ULPGC
Universidad de
Las Palmas de
Gran Canaria

grres ULPGC
group for the research on renewable energy systems

Proceedings of ECOS 2023

36th International Conference on Efficiency, Cost, Optimization, Simulation and Environmental Impact of Energy Systems

Proceedings Book 2 - Preliminary Version

June 25 - 30, 2023
LAS PALMAS DE GRAN CANARIA
SPAIN

ECOS2023

SUPPORTED BY:

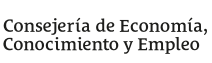

Proceedings of ECOS 2023
36th International Conference on Efficiency, Cost, Optimization, Simulation and Environmental Impact of Energy Systems

Proceedings Preliminary Version
Juny 2023

By
Ana María Blanco-Marigorta, Beatriz Del Rio Gamero, Noemí Melián Martel, Nenna El Kori.

Copyright: Reproduction of this publication in whole or in part must include the customary bibliographic citation, including author attribution, report title, etc.
The editors have included the papers as received from the authors assuming that the presentations only include information without any restrictions on publication in the present collection.
Publisher by: ULPGC – Juan de Quesada, 30 35001 Las Palmas de Gran Canaria
www.ulpgc.es

Conference chairs
Ana María Blanco-Marigorta, ULPGC, Spain
Georte Tsatsaronis, TU-Berlin, Germany
Sotiris Karellas, NTU, Greece
Brian Elmegaard, DTU Technical University of Denmark, Lyngby, Denmark

Honorary chairs
Richard Gaggioli
Ozer Arnas

Local organizing committee
Ana María Blanco-Marigorta
Pedro Jesús Cabrera Santana
Fabián Déniz Quintana
José Antonio Carta González
Julieta Schallenberg Rodríguez
Alexis Lorenzo Medina
Noemí Melián Martel
Baltasar Peñate Suárez
Beatriz del Rio Gamero
Carlos Alberto Mendieta Pino
Sergio Velázquez Medina
Nenna El Kori
Nestor Rubén Florido Suárez
Graciliano Nicolás Marichal Plasencia
Deivis Ávila Prats

ECOS 2023 Scientific Committee Members

Abel Hernandez-Guerrero, Mexico
Adriano Sciacovelli, UK
Alojz Poredoš, Slovenia
Ana María Blanco Marigorta, Spain
Andrea Lazzaretto, Italy
Anna Stoppato, Italy
Antonio Valero Capilla, Spain
Asfaw Beyene, USA
Assaad Zoughaib, France
Brian Elmegaard, Denmark
Daniel Favrat, Switzerland
Eden Mamut, Romania
Edson Bazzo, Brasil
Enrico Sciubba, Italy
Erwin Franquet, France
François Maréchal, Switzerland
George Tsatsaronis, Germany
Giampaolo Manfrida, Italy
Gordana Stefanović, Serbia
Jean-Pierre Bedecarrats, France
José Carlos Teixeira, Portugal
Lydia Stougie, Netherlands
Mauro Reini, Italy
Michel Feidt, France
Na Zhang, China
Noam Lior, USA
Ofira Ayalon, Israel
Ozer Arnas, USA
Pascal Stouffs, France
Rene Hofmann, Austria
Ron Zevenhoven, Finland
Ryohei Yokoyama, Japan
Senhorinha Teixeira, Portugal
Silvia Nebra, Brazil
Silvio de Oliveira Júnior, Brazil
Soteris Kalogirou, Cyprus
Sotirios Karellas, Greece
Sylvain Quoilin, Belgium
Tetyana Morosuk, Germany
Umberto Desideri, Italy
Vittorio Verda, Italy
Vladimir Stevanović, Serbia
Wojciech Stanek, Poland
Yoshiharu Amano, Japan
Young Duk Lee, Korea
Zornitza Kirova-Yordanova, Bulgaria

ULPGC
Universidad de
Las Palmas de
Gran Canaria

grres ULPGC
group for the research on renewable energy systems

Special session. The future of thermoeconomics

ECOS2023

The Exergy Footprint and the resource cost of Externalities

Enrico Sciubba
Niccolò Cusano University, Roma
enrico.sciubba@unicusano.it

This paper provides a review of the concept of the Exergy Footprint, a novel Environmental Indicator formulated in a Thermo-Economic perspective. Every effort is made to present it as the latest -even if probably not the final- development of the brilliant intuition by Rant (formulated in 1955, almost 70 years ago) to use Thermodynamic principles to obtain a more rational cost allocation in multi-products lines. The ExF maintains that the real cost of a material or immaterial commodity is measured by the primary resource cumulatively consumed in its production, operation and disposal, i.e. in a life-cycle sense. Its novelty: it explicitly includes the externalities.

Starting from simple but rigorous examples, it is shown that if sufficient econometric data are available, a primary resource cost can be calculated for the Labour and Capital Externalities. It is then argued that the calculation of the Environmental Cost can be formulated in terms of an "extended exergy balance" in which the streams entering and leaving the system are either physical (material, energy) and "equivalent" (Labour, Capital). Once this step is completed, all three externalities are expressed by their equivalent primary exergy consumption.

For any technological chain it is then possible to calculate the actual amount of primary resource exergy "embodied" (in an extended sense) into a commodity. This amount is clearly a cost proper, and is called "Extended Exergy Cost" or, to better signify its importance, "Exergy Footprint", ExF.

For any human agglomerate it becomes then possible to derive an effective measure of its environmental impact, given by the weighted sum of the ExF of all of its "products". The Exergy Footprint can thus be also viewed as an Environmental Indicator and can be applied to every scale of a society, from the single production line to an entire city or region or nation.

Keywords: Environmental indicators; Non-equilibrium systems; Second Law; Sustainability; Exergy Footprint

1 – A NECESSARY HISTORICAL PRELUDE

Exergy definition by Bosniakovic [1961] & Rant [1955]: *The exergy of a system is the maximum useful work that can be extracted from a system by a process that brings it into equilibrium with a heat reservoir*.
And a more rigorous definition may add: "… (heat reservoir) *of infinite capacity, while the system interacts only with this heat reservoir* ".
I like also Szargut' definition: "*Exergy is the amount of work obtainable when some matter is brought to a state of thermodynamic equilibrium with the common components of the natural surroundings by means of reversible processes*" [Szargut 1988]

But important: *Exergy of a system in a state **x** is also the minimum reversible work that must be done on it to bring it from its equilibrium with the heat reservoir to state **x***.

Gibbs Available Energy "*The greatest amount of mechanical work that ideally can be obtained merely by proceeding from the given condition of the body to one on the surface of dissipated energy that has the same S and V*." [gaggioli 2002]. If we accept this definition, Exergy is NOT equal to Available Energy (but, see also [Keenan 1941])

(The word ‘‘availability’’ was introduced by Tait in 1868 and ‘‘available energy’’ by Maxwell ~1871. For over three decades, 1970-2008, “Availability” and “Exergy” were used to define the same thermodynamic function)

First mention of *economic value of exergy*, [Rant 1955]: “*Exergy is the part of energy having value. Energy without exergy is valueless*”
Exergists were criticized in Europe & Germany in the ’60-‘70s [Tuma 2016] (but they did not give up: in Germany Elsner [1965-1972], Fratzscher [1965-1977, Beyer [1972-1980] and many others; in Russia, Kalinina [1973-1978], Brodianskyi [1965], Nikul’shin [1980]; in Poland, Szargut [1957-1973]…
1962-1971: Tribus, Sama, Evans proposed a monetary cost balance based on exergy content of streams (=> there is a cost in destroyed exergy!) [1962-1981]
Exergists were criticized in Europe & US, 1980-1990, but Gaggioli founded the Second Law Group (1984) whose members did an impressive amount of scientific works and engineering applications that last until today.
Tsatsaronis (& Knoche) 1984/85 and Valero 1986 laid the basis for a) the exergy flowchart of a process; b) the TE assessment and optimization of a process.
Frangopoulos & von Spakovski: Environomics, ~1997: an attempt to explicitly include externalities in a TE formulation. Szargut had already proposed the inclusion of environmental effects in 1973, but his work did not obtain the due recognition until much later.
In fact, Gaggioli (& Petit, Reistad, Wepfer) had already presented an initial structuring of Exergy Economics between 1970-80:
Valero (& Valero-Delgado, Stanek) improved, completed and formalized Szargut’s idea of Exergo-ecological cost [1995-2014]
Jørgenssen proposed a niche application under the name of Eco-exergy, ~2005.
Many other contributions, most of which are included in the Reference list, were published between 1990 and 2021. TE-based Diagnostics paradigms were formulated [Lazzaretto, Serra, Valero, Verda, 1994-2004], the loss structure was more accurately identified [Lazzaretto, Tsatsaronis, Valero, Verda, 1996-2002], applications to more complex systems and the links to the emerging “sustainability” concept was proposed [Wall, Whiting, Dai et al., Nowak, Sciubba, Stanek, Valero, Morosukk, Petrakopoulos, 1977-2014]
The first explicit inclusion of the Labour, Capital and Environmental costs into a non-monetary framework, called Extended Exergy, was proposed by Sciubba [1998]
One possible description (NOT a definition!): Thermoeconomics, TE, is a versatile concept that provides a general, systematic and integrated approach for the analysis of design systems. Being an exergy-aided costing method, TE offers additional insight on the cost formation of primary and secondary streams in energy conversion plants, as well as on the interactions among thermodynamics and economics and among the various plant components, all of which are important for improvement of energy system design.

2 – MONETARY THERMO-ECONOMICS

Every process admits of a **cost balance** equation:

$$C_P = C_F + Z_K \qquad \text{(in €/yr, neglecting profit)} \qquad (1)$$

Z_K [€/s] is the capital repayment cost flow (it may include scheduled maintenance, insurance & Labour).
Consider as a simple example the heating of a room: the Product is Q_{room}, the Fuel Q_{source}

$$c_{source} * Q_{source} + Z_K = c_{room} * Q_{room} \qquad (2)$$

Since we are interested in the cost of space heating, we can run an **energy cost balance** (“how many kWh it takes to generate the desired product?”):

$$c_{source} * Q_{source} + Z_K = c_{room} * Q_{room} \qquad (3)$$

…c in €/kWh, Q may be expressed as Δh, in kWh

$$c_{room} = \frac{c_{source} Q_{source} + Z_K}{Q_{room}} \qquad \text{in €/kWh} \qquad (4)$$

Rant [1955] argued that the real “value” of a commodity is its exergy content. The cost equation can be rephrased in terms of exergy:

$$c_{source} * E_{Qsource} + Z_K = c_{room} * E_{Qroom} \quad (5)$$

…*c* in €/kWh, *E* in kWh

E_{Qroom} is rather low because the room is almost at its dead state (p_0, T_0), $E_{Qsource}$ is much higher because there is indeed some work-generating capacity in the hot source … so:

$$c_{room} = \frac{c_{source} E_{Qsource} + Z_K}{E_{Qroom}} \quad \text{in €/kWh} \quad (6)$$

The same formula, very different meanings! In fact, $E_Q = Q - T_0 \Delta s$ is always lower than the enthalpy of an amount equal to the Gouy-Stodola irreversibly "lost work". As a consequence, the c_{room} given by eqtn. (6) is higher than its energy equivalent given by eqtn. (4).

It is interesting to quote [Rant 1955]: "*A system, let us say a heated room, requires a given quantity of heat (Q_{room}) at temperature T_{room} (Sl. 2). This heat is represented in the s-T diagram by the area of rectangle 1-2-3-4. The heat is available at temperature T_{source} (e.g. the average temperature of flue gases in a furnace) and the environment temperature is T_0. The simplest method of heating involves direct removal of heat from the heat source and its transfer to the user. In this way, the amount of thermal energy Q_{source} removed from the source at temperature T_{source} equals the amount of heat supplied to the heated system:*

$$Q_{source} = Q_{room} \quad (7)$$

In Sl.2, Q_{source} is represented by the area 7-8-9-10, which is obviously equal to the area 1-2-3-4. There are no losses as far as energy is concerned.

What about the exergies? The exergy of heat Q_{room} is $E_{room} = Q_{room}\ (T_{room} - T_0)/T_{room}$, equal to area 1-2-5-6; the exergy of the thermal energy Q_{source} used for heating is $E_{source} = Q_{source}(T_{source} - T_0)/T_{source}$,; E_{source}=7-8 -11-12; considering $Q_{room} = Q_{source}$ and $T_{room} < T_{source}$, we can also establish that $E_{room} < E_{source}$. The exergy has been reduced in this process. The cause for the loss of exergy is the irreversible transfer of heat from the source to the system at a limited and, usually, quite large temperature differences $T_{source} - T_{room}$. Wherever irreversibilities are present, things are not in order energetically, even if it seems otherwise. The method of heating can be improved significantly as follows (Sl. 3):

Only as much heat Q'_s is removed from the source at temperature T_{source}, so that its exergy E'_s equals the exergy E_{room} of thermal energy Q_{room} used for heating. We get:

$$Q'_s = Q_{source} \frac{T_{room} - T_0}{T_{room}} \frac{T_{source}}{T_{source} - T_0} \quad (8)$$

The exergy E'_s coming from the source of removed heat Q'_s is converted to work using a power cycle, and this work is then used to drive a reversed Carnot cycle 1-6-5-2. Valueless heat 6-5-3-4 is removed from the environment in this process (this heat has zero exergy). The heated system is provided with heat Q_{room} =1-2-3-4 having the necessary exergy E_{room} = 1-2-5-6. This method of heating removes less energy from the heat source than that required for heating; but the exergy removed from the heat source equals the spent exergy. This is the operating principle of a Heat Pump." And in the conclusions: … "*The existing method for energy pricing (accounting) in combined plants on the basis of used enthalpies is fundamentally wrong. It has to be replaced with pricing (accounting) on the basis of used exergies, which is the only proper way.*"

(text slightly adapted by this author)

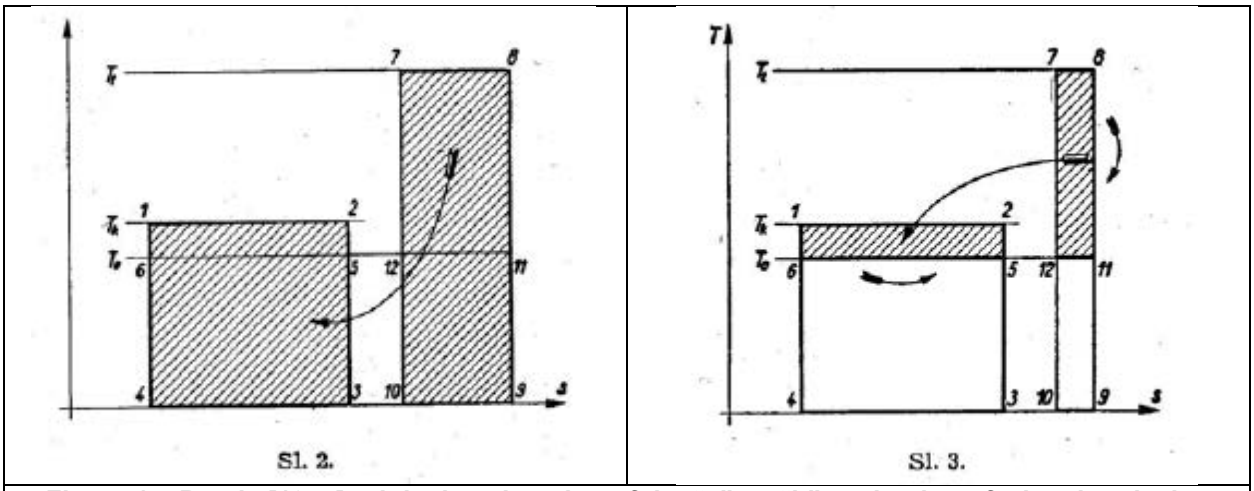

Figure 1 – Rant's [1955] original explanation of the "e" vs "h" evaluation of a heating device

Since realistic processes are much more complex, some "cost rules" must be introduced to maintain rigor and abide to common engineering sense. This was done by Gaggioli & coworkers, Lazzaretto, Tsatsaronis-Cziesla, Morozyuk, Reini [2021-2023],Valero.

In real processes, there are inevitably some material or immaterial discharges. The corresponding term C_D must be included in the cost balance, eqtn. (1), as well.

$$C_P=C_F+Z_K+Z_{ENV}+C_D \qquad (9)$$

There are additional prescriptions on how to handle the C_D term, but they are not essential to our scope here.

Let us provide a simplified outline of the procedure proposed by Tsatsaronis & Valero: (the following treatment is simplified for conciseness & clarity and is not completely rigorous!).

Let us write the cost equations for each individual component in figure 2:

$$\begin{aligned} c_1\dot{E}_1 - c_2\dot{E}_2 + c_7\dot{E}_7 + Z_A &= 0 \\ c_3\dot{E}_3 + c_4\dot{E}_4 - c_5\dot{E}_5 + Z_B &= 0 \\ c_5\dot{E}_5 - c_6\dot{E}_6 - c_7\dot{E}_7 - c_8\dot{E}_8 + Z_C &= 0 \\ c_2\dot{E}_2 - c_3\dot{E}_3 + c_8\dot{E}_8 - c_9\dot{E}_9 + Z_D &= 0 \end{aligned} \qquad (10)$$

Where $C_j = c_j\dot{E}_j = c_j\dot{m}_j e_j$ for material streams and $C_j = c_j P_j$ for immaterial ones (P being the power). Assuming the Z_j are known, system (10) has 4 eqtns. (the cost balances, 1 for each component) and 9 unknowns (the c_i). A possible set of 5 auxiliary equations needed to make its coefficient matrix square is:

$$\begin{aligned} c_1 &= \xi \\ c_4 &= \psi \\ c_6 - c_7 &= 0 \\ c_6 - c_8 &= 0 \\ c_9 &= \varphi \end{aligned} \qquad (11)$$

If the system (10+11) has a $Det(M_{coeff})\neq 0$, the system admits of a solution.
The auxiliary equations are derived on the basis of a proper set of general rules on the *function* of a stream in the component's operation.

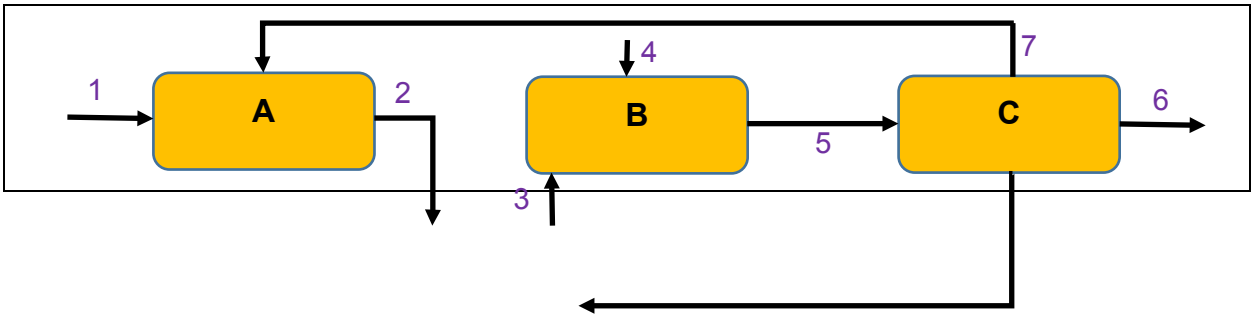

Figure 2 – Generic process scheme

3 – THE PROBLEM OF THE EXTERNALITIES

In Economics, *an **externality*** is *"a fact or an event that impacts a system or a procedure and that is not directly involved in the 'state of the universe' that causes that event"*.

In Engineering Economics it is customary to separate ***internal*** production costs, directly related to the machinery used, the physical parameters of the process and of the participating streams, from ***external*** costs, grouping under this denomination all cost items not depending directly from the installed process. Examples of external costs are land preparation, transportation, electrical connection to the grid, wages and salaries, start-up costs, financial flows, disposal of discharges, etc.

Engineers have borrowed the term "externality" from Economics, making it more precise and itemized. In a cost/benefit evaluation, there are thus three types of "externalities":

a) *Labour*, i.e., the cost of wages and salaries, usually expressed in €/yr or €/unit;
b) *Capital*, i.e. the financial costs necessary to operate the process: repayment of loans, amortization, differed cash flows, etc.
c) *Environmental costs*, neglected until the '70s and still lacking a universally accepted definition: in general, these are the monetary costs caused by actual or potential environmental harm caused by the process operation (most commonly, "emissions" and "discharges").

TE needs special additional procedures to handle these costs:

a) Capital costs are calculated as repayment rates on the TIC (Total Installed Costs) and accounted for in Z_K;
b) Scheduled maintenance, insurance, taxes, start-up, etc. costs can be added to Z_K and possibly adjusted to annual rates;
c) Labour costs can be included -with some caution- in Z_K as well;
d) Environmental costs can be accounted for in three different ways:
   - Z_{ENV} is set equal to the foreseen "pollution fees" set by national or international regulations;
   - Z_{ENV} is set equal to the calculated "remediation" costs directly and indirectly related to the process effluents;
   - Z_{ENV} is set equal to the avoidance costs, i.e. to the remedial actions to be taken within the process boundaries.

Depending on the mode of calculation, Z_{ENV} may vary of orders of magnitude; it is generally accepted that there are non-trivial problems in its calculation [Innes 2013]

4 – EXERGY COST, EXERGO-ECOLOGICAL COST, EXERGY FOOTPRINT

The following example is a simplified rendering mainly based on the works of Valero & coworkers [reff]. Notice though that already Rant [1955], Szargut [1965] and Gaggioli [1980] proposed the same -or a very similar- approach.

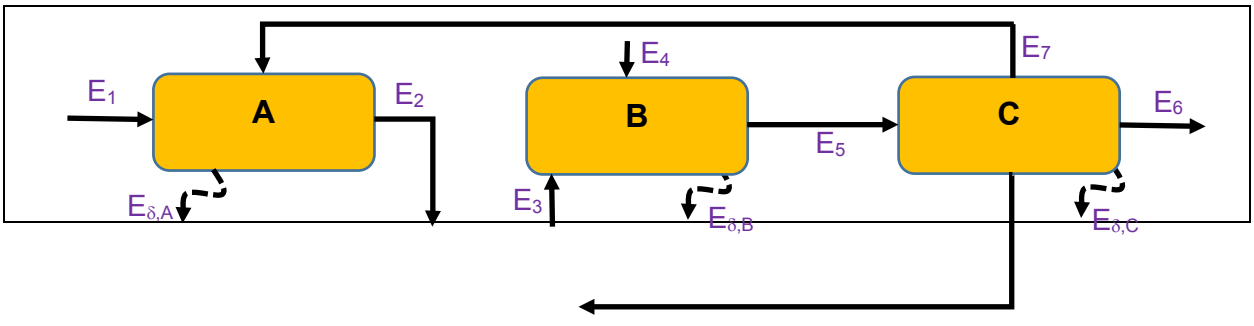

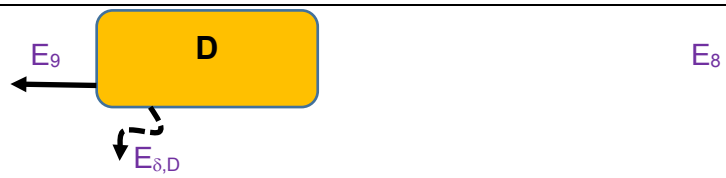

Figure 3 – Exergy flow diagram for the process of figure 3

Table 1 – Flow type identification ("production structure")				
	A	**B**	**C**	**D**
Fuel	**E_1+ E_7**	**E_3+ E_4**	**E_5**	**E_8- E_9**
Product	**E_2**	**E_5- E_3**	**E_6+ E_7+ E_8**	**E_3- E_2**

For the system of figure 3, a purely thermodynamic representation may be chosen: from the exergy flowchart an exergy budget can be derived ($\dot{E}_{in} = \dot{E}_{out} + \dot{E}_{\delta}$). In canonical form (see fig. 4), all terms in [W]:

$$\begin{aligned} \dot{E}_1 - \dot{E}_2 + \dot{E}_7 - \dot{E}_{\delta,A} &= 0 \\ \dot{E}_3 + \dot{E}_4 - \dot{E}_5 - \dot{E}_{\delta,B} &= 0 \\ \dot{E}_5 - \dot{E}_6 - \dot{E}_7 - \dot{E}_8 + \dot{E}_{\delta,C} &= 0 \\ \dot{E}_2 - \dot{E}_3 + \dot{E}_8 - \dot{E}_9 + \dot{E}_{\delta,D} &= 0 \end{aligned} \qquad (12)$$

(mass- and energy balances are assumed to have been successfully closed)

Now, what is the primary exergy required for the formation of the streams $\dot{E}_1, \dot{E}_2 \ldots$ etc.? Solution:

Call k_j the *exergy cost, defined as the amount of primary exergy required to generate the unit exergy* e_j: it is clear that while the *k* of streams 1 and 4 must be assigned somehow because they are entering the process boundary from the "outside" (the environment in this case), the k_j of all other streams depend on the cost balance of each component and on the process structure.

Identify the so-called "productive structure" of each component (Table 1), and consider that an exergy cost conservation rule applies:

$$\sum_j F_j = \sum_i P_i \qquad (13)$$

Applying (132) to the single component/process **B** of figure 3:

i- Case 1, design goal is to increase E_3 to E_5: $F_1=k_4E_4$; $P_1=k_5E_5-k_3E_3$
ii- Case 2, design goal is to mix E_3 & E_4 to produce E_5: $F_1= k_3E_3$; $F_2= k_4E_4$; $P_1= k_5E_5$

Cost balance: $$k_3\dot{E}_3 + k_4\dot{E}_4 - k_5\dot{E}_5 = 0 \qquad (14)$$

1 eqtn., 3 unknowns, need 2 auxiliary eqtns.:
Case 1: $k_4=CExC_4$; $k_3=k_5$
Case 2: $k_4=CExC_4$; $k_3=f(k_5,k_8,k_9)$

The procedure only makes sense if extended to the entire process:

$$\begin{aligned} k_1\dot{E}_1 - k_2\dot{E}_2 + k_7\dot{E}_7 &= 0 \\ k_3\dot{E}_3 + k_4\dot{E}_4 - k_5\dot{E}_5 &= 0 \\ k_5\dot{E}_5 - k_6\dot{E}_6 - k_7\dot{E}_7 - -k_8\dot{E}_8 &= 0 \\ k_3\dot{E}_2 - k_3\dot{E}_3 + k_8\dot{E}_8 - k_9\dot{E}_9 &= 0 \end{aligned} \qquad (15)$$

Number of equations: 4 (1 for each component); number of unknowns: 9 (1 for each stream) $\Rightarrow$ Need 5 auxiliary eqtns: "exergy costing rules" that take into account the origin of the stream and its "function" in the economy of the production process.

Case 1: $k_1=0$; $k_4=CExC_4$; $k_3=k_5$; $k_2=k_3$; $k_8=k_9$
Case 2, $k_1=0$; $k_4=CExC_4$; $k_3=k_4$; $k_2=k_3$; $k_8=k_9$

The exergy cost method does not solve the problem of the externalities. Internalization procedures have been proposed by Szargut [1973], Frangopoulos [1997], Valero & Stanek [1998-2010]. The basic idea is mutuated from Szargut' work: link the mass flow rate of the emissions to a specific "cost of the pollution" using local or national monetary databases. As of today, the environmental externality problem has not found a universally accepted solution [Innes 2013].

The Extended Exergy formulation is an attempt to solve this problem by calculating the Labour and Capital costs in terms of the primary exergy budget of a society (a city, a region, a Country). Once these parameters (ee_L, primary exergy equivalent of 1 workhour) and ee_K (primary exergy equivalent of 1 unit of monetary circulation) are known, the environmental cost can be assessed by using a remediation approach: how much primary exergy (EE'_{fuels}, EE'_L, EE'_K) would be necessary to reduce the effluents' exergy to the limits prescribed by the locally applicable regulations. This solves the Externality problem, but the calculations depend on the availability and accuracy of an additional, very disaggregated, data set. The resulting cost of a commodity is in kJ_p/unit, kJ_p/kg or kJ_p/kJ, "kJ_p" being the primary exergy needed to generate that commodity.

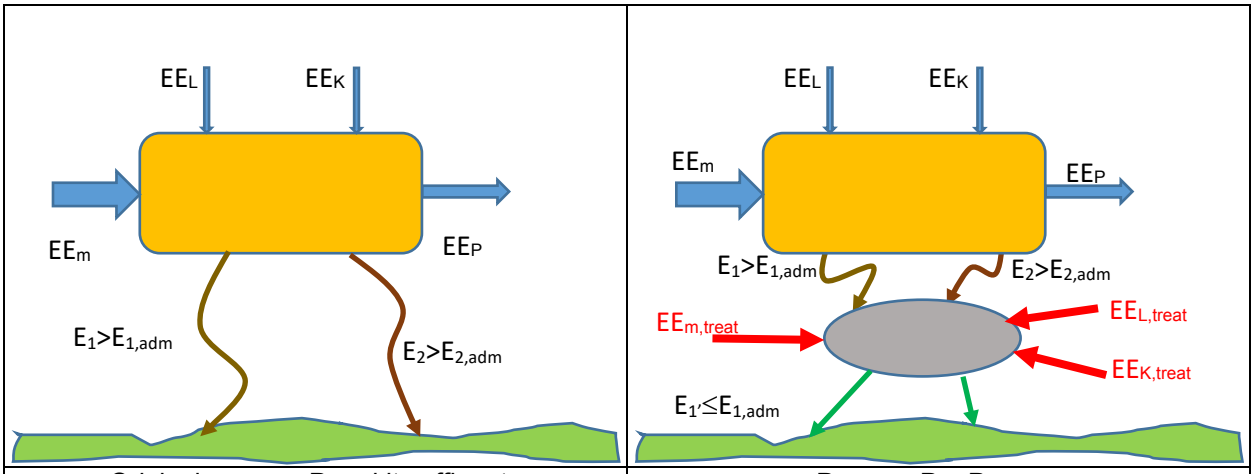

Original process P and its effluents | Process P + $P_{treatment}$

Figure 4 – Treatment of the Environmental externality in EEA

This EEA cost has been called "Exergy Footprint", ExF, because it represents the burden on the Environment caused by the production. Here "burden" is literally meant to signify "the amount of primary resources subtracted from the overall Earth's budget".

5 – WHAT NEXT?

Exergy analysis generally accepted today as best analysis tool;

TE still not practiced by industry and Energy Agencies;

TE diagnostics still considered a niche topic;

Exergy cost and ExF can be valid "sustainability" indicators: ECOS community ought to push for this recognition;

Need to work with media, institutions, schools to clarify correlation between exergy consumption & degree of unsustainability;

Need to aggressively address water-nexus and material replacement & substitution issues.

6 – REFERENCES

The reference list comprises almost 300 items. Not all of them are quoted in the paper, but they represent a useful compendium of the exergy literature over the years. I will make available on a digital support upon request.

PROCEEDINGS OF ECOS 2023 - THE 36TH INTERNATIONAL CONFERENCE ON
EFFICIENCY, **C**OST, **O**PTIMIZATION, **S**IMULATION AND ENVIRONMENTAL IMPACT OF ENERGY SYSTEMS
25-30 JUNE 2023, LAS PALMAS DE GRAN CANARIA, SPAIN

The Future of Thermoeconomics after the School of Zaragoza

A. Valero[a], A. Valero-Delgado[b] and C.Torres[c]

[a] CIRCE Institute, University of Zaragoza, Spain, valero@unizar.es
[b] CIRCE Institute, University of Zaragoza, Spain, avdelgado@unizar.es, CA
[b] CIRCE Institute, University of Zaragoza, Spain, ctorresc@unizar.es

Abstract:

Thermoeconomics was born as a combination of the Second Law of Thermodynamics and Economics in search of the process of cost formation. Linking the physical origin of cost with irreversibility is the central paradigm of Thermoeconomics. Irreversibility is best identified in energy systems, so Thermoeconomics has concentrated on them without extending its scope to other industrial systems, such as chemical or metallurgical processes. As well as to cost accounting for the irreversibilities of all commodities from the cradle to the grave. The concept of cost is universal, so there is no reason not to extend applications to geological, biological, or purely economic systems. The accumulation of irreversibilities can quantify (in kWh) the destruction of the (natural) resources used to produce a commodity, from the cradle to the market and beyond its degradation as waste and its return to the cradle. It is the natural cost of any human activity - subject to its calculation assumptions. This requires an extension of thermodynamics, which we could reasonably call thermoeconomics. At the University of Zaragoza, we have developed the concepts of Thanatia and thermodynamic rarity to identify the loss of the Mineral Capital of the Planet. We also have identified the idea of waste as external irreversibility, the basis of Circular Thermoeconomics. We have also proposed the idea of a new and more precise function that could be used for the diagnosis of processes that we call Relative Free Energy. All these new concepts need further development, which we invite future researchers to develop. Today's economy is disconnected from physics; prices do not internalise the destruction of natural resources. Our vision is that thermoeconomics provides a bridge between the two, valuing nature in such a way as to replace what has been destroyed and regenerate what has been degraded. In effect, thermoeconomics becomes the economics of physics.

Keywords:

Exergy, Dead State, Thanatia, Pristinia, Circular Thermoeconomics, Relative Free Exergy

1. Preamble

Cost, in its physical expression, accounts for the loss of natural resources. In other words, cost accounts for the irreversibilities accumulated in the formation of any product or service. This is the central paradigm of thermoeconomics, which will be analysed in section 4..

The economy sees nature as a supplier of raw materials or solace. It is designed to value the exchange of services between humans. We do not pay nature for its resources, we only pay the extractor, not what is extracted. Nor do we pay for its regeneration or even its depreciation. To overcome this shortcoming, the economy includes as externalities those unavoidable repairs of the natural environment. Money has been created to measure exchanges between individuals or organisations, it is a human construct that nature does not understand, as it only follows the principle of action and reaction.

The second law of thermodynamics is conclusive: degradation is a physical and unavoidable process in any real activity, and this degradation can be measured with entropy generation. So why not use thermodynamics to account for the loss of the planet's natural resources?

As not all energy is usable, exergy is a better alternative analysis when dealing with natural systems. Exergy is not a conservative property and is partly destroyed in every real process. We call the destroyed exergy irreversibility, which, in turn, is related to the entropy generated in the process and thus its degradation (Gouy-Stodola Law): $I = T_0 S_g$.

While the cost accounts for the loss of natural resources, this loss could be identified with the accumulated irreversibility from cradle to commodity. To do this, we need only extend the concept of dead state to assess exergies. In other words, we have opened up thermodynamics to evaluate the planet's resources. The expectations are immense.

From the intersection of thermodynamics and economics comes thermoeconomics, which we consider the concept of cost to be central. Thermoeconomics, in our opinion, is not only about valuing the physical cost in

monetary units but the more objective cost can and should be measured in physical units, kWh. In this way, costs are left out of the vagaries and fluctuations of money. Strange as it may seem, it is linking economics with nature again, as the early physiocrats did, who considered nature as the source of all wealth because they believed that it regenerated itself. Interestingly, when the value of a currency is in doubt, the gold carat is used as a safe haven.

Thermoeconomics should draw on and recognise many concepts of economics, but it can also complement and illuminate others that conventional economics calls shadow costs, i.e. those that are not accountable or are subjectively valued as externalities.

On the other hand, many authors have built bridges between thermodynamics and economics, among them Nicholas Georgescu-Roegen with his book "The Law of Entropy and the Economic Process" [1] marked the foundation of ecological economics, although he called it bioeconomics. However, this term has been used more recently to relate biology to economics for better utilisation of biological resources and by extension natural resources. Another important author and father of biophysical economics is Charles Hall who developed the concept of energy return on energy investment (EROI) and described its Implications in the book "Energy and the Wealth of Nations: An Introduction to Biophysical Economics". [2]. Incidentally, he previously called it Thermoeconomics. Nor should we forget the contributions of Howard Odum [3] and collaborators on the concept of emergy, to say the least.

In this paper, we do not seek to make an extensive review of the use of the name Thermoeconomics and the work of numerous authors who linked thermodynamics, biology, ecology, physics, etc., with economics. We simply focus on a view of thermoeconomics from the concept of exergy and the immense room for future development by integrating the extraction of geological resources with economics. This new view of thermoeconomics allows us to assess the planet's mineral resources and can be a guide to evaluate the damage our civilisation is inflicting on it. It helps to clarify its costs and to act accordingly.

The purpose of this article is twofold: on the one hand, we describe, from the Zaragoza school of thermoeconomics, its conceptual advances and the needs for future development based on them. We have divided it into four parts: The first deals with Thanatia, exergy costs and rarity. The second is Pristinia, a planetary model for assessing the degradation of fertile soils. The third is the principles of a new Circular Thermoeconomics based on the thermodynamic concept of waste. And finally, an introduction to Relative Free Energy as a new thermodynamic function that depends on both the fluid and the machine at work. It opens a new perspective on the diagnosis of thermal systems.

2. Thanatia, a planetary reference state for exergy calculation

One of humanity's biggest problems in the coming decades, if not centuries, is the fast destruction of the planet's natural resources, especially non-renewable minerals. In fact, they are extracted, processed, used and, in the last stage, we disperse them into the earth's crust, the oceans or pollute the atmosphere and fresh waters. Therefore, it would be an immense contribution of thermoeconomics to planetary sustainability to construct a physical theory to evaluate the periodic cost of this destruction to at least minimise and manage it.

Ecological economists have resorted to the law of entropy as an uncountable and even immeasurable metaphor. On the contrary, we believe that thermoeconomics can expand its explanatory capacity and appraise this destruction based on the concepts of cost and irreversibility.

We note that the entropic generation, and with it, the irreversibility of the processes, depends on the reference state we choose. In conventional process exergy analysis, the choice of a reference state is linked to the type of problem we want to solve, i.e. we explicitly or implicitly delimit the relevant costs/irreversibilities. Consequently, if we want to evaluate the destruction of the planet's resources, we need to define a reference environment, also called *dead state*, that allows us to evaluate the costs of both resource depletion and waste generation at the planetary level.

The most important property of a reference environment, RE, is that it actually acts as an attractor of our system's intensive properties. Spontaneous evolution is found in the difference in temperatures, or pressures, or concentration, or composition, of a system with its environment. Therefore, it is necessary to define the temperature, pressure, composition and concentration of all chemical substances composing the reference state that can interact with the system. Their exergy loss in both quantity and quality will make it possible to assess the degradation of the planet's mineral resources.

Thanatia would represent a hypothetical end state of the current exponential trajectory of human-induced degradation: The Earth's crust, hydrosphere and atmosphere would have reached the maximum dissipation of all spent materials [4]. Although this scenario is hypothetical and indicates a final depletion, it is purely instrumental and devoid of social or economic connotations, which would obviously take place long before it is reached. This model was developed by Alicia Valero in her PhD thesis in 2008 [5], with the current geochemical

and geological information on the atmosphere, hydrosphere and crust described below.

The crepuscular or twilight atmosphere would be produced after all conventional fossil fuel reserves have been depleted, with an atmospheric injection of about 2,000 Gigatonnes of carbon. According to previously published simulations, the crepuscular atmosphere would have a carbon dioxide content of 683 ppm, an average surface temperature of 17℃ (maximum carbon dioxide-induced warming of 3.7℃ above pre-industrial temperatures), a pressure of 1.021 bar and a composition, by volume, of 78.8% N2, 20.92% O2, 0.93% Ar and 0.0015% trace gases. (Note that, even if the atmosphere were filled with anthropogenic CO_2, it would be "only" 0.07% [6]).

Saline water accounts for about 97.5% of the entire hydrosphere; the other 2.5% is kept as freshwater, almost all of it in the form of ice, mainly in Antarctica and Greenland. The rest is marginal, although it may seem immense to us, found in groundwater, lakes, rivers, soil and moisture in the atmosphere and biosphere. Only 0.3% of the total amount of freshwater is concentrated in lakes, reservoirs and river systems, yet this is the part of the hydrosphere that we all need to live and is most at risk of being polluted. In addition, due to climate change, a significant part of the glaciers and other ice in the cryosphere is melting. Therefore, we assume that the crepuscular hydrosphere would have the current chemical composition of the oceans at an average temperature of about 17℃. That is, it is implicitly assumed that all ice sheets will have molten and dissolved into saline waters.

According to the US Geological Survey [7] the mass of non-fuel industrial mineral resources worldwide is of the order of 10^{15} kg. Furthermore, the World Energy Council [8] estimates the amount of available conventional and unconventional fossil fuels to be about 10^{16} kg. This means that all concentrated mineral resources of fuel and non-fuel origin represent only 0.001% of the total mass of the Earth's upper continental crust (about 10^{22} kg, according to [9]. Therefore, without any significant error, we can state that the crepuscular continental crust can approximate the average mineralogical composition of the present-day Earth's upper crust [10].

The problem we faced was to identify what type and how many significant and distinct (in a thermodynamic sense) minerals are present in the upper continental crust. To do so, we proposed a model based on the mineralogical composition studied by Grigoriev [11], which would ensure consistency between species and chemical elements. The resulting crustal model comprises at least the 292 most common minerals.

In short, the current state of the biosphere is incredibly close to Thanatia. In our hypothetical reference state, the atmosphere would have reached the state predicted by long-term climate change models. Even if the amount of CO_2 doubled, there would be less carbon dioxide than argon, and this noble gas is considered a trace element. Even if all mineral deposits were increased tenfold in the Earth's crust, the crust would contain no more than 0.01% of them (less than the crustal mass estimation error). Thus, whereas if all commercially exploitable mineral deposits disappeared, the composition of the crust would be virtually the same. Accordingly, the dispersion and degradation of all already used materials mean nothing compared to the amount of common rocks (mostly silicates) that are mostly found in the crust.

As for the hydrosphere, the pollution of all freshwaters and the melting of the Arctic, Greenland and Antarctic ice would have a quantitatively more significant effect, but not more than 2.5% of the total waters of the blue planet. The hydrological cycle driven by solar radiation would still exist, but it must be accountable that water in the atmosphere is only 0.00093% of the total water while rivers account for 0.00015% of all the water on the planet [5]. Therefore, we hold that the hydrosphere of Thanatia would be composed almost entirely of standard salt water.

The present Earth is not in the equilibrium state, whose continental masses evolve slowly in geological times, but more rapidly and spontaneously in chemical terms towards Thanatia. This is by the logic of the second law and there is no catastrophism in it. How fast we get to Thanatia does depend on human beings. But before we get there, one can imagine, without too much difficulty, that economic and perhaps civilisational collapse will be reached sooner as a possible end of the Anthropocene period [12].

2.1. The exponential behaviour of mining demand and the exergetic "U".

Our society does not comprehend exponential behaviour. The extraction of minerals on the planet is growing at such a rate that by 2050 more than twice (or perhaps three times) as much will be consumed as is extracted today, and by 2050 more minerals will have been extracted than in the entire history of human civilisation. Agriculture is heavily dependent on phosphate mines. A mobile phone requires more than 35 chemical elements; a conventional or electric vehicle requires more than 50; and renewable energies, electrochemical storage, and green hydrogen production require huge quantities of rare metals. Therefore, it is necessary to review the message of entropy: its exponential character will help us to understand and assess those behaviours.

It is relevant to analyse the phenomenon of mixtures thermodynamically. As is well known, the irreversibility of a mixing process takes the form:

$$I = -R\,T_0 \sum_{i=1}^{n} x_i \ln x_i = -R\,T_0\,\ln 10 \sum_{i=1}^{n} x_i \log_{10} x_i,$$

where x_i are the mole fractions of the n substances to be mixed. And for the case of a mixture between two substances A and B

$$I = -R\,T_0\,[x_A \ln x_A + (1 - x_A)\ln(1 - x_A)] \quad \text{(kWh)} \qquad \text{and} \qquad \frac{dI}{dx_A} = -R\,T_0\left[\ln \frac{x_A}{1 - x_A}\right]$$

This equation is symmetric around x = 0.5, where it has a minimum, and is asymptotic with x_i = 0. This means that the irreversibility increases exponentially when wanting to decontaminate A from B, or B from A. The separation of the last contaminating particles requires an exponentially increasing exergy. We call this behaviour the exergetic “U”.

This exergetic ”U” is incredibly important from a practical point of view. Oregrades of many mineral deposits are usually at very low concentrations of the 10^{-1}, 10^{-2},...,10^{-n} type. These low ranges imply that when depleting a mine with an initial concentration of 10^{-1} and reducing it to one of 10^{-2}, the exergy required for the same amount of extraction is multiplied by 10, and so on by 100, 1000,..., whereas what remains are declining residual traces. For example, this trend is historically proven with gold, where its ore grades have been reduced by several orders of magnitude over the last 120 years [13]. In addition, as the actual processes are far from reversible, extraction and beneficiation of minerals require an amount of energy several orders of magnitude higher than the thermodynamic minimum.

It is not our technological ignorance that imposes such behaviour, but thermodynamics, which describes the ideal case of separation. In other words, even if today’s mining operations operate gigantic equipment, the physical decline of global oregrades will require more and more energy per tonne of ore extracted.

Unfortunately, metallurgical processes are also subject to the law of entropy. The energy costs for the reduction, purification and refining of metals are even much higher and always far from their thermodynamic minimum the more we want to purify them.

In other words, the law of entropy is evident in the earth’s crust. It is not an orderly reservoir of minerals, like in a ”department store”. This phenomenon had to be added to the Thanatia theory. Many techno-optimistic messages say that there are enough minerals to sustain global development based on new technologies because abundant minerals are in the earth’s crust. Apart from the fact that there are unexplored areas with some constraints, they forget that mineral concentrations are not homogeneous, but declining. The best oregrades are first exploited -”low-hanging fruits”- then decline until they become unviable. So energy, water, tailings movement, environmental, social and economic impacts will grow exponentially, perhaps in decades or centuries.

2.2. Exergy, extraction and replacement costs and thermodynamic rarity

The chemical reactivity of non-fossil minerals is very weak and undistinguishable among them. Therefore, their chemical exergy cannot be used to create a theory to value them. Their demand is linked to the physicochemical properties of the chemical elements or compounds obtained from them. To become useful, they are extracted, beneficiated, processed and refined. And all these operations require energy from chemical or electrical sources. So instead of valuing minerals by their exergy content, through, for instance, the well-known Reference Environment by Szargut [14], we have to value them by the amount of exergy needed to process them from cradle to market, i.e. by their exergy cost of extraction, which can be measured in kWh.

The value of a mine is linked to its mineral concentration or oregrade. This value decreases as the mine is exploited. So, the variation of their costs is also important because it is an indicator of mine depletion and, by extrapolation, of the loss of the planet’s mineral capital.

However, extracting cobalt is not the same as extracting aluminun. The latter is abundant in the earth’s crust, and the former is very scarce. So scarcity is also an indication of value. Whereas we relate the value of scarcity to the physical cost of forming it, we have a problem because the exergy cost depends on the limits of analysis we choose. The resources used to measure it have a cost that expresses the amount of resources used to produce them, and so on, down to the cradle. This accounting has to start from the earth’s crust, which can only be measured in exergetic terms once a reference state describing the dead state of the crust itself has been defined.

Note the linkage of the search for natural costs with the need to identify the terrestrial biosphere as the cradle or reservoir and the origin of all chemical elements. To value these costs, a theory is needed to define the ”physical effort” in extracting the minerals. Exergy is the key, but quantifying it requires a reference environment, which we call *Thanatia*, as previously explained. An economic theory of costing mineral scarcity without defining a physical reference environment would be highly controversial.

In addition, mineral deposits often contain a variety of metallic compounds that are extracted together (metal companions). In the beneficiation or downstream processes, allocating costs between products and waste is necessary. This brings us back to the exergy analysis.

Let us clarify concepts. We call *exergetic cost of extracting and processing a mineral* the amount of exergetic

resources needed to extract a mineral and process it until the market of a given commodity. Therefore, all commodities should have their cost measured in kWh, for example. Whereas, if standardised energy consumption data were available for all mines, it would be possible to classify and catalogue these costs. The lack of standardised data from mines around the world is disappointing.

However, these costs do not consider the scarcity of metals in the upper crust. Indeed, whereas a metal is very scarce, its composition in Thanatia will be of the 10^{-n} type, with a very high n. For example, n is 9 for cobalt, while aluminium is 3. In other words, aluminum is a million times more abundant in the crust than cobalt. Extracting 1 kg of cobalt from Thanatia with the same technology would require a million times more waste rock removal than 1 kg of aluminum. However, the price of cobalt is not a million times higher than that of aluminum, which shows that the market may be more or less sensitive to extraction costs but not at all to geological scarcity. Therefore, the loss of mineral capital from the earth must be sensitive to genuine geological scarcity to know the limits of depletion.

To properly assess geological scarcity, it is necessary to resort to the exergetic "U", which formulates an exponential behaviour for the consumption of exergy in the systematic replenishment from Thanatia to the mine. Continuing with the example of cobalt, its concentration in present-day mines is of the order of 10^{-3}, so the cost of replenishing that mine from Thanatia would require one million times the energy of current cobalt extraction. No current or future economy could bear such costs, which makes cobalt management a global problem.

Consequently, we define "replacement cost of an ore (at zero level)" as the exergy that would be necessary to replace, with current technology, the concentration of an ore found in its mine from its concentration in Thanatia [15]. In essence, this cost is an avoided cost or bonus that nature offers us for free (see Figure 1). An imaginary cost can be assessed by measuring the energy it would take to concentrate a chemical from a common rock to a concentration equal to that of the mine. Examples of these avoided costs are presented in Thanatia's books [4, 16].

When the replacement costs of metals that are not as scarce as cobalt or gold are assessed, the replacement cost of some metals is close to their extraction cost. This is the case for rare earths, which are more common than copper but very expensive to extract and separate. To solve this paradox, we proposed the concept of thermodynamic rarity [17], which is defined as the sum of the replacement cost plus the extraction cost. Indeed, some metals are scarce but feasible to obtain, such as cobalt, and others are abundant but difficult to separate, such as rare earths. And all the others are in the middle of this range.

However, the idea of replacement from Thanatia is extremely radical because long before reaching Thanatia, extraction would be stopped as technically unfeasible. Therefore, we scale the concept of rarity to an R_1, R_2, R_3 that would correspond to a replacement cost from a concentration 10, 100 or 1000 times higher than that of the metal in Thanatia. Logically, the rarity calculated from the concentration in Thanatia would be R_0.

Skinner [18] and others consider that there is a mineralogical barrier whereby the extraction of a metal does not make sense because of the immense impacts it would cause. Although this barrier can be variable, we consider it one-for-all-metals with a concentration ten times lower than the current minimum for gold extraction. That is, 0.2 gr/tn rock. This would imply removing and treating 500 tn of waste rock per kg of metal.

Moreover, some authors, [19,20] and notably UNEP [21] have focused their concerns based on "mass" scarcity. We believe it is better to approach the concept of energy scarcity, which we call thermodynamic rarity. This concept considers the actual ore grades and is based on physical phenomena. On the contrary, geological mass scarcity becomes meaningless when we look at the magnitude of the earth's crust. Whereas the crust contains 10^{22} tn of rocks and, for example, cobalt has a concentration of 10^{-9} /ton crust, what is several thousand tons of annual extraction versus 10^{11} tn total cobalt, most of it dispersed in the crust that can never be mined?. i.e. cobalt is not massively scarce, but exergetically scarce. It is rare.

The accompanying figure explains the exergetic path of a metal from Thanatia to the mine and then to the market. X represents the concentration of the metal. X=1 would be the pure metal. X_B is the concentration after the beneficiation process. X_m is the metal concentration in current mines; X_L is the concentration in landfills, while X_C is the concentration in the crust (in Thanatia). The mineralogical barrier is somewhere in the red zone for each metal.

Unfortunately, the lack of statistics on mining and metallurgical energy consumption means that many concepts described here have yet to be developed. We leave it to young researchers to assess the mineral capital losses of the planet, as well as to outline and evaluate the mining capital losses of countries or mines over time, as well as market failures, and why not, a different way to hold nature's value. The theory outlined here does not ignore the databases of Life Cycle Analyses but complements them. Their data are fundamental to assessing all the physical impacts of mining. Indeed, water consumption, waste rock movement, reagent use, greenhouse gas emissions, ecosystem destruction and other pollution and consumption are necessary to fully assess the current degradation of mineral resources and the need to conserve them for future generations.

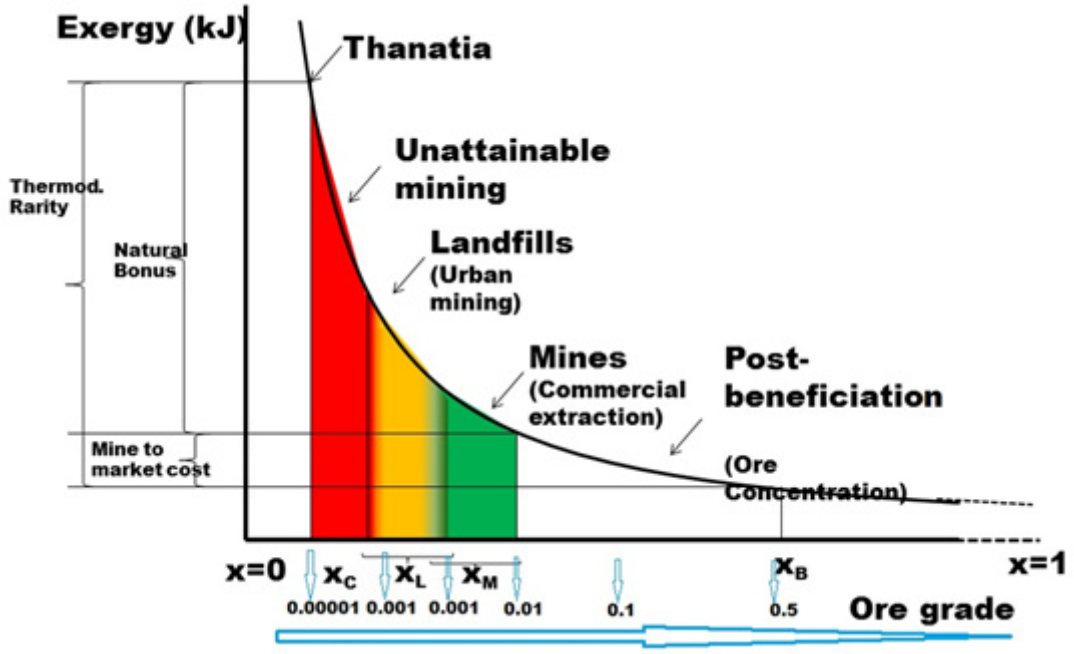

Figure 1: The concept of Thermodynamic Rarity

A final thought in this section: What has been described could perfectly well be called a Thermodynamics of Sustainability. According to the ecological economist J.M.Naredo [22] "Thermodynamics is the Economics of Physics". However, by introducing the concept of cost with all its meanings, in our opinion, the name Thermoeconomics fits better. Not only does it live up to the name it was given in the sixties, but thermodynamics extends its applications to the field of economics, not with metaphors but by quantifying the value of nature that our society ignores, perhaps due to a lack of method, or an excessive interest in forgetting it. It must also be said that by incorporating the word economy in the name, we are honouring all economic mathematics and all the concepts that have been developed until today, for example, input-output analysis, or Lagrange multipliers, to say the least.

3. Pristinia, is exergy appropriate for assessing soil fertility?

When we studied the use of exergy to assess the loss of the planet's mineral capital, we found that fertile soils were left out of our analysis. The problem of soil degradation is even faster than that of mineral depletion, Fertile soils are neither abiotic nor biotic but an amazing mixture. Could soil fertility be assessed through exergy? We have done so, but there is a lack of researchers in soil science and thermodynamicists who want to go into this area.

The sustainability of agroecosystems is an important issue considering that food demand will continue growing as the global population increases. A 49 per cent increase in agricultural production is expected to be required by 2050 [17]. In the last decades, crop production yield has been raised by means of employing intensive agriculture based on high inputs of inorganic fertilizers and pesticides, resulting in severe environmental impacts, erosion, and soil quality loss. In fact, the agricultural sector causes approximately 25 per cent of the global greenhouse gases [23]. Besides, degradation caused in soils threatens around 40 per cent of the land area. In Europe, it is estimated that there are 12 million hectares affected by erosion [24].

Compared with the 15 km de upper crust, fertile soils only occupy, on average 15 cm, of topsoil. They are a complex system composed of three main structures: physical, chemical and biological structures. First, their physical texture comprises a variable clay, sand and silt composition. Second, its chemical composition with an inorganic part of at least 19 nutrients and a rich and varied organic part is essential to improve the physical characteristics and as food for the soil biota. The 19 inorganic nutrients are divided into macronutrients like N, P, K, Mg, Ca and S, then micronutrients like Fe, Mn, Cu, Ni, Mo, B, Zn and Cl, and then, other beneficial elements essential for certain species or under specific conditions like Na, Si, Co, Se and Al. Third, their biological content consists of macro and microbiota with bacteria, fungi and viruses. Besides that, water, air and a specific range of temperatures are vital needs.

It is clear that the Thanatia model is not suitable for assessing soil fertility. Moreover, each area of the globe has different local textures and fertility also depends on climate. Therefore, it is necessary to establish a suitable

methodology to serve as a starting point for assessing soil degradation. We adopt a new strategy, proposing an optimum soil that allows us to analyse all real soils as deviations from an optimum towards Thanatia, Figure 2. Accordingly, we introduce a perfect fertile planetary crust, OPTSOIL [25], composed of nutrients, OPTNUT, and organic matter, OPTSOM, that is invariant and independent of different local textures, but not independent of its water content and aeration. We call this imaginary, copiously fertile crust Pristinia as opposed to Thanatia, a dead state referring to abiotic resources. Thus, any real agricultural soil will be in an intermediate state between Pristinia and Thanatia.

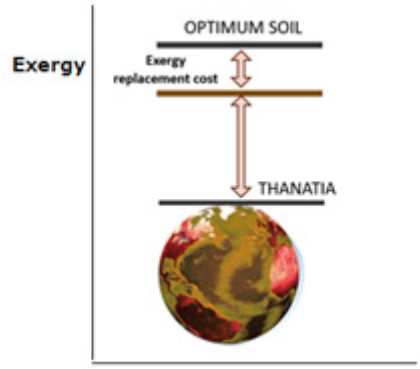

Figure 2: Degraded soils are between Thanatia and an optimal soil in nutrients, organic matter and biota.

The departure of each agricultural soil from the optimum soil can be associated with a sum of physical, chemical and biological causes that can be assessed exergetically. The idea is to evaluate a spectrum of actual degradations of agroecosystems, including those occurring in the soil, and to see the physical cost of their regeneration. For this purpose, the concept of exergy replacement cost is used. As shown in Figure 3, the exergy costs of mechanical processes, fertilisers, pesticides and plant protection products, water and diffuse emissions generated in the agricultural process are quantified. In addition, the substitution processes necessary to return the soil from the final state to the initial state (or optimum state) have been defined and evaluated. In this sense, losses due to erosion, nutrient amendments, organic matter, salinity and acidification are quantified through their exergy costs.

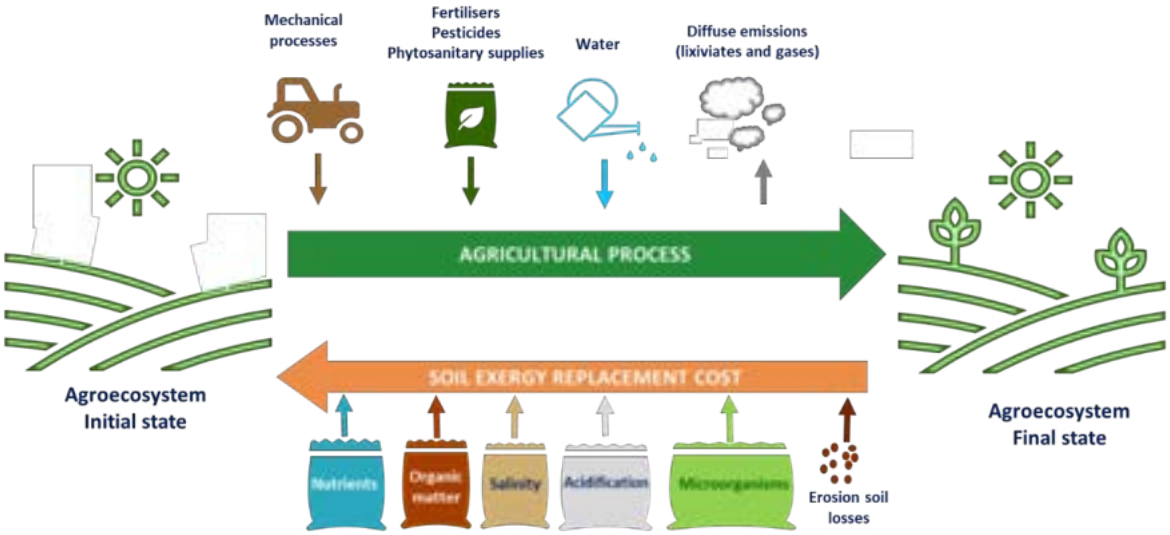

Figure 3: Graphical summary of the exergy-based methodology for the evaluation of agroecosystems.

These are the foundations of an incipient line of work. The next steps should focus on the importance of soil microbiota, OPTMIC, using Jorgensen's concept of eco-energy [26], also in evaluating organic matter in terms

of CO_2 sequestration achieved, which is controversial because of the difficulty of demonstrating its long-term stabilisation. Further development will aim to assess soil considering not only its agricultural production and carbon sequestration functions but all the different ecosystem services it provides, such as habitat provision, biodiversity, water regulation and purification, and environmental quality, among others.

Even with these drawbacks, our methodology has been awarded with a recognition of a reference document from the European Committee for Standardization (CEN).with the title: “Methodology to quantify the global agricultural crop footprint including soil impacts” [27].

This European CWA specifies a methodology for identifying, characterising, and implementing a single indicator to assess the quality and degradation of agricultural soils and the overall impact of the agriculture processes. The agriculture impacts are assessed through the associated mechanical, fertilisation and irrigation activities. Furthermore, soil impacts are evaluated accounting for soil erosion and parameters such as nutrients, texture, and organic matter. The developed methodology allows a simple but robust assessment of soil biogeochemical processes and the loss of fertility and degradation

4. Waste and Circular Thermoeconomics

The concept of waste has not been sufficiently analysed in thermoeconomics. By waste, we mean any unwanted material or energy flow, solid, liquid or gaseous, or a heat, noise or any radiative flow. From a thermodynamic point of view, it is simply the external irreversibility that generates entropy outside the system under analysis. Waste is harmful because it still has exergy and we have to consume it to get rid of it.

Every time we produce, we generate waste. And every product, sooner or later, also becomes waste. This consideration is important because it allows us to distinguish between waste from production processes and the end-of-use waste of material goods. The former corresponds to the remains of the resources used in the processes; let us call them primary waste because they are produced simultaneously as the products are obtained. The latter corresponds to the degradation or elimination of material goods of an inorganic nature or to the discarding of parts of organic substances. Municipalities usually collect this type of waste, and we call it here secondary waste. Their treatment, reduction and disposal require more energy, water and raw materials, which constitute the input for their processing, while new products and tertiary waste are produced, which constitute their output. Thermoeconomic analysis can therefore be applied to them.

Thermoeconomics enables to obtain a coherent and significant set of costs in a given energy structure [28]. Costing allocation essentially looks for the amount of resources needed to produce both intermediate and final products. The irreversibility cost formula [29] allows to calculate the (direct) exergy cost as the exergy content of a flow plus the sum of the irreversibilities generated to produce that flow.

$$B_i^* = B_i + \sum_j^n \phi_{ij}\, I_j \tag{1}$$

The coefficients ϕ_{ij} represent the part of the irreversibility of the equipment -j- that has been generated to produce one unit of the flow -i-. These coefficients depend exclusively on the definition of the production structure of the plant and the definition of the efficiency of each of its components. Therefore, this formula is the connection between thermodynamics and the second law (exergy and irreversibility) and economics (costs) derived from the definition of the productive purpose of the plant components.

As waste is an integral part of the production, just as one assesses the process of product cost formation, the process of waste cost formation must also be evaluated. Considering that waste has exergy, it is rational to think it could still be used for production. But there is a lack of technology and a surplus of ignorance of nature. Externalisation’ is the endorsement of the harms we cause outside the production system. At best, we pay money, in the form of taxes or fines, for society to mitigate them, or we send them to those countries that accept them in return for payment, thus creating an increasingly unequal world. Otherwise, society must adapt to environmental degradation, leaving the burden on future generations.

A responsible society must ”internalise” waste and its costs. For this, it is necessary to develop techniques that rigorously assess, for example, both the CO_2 emitted and the CO_2 avoided in each waste treatment process.

Many thermoeconomic analysts have focused on proposing costing assessment procedures for polygeneration plants [30, 31]. Some of these analyses assess the costs of waste remediation or abatement [32], which must then be added to the cost of the products. The result is clear: the cost of the products increases. And the more complex the waste, the higher the costs added to production and, thus the higher the prices of all goods. This is something that today’s society does not easily accept.

However, whereas waste has exergy, it can be used to improve the plant’s or plants’ efficiency in a cyclical production chain and thus reduce production costs, creating the positive effect of reducing resource consumption and waste emissions.

In many cases, this use of waste energy requires new industrial processes and/or new companies that make up the links in the industrial chains. It is clear that innovation can come from the thermoeconomic analysts themselves, leaving behind more or less irrelevant procedural discussions on achieving a better cost allocation.

The process of waste cost formation must be a priority objective in this new Circular Thermoeconomics. Waste costs must be rigorously assessed because they are the compass for decisions to improve production processes, both within production plants and/or in increasingly complex industrial chains. Whereas we internalise waste costs, eq. (1) will also be accountable for these wastes as (external) irreversibilities. The coefficients ϕ_{ij} also contain information on the internalisation of waste. Therefore, if external irreversibilities (wastes) are recovered, the production costs are reduced. The keyword recycling must be intrinsically related to efficiency and cost. It can be used interchangeably by thermoeconomics, circular economy and industrial symbiosis.

Although it may seem to direct ideas to one's advantage, using exergy makes it possible to quantify any material or energy waste in kWh. This makes it possible to create a general theory based on exergy. Furthermore, exergy can be evaluated with any other energy indicator, e.g. in kg or natural gas equivalent. This allows us to convert it into CO_2 equivalent emitted in the production or, alternatively, to evaluate the CO_2 equivalent savings between two production structures. This is important because it gives rigour to the huge simplifications of GHG emission calculations that are made today in increasingly complex systems.

When applying thermoeconomics to the exergy recovery process of waste, a pinch point of recoverability always appears where total recycling is unattainable because a further increase in recycling does not correspond to the same efficiency increase. The "pinch points" of waste must be identified and systematically diminished. Reality imposes the fact that it is not possible to recycle everything. Hence we should not speak of Circular Economy but of Spiral Economy [33]. The latter makes it possible to assess the degree of spiralling of a material cycle, understood as the percentage of exergy loss with respect to the exergy brought into play in the whole cycle. In this way, spirality can be related to the concept of pinch point, as the economically viable exergy percentage of recovery of a residual flow, measured in the potential for narrowing of its intensive properties of the type ΔT, ΔP, etc.

It is remarkable to see that the search for better energy efficiency is often linked to reduced material efficiency. Nonetheless, this fact has been systematically forgotten. For example, cars, which are nothing more than mobility production plants, consume less and less fuel per kilometre, but we forget that the material complexity of their digitisation has radically reduced their material efficiency. A vehicle from 50 years ago contained only steel, aluminium, copper, rubber, glass, wood and some plastic. Today's vehicles contain more than 55 chemical elements, with a myriad of plastics, alloys and micro-components full of critical raw materials. Their non-recyclability is notorious, and they are not designed to recover their spare parts. Circular thermoeconomics can provide striking answers to this problem because whereas the exergy costs of extraction and replacement of the materials are involved in the analysis, it is possible to assess the relationship between exergy savings and the exergy invested in obtaining them, ExROI. The results obtained yield important conclusions on how our society is squandering the earth's mineral capital in favour of a pseudo-energy efficiency of all processes. This is a strong reason to recycle materials, especially the most critical ones.

The message we can give is that goods are cheap because we internalise the price of products, neither the cost of the scarcity of natural resources nor the impact our waste has on planetary habitability.

Nature closes its material cycles, because the waste generated by one living becomes the resources of others, making the biosphere-geosphere complex a sustainable system driven by solar energy and the planet's internal heat. Nature has its rhythms and the closing of these cycles can even take geological time, as is the case with fossil resources. On the contrary, our society is in a hurry and lets its waste go underground (landfills), turn into gases (incineration) or be diluted in the atmosphere and the hydrosphere.

This is no small task, the production of waste and the depredation of natural resources are closely related to the nine planetary boundaries that Rockstrom et al, [34] point out: climate change, ocean acidification, stratospheric ozone, nitrogen and phosphorous cycle, global freshwater use, deforestation and topsoil degradation, biodiversity loss, chemical pollution, and atmospheric aerosol loading. To these must be added, among others, the more recently reported phenomena such as oceanic pollution by microplastics or the massive extraction of critical raw materials to sustain new digital and renewable technologies.

Against this scenario, thermoeconomicists cannot close their eyes to the most efficient use of waste. Beyond the processes of remediation or abatement of waste, it is necessary to think about the use and reuse of industrial and individual waste. This is the origin of Circular Thermoeconomics. We must learn from nature. The waste of one production plant should be the resource of another. We must design to make the use of waste materially and energetically viable. Cyclical industrial chains must be created to give new life to waste. The concepts of industrial symbiosis and urban-industrial symbiosis must be extended to the whole productive system, which will affect a social change of attitudes.

An introduction to Circular Thermoeconomics can be found in [35]. We invite new researchers to develop both

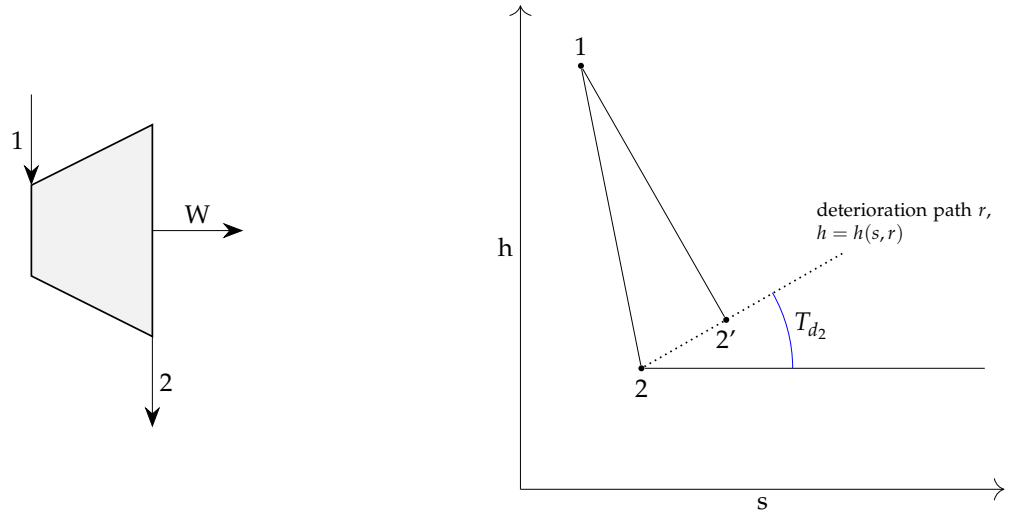

Figure 4: The deterioration path of a turbine.

this theory and its multiple applications that have been proposed with these reflections.

5. Exergy or Relative Free Energy?

There is a consensus among practitioners that exergy is the thermodynamic property that best distributes production costs among various streams, which then helps to establish the economic costs of the streams that interact in any energy system. However, the exergy calculation has the shortcoming that it depends on the reference environment applied, which in turn is an arbitrary selection of the user and not a physical behaviour of the system under analysis. If this is the case, the concept of exergy efficiency, although more precise than the first law efficiency, still depends on the chosen reference environment.

This problem is even worst in thermoeconomic diagnoses of very complex plants using exergy costs, since the chains of causation may induce wrong malfunctions and dysfunctions. There might be a consensus regarding which is the most suitable. However, convergent opinions are not mathematical proofs. Is it possible to find a better function to get rid of this problem? The answer will need future research, perhaps the “relative free energy function” has the ”way” of solving this problem. This section explains why is it.

Any machine that uses a working fluid is designed to change its intensive properties, such as its pressure, temperature, chemical potential or electromagnetic potential, making its energy transfer to another part of the machine.

Suppose now that the working fluid malfunctions due to intrinsic reasons of the machine. If the fuel quality, f, does not change, it will be necessary to increase the amount of fuel to get the same product, P. Then, this excess fuel becomes dissipated in the form of heat.

The enthalpy and entropy balances of the working fluid process, under the conditions (h_1, s_1) and P constant, will be:

$$(h_1 - h_2)\, dm = m\, dh_2$$
$$(s_2 - s_1)\, dm + m\, ds_2 = dS_g$$

As the deterioration process of the machine is compensated by higher fuel consumption, both dm and the entropy generated are positive. So is the heat dissipated, $m\, dh_2$, and the entropy increase of the fluid, $m\, ds_2$. If one defines the deterioration temperature of flow in state #2 as the quotient:

$$T_{d_2} \equiv dh_2 / ds_2$$

the result of the combined balances is as follows:

$$\left(\frac{dm}{dS_g}\right)_r = \frac{T_{d_2}}{(h_1 - h_2) - T_{d_2}\,(s_1 - s_2)}\,, \tag{2}$$

where r is the deterioration path in the (h, s) plane of the outflow, as show in Figure 4 for the case of a turbine.

Equation (2) states that any deterioration process in an energy component has an associated T_d in the exit stream of supplying fuel. This parameter possesses temperature dimensions even if it is not a gauging temperature; it can be calculated by measuring the quotient dh_2/ds_2 experienced by the output stream of the component’s fuel.

This equation is the mathematical expression of the relationship between the additional consumption of the resource needed to compensate for an internal degradation of the machine when the output of the machine is kept constant.

Equation (2) and the function ℓ, whose variation is defined as:

$$\ell_1 - \ell_2 \equiv h_1 - h_2 - T_d(s_1 - s_2)$$

where presented in [36], and was called the *relative free energy*, RFE. It is surprisingly similar to the exergy variation of the working fluid, which may explain the attachment and intuition of process analysts to exergy. However, RFE is mathematics while exergy comes from consensus.

However, the deterioration temperature no longer depends on the chosen reference temperature for exergy calculations. Although T_d has temperature dimensions, is not a gauging temperature; it can be calculated by measuring the ratio dh_2/ds_2 experienced by the machine´s fuel at its output.

For a given deterioration cause r of a machine, a geometric path in the (h, s) plane of the possible exit flow states can be identified. Let $h_2 = h_2(s_2, r)$ be the function describing this outflow deterioration path, and it can be considered as the mathematical description of the effects on the exiting flow caused by such deterioration.

As it is shown in Figure 5 the intersection of the tangent line of the deterioration path r with the h- axis is and its slope is T_d:

$$\ell = h - T_d\, s \tag{3}$$

It means ℓ is a function of T_d, with the caveat that both l, h and s refer to the same zero state.

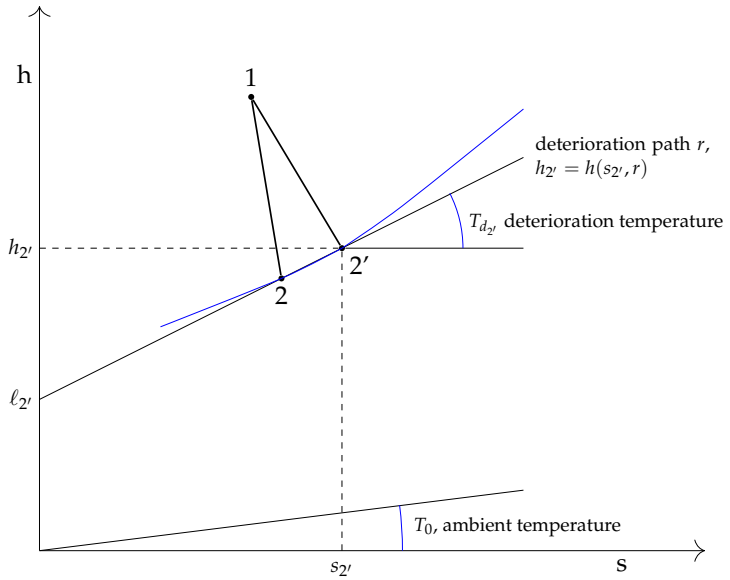

Figure 5: Geometric representation of relative free energy and deterioration temperature.

In reference [37] is shown that (3) is the Legendre transform of the deterioration r.

According to the definition of relative free energy (3), the expression (2) could be written as:

$$\left(\frac{dm}{dS_g}\right)_r = \frac{T_d}{\ell_1 - \ell_2} \tag{4}$$

Note that this equation is always positive, under the specified conditions. Moreover, since $T_d > 0$, then $\ell_1 > \ell_2$, i.e., the working flow has lost part of its relative free energy. In fact, for the same deterioration, $dS_g = const$, the higher the T_d, the greater the amount of resource required to yield the same product. This trade-off is not linear because whereas the numerator increases, the denominator also decreases. On the contrary, when T_d tends to T_0, the impact of this compensation will decrease. Only in the case where $T_d = T_0$, the decrease of relative free energy will coincide with the exergy decrease.

As the environment is an attractor, the T_d of the components of an installation will decrease until it reaches T_0, just as the relative free energy will tend to exergy.

In order to evaluate T_d, it is necessary to know the cause(s) of machine deterioration and its behaviour, which is additional information to be incorporated into the plant diagnosis. In other words, the cost of a malfunction is directly related to the physical behaviour of the machine.

The relative free energy function, ℓ, is the amount of specific energy of the exiting stream of a fuel, which is not affected by the deterioration of the machine. In fact, when the exit flow changes its state owing to the deterioration, h and s, vary by following the path $h_r = h_r(s_r)$. Consequently, the following expression is obtained:

$$d\ell_2 = dh_r - \left(\frac{dh}{ds}\right)_r ds_r = 0 \qquad \text{or} \qquad \ell_2 = \text{const.} \tag{5}$$

Besides that, a new definition of efficiency (or its inverse specific consumption), For example, in a turbine it is:

$$k_L = \frac{F_L}{P_L} = \frac{\mathcal{L}_1 - \mathcal{L}_2}{W} = \frac{H_1 - H_2 - T_d\,(S_1 - S_2)}{W} \tag{6}$$

Where $\mathcal{L}$ is the corresponding extensive property of ℓ, i.e. $\mathcal{L} = m\ell$. This "relative" efficiency, k_L, has an astounding property that exergy lacks.

When a malfunction in the turbine follows a trajectory r at W constant, it follows:

$$\ell_1\, dm = \ell_2\, dm + W\, dk_L \tag{7}$$

because $\ell_1 - \ell_2$ is constant along trajectory r. Therefore:

$$\frac{dk_L}{k_L} = \frac{dm}{m} \tag{8}$$

in other words, any additional percentage of malfunction following a trajectory r at W constant result in an additional percentage of the mass of fuel entering the turbine. This property is very promising for simplifying the mathematical apparatus of plant diagnosis. Note instead that exergy does not fulfil this property since:

$$ex_1\, dm = ex_2\, dm + m\, dex_2 + W\, dk \qquad dex_2 \neq 0$$

which may induce false dysfunctions. Furthermore, the definition of k_L incorporates the information of the physical behaviour of the machine through T_d, whereas the unit exergy consumption is a black box to what happens inside the machine.

A noteworthy observation is that companies usually account for the resource consumption per unit of output of their installation. This accounting at the facility level is the one we propose in this section at the component machine level. Therefore, whereas we have for each cause of deterioration, r, the derivative $(\partial m_{local}/\partial S_g)$ and whereas we could evaluate how the amount of local equipment resources is related to the facility resources (of the same quality), i.e., $(\partial m_{plant}/\partial m_{local})$, we could obtain a new theory of energy system diagnostics. In theory our proposal would obtain the derivative: $(\partial m_{plant}/\partial S_g)$,that is $(\partial F_T/\partial S_g)$, where F_T are the plant resources. Note that what says "plant" here could also mean any disaggregated part of the overall plant structure, without needing to resort to the reference environment. This is what companies need for good energy consumption management, i.e. the genuine costs of the deterioration of each and every component of their installation.

Perhaps, the described procedure is much simpler than assessing the diagnosis using exergy costs:

$$\left(\frac{\partial Ex_{plant}}{\partial Ex_{local}}\right)_r$$

Regrettably, actual installations may have several simultaneous causes of degradation and their impact on overall efficiency would not necessarily be the sum of each cause separately.

Thanks to the Legendre transform we have shown that the RFE and the deterioration temperature are as real as the actual path of degradation of the working fluid in a machine. They have a physical basis and are not merely theoretical inventions. Unlike other thermodynamic functions that only depend on the equilibrium states of the system, the pair (RFE, T_d) only exists whereas the machine exists. It is like transferring the deterioration message from the machine to thermodynamics,

Incredibly, it was first presented in 1992 at the ECOS conference [36], with the earliest work by Alefeld at the University of Munich [38] that went almost unnoticed, perhaps because of the excessive cult of exergy. In spite of this, the use of this function in diagnostic applications and cost assessment of malfunctions in industrial energy systems is still to be developed. We leave it to future thermoeconomics practitioners to develop such ideas.

6. Conclusions

Science to be positive must be quantifiable and predictive. In general, the use of the messages of the second law of thermodynamics in the social sciences and in economics is more philosophical than operational. In

contrast, by redefining cost as a sum of irreversibilities and setting it up from the cradle to the market, we are connecting Thanatia with economics. That is Physics with Economics in a quantifiable and predictive way.

The first ideas of thermoeconomics and its very name are due to Myron Tribus, Robert Evans and Yehia El-Sayed in the sixties of the last century [39, 40]. It was created before Georgescu-Roegen published his book *The law of entropy and the economic process* [1] which claimed that economics had forgotten the concept of irreversibility. Unfortunately, thermoeconomics focused mainly on analysing industrial thermal systems, forgetting the message of its own name.

We believe that beyond converting irreversibility into money and weighing it against investments in production equipment, it is necessary to measure economic activities in terms of irreversibility in order to give value to the services provided by the planet.

The concept of a planetary dead state, Thanatia, allows the loss of mineral capital to be assessed in terms of quality and quantity. What is rare is valuable and must be conserved. We can move from the yes/no dichotomy to the physical quantification of nature's losses. And thus weigh the nature we lose against what we gain by engaging in any activity. And in doing so we will give value to the regeneration, repair, replacement and restoration of materials that are key to sustaining humanity for many generations to come. The supply of planetary wealth is not of an economic origin of the demand/supply equilibrium type, but of planetary limits. And in the face of this phenomenon, agreements between people or between countries are not valid, but rather in the assumption of the irreversibility that will condition the future of humanity itself.

Available mineral phosphates are limited to sustain the supply of a few generations. Electric mobility is limited by the enormous amount of chemical elements, more than 50, needed for high-tech vehicles. The digital economy is based on the profusion of non-recyclable microchips and printed circuit boards, extremely short-lived and full of rare metals. The same is true for renewable energy. The energy transition must be accountable for its material impact.

Similarly, current agricultural practices are degrading fertile soils which are the scarcest natural resource of all. Again, it is the second law that allows us to objectively evaluate all deviations from a model copiously fertile crust, called Pristina, as opposed to Thanatia. With the exergy methodology, we have a single indicator to value all the factors that intervene and form the soil. The recognition of this methodology awarded as a reference document from the European Committee for Standardization opens the door to refining and developing its applications.

Another major global problem is the production of waste, not only solid but also liquid, gaseous, noise, heat and radiation of all kinds. They are produced at the same time as we manufacture goods and consume them. They disturb and above all affect the planet in the form of climate change, pollution and the degradation of ecosystems. Whereas they do this damage, it is because they still have exergy. Harnessing them minimises remediation and abatement costs. Society must learn to internalise waste in order to give it new life and avoid its effects. To this end, industrial symbiosis must be generalised, in which the waste or by-product of one company is the resource of another, trying to close cycles (spirals) of all materials. This activity implies the promotion of a new industrial sector that will need to assess (and optimise) all the losses and savings that occur. The circular thermoeconomics outlined here will be an important branch of the future of second law analysis.

Last but not least, the relative free energy and its conjugate, the deterioration temperature, can take a step beyond the use of exergy in the diagnosis of energy systems, and above all to explain why the diagnosis should not depend on the analyst's choice of reference state. Throughout history, the emergence of new basic functions has been a far-reaching scientific event that has opened up new avenues and applications of thermodynamics. As such, it deserves to be welcomed by the thermoeconomic community.

In short, we at the Zaragoza School of Thermoeconomics believe that the "second law analysis" should be expanded to apply it to important problems facing our civilisation, such as the conservation of the planet's energy, water and material resources; the diagnosis and intelligent management of fertile soils to feed current and future living beings; and the minimisation of waste by closing material supply chains, promoting new industrial sectors for waste recovery, still in its infancy. The Thermodynamics of Sustainability of the future must include Thermoeconomics and all theoretical developments that help with these problems are welcome.

Acknowledgments

This paper has been funded by the Spanish Ministry of Science and Technology under project RESET PID-116851RB-100

References

[1] Georgescu-Roegen N., *The Entropy Law and the Economic Process*. Harvard University Press, Cambridge, MA, 1971

[2] Hall C., Klitgaard K., *Energy and the Wealth of Nations: An Introduction to Biophysical Economics* Springer, Cham, Switzerland, 2018

[3] Odum H.T., Odum E.C Energy Basis for Man and Nature. McGraw-Hill, NY, 1976

[4] Valero A, Valero-Delgado A., *Thanatia: the destiny of the Earth's mineral resources* World Scientific Publishing, London U.K., 2014

[5] Valero-Delgado A., *Exergy evolution of the mineral capital on earth* Phd Thesis, University of Zaragoza, University of Zaragoza, 2008

[6] Valero A., Agudelo A., Valero-Delgado A., *The crepuscular planet. A model for the exhausted atmosphere and hydrosphere* Energy, 2011, 36:3745-3753

[7] USGS *Mineral Commodity Summaries* US Geological Survey, US Geological Survey, 2007

[8] WEC *Survey of Energy Resources 2007* World Energy Council, World Energy Council, 2007

[9] Yoder C., Global Earth Physics: A handbook of physical constants Astrometic and geodetic properties of the Earth and Solar system. American geophysical union, 1995:1-31

[10] Valero-Delgado A., Valero, A. *The crepuscular planet. A model for the exhausted continental crust* Energy, 2010, 36:694-707

[11] Grigor'ev N. The average mineralogical composition of the upper continental crust, Uralian Geological Journal, 2000, 3:3-21

[12] Crutzen, P., Stoermer, E., *The "Anthropocene"* Global Change Newsletter, 2000, 41:7-18

[13] Calvo G., Mudd G., Valero-Delgado A., Valero, A., *Decreasing Ore Grades in Global Metallic Mining: A Theoretical Issue or a Global Reality?* Resources, 2016, 5,

[14] Szargut, J., *Chemical Exergies of the Elements* Applied Energy, 1989:269-286

[15] Valero-Delgado A., Valero A., Domínguez A., *Exergy Replacement Cost of Mineral Resources* Journal of Environmental Accounting and Management, 2013, 1:147-158

[16] Valero-Delgado A., Valero A., Calvo G., *The Material Limits of Energy Transition: Thanatia* Springer Nature, 2021

[17] Valero-Delgado A., Valero, A. Thermodynamic Rarity and the Loss of Mineral Wealth. Energies, 2015, 8:821-836

[18] Skinner, B.J., A second iron age ahead? Am.Sci. 1976, 64:158–169.

[19] Henckens, M.L.C.M., Driessen,P.P.J., Worrell,E., Metal scarcity and Sustainability. Analyzing the necessity to reduce the extraction of scarce metals. Resources Conserv. Recycl., 2014, 93:1–8.

[20] Henckens M.L.C.M., van Ierland E.C., Driessen P.P.J., Worrell E. Mineral resources: Geological scarcity, market price trends, and future generations. Resources Policy 2016, 49:102–111.

[21] UNEP International Panel on Sustainable Resource Management, Working group on geological stocks of metals, Working Paper. 2011 April.

[22] Naredo, J.M. , La Economía en Evolución. Ed. Siglo XXI, Madrid, 1987

[23] FAO *FAO's Work on Climate*, 2019.

[24] Görlach B., Landgrebe-Trinkunaite R., Interwies E., Bouzit M., Darmendrail D., and J. D. Rinaudo, *Assessing the Economic Impacts of Soil Degradation*, Berlin: Ecologic, 2004. doi: ENV.B.1/ETU/2003/0024.

[25] Valero An., Palacino B., Ascaso, S., Valero, Al., *Exergy assessment of topsoil fertility*, Ecological Modelling, 2022, 464: 109802

[26] Jørgensen S.E., *Introduction to systems ecology*, CRC Press Book, First edit. Boca Raton, Florida 2012.

[27] CEN/WS CROP, *Methodology to quantify the global agricultural crop footprint including soil affection*, Available at: `https://standards.iteh.ai/catalog/tc/cen/8fd61ae8-11c2-45c1-88bf-24fba4106e0e/cen-ws-crop`, [accessed 21.3.2023]

[28] Valero A., Torres C., Serra L., *A general theory of thermoeconomics: Part I. Structural analysis* Proceedings of the International Symposium on Efficiency, Costs, Optimization and Simulation of Energy Systems, 1992:137-154

[29] Torres C., Valero A., The Exergy Cost Theory Revisited, Energies, 2021, 14:1594.

[30] Calise F., Cappiello F.L., Vicidomini M., Petrakopoulou-Robinson F., Water-energy nexus: A thermoeconomic analysis of polygeneration systems for small Mediterranean islands Energy Conversion and Management, 2020, 220:113043

[31] Amidpour, M., Khoshgoftar Manesh, M. H., *Exergy and thermoeconomic evaluation of cogeneration and polygeneration systems* In: Amidpour, M., Khoshgoftar Manesh, M. H. editors. Cogeneration and Polygeneration Systems, Academic Press, 2021, p. 55-74

[32] Valero-Delgado A., Valero A. *What are the clean reserves of fossil fuels?* Resources, Conservation and Recycling, 2012, 68:126–131

[33] Valero A., Valero-Delgado A. Thermodynamic Rarity and Recyclability of Raw Materials in the Energy Transition: The Need for an In-Spiral Economy. Entropy, 2019, 21(9):873

[34] Rockström, J., Steffen, W., Noone, K., Persson, Å., Chapin, III, F. S., Lambin, E., Lenton, T. M., Scheffer, M., Folke, C., Schellnhuber, H., Nykvist, B., De Wit, C. A., Hughes, T., van der Leeuw, S., Rodhe, H., Sörlin, S., Snyder, P. K., Costanza, R., Svedin, U., Falkenmark, M., Karlberg, L., Corell, R. W., Fabry, V. J., Hansen, J., Walker, B., Liverman, D., Richardson, K., Crutzen, P., Foley, J., *A safe operating space for humanity*, Nature, 2009, 461:472–475

[35] Valero A., Torres C., *Thermoeconomics as a cost accounting methodology for Spiral Economy and Industrial Symbiosis*. ECOS 2021, 34th International Conference on Efficiency, Cost, Optimization, Simulation and Environmental Impact of Energy Systems, June 27-July 2, Taormina, Italy: 656-666.

[36] Valero A., Lozano M.A., *General theory of thermoeconomics: Part II. The Relative Free Energy Function*, Proceedings of ECOS 1992 International Symposium, Zaragoza, Spain:147-154

[37] Valero A., Torres C., *Relative Free Energy Function and Structural Theory of Thermoeconomics* Energies, 2020, 13:2024.

[38] Alefeld, G., *Problems with the exergy concept (or the missing Second Law)* IEA Heat Pump Newsletter, 1988, 6(3):19–23.

[39] Evans, R.B., and Tribus, M., *Thermoeconomics of Saline Water Conversion* Process Design and Development, Vol 4, April 1965:195-206.

[40] El-Sayed, Y. and Evans, R., *Thermoeconomics and the Design of Heat Systems*, Journal of Engineering for Power, January 1970, pp.27-35.

From thermoeconomics to environomics and beyond

Daniel Favrat[a]

[a] EPFL, Ecole Polytechnique Fédérale de Lausanne,(Energy center) Lausanne, Switzerland, daniel.favrat@epfl.ch

Abstract:
Modern energy systems are more and more based on integrated technologies in a world evolving towards increasing concerns not only for economics but also for environmental issues with a growing focus on resources and emissions. In parallel, information technologies including advanced simulation and optimization algorithms develop at a rapid pace. Thermoeconomics based on either the First Law or exergy, together with cost factors distributed through its equipment, also evolved during the last 30 years. However modern muti-objective evolutionary optimization techniques, extending the capacity to tackle optimization considering a growing number of parameters including the internalization of the costs of emissions of whole systems has also emerged. The latter is called environomics. So far, the supply of energy services was essentially dominated by fossil-based resources with a high focus on operational costs. The new trends towards renewable energies requires a growing need to consider the embedded exergies since renewable energy, like solar energy, is economically free and operational costs are inherently low. While economic factors can vary over a broad spectrum throughout the years of operation, the embedded exergies are more stable values, particularly because the systems are built in a known economic and energetic environment. A new class of methods is only emerging to deal with more complete exergy approaches to formulate more holistic exergy life cycle analyses. Those should provide a lower bound of the expected exergy payback over the lifetime of the systems to be compared with thermoeconomic or environomic optima. It is still a huge challenge ahead to provide practical tools to do it.

Keywords:
Thermodynamics; Exergy; Environomics; Thermoeconomics; Second Law.

1. Introduction

The world is facing major challenges regarding environmental threats and resource constraints at a time where geopolitics tends to have a growing influence and globalization is questioned. In this context there is a growing need for efficient integrated systems. Apart from technical progress, engineering methods have to constantly evolve to account for energy efficiency, economic viability and environmental constraints, taking in particular advantage of progress made in optimisation schemes and data processing.

During the early days of thermoeconomics, with pioneers like Tribus and El-Sayed referred to in Frangopoulos [1], as well as Tstsaronis [2], Valero [3], and von Spakovsky [4], a strong emphasis was put on thermodynamic formulations that would favour the decentralisation of the optimisation of each component due to the lack of available adequate algorithms. In terms of Second Law of thermodynamics each component of a system has to “pay” for its inefficiencies, that is for the entropy it created, and the cost associated with its dumping to the environment. The earlier energy systems considered were primarily fossil based and for systems in steady-state conditions.

The broad name of thermoeconomics includes both energy analyses and optimisation based on the First Law with costs minimisations, while a narrower approach considers only exergy consideration with cost minimization.

Quickly the need for developing methods accounting for the increasing complexity of investment and operation of real energy systems arose to deal in particular with:

- Environmental emissions both local and global (environomics).
- Time dependent operating conditions.
- Reliability constraints implying both active and passive redundancy for example.
- Global resource considerations including considerations of the embedded exergy of components.

2. Competing methods

While the Second Law fundamentals with the exergy theory were rarely questioned two different methodology paths were pursued.

- The mathematical approach with the continuous development of Second Law based thermoeconomics [5] in parallel to First Law thermoeconomics, and
- The graphical approach using a simplified second Law approach, called pinch technology, with an emphasis on minimizing the costs linked to the heat transfer exergy losses. The latter is a clever graphical application of the Second Law to optimize the energy integration of industrial processes [6-10].

Ultimately all benefitted from the considerable progress made by the optimisation algorithms with, in particular, evolutionary algorithms able to reliably tackle problems with non-linear and even discontinuous solution spaces. With such computational capabilities the need for decomposition of the problems to allow easier optimisation faded somewhat. Methods based on non-linear mono- and later multi-objective optimisation emerged allowing to deal with both design and operation factors, even for expected changes in operation over the lifetime of the energy systems [11,13].

2.1 Second Law and environmental aspects

One problem in trying to include environmental pollutants with the Second Law approaches of exergy-based thermoeconomics is that the detrimental effects of local pollution are generally not linked to the entropy of the substances in the environment. Therefore, the need to express the cost of emissions with complementary factors was identified and Frangopoulos coined the term environomics [1] for methods dealing with the internalization of the specific individual costs of pollutants. This allowed to do sensitive analyses on specific pollutants and the economic penalties when having to reduce the emissions. Individual pollutant costs could even be modelled with functions accounting for the distance between the pollutant source and the density of the population directly affected [14] as illustrated in [15-16]. The impact of pollutant could also be accounted for when dealing with downstream pollutant capture as shown for the optimisation of combined cycle plants with or without considering pollutant costs by Pelster et al. [17]. The internalisation of pollutant costs is important in the context of the introduction of taxes like the CO_2 tax. It can also be of great help in assessing new measures for decision makers or in studying the potential financial risk differences between competing designs. Pareto frontier representations of the solutions developed with environomic bi-objective optimisation is a powerful tool as shown in Figure 1. This illustrates the trade-offs related to the design of District heat system [11] and their effects, among others on the temperature of heat distribution. These results nicely complement the mono-objective optimisation initially made by Curti [15-16].

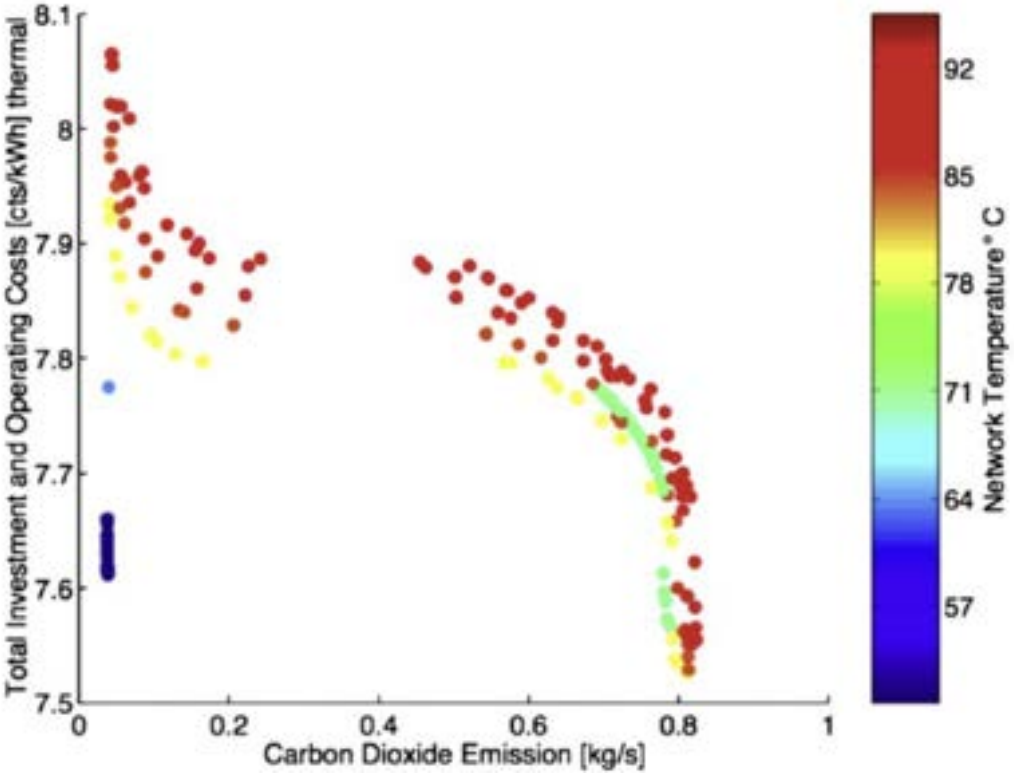

Figure 1. Solutions for a District Heating network with both centralized and decentralized heat pumps. Each dot represents a configuration of components both centralized and decentralized in individual buildings [11].

It particularly highlights the switch that can be observed in District heating networks from central plant with relatively high distribution temperatures to networks operated at “ground temperature levels” with decentralized heat pumps in each building (blue dots on the left). These low temperature networks, sometimes called District Energy Networks of fifth generation or anergy networks, not only increase the synergy between providers and users of energy services but also allow direct air-conditioning services with simple heat exchangers. Operating networks at low temperatures limits the need for thermal insulation and opens the opportunity to capture all kind of waste heat. It further favours some seasonal storage with, for example, fields of shallow geothermal wells. District heating and cooling networks (DHC) are expected to grow fast in the light of the enhanced decarbonization policies.

In Figure 1 the most cost-effective solutions but with the highest emissions are shown on the right and correspond to a central plant with a heat pump for 50%, a cogeneration gas turbine for 20% and ancillary gas boilers for 30% of the heat demand. In this particular case, the peak heating power considered was 63 MW, the specific electricity price was 0.13 $/kWh for a natural gas cost of 0.05 $/kWh. A NOx pollution cost of 13$/kg and a CO_2 cost of 0.03 $/kg [11] was also considered. It is easy to see on the graph that the recent increase of energy prices, that is likely to be maintained in the search for regional independence in energy supply, will further improve the importance of the electric heat pump only solutions.

2.2 Thermoeconomic analysis of time-dependent processes

Obviously, energy systems must be designed for a proper adjustment over time between the needs of the users and the constraints of the suppliers. Hence the need for multi-period/multi time optimization as described in [12,18]. This can be approached with sequential optimization inside the more global optimization. Employing typical operating time periods, like typical days throughout the season, is often the way to reduce the computational efforts. The introduction of energy storage components often generates alternatives to the strategies based on the power modulation of oversized supplying technologies that need to be compared with. Seasonal storage needs often to consider synthetic fuels easy to store over long periods of time. This is part of the actual discussion occurring around energy and cost intensive synthetic fuels compared to the investments in an overcapacity of power production like was favored previously by France with nuclear or Germany with coal plants.

In process engineering a hybrid approach between pinch technology and evolutionary algorithm optimization was proposed by [19] for batch processes including graphical representation of the solutions with multi-storage tanks.

Needless to say that these brief comments are by no means exhaustive and further methodological improvements of these broader thermoeconomic approaches accounting for time variations are needed.

2.3 Thermoeconomic optimisation accounting for reliability

It is imperative for many energy systems to provide reliability guaranties and liabilities could be quite costly during operation. Therefore, including elements like active or passive redundancies of components might significantly modify the thermoeconomic or environomic optimisation of designs. Examples applied to waste incineration plants are shown in [12,13], where increasing the number of furnaces that is less economic at first sight can finally be among the most adapted options.

For all the above requirements a first phase based on exergy considerations is required to build the super-structures (or super-configuration) on which the optimisation problems are based.

3. Influence of the current energy system trends on the thermoeconomic methods

With increasing concerns about greenhouse gases and following the Paris international agreement, the trends are going for an increasing pressure to improve the efficiency of systems and rely more and more on renewables. While the present thermoeconomic or environomic methods based on exergy are already adequate for efficiency, new considerations regarding resources and the increasing ratio between investment versus operational cost with renewables modify the relative importance of the different factors.

If, as mentioned above, the polluting emissions are not directly linked to entropy, the material resources are linked to the concentration of the elements in the Earth crust and therefore to entropy. So, at a time where humans increase the use of most parts of the Mendeleev chart of elements, all the present efforts to account for this in exergy approaches should be pursued. The Second Law approaches for processes, from the early work of [20] to the deeper considerations of materials in [21] represent valuable background approaches that are well initiated. The recent update of [22] adequately complement the methodological aspects on how to deal with resources with the Second Law in mind. Those approaches provide a methodological answer to the crucial problem of the scarcity of materials, like the Rare Earth Elements, in the development of renewable energies and the efficiency improvements links to the growing electrification of our societies. This cannot be

dissociated from the recycling processes or even the material substitutions that follow the fast growth of specific storage components like those used in the electric batteries, often with a significant time delay.

When it comes to graphical approaches the earlier work on extended composites in [8] provides some examples on how embedded exergies of components could be accounted for. Figure 2 illustrates the extended composites related to the implementation of an industrial heat pump in a drying process together with a gas engine (410 kW) to provide the power (265 kW) needed for the compressor of the heat pump as well as the power (145kW) requested by the various fans of the dryer tunnel. It relies on two related diagrams, the main one related to pinch technology approach completed by a second one (electric power versus a pseudo-Carnot factor to illustrate the exergy losses including embedded exergy linked to the compressor of the heat pump. It has also the advantage of visualizing the electricity balance in each process. The exergy losses in the evaporator and condenser of the heat pump are directly shown in the main pinch composite diagram while the exergy losses linked to the engine are shown in the top diagram with a pseudo-Carnot factor superior to one.

A similar diagram was made in [9] for the dryer equipped only with gas furnaces and the exergy losses with the retrofit solution given in Figure 2 were reduced from 1725 kW to 1040 kW.

Note that the notion of embedded exergy losses is strongly inspired by the earlier of work of Bejan [23] when discussing the optima in heat exchangers accounting for heat transfer, friction losses and embedded energy losses.

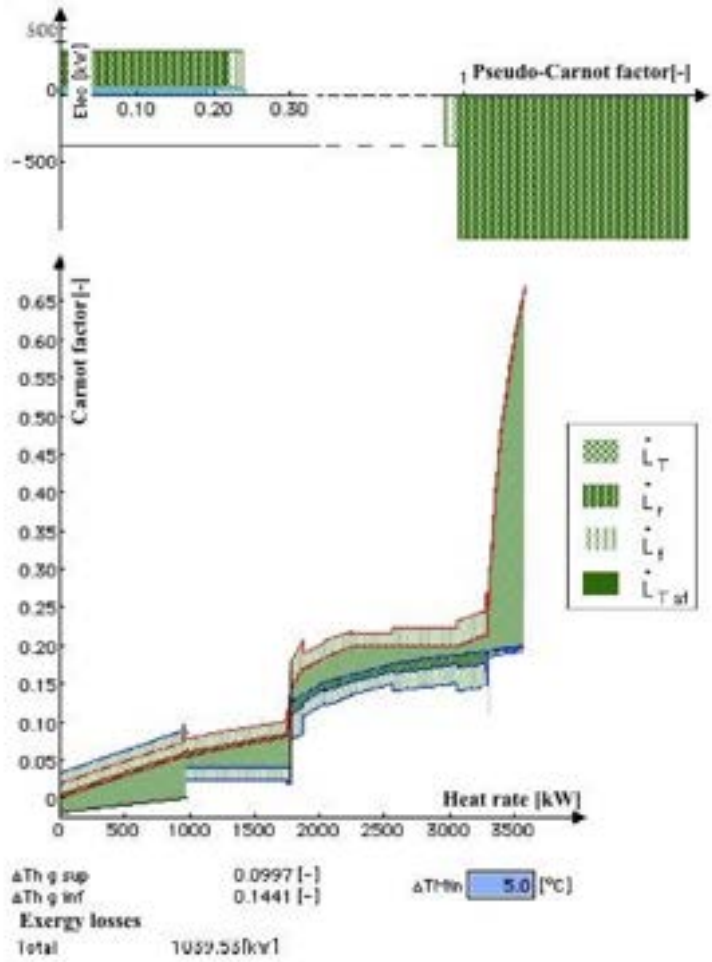

Figure 2. Extended composites proposed in with a visualisation of the exergy losses of heat transfer $\dot{L}_T$, friction $\dot{L}_F$ and embedded exergy losses $\dot{L}_f$ for a plaster drying case with gas engine and heat pump [9]

Contrary to fuel-based approaches, for many renewable technologies like solar or wind the actual resource is free and the embedded exergies together with the implementation, the maintenance and disposal costs are to be accounted for. One earlier paper [24] advocates that the best way to deal with such renewable is to include the rate of embedded exergy divided by the expected lifetime of the equipment among the exergy losses to be taken into consideration. This is particularly valid for solar and wind where the resource does not cost anything. The situation is more complex for biomass for which the resource has a cost and a hybrid approach needs to be taken.

The major hindrance when it comes to embedded exergies is the large inventories of data on materials and processes that are often to be considered. There is a place for advanced methods of data mining in this context.

The extension of exergy-based methods including exergy LCA aspects is particularly interesting in the present context of the implementation of Carbon Capture and Storage or utilisation technologies [25]. The exergy of diffusion of CO_2 in the atmosphere as expressed in [26,27] is providing an absolute minimum of exergy (work) required to extract CO_2 from the atmosphere as is promoted by some companies. It allows an immediate comparison with the extraction from flue-gas pipes in advanced concepts like published in [28]. In the latter CO_2 extraction can be made at negligeable exergy requirements. However, introducing the embedded exergy in the components would allow a much better estimates when comparing these technologies, since the amount of heat exchanger surfaces is high. Synergies with the recent efforts in so-called exergoenvironmental methods [25,29] should be exploited. Nevertheless, optimization based on exergy life cycle analyses can only provide a minimum value that always needs to be compared with economically based optima. They are however much more robust knowing that monetary costs are subject to significant variations linked to geopolitical influences and potential speculation on resources among others.

4. Conclusions on the future of thermoeconomics or environomics

In spite of the interest of “narrow” thermoeconomic approaches, that also include exergoeconomics, from an academic thermodynamic standpoint, the future lies in extended environomic approaches ideally including embedded exergy considerations in connection with broader use of exergy LCA analysis. Furthermore, researchers should be encouraged to further develop graphical tools for easier interpretation of the optimized results. Researchers should also question the results of their methodological approaches when the optimized solution only vary in the range of uncertainties of the major variables. There is also a major effort to be made to try to simplify the approaches and tools, for engineers in practice to be able to concentrate on innovation with new integrated concepts, rather than on the development of sophisticated computer formulations.

References

[1] Frangopoulos C.A., Introduction to Environomics. ASME-AES 1991; 25 : 49-54.

[2] Tsatsaronis, G., Exergoeconomics: Is it only a new name?. Chemical Engineering &Technology 1996; 19 (2):163-169.

[3] Valero A. et al. Fundamentals of exergy cost accounting and thermoeconomics. J. of Energy Resources Technology 2006;128(1):9-15.

[4] Von Spakovsky M.R., Evans R.B., Engineering Functional Analysis, J. of Energy Resources Technology, Transactions of the ASME 1993;115(2): 86-92.

[5] Lazzaretto A., Tsatsaronis G. SPECO: A systematic and general methodology for calculating efficiencies and costs in thermal systems. Energy 2006;31:1257-1289.

[6] Linnhoff B., A user guide on process integration for the efficient use of energy. The institution of chemical engineers, UK; 1982.

[7] Favrat D., Staine F., An interactive approach to the energy integration of thermal processes. Int. Conf. on Computer Aided Learning and Instruction in Science and Engineering;1991 Sept 9-11; Lausanne.

[8] Staine F., Favrat D., Energy Integration of Industrial Processes based on a Graphic Representation of Exergy Factors. Conference on "Energy Systems and Ecology". 1993 July; Poland.

[9] Staine F., Intégration énergétique des procédés industriels par la méthode du pincement étendue aux facteurs exergétiques [Dissertation]. Lausanne, Switzerland: EPFL No 1318, 1994.

[10] Marechal F., Kalitventzeff B., Targeting the minimum cost of energy requirements: A new graphical technique for evaluating the integration of utility systems. Computers and chemical engineering 1996; 20(suppl 1):225-230.

[11] Molyneaux A., Leyland G., Favrat D. Environomic multi-objective optimisation of a district heating network considering centralized and decentralized heat pumps. Energy 2010;35(2):751-758.

[12] Olsommer B., von Spakovsky M.R., Favrat D., An Approach For The Time-Dependent Thermoeconomic Modeling And Optimization Of Energy System Synthesis, Design And Operation (Part I: Methodology and results). International Journal of Applied Thermodynamics 1999; 2(3):97-114.

[13] Olsommer B., von Spakovsky M.R., Favrat D., An Approach For The Time-Dependent Thermoeconomic Modeling And Optimization Of Energy System Synthesis, Design And Operation (Part II: Reliability And Availability). International Journal of Applied Thermodynamics 1999;2(4):177-186.

[14] Kummel R. Growth dynamics of the energy dependent economy. Mathematical systems in economics No 54, Oelgeschlager, Gunn & Hein Publishers, Cambridge MA, 1980.

[15] Curti V., von Spakovsky M.R., Favrat D., An environomic approach for the modeling and optimization of a district heating network based on centralized and decentralized heat pumps, cogeneration and/or gas furnace. Part I: Methodology. International Journal of Thermal Sciences 2000;39(7):721730.

[16] Curti V., von Spakovsky M.R., Favrat D., An environomic approach for the modeling and optimization of a district heating network based on centralized and decentralized heat pumps, cogeneration and/or gas furnace. Part II: Results. International journal of Thermal Sciences 2000;39(7):731-741.

[17] Pelster S., Favrat D., von Spakovsky M.R., The thermoeconomic and environomic modeling and optimization of the synthesis, design and operation of combined cycles with advanced options. Journal of Engineering for Gas turbine and Power 2001;123(4):717-726.

[18] Raluca S., Stadler P., Girardin L., Marechal F., Multi-period multi-time optimization of CO_2 based district energy systems. Computer aided Chemical Engineering 2018;43:1057-1062.

[19] Krummenacher P., Favrat D., Renaud B., Design & optimisation of indirect heat integration of batch processes using genetic algorithms. In Favrat D., Marechal F. editors. ECOS 2010: Proceedings of the 23rd International Conference on Efficiency, Cost, Optimization, Simulation and Environmental Impact of Energy Systems Vol 1; 2010 June 14-17; Lausanne, Switzerland: 97-106.

[20] Szargut J. Morris DR., Steward FR. Exergy analysis of thermal, chemical and metallurgical processes. USA: Edwards Brothers Inc. 1988.

[21] Valero A., Valerio A., Thanatia: The destiny of the Earth's mineral resources. Zaragoza: World Scientific Publishing. 2014.

[22] Torres, C., Valero A., The exergy cost theory revisited. Energies 2021; 14(6):1594-2021.

[23] Bejan A., Thermodynamics of heat transfer devices. Proceedings of the IVth International Symposium on the Second Law Analysis of Thermal Systems; 1987. ASME. Washington.

[24] Haldi P.A., Favrat D., Methodological aspects of the definition of a 2 kW society. Energy 2006;31(15): 3159-3170.

[25] Huang Y, Zhu L., He Y., Wang Y., Hao Q., Zhu Y., Carbon dioxide utilization based on exergoenvironmental sustainability assessment: A case study of CO_2 hydrogenation to methanol. Energy 2023;273. 127219.

[26] Borel L., Favrat D., Thermodynamics and energy systems analysis. EPFL Press, 2010.

[27] Favrat D.,Kane M., From the fuel heating values to the fuel exergy value in advanced energy systems. In: ECOS 2023: Proceedings of the 36th International Conference on Efficiency, Cost, Optimization, Simulation and Environmental Impact of Energy Systems; 2023 June 25-30; Las Palmas de Gran Canaria (Spain).

[28] Facchinetti E., Favrat D., Marechal F., Design and optimization of an innovative solid oxide fuel cell-gas turbine hybrid cycle for small scale distributed generation. Fuel cells 2014;14(4):595-606.

[29] Blumberg T., Lee Young Duk, Morosuk T., Tsatsaronis G., Exergoenvironmental analysis of methanol production by steam reforming and autothermal reforming of natural gas. Energy 2019;181:1273-1284.

A contribution to the discussion on the Future of Thermoeconomics

Christos A. Frangopoulos[a] and George Dimopoulos[b]

[a] National Technical University of Athens, School of Naval Architecture and Marine Engineering Athens, Greece, caf@naval.ntua.gr, CA
[b] National Technical University of Athens, School of Naval Architecture and Marine Engineering Athens, Greece, george_dimopoulos@mail.ntua.gr

Abstract:

'Thermoeconomics' was introduced and its foundations were laid down by Tribus, Evans and El-Sayed in the late 1950's – early 1960's as a method that combines Thermodynamics (in particular Second-Law quantities) and Economics for the analysis, evaluation and optimization of thermal systems. Since that time, many researchers throughout the world taking various roads helped in developing Thermoeconomics from theoretical point of view and applying it in a variety of systems, thus establishing it as a particular field.

Today, questions such as the following may be posed:

- Is there room for further theoretical development of Thermoeconomics?
- Are there areas where Thermoeconomics has not been applied yet, however its application would be beneficial?
- What additional features should Thermoeconomics have, in order to be applied to these areas?
- Is it possible to introduce other considerations, in addition to thermodynamic and economic, in a more holistic approach? If yes, which are they?

In this paper, the authors present in brief their own approach to Thermoeconomics and then they attempt to give answers to the questions, without any claim of completeness.

Keywords:

Thermodynamics; Economics; Thermoeconomics; Second-Law analysis; Optimization.

1. Introduction

'Thermoeconomics' has been coined by M. Tribus as a name for the technique that combines thermodynamic with economic considerations for the analysis and optimization of thermal systems. As it is written by El-Sayed [1], the first landmark of work on thermoeconomics was by Tribus and Evans [2,3] and dealt with seawater desalination processes. The seeds of this work, however, are found in an earlier report by Tribus and co-workers [4], while Evans and El-Sayed developed it further [5-7] and extended the application to thermal systems in general. Significant contributions along these lines in the US were made also by R. Gaggioli and W. Wepfer [8,9].

As it is written by R. Gaggioli [10], the idea of using exergy (availability in the US) for costing energy products appeared in the US in the 1930's:

'… Keenan, who refers to the costing idea in the appendix to his 1932 paper [11]*. (As others have informed us, while teaching at Stevens Institute, Keenan had informed a perplexed cost accountant from a local cogeneration utility, how to charge fuel costs to its steam and electricity products).'*

The idea of combining second law (and exergy, in particular) with economics appeared also in Europe in the same period with thermoeconomics. It is interesting to quote a statement written in a paper by Z. Rant published in Slovenian [12] and translated in English:

'The existing method for energy pricing (accounting) in combined plants on the basis of used enthalpies is fundamentally wrong. It has to replace with pricing (accounting) on the basis of used exergies, which is the only proper way.'

It is worth noting that the word 'exergy' ('eksergij' in Slovenian) appears already in this article, one year before Rant's landmark article [13], where he explains how he coined the word 'exergy'.

Important contributions in these early years in Europe were made also by Szargut [14,15], Beyer [16], Borel [17] and Fratzscher [18].

As written by El-Sayed [1], thermoeconomics rises on three main pillars:

1. Improved thermodynamic analysis (includes second law of thermodynamics quantitatively rather than qualitatively).
2. Improved costing analysis (a closer look at the interaction between fuel and equipment).
3. Enhanced optimization (interdisciplinary approach: thermodynamics, design, manufacture, economics).

In the decades following the early years, the interest in thermoeconomics has increased internationally, a variety of methods have been developed and many applications have demonstrated the usefulness and importance of thermoeconomics.

Today, questions such as the following may be posed:

- Is there room for further theoretical development of Thermoeconomics?
- Are there areas where Thermoeconomics has not been applied yet, however its application would be beneficial?
- What additional features should Thermoeconomics have, in order to be applied to these areas?
- Is it possible to introduce other considerations, in addition to thermodynamic and economic, in a more holistic approach? If yes, which are they?

In the following, the authors present in brief their own approach to Thermoeconomics and then they attempt to give answers to the questions, without any claim of completeness.

The structure of the paper is as follows. The main methodologies are mentioned in Section 2 with emphasis on the functional approach developed by the authors. Section 3 presents thermoeconomics with additional aspects at an early stage and the needs of further development. In Section 4, further considerations and application areas of thermoeconomics are presented together with needs for proper methodological development. The paper closes with remarks regarding the aforementioned four questions and a more or less comprehensive list of references.

2. Progress to date

2.1. Thermodynamic and economic considerations

Several schools of thought have been evolved in the last four decades [1,19], each one characterized by the particular approach it follows, such as the exergoeconomic analysis [20], thermoeconomic functional analysis [21-25], structural theory [26], specific exergy costing (SPECO) [27,28].

2.2. Environmental considerations in addition to thermodynamic and economic

The concern for the depletion of energy / exergy resources led to the development of the aforementioned methods, in an attempt to save energy / exergy by proper analysis and optimization of energy systems.

Soon became evident that energy-related activities cause depletion of other scarce natural resources, in addition to energy, as well degradation of the environment. In order to take these effects into consideration, thermoeconomics had to broaden its basis and methods such as the following appeared in the literature: Cumulative Exergy Consumption [29-31], Thermo-ecological Analysis [31-34], Extended Exergy Accounting [35-37], Environomics [38-41], Exergo-environmental Analysis [42].

Since other contributors to the development of thermoeconomics participate in the discussion about its future, the presentation in this section is not intended to be a general review of thermoeconomics and, therefore, only certain characteristic publications are cited, while more emphasis is given to the functional approach developed by the authors.

2.3. Thermoeconomic functional analysis and optimization

2.3.1. The basic formulation

The basic formulation of thermoeconomic functional analysis (TFA) appears in [21-22]. In TFA, it is considered that the system consists of a set of inter-related units, with each unit having one particular function (purpose or product). Functional analysis is the formal, documented determination of the function of each unit and of the function of the system as a whole.

The functional diagram is a picture of the system consisting of geometrical figures representing the units and a network of lines representing the distribution of the unit functions (Figure 1). Junctions connecting the functions of two or more units and branching points distributing the function of a unit to two or more units are additional features of the functional diagram. The functions of units are quantified by means of second-law properties such as exergy and negentropy.

Since the beginning, TFA is formulated so that it can be applied for analysis, evaluation, product costing [44] and optimization of energy systems. If needed, decomposition of the system into subsystems facilitates the

solution of the optimization problem [23]. Even though the formulation is such that physical economics can be used (every cost is measured in physical units such as exergy), the method has been applied with monetary economics.

It is interesting to note that the productive structure introduced later on by Valero and his co-workers is based on the functional diagram, as written in Ref. [45].

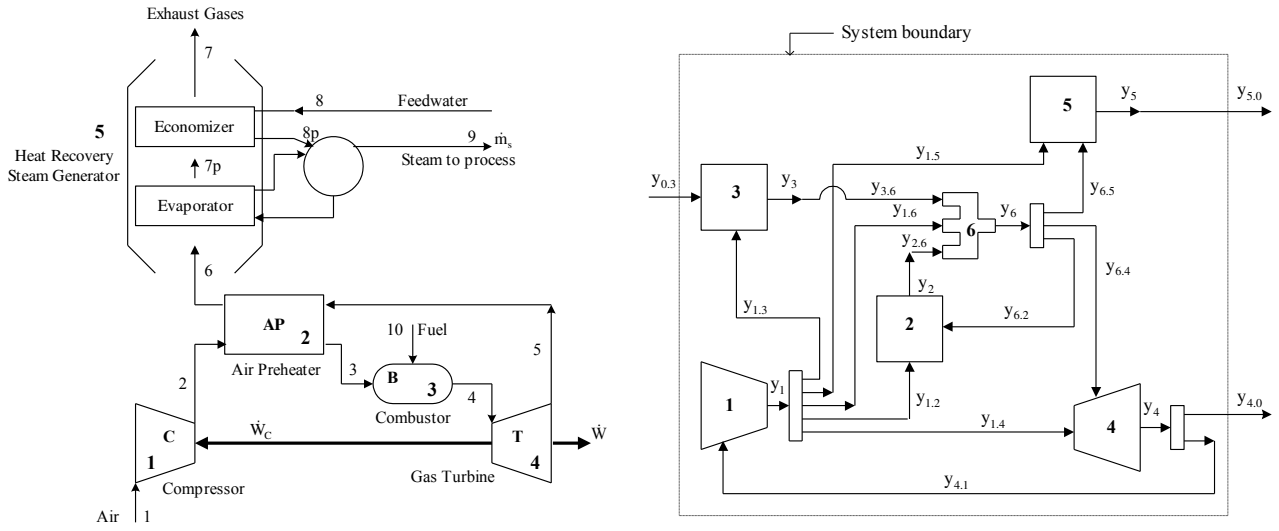

Figure 1. Example of a functional diagram: a) flow diagram of a gas-turbine cogeneration system, b) the functional diagram of the system [43].

2.3.2. The intelligent functional approach (IFA)

Optimization can be considered at three levels (Figure 2): synthesis (components and their interconnections), design (nominal technical characteristics of each component and of the whole system) and operation (operating state at each instant of time): SDO optimization. If complete optimization is the goal, each level cannot be considered in isolation from the others. Thus, the optimization problem can be stated by the following question:

> *What is the synthesis of the system, the design specifications of the components as well as of the whole system and the operating state at each instant of time that lead to the overall optimum?*

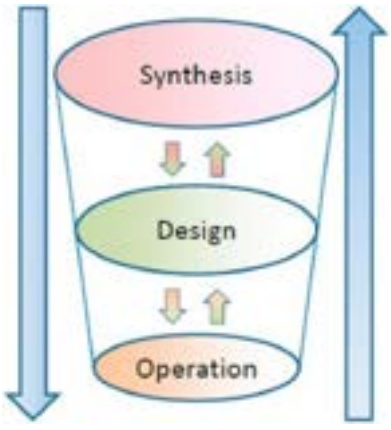

Figure 2. The three interrelated levels of optimization.

Thus, TFA was further developed, in order to address this complex optimization problem [46,47]. The name ‘intelligent’ is due to (i) the information (‘intelligence’) obtained by the analysis and during the optimization procedure in the form of proper indexes (e.g. Lagrange multipliers) and (ii) the intelligent (guided by intellect,

rational) use of this information for the solution of the optimization problem. The superstructure approach is followed for the synthesis optimization.

Of course, if the synthesis of the system is given, the optimization determines the optimal design and operation. If both the synthesis and design are fixed, operation optimization is performed. IFA can be applied for any of these problems.

2.3.3. Environomic functional analysis and optimization

IFA was further developed, in order to take into consideration environmental aspects quantitatively, in addition to the thermodynamic and economic considerations [38-41].

Pollution indexes and degrees of abatement of the various pollutants are defined, and pollution abatement equipment is included in the system. Thus the total cost consists of the (i) installed cost of components including pollution abatement equipment, (ii) cost of resources, (iii) environmental and social cost due to pollution. Complete optimization (synthesis, design, operation) can be performed. The degrees of abatement are among the independent variables of the optimization problem, which determine the design and operation characteristics of the pollution abatement equipment.

The costs to the environment and the society due to damages caused by pollutants emitted from energy conversion systems are called 'external costs' (external to the system) or 'externalities'. It is noted that damages are caused not only in the vicinity of the system, but also in distant areas, even in other countries, that are in the trajectory of pollutants dispersion. Methods for estimation of these costs and publications with first results are mentioned in [48], while joint systematic research at the European Union level led to the development of a method for environmental impact analysis [49] and estimation of externalities [50] supported by related software. More information and an application are presented in [51]. It has to be recognized, however, that this is an effort that has to be continued for improving the methods and decreasing the uncertainty of the results.

Numerical examples including sensitivity analysis demonstrated that, in spite of the uncertainty, it is prudent to take environmental and social costs into consideration in the analysis and optimization of energy systems, than to ignore those.

2.4. Other approaches to the thermoeconomic optimization of synthesis, design and operation of energy systems

The SDO optimization of energy systems requires the derivation of the system configuration either through the automated synthesis during the optimization process or by the definition of a generic super-configuration – consisting of all possible alternatives examined – with the optimal one determined as the output of the optimization procedure. The former approach has been followed in [52,53], while the latter was used in [54-57]. Further, the complex optimization problem of three levels (SDO) can be reformulated in two levels: (A) synthesis and design, and (B) operation. The solution is obtained by iteration between the levels A and B [54-56]. This improves significantly the computational cost of thermoeconomic optimization allowing for complex models of systems and cost functions to be used.

The works presented in [54-56] introduced thermoeconomic optimization in marine energy systems for cruise ships and LNG carriers. In further works, thermoeconomic optimization was applied to Organic Rankine Cycles for low temperature waste heat recovery from ship energy systems [57] and to a marine combined cycle system [58]. In [59] the complete SDO optimization problem is tackled at a single step, with no need of reformulating it in the aforementioned levels A and B. Of course, higher computer capabilities are required for such an approach.

Further developments appear in [60-61] with the introduction of dynamic and intertemporal optimization in the SDO optimization. Dynamic and intertemporal optimization describes situations where subsequent decisions are affected by decisions taken earlier in the time horizon of the optimization problem. Coupling this class of problems to thermoeconomics allows for a wider and more realistic range of energy systems applications to be addressed.

The application of thermoeconomic SDO optimization to ship energy systems is an important contribution to the extension of thermoeconomic approaches due to the complexity of the marine environment. Ship energy systems are isolated (sailing at sea), resource constrained, and highly interconnected with many space, weight and safety constraints. Further, they have many operational modes and wide mission profiles. Therefore, the thermoeconomic methodologies and optimization algorithms often need special adaptation to be successful in marine applications, as the referenced works suggest.

2.5. Achievements not possible without thermoeconomics

The use of thermoeconomics in the analysis and optimization of energy conversion systems acts as a "common denominator" in identifying the sources of losses and their impact on efficiency and costs throughout the system. The major achievement of thermoeconomics lies in to having a methodology that can attribute both costs and energy / exergy efficiency to components and products of a system in a rational and

uniformly applicable manner. This increases the objectivity, trust and transparency of the engineering decision making process when assessing, comparing and optimizing various design and technology alternatives.

Thermoeconomics also uses correlations, i.e. cost functions, of the capital expenditure for the various components of an energy conversion system with their respective design characteristics and performance figures. This is a unique way to assess the impact of technology both in the performance and energy efficiency as well as the cost of the products per unit of energy or exergy. More simple technoeconomic analyses often fail to reveal the dependency of technology with performance and cost of useful products. Therefore, thermoeconomics offers the means for a more robust and informed decision-making process when considering the synthesis, design and operation of energy conversion systems.

3. Thermoeconomics with additional aspects at an early stage of development

Formulations and applications of thermoeconomics with reliability analysis, risk analysis and control of energy systems are presented in brief here. These are interesting subjects but they are at an early stage of development with very few publications. Further development of methodologies combined with more applications would be more than welcome.

3.1. Thermoeconomics with reliability analysis and optimization

In optimization of energy systems it is usually considered that the equipment is not subject to failure and, consequently, it is available for operation at any instant of time, except of predetermined periods of maintenance. Redundancy is provided empirically and as a consequence the configuration of the system may be non-optimal. Let it be mentioned that the reliability and availability of energy systems is a critical economic and efficiency factor.

In [62], reliability and availability are introduced in the thermoeconomic model (IFA formulation) of the system and optimization of synthesis, design and operation under time-varying conditions is performed. The IFA facilitates the solution. A numerical example with a cogeneration system shows that the introduction of reliability leads to an entirely different optimal solution for each one of the three levels (synthesis, design, operation), while profits from selling the products of the system (electrical and thermal energy) are overestimated, if reliability aspects are ignored. More recently in [63], thermoeconomic optimization is coupled with availability considerations for the assessment of a compressed air storage system. Though no optimization is attempted, the differences in expected cost of electricity and profits are assessed with and without reliability considerations highlighting important differences.

Incorporation of reliability into thermoeconomics requires methodological advances on the reliability modelling of energy systems. The most suitable approach, the state-space-method appearing in [62], exhibits an exponential computational burden when the number of system components is increased. There is need of developing reliability assessment methodologies that have significantly lower computational cost and, at the same time, are capable of describing the multiple states of partial failures and reduced output that the whole system may encounter.

In addition, reliability considerations need to be also coupled with the individual component cost functions allowing for increased time between failures or reduced time to maintain a system component, factors that affect the capital cost per unit of time. A revision is also needed on how the maintenance operational expenses are considered up to now, incorporating the mean time to repair as a component of the maintenance costs.

3.2. Thermoeconomics with risk analysis – Thermorisk

Combined quantitative risk and exergy analysis is proposed in [64-65], in order to assess impacts from major accidents in energy systems. Impacts on human health are considered. The method is used to minimize damages of major accidents by proper energy system design. An application example is presented in [64] that minimizes the specific risk (risk per unit exergy of the plant product) of a geothermal drilling plant connected to an organic Rankine cycle system.

In [66], a power and fresh water cogeneration system is studied, consisting of a Rankine cycle, an organic Rankine cycle and a reverse osmosis module. Exergy, economic and risk analyses are performed, followed by multi-objective optimization of the system with the total cost rate and the total specific risk as objective functions.

The work initiated in [64-66] introduces an important dimension in thermoeconomic analysis. In real-world applications the decisions affecting the selection, design and operation of a system also address the total cost of ownership (TCO). The present forms of thermoeconomics account for many of the TCO dimensions such as capital expenditure, operational, maintenance and environmental costs. However, the implicit costs due to safety, major accidents, regulatory compliance and loss of production due to spares availability are

not addressed in a thermoeconomic context up to now. These dimensions are typically assessed via risk assessments methodologies either qualitatively or quantitatively.

The expansion of thermoeconomics towards incorporating risk assessment elements and results will allow for a more holistic framework of analysis, insight and optimization of energy conversion systems. The main extensions required are in the areas of correlating the probability (likelihood) and severity with cost incurred to the system and its components. Then the well-established thermoeconomic methodologies can incorporate and correlate these costs with exergy flows and technical characteristics of the components of the system. Such an extension of thermoeconomics with risk assessment elements will further increase the applicability of the methodology to realistic decision making processes.

3.3. Thermoeconomics with control of a system

Only few publications are mentioned here, but they are adequate for understanding the current state of development.

In [67,68] the thermoeconomic approach is used to evaluate compare and improve the performance of alternative control strategies. An exergetic cost and a monetary cost are associated with the control system. Application to a gas turbine unit driving a generator shows that, with proper control, fuel consumption and operational cost at part load can be significantly reduced in comparison with typical control strategies.

In [67] the effects of the control system on the thermoeconomic diagnosis of a power plant are studied. The role played by the control system on the propagation of malfunctions is analyzed. The control system sometimes forces the plant to operate in a less efficient mode, inducing inefficiencies and malfunctions in the components. In order to avoid these effects, thermoeconomic diagnosis is applied that takes the control system behavior into consideration in the analysis directly. The procedure is applied to a gas turbine cogeneration system.

A review of applications of the second law of thermodynamics to control of energy systems is given in [69], primarily in the building sector. Out of 58 papers reviewed, only three papers apply thermoeconomics / exergoeconomics. In [70] an economic analysis of the exergy-efficiency control strategy of a geothermal district heating system is performed and it is estimated that the new controller (PID) has a payback period of 3.8 years. In [71] the structural theory of thermoeconomics is applied in order to determine the optimal load allocation strategy of the HVAC system of an airport terminal. In [72] energy-based, exergy-based and exergoeconomic-based control strategies of an HVAC system in the built environment is performed and it is shown that the last one could reduce the annual operation costs by up to 23%.

It is noted that in the literature, the words ‘control’ and ‘dynamic’ are used with two different meanings: (a) control of multi-stage operation with steady state in each stage; it sets the operating point of a system at each stage as the conditions (load, environmental temperature, etc.) change from stage to stage, without taking into consideration the transients; (b) control of transients; it specifies the trajectory that a system will follow, in order to go from a steady state to another one. References [67,71-73] belong to the first category, while Refs. [68,70] belong to the second category. In the following, the word will be used with the meaning ‘control of transients’, while setting the operating point of a system in each stage of a multi-stage process is covered by the intertemporal SDO optimization. Needs of further development are presented in brief.

Thermoeconomic control optimization can be considered either in isolation, i.e. optimization of the transient(s) only, or integrated with the intertemporal SDO optimization of the system. In both cases the control unit itself is subject to SDO optimization. There are several configurations of controllers depending on the required control action such as on-off, proportional (P), integral (I), derivative (D) and combinations of those (e.g. PID). The optimal configuration of the control unit is requested (synthesis). For each configuration, the optimal specifications of the components have to be determined (design), followed by optimal adjustment of characteristics (e.g. time constant, gain, damping ratio) in particular periods (operation).

Of course in order for the optimal control to be thermoeconomic, a proper objective function has to be defined. An example of such a function is formulated as follows. During a transient operation along a trajectory specified by the control unit, exergy is used by the whole system including the control unit. Minimization of this exergy is desirable, but such a control action may overstress certain components of the system, thus increasing the frequency and cost of maintenance and/or decreasing their lifetime; the last one causes an increase of the capital cost per unit of time. The total cost (exergy+maintenance+capital) is a very proper thermoeconomic objective function. With appropriate selection of the additive terms, such a function can be defined for the optimization of a single transient operation or for the optimization of the whole period of operation, including transients, as written in Subsection 4.2.

4. Further considerations and application areas of thermoeconomics with proper development of methodology

4.1. Social aspects in thermoeconomics

Currently, thermoeconomics includes thermodynamic, economic and environmental considerations. In the last one, the cost to the society due to emission of pollutants and depletion of natural resources is included either in physical units (exergo-environmental analysis, extended exergy accounting) or in monetary units (environomics). However, the construction and operation of energy systems has not only adverse effects but also benefits to the society. Therefore, an interesting and important extension of thermoeconomics is to include both cost and benefit to society.

Evaluation of projects for their effect on the society with criteria such as job creation, general welfare, standard of living, etc., is widely performed, but the quantitative inclusion of these aspects in thermoeconomic analysis and optimization needs to be developed. Hints of how this can be performed are given by the following publications (indicative only).

In [74] a system of forest-based biorefineries and biofuel supply chain is studied and a multi-objective optimization is performed with three objective functions: (i) maximization of newly created jobs, (ii) maximization of the net present value, and (iii) maximization of the GHG emission savings compared to the current supply chain.

Closer to the energy systems studied by thermoeconomics is the work presented in [75]. Optimization of a thermal-solar-wind combined power system is performed with two objectives: (i) Minimization of economic cost (construction, operation and maintenance, CO_2 cost) and (ii) maximization of social benefits that consist of consumer surplus, government revenue and environmental benefits brought by CO_2 reduction.

The effort is still at its infancy and there is need of significant methodological development for inclusion of social aspects in thermoeconomic analysis and optimization of energy systems.

4.2. Thermoeconomic dynamic optimization of synthesis, design and operation including transients

Even though very few, there are publications on thermoeconomic SDO optimization with multi-stage operation or on optimization of transients, but the complete problem of thermoeconomic SDO optimization addresses the whole life of an energy system taking the complete operating profile into consideration that consists of interrelated periods (stages) of practically stead-state operation as well as transients.

The only publications known to the authors with such an approach are two papers [76,77], where optimization of the energy system of an aircraft that includes the phases of take-off, flight and landing is presented. Each phase is described by a different system of differential and algebraic (DAE) equations and the optimization must be performed for the whole trip. The method is open to further improvement and adaptation to other applications.

The required simulation model of an energy system may contain hundreds even thousands of differential and algebraic equations, making it computationally heavy and very time consuming. Therefore for practical applications there may be need of developing reduced models that are fast, yet with satisfactory accuracy. Examples of methods for developing reduced models are given in [70,78].

4.3. Thermoeconomic SDO optimization of energy systems including synthesis of the working fluids

In the preceding, the optimization of energy systems refers to the components, their interconnections, the technical specifications and the operating state at any instant of time, while the working fluids are selected in advance. If there are several fluids appropriate for the particular system, optimization is performed for each fluid in separate and the one with the best performance is selected.

In [79] computer-aided molecular design (CAMD) of the working fluid in an ORC system is applied that makes it possible to optimize the fluid and the thermodynamic system simultaneously in a single CAMD-ORC framework. The fluid is synthesized during the optimization procedure using several molecular groups (e.g. –CH3, –CH2–, =CH2, =CH–, etc.). The thermodynamic properties of the fluid are calculated by the group-contribution equation of state, SAFT-γ Mie, while critical and transport properties such as thermal conductivity, dynamic viscosity and surface tension are estimated using empirical group-contribution methods. The aim of the optimization is to determine the optimal combination of the molecular groups and thermodynamic variables that maximize the power output generated by the ORC for specified heat source and heat sink.

In a subsequent paper [80], the same system is studied, and two optimization problems are solved: (a) single-objective, minimization of the specific investment cost, and (b) double-objective, minimization of the specific investment cost and maximization of the power output generated by the ORC.

In these works, the synthesis of the system is fixed and operation is considered at the nominal power. It would be very interesting to extend the method by applying thermoeconomic analysis and optimization of synthesis, design and operation under time varying conditions.

It should be mentioned that the term 'thermoeconomic optimization' is used in [80], but neither exergy is used, nor the second law is mentioned explicitly. This fact raises the question as to whether the use of the word 'thermoeconomic' is justified.

4.4. Thermoeconomic SDO optimization with variable synthesis through time

The recent decarbonization concerns for land-based and marine energy systems introduce new fuels, technologies and energy improvement measures to be considered. International and regional decarbonization regulations are introduced in gradual manner, becoming stricter and stricter over time. This entails that the environmental performance of a system has to gradually improve, usually staying below a regulatory trajectory over time. Therefore, a system that is compliant and cost effective now, may not be any more at some point during its economic lifetime. The question that arises is when to invest or re-invest in energy efficiency measures and environmental technologies in order to optimize the system throughout its lifetime.

This question becomes even more important under the new requirements for environmental performance goals with stricter limits (trajectories) over time. Thermoeconomic optimization methodologies should be adapted to identify the optimal point in the economic life of the system, in which a suitable technology is introduced. This needs to be extended also to the selection of the right type of technology or measure from a set of available and feasible technologies. Examples of technologies and measures that affect the environmental performance of energy systems are carbon capture systems, alternative fuels like hydrogen or ammonia (and their auxiliary systems), fuel cells, advanced waste heat recovery.

A further cause of complexity, especially in marine systems, is that some technologies cannot be introduced (retrofitted) later in the lifecycle of the system, unless the system is suitably prepared (becomes "ready") during construction to accept this technology afterwards. For example, introducing a carbon capture system in a ship is significantly less costly if there is an initial provision of space, strengthening of structures and sizing of the energy conversion system to deliver more thermal and electric energy when needed by the carbon capture system.

The above considerations indicate that the standard formulations of thermoeconomic optimization problems need to be revised to account for variable investment points in the time horizon. In addition, the synthesis part of the optimization becomes more important with larger sets of available technology alternatives.

4.5. Low and zero carbon fuels and cryogenic systems

In close relationship with the Subsection 4.4, decarbonization concerns have introduced new fuels, technologies and systems that require analysis, assessment and optimization. Although thermoeconomics has proven its general applicability, there is need for a refinement of methodologies in conjunction with decarbonization considerations.

The decarbonization of land-based, offshore and ship energy conversion systems introduces a multitude of new fuels with low or zero carbon footprint such as hydrogen, ammonia, methanol and synthetic gas or liquid fuels. The actual emissions footprint of these fuels depend on their production, storage, transportation and energy conversion processes. Each of these stages consumes energy and has an inherent efficiency that affects the carbon footprint, the efficiency and cost of the fuel. Introducing exergy analysis and thermoeconomics to the assessment of the value chain of the production, delivery and use of the fuels will significantly enhance the rational and uniform evaluation of their value chain impact on greenhouse gas emissions and overall costs – including the effect of capital expenditure of production and storage infrastructure. Further, the introduction of novel fuels with novel production methods like hydrogen and ammonia poses some challenges with respect to their exergetic analysis and reference state selection that need to be revised and updated accordingly.

Furthermore, most of these new fuels require cryogenic transportation, permanent or temporary storage and fuel gas handling systems. This is also true for liquified natural gas with its global transportation and use intensified due to the recent geopolitical developments. The thermoeconomic analysis of cryogenic and refrigeration systems, although it is well established, poses some challenges related to states below the reference [81,82]. One additional complexity is also related to the muti-component mixtures, with real gas behavior that need to be assessed in vapor-liquid equilibrium conditions, often appearing when assessing the cryogenic storage and handling of the new fuels.

Finally, in terms of component cost functions, there is a significant gap in research and literature. Namely, cryogenic heat exchangers and equipment, natural gas and hydrogen compressors, and many of the associated auxiliary equipment cannot be described or extrapolate their cost functions from conventional power generation ones, used in most of the literature. Efforts should be made to develop representative cost functions describing new equipment and technologies associated with these decarbonization options.

Closure

In a discussion on the future of thermoeconomics, the fundamental question that can be posed is: “does thermoeconomics have a future?” After the fundamental question, other questions such as the four questions written in the Introduction can be posed.

In order to help in answering the four questions, the preceding sections give arguments regarding the necessity of applying thermoeconomics and a few suggestions regarding the introduction of considerations in addition to thermodynamic and economic, areas where the application of thermoeconomics can be extended, and needs of further development of thermoeconomics. Of course, the whole subject is open to additional ideas and suggestions.

After the aforementioned, the answer to the fundamental question is clear: “Yes, thermoeconomics has a future”.

Acknowledgments

The authors are thankful to Prof. Enrico Sciubba for making them aware of early works in European countries combining exergy with economics.

References

[1] El-Sayed Y.M., The thermoeconomics of energy conversions. Oxford, UK: Elsevier, 2003.

[2] Tribus M., Evans R.B., A contribution to the theory of thermoeconomics. Los Angeles, USA: University of California at Los Angeles, 1962. UCLA Report No. 62-36.

[3] Tribus M., Evans R.B., The thermoeconomics of sea-water conversion. Los Angeles, USA: University of California at Los Angeles, 1963 Feb. UCLA Report No. 62-53.

[4] Tribus M. et al., Thermodynamic and economic considerations in the preparation of fresh water from sea water. First draft. Los Angeles, USA: University of California at Los Angeles, 1956. UCLA Report No. 56-16.

[5] Evans R.B., Crellin G.L., Tribus M., Thermoeconomic considerations of sea water demineralization. In: Spiegler K.S., editor. Principles of desalination. New York, USA: Academic Press; 1966: Ch. 2, p. 21-76.

[6] El-Sayed Y.M., Aplenc A.J., Application of the thermoeconomic approach to the analysis and optimization of vapor-compression desalting system. Transactions of the ASME, Journal of Engineering for Power 1970 Jan.;92(1):17-26.

[7] El-Sayed Y.M., Evans R.B., Thermodynamics and the design of heat systems. Transactions of the ASME, Journal of Engineering for Power 1970 Jan.;92(1):27-35.

[8] Gaggioli R.A., Wepfer W.J., Exergy economics. Energy 1980;5(8/9):823-837.

[9] Gaggioli R., editor, Efficiency and costing. ACS Symposium Series 122; 1983.

[10] Gaggioli R., Reflections on the history and future of exergy. In: Ishida M. et al., editors. Proceedings of ECOS’99, 1999, June 8-10. Tokyo, Japan: 5-13.

[11] Keenan J.H., A steam chart for second law analysis. Mechanical Engineering 1932;54:194-204.

[12] Rant Z., Vrednost in obračunavanje energije (Energy value and pricing). Strojniški Vestnik – Journal of Mechanical Enginering 1955;1(1):4-7. In Slovenian.

[13] Rant Z., Exergie, ein Neues Wort für Technische Arbeitsfähigkeit. Forschung auf dem Gebiete des Ingenieurwesens 1956;32(1):36–37.

[14] Szargut J., Towards a rational evaluation of steam prices. Gospodarka Cieplna 1957;5(3):104-106. In Polish.

[15] Szargut J., Generalized method of cost distribution in complex processes. Gospodarka Paliwami, Energia,1969;17(34):4-6. In Polish.

[16] Beyer J., Zur Aufteilung der Primärenergykosten in Koppelprozessen auf der Strukturanalyse. (On the configuration-based allocation of primary energy costs in coupled processes.) Energieanwendung. 1972;21(6):179-183.

[17] Borel L., Economie énergétique et exergie. In: Espoirs limites sources énergétiques non conventionnelles. Lausanne, Switzerland: Assoc. Suisse Electr. 1974. p. 27.

[18] Fratzscher W., Bedeutung der thermoeconomischen Modellierung zur Loesung energie- und verfahrentechnischer Aufgaben. Energieanwendung 1973;22:243-246.

[19] Torres C., Valero A., Serra L., Royo J., Structural theory and thermoeconomic diagnosis; Part I: On malfunction and dysfanction analysis. Energy Conversion and Management 2002;43:1503-1518.

[20] Tsatsaronis G., Winfold M., Exergoeconomic analysis and evaluation of energy conversion plants. Energy 1985;10:69-94.

[21] Frangopoulos C.A., Thermoeconomic Functional Analysis: A Method for Optimal Design or Improvement of Complex Thermal Systems. Ph.D. Thesis. Atlanta, Ga., USA: Georgia Institute of Technology; 1983.

[22] Frangopoulos C.A., Thermoeconomic Functional Analysis and Optimization. Energy 1987;12(7):563-571.

[23] Frangopoulos C.A., Functional Decomposition for Optimal Design of Complex Thermal Systems. Energy 1988;13(3):239-244.

[24] von Spakovsky M.R., A practical generalized analysis approach to the optimal thermoeconomic design and improvement of real-world thermal systems. Ph.D. Thesis. Atlanta, Ga., USA: Georgia Institute of Technology; 1986.

[25] von Spakovsky M.R., Evans R.B., The foundations of engineering functional analysis (Part I and II). In Stecco S., Moran M., editors. A future for Energy, FLOWERS'90, 1990; May 28 – June 1, Florence, Italy. Pergamon Press:445-472.

[26] Valero A., Torres C., Serra L., A general theory of thermoeconomics: Part I: Structural analysis. Part II: The relative free energy function. In: Valero A., Tsatsaronis G. editors. International symposium on efficiency, costs, optimization and simulation of energy systems, ECOS'92, 1992; June 15-18, Zaragoza, Spain. ASME: 137-154.

[27] Lazzaretto A., Tsatsaronis G., SPECO: A systematic and general methodology for calculating efficiencies and costs in thermal systems. Energy 2006;31:1257-1289.

[28] Lazzaretto A., Manente G., Toffolo A., SYNTHSEP: A general methodology for the synthesis of energy system configurations beyond superstructures. Energy 2018;147:924-949.

[29] Szargut J., Minimization of the consumption of natural resources. Bull Polish Acad Sci, Ser Technol 1978;26(6):41-45.

[30] Szargut J., Morris D.R., Cumulative exergy consumption and cumulative degree of perfection of chemical processes. Int J Energy Res 1987;11:245-61.

[31] Szargut J., Ziebik A., Stanek W., Depletion of non-renewable natural exergy resources as a measure of the ecological cost. Energy Conversion and Management 2002;43:1149-63.

[32] Szargut J., Optimization of the design parameters aiming at the minimization of the depletion of non-renewable resources. Energy 2004;29(12-15):2161-9.

[33] Szargut J., Exergy method – technical and ecological applications. Southampton, UK: WIT Press; 2005.

[34] Valero An., Usón S., Torres C., Valero Al., Application of thermoconomics to industrial ecology. Entropy 2010;12:591-612.

[35] Sciubba E., Extended exergy accounting: towards an exergetic theory of value. In: Ishida M. et al., editors. Proceedings of ECOS'99, 1999, June 8-10. Tokyo, Japan: 105-112.

[36] Sciubba E., Beyond thermoeconomics? The concept of extended exergy accounting and its application to the analysis and design of thermal systems. International Journal of Exergy 2001;2:68-84.

[37] Sciubba E., Exergy-based ecological indicators: From Thermo-Economics to cumulative exergy consumption to Thermo-Ecological Cost and Extended Exergy Accounting. Energy 2019;168:462-476.

[38] Frangopoulos C.A., Introduction to Environomics. In Reistad G.M. et al., editors. Symposium on Thermodynamics and Energy Systems; ASME Winter Annual Meeting; 1991 December 1-6; Atlanta, Ga. ASME AES-Vol. 25/HTD-Vol. 191:49-54.

[39] Frangopoulos C.A., An Introduction to Environomic Analysis and Optimization of Energy-Intensive Systems. In Valero A., Tsatsaronis G., editors. ECOS'92: Proceedings of the International Symposium on Efficiency, Costs, Optimization and Simulation of Energy Systems; 1992 June 15-18; Zaragoza, Spain. ASME:231-239.

[40] Frangopoulos C.A., von Spakovsky M.R., A global environomic approach for energy systems analysis and optimization - Part I. In Szargut J., Kolenda Z., Tsatsaronis G., Ziębik A., editors. ENSEC'93: Energy Systems and Ecology; 1993 July 5-9; Cracow, Poland:123-132.

[41] von Spakovsky M.R., Frangopoulos C.A., A global environomic approach for energy systems analysis and optimization - Part II. In Szargut J., Kolenda Z., Tsatsaronis G., Ziębik A., editors. ENSEC'93: Energy Systems and Ecology; 1993 July 5-9; Cracow, Poland:133-144.

[42] Meyer L., Tsatsaronis G., Buchgeister J., Schebek L., Exergoenvironmental analysis for evaluation of environmental impact of energy conversion systems. Energy 2009;34:75-89.

[43] Frangopoulos C.A., Application of the thermoeconomic functional approach to the CGAM problem. Energy 1994;19(3):323-342.

[44] Frangopoulos C.A., Costing of Heat and Electricity from a Cogeneration System. In Serovy G.K., Fransson T.H., editors. 2nd. Intern. Symposium and Exposition on Turbomachinery, Combined-Cycle

Technologies and Cogeneration; 1988 Aug. 30 - Sept. 1 Montreaux, Switzerland. A.S.M.E. IGTI-Vol. 3:349-356.

[45] Lozano M.A., Valero A., Thermoeconomic analysis of gas turbine cogeneration systems. In Richter H.J., editor. Thermodynamics and the Design, Analysis and Improvement of Energy Systems AES-Vol. 30, Book No. H00874-1993. New York, USA. American Society of Mechanical Engineers: 311-320.

[46] Frangopoulos C.A., Intelligent Functional Approach: A Method for Analysis and Optimal Synthesis-Design-Operation of Complex Systems. In Stecco S.S., Moran M.J., editors. Proceedings of FLOWERS'90: A Future for Energy, Florence World Energy Research Symposium; 1990 May 28-June 1; Florence, Italy. Pergamon Press: 805-815. Published also in International Journal of Energy•Environment•Economics 1991;1(4):267-274.

[47] Frangopoulos C.A., Optimization of Synthesis-Design-Operation of a Cogeneration System by the Intelligent Functional Approach. In FLOWERS'90: 597-609. Published also in International Journal of Energy•Environment•Economics 1991;1(4):275-287.

[48] Frangopoulos C.A., Caralis Y.C., A method for taking into account environmental impacts in the economic evaluation of energy systems. Energy Conversion and Management 1997;38(15-17):1751-1763.

[49] Krewitt W, Trukenmueller A, Mayerhofer P, Friedrich R. ECOSENSE – An integrated tool for environmental impact analysis. In: Kremers H., Pillmann W., editors. Space and Time in Environmental Information Systems. Umwelt-Informatik aktuell, Band 7. Marburg: Metropolis-Verlag; 1995.

[50] Bickel P, Friedrich R., ExternE: externalities of energy, methodology update. European Commission, 2005.

[51] Czarnowska L., Frangopoulos C.A., Dispersion of pollutants, environmental externalities due to a coal power plant and their effect on the cost of electricity. Energy 2012;41:212-219.

[52] Sciubba E., Melli R., Artificial intelligence in thermal system design. New York, US: Nova Scientific Publishers; 1998.

[53] Grekas D.N., Frangopoulos C.A., Automatic synthesis of mathematical models using graph theory for optimisation of thermal energy systems. Energy Conversion and Management 2007;48(11):2818-2826.

[54] Dimopoulos G.G., Kougioufas A.V., Frangopoulos C.A., Synthesis, design and operation optimization of a marine energy system. Energy 2008;33(2):180-188. (Special Issue on ECOS 2006)

[55] Dimopoulos G.G., Frangopoulos C.A., Synthesis, design and operation optimization of the marine energy system for a liquefied natural gas carrier. International Journal of Thermodynamics 2008;11(4):203-211. (Special Issue on ECOS 2007)

[56] Dimopoulos G.G., Frangopoulos C.A., Optimization of propulsion systems for modern LNG carriers considering multiple technology and design alternatives. In: Stein Ove Erikstad, ed. IMDC 2009: Proceedings of the 10th International Marine Design Conference; 2009 May 26-29; Trondheim, Norway: 705–722.

[57] Kalikatzarakis M., Frangopoulos C.A., Thermo-economic optimization of synthesis, design and operation of a marine organic Rankine cycle system. Journal of Engineering for the Maritime Environment 2017;231(1):137-152.

[58] Dimopoulos G.G., Georgopoulou C.A., Kakalis N.M.P., Modelling and optimisation of an integrated marine combined cycle system. In Bojić M., Lior N., Petrović J., Stefanović G., Stevanović V. editors. ECOS 2011: Proceedings of the 24th International Conference on Efficiency, Cost, Optimization, Simulation and Environmental Impact of Energy Systems; 2011 July 4-7; Novi Sad, Serbia: 1283-1298.

[59] Sakalis G.N., Frangopoulos C.A., Intertemporal optimization of synthesis, design and operation of integrated energy systems of ships: General method and application on a system with Diesel main engine. Applied Energy 2018;226:991-1008.

[60] Sakalis G.N., Tzortzis G.J., Frangopoulos C.A., Intertemporal static and dynamic optimization of synthesis, design and operation of integrated energy systems of ships. Energies 2019;12:265-314.

[61] Sakalis G.N., Tzortzis G.J., Frangopoulos C.A., Synthesis, design and operation optimization of a combined cycle integrated energy system including optimization of the seasonal speed of a VLCC. Proceedings of the Institution of Mechanical Engineers, Part M: Journal of Engineering for the Maritime Environment 2021;235(1):41-67.

[62] Frangopoulos C.A., Dimopoulos G.G., Effect of reliability considerations on the optimal synthesis, design and operation of a cogeneration system. Energy 2004;29(3):309-329.

[63] Razmi A.R., Janbaz M., Exergoeconomic assessment with reliability consideration of a green cogeneration system based on compressed air energy storage (CAES). Energy Conversion and Management 2020;204:112320.

[64] Cassetti G., Colombo E., Minimization of local impact of energy systems through exergy analysis. Energy Conversion and Management 2013;76:874–882.

[65] Cassetti G., Colombo E., Zio E., A Thermorisk framework for the analysis of energy systems by combining risk and exergy analysis. Energy Conversion and Management 2016;117:281–288.

[66] Safder U., Ifaei P., Kyoo Yoo C., Multi-objective optimization and flexibility analysis of a cogeneration system using thermorisk and thermoeconomic analyses. Energy Conversion and Management 2018;166:602–636.

[67] Verda V., Borchiellini R. Exergetic and economic evaluation of control strategies for a gas turbine plant. Energy 2004;29: 2253–2271.

[68] Verda V., Baccino G., Thermoeconomic approach for the analysis of control system of energy plants. Energy 2012;41:38-47.

[69] Sangi R., Müller D., Application of the second law of thermodynamics to control: a review. Energy 2019;174:938-953.

[70] Keçebaş A., Yabanova İ., Economic analysis of exergy efficiency based control strategy for geothermal district heating system. Energy Conversion and Management 2013;73:1-9.

[71] Fan B., Fang X., Du Z., The method of evaluating operation performance of HVAC system based on exergy analysis. Energy Build 2014;77:332-42.

[72] Sayadi S., Morosuk T., Tsatsaronis G., Exergy-based control strategies for HVAC systems. In: Stanek W., Gładysz P., Czarnowska L., Petela K., editors. Proceedings of the 4th International Conference on Contemporary Problems of Thermal Engineering; 2016 Sept. 14-16; Gliwice – Katowice, Poland.

[73] Verda V., Serra L., Valero A., The effects of the control system on the thermoeconomic diagnosis of a power plant. Energy 2004;29:331–359.

[74] Cambero C., Sowlati T., Incorporating social benefits in multi-objective optimization of forest-based bioenergy and biofuel supply chains. Applied Energy 2016;178:721-735.

[75] Wei Y., Ye Q., Ding Y., Ai B., Tan Q., Song W., Optimization model of a thermal-solar-wind power planning considering economic and social benefits. Energy 2021;222:119752.

[76] Munoz J.R., von Spakovsky M.R., A decomposition approach for the large scale synthesis/design optimization of highly coupled, highly dynamic energy systems. International Journal of Applied Thermodynamics 2001;4(1):19-33.

[77] Munoz J.R., von Spakovsky M.R., The application of decomposition to the large scale synthesis/design optimization of aircraft energy systems. International Journal of Applied Thermodynamics 2001;4(2):61-76.

[78] Mitsos A., Asprion N., Floudas C.A., Bortz M., Baldea M., Bonvin D., Caspari A., Schäfer P., Challenges in process optimization for new feedstocks and energy sources. Computers and Chemical Engineering 2018;113:209-221.

[79] White M.T., Oyewunmi O.A., Haslam A.J., Markides C.N., Industrial waste-heat recovery through integrated computer-aided working-fluid and ORC system optimisation using SAFT-γ Mie. Energy Conversion and Management 2017;150:851-869.

[80] van Kleef L.M.T., Oyewunmi O.A., Markides C.N., Multi-objective thermo-economic optimization of organic Rankine cycle (ORC) power systems in waste-heat recovery applications using computer aided molecular design techniques. Applied Energy 2019:251(112513):1-21.

[81] Marmolejo-Correa D., Gundersen T., New graphical representation of exergy applied to low temperature process design. Industrial & Engineering Chemistry Research, 2013;52(22):7145-7156.

[82] Marmolejo-Correa D., Gundersen T., A comparison of exergy efficiency definitions with focus on low temperature processes. Energy 2012;44(1):477-489.

The future of Thermoeconomics: from industrial cost minimization toward cumulative resources accounting and sustainability assessment

Mauro Reini[a] and Melchiorre Casisi[b]

[a] Dept. of Engineering and Architecture, University of Trieste, Italy, reini@units.it
[b] Polytechnic Dept. of Engineering and Architecture, University of Udine, Italy, melchiorre.casisi@uniud.it

Abstract:
Thermoeconomics has been developed with the main object of first identifying, and then reducing the costs of the energy produced by industrial power plants. More recently, the same approach formalized in the Exergy Cost Theory has been recognized as a useful tool also in a wider field, like industrial symbiosis and sustainability assesment. To do this, exergy supply chains have been tracked backward and backward, to include in the primary resource consumption a more and more complete inventory of the indirect consumption. In Authors' opinion, the future of Thermoeconomics is to go on in this directions. If a very complete inventory of all indirect consumption were obtained, the sustainability assessment of a production process could be performed (at least in principle) by applying the idea that the lower its consumption (direct and indirect) of scarce primary resources, the more sustainable a production process is.
In this paper, the idea of the Thermoeconomic Environment (TEE) is summarized, to highlight as it is a consistent ultimate boundary of the exergy cost accounting, where the origin of the exergy supply chains can be properly placed. Then, the frame of the TEE is used to discuss some possible options for obtaining a more complete inventory of all indirect consumption, and to outline possible perspective connections with some relevant environmental models, coming from Biology, Dynamic of Populations, or Climatology.

Keywords:
Thermoeconomics; Exergy Replacement Cost; Exergy equivalent of capital and labour; Exergy costs of bioproducts; Sustainability.

1. Introduction

Thermoeconomics has been developed with the main object of first identifying, and then reducing the costs of the energy produced by industrial power plants (see, for instance [1-3]). From the beginning, the very fundamental ideas of this approach were:

- All *Fuels* (local resource consumed by a process, or by a component) have to be evaluated in term of the exergy of the streams entering (or leaving) the considered control volume, and the same for the *Products* (goods or commodities locally obtained for the usage in a different part of the system, or for the outside).
- For a process, or a component, the exergy cost of the Products have to be calculated taking all Fuels into account, with their specific exergy costs, disregarding if some Fuels come from the upstream, or the downstream part of the production chain.
- The total cost of the Fuels is allocated on the Products. If a process, or a component, obtains more than one Product at the same time, the total cost is allocated in proportion to the exergy content of each Product.

As a consequence of the previous assumptions, the exergy cost is a conservative magnitude, and the exergy costs obtained by aggregating contiguous control volumes, are consistent with the exergy costs obtained by the previous, smaller, control volumes. These are similar to the properties of the monetary cost, in a closed economy without profit. This analogy is at the basis of the name *Thermoeconomics*.

From the very beginning of Thermoeconomics, the problem arose of including in the exergy cost balance also the resources consumed for owning, operating and maintaining the hardware of the system, i.e. the capital costs of all its parts. The first solution found was consistent with the objective of limiting the Thermoeconomic Analysis to the control volume of a power plant, converting all input flows of resource in terms of monetary costs, using the known values of the unit costs of the energy carriers at the control volume frontier.

In the 80s, a lot of previous ideas about Thermoeconomics have been clarified and organized in an algebraic formulation, named the Exergy Cost Theory (ECT) [4-6].

More recently, the same approach formalized in the ECT has been recognized as a useful tool also in a wider field, like the Industrial Symbiosis [7] and the analysis of eco-industrial parks [8].

In the ECT formulation (as well as in other accounting methodologies, based on the input/output approach [9]) the space boundaries of the analysis are not defined in advance, but they can be adapted case-by-case. In this way, it should be possible, at least in principle, to extend the space boundaries of the analysis, so that the exergy supply chains can be tracked backward and backward, to reach the real primary resources, directly and indirectly consumed, like the raw minerals, the solar radiation, or the biomass in the living ecosystems. If a very complete inventory of all direct and indirect consumption were obtained, the sustainability assessment of a production process could be performed by applying the idea that the lower its consumption (direct and indirect) of scarce primary resources, the more sustainable a production process is. Notice that the idea of *scarcity* plays an important role for assessing sustainability, because the consumption of a certain amount of a very abundant, not renewable resource has to be regarded as more sustainable than the consumption of the same amount of a scarce not renewable one. If this concept is disregarded, we go towards a poor on/off evaluation of sustainability: Goods and process completely based on renewable resources (very few) are identified as sustainable, while all the others, completely, or partially, based on non-renewable resources, are identified as unsustainable!

In view of using the Thermoeconomic approach for cumulative resources accounting and assessing sustainability, a common boundary for the analysis of different goods and processes should be defined. Very recently, the idea of Thermoeconomic Environment (TEE) has been presented [10], highlighting that it may be regarded as a consistent ultimate boundary of the exergy cost accounting, where the origin of the exergy supply chains can be placed, consistently with different exergy accounting methodologies.

In the following, the idea of the Thermoeconomic Environment (TEE) is summarized and then it is used to outline some possible answers to the questions still under discussion in the scientific ambit of exergy accounting. In particular:

- the exergy cost embodied into money capital and human work,
- the proper specific exergy cost to be used for of non-fuel mineral resources,
- the proper approach to be used for the exergy cost accounting of externalities like polluting emissions,
- the proper specific exergy cost to be used for the products of biological systems, which cannot be regarded as supplied “for free” by the ecosystems, neglecting the consumptions and the environmental effects for the production of living stocks, or biomass, inside the ecosystem.

Finally, some possible perspective connections with some relevant environmental models, coming from Biology, Dynamic of Populations, or Climatology are also outlined.

2. The Thermoeconomic Environment

Ones the cost allocation rules have been defined, consistently with the conservative cost balances of all control volumes, the ultimate boundaries of the exergy cost accounting have to be defined, consistently with the purpose of assessing the impact in primary exergy resources of a good, or a service [11].

In the perspective of exergy cost accounting for assessing sustainability, it is evident that the Reference Environment, used in the basic exergy analysis [12], is not well suited for representing the ultimate boundary of the exergy cost accounting analysis. In fact, (i) it is perfectly homogeneous, (ii) its temperature and pressure cannot be modified and (iii) by hypothesis, it cannot be affected in any way by the interaction with the considered system, neither technological nor biological.

Although these characteristics are often considered mandatory for a precise definition of the exergy magnitude, it must also be recognized that they mean that:

- the Reference Environment does not contain any resource; in fact, it is perfectly homogeneous while a resource is generally a concentrated reservoir of some useful substance, or a localized energy flow, which is able to produce useful work while its thermodynamic state is transformed approaching the equilibrium with the defined reference conditions;
- the global warming cannot be accounted for, even in theory, because the temperature of the Reference Environment cannot be modified, in contrast with the evidence of a global temperature change that is happening as a consequence of the interaction of the real environment with the industrial system made by man [13];
- any polluting emissions from the considered production systems have no effect at all on the Reference Environment.

The last point in particular may be regarded as inconsistent, in Authors’ opinion, with the target of an appropriate exergy evaluation of the environmental impact of the industrial processes, at global scale.

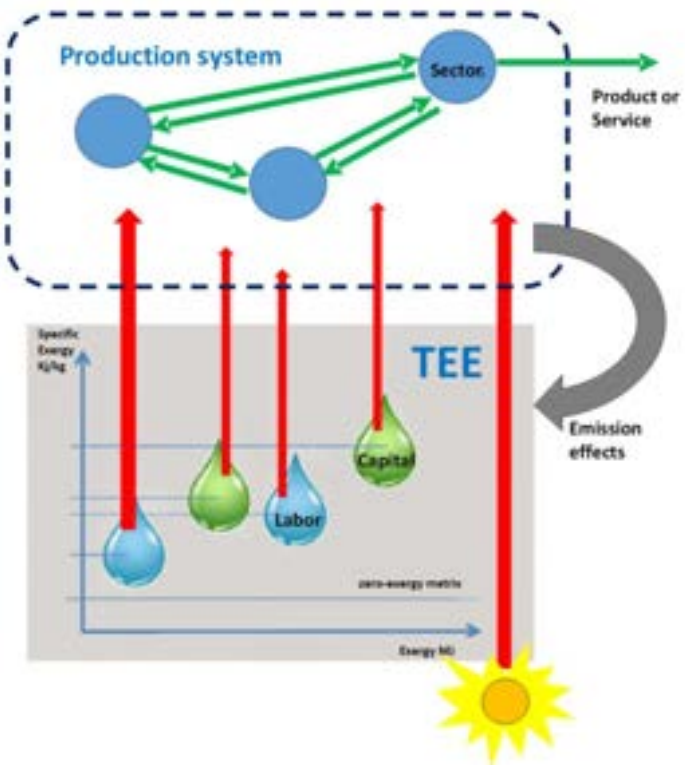

Fig. 1. A qualitative description of some reservoirs in the TEE [10].

To overcome the drawbacks highlighted previously, the TEE has been recently proposed. It is a model of environment, defined as a set of reservoirs, where different kind of natural resources are confined, consistently with the physical nature of the real-world energy systems, which do not operate in a homogeneous environment, but they are fully immersed in the biosphere. All reservoirs are surrounded by the zero-exergy matrix, which plays the role of the dead state for calculating the exergy of all flows inside the energy systems, as well as of all reservoirs (Fig.1). Notice that a specific exergy content greater than zero has to be assigned to each available resource.

From the previous definition, it can be easily inferred that the TEE is not too big to be modified by the interactions with the production processes, because the amount of exergy in each reservoir is limited and because the confined conditions of the reservoirs can be compromised, directly or indirectly, by the production processes. In addition, it must be recognized that even the zero-exergy matrix may change its temperature T° and composition in consequence of some real-world phenomena, like the periodic oscillations of the availability of solar energy or the global warming, which is nowadays increasing as consequence of GHG emissions.

3. Extending the boundary of Thermoeconomic Analysis

If the history of Thermoeconomics and of all exergy-based cost allocation techniques is revised (see, for instance [14]), it clearly appears that this historical development may be regarded as a continuous effort to extend backward the exergy supply chains, toward the primary resources available in the environment (i.e. the reservoirs included inside the TEE).

Very few years after the first application of the Thermoeconomic thinking (1973), the effort of extending the control volume from the gates of the industrial plants, toward the primary resources was formalized by Szargut [15]. He proposed an accounting method based solely on exergy, and properly named it Cumulative Exergy Consumption (CExC): its objective is to compute the cumulative consumption of natural resources, quantify this consumption in units of exergy, and attribute the total resource cost to the products. In its original formulation, CExC focused mainly on mineral resources, assuming an exergy cost equal to one for the chemical exergy of those resources, and it did not include any externalities. A list of CExC values for a large number of finished materials and energy vectors are available in literature [16].

At that point, it appeared as evident that the industrial plants do not consume only the conventional productive factors passing the gates of the plants. Also the polluting emissions, generated during the production process do consume natural resources, to be dispersed and neutralized in the biosphere. To consider this additional resource consumption, the Thermo-Ecological Cost (TEC) [17] was introduced by Szargut. In this last approach, a fictitious extension of the plant is considered, where the polluting emissions are treated in order of obtaining a completely neutralized effluent (or at least an effluent respecting the more restrictive prescriptions actually operating) which can be released in the environment without any damage. The resources

expected to be consumed for the fictitious extension of the plant constitute the ecological cost for polluting emissions, which is used to complement the CExC and to obtain the TEC.

Notice that other Authors, too, use the same procedure for an exergy evaluation of polluting emissions, in particular Sciubba [11] in the Extended Exergy Accounting (EEA), where special emphasis is put in taking into account the entire life cycle of a good, or a service.

After including in the total consumption the effect of polluting emissions and all the main direct and indirect exergy resources supplied to the plant (being the exergy content of some non-fuel minerals quantitatively negligible) the picture could seem complete. Nevertheless, it is not. In fact, even if the hypothesis of a specific exergy cost equal to one for all reservoirs inside the TEE is accepted (as implicitly assumed by TEC and EEA), the operation of tracking back all supply chains towards the indirect primary exergy consumptions may be a very difficult task. In particular, when money capital and human work are considered among the production factors involved in those chains. Money links all sectors of an industrial economy to each other and is used at different stages in the construction and operation of manufacturing facilities. The availability of human work requires food, clothes, instruction, houses, transports, healthcare, etc. All of them are complex products in an industrial economy. To untie all these tangled links, the EEA introduces the exergy equivalent of work and the exergy equivalent of capital, which can be computed based on the Human Development Index (HDI) and the total quantity of circulating money and financial activities that can perform the same functions as money (M2) [18]. Notice that, in the frame of the TEE, this approach means that the TEE contains a reservoir of capital and another of human work and that the specific exergy costs of both resources is known.

4. The proper exergy cost of primary resources

Not only the specific exergy costs of capital and human work have to be known, but also those of all available resource inside the TEE have to be identified, in order of obtaining a meaningful set of product costs by applying the exergy accounting. A straightforward option is considering equal to one by hypothesis (see, for instance, [5]) the specific exergy costs of all exergy reservoirs present in the TEE. This approach expresses the idea that a certain exergy stock of non-renewable resources is available in the TEE at the present moment, jointly with a set of exergy flows of renewable resources (including the renewable part of all partially renewable reservoirs). It is consistent with the CExC and the derived approaches, and with the EEA, too. Then, the exergy cost of a good, or service, is the part of the exergy available in the TEE that is consumed directly or indirectly for obtaining it. This may be correct if the dynamic processes allowing the exergy accumulation inside the reservoirs can be neglected. This is possible, for instance, when the accumulation process is very slow, compared with the production process considered in the analysis, like for natural fossil fuel, or other mineral reservoir. Otherwise, if a dynamic exists inside the TEE and it provides an exergy accumulation inside the reservoirs at a time scale comparable with that of the considered good, or service, it should be taken into account. In fact, the exergy extraction from a certain reservoir may produce an exergy destruction in some other reservoirs of the TEE, in addition to the extraction up from the former reservoir. In this second case, two options can be immediately identified: (i) to extend the supply chain describing the indirect consumption of resources, or (ii) to define a set of specific exergy costs, not equal to one, which takes into account the effect of the mechanism of additional exergy resource consumption. As previously noted, this second option has been used for introducing the externalities of capital and human work consumptions into the EEA.

The meaning of the first option is that the TEE has its own internal production processes. In this case, the specific exergy costs of the exergy reservoirs should be determined by applying the same exergy accounting techniques considered for the manufacturing systems.

Various Authors, in particular Valero A. C. and Valero A. D. [19], have highlighted that, if the specific exergy costs of all exergy reservoirs present in the TEE were fixed at a value equal to one, a sort of inconsistency would arise: all non-fuel mineral resources would have a very low exergy cost, because of their poor chemical exergy content. This happens although some of them are quite rare and someone even valuable. Consequently, some industrial products appear to have an exergy cost that is extremely little dependent on the presence of rare materials and this is in strong contrast with the technological effort undertaken to reduce the presence of such materials, or to replace them with non-rare ones. This effort implies actions in parallel, or in competition with those for increasing the exergy efficiency of the modern production of goods and services, so that, it cannot be simply disregarded.

Paying attention to the rare or valuable characteristic of some minerals may seem irrelevant to the issue of accounting for exergy costs, and only meaningful in relation to the market economy. However, consider the conceptual example of an industrial economy fed by a TEE with only two non-renewable reservoirs, let's say coal and iron ore. That economy could obtain many technological products, but certainly not all the modern industrial goods. This example allows us to infer easily that the availability inside the TEE of many abundant reservoirs of *different* chemical nature is an asset for the industrial system, just like the availability of fossil fuels. In few words, the *Chemiodiversity* (that can be defined analogously to the most popular *Biodiversity*) of the TEE is a resource and has to be accounted for in the calculation of the exergy costs. In addition, consuming

a scarce resources is different (less sustainable) that consuming an abundant one, even if they both were, for instance, not renewable.

The proper specific exergy cost to be used for non-fuel mineral resources has been proposed by Valero A. C. and Valero A. D. [19], by introducing the exergy replacement cost (ERC) of mineral resources. The ERC has to be regarded as the exergy cost required for producing a reservoir of a certain mineral resource, from the conditions defined for the Thanatia planet, where the confining constraints of all reservoirs have been destroyed and all mineral resources are mixed together. In other words, the reconstruction of the mineral deposits (i.e. the cradle of the resources consumed by the production process) requires an exergy expenditure, because real-world, irreversible technologies are used. An exergy cost greater than the mere content of chemical exergy can be identified in this way for all mineral reservoirs in the TEE. In its original formulation, the ERC calculation implicitly assumes that the input exergy is available for the ideal process of reconstruction of a mineral resource as it is in the real-world industrial system, being the process constrained only by the concentration of each chemical substance in the Thanatia environment. Notice that this makes sense (at least for an ideal experiment) if the replacement of a small sample of a certain mineral resource is considered. On the contrary, the replacement of *all the mineral resources consumed* by the global industrial system is not possible, neither in principle, because of the exergy losses in both cradle-to-grave and grave-to-cradle conversion processes. To make it possible (at least for an ideal experiment) an exergy source external to the bio-geosphere of the planet Earth should be considered.

4. The future of Thermoeconomics

In Authors' opinion, the future of Thermoeconomics must continue in the directions outlined above, in particular:

a) integrate the ERC concept into exergy cost accounting methodologies and sustainability assessment,
b) identify an appropriate specific exergy cost to be used for products of biological systems,
c) develop the exergy assessment of the environmental impact of industrial processes, on a global scale,
d) explore alternatives to evaluate the exergy cost embedded in money capital and human labour.

4.1. ERC integration

A first progress in the direction indicated in point a) has been recently obtained by integrating the ERC with the CExC approach, obtaining the new thermoecological-cost methodology [20].

When the object of the analysis is assessing the sustainability of a technology, or of an industrial sector, it is important to pay attention to the replacement of all the mineral resources consumed by the industrial sectors, directly or indirectly connected inside the global system.

As just mentioned, this is possible only if an exergy source external to the bio-geosphere of the planet Earth is considered. The only exergy input external to the geo-biosphere is solar energy (and possibly tidal and geothermal energy). Thus, the ERC may be understood as the exergy cost that should be payed to re-obtain a certain non-renewable resource by using additional renewable external exergy input [10], i.e. to allow its usage as it were renewable, excluding its exhaustion, on a human time scale. This interpretation does not require any conceptual modification of the ERC definition and is consistent with the idea that unit exergy costs greater than one can be considered for the reservoirs in the TEE. The numerical values of the ERCs of the different mineral resources may result amplified by a factor equal to the inverse of the exergy efficiency of the conversion process that produces the form of exergy required by the replacement process starting from solar radiation. Notice that this occurrence is implicit in the idea of using real-word technologies, so that, when the technologies change, also the values of the ERCs may change.

4.2. Products of biological systems

For what concern the direction indicated in point b), it has to be recognized as a difficult task, with few suggestions available in Literature. In fact, the products of the biological systems are resources of the kind having their own dynamic connecting many different reservoirs each other inside the TEE, for which a natural exergy accumulation may be present, at a time scale comparable with that of goods production by the industrial economy. Bakshi and co-workers [21] have proposed one of the few historical contribution in this direction. They have defined the approach named Ecological Cumulative Exergy Consumption (ECEC), that is identical to the CExC for what concern the contribution of mineral resources, whilst the exergy cost of the products of the biological systems are assumed to be equal to the emergy of the same products, calculated in the ambit of the EMergy Analysis (EMA) [22].

The EMA allows overcoming the difficulties related to a detailed knowledge of the exergy flow network that is required to apply The CExC, or the ECT. In fact, only the inputs to the whole ecosystem have to be known in detail. Unfortunately, in the EMA approach, the ultimate boundary of the accounting analysis is placed in the solar energy that fed the whole geo-biosphere from the distant past to now, not in the TEE as it is at present time. In addition, special allocation rules (the Emergy Algebra), are used, which are only in part analogue to a conservative cost balance. In summary, the EMA has some characteristics that make energy engineers often

sceptical about the option of incorporating the results of this approach inside the exergy cost accounting of goods and services [23].

The frame of the TEE offers an alternative for the calculation of the exergy costs of the products of biological systems, similar to the ERC of the mineral resources and consistent with the EEA approach. In this case, too, some information is required about the ecosystem dynamic, but it mainly consists of the parameters of natural growth rate and of extraction rate, which are not difficult to obtain (see, for instance [24]).

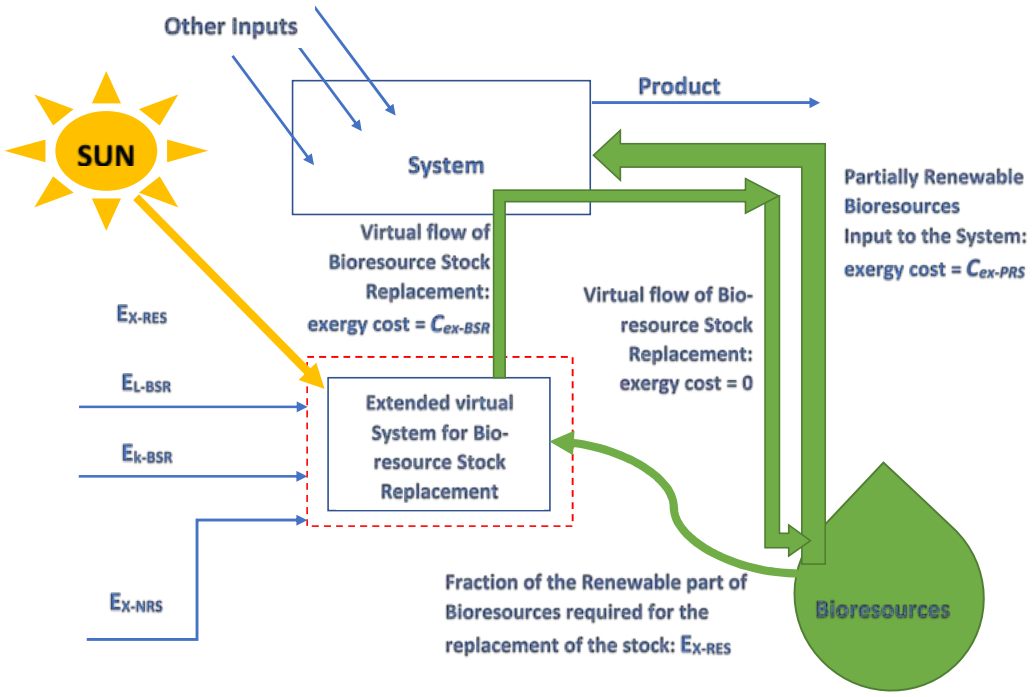

Fig. 2 The concept of Bioresources Stock Replacement Cost [10].

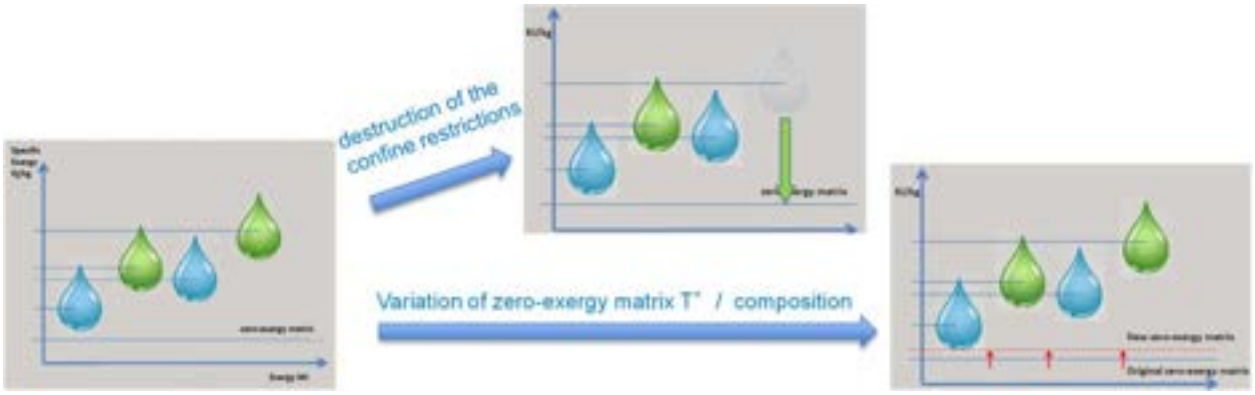

Fig. 3 A qualitative description of possible depletion of the exergy stock inside the TEE.

An extension of the system is considered (see Fig. 2), the function of which is to replace the stock of the bioresource reservoir in the TEE, if the stock has been affected by the operation of the system. In fact, if the bioresource is consumed at an extraction rate lower than (or equal to) its growth rate, the stock is not affected and the input to the production system can be regarded as completely renewable, like solar radiation, and its exergy cost can be equal to one as that of the solar radiation. On the contrary, if the extraction rate is greater than the growth rate, the exergy stock of the TEE is consumed and the extended system has to cultivate the ecosystem, to produce the biomass required to replace the original stock. The bioresource stock replacement cost (BSR) can be calculated because the exergy costs of the inputs of the extended system can be known [10, 25].

4.3. Environmental impact

To develop the exergy assessment of the environmental impact of industrial processes (point c), it is worth noting that the remediation cost for neutralizing the chemical and physical exergy of waste (the cost considered by both the CExC and the EEA, among others) may be the same whether or not waste treatment strategies

are actually applied. In fact, part of the costs are actually incurred within the real plant, while the other part (so as, to have virtually neutralized emissions) is incurred in the fictitious extension of the plant. In other words, the cost charged on the plant products because of polluting emissions may independent by the degree of emission cleaning actually operated. Moreover, the cost for the actual treatment may be even higher, because real processes are generally less efficient than virtual ones. The result is that a highly polluting plant may appear to be less resource-consuming (more sustainable) than a plant that obtains the same product cleanly. To avoid this inconsistency, an alternative approach has been suggested in the frame of the TEE [10, 25], where the actual exergy cost of polluting emissions has to be defined as the real exergy stock depletion produced by the polluting emissions. Bearing in mind the definition of TEE, it is easy to deduce that a certain depletion of the exergy stock can be caused, besides consumption, also by:

- destruction of the confine restrictions of reservoirs (see Fig. 3),
- variation in the zero-exergy matrix temperature or composition(see Fig. 3),
- dilution of substances inside the reservoirs, reducing their concentration,
- indirect destruction of the (living) biomass stock inside the reservoirs.

In this way, virtuous plants, which effectively include emission neutralization systems, may have a specific exergy cost of their products lower than polluting plants, highlighting that the former requires less consumption of resources (i.e., they are more sustainable).

It is worth noting that the suggested alternative approach requires an inventory of the effects of the identified polluting emissions and then the translation of those effects in terms of depletion of the exergy content of the reservoirs inside the TEE. The effort of the first step is similar to that required by the LCA [26] of a process, whilst the second step requires an appropriate evaluation of the specific exergy cost attributed to each reservoir, in order of obtaining the total exergy cost of the polluting emissions [27]. Moreover, the evaluation of the exergy stock depletion produced by some pollutant may vary, because new effects may be discovered. This may be regarded as a negative point, because the evaluation is, to some extent, dependent on the historic moment. Or as a positive point, because new discoveries can be integrated in the evaluation, allowing well supported decision for improving the sustainability of the production processes. It is worth noting that this alternative approach define a connection among Thermoeconomics and the ecological models developed in different scientific fields, in particular with the climatic models, that have assumed increasing importance in the recent years [13] because of the arising of the global warming.

4.4. Money capital and human labour

The final topic (d) of the future development of Thermoeconomics will be, in Authors opinion, the development of alternatives to evaluate the exergy cost embedded in money capital and human labour. The exergy equivalent of money capital and of human work following the methodology of the EEA have been presented in the previous sections. Rocco and Colombo [28] have proposed an alternative approach, which can be regarded as an exergy extension of the input/output analysis, originally formulated by Leontief [9]. In this approach, the interactions among the sectors of the whole production system are described by the monetary magnitudes, usually adopted in the economic analysis. Then, the exergy cost accounting of each flow in the model is obtained considering the exergy of all inputs coming from the environment and feeding the sectors (the nodes) of the production network. The exergy equivalent of capital has not to be evaluated explicitly in this procedure and (if it is evaluated *a posteriori*) it may result different for the different production sectors considered.

As far as the exergy cost accounting of human work is concerned, the suggestion by Rocco and Colombo [28] is again a direct extension of their exergy input/output analysis. Human labour is embedded as an additional sector, without the need of any arbitrary assumption. Obviously, additional information is required, in particular the quantitative evaluation of the inputs required by the human working activities from each one of the other sectors and, likewise, the human working hours required by each of them.

It has been previously highlighted that the development of the exergy assessment for the environmental impact of polluting emissions will imply a more strict connection with the ecological models developed in different scientific fields. In conclusion, it is worth noting that, in the same way, the identification of a detailed information about the exergy cost embedded in money capital and human labour will imply a strict integration with the input/output models coming from the economic analysis.

5. Is Thermoeconomics a science?

This question has been always present, even not explicitly asked, from the very beginning of the exergy based cost accounting methodologies:

Is Thermoeconomics a science?

The question may appears as inappropriate, out of place, and even insulting. Thermoeconomics comes from the exergy analysis that means from the Second Law of Thermodynamics. It has to be close to the holy hart of Physics.

Unfortunately, the exergy cost cannot be measured like mass, or energy. In fact, these magnitudes can be measured independently from the thesis to be demonstrated. By using the measured values of two masses, it can be demonstrated that the gravitational attraction between them is proportional to the product of the two masses. By using the measured value of the potential energy of a body, the Joule experiment can be performed, demonstrating the energy equivalent of heat. On the contrary, the exergy cost cannot be measured independently by the cost allocation rules, the inventory of the flows regarded as relevant (whilst a lot of others are disregarded), the hypotheses about the exergy equivalent of money capital and of human labour, and so on. Ones the cost allocation rules are defined, together with all other required information, the calculated exergy costs cannot be wrong, *they are right by hypothesis*. They may be more or less useful from an engineering point of view (this is true), but this is far from a clear scientific result.

To claim Thermoeconomics as a science, it should be shown that the exergy costs (or the specific exergy costs) are involved in some physical phenomena different from their calculation procedure. Perhaps, this could be investigated referring to a process without any requirement of money capital or human labour, and with a clearly identified environment, where all resources come from. Such a process could be a network of chemical reactions, where reactants and products could be identified for each reaction, or better, the metabolic network of a simple bacterium in a Petri dish.

This investigation line is nowadays under development [29, 30]. The object is to show that, under well-identified conditions, the minimization of the specific exergy costs of the products plays a role [31, 32] analogous to the Constructal Principle, formulated by Bejan [33] and often considered to be a physical principle of the same rank of the First and Second Law of thermodynamics [34]. If this hypothesis were confirmed, it would be definitely demonstrated that Thermoeconomics is more than a useful engineering tool, but a real scientific field.

6. Conclusions

In the paper the history of Thermoeconomics is quickly summarized, highlighting how its development may be regarded as a continuous effort to extend backward the exergy supply chains, toward the primary resources available in the environment. In fact, this allows including in the economic and sustainability assessment a more and more complete inventory of direct and indirect consumption. If a very complete inventory of all direct and indirect consumption were obtained, the sustainability assessment of a production process could be performed by applying the idea that the lower its consumption (direct and indirect) of scarce primary resources, the more sustainable a production process is. In spite of being apparently a simple idea, this effort is still not completed.

In Authors' opinion, the future of Thermoeconomics will be going on in the direction of improving the inventory of all direct and indirect consumption related to a production process, in order to supply a more complete information to the decision-makers in the field of industrial sustainability. In the paper, some specific directions have been identified, like:

a) The integration of the Exergy Replacement Cost of rare mineral resources into the exergy cost accounting methodologies and sustainability assessment.
b) The identification of an appropriate specific exergy cost to be used for the products of the biological systems. In this direction, the exergy Bioresources Stock Replacement Cost has been presented as an alternative to other approaches, keeping the consistency with the exergy cost accounting and the Exergy Replacement Cost formulations.
c) The continuous improving of the exergy assessment for the environmental impact of industrial processes, on a global scale. In this direction, the frame of the Thermoeconomic Environment may help overcoming a drawback of the exergy assessment of pollution, in which a highly polluting plant may appear to be less resource-consuming (more sustainable) than a plant that obtains the same product cleanly.
d) The exploration of alternatives to evaluate the exergy cost embedded in money capital and human labour.

Is worth noting that the development of the exergy assessment for the environmental impact of the production processes will imply a more strict connection with the ecological models developed in different scientific fields. In the same way, the identification of a detailed information about the exergy cost embedded in money capital and human labour will imply a strict integration with the input/output models coming from the economic analysis. In addition, all these improvements of the inventory of direct and indirect consumption have to be integrated into a unique frame. For instance, the exergy cost embedded in human labour should be accounted for in the Exergy Replacement Cost of rare mineral resources, and Bioresources Stock Replacement Cost should be accounted for in the assessment for the environmental impact of industrial processes, if even distant ecosystems are affected by their emissions.

In conclusion, the question if Thermoeconomics has to be regarded as a science, or not, is briefly discussed and a possible path to demonstrate that Thermoeconomics is more than a useful engineering tool, but a real scientific field, is outlined.

Acronyms

BSR Bioresource Stock Replacement Cost,
CExC Cumulative Exergy Consumption CExC,
ECEC Ecological Cumulative Exergy Consumption,
ECT Exergy Cost Theory,
EEA Extended Exergy Accounting,
EMA EMergy Analysis,
ERC Exergy Replacement Cost,
GHG Greenhouse Gases,
LCA Life Cycle Assessment,
TEC Thermo-Ecological Cost,
TEE Thermoeconomic Environment.

References

[1] Fehring T. H., Gaggioli R. A., Economics of feedwater heater replacement, Trans. ASME, J. Eng. Power, vol. 99, pp. 482-489, July 1977.

[2] Gaggioli R.A. and Petit P.J., 1977, Use The Second Law First, Chemtech, 7, 496-506.

[3] Rodríguez L. S. J., Gaggioli R. A.,1980, Second law of a coal gasification process, Can. J. Chem. Eng., vol. 58, p. 376.

[4] Valero A, Lozano M A, Munoz M., A general theory of exergy savings - 1. On the exergetic cost, Proc. ASME Computer-Aided Engineering of Energy Systems, v. 3, Second law analysis and modelling, pp. 1-8, Anaheim, Ca., 1986.

[5] Valero A., Serra L., Uche J., Fundamentals of Exergy Cost Accounting and Thermoeconomics. Part I: Theory, Journal of Energy Resources Technology, March 2006, Vol. 128.

[6] Lozano M, Valero A. Theory of the exergetic cost. Energy 1993, 18, 939–960.

[7] Usón S, Valero A, Agudelo A, Thermoeconomics and Industrial Symbiosis. Effect of by-product integration in cost assessment, Energy Vol. 45, Issue 1, September 2012, Pages 43-51.

[8] Valero A. et. Al., Thermoeconomic tools for the analysis of eco-industrial parks, Energy, Volume 62, 1 December 2013, Pages 62-72.

[9] Leontief W. W., The structure of the American economy, 1919–1939, 2nd Ed., Oxford University Press, New York, 1951.

[10] Casisi M., Khedr S., Reini M., The Thermoeconomic Environment and the exergy-based cost accounting of technological and biological systems, Energy 2023, Volume 262, Part A (available on line: 14 August 2022).

[11] Sciubba E, Bastianoni S, Tiezzi E., Exergy and extended exergy accounting of very large complex systems with an application to the province of Siena, Italy. J Environ Manage 2008;86:372–82.

[12] Kotas T., The Exergy Method of Thermal Plant Analysis, New Publisher, 2021.

[13] Giorgi F., Coppola E. and Raffaele F., A consistent picture of the hydroclimatic response to global warming from multiple indices: Model sand observations, J. Geophys. Res. Atmos. (2014), 119,11,695–11,708, doi:10.1002/2014JD022238.

[14] Sciubba E., Wall G., A brief Commented History of Exergy From the Beginnings to 2004, Int. J. of Thermodynamics ISSN 1301-9724, Vol. 10 (No. 1), pp. 1-26, March 2007.

[15] Szargut J., Morris D. R., Steward F. R., Exergy analysis of thermal, chemical, and metallurgical processes. Hemisphere; 1988.

[16] Szargut J., Exergy method: technical and ecological applications. WIT Press; 2005.

[17] Szargut J., Ziebik A., Stanek W., Depletion of the non-renewable natural exergy resources as a measure of the ecological cost. Energy Convers Management 2002; 43:1149–63.

[18] Sciubba E., A revised calculation of the econometric factors □- and □ for the Extended Exergy Accounting method. Ecological Modelling 222 (2011) 1060–1066.

[19] Valero A. C., Valero A. D., Thanatia-The destiny of the earth's mineral resources - a thermodynamic cradle-to-cradle assessment, Ed. World Scientific Publishing Company, 2014, 670 pp.

[20] Valero A., Valero A., Stanek W., Assessing the exergy degradation of the natural capital: From Szargut's updated reference environment to the new thermoecological-cost methodology. Energy 2018, 163, 1140–1149.

[21] Hau Jorge, Bhavik L., Bakshi R., Expanding exergy analysis to account for ecosystem products and service, Environ. Sci. Technol. 38 (2004) 3768-3777.

[22] Odum H.T., Environmental Accounting: Emergy and Environmental Decision Making (1st edition). John Wiley & Sons, New York, 1996, 370 pp.

[23] Sciubba E., Ulgiati S., Emergy and exergy analyses: Complementary methods or irreducible ideological options? Energy, Volume 30, Issue 10, July 2005, Pages 1953-1988.

[24] Cordier M. et al., An Input-output Economic Model Integrated Within a System Dynamics Ecological Model: Feedback Loop Methodology Applied to Fish Nursery Restoration, Ecological Economics Volume 140, October 2017, Pages 46-57.

[25] Khedr S., Casisi M., Reini M., The Thermoeconomic Environment Cost Indicator (iex-TEE) as a One-Dimensional Measure of Resource Sustainability, Energies 2022, 15, 2260.

[26] Klöpffer W., Life cycle assessment. Environmental Science & Pollution Research 4, 223–228 (1997). https://doi.org/10.1007/BF02986351.

[27] Dewulf J. et al., Cumulative Exergy Extraction from the Natural Environment (CEENE): a comprehensive Life Cycle Impact Assessment method for resource accounting, Environ. Sci. Technol. 2007, 41, 8477–8483.

[28] Rocco M., Colombo E., Internalization of human labor in embodied energy analysis: Definition and application of a novel approach based on environmentally extended Input-Output analysis, Applied Energy 182 (2016) 590–601.

[29] Assal S., Malfatti F., Giani M., Reini M., Exergy and exergy cost analysis of biochemical networks in living systems far from equilibrium, Proceedings of the 9th International Conference on Bioinformatics Research and Applications - ICBRA '22, September 2022 Pages 36–40 https://doi.org/10.1145/3569192.3569199.

[30] Assal S., Application of exergy analysis in living cells: A case study with Escherichia coli as a biofuel source, Journal of Fundamentals of Renewable Energy and Applications, 2023, Vol. 13.

[31] Reini M., Constructal Law & Thermoeconomics, International Journal of Heat and Technology, Volume 34 (January 2016), Special Issue 1, pp. S141-S146. Presented at the Constructal Law & Second Law Conference 2015 CLC 2015, Parma (Italy), 18 - 19 May 2015.

[32] Reini M., Casisi M., Is the evolution of energy system productive structures driven by a physical principle?, Front. Sustain., 25 March 2021, https://doi.org/10.3389/frsus.2021.599173.

[33] Bejan A., Evolution in thermodynamics, Applied Physics Reviews, Vol. 4, No. 1, 011305, 2017.

[34] Reis A. H., Use and validity of principles of extremum of entropy production in the study of complex systems, Annals of Physics 346 (2014) 22–27.

From Exergoeconomics to Thermo-X Optimization of Energy Systems in the transition to a fully renewable system

Andrea Lazzaretto[a], Massimo Masi[b], Sergio Rech[a], Gianluca Carraro[a], Piero Danieli[b], Gabriele Volpato[a], Enrico Dal Cin[a]

[a] University of Padova, Department of Industrial Engineering
Via Venezia 1, 35131 Padova, Italy
[b] University of Padova, Department of Management and Engineering, Stradella S. Nicola 3, 36100 Vicenza, Italy
andrea.lazzaretto@unipd.it, massimo.masi@unipd.it, sergio.rech@unipd.it, gianluca.carraro@unipd.it, piero.danieli@unipd.it, gabriele.volpato.1@phd.unipd.it, enricodalcin@phd.unipd.it

Abstract:

Exergoeconomics has played an important role in the analysis and optimization of energy systems in the last decades. The idea of using exergy as a “carrier of value” allowed defining an unambiguous criterion to allocate costs among the products of energy systems and paved the way to a deeper analysis of the losses of potential work within the systems. With the development of efficient optimization algorithms, the exergoecomic procedures of analytic optimization and the design improvement procedures based on heuristic exergoeconomic criteria have been gradually replaced by more efficient optimization procedures aimed at minimizing a “cost” objective function, leaving the calculation of exergoecomic costs in the optimum as final step. The increasing attention to the mitigation of the effects of human activities on climate change, together with increasingly higher disparity in the availability and use of energy, enlarged the perspective to a wider set of goals of the energy system designer, which has to consider the energy systems as a part of the whole society. This asks the energy systems designer to move the attention also towards energy users, integrating the design and operation optimization of energy conversion systems with smarter methodologies to reduce energy consumption. Therefore, we propose the Exergoeconomic methodologies to evolve towards Thermo-X Optimization methodologies involving a wider set (X) of goals and constraints than the economic ones, to solve the “energy problems” of our society with a wider perspective. The paper briefly summarizes the history of Exergoeconomic analysis and optimization methodologies and outlines the path for developing a general methodology including all the aspects mentioned above.

Keywords:

Exergoeconomics, design optimization, UN goals

1. Introduction: exergoeconomic methods

Exergoeconomics aims to evaluate the exergetic and monetary costs associated with mass and energy flows in the energy system. Building on the pioneering work of [1–4], the idea is to allocate the input costs of the total system between the internal mass and energy flows of the system, up to the final products, in proportion to the associated exergy flows. The principle that exergy is the most appropriate variable for cost allocation actually needs to be supplemented with the definition of the desired exergetic "Product" and the exergetic resources needed to obtain it ("Fuel"). Thus, all exergoeconomic methodologies proposed in the literature suggest allocating the costs of the input streams based on the exergy carried by the Fuel and the Product of the system components. However, this introduces an inherent degree of subjectivity, as the definitions of Product and Fuel that satisfy the energy balance of each component are not unique. The various exergoeconomic methodologies in the literature ultimately differ each other only in the ways of defining or representing the Fuel and the Product of the components. The "algebraic" approach initially suggested in [4] and [5,6] as well as the "algebraic theory" proposed by [7,8] leaves a fairly large degree of freedom on these definitions and their representation, i.e., on the so-called production structure, specifying some rules only to avoid other arbitrariness at the system level (e.g., to handle energy losses - "residuals" - of the total system). The SPECO method, proposed by Lazzaretto and Tsatsaronis [9–13], avoids any ambiguity in the definitions of Fuel and Product by providing specific rules for obtaining them, simply based on the principle that any addition of energy by the considered component belongs to the Product, while any removal belongs to the Fuel. The resulting representation of the production structure is also unique and keeps every interaction

between Fuel and Product and the flows of exergy into and out of each component within the boundaries of the component itself.

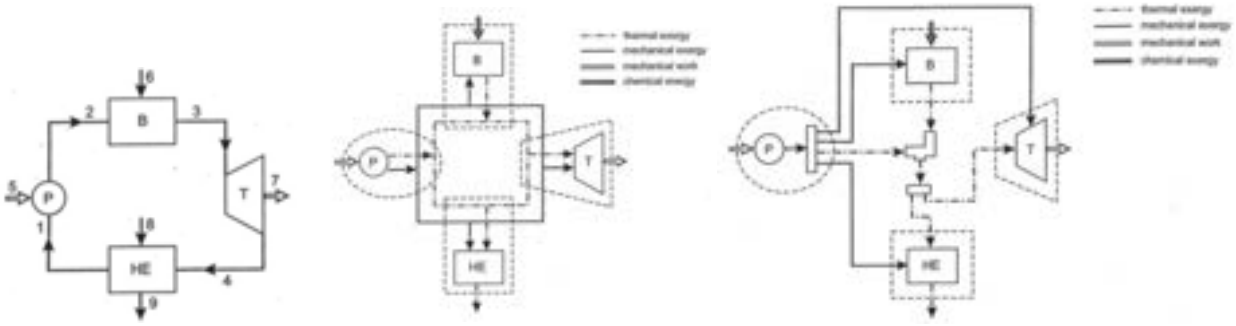

(a) (b) (c)

Figure 1. Simplified physical structure of a steam power plant with “hot” heat exchanger (a) and corresponding productive structures according to the SPECO (b) and Functional (c) approaches [14].

A substantially different approach has been proposed by the "functional" approaches [3,15–19], where functions (i.e., product) are defined according to a “purpose” of the component in the system in which it operates, i.e. considering how the single component “serves”, and therefore interacts, with the rest of the system structure. In this way, the same component does not have the same "function" independently of the system in which it operates, as the SPECO approach states, but it may have different functions depending on the system in which it is embedded. In this way, a "functional diagram" is constructed that has the same logical meaning as the productive structure of the SPECO criterion or other thermoeconomic approaches, but is generally different from it, thus involving a different cost allocation criterion [14,20–23]. For any functional or production structure, costing requires formulating a conservative balance of the cost streams entering and leaving the component under consideration and formulating auxiliary equations equal in number to the number of exergetic streams leaving the component minus one (since the balance equation is always available). For example, for the k_{th} component receiving a heat transfer ($\dot{E}_{q,k}$) and generating power ($\dot{W}_k$), the cost balance is [24].

$$\sum_e \left(c_e \dot{E}_e\right)_k + c_{w,k}\dot{W}_k = c_{q,k}\dot{E}_{q,k} + \sum_i \left(c_i \dot{E}_i\right)_k + \dot{Z}_k$$

where $\dot{E}_i$, $\dot{E}_e$ and c_i, c_e denote exergy flow rates (*kJ/s*) and costs per monetary unit (*$/kJ*), respectively, at the inlet (*i*) and exit (*e*) of the k-*th* component, $\dot{Z}_k$ is the amortization cost for the investment and maintenance and $c_{w,k}$ and $c_{q,k}$ are costs per monetary unit of the work and heat, respectively.

Auxiliary equations are formulated according to the *F* and *P* rules [7,10–12]. Referring to the SPECO approach, the *F* rule states that the exergy removal in a component occurs at the average unit cost at which the exergy removed was supplied in the upstream components, whereas the *P* rule states that every exergy unit belonging to the product has the same unit cost (Fig. 2).

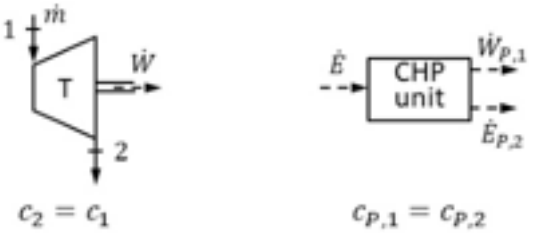

Figure 2. F rule applied to a turbine (left) and P rule applied to a CHP engine (right).

The result is an overall picture of the exergetic or monetary cost flows associated with the different mass and energy flows in the system. In particular, this makes it possible to estimate product costs, showing that products of components further downstream in the energy conversion system are loaded with higher costs as they are affected by all the irreversibilities generated by upstream components. Regardless of the differences between the different methods, which are generally quite small, they have had the merit of calculating the least ambiguous possible cost of the different energy products of a system, and thus of being able to make comparisons about the ability of different systems to generate products at higher or lower costs.

The method of design improvement proposed in [6] and subsequently included in [24] is based on finding the best efficiency-cost trade-off at the component level, so as to create an overall picture of the main sources of irreversibility and costs in the various components of the energy system, and intervene mainly on those

components with the highest values of the sum of depreciation costs and energy destruction costs. This method may require some iteration steps to improve the system design, driven by the designer's ability to choose the appropriate performance modification of the components responsible for the highest destruction of exergy and cost.

On the other hand, starting from the 70ies several researchers proposed to optimize the system design with a Lagrangian analytical approach [3,15–19] that searches for the minimum unit cost of the total system product as objective function. Compared with the design improvement criterion proposed by Tsatsaronis and co-workers [6,24], this approach has the advantage of finding the optimal values of the system design variables (pressures, temperatures, flow rates) without the need for iterations, but at the expense of a quite difficult search for the analytical solution. Langrange multipliers in this case take the meaning of marginal costs at the point of optimality found. However, setting up and solving an optimization problem with an analytical method limits the use of this approach to relatively simple system configurations, or requires strong simplifying assumptions.

An evolution of this approach was the development of “Environomics”, which, in addition to the exergetic and monetary costs of mass and energy streams in the system, considers the costs associated with the consumption of other resources and the emission of pollutants [25]. The thermo-economic objective function is still used with the addition of one or more terms, which depend on: the environmental and social costs of undesired emissions [26]; on the pollution costs associated with system manufacturing and dismantling system equipment; the costs associated with resource preparation and transport [27]. Since all these terms are costs, the objective function is still economic (in this sense, the unabbreviated term thermo-enviroeconomics would be more appropriate, as recognized by Frangopoulos [25]), with penalties applied according to the pollution generated. A variant of the environomic approach is used in [28], where the objective function considers a carbon tax on CO2 production as a penalty term and includes the costs of pollutant abatement devices and CO2 sequestration in the cost of equipment. A different penalty term linked to operational inefficiencies is considered in [29].

Going back to the design improvement methods, from the beginning of 2000s onward, Tsatsaronis and co-workers introduced the concepts of "avoidable" and "not avoidable" exergy destruction to understand the actual margins of improvement achievable in the iterative design based on the calculation of exergoeconomic variables [30]. Moreover, they suggested overcoming the problem associated with the mutual interdependence of the components behavior by splitting the total exergy destruction within a component into its endogenous and exogenous parts [31]. The former refers to the exergy destruction occurring within the component when all other components operate in an ideal way, whereas the latter is the difference between total and endogenous exergy destruction in the same component. In spite of the interesting conceptual approach, the practical applicability of this exergy splitting is not trivial. Several papers were written in the last years on these advanced exergy-based methods for developing, evaluating, understanding, and improving energy conversion systems by Tsatsaronis and Morosuk. A good review of these approaches is supplied in [32].

Other important developments have also been made to use exergoeconomics in the diagnosis of energy systems malfunctions. The paper by [6] first evaluated the effects of variations in exergy destruction in a component of a complex system on the total system fuel in the system design. This concept was later applied by Valero and co-workers [33] to evaluate the system-level effects of malfunctions, understood as changes in efficiency or product in a component relative to the design condition. Reini in 1994 [34] fully formalized how to calculate the "impact" on total system fuel due to changes in the efficiency or product of its components for any system configuration. Torres at al. [35] introduced the concepts of malfunction and dysfunction to distinguish between variation of the component behavior that depend on the component in hand or originate in other components. In [36] a criterion was proposed to identify and localize malfunctions using exergoeconomic performance variables.

However, as already in the iterative design improvement procedures mentioned earlier [6] the main drawback in the application of exergoeconomics to the search of malfunctions lies in the dependency relationship between the exergetic performance variables (exergetic efficiency and exergetic product) of different components. This implies that a variation in one of these variables due to changes in one of more design variables (pressure, temperature, mass flow rate..) generally results in induced changes in the exergetic variables of other components as well, thus “hiding” the “real” malfunctions and making their identification difficult. To overcome this intrinsic drawback, Toffolo and Lazzaretto suggested a fundamentally different approach to detect malfunctions, based simply on identifying components that vary their characteristic curve through an exergetic indicator that accounts for the changes in the derivatives of irreversibilities at the design point of this curve with respect to the independent variables of the component under consideration [36].They also reviewed all exergoeconomic diagnostic methodologies to highlight their strength and limitations [37]. A good synthesis of different points of view on the use of exergoeconomics in the detection of malfunctions and evaluations of their effects is presented in [38,39].

Most of the mentioned drawbacks either of the exergoeconomic method for the design improvement or of the Langrangian optimization approaches were subsequently overcome by the introduction of new optimization

algorithms that allowed researchers to develop new and often more efficient methods for the design optimization of energy conversion systems, as shown in this paper.

In this context, the goals of the paper are:

- To demonstrate that exergoeconomics has paved the way for the recent design optimization methods and can still be used to obtain more in-depth information for a comprehensive understanding of the optimal design of single energy conversion systems;

- To understand the direction in which newer optimization methods have developed;

- To foresee how these optimization methods may develop in the future to include not only energy and economic performance aspects of individual systems but also all the other aspects that must necessarily be considered when designing groups of energy conversion systems that fulfil the time-varying demands of multiple users, in larger or smaller geographic areas, through different energy distribution networks.

- To emphasize the need to focus on reducing energy demand, avoiding energy waste in wealthier countries, and instead help increase consumption in poor countries while maintaining a good balance with the environment.

The paper identifies themes and asks questions about these problems without claiming to give exhaustive answers, which are impossible given the complexity and enormity of the problems, which involve virtually all human activities. Rather, it aims to retrace the evolution of research in order to identify lines of development that are respectful of the developmental needs of individual states, but at the same time narrow their limits in order to give every human being the same opportunities, not only now but also in the future.

2. Critical aspects and limitations of the exergoeconomic methods

Exergoeconomics is based on concepts and assumptions that have a certain degree of subjectivity, which is reflected in the results obtained and in their utilization for improving the design and operation of energy conversion systems. The critical issues associated with this subjectivity are discussed in the following, separating those associated with simple cost accounting from those involved in the use of exergoeconomics for the design improvement according to the criteria proposed by Tsatsaronis and co-workers [6,24].

2.1. Cost accounting

As shown in the Introduction, the cost balance and the auxiliary equations obtained by the *F* and *P* rules allows calculating the exergetic and monetary costs associated with mass and energy streams. Given that the *F* and *P* rules require the definition of Fuel and Product of each component, these definitions become crucial for an effective and unambiguous cost allocation criterion [9–12].

The criteria for defining Fuel and Product, and consequently the exergetic efficiency (ratio of Product to Fuel), have been extensively discussed in the literature and converge toward the general idea that the Fuel and Product of a component consist of the decreases and increases, respectively, in each form of exergy between the input and output of that component. This general criterion and the very few exceptions to it are discussed in detail in [11,12,40]. On the other hand, the *F* and *P* rules used to define the auxiliary equations are essentially based on the principle that every unit of exergy removed or added by the component has the same cost. Although consistent with the idea that exergy is the “carrier of value”, this principle is arbitrary and does not take into account the fact that exergy is the maximum work "ideally obtainable" from a mass or energy stream, which differs from the maximum work actually obtainable from such streams. In particular, the exergy destruction to Product ratio associated with real world processes, decreases as the temperature of the process decreases, more than what expected by theoretical thermodynamics. Accordingly, a unit of thermal exergy does not have the same "value" in reality as a unit of mechanical energy, so that units of thermal exergy at lower temperatures have less "value" than those at higher temperatures or, even more, units of mechanical work (Fig. 3).

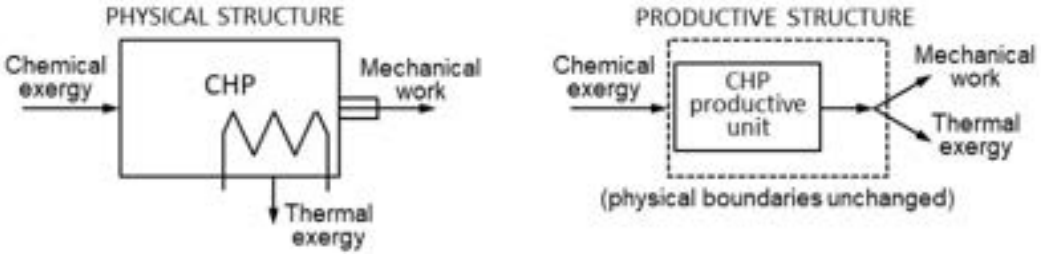

Figure 3. According to exergoeconomic accounting methodologies, a unit of thermal exergy at the outlet of a CHP engine has the same exergetic cost of a unit of mechanical work.

Moreover, this allocation criterion is normally applied at design conditions, whereas more reliable results could be obtained considering the hour by hour operation, throughout the year, as only few papers in the literature

highlighted [41,42]. On the other hand, other equally meaningful allocation criteria than the exergoeconomic one could be used for multi-product systems, as shown in [43,44].

2.2. Design improvement

As reported in the Introduction, the picture of the costs associated with the individual components employed in the procedure of design improvement [6,24] provides information for design improvement that does not allow to obtain the best design in a single iterative process. This is because the improvement in either the exergetic or exergoeconomic performance of one component does not necessarily result in a corresponding improvement for the overall system, since it may have a worsening influence on the exergoeconomic performance of the other components. In fact, there is a dependency link between the exergetic variables of the different components, and thus between the costs associated with them, since exergy values depend, to a greater or lesser extent, on the set of values of the independent design variable set (including temperatures, pressures, flow rates) on which the designer has the ability to act.

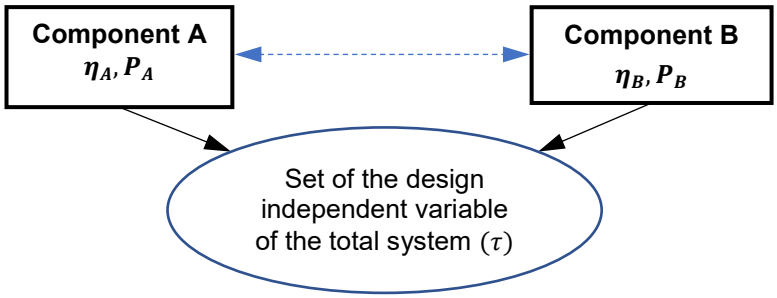

Figure 4. In general, the exergetic performance variables of different components (e.g., η_A, P_A and η_B, P_B) depend on the set of independent variables of the total system (τ), so that they depend on each other (dotted line).

Moreover, the need to guide the different iterations by the designer's "experience" limits the applicability to the more experienced designers in the exergoeconomic field. Furthermore, as already pointed out about cost accounting, the scope of these exergoeconomic procedures concerns the behavior of the plant under design point conditions only, because of the major complication that would result with an application under off-design operation.
However, these limitations do not negate the usefulness of exergoeconomic accounting and exergoeconomic design improvement procedures, but suggest a partially different use for them, as shown in Section 6 (Fig. 9).

3. Single or multi-objective design optimization of individual energy conversion systems

This section briefly describes why, starting in the late 1980s-early 1990s, the design of advanced energy conversion systems shifted from the iterative exergoeconomic design improvement described in Section 2 to the more efficient numerical optimization approach. At that time, the difficulty of setting up and executing design constrained optimization with the Lagrangian analytical method was overcome first with the development of efficient descent optimization algorithms and then with the new and more efficient genetic algorithms.

3.1. Single economic objective

The work of Lazzaretto and Macor [21] showed that, unlike the Lagrangian approach used up to that time for thermoeconomic design optimization, the search for the economic optimum can be separated from the cost calculation by first setting up and solving the following optimization problem, and then calculating the costs in the optimum.

$$\text{Find } \mathbf{x}^* \in \mathbb{R}^n \text{ that minimizes } f(\mathbf{x}) \tag{1}$$

$$\text{subject to } \begin{matrix} g_i(\mathbf{x})=0, & i=1,\ldots,p \\ k_j(\mathbf{x})\geq 0, & j=1,\ldots,q \end{matrix} \tag{2}$$

where $f(\mathbf{x})$ in Eq. (1) is the objective function, the equality and inequality constraints in Eqs (2) represent the energy system model including mass and energy balances of its components and the equations describing the properties of the working fluids, and $\mathbf{x}$ is the set of the design decision variables including pressures, temperature, mass flow rates and fluid properties.

The objective function $f(\mathbf{x})$ is the total cost flow rate ($\dot{C}_{total}(x)$) associated with the amortization of the investment and maintenance costs and of the costs for the fuel utilized by the system.

$$\dot{C}_{total} = \dot{C}_{fuel}(x) + \dot{C}_{inv+maint}(x) \quad (3)$$

3.2. Multi-objective optimization: energetic, economic, environmental

Multi-objective optimization techniques have been introduced into energy system design optimization since the end of 1990s-early 2000s, with the concomitant development of evolutionary algorithms. In particular, the paper [45] expands the perspective of traditional thermoeconomic optimization, by applying a multi-objective approach to evaluate the complete spectrum of solutions that satisfies both the economic and energetic objectives. In fact, a "pure" single-objective approach that considers only the economic objective or only the thermodynamic one is able to find one of the two extreme points on this spectrum of optimal solutions: the minimum of the cost objective function, or the maximum of the efficiency objective function. In [45] the Pareto approach is used to find the optimal set of design variables, since the concepts of Pareto dominance and optimality are straightforward tools for determining the best trade-off solutions between conflicting objectives. An evolutionary algorithm is then chosen to carry out the search for the Pareto optimal solution (Fig. 5) for the cogeneration gas turbine used in [46], since evolutionary optimization techniques were conceived to deal with a set of solutions (a "population") to pursue their task. Consequently, a multi-objective Pareto-based evolutionary algorithm is able to make the population converge to the entire set of optimal solutions in a single run.

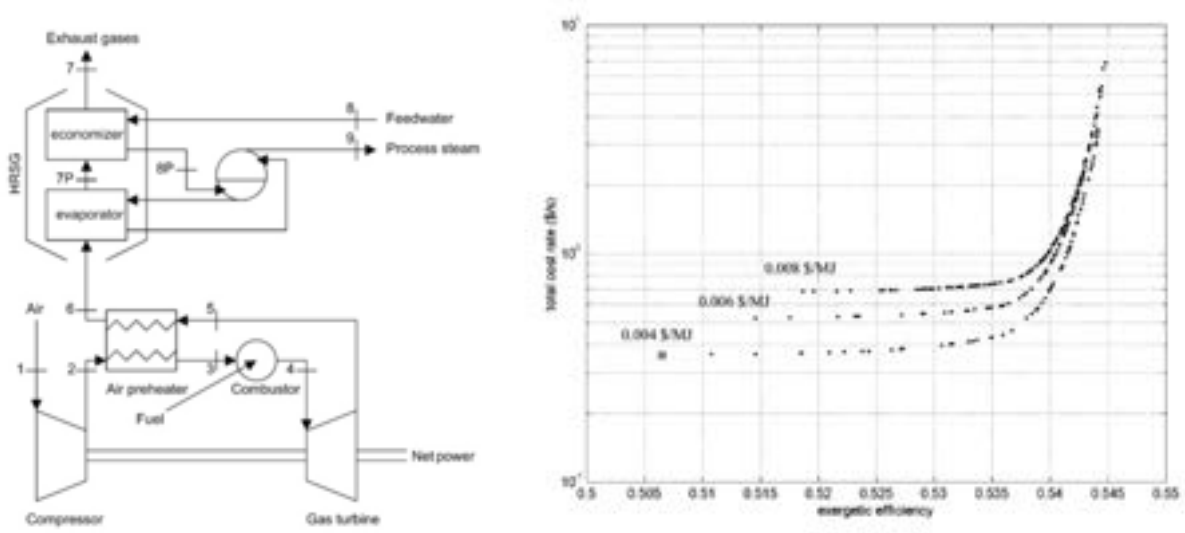

Figure 5. Pareto front (on the right) for different unit costs of fuel of a cogeneration gas turbine (on the left) [45] considering the total system cost rate ($/s) and the exergetic efficiency as objective functions.

The paper [47] shows how the design of the same cogeneration gas turbine in Fig. 5, as well as that of any thermal system, modifies if the optimization capabilities of the multi-objective approach are further exploited by adding an environmental objective function to the energetic and economic ones. The work compares and discusses the three-objective approach with a single-objective thermo-economic optimization and a two-objective energetic and economic optimization. In particular, the energetic, economic and environmental objective functions were defined as:

Energetic $$\varepsilon = \frac{\dot{W}_{NET} + \dot{m}_{steam}(e_9 - e_8)}{\dot{m}_{fuel} \cdot e_{9fuel}} \quad (4)$$

Economic $$\dot{C}_{total} = \dot{C}_{fuel} + \sum_i \dot{Z}_i \quad (5)$$

Environmental $$\dot{C}_{env} = c_{CO_2}\dot{m}_{CO_2} + c_{NO_x}\dot{m}_{NO_x} \quad (6)$$

The environmental one is expressed in terms of cost, weighting carbon dioxide and nitrogen oxide emissions according to their unit damage costs. Thus, a three dimensional spectrum of optimal solutions can be extracted from the space defined by the three objective functions by an evolutionary algorithm (Fig. 6).

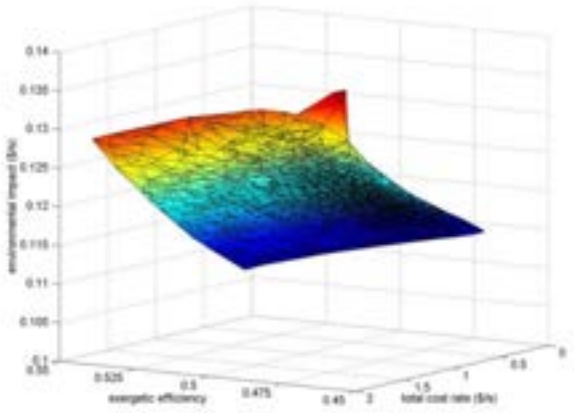

Figure 6. Optimal values of the three-objective functions (Pareto front) in Eqs (4), (5) and (6) [47].

The main novelty in that paper consists in considering the environmental impact no longer as a limitation to be met, according to legal regulations, but as an objective to be pursued. This paradigm shift, however, requires the correct formulation of the environmental objective function. Eq. (6) indicates that on the one hand it is necessary to consider local pollution related to toxic emissions, and on the other hand the impact on the atmosphere of elements that have a high global warming potential. In the design procedure this environmental goal is only partially independent from that of maximum efficiency, because achieving too high temperatures is environmentally pejorative. Of course, considering environmental impact as an objective instead of a constraint leads to a general rethinking of objective functions, as discussed below.

4. The need of proper objective functions for the whole society

The previous section showed how the design of energy conversion systems has naturally moved toward goals other than just maximum efficiency or maximum profit/cost. Indeed, the use of the design and operation of these systems have implications that go far beyond these goals. Thus, some questions naturally arise:

“Is efficiency the best energy goal? or is it instead absolute energy consumption? Are thermo-economic analyses sufficient, or should we better move toward thermo-X analysis? Which are the right environmental goals? Is decarbonization the best one? Is it sufficient to measure the environmental impact?”

As much as conversion technologies continually evolve over time, many of those involving the bulk of global consumption, and particularly those using fossil fuels, have reached levels close to the maximum achievable ones relative to unavoidable physical constraints (e.g., the Second Law of thermodynamics in case of thermal systems). Thus, it is reasonably not conceivable that further developments in technologies could contribute to efficiency gains for these systems that are relevant to the overall system. Moreover, the introduction of more efficient technologies often leads to the so-called “rebound effect” that, in turn, can offset, at least partially, the reduction in primary energy consumption associated with the efficiency gains [48]. On the other hand, it is certainly desirable that there be major increases in the efficiency of technologies based on renewable sources, but it is hardly conceivable that these can really become complete replacements for fossil fuels in a short period of time. Following the 2015 Paris Agreement on climate change mitigation actions adopted at the 21st Conference of the Parties [49], the legislations of the most technologically advanced states have evolved in the direction of promoting the development of renewable sources, and they have certainly been successful in terms of total installed capacity. However, the share of renewable energy consumption is struggling to grow significantly still remaining in the minority worldwide due to the concomitant increase in overall consumption together with the inherent low capacity factor of renewable sources (solar, wind, hydro in some cases). We can therefore state that,

"*From an energy perspective, the goal of efficiency should be considered concurrently with that of reducing overall consumption*."

Without this reduction, it will be difficult to achieve the increase in renewable share stated in the legislations, as, for instance, the European Green Deal [50], which aims at reaching carbon neutrality for European countries in 2050. Thus, the limitedness of the atmosphere and of every other natural element involved in energy generation (water, raw materials, ...) must necessarily direct us towards the search for new consumption patterns that reduce the overall energy consumption, which is the primary cause of changes in environmental balance.

The focus must then shift to the whole of society, no longer to the individual conversion plant, seeking the best interaction between different energy conversion and storage systems according to the objectives we want to pursue. Therefore, starting from the consideration that our society requires a complex multi-energy system and its associated energy distribution networks, we certainly cannot proceed only with a "plant-by-plant" optimization, and we must necessarily ask the following question:

"Which are the objectives of the society?"

Figure 7 shows a block scheme of the Italian energy system. The blocks included in the red-dotted box represent different types of energy conversion units, energy storage capacities and energy transport infrastructures. In the left side of the box, all categories of renewable and traditional energy sources are shown, while in the right side, all the energy demands. Each part of this very complex system can be modeled with the desired level of detail depending to the number and type (linear, bi-linear, non-linear) of the utilized equations. For example, it is possible to include many kinds of external constraints (e.g., the transportation limits imposed by the capacity of the energy networks). This flexibility allows build statewide models of design and operation that predict what the future system might look like, in relation to variations in boundary conditions that depend on human activities (demands, costs, legislation, ...) and more or less predictable changes in the availability of energy resources.

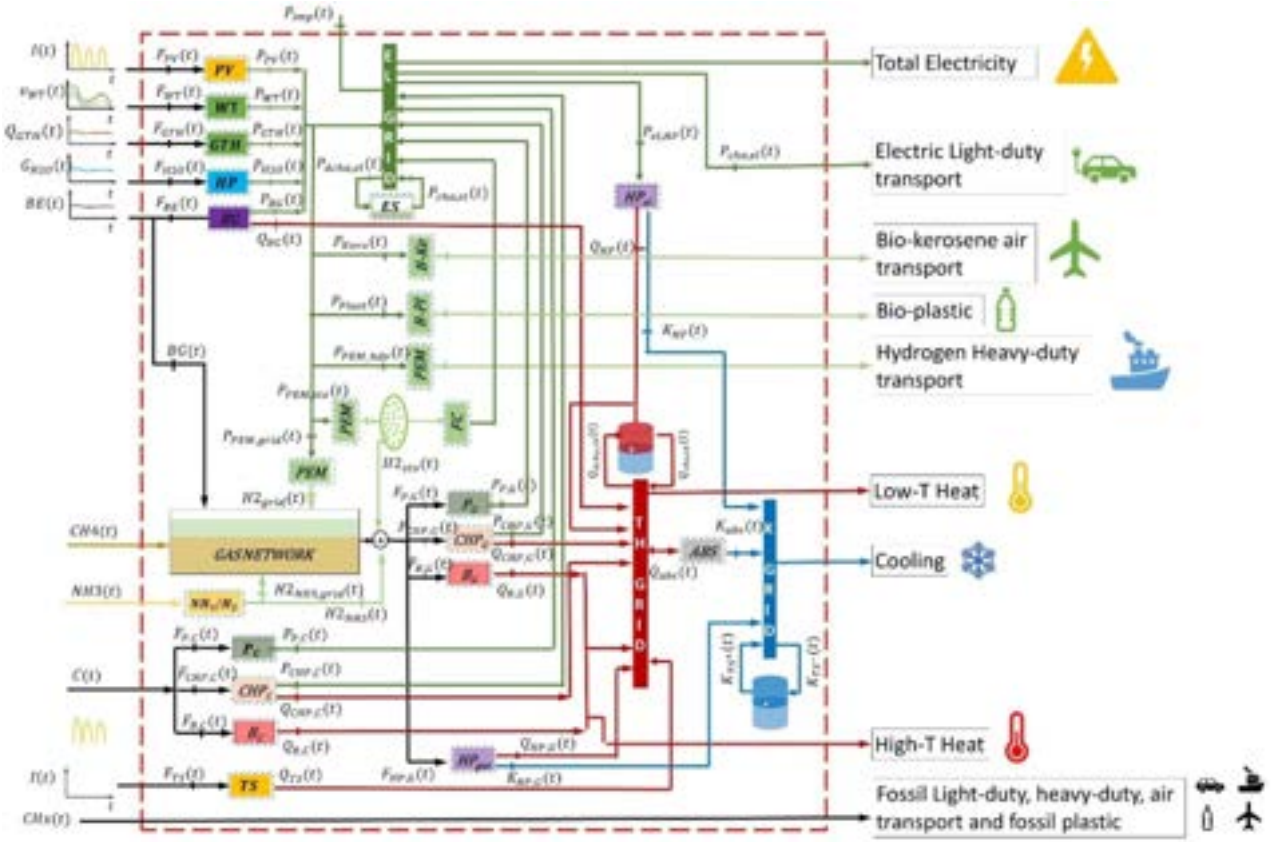

Figure 7. Superstructure of a multi-energy system representing the Italian energy system.

A representation like the one in Figure 7 could be made for any country, region, city, industrial or housing district in the world. However, certainly, this model would be very different from zone to zone. How might it look, for example, for a developing country? Again, some questions arise, which are not easy to answer:

"*What are the most sensible objective functions to consider for those systems that barely achieve survival conditions for the majority of the population?"*

"Are there universal goals toward which every state should converge?"

Certainly the goals must be enlarged, and thermo-economic or environomic analyses must also include other constraints than those strictly associated with the energy conversion (e.g., social and political ones) in addition

to the evolution of these constraints over time (dynamic optimization). Figure 8 shows shows the well-known seventeen goals of the United Nations [51] stated in 2015 as part of the 2030 Agenda for Sustainable Development. Those most directly related to energy conversion and consumption are the seventh (affordable and clean energy) and twelfth (responsible consumption and production). All the others are actually closely related to them because of any interaction with the environment and the socio-economic conditions of humanity. All 17 goals are well summarized, in the following three: **end poverty, protect the environment and ensure prosperity for all** [52]**.**

Figure 8. UN sustainable development goals [51].

The question is,

"*What can researchers, and particularly engineers, do to find realistic solutions to make the overall energy system as consistent as possible with these three general goals?*"

A certain and unambiguous answer is impossible, and would require investigating and establishing the meaning of "prosperity," and "poverty" in addition to knowing in a general sense what the best criteria are for truly defending the environment. What is certain is that some problems (poverty eradication) have a much higher priority than others, and this requires innovative models of intervention and development, which can also develop within market logic [53], and certainly a comprehensive global view of energy and environmental problems. On the other hand, it is equally certain that in every country, region, area of the World, there is the need to satisfy the current energy demands with an appropriate energy conversion system [54].

However, different countries have different "energy needs" and more or less urgent actions to undertake. We can measure prosperity with the Human Development Index [55], and increase this Index by increasing availability and consumption of energy of poor countries while keeping their already existing good equilibrium with environment. Conversely, to drastically reduce the environmental impact of "rich" (developed) countries, with high HDI but too high energy consumption, we must first rationalize the usage of energy to decrease the absolute value of primary energy consumption. This can be done by pushing low-consumption/low-environmental impact technologies. This necessity requires us to ask several questions, including:

"What does it mean to "waste" energy?" "How can the "minimum waste" goal (objective function) be defined?" Are there criteria for defining the minimum/proper energy needs of a human being regardless of location? What are the acceptable levels of consumption for the planet? "

Independently of the definition, the "waste objective function" must be minimized everywhere to meet the three general objectives mentioned above (end poverty, ensure prosperity for all, protect the environment).

Dealing with the *energy conversion process*, a *waste* can be defined as *the use of an excess of energy compared to the minimum required to fulfill a specified energy demand or to obtain a certain product*. All research in the field of energy conversion systems is, and has been, aimed at maximizing efficiency, which is equivalent to minimizing waste, defined in this way. However, this definition covers the energy conversion only, and does not consider the demand side, that is the way in which energy is consumed by the end users. Clearly, it has little effectiveness to seek waste reduction in energy conversion without seeking waste reduction in the use of energy itself. This issue obviously invokes the need to evaluate without conditioning or mistaken habits the ways in which energy is actually used, questioning the uses that are "not properly necessary" because they are overabundant compared to real needs. As such, they cannot be proposed to everybody, because

they would not be bearable by the ecosystem. Spreng [56] proposed a primary energy consumption target of 2000 W per capita ("*the 2000 W/capita society*") to be applied worldwide and that can be sustainable for both environment and society. However, this target is utopistic for the Author himself.

This article was written a few years ago, but this still open problem has subsequently been only much discussed but little addressed, thus greatly lengthening the energy transition towards a renewable system. The delay in becoming aware of the impossibility for the environment to bear an excessive consumption of energy (and consumer goods in general) now leads to the need to intervene "immediately" to avoid even catastrophic consequences [57]. However, this is not rationally possible due to the long installation times of the plants generating the huge renewable energy needed to replace all fossil energy, and requires first considering those interventions that have the best impact on the environment and society as a whole. Given the complexity of the problem, experts from the various disciplines involved propose different recipes, including the need to accept these catastrophic events, or to return to technologies already abandoned for safety and health reasons (nuclear) [58].

In the final analysis, it is a matter of considering the energy problem as a global problem involving all humanity, where the excessive consumption of some leads to energy shortages for others, and thus results, if nothing else, in a "lack of respect" toward them. Of course, these considerations cannot disregard the "models" of societies of individual countries. Many countries have acquired the so-called "western" model based on the search for GDP growth as the only criterion for increasing the individual's wealth, although often disregarding adequate wealth distribution criteria. Is this the way? Certainly, this approach has led to an enormous improvement in the well-being of many people, and of entire countries as a whole. However, at the same time, it can be certainly be improved to ensure a more equitable distribution of energy use and the benefits that come with it. Can "prosperity for all" be ensured by increasing GDP, regardless of appropriate distribution criteria and regardless of the fact that there are other cultural and developmental patterns of individual countries? Interesting ideas on this issue have been proposed and applied by a former president of Uruguay, Mujica (see for example his speech to the United Nations General Assembly on September 24, 2013 [59]). Moreover, some Authors proposed to integrate social science in energy research and energy policy (see, e.g., Sovacool et al. [60] and Spreng [61]). In any case, this issue must shift the attention of engineers to the "consumption" side, as highlighted in the following Section.

5. From engineering of "energy conversion" to engineering of "energy utilization"

Most of the discussion in Section 4 focused on the critical need to reduce overall energy consumption, while improving the efficiency of individual energy conversion systems, with an effort to achieve as much as possible the three general principles enunciated in that section: end poverty, ensure prosperity for all, and protect the environment."

Having established that the generation efficiency of individual energy conversion systems is generally very difficult to improve for most existing systems, attention must necessarily shift to what might be the most effective actions to reduce our society's total energy consumption. Below we try to list some of them:

- Actions aimed at better integrating individual conversion and storage units to take advantage of potential generation synergies between them, thereby optimizing the design and operation of multi-energy systems that supply energy to our society [62–64];
- Actions aimed at aggregating different local generation and demand loads of different energy users into "energy communities" to reduce demand peaks and thus the required power to be installed [65–67]. Consequently, also the efficiency of the plant and the environmental impact in the operation would be improved, as they it would work at more constant load.
- Actions aimed at more efficiently coupling the entire generation system with the entire "demand system" [54] to size and deploy each plant in the most efficient, least costly, and least impactful way for the entire generation-demand system.
- Actions and criteria aimed at reducing the absolute value of demand, such as through appropriate price- and incentive-based demand-response programs [68,69], or appropriate incentive policies, public awareness and education on proper energy use starting from elementary school training levels.

Actions to limit the maximum amounts of energy available for individual use should not be ruled out either, since it is quite inconceivable that a reduction in overall consumption (particularly, but not only, of fossil fuels) could take place without limitations on the consumption of individuals. However, it should be considered that these limitations on direct energy consumption (for individual use, as heating, cooling, etc.) would still not include all indirect energy consumption, associated with the purchase of goods (and even devices that use renewable energy but are not "strictly necessary," still involve energy consumption for construction and disposal of materials).

The list of actions listed can be summarized as the search for the best possible integration among the elements that make up a society's energy system, namely the energy conversion plants, the networks that distribute it, and the users who consume it. This integration requires a substantial paradigm shift in the overall design and

management of the energy system. The system based on individual production facilities for individual users must be replaced by a system designed to serve the whole society, and the whole society must constitute itself as a community of people who consume energy to improve (or maintain) a better living condition. The design of the system must therefore be unique and optimized for the common good. This vision, which is reasonably utopian, can nevertheless be a reference to be pursued. Actions concerning aggregations of users into energy communities certainly go in this direction.

We stress the importance of aggregation as a key element for a prosperous future of society. In this regard, actions should start from local communities with the support of politicians. Local governments should rank different utilities (i.e., energy users acting as consumers or prosumers) to identify those with the greatest synergies and coupling possibilities. The energy “demand system” could then consists of the aggregation of these local communities, rather than being composed of individual utilities, with the ultimate goal of achieving an overall energy demand curve that is more consistent with the total renewable availability curve, and at the same time, leading to a net reduction of the total consumption. This would have the added benefit of reducing the need for energy storage, resulting in lower costs for the system as a whole. The search for mechanisms ensuring a fair distribution of benefits from user aggregations, as well as a fair distribution of costs associated with the installation of new renewable plants among those who benefit from them, must therefore become a central theme of research in the field of energy conversion systems. Efforts in this direction have been already the subject of several research [66,67], and may also benefit from allocation criteria based also on exergoeconomics analysis [44]. It is natural to think that every place in the world is different in habits, religions, customs, but every place can benefit from aggregation and interaction, while respecting and recognizing individual specificities. Energy policies must therefore seek universal means of aggregation, such as the identification of the most suitable energy users that could participate into energy communities, fair criteria for the distribution of profits resulting from aggregation, and compensation mechanisms for those who may suffer damages as a result of aggregation itself, or for those who may not be able to fulfill their commitments due to force majeure (e.g., illness).

6. The dynamic optimization model of the society or of its portions

The need for an integrated design and management of the whole energy system, including generation and storage plants, energy distribution networks and users (with different habits and customs), requires the development of tools that allow modelling this complex system in its totality by considering in it all variables involved, and especially those on which actors from different disciplines (i.e., engineering, economics, sociology, philosophy, politics) can intervene. The models should take into account contextually, on one hand, all the laws of physics, thermodynamics, and chemistry that govern the energy processes and, on the other hand, the design and operational constraints related to the above-mentioned disciplines, and the laws of the countries in which the energy systems operate. Eventually, these models represent the society in its entirety because of their capability to describe the relationship between energy problems and society [70].

Given the potentially huge size of the optimization problem, the degree of detail of the models will necessarily have to decrease as the size of the geographical area under consideration increases. Thus, if the size is that of an entire country or region, plants of the same type may be aggregated into categories, users may be aggregated by types (e.g., low-temperature thermal, high-temperature thermal, electric), and networks may be considered by common characteristics (e.g., high, medium, and low-pressure gas network, or high-, medium-, low-voltage electric networks). Conversely, if the size of the geographic area is narrower, such as housing or industrial districts, all individual energy systems (i.e., energy conversion and storage units) and interconnections (i.e., electric, thermal and gas grids) can be modeled precisely, without approximations. For municipal governments, the boundaries of analysis could be whole municipalities or parts of them, in which it will be possible to model in detail not only the associated plants and distribution networks with each specific existing constraint, but also the utilities, proposing aggregation mechanisms to create benefits for both individual members and the community.

In such a complex reality, it is certainly useful for the individual (or entity, company,..) to decide on the "energy interventions" that are most convenient locally, but it is difficult to think that these local interventions can always be consistent with the search for the overall optimum of the society in which they are implemented.

Thus, there is a clear need to operate both locally and globally, so that local interventions are consistent with those of a global nature, i.e., relating to the region-state, or in general to the overall context/society in which they are carried out.

This coherence highlights the pressing need to start from global models, which give the general guidelines for appropriate energy policies, within which local interventions fit.

Several questions can be asked here as well:

What kind of structure, equations, variables, and what kind of evaluations can this model perform? Is it possible to build models that include all the variables involved without becoming overly complex and such that they

require excessive computational time, preventing their simple use, and such that the benefits that can be achieved at the overall level can be immediately assessed? What are the objectives in using these models and what is the actual utility of the evaluations produced?

Below an attempt to answer:

- The overall model must certainly include sub-models that are capable of evaluating the behavior of all the conversion and storage systems included in them, both under design and off-design conditions. These sub-models include mass and energy balances of these components and the chemical and physical properties of the fluids involved, and should be included in databases that can be used by the overall model.

- The model arranges these sub-models so that the individual conversion and storage units can be aggregated not only with each other but with the distribution networks in order to form the model of the overall system;

- The model must include time series of users' energy demands, evaluated on a deterministic or stochastic basis when necessary. The model must also be capable of "managing" these demands according to utility aggregation criteria [71] and demand-response programs [72].

- The overall model is part of an optimization problem that must be solved by an algorithm capable of considering different sets of decision variables.

- The model must consider also all constraints other than energy-technology constraints, i.e. those associated with the economic environment (investment costs, costs and prices of different forms of energy and their variability over time,..) and the natural and regulatory environment (limitations on emissions, incentives,..) as well as arising from social issues (acceptability and acceptance and consequent time for installation, use of labor, working conditions, etc....).

- Goals (objective function(s)) should be clearly established (Section 4) and properly expressed in mathematical terms.

Figure 9 shows the conceptual scheme of a computational platform capable of building an energy system model that includes the above-mentioned features.

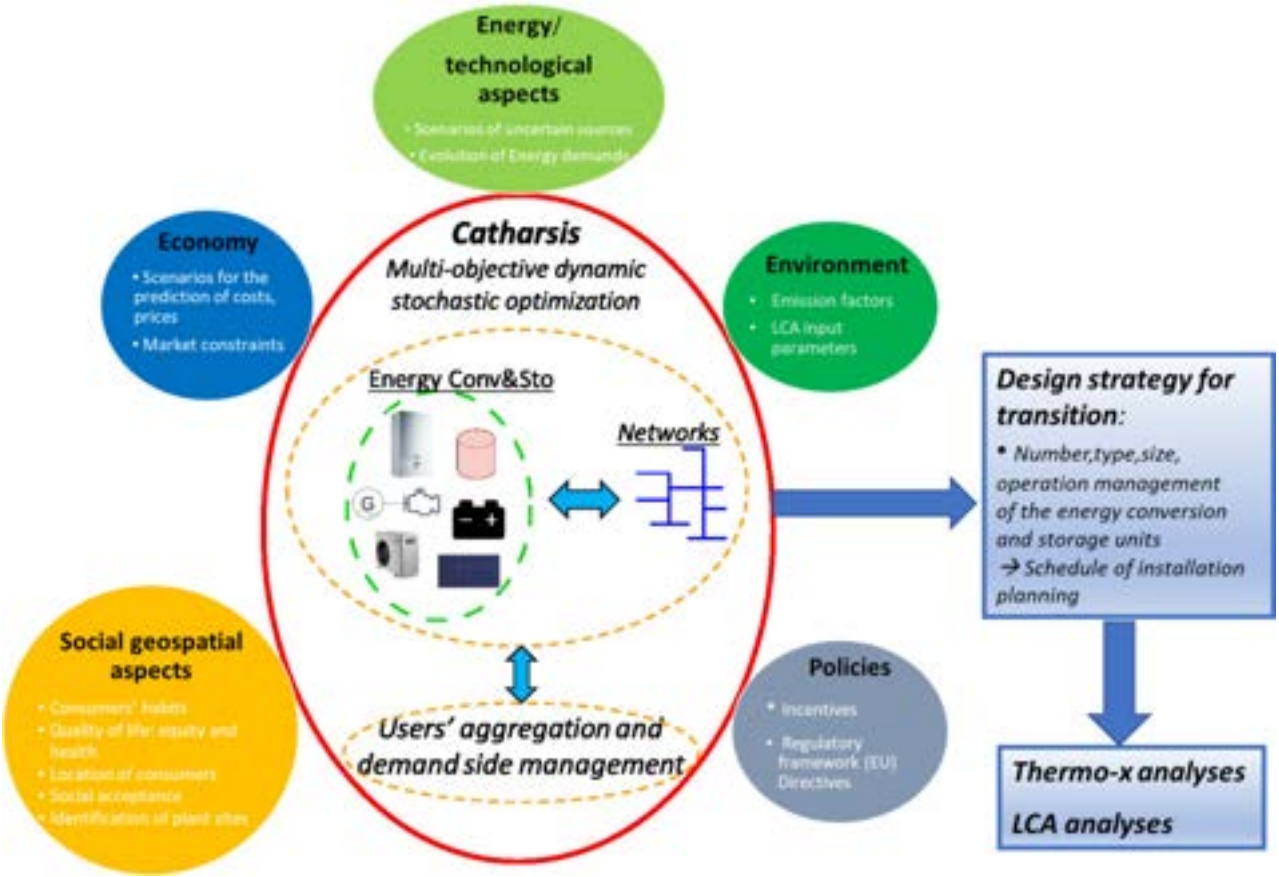

Figure 9. Calculation platform to evaluate the schedule of installation planning of new energy conversion/storage systems and network in the future.

The platform builds the model of the considered system from a superstructure (red part in the center) containing (in a database) all available conversion and storage units in the considered geographical area. The platform chooses the optimal number, type, and size of these units and builds the network to connect them together and distribute power to users according to the optimal value (minimum or maximum) of one or more target functions.. The same central part (red) of the superstructure includes the optimization procedure driven by an appropriate algorithm capable of evaluating the objective function for each set of values of the system's independent/decision variables. The construction of the model requires setting all constraints arising not only from the technological-energy limitations of individual conversion and storage facilities, but also economic (investment costs, costs and prices of energy consumed and sold,...), environmental (limitations on emissions, materials to be used...), social (acceptability of renewable and fossil fuel based plants, occupation of areas intended for other uses,...), political-legislative (restrictions imposed by legislation, incentives, taxes,...) constraints. The nature of the model is dynamic, since all variables involved are time-dependent. As highlighted in Section 4, this feature is crucial given the need to shape the energy system of the future, especially in the "energy transition", by progressively choosing the energy conversion units that best fit to a specific location at a specific time. The model has a Mixed-Integer Linear Programming formulation, where integer variables are used to decide the inclusion or exclusion of conversion and storage units in design problems, and their activation or deactivation in operation problems. General features of the models have been presented in [73,74]. The last stage of development of the platform [75] concerns the contextual search for the optimal configuration of the energy generation and storage system and the configuration of the networks that distribute the energy produced. This comprehensive view of the system can also include utility management, through organization into energy communities or membership in demand-response programs. Once the optimal configuration and design variables of the generation/accumulation units and energy networks are defined, a final thermoeconomic/environmental or life-cycle assessment of the overall system is performed to obtain a complete picture of its performance and environmental compatibility (bottom right in Fig. 9). In this way, the platform stands as an essential tool for designing and managing the energy system, from generation to demand for the portion of "society" under consideration.

7. Conclusions

This paper is an attempt to trace in a simple way the extraordinary evolution in the research on energy conversion systems that has taken place in recent years. In particular, the purpose was to see how thermoeconomic analyses have played a pioneering role in expanding energy-only analyses toward the whole set of disciplines that are necessarily involved in the design and use of an energy system, starting with economics. The initial focus on increasing the exergetic efficiency of large fossil fuel plants that supplied almost all of the energy for end uses necessarily shifted to the simultaneous search for the best trade-off between this increase and cost reduction, taking into account all the environmental issues involved in the conversion and use of the energy generated. It is precisely this necessary consideration of the "environment," understood not only as “nature” but also as "humanity" inhabiting the world, that has shifted the focus from the individual plant to larger geographic portions in which there are different individuals with different energy needs. These portions of the universe, and ultimately the whole world, require that we design the overall energy system of the future in the most sustainable way possible, to give future generations the same or even better opportunities for consumption and well-being as existing ones. To this end, the work of the energy engineer must not be concerned with the individual plant but with all the plants included in the geographical portion under consideration and the distribution networks to users, integrating closely with that of all the actors involved in the design of the society of the future. Thus, the paper shows that other types of "X" analysis should be added to exergoeconomic analyses to include all aspects involved in energy use, with the ultimate goal of reducing overall consumption and distributing it more evenly around the world as the only means of achieving a truly sustainable system. In this direction, the paper also demonstrates the importance of forecasting models that are capable of predicting and optimizing the design and operation of the energy system of the future by considering the real physical processes involved along with all the external constraints, while maintaining a simple structure. This feature allows useful and realistic results to be obtained quickly and in a way that is easily understood even by non-"insiders." The ambition is for these models to become commonly used, especially in public administrations and private companies, to build an overall system that is as consistent as possible with the sustainability needs of society as a whole.

Nomenclature

c	cost per monetary unit (*$/kJ*)
$\dot{C}$	total cost flow rate (*$/s*)
CHP	Combined Heat and Power
e	specific exergy (*kJ/kg*)
$\dot{E}$	exergy flow rate (*kJ/s*)
$\dot{m}$	mass flow rate (*kg/s*)

$MINLP$ Mixed-Integer Non-Linear Programming

$\dot{W}$ mechanical power (*kW*)

$\dot{Z}$ amortization cost flow rate (*$/s*)

ε energetic efficiency

η exergetic efficiency

Subscripts and superscripts

$e, 2$ exit

F related to a fuel stream

$i, 1$ inlet

k related to k-th component

P related to a product stream

q heat

w work

References

[1] Keenan JH. A steam chart for second law analysis. Mech Eng 1932;54:11.

[2] Evans RB, Tribus M. A Contribution to the Theory of Thermoeconomics, UCLA, Dept. of Engr. Report; 1962.

[3] El-Sayed YM, Evans RB. Thermoeconomics and the Design of Heat Systems. Journal of Engineering for Power 1970;92:27–35. https://doi.org/10.1115/1.3445296.

[4] Gaggioli RA, Wepfer WJ. Exergy economics: I. Cost accounting applications. Energy 1980;5:823–37. https://doi.org/10.1016/0360-5442(80)90099-7.

[5] Tsatsaronis G, Winhold M. Exergoeconomic analysis and evaluation of energy-conversion plants-II. Analysis of a coal-fired steam power plant. Energy 1985;10:81–94. https://doi.org/10.1016/0360-5442(85)90021-0.

[6] Tsatsaronis G, Winhold M. Exergoeconomic analysis and evaluation of energy-conversion plants. Part I: A new general methodology. Part II: Analysis of a coal-fired steam power plant. Energy 1985;10:69–94. https://doi.org/10.1016/0360-5442(85)90020-9.

[7] Valero A, Lozano MA, Muñoz M. A general theory of exergy saving. Part I: On the exergetic cost. Part II: On the thermoeconomic cost. Part III: Energy saving and thermoeconomics. Computer-Aided Engineering and Energy Systems: Second Law Analysis and Modelling 1986;3:1–22.

[8] Lozano MA, Valero A. Theory of the exergetic cost. Energy 1993;18:939–60. https://doi.org/10.1016/0360-5442(93)90006-Y.

[9] Lazzaretto A, Tsatsaronis G. On the Calculation of Efficiencies and Costs in Thermal Systems. ASME International Mechanical Engineering Congress and Exposition, Proceedings (IMECE) 1999;1999-B:421–30. https://doi.org/10.1115/IMECE1999-0852.

[10] Lazzaretto A, Tsatsaronis G. On the Quest for Objective Equations in Exergy Costing. ASME International Mechanical Engineering Congress and Exposition, Proceedings (IMECE) 1997;1997-G:197–210. https://doi.org/10.1115/IMECE1997-0989.

[11] Lazzaretto A, Tsatsaronis G. A general process-based methodology for exergy costing. ASME Advanced Energy Systems Division, Ed. A.B. Duncan, J.Fiszdon, D. O'Neal, K.Den Braven. AES-vol. 36 pp. 413- 428. Atlanta (USA), November 17-22. ISBN: 0-7918-1527-7, United States: American Society of Mechanical Engineers, New York, NY (United States); 1996.

[12] Lazzaretto A, Tsatsaronis G. SPECO: A systematic and general methodology for calculating efficiencies and costs in thermal systems. Energy 2006;31:1257–89. https://doi.org/10.1016/j.energy.2005.03.011.

[13] Lazzaretto A, Andreatta R. Algebraic Formulation of a Process-Based Exergy Costing Method. Thermodynamics and the Design, Analysis, and Improvement of Energy Systems, AES-Vol. 35, 1995.

[14] Lazzaretto A, Tsatsaronis G. Comparison Between Speco-Based and Functional Exergoeconomic Approaches. American Society of Mechanical Engineers, Advanced Energy Systems Division (Publication) AES 2001;41:463–78. https://doi.org/10.1115/IMECE2001/AES-23656.

[15] Frangopoulos CA. Thermoeconomic functional analysis: a method for optimal design or improvement of complex thermal systems. Georgia Institute of Technology; 1983.

[16] Frangopoulos CA. Thermo-economic functional analysis and optimization. Energy 1987;12:563–71. https://doi.org/10.1016/0360-5442(87)90097-1.

[17] Von Spakovsky MR. A practical generalized analysis approach to the optimal thermoeconomic design and improvement of real-world thermal systems. Georgia Institute of Technology; 1986.

[18] Von Spakovsky MR, Evans RB. The foundations of engineering functional analysis. Proceedings of FLOWERS, vol. 90, 1990, p. 445–72.

[19] von Spakovsky MR, Evans RB. The Design and Performance Optimization of Thermal Systems. J Eng Gas Turbine Power 1990;112:86–93. https://doi.org/10.1115/1.2906482.

[20] Lazzaretto A, Macor A. Marginal and Average Unit Costs in Thermoeconomic Functional Analysis. In: Carnevale E, Manfrida G, Martelli F, editors. Florence World Energy Research Symposium (FLOWERS), Florence: SGEditoriali Padova; 1994, p. 133–48.

[21] Lazzaretto A, Macor A. Direct Calculation of Average and Marginal Costs From the Productive Structure of an Energy System. J Energy Resour Technol 1995;117:171–8. https://doi.org/10.1115/1.2835337.

[22] Reini M, Lazzaretto A, Macor A. Average structural and marginal costs as result of a unified formulation of the thermoeconomic problem. Proc. of Second Law Analysis of Energy Systems: Towards the 21-st Century, Esagrafica Roma; 1995, p. 307–23.

[23] Lazzaretto A. Fuel and product definitions in cost accounting evaluations: Is it a solved problem. Proc. 12th Joint Eur. Thermodyn. Conf., Brescia, 2013, p. 244–50.

[24] Bejan A, Tsatsaronis G, Moran MJ. Thermal design and optimization. John Wiley & Sons; 1995.

[25] Frangopoulos CA. Introduction to environomic analysis and optimization of energy-intensive systems. ASME, NEW YORK, NY(USA) 1992:231–9.

[26] Frangopoulos C, von Spakovsky M. A global environomic approach for energy systems analysis and optimization (Part I). Energy systems and ecology: proceedings of the International Conference ENSEC'93, 1993, p. 123–32.

[27] Curti V, Favrat D, von Spakovsky MR. An environomic approach for the modeling and optimization of a district heating network based on centralized and decentralized heat pumps, cogeneration and/or gas furnace. Part I: Methodology. Part II: Application. International Journal of Thermal Sciences 2000;39:721–41.

[28] Borchiellini R, Massardo AF, Santarelli M. Carbon tax vs CO2 sequestration effects on environomic analysis of existing power plants. Energy Convers Manag 2002;43:1425–43.

[29] Borchiellini R, Massardo A, Santarelli M. A carbon exergy tax evaluation based on the efficient use of energy resources: a case study. International Journal of Thermodynamics 2000;3:129–45.

[30] Tsatsaronis G, Park M-H. On avoidable and unavoidable exergy destructions and investment costs in thermal systems. Energy Convers Manag 2002;43:1259–70.

[31] Kelly S, Tsatsaronis G, Morosuk T. Advanced exergetic analysis: Approaches for splitting the exergy destruction into endogenous and exogenous parts. Energy 2009;34:384–91.

[32] Morosuk T, Tsatsaronis G. Advanced exergy-based methods used to understand and improve energy-conversion systems. Energy 2019;169:238–46. https://doi.org/10.1016/j.energy.2018.11.123.

[33] Valero A, Torres C, Lozano M. On causality in organized energy systems. Part III: Theory of perturbations. Proceedings of Flowers90: A Future for Energy 1990:401–10.

[34] Reini M. Analisi e Sviluppo dei Metodi Termoeconomici per lo Studio degli Impianti di Conversione dell'Energia (in Italian). University of Padova, 1994.

[35] Torres C, Valero A, Serra L, Royo J. Structural theory and thermoeconomic diagnosis: Part I. On malfunction and dysfunction analysis. Energy Convers Manag 2002;43:1503–18.

[36] Toffolo A, Lazzaretto A. A New Thermoeconomic Method for the Location of Causes of Malfunctions in Energy Systems. J Energy Resour Technol 2007;129:1–9. https://doi.org/10.1115/1.2424960.

[37] Lazzaretto A, Toffolo A. A Critical Review of the Thermoeconomic Diagnosis Methodologies for the Location of Causes of Malfunctions in Energy Systems. J Energy Resour Technol 2006;128:335–42. https://doi.org/10.1115/1.2358148.

[38] Valero A, Correas L, Zaleta A, Lazzaretto A, Verda V, Reini M, et al. On the thermoeconomic approach to the diagnosis of energy system malfunctions Part 1: The TADEUS problem. Energy 2004;29:1875–87. https://doi.org/10.1016/j.energy.2004.04.053.

[39] Valero A, Correas L, Zaleta A, Lazzaretto A, Verda V, Reini M, et al. On the thermoeconomic approach to the diagnosis of energy system malfunctions Part 2. Malfunction definitions and assessment. Energy 2004;29:1889–907. https://doi.org/10.1016/j.energy.2004.03.008.

[40] Borel L, Favrat D. Thermodynamics and energy systems analysis: from energy to exergy. EPFL press; 2010.

[41] Lazzaretto A, Macor A, Mirandola A, Reini M. Thermoeconomic Analysis of energy recovery and cogeneration plants under variable load conditions. Proc. of Analysis of THermal and ENergy Systems "ATHENS '91," ASME; 1991, p. 383–94.

[42] Lazzaretto A. Studio, Dimensionamento e Criteri di Valutazione Tecnico-Economica di un Nuovo Tipo di Impianto di Recupero Energetico con Cogenerazione (in Italian) ("Study, Sizing and Technical-Economic Evaluation Criteria of a New Type of Energy Recovery Plant with Cogeneration"). University of Padova, 1992.

[43] Lazzaretto A. A critical comparison between thermoeconomic and emergy analyses algebra. Energy 2009;34:2196–205. https://doi.org/10.1016/j.energy.2008.10.020.

[44] Lozano MA, Serra LM, Pina EA. Optimal design of trigeneration systems for buildings considering cooperative game theory for allocating production cost to energy services. Energy 2022;261. https://doi.org/10.1016/j.energy.2022.125299.

[45] Toffolo A, Lazzaretto A. Evolutionary algorithms for multi-objective energetic and economic optimization in thermal system design. Energy 2002;27:549–67. https://doi.org/10.1016/S0360-5442(02)00009-9.

[46] Valero A, Lozano MA, Serra L, Tsatsaronis G, Pisa J, Frangopoulos C, et al. CGAM problem: Definition and conventional solution. Energy 1994;19:279–86. https://doi.org/10.1016/0360-5442(94)90112-0.

[47] Lazzaretto A, Toffolo A. Energy, economy and environment as objectives in multi-criterion optimization of thermal systems design. Energy 2004;29:1139–57. https://doi.org/10.1016/j.energy.2004.02.022.

[48] Greening LA, Greene DL, Difiglio C. Energy efficiency and consumption — the rebound effect — a survey. Energy Policy 2000;28:389–401. https://doi.org/10.1016/S0301-4215(00)00021-5.

[49] The Paris Agreement | UNFCCC n.d. https://unfccc.int/process-and-meetings/the-paris-agreement (accessed May 15, 2023).

[50] A European Green Deal n.d. https://commission.europa.eu/strategy-and-policy/priorities-2019-2024/european-green-deal_en (accessed May 15, 2023).

[51] THE 17 GOALS | Sustainable Development n.d. https://sdgs.un.org/goals (accessed May 15, 2023).

[52] Take Action for the Sustainable Development Goals - United Nations Sustainable Development n.d. https://www.un.org/sustainabledevelopment/sustainable-development-goals/ (accessed May 15, 2023).

[53] Yunus M. Creating a world without poverty: Social business and the future of capitalism. Public affairs; 2009.

[54] Lazzaretto A, Toffolo A. Optimum Choice of Energy System Configuration and Storages for a Proper Match between Energy Conversion and Demands. Energies (Basel) 2019;12:3957.

[55] Human Development Index | Human Development Reports n.d. https://hdr.undp.org/data-center/human-development-index#/indicies/HDI (accessed May 15, 2023).

[56] Spreng D. Distribution of energy consumption and the 2000 W/capita target. Energy Policy 2005;33:1905–11. https://doi.org/10.1016/J.ENPOL.2004.03.023.

[57] Mercalli L. Non c'è più tempo: come reagire agli allarmi ambientali (in Italian)("There is no more time: how to react to environmental alarms"). 2020.

[58] Gates B. How to Avoid a Climate Disaster: The Solutions We Have and the Breakthroughs We Need. 2021.

[59] Uruguayan President focuses on climate change, environment in UN Assembly speech | UN News n.d. https://news.un.org/en/story/2013/09/450362 (accessed May 15, 2023).

[60] Sovacool BK, Ryan SE, Stern PC, Janda K, Rochlin G, Spreng D, et al. Integrating social science in energy research. Energy Res Soc Sci 2015;6:95–9. https://doi.org/10.1016/J.ERSS.2014.12.005.

[61] Spreng D. On physics and the social in energy policy. Energy Res Soc Sci 2017;26:112–4. https://doi.org/10.1016/J.ERSS.2017.01.011.

[62] Rech S, Lazzaretto A. Smart rules and thermal, electric and hydro storages for the optimum operation of a renewable energy system. Energy 2018;147:742–56. https://doi.org/10.1016/j.energy.2018.01.079.

[63] Gabrielli P, Gazzani M, Martelli E, Mazzotti M. Optimal design of multi-energy systems with seasonal storage. Appl Energy 2018;219:408–24. https://doi.org/10.1016/j.apenergy.2017.07.142.

[64] Rech S, Casarin S, Silva CS, Lazzaretto A. University campus and surrounding residential complexes as energy-hub: a MILP optimization approach for a smart exchange of solar energy. Energies (Basel) 2020;13:2919.

[65] Cosic A, Stadler M, Mansoor M, Zellinger M. Mixed-integer linear programming based optimization strategies for renewable energy communities. Energy 2021;237. https://doi.org/10.1016/j.energy.2021.121559.

[66] Volpato G, Carraro G, Cont M, Danieli P, Rech S, Lazzaretto A. General guidelines for the optimal economic aggregation of prosumers in energy communities. Energy 2022;258:124800. https://doi.org/10.1016/J.ENERGY.2022.124800.

[67] Dal Cin E, Carraro G, Volpato G, Lazzaretto A, Danieli P. A multi-criteria approach to optimize the design-operation of Energy Communities considering economic-environmental objectives and demand side management. Energy Convers Manag 2022;263. https://doi.org/10.1016/j.enconman.2022.115677.

[68] Niu J, Tian Z, Zhu J, Yue L. Implementation of a price-driven demand response in a distributed energy system with multi-energy flexibility measures. Energy Convers Manag 2020;208. https://doi.org/10.1016/j.enconman.2020.112575.

[69] Luo Z, Hong SH, Ding YM. A data mining-driven incentive-based demand response scheme for a virtual power plant. Appl Energy 2019;239:549–59. https://doi.org/10.1016/j.apenergy.2019.01.142.

[70] Nadesan M, Pasqualetti M, Keahey J. Energy Democracies for Sustainable futures. Elsevier; 2022. https://doi.org/10.1016/B978-0-12-822796-1.09983-6.

[71] Hoffmann M, Kotzur L, Stolten D, Robinius M. A review on time series aggregation methods for energy system models. Energies (Basel) 2020;13:641.

[72] Bahlawan H, Castorino GAM, Losi E, Manservigi L, Spina PR, Venturini M. Optimal management with demand response program for a multi-generation energy system. Energy Conversion and Management: X 2022;16. https://doi.org/10.1016/j.ecmx.2022.100311.

[73] Rech S. Smart energy systems: Guidelines for modelling and optimizing a fleet of units of different configurations. Energies (Basel) 2019;12:1320.

[74] Danieli P, Lazzaretto A, Al-Zaili J, Sayma A, Masi M, Carraro G. The potential of the natural gas grid to accommodate hydrogen as an energy vector in transition towards a fully renewable energy system. Appl Energy 2022;313:118843. https://doi.org/10.1016/J.APENERGY.2022.118843.

[75] Dal Cin E, Carraro G, Lazzaretto A, Tsatsaronis G, Volpato G, Danieli P. Integrated design and operation optimization of multi-energy systems including energy networks. Submitted to ECOS2023, The 36th International Conference on Efficiency, Cost, Optimization, Simulation and Environmental Impact of Energy Systems, 2023.

On the Future of Exergy-based Methods

George Tsatsaronis

Chair of Energy Engineering and Environmental Protection
Technische Universität Berlin, Berlin, Germany
georgios.tsatsaronis@tu-berlin.de

Abstract:

In 1984 the author coined the term *exergoeconomics* to replace the term *thermoeconomics* when *exergy costing* is used in the combination of an exergetic analysis with a cost analysis and to emphasize the role of exergy in the efforts to reduce the product cost. He also developed a general exergoeconomic methodology based on appropriate definitions of the "product" and "fuel" for each component of an energy conversion system and on exergy-based variables. These definitions and the application of exergoeconomics were generalized by A. Lazzaretto and the author in 2006 in an approach based on specific costs (*SPECO approach*).

Mayer and the author coined in 2009 the term exergoenvironmental analysis for a combination of an exergy analysis with a life-cycle analysis when exergy is used to assign environmental impacts to streams. An exergoenvironmental analysis uses the methodological background of the above exergoeconomic methods.

Starting in 2002, the author and later, in cooperation with T. Morosuk and co-workers at TU Berlin, developed the advanced exergy-based methods, which are based on the notion that the inefficiencies (exergy destruction and exergy loss), the costs, and the environmental impacts can be split into avoidable/unavoidable and endogenous/exogenous parts, to improve understanding of the formation process of inefficiencies, costs and environmental impacts within an energy conversion system, to reduce the limitations of the conventional exergy-based methods, and to facilitate system optimization.

As often happens, after their introduction, all the above terms and methods have been misused and misinterpreted by some other authors.

This paper very briefly reviews past contributions by the author and some other exergy practitioners and discusses future developments.

The exergy-based methods allow for a comprehensive and consistent simultaneous evaluation of the performance of an energy conversion system from the thermodynamic, economic, and environmental viewpoints. However, the advanced exergy-based methods need further investigations to be generalized, integrated and to reduce their subjectivity as well as the efforts and time required for their application. Development of appropriate software and short-cut methods will facilitate their use by researchers and engineers in industry and the applications of exergy-based methods in energy-intensive industrial processes for multiobjective optimization purposes.

Keywords:
Thermoeconomics; Exergoeconomics; Exergoenvironmental analysis; Advanced exergy-based methods; Optimization of energy systems.

1. Introduction

In the analysis, evaluation and optimization of energy-conversion systems (ECS), progress has been made every time the limitations of an existing method have been identified and solutions for overcoming at least some of these limitations have been developed. Thus, after realizing that an energy-based method can lead to misleading results and conclusions, the exergetic analysis, which combines the concepts of energy and entropy, was adopted as the appropriate method for analyzing and evaluating ECS from the thermodynamic viewpoint. All alternative terms used to characterize an exergetic analysis (e.g., the term "second-law analysis") are not accurate, because this analysis combines the second *and* the first laws of Thermodynamics.

An exergetic analysis identifies the location, magnitude and causes of inefficiencies within an ECS. The inefficiencies are measured in terms of exergy destruction and exergy loss [1]. Based on the results received by an exergetic analysis, changes in the design and operation of an ECS can be identified to improve its exergetic efficiency, which is the best variable for evaluating the thermodynamic performance of an ECS. An exergetic analysis can be applied also to very complex systems and is the most effective method for evaluating and improving the thermodynamic performance of a system. Various variables can be used to measure the performance of an ECS (for example, thermodynamic efficiency, cost of product(s), environmental impact, rate of return on investment, and payback time). An exergy-based method should be able to consider all of these measures of performance. Finally, an exergetic analysis can stimulate and guide creativity and innovation [2].

In order to predict future developments, we must first understand and evaluate what has happened up to now. Therefore, the following two sections refer to past contributions to the exergy-based methods by the author and his co-workers as well as by other authors, before in section 4 the needs for future developments are discussed. It is important to keep in mind that all analyses of an ECS should consider the entire life time of the system.

This is a brief review paper. Because of space limitations no equations to describe the methods are given. The equations are available in the literature cited for each method. Also the mathematical cost minimization methods developed for an ECS are not discussed here (even the ones using exergy) because in these methods (a) we need to know the investment costs of components as functions of thermodynamic variables and such information is not readily available, and (b) we cannot include in the optimization considerations related to safety, maintainability, and operability of the plant, considerations that could be easier incorporated into an iterative improvement approach, such as the approaches discussed here.

2. Contributions by the author and his co-workers: From exergetic analysis to the advanced exergy-based methods

An exergetic analysis assists in the *thermodynamic* optimization of an ECS. In real-world applications, however, realization of the thermodynamic optimum would result in very high investment and product costs. Therefore, we are interested in a solution that minimizes the product cost and not in a solution that maximizes efficiency. Thus, an economic analysis must be considered in parallel and in addition to the exergetic one. From a combination of the two analyses, we obtain the maximum useful information, when both following conditions are fulfilled: (a) the two methods are combined using the exergy-costing principle [1], and (b) the analysis is conducted at the system component or a lower level. The term *thermoeconomics* was initially used for this combination (e.g., [3]). However, after noticing that the term “thermoeconomic analysis” was used also in publications that were not employing the exergy-costing principle, which is essential here, the author introduced in 1984 the term *exergoeconomics* (or *exergoeconomic analysis*) to more accurately characterize this combination, to emphasize the role of exergy in cost minimization, and to clearly distinguish the different approaches [4]. In the same publication, the terms *fuel* and *product* were generalized, the variables *cost per unit of exergy for fuel and product*, *cost difference* (which later was replaced by the *relative cost difference*) and *exergoeconomic factor* were introduced, and the formulation of the exergy balances and cost balances was generalized. These generalizations allowed later a consistent evaluation of the thermodynamic, economic, and environmental performance of an ECS. For a long time the terms thermoeconomics and exergoeconomics were used in parallel as synonyms by the author (e.g., [1]). Unfortunately the term exergoeconomics has been used in the past by some other authors in cases where only an exergetic analysis and an economic one were conducted without using the exergy costing principle and without using an appropriate combination of the two analyses, thus contributing to a certain confusion surrounding the meaning and use of these terms.

Purpose plays a central role in exergy-based analyses, where a *product* is defined unambiguously for every system component and process according to its purpose [4-8]. The ratio between *product* and *fuel* is the exergetic efficiency of the thermodynamic system being considered. An exergetic analysis provides the most rigorous definition of thermodynamic efficiency and the foundation for assigning costs (in an exergoeconomic analysis, e.g., [1, 4-9]) and environmental impacts (in an exergoenvironmental analysis [10,11]) to energy carriers. The definitions of exergetic efficiency have been generalized in the SPECO method [9].

The continuously increasing interest in environmental considerations in the last decades led to the development of the exergoenvironmental analysis, which identifies the location, magnitude and causes of environmental impacts associated with an ECS [10-12]. Thus, using an appropriate definition for *product* and *fuel* for each component of an ECS [9], engineers obtain *consistent*, informative, and powerful analyses and evaluations from the viewpoints of thermodynamics, economics and envirnmental impact.

A conventional exergy-based method, however, does not assess (a) the parts of exergy destruction, cost and environmental impact that can be realistically avoided in a component or a process (by increasing the capital investment), and (b) the interactions among components with respect to exergy destruction, cost and environmental impact. These drawbacks of a conventional analysis are corrected in the *advanced exergy-based methods* (AEBM) (see, for example, [13-19]). By considering the avoidable/unavoidable values, the endogenous/exogenous values and their combinations (endogenous avoidable, exogenous avoidable, etc.) and by applying these concepts to the exergetic, exergoeconomic, and exergoenvironmental analyses, we obtain the most comprehensive set of analyses and evaluations of an ECS available today.

When dealing with exergy streams carrying a significant amount of *useful* chemical exergy, a distinction in the costs and environmental impacts associated with chemical and physical exergy might be meaningful. In addition, the chemical exergy should sometimes be split into reactive and non-reactive exergy [1] (e.g., in a gasification or chemical process), and the physical exergy, into thermal and mechanical exergy [20] (e.g., in a refrigeration process) to enable the definition of meaningful efficiencies, to improve the accuracy of calculations, to make fairer the calculation of costs and environmental impacts, and to improve the quality of conclusions drawn from the results of applications of exergy-based methods to an ECS.

Recently R. Castillo developed the *thermodynamic cost accounting* (TCA) approach, a novel exergy-based approach to determine the cost formation process and the formation of environmental impacts within an ECS [21]. Compared to the approaches discussed above, this approach emphasizes the boundaries to the overall system (instead of the component level), takes a different approach to the interactions among components, extracts useful conclusions from the Castillo Paz diagram, and clearly reveals the importance of recirculating streams to the thermodynamic, economic, and environmental performances (see, for example, the application of the TCA to the CGAM problem [7, 21]).

3. Contributions by other authors

Based on the ratio between the cost per unit of exergy of a stream and the cost per unit of exergy of fuel to the overall ECS when only fuel costs (but no investment or operation and maintenance costs) are considered (cases the author studied, for example, in [6] and [22]), the Zaragoza group under the leadership of Antonio Valero developed the *exergetic cost theory* (ECT) [7, 23-24], which calculates the amount of exergy needed to provide each exergy stream in an ECS. The contributions of ECT complement the ones by the author and his co-workers. The group from Zaragoza also developed a method for the *diagnosis of malfunctions and disfunctions* around the operating point of an ECS [25-26].

The approach of *cumulative exergy consumption* (CEC) considers all thermodynamic inefficiencies that occur in the entire chain between the point where all natural resources used in the process are obtained from the natural environment to the point where the final product is generated [27]. This approach extends the system boundaries of the thermodynamic analysis to include all processes that previously were used to provide the feeds to the process under investigation. CEC accounts for how the inefficiencies of the process being analyzed affect the inefficiencies of the processes that provide the feeds, and vice versa. This information is used in calculating environmental impacts associated with the process that is being considered.

The *extended exergy accounting* (EEA) method is also based on the calculation of the cumulative exergy consumption, but takes into consideration additional aspects such as the exergy associated with capital (investment costs) and human activity (labor) [28-29]. The *extended cumulative exergy consumption* associated with the investigated system is minimized.

Environomics, *thermoecology*,and *exergoenvironmental analysis* deal with the reduction of the environmental impact. [30-37]. When more than one pollutant (e.g., CO2, CO, NOx, SO2, and solid particles) are considered in the analysis, the question arises how to compare (to establish the equivalence of) 1 kg of one pollutant with 1 kg of another. A common currency is needed here: In *environomics* [30, 31], monetary values (costs) are assigned to the environmental impact associated with each pollutant, then an exergoeconomic model is extended to include the costs of pollutants, and finally a cost minimization problem is solved. In *thermoecology* [32], or *exergoecology* [33], the depletion of non-renewable natural resources and the effects of pollutants are expressed in exergy terms. The resulting thermoecological (or exergoecological) cost (expressed in exergy units) is based on the cumulative consumption of non-renewable exergy, and includes the cost associated with the rejection of harmful substances to the natural environment. In the *exergoenvironmental analysis* [10-12, 34, 35], a one-dimensional characterization indicator is obtained using a *life cycle assessment* (LCA); this indicator is used in the *exergoenvironmental analysis* in a similar way as the cost is used in *exergoeconomics*.

An index (a single number), for example, the Eco-indicator 99 describes the overall environmental impact associated with each exergy carrier and with the manufacturing of each system component.

4. Future developments

Before discussing any future development we must point out that all methods mentioned in sections 2 and 3 have not yet received the same acceptance and reception by the scientific, engineering, and political communities as other methods, for example the pinch method and the method of LCA. The reasons for this lie probably in the facts that (a) exergy, not being introduced and discussed properly or sufficiently in engineering curricula, remains a variable and a concept that is not understood and used easily, and (b) the extraction of useful information from an exergy-based method requires good understanding of the limitations of the method being used and critical thinking, contrary to other more popular methods that can be applied as "recipes". Finally, the disagreements among the exergy practitioners, the plethora of available approaches, the misinterpretations and misuses of these methods certainly have not contributed to their wider acceptance. In 2007 the author coordinated the responses received from several exergy practitioners in an effort to standardize the definitions and nomenclature in exergy-based methods [36]. The applications that followed showed a very limited success of this effort.

One development is certain for the future: The number of cases in which exergy-based methods could be applied will be lower because more electricity will be generated using direct energy conversion, for example, photovoltaics, wind energy, and hydropower, and more electricity will be used in the sectors of transportation, industry, and buildings in every future year. Thus, the exergy-based methods, which show their strength and are more useful when thermal energy is involved, will follow the decline in relative importance we have experienced for thermodynamics and thermal sciences in the engineering curricula in the last years.

The diversity of the methods mentioned in sections 2 and 3 indicates that there is not a single generally accepted method for evaluating the design and the performance of an ECS. All methods have weak points: For example, the *advanced exergy-based methods* often use some subjective estimates, *the exergetic cost theory* does not explicitly consider the investment cost, the assignment of costs to environmental impacts in *environomics* is more or less arbitrary, as is the conversion of monetary values (e.g., capital investment and salaries) and environmental impact into exergy values in the *extended exergy accounting method*. In addition, it is very time consuming to apply most of the above methods. All these weak points reduce the usefulness of the corresponding methods. In the future we should expect developments that will reduce the weak points associated with each approach.

It should be emphasized that the evaluation of costs, which will incur in the future, and of environmental impacts will always be somehow subjective and associated with limitations because of the uncertainties involved in their estimation. However, even the imperfect information extracted from an exergoeconomic or an exergoenvironmental analysis is always useful for reducing the costs and the environmental impacts associated with an ECS.

The *advanced exergy-based methods* are expected to be further developed in the future, so that their subjectivity and the time required for their application will be reduced. Through applications to different ECS, we should expect a higher degree of method generalization and the development of short-cuts to reduce the time required for their application. Also the development of new software specialized in the application of these methods will facilitate application of the methods to many different energy-intensive processes. Because environmental considerations will become more important on future applications, a further integration of these methods (see, e.g., [37, 38]) will enable a fast and consistent multiobjective optimization of an ECS, for example an optimization (improvement procedure) that will simultaneously consider costs and environmental impacts in the optimization to reveal actions that could decrease the cost(s) of the overall product(s), while, at the same time, enhancing the efficiency, and decreasing the environmental impact of the ECS being evaluated. Finally, decision making procedures referring to an ECS will be further improved through applications of advanced exergy-based methods.

5. Conclusions

Various methods have been developed using exergy for the evaluation and improvement of an ECS from the viewpoints of thermodynamics, economics and ecology. Brief reviews of the methods show that all of them have some limitations while focusing on specific aspects of the ECS being considered. The *advanced exergy-based methods* provide the most comprehensive and powerful set of methods available today for evaluating

and improving an ECS. All these methods have not yet received from the industry and politicians the recognition they deserve as tools for decision making.

Future work is expected to include the reduction of the limitations associated with each method, a generalization and integration of the methods and the development of appropriate software and short-cut approaches to reduce the time required for the applications.

Abbreviations

AEBM Advanced Exergy-Based Method(s)
CEC Cumulative Exergy Consumption
CGAM An energy-conversion system used to compare the application of exergoeconomic methods in [7]. The name was formed by combining the first letters of the first name of the four main contributors to [7]: **C**hristos Frangopoulos, **G**eorge Tsatsaronis, **A**ntonio Valero and **M**ichael von Spakovsky.
ECS Energy-conversion system(s)
ECT Exergetic Cost Theory
EEA Extended Exergy Accounting
LCA Life-Cycle Assessment
SPECO Specific Cost (method)
TCA Thermodynamic Cost Accounting (method)

References

[1] Bejan, A., Tsatsaronis, G., and Moran, M.,Thermal Design and Optimization, J. Wiley, New York, 1996.
[2] Tsatsaronis, G. Strengths and Limitations of Exergy Analysis. In Thermodynamic Optimization of Complex Energy Systems; Bejan, A., Mamut, E., Eds.; Kluwer Academic Publishers: Dordrecht, The Netherlands, 1999. p. 93–100.
[3] Evans, R.B., Tribus, M. A contribution to the theory of thermoeconomics, UCLA, Dept. of Engineering Report No. 6243, Los Angeles, 1962.
[4] Tsatsaronis G., Combination of Exergetic and Economic Analysis in Energy-Conversion Processes. In Energy Economics and Management in Industry, In: Proceedings of the European Congress, Algarve, Portugal, April 2-5, 1984, Pergamon Press, Oxford, England, Vol. 1: 151-157.
[5] Tsatsaronis, G. and Winhold, M., Exergoeconomic Analysis and Evaluation of Energy Conversion Plants. Part I-A New General Methodology, Energy 1985; 10 (1): 69-80.
[6] Tsatsaronis, G. and Winhold, M., Exergoeconomic Analysis and Evaluation of Energy Conversion Plants. Part II - Analysis of a Coal-Fired Steam Power Plant. Energy 1985; 10 (1): 81-94.
[7] Tsatsaronis, G. (Guest editor), Invited papers on exergoeconomics, Energy 1994; 19 (3): 279-381.
[8] Tsatsaronis, G. "Exergoeconomics: Is It Only a New Name?", Chemical Engineering and Technology, 19 (1996), No. 2, pp. 163-169.
[9] Lazzaretto, A. and Tsatsaronis, G., SPECO: A Systematic and General Methodology for Calculating Efficiencies and Costs in Thermal Systems, Energy 2006; 31: 1257-1289.
[10] Meyer, L., Tsatsaronis, G., Buchgeister, J., and Schebek, L. Exergoenvironmental Analysis for Evaluation of the Environmental Impact of Energy Conversion Systems**.** Energy 2009; 34 (1): 75-89.
[11] Meyer, L., “Exergiebasierte Untersuchung der Entstehung von Umweltbelastungen in Energieumwandlungsprozessen auf Komponentenebene: Exergoökologische Analyse“, Universität Darmstadt, Ph.D. dissertation, 2006.
[12] Meyer, L., Castillo, R., Buchgeister, J., Tsatsaronis, G., Application of Exergoeconomic and Exergoenvironmental Analysis to a SOFC System with an Allothermal Biomass Gasifier. International Journal of Thermodynamics 2009; 12(4): 177-186.
[13] Tsatsaronis, G., Park, M.-H. On avoidable and unavoidable exergy destructions and investment costs in thermal systems. Energy Conversion and Management 2002; 43: 1259–1270.
[14] Kelly, S.; Tsatsaronis, G.; Morosuk, T. Advanced exergetic analysis: Approaches for splitting the exergy destruction into endogenous and exogenous parts. Energy 2009, 34: 384–391.
[15] Morosuk, T.; Tsatsaronis, G. Advanced Exergetic Analysis is a Modern Tool for Evaluation and Optimization of Refrigeration Systems. In Handbook of Research on Advances and Applications in Refrigeration Systems and Technologies; Gaspar, P.D., da Silva, P.D., Eds.; IGI Global: Hershey, PA, USA, 2015: 5–105.
[16] Tsatsaronis, G. Exergoeconomics and Exergoenvironmental Analysis. In Thermodynamics and the Destruction of Resources; Bakshi, B.R., Gutowski, T., Sekulic, D., Eds.; Cambridge University Press: Cambridge, UK, 2011; 377–401.
[17] Tsatsaronis, G., Morosuk, T. Understanding and Improving Energy Conversion Systems with the Aid of

Exergy-Based Methods. International Journal Exergy 2012; 11(4): 518-542.
[18] Penkuhn, M., Tsatsaronis, G., A Decomposition Method for the Evaluation of Component Interactions in Energy Conversion Systems for Application to Advanced Exergy-Based Analyses. Energy 2017; 133: 388-403.
[19] Penkuhn, M., and Tsatsaronis, G., Application of Advanced Exergetic Analysis to the Improvement of Chemical Processes. Chemie Ingenieur Technik 2017, 89(5); 607-619.
[20] Morosuk, T., and Tsatsaronis, G., Splitting Physical Exergy: Theory and Application. Energy 2019, 167: 698-707.
[21] Castillo, R., and Tsatsaronis, G., The Exergy-based Thermodynamic Cost Accounting Approach for Improving the Design of Thermal Systems. In Proceedings of ECOS 2023 - The 36th International Conference on Efficiency Cost, Optimization, Simulation and Environmental Impact of Energy Systems, June 25-30, 2023, Las Palmas de Gran Canaria, Spain.
[22] Tsatsaronis, G., Winhold, M., Thermoeconomic Analysis of Power Plants. EPRI AP-3651, RP 2029-8, Electric Power Research Institute, Palo Alto, CA, USA, August 1984.
[23] Lozano, M.A., Valero, A., Theory of the exergetic cost. Energy 1993; 18: 939-960.
[24] Valero, A., Lozano, M.A., Serra, L., Torres, C., Application of the exergetic cost theory to the CGAM problem. Energy 1994, 19: 365–381.
[25] Torres, C., Valero, A., Serra, L., Royo, J., Structural theory and thermoeconomic diagnosis-Part I. On malfunction and dysfunction analysis. Energy Conversion and Management 2002, 43: 1503-1518.
[26] Valero, A., Correas, L., Zaleta, A., Lazzaretto, A., Verda, V., Reini, M., Rangel, V., On the thermoeconomic approach to the diagnosis of energy system malfunctions - Part 1: the TADEUS problem. Energy 2004, 29: 1875–1887
[27] Szargut, J., Analysis of cumulative exergy consumption. Int. J. Energy Res. 1987, 11: 541–547.
[28] Sciubba, E., Beyond thermoeconomics? The concept of Extended Exergy Accounting and its application to the analysis and design of thermal systems. Exergy Int. J. 2001, 1 (2): 68–84.
[29] Rocco, M.V., Colombo, E., Sciubba, E., Advances in exergy analysis: A novel assessment of the Extended Exergy Accounting method. Appl. Energy 2014, 113: 1405–1420.
[30] Frangopoulos, C.A., Introduction to environomics. In Symposium onThermodynamics of Energy Systems; Reistad, G.M., Ed.; ASME: Atlanta, GA, USA, 1991: 49–54.
[31] Frangopoulos, C.A., von Spakovsky, M.R., A global environomic approach for energy systems analysis and optimization. In Proceedings of the Energy Systems and Ecology: Proceedings of the International Conference (ENSEC 93), Cracow, Poland, 5–9 July 1993; Szargut, J., Ed.; Advanced Energy Systems Division, American Society of Mechanical Engineers: Atlanta, GA, USA, 1993; pp. 123–132.
[32] Valero, A., Valero, A., Stanek, W., Assessing the exergy degradation of the natural capital: From Szargut's updated reference environment to the new thermoecological-cost methodology. Energy 2018, 163: 1140–1149.
[33] The Exergoecology Portal. Available online: http://www.exergoecology.com
[34] Boyano, A., Blanco-Marigorta, A.M., Morosuk, T., Tsatsaronis, G., Exergoenvironmental analysis of a steam methane reforming process for hydrogen production. Energy 2011, 36: 2202–2214.
[35] Petrakopoulou, F., Tsatsaronis, G., Morosuk, T., Assessment of a power plant with CO2 capture using an advanced exergoenvironmental analysis. J. Energy Resour. Technol. 2014, 136: 022001.
[36] Tsatsaronis G, Definitions and Nomenclature in Exergy Analysis and Exergoeconomics. Energy 2007, 32: 249–53.
[37] Morosuk T, Tsatsaronis G, 3-D Exergy-Based Methods for Improving Energy-Conversion Systems. Int J Thermodynamics 2012, 5 (4): 201–213
[38] Lara, Y., Morosuk, T., Petrakopoulou, F., Boyano, A., Tsatsaronis, G., An exergy-based study on the relationship between costs and environmental impacts in power plants. Energy 2017,138: 920-928.

ULPGC
Universidad de
Las Palmas de
Gran Canaria

grres ULPGC
group for the research on renewable energy systems

A. Basic and applied thermodynamics

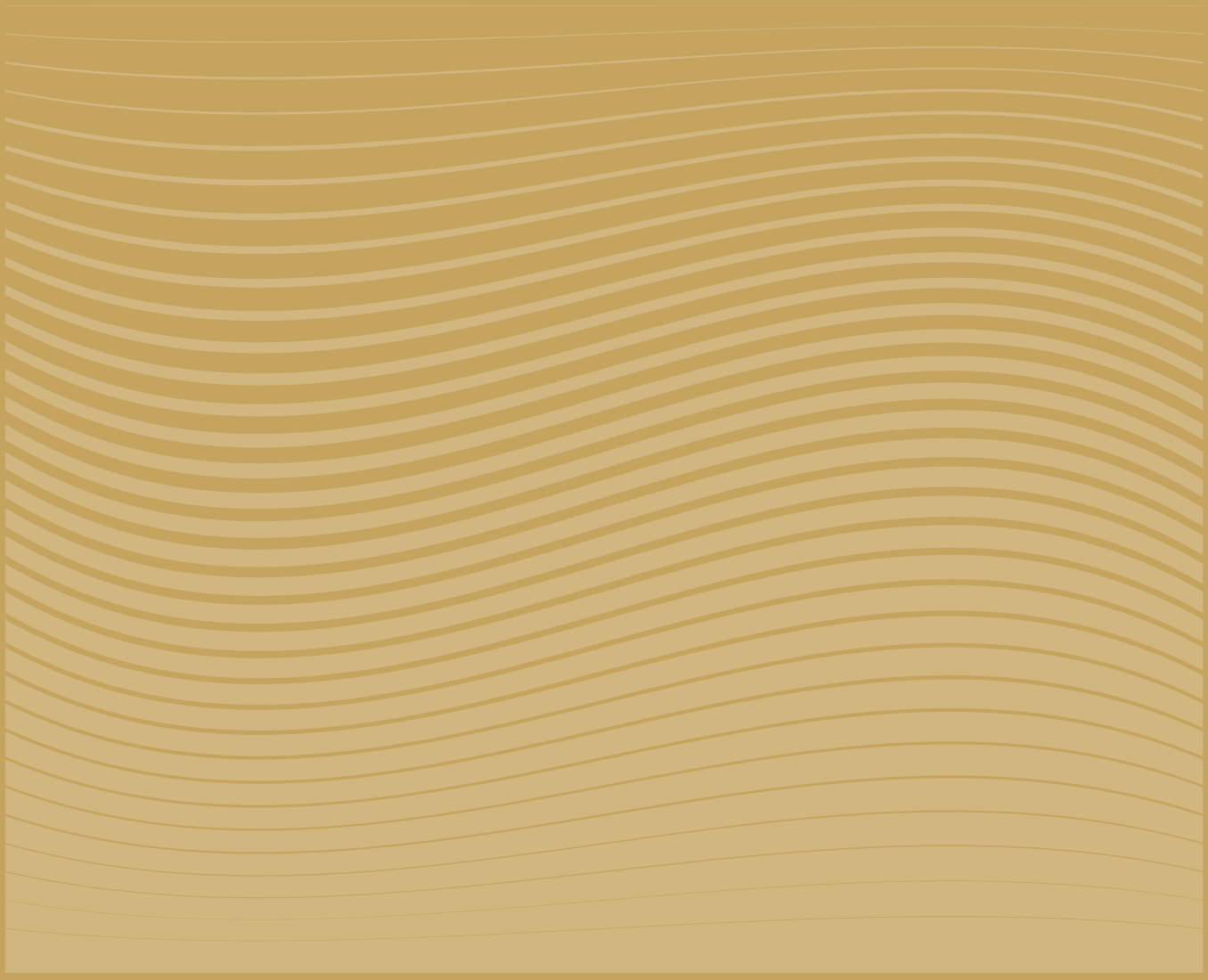

ECOS2023

A comparative study of thermophysical properties of amine aqueous solutions for CO_2 mitigation

Eduardo I. Concepción[a,b], Alejandro Moreau[a], José J. Segovia[a], Yisel Pérez[a], Juan D. Arroyave[a], M. Carmen Martín[a]

[a] TERMOCAL Research Group, Research Institute on Bioeconomy, Universidad de Valladolid, Valladolid, Spain, mcarmen.martin@eii.uva.es, CA
[b] Universidad Tecnológica de Panamá, Panamá, Panama, eduardo.concepcion1@utp.ac.pa.

Abstract:

Research on carbon capture is increasing interest due to its impact in the search of net-zero carbon economy. In this sense, amine solutions play an important role in the post-combustion CO_2 capture, using them as chemical absorbents. There are different amines or mixed amines that are studied to substitute MEA, which is the best well-known despite some drawbacks such as its high energy demand or its low potential of CO_2 absorption. On the other hand, key properties such as density, viscosity or heat capacity are necessary for the design and optimization of the separation plant; the accuracy of the calculations is directly related to the accuracy of the properties. In this work, these properties, which were determined by means of experimental techniques of low uncertainty, are presented and compared for three tertiary amines: Triethanolamine (TEA), N-Methyldiethanolamine (MDEA) and 2-Dimethylaminoethanol (DMAE). Densities were measured using a commercial vibrating tube densimeter that was completed with different devices allowing the determination of density with a standard uncertainty of 0.35 kg/m^3. A falling body viscometer was used for viscosity measurements with a standard uncertainty of 1.6%. Finally, a flow calorimeter, developed in our laboratory, measured isobaric heat capacities with a standard uncertainty of 0.5%. The comparison is done in a temperature range from 293.15 K to 353.15 K and pressures up to 25 MPa. In addition, different mass fractions of amine in the mixture (amine +water) are studied (w_{amine} = 0.1 to 0.4).

Keywords:

Density; Viscosity; Heat capacity; 2-Dimethylaminoethanol (DMAE); N-Methyldiethanolamine (MDEA); Triethanolamine (TEA).

1. Introduction

The objective of a net-zero carbon economy is fostering the research on carbon capture as a measure to promote the energy transition. In this context, alkanolamine solutions play an important role as chemical absorbents for CO_2 capture in the post-combustion. Although this technology is industrially mature, there are some key points to address to reduce the associated cost such as the search for solvents with less energy requirements, better stability, and less harmful emissions, in addition to the process optimization, and integration with the CO_2-emitting plant [1].

There are different amines or mixed amines that are studied to substitute MEA, which is the best well-known despite some drawbacks such as its high energy demand or its low potential of CO_2 absorption. However, the design and optimization of the separation plant require the knowledge of key properties such as density, viscosity or heat capacity of these new potential absorbents. Moreover, the accuracy of the calculations is directly related to the accuracy of the properties.

Our research group has been involved during the last decade in the accurate measurement of these properties as can be seen in previous papers. Density and viscosity of different aqueous solutions of alkanolamines were already measured at wide ranges of temperature and pressure: Ethanolamine (MEA) and N-Methyldiethanolamine (MDEA) in [2]; Diethanolamine (DEA), Triethanolamine (TEA) and 2-Dimethylaminoethanol (DMAE) in [3]; Piperazine (PZ) in [4] and blended amines (PZ+ DMAE) in [4] and (MDEA+DEA) in [5]. Heat capacities of 30% weight of amine up to 25 MPa for aqueous solutions of MEA, DEA and TEA were presented in [6], and heat capacities of aqueous solutions of six different amines are reported in [7].

In this work, a comparison of the behaviour of the three tertiary amines: Triethanolamine (TEA), N-Methyldiethanolamine (MDEA) and 2-Dimethylaminoethanol (DMAE) in terms of density, viscosity and heat capacity is presented and discussed. The comparison is done in a temperature range from 293.15 K to 353.15 K and pressures up to 25 MPa. In addition, different mass fractions of amine in the mixture (amine +water) are studied (w_{amine} = 0.1 to 0.4).

2. Experimental section

2.1. Materials

The materials used in the measurements were purchased from Sigma-Aldrich of the highest purity available and used without further purification. Their purities in mass fraction (as stated by the supplier) were: Triethanolamine (TEA) ≥ 0.99, N-Methyldiethanolamine (MDEA) ≥ 0.99, and 2-Dimethylaminoethanol (DMAE) ≥ 0.995.

A precision balance (RADWAG PS750/C/2) was used to make the mixtures by weighting, estimating an expanded uncertainty (k=2) of 0.0002 in mass fraction.

2.2. Equipment

Three accurate techniques are used to perform the measurements: densities are determined using a commercial vibrating tube densimeter, viscosities by means of a falling body viscometer and heat capacities using a flow calorimeter. All the techniques are calibrated and checked regularly. A brief description of the main features of these techniques is explained below.

An Anton Paar DMA HPM densimeter is employed to carry out the density measurements, the technique is completed with an automatization system in such a way that, through the computer program, ramps of pressures and temperatures can be programmed, and the frequency measurements are recorded for the sample. The technique can measure density in a temperature range from 240 K to 420 K and up to 140 MPa with a relative standard uncertainty of 0.35 kg/m^3. Details of the technique and the uncertainty budget are published in [8].

Density, ρ, of a fluid is related to the vibration period, τ, through (1):

$$\rho(T,p) = A(T)\tau^2(T,p) - B(T,p) \quad (1)$$

where $A(T)$ and $B(T,p)$ are two characteristic parameters of the apparatus which can be determined by a calibration procedure, in this case, water and vacuum were used for calibration.

Viscosity measurements are undertaken in a falling body viscometer whose principle of measure is based on the fall time of a body in a vertical tube filled with the sample [3,9]. The apparatus can perform measurements between 240 K to 475 K and up to 140 MPa, with a relative expanded uncertainty (k = 2) of 3%.

The model used for this viscometer is given by (2):

$$\eta = a + b\Delta\rho\Delta t \quad (2)$$

Where viscosity (η) is related to fall time (Δt) and the difference of density between the falling body and the liquid ($\Delta\rho$) and the parameters a and b are obtained by calibration using water and dodecane.

Finally, an automated flow calorimeter, fully developed in our laboratory, is used for isobaric heat capacity measurements. Its working principle lies in balancing the heating and cooling power of the calorimetric cell to maintain a fixed difference between the inlet and exit temperatures of the circulating fluid. at constant flow rate and, heat capacity is calculated by the determination of the net power exchanged.

The value of net power ($\dot{Q}_{net}$) is directly related to the isobaric heat capacity as shown in equation (3):

$$C_p = \dot{Q}_{net}/(\dot{V} \times \rho \times \Delta T) = \left[a + b\left(\dot{Q}_{base} - \dot{Q}_{measured}\right)\right]/(\dot{V} \times \rho \times \Delta T) \quad (3)$$

where $\dot{V}$ is the volumetric flow of the fluid, ρ is the density of the fluid at the pump temperature, ΔT is the temperature decrease and, a and b are the calibration constants calculated by an electric calibration. The relative expanded uncertainty of the heat capacity obtained with this technique is 1%. This equipment works in the temperature range from 240 K to 420 K and up to 25 MPa, the details are described in [6,10].

3. Results and discussion

This work is focus on the thermophysical behaviour of aqueous solutions of three ternary amines (TEA, MDEA, DMAE), based on the experimental data of densities, viscosities, and isobaric heat capacities. These properties will be compared in the range of temperatures from 293.15 K to 353.15 K, pressures from 0.1 MPa to 30 MPa and mass fractions from 0.1 to 0.4.

Experimental values of density and viscosity for (TEA+ water) and (DMAE+ water) are published in [3] at mass fractions from 0.1 to 0.4, in the range of temperatures from 293.15 K to 393.15 K and pressures up to 140 MPa for density and up to 100 MPa for viscosity. On the other hand, data for (MDEA + water) mixtures (w_{amine} = 0.1 to 0.4) can be found in [2] where densities from 293.15 K to 393.15 K and pressures up to 140 MPa and viscosities from 293.15 K to 353.15 K and pressures up to 120 MPa are reported.

Data of isobaric heat capacities of the aqueous solutions of the three ternary amines of this study (w_{amine} = 0.3) from 313.15 K to 353.15 K and up to 25 MPa are given in [6].

Although the experimental values can be found in different papers [2,3,6,7], to report the complete information, Tables 1-3 contains the experimental values of heat capacities, viscosities and densities of the amine solutions under study.

Table 1. Isobaric heat capacities for amine + water mixtures [6,7].

	c_p, kJ/kgK							
P, MPa	293.15 K	313.15 K	333.15 K	353.15 K	293.15 K	313.15 K	333.15 K	353.15 K
		w_{TEA} = 0.1001				w_{TEA} = 0.2000		
0.10	4.064	4.041	4.054	4.071	3.784	3.907	3.961	3.983
5.0	4.055	4.03	4.046	4.064	3.774	3.883	3.961	3.975
10.0	4.041	4.023	4.038	4.055	3.764	3.880	3.954	3.965
15.0	4.029	4.010	4.030	4.049	3.760	3.876	3.942	3.963
20.0	4.016	3.998	4.019	4.035	3.758	3.868	3.934	3.961
25.0	4.004	3.992	4.010	4.032	3.756	3.866	3.933	3.949
		w_{TEA} = 0.2991				w_{TEA} = 0.4000		
0.10		3.803	3.871	3.934	3.492	3.554	3.611	3.646
5.0		3.787	3.861	3.928	3.416	3.484	3.533	3.563
10.0		3.775	3.854	3.925	3.352	3.404	3.457	3.502
15.0		3.757	3.847	3.922	3.293	3.355	3.403	3.451
20.0		3.749	3.834	3.917	3.238	3.297	3.362	3.400
25.0		3.732	3.831	3.914	3.199	3.260	3.318	3.354
		w_{MDEA} = 0.1001				w_{MDEA} = 0.2001		
0.10	4.065	4.126	4.096	4.179	3.880	3.987	4.051	4.098
5.0	4.060	4.113	4.080	4.169	3.867	3.965	4.050	4.085
10.0	4.050	4.108	4.077	4.157	3.861	3.964	4.043	4.084
15.0	4.049	4.094	4.069	4.144	3.855	3.949	4.034	4.074
20.0	4.046	4.090	4.068	4.137	3.836	3.943	4.033	4.070
25.0	4.041	4.077	4.065	4.127	3.847	3.934	4.026	4.066
		w_{MDEA} = 0.2998				w_{MDEA} = 0.4001		
0.10		3.890	3.965	4.057	3.601	3.727	3.810	3.897
5.0		3.857	3.946	4.040	3.591	3.722	3.797	3.886
10.0		3.836	3.930	4.028	3.577	3.718	3.784	3.881
15.0		3.814	3.920	4.010	3.566	3.713	3.780	3.882
20.0		3.782	3.908	4.000	3.554	3.706	3.777	3.879
25.0		3.775	3.900	3.977	3.549	3.701	3.773	3.875
		w_{DMAE} = 0.1000				w_{DMAE} = 0.2005		
0.10	4.187	4.228	4.172	4.253	4.017	4.101	4.179	4.229
5.0	4.180	4.218	4.166	4.244	4.010	4.095	4.177	4.223
10.0	4.168	4.209	4.155	4.234	4.006	4.087	4.171	4.222
15.0	4.161	4.202	4.150	4.227	4.000	4.086	4.167	4.222
20.0	4.152	4.192	4.140	4.220	3.993	4.085	4.163	4.216
25.0	4.143	4.184	4.131	4.214	3.989	4.079	4.161	4.211
		w_{DMAE} = 0.3005				w_{DMAE} = 0.4000		
0.10		4.072	4.123	4.272	3.812	3.931	3.948	4.093
5.0		4.059	4.116	4.257	3.811	3.929	3.945	4.091
10.0		4.043	4.090	4.242	3.813	3.922	3.941	4.085
15.0		4.028	4.072	4.232	3.814	3.917	3.939	4.079
20.0		4.012	4.054	4.220	3.815	3.914	3.931	4.068
25.0		3.997	4.039	4.205	3.812	3.910	3.927	4.057

Table 2. Viscosities for amine + water mixtures [2,3].

				η, mPa·s				
P, MPa	293.15 K	313.15 K	333.15 K	353.15 K	293.15 K	313.15 K	333.15 K	353.15 K
		w_{TEA} = 0.0992				w_{TEA} = 0.2000		
0.10	1.429	0.909	0.612		2.038	1.203	0.808	0.581
5.0	1.459	0.894	0.611		2.036	1.208	0.808	0.583
10.0	1.455	0.896	0.615		2.035	1.210	0.813	0.588
20.0	1.450	0.897	0.618		2.042	1.220	0.820	0.594
30.0	1.446	0.899	0.622		2.046	1.228	0.828	0.601
		w_{TEA} = 0.2991				w_{TEA} = 0.4000		
0.10	3.208	1.786	1.147	0.805	5.317	2.788	1.670	1.124
5.0	3.213	1.797	1.155	0.799	5.311	2.794	1.680	1.125
10.0	3.229	1.808	1.164	0.805	5.331	2.797	1.698	1.136
20.0	3.234	1.832	1.178	0.814	5.417	2.852	1.720	1.154
30.0	3.245	1.846	1.189	0.827	5.500	2.889	1.748	1.174
		w_{MDEA} = 0.1000				w_{MDEA} = 0.2000		
0.10	1.476	0.912	0.624		2.350	1.345	0.872	0.617
5.0	1.475	0.914	0.627		2.353	1.347	0.876	0.620
10.0	1.475	0.915	0.630		2.357	1.349	0.881	0.625
20.0	1.471	0.920	0.634		2.364	1.358	0.890	0.633
30.0	1.472	0.923	0.638		2.372	1.367	0.898	0.640
		w_{MDEA} = 0.3000				w_{MDEA} = 0.4000		
0.10	3.999	2.095	1.271	0.854		3.238	1.843	1.181
5.0	4.018	2.106	1.278	0.862		3.270	1.861	1.193
10.0	4.038	2.118	1.286	0.869		3.302	1.880	1.204
20.0	4.077	2.144	1.302	0.881		3.365	1.921	1.229
30.0	4.114	2.168	1.316	0.894		3.428	1.956	1.253
		w_{DMAE} = 0.1005				w_{DMAE} = 0.2020		
0.10	1.559	0.940	0.634	0.462	2.533	1.368	0.873	0.606
5.0	1.564	0.942	0.634	0.464	2.547	1.374	0.877	0.606
10.0	1.564	0.944	0.637	0.467	2.557	1.382	0.886	0.614
20.0	1.562	0.948	0.643	0.472	2.574	1.395	0.897	0.623
30.0	1.564	0.953	0.648	0.477	2.589	1.412	0.906	0.634
		w_{DMAE} = 0.3005						
0.10	4.211	2.042	1.217	0.806				
5.0	4.223	2.063	1.223	0.812				
10.0	4.258	2.084	1.239	0.821				
20.0	4.330	2.121	1.260	0.841				
30.0	4.405	2.161	1.283	0.856				

Table 4. Densities for amine + water mixtures [2,3].

				ρ, kg/m^3				
	293.15 K	313.15 K	333.15 K	353.15 K	293.15 K	313.15 K	333.15 K	353.15 K
P, MPa		w_{TEA} = 0.0992				w_{TEA} = 0.2000		
0.1	1013.3	1006.9	997.2	985.7	1029.5	1021.9	1011.6	999.5
0.5	1013.5	1007.0	997.5	985.7	1029.5	1022.1	1011.8	999.6
1	1013.7	1007.2	997.7	985.9	1029.7	1022.3	1012	999.8
2	1014.2	1007.6	998.1	986.4	1030.2	1022.7	1012.4	1000.1
5	1015.5	1008.9	999.3	987.7	1031.4	1023.9	1013.6	1001.5
10	1017.6	1010.9	1001.4	989.9	1033.4	1025.9	1015.7	1003.7

Table 4. (cont.) Densities for amine + water mixtures [2,3].

	ρ, kg/m^3							
	293.15 K	313.15 K	333.15 K	353.15 K	293.15 K	313.15 K	333.15 K	353.15 K
P, MPa	w_{TEA} = 0.0992				w_{TEA} = 0.2000			
15	1019.6	1013.0	1003.5	992.1	1035.4	1027.8	1017.7	1005.8
20	1021.8	1015.0	1005.5	994.1	1037.4	1029.7	1019.7	1007.8
30	1026.0	1019.1	1009.6	998.2	1041.4	1033.7	1023.6	1011.9
	w_{TEA} = 0.2991				w_{TEA} = 0.4000			
0.1	1046.1	1037.4	1026.3	1013.6	1065.2	1055.1	1043.1	1029.7
0.5	1046.2	1037.5	1026.5	1013.7	1065.3	1055.3	1043.3	1029.8
1	1046.4	1037.7	1026.7	1013.9	1065.4	1055.4	1043.5	1030
2	1046.8	1038.1	1027.2	1014.3	1065.8	1055.8	1043.9	1030.4
5	1047.9	1039.3	1028.3	1015.6	1066.9	1056.9	1045.1	1031.7
10	1049.8	1041.2	1030.4	1017.8	1068.7	1058.8	1047.1	1033.9
15	1051.7	1043.1	1032.4	1019.9	1070.5	1060.6	1049	1035.8
20	1053.7	1045	1034.3	1021.9	1072.3	1062.4	1050.9	1037.9
30	1057.4	1048.8	1038.2	1025.9	1075.8	1066	1054.7	1041.9
	w_{MDEA} = 0.1000				w_{MDEA} = 0.2002			
0.1	1007.0	1000.2	990.5	978.6	1016.5	1008.5	997.8	985.3
0.5	1007.2	1000.4	990.6	978.7	1016.6	1008.6	998.0	985.3
1	1007.4	1000.6	990.8	978.9	1016.8	1008.8	998.2	985.5
2	1007.8	1001.0	991.3	979.3	1017.2	1009.2	998.6	985.9
5	1009.0	1002.2	992.5	980.6	1018.4	1010.4	999.8	987.2
10	1011.1	1004.3	994.6	982.8	1020.3	1012.3	1001.8	989.4
15	1013.2	1006.3	996.6	984.9	1022.2	1014.2	1003.8	991.5
20	1015.3	1008.2	998.6	987.0	1024.2	1016.1	1005.7	993.5
30	1019.4	1012.3	1002.6	991.2	1028.0	1019.9	1009.7	997.6
	w_{MDEA} = 0.3000				w_{MDEA} = 0.4000			
0.1	1026.7	1017.2	1005.4	992.0	1036.6	1025.5	1012.4	998.1
0.5	1026.9	1017.4	1005.6	992.0	1036.8	1025.6	1012.7	998.2
1	1027.1	1017.5	1005.7	992.2	1036.9	1025.8	1012.8	998.4
2	1027.4	1017.9	1006.2	992.7	1037.3	1026.2	1013.2	998.8
5	1028.6	1019.1	1007.3	993.9	1038.3	1027.3	1014.4	1000.1
10	1030.4	1020.9	1009.3	996.1	1040.1	1029.2	1016.4	1002.3
15	1032.2	1022.8	1011.3	998.2	1041.9	1031.0	1018.4	1004.4
20	1034.1	1024.6	1013.2	1000.3	1043.6	1032.8	1020.3	1006.5
30	1037.7	1028.4	1017.0	1004.3	1047.1	1036.3	1024.1	1010.5
	w_{DMAE} = 0.1005				w_{DMAE} = 0.2020			
0.1	994.5	987.4	977.4	965.2	992.6	983.2	971.5	958.1
0.5	994.7	987.6	977.6	965.3	992.7	983.4	971.8	958.1
1	994.8	987.8	977.8	965.6	992.9	983.6	972.0	958.4
2	995.3	988.3	978.2	966.0	993.3	984.0	972.4	958.8
5	996.5	989.5	979.5	967.3	994.4	985.2	973.7	960.1
10	998.5	991.5	981.5	969.5	996.3	987.2	975.7	962.4
15	1000.5	993.4	983.6	971.6	998.2	989.1	977.7	964.5
20	1002.6	995.4	985.6	973.8	1000.0	990.9	979.7	966.7
30	1006.6	999.4	989.7	978.0	1003.7	994.8	983.7	971.0

Table 4. (cont.) Densities for amine + water mixtures [2,3].

	ρ, kg/m^3							
	293.15 K	313.15 K	333.15 K	353.15 K	293.15 K	313.15 K	333.15 K	353.15 K
P, MPa	w_{DMAE} = 0.3005				w_{DMAE} = 0.3995			
0.1	990.6	978.8	965.2	950.2	986.6	972.7	957.4	941.1
0.5	990.7	979.0	965.4	950.3	986.7	972.9	957.6	941.2
1	990.9	979.2	965.6	950.6	986.9	973.1	957.9	941.4
2	991.3	979.6	966.1	951.0	987.3	973.5	958.3	941.9
5	992.4	980.8	967.3	952.4	988.4	974.7	959.6	943.3
10	994.2	982.7	969.5	954.7	990.3	976.7	961.8	945.8
15	996.0	984.6	971.5	956.9	992.1	978.6	963.9	948.1
20	997.8	986.5	973.5	959.1	994.0	980.6	966.0	950.5
30	1001.4	990.3	977.5	963.4	997.5	984.4	970.2	954.9

To better illustrate the comparison in the behaviour of the mixtures under study, some experimental results are presented graphically. Figure 1 presents the density as a function of pressure at different temperatures for the aqueous solutions of MDEA, DMAE and TEA at mass fractions of 0.2 and 0.4 as an example.

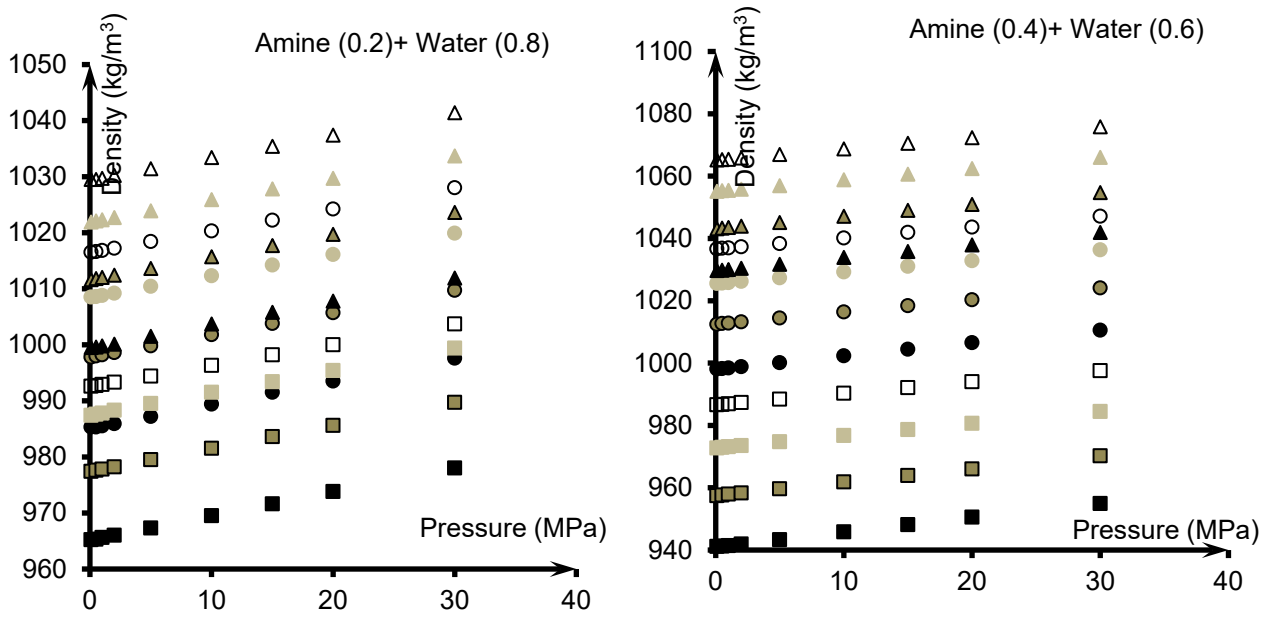

Figure. 1. Densities of the amine + water mixtures, TEA (triangle), MDEA (circle) and DMAE (square), as a function of pressure at different temperatures: (empty symbol) 293.15 K, (clear grey) 313.15 K, (dark grey) 333.15 K and (black) 353.15 K.

As can be seen in Figure 1, whether the aqueous solutions of amines are compared at the same conditions of temperature, pressure and compositions, densities follow the following sequence ρ(TEA) > ρ(MDEA) > ρ(DMAE) which is the same as the pure amines. TEA and MDEA have densities higher than water whereas DMAE density is lower than water, therefore, when the mixture is enriched in amine the density is enhanced for TEA and MDEA solutions and is decreased for DMAE mixtures. When the mass fraction of the amine is changed from 0.1 to 0.4, the increase of density ranges from 1.9% up to 2.9% for MDEA solutions and from 4.4% up to 5.1% for TEA solutions, the maximum effect is obtained at 293.15 K. In the case of DMEA solutions, the decrease of density varies from 0.8% up to 2.5%, and the maximum decrease is found at 353.15 K.

Concerning the effect of pressure, the density increases lineally with pressure, in the range of this study; this increment varies between 1% and 1.5% when the pressure is changed from 0.1 MPa to 30 MPa, being similar, regardless the amine or its amount. This effect is well quantified since the uncertainty in density is less than 0.1%.

On the other hand, density decreases with increasing temperature as expected. When temperature is increased from 293.15 K to 353.15 K, the density for the mixtures under study decreases between 2.7% up to

4.5%. In this case, a slightly different behaviour between the amines is observed. The density of TEA mixtures decreases between 2.7% up to 3.3% whereas the decrease ranges from 3% up to 3.6% for MDEA solutions and from 3.4% up to 4.5% for DMAE solutions. For the three amines, the highest effect is observed for the mixture of the highest amine content (w_{amine} = 0.4).

Results for viscosity are illustrated in Figure 2 in a similar way than for density. Viscosity is presented as a function of pressure at different isotherms for two mixtures of amine mass fraction of 0.2 and 0.4. It should be clarified that isotherm at 293.15 K for the system {MDEA (0.4) + water (0.6)} was not measured.

If the viscosities are compared for the different amine solutions at the same conditions (p, T, and w), TEA solutions are less viscous than MDEA solutions in the whole ranges of studied, and the same is true in comparison to DMAE solutions except at w_{amine} = 0.4 and T = 353.15 K; at these conditions, viscosity of DMEA mixture is less than TEA mixture. Moreover, the comparison of TEA and DMAE solutions at w_{amine} = 0.4 and T = 333.15 K, indicates that viscosity of DMAE mixture is less than TEA up to 10 MPa and above 15 MPa TEA solutions are less viscous but the differences in viscosity at this isotherm are below the uncertainty of the measurements.

The comparison between MDEA and DMAE solutions in terms of viscosity, let conclude that viscosity of DMAE solutions is higher than MDEA solutions for w_{amine} = 0.1 and 0.2 at T = 293.15 K, 313.15 K and 333.15 K, and w_{amine} = 0.3 at T = 293.15 K, and the whole pressure range (0.1 MPa to 30 MPa). On the contrary, viscosity of MDEA solutions is higher than DMAE solutions for w_{amine} = 0.2 and T = 353.15 K; w_{amine} = 0.3 and 0.4 and T = 313.15 K, 333.15 K and 353.15 K; and the whole pressure range (0.1 MPa to 30 MPa).

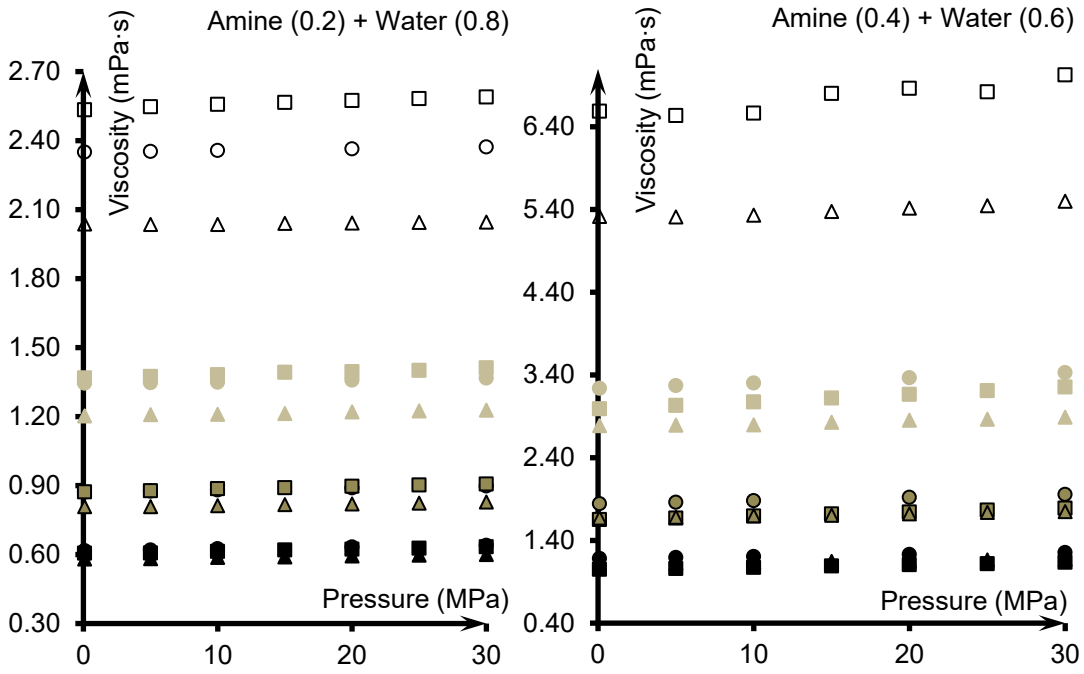

Figure. 2. Viscosities of the amine + water mixtures, TEA (triangle), MDEA (circle) and DMAE (square), as a function of pressure at different temperatures: (empty symbol) 293.15 K, (clear grey) 313.15 K, (dark grey) 333.15 K and (black) 353.15 K.

If we compare the effect on viscosity of increasing the amine composition from 0.1 to 0.4, the result is a remarkable increase: from 145% (at 353.15 K and 0.1 MPa) up to 280% (293.15 K and 30 MPa) for TEA, from 195% (at 333.15 K and 0.1 MPa) up to 271% (313.15 K and 30 MPa) for DMAE and, from 127% (at 353.15K and 0.1 MPa) up to 349% (293.15K and 30 MPa) for MDEA.

Analysing the effect of increase pressure from 0.1 MPa up to 30 MPa in the viscosity, the results are as follows: There is an increase in viscosity whose value depends on the amine and its quantity in such a way that the highest increased is observed for w_{amine} = 0.4. For the mixtures with this composition, the increase of viscosity ranges from 3.4% to 4.6% for TEA, 5.9% to 6.1% for MDEA and 6.7% up to 8.8% for DMAE, whereas the increase ranges from 1.2% to 3.6% for TEA, 2.9% to 4.7% for MDEA and 4.6% up to 6.2% for DMAE, for the w_{amine} = 0.3 mixtures. In contrast with the mixtures with w_{amine} = 0.1, whose increments in viscosity are between -1.1% up to 3.2%, being these values within the uncertainty of the measurements.

As clearly shown in Figure 2, the higher the temperature, the lower the viscosity, being the average decrease, when temperature is increased from 293.15 K up to 353.15 K, between 68.5% and 83.8% for w_{TEA} = 0.1 and

w_{DMAE} = 0.4, respectively. Moreover, the effect is greater for solutions richer in amine, for example the average decrease is 69.9 % for w_{DMAE} = 0.1 and 78.7% for w_{TEA} = 0.4.

Finally, it can be concluded that the viscosity of DMAE solutions is the most sensitive to pressure and temperature changes. For example, the viscosity varies, at T=353.15 K, from 1.050 mPa/s at *p*=0.1 MPa to 1.135 mPa/s at p= 30 MPa, and, at T=293.15 K, from 6.587 mPa/s at p=0.1 MPa to 7.027 mPa/s at p= 30 MPa, for the w_{DMAE} = 0.4 mixture.

The last comparison refers to the isobaric heat capacity that is shown in Figure 3, where this property is represented for the three amines at different conditions.

At the same conditions of temperature, pressure and composition, the isobaric heat capacity of the amine solutions studied is ordered as follows: c_p (DMAE) > c_p (MDEA) > c_p (TEA) which is the opposite to the behaviour of density and different from viscosity, as well.

When the effect of increasing pressure from 0.1 MPa to 25 MPa is quantified, the general trend is a slight decrease which is within the uncertainty of the measurements (1%) except for the mixtures w_{DMAE} = 0.3, w_{MDEA} = 0.3; and w_{TEA} = 0.4. The average decrement of isobaric heat capacity is 1.8%, 2.2% and 8.2%, respectively. This remarkable effect for the w_{TEA} = 0.4 solution is clearly shown in Figure 3.

In relation to the variation of the heat capacity with the temperature, it should be noted that for mixtures of composition 0.1, a minimum is observed at 313.15 K for TEA and at 333.15 K for MDEA and DMEA; for the other compositions, the heat capacity increases with increasing temperatures.

In order to discuss the effect of temperature on the isobaric heat capacity values, this is computed when the temperature is changed from 313.15 K to 353.15 K: The heat capacity of TEA aqueous solutions increases an average of 2.2% (w_{TEA} = 0.2), 4.1% (w_{TEA} = 0.3) and 2.8% (w_{TEA} = 0.4); the effect for MDEA solutions is an average increment of 3.1% (w_{MDEA} = 0.2), 5% (w_{MDEA} = 0.3) and 4.5% (w_{MDEA} = 0.4); and for DMAE mixtures is 3.2% (w_{DMAE} = 0.2), 5% (w_{DMAE} = 0.3), and 4% (w_{DMAE} = 0.4).

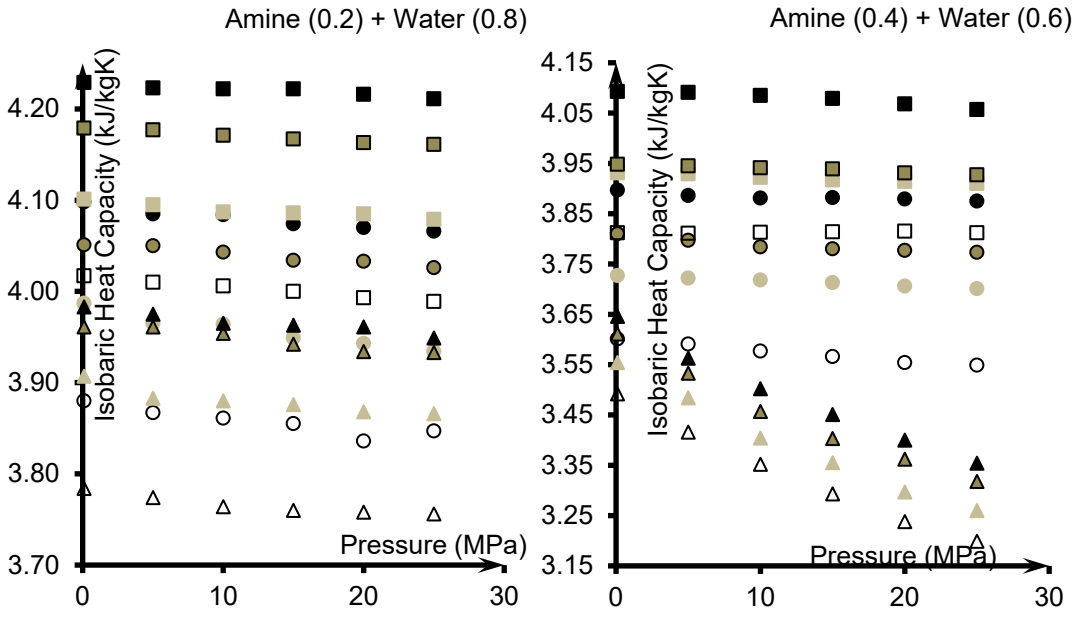

Figure. 3. Isobaric heat capacities of the amine + water mixtures, TEA (triangle), MDEA (circle) and DMAE (square), as a function of pressure at different temperatures: (empty symbol) 293.15 K, (clear grey) 313.15 K, (dark grey) 333.15 K and (black) 353.15 K.

Therefore, no significant differences are observed for the three amines, at a given composition, in relation to the effect of temperature, however, it is the amount of amine that matters. If the mass fraction of amine is increased from 0.1 to 0.4, the heat capacity of the mixtures decreases between 4% and 9% for DMAE solutions, 6% and 9% for MDEA solutions and 10% and 20% for TEA solutions.

Besides, the experimental data are fitted to semiempirical equations. The modified Tammann-Tait equation (Eq. 1) is used for density for each composition:

$$\rho(T,p) = (A_0 + A_1 T + A_2 T^2)/1 - C\, ln\left(\frac{B_0+B_1 T+B_2 T^2+p}{B_0+B_1 T+B_2 T^2+0.1MPa}\right) \quad (1)$$

On the other hand, viscosity data are correlated using the modified VFT (Vogel-Fulcher-Tammann) model, Eq. (2), for each composition, that was used by other authors [11]:

$$\eta(T,p) = \exp\left[\mathrm{a} + \mathrm{b}p + (\mathrm{c} + \mathrm{d}p + \mathrm{e}p^2)/(T - \mathrm{f})\right] \quad (2)$$

Regarding isobaric heat capacities, the following empirical correlation is used [7]:

$$c_p(p,T) = a_0 + a_1 p + a_2 T + a_3 p^2 + a_4 T^2 + a_5 pT \quad (3)$$

The fitting parameters are reported in [2,3,7], and the standard deviations obtained for the three thermophysical properties under study are summarized in Table 5.

Table 5. Results of the standard deviations σ obtained by the different fitting equation of the experimental data: density Eq. (1), viscosity Eq. (2) and isobaric heat capacity Eq. (3).

MDEA (1) + H_2O (2)	w_1 = 0.1	w_1 = 0.2	w_1 = 0.3	w_1 = 0.4
Density, Eq. (1): σ (kg/m^3)	0.029	0.018	0.0046	0.026
Viscosity, Eq. (2): σ (mPa·s)	0.0042	0.0035	0.017	0.026
Heat capacity, Eq. (3): σ (kJ/kgK)	0.023	0.006	0.008	0.013
TEA (1) + H_2O (2)	w_1 = 0.1	w_1 = 0.2	w_1 = 0.3	w_1 = 0.4
Density, Eq. (1): σ (kg/m^3)	0.164	0.146	0.130	0.0915
Viscosity, Eq. (2): σ (mPa·s)	0.0022	0.012	0.015	0.057
Heat capacity, Eq. (3): σ (kJ/kgK)	0.005	0.004	0.002	0.005
DMAE (1) + H_2O (2)	w_1 = 0.1	w_1 = 0.2	w_1 = 0.3	w_1 = 0.4
Density, Eq. (1): σ (kg/m^3)	0.162	0.119	0.0849	0.0881
Viscosity, Eq. (2): σ (mPa·s)	0.0080	0.0122	0.0213	0.0190
Heat capacity, Eq. (3): σ (kJ/kgK)	0.029	0.004	0.005	0.027

Table 5 shows that the standard deviations obtained are always lower than the expanded uncertainty of the experimental measurements: 0.7 kg/m^3 for density; 3% for viscosity or 1% for heat capacity, proving the goodness of these equations.

4. Conclusions

Experimental thermophysical properties, for amine aqueous solutions of MDEA, TEA and DMAE (at amine mass fractions of 10%, 20%, 30% and 40%) are reported and the behaviour is compared. Whether the aqueous solutions of amines are compared at the same conditions of temperature, pressure and compositions, the density of the mixtures follows the same behaviour than the pure amines: ρ(TEA) > ρ(MDEA) > ρ(DMAE) which is the same as the pure amines and wide ranges of temperature and pressure. Densities increase for richer amine solutions for MDEA and TEA but decrease for DMEA. In contrast, the heat capacity of the mixtures varies in a different order: c_p (DMAE) > c_p (MDEA) > c_p (TEA), and the heat capacity decreases for richer amine solutions for the three amines being TEA more sensitive. Finally, viscosity shows different tendencies and some differences observed are within the uncertainty of the measurements, however, viscosities of these mixtures increase with increasing amine weight fraction.

Finally, it should be noted the importance of having accurate data of these properties, since the results of these calculations will be as accurate as the properties involved in them. These measurements enrich data bases and allow to check the models which are used in the software for designing and optimizing industrial plants.

Acknowledgments

This work was supported by the Regional Government of Castilla y León and the EU-FEDER programs (VA280P18 and CLU-2019-04) and by European Union (EURAMET), Project Number: 21GRD06.

References

[1] de Meyer F., Jouenne S., Industrial carbon capture by absorption: recent advances and path forward. Current Opinion in Chemical Engineering 2022;38:100868.

[2] Sobrino M., Concepción E.I., Gómez-Hernández A., Martín M.C., Segovia J.J., Viscosity and density measurements of aqueous amines at high pressures: MDEA-water and MEA-water mixtures for CO_2 capture. J Chem Thermodyn 2016;98:231-41.

[3] Concepción E.I., Gómez-Hernández A., Martín M.C., Segovia J.J., Density and viscosity measurements of aqueous amines at high pressures: DEA-water, DMAE-water and TEA-water mixtures. J Chem Thermodyn 2017;112:227-39.

[4] Concepción E.I., Moreau A., Martín M.C., Bermejo M.D., Segovia J.J., Density and viscosity measurements of (piperazine + water) and (piperazine + 2-dimethylaminoethanol + water) at high pressures. J Chem Thermodyn. 141 (2020) 105960.

[5] Concepción E.I., Moreau A., Martín M.C., Vega-Maza D., Segovia J.J., Density and viscosity of aqueous solutions of methyldiethanolamine (MDEA) + diethanolamine (DEA) at high pressures, J. Chem. Thermodyn. 148 (2020) 106141.

[6] Concepción E.I, Moreau A., Segovia J.J., Villamañán R.M., Chamorro C.R., Martín M.C., Heat capacities of amine solutions for CO_2 capture. In: Yokoyama R., Amano Y., Editors ECOS 2020. Proceedings of the 33rd International Conference on Efficiency, Cost, Optimization, Simulation, and Environmental Impact of Energy Systems; 2020 Jun 29-July 3 Osaka, Japan. Currant Associates, Inc :1932-7.

[7] Concepción E.I., Moreau A., Vega-Maza D., Paredes X., Martín M.C. Heat capacities of different amine aqueous solutions at pressures up to 25 MPa for CO_2 capture, J. Mol. Liquids (accepted for publication) https://doi.org/10.1016/j.molliq.2023.121575.

[8] Segovia J.J., Fandiño O., López E.R., Lugo L., Martín M.C., Fernández J., Automated densimetric system: Measurements and uncertainties for compressed fluids. J Chem Thermodyn 2009;41:632-8.

[9] Zambrano J.R., Sobrino M., Martín M.C., Villamañán M.A., Chamorro C.R., Segovia J.J., Contributing to accurate high pressure viscosity measurements: Vibrating wire viscometer and falling body viscometer techniques. J Chem Thermodyn 2016;96:104-16.

[10] Segovia J.J., Vega-Maza D., Chamorro C.R., Martín M.C., High-pressure isobaric heat capacities using a new flow calorimeter. J. Supercrit. Fluids 2008;46:258-64.

[11] Harris K.R., Woolf L.A., Kanakubo, M., Temperature and pressure dependence of the viscosity of the Ionic Liquid 1-Butyl-3-methylimidazolium Hexafluorophosphate. J. Chem. Eng. Data 2005;50:1777–82.

PROCEEDINGS OF ECOS 2023 - THE 36TH INTERNATIONAL CONFERENCE ON
EFFICIENCY, **C**OST, **O**PTIMIZATION, **S**IMULATION AND ENVIRONMENTAL IMPACT OF ENERGY SYSTEMS
25-30 JUNE, 2023, LAS PALMAS DE GRAN CANARIA, SPAIN

Hybrid thermochemical cycle for cold and electricity cogeneration: experimental analysis of the process behavior and expander-reactor coupling

Hasan Ghazale[a], Nathalie Mazet[b], Pierre Neveu[c] and Maxime Perier-Muzet[d]

[a] CNRS-PROMES. Laboratoire PROcédés, Matériaux et Energie Solaire, Perpignan, France, Hasan.ghazale@promes.cnrs.fr, CA

[b] CNRS-PROMES. Laboratoire PROcédés, Matériaux et Energie Solaire, Perpignan, France, mazet@univ-perp.fr

[c] CNRS-PROMES. Laboratoire PROcédés, Matériaux et Energie Solaire, Perpignan, France, neveu@univ-perp.fr

[d] CNRS-PROMES. Laboratoire PROcédés, Matériaux et Energie Solaire, Perpignan, France, maxime.perier-muzet@univ-perp.fr

Abstract :

The valorisation of waste heat to respond to the increase demand on electricity and cooling is an important energetic challenge. For this purpose, an original hybrid thermochemical cycle is proposed: this sorption cycle is based on reversible endothermic/exothermic solid-gas reactions, and its originality lies in the integration of an expander on the gas line to provide mechanical work. This tri-thermal discontinuous cycle is able to recover medium grade waste heat (between 150 and 250 °C) to valorise it in a second step by providing cold production at its endothermic component and mechanical work - thanks to the expander - on the gas flow. Moreover, its two step operation leads to a storage functionality. While a previous study holds the thermodynamic stationary analysis of this cycle (Godefroy et al., ECOS 2019), this paper presents the experimental study part. A prototype of the hybrid thermochemical cycle, with $MnCl_2(6/2)NH_3$ (solid-gas reactants) and 1 kWe scroll expander, is developed at the laboratory. First experimentations on the prototype proved on a side the hybrid thermochemical concept by the simultaneous cold and mechanical productions during the whole reaction of the production phase, and on the other side they showed experimentally the mass coupling behaviour between the reactor and the expander in several operating conditions.

Keywords: Hybrid thermochemical cycle; Heat waste recovery; Cold and work productions; Experimental prototype.

1. Introduction

1.1. Background and state of the art

Sustainable development that meets the needs of the present without promising the ability of future generations to meet their own needs has been announced in 1987 by the World Commission on Environment and Development [1]. The acceptance and reliability of solar energy and waste heat come in the same context while considering such sources of energies as emerging sources since they are always free, endless and convertible [2]. Waste heat is highly discharged at the industrial sectors in a wide temperature range and thus participating in the increase of greenhouse gas emissions and more resource consumptions while left useless. As a step in responding to this issue, the United Nations Environment Program proposed industrial ecology, which involves studying the relationships and interactions within and between industrial systems and natural ecological systems from a systems-oriented perspective [3]. On this way also, conversion technologies and cycles based on the wide temperature ranges of the released heat at the industries were developed and set under study. Absorption chillers, adsorption beds, thermochemical reaction processes were exploited in this theme showing their adaptability in such temperature ranges (even low and medium) as chemical heat pumps for temperature upgrading. Besides, steam and organic Rankine cycles were investigated also but for power generation purposes.

As industrial waste heat has an intermittent regime, processes like thermochemical attract attention due to the storage functionality they offer.

Among such solid-gas thermochemical processes, ammoniated ones have a large diversity due to the variety of solid salts that can react with ammonia – especially the chlorides [4]. Being integrated with an expander, hybrid thermochemical cycles were defined to valorise mass and heat transfers in thermal and electrical productions. In [5], a novel "resorption" (two-salt bed reactors) cycle for cogeneration of electricity and refrigeration was proposed featuring a turbine between the high and low temperature salt reactors. Numerical analysis of a single sorption cycle was performed and investigated in [6]. Results showed a limited performance of the cycle resulted from the mutual constraint between the expansion device and the sorption unit with a detectable mismatch between them. Experimentally, by having $CaCl_2$ and activated carbon as the sorbent unit and a scroll expander, the challenges were confirmed by [7] where only unstable and weak work production was achieved during the experiment. A second experiment was performed in [8], the resorption pairs was $MnCl_2$ & $CaCl_2$, and similarly unstable work production was noticed during the short process. Such challenges haven't stopped the research, so that in [9] the use of phase change material in a heat storage system combined with a thermochemical hybrid process was addressed. In [10], more than one hundred reactive ammoniated salts were scanned and analysed in a hybrid thermochemical cycle that can recover heat below than 250 °C. Moreover, it was shown that these hybrid thermochemical cycles offer inherent cogeneration and storage capabilities, as demonstrated in [11] and [12], representing an added value compared to more traditional solutions. This paper continues the research in hybrid thermochemical processes, where an experimental prototype is developed at CNRS-PROMES permitting to validate the hybrid concept by continuous cold and mechanical productions during the production phase, and to analyse the cycle's behaviour and the coupling between the expander and the reactor in different operating conditions.

1.2. The proposed cycle

Several architectures were defined for the hybrid thermochemical cycle [13] depending on the preferred energy production: cold or mechanical. In this study, the simultaneous mode is chosen for the developed prototype: it allows a cogeneration of cold and mechanical energy as presented on the Clausius Clapeyron diagram, Figure. **1**. Figure. **2** shows the main components of the prototype: thermochemical reactor, condenser, evaporator, volumetric expander and fluid tank. The decomposition reaction of the solid-gas reactant is the charging phase where heat Q_h is supplied to the reactor at T_{hot} and the gas desorbs toward the condenser to be condensed and stored at ambient conditions T_{amb}. During the discharging phase (synthesis reaction), cold is produced by the evaporation of the condensed liquid at T_{cold} at the evaporator. This vapor flow produces then mechanical work at the expander, and after it is then involved in the synthesis reaction occurring at ambient conditions (or at a medium temperature). $MnCl_2$, (6/2) NH_3 is the chosen reactive ammoniated salt, based on its interesting thermodynamic properties and stability as shown in the analysis of [10]. The thermochemical reaction that takes place is:

$$MnCl_2.6NH_3 + \Delta h_r \rightleftarrows MnCl_2.2NH_3 + 4NH_3 \qquad (1)$$

The diagram, Figure. **1**, presents the NH3(L/G) and MnCl2(6/2) NH3 equilibrium lines for ammonia and the reaction respectively, based on the Clausius Clapeyron equilibrium equation:

$$\ln\left(\frac{p}{p_0}\right) = -\frac{\Delta h_r}{RT_r} + \frac{\Delta s_r}{R} \qquad (2)$$

where, p is the equilibrium pressure, p_0 is the reference pressure (1 bar), R is the ideal gas constant, Δh_r and Δs_r are respectively the enthalpy and the entropy of the solid gas reaction or the phase change of ammonia and T_r is the reactant temperature.

A scroll expander is integrated within the thermochemical cycle between the evaporator and the reactor. The control parameter of the bench are the temperatures and flowrates of all heat transfer fluids (HTF), with the electrical resistance at the generator bounds. Temperatures are measured with PT100 probes for the inlet/outlet of HTFs, and by numerous thermocouples inside the reactor (in the reactive solid (12 thermocouples), at the reactor wall (8 thermocouples) and in the HTF (8 thermocouples)). The pressure of the main components (evaporator, expander, condenser and reactor) and the level of liquid ammonia in the tank (linked to the reaction advancement) are also monitored.

In what follows, experimental analysis of cycle is done showing the proved concept of the hybrid thermochemical cycle and the coupling between its components.

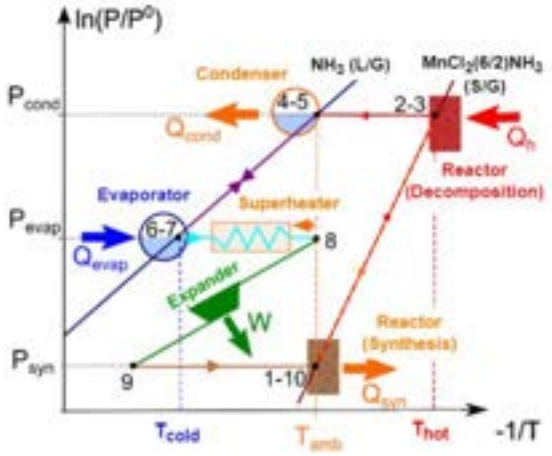

Figure. 1. Simultaneous hybrid thermochemical cycle described on the Clausius Clapeyron diagram.

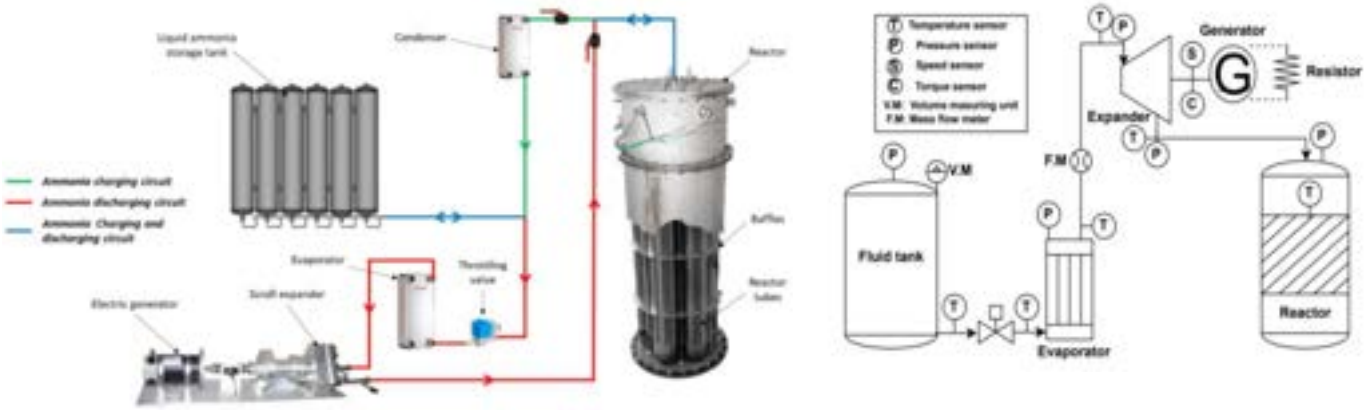

Figure. 2. Left: Schematic description of the developed prototype: reactor with 29 Kg of $MnCl_2$ & 23 kg of NH_3, 1 kWe scroll expander (bought from Air squared), condenser, evaporator, throttling valve & fluid tanks. Right: Process flow diagram: cold and mechanical productions phase.

2. Numerical analysis of the expander/reactor coupling

To analyse from a theoretical point of view the coupling between the expander and the reactor, a simplified modelling of these components has been developed.

The main hypotheses of this analysis are as follows:

- Steady state operation;
- The working fluid is considered as an ideal gas with constant heat mass capacity;
- Uniform pressure, temperature and composition are considered in each component;
- Heat losses and pressure drops are neglected;
- Variation of kinetic and potential energy are neglected.

By applying the first law on the expander, the expansion power of the working fluid can be expressed as:

$$\dot{W}_{NH_3} = \dot{m}_{swept} \cdot \Delta h_{swept} \tag{3}$$

Having the mass flow rate expression as:

$$\dot{m}_{NH_3} = \dot{m}_{swept} + \dot{m}_{leak} = \frac{p_{adm} . M_{NH_3}}{R \cdot T_{adm}} \left(\dot{V}_{swept} + \dot{V}_{leak} \right) = \frac{p_{adm} . M_{NH_3}}{R \cdot T_{adm}} \left(V_{swept} \cdot \omega + K_{leak} \cdot \sqrt{p_{adm} - p_{exh}} \right) \tag{4}$$

With p_{adm} and T_{adm} are the pressure and temperature at the expander admission, V_{swept} is the swept volume and ω the rotational speed, K_{leak} is the coefficient of internal leakage of the expander and p_{exh} is the pressure at the expander exhaust.

The enthalpy variation is expressed, considering a constant isentropic efficiency:

$$\eta_{is} = \frac{\Delta h_{swept}}{\Delta h_{is}} \rightarrow \Delta h_{swept} = \eta_{is} \cdot \Delta h_{is} \tag{5}$$

With the ideal gas assumption and a constant Cp, the swept enthalpy variation is as:

$$\Delta h_{swept} = \eta_{is} \cdot Cp_{NH3} \cdot T_{adm} \cdot \left(\left(p_{adm} / p_{exh} \right)^{\frac{1-\gamma}{\gamma}} - 1 \right) \tag{6}$$

The exhaust pressure can be expressed, thanks to the kinetic law of the reactor, as:

$$\dot{m}_{NH3} = M_{NH_3} \cdot n_{sal} \cdot \nu_r \cdot \tilde{k}_{cin} \cdot \frac{p_{exh} - p_{eq}\left(T_r\right)}{p_{exh}} \text{ and thus: } p_{exh} = \frac{p_{eq}\left(T_r\right)}{\left(1 - \frac{\dot{m}_{NH3}}{M_{NH_3} \cdot n_{salt} \cdot \nu_r \cdot \bar{k}_{cin}} \right)} \tag{7}$$

Where:

- $n_{salt,}$ $\nu_{r,}$ and $\bar{k}_{cin}$ are the number of mole of the reactive salt in the reactor, the stoichiometric coefficient of the reaction (eq. 1), and the average kinetic coefficient of the reaction;

- the solid/gas equilibrium pressure is calculated, thanks to the Clausius-Clapeyron equation (eq. 2), as a function of the reactant temperature (T_r).

The temperature T_r is calculated by applying the 1st law on the reactor wall and on the reactants:

$$\dot{m}_{NH3} \cdot \left(\frac{\Delta h_r}{M_{NH3}} - Cp_{NH3}\left(T_r - T_{exh}\right) \right) = \left(UA\right)_r \cdot \left(T_r - \bar{T}_{htf;r}\right) \quad \text{with } \bar{T}_{htf;r} = \frac{T_{out;htf;r} + T_{in;htf;r}}{2} \tag{8}$$

$$\dot{m}_{NH3} \cdot \left(\frac{\Delta h_r}{M_{NH3}} - Cp_{NH3}\left(T_r - T_{exh}\right) \right) = \left(\dot{m}Cp\right)_{htf;r} \cdot \left(T_{out;htf;r} - T_{in;htf;r}\right) \tag{9}$$

Taking into account that $\frac{\Delta h_r}{M_{NH3}} >> Cp_{NH3}\left(T_r - T_{exh}\right)$:

$$T_r \approx T_{in;htf;r} + \frac{\dot{m}_{NH3}.\Delta h_r}{M_{NH3}} \cdot \left(\frac{1}{2.\left(\dot{m}Cp\right)_{htf;r}} + \frac{1}{\left(UA\right)_r} \right) \tag{10}$$

Where $T_{out;htf;r}$ and $T_{in;htf;r}$ are the outlet and inlet temperatures of the reactor heat transfer fluid; $\left(\dot{m}Cp\right)_{htf;r}$ is the heat capacity flow of the reactor HTF; $\left(UA\right)_r$ is the heat transfer parameter of the reactor.

By combining eq.3, 6, 7 and 10, the power of working fluid expansion can be expressed as:

$$\dot{W}_{NH_3} = \dot{m}_{swept} \cdot \eta_{is} \cdot Cp_{NH3} \cdot T_{adm} \cdot \left(\left(\frac{p_{adm} \cdot \left(1 - \frac{\dot{m}_{NH3}}{M_{NH_3} \cdot n_{salt} \cdot \nu_{react} \cdot \tilde{k}_{cin}} \right)}{p_{eq}\left(T_r\right)} \right)^{\frac{1-\gamma}{\gamma}} - 1 \right) \qquad (11)$$

The eq. 4, eq.10 and eq.11 show that the power of working fluid expansion $\left(\dot{W}_{NH_3}\right)$ is mainly a function of two operating parameters: the admission pressure (p_{adm}), the expander rotational speed (ω), and one design parameter which is the heat transfer parameter $\left(UA\right)_r$ of the reactor HTF. An analysis of the evolution of $\dot{W}_{NH_3}$ by varying these 3 parameters has been carried out. All other parameters are kept constant and their values represent the characteristics of the prototype (design values or values identified from the first experiments), as shown below in Table 1.

Table 1. Main design and operating parameters for the numerical coupling analysis

Expander parameter	Value	Reactor parameter	Value
Swept volume V_{swept}	1.45×10^{-5} m^3	Number of mole of salt n_{salt}	235.9 mol
Coef. of internal leakage K_{leak}	1×10^{-6} m^{3}s^{-1}.Pa$^{0.5}$	Kinetic of the reaction $\overline{k}_{cin}$	1.5×10^{-4} s^{-1}
Isentropic efficiency η_{is}	0.6	Enthalpy of the reaction Δh_r	50.59 kJ.mol^{-1}
Admission temperature T_{adm}	20 °C	HTF heat capacity flow $\left(\dot{m}Cp\right)_{htf;r}$	1000 W.K^{-1}
		HTF inlet temperature $T_{in;htf;r}$	40 °C

The increase of the expander rotation speed (ω), (Figure. **2**), induces an increase of the swept flow and thus an increase of the working fluid mass flow $\left(\dot{m}_{NH_3}\right)$, (cf. eq. 4). This increase in the mass flow rate causes a decrease of the pressure ratio (R_p) due to the increase of the reactor's temperature (T_r), (cf. eq. 10), and an increase of the pressure difference between the exhaust pressure and the equilibrium pressure of the reaction, (cf. eq. 7). These two antagonism evolutions generate an optimum of the expansion power $\left(\dot{W}_{NH_3}\right)$. For a given rotation speed, the swept mass flow rate $\left(\dot{m}_{swept}\right)$ is fixed, and thus the increase of the total mass flow rate $\left(\dot{m}_{NH_3}\right)$ with the rise of $\left(UA\right)_r$ is related to the increase in the leaked flow $\left(\dot{m}_{leak}\right)$ generated by the higher pressure ratio. While the admission pressure is fixed (p_{adm} =1.5×10^5 Pa), the enhancement of the reactor heat transfer parameter $\left(\left(UA\right)_r\right)$ allows the decrease of the reactor temperature (T_r), (cf. eq. 10), and thus a decrease of the exhaust pressure (p_{exh}) resulting in a higher-pressure ratio. Thus, this higher-pressure ratio generates a rise in the power output with $\left(UA\right)_r$.

On the other hand, increasing the inlet pressure of the expander (Figure. **3**) induces an increase of the mass flow (cf. eq. 4). As for the previous analysis, this higher mass flow generates a decrease in the pressure ratio (Figure. **3** centre). In the case of low heat transfer parameter $\left(UA\right)_r$ at the reactor, these two behaviours lead to a decrease in the produced power, but for higher heat transfer parameters, an optimum of power production is detected (Figure. **3** right).

This coupling between the expander and the reactor has also been analysed experimentally, and presented in the following section. Experimentally, the rotational speed of the expander is modulated by a variable electrical resistor

which is connected to the electrical generator at the expander's extremities. The variation of the admission pressure is generated by a modification of the cold source temperature T_{cold}.

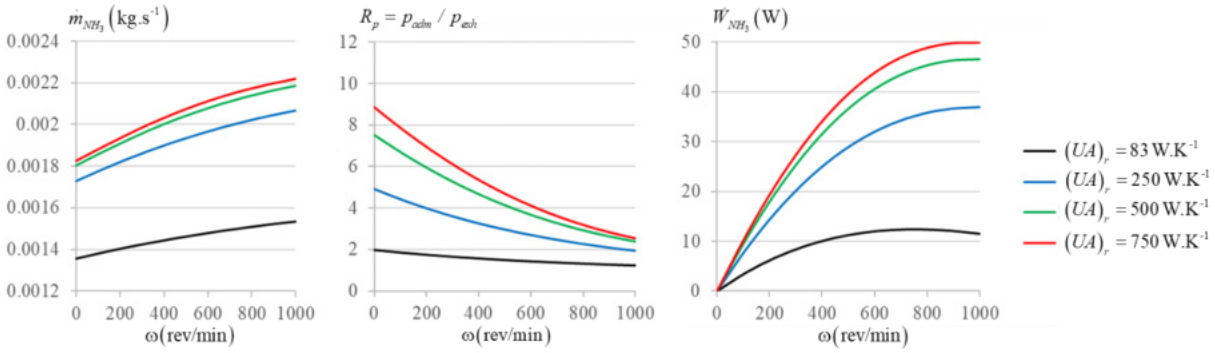

Figure. 2. Evolution of the working fluid flow rate (left), the pressure ratio (centre), the power of working fluid expansion (right) as function of the expander rotational speed for different reactor heat transfer parameter with p_{adm} =1.5×10^5 Pa.

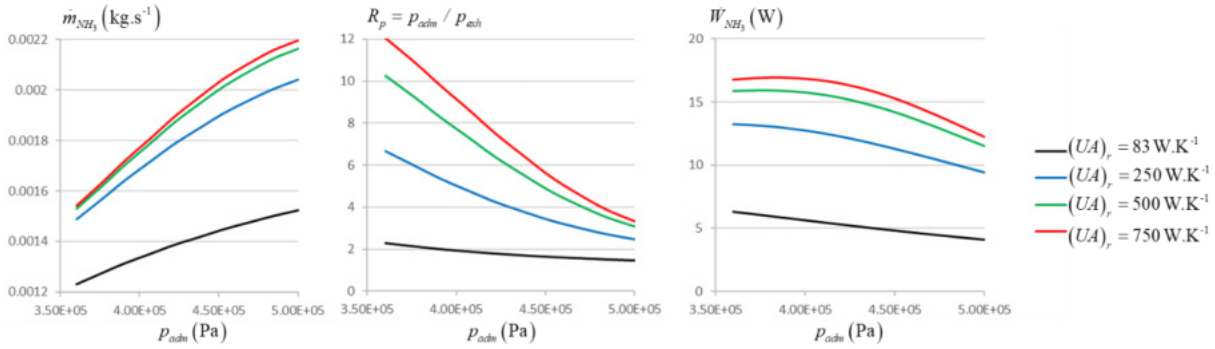

Figure. 3. Evolution of the working fluid flow rate (left), the pressure ratio (centre), the power of working fluid expansion (right) s function of the admission pressure for different reactor heat transfer parameter with ω =200 rev/min.

3. Experimental Analysis

The thermochemical cycle (reactor – condenser – evaporator) was set firstly under experimentations, by bypassing the expander. Several decomposition and synthesis reactions were done to check the reproducibility and the kinetics of the phases. Once validated [14], the expander was integrated to exploit the hybrid cycle in the discharging phase, where ammonia passes from the liquid tank to the evaporator, expander, and then to the reactor. Two protocols are set to be followed during the test of the hybrid cycle:

- The first is to fix the inlet pressure at the expander (and thus T_{cold} i.e. T^{in} and P^{in} of the expander) while varying the electrical load at the generator which will vary the coupling force with the expander, and its mechanical power. While the mechanical power is expressed as function of the pressures at the extremities of the expander, as shown in the following equation, this protocol leads to vary the outlet pressure at the expander with the electrical load and thus permits to analyse the behaviour of the cycle in such conditions.

$$\dot{W}_{mec} = \mathbf{T}_{mec}.\omega = \dot{W}_{NH_3}.\eta_{mec}$$

where $\dot{W}_{mec}$is the produced mechanical power, $\mathbf{T}_{mec}$ is the torque force between the generator and the expander, ω is the rotational speed, η_{mec} is the mechanical efficiency of the expander.

- The second is to vary the inlet pressure at the expander (and thus T_{cold}), permitting to analyse the behaviour of the expander during the discharging phase while coupled to a fixed electrical load, and thus the same coupling force with the generator.

3.1. Fixed Tcold and variable electrical charge

A first experiment with an electrical resistor of 7 Ω, connected to the generator, is done while exploiting the expander in the hybrid cycle, for a fixed T_{cold} at 10 °C at the evaporator's inlet. The inlet temperature at the reactor is set to be maintained at a medium temperature 40 °C. After the concept's validation in this experiment, more experiments are done with changing the electrical resistance to: 3.4, 31, 57, 85, 100 Ω. An experiment with a blocked expander is conducted to simulate short circuit electrical conditions, and another one without electrical charge to simulate open circuit electrical conditions, i.e. a resistor of ∞ Ω, leading to define the behaviours of the cycle at the electrical condition boundaries. In Figure. **4**, results of this first experiment are presented. The expander is rotating continuously during the whole synthesis reaction stage i.e. for a reaction advancement X between 0.1 and 0.9, proving the concept of the hybrid thermochemical cycle. After the start-up phase, the rotational speed ω of the expander decreases from 600 tr/min (i.e. the classical peak of a reaction at its beginning) till 80 tr/min for an advancement X < 0.3. Behind, an acceleration in the production is noticed where the rotational speed increased to reach 300 tr/min. Such two-level profile is also repeated in the other experiments, where the cold production and the mechanical work have always two levels during the reaction – under actual analysis. For this system analysis, results are treated as average values between the minimum and the maximum level production limits that correspond to an average of the production during an advancement of the reaction between 0.2 & 0.8.

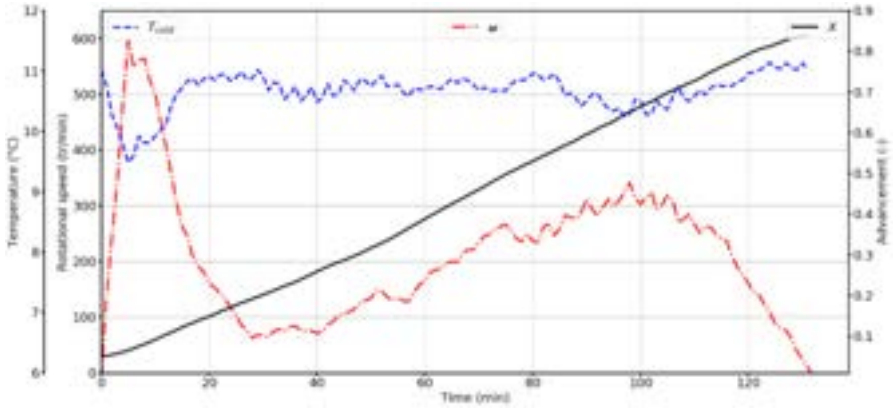

Figure. 4. Cold temperature, rotational speed of the expander during the discharging phase.

Figure. **5**, Figure. **6**, and Figure. **7** present the behaviour of the hybrid cycles for different electrical resistances. Figure. **5** presents the variation of the rotational speed ω_{av} of the expander, and the torque force $T_{mec,av}$ with the generator as function of the electrical resistor. When the expander is free, or the generator is in an open circuit electrical condition, the rotational speed reaches its maximum value while the torque force has its minimum. Coupling the electrical resistor to the generator increases the torque force on the expander and decreases its rotational speed. The maximum average rotational speed achieved by the expander was at 480 tr/min in an open circuit electrical condition. Regarding the average torque force, its maximum was at 1 N.m for a blocked expander, while the minimum was at 0.1 N.m for the open circuit experiment.

Figure. **6** shows the variation of the average mass flow rate of ammonia $\dot{m}_{av}$ and the average pressure ratio $R_{p,av}$ at the expander as function of the electrical resistor. The average mass flow rate has an increasing profile as the electrical resistance increases, whereas the pressure ratio has a decreasing one. The maximum pressure ratio achieved during the experiments is for the blocked case experiment, where $R_{p,av}$ = 1.5 and the minimum is for an open circuit electrical condition experiment, $R_{p,av}$ = 1.2. Regarding the mass flow rate of ammonia, the difference between experimental boundaries (blocked and open circuit conditions) is of 0.175 g/s. On the other side, concerning the productions of the cycle, Figure. **7**, the cold production has a negligible variation between the boundaries of the experiments, but although it shows an increasing profile while the electrical resistance increases ($Q_{c,av}$ from 1.98 to 2.1 kW). This slight increase in the cold production results from the slight increase in the mass flow rate of ammonia as the conditions changes from blocked to an open circuit. No mechanical productions are achieved while the expander is blocked, an average of 6 W is produced in open circuit conditions, and a maximum of 10.5 W is reached for a resistance of 7 Ω. The mechanical production increases to reach a maximum and then decreases while the electrical load at the generator increases presenting an optimum of the mechanical production between the blocked conditions and the experiment with an electrical resistor of 31 Ω, contrary to the cold production that increases always with the electrical resistance. This cycle's behaviour, shows the antagonistic coupling behaviour between the cold production and the mechanical power as the electrical resistance varies,

determining an optimum of the mechanical power production dependent on the mass flow rate of the gas, the coupling force and the pressure ratio at the expander.

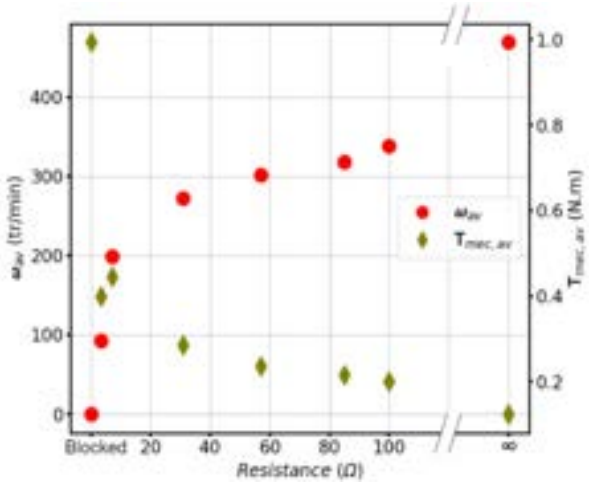

Figure. 5. Variation of the rotational speed and the mechanical torque at the expander with the electrical resistance.

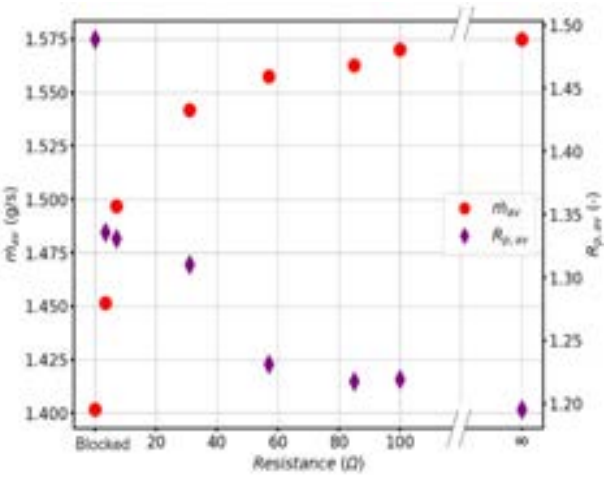

Figure. 6. Average ammonia flow rate and pressure ratio variations with the electrical resistance.

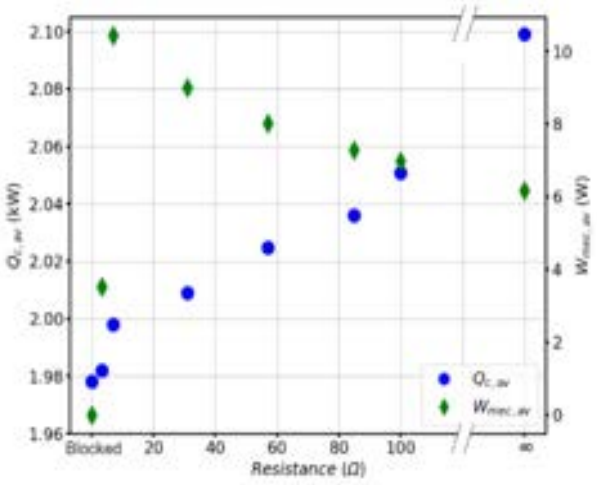

Figure. 7. Variation of the average cold and mechanical productions with the electrical resistance.

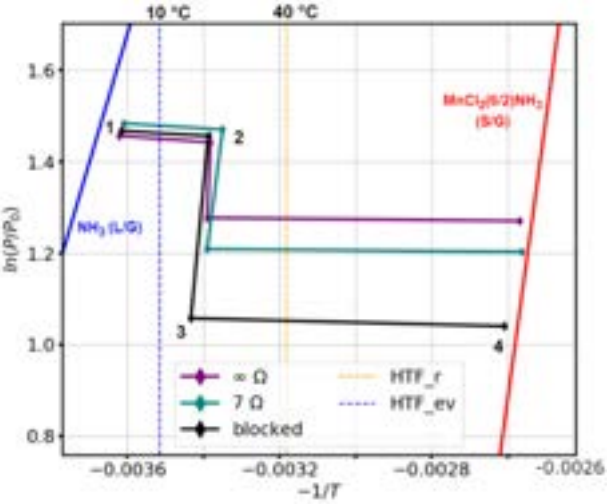

Figure. 8. Clausius Clapeyron diagram: experiments with constant Tcold but variable electrical conditions.

Whereas, the cold production is shown to be dependent on the mass flow rate as the evaporating pressure is set to be fixed by T_{cold}. These experimental results that show weak pressure ratios and mechanical productions highlight the importance of the expander's technology necessary for such hybridization objective, where such results determine an important internal leakage inside the scroll expander that affects the mechanical behaviour and the mass coupling between the components. Additionally, Figure. **5**, Figure. **6** and Figure. **7**, show that experiments done between a blocked resistor and a resistor of 31 Ω, have more important and interesting evolution of the cycle's behaviour since after this boundary its seems that the behaviour don't have a significant change - stable. Therefore, this demands to define operating electrical conditions more adaptable to the range of production of the expander in such cycles of small gas flow rates.

Within such limitation and weak productions, Clausius Clapeyron diagram in Figure. **8** still shows the mass coupling between the components of the hybrid cycle at the electrical boundary conditions and at 7 Ω (chosen since it's the cycle that achieved the maximum mechanical power). For each experiment representation on this diagram:

HTF_ev and HTF_r represents the heat transfer fluid conditions at the evaporator and the reactor respectively, points 1, 2, 3, represent respectively the temperature and pressure of ammonia at the evaporator, at the inlet of the expander, at the outlet of the expander and point 4 represents the salt's temperature and pressure during the reaction. This diagram presents clearly the difference with the classical one (where the synthesis pressure is the same as the evaporating pressure in a classical cycle but different in a hybrid one - points 1 & 4) and shows the expansion of ammonia at the expander (points 2 – 3) even with its weak ratio. Furthermore, it sheds attention to the importance of the heat sink and exchange at the reactor (to evacuate the heat of the synthesis reaction) while the salt's temperature is closer to the equilibrium temperature of the reaction than the heat transfer fluid temperature at the reactor's level.

3.2. Variable cold temperature and fixed electrical charge

Three experiments were done at three different cold temperatures: 5, 10, and 15 °C (by the glycolic water heat transfer fluid loop of the evaporator) corresponding to $P_{sat,evap}$: 5.12, 6.12, and 7.28 bar respectively. An electrical resistor of 7 Ω is connected to the generator that's coupled to the expander. The inlet temperature at the reactor is set to be maintained at a medium temperature of 40 °C (by an oil HTF loop). The following figures (Figure. **9** and Figure. **10**) present the behaviour of the hybrid cycles for these 3 cold temperatures. For a better analysis, the experimental operating conditions are plotted on the Clausius Clapeyron diagram, Figure. **11**.

The average cold production $Q_{c,av}$ at the evaporator and the average mass flow rate of ammonia $\dot{m}_{av}$ are shown in Figure. **9** and Figure. **10** for the three experiments. As T_{cold} increases (i.e. P_1 in Figure. **11**), the average mass flow rate of ammonia increases. This is due to a larger deviation from the equilibrium conditions of the synthesis reaction (i.e. the difference between $T_{HTF\text{-}r}$ and $T_{eq}(P_3)$ in Figure. **11**). This increase in the flow rate of the gas increases the average cold power production, as expected. Despite in these experiments the minimum cold temperature is fixed at 5 °C and the maximum at 15 °C, corresponding to 2.16 bar as a pressure difference between the minimum and maximum operating conditions at the evaporator' level, the difference between the average cold productions slightly changed where the average production increases from 1.85 to 2.25 kW with the increase of the average mass flow rate from 1.4 to 1.75 g/s as the cold temperature increases. At the level of the expander, the average mechanical production $\dot{W}_{mec,av}$ and the average pressure ratio $R_{p,av}$ between the inlet and the exhaust pressures are shown in Figure. **9** and Figure. **10**. The average mechanical power decreases from 10.2 to 9.6 W and the average pressure ratio from 1.55 to 1.22, as the cold temperatures increases from 5 to 15 °C. The Clausius Clapeyron diagram Figure. **11** shows for the three experiments that the salt's temperature is mostly close to its equilibrium and far from the imposed heat transfer fluid temperature HTF_r. This increase of the temperature difference between the reactive medium and the HTF, that's proposed to be a result of the weak heat transfer parameters at the reactor, imposes a higher pressure at the expander's exhaust. In the ideal case, without heat transfer limitations at the reactor, the pressure in the reactor P_3 would be smaller for the 3 cases and thus the pressure ratio of the expander $R_p = P_{in}/P_{out} = P_2/P_3$ would increase with T_{cold}, but, the experimental results show the inverse ($R_{p,av}$ = 1.49, 1.26, 1.19 for T_{cold} = 5, 10 and 15 °C respectively).

Therefore, while T_{cold} and the evaporating pressure P_1 increases, the mass flow rate of ammonia increases, which must favour in terms the mechanical power at the expander, but while on the other hand the pressure ratio of the expander decreases, the mechanical power is reduced. This behaviour demonstrates the coupling between the reactor and the expander, and numerical studies are in progress to deeper analyse this coupling, thanks to these experimental results. Besides the effect of the hot reactive medium temperature, the decrease in the pressure ratio while the evaporating pressure increases results from an important internal leakage through the scroll expander. Therefore, the leaked flow rate which flows directly to the reactor is significantly higher than the effective mass flow rate, rising the pressure at the reactor inlet, and thus resulting in low pressure ratios and an unexpected decrease in the mechanical work. This analysis, in this protocol, highlight again the important mass coupling between the expander and the reactor, with an attention to the expander's technology and the heat exchange at the thermochemical reactor during the synthesis reaction.

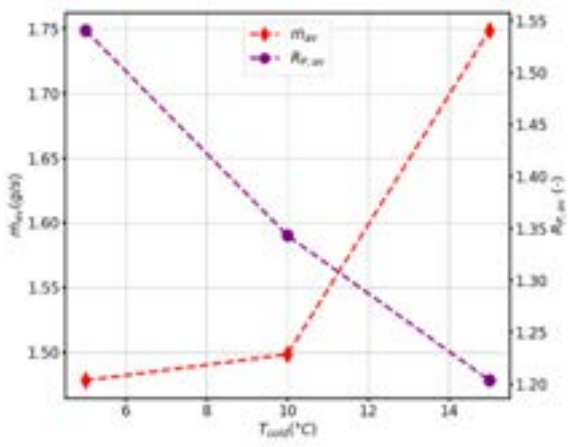

Figure. 9. Variation of the average mass flow rate and pressure report with Tcold.

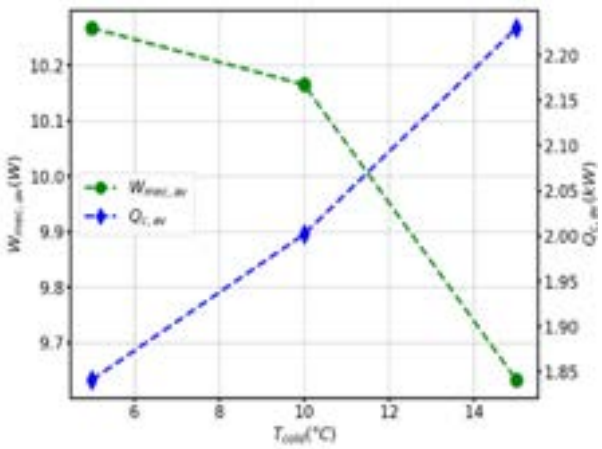

Figure. 10. Average mechanical and cold power variations with Tcold.

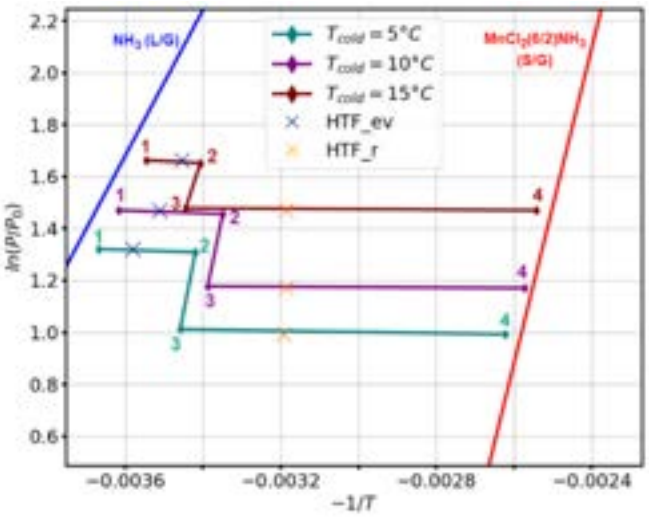

Figure. 11. Clausius Clapeyron diagram: Fixed electrical condition but variable Tcold.

4. Conclusion

A hybrid thermochemical prototype was developed at CNRS-PROMES laboratory, providing the reliability and concept validation of such hybrid cycles. Such cycle is able to recover heat at low and medium ranges below 250 °C, showing its adaptability to the integration in industrial parks for heat waste recovery. After a steady state analysis of the coupling between the expander and the reactor, first experimental tests at the laboratory showed this mass coupling behaviour between the expander and the reactor in several operating conditions. At their limits, the experiments highlight the importance of the heat sink and thermal exchanges at the reactor's level and shed attention on the technology of the expander regarding its internal leakage, as concluded from the experiments done with a fixed electrical load and variable evaporating pressures. On the other side, the experiments with a fixed evaporating pressure and variable electrical resistances defined an optimum of the mechanical production at the expander's level and showed the possibility of a control methodology at the generator's level to maintain the pressure of the synthesis reaction (or the expander's exhaust). While it could be noted that such hybrid cycle achieves the first experimental success based on what's presented in the literature, motivations to perform experimental tests on other hybrid thermochemical architectures are considered. In parallel, a numerical model developed in a previous study is set to be validated in order to go deeper in the energetic and exergetic analysis of the cycle.

Acknowledgments

This work has been financially supported by the French National Research Agency (ANR) for the purpose of the ThermHyVal project under contract ANR-20-CE05-0036 (https://anr.fr/Projet-ANR-20-CE05-0036) and by a prematuration program of the French National Centre for Scientific Research (CNRS).

Nomenclature

$CaCl_2$	calcium chloride
C_p	specific heat capacity
h	enthalpy
htf	heat transfer fluid
HTF_ev	heat transfer fluid at the evaporator
HTF_r	heat transfer fluid at the reactor
K_{leak}	leakage loss coefficient
$\bar{k}_{cin}$	kinetics of the reaction
$\dot{m}$	mass flow rate
M	molar mass, kg/mol
$MnCl_2$	Manganese (II) chloride
n	number of moles, mol
NH_3	ammonia
P	pressure, bar
Q	thermal power
R	ideal gas constant, J/(K.mol)
Rp	pressure ratio
T	temperature, °C
T	torque, N.m
UA	conductance parameter, W/K
$\dot{W}$	expansion power, W
$\dot{W}_{mec}$	mechanical power, W
X	advancement, -

Greek symbols

η	efficiency
$\boldsymbol{\omega}$	rotational speed, tr/min
ν	stoichiometric coefficient
Δ	variation
γ	adiabatic coefficient

Subscripts

av	average
cond	condensation
evap	evaporation
h	hot
cold	cold
syn	synthesis
swept	suction chambers
leak	leakage
adm	admission
exh	exhaust
is	isentropic

r	reactor
eq	equilibrium
sat	saturation
c	cold
in	inlet
out	outlet
mec	mechanical
amb	ambient

References

[1] Brundtland G, Khalid M, Agnelli S, *et al*. Our common future: the world commission on environment and development. Oxford: Oxford University Press; 1987.

[2] M.S. Choudhari, V.K. Sharma, M. Paswan, Metal hydrides for thermochemical energy storage applications, Int. J. Energy Res. 45 (2021)1–28.

[3] United Nation Environment Program. Division of technology, industry, and economics (UNEP DTIE), cleaner production (CP) activities; 2004

[4] Neveu P, Castaing J. Solid-gas chemical heat pumps: Field of application and performance of the internal heat of reaction recovery process. Heat Recover Syst CHP 1993;13(3):233–51. doi.org/10.1016/0890-4332(93)90014-M.

[5] Wang L, Ziegler F, Roskilly AP, *et al*. A resorption cycle for the cogeneration of electricity and refrigeration. Appl Energy 2013;106:56–64. doi.org/10.1016/j.apenergy.2013.01.041.

[6] Bao H, Wang Y, Roskilly AP. Modelling of a chemisorption refrigeration & power cogeneration. Appl Energy 2014;119:351–62 doi.org/10.1016/j.apenergy.2014.01.012

[7] Bao H, Wang Y *et al.* Chemisorption cooling and electric power cogeneration system driven by low grade heat. Energy 2014;72:590–8. doi.org/10.1016/j.energy.2014.05.084.

[8] Jiang L, Wang LW *et al*. Experimental study on a resorption system for power and refrigeration cogeneration. Energy 2016;97:182–90. doi.org/10.1016/j.energy.2015.12.128

[9] Jiang L, Wang LW, *et al*. Performance prediction on a resorption cogeneration cycle for power & refrigeration. Renew. Energy 2015;83. doi.org/10.1016/j.renene.2015.06.028.

[10] Godefroy A, Perier-Muzet M *et al*. Thermodynamic analyses on hybrid sorption cycles for low-grade heat storage & cogeneration of power & refrigeration. Appl Energy 2019;255:113751. doi.org/10.1016/j.apenergy.2019.113751.

[11] Godefroy A, Perier-Muzet M, Mazet N. Novel hybrid thermochemical cycles for low-grade heat storage and autothermal power generation. Appl Energy 2020;270:115111. doi.org/10.1016/j.apenergy.2020.115111.

[12] Godefroy A, Perier-Muzet M *et al*. Hybrid thermochemical cycles for low-grade heat storage & conversion. ECM 2020;225 doi.org/10.1016/j.enconman.2020.113347

[13] Godefroy A. Analyse thermodynamique et performances dynamiques de cycles hybrides impliquant des procédés sorption. PhD, U.Perpignan,2020.theses.hal.science/tel-03051549

[14] Ghazale H., Morel G., Godefroy A., *et al*. Procédé thermochimique hybride de stockage et conversion en froid et électricité d'une source thermique basse température. (SFGP 2022). sfgp2022.fr/fr/soumissions/resumes-a-telecharger.html - Transition energétique/

Finite Dimension Thermodynamics for optimizing power plants including heat storage device

Pierre Neveu[a], Baptiste Rebouillat[b], Quentin Falcoz[c]

[a] University of Perpignan Via Domitia,,Perpignan, France, pierre.neveu@univ-perp.fr
[b] PROMES-CNRS, Perpignan, France, baptiste.rebouillat@univ-perp.fr
[c] PROMES-CNRS, Odeillo, France, quentin.falcoz@promes.cnrs.fr

Abstract:

- This paper deals with the optimal integration of power plants including a storage device such as concentrated solar power plants. For such systems, numerous structures are possible, involving different number of heat exchangers, and for each of them, optimal operating temperatures to be found. Moreover, the heat storage system can be located at different temperature levels offering another degree of freedom when optimizing the whole system. If process simulators are nowadays very powerful tools for optimizing complex processes, they require to propose a primary design before any optimization steps. Finite-Dimension Thermodynamics (FDT) could help engineers to propose this primary design, close to the optimal one. To this aim, FDT method have been generalized for power generation systems including a storage device and any number of heat exchangers. An model of thermal storage system is also proposed which can be included in the FDT modelling. The optimization step consists in maximizing the power generation submitted to the thermodynamics constraints (first and second Laws) related to each heat exchangers, power block and thermal storage system. Remarkable results have been found: i) all the studied structures lead to the Curzon-Ahlborn efficiency when optimized, ii) for the same driving source (same temperature and same power), the output power production varies with N^{-2}, N being the number of the heat exchangers, iii) Charge and discharged times scenarios have a big impact on the optimal operating temperatures and on the resulting daily energy production.

Keywords:

Finite dimension thermodynamics, optimal integration, thermal storage, solar power plant.

1. Introduction

Finite-Time Thermodynamics aims to overpass the assumption of reversible, and consequently infinitely slow, transformations inherent to the Carnot cycle definition [1]. Chambadal [2] and Novikov [3] were the pioneers in 1957, proposing a power plant model that associates a reversible Carnot cycle driven by a heat source at high temperature T_H through an irreversible thermal resistance. These works were rediscover and completed by Curzon and Ahlborn [4] in 1975, who added a second thermal resistance coupling the reversible power block with the heat sink at low temperature T_L. All these previous studies were seeking the optimal temperatures between which the Carnot cycle must operate to ensure maximum power production. They demonstrated that at this maximum power point (MPP), the efficiency is equal to the so called 'nice radical efficiency' $\eta_{MPP} = 1 - \sqrt{T_L/T_H}$. De Vos [5] and Bejan [6] extended the Finite-Time Thermodynamics (FTT) to the Finite-Size or Finite-Dimension Thermodynamics (FDT) [7], [8]. The main difference is that the energy and entropy balances are here applied to the power plant itself, operating in a steady state, and not to the working fluid evolving in time over a cycle as done in FTT studies. Consequently, the method is no longer limited to Carnot engines, but can be applied for all types of engines. This leads to define endoreversible engine [5] for those internal entropy production is null or negligible. In that case, FTT and FDT lead to similar results, in particular to the nice radical efficiency at the MPP.

From these first studies, FTD/FDT methods have been successfully applied to a wide variety of systems such as refrigerators and heat pumps [9], distillation systems [10], chemical reactions [11] , wind power [12] or solar power [13]

However, the reliability of the results is often subjected to much criticism due to the assumptions underlying the FTT/FDT:

1. Linear driving force.
2. Endoreversible nature of the cycle.
3. Availability of powerful tools for industrial process optimization such as Aspen, Dymola or TRNSYS.

We obviously agree with these limitations. However, process simulators/optimisers require a mandatory first step: to propose a guessed design for initiating the optimisation process. This is the main objective of the FTT/FDT methodology: to define an initial design, deduced from thermodynamics, which could be used as a basis for further optimisation. Following this objective, the two first items seems reasonable: linear laws are commonly used in engineering pre-design, and endoreversible cycles are quite close to actual cycles as main irreversibility sources appear in the heat exchangers linking the process with the external heat sources . Moreover, Meunier et al. [14] and Castaing et al. [15] showed that an equivalent endoreversible cycle could be substituted to any sorption refrigeration irreversible cycles. This result also applies to any thermodynamics cycles. Conversely, passing from an endoreversible cycle to an actual cycle is also possible: in Reference [16], FDT method was used in order to find the optimal operating conditions of a endoreversible cycle, from which the optimal operating conditions of an actual Hirn cycle were deduced (i.e condensing and evaporating pressures and inlet turbine temperature). Nevertheless, FDT models are restricted to basic architectures of power plant: a single power cycle exchanging heat with two reservoirs through two heat exchangers (HX) whereas actual power plants often include more heat exchangers. PWR nuclear power plants use a primary heat transfer fluid (HTF), that induces two heat exchangers in the hot side: the reactor and the steam generator. In contrast, BWR use a single heat exchanger in the hot side: the reactor itself. The cooling loop can also involve one (condenser for direct through cooling) or two HXs (condenser and cooling tower for indirect cooling). A question then rises: does the HX number affect the optimal operating temperatures, the output power, and the efficiency of the cycle at the MPP? Similar issue appears for Concentrated Solar Power (CSP) plants, which can also involve one (Direct Steam Generator, DSG) or two (indirect heating) hot HXs. In addition, most of CSP plants include a thermal energy storage (TES) system, which adds complexity and diversity in possible architecture: the storage system can be direct (same fluid acts as HTF and storage medium) or indirect (two different HTFs flow in the solar loop and in the power block hot loop). Consequently, thermal storage device should be integrated in the FDT analysis. Therefore, the objectives of this work are twofold:

1. Extend the FDT methodology to processes that include a heat storage device.
2. Investigate the impact of TES and number of HX on the power plant optimal temperatures, power output and efficiency at the MMP.

In addition to these two original contributions, the optimization problem is solved without any assumption concerning the endoreversibility of the TES and the power block: the second law is treated here as an inequality while endoreversibility is usually assumed in FDT studies.

2. Problem definition

The FDT formalism requires to substitute a thermodynamic equivalent system to the real components involved in the power plant. The method is detailed in [16] and is briefly outlined here for heat exchangers and power blocks. An equivalent system is then proposed for TES systems. Finally, the optimisation problem is defined.

2.1. Equivalent heat exchanger and power block

Heat exchangers can be modelled by a thermal conductance K, transferring the heat flux $\dot{q}$ between two thermostats whose temperatures are equal to the mean entropic temperatures ($\tilde{T} = \Delta h/\Delta s$) of the cold and hot fluids. The heat flux can then be simply expressed by a Newton law:

$$\dot{q} = \mathrm{K}\left(\tilde{T}_H - \tilde{T}_L\right) \tag{1}$$

For power blocks, the same concept applies: any power cycle can be assessed through an equivalent cycle operating between two reservoirs à $\tilde{T}_H$ and $\tilde{T}_L$. For Rankine or Hirn cycles, these two temperatures are the entropic mean temperatures related to the working fluid when crossing respectively the steam generator and the condenser. First and Second Laws then write:

$$\dot{q}_H - \dot{q}_L = \dot{w} \tag{2}$$

$$\frac{\dot{q}_H}{\tilde{T}_H} - \frac{\dot{q}_L}{\tilde{T}_L} = -\dot{\sigma}_i \leq 0 \tag{3}$$

with $\dot{\sigma}_i$: internal entropy production (W/K)

$\dot{w}$: output power (W)

Notice that if $\dot{\sigma}_i$ = 0, Eqs. (2) and (3) define the endoreversible cycle.

2.2. Equivalent Thermal Energy Storage system

A two-tank heat storage device is considered (**Figure 1a**). Upstream, $\dot{m}^H$ flow enters the high temperature loop at temperature T_{out}^H, and returns to the TES system at higher temperature T_{in}^H. Downstream, $\dot{m}^M$ flow enters the medium temperature loop at T_{out}^M, and returns to the TES system at lower temperature T_{in}^M. The difference between the two mass flows is stored in or taken from either of the two tanks, hot at T^H. and cold

T^C. **Figure 1b** presents the operation scenario. Constant thermal powers are assumed here, but the method applies also for varying power. Hot loop operates during the duration t^H and the user demand is active during the duration t^M.

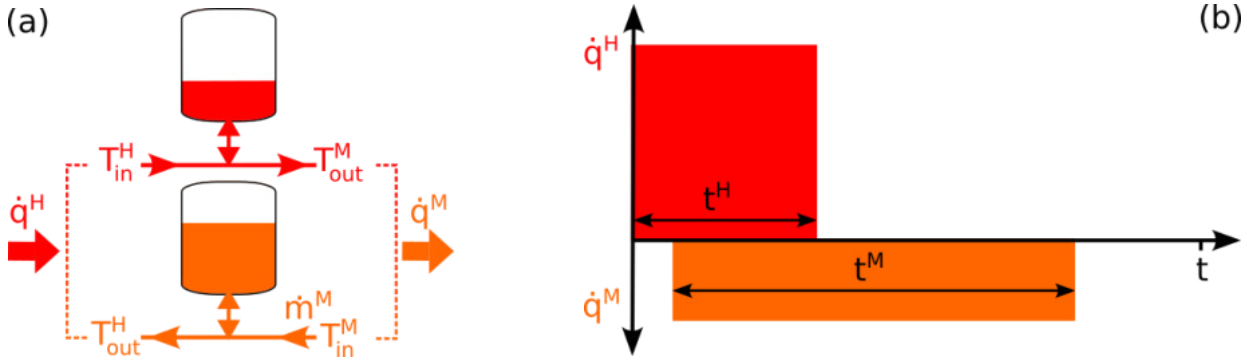

***Figure 1**. (a) 2-Tank TES system, (b) operation scenario*

Assuming a periodic stationary regime and no heat losses, energy and entropy balances related to the TES system write, on a period t:

$$\Delta U = \int_{t^H} \dot{m}^H \, (h^H_{in} - h^H_{out}) \, dt + \int_{t^M} \dot{m}^M \, (h^M_{in} - h^M_{out}) \, dt = 0 \tag{4}$$

$$\Delta S = \int_{t^H} \dot{m}^H \, (s^H_{in} - s^H_{out}) \, dt + \int_{t^M} \dot{m}^M \, (s^M_{in} - s^M_{out}) \, dt + \int_{t} \dot{\sigma}_{irr} \, dt = 0 \tag{5}$$

Posing

$$\dot{q}^H = \frac{1}{t^H} \int_{t^H} \dot{m}^H \, (h^H_{in} - h^H_{out}) \, dt \qquad \dot{q}^M = \int_{t^M} \dot{m}^M \, (h^M_{in} - h^M_{out}) \, dt \tag{6}$$

$$\tilde{T}^H = \frac{\int_{t^H} \dot{m}^H \, (h^H_{in} - h^H_{out}) \, dt}{\int_{t^H} \dot{m}^H \, (s^H_{in} - s^H_{out}) \, dt} \qquad \tilde{T}^M = \frac{\int_{t^M} \dot{m}^M \, (h^M_{in} - h^M_{out}) \, dt}{\int_{t^M} \dot{m}^M \, (s^M_{in} - s^M_{out}) \, dt} \tag{7}$$

Eqs. (3) and (4) simplify in:

$$\dot{q}^H t^H - \dot{q}^M t^M = 0 \tag{8}$$

$$\frac{\dot{q}^H t^H}{\tilde{T}^H} - \frac{\dot{q}^M t^M}{\tilde{T}^M} = - \int_{t} \dot{\sigma}_{irr} \, dt \leq 0 \tag{9}$$

Energy conservation (Eq. (8)) permits to express the 2nd law inequality according to the equivalent temperatures $\tilde{T}^H$ and $\tilde{T}^M$:

$$\tilde{T}^M - \tilde{T}^H \leq 0 \tag{10}$$

2.3. Equivalent power plant

The equivalence models allow any heat transfer fluid that undergoes a temperature change to be replaced by a thermostat whose temperature corresponds to the equivalence temperatures defined above. As an example, **Figure 2** presents the flowsheet of a CSP plant with indirect storage and its related equivalent model. All heat exchangers are replaced by a conductance, and every heat transfer fluid inlet/outlet by a thermostat. The process can be divided in three loops:

In the high temperature (HT) loop, the solar thermal flux $\dot{q}^H$ is collected and transferred to the TES system. The medium temperature (MT) loop picks up the thermal flux $\dot{q}^M$ from the TES system and transfers it to the power block. The power block consumes $\dot{q}^M$, and converts it in power $\dot{w}$ and thermal flux $\dot{q}^L$. The low temperature (LT) loop cools the power block and transfers the thermal flux $\dot{q}^L$ to the air through the cooling tower.

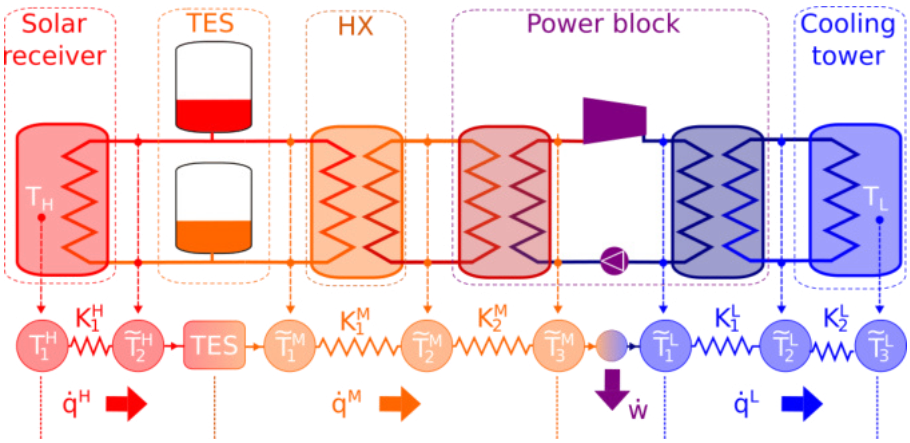

***Figure 2**. CSP plant with indirect storage. Schematic flowsheet and related equivalent system.*

2.3. Optimisation problem

To be as general as possible, the problem is defined for any number of heat exchangers in each loop. Thence, the power plant to be optimised includes (**Figure 3**):

- h heat exchangers in the HT loop,
- m heat exchangers in the MT loop,
- l heat exchangers in the LT loop.

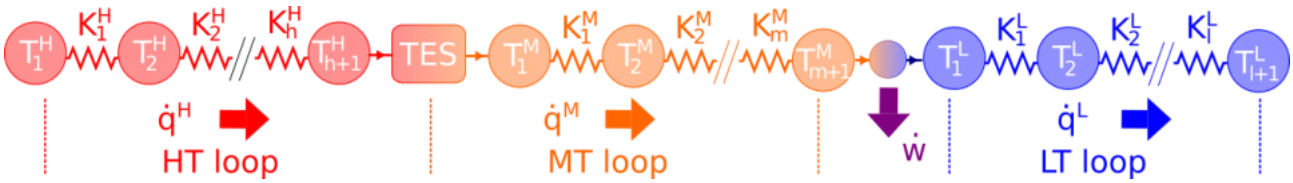

***Figure 3**. Equivalent system to be optimised.*

According to the operation scenario displayed **Figure 1b**, the mechanical energy produced per cycle is:

$$w = \dot{w}\, t^M \tag{11}$$

This quantity is maximised subjected to the following equality constraints:

1. conservation of energy for the TES, Eq. (8),
2. Newton's Law, Eq. (1), for each heat exchanger, in each loop,
3. conservation of energy for the power block, Eq. (2),
4. Equality of T_1^H and T_l^L with the temperature of the hot and cold sources,

$$T_1^H = \mathrm{T_H}, \qquad T_{l+1}^L = \mathrm{T_L} \tag{12}$$

Three inequality constraints also apply:

5. 2nd law related to the power block, Eq. (3),
6. 2nd law related to the TES system, Eq. (10),
7. Finite dimensions constraint: as each conductance must be finite, their sum is necessary also finite. Then, there exists a finite positive number K_Σ such as:

$$\sum_{i=1}^{h} K_i^H + \sum_{i=1}^{m} K_i^M + \sum_{i=1}^{l} K_i^L - K_\Sigma \leq 0 \tag{13}$$

The resolution of this optimisation problem is detailed in Appendix A. It involves $7 + 2 \cdot (h + m + l)$ optimisation variables (output power $\dot{w}$, heat fluxes $\dot{q}^H, \dot{q}^M$ and $\dot{q}^L$, $h + m + l$ conductances K_i^J, $h + m + l + 3$ temperatures T_i^J), and four optimisation parameters (durations t^H and t^M related to the operating scenario, and temperatures

of the heat source T_H and heat sink T_L). An optimal solution exists whatever the number of heat exchanger is. The main results are presented and discussed in the next section.

3. Results and discussion

The optimal solution is obtained for saturated inequality constraints (Eq. (A 31)-(A 33)).This shows logically that the TES system and the power block must be endoreversible, and that a higher K_Σ implies a higher output power. This last item appears clearly through the expression of the optimal power output (Eq. (A 66)):

$$\dot{w}^* = \frac{1}{\left(h\sqrt{t^M/t^H} + m + l\right)^2} K_\Sigma \left(\sqrt{T_H} - \sqrt{T_L}\right)^2 \tag{14}$$

which depends linearly on K_Σ. Equation (A 14) also shows how the number of heat exchangers affects the output power $\dot{w}^*$. As t^H and t^M are of same order of magnitude, the denominator represents approximatively the total number of heat exchangers $N_{HX} = h + m + l$. Thence, output power produced by the plant is approximately inversely proportional to N_{HX}. Impact of the TES can also be analysed. Increasing the ratio t^M/t^H, (i.e., increasing the storage capacity), reduces the capacity of the power block, but increases the mechanical energy provided during a cycle given by Eq. (11). **Figure 4** presents the evolution of output power $\dot{w}^*$ and mechanical energy $\dot{w}^*$ produced per day according to the production duration t^M and assuming t^H = 10 h (sunny hours in the case of CSP plant) for K_Σ = 10 MW/K, T_H = 30°C and T_H = 400°C. Three architectures are compared, all integrating an indirect cooling (cooling tower):

- Direct Steam Generation with direct storage, involving 3 HXs (h = 1, m = 0, l = 2)
- Indirect Steam Generation with direct storage, involving 3 HXs (h = 1, m = 1, l = 2)
- Indirect Steam Generation with indirect storage, involving 4 HXs (h = 1, m = 2, l = 2)

As t^H = 10h, t^M = 10 h correspond to no TES and t^M = 24 h to a continuous production implying a 14 h storage capacity.

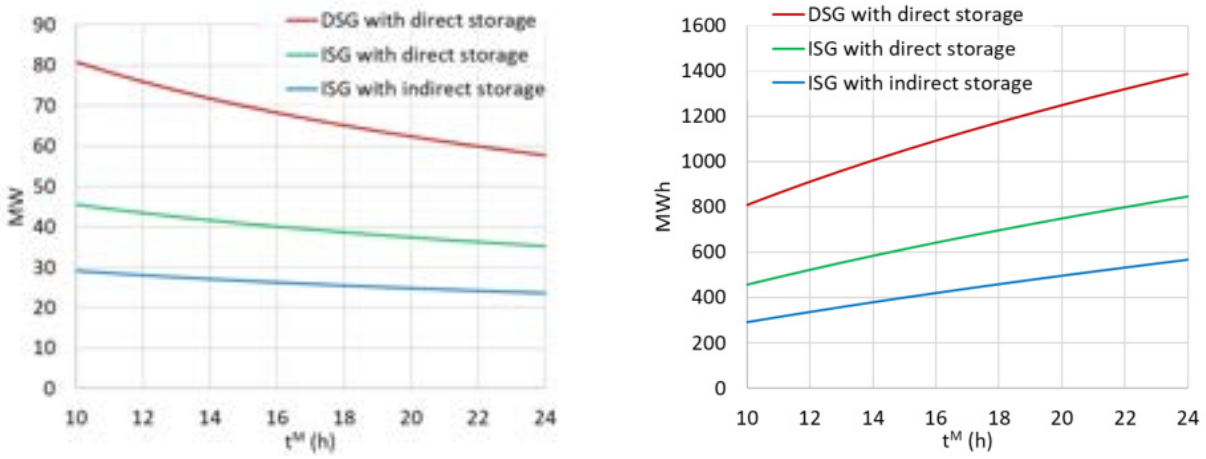

Figure 4. *Output power $\dot{w}^*$(a) and mechanical energy per day (b) according to the production duration.*

Influence of the number of HX is clearly displayed. For a constant K_Σ, which reflects the cost of the HXs, the output power or energy production evolves approximately with N_{HX}^{-2}, as mentioned above. Concerning the production duration, it decreases the power block capacity, but increases the daily production due to a longer production duration.

Another interesting result concerns the optimal conductances and driving forces. In each loop, all conductances (and consequently all driving forces because of Newton's Law) are equal. From Eqs. (A 43),(A 46) and (A 55) we have:

$$K^{L*} = K^{M*} \qquad \Delta T^{L*} = \sqrt{T_L/T_H}\ \Delta T^M \qquad \dot{q}^{L*} = \sqrt{T_L/T_H}\ \dot{q}^M \tag{15}$$

$$K^{H*} = \sqrt{t^M/t^H}\ K^* \qquad \Delta T^{H*} = \sqrt{t^M/t^H}\ \Delta T^M \qquad \dot{q}^{H*} = (t^M/t^H)\ \dot{q}^M \tag{16}$$

For the MT and LT loop downstream the TES, conductances are equal. Heat flux $\dot{q}^{L*}$ is lower $\dot{q}^{M*}$ because part of $\dot{q}^{M*}$ has been converted in power $\dot{w}^*$. Consequently, the driving force ΔT^{L*} is also lower than ΔT^{M*}.

For the HT loop, heat flux $\dot{q}^{H*}$ is higher then $\dot{q}^{M*}$, but here, the optimal solution shares equally this increase between the driving force ΔT^{K*} and the conductances K^{H*}

Finally, the energy efficiency of the plant can be deduced from (A 65) and (A 66):

$$\eta^* = \frac{\dot{w}^* t^M}{\dot{q}^{H*} t^H} = \frac{\dot{w}^*}{\dot{q}^{M*}} = 1 - \sqrt{\frac{T_L}{T_H}} \tag{17}$$

Thus, the optimal efficiency neither depends on the number of HXs, nor on the operating scenario, and is equal to the Curzon-Ahlborn efficiency. **Figure 5** compares the efficiency given by Eq.(17) with experimental efficiencies evaluated from available data sets covering many power plant architectures. The ORCs [17] correspond to the simpler structure: no TES ($t^M = t^H$), no MT loop ($m = 0$), direct or indirect cooling ($l = 1\ or\ 2$). Most of those displayed are laboratory prototypes. This could explain efficiencies sometimes much lower than η^*. For nuclear power plants [18], the hot source temperature (cladding maximum temperature) has been supposed to be 50°C higher than the reactor outlet temperature. Two architectures are presented, BWR ($h = 1$) and PWR ($h = 2$), the other parameters being similar ($t^M = t^H, m = 0, l = 1\ or\ 2$). Most of them reach or even overcome the optimal efficiency. Solar power plant [19] are also commercial plants, all including a TES, with various storage capacity ($2\ h\ < t_{storage}\ < 13\ h$), storage technology (m = 1 or 2), and involving a cooling tower (l = 2). Similarly to nuclear, the only hot temperature available in database was the solar field outlet temperature. Hot source temperatures (maximum temperature of the receiver wall) have been supposed to be 20°C (parabolic trough) or 50°C (tower) higher than the solar field outlet temperature. This figure clearly displays the fact that commercial plants, which have benefited for more than 40 years (solar) or 70 years (nuclear) of R&D fit quite well the η^* curve. That proves that Eq. (17) gives a good approximation of the efficiency of heat engines that have benefited from several decades of research and development. Therefore, we can reasonably assume that it also gives a good assessment of what the efficiency of emerging technologies will be in their future commercial form.

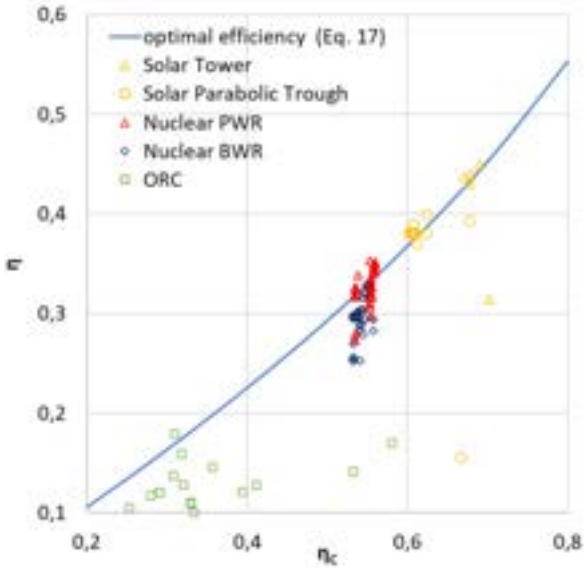

***Figure 5** : Energy efficiency of power plants from [17], [18], [19] data.*

4. Conclusion

This study aimed to extend FDT results to many power plant structures that may involve different numbers of heat exchangers and may operate with or without a TES. A general model was developed that determined the operating temperatures maximizing the power plant's output energy. A remarkable result is that the optimal efficiency is equal to the Curzon-Ahlborn efficiency, regardless the architecture of the plant and the operation scenario. However, the architecture of the plant impacts a lot the output power which varies approximatively with N_{HX}^{-2}. Concerning the operation scenario, increasing the storage capacity decreases the installed capacity of the power block but increases the daily energy output. Finally, the comparison of the actual efficiency of power plants shows that technologies that have benefited from several years of R&D achieve the Curzon Ahlborn efficiency. The latter could then be used to estimate the future performance of emerging technologies, such as combined cycles, or supercritical cycles. These technologies could take advantage of a higher temperature provided by generation IV nuclear reactors or future solar towers. Integrating these new technologies in the present analysis is one of the perspectives of this work.

Appendix A

The optimization problem is:

$\min(-\dot{w}\ t^M)$

s.t. $\dot{q}^H\ t^H - \dot{q}^M\ t^M = 0$ (A 1)

$K_i^J\left(T_i^J - T_{i+1}^J\right) - \dot{q}_i^J = 0\ , \forall\ J\ \in \{H,\ M, L\}, \forall\ i\ \in\ [1 \cdots n^J]$ (A 2)

$\dot{q}^H\ -\ \dot{q}^L -\ \dot{w} = 0$ (A 3)

$T_1^H = \mathrm{T_H}$ (A 4)

$T_{l+1}^L = \mathrm{T_L}$ (A 5)

$T_1^M - T_{h+1}^H \leq 0$ (A 6)

$\dot{q}^M/T_{m+1}^M - \dot{q}^L/T_1^L \leq 0$ (A 7)

$$\sum_{J=H,M,L}\left(\sum_{i=1}^{n^J} K_i^J\right) - K_\Sigma \leq 0 \quad \text{(A 8)}$$

The durations (t^H, t^M), the heat source temperatures ($\mathrm{T_H}$,$\mathrm{T_L}$) and the numbers of heat exchangers $n^H = h$, $n^M = m,\ n^L = l$) being taken as parameters, the Lagrangian function of this optimization problem writes:

$$\mathcal{L}\left(\dot{w}, \dot{q}^J, K_i^J, T_i^J, \lambda_i^J, \lambda_k, \mu_n\right) = \left\{\begin{array}{l} -\dot{w}\ t^M + \lambda_1(\dot{q}^H\ t^H -\ \dot{q}^M\ t^M) + \sum_{J=H,M,L}\left\{\sum_{i=1}^{n^J}\lambda_i^J\left[K_i^J\left(T_i^J - T_{i+1}^J\right) - \dot{q}^J\right]\right\} \\ +\lambda_2(\dot{q}^M -\ \dot{q}^L -\ \dot{w}) + \lambda_3(T_1^H - \mathrm{T_H}) + \lambda_4(T_{l+1}^L - \mathrm{T_L}) \\ +\mu_1(T_1^M - T_{h+1}^H) + \mu_2(\dot{q}^M/T_{m+1}^M - \dot{q}^L/T_1^L) + \mu_3\left[\sum_{J=H,M,L}\left(\sum_{i=1}^{n^J} K_i^J\right) - K_\Sigma\right] \end{array}\right\} \quad \text{(A 9)}$$

where $J\ \in \{H,\ M, L\}$, $i\ \in\ [1 \cdots n^J]$, $k\ \in\ [1 \cdots 5]$, $n \in\ [1 \cdots 2]$. The optimal conditions are:

$$\frac{\partial \mathcal{L}}{\partial \dot{w}} = -t^M -\ \lambda_2 = 0 \quad \text{(A 10)}$$

$$\frac{\partial \mathcal{L}}{\partial \dot{q}^H} = \lambda_1\ t^H - \sum_{i=1}^{h}\lambda_i^H = 0 \quad \text{(A 11)}$$

$$\frac{\partial \mathcal{L}}{\partial \dot{q}^M} = -\lambda_1\ t^M - \sum_{i=1}^{m}\lambda_i^M + \lambda_2 + \mu_2/T_{m+1}^M = 0 \quad \text{(A 12)}$$

$$\frac{\partial \mathcal{L}}{\partial \dot{q}^L} = -\sum_{i=1}^{l}\lambda_i^L - \lambda_2 - \mu_2/T_1^L = 0 \quad \text{(A 13)}$$

$$\frac{\partial \mathcal{L}}{\partial K_i^J} = \lambda_i^J\left(T_i^J - T_{i+1}^J\right) + \mu_3\ = 0, \forall\ J\ \in \{H, M, L\}, \forall\ i\ \in\ [2 \cdots n^J] \quad \text{(A 14)}$$

$$\frac{\partial \mathcal{L}}{\partial T_i^J} = \lambda_i^J K_i^J - \lambda_{i-1}^J K_{i-1}^J = 0, \qquad \forall\ J\ \in \{H, M, L\}, \qquad \forall\ i\ \in\ [2 \cdots n^J] \quad \text{(A 15)}$$

$$\frac{\partial \mathcal{L}}{\partial T_1^H} = \lambda_1^H K_1^H + \lambda_3 = 0 \quad \text{(A 16)}$$

$$\frac{\partial \mathcal{L}}{\partial T_{h+1}^{H}} = -\lambda_h^H K_h^H - \mu_1 = 0 \quad \text{(A 17)}$$

$$\frac{\partial \mathcal{L}}{\partial T_1^M} = \lambda_1^M K_1^M + \mu_1 = 0 \quad \text{(A 18)}$$

$$\frac{\partial \mathcal{L}}{\partial T_{m+1}^M} = -\lambda_m^M K_m^m - \mu_2 \, \dot{q}^M / (T_{m+1}^M)^2 = 0 \quad \text{(A 19)}$$

$$\frac{\partial \mathcal{L}}{\partial T_1^L} = \lambda_1^L K_1^L + \mu_2 \, \dot{q}^L / (T_1^L)^2 = 0 \quad \text{(A 20)}$$

$$\frac{\partial \mathcal{L}}{\partial T_{l+1}^L} = -\lambda_l^L K_l^L + \lambda_4 = 0 \quad \text{(A 21)}$$

$$\dot{q}^H \, t^H - \, \dot{q}^M \, t^M = 0 \quad \text{(A 22)}$$

$$K_i^J \left(T_i^J - T_{i+1}^J\right) - \dot{q}^J = 0, \qquad \forall \, J \in \{H, M, L\}, \qquad \forall \, i \in [1 \cdots n^J] \quad \text{(A 23)}$$

$$\dot{q}^H - \dot{q}^L - \dot{w} = 0 \quad \text{(A 24)}$$

$$T_1^H - \mathrm{T_H} = 0 \quad \text{(A 25)}$$

$$T_{l+1}^L - \mathrm{T_L} = 0 \quad \text{(A 26)}$$

$$\mu_1 (T_1^M - T_{h+1}^H) = 0, \qquad \mu_1 \geq 0, \quad \text{(A 27)}$$

$$\mu_2 (\dot{q}^M / T_{m+1}^M - \dot{q}^L / T_1^L) = 0, \qquad \mu_2 \geq 0 \quad \text{(A 28)}$$

$$\mu_3 \left(\sum_{J=H,M,L} \left(\sum_{i=1}^{n^J} K_i^J \right) - K_\Sigma \right) = 0, \qquad \mu_3 \geq 0 \quad \text{(A 29)}$$

We first demonstrate that μ_1, μ_2 and μ_3 cannot be null and then solve this system.

1. $\mu_3 = 0$

Equation (A 14) shows that all the λ_i^J should be zero, as $T_i^J - T_{i+1}^J = 0$ would imply, from (A 23), $\dot{q}^J = 0$ which is not acceptable. Therefore, $\mu_2 = 0$ from (A 19) or (A 20), and (A 13) implies that $\lambda_2 = 0$,which is forbidden from (A 10), the duration t^M being strictly positive:

$$\lambda_2 = -t^M \quad \text{(A 30)}$$

Hence, $\mu_3 \neq 0$

2. $\mu_1 = 0$

Equation (A 18) shows that λ_1^M should be zero as $K_1^M = 0$ would imply, , from (A 23), $\dot{q}^M = 0$, which is not acceptable. Therefore, Eq. (A 15) implies that all $\lambda_i^M = 0$ because $K_{\mathrm{j}}^M = 0$ would also implies $\dot{q}^M = 0$. Thence, $\mu_2 = 0$ from Eq. (A 19), which is not acceptable as seen above. Hence, $\mu_1 \neq 0$

3. $\mu_2 = 0$

Equations (A 19) shows that $\lambda_m^M = 0$ as $K_m^M = 0$ is not acceptable, because it would imply, from (A 23), $\dot{q}^M = 0$. Therefore, $\mu_2 = 0$ from (A 14), which is forbidden as seen above. Hence, $\mu_2 \neq 0$

4. $\mu_1 \neq 0$ and $\mu_2 \neq 0$ and $\mu_3 \neq 0$

Equations (A 28) and (A 29) then write:

$$T_1^M = T_{h+1}^H = \mathrm{T_{TES}}, \qquad \mu_1 \geq 0 \quad \text{(A 31)}$$

$$\frac{\dot{q}^M}{T_{m+1}^M} - \frac{\dot{q}^L}{T_1^L} = 0, \qquad \mu_2 > 0 \quad \text{(A 32)}$$

$$\sum_{i=1}^{h} K_i^H + \sum_{i=1}^{m} K_i^M + \sum_{i=1}^{l} K_i^L - K_\Sigma = 0, \quad \mu_3 > 0 \tag{A 33}$$

Equations (A 31) and (A 32) demonstrates that, quite logically:

- the optimal TES system operates reversibly,
- the optimal power block is an endoreversible engine.

Equations (A 14) and (A 23) imply:

$$\lambda_i^J = -\frac{\mu_3}{\left(T_i^J - T_{i+1}^J\right)} = -\mu_3 \frac{K_i^J}{\dot{q}^J}, \qquad \forall\, J \in \{H, M, L\}, \qquad \forall\, i \in [2 \cdots n^J] \tag{A 34}$$

Replacing λ_i^J in Eq. (A 15) gives:

$$-\frac{\mu_3}{\dot{q}^J}\left[\left(K_i^J\right)^2 - \left(K_{i-1}^J\right)^2\right] = 0, \qquad \forall\, J \in \{H, M, L\}, \qquad \forall\, i \in [2 \cdots n^J] \tag{A 35}$$

showing that, in each loop (i.e., HT, MT, or LT loops), all the conductances are equal.

$$K_i^H = K^H, \quad K_i^M = K^M, \quad K_i^L = K^M, \qquad \forall\, i \tag{A 36}$$

That also implies, from Eq. (A 34):

$$\lambda_i^H = -\mu_3 \frac{K^H}{\dot{q}^H} = \lambda^H, \qquad \lambda_i^M = -\mu_3 \frac{K^M}{\dot{q}^M} = \lambda^M, \qquad \lambda_i^L = -\mu_3 \frac{K^L}{\dot{q}^L} = \lambda^L, \qquad \forall\, i \tag{A 37}$$

$$T_i^H - T_{i+1}^H = \frac{\dot{q}^H}{K^H} = \Delta T^H, \quad T_i^M - T_{i+1}^M = \frac{\dot{q}^M}{K^M} = \Delta T^M, \quad T_i^L - T_{i+1}^L = \frac{\dot{q}^L}{K^L} = \Delta T^L, \quad \forall\, i \tag{A 38}$$

Introducing the expressions of λ_i^J in Eqs.(A 11) (A 16),(A 17),(A 18) and (A 21) gives:

$$\lambda_1 = -\mu_3 \frac{h\, K^H}{\dot{q}^H\, t^H} \tag{A 39}$$

$$\lambda_3 = \mu_3 \frac{(K^H)^2}{\dot{q}^H} \tag{A 40}$$

$$\mu_1 = \mu_3 \frac{(K^H)^2}{\dot{q}^H} = \mu_3 \frac{(K^M)^2}{\dot{q}^M} \tag{A 41}$$

$$\lambda_4 = -\mu_3 \frac{(K^L)^2}{\dot{q}^L} \tag{A 42}$$

Equations (A 22), (A 41) and (A 38) imply:

$$\dot{q}^H = \tau\, \dot{q}^M, \qquad K^H = \sqrt{\tau}\, K^M, \qquad \Delta T^H = \sqrt{\tau}\, \Delta T^M \tag{A 43}$$

with $\tau = t^M / t^H$

Expressing μ_2 from Eqs. (A 19) and (A 20), and using (A 36) and (A 37) gives:

$$\mu_2 = \mu_3\, (K^M)^2 \left(\frac{T_{m+1}^M}{\dot{q}^M}\right)^2 = \mu_3\, (K^L)^2 \left(\frac{T_1^L}{\dot{q}^L}\right)^2 \tag{A 44}$$

showing that, using (A 32):

$$K^M = K^L = K^* \tag{A 45}$$

Introducing Eqs. (A 43) and (A 45) in Eq. (A 33) gives the optimal values of the conductance K^*:

$$\mathrm{h} \cdot \sqrt{\tau}\, \mathrm{K}^* + \mathrm{m} \cdot\, \mathrm{K}^* + \mathrm{l} \cdot\, \mathrm{K}^* = K_\Sigma \implies \mathrm{K}^* = \frac{K_\Sigma}{\mathrm{h} \cdot \sqrt{\tau} + m + l} \tag{A 46}$$

Introducing the expression of λ_1(A 39), λ_2 (A 30), μ_2(A 44) and λ_i^J(A 37) in Equations (A 12) and (A 13) gives:

$$\mu_3 \left[h \frac{K^H}{\dot{q}^H} \frac{t^M}{t^H} + \mathrm{m} \ \frac{K^M}{\dot{q}^M} + T_{m+1}^M \left(\frac{K^M}{\dot{q}^M} \right)^2 \right] = t^M \tag{A 47}$$

$$\mu_3 \left[-l \ \frac{K^L}{\dot{q}^L} + T_1^L \left(\frac{K^L}{\dot{q}^L} \right)^2 \right] = t^M \tag{A 48}$$

Using (A 38) and (A 43), Equations (A 47) and (A 48) write:

$$\frac{\mu_3}{\Delta T^M} \left[h\sqrt{\tau} \ + \mathrm{m} + \frac{T_{m+1}^M}{\Delta T^M} \right] = t^M \tag{A 49}$$

$$\frac{\mu_3}{\Delta T^L} \left[-l \ + \frac{T_1^L}{\Delta T^L} \right] = t^M \tag{A 50}$$

Thence,

$$\mu_3 = \frac{t^M (\Delta T^M)^2}{\left(h\sqrt{\tau} \ + m \right) \Delta T^M + T_{m+1}^M} = \frac{t^M (\Delta T^L)^2}{-l \ \Delta T^L + T_1^L} \tag{A 51}$$

Combining (A 43), (A 25) and (A 31) gives:

$$\left(h\sqrt{\tau} \ + m \right) \Delta T^M = h \ \Delta T^H + \ m \ \Delta T^M = T_1^H - T_{h+1}^H + T_1^M - T_{m+1}^M = T_H - T_{m+1}^M \tag{A 52}$$

In a similar way, we have, using (A 26)

$$l \ \Delta T^L = T_1^L - T_{l+1}^L = T_1^L - T_L \tag{A 53}$$

Thence, Eq. (A 51) simplifies in:

$$\mu_3 = \frac{t^M (\Delta T^M)^2}{T_H} = \frac{t^M (\Delta T^L)^2}{T_L} \tag{A 54}$$

showing that:

$$\Delta T^L = \sqrt{\frac{T_L}{T_H}} \ \Delta T^M \ . \tag{A 55}$$

Combining (A 38), (A 44) and (A 55) gives:

$$\mu_2 = \mu_3 \left(\frac{T_{m+1}^M}{\Delta T^M} \right)^2 = \mu_3 \left(\frac{T_1^L}{\Delta T^L} \right)^2 \implies T_1^L = \frac{\Delta T^L}{\Delta T^M} \ T_{m+1}^M = \sqrt{\frac{T_L}{T_H}} \ T_{m+1}^M \tag{A 56}$$

Introducing (A 55) and (A 56) in (A 53) gives

$$l \sqrt{\frac{T_L}{T_H}} \ \Delta T^M = \sqrt{\frac{T_L}{T_H}} \ T_{m+1}^M - T_L \ \Rightarrow \ T_{m+1}^M = \sqrt{T_H T_L} + l \ \Delta T^M \tag{A 57}$$

Thence, (A 52) writes :

$$\left(h\sqrt{\tau} \ + m \right) \Delta T^M = T_H - \sqrt{T_H T_L} - l \ \Delta T^M \tag{A 58}$$

which gives the optimal expressions of ΔT_M^*:

$$\Delta T^{M*} = \frac{T_H - \sqrt{T_H T_L}}{h\sqrt{\tau} \ + m + l} \tag{A 59}$$

ΔT^{H*} and ΔT^{L*} are deduced respectively from (A 43) and (A 55):

$$\Delta T^{H*} = \sqrt{\tau} \frac{T_H - \sqrt{T_H T_L}}{h\sqrt{\tau} \ + m + l}, \qquad \Delta T^{L*} = \frac{\sqrt{T_H T_L} - T_L}{h\sqrt{\tau} \ + m + l} \tag{A 60}$$

All the optimization variables can be now deduced.

Conductances

Optimal conductances are given by Eqs (A 43), (A 45) and (A 46):

$$K_i^{L*} = K_i^{M*} = K^* = \frac{K_\Sigma}{\mathrm{h}\cdot\sqrt{\tau}+m+l}, \qquad K_i^{H*} = \sqrt{\tau}\,K^* = \frac{\sqrt{\tau}\,K_\Sigma}{\mathrm{h}\cdot\sqrt{\tau}+m+l} \tag{A 61}$$

Temperatures

The optimal temperature bounding the power block write, using (A 56) and (A 57):

$$T_{m+1}^{M*} = \frac{l\,T_H + \left(h\sqrt{\tau}\,+m\right)\sqrt{T_H T_L}}{h\sqrt{\tau}\,+m+l}, \qquad T_1^{L*} = \frac{l\,\sqrt{T_H T_L} + \left(h\sqrt{\tau}\,+m\right)T_L}{h\sqrt{\tau}\,+m+l}, \tag{A 62}$$

The optimal temperature of the TES ($T_{TES} = T_{h+1}^{H} = T_1^{M}$) can be deduced from (A 59) and (A 62) reminding that $m\,\Delta T^M = T_1^M - T_{m+1}^M$:

$$T_{TES}^* = \frac{(l+m)\,T_H + h\sqrt{\tau}\,\sqrt{T_H T_L}}{h\sqrt{\tau}\,+m+l} \tag{A 63}$$

General expressions for the temperatures are:

$$\begin{aligned} T_{i+1}^{H*} &= T_H - i\;\Delta T^{H*}, & i &= 0..h \\ T_{i+1}^{M*} &= T_{TES} - i\,\Delta T^{M*} & i &= 0..m \\ T_{i+1}^{L*} &= T_L + (l-i)\,\Delta T^{L*}, & i &= 0..l \end{aligned} \tag{A 64}$$

Heat flows and mechanical power

The heat flows are obtained using (A 43), (A 45),(A 46),(A 59) and (A 60):

$$\dot{q}^{H*} = \tau\,K_\Sigma\frac{T_H - \sqrt{T_H T_L}}{\left(h\sqrt{\tau}\,+m+l\right)^2}, \quad \dot{q}^{M*} = K_\Sigma\frac{T_H - \sqrt{T_H T_L}}{\left(h\sqrt{\tau}\,+m+l\right)^2}, \qquad \dot{q}^{L*} = K^*\frac{\sqrt{T_H T_L} - T_L}{\left(h\sqrt{\tau}\,+m+l\right)^2} \tag{A 65}$$

Mechanical power is obtained from (A 24). Using (A 65), we get:

$$\dot{w}^* = K_\Sigma\frac{\left(\sqrt{T_H} - \sqrt{T_L}\right)^2}{\left(h\sqrt{\tau}\,+m+l\right)^2} \tag{A 66}$$

Lagrange multipliers

Combining Eqs. (A 41), (A 54) and (A 56) gives:

$$\mu_1^* = t^M\frac{\dot{q}^{M*}}{T_H} > 0 \qquad \mu_2^* = \frac{t^M}{T_H}(T_{m+1}^{M*})^2 > 0 \qquad \mu_3^* = \frac{t^M}{T_H}(\Delta T^{M*})^2 > 0 \tag{A 67}$$

From Eqs. (A 37) to (A 42), combined with (A 54),(A 55) and (A 61) , we get

$$\begin{aligned} &\lambda_1^* = -\,h\,\frac{\Delta T^{H*}}{T_H}, \qquad \lambda_2^* = -t^M, \qquad \lambda_3^* = t^M\frac{\dot{q}^{M*}}{T_H}, \qquad \lambda_4^* = -t^M\frac{\dot{q}^{L*}}{T_L} \\ &\lambda_i^{H*} = -\,t^H\frac{\Delta T^{H*}}{T_H}, \qquad \lambda_i^{M*} = t^M\frac{\Delta T^{M*}}{T_H}, \quad \lambda_i^{L*} = -\,t^M\frac{\Delta T^{L*}}{T_L}, \qquad \forall\, i \end{aligned} \tag{A 68}$$

Nomenclature

h specific enthalpy, J/kg

K conductance, W/K

$\dot{m}$ mass flow rate, kg/s

$\dot{q}$ thermal flux, W

s specific entropy, J/(kg.K)

T temperature, °C

U Internal energy , J

S Entropy, J/K

$\dot{w}$ output power, W

Greek symbols

λ Lagrange multiplier (equality constraint)

Δ difference

η efficiency

μ Lagrange multiplier (inequality constraint)

$\dot{\sigma}$ internal entropy generation, W/K

τ operating durations ratio, $= t^M/t^H$

Subscripts and superscripts

H high temperature

h HX number in the high temperature loop

L low temperature

l HX number in the low temperature loop

M medium temperature

m HX number in the medium temperature loop

References

[1] S. Carnot, *Réflexions sur la puissance motrice du feu et sur les machines propres à développer cette puissance*. Bachelier Libraire, 1824.

[2] P. Chambadal, *Les centrales nucléaires*, Paris : A. Colin, 1957. in Armand Colin, 321. Section physique.

[3] I. I. Novikov, 'The efficiency of atomic power stations (a review)', *Journal of Nuclear Energy (1954)*, vol. 7, no. 1–2, pp. 125–128, Aug. 1958, doi: 10.1016/0891-3919(58)90244-4.

[4] F. L. Curzon and B. Ahlborn, 'Efficiency of a Carnot engine at maximum power output', *American Journal of Physics*, vol. 43, no. 1, pp. 22–24, Jan. 1975, doi: 10.1119/1.10023.

[5] A. D. Vos, 'Reflections on the power delivered by endoreversible engines', *J. Phys. D: Appl. Phys.*, vol. 20, no. 2, p. 232, Feb. 1987, doi: 10.1088/0022-3727/20/2/014.

[6] A. Bejan, 'Theory of heat transfer-irreversible power plants', *International Journal of Heat and Mass Transfer*, vol. 31, no. 6, pp. 1211–1219, Jun. 1988, doi: 10.1016/0017-9310(88)90064-6.

[7] A. Bejan, 'Entropy generation minimization: The new thermodynamics of finite-size devices and finite-time processes', *Journal of Applied Physics*, vol. 79, no. 3, pp. 1191–1218, Feb. 1996, doi: 10.1063/1.362674.

[8] M. Feidt, *Finite Physical Dimensions Optimal Thermodynamics 2 : Complex Systems*. Elsevier Science, 2018.

[9] C. H. Blanchard, 'Coefficient of performance for finite speed heat pump', *Journal of Applied Physics*, vol. 51, no. 5, p. 2471, 1980, doi: 10.1063/1.328020.

[10] M. Schaller, K. H. Hoffmann, R. Rivero, B. Andresen, and P. Salamon, 'The Influence of Heat Transfer Irreversibilities on the Optimal Performance of Diabatic Distillation Columns', *Journal of Non-Equilibrium Thermodynamics*, vol. 27, no. 3, Jan. 2002, doi: 10.1515/JNETDY.2002.015.

[11] M. J. Ondrechen, B. Andresen, and R. S. Berry, 'Thermodynamics in finite time: Processes with temperature-dependent chemical reactions', *The Journal of Chemical Physics*, vol. 73, no. 11, pp. 5838–5843, Dec. 1980, doi: 10.1063/1.440026.

[12] J. M. Gordon and Y. Zarmi, 'Wind energy as a solar-driven heat engine: A thermodynamic approach', *American Journal of Physics*, vol. 57, no. 11, pp. 995–998, Nov. 1989, doi: 10.1119/1.15783.

[13] D. Vos and A, 'Endoreversible thermodynamics of solar energy conversion', Jan. 1992, Accessed: Mar. 21, 2023. [Online]. Available: https://www.osti.gov/biblio/6010938

[14] F. Meunier, P. Neveu, and J. Castaing-Lasvignottes, 'Equivalent Carnot cycles for sorption refrigeration: Cycles de Carnot équivalents pour la production de froid par sorption', *International journal of refrigeration*, vol. 21, no. 6, pp. 472–489, 1998.

[15] J. Castaing-Lasvignottes and P. Neveu, 'Equivalent Carnot cycle concept applied to a thermochemical solid/gas resorption system', *Applied thermal engineering*, vol. 18, no. 9–10, pp. 745–754, 1998.

[16] P. Neveu, F. Ayachi, C. Leray, and Y. Azoumah, 'Optimal integration of rankine cycles in concentrated sol power plant', presented at the ECOS 2015 - 28th International Conference on Efficiency, Cost, Optimization, Simulation and Environmental Impact of Energy Systems, 2015.

[17] A. Landelle, N. Tauveron, P. Haberschill, R. Revellin, and S. Colasson, 'Organic Rankine cycle design and performance comparison based on experimental database', *Applied Energy*, vol. 204, pp. 1172–1187, Oct. 2017, doi: 10.1016/j.apenergy.2017.04.012.

[18] I. A. E. Agency, 'Operating Experience with Nuclear Power Stations in Member States', International Atomic Energy Agency, Text, 2020. Accessed: Mar. 30, 2023. [Online]. Available: https://www.iaea.org/publications/14782/operating-experience-with-nuclear-power-stations-in-member-states

[19] J. Thonig and R. Lilliestam, 'CSP.guru 2022-07-01 (2022-07-01) [Data set]. Zenodo.https://doi.org/10.5281/zenodo.7112761'. 2022.

New approach for a general expression of effectiveness

Malick Kane[a], Daniel Favrat[b]

*[a] HES-SO//FR, University of Applied Science in Fribourg, Mechanical Engineering Department (ENERGY institute), Fribourg, Switzerland, malick.kane@hefr.ch, **CA***
[b] EPFL, Ecole Polytechnique Fédérale de Lausanne, Switzerland, daniel.favrat@epfl.ch

Abstract:

Providing energy services can be achieved by various technologies or combinations of technologies and it is important to be able to characterize the quality of these different options. In practice, different indicators of the quality of energy processes can be defined: the effectiveness based only on the First Law of thermodynamics or the exergy efficiency based on the exergy balance, thus accounting for both the First and the Second Laws of thermodynamics. While the exergy efficiency definition is general and applies to all systems with values always ≤1, it is not the case of the effectiveness. Today, there is no general definition and formulation of effectiveness that can be applied to all technologies and/or energy conversion systems. The most general formulation of effectiveness given in the literature is indeed mainly valid for processes that take place above the atmospheric temperature. It must however be adapted for refrigeration systems and also for any conversion systems providing simultaneously energy services for both heating and cooling. In this article, we propose a new approach for a general expression of the effectiveness suitable for any energy conversion systems including heat pumps and cogeneration systems with combined heating and cooling. The main advantage of such a method is therefore to provide simple and generic expressions of global exergy losses and efficiencies of any systems in relation to the conventional performance indicator (the effectiveness) most commonly used by engineers to estimate energy losses of a system.

Keywords:

Thermodynamics; Exergy losses; Exergy efficiency; Effectiveness; Explicit relations of exergy

1. Introduction

Energy services can be provided by a variety of types of processes, technologies or combinations of technologies, including boilers, powerplants and heat pump/refrigeration systems with or without cogeneration(combining power, heating and/or cooling). The energy processes can take place in various forms, accompanied by different losses: internal and external losses. The internal losses are resulting from various irreversibilities (dissipations, thermal devaluation and others) while the external losses are related to the energy released to the atmosphere (heat losses, exhaust losses, energy evacuated by a cooling media). In practice, different indicators of the quality of energy processes can be defined [1,2]: the effectiveness based only on the First Law of thermodynamics or the exergy efficiency based on the exergy balance, thus accounting for both the First and the Second Laws of thermodynamics. Different approaches, formalisms and nomenclatures of the exergy analysis to identify losses in a system are reported in [3]. The exergy method applied by some authors [4, 5] consists of quantitatively evaluating the global exergy losses $\dot{L}$ on the basis of internal exergy losses $\dot{L}_D$ called also exergy destruction inside the strictly defined system and external exergy losses $\dot{L}_E$ or exergy destroyed between the system and the atmosphere and calculating the overall exergy efficiency. A general approach of exergy formulation has also been proposed in [1, 2] on the basis of an exergy balance carried out on the boundary of the system extended to the atmosphere in order to internalize and attribute all losses to the system and also by subdividing $\dot{L}$ in two subcategories: the dissipation exergy losses inside the system and the heat transfer exergy losses. Based on this approach, the performance of a system can be determined using a general formulation of efficiency by identifying all exergy services (work, heat and flow exergies) received or provided by the system. All these approaches or methods are equivalent in term of using entropy to estimate the global exergy losses and are still not frequently used in industrial sectors, as it may seem too theoretical. Besides, its application, although ideal for comparing different technologies and locating losses, is not easy for practitioners for different reasons: the concept of entropy and the potential maximum of work associated to a flow-energy (co-enthalpy) are not well understood [1].

The effectiveness (based on the First Law of thermodynamics) is most commonly used by partitioners because of the simplicity of using the energy balance equation to identify external energy losses without any knowledge of entropy. It is however not applicable to compare different technologies because of the multiple definitions that exist (engine efficiency, efficiency based on Lower Heating Value or on Higher Heating Value, heating coefficient of performance, cooling coefficient of performance). Today, there is no general definition and formulation of effectiveness that can be applied to all technologies. The most general formulation of effectiveness given in [5] is indeed only valid for processes that take place above the atmospheric temperature. It must therefore be adapted for refrigeration systems but also for any conversion systems providing simultaneously energy services for both heating and cooling.

In this article, we propose a **new approach for a general expression of the effectiveness** applied to all technologies including heat pumps when used in cogeneration with combined heating and cooling. This new approach facilitates the use of exergy theory in a way to highlight, with explicit equations, the existing link and relationship between energy and exergy losses of any system. Results of using such a method are shown for different examples of cogeneration systems with integrated technologies but also for particular basic components like boilers, heat exchangers and air-coolers. The overall exergy losses and efficiencies explicitly are expressed in function of the effectiveness and the energy services balance which can be determined in any case without any knowledge of the entropy. This can be useful for practitioners to determine and know the exergy performance of any energy system based solely on energy balance terms and the effectiveness of the system.

2. Commonly used indicators of the quality of energy processes

In practice, two different indicators of the quality of energy processes can be defined: the effectiveness (ε: so-called "thermal efficiency" or "coefficient of performance") based only on the First Law of thermodynamics or, better, the exergy efficiency (η) based on the exergy balance, thus accounting for both the First and the Second Laws of thermodynamics. The basic idea of the exergy performance indicator given in [1,2] is to use:

$$\eta = \frac{\sum_t \left[\dot{E}^-_{u,t}\right]}{\sum_t \left[\dot{E}^+_{u,t}\right]} \tag{1}$$

Where $\sum_t \left[\dot{E}^-_{u,i}\right]$ represents the total exergy services provided or delivered by the system to consumers in the form of work ($\dot{E}^-_w$), heat ($\dot{E}^-_q$) and transformation ($\dot{E}^-_y$) exergies and $\sum_t \left[\dot{E}^+_{u,t}\right]$ represents the total exergy services received by the system from utilities in the form of work ($\dot{E}^+_w$), heat ($\dot{E}^+_q$) and transformation ($\dot{E}^+_y$) exergies. All terms here are numerically positive. Considering the global exergy loss ($\dot{L}$) in the system, the ***exergy efficiency*** can then simply be formulated as follows:

$$\eta = \frac{\dot{E}^-_w + \dot{E}^-_q + \dot{E}^-_y}{\dot{E}^+_w + \dot{E}^+_q + \dot{E}^+_y} = 1 - \frac{\dot{L}}{\sum_t \left[\dot{E}^+_{u,t}\right]} \tag{2}$$

When any exergy term of the numerator exits the system without being used, the boundary of the system needs to be extended to the atmosphere and this exergy term becomes zero, but the corresponding exergy losses are still accounted for in $\dot{L}$ since the denominator has not changed. We can say that the related exergy loss is internalized and attributed to the system. For example, if the system is a combustion engine with a generator, its main service is to provide electricity, even though the cooling network has exergy that could potentially be used by others. However, if the exergy of the cooling network is not used but is destroyed in a cooling tower, it is automatically included in the exergy losses $\dot{L}$. Some authors [4, 5] subdivide $\dot{L}$ into:

$$\dot{L} = \dot{L}_D + \dot{L}_E$$

Where $\dot{L}_D$ includes the exergy destruction inside the strictly defined system and $\dot{L}_E$ includes the exergy destroyed between the system and the atmosphere. For example, if the designer knows that there is no use of the heat of an engine thermal cycle he should not only try to limit the exergy destruction inside the cycle itself but also design the cycle in such a way to try to minimize the heat exergy exiting the system.

Although different definitions of exergy efficiency can be found in the literature, a simple example will show the interest of having introduced the transformation exergy concept in its formulation. Take the heat exchanger of Figure 1 used to heat a substance (c) such as cold milk with another substance (h) e.g. hot water (two-stream heat transfer process with no phase-change).

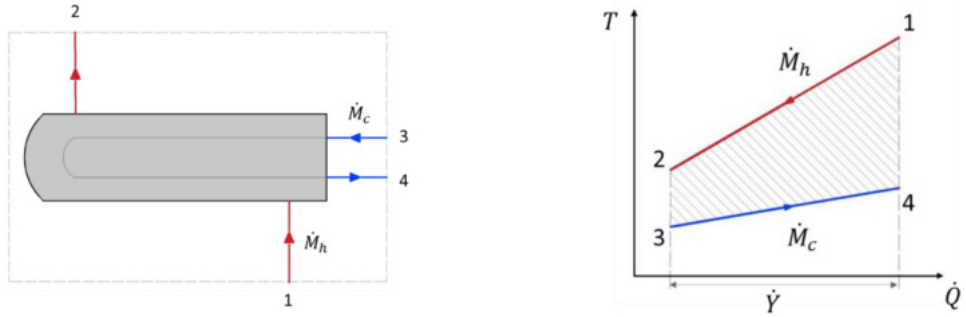

Fig. 1: Example of a heat transfer process through a heat exchanger
a) Schematic heat exchanger process, b) T-Q diagram of the hot and cold streams

The transformation (also called flow) energy ($\dot{Y}_h^+$) received by the system from the hot stream at a given temperature (T_h) is transferred through the heat exchanger to a cold stream ($\dot{Y}_c^-$) at a useful temperature (T_c). The above formulation of efficiency Eq. (2) reduces to:

$$\eta = \frac{\dot{E}_{yc}^-}{\dot{E}_{yh}^+} = \frac{\dot{M}_c\,(k_4 - k_3)}{\dot{M}_h\,(k_1 - k_2)} \leq 1 \tag{3}$$

Where $\dot{E}_{yh}^+$ is the exergy received from the hot stream (water), $\dot{E}_{yc}^-$ represents the one transferred to the cold stream (milk) through the heat exchanger and $k_j = h_j - T_a s_j$ represents the coenthalpy of the fluid in State j. That is coherent with the services provided and avoids discrepancies due to the fact that different thermodynamic references exist for the substances milk and water. Therefore an efficiency defined like:

$$\eta^* = \frac{\dot{M}_c\,k_4 + \dot{M}_h\,k_2}{\dot{M}_h\,k_1 + \dot{M}_c\,k_3} \tag{4}$$

would not be adequate to provide a coherent view of the exergy service to be provided. Furthermore, if two users refer to different thermodynamic databases they would get, for the same system, different values for the efficiency η^*. Such a confusion is avoided when using the definition η (Eq.3). It is interesting to note that the general exergy efficiency Definition (Eq.2) remains valid when a refrigeration service is demanded. In Figure 1 the milk could be cooled typically from the atmospheric temperature to a lower temperature by a water or brine achieving thus the required refrigeration service. Equation (3) remains unchanged since the cooled milk leaves with a higher exergy level while, on the other side the water loses some of its exergy from inlet to exhaust of the heat exchanger. This results from the fact that, as was shown in [1], the further the thermodynamic state of a substance, at a given pressure, is away from the dead state (atmosphere) the higher is its exergy level represented here by the coenthalpies.

It is not the same for the energy terms that do not change sign below and above the atmospheric temperature, with the exception of the heat losses to the atmosphere. The basic idea of the effectiveness is that all energy exchanges between a system and its atmospheric environment (taken from and/or released to the environment) are considered as losses. The general formulation of the ***effectiveness*** given in [1,2] (based on First Law only) in a similar manner to what has been done for the exergy efficiency would give:

$$\varepsilon = \frac{\dot{E}_w^- + \dot{Q}_i^- + Y_n^-}{\dot{E}_w^+ + \dot{Q}_i^+ + Y_n^+} \qquad T > T_a \tag{5}$$

This expression is indeed only valid for processes that take place above the atmospheric temperature and can take values between 0 and ∞. The effectiveness, as defined from the general Equation (Eq.2), is not an absolute quality indicator like the exergy efficiency is. It is still commonly used but mainly for relative comparison between system alternatives providing the same service. To illustrate this, let us consider the case of a simple heat pump for heating (a) and cooling (b) applications given in Figure 1.

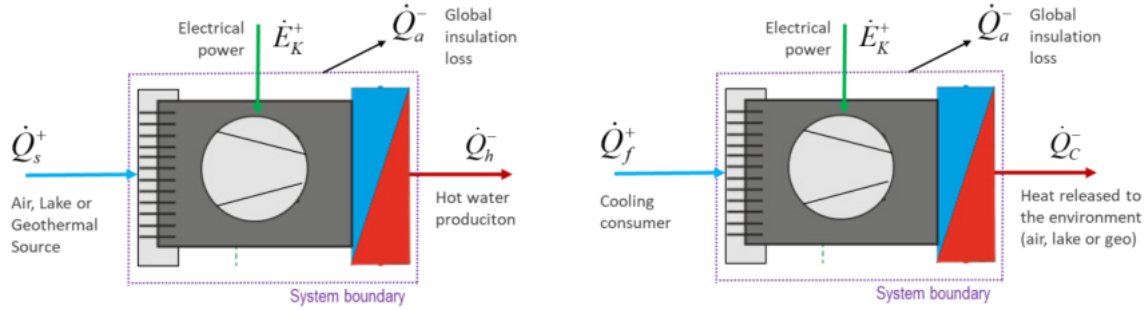

Fig. 2: Example of a vapor compression simple heat pump system: (a) for a heating, (b) for a cooling

For this case of a heat pump, the system boundary is defined by the closed cycle refrigerant (working fluid), so that the thermal energy exchanges with the exterior (with the user and/or the environment) are represented by thermal-heat only ($\dot{Q}$); there is no flow-energy ($\dot{Y}$) exchanged between the system and the exterior.

For the **heating** application, the system receives electricity ($\dot{E}_w^+ = \dot{E}_K^+$) and captures heat-energy ($\dot{Q}_s^+$) from the environment to deliver thermal heat ($\dot{Q}_h^-$) to a user for hot water production. Knowing that $\dot{Q}_s^+$ heat energy comes from the environment and is therefore "free" and thus not accounted for, the heating effectiveness $\boldsymbol{\varepsilon_h}$ obtained from Eq. (5) becomes:

$$\varepsilon_h = \frac{\dot{Q}_h^-}{\dot{E}_w^+} \geq 1 \quad (6)$$

Because the numerical value of this indicator is always higher than one and thus can no more semantically be called an "efficiency", this heating effectiveness is commonly called "coefficient of performance of heating (COP_h)".

The situation is different for the heat pump with **cooling** application of Figure 2b. The system receives electricity ($\dot{E}_w^+ = \dot{E}_K^+$) and provides cooling service to consumer by extracting energy ($\dot{Q}_f^+$) at low temperature and rejecting heat ($\dot{Q}_c^-$) to the environment at higher temperature. For this basic application, the cooling effectiveness $\boldsymbol{\varepsilon_f}$ is commonly defined in the literature by the following equation (Eq. 7) and is therefore not coherent for an effectiveness determined from the Eq. (5):

$$\varepsilon_f = \frac{\dot{Q}_f^+}{\dot{E}_w^+} \geq 1 \quad (7)$$

It can also take any numerical value between 0 and ∞, reason why it is commonly called *coefficient of performance of cooling* (COP_f) instead. For both applications of heating and cooling, the exergy efficiency based on Eq. (2) can be applied and the numerical value of these indicators are always lower than one, reason why we use the term of efficiency with the difference of the effectiveness:

$$\eta_h = \frac{\dot{E}_{qh}^-}{\dot{E}_w^+} < 1 \quad (8)$$

$$\eta_f = \frac{\dot{E}_{qf}^-}{\dot{E}_w^+} < 1 \quad (9)$$

While the exergy efficiency definition Eq. (2) is general and applies to all systems, it is not the case of the effectiveness (Eq. 5). The latter cannot be applied to all technologies and/or energy conversion systems. It is indeed only valid for processes that take place above the atmospheric temperature ($T \geq T_a$) and therefore must be adapted for refrigeration systems and also for any conversion systems providing simultaneously energy services for both heating and cooling.

3. New approach for a general expression of the effectiveness

3.1. A general expression of effectiveness applied to all technologies

To circumvent some of the difficulties to define a general expression for the effectiveness we propose the following expression in such a way to highlight $(\dot{U}_{0t})$ which represents the difference between the inlet services (work, gas, biomass…) expended for the system and the outlet services (work, heating and/or cooling) delivered by the system:

$$\varepsilon = \frac{\sum_t [\dot{U}_t^-]}{\sum_t [\dot{U}_t^+]} = 1 - \frac{\dot{U}_{0t}}{\sum_t [\dot{U}_t^+]} \quad (10)$$

Where $\sum_t [\dot{U}_t^-]$ is the total energy services provided or delivered by the system to users and $\sum_t [\dot{U}_t^+]$ represents the total energy services received by the system from utilities. Considering the different form of outlet energy services, the inlet/outlet ***energy services balance*** ($\dot{U}_{0t}$) can then clearly be formulated as follows:

$$\dot{U}_{0t} = \sum_t [\dot{U}_t^+] - \left(\sum_w [\dot{E}_w^-] + \sum_h [\dot{U}_h^-] + \sum_f [\dot{U}_f^+] \right) \quad (11)$$

Where each term (given in bracket) is a numerically positive value and the indices w, h and f refer to the types of energy services delivered or supplied by the system:

- $\sum_w [\dot{E}_w^-]$ mechanical or electrical energy services that can be **delivered** by the system
- $\sum_h [\dot{U}_h^-]$ hot services **delivered** by a system for a heating application
- $\sum_f [\dot{U}_f^+]$ cold services **supplied** by a system for a cooling application

This later term corresponds to a positive value because the main service in a cooling application is not to deliver heat but to capture heat at a temperature T_f lower than that of the ambient like in a fridge or any refrigeration system.

The inlet/outlet ***energy services balance*** ($\dot{U}_{0t}$) could also be obtained by using the First Law equation [1] and by separating the energy service terms from the total energy exchanged with the environment ($\dot{Q}_a^-$):

$$\sum_k \dot{E}_{w_k}^+ + \sum_i \dot{Q}_i^+ + \sum_n \dot{Y}_n^+ = \dot{Q}_a^- \quad (12)$$

$\dot{Q}_a^-$ may be exchanged in different forms such as heat transferred between the system and the environment, e.g. water, soil, air ($\dot{Q}_0^-$) and/or flow energy evacuated to the atmosphere, e.g. exhaust gases ($\dot{Y}_0^-$). The term $\dot{Q}_0^-$ may also include thermal losses due for example to the imperfection of the insulation.

A distinction is made because the terms $\dot{Q}_0^- and\ \dot{Y}_0^-$ may include some valuable energies taking into account that the level of temperature of the fluid T_0 could be higher or lower than the ambient temperature T_a. This expression of the First Law Eq. (12) could also be reformulated by using the numerically positive values of energy services defined above and by highlighting the balance of energy exchanges with the environment:

$$\sum_t \left[\dot{U}_t^+\right] - \left(\sum_w \left[\dot{E}_w^-\right] + \sum_h \left[\dot{U}_h^-\right] + \sum_f \left[\dot{U}_f^-\right]\right) = \dot{Q}_0^- + \dot{Y}_0^- \quad (13)$$

By subtracting the First law equation Eq. (13) from the inlet/outlet energy services equation Eq. (11), the inlet/outlet energy services balance ($\dot{U}_{0t}$) can lead to the following general equation, as function of the total energy exchanged between the system and its environment:

$$\dot{U}_{0t} = \dot{Q}_0^- + \dot{Y}_0^- - 2\sum_f \left[\dot{U}_f^+\right] \quad (14)$$

This result shows clearly the difference between the heating and cooling application in term of the effectiveness. In a heating application, $\dot{U}_{0t}$ is equal to the total energy exchanged with the environment ($\dot{Q}_a^- = \dot{Q}_0^- + \dot{Y}_0^-$) but it is not the case for a cooling application where $\dot{U}_f^+ \neq 0$. This result can be interpreted by the fact that the cold utility (or refrigerant) in the system is considered in the balance for both capturing heat from the user and providing cooling services to the same user.

Example of a simple heat pump system for heating application

Let us apply this definition to the previous examples, starting with the case of the heat pump for heating (Figure 2a). The energy service provided to customers corresponds to $\dot{Q}_h^-$ and the energy service received by the system is the electrical power ($\dot{E}_k^+$). There are no cooling services and no work or electric production for this application:

- $\sum_h \left[\dot{U}_h^-\right] = \dot{Q}_h^-$ Heating service
- $\sum_f \left[\dot{U}_f^+\right] = 0$ No cooling service for this application
- $\sum_w \left[\dot{E}_w^-\right] = 0$ No work or electrical production

There is no flow exchanged with environment ($\dot{Y}_0^- = 0$) and the heat exchanged with environment is represented by $\dot{Q}_0^- = \dot{Q}_s^-$. The energy balance based on the two equations of energy services Eq. (11) and energy exchange between the system and the environment Eq.(14) can be done as:

$$\dot{U}_{0t} = \dot{E}_k^+ - \dot{Q}_h^- = \dot{Q}_a^- - \dot{Q}_s^+ \quad (16a)$$

Therefore, the effectiveness of the general Equation Eq. (10) corresponds to COP_h according to:

$$\varepsilon_h = 1 - \frac{\dot{E}_k^+ - \dot{Q}_h^-}{\dot{E}_K^+} = \frac{\dot{Q}_h^-}{\dot{E}_K^+} = COP_h \quad (16b)$$

$$\varepsilon_h = 1 + \frac{\dot{Q}_s^+}{\dot{E}_K^+} \quad (16c)$$

A same result can be obtained by using Eq. 5 for this process of heating services which takes place above the atmospheric temperature.

Example a simple refrigeration system for cooling application:

In the case of the refrigeration unit of Figure 2b, the energy service provided to customers corresponds to $\dot{Q}_f^+$ and the energy service received by the system is the electrical power ($\dot{E}_k^+$). There are no heating services and no work or electric production for this application:

- $\sum_f \left[\dot{U}_f^+\right] = \dot{Q}_f^+$ Cooling service
- $\sum_h \left[\dot{U}_h^-\right] = 0$ No heating service for this application

- $\sum_w[\dot{E}_w^-] = 0$ No work or electrical production

There's no flow exchanged with environment ($\dot{Y}_0^- = 0$) and the heat exchanged with environment is represented by $\dot{Q}_0^- = \dot{Q}_c^-$. The energy balance based on the two equations of energy services Eq. (11) and energy exchange between the system and the environment Eq. (14) can be done as:

$$\dot{U}_{0t} = \dot{E}_k^+ - \dot{Q}_f^+ = \dot{Q}_c^- - 2\,\dot{Q}_f^+ \tag{17a}$$

Therefore, the effectiveness of the general Equation (Eq.10) corresponds to COP_f according to:

$$\varepsilon_f = 1 - \frac{\dot{E}_k^+ - \dot{Q}_f^+}{\dot{E}_K^+} = \frac{\dot{Q}_f^+}{\dot{E}_K^+} = COP_f \tag{17a}$$

$$\varepsilon_f = 1 - \frac{\dot{Q}_c^- - 2\,\dot{Q}_f^+}{\dot{E}_K^+} \tag{17a}$$

This result could not be obtained with Eq. (5) for this process of refrigeration that take place at a temperature level below the atmospheric temperature and also for any energy conversion processes providing simultaneously energy services for both heating and cooling (for example with heat pumps in cogeneration). For such cogeneration applications, the energy balance based on Eq. (11) and Eq. (14) can be done as:

$$\dot{U}_{0t} = \dot{E}_k^+ - \dot{Q}_h^- - \dot{Q}_f^+ = -2\,\dot{Q}_f^+ \tag{18a}$$

Therefore, the effectiveness of the general Equation Eq. (10) corresponds to $\varepsilon = \varepsilon_h + \varepsilon_f$ according to:

$$\varepsilon = 1 - \frac{\dot{E}_k^+ - \dot{Q}_h^- - \dot{Q}_f^+}{\dot{E}_K^+} = \frac{\dot{Q}_h^- + \dot{Q}_f^+}{\dot{E}_K^+} = \varepsilon_h + \varepsilon_f \tag{18b}$$

$$\varepsilon = 1 + \frac{2\,\dot{Q}_f^+}{\dot{E}_K^+} = 1 + 2\,\varepsilon_f \tag{18c}$$

Considering Eq. (18b) and Eq. (18c), we can deduce the well-known simple relation between the effectiveness for heating (ε_h) and cooling (ε_f):

$$\varepsilon_h = \varepsilon_f + 1 \tag{19}$$

3.2. A general relationship between energy and exergy indicators

From the equations of exergy efficiency (Eq.2) and effectiveness (Eq.10), a generic relationship can be deduced for the overall exergy losses and efficiencies of any energy conversion technologies as a function of the conventional performance indicators (engine efficiency, efficiency based on Lower Heating Value or on Higher Heating Value, heating coefficient of performance, cooling coefficient of performance) most commonly used by engineers to estimate various energy losses of a system:

$$\frac{\dot{L}}{\dot{U}_{0t}} = \frac{1-\eta}{1-\varepsilon}\,.\,R_{E/X} \tag{20}$$

Where $R_{E/X}$ represents the ratio of exergy services received by the system ($\sum_t[\dot{E}_{ut}^+]$) to the energy services expanded for the system ($\sum_t[\dot{U}_t^+]$). This ratio of exergy/energy is generally known for different sources and/or technologies. For electric vapor compression heat pumps, it is equal to the unity ($R_{E/X} = 1$); for thermal power cycle units, it corresponds to the Carnot factor related to the temperature level of the source ($R_{E/X} = 1 - T_a/\bar{T}_g$); For industrial fuels in combustion boilers, it can be determined by the coefficients given in [6, 7].

Such a general formulation of Eq. (20) can be applied to develop explicit relations between the global exergy losses ($\dot{L}$) and the external energy exchanges ($\dot{U}_{0t}$) with the environment (taken from and/or released to environment) and for any energy conversion technologies.

In fact, $\dot{U}_{0t}$ represents the difference between the inlet and the outlet energy services and can be determined or estimated in any case without any **knowledge of the entropy**. This can be very useful for practitioners to determine and know the exergy performance of any energy system based solely on energy balance terms and the effectiveness of the system.

4. Explicit relations of exergy losses for cogeneration technologies

4.1. Combined heat and power cogeneration systems

Any energy conversion system receiving heat-energy services ($\dot{Q}_g^+$) from a **hot** source at a given temperature level ($\bar{T}_g$) to both produce mechanical or electrical energy services ($\dot{E}_w^-$) and supply heat energy services ($\dot{Q}_h^-$) to a heating system at a lower temperature level ($\bar{T}_h$) is considered as a combined heat and power system.

There are many types of power-heat cogeneration plants based on steam turbine (ST) or organic fluid turbine (ORC), gas turbine (GT) and combined gas-steam cycle power plant technologies (CC), which can be found in particular in the chemical or food industry, in household waste incineration plants and of course in district heating thermal power stations. Figure 3 shows an example of a cogeneration plant with a power plant combining electricity and heat using the thermal energy of combustion gases in a boiler to generate steam which drives a power generation turbine. Steam extraction at an intermediate enthalpy level is used to provide energy services for the production of superheated water for a district heating network.

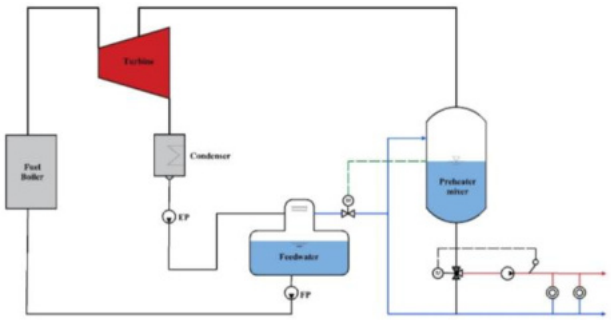

Figure 3: Schematic diagram of the example of steam turbine cycle cogeneration system

Other more decentralized cogeneration systems based on internal combustion engine or fuel cell technologies are used for small scale applications, e.g. in building.

For the example of the cogeneration system given in figure 3: the hot source is represented by the combustion gases ($\dot{Q}_g^+$) in the boiler, the output energy services are the net electricity production ($\dot{E}_w^- = \dot{E}_T^- - \dot{E}_P^+$, meaning the balance between the production in the turbine and the consumption in the various pumps) and the heat energy ($\dot{Q}_h^-$) obtained from the vapor extraction is to supply the heating circuit in the network.

Let us consider the general case of cogeneration where $\dot{Q}_a^-$ represents the heat losses to the atmosphere because of non-perfect insulated components, $\dot{Q}_0^-$ the quantity of energy released from the condenser and $\dot{Y}_0^-$ the exhaust energy out of the boiler. In this case, $\dot{U}_{0t}$ can be expressed by the following relations for steady state operation and based on Eq. (11) and Eq. (14):

$$\dot{U}_{0t} = \dot{Q}_g^+ - \left(\dot{E}_w^- + \dot{Q}_h^-\right) \qquad \dot{U}_{0t} = \dot{Q}_a^- + \dot{Q}_0^- + \dot{Y}_0^- \tag{21}$$

Thus, the effectiveness for cogeneration (ε) based on Eq. (10) can be given by:

$$\varepsilon = 1 - \frac{\dot{U}_{0t}}{\dot{Q}_g^+} = \frac{\dot{E}_w^- + \dot{Q}_h^-}{\dot{Q}_g^+} = \varepsilon_e + \varepsilon_h \tag{22}$$

Where $\varepsilon_e = \dot{E}_w^- / \dot{Q}_g^+$ represents the effectiveness for electricity production and $\varepsilon_h = \dot{Q}_h^- / \dot{Q}_g^+$ represents the effectiveness for heating. A same result can be obtained by using Eq. 5 for this process of cogeneration which takes place above the atmospheric temperature.

Same reasoning can be applied to determine the overall exergy efficiency (η) by the general equation (Eq. 2):

$$\eta = \frac{\dot{E}_w^- + \dot{E}_{qh}^-}{\dot{E}_{qg}^+} \tag{23}$$

Where $\dot{E}_{qg}^+$ represents the heat-exergy received by the system from the hot source and $\dot{E}_{qh}^-$ represents the heat-exergy provided by the system to the user for heating.

The exergy efficiency can then be determined by considering the Carnot factors related to the temperature levels of the hot source ($\bar{T}_g$) and of the heating system ($\bar{T}_h$):

$$\eta = \frac{\dot{E}_w^- + \left(1 - \frac{T_a}{\bar{T}_h}\right) \dot{Q}_h^-}{\left(1 - \frac{T_a}{\bar{T}_g}\right) \dot{Q}_g^+} = \frac{\varepsilon_e + \left(1 - \frac{T_a}{\bar{T}_h}\right) \varepsilon_h}{1 - \frac{T_a}{\bar{T}_g}} \tag{24}$$

In general, these temperature levels of the source and the heating system are initially known. Thus, improving the exergy performance of a cogeneration system shall involve also improving the effectiveness ($\varepsilon = \varepsilon_e + \varepsilon_h$) and therefore minimizing the total energy released to the environment Eq. (21). To illustrate this, we can apply the general expression for exergy losses Eq. (10) by replacing the exergy efficiency η by its value defined in Eq. (24). We can thus express the exergy losses in the most general form by the following relations:

$$\dot{L}_g = \left[1 + \frac{T_a}{1 - \varepsilon}\left(\frac{\varepsilon_h}{\bar{T}_h} - \frac{1}{\bar{T}_g}\right)\right] \dot{U}_{0t} \tag{25}$$

Or on the basis of the system input energy:

$$\dot{L}_g = \left[1 - \varepsilon + T_a\left(\frac{\varepsilon_h}{\bar{T}_h} - \frac{1}{\bar{T}_g}\right)\right] \dot{Q}_g^+ \tag{26}$$

Two components of exergy losses can be distinguished: external exergy losses that are exactly equal to the energy releases to the environment (and therefore become zero for a system without energy exchange with the atmosphere) and internal exergy losses (exergy destruction) that are related to the temperature difference between source and user. The exergy losses by destruction in the system increase not only with the temperature difference but are lower the higher the source and user temperature levels are. The lower the temperature levels, the higher the losses for the same temperature difference.

Equation (24), Eq. (25) and Eq. (26) are general for any cogeneration system with or without combustion exhaust gases, using for example boiler, gas turbine or internal combustion engine technologies for which the overall effectiveness is less than unity (ε<1) taking into account the exhaust losses to the chimney ($\dot{Y}_0^-$) as well as the possible heat losses to the atmosphere ($\dot{Q}_a^-$) because of the high gas temperature. They can also be used for various particular or supposed cases for power generation only (powerplants), for small organic ranking cycles with cogeneration effectiveness close to unity (ε<1) and/or for simple heating applications with boilers or network substations with a perfectly insulated heat exchanger.

Case of **a powerplant:** Zero effectiveness for heating (ε_h=0) corresponds to a **power system** where the energy received from the hot source is only for producing mechanical or electrical energy and all energy that can be recovered from the cold source at lower temperature Th is destroyed to the atmosphere. This is the case for example for many **power-plants**. Thus, Eq. (24) and Eq. (26) become:

$$\eta = \frac{\varepsilon_e}{1 - T_a/\bar{T}_g} \qquad \dot{L}_g = \left[1 - \varepsilon_e - \frac{T_a}{\bar{T}_g}\right] \dot{Q}_g^+ \tag{27}$$

This is a well-known and particular relationship between the exergy efficiency of a power system, the effectiveness and the ideal effectiveness based on the Carnot factor.

Case of **a cogeneration system** based on **Organic Rankine Cycle:** Effectiveness of cogeneration equal to unity (ε=1) corresponds to a perfectly insulated–cogeneration system ($\dot{Q}_a^- = 0$) without any exhaust energy to the atmosphere ($\dot{Y}_0^- = 0$) and where the energy received from the hot source is totally used for producing mechanical or electrical energy and all residual and available energy of the cold source at lower temperature $\bar{T}_h$ is recovered for cogeneration. The external energy losses are zero ($\dot{U}_{0t} = 0$) and part of the exergy received is destroyed in the system. It is the case for example for cogeneration systems using **closed power-cycles e.g. with organic rankine cycles** which are supposed to be perfectly insulated. Equations (24) and Eq. (26) become:

$$\eta = \frac{1 - T_a/\bar{T}_h\,(1 - \varepsilon_e)}{1 - T_a/\bar{T}_g} \qquad \dot{L}_g = \left[T_a\left(\frac{1 - \varepsilon_e}{\bar{T}_h} - \frac{1}{\bar{T}_g}\right)\right] \dot{Q}_g^+ \tag{28}$$

Case of a **heating system with boiler or heat exchanger only:** Zero effectiveness for electricity (ε_e=0) corresponds to a **heating system** where the energy received from the hot source is only for supplying heat energy services ($\dot{Q}_h^-$) to a heating system at a lower temperature level ($\bar{T}_h$). Losses to the atmosphere ($\dot{U}_{0t}^-$) can take place in different forms, due for example to a defect in the insulation of system components ($\dot{Q}_a^- = 0$) or for exhaust gases ($\dot{Y}_0^- = 0$). This is the case for example for **heat transfer process with boiler or heat exchanger**. Thus, Eq. (26) and Eq. (28) become:

$$\eta = \frac{1 - T_a/\bar{T}_h}{1 - T_a/\bar{T}_g}\,\varepsilon_h \qquad \dot{L}_g = \left[1 - \varepsilon_h + T_a\left(\frac{\varepsilon_h}{\bar{T}_h} - \frac{1}{\bar{T}_g}\right)\right]\dot{Q}_g^+ \tag{29}$$

For all these above applications, one can show the important role of the temperature in the assessment of the overall exergy losses or efficiencies. To illustrate this, let us consider for example Eq. (31) by using the temperature difference ($\Delta T = \bar{T}_g - \bar{T}_h$) between the hot gases and the heating process. The following expressions are obtained:

$$\dot{L}_h = \left[(1 - \varepsilon_h)\left(1 - \frac{T_a}{\bar{T}_g}\right) + \varepsilon_h\,\frac{T_a}{\bar{T}_g}\,\frac{\Delta T}{\bar{T}_h}\right]\dot{Q}_g^+ \tag{30}$$

$$\eta_h = \varepsilon_h\left[1 - \frac{T_a}{\bar{T}_g - T_a}\,\frac{\Delta T}{\bar{T}_h}\right] \tag{31}$$

Two components of exergy losses can be distinguished: external heat transfer exergy losses that are rather related to the temperature level of the source (and therefore become zero for a system without energy exchange with the atmosphere) and internal heat losses (devaluation of energy) that are related to the temperature difference between source and user. The exergy losses by external transfer do increase with the temperature level of the source while the exergy losses by internal heat devaluation increase not only with the temperature difference but are lower the higher the source and user temperature levels are. The lower the temperature levels, the higher the exergy losses for the same temperature difference. The temperature therefore plays an important role in the assessment of the overall exergy losses and irreversibilities.

These expressions of exergy losses Eq. (30) and efficiency Eq. (31) for a heat transfer process not only classify but also define the qualities that any heat transfer system between a source and a user must have. Figures 4 show for a given effectiveness like in a heat exchanger ($\varepsilon_h = 1$) the influence of temperature difference between hot and cold streams on the specific exergy loss and efficiency in the heat transfer process, by considering respectively the parametric curves of the consumer's useful temperature ($\bar{T}_h$) and the temperature level of the hot source ($\bar{T}_g$). The specific exergy loss is given by the following $\alpha_L = \dot{L}_g/\dot{Q}_g^+$.

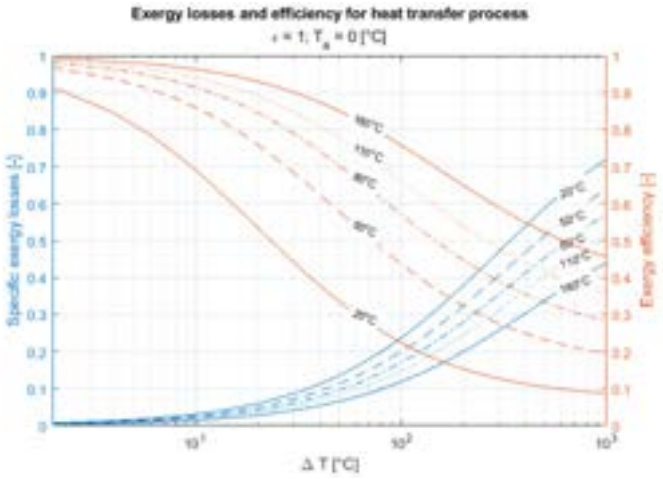

Fig. 5: The effect of the differential temperature on the exergy performance of a heat transfer process with parametric curves corresponding to the consumer's useful temperature ($\bar{T}_h$)

Zero heating effectiveness ($\varepsilon_h = 0$) corresponds to a heat transfer system where all energy received from the hot stream is destroyed to the atmosphere. It is the case for example for an **air-cooler**. Thus, Eq. (24) and Eq. (26) become:

$$\dot{L}_g = \left[\left(1 - \frac{T_a}{\bar{T}_g}\right)\right]\dot{Q}_g^+ \qquad \eta = 0 \tag{32}$$

In the case of a **perfectly insulated heat exchanger**, the effectiveness is assumed to be equal to unity ($\varepsilon_h = 1$). The external heat transfer losses are zero and part of the exergy received is destroyed by internal heat devaluation. Equation (32) and Eq. (33) become:

$$\dot{L}_g = \frac{T_a}{\bar{T}_g}\,\frac{\Delta T}{\bar{T}_g - \Delta T}\,\dot{Q}_g^+ \qquad \eta_t = 1 - \frac{T_a}{\bar{T}_g - T_a}\,\frac{\Delta T}{\bar{T}_g - \Delta T} \tag{33}$$

For the same temperature difference between the hot source (hot gases) and user (heating system), the heat exchange is better for a hot source at higher temperature. This is why, for the same temperature difference, the exergy losses in a heat exchanger for domestic hot water production or for LT heating system are greater than those in a substation of a HT district heating system.

This is also the case for example with heat exchangers for the production of domestic hot water, for heating in district heating substations between the superheated water and the water for heating or for heat production in water-cooled boilers.

4.2. Heating and cooling with heat pump cogeneration systems

Heating and/or cooling installations are often composed of many components that exchange energy with a thermodynamic circuit. These energy exchanges can take place in various forms, involving different processes, including vapor compression and absorption heat pump/refrigeration cycles most commonly investigated by engineers. Modern installations of heat pumps are used in cogeneration with combined heating and cooling. Figure 6 shows an example of such a system with a heat pump combining heating and cooling. It allows to capture low temperature energy from the environment $\dot{Q}_s^+$ (i.e. Lake or geothermal) at a certain temperature level ($\bar{T}_0$), to transfer heat to a fluid (principal circuit) via a heat exchanger and to use it as a cold source in a heat pump to provide a heating service ($\dot{Q}_h^-$) necessary for hot water production ($\bar{T}_h$). The cold fluid out of the heat pump is transported through a network of pipes to supply cooling energy to the consumer and returns back to the heat exchanger. The cooling service are represented with the flow or transformation energy service ($\dot{Y}_f^+$) at temperature level ($\bar{T}_f$).

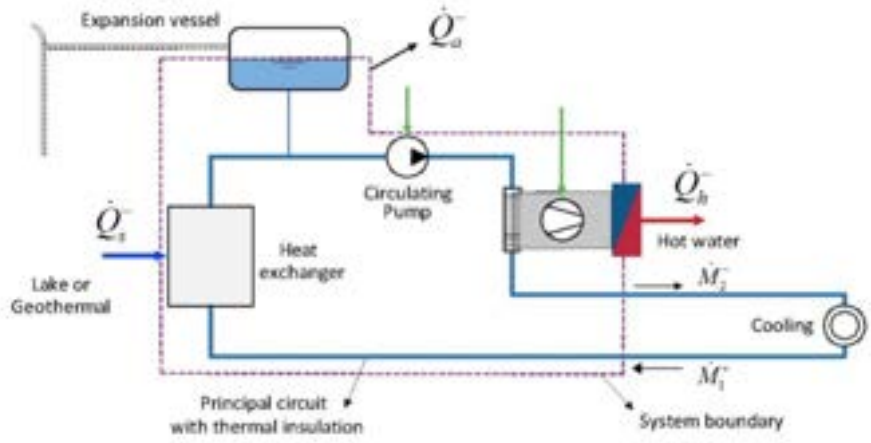

Fig. 6 *Example of a combined heating and cooling system*

The circulation of the heat transfer fluid is ensured by a circulating pump that overcomes the total pressure losses of the network. $\dot{E}_P^+$ represents the electrical power consumed by the circulating pump and $\dot{E}_K^+$ is the electrical power consumed by the heat pump. The input energy services are the net electricity consumption ($\dot{E}_w^+ = \dot{E}_P^+ + \dot{E}_K^+$). There is no work or electric production for this application:

- $\sum_f [\dot{U}_f^+] = \dot{Y}_f^+$ Cooling service, $\dot{Y}_f^+ = \dot{M}\left(h_{cz_1} - h_{cz_2}\right)$
- $\sum_h [\dot{U}_h^-] = \dot{Q}_h^-$ Heating service for this application
- $\sum_w [\dot{E}_w^-] = 0$ No work or electrical production

As the system is considered perfectly insulated (heat losses to the atmosphere are null) and there is no flow exchanged with environment ($\dot{Y}_0^- = 0$), the heat exchanged with environment is represented by $\dot{Q}_0^- = \dot{Q}_s^-$. The energy balance based on the two equations of energy services Eq. (11) and energy exchange between the system and the environment Eq. (14) can be done as:

$$\dot{U}_{0t} = \dot{E}_w^+ - \dot{Q}_h^- - \dot{Y}_f^+ \qquad \dot{U}_{0t} = -\left(\dot{Q}_s^+ + 2\,\dot{Y}_f^+\right) \tag{34}$$

Therefore, the effectiveness of the general Equation Eq. (10) corresponds to the total effectiveness according to:

$$\varepsilon = 1 - \frac{\dot{U}_{0t}}{\dot{E}_w^+} = \frac{\dot{Q}_h^- + \dot{M}\left(h_{cz_1} - h_{cz_2}\right)}{\dot{E}_w^+} = \varepsilon_h + \varepsilon_f \tag{35}$$

$$\varepsilon = 1 + \frac{\dot{Q}_s^+ + 2\,\dot{M}\left(h_{cz_1} - h_{cz_2}\right)}{\dot{E}_w^+} = \varepsilon_0 + 2\varepsilon_f \tag{36}$$

Where $\varepsilon_h = \dot{Q}_h^- / \dot{E}_w^+$ and $\varepsilon_f = \dot{Y}_f^+ / \dot{E}_w^+$ respectively represent the effectiveness for heating and cooling and the term given by the following $\varepsilon_0 = 1 + \dot{Q}_s^+ / \dot{E}_w^+$ characterizes the amount of energy taken from the environment.

When considering equation Eq. 34, one also can demonstrate that ε_0 represents the difference between the effectiveness for heating and cooling ($\varepsilon_0 = \varepsilon_h - \varepsilon_f$). In the case of adiabatic components with no heat transfer losses and no energy withdrawal from the source ($\dot{Q}_s^+ = 0,\ \varepsilon_0 = 1$), we find the same relation Eq. (19) between the effectiveness of heating (ε_h) and cooling (ε_f) for a simple heat pump. This shows that the total effectiveness (ε) of such a combined heating/cooling cogeneration system also depends on this percentage of energy taken from the environment ($1 - \varepsilon_0$). These results based on Eq. (35) and Eq. (36) could not be obtained by using Eq. (5) for this process of cogeneration involving cooling services which take place at a temperature level below the atmospheric temperature.

Same reasoning can be applied to demonstrate that, the exergy performance of the system not only depends on the effectiveness of heating (ε_f) and cooling (ε_f) but also on the energy exchanged the environment ($1 - \varepsilon_0$). To illustrate that, let us first apply the general expressions of exergy efficiency Eq. (2) by considering the Carnot factors related to the temperature level of heating ($\bar{T}_h$) and cooling ($\bar{T}_f$). The overall exergy efficiency for heating/cooling cogeneration (η) is:

$$\eta = \frac{\dot{E}_{qh}^- + \dot{E}_{yf}^-}{\dot{E}_w^+} = \left(1 - \frac{T_a}{\bar{T}_h}\right) \varepsilon_h + \left(\frac{T_a}{\bar{T}_f} - 1\right) \varepsilon_f \tag{37}$$

Or then:

$$\eta = \varepsilon_0 - T_a \left(\frac{\varepsilon_h}{\bar{T}_h} - \frac{\varepsilon_f}{\bar{T}_f}\right) \tag{38}$$

Where $\dot{E}_w^+$ represents the work-exergy received by the system, $\dot{E}_{qh}^-$ represents the heat-exergy provided by the system to the user for heating and $\dot{E}_{yf}^-$ represents the flow-exergy provided by the system to the user for cooling.

By replacing the exergy efficiency η by its value defined in Eq. (20). We can thus express the exergy losses in the most general form by the following relations:

$$\dot{L}_g = \left[1 - \varepsilon_0 + T_a \left(\frac{\varepsilon_h}{\bar{T}_h} - \frac{\varepsilon_f}{\bar{T}_f}\right)\right] \dot{E}_w^+ \tag{39}$$

Two components of exergy losses can be distinguished: external exergy losses that are exactly equal to the energy taken from the environment and internal exergy losses (with irreversibilities) that are related to the temperature difference between heating and cooling consumers. The internal exergy losses in the system increase not only with the temperature difference but are lower the higher the temperature levels.

Equations (38) and (39) are general for any combined heating and cooling system using a heat pump technology with additional energy taken from the environment e.g. $\varepsilon_0 \neq 1$. For a particular case of a simple heat pump cogeneration application without any energy captured from the environment ($\dot{Q}_s^+ = 0, \varepsilon_0 = 1$), Eq. (38) and Eq. (39) become:

$$\eta = 1 - T_a \left(\frac{\varepsilon_h}{\bar{T}_h} - \frac{\varepsilon_f}{\bar{T}_f}\right) \qquad \dot{L}_g = \left[T_a \left(\frac{\varepsilon_h}{\bar{T}_h} - \frac{\varepsilon_f}{\bar{T}_f}\right)\right] \dot{E}_w^+ \tag{40}$$

Equations (38) and (39) can also be used for particular cases of a thermopump for heating only ($\varepsilon_0 = 1, \bar{T}_f = T_a$) or of a frigopump for cooling only ($\varepsilon_0 = 1, \bar{T}_h = T_a$). For example, by combining Eq. (20) and Eq. (38), we found the well-known and particular relationships between the exergy efficiency of a heat pump cycle, the coefficient of performance (effectiveness) and the ideal effectiveness based on the Carnot factor:

For a thermopump ($\bar{T}_f = T_a$):

$$\eta_h = \varepsilon_h \left(1 - \frac{T_a}{\bar{T}_h}\right) \qquad COP_h = \eta_h \cdot \frac{\bar{T}_h}{\bar{T}_h - T_a} \tag{41}$$

For a frigopump ($\bar{T}_h = T_a$):

$$\eta_f = \varepsilon_f \left(\frac{T_a}{\bar{T}_f} - 1\right) \qquad COP_f = \eta_f \cdot \frac{\bar{T}_f}{T_a - \bar{T}_f} \tag{42}$$

5. Conclusion

A general expression of the effectiveness applied to all technologies is proposed in this study. It is based on the First Law of thermodynamics by separating the energy service terms (inlet services in term of work, gas and/or biomass expended for a system and outlet services in term of work, heating and/or cooling delivered by the system) from the total energy exchanged with the environment. A clear difference between the heating and cooling processes is observed based on a general formula of energy services balance. In the case of a heating process, the difference between the inlet and outlet energy services is exactly equal to the total energy exchanged with the environment but it is not the case for a cooling application for which the energy exchanged with the refrigerant (cold utility) need properly to be considered in the balance by accounting for both the cooling services supplied by system to the user and the same quantity of energy received or captured by the system from the user.

Based on this new approach of effectiveness and the existing exergy efficiency formulation, a generic relationship between energy and exergy losses has been proposed. It allows to provide simple and generic expressions of exergy losses and efficiencies of any energy systems in relation to the conventional performance indicators (thermal efficiency, heating coefficient of performance, cooling coefficient of performance) most commonly used by engineers to estimate the various losses of a system. Such a method has been applied for complex cogeneration systems (combining power, heating and/or cooling) but also for single energy components, e.g. boilers, heat exchangers and air-coolers to show the benefit. The overall exergy efficiency and losses of such systems explicitly are given in function of the effectiveness.

Main results and advantages of such an approach are: Having a unique formula of effectiveness for both heating and cooling applications and creating the link between the known performance indicators; Providing a general relationship between exergy efficiency and effectiveness of any system; Performing the exergy analysis of common installations without any knowledge of entropy; Providing simple and generic relations of exergy efficiencies and losses and/or estimating the detailed distribution of the exergy losses of a system according to the different forms of energy losses (heat losses, exhaust gases, heat energies taken from or released to the environment, e.g. water, soil and air).

These can be very useful for practitioners to determine and know the exergy performance of any energy system based solely on energy balance terms and thus the effectiveness of the system.

Nomenclature

Roman symbols

E work energy, exergy, J

k co-enthalpy, J

L global exergy losses, J

$\dot{M}$ mass flow rate, kg/s

Q heat energy, J

Y flow or transformation energy, J

T temperature, K

U utility, energy service, J

Greek symbols

η exergy efficiency

ε effectiveness

Subscripts and superscripts

a ambient, atmosphere

f cooling service

h heating service

K compressor

References

[1] Favrat D., Kane M., Clear paths to teach exergy. Proc. of ECOS2023

[2] Borel, L., Favrat, D., (2010). Thermodynamics and energy systems analysis. EPFL Press,

[3] Adihou Y. (2022). Modélisation et optimisation exergétique des réseaux thermiques basse température. Thèse Doctorat USMB

[4] Bejan, A., Tsatsaronis, G., Moran, M.J., (1995). Thermal Design and Optimization. John Wiley & Sons

[5] Moran M.J., Shapiro H.N., Boettner D.D, Bailey M.B. Fundamentals of engineering thermodynamics. Wiley 9th edition 2018

[6] Szargut J., Moris D.R., Steward F.R, (1979). Exergy analysis of thermal, chemical, and metallurgical processes. Hemisphere &Springer-Verlag, 397 pages, ISBN 0-89116048-5

[7] Kotas, T.J., (1985). The Exergy Method of Thermal Plant Analysis. Elsevier ,

Internal cooling of a gas turbine blade using Ranque-Hilsch vortex flow

Daisy Galeana[a], Ashenafi Abebe[b], and Asfaw Beyene[c]

[a] Solar Turbine Inc., San Diego CA, USA, Galeana_Daisy@solarturbines.com
[b] Debre Berhan University, Debre Berhan, Ethiopia, abebeashenafi7@gmail.com
[c] Department of Mechanical Engineering, San Diego State University, San Diego CA, USA, abeyene@sdsu.edu

Abstract:

Efficiency of a gas turbine engine is directly impacted by the turbine inlet temperature and the corresponding pressure ratio. A major strategy, aside from use of costly high-temperature blade materials, is increasing the turbine inlet temperature by internally cooling the blades using pressurized air from the engine compressor. Understanding the fluid mechanics and heat transfer of internal blade cooling is therefore, of paramount importance for increasing the temperature threshold, hence increasing engine efficiency. This paper presents results of a novel cooling approach, i.e., the use of Ranque-Hilsch vortex flow for first row gas turbine blade cooling. Test results clearly demonstrate the successful formation of continuous Ranque-Hilsch vortex flow by injecting compressed air into a cylindrical chamber equipped with seven air inlets. Separated boundaries of the reversed flow with detectable boundaries were accompanied by a significant drop in temperature on the cold stream side. At inlet pressure of 63 kPa, the outlet temperature from the vortex tube dropped below 0°C, which allowed blade temperature drop of about 200 °C. The thermal efficiency of the gas turbine increased from 40% to 43% by vortex-cooling the blades with 10% mass of compressed air extracted at about 910 kPa. For the tested scenario of a 17 MW engine, the partial extraction had a better efficiency increment than extraction at full compression which was 1200 kPa.

Keywords:

Thermodynamics; Gas turbine engine, internal blade cooling, thermal efficiency, power output, Ranque-Hilsch vortex flow, experiment.

1. Introduction

The life cycle of a gas turbine engine blade is most affected by high the operating temperature, constant centripetal loading, and thermally induced stresses, particularly during start-up and shutdown. The thermal efficiency of the engine increases with the increase of the pressure ratio and the firing temperature which increases the turbine rotor inlet temperature (TRIT). As the firing temperature increases, the heat transferred to the turbine also increases, rising above the material temperature threshold which requires mitigation measures of material failure if upholding the high temperature is desired to maintain high efficiency. This requires internal cooling of the rotor blades. Significant research has been going on for decades to design an internal cooling system particularly for the first-stage blades, to achieve higher firing temperature. Effective internal cooling of the rotating blades is a significant challenge, compounded by wake-induced turbulence and unfavorable area ratios between inner and outer surfaces [1] [2]. This can cause formidable challenges to turbine internal cooling.

Various cooling techniques are applied on the turbine blade to keep the working temperature within a safety limit [3] [4] [5]. It is a common practice to cool high-pressure turbine blades using air from the compressor which is routed through the turbine blades thereby lowering its temperature. Swirl cooling is one of the many techniques used for such cooling. The idea is to route swirling air from the compressor through the turbine blade's internal passages [6]. The first rows of turbine blades typically operate at a temperature that exceeds 1,200 °C [7] [8] [9], and therefore, may greatly benefit from internal cooling if higher firing temperature is to be entertained.

Analytical and experimental modeling in the leading-edge area of the blade, with regard to internal swirl cooling systems, could result in optimization of turbine blade designs with respect to heat transfer, cost, and performance, as well as reduced downtime [10] [11] [12]. Adding complexity to the demanding task of managing high temperature without its accompanying penalties is the driving desire for a long-term life cycle without frequent inspections and overhauls. Turbine blades withstanding high temperatures and constant mechanical stresses, which limit the turbine blade life cycle, may also cause permanent material deformation

[13] [14]. These can also cause local plastic yielding while contributing to material creep [15]. Some innovative techniques have been proposed to improve the convective heat transfer for internal cooling of gas turbine airfoils, including rib turbulators, pin fins, dimpled surfaces, impingement cooling, and swirl flow cooling [16] [17] [18] [19] [20].

Of particular interest here, the topic of our research, is “swirl cooling” which induces a reverse flow. One such innovative approach is discussed by Glezer et al. [14] who present experimental results comparing three separate studies. The research provided a better understanding of the screw-shaped swirl cooling technique for heat transfer in internal swirl flow, where heated walls were applied and a screw-shaped cooling swirl was generated, introducing flow through discrete tangential slots. The authors mention that the Coriolis forces play an important role in enhancing the internal heat transfer when their direction coincides with a tangential velocity vector of the swirl flow.

Another paper on the same subject of swirl cooling, [21] states that the local surface Nusselt numbers increase when increasing the Re number (the range in this study was from 6,000 to about 20,000). As a result, the local swirl chamber heat transfer and flow structure are linked to increased advection as well as notable alterations to vortex behavior near the concave surfaces of the swirl chamber. One key result was that, along with the Nusselt number, the changes of surface heat transfer downstream of each inlet increased sharply when compared to other locations. Hedlund et al. [21] observe that as the turbulent flow becomes more pronounced, the axial and circumferential velocities get larger and intensify the turning of the flow from each inlet.

Other studies show that blade internal swirl cooling is effective and can afford long term life to blades especially if employed in tandem with advanced blade alloys [22] [23]. Experiments conducted by Ligrani et al. [3], Moon et al. [1], and Glezer et al. [13] introduced an internal cooling structure as one way to attend to high temperature management in gas turbine cooling, Fig. 1.

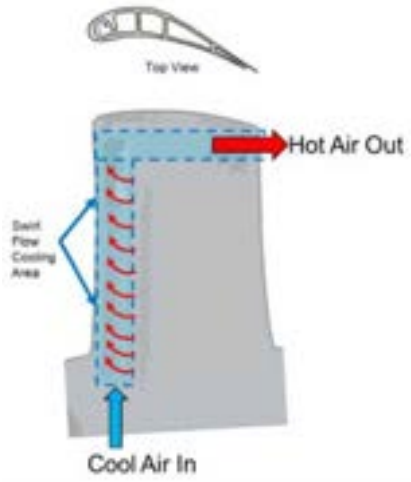

Figure 1: Turbine blade leading edge internal cooling design, [4].

The above summaries of recent developments in turbine blade internal cooling show advances in several fronts. However, the idea of applying the Ranque-Hilsch vortex flow for internal blade cooling has never been investigated. Thus, the focus of this study is to conclusively prove that sustained reverse flow with accompanying temperature drop can be produced, which allows the use of the cold stream for a gas turbine blade internal cooling. The vortex flow is injected tangentially through holes to induce the vortices, as shown in Fig. 2.

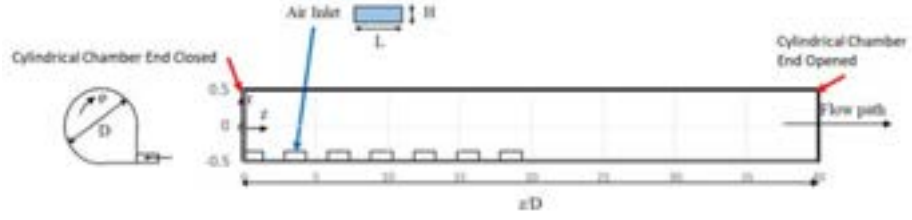

Figure 2: Cylindrical chamber geometry with seven air inlets, [24].

2. Experimental setup

The main piece of the lab setup for the vortex flow cooling experiment is LaVision Stereo-PIV system, which includes a LaVision PC, two ImagerproX cameras, two Nd-YAG lasers, and LaVision particle seeder as shown in Fig. 3. The cameras are mounted on a stand equipped with stepper motors, allowing it to travel freely along the chamber length. The fluid is seeded with olive oil particles that have diameters in the range of 1-3 μm and specific gravity of 0.703. These oil tracer particles are chosen because they are small enough that they have little inertia; validating the tracer particle motion best reflects the actual flow path. The seeding particles in the fluid distribute the laser light, which is captured by the video acquisition system. The Nd-YAG laser is a Pegasus PIV with a wavelength of 527 nm and maximum energy of 20 mJ per pulse. The Nd-YAG laser serves as the illumination source for the PIV system and is manipulated through the appropriate use of optical instruments to produce a laser sheet of 2 mm thickness on the chamber's bottom wall. This setup allows the illumination of planes parallel to the vertical axis. Two high-speed and high-resolution CCD cameras (Phantom v7.3. 800_600 pixels, 12 bit) capture images of the illuminated PIV particles at a rate of 100 frames per second. With that frame rate, 2000 images are acquired over a period of 10 seconds, similar to the measurement duration in the experiment conducted by others [12-13].

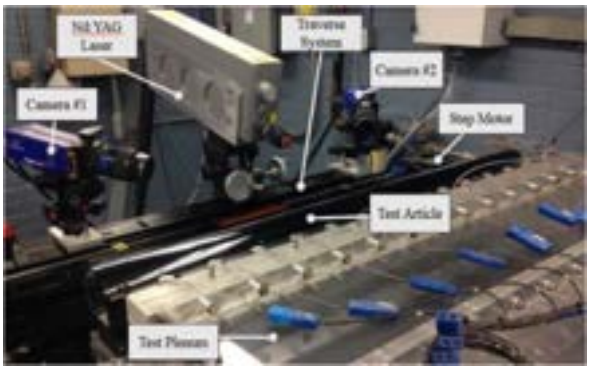

Figure 3: Hardware setup.

DaVis is utilized to collect PIV data, all data points are taken and collected in one file set which exports time-average velocity and is post-processed in DaVis to be transferred into MATLAB. MATLAB cleans up DaVis raw data and allows the calculation of crucial flow field variables. All velocity calculations are conducted in MATLAB, followed by a file structure that prepares data for visualization in Tecplot 360, which is used for data visualization. One advantage of using Tecplot 360 is that it provides powerful flow visualization options. Created some macros to automate visualization procedures. To create smooth transitions in between data points, a data interpolation scheme was employed.

3. Generating a Ranque-Hilsch vortex flow

Before committing to the use of the cold stream of the Ranque-Hilsch flow, it would behoove us to first scrutinize its occurrence within the theoretical scope presented above, with an accompanying temperature drop - significant enough to cool the gas turbine blades.

3.1. Theoretical justification, Navier Stokes Eq. and CFD

The Navier-Stokes, centrifugal force, and centrifugal velocity equations can be used to show prevalence of the reverse flow in the cylindrical chamber. Once preliminary values were entered, the results show a radial pressure drop of about 140 Pa, which spans from the gauge pressure at the inlet of approximately 340 Pa, as clearly illustrated in Fig. 4.

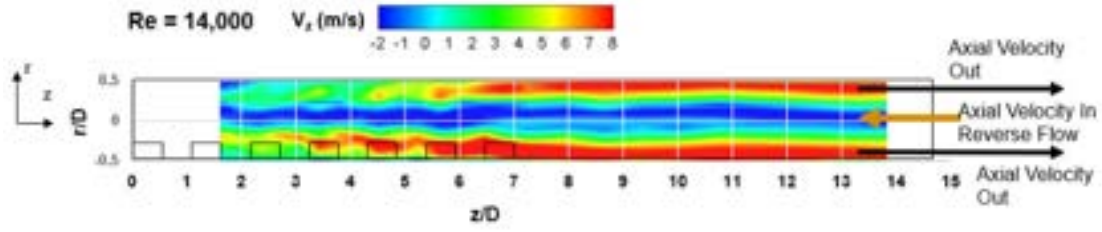

Figure 4: Radial pressure drop estimate.

CFD simulations can further lay evidence to predict the loadings and flow distributions of blade rows, including for end-wall regions. As a tool, CFD can produce valuable outputs, albeit its limitations in predicting turbine heat transfer, mainly because of constraints in modeling turbulence and vortices, uncertainty of boundary conditions, and the inherent flow unsteadiness in turbomachinery. Here we simulate velocity, temperature, and pressure distributions to show if their profiles support the notion of existence of a reverse flow, and if the continuity equation is satisfied.

Velocity: The velocity streamline for the entire fluid domain is presented in **Error! Reference source not found.**5. The largest velocity value is noticed at inlet 7 at 30.457 m/s. There are three reversed flow cases at the inlets 1, 2 and 3. The velocity is minimum near the end of the chamber.

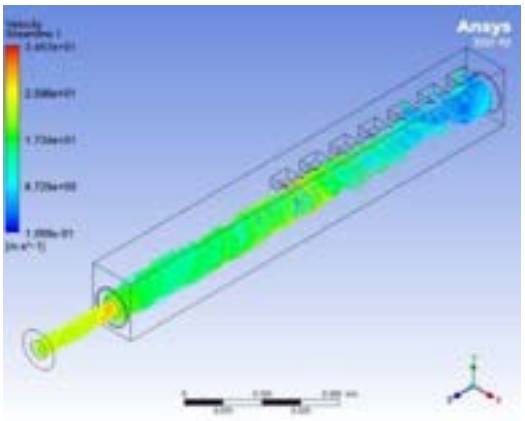

Figure 5: Velocity streamline of the fluid domain.

Temperature and Pressure: The temperature and pressure distribution along the cylindrical chamber are given in Fig. 6. The highest pressure is observed in front of inlet seven reading 979 Pa. However, after air inlet seven the cross-section of the chamber, the pressure distribution shows significant drop resulting in -30.870 Pa. The temperature contour indicates separated cold and hot streams. These temperature and pressure show existence of a reverse flow with a temperature drop.

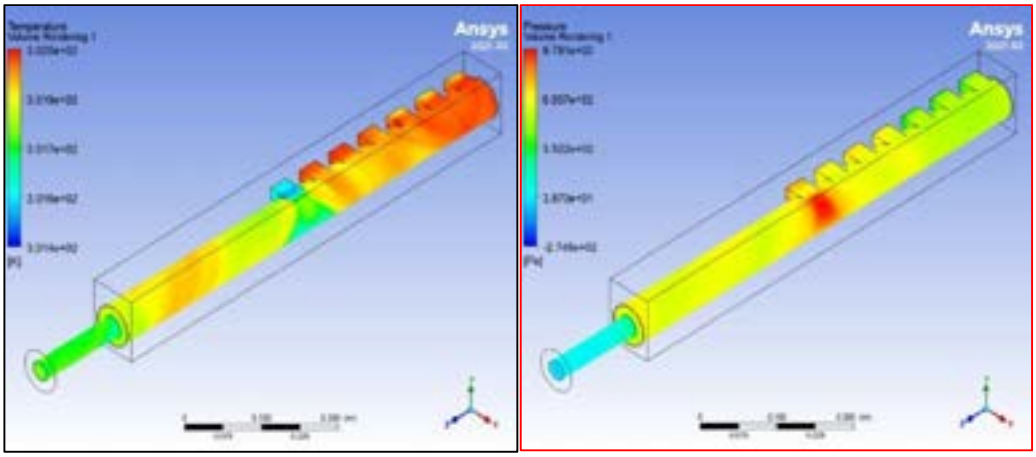

(a) (b)

Figure 6: Temperature (a) and pressure (b) contour of the vortex chamber and tube

Continuity Eq.: To confirm the mass is balanced, we assess the mass flow rate at some distance “z” downstream of the flow. The goal here is to plot the mass flow rate at the three assumed Re numbers to confirm that the mass flow rate going into the cylindrical chamber matches the total mass flow rate going out of the chamber as cold and hot streams. Figure 7 shows that the mass flow rate going into the chamber matches the sum of reversed and unreversed flows leaving the chamber, which proves the reverse vortex flow takes place inside the cylindrical chamber.

The total mass inflow rate through the system is 0.0535 kg/s. This is also the sum of the flow rate through each inlet, which again is the same as the flow rate at the outlet, as shown in Tab 2.

Table 2: Summary of mass flow rate at the inlets and outlets.

Location	Inlet 1	Inlet 2	Inlet 3	Inlet 4	Inlet 5	Inlet 6	Inlet 7	Outlet
Flow Rate, kg/s	-0.0085	-0.0088	-0.0075	0.0096	0.0033	0.0063	0.0343	0.0287

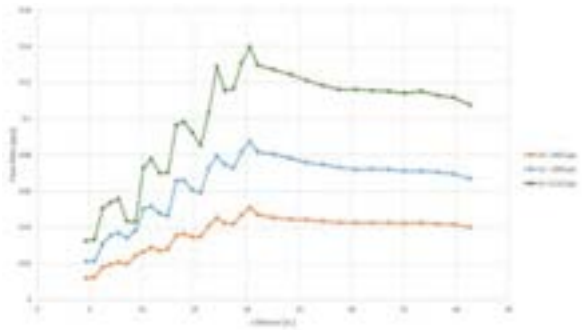

Figure 7: Mass flow rate vs. z-Distance at all three Re numbers of cylindrical chamber.

4. Evidence of prevalence of reverse flow

4.1. Thermochromic Liquid Crystal (TLC)

The cylindrical chamber is made of clear acrylic material, painted with TLC to allow visualization of color changes within the required time range. As the air enters the plenum, Fig. 8, it passes into a rectangular heating mesh, leading to rectangular cross-sectional air inlets with individual hydraulic diameters (D_H) of 0.011 m. These inlets are connected to the principal vortex chamber so that one surface is tangent to the chamber inner circumference.

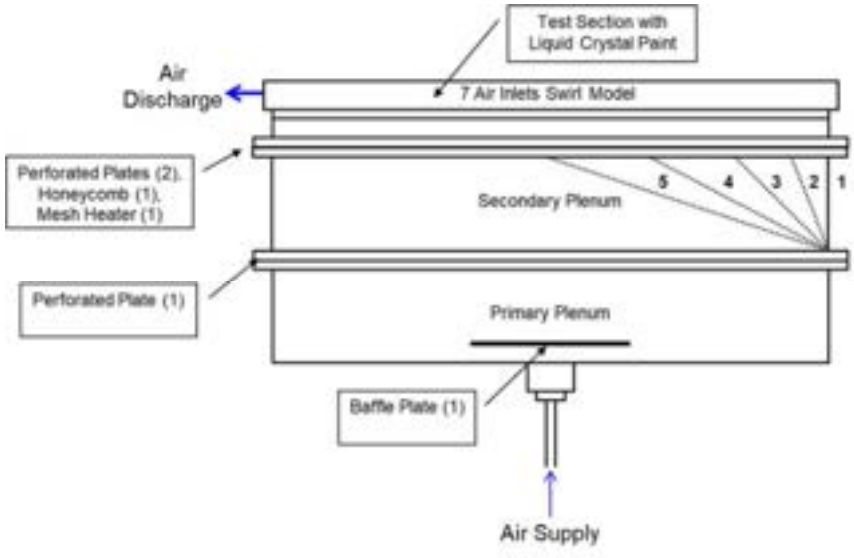

Figure 8: TLC painted test stand with plenums attached.

The surface area optics suitable for the spatial resolution are painted, first the cylindrical chamber is coated with liquid crystal paint, followed by black paint. A coupon is built, following the same process for calibration purposes, coated with liquid crystal paint, and followed by black paint.

TLC Data Collection: An in-house software is used to synchronize the entire liquid crystal experiment. The data is collected by continuously polling after the system is heat-soaked to the required temperature. The data acquisition step size is 0.5 seconds and the VXI is set to a time interval of 0.2 seconds. The video file is converted to an AVI file, imported into the “Liquid Crystal Image Analyzer (LCIA),” as shown in Fig. 9. Contact resistance and temperature drop through the wall are determined experimentally from the calibration process

and green time is measured simultaneously. Using seven calibrated thermocouples equally separated across the length of the cylindrical chamber, the temperature of the air entering the cylindrical chamber is measured. All measurements are collected when the cylindrical chamber is at steady state and when the heating mesh on the plenum reaches 35°C.

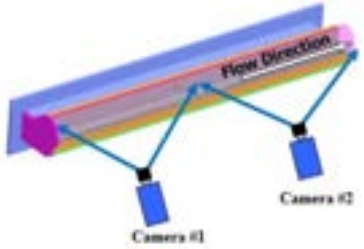

Figure 9: heat transfer data collection by two cameras for the painted test stand.

Once the green time image is calculated, then the probe locations are associated with columns of temperature readings in the temperature probe data file. Noise is edited out with an eraser image mask, followed by the region of interest definition using a polygon mask. These final images are then exported as JPEG image files. Cameras recording in DV format are set up to view the liquid crystal coated surface of the test stand, capturing 10 samples per second. The air flow rate is set as the liquid crystal transitions at 35°C and regulator pressure at 6.89 KPa. Once the system is heat soaked, cameras start recording. When the paint has fully transitioned to blue, the cameras and data acquisition system are stopped manually.

The data points were taken at 33 locations at a distance of 19.81 mm from each other, as shown in Figure 10 and Fig. 11. Data were collected at both locations, in between air inlets and at the middle of the air inlets (i.e., data point #2 and data point #4, respectively) to show the complicated flow and its variation.

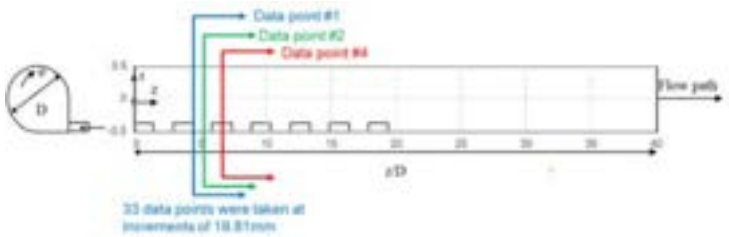

Figure 10: Data point locations in increments of 19.81 mm.

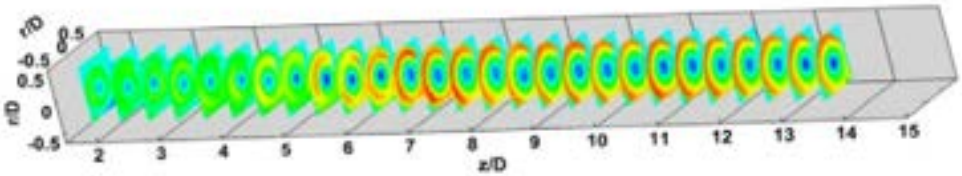

Figure 11: Cross-sectional area of data points.

4.1.1. Axial Velocity Distribution

As the Re number increases, the axial velocity, V_Z, intensifies, measuring higher on the outer wall region, as shown in Figure 12. From upstream to downstream, the V_Z ranges from -2 to 7 m/s in all three Re numbers, as is expected in a cylindrical chamber. The outer wall region velocity increases across the length, reaching a maximum velocity at the second half of the vortex chamber. Another observation is the high V_Z in the direction of the outer wall region. Between the core and the chamber wall in the outer wall region, an inertia-driven vortex was observed and measured a flow field pattern that is critically different between high to low Re numbers.

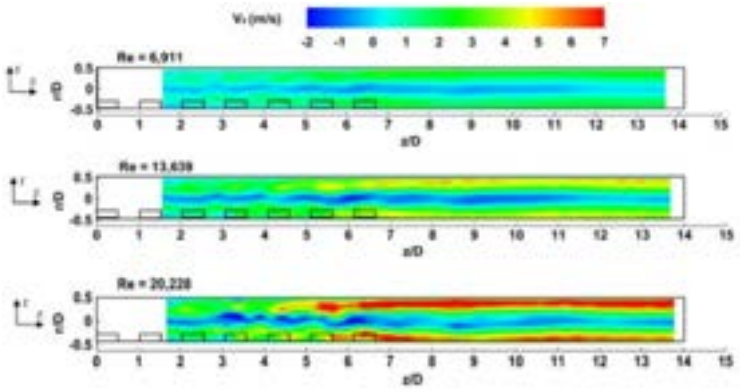

Figure 12: Axial velocity distribution of cylindrical chamber at all three Re numbers.

4.1.2. Reverse Vortex Flow at the Center of the Cylindrical Chamber

With this geometry, the vortex flow cooling has important axial and circumferential components of velocity, and the overall flow pattern through the cylindrical chamber behaves similar to a vortex tube, also known as the Ranque-Hilsch vortex tube, a mechanical device that separates a compressed air into hot and cold streams with temperature difference reaching over 250°C. Although unintended, the detailed flow behavior inside a Ranque-Hilsch vortex tube and flow reversal in the cylindrical chamber share similitudes. The velocity profile was measured for both air and water operated Ranque-Hilsch vortex tube. Based on this study, there was a remarkable agreement between theoretical estimation and experimental results. Furthermore, the unintended consequence of the vortex flow behavior needed more analysis; utilizing 3-D stereo-PIV at the nominal Re = 13,639, three cross-sectional areas were chosen. **Error! Reference source not found.** 10 shows the three cross-sectional areas z/D = 3, 6, and 13 carefully studied looking for evidence of the reverse flow and captured it and all three cross-sectional areas to show reverse flow. Stereo-PIV is a powerful tool able to capture in great detail how each droplet behaves and map the axial velocity field flow. The discovery of this unintended behavior is so astronomically important that more research and analysis had to be completed to satisfy the minds of the experts. The next step is to understand the vortex flow behavior where the reverse flow exists.

Figure 13 presents the normalized axial velocity against the cylindrical chamber length, downstream of the flow. The pressure decreases downstream on the outer chamber wall, the reverse flow at the centerline is increasingly visible.

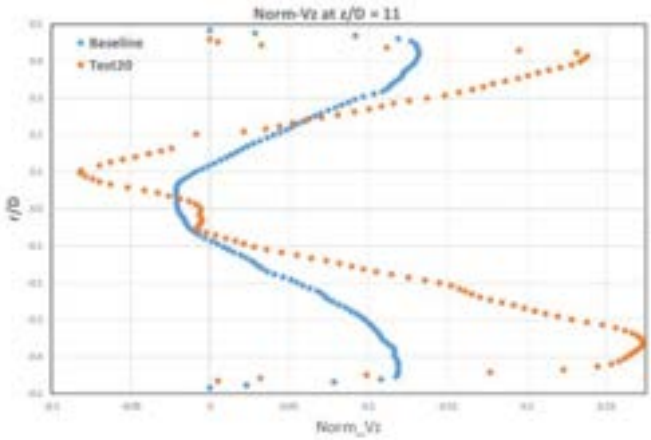

Figure 13: Normalized V_z at z/D = 11 of cylindrical chamber.

4.2 Video Evidence

In addition to the above listed techniques, the existence of a reverse flow was also validated using a video. For this purpose, we prepared a wire with a piece of light string, rag attached at the end of the wire. The wire is then inserted at three different locations to see its motion. The string moved in the direction of the flow in all the three locations. The string changes direction as it is moved across the internal boundary of the reversed flow.

Figure 14: Video evidence of the reverse vortex flow using a wire and a soft yarn attached.

5. Conclusion

The results show that for an incoming air of 100kPa, the temperature and pressure drops are significant. The exit temperature depends on the input pressure with a nearly linear relationship. As the input pressure increases, the outlet temperature of the cold stream decreases. For validation purposes, the compressed air temperature at inlet was kept constant at a value of 28°C for the simulation. When the air at 1kPa was admitted to the vortex chamber, the exit temperature remained the same for both the simulation and the experimental test. However, at 63kPa inlet pressure, the stream temperature cooled to 0°C i.e., yielding a temperature drop of about 29°C.

Experimental data collected from the cylindrical vortex chamber which models internal cooling passage of a blade located near the leading edge of a gas turbine blade, for Re range of 7,000 to 21,000 show outstanding accuracy and 3-D resolution obtained with the Stereo-PIV imaging techniques employed here. The combination of CFD and experimental data reveal distinct advantages of the vortex cooling concept introduced here, over other cooling methods.

The versatility of the vortex cooling design to redistribute a different path of heat load profile without major casting changes was demonstrated by using seven air inlets. The span of the outer-wall velocity flow fields increases, due to the enlargement of the vortex flow core. The TLC heat transfer test results exemplify how the Nu were measured favourably at the middle length of the chamber and values decline downstream.

The primary objective of this research has been met by performing tests to prove prevalence of a reverse flow in the swirl chamber. The channel served as a Ranque-Hilsch vortex tube. As a result, the compressed air was separated into hot and cold streams with temperature difference reaching over 250°C. The detailed flow behaviour inside a Ranque-Hilsch vortex tube and flow reversal in the cylindrical chamber share similarities. Based on this study there was an impressive and conclusive presence of reverse axial flow at the core as illustrated in the experimental results. Simulation results correlated the experiment results and validated the reverse flow with similar mass flow rate and pressure gradients of 0.0535 kg/s and 979 Pa, respectively. The CFD recreated the reverse flow at Re = 14,000. The results affirm that higher pressure input can contribute to lowering the temperature at the exit from the chamber, favouring the cooling process. The thermal efficiency increased by about 3% when the blade is cooled by extracting 10% partially compressed air. This is a significant gain.

Nomenclature

D	Circular chamber diameter, m
D_H	Hydraulic diameter of one swirl chamber inlet, m
Q	Mass flow rate, kg/s
H	Height, m
k	Turbulent kinetic energy, m^2/s^2
L	Cylindrical chamber length, m
P	Pressure, Pa
R	Radial distance measured from chamber centreline, m
Re	Reynolds number
r	Radial distance, m
S_N	Swirl number
V_z	Axial velocity, m/s
V_ϕ	Circumferential velocity, rad/s
W	Air inlet width, m
r, θ, z	Cylindrical coordinates
ρ	Density, kg/m^3
v	Kinematic viscosity, m^2/s
$\delta_f = m_f/m_a$	Mass of fuel to mass of air ratio
P_{ra}	Pressure ratio at the point of extraction
T	Temperature, K
η	Efficiency

Subscripts and superscript

a	Air
f	Fuel
CA	Cooling air fraction
t	Turbine
c	Compressor
‘	Ideal compression/expansion process

References

[1] Moon, H.K., O'Connell, T., and Glezer, B., "Heat Transfer Enhancement in a Circular Channel Using Lenghtwise Continuous Tangential Injection," *Heat Transfer,* vol. 6, pp. 559-564, 23-28 August 1998.

[2] Moon, H.K., O'Connell, T., and Glezer, B., "Channel Height Effect on Heat Transfer and Friction in a Dimpled Passage," *Journal of Engineering for Gas Turbines and Power, ASME,* vol. 122, pp. 307-313, 2000.

[3] Ligrani, P., "Heat Transfer Augmentation Technologies for Internal Cooling of Turbine Components of Gas Turbine Engines," *International Journal of Rotating Machinery,* vol. 1, pp. 1-33, 2013.

[4] Ligrani, P., Goodro, M., Fox, M., and Moon, H.-K., "Full-Coverage Film Cooling: Film Effectiveness and Heat Transfer Coefficients for Dense Hole Arrays at Different Hole Angles, Contraction Ratios, and Blowing Ratios," *Journal of Heat Transfer, ASME,* pp. 031707-1 - 031707-14, 2013.

[5] Ligrani, P., Goodro, M., Fox, M.D., and Moon, H.-K, "Full-Coverage Film Cooling: Heat Transfer Coefficients and Film Effectiveness for a Sparse Hole Array at Different Blowing Ratios and Contraction Ratios," *Journal of Heat Transfer, ASME,* vol. 137, pp. 032201-1 - 032201-12, 2015.

[6] Kumar, S. and Singh, O., "Thermodynamic Evaluation of Different Gas Turbine Blade Cooling Techniques," *Thermal Issues in Emerging Technologies,* pp. 237-244, 2008.

[7] Kurz, R., "Gas Turbines Performance," *Proceedings of the Thirty-Fourth Turbomachinery Symposium,* pp. 131-145, 2005.

[8] Gao, Z., Narzary, D.P., and Han, J.-H., "Film Cooling on a Gas Turbine Blade Pressure Side or Suction Side with Axial Shaped Holes," *International Journal of Heat and Mass Transfer,* vol. 51, pp. 2139-2152, 2008.

[9] Garg, V. and Gaugler, R., "Effect of Coolant Temperature and Mass Flow on Film Cooling of Turbine Blades," *International Journal of Heat and Mass Transfer,* vol. 40, no. 2, pp. 435-445, 1997.

[10] Kusterer, K., Lin, G., Bohn, D., Sugimoto, T., Tanaka, R., and Kazari, M., "Leading Edge Cooling of a Gas Turbine Blade with Double Swirl Chambers," *Proceedings of ASME Turbo Expo 2014: Turbine Technical Conference and Exposition,* pp. 1-11, 2014.

[11] Ahn, J., Schobeiri, M.T., han, J.-C., and Moon, H.-K., "Effect of Rotation on Leading Edge Region Film Cooling of a Gas Turbine Blade with Three Rows of Film Cooling Holes," *International Journal of Heat and Mass Transfer,* vol. 50, pp. 15-25, 2007.

[12] Chung, H., Park, J.S., Sohn, H.-S., Rhee, D.-H., and Cho, H.H., "Trailing Edge Cooling of a Gas Turbine Blade with Perforated Blockages with Inclined Holes," *International Journal of Heat and Mass Transfer,* vol. 73, pp. 9-20, 2014.

[13] Glezer, B., Moon, H.K., and O'Connell, T., "A Novel Technique for The Internal Blade Cooling," *The American Society of Mechanical Engineers,* pp. 1-10, 10-13 June 1996.

[14] Glezer, B., Moon, H.K., Kerrebrock, J., Bons, J., and Guenette, G., "Heat Transfer in a Rotating Radial Channel with Swirling Internal Flow," *ASME,* pp. 1-7, 1998.

[15] Han, J.-C., and Chen, H.-C., "Turbine Blade Internal Cooling Passages with Rib Turbulators," *Journal of Propulsion and Power,* vol. 22, no. 2, pp. 226-248, 2006.

[16] Ligrani, P.M., Hedlund, C.R., Babinchak, B.T., Thambu, R., Moon, H.-K., and Glezer, B., "Flow Phenomena in Swirl Chambers," *Experiments in Fluids,* vol. 24, pp. 254-264, 1998.

[17] Ligrani, P.M., Choi, S., Schallert, A.R., and Skogerboe, P., "Effects of Dean Vortex Pairs on Surface Heat Transfer in Curved Channel Flow," *Internationl Journal of Heat and Mass Transfer,* vol. 39, no. 1, pp. 27-37, 1996.

[18] Ligrani, P.M., Mahmood, G.I., Harrison, J.L., Clayton, C.M., and Nelson, D.L., "Flow Structure and Local Nusselt Number Variations in a Channel with Dimples and Protrusions on Opposite Walls," *International Journal of Heat and Mass Transfer,* vol. 44, pp. 4413-4425, 2001.

[19] Ligrani, P.M., Oliveira, M.M., and Blaskovich, T., "Comparison of Heat Transfer Augmentation Techniques," *AIAA JOURNAL,* vol. 41, no. 3, pp. 1-26, March 2003.

[20] Li, S.-J., Lee, J., Han, J.-C., Zhang, L., and Moon, H.-K., "Turbine Platform Cooling and Blade Suction Surface Phantom Cooling from Simulated Swirl Purge Flow," *Journal of Turbomachinery,* vol. 138, pp. 1-11, 2016.

[21] Hedlund, C.R. and Ligrani, P.M., "Local Swirl Chamber Heat Transfer and Flow Structure at Different Reynolds Numbers," *Journal of Turbomachinary,* vol. 122, pp. 374-385, April 2000.

[22] Nasir, H., "Turbine Blade Tip Cooling and Heat Transfer," Doctoral Dissertation, *Louisiana State University,* 2004.

[23] Morris, W.D. and Chang, S.W., "An Experimental Study of Heat Transfer in a Simulated Turbine Blade Cooling Passage," *International Journal of Heat and Mass Transfer,* vol. 40, no. 15, pp. 3703-3716, 1997.

[24] Mebrat A.A., Galeana D., and Beyene A., "Vortex cooling of a gas turbine blade: comparison of single and bidirectional swirl formation," *Proceedings of ECOS 2022 - The 35rth International Conference on Efficiency, Cost, Optimization, Simulation and Environment,* 2022.

PROCEEDINGS OF ECOS 2023 - THE 36TH INTERNATIONAL CONFERENCE ON
EFFICIENCY, **C**OST, **O**PTIMIZATION, **S**IMULATION AND ENVIRONMENTAL IMPACT OF ENERGY SYSTEMS
25-30 JUNE, 2023, LAS PALMAS DE GRAN CANARIA, SPAIN

From the fuel heating values to the fuel exergy value in advanced energy systems

Daniel Favrat[a], Malick Kane[b],

[a] EPFL, Ecole Polytechnique Fédérale de Lausanne,(Energy center) Lausanne, Switzerland, daniel.favrat@epfl.ch
[b] HES-SO//FR, University of Applied Science in Fribourg, Mechanical Engineering Department (ENERGY Institute), Fribourg, Switzerland, malick.kane@hefr.ch

Abstract:

Several advanced energy systems include less standard fuel oxidation conditions. This is particularly true when partial oxy-combustion, post-combustion of anodic gases of SOFC or CO_2 gas separation are considered. This paper reviews the theoretical basis for the determination of the heating values and of the exergy values of various fuels. As a reminder, the exergy value of fuels is developed using Gibbs free energies of formation and is illustrated with a van't Hoff box with compressors and turbines. The paper also discusses the molar exergy of diffusion which is important when assessing various CO_2 separation technologies as well as the relative importance of the reference environment. The concepts of fuel exergy for fuels and exergy of diffusion for inert species is clearly established. The choice of the value of the exergy of diffusion of liquid water is particularly sensitive when calculating the exergy value of hydrocarbon fuels in systems with gas condensation.

Keywords:

Thermodynamics; Fuel; Heating value; Exergy; Oxidation.

1. Introduction

In practice processes occurring within real energy system take place in a given surrounding environment (e.g. the atmosphere characterized by the pressure P_a, the ambient temperature T_a and its chemical composition). The latter is considered large enough for its main features like the pressure, the temperature and the mass concentrations to remain constant. Whatever resources are considered in energy systems their ultimate fate will end up to be in equilibrium with the environment.

Combustion gases from a fuel boiler will reach an equilibrium with the atmosphere after passing through the chimney exhaust. Energy and masses are conserved, but their potential to do work is ultimately degraded to be cancelled when the equilibrium with the atmosphere is reached, a thermodynamic state that is called the dead state. Therefore, every technical energy system, aim at exploiting at its best the potential of a resource from its original state to the ultimate state of the environment. For example, a fuel is interesting because its initial thermodynamic state is different from that of the one from the stable inert gasses of the atmosphere. The objective of the energy system designer is therefore to make the most of the chemical potential of the fuel for delivering energy services. The challenge lies on the manner that the fuel energy or the exergy potential can be coherently represented in the expressions of the Laws of thermodynamics.

Most publications like [2] apply the terminology of chemical exergy for fuels as well as for inert gases like molecular N_2. The objective of this paper is to reformulate a coherent and concise approach of the problem of the comparison between energy and exergy evaluation of fuels in modern energy systems. The paper advocates a clear differentiation between diffusion and reactive phenomena in the exergy analysis of fuel-based energy systems. It also expresses the interest of having a symmetry between energy and exergy approaches of fuels. In so doing the paper also highlights the importance of an existing model of reversible combustion for a proper understanding of the main concepts.

2. Combustion

Combustion is an oxidation process, air oxygen (O) being the dominant oxidizer used. The input mixture (M) is made of fuel and oxidizer, called "reactants" in chemistry, while the output combustion or oxidation gases (G) are the reaction "products", generally emitted directly to the atmosphere. When all fuel components are fully oxidized (reactants in *stoichiometric* proportions, see below) the combustion or oxidation is said to be complete and the reaction products are designated by Gc.

For simplicity of analysis, the most common fuels are often reduced to their main component only, i.e. natural gas to methane CH_4, gasoline to octane C_8H_{18} and diesel fuel (or heating oil) to dodecane $C_{12}H_{26}$. More

generally, a generic molecule $\boldsymbol{C_aH_bO_cN_d}$ can be used. The stoichiometric coefficients, stoichiometric air amount and volume ratio of the combustion products for such a generic molecule are given below. Note that for energy analyses a simple composition of air is assumed, with a molar fraction of O_2 of 0.21, the rest being essentially nitrogen with a molar fraction of 0.79.

2.1 Energy (heating value of fuel)

A convenient way to assess the energy that can be obtained from a fuel in basic energy analyses is the concept of "Heating Value, HV". Although there are several different heating value concepts that can be developed [1], heating and cooling systems are usually open systems, such as typical burners, and the combustion can be considered to take place at constant pressure (isobaric). Heating values are defined with respect to a given reference state (standard conditions) that is usually:

$$Standard\ pressure\ P^0 = 1\ atm = 1.01325\ bar \text{ and } standard\ temperature\ T^0 = 25°C$$

However, most fuels include hydrogen atoms that oxidize to give H_2O vapor in the combustion products. When cooling the combustion gases to recover their heat energy, this water vapor can condense - totally or partially- depending on its partial pressure in the gases P_v and the lowest temperature of the cooling medium. In fact, water vapor starts to condense as soon as its partial pressure corresponds to the saturation pressure P_v'' at what is called the ***dew point***. In calorimeters, condensation takes place each time that the dew point temperature is higher than the standard temperature. This corresponds to:

$$\frac{P_v}{P} = \tilde{c}^G_{H2O}\ with\ P_v = P_v''(T)\ at\ the\ dew\ point \quad (1)$$

In which $\tilde{c}^G_{H2O}$ is the molar fraction of H_2O in the combustion gases.

The saturation pressure of water $P_v''(T)$ can be calculated on the basis of the following approximation of the Clausius-Clapeyron Eq. (2) [1]:

$$ln\left(\frac{P_v''}{140974}\right) = \frac{-3928.5}{231.667+T} \quad (2)$$

Where P_v'' is in bar and T in degree Celsius. Equation valid for the temperature range from 0°C and 150°C.

2.1.1. Air factor and its influence on gas condensation

A minimum proportion of oxygen, called ***stoichiometric,*** is required to achieve a complete combustion of the fuel. When air is the oxidant source the ratio between the input air amount (A) and the stoichiometric amount (Ast) is the ***air factor*** λ defined by:

$$\lambda = \frac{N_A}{N_{Ast}} = \frac{M_A}{M_{Ast}} \quad (3)$$

Another parameter called ***equivalence ratio*** ϕ is also often used; it is defined by:

$$\phi = \frac{1}{\lambda} \quad (4)$$

Note that the quantity of air corresponding to the stoichiometric quantity of oxygen is also called ***theoretical air*** [2].

Another ratio commonly used is the air-fuel ratio that is the ratio between the amount of air and the amount of fuel in mass (AF) or molar ($\widetilde{AF}$) units. The conversion between the mass and the molar air-fuel ratios corresponds to:

$$AF = \widetilde{AF}\ \frac{\tilde{m}_A}{\tilde{m}_F} \quad (5)$$

2.1.2. Isobaric heating values

Heating values are typically measured in calorimeter at constant volume or at constant pressure [1]. In order to simplify the discussion in this paper and since the majority of oxidation-based energy systems are open systems in quasi-steady operation this paper focusses on constant pressure (isobaric conditions).

For hydrocarbons the dew point is higher if the hydrogen/carbon ratio is higher and lower if the degree of dilution of water vapor is high in combustion gases (high air factor λ). This is the reason why there is a need to introduce two different isobaric heating values:

- ***higher heating value HHV*** when all H_2O formed during combustion is condensed;
- ***lower heating value LHV*** when none of H_2O formed during combustion is condensed

Those are defined by the following equations:

Specific isobaric Heating Value. $HHV(or\ LHV) = \Delta h^0 = \frac{H_M^0 - H_{Gc}^0}{M_F}\ \left[\frac{J}{kgF}\right]$ (6)

Molar isobaric Heating Value. $HHVm\ (or\ LHVm) = \Delta \tilde{h}^0 = \frac{H_M^0 - H_{Gc}^0}{N_F}\ \left[\frac{J}{kmolF}\right]$ (7)

The exponent $()^0$ reminds that those values are determined at a given reference state and H_{Gc}^0 varies depending on whether there is full or no condensation of the formed vapor from hydrogen. The following relation links the higher and lower heating values:

$$HHV = LHV + \dot{M}_{H2Op}\, q_{vap}^0 / \dot{M}_F \quad (8)$$

In which:

- $\dot{M}_{H2Op}$ is the total mass flow of H_2O produced during combustion,
- q_{vap}^0 is the latent heat of H_2O at the standard temperature.

The heating values of most common fuels can be found in the literature with specific or molar values.

The energy balance with all terms numerically positive can be expressed by:

$$\sum_k \dot{E}_k^+ + \sum_i \dot{Q}_i^+ + \dot{\boldsymbol{Y}}_{\boldsymbol{comb}}^+ + \sum_n \dot{Y}_n^+ - Q_a^- = \sum_k \dot{E}_k^- + \sum_i \dot{Q}_i^- + \sum_n \dot{Y}_n^- \quad (9)$$

Considering separately the network denominated with the subscript $()_{comb}$ in which combustion takes place:

$$\dot{\boldsymbol{Y}}_{\boldsymbol{comb}}^+ = \dot{M}_F\left(HHV + \hat{h}_F\right) + \dot{M}_A \hat{h}_A - \dot{M}_G \hat{h}_G - \sum(\dot{M}_I\, HHV_I) - (\dot{M}_{H2Op} - \dot{M}_{cond}) q_{vap}^0 \quad (10)$$

Where:

- $\hat{h}_F = \int_{T^0}^{T^F} dh_F$ (11) and $\hat{h}_A = \int_{T^0}^{T^A} dh_A$ (12) and $\hat{h}_G = \int_{T^0}^{T^G} dh_G$ (13) are accounting for the fact that the entering reactants and exiting products in practice have a temperature different from that of the reference standard state,
- $\dot{M}_I$ and HHV_I are the mass-flows of unburned hydrocarbons and their higher heating value, in the case of incomplete combustion,
- $\dot{M}_{H2Op}$ is the total mass-flow of H_2O produced during combustion,
- $\dot{M}_{cond}$ is the mass-flow of H_2O effectively condensed.

Figure 1 illustrates the heat gains that can be obtained by condensing the combustion gases in a condensing boiler for various fuels. The same applies to the exhaust gases of cogeneration units (engines or gas fed fuel cells) and gas fired heat pumps. The more diluted the resulting water vapor is (high λ), the less heat can be recovered from condensation and the lower is the dew point temperature. The higher the H/C ratio, the higher the dew point temperature. We can see, for example, that stoichiometric gas engines ($\lambda = 1$) allow to potentially recover more condensation heat and at a higher temperature than lean burn gas engines ($\lambda \cong 1.6$).

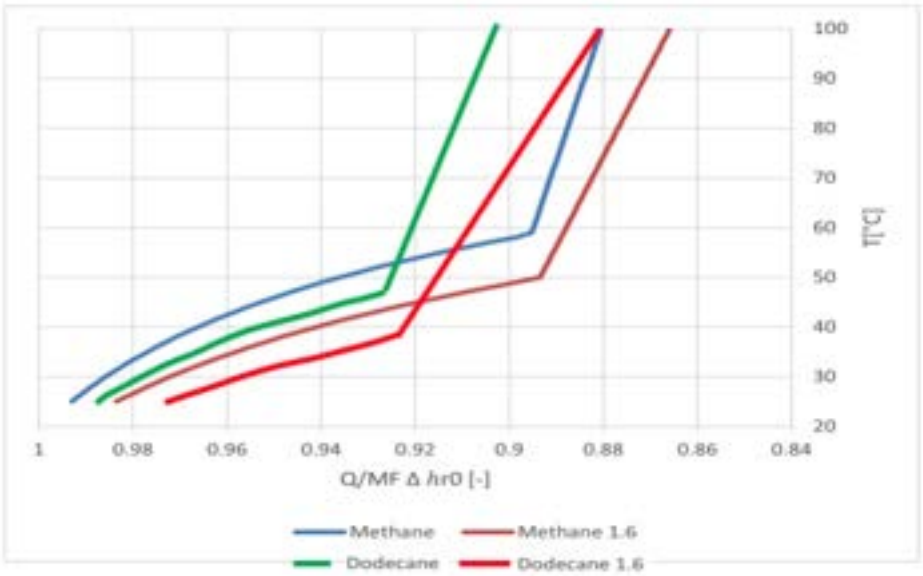

Figure. 1. Parts of the higher heating value recoverable when cooling the combustion gases from a condensing boiler down to 25°C with $\boldsymbol{\lambda = 1}$ (blue &green) or $\mathbf{1.6}$ (red & brown) for methane CH_4 (close to natural gas) and $C_{12}H_{26}$ (close to fuel oil). Here Q is the heat rate obtained, MF is the mass flow rate of fuel and $\Delta hr0$ is the isobaric higher heating value.

2.1.3. Enthalpies of formation and absolute entropies

In processes that do not involve chemical reactions, no species is modified and therefore all are considered inert, thus the reference of each of their thermodynamic state properties cancels out between inlet et outlet in energy or exergy balances. This is not the case anymore when reactions take place and new species are formed. In such conditions it becomes important to define coherent references. Hence the use of the definition of ***standard enthalpies of formation***, given per molar units in thermodynamic tables. Since entropy is also

essential in the Second Law and exergy analyses, the use of ***absolute entropies*** for all species is also of prime importance.

The values of enthalpies of formation of species that can be considered stable in the environment are arbitrarily assigned a zero value at the standard state. When this is not the case, they are determined either from calorimetric experiments or based on methods of statistical thermodynamics using spectroscopic measures. The fact that the reactions are exo- or endo-thermic influences the sign of the enthalpies of formation. For example, the reaction $2H_2 + O_2 \rightarrow 2H_2O$ is exothermic, which implies that heat needs to be extracted to come down to the standard temperature after reaction. Therefore, the enthalpy of formation of H_2O is negative, which is coherent with the convention of "positive entering" in a calorimeter for example.

The isobaric molar $\Delta\tilde{h}^0$ and specific heating value Δh^0 can then be determined by the following generic equations:

$$\Delta\tilde{h}^0 = \sum_i \left[\frac{N_i\ \tilde{h}^0_{fi}}{N_F}\right] - \sum_j \left[\frac{N_j\ \tilde{h}^0_{fj}}{N_F}\right] \qquad \left[\frac{J}{kmol_F}\right] \tag{14}$$

$$\mathrm{HHV} = \Delta h^0 = \sum_i \left[\frac{N_i\ \tilde{h}^0_{fi}}{M_F}\right] - \sum_j \left[\frac{N_j\ \tilde{h}^0_{fj}}{M_F}\right] \qquad \left[\frac{J}{kg_F}\right] \tag{15}$$

In which all the H_2O formed during combustion is condensed and, as before:

- subscript i refers to all compounds of the reactants (fuel and air)
- subscript j refers to all compounds of the reaction products (combustion gases)

3. Exergy value and exergy of diffusion (also called chemical exergy)

The **advantage of the heating values based on the First Law of thermodynamics is that they are independent from the presence of inert gases as long as enough oxygen is provided to allow for a complete combustion**. As such they do not account for the level of purity of the oxygen (pure or mixed with air) or for the concentration of CO_2 in the combustion gases. These parameters however play an increasing role in all energy systems that include CO_2 separation or oxy-combustion for example. Then the Second Law starts to be of primary importance and exergy analyses can provide a more coherent framework to evaluate advanced systems.

3.1 Convention regarding the exergy value

The objective is not only to consider thermomechanical equilibrium with the environment (P^0, T^0) (thermo-mechanical dead state) but also physico-chemical equilibrium (P^{00}, T^0, s^{00}) (dead states of each species). Hence, the need to precise a more complete reference of the environment considered, as described in Table1.

Table 1. Partial pressure and molar fractions of the main gaseous constituents of the standard atmosphere (at the standard conditions with $P^0 = 1.01325\ bar$ and $T^0 = 25°C$)

Substance	$P_i\ [bar]$	$\tilde{c}_i^A\ [kmol_i/kmol_A]$
N_2	0.7665	0.7565
O_2	0.2056	0.2030
Ar	0.0091	0.0090
$H_2O(g)$	0.0316	0.0312
CO_2	0.0003	0.0003

One further component to account for is liquid water resulting for example from condensation of combustion gases. It will be discussed later.

Furthermore, a convention is established to clarify the following conditions for the evaluation of the exergy value resulting from reactive processes:

- The fuel F and the air A enter separately (no premixing with the fuel)
- Each constituent of the reaction products Gc (combustion gases) ends up physically mixed with the standard atmosphere, i.e. at its partial pressure P_i^{00}
- Water exists in the final combustion products Gc either in liquid or vapor form at the limit of saturation, i.e. at the partial pressure of saturation in the standard atmosphere.

These conditions being set, the corresponding values for the **exergy value of a fuel** are the following:

$$\widetilde{EXV} = \Delta\tilde{k}^0 = \sum_i \left[\frac{N_i\ \tilde{k}^{00}_{fi}}{N_F}\right] - \sum_j \left[\frac{N_j\ \tilde{k}^{00}_{fj}}{N_F}\right] \qquad \left[\frac{J}{kmol_F}\right] \tag{16}$$

$$\mathrm{EXV} = \Delta k^0 = \sum_i \left[\frac{N_i\ \tilde{k}^{00}_{fi}}{M_F}\right] - \sum_j \left[\frac{N_j\ \tilde{k}^{00}_{fj}}{M_F}\right] \qquad \left[\frac{J}{kg_F}\right] \tag{17}$$

In accordance with the basic definition of exergy, the specific exergy value Δk^0 corresponds to the maximum work e^F_{max} that can be recovered from a fuel in an open reversible combustion in steady state, like in Figure 2. In principle, we should also consider whether or not there is condensation of the water formed during combustion. However as shown in [1] the difference between a higher and a lower exergy value is negligible, in particular when $T_a = T^0$. This is logical since the Carnot factor $(1 - {}^{T_a}/_{T^0})$ is zero. Hence t**he advantage of the exergy analysis of systems including oxidation processes is that a single exergy value can be considered in first approximation for fuels.**

Table 2. Features of the main species involved in combustion [5]

Species	Symbol	State	Molar mass [kg/kmol]	Enthalpy of formation [kJ/kmol]	Absolute entropy [kJ/(kmol K)]	Standard free enthalpy* [kJ/kmol]	**Exergy value** or Exergy of diffusion
Graphite	C	Solid	12.01	0	5.6944	0	**410545**
Molecular hydrogen	H_2	Gas	2.02	0	130.586824	0	**235210**
Molecular nitrogen	N_2	Gas	28.01	0	191.50168	0	691.066
Molecular oxygen	O_2	Gas	32	0	205.028552	0	3946.5
Carbon monoxide	CO	Gas	28.01	-110541	197.9032	-137277	**275241**
Carbon dioxide	CO_2	Gas	44.01	-393505	213.67688	-394383.8	20107.5
Water liq.	H_2O	Liquid	18.02	-285830	69.91464	-237178.4	5.10164
Water vap.	H_2O	Gas	18.02	-241818	188.715136	-228588.6	8594.9
Methane	CH_4	Gas	16.04	-74851.76	186.27168	-50835.6	**830130**
Ethane	C_2H_6	Gas	30.07	-84684.16	229.11584	-32802.6	**1493918**
Propane	C_3H_8	Gas	44.1	-103846.9	270.20272	-23555.9	**2148920**
n-butane	n-C_4H_{10}	Gas	58.12	-126147.6	310.11808	-17.1544	**2818213**
Heptane	C_7H_{16}	Liquid	100.2	-224387.9	326.01728	1757.28	**4757253**
n-octane	C_8H_{16}	Gas	114.2	-208446.9	466.7252	16401.28	**5417652**
n-octane	C_8H_{16}	Liquid	114.2	-249952.2	357.732	7405.68	**5408656**
dodecane	$C_{12}H_{26}$	Liquid	170.33	-352100	490.66	50160	**8034431**
Methanol	CH_3OH	Gas	32.04	-201083	239.70136	-162422.9	**720516**
Methanol	CH_3OH	Liquid	32.04	-239031.9	127.23544	-166816.1	**716122**
Ethanol	C_2H_5OH	Gas	46.07	-234429.5	282.58736	-167903.9	**1360790**
Ethanol	C_2H_5OH	Liquid	46.07	-276980.8	161.04216	-174179.92	**1354514**
Ammonia	NH_3	Gas	17.03	-46107.7	192.33848	-16484.96	**336676**

*also called Gibbs function of formation or Gibbs free energy of formation

Table 2 provides the molar masses $\tilde{m}$, the enthalpies of formation $\tilde{h}_f^0$,the absolute entropies $\tilde{s}^0$, the standard free enthalpies $\tilde{g}_f^0$, the exergy values $\widetilde{EXV}(= \Delta\tilde{k}^0)$, resp. the exergies of diffusion $\tilde{e}_d^0$ of a number of compounds considered in practice. For reference, the calculator [12] provides slightly different values with a fairly high value for the entropy of diffusion of H_2O liquid, reason why we kept here the original values of [5].

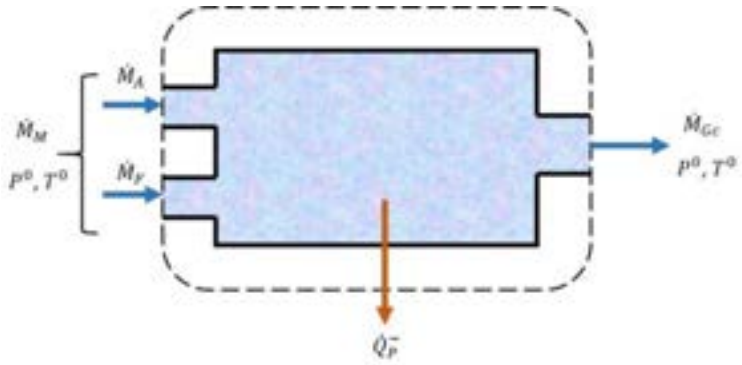

Figure. 2. Example of combustion in steady-state operation at constant pressure

3.2 Model of reversible combustion or oxidation

According to the definition of exergy the maximum work to be considered is the ideal work that could be recovered from reversible processes. In this context the idea of a ***reversible combustion*** is not obvious but can be explained with the use of a so-called van't Hoff box (cited in [3]) with compressors and turbines and semi-permeable membranes (Figure 3). Semi-permeable membranes are membranes that let only one species go through when the partial pressure of that species is not balanced on both sides of the membrane. One practical example of semi-permeable membrane is the solid electrolyte of a Solid Oxide Fuel Cell (ionic conductor) that, in certain conditions of temperatures, let only oxygen go through. The principle of a van't Hoff box is that the species inside the box are near the chemical equilibrium when reactions occur in the direction of the arrows shown in Figure 3, but the process can be reversed with only a slight change in the pressure between inlet and outlet with in this case arrows being reversed. For example, the species i2 in Figure 3 could be oxygen taken from the atmosphere and i1 a gaseous fuel like CH_4. Then j2 could be CO_2 and j1 would be H_2O according to the well-known reaction:

$$CH_4 + 2O_2 \rightleftarrows CO_2 + 2H_2O \tag{18}$$

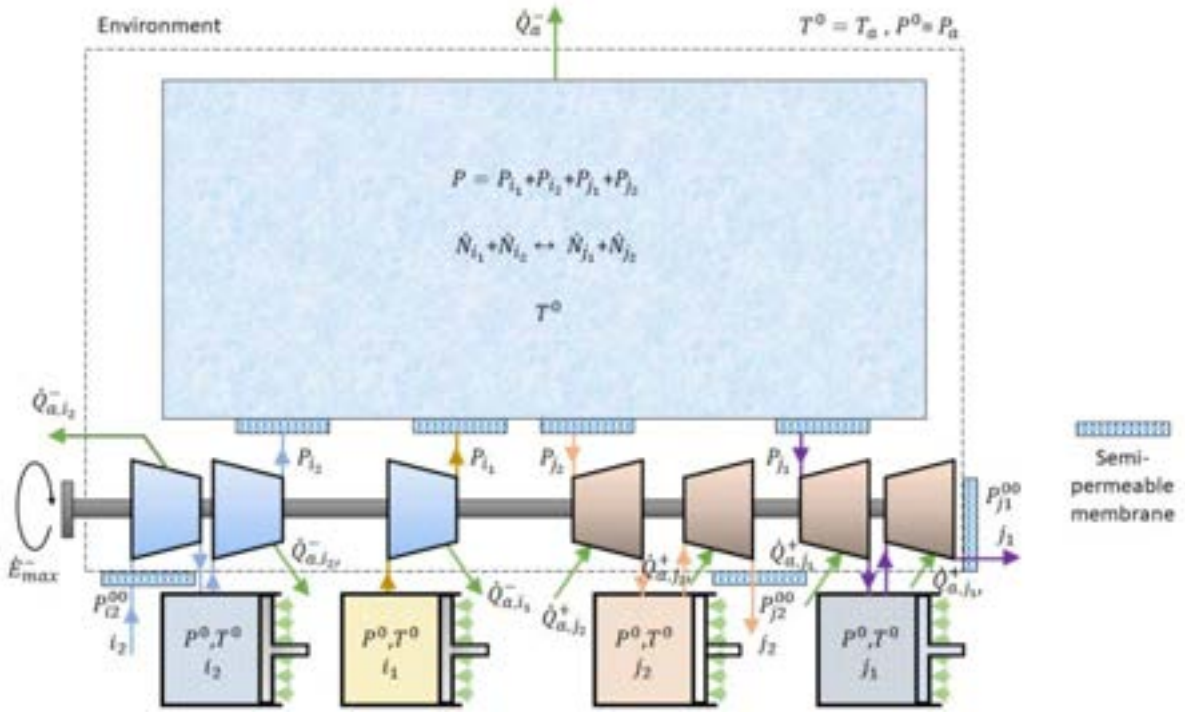

Figure. 3. Schematic representation of the reversible combustion of a fuel

The double arrow in the above equation indicates that the reaction is reversible close to equilibrium. Mechanically the first compressor is used to suck O_2 from its partial pressure P_{i2}^{00} in the atmosphere to a dedicated storage at pressure P^0, and the second compressor is pushing O_2 into the box at pressure *P*. The third compressor is pushing CH_4 from pressure P^0 to pressure *P* in the box. Then, on the same shaft one could imagine 4 turbines, 2 for CO_2 and 2 for H_2O, all gases ending up at their partial pressure in the atmosphere. All these machines are supposed to be isothermal, exchanging heat only with the atmosphere. Reversing the processes would mean that the turbines become compressors and the compressors become turbines. The net

mechanical power $\dot{E}^{-}_{max}$ that can be obtained from the process corresponds to an exergy rate equal to the specific exergy value of the fuel multiplied by the mass flow of fuel.

Through this representation one sees that if the oxidant is pure oxygen, more work can be obtained since the work required by the first compressor is not needed. On the other end if the concentrated CO_2 or H_2O exiting the system are just mixed with the atmosphere, then an opportunity to recover more work is lost. It is interesting to note that the theoretical work delivered by the second CO_2 turbine is equivalent to the minimum amount of work required to separate the same amount of CO_2 from the atmosphere for separate storage.

Let us first calculate the work recovered in steady-state operation for the simple case without the first compressor and the two turbines adapting the state of the exhaust gases to the atmospheric conditions:

$$\dot{E}^{-} = \dot{Q}^{+}_{a} + \sum_i [\dot{M}_i \, h^0_{fi}] - \sum_j [\dot{M}_j \, h^0_{fj}] \tag{19}$$

Assuming that the processes are reversible, then the Second Law gives:

$$\dot{Q}^{+}_{a} = T^0 \, (\sum_j [\dot{M}_j \, s^0_j] - \sum_i [\dot{M}_i \, s^0_i]) \tag{20}$$

Therefore:

$$\dot{E}^{-} = \dot{E}^{-}_{max} = \sum_i [\dot{M}_i \, (h^0_{fi} - T^0 s^0_i)] - \sum_j [\dot{M}_j \, (h^0_{fj} - T^0 s^0_j)] \tag{21}$$

$$\dot{E}^{-} = \dot{E}^{-}_{max} = \sum_i [\dot{M}_i \, g^0_{fi}] - \sum_j [\dot{M}_j \, g^0_{fj}] \tag{22}$$

Where g^0_f is the Gibbs free energy (also called free enthalpy) of formation.

For ideal gases the reversible mechanical power of an isothermal compressor is known to be:

$$\dot{E}^{+} = \dot{N} \int_{P_{in}}^{P_{out}} \tilde{v} dP = \dot{N} \int_{P_{in}}^{P_{out}} \tilde{\boldsymbol{r}} T^0 \frac{dP}{P} = \dot{N} \tilde{\boldsymbol{r}} T^0 ln\left(\frac{P^{out}}{P_{in}}\right) \tag{23}$$

Where $\tilde{\boldsymbol{r}}$ is the molar universal gas constant and the species behave like an ideal gas.

Inversing the integral limits give the equivalent equation for turbine.

Therefore, the net maximum work of the case of Figure 3 corresponds to:

$$\dot{E}^{-}_{max} = \sum_i [\dot{N}_i \, \tilde{g}^0_{fi}] - \sum_j [\dot{N}_j \, \tilde{g}^0_{fj}] + \dot{N}_{j1} \tilde{\boldsymbol{r}} T^0 ln\left(\frac{P^0}{P^{00}_{j1}}\right) + \dot{N}_{j2} \tilde{\boldsymbol{r}} T^0 ln\left(\frac{P^0}{P^{00}_{j2}}\right) - \dot{N}_{i2} \tilde{\boldsymbol{r}} T^0 ln\left(\frac{P^0}{P^{00}_{i2}}\right) \tag{24}$$

Let us also introduce the ***molar exergy of diffusion*** $\tilde{e}^0_{dk}$ for a species k:

$$\tilde{e}^0_{dk} = \frac{\dot{N}_k}{\dot{N}_F} \tilde{\boldsymbol{r}} T^0 ln\left(\frac{P^0}{P^{00}_k}\right) \tag{25}$$

The ratio $\frac{\dot{N}_k}{\dot{N}_F} = \nu_k$ is called stoichiometric coefficient and the ***molar exergy value of a fuel*** can be written in the following compact form:

$$\frac{\dot{E}^{-}_{max}}{\dot{N}_F} = \Delta\tilde{k}^0 = \sum_i [\nu_i \, \tilde{g}^0_{fi}] - \sum_j [\nu_j \, \tilde{g}^0_{fj}] + \sum_j [\tilde{e}^0_{dj}] - \sum_i [\tilde{e}^0_{di}] \tag{26}$$

$$\widetilde{EXV} = \Delta\tilde{k}^0 = \Delta\tilde{g}^0_f + \sum_j [\tilde{e}^0_{dj}] - \sum_i [\tilde{e}^0_{di}] \tag{27}$$

The absolute free enthalpy $\tilde{g}^0_f$ can be calculated from the absolute enthalpies and the absolute entropies according to the following relation:

$$\tilde{g}^0_f = \Delta\tilde{h}^0_f - T^0 \sum(\tilde{s}^0_P - \tilde{s}^0_R) \tag{28}$$

Note that in the literature [4], [2] all terms of the equation (3.114) are called **standard chemical exergies** although they refer to chemically stable substances and their exergy potential only lies in their partial pressure relative to the environment. Hence our terminology of ***exergy value*** $\widetilde{EXV} = \widetilde{\Delta k}^0$ of the fuels and ***exergy of diffusion*** for the other terms like the oxidants (i.e. O_2) or the stable combustion products like CO_2 or H_2O(g). In that way the symmetry between the heating values of fuels and their exergy value is kept, since the expression “heating value” is not to be used for inert components.

We also have the relation [2]:

$$\tilde{s}^{00}_i(T, P_i) = \tilde{s}^0_i(T) - \tilde{\boldsymbol{r}} ln\left(\frac{P_i}{P^0}\right) = \tilde{s}^0_i(T) - \tilde{\boldsymbol{r}} ln\left(\frac{\tilde{c}^A_i P}{P^0}\right) \tag{29}$$

Note that, in practice, real fuels are often mixtures of monomolecular fuels. Natural gas being the most common example. Since mixing implies diffusion losses, the exergy value of such a real fuel cannot be the simple addition of the relative exergy values of the n fuel components but corresponds to:

$$\Delta\tilde{k}^0 = \sum_1^n \tilde{c}_i \, \Delta\tilde{k}^0_i + \tilde{\boldsymbol{r}} T_a \sum_1^n \tilde{c}_i \ln \tilde{c}_i \tag{30}$$

3.3 Exergy values of more complex technical fuels

However, the exergy value of most solid or liquid technical fuels, which are complex mixtures of chemical compounds, is often difficult to determine. Various evaluations have been made on the basis of statistical

methods [4] using the concentration of basic components in the fuel like C, H, O, N and S as well as their LHV or HHV.

Table 3. Energy (heating) and exergy values of common fuels at the standard conditions of 1 atm and 25°C [5]

Fuel	State	LHV $= \Delta h_i^0$ [kJ/kg]	HHV $= \Delta h_s^0$ [kJ/kg]	$\widehat{LHV} = \Delta \tilde{h}_i^0$ [kJ/kmol]	$\widehat{HHV} = \Delta \tilde{h}_s^0$ [kJ/kmol]	$\mathrm{EXV} = \Delta k^0$ [kJ/kg]	$\widehat{EXV} = \Delta \tilde{k}^0$ [kJ/kmol]
C	Solid	32765	32765	393510	393510	34183	410545
CO	Gas	10103	10103	282980	282980	9831	275241
H_2	Gas	119716	141500	241826	285830	116441	235210
S	Solid	9250	9250	296600	296600	19011	609600
CH_4	Gas	50018	55505	802292	890300	51757	830130
C_2H_6	Gas	47512	51903	1428698	1560710	49678	1493418
C_7H_{16}	Liquid	44559	48072	4464778	4816810	47460	4757253
C_2H_6	Gas	47512	51903	1428698	1560710	49678	1493418
C_8H_{18}	Liquid	44788	48255	5116144	5512150	47435	5408656
$C_{12}H_{26}$	liquid	44574	47838	7592289	8148246	47169	8034431
CH_3OH	Gas	21110	23850	676364	764154	22544	720516
CH_3OH	Liquid	19936	22683	638762	726770	22367	716122
C_2H_5OH	Gas	27720	30590	1277060	1409281	29605	1360790
C_2H_5OH	Liquid	26818	29683	1235498	1367510	29386	1354514

However, a simplified approach to evaluate the chemical exergy of common combustible raw materials has been also proposed by [4].

$$\Delta k^0 = \alpha(LHV) \quad or \quad \Delta k^0 = \beta(\mathrm{HHV}) \tag{31}$$

Table 4. Coefficients to evaluate the exergy value of fuels [4]

Fuel	Coefficient	
	$\boldsymbol{\alpha}$	$\boldsymbol{\beta}$
Wood	1.15	1.05
Fuel oil	1.07	0.99
Natural gas (high methane)	1.04	0.99
Hard coal	1.09	1.03
Coke	1.06	1.04
Lignite	1.17	1.04
Coke-oven gas	1	0.89
Blast furnace gas	0.98	0.97

The following more detailed approach is also proposed for wood by [4].

$$\beta = \frac{1.0412+0.2160\left(c_{H_2}^F/c_C^F\right)-0.2499\left(c_{O_2}^F/c_C^F\right)\left[1+0.7884\left(c_{H_2}^F/c_C^F\right)\right]+0.0450\left(c_{N_2}^F/c_C^F\right)}{1-0.3035\left(c_{O_2}^F/c_C^F\right)} \qquad \text{valid for } \frac{c_{O_2}^F}{c_C^F} \le 2.67 \tag{32}$$

3.4 Exergy balance for a generic fuel molecule $C_aH_bO_cN_d$

$$C_aH_bO_cN_d + \left[a+\frac{b}{4}-\frac{c}{2}\right]O_2 \rightarrow a\ CO_2 + \frac{b}{2}H_2O(g) + \frac{d}{2}N_2 \tag{33}$$

$$\frac{\dot{E}^-}{\dot{N}_F} = \frac{\dot{Q}^+}{\dot{N}_F} + \tilde{h}_F^0 + \left[a+\frac{b}{4}-\frac{c}{2}\right]\tilde{h}_{O_2}^0 - a\tilde{h}_{CO_2}^0 - \frac{b}{2}\tilde{h}_{H_2O}^0 - \frac{d}{2}\tilde{h}_{N_2}^0 \tag{34}$$

Second Law for steady-state operation:

$$0 = \frac{\dot{Q}^+}{\dot{N}_F T^0} + \tilde{s}_F^{00} + \left[a+\frac{b}{4}-\frac{c}{2}\right]\tilde{s}_{O_2}^{00} - a\tilde{s}_{CO_2}^{00} - \frac{b}{2}\tilde{s}_{H_2O}^{00} - \frac{d}{2}\tilde{s}_{N_2}^{00} + \frac{\dot{s}^i}{\dot{N}_F} \tag{35}$$

By substituting the value $\frac{\dot{Q}^+}{\dot{N}_F}$ in Equation (34) one gets:

$$\frac{\dot{E}^-}{\dot{N}_F} = \tilde{h}_F^0 + \left(a+\frac{b}{4}-\frac{c}{2}\right)\tilde{h}_{O_2}^0 - a\tilde{h}_{CO_2}^0 - \frac{b}{2}\tilde{h}_{H_2O}^0 - \frac{d}{2}\tilde{h}_{N_2}^0 - T^0\left[\tilde{s}_F^{00} + \left(a+\frac{b}{4}-\frac{c}{2}\right)\tilde{s}_{O_2}^{00} - a\tilde{s}_{CO_2}^{00} - \frac{b}{2}\tilde{s}_{H_2O}^{00} - \frac{d}{2}\tilde{s}_{N_2}^{00}\right] - T^0\frac{\dot{s}^i}{\dot{N}_F} \tag{36}$$

The transition of the absolute entropy from the thermomechanical dead state to the global dead state is given by Equ.(34).

For a generic molecule, Equ. (36) can also be written as:

$$\Delta\tilde{k}^0(or\ \tilde{e}_d^0) = \left[\tilde{g}^0_{f\,C_aH_bO_cN_d} + \left(a + \frac{b}{4} - \frac{c}{2}\right)\tilde{g}^0_{f\,O_2} - a\tilde{g}^0_{f\,CO_2} - \frac{b}{2}\tilde{g}^0_{f\,H_2O} - \frac{d}{2}\tilde{g}^0_{f\,N_2}\right] + \tilde{\boldsymbol{r}}T^0 ln\left[\frac{\left(\tilde{c}^A_{O_2}{}^{\left(a+\frac{b}{4}-\frac{c}{2}\right)}\right)}{\left(\tilde{c}^A_{CO_2}\right)^a\left(\tilde{c}^A_{H_2O}\right)^{\frac{b}{2}}\left(\tilde{c}^A_{N_2}\right)^{\frac{d}{2}}}\right] \quad (37)$$

All data from species involved in combustion (Table 2), either exergy values for fuels or exergies of diffusion for inert species can typically be generated by Eq. (37).

3.5 Liquid water as a special case

Table 1 provides the values for a standard gaseous environment. We all know, however, that the environment consists of various equilibria like the equilibrium between surface water and the local gaseous atmosphere that usually shows a temperature difference. When dealing in particular with heating and cooling services, but also with power plants, the gaseous atmosphere is the most important environment since heat losses or gains as well as oxidant input and gas exhausts take place with the atmosphere. Because of that practical choice it is logical to also define the exergy of diffusion of liquid water by the exergy required for its release to the standard atmosphere.

Equation (37) can also be used to calculate the exergy of diffusion of liquid water. Even though there is no chemical change involved, the expression of the generic molecule can be used. Note that various attempts have been made in the literature [10], [4], [2] to find a global equilibrium between gaseous, liquid and solid species on Earth even going as far as considering various depth in the Earth crust[1].

Song et al. [9] developed new correlations based on a broad range of data bases. As a result of these various analyses the exergy of diffusion of liquid water varies between 5 et 950 kJ/kmol. Using the higher values results in a variation of the exergy values of fuels like hydrocarbons. From a practical standpoint this introduces complications that are not worth the efforts and we propose to limit the exergy of diffusion (chemical exergy in the literature) to the lower bound following the calculation shown below.

Example: Calculation of the exergy of diffusion of liquid water

We consider a system in which the water is evaporated and expanded in an isothermal turbine. For liquid water, a=0, b=2, c=1 and d=0. Equ. (37) becomes:

$$\tilde{e}_{d,H_2Oliq} = \left[\tilde{g}^0_{f\,H_2Oliq} - \frac{b}{2}\tilde{g}^0_{f\,H_2Og}\right] + \tilde{\boldsymbol{r}}T^0 ln\left[\frac{1}{\left(\tilde{c}^A_{H_2O}\right)^1}\right] = 5.1\ \text{[kJ/kmol]}$$

Conclusions

The concepts of fuel lower and higher heating values are compared with the fuel exergy value that has the advantage of being independent from the amount of condensation taking place in combustion or oxidation gases. The mechanistic model of reversible combustion presented allows a better interpretation of phenomena than a blind application of the concept of fuel exergy. Furthermore, and by coherence with First Law approaches it is recommended to separate the notions of exergy values for fuels from the concept of exergy of diffusion for chemically stable substances. In these definitions, one uncertainty remains that is linked to the broad range of exergy of diffusion of liquid water found in the literature.

References

[1] Borel L.,Favrat D. Thermodynamics and energy systems analysis. EPFL Press 2010.

[2] Moran M.J., Shapiro H.N., Boettner D.D., Bailey M.B. Fundamentals of engineering thermodynamics. Wiley 9th ed. 2018

[3] Kotas T.J. The exergy method of thermal plant analysis. Krieger, Mlabar (Florida), 1995 (original 1985)

[4] Szargut J. Morris DR., Steward FR. Exergy analysis of thermal, chemical and metallurgical processes. USA: Edwards Brothers Inc (1988)

[5] Dean J.A. Lange's Handbook of chemistry, 12th ed.; MacGraw-Hill: New York, 1979; p9.4-9.94

[6] Szargut J.,Valero A., Stanek W.,Valero A. Towards an international legal reference environment. Proceedings of the 18th International Conference on Efficiency, Cost, Optimization, Simulation, and

[1] Ertesvag [8] did a sensitivity analysis of the so-called chemical exergy for atmospheric gases with regards to variations of the ambient conditions. Regarding liquid and solids, Valero et al [7], updated the chemical exergies while proposing a new thermoecological-cost method

Environmental Impact of Energy Systems; 2005 Jun 20-25; Trondheim, Norway. 20-22 June 2005. Tapir Academic Press:409-17.

[7] Valero Al., Valero An., Stanek W. Assessing the exergy degradation of the natural capital: From Szargut's updated reference environment to the new thermoecological-cost methodology. Energy 2018; 163:1140-1149.

[8] Ertesvag, I.S. Sensitivity of the chemical exergy for atmospheric gases and gaseous fuels to variation of ambient conditions. Energy Conversion and Management 2017; 48(7): 1983-1995.

[9] Song G.,Xiao J.,Zhao H.,Shen L. A unified correlation for estimating specific chemical exergy of solid and liquid fuels. Energy 2012; 40:164-173.

[10] Ahrendts J., Reference states. Energy 1980;5(8-9):793-802.

[11] Ahrendts J., Thermodynamics of chemical reactive systems [die Exergie Chemisch Reaktionsfaehiger Systeme]. VDI Forschungsh, 579, 1977.

[12] http://www.exergoecology.com/excalc.

Liquefaction of natural gas in offshore installations: effects of irreversibilities and composition of natural gas

Rafael Dias Assunção[a], Waldyr Luiz Ribeiro Gallo[b]

[a] University of Campinas, Campinas, Brazil, rafassunc@gmail.com
[b] University of Campinas, Campinas, Brazil, gallo@fem.unicamp.br ***(CA)***

Abstract:

The use of natural gas in the energy matrix has been gaining prominence on the world scenery, due to being a fuel with available reserves and being less pollutant than other fossil fuels. Gas pipelines can be hard to build when oil and gas production takes place in deep waters and at a great distance from the coast. An alternative is to liquefy natural gas at the production site (LNG). The LNG can then be transferred to land by methane tankers. Offshore natural gas liquefaction is strongly limited by weight and available space on vessels. In this work, three natural gas liquefaction processes are evaluated (Joule-Thomson cycle, reverse Brayton cycle and Claude cycle). The main objective is to evaluate the sensitivity of each type of technology to the main irreversibilities present: isentropic efficiencies, pressure drop and minimum temperature differences in heat exchangers. Each system is modeled in the ASPEN-Hysys environment, with Peng-Robinson equations of state. After validating the modeled systems, sensitivity studies are performed on the main sources of irreversibility for each system. The effect of the composition of the natural gas to be liquefied on the performance of the systems was also analyzed. The obtained results showed that design parameters (and the irreversibilities associated with them) produce enormous effects on the performance of the liquefaction systems, indicating that compromises between weight and space available in the FPSO may imply the adoption of non-optimized systems in terms of exergy efficiency.

Keywords:

Offshore oil and gas production; Natural gas liquefaction systems; LNG; Exergy efficiency.

1. Introduction

Natural gas (NG) is increasing it's participation in the world energy matrix. Among the fossil fuel, NG is the less pollutant and have the smaller CO_2 footprint. Although the COVID-19 pandemic decreased the economic activities in the world, the war among Russia and Ucrania introduced large concerns on NG availability and energy security. The international trade of NG was greatly affected, specially in Europe.

As any gaseous fuel, NG presents difficulties concerning its transport and distribution. The most used form of transport today is the use of gas pipelines as a link between producers, intermediaries and consumers. However, this solution has as its main disadvantage the fact that when the distances involved are large, the risks involving gas pipelines, such as leaks, increase significantly [1]. This problem is amplified when the production is made offshore, due to the difficulties associated with the launching pipelines at deep water and at long distances from the coastline. This is the case for NG produced in the Brazilian Pre-Salt oil and gas fields. Today, most of the gas produced (associated gas) is re-injected in the oil field. Although this is positive to maintain the pressure in the oil field, the gas is not delivered to the market and is not monetized.

There are a considerable international experience in the transport and trade of NG in liquefied form (LNG) using specialized ships. Various LNG production and export facilities are distributed in producing countries and various re-gasification facilities exists in importing countries. This is the only viable form to deliver natural gas for long distances. LNG production facilities are positioned aside the production fields, onshore. However, when the gas field is offshore, some specialized floating production units (FLNG) were proposed and constructed. An analysis presented by [2] points to this option as a "game changer" in the same way that FPSO enabled oil production in deep water. However, this will depend on the performance and economics of the few pioneer FLNG in operation. There are great challenges to be overcome: weight, topside deck available space, meteorologic and oceanographic conditions. Figure 1 shows preliminary CAPEX and capacity figures of some FLNG units. As for 2022, there are six units in operation: Prelude (Australia), Satu and Dua (Malaysia), Hilli Episeyo (Cameroon), Coral Sul (Mozambique) and Tango (Congo Brazzaville - a barge).

Figure 1. CAPEX and capacity for FLNG in operation or construction. Source: [3]

The heart of a FLNG is the cryogenic system. There are many different cryogenic cycles being proposed to LNG production, both for land or offshore units. The cycles can be classified by the type of refrigerating fluid (pure substances, or mixed substances) and by the type of expansion adopted: Joule-Thomson effect obtained by expansion valves, or adiabatic expansion obtained by turbo-expanders. There is also the possibility to use both effects, like in the Claude cycle.

For land systems, weight, size and complexity are not great concerns, and various researchers presented comparison among different system [4], or optimization of systems [5,6]. A comprehensive review for cryogenic cycles can be found in [7]. Due to the restrictions posed by floating production, specific FLNG systems have been explored. A simplified mixed refrigerant cycle (N_2, CH_4, C_2H_6 and C_3H_8) with dual pressure is proposed in [8] and a good specific power consumption of 1150 kJ / kg of LNG was obtained. A cryogenic cycle based on a reverse Brayton cycle is presented and analyzed in [9]. This cycle uses N_2 as working fluid.

Usually the NG to be liquefied is also pressurized, to reduce the size of the equipment. Using this characteristic, [10] proposes that the last stage for LNG production uses of an expansion valve in the NG line to obtain the final product, LNG at near atmospheric pressure.

Looking for small systems, [11] compares three cycles: one with mixed refrigerant and dual expansion, and two reverse Brayton cycles also with dual expansion, one of them with N_2 and another with CH_4 as working fluids. Based on the hypothesis adopted, the mixed refrigerant presents a better performance: ~1500 kJ / kg of LNG versus 2500 and 2100 kJ / kg of LNG for mixed refrigerant, dual expansion with N2 and dual expansion with CH4. Another work [12] uses data from a Brazilian FPSO gas production and composition, and obtains similar results.

It is difficult to compare the performance of the various systems due to different hypothesis adopted by each author. Some papers does not present all hypothesis adopted, specially those associated with the main irreversibilities: compressors and expanders isentropic efficiencies, pressure losses in the heat exchangers and pipes, approach temperatures in heat exchangers. This work intends to evaluate the effect of irreversibilities and the effect of NG composition on the performance of three cryogenic cycles.

2. Methodology

The cryogenic systems analyzed in this work are described in the next section. All equipment are supposed to operate in the steady-state. Mass and energy conservation was the first step in the simulation of each control volume identified in the flowsheets. Using the entropy balance, entropy generation was calculated to avoid thermodynamic pitfalls in heat exchangers. The exergy balance was used to calculate the irreversibilities and exergy components to obtain performance parameters.

Aspen-Hysys software was adopted to calculate thermodynamic properties of the different flows, using the Peng-Robinson equation of state. All simulated cycles were validated using the same cycles, hypothesis and values of parameters present in [7].

Equation (1) shows the exergy balance for a control volume in the steady-state

$$0 = \dot{Ex}_Q - \dot{Ex}_W + \sum_{in}(\dot{Ex}) - \sum_{out}(\dot{Ex}) - \dot{ExD}, \quad (1)$$

where $\dot{Ex}_Q$ is the exergy associated with a heat flow, $\dot{Ex}_W$ is the available power, $(\dot{Ex})$ are the exergy flow associated with the masses crossing the control surface and $\dot{ExD}$ is the destroyed exergy inside the control volume, also known as irreversibility. The exergy flow $(\dot{Ex})$ is determined by the Eq.(2):

$$\dot{Ex} = \dot{m}[h - h_0 - T_0(s - s_0) + ex^{ch}], \quad (2)$$

where ex^{ch} is the chemical exergy per mass unit. The environment is supposed at 25ºC and 1 atm and the chemical exergy, when needed, was obtained according to [13] methodology.

Three performance parameters were calculated: the exergy efficiency, shown in the Eq. (3), the liquid power needed to produce 1 kg of LNG in the Eq.(4), and the energy needed to produce LNG as a percentual of the Lower Heating Value (LHV) of LNG, Eq. (5):

$$\eta_{Ex} = \frac{\dot{Ex}_{LNG} - \dot{Ex}_{NGin}}{|\dot{W}_{net}|} \quad (3)$$

$$\frac{W}{m} = \frac{\dot{W}_{net}}{\dot{m}} = \frac{\dot{W}_{compressors} - \dot{W}_{expanders}}{\dot{m}_{LNG}} \left[\frac{kJ}{kg\ LGN}\right] \quad (4)$$

$$\%\text{LHV} = \frac{\dot{W}_{net}}{\dot{m}_{LNG} * LHV} \ . \quad (5)$$

3. Simulated cycles and its validation

Three cycles were selected in this study: one based in the Joule-Thomson effect, one reverse Brayton cycle and one Claude cycle. All cycles chosen were compatible with [7], which was the reference for model validation.

3.1. Joule-Thomson cycle

The J-T cycle flowsheet in presented in the Fig. 2. The working fluid is compressed in three stages K- , with water cooling E- , and the expansion valve VLV-100 produces the final cooling effect. The working fluid in the cycle is a mixture of components, with the composition given in the Table 1. The composition of the mixture can be changed if desired, to obtain a better match with the NG cooling temperature path. The NG to be liquefied enters the cold box LNG-100 in the state 10 at 5 MPa and 298 K and exits in state 11 at 5 MPa and 113 K.

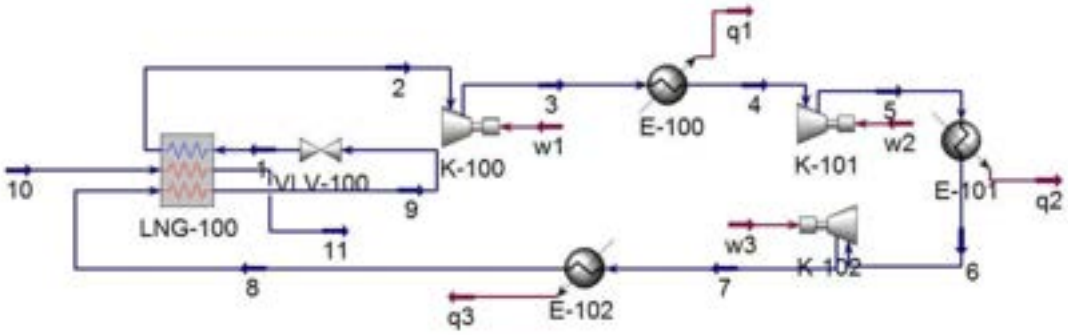

Figure 2. Joule-Thomson cycle.

Table 1. Mixed refrigerant composition for the J-T cycle

Substance	Molar fraction (%)
N_2	8.6
CH_4	30.1
C_2H_6	24.3
C_3H_8	37.0

3.2. The reverse Brayton cycle

The flowsheet of this cycle is presented in the Fig.3. In the reverse Brayton cycle, the working fluid is N_2. The refrigerant in compressed in three stages, with water cooling. The expansion is done by a turbo-expander (K-103). The NG to be liquefied enters the first heat exchanger LNG-100 and is pre-cooled. The final liquefaction occurs in the heat exchanger LNG-101. Again, the NG is at a constant pressure of 5 MPa, enter the system at 298 K and exits at 113K.

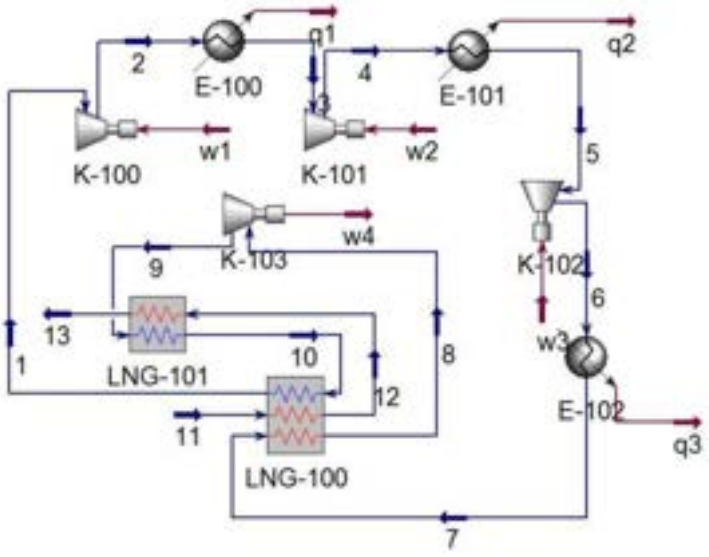

Figure 3. Reverse Brayton cycle

3.3. The Claude cycle

The Claude cycle is shown in the Fig.4. The NG to be liquefied is cooled through the heat exchangers LNG-100 to LNG103. The inlet and outlet conditions of the NG is the same as the two previously presented cycles: 5 MPa, constant, 298 K at inlet and 113 K at outlet. The cooling cycle is somewhat more complex, with four stages of compression, with water cooling, and the expansion process is made by expansion valves and turbo-expanders. The working fluid is pre-cooled in the heat exchanger LNG-100 and then is splitted in two streams. One of them goes to the turbo-expander K-104, mixes with the return stream in the MIX-100 and then passes in the heat exchanger LNG-101. The second stream passes LNG-101, LNG-102 where is cooled, goes to the expansion valve VLV-100 and finally enters the heat exchanger LNG-103. The return stream goes to LNG-102, LNG-101 and LNG-100 to close the cycle.

This cycle uses a NG as the working fluid, with composition given in the Table 2, which is the same adopted for the NG to be liquefied.

Table 2. Natural gas composition adopted for model validation.

Substance	N_2	CH_4	C_2H_6	C_3H_8	$n-C_4H_{10}$	$i-C_4H_{10}$
Molar composition (%)	1.0	91.0	5.0	2.0	0.6	0.4

3.4. Validation of the simulation

It is important to mention that [7] presents results for a great number of **ideal** cycles, always considering the production of 1 kg/s of LNG. Pressure losses, minimum approach temperatures and isentropic efficiencies for compressors and expanders are not considered. The cycles simulated in this work were validated against the values presented in [7] for the simplest cycle of each type (J-T, Brayton, Claude) using the same data, and good results were obtained. The relative deviations on exergy efficiency, Eq. (3), were -1.2% for the J-T cycle, +0.2% for the reverse Brayton cycle and 0,0% for the Claude cycle. Main results of the validation of this work are presented in the Table 3, showing also the exergy efficiency of [7].

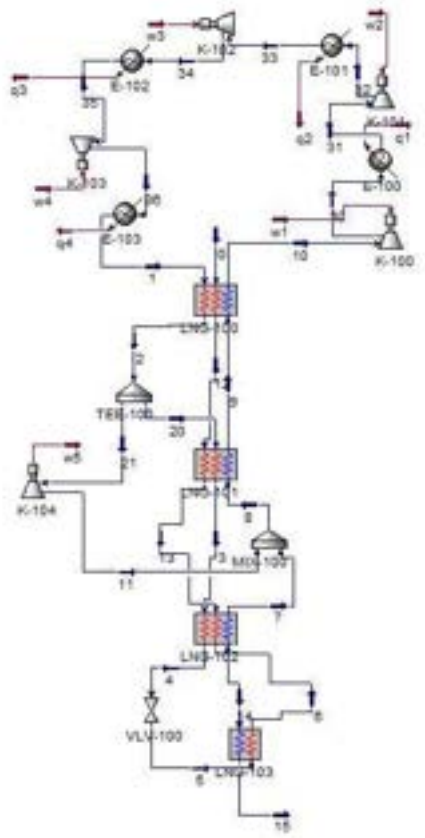

Figure 4. The Claude cycle

The obtained results are overestimated, since important sources of irreversibility were not considered. The use of exergy efficiency is not usual outside academic circles. The most usual parameter to define a good performance for LNG production is presented in the third column in the Table 4: energy expressed in kWh needed to produce 1 kg of LNG. The best practical systems developed for onshore complex installations are in the range of 0.2545 - 0.3572 [4] and for offshore values in the range of 0.400 to 0.474 according to one equipment provider [14].

Table 3. Main results from the validation process

Parameter Cycle	W/m [kJ / kg LNG]	W/m [kWh / kg LNG]	Energy/ LHV %	η_{Ex} %	η_{Ex} % [7]
J-T	795.9	0.2211	1.64	56.4	57.1
Reverse Brayton	743.4	0.2065	1.53	60.4	60.3
Claude	752.8	0,2091	1.56	59.7	59.7

4. Results and discussion

This section shows the effects of irreversibilities as well as the effects of the NG composition on the performance of the basic cryogenic cycles presented.

4.1. Influence of the irreversibilities on cycle performance

This work evaluates three types of irreversibilities: isentropic efficiencies of compressors and expanders, pressure losses in heat exchangers, and minimum approach temperatures in heat exchangers. To evaluate the isolated effect of each irreversibility source, a parametric study was made. The isentropic efficiency was varied in the range from 80-100%; pressure losses were evaluated in the range 0-5% as a percentage of

inlet pressure of each stream; minimum approach temperatures in the heat exchangers were evaluated in the range 0-10°C. Ideal cycles have 100% isentropic efficiencies, 0% pressure losses and minimum approach temperatures of 0°C. To analyze each parameter, the other ones were maintained at the ideal values.

It is important to note that the results for exergy efficiency presented in this section for ideal (base) cycles are different from the results presented for the same ideal cycles presented in the Table 3. This is due the fact that the NG composition is different from the one adopted in [7] and presented in Table 2. To this study, a typical composition of the NG produced in the Brazilian Pre-Salt was adopted. So, to obtain the maximum exergy efficiency a new optimization should be made. This is a clear proof of the dependency of the performance of each cycle to the NG composition, effect which will be analyzed in the next section.

Table 4 presents the results of the parametric analysis for the Joule-Thomson cycle. This cycle uses mixed refrigerant with the composition given in Table 1 and reaches a maximum pressure of 5,0 MPa. From the results, it is clear that the minimum approach temperature is the main irreversibility effect, followed by the isentropic efficiency of the compressors. Pressure losses are also relevant, although less important than the other effects. The importance of the minimum approach temperature is due to the mismatch among the NG composition and the composition of the mixed refrigerant, and emphasize the importance of the adjustment of the working fluid composition to each NG composition.

Table 4. Parametric analysis for the Joule-Thomson cycle.

Parameter	Value	Exergy Efficiency	W/m [kJ/kg LNG]	W/m [kWh/kg LNG)	Energy / LHV %
Isentropic efficiency	100%	49.5	720.1	0.2000	1.49
	90%	44.6	800.1	0.2223	1.65
	80%	39.6	900.1	0.2500	1.86
Pressure loss	0%	49.5	720.1	0.2000	1.49
	2%	48.0	738.7	0.2052	1.53
	5%	45.9	766.9	0.2130	1.58
Approach T (°C)	0.0	49.5	720.1	0.2000	1.49
	5.0	30.1	1185.3	0.3293	2.45
	10.0	22.2	1604.0	0.4455	3.31

The results obtained for the reverse Brayton cycle are presented in the Table 5. This cycle operates with N2 as working fluid and its maximum pressure is very high: 10 MPa. The cycle adopts a turbo-expander to obtain the desired minimum temperature. Due to the high pressure needed from compressors and the use of the turbo-expander, the main irreversibility in this cycle is the isentropic efficiency of the rotating machines. Minimum approach temperatures and pressure losses are clearly secondary effects, although important.

Table 5. Parametric analysis for the reverse Brayton cycle.

Parameter	Value	Exergy Efficiency	W/m [kJ/kg LNG]	W/m [kWh/kg LNG)	Energy / LHV %
Isentropic efficiency	100%	52.2	683.4	0.1898	1.41
	90%	31.7	1124.0	0.3122	2.32
	80%	19.2	1859.6	0.5165	3.84
Pressure loss	0%	52.2	683.4	0.1898	1.41
	2%	47.5	742.9	0.2064	1.53
	5%	41.7	833.9	0.2316	1.72
Approach T (°C)	0.0	52.2	683.4	0.1898	1.41
	5.0	48.4	736.8	0.2047	1.52
	10.0	44.9	794.6	0.2207	1.64

Table 6 presents the results obtained for the Claude cycle. The working fluid for the Claude cycle is NG, but with composition as given by Table 2. There is a mismatch among composition of the NG as working fluid and the NG to be liquefied. This cycle also operates with very high pressure (10 MPa) and uses a turbo-expander as well as a expansion valve to obtain the needed minimum temperature. Since there are rotating machines, mismatch among the working fluid and NG to be liquefied, and a great number of heat exchangers, all irreversibilities are important, including pressure losses.

As seen in Tables 4 to 6, the irreversibilities can have a huge effect on the performance of the cycles.

Table 6. Parametric analysis for the Claude cycle.

Parameter	Value	Exergy Efficiency	W/m [kJ/kg LNG]	W/m [kWh/kg LNG)	Energy / LHV %
Isentropic efficiency	100%	44.3	805.1	0.2236	1.66
	90%	30.9	1154.4	0.3207	2.39
	80%	21.4	1662.2	0.4617	3.43
Pressure loss	0%	44.3	805.1	0.2236	1.66
	2%	41.6	839.6	0.2332	1.73
	5%	37.9	893.8	0.2483	1.85
Approach T (°C)	0.0	44.3	805.1	0.2236	1.66
	5.0	41.9	851.9	0.2366	1.76
	10.0	39.5	903.7	0.2510	1.87

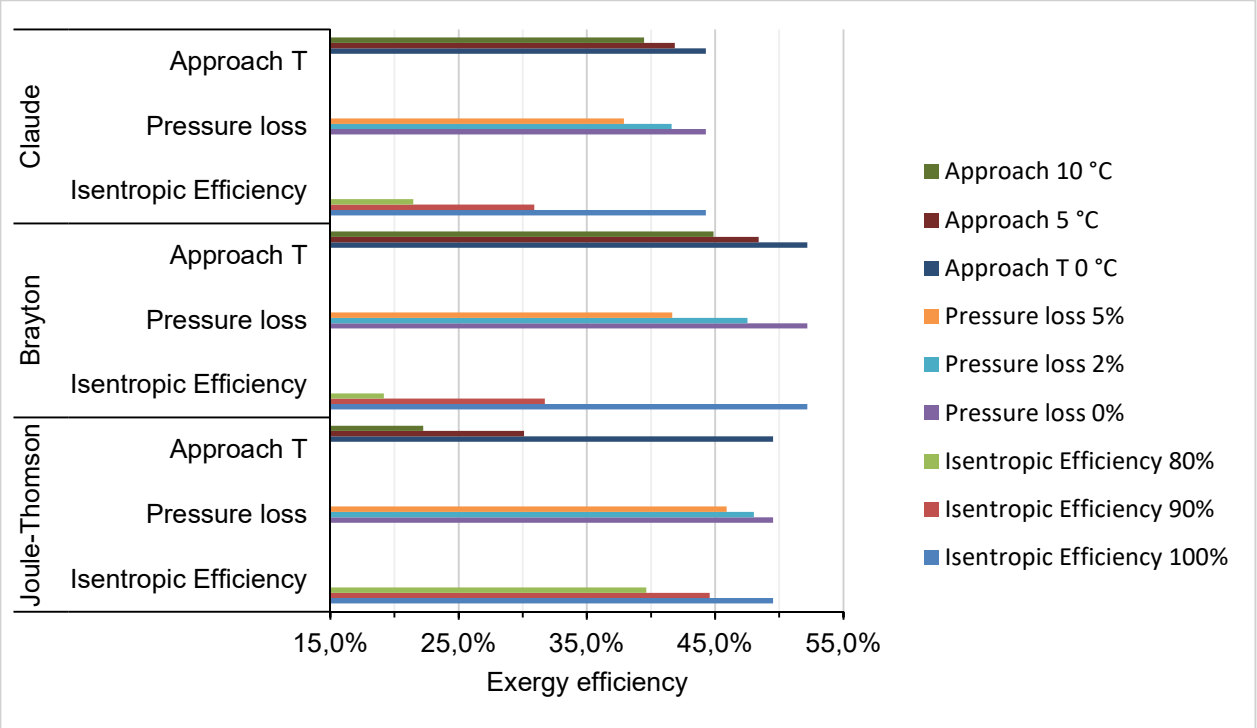

Figure 5. Effects of irreversibilities on the exergy efficiency for the three cycles.

Figure 5 shows the effects of irreversibilities on the exergy for the three cycles. As can be observed, each cycle presents different impacts from each parameter. Since all cycles use compressors, the isentropic efficiency is relevant for all of them. The mismatch of working fluid and NG properties can induce a great impact on performance due to high values of minimum approach temperatures.

4.2. Influence of the natural gas composition

The operation of a FLNG is foreseen to 20 to 25 years in a given gas oil and gas field. The composition of the NG to be liquefied varies during the field operation, even after the needed treatment before liquefaction. As became clear in the previous section, NG composition impacts the performance of the cryogenic cycles.

To evaluate the effect of NG composition, five NG compositions were adopted. These compositions are presented in the Table 7 and are associated to different years of a typical production curve. The first one corresponds to the third year, when occurs the maximum production of oil and gas. The second composition is for the production year 12. The third composition corresponds to the year 15, when the oil and gas production begins to fall and water content increases. The fourth composition occurs at the 50% BSW (Basic Sediment and Water) condition. Finally, the fifth composition corresponds to year 21, in a condition with maximum water and CO_2 in the oil field. It must be said that all compositions are obtained after the pretreatment phase.

Table 7. NG composition for five field operation conditions.

	NG molar Composition (%)				
Substance	1	2	3	4	5
H_20	0.0000	0.0000	0.0000	0.0000	0.0000
N_2	0.7288	0.7370	0.7516	0.6706	0.7092
CO_2	2.6845	2.8480	2.9941	2.9861	3.2325
C1	75.0549	75.5498	75.9309	75.7151	78.3747
C2	10.8992	10.6941	10.6156	10.0091	9.3585
C3	7.1086	6.7848	6.4926	6.9561	5.5985
i-C4	0.9802	0.9244	0.8666	1.0153	0.7384
n-C4	1.6498	1.5593	1.4594	1.7246	1.2269
i-C5	0.2859	0.2763	0.2620	0.3035	0.2189
n-C5	0.4886	0.4795	0.4590	0.5156	0.3830
C6	0.0616	0.0697	0.0733	0.0592	0.0648
C7	0.0481	0.0632	0.0767	0.0383	0.0760
C8	0.0084	0.0119	0.0155	0.0057	0.0160
C9	0.0012	0.0017	0.0023	0.0007	0.0023
C10+	0.0002	0.0003	0.0004	0.0001	0.0004

Three scenarios for irreversibilities effects were explored. The Base Case is the ideal condition: isentropic efficiencies of 100% for all rotating machines, no pressure loss, and minimum approach temperature of 0°C whenever possible. For the Case 1, irreversibility parameters are in an intermediate value. Isentropic efficiencies are 90%, pressure losses are 2% of the inlet pressure for each heat exchanger, and minimum approach temperature is 5°C. Case 2 represents the worst condition for all parameters: isentropic efficiencies are 80%, pressure losses are 5% of the inlet pressure for each heat exchanger, and minimum approach temperature is 10°C.

As an example of the thermodynamic states for each stream, Table 8 presents the results for condition 1 (NG composition for the third year of field operation) for the three scenarios using Joule-Thomsom cycle. The streams are numbered according to Fig.2.

The thermodynamic states for the reverse Brayton and Claude cycle are not presented here due to space limitation for the paper.

The effect of NG composition and degree of irreversibilities on the performance of the Joule-Thomson cycle is presented in the Table 9. The degree of irreversibility is the dominant effect, causing huge reductions on the exergy efficiency, whatever is the NG composition. As an example, for NG composition 2, the exergy efficiency falls from 52.5% (base case) to 27.6% for case 1 and to 14.4% to case 2. The effect of NG composition, however, for the same level of irreversibility (case), is also relevant. In the example, the exergy efficiency vary in the range from 5 to 17% depending on the NG composition. And it must be remembered that the NG composition didn't vary so much, as can be seen in the Table 7. The J-T cycle uses mixed refrigerant. To improve the performance of the cycle, the molar percentage of the constituents of the working fluid should be optimized for each NG composition, bringing operational complexity for the FLNG.

Table 8. Thermodynamic conditions of the streams. Joule-Thomson cycle, NG composition 1

	Stream	**1**	**2**	**3**	**4**	**5**	**6**	**7**	**8**	**9**	**10**	**11**
Base case	vapor fraction	0.045	1.000	1.000	1.000	1.000	1.000	1.000	0.564	0.000	1.000	0.000
	Temperature (C)	-160.2	24.9	67.4	24.9	70.3	24.9	77.2	24.9	-160.2	24.9	-160.2
	Pressure (kPa)	402.3	402.3	949.5	949.5	2241	2241	5300	5300	5300	5000	5000
Case 1	vapor fraction	0.101	1.000	1.000	1.000	1.000	1.000	1.000	0.564	0.000	1.000	0.000
	Temperature (C)	-165.2	19.9	89.3	24.9	97	24.9	106.2	24.9	-160.2	24.9	-160.2
	Pressure (kPa)	111.8	109.8	406.1	398.1	1473	1443	5410	5300	5194	5102	5000
Case 2	vapor fraction	0.139	1.000	1.000	1.000	1.000	1.000	1.000	0.564	0.000	1.000	0.000
	Temperature (C)	-170.2	14.9	112.7	24.9	125.4	24.9	135.8	24.9	-160.2	24.9	-160.2
	Pressure (kPa)	41.9	39.9	211.6	200.6	1063	1010	5570	5300	5035	5236	5000

Table 9. Performance of the Joule-Thomson cycle. Different NG compositions and degrees of irreversibilities

NG Composition	Degree of irreversibility	Exergy efficiency	W/m [kJ /kg LNG]	W/m [kWh/kg LNG]	Energy / LHV %
1	Ideal	49.52%	720.1	0.200	1.49
	Case 1	26.48%	1339.9	0.372	2.77
	Case 2	16.90%	2082.4	0.579	4.30
2	Ideal	52.48%	684.2	0.190	1.41
	Case 1	27.59%	128.1	0.358	2.66
	Case 2	14.41%	2426.8	0.674	5.01
3	Ideal	50.09%	721.6	0.200	1.49
	Case 1	26.78%	1342.8	0.373	2.77
	Case 2	17.10%	2086.6	0.580	4.31
4	Ideal	49.71%	719.3	0.200	1.49
	Case 1	26.58%	1338.5	0.372	2.77
	Case 2	16.96%	2080.4	0.578	4.30
5	Ideal	51.31%	727.5	0.202	1.50
	Case 1	27.42%	1354.0	0.376	2.80
	Case 2	17.50%	2105.0	0.585	4.35

Table 10 shows the performance for the reverse Brayton cycle. The overall tendencies are similar to J-T cycle - that is, the degree of irreversibility is the main effect. Since the working fluid for this cycle is N_2, the effects of NG composition is near 3.5%, not so great as for J-T cycle. Since this cycle operates with very high pressures and uses various rotating machines, the effects of irreversibilities on exergy efficiencies are even greater than for the J-T cycle: from 54% (base case) to 28% in case 1 and 14% in the case 2.

The performance of the Claude cycle is presented in the Table 11. The effect of irreversibilities on performance is again the predominant: the exergy efficiency drops from 45% in the base case to 31.5% in case 1 and to 20.3% for case 2. The effect of the NG composition for a given level of irreversibility is in the range of 3.7 to 6.0%.

Table 10. Performance of the reverse Brayton cycle for different NG compositions and different degrees of irreversibilities

NG Composition	Degree of irreversibility	Exergy eff	W/m [kJ /kg LNG]	W/m [kWh/kg LNG]	Energy / LHV %
1	Ideal	52.2%	683.4	0.190	1.41
	Case 1	27.4%	1286.6	0.357	2.66
	Case 2	14.3%	2423.7	0.673	5.01
2	Ideal	52.5%	684.2	0.190	1.41
	Case 1	27.6%	1288.1	0.358	2.66
	Case 2	14.4%	2426.8	0.674	5.01
3	Ideal	52.7%	685.5	0.190	1.42
	Case 1	27.7%	1289.7	0.358	2.66
	Case 2	14.5%	2430.0	0.675	5.02
4	Ideal	52.4%	682.7	0.190	1.41
	Case 1	27.5%	1285.3	0.357	2.66
	Case 2	14.4%	2421.4	0.673	5.00
5	Ideal	54.1%	690.6	0.192	1.43
	Case 1	28.4%	1300.6	0.361	2.69
	Case 2	14.8%	2451.7	0.681	5.07

Table 11. Performance of the Claude cycle for different NG compositions and different degrees of irreversibilities

NG Composition	Degree of irreversibility	Exergy eff	W/m [kJ /kg LNG]	W/m [kWh/kg LNG]	Energy / LHV %
1	Ideal	44.3%	804.6	0.224	1.66
	Case 1	31.2%	1118.9	0.311	2.31
	Case 2	20.3%	1669.8	0.464	3.45
2	Ideal	44.3%	809.6	0.225	1.67
	Case 1	31.3%	1124.2	0.312	2.32
	Case 2	21.3%	1596.6	0.444	3.30
3	Ideal	44.6%	810.7	0.225	1.68
	Case 1	31.6%	1120.7	0.311	2.32
	Case 2	20.2%	1694.3	0.471	3.50
4	Ideal	44.7%	799.4	0.222	1.65
	Case 1	31.3%	1117.9	0.311	2.31
	Case 2	20.0%	1695.7	0.471	3.50
5	Ideal	46.4%	803.8	0.223	1.66
	Case 1	32.4%	1126.7	0.313	2.33
	Case 2	20.6%	1714.9	0.476	3.54

Figures 6 and 7 present comparisons among the three cycles, focusing on exergy efficiency and work to produce 1 kg of LNG respectively. As expected, the work needed increases (and the exergy efficiency decreases) when the irreversibilities increases. It is interesting to note, however, that for a given cycle and a given level of irreversibility, the NG composition can produce a higher exergy efficiency associated with a smaller work to produce 1 kg of LNG. Mass, energy and approach temperatures details can explain this.

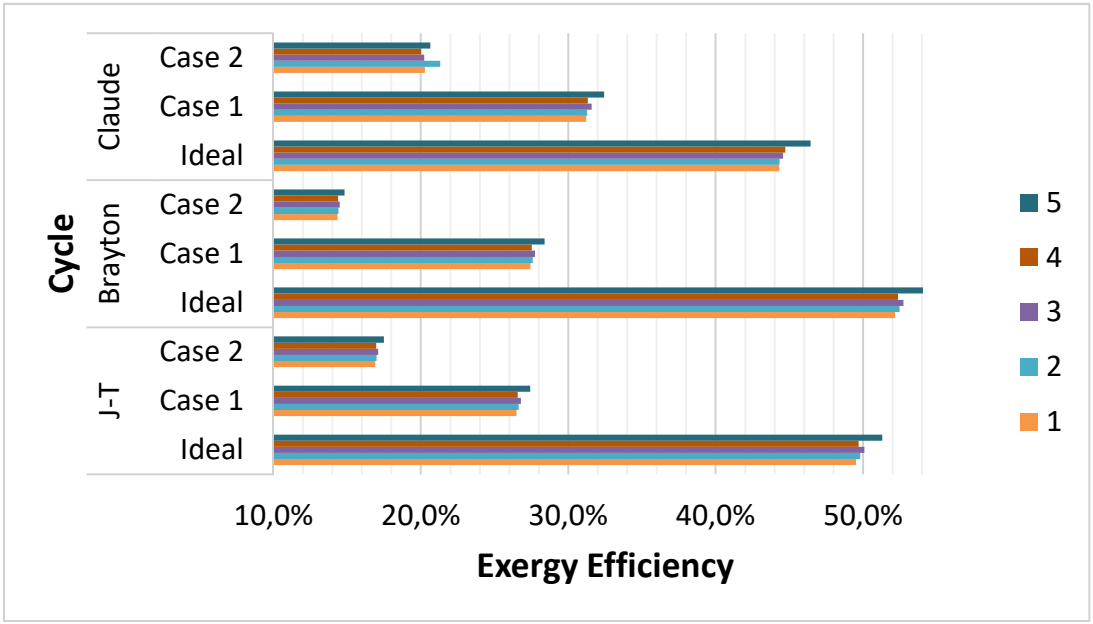

Figure 6. Performance comparisons among the three cycles: exergy efficiency.

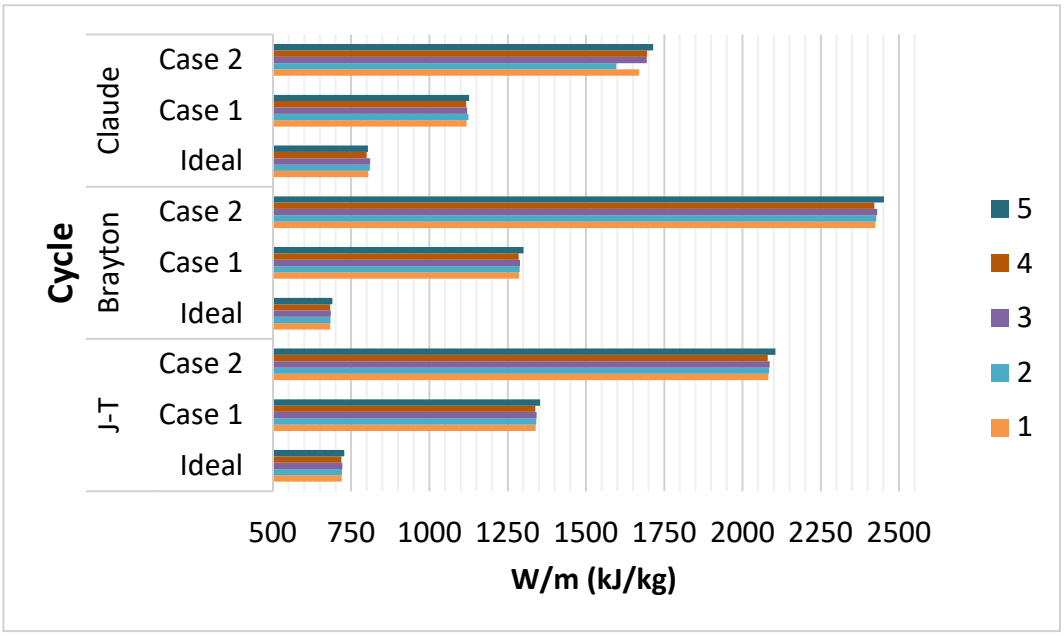

Figure 7. Performance comparisons among the three cycles: work to produce 1 kg of LNG.

5. Concluding remarks

The analysis developed in this work showed the huge influence of the irreversibility level on the performance of three cycles proposed to produce LNG offshore. The limitation of weight and size induces a design which uses as few components as possible. Then, the three cycles studied were the simplest of each class. The influence of the NG composition, although smaller, is also relevant.

The use of mixed refrigerants is interesting to reduce the internal heat transfer irreversibilities in heat exchangers, but requires an optimization of the working fluid composition (molar fractions of the components) associated with the NG composition. This is the case for the analyzed J-T and Claude cycles.

The use of N_2 in a reverse Brayton cycle presented less dependency of the NG composition. However, this cycle proved to be the most sensitive to the isentropic efficiencies of the rotating machines - that is, the design of highly efficient compressors and turbo-expanders must be the focus for a better performance of this cycle.

The prime movers to run the compressors can be electrical motors, or thermal machines as gas turbines. The work needed to produce 1 kg of LNG didn't take into account the use of fuel to run the prime mover or to generate the electricity. As an example, if a gas turbine fueled by NG, with 35% of efficiency, is used as mechanical drive, the use of fuel can be in the range of 5-15% of the available NG, depending on the cycle and level of irreversibilities.

To reduce the volume of the equipment, the NG to be liquefied was assumed at 5 Mpa to increase its density. The power needed to compress the NG to this pressure was not taken into account. Depending on details of the FLNG design and pretreatment processes, the NG can be at some pressure grater than atmospheric.

For the cycles analyzed, in the conditions specified in this work, the exergy efficiency varied from 43 to 52% for the ideal cycles, to 14 to 17% for cycles with high level of irreversibilities. This indicates that the feasibility of FLNG is quite sensible to a balance among high efficiency and cycles as simple as possible to save size, weight and economic costs.

Nomenclature

h -	Enthapy [kJ/kg]	LHV -	Lower heating value [kJ/kg]	$\dot{E}x$	Exergy flow [kJ/s]
$\dot{m}$ -	Mass flow [kg/s]	$\dot{E}x_Q$ -	Exergy flow -heat transfer [kJ/s]	η_{Ex}	Exergy efficiency
s -	Entropy [kJ/(kg.K)]	$\dot{E}x_W$ -	Exergy of power [kJ/s]	NG	Natural gas
T -	Temperature [K]	$\dot{E}xD$ -	Destryed exergy [kJ/s]	LNG	Liquified natural gas
$\dot{W}$ -	Power [kW]	ex^{ch} -	Chemical exergy [kJ/kg]	FPSO	Oil and gas platform

References

[1] Cipolato, L.; Lirani, M.C.A.; Costa, T.V.; Fabrega, F.M.; D'Angelo, J.V.H. Exergetic optimization of a refrigeration cycle for natural gas liquefaction. Proceedings of the 11th International Symposium on Process Systems Engineering, 15-19 July 2012, Singapore, p.440-444.

[2] Songhurst, B. Floating Liquefaction (FLNG): Potential for Wider Deployment. OIES paper: NG 107. Oxford Institute for Energy Studies, UK, 2016.

[3] Bonelli, C.M.C. FLNG as an option to monetizing the natural gas from Pre-Salt in Brazil. Empresa de Pesquisa Energética (EPE) stand on Rio Pipeline 2019. Rio de Janeiro, Brazil.

[4] Vatani, A.; Mehrpooya, M.; Palizdar, A. Advanced exergetic analysis of five natural gas liquefaction processes. Energy Conversion and Management 2014 78, 720–737

[5] Nguyen, T.-V., & Elmegaard, B. Assessment of thermodynamic models for the design, analysis and optimisation of gas liquefaction systems. Applied Energy, 2016, 183, 43–60.

[6] He, T.; Karimi, I.A.; JU, Y. Review on the design and optimization of natural gas liquefaction processes for onshore and offshore applications. Chemical Engineering Research and Design, 2018, 132, 89–114.

[7] Chang, H.-M. A thermodynamic review of cryogenic refrigeration cycles for liquefaction of natural gas. Cryogenics, 2015, 72, 127-147.

[8] Lee, S.; Long, N.V.D.; Lee, M. Design and Optimization of Natural Gas Liquefaction and Recovery Processes for Offshore Floating Liquefied Natural Gas Plants. Ind. Eng. Chem., 2012, Res. 51, 10021−10030.

[9] Qyyum, M.A.; Qadeer, K.; Minh L.Q.; Haider, J.; Lee, M. Nitrogen self-recuperation expansion-based process for offshore coproduction of liquefied natural gas, liquefied petroleum gas, and pentane plus. Applied Energy, 2019, 235 247-257.

[10] Xiong, X.; Lin, W.; Gu, A. Design and optimization of offshore natural gas liquefaction processes adopting PLNG (pressurized liquefied natural gas) technology. Journal of Natural Gas Science and Engineering, 2016, 30 379-387.

[11] Nguyen, T.V; Rothuizen, E.D.; Markussen, W.B.; Elmegaard, B. Thermodynamic comparison of three small-scale gas liquefaction systems. Applied Thermal Engineering, 2018, 128, 712–724.

[12] Nguyen, T.V.; De Oliveira Jr, S. System evaluation of offshore platforms with gas liquefaction Processes. Energy, 2018, 144, 594-606.

[13] Kotas, T. J. The Exergy Method of Thermal Plant Analysis. London, UK: Anchor Brendon, 1985.

[14] Walther, S.; Franklin, D.; Ross, P.; Hubbard, B. Liquefaction solutions for challenge of new offshore FPSO developments. LNG Journal, Feb.2008, 31-34.

Trilateral Flash Cycle for efficient low-temperature solar heat harvesting- A case study.

Anastasios Skiadopoulos[a], Christina Antonopoulou[b], Konstantinos Atsonios[c], Panagiotis Grammelis[d], Apostolos Gkountas[e], Panteleimon Bakalis[f], George Kosmadakis[g], and Dimitris Manolakos[h]

[a] Agricultural University of Athens, Athens, Greece, tskiado@aua.gr, CA
[b] Centre of Research and Technology Hellas, Athens, Greece, antonopoulou@certh.gr
[c] Centre of Research and Technology Hellas, Athens, Greece, atsonios@certh.gr
[d] Centre of Research and Technology Hellas, Athens, Greece, grammelis@certh.gr
[e] Psyctotherm SME, Piraeus, Greece, agountas@psyctotherm.gr
[f] Psyctotherm SME, Piraeus, Greece, pbakalis@psyctotherm.gr
[g] Ricreation IKE, Agia Paraskevi, Greece, gkosmad@ipta.demokritos.gr
[h] Agricultural University of Athens, Athens, Greece, dman@aua.gr

Abstract:

In this work, the annual performance of a solar thermal power system in Greece is numerically studied. The system consists of a field of Evacuated Tube Collectors and a Trilateral Flash Cycle engine. The main target of this study is to assess the potential of the Trilateral Flash Cycle, a promising higher efficiency alternative to the Organic Rankine Cycle, for solar energy exploitation. The effects of the solar irradiance, the temperature of the heat source, and the flashing efficiency on the total solar energy conversion efficiency are monitored. The economics of the system is preliminarily studied taking into account its scale and the anticipated annual power output. Simulations indicate that the combined Solar-Trilateral Flash Cycle system can achieve an average annual total solar energy conversion efficiency of 5%, outperforming a Solar-Organic Rankine Cycle system of similar architecture at the examined location. It is demonstrated that the efficiency of the Trilateral Flash Cycle engine is highly dependent on the quality of the Working Fluid at the onset of expansion, and the operating pressure ratio. Moreover, the Trilateral Flash Cycle can achieve a thermal efficiency of up to 11%. The Levelized Cost of Electricity of the power system is estimated to lie in the region of 0.26 - 0.32 €/kWh, based on its scale, indicating that it may be a competitive solution for solar energy exploitation.

Keywords:

Solar Energy; Trilateral Flash Cycle; Two-Phase Expansion; Evacuated Tube Collectors; Solar Efficiency; Thermal Efficiency.

1. Introduction

Solar energy presents a huge potential for green power generation, especially in locations with low to middle latitudes, and it may be efficiently exploited by solar thermal power systems. In these systems, solar thermal collectors generate heat that is utilized for power production by a heat-to-power conversion technology. Several types of solar thermal collectors, with different ranges of applications each, have been developed [1], and they are currently considered to be at a mature technological level [2]. These collectors provide heat at rather low temperatures (<400^{o}C), a range where the traditional water-steam Rankine power cycles of centralized power stations cannot operate efficiently. The overall solar energy conversion efficiency of solar thermal power systems depends on the collectors' efficiency and the thermal efficiency (heat-to-power ratio) of the power generation technology. Bottoming power cycles are a widely applied solution for the efficient exploitation of low-temperature heat, with the Organic Rankine Cycle (ORC) indicated as a robust solution because of its flexible design, low maintenance cost, and nearly unsupervised operation [3].

Many works have been published in the literature (e.g. [4–7]) assessing the potential and efficiency of the ORC, both numerically and experimentally, with different heat sources. The main drawback of the ORC is the drop in its thermal efficiency at lower heat source temperatures. Several studies have been published in the literature (e.g. [8]) aiming to identify the causes for this efficiency drop. The consensus is that the energy losses in the ORC are mainly ought to the isothermal vaporization process of the Working Fluid (WF) at the evaporator of the cycle. During this process, the temperature of the WF remains constant while the temperature of the Heat Transfer Fluid (HTF) drops, leading to a sub-optimal match between the finite heat source and the WF. The optimal match between the heat source and the WF may be accomplished when the power cycle obtains

a trilateral shape [8], where the vaporization of the WF is omitted. One such possible high-efficiency power cycle variant is the Trilateral Flash Cycle (TFC), initially conceptualized by Smith et al. [9].

The TFC consists of the same components as the ORC but the WF enters the power generator in the saturated liquid state, or partially evaporated in the generalized version of the TFC, where it undergoes two-phase expansion, also known as flashing. The TFC is not technologically mature, mainly because of the lack of fundamental knowledge about the complex flashing phenomenon in the expander. Only a few experimental works ([10–12]) have been performed in two-phase expansion until now, with the quality of the WF at the onset of expansion identified as the most significant factor affecting the efficiency of the two-phase expander. Higher vapor qualities result in increased efficiencies of the two-phase expansion, which can reach 80% [11]. Furthermore, only a few numerical models [13–16] have been developed to simulate two-phase expansion, all of which simulate flashing in twin-screw expanders. In the work of Skiadopoulos et al. [16], a semi-empirical thermodynamic low-order model was developed to simulate two-phase expansion in twin-screw expanders. In this model, a segmental approach is applied to monitor the evolution of flashing in the expansion chamber. Moreover, the liquid and vapor phases are assumed to be in thermal non-equilibrium and a two-fluid model approach is followed for the formulation of the governing equations.

The purpose of this work is to assess the performance of a small-scale solar thermal power system in Athens, Greece, driven by low-temperature solar heat, which is provided by a field of Evacuated Tube Collectors (ETCs), and exploited by a TFC bottoming power cycle. To the best of the authors' knowledge, this is the first work in the literature systematically investigating the promising TFC power cycle for solar heat exploitation. The ETCs are selected for the system, because of their increased efficiency in comparison to Flat Plate Collectors, which are typically preferred for small-scale systems because of their lower cost. An integrated numerical tool simulating the annual performance of the combined Solar-TFC system is developed, in the software environment of Matlab (R2022b). The numerical model utilizes meteorological data for the installation site, provided by the National Observatory of Athens. Another novel feature of this work is that in TFC modeling, the performance of the two-phase expander, under varying operating conditions, is accurately monitored, by applying the novel thermodynamic low-oder model developed by Skiadopoulos et al. [16]. This approach in two-phase expansion modeling comes to fill a gap in the relevant literature since several theoretical works studying the performance of the TFC have been published, but the two-phase expander is usually treated as a black box with isentropic efficiencies achieved in the dry-vapor region [17,18]. R245fa is selected as the WF of the TFC, because it has been tested as a WF in Solar-ORC systems, numerically and experimentally, demonstrating very good thermodynamic behavior within the range of temperature and operating pressure ratios of low-temperature solar systems [6,7].

This paper is organized as follows. In Section 2, the architecture of the integrated system, the governing equations, and the numerical methodology are presented in detail. Moreover, the methodology for the economic assessment of the Solar-TFC system is presented. In Section 3, the performance of the ETCs, the TFC, and the integrated system are investigated in detail. Thereafter, the annual electricity output of the unit and the achievable total solar energy conversion efficiency, along with the thermal efficiency of the TFC and the second law efficiency of the Solar-TFC system, under optimal operating conditions, throughout the year are estimated. Finally, a short economic analysis of the Solar-TFC system is presented. General conclusions and remarks are presented in Section 4.

2. Materials and Methods

2.1. Description of the Solar-TFC system

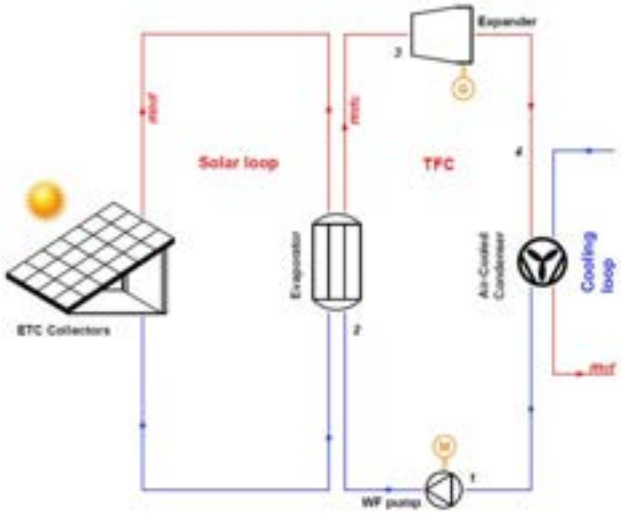

Figure 1. Schematic layout of the Solar-TFC system.

A schematic layout of the modeled Solar-TFC system is presented in Figure 1. The unit operates in HTF mode, i.e. solar thermal energy is transferred from the field of the ETC to the evaporator of the TFC through an HTF. In the evaporator of the TFC, the WF is heated up, at high pressure, reaching the state of the saturated liquid or the two-phase mixture. Thereafter, it flows through the two-phase expander, where flashing occurs and power is generated. The two-phase mixture at the expander's discharge dissipates heat to the environment through the air-cooled condenser. Finally, the WF is pumped to the operating pressure of the evaporator, and the power cycle starts anew. The thermodynamic states of the WF in the TFC (numbered 1÷4) are presented in Figure 1. Details regarding the thermodynamic processes of the WF in the TFC are given in Section 2.2.2. The thermodynamic properties of the HTF, the WF, and the CF are calculated by utilizing the CoolProp library [19] wrapper for Matlab.

2.2. Modeling

2.2.1. ETC collectors

The Thermomax DF 100 30, developed by Kingspan Thermomax, ETCs are selected for the solar field. The technical specifications of the selected ETCs are listed in Table 1. The inclination angle β is selected to maximize the annually absorbed solar energy at the installation site [7]. The values of T_{min} and T_{max} are typical of low-temperature solar power systems, ensuring low thermal losses towards the ambient, and, at the same, subcritical operation of the power cycle (taking into consideration that the critical temperature of R245fa is equal to 154 °C). Based on T_{max}, H_2O pressurized at 4 bar, to avoid boiling in the solar loop, is selected as the HTF. Finally, $\dot{m}_{htf}/A_{col}$ takes the average value of the recommended, by the collectors' developer, mass flowrate range for the solar cooling loop.

Table 1. Technical specifications of the ETCs.

Parameter	Symbol	Value [Units]
Aperture area	A_{ap}	3.228 [m^2]
Optical efficiency at normal incidence	η_o	0.779 [-]
First-order losses coefficient (based on A_{ap})	a_1	1.07 [W/m^2-K]
Second-order losses coefficient (based on A_{ap})	a_2	0.0135 [W/m^2-K^2]
Heat Transfer Fluid	HTF	H_2O [-]
Collector Area- Specific HTF flowrate	$\dot{m}_{htf}/A_{col}$	$2.95 \cdot 10^{-2}$ [kg/m^2-s]
Inclination angle	β	32 [°]
Minimum collectors' temperature	T_{min}	80 [°C]
Maximum collectors' temperature	T_{max}	130 [°C]

The thermal efficiency η_{col} of the collectors is calculated by Eq. (1). This empirical formula is applied commonly in solar collectors' modeling because the value of the coefficients η_o, a_1, and a_2 are available from the collectors' certification experiments.

$$\eta_{col} = \eta_o - a_1 \cdot \frac{(T_m - T_{amb})}{G_{tot}} - a_2 \cdot \frac{(T_m - T_{amb})^2}{G_{tot}} \quad (1)$$

In Eq. (1) G_{tot} is the total solar irradiance on the collectors' surface, T_m is their average temperature, and T_{amb} is the ambient temperature. The heat gain $\dot{Q}_{col}$ of the collectors is then given by Eq. (2), where A_{col} is the total area of the collectors.

$$\dot{Q}_{col} = \eta_{col} \cdot A_{col} \cdot G_{tot} \quad (2)$$

A common assumption in solar power system simulations is that T_m is equal to the average temperature of the HTF flowing in the solar loop. This assumption is expressed by Eq. (3), where $T_{htf,in}$ and $T_{htf,out}$ are the temperatures of the HTF flowing in and out of the solar cooling loop, respectively.

$$T_m = \frac{T_{htf,in} + T_{htf,out}}{2} \quad (3)$$

During steady-state operation of the Solar-TFC system, and if the heat losses at the HTF circuit are assumed negligible, $\dot{Q}_{col}$ is equal to the heat transfer rate $\dot{Q}_{ev}$ to the evaporator of the TFC engine. $\dot{Q}_{ev}$, on the HTF side, is given by Eq. (4), with $c_{p,htf}$ representing the specific heat capacity, under constant pressure, of the HTF, calculated at T_m.

$$\dot{Q}_{ev} = \dot{m}_{htf} \cdot c_{p,htf}\left(T_{htf,out} - T_{htf,in}\right) \quad (4)$$

The total irradiance G_{tot} on the inclined surface of the collectors is given by Eq. (5), where G_b and G_d are the beam irradiance normal on the collectors, and the diffuse irradiance, respectively (ground-reflected irradiance is not considered).

$$G_{tot} = G_b + G_d \quad (5)$$

G_b is calculated based on the available meteorological data at the installation site. Specifically, G_b is given by Eq. (6), where G_h is the beam irradiance on a horizontal surface, and R_b is the beam radiation tilt factor.

$$G_b = G_h \cdot R_b \tag{6}$$

R_b is given at each instance by applying Eq. (7), where L is the local latitude, δ the solar declination, and hr the hour angle. Detailed methodology concerning the calculation of R_b is presented by Kalogirou [20].

$$R_b = \frac{\sin(L-\beta)\cdot\sin(\delta) + \cos(L-\beta)\cdot\cos(\delta)\cdot\cos(hr)}{\sin(L)\cdot\sin(\delta) + \cos\cdot(L)\cdot\cos(\delta)\cdot\cos(hr)} \tag{7}$$

2.2.2. TFC

A qualitative Temperature- Entropy (T-s) diagram of the TFC power cycle with R245fa as the WF is presented in Figure 2, where the thermodynamic processes undergone by the WF, the HTF, and the Cooling Fluid (CF) are drawn. The thermodynamic processes of the TFC are the following:

- 1→2: Adiabatic pumping
- 2→3: Heat absorption in the evaporator at constant pressure p_{ev}
- 3→4: Adiabatic expansion in the two-phase expander
- 4→1: Heat rejection in the condenser at constant pressure p_{con}

The WF is sub-cooled at the suction port of the pump to prevent cavitation. Heat is transferred to the evaporator of the TFC engine by the HTF of the solar cooling loop, leading to a drop in its temperature from $T_{htf,out}$ to $T_{htf,in}$. Heat is dissipated from the TFC in the condenser, resulting in the temperature rise of the CF from $T_{cf,in}$ to $T_{cf,out}$. Herein, the term TFC is generalized to engulf the power cycle architectures where the WF at the onset of expansion can be in a state ranging from saturated liquid to saturated vapor.

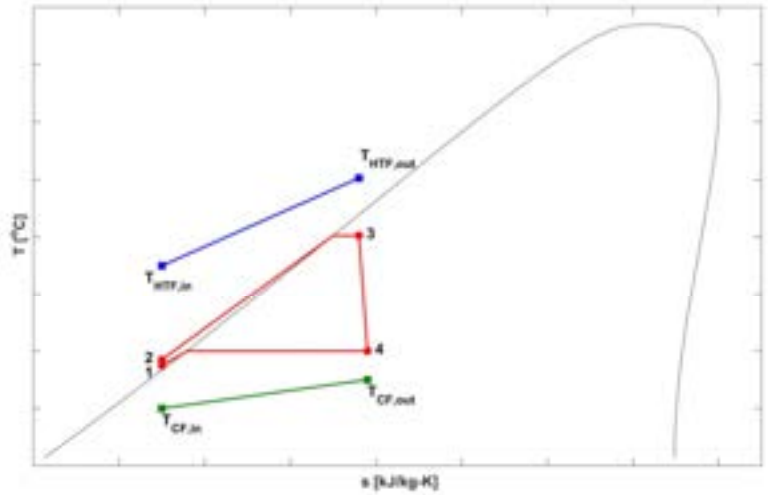

Figure 2. T-s diagram of the TFC with R245fa as the WF.

The parameters, along with their values and symbols, for the numerical modeling of the TFC are listed in Table 2. Assuming negligible heat losses at the TFC evaporator, $\dot{Q}_{ev}$ will be equal to the heat absorbed by the WF of the TFC, equality expressed by Eq. (8), where $\dot{m}_{wf}$ is the mass flowrate of the WF, whereas h_3 and h_2 are the specific enthalpies of the WF at thermodynamic states 2 and 3 of the power cycle, respectively.

$$\dot{Q}_{ev} = \dot{m}_{wf} \cdot (h_3 - h_2) \tag{8}$$

Table 2. Modeling parameters of the TFC cycle.

Parameter	Symbol	Value [Units]
Pinch point temperature difference at the evaporator	PP_{ev}	5 [°C]
Pinch point temperature difference at the condenser	PP_{con}	5 [°C]
Pump isentropic efficiency	$\eta_{pu,is}$	0.75 [-]
Working Fluid	WF	R245fa
Cooling Fluid	CF	Air [-]
Temperature rise of the Cooling Fluid	ΔT_{cf}	10 [°C]
Working fluid sub-cooling at pump suction	ΔT_{sub}	5 [°C]

The temperature T_4 of the WF at the onset of condensation is derived from PP_{con}, as in Eq. (9)

$$T_4 = T_{cf,out} + PP_{con} \tag{9}$$

where $T_{cf,out}$ is the temperature of the CF at the outlet of the condenser's cooling loop, given by Eq. (10). In Eq. (10), $T_{cf,in}$ is the temperature of the CF at the inlet of the cooling loop, equal to T_{amb} for the modeled case of the air-cooled condenser in this work.

$$T_{cf,out} = T_{cf,in} + \Delta T_{cf} \tag{10}$$

After applying Eq. (9), p_{con} is readily calculated, as the saturation pressure of the WF at T_4. The coupling between the TFC and the solar cooling cool is accomplished by PP_{ev}, as expressed by Eq. (11), where $T_{htf,pr}$ is the temperature of the HTF at the end of the preheating stage, and $T_{sat,wf}(p_{ev})$ is the saturation temperature of the WF at p_{ev}. In the ideal trilateral cycle, $T_{htf,pr}$ becomes equal to $T_{htf,out}$.

$$T_{htf,pr} = T_{sat,wf}(p_{ev}) + PP_{ev} \tag{11}$$

Equation (12) must be satisfied along with Eq. (8). In Eq. (12), $\dot{Q}_{pr}$ is the heat transfer rate from the HTF to the WF during the preheating stage, and $h_{l,sat}(p_{ev})$ is the enthalpy of the saturated liquid at p_{ev}.

$$\dot{Q}_{pr} = \dot{m}_{wf} \cdot \left(h_{l,sat}(p_{ev}) - h_2\right) = \dot{m}_{htf} \cdot c_{p,htf} \cdot \left(T_{htf,pr} - T_{htf,in}\right) \tag{12}$$

The numerical procedure for the determination of $\dot{m}_{wf}$ and p_{ev}, for a desired quality x_3 of the two-phase mixture at the onset of expansion is as follows. The value of p_{ev} is varied iteratively in a stepwise manner. For a guess intermediate value of p_{ev}, the saturation temperature $T_{sat,wf}(p_{ev})$ of the WF is calculated, and, subsequently, $T_{ht\ ,pr}$ is derived by applying Eq. (11). Thereafter, two values for $\dot{m}_{wf}$ are calculated by simultaneously applying Eqs. (8) and (12). The iterations on p_{ev} terminate when the two values of $\dot{m}_{wf}$ converge.

After the values of $\dot{m}_{wf}$ and p_{ev} have been determined, the thermodynamic low-order two-phase expansion model (details about the methodology applied in the two-phase expansion model can be found in Ref. [16]), is run. The outcome of the simulation is the rotational speed of the expander for the given mass flowrate, and the specific enthalpy h_4 of the WF at the discharge port. Thereafter, the isentropic efficiency $\eta_{ex,is}$ of expansion is calculated by Eq. (13), where $h_{4,is}$ is the specific enthalpy of the WF corresponding to an isentropic expansion from state 3 at p_{ev} to p_{con}.

$$\eta_{ex,is} = \frac{h_3 - h_4}{h_3 - h_{4,is}} \tag{13}$$

The power $\dot{w}_{ex}$ generated by the two-phase expander is given by Eq. (14)

$$\dot{w}_{ex} = \dot{m}_{wf} \cdot (h_3 - h_4) \tag{14}$$

whereas the power $\dot{w}_{pu}$ absorbed by the pump is calculated by Eq. (15), in which h_1 is the specific enthalpy of the WF at its suction.

$$\dot{w}_{pu} = \dot{m}_{wf} \cdot (h_2 - h_1) \tag{15}$$

h_2 is derived by applying the formula for the isentropic efficiency $\eta_{pu,is}$ of the pump, as in Eq. (16).

$$\eta_{pu,is} = \frac{h_{2,is} - h_1}{h_2 - h_1} \tag{16}$$

In Eq. (16), $h_{2,is}$ is the specific enthalpy of the WF corresponding to its isentropic pumping from state 1 at p_{con} to p_{ev}. The thermal efficiency η_{th} of the TFC is given by Eq. (17), where $\dot{w}_{net}$ is the net power generated by the TFC engine.

$$\eta_{th} = \frac{\dot{w}_{net}}{\dot{Q}_{ev}} = \frac{\dot{w}_{ex} - \dot{w}_{pu}}{\dot{Q}_{ev}} \tag{17}$$

The heat transfer rate $\dot{Q}_{con}$ at the condenser is calculated by Eq. (18), leading to the evaluation of the necessary mass flowrate $\dot{m}_{cf}$ of the CF. In Eq. (18) $c_{p,cf}$ is the specific heat capacity, under constant pressure, of the CF.

$$\dot{Q}_{con} = \dot{m}_{wf} \cdot (h_4 - h_1) = \dot{m}_{cf} \cdot c_{p,cf} \cdot \Delta T_{cf} \tag{18}$$

2.2.3. Solar-TFC system

At any operating instance of the Solar-TFC system, the overall solar energy conversion efficiency η_{tot} is given by Eq. (19).

$$\eta_{tot} = \eta_{col} \cdot \eta_{th} = \frac{\dot{Q}_{col}}{A_{col} G_{tot}} \cdot \frac{\dot{w}_{net}}{\dot{Q}_{ev}} = \frac{\dot{w}_{net}}{A_{col} \cdot G_{tot}} \quad (19)$$

Moreover, the exergy efficiency η_{II} of the unit is given by Eq. (20)

$$\eta_{II} = \frac{\dot{w}_{net}}{\left(1 - \frac{T_{amb}}{T_{sol}}\right) A_{col} \cdot G_{tot}} \quad (20)$$

where T_{sol} is the solar reference temperature, taken equal to 5770 K for this work [7].

The average thermal efficiency $\eta_{th,av}$ of the TFC engine, and the average solar energy conversion efficiency $\eta_{tot,av}$ and average exergy efficiency $\eta_{II,av}$ of the combined unit over a period are calculated by integrating Eqs. (17), (19), and (20), respectively.

2.3. Economic analysis

The economics of the Solar-TFC system is assessed by evaluating the Levelized Cost of Electricity ($LCOE$), an estimation of the average cost that the owner-operator of the system will have to pay for every kWh produced during its anticipated lifetime N. $LCOE$ is given by Eq. (21)

$$LCOE = \frac{C_{inv} + \sum_{i=1}^{N} \frac{M}{(1+i)^r}}{\sum_{i=1}^{N} W} \quad (21)$$

where C_{inv} is the total initial investment cost, W is the total electricity produced at year i, M is the annual maintenance cost at year i, and r is the annual discount rate. In this work, it is assumed that W, as well as M and r remain constant throughout N. C_{inv} is given by Eq. (22), where sc_{tfc} and sc_{col} are the specific costs of the TFC and the ETC collectors, respectively, whereas P_{tfc} is the nominal electric capacity of the TFC.

$$C_{inv} = sc_{tfc} \cdot P_{tfc} + sc_{col} \cdot A_{col} \quad (22)$$

The values of the parameters for the economic analysis are listed in Table 3. Analysis concerning the estimation of sc_{tfc}, based on the nominal capacity of the TFC is presented in Section 3.3.3.

Table 3. Parameters of the economic analysis.

Parameter	Symbol	Value [Units]
Lifetime	N	20 [yr]
Annual discount rate	r	5 [%] [7,21]
Annual maintenance cost	M	$0.01 C_{inv}$ [€]
Specific cost of collectors	sc_{col}	260 [€/m^2] [6]

3. Results & Discussion

3.1. Solar field

The performance of the solar field is assessed based on the achievable values for η_{col} as a function of G_{tot}, T_{amb}, and T_m for a clear-sky day at the installation site. The variation of G_{tot}, G_d, and T_{amb} from sunrise to sunset, with an hourly time step, as a function of solar time for the reference day is presented in Figure 3. The fluctuation of η_{col} and $\dot{Q}_{ev}/A_{col}$ versus solar time for the reference day and different desired operating temperatures T_m is presented in Figure 4. It is assumed that the TFC engine operates when the temperature of the collectors reaches the desired value of T_m, and, thereafter, T_m remains constant for as long as possible, based on the values of G_{tot} and T_{amb}. Therefore, during the heating up of the collectors, it is assumed that the solar irradiance is exploited initially only to increase T_m ($\dot{Q}_{ev} = 0$) until its desired value has been reached. Subsequently, (and for as long as $\dot{Q}_{col} > 0$) all the heat gain $\dot{Q}_{col}$ is delivered to the TFC engine ($\dot{Q}_{col} = \dot{Q}_{ev}$), and T_m is kept constant. When $\dot{Q}_{col} < 0$, the collectors are cooled down, and the operation of the TFC engine stops.

After sunrise, the temperature of the collectors begins to increase, with a gradual drop in η_{col} because the temperature difference $T_m - T_{amb}$ rises and the heat losses towards the ambient are increased. After the desired operating temperature T_m has been reached, η_{col} rises as G_{tot} and T_{amb} increase, and it drops gradually after solar noon. The maximum values of η_{col} and $\dot{Q}_{ev}/A_{col}$ (while the TFC engine is operating), equal to 0.664 and 676.84, respectively, are obtained for T_m equal to 80 °C. Increasing T_m reduces η_{col} and $\dot{Q}_{ev}/A_{col}$ because the heat losses towards the ambient are also higher. However, reducing T_m may harm η_{th}, as the

operating pressure ratio of the TFC will drop. The effect of T_m, along with other identified crucial parameters, on the efficiency of the TFC is described in detail in Section 3.2.

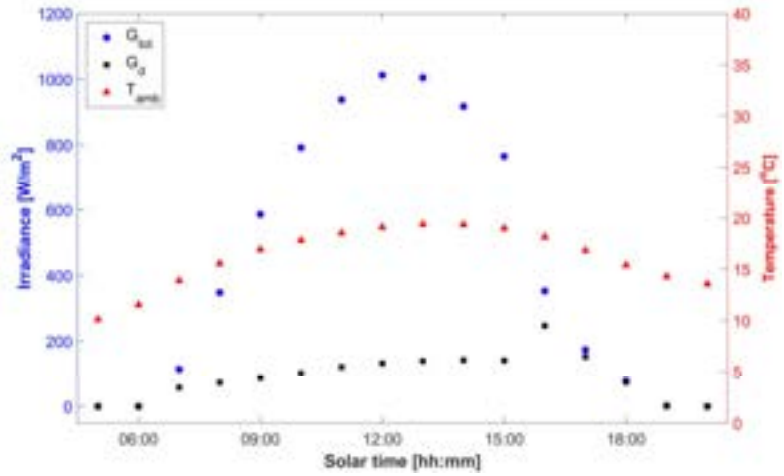

Figure 3. Irradiance on ETC collectors and T_{amb} as a function of solar time on a clear-sky spring day.

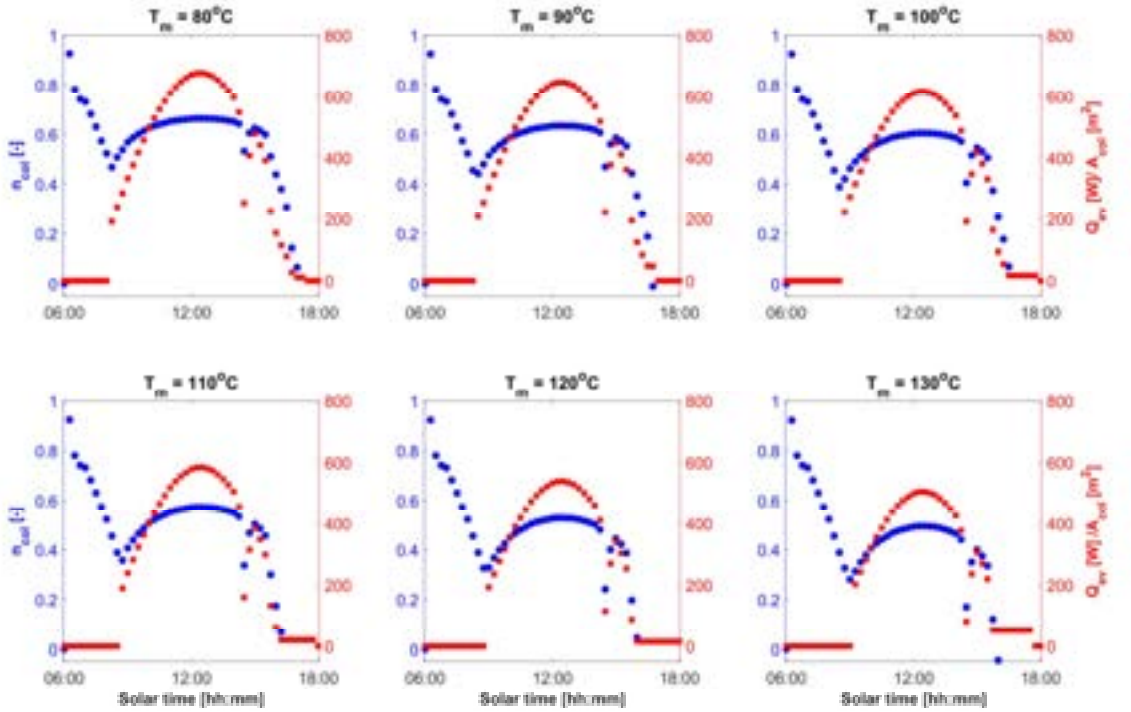

Figure 4. η_{col} and $\dot{Q}_{ev}/A_{col}$ as a function of solar time for different values of T_m.

3.2. TFC

The performance of the TFC is assessed based on its efficiency at solar noon, when the irradiance on the collectors is maximized, of the reference day presented in Section 3.1. The value of η_{th} depends on the isentropic efficiency $\eta_{ex,is}$ of the two-phase expansion, which, in turn, is directly related to x_3 and T_m, as can be seen in Figure 5. Low vapor quality at the suction port of the two-phase expansion leads to very low values of $\eta_{ex,is}$. This is attributed to the increased pressure losses at suction and the increased mass flowrates $\dot{m}_{wf}$ of the WF, which cannot be accommodated by the modeled expander [11,16]. Furthermore, as T_m and x_3 vary, the deviation of the WF volume ratio from the built-in volume ratio of the two-phase expander varies as well. For every T_m there is a value of x_3 for which an optimal match between the two values is obtained, and the over-under expansion losses are minimized.

Increasing $\eta_{ex,is}$ has an obvious positive effect on η_{th}, and values as high as 0.11 can be achieved. The variation of $\eta_{ex,is}$ and η_{th} with x_3, for the range of values for T_m, indicates that the optimal operating point of

the unit lies always within the two-phase region, as their values are systematically reduced towards the saturated vapor state.

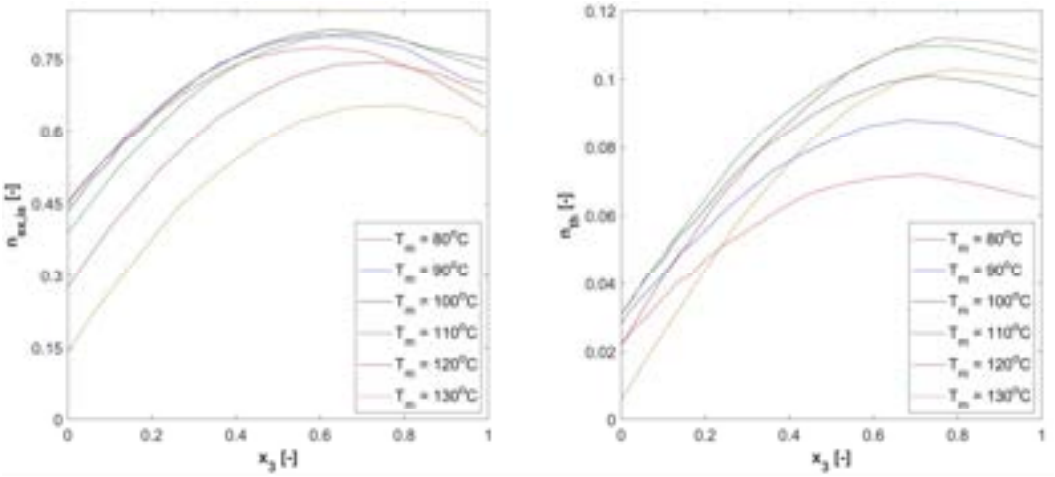

Figure 5. $\eta_{ex,is}$ and η_{th} versus x_3 for different values of T_m.

3.3. Solar-TFC

3.3.1. Performance optimization

The analysis presented in Sections 3.1 and 3.2 highlighted that there are two degrees of freedom, i.e. T_m and x_3, in the Solar-TFC system, the determination of which leads to the maximization of η_{tot} for given irradiance and T_{amb} values. The system of Eqs. presented in Sections 3.1, 3.2, and 3.3 is formulated in Matlab, wherein a native genetic algorithm, which leads to the determination of the global optimum, is applied aiming to maximize η_{tot}, with T_m and x_3 the iteration variables. The optimization problem is solved throughout the year with a fifteen minute interval.

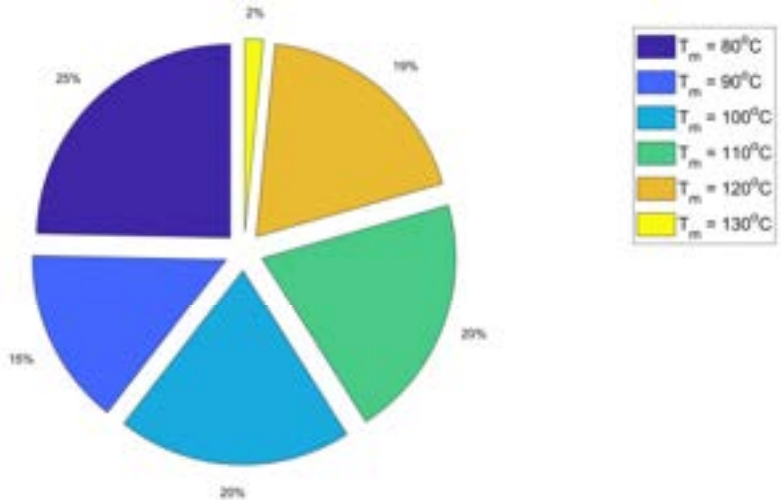

Figure 6. Frequency distribution of optimal T_m value per year.

The simulations reveal that the Solar-TFC system can be operational for a total of 2835 hours per year in Athens. The frequency distribution of the optimal T_m on the annual basis is presented in Figure 6. It can be deduced that T_{min} is the most frequent optimal operating temperature of the collectors. This is justified since an annual optimization is undertaken, and days with low values of irradiance and T_{amb} are also considered. On the other hand, it must be stressed that it is optimal to operate the system at T_{max} for only about 2% of the unit's operating time around the year. This is because, as analyzed in Sections 3.1 and 3.2, the heat losses of the solar field towards the ambient are very high, and, at the same time, the efficiency of the TFC is rather low, because of low $\eta_{ex,is}$ values. T_{max} is optimal only in a few instances during summer, when $\dot{Q}_{ev}/A_{col}$ is maximized because of the high irradiance, and, T_{amb} is high enough to ensure a favorable WF volume ratio, and, therefore, an operating pressure ratio for the TFC. The variation of the optimal x_3 throughout the year is presented in Figure 7, and it ranges from 0.59 to 0.83. As analyzed in Section 3.2, high values of x_3 ensure satisfying $\eta_{ex,is}$, and, as a result, increased η_{th}, a finding consistent with experiments [11].

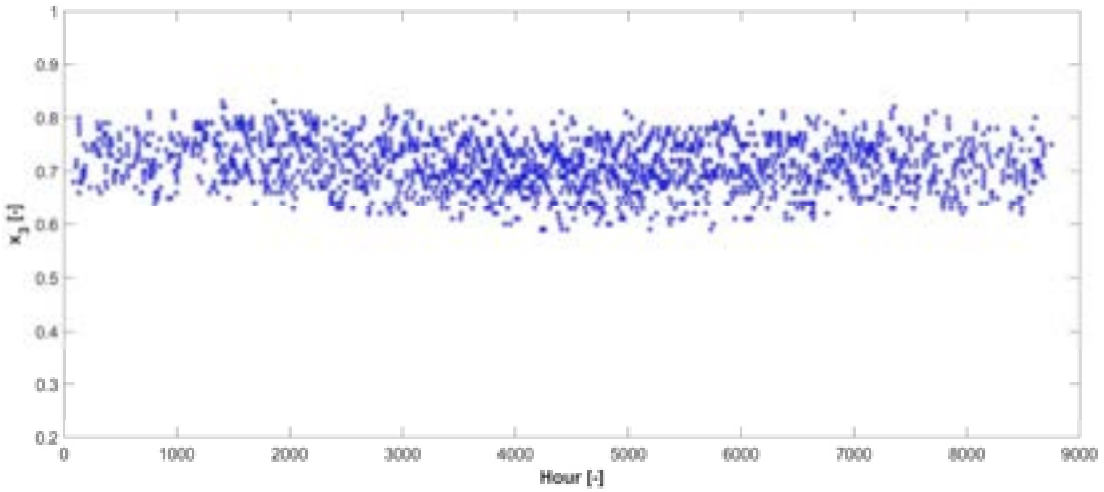

Figure 7. Optimal vapor quality x_3 at the suction port of the expander throughout the year.

3.3.2. Annual yield and efficiency

The total collectors' area- specific solar energy E_{sol}/A_{col} incident on the ETCs monthly, for the operational time of the Solar-TFC system, along with the average monthly $\eta_{tot,av}$ are presented in Figure 8.

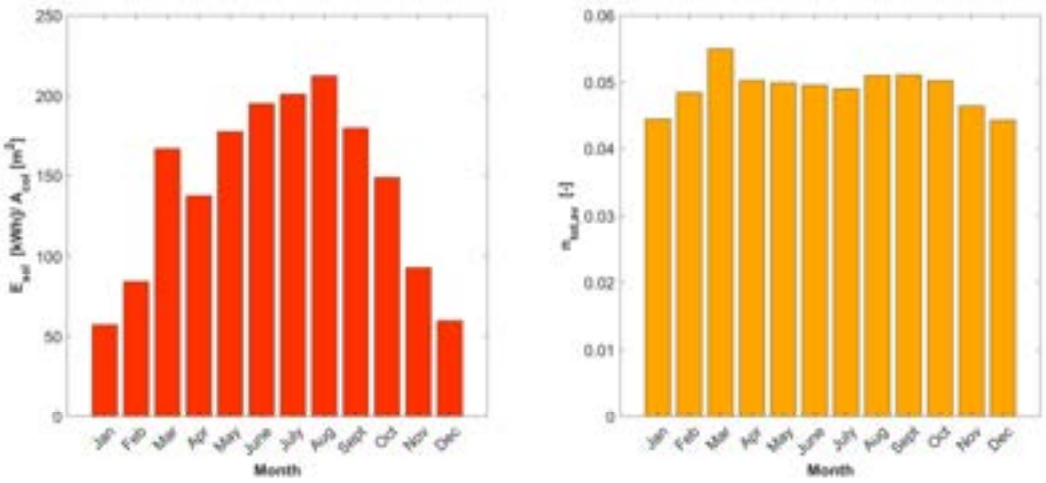

Figure 8. Monthly variation of E_{sol}/A_{col} and $\eta_{tot,av}$.

E_{sol}/A_{col} is maximized in August, however, the combined system is most efficient in solar energy harvesting during March. This can be explained as follows. The irradiance on the collectors may be higher during summer, but the utilization of an air-cooled condenser increases the condensation temperature and pressure (see Eqs. (9) and (10)), and the operating pressure ratio p_{ev}/p_{con} of the TFC is reduced, with adverse effects on the power generation potential. If the condensation temperature was kept constant throughout the year, it is expected that $\eta_{tot,av}$ would be higher in summer.

The average annual solar energy conversion efficiency $\eta_{tot,av}$ of the Solar-TFC system is equal to 0.05, which is substantially higher than the one estimated (0.03) for a small-scale Solar-ORC system at the installation site [6], which consists of the same ETCs and two scroll expanders, installed in series, as power generators. The monthly distribution of the total collectors' area-specific W/A_{col} electricity produced by the TFC, and the values of $\eta_{II,av}$ and $\eta_{th,av}$ are presented in Figure 9. The annual yield of electricity is equal to 86 kWh per m^2 of collectors, with an average $\eta_{th,av}$ equal to 0.10. This average annual efficiency is again higher than the calculated (0.089) from the simulations of the aforementioned small-scale Solar-ORC system at the same location, demonstrating the potential of the TFC for higher-efficiency solar thermal power systems. The annual average exergy efficiency $\eta_{II,av}$ is approximately 0.05, a value slightly lower than the one simulated for a small-scale Solar-ORC system with R245fa as the WF in Athens [7]. However, that unit utilizes Parabolic Trough Collectors, which achieve higher values of η_{col}, but are most costly.

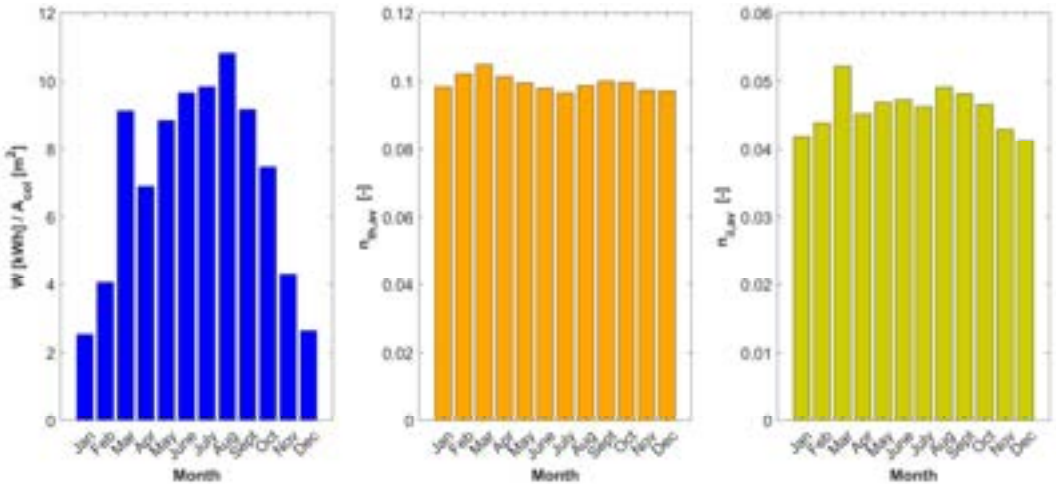

Figure 9. Monthly variation of W/A_{col}, $\eta_{th,av}$, and $\eta_{II,av}$.

3.3.3. Economic assessment

The economics of the Solar-TFC system is assessed by performing a parametric analysis, with A_{col} and sc_{tfc} the degrees of freedom. A_{col} implicitly determines the value of P_{tfc}. It is assumed that G_t, T_m, and T_{amb} are equal to 1000 W/m^2, 110 ^{o}C, 20 ^{o}C, respectively, at the design point of the unit. By applying Eq. (1), η_{col} is calculated and, assuming a gross value, i.e. neglecting $\dot{w}_{pu}$, of η_{th} equal to 0.08, the value of P_{tfc} may be readily calculated. Thereafter, sc_{tfc} is estimated based on the values of P_{tfc}, the nominal heat capacity, and the temperature of the heat source, according to the work of Braimakis et al. [22]. The values of P_{tfc} and sc_{tfc} as a function of A_{col} are listed in Table 4. It must be noted that the parametric values of A_{col} were selected to ensure that P_{tfc} lies within the operating nominal electric capacities of twin screw expanders [23].

$LCOE$ versus A_{col} is plotted in Figure 10. As A_{col} increases, $LCOE$ drops because sc_{tfc} is diminished. The estimated $LCOE$ values are considered competitive against the current electricity prices at the European Union, and also against the reported $LCOE$ values of Solar-ORC systems in the literature, that range between 0.25 and 0.95 €/kWh [6,7,24]. The penetration of the Solar-TFC system in the market could be further assisted in the future, considering the European policies to assist the participation of renewables in the energy mix and promote decentralized energy production.

Table 4. Parametric values of A_{col}, P_{tfc}, and sc_{tfc} at the Solar-TFC system design point.

A_{col} [m^2]	200	300	400	500	600
P_{tfc} [kW$_{el}$]	9	14	18	23	28
sc_{tfc} [€/kW$_{el}$]	4850	4300	3800	3300	3000

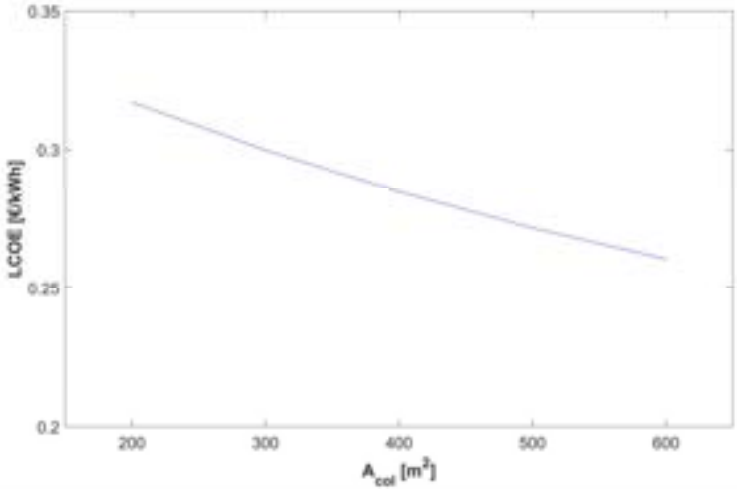

Figure 10. $LCOE$ as a function of A_{col}.

4. Conclusions

In the present work, the annual performance of a Solar-TFC power system located in Athens was numerically studied. The operation of the system was optimized throughout the year to maximize solar energy conversion efficiency. Particular attention was paid to the two-phase expansion efficiency, which mainly affects the thermal efficiency of the TFC, with flashing simulations indicating that higher vapor qualities (59-83%) of the WF at the onset of expansion have a positive effect on the power cycle performance. The numerical results indicated that 86 kWh of green power per m^2 of collectors can be generated by the Solar-TFC system annually, with the average solar energy conversion efficiency reaching 5%, higher than the one estimated for a Solar-ORC system with similar architecture in Athens. The average annual thermal efficiency of the TFC and exergy efficiency of the combined Solar-TFC system were calculated approximately equal to 10% and 5%, respectively.

The preliminary economic analysis of the Solar-TFC system demonstrated the potential of the TFC as a competitive replacement of the ORC for solar heat recovery. Indeed, $LCOE$ values in the range of 0.26 - 0.32 €/kWh can be anticipated for an operation reaching 20 years. The economics of the system is better as its size increases, because of the TFC engine's lower specific cost at higher capacities.

Concluding, the analysis presented in this work highlighted the potential of the TFC for efficient solar energy conversion, and its competitiveness compared to the ORC. However, it must be noted that additional research work is necessary for the TFC to reach a technologically mature level. This research work must mainly focus on the comprehension of the flashing phenomenon and the development of expanders that will operate efficiently in the two-phase region.

Acknowledgments

This research work was supported by the *Operational Programme Competitiveness, Entrepreneurship, and Innovation 2014-2020 (EPAnEK)*. (Project Number: T2EΔK-00351, Acronym: TRI-MAX).

Nomenclature

Symbols

p	Pressure [bar]
T	Temperature [°C]
A	Collectors' area [m^2]
h	Specific enthalpy [kJ/kg]
s	Specific entropy [kJ/kg-K]
G	Irradiance [W/m^2]
c_p	Specific heat [kJ/kg-K]
$\dot{m}$	Mass flow rate [kg/s]
$\dot{w}$	Power [kW]
x	Vapor quality [-]
W	Electricity [kWh]
$\dot{Q}$	Heat transfer rate [kW]
C	Cost [€]
r	Discount rate [%]
L	Latitude [°]
P	Nominal power [kW]
sc	Specific cost [€/m^2] [€/kW]
hr	Hour angle [°]
R	Radiation tilt factor [-]
E	Solar energy [kWh]

Subscripts

in	Inlet
out	Outlet
is	Isentropic
ex	Expander
ev	Evaporator
con	Condenser
sub	Subcooling
pr	Preheating
pu	Pump
sat	Saturated
th	Thermal
l	Liquid
amb	Ambient
m	Mean
col	Collector
d	Diffuse
b	Beam
tot	Total
inv	Investment
h	Horizontal
II	Second Law
av	Average
ap	Aperture
sol	Solar
htf	Heat Transfer Fluid
wf	Working Fluid
cf	Cooling Fluid

Greek letters

δ	Solar declination [°]
η	Efficiency [-]
β	Inclination angle [°]
α	Losses Coefficient [-]

Abbreviations

TFC	Trilateral Flash Cycle
ETC	Evacuated Tube Collector
HTF	Heat Transfer Fluid
CF	Cooling Fluid
WF	Working Fluid
PP	Pinch point [°C]
ORC	Organic Rankine Cycle
LCOE	Levelized Cost of Electricity

References

[1] Kalogirou S.A., Solar thermal collectors and applications. Prog Energy Combust Sci 2004;30:231–95.

[2] Karellas S., Roumpedakis T.C., Solar thermal power plants. Solar Hydrogen Production: Processes, Systems and Technologies 2019:179–235.

[3] Tchanche B.F., Lambrinos G., Frangoudakis A., Papadakis G., Low-grade heat conversion into power using organic Rankine cycles – A review of various applications. Renewable and Sustainable Energy Reviews 2011;15:3963–79.

[4] Golonis C., Skiadopoulos A., Manolakos D., Kosmadakis G., Assessment of the performance of a low-temperature Organic Rankine Cycle engine coupled with a concentrating PV-Thermal system. Renew Energy 2021;179:1085–97.

[5] Manolakos D., Kosmadakis G., Kyritsis S., Papadakis G., Identification of behaviour and evaluation of performance of small scale, low-temperature Organic Rankine Cycle system coupled with a RO desalination unit. Energy 2009;34:767–74.

[6] Soulis K.X., Manolakos D., Ntavou E., Kosmadakis G., A geospatial analysis approach for the operational assessment of solar ORC systems. Case study: Performance evaluation of a two-stage solar ORC engine in Greece. Renew Energy 2022;181:116–28.

[7] Roumpedakis T.C., Loumpardis G., Monokrousou E., Braimakis K., Charalampidis A., Karellas S., Exergetic and economic analysis of a solar driven small scale ORC. Renew Energy 2020;157:1008–24.

[8] Schuster A., Karellas S., Aumann R., Efficiency optimization potential in supercritical Organic Rankine Cycles. Energy 2010;35:1033–9.

[9] Smith I.K., Development of the trilateral flash cycle system: Part 1: Fundamental considerations. Proceedings of the Institution of Mechanical Engineers, Part A: Journal of Power and Energy 1993;207:179–94.

[10] Kanno H., Shikazono N., Experimental study on two-phase adiabatic expansion in a reciprocating expander with intake and exhaust processes. Int J Heat Mass Transf 2016;102:1004–11.

[11] Smith I.K., Stošić N., Aldis C.A., Development of the trilateral flash cycle system. Part 3: The design of high-efficiency two-phase screw expanders. Proceedings of the Institution of Mechanical Engineers, Part A: Journal of Power and Energy 1996;210:75–92.

[12] Öhman H., Lundqvist P., Experimental investigation of a Lysholm Turbine operating with superheated, saturated and 2-phase inlet conditions. Appl Therm Eng, vol. 50, Pergamon; 2013, p. 1211–8.

[13] Bianchi G., Kennedy S., Zaher O., Tassou S.A., Miller J., Jouhara H., Numerical modeling of a two-phase twin-screw expander for Trilateral Flash Cycle applications. International Journal of Refrigeration 2018;88:248–59.

[14] Vasuthevan H., Brümmer A., Theoretical investigation of flash vaporisation in a screw expander. IOP Conf Ser Mater Sci Eng, vol. 232, Institute of Physics Publishing; 2017.

[15] Taniguchi H., Kudo K., Giedt W.H., Park I., Kumazawa S., Analytical and experimental investigation of two-phase flow screw expanders for power generation. J Eng Gas Turbine Power 1988;110:628–35.

[16] Skiadopoulos A., van Heule X., Kosmadakis G., Manolakos D., de Paepe M., Lecompte S., Thermodynamic low-order model for the simulation of two-phase expansion within a TFC unit. In: of Munich TU, editor. Proceedings of the 6th International Seminar on ORC Power Systems, Technical University of Munich; 2021.

[17] Baccioli A., Antonelli M., Desideri U., Technical and economic analysis of organic flash regenerative cycles (OFRCs) for low temperature waste heat recovery. Appl Energy 2017;199:69–87.

[18] Lai K.Y., Lee Y.T., Chen M.R., Liu Y.H., Comparison of the trilateral flash cycle and Rankine cycle with organic fluid using the pinch point temperature. Entropy 2019;21.

[19] Bell I.H.,Wronski J., Quoilin S., Lemort V., Pure and pseudo-pure fluid thermophysical property evaluation and the open-source thermophysical property library coolprop. Ind Eng Chem Res 2014;53:2498–508.

[20] Kalogirou S.A., Solar energy engineering: Processes and systems. Solar Energy Engineering: Processes and Systems 2009:1–760.

[21] Tzivanidis C., Bellos E., Antonopoulos K.A., Energetic and financial investigation of a stand-alone solar-thermal Organic Rankine Cycle power plant. Energy Convers Manag 2016;126:421–33.

[22] Braimakis K., Karellas S., Integrated thermoeconomic optimization of standard and regenerative ORC for different heat source types and capacities. Energy 2017;121:570–98.

[23] Quoilin S., Broek M. Van Den, Declaye S., Dewallef P., Lemort V., Techno-economic survey of Organic Rankine Cycle (ORC) systems. Renewable and Sustainable Energy Reviews 2013;22:168–86.

[24] Delgado-Torres A.M., García-Rodríguez L., Analysis and optimization of the low-temperature solar organic Rankine cycle (ORC). Energy Convers Manag 2010;51:2846–56.

ULPGC
Universidad de
Las Palmas de
Gran Canaria

grres ULPGC
group for the research on renewable energy systems

B. Exergy-based analysis-Applications and teaching in academia

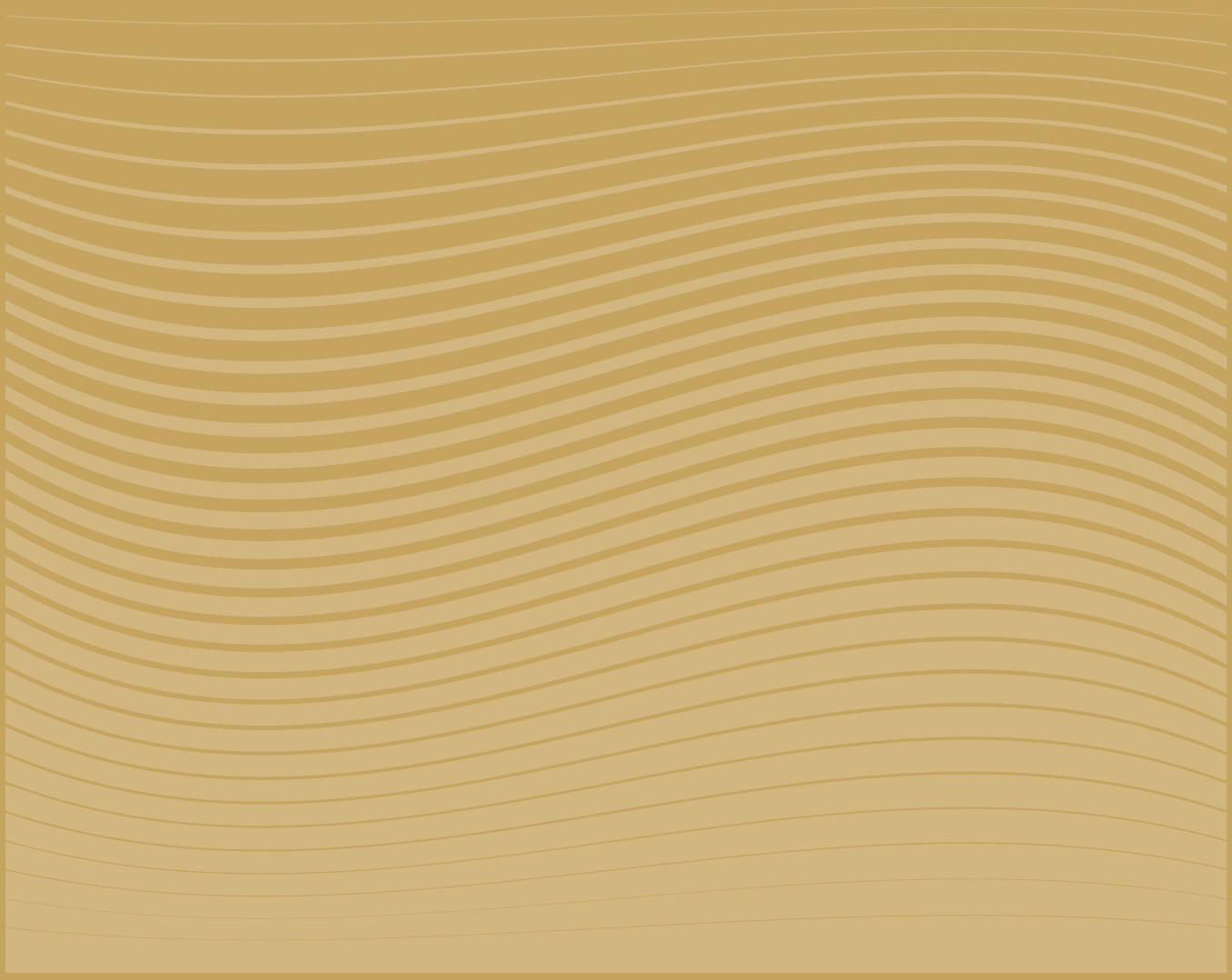

ECOS2023

TaesLab: An advanced software tool for circular thermoeconomics

C.Torres[a], A. Valero[b] and A.Valero-Delgado[c]

[a] CIRCE Institute, University of Zaragoza, Spain, ctorresc@unizar.es, CA
[b] CIRCE Institute, University of Zaragoza, Spain, valero@unizar.es
[c] CIRCE Institute, University of Zaragoza, Spain, avdelgado@unizar.es

Abstract:

Circular thermoeconomics encompasses the physical principles of the circular economy (strictly spiral economy), industrial symbiosis, and second law costing and diagnosis of complex energy systems.
This article describes a new software tool for circular thermoeconomics distributed as a MATLAB package. The software implements the algorithms described in the latest revisions of the exergy cost theory. In addition to production cost calculation and diagnostics functions, TaesLab incorporates new ones for determining energy savings due to waste recovery and process integration. The production structure model makes it possible to analyse different plant configurations, integrating other processes for waste recovery or energy storage. For demonstration purposes, the article presents a short example of a cogeneration plant with waste recovery and describes its data model and the functionality of this software tool.

Keywords:

thermoeconomics, waste cost allocation, circular economy, software tools.

1. Introduction

Thermoeconomics, an energy analysis methodology combining thermodynamics and economics, support energy systems' design, synthesis, and operation with higher efficiency and lower production costs. Thermoeconomics methods are usually applied to assess the energy and monetary cost of energy systems' internal flows and final products. These methods detect inefficiencies and evaluate their economic effects using thermoeconomic diagnosis [1]. Environmental issues have been incorporated into the analysis [2] to consider waste treatment and emission cost allocation. Classic exergy cost theory [3] has been recently revisited to include general waste cost allocation methods [4].

This methodology, called Circular Thermoeconomics [5], is based on the theory of exergy cost and its generalisation, the *structural theory*, which allows the accounting of physical or thermodynamic costs, both of functional products and waste generated in parallel. It makes it possible to identify which part of these costs are due to internal irreversibilities and which are due to the waste produced or external irreversibilities. Each of these irreversibilities can be reduced to certain limits: Internal irreversibilities by improving the efficiency of the processes or changing the technology, but always up to a specific limit; External irreversibilities by recycling waste. Internal irreversibilities are, at the same time, also the cause of waste and their transfer and disposal increment costs.

The word "recycling" is used interchangeably by Thermoeconomics, Circular Economy and Industrial Symbiosis. One may wonder if it means the same thing in all three fields of activity. Recycling means efficient use of resources. What is different is the type of systems it studies. In general, the objective of the circular economy is the recovery of any solid waste, while the system analysed is the recovery plant. Industrial symbiosis deals with reusing waste or by-products from one plant by other plants. In this case, the system under study is the set of interacting plants. Thermoeconomics cover the general use, no matter how complex the subsystems and flow interconnections are.

If a waste leaves the boundaries of a plant, it is dissipated into the environment, but its formation and disposal costs must be accounted for by identifying its origin. Some of this waste could be reused in other processes or plants. This theory allows for calculating its formation costs and providing a target cost as a basis for discussion with other plants interested in using it.

There is a wide range of software for the modelling, process integration, simulation, and optimisation of energy systems, such as EES [6], HSC Chemistry [7], or ASPEN PLUS [8]. Still, in general, they do not include thermoeconomic analysis. Torres et al. [9] provide the guidelines for developing thermoeconomic

analysis software and present an Excel-based application [10] that implements these ideas. These ideas are applied in some specific tools for energy analysis software [11].

This paper describes a new software tool, called TaesLab, that implements the algorithms described in [4], including waste cost allocation and recycling analysis. The software is presented as a MATLAB package or as a stand-alone application. TaesLab provides a set of functions and tools that allow a complete thermo-economic analysis of an energy system, starting from the definition of its thermoeconomic model, a collection of plant states defined by the exergies of its mass and energy flows, and the costs of its external resources. The main functions are:

- Read and Check the Thermoeconomic Data Model.
- Compute Exergy Balances and Fuel Product table.
- Compute Exergy Cost.
- Analyse the Cost Formation Process of Products and Waste.
- Recycling Analysis.
- Thermoeconomic Diagnosis.

The results are presented in the form of graphs and tables. These can be saved in Excel sheets or text files for further analysis.

An Organic Rankine Cycle (ORC) is used as an example to illustrate the application's functionality. It uses waste heat to produce electricity. Part of the heat dissipated in the condenser could be recycled and used to produce air conditioning in another plant process, for example, an ejector refrigeration cycle [12].

2. Thermoeconomic Data Model

To make a thermoeconomic analysis of an energy system. a set of information that constitutes the thermoeconomic data model is needed.

2.1. Physical structure

For a given level of aggregation, an energy system can be represented by a directed graph, whose nodes are the thermodynamic processes and edges are the flows of matter and energy exchanged. Figure 1 depicts the physical structure of the plant used as example.

2.2 Thermodynamic model

To perform the thermoeconomic analysis of an energy system, it is necessary to define the exergy of each flow specified in the physical structure. The thermodynamic model of the plant is described by a set of equations (including mass, energy and entropy balances) that allow the determination of each mass, heat and work stream involved in the physical structure of the plant from a set of input variables, which define a thermodynamic state of the plant. In this example, an EES model obtains the exergy flows. The main parameters of the plant are also shown in Figure 1.

2.3 Productive structure

Each component or process of the system has a productive purpose established by its exergy efficiency, defined as the amount of exergy produced per unit of exergy of resources used, and which measures the quality of the process. Thus, for each process of the system, it is necessary to identify which flows constitute the product or products of the process and which resources or fuels are used to produce them. In this definition, it is also necessary to indicate which flows are waste and which processes are used to eliminate them, called dissipative processes [13]

2.4 Waste Cost Allocation

How the waste cost is allocated to the production processes of a system depends on the type and nature of the waste. There is no general criterion for assigning the cost of system waste. For example, in the case of heat dissipated in the condenser of a Rankine cycle, we can distribute the cost proportionally to the entropy generated by each process. On the other hand, the flue gases removed by the stack of the combined cycle are allocated to the combustion process. Therefore, the allocation of the residual costs should be based on the following criteria:

- The waste cost must be allocated to the production units that have generated it. Here, it is essential to establish a conceptual difference between the exergy of waste and its cost. Costs also encompass exergy consumption to be involved in eliminating the system waste. Therefore, the cost, not its exergy, is of actual interest. It raises a need that is expressed in the second premise.
- It is needed to identify the process of cost formation of waste. It parallels the production cost formation process because the residues are removed in the dissipative components but are formed together with the production processes. The responsibility of a productive component for waste generation lies in its contribution to the formation cost of waste.

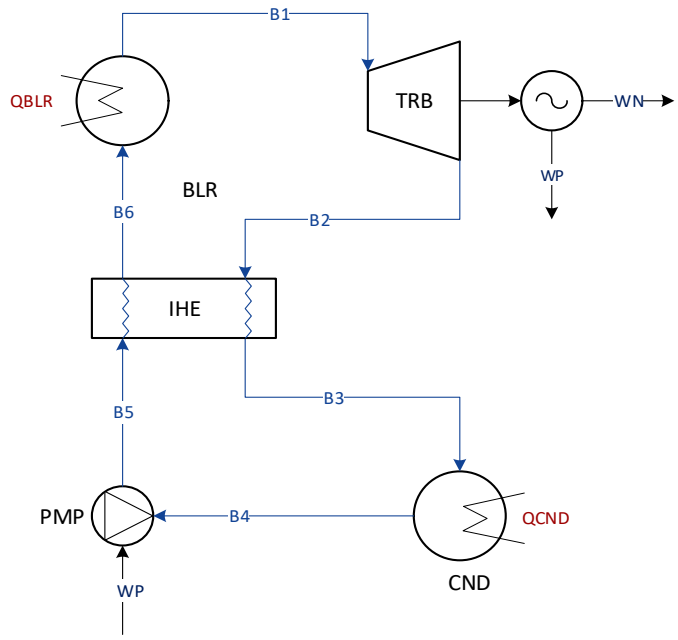

Parameter	Value
ORC fluid	R245fa
Generator pressure P_{blr} (bar)	20
Inlet waste gases temperature T_G (ºC)	160
Generator pinch point ΔT_{blr} (ºC)	20
Condenser outlet temperature T_{cnd} (ºC)	30
Turbine isentropic efficiency η_{trb} (%)	80
Pump isentropic efficiency η_{pnp}(%)	85
Internal Heat Exchange efficiency ε_{ihe}(%)	80
Net Power (kW)	50
Reference temperature T_0 (ºC)	15.94
Reference pressure P_0 (bar)	1.013

Figure. 1. Thermodynamic diagram of the ORC plant and main operational parameters,

To identify waste flows at the process level, relating each flow with the physical and chemical processes in dissipative units is necessary. We must define as many dissipative units as waste flows. Dissipative units are defined in such a way that the output product stream is a waste flow, and input fuel streams are these flows that one wants to be eliminated and the resources required to do that. The irreversibility carriers allow one to identify the waste stream's origin, path, and end. The Fuel-Product and the Irreversibility-Cost tables can help to determine the cost formation process of products and wastes.

TaesLab uses the following methods, described in detail in reference [4]

- EXERGY: This method looks for the immediate cause and distributes the waste's costs to the components that have produced it directly and in proportion to their exergy.
- COST: This allocation method is like the previous one but distributes the cost proportionately to its exergy cost instead of its exergy. It should be noted that, in many cases, a waste's exergy is irrelevant, but its cost is relevant.
- RESOURCES: This method is based on the definition of cost, i.e. the cost of a waste is the amount of external resources expended to produce it. The method internalises the waste cost to the external resources proportionally to the amount used to make it. This is the DEFAULT method used by TaesLab if no waste definition is provided.
- IRREVERSIBILITY: This method identifies the waste cost formation process from the cost-irreversibility table and distributes the cost according to the irreversibility carriers of waste streams.
- HYBRID: This method combines the IRREVERSIBILITY and EXERGY methods. The method considers the full path of the waste cost formation. See reference [14]

2.5. Economic and environmental model

The exergy cost is relative to the limits of the system. Therefore, we must define the thermodynamic system's boundaries that constitute the installation and its environment. The exergy cost, also called direct exergy cost, only considers the irreversibility of the processes (both internal and external) within the system boundaries.

From the viewpoint of natural resource management, the system boundaries should be set at the level of extraction of non-renewable resources from nature [15]. The exergy cost of natural gas processed in a gas turbine will be higher than its exergy due to the extraction, storage and transportation processes required to use it. Moreover, the direct exergy cost does not consider that the installation processes have their own exergy cost because additional exergy will be needed to keep them in operation. On the other hand, when considering the economic aspects, the perspective is broadened by the introduction of two additional factors: the market prices of fuels (€/MWh) that are not linked to the exergy of the resources processed and the cost of investment, maintenance and operation of the facility necessary for the production process (€/h) For these

reasons, the concept *generalised exergy cos*t is presented as a broader view of the exergy cost, in which the costs of the system flows take into account the interactions with the physical and economic environment. Therefore, the external valuation of resources could be measured in mass, energy or monetary units per unit of time; and the costs of the plant processes, measured in terms of mass, energy or monetary units and levelized per unit of time, must be considered.

Some examples of generalised exergy costs are the thermo-ecological cost [16] or the exergoeconomic cost [17], which assesses the monetary cost of internal flows and outputs of complex plants.

2.6 Thermoeconomic Data Model

Defining this thermoeconomic model requires a collection of structured data or tables that provide the information needed to analyse a system using TaesLab. The data model can be saved in an XLSX spreadsheet workbook, but other formats, such as CSV, JSON or XML, can also be used. The required tables, defined for the ORC plant in Appendix A, are:

- *Flows*: Enumerate the flows of the system. See Table A1 (a). The *type* field indicates if the flow connects to the plant process (INTERNAL), is an external resource (RESOURCE), is a final product (OUTPUT) or a waste leaving the system (WASTE).
- *Processes*: Enumerate the process of the system. See Table A1 (b). The *type* field indicates if the process is PRODUCTIVE or DISSIPATIVE. The productive structure is defined in the fields: *fuel* and *product*. We show which flows, described in the previous table, constitute the fuel and which flows are the product. For example, in the case of the Steam Generator (BLR), the fuel is the waste heat (QBLR), and the product is (B1-B6), the exergy difference between flows B1 and B6.

  These two tables define the productive structure of the plant.
- *Format*: The numerical format used for the results tables and the units in which the different quantities appear are indicated. For example, exergy values (EXERGY) are expressed in (kW) and are shown with up to ten significant digits and three decimal places. See Table A4
- *Exergy*: It contains the values of the flow exergies for different plant states or simulations. See Table A2. Each column represents a plant state. The first column of values is used as the reference state, and the column name serves as a key to identify that state. TCND45 use T_{cnd}=45ºC, ETAT75 simulates the plant with η_{trb}=75%, PBLR15 use P_{blr}=15 bar, noIHE bypasses the internal heat interchange, and n-Butane uses that fluid instead R234fa.

The rest of the tables described below are optional:

- *WasteDefinition*: Defines how the waste cost is allocated; see table A3. The different types of waste cost allocation have been described in section 2.5
- *WasteAllocation:* It manually defines the ratios for allocating waste costs to production processes. See also Table A.5
- *ResourcesCost*: Values of external resource costs, both flow costs (FLOW) and process costs (PROCESS). The units must be those indicated in the Format table for GENERALIZED_UNIT_COST and GENERALIZED_COST, respectively. Table A5 shows the economic costs of the processes in c€/kWh, according to the reference [18]. In the case of waste gases, they are considered amortised in the plant that produces them. Therefore the unit cost of the external resource flow QBLR is zero.

3. The TaesLab Application

TaesLab is a MATLAB package compatible with Octave, which provides a set of functions to perform the thermoeconomic analysis of a plant interactively from the MATLAB console. It also provides an application with a graphical user interface, see Figure 2, where the essential functions can be performed. See reference [10] for complete information on the use of the package, the user guide and its download.

TaesLab GUI has three panels. In the left panel, select the status to be calculated and the rest of the parameters. In the right panel, select the tables and graphs of the current state to be displayed in the central panel.

TaesLab has three groups of functions.

- Read and check the thermoeconomic model files.
- Cost analysis and thermoeconomic diagnosis.
- Show and save the results.

There are five blocks of results:

- Productive Structure.
- Thermoeconomic State.

- Thermoeconomic Analysis
- Thermoeconomic Diagnosis
- Summary Results

For each of these blocks, we can show the tables obtained, graph representations, and see internal information of the calculations using the workspace inspector. All the results could be saved into text files or XLSX spreadsheet workbooks for further analysis. The complete list of tables and graphs that could be obtained is explained in the user manual [10] mentioned above.

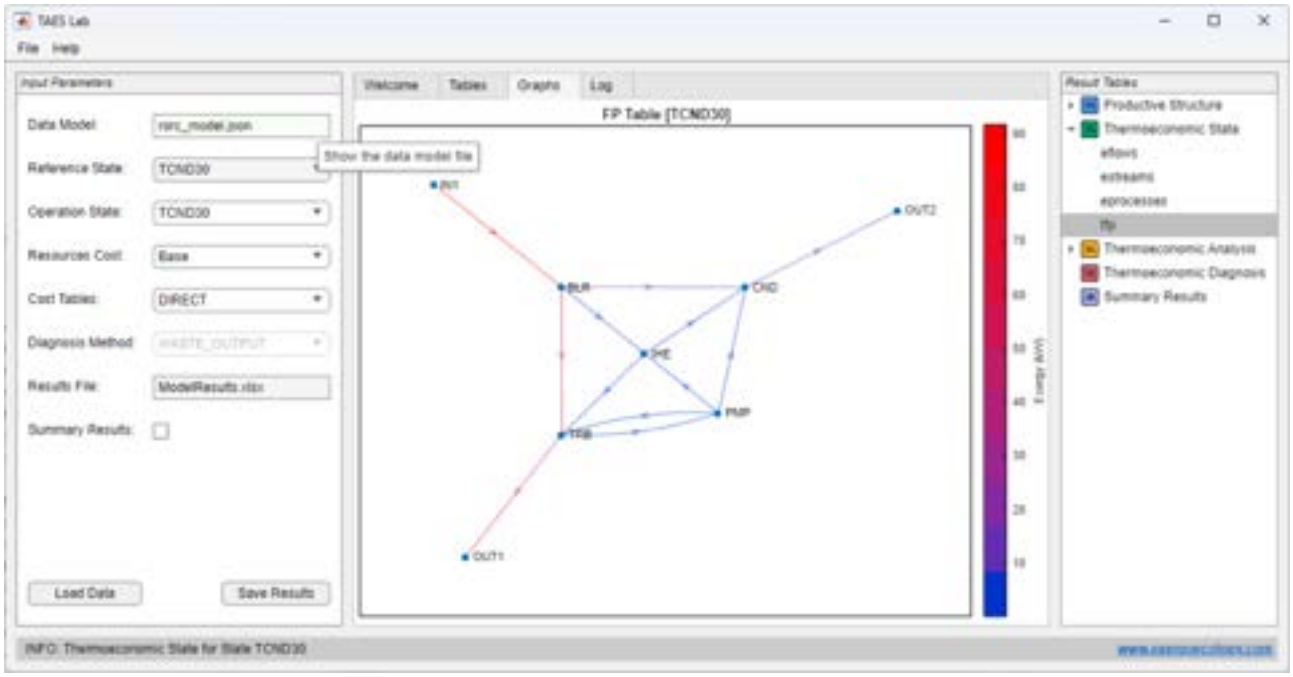

Fig.2 Screenshot of the GUI Application of TaesLab

3.1. Input Parameters

The application has several parameters that can be modified interactively.

- *State*: Indicates the state where we want to perform the analysis.
- *CostTables*: Indicates which types of tables we want to generate.
  - DIRECT: Only direct exergy costs are calculated
  - GENERALIZED: If external resources data are available, obtain generalised exergy costs
  - ALL: Both cost types are selected.
- *ResourcesCost*: Allows selecting the data to calculate the generalised costs.
- *ReferenceState*: Indicates which state will be used as the reference when running the thermoeconomic diagnosis.
- DiagnosisMeth*od*: Indicates the method used to make the thermoeconomic diagnosis.
  - NONE: The thermo-economic diagnosis calculations are deactivated.
  - WASTE_OUTPUT: Waste is considered as plant output flows.
  - WASTE_INTERNAL: The cost of waste is assessed according to the chosen waste cost allocation.
- Summary Results: Activate Summary Results tables and graphs.

Appendix B shows the Live Script used to obtain the tables and figures obtained below.

3.2. Productive Structure

In this block of results, the information on the production structure graph, including the production groups, also called streams, is shown. The construction of the adjacency matrix of the production structure graph is explained in detail in reference [4]. Figure 3 shows the production structure of the example plant. It has been drawn with yEd graph software [19] from a file obtained by the app function `SaveProductiveDiagram`.

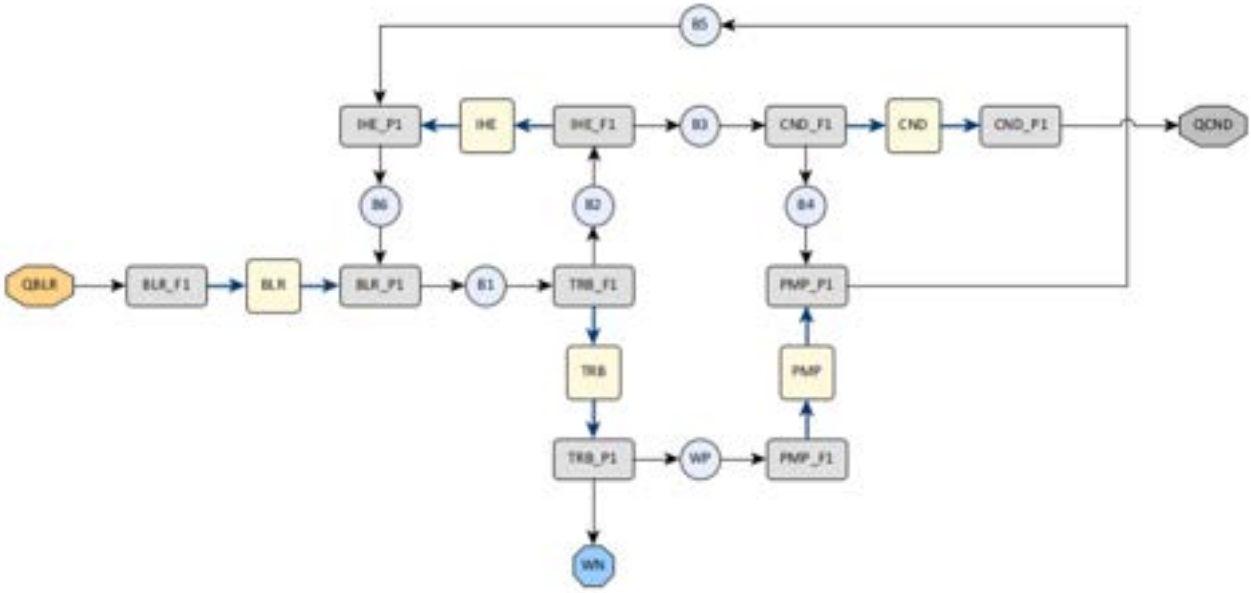

Figure 3. *Productive structure graph of the ORC plant,*

In this graph, the yellow squares represent the processes, the gey rectangles the productive groups, and the blue circles the flows. Resources are drawn as an orange octagon, waste as a grey octagon, and Final products as a blue octagon. Each Internal flow connects two productive groups, and each process connects to one or several fuel and product groups.

3.3 Thermoeconomic State

This results block shows the plant's exergy balances and its Fuel-Product table. Table 1 shows the exergy balance of the example ORC plant.

Table 1. Process Exergy Balance of ORC plant

Key	F(kW)	P(kW)	I(kW)	k(J/J)	η (%)
BLR	99.53	73.70	25.84	1.3506	74.04
TRB	65.67	52.43	13.24	1.2525	79.84
IHE	2.07	1.51	0.57	1.3754	72.71
PMP	2.43	2.08	0.35	1.1698	85.49
CND	9.54	9.54	0.00	1.0000	100.00
ENV	99.53	50.00	49.53	1.9906	50.24

The application checks if fuel (F), product (P) and irreversibility (I) are non-negative values. If both fuel and product are zero, the component is bypassed and not considered in the calculation. It permits to analyse of several plant configurations in the same data model.

Table 2. Fuel-Product Exergy Table (kW)

Key	BLR	TRB	IHE	PMP	CND	ENV	Total
BLR	0.00	62.62	1.97	0.00	9.10	0.00	73.70
TRB	0.00	0.00	0.00	2.43	0.00	50.00	52.43
IHE	0.00	1.28	0.04	0.00	0.19	0.00	1.51
PMP	0.00	1.77	0.06	0.00	0.26	0.00	2.08
CND	0.00	0.00	0.00	0.00	0.00	9.54	9.54
ENV	99.53	0.00	0.00	0.00	0.00	0.00	99.53
Total	99.53	65.67	2.07	2.43	9.54	59.54	238.78

Table 2 shows the Fuel-Product table of the plant. This table shows the role of each plant's processes. The most important ones are the steam generator (BLR) and the turbine (TRB), while the IHE and the pump (PMP) recover a small part of the exergy.

3.4. Thermoeconomic analysis

This section presents the results of calculating a plant state's direct and generalised energy costs. There are several types of tables:

- Summary tables of costs for flows and processes.
- Fuel-Product Cost Tables
- Irreversibility Cost Tables

The values of direct exergy costs are decomposed between the part due to internal irreversibilities B^*_{IN} and the costs due to waste B^*_{EX}, applying the selected criterion for waste cost allocation.

$$B^* = B^*_{IN} + B^*_{EX} \quad (1)$$

In the case of generalised exergy costs, they are broken down into the part due to the cost of external resources C_e, the costs associated with processes, C_z, and the cost due to waste, C_r, see Table 3.

$$C = C_e + C_z + C_r \quad (2)$$

Table 3. *Generalised (exergoeconomic) cost of ORC flows.*

Key	B(kW)	C(c€/h)	Ce(c€/h)	Cz(c€/h)	Cr(c€/h)	c(c€/kWh)	ce(c€/kWh)	cz(c€/kWh)
B1	82.99	37.96	0.00	20.96	17.01	0.4574	0.0000	0.2525
B2	17.32	7.92	0.00	4.37	3.55	0.4574	0.0000	0.2525
B3	15.25	6.98	0.00	3.85	3.12	0.4574	0.0000	0.2525
B4	5.71	2.61	0.00	1.44	1.17	0.4574	0.0000	0.2525
B5	7.79	13.37	0.00	11.36	2.01	1.7163	0.0000	1.4589
B6	9.30	17.19	0.00	14.45	2.74	1.8491	0.0000	1.5542
QBLR	99.53	0.00	0.00	0.00	0.00	0.0000	0.0000	0.0000
WP	2.43	8.45	0.00	7.81	0.64	3.4736	0.0000	3.2105
WN	50.00	173.68	0.00	160.52	13.16	3.4736	0.0000	3.2105
QCND	9.54	15.11	0.00	13.16	1.95	1.5841	0.0000	1.3791

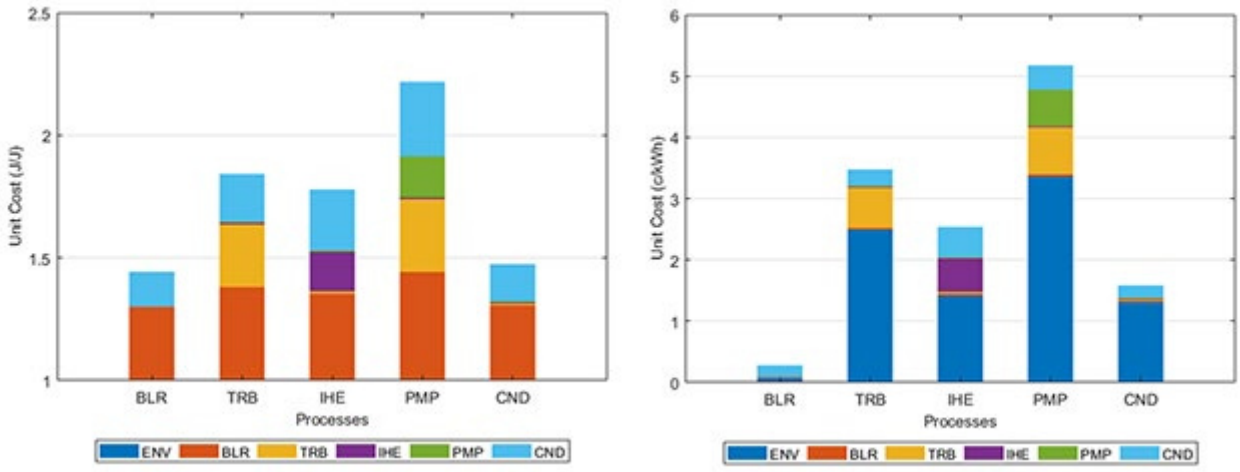

Fig. 4 *Direct and Generalized irreversibility cost graphs*

Table 3 shows the generalised cost of flows. The main contribution is the investment and maintenance costs of the equipment. Here the cost of waste does not reach 10%, and it is assumed that the heat used in the steam generator has no cost. Then the electricity cost is 34.73 €/MWh and the heat 15.84 €/MWh.

The irreversibility cost charts analyse the cost formation process, considering the effect of each process's internal and external irreversibilities. In the case of generalised cost, the impact of the cost of external resources associated with flows and processes is also considered. See Fig. 4.

In the case of direct cost, the main contribution to the cost of each component is the steam generator, as it is the least efficient component located at the beginning of the production chain, also noting that waste costs have a significant weight. In the case of exogenous economic costs, an essential part, as already mentioned, is the equipment costs, together with the irreversibilities of the turbine, due to its high cost.

The application provides an additional function (Summary of Results) that allows the generation of comparative tables and graphs for the different states of the plant.

3.5. Waste Recycling Analysis

As long as residual streams have exergy, they can be retrieved in *recovery units*; the condenser/heat exchange is in the ORC example. These recovery units are integrated into the plant and constitute productive units. Instead of expending exergy to dispose of waste, their exergy is recovered to produce another by-product. In the case of the ORC plant, the recovery unit could produce steam for an ejector refrigeration system. The potential savings from waste recycling can be estimated if one knows the production costs due to external irreversibilities. The production cost due to waste k^*_{EX} indicates the maximum amount of resources that could be saved if waste were recycled.

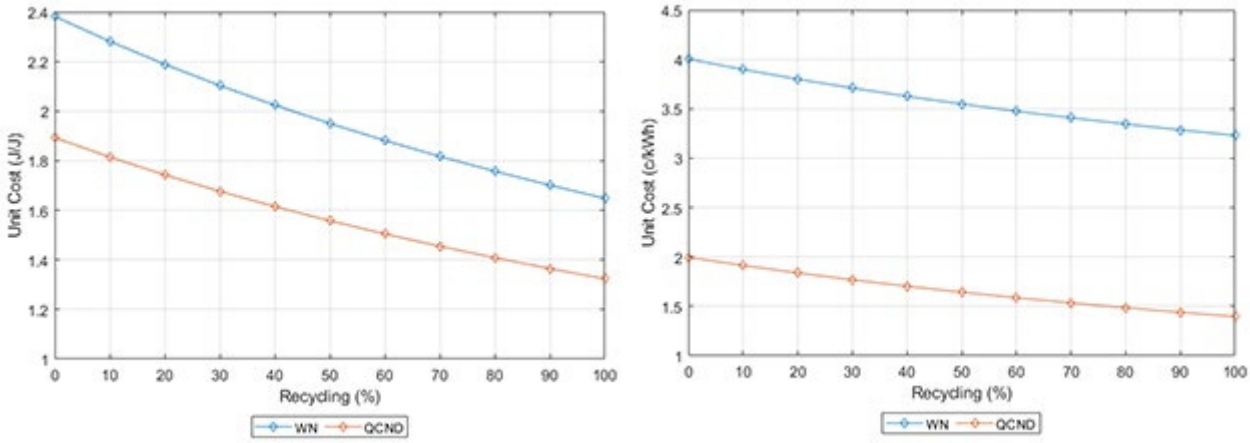

Fig. 5 *Direct and Generalized cost of output flows as a function of waste QCND recycled for TCND45 state.*

It is well known that not all waste can be saved for technical and economic reasons. But, using process integration and Industrial Symbiosis[21], other systems may convert this waste into resources. The exergy cost theory allows for evaluating the waste cost, accounting for resource savings, and providing fair prices to waste becoming by-products.

TaesLab allows computing the production costs if a part of the waste stream is recycled. Figure 6 shows the plots of the output system flows as a function of the portion of waste recycled for the TCND45 state. In the case of recycling up to 66% of the heat, the cost of electricity is 34.35 €/MWh, which is lower than operating the plant under reference conditions.

3.6 Thermoeconomic Diagnosis

The thermoeconomic diagnosis allows for comparing two states of the plant, identifying the causes of the increase in resource consumption between a reference state and another state (operating state). It also allows for evaluating the cost of production increase and the increase of the waste cost.

Diagnosis results are generated when `DiagnosisMethod` is active, and the `ReferenceState` and `State` parameters have different values. The application provides two methods for the analysis of waste cost variation. The first one, WASTE_OUTPUT, is the standard method of thermoeconomic diagnosis, in which the impact on fuel is the sum of the cost of malfunctions caused by the variation of internal irreversibilities MF_i^*, plus the cost of the variation of external outputs, including final products and wastes. The increase in the waste cost implies a useless consumption of resources but not an increase in the final product.

$$\Delta F_T = \sum_i MF_i^* + \sum_i k^*_{P,IN}\Delta\omega_s \tag{3}$$

The second method, WASTE_INTERNAL, addresses this limitation. It is a new implementation of the fuel impact calculation. The cost of waste variation is reallocated to the plant's production processes and final products, according to the defined waste cost allocation criteria.

$$\sum_j k^*_{IN,j}\Delta\omega_{R,j} = \sum_i MR_i^* + \sum_j k^*_{EX,j}\Delta\omega_{T,j}\ , \tag{4}$$

where MR_i^* is the cost of process malfunctions due to the external irreversibility increase, and $\Delta\omega_T$ is the variation of the final products. In such a case, the fuel impact formula is rewritten as follows:

$$\Delta F_T = \sum_i MF_i^* + \sum_j MR_i^* + \sum_j k_{P,j}^* \Delta\omega_{T,i} \quad (5)$$

If we compare the waste heat consumption of the plant in the reference state with that used in the TCND45 (66% recycling) state condition, we can see a fuel impact of 19.47 kW. However, in Table 4 and Figure 8, it can be seen that there is also an extra production of 18.17 kW and a real exergy saving of 7.398 kW.

Table 4. *Diagnosis table comparison between Reference and TCND45 (%66 Recycling) states*

Key	MF (kW)	ΔI (kW)	ΔP_S(kW)	MF* (kW)	MR* (kW)	ΔP_T* (kW)
BLR	-3.679	1.695	0.000	-3.679	-2.712	0.000
TRB	-0.385	-0.240	0.000	-0.368	0.041	0.000
IHE	-0.330	-0.125	0.000	-0.433	-0.226	0.000
PMP	-0.016	0.068	0.000	-0.027	-0.024	0.000
CND	0.000	0.000	18.172	0.021	0.010	26.968
ENV	-4.410	1.398	18.172	-4.486	-2.912	26.968

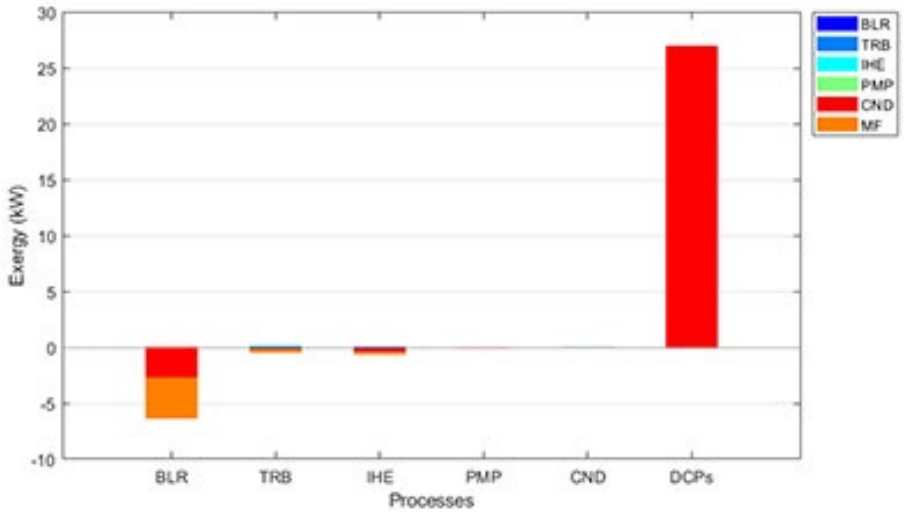

Fig. 6. *Malfunction Cost graph comparison between Reference and TCND45 (%66 recycling) states*

4. Conclusions

This paper presents a new software application for the thermoeconomic analysis of energy systems. The application follows the methodology described in [9]. It is an evolution of the TAESS application [web], which implements the new algorithms for circular thermoeconomics described in [4], with particular emphasis on analysing the waste cost formation process and its effect on production costs.

The application is presented as a MATLAB package, which includes both applications with a graphical user interface (GUI) and interactive functions that can be used in the MATLAB environment. The fact that it is written in MATLAB language facilitates the calculations of mathematical structures and provides an efficient environment for visualising the results obtained. Through notebooks or Live Scripts, it is possible to use TaesLab for educational purposes and applications adapted to users' needs. In addition, a library of classes is available, allowing new applications and functions to be developed by reusing the source code already generated. Most of the functionality of this software is also compatible with Octave, the open-source alternative to MATLAB.

TaesLab allows focusing on obtaining results without defining the cost equations as in other methodologies. The paper describes the data model, including its physical and productive structure and thermodynamic, economic and environmental data, and shows with an example its capabilities.

As future perspectives for TaesLab, besides adding new functionalities such as aggregation and integration of systems and models with energy storage..., is to integrate it with other simulation packages of energy systems such as Simulink [22], ASPEN or HSC.

Acknowledgements

This paper has been funded by the Spanish Ministry of Science and Technology under project RESET PID-116851RB-100, and project G/5423/740121/32444 funded by the Aragon Government under the Renewable Energy and Hydrogen program within the framework of the complementary plans foreseen in the plan for recovery, transformation and resilience-MRR

Appendix A

This appendix shows the data model tables of the ORC plant example.

Table A1. Physical and Productive Structure definition.

(a) Flows definition

key	type
B1	INTERNAL
B2	INTERNAL
B3	INTERNAL
B4	INTERNAL
B5	INTERNAL
B6	INTERNAL
QBLR	RESOURCE
WP	INTERNAL
WN	OUTPUT
QCND	WASTE

(b) Process definition

key	fuel	product	type	description
BLR	QBLR	B1-B6	PRODUCTIVE	Steam Generator
TRB	B1-B2	WN+WP	PRODUCTIVE	Turbine
IHE	B2-B3	B6-B5	PRODUCTIVE	Internal Heat Exchanger
PMP	WP	B5-B4	PRODUCTIVE	Pump
CND	B3-B4	QCND	DISSIPATIVE	Condenser

Table A2. Exergy States values (kW)

Key	Reference	TCND45	ETAT75	PBLR15	NoIHE	N-Butane
B1	82.99	106.70	88.81	84.14	82.99	103.5
B2	17.32	40.68	18.92	18.96	17.32	37.2
B3	15.25	37.42	16.36	17.02	17.32	35.03
B4	5.71	9.71	6.11	6.39	5.711	24.87
B5	7.79	12.31	8.34	8.09	7.79	27.41
B6	9.30	15.13	10.17	9.51	7.79	29.02
QBLR	99.53	119.10	105.80	102.80	106.4	100.8
WP	2.43	3.02	2.60	1.98	2.432	2.967
WN	50.00	50.00	50.00	50.00	50	50
QCND	9.54	27.71	10.25	10.63	11.609	10.16

Table A3. Waste Definition and allocation (values in %)

key	type	recycle
QCND	IRREVERSIBILITY	0.00

key	QCND
BLR	94.40
TRB	2.24
IHE	2.06
PMP	1.29

Table A4. Format definition

key	width	precision	unit
EXERGY	10	3	(kW)
EXERGY_COST	10	3	(kW)
EXERGY_UNIT_COST	10	4	(J/J)
GENERALIZED_COST	10	3	(c€/h)
GENERALIZED_UNIT_COST	10	4	(c€/kWh)
DIAGNOSIS	10	4	(kW)

Table A5. Resources Cost Values (The units of the values are as defined in the format table)

key	type	Base
QBLR	FLOW	0.00
BLR	PROCESS	6.51
TRB	PROCESS	151.75
IHE	PROCESS	2.56
PMP	PROCESS	2.11
CND	PROCESS	10.75

Appendix B

This appendix shows the LiveScript commands of the TaesLab application used to generate the figures and tables of the paper.

Read and check the Data Model file.

Read the data model `rocr_model.xlsx`, select all tables and deactivate diagnosis

```
model=ThermoeconomicTool('rorc_model.xlsx', 'CostTables', 'ALL',...
'DiagnosisMethod', 'NONE', 'Debug',false);
```

Get tables and graphs for the reference state TCND30.

Save results tables in an Excel workbook. Tables 1-3 and Figure 3

```
SaveResults(model,'rorc_results.xlsx');
model.saveProductiveDiagram('rorc_ps.xlsx');
```

Generate Irreversibility Cost Graph. Figure 4

```
model.graphCost(cType.Tables.PROCESS_EXERGY_COST);
model.graphCost(cType.Tables.PROCESS_GENERAL_COST);
```

Recycling Analysis

Get the recycling graphs for state **TCND45**. Figure 5

```
model.State='TCND45';
res=recyclingAnalysis(model);
res.graphRecycling(cType.Tables.WASTE_RECYCLING_DIRECT);
res.graphRecycling(cType.Tables.WASTE_RECYCLING_GENERAL);
```

Thermoeconomic Diagnosis

Compare **TCND30** (reference state) with **TCND45**, recycling 66% of the condenser heat.

```
mode.setRecycledRatio('QCND',0.66)
model.DiagnosisMethod='TCND45';
```

Save the thermoeconomic diagnosis results, table 4, and show the malfunction cost graph, figure 6.

```
SaveResults(model,'rorc_TCND45.xlsx');
model.graphDiagnosis(cType.Tables.MALFUNCTION_COST);
```

References

[1] Torres C., Valero A., Serra L., Royo J., Structural theory and thermoeconomic diagnosis: Part I. On malfunction and dysfunction analysis. Energy Conver Manag. 2002; 43(9-12): 1503-1518.

[2] Stanek W., Thermodynamics for Sustainable Management of Natural Resources; Springer: Cham, Switzerland, 2017.

[3] Lozano, M.; Valero, A. Theory of the exergetic cost. Energy 1993, 18, 939–960.

[4] Torres C., Valero A., The Exergy Cost Theory Revisited. Energies, 2021, 14, 1594.

[5] Valero A., Torres C., Thermoeconomics as a cost accounting methodology for Spiral Economy and Industrial Symbiosis. ECOS 2021, 34th International Conference on Efficiency, Cost, Optimization, Simulation and Environmental Impact of Energy Systems, June 27-July 2, Taormina, Italy: 656-666.

[6] EES: Engeeniering Equation Solver. Available at https://fchartsoftware.com/ees/ [accessed 20.3.2023]

[7] HSC Chemistry Software for Process Simulation. Available at: http://www.hsc-chemistry.net/ [accessed 20.3.2023]

[8] Aspen PLUS. Available at: https://www.aspentech.com/en/products/engineering/aspen-plus [accessed 20.3.2023]

[9] Torres, C., Valero, A., Perez, E., Guidelines to developing software for thermoeconomic analysis of energy systems, ECOS 2007, 20th International Conference on Efficiency, Cost, Optimization, Simulation and Environmental Impact of Energy Systems, June 24-28, Padova Italy, vol. 1:435–490.

[10] TAESS. Thermoeconomic Analysis of Energy Systems Software. The Exergoecology Portal. Available online: https://www.exergoecology.com/ [accessed 10/3/2023].

[11] Picallo A., Sala J.M., Portillo L., Development of a tool based on thermoeconomics for control and diagnosis build thermal facilities, Energy, 2022, 239, 122304.

[12] Rostamzadeh H., Ebadollahi M., Ghaebi H., Amidpour M., Kheiri R. Energy and exergy analysis of novel combined cooling and power Cycles. Applied Thermal Engineering, 2017, 124, 152–169

[13] Torres C., Valero A., Rangel V., Zaleta A. On the cost formation process of the residues. Energy 2008, 33, 144–152.

[14] Agudelo, A.; Valero, A.; Torres, C. Allocation of waste cost in thermoeconomic analysis. Energy 2012, 45, 634–643.

[15] Usón, S.; Kostowski, W.J.; Stanek, W.; Gazda, W. Thermoecological cost of electricity, heat and cold generated in a trigeneration module fuelled with selected fossil and renewable fuels. Energy 2015, 92, 308–319.

[16] Szargut, J. Exergy Method: Technical and Ecological Applications; WIT Press: Southampton, UK, 2005.

[17] Tsatsaronis, G., Winhold, M. Exergoeconomic analysis and evaluation of energy-conversion plants-I. A new general methodology. Energy 1985, 10, 69–80.

[18] Ghaebi H., Parikhani T., Rostamzadeh H., Farhang B., Thermodynamic and thermoeconomic analysis and optimization of a novel combined cooling and power (CCP) cycle by integrating of ejector refrigeration and Kalina cycles. Energy 2017, 139, 262-276

[19] yWorks. yEd Graph Editor. Available online: https://www.yworks.com/products/yed [accessed on 10.3.2023].

[20] e!Sankey – Show the Flow. Available online: https://www.ifu.com/e-sankey/ [accessed on 10.3.2023].

[21] Valero, A.; Uson, S.; Torres, C.; Valero, A.; Agudelo, A.; Costa, J. Thermoeconomic tools for the analysis of eco-industrial parks. Energy 2013, 62, 62–72.

[22] Simulink, Available at: https://www.mathworks.com/products/simulink.html [accessed on 10.3.2023]

PROCEEDINGS OF ECOS 2023 - THE 36TH INTERNATIONAL CONFERENCE ON
EFFICIENCY, **C**OST, **O**PTIMIZATION, **S**IMULATION AND ENVIRONMENTAL IMPACT OF ENERGY SYSTEMS
25-30 JUNE 2023, LAS PALMAS DE GRAN CANARIA, SPAIN

Advanced Exergy Analysis of the Flash Ironmaking Process

Jannik Neumann, Frank Dammel, Peter Stephan

Institute for Technical Thermodynamics, Technical University of Darmstadt, Darmstadt, Germany, (neumann, dammel, pstephan)@ttd.tu-darmstadt.de

Abstract:
The growing demand for renewable energy highlights the importance of green energy carriers in mitigating the temporal and geographic imbalances between renewable energy supply and demand. Iron, as a metal fuel, offers a promising solution by enabling the storage of electrical energy from renewables through the thermochemical reduction of iron oxides with green hydrogen. This stored energy can be later converted back into electricity via thermochemical oxidation, such as in retrofitted coal-fired power plants. Transporting the iron/iron oxide in a closed cycle allows for spatial and temporal separation of renewable energy storage and release. To maximize the system efficiency of this energy-iron cycle, it is crucial to achieve high storage efficiencies during the thermochemical reduction of iron oxides. The flash ironmaking process is a promising method for this, as it allows for the reduction of fine iron oxide particles with green hydrogen without the need for pre- or post-treatment. Conventional exergy analyses, as well as advanced exergy analysis, are used to analyze the flash ironmaking process. The results reveal an exergetic system efficiency of 53.7 % for a defined base case, with the largest share of exergy destruction attributed to unavoidable exergy destruction at 82.2 % of the total exergy destruction. Additionally, most of the exergy destruction was endogenous at 89.4 % of the total exergy destruction. These assessments indicate that the overall potential for improvement of the reduction plant is moderate, and component improvements should be prioritized over structural improvements to reduce avoidable endogenous exergy destruction.

Keywords:
Direct Reduction of Iron; Exergy Analysis; Green Iron; Iron as Energy Carrier; Metal Fuels.

1. Introduction

The impact of climate change on both ecosystems and humans is becoming increasingly concerning, with approximately 3.3 to 3.6 billion people residing in highly susceptible areas [1]. Governments worldwide are facing the challenge of balancing electricity security and meeting the rising demand for electricity while simultaneously reducing emissions. This becomes even more challenging due to the recent global energy crisis triggered by Russia's invasion of Ukraine which highlights the vulnerability of the current energy system [2]. At the center of the required clean energy transition is the significant increase in renewable energy soruces paired with the electrification of end-uses. However, due to the inherent variability of renewable energy sources, a secure and decarbonized power sector requires much larger-scale flexible resources than currently exist [3]. One cornerstone of future energy systems might be the use of carbon-free chemical energy carriers (ECs), which can convert clean electricity into stable media for energy storage and transport. By connecting various low-cost production regions with users of green ECs through global value chains, the future energy supply security can be ensured [3]. Iron is being considered as a potential alternative to frequently discussed ECs such as hydrogen and hydrogen-based ECs for the global transport and seasonal storage of renewable energy [4–7]. The energy-iron cycle consists of the storage of electrical energy via thermochemical reduction of iron oxides using green hydrogen, which can subsequently be converted back into electricity through thermochemical oxidation. This conversion process can take place in coal-fired power plants that have been retrofitted for this purpose [8]. This reuse of existing assets and infrastructure can lead to significantly reduced implementation times and costs compared to alternative ECs [7]. Furthermore, the transport and storage of iron/iron oxide is comparatively easy and does not require liquefaction or elevated pressures, which is an advantage over other ECs. The round trip efficiency and the cost of such an energy-iron cycle depend strongly on the regeneration (thermochemical reduction) of the iron oxides [7].
Thermochemical reduction of iron oxide is a well-established process that primarily utilizes coal in blast furnaces, resulting in a significant contribution of 7 % to global CO_2 emissions [9]. However, an alternative method is to employ shaft furnace processes that use natural gas instead of coal, which offer a promising solution to reduce associated CO_2 emissions from ironmaking [9]. This approach is particularly useful in regions with access to cheap natural gas.

Among various routes towards carbon-neutral ironmaking, the shaft furnace process is considered the most promising due to its ability to operate with green hydrogen instead of natural gas and its comparatively high technological readiness level [10]. One drawback of the shaft furnace reduction process is the necessity of iron oxide pellets as feedstock, which must be prepared beforehand and adds to the costs and emissions (although the potential for carbon neutrality exists through the use of hydrogen or bio-mass [11]). Further processing is needed to obtain the required iron powder [8], typically by melting the reduced iron pellets in an energy-intensive electric arc furnace and subsequently water-atomizing the melt.
At the University of Utah a promising alternative technology called the flash ironmaking process [12, 13] has been developed, which can reduces energy consumption and capital investment requirements. This innovative process allows for the direct utilization of fine iron oxide particles without requiring additional pre- and post-treatment, eliminating the need for pelletization and iron powder production. The reaction rate is rapid, and residence times are short, typically just a matter of seconds [12, 14], compared to the minutes to hours required in shaft furnace reactors, thanks to the small particle size (ranging from 10 to 100 microns). The flash reactor reduction technology is a high-intensity process that is free from problems associated with operating at high temperatures, such as particle sticking, unlike other gas-based ironmaking processes that use fluidized bed or shaft furnace reactors. As a result, the process can be operated at elevated temperatures (i.e. above 1150 °C), resulting in a more intensive process. The flash ironmaking process offers several advantages, including dispensing with the requirement for pre- and post-treatment, low energy consumption and capital investment, and high-intensity. Given these advantageous features, the flash ironmaking process aligns perfectly with the described energy-iron cycle as a promising reduction process.
To improve the understanding, identify the sources of irreversibility, and estimate the real improvement potential of this energy-intensive process, exergy-based analyses are performed. For this purpose the methodology and process are described in detail before the analyses are performed.

2. Methodology

The flash ironmaking process will be analyzed using both conventional and advanced exergy analyses. These two analyses will be briefly summarized subsequently before the flash ironmaking process is described in more detail.

2.1. Exergy Analysis

An exergetic analysis is widely recognized as the most efficient method for evaluating the efficiency of energy conversion processes [15–17]. It provides insights by analyzing the real thermodynamic inefficiencies in a system and its components, which are not available by means of an energetic analysis. These can greatly enhance energy-intensive processes from a thermodynamic, an economic, and an ecological perspective. When evaluating systems that involve chemical reactions, the total specific exergy e_{tot} of a material stream, is a combination of both physical exergy e_{ph} and chemical exergy e_{ch}, as represented by

$$e_{\text{tot}} = e_{\text{ph}} + e_{\text{ch}} \,. \tag{1}$$

Physical exergy is calculated based on the current enthalpy h and entropy s as well as their reference state values (h_0 and s_0), using the following equation

$$e_{\text{ph}} = (h - h_0) + T(s - s_0) \,. \tag{2}$$

Chemical exergy, on the other hand, has two components: a reactive part, which is represented by the standard chemical exergies, and a non-reactive part due to mixing. This can be expressed as

$$e_{\text{ch}} = \sum_l \omega_l e^0_{\text{ch},l} + T_0 \sum_l R_l x_l ln(x_l) \,. \tag{3}$$

The standard chemical exergy $e^0_{\text{ch},l}$ for each species l can be obtained from tables for standard reference environments [15, 18, 19] or it can be calculated for a process-specific reference environment. In this case, the latter approach is used, with the reference species being liquid H_2O, Fe_2O_3, and ambient air. For iron and hydrogen, the standard chemical exergies based on the process-specific reference environment are 6448 kJ kg^{-1} and 118 246 kJ kg^{-1}, respectively.

The exergy balance of a generic open control volume can be expressed by

$$\dot{E}_{\text{D}} = P + \dot{E}_{\text{Q}} + \sum_{in,i} \dot{m}_i e_{i,\text{tot}} - \sum_{out,j} \dot{m}_j e_{j,\text{tot}} - \dot{E}_{\text{L}} \,, \tag{4}$$

where $\dot{E}_{\text{Q}}$ and P correspond to the time rates of exergy transfer associated to heat and work transfer, respectively. The exergy loss rate $\dot{E}_{\text{L}}$ and exergy destruction rate $\dot{E}_{\text{D}}$ depend on the chosen system boundary. For

this evaluation, the system boundaries extend into the environment with the constant reference temperature T_0. Therefore, any exergy reduction due to heat losses to the environment is considered as exergy destruction, and only the material streams leaving the system correspond to exergy losses. To determine the exergetic efficiency of a system or component, it is necessary to define a fuel (F) and a product (P) for the analyzed system or component. Then, the overall exergy balance can be expressed by

$$\dot{E}_\mathrm{D} = \dot{E}_\mathrm{F} - \dot{E}_\mathrm{P} - \dot{E}_\mathrm{L}\,, \tag{5}$$

where the definition of the product must be consistent with the purpose of the system/component. The exergetic efficiency is defined as the ratio of the rate of exergy transfer associated with the product to the rate of exergy transfer associated with the fuel

$$\epsilon = \frac{\dot{E}_\mathrm{P}}{\dot{E}_\mathrm{F}} = 1 - \frac{\dot{E}_\mathrm{D} + \dot{E}_\mathrm{L}}{\dot{E}_\mathrm{F}}\,. \tag{6}$$

To compare the exergy destruction $\dot{E}_{\mathrm{D},k}$ of individual components k and losses associated to material streams leaving the system $\dot{E}_\mathrm{L}$ to the total fuel exergy $\dot{E}_{\mathrm{F,tot}}$ of the overall system, exergy destruction $y_{\mathrm{D},k}$ and exergy loss y_L ratios can be defined

$$y_{\mathrm{D},k} = \frac{\dot{E}_{\mathrm{D},k}}{\dot{E}_{\mathrm{F,tot}}}\,, \qquad y_\mathrm{L} = \frac{\dot{E}_\mathrm{L}}{\dot{E}_{\mathrm{F,tot}}}\,. \tag{7}$$

This allows for the assessment of the relative contribution of each component to the total exergy destruction of the system and can be used to define the total exergetic system efficiency

$$\epsilon_\mathrm{tot} = 1 - \sum_k y_{\mathrm{D},k} - y_\mathrm{L}\,. \tag{8}$$

Conventional exergy analysis provides valuable insights into how energy systems can be improved, but it falls short in illustrating the impact of interactions among components within the overall system and the real potential (including technological limitations) for improvement [20, 21]. To overcome these limitations, advanced exergy analysis has been developed. This approach provides a more comprehensive view of the origin of exergy destruction, taking into account the interactions between components and offering a clearer picture of the potential for improvement.

2.2. Advanced Exergy Analysis

An advanced exergy analysis goes beyond conventional analysis by breaking down the exergy destruction within each component into its endogenous and exogenous parts, as well as its avoidable and unavoidable parts and their combinations. Determining the unavoidable and endogenous fractions of exergy destruction entails making certain discretionary judgments, and thus, is somewhat subjective. Nonetheless, the insights obtained from this division surpasses the drawbacks of partial subjectivity [22]. The methodology of advanced exergy analysis was developed at the Institute for Energy Engineering of Technical University Berlin [20–25] and will be briefly summarized before been applied to the flash ironmaking process.

2.2.1. Unavoidable and Avoidable Exergy Destruction

Although it may be possible to mitigate a fraction of the exergy destruction rate in a component, there is usually a residual amount that cannot be avoided due to a variety of limitations. These limitations can include techno-economic constraints such as material availability and cost, as well as thermodynamic restrictions. For instance, the maximum achievable efficiencies of turbo-machinery or electrolyzers may be limited by current or future technology, resulting in unavoidable exergy destruction. By segregating the exergy destruction into two distinct parts – unavoidable $\dot{E}^{\mathrm{UN}}_{\mathrm{D},k}$ and avoidable $\dot{E}^{\mathrm{AV}}_{\mathrm{D},k}$ – in the k$^{\mathrm{th}}$ component

$$\dot{E}_{\mathrm{D},k} = \dot{E}^{\mathrm{UN}}_{\mathrm{D},k} + \dot{E}^{\mathrm{AV}}_{\mathrm{D},k}\,, \tag{9}$$

a more precise evaluation of the potential to enhance the component's thermodynamic efficiency can be achieved. To estimate the value of $\dot{E}^{\mathrm{UN}}_{\mathrm{D},k}$ within each system component, the most favorable operating conditions that just cannot be achieved in the near future are assumed.

2.2.2. Endogenous and Exogenous Exergy Destruction

Additionally, the impact of interdependencies of the system component can be analyzed by separating the total exergy destruction within the k$^{\mathrm{th}}$ component into endogenous $\dot{E}^{\mathrm{EN}}_{\mathrm{D},k}$ and exogenous $\dot{E}^{\mathrm{EX}}_{\mathrm{D},k}$ parts

$$\dot{E}_{\mathrm{D},k} = \dot{E}^{\mathrm{EN}}_{\mathrm{D},k} + \dot{E}^{\mathrm{EX}}_{\mathrm{D},k}\,. \tag{10}$$

The endogenous share refers to the exergy destruction that takes place within the kth component while all other components are ideal, and the component under assessment is performing at its designated efficiency. In contrast, the exogenous fraction represents the discrepancy between the overall exergy destruction and the endogenous exergy destruction for the specific component. Determining exogenous and endogenous exergy destruction values for individual components is a critical aspect of advanced exergy analysis. Traditionally, two methods, based on thermodynamic cycles and the engineering approach, have been employed [24]. However, these approaches have limitations such as computational difficulties, theoretical deficiencies, and the need for a large number of non-standard simulations, rendering them impractical [21, 25]. To overcome these limitations, a novel decomposition-based approach was recently developed [25] and successfully applied [26] by Penkuhn and Tsatsaronis. This method involves calculating the exogenous exergy destruction for a given component by applying a modified exergy balance equation

$$0 = \sum_j \dot{E}^{\mathrm{EN}}_{\mathrm{Q},j,k} + P^{\mathrm{EN}}_k + \sum_i (\dot{m}e)^{\mathrm{EN}}_{i,k} - \sum_o (\dot{m}e)^{\mathrm{EN}}_{o,k} - \dot{E}^{\mathrm{EN}}_{\mathrm{D}k} \,. \tag{11}$$

This equation takes into account the endogenous operation parameters, which include composition, pressure, temperature, mass flow rate, and exergy transfer to or from the components. It is crucial to define these endogenous parameters for each component in relation to the remaining idealized system. Additionally, the exergetic efficiency ϵ_k of the component must be identical in both the endogenous case and the base case design. By using this novel approach, the drawbacks of previous methods can be avoided, providing a more accurate and practical solution to determine endogenous and exogenous exergy destruction values.

2.2.3. Combination of the Exergy Splitting Approaches

The combination of the two previous concepts results in the following equation for exergy destruction

$$\dot{E}_{\mathrm{D},k} = \dot{E}^{\mathrm{UN,EN}}_{\mathrm{D},k} + \dot{E}^{\mathrm{UN,EX}}_{\mathrm{D},k} + \dot{E}^{\mathrm{AV,EN}}_{\mathrm{D},k} + \dot{E}^{\mathrm{AV,EX}}_{\mathrm{D},k} \,. \tag{12}$$

When optimizing a system based on the results of an advanced exergy analysis, it is important to focus on reducing the avoidable endogenous (that can be reduced by improving the efficiency of the component being considered) and avoidable exogenous (that can be reduced by changes to the system topology) exergy destruction. With these considerations in mind, the exergetic efficiency given in 6 can be adjusted

$$\epsilon^{\mathrm{AV,EN}}_k = \frac{\dot{E}_{\mathrm{P},k}}{\dot{E}_{\mathrm{F},k} - \dot{E}^{\mathrm{UN}}_{\mathrm{D},k} - \dot{E}^{\mathrm{AV,EX}}_{\mathrm{D},k}} \,. \tag{13}$$

Similarly to the differentiation of different parts of exergy destruction (see 12), the exergy destruction ratios can be further differentiated as follows

$$y_{\mathrm{D},k} = y^{\mathrm{UN,EN}}_{\mathrm{D},k} + y^{\mathrm{UN,EX}}_{\mathrm{D},k} + y^{\mathrm{AV,EN}}_{\mathrm{D},k} + y^{\mathrm{AV,EX}}_{\mathrm{D},k} \,. \tag{14}$$

The important information is conveyed through the unavoidable, endogenous exergy destruction $\dot{E}^{\mathrm{UN,EN}}_{\mathrm{D},k}$, which represents the smallest possible endogenous exergy destruction resulting from techno-economically constraints of the component as well as its interactions with other components [21, 26].

$$\dot{E}^{\mathrm{UN,EN}}_{\mathrm{D},k} = \dot{E}^{\mathrm{UN}}_{\mathrm{D},k} \frac{\dot{E}^{\mathrm{EN}}_{\mathrm{D},k}}{\dot{E}_{\mathrm{D},k}} \,. \tag{15}$$

The remaining different parts of exergy destruction can then be calculated by the introduced set of equations.

3. Flash Ironmaking

As prevousliy mentioned the utilization of green hydrogen for green ironmaking is an emerging technology. This section provides a brief overview of the thermochemical reduction of iron oxides using hydrogen, followed by a detailed introduction to the flash ironmaking process.

3.1. Reduction of Iron Oxides with Hydrogen

The step-wise direct reduction of iron oxides with hydrogen at temperatures above 843 K proceeds through a series of intermediate stages, starting from hematite Fe_2O_3, then magnetite Fe_3O_4, followed by wüstite $Fe_{(1-z)}O$, and finally to metallic iron Fe [27]. The global reaction for the reduction of hematite is described by

$$\mathrm{Fe_2O_3} + 3\,\lambda_{\mathrm{H_2}}\mathrm{H_2} \longrightarrow 2\,\mathrm{Fe} + 3\,\lambda_{\mathrm{H_2}}\mathrm{H_2O} + 3\,(\lambda_{\mathrm{H_2}}\text{-}1)\,\mathrm{H_2} \qquad \Delta H_{\mathrm{r}}(\lambda_{H_2} = 1) = 98.77\,\mathrm{J\,mol^{-1}} \,. \tag{R1}$$

Here, λ_{H_2} represents the hydrogen equivalence ratio. However, to achieve full conversion of the iron oxides to iron, an overstoichiometric ($\lambda_{H_2} > 1$) amount of hydrogen is required, since the reaction is limited by the chemical equilibrium [27]. It should be noted that the applied thermodynamic data [28] assume that wüstite exists only as $Fe_{0.947}O$ ($z = 0.053$). The progress of reduction can be quantified by the reduction degree, denoted as X, which is given by

$$X = 1 - \frac{N_O}{1.5 \cdot N_{Fe}}, \tag{16}$$

where N_{Fe} represents the molar amount of iron and N_O corresponds to the molar amount of oxygen bound to the iron. For example, the reduction degree of pure iron would be 1 ($N_O = 0$), and for a mixture of wüstite and iron ($\omega_{Fe} = 0.83$, $\omega_{Fe_{0.947}O} = 0.17$), the reduction degree is 0.9.

3.2. Process Description, Modeling, and Parameterization

Figure 1 illustrates the flowsheet of the flash ironmaking process under investigation. The process begins with fine iron oxide powder (the product of the prior oxidation process) as feedstock which is preheated in an iron oxide preheater. The powder is then directed to the flash reactor, where it reacts with a hydrogen stream to iron and water, as represented by R1. Due to the endothermic nature of the reduction reaction, an external heat source is required. This heat can be generated internally by burning a portion of the reducing agent through partial oxidation, a technique commonly used in various industrial processes, such as natural gas reforming. The reactor effluent is separated through a cyclone, with the hot iron leaving the cyclone being cooled down by an air heater, which utilizes the available heat to preheat the iron oxide feed using a secondary fluid (air). The hot hydrogen leaving the cyclone is then utilized in a regenerative heat exchanger (hydrogen preheater) to preheat the gaseous reactants before entering the flash reactor. The majority of the water in the recycle stream is removed through a simple condenser and the remaining hydrogen is merged with hydrogen generated by the electrolyzer.

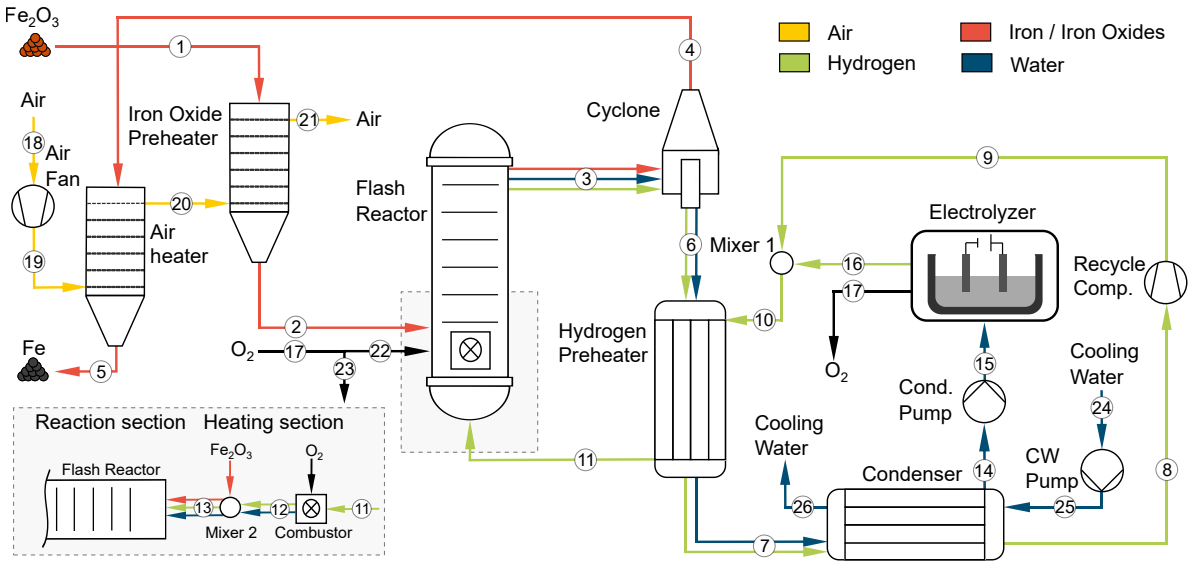

Figure 1: Flowsheet of the investigated flash ironmaking process

3.2.1. Modeling and Assumptions

The flash reactor is the key component of the investigated process. Experimental and numerical evidence suggests that it is possible to fully convert iron oxides to iron using hydrogen at atmospheric pressure [13]. However, for the reference design, a reduction degree of $X = 90\,\%$ is assumed. The flash reactor is modeled as a sequence of a combustor, a heating section (adiabatic mixer), and a reaction section (adiabatic yield reactor), as highlighted in Fig. 1. The adiabatic mixing of the heating section is a reasonable simplification since the heating period is very brief, as supported by numerical investigations [14]. The oxygen flow into the combustor is adjusted to achieve a defined temperature of 1300 °C at the reactor section inlet (Stream 13). In addition, the hydrogen equivalence ratio is set to $\lambda_{H_2} = 3$, so there are no conversion restrictions due to chemical equilibrium limitations. The mass flow rate of solid product leaving the process (Stream 5) is set to $\dot{m}_5 = 35\,\mathrm{kg/s}$, which corresponds to an annual production of approximately 1 million tons (industrial plant scale). All heat exchangers are assumed to have a pressure drop of $\Delta p = 0.15\,\mathrm{bar}$ and a relative heat flow loss $\dot{Q}_{rel}$ equivalent to 2.5 % of the heat flow of combustion/transferred heat flow, is introduced to account for heat losses in both the combustor and heat exchangers. Additional details on the process components are presented in Table 2, and the corresponding stream table is provided in Appendix A.

To enable comparisons between energy-based and exergy-based analyses, a system efficiency parameter is defined, denoted as η_{tot}, for the given process. This parameter is calculated using the following equation

$$\eta_{tot} = \frac{\dot{m}_5 \cdot HV_5}{\sum_k P_k}, \tag{17}$$

where the numerator simply represents the product of the mass flow rate and the corresponding heating value of the product stream, and the denominator accounts for the sum of all energy supplied to the system.

The required definition of fuel and product for the exergy analyses, taking into account the splitting of chemical and physical exergy, for each component and at the system level is defined in Table 1. The unavoidable exergy destruction for each component is calculated individually at the component level, under the best conditions possible, to define the unavoidable exergy destruction. The technological limitations and associated assumptions are given in Table 2. For components where an exergetic efficiency cannot be defined (such as mixer 1 and the cyclone), as they do not serve any meaningful purpose from a thermodynamic perspective, the unavoidable exergy destruction is set equal to the endogenous exergy destruction. The same assumption was made for the flash reactor (consisting out of the combustor, mixer 2 and the reaction section). Another approach to defining unavoidable conditions for the flash reactor could be to assume full conversion ($X = 1$) at the minimum possible hydrogen equivalence ratio. However, such an assumption would result in higher specific exergy destruction due to the inherent irreversibilities associated with the chemical reactions involved. Consequently, this approach would lead to negative avoidable exergy destruction, the interpretation of which is not clear.

To calculate the endogenous and exogenous exergy destruction, individual components with their corresponding exergetic efficiency are simulated in conjunction with an idealized system [25]. The real process takes into account factors such as incomplete conversion of iron oxides in the reactor, incomplete separation of water from the residual gaseous stream in the condenser, and a higher hydrogen equivalence ratio than thermodynamically required. In contrast, in the idealized process, full conversion is achieved ($X = 1$), complete separation of water out of the recycle stream, and the minimal possible hydrogen equivalence ratio are assumed. The minimal hydrogen equivalence ratio $\lambda_{H_2} = 2.6$ is obtained using chemical equilibrium calculation for the idealized system under the corresponding conditions ($t = 1300\,^{\circ}\mathrm{C}, \omega_{H2} = 57\,\%$, $\omega_{H2O} = 43\,\%$). These idealizations result in different mass flow rates and compositions. To ensure a fair comparison, the overall main product of the process is kept constant, corresponding in this case to the chemical exergy in stream 5 leaving the system ($\dot{E}_{ch,5} = 196.4\,\mathrm{MW}$). Due to the full conversion and the corresponding higher specific chemical exergy of the product, the material flow is reduced to meet the same main product for both the idealized and real processes. To determine the endogenous exergy destruction within the air heater, we assume that the upstream air fan is operating isentropically and adjust the pressure accordingly, as pressure drops downstream should not be attributed to the air heater. The inlet of the hot stream is determined by the idealized reactor ($X = 1$), while the approach temperature is adjusted to achieve the same exergetic efficiency as in the base case design. Similarly, the endogenous exergy destruction of the other heat exchangers are determined by using the streams of the idealized system and adjusting the approach temperature to achieve the same exergetic efficiency as in the base case design. For the reaction section and the combustor, the hydrogen equivalence ratio and the associated heat losses are adjusted to meet the same exergetic efficiency between the base case design and the idealized system in conjunction with the component, respectively. Since the reactor operates at atmospheric pressure, the pressure levels generated by the turbo-machinery are not required for the overall process and are associated with pressure drops in other components. Therefore, the entire exergy destruction within the turbo machinery is exogenous. The specifications for the calculation of endogenous exergy destruction and the resulting streams are given in Appendix B.

The results are derived using EBSILON® *Professional* [30] applying the thermodynamic data given in [28] and user defined routines for the calculation of physical and chemical exergies. The reference temperature and pressure is set to $T_0 = 298.15\,\mathrm{K}$ and $p_0 = 1.013\,\mathrm{bar}$, respectively.

4. Results and Discussion

The energetic system efficiency of the base case design was determined to be $\eta_{tot} = 61.7\,\%$ based on a conventional mass and energy-based analysis (not explicitly shown here). The energetic analysis identified the electrolyzer as the component with the highest losses, followed by the residual energy of the material streams leaving the system, and the heat losses of the combustor and heat exchangers. To get an impression of the achievable energetic system efficiency, the process was parameterized according to the assumed unavoidable technological constraints given in Table 2. This resulted in an energetic system efficiency of $\eta_{tot} = 68.5\,\%$, a significant improvement potential from the base case design.

Based on the conventional exergy analysis presented in Table 3, the exergetic system efficiency of $\epsilon_{tot} = 53.7\,\%$ indicates significant inefficiencies within the process. The electrolyzer is responsible for the largest exergy de-

Table 1: Definition of fuel and product according to [29] for each component given in Fig. 1

Component	**Fuel $\dot{E}_F$**	**Product $\dot{E}_P$**
Electrolyzer	$P_{el} + \dot{E}_{15,ch} - (\dot{E}_{16,ph} + \dot{E}_{17,ph} - \dot{E}_{15,ph})$	$\dot{E}_{16,ch} + \dot{E}_{17,ch}$
Mixer 1	NA	NA
Hydrogen Preaheater	$\dot{E}_{6,ph} - \dot{E}_{7,ph}$	$\dot{E}_{11,ph} - \dot{E}_{10,ph}$
Combustor	$\dot{E}_{11,ch} + \dot{E}_{23,ch} - \dot{E}_{12,ch}$	$\dot{E}_{12,ph} - \dot{E}_{11,ph} - \dot{E}_{13,ph}$
Mixer 2	$\dot{m}_{12}(e_{12,ph} - e_{13,ph}) + (\dot{E}_{2,ch} + \dot{E}_{12,ch} - \dot{E}_{13,ch})$	$\dot{m}_2(e_{13,ph} - e_{2,ph})$
Flash Reactor	$\dot{E}_{13,ch} + \dot{E}_{13,ph} - \dot{E}_{3,ph}$	$\dot{E}_{3,ch}$
Cyclone	NA	NA
Air Heater	$\dot{E}_{4,ph} - \dot{E}_{5,ph}$	$\dot{E}_{20,ph} - \dot{E}_{19,ph}$
Air Fan	P_{el}	$\dot{E}_{19,ph} - \dot{E}_{18,ph}$
Iron Oxide Preheater	$\dot{E}_{20,ph} - \dot{E}_{21,ph}$	$\dot{E}_{2,ph} - \dot{E}_{1,ph}$
Condensate Pump	P_{el}	$\dot{E}_{15,ph} - \dot{E}_{14,ph}$
Cooling Water Pump	P_{el}	$\dot{E}_{25,ph} - \dot{E}_{24,ph}$
Recycle Compressor	P_{el}	$\dot{E}_{9,ph} - \dot{E}_{8,ph}$
Condenser	$\dot{E}_{7,ch} + (\dot{E}_{7,ph} - \dot{E}_{14,ph} - \dot{E}_{8,ph}) - (\dot{E}_{26,ph} - \dot{E}_{25,ph})$	$\dot{E}_{8,ch} + \dot{E}_{14,ch}$
Overall System	$\sum_k P_{el,k} + \dot{E}_{1,tot} + \dot{E}_{18,tot} + \dot{E}_{24,tot}$	$\dot{E}_{5,ch}$

Table 2: Technological assumptions for determination of avoidable and unavoidable exergy destruction

Component	**Parameter**	**Base Case**	**Unavoidable Inefficiency**
Pumps	Isentropic efficiency η_{is}	75 %	85 %
Compressors	Isentropic efficiency η_{is}	80 %	90 %
Condenser	Approach temp. ΔT	10 K	1 K
Heat exchangers	Approach temp. ΔT	50 K	3 K
Heat exchangers	Relative heat loss $Q_{rel,L}$	2.5 %	1 %
Electrolyzer	System efficiency η_{LHV}	70 %	74 %
Electric motors	Efficiency η	90 %	95 %

struction, followed by the condenser, hydrogen preheater, reactor, combustor, and the other heat exchangers. Figure 2 illustrates the exergy destruction ratios of all components, starting from the overall process fuel, in descending order leading to the defined product of the process. The analysis reveals that the turbo-machinery and the cyclone only cause insignificant exergy destruction. The exergy losses associated with streams leaving the system result in an exergy loss ratio of y_L = 1 %, with the chemical exergy of the oxygen leaving the system having the highest share. In contrast to the energetic analysis, which pointed to the material streams leaving the system, the exergy analysis quantifies the low quality of the energy within these streams due to the low associated temperatures. The exergetic efficiencies of the different components are mostly high, with the exception of the flash reactor, which suffers from the high inherent irreversibilities associated with the reduction reaction. Interestingly, the exergetic efficiency of the combustor is comparatively high, which is due to the partial oxidation and the high temperature of stream 11 entering the combustor.

Based on the analysis of unavoidable and avoidable exergy destruction, it is concluded that the total unavoidable and avoidable exergy destruction account for 82.2 % ($\dot{E}^{UN}_{D,tot}$ = 136.1 MW) and 17.8 % ($\dot{E}^{AV}_{D,tot}$ = 29.4 MW) of the exergy destruction, respectively. After factoring in the unavoidable exergy destruction, a modified exergetic efficiency of 85.8 % can be determined for the base case (cf. Table 3). The highest unavoidable exergy destruction is associated with the electrolyzer, the condenser, the flash reactor and the combustor, while the highest avoidable exergy destruction is related to the elctrolyzer, the hydrogen preaheater, the combustor and the iron oxide preheater. The share between endogenous and exogenous exergy destruction is even more one-sided, with endogenous exergy destruction accounting for 89.4 % and exogenous exergy destruction for 10.6 % of the total exergy destruction. These findings suggest that a large share of the exergy destruction is unavoidable. However, the assessments point out that improving individual components should have a higher priority over structural improvements.

When combining the two exergy splitting approaches, the total share of avoidable endogenous and avoidable exogenous exergy destruction in relation to the total avoidable exergy destruction is 87.1 % and 12.9 %, respectively. The electrolyzer, hydrogen preheater, and the combustor exhibit the highest potential for reducing endogenous avoidable exergy destruction. This highlights the potential for improvement through technological

Table 3: Results of conventional and advanced exergy analysis

Component	Conventional Exergy Analysis						Advanced Exergy Analysis				
	$\dot{E}_F$ [MW]	$\dot{E}_P$ [MW]	$\dot{E}_D$ [MW]	$\dot{E}_L$ [MW]	ϵ [-]	y_D [-]	$\dot{E}_{D,k}^{UN,EN}$ [MW]	$\dot{E}_{D,k}^{UN,EX}$ [MW]	$\dot{E}_{D,k}^{AV,EN}$ [MW]	$\dot{E}_{D,k}^{AV,EX}$ [MW]	$\epsilon_k^{AV,EN}$ [-]
Electrolyzer	358.2	248.0	110.2	0.0	0.69	0.30	87.0	4.0	18.5	0.8	0.93
Condenser	460.7	449.0	11.7	0.0	0.97	0.0	7.8	3.5	0.2	0.1	1.00
Hydrogen Preheater	67.7	57.2	10.5	0.0	0.84	0.03	5.6	1.9	2.3	0.7	0.96
Flash Reactor	14.9	4.5	10.4	0.0	0.30	0.03	9.6	0.4	0.4	0.0	0.92
Combustor	53.4	43.2	10.2	0.0	0.81	0.03	5.5	2.0	2.0	0.7	0.96
Air Preheater	17.6	12.7	4.9	0.0	0.72	0.01	3.5	0.6	0.6	0.1	0.95
Iron Oxide Preheater	13.0	10.5	2.6	0.0	0.80	0.01	1.0	0.2	1.1	0.2	0.90
Mixer 2	80.9	78.3	2.6	0.0	0.97	0.01	1.8	0.4	0.4	0.1	1.00
Recycle Compressor	4.8	3.6	1.2	0.0	0.75	0.00	0.0	0.5	0.0	0.7	1.00
Cyclone	741.5	740.7	0.8	0.0	0.00	0.0	0.5	0.1	0.1	0.0	0.00
Air Fan	1.5	1.1	0.4	0.0	0.74	0.00	0.0	0.2	0.0	0.2	1.00
Mixer 1	0.0	0.0	0.0	0.0	0.00	0.00	0.0	0.0	0.0	0.0	0.00
Cooling Water Pump	0.0	0.0	0.0	0.0	0.67	0.00	0.0	0.0	0.0	0.0	1.00
Condensate Pump	0.0	0.0	0.0	0.0	0.68	0.00	0.0	0.0	0.0	0.0	1.00
Total	365.3	196.6	165.5	3.5	0.54	0.45	122.4	13.7	25.6	3.8	0.86*

*) Exergetic system efficiency adjusted by the unavoidable parts: $\epsilon_{tot}^{AV} = \frac{\dot{E}_{P,tot}}{\dot{E}_{F,tot} - \dot{E}_{D,tot}^{UN}}$

advances in water-electrolysis, heat recovery measures, and the importance of proper reactor design and operation, including internal combustion.

The exergy-based evaluations presented here demonstrate the potential for enhancement of the analyzed flash ironmaking process. While technological advancements in water-electrolysis and lower approach temperatures lead to obvious improvements in overall performance, it is evident that there is still potential for improvement of the flash reactor (sequence of combustor, mixer 2, and reaction section). The attained conversion and reaction conditions (reaction temperature, hydrogen equivalence ratio) result in exergy destruction upstream and downstream of the reactor, which could be reduced. However, it should be noted that although these assessments are thermodynamically correct, economic considerations remain the driving force in real-world process synthesis.

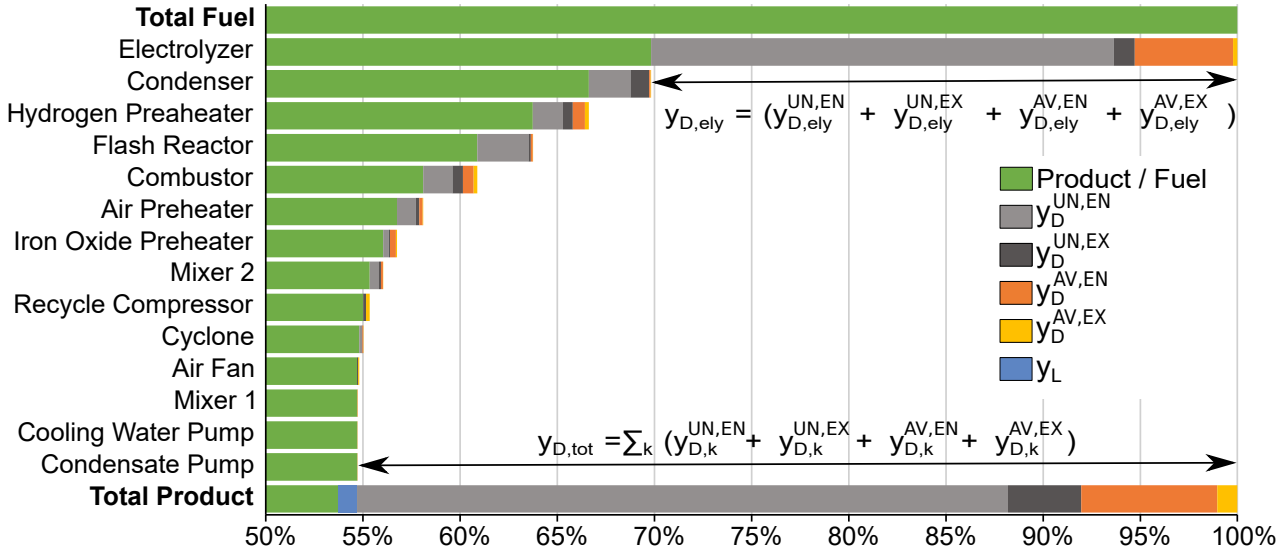

Figure 2: Waterfall diagram to visualize the results of the conventional and advanced exergy analysis

5. Conclusion

The present study focuses on the thermodynamic assessment of flash ironmaking, a promising method for sustainable iron oxide reduction using green hydrogen. To this end, conventional energy and exergy analyses, as well as an advanced exergy analysis, are conducted. A defined based case is used to determine an energetic efficiency of 61.7 % and an exergetic efficiency of 53.7 % for a given parameterization. For a scenario with foreseeable best case technological constraints, an energetic efficiency of 68.5 % and an exergetic efficiency of 59.7 % can be determined.

The informative value of the employed methods can be demonstrated by the assessment of the condenser, which separates the undesired water out of the recycle stream. While the energetic analysis points to the high energy content of the cooling water leaving the condenser, the exergetic analysis indicates significantly lower potential, which is further deemed as mainly unavoidable exergy destruction by the advanced exergy analysis. The overall potential for improvement of the plant is found to be moderate, mainly due to the high unavoidable exergy destruction (i.e. 82.2 % of the total exergy destruction), and the improvement potential is primarily associated with the internal operational conditions of the components. The highest avoidable exergy destruction is observed in the electrolyzer, the hydrogen preheater, and the combustor, which is also endogenous.
The findings of these analyses confirm that the flash ironmaking process is a promising alternative to the conventional shaft furnace process, particularly in the context of a circular energy-iron economy, given its dispensation of the requirement for pre- and post-treatment of iron oxides (required for the shaft furnace process), low energy consumption, and high-intensity. The performed assessments provide insights into the sources of irreversibility and estimate the potential for improvement in this energy-intensive process. However, for a more comprehensive assessment, it is crucial to consider economic factors in the synthesis of the analyzed flash ironmaking process. In addition to reliable techno-economic models, this requires a comprehensive reactor model that takes reaction kinetics and transport phenomena into account.

Acknowledgments

The funding of the cluster project Clean Circles by the Hessian Ministry of Higher Education, Research, Science and the Arts is gratefully acknowledged.

Appendix A Base Case Design

Table 4: Thermodynamic data for the base case design of the flash ironmaking process. Only selected mass fractions are shown. Missing fraction are obvious from the flow sheet (e.g. liquid water stream: $\omega_{H_2O(l)} = 1$).

Stream	$\dot{m}$	p	t	e_{tot}	e_{ph}	e_{ch}	Mass Fractions ω_i				
	[kg/s]	[bar]	[°C]	[kJ/kg]	[kJ/kg]	[kJ/kg]	Fe_2O_3	Fe	$Fe_{0.947}O$	H_2	H_2O(g)
S1	48.0	1.01	25.0	0.0	0.0	0.0	1.00	0.00	0.00	0.00	0.00
S2	48.0	1.01	584.2	218.2	218.2	0.0	1.00	0.00	0.00	0.00	0.00
S3	59.4	1.01	1190.3	12490.9	1599.5	10891.5	0.00	0.49	0.10	0.06	0.35
S4	35.0	1.01	1190.3	6120.7	508.5	5612.1	0.00	0.83	0.17	0.00	0.00
S5	35.0	1.01	106.7	5617.0	4.9	5612.1	0.00	0.83	0.17	0.00	0.00
S6	24.4	0.91	1190.3	21610.0	3134.6	18475.4	0.00	0.00	0.00	0.16	0.84
S7	24.4	0.76	258.9	18830.8	355.4	18475.4	0.00	0.00	0.00	0.16	0.84
S8	5.7	0.61	25.0	78687.2	-433.1	79120.2	0.00	0.00	0.00	0.67	0.33
S9	5.7	1.16	99.4	79327.7	207.5	79120.2	0.00	0.00	0.00	0.67	0.33
S10	7.8	1.16	86.0	89667.0	196.3	89470.6	0.00	0.00	0.00	0.76	0.24
S11	7.8	1.01	1115.5	97029.7	7559.1	89470.6	0.00	0.00	0.00	0.76	0.24
S12	11.4	1.01	1598.8	65343.9	8957.2	56386.7	0.00	0.00	0.00	0.48	0.52
S13	59.4	1.01	1300.0	12666.8	1851.2	10815.6	0.81	0.00	0.00	0.09	0.10
S14	18.7	0.61	25.0	0.0	0.0	0.0	0.00	0.00	0.00	0.00	0.00
S15	18.7	1.16	25.0	0.0	0.0	0.0	0.00	0.00	0.00	0.00	0.00
S16	2.1	1.16	60.0	117722.0	196.9	117525.1	0.00	0.00	0.00	1.00	0.00
S17	16.6	1.16	60.0	134.6	12.4	122.1	0.00	0.00	0.00	0.00	0.00
S18	40.8	1.01	25.0	0.0	0.0	0.0	0.00	0.00	0.00	0.00	0.01
S19	40.8	1.35	56.7	26.3	26.3	0.0	0.00	0.00	0.00	0.00	0.01
S20	40.8	1.20	666.1	338.4	338.3	0.0	0.00	0.00	0.00	0.00	0.01
S21	40.8	1.05	130.3	18.5	18.5	0.0	0.00	0.00	0.00	0.00	0.01
S22	3.6	1.16	60.0	134.6	12.4	122.1	0.00	0.00	0.00	0.00	0.00
S23	13.0	1.16	60.0	134.6	12.4	122.1	0.00	0.00	0.00	0.00	0.00
S24	648.1	1.01	15.0	0.7	0.7	0.0	0.00	0.00	0.00	0.00	0.00
S25	648.1	1.20	15.0	0.7	0.7	0.0	0.00	0.00	0.00	0.00	0.00
S26	648.1	1.05	40.0	1.5	1.5	0.0	0.00	0.00	0.00	0.00	0.00

P_{Ely} = 358.82 MW, P_{AF} = 1.46 MW, P_{CWP} = 0.02 MW, P_{RC} = 4.83 MW, P_{CP} = 0.0 MW

Appendix B Calculation of Endogenous Exergy Destruction

Table 5: Thermodynamic data used for the calculation of endogenous exergy destruction. Only selected mass fractions are shown. Missing fraction are obvious from the flow sheet (e.g. liquid water stream: $\omega_{H_2O(l)} = 1$).

Stream	$\dot{m}$	p	t	e_{tot}	e_{ph}	e_{ch}	Mass Fractions ω_I				
	[kg/s]	[bar]	[°C]	[kJ/kg]	[kJ/kg]	[kJ/kg]	Fe_2O_3	Fe	$Fe_{0.947}O$	H_2	H_2O(g)
Air heater (AH): $\epsilon_{AH} = 72.2\,\%$, $T'_{19} = f(p'_{19}, \eta_{is,AF} = 1)$, $p'_{19} = p_0 + \Delta p_{AH}$, $T'_{20} = f(\epsilon_{AH})$, $T'_5 = f(\epsilon_{AH})$											
S4	30.46	1.013	1175.5	6937.1	489.6	6447.4	0.00	1.00	0.00	0.00	0.00
S5	30.46	1.013	49.7	6447.9	0.4	6447.4	0.00	1.00	0.00	0.00	0.00
S19	37.02	1.163	36.9	12.1	12.1	0.0	0.00	0.00	0.00	0.00	0.01
S20	37.02	1.013	623.1	290.8	290.8	0.0	0.00	0.00	0.00	0.00	0.01
Iron oxide preheater (IOPH): $\epsilon_{IOPH} = 80.3\,\%$, T'_{20}, $p'_{20} = p_0 + \Delta p_{IOPH}$, $T'_2 = f(\epsilon_{IOPH})$, $T'_{21} = f(\epsilon_{IOPH})$											
S1	43.55	1.01	25.0	0.0	0.0	0.0	1.00	0.00	0.00	0.00	0.00
S2	43.55	1.01	560.6	202.7	202.7	0.0	1.00	0.00	0.00	0.00	0.00
S20	37.02	1.16	641.0	316.3	316.3	0.0	0.00	0.00	0.00	0.00	0.01
S21	37.02	1.01	144.1	19.3	19.2	0.0	0.00	0.00	0.00	0.00	0.01
Combustor (Comb): $\epsilon_{IOPH} = 80.9\,\%$, $e'_{11} = f(\lambda)$, $e'_{12} = f(X, \lambda, T'_{12})$, $m'_{22} = f(\lambda)$, $m'_{11} = f(\lambda)$, $T'_{12} = f(\epsilon_{Comb})$											
S11	4.63	1.01	1171.2	127713.5	10188.4	117525.1	0.00	0.00	0.00	1.00	0.00
S12	7.30	1.01	1644.2	79993.5	10821.7	69171.8	0.00	0.00	0.00	0.59	0.41
S22	2.67	1.01	60.0	123.9	1.7	122.1	0.00	0.00	0.00	0.00	0.00
Flash Reactor (FR): $\epsilon_{FR} = 30.2\,\%$, $\lambda = f(\epsilon_{FR})$, $e'_{13} = f(\lambda)$, $e'_3 = f(\lambda)$											
S3	54.77	1.01	1154.6	9356.1	1270.4	8085.7	0.00	0.53	0.11	0.04	0.32
S13	54.77	1.01	1300.0	9539.2	1533.2	8006.0	0.88	0.00	0.00	0.07	0.06
Cyclone (Cyc): $\epsilon_{Cyc} = NA$, $m'_3 = f(X, \lambda)$, $T'_3 = T'_4 = T'_5$											
S3	51.43	1.01	1175.2	11332.5	1460.8	9871.7	0.00	0.59	0.00	0.05	0.36
S4	30.47	1.01	1175.2	6936.9	489.5	6447.4	0.00	1.00	0.00	0.00	0.00
S6	20.96	0.91	1175.2	17691.5	2843.8	14847.7	0.00	0.00	0.00	0.13	0.87
Hydrogen Preaheater (HPH): $\epsilon_{HPH} = 84.5\,\%$, T'_6, T'_7, $p_{10} = p_0 + \Delta p_{HPH}$, $p_6 = p_0$, $T'_7 = f(\epsilon_{HPH})$, $T'_{11} = f(\epsilon_{HPH})$											
S6	20.77	1.01	1173.3	17859.1	2875.0	14984.1	0.00	0.00	0.00	0.13	0.87
S7	20.77	0.86	272.3	15409.4	425.3	14984.1	0.00	0.00	0.00	0.13	0.87
S10	4.67	1.16	55.3	117715.3	190.2	117525.1	0.00	0.00	0.00	1.00	0.00
S11	4.67	1.01	1107.9	126920.9	9395.8	117525.1	0.00	0.00	0.00	1.00	0.00
Condenser (Cond): $\epsilon_{Cond} = 97.5\,\%$, $T'_8 = T'_{14} = f(p'_8, \epsilon_{cond})$, $p'_7 = p_0$, $p'_8 = p_0 - \Delta p_{Cond}$											
S7	20.79	1.01	189.6	15319.2	349.9	14969.2	0.00	0.00	0.00	0.13	0.87
S8	3.12	0.91	16.0	99402.9	-108.9	99511.8	0.00	0.00	0.00	0.85	0.15
S14	17.68	0.91	16.0	0.6	0.6	0.0	0.00	0.00	0.00	0.00	0.00
S25	536.83	1.20	15.0	0.7	0.7	0.0	0.00	0.00	0.00	0.00	0.00
S26	536.83	1.10	40.0	1.5	1.5	0.0	0.00	0.00	0.00	0.00	0.00
Electrolysis (Ely): $\epsilon_{Ely} = 69.2\,\%$, $P_{Ely} = 342.5\,\text{MW}$, T'_{15}, $m'_{15} = f(X)$											
S15	17.87	1.01	16.0	0.6	0.6	0.0	0.00	0.00	0.00	0.00	0.00
S16	2.00	1.01	60.0	117552.1	27.1	117525.1	0.00	0.00	0.00	1.00	0.00
S17	15.87	1.01	60.0	123.9	1.7	122.1	0.00	0.00	0.00	0.00	0.00
Mixer 2 (Mix2): $\epsilon_{Mix2} = 96.8\,\%$, $m_{12} = f(\lambda)$, $e'_{12} = f(\lambda)$, T'_2											
S2	43.56	1.01	618.3	241.8	241.8	0.0	1.00	0.00	0.00	0.00	0.00
S12	7.31	1.01	1639.1	81332.6	10918.9	70413.7	0.00	0.00	0.00	0.60	0.40
S13	50.86	1.01	1300.0	11849.3	1733.8	10115.5	0.86	0.00	0.00	0.09	0.06

Nomenclature

e	specific exergy, $\mathrm{J\,kg^{-1}}$
$\dot{E}$	time rate of exergy transfer, $\mathrm{J\,s^{-1}}$
h	specific enthalpy, $\mathrm{J\,kg^{-1}}$
HV	heating value, $\mathrm{J\,kg^{-1}}$
$\dot{m}$	mass flow rate, $\mathrm{kg\,s^{-1}}$
N	molar amount, mol
P	electrical/mechanical power, $\mathrm{J\,s^{-1}}$
R	specific gas constant, $\mathrm{J\,kg^{-1}\,K^{-1}}$
s	specific entropy, $\mathrm{J\,kg^{-1}\,K^{-1}}$
t	temperature, ℃
T	temperature, K
x	mole fraction
X	reduction degree
y	exergy destruction/loss ratio

Greek symbols

Δ	difference
ϵ	exergetic efficiency
η	efficiency
λ	hydrogen equivalence ratio
ω	mass fraction

Subscripts and superscripts

AV	avoidable
ch	chemical
D	destruction
el	electrical
EN	endogenous
EX	exogenous
Fe	iron
F	fuel
is	isentropic
L	loss
O	oxygen
ph	physical
P	product
Q	heat
rel	relative
tot	total
UN	unavoidable
0	standard, reference

References

[1] Pörtner, H.-O., D.C. Roberts, H. Adams, I. Adelekan, C. Adler, R. Adrian, P. Aldunce, E. Ali, R. Ara Begum, B. Bednar-. *IPCC, 2022: Summary for Policymakers*. 2022. URL: https://www.ipcc.ch/report/ar6/wg2/downloads/report/IPCC_AR6_WGII_SummaryForPolicymakers.pdf (visited on Feb. 24, 2023).

[2] IEA. *World Energy Outlook 2022*. URL: https://iea.blob.core.windows.net/assets/830fe099-5530-48f2-a7c1-11f35d510983/WorldEnergyOutlook2022.pdf (visited on Feb. 24, 2023).

[3] IEA. *The role of low-carbon fuels in the clean energy transitions of the power sector*. 2022. URL: https://iea.blob.core.windows.net/assets/01ca16c8-e493-475c-81c4-04ac5d3b9882/Theroleoflowcarbonfuelsinthecleanenergytransitionsofthepowersector.pdf (visited on Feb. 24, 2023).

[4] Bergthorson J. M. *Recyclable metal fuels for clean and compact zero-carbon power*. In: Progress in Energy and Combustion Science 68 (2018), pp. 169–196. DOI: 10.1016/j.pecs.2018.05.001.

[5] Debiagi P. et al. *Iron as a sustainable chemical carrier of renewable energy: Analysis of opportunities and challenges for retrofitting coal-fired power plants*. In: Renewable and Sustainable Energy Reviews 165 (2022), p. 112579. ISSN: 13640321. DOI: 10.1016/j.rser.2022.112579.

[6] Kuhn C. et al. *Iron as recyclable energy carrier: Feasibility study and kinetic analysis of iron oxide reduction*. In: Applications in Energy and Combustion Science 12 (2022), p. 100096. ISSN: 2666352X. DOI: 10.1016/j.jaecs.2022.100096.

[7] Neumann, J. and da Rocha, R. C. et al. *Techno-economic assessment of long-distance supply chains of energy carriers: Comparing hydrogen and iron for carbon-free electricity generation*. In: Applications in Energy and Combustion Science 14 (2023), p. 100128. DOI: 10.1016/j.jaecs.2023.100128.

[8] Janicka J. et al. *The potential of retrofitting existing coal power plants: a case study for operation with green iron*. In: Applied Energy (2023). DOI: 10.1016/j.apenergy.2023.120950.

[9] IEA. *Global crude steel production by process route and scenario, 2019-2050 – Charts – Data & Statistics - IEA*. 2019. URL: https://www.iea.org/data-and-statistics/charts/global-crude-steel-production-by-process-route-and-scenario-2019-2050 (visited on Feb. 9, 2023).

[10] Suer J. et al. *Carbon Footprint and Energy Transformation Analysis of Steel Produced via a Direct Reduction Plant with an Integrated Electric Melting Unit*. In: Journal of Sustainable Metallurgy 8.4 (2022), pp. 1532–1545. ISSN: 2199-3823. DOI: 10.1007/s40831-022-00585-x.

[11] Wiinikka H. et al. *Combustion Evaluation of Renewable Fuels for Iron-Ore Pellet Induration*. In: Energy & Fuels 33.8 (2019), pp. 7819–7829. ISSN: 0887-0624. DOI: 10.1021/acs.energyfuels.9b01356.

[12] Sohn H. Y., Fan D.-Q., and Abdelghany A. *Design of Novel Flash Ironmaking Reactors for Greatly Reduced Energy Consumption and CO2 Emissions*. In: Metals 11.2 (2021), p. 332. DOI: 10.3390/met11020332.

[13] Sohn H. Y., Elzohiery M., and Fan D.-Q. *Development of the Flash Ironmaking Technology (FIT) for Green Ironmaking with Low Energy Consumption*. In: Journal of Energy and Power Technology 03.03 (2021), p. 1. ISSN: 26901692. DOI: 10.21926/jept.2103042.

[14] Wang X. et al. *Numerical simulation of effect of operating conditions on flash reduction behaviour of magnetite under H2 atmosphere*. In: International Journal of Hydrogen Energy 44.48 (2019), pp. 26261–26270. ISSN: 03603199. DOI: 10.1016/j.ijhydene.2019.08.089.

[15] Kotas T. J. *The exergy method of thermal plant analysis*. Butterworths, 1985. ISBN: 9780408013505.

[16] Bejan A., Tsatsaronis G., and Moran M. J. *Thermal design and optimization*. New York and Chichester: John Wiley, 1996. ISBN: 0471584673.

[17] Tsatsaronis G. *Thermoeconomic Analysis and Optimization of Energy Systems*. In: Progress in Energy and Combustion Science 19 (1993), pp. 227–257. DOI: 10.1016/0360-1285(93)90016-8.

[18] Ahrendts J. *Reference states*. In: Energy 5.8-9 (1980), pp. 666–677. ISSN: 0360-5442. DOI: 10.1016/0360-5442(80)90087-0.

[19] Jan Szargut. *Towards an International Reference Environment of Chemical Exergy*. In: (2005). URL: https://www.exergoecology.com/exergoecology/szargut2005 (visited on June 21, 2021).

[20] Tsatsaronis G. and Morosuk T. *Understanding and improving energy conversion systems with the aid of exergy-based methods*. In: International Journal of Exergy 11.4 (2012), p. 518. ISSN: 1742-8297. DOI: 10.1504/IJEX.2012.050261.

[21] Morosuk T. and Tsatsaronis G. *Advanced exergy-based methods used to understand and improve energy-conversion systems*. In: Energy 169 (2019), pp. 238–246. ISSN: 0360-5442. DOI: 10.1016/j.energy.2018.11.123.

[22] Tsatsaronis G. et al. *Understanding the thermodynamic inefficiencies in combustion processes*. In: Energy 62 (2013), pp. 3–11. ISSN: 0360-5442. DOI: 10.1016/j.energy.2013.04.075.

[23] Tsatsaronis G. *Recent developments in exergy analysis and exergoeconomics*. In: International Journal of Exergy 5.5/6 (2008), p. 489. ISSN: 1742-8297. DOI: 10.1504/IJEX.2008.020822.

[24] Kelly S., Tsatsaronis G., and Morosuk T. *Advanced exergetic analysis: Approaches for splitting the exergy destruction into endogenous and exogenous parts*. In: Energy 34.3 (2009), pp. 384–391. ISSN: 0360-5442. DOI: 10.1016/j.energy.2008.12.007.

[25] Penkuhn M. and Tsatsaronis G. *A decomposition method for the evaluation of component interactions in energy conversion systems for application to advanced exergy-based analyses*. In: Energy 133 (2017), pp. 388–403. ISSN: 0360-5442. DOI: 10.1016/j.energy.2017.03.144.

[26] Penkuhn M. and Tsatsaronis G. *Comparison of different ammonia synthesis loop configurations with the aid of advanced exergy analysis*. In: Energy 137 (2017), pp. 854–864. ISSN: 0360-5442. DOI: 10.1016/j.energy.2017.02.175.

[27] Spreitzer D. and Schenk J. *Reduction of Iron Oxides with Hydrogen—A Review*. In: steel research international 90.10 (2019), p. 1900108. ISSN: 1611-3683. DOI: 10.1002/srin.201900108.

[28] McBride B. J., Zehe M. J., and Gordon S. *NASA Glenn Coefficients for Calculating Thermodynamic Properties of Individual Species*. 2002. URL: https://ntrs.nasa.gov/citations/20020085330 (visited on Feb. 22, 2022).

[29] Lazzaretto A. and Tsatsaronis G. *SPECO: A systematic and general methodology for calculating efficiencies and costs in thermal systems*. In: Energy 31.8-9 (2006), pp. 1257–1289. ISSN: 0360-5442. DOI: 10.1016/j.energy.2005.03.011.

[30] Iqony GmbH. *EBSILON Professional*. URL: https://www.ebsilon.com/en/ (visited on Mar. 14, 2023).

PROCEEDINGS OF ECOS 2023 - THE 36TH INTERNATIONAL CONFERENCE ON
EFFICIENCY, **C**OST, **O**PTIMIZATION, **S**IMULATION AND ENVIRONMENTAL IMPACT OF ENERGY SYSTEMS
25-30 JUNE 2023, LAS PALMAS DE GRAN CANARIA, SPAIN

Exergoeconomic analysis of a system for liquefaction and purification of captured CO_2

Rikke C. Pedersen [a], Torben Ommen [b], Erasmus Rothuizen [c], Brian Elmegaard [d] and Jonas K. Jensen [e]

[a] Technical University of Denmark, Dept. of Civil & Mechanical Engineering, Kgs. Lyngby, DK, rikpe@dtu.dk, CA
[b] Sensible Energy A/S, Ballerup, DK, tso@sensibleenergy.dk
[c] Sensible Energy A/S, Ballerup, DK, edr@sensibleenergy.dk
[d] Technical University of Denmark, Dept. of Civil & Mechanical Engineering, Kgs. Lyngby, DK, brel@dtu.dk
[e] Technical University of Denmark, Dept. of Civil & Mechanical Engineering, Kgs. Lyngby, DK, jkjje@dtu.dk

Abstract:

The most severe reason for global warming is the release of anthropogenic CO_2 emissions to the atmosphere. One way to mitigate these emissions is to capture CO_2 directly at an emitting source using carbon capture technologies. An important process in the carbon capture value chain is to condition the captured CO_2 to the following transportation. In this study, a system for liquefaction and purification of CO_2 is of focus and an exergoeconomic analysis is made. In the system, CO_2 is compressed through two-stage compression with intercooling, while water condensate is removed. The liquefaction is performed using an external two-stage refrigeration cycle. The compressors were found to be the greatest source of exergy destruction and were the greatest cost contributors. An overall exergy efficiency of 39 % was found and it was seen that 13 % of the fuel supplied was lost in external coolers. To improve the system and utilise the exergy loss, two configurations for district heat integration were investigated. It was found to increase the exergy efficiency to 45 % and 50 %, respectively, depending on the configuration. Integration of district heating in the intercoolers could be made without additional costs for the system. A cost increase of the overall system of 11 % was seen when the heat discharged in the refrigeration cycle was also utilised for district heat production. This shows that there is a potential for utilising the waste heat from the system and adding revenue from district heat sales.

Keywords:

CO_2 liquefaction and purification; CO_2 conditioning; District heat integration; Exergoeconomic analysis; Thermoeconomic analysis.

1. Introduction

In 2016, anthropogenic CO_2 emissions accounted for 75 % of the total greenhouse gas emissions in the world [1]. Some of the sectors responsible for the majority of the CO_2 emissions are the electricity and heating sector and the manufacturing and construction sector accounting for 41 % and 17 %, respectively. Carbon capture technologies are expected to play an important role in reducing emissions from these sectors, as the technology allows for continuous utilisation of existing fossil-based facilities and can provide deep emission reductions that are difficult to mitigate with technological advances (e.g. for production of iron, steel, cement, and various chemicals) [2]. Furthermore, the technology can be used to achieve negative emissions by capturing and storing CO_2 from biogenic sources. A capture capacity of 7.6 Gt CO_2 per year is expected in 2050 [3], of which only 0.5 % was realised in 2021 [4]. This indicates that all process steps of the carbon capture value chain must be scaled up and become more cost-effective to reach the required capacity. The focus of this study is the liquefaction and purification process, which ensures that captured CO_2 is conditioned to the correct state and quality before transport. The process is highlighted in the carbon capture value chain in Fig. 1. The conditioning process accounts for between 20 % and 70 % of the costs when also considering the following transportation [5, 6, 7]. Therefore, an improvement of this process step can potentially have a significant influence on the overall costs.

The captured CO_2 is typically in a gaseous state after separation. To reduce the cost of transportation, the density can be increased. This can be achieved in the conditioning process by increasing the pressure or decreasing the temperature of CO_2. In the food and beverage industry today, CO_2 is transported in a liquid state at 15 bar and –30 °C [8]. Furthermore, impurities such as water, volatiles, and incondensable gasses could be removed before transportation [9].

Several studies have compared different layouts of the liquefaction and purification system on energy [10, 11]

Figure 1: Position of the liquefaction and purification process in the carbon capture value chain.

and economic [12, 13] performance parameters when different requirements for the end-state of CO_2 exist. At a delivery pressure of 15 bar, a system with an external refrigeration cycle generally shows the best performance. The effects of impurities and final quality requirement are investigated by Deng et al. [8], they find that the process costs increase when impurities in the source increase at lower delivery pressures. Aspelund and Jordal [9] investigate the effects of impurities and pressure level of the CO_2 feed gas. They find that a decrease in the inlet pressure and an increase in impurities increase power consumption. Energy, exergy, and economic analyses have been performed on different layouts of a CO_2 liquefaction system by Chen and Morosuk [14], showing that the majority of the exergy destruction ($>$80 %) occurs in coolers and compressors and that it is equally distributed between these two types of components. The highest exergy efficiency of 67 % was found for a system with an external refrigeration cycle. An exergoeconomic analysis was made on a liquefaction system using an absorption refrigeration cycle by Aliyon et al. [15] having an exergy efficiency of 86 % with heat exchangers showing the highest cost improvement potential. Exergy analyses have also been performed on liquefaction systems by Muhammad et al. [16, 17] resulting in total exergy efficiencies of 68 % and 56 %, respectively. It is seen that the highest exergy destruction occurs during compression of the captured CO_2 and that potential for utilisation of heat from intercooling exists. It is of interest to determine where cost inefficiencies exist in a liquefaction system using an external refrigeration cycle to deliver purified liquid CO_2 at 15 bar, and whether it is possible to recover heat through the integration of district heat (DH) production. Therefore, an exergoeconomic analysis of a liquefaction and purification system was made in the present study. It was investigated which components were of most importance for the overall costs of the system and whether thermodynamic inefficiencies or capital expenses were dominating sources of costs. The potential of DH integration was evaluated to determine the economic benefit for the system.

2. Methods

2.1. System description

A process flow diagram of the baseline liquefaction and purification system is illustrated in Fig. 2. The CO_2 product stream is compressed through two-stage compression (COMP) with intercooling (COOL). During intercooling, the remains of water in the captured CO_2 are condensed and removed in gas-liquid separators (SEP). The compressed and purified CO_2 is then liquefied in a heat exchanger (LIQHEX) which works as the evaporator of an external transcritical CO_2 refrigeration cycle. Finally, the liquid CO_2 is pumped to the transport pressure. The incoming mass flow rate of 1.8 th^{-1} of gaseous CO_2 was at 40 °C and 1.7 bar containing 4.3 %(mol) water. Remaining impurities were neglected. The system should deliver liquid CO_2 at 15 bar and 2 K subcooling, and the liquefaction was set to occur at 14.5 bar. In the baseline system, cooling water was heated from 20 °C to 70 °C in the intercoolers, while air was heated from 15 °C to 40 °C in the gascooler (GC). DH was integrated in two alternative ways; in all intercoolers and the gascooler (COOL1, COOL2, COOL3, and GC), and only in intercoolers (COOL1, COOL2, and COOL3). DH water was assumed to be heated from 35 °C to 70 °C. The high pressure in the refrigeration cycle was optimised to the temperature of the available cooling media through cost minimisation. The optimal pressure with air as cooling media in the GC was 75 bar, while the optimal pressure was 110 bar when DH was integrated in the GC. In two-stage compression, the same pressure ratio was applied for each stage, and the intermediate pressure levels (p_{int}) were given by: $p_{int} = \sqrt{p_{low} \cdot p_{high}}$ [18].

2.2. Energy analysis

The system was modelled in steady state by applying mass and energy balances to control volumes for all components. Pressure and heat losses were neglected in pipelines, heat exchangers, and separators. The model was implemented in Engineering Equation Solver [19], and the thermodynamic properties of the CO_2 stream with water impurities were determined using Dalton's law and an ideal gas mixture assumption.

Reciprocating compressors were used in the system and were modelled using a heat loss factor, an isentropic efficiency (η_s), and a volumetric efficiency (η_{vol}). A heat loss factor of 3 % was applied and defined as the ratio of the compressor heat loss to the supplied compressor power. The estimated efficiencies for compressors and pump are presented in Table 1.

The heat exchangers were modelled with a minimum temperature approach of 5 K^1 and a constant overall heat transfer coefficient (U), as shown in Table 2.

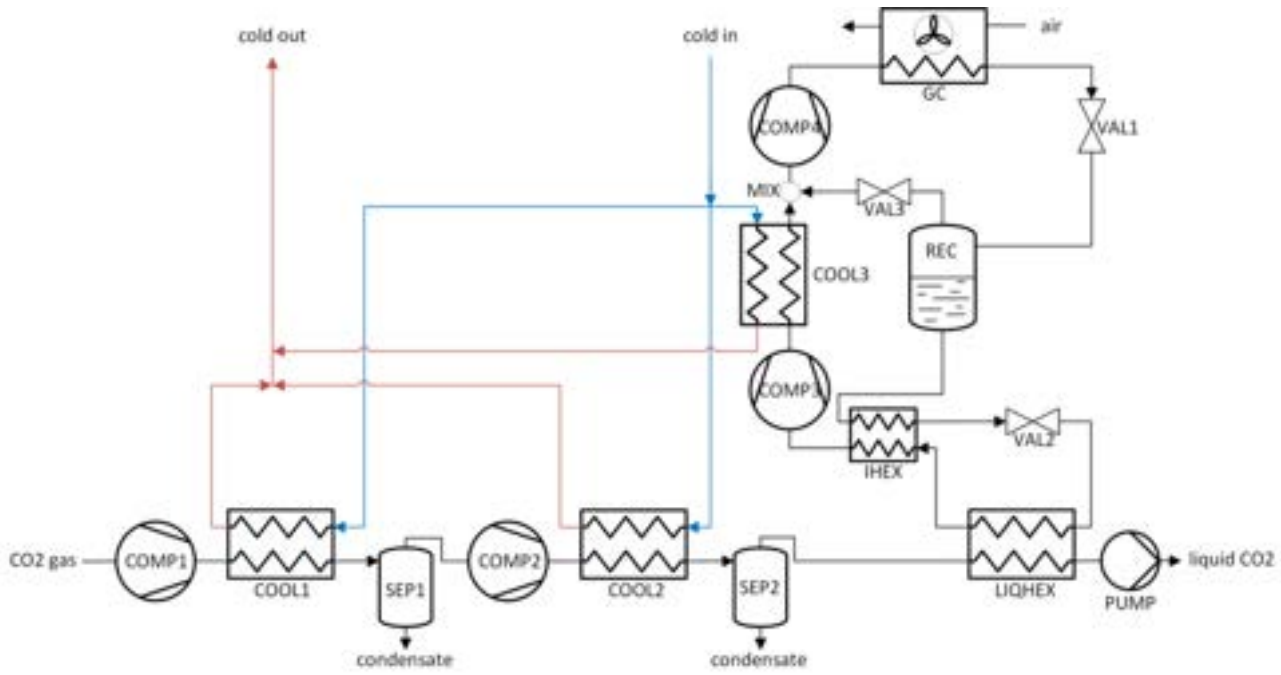

Figure 2: Process flow diagram of the baseline liquefaction and purification system.

Table 1: Assumed efficiencies. Component names refer to Fig. 2.

Component	η_s [%]	η_{vol} [%]
COMP1, COMP2	65	80
COMP3, COMP4	67	83
PUMP	85	100

The gas-liquid separators were assumed to collect all liquid from the two-phase mixture at the bottom of the tank by gravitational forces. The vertical velocity (v) was assumed to be 0.30 ms^{-1} for SEP1, 0.05 ms^{-1} for SEP2 and, 0.13 ms^{-1} for the receiver in the refrigeration cycle (REC). SEP2 in the CO_2 product stream was assumed to remove all remains of water so that pure CO_2 entered the liquefaction heat exchanger.

The required size of each component was determined using the relations given in Table 3. The compressors and pump were defined by a displacement volume ($\dot{V}_{disp}$) required to deliver the actual volume flow rate at the suction line ($\dot{V}_{in}$). The required heat transfer area (A) of the heat exchangers were determined from the required heat transfer rate ($\dot{Q}$), the overall heat transfer coefficient and the logarithmic mean temperature difference of the process (ΔT). The gas-liquid separators had a cross-sectional area (A_{cross}) which ensured the assumed vertical velocity of the volume flow of gas ($\dot{V}_{gas,out}$).

Table 2: Assumed overall heat transfer coefficients. Component names refer to Fig. 2.

Component	U [$kW(m^2K)^{-1}$]	**Source**
LIQHEX	1.20	[20]
IHEX	0.46	[20]
COOL1	0.46	*NDA*
COOL2, COOL3	0.68	*NDA*
GC (air as cooling media)	0.04	[21]
GC (DH water as cooling media)	2.30	*NDA*

2.3. Exergy analysis

The exergy of a given system is the useful work that can potentially be utilised in a process where the system interacts and reaches equilibrium with the surroundings, while heat transfer only occurs to the surroundings [22].

[1] To allow the model to reach the optimal pressure of 110 bar when DH was integrated in the GC, the pinch point temperature difference in the internal heat exchanger (IHEX) was increased from 5 K to 8 K.

Table 3: Relations for calculation of required component sizes.

Component type	Size relation
Compressors and pump	$\dot{V}_{\text{disp}} = \dot{V}_{\text{in}}/\eta_{\text{vol}}$
Heat exchangers	$A = \dot{Q}/U\Delta T$
Gas-liquid separators	$A_{\text{cross}} = \dot{V}_{\text{gas,out}}/v$

An exergy analysis helps identify which components and material streams are the cause of inefficiencies and losses in the system. The surroundings (denoted state 0) were defined with a temperature and pressure of 15 °C and 1 atm. An exergy reference environment was chosen and the standard chemical exergy (e_0^{CH}) of CO_2 and H_2O was given as 19 870 kJ/kmol and 9500 kJ/kmol, respectively [22]. The specific exergy (e) was calculated by Eq. (1) [22] taking the physical (PH) and chemical (CH) exergy into account. This was used together with the mass flow rate ($\dot{m}$) to determine the exergy flow rates ($\dot{E}$) through the system: $\dot{E} = e \cdot \dot{m}$.

$$e = \underbrace{(h - h_0) - T_0\,(s - s_0)}_{e^{\text{PH}}} + \underbrace{\sum_n \left(y_n e_{0,n}^{\text{CH}}\right) + \left(h_0 - \sum_n y_n h_{n,0}\right) - T_0 \left(s_0 - \sum_n y_n s_{n,0}\right)}_{e^{\text{CH}}} \tag{1}$$

The exergy destruction within the system was determined using the product (P) and fuel (F) concepts [23]. The rate of fuel exergy should be sufficient to generate the product and overcome the exergy destruction (D) and exergy losses (L), as given by Eq. (2) [22]. Losses were considered as material streams which transfer exergy directly to the surroundings without further use and were only considered on a system level. Therefore, the last term of Eq. (2) was omitted on a component level.

$$\dot{E}_{\text{F}} = \dot{E}_{\text{P}} + \dot{E}_{\text{D}} + \dot{E}_{\text{L}} \tag{2}$$

The definitions of product and fuel exergy flow rates are given in Table 4. The external coolers, mixer and valves were considered to be dissipative components, therefore no product was defined. The overall product of the baseline system was the increase in exergy of the CO_2 product stream, while the exergy fuel accounted electricity consumption and cooling water (denoted COOL). When DH was integrated in the system, the heating of the cooling water was also considered as a product and the fuel reduced to only being the electricity consumption. For the baseline system, the overall losses were given as the sum of the condensate of water leaving the separators, all leaving streams of cooling water, and the air stream leaving the GC, as given by Eq. (3).

$$\dot{E}_{\text{L}} = \sum \left(\dot{E}_{\text{liq,out}} + \dot{E}_{\text{COOL,out}}\right) + \dot{E}_{\text{GC,out}} \tag{3}$$

Table 4: Definitions of fuel and product exergy rates. Component names refer to Fig. 2.

Component type	$\dot{E}_{\text{F}}$	$\dot{E}_{\text{P}}$
COMP	$\dot{W}$	$\dot{E}_{\text{out}} - \dot{E}_{\text{in}}$
PUMP	$\dot{W}$	$\dot{E}_{\text{out}} - \dot{E}_{\text{in}}$
SEP	$\dot{E}_{\text{in}} - \dot{E}_{\text{liq,out}}$	$\dot{E}_{\text{gas,out}}$
REC	$\dot{E}_{\text{in}}$	$\dot{E}_{\text{gas,out}} + \dot{E}_{\text{liq,out}}$
LIQHEX (cooling across T_0)	$(\dot{E}_{\text{ref,in}} - \dot{E}_{\text{ref,out}}) + \dot{E}_{\text{CO2,in}}$	$\dot{E}_{\text{CO2,out}}$
IHEX (cooling at $T < T_0$)	$\dot{E}_{\text{cold,in}} - \dot{E}_{\text{cold,out}}$	$\dot{E}_{\text{hot,out}} - \dot{E}_{\text{hot,in}}$
COOL (cooling at $T > T_0$)	$\left(\dot{E}_{\text{CO2,in}} - \dot{E}_{\text{CO2,out}}\right) - \left(\dot{E}_{\text{COOL,out}} - \dot{E}_{\text{COOL,in}}\right)$	–
GC (cooling at $T > T_0$)	$\left(\dot{E}_{\text{ref,in}} - \dot{E}_{\text{ref,out}}\right) + \dot{W} - \dot{E}_{\text{a,out}}$	–
MIX	$\dot{E}_{\text{hot,in}} + \dot{E}_{\text{cold,in}} - \dot{E}_{\text{out}}$	–
VAL	$\dot{E}_{\text{in}} - \dot{E}_{\text{out}}$	–
Baseline system	$\sum \left(\dot{W} + \dot{E}_{\text{COOL,in}}\right)$	$\dot{E}_{\text{CO2,out}} - \dot{E}_{\text{CO2,in}}$
DH integration	$\sum \dot{W}$	$\left(\dot{E}_{\text{CO2,out}} - \dot{E}_{\text{CO2,in}}\right) + \sum \left(\dot{E}_{\text{COOL,out}} - \dot{E}_{\text{COOL,in}}\right)$

For the system with DH integration in the intercoolers, the losses reduced to only account the condensate of water leaving the separators and the air stream leaving the GC, as given by Eq. (4).

$$\dot{E}_{\mathrm{L}} = \sum \dot{E}_{\mathrm{liq,out}} + \dot{E}_{\mathrm{GC,out}} \tag{4}$$

When DH was integrated in all external coolers, the losses only included the condensate of water leaving the separators, as given by Eq. (5).

$$\dot{E}_{\mathrm{L}} = \sum \dot{E}_{\mathrm{liq,out}} \tag{5}$$

A set of exergy performance indicators can be defined to evaluate individual components and the system as a whole. An exergy destruction ratio (γ_{D}) was defined for each component and on a system level, see Eq. (6) [22]. An exergy loss ratio (γ_{L}) was similarly defined for each material stream considered as a loss and on a system level as seen in Eq. (7). An exergy efficiency (ε) was defined for all non-dissipative components and on a system level and was given as the ratio of the exergy product rate to the exergy fuel rate: $\varepsilon = \dot{E}_{\mathrm{P}}/\dot{E}_{\mathrm{F}}$. For the dissipative components, no exergy efficiency was defined.

$$\text{component level}: \quad \gamma_{\mathrm{D}} = \frac{\dot{E}_{\mathrm{D}}}{\dot{E}_{\mathrm{D,sys}}}, \qquad \text{system level}: \quad \gamma_{\mathrm{D,sys}} = \frac{\dot{E}_{\mathrm{D,sys}}}{\dot{E}_{\mathrm{F,sys}}} \tag{6}$$

$$\text{stream level}: \quad \gamma_{\mathrm{L}} = \frac{\dot{E}_{\mathrm{L}}}{\dot{E}_{\mathrm{L,sys}}}, \qquad \text{system level}: \quad \gamma_{\mathrm{L,sys}} = \frac{\dot{E}_{\mathrm{L,sys}}}{\dot{E}_{\mathrm{F,sys}}} \tag{7}$$

2.4. Economic analysis

For each component, the purchased equipment cost (PEC) was estimated by the cost relation in Eq. (8) [22]. The PEC of a component with a given size (X) was estimated using the list price of a similar component (denoted z) with a known size. The scaling exponent (α) is specific for each component type and is given in Table 5. The PEC of the reference components are presented in Table 6. All monetary values are given in 2022€.

$$\mathrm{PEC} = \mathrm{PEC}_z \left(\frac{X}{X_z} \right)^{\alpha} \tag{8}$$

Table 5: Scaling exponents used for different types of components.

Component type	**Scaling exponent** (α)	**Source**
Compressors	0.77	[24]
Pump	0.59	[25]
Heat exchangers with CO_2 or water	0.78	[25]
External cooler with air	0.39	[25]
Gas-liquid separators	0.30	[22]

To account for additional costs besides the investment of the component, the PEC was adjusted to a total capital investment of TCI = 4.16 · PEC [22]. The levelised cost rate associated with the capital investment ($\dot{Z}^{\mathrm{CI}}$) was then given by Eq. (9). Here, the TCI was discounted and annualised using a real discount rate (i) of 3 % and a lifetime (L) of 25 years. An annual operating time (H) of 8000 h was assumed. The cost rate of operation and maintenance was given by $\dot{Z}^{\mathrm{OM}} = 0.15 \cdot \dot{Z}_k^{\mathrm{CI}}$ [25]. The total costs associated with owning a component ($\dot{Z}$) was the sum of capital investment and operation and maintenance: $\dot{Z} = \dot{Z}^{\mathrm{CI}} + \dot{Z}^{\mathrm{OM}}$.

$$\dot{Z}^{\mathrm{CI}} = \frac{\mathrm{TCI}\left(\frac{i(1+i)^L}{(1+i)^L-1}\right)}{H\,3600\mathrm{sh}^{-1}} \tag{9}$$

The electricity price was assumed to be 0.08 €kWh^{-1} based on [29] and [30]. The cost of the cooling media was 7.83 €kWh^{-1} and was calculated from the TCI and operational costs of a drycooler required to discharge the heat to the surroundings. The entering gaseous CO_2 and the entering DH water were assumed to be free of charge.

Table 6: Purchased equipment cost and size of reference component for all components in the system. Component names refer to Fig. 2.

Component	PEC of reference [€]	Size of reference (X)	Source
COMP1, COMP2, COMP3	34 393	150.5 m^3h^{-1}	[26]
COMP4	66 731	112.8 m^3h^{-1}	[26]
PUMP	4956	5.7 m^3h^{-1}	[27]
LIQHEX	2426	13.5 m^2	[28]
IHEX	452	1.97 $m^{2\dagger}$	[28]
COOL1	2177	7.69 $m^{2\dagger}$	*NDA*
COOL2, COOL3	1128	6.07 $m^{2\dagger}$	*NDA*
GC (air as cooling media)	14 695	464 m^2	[21]
GC (DH water as cooling media)	2223	17.1 m^2	*NDA*
SEP1	5335	0.29 m^3	*NDA*
SEP2	6018	0.29 m^3	*NDA*
REC	1228	0.03 m^{3*}	[26]
VAL1	1926	–	[26]
VAL2, VAL3	1110	–	[26]
MIX	68	–	[26]

Range of cost function: *0.07 m^3 to 150 m^3, †8.3 m^2 to 373 m^2. It was assumed that prices were still representative.

2.5. Exergoeconomic analysis

An exergoeconomic analysis is a way to determine cost flows throughout a thermal energy system and to investigate how inefficiencies in the system affect the cost of the final product [22]. The cost rates ($\dot{C}$) were determined throughout the system, and are given as the product of the average cost per unit of exergy (c) and the exergy flow rate: $\dot{C} = c \cdot \dot{E}$ [22]. The cost balances applied to all types of components are given in Table 7. Auxiliary cost equations were made for components with more than one exiting exergy stream using the product and fuel principles according to the approach in [23]. The cost balances of dissipative components (coolers, mixer, and valves) were adjusted so that all costs were assigned to an auxiliary variable ($\dot{C}_{\mathrm{dif,dc}}$), which was added to the final product. The costs of all loss streams were set to 0 €s^{-1} in the analysis, thereby the costs were assigned directly to the overall product. On a system level, the economic value of the losses was estimated by assuming an overall constant product rate and that changes in losses result in changes in the fuel supply: $\dot{C}_{\mathrm{L}} = c_{\mathrm{F}} \cdot \dot{E}_{\mathrm{L}}$, where c_{F} is the average cost per unit of exergy fuel. A similar assumption was used for estimating the costs of exergy destruction: $\dot{C}_{\mathrm{D}} = c_{\mathrm{F}} \cdot \dot{E}_{\mathrm{D}}$ [22].

The cost balance of the general form: $\dot{C}_{\mathrm{P}} = \dot{C}_{\mathrm{F}} + \dot{Z}$ was applied on a system level with the definitions of product and fuel costs given in Table 8. For the systems with DH integration, the cost rate of the total product was given as the sum of the cost rate of CO_2 and DH production: $\dot{C}_{\mathrm{P}} = \dot{C}_{\mathrm{P,CO2}} + \sum \dot{C}_{\mathrm{P,DH}}$. The definition of product and fuel exergy used for the external coolers was the same in both the baseline system and with DH integration, as this allowed for allocation of the component costs to both DH production and the CO_2. When DH was produced

Table 7: Cost balances and auxiliary equations for each component. Component names refer to Fig. 2.

Component type	Cost balance	Auxiliary equation (*F/P principle*)
COMP	$\dot{C}_{\mathrm{out}} = \dot{C}_{\mathrm{in}} + \dot{C}_{\mathrm{w}} + \dot{Z}$	–
PUMP	$\dot{C}_{\mathrm{out}} = \dot{C}_{\mathrm{in}} + \dot{C}_{\mathrm{w}} + \dot{Z}$	–
SEP	$\dot{C}_{\mathrm{gas,out}} = \dot{C}_{\mathrm{in}} + \dot{Z}$	
REC	$\dot{C}_{\mathrm{gas,out}} + \dot{C}_{\mathrm{liq,out}} = \dot{C}_{\mathrm{in}} + \dot{Z}$	(P) $c_{\mathrm{gas,out}} = c_{\mathrm{liq,out}}$
LIQHEX	$\dot{C}_{\mathrm{CO2,out}} + \dot{C}_{\mathrm{ref,out}} = \dot{C}_{\mathrm{CO2,in}} + \dot{C}_{\mathrm{ref,in}} + \dot{Z}$	(F) $c_{\mathrm{ref,in}} = c_{\mathrm{ref,out}}$
IHEX	$\dot{C}_{\mathrm{hot,out}} + \dot{C}_{\mathrm{cold,out}} = \dot{C}_{\mathrm{cold,in}} + \dot{C}_{\mathrm{hot,in}} + \dot{Z}$	(F) $c_{\mathrm{cold,in}} = c_{\mathrm{cold,out}}$
COOL	$\dot{C}_{\mathrm{dif,dc}} + \dot{C}_{\mathrm{CO2,out}} = \dot{C}_{\mathrm{CO2,in}} + \dot{C}_{\mathrm{COOL,in}} + \dot{Z}$	(F) $c_{\mathrm{CO2,in}} = c_{\mathrm{CO2,out}}$
GC	$\dot{C}_{\mathrm{dif,dc}} + \dot{C}_{\mathrm{ref,out}} = \dot{C}_{\mathrm{ref,in}} + \dot{C}_{\mathrm{w}} + \dot{Z}$	(F) $c_{\mathrm{ref,in}} = c_{\mathrm{ref,out}}$
MIX	$\dot{C}_{\mathrm{dif,dc}} + \dot{C}_{\mathrm{out}} = \dot{C}_{\mathrm{hot,in}} + \dot{C}_{\mathrm{cold,in}} + \dot{Z}$	(F) $c_{\mathrm{out}} = \frac{\dot{E}_{\mathrm{hot,in}} c_{\mathrm{hot,in}} + \dot{E}_{\mathrm{cold,in}} c_{\mathrm{cold,in}}}{\dot{E}_{\mathrm{hot,in}} + \dot{E}_{\mathrm{cold,in}}}$
VAL	$\dot{C}_{\mathrm{dif,dc}} + \dot{C}_{\mathrm{out}} = \dot{C}_{\mathrm{in}} + \dot{Z}$	(F) $c_{\mathrm{in}} = c_{\mathrm{out}}$

Table 8: Cost flow rates for the overall system.

System	$\dot{C}_F$	$\dot{C}_{P,CO2}$	$\dot{C}_{P,DH}$
Baseline	$\sum \dot{C}_w + \sum \dot{C}_{COOL,in}$	$\dot{C}_{CO2,out} + \sum \dot{C}_{dif,dc}$	–
DH integration	$\sum \dot{C}_w$	$\dot{C}_{CO2,out} + \frac{\dot{E}_{CO2,out} - \dot{E}_{CO2,in}}{\dot{E}_P} \sum \dot{C}_{dif,dc}$	$\dot{C}_{COOL,out} + \frac{\dot{E}_{COOL,out} - \dot{E}_{COOL,in}}{\dot{E}_P} \sum \dot{C}_{dif,dc}$

in a cooler, the fuel principle was applied to both the CO_2 stream and the DH water stream, to keep all costs in the auxiliary variable. The allocation of the total sum of $\dot{C}_{dif,dc}$ was made using the exergy value of the CO_2 product and DH as weighting factors in the absence of other valuation methods.

A set of exergoeconomic performance indicators were defined to evaluate the system. The relative cost difference (r) indicates the increase in average cost per exergy unit between fuel and product of a productive component or system, relative to the average cost of fuel supplied [22]. It is given by Eq. (10), here c_P is the average cost per unit of exergy product.

$$r = \frac{c_P - c_F}{c_F} = \frac{1-\varepsilon}{\varepsilon} + \frac{\dot{Z}}{c_F \dot{E}_P} \tag{10}$$

An exergoeconomic factor (f) was defined, as given in Eq. (11). It is the ratio between the costs coming from investment and operation to the total costs of the component or system. By using this factor, the dominating source of costs in a component can be evaluated [22]. Since costs of losses were only considered on a system level, the last term of the denominator was omitted on a component level.

$$f = \frac{\dot{Z}}{\dot{Z} + \dot{C}_D + \dot{C}_L} \tag{11}$$

3. Results

3.1. Baseline system

The baseline system had a total power consumption of 210 kW and a cooling load on the refrigeration cycle of 177 kW. Furthermore, the total cooling load in COOL1 and COOL2 was 137 kW. The total capital investment of the system was 1.7 M€. The results of the exergy and exergoeconomic analyses of the baseline system are shown in Table 9. The greatest exergy destruction was seen in the compressors and the GC, with the three highest rates of exergy destruction in COMP4 (15.1 kW), COMP1 (14.2 kW), and the GC (14.2 kW). The four compressors accounted for 56 % of the exergy destruction in the system, while the GC accounted for 14 %. Less significant contributions were found in the LIQHEX, COOL1, COOL2, VAL1, and VAL2 ranging between approx. 3 % to 8 %, while the remaining components each contributed less than 1 % to the overall exergy destruction. The results for the PUMP and the MIX were excluded from Table 9 as these components only accounted for a total of less than 0.4 % of the total exergy destruction, and less than $6 \cdot 10^{-3}$ % of the total capital investment.

The results for all material streams considered as losses are seen in Table 10. The greatest exergy losses were discharged in the GC (9.9 kW) and COOL1 (7.6 kW) accounting for 32 % and 24 % of the total losses, respectively. Losses related to cooling accounted for 85 % of the total losses in the system, while the removal of water constituted the remaining 15 %. On a system level, an exergy efficiency of 39 % was found, while 46 % of the fuel exergy being supplied was destroyed through irreversibilities in the system. The exergy losses constituted 15 % of the fuel supply on a system level.

The results of the exergy analysis indicated that the performance of the system could be improved by reducing exergy destruction, with the highest reduction potential seen in compressors and the GC and somewhat lower reduction potentials in the LIQHEX, COOL1, and COOL2. By increasing the efficiencies of compressors and decreasing the temperature difference in the LIQHEX, the exergy efficiency of the system could be directly improved. However, an improvement of the GC, COOL1, and COOL2, would reduce the destruction in these components while increasing the exergy losses. The temperature of the working media at the outlet of the components would in such case decrease and therefore a greater cooling load would be needed in the components, resulting in a greater discharge of heat to the cooling media. The analysis also showed a potential for utilising losses associated with cooling, as approx. 13 % of the fuel supply was lost in the cooling water.

Table 9: Exergy and exergoeconomic results of the baseline system. Component names refer to Fig. 2.

Component	$\dot{E}_F$ [kW]	$\dot{E}_P$ [kW]	$\dot{E}_D$ [kW]	ε [%]	γ_D [%]	$\dot{C}_F$ [€h^{-1}]	$\dot{C}_P$ [€h^{-1}]	$\dot{C}_D$ [€h^{-1}]	$\dot{Z}$ [€h^{-1}]	r [%]	f [%]
COMP1	55.9	41.7	14.2	74.6	14	4.5	12	1.1	7.24	250	86
COMP2	50.3	37.0	13.3	73.6	14	4.1	7.0	1.1	2.95	130	73
COMP3	46.1	33.1	13.0	71.8	13	3.8	4.7	1.1	0.93	74	47
COMP4	57.3	42.3	15.1	73.7	15	4.6	5.9	1.2	1.31	74	52
SEP1	264	264	0.836	99.7	0.85	11	11	0.035	0.219	2.3	86
SEP2	291	291	0.283	99.9	0.29	18	19	0.018	0.243	1.4	93
REC	162	162	0.0	100	0.0	23	23	0.0	0.0323	0.14	100
LIQHEX	328	320	8.19	97.5	8.3	23	24	0.59	0.132	3.1	18
IHEX	1.52	0.947	0.574	62.3	0.58	0.22	0.24	0.08	0.0207	76	20
COOL1	3.12	–	3.12	–	3.2	1.0	–	1.0	0.0624	–	5.9
COOL2	3.64	–	3.64	–	3.7	0.92	–	0.92	0.0245	–	2.6
COOL3	0.719	–	0.719	–	0.73	0.88	–	0.88	0.0831	–	8.7
GC	14.2	–	14.2	–	14	3.2	–	3.2	0.527	–	14
VAL1	5.77	–	5.77	–	5.9	0.82	–	0.82	0.0657	–	7.4
VAL2	3.93	–	3.93	–	4.0	0.57	–	0.57	0.0378	–	6.3
VAL3	0.894	–	0.894	–	0.91	0.13	–	0.13	0.0378	–	23
System	212	82.7	98.1	39.0	46	18	32	8.5	14.0	350	56

The results of the exergoeconomic analysis seen in Table 9 showed that the highest cost sources were the compressors and the GC, as these components had both relatively high costs associated with exergy destruction and capital investment. The CO_2 product compressors, COMP1 and COMP2, showed high relative cost differences of 250 % and 130 % meaning that the specific cost of the product stream was significantly increased compared to the fuel costs in these two components. Furthermore, COMP1 and COMP2 showed exergoeconomic factors of 86 % and 73 %, respectively, indicating that the highest cost sources in these components were capital investment. The relative cost increase in COMP3 and COMP4 of 74 % were less significant. The costs of irreversibilities and capital investment in these two components were well balanced with exergoeconomic factors of 47 % and 52 %, respectively. Looking at the heat exchangers in the system, these were generally dominated by costs associated with exergy destruction, with the greatest contributions in the GC, COOL1, COOL2, and COOL3 showing exergoeconomic factors ranging between 2 % to 14 %. At a system level, the cost rate of the product was 32 €h^{-1}, corresponding to 18.3 €t^{-1} CO_2 at the liquid product mass flow rate of 1.77 th^{-1}. The exergoeconomic factor of the overall system was 56 % indicating, that the costs associated with capital investment and inefficiencies were balanced.

The exergoeconomic analysis showed that the components in which fuel was supplied to the system were of most importance for the overall costs. The analysis indicated that the overall product cost could be reduced if the costs associated with the CO_2 product stream compressors, COMP1 and COMP2, were decreased. The

Table 10: Results for losses of the baseline system. Component names refer to Fig. 2.

Component source	$\dot{E}_L$ [kW]	γ_L [%]	$\dot{C}_L$ [€h^{-1}]
SEP1	4.1	13	0.35
SEP2	0.7	2.3	0.062
COOL1	7.6	24	0.66
COOL2	5.2	17	0.45
COOL3	3.6	12	0.31
GC	9.9	32	0.85
System	31	15	2.7

greatest cost contribution in these components was the capital investment, therefore, this could be decreased to potentially reduce the costs of the overall product. The external coolers showed moderate cost contributions stemming from inefficiencies. However, a reduction in exergy destruction and thereby costs associated with inefficiencies would result in increased costs of exergy losses. An alternative way of reducing the costs of inefficiencies in the external coolers could be to reduce the average cost of fuel supply to the components. This could be done if the costs of the available cooling media could be reduced.

3.2. Integration of district heat

Based on the results of the exergy and exergoeconomic analyses, it was chosen to implement DH in the external coolers to utilise the exergy loss associated with cooling and to eliminate the costs of the cooling water. The effects on the overall system costs were evaluated when DH was integrated in all coolers (COOL1, COOL2, COOL3, and the GC) and when it was only integrated in the intercoolers (COOL1, COOL2, and COOL3).

The results of the exergy and exergoeconomic analyses for the overall systems are presented in Table 11. It is seen, that the overall exergy product was increased for both DH integration options compared to the baseline system because the heating of water was now considered a product for the overall system. Therefore, the total losses were reduced to 5.0 kW and 16 kW when implementing DH in all external coolers and only in intercoolers, respectively. As a consequence, also the exergy efficiency increased for both integration options, with the highest exergy efficiency seen for the system with DH integration in all coolers because this option also utilised the heat discharged in the GC. The cooling was provided at a higher temperature with DH water. Therefore, an increase in exergy destruction was seen for both integration options which was primarily caused by increased exergy destruction in compressors and in the LIQHEX, because the temperatures at the component inlets increased. A significantly higher total exergy destruction was seen for the integration of DH in all coolers. This was caused by an increase in the optimal high pressure in the refrigeration cycle when the GC should use DH water for cooling (see Section 2.1). This significantly increased the load on COMP4, and also increased the throttling losses in VAL1.

Considering the overall system costs in Table 11, it was seen that the costs of the total system increased 11 % to 36 €h^{-1}, when DH was integrated in all coolers. This was caused by the increase of the high pressure in the refrigeration cycle, resulting in higher electricity consumption in compressors. This was also seen from the higher cost of exergy fuel of 22 €h^{-1}. The costs of the total system remained constant when DH was only implemented in intercoolers. In this integration option, the costs associated with cooling water were eliminated and outweighed the increased power consumption of compressors, meaning that the overall fuel costs remained closed to constant. The increased temperature at the suction line of COMP2 and COMP4 increased the volume flow rates, which led to greater component sizes and increased capital investment. This resulted in a cost rate of capital investment of 14.3 €h^{-1} when DH was integrated in intercoolers. For the alternative option, the capital investment showed an overall small decrease to 13.9 €h^{-1} which was caused by the GC being significantly smaller when water was used as cooling media.

When considering the costs assigned to the liquefaction and purification of CO_2, it was reduced for both implementation options. For the system with DH integration in all coolers, the CO_2 product cost was found to be $\dot{C}_{P,CO2}$ = 31.1 €h^{-1}, while it was $\dot{C}_{P,CO2}$ = 30.9 €h^{-1} when only integrating DH in existing water coolers. These costs corresponded to a specific cost of liquefaction and purification of 17.6 €t^{-1} CO_2 and 17.5 €t^{-1} CO_2, respectively. The remaining costs were assigned to the DH product. The total DH production was 168 kW at 10.1 €MWh^{-1} and 160 kW at 9.2 €MWh^{-1} when implementing DH in all coolers and only in intercoolers, respectively.

The results showed that integration of DH in the existing water coolers could be made without increasing the costs of the overall system, when assuming that the DH operators would pay for additional components needed to operate the DH. The increase in available cooling temperature increased the power consumption and the required size of the subsequent compressors, which increased the costs associated with these components. However, the costs associated with cooling were reduced, thereby reducing the costs stemming from ineffi-

Table 11: Exergy and exergoeconomic results for systems with DH integration.

DH integration	$\dot{E}_F$ [kW]	$\dot{E}_P$ [kW]	$\dot{E}_D$ [kW]	ε [%]	γ_D [%]	$\dot{C}_F$ [€h^{-1}]	$\dot{C}_P$ [€h^{-1}]	$\dot{C}_D$ [€h^{-1}]	$\dot{Z}$ [€h^{-1}]	r [%]	f [%]
COOLs and GC	272	137	130	50.2	48	22	36	11	13.9	220	56
COOLS only	224	101	107	45.2	48	18	32	8.6	14.3	300	59

ciencies in the system. The results also showed that integration of DH in the GC increased the overall system costs, due to an increased load on the high-pressure compressor. Therefore, this integration option would only be more feasible than the baseline system, if the revenue from DH sales was greater than the additional costs of the electricity consumption.

4. Discussion

The definitions of product and fuel for all components were chosen as total exergy streams. In some components and on the system level it would be more correct to divide the streams of exergy into thermal, mechanical, and chemical parts. As an example, the correct product definition of the CO_2 liquefaction and purification would be the sum of the thermal exergy in the liquid outlet stream and the increase in mechanical and chemical exergy from inlet to outlet, while the thermal exergy in the gaseous inlet stream should be considered as a fuel. This would give a negligible increase in the overall exergy product rate to 85 kW and the exergy efficiency to 39.7 %. It would result in a slightly lower product cost rate, as the costs of fuel and capital investment would not be affected by a split in exergy streams. Furthermore, it would affect the systems with DH integration in a similar way. The higher level of detail would significantly increase the computational effort of the model, and would not affect the overall conclusions of the study.

The cost balances for the external coolers were the same for both the baseline system and the systems with DH integration, even though a useful exergy product could be defined with DH integration. This approach allowed for allocation of the cooler costs between the liquefaction and purification of CO_2 and the DH production. Alternatively, all costs could be assigned to the DH product in each cooler. This would not affect the overall costs of the system, but reduce the costs assigned to the liquefaction and purification of CO_2. Furthermore, alternative methods for allocation of the costs could be used, which could distribute the costs of coolers and dissipative components in a different way between the DH product and the CO_2 product.

In both systems with DH integration, it was expected that the DH can generate positive revenue. DH integration in intercoolers would make the system more economically feasible than the baseline system, while the revenue from DH should at least exceed the additional expenses when implementing DH in all coolers. The additional costs of this system corresponded to a minimum selling price of DH of 21 €MWh^{-1}. In 2022, around 100 of the Danish DH networks had heat prices higher than 21 €MWh^{-1} [31], assuming that the heat price constituted 25 % of the price paid by consumers [32]. This indicated that the feasibility of integrating DH in all coolers depends on the local DH network. To make the conclusions on DH integration more robust, a sensitivity analysis of the ambient temperature and the yearly operating hours of the plant could be made.

The analysis also showed that the compressors were a major cost source. If the components of the systems should be changed, these should be of focus. In the systems with DH integration, it could also be beneficial to improve the performance of the coolers, as these showed moderate costs associated with inefficiencies. This would increase DH production and revenue. It would also result in a reduction of the exogenous contribution to exergy destruction in COMP2, COMP4, and the LIQHEX because the temperature at the inlet of these components would be reduced. To investigate the interdependencies between components, it could be of interest to perform an advanced exergy analysis [33]. In the present study, it was assumed that all water was removed from the CO_2, however, the amount of water that can be removed by condensation is limited by the temperature of the available cooling water. It would be relevant to also consider this influence when evaluating the effect of DH integration.

5. Conclusion

An exergoeconomic analysis of a system for liquefaction and purification of CO_2 was made. The system consisted of two-stage compression with intercooling and an external two-stage refrigeration cycle used for liquefaction. The analysis showed an exergy efficiency of 39 %, while 15 % of the supplied exergy fuel was considered as losses with the dominating part associated with external cooling. The compressors throughout the system were responsible for 56 % of the total exergy destruction and were found to be the most significant for costs. The analysis suggested that the capital investment of the two-stage compressors in the CO_2 product stream should be reduced to reduce the costs of the overall process.

It was found that integration of DH could increase the exergy efficiency to 45 % and 50 % and that the highest efficiency was achieved when all external coolers were used for DH production. However, it was seen that implementation of DH in the gascooler of the refrigeration cycle resulted in an 11 % increase in the total system costs, while DH could be integrated only in the water coolers without affecting the total costs of the system. Integration of DH increased the costs associated with compressors but reduced the costs of cooling. The analysis of the initial system also suggested that the performance of the coolers should be improved, which was expected to have a positive impact on the overall system only if DH was integrated. The study showed, that production of DH from the waste heat of the liquefaction and purification process could potentially have a positive economic impact on the system and that this was depending on the choice of integration.

Nomenclature

Roman Letters

$\dot{C}$	Cost rate [€s^{-1}]
$\dot{E}$	Exergy flow rate [kW]
$\dot{m}$	Mass flow rate [kgs^{-1}]
$\dot{Q}$	Heat transfer rate [kW]
$\dot{V}$	Volumetric flow rate [m^{3}s^{-1}]
$\dot{W}$	Power [kW]
$\dot{Z}$	Cost rate of owning component [€s^{-1}]
A	Area [m^2]
c	Average cost per exergy unit [€kJ^{-1}]
e	Specific exergy [kJkg^{-1}]
f	Exergoeconomic factor [%]
H	Annual operating hours [h]
h	Specific enthalpy [kJkg^{-1}]
i	Real interest rate [%]
L	Lifetime [y]
r	Relative cost difference [%]
s	Specific entropy [kJ(kgK)$^{-1}$]
T	Temperature [℃]
U	Overall heat transfer coefficient [kW(m^{2}K)$^{-1}$]
v	Velocity [ms^{-1}]
X	Primary design variable
y	Mass fraction [–]

Greek Letters

α	Scaling exponent [–]
η	Efficiency [%]
γ	Exergy ratio [–]
ε	Exergy efficiency [%]

Subscripts and superscripts

n	Chemical component
0	Reference state
a	air
CH	Chemical
CI	Capital investment
cross	Cross-sectional
D	Destruction
dc	Dissipative component
dif	Difference
disp	Displacement
F	Fuel
int	Intermediate
OM	Operation and maintenance
P	Product
PH	Physical
s	Isentropic
sys	Overall system
vol	Volumetric

Abbreviations

COMP	Compressor
COOL	Intercooler
DH	District heating
GC	Gascooler
IHEX	Internal heat exchanger
LIQHEX	Liquefaction heat exchanger
PEC	Purchased equipment cost [€]
REC	Receiver
SEP	Gas-liquid separator
TCI	Total capital investment [€]
VAL	Expansion valve

References

[1] Ritchie H., Roser M., *CO_2 and Greenhouse Gas Emissions 2020.* Available at: `https://ourworldindata.org/greenhouse-gas-emissions` [accessed 03.01.2022].

[2] International Energy Agency, *20 Years of Carbon Capture and Storage.* 2015 Nov. Available at: `https://www.iea.org/reports/20-years-of-carbon-capture-and-storage`.

[3] International Energy Agency, *Net Zero by 2050.* 2021 Oct. Available at: `https://www.iea.org/reports/net-zero-by-2050`.

[4] International Energy Agency, *About CCS, 2021.* Available at: `https://www.iea.org/reports/about-ccus`.

[5] Aspelund A., Mølnvik MJ., De Koeijer G., *Ship transport of CO_2: Technical solutions and analysis of costs, energy utilization, exergy efficiency and CO_2 emissions.* Chemical Engineering Research and Design 2006;84(9A):847-855.

[6] Seo Y., Huh C., Lee S., Chang D., *Comparison of CO_2 liquefaction pressures for ship-based carbon capture and storage (CCS) chain.* International Journal of Greenhouse Gas Control 2016;52:1-12.

[7] Roussanaly S., Deng H., Skaugen G., Gundersen T., *At what pressure shall CO_2 be transported by ship? An in-depth cost comparison of 7 and 15 barg shipping*. Energies 2021;14(18)5635.

[8] Deng H., Roussanaly S., Skaugen G., *Techno-economic analyses of CO_2 liquefaction: Impact of product pressure and impurities*. International Journal of Refrigeration 2019;103:301-315.

[9] Aspelund A., Jordal K., *Gas conditioning – The interface between CO_2 capture and transport.* International Journal of Greenhouse Gas Control 2007;1(3):343-354.

[10] Gong W., Remiezowicz E., Fosbøl PL., von Solms N., *Design and Analysis of Novel CO_2 Conditioning Process in Ship-Based CCS.* Energies 2022;15(16):5928.

[11] Alabdulkarem A., Hwang Y., Radermacher R., *Development of CO_2 liquefaction cycles for CO_2 sequestration.* Applied Thermal Engineering 2012;33-34(1):144-156.

[12] Øi LE., Eldrup N., Adhikari U., Bentsen MH., Badalge JL., Yang S., *Simulation and Cost Comparison of CO_2 Liquefaction.* Energy Procedia 2016;86:500-510.

[13] Seo Y., You H., Lee S., Huh C., Chang D., *Evaluation of CO_2 liquefaction processes for ship-based carbon capture and storage (CCS) in terms of life cycle cost (LCC) considering availability.* International Journal of Greenhouse Gas Control 2015;35:1-12.

[14] Chen F., Morosuk T., *Exergetic and economic evaluation of CO_2 liquefaction processes.* Energies 2021;14(21):7174.

[15] Aliyon K., Mehrpooya M., Hajinezhad A., *Comparison of different CO_2 liquefaction processes and exergoeconomic evaluation of integrated CO_2 liquefaction and absorption refrigeration system.* Energy Conversion and Management 2020;211:112752.

[16] Muhammad HA., Roh C., Cho J., Rehman Z., Sultan H., Baik YJ., Lee B., *A comprehensive thermodynamic performance assessment of CO_2 liquefaction and pressurization system using a heat pump for carbon capture and storage (CCS) process*. Energy Conversion and Management 2020;206:112489.

[17] Muhammad HA., Lee B., Cho J., Rehman Z., Choi B., Cho J., Roh C., Lee G., Imran M., Baik YJ., *Application of advanced exergy analysis for optimizing the design of carbon dioxide pressurization system.* Energy 2021;228:120580.

[18] Granryd E:, Ekroth I., Lundqvist P., Melinder Å., Palm B., Rohlin P., *Refrigerating Engineering.* Stockholm, Sweden: Royal Institute of Technology, KTH; 2011.

[19] Klein S.A., *EES: Engineering Equation Solver.* Available at: `https://fchartsoftware.com/ees/`.

[20] SWEP International, *SSP G8 Calculation Software*. Available at: `https://www.swep.net/support/ssp-calculation-software/ssp-g8/` [accessed 13.05.2022].

[21] Kelvion Holding, *Select RT.* Available at: `https://selectrt.kelvion.com/selector/system` [accessed 21.04.2022].

[22] Bejan A., Tsatsaronis G., Moran M., *Thermal Design & Optimization*. John Wiley & Sons, Inc.;1996.

[23] Lazzaretto A., Tsatsaronis G:, *SPECO: A systematic and general methodology for calculating efficiencies and costs in thermal systems*. Energy 2006;31(8-9):1257-1289.

[24] Woods DR., *Rules of Thumb in Engineering Practice*. Wiley-VCH Verlag GmbH & Co.; 2007.

[25] Garrett DE., *Chemical engineering economics*. Van Nostrand Reinhold; 1989.

[26] H. Jessen Jürgensen, *Prisliste 2022*. Available at: `https://www.hjj.dk/downloads-og-prislister/prisoverblik-prisbog-og-prisliste` [accessed 17.04.2022].

[27] Anderson Process, *Cat 2530 Pump*. Available at: `https://shop.andersonprocess.com/cat-2530-pump.html` [accessed 30.05.2022].

[28] SWEP International, *Heat exchangers range*. Available at: `https://www.heat-exchanger.eu/range/` [accessed 13.05.2022].

[29] Dansk Energi, *Elforsyningens nettariffer & priser pr. 1. januar 2021*. 2021 May.

[30] Danish Energy Agency, *Baggrundsnotat om elprisfremskrivninger i Analyseforudsætninger til Energinet 2021 (AF21).* 2021 Dec. Technical Report No.: 2021-6416.

[31] The Danish Utility Regulator, *Varmeprisstatistik Januar 2022*, Available at: `https://forsyningstilsynet.dk/tal-fakta/priser/varmepriser/priser-pr-1-januar-2022`.

[32] Gentofte Gladsaxe Fjernvarme, *Takstsammensætning 2022.* Available at: `https://gladsaxefjernvarme.dk/privat/faq/det-med-smaat/` [accessed 14.03.2023].

[33] Morosuk T., Tsatsaronis G., *Advanced exergy-based methods used to understand and improve energy-conversion systems*. Energy 2019;169:238-246.

Clear paths to teach exergy

Daniel Favrat[a], Malick Kane[b],

[a] Ecole Polytechnique Fédérale de Lausanne (energy center), Lausanne, Switzerland, daniel.favrat@epfl.ch
[b] HES-SO//FR, University of Applied Science in Fribourg, Mechanical Engineering Department (ENERGY Institute), Fribourg, Switzerland, malick.kane@hefr.ch

Abstract:

This paper proposes a clear path to the exergy balance by subtracting the second Law balance (multiplied by Ta) to the first Law that let appear all the exergy terms. In each exergy terms it is shown that it is essential to clearly distinguish the process-dependent entities from the state functions and how the latter can be visualized in parametric representations including 3D. An opportunity is shown to superpose the various dead states (thermo-mechanical or physicochemical equilibrium). The typical First Law indicators (Effectiveness, coefficient of performance) are compared with the corresponding exergy efficiency for integrated processes including house heating with cogeneration and heat pumps or the valorization of LNG evaporation. From this strong basis the development of both First Law and Exergy efficiencies is shown for a variety of systems providing different energy services in the whole range of temperatures. A much greater coherence of the exergy approach for modern systems including co-or tri-generation is highlighted. The power of the notion of exergy efficiency is further illustrated by comparing various heating or air-conditioning energy systems in urban areas with the possibility to multiply the exergy efficiency of the subsystems to get a coherent ranking of the active technology options. Ultimately, we briefly show how one specific emerging platform (nolej) based on AI could simplify the work of teachers in thermodynamics in general.

Keywords:

Thermodynamics; Teaching; Exergy; Entropy; Exergy efficiency; Effectiveness.

1. Introduction

Exergy is too complicated! That is the too frequent comment coming from practitioners or even physics colleagues. One potential explanation is the fact that, to start with, the entropy concept is often not well understood. In many studies in physics, entropy is essentially introduced in relation to closed system. However, most of the energy systems the engineers deal with, are open systems with the importance of considering the entropy of the masses transiting through the boundaries of the system. As a matter of fact, when asked if they, themselves, have seen their own entropy increase in average during the last year, many would answer yes instead of considering that it is vital for them to keep their entropy constant (at least at constant weight!!). They are also unable to explain why human can still live by 45°C atmospheric temperature or more, while their own body is at 37°C. Heat transfer is not the only way to get rid of one's entropy creation.

One second potential explanation is that while, in the First Law of thermodynamics, the distinction between state functions and process-dependent entities is clearly done with differentiated names, it is often not done with the exergy balance where all terms are called exergy.

One third potential explanation is that the exergy efficiencies, in particular for combustion systems, are numerically much lower than the performance indicators based on the First Law of thermodynamics, reason why the practitioners do not like it. This is in particular relevant for condensing fuel boilers, where First Law "efficiencies" are sometimes quoted with values above 100% due to their use of the Lower Heating Value to characterize the fuel energy input while they condense part of the vapor produced during combustion.

Other obstacles might also be a confusion with the many First Law performance indicators that exist (engine efficiency, efficiency based on Lower Heating Value or on Higher Heating Value, heating coefficient of performance, cooling coefficient of performance) that can be replaced by a single indicator, the exergy efficiency. Also comes into play the potential maximum work that is easily associated to work but not well understood for the other energy outputs like those linked to exiting masses.

2. Exergy balance

2.1. Definition of exergy

The historical path that resulted in a correct and complete interpretation of the First and Second Laws of thermodynamics and their implications has been a lengthy one. It ultimately led to the following definition of exergy, a fundamental concept in the modern approach of the management and proper use of energy:

Exergy: the potential of maximum work that could ideally be obtained from each amount of energy being transferred or stored, using reversible cycles with the environment (atmosphere) as one of the energy sources, either hot or cold.

2.2. Equation of exergy balance

Let us look at a given system surrounded by an environment characterized by its temperature T_a and its pressure P_a.

The First Law of thermodynamics (energy balance) is given by:

Energy storage work heat energy of transiting masses

$$\frac{d(U_{cz}+P_aV)}{dt} = \sum_k \dot{E}^+_{wk} + \sum_i \dot{Q}^+_i - \dot{Q}^-_a + \sum_j \dot{M}^+_j h_{cz_j} \quad (1)$$

Or to express the energy conservation:

$$\sum_k \dot{E}^+_{wk} + \sum_i \dot{Q}^+_i - \dot{Q}^-_a + \sum_j \dot{M}^+_j h_{cz_j} - \frac{d(U_{cz}+P_aV)}{dt} = 0 \quad (2)$$

$$\underbrace{\sum_k \dot{E}^+_{wk} + \sum_i \dot{Q}^+_i - \dot{Q}^-_a + \sum_j \dot{M}^+_j h_{cz_j} - \frac{d(U_{cz}+P_aV)}{dt}}_{\dot{Y}^+} = 0$$

Power transformation

The state functions U_{cz} and h_{cz_j} are defined here as:

$$U_{cz} = U + M\frac{C^2}{2} + MgZ \quad (3)$$

$$h_{cz_j} = h_j + \frac{C_j^2}{2} + gZ_j \quad (4)$$

Where U_{cz} is the total internal energy including the internal energy *U*, as well as the kinetic and potential energies. h_{cz_j} is the total enthalpy per unit mass of the flowing fluid including the specific enthalpy *h* as well as the specific kinetic and potential energies at the specified state *j*.

The specific enthalpy *h* accounts for the specific internal energy and the specific work required to push it into or out of the system, *C* represents the absolute velocity and *Z* the altitude. In most practical cases the kinetic and potential terms can be neglected, except when the conditions vary significantly through time or in off-design conditions.

In the above equations, the entities $\dot{E}^+_w, \dot{Q}^+, \dot{M}^+$ can be numerically positive or negative using the convention positive entering indicated by the exponent $()^+$. This allows very compact formulations of the laws. (Later when defining the performance indicators requiring only numerically positive terms the convention positive exiting $()^-$ will also be introduced for some entities).

- $\dot{E}^+_w$ represents the mechanical energy rate ("work") given to or retrieved from the system (through volume change or rotating shaft for examples),
- $\dot{Q}^+$ represents the heat rate entering or retrieved from the system from any hot source different from the atmosphere,
- $\dot{M}^+$ is the input or output (fluid) mass flow of the system,

The notion of *power transformation* $\dot{Y}$ introduced here allows to group all terms concerned with similar masses in networks [1], making sure that the thermodynamic references are coherent, and allowing a simpler definition of the energy services received or provided. A network groups all the masses in a subsystem that are in direct contact with each other. For example, a simple heat exchanger has two networks, one for the fluid being heated and one for the fluid being cooled.

The Second Law of thermodynamics is given by:

Entropy storage entropy of heat entropy of masses entropy creation

$$\frac{dS}{dt} = \sum_i \frac{\dot{Q}^+_i}{T_i} - \frac{\dot{Q}^-_a}{T_a} + \sum_j \dot{M}^+_j s_j + \dot{S}^i \quad (5)$$

Where:

- S is the entropy of the system and is a state function while *s* is a specific state function attached to each mass of the system or moving through its boundary.

- $\dot{S}^i$ is the creation of entropy inside the system, exponent i for internal or irreversibility, and is not a state function but a process-dependent entity. As such $\dot{S}^i$ cannot be determined at a time t, since it needs to be integrated over a time lapse like for work or heat.

In both formulas, the energy or entropy exchanges with the surrounding (atmosphere) have been separated from the other entities, in the same way as Carnot did not include them in his definition of the Carnot efficiency. In quasi-steady operation of open systems, the time derivatives of the state functions *S*, U_{cz} and *V* are equal to 0. However, it is not the case for the rate of entropy creation $\dot{S}^i$ since it is not a state function but a process-dependent entity, that requires an integration over time to be quantified. Equation 2 then allows to highlight that any open system needs, not only a cold source but an entropy bin for the entropy of both the heat and the entropy of masses crossing the boundary to compensate for its entropy creation. In quasi-steady operation the entropy of an adiabatic steam turbine does not change, thanks to the fact that the exiting steam has a higher entropy and therefore carry with it the entropy creation occurring in the turbine itself. The same applies to humans or other living creatures that can get rid of their entropy creation through mass transfer [2,3].

Let us multiply the two members of the entropy balance of Equ. (5) by the environmental (atmospheric) temperature T_a so that each term is expressed in energy per unit of time (W), like in the energy balance. Furthermore, since entropy is not conserved in real processes, the term of entropy creation is moved to the right member of the equation:

$$T_a \sum_i \frac{\dot{Q}_i^+}{T_i} - \dot{Q}_a^- + T_a \sum_j \dot{M}_j^+ s_j - T_a \frac{dS}{dt} = -T_a \dot{S}^i \qquad (5)$$

Subtracting the latter from the energy balance (Equ. (2)) leads to the ***exergy balance*** for a system including n networks:

$$\sum_k \dot{E}_{wk}^+ + \sum_i \dot{Q}_i^+ - \dot{Q}_a^- + \sum_j \dot{M}_j^+ h_{cz_j} - \frac{d(U_{cz} + P_a V)}{dt} = 0$$

$$-\left\{ T_a \sum_i \frac{\dot{Q}_i^+}{T_i} - \dot{Q}_a^- + T_a \sum_j \dot{M}_j^+ s_j - T_a \frac{dS}{dt} = -T_a \dot{S}^i \right\}$$

$$\sum_k \dot{E}_{wk}^+ + \sum_i \left(1 - \frac{T_a}{T_i}\right) \dot{Q}_i^+ + \sum_n \left[\sum_j \dot{M}_j^+ (h_{cz_j} - T_a s_j) - \frac{d(U_{cz} + P_a V - T_a S)}{dt} \right] = T_a \dot{S}^i \qquad (6)$$

Coenthalpy coenergy

Work exergy Heat exergy Flow exergy Storage exergy Exergy loss

Exergy transformation $\dot{E}_y^+$ for each of n network

In Equ. (6) all the terms are now ***exergy*** terms in the same way as all the terms of the First Law are energy terms. However, there is the need to clearly differentiate between state functions and process-dependent entities with a clear denomination. For systems with only work exchange and heat exchanges, these state functions can be expressed as a function of two other state functions (in a given atmosphere for exergy state functions)

Table 1. State functions

First Law and Second state functions	Exergy state functions
Internal energy *U* or *u*	*Coenergy* $J = U + P_aV - T_aS$ or $j = u + P_av - T_as$
Total internal energy U_{cz} or u_{cz}	Total coenergy $J_{cz} = U_{cz} + P_aV - T_aS$ or $j_{cz} = u_{cz} + P_av - T_as$
Enthalpy *H* or *h*	Coenthalpy $K = H - T_aS$ or $k = h - T_as$
Total enthalpy H_{cz} or h_{cz}	Total coenthalpy $K_{cz} = H_{cz} - T_aS$ or $k_{cz} = h_{cz} - T_as$

The rate of mechanical (or electric) energy, $\dot{E}_w^+$, represents a transfer of energy of the highest thermodynamic quality, such as technical work or electricity, with the system, and as long as such a transfer is done without friction.

According to the definition of exergy given in the introduction, the quantitative values of energy and exergy, for mechanical work or electricity for example, $\dot{E}_w^+$, are identical. Let us emphasize that, in this paper, the E_w terms represent the energy terms with the highest potential to provide all kinds of energy services (in this case, equivalent in quantity to exergy). Therefore, it applies to work or electricity terms. The letter *E*, contrary to many books, is not used to express the total internal energy, which is defined here as U_{cz}. In most practical cases the kinetic and potential terms can be neglected, except when the conditions vary significantly through time or space, or in off-design conditions. This way of writing has also the advantage that the same subscript $()_{cz}$ can be applied to the total enthalpy by symmetry.

The ***heat exergy*** term $(1 - T_a/T_i)\dot{Q}_i^+$ is the work equivalent of the thermal energy given to the system from a heat reservoir at temperature T_i different from T_a. This expression highlights the multiplicative factor $(1 - T_a/T_i)$ that is nothing other than the so-called *Carnot factor*. This one determines the maximum work that can be produced from a heat rate $\dot{Q}_i^+$ at temperature T_i when working in an environment at temperature T_a (*Carnot cycle*) with $T_i > T_a$. One key element that needs to be highlighted is that as soon the temperature of the source at T_i is below T_a then $\dot{E}_q^+$ becomes numerically negative which means that for the system to accept heat, it must provide work, like typically for cooling or refrigeration.

The ***flow exergy*** term $\dot{M}^+(h_{cz} - T_a s)$, in the absence of chemical reactions, is the maximum work that can be recovered if the considered flow is reversibly brought to a thermal and mechanical equilibrium with the atmosphere. This fact is not obvious at first sight and deserves a demonstration. Figure 1 illustrates the reversible processes that could be used to verify that this expression is the maximum potential work that can be recovered. Those consist first of an isentropic expansion in a turbine until the exit temperature corresponds to T_a, followed by a further expansion in an isothermal turbine until P_a is reached.

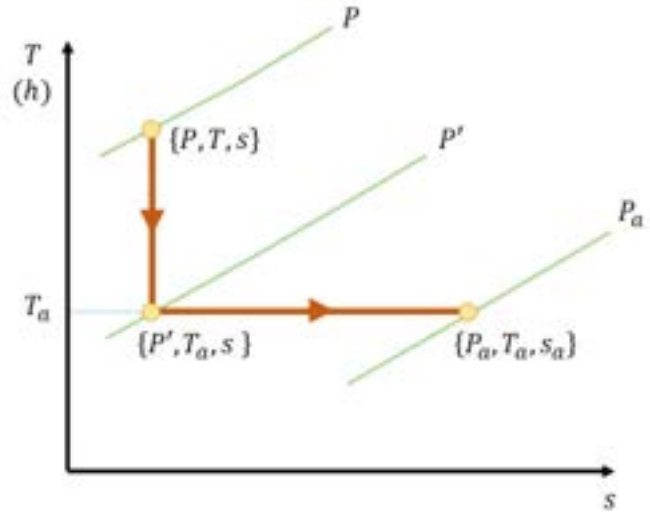

Figure 1. Reversible processes to illustrate that the coenthalpy ($k = h - T_a s$) corresponds to the maximum specific work (exergy) that can be recovered from a mass flow.

The ***storage exergy term,*** *the total coenergy* $J_{cz} = U_{cz} + P_a V - T_a S$ is the maximum work that is stored in the system and could be recovered at a later stage. It accounts for the internal energy (*U*), including the kinetic and potential energy (*cz*), and the mechanical exergy linked to the exchange at the flexible system boundary (like with a piston) with the atmosphere. Again, this concept is not obvious and needs a demonstration to accept it.

Figure 2 illustrates in a (T-s) diagram the reversible processes that could be used to verify that this expression is the maximum potential work that can be recovered from a mass stored in the system. Those consist first of an isentropic expansion in an expander until the exit temperature corresponds to T_a, followed by a further expansion in an isothermal heated expander until P_a is reached. The term $T_a s$ corresponds to the heat received from the atmosphere during these processes. Finally, if the downstream pressure in a general case does not correspond to the atmospheric pressure, then an isentropic compressor might be required as illustrated in Figure 2. Releasing or capturing heat to or from the atmosphere does not, in-itself, imply any exergy exchange since $T = T_a$ and the Carnot factor is null. When it comes to $P_a V$ it should be easy to understand that when the piston of an engine moves downwards, some of the work from the expanding gas is used to push the surrounding atmosphere ($-P_a\, dV$) but is recovered when the piston goes up, the atmosphere helping. Therefore, it is a true form of energy storage and can be associated to any of the networks in the system.

The ***exergy loss term*** $T_a \dot{S}^i = \dot{L}$ includes all the exergy losses taking place in the system.

In the same way that the notion of *power transformation* was introduced in the First Law, the corresponding notion of *exergy transformation* grouping the flow exergy and storage exergy terms for each network is also quoted.

Demonstration that the exergy transformation between two different pressures of a gas bottle corresponds to the maximum work that could be retrieved. This case of energy storage with an inert gas, like air, initially pressurized, can be represented by the cylinder-piston device of Figure 2. Equations are the same as for the case of Figure 1 except that the end point is not the state of the atmosphere and we have thus to add a compression process from 2' to 2. The kinetic and potential energies $()_{cz}$ are neglected.

a) *isentropic* expansion in an adiabatic expander from $\{P_1, v_1, T_1, s_1\}$ to $\{P_{1'}, v_{1'}, T_a, s_1\}$, that is until the temperature T_a is reached:

$$E_w^- = -(U_{1'} - U_1) - P_a(V_{1'} - V_1) = -M\big((u_{1'} - u_1) - P_a(v_{1'} - v_1)\big) \tag{7}$$

b) *isothermal* expansion in a diabatic compressor from $\{P_{1\prime}, v_{1\prime}, T_a, s_1\}$ to $\{P_{2\prime}, v_{2\prime}, T_a, s_2\}$, heat being received from the atmosphere:

$$E_w^- = -(U_{2'} - U_{1'}) + Q_a^+ - P_a(V_{2'} - V_{1'}) = (U_{1'} - U_{2'}) + T_a(S_2 - S_1) + P_a(V_{1'} - V_{2'}) \quad (8)$$

c) *isentropic* compression in an adiabatic compressor from $\{P_{2\prime}, v_{2\prime}, T_a, s_2\}$ to $\{P_2, v_2, T_a, s_2\}$:

$$E_w^+ = (U_2 - U_{2\prime}) + P_a(V_2 - V_{2\prime}) \quad (9)$$

Hence the maximum work that can be recovered is:

$$E_{wmax}^- = -(U_{1'} - U_1) - P_a(V_{1'} - V_1) + (U_{1'} - U_{2'}) + T_a(S_2 - S_1) + P_a(V_{1'} - V_{2'})\ (U_2 - U_{2'}) + P_a(V_2 - V_{2'})$$
$$= (U_1 - U_2) - T_a(S_1 - S_2) + P_a(V_1 - V_2) = J_1 - J_2 = E_y^- \quad (10)$$

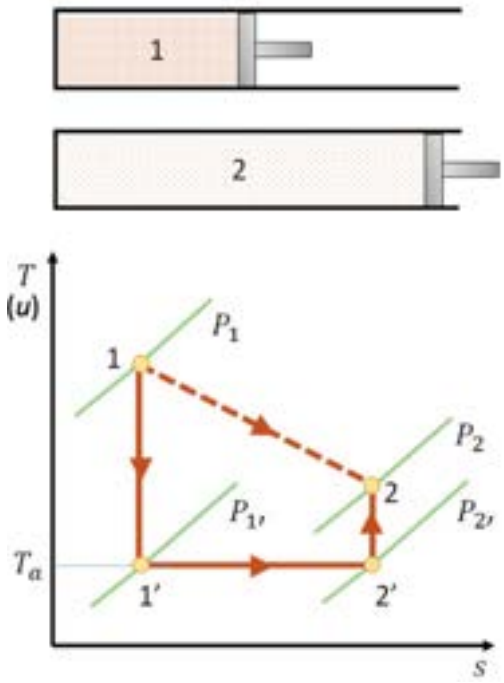

Figure 2. Reversible processes leading to the production of maximum work from the expansion of a given mass of gas in a closed system.

The net maximum work is therefore also the difference of the total coenergies. This is typically the term that will allow us to assess the work that can ideally be recovered in compressed air storage schemes, or from a compressed inert gas in a compressed air car, a technology that some researchers are presently developing for urban driving [4].

2.3 State functions versus process-dependent entities

Note that in the above equations the symbol δ is used in derivatives for process-dependant entities while d is used for state functions.

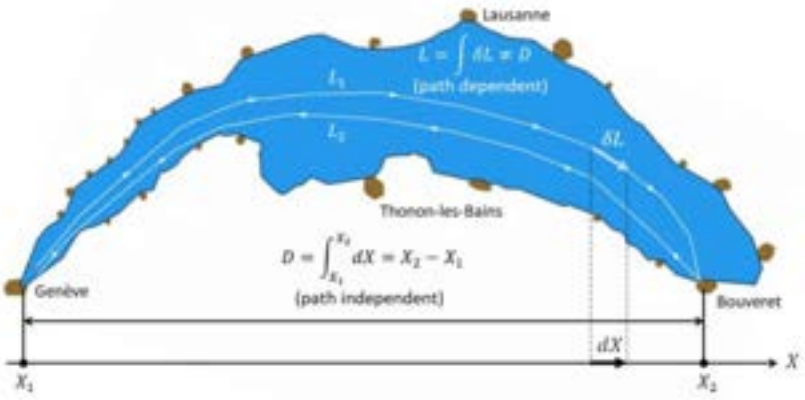

Figure 3. Illustration of the difference between a state function and process-dependent entity

State functions can be defined in any position during a process while process-dependant entities require an integration over the chosen thermodynamic path. Figure 3 symbolically illustrates this difference in the simple example of a boat going from point 1 ("Geneva") to point 2 ("Bouveret") and return following a different path, thus of different length ($L_1 \neq L_2$) while the "distance as the crow flies" D between the two cities remains of course unchanged.

In this case the length of the path L is a process-dependent entity while the reference of its horizontal position X is a state function. X_1 and X_2 can be clearly defined, but this is not the case for L that will depend on the path chosen by the skipper that day.

One interesting feature is: $\oint dX = 0$ while $\oint \delta L > 0$

Therefore, we will also have: $\oint dS = 0$ while $\oint \delta S^i > 0$

It is important to realize that, even though we are in both cases speaking of entropy, the entropy *S* within the system is a state function while the creation of entropy **inside** the system S^i is a process-dependent entity.

Q, E_w are also process dependent entities while S, U, H with their specific mass counterparts s, u, h are state functions.

When expressed in function of time we have:

$$\dot{Q}^+ = \frac{\delta Q^+}{dt} \quad (11) \; ; \qquad \dot{E}_w^+ = \frac{\delta E_w^+}{dt} \quad (12) \; ; \qquad \dot{S}^i = \frac{\delta S^i}{dt} \quad (13)$$

Figures 4 and 5 show the state function *coenergy* of air in function of the temperature and its specific entropy. Similar diagrams can be made for any substance or mixtures of substances.

Energy and masses are conserved, but their potential to do work is ultimately degraded to be cancelled when the equilibrium with the atmosphere is reached, a thermodynamic state that is called the *dead state*.

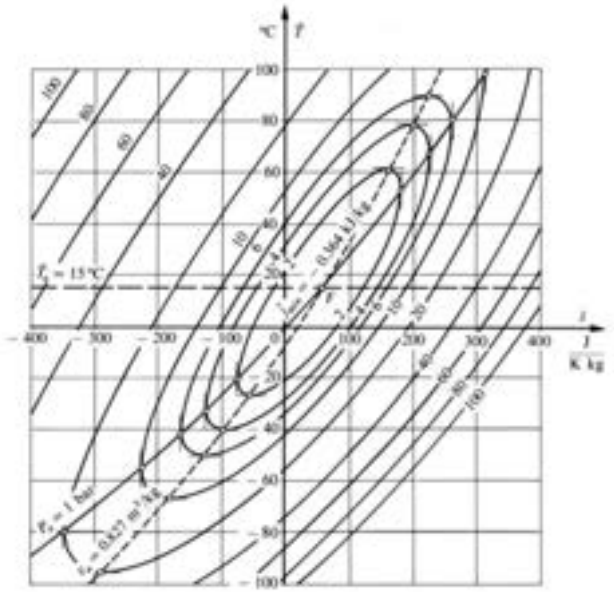

Figure 4. Coenergy of air in a T-s diagram [1]

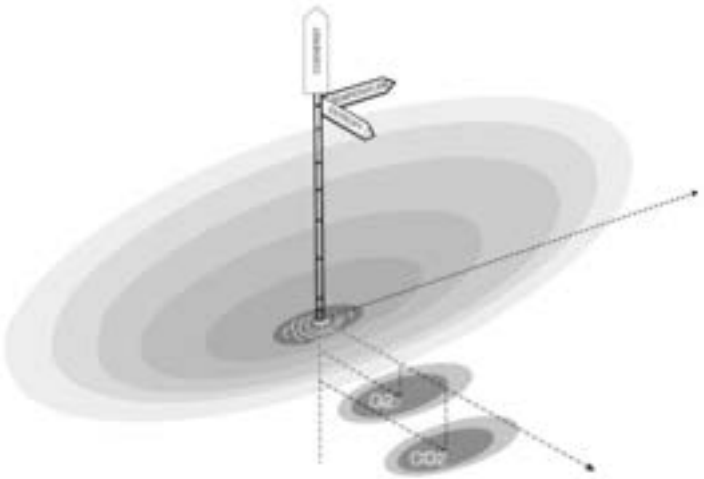

Figure. 5. Approximate representation of the coenergy function (here for air) with the thermomechanical dead state at the centre of the bowl, as well as the individual dead states for O_2 and CO_2

Those diagrams illustrate the existence of different *dead states*:

- The *dead state* of the mixture corresponding to the thermo-mechanical equilibrium with the environment (atmosphere). It corresponds to the bottom of a bowl where the coenergy has a minimum value. The higher the difference between the absolute value of (s-s_a) or the difference (T-T_a), the higher is the value of the coenergy.
- Two other *dead states* are approximatively represented, one for the physico-chemical equilibrium of the component H_2O of the air mixture and one other for the physico-chemical equilibrium of the component CO_2.The exergy analysis requires then the definition of a reference composition of the atmosphere shown in Table 2. The latter illustrates the minimum work required to separate CO_2 from air that is now discussed in the context of CO_2 separation for either reuse or storage.

3. Extension to chemical processes

Chemical processes like combustion or oxidation in fuel cells imply a change of substance between the input substances and the products of the reactions. While the sum of the enthalpies of the flows through an open adiabatic system with a combustion process does not change, the reference states for each products have lower values.

Table 2. Partial pressure and molar fractions of the main gaseous constituents of the standard atmosphere (at the standard conditions with $P^0 = 1.01325$ bar and $T^0 = 25°C$)

Substance	$P_i\ [bar]$	$\tilde{c}_i^A\ [kmol_i/kmol_A]$
N_2	0.7665	0.7565
O_2	0.2056	0.2030
Ar	0.0091	0.0090
$H_2O(g)$	0.0316	0.0312
CO_2	0.0003	0.0003

3.1. Fuel exergy value

The analysis of reactive processes, like combustion, can be dealt with by introducing a combustion network with a power transformation term $\dot{Y}_{comb}^{+}$ in the energy balance et a combustion exergy transformation term $\dot{E}_{y\,comb}^{+}$ in the exergy balance. For the latter not only the standard atmosphere (Table 2) should be considered but also the following set of hypotheses:

- The fuel F and the air A enter separately (no premixing with the fuel)
- Each constituent of the reaction products Gc (combustion gases) ends up physically mixed with the standard atmosphere, i.e. at its partial pressure P_i^{00}
- Water exists in the final combustion products Gc either in liquid or vapor form at the limit of saturation, i.e. at the partial pressure of saturation in the standard atmosphere.

These conditions being set, the corresponding values for the **exergy value of a fuel** EXV are the following:

$$\mathrm{EXV} = \Delta k^0 = \sum_i \left[\frac{N_i\ \tilde{k}_{fi}^{00}}{M_F}\right] - \sum_j \left[\frac{N_j\ \tilde{k}_{fj}^{00}}{M_F}\right] \qquad \left[\frac{J}{kg_F}\right] \tag{14}$$

In accordance with the basic definition of exergy, the specific exergy value Δk^0 corresponds to the maximum work e_{max}^F that can be recovered from a fuel in an open reversible combustion in steady state (Fig.6).

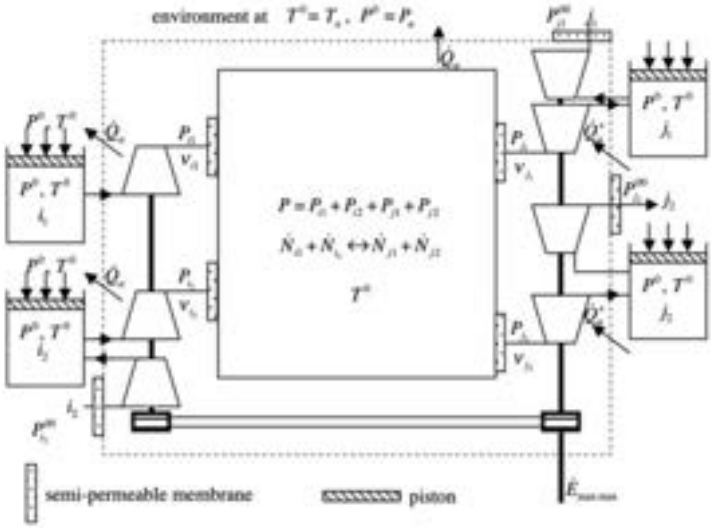

Figure 6. Mechanistic model of a reversible combustion using a van'Hoff's box [1,5]

3.2. Energy and exergy balances including power- or exergy- transformation for the combustion network

In principle, we should also consider whether or not there is condensation of the water formed during combustion. However as shown in [1] the difference between a higher and a lower exergy value is negligible in particular when $T_a = T^0$. This is logical since the Carnot factor $(1 - \frac{T_a}{T^0})$ is zero. Hence t**he advantage of the exergy analysis of systems including oxidation processes is that a single *fuel exergy* value can be considered in first approximation.**

Energy balance

$$\sum_k \dot{E}^-_{w_k} + \sum_i \dot{Q}^-_i \left(+\dot{Q}^-_a\right) + \sum_n \dot{Y}^-_n = \sum_k \dot{E}^+_{w_k} + \sum_i \dot{Q}^+_i \left(+\dot{Q}^+_a\right) + \sum_n \dot{Y}^+_n + \dot{Y}^+_{comb} \quad (15)$$

$\dot{Y}^+ = \sum_l \left[\dot{M}^+_l h_{cz_l}\right] - \mathrm{d}(U_{cz} + P_a V)/dt$ (16) for each of the n system networks, except for the combustion network that is treated separately:

$$\dot{Y}^+_{comb} = \dot{M}_F\left(HHV + \hat{h}_F\right) + \dot{M}_A \hat{h}_A - \dot{M}_G \hat{h}_G - \sum(\dot{M}_I\, HHV_I) - (\dot{M}_{H2Op} - \dot{M}_{cond}) q^0_{vap} \quad (17)$$

Where:

- $\hat{h}_F = \int_{T^0}^{T^F} dh_F$ and $\hat{h}_A = \int_{T^0}^{T^A} dh_A$ and $\hat{h}_G = \int_{T^0}^{T^G} dh_G$ are the enthalpy differences between the state of the entering or exiting entities considered in the power transformation $\dot{Y}^+_{comb}$ and the standard conditions. The species in $\hat{h}_A$ and $\hat{h}_G$ are considered to be perfect gases
- $\dot{M}_I$ and HHV_I are the mass-flows of unburned hydrocarbons and their higher heating value, in the case of incomplete combustion,
- $\dot{M}_{H2Op}$ is the mass-flow of *H₂O* produced during combustion,
- $\dot{M}_{cond}$ is the mass-flow of *H₂O* effectively condensed.

Exergy balance

$$\sum_k \dot{E}^-_{w_k} + \sum_i \dot{E}^-_{q_i} + \sum_n \dot{E}^-_{y_n} = \sum_k \dot{E}^+_{w_k} + \sum_i \dot{E}^+_{q_i} + \sum_n \dot{E}^+_{y_n} + \dot{E}^+_{y,comb} - \dot{L} \quad (18)$$

$$\dot{E}^+_y = \sum_l \left[\dot{M}^+_l (h_{cz_l} - T_a s_l\right] - \mathrm{d}(U_{cz} + P_a V - T_a S)/dt = \sum_l \left[\dot{M}^+_l k_{cz_l}\right] - \mathrm{d}J_{cz}/dt \quad (19)$$

for each of the *n* system networks except for the combustion network that is treated separately:

$$\dot{E}^+_{y,comb} = \dot{M}_F\left(\mathrm{EXV} + \hat{k}_F\right) + \dot{M}_A \hat{k}_A - \dot{M}_G \hat{k}_G - \sum\left[\dot{M}_I \Delta k^0_I\right] \quad (20)$$

(Specific isobaric) fuel exergy value

$$\mathrm{EXV} = \Delta k^0 = \sum_i \left[\frac{N_i\ \tilde{k}^0_{fi}}{M_F}\right] - \sum_j \left[\frac{N_j\ \tilde{k}^0_{fj}}{M_F}\right] \quad \text{in } \left[\frac{J}{kg_F}\right] \quad (21)$$

or

$$\Delta\tilde{k}^0 = \Delta\tilde{g}^0_F + \sum_j [\,\tilde{e}^0_{dj}] - \sum_i [\,\tilde{e}^0_{di}] \text{ in } \left[\frac{J}{kmol_F}\right] \text{ with } \tilde{e}^0_{dk} = \frac{\dot{N}_k}{\dot{N}_F} \tilde{r} T^0 ln\left(\frac{P^0}{P^{00}_k}\right) \quad (22)$$

Where $\Delta\tilde{g}^0_F$ is the Gibbs free energy (free enthalpy) of the fuel based on the enthalpies of formation and the absolute entropies. $\tilde{e}^0_{dk}$ is the exergy of diffusion (often called chemical exergy of the inert species).

4. Energy and exergy performance indicators

Historically Carnot developed its engine efficiency based only on energy terms. When the process is reversed this definition of efficiency becomes higher than 1 for heating or $\lessgtr 1$ for cooling, reason why COP heating or COP cooling have been introduced. We prefer the introduction of the concept of effectiveness adapted to all cases even if there is still the need to differentiate between heating and cooling effectivenesses when dealing with First Law energy terms.

This issue is not a problem with the notion of exergy efficiency where one definition only can be used for all systems with values remaining lower or equal to 1.

Providing energy services can be achieved by various technologies or combinations of technologies and it is important to be able to characterize the quality of these different options. In practice, two different indicators of the quality of energy processes can be defined: the *(energy)* ***effectiveness*** (so-called "thermal efficiency" or "coefficient of performance") based on the First Law of thermodynamics only or, better, the ***exergy efficiency*** based on the exergy balance, thus accounting for both the First and the Second Laws of thermodynamics. The basic idea of these sets of performance indicators is to use:

$$\varepsilon\ (or\ \eta) = \frac{energy\ (or\ exergy)\ services\ \boldsymbol{provided\ by}\ the\ system}{energy\ (or\ exergy)\ services\ \boldsymbol{received\ by}\ the\ system} \quad (22)$$

The *energy* ***effectiveness*** can be formulated as follows:

$$\varepsilon = \frac{\sum_k \dot{E}^-_{w_k} + \sum_i \dot{Q}^-_i + \sum_n \dot{Y}^-_n}{\sum_k \dot{E}^+_{w_k} + \sum_i \dot{Q}^+_i + \sum_n \dot{Y}^+_n} \quad \text{valid for processes at } T \geq T_a \quad (23)$$

Written that way, this expression is indeed only valid for processes that take place above the atmospheric temperature and can take values between 0 and ∞. This formulation can be directly used for engine or heating heat pump cycles. An exception needs to be done for refrigeration for which the refrigeration service $\dot{Q}_f^+$ or $\dot{Y}_f^+$ with temperature values lower than T_a must be only considered in the numerator as an energy service provided by the system.

The ***exergy efficiency*** can then simply be formulated as follows:

$$\eta = \frac{\sum_k \dot{E}_{w_k}^- + \sum_i \dot{E}_{q_i}^- + \sum_n \dot{E}_{y_n}^-}{\sum_k \dot{E}_{w_k}^+ + \sum_i \dot{E}_{q_i}^+ + \sum_n \dot{E}_{y_n}^+} = 1 - \frac{\dot{L}}{\sum_k \dot{E}_{w_k}^+ + \sum_i \dot{E}_{q_i}^+ + \sum_n \dot{E}_{y_n}^+} \leq 1 \quad (24)$$

Note that we consider in the numerator only the exergy services provided to users of the system. When any exergy term of the numerator exits the system without being used, the boundary of the system needs to be extended to the atmosphere and this exergy term becomes zero, but the corresponding exergy losses are still accounted for in $\dot{L}$ since the denominator has not changed. We can say that the related exergy loss is internalized and attributed to the system. For example, if the system is a combustion engine with a generator, its main service is to provide electricity, even though the cooling network has exergy that could potentially be used by others. However, if the exergy of the cooling network is not used but is destroyed in a cooling tower, it is automatically included in the exergy losses $\dot{L}$. Some authors like [6] subdivide $\dot{L}$ into:

$$\dot{L} = \dot{L}_D + \dot{L}_E \quad (25)$$

Where $\dot{L}_D$ includes the exergy destruction inside the strictly defined system and $\dot{L}_E$ includes the exergy destroyed between the system and the atmosphere. We do not consider this subdivision as useful in practice, since the objective is in fine the reduction of the total exergy loss $\dot{L}$.

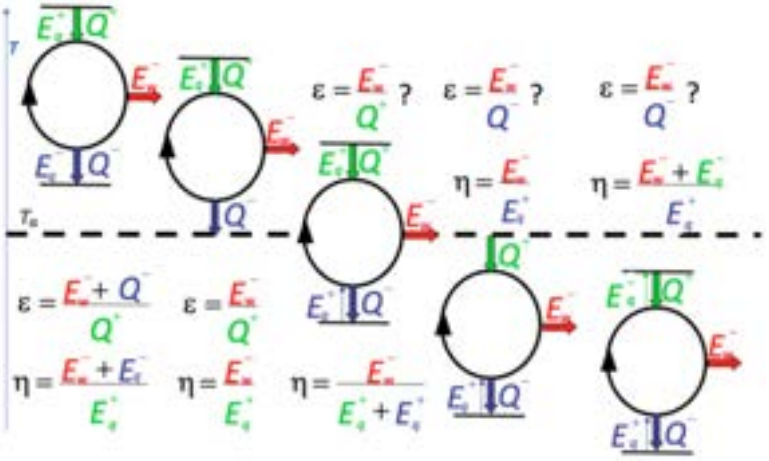

Figure 7. Simple representation of the energy effectiveness and the exergy efficiency of engine cycles in function of the temperature range [1]

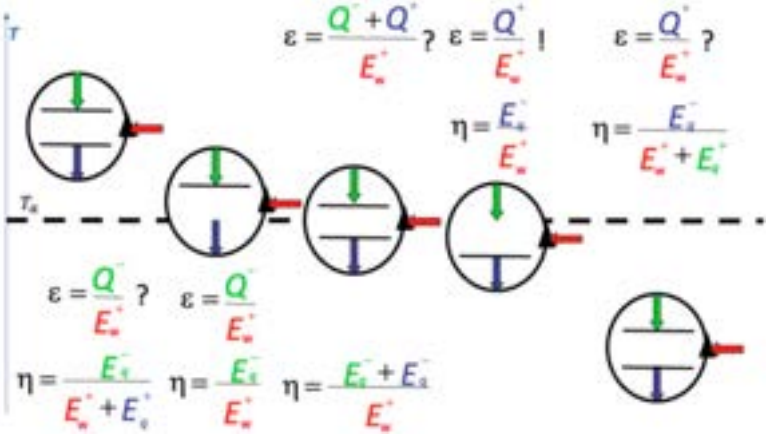

Figure 8. Simple representation of the energy effectiveness and the exergy efficiency of heat pump cycles in function of the temperature range [1]

Figures 7 and 8 show the performance indicators for simple engine cycles and heat pumps cycles in the various temperature ranges. There are clearly situations where defining an effectiveness is problematic while exergy efficiencies are coherent for all cases.

Figure 9 shows a symbolic representation of some common technologies in a 3D bowl diagram. This is inspired from the earlier representations of [1] with an analogy between exergy levels and the gravity field. Mass units are represented by little men. The red arrows show a typical fuel boiler situation starting with a high exergy level fuel combined to give combustion gases at relatively high temperature and specific exergy to provide

heat for a building at low exergy level. Finally heat losses through the walls of the building let energy leak to the dead state. The green arrows represent the processes of an engine requiring, to elevate some of the little men to the high exergy level of electricity some little men need to be going to the dead state all the greater as the initial exergy level is low. An alternative is shown with the downward little men being deviated at the level of the house heating and that corresponds to a cogeneration system. The blue arrows illustrate a direct electric heating based on Joule's effect. The yellow arrow illustrates an electrical heat pump. Finally on the left of the figure is a representation of a sub-atmospheric temperature Rankine engine cycle using the environmental heat as a heat source and the lower temperature of liquid natural gas (LNG) to be evaporated as a cold source.

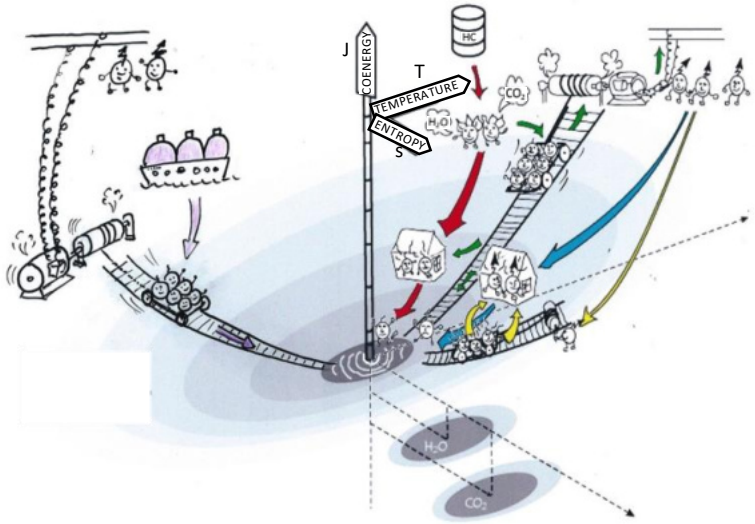

Figure 9: Symbolic representation of the exergy bowl with different heating and power generation technologies [7]. (Rigorously the coenergy bowl should be redrawn for each change of substance)

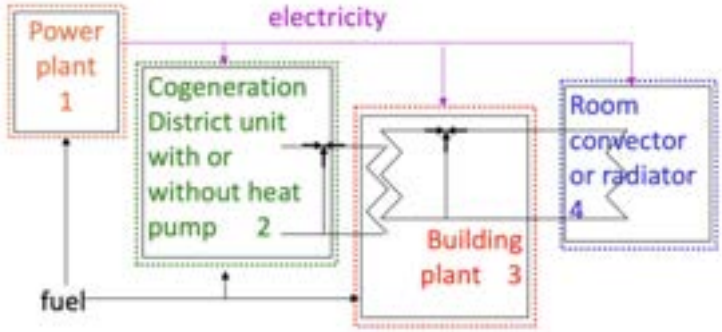

Figure 10. Division in 4 subsystems of the problem of heating or cooling of a building with a multiple choice of technologies [8].

Table 2: Examples of overall technologies for heating

Technologies	Power plant	DH plant	Building plant		Room convector		Overall exergy efficiency (%)	
Supply/return temperatures			45°/35°	65°/55°	45°/35°	65°/55°	45°/35°	65°/55°
Direct electric heating (hydro power)	0.88				0.07	0.07	6.0	6.0
Building non-condensing boiler			0.11	0.16	0.53	0.38	6.1	6.1
Building condensing boiler			0.12		0.53		6.6	
District heat pump (combined cycle plant)	0.54	0.61	0.54	0.76	0.53	0.38	9.4	9.4
Domestic heat pump (cogeneration combined cycle power)	0.54		0.45	0.45	0.53	0.38	12.9	9.2
District heat pump(hydropower)	0.88	0.61	0.54	0.76	0.53	0.38	15.4	15.4
Domestic heat pump (hydropower	0.88		0.45	0.45	0.53	0.38	21.2	15.1

Figure 10 and Table 2 responds to a basic question asked by the architect. Since exergy is higher at a higher heating temperature why is it interesting to use low temperature heating systems like floor heating? Exergy

analysis provides a coherent answer. As shown in [7] the overall exergy efficiency can be obtained by multiplying the exergy efficiencies of each subsystem.

$$\eta = \eta_1 \eta_2 \eta_3 \eta_4 \tag{26}$$

Example: Combined cycle power plant without cogeneration (1) + District heating heat pump (2) + DH heat exchanger in the building (3) + Convector (4).

$$\eta = \left(\frac{\dot{E}^-_{el,1}}{\dot{E}^+_{y,1}}\right)\left(\frac{\dot{E}^-_{y,2}}{\dot{E}^+_{el,2}}\right)\left(\frac{\dot{E}^-_{y,3}}{\dot{E}^+_{y,3}}\right)\left(\frac{\dot{E}^-_{q,4}}{\dot{E}^+_{y,4}}\right) = \frac{\dot{E}^-_{q,4}}{\dot{E}^-_{y,1}} \tag{27}$$

Table 11 illustrates the case for cooling.
The net conclusion from such analysis and which corresponds well to the second Law of thermodynamics is:

Heat at the lowest temperature as possible and cool at the highest temperature as possible

Table 11 Examples of overall technologies for air-conditioning [8]

Power plant technologies	Power plant	Dist. plant	Building plant			Room convector			Overall exergy efficiency [%]		
Supply/return temperatures			*10°/15°*	5°/10°	0°/5°	*10°/15°*	5°/10°	0°/5°	*10°/15°*	5°/10°	0°/5°
Nuclear power	0.32		*0.4*	0.4	0.4	*0.56*	0.43	0.34	*7.1*	5.4	4.3
Gas motors	0.36		*0.4*	0.4	0.4	*0.56*	0.43	0.34	*8.1*	6.2	4.9
Combined cycle power plant without cogeneration	0.54		*0.4*	0.4	0.4	*0.07*	0.07	0.07	*12.1*	9.3	7.3
Hydropower	0.88		*0.4*	0.4	0.4	*0.53*	0.38	0.33	*19.8*	15.2	12.0

Further application of the concept of exergy efficiency that is often motivating students is the application to vehicle drives as shown in [9,10] where alternative of power drives from electric to liquid nitrogen cars and others are compared. Estimates of exergy efficiencies of electric cars of the order of 69% (without accounting for the efficiency of power generation) are compared with an average of 18% for thermal engine cars based on road tests. In [10] these values are introduced into regional energy scenarios to estimate the future influence on the electricity consumption for example.

5. AI platform for teaching exergy

An attempt was made to apply an AI emerging platform [11] to assist educators. It was applied to the first part of this paper noticing that this beta version did not yet allow equations in a MS Word environment so those had to be described in a written format. However, this early approach illustrates the potential interest of this fast-developing tool at a time where ex-cathedra courses are recognized to be inefficient. The platform proposes a number of tools including automatically generated glossary, concept cards, Quiz, Drag the word, flash cards and crosswords that the author can then freely modify to increase the accuracy or the pertinence.

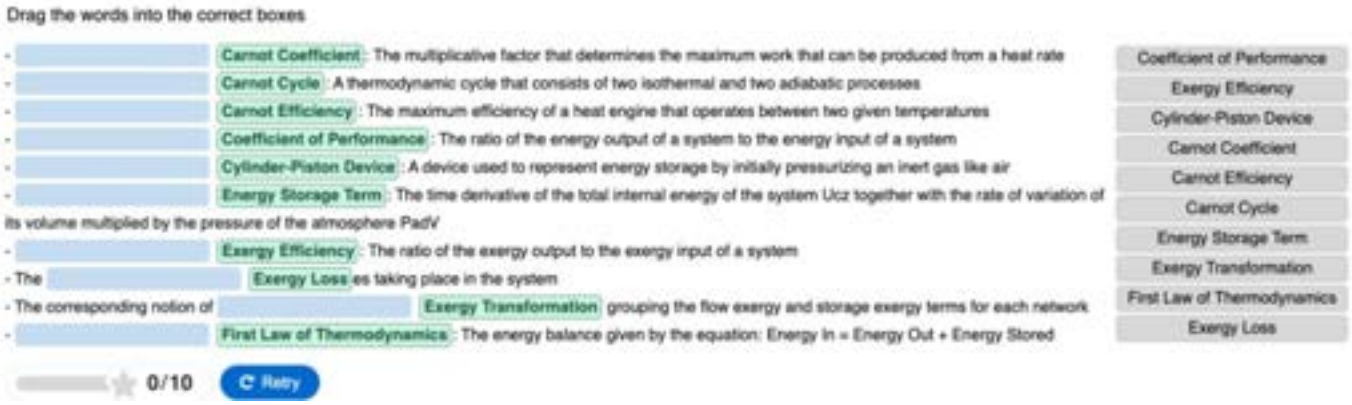

Figure 10. Non modified proposal from the platform for a “drag the word” exercise

Figure 10 shows one of the “Drag the word” proposal with here the solution superposed in green. Some of the definition obviously need to be improved but the structure is there and the effort from the educator is significantly reduced. Figure 11 provides another presentation with the crossword that can break the monotony during the course. Here again some definitions need to be improved. Of particular interest is the 40 questions with multiple choice of answers among which about one third still need to be discarded, mainly because they refer to the descriptive of equations that are not ideal at this stage.

One additional benefit for the educator could be to highlight the parts of his paper that are not clear enough and need to be improved.

Conclusions

Teaching exergy for a broad range of users is still a challenge. The approach proposed in this paper tries to have a rigorous symmetry between the First Law balance and the exergy balance in cases of open systems with a clear distinction between state functions and process-dependent entities. Applications linked to the ranking of technology combinations for heating and air-conditioning are, among others, good examples for the use of the exergy concept. Finally, an attempt is made to exploit for teaching purposes the fast-developing use of AI tools with the present limitations.

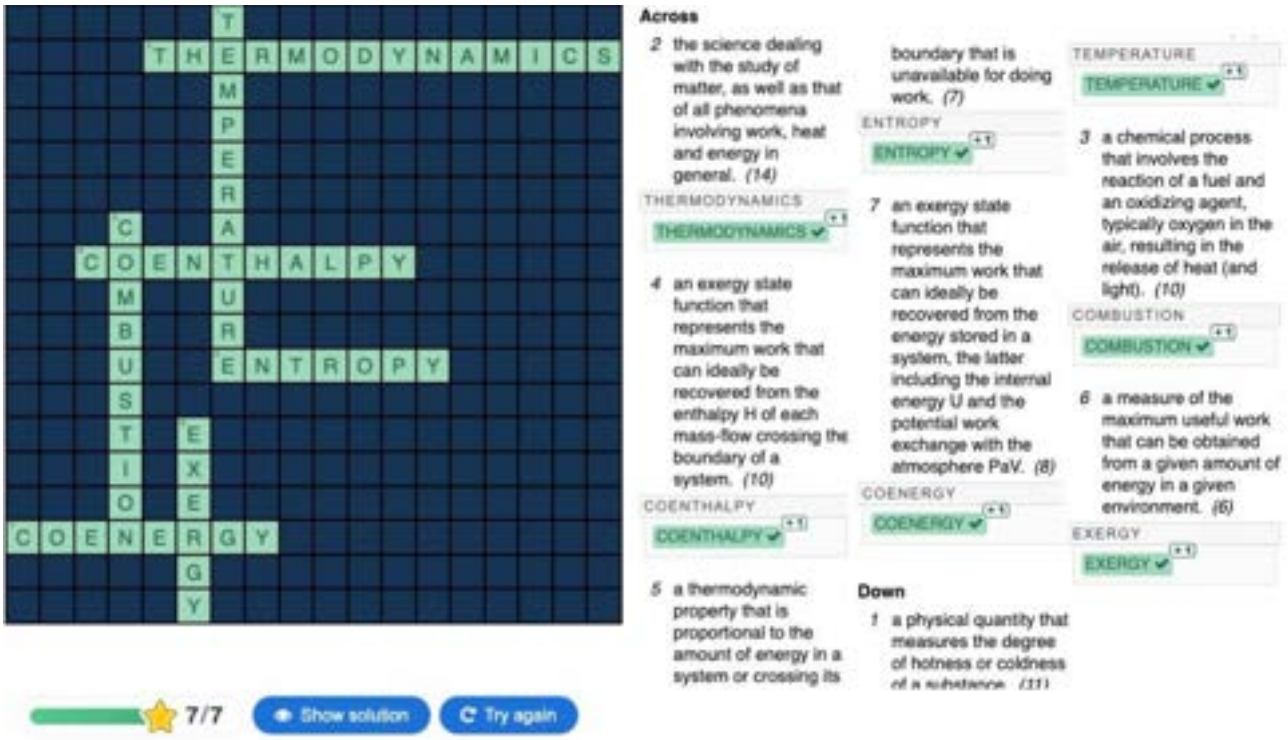

Figure 11. Example of crossword generated by the platform (text yet unmodified)

References

[1] Borel L., Favrat D., Thermodynamics and energy system analysis. EPFL Press, Lausanne,Switzerland; 2011

[2] Batato M., Energétique du corps humain. Ed. PPUR, Lausanne, 1989. ISBN 2-88074-177-7

[3] Nielsen S,N., Müller F., Marques J,C., Bastianoni S., Jorgensen S.E., Thermodynamics in Ecology - An introductory Review. Entropy 2020;22(820).

[4] Rufer A., Energy storage. CRC Press, London UK; 2018

[5] Favrat D., Kane M., From the fuel heating values to the fuel exergy value in advanced energy systems. In ECOS 2023: Proceedings of the 36th International Conference on Efficiency, Cost, Optimization, Simulation and Environmental impacts of Energy Systems, 2023 June 25-30; Las Palmas de Gran Canaria (Spain).

[6] Moran M.J., Shapiro H.N., Boettner D.D, Bailey M.B. Fundamentals of engineering thermodynamics. Wiley 9th edition ,US; 2018.

[7] Favrat D., Marechal F., Exergy representation in thermodynamics. In: Meyer J.P. editor. HEFAT 2015: Proceedings of the 11th International Conference on Heat Transfer, Fluid Mechanics and Thermodynamics, Skukuza, South Africa, 2015 July 20-23. (ISBN: 978-1-77592-108-0)

[8] Favrat D., Marechal F., Epelly O., The challenge of introducing an exergy indicator in a local law on energy. Energy 2008;33(2):130-136

[9] Iglesias A., Favrat D., Comparative exergy analysis of compressed air, liquid nitrogen and classical power cycle for urban vehicles. In: ECOS 2013: Proceedings of the 26th International Conference on Efficiency, Cost, Optimization, Simulation and Environmental impact of Energy Systems, 2013 July 16-19; Guilin (China).

[10] Codina V., Allais M., Favrat D.,Vuille F., Marechal F. Exergy assessment of future energy transition scenarios with application to Switzerland. In : ECOS 2017 : Proceedings of the 30th International Conference on Efficiency, Cost, Optimization, Simulation and Environmental impact of Energy Systems; 2017 July 2-6, San Diego, USA

[11] Nolej.io (tested on May 1, 2023)

Exergy and exergy cost analysis of biochemical energy conversion process: Application to the metabolic model of living cells

Assal SELMA[a], Mauro REINI[b], Michele GIANI[c] and Francesca MALFATTI[d]

[a] Dept. of Engineering and Architecture, University of Trieste, Polo di Pordenone-Italy, assal.selma@phd.units.it,
[b] Dept. of Engineering and Architecture, University of Trieste, Polo di Pordenone-Italy, reini@units.it,
[c] Instituto nazionale di oceanografia e di geofisica sperimentale - (TS) - Italy, mgiani@inogs.it,
[d] Instituto nazionale di oceanografia e di geofisica sperimentale - (TS) - Italy, fmalfatti@ogs.it,

Abstract:

The idea of a Thermodynamic cost associated with flows in a network of irreversible thermodynamic processes is widely developed in the context of energy engineering, but the general formulation of the Exergy Cost Theory-ECT allows in principle its application also to the biochemical networks.
This paper describes the application of the exergy analysis to a generic metabolic network and an approach for calculating the exergy costs associated with all the flows present in the network, according to the ECT. The main perspective is to use the exergy cost information for defining additional constraints in the Flux Balance Analysis- FBA of the bacterial metabolic network. Which could help identifying directions for the optimization of the biomass production process, and the enhancement of the biofuel use in industry. In fact, this approach mainly relays on the maximization of the produced biomass, for identifying all metabolites fluxes in a biochemical network, with the constraints expressed by the stoichiometric relations of all reactions within the network. Therefore, some additional constraints have to be introduced, in order for guiding the optimization algorithm towards thermodynamically feasible solutions.
The expectation is that, by introducing the actual exergy cost, with their clear physical meaning, the results would be more consistent with the experimental finding, reported in literature, for a wide range of possible environmental conditions.
By applying the unit exergy cost concept, a deeper understanding of the reason why the reaction paths of the same metabolic network changes, in different environmental conditions, is also expected to be achieved.

Keywords:

Exergy analysis; Exergy Cost Theory-ETC; Energy Conversion Process; Thermodynamic Cost, Biomass Production Optimization; Biofuel; Flux Balance Analysis-FBA; Biochemical Networks Of Living Systems Far From Equilibrium.

1. Introduction

Living cells are known as complex and dynamic systems that play a vital role in maintaining the balance of life on Earth. They are composed of various subsystems that interact with each other in a coordinated manner, with each subsystem contributing to the overall functioning of the cell.

Understanding the behavior and performance of these systems is critical for comprehending the underlying mechanisms of cellular processes and for improving the efficiency of biotechnological processes. One approach to analyzing the behavior and performance of living cells is exergy analysis. Exergy analysis is a thermodynamic method that quantifies the amount of energy available for conversion from one form to another and has been widely used in the analysis of energy systems, such as power plants and industrial processes.

In recent years, exergy analysis has been applied to the study of living cells, it has been widely used in the study of living cells, providing a comprehensive understanding of the thermodynamics of these complex and dynamic systems. The application of exergy analysis to living cells has resulted in new insights into cellular behavior and performance, and has led to improvements in the design and operation of bioreactors and bioprocesses. One of the key areas where exergy analysis has been applied to the study of living cells is in the analysis of metabolic pathways.

By quantifying the energy inputs, outputs, and losses in cellular processes, exergy analysis can provide a detailed understanding of the efficiency of metabolic pathways, and identify areas for improvement. This

information can be used to optimize cellular processes, leading to improved performance and greater sustainability. Another area where exergy analysis has been applied to the study of living cells is in the analysis of ion transport processes, such as ion pumps and channels. By quantifying the energy inputs and outputs of these processes, exergy analysis provides a valuable framework for assessing their efficiency and optimizing their performance.

In this context, exergy analysis has also been used in the study of bioreactors and bioprocesses, providing a thermodynamic framework for the analysis of energy and matter exchange in these systems.

In this paper, we describe the application of exergy analysis to a generic metabolic network, with a focus on calculating the exergy costs associated with all the flows present in the network.

The Exergy Cost Theory (ECT) provides a framework for this analysis, allowing for the formulation of a thermodynamic cost associated with flows in a network of irreversible thermodynamic processes. While the ECT has been widely used in energy engineering, this paper explores its application to biochemical networks. Our main perspective is to use the exergy cost information to define additional constraints in the Flux Balance Analysis (FBA) of the bacterial metabolic network, which is a powerful technique in bioinformatics, used for identifying directions for the optimization of biomass production processes and the enhancement of biofuel use in industry. Nevertheless, the approach mainly relies on the maximization of the produced biomass, with the constraints expressed by the stoichiometric relations of all reactions within the network. This approach requires the introduction of additional constraints for guiding the optimization algorithm towards thermodynamically feasible solutions.

We expect that by introducing the actual exergy cost, with their clear physical meaning, the results would be more consistent with experimental findings reported in literature for a wide range of possible environmental conditions. We also expect to achieve a deeper understanding of why the reaction paths of the same metabolic network change in different environmental conditions by applying the concept of unit exergy cost. Overall, our paper demonstrates the potential of exergy analysis, and the ECT in particular, for optimizing metabolic networks in bioengineering.

2. Exergy analysis of cellular process

Exergy analysis of cellular processes starts with a thermodynamic analysis of the energy exchanges that take place in the cell, including the inputs and outputs of energy, matter, and entropy[1].

The exergy of a process is defined as the maximum useful work that can be obtained from a system, and it is calculated as the difference between the actual enthalpy of the system and the reference enthalpy[2]. The reference enthalpy is the enthalpy of the system in a state of equilibrium at a reference temperature and pressure, usually taken to be the temperature and pressure of the environment.

Exergy analysis can be used to assess the efficiency of various cellular processes, such as metabolic pathways, ion transport, and biochemical reactions[3]. For instance, it is possible to use it to determine the energy conversion efficiency of metabolic pathways, as well as the exergy losses due to internal irreversibilities, [4] [13] such as entropy production.

Additionally, exergy analysis can be used to assess the efficiency of ion transport processes, such as ion pumps and channels, by quantifying the inputs and outputs of these processes from an energetic point of view [5]. By quantifying the energy inputs, outputs, and losses in cellular processes, exergy analysis could be utilized for assessing theefficiency of various metabolic pathways [6].

The late mentioned method provides a valuable framework for the optimization of cellular processes, by identifying areas for improvement in energy and matter exchange. This information can be used to improve the efficiency of cellular processes [7].

3. Exergy Analysis of Biotechnological Processes

Evaluating the potential for energy utilization and efficiency in a given system or process is a key point to fulfill optimization. In the context of biotechnology, exergy analysis is a suitable tool to evaluate the performanceof bioprocesses such as fermentation, biorefining, and biogas production, etc..

The basic principle of exergy analysis is to calculate the maximum useful work that can be obtained from a system or process, based on the availability of energy in the system and the environment.
In bioprocesses,[7] the exergy of the process inputs (such as substrates and nutrients) and the exergy losses (such as waste heat and other by-products) can be quantified. These information can then be employed to identify areas for improvement in terms of energy efficiency and sustainability.

There are several benefits to using exergy analysis in biotechnology. One of the main benefits is that it provides a comprehensive and quantitative assessment of the energy utilization and efficiency of a bioprocess.

Such information is quite useful for enhancement the process conditions, reduce energy costs, and minimize environmental impact.

These kind of analysis is indeed, a valuable tool for evaluating the performance of bioprocesses in terms of energy utilization and efficiency. As the information obtained from an exergy analysis could provide meaningful insights to optimize the process conditions, reduce energy costs, and minimize environmental impact, making bioprocesses more sustainable and environmentally friendly.

4. Glycolysis pathway of Escherichia coli

Escherichia coli is a type of bacterium that uses glycolysis as its primary source of energy, which is a metabolic pathway that breaks down glucose (a simple sugar) into pyruvate, producing energy in the form of ATP [9]. The following is a summary of the glycolysis pathway in *E. coli*:

• Conversion of glucose to fructose-1,6-bisphosphate: Glucose is converted to fructose-1,6-bisphosphate through the action of hexokinase, which adds a phosphate group to the molecule.

• Cleavage of fructose-1,6-bisphosphate: The next step is the cleavage of fructose-1,6- bisphosphate into two three-carbon molecules, glyceraldehyde-3-phosphate and dihydroxyacetone phosphate, by the action of aldolase;

• Phosphorylation and isomerization: Both glyceraldehyde-3-phosphate and dihydroxyacetone phosphate are converted to their isomer, 1,3-bisphosphoglycerate, by the action of triose phosphate isomerase. This reaction is also accompanied by the addition of a phosphate group, producing energy in the form of ATP.

• Conversion of 1,3-bisphosphoglycerate to 3-phosphoglycerate: The next step is the conversion of 1,3-bisphosphoglycerate to 3-phosphoglycerate through the action of phosphoglycerate kinase, which adds another phosphate group, producing more ATP.

• Conversion of 3-phosphoglycerate to 2-phosphoglycerate: The next step is the conversion of 3-phosphoglycerate to 2-phosphoglycerate through the action of phosphoglycerate mutase.

• Conversion of 2-phosphoglycerate to phosphoenolpyruvate: The final step of glycolysis is the conversion of 2-phosphoglycerate to phosphoenolpyruvate (PEP) through the action of enolase. This reaction releases energy in the form of ATP.

• Conversion of phosphoenolpyruvate to pyruvate: The conversion of phosphoenolpyruvate to pyruvate is catalyzed by the enzyme pyruvate kinase. This final step of glycolysis completes the degradation of glucose to pyruvate, producing a net gain of two ATP molecules.

In addition to producing ATP, the degradation of glucose in glycolysis also generates the building blocks for other metabolic processes, including the citric acid cycle, which generates more energy.

Figure. 1. Glycolysis pathway of *Escherichia. Coli*.

4.1. Exergy analysis and exergy cost of the glycolysis metabolic pathway of *Escherichia coli*

Exergy analysis is a thermodynamic method that assesses the maximum useful work that can be obtained from a system. In the context of the glycolysis metabolic pathway of *E. coli*, the exergy analysis would involve calculating the change in exergy (useful work potential) for e each step of the reaction sequence.

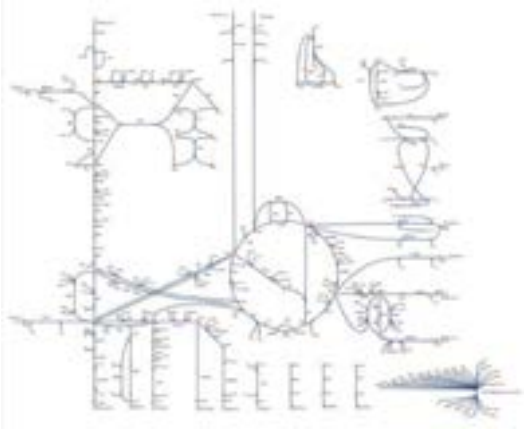

Figure. 2. ESCHER map of the metabolic pathway of *E.coli*. core (**a simplified model**).

(https://escher.github.io/#/app?map=e_coli_core.Core%20metabolism&tool=Builder&model=e_coli_core)

Performing the exergy analysis of the glycolysis pathway involves estimating the change in exergy (by representing the useful work potential) at each step of the whole reaction sequence.

In order to perform exergy analysis, it is necessary to determine the chemical exergy values of the involved compounds in the metabolic pathway. These values represent the maximum amount of work that can be obtained from each compound through chemical reactions under standard conditions.

By taking into account the exergy inputs and outputs of each reaction, the exergetic cost associated with the targeted pathway could be calculated.

Identifying possible relevant compounds in the pathway is also possible through the exergy of the metabolic compounds. (Figure3)

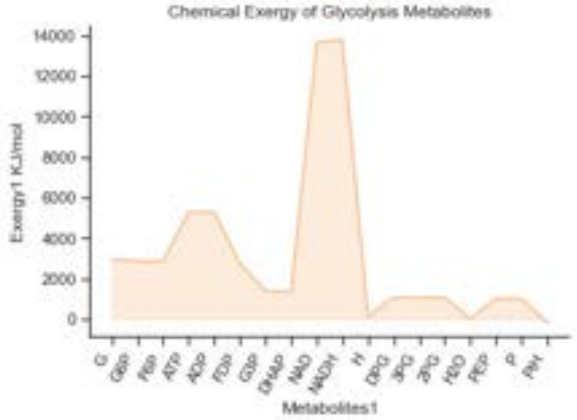

Figure. 3. The chemical exergy of the glycolysis metabolites in standard conditions.

The chemical exergy values in the plot represent the maximum amount of work that can be obtained from the metabolites through chemical reactions, and under standard conditions (298 K, 1 atm, pH 7). The data used toproduce the plot was originally extracted from literature [11].

It demonstrate that the higher the chemical exergy value of a metabolite, the greater its potential for doing useful work. Based on the plot, we can see that glucose-6-phosphate (G6P) has the highest chemical exergy value among all the metabolites in the glycolysis pathway, followed by fructose-6-phosphate (F6P) and 3-phosphoglycerate (3PG).

Which could suggests that these metabolites have the greatest potential for performing useful work in the pathway. In contrast, the lowest chemical exergy values are observed for pyruvate and ATP, indicating that these metabolites have less potential for performing useful work in the pathway.

However, it is important to note that ATP is a crucial energy carrier in the cell and plays a key role in energy metabolism, as showed, the plot gives insight into the chemical potential of the metabolites in the glycolysis pathway and can be used to guide the optimization of the pathway for increased efficiency and energy utilization. (View Figure.3)

The exergy cost represents the irreversibilities or inefficiencies within a giving system and it is a good tool to quantifies the amount of available work that is lost or degraded during the process. Exergy cost calculation involves the comparison between the exergy values of the reactants and the exergy of the products for each reaction in the metabolic pathway.

For accurate K* calculations, reliable chemical exergy values for the compounds involved in glycolysis are crucial as a primary step.

By applying exergy analysis approach and calculating the exergetic cost for each compound in the glycolysis pathway, it is possible to determine the steps with the highest exergy losses.

This sort of information is a suitable way to guide efforts for the optimization of certain pathways and improvement of the overall efficiency and energy utilization of the whole process.

Using the exergy analysis and exergy cost calculation of compounds in the glycolysis metabolic network may be a way to provide valuable insights into the thermodynamic efficiency and sustainability of this essential metabolic process. Furthermore, It enables researchers to evaluate the performance of the pathway, determine areas for potential improvement, and to develop more efficient strategies, especially for metabolic engineering and optimization.

Through the optimizing the glycolysis pathway based on exergy analysis, it is possible to enhance energy efficiency, reduce waste, and improve the utilization of resources in *Escherichia coli* metabolism.

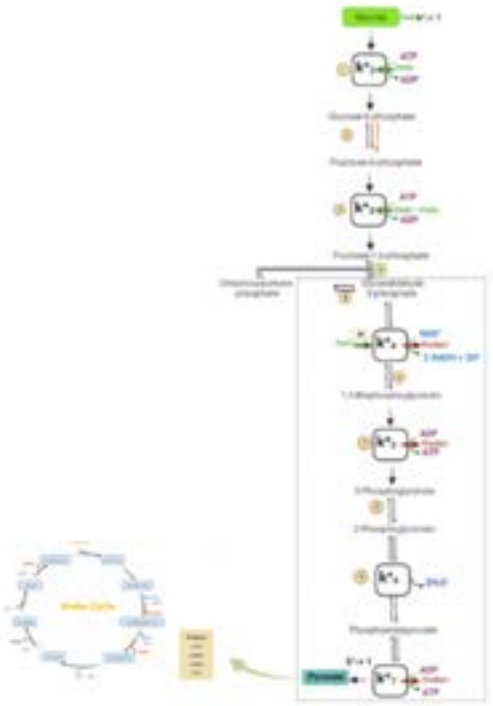

Figure. 4. Reproductive structure of the glycolysis pathway.

K* represents the exergy cost

In this context, glycolysis pathway can be seen as a reproductive structure within cellular metabolism, where the participated metabolic compounds act as fuels and products.

This pathway is one of the important and relevant pathways in most metabolic networks, as it serves as a central hub for energy generation and the production of essential molecules that sustain cellular functions.

In glycolysis, glucose, is regarded as a primary fuel source, it is initially converted into two molecules of pyruvate through a series of enzymatic reactions. This breakdown of glucose generates energy in the form of ATP and NADH. These energy-rich compounds are considered as vital fuels for various cellular processes in biology.

Moreover, the selected pathway is responsible for the production of other important metabolic compounds (that act as products). For instance, during the conversion of glucose to pyruvate, intermediates such as glucose-6-phosphate (G6P), fructose-6-phosphate (F6P), and 3-phosphoglycerate (3PG) are formed and regarded as “internal products” in this process. These compounds play crucial roles in biosynthetic pathways, providing building blocks for the synthesis of essential molecules such as nucleotides, amino acids, and lipids, etc..

The reproductive nature of the glycolysis metabolic network is evident in the recycling of metabolic compounds, where NADH, generated during glycolysis, is further oxidized to NAD+ in a subsequent cellular processes, such as oxidative phosphorylation. This recycling mechanism ensures the continuous availability of key cofactors and maintains the energy flow within the metabolic network.

The identification of metabolites as fuels and products highlights the dynamic and interconnected nature of cellular metabolism.

Glycolysis not only generates ATP, the primary energy currency of the cell, but also provides essential precursors for the synthesis of biomolecules involved in the cellular growth.

Consequently, understanding the reproductive structure of the glycolysis pathway and the roles of its compounds (By its identification as fuels and products in the process) is vital for comprehending cells from an energetic point of view, optimizing certain metabolic pathways, and also designing strategies for metabolic engineering and biotechnological applications.

Therefore, by manipulating the glycolysis pathway and its associated metabolic compounds, it would make possible to ameliorate energy production, redirect metabolic fluxes, and achieve desired cellular outcomes.

4.2. Exergy and exergy cost analysis of biochemical networks in living systems far from equilibrium

These kind of analyses represents a potential approach to understand the thermodynamic behavior of biological systems and to identify the most energetically efficient pathways for energy conversion and utilization. In living systems, biological processes often occur far from thermodynamic equilibrium, which means that traditional exergy analysis approaches may not be applicable.

For this matter, it is important to develop new methods and theoretical frameworks for exergy analysis in far from- equilibrium systems. One example of a theoretical framework is the concept of exergy efficiency, which is utilized to quantify the efficiency of energy conversion and utilization in living systems. This framework takes into account the entropy production of the system, as well as the exergy changes that occur in the system. Another important area of research is the application of exergy and exergy cost analysis to specific biological systems, such as metabolic pathways, cellular respiration, and photosynthesis. As these sort of studies can provide wider insights into the energetics of these processes and furthermore, help in the identification of potential targets for improvement in terms of energy and energy efficiency.

Despite that the approach of exergy analysis of biochemical networks in living systems far from equilibrium is still developing, it has already produced valuable insights into the energetics of these systems and has the potential to provide important guidance for energy-efficient design and operation in a wide range of biological and biotechnological application.

5. Analogical analysis: Industrial system (Engine) vs Biological system (Bacterial environment)

One of the fascinated things about nature is that it is the origin of all human kind works, same as industrial systems that has been inspired from the biological system present in our environment, as understanding the nature of the work process in a biological environment could be the key to make a development and a step forward in Human work, and vice- versa. In an engine, the exergy analysis would involve quantifying the energy losses and inefficiencies that occur as fuel is converted into useful work. This analysis can help identify areas where energy is being wasted, such as through heat losses or frictional losses, and guide efforts to optimize the engine for improved efficiency.

Similarly, in a bacterial environment, the exergy analysis would involve quantifying the energy losses and inefficiencies that occur as nutrients are converted into biomass or other bioproducts. This analysis can help identify areas where energy is being wasted, such as through the production of useless bi-products, and guide efforts to optimize the metabolic pathways of the bacteria for improved efficiency.

A key difference between the two mentioned systems is that an engine is a closed system, whereas a bacterial environment is an open system that interacts with its surroundings.

This means that the exergy analysis of a bacterial environment must take into account the energy inputs and outputs from the surrounding environment, such as through the exchange of nutrients, gases, and heat. To say better, the analogy between the exergy analysis of an industrial system and a biological system highlights the importance of understanding the thermodynamic efficiency of systems, whether they are designed by humans or evolved through natural selection.

By optimizing the efficiency of these systems, we can minimize energy losses and waste, and improve our ability to produce useful work or bioproducts.

6. Microbial production of fuels

Microbial production of fuels refers to the process of using microorganisms, such as bacteria and yeast, to convert biomass into biofuels. The most common type of biofuel produced using this method is bioethanol, which is made from sugars or starches in crops such as corn, sugarcane, and wheat.

The process of microbial production of bioethanol involves the fermentation of sugars by yeast or bacteria to produce ethanol and carbon dioxide. In addition to bioethanol, other biofuels such as butanol and biomethane can also be produced using microbial processes. Butanol, for example, can be produced by the

fermentation of sugars and starches by bacteria such as Clostridium. Biomethane can be produced by the anaerobic digestion of organic matter by microorganisms, producing methane that can be used as a fuel source. Microbial production of biofuels has gained increasing attention as a sustainable and renewable alternative to traditional fossil fuels.[13]

The use of biomass as a feedstock reduces the carbon footprint of biofuels and helps to reduce dependence on finite fossil fuel resources. However, the efficiency and scalability of microbial production of biofuels still pose challenges, and further research and development is needed to make this technology more economically viable.

7. The challenges

The efficiency and scalability of microbial production of biofuels are two important factors that determine the commercial viability of this technology. Efficiency refers to the amount of biofuel produced per unit of biomass used as a feedstock. Improving the efficiency of the process is crucial in order to make it economically viable, as it directly affects the cost of production.

The efficiency of microbial production of biofuels is influenced by a number of factors, such as the type of microorganisms used, the composition of the feedstock, and the conditions of the fermentation process. The efficiency and scalability of microbial production of biofuels are two important factors that determine the commercial viability of this technology.

Efficiency refers to the amount of biofuel produced per unit of biomass used as a feedstock. Improving the efficiency of the process is crucial in order to make it economically viable, as it directly affects the cost of production. The efficiency of microbial production of biofuels is influenced by a number of factors, such as the type of microorganisms used, the composition of the feedstock, and the conditions of the fermentation process.

Scalability refers to the ability to increase the production of biofuels as demand increases. Scalability is a challenge for microbial production of biofuels, as the process is often limited by factors such as the availability of suitable feedstocks, the cost and availability of the microorganisms used, and the cost of the necessary equipment and infrastructure. Additionally, scaling up the production process can also affect the efficiency of the process, as the conditions required for optimal growth and fermentation of microorganisms may change at larger scales.

Despite these challenges, research and development in the field of microbial production of biofuels continues, with the goal of improving both the efficiency and scalability of the process. Advances in genetic engineering and synthetic biology have led to the development of more efficient microorganisms, and the development of new technologies such as consolidated bioprocessing and metabolic engineering have the potential to significantly improve the efficiency and scalability of the process in the future.

Conclusion

Exergy analysis is a powerful tool for the analysis of living cells and biotechnological processes. It provides a thermodynamic framework for quantifying the efficiency of cellular processes and biotechnological systems, and it has been widely applied to the study of energy systems, such as power plants and industrial processes. lately, exergy analysis has been applied to the study of living cells, providing new insights of the metabolic behavior, and offering new avenues for optimization and improvement.

It has been used to assess the efficiency of metabolic pathways, ion transport, and biochemical reactions, and to identify areas for improvement in bioreactor design and operation. The application of exergy analysis to living cells and biotechnological processes continues to grow, as researchers seek to gain deeper insights into the complex and dynamic nature of these systems. With its ability to provide a thermodynamic framework for the analysis of energy and matter exchange, exergy analysis is poised to play an increasingly important role in the study of living cells and biotechnology in the years to come.

The application of exergy analysis to living cells and biotechnological processes continues to grow, as researchers seek to gain deeper insights into the complex and dynamic nature of these systems. With its ability to provide a thermodynamic framework for the analysis of energy and matter exchange, exergy analysis is poised to play an increasingly important role in the study of living cells and biotechnology.

References

[1] Chen, W., & Chen, Q. (2019). Exergy analysis of biological systems: A review. Renewable and Sustainable Energy Reviews, 111, 238-249.

[2] Wang, Y., & Chen, Q. (2018). Exergy analysis of metabolic pathways in biological systems: A review. Bioresource Technology, 262, 170-178.

[3] Smith, B. H., & van der Meer, A. D. (2018). Thermodynamics and exergy analysis of living cells. Journal of The Royal Society Interface, 15(143), 20170912.

[4] Bianchi, G., & Manfrida, G. (2019). Exergy analysis of cellular metabolism: A comprehensive review. Entropy, 21(7), 655.

[5] Chi, M., & Chen, Q. (2018). Exergy analysis of biological systems: A brief review and future perspectives. Applied Energy, 228, 1435-1441.

[6] Bejan, A. (1996). Entropy generation minimization: The new thermodynamics of finite size devices and finite-time processes. Journal of Applied Physics, 79(3), 1191-1218.

[7] Farkas, I., Hardy, G., & Weiss, J. N. (1992). The exergetic costs of ion pumping by Ca2+- ATPase of sarcoplasmic reticulum. Journal of Biological Chemistry, 267(17), 11827-11834.

[8] Özgür, E., Gökçay, C. F., & Can, Ö. (2006). Exergy analysis of biological systems: An overview. Proceedings of the Institution of Mechanical Engineers, Part A: Journal of Power and Energy, 220(6), 539-550.

[9] Berg, J. M., Tymoczko, J. L., & Stryer, L. (2002). Biochemistry. New York: W.H. Freeman and Company.

[10] Wu, H., Li, H., Li, C., Li, D., & Wang, Y. (2019). Exergy analysis and optimization of membrane bioreactor for wastewater treatment. Chemical Engineering Research and Design, 145, 187-197.

[11] Borgert, J.A. and Moura, L.M., 2013. Exergetic analysis of glucose metabolism. Chemical Engineering Science, 101, pp.782-791

[12] Wang, Jiaying, Zhiqiang Chen, Xiaogui Deng, Qianqian Yuan, and Hongwu Ma. 2023. "Engineering Escherichia coli for Poly-β-hydroxybutyrate Production from Methanol" Bioengineering 10, no. 4: 415. https://doi.org/10.3390/bioengineering10040415.

[13] Selma, Assal, Francesca Malfatti, Michele Giani, and Mauro Reini. "Exergy and exergy cost analysis of biochemical networks in living systems far from equilibrium." In *Proceedings of the 9th International Conference on Bioinformatics Research and Applications*, pp. 36-40. 2022.

PROCEEDINGS OF ECOS 2023 - THE 36TH INTERNATIONAL CONFERENCE ON
EFFICIENCY, **C**OST, **O**PTIMIZATION, **S**IMULATION AND ENVIRONMENTAL IMPACT OF ENERGY SYSTEMS
25-30 JUNE, 2023, LAS PALMAS DE GRAN CANARIA, SPAIN

Free and Open-Source Teaching: Understanding Exergy using Thermal Engineering Systems in Python (TESPy)

Mathias Hofmann[a], Francesco Witte[b], Malte Fritz[c,d], Jonas Freißmann[c,d], Ilja Tuschy[c,d], George Tsatsaronis[e]

[a] Technische Universität Berlin, Berlin, Germany, hofmann@iet.tu-berlin.de, CA
[b] German Aerospace Center (DLR), Institute of Networked Energy Systems, Oldenburg, Germany
[c] Hochschule Flensburg, University of Applied Sciences, Flensburg, Germany
[d] Center for Sustainable Energy Systems (ZNES), Europa-Universität & Hochschule Flensburg, Flensburg, Germany
[e] Technische Universität Berlin, Berlin, Germany

Abstract:

In energy or chemical engineering, a representation of highly complex processes is often only possible through a simulation. Conducting experiments or building demonstrators is far too costly and time-consuming. Applying exergy-based methods is beneficial to reveal thermodynamic inefficiencies and to propose appropriate optimization approaches for energy conversion processes. Therefore, teaching theory and software-based application of such methods are essential in engineering study programs.

This paper presents a didactic concept for open educational resources on exergy analysis covering the introduction to the exergy method, its distinction from the energy analysis, and its application to various case studies. The course aims to combine thermodynamic understanding with numerical mathematics and object-oriented programming. Students learn to build and run models of energy conversion systems and conduct respective exergy analyses using the software Thermal Engineering Systems in Python (TESPy). The course material is developed using Jupyter notebooks, which offer a flexible connection between theory and code. Results are reproducible and can be tested and developed further by the open-source community.

The advantages of exergy-based methods can be illustrated by evaluating and visualizing real thermodynamic losses using Grassmann or waterfall diagrams. Process understanding can be deepened further by parameter analysis showing their impact on components and the overall process. Finally, the acquired knowledge is transferred to more complex problems with multiple components or more than one product.

Keywords:

Thermodynamics, Exergy, Exergy-based methods, Simulation, Python, Online class

1. Introduction and Motivation

In the last years, particularly since the start of the COVID-19 pandemic, the need for using electronically-based teaching materials has increased. Nevertheless, the didactic concepts for teaching events have also changed fundamentally in a concise time [1, 2]. Specific methods, e.g., flipped/inverted classroom, were previously only used by an interested group of lecturers and played a subordinate role. The pandemic has significantly accelerated the development and led to the increased use of numerous previously underrepresented didactic methods. As a result, the didactic quality of teaching courses was improved almost imperceptibly, especially in the field of engineering.

But what principles should be applied to the design of a lecture or seminar at a university today? Von Thun [3] gives some advice on this. He considers the development of one's own design principles as fundamental, which correspond to the requirements and possibilities of your subject, your contents, and your person. The lecture or seminar should not only be given but also created. Developing those design principles is an exciting and valuable part of the professional biography of a university teacher.

When designing a course, it is necessary to determine which competency goals are to be achieved. According to Anderson and Krathwohl [4] there are six categories of cognitive process dimensions to choose from: first remember, second understand, third apply, fourth analyze, fifth evaluate, sixth create. Many courses at universities, especially introductory classes, usually are within the third category. However, the study's goal should be to reach the 6th level, i.e., to plan a research paper on a given topic, i.e., to work scientifically on one's own. Concerning engineering sciences, it is, therefore, essential to get into independent practice-relevant action as early as possible in the curriculum, e.g., to be able to program independently.

In engineering programs, especially in the field of energy and chemical engineering, thermodynamics is a fundamental discipline. In many of these courses, the exergy concept [5–9] is taught to aspiring engineers as a helpful and powerful tool. In this context, the conclusive teaching of the concept is one of the major challenges for the lecturers. There needs to be more than a conventional thermodynamics lecture to make the students apply the exergy concept and explore exergy. Following the previous remarks, we need at least one more advanced course for teaching the exergy concept. Independent activities such as programming should be included. The students must be enabled to apply general principles of thermodynamics independently, evaluate them, and finally, create energy conversion processes independently according to the given requirements and check them with the help of exergy-based methods.

In today's highly interconnected and globalized world, it should be widely accepted that research and teaching are not the exclusive preserve of established societies or segregated groups with limited social access. Indeed, even in the beginnings of the universities in the Middle Ages, admission restrictions were unusual [10, 11]. Ultimately, the composition of the student body was shaped by social realities, such as the exclusion of women. Of course, numerous social barriers have been dismantled in the meantime. That it is nevertheless not self-evident is shown by the 4th United Nations Sustainable Development Goal[1]: "Ensure inclusive and equitable quality education and promote lifelong learning opportunities for all." Addressing lifelong learning shows a need to make knowledge and knowledge transfer accessible to all without barriers, even outside appropriate institutions. For example, this can be made possible through a digital offering independent of end devices. Free and open-source access should be a standard feature.

Furthermore, in research projects funded by third parties, work is often expected today to be transdisciplinary. Consequently, social shareholders are also involved, and data and results should be available to everyone for subsequent use. For such cooperative collaboration across spatial or temporal distances, several technical solutions (cloud, git, web) exist today that enable participation and curation in various forms simultaneously. Remember, understand, apply, analyze, evaluate, and create no longer necessarily have to take place in the lecture hall or seminar room on the chalkboard.

An online course was developed based on the findings formulated up to this point. The open educational resources on exergy analysis covering the introduction to the exergy method, its distinction from the energy analysis, and its application to various case studies. The interactive digital learning experience offered to students in the course described here is a building block in the development of professional competencies for future engineers.

The present contribution is structured as follows: A didactic concept for the developed online course is presented in the next section. Information about the online implementation based on Python and Jupyter Notebooks is collected in Section 3. Some illustrative results from the course material are shown in the results section, followed by the conclusions.

All developed materials and used libraries are available on a free and open-source basis. If researchers, practitioners, teachers, or students use the content, the CC BY 4.0 guidelines[2] should be respected. The prepared content can be accessed online in a textbook format.[3] Furthermore, everyone is invited to join the developer team, share ideas and suggestions, or even bug reports via the GitHub repository.[4]

2. Didactic Concept

2.1. Target Group, Prerequisites and Integration into Curriculum

The course is intended for students in undergraduate engineering programs, especially power engineering, process engineering, and chemical engineering. In addition, the course can be a possible advanced training, since it is available in an open-source form. Nevertheless, the content is not primarily aimed at that, meaning that examples could seem too simple for a practitioner.

Students should already completed coursework in basic mathematics, thermodynamics, and object-oriented programming knowledge. Furthermore, they should be familiar with the purpose of using apparatus and machines as well as processes of energy engineering. Finally, they are expected to be interested in going deeper into the exergy concept.

Consequently, the course fits into the curriculum of the study program according to Figure 1. In deviation from the illustration, it is conceivable that the course is offered in the third or fourth semester. In any case, the stated prerequisites should be taken into account. The advantage of an early start of the course is the practice-oriented relevance of the contents. Thus, a hands-on mentality is developed, and the students are taught the relevant engineering skills at an early stage. They learn to solve problems in teams and practice modeling, programming,

[1] https://sdgs.un.org/goals/goal4
[2] https://creativecommons.org/licenses/by/4.0/
[3] https://fwitte.github.io/TESPy_teaching_exergy/
[4] https://github.com/fwitte/TESPy_teaching_exergy

and scientific computing. Also, they get familiar with from scratch process design and find alternative solutions. Finally, the students further develop existing structures.

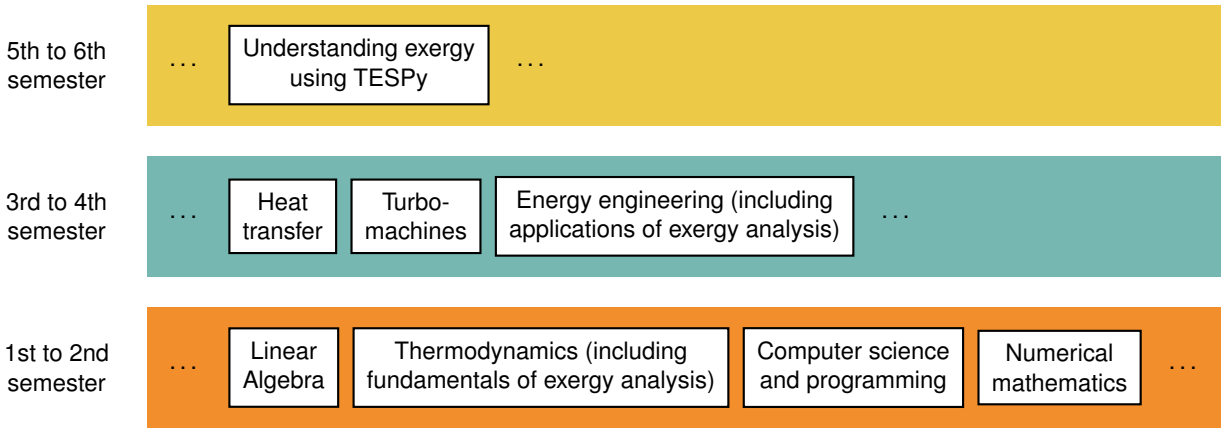

Figure 1: Integration into the curriculum of a typical engineering undergraduate program

2.2. Learning Outcomes

After finishing the course, the students are familiar with the basics of steady-state process simulation and know different methods for calculating the thermodynamic properties of substances. Also, they can build, initialize and solve process flowsheets independently, using the software Thermal Engineering Systems in Python (TESPy) as a process simulation tool for modeling, calculating, and analyzing complex energy engineering processes and interpreting the results obtained. The participants identify and solve problems that occur during process simulation and can independently use aspects of the exergy concept for their future research questions. They are familiar with physical and chemical exergy and the splitting of physical exergy. They can evaluate processes and components with the help of exergy analysis and exergy-based parameters and present the analyses graphically. Finally, using a version control system, the students apply group work methods such as team communication, milestone processing, and cooperative programming.

In their best efforts, students complete the module by adding new elements to the existing course, and thus reach the highest level of competence according to Anderson and Krathwohl [4], see Section 1.

2.3. Content and Competencies

Following the course content of fundamentals of thermodynamics and energy conversion, the focus is on simulating single state changes, simple cycles, and complex energy conversion systems. At the same time, the participants will practice methods of exergetic process evaluation.

The mathematical representation of individual components of energy engineering processes, e.g., heat exchangers, pumps, turbines, waste heat boilers, steam generators, condensers, is subsequently combined into the representation of overall processes, e.g., gas turbines, gas and steam turbine power plants, steam power processes, and integration of renewable energy sources. The methods of setting up process simulations, solving mass and energy balances, and calculating thermodynamic property data are covered. The simulation program used is the free and open-source software TESPy, see Section 3.

The work can be done individually or in small groups. We recommend working in teams of 2 to 3 people to intensify social skills and test suitable collaboration methods. Figure 2 shows the distribution of the competence fields addressed during the course. Depending on the individual characteristics of the course, shares may shift slightly.

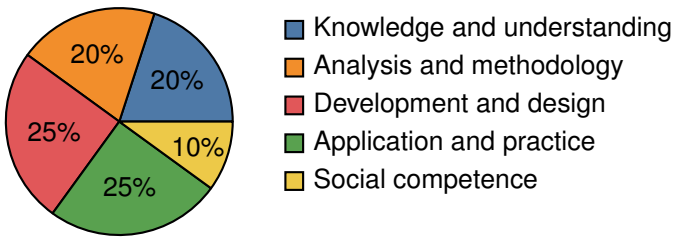

Figure 2: Pie chart showing the competency fields addressed in the progress of the course.

2.4. Schedule

The Gannt chart in Figure 3 shows a sample schedule for designing the class for one semester (2 contact hours per week). In its first version, the course includes four sections and three milestones. The kick-off meeting can include a get-to-know-you and orientation session if the students work in teams. Afterward, there is the possibility to configure the own hardware and run tests regarding the functionality of the libraries to be used.

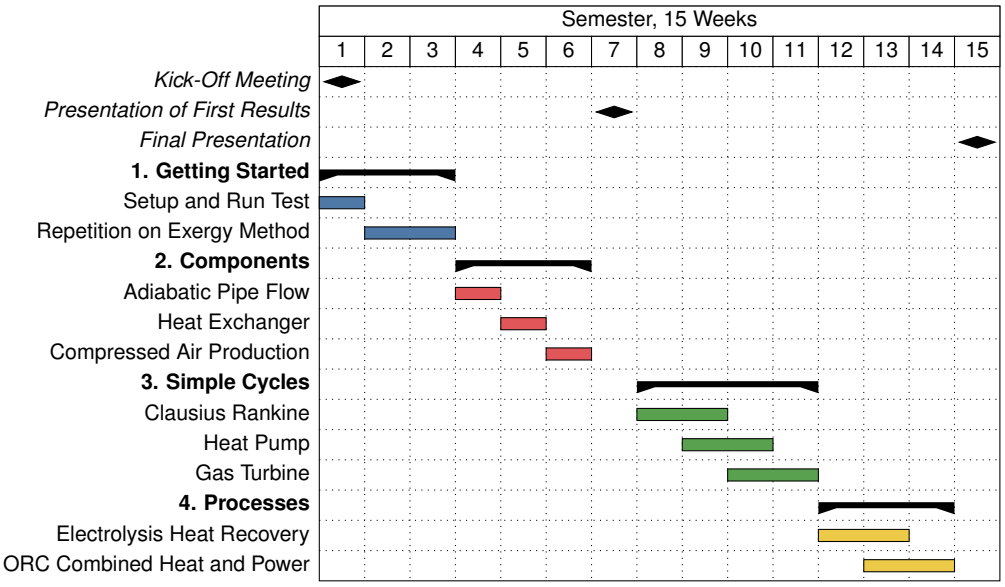

Figure 3: Gannt chart showing the possible progress of the course in one term.

In the second section, students are encouraged to investigate thermodynamic fundamentals for simple applications and program them independently. All analyses are carried out at the component level and usually involve exactly one thermodynamically describable change of state. With the help of simple exergetic analyses based on the solution of the mass and energy balances and simple graphical evaluations, differences between energetic and exergetic descriptions can be made easily understandable.

In the second section, the students will partially write down the correlations in an elementary way and later moving forward to a object-oriented programming. The advantages of a Python library (e.g., TESPy) become clear with the transition from the second to the third section.

In the third section of the course, the exergy analysis is to be applied to simple multi-component systems. At the latest in this section, the students should be aware of the advantages of the exergy-based evaluation compared to a purely energetic consideration. A further focus is then on the graphical evaluation of the results. How can the findings be visualized in the best possible way? The students can try out various approaches independently here.

Since the interaction of several components is now being investigated, the focus is on how the components' properties impact the overall process. For instance, which components significantly influence the exergy destruction of the overall process and why. It is necessary to determine which thermodynamic parameters are the most important for improving the overall process.

The last section examines complex processes with more than one product. If a process provides different forms of energy as products, for example electricity and district heating, an energy-based assessment of the quality of the overall process is misleading. Exergy is the only way to ensure comparability of the different material and energy flows. The students are to conduct these evaluations for processes such as heat recovery in electrolysis or processes with combined heat and power.

2.5. Further Reading, Online Tutorials, Hardware, Software

During their work the students can use several textbooks or online tutorials for fundamental or further reading. We recommend the following:

- Thermodynamic fundamentals [12, 13]
- Exergy concept [6–9]
- Python [14] and Jupyter Notebooks [15]
- TESPy [16–18]

For scientific computing in Python environments, it is a convenient option to use ready-made distributions that integrate relevant packages and library management in a user-friendly way. A simple start succeeds with miniforge[5], available for all current operating systems. To edit and run the code students can install a code editor such as Pycharm[6] (free of charge for university members) or Visual Studio Code[7] or run a local server allowing them to work in a browser. The online documentation of the course includes all relevant installation instructions.

3. Implementation

In recent years, there has been a concern [19] in the energy system analysis community, among others, with the public provision of data and publicly funded research's traceability. Various initiatives are engaging in this area, developing free and open-source work paradigms and taking them into other domains. Aspects initially discussed only in research are spilled into teaching. For example, the Journal of Open Source Education [20] specifically addresses lecturers to publish online educational resources connected with free and open-source software. In a proposal, Morrison [21] formulates the idea of combining publicly available data and voluntary contributions from experts into a "student-centered" energy system model for education. The actual energy system model will be programmed in Julia, and the workflow will be set up in Jupyter. It is explicitly not a web-based scenario generator or gamification exercise. The students will perform exercises in a curated way and develop the code of the energy system model piece by piece.

Inspired by these ideas, the present course for energy technology and exergy analysis was developed. In particular, the idea for the structural content and the technical project architecture is based on Morrison's proposal. The entire content of the course is embedded in a Python-based structure. The prepared content can be accessed online in a textbook format[8] and the source files are available through the respective GitHub repository.[9] Figure 4 shows the implementation.

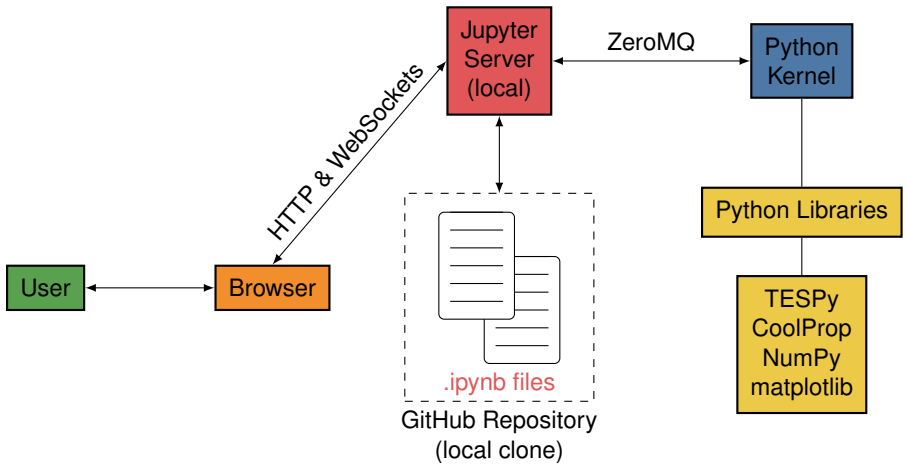

Figure 4: Implementation of the resources into a Python-based architecture including a powerful and user-friendly front-end

The files[10] are provided as a Jupyter notebook. It is an editable format where not only Python code is stored and can be executed, but visualization, markdown, and collaboration capabilities exist. Consequently, this format is particularly suitable for course formats like the one presented here. Outlines can be created, and text can be formatted, images and videos can be added, mathematical formulas and referencing can be used.

To create their own code, students can download the Jupyter files to their machine and locally run a Jupyter server, which allows to access a Python kernel and run their code in the browser or in code editors.

The open-source software TESPy [16] is used for the component-based simulation of the considered energy conversion processes. The software is developed as part of the open energy modeling framework (oemof) in the scientific field and by industrial users.[11] The user can build up arbitrary thermodynamic processes from single predefined components like heat exchangers, compressors, valves, or turbines. In addition to heat pumps, geothermal or solar thermal power plants, heat networks, or chillers can also be mapped. The software

[5] https://github.com/conda-forge/miniforge
[6] https://www.jetbrains.com/community/education/#students
[7] https://code.visualstudio.com/
[8] https://fwitte.github.io/TESPy_teaching_exergy
[9] https://github.com/fwitte/TESPy_teaching_exergy
[10] file extension .ipynb
[11] https://oemof.org

accesses the likewise open-source substance properties database CoolProp [22]. Detailed documentation with more examples and tutorials is available for the software.[12]

Following process simulation and design, exergy analysis can be used to identify sources of thermodynamic losses. The exergy analysis is performed automatically. Only the exergetic fuel, product, and loss of the overall process have to be passed to the tool [17, 18]. Furthermore, the simulation models can be combined with optimization methods [23].

4. Featured Course Material

The course is based on three relevant pillars whose approach enables change management and innovation processes in their respective disciplines or application areas. The three pillars are

- object-oriented programming with Python,
- steady-state power plant simulation with open-source software (TESPy, CoolProp), and
- thermodynamic evaluation using exergy-based methods.

As a consequence, the contents of the course lead to the conclusion that these three pillars can be interlinked with each other exceptionally well for prospective engineers to teach the exergy concept. We want to summarize this by presenting selected tasks from the course and illustrating the results comprehensibly.

Within all listed thermodynamic models below we assume steady-state processes, all components are adiabatic, there are no pressure losses in the heat exchangers, and changes in kinetic and potential energies can be neglected. Ambient conditions are set to $T_0 = 25\,^\circ\mathrm{C}$ and $p_0 = 1.013\,\mathrm{bar}$. For the calculation of chemical exergies the model of Ahrendts [24] is used. The corresponding flow diagrams and parameters of the processes can be found in Figures 5, 8, 11, and 12 as well as Tables 1, 2, and 3. Due to space limitations, not all source codes are given below. All tasks and solutions can be obtained from the git repository.

4.1. Highlight 1: Adiabatic Pipe Flow

Consider a well insulated pipeline transporting a fluid, i.e., water steam or air. The state change from 1 to 2 because of friction can be described as an adiabatic throttling valve as shown in 5.

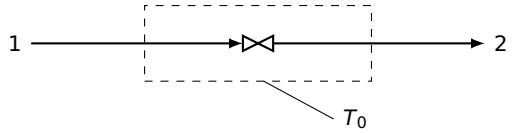

Figure 5: Flowchart of adiabatic pipe flow

Table 1: Adiabatic pipe flow parameters

Parameter	Symbol	Unit	Value
Inlet temperature	T_1	°C	195
Inlet pressure	p_1	bar	10
Constant (or varying) outlet pressure	p_2	bar	6 (or p_1 ... p_0)
Mass flow rate	m_1	kg/s	1

First, setting up the parameters of the pipe flow and calculating the inlet enthalpy, if necessary install CoolProp.[13]

```
from CoolProp.CoolProp import PropsSI as PSI
fluid = "water"
p_in = 10 * 1e5
T_in = 195 + 273.15
h_in = PSI("H", "P", p_in, "T", T_in, fluid)
p_out = 6 * 1e5
```

Considering the above assumptions, and the energy balance, we determine the outlet temperature for isenthalpic throttling using CoolProp.

```
h_out = h_in
PSI("T", "P", p_out, "H", h_out, fluid) - 273.15
```

[12] https://tespy.rtfd.io

[13] As an alternative a simple, full-featured, lightweight CoolProp wrapper for Python is available via https://pypi.org/project/pyfluids/.

Subsequently, the following exercises, among others, can be performed. Implementing a function that splits the physical exergy in its thermal and mechanical parts [25]. Creating a plot showing how the thermal and mechanical exergies are affected within a range from ambient pressure to inlet pressure. And re-performing the tasks by using air instead of water steam.

Using a Python function the calculation of thermal and mechanical exergy can be performed for different temperatures, pressures and fluids.

```
def calc_splitted_physical_exergy(p, h, p0, T0, fluid):
    r"""Calculate specific physical exergy according to splitting rule."""
    s = PSI("S", "P", p, "H", h, fluid)
    h_T0_p = PSI("H", "P", p, "T", T0, fluid)
    s_T0_p = PSI("S", "P", p, "T", T0, fluid)
    ex_therm = (h - h_T0_p) - T0 * (s - s_T0_p)
    h0 = PSI("H", "P", p0, "T", T0, fluid)
    s0 = PSI("S", "P", p0, "T", T0, fluid)
    ex_mech = (h_T0_p - h0) - T0 * (s_T0_p - s0)
    return ex_therm, ex_mech

ex_T_in, ex_M_in = calc_splitted_physical_exergy(p_in, h_in, p0, T0, "water")
```

Figure 6a and 6b show the difference in the values between inlet and outlet of the thermal and mechanical exergies, representing the corresponding exgery destruction in the pipe flow for varying pressure ratios. Note the different scales of the y-axes. The thermal exergy of water steam changes by up to 300 kW, while the mechanical exergy difference is 0.9 kW at maximum. For air the thermal exergy difference reaches a maximum of around 0.5 kW, the mechanical exergy changes up to 200 kW.

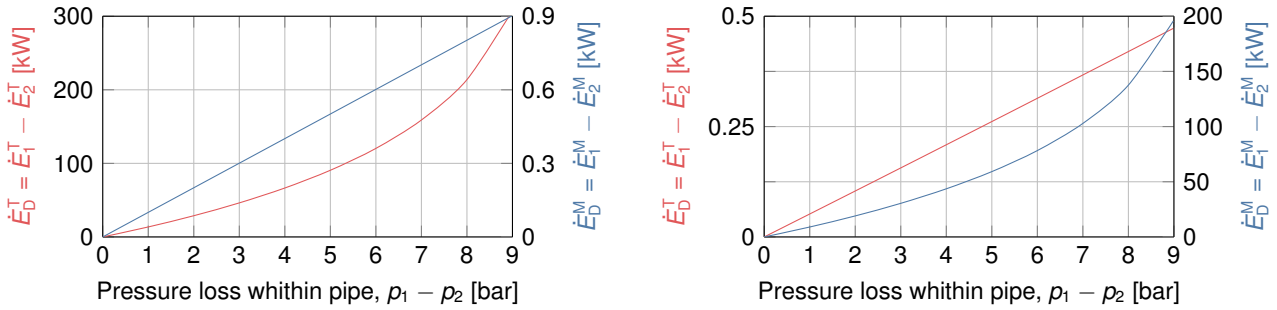

(a) Water steam

(b) Air

Figure 6: Thermal and mechanical exergy destruction within the the pipe for varying pressure losses

The fundamental difference of the substance characteristic leads to the fact that the exergy destruction for water steam in the pipe flow is mainly triggered by a decrease of the thermal exergy. In the case of air, the mechanical exergy decreases significantly more.

A comparison of the exergy destruction rate for the pipe flow of water steam and air is shown in Figure 7. The ratio of both exergy destruction rates is almost constant and is about 1.5.

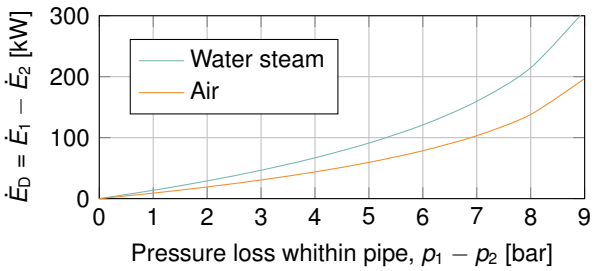

Figure 7: Exergy destruction for water steam and air within the adiabatic pipe flow

Lessons Learned from this task:

- Physical exergy of a mass flow can be split into a thermal and a mechanical part.
- At the same pressure and temperature, the shares of thermal and mechanical exergies depend on the working fluid.

4.2. Highlight 2: Open-Cycle Gas Turbine

A simple gas turbine model should be developed within this task. Compressed ambient air is mixed up with methane. The gases after the combustion are used in a gas turbine expander to supply mechanical, respectively electrical energy.

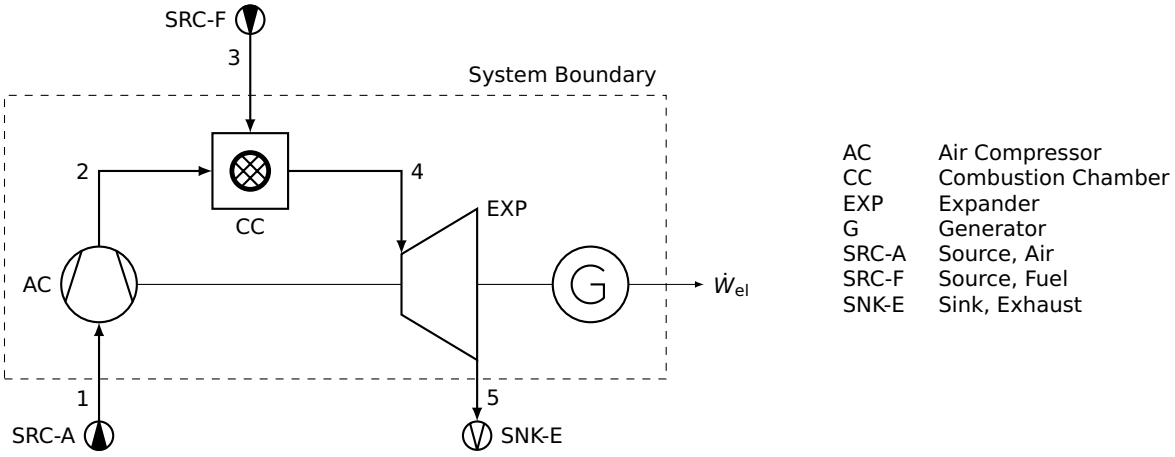

Figure 8: Flowchart of open-cycle gas turbine

Table 2: Open-cylce gas turbine parameters

Parameter	Symbol	Unit	Value
Net power output	$\dot{W}_{net}$	MW	150
Air compressor, isentropic efficiency	$\eta_{s,AC}$	–	0.85
Air compressor, pressure ratio	$r_{p,AC}$	–	18
Combustion chamber, thermal efficiency	η_{CC}	–	0.98
Combustion chamber, pressure ratio	$r_{p,CC}$	–	0.95
Expander, isentropic efficiency	$\eta_{s,AC}$	–	0.9
Expander, inlet temperature	T_4	°C	1400
Expander, outlet pressure	p_5	bar	1.013
Fuel, inlet pressure	p_3	bar	20
Fuel, inlet temperature	T_3	°C	25
Fuel, mass analysis[a]	$y_{i,fuel}$	–	$(\dots, 1.0)$
Air, mass analysis[a]	$y_{i,air}$	–	$\begin{pmatrix} 0.7551 \\ 0.2314 \\ 0.0129 \\ 0.0006 \\ 0.0 \\ 0.0 \end{pmatrix}$

[a] All fluid compositions are given as $y_i = \left(y_{N_2}, y_{O_2}, y_{Ar}, y_{CO_2}, y_{H_2O}, y_{CH_4}\right)^T$

TESPy is used to set up the thermodynamic model of the gas turbine. The solution is carried out for the full load case. The documentation of the source code can be found in the appendix.

A parameter study should be performed based on the results for the air compressor pressure ratio and expander inlet temperature. The solution is a multiple run of the simulation above, while varying pressures and temperatures.

Figure 9 depicts a parameter plot for the given gas turbine system varying expander inlet temperature from 900 °C to 1400 °C and the air compressor pressure ratio from 5 to 30. The reference point corresponds to the data from Table 2. For the plot only the marked points were calculated, the lines in between are linear regressions. If necessary, the accuracy of the graph can be increased by performing more calculations. An optimal combination of expander inlet temperature and pressure ratio exists to maximize the specific work and the efficiency of the gas turbine.

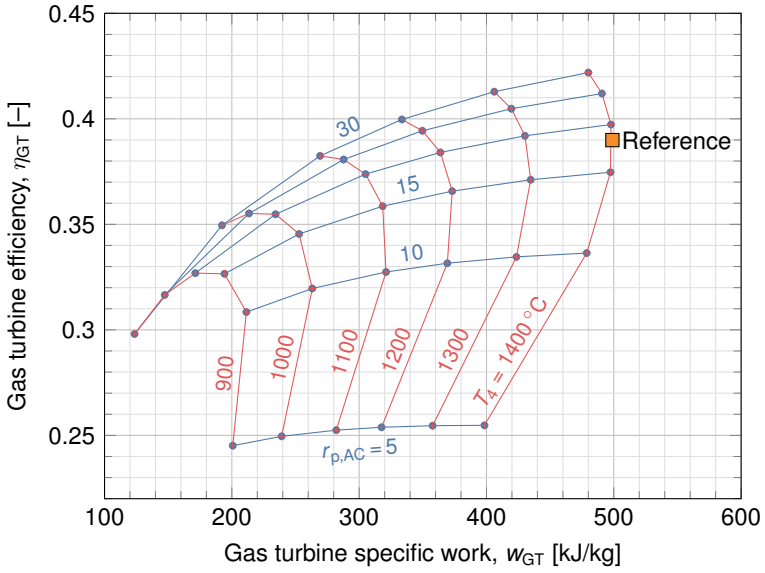

Figure 9: Gas turbine parameter plot for varying expander inlet temperature air compressor pressure ratio

However, with this initially only energetic evaluation of the process, based on the specific power and the net efficiency, the real thermodynamic losses cannot be quantified and the performance of the system components cannot be compared with each other. The exergy analysis answers these open questions.

In case TESPy is used for the simulation of the thermodynamic performance, an exergy-based evaluation can be carried out using the class ExergyAnalysis. The students have to set up the exergy flow rates crossing the system boundary and define the exergetic fuel, the exergetic product and the exergetic loss of the overall process.

The busses for the net work rate and the fuel input are already defined. In case of fuel the chemical exergy must be considered. Additionally, an exergy loss bus must be defined for the exhaust gas.

The generic exergy analysis of TESPy can be set up within a few lines of code, defining the above mentioned exergy flow rates and the ambient conditions.

```
from tespy.tools import ExergyAnalysis
ean = ExergyAnalysis(gas_turbine, E_P=[work_net], E_F=[ex_fuel], E_L=[ex_loss])
ean.analyse(pamb=1.013, Tamb=25)
```

The graphical evaluation of the exergy analysis can be done, for example, with a waterfall diagram. Penkuhn et al. [26] show this for a cogeneration plant. Another form of visualization is the representation of exergy rates in a Sankey diagram, often called a Grassmann diagram.[14] The exergy analysis results are linked to the representation of the process flow diagram. The different material and energy streams of the flowsheet are brought to a uniform basis with the help of the exergy. The width represents the exergy rate. In addition, the exergy destruction is directly assigned to each component. Figure 10 shows this for the gas turbine process under investigation. The highest exergy destruction rate occurs in the combustion chamber, followed by the expander and air compressor. The exhaust gases represent an exergy loss for the overall process.

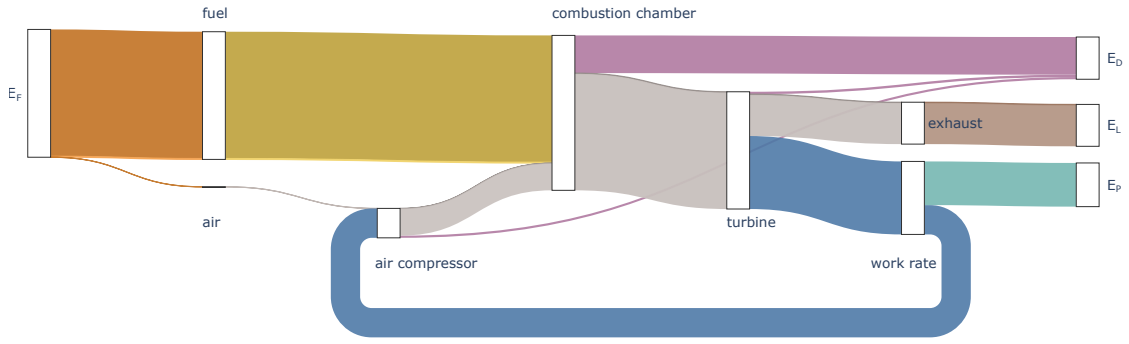

Figure 10: Grassmann diagram of gas turbine process showing the results of the exergy-based assessment

[14] Grassmann [27] transferred the idea of Sankey to the exergy concept. Exergy flow diagrams are therefore associated with his name.

The light tint indicates physical exergy, and the dark tint indicates chemical exergy, for example, visible in the fuel exergy flow rate or the exergy flow rate between the combustion chamber and the expander. It can be observed that all flows are either nearly pure chemical or pure physical exergy.

Lessons Learned from this task:

- Learn that TESPy can do a lot of work for you.
- Relevant thermodynamic process parameters identified and numerically evaluated.
- Applied exergy analysis for a simple process for the first time, and identified the locations and magnitudes of real thermodynamic inefficiencies.

4.3. Highlight 3: Process Design Study for a Combined Heat and Power Plant

This example contains a process design study. A proposal for a power plant to supply electricity and district heating is to be developed. The heat source is a geothermal field.

The design proposal is to be modeled, simulated, and evaluated independently by the students. The design based on the principle of cogeneration is to be compared with a process design with complete condensation operation (without heat extraction). For this purpose, the energetic and exergetic efficiency of the overall process will be defined.

$$\eta = \frac{\dot{W}_{\text{net}} + \dot{Q}_{\text{DH}}}{\dot{H}_1 - \dot{H}_2} \tag{1}$$

$$\varepsilon = \frac{\dot{W}_{\text{net}} + \left(\dot{E}_{\text{FL}} - \dot{E}_{\text{RL}}\right)}{\dot{E}_1 - \dot{E}_2} \tag{2}$$

All predefined parameters and boundary conditions can be found in Figure 11 and Table 3.

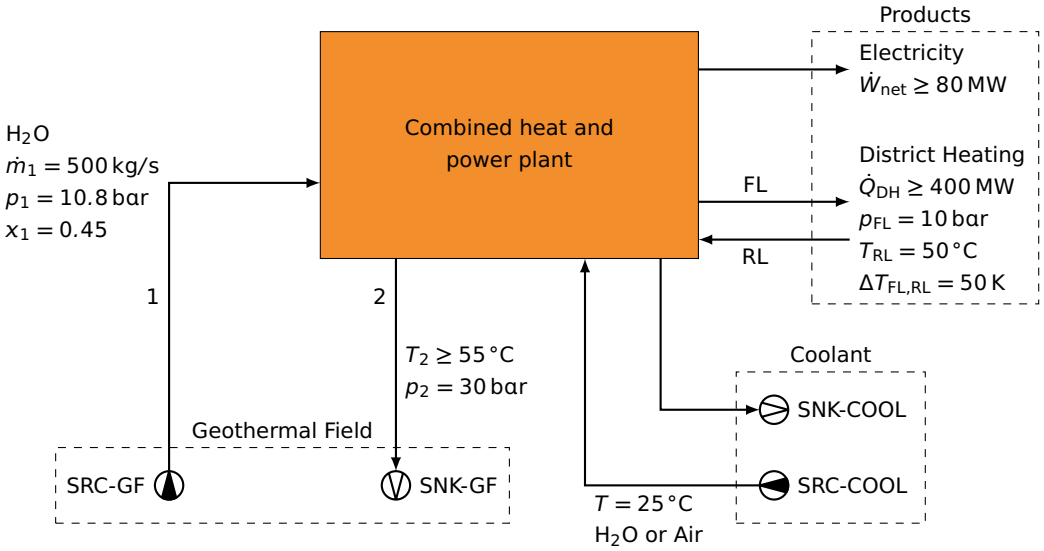

Figure 11: Process design study for a combined heat and power plant to provide electricity and district heating.

The following subtasks are to be solved within the scope of the assigned problem: Selection of suitable working fluids and selection and reasoning of the use of thermodynamic properties models for the simulation; creation of a process design, modeling, and simulation in TESPy; definition and use of relevant variables for the evaluation of the process designs and subsequent comparison and discussion.

There is no generally valid standard solution for solving this task. Two possible designs with and without heat extraction are shown in Figure 12. In both variants, the heat flow of the liquid part of the geothermal fluid is absorbed by an upstream organic Rankine cycle (ORC) and used to produce electricity. The steam phase is expanded in a steam turbine. In the case of simultaneous provision of district heating, a heating condenser with preheating follows before the geothermal fluid is returned. In the design for electricity generation only, a second ORC is inserted after the steam turbine.

Both process designs are simulated and compared both energetically and exergetically. The results are shown in Table 4. According to Eq. (1), the energetic evaluation treats two different energy flows (electricity and heat)

Table 3: Process design study specifications and constraints

Component	Parameter		Unit	Value
Auxiliary installations	Electrical power requirements		MW	3
Generators	Mechanical-electrical efficiency		–	0.985
Motors	Electrical-mechanical efficiency		–	0.975
Steam turbines	Isentropic efficiency		–	0.9
	Mechanical efficiency		–	0.99
	Minimum steam quality		–	0.9
Pumps	Isentropic efficiency		–	0.8
	Mechanical efficiency		–	0.99
Heat exchangers	Minimal temperature difference	liquid–liquid	K	10
		liquid–condensing	K	5
		liquid–steam	K	20
		liquid–gaseous	K	25

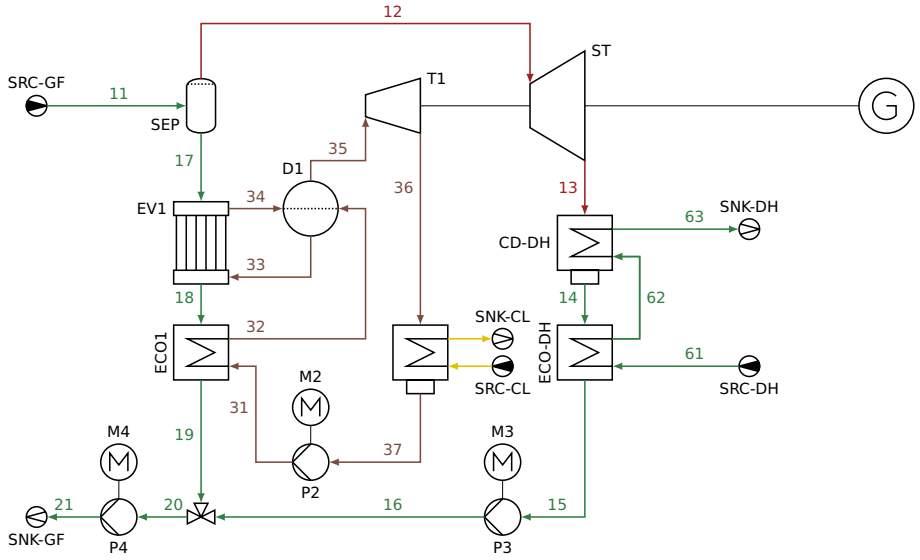

(a) Geothermal combined heat and power plant

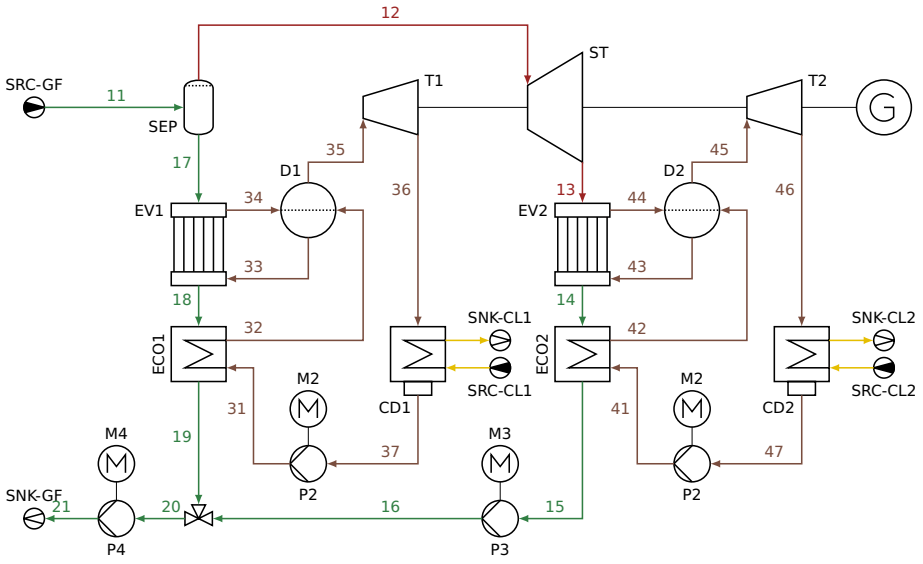

(b) Geothermal power plant

Figure 12: Flowcharts of possible process designs

equally. The efficiency is significantly higher in the case of heat extraction. It gives the impression that the process is much closer to the thermodynamic optimum, which is not the case, as the comparison of the exergetic efficiencies shows. Here, both exergetic products can be directly converted into each other. The result is that the process designs have approximately similar range of exergetic efficiencies, and therefore the misestimation of the energetic evaluation can be revealed.

Table 4: Comparison of energetic and exergetic efficiency for developed process designs

Process design	Energetic efficiency η [%]	Exergetic efficiency ε [%]
Geothermal combined heat and power plant	80.4	70.3
Geothermal power plant	19.0	62.8

Lessons Learned from this task:

- The exergy analysis assists in the selection and improvement of a suitable process design.
- Different material and energy streams can be consistently evaluated based on exergy.
- Various process designs with different fuels or products remain comparable with the help of exergy.

5. Conclusion

The idea presented in this article is based on the notion that research and teaching should be accessible to all with as few barriers as possible. At the same time, the paper addresses the exergy concept, one of the essential analysis tools of thermodynamic engineering. Object-oriented programming with Python, particularly steady-state power plant simulation with open-source software, is linked to exergy as an established thermodynamic quantity in the concept presented.

A modular structure is developed to facilitate the integration of the resources into existing courses and for self-learners to choose their appropriate entry point. The modular structure covers exergy analysis of single component operation as the entry-level, where the fundamental understanding of the exergy concept is conveyed. Based on that, students will learn to model simple thermodynamic cycles and to carry out first and second-law analyses by evaluating the simulation results. It is further supported by applying parametric analysis to understand the connection between individual component parameters to the thermodynamic performance of the overall process.

Further processing possibilities arise from the potential integration of additional exercises, the extension to the exergoeconomic analysis [28], the exergoenvironmental analysis [29], or the advanced exergy analysis [30]. At the same time, all interested students, researchers, and practitioners are invited to try the course, and to contribute by making comments or reporting bugs and developing it further collaboratively.

CRediT author statement

Mathias Hofmann: Conceptualization, Methodology, Software, Validation, Formal analysis, Investigation, Resources, Data Curation, Writing - Original Draft, Writing - Review & Editing, Visualization **Francesco Witte:** Conceptualization, Methodology, Software, Validation, Formal analysis, Data Curation, Writing - Review & Editing **Malte Fritz:** Software, Validation, Formal analysis, Data Curation **Jonas Freißmann:** Software, Validation, Formal analysis, Data Curation **Ilja Tuschy:** Review & Editing, Supervision **George Tsatsaronis:** Review & Editing, Supervision

Malte Fritz and **Jonas Freißmann** contributed equally to this work.

Acknowledgments

The authors would like to thank Björn Kiehne (Berliner Zentrum für Hochschullehre) for his remarks on Section 1. and 2. Mathias Penkuhn (Technische Universität Berlin) has to be credited for the conceptual design of the task given in Section 4.3.

Nomenclature

Abbreviations

A Air
AC Air compressor
CC Combustion chamber

CD Condenser
CL Coolant
D Drum
DH District heating
E Exhaust
ECO Economizer
EXP Expander
EV Evaporator
F Fuel
FL Feed line
G Generator
GF Geothermal fluid
GT Gas turbine
M Motor
ORC Organic Rankine cycle
P Pump
SEP Separator
SNK Sink
SRC Source
ST Steam turbine
T Turbine
RL Return line

Letter symbols

$\dot{E}$ Exergy rate, W
$\dot{H}$ Enthalpy rate, W
$\dot{m}$ Mass flow rate, kg/s
p Pressure, bar
$\dot{Q}$ Heat rate, W
r Ratio, –
T Temperature, °C
w Specific work, kJ/kg
$\dot{W}$ Work rate, W
x Quality, –
y_i Mass fraction, –

Greek symbols

Δ Difference
ε Exergetic efficiency
η Energetic efficiency

Subscripts and superscripts

0 At ambient state
D Destruction
F Fuel
i Stream
p Pressure
P Product
s Isentropic

References

[1] D. Abdrasheva, M. Escribens, E. Sabzalieva, D. V. do Nascimento, and C. Yerovi. *Resuming or Reforming? Tracking the global impact of the COVID-19 pandemic on higher education after two years of disruption*. Retrieved: January 27th, 2023. 2022. URL: https://unesdoc.unesco.org/ark:/48223/pf0000381749.

[2] K. H. Mok. "Impact of COVID-19 on Higher Education: Critical Reflections". In: *High. Educ. Policy* 35 (2022), pp. 563–567. DOI: 10.1057/s41307-022-00285-x.

[3] F. S. von Thun. "Wie gestalte ich meine Vorlesung – und halte die Hörerschaft und mich selbst bei Laune?" In: *Die Qualität Akademischer Lehre*. Ed. by M. Merkt and K. Mayrberger. in German. Innsburck, Austria: Studienverlag, 2007, pp. 115–131.

[4] L. W. Anderson and D. R. Krathwohl, eds. *A Taxonomy for Learning, Teaching, and Assessing: A Revision of Bloom's Taxonomy of Educational Objectives*. New York: Longman, 2001.

[5] Z. Rant. "Exergie, ein neues Wort für technische Arbeitsfähigkeit". In: *Forschg. Ing.-Wes.* 22.1 (1956). in German, pp. 36–37.

[6] T. J. Kotas. *The Exergy Method of Thermal Plant Analysis*. London, UK: Butterworths, 1985.

[7] W. Fratzscher, M. Brodjanskij, and K. Michalek. *Exergie*. in German. Leipzig, Germany: Verlag für Grundstoffindustrie, 1986.

[8] A. Bejan, G. Tsatsaronis, and M. Moran. *Thermal design and optimization*. New York, USA: Wiley, 1996.

[9] J. Szargut. *Exergy Method*. Southampton, UK: WIT Press, 2005.

[10] W. Rüegg, ed. *Geschichte der Universität in Europa*. Vol. 1, Mittelalter. in German. München, Germany: Beck, 1993.

[11] R. A. Müller. *Geschichte der Universität*. in German. München, Germany: Callwey, 1990.

[12] M. J. Moran, H. N. Shapiro, D. D. Boettner, and M. B. Bailey. *Fundamentals of Engineering Thermodynamics*. 9th ed. New York, USA: John Wiley, 2018.

[13] H. D. Baehr and S. Kabelac. *Thermodynamik*. in German. Berlin, Germany: Springer, 2016. DOI: 10.1007/978-3-662-49568-1.

[14] E. Matthes. *Python Crash Course*. San Francisco, USA: No Starch Press, 2023.

[15] A. Galea. *Beginning Data Analysis with Python and Jupyter*. Birmingham, UK: Packt Publishing, 2018.

[16] F. Witte and I. Tuschy. "TESPy: Thermal Engineering Systems in Python". In: *J. Open Source Softw.* 5 (2020), p. 2178. DOI: 10.21105/joss.02178.

[17] F. Witte, M. Hofmann, J. Meier, I. Tuschy, and G. Tsatsaronis. "Generic and Open-Source Exergy Analysis—Extending the Simulation Framework TESPy". In: *Energies* 15 (2022), p. 4087. DOI: 10.3390/en15114087.

[18] M. Hofmann, F. Witte, K. Shawky, I. Tuschy, and G. Tsatsaronis. "Thermal Engineering Systems in Python (TESPy): The implementation and validation of the chemical exergy". In: *Proceedings of ECOS 2022*. Copenhagen, Denmark, 2022, pp. 257–269.

[19] S. Pfenninger, J. DeCarolis, L. Hirth, S. Quoilin, and I. Staffell. "The importance of open data and software: Is energy research lagging behind?" In: *Energy Policy* 101 (2017), pp. 211–215. DOI: 10.1016/j.enpol.2016.11.046.

[20] *The Journal of Open Source Education*. Retrieved: March 23rd, 2023. URL: https://jose.theoj.org/.

[21] R. Morrison. *einfach : an energy system model for education*. 2020. DOI: 10.5281/zenodo.7746137.

[22] I. H. Bell, J. Wronski, S. Quoilin, and V. Lemort. "Pure and Pseudo-pure Fluid Thermophysical Property Evaluation and the Open-Source Thermophysical Property Library CoolProp". In: *Ind. Eng. Chem. Res.* 53.6 (2014), pp. 2498–2508. DOI: 10.1021/ie4033999.

[23] F. Biscani and D. Izzo. "A parallel global multiobjective framework for optimization: pagmo". In: *J. Open Source Softw.* 5.53 (2020), p. 2338. DOI: 10.21105/joss.02338.

[24] J. Ahrendts. "Reference states". In: *Energy* 5 (1980), pp. 666–677. DOI: 10.1016/0360-5442(80)90087-0.

[25] T. Morosuk and G. Tsatsaronis. "Splitting physical exergy: Theory and application". In: *Energy* 167 (2019), pp. 698–707. DOI: 10.1016/j.energy.2018.10.090.

[26] M. Penkuhn, M. Hofmann, S. Meinke, and C. Lösche. "Prozessbewertung und Exergieanalyse für ein Heizkraftwerk". In: *Kraftwerkstechnisches Kolloquium*. Dresden, Germany, 2021, pp. 1–12. DOI: 10.14279/depositonce-15966.

[27] P. Grassmann. "Die Exergie und das Flussbild der technisch nutzbaren Leistung". In: *Allg. Wärmetechn.* 9.4/5 (1959). in German, pp. 79–86.

[28] G. Tsatsaronis. "Thermoeconomic analysis and optimization of energy systems". In: *Prog. Energy Combust. Sci.* 19 (1993), pp. 227–257. DOI: 10.1016/0360-1285(93)90016-8.

[29] L. Meyer, G. Tsatsaronis, J. Buchgeister, and L. Schebek. "Exergoenvironmental analysis for evaluation of the environmental impact of energy conversion systems". In: *Energy* 34 (2009), pp. 75–89. DOI: 10.1016/j.energy.2008.07.018.

[30] M. Penkuhn and G. Tsatsaronis. "A decomposition method for the evaluation of component interactions in energy conversion systems for application to advanced exergy-based analyses". In: *Energy* 133 (2017), pp. 388–403. DOI: 10.1016/j.energy.2017.03.144.

A Appendix: Open-Cycle Gas Turbine – TESPy Source Code

```
from tespy.networks import Network
from tespy.components import (Sink, Source, Compressor, DiabaticCombustionChamber, Turbine)
from tespy.connections import Connection, Bus

# general configurations
# substances, fluids, network, units
fluid_list = ['N2', 'O2', 'Ar', 'CO2', 'H2O', 'CH4']
gas_turbine = Network(fluids=fluid_list, p_unit='bar', T_unit='C', h_unit='kJ / kg')

# composition of given fluids
air = {'N2': 0.7551, 'O2': 0.2314, 'Ar': 0.0129, 'CO2': 0.0006, 'H2O': 0, 'CH4': 0}
fuel = {'N2': 0, 'O2': 0, 'Ar': 0, 'CO2': 0, 'H2O': 0, 'CH4': 1}

# define sources and sinks
src_air = Source('air')
src_fuel = Source('fuel')
snk_exhaust = Sink('exhaust')

# define components
cmp_AC = Compressor('air compressor')
cmp_CC = DiabaticCombustionChamber('combustion chamber')
cmp_EX = Turbine('expander')

# define connections
c1 = Connection(src_air, 'out1', cmp_AC, 'in1', label='1')
c2 = Connection(cmp_AC, 'out1', cmp_CC, 'in1', label='2')
c3 = Connection(src_fuel, 'out1', cmp_CC, 'in2', label='3')
c4 = Connection(cmp_CC, 'out1', cmp_EX, 'in1', label='4')
c5 = Connection(cmp_EX, 'out1', snk_exhaust, 'in1', label='5')

# add connections to network
gas_turbine.add_conns(c1, c2, c3, c4, c5)

# parameter of components
cmp_AC.set_attr(eta_s=0.85, pr=18)
cmp_CC.set_attr(eta=0.98, pr=0.95)
cmp_EX.set_attr(eta_s=0.9)

# parameter of connections
c1.set_attr(p=1.013, T=25, fluid=air)
c3.set_attr(p=20, T=25, fluid=fuel)
c4.set_attr(T=1400)
c5.set_attr(p=1.013)

# busses
work_net = Bus('work netto')
fuel_in = Bus('fuel input')

work_net.add_comps(
    {'comp': cmp_AC, 'base': 'bus', 'char': 1},
    {'comp': cmp_EX, 'char': 1})

fuel_in.add_comps(
    {'comp': cmp_CC, 'base': 'bus'})

gas_turbine.add_busses(work_net, fuel_in)

# parameter of busses
work_net.set_attr(P=-150e6)

# solve network
gas_turbine.solve('design')

# print network results
gas_turbine.print_results()
```

Exergetic analysis of the nCO_2PP cycle with particular reference to the exergy destruction of sewage sludge due to gasification

Kamil Stasiak[a], Ivar Ståle Ertesvåg[b], Paweł Ziółkowski[a], and Dariusz Mikielewicz[a]

[a] Gdańsk University of Technology, Gdańsk, Poland, kamil.stasiak@pg.edu.pl, CA, pawel.ziolkowski1@pg.edu.pl, dariusz.mikielewicz@pg.edu.pl,
[b] Norwegian University of Science and Technology, Trondheim, Norway, ivar.s.ertesvag@ntnu.no

Abstract:

An exergy analysis is carried out on the negative CO_2 emission gas power plant (nCO_2PP), which integrates the process sections of fuel preparation, power generation and carbon capture. Processes of exergy destruction are studied with particular focus on the process in the gasification unit of the fuel preparation section, where a large amount of exergy is destroyed in various chemical reactions from sewage sludge to producer gas conversion. The largest exergy losses are observed in the wet combustion chamber and in the fuel line with the gasification process and water condensation in the gas scrubber, amounting to 126 kW, 43-45 kW and 56 kW respectively, which corresponds to efficiencies of 62%, 89% and 84% of these units, while the exergy efficiency of the power plant is 29.5%. The integration of the gasification unit with the gas scrubber is investigated, and a heat exchanger combination is considered. Ambient air changes in relative humidity and, due to increasing global greenhouse gas emissions, CO_2 concentration are analysed. Insight into the theoretical operation of the power plant through exergy analysis allows energy efficiency to be increased by improving areas of highest exergy destruction. To represent real power plant operation, the analysis is based on an optimised process simulation calculated using the most accurate published equations of state, verified with experimental thermophysical property data from the literature.

Keywords:

Exergy Analysis; Efficiency; Gasification; Sewage Sludge; CO_2; Process Simulation; Integration; Power Plant.

1. Introduction

The Negative CO_2 emission Gas Power Plant (nCO_2PP) shown in Figure 1 is the subject of intensive research in a project dedicated to the disposal of sewage sludge with simultaneous generation of electricity and CO_2 capture [1]. The nCO_2PP cycle has already been described in several articles [2–4] as it offers the hope of simultaneously disposing of the harmful products of human activity (e.g., sewage sludge), then allowing the production of useful electricity, and finally allowing the capture of carbon dioxide in a dedicated part of the CCS. A contribution to the field was made in [5], where an exergy analysis of the nCO_2PP system was conducted, investigating aspects of energy efficiency and CO_2 capture. The basic equipment includes: (1) the working medium generator - i.e., the wet combustion chamber (WCC), the steam-gas expander ($GT+GT^{bap}$), the spray-ejector condenser (SEC), and the gasifier in which the sewage sludge is converted into syngas by means of a converter, which is a bleed stream (Fig.1.). Additional equipment includes oxygen, fuel and CO_2 compressors, water pumps and heat exchangers. It is extremely important not only to test the syngas production experimentally, but also to model the gasification process correctly to indicate its contribution to the energy conversion chain.

The nCO_2PP cycle is consistent with the idea of a bioenergy with a carbon capture and storage (BECCS) power cycle. This involves using a renewable energy source in the form of biomass in combustion processes and then capturing the carbon dioxide produced in this way, ultimately achieving negative CO_2 emissions. However, in addition to carbon performance, an important parameter for the sustainable conversion of fuel energy is exergy destruction. One of the critical parameters influencing exergy destruction are ambient parameters such as temperature, humidity and pressure, which have already been classified in many works by some well-known authors on the subject [6,7]. It is worth noting that the effect of CO_2 in the air is also beginning to play an increasingly important role in exergy analyses, while the issue of determining the chemical exergy of individual elements still lacks a sufficiently reliable physical basis, and most scholars rely on Szargut

[7] in this area. The situation is even more complicated when determining the chemical exergy of different types of biomass [8]. First of all, there is a lack of a clear chemical and physical foundation to move from well-established methods to determine the composition of the ultimate and proximate type to the exergy, because here, entropy relating to the atomic level plays a role [9]. In the case of the present work, the analyses will focus on a significantly challenging biomass, which is sewage sludge. Attempts to model this process appropriately are being developed particularly intensively in the Aspen Plus environment, where, using mass, momentum and energy balance and the entropy production equation, the exergy destruction due to gasification can be determined [10]. Using these models, it is important to determine the components of the syngas at the reactor outlet and the input supplied to the gasifier. Due to the varying composition of sewage sludge, depending on the region of the world, the calorific value of the sludge and thus, the exergy that is stored in it, also changes [11]. In addition, there is great hope in the production of alternative fuels using sewage sludge, where exergetic analyses supplement information on the quality of energy conversion to useful products such as hydrogen [12] or methanol [13]. With respect to exergetic efficiency, it is possible to provide feedback about sustainable energy conversion. This is because it is necessary to identify possible ways of reducing the destruction of exergy, especially in devices where an alternative solution can be proposed.

In the case of the oxyfuel cycle, which is the subject of this study, it is also important to determine the impact of exergy destruction in separation processes either in an air separation unit (ASU) and a spray-injection condenser (SEC). Industrial ASUs rely on cryogenic methods in order to be able to supply the required amount of oxygen, and methods to reduce power consumption are also found in this part of the system [14]. Thus, exergetic analyses undoubtedly provide an opportunity to study technical and environmental aspects related to energy systems [15]. Therefore, this approach was chosen to analyse the nCO_2 cycle integrated with syngas production in the sludge gasification process.

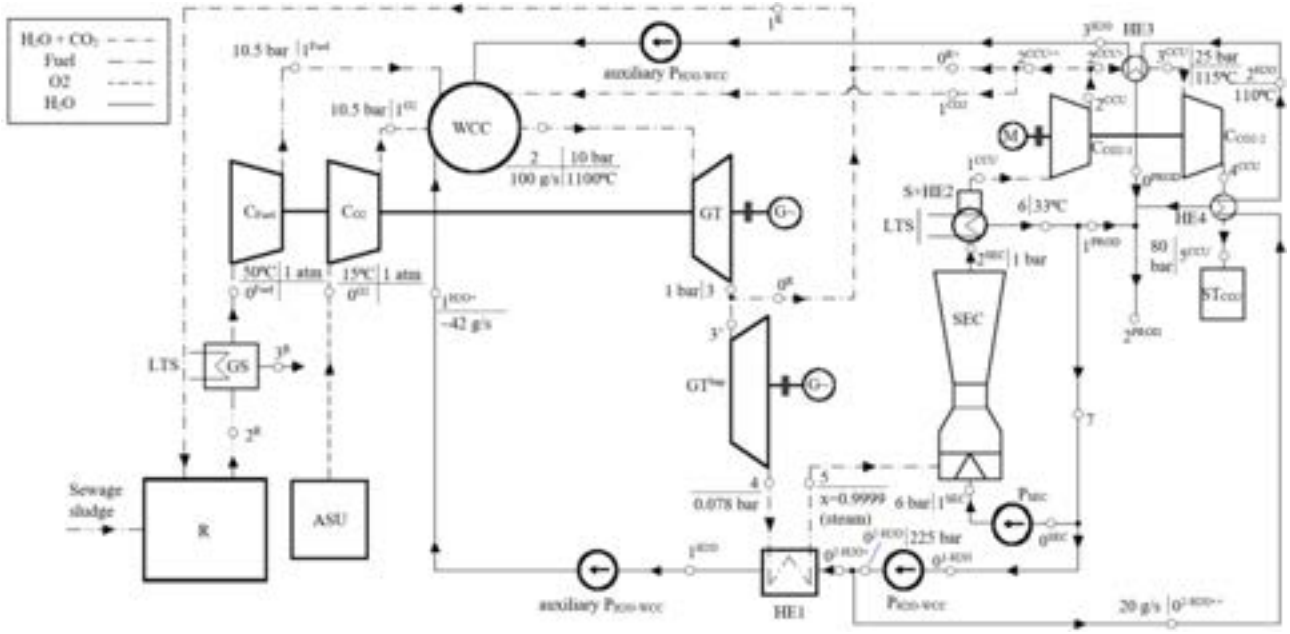

Figure. 1. nCO_2PP process flow diagram [16] where main devices are: WCC – wet combustion chamber, GT – gas turbine, GT^{bap} – low-pressure turbine, R – gasifier, SEC – spray-ejector condenser. Additional devices includes: C_{O2} – oxygen compressor, C_{fuel} – fuel compressor, HE1 – heat exchanger 1, G – generator, $P_{H2O\text{-}WCC}$ – WCC water pump, P_{SEC} – SEC pump, S+HE2 – separator connected with heat exchanger 2, $C_{CO2\text{-}1}$ and $C_{CO2\text{-}2}$ – CO_2 compressors, HE3 – heat exchanger 3, HE4 – heat exchanger 4, GS – gas scrubber, ASU – air separation unit, LTS – lower temperature source.

2. Methodology

2.1. Principal equations

The flow exergy is usually split into a thermomechanical part and a chemical exergy. The latter consists of a mixing part and the chemical exergy component.

$$E^{tot} = E^{th} + E^{ch} \tag{1}$$

The chemical exergy of sewage sludge was calculated as [13]

$$E_{ss}^{ch} = \dot{m}_{ss} \cdot LHV_{ss} \frac{1.0412+0.2160\cdot\left(\frac{H}{C}\right)-0.2499\cdot\left(\frac{O}{C}\right)\cdot\left[1+0.7884\cdot\left(\frac{H}{C}\right)\right]+0.0450\cdot\left(\frac{N}{C}\right)}{1-0.3035\cdot\left(\frac{O}{C}\right)} \tag{2}$$

The power plant was simulated using Aspen Plus with REFPROP equations of state. A part of the exergy was derived from this software. However, due to the lack of proper documentation of exergy in Aspen software, it was investigated whether this was total exergy, thermomechanical exergy or some part of it. Essentially, total flow exergy is the reversible work done when a flow is brought into equilibrium with its environment. The "Aspen exergy" is the reversible work done when the flow is brought from the relevant state to the Aspen dead state. Due to condensation and phase separation when the flow contains H_2O, the mixture is partially separated. This means that the Aspen exergy calculation includes part of the mixing exergy together with the thermomechanical component. The remaining flow exergy is the reversible work obtained when the flow is brought from the Aspen Plus restricted dead state to equilibrium with the environment:

$$W_{\text{rev}} = T_0 \cdot \bar{R} \cdot \left[\sum_{i \neq H_2O} n_i \cdot ln \frac{n_i}{n - n_{H_2O(liq0)}} + \left(n_{H_2O(\text{g0})} + n_{H_2O(\text{liq0})}\right) \cdot ln \frac{p_{s0:\,H_2O}(T_0)}{p_0}\right] + n_{H_2O(\text{liq0})} \cdot (p_0 - p_{s0}) \cdot \bar{v}_{f:\,H_2O}(T_0) + \sum_i n_i \cdot \bar{e}_i^{\text{ch}} \quad (3)$$

For streams consisting only of liquid water, the equation reduces to the chemical exergy:

$$W_{\text{rev}} = n_{H_2O(liq0)} \cdot \bar{e}_{H_2O(liq0)}^{\text{ch}} \quad (4)$$

Including the exergy part calculated by Aspen Plus, the total exergy is as follows:

$$E^{\text{tot}} = E^{\text{Aspen}} + W_{\text{rev}} \quad (5)$$

For the purposes of analysis, exergy destruction was obtained from the steady-state exergy balance,

$$E_d = \sum E_{in}^{\text{tot}} - \sum E_{out}^{\text{tot}} + \sum W_{in} - \sum W_{out} \quad (6)$$

The exergy efficiency of a unit is expressed as the outflow-to-inflow ratio of exergy rates,

$$\eta_{ex} = \frac{\sum E_{out}^{\text{tot}} + \sum W_{out}}{\sum E_{in}^{\text{tot}} + \sum W_{in}} \quad (7)$$

A benefit of the outflow-to-inflow efficiency (compared to the “task efficiency”) is that the efficiency of two or more combined units (subsystems) is simply the product of the efficiencies of the individual units. The exergy efficiency of the power plant is then expressed as

$$\eta_{ex|nCO_2PP} = \frac{\sum W_{out} - \sum W_{in}}{E_{fuel,in} + E_{O_2,in}} \quad (8)$$

Here, to appreciate the CO_2 capture, the thermodynamic value (pressure and chemical exergy) of the captured CO_2 could be added in the denominator.

2.2. Input data

For exergy analysis, the Aspen Plus dead state was set to the T_0 temperature of 15ºC and p_0 pressure of 1 atm (at sea level 0), which corresponds to most standards. Thus, read values from Aspen Plus with REFPROP equations of state, such as saturation pressure $p_{s0:\,H_2O}(T_0)$ was 0.0170579 bar and $\bar{v}_{f:\,H_2O}(T_0)$ was 0.018031 m^3/kmol. The exergy calculation also uses the universal gas constant $\bar{R}$ equal to 8.31433 kJ/(kmol K). The chemical exergy calculations used the composition of dry air [17] based on the US Standard Atmosphere, with the CO_2 concentration assumed to be 375 ppm [6] for the year 2004. For comparison, a global average of 417 ppm was used for the year 2022 [18] and a worst-case scenario of 1000 ppm was predicted for the year 2100 [19].

The composition of sewage sludge digested in the gasification unit and fueling the whole power plant, was assumed as mass fractions 27.9% C, 6.7% H, 28.9% O, 4.4% N, 32.2% Ash, with an LHV of 9.8 MJ/kg. The synthesis gas produced by gasification in a steam atmosphere at 760 °C and, after cleaning in the gas scrubber, a volumetric composition of 9.3% CO, 46.8% H_2, 13.9% CH_4, 26.4% CO_2 and 3.5% C_3H_8.

Table 1. Assumptions for the thermodynamic cycle

Parameter	Symbol	Unit	Value
Temperature exhaust after WCC (before GT)	t_2	ºC	1100
Mass flow of the exhaust gas from the WCC	$\dot{m}_2$	g/s	100
Exhaust pressure after WCC	p_2	bar	10
Oxygen-fuel excess ratio in WCC	λ	-	1
Initial syngas temperature, after gas scrubber	t_{fuel}	ºC	50
Initial oxygen temperature	t_{O2}	ºC	15

Syngas fuel pressure before C_{fuel} compressor	p_{0-fuel}	bar	1
Oxygen pressure before C_{O2} compressor	p_{0-O2}	bar	1
Fuel to WCC pressure loss factor	δ_{fuel}	-	0.05
Oxygen to WCC pressure loss factor	δ_{O2}	-	0.05
Regenerative water pressure to WCC	p_{1-H2O}	bar	225
Exhaust vapor quality after HE1	x_5	-	0.999
Exhaust temperature after HE1, before SEC	t_5	ºC	33
CO_2 pressure after compressor C_{CCU1}	p_{2-CCU}	bar	25
CO_2 pressure after compressor C_{CCU2}	p_{4-CCU}	bar	80
H_2O temperature after HE4	t_{2-H_2O}	ºC	110
CO_2 temperature after HE3	t_{3-CCU}	ºC	115
Water vapor from Separator in 1^{CCU} mixed with CO_2 vapor	-	%	100% humid
Pressure after GT^{bap}	p_4	bar	0.078
Temperature after SEC	t_6	ºC	35
Turbine GT, internal efficiency (η_i)	η_{iGT}	-	0.89
Turbine GT^{bap}, η_i	$\eta_{iGT-bap}$	-	0.89
Fuel compressor C_{fuel}, η_i	$\eta_{iC-fuel}$	-	0.87
Oxygen compressor C_{O2}, η_i	η_{iC-O2}	-	0.87
WCC water pump $P_{H2O-WCC}$, η_i	$\eta_{iP-H2O-WCC}$	-	0.8
SEC water pump P_{SEC}, η_i	η_{iP-SEC}	-	0.8
CO_2 compressor C_{CO2-1}, η_i	$\eta_{iC-CO2-1}$	-	0.87
CO_2 compressor C_{CO2-2}, η_i	$\eta_{iC-CO2-2}$	-	0.87
Mechanical efficiency for all devices	η_m	-	0.99

3. Results and discussion

Table 2. Calculated chemical components exergy in changing air relative humidity or CO_2 concentration according to [6] and based on Szargut model [7].

Parameter	Symbol	Unit	Value				
Relative Humidity	RH	%	40	50	60	50	50
Atmospheric CO_2 concentration	X_{aCO_2}	ppm	375	375	375	417	1000
Chemical exergies of substances	$\bar{e}^{ch}_{O_2}$	kJ/kmol	3762	3766	3770	3766	3766
	$\bar{e}^{ch}_{CO_2}$	kJ/kmol	18915	18920	18924	18665	16570
	$\bar{e}^{ch}_{H_2O(liq0)}$	kJ/kmol	2195	1661	1224	1661	1661
	$\bar{e}^{ch}_{H_2O(g0)}$	kJ/kmol	11980	11446	11009	11446	11446
	$\bar{e}^{ch}_{H_2}$	kJ/kmol	239121	238585	238146	238585	238585
	$\bar{e}^{ch}_{CO}$	kJ/kmol	275120	275122	275124	274868	272772
	$\bar{e}^{ch}_{CH_4}$	kJ/kmol	836442	835368	834491	835114	833019
	$\bar{e}^{ch}_{C_3H_8}$	kJ/kmol	2157893	2155747	2153991	2154984	2148697

To complete the exergy analysis, the next step was to calculate the chemical exergy of the sludge and calculate the total exergy and efficiency by substituting the chemical exergies from Table 2 above, with the Aspen Plus exergy known from the models. Relative humidities of 40%, 50% and 60% were used for the chemical exergy calculations. For comparison, the changing atmospheric CO_2 concentration of 417 ppm for the global near-surface average in 2022 and the worst-case scenario of 1000 ppm predicted for 2100 were added.

The following tables (Tables 3-13) show the change in exergy rates as a function of the change in dead state parameters. Note that the parameters in Table 1 do not change.

For the gasification unit shown in Table 3, the syngas composition results came from the experiment presented in the authors' other work [2]. Some simplifications were applied: neglecting the exergy of moisture, ash, nitrogen and sulphur, focusing only on the most important aspect from the power generation point of view. A special attention to this process was due to the high water content in the producer gas and its subsequent treatment in a gas scrubber, the exergy analysis of which is shown in Table 4. While applying the simplifications mentioned above, the gas scrubber is simply a condenser in this case. While the producer gas has a high temperature, the waste heat can be recovered during the condensation process, which was not foreseen in the nCO_2PP concept, as the power plant efficiency of BECCS was usually calculated in the literature without

the gasification unit and gas scrubber and overlooked, thus opening a way to increase the overall energy efficiency of the power plant. The exergy efficiency of the gasification unit decreases with higher humidity or CO_2 concentration, and the same is true for the gas scrubber. The exergy destruction had among the largest exergy destruction rates after the WCC, amounting to 43-45 kW and 56 kW for the gasification unit and the gas scrubber, respectively. The exergy efficiency of the gasification unit was close to 89%, while that of the gas scrubber was 84%. The latter can be increased together with the exergy efficiency of the power plant by using water condensation waste heat for the power plant processes.

The following points show the exergy rates as a function of the relative humidity and as a function of the CO_2 content in the air. As can be seen from Tables 5 and 6, the variation of the above parameters did not affect the compressors. In the whole range of the analyzed parameters, the O_2 compressor exergy destruction remained at the level of 0.45 kW, giving an exergy efficiency of 94.6%, while for the fuel compressor the exergy destruction was 0.67 kW and the exergy efficiency 99.8%. It is worth noting that the influence of the environment on the operation of the compressors was reduced to a negligible level due to the lowest exergy rates. Table 7 applies to water pumps, where the effect of the dead state was much more significant. Despite the constant value of exergy destruction, there is a decrease in exergy efficiency with increasing relative humidity. This is related to the change in the value of the exergy rates carried in the water pumped by the pumps. In contrast, a “task efficiency” would give identical results, independent of atmospheric composition.

Heat exchanger 1 (HE 1) results are given in Table 8, with a heat load of 48.6 kW. In this case, the changes in exergy flux were not only for water, but also for the mixture of water vapour and CO_2. A mixture flowed on one side of the exchanger, so the exergy efficiency decreased as both the relative humidity and the proportion of CO_2 in the dead state increase. Also here, a “task efficiency” would be independent of the atmospheric composition.

Table 9, which refers to the water-injected oxy-fuel combustor, is of particular interest as it has several functions in this power plant. Apart from producing working medium with desired parameters for gas turbines, it has oxy-combustion destined for CCU unit, also it reuses water collecting waste heat from other parts of the power plant and cools down the oxy-combustion flame to desired temperature. Hence, it is called a 'wet' combustor. The combustion was assumed stoichiometric with perfect mixing of oxygen and fuel. In reality, some dissociation and kinetics (non-completed reactions) will give a somewhat lower adiabatic flame temperature. The exergy destruction rate of this unit was the largest in the whole power plant yielding about 126 kW, and its exergy efficiency was about 62%, indicating that special attention needs to be paid to improving this process. In relation to the exergy of the sewage sludge fed to the system, this exergy efficiency was 50% when taking into account the whole process from gasification through water condensation in the gas scrubber, compression and mixing effects in the WCC before ignition and after flame generation. It is worth noting that while oxygen mixing with fuel did not cause significant exergy destruction, water mixing into the flame exhaust caused the largest exergy drop in the range of 64-67 kW. Therefore, to increase efficiency, solutions should be sought in the area of water injection to the WCC.

Tables 10 and 11 refer to the main useful energy generator, the high pressure (GT) and low pressure (GT^{bap}) expander with output power of 90.4 kW and 65.7 kW, respectively. The total exergy rates depended slightly on the amount of CO_2 and relative humidity of the atmosphere at dead state. Increasing these parameters gave insignificant changes and virtually no effects on the exergy destruction rates, which were 4.7 kW and 4.8 kW, respectively. In addition, as expected, the gas turbine expanders were characterized by high exergy efficiencies of 97.9% (GT) and 95.6% (GT^{bap}), respectively, at RH=0.4 and 375 ppm CO_2.

Despite significant exergy rates flowing into the SEC, the exergy destruction within this device was negligible. The value of the exergy efficiency, as shown in Table 12, varied from 99.5% to 99.7% in inverse proportion to the increase in relative humidity. It can also be seen that the increase of CO_2 to 1000 ppm in the dead state did not affect the exergy efficiency.

One of the main objectives of the nCO_2PP cycle is to capture carbon dioxide. Therefore an indispensable part is to determine the exergy conversion in the Carbon Capture Unit (CCU) island, where the following should be distinguished: heat exchangers HE3 and HE4 (heat duty 12.3 kW), compressors C_{CO2-1} and C_{CO2-2} (power consumption 10.1 kW). The results of the analysis of the exergy destruction rates and the exergy efficiency are presented in Table 13. It can be noted that for the CCU island, there was a clear effect of the amount of CO_2 in the dead state on the exergy efficiency, which decreased from 74.8% for 375 ppm CO_2 (RH=0.5) to 73.2% for 1000 ppm CO_2. This is due to the definition of the efficiency, as the inflow and outflow exergies both decrease with the chemical exergy when increasing atmospheric CO_2. A task efficiency (changed exergy rate by input power) would be unaltered.

3.1. Fuel supply line with gasification process

Table 3. Gasifying unit (R).

	RH, %				40	50	60	50	50
	X_{aCO_2}, ppm				375	375	375	417	1000
Function	Medium	t, °C	p, bar	$\dot{m}$, g/s			E^{tot}, kW		
Inlet	Sewage Sludge	15	1.013	33.2	375.7	375.7	375.7	375.7	375.7
Inlet	H_2O(g)	100	1.013	27.1	18.0	17.3	16.6	17.3	17.3
Outlet	H_2O(g), CO, CO_2, CH_4, C_3H_8, H_2, without ash	760	1.013	49.6	350.6	349.1	347.9	349.0	347.9
	E_d, kW				43.1	43.8	44.4	43.9	45.0
	η_{ex},%				89.1	88.9	88.7	88.8	88.5

Table 4. Heat exchanger of Gas Scrubber (GS), Heat Duty = 112.1 kW.

	RH, %				40	50	60	50	50
	X_{aCO_2}, ppm				375	375	375	417	1000
Function	Medium	t, °C	p, bar	$\dot{m}$, g/s			E^{tot}, kW		
Inlet	H_2O(g), CO, CO_2, CH_4, C_3H_8, H_2	760	1.013	49.6	350.6	349.1	347.9	349.0	347.9
Outlet	CO, CO_2, CH_4, C_3H_8, H_2	50	1.013	16.6	289.8	289.4	289.1	289.3	288.2
Outlet	H_2O(liq)	50	1.013	33.0	4.7	3.7	2.8	3.7	3.7
	E_d, kW				56.1	56.1	56.1	56.1	56.1
	η_{ex},%				84.0	83.9	83.9	83.9	83.9

Table 5. Fuel Compressor (C_{fuel}), Work = 8.5 kW.

	RH, %				40	50	60	50	50
	X_{aCO_2}, ppm				375	375	375	417	1000
Function	Medium	t, °C	p, bar	$\dot{m}$, g/s			E^{tot}, kW		
Inlet	CO, CO_2, CH_4, C_3H_8, H_2	15	1.013	16.6	289.8	289.4	289.1	289.3	288.2
Outlet	CO, CO_2, CH_4, C_3H_8, H_2	306	10.5	16.6	297.7	297.2	296.9	297.1	296.0
	E_d, kW				0.7	0.7	0.7	0.7	0.7
	η_{ex},%				99.8	99.8	99.8	99.8	99.8

3.2. Oxygen supply line

Table 6. Oxygen Compressor (C_{O2}), Work = 5.9 kW.

	RH, %				40	50	60	50	50
	X_{aCO_2}, ppm				375	375	375	417	1000
Function	Medium	t, °C	p, bar	$\dot{m}$, g/s			E^{tot}, kW		
Inlet	O_2	15	1.013	20.6	2.4	2.4	2.4	2.4	2.4
Outlet	O_2	313	10.5	20.6	7.9	7.9	7.9	7.9	7.9
	E_d, kW				0.5	0.5	0.5	0.5	0.5
	η_{ex},%				94.6	94.6	94.6	94.6	94.6

3.3. Water to Wet Combustion Chamber supply line with heat recovery

Table 7. WCC pump ($P_{H2O\text{-}WCC}$), Work = 1.8 kW.

	RH, %				40	50	60	50	50
	X_{aCO_2}, ppm				375	375	375	417	1000
Function	Medium	t, °C	p, bar	$\dot{m}$, g/s	E^{tot}, kW				
Inlet	H_2O(liq)	33	1	62.9	2.4	2.4	4.4	5.9	5.9
Outlet	H_2O(liq)	35	225	62.9	9.2	7.4	5.8	7.4	7.4
	E_d, kW				0.4	0.4	0.4	0.4	0.4
	η_{ex},%				96.2	95.2	94.1	95.2	95.2

Table 8. Heat Exchanger (HE1), Heat Duty = 48.6 kW

	RH, %				40	50	60	50	50
	X_{aCO_2}, ppm				375	375	375	417	1000
Function	Medium	t, °C	p, bar	$\dot{m}$, g/s	E^{tot}, kW				
Inlet	H_2O(liq)	35	225	42.9	6.3	5.0	4.0	5.0	5.0
Outlet	H_2O(liq)	294	225	42.9	22.2	20.9	19.9	20.9	20.9
Inlet (exhaust)	H_2O(g), CO_2	323	0.078	100	41.9	39.7	37.8	39.5	38.4
Outlet (exhaust)	H_2O(g), CO_2	40	0.078	100	25.0	22.8	20.9	22.6	21.5
	E_d, kW				1.0	1.0	1.0	1.0	1.0
	η_{ex},%				98.0	97.8	97.6	97.8	97.7

3.4. Wet Combustion Chamber and expansion

Table 9. Wet Combustion Chamber (WCC) with chemical energy rate according to LHV = 282 kW, and according to HHV = 317 kW

	RH, %				40	50	60	50	50
	X_{aCO_2}, ppm				375	375	375	417	1000
Function	Medium	t, °C	p, bar	$\dot{m}$, g/s	E^{tot}, kW				
Inlet (syngas)	CO, CO_2, CH_4, C_3H_8, H_2	306	10.5	16.6	297.7	297.2	296.9	297.1	296.0
Inlet	O_2	313	10.5	20.6	7.9	7.9	7.9	7.9	7.9
Inlet	H_2O(liq)	181	225	20	5.8	5.2	4.7	5.2	5.2
Inlet	H_2O(liq)	294	225	42.9	22.2	20.9	19.9	20.9	20.9
Intermediary	O_2 (mixing with:), CO, CO_2, CH_4, C_3H_8, H_2	308	10.5	37.2	303.0	302.6	302.3	302.5	301.4
Flame	H_2O(g), CO_2	4260	10	37.2	271.1	270.7	270.4	270.6	269.5
Outlet	H_2O(g), CO_2	1100	10	100	207.3	205.0	203.1	204.9	203.7
	E_d, kW				126.3	126.3	126.3	126.3	126.3
	η_{ex},%				62.1	61.9	61.7	61.9	61.7

Table 10. Gas Turbine (GT), Work = 90.4 kW

	RH, %				40	50	60	50	50
	X_{aCO_2}, ppm				375	375	375	417	1000
Function	Medium	t, °C	p, bar	$\dot{m}$, g/s	E^{tot}, kW				
Inlet	H_2O(g), CO_2	1100	10	100	207.3	205.0	203.1	204.9	203.7
Outlet	H_2O(g), CO_2	672	1	100	112.5	110.2	108.3	110.0	108.9
	E_d, kW				4.7	4.7	4.7	4.7	4.7
	η_{ex},%				97.9	97.8	97.8	97.8	97.8

Table 11. Gas Turbine below ambient pressure (GT^{bap}), Work = 65.7 kW

	RH, %				40	50	60	50	50
	X_{aCO_2}, ppm				375	375	375	417	1000
Function	Medium	t, °C	p, bar	$\dot{m}$, g/s	E^{tot}, kW				
Inlet	H_2O(g), CO_2	672	1	100	112.5	110.2	108.3	110.0	108.9
Outlet	H_2O(g), CO_2	323	0.078	100	41.9	39.7	37.8	39.5	38.4
	E_d, kW				4.8	4.8	4.8	4.8	4.8
	η_{ex},%				95.7	95.6	95.6	95.6	95.6

3.5. Ending of the expansion with CO_2 processing

Table 12. Spray Ejector Condenser (SEC) with Separator, Pump Work = 18.2 kW

	RH, %				40	50	60	50	50
	X_{aCO_2}, ppm				375	375	375	417	1000
Function	Medium	t, °C	p, bar	$\dot{m}$, g/s	E^{tot}, kW				
Inlet (motive fluid)	H_2O(liq)	33	1	28740	3564.3	2712.1	2015.8	2712.1	2712.1
Inlet (exhaust)	H_2O(g), CO_2	40	0.078	100	25.0	22.8	20.9	22.6	21.5
Outlet	H_2O(g)+CO_2	35	1	23.7	10.0	10.0	10.0	9.8	8.7
Outlet	H_2O(liq)	35	1	28816	3586.2	2731.8	2033.6	2731.8	2731.8
	E_d, kW				11.3	11.3	11.3	11.3	11.3
	η_{ex},%				99.7	99.6	99.5	99.6	99.6

Table 13. Carbon Capture Unit (CCU), HE3 and HE4 cooling heat duty = 12.3 kW, compressors $C_{CO2\text{-}1}$ and $C_{CO2\text{-}2}$ Work = 10.1 kW

	RH, %				40	50	60	50	50
	X_{aCO_2}, ppm				375	375	375	417	1000
Function	Medium	t, °C	p, bar	$\dot{m}$, g/s	E^{tot}, kW				
Inlet	H_2O(g)+CO_2	35	1	23.7	10.0	10.0	10.0	9.8	8.7
Outlet	H_2O(liq)	65	80	0.5	0.07	0.06	0.04	0.06	0.06
Outlet	H_2O(g)+CO_2	65	80	23.2	15.0	15.0	15.0	14.8	13.7
	E_d, kW				7.4	7.4	7.3	7.4	7.4
	η_{ex},%				74.8	74.8	74.8	74.6	73.2

3.6. nCO₂PP exergy efficiency

While the cumulative efficiency of the power plant in the studied combination is 27.88% [16], its exergy efficiency according to Eq. (8) is 29.48% when related to the exergy of the sewage sludge used as input and is constant for varying RH or CO_2 concentration, although the value starts to vary when related to the producer gas.

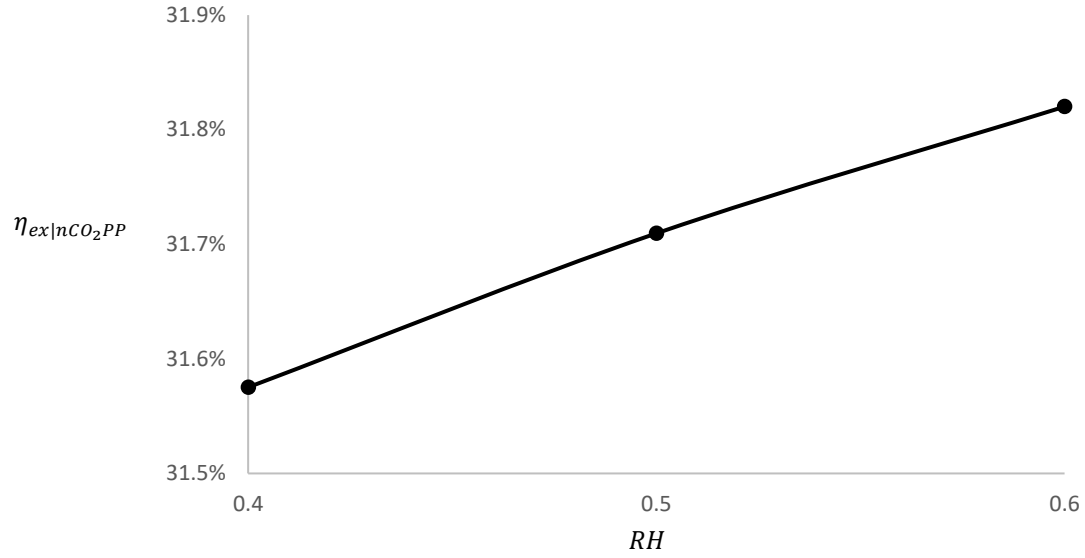

Figure. 2. nCO₂PP exergy efficiency in changing air humidity conditions

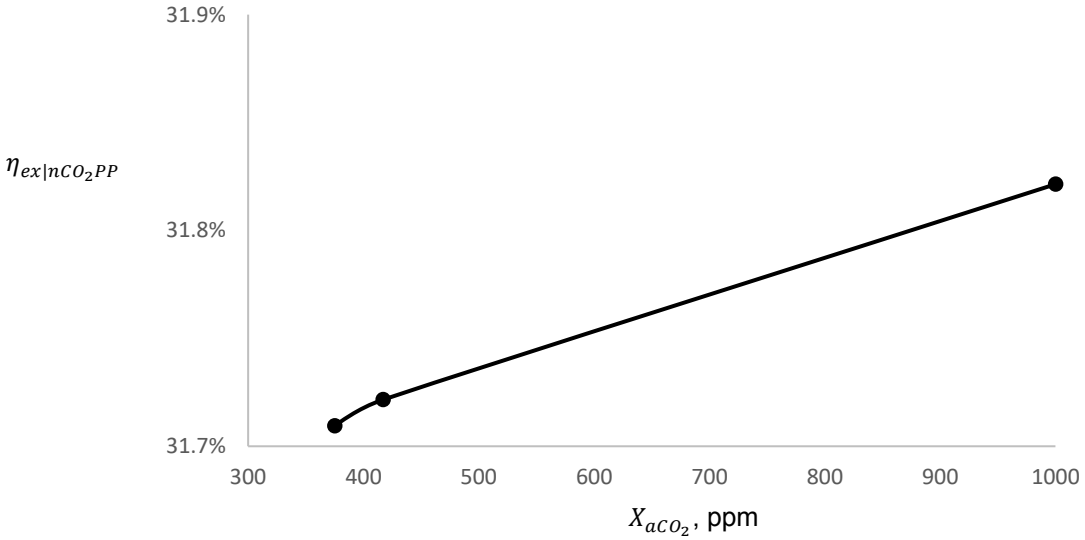

Figure. 3. nCO₂PP exergy efficiency in changing air CO_2 concentrations

4. Conclusions

Second law analysis has been conducted on nCO₂PP. The analyses gave an insight into the integrated system of the gasifier and the nCO₂PP cycle, taking into account the influence of relative humidity and CO_2 content in the air, which translated into chemical exergy of the components in relation to the dead state. The conducted analyses showed that the lowest exergy efficiency is characterized by a wet combustion chamber with a value of about 62%. However, exergy losses affecting the efficiency of this device are unavoidable. Another significant loss is the CO_2 conditioning system for later storage with an exergy efficiency value of 75%. Also, in this set of devices, the possibilities of reducing exergy destruction are limited. Another device with a relatively low exergy efficiency is the gasifier unit and the heat exchanger of gas scrubber with efficiencies of 89% and 84%, respectively. Significant prospects for reducing exergy destruction are offered by the Heat exchanger of Gas Scrubber because the waste heat from this device can be used to drive organic Rankine cycles or to produce oxygen in oxygen transport membranes.

Acknowledgments

The research leading to these results has been funded by the Norway Grants 2014-2021 via the National Centre for Research and Development. This article has been prepared within the project "Negative CO_2 Emission Gas Power Plant" — NOR/POLNORCCS/NEGATIVE-CO2-PP/0009/2019-00, which is co-funded by the "Applied Research" programme under the Norwegian Financial Mechanism 2014-2021 POLNOR CCS 2019 for the development of CO_2 capture solutions integrated in power and industrial processes.

Nomenclature

E	flow exergy rate, kW
E_d	exergy destruction rate, kW
$\bar{e}$	specific molar exergy, kJ/kmol
$\dot{m}$	mass flow rate, g/s
p	pressure, bar
RH	air relative humidity, %
t	temperature, °C
W	work rate (power), kW

Greek symbols

η	efficiency

Subscripts and superscripts

aCO_2	CO_2 in atmospheric air
$Aspen$	derived from Aspen Plus
ch	chemical
ex	exergetic
$fuel, in$	either sewage sludge or producer gas input to the power plant system
nCO_2PP	negative CO_2 emission gas power plant project
O_2, in	oxygen input to the power plant system
rev	reversible
th	thermomechanical
tot	total

References

[1] Negative CO2 Emission Gas Power Plant Project site 2023. nco2pp.com (accessed February 26, 2023).

[2] Ziółkowski P, Badur J, Pawlak- Kruczek H, Stasiak K, Amiri M, Niedzwiecki L, et al. Mathematical modelling of gasification process of sewage sludge in reactor of negative CO2 emission power plant. Energy 2022;244. https://doi.org/10.1016/j.energy.2021.122601.

[3] Ziółkowski P, Madejski P, Amiri M, Kuś T, Stasiak K, Subramanian N, et al. Thermodynamic analysis of negative CO2 emission power plant using aspen plus, aspen Hysys, and ebsilon software. Energies (Basel) 2021;14. https://doi.org/10.3390/en14196304.

[4] Stasiak K, Ziółkowski P, Mikielewicz D. Carbon Dioxide Recovery Skid. Progress in Petrochemical Science 2020;3:362–4. https://doi.org/10.31031/pps.2020.03.000570.

[5] Ertesvåg IS, Madejski P, Ziółkowski P, Mikielewicz D. Exergy analysis of a negative CO2 emission gas power plant based on water oxy-combustion of syngas from sewage sludge gasification and CCS. Energy 2023;278:127690. https://doi.org/10.1016/J.ENERGY.2023.127690.

[6] Ertesvåg IS. Sensitivity of chemical exergy for atmospheric gases and gaseous fuels to variations in ambient conditions. Energy Convers Manag 2007;48:1983–95. https://doi.org/10.1016/J.ENCONMAN.2007.01.005.

[7] Szargut J. Chemical exergies of the elements. Appl Energy 1989;32:269–86. https://doi.org/10.1016/0306-2619(89)90016-0.

[8] Aghbashlo M, Tabatabaei M, Nadian MH, Soltanian S, Ghasemkhani H, Shafizadeh A, et al. Determining biomass chemical exergy using a novel hybrid intelligent approach to promote biomass-

based biorefineries. J Clean Prod 2020;277:124089. https://doi.org/10.1016/J.JCLEPRO.2020.124089.

[9] Qian H, Zhu W, Fan S, Liu C, Lu X, Wang Z, et al. Prediction models for chemical exergy of biomass on dry basis from ultimate analysis using available electron concepts. Energy 2017;131:251–8. https://doi.org/10.1016/J.ENERGY.2017.05.037.

[10] Zhang F, Wang S, Li Y, Chen W, Qian L. Thermodynamic analysis of a supercritical water gasification – oxidation combined system for sewage sludge treatment with cool wall reactor. Energy Convers Manag 2021;247:114708. https://doi.org/10.1016/J.ENCONMAN.2021.114708.

[11] Ruya PM, Purwadi R, Lim SS. Supercritical water gasification of sewage sludge for power generation–thermodynamic study on auto-thermal operation using Aspen Plus. Energy Convers Manag 2020;206:112458. https://doi.org/10.1016/J.ENCONMAN.2019.112458.

[12] Abuşoğlu A, Özahi E, Kutlar Aİ, Demir S. Exergy analyses of green hydrogen production methods from biogas-based electricity and sewage sludge. Int J Hydrogen Energy 2017;42:10986–96. https://doi.org/10.1016/J.IJHYDENE.2017.02.144.

[13] Ptasinski KJ, Hamelinck C, Kerkhof PJAM. Exergy analysis of methanol from the sewage sludge process. Energy Convers Manag 2002;43:1445–57. https://doi.org/10.1016/S0196-8904(02)00027-4.

[14] Fu C, Gundersen T. Using exergy analysis to reduce power consumption in air separation units for oxy-combustion processes. Energy 2012;44:60–8. https://doi.org/10.1016/J.ENERGY.2012.01.065.

[15] Szargut J. Exergy method: technical and ecological applications. International Series on Developments in Heat Transfer 2005;18.

[16] Ziółkowski P, Stasiak K, Amiri M, Mikielewicz D. Negative carbon dioxide gas power plant integrated with gasification of sewage sludge. Energy 2023;262:125496. https://doi.org/10.1016/j.energy.2022.125496.

[17] David R. Lide. CRC Handbook of Chemistry and Physics 80th Edition. 1999.

[18] Friedlingstein P, O'Sullivan M, Jones MW, Andrew RM, Gregor L, Hauck J, et al. Global Carbon Budget 2022. Earth Syst Sci Data 2022;14:4811–900. https://doi.org/10.5194/essd-14-4811-2022.

[19] Schneider S. The worst-case scenario. Nature 2009;458:1104–5. https://doi.org/10.1038/4581104a.

Teaching Exergy to Engineering Students in view of the Energy Transition

Lydia Stougie[a], Brendon de Raad[b], Hedzer van der Kooi[c] and Gijsbert Korevaar[d]

[a] Delft University of Technology, Delft, Netherlands, l.stougie@tudelft.nl, CA
[b] Rotterdam University of Applied Sciences, Rotterdam and Delft University of Technology, Delft, Netherlands, b.w.de.raad@hr.nl,
[c] Delft University of Technology, Delft, Netherlands (retired), jvdkooi@casema.nl,
[d] Delft University of Technology, Delft and Rotterdam University of Applied Sciences, Rotterdam, Netherlands, g.korevaar@tudelft.nl

Abstract:

In view of the energy transition, it is important that engineering students are familiar with the concept of exergy and the added value of exergy analysis compared to energy analysis. Exergy analysis tells the truth about energy efficiency and exergy is directly related to sustainable development. This paper focuses on teaching exergy to students at the Delft University of Technology (TU Delft), but the contents are valuable to other engineering students as well. To encourage the teaching of exergy, the basics of exergy and exergy analysis are presented, as well as examples and ideas for teaching exergy to BSc students that are related to the topics of their BSc programme. It is recommended that the contents of this paper be discussed with many teachers of BSc programmes, especially teachers of BSc programmes that do not yet seem to include the teaching of exergy, and that attention be paid to teaching exergy to MSc students as well.

Keywords:

Teaching; Exergy; Academia; Energy Transition; Added Value; Basics; Examples.

1. Added value of exergy

In view of the energy transition, it is of utmost importance that students graduating from technical universities are well aware of energy-related concepts such as heat, work, energy conservation and the work potential, or quality, of energy. This work potential is important since it is needed for all processes and activities to take place. Preferably, all students who become policy makers, whether they graduate from technical or from non-technical universities, are familiar with these concepts. The work potential of energy is known as exergy; a term proposed in 1953 by Z. Rant [1].

According to the Science Europe Physical, Chemical and Mathematical Sciences Committee, our society does not have an energy crisis, but an exergy crisis [2]. As they put it [2, p.2]: “It is, however, not energy per se that needs to be secure, affordable and sustainable but rather exergy.” and “Exergy analysis not only tells the truth about energy efficiency, but, in an extended perspective, potentially leads to resource accounting on a global scale: a common scale for our common future.”

Exergy analysis tells the truth about energy efficiency because it, in contrast with energy analysis, takes into account the work potential of the ingoing and outgoing flows of a process or system, and shows where work potential is lost. This loss of work potential cannot be made visible with energy analysis. Besides, the law of energy conservation tells that energy cannot be lost nor created. It can only change forms.

Knowing that work potential is needed for all processes and activities and that each process and activity is accompanied with the loss of work potential raises the question whether enough work potential is available to current and future generations. Sources of work potential are fossil fuels such as gas and oil, but these are not renewable and their use causes carbon dioxide emissions. An example of an infinite and renewable source of work potential is solar energy. Solar radiation is also essential for photosynthesis; for plants and trees to grow and to produce the substances necessary in living organisms. Like human processes and activities, photosynthesis and related natural processes involve loss of work potential as well.

Exergy analysis can be used to investigate the causes of the loss of work potential and whether there are possibilities to limit this loss, and thus limit the amount of work needed for the process or activity to take place. In this way, exergy analysis can also be helpful in the choice of which product(s) must preferably be produced,

in the assessment of the reparability, reusability of products and the selection of, e.g., minerals that are used to produce a product.

The results of energy and exergy analyses may very well indicate different parts of processes or systems that have the largest room for improvement. For example, the results of an energy analysis of a methanol production process show that the distillation section needs improvement, while the results of an exergy analysis of the same process clearly indicate that the reforming section causes the highest exergy loss [3].

Furthermore, according to Dincer and Rosen [4, p.61]: “Many suggest that mitigating the environmental impact of energy resource utilization and achieving increased resource-utilization efficiency are best addressed by considering exergy. The relations between exergy and both energy and the environment make it clear that exergy is directly related to sustainable development.”

The calculation of exergy values of amounts of mass and/or energy is based on thermodynamic equations, which makes it a more fundamental method than other sustainability assessment methods because, e.g., the environmental impact is calculated by making use of models and weighting factors, the economic performance is based on costs that vary over time because of market developments, and the calculation of the societal impact of processes or systems is hampered by the limited availability and qualitative nature of data.

This paper focuses on teaching exergy to students at Delft University of Technology (TU Delft), Delft, Netherlands, because all authors have graduated from this university and are, or were, employed by this university. Chapter 2 considers the current status of exergy teaching at TU Delft. Chapter 3 deals with teaching exergy in general, while chapter 4 provides examples and ideas dedicated to students taking specific BSc programmes at TU Delft. This is followed by discussion, conclusions and recommendations.

2. Current exergy teaching at TU Delft

In the academic year 2022-2023, TU Delft offers 16 BSc programmes and more than 30 MSc programmes. The TU Delft study guide [5] was used to determine which of these programmes discusses exergy in one or more of their courses by searching the study guide for courses with the search text “exerg*”, thus with a wildcard at the end. This search resulted in the following eight programmes.

The BSc Mechanical Engineering includes the course Process Engineering & Thermodynamics (WB2543), with the ability to perform energy and exergy calculations of energy and process equipment being one of the learning objectives. The BSc Molecular Science & Technology comprises the course Energy, Recycling and Safety (4052ENRV6), where exergy is mentioned in the Dutch description (not in the English version) of the course contents as part of the topic energy, i.e. together with the energy balance of the earth, greenhouse effect and climate change. The BSc Systems Engineering, Policy Analysis & Management offers the course Processes in the Energy Sector (TB242EB), of which one of the learning objectives is dedicated to exergy, i.e. to be able to explain what exergy and exergy loss is and to calculate exergy losses, values and efficiencies. The BSc minor programme Engineering for Large-scale Energy Conversion and Storage (ELECS) comprises two courses that deal with exergy: the course Energy Conversion: Devices, Systems and Efficiencies (WB3575) applies exergy analysis to energy conversion systems, devices and processes and the course Assessment of Energy Systems (WB3585) applies several assessment methods, i.e. life cycle assessment and exergy analysis, to large scale energy conversion and storage systems. The MSc Applied Earth Sciences contains a course Energy Transition (AESM1315), of which exergy analysis belongs to the course contents, but in 2022/2023 only exam opportunities are offered because this course is discontinued. The MSc Architecture, Urbanism and Building Sciences offers the course User-centred Sustainability Studio (AR3B015), where exergy is mentioned in one of the titles listed as literature and study materials, i.e. Energy Potential Mapping - Visualising Energy Characteristics for the Exergetic Optimisation of the Built Environment [6]. The MSc Mechanical Engineering includes the course Equipment for Heat & Mass Transfer (ME45165), which deals with the principles of heat integration, exergy analysis and pinch technology for heat exchanger networks. The MSc Sustainable Energy Technology programme’s course The Necessity of Storage Technology (SET3080) investigates energy densities, efficiencies, capacities, exergies of thermal storage and combined heat and power possibilities.

This does not mean that teaching exergy is part of the aforementioned programmes only, since exergy could be taught in other programmes without mentioning it in the study guide. E.g. it is expected that the BSc Architecture, Urbanism and Building Sciences pays attention to exergy by means of the Exergy guidebook for building professionals [7]. Because of the strong relationship between exergy and thermodynamics, especially entropy (Section 3.1.1), the study guide was used to find programmes that contain courses in this field by using the search texts “thermodynamic*” and “entrop*”. This has been complemented with a search for courses dealing with “energ*” for BSc programmes which don’t seem to teach exergy, thermodynamics nor entropy. The reason for looking in more detail at the BSc programmes is that TU Delft offers 16 BSc programmes, while the number of MSc programmes is considerably larger, i.e. more than 30. This makes it more feasible to start with all BSc students being well aware of work potential, exergy, in view of the energy transition. Table 1 presents an overview of the results of the search for courses and programmes.

Table 1. Overview of exergy and/or exergy related education per BSc and/or MSc programme according to the TU Delft study guide 2022-2023.

BSc programmes	**Exerg***	**Thermodynamic***	**Entrop***	**Energ***
Aerospace Engineering		x	x	
Applied Earth Sciences		x	x	
Applied Mathematics				x[1]
Applied Physics		x	x	
Architecture, Urbanism and Building Sciences				x[2]
Civil Engineering				x[3]
Clinical Technology		x		
Computers Science & Engineering				x[4]
Electrical Engineering				x[5]
Industrial Design Engineering				x[6]
Life Science & Technology		x	x	
Marine Technology		x		
Mechanical Engineering	x	x		
Molecular Science & Technology	x	x	x	
Nanobiology			x	
Systems Engineering, Policy analysis & Management	x	x		
MSc programmes	**Exerg***	**Thermodynamic***	**Entrop***	
Applied Earth Sciences	x	x		
Applied Mathematics			x	
Applied Physics		x		
Architecture, Urbanism and Building Sciences	x		x	
Chemical Engineering		x	x	
Civil Engineering		x		
Electrical Engineering			x	
Environmental Engineering		x		
Integrated Product Design		x		
Marine Technology		x	x	
Materials Science and Engineering		x	x	
Mechanical Engineering	x	x		
Sustainable Energy Technology	x	x		
Systems and Control			x	
Other	**Exerg***	**Thermodynamic***	**Entrop***	
Minor Engineering for Large-scale Energy Conversion and Storage	x			

[1] The course Mathematical Physical Models (AM3510) contains the derivation of differential equations from physical laws such as mass and energy conservation
[2] Several courses (codes with BK*) deal with energy use, in-house climate etc.
[3] Several courses (codes CTB*) deal with energy, e.g. energy balances, energy dissipation etc.
[4] The course Computer Organisation (CSE1400) deals with the design of digital computers and their energy use.
[5] E.g. the course Electrical Energy Conversion (EE2E11).
[6] The course Sustainable Impact (IOB3-5) considers the energy effectiveness in products, energy efficiency etc.

It can be concluded from the results in Table 1 that nine of the sixteen BSc programmes teach exergy and/or thermodynamics and that teaching entropy is part of the BSc Nanobiology. The other six BSc programmes do at least pay attention to energy, though it sometimes seems quite specific. Nevertheless, the contents of all BSc programmes provide starting points for teaching exergy.

3. Teaching exergy in general

General information about exergy can be found in literature (section 3.1). As an alternative, this chapter provides basic knowledge about thermodynamics (section 3.2), exergy calculations (section 3.3) and methods that apply exergy analysis (section 3.4).

3.1. Where to start?

Several textbooks about thermodynamics pay attention to exergy, e.g. the books by Moran and Shapiro [8], Smith, Van Ness and Abbott [9] and Cengel and Bowles [10]. Textbooks about exergy have been published as well, e.g. by Dincer & Rosen [4], Szargut, Morris & Steward [11], Kotas [12] and Sankaranarayanan, Van der Kooi and De Swaan Arons [13]. PhD theses may also be a valuable source of information, e.g. [3,14-16]. Many scientific papers about exergy have been published and even a journal dedicated to exergy analysis exists: the International Journal of Exergy [17]. More informal information can be found on websites such as

the website ‘Do more with the quality of energy’, which explains in plain words, in Dutch, what exergy is [18] and the website tudelft.nl/exergy.

3.2. Basic thermodynamics

The concepts of energy, energy conservation, heat and work can in plain words be explained by an example from daily practice, such as the following example about bicycling. When someone wants to make a ride on their bike, they must exert a continued force on the pedals, in other words: they perform work. The larger the friction with the road, the larger the force that they need to exert on the pedals of the bicycle (be it by keeping the same speed, or by lowering the force and distance per revolution and making more revolutions). On the other hand, without friction, they would not start moving forward because the friction between the tires of the bicycle and the road is essential to start riding. Once started bicycling, it would be possible to bike at constant speed without using the pedals in case of a flat and frictionless road and the absence of any other friction effects. In reality, different types of friction occur and they must continue to exert a force on the pedals to continue biking, i.e. a continual work input is necessary. This work input is a form of energy. The law of energy conservation states that the total amount of energy remains the same. So, where does this work input go to? The exerted work causes deformation of the tires and road, and finally becomes heat at the temperature of the environment. Thus, the work input is transformed into other types of energy. This degradation of work is a general characteristic of processes that occur in reality.

The law of energy conservation is also known as the first law of thermodynamics. However, being more precise: the first law of thermodynamics results from applying the law of energy conservation to a system and its surroundings. Another important law of thermodynamics related to the concept of work is the second law of thermodynamics. This 2nd law can be expressed as follows: in every real process degradation of work takes place, only in the limiting case of a reversible process the amount of work remains the same. In reality, reversible processes cannot take place because it is impossible to return both the system and the surroundings to the state before the process started. Examples of irreversibilities and driving forces are the following [7]: friction, heat transfer through a finite temperature difference, spontaneous chemical reactions and spontaneous mixing of substances with different compositions and unrestrained expansion of a gas or liquid to a lower pressure.

The transfer of energy between a system and its surroundings can be classified as work or as heat. The latter is caused by a temperature difference between the system and surroundings and always occurs in the direction of decreasing temperature. Examples of forms of energy that are different from work and heat are the following: kinetic energy, potential energy due to gravity, chemical potential energy, electrical energy etc.

3.3. Basic exergy calculations

This section is a selection of what 2nd year BSc students Systems Engineering, Policy analysis & Management is taught about exergy analysis. After an introduction about the difference between energy and exergy and the added value of exergy, they learn how to calculate exergy values of mass and/or energy, which starts with the definition of exergy. Exergy is defined as the maximum theoretical amount of work that can be obtained when an amount of energy or mass is brought into total equilibrium with the reference environment. It follows from this definition that energy in the form of work resembles 100% exergy. The same holds for kinetic energy, potential energy due to gravity and electrical energy. To be able to calculate the maximum amount of work that can be obtained from other forms of energy, the reference environment needs to be defined. This reference environment is a model of the atmosphere, oceans and earth’s crust. It consists of components in total equilibrium with each other and at a certain pressure, p_0, and temperature, T_0, mostly 1 atm. and 25 °C, respectively. In some applications, e.g. in analyses related to the built environment, the actual pressure and temperature are used. The composition of the reference environment is chosen in such a way that by no means work can be obtained from the reference environment. A well-known and commonly used model of the reference environment has been developed by Szargut et al. [11].

3.3.1. Calculation of exergy values

The exergy value of heat is calculated from its energy value and the Carnot efficiency. Assuming a constant temperature of the heat, the exergy value of heat at a higher temperature than the temperature of the reference environment is calculated as shown in Eq. (1). N.B.: when temperature T is lower than T_0 the absolute value of the Carnot factor has to be used.

$$Ex_{\mathrm{Q}} = Q \cdot \left(1 - \frac{T_0}{T}\right) \quad (1)$$

with:
Ex_{Q} = exergy value of heat [J]
Q = energy value of heat [J]
T = temperature of the heat (assumed constant) [K]
T_0 = temperature of the reference environment [K]

The exergy value of mass flows consists of a physical contribution, Eq. (2), a chemical contribution, Eq. (3) and/or a contribution due to mixing, Eq. (4), when the mass flow consists of more than one substance.

$$Ex_{\mathrm{m,phys}} = (H - H_0) - T_0(S - S_0) \quad (2)$$

with:
$Ex_{\mathrm{m,phys}}$ = physical exergy value of the substance [J]
H = enthalpy of the substance at its conditions [J]
H_0 = enthalpy of the substance at the pressure and temperature of the reference environment [J]
S = entropy of the substance at its conditions [J/K]
S_0 = entropy of the substance at the pressure and temperature of the reference environment [J/K]
T_0 = temperature of the reference environment [K]

$$ex^0_{\mathrm{ch},i}(T_0) = \sum(N_e ex^0_{\mathrm{ch},e}(T_0)) + \Delta_{\mathrm{f}} g^0_i(T_o) \quad (3)$$

with:
$ex^0_{\mathrm{ch},i}(T_0)$ = standard chemical exergy value of substance i at T_0 [J/mol]
$ex^0_{\mathrm{ch},e}(T_0)$ = standard chemical exergy value of element e at T_0 [J/mol]
$\Delta_{\mathrm{f}} g^0_i(T_o)$ = Gibbs energy of formation of substance i at T_0 [J/mol]
N_e = number of moles of element e per mole of substance i [-]

$$ex_{\mathrm{mixing}} = RT_0 \sum(x_i \ln(x_i)) \quad (4)$$

with:
ex_{mixing} = mixing contribution in case of ideal mixing [J/mol of mixture]
R = universal gas constant, 8.314 [J/mol·K]
T_0 = temperature of the reference environment [K]
x_{i} = molar fraction of substance i

3.3.2. Calculation and presentation of exergy losses and efficiencies

The loss of exergy can be subdivided into internal exergy loss and external exergy loss. The internal exergy loss, Eq. (5), is caused by irreversibilities (Section 3.2) and is also known as exergy destruction. The external exergy loss is the exergy that is lost with waste flows.

$$Ex_{\mathrm{loss,internal}} = \sum Ex_{\mathrm{in}} - \sum Ex_{\mathrm{out}} \quad (5)$$

Universal as well as functional exergy efficiencies of a system can be calculated. Where the universal exergy efficiency compares all ingoing and outgoing amounts of exergy, Eq. (6), the functional exergy efficiency takes into account the purpose of the system [19], e.g. the exchange of heat in a heat exchanger, Eq. (7).

$$\Psi_{\mathrm{univ}} = \frac{\sum Ex_{\mathrm{out}}}{\sum Ex_{\mathrm{in}}} \quad (6)$$

$$\Psi_{\mathrm{funct,heat\ exchanger}} = \frac{(Ex_{\mathrm{p,out}} - Ex_{\mathrm{p,in}})}{(Ex_{\mathrm{s,in}} - Ex_{\mathrm{s,out}})} \quad (7)$$

with:
Ex_{p} = exergy amount of the mass flow that is heated in the heat exchanger [J]
Ex_{s} = exergy amount of the mass flow that is cooled in the heat exchanger [J]

Besides numerical representation of the results of exergy analyses, the loss of exergy can be shown in a Grassmann diagram, i.e. the exergy variant of the Sankey diagram, and/or in a value diagram. Originally, value diagrams were used for heat transfer processes, as they show the $(1-T_0/T)$ value of heated and cooled flows versus the amount of heat that is transferred, but they can be used for the evaluation of thermal power plants as well [16].

3.4. Exergy methods

Scientists from all over the world have developed assessment methods that pay attention to exergy losses [3]. The following presents a brief overview of some important exergy analysis methods. The Cumulative Exergy Consumption (CExC) method was introduced in 1988 by Szargut et al. [11] and takes into account all exergy needed to produce a product, i.e. attention is paid to the exergy needed in its supply chains as well. A method that is considered equivalent [1] is the Exergetic Cost method developed by Valero et al. [20] in 1986. The CExC method was extended in 2001 with the abatement of emissions and the system itself by Dewulf et al. [21] resulting in the Cumulative Exergy Consumption for Construction and Abatement (CExCA) method. Around the same time, Sciubba [22] introduced the Extended Exergy Accounting (EEA) method which expands the CExC method by integrating thermo-economic methods and the inclusion of labour and environmental impact. The Cumulative Exergy Extraction form the Natural Environment (CEENE) method extends the CExC method with land use and was developed in 2007 by Dewulf et al. [23] to be used in combination with the ecoinvent database [24]. Examples of assessment methods related to the standard Life Cycle Assessment (LCA) method [25] are the following: Exergetic Life Cycle Analysis (ELCA) developed in 1997 by Cornelissen [26] includes the calculation of internal exergy losses, Life Cycle Exergy Analysis (LCEA) developed around the same time by Gong and Wall [27] calculates the exergetic pay-back time and the Exergoenvironmental analysis method introduced in 2009 by Meyer et al. [28] combines LCA with the Exergoeconomic analysis method by Tsatsaronis and Winhold [29]. This Exergoeconomic analysis method was introduced in 1984 for the combined exergetic and economic analysis of energy conversion processes and determines the costs of the exergy losses in the components of a system. The method was the basis of the Advanced exergoeconomic analysis method introduced in 2008, which splits the internal exergy losses into avoidable and unavoidable exergy losses and makes a distinction between exergy losses caused by the component itself and exergy losses caused by connected components [30]. The Total Cumulative Exergy Loss (TCExL) method can be regarded as combination of, or extension to, the CExC, CExCA, CEENE and ELCA methods and calculates all exergy losses caused by a technological system during its life cycle [3].

4. Examples and ideas for teaching exergy at TU Delft

The examples and ideas for teaching exergy presented in this chapter vary in difficulty, i.e. for students with no background in thermodynamics at all, for students with a background in thermodynamics but who are unfamiliar with exergy and some illustrative examples for students who have been taught how to carry out exergy analysis. Section 4.1 provides an overview of which examples/ideas are recommended for students from which BSc programme. Sections 4.2 to 4.8 introduce and explain these examples/ideas. Many more examples and applications of exergy analysis can be found in textbooks about exergy, e.g. [4].

4.1. Overview of examples/ideas and educational programmes

The results of the search for current education in the field of exergy, thermodynamic, entropy and/or energy presented in chapter 3 has been used as the starting point for providing examples/ideas for the teaching of exergy at TU Delft. The goal was to find examples/ideas that are related to the subjects the students are being taught during their BSc programme. The examples/ideas mentioned in Table 2 are based on examples used by the authors when teaching exergy to their students, complemented with examples that are expected to be interesting to students from other BSc programmes.

The authors recommend teachers to make the lectures interesting by interacting frequently with the students and to visualise the theory as much as possible, e.g. by visualising the difference between physical and chemical exergy or how the chemical exergy of a substance can be calculated from the standard exergy values of the elements. It is also recommended to alternate between explaining theory and letting the students make calculations based on the examples/ideas provided in this chapter during the lectures. The assessment can consist of theoretical questions about the concept of exergy as well as questions that require calculations by the students. The students may be expected to know the equations by heart before taking the exam, but another option would be to provide a formula sheet. In the latter case, it can still be tested whether the students understand the theory correctly, e.g. by providing a schematic overview of an energy system including the thermodynamic properties of the flows and asking the students to calculate the internal and external exergy losses, which implies that they e.g. need to understand which temperature and enthalpy and entropy values should be used for the calculation of the physical exergy of a mass flow.

Table 2. Overview of examples per BSc programme.

BSc programmes	Section(s)	Example(s)
Aerospace Engineering	4.7	Hydrogen combustion
Applied Earth Sciences	4.6	Heat exchanger
Applied Mathematics	4.2, 4.3.2	Energy/exergy, Electricity to heat
Applied Physics	4.6	Heat exchanger
Architecture, Urbanism and Building Sciences	4.2, 4.3.1, 4.6	Energy/exergy, Mixing hot/cold water, Heat exchanger
Civil Engineering	4.2, 4.3.1, 4.4, 4.6	Energy/exergy, Mixing hot/cold water, Iron production, Heat exchanger
Clinical Technology	4.2, 4.5	Photosynthesis
Computers Science & Engineering	4.2, 4.3.2	Energy/exergy, Electricity to heat
Electrical Engineering	4.2, 4.3.2	Energy/exergy, Electricity to heat
Industrial Design Engineering	4.2, 4.4	Energy/exergy, Iron production
Life Science & Technology	4.2, 4.5	Photosynthesis
Marine Technology	4.2, 4.4, 4.7	Iron production, Hydrogen combustion
Mechanical Engineering	4.6, 4.8	Heat exchanger, Heat pump
Molecular Science & Technology	4.7	Hydrogen combustion
Nanobiology	4.2, 4.5	Photosynthesis
Systems Engineering, Policy analysis & Management	4.2, 4.6, 4.7	Heat exchanger, Hydrogen combustion

4.2. Energy versus exergy

The teaching of exergy could start with the following example, which proved to be insightful to students who have never heard of exergy before (and maybe think the “x” is just a typo).

This example starts with telling that different types of energy exist and that one type of energy may be more valuable, or useful, than another type of energy. This could be followed by the teacher asking the students to mention some types of energy, i.e. electrical energy, heat, kinetic energy etc. Then the teacher tells the students that the valuable or useful part of energy has its own name: exergy.

After that, the teacher shows a sandwich, or a picture of a sandwich, and asks the students whether they know how many calories the sandwich provides and where these calories come from, i.e. from carbohydrates, proteins and oils/fats. Finally, the teacher tells the students that you could look at energy and exergy like the following: the energy represented by the sandwich are the calories and one of the components, e.g. the carbohydrates, is the exergy (although in reality all three components contain more or less exergy). So, exergy is a part of energy. The amount of exergy could be large or even 100%, i.e. many calories and many or all, in this case, carbohydrates such as with a sugar cube. And the amount of exergy could be small or even zero, i.e. calories without these carbohydrates such as with a piece of fish.

4.3. Energy conservation versus exergy loss

4.3.1. Mixing of hot and cold water

The difference between energy and exergy analysis can easily be shown with the following example about the mixing of hot and cold water. The example is about filling a bath tub, but of course the teacher can think of another situation that is applicable.

An empty and well-isolated bath tub is filled with two buckets of hot water of 60 °C and two buckets of cold water of 20 °C, resulting in warm bath water with a temperature of 40 °C, i.e. there are no heat losses from the hot or warm water to the bathroom. The temperature in the bathroom equals 20 °C. Table 3 presents an overview of the energy and exergy values of the water in the buckets.

Table 3. Energy and exergy values of buckets filled with water.

Water temperature [°C]	Energy [kJ/bucket]	Exergy [kJ/bucket]
60 °C (hot)	2511	105
20 °C (cold)	839	0
40 °C (warm)	1675	28

The question to be asked to the students would be: calculate the total amounts of energy and exergy before the mixing of water and after the mixing of the water, and compare the results. The answer is quite straightforward since the total amount of energy before mixing equals 2*2511+2*839 = 6700 kJ, which is the same as the amount of energy after mixing, i.e. 4*1675 = 6700 kJ. In case of exergy, these values are different, i.e. 2*105+2*0 = 210 kJ before mixing and only 4*28 = 112 kJ after mixing. With this example, the teacher can let the students experience that the total amount of energy stays the same, is conserved, but that this does

not hold for the total amount of exergy. The mixing of hot and cold water causes exergy loss. This exergy loss is of the type internal exergy loss, also known as exergy destruction, and the driving force that causes this exergy loss is the difference in temperature between the hot and cold water (Section 3.2).

4.3.2. From electricity to heat

The following example is about a laptop, but it is applicable to many more electrical devices, such as an electrical heater, a television, a vacuum cleaner etc. The only thing is that the power of the device and the temperature of the emitted heat will be different.

Assume that a laptop is used to write a conference paper about teaching exergy, that the power of this laptop equals 50 W and that the room in which the author writes their paper has a constant temperature of 18 °C. The laptop gets warm during the writing of the paper and constantly emits heat of 60 °C.

The question to be asked to the students would be: perform an energy and exergy analysis of this warm laptop. The answer to the first part of the question is, again, quite straightforward since the power consumed by the laptop will be fully converted into heat, i.e. the heat generation equals the electric power and both equal 50 W. The results of the exergy analysis are, again, different, since electric power represents 100% exergy, while the exergy content of heat depends on the temperature of the heat and the temperature of the reference environment (Section 3.3.1), in this case the temperature of the room since no other information is available. The amount of heat represents an exergy amount of (1-(18+273.15)/(60+273.15))*50 = 0.13*50 = 6.3 W. Thus, the internal exergy loss equals 50-6.3 = 44 W, i.e. 87% of the exergy input, which is very different from the 0% loss according to the energy analysis.

4.4. Iron production

The usual way of producing iron, e.g. to be used in parts of a bicycle or for large constructions, is the blast furnace process, which converts iron ore into pure iron by burning coke (carbon) and results in the emission of carbon dioxide, Eq. (R1). The reactants are at 298 K and the products at 1809 K.

$$\mathrm{Fe_2O_3(s) + 5.7C(s) + 4.2O_2(g) + 17N_2(g) \rightarrow 2Fe(l) + 5.7CO_2(g) + 17N_2(g)} \quad \text{(R1)}$$

In view of the energy transition, attention is paid to an alternative way of producing iron, i.e. with hydrogen instead of coke, Eq. (R2).

$$\mathrm{Fe_2O_3(s) + 8.1H_2(g) + 2.5O_2(g) + 10N_2(g) \rightarrow 2Fe(l) + 8.1H_2O(g) + 10N_2(g)} \quad \text{(R2)}$$

Table 4 provides the exergy values of the reactants and products of Eqs. (R1) and (R2). The question to be asked to the students would be: calculate the total exergy input of the original blast furnace process and the alternative process with hydrogen, the percentage of exergy that is lost and compare the results with regard to exergy and emitted components.

Table 4. Chemical exergy values of the substances of Eqs. (R1) and (R2) [31,32].

Reactants at 298 K	Exergy [kJ/mol]	Products at 1809 K	Exergy [kJ/mol]
Fe_2O_3(s)	12.4	Fe(l)	415
C(s)	411	CO_2(g)	73
O_2(g)	3.97	H_2O(g)	51
N_2(g)	0.72	N_2(g)	33
H_2(g)	236		

The exergy inputs of the original and alternative processes equal 2384 kJ/mol iron ore and 1941 kJ/mol iron ore, resp., and are obtained by multiplying the exergy values of the components with the stoichiometric coefficients shown in the reaction equation. The total exergy of the products is calculated analogously and comparing the exergy input with the exergy output results in exergy losses of 24% and 19%, respectively.

4.5. Photosynthesis

Each and every process is accompanied with exergy losses: technological processes as well as natural, biological processes such as photosynthesis. In his PhD thesis [14], Lems provides a detailed exergy analysis of photosynthesis. He assesses the light and dark reactions of photosynthesis separately and combines them into the following overall reaction equation, Eq. (R3):

$$\mathrm{6CO_2 + 6H_2O + 6P + 24h\nu_{680nm} + 24h\nu_{700nm} \rightarrow 6C_6H_{12}O_6 + 6O_2 + 6P_{ATP}} \quad \text{(R3)}$$

with:

$h\nu_{680nm}$ and $h\nu_{700nm}$ = photons with a wavelength of 680 nm and 700 nm, respectively

P = inorganic phosphate

P_{ATP} = terminal phosphate group of ATP (adenosine triphosphate)

Table 5 shows the exergy values of the substances. The exergy value of photons can be calculated in the same way as the exergy value of heat, i.e. from the energy value of the photons times the Carnot factor, with T_{low} and T_{high} being the surface temperatures of the earth (298.15 K) and the sun (5762 K), respectively. The Planck constant equals 6.626×10^{-34} Js.

Table 5. Exergy values of the substances occurring in the overall photosynthesis reaction.

Substance	Exergy [kJ/mol]	Comment [14]
$C_6H_{12}O_6$ (glucose)	2955	
CO_2	≈ 0	almost in equilibrium with the concentration in the atmosphere
H_2O	0	taken at zero
O_2	≈ 0	considered to be in equilibrium with air
P_{ATP}	306	compared to P

The question to be asked to the students would be: calculate the exergy loss caused by the overall photosynthesis reaction.

The answer can be calculated as follows. The exergy value of one mole of photons with a wavelength of 680 and 700 nm equals 6.26x10-34*680/1E9*(1-298.15/5762)* 6.022x10^23 = 162 kJ and, analogously, 167 kJ, respectively. This results in a total exergy input of 24*162 + 24*167 = 7896 kJ. The total exergy output equals 2955 + 6*306 = 3261 kJ. Combining these answers results in an exergy loss of 7896 – 3261 = 4635 kJ per mole of glucose formation.

4.6. Energy and exergy analysis of a heat exchanger

An interesting example of the differences between energy and exergy analysis and between universal and functional efficiencies (Section 3.3.2) is the assessment of an ideal counter current heat exchanger. Table 6 shows the enthalpy (i.e. energy) and entropy values of the primary and secondary flows, i.e. steam and flue gas, respectively. The steam is heated from 138 to 234 °C, the flue gas cooled from 436 to 220 °C and the temperature of the reference environment equals 15 °C. The chemical exergy value of flue gas equals 69 kJ/kg.

Table 6. Enthalpy and entropy values of flue gas (41 kg/s) and steam (29 kg/s).

Substance	h_{in} [MJ/kg]	h_{out} [MJ/kg]	h_0 [MJ/kg]	s_{in} [kJ/kg·K]	s_{out} [kJ/kg·K]	s_0 [kJ/kg·K]
Flue gas	-3.5	-3.8	-4.3	7.9	7.5	6.0
Steam	0.58	1.0	0.063	1.7	2.6	0.22

The question to be asked to the students would be: calculate and compare the universal and functional energy and exergy efficiencies of the heat exchanger. Table 7 shows the results obtained by using the enthalpy values of the in- and outgoing flows to calculate the energy flows, Eq. (2) to calculate the exergy flows and Eqs. (6) and (7) for the calculation of the universal and functional efficiencies. The differences between the energy and exergy efficiencies as well as between the universal and functional exergy efficiencies are remarkable.

Table 7. Universal and functional energy and exergy efficiencies of the heat exchanger.

	Universal [%]	Functional [%]
Energy	100	99
Exergy	82	62

4.7. Hydrogen combustion

One of the energy carriers that has gained interest in view of the energy transition is hydrogen, since it can be produced when there is an excess of wind energy, stored, and combusted in a power plant when there is a shortage of electricity from renewable energy sources, although the round-trip efficiency is low.

The following example is about calculating the exergy loss during hydrogen combustion with pure oxygen. It is assumed that the combustion temperature equals 1100 °C. The temperature of the reference environment is set at 25 °C and the Gibbs energy of formation of water at 25 °C equals -237 kJ/mol. Table 8 shows the other thermodynamic data needed for this example.

Table 8. Exergy values of the substances related to hydrogen combustion, at 1 atm [31].

Substance	Enthalpy at 1100 °C [kJ/mol]	Enthalpy at 25 °C [kJ/mol]	Entropy at 1100 °C [J/mol·K]	Entropy at 25 °C [J/mol·K]	Standard chemical exergy [kJ/mol]
H_2 (hydrogen)	32	0	176	131	236
O_2 (oxygen)	36	0	255	205	3.97
H_2O (water)	-200	-286	246	70	to be calculated

The question to be asked to the students would be: calculate the exergy loss caused by the combustion of hydrogen when the effect of mixing is neglected. The solution to this example consists of the following steps: 1) calculate the physical exergy values of the reactants (H_2, O_2) and product (H_2O) with Eq. (2), 2) calculate the chemical exergy value of H_2O with Eq. (3), 3) calculate the total exergy value of the reactants and product, 4) calculate the amount of heat that is released during combustion and calculate its exergy value with Eq. (1), 5) calculate the exergy loss by subtracting the total amount of exergy out from the total amount of exergy in. Table 9 shows the results.

Table 9. Results of the example about hydrogen combustion.

	Energy [kJ/mol H_2]	Physical exergy [kJ/mol]	Chemical exergy [kJ/mol]	Total exergy [kJ/mol]	Total exergy [kJ/mol H_2]	**Total**
IN						**268**
H_2		19	236	255	255	
O_2		21	3.97	25	13	
OUT						**203**
H_2O		34	0.99	35	35	
Heat of combustion	214			168	168	
Exergy loss						**65**

4.8. Energy and exergy analysis of a heat pump

The implementation of electric heat pumps in industry and households is very relevant in view of the energy transition. In this example, operational costs are allocated to the exergy destruction in the heat pump components. Assume that the heat pump operates 8.000 hrs per year, during 5 years at an electricity price of 0.041 €/kWh. The efficiency of the compressor drive, η_m, equals 85%. The temperature of the reference environment is set at 20 °C. Table 10 shows the mass flows and thermodynamic data of the flows.

Table 10. Mass flows and thermodynamic data needed for the heat pump example.

Component[1]	Working medium (2.1 kg/s)		Source or Sink (30 kg/s)			
	h_{in} [kJ/kg]	s_{in} [J/kg·K]	h_{in} [kJ/kg]	s_{in} [J/kg·K]	h_{out} [kJ/kg]	s_{out} [J/kg·K]
Evaporator	322	1,421	126	437	108	378
Compressor	581	2,305	n/a	n/a	n/a	n/a
Drive	n/a	n/a	n/a	n/a	n/a	n/a
Condenser	626	2,347	168	572	189	639
Expansion valve	322	1,406	n/a	n/a	n/a	n/a

[1] The working medium leaving the evaporator has the conditions of the working medium entering the compressor, etc.

The question to be asked to the students would be: calculate per component the amount of energy transferred, the exergy destruction and the related operational losses (costs). Table 11 presents the results, which have been calculated as follows. The energy transfer by the evaporator, compressor, condenser and expansion valve follows from the difference in enthalpy of the ingoing and outgoing working medium. The energy transfer by the drive has been calculated with $W_D = W_C/\eta_m$. The exergy destruction caused by the evaporator, compressor, condenser and expansion valve has been calculated with Eqs. (2) and (5), where H_0 and S_0 cancel out. The exergy destruction caused by the drive is taken as the difference with the compressor duty, i.e. W_D minus W_C. The operational losses are calculated by multiplying the exergy destruction with the number of operating hours per 5 years and the costs per kWh.

Table 11. Results of the heat pump example.

Component	Energy transfer [kW]	Exergy destruction [kW]	Operational losses [k€]
Evaporator	544	21	35
Compressor	95	26	42
Drive	111	16	27
Condenser	638	18	30
Expansion valve	0	9	15

5. Discussion and conclusions

It is said that our society does not have an energy crisis, but an exergy crisis, and that exergy is directly related to sustainable development. Despite the added value of exergy analysis compared to energy analysis, it is

important to pay attention to all three pillars of sustainability, i.e. to the environmental, economic as well as the social sustainability of processes and activities.

The reader of this paper may get the impression that exergy losses should be avoided by all means, but the loss of exergy is unavoidable; it is needed to overcome friction and to achieve a reasonable speed of processes and activities. However, too large driving forces, e.g. differences in pressure and/or temperature, should be avoided because this would lead to a too large input of work.

Although exergy analysis, paying attention to the loss of work potential, is relevant in view of the energy transition, it seems that teaching exergy is not common practice at TU Delft. It was learnt from the TU Delft study guide that probably just 4 of the 16 BSc programmes, 1 BSc minor programme and 4 of the more than 30 MSc programmes pay attention to exergy and exergy analysis. However, a more detailed investigation is needed before firm conclusions can be drawn about the extent to which teaching exergy is part of the TU Delft educational programmes.

The basics of thermodynamics and exergy calculations presented in this paper are meant as a first step in teaching exergy in academia, but it cannot be ruled out that (essential) information is missing. The same holds for the brief overview of exergy methods.

The authors like to emphasize that the understanding of the exergy concept is highly valuable for both engineering professionals and policy makers that have to decide about the energy transition. Exergy analysis provides a more thorough understanding of the improvement potential of processes and systems. It helps to better understand how to reach sustainability goals such as the reduction of carbon dioxide emissions and improving resource efficiency.

6. Recommendations

It is recommended that a more detailed investigation of the teaching of exergy at TU Delft be carried out and that the contents of this paper be discussed with many teachers of BSc programmes, especially teachers of BSc programmes that do not yet seem to include the teaching of exergy. Based on these discussions, dedicated examples and ideas can be developed for teaching exergy as part of BSc programmes. It is recommended that attention be paid to teaching exergy to MSc students as well.

References

[1] Sciubba E., Wall, G., A brief commented history of exergy from the beginnings to 2004, International Journal of Thermodynamics 2007;10(1):1-26.

[2] Science Europe physical, chemical and mathematical sciences committee, A common scale for our common future: exergy, a thermodynamic metric for energy. Brussels, Belgium: Science Europe; 2015 Sep. Report No.: D/2015/13.324/6.

[3] Stougie L., Exergy and Sustainability – Insights into the value of exergy analysis in sustainability assessment of technological systems [dissertation]. Delft, Netherlands: Delft University of Technology; 2014.

[4] Dincer I., Rosen M.A., Exergy: Energy, Environment and Sustainable Development. Amsterdam: Elsevier Ltd.; 2021.

[5] Delft University of Technology. Study guide - Available at:<http://studyguide.tudelft.nl> [accessed 1.12.2022].

[6] Broersma S., Fremouw M., van den Dobbelsteen A., Energy potential mapping: visualising energy characteristics for the exergetic optimisation of the built environment. Entropy 2013;15(2):490-510.

[7] Jansen, S., Exergy guidebook for building professionals - How to use exergy to analyse and develop energy systems for the built environment, Delft, Netherlands. Delft University of Technology; 2014.

[8] Moran M.J., Shapiro H.N., Boettner D.D., Bailey M.B., Principles of engineering thermodynamics. Singapore: John Wiley & Sons Singapore Pte. Ltd.; 2015.

[9] Smith J.M., van Ness H.C., Abbott M., Introduction to chemical engineering thermodynamics. Singapore: McGraw-Hill Book Co.; 1987.

[10] Cengel Y.A., Bowles M.A., Thermodynamics: an engineering approach. New York, USA: McGraw-Hill; 2011.

[11] Szargut J., Morris D.R., Steward F.R., Exergy analysis of thermal, chemical and metallurgical processes. New York, USA: Hemisphere Publ. Corp; 1988.

[12] Kotas T.J., The exergy method of thermal plant analysis. Malabar, USA: Krieger Publishing Co.; 1995.

[13] Sankaranarayanan K., Kooi H.J. van der, Swaan Arons J. de, Efficiency and sustainability in the energy and chemical industries: scientific principles and case studies. Boca Raton, USA: CRC Press; 2010.

[14] Lems S., Thermodynamic explorations into sustainable energy conversion: Learning from living systems [dissertation]. Delft, Netherlands: Delft University of Technology; 2009.

[15] Jansen S.C., Exergy in the built environment. The added value of exergy in the assessment and development of energy systems for the built environment [dissertation]. Delft, Netherlands: Delft University of Technology; 2013.

[16] Woudstra N., Sustainable energy systems: limitations and challenges based on exergy analysis [dissertation]. Delft, Netherlands: Delft University of Technology; 2012.

[17] Inderscience Publishers. International Journal of Exergy – Available at: <https://www.inderscience.com/jhome.php?jcode=ijex> [accessed 01.03.2023].

[18] Stougie L., Stikkelman R.M., Woudstra N., van der Kooi H.J., Do more with the quality of energy (in Dutch) – Available at:<https://www.tudelft.nl/en/tpm/exergy/do-more-with-the-quality-of-energy> [accessed 01.03.2023].

[19] Woudstra N., Exergetische rendementen (in Dutch), Delft, Netherlands: Delft University of Technology, Faculty of Mechanical Engineering and Maritime Technology; 1995. Technical Report No.: EV-1809.

[20] Valero A., Lozano M.A., Munoz M., A general theory of exergy saving. I. On the exergetic cost. Computer-Aided Engineering and Energy Systems: Second Law Analysis and Modelling 1986;3: 1-8.

[21] Dewulf J., Van Langenhove H. and Dirckx J., Exergy analysis in the assessment of the sustainability of waste gas treatment systems, Science of the Total Environment 2001;273(1-3): 41-52.

[22] Sciubba E., Beyond thermoeconomics? The concept of extended exergy accounting and its application to the analysis and design of thermal systems. Exergy, an International Journal 2001;1(2): 68-84.

[23] Dewulf J., Bösch M., De Meester B., Van der Vorst G., Van Langenhove H., Hellweg S., Huijbregts M.A.J., Cumulative exergy extraction from the natural environment (CEENE): a comprehensive life cycle impact assessment method for resource accounting. Environmental Science & Technology 2007;41(24): 8477-8483.

[24] Ecoinvent Centre (Swiss Centre for Life-Cycle Inventories) St-Gallen, Switzerland. Ecoinvent database – Available at: <http://www.ecoinvent.org> [accessed 1.3.2023].

[25] Life Cycle Initiative (hosted by the UN environment programme) – Available at: <https://www.lifecycleinitiative.org> [accessed 1.3.2023].

[26] Cornelissen R.L., Thermodynamics and sustainable development; the use of exergy analysis and the reduction of irreversibility [dissertation]. Enschede, Netherlands: Twente University; 1997.

[27] Gong M., Wall G., On exergetics, economics and optimization of technical processes to meet environmental conditions. In: R. Cai et al., editors. TAIES '97: Proceedings of the Internatinal Conference on Thermodynamic Analysis and Improvement of Energy Systems; 1997 June 10-13; Beijng, China. Beijing World:453-460.

[28] Meyer L., Tsatsaronis G., Buchgeister J., Schebek L., Exergoenvironmental analysis for evaluation of the environmental impact of energy conversion systems, Energy 2009;34(1): 75-89.

[29] Tsatsaronis G., Winhold M., Exergoeconomic analysis and evaluation of energy-conversion plants-I. A new general methodology, Energy 1985;10(1): 69-80.

[30] Tsatsaronis G., Recent developments in exergy analysis and exergoeconomics, International Journal of Exergy 2008;5(5): 489-499.

[31] National Institute of Standards and Technology. NIST Chemistry WebBook – Available at: <https://webbook.nist.gov> [accessed 10.03.2023]

[32] Szargut J., Egzergia. Poradnik obliczania I stosowania, Widawnictwo Politechniki Shlaskej, Gliwice 2007 – Available at: <http://web.mit.edu/2.813/www/readings/APPENDIX.pdf> [accessed 10.03.2023].

Exergoeconomic assessment of green hydrogen production via high-temperature electrolysis powered by solar and wind energy

Diego Luis Izidoro[a,b], Silvio de Oliveira Junior[c]

[a] Instituto Federal de Educação Ciência e Tecnologia de Minas Gerais - Campus Formiga, Formiga - MG, Brasil, diego.izidoro@ifmg.edu.br
[b] Escola Politécnica, Universidade de São Paulo, São Paulo - SP, Brasil, diego.izidoro@usp.br
[c] Escola Politécnica, Universidade de São Paulo, São Paulo - SP, Brasil, soj@usp.br

Abstract:
Hydrogen is considered a promising alternative as an energy carrier for the transition to a renewable energy matrix. However, most of the hydrogen is currently produced using fossil fuels, making it essential to develop green hydrogen production routes. Therefore, this study aims to perform an exergoeconomic analysis of the high-temperature electrolysis (HTE) process for hydrogen production using solar and wind energy. To this end, it is proposed novel plant arrangements for solid oxide electrolysis cells (SOEC). To supply the plant's electrical demand, two options are considered: a wind farm (WF) and a photovoltaic system (PV). A solar concentration system is considered for the thermal demand. As another contribution to the area, the analysis is carried out considering the Brazilian scenario, specifically Pecém (Ceará), a coastal district located in the northeast of Brazil. It was selected due to the high availability of solar and wind resources and the existing industrial and port infrastructure. Energy and exergy analyses are performed to identify the components with the highest level of irreversibility. Finally, an exergoeconomic assessment is accomplished to determine the exergy costs of hydrogen production. For the WF-SOEC arrangement, the total exergy efficiency obtained is 26.53%, and the unit exergy cost of hydrogen is 3.89 kJ/kJ. For the PV-SOEC arrangement, the corresponding values are 13.74% and 7.53 kJ/kJ, respectively. Overall, the results demonstrate that HTE route using solar and wind energy can be a viable and sustainable alternative to produce hydrogen from 100% renewable sources and without direct CO_2 emissions.

Keywords:
Exergoeconomic assessment; Green hydrogen; Solar energy; Wind energy.

1. Introduction

Hydrogen plays an important role in the chemical industry. Industrial hydrogen is utilized for various purposes such as producing fertilizers and ammonia, refining petrochemicals, processing food, cooling power generators in power plants, metallurgical processes, as a fuel for space exploration, and manufacturing semiconductors [1][2].

In addition to being an important industrial raw material, hydrogen has the potential to become a key energy source for achieving sustainable decarbonization, particularly in sectors where electrification is difficult [3][4] From a total cost perspective (including production, distribution and retail costs), hydrogen could be the most cost-effective low-carbon solution for more than twenty different applications, including long-distance transportation by road and sea, urban vehicles, trains, the steel industry, energy storage, and residential heating [5][6].

Hydrogen can be produced using different non-renewable (coal, oil, nuclear and natural gas) or renewable (biomass, solar, wind, hydro, geothermal, wave energy, etc.) resources through a wide variety of technological routes (reforming, gasification, electrolysis, etc.) [7]. To be considered low-carbon hydrogen, it must be produced from renewable electricity, nuclear, biomass or fossil fuels with carbon capture, storage and utilization (CCUS). However, almost all the hydrogen is currently generated from fossil fuels without CCUS [8].

Electrolysis is one of the oldest and most mature processes and has the versatility to use electricity from different renewable sources to produce H_2. Alkaline electrolysis stands out for being the one with the greatest maturity and the greatest commercial reach [9]. PEM (polymer electrolyte membrane) electrolysis have many advantages such as lower gas permeability, high proton conductivity, and high pressure operation [10]. However, as the temperature rises, the electrolysis process becomes more endothermic and a greater proportion of the total energy needed for the system can be provided in the form of heat, leading to increased efficiency in the process [11].

In this way, high-temperature electrolysis (HTE) offers higher efficiency by operating at reduced electrical potentials, thereby minimizing irreversibilities. The high operating temperature is an important feature of this process, giving rise to its two main advantages over alkaline and polymeric membrane electrolyzers: higher exergy efficiencies and faster chemical kinetics [12]. Despite being a process under development, it is approaching maturity. HTE occurs through solid oxide electrolyzer cells (SOEC) operating in the range of 600°C to 900°C. SOECs can convert steam (H_2O), carbon dioxide (CO_2), or a combination of both, directly into hydrogen (H_2) or syngas (H_2+CO), respectively. HTE can be integrated with various renewable energy sources and industrial processes. These can serve as feedstocks for fuel synthesis plants and the chemical industry, thus enabling different Power-to-X scenarios. They can also be integrated with various chemical synthesis processes for the recycling of captured CO_2 and H_2O into synthetic fuels such as methane, methanol, and ammonia. When operating in reverse, the electrolyzer cell acts as a solid oxide fuel cell (SOFC) [13].

Some authors [14][15][16][17][18][19] have previously proposed plant layouts for solid oxide electrolyzer cells that operate from renewable sources, specially solar energy. However, these studies have mainly focused on technical and economic analysis, with an emphasis on energy and capital costs. In general, energy balances treat all energy forms as equal without distinguishing between different degrees of energy that pass through the system boundary and do not provide information on internal losses. Exergy analysis, which is an alternative technique based on the concept of exergy, can be used to address this limitation [20][21]. And from the perspective of modeling, simulating, and optimizing energy systems, exergoeconomic assessment is also important in determining the average cost per unit of exergy of each exergy stream [22].

Based on this background, the present study makes a significant contribution to the area by employing a comprehensive evaluation methodology based on energy, exergy, and exergoeconomic assesment for two novel plant arrangements for H_2 production based on the HTE route, powered by solar and wind energy. This assessment provides a comprehensive thermodynamic evaluation of the plant processes. In addition, the study focuses on the Brazilian scenario, specifically Pecém (Ceará), which is a location in northeastern Brazil with high availability of solar and wind resources and existing industrial and port infrastructure - optimal conditions for a hydrogen production plant.

2. Method

2.1. SOEC modelling

The process of electrolyzing water to produce hydrogen and oxygen gases is a long-standing and established method. The basic principle of an electrolyzer is to use electricity to split water molecules. This phenomenon was initially demonstrated by Nicholson and Carlisle in 1800, and further expounded upon by Faraday in the 1820s, who coined the term "electrolysis" in 1834. However, it was only in 1902 that the Oerlikon Engineering Company began the commercial use of electrolysis [11]. The reaction for water electrolysis can be represented by the Eq. (1):

$$H_2O \rightarrow H_2 + 1/2\, O_2 \tag{1}$$

Solid oxide electrolyzer models can be classified into several types. Geometrically, they are categorized into zero-dimensional (0D), one-dimensional (1D), two-dimensional (2D), and three-dimensional (3D) models. They can also be classified as physical models (white-box), empirical models (black-box), and semi-empirical models (gray-box). Additionally, in terms of length scale, SOEC models can be classified into microscale, mesoscale, and macroscale models, with the latter further subdivided into cell-level, stack-level, and system-level models [23]. In this study, a semi-empirical SOEC (zero dimension) system model was developed according to the studies of O'Brien [12], Petipas, Brisse and Bouallou [24], and Hansen [25].

The minimum electrical energy (W_{min}) required for electrolysis (reversible process) is equal to the change in Gibbs free energy (G), shown in Eq. (2), where H represents the enthalpy, T is the absolute temperature and S the entropy of the reactants and products of the chemical reaction. With increasing temperature, the electrolysis process becomes progressively endothermic.

$$\dot{W}_{min} = \Delta G = G_{prod} - G_{react} = H_{prod} - H_{react} - T(S_{prod} - S_{react}) \tag{2}$$

For the electrolysis process to take place, the minimum voltage required is the standard state open-cell voltage or reversible voltage (V_0) given by Eq. (3), where ΔG is the Gibbs free energy change, F is the Faraday constant (96,486 C/mol) and j is the number of electrons transferred per molecule of hydrogen produced.

$$V_0 = \frac{\Delta G}{jF} \tag{3}$$

When reactants and pure products are separated, the reversible voltage (V_0) is applicable [26]. However, to account for the variety of gas compositions present in real electrolyzers, the Nerst open cell potential (V_N) must

be considered, as given by Eq. (4), where R_u is the universal gas constant, y represents the molar fractions and T is the absolute temperature during the reaction.

$$V_N = \frac{\Delta G}{jF} - \frac{R_u T}{jF} ln\left(\frac{y_{H_2O}}{y_{H_2} y_{O_2}^{0,5}}\right) \quad (4)$$

The thermoneutral voltage (V_{TN}), as a function of the enthalpy of reaction (ΔH), is given by Eq. (5). The electrolysis of water is an endothermic process. Therefore, the heat flux of the reaction ($q"_R$) is negative. However, the heat flux resulting from irreversibilities ($q"_{OHM}$), is positive. At thermoneutral voltage, the net heat flux is zero, as these heat fluxes cancel each other out [26]. Their values can be calculated using Eq. (6) where i is the current density (A/m²).

$$V_{TN} = \frac{\Delta H}{jF} \quad (5)$$

$$q"_R = -q"_{OHM} = i(V_N - V_{TN}) \quad (6)$$

The electrical power ($\dot{W}_{TN}$) required for the electrolysis process considering the thermoneutral voltage can be calculated using Eq. (7), where I is the current (A) in the electrolyzer and $\dot{m}_{H_2}$ is the mass flow rate of hydrogen.

$$\dot{W}_{TN} = V_{TN} I = \dot{m}_{H_2} \Delta H \quad (7)$$

The modelling and simulation of the electrolysis process is performed via Python using the suite Cantera [27] and the Coolprop library [28].

2.2. Proposed plants

An electrolysis plant is basically composed of electrolyzers and the Balance of Plant (BoP), which includes energy supply, water supply and purification, compression, processing, and storage of gases. Figure 1 illustrates two hydrogen production plants. The first involves a wind farm supplying electricity to solid oxide electrolysis cells (WF-SOEC), proposed initially in a previous study [29]. In the second plant, photovoltaic panels (PV-SOEC) supply all the electrical energy needed. In both cases, to provide the necessary thermal energy, a solar tower system is used, whereby solar radiation is collected by heliostats in the solar field and reflected to superheat steam at a temperature of 850°C in the solar receiver (SR).

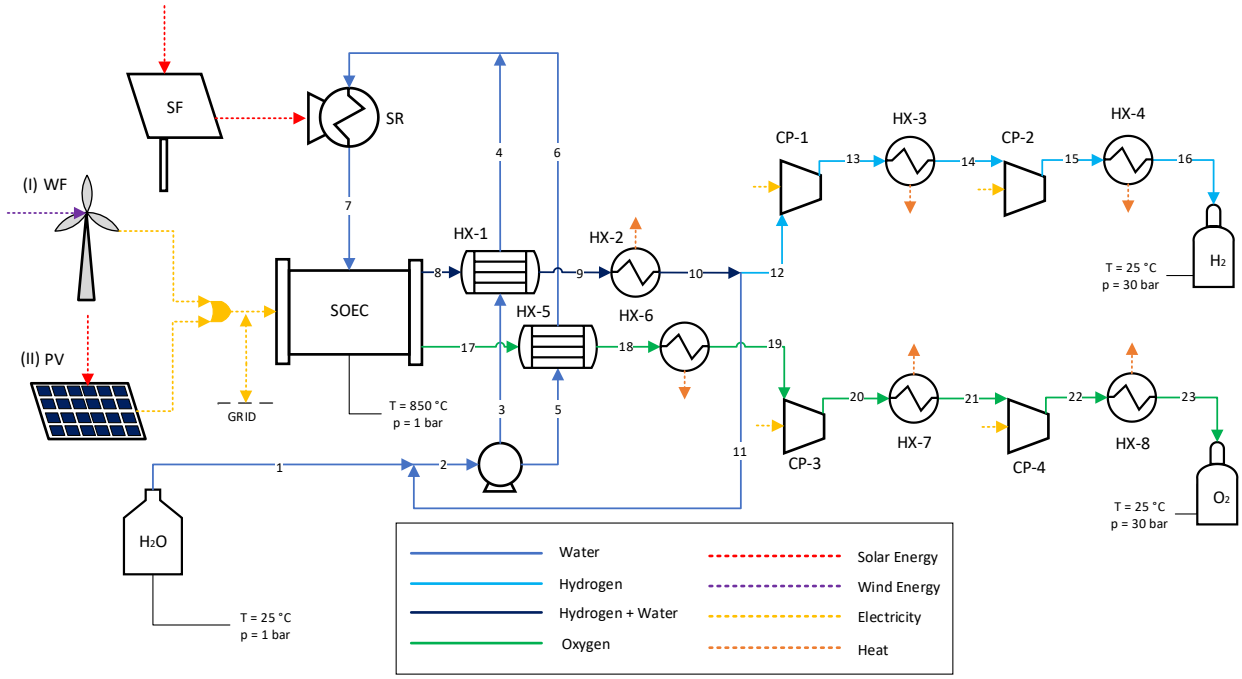

Figure 1. Proposed plants: (I) WF-SOEC (II) PV-SOEC

The electrolyzer produces two streams, one containing a mixture of hydrogen (H_2) and steam, and the other containing oxygen (O_2), which are then directed to recovery heat exchangers (HX-1 and HX-5, respectively) to preheat the water used in the process. The H_2/H_2O mixture is then cooled in HX-2, and the condensed steam is separated from hydrogen and recycled. Finally, hydrogen and oxygen are compressed (H_2 in CP-1 and CP-2, and O_2 in CP-3 and CP-4) and cooled (H_2 in HX-3 and HX-4, and O_2 in HX-6, HX-7, and HX-8)

before being stored at a pressure of 30 bars. The main differences in relation to other arrangements proposed in the literature are related to the direct recovery of heat from the electrolyzer outlet gases and the processing and storage of oxygen as a co-product.

The wind farm (or photovoltaic panels) also provides the necessary electricity to power the compressors, but due to the intermittent nature of electricity production, a connection to the electrical grid is also included. For the analysis of the proposed systems, the following conditions are considered:

- The hydrogen production plant is designed to operate for eight hours a day according to the supply of concentrated solar energy [30].
- In the WF-SOEC arrangement, the installed capacity of the wind farm is 10 MW (five Vestas V100-2MW wind turbines) [31].
- In the PV-SOEC arrangement, the installed capacity is considered the minimum necessary to produce the equivalent amount of H_2 in the WF-SOEC arrangement.
- The efficiency of PV system, defined as the ratio between the output electricity and the input of solar energy, is 15%.
- The AC-DC electricity conversion efficiency is 95%.
- The solar field (SF) has an energy efficiency of 60% [17], which means that only 60% of the solar energy reaching the heliostats is directed to the receiver (the remaining 40% are heat and optical losses).
- The solar receiver (SR) has an energy efficiency of 85% [32], which is the percentage of energy absorbed by the steam in the component (the remaining 15% are heat and optical losses).
- The electrolyzer operates at a thermoneutral voltage to minimize thermal stress [12]. Consequently, the process is isothermal at T = 850ºC and p = 1 bar.
- The molar steam conversion ratio (SC) is 75%, i. e., the molar fraction of H_2 at the SOEC outlet is 0.75 [24].
- Each compressor has an isentropic efficiency of 80%.
- Heat recovery exchangers HX-1 and HX-5 do not transfer heat to the environment, and pinch point is 10°C. The thermodynamic state of the water is the same at the outlet of these both heat exchangers.
- Pressure losses, as well as changes in kinetic and potential energy are not considered.

3.3. Solar and wind data

The study is being carried out for Pecém, a coastal district located in north-eastern Brazil. This location was selected due to its established industrial, electrical, and port infrastructure, as well as its abundance of solar and wind energy resources. Furthermore, there is a project to establish a green hydrogen hub in the area [33].

Data for solar resource evaluation are taken from The National Solar Radiation Data Base (NRSDB) through System Advisor Model (SAM) software considering a typical meteorological year (TMY) [34][35]. The average daily global horizontal irradiation (GHI) is estimated at 6.19 kWh/m²/day and the average daily direct normal irradiation (DNI) is estimated at 5.95 kWh/m²/day.

For the wind resource evaluation, it was used the data from the atlas of Brazilian wind potential [36]. The wind speed distribution can be represented by the Weibull density probability function, given by Eq. (8), where v is the wind speed, c is the scale factor and k is the form factor [37]. The main wind parameters for Pecém considering a height of 100 meters are presented in Tab. 1.

$$f(v) = \frac{K}{C}\left(\frac{v}{C}\right)^{K-1} e^{-(v/C)^K} \tag{8}$$

The monthly mean values of direct normal irradiance (DNI) and global horizontal irradiance (GHI) for Pecém in a TMY are shown in Figure 2a. The annual wind speed distribution is shown in Figure 2b, considering the number of annual hours for different speed intervals.

Table 1. Main wind parameters

Parameter	Unit	Value
Average wind speed ($\bar{v}$)	m/s	8.87
Scale factor (C)	-	9.76
Form factor (K)	m/s	4.20
Average air density (ρ)	kg/m³	1.17

Source: [36]

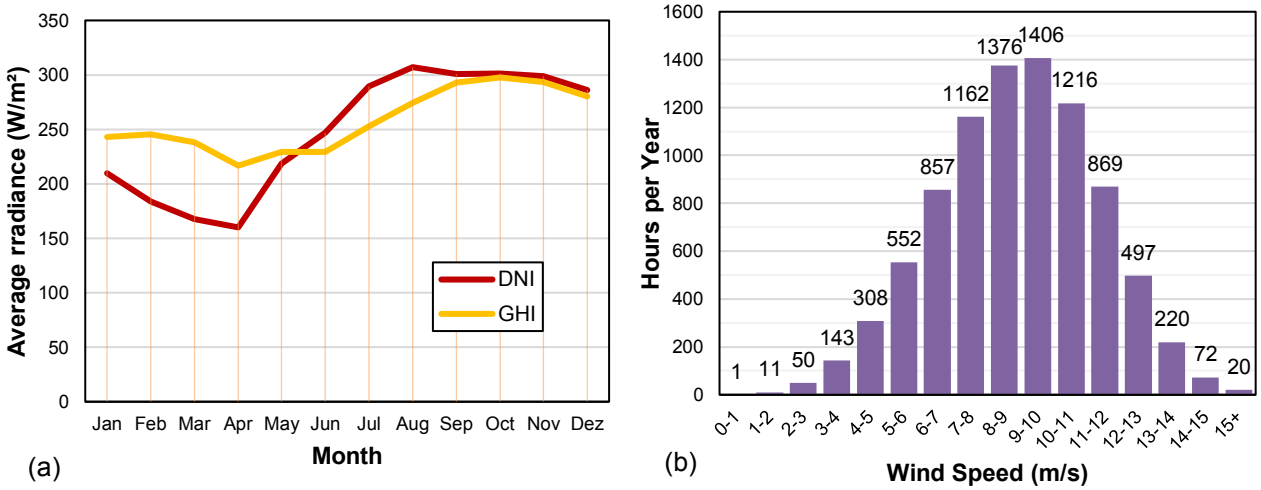

Figure 2. Solar and wind data for Pecém: (a) Solar irradiance [34][35] *and (b) Wind speed distribution* [36].

3.4. Energy and exergy analysis

The efficiency of energy conversion in SOEC system (η_{SOEC}) can be defined analogously to the definition for fuel cells in terms of the enthalpy of reaction according to Eq. (9) and the solar/wind-to-hydrogen conversion efficiency can be calculated in terms of the higher heating value of hydrogen (HHV) with Eq. (9):

$$\eta_{SOEC} = \frac{\dot{m}_{H_2} \Delta H}{\dot{W}_{SOEC}} \tag{9}$$

$$\eta_{solar/wind\_H_2} = \frac{\dot{m}_{H_2} HHV_{H_2}}{\dot{W}_{WF/PV} + \dot{Q}_{SF}} \tag{10}$$

The exergy efficiency of the electrolysis process can be defined according to the expression of Eq. (11), called the degree of perfection, being the ratio between the exergy of the products and the input exergy:

$$\eta_{B,SOEC} = \frac{B_{prod}}{B_{input}} = \frac{\dot{B}_8 + \dot{B}_{17}}{\dot{B}_7 + \dot{W}_{SOEC}} \tag{11}$$

The wind turbine exergy ($\dot{B}_{WF,in}$) is expressed by Eq. (12), which is a function of the air specific mass (ρ), the turbine swept area (A), and the wind speed (v) [38]. For the exergy analysis of solar field (SF) and photovoltaic panels (PV), the relation between energy and exergy fluxes in Eq. (13) is considered [39], where *T* is the solar surface temperature (5778 K) and T_0 is the ambient temperature (298 K). For these specific values, the ratio between exergy and energy fluxes is 0.9312.

$$\dot{B}_{WF,in} = \frac{1}{2} \rho A v^3 \tag{12}$$

$$\frac{\dot{B}_{SF/PV,in}}{\dot{E}_{SF/PV,in}} = 1 - \frac{4}{3}\frac{T_o}{T} + \frac{1}{3}\left(\frac{T_0}{T}\right)^4 \tag{13}$$

The exergy efficiencies for the solar field (SF), solar receiver (SR), wind farm (WF), photovoltaic panels, electrolyzer (SOEC), and heat exchangers HX-1 e HX-5 are defined as the ratio between output and input exergy. As for the compressors, their exergy efficiencies were determined by the ratio of the exergy change and the power provided. The total exergy efficiency of the plant was calculated as a function of the total fluids exergy rates and the solar radiation exergy rates with Eq. (14):

$$\eta_{B,total} = \frac{\dot{B}_{H_2.16} + \dot{B}_{O_2.23}}{\dot{B}_{WF/PV,in} + \dot{B}_{SF,in} + \dot{B}_{water.1}} \quad (14)$$

3.5. Exergoeconomic assessment

Based on Fig. 3, the exergoeconomic balance can be written according to Eq. (15), where $\dot{C}_{inp,i}$ and $\dot{C}_{prod,i}$ are the cost rates of inputs and products, respectively.

Figure 3. Exergoeconomic balance components

$$\sum_i \dot{C}_{inp,i} = \sum_i \dot{C}_{prod,i} \quad (15)$$

Eq. (15) can be rewritten, inserting the unit exergy cost, c_i, (in kJ/kJ) for each stream, according to Eqs. (16) and (17). It represents the amount of exergy required to produce a unit of the respective exergy stream. In this way, it is considered that the input used in the first process of a plant has an exergy cost equal to the unit.

$$c_i = \frac{\dot{C}_i}{\dot{B}_i} \quad (16)$$

$$\sum_i (c_{inp} \cdot \dot{B}_{inp})_i = \sum_i (c_{prod} \cdot \dot{B}_{prod})_i \quad (17)$$

When necessary, partition methods are applied, as proposed by [40]: Equality method: the costs are divided among the products according to their exergy content; (ii) Extraction method: the costs are discharged in a single exergy stream.

The product of multiplying the unit exergy cost (kJ/kJ) by the specific exergy of a given stream (kJ/kg) produces an exergy intensity indicator in kJ/kg that specifies the amount of exergy required to obtain a unit of mass of a certain stream [41], according to Eq. (18):

$$\varphi_i = c_i b_i \quad (18)$$

4. Results and Discussion

Figure 4a illustrates the wind exergy and generated electricity for the analysed wind farm as function of wind speed. Figure 4b shows the corresponding exergy efficiencies. The maximum net power output of 10 MW is achieved only when wind speed exceeds 11.6 m/s, which happens 12.7% of the time, or approximately 1110 hours per year. The average net power output is estimated as 6.38 MW. The total yearly electricity generation in the wind farm is estimated as 55.88 GWh. Considering a total of 170.5 GWh of wind exergy available annually, this represents an average exergy efficiency of 32.8%.

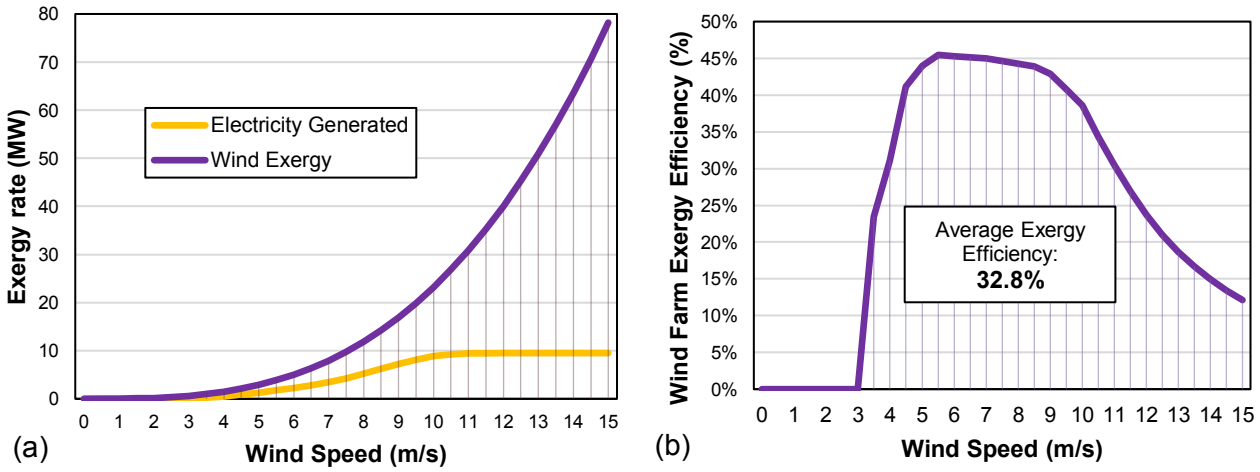

Figure 4. Wind farm results: (a) Wind exergy and electricity generated and (b) Exergy efficiency

The estimated electricity generation over a typical meteorological year (TMY) is shown in Fig. 5 in GWh for the two considered systems (WF and PV). The months with the highest and lowest levels of generation coincide for both forms of generation. However, the variability of wind energy is slightly higher. Fig. 6 illustrates the hydrogen production of the proposed plant. The estimated average daily production of hydrogen is 4.13 t, which results in a daily production of 23.7 t of oxygen and a water consumption of 36.8 m³/day. Due to the variation in direct irradiation throughout the year, the production in April tends to be 48% lower than in August. In practice, it means that the plant would operate at about half of its capacity during this month.

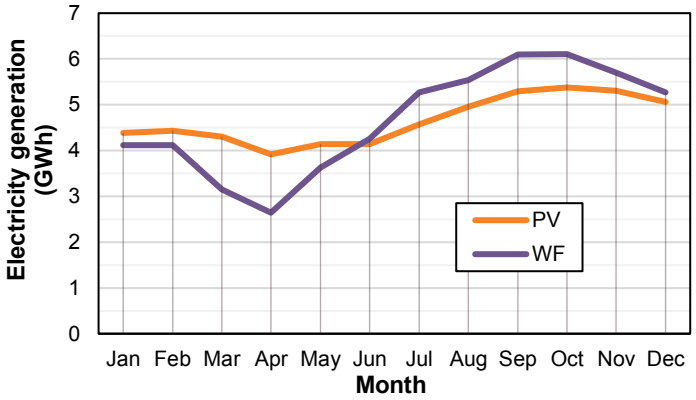

Figure 5. Estimated electricity generation over a typical meteorological year (TMY)

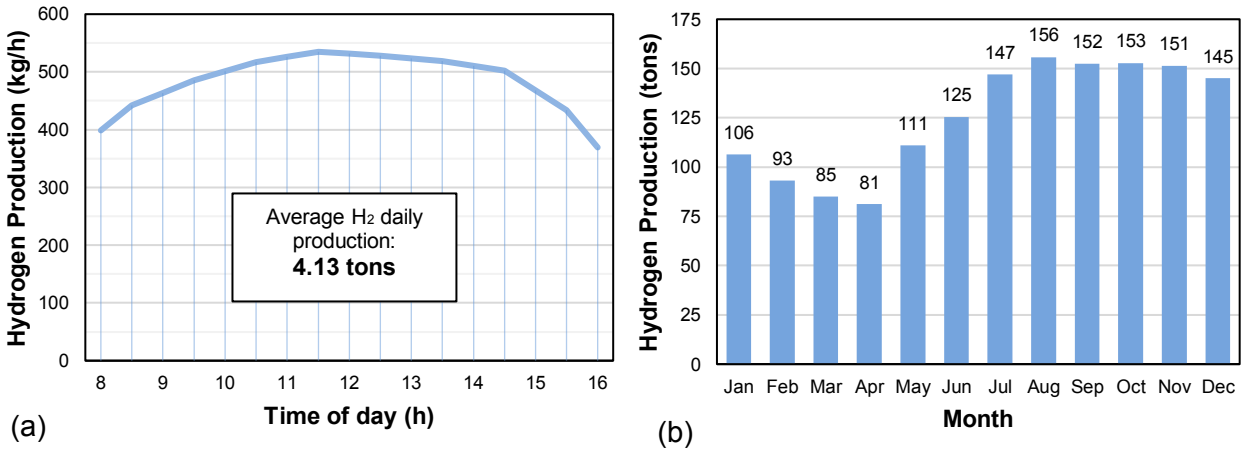

Figure 6. Hydrogen production: (a) Average hourly production and (b) Average production per month

Table 2 summarizes the results of the energy and exergy analysis conducted for the plant's power and heat supply components. The irreversibilities observed in wind turbines are associated with the interaction between air and blades, as well as the efficiencies of mechanical and electrical conversion. In the PV panels and solar concentrators there are optical losses such as attenuation, blocking, or shadowing, as well as losses related to heat convection and conduction [39]. For the wind farm, the values from the energy and exergy analysis are the same since wind exergy and electrical work are equal to the values in the exergy balance. For the PV panel, solar field and solar receiver, the ratio between exergy and input energy is given by Eq. (13). Specifically for the solar receiver, the exergy efficiency is much lower than the energy efficiency due to the irreversibility of the process of converting solar radiation into exergy of the steam.

Table 2. Energy and exergy analysis: power supply components

Components[1]	Energy Analysis			Exergy Analysis		
	Received (MWh/day)	Delivered (MWh/day)	Energy Efficiency (%)	Received (MWh/day)	Delivered (MWh/day)	Exergy Efficiency (%)
Wind Farm (WF)	467.19	153.09	32.8	467.19	153.09	32.8
Photovoltaic System (PV)	1020.63	153.09	15.0	950.41	153.09	16.1
Solar Field (SF)	55.67	33.40	60.0	51.84	31.10	60.0
Solar Receiver (SR)	33.40	28.39	85.0	31.10	13.78	44.3[2]

[1] The wind farm is part of the arrangement (I) WF-SOEC, and the photovoltaic system is part of the arrangement (II) PV-SOEC.
[2] Only physical exergy of the steam was considered for the calculation for the solar receiver.

The results of the analysis conducted for the electrolyzer, heat exchangers, and compressors are presented in Tab. 3. The SOEC exergy efficiency is 89.4%. The losses in the electrolyzer occurs due to overvoltage at the anode and cathode, as well as ohmic resistance of the cells [26]. The thermoneutral voltage (V_{TN}) is 1.288 V, the ohmic heat flux ($q"_R$) is 0.163 W/cm², and the average power consumed ($\dot{W}_{TN}$) is 17.67 MW, which corresponds to 92.3% of the electricity demanded in the plant.

Table 3. Energy and exergy analysis: SOEC, heat exchangers, and compressors

Components	Energy Analysis			Exergy Analysis		
	Power (kW)	Rejected (kW)	Energy Efficiency (%)	Destroyed (kW)	External Losses (kW)	Exergy[(2)] Efficiency (%)
Electrolyzer (SOEC)	17671.20	0	100.0	1864.69	0	89.4
Heat Exchanger 1 (HX-1)	-	0	100.0	729.33	0	40.2
Heat Exchanger 2 (HX-2)	-	878.64	-	0	153.45	-
Compressor 1 (CP-1)	483.97	0	100.0	56.17	0	88.4
Heat Exchanger 3 (HX-3)	-	483.70	-	0	131.03	-
Compressor 2 (CP-2)	496.38	0	100.0	57.26	0	88.5
Heat Exchanger 4 (HX-4)	-	505.10	-	0	135.82	-
Heat Exchanger 5 (HX-5)	-	0	100.0	332.23	0	34.9
Heat Exchanger 6 (HX-6)	-	6.54	-	0	0.18	-
Compressor 3 (CP-3)	240.25	0	100.0	28.40	0	88.2
Heat Exchanger 7 (HX-7)	-	241.46	-	0	63.99	-
Compressor 4 (CP-4)	245.28	0	100.0	28.72	0	88.3
Heat Exchanger 8 (HX-8)	-	257.42	-	0	67.50	-
Total	19137.10	2372.86	87.6	3096.80	551.97	80.9

[(2)] Only physical exergy was considered for the calculation of the heat exchangers.

Heat recovery exchangers HX-1 and HX-5 achieved low exergy efficiencies due to the high mean temperature difference between the fluids. Therefore, one of the enhancements that can be made in this plant involves modifying the configuration of these exchangers or changing the method of heat recovery. In the other exchangers, the heat is rejected to the environment, which represents an exergy rate of 552 kW, enough to feed at least one of the compressors. Despite this, the efficiency of the set of electrolyzer, exchangers and compressors is 80.9%.

The overall energy efficiency for the WF-SOEC configuration is 31.08%, and 15.10% for the PV-SOEC arrangement. The overall exergy efficiency is 26.53% and 13.74%, respectively. The energy losses and exergy destroyed are detailed in the Sankey and Grassmann diagrams in Fig. 7 and 8 for both configurations.

Regarding other studies, Lin and Haussener [14] obtained an energy efficiency of 9.9% for a different PV-SOEC arrangement. Restrepo et al. [17] obtained an efficiency of 31.8% for a PV-SOEC system but used PV panels with solar concentration (CPV) that achieve efficiencies far above conventional PV cells (36.3% versus 15.0%). Nasser and Hassan [19] obtained an efficiency value of 18.6% considering a WF-SOEC plant configuration. However, it is difficult to make direct comparisons among these studies due to variations in plant configuration, modes of operation, and locations considered for the analyses.

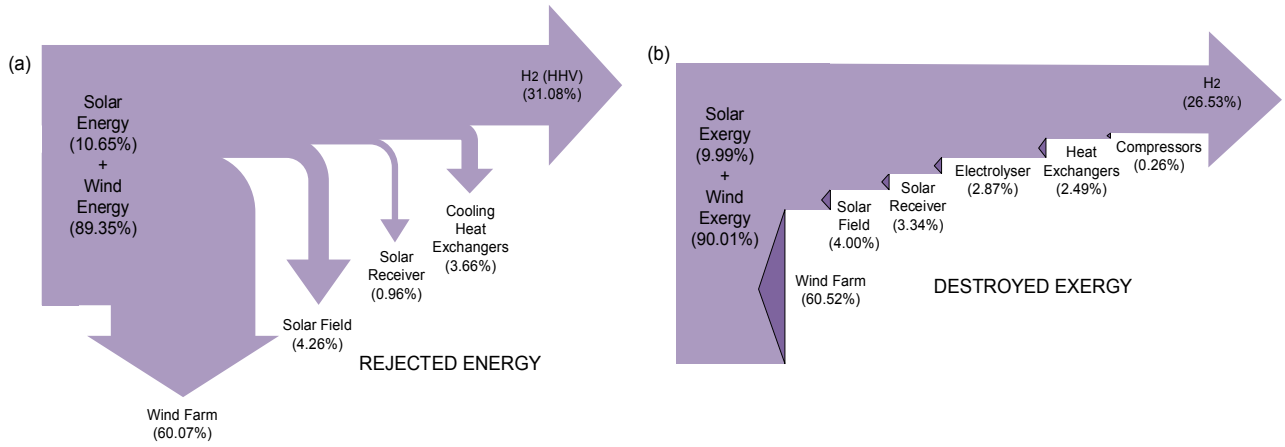

Figure 7. Energy and Exergy Diagrams for the WF-SOEC plant: (a) Sankey and (b) Grassmann

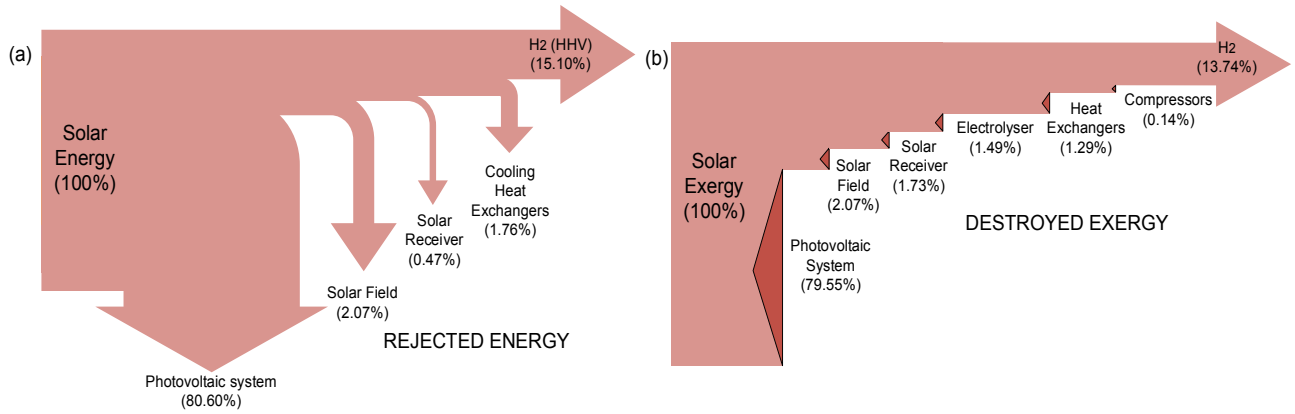

Figure 8. Energy and exergy diagrams for the PV-SOEC plant: (a) Sankey and (b) Grassmann

In the exergoeconomic analysis, the extraction method is adopted in the electrolyzer since hydrogen is considered the main product of the plant. However, as the total exergy of hydrogen at the electrolyzer outlet is almost 30 times higher than the total exergy of oxygen, there will be no significant differences in costs if the equality method is applied.

The unit exergy costs for each stream are presented in Fig. 9a for the WF-SOEC arrangement, where A and B are the exergy fluxes of solar irradiation, C is the flow of wind exergy, and D is the electricity generated by the wind turbines. As the streams A, C, and 1 are the inputs used in the first process of the plant, their exergy costs are considered equal to the unit. The unit exergy costs obtained for solar exergy in the solar receiver, electricity, and steam are 1.67, 3.30, and 4.26 kJ/kJ, respectively. For oxygen, the estimated unit exergy cost is 4.78 kJ/kJ, and for hydrogen at the end of the process, it is 3.89 kJ/kJ.

The unit exergy costs for the PV-SOEC plant are presented in Fig. 9b. As the efficiency of the photovoltaic system is less than half that of the wind system, the exergy costs are significantly higher. The unit cost of electricity is 6.72, steam is 6.35, and for oxygen, it is 9.61 kJ/kJ. For hydrogen, it is 7.53 kJ/kJ, which is 94% higher than in the previous configuration.

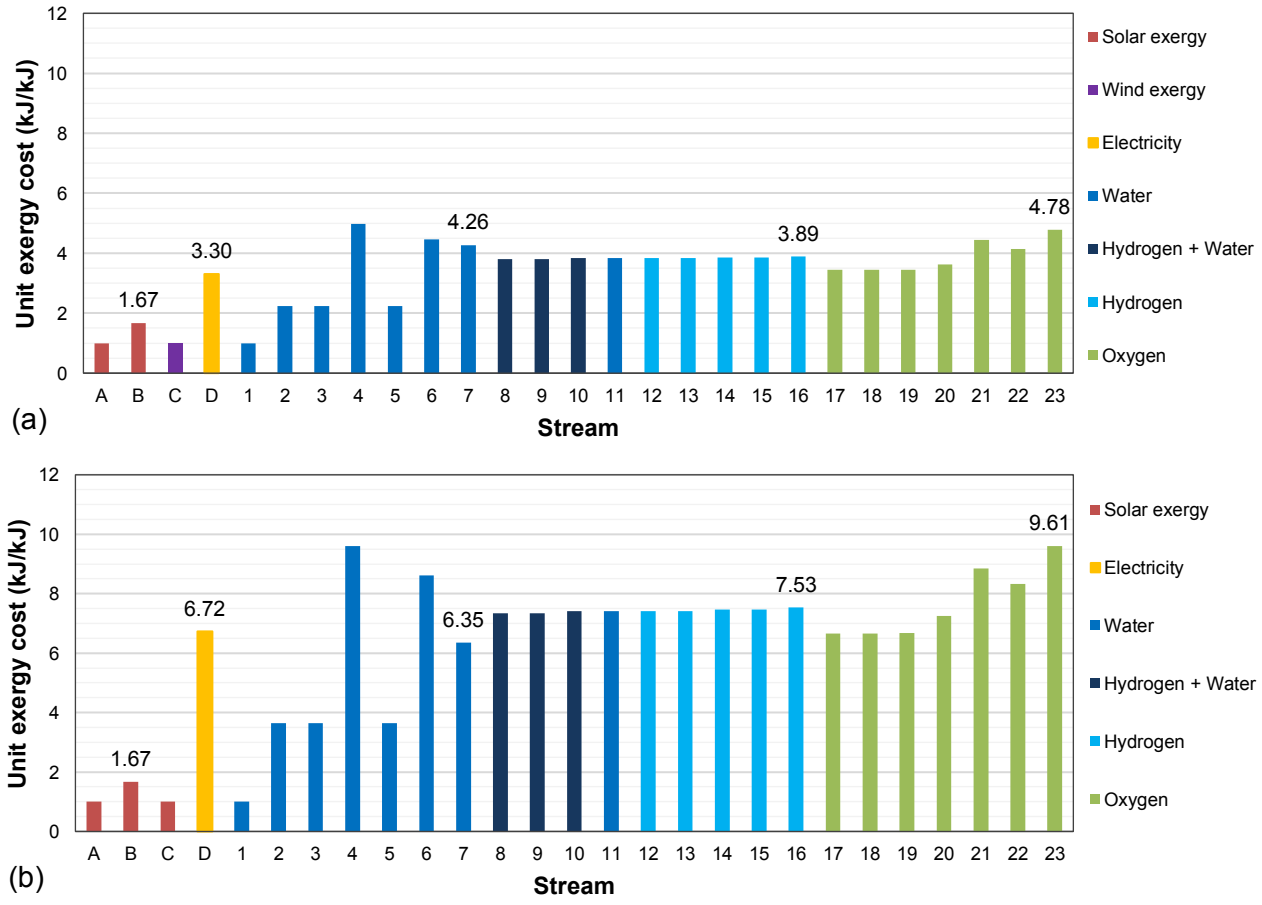

Figure 9. Unit exergy costs: (a) WF-SOEC and (b) PV-SOEC

Finally, Tab. 4 shows the exergy intensity values for the superheated steam used in the electrolysis process and the gases oxygen and hydrogen produced. In the WF-SOEC plant, 471.96 MJ of exergy is necessary to produce 1 kg of hydrogen, while for the PV-SOEC plant, it is 913.69 MJ. Although these values are high compared to the chemical exergy of H_2, in both cases, the exergy used is 100% obtained from renewable resources and without direct CO_2 emissions, which gives a significant advantage compared to the currently predominant production processes in the hydrogen industry. Moreover, these arrangements can be optimized to achieve higher levels of efficiency and lower exergy costs.

Table 4. Exergy Intensity

Plant	Stream	Exergy intensity (MJ/kg)
WF-SOEC	H_2O (850ºC, 1 bar)	8.00
	O_2 (25ºC, 30 bar)	1.84
	H_2 (25ºC, 30 bar)	471.96
PV-SOEC	H_2O (850ºC, 1 bar)	11.91
	O_2 (25ºC, 30 bar)	3.69
	H_2 (25ºC, 30 bar)	913.69

5. Conclusions

This study provides a comprehensive energy, exergy, and exergoeconomic assessment for two hydrogen production plants based on the high-temperature electrolysis (HTE) route. The analyses were carried out for Pecém, a coastal district located in north-eastern Brazil. In the proposed plants, the thermal demand is supplied by solar energy from a solar tower system. For the electrical demand, wind turbines and photovoltaic panels were evaluated.

Assuming the generation of a wind farm with 10 MW of installed capacity as a reference, the daily H_2 production was estimated at 4.13 t. The SOEC exergy efficiency was 89.4%. The overall energy efficiency for the WF-SOEC configuration was 31.08%, and 15.10% for the PV-SOEC arrangement. The overall exergy efficiency was 26.53% and 13.74%, respectively. In the exergoeconomic analysis, the unit exergy cost of hydrogen was 3.89 for the WF-SOEC, and 7.53 for the PV-SOEC configuration.

Regardless the efficiencies and the exergy costs achieved, it is important to note that in both arrangements evaluated, the exergy used is obtained 100% from renewable resources and without direct CO_2 emissions. This gives a significant advantage over the predominant production processes in the hydrogen industry. The SOEC technology, while still undergoing research and development, offers a promising alternative for hydrogen production with the potential for further optimization of efficiency levels and lower exergy costs. Furthermore, this study provides a basis for future investigations into HTE-based hydrogen production plants and serves as a contribution to the transition towards sustainable energy systems.

Acknowledgments

The first author acknowledges Instituto Federal de Educação, Ciência e Tecnologia de Minas Gerais (IFMG) - Campus Formiga for its support during the development of this study. The second author acknowledges CNPq (Conselho Nacional de Desenvolvimento Científico e Tecnológico) for the grant 306484/2020-0.

Nomenclature

A area, m²
b specific exergy, kJ
B exergy, kJ
$\dot{B}$ exergy rate, kW
c unit exergy cost, kJ/kJ
C scale factor
$\dot{C}$ exergy cost rate, kW
$\dot{E}$ energy rate, kW
F Faraday constant, 96,486 C/mol
G Gibbs free energy, kJ
H enthalpy, kJ
i current density, A/cm²
I current, A
j number of electrons
K form factor, m/s
$\dot{Q}$ heat transfer rate, kW
v wind speed, m/s
V voltage, V
W work, kJ
$\dot{W}$ power, kW
$\dot{m}$ mass flow rate, kg/s
q" heat flux, W/cm²

R universal gas constant, 8.314 kJ/(kmol·K)
S entropy, kJ/K
T temperature, °C
y molar fraction

Greek symbols

Δ variation
η efficiency
ρ specific mass, kg/m³
φ exergy intensity, MJ/kg

Subscripts and superscripts

0 standard
inp input
min minimum
N Nerst
O ohmic
$prod$ products
PV photovoltaic system
R reaction
$react$ reactants
SF solar field
TN thermoneutral
WF wind farm

References

[1] F. Dawood, M. Anda, and G. M. Shafiullah, "Hydrogen production for energy: An overview," *Int. J. Hydrogen Energy*, vol. 45, no. 7, pp. 3847–3869, 2020, doi: 10.1016/j.ijhydene.2019.12.059.

[2] E. S. Hanley, J. P. Deane, and B. P. Ó. Gallachóir, "The role of hydrogen in low carbon energy futures–A review of existing perspectives," *Renew. Sustain. Energy Rev.*, vol. 82, no. July, pp. 3027–3045, 2017, doi: 10.1016/j.rser.2017.10.034.

[3] J. Töpler and J. Lehmann, *Hydrogen and Fuel Cells*. New York: Springer, 2016.

[4] IEA, "Net zero by 2050: a roadmap for the global energy sector," International Energy Agency, Paris, 2021. [Online]. Available: https://www.iea.org/reports/net-zero-by-2050

[5] Z. Abdin, A. Zafaranloo, A. Rafiee, W. Mérida, W. Lipiński, and K. R. Khalilpour, "Hydrogen as an energy vector," *Renew. Sustain. Energy Rev.*, vol. 120, no. November 2019, 2020, doi: 10.1016/j.rser.2019.109620.

[6] Hydrogen Council, "Hydrogen for Net-Zero A critical cost-competitive energy vector," Hydrogen Council and McKinsey & Company, Brussels, 2021.

[7] J. O. Abe, A. P. I. Popoola, E. Ajenifuja, and O. M. Popoola, "Hydrogen energy, economy and storage: Review and recommendation," *Int. J. Hydrogen Energy*, vol. 44, no. 29, pp. 15072–15086, 2019, doi: 10.1016/j.ijhydene.2019.04.068.

[8] IEA, "Global Hydrogen Review 2021.," International Energy Agency, Paris, 2021. doi: -.

[9] M. David, C. Ocampo-Martínez, and R. Sánchez-Peña, "Advances in alkaline water electrolyzers: A review," *J. Energy Storage*, vol. 23, no. April, pp. 392–403, 2019, doi: 10.1016/j.est.2019.03.001.

[10] M. Carmo, D. L. Fritz, J. Mergel, and D. Stolten, "A comprehensive review on PEM water electrolysis," *Int. J. Hydrogen Energy*, vol. 38, no. 12, pp. 4901–4934, 2013, doi: 10.1016/j.ijhydene.2013.01.151.

[11] M. A. Laguna-Bercero, "Recent advances in high temperature electrolysis using solid oxide fuel cells: A review," *J. Power Sources*, vol. 203, pp. 4–16, 2012, doi: 10.1016/j.jpowsour.2011.12.019.

[12] J. E. O'Brien, "Thermodynamics and transport phenomena in high temperature steam electrolysis cells," *J. Heat Transfer*, vol. 134, no. 3, pp. 1–11, 2012, doi: 10.1115/1.4005132.

[13] A. Hauch *et al.*, "Recent advances in solid oxide cell technology for electrolysis," *Science (80-.).*, vol. 370, no. 6513, 2020, doi: 10.1126/science.aba6118.

[14] M. Lin and S. Haussener, "Techno-economic modeling and optimization of solar-driven high-temperature electrolysis systems," *Sol. Energy*, vol. 155, pp. 1389–1402, 2017, doi: 10.1016/j.solener.2017.07.077.

[15] D. Yadav and R. Banerjee, "Economic assessment of hydrogen production from solar driven high-temperature steam electrolysis process," *J. Clean. Prod.*, vol. 183, pp. 1131–1155, 2018, doi: 10.1016/j.jclepro.2018.01.074.

[16] L. Mastropasqua, I. Pecenati, A. Giostri, and S. Campanari, "Solar hydrogen production: Techno-economic analysis of a parabolic dish-supported high-temperature electrolysis system," *Appl. Energy*, vol. 261, no. December 2019, p. 114392, 2020, doi: 10.1016/j.apenergy.2019.114392.

[17] J. C. Restrepo, D. Luis Izidoro, A. Milena Lozano Násner, O. José Venturini, and E. Eduardo Silva Lora, "Techno-economical evaluation of renewable hydrogen production through concentrated solar energy," *Energy Convers. Manag.*, vol. 258, p. 115372, Apr. 2022, doi: 10.1016/j.enconman.2022.115372.

[18] M. Mohebali Nejadian, P. Ahmadi, and E. Houshfar, "Comparative optimization study of three novel integrated hydrogen production systems with SOEC, PEM, and alkaline electrolyzer," *Fuel*, vol. 336, no. November 2022, p. 126835, 2023, doi: 10.1016/j.fuel.2022.126835.

[19] M. Nasser and H. Hassan, “Techno-enviro-economic analysis of hydrogen production via low and high temperature electrolyzers powered by PV/Wind turbines/Waste heat,” *Energy Convers. Manag.*, vol. 278, no. November 2022, p. 116693, 2023, doi: 10.1016/j.enconman.2023.116693.

[20] T. J. Kotas, *The exergy method of thermal plant analysis*, no. 1. London: Butterworths, 1985. doi: 10.1016/0378-3804(88)90147-7.

[21] J. Szargut, *Exergy method: technical and ecological applications*, vol. 18. Southampton, UK: WIT Press, 2005.

[22] S. Oliveira Jr., *Exergy: Production, cost and renewability*. London: Springer, 2013. doi: 10.1007/978-1-4471-4165-5.

[23] Z. Li, H. Zhang, H. Xu, and J. Xuan, “Advancing the multiscale understanding on solid oxide electrolysis cells via modelling approaches: A review,” *Renew. Sustain. Energy Rev.*, vol. 141, no. February, p. 110863, 2021, doi: 10.1016/j.rser.2021.110863.

[24] F. Petipas, A. Brisse, and C. Bouallou, “Model-based behaviour of a high temperature electrolyser system operated at various loads,” *J. Power Sources*, vol. 239, no. 2013, pp. 584–595, 2013, doi: 10.1016/j.jpowsour.2013.03.027.

[25] J. B. Hansen, “Solid oxide electrolysis - a key enabling technology for sustainable energy scenarios,” *Faraday Discuss.*, vol. 182, pp. 9–48, 2015, doi: 10.1039/c5fd90071a.

[26] J. E. O’Brien, “Thermodynamic considerations for thermal water splitting processes and high temperature electrolysis,” *ASME Int. Mech. Eng. Congr. Expo. Proc.*, vol. 8, pp. 639–651, 2009, doi: 10.1115/IMECE2008-68880.

[27] D. G. Goodwin, H. K. Moffat, I. Schoegl, R. L. Speth, and B. W. Weber, “Cantera: An object-oriented software toolkit for chemical kinetics, thermodynamics, and transport processes.” 2022. doi: 10.5281/zenodo.6387882.

[28] I. H. Bell, J. Wronski, S. Quoilin, and V. Lemort, “Pure and pseudo-pure fluid thermophysical property evaluation and the open-source thermophysical property library coolprop,” *Ind. Eng. Chem. Res.*, vol. 53, no. 6, pp. 2498–2508, 2014, doi: 10.1021/ie4033999.

[29] D. Izidoro and S. Oliveira Jr., “Energy and Exergy Analysis of Hydrogen Production Via High-Temperature Electrolysis Powered By Solar and Wind Energy,” 2021. doi: 10.26678/abcm.cobem2021.cob2021-0368.

[30] M. Lin and S. Haussener, “Techno-economic modeling and optimization of solar-driven high-temperature electrolysis systems,” *Sol. Energy*, vol. 155, pp. 1389–1402, 2017, doi: 10.1016/j.solener.2017.07.077.

[31] Vestas, “2 MW platform - V100,” 2023. https://www.vestas.com/en/products/2-mw-platform/V100-2-0-MW

[32] C. Xu, Z. Wang, X. Li, and F. Sun, “Energy and exergy analysis of solar power tower plants,” *Appl. Therm. Eng.*, vol. 31, no. 17–18, pp. 3904–3913, 2011, doi: 10.1016/j.applthermaleng.2011.07.038.

[33] Governo do Ceará, “Complexo Portuário do Pecém: Hub de Hidrogênio Verde,” 2023. https://www.complexodopecem.com.br/hubh2v/

[34] M. Sengupta, Y. Xie, A. Lopez, A. Habte, G. Maclaurin, and J. Shelby, “The National Solar Radiation Data Base (NSRDB),” *Renew. Sustain. Energy Rev.*, vol. 89, no. March, pp. 51–60, 2018, doi: 10.1016/j.rser.2018.03.003.

[35] NREL, “National Solar Radiation Database (NSRDB),” 2022. nsrdb.nrel.gov/ (accessed Jan. 13, 2022).

[36] CEPEL, “Atlas do Potencial Eólico Brasileiro: Simulações 2013,” Centro de Pesquisas de Energia Elétrica, Rio de Janeiro, 2017.

[37] M. O. Pinto, "Wind Energy Fundamentals", 1st ed. Rio de Janeiro: LTC, 2018.

[38] K. Christopher and R. Dimitrios, “A review on exergy comparison of hydrogen production methods from renewable energy sources,” *Energy Environ. Sci.*, vol. 5, no. 5, pp. 6640–6651, 2012, doi: 10.1039/c2ee01098d.

[39] R. Petela, *Engineering Thermodynamics of Thermal Radioation For Solar Power Utilization*. New York: McGraw Hill, 2010.

[40] R. A. Gaggioli and W. J. Wepfer, “Exergy economics: I. Cost accounting applications,” *Energy*, vol. 5, no. 8–9, pp. 823–837, 1980, doi: 10.1016/0360-5442(80)90099-7.

[41] J. A. M. Silva, “Exergo-environmental performance of oil processing and its derivatives,” Department of Mechanical Engineering" Departament of Mechanical Engineering, Escola Politécnica, Universidade de São Paulo. São Paulo, PhD Thesis, 2013.

Thermodynamic assessment of Latin American cities applying exergetic efficiency: effects of information availability on efficiency evaluation

Ricardo Morel Hartmann[a], Luis Evelio Garcia-Acevedo[a], Amir Roberto De Toni Jr[b]

*[a] Federal University of Latin-America Integration, Faculty of Energy Engineering, Foz do Iguaçu, Brazil, ricardo.hartmann@unila.edu.br **CA**, luis.acevedo@unila.edu.br*
[b] Federal University of Rio Grande do Sul, Interdisciplinary Department, Tramandaí, Brazil, amir.detoni@ufrgs.br

Abstract:

Energetic analysis of cities is a challenging task, due to the lack of a concise, general thermodynamic parameter to evaluate energetic output streams that is applicable to every city. Therefore, exergetic efficiency was applied as a comparative index, given that it encompasses concepts of first and second laws of thermodynamics, thus providing a figure of merit similar to those applied to thermal systems. The proposed concept was employed to assess five metropolitan areas in Latin America: Bogotá, Buenos Aires, Rio de Janeiro, Santiago de Chile and São Paulo. Comparisons among the five cities show a linear trend of increasing per capita CO_2 emissions with increasing *per capita* inlet exergy, as well as the importance of electric mobility to the overall exergetic efficiency. Also noteworthy is the complexity of observing and assessing internal exergetic streams and the evaluation of a usefulness of industrial production in terms of thermodynamic properties. According to the analysis, São Paulo presented the highest exergetic efficiency, 22.43 %, while Santiago de Chile presented the lowest, 17.94 %. This result is somewhat unexpected, since São Paulo is a warmer city, with significant HVAC use during Spring and Summer, but at the same time reflects São Paulo's exergetic data availability, thus allowing a more detailed evaluation.

Keywords:

Thermodynamics of cities; Smart cities; Exergetic efficiency, Data availability.

1. Introduction

Around 5,000 BC the first cities were formed as primitive centers for trade and religious activities [1] and, as time elapsed, certain cities became specialized centers, e.g., Sidon and Tyre, in modern-day Lebanon, which were well established maritime cities circa 2,000 BC. Since then, urban centers evolved as *locus* for several economic activities like shipping, manufacturing, mining, education, finance, health and many others, with capitals and metropolitan areas being relevant in one or more of these economic sectors. According to the United Nations [2], in 2014, urban dwellers were 54 % of the global population, and this share is projected to be 66 % by 2050. Such an increase in urban density will demand better solutions for mobility, water supply, and waste management, all of which are related to energetic and exergetic efficiency and sustainable development.

Eger [3] and Susanti et. al. [4] pointed out that only in the last four decades have cities been analyzed from a multidisciplinary perspective, instead of being an exclusive subject of demography, and, currently, economic discussions involving concepts such as circular economy [5-7] provide additional tools for the study of cities. Beyond these views in terms of economic roles and sectors, cities can also be seen as living organisms that consume and discard mass and energy, thus being amenable to the laws of conservation which underpin the science of thermodynamics.

Issues with municipal solid waste (MSW) and sewage management are much older than the formal statements of mass and energy conservation, which may help explain why these problems are seldom investigated from a thermodynamics standpoint. Though the number of studies exploring thermodynamics of cities increased in recent years, such assessments are sparse compared to analysis focused on Information and Communication Technology (ICT), which is one of the features of so-called Smart Cities (SC). The

concept of Smart City is not unequivocal [8,9] but there is consensus regarding the key role of ICT, Artificial Intelligence (AI), and Internet of Things (IoT) to enhance governance, transparency, and mobility, among other interactions of citizens with the urban environment. Albino et. al. [9] argue that a comprehensive approach to SC must also include personal and community needs, considering sustainability in a broader sense. Also relevant is the role of renewable energy, distributed generation and electrical mobility, aiming to improve exergetic efficiency and to achieve net zero emissions.

1.1. Thermodynamic assessment of cities

In this subsection a brief overview of recent studies regarding thermodynamic assessments of cities is provided. Pelorosso et al. [10] presented a discussion involving the concepts of circular economy, low-entropy city and complex socio-ecological systems. The authors also discuss the role of urban green infrastructure (UGI) to increase exergetic efficiency and the possibility of devising a generic strategy applicable to every city. Purvis and Mao [11] examined the application of entropy as an indicator of urban sustainability, by means of assessing exergy and generation of irreversibilities. Cities were analyzed as dynamic entities consisting of dissipative structures, thus showing the limits of a straightforward evaluation of entropy in urban systems. The authors argued that it is not possible to use entropy to assess material flows and degradation in a meaningful way, given the absence of 'utility' or 'usefulness' metrics in thermodynamics, which only has exergy, that corresponds to energetic availability. Regardless, Purvis and Mao agree with the use of exergetic assessments and circular economy strategies to improve urban sustainability.

Bristow and Kennedy [12] presented a nonequilibrium thermodynamics evaluation based on the concept of dissipative structures as stated by Kondepudi and Prigogine [13]. The authors conducted a macro-scale analysis, presenting results of energetic intensity as function of population density for 22 global cities. Results showed that energy intensity increases at a higher rate than population growth, which is a characteristic behavior of dissipative structures. Additionally, Bristow and Kennedy emphasized the need for further studies, with a consistent methodology, to assess exergetic flows in cities, especially regarding micro-scale processes occurring within their control volume.

Regarding Smart Cities, Zheng et al. [8] reported a scientometric review of smart city literature between 1990 and 2019, encompassing 7,380 articles. Publications were classified according to Web of Science criteria, with 35.05 % of studies being in the 'engineering electrical electronics' area, 21.98 % in 'computer science information systems', 20.18 % in 'telecommunications', and 19.95 % in 'computer science theory methods', with no category dedicated to thermodynamics. Yu and Zhang [14] evaluated the energetic efficiency in 251 Chinese cities, given their adoption of smart city policies, between 2003 and 2016. The authors developed a non-convex metafrontier data envelopment analysis to examine energy consumption data, but no analysis of thermodynamic behavior was conducted. Yu and Zhang claim to present the first systematic analysis of energetic efficiency of cities in China and concluded that the adoption of SC policies positively affected energetic efficiency.

Hartmann et al. [15] assessed the exergetic efficiency of a coastal city in Brazil (Florianópolis), focused on the effect of MSW management, showing that a proper waste separation combined with waste-to-energy generation could increase exergetic efficiency by 1.5 %, resulting in a yearly mitigation of 15,761 tons of carbon dioxide. Hartmann and Garcia-Acevedo [16] further developed the methodology for evaluation of the exergetic efficiency of urban centers, presenting results for five cities with different main economic sectors: electricity generation (Foz do Iguaçu), manufacturing (Ingolstadt), services/ICT (Florianópolis), tourism (Hawaii), and oil refining (Singapore), the latter also being a Smart City. The results indicate a linear trend of increasing per capita CO_2 emissions with increasing per capita production of MSW. Also noteworthy is the impact of electric mobility to reduce exergy destruction within the city.

Given this brief overview, the present paper aims to add to the scientific literature by reporting an assessment of the exergetic profile of five major cities in Latin America, thus providing subsidies to improve their exergetic performances. Additionally, it intends to compare and discuss the influence of available data on exergetic evaluation of the cities, given that availability of reliable data is one of the key issues of smart cities [3,4,8,9,14].

2. Theoretical background

Among the reasons to employ exergetic efficiency as an 'energy smartness index' one can emphasize that i) it encompasses both the first and second laws of thermodynamics; ii) it can be related to carbon dioxide emissions and fuel savings; iii) it is a positive number between zero and one, thus easy to communicate. Purvis and Mao [11] pointed out that an energetic efficiency analysis based only on the first law of thermodynamics is not adequate to every urban center, given the impossibility to evaluate the 'usefulness' of intangible products such as software and services. On the other hand, every city consumes exergy through

internal irreversibilities, thus it is possible to apply exergetic assessments regardless of the main economic sector.

The thermodynamic analysis applied here involves: a) definition of the metric to be evaluated; b) setting of adequate control volume; c) description of simplification hypothesis; d) mathematical model; and e) analysis of results. The preceding sections have shown that exergy is the thermodynamic property that fulfils a). Regarding b), a proper control volume, which includes streams of energy, enthalpy, entropy, exergy, heat, mass, water, pollutants, among others, is illustrated in Fig. 1.

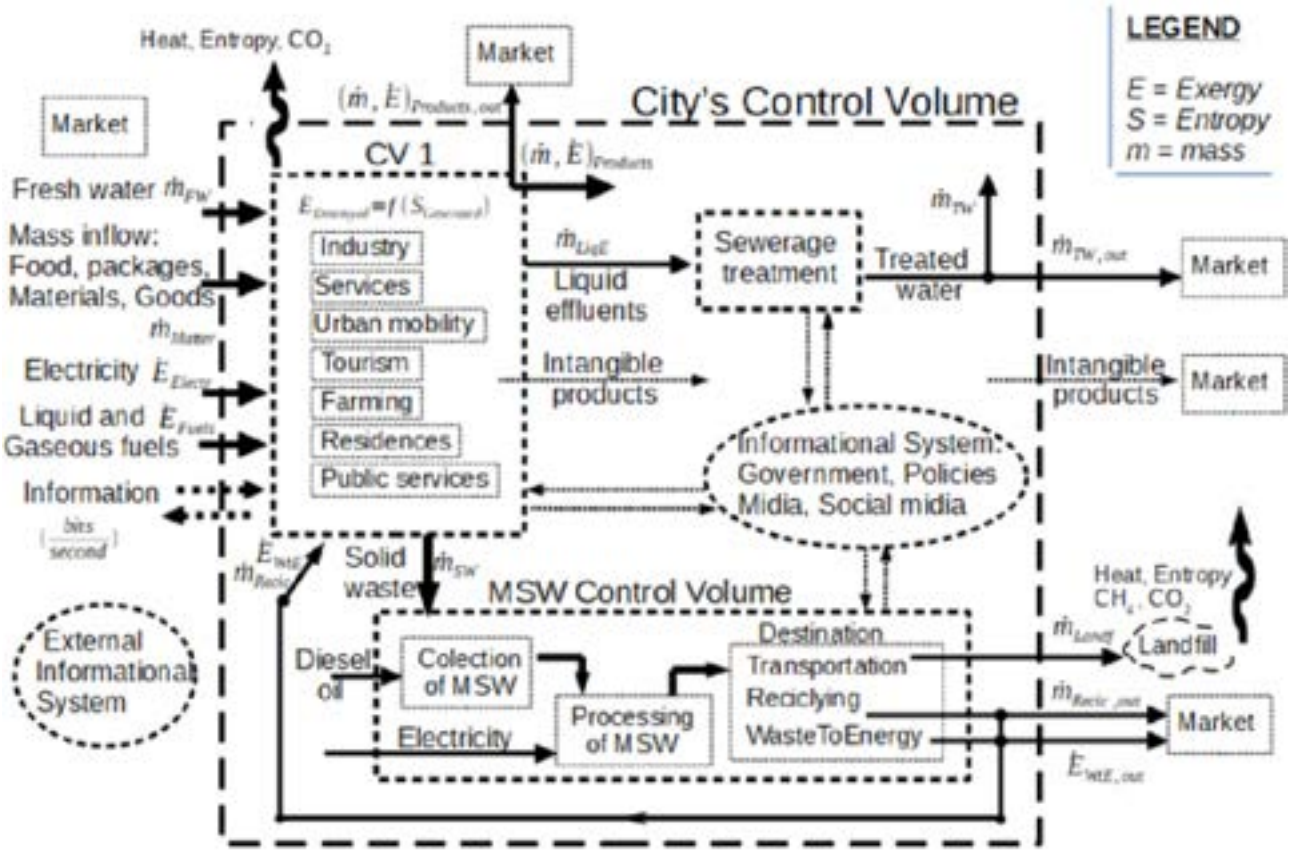

Fig. 1. Representative control volume for the thermodynamic assessment of cities.

The proposed simplification hypothesis are as follows:

(i) Inlets and outlets are considered in terms of yearly average, steady-state streams of exergy;
(ii) Exergy streams are limited to the concepts presented in Hartmann et al. [15], Moran et al. [17] and Szargut et al. [18], i.e., exergy related to altitude, kinetic exergy, electrical exergy, physical exergy related to temperature difference, and chemical exergy (heating value of fuels);
(iii) Vehicles, house appliances and other equipment are considered in terms of annual exergy consumption;
(iv) Analysis will be limited to classical thermodynamics, thus information streams will not be assessed.

2.1. Mathematical formulation

Given the proper control volume and the set of hypotheses, the mathematical model can be formalized. Exergetic efficiency is calculated in terms of inlet and outlet streams,

$$\eta_{II} = \frac{\dot{E}_{out}}{\dot{E}_{inlet}} \qquad (1)$$

$$\eta_{II} = 1 - \left(\frac{\dot{E}_{dest}}{\dot{E}_{inlet}} \right) \qquad (2)$$

where η_{II} is exergetic efficiency, $\dot{E}_{out}$ is produced exergy, $\dot{E}_{inlet}$ is inlet exergy and $\dot{E}_{dest}$ is exergy destroyed within the control volume. Equation (1) is convenient for evaluating cities which export exergy, like ones with an oil refinery or a power plant, while Eq. (2) shows a general case. The inlet rate of exergy, $\dot{E}$, is simply the sum of all exergetic streams, e.g. electricity, coal, oil, liquid and gaseous fuels, as well as river streams. The exergy rate for electricity is equal to its power, while that for water and other mass streams includes kinetic exergy, physical exergy due to temperature difference in relation to a dead state, and potential exergy [17]. Chemical exergy of liquid and gaseous fuel is calculated following Szargut et al. [18],

$$\dot{E}_{fuel,i} = \dot{E}_{chem} = \beta_{fuel,i} \cdot LHV_{fuel,i} \qquad (3)$$

where $\dot{E}_{chem}$ is the rate of chemical exergy, LHV is the lower heating value, and β is the ratio of chemical exergy to LHV, which is given by Rakopoulos and Giakoumis [19], for liquid and gaseous fuels, respectively, as,

$$\beta_{liq} = 1.0334 + 0{,}0144\left(\frac{H}{C}\right) \qquad (4)$$

$$\beta_{gas} = 1.0334 + 0{,}0144\left(\frac{H}{C}\right) - 0.0694\left(\frac{1}{N_C}\right) \qquad (5)$$

where H/C is the hydrogen to carbon ratio in the fuel, and N_C is the number of carbon atoms in the fuel molecule. Exergy outlet evaluation is analogous to the exergy inlet one, plus the streams of wastewater and MSW, when useful data is available. The evaluation of the rate of exergy destruction is expressed as,

$$\dot{E}_{dest,i} = \left(1 - \eta_{II,i}\right)\dot{E}_{Inlet,i} \qquad (6)$$

where $\eta_{II,i}$ is the exergetic efficiency of a process i. Representative values of exergetic efficiencies of processes and appliances, as well as the source of data are presented in Tab. 1.

Table 1. Exergetic efficiencies for processes and appliances

Process/Appliance	Exergy type	%	Reference
Motors (industrial, mobility)	electric	76.00	[20,21]
Air conditioner	electric	01.90	[22]
Personal computer	electric	75.00	[22]
Lighting	electric	20.00	[22]
Refrigerator	electric	07.20	[22]
Cooking oven	electric	24.20	[22]
Television	electric	80.00	[22]
Vacuum cleaner	electric	70.00	[22]
Water heater	electric	10.50	[22]
Heater/boiler	combustion	06.00	[23]
Internal combustion engines/vehicles	combustion	25.00	[19,20]
Ovens	combustion	14.88	[24]
Combustion/chemical reactions	combustion	70.00	[25]

Assessment of carbon dioxide emissions due to combustion considered stoichiometric combustion [26] with dry air, thus the emissions, in kilograms of CO_2 emissions per kilogram of fuel, are: 3.09 for gasoline, 3.12 for Diesel oil, 1.91 for hydrated ethanol, 3.02 for liquefied petroleum gas (LPG), and 2.75 for natural gas. Emissions from coal, when necessary, were obtained from data available for each analysed city.

3. Results and discussions

The proposed methodology [16] was applied to assess five global cities in Latin America: Bogotá, Buenos Aires, Rio de Janeiro, Santiago de Chile and São Paulo. The selection of these cities considered their presence in the IMD-SUTD Smart City Index Report 2021 [27], and the energy data used as input for the present analysis were obtained from their respective open data/transparency websites and reports, which are referenced in each subsection. However, the availability and specificity of municipal data varied significantly between cities, thus hampering a thorough assessment. In order to check the reliability and consistency of some metrics calculated in the present assessment, like per capita emissions, data available at the US Energy Information Agency [28], the Our World in Data Project [29] and the International Energy Agency [30] served as baseline values. Each of the following subsections provides details regarding these differences of available information. The analysis was carried out based on data of the year 2019, before the Covid-19 pandemic.

3.1. Bogotá

Bogotá is the capital and largest city of Colombia, with 7.2 million inhabitants in the city proper (Geoportal del DANE - Geovisor CNPV 2018) and 10.7 million in the metropolitan area. The urban centre covers 307.3 km², resulting in a population density above 24,000/km². Bogotá is located in a high plateau of the Andes, with an average altitude of 2,640 metres and typical temperatures between 5 and 20 °C. The metropolitan region is responsible for 24.7 % of national gross domestic product and the El Dorado International Airport handles the largest cargo volume in Latin America.

According to the Smart City Index [27], Bogotá ranks 116 out of 118, with a 'D' rating, in a tier shared with Nairobi, Lagos, Rio de Janeiro and São Paulo. Energy and emissions data for Bogotá are available on open data websites <http://www.sui.gov.co/web/energia> [31] and <https://public.tableau.com/app/profile/upme> [32]. It is worth noting that the website hosted by the government [31] has many features, allowing detailed searches considering income level (in Spanish, *estrato*), rural and urban locations, government buildings, and many others. On the other hand, the website was frequently offline, usually at night and during weekends. Table 2 summarizes the results of the exergetic assessment of Bogotá.

Table 2. Exergetic assessment of Bogotá, year 2019.

Energy source	Exergy input, TJ/yr	Exergy destroyed, TJ/yr	$CO_{2,\ equi}$, Mton/yr
Gasoline	30,552.7	22,761.8	2.253
Diesel oil	33,926.1	25,274.9	2.353
Ethanol	416.1	310.0	0.028
LPG	1,765.4	1,502.7	0.109
Natural gas	25,201.8	23,689.7	1.844
Electricity	27,273.7	24,137.2	1.287
Total	**119,135.8**	**97,676.3**	**7.874**
Exergetic efficiency	**18.01 %**	**$CO_{2,\ equi}$, ton/person-yr**	**1.096**

From data on Tab. 2, one can notice how the inhabitants of Bogota have an almost equal reliance on gasoline and Diesel for urban mobility, as well as a limited use of LPG. It is important to note that per capita emissions available elsewhere [29] include all emissions sources. In the case of Colombia, more than 50 % of emissions are associated with land-use changes and agriculture, which are not included in our assessment.

3.2. Buenos Aires

Buenos Aires is the capital and largest city of Argentina, with 2.9 million inhabitants in the city proper and 12.8 million in the metropolitan area. The city covers 20,300 km², resulting in a population density above 14,000/km². The metropolitan area has Argentina's two main maritime ports and represents around a quarter of the country's gross domestic product. Buenos Aires has a humid subtropical climate, with typical temperatures between 10 and 25 °C, though summers have highs above 35 °C and record highs reaching 43 °C, while record lows are near -5 °C.

According to the Smart City Index [27], Buenos Aires ranks 98 out of 118, with a 'CC' rating, in a tier shared with Mumbai, Jakarta, Istanbul, Lisbon, and Budapest. Energy and emissions data for Buenos Aires are supposedly available on open data website <estadisticaciudad.gob.ar>, though it has been down/inaccessible for several months. Therefore, the authors had to use national level data [33-36] to evaluate municipal values, which is likely to produce biased results. Table 3 presents the exergy assessment for Buenos Aires.

Table 3. Exergetic assessment of Buenos Aires, year 2019.

Energy source	Exergy input, TJ/yr	Exergy destroyed, TJ/yr	$CO_{2,\ equi}$, Mton/yr
Gasoline	16,458.6	12,261.7	1.214
Diesel oil	22,478.9	16,746.8	1.559
LPG	2,463.0	2,096.5	0.153
Natural gas	71,949.8	61,229.3	5.265
Electricity	31,880.5	23,910.4	3.099
Total	**145,230.8**	**116,244.6**	**11.290**
Exergetic efficiency	**19.96 %**	**$CO_{2,\ equi}$, ton/person-yr**	**3.690**

From the data in Tab. 3 one can notice Buenos Aires', hence Argentina's, reliance on natural gas, which corresponds to 64 % of the electric mix [29]. It is also noteworthy that about 1.72 million vehicles in Argentina, roughly 17 % of the passenger fleet, are fuelled by compressed natural gas (CNG). Electricity generation in Argentina consumed approximately 590,000 TJ of natural gas in 2019, followed by industries, with a consumption close to 523,000 TJ [34]. Regarding emissions, the electricity generation in Argentina is more carbon intensive than natural gas burning for final uses.

3.3. Rio de Janeiro

Rio de Janeiro is the second-most populous city in Brazil, with a population of 6.72 million, while its metropolitan area is home to 12.28 million. The city proper covers 1,221 km², with a population density around 5,500/km². The city is known for its tropical, humid climate, with daily means above 20 °C, record lows around 10 °C and record highs above 42 °C, thus having significant demand for HVAC.

According to the Smart City Index [27], Rio de Janeiro ranks 118 out of 118, with a 'D' rating, in a tier shared with Nairobi, Lagos, Bogotá and São Paulo. Energy and emissions data for Rio de Janeiro were obtained from its open data website <www.data.rio> [37] and also from state level data [38]. The Data Rio website is not user friendly, since it does not offer data visualization on graphs or tables online, thus working more like a repository of spreadsheets. Table 4 presents the exergetic assessment for Rio de Janeiro.

Table 4. Exergetic assessment of Rio de Janeiro, year 2019.

Energy source	Exergy input, TJ/yr	Exergy input, %	Exergy destroyed, TJ/yr	$CO_{2,\ equi}$, Mton/yr
Gasoline	23,451.4	15.6	17,471.3	1.729
Diesel oil	24,575.5	16.3	18,308.8	1.704
Ethanol	6,936.1	4.6	5,167.4	0.468
LPG	5,568.1	3.7	4,739.6	0.345
Natural gas	35,575.0	23.6	26,532.3	2.603
Electricity	54,453.6	36.2	51,186.4	2.508
Total	**150,559.8**	**100.0**	**123,405.7**	**9.357**
Exergetic efficiency	**18.03 %**		**$CO_{2,\ equi}$, ton/person-yr**	**1.393**

Regarding data on Tab. 4, it is important to note that Brazilian gasoline, available at the pump, is mixed with ethanol, in proportions up to 27.5 %. Hydrated ethanol is also available in gas stations, and most passenger vehicles produced in Brazil since 2006 can run on any mixture between E20 gasoline to E100. Also noteworthy are the low emissions associated with electricity, which are due to Brazil's reliance on hydropower.

3.4. Santiago de Chile

Santiago is the capital and largest city of Chile, and its population of 6.3 million people corresponds to some 32 % of the country. The city has an area of 641 km² with a population density close to 10,000/km². Santiago is located in a valley, with an average elevation of 570 metres, and has a cool, semi-arid climate, with daily averages between 7 and 21 °C, record lows below -5 °C and record highs around 40 °C. According to the Smart City Index [27], Santiago ranks 110 out of 118, with a 'C' rating, in a tier shared with Cape Town, Bucharest, Sofia, Mexico City, Athens, and Rome.

Energy statistics for Santiago de Chile and its metropolitan region are available in reports [39] and on an open data website <energiaregion.cl> [40], which is very user friendly even though it mostly presents per

capita data, thus lacking the extensive searching features of its Colombian counterpart. Table 5 presents the exergetic assessment for Santiago.

Table 5. Exergetic assessment of Santiago de Chile, year 2020.

Energy source	Exergy input, TJ/yr	Exergy destroyed, TJ/yr	$CO_{2,\ equi}$, Mton/yr
Gasoline	50,141.0	37,355.0	3.697
Diesel oil	53,816.3	40,093.1	3.732
LPG	22,839.1	19,440.6	1.415
Natural gas	25,201.8	23,689.7	1.844
Electricity	64,317.0	56,920.5	19.777
Total	**216,315.2**	**177,499.0**	**30.465**
Exergetic efficiency	**17.94 %**	**$CO_{2,\ equi}$, ton/person-yr**	**4.859**

From Tab. 5 one can notice that Santiago, in comparison with Rio de Janeiro, has a similar population, but its population density is 80 % higher than Rio's and its exergy input is 43 % higher. Per capita emissions are quite high since half of the Chilean electricity generation comes from fossil fuels (22 % coal, 15 % oil, and 14 % gas) [29,30].

3.5. São Paulo

São Paulo is the largest city in Brazil and the Southern Hemisphere, with 12.4 million inhabitants and a population density of 8,000/km². The city comprises around 5.8 % of the country's population but it represents some 10.7 % of the national GDP. São Paulo is located on a plateau close to the Atlantic Ocean, with an average elevation of 800 metres, and has a humid subtropical climate, with daily averages between 12 and 30 °C, record lows around 0 °C and record highs around 40 °C.

According to the Smart City Index [27], São Paulo ranks 117 out of 118, with a 'D' rating, in a tier shared with Nairobi, Lagos, Bogotá and Rio de Janeiro. Energy statistics for the city of São Paulo are available on the São Paulo state open data website [41], though only as a repository for reports and spreadsheets. Table 6 shows the exergetic assessment of São Paulo.

Table 6. Exergetic assessment of São Paulo, year 2019.

Energy source	Exergy input, TJ/yr	Exergy input, %	Exergy destroyed, TJ/yr	$CO_{2,\ equi}$, Mton/yr
Gasoline	61,789.5	20.0	46,033.2	4.556
Diesel oil	64,263.1	20.8	47,876.0	4.456
Ethanol	56,944.7	18.4	42,423.8	3.842
LPG	13,907.9	4.5	11,838.4	0.862
Natural gas	19,753.5	6.4	14,738.6	1.446
Electricity	92,516.0	29.9	76,912.7	4.221
Total	**309,174.7**	**100.0**	**239,882.7**	**20.828**
Exergetic efficiency	**22.43 %**		**$CO_{2,\ equi}$, ton/person-yr**	**1.707**

Regarding data on Tab. 6, it is noteworthy the relevance of ethanol in the São Paulo energy mix, due to the state being Brazil's largest producer of sugarcane, thus making E100 price competitive with gasoline.

The state government of São Paulo publishes monthly data of its energetic profile, which allows more comprehensive analysis compared to the other four cities. Table 7 shows a detailed exergetic profile of natural gas use and Tab. 8 shows a detailed exergetic profile of electricity consumption in São Paulo for the year 2019.

Table 7. Exergetic assessment of natural gas utilization in São Paulo, year 2019.

Energy source	Exergy input, TJ/yr	Exergy input, % of city	Exergy destroyed, TJ/yr
Residential	5,781.8	1.9	5,178.2
Commercial	2,241.9	0.7	1,908.3
Industrial	5,481.9	1.8	3,837.4
Automotive	2,042.0	0.7	1,521.3
Cogeneration	131.7	0.0	52.7
Thermogeneration	4,074.2	1.3	2,240.8

Table 8. Exergetic assessment of electricity consumption in São Paulo, year 2019.

Energy source	Exergy input, TJ/yr	Exergy input, % of city	Exergy destroyed, TJ/yr
Residential	41,313.5	13.4	37,430.0
Commercial	32,788.1	10.6	28,525.7
Industrial	8,718.0	2.8	2,615.4
Rural	6.8	0.0	2.0
Public lightning	1,643.3	0.5	1,339.3
Public buildings	8,046.3	2.6	7,000.3

It is possible to observe in Tab. 7 that there is no prominent sector using natural gas, since none of them represents more than 2 % of inlet of exergy into São Paulo's control volume. Observation of Tab. 8, on the other hand, reveals that, in the case of electricity use, there are some sectors more suitable for exergetic improvements. Residential and commercial sectors presented higher shares of electricity use, thus offering more opportunities for improvements related to renewable energy microgeneration, wall insulation, smart building management, and general strategies for energy efficient buildings. These initiatives are also applicable to public buildings.

Regarding urban mobility, São Paulo presents a higher share of ethanol use, about 18.4 %, compared to 4.6 % in Rio de Janeiro. On the other hand, Rio de Janeiro has a higher share of vehicular natural gas, about 18.8 %, while in São Paulo it is only 0.7 %. These differences are due to the distinct energetic profile of the states, e.g. São Paulo is the main producer of ethanol, while Rio de Janeiro is the main producer and industrial centre of petroleum and natural gas in Brazil.

Regarding electromobility, both cities present a very low percentage of electric vehicles, lower than 0.05 %. It is important to note that for Rio de Janeiro and São Paulo summation of all fuels for mobility (ethanol, Diesel oil, gasoline and natural gas) is in the range of 55 – 60 %, thus offering a significant room for exergetic improvement by means of electromobility adoption. In fact, this observation is also valid for Bogotá, Buenos Aires and Santiago de Chile. Table 9 presents the comparison of exergetic efficiency, CO_2 emissions and population of the five cities analyzed.

Table 9. Exergetic comparison of the five assessed cities.

City	Population, Million people	Total Exergy input, TJ/yr	Exergetic efficiency, %	CO_2 Emission, Ton/person-yr
Bogotá	7.2	119,135.8	18.01	1.096
Buenos Aires	2.9	145,230.8	19.96	3.690
Rio de Janeiro	6.7	150,559.8	18.03	1.393
Santiago de Chile	6.3	216,315.2	17.94	4.859
São Paulo	12.4	309,174.7	22.43	1.707

In Tab. 9 one can notice that, even though Buenos Aires has less than half of the population of Bogotá, it presents higher input of exergy. Also, comparing the Brazilian metropoles, São Paulo presents noticeably higher exergetic efficiency compared to Rio de Janeiro. The likely culprit for this difference is Rio de Janeiro's warmer climate, which increases electricity consumption by very exergetic inefficient (1.9 %) air conditioners.

3.6. Effects of geographic location and data availability on the calculation of exergetic efficiency

Geographic location has a strong influence on the exergetic performance of cities, mainly due to different HVAC needs of each climate. According to Table 1, comparing electric devices, exergetic efficiency of air conditioners is 1.9 % while for water heaters the value is 10.5 %. For gas boilers applied for water heating, the exergetic efficiency is around three times higher, which means that colder cities are likely to present higher exergetic efficiencies, but the present assessment does not reproduce this expectation. For instance, the exergetic efficiency of São Paulo, located in Köppen's 'Cwa' (dry winter) climate zone, was evaluated as 22.43 %, while Buenos Aires, located in Köppen's 'Cfa' (humid year round) climate zone, has an exergetic efficiency of 19.93 %. This discrepancy could be due to differences in mobility systems, which has been previously observed by Hartmann and Garcia-Acevedo [16] when evaluating the exergetic efficiency of Ingolstadt, Germany, where an extensive system of electric trams operates. However, in the current

comparison, Tables 3 and 6 shows that Buenos Aires and São Paulo present similar amounts of combustion exergy on their transportation sectors. It is noteworthy that combustion exergetic efficiency of any fuel is almost the same because of the dynamic behaviour of machines for mobility, as pointed out by Rakopoulos and Giakoumis [19]. Thus the unexpected difference in the results for Buenos Aires and São Paulo must be related to a different source of exergy destruction.

One possible reason for such difference could be attributed to errors on data collection and/or miscalculations. In order to check for possible discrepancies, some results were compared to the literature, e.g., Figure 2 shows the plot of *per capita* CO_2 emission as function *per capita* inlet exergy.

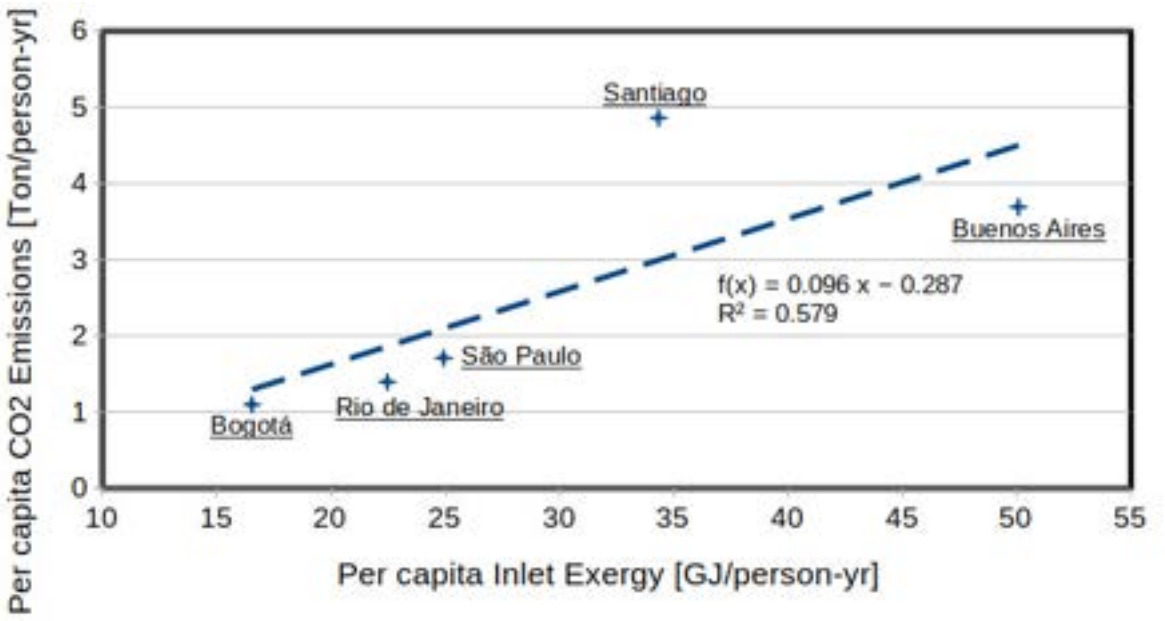

Fig. 2. Plot of per capita CO_2 emission as function per capita inlet exergy.

Figure 2 shows a linear trend of increasing *per capita* CO_2 emission with increasing *per capita* inlet exergy, with a similar trend being reported by Hartmann and Garcia-Acevedo [16]. It is noteworthy that Santiago de Chile presented the highest *per capita* emission of CO_2, of 4.859 Mton of CO_2 per person-year, visible as an 'outlier' well above the trend line on Fig. 2. This high volume of emissions is due to significant consumption of coal and Diesel oil for electricity generation.

Thus, the exergetic efficiency comparison between Buenos Aires and São Paulo, considering their distinct climates, further comparisons with literature data, and with the observed lack of reliable exergetic data for Buenos Aires, as discussed in section 3.2, allows us to conclude that the differences on exergetic efficiency between these two cities is mainly due the lack of comprehensive and reliable exergetic information for the city of Buenos Aires. For instance, data presented on Tables 7 and 8 for São Paulo allowed a better assessment of São Paulo, being on accordance with a previous analysis carried out for a well established Smart City, Singapore [16]. Therefore, one can expect that, as smart grids and smart city initiatives are implemented in the major metropolitan areas of Latin America, it will be possible to improve the quality and thoroughness of this kind of exergetic assessment.

4. Conclusions

An exergetic assessment of five Latin American cities was carried out by comparing their inlet and outlet exergetic fluxes and then calculating the exergetic efficiency and carbon dioxide emissions in CO2 equivalent ton by person per year.

The methodology for evaluation of the exergetic efficiency of urban centers takes as a metric to be evaluated the major energetic fluxes, i.e. gas and liquid fuels as well as electricity; it assumes the city border as a control volume; applies the mathematical model developed by Hartmann and Garcia-Acevedo [16], which follows the basic principles for the evaluation of machines and thermal systems, resulting in an overall exergetic efficiency for each analised city.

São Paulo, rated "d" in the smart index, has the highest exergy efficiency among the cities studied, 22,43%. This result is likely due to the highest participation of ethanol in its mobility-related consumption, since ethanol's share is of the same order of magnitude as gasoline and diesel, as shown on Table 6. Other cities also rated "d" in the smart index, as Bogotá (18,01%) and Rio de Janeiro (18,03%), have medium value of exergy efficiency. On the other hand, Santiago de Chile has the lowest exergy efficiency (17,94%) and

highest carbon dioxide emissions index (30,46 MTon CO2 per year), even though its population is about half of Sao Paulo's. This result is probably due to the low use of ethanol combined with the extensive use of natural gas as a main fuel of the automobile fleet.

It is also possible to observe a relationship between the cities' high temperatures and their low exergetic efficiency. This phenomena could be explained due to the massive use of air conditioning systems while also related to the type of primary source for the electricity production. Such a scenario presents an opportunity to improve the city's Smart City Index, by means of investing, for example, in constructive systems aimed at improving the energy efficiency of buildings. The methodology has been demonstrated to be applicable for an initial assessment of the smartness of cities, but further data granularity is required to provide a thorough analysis.

References

1 Benevolo L., The history of the city. Cambridge, US: MIT Press; 1980.

2 United Nations. World Urbanization Prospects – Available at: < https://population.un.org/wup/Publications/Files/WUP2014-Highlights.pdf>. [accessed 10.2.2022].

3 Eger JM. Smart Growth, Smart Cities, and the Crisis at the Pump: A Worldwide Phenomenon. I-WAYS, Dig Electron Commer Policy Regul 2009;32:47-53. doi: 10.3233/iwa-2009-0164.

4 Susanti R., Soetomo S., Buchori I., Brotosunaryo P.M. Smart Growth, Smart City and Density: In Search of the Appropriate Indicator for Residential Density in Indonesia. Procedia – Soc Behav Sci 2016;227:194-201. doi: 10.1016/j.sbspro.2016.06.062.

5 Malinauskaite J., Jouhara H., Czajczyńska D., Stanchev P., et al. Municipal solid waste management and waste-to-energy in the context of a circular economy and energy recycling in Europe. Energy 2017;141:2013-44. doi: 10.1016/j.energy.2017.11.128.

6 Nelles M., Grünes J., Morscheck G. Waste management in Germany – Development to a sustainable circular economy? Procedia Environ Sci 2016;35:6-14. doi: 10.1016/j.proenv.2016.07.001.

7 Khan I., Kabir Z. Waste-to-energy generation technologies and the developing economies: A multi-criteria analysis for sustainability assessment. Renew Energy 2020;150:320-33. doi: 10.1016/j.renene.2019.12.132.

8 Zheng C., Yuan J., Zhu L., Zhang Y., Shao Q. From digital to sustainable: a scientometric review of smart city literature between 1990 and 2019. J Clean Prod 2020;258:120689. doi: 10.1016/j.jclepro.2020.120689.

9 Albino V., Berardi U., Dangelico R.M. Smart Cities: Definitions, Dimensions, Performance, and Initiatives. J Urban Technol 2015;22:3-21. doi: 10.1080/10630732.2014.942092.

10 Pelorroso R., Gobattoni F., Leone A. The low-entropy city: a thermodynamic approach to reconnect urban systems with nature. Landsc Urban Plan 2017;168:22-30. doi: 10.1016/j.landurbplan.2017.10.002.

11 Purvis B., Mao Y. Thermodynamic entropy as an indicator for urban sustainability? Procedia Eng 2017;198:802-12. doi: 10.1016/j.proeng.2017.07.131.

12 Bristow D., Kennedy C. Why Do Cities Grow? Insights from Nonequilibrium Thermodynamics at the Urban and Global Scales. J Ind Ecol 2015:19:211-21. doi: 10.1111/jiec.12239.

13 Kondepudi D., Prigogine I. Modern Thermodynamics: From Heat Engines to Dissipative Structures. Hoboken, US: Wiley; 2014.

14 Yu Y., Zhang N. Does smart city policy improve energy efficiency? Evidence from a quasi-natural experiment in China. J Clean Prod 2019;229:501-12. doi: 10.1016/j.jclepro.2019.04.316.

15 Hartmann R.M., Garcia-Acevedo L.E., Bazzo E. Assessment of municipal solid waste management system using a mixing index as indicative of urban sustainability analysis. In: Stanek W., Gładysz P., Werle S., Adamczyk W., editors. ECOS 2019: Proceedings of 32nd International Conference on Efficiency, Cost, Optimization, Simulation and Environmental Impact of Energy Systems; 2019 Jun 23-28; Wrocław, Poland. Silesian University of Technology: 1715-29.

16 Hartmann R.M., Garcia-Acevedo L.E. Thermodynamic assessment of cities applying exergetic efficiency as evaluation index. Sustain Energy Technol Assess 2022;50:101801. doi: 10.1016/j.seta.2021.101801.

17 Moran M.J., Shapiro H.N., Boettner D.D., Bailey M.B. Fundamentals of Engineering Thermodynamics. Hoboken, US: Wiley; 2014.

18 Szargut J., Morris D.R., Steward F.R. Exergy analysis of thermal, chemical, and metallurgical processes. New York, US: Hemisphere; 1988.

19 Rakopoulos C.D., Giakoumis E.G. Second-law analyses applied to internal combustion engines operation. Prog Energy Combust Sci 2006;32:2-47. doi: 10.1016/j.pecs.2005.10.001.

20 ElBahloul M.A., Aziz E.S., Chassapis C. Mechanical efficiency prediction methodology of the hypocycloid gear mechanism for internal combustion engine application. Int J Interact Des Manuf 2019;13:221-33. doi: 10.1007/s12008-018-0508-2.

21 Michaelides E.E. Thermodynamics and energy usage of electric vehicles. Energy Convers Manag 2020;203:112246. doi: 10.1016/j.enconman.2019.112246.

22 Almasri R.A., Almarshoud A.F., Omar H.M.,Esmaeil K.K., Alshitawi M. Exergy and Economic Analysis of Energy Consumption in the Residential Sector of the Qassim Region in the Kingdom of Saudi Arabia. Sustainability 2020;12:2606. doi: 10.3390/su12072606.

23 Kallert A., Schmidt D., Bläse T. Exergy-based analysis of renewable multi-generation units for small scale low temperature district heating supply. Energy Procedia 2017;116:13-25. doi: 10.1016/j.egypro.2017.05.051.

24 Mahlia T.M.I., Taufiq B.N., Ong K.P., Saidur R. Exergy analysis for day lighting, electric lighting and space cooling systems for a room space in a tropical climate. Energy Build 2011;43:1676-84. doi: 10.1016/j.enbuild.2011.03.011.

25 Hartmann R.M., Oliveira E.J., Rocha M.I., Oliveira A.A.M. Customized software and hardware applied to assessment of outwardly spherical flames using the pressure trace: a thermodynamic approach to improve accuracy of laminar flame speed measurements. Int J Thermodyn 2017;20:121-30. doi: 10.5541/eoguijt.324163.

26 Turns S.R. An Introduction to Combustion: Concepts and Applications. New York, US: McGraw Hill; 2011.

27 International Institute for Management Development. Smart City Index 2021 – Available at: < https://www.imd.org/smart-city-observatory/home/>. [accessed 14.2.2022].

28 U.S. Energy Information Administration - International. Available at: <https://www.eia.gov/international/data/world>. [accessed 10.3.2022]

29 Ritchie H., Roser M. Energy. Published online at OurWorldInData.org. Available at: <https://ourworldindata.org/energy>. [accessed 10.3.2022]

30 International Energy Agency - Data and statistics. Available at: <www.iea.org/data-and-statistics>. [accessed 11.03.2022].

31 Sistema Único de Información de Servicios Públicos Domiciliarios. Available at: <www.sui.gov.co>. [accessed 07.03.2022].

32 Unidad de Planeación Minero Energética UPME - BECO Consulta. Available at: <public.tableau.com/app/profile/upme>. [accessed 07.03.2022].

33 Secretaría de Energía. Datos Energía - Available at: <datos.minen.gob.ar>. [accessed 16.02.2022].

34 Instituto Nacional de Estadística y Censos. Anuario Estadístico de la República Argentina 2019 - Available at: <https://www.indec.gob.ar › anuario_estadistico_2019>. [accessed 16.02.2022].

35 Muzio M.M., Gaioli F., Galbusera S. Inventario Nacional de Gases de Efecto Invernadero: Argentina - 2019. Secretaria de Ambiente y Desarrollo Sustentable de la Nación. Available at : <https://www.argentina.gob.ar/sites/default/files/inventario_de_gei_de_2019_de_la_republica_argentina.pdf>. [accessed 17.02.2022].

36 Instituto Nacional de Estadística y Censos. Informes técnicos / Vol. 5, nº 232 : Energía Vol. 5, nº 4. Available at: <https://www.indec.gob.ar/uploads/informesdeprensa/indicadores_energeticos_12_21B2A18B6098.pdf>. [accessed 17.02.2022].

37 Instituto Pereira Passos. Data Rio - Available at: <www.data.rio>. [accessed 20.02.2022].

38 Empresa de Pesquisa Energética. Anuário Estatístico de Energia Elétrica 2020, ano base 2019 - Available at: <https://www.epe.gov.br/pt/publicacoes-dados-abertos/publicacoes/anuario-estatistico-de-energia-eletrica>. [accessed 21.02.2022].

39 Comisión Nacional de Energía. Anuario Estadístico de Energía 2020 – Available at: <https://www.cne.cl/wp-content/uploads/2021/12/AnuarioCNE2020.pdf>. [accessed 16.02.2022].

40 Comisión Nacional de Energía. Energía Región - Available at: <energiaregion.cl>. [accessed 16.02.2022].

41 Serviço de Informação ao Cidadão. Governo Aberto SP - Available at: <http://catalogo.governoaberto.sp.gov.br/group/energia>. [accessed 19.02.2022].

Thermoeconomic Cost Allocation Approaches in a Simultaneous Heating and Cooling Heat Pump System.

Rodrigo Guedes dos Santos[ab], Miguel Ángel Lozano[c], Luis María Serra[d], Atílio Barbosa Lourenço[e] and José Joaquim C. S. Santos[f].

[a] Federal Institute of Espírito Santo, Vitória, Brazil, guedes.rodrigo88@gmail.com CA
[b] Federal University of Espírito Santo, Vitória, Brazil
[c] GITSE I3A, Dept. Mech. Eng, Universidad de Zaragoza, Zaragoza, Spain, mlozano@unizar.es
[d] GITSE I3A, Dept. Mech. Eng, Universidad de Zaragoza, Zaragoza, Spain, serra@unizar.es
[e] Federal University of Espírito Santo, Vitória, Brazil, atilio.lourenco@ufes.br
[f] Federal University of Espírito Santo, Vitória, Brazil, jose.j.santos@ufes.br

Abstract:

Thermoeconomics is a branch of engineering that combines concepts from thermodynamics and economics to tackle problems that are hard or cannot be solved by these sciences, separately. The main applications of thermoeconomics are cost allocation, optimization, and malfunction diagnosis of energy systems. Defining the productive structure plays a critical role in thermoeconomic modeling, and exergy is a highly appropriate thermodynamic quantity to correlate with costs. For systems containing dissipative equipment, the use of total exergy in conventional productive diagrams need a subsequent decision, by the analysts, on how to define its fuel and product. In some applications, exergy disaggregation can be elegant options, mostly to deal with dissipative components. Nevertheless, all of them increase the complexity in thermoeconomic modelling. In this work, thermoeconomic cost allocation approaches in a simultaneous heating and cooling heat pump system were performed from the application of some thermoeconomics methodologies. The studied system has one dissipative component (valve) and generates no waste. There are three specific objectives. Firstly, to present the different possibilities to treat and isolate the valve in the thermoeconomics modelling. Secondly, to compare the methodologies presented from the thermoeconomic point of view through the cost allocation in a simultaneous heating and cooling heat pump system. And finally, to show the pros and cons of each methodology applied in this study to support future decision-makings in thermoeconomic modelling. The research demonstrates that the differences between the methodologies used were not significant, and the choice of methodology should depend on factors such as the need for disaggregated equipment. In conclusion, the findings of this study indicate that without certain models that may overestimate the cost of particular components, the thermoeconomic results fall within a narrow range of 4% of the solution line. This suggests that the methodologies used did not yield significantly different results.

Keywords:

Thermoeconomic Approach, Cost Allocation, Physical Exergy Disaggregation, Modelling Complexity, Dissipative Component.

1. Introduction

Thermoeconomics is a branch of engineering that combines concepts from thermodynamics and economics to tackle problems that are hard to solve or cannot be solved by these sciences, separately. The main applications of thermoeconomics are cost allocation, local and global optimization, and malfunction diagnosis of energy systems.

Historically, Keenan [1] was the first researcher to associate the exergy (availability) of the final products of an energy system with their respective costs [2]. Since then, this idea has been applied to several different problems [3], including optimisation of energy systems [4,5]. However, it was only in the late 1980s and early 1990s that modern thermoeconomic methodologies were proposed. In 1994, the CGAM problem was defined to compare results by the application of such methodologies [6]. Since then, thermoeconomics has been widely applied to many energy system problems.

Frangopoulos proposed the Thermoeconomic Functional Analysis (TFA) [7,8], which is originally a methodology for energy systems optimisation. Nevertheless, TFA can be adapted to solve cost allocation problems. Von Spakovsky proposed the Engineering Functional Analysis (EFA) [9], which is an optimisation methodology, but it can be used for cost allocation as well as TFA. Lozano and Valero proposed the Theory

of Exergy Cost (TEC) [10,11] which was originally developed for cost allocation and malfunction diagnosis, but it can be also applied to formulate optimisation problems. Tsatsaronis and co-workers proposed some exergoeconomic methods [12,13] that became the SPECO method [14], which is a methodology for cost allocation and energy systems optimisation. The methodologies were adapted to deal with environmental impact problems in the same energy systems as well [15–17].

Other thermoeconomic approaches were proposed besides the ones. Erlach et al. proposed the Structural Theory [18], which is a unification approach of the methodologies applied to the CGAM problem. Santos et al. proposed the H&S model [19], which is a modification of the Structural Theory regarding the application of negentropy. Lourenço et al. proposed the UFS model [20], which is an extension of the H&S model. Recently, a method of localized physical disaggregation [21] was proposed to isolate dissipative equipment with less complexity when compared with total disaggregation. However, it can incur a loss in the accuracy of the results. Finally, the latest thermoeconomic methodology presented in the literature is the A&F model [22], a methodology proposed to isolate dissipative components with less modelling complexity.

A key concept used in most thermoeconomic methodologies and approaches is the functional diagram, also known as the productive diagram. The productive diagram is a graphical representation of the inter-relations between the subsystems of the global system and its surroundings. Subsystems are connected according to their respective purposes. Frangopoulos [7] proposed this key concept first in the 1980s, but it has been applied since then until nowadays. The way in which the productive structure is defined is a key point of thermoeconomic modelling. One of the most adequate thermodynamic magnitudes to be associated with the cost is exergy since it contains information from both the first and the second laws of thermodynamics. Most thermoeconomicists agree that exergy is the most appropriate thermodynamic magnitude to associate with cost since it contains information from both the first and the second laws of thermodynamics, qualifies the energy streams, and identifies the irreversibility of the subsystems [23].

The utilization of total exergy in conventional productive diagrams can become a hard task when the systems include dissipative equipment, such as valves. This is because the analyst needs to decide on how to define the fuel and product for the dissipative component, which can be challenging. One solution to this issue is the use of physical exergy disaggregation. Despite the improvement in result accuracy, when the exergy streams are disaggregated, the modelling complexity is increased [14].

In this study, different thermoeconomic methodologies are applied to a simultaneous heating and cooling heat pump system, which contains a dissipative valve and generates no waste. The study has three specific objectives. Firstly, the research presents the different methodological possibilities for treating and isolating the valve. Secondly, it compares the various thermoeconomic methodologies based on cost allocation in the simultaneous heating and cooling heat pump system. Finally, it demonstrates the advantages and disadvantages of each methodology, which can help guide future decision-makings in thermoeconomic modelling.

By presenting and comparing different cost allocation approaches, this study provides guidance for analysts in their future work and contributes to the development of more effective thermoeconomic modelling.

2. Physical exergy disaggregation

Since 1990, thermoeconomics has used physical exergy disaggregation, which was initially introduced by Kotas [24]. In agreement with [14], disaggregate exergy components enhance the precision of results in thermoeconomics. Physical exergy, disregarding kinetic, potential, and other energy forms, is expressed by Eq. (1), as used by H&S Model approach. It is worth mentioning that all components of exergy presented in this study depend solely on the thermodynamic properties of the flows, previously known.

$$\dot{E}_i^{PH} = \dot{E}_i^{H} - \dot{E}_i^{S} = \dot{m}_i \cdot \left[\left(h_i - h_0 \right) - T_0 \cdot \left(s_i - s_0 \right) \right] \tag{1}$$

Applying the definition of specific enthalpy in Eq. (1), h = u + Pv, Eq. (2) is written. Rearranging Eq. (2), the three terms of UFS Model are obtained and given by Eq. (3).

$$\dot{E}_i^{PH} = \dot{m}_i \cdot \left\{ \left[\left(u_i + P_i \cdot v_i \right) - \left(u_0 + P_0 \cdot v_0 \right) \right] - T_0 \cdot \left(s_i - s_0 \right) \right\} \tag{2}$$

$$\dot{E}_i^{PH} = \dot{E}_i^{U} + \dot{E}_i^{F} - \dot{E}_i^{S} = \dot{m}_i \cdot \left[\left(u_i - u_0 \right) + \left(P_i \cdot v_i - P_0 \cdot v_0 \right) - T_0 \cdot \left(s_i - s_0 \right) \right] \tag{3}$$

Furthermore, Eq. (4) can be obtained by rearranging Eq. (2) in a different way, specifically by combining the first and third terms of Eq. (3).

$$\dot{E}_i^{PH} = \dot{m}_i \cdot \left\{ \left[\left(u_i - T_0 \cdot s_i \right) - \left(u_0 - T_0 \cdot s_0 \right) \right] + \left(P_i \cdot v_i - P_0 \cdot v_0 \right) \right\} \tag{4}$$

The specific Helmholtz energy of a closed system under a heat bath (reservoir at T_0) is given by $a = u - T_0 s$. This can be applied for both i-th and dead states. Eqs. (5) and (6) show the Helmholtz energy term and flow

work term, respectively. Thus, the physical exergy could be written as in Eq. (7), according to the A&F Model. It is important to highlight that the principle used in applying the A&F Model to disaggregate physical exergy into its Helmholtz energy terms (Eq. (5)) and flow work term (Eq. (6)) is similar to that used in the H&S and UFS Models.

$$\dot{E}_i^A = \dot{m}_i \cdot (a_i - a_0) = \dot{m}_i \cdot \left[(u_i - T_0 \cdot s_i) - (u_0 - T_0 \cdot s_0) \right] \tag{5}$$

$$\dot{E}_i^F = \dot{m}_i \cdot (P_i \cdot v_i - P_0 \cdot v_0) \tag{6}$$

$$\dot{E}_i^{PH} = \dot{E}_i^A + \dot{E}_i^F = \dot{m}_i \cdot \left\{ \left[(u_i - T_0 \cdot s_i) - (u_0 - T_0 \cdot s_0) \right] + (P_i \cdot v_i - P_0 \cdot v_0) \right\} \tag{7}$$

3. Thermoeconomic modelling

The productive structure is a representation that elucidates the purpose of subsystems by explicitly revealing their input (fuels) and output (products) components in terms of productive flows. In thermoeconomic methodologies, physical or/and productive flows are conventionally utilized to graphically illustrate the productive interconnections among subsystems. This study employs productive and physical flows to construct productive/physical diagrams that facilitate the visualization of the productive structure. Fictitious units (junctions and bifurcations) are used to assist the drawing up of the productive diagrams.

After the definition of the productive structure, each subsystem is represented by means of a cost equation balance relating a thermodynamic magnitude and the unit cost of external resources, and internal flows. The mathematical model lists a set of cost equation balances in each subsystem to calculate the unit costs. A thermoeconomic model should be performed by using Eq. (8).

$$\sum (k_{out} \cdot Y_{out}) - \sum (k_{in} \cdot Y_{in}) = k_F \cdot E_F \tag{8}$$

In Eq. (8), E_F is the external fuel exergy consumption (in kW); and Y_{out} and Y_{in} means the generic thermodynamic magnitude of the internal flows at inlet and outlet (including final products) of each subsystem. The solution of the set of equations results in the unit exergy costs of each internal flow and each final product. In this paper, *Y* assumes the thermodynamic magnitudes, such as power (W), total exergy (E), Helmholtz energy term (E^A), flow work term (E^F), internal energy (E^U), and entropic term (E^S). The unknown k_{out} and k_{in} are the unit exergy costs of the internal flows at the outlet and the inlet of each subsystem. The unit exergy cost of a flow is the amount of external exergy unit required to obtain one unit of this flow, meaning that the unit exergy costs of a flow is a measure of the thermodynamic efficiency of the production process when producing this flow [25]. Each subsystem provides a single cost balance equation, thus auxiliary equations are necessary when several products are obtained in a component. Thermoeconomic models which use physical exergy disaggregation, based on the productive diagrams, consider the equality criteria [8,14,26], where productive flows exiting the same productive unit must have the same unit cost. It is worth mentioning that for all the methodologies studied in this research, in the absence of external assessment, the exergy cost of the mass and energy streams entering the plant equals their exergy *(k_w = 1 [kJ/kJ]).*

4. Case study

A simultaneous heating and cooling heat pump system is studied to exemplify the proposal of this paper. This is the same system studied by Nguyen et al. [27]. The flowsheet of the system is shown in Figure 1. The heat pump consists of four components: evaporator, motor-compressor, condenser, and valve. The working fluid of the system is ammonia. The evaporator and the condenser are two water-coupled systems designed for district cooling and heating, respectively. In Figure 1, 'H', 'C', 'r' and 's' correspond to hot, cold, return and supply, respectively, and 'em' corresponds to electric motor.

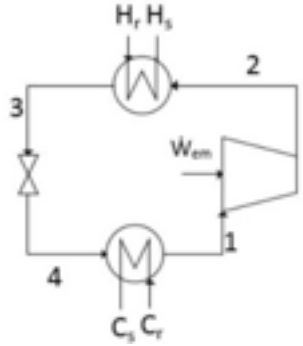

Figure. 1. The physical structure of the heat pump system

Certain assumptions have been made, including the assumption that the processes are in a steady state. Additionally, it is assumed that ammonia is a saturated vapor at state 1 and a saturated liquid at state 3, there is no heat exchange with the environment, there are no changes in kinetic and potential energy, there is no pressure drop for flow through heat exchangers, and chemical exergy is not considered.

Table 1 shows the parameters of the heat pump system.

Table 1: System parameters

Parameter	Symbol	Value	Unit
Condensation temperature	T_{cnd}	70	°C
Evaporation temperature	T_{evp}	7	°C
Evaporator heat transfer rate	$\dot{Q}_{evp}$	250	kW
Compressor isentropic efficiency	η_{cmp}	75	%
Electric motor efficiency	η_{em}	90	%
Water streams pressure	P_{H2O}	300	kPa
Environment pressure	P_0	100	kPa
Environment temperature	T_0	20	°C

Avoiding pinch problems, Eqs. (10)-(13) are used to model the condenser and the evaporator:

$$T_{Hs} = T_{cnd} + 0°C \tag{10}$$

$$T_{Cs} = T_{evp} + 3°C \tag{11}$$

$$T_{Hr} = T_{Hs} - 30°C \tag{12}$$

$$T_{Cr} = T_{Cs} + 6°C \tag{13}$$

Conventional mass, energy and exergy balance equations are applied from the data to each control volume. The simulation is done in Engineering Equation Solver [28]. Table 2 shows the values of electrical power input and mass flow rates of ammonia, hot water, and cold-water streams.

Table 2. Electrical power input and mass flow rates

Variable	Symbol	Value	Unit
Electrical power	$\dot{W}_{cmp}$	110.181	kW
Ammonia mass flow rate	$\dot{m}_{NH3}$	0.271	kg/s
Hot water mass flow rate	$\dot{m}^{H}_{H2O}$	2.783	kg/s
Cold water mass flow rate	$\dot{m}^{C}_{H2O}$	9.958	kg/s
Hot water stream exergy	$\dot{E}_{Qcond}$	37.026	kW
Cold water stream exergy	$\dot{E}_{Qevp}$	6.125	kW

Table 3 shows the thermodynamic properties of ammonia.

Table 3. Thermodynamic properties of the main physical flows of the heat pump system

Flow	P [kPa]	T [°C]	E [kW]	E^A [kW]	E^F [kW]	E^S [kW]	E^U [kW]
1	554	7.00	64.50	68,76	-4,27	-82,50	-13,74
2	3312	179.80	147	129,95	17,04	-65,84	64,11
3	3312	70.00	86.17	122,73	-36,57	-354,08	-231,39
4	554	7.00	76.09	105,58	-29,51	-344,08	-238,47

5. Thermoeconomic methodologies

In this Section, five thermoeconomic methodologies will be studied for the case study presented in this work. One of these methodologies will be presented in a physical diagram (TEC), while the others will be presented using a productive diagram (E Model, UFS Model, A&F Model, and localized physical exergy disaggregation). The aim is to develop the methodologies for the exergy cost allocation of the electrical power to the final products of the system, i.e., heating and cooling. In agreement with [29], this work also concurs that the best productive structure would be one that explains with the greatest depth and simplicity the productive function of the subsystems and flows present in the physical structure of the plant under examination.

5.1. TEC

According to original formulation of TEC [10], one can apply the exergy cost balance equation to each control volume of the system. In addition, it is considered that the final products of the system are the exergy flow increase of both hot and cold-water streams, respectively. In this methodology, the sum of the inlet cost streams is equal to the sum of the exit cost streams for each control volume shown, such as Eq. 8. However, the interpretation of which flows are fuels or products for each subsystem is not a trivial task. Therefore, equations Eqs. (14) - (17) are formulated with the aim of performing the proposed study and Figure 2 shows the physical structure of the heat pump system using TEC.

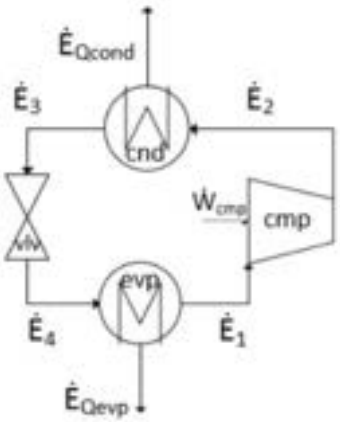

Figure. 2. Physical structure of the heat pump system using TEC

$$k_w \cdot \dot{W}_{cmp} + k_1 \cdot \dot{E}_1 = k_2 \cdot \dot{E}_2 \tag{14}$$

$$k_2 \cdot \dot{E}_2 = k_3 \cdot \dot{E}_3 + k_{cnd} \cdot \dot{E}_{Qcond} \tag{15}$$

$$k_3 \cdot \dot{E}_3 = k_4 \cdot \dot{E}_4 \tag{16}$$

$$k_4 \cdot \dot{E}_4 = k_1 \cdot \dot{E}_1 + k_{evp} \cdot \dot{E}_{Qevp} \tag{17}$$

Whether there is removal of exergy from a mass stream within the control volume being considered then the unit exergy cost of the output stream is equal to the unit exergy cost of the correspondent input stream. Therefore, Eqs. (18)-(19) are written.

$$k_3 = k_2 \tag{18}$$

$$k_1 = k_4 \tag{19}$$

According to the authors [29], a limitation of the theory of exergetic cost, as it was originally formulated, consisted of defining the productive structure in relation to the same flows and components present in the physical structure. One of the resulting difficulties lies mainly in the adequate treatment of the dissipative units and of the residues of the plant [29].

5.2. E Model

The E Model utilizes total exergy to define fuels and products of the subsystems of the plant. However, when a valve is present in the system as a dissipative equipment, the analyst must decide how to treat the valve. It is not possible to assign a productive purpose to the valve using only total exergy. Usually, dissipative equipment is combined with other subsystems to aid in the production of the final product. Moreover, this plant has the characteristic of having two products, which makes the analyst's decision more difficult. Therefore, this study presents three options to treat the valve using total exergy, as illustrated in Figure 3. The first option (Figure 3a) is to combine the valve with the condenser (where the valve's irreversibility is entirely attributed to heat), the second (Figure 3b) is to combine it with the evaporator (where the valve's irreversibility is entirely attributed to cold), and the third option (Figure 3c) is to separate it until temperature T_0 (ambient temperature), where the valve's irreversibility up to that point will be attributed to the condenser, and below temperature T_0, it will be attributed to the evaporator. This third option appears to be more reasonable since it is consistent to consider (from a thermodynamic point of view) that until temperature T_0, the valve contributes to the heat production and below the ambient temperature, it contributes to the cooling production.

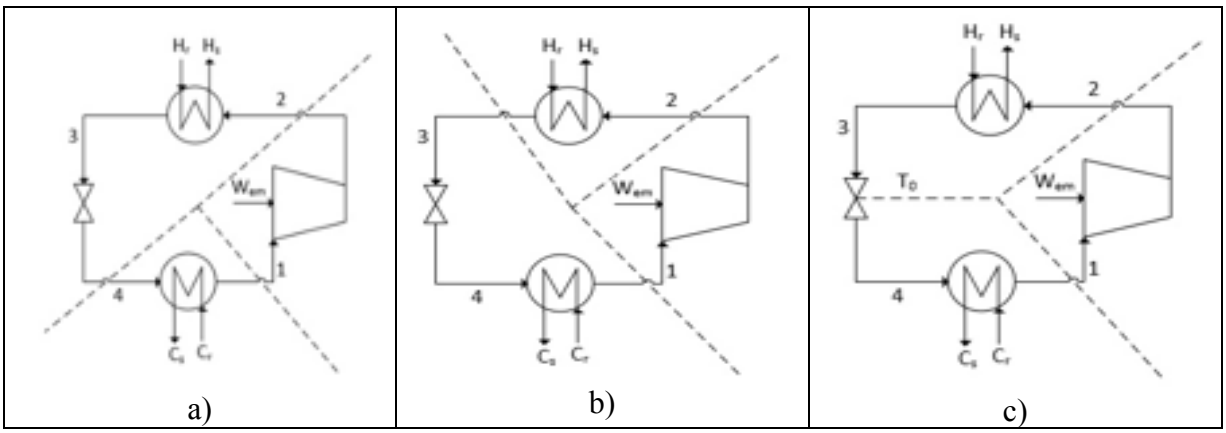

Figure. 3. Three physical structure layouts for the treatment of the valve: a) *valve with the condenser; b) valve with the evaporator; c) valve until T_0 with condenser, below T_0 with evaporator.*

Figures 4 to 6 depict the production diagram for the three possible treatments of the valve using Model E. It is worth noting that the main difference between the three diagrams is the input of the subsystem where the valve is merged. As previously explained, however now represented in the productive diagram, in Figure 4 the valve is merged with the Condenser (*E Model - CV*), in Figure 5 it is merged with the evaporator (*E Model – VE)*, and in Figure 6 the irreversibility of the valve is divided between the condenser and the evaporator.
In all the productive diagrams analysed in this research, the rectangles represent the actual units or subsystems that correspond to the physical equipment of the system. The rhombus and circles are fictitious units utilized to connect and/or divide the productive streams. Each subsystem includes input arrows to indicate its fuel or resources, and output arrows to indicate its products. The determination of productive streams is based on the specific exergy term variation between the inlet and outlet, with positive variation classified as a product and negative variation as fuel [19]. In this research, the auxiliary equation for each bifurcation is formulated using the multiproduct method, which assumes that the same unit costs apply to all productive streams that leave the same subsystem, owing to shared resources and irreversibilities inherent within the subsystem [30].

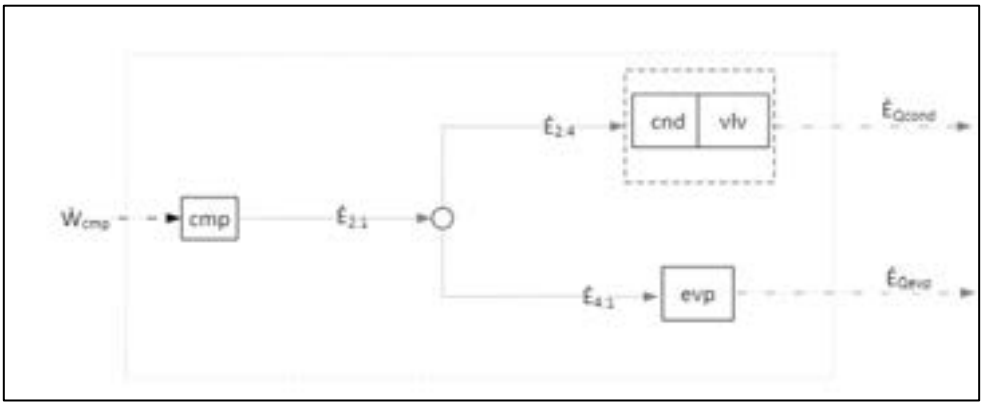

Figure. 4. Productive diagram for the heat pump system using E Model - CV.

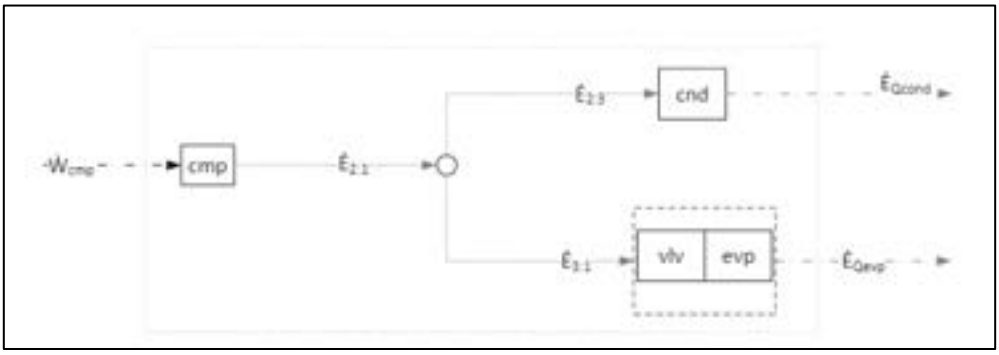

Figure. 5. Productive diagram for the heat pump system using E Model - VE.

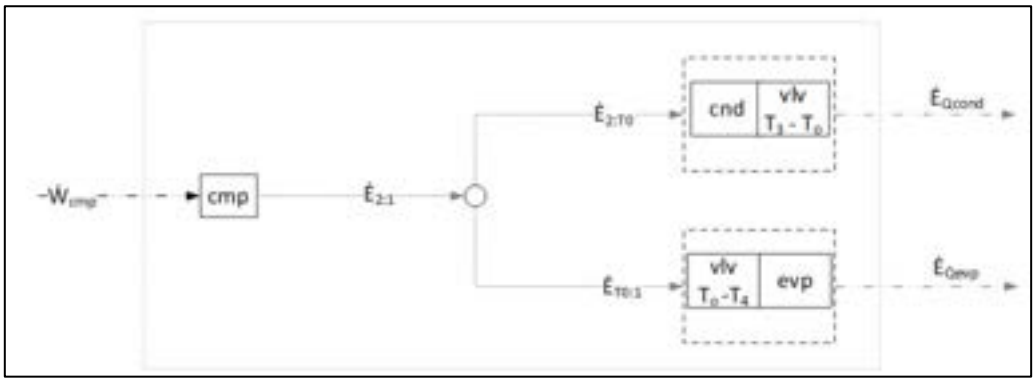

Figure. 6. Productive diagram for the heat pump system using E Model - CVE.

5.3. UFS Model

Despite the increased computational effort required and modelling complexity compared with the E Model, the application of the UFS Model [20] is justified because there is a valve in the system. To be more specific, there are two additional exergy terms for every equipment in the productive diagram to define fuel and product, compared to the E Model. The valve is now isolated, and there is no longer a need to merge this component with another to achieve its intended production purpose. Figure 7 represent the productive diagram of the heat pump system using the UFS Model. As already explained, this model utilizes physical exergy disaggregated into internal energy (E^U), flow work (E^F), and entropic term (E^S).

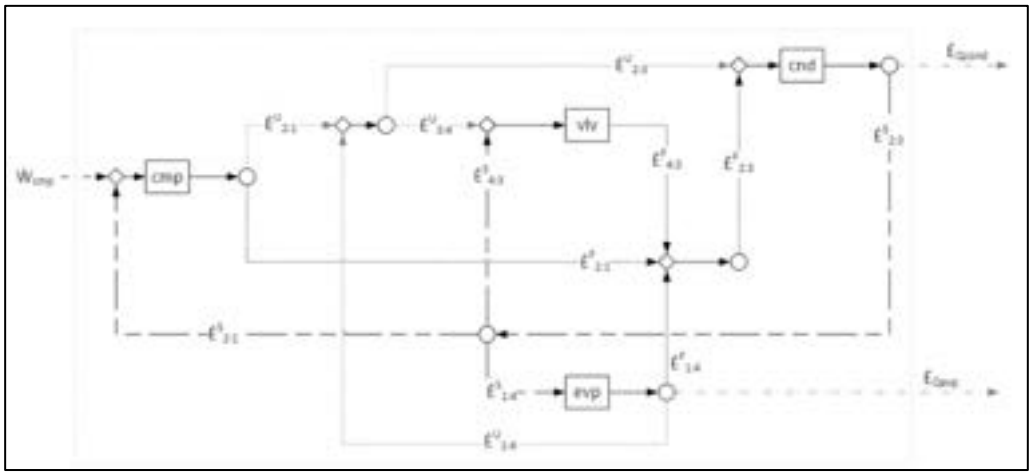

Figure. 7. Productive diagram for the heat pump system using UFS Model.

5.4. A&F Model

The diagram depicted in Figure 8 showcases the use of the A&F Model [22] in the heat pump system for the isolation of valves and the determination of their products and fuels via the utilization of Helmholtz energy (E^A) and flow work (E^F) terms.

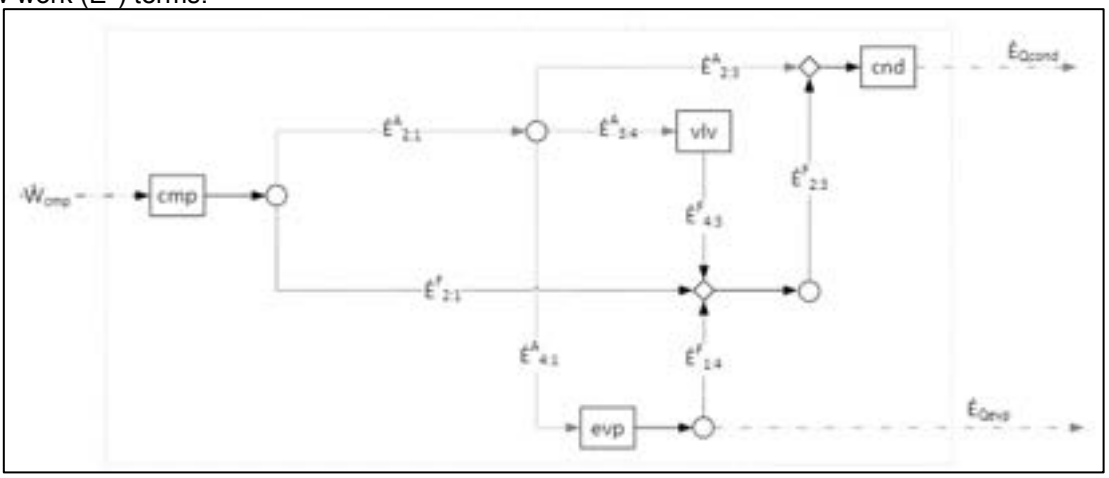

Figure. 8. Productive diagram for the heat pump system using A&F Model.

By employing these terms, the model allows for the appropriate handling of this dissipative component. The pro of the A&F Model over the E Model, in this study, is attributed to its ability to isolate valves. Regarding the UFS model, both models can isolate dissipative components, but the A&F Model achieves this via a simpler exergy disaggregation using only two terms, as opposed to the three terms used by UFS. Consequently, the A&F Model's simplicity and universality are its main advantages. Furthermore, compared to the UFS Model, the A&F Model reduces the number of flows, junctions-bifurcations, and cost equations, resulting in a significantly lower degree of complexity and computational requirements.

5.5. Localized physical exergy disaggregation (E Model – LD).

The localized physical exergy disaggregation [21] is used to disaggregate physical exergy only in dissipative equipment where the total exergy is not enough to define a productive purpose for the equipment. In this case study, the valve is a dissipative equipment, and therefore, the disaggregation of physical exergy into its Helmholtz energy (E^A) and flow work (E^F) terms was only used in the definition of fuel and product for this equipment. It should be noted that other methodologies could be used to isolate the valve as long as fuel and products could be defined. However, in this work, the A&F model was chosen, which is the thermoeconomic model with the fewest exergy terms capable of defining input and output for the valve. In other words, where total exergy can be used, it is used; where it is not possible, the disaggregation of physical exergy is a viable solution. This model has an advantage over other models that use physical exergy disaggregation, as it can isolate the valve with fewer flows. The Figure 9 shows the productive diagram for the heat pump system using localized physical exergy disaggregation.

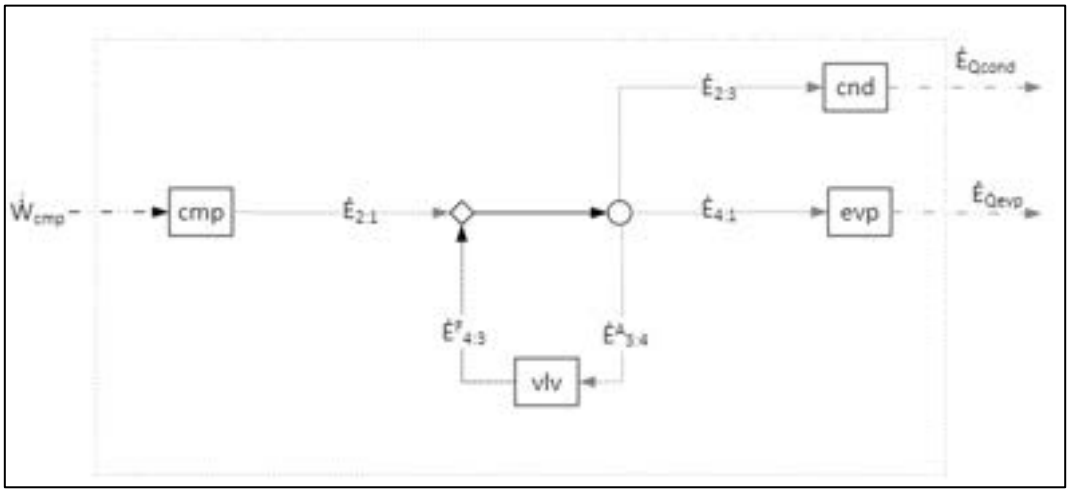

Figure. 9. Productive diagram for the heat pump system using localized physical exergy disaggregation.

6. Results and discussions

The cost allocation models had to determine the unit exergy cost for both heating and cooling, which was a challenge. Regardless of the method used for allocation, the result was a pair of unit exergy costs for both final products that lie along a defined straight line, which can be mathematically represented by Eq. (20).

$$\dot{W}_{cmp} = k_{E_{Qcond}} \cdot \dot{E}_{Q_{cond}} + k_{E_{Qevp}} \cdot \dot{E}_{Q_{evp}} \rightarrow k_{E_{Qcond}} = -\frac{\dot{E}_{Q_{evp}}}{\dot{E}_{Q_{cond}}} \cdot k_{E_{Qevp}} + \frac{\dot{W}_{cmp}}{\dot{E}_{Q_{cond}}} \quad (20)$$

Thus, for each model, as the unit exergy cost of heating increases (k_{EQcond}), the unit exergy cost of cooling (k_{EQevp}) decreases. The six points in Figure 10 represent pairs of unit exergy costs for heating and cooling obtained from the different methods analysed in the study, and they are consistent from a thermoeconomic point of view since they belong to the same straight-line solution.

In Figure 10, it can be observed in the upper corner that when assigning the entire cost of the fuel of the system to a single final product, the unit exergy costs will be (0;2.98) and (17.99;0) for the separately produced of heating and cooling, respectively. In this same region of the Figure 10, it is possible to identify a green square that delimits an area where the costs allocation corresponding to all thermoeconomic methodologies presented in this work are contained, highlighting that the results obtained for the unit exergy costs do not present significant differences. More specifically, when considering all possible thermoeconomic results for the unit exergetic costs of heating and cooling, it is possible to notice that the employed methodologies are concentrated within a specific range, with a variation of around 17.5% for heating and cooling. This observation can be interpreted as an additional indication that these methodologies demonstrate yield similar results with respect to the values found.

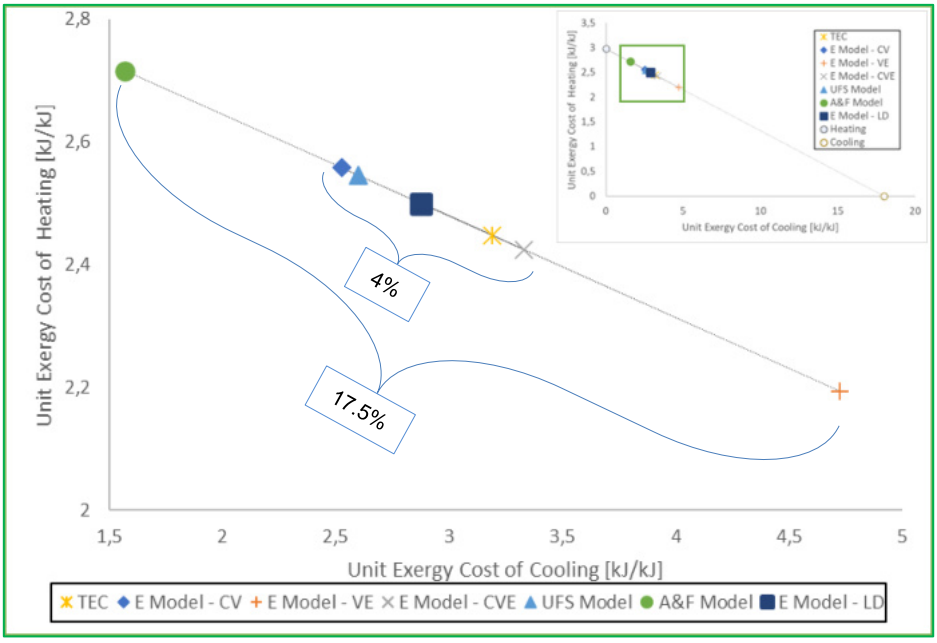

Figure. 10. Results of final unit exergy costs of products

It is not possible to determine which methodology presents the best/right cost through cost allocation, as all the methodologies presented in this study produce coherent results. However, some comparative analysis can be made such as among the three possibilities for using Model E presented in the study. It is observed that associating the valve with the condenser results in the highest cost of heating among the three possibilities, which was expected because all the irreversibility related to the valve is associated with heat, which increases his cost. Associating the valve with the evaporator leads to an increase in the cost of cooling, as all the valve irreversibility is associated with the evaporator. When there is a rational criterion for dividing the irreversibility of the valve (Model E-CVE), an intermediate value is obtained for the costs. It can be observed that the A&F model exhibits the highest unit exergy cost of heating. This can be attributed to the fact that all the irreversibility of the valve is associated as fuel to the condenser, along with a portion of the irreversibility of the evaporator that is also linked as fuel to the condenser (see Figure 8). This is similar to the UFS model. However, in the UFS model diagram, a part of the irreversibility of the condenser returns to the cycle as fuel to the compressor, which slightly reduces the cost of the condenser product.

When analysing the TEC, E Model - CVE, and E Model - LD, it is noted that all of them have an implicit or explicit rule for dividing the irreversibility of the valve for both final products, which results in intermediate costs for these products. It is worth noting that it is more thermodynamically reasonable for the irreversibility of the valve to be divided between both final products. However, not all methodologies presented in this study follow this procedure, possibly due to the subjectivity of the productive diagram, regarding the productive unit interconnection, adopted by the analyst during the implementation of these methodologies. By conducting a more detailed analysis of cost allocation, excluding methodologies that overload the cost of heating (A&F Model and E - CV Model) or cooling (E Model - VE), it can be observed that the methodologies that apply a more rational criterion for dividing valve irreversibility among final products (TEC, E Model - VCE, E MODEL - LD, and UFS Model) are concentrated within a specific range, with a variation of about 4% for heating and cooling. This conclusion is the result of a more rigorous and precise analysis, which allowed for a clearer identification of the methodologies that may be more effective in allocating these costs.

The information presented in Tables 4 – 5 displays the values of fuel (Fu), product (Pr) and irreversibility (Ir) for each individual component of the plant, for each used methodology. It should be noted that although different productive structures (fuel and product) are defined, no matter the methodology, the irreversibility (fuel-product difference) of each component remains the same. Irreversibility is one of the responsible for generating costs in thermoeconomics. However, the methodologies obtain different results since different fuels and products are used for the productive units. It is important to highlight that the costs generated by each productive units depend on the product-fuel ratio (efficiency). Thus, different cost values are obtained for each methodology.

Table 5 presents a comparison between the subsystems merged in the E model. It is observed that, in the E-Model-CV, the irreversibility of the Condenser-Valve subsystem is exactly equal to the sum of the irreversibility of the equipment when they are separated in the other thermoeconomic methodologies. Similarly, the same result can be observed in the E-Model-VE. For the E-Model-CVE, two inputs, two outputs, and two irreversibilities were presented, as the valve is partly merged with the condenser and partly with the valve. Nevertheless, it is still possible to compare the irreversibility, as the sum of the two irreversibilities presented in the E-Model-CVE is the same as the sum of the irreversibility of these subsystems when separated in the other thermoeconomic methodologies.

Table 4. Exergy balances of each productive units of the heat pump system.

Model	Condenser			Valve			Evaporator			Compressor		
	Fu [kW]	Pr [kW]	Ir [kW]	Fu [kW]	Pr [kW]	Ir [kW]	Fu [kW]	Pr [kW]	Ir [kW]	Fu [kW]	Pr [kW]	Ir [kW]
TEC	60.8	37.0	23.8	86.2	76.1	10.1	11.6	6.1	5.5	110.2	82.5	27.7
UFS	349.1	325.3	23.8	17.1	7.1	10.1	261.6	256.1	5.5	126.8	99.2	27.7
A&F	60.8	37.0	23.8	17.1	7.1	10.1	36.8	31.4	5.5	110.2	82.5	27.7
E - LD	60.8	37.0	23.8	17.1	7.1	10.1	11.6	6.1	5.5	110.2	82.5	27.7

Table 5. Exergy balances of the E Models with heat pump subsystem division.

Model	Condenser Valve			Valve Evaporator			Condenser Valve Evaporator			Compressor		
	Fu [kW]	Pr [kW]	Ir [kW]	Fu [kW]	Pr [kW]	Ir [kW]	Fu [kW]	Pr [kW]	Ir [kW]	Fu [kW]	Pr [kW]	Ir [kW]
E - CV	70.9	37.0	33.9	-	-	-	-	-	-	110.2	82.5	27.7
E - VE	-	-	-	21.7	6.1	15.6	-	-	-	110.2	82.5	27.7
E - CVE	-	-	-	-	-	-	67.2 15.2	37 6.1	30.2 9.1	110.2	82.5	27.7

7. Conclusions

This study aimed to present and compare different thermoeconomic methodologies for unit exergy cost allocation in a heat pump system with a dissipative valve. The study focused on presenting different options for treating the valve in thermoeconomic modelling and comparing the advantages and disadvantages of each methodology. The methodologies presented in this study were TEC, E Model, UFS Model, A&F Model, and localized physical exergy disaggregation.

Different models can be used to define fuels and products of subsystems in the presence of a dissipative equipment like a valve. The E Model uses total exergy, but it can be challenging to assign a productive purpose to the valve. The UFS Model is more complex but allows for the isolation of the valve. The A&F Model isolates valves using Helmholtz energy and flow work terms, reducing complexity and computational requirements when compared with UFS Model. Finally, localized physical exergy disaggregation can disaggregate physical exergy only in dissipative equipment, like valves, where total exergy is not enough to define a productive purpose. It is important to observe that while the models define different productive structures, with different fuels and products utilized in each production unit, the irreversibility of each component remains constant. Therefore, it can be concluded that the models are consistent with thermodynamic principles.

The results demonstrate that although each methodology presents different results, the differences are not significant. Therefore, the methodology to be used will depend on various factors, such as the need to have disaggregated equipment or not. Regarding the E Model - CV and E Model - VE, it was observed that they tend to overload the cost of heating and cooling, respectively. Conversely, the UFS and A&F Models disaggregate the valve but were presented in this study using the productive diagram, which may have some arbitrariness in relation to connections, due to the use of productive flow only. Thus, for these methodologies, the use of the comprehensive diagram, which combines both productive and physical flows, may be a more appropriate option, since the TEC method, which uses physical flows, presents an intermediate cost.

When considering all possible thermoeconomic results, i.e., all the solution straight line, the obtained results are concentrated within approximately 17.5% of the line. However, excluding methodologies that overload the cost of heating or cooling, this value would drop to 4%, which indicates that these methodologies did not produce significantly distinct results.

In conclusion, this study provides valuable insights for future decisions in thermoeconomic modelling and highlights the importance of a suitable productive structure to explain the productive function of the subsystems and flows present in the physical structure of the plant.

Acknowledgments

The authors would like to thank the Support Foundation of Espírito Santo Research (FAPES), the Federal University of Espírito Santo (UFES), the Federal Institute of Espírito Santo (IFES), the National Council for Scientific and Technological Development (CNPq, Brazil), This study was financed in part by the Coordenação de Aperfeiçoamento de Pessoal de Nível Superior – Brasil (CAPES) – Finance Code 001, the University of Zaragoza (Unizar), the Government of Aragon (Ref: T55-20R) and Viana S.A. Thermoelectric Power Plant - TEVISA for their financial support.

Nomenclature

Latin

A	Helmholtz energy [kJ]
a	Specific Helmholtz energy [kJ/kg]
A&F	Helmholtz energy and flow work
cmp	compressor
cnd	condenser
E	Physical exergy
evp	evaporator
evp	evaporator
F	Flow work [kJ]
H	Enthalpic term [kJ]
h	Specific enthalpy [kJ/kg]
Ir	Irreversibility
k	Exergetic unit cost [kW/kW]
LD	Localized physical exergy disaggregation
P	Pressure [kPa]
Q	heat exergy
S	Entropy [kJ/K]
s	Specific entropic [kJ/kgK]
T	Temperature [°C or K]
TEC	Theory of the exergetic cost
trb	turbine
U	Internal energy [kJ]
UFS	Internal energy, flow work, entropic term
v	Specific volume [m³/ kg]
vlv	valve
Y	thermodynamic magnitudes
$\dot{m}$	Mass flow [m³ /s]

Greek

η	efficiency
x	quality

Subscript

0	Environmental conditions
cnd	condenser
evp	evaporator
F	Fuel
i	Internal flow
in	Inlet
out	Outlet
ph	Physical
trb	turbine
vlv	valve

References

[1] Keenan, J.H. A Steam Chart for Second Law Analysis. Mechanical Engineering 1932, 54, 195–204.

[2] Abusoglu, A.; Kanoglu, M. Exergoeconomic Analysis and Optimization of Combined Heat and Power Production: A Review. Renewable and Sustainable Energy Reviews 2009, 13, 2295–2308, doi:10.1016/j.rser.2009.05.004.

[3] Tribus, M.; Evans, R.B. A Contribution to the Theory of Thermoeconomics.; Los Angeles, CA, USA, 1962;

[4] El-Sayed, Y.M.; Evans, R.B. Thermoeconomics and the Design of Heat Systems. Journal of Engineering for Power 1970, 92, 27–35, doi:10.1115/1.3445296.

[5] El-Sayed, Y.M. The Thermoeconomics of Energy Conversions; Elsevier: Amsterdam ; Boston, 2003; ISBN 978-0-08-044270-9.

[6] Valero, A.; Lozano, M.A.; Serra, L.; Tsatsaronis, G.; Pisa, J.; Frangopoulos, C.A.; von Spakovsky, M.R. CGAM Problem: Definition and Conventional Solution. Energy 1994, 19, 279–286, doi:10.1016/0360-5442(94)90112-0.
[7] Frangopoulos, C.A. Thermo-Economic Functional Analysis and Optimization. Energy 1987, 12, 563–571, doi:10.1016/0360-5442(87)90097-1.
[8] Frangopoulos, C.A. Application of the Thermoeconomic Functional Approach to the CGAM Problem. Energy 1994, 19, 323–342, doi:10.1016/0360-5442(94)90114-7.
[9] von Spakovsky, M.R. Application of Engineering Functional Analysis to the Analysis and Optimization of the CGAM Problem. Energy 1994, 19, 343–364, doi:10.1016/0360-5442(94)90115-5.
[10] Lozano, M.A.; Valero, A. Theory of the Exergetic Cost. Energy 1993, 18, 939–960, doi:10.1016/0360-5442(93)90006-Y.
[11] Valero, A.; Lozano, M.A.; Serra, L.; Torres, C. Application of the Exergetic Cost Theory to the CGAM Problem. Energy 1994, 19, 365–381, doi:10.1016/0360-5442(94)90116-3.
[12] Tsatsaronis, G.; Winhold, M. Exergoeconomic Analysis and Evaluation of Energy-Conversion Plants—I. A New General Methodology. Energy 1985, 10, 69–80, doi:10.1016/0360-5442(85)90020-9.
[13] Tsatsaronis, G.; Pisa, J. Exergoeconomic Evaluation and Optimization of Energy Systems - Application to the CGAM Problem. Energy 1994, 19, 287–321, doi:10.1016/0360-5442(94)90113-9.
[14] Lazzaretto, A.; Tsatsaronis, G. SPECO: A Systematic and General Methodology for Calculating Efficiencies and Costs in Thermal Systems. Energy 2006, 31, 1257–1289, doi:10.1016/j.energy.2005.03.011.
[15] Frangopoulos, C.A.; von Spakovsky, M.R. A Global Environomic Approach for Energy Systems Analysis and Optimization (Part I and Part II). In Proceedings of the Proceedings of International Conference on Energy Systems Analysis and Ecology; Cracow, Poland, 1993.
[16] Valero, A.; Usón, S.; Torres, C.; Stanek, W. Theory of Exergy Cost and Thermo-Ecological Cost. In Thermodynamics for Sustainable Management of Natural Resources; Stanek, W., Ed.; Springer, 2017; pp. 167–202.
[17] Boyano, A.; Morosuk, T.; Blanco-Marigorta, A.M.; Tsatsaronis, G. Conventional and Advanced Exergoenvironmental Analysis of a Steam Methane Reforming Reactor for Hydrogen Production. J Clean Prod 2012, 20, 152–160, doi:10.1016/j.jclepro.2011.07.027.
[18] Erlach, B.; Serra, L.; Valero, A. Structural Theory as Standard for Thermoeconomics. Energy Convers Manag 1999, 40, 1627–1649, doi:10.1016/S0196-8904(99)00057-6.
[19] Santos, J.J.C.S.; Nascimento, M.A.R.; Lora, E.E.S.; Martínez-Reyes, A.M. On the Negentropy Application in Thermoeconomics: A Fictitious or an Exergy Component Flow? International Journal of Thermodynamics 2009, 12, 163–176.
[20] Lourenço, A.B.; Nebra, S.A.; Santos, J.J.C.S.; Donatelli, J.L.M. Application of an Alternative Thermoeconomic Approach to a Two-Stage Vapour Compression Refrigeration Cascade Cycle. Journal of the Brazilian Society of Mechanical Sciences and Engineering 2015, 37, 903–913, doi:10.1007/s40430-014-0210-7.
[21] Santos, R.G.; Faria, P.R.; Belisario, I.C.; Barrone, M.A.; Santos, J.J.C. On the Localized Physical Exergy Disaggregation for Dissipative Component Isolation in Thermoeconomics. Revista de Engenharia Térmica 2020, 19, 63–69, doi:10.5380/reterm.v19i2.78618.
[22] dos Santos, R.G.; Lourenço, A.B.; de Faria, P.R.; Barone, M.A.; Santos, J.J.C.S. A New Exergy Disaggregation Approach for Complexity Reduction and Dissipative Equipment Isolation in Thermoeconomics. Entropy 2022, 24, 1672, doi:10.3390/e24111672.
[23] Valero, A.; Serra, L.; Uche, J. Fundamentals of Exergy Cost Accounting and Thermoeconomics. Part I: Theory. J Energy Resour Technol 2006, 128, 1–8, doi:10.1115/1.2134732.
[24] Kotas, T.J. The Exergy Method of Thermal Plant Analysis; 2nd ed.; Elsevier, 1985; ISBN 9780408013505.
[25] Valero, A.; Serra, L.; Uche, J. Fundamentals of Exergy Cost Accounting and Thermoeconomics. Part I: Theory. J Energy Resour Technol 2006, 128, 1–8, doi:10.1115/1.2134732.
[26] Wang, Y.; Lior, N. Fuel Allocation in a Combined Steam-Injected Gas Turbine and Thermal Seawater Desalination System. Desalination 2007, 214, 306–326, doi:10.1016/j.desal.2007.01.001.
[27] Nguyen, C.; Veje, C.T.; Willatzen, M.; Andersen, P. Exergy Costing for Energy Saving in Combined Heating and Cooling Applications. Energy Convers Manag 2014, 86, 349–355, doi:10.1016/j.enconman.2014.05.040.
[28] F-Chart Software Engineering Equation Solver - EES 2017.
[29] Lozano, M.A.; Valero, A. Thermoeconomic Analysis of Gas Turbine Cogeneration Systems. ASME, NEW YORK, NY,(USA). 1993, 30, 311–320.
[30] Barone, M.A.; Santos, R.G. dos; Faria, P.R. de; Lorenzoni, R.A.; Lourenço, A.B.; Santos, J.J.C.S. On the Arbitrariness and Complexity in Thermoeconomics Due to Waste Cost and Supplementary Firing Treatment. Engineered Science 2022, 17, 328–342, doi:10.30919/es8e624.

ULPGC
Universidad de
Las Palmas de
Gran Canaria

grres ULPGC
group for the research on renewable energy systems

C. Heat and mass transfer

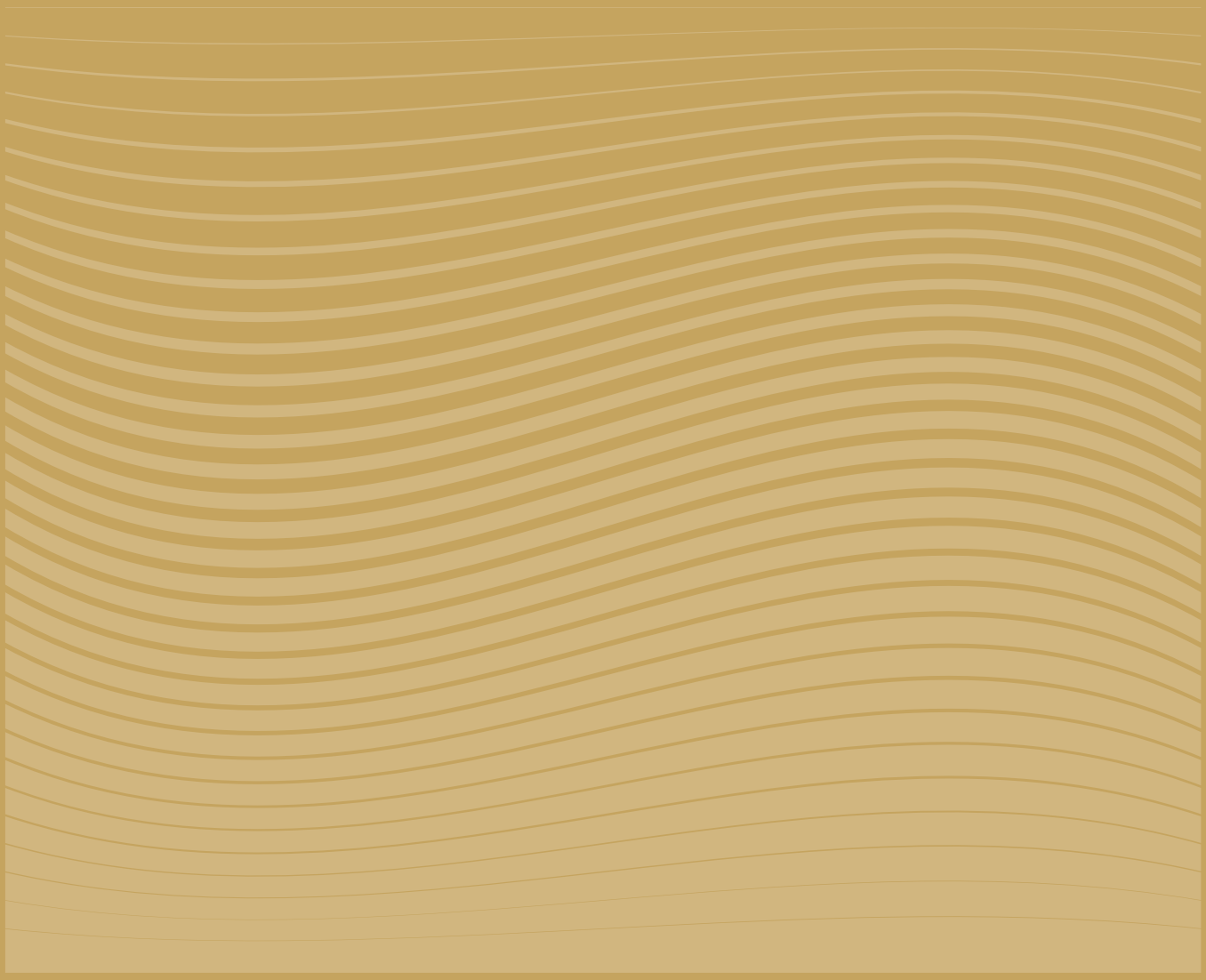

ECOS2023

Application feasibility of low temperature cooling tower for high-temperature buildings to daytime ventilation

Tejero-González, Ana[a]; Andrés-Chicote, Manuel[b]; Velasco-Gómez, Eloy[c]; Salins, Sampath Suranjan[d]

[a] Dept. Energy Engineering and Fluidmechanics, Universidad de Valladolid, Valladolid, Spain, ana.tejero@uva.es, CA
[b] Dept. Energy Engineering and Fluidmechanics, Universidad de Valladolid, Valladolid, Spain, manuel.andres.chicote@uva.es
[c] Dept. Energy Engineering and Fluidmechanics, Universidad de Valladolid, Valladolid, Spain, eloy.velasco.gomez@uva.es
[d] School of Engineering and IT, Manipal Academy of Higher Education, Dubai Campus, UAE, sampath@manipaldubai.com

Abstract:

An experimental study has been carried out to characterise a laboratory-scale cooling tower (CT) intended to provide water to a high temperature radiant cooling system during night-time. The present study evaluates the possibility of broadening its operation during daytime to precool the outdoor airflow required for ventilation during occupation periods. The performance of the CT combined with a water-to-air coil demonstrates that its operation within a water-economiser cycle would result into energy savings and better indoor air quality (IAQ) for most summer conditions studied, with the only exception of humid tropical climates. The few non-interesting locations can be easily identified regarding the corresponding Köppen-Geiger climate classification, and relative energy efficiency of the system at different climates is rather foreseeable through the local wet bulb depression (WBD) bin data. This leads to the conclusion that a CT designed to fed TABS during night-time can efficiently operate during diurnal occupation periods to remove ventilation loads of the required dedicated outdoor air system (DOAS) or support the additional mechanical cooling if required, with little initial cost.

Keywords:

Cooling Tower; Free cooling; Water-side economiser; Ventilation air cooling; ANOVA.

1. Introduction

Current research and policies being developed towards less energy-consuming buildings aim for energy efficient strategies to achieve indoor comfort. Improvements in cooling systems are key steps on this path, given the growing trends on energy consumption for space cooling due to global warming and urban heat islands, in addition to the quality of life expectations of a population that spends more and more time indoors.

Ventilation rates have such an impact on buildings energy requirements that it may result appealing to try to minimise them. However, it is essential to avoid compromising IAQ, and in this sense strategies such as heat recovery, demand control or free cooling are targeted as possible solutions (1).

Research conducted on Thermally Activated Building Systems (TABS) for space cooling is gaining interest due to higher cool water temperatures required, but a Dedicated Outdoor Air System (DOAS) would be always required to fulfil ventilation rates established in the standards (2).

Among the number of existing alternatives designed to simultaneous and efficiently achieve indoor thermal comfort and IAQ, those based in the free-cooling potential of outdoor conditions are particularly appealing. Low temperature cooling towers (CT) can efficiently exploit this free-cooling potential for either cool ventilation air or fed high temperature water cooling systems, though to date little research work has been focused on the characterisation of these CT (3,4). In the present paper it is aimed to maximise this free-cooling potential by enabling a CT designed to operate during favourable night-time outdoor conditions for TABS cooling, to extend its operating hours during daytime within a water-economiser cycle for ventilation air cooling.

1.1. Water-Economiser cycles

The simplest solution of directly use cool outdoor air as ventilation air is the only one that could simultaneously improve energy efficiency and IAQ when higher airflows are supplied (5,6). The implementation of this all-air free-cooling solution is called air-side economiser cycle, and in principle it is always interesting in ventilation

systems because it can minimise or even avoid mechanical cooling requirements if outdoor conditions are favourable. However, it incurs in also higher fan requirements.

Some research work focused on this particular issue. Wang and Song (7) approached it considering a steady-state study in terms of operating conditions and auxiliary fan power consumption, to design the optimal control for an air handling unit (AHU) equipped with an economiser cycle. They determined the optimal supply temperature and airflow for three different operating zones of (I) 100% free-cooling, (II)partially assisted mechanical cooling and (III) minimum airflow supplied, obtaining energy savings of up to 90%. Rackes and Waring (8) also defined ranges of optimal temperature set-points and airflows for different building zones and periods along a representative day in different seasons. On contrary, from their analysis of the impact of changing the ventilation rate on the energy demand, Santos and Leal (1)obtained for the European climatology a general lowering of the yearly cooling demand if ventilation rates are increased. Hence, their results showed variations on the cooling demand from -0.01 to -0.16 kWh/(m^2·year) when ventilation rate was changed in 1m^3/(h·person). Besides being favourable for every case studied, they concluded that, although results depended on the building type and use, climate is the determinant factor in the case of new buildings in general. They all nonetheless agreed in combining different systems with an adequate control to optimise energy savings at each operating conditions.

Control is the core in economiser cycles, which can be on a temperature or enthalpy basis. Although the latter can in principle be more energy-saving, its further complexity and relative precision make temperature control generally more interesting, provided that climate is not excessively humid. A fixed-dry bulb temperature control can then be interesting if set-temperatures are adequately defined according to the climate (5). Hence, limitations of these systems are intrinsically related to climate conditions. When outdoor conditions are beyond the psychrometric region of interest for air-side economisers applicability, they can still be interesting for water-side economisers operation. This is because water-side economisers exploit outdoor air free-cooling potential indirectly, by cooling water in a CT that later passes through a coil where ventilation air is cooled. However, additional electric power requirements due to fans and pumps would have considerable weight in this case, thus restricting the range of applicability more importantly.

Although free-cooling potential for different climate conditions and the related energy savings have been extensively studied for air-side economisers for different locations and cases (9), water-economisers have not been so widely approached.

Kim et al. (10) proposed a water-side free-cooling system to provide cooling water required in a liquid desiccant system assisted with evaporative cooling that operates with 100% outdoor air. A range of hot and humid conditions of dry bulb temperature (DBT) between about 20 and 32°C, and wet bulb temperature (WBT) from about 20 to 25°C were tested for the CT operation. With this combined system they obtained COPs of 3 to 20 times those expected for a conventional chiller. They also obtained important reductions in the chilling demand through a similar system proposed for a Data Centre (11).

Most research work on economisers applications focused on Data Centres, due to the large cooling demands involved in these applications, which lead to the existence and development of further numerous technologies to efficiently provide the required cooling (12–14). Air-side economisers are particularly appealing for higher energy savings are expected, as demonstrated by Cho et al. (15) for subtropical climates. However, some authors have directed their studies to specific implementations of water-side economisers because of the requirements on air cleanliness and humidity, besides the advantages on the system's integration within the central cooling system (16). Ham and Jeong (16) demonstrated through an annual simulation of a water-side economiser modelled in EnergyPlus, that this system would always result into energy savings with respect to cooling consumptions in Data Centres. If a proper design of the Data Centre is developed (that is, an aisle contained instead of uncontained Data Centre) higher supply temperatures could be set, thus enlarging the number of operating hours and consequently the energy savings. Agrawal et al. (17) compared various strategies to improve efficiency in air cooling for Data Centres at different locations of 17 climate types. Among them, they proposed configurations of 1 or 2 cooling towers to provide cooling water that is later used to precool water used in the AHU. Results showed that interest of water-side economisers increased for colder climates and that a two-cooling tower configuration would improve energy savings in some cases. Interest of water-side economiser over indirect evaporative cooling strategies focused on its less water consumptions.

As could be expected, efficiency of water-side economisers also depends on the season. Durand-Estebe et al. (18) obtained, through simulation in TRNSYS of different water-side economiser strategies in a Data Centre, optimal temperature set-points of 20°C during Winter, whereas it rises to 24°C for mid-season operation at a Mediterranean mild climate. However, these optimal set-points would differ for different case studies in terms of air-cooling production or control strategy. Hence, they proposed a control that adapts to the outdoor climate operating conditions.

On the overall, water-side economisers have been demonstrated to be effective. However, as also stated for air-side economisers, actual energy savings may not always be significant due to extra fan and pump power consumption. Durand-Estebe et al. (18) disregarded the power required by water pumps in water-side

economiser cycles, though payed close attention to extra fan power required when air temperature set is raised. They in fact obtained an increase in the fan energy consumption of 43% when air temperature is modified from 16°C to 24°C to optimise energy savings by reducing heat pump energy requirements by 78%.

Besides, the installation is voluminous and costly, so it would be only reasonable if energy savings obtained balance out the initial investment, costs of water consumption and maintenance of the CT (17–19). Nonetheless, initial cost can be justified through the expected energy savings (10).

The aim of the present study is to assess the energy savings potential of expanding the operation of a CT designed for TABS, towards daytime operation in a water-economiser cycle, either to remove ventilation loads or to precool supply air when thermal comfort is not achieved by means of the TABS and additional cooling is required.

2. Methodology

A laboratory-scale device has been designed and constructed. It consists of a low temperature CT combined with an external finned coil as a water-to-air heat exchanger. This system would permit the pre-cooling of ventilation air through the coil with water previously cooled in the tower.

The target was to experimentally characterise the operation of this system in diurnal summer air conditions, to study the possibilities of expanding the operating period of low temperature cooling towers implemented for night-time water cooling for TABS, to daytime operation for cooling ventilation air.

2.1. Cooling tower

The experiments are conducted with the open, forced draft wet cooling tower shown in Figure 1.

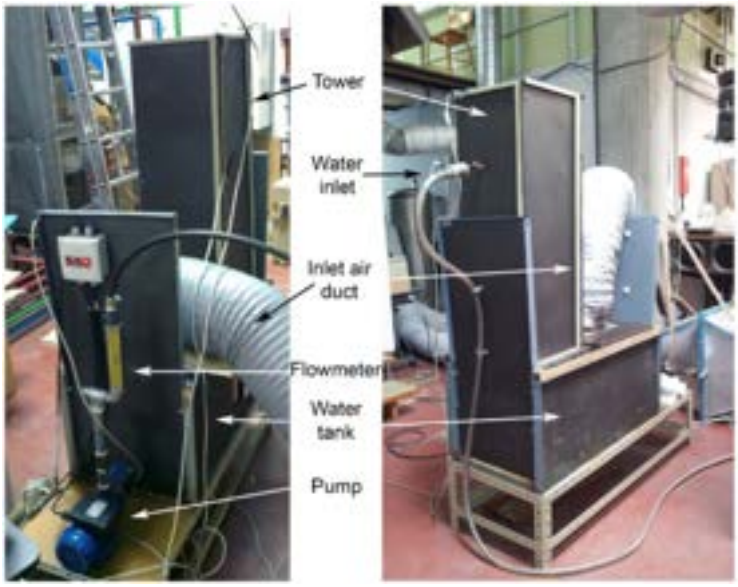

Figure. 1. Low temperature cooling tower used for the tests.

Water is sprayed from the upper part of the tower with the aid of a set of nozzles. The tower is equipped with a droplet separator at the air outlet to avoid generation of aerosols and unnecessary water losses. The packing consists of polycarbonate panels with a structure of hexagonal cells, offering a total exchange area of 13,5 m^2, which results in a surface density of 370 m^2/m^3. The water tank has a total capacity of 100 l; water level can be controlled with a level-viewer in the tank and is maintained at 60 l. Air enters the tower through a separate orifice in the same water tank, generating the desired counter-flow through the tower filling. Cooled water in the tank is then driven to the coil by a water pump placed at the water tank exit, and from the coil to the tower nozzles.

A copper-tube aluminum-fin coil is employed to pre-cool ventilation air with the aid of water cooled in the tower. It consists of staggered tubes of 3/8'' and 3.2mm separation between fins, arranged in 4 columns and 12 rows. Its total dimensions are 320x320x90mm. The coil is assembled within a structure to which the air ducts for ventilation air are connected.

The approach of the tower results to be about 5°C, which falls within the expected achievable range in practice (20). This high value is due to the also high outdoor air operating temperatures tested in the study, which has an important influence on the CT performance owing to results in existing literature (3,10). The outdoor DBT is also decisive for the approaching temperature, according to the Analysis of Variance (ANOVA) performed from the experimental results obtained in the present work (figure 2.a). However, the approaching temperature could be reduced by increasing the air flow rate (3,4), as observed in figure 2.b.

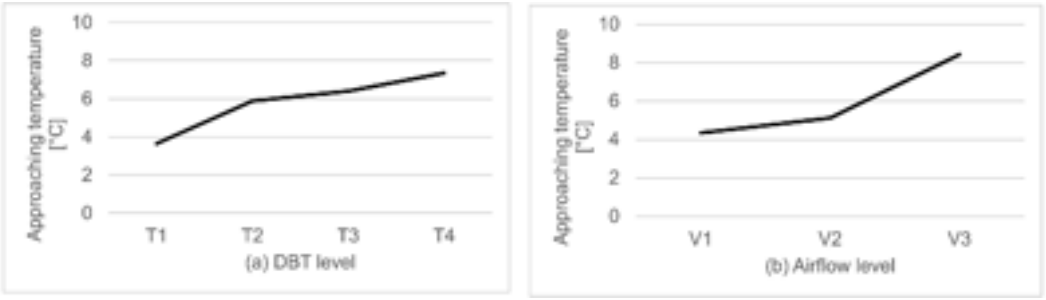

Figure. 2. Average approaching temperatures in the CT for increasing (a) outdoor air DBT; and (b) air flow rate.

This high approach justifies the limited effectiveness obtained in the tower (figure 3), as the effectiveness of the tower is calculated from the water temperature drop achieved in the tower to the maximum temperature drop achievable (1):

$$\varepsilon_T = (T_{Tw\,i} - T_{Tw\,o})/(T_{Tw\,i} - \mathrm{T}_{wb\,Ta\,i}) \quad (1)$$

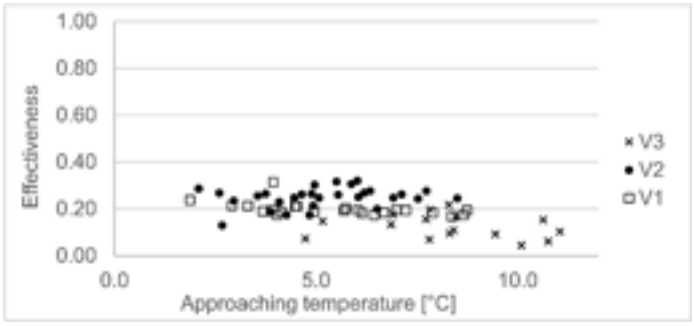

Figure. 3. CT effectiveness to approaching temperatures obtained for different air flows.

2.2. Test bench

The cooling tower and the coil are connected together as illustrated in figure 4. Air supplied to both the CT and the coil is conditioned by an Air Handling Unit that enables the system to operate at the different outdoor conditions defined in the design of experiments. Water cooled in the tower would be automatically driven to the TABS during night-time, and to the coil for diurnal operation, switched when the building becomes occupied. Ventilation air pre-cooled in the coil would be supplied to the conditioned space.

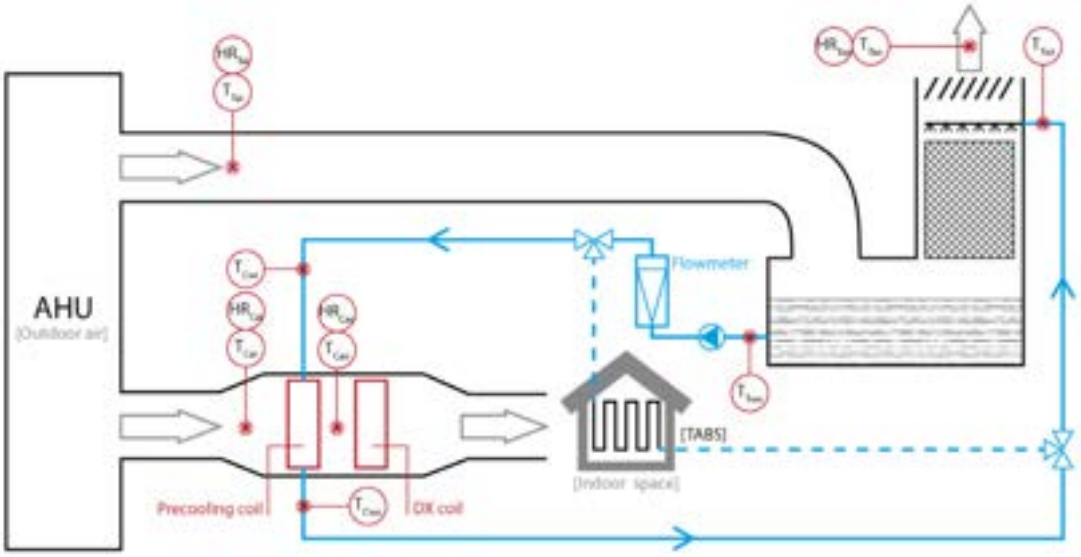

Figure. 4. Configuration of the combined system.

Measurements of air DBT and RH are acquired at the air inlet and outlet of the CT and the coil, as indicated in figure 4. Also, water temperatures are measured in the water circuit at the inlet and outlet of both the coil

and the tower. Water flow is measured with a variable area flowmeter at the outlet of the water tank, with ±2% accuracy and range from 1.5 to 10 l/min. Air flow is measured through the pressure drop obtained in orifice plates placed in the air ducts downstream the AHU plenum for air distribution.

Temperature sensors are 4-wired Pt-100 with accuracy of ±0.1°C and range from 50 to 250°C. They have been calibrated before the tests with a calibration oven.

RH sensors are capacitive type, ±2% stability and 0 to 100% range, also previously calibrated to a reference sensor.

Pressure drop is measured with differential pressure sensors placed upstream and downstream enough of the two orifice plates. These orifice plates have been previously calibrated with a reference nozzle.

2.3. Design of experiments

Table 1 presents the design of experiments. Three levels of airflow are studied, while the water flow is fixed at 4 l/min (and thus not reflected in table 1). This is because only water-to-air flow ratios are of interest (3). The consequent operating water-to-air ratios are of about 1.5, 0.9 and 0.8 for levels V1, V2 and V3, respectively. Four levels of outdoor air DBT and another four levels of wet bulb temperature (WBT) are proposed. These levels are selected to cover the widest range of probable diurnal outdoor air conditions during summer period. Conditions for the set T1-W4 belong to the fog region and are thus disregarded; consequently, a total of 90 tests have been developed.

Table 1. Design of experiments.

FACTORS					
V	(m^3/h)	DBT	(°C)	WBT	(°C)
V1	150	T1	25	W1	18
V2	250	T2	30	W2	21
V3	300	T3	35	W3	24
		T4	40	W4	27

An AHU is used to reproduce the desired outdoor conditions, as shown in figure 4. Because the variable controlled in the AHU was the relative humidity, for each pair of DBT – WBT the corresponding RH was calculated, then established as the set condition in the AHU together with the DBT. These operating conditions are tested in an arbitrary order and twice to check repeatability. Those tests where repeatability was not observed, were developed again and the less reliable tests were disregarded.

3. Results and discussion

3.1. Ventilation and cooling potential

3.1.1. Air temperature drop in the coil

Figures 5.a) to c) show the air temperature drop obtained in the coil for the different inlet airflow rate, DBT and WBT. It can be observed that ventilation air cooling in the coil is influenced by its initial DBT (T_{Cai}) and WBT ($T_{wb\ Cai}$). Higher T_{Cai} result into larger temperature drops because the air DBT at the inlet determines the logarithmic mean temperature difference (LMTD). But, to understand how $T_{wb\ Ca\ i}$ affects air cooling achieved in the coil, it must be noticed that outdoor air is used both as operating air in the tower and as ventilation air in the coil ($T_{Cai}=T_{Tai}$; $T_{wb\ Cai}=T_{wbTai}$). Because the WBT determines the water temperature achieved at the outlet of the cooling tower (T_{Two}), then driven to the coil, $T_{wb\ Ca\ i}$ also influences the LMTD, though indirectly. Increasing T_{ai} yields larger air-to-water temperature differences in the coil. Likewise, both higher T_{ai} and lower $T_{wb\ a\ i}$ foresee larger water cooling in the tower, hence larger air-to-water temperature differences and then air temperature drops in the coil.

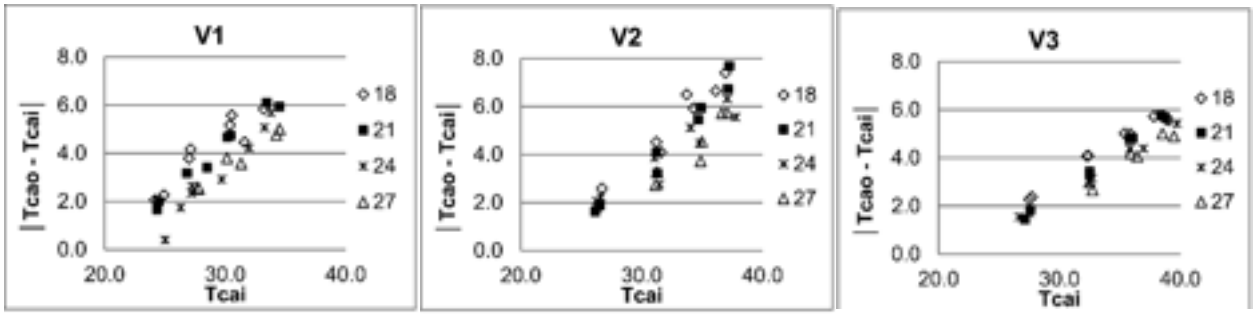

Figure. 5. Experimental air temperature drop through the coil for airflows (a) V1, (b) V2, and (c) V3.

The ANOVA demonstrate a main contribution of T_{Cai}, of 65% on the temperature drop, and a contribution of $T_{WB\ C\ ai}$ of 15%. Effect of airflow is limited to 8%, and the remaining effect comprehends the effect of dual and three factors interactions, as well as a remaining non-determined contribution.

3.1.2. Ventilation air cooling capacity

Because only sensible cooling is performed through the coil, x_{Ca} would be constant and ventilation air cooling can be obtained as expressed in equation (2):

$$\dot{Q}_{Ca} = \dot{m}_{Ca} \cdot (Cp_a + Cp_v \cdot x_{Ca}) \cdot \Delta T_{Ca} \quad (2)$$

Figure 6 represents air cooling achieved in the coil in terms of the the wet bulb depression (WBD), which is defined as the difference between the outdoor air DBT and its WBT. For the same reason derived from previous figures 5.a) to c), it can be observed that increasing the outdoor air WBD result in larger heat transferred from the air cooled in the coil. This is due to better evaporative cooling potential in the tower under larger WBD, hence larger water temperature range, which is afterwards used to cool the ventilation airstream in the coil. In this case, there is greater influence of the airflow rate, due to the same definition of equation (2).

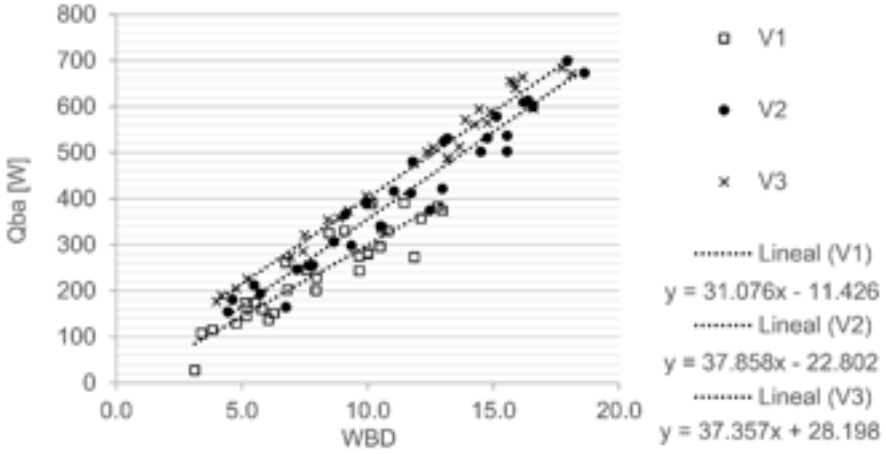

Figure. 6. Air cooling achieved in the coil at different outdoor air conditions and ventilation airflows.

The ANOVA developed on this parameter showed a main dependency on airflow, of 50%, being the contribution of T_{Cai} a 35% whereas $T_{wb\ Ca\ i}$ accounts for only 8%. The remaining effect is similarly distributed between the effect of the three possible pairs of factors interaction and a non-determined error.

Consequently, although harsher outdoor air conditions entrain larger thermal loads, they also yield better performance. This point agrees with the idea stated by Ma et al. (21) that the external environment at the same time hinders the building autonomy and benefits the building homeostasis.

3.1.3. Coil thermal effectiveness.

Another interesting parameter to be considered concerning the coil operation is its thermal effectiveness. According to the ε-NTU method, thermal effectiveness of the coil can be defined as (3):

$$\varepsilon_c = (T_{Cao} - T_{Cai})/(T_{Cao} - T_{Cwi}) \quad (3)$$

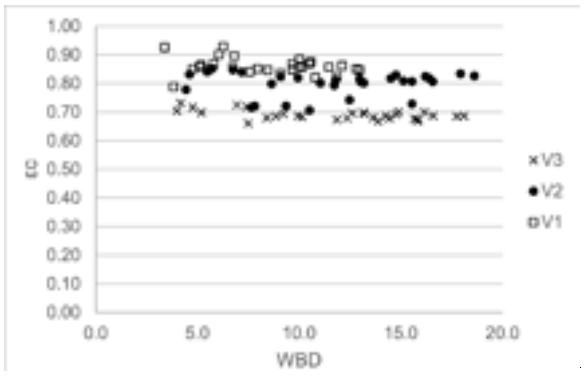

Figure. 7. Thermal effectiveness in the coil.

Figure 7 shows that the difference between T_{Cai} and the $T_{wb\ Ca\ i}$ has no effect. However, higher airflows imply shorter residence times and thus lower air temperature drops, hence smaller thermal efficiencies. This idea agrees with the results of the ANOVA on this parameter, as the contribution of the airflow rate is 82%.

3.2. Total cooling application

In this section, daytime operation of the cooling tower is studied as a mean to remove the ventilation loads generated by the required DOAS for TABS. The TABS are cooled with the night-time operation of the CT as the only cooling source and no further mechanical cooling is required during occupation times. The adaptive thermal comfort criteria can be fairly considered under these conditions.

The adaptive thermal comfort criteria is regarded in the existing European standards on indoor environment ([23] EN 16798-1:2019 Standard: Energy Performance of Buildings. Ventilation for Buildings. Part 1: Indoor Environmental Parameters for Design and Assessment of Energy Performance of Buildings Addressing Indoor Air Quality, Thermal Environment, Lighting and Acoustics. Module M1-6., n.d.) as suitable when there is no mechanical cooling and occupants can adapt to the thermal conditions by operating windows or modifying their clothing.

Some authors conceive adaptive comfort for buildings where TABS are implemented for thermal mass cooling, if water cooling demand is supported through low energy means. Whether considering adaptive or conventional thermal comfort models for TABS is thoroughly studied by Sourbron and Helsen (23). According to these authors every criterion would be valid in these cases, but they highlight that the key of the decision among existing models lays on the conflict between energy savings and strict comfort requirements. Pfafferot et al. (24) state that buildings with TABS fed by ground cooling should be considered as ‘‘mixed-mode buildings’’, and decide to consider the adaptive models. They nonetheless concede that further research on their applicability for these cases would be needed. The suitability of adaptive thermal comfort models for radiant cooling panels with water cooled in a CT is evaluated by Memon et al. (25), obtaining adequate indoor conditions in naturally ventilated spaces.

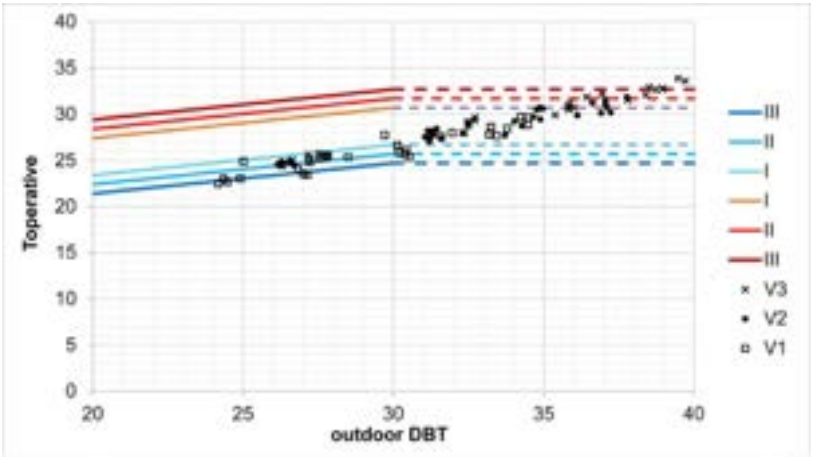

Figure. 8. Temperatures achieved in the ventilation air precooled in the coil and adaptive comfort ranges to be expected.

To study whether the cooling tower could support ventilation loads during its daytime operation, it would be enough to pay attention to supply air temperatures reached in the coil. These are represented in figure 8 within the ranges of adaptive comfort defined in the European standard ([23] EN 16798-1:2019 Standard: Energy Performance of Buildings. Ventilation for Buildings. Part 1: Indoor Environmental Parameters for Design and Assessment of Energy Performance of Buildings Addressing Indoor Air Quality, Thermal Environment, Lighting and Acoustics. Module M1-6., n.d.). Because comfort ranges for the adaptive criterion are not defined for outdoor air DBT over 30°C, trends have not been extrapolated, and the corresponding limits for 30°C have been considered for temperatures over this value. Besides, cases between 25°C and 30°C are scarce, being anyhow limited the validity of its application.

Figure 8 shows that supply air temperatures are maintained within the comfort ranges, except from the cases when the harshest outdoor conditions occur working with the highest airflow rate. For these cases, as well as for those when TABS and the night-time operation cooling tower as the only cooling source are insufficient, additional cooling would be needed during daytime occupation, and adaptive comfort criteria would not be acceptable.

3.3. Air precooling application

If additional mechanical cooling is required to achieve comfort, then the adaptive thermal comfort criteria would no longer be applicable, and the water-economiser cycle would just reduce the energy demand required by the conventional chilling system.

The energy savings achievable through the water-economiser cycle are calculated for various locations at different summer climate types. Four cities Worldwide and then seven Spanish cities have been selected and compared to assess the climate applicability of the CT. The considered cooling season spans from May to September for the Northern Hemisphere and from November to March for the Southern Hemisphere.

Worldwide cities selected correspond to the following Köppen-Geiger climate classification (26): (a) London, UK (Cfb: Temperate climate without dry season, warm summer); (b) Sydney, Australia (Cfa: Temperate climate without dry season, hot summer); (c) Las Vegas, US (Bwh: Arid, desert, hot climate); and (d) Singapore (Af: Tropical, rainforest). Climate data used in the study is obtained from Meteonorm databases (27).

Results obtained for the three airflow levels tested are gathered in table 2. Operating periods are calculated for a base temperature of 25°C, as an upper limit set-temperature for indoor thermal comfort in offices in summer ([23] EN 16798-1:2019 Standard: Energy Performance of Buildings. Ventilation for Buildings. Part 1: Indoor Environmental Parameters for Design and Assessment of Energy Performance of Buildings Addressing Indoor Air Quality, Thermal Environment, Lighting and Acoustics. Module M1-6., n.d.). Consequently, number of operating hours corresponds to the summer occupation periods (May to September between 8 a.m. and 8 p.m.) when outdoor DBT is over 25°C. If outdoor air DBT falls below 25°C, the system would operate under an air-economiser cycle, while for temperatures above 25°C, the water-economiser cycle would start operating. This temperature control is considered over enthalpy control due to its simplicity and less cost; however, enthalpy control would be recommendable in humid climates (S. K. Wang, 2001).

Energy savings are calculated through the correlations obtained for the total air-cooling capacity (Figure 6) applied to the climate data at each location on an hourly basis. The corresponding electric energy savings in the conventional water chilling system are estimated for a seasonal COP of 2.5.

Finally, actual energy savings are calculated deducting the electric energy consumption of the circulation devices: the water pump and the additional fan power required to support the pressure drop in the cooling tower. No additional fan requirements are considered through the coil because it is part of the existing ventilation system.

The power of the water pump (W_{pump}) used in the tower is of 46W. To obtain the additional fan power requirements (W_{fan}), equation (4) is used:

$$W_{fan} = \Delta P_T \cdot \dot{V}_T \tag{4}$$

The pressure drop in the cooling tower has been experimentally characterised through equation (5) for different air volume flows in the tower. A constant of K_T=200 has been obtained, for the pressure drop ΔP_T in [hPa]:

$$\dot{V}_T = K_T \cdot \sqrt{\Delta P_T} \tag{5}$$

Table 2. Operating periods and expected energy savings (World)

CITY	Water-economiser cycle operating period No. hours / % summer	Air cooling [kWh]	Energy savings (no aux.)* [kWh$_e$]	Energy savings [kWh$_e$]	Airflow level
LONDON	58	11.6	4.6	1.8	V1
(Cfb)	2.9%	13.6	5.4	2.1	V2
		16.3	6.5	2.8	V3
SYDNEY	540	91.6	36.6	10.5	V1
(Cfa)	27.5%	106.8	42.7	12.0	V2
		132.7	53.1	18.0	V3
LAS VEGAS	1772	935.8	374.3	288.6	V1
(BWh)	89.1%	1124.7	449.9	348.9	V2
		1199.7	479.9	364.8	V3
SINGAPORE	1846	159.1	63.6	-25.6	V1
(Af)	92.8%	177.8	71.1	-34.0	V2
		268.6	107.4	-12.4	V3

*Without considering additional power consumption of the auxiliary devices.

Table 2 shows how harsh climate conditions may enable the cooling tower to operate during longer daytime periods with larger energy savings. Indeed, the system would operate during around 90% of the summer -daytime occupation- period at Las Vegas. However, particularly humid climates like Singapore would have long operating periods but low effectiveness, yielding negative energy savings. It can also be observed that increasing airflows always allow larger energy savings, despite also larger pressure drops in the CT and the consequent extra fan power requirements.

A second study has been conducted for seven Spanish climates according to the Spanish building code (28) and the Köppen-Geiger classification (26): (i) Avila – E1/Csb (Temperate climate, dry warm summer); (ii) Barcelona – C2/ Csa (Temperate climate, dry hot summer); (iii) Bilbao – C1/ Cfb (Temperate climate without dry season, warm summer); (iv) Madrid – D3/ Csa (Temperate climate, dry hot summer); (v) Sevilla – B4 / Csa (Temperate climate, dry hot summer); (vi) Valencia – B3/ Csa (Temperate climate, dry hot summer); (vii) Valladolid – D2 / Csb (Temperate climate, dry warm summer). Concerning the Spanish building code climate index (composed by a letter and a number), only the number is of interest here, which refers to the summer climate harshness. Climate data used in this study has been obtained from the Spanish building code. Results are gathered in Table 3.

Table 3. Operating periods and expected energy savings (Spain)

CITY	Water-economiser cycle operating period No. hours / % summer	Air cooling [kWh]	Energy savings (no aux.)* [kWh]	Energy savings [kWhe]	Airflow level
Avila (E1/ Csb)	323 16.2%	133.1	53.3	37.6	V1
		159.4	63.7	45.4	V2
		173.6	69.5	48.5	V3
Bilbao (C1/ Cfb)	288 14.5%	65.0	26.0	12.1	V1
		76.6	30.6	14.2	V2
		90.2	36.1	17.4	V3
Barcelona (C2/ Csa)	579 29.1%	120.5	48.2	20.2	V1
		141.7	56.7	23.7	V2
		169.2	67.7	30.1	V3
Valladolid (D2/ Csb)	715 35.9%	280.9	112.4	77.8	V1
		336.0	134.4	93.7	V2
		367.8	147.1	100.7	V3
Valencia (B3/ Csa)	924 46.5%	205.5	82.2	37.5	V1
		242.2	96.9	44.3	V2
		285.8	114.3	54.4	V3
Madrid (D3/ Csa)	873 43.9%	353.7	141.5	99.3	V1
		423.3	169.3	119.6	V2
		462.0	184.8	128.1	V3
Sevilla (B4/ Csa)	1405 70.6%	519.1	207.7	139.7	V1
		620.1	248.1	168.0	V2
		683.2	273.3	182.1	V3

*Without considering additional power consumption of the auxiliary devices.

Again, increasing airflow levels entrain larger energy savings, despite additional consumption of the fan. On the other hand, longer operating periods do not necessarily involve larger savings. This is because a simple fixed DBT control is performed whereas it has been demonstrated that the system performance is highly dependent on the WBD. However, despite an enthalpy control of the cooling tower operating periods would provide more coherent results concerning number of operating hours and energy savings achieved, it would not be interesting due to its greater complexity and given that energy savings are anyway positive.

Hence, the achievable energy savings cannot be foreseen in detail if only the climate harshness index of the Spanish building code and the operating hours are considered. More humid climates incur into worse results than those expected regarding the operating hours. The cases of Madrid and Valencia, Avila and Bilbao, and Valladolid and Barcelona have the same climate classification in summer, but Valencia, Bilbao, and Barcelona are more humid climates. Hence, energy savings are of about 2.5, 3, and near 4 times higher for Madrid, Avila, and Valladolid, respectively. This lack of direct connection among operating hours and energy savings highlights the importance of carefully considering the climate of the location, to avoid excessive energy

consumptions of the circulation devices. For this reason, summer climate classification in the Spanish building code would be insufficient to foresee the applicability of this system. Consequently, to better study the interest of the cooling tower diurnal operation, the WBD bin-data of the target location rises as a key point of study, if faced to the experimental results of the system (9). This comparison is illustrated in figures 9 (a) to (g).

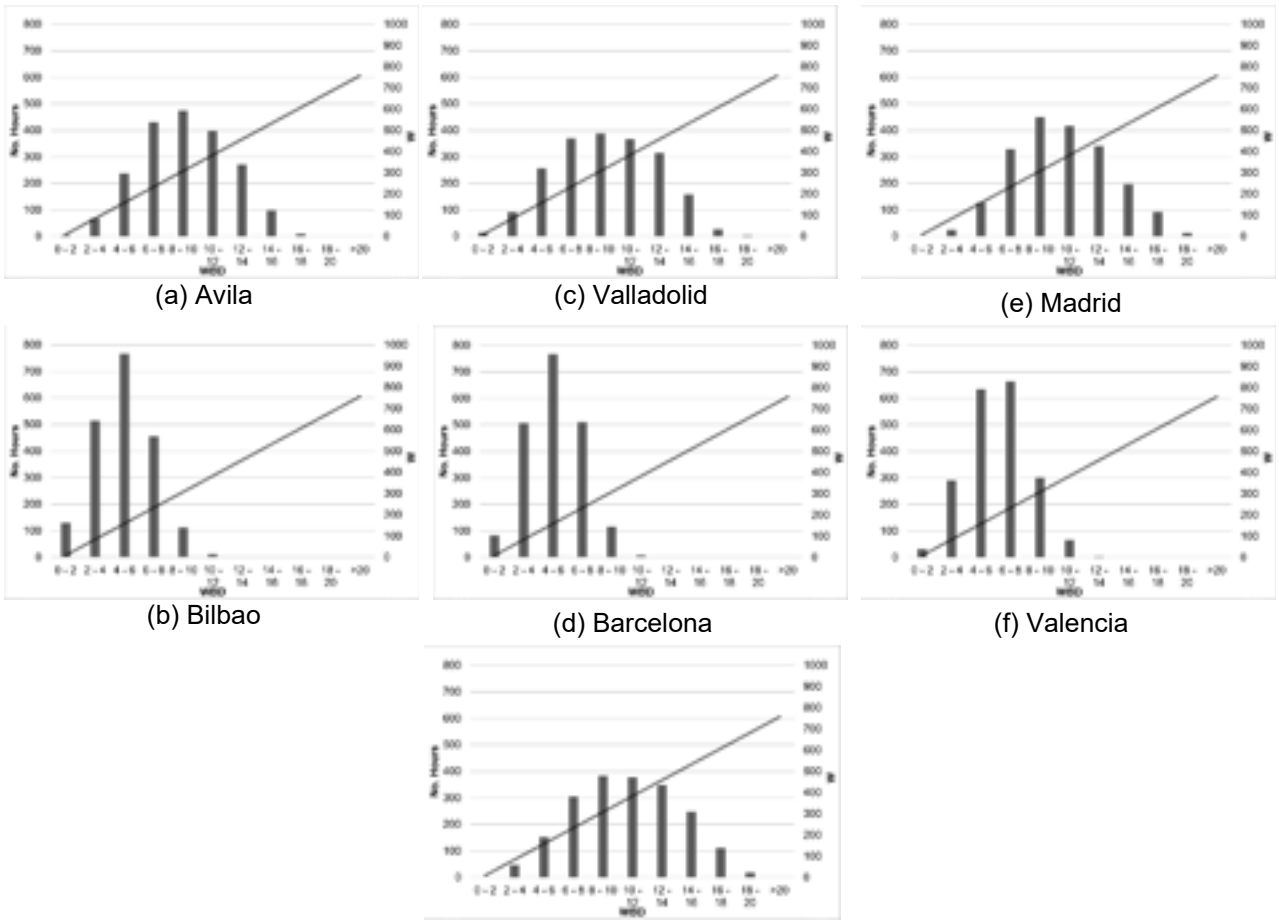

(a) Avila (c) Valladolid (e) Madrid

(b) Bilbao (d) Barcelona (f) Valencia

(g) Sevilla

Figure. 9. WBD-bin data of the selected Spanish cities compared to the system's cooling capacity.

In these figures, WBD of up to 20°C are considered, for being these the ones experimentally characterised. The cooling capacity of the system at V3 is represented, deducting the additional fan and pump power requirements. It can be seen how climates with larger WBD ranges would enable more energy savings, thereby justifying the values obtained in table 3. Therefore, from figure 9 Avila, Valladolid, Madrid and Sevilla would appear to be the most interesting locations for day-time operation of the cooling tower to pre-cool ventilation air, and actually are the ones with better results (table 3).

4. Conclusions and future work

A low temperature cooling tower has been experimentally characterised at a laboratory scale. Water cooled in the CT is used for ventilation air cooling in a water-to-air coil through a water-economiser cycle.

The performance of the CT is studied for three water-to-airflow rates of 0.8, 0.9 and 1.5, keeping the water flow constant, four DBT and four WBT. An ANOVA demonstrates that the airflow factor has the largest contribution to the water-economiser cycle thermal effectiveness and cooling capacity. Increased airflow yields larger energy savings, together with better IAQ expectations, despite higher fan power requirements.

Energy savings have been calculated for 4 cities Worldwide (London, Sydney, Las Vegas and Singapore) and seven Spanish cities. It was seen that, although the best results were obtained for the driest climates, broadening the operation period of the CT would result into positive energy savings for all cases studied but for Singapore.

Non-interesting humid climates can be easily identified regarding the WBD-bin data. On contrary, the Spanish building code climate classification for summer is not detailed enough to foresee the locations where the system proposed would have better potential, as it does not consider the humidity of the summer season.

At those climates where the water-economiser cycle is effective, the use of fixed DBT control is enough to switch between an air or a water-economiser cycle. This option is preferable over an enthalpy control, due to its higher simplicity and the positive energy savings obtained at these climates.

Thanks to positive energy savings and no significant investment required, it is interesting in most cases to expand to daytime operation of an existing CT for night-time TABS cooling, either to simply supply ventilation loads or to pre-cool air if auxiliary mechanical cooling is needed.

Acknowledgments

This work has been developed within the research project TED2021-129652A-C22, funded by MCIN/AEI/10.13039/501100011033 and the European Union through the “NextGenerationEU”/PRTR.

Nomenclature

$\dot{Q}$ heat transfer rate, W

$\dot{m}$ mass flow, kg/s

$\dot{V}$ volume flow, m^3/s

T dry bulb temperature, °C

T_{wb} wet bulb temperature, °C

x absolute humidity, $kg_{vapor}/kg_{dry\ air}$

c_p heat capacity, $kJ/(kg_{dry\ air} \cdot K)$

RH Relative Humidity, %

P fan/pump power, W

ΔP Pressure drop, Pa

K_T pressure drop constant in the tower

ε Thermal effectiveness

Subscripts and superscripts

o outlet

i inlet

T tower

C coil

a air

w water

v vapor

Abbreviations:

AHU=Air handling unit

ANOVA= Analysis of Variance

COP=Coefficient of Performance

CT=cooling tower

DBT=Dry bulb temperature

DOAS=Dedicated Outdoor Air System

IAQ= Indoor air quality

RH=Relative Humidity

TABS=Thermally Activated Building Systems

WBD=Wet bulb depression

WBT= Wet bulb temperature

References

[1] Santos HRR, Leal VMS. Energy vs. ventilation rate in buildings: A comprehensive scenario-based assessment in the European context. Energy Build [Internet]. 2012 Nov;54:111–21. Available from: https://linkinghub.elsevier.com/retrieve/pii/S0378778812003854

[2] Babiak J, Olesen BW, Petras D. REHVA Guidebook No.7: Low temperature heating and high temperature cooling. 2nd ed. Forssa; 2009.

[3] Nasrabadi M, Finn DP. Mathematical modeling of a low temperature low approach direct cooling tower for the provision of high temperature chilled water for conditioning of building spaces. Appl Therm Eng. 2014;64(1–2):273–82.

[4] Nasrabadi M, Finn DP. Performance analysis of a low approach low temperature direct cooling tower for high-temperature building cooling systems. Energy Build. 2014;84:674–89.

[5] Wang SK. Handbook of air conditioning and refrigeration. 2nd ed. New York: McGraw-Hill; 2001.

[6] Bulut H, Aktacir MA. Determination of free cooling potential: A case study for İstanbul, Turkey. Appl Energy. 2011;88(3):680–9.

[7] Wang G, Song L. Air handling unit supply air temperature optimal control during economizer cycles. Energy Build. 2012 Jun;49:310–6.

[8] Rackes A, Waring MS. Using multiobjective optimizations to discover dynamic building ventilation strategies that can improve indoor air quality and reduce energy use. Energy Build. 2014;75:272–80.

[9] Tejero-González A, Andrés-Chicote M, García-Ibáñez P, Velasco-Gómez E, Rey-Martínez FJ. Assessing the applicability of passive cooling and heating techniques through climate factors: An overview. Renewable and Sustainable Energy Reviews. 2016;65.

[10] Kim MH, Park JY, Ham SW, Jeong JW. Energy conservation benefit of water-side free cooling in a liquid desiccant and evaporative cooling-assisted 100% outdoor air system. Energy Build. 2015 Aug 4;104:302–15.

[11] Kim MH, Ham SW, Park JS, Jeong JW. Impact of integrated hot water cooling and desiccant-assisted evaporative cooling systems on energy savings in a data center. Energy. 2014 Dec 15;78:384–96.

[12] Ebrahimi K, Jones GF, Fleischer AS. A review of data center cooling technology, operating conditions and the corresponding low-grade waste heat recovery opportunities. Vol. 31, Renewable and Sustainable Energy Reviews. Elsevier Ltd; 2014. p. 622–38.

[13] Zhang H, Shao S, Xu H, Zou H, Tian C. Free cooling of data centers: A review. Vol. 35, Renewable and Sustainable Energy Reviews. Elsevier Ltd; 2014. p. 171–82.

[14] Capozzoli A, Primiceri G. Cooling systems in data centers: State of art and emerging technologies. In: Energy Procedia. Elsevier Ltd; 2015. p. 484–93.

[15] Cho J, Lim T, Kim BS. Viability of datacenter cooling systems for energy efficiency in temperate or subtropical regions: Case study. Energy Build. 2012 Dec;55:189–97.

[16] Ham SW, Jeong JW. Impact of aisle containment on energy performance of a data center when using an integrated water-side economizer. Appl Therm Eng. 2016 Jul 1;105:372–84.

[17] Agrawal A, Khichar M, Jain S. Transient simulation of wet cooling strategies for a data center in worldwide climate zones. Energy Build. 2016 Sep 1;127:352–9.

[18] Durand-Estebe B, Le Bot C, Mancos JN, Arquis E. Simulation of a temperature adaptive control strategy for an IWSE economizer in a data center. Appl Energy. 2014 Dec 1;134:45–56.

[19] Costelloe B, Finn D. Indirect evaporative cooling potential in air-water systems in temperate climates.

[20] Feng J, Chuang F, Borrelli F, Bauman F. Model predictive control of radiant slab systems with evaporative cooling sources. Energy Build. 2015 Jan 1;87:199–210.

[21] Ma P, Wang LS, Guo N. Modeling of hydronic radiant cooling of a thermally homeostatic building using a parametric cooling tower. Appl Energy. 2014 Aug 15;127:172–81.

[22] EN 16798-1:2019 Standard: Energy performance of buildings. Ventilation for buildings. Part 1: Indoor environmental parameters for design and assessment of energy performance of buildings addressing indoor air quality, thermal environment, lighting and acoustics. Module M1-6.

[23] Sourbron M, Helsen L. Evaluation of adaptive thermal comfort models in moderate climates and their impact on energy use in office buildings. Energy Build. 2011 Feb;43(2–3):423–32.

[24] Pfafferott JÜ, Herkel S, Kalz DE, Zeuschner A. Comparison of low-energy office buildings in summer using different thermal comfort criteria. Energy Build. 2007 Jul;39(7):750–7.

[25] Memon RA, Chirarattananon S, Vangtook P. Thermal comfort assessment and application of radiant cooling: A case study. Build Environ. 2008 Jul;43(7):1185–96.

[26] Peel MC, Finlayson BL, McMahon TA. Updated world map of the Köppen-Geiger climate classification. Hydrol Earth Syst Sci. 2007;11(5):1633–44.

[27] Meteonorm TMY2 database [Internet]. 2023 [cited 2023 Mar 13]. Available from: www.meteonorm.com

[28] Spanish Building Code [Internet]. 2023 [cited 2023 Mar 13]. Available from: https://www.codigotecnico.org/

Application of Feed Forward Neural Networks for modeling of heat transfer coefficient during flow condensation for low and high values of saturation temperature

Stanisław Głuch[a], Tacjana Niksa-Rynkiewicz[b], Dariusz Mikielewicz[c] and Piotr Stomma[d]

[a] Gdańsk University of Technology, Gdańsk, Poland stanislaw.gluch@pg.edu.pl
[b] Gdańsk University of Technology Gdańsk, Poland tacjana.niksa@pg.edu.pl
[c] Gdańsk University of Technology Gdańsk, Poland dariusz.mikielewicz@pg.edu.pl
[d] University of Bialystok, Białystok, Poland, p.stomma@uwb.edu.pl

Abstract:

Most of the literature models for condensation heat transfer prediction are based on specific experimental parameters and are not general in nature for applications to fluids and non-experimental thermodynamic conditions. Nearly all correlations are created to predict data in normal HVAC conditions below 40°C. High temperature heat pumps operate at much higher parameters. This paper aims to create a general model for the calculation of heat transfer coefficients during flow condensation which could be applied to a wide range of fluids and thermodynamical parameters up to the vicinity of the critical point. To achieve this goal authors present a model based on Feed Forward Neural Network. The designed neural network consists of 5 hidden layers and utilizes ReLu and linear activation functions. The first four layers consist of 50 neurons, and the last layer consists of 1 neuron. The network was trained on a consolidated database which consists of 4659 data points for 25 fluids and covers a range of reduced pressure from 0.1 to 0.9 for various mass velocities and diameters. Two input variants were considered. For randomly selected test data Mean Square Root achieved 0.1093 and Mean Absolute Error MAE achieved 0.2243 for the first configuration which consist of 4 parameters. For the second variant, which consists of 17 parameters, MSE achieved 0.0452 MAE achieved 0.1028.

Keywords:

condensation; heat transfer coefficient; high value of reduced pressure; increased saturation pressure; artificial neural network.

1. Introduction

The condensation process in high temperature heat pumps occurs at temperatures higher than 80˚C. There is a knowledge gap in the literature for increased saturation temperatures above 90˚C. There is sparse data for the corresponding high reduced pressures for lower values of saturation temperature. Most of existing experimental data is collected for temperatures below 40 ˚C, which is related to the refrigeration applications of low boiling agents. For temperatures higher than 120 ˚C most refrigerants operate around the thermodynamic critical point, where rapid changes in viscosity and density of the liquid and vapor phases occur, which has a significant impact on interfacial interactions. During the 2022 energy price crisis increased demand could be observed for industrial high temperature heat pumps (HTHP). These devices enable energy recovery and further utilization in industrial processes. High temperature heat pumps operate in the vicinity of the critical point. Among the others, the thermal and hydraulic issues close to the critical point are the least recognized. The larger amount of works are related only to carbon dioxide, much smaller to water. Studies for other fluids are very scarce. The ones published are presented in a consolidated database. Only a few experiments regard condensation at high saturation temperatures in the near critical area. The basic characteristics in flows through the channels at close to critical parameters have been studied since the 50s of last century. Nevertheless, the phenomena presenting the specific challenges for the successive researchers have been observed and can be outlined as follows: 1) The fluid is very expandable, while the thermal diffusivity tends to zero due to very low thermal conductivity and high specific heat. 2) The thermal properties change nonlinearly, which is different from the normal liquid or gas flow and leads to new flow structures. 3) The absence of surface tension and a capillary effect leads to low pressure loss and low flow friction. 4) The buoyancy effect can be more complex. 5) There are expected thermal-mechanical effects and

several time and spatial scales, related to thermal equilibrium or stability evolution in confined spaces. Recently, because of environmental protection requirements, it's an obligation to look for new working fluids, in the case in which physical characteristics are not sufficiently studied. In addition, a large group of these fluids are mixtures. In such a case, the issue is further complicated. It's hard to define the close to the critical area due to the temperature glide effect as well as the different thermal and flow properties of the mixture components. As a result, there is a risk of the formation of vapor-liquid mixtures with dynamics difficult to control. This may happen when one (or more) of the mixture components passes the critical point, while the other components remain in the subcritical area. The situation is similar for media containing additives, i.e. refrigerant oils, air, or inert gases. Untypical character and high dynamics of phenomena taking place in the area close to critical require the selection of working parameters of installation to be chosen very carefully. The authors aim to create a general model which can accurately predict the heat transfer coefficient during condensation at various values of reduced pressure. A special focus on parameters in the vicinity of critical point is a novelty of this research. The authors utilized Feed forward Neural Network which has a different structure than the neural network presented by other authors. The new FNN is also significantly smaller.

Work carried out by other researchers is described in paragraph 1. The consolidated database is described in the second paragraph. Feed-forward network model is presented in the next paragraph. The results are discussed in the fourth paragraph.

1.1. Prediction methods that utilize neural networks.

The study presented by [1] uses machine learning (ML) methods to predict heat transfer coefficients (HTCs) for flow condensation in horizontal tubes. A database with a wide range of fluids and experimental conditions is compiled to evaluate five ML models. Using XGBoost models, a new universal correlation is developed based on the analysis of the most important parameters. The study finds that the ML models perform well in predicting the 1213 test data points, with convolutional neural network CNN achieving the best mean absolute relative deviation (MARD) of 5.82% and the coefficient of determination (R2) of 0.98 or higher for both XGBoost models. XGBoost is better at extrapolating data with reliable performance and the lowest MARD of 19.64%. They also created a conventional correlation which mean absolute relative difference achieved 19.21%. Qiou et al. [2] gathered a consolidated database of 16953 data points. The consolidated database was divided into training and testing data, and an optimization is performed to create the final model architecture consisting of dimensionless input parameters and hidden layers. The artificial neural network (ANN) model demonstrates excellent accuracy in predicting the test data with a mean absolute error (MAE) of 14.3%, and 92.0%, and 97.4% of the predicted data fall within ±30% and ±50%, respectively. The performance of the ANN model was compared with universal correlations for saturated flow boiling heat transfer which was outperformed by ANN. Zhou et al. [3] proposed a new method for predicting heat transfer coefficients in flow condensation in mini/microchannels using a consolidated database of 4,882 data points from 37 sources. The data includes various parameters such as working fluid, reduced pressures, hydraulic diameters, and mass velocities. Four machine learning models were developed and compared, and the ANN and XGBoost models showed the best predicting accuracy. These models were able to predict test data with MAEs of 6.8% and 9.1%, respectively. The models were also compared to a highly reliable universal correlation and were found to perform better in predicting heat transfer coefficients for individual datasheets and different condensation flow regimes. The models were able to accurately predict heat transfer coefficients for datasets outside their training database when fluid specific information was available. The study shows that machine learning algorithms can be used to develop a robust new tool for predicting heat transfer coefficients in flow condensation in mini/micro channels. Moradkhani et al. [4] presented a study which focused on the creation of accurate models for estimating the condensation heat transfer coefficient (HTC) inside conventional and mini/micro channel heat exchangers using machine learning methods. The study evaluated the performance of three different models: gaussian process regression (GPR), hybrid radial basis function (HRBF), and interpolating-based radial basis function (RBF). The study also presented a new general correlation using the least square fitting method (LSFM). The study evaluated the accuracy of earlier HTC models and found a lack of more accurate models for condensation heat transfer coefficient (HTC) in conventional and mini/micro channels. Among the intelligent method-based models, the GPR model showed the highest accuracy for the testing dataset with an average absolute relative deviation of 4.50%, and it was selected as the most reliable model for predicting the HTC in different channels. The study also developed a new conventional general HTC correlation.

2. Consolidated database

The consolidated database is presented in the Table 1. It consists of data presented in 28 publications for 21 fluids. Mass velocity varies from 75 to 1400 kg/(m^2 ·s), reduced pressure varies from 0.1 to 0.9 and diameters vary from 0.76 mm to 15 mm. The first 22 sources which consist form almost 2900 data points were used to train neural networks. 6 last sources are intended for ANN testing

Table 1. Consolidated Database.

number	Authors	Diameter [mm]	Fluid [-]	Mass Velocity G [kg/(m^2·s)]	Reduced Pressure Pr [-]	Number of Points [-]
1	Mcdonald et al. [5,6]	0.76-1.45	R290	150-450	0.254-0.809	260
2	Aroonat [7]	8.1	R134a	300-500	0.251-0.325	54
3	Cavallini et al. [8]	8	R22, R410a, R32, R236ea,R134a, R125	100-800	0.307-0.55	251
4	Cavallini et al. [9]	1.4	R134a, R410a	200-1400	0.251	77
5	Cavallini et al. [10]	0.96	R32, R254fa	100-1200	0.068-0.428	117
6	Keiratch [11]	0.86-3	R404a	200-800	0.382-0.618	522
7	Garimella et al.[12]	0.76-1.52	R410a	200-800	0.805-0.899	214
8	Jiang et al. [13]	9.4	R410a, R404a	200-800	0.8005-0.9	416
9	Fonk and Garimella[14]	1.4	R717	75-150	0.103-0.231	75
10	Andersen [15]	3.05	R410a	400-800	0.8	52
11	Del Co et al. [16]	0.96	R1234yf	200-1000	0.3007	67
12	Del Co et al. [17]	0.762	Propane	100-1000	0.3225	63
13	Longo et al. [18]	4	R290, PROPYLENE, R404a	75-300	0.25-0.322	194
14	Longo et al. [19]	4	R32, R410a	100-800	0.33-0.49	159
15	Longo et al. [20]	4	R134a, R152a, R1234yf, R1234ze(e)	75-600	0.13-0.3	280
16	Ghim and Lee [21]	7.75	R245fa	150-500	0.093	20
17	Patel et al. [22]	1	R134a, R1234yf	202-811	0.256-0.3	77
18	Zhuang et al. [23]	4	Ethane	101-255	0.22-0.522	230
19	Song et al. [24]	4	R14	200-650	0.27-0.79	189
20	Zhuang et al. [25]	4	Methane	99-254	0.43-0.76	286
21	Milkie et al. [26]	7.75	R245fa, n-PENTANE	150-600	0.04-0.17	266
22	Keniar and Garimella [27]	1.55	R245fa, R134a, R1234ze(E)	50-200	0.05-0.32	149
23	Moriera et al. [28]	9.43	R134a, PROPYLENE, R290, R600a	50-250	0.12-0.32	140
24	Huang et al. [29]	0.00418	R410a	200-600	0.49	35
25	Illan-Gomez et al. [30]	1.16	R1234yf	350-945	0.23-0.43	219
26	Del Col et al. [31]	1	Propylen	80-1000	0.35	109
27	Azzolin et al. [32]	3.4	R134a	50-200	0.25	73
28	Berto et al. [33]		R245fa	30-150	0.68	124
		0.76-9.4	25 fluids	75-1400	0.103-0.9	1916

3. Neural network model

The previously cited studies [1–4]show that the use of the artificial intelligence method can give better results than conventional correlations for predicting the heat transfer coefficient. During the initial tests, 3 methods were investigated: Feedforward Neural Networks (FNN), Convolutional Neural Networks (CNN), and the k-means clustering algorithm. The results provided by FNN were the most promising and the authors decided to

pursue this approach. Artificial Neural Network ANN showcased high quality results also in [34,35]. A multi-layer neural network was developed to train the prediction of the heat transfer coefficient during flow condensation. The scheme of this network is presented in the Figure 1.

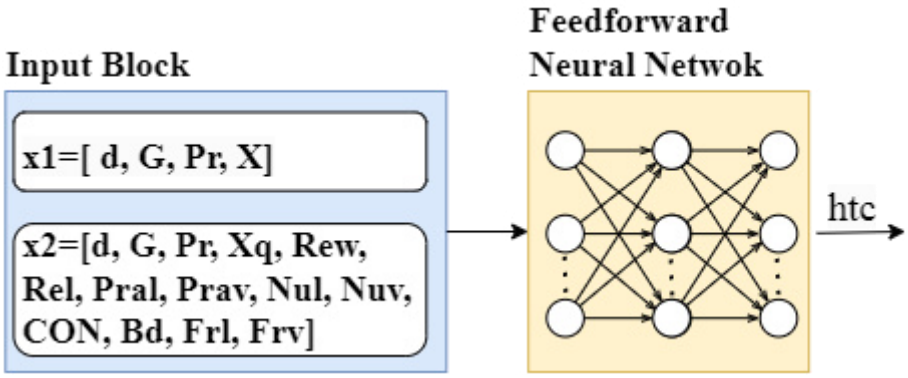

Figure. 1. Scheme of designed neural network.

The applied neural network uses activation functions (FA), such as ReLu (fR) $fR(x) = \max(0, x)$ and Linear $fL(x) = x$. ReLu is used on 4 first layers, and the last layer utilizes linear function. The authors of the work tried to make the architecture of the network used as simple as possible, and at the same time give the best results. Finally, 5 hidden layers were used with 50 neurons in the first layer (M=50), 50 neurons in the second layer (N=50), 50 neurons in the fourth layer (D=50), 50 neurons in the third layer (P=50), and 1 neuron in the last layer (Q=1). The output (y_{out})signal from the network is described by the relation:

$$y_{out}(x,\omega) = fL\left(\sum_{i=1}^{Q} \omega_{ji}^{I} \cdot x_i \left(\sum_{l=1}^{P} \omega_{out} fL\left(\sum_{k=1}^{D} \omega_{lk}^{III} fR\left(\sum_{j=1}^{N} \omega_{kj}^{II} fR\left(\sum_{i=1}^{M} \omega_{ji}^{I} \cdot x_i + \omega_{j0}^{I}\right) + \omega_{k0}^{II}\right) + \omega_{l0}^{III}\right) + \omega_{0utO}^{iv}\right) + \omega_{l0}^{III}\right) \quad (1)$$

Signals $x(k) = [x_1, \ldots, x_M]$ given to the input k neuron multiplied by sets of weights $\omega(k)$ are sent to the next fully connected layer. The vector of initial weights $\omega(k) = [\omega_1, \ldots, \omega_M]$ is randomized from the range (0,1). Given the research results described in [36] the Adam algorithm was used to teach the networks under study. The network performance error was calculated as the difference between expected y and output $\hat{y}$ based on Mean Squared Error (MSE) and Mean Average Error (MAE) for all n observations i;i = 1.. n;

$$MSE(y, \hat{y}) = 1/n \sum_{i}^{n} (y(i) - \hat{y}(i))^2 \quad (1)$$

4. Results

FNN was trained for two input data configurations. The first one consisted only of basic thermodynamical parameters: diameter, flow rate, quality, and reduced pressure (in comparison to critical pressure). The second configuration feature also a set of criteria numbers. From the learning database, nearly 800 measurements were randomly selected to test the database. A comparison of the two input configurations is presented in the Table 2. Both configurations achieved good results for the test dataset. Case 1 with only 4 basic input parameters achieved accurate output data of its limited input data. The second configuration achieved significantly better results., which are lower than the measurement errors of most experiments. Most experiments regarding measurement of HTC during condensation have measurement errors between 10 and 20%. It is worth mentioning that the presented ANN was much smaller than the artificial intelligence networks presented by [1–4]. Values of MSE and MAE have achieved thanks to data preparation and curation for FNN. The expected value was turned into a logarithmic value and rescaled, which enabled FNN to achieve formidable results.

Table 2. FNN evaluations on the test dataset for different input combinations.

case	number of input parameters	input parameters	MSE	MAE
1	4	d, G, Pr, X	0.1093	0.2243
2	17	d, G, Pr, X, Rev, Rel, Pral, Prav, Nul, Nuv, CON, Bo, Frl, Frv, Frlf, Frvf, Wevf	0.0452	0.1028

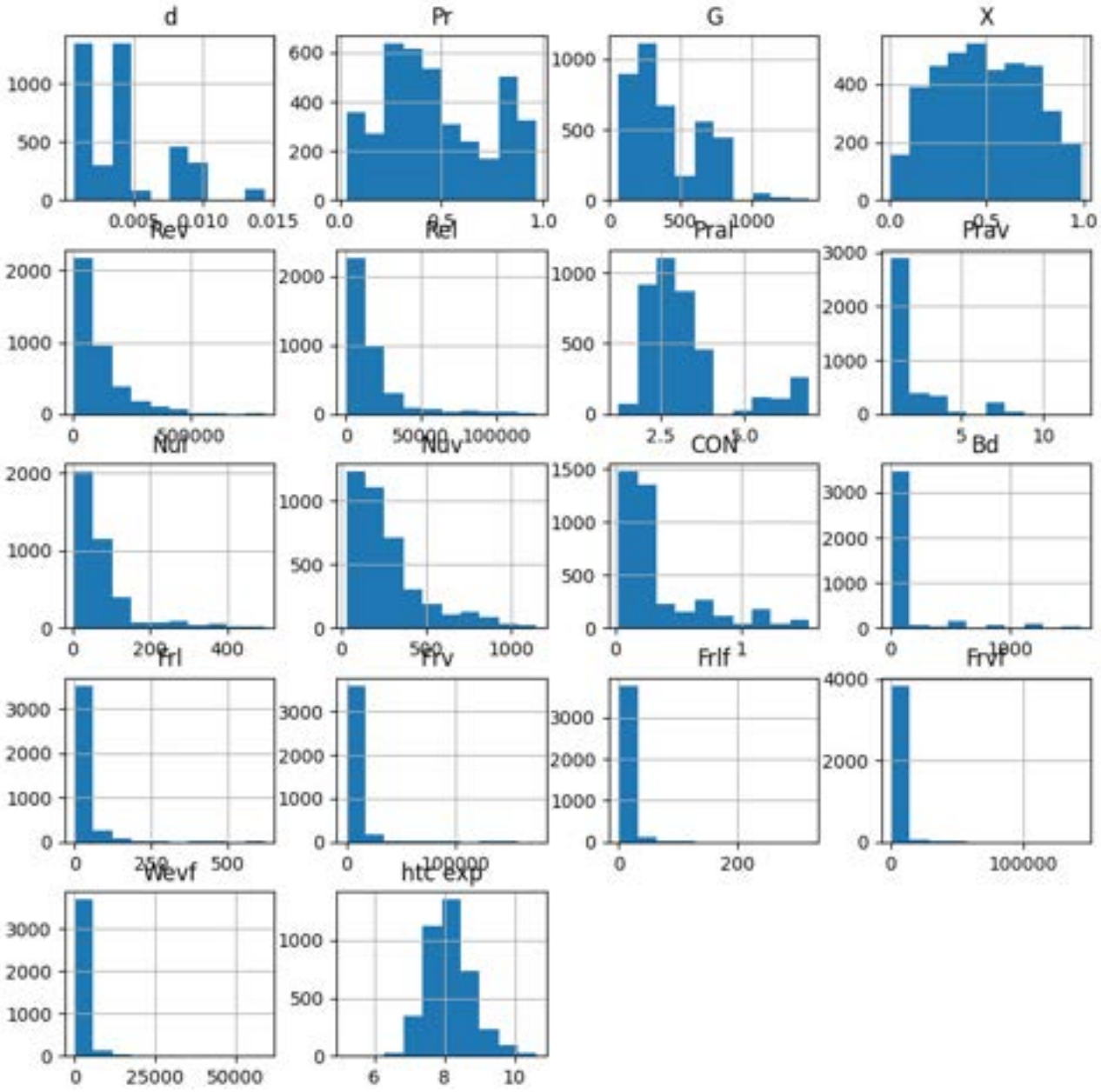

Figure. 2. Histograms that present the distribution of input parameters.

Histograms which present the distribution of input parameters are present in the Figure 2. Parameters are described in the nomenclature section. Most important are diameter, mass velocity, reduced pressure and quality which are measured during the experiment. The rest of the parameters are criteria numbers which are calculated using fluid properties and mentioned experimental parameters. The learning process of the first dataset can be observed in the Fig. 3. Comparison of experimental and calculated values of HTC can be observed in the Fig. 4 and the Fig. 5. Value of the expected value and output value for the training dataset provides good results for sparse input data. Both variants were trained for 100 epochs.

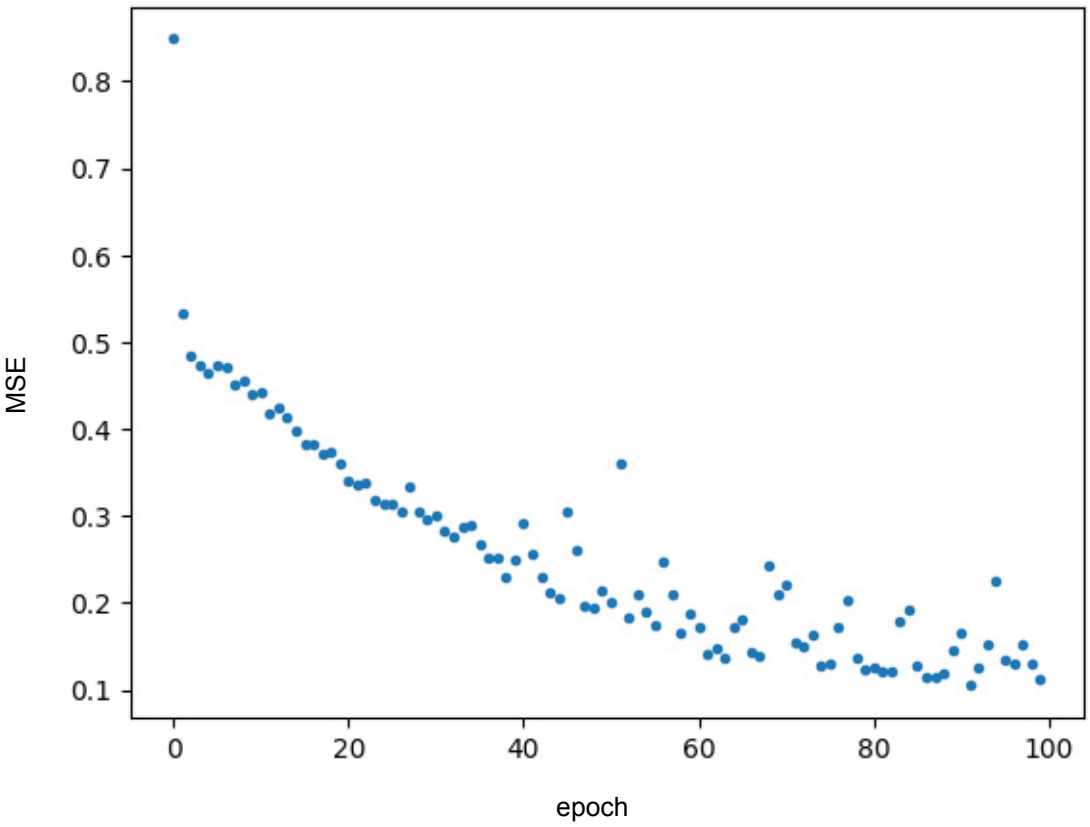

Figure. 3. Learning graph for the first input configuration

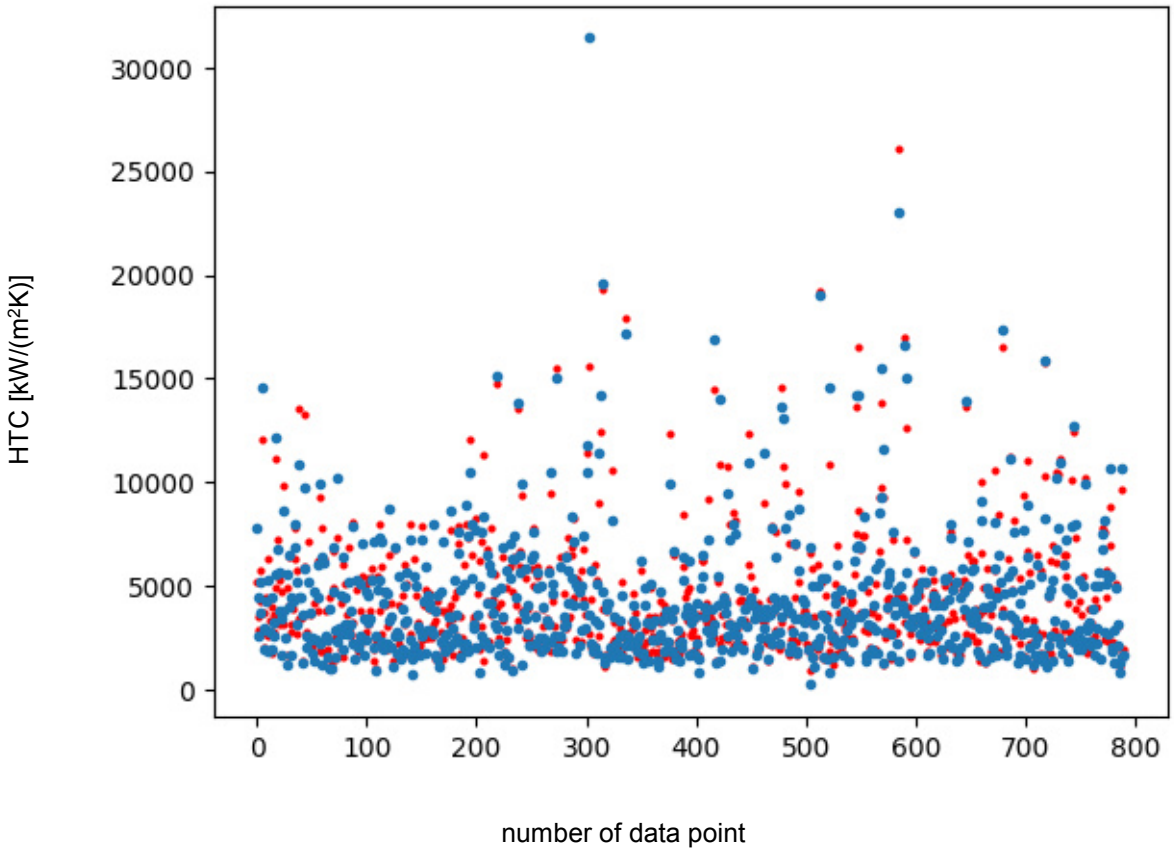

Figure. 4. Comparison of experimental heat transfer coefficient and results for the first input configuration. Experimental values are blue and FNN output values are red.

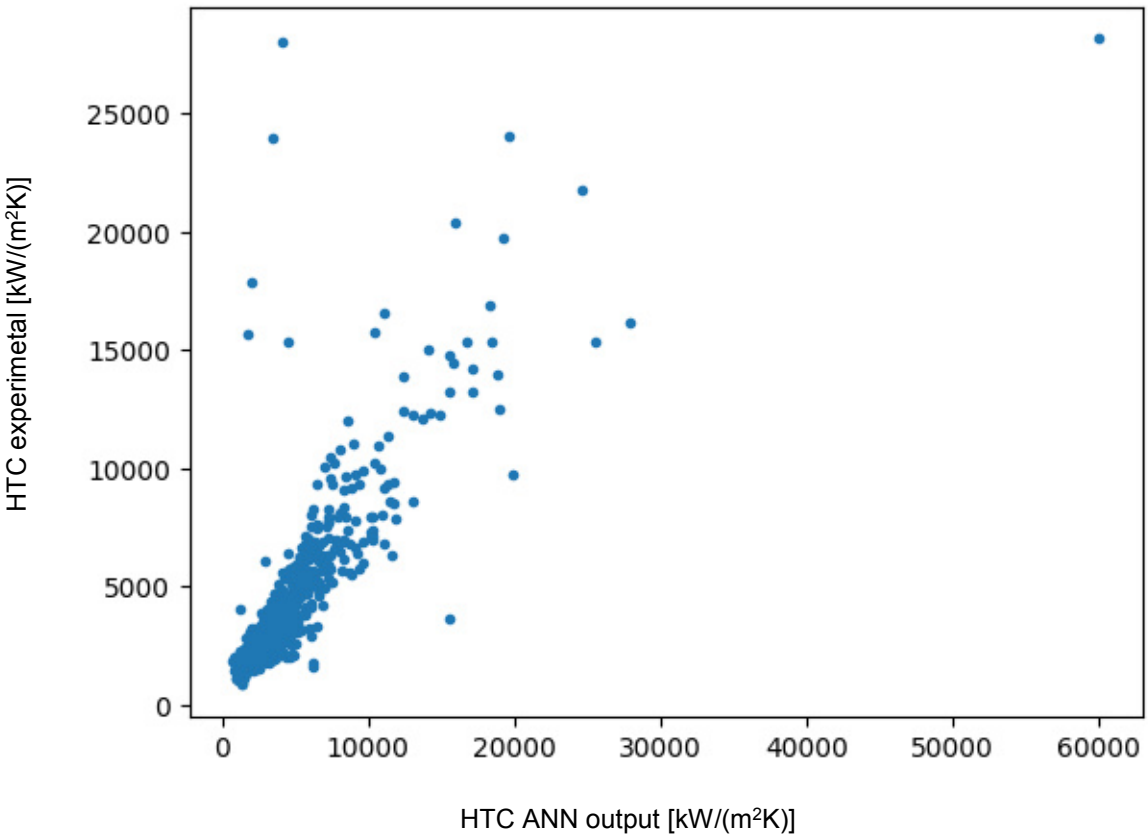

Figure. 5. Comparison of HTC value measured during the experiment and ANN output data for the first input configuration

The learning process of the second dataset can be observed in the Fig. 6. Comparison of experimental and calculated values of HTC can be observed in the Fig. 7 and in the Fig. 6. Better results can be observed in the Fig. 8. than in the Fig. 4. Learning process is significantly faster f second configuration.

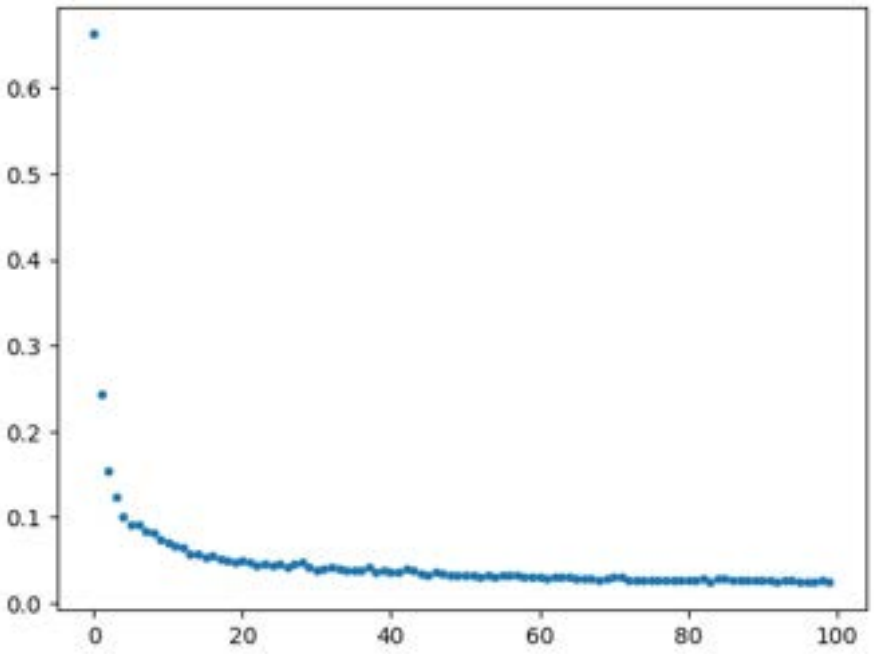

Figure. 6. Learning graph for the second input configuration

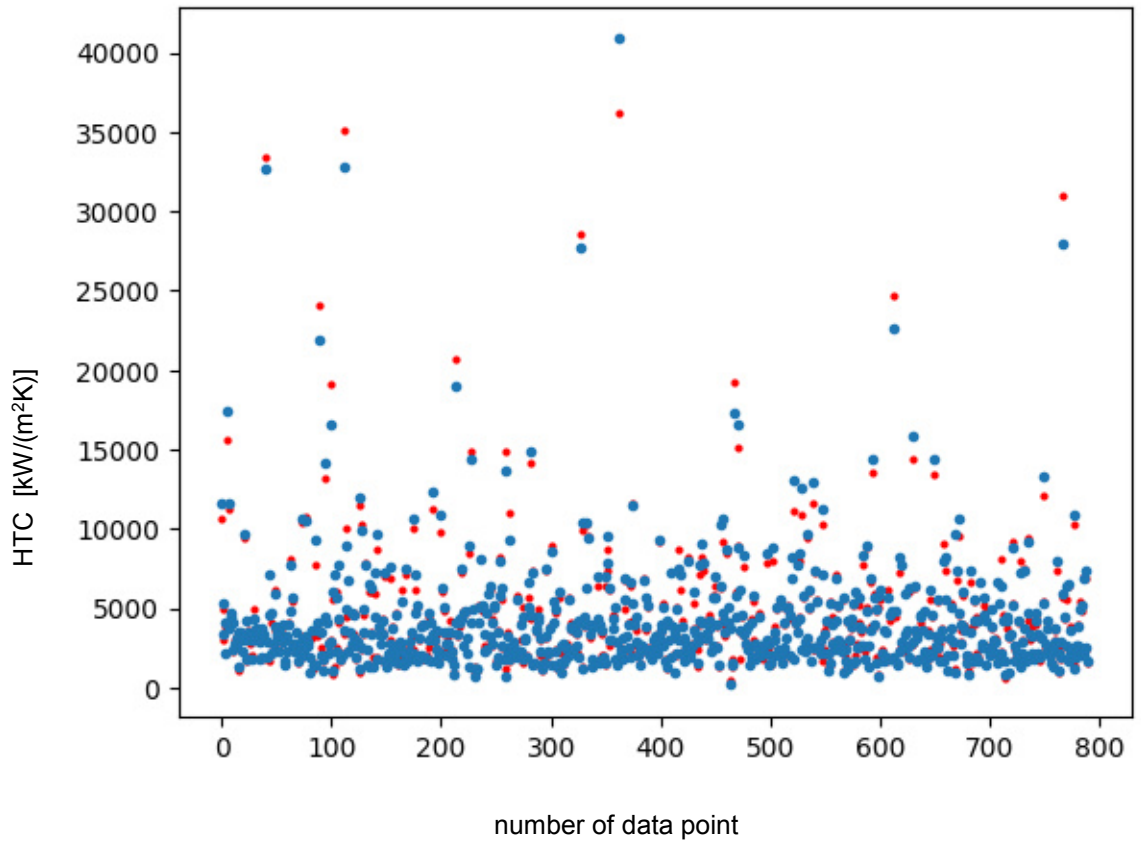

Figure. 7. Comparison of experimental heat transfer coefficient and results in for the second input configuration. Experimental values are blue and FNN output values are red.

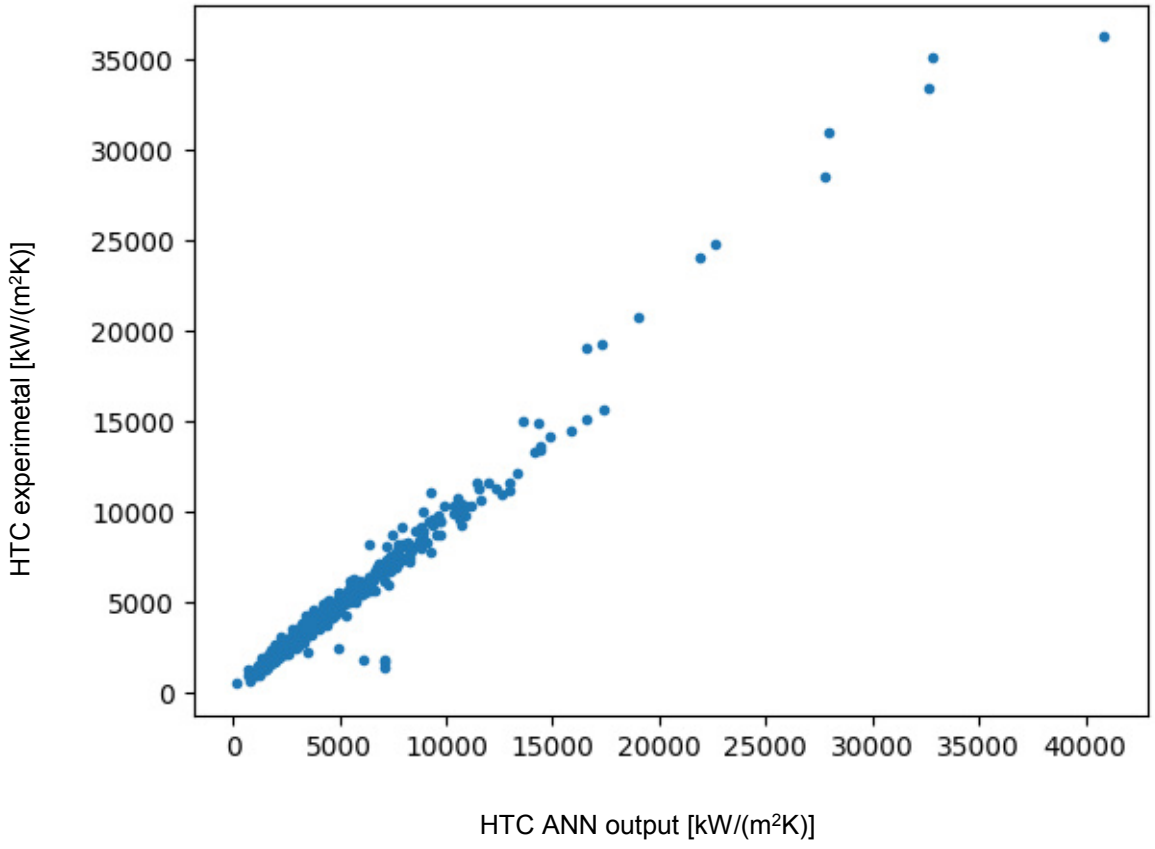

Figure. 8. Comparison of HTC value measured during the experiment and ANN output data for the second input configuration

4. Conclusions

The authors created a model which can predict heat transfer coefficient during flow condensation. The model utilizes Feed Forward Neural Network (FNN). The method was trained on the consolidated experimental database which consists of 4659 data points. The consolidated database covers various parameters of diameter, mass velocities, and reduced pressures ranging from 0.1 to 0.9. The proposed Feed Forward Neural network achieved very good results for randomly selected data points. Designed FNN consists of 5 hidden layers and utilizes ReLu and linear activation functions. ADAM algorithm was used for training. Mean Square Root MSE achieved 0.1093 and Mean Absolute Error MAE achieved 0.2243 for the first variant. For the second variant, MSE achieved 0.0452 MAE achieved 0.1028. The value of MAE achieved by the second configuration is lower than the measurement error of most experiments. It is important to mention that created FNN is relatively small, but it managed to provide good results. The created network consists of 5 layers. Further development of work is required to gather more experimental data points from different experiments than used in testing data and testing created FNN on a new dataset. This will allow to test the new method in a real-case scenario.

Nomenclature

ANN Artificial Neural Network,

d diameter, m

G mass velocity, kg/(m^2·s)

Pr reduced pressure -ratio of pressure to critical pressure, -

Rel Reynolds number for saturated liquid $Rel = \frac{GD}{\mu l}$, -

Rev Reynolds number for saturated vapour $Rev = \frac{GD}{\mu v}$, -

t temperature, °C

Wel Weber number for saturated liquid $Wel = \frac{G^2 D}{\rho l}$, -

x Quality, -

HTC heat transfer coefficient , kW/(m2K)

FNN Feed Forward Neural Network, -

ML Machine Learning, -

CNN Convolutional Neural Network, -

Pral Prandtl number for saturated liquid, -

Prav Prandtl number for saturated vapour, -

Nul Nusselt number for saturated liquid, -

Nuv Nusselt number for saturated vapour, -

CON Confinement Number, -

Bo Bond number, -

Frl Froude number for saturated liquid, -

Frv Froude number for saturated vapour, -

Frlf Froude number for liquid fraction, -

Frvf Froude number for vapour fraction, -

Wevf Weber number for vapour fraction, -

Acknowledgements

This research was funded in whole or in part by National Science Centre, Poland 2021/41/N/ST8/04421

References

[1] Nie F., Wang H., Zhao Y., Song Q., Yan S., Gong M., A Universal Correlation for Flow Condensation Heat Transfer in Horizontal Tubes Based on Machine Learning. International Journal of Thermal Sciences 2023;184:107994.

[2] Qiu Y., Garg D., Zhou L., Kharangate C.R., Kim S.M., Mudawar I., An Artificial Neural Network Model to Predict Mini/Micro-Channels Saturated Flow Boiling Heat Transfer Coefficient Based on Universal Consolidated Data. International Journal of Heat and Mass Transfer 2020;149:.

[3] Zhou L., Garg D., Qiu Y., Kim S.M., Mudawar I., Kharangate C.R., Machine Learning Algorithms to Predict Flow Condensation Heat Transfer Coefficient in Mini/Micro-Channel Utilizing Universal Data. International Journal of Heat and Mass Transfer 2020;162:120351.

[4] Moradkhani M.A., Hosseini S.H., Song M., Robust and General Predictive Models for Condensation Heat Transfer inside Conventional and Mini/Micro Channel Heat Exchangers. Applied Thermal Engineering 2022;201:117737.

[5] Macdonald M., Garimella S., Hydrocarbon Condensation in Horizontal Smooth Tubes: Part i - Measurements. International Journal of Heat and Mass Transfer 2016;93:75–85.

[6] Macdonald M., Garimella S., Hydrocarbon Condensation in Horizontal Smooth Tubes: Part II - Heat Transfer Coefficient and Pressure Drop Modeling. International Journal of Heat and Mass Transfer 2016;93:1248–1261.

[7] Aroonrat K., Wongwises S., Experimental Study on Two-Phase Condensation Heat Transfer and Pressure Drop of R-134a Flowing in a Dimpled Tube. International Journal of Heat and Mass Transfer 2017;106:437–448.

[8] Cavallini A., Censi G., Col D. Del, Doretti L., Longo G.A., Rossetto L., Experimental Investigation on Condensation Heat Transfer and Pressure Drop of New HFC Refrigerants in a Horizontal Smooth Tube Â Rimentale Sur Le Transfert de Chaleur Lors de La Etude Expe Condensation et Sur La Chute de Pression Des Nouveaux Frigorige Da. 2001;24:.

[9] Cavallini A., Del Col D., Doretti L., Matkovic M., Rossetto L., Zilio C., Condensation Heat Transfer and Pressure Gradient inside Multiport Minichannels. Heat Transfer Engineering 2005;26:45–55.

[10] Cavallini A., Bortolin S., Del Col D., Matkovic M., Rossetto L., Condensation Heat Transfer and Pressure Losses of High- and Low-Pressure Refrigerants Flowing in a Single Circular Minichannel. Heat Transfer Engineering 2011;32:90–98.

[11] Keinath B., Void Fraction, Pressure Drop, and Heat Transfer in High Pressure Condensing Flows through Microchannels. 2012;1–353.

[12] Garimella S., Andresen U.C., Mitra B., Jiang Y., Fronk B.M., Heat Transfer During Near-Critical-Pressure Condensation of Refrigerant Blends. Journal of Heat Transfer 2016;138:.

[13] Jiang Y., Garimella S., Heat Transfer and Pressure Drop for Condensation of Refrigerant R-404A at Near-Critical Pressures. ASHRAE Winter Meetings CD, Technical and Symposium Papers 2003;2003:667–677.

[14] Fronk B.M., Garimella S., Heat Transfer and Pressure Drop During Condensation of Ammonia in Microchannels 2012;, 399–409.

[15] Andresen U.C., Supercritical Gas Cooling and Near-Critical-Pressure Condensation of Refrigerant Blends in Microchannels. 2006;

[16] Del Col D., Torresin D., Cavallini A., Heat Transfer and Pressure Drop during Condensation of the Low GWP Refrigerant R1234yf. International Journal of Refrigeration 2010;33:1307–1318.

[17] Del Col D., Bortolato M., Bortolin S., Comprehensive Experimental Investigation of Two-Phase Heat Transfer and Pressure Drop with Propane in a Minichannel. International Journal of Refrigeration 2014;47:66–84.

[18] Longo G.A., Mancin S., Righetti G., Zilio C., Saturated Vapour Condensation of HFC404A inside a 4 Mm ID Horizontal Smooth Tube: Comparison with the Long-Term Low GWP Substitutes HC290 (Propane) and HC1270 (Propylene). International Journal of Heat and Mass Transfer 2017;108:2088–2099.

[19] Longo G.A., Mancin S., Righetti G., Zilio C., Saturated Vapour Condensation of R410A inside a 4 mm ID Horizontal Smooth Tube: Comparison with the Low GWP Substitute R32. International Journal of Heat and Mass Transfer 2018;125:702–709.

[20] Longo G.A., Mancin S., Righetti G., Zilio C., Saturated Vapour Condensation of R134a inside a 4 mm ID Horizontal Smooth Tube: Comparison with the Low GWP Substitutes R152a, R1234yf and R1234ze(E). International Journal of Heat and Mass Transfer 2019;133:461–473.

[21] Ghim G., Lee J., Condensation Heat Transfer of Low GWP ORC Working Fluids in a Horizontal Smooth Tube. International Journal of Heat and Mass Transfer 2017;104:718–728.

[22] Patel T., Parekh A.D., Tailor P.R., Experimental Analysis of Condensation Heat Transfer and Frictional Pressure Drop in a Horizontal Circular Mini Channel. Heat and Mass Transfer/Waerme- und Stoffuebertragung 2020;56:1579–1600.

[23] Zhuang X.R., Gong M.Q., Zou X., Chen G.F., Wu J.F., Experimental Investigation on Flow Condensation Heat Transfer and Pressure Drop of R170 in a Horizontal Tube. International Journal of Refrigeration 2016;66:105–120.

[24] Song Q., Chen G., Xue H., Zhao Y., Gong M., R14 Flow Condensation Heat Transfer Performance: Measurements and Modeling Based on Two-Phase Flow Patterns. International Journal of Heat and Mass Transfer 2019;136:298–311.

[25] Zhuang X.R., Chen G.F., Zou X., Song Q.L., Gong M.Q., Étude Expérimentale Sur La Condensation De L'Écoulement De Méthane Dans Un Tube Horizontal Lisse. International Journal of Refrigeration 2017;78:193–214.

[26] Milkie J.A., Condensation of Hydrocarbons and Zeotropic Hydrocarbon/Refrigerant Mixtures in Horizontal Tubes. 2014;

[27] Keniar K., Garimella S., Experimental Investigation of Refrigerant Condensation in Circular and Square Micro- and Mini- Channels. International Journal of Heat and Mass Transfer 2021;176:121383.

[28] Moreira T.A., Ayub Z.H., Ribatski G., Convective Condensation of R600a, R290, R1270 and Their Zeotropic Binary Mixtures in Horizontal Tubes. International Journal of Refrigeration 2021;130:27–43.

[29] Huang X., Ding G., Hu H., Zhu Y., Peng H., Gao Y., Deng B., Influence of Oil on Flow Condensation Heat Transfer of R410A inside 4.18 Mm and 1.6 Mm Inner Diameter Horizontal Smooth Tubes. International Journal of Refrigeration 2010;33:158–169.

[30] Illán-Gómez F., López-Belchí A., García-Cascales J.R., Vera-García F., Experimental Two-Phase Heat Transfer Coefficient and Frictional Pressure Drop inside Mini-Channels during Condensation with R1234yf and R134a. International Journal of Refrigeration 2015;51:12–23.

[31] Del Col D., Azzolin M., Bortolin S., Berto A., Experimental Results and Design Procedures for Minichannel Condensers and Evaporators Using Propylene. International Journal of Refrigeration 2017;83:23–38.

[32] Azzolin M., Bortolin S., Del Col D., Convective Condensation at Low Mass Flux: Effect of Turbulence and Tube Orientation on the Heat Transfer. International Journal of Heat and Mass Transfer 2019;144:118646.

[33] Berto A., Lavieille P., Azzolin M., Bortolin S., Miscevic M., Del Col D., Liquid Film Thickness and Heat Transfer Measurements during Downflow Condensation inside a Small Diameter Tube. International Journal of Multiphase Flow 2021;140:103649.

[34] Niksa-Rynkiewicz T., Witkowska A., Głuch J., Adamowicz M., Monitoring the Gas Turbine Start-up Phase on the Platform Using a Hierarchical Model Based on Multi-Layer Perceptron Networks. Polish Maritime Research 2022;

[35] Niksa-Rynkiewicz T., Szewczuk-Krypa N., Witkowska A., Cpałka K., Zalasiński M., Cader A., Monitoring Regenerative Heat Exchanger in Steam Power Plant by Making Use of the Recurrent Neural Network. Journal of Artificial Intelligence and Soft Computing Research 2021;

[36] Goodfellow I., Bengio Y., Courville A., Deep Learning. Cambridge: MIT Press, 2016;

Influence of desiccant concentration and temperature on moisture absorption using a multistage dehumidifier

Ana Tejero-González[a]; Shiva Kumar[b]; Sampath Suranjan Salins[c]; S.V. Kota Reddy[d]

[a] School of Engineering, University of Valladolid, Valladolid, Spain, ana.tejero@uva.es CA
[b] Department of Mechanical and Manufacturing Engineering, Manipal Institute of Technology, Manipal Academy of Higher Education, Manipal, India, shiva.kumar@manipal.edu
[c] School of Engineering and IT, Manipal Academy of Higher Education, Dubai Campus, UAE, sampath@manipaldubai.com
[d] Department of Mechanical Engineering, VIT-AP University, Vijayawada, Andhra Pradesh, India, vc@vitap.ac.in

Abstract:

Moisture control is essential for appropriate indoor air quality, mainly in humid regions. Liquid desiccant dehumidification system is among the latest techniques used to minimize the humidity indoors and maintain thermal comfort, requiring less energy than dehumidification through conventional refrigeration. In the current work, a four-stage dehumidifier is constructed, which consists of a dynamic packing soaked in the solution containing the desiccant. The linear motion of packing is induced by a cam spring follower mechanism powered by a motor. Celdek 7090 is used as packing along with Calcium Chloride of different concentrations as desiccant. Experiments are conducted for varying air velocity, desiccant concentration, and inlet dry bulb temperature. Input parameters are noted and performance parameters such as coefficient of performance, moisture removal rate, dehumidification efficiency, and humidity and temperature drops are evaluated. Results indicate that an increase in the desiccant concentration yields larger dehumidification, though 40% desiccant concentration led to adverse effects on the system components and hindered the flow. Rise in the inlet temperature slightly raised the dehumidification. System gave maximum moisture removal rate, dehumidification efficiency, and coefficient of performance equal to 4.83 g/s, 72.74%, and 4.35 respectively. Results also showed that increasing air velocity reduced the dehumidification efficiency. Air quality check conducted on the exit air, it is found that air quality is good and meets ASHRAE standards.

Keywords:

Multistage dehumidifier; desiccant; coefficient of performance; dehumidification effectiveness; air quality.

1. Introduction

Due to the rise in the world's population, there is a significant increase in the energy consumption. Air conditioning (AC) alone comprises 50% of the overall building energy utilization [1]. It is thus critical to improve the energy efficiency when controlling the temperature and humidity within the occupied spaces. In AC, the temperature is maintained below dew point temperature to remove moisture by condensation [2]. Due to water collection, there is a risk of growth of the mold and bacteria, with the consequent undesirable health effects. Therefore, to remove more moisture, reheater is required [3]. Desiccant dehumidification is an alternative approach which can provide high air quality and meet thermal comfort conditions [4]. Liquid desiccant dehumidification system (LDDS) is an alternative option where that dehumidifies the air with the use of liquid desiccant. Humid air is driven through the duct and interacts with the packing, where there moisture condensates [5]. This is due to the vapor pressure difference between the desiccant and the air. As the concentration of the desiccant increases, there is a drop in the vapor pressure of the desiccant and the moisture diffuses from the higher to the lower concentration [6]. Some of the packings which are commercially available are Celdek and Aspen packing. Celdek packing gives high wettability value. Wettability is the desiccant holding capacity of the packing. Lithium bromide (Li Br) and Lithium Chloride (Li Cl) are commonly used desiccants which yielded good dehumidification, but they are corrosive [7]. This issue can be overcome using less corrosive desiccants such as Calcium Chloride ($Ca\ Cl_2$) and potassium formate (HCO_2K) [8]. Thickness of the packing and desiccant concentration are decisive on the dehumidification performance [9].

Outside climate is another factor which determines the dehumidifier performance. In the majority of the systems, the packing is static, single stage, and the type of flow between the air and the desiccant is either counter or cross flow [10]. Counter flow can result into higher performance. Some articles in the literature focus on multistage and dynamic dehumidifiers.

Air can be driven through one or more packings. Similarly, the packing may be static or dynamic. Dong et al. [11] studied a corrugated, S-shaped, PVC, and a globular shaped, polypropylene packing. the performance of the dehumidifier was evaluated for the inlet air flow rate and temperature. In terms of the moisture effectiveness, corrugated packing gave better results than S-shaped packing. Globular packing gave the least performance among all. Wang et al. [12] worked on a counterflow liquid desiccant dehumidifier which used structured packing with wettability of 650 m^2/m^3. Experiments were conducted for variable packing height, climatic conditions, and air velocity. The system gave a moisture effectiveness of 0.6 and moisture removal rate of 0.9 g/s. Jain et al. [13] built a dehumidifier unit which comprised a cooling tower, heat exchanger, regenerator and control unit. The desiccant used by the unit was Ca Cl_2 and Li Cl, and the desiccant concentration and air flow rate were varied. Results indicated that change in the specific humidity of Lithium Chloride and Calcium Chloride was found to be 5.86 and 1.77 g/kg. Bouzenada et al. [14] developed a desiccant air conditioning system which used Ca Cl_2 as desiccant. Operating parameters such as air temperature, humidity and air velocity were varied and found that absorption mass rate varied linearly with the inlet air humidity. Results indicated that the system gave a vapor pressure of 20 Pa. Lu et al. [15] worked on LDDS where the inlet air humidity ratio and temperature were varied. Experimental test rig was developed and found that outlet desiccant and air temperature increased with the inlet conditions. Solution fraction increase gave a drop in the outlet humidity. Seenivasan et al. [16] compared the performance of single and two stage dehumidifiers. Air flow rate were varied and found that there was a drop in the dehumidification effectiveness. There was a rise in the condensation rate with the increase in the desiccant flow rate. Also, the performances varied with the desiccant concentrations and found that moisture removal rate increased significantly. Results inferred that two-stage dehumidifier performed better than single stage dehumidifier. Cheng et al. [17] worked on a multistage dehumidifier and conducted experiments for different number of packing stages. The system used Li Cl solution which interacted with the humid air in cross flow direction. Results indicated that dehumidification efficiency was mainly affected by air flow rate and solution flow rate, and the system gave a dehumidification efficiency of 80%. Li et al. [18] performed an experimental study on a multistage planar membrane dehumidifier both counter and parallel flow arrangements. Nafion 212 membranes were used, and the inlet operating conditions were initially maintained at 27ºC, then varied. Performance parameters were obtained by varying the temperatures, relative humidity, and air flow rate. Results indicated that counter flow dehumidifier gave better performance compared to the parallel type.

After reviewing the literature, it is found that most of the papers used counter and cross flow types, while desiccant used were Li Cl and Ca Cl_2. Celdek packing is widely used, which gave high wettability. Few works focused on the variation of the climatic conditions and the solution flow rate. Most research focus on single stage static dehumidifiers, while research related to multistage dynamic dehumidifiers is scarce. Also, the study of the influence of the desiccant concentration variation and the climatic conditions on the system performance are limited. To overcome these gaps, a multistage reciprocating dehumidifier is constructed where the desiccant concentration and inlet climatic conditions were varied to obtain the performance parameters such as moisture removal rate and moisture effectiveness. Energy efficiency is also studied and expressed in the form of the COP.

2. Methodology

Figure.1 shows the psychrometric process in the desiccant dehumidification system.

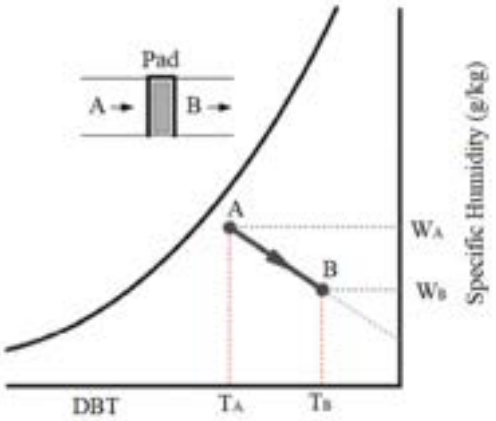

Figure.1. Psychometric process representing dehumidification.

The air gets dehumidified as it passes through the reciprocating packing system. W_A, T_A are the air specific humidity and temperature at the inlet, while W_B, T_B are the air specific humidity and temperature at the outlet. In the dehumidification process, the temperature of air increases as the specific humidity drops.

The moisture removed from the air (MRR) is given by equation (1), which is evaluated by the product of air flow rate and difference in specific humidity.

$$MRR = (\omega_i - \omega_o)\, \dot{m}_a \tag{1}$$

The dehumidification efficiency given in equation (2) is defined as the ratio of the difference between the inlet and outlet specific humidity to the inlet specific humidity and equilibrium specific humidity.

$$\varepsilon = \frac{\omega_i - \omega_o}{\omega_i - \omega_{eq}} \tag{2}$$

The mass transfer coefficient is defined as the product of the MRR to the product of the surface area and the specific humidity difference of average and equilibrium points. It is given by equation (3).

$$K = \frac{MRR}{A\,(\omega_{av} - \omega_{av,eq})} \tag{3}$$

The Coefficient of Performance (COP) is defined as the ratio of the enthalpy difference or heating effect to the total energy required. It is shown in equation (4).

$$COP = \frac{HE}{Energy\ consumed} \tag{4}$$

All the performance parameters are determined using equations (1) to (4) and represented in section 3 in the form of graphical representation.

2.1. Multistage dehumidifier test rig construction and operation

Figure 2 shows the experimental test rig constructed. It mainly consists of an absorber unit where the dehumidification process is carried out, composed by four packings at different positions that reciprocate inside the desiccant solution.

The evaporator of a vapour compression refrigeration system is integrated in the absorber to regulate the desiccant temperature. Celdek 7090 is used for the multistage packing, which rotates thanks to a 0.3HP motor that powers a cam spring follower mechanism. A blower drives the air through a 25cm×25cm and 2.5 m length duct, where it interacts with the packing soaked with desiccant. As the air gets dehumidified, the desiccant concentration drops due to the water condensation. To regain the due concentration, the desiccant is driven to a preheater tank, where it is heated up to approximately 65°C, then driven to the heater tank equipped with an electric coil that supplies 1 kW. A separator consisting of baffled structured plates enables the mass transfer and the hot desiccant is pumped to a contact device system. The contact device consists of four further reciprocating packings where air interacts with the hot desiccant, removing the moisture and cooling it. The desiccant at the original concentration is pumped to a radiator where it is further cooled, then supplied to the absorber unit. The connection of the different systems is represented in Figure 3.

In this system, the reciprocating packing gets dipped inside to increase the wettability. The reciprocating action is enhanced due to cam follower mechanism powered by a 0.3 HP motor. Air is blown by a 0.5 HP blower and interacts with the Ca Cl_2 desiccant, which leads to moisture condensation. High desiccant concentration has low vapor pressure; hence the air moisture diffuses towards the concentrated desiccant. Low concentration desiccant is driven through a regenerator to regain the original concentration. The regenerator consists of a preheater, separator, heater and a contact device. Weak desiccant is preheated using the waste condenser heat from a VCR cycle. It is driven through the heater where the desiccant is heated to the boiling temperature, then enters the separator to eliminate moisture from the solution. The separator contains baffle plates and is insulated using Asbestos covering. This completes a first stage of dehumidification. The desiccant moves into the contact device where it is in contact with the reciprocating packing. Due to the vapor pressure difference between hot desiccant and the fresh air entering the contact device, a second stage dehumidification takes place. In the second stage regeneration, due to the packing action, the temperature of the desiccant slightly drops down. The high temperature concentrated desiccant is made to pass through the radiator to reduce the temperature drastically and the warm desiccant enters the absorber unit where the temperature of the desiccant is in equilibrium temperature due to the evaporator coil. Table.1 gives the operating conditions of the system.

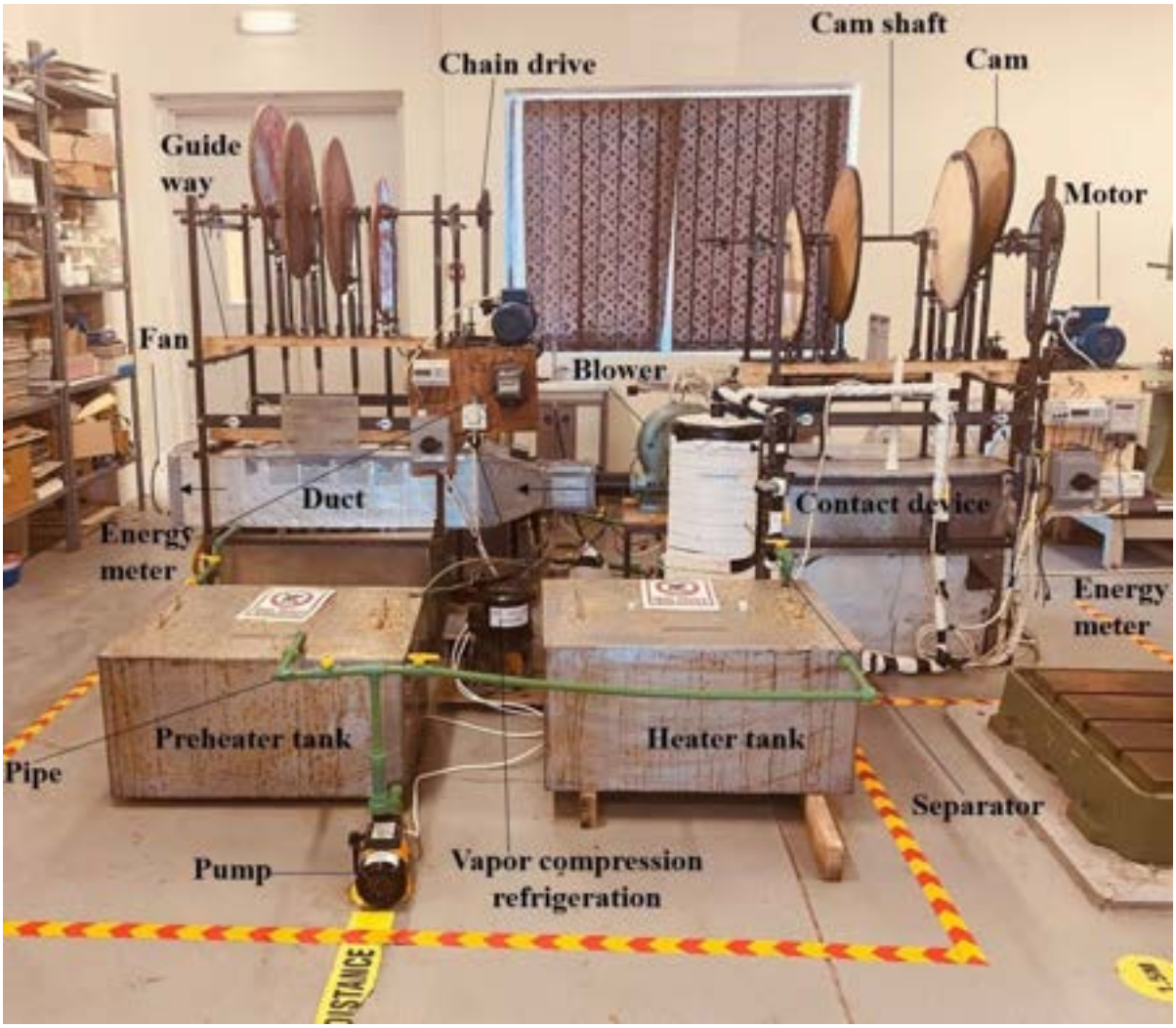

Figure.2: View of the multistage dehumidifier test rig

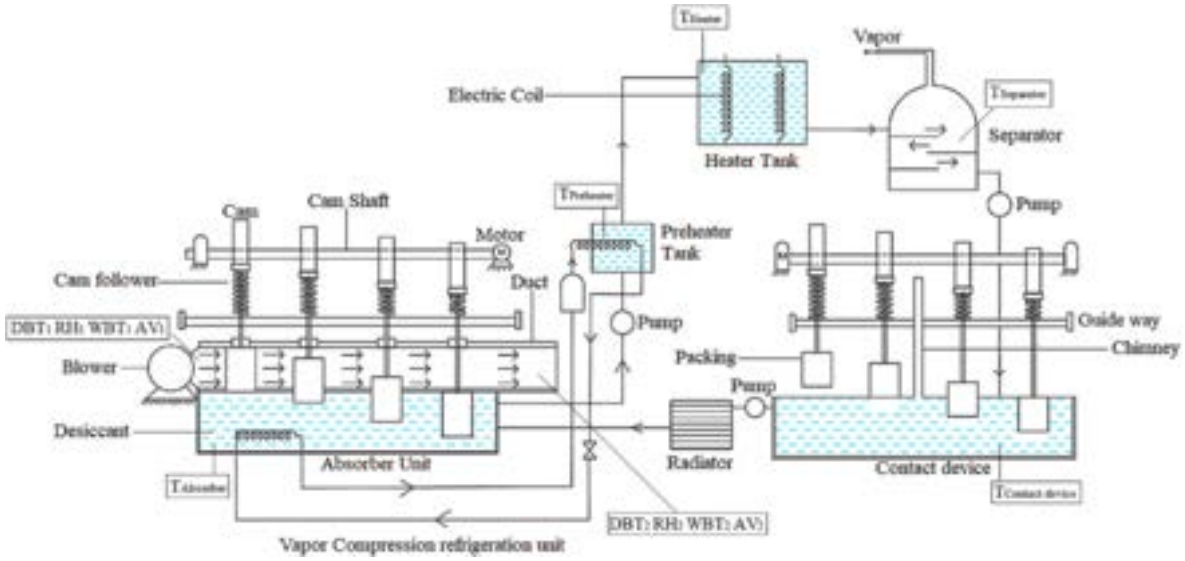

Figure.3: Scheme of the multistage dehumidifier test rig

Table.1. Experimental conditions and parameters studied

Packing, wettability, type of flow and fluids	Inlet conditions	Measuring parameters	Performance parameters
Packing: Celdek 7090, Wettability: 632 m^2/m^3 Type of flow: cross flow Fluids: Air and Calcium Chloride desiccant Cam shaft speed: 10 rpm	Inlet temperature: 30 to 42ºC Mass flow rate: 0.23 to 0.62 kg/s Desiccant concentration: 20%, 30% and 40%	Outlet temperature, relative humidity, wet bulb temperature	Moisture removal rate, COP, dehumidification efficiency, mass transfer coefficient

2.2. Measuring instruments

Several instruments are used to measure the operating parameters. A refractometer is used to measure the concentration of the salt. It measures the salinity range between 1 to 100% and has a resolution of 1%. The desiccant flow is measured using a flow meter which has a range of flow between 10 to 120 LPM and has a pressure value of 20 bar. Dry bulb temperature is measured using Pt100 thermometers with a range from -20 to 80°C, accuracy ± 0.1˚C, and resolution of 0.1˚C. To measure the wet bulb temperature, a Pt100 thermometer with similar specification is used, where the bulb is covered with a soaked cloth. Capacitive hygrometers are used to measure the relative humidity, which has a range of 0 to 99%. Anemometer measures the air velocity of air which has the range of 0.3 to 30 m/s and resolution 0.1 m/s. Tachometer measures the cam shaft speed of rotation which has range of 10 to 9999 rpm and resolution 0.1 rpm. Energy meter measures the total energy consumed by the unit during the operation period. It has voltage of 220 V, frequency 50 Hz and current 80 A.

3. Results and discussion

Experiments have been conducted by varying the mass flow rate of air and desiccant concentration. For a particular concentration, mass flow rate of air is varied from 0.23 kg/s to 0.62 kg/s with an increment of 0.1 kg/s. Air and desiccant conditions such as air temperature, specific humidity, desiccant concentration, and air velocity are measured at the inlet and exit of the system.

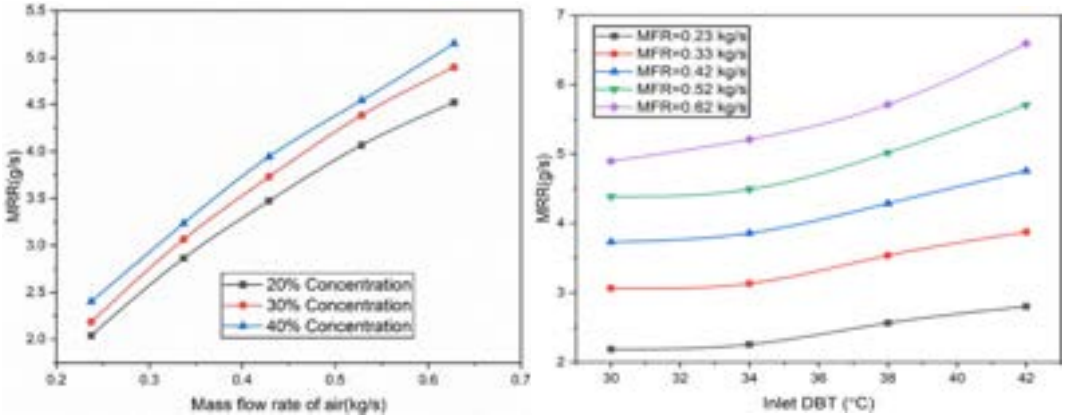

Figure. 4. Variation of MRR with mass flow rate of air and inlet DBT

Figure 4 shows the variation of MRR with the flow rate for different desiccant concentrations. As the concentration and mass flow rate increases, MRR also increases. Higher air velocities have higher mass flow rates. Even though difference in the humidity ratio decreases for higher mass flow rates, increased mass helps to remove more moisture per time unit. This increases the MRR (g/s). As the concentration is increased, vapour pressure difference between air and the desiccant also increase. Higher vapour pressure difference increases the ability to remove more moisture. Hence, 40% concentration desiccant absorbs more moisture than 20 %.

Figure 4 also shows the variation of MRR with the inlet air temperatures. For any value of fixed air relative humidity, as the air temperature increases, humidity ratio also increases. This increases the dehumidification capacity of the air sample. Hence, as the inlet air temperature increases, higher MRR is observed. The results show that for 0.52 kg/s air flow rate, MRR increases by 11.79% for 40% desiccant concentration, as compared to that of 20% concentration. Similarly, when the inlet temperature varies from 30 to 42°C, MRR increases by 30.2%.

3.1. Outlet DBT

Figure 5 shows the variation of the exit DBT with the mass flow rate and the inlet DBT for different desiccant concentrations. Higher concentrated desiccant can absorb more moisture from the air, or, in other words, higher heat of condensation is released. This heat increases the temperature of both the air and the desiccant. This leads to a rise in the exit air temperature for all tested cases. As the mass flow rate of the air increases, the amount of moisture being condensed reduces, which in turn reduces the exit air temperature.

Figure 5 also depicts the variation of the exit DBT for different air inlet temperatures. Higher inlet temperature increases the temperature rise for any fixed air mass flow rate. This is because higher inlet temperature is responsible for higher dehumidification, hence enhanced heat transfer rate, which also increases the air temperature. From the tested values, it is observed that the air exit temperature is 4.5% higher for 40 % desiccant concentration than for 20% concentration and 0.52 kg/s air flow rate. When the inlet temperature varied from 30 to 42°C, exit DBT raises by 83%.

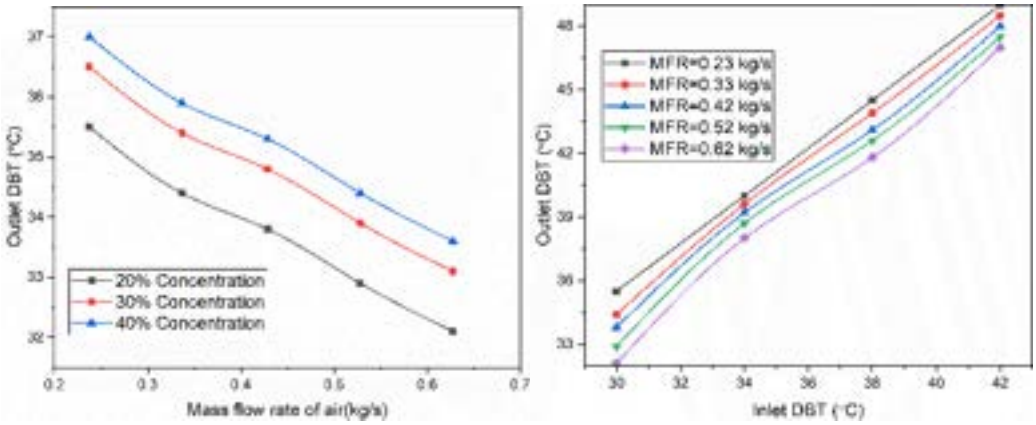

Figure. 5. Variation of outlet DBT of air with mass flow rate and inlet DBT

3.2. Dehumidification or moisture effectiveness (DE)

Dehumidification or moisture effectiveness (DE) is the ratio of moisture absorbed by the desiccant to the difference between the inlet and equilibrium moisture. Equilibrium moisture is the moisture contained by the air sample at the desiccant inlet conditions. It is clearly seen from figure 6 that higher desiccant concentrations show higher moisture effectiveness. This is because as the concentration increases, dehumidification also increases. For a constant value of equilibrium moisture, higher DE will be observed. As the mass flow rate of the moisture increases, DE value decreases resulting in reduced DE.

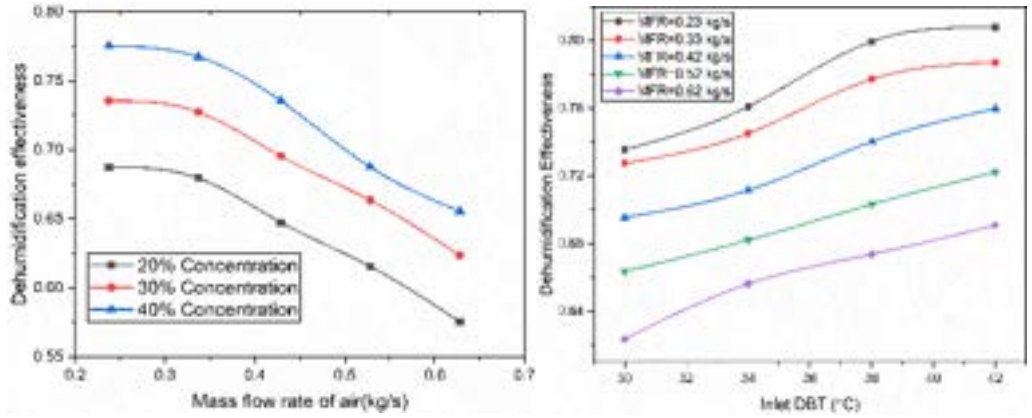

Figure. 6. Variation of Dehumidification effectiveness with mass flow rate and inlet DBT

Figure 6 also depicts the variation of DE for various inlet air temperatures. As the air inlet temperature increases, DE also increases. Similarly, as the inlet temperature increases, dehumidification capacity of air sample increases. For any constant RH condition, specific humidity values are higher for higher temperatures. This increases the dehumidification capacity. Hence higher temperature will have higher tendency for dehumidification. When the concentration is increased from 20% to 40%, DE increases 11.5% for 0.52 kg/s air flow rate. For the same air mass flow rate, when the inlet temperature increases from 30 to 42°C, DE increases by 10.6%.

3.3. COP

COP is the ratio of enthalpy change due to the dehumidification to the total energy input to the system. Total energy input includes the work supplied to the blower and the motor that runs the cams. It is observed from figure 7 that desiccant concentration significantly influences the COP, as the dehumidification values increase when increasing the desiccant concentration. Furthermore, as the air mass flow rate increases, COP tends to rise. Even though energy input to the blower increases for higher mass flow rates, the increased enthalpy difference contributes to higher COP values. It is also seen that higher inlet temperatures tend to enhance the COP. This is mainly due to the higher moisture absorbing capacity of the air sample at higher temperatures with fixed RH conditions. Concerning the energy requirements, these are independent from the inlet temperatures. Consequently, higher inlet DBT increases the enthalpy difference and hence the COP. The experimental results reveal that when the desiccant concentration is enhanced from 20 % to 40%, COP rises by 48%. Similarly, when the inlet temperature increased from 30 to 42°C, the COP is increased by 45% for 0.53 kg/s air flow rate.

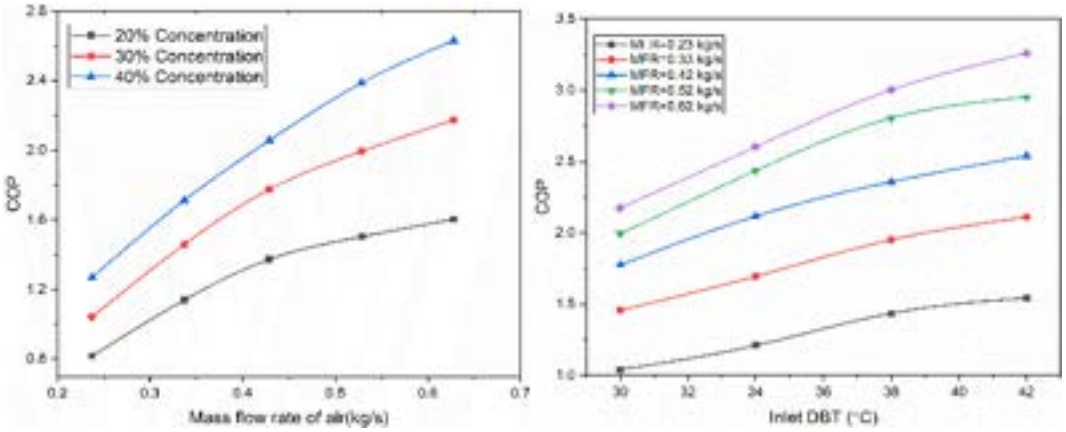

Figure 7. Variation of COP with mass flow rate and inlet DBT

4. Conclusions

Experimental investigations are conducted in a reciprocating multistage dehumidification unit to assess the dehumidification performance for different $CaCl_2$ desiccant concentrations and different air inlet temperatures. The results obtained can be summarized as follows:

- Multistage reciprocating dehumidification shows better performance as compared to that of a single stage stationary type, with higher values of MRR and moisture effectiveness.
- Increasing the concentration from 20 to 40% increases the MRR, DE, and COP by 17.6%, 13.2% and 53.6%, respectively, for 0.23 kg/s air flow rate.
- When the inlet temperature increased from 30 to 42°C, the performance parameters MRR, DE, and COP increased by 27.2%, 34.5% and 49 %, respectively, for 0.23 kg/s air flow rate.
- When the mass flow rate is increased from 0.23 kg/s to 0.72 kg/s, the DBT, humidity ratio, and DE decrease by 9.5%,7.2%,16.1%; whereas the MRR and the COP increase by 80% and 95%, respectively, for 20% desiccant solution and inlet temperature of 34°C.

Hence, it is seen that a multistage reciprocating dehumidification unit offers benefits such as higher performance with reduced desiccant consumption, as the desiccant remains stationary unlike the conventional dehumidification systems. As the four pads are intermittently in contact with air, pressure drop and energy consumption are lower. This contributes to more sustainable dehumidification technologies with minimum energy consumption and environmental pollution.

Acknowledgments

Authors are thankful to the lab support provided by the School of Engineering & IT, Manipal Academy of Higher education, Dubai, UAE.

Nomenclature

$\dot{m}$ mass flow rate, kg/s

T temperature, °C

ΔT temperature difference, °C

RH relative humidity, %

K mass transfer rate, kg/(m^{2}s)

w specific humidity, g/kg

HE Heating Effect, W

Greek symbols

ε dehumidification effectiveness or efficiency, %

Subscripts and superscripts

a air

av average

eq equilibrium

i inlet

o outlet

References

[1] Naik BK, Muthukumar P. Experimental investigation and parametric studies on structured packing chamber based liquid desiccant dehumidification and regeneration systems. Build Environ 2019;149:330-348.

[2] Salins SS, Reddy SVK, Kumar S. Assessment of process parameters in a dehumidification process using biomass-based wood shaving as a packing material. Indoor Built Environ 2022;31(2):496-509.

[3] Ou X, Cai W, He X. Model-based optimization strategy for a liquid desiccant cooling and dehumidification system. Energy Build 2019;194:21-32.

[4] Qasem NAA, Zubair SM. Performance evaluation of a novel hybrid humidification-dehumidification (air-heated) system with an adsorption desalination system. Desalination 2019;461:37-54.

[5] Salins SS, Kota Reddy SV, Shiva Kumar. Experimental Investigation and Neural network based parametric prediction in a multistage reciprocating humidifier. Appl Energy 2021;293.

[6] Kavasoğullari B, Cihan E, Demir H. Novel Packing Materials for Open Liquid Desiccant System. Energy Procedia; 2016.

[7] Zegenhagen MT, Ricart C, Meyer T, Kühn R, Ziegler F. Experimental Investigation of A Liquid Desiccant System for Air Dehumidification Working with Ionic Liquids. Energy Procedia; 2015.

[8] Wu A, Li C, Zhang H. The primary research on liquid desiccant dehumidifier with cooling capacity using compression heat pump system. International refrigeration and air conditioning Conference. 2006.

[9] Mohamed ASA, Ahmed MS, Hassan AAM, Hassan MS. Performance evaluation of gauze packing for liquid desiccant dehumidification system. Case Stud Therm Eng 2016;8:260-276.

[10] Sampath SS, Kumar S, Kota Reddy SV. Influence of Different Desiccants, Flow Type and Packings on the Liquid Desiccant Dehumidification System: A Review. Intl J Air-Conditioning Refrig 2020;28(1).

[11] Dong C, Qi R, Lu L, Wang Y, Wang L. Comparative performance study on liquid desiccant dehumidification with different packing types for built environment. Sc Tech Built Environ 2017;23(1):116-126.

[12] Wang L, Xiao F, Zhang X, Kumar R. An experimental study on the dehumidification performance of a counter flow liquid desiccant dehumidifier. Int J Refrig 2016;70:289-301.

[13] Jain S, Tripathi S, Das RS. Experimental performance of a liquid desiccant dehumidification system under tropical climates. Energy Convers Manage 2011;52(6):2461-2466.

[14] Bouzenada S, Frainkin L, Léonard A. Experimental investigation on vapor pressure of desiccant for air conditioning application. Procedia Computer Science; 2017.

[15] Lu, J., Wang, M., Li, Y. and Yang, L., 2017. Numerical study on dehumidification performance of a crossflow liquid desiccant air dehumidifier. Procedia Engineering, 205, pp.3630-3637.

[16] Seenivasan D, Selladurai V, Arjunan TV. Experimental studies on the performance of dehumidifier using calcium chloride as a liquid desiccant. Int J Energy Technol Policy 2018;14(1):49-63.

[17] Cheng X, Rong Y, Zhou X, Gu C, Zhi X, Qiu L, et al. Performance analysis of a multistage internal circulation liquid desiccant dehumidifier. Appl Therm Eng 2020;172.

[18] Li, C.H., Chen, C.Y., Yang, T.F., Li, W.K. and Yan, W.M., 2020. Experimental study on heat and mass transfer of a multistage planar dehumidifier. International Journal of Heat and Mass Transfer, 148, p.119104.

Solar volumetric receiver coupled to a parabolic dish: heat transfer and thermal efficiency analysis

Judit García-Ferrero [a], Rosa P. Merchán [b], María Jesús Santos [c], Alejandro Medina [d], Antonio Calvo Hernández [e], Paulo Canhoto [f] and Andrea Giostri [g]

*[a] Universidad de Salamanca, Salamanca, Spain, jgferrero@usal.es (**CA**)*
[b] rpmerchan@usal.es
[c] smjesus@usal.es
[d] amd385@usal.es
[e] anca@usal.es
[f] Universidade de Évora, Évora, Portugal, canhoto@uevora.pt
[g] Politecnico di Milano, Milano, Italy, andrea.giostri@polimi.it

Abstract:
Concentrated Solar Power plants are commonly recognized as one of the most attractive options within carbon free power generation technologies because their high efficiency and also because implementation of hybridization and/or storage is feasible. In this work a small-scale system focused on distributed production, in the range of kW_e (5 kW_e to 30 kW_e), is modeled. A parabolic dish collects direct solar power towards a receiver located at its focus. There, the heat transfer fluid increases its temperature for thermal storage or for directly producing electricity at the power block. Thus, this is a crucial component in CSP systems since it greatly influences global efficiency. There is a trade-off in the energy balance within the thermal receiver, since the higher the temperatures it achieves, the higher the radiation losses could be. In this work, a heat transfer analysis for an air volumetric receiver coupled to a parabolic dish is carried out. The solar receiver is modeled under steady-state conditions using a detailed set of equations. The model considers the main losses by convection, conduction and radiation at the glass window and the surrounding insulator. The temperatures and heat transfers along the different receiver zones are computed with a built from scratch in-house code programmed in Mathematica®. The thermal efficiency mainly depends on the incoming solar irradiance at the glass window, the receiver geometry and the type of materials considered, as well as on the ambient temperature. It is expected that this model (precise but not too expensive from the computational viewpoint) could help to identify the main bottlenecks, paving the way for optimization when designing solar volumetric receivers in this kind of systems.

Keywords:
Concentrated Solar Power, Solar receiver, Heat transfer, Parabolic dish, Distributed energy.

1. Introduction

A key element in any concentrated solar power (CSP) system is the solar receiver. It can be considered as a special type of heat exchanger with the aim to convert the input direct solar irradiance into heat for a thermal fluid. Receiver efficiency is essential to obtain a high efficiency in the overall CSP plant and so, commercial interest. Heat transfer processes in the solar receiver are very complicated and during the last years many experimental or simulation studies were conducted in order to propose optimized designs. A recent compilation of those studies is due to Sedighi *et al.* [1].

A particularly interesting application of CSP systems is the possibility of producing distributed electricity at the scale of kW_e, close to the consumption place. Solar dishes, for instance, are capable to perform this task with good efficiencies. A collecting parabolic dish reflects the input solar radiation into a solar receiver located at parabola focus, where it is transferred to a fluid that uses to be a gas running a thermodynamic cycle.

Particularly, Brayton cycles are being investigated due to their promising features as high efficiency, versatility, compactness, and possibility to integrate hybridization or storage schemes. Requirements for solar receivers designed to operate together with Brayton cycles include the necessity to operate at high temperatures (over about 800°C) and relatively high pressures [2].

Pressurized volumetric receivers use closed loops, can be compact and reach large efficiency at large temperatures and pressures adequate for Brayton cycles [3]. Moreover, can operate with gases different from air, as helium, argon, nitrogen or CO_2. Their design continue being a challenge nowadays in order to set the basis for new evolutions of CSP systems, increasingly interesting from an economic perspective. These receivers

are usually closed with a quartz glass window that can reach temperatures about 1200°C and its cooled by the thermal fluid itself or through an extra cooling system [4]. Behind the glass, there is a cavity containing a porous media, the absorber, that is directly impinged by solar radiation. The gas flows through its pores getting a high temperature. Foam can be metallic or ceramic [5]. The first are more economic and can reach temperatures about 1450°C, for instance with Nickel compounds. Other advantages of metal foams include high porosity and specific surface area, as well as, high mechanical strength. Outer walls of the receivers are usually thermally isolated from the ambient to minimize heat losses. Aluminum silicate is a usual material with a low thermal conductivity (around 0.06 W/(m.K) [6]. Bellos *et al.* [7] have reviewed the most recent technologies and advances on cavity receiver designs for solar dish concentrators.

Studies and analysis of solar receivers for solar dish applications include experiments and simulations at different levels. Zhu *et al.* [4, 6] performed both studies for an own design. The experimental study was conducted at Hangzhou, China, and consisted of a compressor, a dish and a receiver with a Ni foam absorber [4]. Variations with time of different parameters as energy and exergy efficiencies, heat losses, temperatures, pressures were performed at real solar conditions in a period with approximately constant direct normal irradiance (DNI). Subsequently, a simplified stationary model for heat transfer in receiver zones was presented [6]. A good agreement between experimental and calculated receiver efficiency (with values about 82%) was obtained.

At a different level of refinement, Wang *et al.* [8] developed a Computational Fluid Dynamics (CFD) model that was validated against experimental measures. A SiC (silicon carbide) absorber was utilized and different porous parameters were analyzed. Maximum temperatures of the outlet air slightly exceeded 1000 K. Solar to thermal efficiencies over 63% were obtained.

The aim of this work is to accurately predict the thermal efficiency of the system made up of a Parabolic Dish Collector (PDC) and a solar volumetric receiver placed at its focus. This system subsequently could be coupled to a thermal cycle, as Stirling or Brayton ones, to produce electric energy for distributed applications. This work is part of a series of studies by our group devoted to a complete modeling of the overall system, including the optics of the parabolic dish, the thermal efficiency of the receiver and the efficiency of the thermodynamic cycle. The methodology intends to be capable of making precise computations for each subsystem at a similar physical level, making clear the bottlenecks of all involved efficiencies with the aim to propose improved designs and operation schemes on the whole system [9]. Special emphasis on subsystems integration is envisaged. For instance, CFD analysis would be an alternative analysis method [10]. However, this would an extensive computational effort and the key physical factors affecting global system efficiency (and the corresponding efficiency bottlenecks) are not always easy to extract. Due to space limitations, in this paper only the model for the efficiency of the solar receiver is exposed.

A detailed set of equations for the heat transfer model in each of the stages during gas heating will be employed. The model includes some features not considered and/or barely touched in previous works, as the volumetric (instead of superficial) heat transfer coefficient for the porous media, different temperatures inside and outside of the glass window, losses across the receiver insulator, more accurate expressions for thermal radiation exchanges and a more complete set of view factors. All these factors are included in appropriate energy balance equations. Most important losses are also incorporated to the model. The models presented in the following paragraphs pursue to be realistic enough to precisely determine the thermal efficiency within a reasonable computational time. They include a comprehensive set of equations with a relatively large number of parameters, but all of them are controllable and with a clear physical origin and meaning.

2. Modelling

The solar receiver model was originally inspired in that from Zhu *et al.* [6], although significant modifications are introduced in order to enlarge its capabilities and to improve model accuracy. The solar receiver model is exposed in the following subsections.

2.1. Energy efficiency equation

The receiver thermal efficiency is the ratio between the heat absorbed by the fluid and the total heat flux impinging at the receiver aperture area, as it is shown in Eq. (1):

$$\eta_{th,rcv} = \frac{\dot{Q}_r}{I_b} = \frac{\dot{m}\,(\bar{h}_o - \bar{h}_i)}{\eta_d\, A_d\, DNI} \tag{1}$$

where $\dot{Q}_r$ stands for the heat flux absorbed by the fluid at the receiver. It can be calculated in terms of the fluid mass flow through the receiver, $\dot{m}$, and the difference between the outlet and inlet fluid specific enthalpies, $\bar{h}_o$ and $\bar{h}_i$, respectively. I_b is the solar radiation power impinging at the solar receiver window. This parameter can be expressed as the product of the parabolic dish optical efficiency, η_d, dish aperture area, A_d, and direct solar irradiance (DNI) [6, 11]. Thus, Eq. (1) encompasses solar receiver efficiency associated with heat losses and parabolic dish optical efficiency.

2.2. Solar volumetric modelling: Heat transfer equations

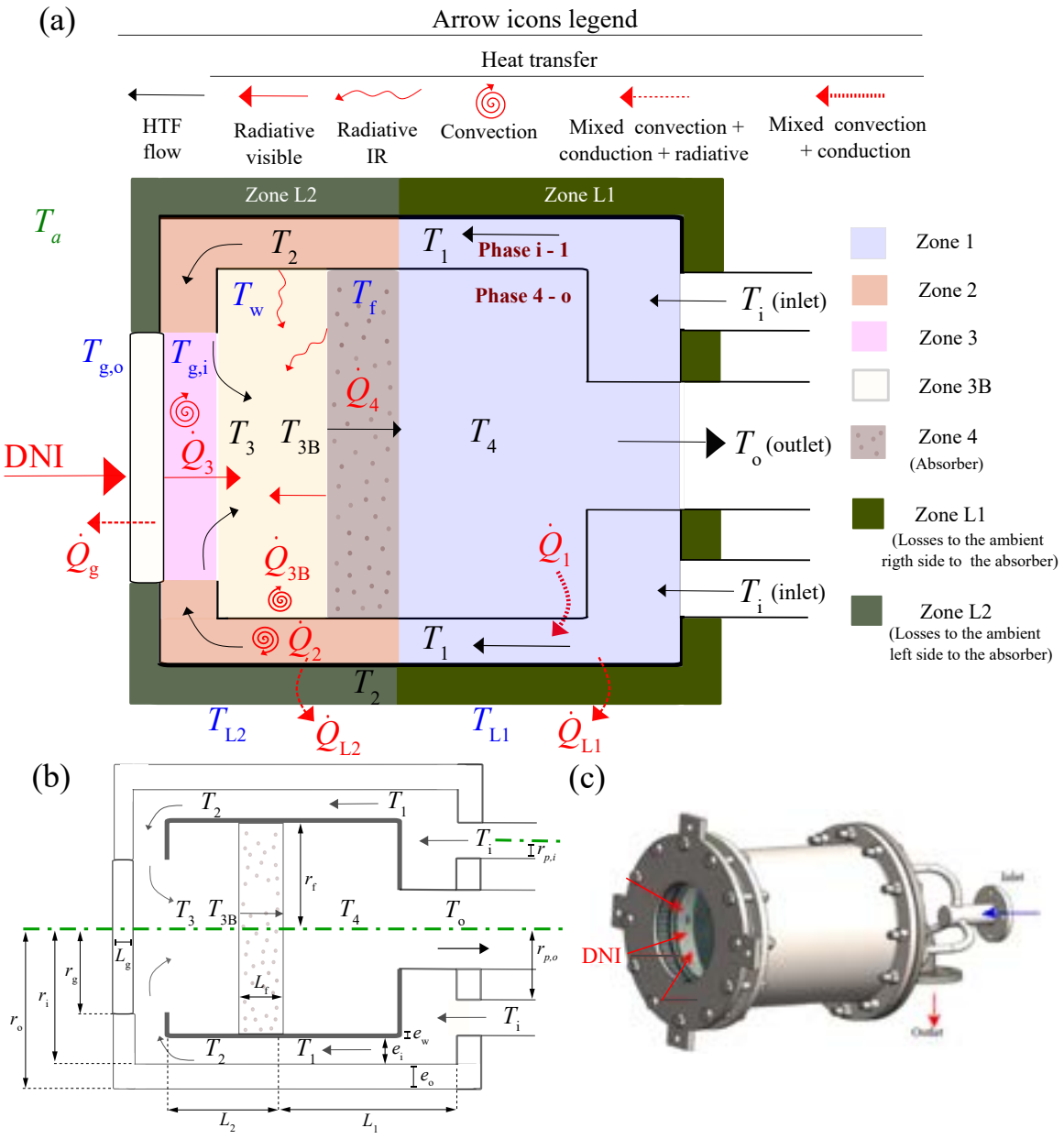

Figure 1: (a) Scheme of the receiver used for this work [6]. Air temperatures (T_i, T_1, T_2, T_3, T_{3B}, T_4 and T_o) are depicted in black. Surfaces temperatures related to glass, internal wall, absorber foam, front external insulator, and back external insulator (T_g, T_w, T_f, T_{L1} and T_{L2}, respectively) in blue and ambient temperature (T_a) is depicted in green. (b) Geometrical parameters used in the heat transfer model of the receiver. (c) 3D image of the receiver (taken from Zhu *et al.* [6]).

The solar receiver model presented hereby considers an axially cylindrical pressurized volumetric receiver with a geometrical design as shown in Fig. 1. For validation and numerical applications the design by Zhu *et al.* [6] will be considered, but the models developed in this paper could be applied to other designs and dimensions in a straightforward manner. The symmetry axis goes through the window centre and it is normal to the window surface. As commented in the Introduction, this kind of receivers are especially interesting for high-temperature applications because aperture quartz glasses can reach temperatures quite above 1000 °C and receiver thermal efficiency at such conditions can be very high. Usually, the heat transfer fluid (HTF) is pressurized air and the receiver core is a metal or ceramic foam that will be considered as a uniform medium with a given porosity (Zone 4 in Fig. 1).

All the temperatures and heat exchanges involved are included and shown in Fig. 1(a). Figure 1(b) displays the main geometric parameters considered. The HTF (air) enters the receiver at T_i temperature and crosses different zones until it arrives at the outlet, at temperature T_o. Next, a brief description of all zones is given.

- Zone 1: It can be split in two parts: phase $i-1$ (from the receiver inlet until the end of Zone 1), and phase $4-o$ (from Zone 1 after the absorbing foam until the receiver outlet). The colder air (at temperature T_i) receives heat ($\dot{Q}_1$) from the flux of air which is crossing the receiver outlet, since the latter has a higher temperature (T_o). Thus, the air arrives at Zone 2 at temperature T_1. Due to this heat exchange, the temperature at the receiver exit, T_o, is slightly lower than the air temperature just after crossing the absorber foam (T_4). The heat transfer can be modeled as a mixed convection and conduction process (similar to a heat exchanger).
- Zone 2: There is a heat transfer ($\dot{Q}_2$) through the inner cylinder wall (at temperature T_w) to the air, which rises its temperature from T_1 to T_2. $\dot{Q}_2$ comes from the thermal and visible radiation emitted by the absorber foam and the glass window to the inner cylinder wall.
- Zone 3: The air receives a heat flux $\dot{Q}_3$ by means of convection with the inner glass surface (at temperature $T_{g,i}$). Thus, the air achieves temperature T_3. Besides, the heat balance at the glass window has to be considered, and it will be further explained in detail in the following paragraphs.
- Zone 3B: The air exchanges a heat flux, $\dot{Q}_{3B}$, through convection with the inner wall surface (at temperature T_w). Hence, the air arrives at the absorber foam at temperature T_{3B}. $\dot{Q}_{3B}$ influences the energy balance at Zone 2.
- Zone 4: Here, the fluid crosses the absorber foam (at temperature T_f), receiving thus a heat flux $\dot{Q}_4$. In this stage, the air rises its temperature up to T_4. The heat transfer corresponds to a convection with the pores inside the absorber foam.

The previous brief explanation serves as an introduction to the set of equations employed for simulating the receiver. The equations are exposed in the following paragraphs but first, some considerations should be noticed:

- This work presents a steady-state model. Hence, mass balance equations ($\dot{m}_i = ... = \dot{m}_o = \dot{m}$) will be indirectly included within heat balance equations.
- Absorber foam (T_f) temperature is considered uniform along the whole material. This assumption means that T_f is the left, right and inside temperature for the absorber foam.
- The wall of the inner cylinder is considered a grey body under thermal-balance conditions. Then, its absorptivity (α_w) and emittance (ϵ_w) are equivalent. This element also possesses a uniform temperature T_w.
- It has been considered negligible the glass thermal radiation transmittance. Thus, there are no radiation losses across the glass (greenhouse effect).

As in any heat transfer process, three equations should be taken into account: heat transfer mechanisms, and mass and energy balances. As previously mentioned, mass balance is included within enthalpy balance. Regarding the pressure, it has been considered a global pressure drop of 0.2 bar [11] across the receiver. However, for each heat transfer, the pressure drop is small enough for considering it constant. Thus, within the equations, the isobaric heat capacity, $\bar{c}_p$, will be considered instead of enthalpies. The following equations describe the volumetric solar receiver model:

2.2.1. Zone 1

The heat exchange in this zone is modeled as a heat exchanger (Logarithmic Mean Temperature Difference, LMTD, expression will be considered). Then, the energy balance can be written as:

$$\dot{Q}_1 = \dot{m}\,\bar{c}_p(T)(T_1 - T_i) + \dot{Q}_{L1} = \dot{m}\,\bar{c}_p(T)(T_4 - T_o) \tag{2}$$

Here, $\dot{Q}_{L1}$ stands for the thermal losses through the insulator (Zone L1, see Fig. 1). Besides, as a heat exchanger, the heat transfer should meet the following relation:

$$\dot{Q}_1 = U_1 A_1 \frac{(T_o - T_i) - (T_4 - T_1)}{\log \dfrac{(T_o - T_i)}{(T_4 - T_1)}} \tag{3}$$

where $\bar{c}_p(T)$ stands for the average isobaric thermal capacity between temperatures T_i and T_1, or between T_4 and T_o. $\bar{c}_p(T_m)$ is calculated through REFPROP coupled with Mathematica® [12, 13]. Regarding U_1, it represents a global conduction and convection heat transfer coefficient, while A_1 stands for the effective Zone 1 area.

2.2.2. Zone 2

The heat transfer in this zone, $\dot{Q}_2$, is also modeled as a heat exchanger, where the air and the inner wall cylinder are involved. The energy balance can be written as:

$$\dot{Q}_2 = \dot{m}\bar{c}_p(T)(T_2 - T_1) + \dot{Q}_{L2} = h_{wo}A_w \frac{(T_w - T_1) - (T_w - T_2)}{\log \frac{(T_w - T_1)}{(T_w - T_2)}} \tag{4}$$

where $\dot{Q}_{L2}$ represents the thermal losses through the insulator (Zone L2 in Fig. 1) and T_1, T_2 are the air temperatures at Zone 1 and Zone 2, respectively. h_{wo} is the convective coefficient at the inner cylinder outer surface wall. A_w stands for the inner cylinder wall area, but it only comprises the wall area in between the absorber foam and the glass window. Temperature T_w is the inner wall temperature.

Finally, heat flux $\dot{Q}_2$ emitted by the wall comes from the absorber foam and from the glass window. The absorber foam releases thermal and visible radiation due to the reflection of the direct sun beam radiation (I_b) impinging on it. It also receives visible radiation from the glass window. At the same time, the wall losses energy due to the convection with the air crossing Zone 3B, and thermal radiation to the glass window are considered. Then, the following heat balance equation can be written:

$$\dot{Q}_2 = \overbrace{\tau_g\, I_b\, F_{gf}\cdot \rho_f\, F_{fw}}^{\text{Visible radiation from foam}} + \overbrace{\tau_g\, I_b\, F_{gw}(1 - \rho_w\, F_{wf} - \rho_w\, F_{wg})}^{\text{Visible radiation from glass window}} + \frac{\overbrace{\sigma(T_f^4 - T_w^4)}^{\text{Thermal radiation from foam}}}{\frac{1-\epsilon_f}{A_f\,\epsilon_f} + \frac{1}{A_f\,F_{fw}} + \frac{1-\epsilon_w}{A_w\,\epsilon_w}} - \frac{\overbrace{\sigma(T_w^4 - T_{g,i}^4)}^{\text{Thermal radiation to the glass}}}{\frac{1-\epsilon_w}{A_w\,\epsilon_w} + \frac{1}{A_w\,F_{wg}} + \frac{1-\epsilon_g}{A_g\,\epsilon_g}} - \underbrace{\dot{Q}_{3B}}_{\text{Convection with air}} \tag{5}$$

where ϵ_w, ϵ_f and ϵ_g are the wall, absorber foam and glass window emissivities, respectively. Note that the wall is being considered as a grey body in thermal equilibrium. Thus, the wall absorptivity (*i.e.* the share of energy that the wall will absorb and transfer to the air) is the same as the wall emissivity ($\alpha_w = \epsilon_w$). The share of visible radiation reflected by the foam and by the wall are represented as ρ_f and ρ_w, respectively, while τ_g is the glass window transmissivity. A_f is the cross-sectional foam area, and σ is the Stefan-Boltzmann constant. The term F_{fw} is the '*view factor*' between the foam and the wall. It represents the ratio between the amount of thermal radiation leaving the foam that hits the wall [14]. Similarly, F_{wg} is the wall-to-glass view factor, and F_{gf} is the glass-to-foam view factor. Finally, T_f and $T_{g,i}$ are the absorbing foam and the inner glass surface temperatures, respectively. $\dot{Q}_{3B}$ is the convection heat exchange between the inner wall and the fluid, which will be defined later.

2.2.3. Zone 3

Here, the air fluxes over the internal surface of the glass window. This prevents the window breakage, since the air flux lowers its temperature. On one hand, there is a convection heat transfer between the air and the inner window surface, which can also be modeled as a heat exchanger. Thus, the following equations can be used:

$$\dot{Q}_3 = \dot{m}\bar{c}_p(T)(T_3 - T_2) = h_{gi}A_g \frac{(T_{g,i} - T_3) - (T_{g,i} - T_2)}{\log \frac{(T_{g,i} - T_3)}{(T_{g,i} - T_2)}} \tag{6}$$

where h_{gi} is the convective coefficient at the glass inner surface, A_g is the cross sectional glass area, T_g is the glass window temperature and T_3, T_2 are the Zone 3 and Zone 2 air temperatures, respectively.

Besides, some other heat transfers occurs at the glass window. It receives visible radiation directly from the Sun (I_b) as well as from the absorber foam ($\sim F_{fg}\,\rho_f\,\tau_g\,I_b$). The window also receives thermal radiation from the wall and the foam. However, it also suffers convection and radiation losses with the ambient. The convection heat transfer with the air can be also considered a 'loss' at the glass window inner surface. All these phenomena can be summarized in the following expression:

$$\begin{aligned}\overbrace{\alpha_g \cdot I_b + \tau_g\, I_b\,(F_{fg}\,\rho_f\,F_{fg} + F_{gw}\,F_{wg}\,\rho_w)}^{\text{Visible radiation}} + \frac{\overbrace{\sigma(T_f^4 - T_{g,i}^4)}^{\text{Thermal radiation from foam}}}{\frac{1-\epsilon_f}{A_f\,\epsilon_f} + \frac{1}{A_f\,F_{fg}} + \frac{1-\epsilon'_g}{A_g\,\epsilon'_g}} + \frac{\overbrace{\sigma(T_w^4 - T_{g,i}^4)}^{\text{Thermal radiation from wall}}}{\frac{1-\epsilon_w}{A_w\,\epsilon_w} + \frac{1}{Aw\,F_{wg}} + \frac{1-\epsilon'_g}{A_g\,\epsilon'_g}} = \\ = \underbrace{\dot{Q}_3}_{\text{Convection with air}} + \underbrace{h_{go}\,A_g\,(T_{g,o} - T_a)}_{\text{Convection with ambient}} + \underbrace{\epsilon'_g\,A_g\,\sigma\,(T_{g,o}^4 - T_a^4)}_{\text{Radiation with ambient}}\end{aligned} \tag{7}$$

where α_g is the glass absorptance at visible wavelength. ϵ'_g is the glass emissivity at long wavelength and F_{fg} is the foam-to-glass view factor. Finally, h_{go} stands for the convective coefficient at the outer glass surface.

2.2.4. Zone 3B

Aiming to model the solar receiver as realistic as possible, it has been considered a convection heat exchange between the internal wall, on the inner side, with the fluid. This heat transfer is not considered in [6]. The energy balance equations describing this phenomena will be related to the energy balance at Zone 2 ($\dot{Q}_{3B}$ in Eq. (5)):

$$\dot{Q}_{3B} = \dot{m}\bar{c}_p(T)(T_{3B} - T_3) = h_{wi}A_w \frac{(T_w - T_3) - (T_w - T_{3B})}{\log \dfrac{(T_w - T_3)}{(T_w - T_{3B})}} \tag{8}$$

where h_{wi} is the convective coefficient at the wall inner surface, A_w is the internal wall area, T_w is the wall temperature and T_{3B}, T_3 are the Zone 3B and Zone 3 air temperatures, respectively.

2.2.5. Zone 4

At this stage, the absorbing foam exchanges heat with the air crossing through it. This occurs through convection, so the energy balance equations are:

$$\dot{Q}_4 = \dot{m}\bar{c}_p(T)(T_4 - T_3) = V_f \cdot h_{vf} \frac{(T_f - T_3) - (T_f - T_4)}{\log \dfrac{(T_f - T_3)}{(T_f - T_4)}} \tag{9}$$

where V_f is the absorber foam vacuum volume $V_f = A_f L_f \phi$. The parameters ϕ and L_f are the foam porosity and foam width, respectively. Zhu *et al.* [4, 6] only provides the pore diameter, d_p, and the Pores Per Inch, (PPI). Thus, Fu *et al.* [15] expression was used for obtaining the absorbing foam porosity: $\phi = (\pi/4)(\text{PPC}\, d_p)^2$ where PPC refers to 'Pores Per Centimeter'. It can be calculated by means of PPI.

The volumetric convective coefficient, h_{vf}, is obtained by following Barreto *et al.* [10], Wu *et al.* [16] and Fu *et al.* [15] works. Similarly to previous equations, T_4 stands for the air temperature at the foam outlet. Besides, an energy balance for the absorber foam system must be established. The foam absorbs the visible radiation coming from the glass window, but it also suffers some losses: visible radiation reflected, convection heat transfer with the air, and thermal radiation emitted to the wall and glass. So, the following equation can be written:

$$\overbrace{\tau_g\, I_b\, F_{gf}(1-\rho_f)}^{\text{Visible from glass to foam}} + \overbrace{\tau_g\, I_b\, F_{gw}\cdot F_{wf}\,\rho_w}^{\text{Visible from wall to foam}} = \dot{Q}_4 + \frac{\overbrace{\sigma(T_f^4 - T_w^4)}^{\text{Thermal radiation to the wall}}}{\frac{1-\epsilon_f}{A_f\,\epsilon_f} + \frac{1}{A_f\,F_{fw}} + \frac{1-\epsilon_w}{A_w\,\epsilon_w}} + \frac{\overbrace{\sigma(T_f^4 - T_{g,i}^4)}^{\text{Thermal radiation to the glass}}}{\frac{1-\epsilon_f}{A_f\,\epsilon_f} + \frac{1}{A_f\,F_{fg}} + \frac{1-\epsilon_g}{A_g\,\epsilon_g}} \tag{10}$$

The air temperatures at all the stages are perfectly characterized by those previous equations. However, losses through the receiver insulator must be modeled in order to obtain more precision when analyzing the system.

2.2.6. Heat losses at the insulator: Zone L1

This zone refers to the cylindrical insulator from the inlet pipes until the absorber foam plane. It also considers the plane surface surrounding the inlet and outlet pipes, as depicted in Fig. 1. The heat transfer across the insulator surfaces will be modeled as a heat exchanger. So, the heat transferred from the air to the insulator (convection and conduction) must be the same as the heat flux from the outer insulator surface to the surroundings (convection and radiation).

$$\dot{Q}_{L1} = A_{iL1}\, U_{L1} \frac{(T_1 - T_{L1}) - (T_i - T_{L1})}{\log \dfrac{(T_1 - T_{L1})}{(T_i - T_{L1})}} \tag{11}$$

where $\dot{Q}_{L1}$ denotes the heat flux that is lost through the Zone L1. A_{iL1} stands for the internal insulator area, including the cylindrical and the circular sectors ones. U_{L1} is an effective heat transfer coefficient, which accounts for the cylindrical and plane zones. Thus, $A_{iL1}\, U_{L1}$ can be written as:

$$A_{iL1}\, U_{L1} = A_{iL1.cyl}\, U_{cyl.L1} + A_{iL1.flat}\, U_{flat.L1} \tag{12}$$

where:

$$A_{iL1.cyl} = 2\,\pi\, r_i\, L_1; \qquad A_{iL1.flat} = \pi\,(r_i^2 - r_{p,o}^2 - 3r_{p,i}^2) \tag{13}$$

$$U_{cyl.L1} = \left[\frac{1}{h_{L1,in}} + \frac{r_i \cdot \log(r_o/r_i)}{k_i}\right]^{-1}; \qquad U_{flat.L1} = \left[\frac{1}{h_{L1,in}} + \frac{e_o}{k_i}\right]^{-1} \tag{14}$$

$U_{cyl.L1}$ and $U_{flat.L1}$, represent two global conduction and convection heat transfer coefficients for the cylindrical and flat areas, respectively. The insulator thermal conductivity (0.06 W/(m.K) for aluminium silicate) is denoted by k_i, e_o stands for the insulator thickness and $h_{L1,in}$ represents an average convection coefficient for the inner insulator surface. r_i denotes the inner insulator cylinder radius while r_o accounts for the external insulator radius, respectively. $r_{p,i}$ and $r_{p,o}$ are the inlet and outlet pipes radius. The effective flat area, $A_{iL1.flat}$, does not include the three inlet pipes nor the outlet pipe (see Eq. (13)). The last heat exchange occurs at the outer insulator surface, where convection and radiation with the surroundings has been considered. Thus, this phenomenon can be described through the following expression:

$$\dot{Q}_{L1} = A_{o1}\,(h_{c,L1} + h_{r,L1})\,(T_{L1} - T_a) \tag{15}$$

where A_{o1} represents the insulator outer surface area in Zone L1, including cylindrical and flat ones:

$$A_{o1} = A_{o1,cyl} + A_{o1,flat} = 2\,\pi\,r_o\,L_1 + \pi\,(r_o^2 - r_{p,o}^2 - 3r_{p,i}^2) \tag{16}$$

$h_{c,L1}$ is the convection coefficient between the outer insulator surface temperature (T_{L1}) and ambient temperature (T_a), while $h_{r,L1}$ stands for the radiation coefficient under the same conditions. This radiation coefficient can be written as follows [17]:

$$h_{r,L1} = \epsilon_{L1}\,\sigma\,(T_{L1} + T_a)(T_{L1}^2 + T_a^2) \tag{17}$$

where ϵ_{L1} is the outer insulator surface emissivity.

2.2.7. Heat losses at the insulator: Zone L2

This zone refers to the cylindrical insulator from the absorber foam plane until the glass window plane. It also takes into account the plane surface surrounding the glass window, as depicted in Fig.1. Similarly to Zone L1, the heat transfer across the insulator surfaces will be considered as heat exchangers.

$$\dot{Q}_{L2} = A_{iL2}\,U_{L2}\,\frac{(T_2 - T_{L2}) - (T_1 - T_{L2})}{\log\dfrac{(T_2 - T_{L2})}{(T_1 - T_{L2})}} \tag{18}$$

where $\dot{Q}_{L2}$ denotes the heat flux lost through the insulator front side. $A_{iL2}\,U_{L2}$ is an effective heat transfer coefficient, which accounts for the cylindrical and flat zones.

The coefficients are analogous to those explained for Eqs. (11) and (13). The only difference is that here, the temperatures involved are T_2, T_1 and T_{L2} (the outer insulator surface temperature in Zone L2) as depicted in Fig. 1. r_g stands for the receiver glass window radius.

Again, the heat released from the outer insulator surface to the surroundings, can be described by:

$$\dot{Q}_{L2} = A_{o2}\,\left(h_{c,L2} + h_{r,L_2}\right)\,(T_{L2} - T_a) \tag{19}$$

where A_{o2} represents the insulator outer surface area within Zone L2, including cylindrical and flat ones.

$h_{c,L2}$ is the convection coefficient between the outer insulator surface temperature (T_{L2}) and ambient temperature (T_a), while $h_{r,L2}$ stands for the radiation coefficient under the same conditions.

2.3. Receiver thermal energy efficiency

All previous equations allow for calculating the receiver efficiency by means of Eq. (1) through the resolution of T_o. However, $\eta_{th,rcv}$ can also be estimated by means of the heat fluxes as follows:

$$\eta_{th,rcv} = \frac{\dot{Q}_1' + \dot{Q}_2' + \dot{Q}_3 + \dot{Q}_{3B} + \dot{Q}_4 - \dot{Q}_1}{I_b} \tag{20}$$

where $\dot{Q}_1' = \dot{Q}_1 - \dot{Q}_{L1}$ and $\dot{Q}_2' = \dot{Q}_2 - \dot{Q}_{L2}$. Within Zone 1, a wall temperature, T_w, it is not considered, and the inner cylinder wall is assumed to be a heat exchanger. So, note that $\dot{Q}_1$ is not a net flux since it is gained by the fluid at the inlet (phase $i-1$) but it is lost at the output (phase $4-o$). Considering this, Eq. (20) can be rewritten as:

$$\eta_{th,rcv} = \frac{\dot{Q}_2 + \dot{Q}_3 + \dot{Q}_{3B} + \dot{Q}_4 - \dot{Q}_{L1} - \dot{Q}_{L2}}{I_b} \tag{21}$$

Finally, the efficiency can also be expressed as a function of heat losses as follows:

$$\eta_{th,rcv} = 1 - \frac{\dot{Q}_g + \dot{Q}_{L1} + \dot{Q}_{L2} + \rho_g I_b}{I_b} \tag{22}$$

where the term $\rho_g I_b$ accounts for the share of solar energy radiation reflected by the glass window.

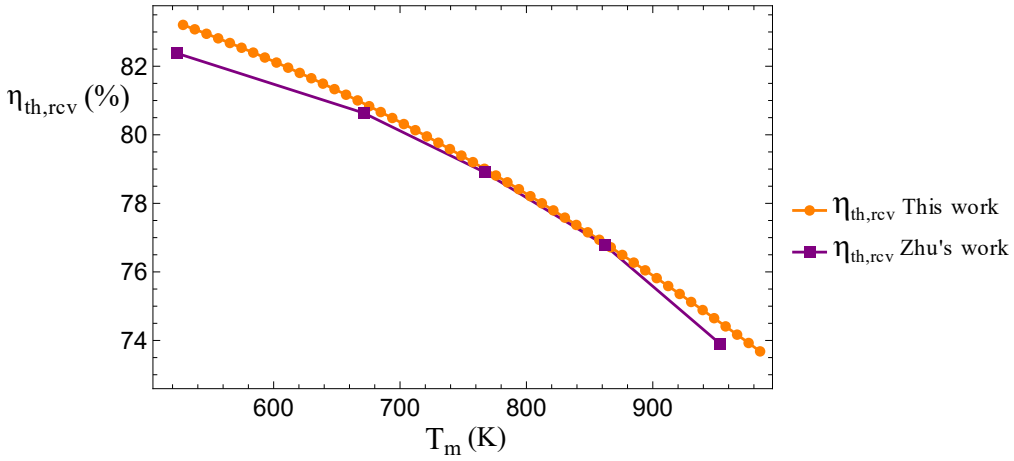

Figure 2: Solar receiver thermal efficiency as a function of mean receiver temperature, T_m: Comparison between Zhu's model (purple) [4] and this work (orange).

3. Validation

In this subsection, the validation of the solar receiver model is presented. As mentioned before, the geometry has been mainly taken from Zhu's work [4]. The optical efficiency will be taken as the same that Zhu *et al.* provide (η_d = 0.8645). In Table 1, the value of the parameters employed for the validation process are exposed. In Fig. 2, a comparison between the values obtained in this work and Zhu *et al.* [6] results is depicted. It shows a good agreement, especially in the medium zone of the temperature interval. The smallest relative difference (0.05%) is found at 861.8 K. The greater relative differences are found at the lowest temperature (1.06% at 523.9 K) and at the highest temperature (0.83% at 953.3 K). The relative difference is below 1.5% for all the cases. Thus, it can be considered that the model presented here has been validated.

4. Application

The model presented here can be used to predict the thermal receiver efficiency at specific locations with different meteorological conditions. In Fig. 3, the receiver thermal efficiency for two days is presented. The mass flow rate remains constant in these simulations. The location selected is Ouarzazate (Morocco) and the days are one day in summer (June 24th, 2021) and one day in winter (December 22th, 2021). The variation of DNI and ambient temperature (T_a) are also attached.

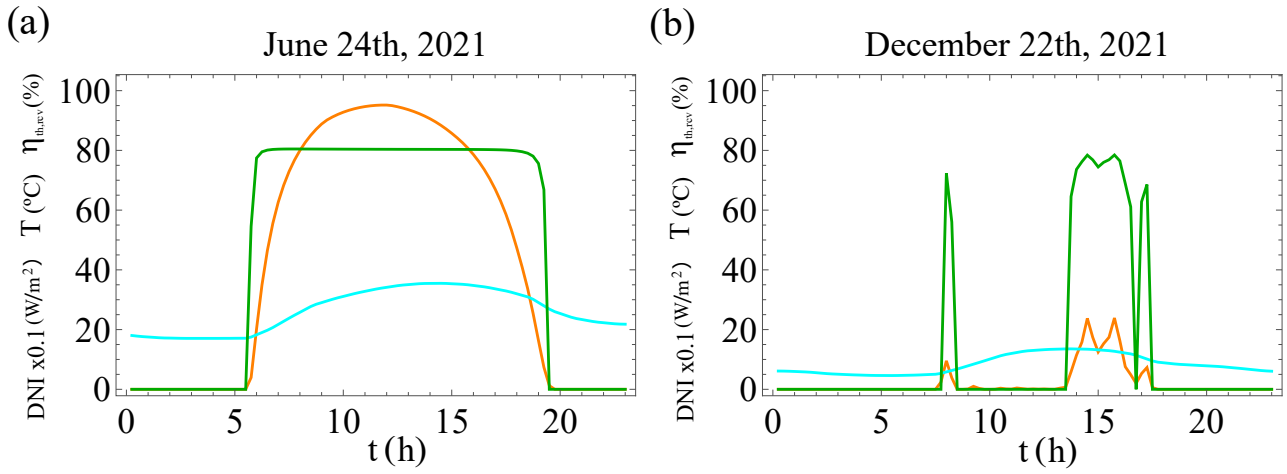

Figure 3: Solar receiver thermal efficiency along one day at Ouarzazate (Morocco). The thermal receiver efficiency, ($\eta_{th,rcv}$, (%), green), DNI (W/m^2) multiplied by 0.1 (orange) and ambient temperature (°C, cyan) are depicted together. (a) June 24th, 2021. (b) December 22th, 2021. December month is exposed for proving that, if DNI overcome a minimum value, receiver's thermal efficiency could achieve values close to the ones obtained in summer.

Table 1: Solar receiver parameters for the validation with Zhu's [6] work.* These parameters are not made explicit within Zhu's work.

Nomenclature	Value (unit)	
DNI	600 W/m^2	Solar heat flux impinging at the glass window
σ	5.67 10^{-8} W/(m^2 K^4)	Stefan Boltzmann constant
$\dot{m}$	0.04 kg/s	Mass flow rate
η_d	0.8645	Dish optical efficiency
A_d	44 m^2	Dish aperture area
Glass window		
ρ_g	0.136	Reflectivity at visible wave
τ_g	0.851	Transmissivity at visible wave
α_g	0.013	Absorptivity at visible wave
$^*\alpha'_g$	1	Absorptivity at long wave (perfect)
r_g	0.125 m	Radius
$^*L_g$	0.015 m	Glass thickness
Inner cylinder wall		
ρ_w	0.2	Reflectivity at visible wave
ϵ_w	0.8	Emissivity (grey body at thermal equilibrium)
A_w	0.1788 m^2	Total wall area (only the share of wall placed in between porous matrix and glass window)
$^*e_w$	0.001 m	Wall thickness
Foam porous matrix		
ρ_f	0.05	Reflectivity at visible wave
ϵ_f	0.95	Emissivity (grey body at thermal equilibrium)
r_f	0.182 m	Radius
L_f	0.065 m	Foam width
ϕ	0.792 (-)	Porosity
PPI / PPC	75 / 29.53	Pores Per Inch / Pores Per Centimeter
d_p	3.40·10^{-4} m	Pore diameter
d_c	1.86·10^{-3} m	Average pore cell diameter
l_s	6.58·10^{-4} m	Strut length
Geometrical parameters*		
L_1	0.195 m	Receiver length for the phase i – 1 (to the right of the foam)
L_2	0.1079 m	Receiver length for the phase 1 – 2 (to the left to the foam)
e_i	0.014 m	Radius difference between inner wall and insulator cylinders
r_i	0.136 m	Internal insulator radius
e_o	0.003 m	Insulator thickness
r_o	0.2 m	External insulator radius
Inlet and outlet pipes		
$r_{p,i}$	0.01 m	Inlet pipe radius
$^*r_{p,o}$	0.042 m	Outlet pipe radius
View factors		
F_{fg}	0.4193	Foam porous matrix to glass window
F_{fw}	0.5807	Foam porous matrix to inner wall
F_{gf}	0.8891	Glass window to foam porous matrix
F_{gw}	0.1109	Glass window to inner wall
F_{wf}	0.6069	Inner wall to foam porous matrix

Meteorological data were taken from MERRA (Modern-Era Retrospective Analysis) for the ambient temperature and from Copernicus Europe's eye on earth for the DNI data. Both of them were provided by Solar Radiation Data (SoDa) Service [18, 19]. If the DNI overcomes the minimum value of 30 W/m^2 (necessary for the set of equations to converge), the receiver thermal efficiency ranges between 80.47 % and 54.57 % in June, and between 78.45 % and 56.01 % in December.

The results in Fig. 3(a) shows an almost constant value for $\eta_{th,rcv}$ during the central hours of the day (a sunny day without DNI oscillations), reaching values above 82%. The day selected in December is a cloudy day with strong oscillations of DNI. Mean temperature is quite lower than in June. In spite of this, maximum thermal efficiency value is 78.45 % (only 2.42 % below the maximum for June, achieved at a DNI value of 768 W/m^2).

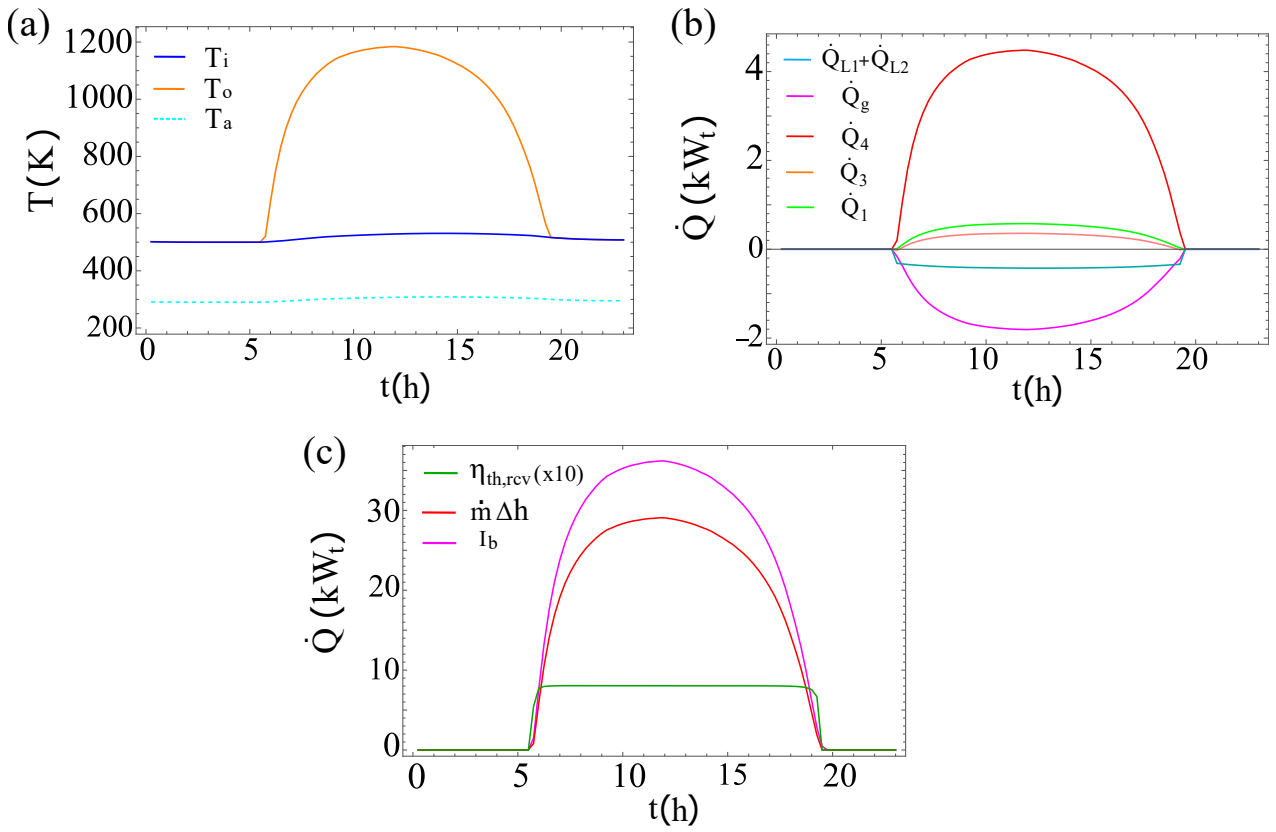

Figure 4: Solar receiver outputs throughout the day June 24th, 2021, at Ouarzazate (Morocco). (a) Inlet (orange), outlet (blue) and ambient temperatures (cyan) in K (T_i,T_o and T_a, respectively). (b) Fluid Heat fluxes ($\dot{Q}_1$ (green), $\dot{Q}_3$ (orange), $\dot{Q}_4$ (red) and losses trough the glass window ($\dot{Q}_g$ (magenta) and trough the insulator $\dot{Q}_{L1}$ + $\dot{Q}_{L2}$ (dark cyan)). $\dot{Q}_4$ is multiplied by $0.2 \cdot 10^{-3}$ and $\dot{Q}_g$ is multiplied by 10^{-3}. (c) Thermal receiver efficiency, ($\eta_{th,rcv}$ in green), is multiplied by 10. The product of mass flow and enthalpy increase ($\dot{m} \cdot \Delta h$) (red) and the solar power at the receiver window, I_b (magenta) are depicted together.

In Fig. 4, some of the output indicators of the receiver model throughout June 24th, 2021 are presented. It has been considered that during night hours, and also for DNI values below 30 W/m^2, the system is turned off. Fig. 4(a) depicts the inlet and outlet temperature (T_i (blue) and T_o (orange), respectively). While T_i seems to follow ambient temperature (T_a) shape (plotted in cyan), the outlet temperature resembles the shape of DNI during the sunlight hours. In Fig. 4(b) it is clear that the heat absorbed inside the porous foam, $\dot{Q}_4$ (red), is the highest heat flux contribution to the fluid for raising its temperature. At the same time, the heat losses through the glass window, $\dot{Q}_g$ (magenta), account for the main losses within the receiver. In Fig. 4(c), aiming to explain the receiver efficiency plateau during the day, the numerator of the Eq. 1 , $\dot{m}(\bar{h}_o - \bar{h}_i)$ was depicted in red, along with the denominator, I_b (magenta). Since the ratio between the numerator and the denominator is almost the same throughout the sunlight hours, the receiver efficiency, $\eta_{th,rcv}$, is also approximately constant during the same hours as it is seen in Fig.4(c) and Fig. 3(a).

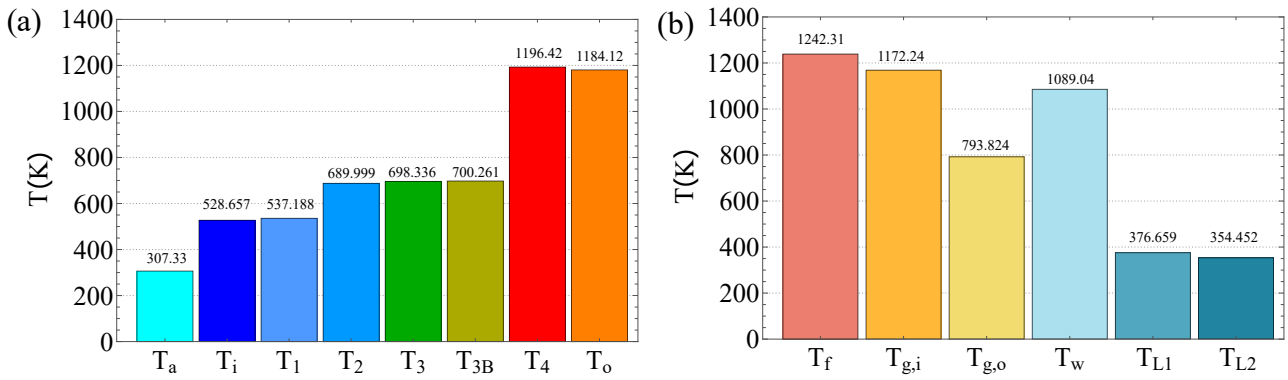

Figure 5: (a) Fluid temperatures during its flow through the receiver (see Fig. 1(a)) for notation. (b) Temperatures on receiver surfaces at the same conditions: June 24th, 2021 at noon.

Finally, in Fig. 5, the profile of the fluid (Fig. 5(a)) and receiver surfaces temperatures (Fig. 5(b)) are shown. These temperature values correspond to June 24th, 2021 at noon (12 h). In Fig. 5(a), it is depicted how the air rises its temperature from 528.7 K (T_i ,temperature at the outlet of the initial compressor) until 1196.42 K (T_4, the temperature after crossing the porous foam). The outlet temperature (T_o) is approximately 12.3 K below T_4, due to the heat exchange between the receiver outlet and inlet (Zone 1). As depicted in Fig. 5(b), the highest temperature among the surfaces is achieved at the porous foam, T_f, (1242.31 K). There is a difference of 378 K between the inner and outter glass surfaces ($T_{g,i}$ and $T_{g,o}$, respectively). This temperature difference is proportional to the heat losses across the glass window ($\dot{Q}_g$). The insulator surface temperatures for Zone L1 (376.66 K) and Zone L2 (354.45 K), are about 70 K above ambient temperature. The wall surface temperature (1089.04 K) is close to the inner glass window surface temperature, but it never overcomes it.

5. Conclusions

A physical model for heat transfers and losses in a closed pressurized solar receiver associated to a parabolic dish, small-scale, CSP system was presented. It can be applied to different receiver geometries and materials at stationary conditions. Particularly, a quartz glass on the window and a metallic foam in the absorber were considered. All the main heat transfer efficiencies are modeled and computed, allowing for a precise estimation of receiver thermal efficiency without paying an excessive computational effort. The physical mechanisms influencing receiver efficiency are identified and modeled within realistic hypotheses. This permits to calculate, for any value of DNI and ambient temperature, the temperatures of the heat transfer fluid and receiver surfaces at any stage, and also, to quantify heat transfer flows and losses to the ambient.

The ultimate goal of this kind of models is to couple it with submodels for the optical efficiency of the dish, for instance by means of a ray tracing software like Tonatiuh [20] and also with thermodynamic models for the power unit associated, as Brayton of Stirling cycles. Thus, it would be possible to analyze the behaviour of the whole system and to propose improvements for design or operation with enough precision and without applying to techniques requiring a huge computational effort.

Acknowledgments

Financial support from the Institute of Fundamental Physics and Mathematics (IUFFYM) and Escuela de Doctorado “Studii Salamantini” from University of Salamanca is acknowledged. “European Union, *Next Generation EU*” financial support, within ’Programa Investigo, Plan de Recuperación, Transformación y Resiliencia’, Junta de Castilla y León and Universidad de Salamanca is also acknowledged. SoDa Transvalor/MINES ParisTech is acknowledged for the meteorological and solar radiation data provided.

References

[1] M. Sedighi, R. Vasquez Padilla, R.A. Taylor, M. Lake, I. Izadgoshasb, and A. Rose. High-temperature, point-focus, pressurised gas-phase solar receivers: A comprehensive review. *Ener. Conv. Manage.*, 185:678–717, 2019.

[2] R. P. Merchán, M. J. Santos, A. Medina, and A. Calvo Hernández. High temperature central tower plants for concentrated solar power: 2021 overview. *Renew. Sust. Ener. Rev.*, 155:111828, 2022.

[3] M. Lubkoll, T.W. von Backström, and D.G. Kröger. Survey on pressurized air receiver development. In *Sol. Ener. Conference*. Sol. Ener. Conference, 2014.

[4] J. Zhu, K. Wang, G. Li, H. Wu, Z. Jiang, F. Lin, and Y. Li. Experimental study of the energy and exergy performance for a pressurized volumetric solar receiver. *Applied Thermal Engineering*, 104:212–221, 2016.

[5] V. R. Patil, F. Kiener, A. Grylka, and A. Steinfeld. Experimental testing of a solar air cavity-receiver with reticulated porous ceramic absorbers for thermal processing at above 1000°C. *Sol. Ener.*, 214:72–85, 2021.

[6] J. Zhu, K. Wang, Z. Jiang, B. Zhua, and H. Wu. Modeling of heat transfer for energy efficiency prediction of solar receivers. *Energy*, 190:116372, 2020.

[7] E. Bellos, E. Bousi, C. Tzivanidis, and S. Pavlovic. Optical and thermal analysis of different cavity receiver designs for solar dish concentrators. *Ener. Conv. Manage. X*, 2:100013, 2019.

[8] P. Wang, J. B. Li, F. W. Bai, D. Y. Liu, C. Xu, L. Zhao, and Z. F. Wang. Experimental and theoretical evaluation on the thermal performance of a windowed volumetric solar receiver. *Energy*, 119:652 – 661, 2017.

[9] R. P. Merchán, M. J. Santos, I. Heras, J. Gonzalez-Ayala, A. Medina, and A. Calvo Hernández. On-design pre-optimization and off-design analysis of hybrid Brayton thermosolar tower power plants for different fluids and plant configurations. *Renew. Sust. Energy Rev.*, 119:109590, 2020.

[10] Germilly Barreto, Paulo Canhoto, and Manuel Collares-Pereira. Three-dimensional CFD modelling and thermal performance analysis of porous volumetric receivers coupled to solar concentration systems. *Applied Energy*, 252:113433, 2019.

[11] A. Giostri and E. Macchi. An advanced solution to boost sun-to-electricity efficiency of parabolic dish. *Solar Energy*, 139:337–354, 2016.

[12] E. W. Lemmon, M. L. Huber, and M. O. McLinden. NIST Standard Reference Database 23: Reference fluid thermodynamic and transport properties-REFPROP, version 9.1. National Institute of Standards and Technology, Standard Reference Data Program, Gaithersburg, 2013.

[13] Wolfram Research, Inc. Mathematica, Version 13.2. Champaign, IL, 2022.

[14] Michael F. Modest. *Radiative Heat Transfer*. Academic Press, Elsevier Science, second edition, 2003.

[15] X. Fu, R. Viskanta, and J.P. Gore. Measurement and correlation of volumetric heat transfer coefficients of cellular ceramics. *Experimental Thermal and Fluid Science*, 17:285–293, 1998.

[16] Z. Wu, C. Caliot, G. Flamant, and Z. Wang. Numerical simulation of convective heat transfer between air flow and ceramic foams to optimise volumetric solar air receiver performances. *International Journal of Heat and Mass Transfer*, 54:1527–1537, 2011. Issues 7–8.

[17] Soteris A. Kalogirou. *Solar energy engineering: processes and systems*. Second edition, 2014.

[18] Global Modeling and Assimilation Office (GMAO) (2015), MERRA-2 tavg1_2d_slv_Nx: 2d,1-Hourly,Time-Averaged,Single-Level,Assimilation,Single-Level Diagnostics V5.12.4, Greenbelt, MD, USA, Goddard Earth Sciences Data and Information Services Center (GES DISC), Accessed 23/02/2023 `https://www.soda-pro.com/web-services/meteo-data/merra`.

[19] Copernicus atmosphere monitoring service (ECMWF), 2023. Accessed 23/02/2023. `https://www.soda-pro.com/web-services/radiation/cams-radiation-service`.

[20] M. J. Blanco, J. M. Amieva, and A. Mancillas. The Tonatiuh software development project: An open source approach to the simulation of solar concentrating systems. In *ASME 2005 International Mechanical Engineering Congress and Exposition*, pages 157–164. American Society of Mechanical Engineers., 2005.

PROCEEDINGS OF ECOS 2023 - THE 36TH INTERNATIONAL CONFERENCE ON
EFFICIENCY, **C**OST, **O**PTIMIZATION, **S**IMULATION AND ENVIRONMENTAL IMPACT OF ENERGY SYSTEMS
25-30 JUNE 2023, LAS PALMAS DE GRAN CANARIA, SPAIN

Modelling and Scaling Laws of cryogenic tank's thermal response to sloshing

Samuel Ahizi[a], Pedro A. Marques[b,c], Miguel A. Mendez[b]

[a] von Karman Institute, Waterloosesteenweg 72, 1640 Sint-Genesius-Rode, Belgium, samuel.ahizi@vki.ac.be, CA
[b] von Karman Institute, Waterloosesteenweg 72, 1640 Sint-Genesius-Rode, Belgium
[c] Université Libre de Bruxelles, Av. Franklin Roosevelt 50, 1050 Bruxelles, Belgium

Abstract:

The storage of cryogenic fuels such as liquid hydrogen (LH_2) or liquefied natural gas (LNG) poses significant thermal and mechanical loads to the tanks that store them because of the considerable temperature gradients produced during filling operation and sloshing. This work presents a numerical investigation of the transient heat conduction within the walls of an insulated cryogenic tank undergoing sloshing. The unsteady heat conduction is analyzed by modeling the sloshing as a spatially distributed and time-varying boundary condition on the inner side of the tank. The scaling laws of the problem are analyzed by combining the characteristic time scale of heat conduction with the characteristic time scales of the sloshing. The modulation of sloshing-induced thermal fluctuations is then analyzed across the wall thickness and in the circumferential direction. The resulting dimensionless modulation map allows for analyzing the tank's thermal response for different designs.

Keywords:

Cryogenics, Cryogenic liquid storage, Heat transfer and thermal insulation, Sloshing,

1. Introduction

Cryogenic tanks store liquefied fuels such as liquid hydrogen (LH_2) or liquefied natural gas (LNG) at extremely low temperatures, ranging from 20 to 110 K. Consequently, the walls of these tanks experience significant temperature gradients during all the phases of their operating cycle (e.g., chill-down, filling, pressurization), and the design and optimization of their thermal response raise many challenges. The tank wall and the insulation layers should minimize the heat ingress to minimize the boil-off of the cryogenic liquid and, thus, the need for venting to avoid overpressurizing the tank. Moreover, the tank weight should be minimized in all transport applications to maximize the payload without compromising its mechanical resistance. The need for these compromises has motivated various experimental and numerical investigations on the thermo-mechanical analysis of these tanks.

Heathman et al. [1] experimentally characterized a cryogenic tank for space applications and measured the effect of boil-off and different insulation strategies on the wall temperature. Murugan, Starvin, and Dhas[2], the authors studied the behavior of a hydrogen tank during the chill-down process using thermo-structural finite elements analysis to estimate the heat transfer and induced deformations. Similarly, Rao and Jagadeesh [3], and Ko [4] used finite elements to characterize the structural and thermal stress of a hydrogen tank under high-pressure loads and heating/cryogenic cooling. Craig and Hanna [5] studied the thermal response of a LH_2 tank subjected to extreme heating profiles using 1D/2D finite differences models to determine the boil-off level as a function of the insulation strategy.

Furthermore, the inner tank material in contact with the fluid must be carefully chosen, especially for hydrogen storage, as its molecules are likely to penetrate through the solid [6] and embrittle the materials [7, 8]. This has promoted using metallic materials such as stainless steel, aluminum alloys, and nickel alloys, combined with multilayer and vacuum insulation [9]. The latter consists of alternating layers of reflective and insulating materials to minimize radiation and conduction heat transfer. For hydrogen tanks, an aluminum alloy inner layer offers a slow permeation rate and is less subject to embrittlement [10]. Such an approach was also shown to minimize boil-off due to "hot spots" by spreading the localized heat leaks through the metal's high conductivity [11]. In the aforementioned studies, the effect of sloshing has not been considered by focusing either on static storage or a perfectly mixed tank. However, an appreciable temperature difference (up to 15 K, [12, 13]) can be produced between the liquid and the ullage gas. Sloshing can thus induce additional time-varying thermal loads on the tank's wall [14]. This is especially critical in metallic alloys, which are known to suffer from crack propagation and *thermal fatigue* when undergoing repeated thermal cycles [15].

This work investigates the thermal response of a horizontal cylindrical tank undergoing lateral sloshing. We consider a simplified model in 2D, leveraging the large aspect ratios in most common tank designs and allowing for fast numerical integration of the heat conduction problem. The thermal response is analyzed in a dimensionless form to link the modulation of temperature fluctuations to the dimensionless numbers scaling the problem.

The rest of the article is structured as follows. Section 2. introduces the problem set, with its simplifying assumptions and the numerical methods and investigated test cases. Section 3. collects the results regarding thermal propagation across the wall's thickness and along the circumferential direction. Finally, section 4. collects conclusions and perspectives for future work.

2. Problem set

The configuration investigated in this work is illustrated in the schematic of Fig. 1a. We consider a horizontal cylindrical tank with radius R and thickness e_1, insulated with a cylindrical shell of thickness e_2 and filled with a liquid up to a level f. The extension of the tank along its axis (i.e. orthogonal to the paper) is large enough to allow considering the problem in 2D, in the plane (x, y) introduced in the figure.

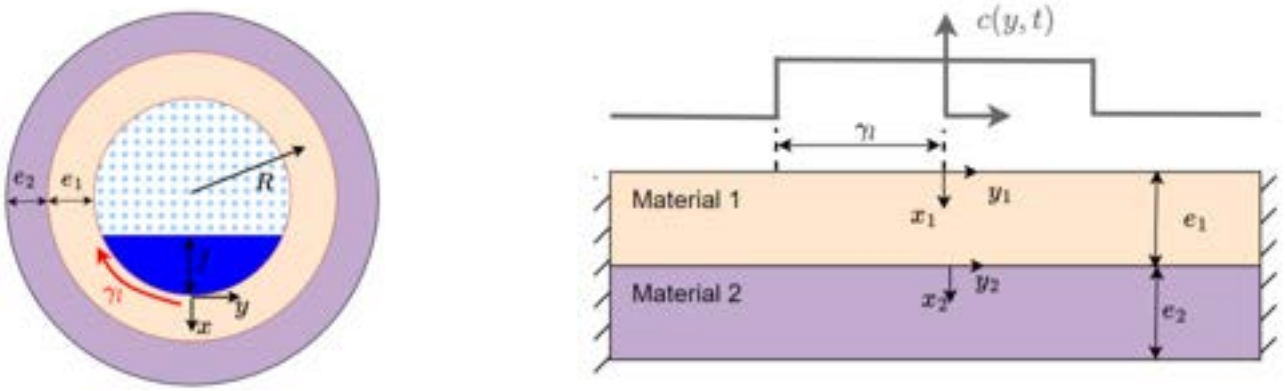

(a) Cross view of the cylinder

(b) Two-dimensional simplification of the tank wall geometry

Figure 1: Schematic views of the tank geometry and 2D domain considered in this work.

Assuming that the tank's thickness is much smaller than its circumference (i.e. $e_1, e_2 \ll 2\pi R$), we replace the curvilinear coordinates with Cartesian ones and construct a 2D domain by unwrapping the cylinder and the shell (see Fig. 1b). We treat the heat conduction problem in the cylinder and the insulation shell with two distinct domains, herein distinguished with subscripts 1 and 2.

On the inner side of the wall, in contact with the liquid and ullage gas, we define the fluid temperature as $T_f(y_1, t) = T_l c(y_1, t) + T_g(1 - c(y_1, t))$, where T_l and T_g are the (constant) temperatures on the liquid and the ullage gas respectively and $c(y_1, t) \in [0, 1]$ is a color function equal to 1 where the solid is contact with the liquid and 0 when it is contact with the gas. The temperature difference $\Delta T = T_g - T_l$ is encountered in cryogenic tanks because of heat leaks and/or pressurization as well as evaporation and the natural tendency of the liquid to be subcooled with respect to the interface [12, 13]. By keeping the temperature of the fluids constant in time, we assume no thermal mixing and no mass exchange (evaporation/condensation) between the two phases, at least within the sloshing time scale of interest.

The 2D heat conduction problem and the boundary conditions considered in this work for the two domains $\Omega_1 := x_1 \in [0, e_1] \times y_1 \in [-\pi R, \pi R]$ and $\Omega_2 := x_2 \in [0, e_2] \times y_2 \in [-\pi R, \pi R]$ are

$$
\begin{cases}
\partial_t T_1(x_1, y_1, t) & = \alpha_1(\partial^2_{x_1} T_1 + \partial^2_{y_1} T_1) \\
T_1(0, y_1, t) & = T_f(y_1, t) \\
\quad \text{or} & \\
\kappa_1 \partial_x T_1(0, y_1, t) & = h_f(T_1(0, y_1, t) - T_f(y_1, t)) \\
T_1(e_1, y_1, t) & = T_2(0, y_2, t) \\
T_1(x_1, -\pi R, t) & = T_1(x_1, \pi R, t)
\end{cases}
\quad \text{and} \quad
\begin{cases}
\partial_t T_2(x_2, y_2, t) & = \alpha_2(\partial^2_{x_2} T_2 + \partial^2_{y_2} T_2) \\
T_2(0, y_2, t) & = T_1(e_1, y_1, t) \\
\kappa_2 \partial_x T_2(e_2, y_2, t) & = h_a(T_2(e_2, y_2, t) - T_a) \\
T_2(x_2, -\pi R, t) & = T_2(x_2, \pi R, t)
\end{cases}
\tag{1}
$$

where α_1, α_2 are the heat diffusivities, and κ_1, κ_2 are the thermal conductivities for the two materials. On the inner condition problem, we consider two scenarios for the boundary conditions on the surface in contact with the fluid: (1) a Dirichlet boundary condition or (2) a Robin boundary condition with heat transfer coefficient h_f. The assumption of Dirichlet conditions on the inner wall is purely demonstrative and rather unphysical. Considering the large differences in the thermal effusivities of the fluid (whether liquid or gas) and the solid, the surface temperature at the contact between the two is expected to be much closer to the latter than the former. However, from the thermal loading point of view, the two investigated problems can be seen as the two extremes between the actual loads are expected.

The two solid domains communicate with a Dirichlet boundary condition at $x_1 = e_1$, $x_2 = 0$ while a Robin boundary condition is considered on the external surface of the insulation, with heat transfer coefficient h_a. Periodic boundary conditions are introduced in $y = -\pi R$ and $y = \pi R$ for both domains, as both locations are at the top of the cylinder.

To model the occurrence of a sloshing event, we treat the color function with an imposed variation in space and time (see Fig. 1b). This is a square wave with half-width γ_l, oscillating with an amplitude A_f and an angular frequency ω. Focusing on lateral sloshing, the oscillation frequency is taken as the one corresponding to the first sloshing mode in potential flow theory [16]. This is usually the first to be triggered and most prominently present in the sloshing response. According to Lamb[17] for an horizontal tank this is $\omega = \sqrt{1.37g/(R - e_1)}$, with g the gravitational acceleration. Concerning the sloshing amplitude A_f and width γ_l, computed from the filling level. Throughout the modeling of the sloshing, we focus on planar waves [16]. Furthermore, the temperature of the fluids is kept constant, thus assuming no thermal mixing between the two phases. Finally, evaporation due to heat ingress or condensation due to thermal mixing are not considered.

2.1. Scaling and dimensionless formulation

To scale the problem, we consider the dimensionless coordinates $\hat{x}_j = x_j/e_j$ and $\hat{y}_j = y_j/2\pi R$, with $j = 1, 2$, the dimensionless temperatures $\theta_j = (T_j - T_l)/(T_g - T_l)$, and the dimensionless time $\hat{t} = \omega t/2\pi$. The resulting dimensionless problem in $\hat{\Omega}_1 := x_1 \in [0,1] \times \hat{y}_1 \in [-1/2, 1/2]$ and $\hat{\Omega}_2 := \hat{x}_2 \in [0,1] \times \hat{y}_2 \in [-1/2, 1/2]$ becomes:

$$
\begin{cases}
\partial_t \theta_1(\hat{x}_1, \hat{y}_1, \hat{t}) & = Fo_1(\partial^2_{\hat{x}_1}\theta_1 + \varepsilon_1^2 \partial^2_{\hat{y}_1}\theta_1) \\
\theta_1(0, \hat{y}_1, \hat{t}) & = 1 - c(\hat{y}_1, \hat{t}) \\
\quad \text{or} & \\
\partial_{\hat{x}_1}\theta_1(0, \hat{y}_1, t) & = Nu_f(\theta_1(0, \hat{y}_1, t) - 1 + c(\hat{y}_1, \hat{t})) \\
\theta_1(1, \hat{y}_1, \hat{t}) & = \theta_2(0, \hat{y}_2, \hat{t}) \\
\theta_1(\hat{x}_1, -1/2, \hat{t}) & = \theta_1(\hat{x}_1, 1/2, \hat{t})
\end{cases}
\quad \text{and} \quad
\begin{cases}
\partial_t \theta_2(\hat{x}_2, \hat{y}_2, \hat{t}) & = Fo_2(\partial^2_{\hat{x}_2}\theta_2 + \varepsilon_2^2 \partial^2_{\hat{y}_2}\theta_2) \\
\theta_2(0, \hat{y}_2, \hat{t}) & = \theta_1(1, \hat{y}_1, \hat{t}) \\
\partial_{\hat{x}_2}\theta_2(1, \hat{y}_2, \hat{t}) & = Nu_a(\theta_2(1, \hat{y}_2, \hat{t}) - \theta_a) \\
\theta_2(\hat{x}_2, -1/2, \hat{t}) & = \theta_2(\hat{x}_2, 1/2, \hat{t})
\end{cases}
\tag{2}
$$

where $Fo_j = 2\pi\alpha_j/(e_j^2\omega)$ are the Fourier numbers in the two domains, $Nu_f = h_f e_1/\kappa_1$ and $Nu_a = h_a e_2/\kappa_2$ are the Nusselt numbers in the inner and outer surfaces, and $\varepsilon_j = e_j/2\pi R$ are the thickness to circumference ratio of the two domains.

The Nusselt number on the outer surface was computed using a classic correlation of natural convection over on horizontal cylinder [18]:

$$
Nu_a = \left(0.6 + \frac{0.387 Ra_a^{1/6}}{[1 + (0.559/Pr_a)^{9/16}]^{8/27}}\right)^2 \tag{3}
$$

where $Ra_a = g\beta_a(T_a - T_2(e_2)(D_o)^3)/(\nu_a^2)Pr_a$ is the Rayleigh number based on the outer diameter $D_o = 2R + e_1 + 2e_2$ as a reference length, the external wall temperature $T_2(e_2)$. This is computed during the simulation and the air properties at ambient temperature while the air's Prandtl number at ambient temperature Pr_a is constant.

The Nusselt number on the inner surface is computed using two correlations depending on the inner Richardson number :

$$
Ri_f = \frac{Gr_f}{Re_r^2} = \frac{g\beta_f(T_a - T_1(0))(R_i)^3)}{A_f^4\omega^2} \tag{4}
$$

where the Reynolds number was defined as in [19] and the properties β_f and ν_f and Pr_f are computed using the color function $c(y_1, t)$ for weight-averaging liquid and gas properties. Natural convection is considered $Ri > 10$, while forced convection is assumed if $Ri_f < 0.1$ [20]. A mixed regime appears between these two boundaries.

Therefore, depending on Ri_f the Nusselt number on the inner surface is

$$\begin{cases} Nu_f = Nu_{f,F} = 0.680 Re^{1/2} Pr^{1/3} & \text{if } Ri < 0.1 \\ Nu_f = Nu_{f,N} = 0.605 Ra_f^{1/3} & \text{if } Ri > 10 \\ Nu_f = (Nu_{f,F}^3 + Nu_{f,N}^3)^{1/3} & \text{if } Ri \in [0.1, 10] \end{cases} \tag{5}$$

All fluid properties used in the above correlations were computed from the library *CoolProp* [21] using air for the ambient side and liquid/gaseous hydrogen or methane for the fluid side. Typical values for the thermophysical properties of the materials considered in this work are summarized in Table 1 while the usual ranges for the Nusselt numbers are given in Table 2.

Table 1: Properties and typical thickness of the materials considered in the composition of the walls.

Material	κ [W/m/K]	α [mm^2/s]	e [mm]
Al 6061 (domain 1) [22]	162	65.4	1-20
SST 316 (domain 1) [22]	16.3	4.1	1-20
Polyurethane foam (domain 2) [23]	0.05	2.2	10-200
High Density Polyethylene (domain 2) [24]	0.04	0.02	10-200

Table 2: Typical Nusselt number range

Fluid	Gas phase	Liquid phase
Air	70-140	-
Hydrogen	100-2500	6000-10000
Oxygen	100-1200	6800 - 7300
Methane	100-800	3800 - 4300

2.2. Numerics and selected test cases

The problems in (2) were solved using the method of lines. This approach consists of discretizing the equation's spatial derivatives and transforming the resulting expressions into a system of ordinary differential equations (ODEs) in time. The spatial derivatives were computed using second-order finite difference while the time integration was carried out using the LSODA solver [25] from the ODEINT package in SciPy [26]. Prior to introducing the sloshing perturbation, the thermal field is initialized with the steady solution at rest, i.e., without fluid motion.

We consider two aspects of the tank's thermal response. First, we focus on the thermal response across the wall thickness. To this end, we reduce the problem to a 1D domain by setting $\varepsilon_1, \varepsilon_2 \to 0$ in (2) and study the dimensionless temperature evolution at the height of the interface at rest, that is $\hat{y}_1 = \gamma_l$). For the half-filled tanks considered in this work, this is $\hat{y}_1 = 1/4$ (or $\hat{y}_1 = -1/4$). In this location, the oscillation of the color function in the dimensionless domain $c(\gamma_l/(2\pi R), \hat{t})$ produces a square wave of unitary amplitude, unitary period and 50% duty cycle (see Fig. 2). Second, we focus on the circumferential propagation of heat by analyzing the full 2D problem. Considering a half-filled tank, the interface is centered at $\hat{y}_1 = \pm 1/4$ and oscillates harmonically in time with unitary period and dimensionless amplitude $\hat{A}_f$. An example of the corresponding spatiotemporal evolution for an amplitude $\hat{A}_f = 0.2$ is shown in Fig. 2.

Table 3: Test matrix summarizing the main parameters for the 1D and 2D simulations presented in this work.

Case	Model	θ_a	ε_1	ε_2	Fo_1	Fo_2	Fluid BC	No. layers
1	1D	28.8	0	0	[7e-5, 300]	-	Dirichlet	1
2	1D	28.8	0	0	[7e-5, 300]	-	Robin	1
3	1D	28.8	0	0	[1e-3, 80]	[1e-5, 30]	Robin	2
4	2D	28.8	1e-3	7e-3	5e-2	6	Robin	2

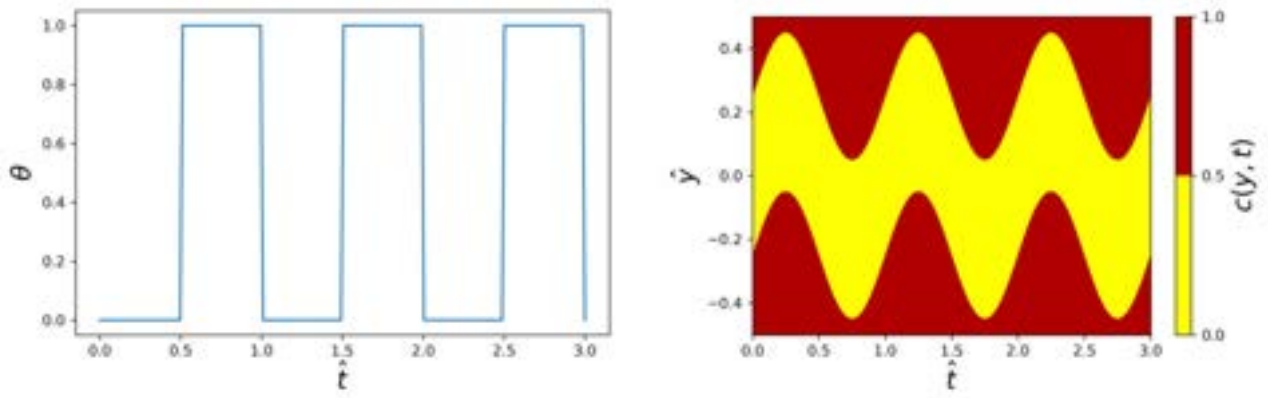

(a) (b)

Figure 2: (a) Dimensionless temperature evolution at $\hat{y}_1 = \gamma_l$ in the 1D problem and (b) spatiotemporal evolution of the color function used to simulate sloshing $c(y, t)$ in the 2D problem. In both cases, the tank is considered to be half-filled.

The simulations were carried out with n_x = 100 grid points across the thickness ($\hat{x}$) and n_y = 70 points across the circumferential coordinate ($\hat{y}$) for a total of 10 oscillation periods. A grid dependence study proved that this discretization was sufficient for our needs. Four test cases are considered, and their settings are reported in Table 3. Case 1 considers a 1D problem with a single layer, with Fourier numbers ranging from 7×10^{-5} to 300. To give an order of magnitude, a representative Al6061 tank from [27], with R = 0.5 m and e_1 = 5 mm (see Table 1), shielded by a shell of e_2 = 3 cm thick Polyurethan foam leads to $Fo_1 \approx 6$ and $Fo_2 \approx 5 \times 10^{-3}$. Dirichlet boundary conditions are considered in Case 1, with a dimensionless ambient temperature of θ_a = 28.8. This represents a test case with T_l = 20K, T_a = 293K, and $\Delta T = T_g - T_l$ = 10 K. Case 2 is identical to Case 1 but considers Robin boundary conditions in the inner wall. Case 3 considers a multi-layer problem, maintaining the 1D formulation, while Case 4 considers the multi-layer problem using a 2D formulation.

To quantify the dimensionless thermal response of the tank wall to the sloshing-induced thermal excitation, we define the dimensionless thermal modulation as

$$\mathcal{H}(\hat{x}, \hat{y}) = \max(\theta(\hat{x}, \hat{y})) - \min(\theta(\hat{x}, \hat{y})). \tag{6}$$

This is only a function of $\hat{x}$ in the 1D problem (having fixed $\hat{y} = \pm 1/4$). Moreover, we define the thermal penetration depth as the distance from $\hat{x}_1 = 0$, or $\hat{x}_2 = 0$, along the wall thickness, within which $\mathcal{H} > 0.1$, hence $\mathcal{H}(\hat{x} = \hat{d}) = 0.1$.

3. Results and discussion

The results for the one-dimensional simulations (Cases 1,2,3 in Table 1) are presented in section 3.1. while the results for the two-dimensional simulations (Cases 4 in Table 1) are presented in section 3.2..

3.1. One-dimensional model

3.1.1. Single layered tank wall response to sloshing excitation

Focusing on the single-layered wall (Cases 1 and 2 in Table 1), Fig. 3a and 3b show the distribution of $\mathcal{H}$ across the tank's thickness $\hat{x}$ with the Dirichlet and Robin boundary conditions on the inner wall, respectively, for a broad range of Fourier numbers. Since only one layer is considered, no subscripts are used in the legends. The colored area in both figures defines the region $\mathcal{H} < 0.1$, indicating where the sloshing-induced thermal oscillations are considered negligible.

These figures show that the penetration depth $\hat{d}$ remains identical with both boundary approaches. Furthermore, in both cases, for $Fo > 3 \times 10^{-1}$, the sloshing perturbation causes the thermal oscillations to propagate through the entire thickness, producing $\mathcal{H}(1) \sim 1$. Then, as $Fo \to 0$, the thermal fluctuations are increasingly damped, pushing the penetration depth to zero (i.e., $\hat{d} \to 0$). In such a case, the time scale of the sloshing excitation is negligible compared to the time scale of diffusion. In fact, as $Fo < 10^{-2}$, the perturbations are significantly damped in the close vicinity of the wall.

The key difference between Cases 1 and 2 is the value of the thermal modulation in the vicinity of the inner wall (i.e., $\mathcal{H}(0)$). While the Dirichlet condition imposes the perturbation to be bounded between 0 and 1, the convective boundary condition can amplify it beyond these bounds. This means that the inner wall becomes

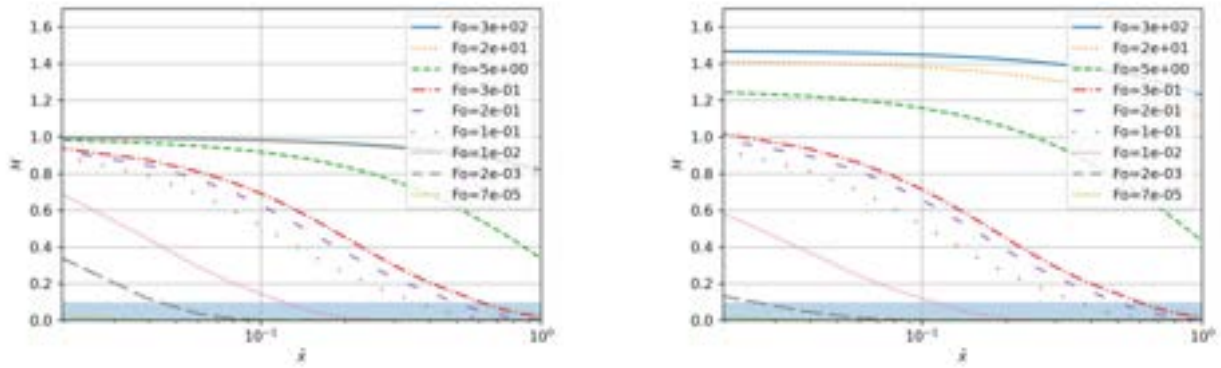

(a) (b)

Figure 3: One-dimensional transfer function along non-dimensional wall thickness for different *Fo* numbers. (a) Dirichlet boundary condition on the fluid side and (b) Robin boundary condition on the fluid side.

warmer than the gas. One can show that the steady state solution of the 1D heat equation (2) with Robin boundary conditions on both ends leads to the following inner wall temperature:

$$\overline{\theta}(0) = \frac{(Nu_f Nu_a - Nu_f)\,(1 - \overline{c}(\gamma_l)) + Nu_a \theta_a}{Nu_f Nu_a + Nu_a - Nu_f}. \tag{7}$$

Therefore, provided that $\theta_a > 1$, the inner temperature is always warmer than the fluid at equilibrium, i.e. $\overline{\theta}(0) > 1 - \overline{c}(\gamma_l)$ with $\overline{c}(\gamma_l) = 0$ for the gas and 1 for the liquid. From Equation (7), it is clear that temperature overshoot increases as Nu_f decreases. Thus, since the Nusselt number of the gas is one order of magnitude lower than the liquid's (see Table 2), the temperature overshoot in the regions in contact with the gas is larger than in the liquid phase. Consequently, as shown in Fig. 3b, the thermal modulation reaches values greater than unity for $Fo > 3 \times 10^{-1}$.

This phenomenon is more evident in Fig. 4, which shows the dimensionless evolution of temperature in time at $\hat{x}_1 = 0, 0.5, 1$ with Dirichlet (a) and Robin (b) boundary conditions for $Fo = 3.9$. This case is representative of an aluminum layer within the typical thickness in Table 1. The Robin boundary condition introduces a delay in the transfer of the perturbation to the inner side of the wall, as depicted by the solid line in Fig. 4b. This delay further attenuates the perturbation when the time scale of the excitation is much smaller than the one of diffusion, i.e. $Fo << 1$, compared to the Dirichlet approach. This effect can be visualized for $Fo = 10^{-2}$ and $Fo = 2 \times 10^{-3}$ on Fig. 3.

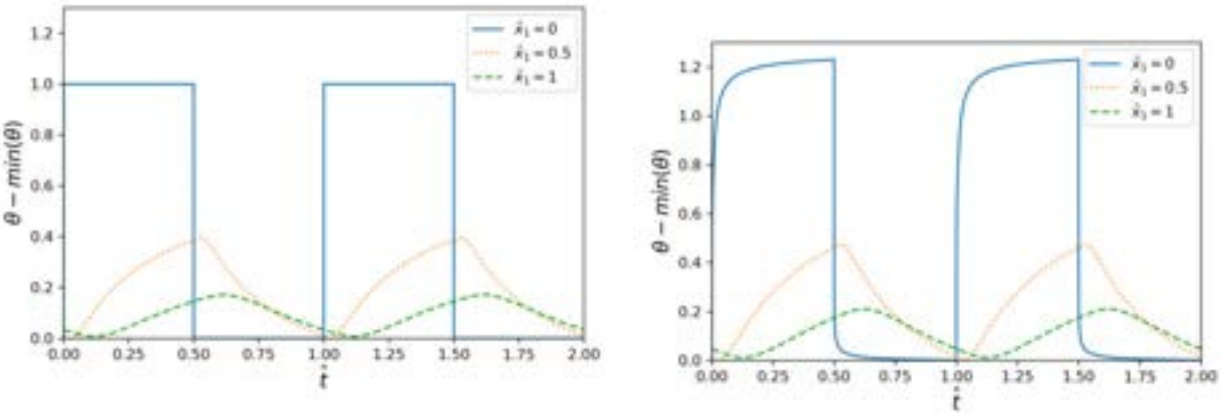

(a) (b)

Figure 4: Evolution of the temperature with dimensionless time at different depths of the single-layered wall, $Fo = 3.9$. (a) Dirichlet boundary condition on the fluid side and (b) Robin boundary condition on the fluid side.

While the Dirichlet simplification provides a good estimate of the penetration depth and allows for identifying the critical Fourier number above which the perturbation reaches the ambient side as $Fo = 3 \times 10^{-1}$, it fails

at representing the amplification/attenuation phenomena. Indeed, as this approach forces the inner side of the wall to be at the fluid temperature, the wall overheating due to external heat flux cannot be considered. In addition, the delay introduced by the thermal inertia is under-predicted. In the following, we focus on the convective boundary condition on the fluid side.

3.1.2. Multi-layered tank wall response to sloshing excitation

As cryogenic tanks are usually made of multi-layered materials, we investigate the influence of the different layer compositions and thicknesses for the dual-layered tank (Case 3 in Table 3). To represent the state-of-art tank layout, a conductive material is placed on the fluid side while an insulating material is placed on the ambient side. Thus, we study the thermal response of the two layers as a function of their respective Fourier numbers for the ranges indicated in Table 3. Figure 5 shows contour maps of the penetration depth within the two layers as a function of the Fourier number combination. Similarly, Fig. 7 represents the maximum value of thermal modulation encountered in each layer, i.e. $\mathcal{H}_1(0)$ and $\mathcal{H}_2(0)$. In these figures, the circle and cross points locate existing hydrogen tanks of respective dimensions $R \approx 0.5$ meters [27] and $R \approx 1.5m$ [28]. The dimensionless temperature evolution of the circle point is depicted in Fig. 6.

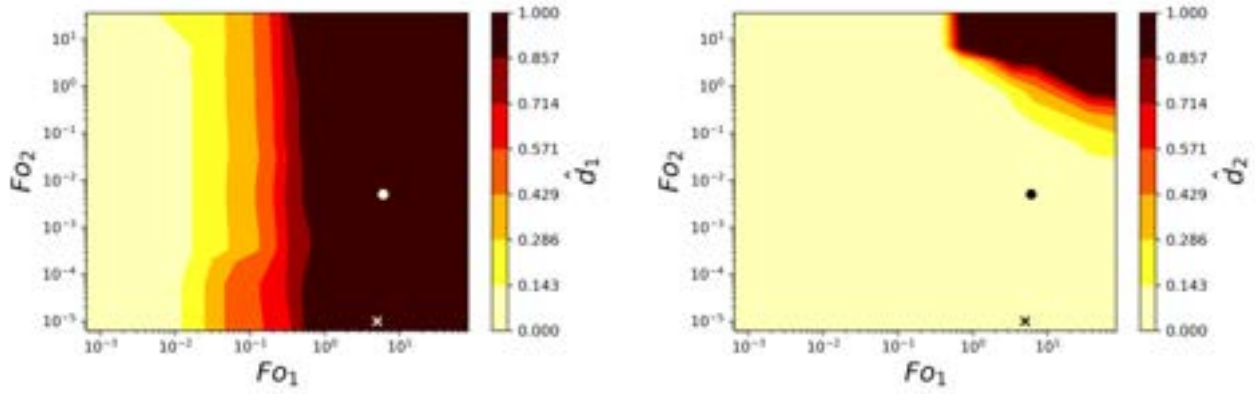

(a) (b)

Figure 5: Contour plot of dimensionless penetration depths of a dual-layered cryogenic tank wall as a function of the layer *Fo* numbers. (a) Penetration depth on the fluid side material and (b) penetration depth on the ambient side material

Figure 5a shows the penetration depth in the first layer (material 1 in Figure 1), computed as in the previous condition, while Figure 5b shows the same quantity in the second layer (material 2 in Figure 1). The thermal fluctuation reaches the second layer by traveling the first layer only if $Fo_1 > 3 \times 10^{-1}$. When this occurs, the fluctuation can travel through the second layer if $Fo_2 > 10^{-1}$ (note that one has $\hat{d}_2 > 1/3$ for $Fo_2 > 10^{-1}$ 5b).

Figures 6 shows the dimensionless temperature fluctuation at $\hat{x}_1 = 0, 0.5, 1$ for the multilayer condition in the case of $Fo_1 = 3.9$, $Fo_2 = 10^{-5}$ (configuration labelled with a circle in figures 5). In this condition, the oscillation period is large enough to let the wall reach equilibrium before the solid comes into contact with a different

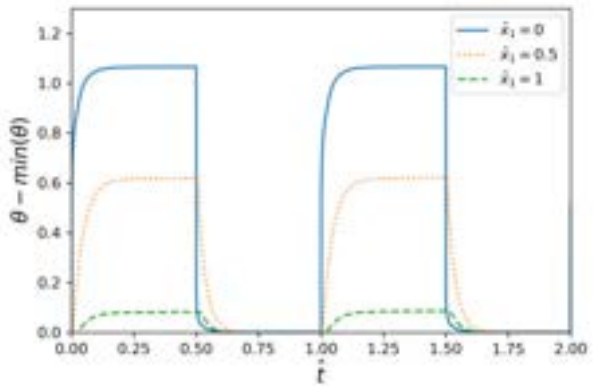

Figure 6: Evolution of the temperature with dimensionless time at different depths of the fluid side material for a dual-layered wall, $Fo_1 = 3.9$, $Fo_2 = 10^{-5}$ (circle marker in Figure 5).

phase. Figures 7a and 7b show the maximum value of the dimensionless modulation $\mathcal{H}$ in both materials for the same range of Fourier numbers considered in the previous figures. These figures show that the penetration length for the inner material is almost independent of the outer one, but the amplification in the inner (more conductive) material is influenced by the Fourier number of the outer (insulation) layer. The amplification of the thermal oscillation is reduced as $Fo_2 \to 0$. As Fo_2 tends to 0, the ambient side material mitigates the external heat ingress, thus tempering the overheating of the inner side with respect to the ullage gas. It is interesting to note that the insulation layer always receives an attenuated perturbation, as depicted in Fig. 7b, except for extreme Fourier number values, i.e. $Fo_{1,2} > 10$.

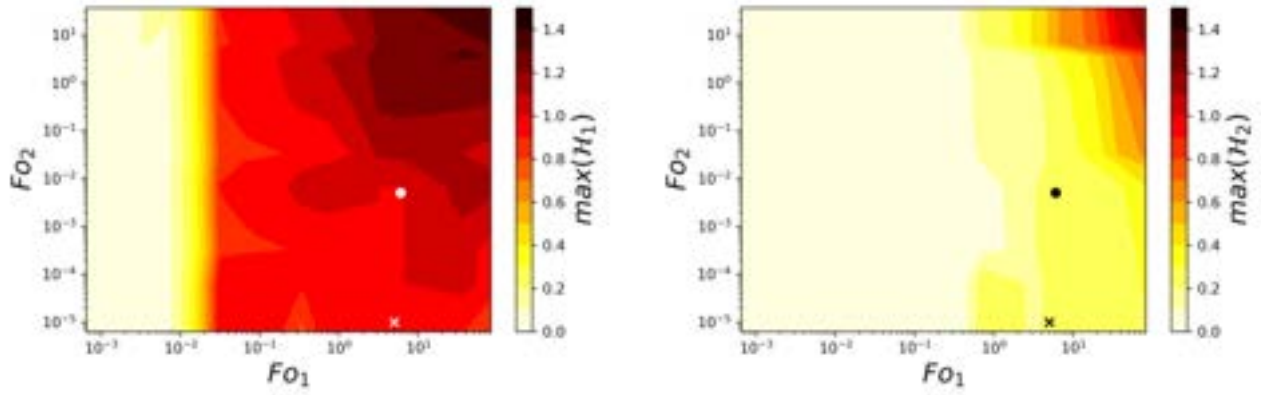

(a) (b)

Figure 7: Contour plot of dimensionless thermal modulation of a dual-layered cryogenic tank wall as a function of the layer *Fo* numbers, (a) maximum value in fluid side material, and (b) maximum value in the ambient side material

3.2. Two-dimensional model

We conclude this investigation with the two-dimensional response of the wall to sloshing with varying dimensionless excitation amplitudes $\hat{A}_f$. We focus on the configuration with $Fo_1 = 3.9$, $Fo_2 = 10^{-5}$ (circle marker in Fig. 5) because similar results were found for the one with $Fo_1 = 3.9$, $Fo_2 = 10^{-5}$ (cross marker in Fig. 5).

The resulting thermal modulation maps in 2D are depicted in Fig. 8a. The boundary between the two materials is represented by a horizontal solid line, while vertical dashed lines delimit the region spanned by the oscillation of the temperature distribution (color function). The results of the 2D approach align with the maps 7 and 5. Indeed, while the perturbation enters the insulation layer with a thermal modulation $\mathcal{H}_2 \approx 0.4$, it is quickly damped so that $\hat{d}_2 \approx 0$. Regardless of the oscillation amplitude, and despite the large diffusivity of the inner layer, we observe that the response of the wall remains extremely localized to the region covered by the sloshing. In other words, at the scale of the sloshing, heat conduction in the circumferential direction can be neglected.

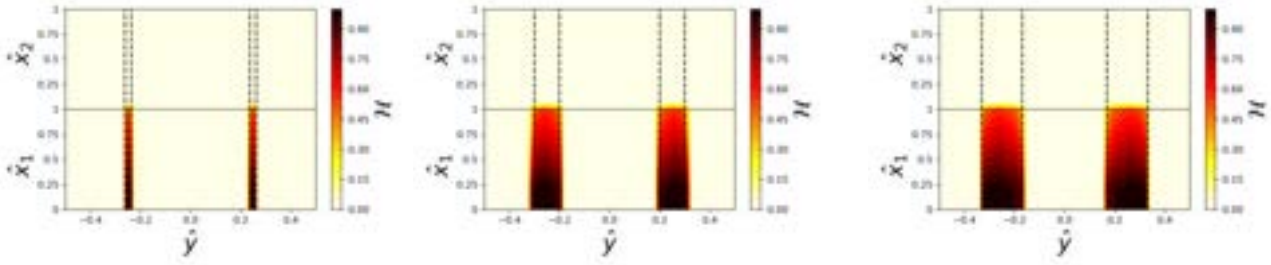

(a) $\hat{A}_f = 0.016$ (b) $\hat{A}_f = 0.064$ (c) $\hat{A}_f = 0.087$

Figure 8: 2D contour plot of transfer function value of a dual-layered cryogenic tank wall subjected to sloshing excitation of different non-dimensional amplitudes.

4. Conclusions

This study analyzed the transient heat conduction with cryogenic sloshing perturbation within a multi-layered tank, considering both one and two-dimensional cases. A dimensionless analysis was performed to identify the scaling parameters on the thermal behavior of the tank.

The study identified a threshold on the Fourier number for inner layer material, namely $Fo_1 \approx 3 \times 10^{-1}$, above which the thermal excitation is amplified and crosses the entire layer thickness. This amplification is attributed to the inner wall overheating due to heat ingress from the outside. It can be minimized by increasing the insulation, i.e. decreasing the Fourier number of the ambient side material Fo_2. This finding suggests that careful consideration must be given to the thermal properties of the tank walls and the operating conditions to minimize the effects of sloshing on the thermal cycling of the inner tank shell.

Furthermore, the study revealed that the perturbation caused by sloshing remains localized in the excitation region and barely spreads along the circumference of the inner shell. This means that the time scale of the sloshing is usually much shorter than the time scale for the heat conduction in the circumferential direction for most material combinations considered in this work.

Overall, the single and multi-layered tank walls' dimensionless analysis has provided an understanding of the thermal behavior of cryogenic storage tanks subjected to sloshing. In particular, thermal modulation and penetration depth maps are valuable tools for designers. The maps can be used to determine the tank's response to such perturbation excitation as a function of the Fourier number of each layer and can help optimize the design of the tank walls by minimizing the effects of sloshing on the temperature distribution within the tank. The findings of this study can be used to improve the design and operation of cryogenic storage systems, to enhance their safety and efficiency. Further research will be focused on extending this work to a complete thermodynamic model accounting for fluid phase and temperature changes.

Acknowledgments

This work has been funded by the Flemish Agentschap Innoveren & Ondernemen in the framework of the cSBO project HBC.2021.0680 "Clean Hydrogen Propulsion for Ships (CHyPS)". Pedro Marques is supported by the FRIA grant 40009348 from the 'Fonds de la Recherche Scientifique (F.R.S. -FNRS)'. The authors gratefully acknowledge the fruitful conversations with Prof. Jean Marie Buchlin on unsteady heat conduction.

Nomenclature

Letter symbols

A	sloshing amplitude, m
$\mathcal{C}$	interface location at rest, m
c_p	specific heat capacity, J/(kgK)
$\hat{d}$	dimensionless penetration depth
f	liquid fill height, m
Fo	Fourier number
g	gravitational acceleration, m/s^2
Gr	Grashof number
h	heat transfer coefficient, W/(m^{2}K)
$\mathcal{H}$	thermal modulation
Nu	Nusselt number
e	tank wall thickness, m
Pr	Prandtl number
R	tank radius, m
Ra	Rayleigh number
Re	Reynolds number
Ri	Richardson number

T temperature, K

U fluid velocity, m/s

Greek symbols

α thermal diffusivity, m^2/s

β volumetric thermal expansion, K^{-1}

ε tank aspect ratio

ρ density, kg/m^3

ν kinematic viscosity, m^2/s

κ thermal conductivity, W/(mK)

θ dimensionless temperature

ω sloshing frequency, rad/s

Subscripts and superscripts

f fluid

g gas

l liquid

i interface

a ambient

References

[1] Heathman JH, Nau RA, Yates GB, Egli WA, Christian JL, Neff D, Rose J, and Stockham TL. *Hydrogen tankage for hypersonic cruise vehicles - Phase 1.* Technical report. General Dynamics San Diego CONVAIR DIR, 1966 Aug

[2] Murugan S, Starvin MS, and Dhas K. *Thermo structural analysis of high pressure cryogenic tank.* International journal of engineering research and technology 2013; 2

[3] Rao KS and Jagadeesh C. *Analysis of Thermal Criteria on Cryogenic Pressure Vessel.* International Journal of Trend in Scientific Research and Development 2019

[4] Ko W. *Thermocryogenic buckling and stress analyses of a partially filled cryogenic tank subjected to cylindrical strip heating.* NASA Technical Memorandum 4579, 1994

[5] Craig S and Hanna G. *Thermal Modeling and Analysis of a Cryogenic Tank Design Exposed to Extreme Heating Profiles.* Technical report NASA Dryden Flight Research Facility, 1991

[6] Mital S, Gyekenyesi J, Arnold S, Sullivan R, Manderscheid J, and Murthy P. *Review of Current State of the Art and Key Design Issues with Potential Solutions for Liquid Hydrogen Cryogenic Storage Tank Structures for Aircraft Applications.* Technical report NASA-TM-2006-214346., 2006

[7] Stroe ME. *Hydrogen embrittlement of ferrous materials.* PhD thesis. Université libre de Bruxelles, Faculté des sciences appliquées – Matériaux, 2005

[8] Pressouyre G. *Trap theory of Hydrogen embrittlement.* Acta Metallurgica 1980; 28:895–911. DOI: 10 . 1016 / 0001 - 6160(80) 90106 - 6.

[9] Winnefeld C, Kadyk T, Bensmann B, Krewer U, and Hanke-Rauschenbach R. *Modelling and Designing Cryogenic Hydrogen Tanks for Future Aircraft Applications.* Energies 2018 Jan; 11:105. DOI: 10.3390/en1101005

[10] Zielinski A. *Hydrogen-assisted degradation of some non-ferrous metals and alloys.* Journal of Materials Processing Technology 2001 Feb; 109:206–14.

[11] Johnson WL, Balasubramaniam R, and Grotenrath R. *Analysis of heat transfer from a local heat source at cryogenic temperatures.* IOP Conference Series: Materials Science and Engineering 2022 May; 1240:012013. DOI: 10.1088/1757- 899X/1240/1/012013.

[12] Lin C and Hasan M. *Self-pressurization of a spherical liquid hydrogen storage tank in a microgravity environment.* 30th Aerospace Sciences Meeting and Exhibit. DOI: 10.2514/6.1992-363. eprint: https://arc.aiaa.org/doi/pdf/10.2514/6.1992-363.

[13] Seo M and Jeong S. *Analysis of self-pressurization phenomenon of cryogenic fluid storage tank with thermal diffusion model.* Cryogenics 2010; 50. 2009 Space Cryogenic Workshop:549–55. DOI: 10.1016/j.cryogenics.2010.02.021.

[14] Kartuzova O, Kassemi M, Umemura Y, Kinefuchi K, and Himeno T. *CFD Modeling of Phase Change and Pressure Drop during Violent Sloshing of Cryogenic Fluid in a Small-Scale Tank.* AIAA Propulsion and Energy Forum, 2020

[15] Mukai Y and Nishinura A. *Mechanical Properties of SUS304 Stainless Steel Under Cold Thermal Cycles.* 11th International Conference on Magnet Technology (MT-11): Volume 1. Ed. by Sekiguchi T and Shimamoto S. Dordrecht: Springer Netherlands, 1990 :743–8. DOI: 10.1007/978- 94- 009- 0769- 0128.

[16] Miles JW. *Resonantly forced surface waves in a circular cylinder.* Journal of Fluid Mechanics 1984; 149:15–31.

[17] Lamb H. *Hydrodynamics. 3rd ed.* Cambridge University Press, 1945

[18] Churchill SW and Chu HH. *Correlating equations for laminar and turbulent free convection from a horizontal cylinder.* International Journal of Heat and Mass Transfer 1975; 18:1049–53. DOI: 10.1016/0017-9310(75)90222- 7

[19] Ludwig C, Dreyer M, and Hopfinger E. *Pressure variations in a cryogenic liquid storage tank subjected to periodic excitations.* International Journal of Heat and Mass Transfer 2013 Aug; 66:223–34.

[20] Bergman TL, Lavine AS.,*Fundamentals of heat and mass transfer*. 7th ed. John Wiley & Sons, 2011

[21] Bell IH, Wronski J, Quoilin S, and Lemort V. *Pure and Pseudo-pure Fluid Thermophysical Property Evaluation and the Open-Source Thermophysical Property Library CoolProp.* Industrial & Engineering Chemistry Research 2014; 53:2498–508. DOI: 10.1021/ie4033999.

[22] Verstraete D. *The Potential of Liquid Hydrogen for long range aircraft propulsion.* PhD thesis. Cranfield University, 2009

[23] Prasad K, Kramer R, Marsh N, Nyden M, Ohlemiller T, and Zammarano M. *Numerical simulation of fire spread on polyurethane foam slabs.* Conference Proceedings - Fire and Materials 2009, 11th International Conference and Exhibition 2009 Jan; 28

[24] Araujo J, Waldman W, and De Paoli M. *Thermal properties of high density polyethylene composites with natural fibres: Coupling agent effect.* Polymer Degradation and Stability 2008; 93:1770–5

[25] Hindmarsh A and Petzold L. *LSODA, Ordinary Differential Equation Solver for Stiff or Non-Stiff System.*, 2005

[26] Virtanen P, Gommers R, Oliphant TE, Haberland M, Reddy T, Cournapeau D, Burovski E, Peterson P, Weckesser W, Bright J, van der Walt SJ, Brett M, Wilson J, Millman KJ, Mayorov N, Nelson ARJ, Jones E, Kern R, Larson E, Carey CJ, Polat I, Feng Y, Moore EW, VanderPlas J, Laxalde D, Perktold J, Cimrman R, Henriksen I, Quintero EA, Harris CR, Archibald AM, Ribeiro AH, Pedregosa F, van Mulbregt P, and SciPy 1.0 Contributors. *Fundamental Algorithms for Scientific Computing in Python.* Nature Methods 2020; 17:261–72.

[27] Meneghelli B, Tamburello D, Fesmire J, and Swanger A. *Integrated Insulation System for Automotive Cryogenic Storage Tanks.* Technical report IV.D.4. Kennedy Space Center, 2016

[28] Swanger A, Notardonato W, and Jumper K. *ASME Section VIII Recertification of a 33,000 Gallon Vacuum-Jacketed LH2 Storage Vessel for Densified Hydrogen Testing at NASA Kennedy Space Center* NASA Kennedy Space Center. 2015

Heat transfer of the multicolor-laser-sources-irradiated nanoparticles in reference to thermal processes

Piotr Radomski[a], Federica Zaccagnini[b], Paweł Ziółkowski[a], Francesca Petronella[c], Luciano de Sio[b] and Dariusz Mikielewicz[a]

[a]Gdansk University of Technology, Faculty of Mechanical Engineering and Ship Technology, Energy Institute, Poland;
[b]Sapienza University of Rome, Department of Medico-surgical Sciences and Biotechnologies, Italy;
[c]Insitute of Crystallography of National Research Council, Department Chemical Sciences and Material Technologies, Italy

Abstract:

Unlike the standard materials, metallic nanoparticles offer enhancing the heat convertion rate which implies the maximum and average temperature boost significantly in the considered system. The work's purpose is to examine heat transfer in the metallic nanoparticles which have been deposited on a glassy substrate, enabling the nanostructures thermoablation. Furthermore, the functionalized substrate is irradiated with multicolor-laser-sources, with a future perspective to develop a solar model. This is particularly crucial at improving efficiency in solar-collectors-based renewable energy sources. On the other hand, the theoretical investigations which have been previously verified for a single laser source aim to demonstrate the unsteady temperature and entropy increase in selected geometry cross-sections. The produced heat and the appropriate boundary conditions are calculated based on the advanced optics (Mie-Lorentz and Rayleigh-Drude theories) using an analytical approach. On the other hand, the temperature field and entropy production for the case study is being achieved via CFD simulations. The obtained results will be subsequently being applied in order to optimize the appropriate nanoparticle size and shape in operational work conditions.

Keywords:

heat transfer, light ablation, energy convertion, nanostructures

1. Introduction

The world sources of energy were grounded on fossil fuels above one hundred years ago due to their efficiency and common availability. It has been discovered, however, that their exploitation and extensive utilization is contributing to have the greenhouse effect accelerated. Therefore, the diligent search of new alternate energy sources and their diversification has been a burning issue nowadays. Nonetheless, the majority of the renewable sources of energy do not provide the instant and powerful temperature increase at the same time, which may last either long hours or explode the costs of usage. Regrettably, many of the available techniques are based on the heat flux supply to the fluid-solid boundary, which implies a slow temperature increase in the whole system [1].

On the other hand, since the COVID-19 pandemic situation began, the peoples have realized the necessity of hand and room disinfections. Unlike the powerful chemical compounds, the overheating of viruses by reaching an appropriate temperature may reduce number of germs in a selected volume to virtually zero. In a similar way, tumors and cancers could be damaged completely, however there is the same problem with penetration in order not to kill healthy cells at the same time and in order to provide the noninvasiveness [2–3].

In this moment, metallic nanoparticles emerge as a new strategy by using their own radiative properties. Their advantage is that they may freely travel through a microscale pipe, which increases temperature much faster than it is performed with a standard metal sheet. The future perspective is to apply them as an agent for solar collectors, steam production or germs inactivation. Although there are several papers which propose the nanofluidic flows in the context of mass and heat transfer [4 – 5], heat generation and nanoparticles' shape optimization are an abstruse issue and require to compute sophisticated formulas and equations that would be calculated numerically.

Therefore, this work introduces and offers step by step some theoretical methods which are joined following the available models, which is Cattaneo-Vernotte equation for nanoparticles, Rayleigh-Drude approximation, Royer-Yamaguchi approach for a surface effect and the electromagnetic energy convertion into heat, which has been developing in authors' papers. Likewise, the proposed theory is capable of being shifted for bulbs

and solar models. Moreover, the obtained results for the selected theory are revealed for the specially-prepared system which was thermoablated using three lasers and which enables to study both convection moves and microscale heat transfer effects.

2. Theoretical models

Heat transfer of light-ablated metallic nanoparticles is calculated in different methods, depending on the considered model. Nevertheless, most of them require using the hyperbolic energy equation, which is known as Cattaneo-Vernotte equation [7 – 8], and frequently is dedicated for pulsed light sources where temperature inside nanoparticles cannot be written as constant the whole time. For AuNRs, this equation is presented as follows:

$$\mathrm{r}\cdot\frac{\partial^2}{\partial t^2}(\rho\cdot e)+\frac{\partial}{\partial t}(\rho\cdot e)=\mathrm{div}\big(k_{\mathrm{eff}}\cdot\mathrm{grad}(T)\big)+S_e^{\mathrm{np}} \tag{1}$$

$$\mathrm{r}=3\cdot\frac{k_{\mathrm{eff}}}{\rho\cdot c_p}\cdot\frac{1}{{v_{\mathrm{sound}}}^2} \tag{2}$$

On the other hand, for the continuous light sources, like CW-lasers, the delivered heat is sufficiently low so as to have the hyperbolic energy equation reduced into the standard parabolic one. In this work, including gravity forces and Boussinesq approach, the utilized continuity, momentum and energy, turbulence and dissipation equations are written by [5]:

$$\frac{\partial}{\partial t}\begin{Bmatrix}\rho\\ \rho\vec{v}\\ \rho e\\ \rho\mathbb{k}\\ \rho\epsilon\end{Bmatrix}+\mathrm{div}\begin{Bmatrix}\rho\vec{v}\\ \rho\vec{v}\otimes\vec{v}\\ \rho e\vec{v}\\ \rho\mathbb{k}\vec{v}\\ \rho\epsilon\vec{v}\end{Bmatrix}=\mathrm{div}\begin{Bmatrix}0\\ \overleftrightarrow{\tau}-p\overleftrightarrow{I}\\ \left(\overleftrightarrow{\tau}-p\overleftrightarrow{I}\right)\cdot\vec{v}+(k_{\mathrm{eff}}+k_{\mathrm{t}})\cdot\mathrm{grad}(T)\\ \left(\mu+\frac{\mu_{\mathrm{t}}}{\mathrm{Pr}_{\mathbb{k}}}\right)\cdot\mathbb{k}\\ \left(\mu+\frac{\mu_{\mathrm{t}}}{\mathrm{Pr}_{\epsilon}}\right)\cdot\epsilon\end{Bmatrix}+\begin{Bmatrix}0\\ (\rho-\rho_o)\cdot\vec{g}\\ S_e^{\mathrm{f}}+S_e^{\mathrm{np}}\\ G_{\mathbb{k}}-\rho\epsilon+G_{\mathrm{Б}}\\ C_{1\epsilon}\cdot\frac{\epsilon}{\mathbb{k}}\cdot\left(G_{\mathbb{k}}+C_{3\epsilon}\cdot G_{\beta}\right)-C_{1\epsilon}\cdot\rho\cdot\frac{\epsilon^2}{\mathbb{k}}\end{Bmatrix} \tag{3}$$

where:

$$\overleftrightarrow{\tau}=\mathrm{grad}\left(\overrightarrow{X^{\dagger}}\right)-\frac{2}{3}\mu I_{\vec{d}}\overleftrightarrow{I}+2\mu\overleftrightarrow{d}-\frac{2}{3}(\rho\mathbb{k}+\mu_{\mathrm{t}}\cdot I_{\vec{d}})\cdot\overleftrightarrow{I}+2\mu_{\mathrm{t}}\cdot\overleftrightarrow{d} \tag{4}$$

$$G_{\mathbb{k}}=2\mu_{\mathrm{t}}\cdot\overleftrightarrow{d}\cdot\overleftrightarrow{d^{\dagger}} \tag{5}$$

$$G_{\mathrm{Б}}=\mathrm{Б}\cdot\frac{\mu_{\mathrm{t}}}{\mathrm{Pr}}\cdot\vec{g}\cdot\mathrm{grad}(T) \tag{6}$$

The most relevant factors, however, estimate this part of energy which is directly converted into heat from the incident light. Likewise, the formulas may be presented for fluids (and solids as well) and particles, respectively as follows:

$$S_e^{\mathrm{f}}=A_{abs_M}\cdot I_{abs_M}=A_{abs_M}\cdot I_o(\vec{r})\cdot(1-R_M)\cdot\left(1-\exp\left(-A_{abs_M}\cdot\delta\right)\right) \tag{7}$$

$$S_e^{\mathrm{np}}=\sum_{i=1}^{N}A_{abs_i}\cdot I_{abs_i}=\sum_{i}^{N}w_i\cdot\left(\xi\cdot C_{abs_i}\cdot I_o(\vec{r})\cdot(1-R_i)\cdot\left(1-\exp\left(-A_{abs_i}\cdot l_{ph}\right)\right)\right) \tag{8}$$

The difference is visible as well in the absorption coefficient whose value is calculated via different ways. For continuous media, like homogeneous fluids or solids, the formula may be described by:

$$A_{abs_M}=\frac{4\pi\cdot\mathbb{im}\left(n_M(\lambda)\right)}{\lambda} \tag{9}$$

For particles, however, the formula implies counting particle by particle, which obviously cannot be performed. This is the reason why N refers to the number of the grouped particles which possess the same or similar dimensions. The commonly utilized theory, which solves the problem, is based on Rayleigh-Drude approximation whose advantage is the simplicity in adjusting both size, shape and distance effects [9 – 10]. The general formula are followed by [11 – 12]:

$$A_{abs_i}=\xi\cdot\left(\left(C_{ext_i}\right)-\left(C_{sca_i}\right)\right)=\xi\cdot\left(\left(4\pi\cdot\left(\frac{2\pi}{\lambda}\right)\cdot\mathbb{im}(\alpha_i)\right)-\left(\frac{8\pi}{3}\cdot\left(\frac{2\pi}{\lambda}\right)^4\cdot|\alpha_i|^2\right)\right) \tag{10}$$

Nevertheless, the situation which significantly distinguishes the converted rate is how far from the surface nanoparticles are located. For microsize pipes this effect is relevant only near walls, and here only nanofluidic theories are utilized based on the heat transfer coefficient between fluid and particles [4 – 5]. Amongst many theories where the topic has been investigated, Smoluchowski theory, which is presented in [13 – 14], provides satisfactory solutions.

On the other hand, when nanoparticles are deposited on a surface, the interaction should be included with the surface effect which generally increases the optical cross sections, especially for elongated shapes, like nanodisks or nanorods. Here, Royer-Yamaguchi approach [15 – 16] appears to be a perfect solution due to the fact it includes both the surface and distance effect. In this work, the adjusted polarizabilities for rods are presented in the Appendix A. Nevertheless, it should be mentioned that this method is immature for prolate structure, and provides the validity only for the symmetrical alignment of nanoparticles to each other. The other configurations, although they correspond much more to reality, are not supported with the abovementioned formulas, and this aspect would be under further investigations.

Furthermore, total entropy generation, $\mathbb{S}$, is investigated using formula [21,33 – 35] for Boussinesq and turbulent approach:

$$\mathbb{S} = \left(\frac{k_{\mathrm{eff}} + k_{\mathrm{t}}}{T^2}\right) \cdot \left(\mathrm{grad}(T)\right)^2 + \left(\frac{\mu}{T}\right) \cdot \left(-\frac{2}{3} I_{\vec{a}} \cdot \overrightarrow{I} + 2\overrightarrow{d}\right) + \left(\frac{1}{T}\right) \cdot \left(-\frac{2}{3}(\rho \mathbb{k} + \mu_{\mathrm{t}} I_{\vec{a}})\overrightarrow{I} + 2\mu_{\mathrm{t}}\overrightarrow{d}\right) \tag{11}$$

This parameter determines the irreversibility rate of each process, and may reveal which irreversible processes, friction in movement or heat transfer with conduction and forced or natural convection is dominant at each stadium of the simulations.

3. Numerical proceedings

3.1. Considered system

In order to reduce the number of examined systems and to investigate the heat and mass transfer particularly at the same time, it has been decided to create the model which is both simple to prepare, to simulate and to be proceeded in the target application. Fig. 1. outlines the system's scheme from two sides. Gravitational forces works along the x direction in this model.

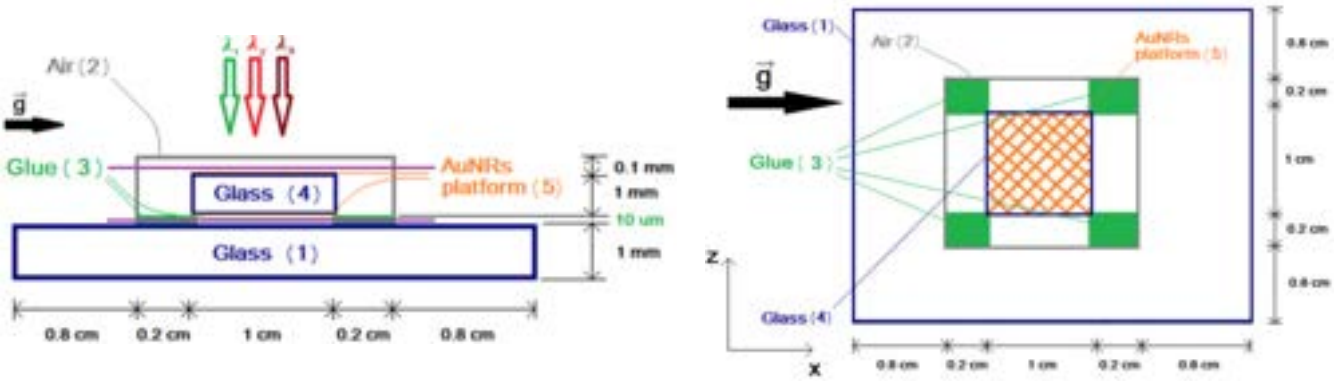

Figure. 1. Scheme of the created geometry and domains with boundary conditions applied in the simulations (scale has not been saved). Violet lines highlight the considered planes in section "Results".

3.2. Boundary conditions

In order to compute the results numerically, the considered system has been discretized into three grids. The calculations have been performed via *Ansys.Fluent* software (version 22.1) on the *Tryton* supercomputer of the TASK resources consisted of 72 cores (Intel®Xeon®Processor E5 v3 @ 2,3GHz) using the SIMPLE algorithm and the second-order scheme for the (2) – (9) equations. The control parameters have been established on 0.5 excepting pressure and density whose values equals 0.3. The space and time tests are based on Roacher's and Richardson's extrapolations [17] so as to verify and minimize the numerical error. The utilized mesh for results is visible in fig. 2.

Likewise, boundary conditions are specified assuming the system is kept in the adiabatic conditions, excepting the irradiated walls where mixed conditions are expected. Moreover, diffusive momentum flux, although they are coated on the glassy base, require using Marangoni's stress for gold nanoparticles due to the presence of the organic compound (CTAB):

$$\overrightarrow{X^{\dagger}} \rightarrow \frac{d\vec{\sigma}}{dT} \cdot \mathrm{grad}(T) \tag{13}$$

where surface tension coefficient equals $\frac{d\vec{\sigma}}{dT} = -0.00005263\ \mathrm{N} \cdot \mathrm{m}^{-1} \cdot \mathrm{K}^{-1}$ [21].

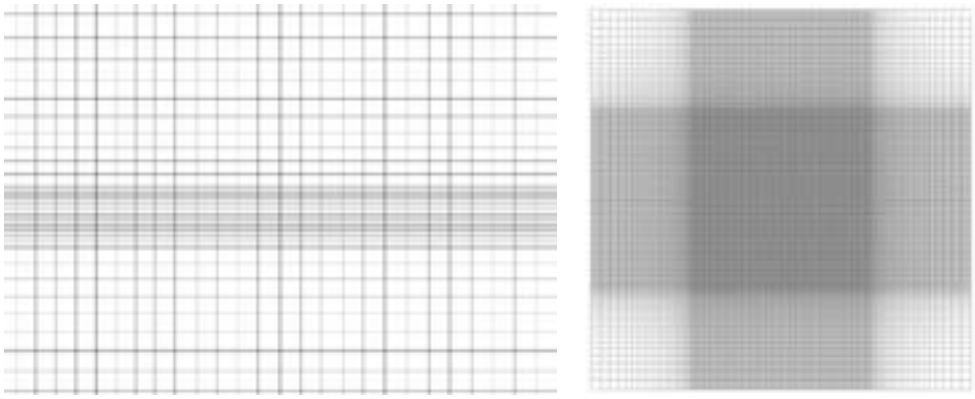

Figure. 2. Applied discretized grid in the simulations from two sides.

Furthermore, heat source, which are three lasers here with the incident wavelengths, $\lambda_{L=1} = 532\ \mathrm{nm}$, $\lambda_{L=2} = 640\ \mathrm{nm}$, $\lambda_{L=3} = 808\ \mathrm{nm}$, undergo the gaussian distribution in the space regime, accordingly:

$$S_e^{\mathrm{np}} = \sum_{L=1}^{3}\left(\sum_{i}^{N} w_i \cdot \left(\xi \cdot C_{abs_i}(\lambda_L) \cdot I_{oL} \cdot \exp\left(-2\left(\frac{\vec{r}}{R_{\phi L}}\right)^2\right) \cdot \left(1 - R_i(\lambda_L)\right) \cdot \left(1 - \exp\left(-A_{abs_i}(\lambda_L) \cdot l_{ph}\right)\right)\right)\right) \tag{14}$$

where each laser output power has been established on $80\ \mathrm{mW}$. These three lasers deliver the heat flux during 90 seconds (irradiation time). After this time, the system is being cooled.

Table 1. details all mentioned assumptions, whereas table 2. reveals material thermal properties from literature.

Table 1. Specified boundary conditions in the considered simulations

No.	Material	Type of boundary conditions	Details
(1)	Bottom borosilicate glass	Mixed	$T_o = 297.15\ \mathrm{K}\ (75.20^{\mathrm{o}}\mathrm{F})$ $h = 13.6\ \mathrm{W \cdot m^{-2} \cdot K^{-1}}$ $\delta = 0.001\ \mathrm{m}$ $S_e^{\mathrm{f}} \approx 0\ \mathrm{W \cdot m^{-3}}$ $R_{\phi L} = 0.0015\ \mathrm{m}$
(2)	Air	Outlet (Neumann)	$T_o = 297.15\ \mathrm{K}\ (75.20^{\mathrm{o}}\mathrm{F})$ $v_o = 0$ $S_e^{\mathrm{f}} \approx 0\ \mathrm{W \cdot m^{-3}}$
(3)	Glue	Neumann	$T_o = 297.15\ \mathrm{K}\ (75.20^{\mathrm{o}}\mathrm{F})$ $S_e^{\mathrm{f}} \approx 0\ \mathrm{W \cdot m^{-3}}$
(4)	Top borosilicate glass	Mixed	$T_o = 297.15\ \mathrm{K}\ (75.20^{\mathrm{o}}\mathrm{F})$ $h = 13.6\ \mathrm{W \cdot m^{-2} \cdot K^{-1}}$ $\delta = 0.001\ \mathrm{m}$ $S_{e_1}^{\mathrm{f}} = 0.0006956\ \mathrm{W \cdot m^{-3}}$ $S_{e_2}^{\mathrm{f}} = 0.0015740\ \mathrm{W \cdot m^{-3}}$ $S_{e_3}^{\mathrm{f}} = 0.0003483\ \mathrm{W \cdot m^{-3}}$ $R_{\phi L} = 0.0015\ \mathrm{m}$
(5)	Gold surface	Neumann	$T_o = 297.15\ \mathrm{K}\ (75.20^{\mathrm{o}}\mathrm{F})$ $l_{ph} = 26.0\ \mathrm{nm}$ $S_{e\ 1}^{\mathrm{np}} = 1.45745 \cdot 10^{11}\ \mathrm{W \cdot m^{-3}}$ $S_{e\ 2}^{\mathrm{np}} = 1.90629 \cdot 10^{9}\ \mathrm{W \cdot m^{-3}}$ $S_{e\ 3}^{\mathrm{np}} = 3.22348 \cdot 10^{11}\ \mathrm{W \cdot m^{-3}}$ $R_{\phi 1} = 0.0015\ \mathrm{m}$ $R_{\phi 2} = 0.0015\ \mathrm{m}$ $R_{\phi 3} = 0.0015\ \mathrm{m}$ $\frac{d\vec{\sigma}}{dT} = -0.00005263\ \mathrm{N \cdot m^{-1} \cdot K^{-1}}$

Table 2. Material properties in the considered simulations.

Material	Density, ρ $(\mathbf{kg \cdot m^{-3}})$	Specific heat capacity, c_p $(\mathbf{J \cdot kg^{-1} \cdot K^{-1}})$	Thermal conductivity coefficient, $k_{\mathbf{eff}}$ $(\mathbf{W \cdot m^{-1} \cdot K^{-1}})$	Dynamic viscosity, μ $(\mathbf{Pa \cdot s})$	References
Borosilicate glass	2124.9	779.74	$0.9245251 + 0.0004777689 \cdot T + 9.178795 \cdot 10^{-7} \cdot T^2$	-	[22,23]
Gold nanorods	19320	129.81	317	-	[24,25]
Air	$352.965 \cdot T^{-1}$	1006.43	$0.004204762 + 7.242857 \cdot 10^{-5} \cdot T$	$7.29 \cdot 10^{-6} + 4.0 \cdot 10^{-8} \cdot T$	[26-28]
Glue	1231	1100	0.50	0.30	[29,30]

4. Results

Heat transfer results may be described by the mathematical functions whose solutions are determined by specified boundary conditions. Some results are based on Green's or gaussian functions and are presented in [19 – 20]. The presence of forced and natural convection, however, which occurs in this work, implies the major functions' complicity and therefore numerical methods are advisable.

Results are being considered 5 μm above (top) (red color) and under (bottom) (blue color) glassy base, near the AuNRs platforms respectively. Fig. 3a. highlights maximum temperature vs time response, fig. 3b. presents the entropy changes, whereas fig. 3c outlines maximum velocity fluctuations. As may be noticed, maximum temperature reaches 33.225°C and 31.795°C above and under the top glass respectively, which is a promising temperature increase since the operating laser power is quite low. It is expected that higher values of power would significantly increase the maximum temperature of the system. On the other hand, this work assumes using the three wavelengths which do not correspond perfectly for the sun spectrum distribution.

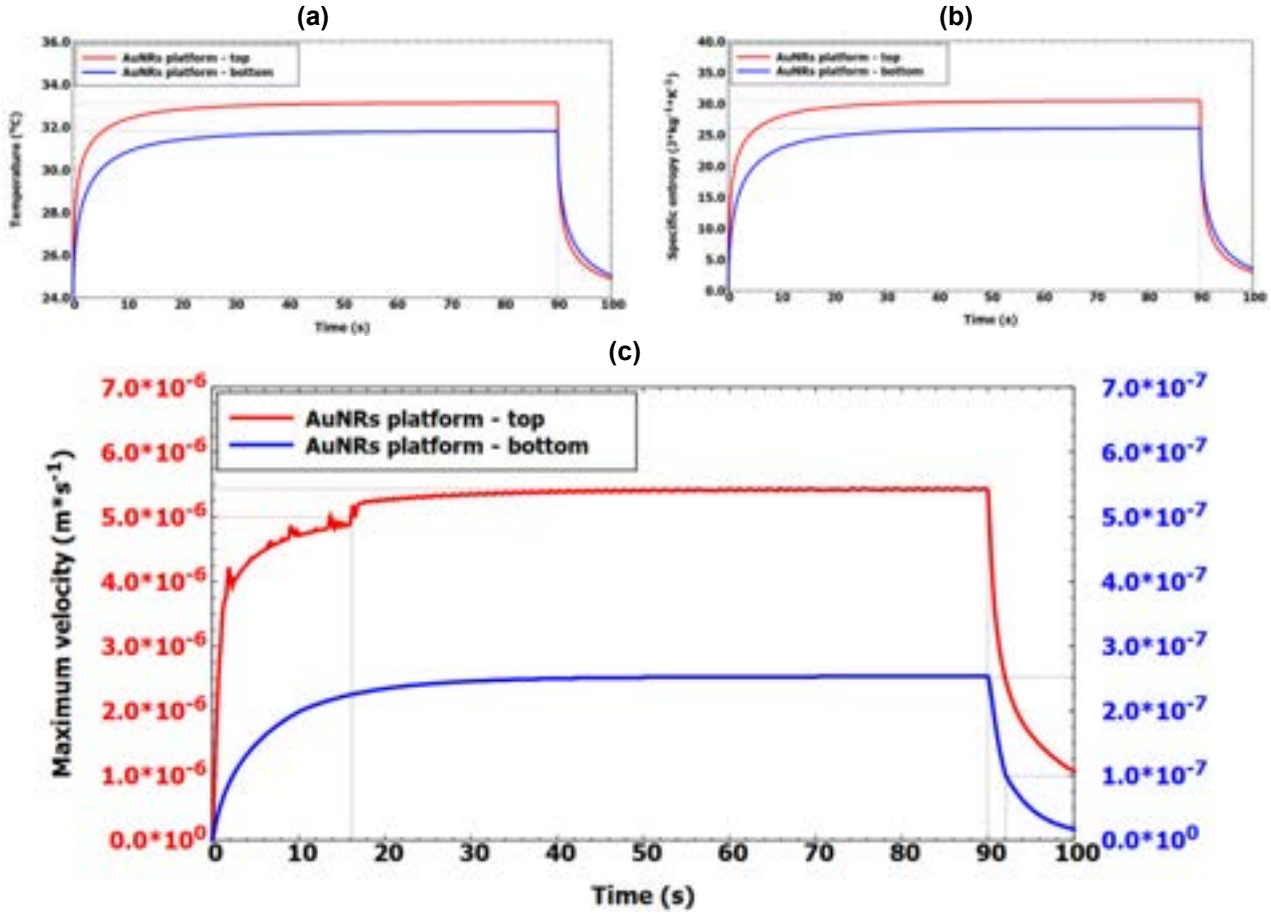

Figure. 3. (a) Maximum temperature, **(b)** specific total entropy and **(c)** maximum velocity vs. time results 5 μm above (top) (red color) and 5 μm under (bottom) (blue color) glassy base of the AuNRs platforms respectively. Using dotted lines, sensitive moments in time are raised.

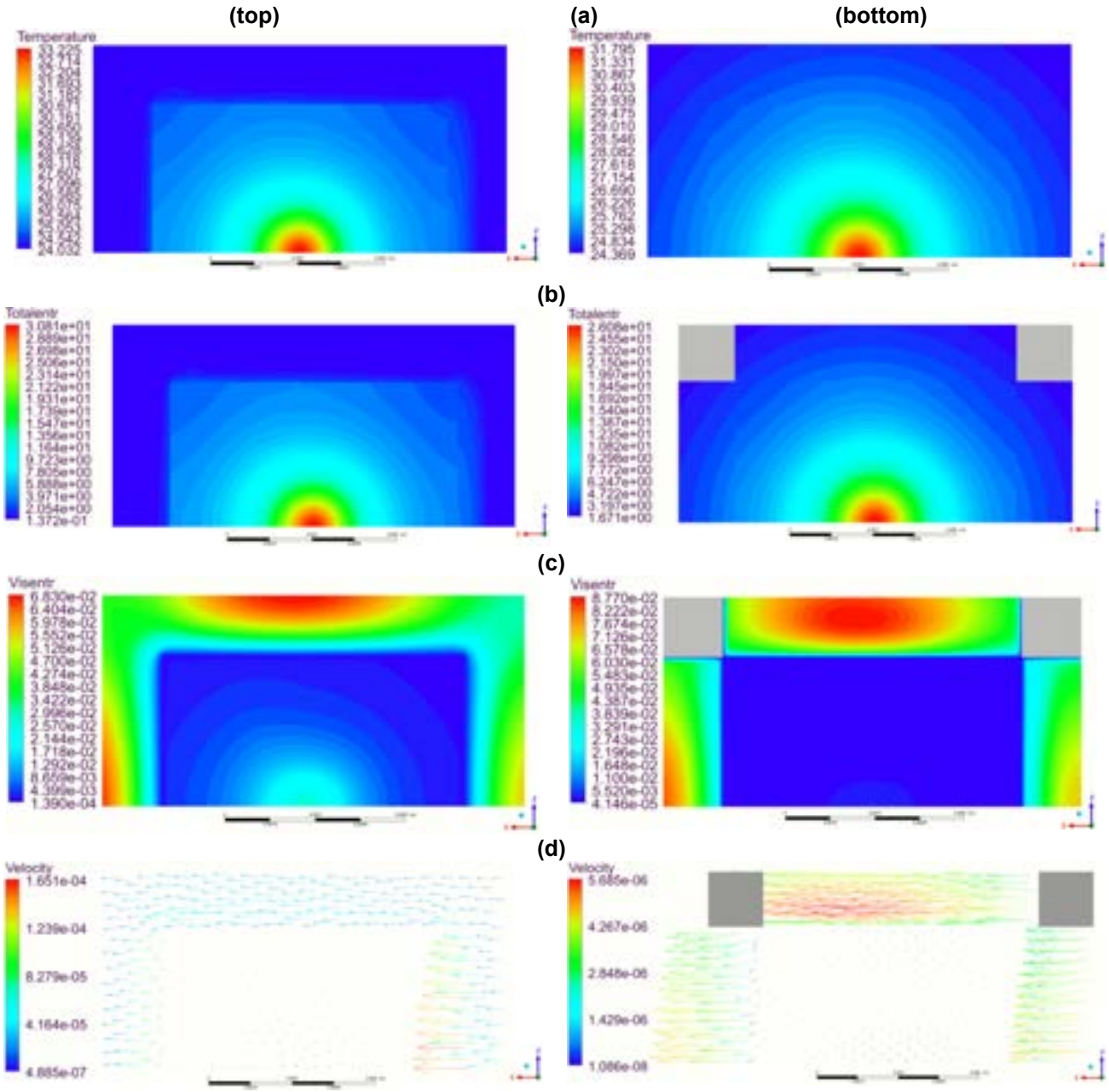

Figure. 4. (a) Temperature, **(b)** specific total and **(c)** dynamic entropy, **(d)** velocity contour plots 5 μm above (top) (red color) and 5 μm under (bottom) (blue color) glassy base of the AuNRs platforms respectively after 90 seconds of the system irradiation.

Furthermore, curve shapes are responsible for the heat rate and thermal properties of that the considered system consisted. As long as the quick temperature increase is explained via high value of material's thermal diffusivities compared to gold, the steady state is obtained as a result of assumed adiabatic and insulated conditions at walls and of the air domains, respectively. Nonetheless, under the discussed theory in Appendix A, many parameters, like nanoparticle's dimensions or surface material, can be adjusted ensuring different temperature changes and curve shapes. Each of these aspects should be examined particularly in the near future.

Likewise, the obtained low values of velocity imply weak impact on the heat rate. As a matter of fact, thermal effects may have triggered the natural convective movement of the fluid associated with the distribution of the plate. Moreover, the results are expected to be distinguishable in the microscale region between glass and above the AuNRs-platform respectively. This may be noticed peering into both the differences of the maximum temperature and specific entropy for the considered surfaces. The explanations are searched in the thickness of the AuNRs platforms and the heat transfer coefficient which implies a lower value if the flow is weaker, which is clearly visible in fig. 3c. The flow, however, is governed by different phenomena. The top-AuNRs-platform is exhibited for the forced convection and turbulence effects which is due to the gravity forces.

This is the reason why dynamic entropies, which are presented in figs. 4c and 5c, are distinguishable to each other, and why are visible only very close to AuNRs platforms. In order to enforce the flow inside the microscale region, significantly higher pressures should be applied, which is not necessary for the top-AuNRs-platform due to the assumed outlet condition. On the other hand, dynamic entropy is not a dominant process, which may be realized from total entropy contours which implies that and mainly heat transfer does the lion's share in the whole simulation.

Hence, heat is generally transported by conduction, whereas natural convection is directly responsible for the entropy generation. Dynamic entropy, which is caused by friction, is a few ranks lower than the static one. However, asymmetrical heat wave front, which is visible in the figures 4c and 5c, appears to be due to the natural convection, both near the top- and bottom-AuNRs-platforms.

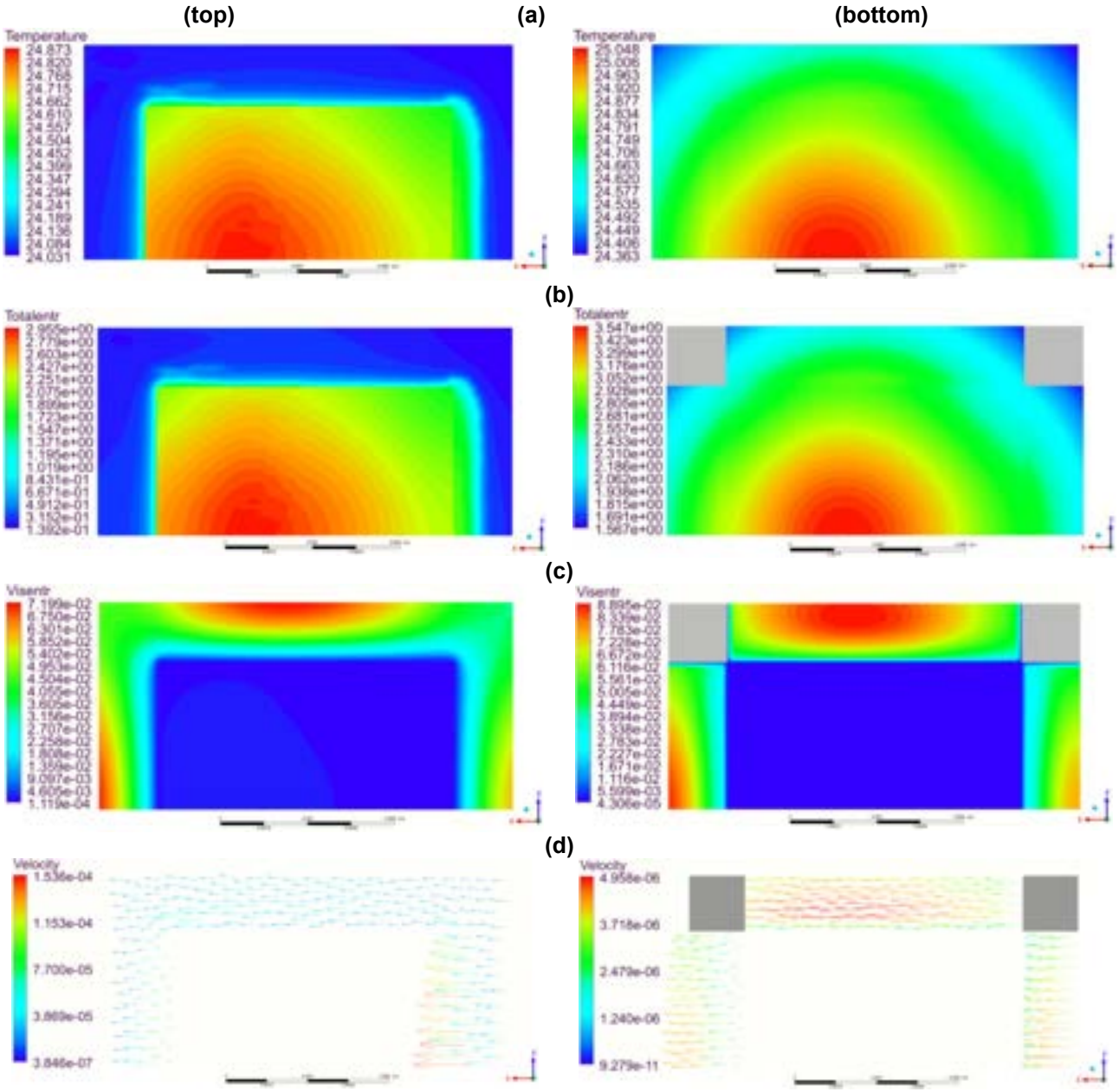

Figure. 5. (a) Temperature, **(b)** specific total and **(c)** dynamic entropy, **(d)** velocity contour plots 5 μm above (top) (red color) and 5 μm under (bottom) (blue color) glassy base of the AuNRs platforms respectively after 10 seconds of the system cooling.

Jagged contours may be explained following that Marangoni's stress is responsible for the fluctuations presence which are intensified as a result of the turbulence effects due to convection forces. Moreover, it is supposed that heat is transported as a result of the convection processes which implies the turbulence influence, even if the flow takes low values. Another issue occurs at the rectangular boundaries where the contours appear to be discontinuous due to the fact that there are located the material boundaries, and the material properties abruptly vary. These discontinuities are common phenomena manifested at the micro- and

nanoscale, with velocity slip, transpiration mobility and Marangoni's stress among the dominant effects [36-39].

Furthermore, the jumpy variations may be noticed in the velocity vs time plot where the curve does not possess a smooth character. This is not observed in the bottom-AuNRs platform where the curve is deprived of the discontinuities, and where the turbulence is significantly weaker. It is also worth mentioned that the curves have been improved via decreasing mesh size as long as the satisfactory quality obtains, and every simulation has provided a similar feedback.

5. Summary

Metallic nanostructures, although they are followed with standard Boltzmann transport equations, require utilizing sophisticated mathematics which implies the problem complexity in boundary conditions. In this work, microscale heat transfer and convection moves have been raised and discussed. This paper suggests that there is a possibility to apply metallic nanoparticles in real energy or biomedical applications. Their unquestionable advantage is heating them inside pipes, which omits the problem of the low heat transfer coefficient of the exterior surfaces. Moreover, the utilized model, although NRs are not truly present, the interaction between NRs and light is the response based on the physical phenomena. The approach, however, does not require to calculate many equations, which definitely may accelerate the simulation compared to the available full optical approaches, like DO model.

Furthermore, the outlined theoretical results reveal that even relatively low values of the laser powers are sufficient so as to obtain a significant temperature increase. In this work, the maximum value has reached ΔT=9.225^{o}C. Although higher temperature may be provided by manipulation of nanoparticle's properties or stronger light sources, it should be taken into account the heat transfer is strictly conjugated with the conduction where heat spreads decreasing the maximum value supporting the average one. On the other hand, the competition between force and natural convection also is not trivial, which has been present and been studied thoroughly in this work as well. In this work, the forced convection influence has been discovered not to do the lion's share due to the weak flow near the AuNRs platforms.

It is being predicted, however, this effect would be much more visible e.g. in solar collectors where AuNRs shall move freely and be exposed to the high stresses due to the forced convection. Nonetheless, the considered topic takes the advantage and encourages further investigations due its promising temperature increase in the imitating-systems which may be used in energy or biomedical applications.

Acknowledgments

The work was supported by the National Science Centre, Poland, under research project „Shape and displacement optimization of gold nanorods in the killing chamber in order to phototermoablation processes", no UMO-2021/43/D/ST8/02504.

Computations were carried out using the computers of Centre of Informatics Tricity Academic Supercomputer & Network (CI TASK) in Gdansk.

Appendix A

This part studies the applied formula for electrical polarizabilities applied for the substrate effect of the used nanostructures. Due to the surface effect and anisotropy of considered nanostructures, several formulas are calculated and specified for 130 x 130 different sizes of d_{s_i} and d_{l_i}. The general boundary condition for the total polarizability is described as follows:

$$\alpha_i = \frac{2}{3}\left(\frac{2}{3}\cdot\left(\left(\alpha_{i,y}\right)_{Ya}+\left(\alpha_{i,z}\right)_{Ya}\right)+\frac{1}{3}\cdot\left(\left(\alpha_{i,x,dl}\right)_{Ya}\right)\right)+\frac{1}{3}\cdot\left(\frac{2}{3}\cdot\left(\left(\alpha_{i,y,ds}\right)_{Ya}+\left(\alpha_{i,z,ds}\right)_{Ya}\right)+\frac{1}{3}\cdot\left(\left(\alpha_{i,x}\right)_{Ya}\right)\right) \tag{A.1}$$

The substrate and distance effects are described by Royer-Yamaguchi approach [15 -16], where the anisotropic factor, β_i, is perpendicular along the y-axis, as follows:

$$\left(\alpha_i\right)_{Yam} = \frac{\left(\alpha_i\right)_{sur}}{1+\left(\frac{\left(\alpha_i\right)_{sur}}{\frac{4}{3}\pi\cdot {d_{s_{1i}}}^2\cdot d_{l_{1i}}}\right)\cdot\beta_i} \tag{A.2}$$

Surface polarizabilities are assumed for the prolate ellipsoids which are the complex functions, as follows:

$$\left(\alpha_{i,x,z}\right)_{sur}\rightarrow\left(\alpha_{i,x,z}\right)_{sur}\left(\mathbb{p}_{11},\mathbb{q}_{11},\mathbb{e}_{11},\varepsilon_h,\varepsilon_{sur},d_{s_{1i}},d_{s_{2i}},d_{l_{1i}},u_l\right) \tag{A.3}$$

$$\left(\alpha_{i,y}\right)_{sur}\rightarrow\left(\alpha_{i,y}\right)_{sur}\left(\mathbb{p}_{10},\mathbb{e}_{10},\varepsilon_h,\varepsilon_{sur},d_{s_{1i}},d_{s_{2i}},d_{l_{1i}},u_l\right) \tag{A.4}$$

Contrary to ellipsoids, rods possess the flat long dimension which contributes to appear new dipole configurations. It was discovered by Fuchs publication [18] in which the charge arrangements of edgy shapes (triangles, cubes, octahedrons etc.) The publication implies that the dipole arrangement in a nanoparticle may be

specified by a certain parameter in order to solve and establish the other dipole configurations. As long as the along axes tend to spherical distribution, $(\phi_i(d_{s_i}, d_{l_i}) \rightarrow \phi_i(d_{s_i}, d_{s_i}) \rightarrow 0)$, the situation changes in rods. It is assumed to exist the new configuration where dipoles are arranged at the very opposites diagonal indicating $\phi_i(d_{s_i}, d_{l_i}) \rightarrow \phi_{i,d_l}\left(d_{l_i} - d_{s_i}, \sqrt{(d_{l_i} - d_{s_i})^2 + (d_{s_i})^2}\right)$ and $\phi_i(d_{s_i}, d_{l_i}) \rightarrow \phi_{i,d_s}\left(d_{s_i}, \sqrt{(d_{l_i} - d_{s_i})^2 + (d_{s_i})^2}\right)$, which are projected on the main space diagonal of a rod for y- and x-, z- axes respectively. Fig. A.1 demonstrates these four assumed charge arrangements which have been adjusted to the x-oriented particles than are deposited on the y-axis surface. The assumed parameters and properties for the abovementioned formulas are highlighted in tables A.1 and A.2.

Table A.1: Nanorods assumed parameters

General parameters	**Assumed value**
NPs general size, d_s x d_s x d_l	15 x 15 x 55 nm
Coating thickness, d_{s_2}	4 nm
Average NP – NP distance, u_l	140 nm
Nanoparticles concentration, ξ	$8.67 \cdot 10^{21}$ m^{-3}

Table A.2: Electrical properties for the utilized three wavelength values

Wavelength dependence parameters		$\lambda_1 = 532$ nm	$\lambda_2 = 640$ nm	$\lambda_3 = 808$ nm	**References**
Permittivity of air (humidity – 15%), ε_h		1.103112	1.102395	1.101639	[30,32]
Permittivity of borosilicate glass, ε_{sur}		2.308880	2.294619	2.281912	[22]
Gold electrical permittivity, ε_1	$\mathbb{re}$	-4.660220	-12.183069	-25.035329	[31]
	$\mathbb{im}$	2.346720	1.1734087	1.564609	

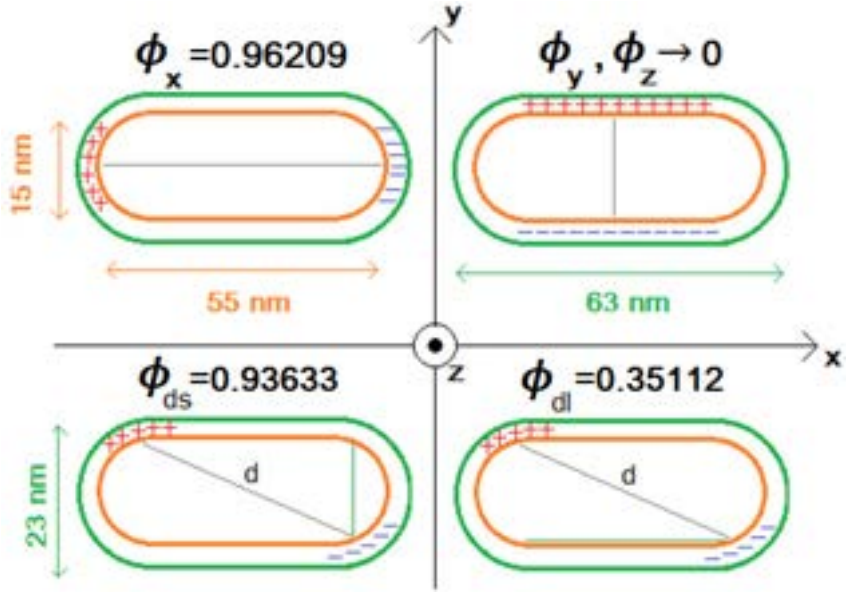

Figure. A.1. Electric dipole configurations which have been considered in the calculations for 15-15-55-nm gold nanorods (orange color) coated by a 4-nm organic compound (green color).

Nomenclature

Roman letters

A_{abs_i}	absorption coefficient of the i-particle, m^{-1}
A_{abs_M}	absorption coefficient of the continuous material, m^{-1}
C_{abs_i}	absorption cross section of the i-particle, m^2
C_{ext_i}	extinction cross section of the i-particle, m^2
C_{sca_i}	scattered cross section of the i-particle, m^2
c_p	specific heat capacity, $\mathrm{J} \cdot \mathrm{K}^{-1} \cdot \mathrm{kg}^{-1}$
$\overleftrightarrow{d}$	symmetric rate of deformation, s^{-1}
d_{l1_i}	longer diameter of the i-nanoparticle, m

d_{s1_i}	shorter diameter of the i-nanoparticle, m
d_{s2_i}	size of the nanoparticle's coating, m
e	specific energy, $\mathrm{J} \cdot \mathrm{kg}^{-1}$
$G_{\mathbb{k}}$	turbulence kinetic energy generation due to velocity gradients, $\mathrm{kg} \cdot \mathrm{m}^{-1} \cdot \mathrm{s}^{-3}$
$G_{\text{Б}}$	turbulence kinetic energy generation due to buoyancy forces, $\mathrm{kg} \cdot \mathrm{m}^{-1} \cdot \mathrm{s}^{-3}$
$\vec{g}$	gravity, $\mathrm{m} \cdot \mathrm{s}^{-2}$
h	heat transfer coefficient, $\mathrm{W} \cdot \mathrm{m}^{-2} \cdot \mathrm{K}^{-1}$
$I_o(\vec{r})$	initial intensity laser profile, $\mathrm{W} \cdot \mathrm{m}^{-2}$
I_{abs_i}	absorbed part of the i-particle, $\mathrm{W} \cdot \mathrm{m}^{-2}$
$I_{\vec{d}}$	first invariant of the strain rate, s^{-1}
$\overleftrightarrow{I}$	unit tensor, -
k_{eff}	effective thermal conductivity coefficient, $\mathrm{W} \cdot \mathrm{m}^{-1} \cdot \mathrm{K}^{-1}$
L	subsequent laser source
l_{ph}	light-NR interaction thickness, m
$Pr_{\mathbb{k}}$	turbulent Prandtl number for kinetic energy, -
Pr_{ϵ}	turbulent Prandtl number for rate of dissipation, -
Pr	Prandtl number, -
p	pressure (Pa)
R_i	reflection coefficient of the i-nanoparticle, m
R_M	reflection coefficient of the continuous material, m
$R_{\phi L}$	beam sizes of laser sources, m
$\overleftrightarrow{R}$	Reynolds stress tensor
$\vec{r}$	radius – spherical coordinate, m
S_e^f	source of energy for fluids, $\mathrm{W} \cdot \mathrm{m}^{-3}$
S_e^{np}	source of energy for the i-particle, $\mathrm{W} \cdot \mathrm{m}^{-3}$
T	temperature, K
T_o	initial temperature at the $t = 0\ \mathrm{s}$, K
t	time, s
u_l	distance between particles, m
$\vec{v}$	velocity of the fluid, $\mathrm{m} \cdot \mathrm{s}^{-1}$
v_{sound}	speed of sound, $\mathrm{m} \cdot \mathrm{s}^{-1}$
$\overrightarrow{X^{\dagger}}$	diffusive momentum flux, $\mathrm{kg} \cdot \mathrm{m} \cdot \mathrm{s}^{-2}$
x, y, z	Cartesian's coordinates, -

Greek letters

α_i	polarizability of the i-particle, m^3
β	anisotropic factor for distance and surface effects, -
δ	thickness of the considered material, m
ε_h	permittivity of the host medium, -
ε_{sur}	permittivity of the base where NRs are embedded, -
ϵ	turbulent energy dissipation, $\mathrm{m}^2 \cdot \mathrm{s}^{-3}$
λ	incident wavelength, m
μ	molecular viscosity, $\mathrm{Pa} \cdot \mathrm{s}$
μ_{t}	eddy viscosity, $\mathrm{kg} \cdot \mathrm{m}^{-1} \cdot \mathrm{s}^{-1}$
ξ	nanoparticles concentration, m^{-3}
ρ	density of a material, $\mathrm{kg} \cdot \mathrm{m}^{-3}$
$\overleftrightarrow{\sigma}$	surface tension parameter, $\mathrm{N} \cdot \mathrm{m}^{-1}$
ψ	prolation parameter, -

Slavic letters

Б	thermal expansion coefficient, K^{-1}
г	relaxation time, s

Others

∂	symbol of partial derivative
$\mathbb{i}$	symbol of imaginary unit
$\mathbb{im}$	imaginary part of a complex expression
$\mathbb{k}$	turbulent kinetic energy
$\mathbb{p}$	associated Legendre polynomials of a first kind
$\mathbb{q}$	associated Legendre polynomials of a second kind
$\mathbb{re}$	real part of a complex expression

Subscripts and superscripts

a	air
d	diffusivity
f	fluid
i	selected number
l	long or distance
M	material
o	in reference to initial conditions
s	short
t	turbulent
†	transposition

Abbreviations

abs	absorption
div	divergence
eff	effective
exp	exponent
ext	extinction
grad	gradient
np	nanoparticle
NRs	nanorods
ph	photon
sca	scattering
sur	surface
Ya	in reference to Yamaguchi approach

References

[1] Coyle E. D., Simmons R.A, Understanding the Global Energy Crisis, Purdue University Press, West Lafayette, USA, 2014

[2] Petronella F., De Biase D., Zaccagnini F., Verrina V., Lim S., Jeong K., Miglietta S., Petrozza V., Scognamiglio V., Godman N.P., Evans D.R., McConneye M., De Sio L., Label-free and reusable antibody-functionalized gold nanorod arrays for the rapid detection of Escherichia coli cells in a water dispersion, Environmental Science: Nano, 2022, 9, 3343-3360

[3] Pontico M.,Conte M., Petronella F., Frantellizzi V., De Feo M.S., Di Luzio D., Pani R., De Vincentis G., De Sio L., 18F-fluorodeoxyglucose (18F-FDG) Functionalized Gold Nanoparticles (GNPs) for Plasmonic Photothermal Ablation of Cancer: A Review, Pharmaceutics, 2023, 15, 319

[4] Mikielewicz D., Hydrodynamics and heat transfer in bubbly flow in the turbulent boundary layer, International.Journal of Heat and Mass Transfer, 2002, 46, 207 – 220, 2

[5] Ziolkowski P., Badur J., A theoretical, numerical and experimental verification of the Reynolds thermal transpiration law, International Journal of Numerical Methods for Heat & Fluid Flow, 2018, 28, 1

[6] De Sio L., Placido T., Comparelli R., Curri M. L., Striccoli M., Tabiryan N., Bunning T. J., Next-generation thermo-plasmonic technologies and plasmonic nanoparticles in optoelectronics, Progress in Quantum Electronics, 2015, 41, 23

[7] Sobhan C.B, Peterson G.P., Microscale and Nanoscale Heat Transfer: Fundamentals and Engineering Applications, CRC Press Taylor&Francis Group, USA, 2008

[8] Cattaneo M.C., A form of heat conduction equation which eliminates the paradox of instantaneous propagation, Compte Rendus, 1958, 247, 431–433

[9] Bohren C.F., Huffman D.R., Absorption and Scattering of Light by Small Particles, A Wiley-Interscience publication, Canada, 1998

[10] Strutt, J.W. (Rayleigh L.), On the scattering of light by small particles, The London, Edinburgh, and Dublin Philosophical Magazine and Journal of Science, 1871, 41, 275, 447 – 454

[11] Radomski P., Ziolkowski P., Mikielewicz D., Theoretical approach of laser-irradiated metallic nanoparticles in selected mixed-convection systems, Progress in heat and mass transfer research, Conference monograph of XVI Heat and Mass Transfer Symposium in Mragowo, Polish Academy of Science (PAN), Bialystok, 2022, 374 – 384

[12] Radomski P. Ziolkowski P., De Sio L., Mikielewicz D., Effects of the laser-ablated metallic nanoparticles shapes on the photo-thermal performances in a selected fluidic medium, 15th Mediterranean Workshop and Topical Meeting "Novel Optical Materials and Applications", University of Calabria, Cetraro (Italy), 2022

[13] Smoluchowski M., On conduction of heat by rarefied gases, Annalen der Physik, 1898, 300, 1

[14] Radomski P., Ziolkowski P., De Sio L., Mikielewicz D., Computational fluid dynamics simulation of heat transfer from densely packed gold nanoparticles to isotropic media, Archives of Thermodynamics, 2021, 42, 87 – 114, 3

[15] Yamaguchi T., Yoshida S., Kinbara A.,Optical Effect Of The Substrate On The Anomalous Absorption Of Aggregated Silver Films, Thin Solid Films, 1974, 21, 173 – 187

[16] Royer P., Bijeon J.L., Goudonnet J.P., Inagaki T., Arakawa E.T., Optical Absorbance of Silver Oblate Particles, Substrate And Shape Effects: Surface Science, 1989, 217, 384 – 402

[17] Roache, P.J., Quantification of Uncertainty in Computational Fluid Dynamics, Annual Review of Fluid Mechanics, 1997, 29, 123 – 160

[18] Fuchs R., Theory of the optical properties of ionic crystal cubes, Physical Review B, 1975, 11, 1732 – 1740, 4

[19] Domański R., Laser Radiation – solid-state interaction, Polish Scientific-Technical Journals, 1990, Warsaw (Poland), 130 – 220 (in Polish)

[20] Carslaw H.S, Jaeger J.C, Conduction of Heat in Solids. Second Edition, Oxford University Press, 1959, London, 50–132

[21] Romanchuk B.J., Computational Modeling of Buble Growth Dynamics in Nucleate Pool Boiling for Pure Water and Aqueous Surfactant Solutions, Master of Engineering dissertation, Division of Research and Advanced of The University of Cincinnati, 2014

[22] Bansal N. P., Doremus R. H., Handbook of Glass Properties, Academic Press, Materials Engineering Department Rensselaer Polytechnic Institute, Troy, New York, 1986

[23] Zaitlin M. P., Anderson A. C., Thermal Conductivity of Borosilicate Glass, Physical Review Letters, 1974, 33, 1158-1161, 19

[24] Reddy H., Temperature-dependent optical properties of gold thin films, Optical Material Express, 2016, 6, 2776 – 2802, 9

[25] Siegel R., Howell J.R., Thermal radiation heat transfer, McGraw-Hill Book Company, USA, 1972

[26] Engineering ToolBox, (2003). Air - Density, Specific Weight and Thermal Expansion Coefficient vs. Temperature and Pressure [accessed 17.2.2023].

[27] Engineering ToolBox, (2009). Air - Thermal Conductivity vs. Temperature and Pressure [accessed 17.2.2023].

[28] Engineering ToolBox, (2003). Air - Dynamic and Kinematic Viscosity [accessed 17.2.2023].

[29] Mark J. E., Polymer Data Handbook, Oxford University Press, 1999, 131, 44

[30] Bengte D. L., The Refractive Index of Air, Metrologia,1966, 8, 71 – 80, 2

[31] Vial A., Laroche T., Description of dispersion properties of metals by means of the critical points model and application to the study of resonant structures using the FDTD method, J. Phys. D: Appl. Phys, 2007, 40, 7152–7158

[32] Fernández-Prini R., Release on the Refractive Index of Ordinary Water Substance as a Function of Wavelength, Temperature and Pressure, The International Association for the Properties of Water and Steam, Erlagen, 1997, 2 – 7

[33] Bejan A., Fundamentals of Exergy Analysis, Entropy Generation Minimization, and the Generation of Flow Architecture, International Journal of Energy Research, 2002, 26, 1–43.

[34] Sciubba E., Use of Exergy Analysis To Compute The Resource Intensity of Biological Systems and Human Societies, 12th Joint European Thermodynamics Conference, Brescia, 2013, 268 – 273

[35] Jou D. Entropy, entropy flux, temperature, and second law in extended irreversible thermodynamics, 12th Joint European Thermodynamics Conference, Brescia, 2013, 211 – 216.

[36] Ziolkowski P., Badur J., On Navier slip and Reynolds transpiration numbers, Archive of Mechanics, 70, 3, 2018, 269–300.

[37] Schneider W., Surfaces as non-autonomous thermodynamic systems, 12th Joint European Thermodynamics Conference, Brescia, 2013, 178 – 185.

[38] A. Sellitto, V. A. Cimmelli and D. Jou, Thermoelectric effects and size dependency of the figure-of-merit in cylindrical nanowires, Int. J. Heat Mass Transfer, 57, 2013, 109-116.

[39] D. Jou, J. Casas-Vazquez and G. Lebon, Extended Irreversible Thermodynamics, Berlin Springer, fourth revised ed., 2010

An IR-based methodology for indirect measurement of average inner temperatures

Elisa Carvajal Trujillo[a], Francisco Jiménez Espadafor Aguilar[a], Ricardo Chacartegui-Ramírez[a]

[a] Universidad de Sevilla, Seville, Spain ecarvajal@us.es
[b] Universidad de Sevilla, Seville, Spain fcojjea@us.es
[c] Universidad de Sevilla, Seville, Spain ricardoch@us.es

Abstract:

In many thermal processes, elements with high temperatures are distributed in a non-uniform way, whose internal surface temperatures must be known. Intrusive through-wall sensors are commonly used, but this technique is not possible in some cases. In addition, it requires numerous sensors distributed over the entire surface to know the temperature of the entire surface adequately. This is the case with the inner surfaces of the cylinder and cylinder head of reciprocating internal combustion engines, where it is relatively easy to measure the external temperature of the surfaces but not the temperature distribution of the inner surfaces. The accurate evaluation of this interior temperature is relevant for the determination of inner processes, such as the rejected heat from the combustion chamber.

In this work, a methodology for the estimation of the average temperature of the interior surfaces of elements is presented. Starting from the experimental measurement of the temperature distribution of the exterior surfaces and measuring the total energy transferred from the interior to the exterior surface, the proposed methodology uses an iterative sequence of simulations using finite element methods. The result is a distribution of temperatures on the interior surfaces, whose average temperature is taken as the temperature of the interior surfaces. The minimum mean square error (MSE) value achieved is of the order of 50. The method converges when an improvement of the MSE by less than 5% is achieved. The convective heat transfer coefficients from the finned surface to the atmosphere is $1{,}4 \cdot 10^{-4}$ W/mm^{2}K, which are normal values associated with natural convection.

This methodology has been validated by building a prototype in the laboratory. The methodology has achieved a high agreement between the measured and the predicted values.

Keywords:

Sensors, Infrared thermal images, thermal engine, temperature indirect measurement

1. Introduction

In thermal systems that are composed of mechanisms and thermal generation within them, the prediction of heat transfer is important as it influences heat losses. An accurate prediction of heat losses are essential to know the performance, power, emissions and stress field [1]. Examples of such systems are heat engines, such as reciprocating internal combustion engines, or thermal storage systems based on thermochemical reactions. Knowing the temperature distribution inside these systems is important to characterise the behaviour of these thermal systems.

Measuring the interior temperatures of walls that are not accessible is quite costly and difficult. Intrusive techniques are normally used, with holes drilled to install the sensors, which can modify the phenomenon and render the model useless [2]. Measurements based on optical techniques are also common [3] but require specific windows or special preparation of the model to be measured, with optical access. An example would be the diode laser sensor [4] or coherent anti-Stokes Raman spectroscopy [5].

Directly measuring temperatures on indoor surfaces using sensors can be complicated and intrusive [6]. In addition, the spatial variation of temperatures on indoor surfaces is important [7,8]. If the measurement is reduced to a few points, the averages can be non-representative of the whole assembly. Moreover, it is challenging for small systems to install a relevant number of sensors on the inner surfaces, with the risk of affecting inner flows. This is especially important for measuring the inner surface of combustion chambers of reciprocating internal combustion engines or high-temperature energy storage systems where the gas temperature could be considered constant for many analyses, but for the purpose of mechanical calculations and heat transfer calculations, the assumption of constant surface temperature is not valid. The smaller the

volume and the higher the temperature, the more complicated the installation and the more intrusive the measurement method.

In addition, when the outer surface of the system whose inner surface temperature is to be measured is not uniform, for instance, air cooling internal combustion engines with an external finned surface, measurement becomes even more difficult due to the more difficult installation conditions of the sensors.

There are indirect methods for the determination of these temperatures based on heat transfer mechanisms. Some authors use resistance-capacitance models [9]. Other authors use models that solve by finite element methods, in stationary or transient regimes. For both types of models, the boundary conditions are varied: constant temperatures on the inner and outer surface, constant heat transfer coefficients on the inner wall and temperature of the outer wall equal to that of the coolant or heat transfer coefficients in different areas of the outer surface of the piston [10, 11, 12].

It should also be noted that the derivation of the values of the boundary conditions for these simulations is varied. In many cases, the authors use values of conditions from the literature, which do not ensure their validity if extrapolated to different engines or systems. Other authors obtain these values through previous simulations of the combustion cycle or the internal process within the system. Obtaining accurate boundary condition values from experimental measurements is challenging [13].

In general, the most usual boundary condition for the outer surface side is to impose either the surface temperatures, the heat transfer coefficient or the coolant temperature. In the literature, most of the studies applied to internal combustion engines are directed to the study of water-cooled systems, in which the water temperature is almost constant or varies slightly, and the outer surfaces are smooth and do not have extended surfaces, unlike the case of air cooling. This work presents a methodology for an accurate evaluation of the inner temperature of high-temperature thermal energy systems. It is a non-intrusive methodology, requiring only infrared imaging, measurement or estimation of total heat and the use of CFD software for heat transfer analysis. Unlike other methodologies, no contact or drilling is required for thermocouple or heat flow meter placement. It is developed for being applied to hard-to-monitor systems, such as internal combustion engines or high-temperature energy storage systems. The methodology is demonstrated in an air-cooled internal combustion engine but is fully applicable to any other thermal system with the characteristics described.

2. Preliminary considerations

Several considerations have to be made before proposing a methodology for the indirect determination of the inner temperature of systems, inside which there is thermal generation or gases at high temperatures and cannot be accessed by simple methods. These considerations are related to the use of the finite element method (FEM), appropriate selection of the boundary conditions, analysis of the theoretical basis of heat transfer through extended surfaces; available experimental techniques; election of the resolution method and setting of admissible errors.

2.1. Application of the finite element method to problems in conduction and convection heat transfer

The following steps are required to solve a thermal problem using FEM:

- Phase 1 "Preprocessing": meshing, development of the equations for each element, creation of the total conductivity matrix and application of the boundary conditions and loads.
- Phase 2 "Equation solving": solving the set of linear algebraic equations to obtain the results at the nodes.
- Phase 3 "Post-processing": extraction of the information required for this research. For example, the total heat loss of a body under study or the temperature distribution on selected surfaces of this system.

Equation (1) is the form of the equations characterizing heat transfer by convection and conduction under stationary conditions:

$$[K]\{u\} = \{P\} + \{N\}, \tag{1}$$

Where [K] is the total conductivity matrix, {u} is the vector of temperatures of the nodes to be known, {P} is the vector of heat loads that are constant and {N} is the vector of nonlinear heat fluxes that depend on temperature. The vector {P} is associated with the heat transfer occurring at the surface of the element as well as the generation within the element. The vector {N} is associated with convection at the surface of the solid and temperature-dependent heat loads.

The chosen software is NC/NASTRAN and uses an iteration scheme based on the Newton-Raphson method. It is useful to follow the following two recommendations so that the iterative process can converge properly:

- Initial temperature estimation: for highly nonlinear problems, the iterative solution is very sensitive to the assumed initial temperature.

- Convergence criterion: the first time a problem is solved, it is advisable to keep the default values of the parameters that control the iterative process. For problems with poor convergence, it is possible to increase the values of the tolerances, although this decreases the accuracy.

2.2. Analytical resolution of heat transfer by conduction and convection of finned surfaces

As a previous step to the determination of the methodology, it is necessary to study the theoretical basis of heat transfer on extended surfaces. This study will allow us to justify the methodology and better interpret the results.

In the conduction analysis for a generic annular fin, Figure1, the following assumptions are adopted:

- One-dimensional conduction in the radial direction of the fin. If the longitudinal dimensions are much larger than the fin thickness t, then the temperature changes in the longitudinal direction are much larger than those in the transverse direction.
- Steady-state conditions.
- Constant and non-temperature-dependent conductivity.
- Radiative transfer from the fin surfaces is negligible.
- There is no energy generation in the volume considered.
- The heat transfer coefficient is constant over the entire surface.

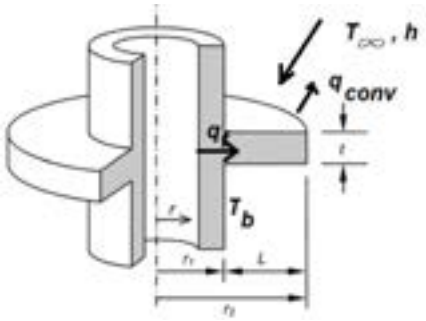

Figure. 2. Fin model and characteristic dimensions.

The conduction equation in the fin is a zero-order modified Bessel equation, Eq. (2):

$$\frac{d^2\theta}{dr} + \frac{1}{r}\frac{d\theta}{dr} - m^2\theta = 0, \tag{2}$$

where $m^2 = 2h/kt$ y $\theta = T - T_\infty$.

The temperature distribution is obtained once the boundary conditions have been chosen. The following four sets of possible boundary conditions can be applied:

- CC1, where heat arriving by conduction at the beginning of the fin is transmitted by convection along the fin;
- CC2, in which the heat arriving at the end of the fin is negligible and, therefore, the fin edge can be considered adiabatic;
- CC3, in which the temperature of the fin edge is known and;
- CC4 represents the ideal case in which the fin extension is so large that it can be considered infinite, and therefore, the temperature at the fin edge is equal to the ambient temperature.

Figure 3 illustrates the temperature distribution for an annular ring case of the inner and outer radius of 50 and 100 mm, respectively, with a heat transfer coefficient equal to 150 W/m^{2}K, the thickness of 5 mm and end temperatures of 100 ºC and 80 ºC, ambient temperature of 50 ºC. The heat fluxes for boundary conditions CC1, CC2, CC3 and CC4 are 244, 238, 230 and 387 W/m^2, respectively. As can be seen, the last boundary condition CC4 differs quite a lot from the remaining ones, as the ratio of the exterior to interior radius is not high.

Considering the objective of this work, the most appropriate boundary condition is CC1 because the transmission at the tip is by convection. However, for the characteristic dimensions of the fins, CC2 and CC3 would also be valid. The distribution can be approximated by straight lines to achieve zero errors at the base and tip of the fin.

In a first approximation, the solution for boundary conditions CC1, CC2 and CC3 can be approximated by straight lines to achieve zero errors at the base and the tip of the fin. The maximum relative approximation

error is 6.5% and occurs at the midpoint of the fin. Because these are small errors, the fins can be made independent, in terms of temperature, of the body to which they are attached.

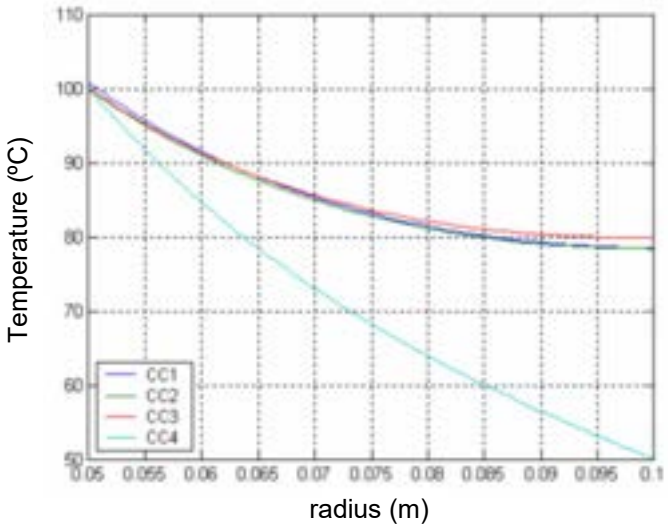

Figure. 3. Evolution of temperatures along an annular fin for different boundary conditions.

2.3. Finite element method (FEM) resolution of conduction and convection heat transfer of extended surfaces

A simple model of a trapezoidal fin is initially simulated to validate and understand the FEM resolution of heat transfer. Figure 3 shows the fin and conditions and simulation results.

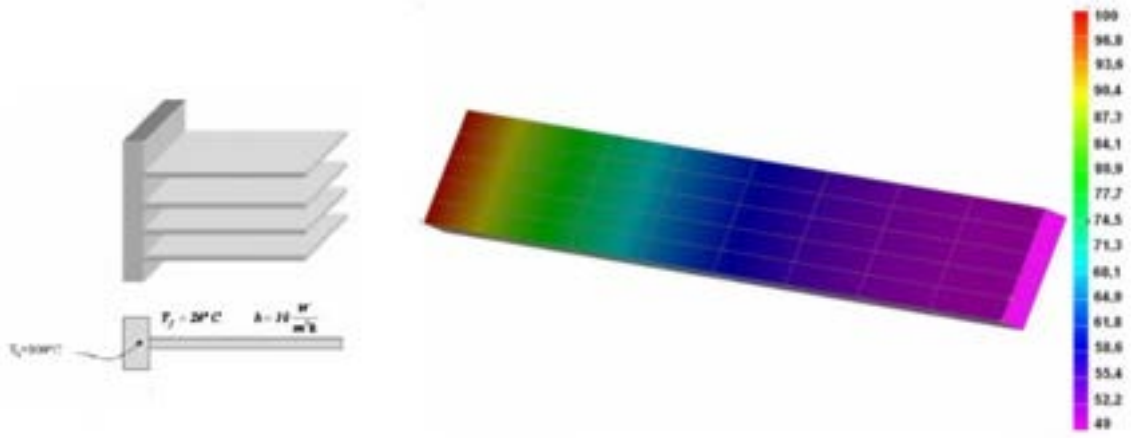

Figure. 3. a) Fin model; b) Simulation results

The temperatures obtained by analytical resolution and by FEM are compared and show divergences of less than 0,5%, which are smaller the more elements the model meshing has, although its complexity and computational load also increase.

2.4. Experimental setup

An experimental installation for the measurement of inner temperatures of systems by means of the methodology proposed in this work and for its validation is carried out., which consists of a large box, in comparison with those of the system to be tested, totally hermetic and thermally isolated from the outside. Inside this box, electrical resistors were placed. On the upper surface of the box, there is an opening in which the inner surface of the component to be tested is fitted. In this way, the box simulates the combustion chamber of the engine in which the electrical resistors generate the released energy. The thermal power chosen is similar to that which would be produced in the real operating conditions of the components to be tested. They simulate the conditions of energy generation by combustion. Thermocouples are placed on the inner and outer surfaces of the system to be tested. Figure 4 shows the installation scheme, and Figure 5 shows photographs of the installation and a detail of the location of thermocouples on the inner surfaces. Thermographs are also taken of the external surfaces, which are the ones visible to the camera. Figure 6 shows thermographs taken from the experiments.

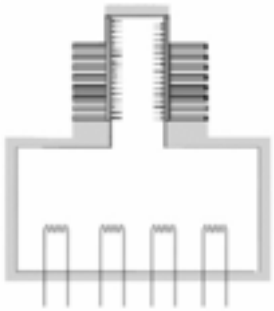

Figure 4. Installation scheme for methodology validation.

Tests were carried out with electrical powers of 150, and 600 W and the cylinder and cylinder head of an air-cooled reciprocating internal combustion engine with finned outer surfaces were chosen as parts. When the temperatures at the thermocouples and the temperature and pressure inside the case reached a steady state, approximately 30 minutes, the thermocouple temperatures and thermographs of all visible surfaces were recorded (Figure 6), and the values of the ambient conditions were also recorded.

3. Selection of the set of boundary conditions

Several sets of boundary conditions can be imposed to estimate the temperature of the inner surface of the cylinder head or cylinder. The proposed ones are:

a) The temperature at the outer surfaces and heat flux at the inner surface.
b) Convective heat transfer coefficient on the outer surfaces and heat flux on the inner surface, such that the temperatures of the outer surfaces match the measured temperatures.
c) The temperature at the outer surfaces and heat flux due to convection at the outer surface.

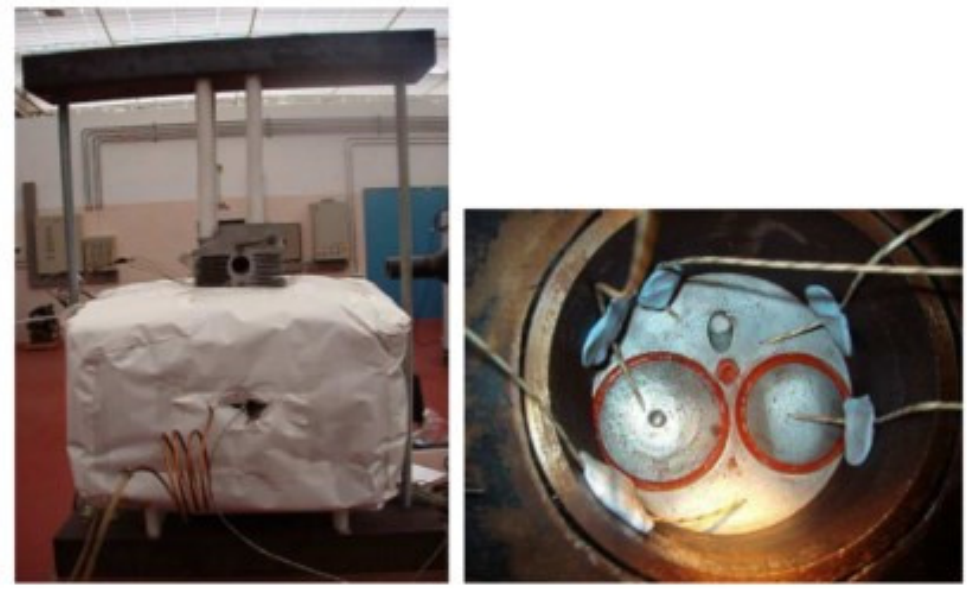

Figure 5. a) Installation setup; b) thermocouples on inner surfaces.

The set of boundary conditions c) is discarded because of the need to impose boundary conditions on all finned surfaces for FEM resolution, which is impossible from a practical point of view.

The two possible sets of boundary conditions, a) and b), are applied to the two chosen components.

3.1 Previous analysis of the boundary conditions

In this case, the set of boundary conditions a) is applied. The external surface temperature field is imposed from the temperature measurements obtained in the test. This field is of the logarithmic type, as shown in Section 2.2:

Step 1: This step intends to obtain a logarithmic-type temperature distribution on the fins by imposing on the bottom and end nodes of the fins the temperatures measured in the test. As discussed in Section 2.2, the errors in the temperature distribution are small regardless of whether a linear or logarithmic distribution is applied. However, the errors in the flow distribution through the surface are relevant. It should be noted that

these are the only boundary conditions applied and that the rest of the surfaces (lateral surface of the fins, inner surface of the cylinder head and non-finned surfaces of the cylinder head) are adiabatic. A scheme of Step 1 is shown in Figure 7.

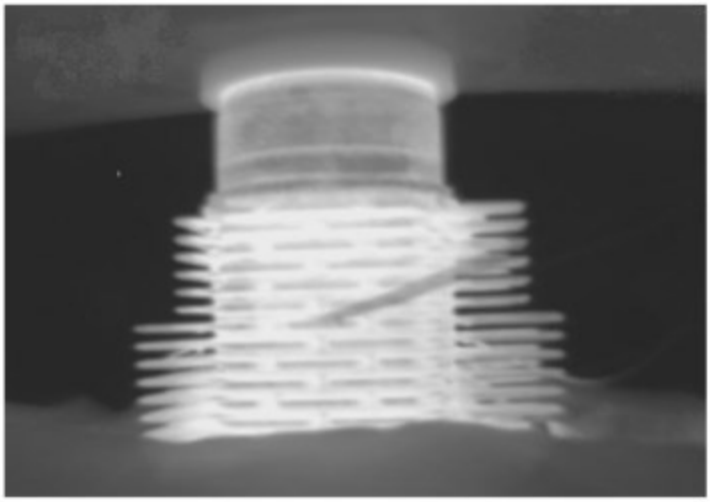

Figure 6. Extended surface cylinder thermograph.

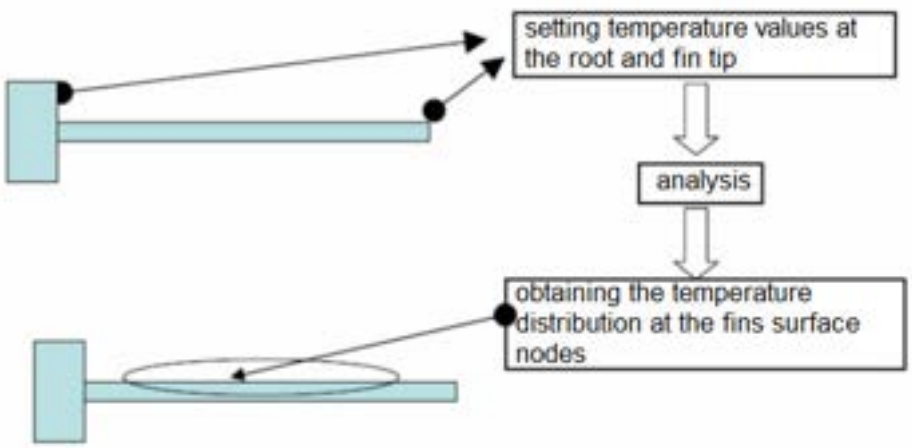

Figure 7. Step 1 of the boundary conditions set election.

Step 2: in this step, the temperatures of the finned surfaces obtained in Step 1 are imposed as a boundary condition; other boundary conditions modelling the test are also imposed, Figure 8:

- heat flow through the inner surface of the cylinder head,
- free convection transfer coefficient from the non-finned outer surfaces to the environment,
- other surfaces are considered adiabatic

3.2. Analysis of the simulation results

The temperature distribution is obtained from the resolution of this model and matches the measured values. However, the heat flux distribution is not valid since it results from solving a one-dimensional conduction problem in the fin in Step 1. This model forces the appearance of local heat fluxes that are transferred from the environment to the root of the fin, called auxiliary fluxes. A scheme of such auxiliary flows is shown in Figure 9. This situation is unrealistic and persists in Step 2 of this resolution and cannot be cancelled.

Therefore, although the temperature field on the outer surfaces is adequate, the heat flux distribution is not. This is the reason why this set of boundary conditions cannot be imposed on the simulation of the cylinder head and cylinder when the engine is under load. The second set of boundary conditions and their validity for the estimation of the average inner surface temperature of the two systems tested is presented below.

In view of the conclusions of the analysis of the application of the set of conditions a), which advise against its use, the set of boundary conditions b), which imposes free convection transfer on the surfaces, is applied. The measured heat power is uniformly distributed on the inner surface.

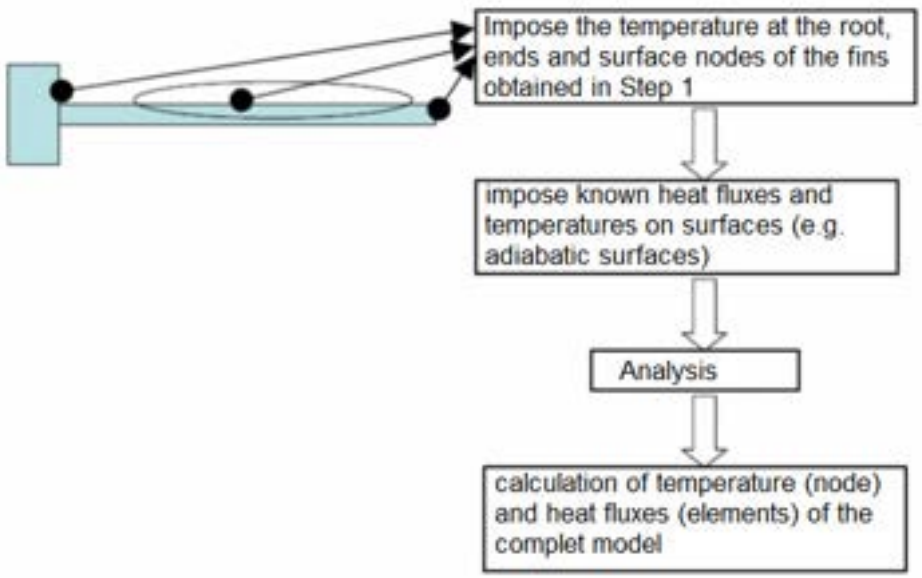

Figure 8. Step 2 of the boundary conditions set election.

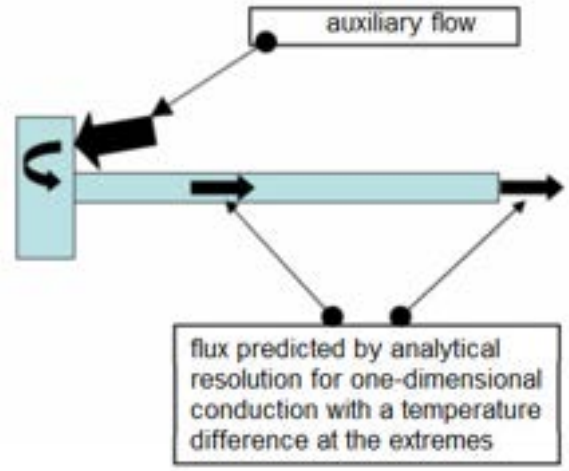

Figure 9. Auxiliary flows representation.

Once the boundary conditions are imposed: uniform heat flux over the elements of the inner surface of the cylinder, which is equal to the heat power generated by the electrical resistors, and the convection coefficient over the elements of the finned surfaces, the model with the applied loads is sent to the NX/NASTRAN solver module.

The temperatures measured on the external surfaces by thermographs and thermocouples will be compared with the temperature field on the external surfaces obtained from the FEM simulation from an initial heat transfer coefficient. If this correspondence does not occur, the comparison is iterated with FEM simulation results with another heat transfer coefficient value.

4. Methodology proposed

A comprehensive review of heat transfer on extended surfaces has been carried out in the previous sections, and the best selection of boundary conditions for temperature determination has been studied. This work aims to determine the average inner surface temperature of systems with extended outer surfaces inside which there is power generation. An inverse method that solves the heat transfer in these systems by means of finite elements is then proposed and described, taking into account the previous considerations exposed in Sections 2 and 3. The main difficulty of this kind of approach is the correct imposition of the boundary conditions in the models and the value of these boundary conditions, whose considerations have been discussed in Section 3. A flow diagram of this methodology is presented in Figure 10.

In the proposed method, the following boundary conditions are chosen:

- Heat flow through the inner walls of the system to the outside, $\dot{Q}_{heat}$

- The heat transfer coefficient on the outer surfaces h_{ext}, which is obtained from an iterative process that converges when the temperatures on the outer surfaces resulting from the FEM model match the measured ones,
- The temperatures of the selected points of the external surfaces and whose values are obtained from the thermographs and those recorded in the thermocouples during the tests, $T_{meas,k}^{outer}$.

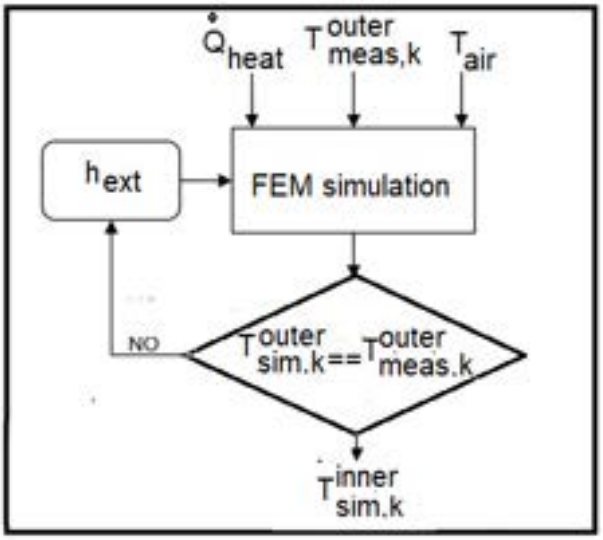

Figure. 10. Methodology flow diagram.

The value of the heat flow through the inner walls of the system, $\dot{Q}_{heat}$, is the heat released by the electrical resistances, whose total value is known but not its distribution along the inner surface. The FEM model requires the heat per unit area and time as a boundary condition. The heat distribution is assumed to be uniform, and the inner surfaces whose outer equivalent are not finned, which is also adiabatic, are considered adiabatic.

The second boundary condition imposed is the convective heat transfer from the outer extended surface to the surrounding air. The heat transfer coefficient h_{ext} is constant and the air temperature is constant.

The cylinder head is an example of those components where there are several parts, and the interaction between surfaces must be considered. In this case, it is considered that the bond between the contact surfaces is perfect and the conductivity is infinite.

Once the boundary conditions have been applied, the model is sent to the NX/NASTRAN solver module.

Once the boundary conditions have been successfully applied, the model is sent to the NX/NASTRAN solver module.

When the simulation is finished, the temperatures of the outer finned surfaces are obtained in the FEMAP post-processing module. Due to the large surface area, points were chosen to compare the measured temperature with the temperature resulting from each simulation. The values of the 9 thermocouples and 10 points on the thermographs were chosen, in total 19 points. The 19 measured temperature values, $T_{meas,k}^{outer}$., are compared with those resulting from the simulation, $T_{sim,k}^{outer}$. k indicates the temperature point being compared. The mean square variation, called MSE, is defined according to Equation (2):

$$MSE = \frac{1}{n}\sum_{k=1}^{k=n}\left(T_{sim,k}^{outer} - T_{meas,k}^{outer}\right)^2, \quad (2)$$

The method attempts to identify the value of h_{ext} that minimizes the mean square error with the temperature measurements MSE_{min}, Figure 11. To calculate such an optimal value of h_{ext} an iterative search process is followed based on interpolations of $MSE(h_{ext})$ as a Cubic Spline type curve. The search is initialized by taking three sufficiently distant values of h_{ext} and calculating the MSE values, they produce.

These $MSE(h_{ext})$ curve values are then interpolated by Spline, and the minimum of the interpolated curve and the corresponding hext,CIL value are calculated. The model is then simulated with this value, and the MSE it produces is calculated. If no significant improvement of MSE is achieved, relative difference below 5%, it is considered to have converged to MSE_{min}. If the improvement is significant, it is incorporated into the interpolation of MSE_{min} by Cubic Spline and iterated again.

As an example, the method when the extended surface cylinder is tested, and the internal thermal generation is equal to 150 kW is illustrated in Figure 12.

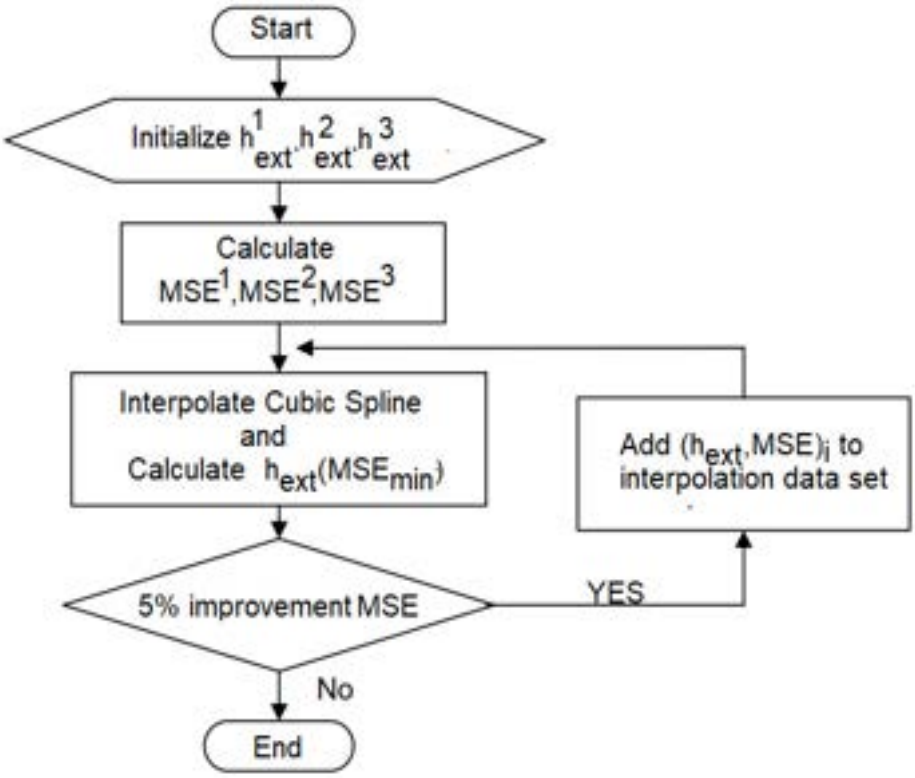

Figure. 11. Heat transfer coefficient iterative method.

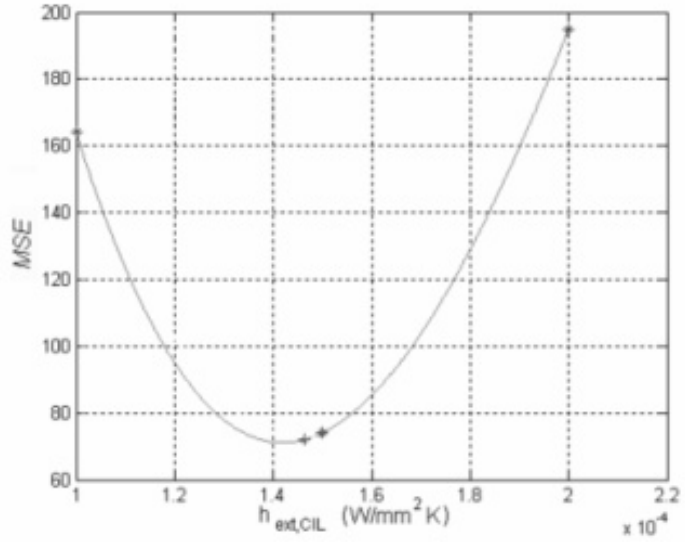

Figure. 12. MSE for different heat transfer coefficients values according to the iteration method

A representation of the temperatures at the chosen points, resulting from experimentation and simulations, for the internal and external surfaces is shown in Figure 13. As can be seen, the difference between the simulation and measured temperatures is quite small. Figure 14 shows a comparison of FEM simulation results with thermography measurements, proving the great similarity between the two.

It is verified that the resulting inner surface temperatures correspond to those measured with thermocouples in the tests. As for the distribution of the heat flows, it is verified that, in all cases, on the whole external surface they are transferred from the environment to the cylinder head and that on the internal surface, the flows are incoming. There are no auxiliary heat flows from the environment to the fins, as in the previous case. The total power transferred through each of the surfaces is also obtained, and it is found that the power transferred through the outer surfaces is equal to that generated by the electrical resistors. It should be noted that the proportion of power transferred to the environment from the finned surfaces is much higher than that associated with the non-finned surfaces. Once this correspondence has been achieved, it is verified that the resulting interior surface temperatures correspond to those measured with thermocouples in the tests.

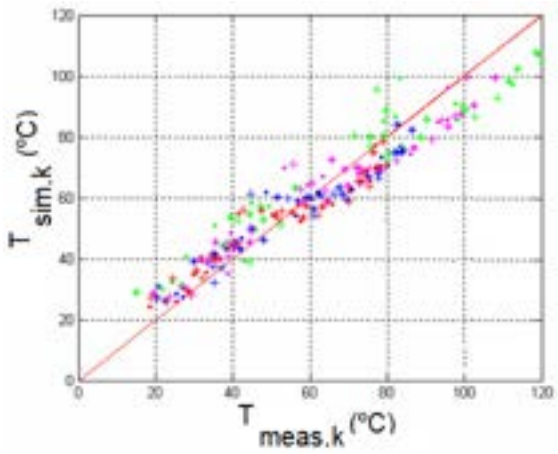

Figure. 13. Representation of temperatures at the points of comparison.

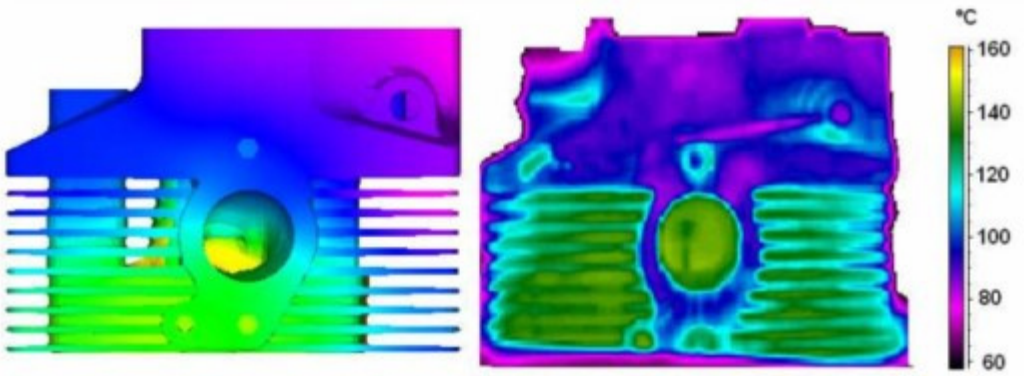

Figure. 14. Comparison of FEM simulation results with thermographs, for tests at 150 W and cylinder head as a component.

5. Conclusions

This work presents a methodology for an accurate evaluation of the inner temperature of high-temperature thermal energy systems. It is developed for being applied to hard-to-monitor systems, such as internal combustion engines or high-temperature energy storage systems. The methodology is demonstrated in an air-cooled internal combustion engine but is fully applicable to any other thermal system with the characteristics described.

Regarding the distribution of the heat flows, it is verified that, for all cases, in all the external surfaces, these are transferred from the environment to the cylinder head and that in the internal surface, the flows are incoming. There are no auxiliary heat flows from the environment to the fins, as in the previous case. The total power transferred through each of the surfaces is also obtained, and it is found that the power transferred through the outer surfaces is equal to that generated by the electrical resistors. It should be noted that the proportion of power transferred to the environment from the finned surfaces is much higher than that associated with the non-finned surfaces.

Therefore, the inverse methodology for determining internal surface temperatures by non-intrusive means has been validated.

Acknowledgments

This work was partially supported by the project MOTHERESE, TED2021-131839B funded by the Spanish Ministry of Science and Innovation and European Union through Plan of Recovery, transformation and resilience funds

References

Journals:

[1] Šarić S, Basara B, Žunič Z. “Advanced near-wall modeling for engine heat transfer”. Int J Heat Fluid Flow 2017; 63:205–211.

[2] Irimescu A, Merola SS, Tornatore C, Valentino G. “Development of a semi-empirical convective heat transfer correlation based on thermodynamic and optical measurements in a spark ignition engine”. Appl Energy 2015; 157:777–788.

[3] Bürkle, Sebastian, et al. "In-cylinder temperature measurements in a motored IC engine using TDLAS." Flow, Turbulence and Combustion 2018; 101: 139-159.

[4] Rieker, G. B., Li, H., Liu, X., Liu, J. T. C., Jeffries, J. B., Hanson, R. K., .& Takatani, S. “Rapid measurements of temperature and H2O concentration in IC engines with a spark plug-mounted diode laser sensor”. Proceedings of the Combustion Institute 2007; 31(2), 3041-3049.

[5] Birkigt, A., Michels, K., Theobald, J., Seeger, T., Gao, Y., Weikl, M. C., ... & Leipertz, A. “Investigation of compression temperature in highly charged spark-ignition engines”. International Journal of Engine Research 2011; 12(3), 282-292.

[6] Finol, C. A., and K. Robinson. "Thermal modelling of modern engines: a review of empirical correlations to estimate the in-cylinder heat transfer coefficient." Proceedings of the institution of mechanical engineers, part D: journal of automobile engineering 2006; 220.12: 1765-1781.

[7] Catto A. G., Prata A. T., A numerical study of instantaneous heat transfer during compression and expansion in piston-cylinder geometry. Numerical Heat Transfer Part A 2000; 38:281-303.

[8] Huang, Cheng-Hung, and Chien-Tsuen Lee. "An inverse problem to estimate simultaneously six internal heat fluxes for a square combustion chamber." International Journal of Thermal Sciences 2015; 88: 59-76.

[9] Bohac, Stanislav V., Douglas M. Baker, and Dennis N. Assanis. "A global model for steady state and transient SI engine heat transfer studies." SAE transactions 1996: 196-214.

[10] Jing, Dong Zhan, and Wei Gang Zheng. "A Numerical Simulation of steady-state temperature field of natural gas engine piston." Applied Mechanics and Materials. Vol. 496. Trans Tech Publications Ltd, 2014.

[11] Fonseca, Leonardo, et al. "Internal combustion engine heat transfer and wall temperature modeling: an overview." Archives of Computational Methods in Engineering 2000; 27.5: 1661-1679.

[12] Liu, Yong, and R. D. Reitz. "Modeling of heat conduction within chamber walls for multidimensional internal combustion engine simulations." *International Journal of Heat and Mass Transfer* 1998; 41.6-7): 859-869.

[13] Cerdoun, Mahfoudh, Carlo Carcasci, and Adel Ghenaiet. "Analysis of unsteady heat transfer of internal combustion engines exhaust valves." International Journal of Engine Research 2018; 19.6: 613-630.

Direct vaporization ORC-evaporator heat transfer model for thermal degradation risk assessment

João S. Pereira* and José B. Ribeiro

Univ Coimbra, ADAI, Department of Mechanical Engineering, Coimbra Portugal,
joao.pereira@dem.uc.pt

Abstract:

For the last decades, Organic Rankine Cycle has been the technological choice of numerous large-scale systems. Due to its characteristics, mainly its simplicity and reliability, the ORC is pointed to be one of the most promising technologies to fulfil the gap of cogeneration systems in domestic dwellings. However, bringing the technology to the domestic scale can raise some difficulties related to its restricted requirements which can go from the system size to the response time. To deal with these questions, the use of direct evaporators is been referenced as an imperative path to follow. The use of these direct evaporators excludes the intermediate circuit that is frequently implemented. The introduction of this is usually justified by the direct exposition of the organic fluid to the high temperatures of the heat source which can degrade it. When the author's objective is to individually study the organic fluid and its properties (including its thermal stability), all the information regarding the system becomes irrelevant. The evaluation of the risk that this option may put to the organic fluid thermal degradation requires the determination of the temperature of the heat-transfer surfaces with which the organic fluid is in contact. As its experimental measure is extremely difficult to accomplish, such determination requires the development of a detailed physical model of the combustion and heat-transfer processes in the ORC-evaporator.Taken this into consideration, the development and validation of such model is presented. This will allow a detailed evaluation of several key features of the combustion and heat-transfer processes as a function of some ORC operating parameters. Among those features is the temperature of the internal surface of the tubes with which the organic fluid is in contact. This temperature, which can be used to assess the risk of the thermal degradation of the organic fluid, has shown to be highly affected by the thermal resistances and by the combustion gases temperature. To reduce that risk, the operating conditions of the ORC should be those allowing the vaporization process to start as early as possible and reducing the superheating phase to the minimum possible.

Keywords:

Organic Rankine cycle, Heat-transfer model, ORC-evaporator, Direct vaporization arrangement, Thermal degradation risk assessment.

1. Introduction

Given the huge dimension of its potential market and the expected economic and environmental benefits associated with its use, the research and development activities on a domestic scale combined heat and power systems (CHP) have increased over the last two decades [1,2]. For the particular case of the systems that are attempting to retrofit the current wall-hang combi-boilers, the most promising solutions involve the use of Organic Rankine Cycles (ORC) [3,4]. Furthermore, due to the extremely demanding requirements imposed on these systems, especially in what refers to the (short) response time and (small) dimensions, it is suggested that the vaporization of the working fluid of the ORC should be done using the high-temperature combustion gases directly [5,6]. One of the major risks associated with this option is the thermal degradation of the organic working fluid [7,8]. The high temperature that these fluids may reach when in contact with the heat transfer surfaces can lead to the disruption of the chemical bonds of its molecules and to the subsequent degradation of their physical properties. In an attempt to minimize this problem, ORC-based micro-CHP systems may be reconfigured into a hybrid arrangement in which the combustions gases are firstly cooled in a combustion gases-water heat exchanger before crossing through the organic fluid heat exchanger [9]. Even so, the evaluation of the magnitude of this problem demands the calculation of the heat-transfer surfaces' temperature with which the organic fluid will be in contact. That risk will be minimum if the temperature of those surfaces is kept below the one of thermal degradation. This limiting temperature,

however, is normally determined by standard tests where the fluid is at rest and in thermal equilibrium with the wall of its container [10–14]; a quite different situation from what happens in real working conditions [15]. Besides the bulk temperature of the organic fluid at the exit of the evaporator (a well-known parameter since it is easy to measure and required for the evaluation of the cycle efficiency), it is also important to know the temperature of the heat-transfer surfaces with which the fluid is in contact. Contrary to the organic fluid temperature, this is very difficult to measure but it can, and should, be controlled. Despite its importance, heat-transfer surface temperatures are rarely measured or calculated. Since its direct measure is very difficult, as are those of any tubes' internal surface, the only option left is its calculation. That, however, is far from being trivial as it results from the mutual dependency of the internal and external heat-transfer mechanisms and demands for the development of an appropriated heat-transfer model. The development of such model, that is crucial for the determination of the operation conditions that should keep the risk of thermal degradation of the organic fluid at an acceptable level, however, is not yet described in the literature.

Acknowledging that the thermal degradation of the organic fluid is the key feature opposing the use of direct vaporization in ORC-based micro CHP systems, the main objective of this paper is to show how the operating conditions of those systems (e.g. the organic fluid mass flow rate or the natural-gas burner combustion power) affect the organic fluid vaporization process and the temperatures of the heat-transfer surfaces. These are compared to the temperature limits referenced in the literature to evaluate the risk of organic fluid thermal degradation. This will be illustrated on a particular ORC-evaporator design but the analysis will be kept as general as possible. Given the importance that the evaluation of the heat-transfer surface temperatures may have on the definition of boundaries for the operating conditions, and given the scarcity of heat-transfer models intended to calculate those temperatures, it is also an objective of this manuscript to contribute to the disclosure and widespread of these type of models through the presentation of the approach followed in its development, namely: disclosing the correlations used for the determination of the heat-transfer coefficients and duly presenting the underlying simplifications, calibration and validation.

2. ORC-evaporator heat-transfer model

The ORC-evaporator domain to be simulated in this study comprises the gas-burner and two heat-exchanger sections: one to complete the water heating process initiated in the ORC-condenser, named the water post-heater section (PH), and the other for the organic fluid vaporization, simply named evaporator heat-exchanger (EHE). A 3-D representation of these two sections can be seen in Figure 1.

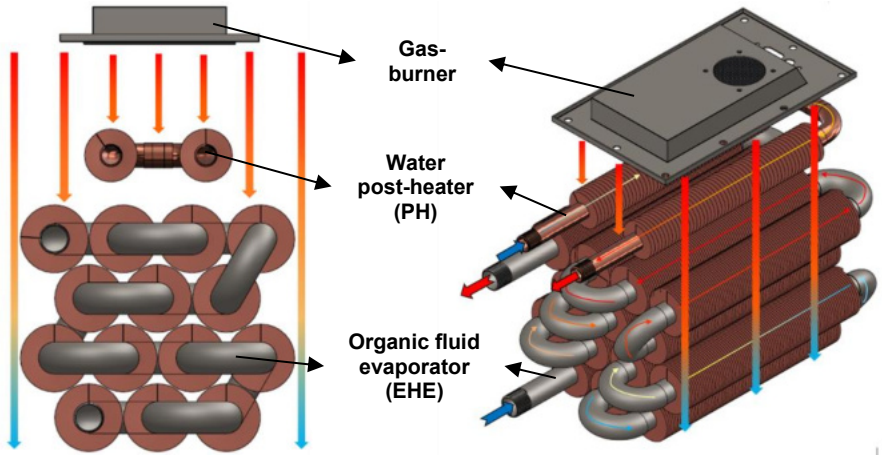

Figure 1. Schematic representation of the two heat-exchanger sections and the natural-gas burner of the ORC-evaporator.

As the PH and the EHE heat-transfer models demand, as input parameters, several combustion gases' characteristics, the thermochemical calculations of the natural gas (NG) combustion process were also included in the overall model. Thus, the overall model includes three different sub-models: i) the gas-burner/combustion model, ii) the PH heat-transfer model and iii) the EHE heat-transfer model. These models were implemented in MatLab® coupled with the RefProp thermodynamic database [16]. According to the physical arrangement, as depicted in Figure 1, the models are run sequentially since the outputs of the combustion model are used as inputs for the PH model and its outputs are used as inputs for the EHE model, as shown in Figure 2.

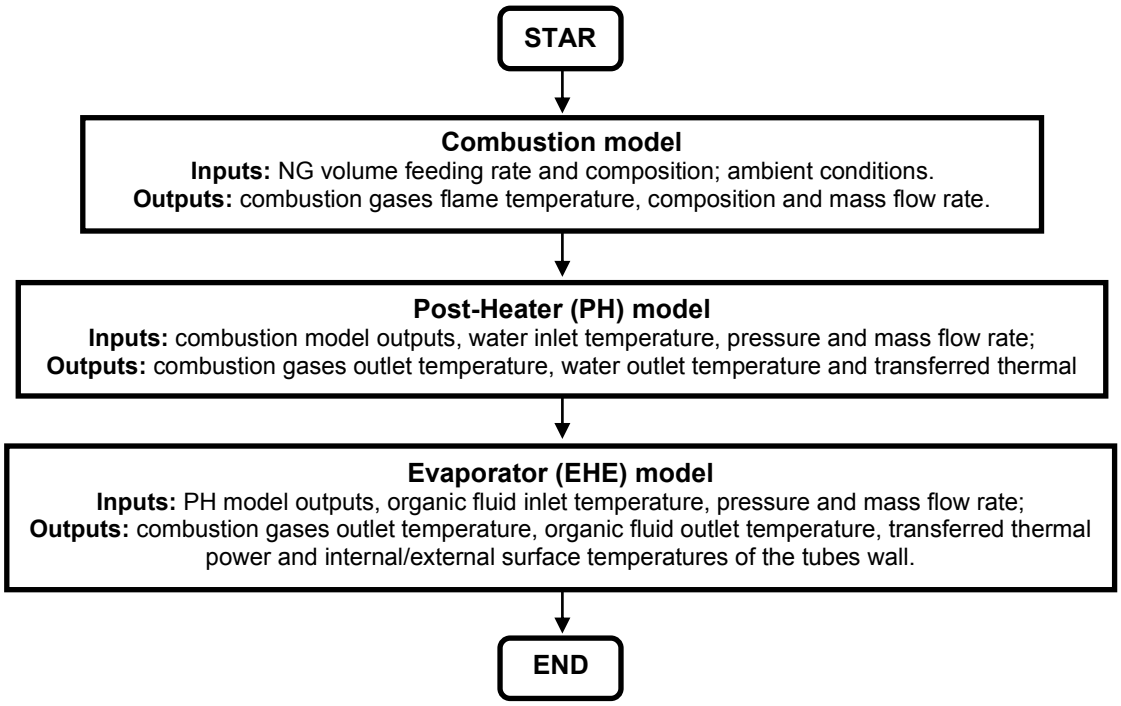

Figure 2. General flowchart of the entire ORC-evaporator model with the main inputs and outputs.

The Post-Heater (PH) is a cross-flow heat exchanger placed between the gas burner and the EHE (see Figure 1). It is composed of a pair of finned tubes within which water, previously heated in the ORC condenser, flows. To calculate the outputs described in Figure 2, the overall heat-transfer coefficient must be determined. This demands the calculation of the heat-transfer coefficient for the water and combustion gases sides. In order to make that determination easier and since it is known that the water inside the PH tubes will remain in the liquid state and its temperature will not drastically rise, the water's physical domain was divided into two control volumes (CV) – one for each tube. For the combustion gases side, however, the physical domain was not divided and the temperature is assumed to have a uniform/ homogeneous distribution in the horizontal direction. The CVs in which the PH domain is divided are illustrated in Figure 3.

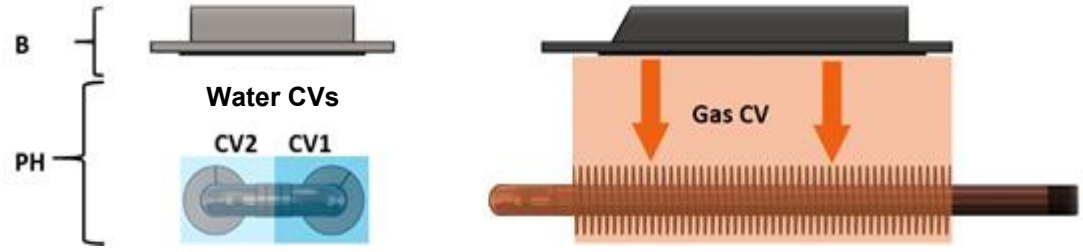

Figure 3. 2D view of the gas-burner (B) and PH assembly with the CVs defined for the water and the combustion gases flow.

The EHE is a compact heat exchanger made of stainless-steel tubes with copper fins presenting a mixed configuration regarding the interaction between the external and internal flows since it can be classified neither as a counter-flow nor as a cross-flow arrangement. Figure 4 shows a detached schematic representation of the EHE with the flow directions for both fluids.

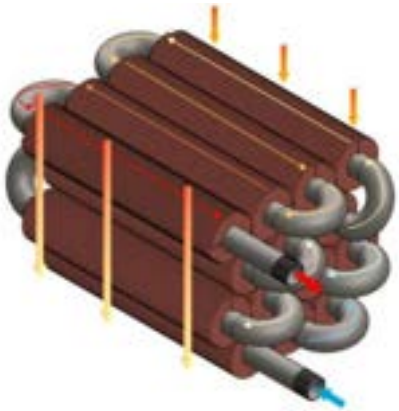

Figure 4. Schematic representation of the (detached) EHE section.

The EHE contains four levels of stainless-steel tubes with copper fins. Each level contains a different number of tubes, as shown in Figure 5. Since the variation of the organic fluid properties is expected to be much bigger than those observed for the water in the PH section (mainly due to the vaporization process), the volume occupied by this inside the EHE tubes was split into a large number of CVs. On the other hand, the volume occupied by the combustion gases was split into as many CVs as levels of tubes.

All the equations and details regarding the model developed are shown in [17].

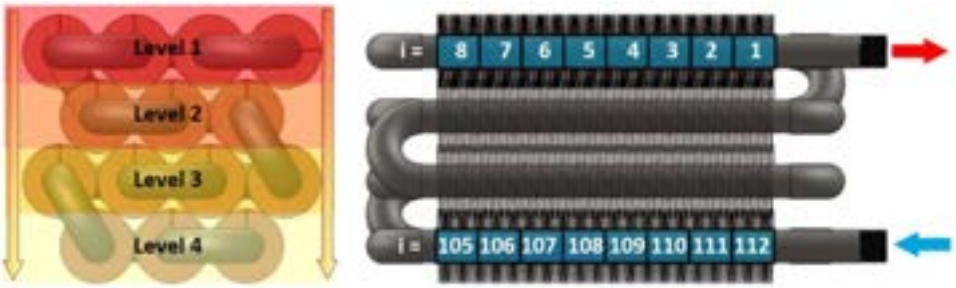

Figure 5. 2D view of the EHE section with the discretization of the gas and organic fluid per CV.

3. Experimental test rig

In order to verify and validate the options taken and the simplification made in the development of the ORC-evaporator physical-mathematical model, a comparison needs to be done between the results retrieved with it and those obtained from the experimental tests. To perform such a task, the designed ORC-evaporator was integrated into a test rig emulating a micro-scale ORC-based CHP system. A schematic diagram, including the instrumentation used, is presented in Figure 6.

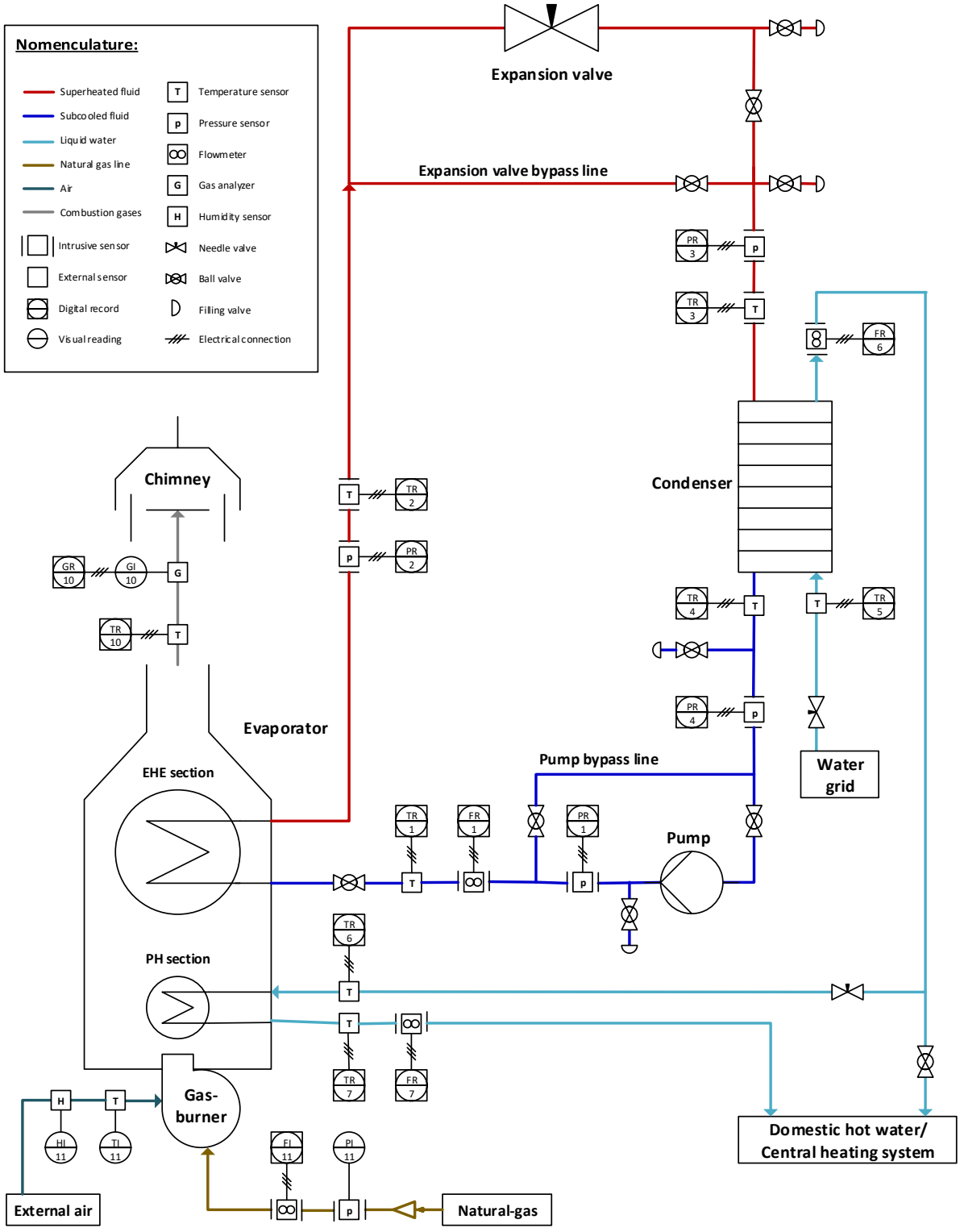

Figure 6. Schematic diagram of the hybrid CHP configuration with the new ORC-evaporator.

As there is a particular interest in the characterization of the ORC-evaporator behaviour, this component is specially monitored and, in addition to the instruments presented in Figure 6, both of its sections have a series of contact thermocouples partially embedded in the wall of the elbows that connect their finned tubes. These thermocouples are kept out from the direct exposition of the combustion gases and are externally surrounded by a quasi-adiabatic media, as is shown in Figure 7. The main characteristics of the instruments used are presented in Table 1.

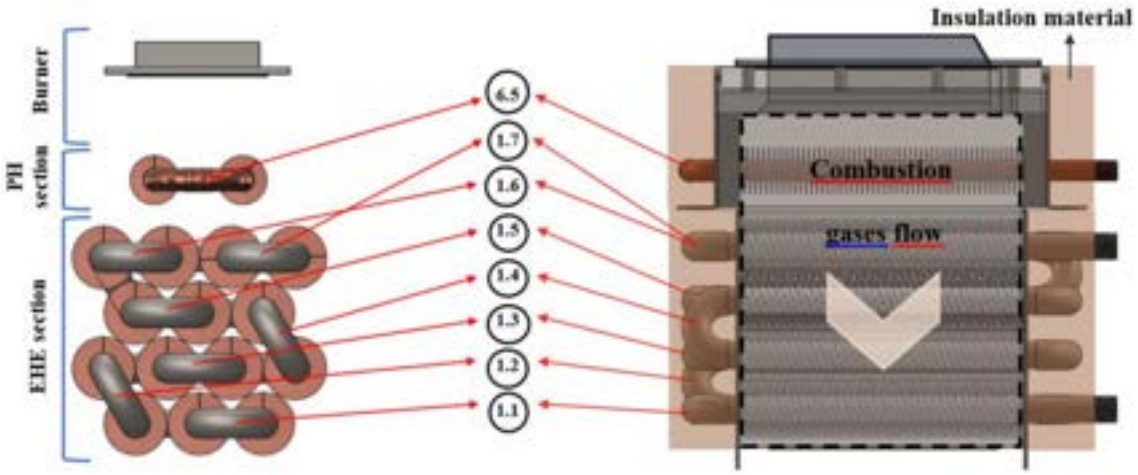

Figure 7. Schematic representation of the ORC-evaporator with the location of the contact thermocouples alongside the PH and EHE sections.

Table 1. Main characteristics of the instruments used in the experimental test rig.

Line number (see Figure 6)	**Measurement**	**Stream**	**Type**	**Range**	**Accuracy**
1	Mass flow rate	Organic fluid	Coriolis	[0 – 2.2] kg/s	0.4 %
[1-4]	Pressure	Organic fluid	Diaphragm	[0 - 10] bar	0.05 % FS
[All]	Temperature	Organic fluid / PH water / combustion gases	Thermocouple type T	[-40 - 300] ºC	0.0075.|T| or 1 °C
7	Volumetric flow rate	PH water	Turbine	[1 - 25] L/min	2 %
10	Oxygen sensor	Combustion gases	Infra-red	[0 - 25] %	1 %
11	Temperature / humidity	Ambient air	Thermistor/ polymer film	[-20 - 40] ºC / [20 - 80] %	5 %
11	Volumetric flow rate	Natural-gas	Diaphragm	[0 – 1.7] dm^3/s	1 %

4. Model validation

The comparison between the experimental and the model results will be done for the water and organic fluid temperatures gathered along the PH and EHE sections of the ORC-evaporator (see Figure 8), respectively. Besides those temperatures, the transferred thermal power in each section will also be used to assess the match between the experimental and the model results as it allows solving the problems arising from the use of temperatures to compare the heat-transfer process when a two-phase state is presented (see Figure 9).

The data shown reveals differences between the calculated and the experimental results smaller than 2% regarding the transferred thermal power, for both sections and, concerning the temperatures, values smaller than 2% and 8% for the PH and EHE sections, respectively. These results end up reflected in the model's capacity to predict the starting point of the organic fluid vaporization process within the ORC-evaporator tubes. This can be seen in Figure 10, in which the measured and calculated temperatures of the organic fluid retrieved along the EHE section are shown for one specific operating point. The error in the identification of the beginning of the phase transition process is less than 1 tube.

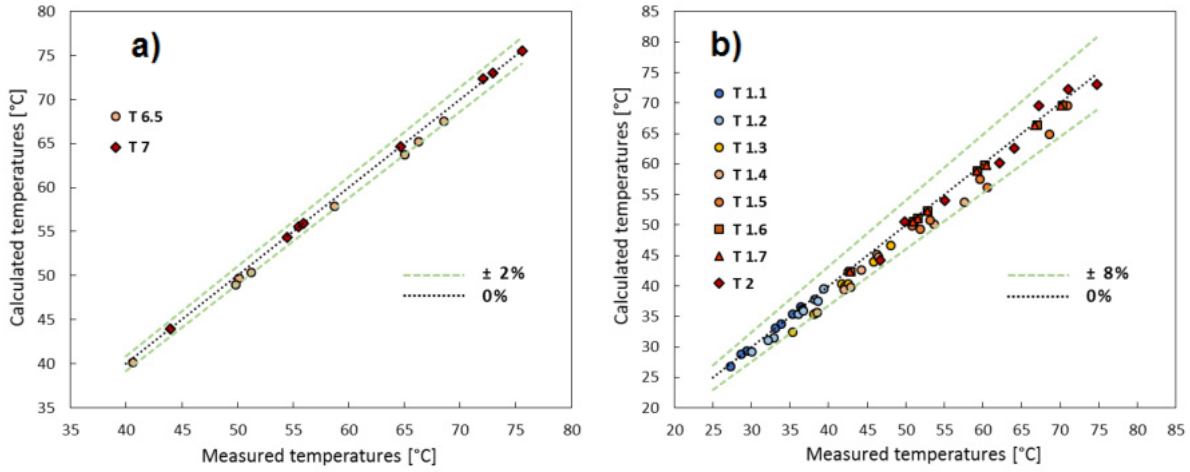

Figure 8. Calculated versus measured temperatures for a) PH and b) EHE.

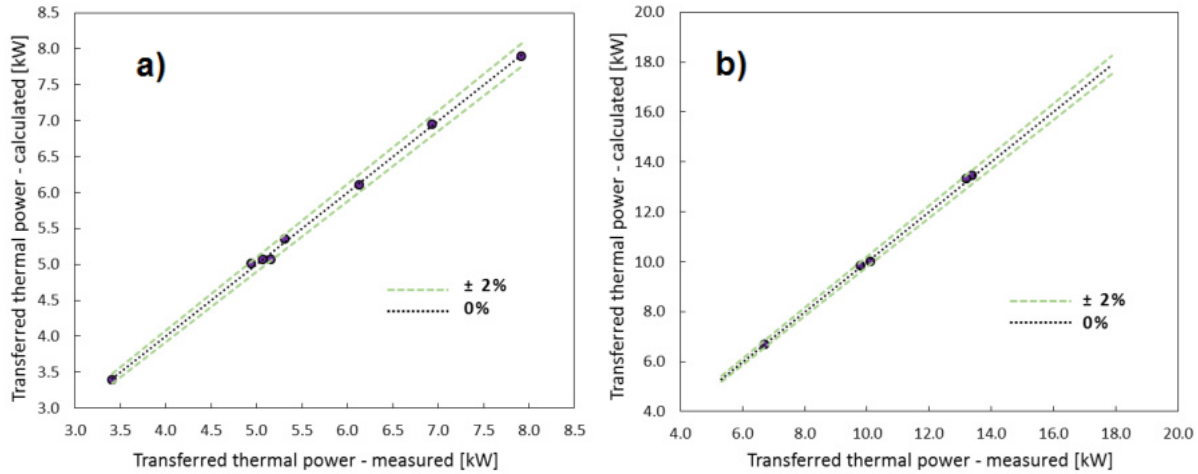

Figure 9. Calculated versus measured transferred thermal power for a) PH and b) EHE.

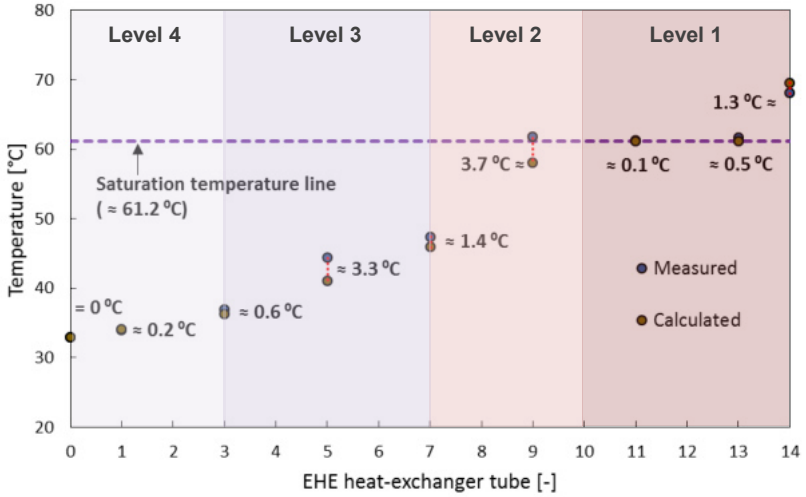

Figure 10. Calculated and measured values of the organic fluid temperatures along the EHE section.

5. Model exploration and conclusions

It is presumed that the reliability shown by the model on the prediction of the organic fluid temperature and of the transferred thermal power is inferable for the prediction of the temperatures of the inner surface of the evaporator tubes since they are mutually dependent. Thus, it will be possible to use it to identify what is and where occurs the maximum value of the inner surface temperature of the evaporator tubes, so that considerations about the risk of thermal degradation of the organic fluid may be taken into account. This temperature, together with both the outer surface and the organic fluid temperatures, is shown in Figure 11 for one specific operating point, as an example. The combustion gases' temperature values, for each of the

levels in which their domain is divided, are also shown in that figure. As their behaviour is essentially determined by the thermal resistances involved in the heat-transfer process, the values of those, evaluated for each of the EHE control volumes, are shown in Figure 12 together with the cumulative transferred thermal power.

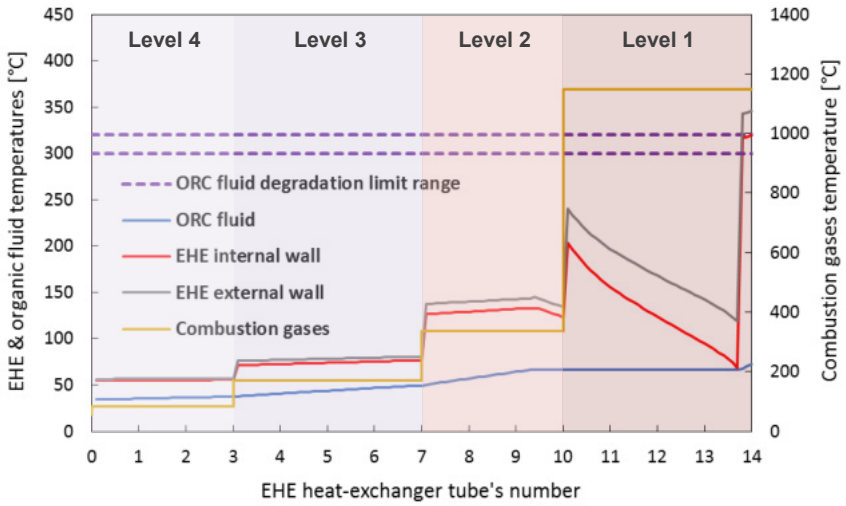

Figure 11. Combustion gases, organic fluid (bulk) and tubes internal and external wall temperatures along the EHE tubes.

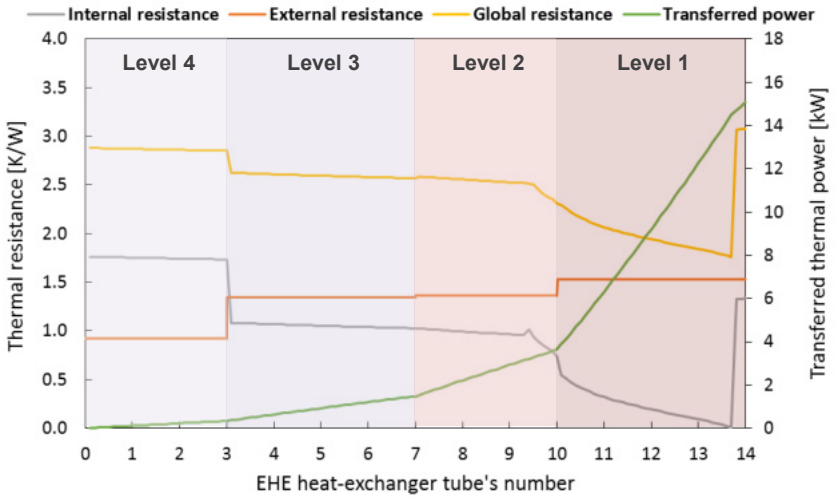

Figure 12. Internal, external and overall thermal resistances and cumulative transferred thermal power along the EHE tubes.

From this analysis, it can be said regarding the main objective of this work, the characterization of the temperature of the internal surface of the EHE tubes, that this parameter is essentially determined by the internal thermal resistance (since the external is essentially constant) and by the combustion gases' temperatures. As the non-boiling heat-transfer processes, occurring when the organic fluid is either in liquid or in gaseous phases, are characterized by similar values of the internal thermal resistance (see Figure 12), the combination of these heat-transfer regimes with high temperatures of the combustion gases may originate very high internal surface temperatures of the EHE tubes (see Figure 11). Therefore, efforts should be made to avoid or, if not possible, to minimize those. That means, reducing the superheating degree to the minimum value possible and avoiding the presence of the organic fluid in a liquid phase on the 1st level of the tubes. It is also important to notice that any reduction in the temperature of the combustion gases in contact with the tubes of this 1st level, as the one induced by the PH section in this case, will help to reduce the maximum temperature of the inner surface of the tubes' wall and with that, the risk of fluid degradation.

References

[1] S. Murugan, B. Horák, A review of micro combined heat and power systems for residential applications, Renew. Sustain. Energy Rev. 64 (2016) 144–162. https://doi.org/10.1016/j.rser.2016.04.064.

[2] T.C. Fubara, F. Cecelja, A. Yang, Modelling and selection of micro-CHP systems for domestic energy supply: The dimension of network-wide primary energy consumption, Appl. Energy. 114 (2014) 327–334. https://doi.org/10.1016/j.apenergy.2013.09.069.

[3] P. Colonna, E. Casati, C. Trapp, T. Mathijssen, J. Larjola, T. Turunen-Saaresti, A. Uusitalo, Organic Rankine Cycle Power Systems: From the Concept to Current Technology, Applications, and an Outlook to the Future, J. Eng. Gas Turbines Power. 137 (2015) 100801. https://doi.org/10.1115/1.4029884.

[4] G. Carraro, V. Bori, A. Lazzaretto, G. Toniato, P. Danieli, Experimental investigation of an innovative biomass-fired micro-ORC system for cogeneration applications, Renew. Energy. 161 (2020) 1226–1243. https://doi.org/10.1016/j.renene.2020.07.012.

[5] J.S. Pereira, J.B. Ribeiro, R. Mendes, G.C. Vaz, J.C. André, ORC based micro-cogeneration systems for residential application – A state of the art review and current challenges, Renew. Sustain. Energy Rev. 92 (2018) 728–743. https://doi.org/10.1016/j.rser.2018.04.039.

[6] J.S. Pereira, J.B. Ribeiro, R. Mendes, G.C. Vaz, J.C. André, Development of a direct concept helical-coil evaporator for an ORC based micro-CHP system, Energy Procedia. 129 (2017) 474–478. https://doi.org/10.1016/j.egypro.2017.09.162.

[7] C.M. Invernizzi, P. Iora, G. Manzolini, S. Lasala, Thermal stability of n-pentane, cyclo-pentane and toluene as working fluids in organic Rankine engines, Appl. Therm. Eng. 121 (2017) 172–179. https://doi.org/10.1016/j.applthermaleng.2017.04.038.

[8] C.M. Invernizzi, D. Bonalumi, Thermal stability of organic fluids for Organic Rankine Cycle systems, Elsevier Ltd, 2016. https://doi.org/10.1016/B978-0-08-100510-1.00005-3.

[9] J.S. Pereira, J.B. Ribeiro, R. Mendes, J.C. André, Analysis of a hybrid (topping / bottoming) ORC based CHP configuration integrating a new evaporator design concept for residential applications, Appl. Therm. Eng. 160 (2019) 113984. https://doi.org/10.1016/j.applthermaleng.2019.113984.

[10] C.M. Invernizzi, P. Iora, D. Bonalumi, E. Macchi, R. Roberto, M. Caldera, Titanium tetrachloride as novel working fluid for high temperature Rankine Cycles: Thermodynamic analysis and experimental assessment of the thermal stability, Appl. Therm. Eng. 107 (2016) 21–27. https://doi.org/10.1016/j.applthermaleng.2016.06.136.

[11] L. Keulen, S. Gallarini, C. Landolina, A. Spinelli, P. Iora, C. Invernizzi, L. Lietti, A. Guardone, Thermal stability of hexamethyldisiloxane and octamethyltrisiloxane, Energy. 165 (2018) 868–876. https://doi.org/10.1016/j.energy.2018.08.057.

[12] M.Z. Irriyanto, H.S. Lim, B.S. Choi, M. Lee, A.A. Myint, J. Kim, Thermal stability study of HFO-1234ze(E) for supercritical organic Rankine cycle: Chemical kinetic model approach through decomposition experiments, J. Ind. Eng. Chem. 90 (2020) 244–250. https://doi.org/10.1016/j.jiec.2020.07.018.

[13] E. Huo, Q. Li, C. Liu, Z. Huang, L. Xin, Experimental and theoretical studies on the thermal stability and decomposition mechanism of HFO-1336mzz(Z) with POE lubricant, J. Anal. Appl. Pyrolysis. 147 (2020) 104795. https://doi.org/10.1016/j.jaap.2020.104795.

[14] M. Preißinger, D. Brüggemann, Thermal stability of hexamethyldisiloxane (MM) for high-temperature Organic Rankine Cycle (ORC), Energies. 9 (2016). https://doi.org/10.3390/en9030183.

[15] J.S. Pereira, M. Santos, R. Mendes, J.C. André, J.B. Ribeiro, Thermal degradation assessment study of a direct vaporization ORC based micro-CHP system under close-to-real operating conditions, Appl. Therm. Eng. 214 (2022). https://doi.org/10.1016/j.applthermaleng.2022.118878.

[16] M.O. Lemmon, E.W., Huber, M.L., McLinden, NIST Reference Fluid Thermodynamic and Transport Properties (REFPROP) - Version 9.1, Natl. Inst. Stand. Technol. (2013).

[17] J.S. Pereira, J. Almeida, J.C. André, R. Mendes, J.B. Ribeiro, Modelling and experimental validation of the heat-transfer processes of a direct vaporization micro-scale ORC-evaporator for thermal degradation risk assessment, Energy Convers. Manag. 238 (2021) 114130. https://doi.org/10.1016/j.enconman.2021.114130.

ACKNOWLEDGEMENTs

In association with the authors' host institutions, this research was also supported by the Energy for Sustainability Initiative (EfS) and, by the Portuguese Recovery and Resilience Plan (PRR) and Next Generation European Funds EU through the project AM2R with the reference 7253 under the title AM2R - Agenda Mobilizadora para a inovação empresarial do setor das Duas Rodas. The financial support is gratefully acknowledged.

Exergy cost analysis of bifurcated circular vessels with permeable walls: beyond the Hess-Murray law

Enrico Sciubba
Università Niccolò Cusano – Roma, Italy
enrico.sciubba@unicusano.it
ORCID 0000-0003-2220-1762

Abstract

Since bi- and trifurcated structures are ubiquitous in nature (from trees to rivers to bronchial alveoli to veins and arteries etc.), the idea that their striking topological similarity originates from a physical principle is appealing and stimulated a great number of theoretical and experimental investigations. The concepts of "nature's economy" and of "goal-driven evolution" can been invoked to conjecture that there must be some "reward" for the effort placed by a biological system to build a bifurcated structure, in the sense that the evolutionary advantage gained by the system must more than compensate the additional resource consumption. The interest of engineers, botanists and biologists in this matter is justified by the expectation that linking the "shape" of these structures to their "function" would allow for better aimed interventions in the case of malfunctions (overflow of rivers and channels, tree roots rotting, poor soil exploitation, circulatory diseases…). Furthermore, provided the quite different boundary conditions are properly taken into account, such an insight may be translated into more accurate and efficient design guidelines of artificial (manufactured) branched structures like pipelines, heat exchangers, biological implants etc..

In the early XX century two physiologists, Walther R. Hess in 1903 and Cecil B. Murray in 1926, independently derived a general correlation between the successive radii of bi- and trifurcated vessels: since their derivation was based on a first-order "energy budget" of the operation of the bifurcated system, their result ($r_{i+1}/r_i=2^{-1/3}$) was seen as a confirmation of the evolutionary biology, then in its infancy. The Hess-Murray Law has undergone since a series of critical reviews both in biology and in engineering, and different researchers strived on the one side to reinforce its physical foundation and on the other side to justify the obvious disagreement of its predictions with experimental data.

In this paper, after a brief discussion of Hess' and Murray's original derivations, experimental evidence and physical considerations are used to argue that the "cubic root of 2" allometry cannot apply to the blood flow in arteries and veins. Its application to capillary flows must be corrected by introducing wall suction. On the same basis, it is argued that the law accurately represents the flow in sap-carrying vessels in leaves, but cannot be applied to tree branchings where the bifurcations are originated by a different sort of evolutionary trade-off.

It is then shown that an exergy cost analysis leads to a more credible quantification of the cost/benefit ratio of creating a bifurcation: an application to realistic models of permeable blood vessels indicate that a) the onset of a bi- or trifurcation always requires a larger use of resources w.r.t. the equivalent non-bifurcated configuration; b) the existence of an optimal radius ratio is not guaranteed; and c) the H-M optimal ratio can be seen as a limit value obtained by neglecting some of the relevant physical variables.

Keywords: Branched Fluid Structures; Hess-Murray law; Permeable wall vessels; Entropy Generation Minimization; Exergy cost

1- Introduction

1.1 - The problem

Bifurcated structures in fluid carrying channels and vessels are ubiquitous in nature: as shown in (Figure 1) the shape of tree roots and branches, leaf veins, circulatory systems in animals, air vessels in the respiratory systems, river deltas…display an amazing degree of geometric similarity, so pervasive to suggest the conjecture that their creation can be explained by some common evolutionary principle. Understanding the underlying physics might lead to a better comprehension of natural evolution and linking the "shape" of these structures to their "function" would allow for better aimed interventions in the case of malfunctions (overflow of rivers and channels, poor health of tree roots and tips, poor soil exploitation, circulatory diseases…). And a clearer insight on the physics of natural bifurcations may pave the way to the formulation of more accurate and efficient design guidelines of artificial (manufactured) branched structures (provided proper provision is made for the quite different boundary conditions).

It is therefore not surprising that a multitude of studies have been -and still are being- published on the topic. In fact, engineers, botanists and biologists have devoted substantial time and resources to search for a general model of bi-, tri- and polyfurcated fluid carrying vessels. From a careful consultation of the archival literature [9,18,24,27,28] it is though apparent that there remain questions to be answered:

a) Why do bifurcated structures appear in nature?
b) Why is the geometry of such structures apparently similar at all scales and in different instantiations?
c) How and to what measure is the shape of a bifurcation independent of the prevailing boundary conditions?
d) Does the functional advantage obtained by repeated bifurcations decrease with the number of splittings?

One of the goals of this paper is to clarify the current state of affairs and suggest possible paths to a solution. To place this study in the correct perspective, it is useful to begin by examining the available empirical evidence collected over decades of valuable experimental campaigns:

1) Although different types of branchings display an amazing degree of large-scale geometric similarity, the specific details (radius- and length ratio of daughter and parent branches, branching angle, complanarity) depend on the type of fluid being transported (newtonian or non-newtonian, pure substance or particle laden), on the material of the channel walls (lignine, muscle fibers, gravel, sand…), and on the flow features (creeping, laminar or turbulent);
2) Although a branched network resembles a fractal structure, there is no indication that the fractal exponent remains constant over successive branching levels. Thus, Fractal models are not considered here;
3) While in plants the flow can be accurately modeled as stationary, in blood and air systems as well as in rivers the non-stationarity of the flow has a substantial influence on the geometry of the bifurcations.

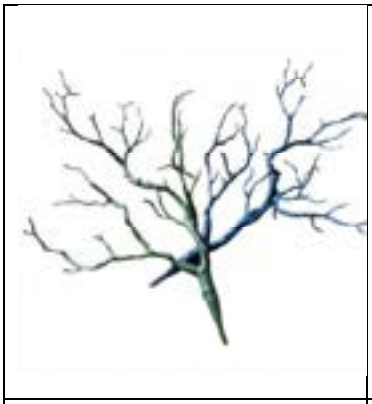

Corals

Fern leaves

Symmetric tree branching

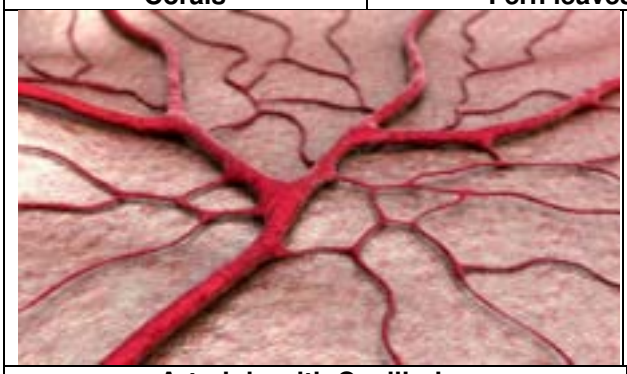

Arteriole with Capillaries

The Mississippi river delta

Figure 1 – Examples of bifurcated topologies appearing in nature (images retrieved from Internet)

1.2 – The currently most popular physical model: the Hess-Murray law

In 1903 the Swiss physiologist Walter Rudolf Hess formulated a model of blood flow in arteries and capillaries that results in an allometric correlation between the radii of successive branchings in bi/trifurcated vessels: the original concept is presented and discussed in Hess' doctoral thesis published in 1903, with expanded versions published in 1914 and 1917 [7,8]. The same correlation was "rediscovered" by the American physiologist Cecil Dunmore Murray in 1926 using a slightly different approach, and later refined and extended in the same year in two other papers [12,13,14]. Since the numerical result, i.e., the allometric rule, is the same, the law came to be referred to as "the Hess-Murray law".

The method proposed by Hess and Murray is described in detail in several review papers [4,20,24,28], and what is of interest here is to underline the novelty of their approach: they assumed that blood or lymph circulation in living organisms is governed by a "work minimization" principle. Although the legacy of the H-M law is considered to be the derivation of an "optimal branching ratio" $\delta = \frac{d_{i+1}}{d_i} = \frac{1}{\sqrt[3]{2}} = 0.7937$ between the daughter-to-parent diameters of symmetrical branchings, the real merit resides in the "energy cost" methods they adopted. As we shall see, their conjecture is in fact only a first approximation of the energy balance of bifurcated systems, but due to the simplicity of their "cubic root of 2" correlation and of its apparent universality, the "H-M radius ratio" is widely employed in biology and even in engineering as a modelling criterion. What goes often unmentioned is that extensive experimental assessments performed in the second half of the 20th century indicate that while the correlation is sufficiently accurate for the smallest vessels (capillaries), it fails for the larger ones (large veins and arteries); moreover, it can be extended to turbulent flows only by changing the exponent of the root [27]. Recent comparisons with numerical investigations of branched flows led to similar conclusions

[2,11,15,16]. It is argued in section 4 here below that this depends on intrinsic limitations of the H-M law and on some hitherto little explored restrictions to its theoretical foundation.

3 – A Brief description of Hess' and Murray's original derivations

3.1 – Hess' problem position and solution

In 1903, in a preparatory paper for his M.D. thesis [7], the Swiss physiologist Walter Rudolf Hess proposed the existence of a physical "optimization criterion" that guides the branching of arterial vessels. This idea was also the topic of later work in his "Habilitation" thesis [8], but the 1903 work already contains a complete derivation of his "cubic root of 2" law. Hess' interest was motivated by previous work by Roux [17] who postulated a "dynamic mechanical principle" to be the driver of vessel bifurcations in animal circulatory systems. To extract physical meaning from Roux' experimental data, Hess suggested that nature would adopt a "minimum resource consumption" criterion to build the human circulatory system and proceeded to calculate how this task can be attained ("*Wie kann die Aufgabe des Blutes mit dem kleinsten Kraftverbrauch erledigt werden*" [7, p.5]). Hess' idea is that the optimal radius of a vessel carrying a given volumetric blood flowrate is the one that minimizes a cost function given by the sum of the pumping work and the metabolic cost of the volume of the pumped blood. Since the former is inversely proportional to the fourth power of the radius and the latter to the square of the radius, an "optimal radius" exists and is proportional to the cubic root of the flowrate. Furthermore, if a vessel splits symmetrically and the mass flowrate is each of the branches is equal to the half of that in the mother vessel, imposing optimality on the daughter branches leads to the allometric law:

$$\delta = \frac{r_1}{r_0} = \frac{1}{\sqrt[3]{2}} \qquad 1)$$

A detailed description of Hess' derivation is provided in [20]: for the purpose of this paper, it suffices here to list the conditions under which the derivation is valid:

a) The flow in arteries, arterioles, veins and capillaries can be described by Poiseuille's law for steady laminar flow in circular vessels with rigid walls;
b) Blood is a Newtonian fluid with constant viscosity;
c) Blood has a metabolic cost proportional to the pumping work performed by the heart (neglecting its thermal content);
d) Since flowrate and pumping power are directly proportional, a larger radius would decrease the pressure drop (and the pumping power) but increase the flowrate. The two effects are opposite, and the problem can be reformulated as a Lagrangian minimization:

$$\mathcal{L}_{Hess} = K_1 \frac{m^2}{r^4} + K_2 r^2 \qquad (2)$$

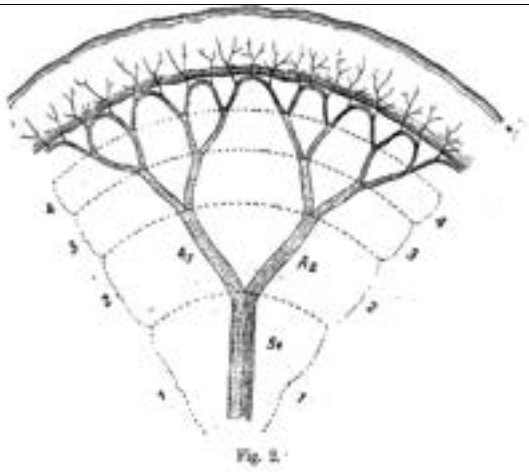

Figure 2 – Hess' concept (original drawing from [8])

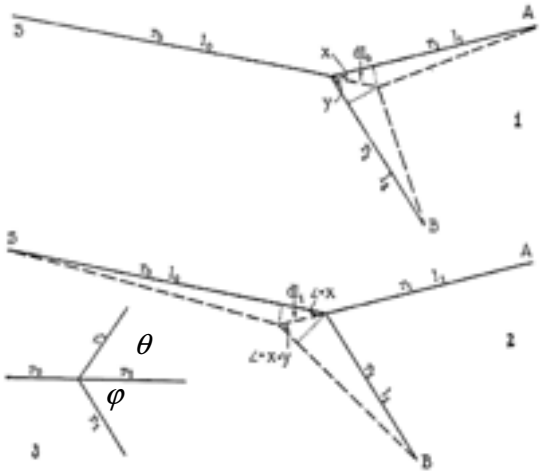

Figure 3 – Murray's calculation of the optimal splitting angle (original drawing from [12])

Which results in:

$$r_{opt} = \left(\frac{2K_1}{K_2}\right)^{1/6} m^{1/3} = \kappa m^{1/3} \quad (3)$$

Where the constant κ depends on the fluid properties and on the metabolic rate.

e) If a vessel bifurcates symmetrically (Figure 2), $m_1=m_2=m_0/2$, the optimality can be extended to the daughter branches:

$$r_0 = \kappa m_0^{1/3}; \quad r_1 = r_2 = \kappa \left(\frac{m_0}{2}\right)^{1/3} \quad (4)$$

Whence equation (1).

Throughout his papers Hess repeatedly states that his result depends on the assumption of validity of Poiseuille pressure drop formula and flow stationarity, and makes reference to selected contemporary literature to support his belief that *i)* a branching does not generate turbulence and *ii)* the low-frequency pulsations do not affect the flow in such a way as to invalidate Eq. (1).

3.2 – Murray's problem position and solution

Murray was aware of Hess' work, and makes his goal explicit in the first lines of his 1926 paper [12]: "*If we examine the arterial system bearing in mind the question of economy, we find that there are two main antagonistic factors. If the vessels are too small, the work required to drive the blood through them becomes too great; if the volume of the vessels is too large, the volume of blood, being equally large, becomes a burden to the whole body*". Murray maintained that his calculation of the blood cost was more accurate than Hess' and based on the latest experimental results. He also derived the "optimal angles" for a symmetric bifurcation using the principle of the minimum virtual work. Again, a detailed description of the mathematical steps is provided in [20].

Proceeding along the same path previously proposed by Hess, Murray obtained an expression for the power required to pump a given mass flowrate of blood in a straight vessel with rigid walls, $P_{pump} = K_1 \frac{m^2}{r^4}$, where K_1 is the same constant as in Hess' formulation. He then proceeded to calculate the metabolic cost of the pumped blood:

$$C_{blood} = bL\pi r^2 = K_3 r^2 \quad (5)$$

Where b is the "cost of blood" calculated on the basis of the then available data on heart rates and varies between 980 and 1980 W/m^3 as per Murray's estimates. For the purpose of this paper, the accuracy of the value of b is though irrelevant.

The optimal radius is again obtained by solving the corresponding Lagrangian:

$$\mathcal{L}_{Murray} = K_1 \frac{m^2}{r^4} + K_3 r^2 \quad (6)$$

Which results in:

$$r_{opt} = \left(\frac{2K_1}{K_3}\right)^{1/6} m^{1/3} = \xi m^{1/3} \quad (7)$$

Where the constant ξ depends on the fluid properties and on the power absorbed by the heart. If a vessel bifurcates symmetrically (Figure 2), i.e., if $m_1=m_2=m_0/2$, the optimality can be extended to the daughter branches and the "cubic root of 2" law $\delta = \frac{r_1}{r_0} = \frac{1}{\sqrt[3]{2}}$ is recovered.

In a second paper [13], Murray calculates the optimal branching angle by applying again the principle of minimum work: as shown in Figure 3, among the possible path lengths the one that minimizes the total work displays branching angles given by:

$$cos\theta = \frac{r_0^4 + r_1^4 - r_2^4}{2r_0^2 r_1^2}; \quad cos\varphi = \frac{r_0^4 + r_2^4 - r_1^4}{2r_0^2 r_2^2} \quad (8)$$

That is:

$$\theta = arccos\left[\frac{r_0^4 + r_1^4 - \left(r_0^3 - r_1^3\right)^{4/3}}{2r_0^2 r_1^2}\right]; \quad \varphi = arccos\left[\frac{r_0^4 + r_2^4 - \left(r_0^3 - r_2^3\right)^{4/3}}{2r_0^2 r_1^2}\right] \quad (9)$$

Introducing the optimal radius ratio δ (Eq. 1):

$$\theta = \varphi = arccos\left[\frac{1 + \delta^4 - \left(1 - \delta^3\right)^{4/3}}{2r_0^2 \delta^2}\right] \sim 37.5° \quad (10)$$

The above result predicts that symmetrical branches should have a total branching angle ($\theta+\varphi$) of about 75°.

If the vessel trifurcates as shown in Figure 4, with two side daughter branches being symmetrical with equal radii $r_1=\gamma r_0$ and the third coaxial with the main and also of radius $r_2=r_1$, the optimal value of the radius ratio is $\gamma = \frac{1}{\sqrt[3]{3}} = 0.6934$ and Murray's optimization procedure provides:

$$\psi = arccos\left[\frac{r_0^2 - \left(r_0^3 - 2r_1^3\right)^{2/3}}{2\gamma^2 r_0^2}\right] \quad (11)$$

with the splitting angle ψ=57°.

Although not mentioned by Murray, Eq. (8) leads to an interesting corollary: if $r_1=r_2$, it reduces to

$$cos\theta = \frac{1}{2\delta^2} \quad (12)$$

Which implies that larger daughter branches ought to form higher angles with the parent vessel.

For future record, consider that Murray's angle formulae (8) and (12) retain their validity if applied to branching ratios different from the "canonical value" ($\delta = 0.7937$; $\theta = 37°$): for example, a $\delta = \frac{1}{\sqrt{2}} = 0.707$ that ensures constant fluid velocity in the parent and daughter branches corresponds (Figure 7) to an angle $\theta=0°$, i.e., to no splitting, while the $\delta=0.5$ derived from a constant Reynolds assumption in parent and daughter branches leads to impossible solutions of Eq. (12): this does though not agree with empirical evidence.

4 – SOME REFLECTIONS ON THE PHYSICS OF FLUID-CARRYING VESSELS

As certified by an impressive experimental database [9,18,23,24,25,27,28,30], the "cubic root of 2" correlation is reasonably accurate in small capillaries and in the small sap-carrying channels of leaves, but it fails in predicting branching ratios in human arteries (typical diameters 0.005-0.025 m) and veins (0.006-0.03 m), as well in smaller vessels in case of turbulent flow [27]. The discrepancies have been traditionally explained by considering that the blood flow is pulsatile, that the vessel walls are non-rigid, that blood is a non-Newtonian fluid with shear thinning characteristics, and that the junctions inevitably generate turbulence in the flow. In fact, in his original paper Hess made a point in stressing that his model was derived by neglecting all of the above.

A possible explanation of the reason for the popularity of the H-M law in spite of its lack of generality may be found in its "robustness" with respect to both the radicand and the exponent of the root: as shown in Figures 5 and 6, changing the radicand from 1.5 to 3.5 results in a maximum difference of about 20% w.r.t. the H-M radius ratio, while changing the exponent 1/n of the root from 0.66 (=1/1.5) to 0.3 (=1/3.3) leads to a maximum derangement of about 17%. Translating these relative values into absolute measurement of the daughter branches, this means that the differences are of the order of fractions of a millimeter and can often be absorbed by the inevitable averaging over large series of *in vivo* measurements.

It is therefore legitimate to question the validity of the H-M model itself: is it missing some relevant variables? Or is its "universality" being overestimated? The remaining sections of this paper present a critical analysis of different physical instantiations.

5 – DIFFERENT TYPES OF BIFURCATED STRUCTURES IN NATURE

5.1 – River flows

The claim that the H.M law ought to apply to river flows appears at least as an arbitrary extrapolation of the principles on which the law is based. First, the flow in rivers is rarely laminar; second, it is an open channel flow rather than a genuinely internal flow; third, the flow characteristics are essentially determined by several factors not contemplated in the H-M derivation: hydraulic head, type of the river bed, structure of the banks, presence of obstacles on the water path; permeability of the terrain. In the absence of a physical model that includes all of the above effects, the similarity between a river delta and -for instance- tree roots is purely topological and the existence of an underlying common physical principle is not justifiable.

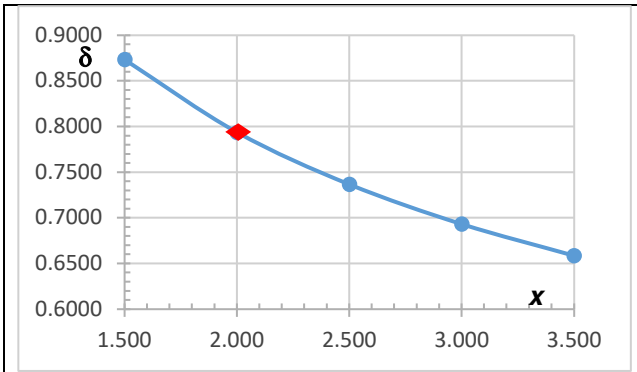

Figure 5 – H-M radius ratio $\delta=r_1/r_0$ vs radicand in $1/x^{1/3}$

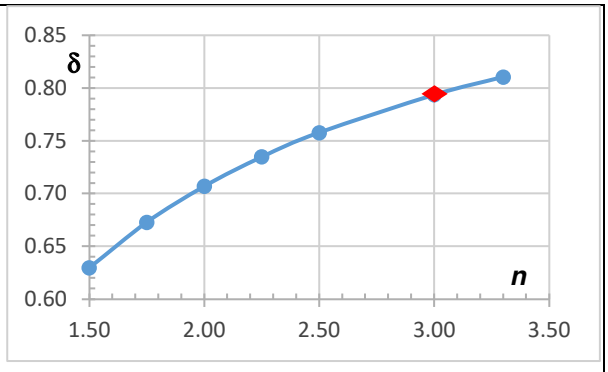

Figure 6 – H-M radius ratio $\delta=r_1/r_0$ vs exponent *n* in Eq. (1).

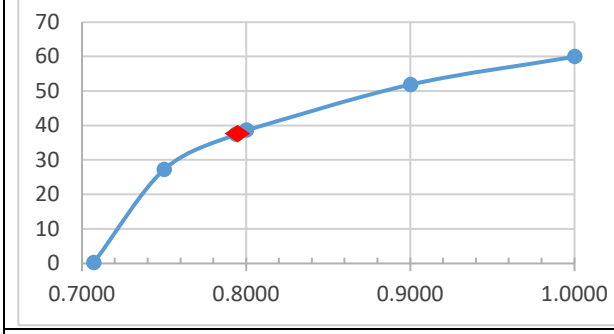

Legenda:
δ=0.707, constant velocity;
δ=0.7937, H-M value;
δ=1, constant vessel radius

Figure 7 - Murray's splitting angle for symmetric branches as f(δ)

5.2 – Blood flow in arteries and veins

Experimental evidence demonstrates that we are dealing here with the unsteady turbulent flow of a non-newtonian fluid in vessels of variable diameter and with non-rigid walls. Again, the H-M model does not account for any of these characteristics. It is therefore legitimate to conclude that the apparent success of "semi-empirical exponent adjustment" of the H-M law is to be abscribed to its arithmetical "robustness" mentioned in section 4.

5.3 – Blood flow in arterioles, venules and capillaries

In these smaller vessels, the flow is with good approximation laminar, and the unsteadiness is strongly damped by the upstream circuit capacity (Figure 8). The H-M law ought to apply here, with a small modification to take into account the effects of permeable walls described in section 6 below.

5.4 – Sap flow in leaves capillary tubules

This is perhaps the most suitable instantiation of H-M flow: laminar, steady, very small flowrates and Reynolds numbers. As for the capillaries, a correction to the H-M model to account for the (significant) amount of wall permeability is in order: the treatment being the same as for blood capillaries, both the model and the results are shown in section 6.

5.5 – Tree branchings, including roots

The attempt to apply the H-M law to these systems is based on wrong premises. To begin with, there is no "fluid branch splitting" here, because the carrying vessels (xylems and phloems) do not bifurcate. The splitting of the woody structure seems to obey some sort of reproducible rule, probably linked to the advantage the plant obtains from a larger crown, that depends in turn on the number of branchings, since the final twigs carry the most leaves. A possible non H-M model is described in [21].

6 – A MODEL BASED ON THE EXERGY COST OF A BIFURCATION

6.1 –Theoretical justification

As stated in the Introduction, the major merit of the Hess-Murray approach is the idea of the existence of an "energy cost" principle that guides the creation of a branching: in essence, a vessel bifurcates in such a way that the energy budget of the main- and of the daughter branches is "optimal". There are two energy cost items in the H-M budget: the energy rate required to overcome friction (pumping power) and that needed to "create" the blood (its metabolic cost). This is a very reasonable physical principle and in fact leads to accurate predictions for the class of flows it has been originally derived for.

It is likely that in capillary flows the permeability of the walls has some influence on the shape of the structure, and in this section we shall examine a model that accounts for these effects. Before doing that though, it is important to consider that when we deal with problems in which different forms of energy are involved (in this case, material energy and pumping work) the proper thermodynamic quantifier is eXergy. The model discussed in the next sections is in fact based on a comparison of the exergy cost [26] of a bifurcated structure w.r.t. to its non-bifurcated counterpart. The results presented here apply to capillary blood flow and sap flow in leaf tubules and -most likely with lesser accuracy- to blood flow in arterioles and venules.

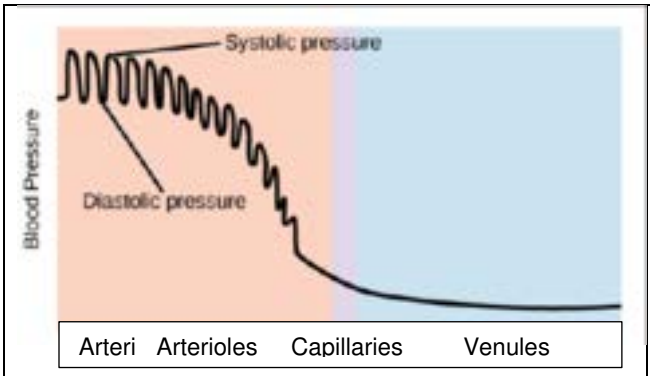

Figure 8 – Representative diagram of the pressure in human blood circulation system

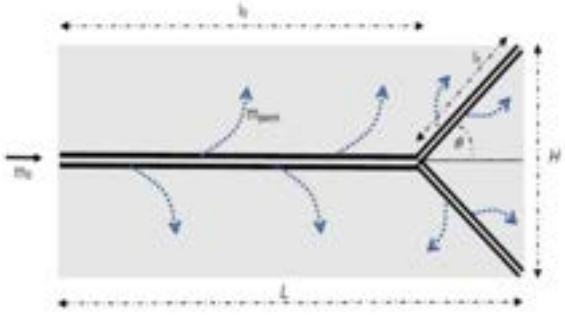

Figure 9 – Conceptual illustration of the proposed model

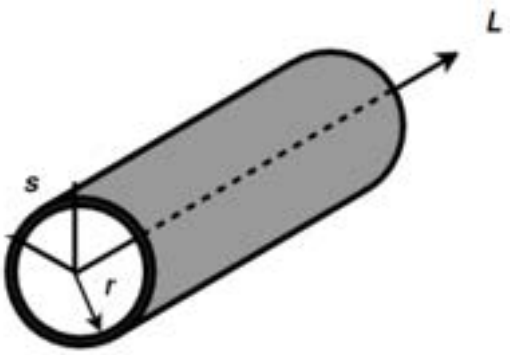

Figure 10 – For the calculation of the tubule volume

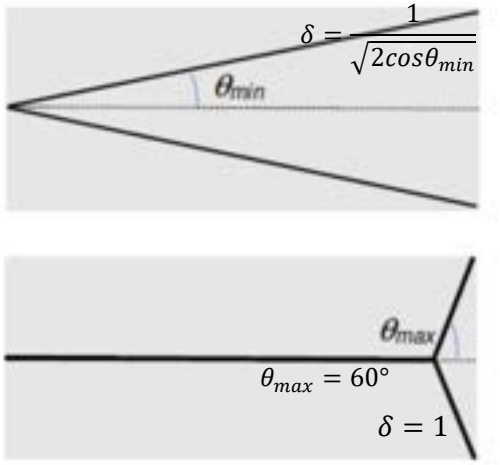

Figure 11 – Minimum- and maximum allowed splitting angles

Consider a straight portion of vessel of length *L* and uniform radius r_0: it will "feed" a domain *H*x*L* as shown in Figure 9. Under steady state conditions, the amount of fluid mass permeated through the wall is proportional to the vessel external surface:

$$m_{perm} = 2\pi r_0 L\xi \tag{13}$$

where ξ [kg/(m^{2}s)] is the wall permeability coefficient.

This mass flowrate must be equal to the difference between the inlet and outlet mass flowrates: for ease of calculation, let us assume that the length *L* is a "terminal" portion and the outlet flowrate is zero:

$$m_{metab} = \gamma HLs \tag{14}$$

where γ [kg/(m^{3}s)] is the local metabolic rate and *s* is the thickness of the surrounding tissue, assumed constant over the domain *H*x*L*.
The inlet mass will be thus equal to:

$$m_0 = m_{metab} = \gamma HLs \tag{15}$$

There are three terms in the exergetic cost of the structure: the first is equal to the pumping power required to propel the fluid through the length *L*:

$$\dot{E}_p = \frac{f m_0^3 L}{4\pi^2 \rho^2 r_0^5} \tag{16}$$

where *f* is the friction factor (in the following calculations the value *f=64/Re* has been assumed throughout). The second cost is the amount of exergy required of the main system (the body, the tree…) to generate the blood or the sap:

$$\dot{E}_f = e_{fluid} m_0 \tag{17}$$

where e_{fluid} [J/kg] is the specific exergy of the blood or sap. The third cost term is the exergy embodied into the walls of the vessel (Figure 10):

$$\dot{E}_{mat} = \frac{e_{fluid} \varphi \pi L r_0^2 (\sigma^2+2)}{\tau} \tag{18}$$

where τ [s] is the assumed operational life of the vessel, φ is a coefficient that accounts for the ratio of the "vessel construction time" to τ and σ=s_0/r_0 is the ratio of the wall thickness to the radius. Thus the total exergy cost (in W) of the "linear vessel segment" of length *L* is:

$$\dot{E}_L = \frac{f m_0^3 L}{4\pi^2 \rho^2 r_0^5} + e_{fluid} m_0 + \frac{e_{fluid} \varphi \pi L r_0^2 (\sigma^2+2)}{\tau} \tag{19}$$

For a symmetrically branched structure the above calculations can be repeated separately for the unsplit length l_0 and for the two branches l_1. The result is:

$$\dot{E}_{BIF} = \frac{f m_0^3 L}{4\pi^2 \rho^2 r_0^5}\left(\lambda_0 + \frac{\lambda_1^4 cos^3(\theta)}{4\delta^5}\right) + e_{fluid} m_0 + \frac{e_{fluid} \varphi \pi L r_0^2 (\sigma^2+2)}{\tau}(\lambda_0 + 2\lambda_1 \delta^2) \tag{20}$$

where $\lambda_0=\ell_0/L=1-a/(2\tan\theta)$; $\lambda_1=\ell_1/L=a/(2\sin\theta)$, $\delta=r_1/r_0$ and $a=H/L$ is the domain aspect ratio.
The difference $\dot{E}_L - \dot{E}_{BIF}$ represents the additional resource cost the main system incurs into when developing a bifurcation in the domain *H*x*L*. It is convenient to use Eq. (12) to eliminate the radius ratio δ and obtain an expression in the angle θ:

$$\Delta\dot{E}_{BIF} = \dot{E}_L - \dot{E}_{BIF} = K_P\left(\frac{a^3 cos^{1.5}(\theta)}{2^{0.5} tan^4(\theta)} - \frac{1}{\tan(\theta)}\right) + K_M\left(\frac{1}{sin(\theta)\cos(\theta)} - \frac{1}{\tan(\theta)}\right) \tag{21}$$

With

$$K_P = \frac{a f m_0^3 L}{8\pi^2 \rho^2 r_0^5}; \qquad K_M = \frac{a e_{fluid} \varphi \pi L r_0^2 (\sigma^2+2)}{2\tau} \tag{22}$$

Plots of ΔE_{BIF} as a function of θ for different aspect ratios are shown in Figures 12 and 13: only the graphs for a=0.25 and a=1 are shown, since the general shape remains similar for the intermediate aspect ratios. As expected, the results are somewhat different for blood and sap:

I. <u>Blood flow</u>

a) The $\Delta\dot{E}_{BIF}$ is always positive, i.e., the construction of a bifurcation <u>always</u> leads to a reduction of the exergy cost born by the system;
b) The cost reduction is of the order of few percentage points for each single bifurcation (see Table 2), with the absolute exergy savings in the range 10^{-7} W/bifurcation: it is clear that the

savings at system level make sense only if the number of branchings is sufficiently high (an estimate of the number of bifurcations in the human blood circulation system is of the order of billions [25]);

c) The aspect ratio of the domain has a direct influence on the resource savings because it sets a limit to the possible splitting lengths: $\theta_{min} = \arctan\left(\frac{a}{2}\right)$ and $\theta_{max} = arccos(0.5)$ as shown in Figure 11;
d) The curve of the saved resource is rather flat and it is shows an optimal value (i.e., maximum resource savings) towards the lowest allowed splitting angles;
e) The optimal radius ratio d lies between 0.715 (narrowest domain, a=0.25) and 0.759 (square domain, a=1): it is interesting that not only these values are consistently lower than the Hess-Murray 0.7937 value, but also that they do not reproduce either the constant Re value (0.5) or the constant velocity (0.707);
f) The value of the ratio K_P/K_M has an important influence on the numerical results (i.e., on the percentage savings), but since all physical quantities in both K_P and K_M are rather rigidly determined for blood and sap (Table 1), this value has a reasonably small variability.

II. <u>Sap flow</u>

a) The $\Delta\dot{E}_{BIF}$ is three orders of magnitude higher than in blood capillaries, with the average value being about 10^{-2}W;
b) Here, too, the aspect ratio plays a significant role in determining the range of θ;
c) The curve of the saved exergy resource is clearly skewed towards the lowest allowed splitting angles;
d) The value of the ratio K_P/K_M has an important influence on the numerical results, but it is rather rigidly determined for the known physical properties of sap and has a small variability.

The above results are somewhat less “deterministic” as those of previously published allometric models [3,4,18,24,28], and lead to an interesting interpretation:

i- The advantage of a single bifurcation is very small, and it becomes relevant at system level only if a sufficiently high number of branchings exist;
ii- While every angle between θ_{min} and θ_{max} leads to exergy savings that differ by few percent points- Blood and sap display different savings for different splitting angles, but the optimal values in both cases are skewed towards the lowest allowable angles (daughter branch length ℓ_1 as long as possible);
iii- For each aspect ratio, the radius ratio δ has a lower limit set by the domain shape and grows with the splitting angle to an upper limit δ=1 (established by experimental evidence) that corresponds to θ_{max}=60°;
iv- Within θ_{min} and θ_{max} thus, solutions are in practice almost equivalent (see Table 2), and different values of the radius ratio are acceptable, possibly influenced by the external boundary condition. For comparison with previous works [1,3,4,19,24,28,29], the H-M solution $\delta = \frac{1}{\sqrt[3]{2}}$ with θ_{max}=35.5°is also shown on the graphs;
v- There is no general allometric rule that governs the branching in ALL blood and sap carrying vessels! The solutions displayed here apply only to capillaries and small leaf tubules. The balance of larger vessels (arteries, veins, larges sap tubes) is much more complicated, due to several other relevant variables that enter the game.

Table 1 – Definition, units and values of the relevant model parameters			
a=H/L, aspect ratio	model parameter	$\delta=r_1/r_0$, radius ratio	calculated
b, kcal/m^3, Murray's "blood cost"	0.39	γ, kg(m^{3}s), metabolic rate	calculated
e, kJ/kg, specific exergy	e_b=1.7; e_s=25.	θ, rad, splitting angle	model parameter
$\dot{E}$, kW, exergy rate	calculated	χ, rad, generic angle	n.a.
f, Moody friction factor	64/(Reynolds #)	$\lambda_j=\lambda_j/L$, length ratio	model parameter
H, m, domain width	model parameter	μ, kg/(ms), dynamic viscosity	μ_b=0.08; μ_s=0.08
ℓ_0, m, 1st splitting length	model parameter	ν, m^2/s, kinematic viscosity*10^5	ν_b=8.05; ν_s=8
ℓ_1, m, 2nd splitting length	model parameter	φ, s, time	φ_b=0.015; φ_s=0.02
L, m, domain length	L_b=0.01; L_s=0.01	ψ, rad, generic angle	n.a.
m, kg/s, mass flowrate	calculated	ρ, kg/m^3, density	ρ_b=105; ρ_s=994
n, Hess-Murray exponent	model parameter	σ=s/r, wall thickness ratio	σ_b=0.125; σ_s=0.125
r_0, m, parent radius[6]	r_{0b}=8*10^{-6}; r_{0s}=0.001	τ, s, lifetime*10^{-7}	τ_b=250; τ_s=3
r_1, m, daughter radius	$=\delta*r_0$	ξ, kg/(m^{2}s), wall permeability	calculated
s, m, tissue thickness	s_b=0.005; s_s=0.0005	ζ, numerical coefficient	n.a.
v, m/s, fluid velocity	v_b=3*10^{-4}; v_s=1*10^{-4}		

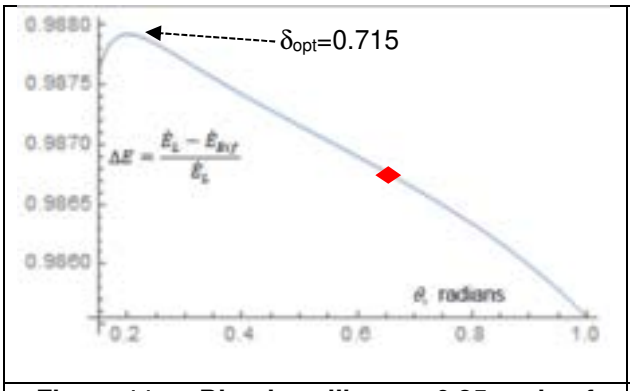

Figure 11a – Blood capillary, a=0.25: ratio of Exergy rate gain to unsplit geometry, $\Delta\dot{E}_{BIF}/\dot{E}_L$

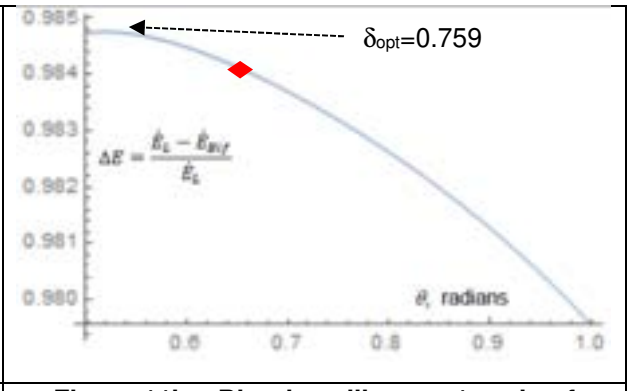

Figure 11b – Blood capillary, a=1: ratio of Exergy rate gain to unsplit geometry, $\Delta\dot{E}_{BIF}/\dot{E}_L$

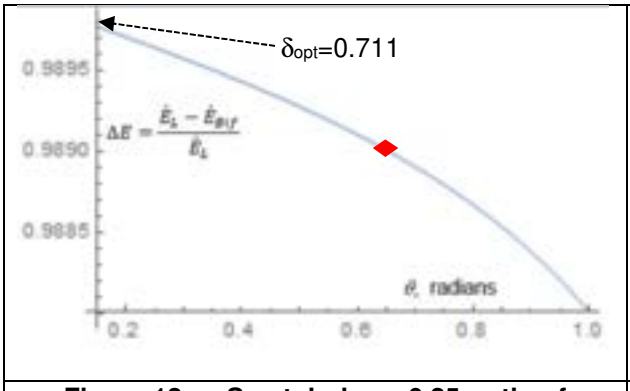

Figure 12a – Sap tubule, a=0.25: ratio of Exergy rate gain to unsplit geometry, $\Delta\dot{E}_{BIF}/\dot{E}_L$

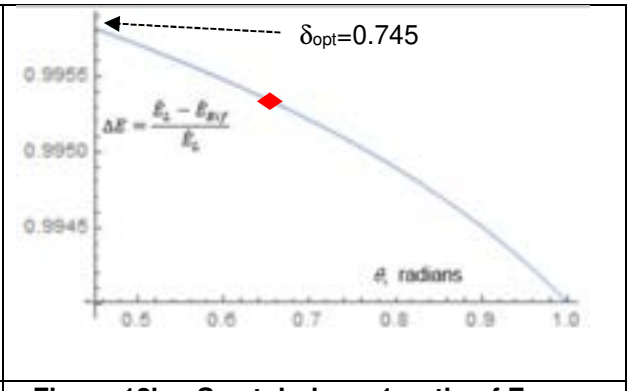

Figure 12b – Sap tubule, a=1: ratio of Exergy rate gain to unsplit geometry, $\Delta\dot{E}_{BIF}/\dot{E}_L$

Legenda: ◆ δ=0.7937, H-M value

Table 2 – Minimum and maximum gain for a single bifurcated structure						
Aspect ratio a=H/L	***Blood capillary***			***Sap tubule***		
	$\Delta\dot{E}_{BIF}/\dot{E}_L$ ***max***	δ_{opt}, Eq. (12)	θ_{opt}	$\Delta\dot{E}_{BIF}/\dot{E}_L$ ***max***	δ_{opt} , Eq. (12)	θ_{opt}

0.25	1.2%	0.715	0.22 rad, 12.60°	1.04%	0.711	0.15 rad, 8.59°
0.5	1.28%	0.730	0.35 rad, 20.05°	0.36%	0.718	0.25 rad, 14.32°
0.75	1.4%	0.745	0.45 rad, 25.78°	0.36%	0.730	0.35 rad, 20.05°
1.	1.52%	0.759	0.52 rad, 29.79°	0.44%	0.745	0.45 rad, 25.78°

7 - CONCLUSIONS

The paper presents a new model to predict the splitting angle and the radius ratio of a single, symmetric bifurcation in small blood vessels and sap tubules. The model consists in the calculation of the exergy cost difference between an unsplit vessel of length L in a domain HxL and the bifurcated configurations in the same domain. The balance is obtained by imposing that the fluid mass flowrate at the inlet is completely permeated to feed the surrounding tissue with the metabolically necessary nutrients. Three "cost terms" are identified: the pumping exergy rate, the exergy rate of the transported fluid and the exergy rate equivalent to the amount embodied in the construction of the vessel structure. The concept is clearly borrowed from the 20th century seminal works of Hess and Murray, but the use of exergy instead of energy and the inclusion of the permeation lead to substantially different results. In conclusion, it can be said that the creation of a bifurcation is -under the boundary conditions specified here- always convenient for the system, in the sense that a bifurcated structure reduces the overall exergy consumption. Furthermore, the resource savings depend on the aspect ratio of the domain, i.e., on the extension of the surrounding tissue the vessels deliver nutrients to. Finally, the concept of "optimal splitting radius ratio" does not apply, because there is a rather wide range of legitimate splitting angles all of which are "convenient" for the system and each one of which corresponds to a different radius ratio. The H-M value falls within the range of allowable angles, but is not optimal in any sense. The advantage for sap vessels is of 3 orders of magnitude higher than for blood capillaries, and this is compensated by a much larger number of capillary junctions w.r.t. those experimentally detectable on leaves and other sap carrying vessels. It must be stressed however that the model does not apply to xylems and phloems that do not bifurcate.

The analysis is performed under rather stringent specifications: laminar flow, rigid permeable walls with constant diameter and constant wall thickness, and an exact balance of the inlet mass flowrate with the permeated one. The inclusion of different levels would imply a major complication in the modelling effort.

8 - REFERENCES

[1] J.A.Adam, 2011: *Blood Vessel Branching: Beyond the Standard Calculus Problem*, Math. Magazine, 84,196–207

[2] A.A.Al-Shammari, E.A.Gaffney, S.Egginton, 2014: *Modelling capillary oxygen supply capacity in mixed muscles: capillary domains revisited*, J. Theor.Biology, 356, 47–61.

[3] A.Bejan, 1997: *Constructal-theory network of conducting paths for cooling a heat generating volume*, Int. J. Heat Mass Transf., 40, 799–816.

[4] A.Bejan, S.Lorente, 2011: *The constructal law and the evolution of design in nature*, Physics of Life Reviews, 8, n.3, 209-240

[5] J.A.Borgert, L.M.Moura, 2013: *Exergetic analysis of glucose metabolism*, Int. J. Exergy, v.12, n.1, 31-53

[6] E.M.Cherry, J.K.Eaton, 2013: *Shear thinning effects on blood flow in straight and curved tubes*, Phys. Fluids v.25, 073104

[7] W.R.Hess, 1903: *Eine mechanisch bedingte Gesetzmäßigkeit im Bau des Blutgefäßsystems*, (A mechanical rule for the construction of the blood circulatory system), Arch. Entwicklungsmech. Org.,*16*, 632–641

[8] W.R.Hess, 1914: *Das Prinzip des kleinsten Kraftverbrauches im Dienste hämodynamischer Forschung* [Habilitation], (The principle of minimum power applied to blood dynamics studies). Veit. Arch. Anat. Physiol., Leipzig, 1–62

[9] W.Huang, R.T.Yen, M.Mclaurine, G.Bledsoe, 1985: *Morphometry of the human pulmonary vasculature*, J. Al. Physiology, 81, n.5, 2123–2133

[10] N.Kunert, L.Schwendenmann, D.Hölscher, 2010: *Seasonal dynamics of tree sap flux and water use in nine species in Panamanian forest plantations*, Agricultural & Forest Meteorology 15, 411–419

[11] M.Massoudi, T.X.Phuoc, 2008: *Pulsatile flow of blood using a modified second-grade fluid model*, Computers and Mathematics with Applications 56 , 199–211

[12] C.D.Murray, 1926a: *The physiological principle of minimum work applied to the angle of branching of arteries*, J. General Physiol., 20 July, 9, n.6, .835–841.

[13] C.D.Murray, 1926b: *The physiological principle of minimum work – I: the vascular system and the cost of blood volume*, Proc. Nat. Acad. Sci., 12, 207–214.

[14] C.D.Murray, 1926c: *The physiological principle of minimum work – II: oxygen exchange in capillaries*, Proc. Nat. Acad. Sci., 12, 299–304.

[15] M.S.Olufsen, C.S.Peskin, W-Y.Kim, E.M.Pedersen, A.Nadim, J.Larsen, 2000: *Numerical Simulation and Experimental Validation of Blood Flow in Arteries with Structured-Tree Outflow Conditions*, Annals Biomedical Engineering, 28, 1281–1299

[16] M.U.Qureshi, G.D.A.Vaughan, C.Sainsbury, M.Johnson, C.S.Peskin, M.S.Olufsen, N.A.Hill, 2014: *Numerical simulation of blood flow and pressure drop in the pulmonary arterial and venous circulation*, Biomech. Model Mechanobiol., n.13, 1137–1154.

[17] W.Roux, 1878: *Über die Verzweigungen der Blutgefässe der Menschen: eine morphologische Studie*, (On the branching of blood vessels in humans: a morphological study), Doctoral thesis, Jena; 1878. in W.Roux Gesammelte Abhandlungen über Entwicklungsmechanik der Organismen. V.1, I-XII, 1-76. Wilhelm Engelmann Verlag Leipzig, 1895

[18] A.G.Roy, M.J.Woldenberg, 1982: *A generalization of the optimal models of arterial branching*, Bull. Math. Biology, 44, n.3, 349–360.

[19] E.Sciubba, 2011: *Entropy Generation Minimization as a Design Tool. Part 1: Analysis of Different Configurations of Branched and Non-branched Laminar Isothermal Flow Through a Circular Pipe*, IJoT 14, 1, 11-20

[20] E.Sciubba, 2016: *A Critical Reassessment of the Hess–Murray Law*, Entropy, 13, 283-300

[21] E.Sciubba, 2023: *A model for bifurcation formation in plants based on a comparative exergy cost analysis,* submitted to Plants, march 2023

[22] E.Sciubba, F.Zullo, 2013: *Stable and periodic solutions of an exergy-based model of population dynamics*, Energy, 58, 202–209

[23] R.S.Seymour, Q-H.Hu, E.P.Snelling, 2020: *Blood flow rate and wall shear stress in seven major cephalic arteries of humans*, J. Anat. 236,522--530

[24] T.F.Sherman, 1981: *On Connecting Large Vessels to Small: The Meaning of Murray's Law*, J. General. Physiol., 78, 431-453

[25] D.F.J. Tees, P.Sundd, D.J. Goetz, 2006: *A flow chamber for capillary networks: leukocyte adhesion in capillary-sized, ligand-coated micropipettes*, Chapter 10 in Principles of Cellular Engineering, 213-231, Acad. Press

[26] C.Torres, A.Valero, 2021: *The Exergy Cost Theory Revisited*, Energies 14 (1594)

[27] H.B.M.Uylings, 1977: *Optimization of diameters and bifurcation angles in lung and vascular tree structures*, Bull. Math. Bio, 39, 509–520.

[28] G.B.West, J.H.Brown, 2005: *The origin of allometric scaling laws in biology from genomes to ecosystems: towards a quantitative unifying theory of biological structure and organization*, J. Exp. Biology, 208, 1575–1592.

[29] T.Young, 1809: *The Croonian Lecture: On the Functions of the Heart and Arteries,* Phil. Trans. R. Soc. London, 99, 1-31

[30] M.Zamir, S.M.Wrigley, B.L.Langille, 1983: *Arterial bifurcations in the cardiovascular system of a rat*, J. General Phys., 81, 325–335

Flow maps and flow patterns of R1233zd(E) in a circular minichannel at low, medium and high values of saturation pressure

Stanisław Głuch[a], Michał Pysz[b], Dariusz Mikielewicz[c]

[a] Gdańsk University of Technology, Gdańsk, Poland stanislaw.gluch@pg.edu.pl
[b] Gdańsk University of Technology Gdańsk, Poland michal.pysz@pg.edu.pl
[c] Gdańsk University of Technology Gdańsk, Poland dariusz.mikielewicz@pg.edu.pl

Abstract:

There is a gap in knowledge regarding the flow pattern of low-boiling working fluids in the range of high saturation temperatures (above 120°C) and medium and high reduced pressures (0.5-0.9). Data are present in the literature for similar values of reduced pressures, but for lower values of saturation temperature. This is due to the existing refrigeration applications of these working fluids. At high values of reduced pressure, the density of the gas phase is relatively high, and the density of the liquid phase is low. There is a low specific volume difference between the liquid and gas phases. The liquid phase has a low surface tension value. The gas phase has a relatively high viscosity, and the liquid phase has a reduced value of viscosity. These changes in the parameters of refrigerants cause significant differences in flow structures. At a low value of reduced pressure, 0.2, the occurrence of annular flow was observed already at a quality of 0.07 for a mass velocity of G=355 [kg/(m^2·s)], while for a reduced pressure of 0.8, annular flow occurs much later, at a quality of 0.47 for the same mass velocity. Mass velocity flow maps in a function of quality for constant values of reduced pressure and flow maps for reduced pressure as a function of quality at constant mass velocity are presented. Flow maps are compared with correlations for transition lines between intermittent and annular flow structures from literature. Authors new correlation for transition line for researched conditions is presented. New prediction method is the only one which managed to predict transition to annular flow at high values of reduced pressure for collected experimental data.

Keywords:

two-phase flow; flow patterns; flow maps; R1233zd(E); high value of reduced pressure; annular flow transition line prediction

1. Introduction

An important trend in the development of new technologies is the miniaturization of technical objects. This effort requires extensive basic knowledge of fluid mechanics and heat transfer in single-phase convection and boiling and condensation in flow. The ability to accurately predict pressure drops and heat transfer, as well as the selection of geometry and operating conditions, are important factors in the design and selection of optimal heat exchanger settings. There is now a growing interest in low global warming potential (GWP) refrigerants. New European regulations require that air conditioning and refrigeration applications cannot be manufactured using fluorinated greenhouse gases with a GWP greater than 150 (EU directive 2019/1937). This leads to the use of new, environmentally friendly agents such as CO2, which operates in the near-critical and supercritical areas. Other applications, such as high-temperature heat pumps or ORC cycles, operate at much higher parameters than refrigeration systems. In 2022 energy price crisis resulted in immense demand for industrial high temperature heat pumps. Data available in the literature on heat transfer by refrigerants at high saturation temperatures are scarce. Studies of structures and flow maps are even more scarce. Many heat transfer correlations such as [1,2]created for specific flow pattern. It is essential to predict flow pattern to accurately calculate heat transfer coefficient.

1.1. Previous research on flow pattern maps

Cheng et al [3]conducted a study of heat transfer coefficients and CO2 flow maps during boiling. The medium was tested for reduced pressure Pr from 0.21 to 0.87, mass velocity G from 170 kg/(m^2·s) to 570 kg/(m^2·s), and temperature from -28°C to 25°C. Nema et al. [4]studied the flow structures of R134a during condensation and proposed a new criterion for the transit of flow structures. Charnay et al. [5] studied the flow structures of R245fa during boiling at 60°C, which corresponds to a pressure of 4.6 bar for a mass velocity of 100 to 1,500 kg/(m^2·s) with an inner diameter of a 3mm round tube. Charnay et al. [6] conducted additional tests for a

saturation temperature of 120°C. They compared the results obtained with annular flow transition lines available in the literature. Although the flow structures more closely resembled those observed at the macroscale, the transition line was similar to that observed in minichannels. Barberi et al.[7] presented research on R134a boiling in in smooth brass tubes for various diameters form 6.2 mm to 12.6 mm for mass velocities from 25 to 500 kg/(m^2·s). El Hajal et al. [8]presented flow pattern map and flow pattern based heat transfer model for condensation inside horizontal plain tubes for CO2 for reduced pressure up to 0.8. Kim et al. [1,9] conducted research on flow maps and heat transfer during condensation of FC-72. They proposed flow patter prediction method which was development of Soliman method [10]Zhang et al. [2] further developed this correlation to predict low patterns for R170 for high saturation pressures from 1.5 to 2.5 MPa what correspond to reduce pressure up to 0.51 MPa. Revelin and Thome [11]in et al presented research of flow patterns of R134a ad R245fa for 26, 30 and 35 °C saturation temperatures inside 0.5 mm and 0.8 mm diameter glass tube. They proposed correlation for pattern prediction method. Ong and Thome [12]proposed new method for pattern flow prediction for R134a, R236fa and R245fa during flow boiling in small channels of 1.03, 2.20 and 3.04 mm diameter.

2. Methodology and laboratory equipment

A study was conducted to visualize the flow of two-phase modern refrigerant R1233zd for reduced pressure values from 0.2 to 0.6. and for mass velocity G [kg/(m^2·s)] from 180 to 445. The critical temperature of the tested refrigerant is 156.6°C, and the critical pressure is 21.4 bar. Its GWP (Global Warming Potential) is 1, and its ODP (Ozone Depleting Potential) is 0 according to the NIST database of Acree et al. (2022). A schematic of the test rig is shown in Figure 1. The prevailing pressure in the system is established through a pressurized nitrogen tank connected to a membrane hydroaccumulator. The main pump ensures that the medium is pumped through the system and overcomes the flow resistance. Behind the pump is a Coriolis mass flow meter. Next is the preheater, followed by a section for measuring heat transfer coefficients during boiling. Behind the measuring section is the visualization section, which is shown in Fig. 2. It consists of a borosilicon tube with an inner diameter of 3mm, a wall thickness of 3mm and a length of 200mm. Behind the visualization section is a condensation section with an intermediate oil system that provides constant condensation conditions. Images were taken with a Photron Fastcam Mini UX100 high-speed camera.

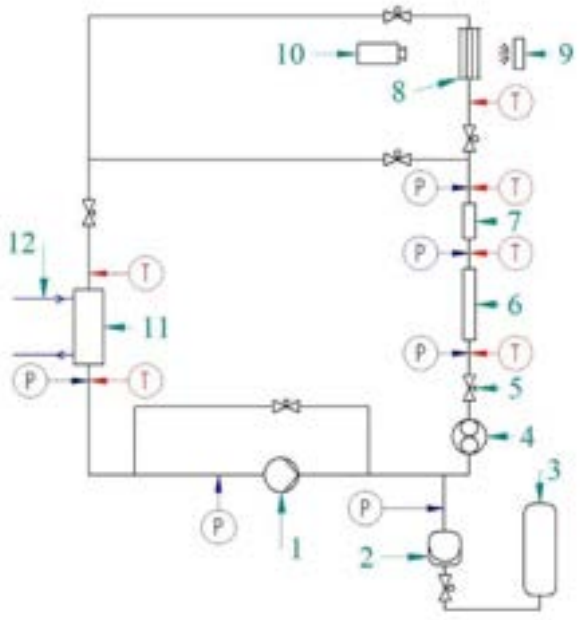

Figure 1. Test stand: 1 - piston diaphragm pump, 2 - diaphragm hydroaccumulator, 3 - pressurized nitrogen tank, 4 - Coriolis flow meter, 5 - control valve, 6 - heater, 7 - heat exchange measurement section, 8 - visualization section, 9 - led light source, 10 - high-speed camera, 11 - condenser, 12 - oil loop.

Figure 2. The visualization section with the Photron Fastcam Mini UX100 high-speed camera. Behind the visualization section is an led light source.

3. Flow patterns

Tests were conducted for reduced pressures Pr from 0.2 to 0.8 of the critical pressure value. The mass velocities tested were 180, 265, 355 and 445 kg/(m^2·s). Figure 3 shows the flow structures for Pr=0.2, while Figure 4 shows the flow structures for Pr=0.4, Figure 5 shows the structures for Pr=0.6, Figure 6 shows the structures for Pr=0.7 and Figure 7 show flow structures for Pr=0.8. All figures show the same mass velocity of G=355 kg/(m^2·s), which makes it possible to compare the differences in flow structures. Due to the large difference in the specific volume ratio of the liquid and gas phases at a reduced pressure of 0.2, annular flow already occurs at a dryness degree of x=7%, while for a quality of 0.8, annular flow occurs at x=45%. Bubble flow was defined as when bubbles alone are present. Slug flow was defined as when single plugs are present. When the flow is dominated by multiple plugs that are close to merging into a ring, or when the ring was not continuous the flow was defined as intermittent. In Fig. 3, one can observe the slug and annular flow. In Fig. 4 and Fig. 5, bubble, plug, intermittent and annular flows can be observed. Fig. 5, Fig. 8, Fig. 9, Fig. 10 show the flow structures for Pr=0.6 and for mass velocities of G=355 kg/(m^2·s), G=180 kg/(m^2·s), G=265 kg/(m^2·s) and G=445 kg/(m^2·s), respectively. In particular, one can observe the later appearance of ring structure for lower mass velocities. This trend is shown in the flow maps in the next section. For reduced pressures 0.7 and 0.8 bubbles can be observed even when annular follow emerged. This is unique structure which can be only observed at vicinity of thermodynamical critical point.

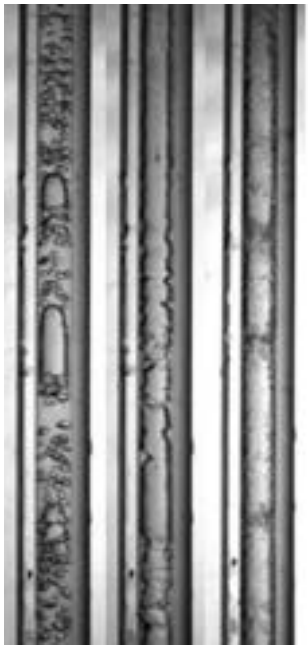

Figure 3. Flow Patterns Pr=0,2 G=355 kg/(m^2·s) Quality respectively: 2%, 7%, 5,03%

Figure 4. Flow Patterns Pr=0,4 G=355 kg/(m^2·s) Quality respectively: 3,1%, 4,2%, 10%, 23,1%, 80,5%

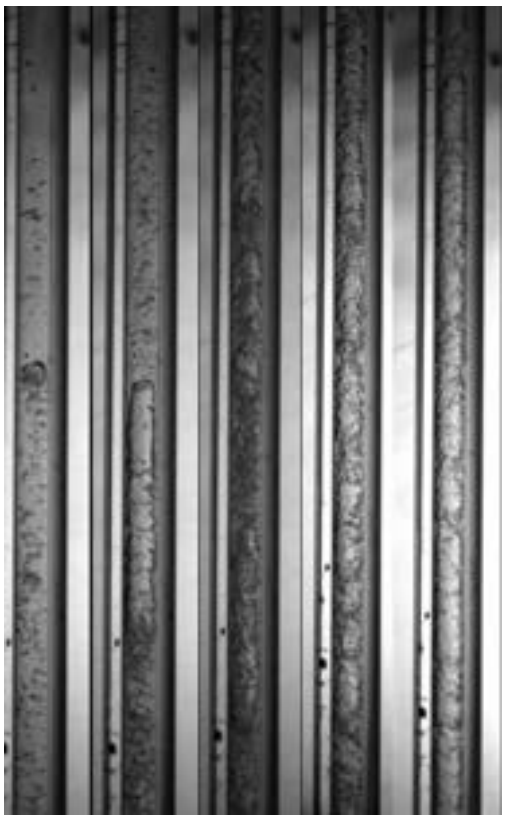

Figure 5. Flow Patterns Pr=0,6 G=355 kg/(m^2·s) Quality respectively: 12%, 15,6%, 19,6%, 23,9%, 36,2%, 60,7%

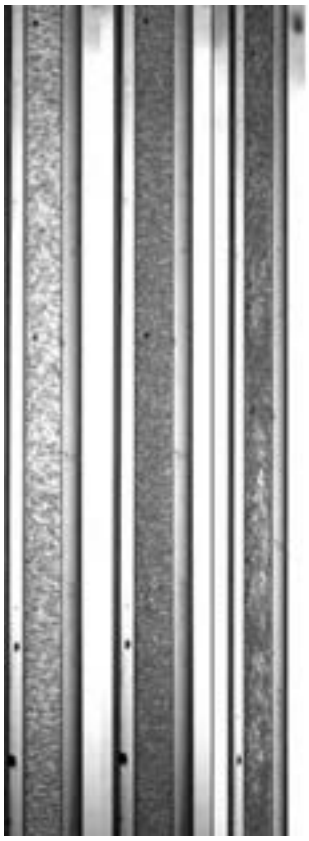

Figure 6. Flow Patterns Pr=0,7 G=355 kg/(m^2·s) Quality respectively: 8.5%, 18.6%, 46%.

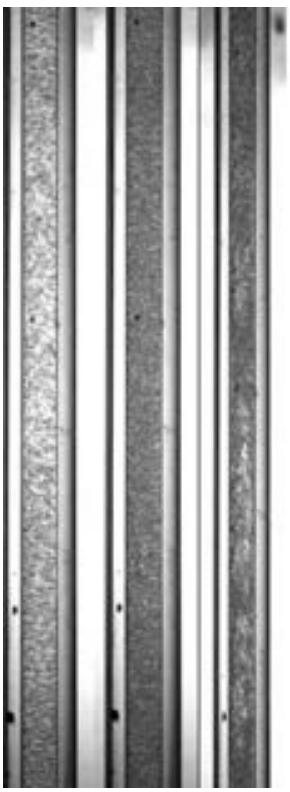

Figure 7. Flow Patterns Pr=0,8 G=355 kg/(m^2·s) Quality respectively: 8.2%, 19%, 33,7%.

Figure 8. Flow Patterns Pr=0,6 G=180 kg/(m^2·s) Quality respectively: 37,2%, 48,6%, 64,6%, 72,8%, 93%

Figure 9. Flow Patterns Pr=0,6 G=265 kg/(m²·s) Quality respectively: 19,6%, 27%, 35,2%, 55,6%

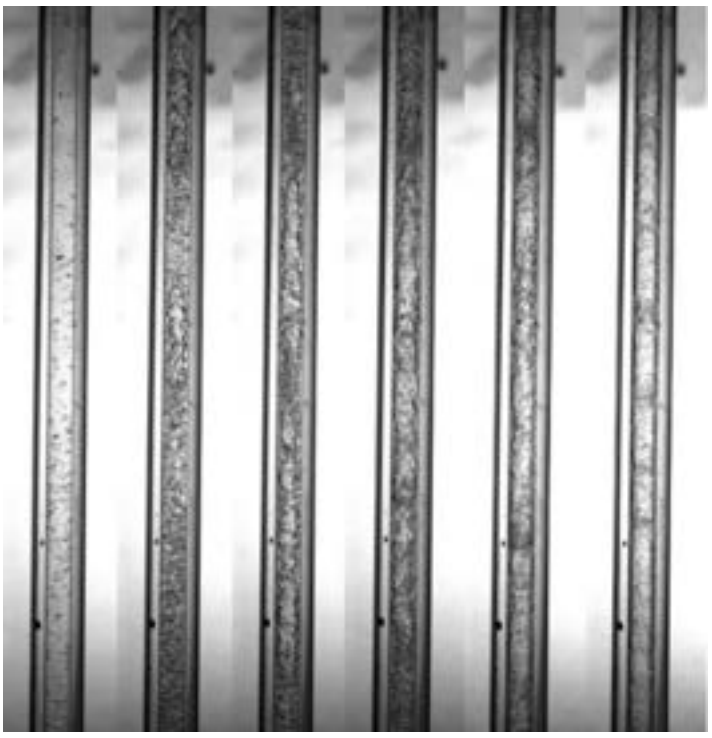

Figure 10. Flow Patterns Pr=0,6 G=445 kg/(m²·s) Quality respectively: 8,5%, 15,9%, 23,7%, 36,5%, 52,4%, 67,6%

4. Flow maps and new annular flow prediction method

In recent years flow maps were primarily presented as Mass flow in function of quality. This presentation method allow to easily compare patterns with experiment and heat transfer coefficient measurements.

4.2. New correlation to determine transition line to annular flow

A new prediction method for determination of flow pattern transition into annular flow is proposed. Its is modification of correlation proposed by Revelin et al. [13] Original correlation presented good prediction at lower values of reduced pressure 0.3 and 0.4 what can be observed in the Figures 12 and 13. Is is good result we take in into account that this method was created for different fluid and different diameter. That correlation is based on fluids R134a and R245fa at 26, 30 and 35 °C saturation temperatures inside 0.5 mm and 0.8 mm diameter glass tube. In the Figure 18 it can be observed that method proposed by Ravelin do not follow trend of annular transition line for different values of reduced pressure. In fact it showed that annular flow occurs fasters at high reduced pressure. Experimental data show opposite trend. Because of that Bond number was introduced to the equation. Bond number represents effect of gravitational forces compared to surface tension forces for the movement of liquid. When significance of surface tension value of this criterial number is higher. Surface tension decreases for higher value of saturation temperature. This change allowed to adapt transition line for all reduced pressures what can be observed in the Fig 18. Formula for transition line between intermittent flow and annular flow is:

$$x_{i/a} = Rel^{1.47}/Wel^{1.23} \cdot Bo^{1.9} \cdot 3.5 \cdot 10^{-7} \quad (1)$$

4.3. Flow maps with transition lines for R1233zd(E)

Fig. 11 shows the flow map for reduced pressure of 0.2, Fig. 12 shows the flow map for Pr=0.3, Fig. 13 shows the flow map for Pr=04, Fig. 14 shows the flow map for Pr=0.5, Fig. 15 shows the flow map for Pr=0.6 Fig. 16 shows the flow map for Pr=0.7, and Fig. 16 shows the flow map for Pr=0.6. Fig. 17 shows the flow map for mass velocity G=355 kg/(m^2*s) as a function of reduced pressure and quality. In Figures 11 through 16, an inverse correlation can be observed between mass velocity and the occurrence of annular flow. Annular flow occurs fastest for a reduced pressure of 0.2, and latest for Pr=0.8. This is a result of the smaller difference between the unit specific volume of the gas phase and the liquid phase, and the lower surface tension of the liquid phase. The delayed occurrence of annular flow also occurs for lower values of mass velocity. 7 correlations for transition of flow pattern into annular flow is presented in the flow maps for various values of reduced pressure and mass velocity. This correlations are proposed by Ong and Thome[12], Revelin and Thome [11],Cheng et al. [3], El Hajal et al. [8]Zhuang et al. [2], Kim and Mundawar [9] and last one is the one

proposed in this article. None of this correlations was created for exact conditions as in experiment conducted by authors. Correlations of El Hajal and Cheng were created for CO_2 for high values of reduced pressure up to 0.8. Zhuang proposed correlation for medium values of reduced pressure for ethane. Other correlations were created for low values of reduced pressure. Correlations proposed by Revelin and Thome and by Ong and Thome showed good results for Pr around0.3 and 0.4. Method proposed by Kim and Mundawar was second best correlation and predicted flow correctly from 0.2 up to 0.5 value of reduced pressure. All correlations expressed correct trend between mass velocity and transition line except from Correlations proposed by El Hajal and Cheng. New correlation correctly predict trends for various value of reduced pressure and various mass velocities.

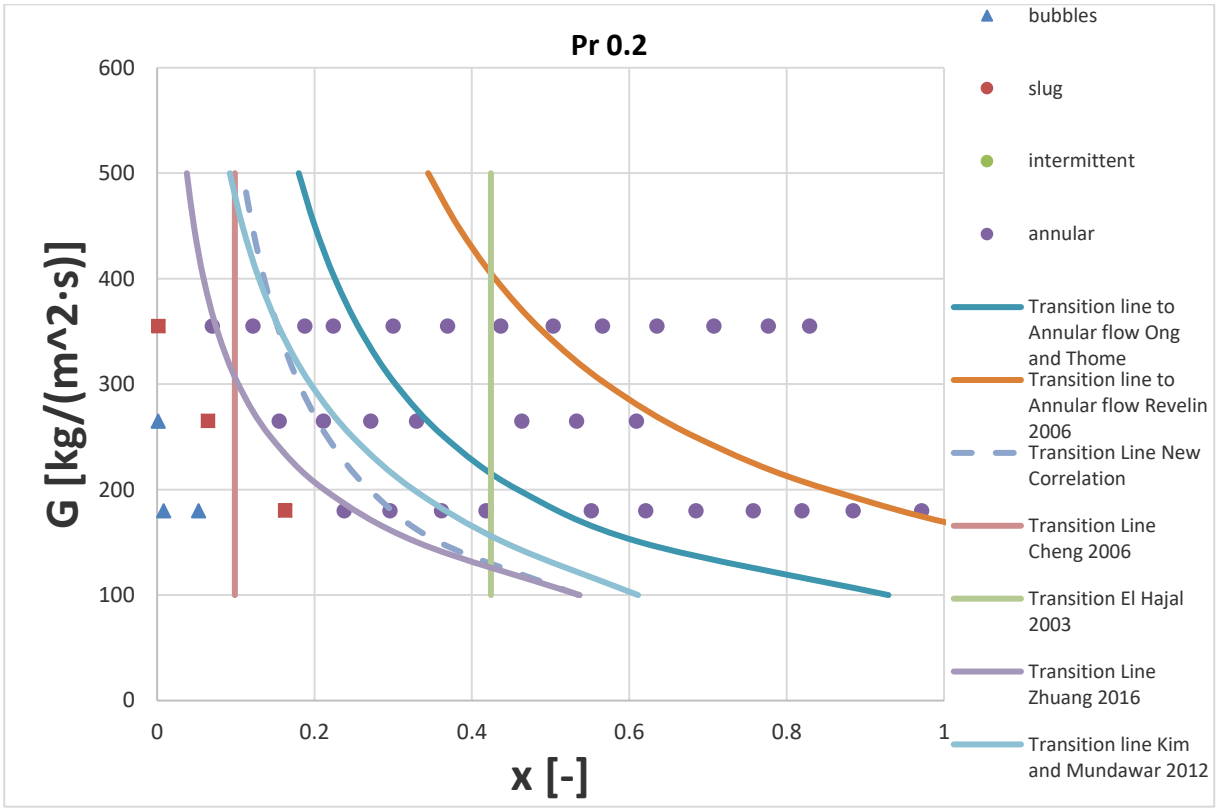

Figure. 11. Flow map for reduced pressure 0.2

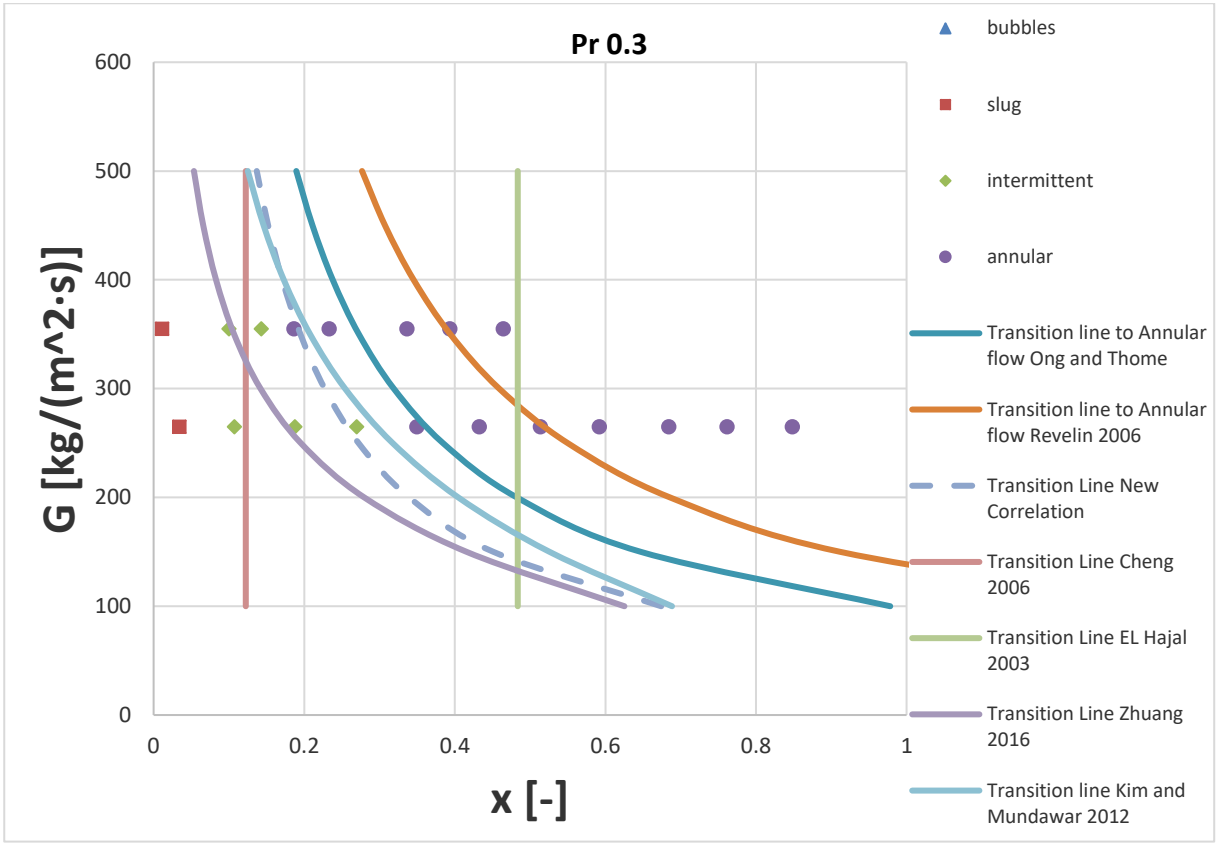

Figure. 12. Flow map for reduced pressure 0.3

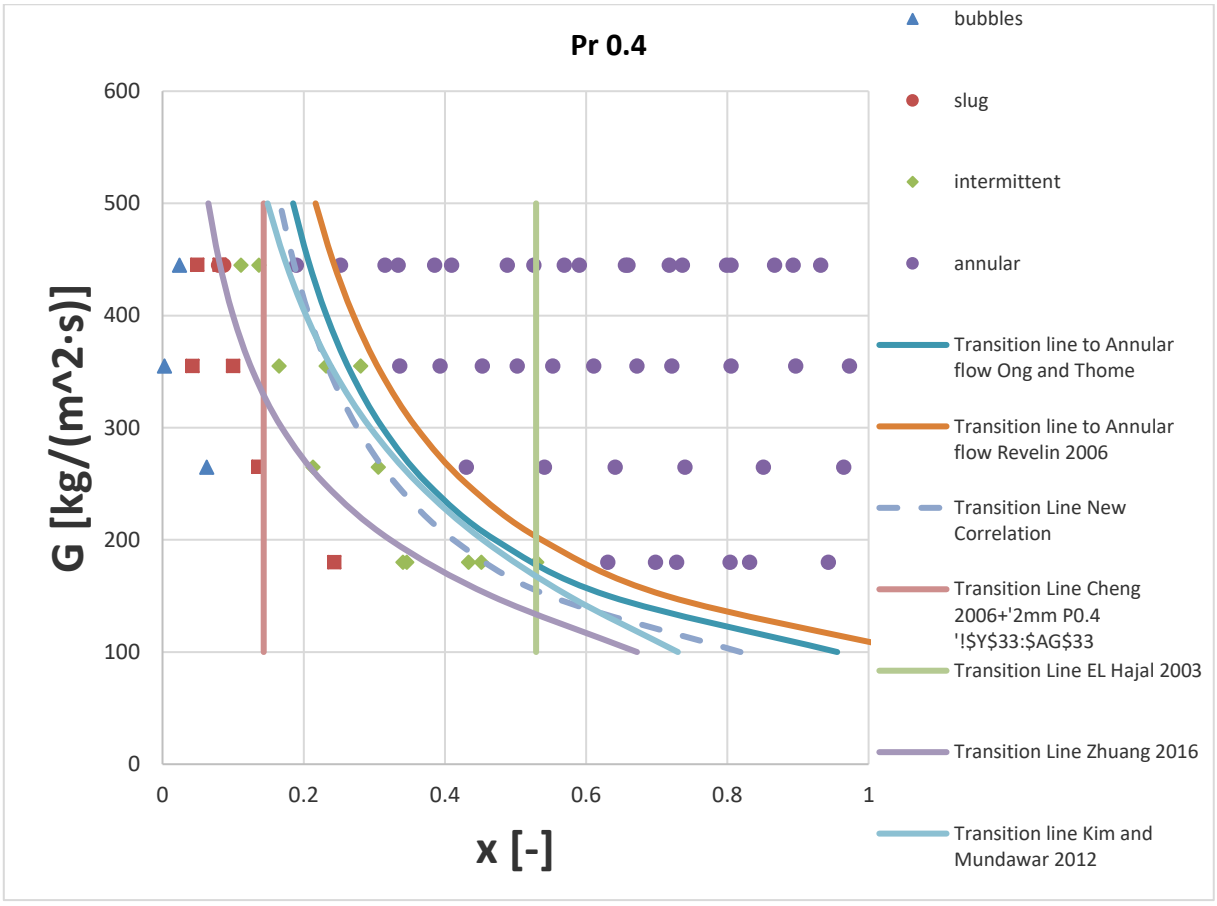

Figure. 13. Flow map for reduced pressure 0.4

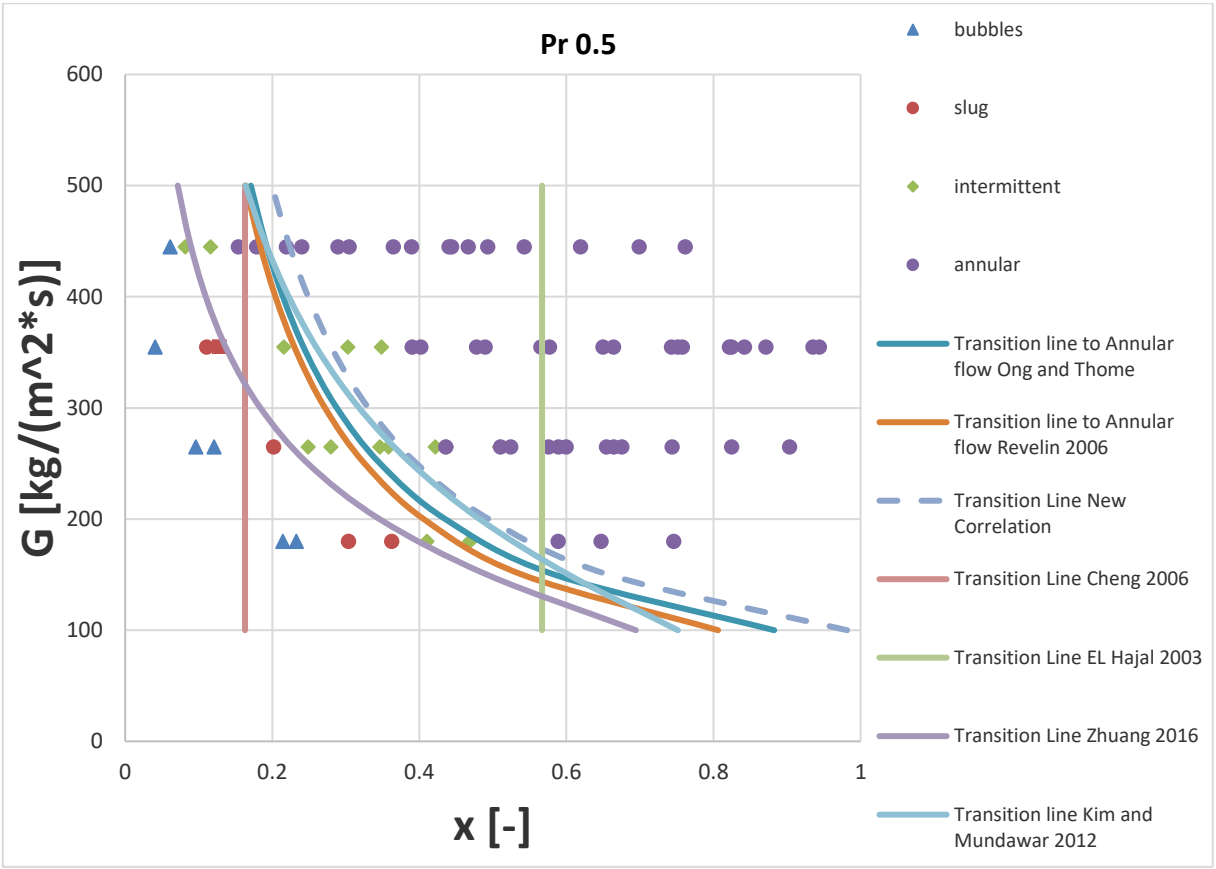

Figure. 14. Flow map for reduced pressure 0.5

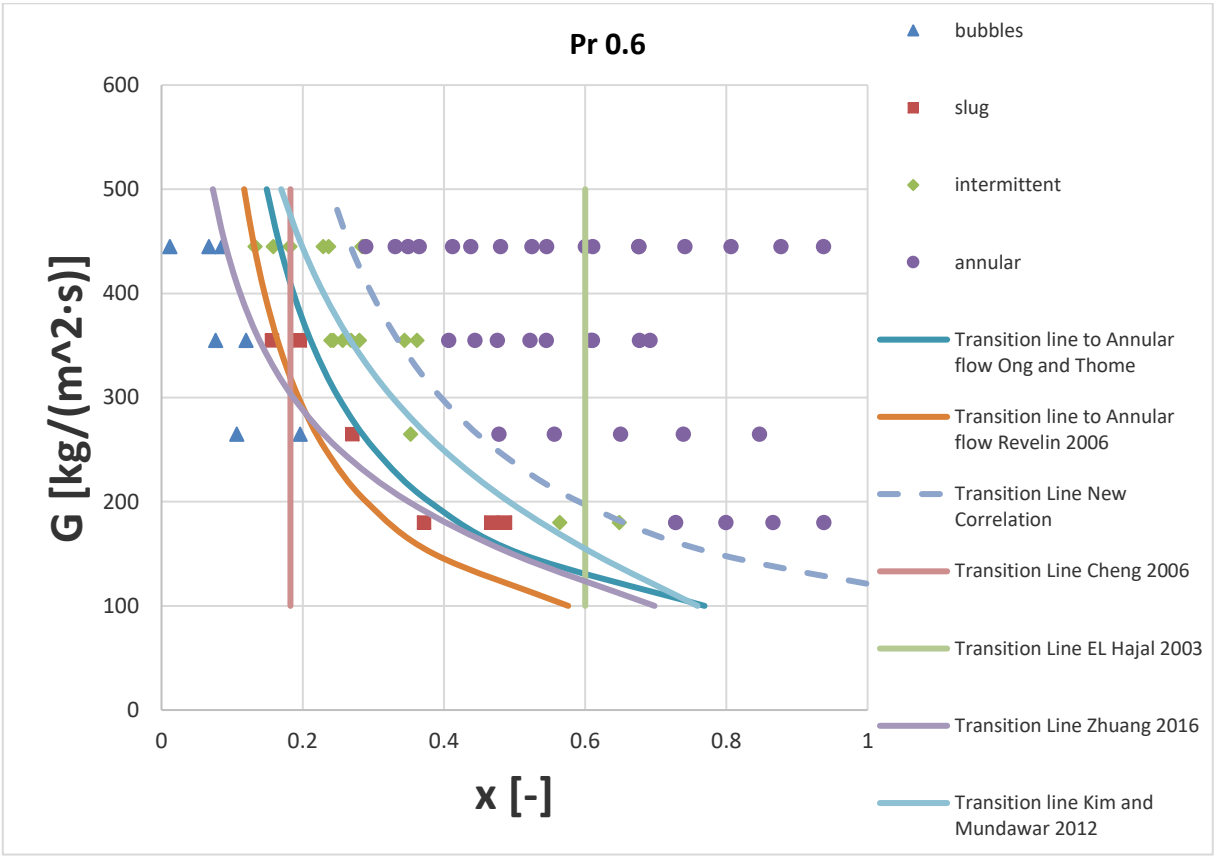

Figure. 15. Flow map for reduced pressure 0.6

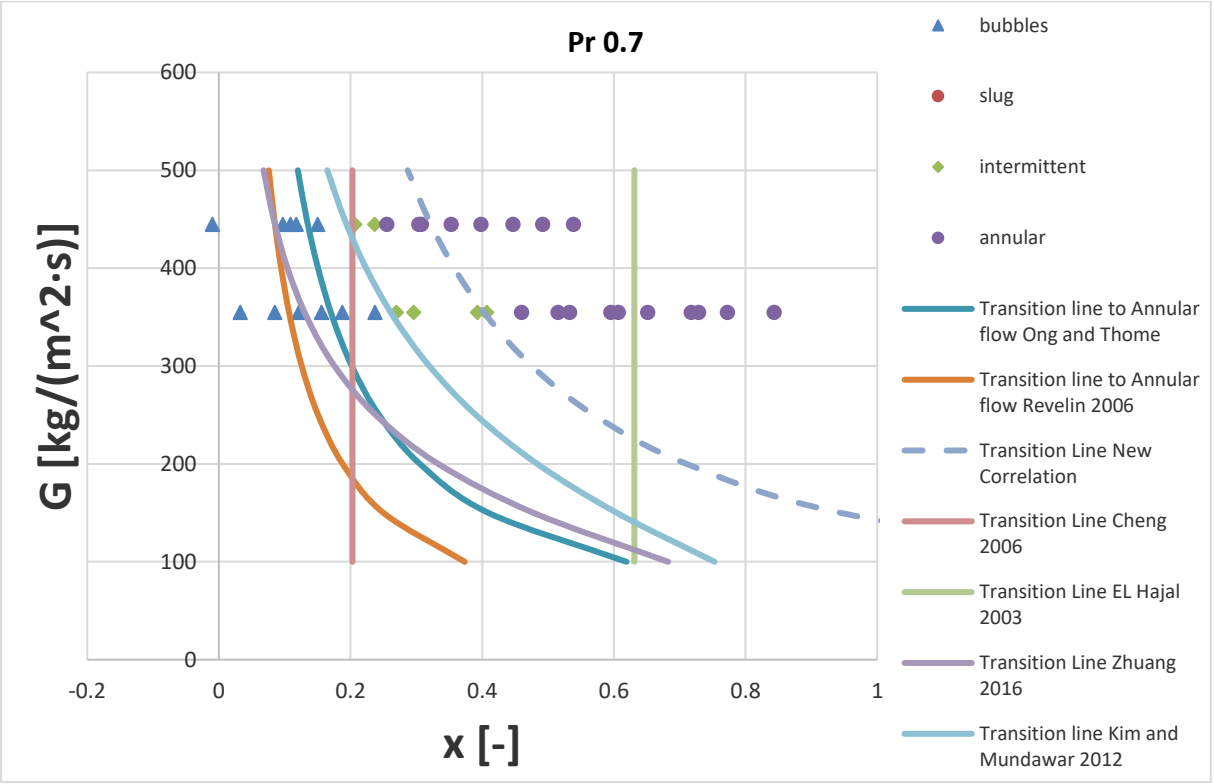

Figure. 16. Flow map for reduced pressure 0.7

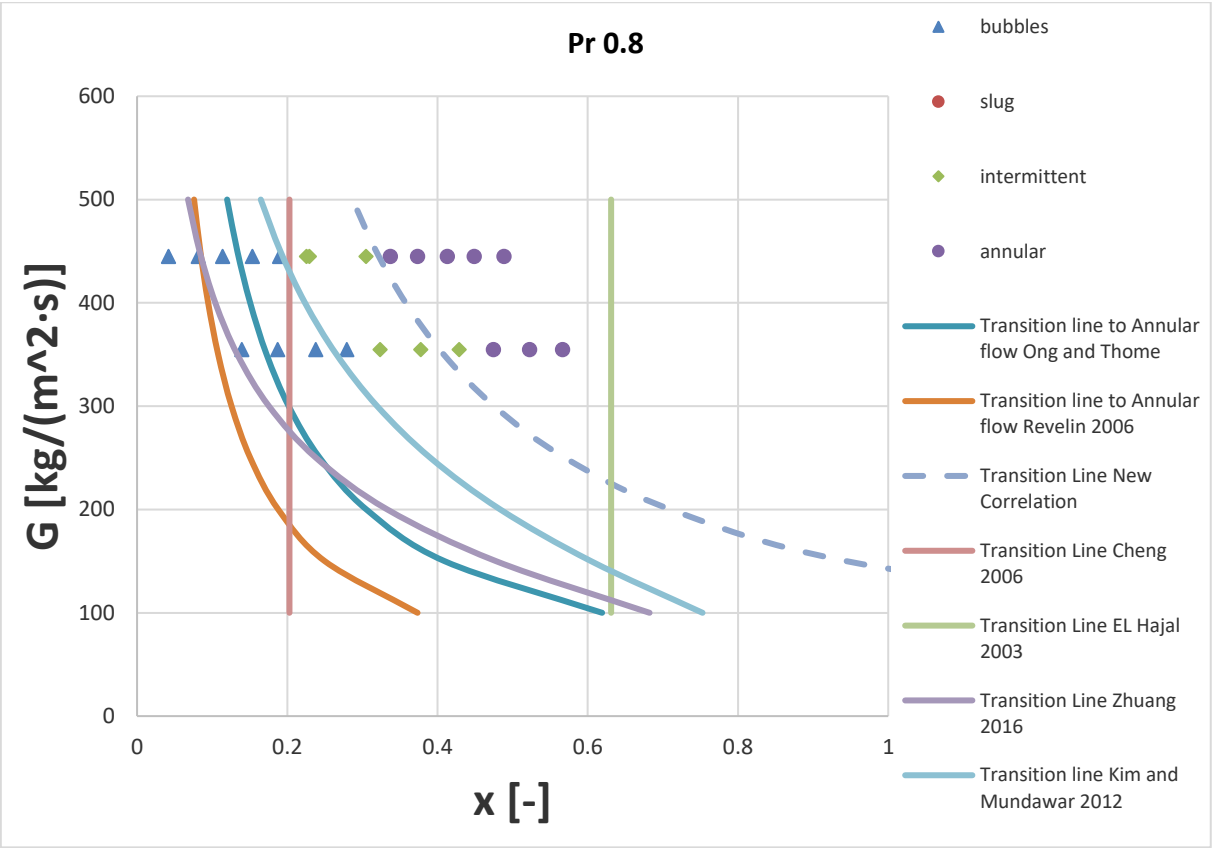

Figure. 17. Flow map for reduced pressure 0.8

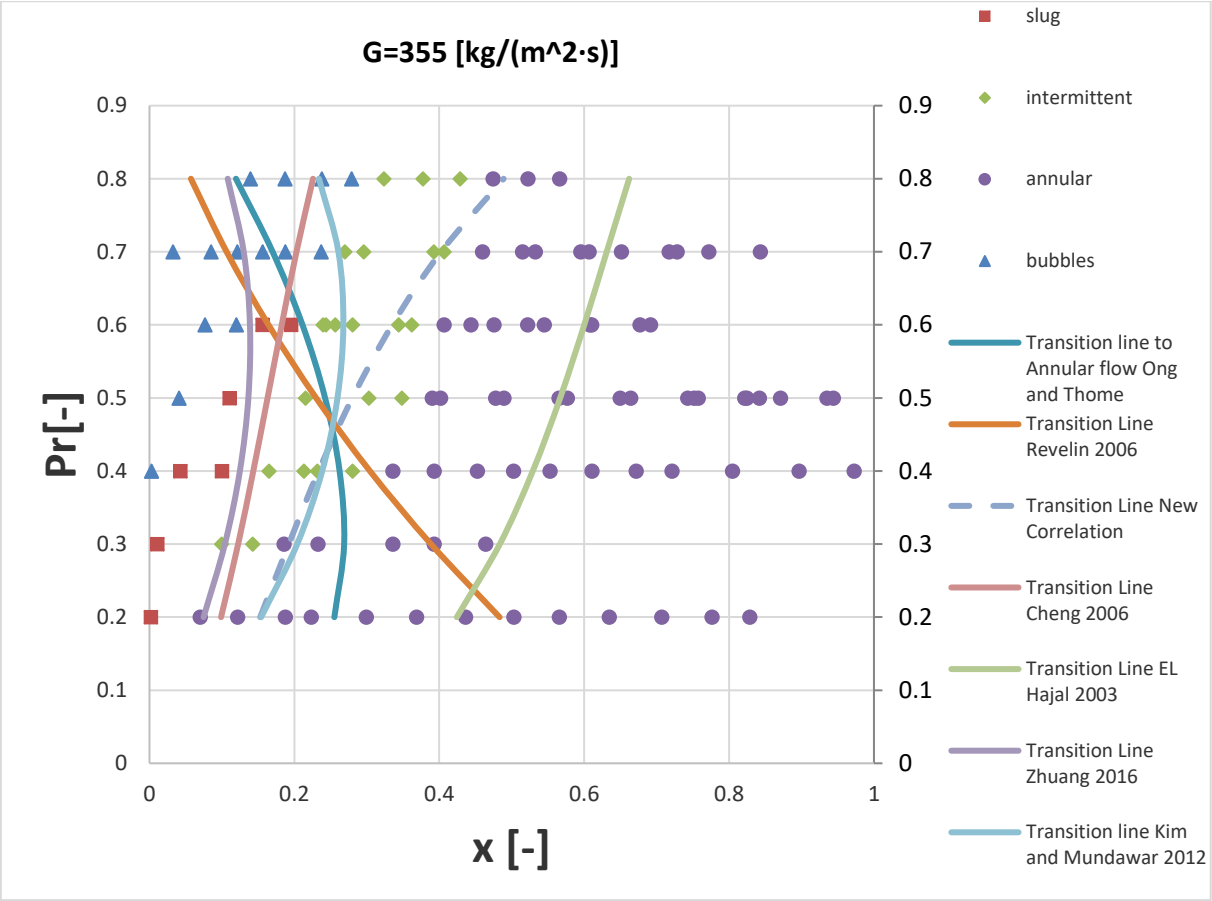

Figure. 18. Flow map for reduced pressure ranging from 0.2 to 0.8 for mass flow 355 [kg/(m^2*s)]

Table 1. Comparison of correlations which predict annular flow for collected database for R1233zd(e).

Correlation	number of experimental data points correctly calculated	percentage of experimental data points correctly calculated
Ong and Thome [12]	238	78.81%
Revelin et al. [11]	214	70.86%
New corelation	276	91.39%
Cheng et al. [3]	236	78.15%
El Hajal et al. [8]	215	71.19%
Zhuang et al. [2]	227	75.17%
Kim and Mundawar [1]	262	86.75%

Comparison of all tested correlations is presented in Table 1. Authors correlation managed to correctly predict 91,39% of collected experimental data points. Second best is correlation presented by Kim and Munawar [1] which predicted 86.75% points. Other correlations managed to predict from 70% to 75% of data point despite not being able to follow experimental transition lines.

4.3. Applicability of new correlation for different fluids.

Applicability of new correlation for different fluids was tested on data collected by Charnay et al.[5,6]. Authors correlation follow experimental transition trend also for this fluid. Experimental lines for all correlations are presented in the Fig 19. Data is presented as function of Reduced pressure and quality

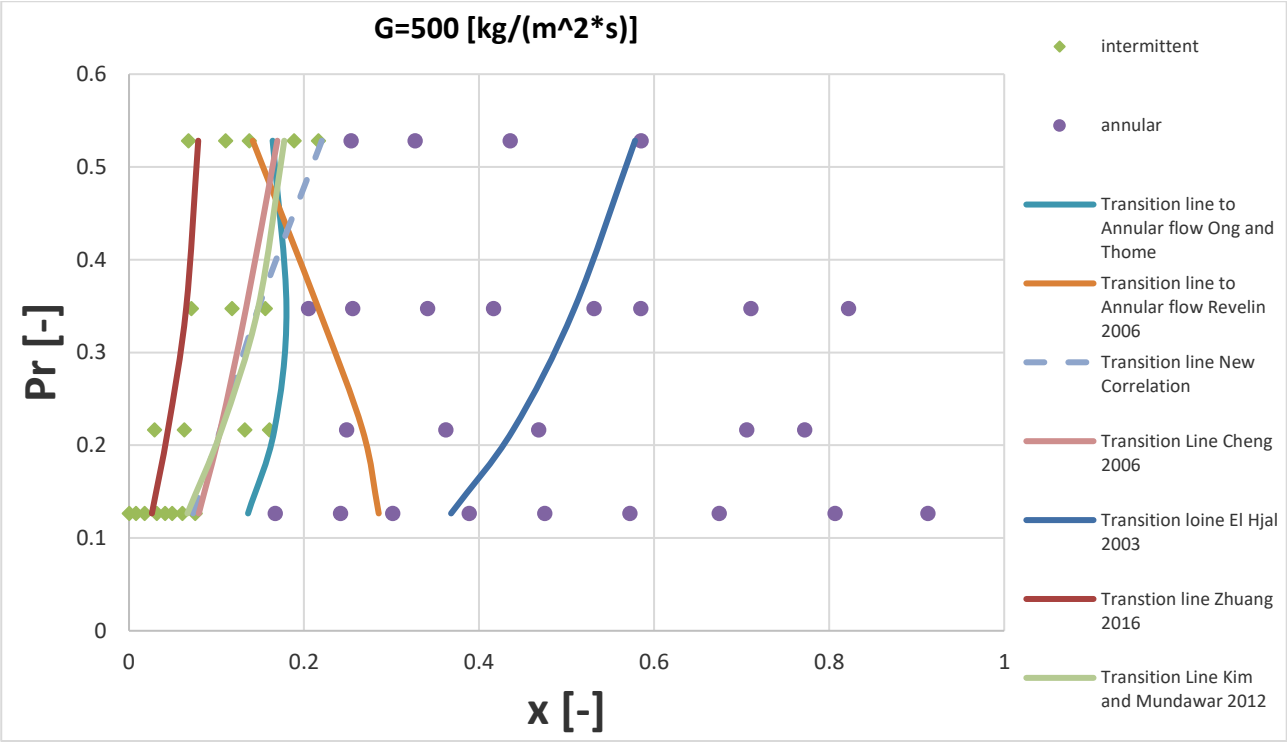

Figure. 19. Flow map for reduced pressure ranging from 0.13 to 0.53 for mass flow 500 [kg/(m^2*s)] for R245fa collected by Charnay et al. [5,6]

5. Conclusions

The change in the physical properties of refrigerants as the saturation temperature increases has a major impact on structures and flow maps. At high values of reduced pressure, the density of the gas phase is relatively high, and the density of the liquid phase is low. There is a low specific volume difference between the liquid and gas phases. These properties cause a delay in the occurrence of annular flow. For reduced pressure 0.8 annular flow occurred at 45% of quality for G=355 [kg/(m^2*s)] and for reduced pressure 0.2 it was visible at 7% of quality. Since the presence of bubbles in the flow occurs for much higher quality at higher reduced pressures nucleation as a heat transfer mechanism is more important for boiling at high saturation temperatures. It is also worth noting the delayed occurrence of annular flow for lower values of mass velocity. Further work should focus on expanding the experimental database. Old correlations for annular transitions lines prediction did not manage correctly to predict transition of flow pattern to annular flow for high reduced pressures. Most of them predicted trend opposite to measured for increasing saturation pressure. They predicted that annular flow occurs faster for high values of reduced pressure, but in fact annular flow occurs later for high saturation pressure. New correlation for annular flow transition line is able to predict transition form intermittent flow into annular flow for all measured reduced pressures and mass velocities. Authors correlation managed to correctly predict 91,39% of collected experimental data points what is best results of all tested correlations.

Nomenclature

Bo Bond, -

G mass velocity, kg/(m^2*s)

Pr reduced pressure -ratio of pressure to critical pressure, -

Rel Reynolds number for saturated liquid $Rel = \frac{GD}{\mu l}$, -

Rev Reynolds number for saturated vapour $Rev = \frac{GD}{\mu v}$, -

t temperature, °C

Wel Weber number for saturated liquid $Wel = \frac{G^2 D}{\rho l}$, -

x Quality, -

Acknowledgements

This research was funded in whole or in part by National Science Centre, Poland 2017/25/B/ST8/00755
This research was funded in whole or in part by National Science Centre, Poland 2021/41/N/ST8/04421

References

[1] Kim S.M., Mudawar I., Flow Condensation in Parallel Micro-Channels - Part 2: Heat Transfer Results and Correlation Technique. International Journal of Heat and Mass Transfer 2012;55:984–994.

[2] Zhuang X., Gong M., Chen G., Zou X., Shen J., Two-Phase Flow Pattern Map for R170 in a Horizontal Smooth Tube. International Journal of Heat and Mass Transfer 2016;102:1141–1149.

[3] Cheng L., Ribatski G., Wojtan L., Thome J.R., New Flow Boiling Heat Transfer Model and Flow Pattern Map for Carbon Dioxide Evaporating inside Horizontal Tubes. International Journal of Heat and Mass Transfer 2006;49:4082–4094.

[4] Nema G., Garimella S., Fronk B.M., Flow Regime Transitions during Condensation in Microchannels. International Journal of Refrigeration 2014;40:227–240.

[5] Charnay R., Revellin R., Bonjour J., Flow Pattern Characterization for R-245fa in Minichannels: Optical Measurement Technique and Experimental Results. International Journal of Multiphase Flow 2013;57:169–181.

[6] Charnay R., Bonjour J., Revellin R., Experimental Investigation of R-245fa Flow Boiling in Minichannels at High Saturation Temperatures: Flow Patterns and Flow Pattern Maps. International Journal of Heat and Fluid Flow 2014;46:1–16.

[7] Barbieri P.E.L., Jabardo J.M.S., Bandarra Filho E.P., Flow Patterns in Convective Boiling of Refrigerant R-134a in Smooth Tubes of Several Diameters. European Thermal-Sciences Conference 2008;9.

[8] El Hajal J., Thome J.R., Cavallini A., Condensation in Horizontal Tubes, Part 1: Two-Phase Flow Pattern Map. International Journal of Heat and Mass Transfer 2003;46:3349–3363.

[9] Kim S.M., Kim J., Mudawar I., Flow Condensation in Parallel Micro-Channels - Part 1: Experimental Results and Assessment of Pressure Drop Correlations. International Journal of Heat and Mass Transfer 2012;55:971–983.

[10] Soliman H.M., On the Annular-to-wavy Flow Pattern Transition during Condensation inside Horizontal Tubes. The Canadian Journal of Chemical Engineering 1982;60:475–481.

[11] Revellin R., Thome J.R., Experimental Investigation of R-134a and R-245fa Two-Phase Flow in Microchannels for Different Flow Conditions. International Journal of Heat and Fluid Flow 2007;28:63–71.

[12] Ong C.L., Thome J.R., Macro-to-Microchannel Transition in Two-Phase Flow: Part 1 - Two-Phase Flow Patterns and Film Thickness Measurements. Experimental Thermal and Fluid Science 2011;35:37–47.

[13] Revellin R., Dupont V., Ursenbacher T., Thome J.R., Zun I., Characterization of Diabatic Two-Phase Flows in Microchannels: Flow Parameter Results for R-134a in a 0.5 Mm Channel. International Journal of Multiphase Flow 2006;32:755–774.

Analysis of first-order model for thermistors in compressible flows temperature measurement

Jorge Valencia-Santana[a], Carlos Mendieta-Pino[b], Alejandro Ramos-Martín[c] and Vicente Henríquez-Concepción[d]

[a] University Institute of Intelligent Systems and Numeric Applications in Engineering, University of Las Palmas de Gran Canaria, Spain, jorge.valencia101@alu.ulpgc.es, (CA)
[b] Process Engineering Department, University of Las Palmas de Gran Canaria, Spain, alejandro.ramos@ulpgc.es
[b] Process Engineering Department, University of Las Palmas de Gran Canaria, Spain, carlos.mendieta@ulpgc.es
[b] Process Engineering Department, University of Las Palmas de Gran Canaria, Spain, vicente.henriquez@ulpgc.es

Abstract:
Thermal variation is assumed to be one of the main source of uncertainty in dimensional measurements and must be controlled in order to analyse and quantify its possible effects. Therefore, as the analysis of temperature control is influenced by different complex non-linear heat transfer effects, the study of this variable is considered a highly application dependent measurement problem. However, temperature measurement devices are often designed primarily to increase their durability, so they remain vulnerable to transient effects. Hence, improvements in mathematical models of general purpose temperature sensors through the knowledge of its response in the application would significantly improve their performance and accuracy.

Keywords:
Thermistor response, Heat transfer, Dynamic response, First-order models.

1. Introduction

One of the coins used to determine the macroscopic state of a system is determined by means of an intensive property known as temperature. This variable has an important dependence on statistical concepts and, for the moment, we shall regard the temperature to be an empirical quantity, measured by a device, such that temperature is proportional to the expansion [1] that occurs whenever energy is added to matter by means of heat transfer. This concept can be understood by imagining a thermometer, where thermal expansion is: liquid metal in a long glass tube, bending of a bimetallic strip or resistivity variation of a semiconductor, among others.
Thermal variation [2] is assumed to be the main source of uncertainty in dimensional measurements and, given these influences, the control of this variable is considered to be a highly application-dependent measurement problem. In fact, it is also known that heat transfer analysis and temperature control is very useful in many engineering systems and that, under stationary conditions, its value does not vary with time at a given point. In contrast, under non-stationary [3] or transient conditions, the temperature varies with time. However, under stationary conditions, effects such as self-heating can occur. For this reason, Darkhaneh [4] proposes a way to quantify the error caused by thermistor self-heating, as it is a problem that generates uncertainty in temperature measurement. In addition, there are areas of thermistor operation that it is preferable to avoid due to certain effects such as blowup, as pointed out in their respective studies by Antontsev and Chipot [5] and Barabanova [6].
On the other hand, nowadays, the precise measurement of the thermal properties of materials is mainly done on the centimetre or millimetre scale [7,8]. It is clear that the miniaturisation of sensors brings undeniable advantages, such as: lower thermal inertia; limited invasiveness of the system to be characterised, which is therefore less disturbed by the sensor; and the possibility of using small amounts of material, which is highly desirable in nanotechnologies, for example. Thus, in this document we refer to miniature sensors as sensor elements whose main dimensions are of the order of a millimetre.
Other problems has been observed that for certain applications involving convection mechanisms, especially in the study of turbulent flows, phenomena are detected during temperature monitoring that introduce uncertainty and lead to confusion in the processes to be analysed. The measurement of transient heat transfer is very important in various areas of scientific importance including the determination of engine temperature,

aerodynamic vehicle temperature in a high velocity flow environment, mentioned by Sanjeev and Kumar [9,10]. From the point of view of analysing the turbulent effects that can occur and generate uncertainty in the temperature measurement, we can refer to the smallest known scale, the Kolmogorov scale. This is the smallest turbulent motion [11] present in a flow and is the scale at which energy is dissipated by molecular viscosity. Taking into account the formation of vorticity at certain points close to the measurement points, near-wall turbulence effects can be considered, as well as the ratio of the velocity and thermal boundary layer established by the Prandtl number.

Hence, improvements in the response of general-purpose temperature sensors through the compensation for response delay would significantly improve their performance and applicability, like mention Tagawa et al. [12]. Thus, this work proposes an experiment to study the turbulence and vorticity generated through the stagnation of a device exposed to an air stream. A device inmersed into the airstream has two built-in thermistors that will measure the stagnation temperature and the static temperature (Fig. 3). In these experiments, it can be seen that an effect is produced that goes against the theory presented and this phenomenon can be associated with a fraction of energy that is dissipated through the leads of the thermistor. This is then corroborated by a series of additional tests in different media with different heat transfer coefficients. Then, this experiment is presented from a mathematical point of view, studying and analysing the effectiveness of first-order models for cases where the sensors are in an airstream. These models provide the necessary tools to approximate real behaviour and by means of a developed algorithm (depending on the selected conditions) it is possible to simulate a thermistor response similar to that of the experiment. However, as will be contrasted with the other tests performed, in certain applications they do not have the necessary precision and induce error in the measurements.

One of the main motivations for the development of this work is that temperature measurement devices are often vulnerable to these transient effects, as they are primarily designed to increase their durability. However, the moderating industry demands smaller and smaller, non-invasive measuring devices for many applications. More accurate measurements of thermal conditions are therefore a real challenge as these companies are demanding more and more complex and precise systems. Accordingly, identifying a suitable mathematical model and the effects that occur in temperature sensors will allow us to evaluate a way to study the effects of turbulence and heat transfer and to be more aware of transient effects.

In the current paper, as a first point of departure, a series of theoretical concepts involved in the test carried out will be described. This is followed by a detailed explanation of the general first-model with the formulation of the governing equations. Next, the description of experiment that has led to the hypotheses put forward in relation to the observed phenomena. Then, the results obtained from such equations will be compared with those of real measurements, thus explaining the phenomena that cause such behaviours. Finally, some perspectives of future are exposed with the conclusions obtained.

1.1. Boundary layer: hidrodynamic and thermal

It is obvious to think that the temperature distribution obtained around a body immersed in a stream will have a similar character to the distribution of velocities in the various layers of a fluid. Therefore, in a flow over a heated surface, both the velocity boundary layer and the thermal boundary layer develop simultaneously (Fig. 1).

This concept of boundary layer was introduced into the science of fluid mechanics by L. Prandtl at the begining of the last century: it has probed to be very fruitful.

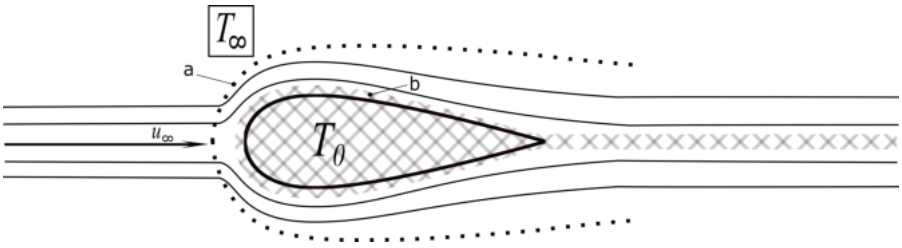

Figure 1: Analogy between temperature and vorticity distribution in the neighbourghood of a body placd in a stream of fluid.

In the Fig. 1, **a** and **b** correspond to the limits of the temperature increase; **a** for low speeds and **b** for high speeds. It should be noted that in the convective transport mechanism two processes take place, the diffusion of heat by the randomly moving molecules in the fluid and the advection of heat due to the overall motion of the fluid. As the molecules of the whole maintain their random motion, the total heat transfer is due to a superposition of the energy transport due to the motion of the molecules and the global motion of the fluid that takes place. Thus, if we imagine a solid body placed in a fluid stream and heated so that its temperature

remains above the surrounding environment, then it is clear that the temperature of the stream will increase only in the layer closest to the boda and in a narrow wake behind it, as shown in Fig. 2. Therefore, the greatest diffusion from the hot body to the surroundings occurs in the layers closest to the hot body, which, in accordance with the flow phenomenon, can be called the thermal boundary layer.

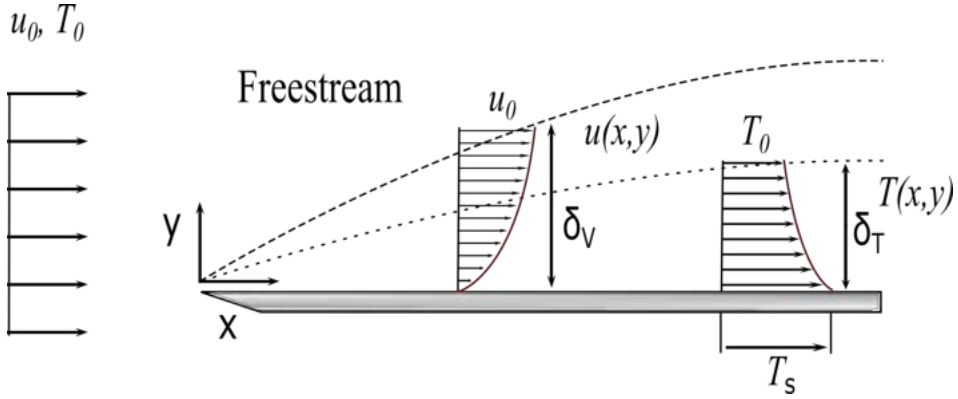

Figure 2: Hidrodynamic and thermal boundary layer.

The thickness of the thermal boundary [13] layer (ΔT) at any location along the surface is defined as the distance from the surface at which the temperature difference ($T - T_s$) is equal to $0.99 \cdot (T_0 - T_s)$, which establishes some relationship to the velocity boundary layer. So, it can be said that the rate of convective heat transfer anywhere along the surface is directly related to the temperature gradient at that location. Hence, the shape of the temperature profile of the thermal boundary layer imposes convective heat transfer between the solid surface and the fluid flowing over it. Since the fluid velocity will have a strong influence on the temperature profile, the development of the velocity boundary layer relative to the thermal boundary layer will have a strong effect on the convective heat transfer. So, it is evident that flow phenomena and thermal phenomena interact to a high degree.

1.2. Temperature increases through adiabatic compression; stagnation temperature.

Temperature changes caused by dynamic pressure variation in a compressible fluid are important from the point of view of heat transfer. In particular, it seems useful to compare the difference in temperatures resulting from heat generation by friction with those caused by compression. For this reason, if we look at Fig. 1, it is logical to think that if the velocity varies along the contour, the temperature will also vary along the shape. If we assume an adiabatic and reversible process due to the low value of conductivity and the high right rate of change in the thermodynamics propierties of state will, in general, prevent any apreciable exchange of heat with the sorroundings. Then, the temperature increase (ΔT) which occurs at the stagnation point of a body in a fluid stream and that is due to the compression that is generated when the fluid makes contact with the solid, as can be deduced from Fig. 1.

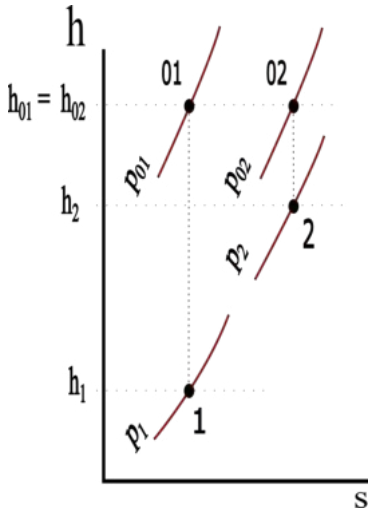

Figure 3: h-s diagram.

The h-s diagram indicates that the stagnation enthalpies - total energy level - are constant, but the area of interest focuses on the static variables and the kinetic energy terms. Thus, it is possible to know the energy state of the fluid and to determine the conditions that are introducing uncertainty into the temperature measurements.

2. First-order model

As mentioned in the introduction, the first model corresponds to the classical approach proposed by the manufacturer to obtain the thermistor properties. It is therefore a generic model that encompasses any situation to which the sensor is subjected. In other words, this type of proposal does not focus on the heat flow through the wires, as well as other thermophysical parameters.
Accordingly, a scenario showing a thermistor immersed in airstream and the heat transfer due to convection process between sensor and surrounding is shown in Fig. 4. In this schematic, it can be seen that the thermistor is in an environment whose fluid temperature is (T_∞) and surrounding temperature (T_{sur}). Also, the boundary layer around of thermistor (control volume) has an associated a convective resistance (R_h).
On the other hand, at this point, it is important to point out that the influences of radiation heat transfer ($\dot{q}_r$) , as well as the self heating (S_h) producing in the thermistor are of minimal relevance in this study, as will be discussed in the conclusions section. Therefore, for now we will focus on the determination of the convection ($\dot{q}_h$) phenomena.

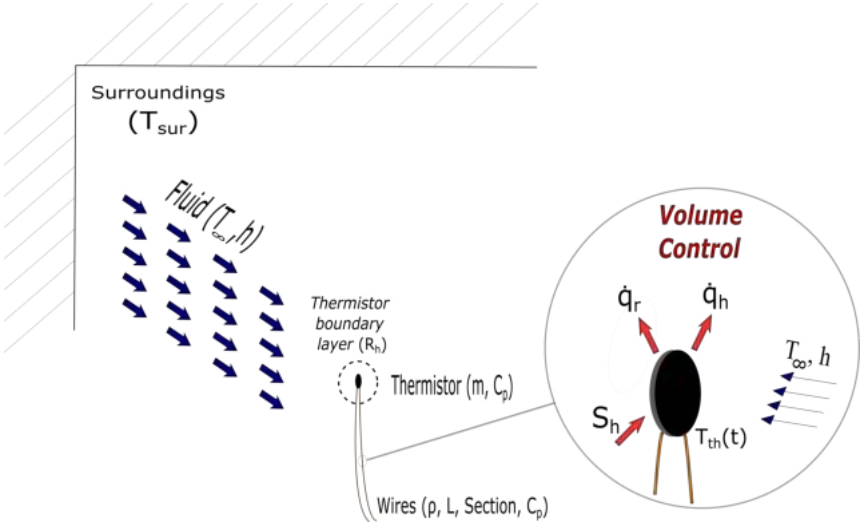

Figure 4: First-order model diagram.

Then, from the energy balance in the control volume (CV) of the last diagram, is deduced:

$$-\dot{q}_h = m \cdot c_p \cdot \frac{dT_{th}}{dt} \tag{1}$$

Keep in mind the minus sign of the equation means that the heat transfer is gave up to surrounding area.
By the other hand, the Newton´s cooling law is:

$$\dot{q}_h = h \cdot A \cdot (T_{th}(t) - T_\infty) \tag{2}$$

So, substituting Eq. (2) into Eq. (1) and developing, it is obtained:

$$-h \cdot A \cdot (T_{th}(t) - T_\infty) = m \cdot c_p \cdot \frac{dT_{th}}{dt} \tag{3}$$

$$(T_{th}(t) - T_\infty) + \frac{m \cdot c_p}{h \cdot A} \cdot \frac{dT_{th}}{dt} = 0 \tag{4}$$

$$(T_{th}(t) - T_\infty) + \tau \cdot \frac{dT_{th}}{dt} = 0 \tag{5}$$

At this point, a linear time-invariant system (LTI) is founded. By this:

$$\frac{1}{\Delta T_{th}} \cdot dT = -\frac{1}{\tau} \cdot dt \tag{6}$$

$$\Delta T_{th_1} = \Delta T_{th_2} \cdot e^{-t/\tau} \tag{7}$$

$$T_{th_1} = (T_{th_2} - T_\infty) \cdot e^{-t/\tau} + T_\infty \tag{8}$$

If $t = \tau$, the equation is:

$$\frac{(T_{th_1} - T_\infty)}{(T_{th_2} - T_\infty)} = 0.632 \tag{9}$$

That is, the time period during which temperature effectiveness ($T_{th_1} - T_\infty$) becomes 63.2% of the temperature width ($T_{th_2} - T_\infty$) is taken as τ.

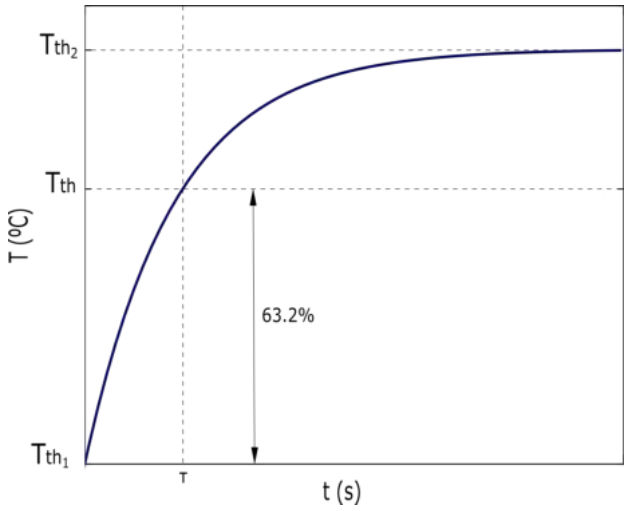

Figure 5: Thermal time constant.

2.1. Thermal-electrical analogy for first-order model

Generally, the manufacturer proposes a first order system as the characteristic response of a temperature sensor. This kind of representation makes it possible to show mathematically and in a simple manner how the thermistor (T_A) behaves over time when an external heat source (E_s) is applied to it. However, this model omits some effects that may be of special interest for the phenomena described in the previous paragraphs. Nevertheless, as a first analysis, to which certain terms will later be introduced and compared, this model is presented in which a series of conditions will be taken into account. Thus, as proposed by Sanjeev and Kumar in [7], the one-dimensional (1D) heat transfer equation for a semi-infinite solid body can be a starting point to obtain the value of the transient temperature at the sensor surface. So, from the schematic shown in Fig. 4, does not involve heat flow through the wires ($\dot{q}_c$), radiation heat transfer ($\dot{q}_r$) and the self heating (S_h). Thus, using the electrical analogy for the study of the heat transfer of a system, this first-order model results as follows:

For this case, initially only convective resistance of the CV (R_h) and heat capacity of thermistor (C_1) will be taken into account.
Therefore, from the energy balance at point A it is obtained:

$$E_s - \dot{q}_h = C_1 \cdot \frac{dT_A}{dt} \tag{10}$$

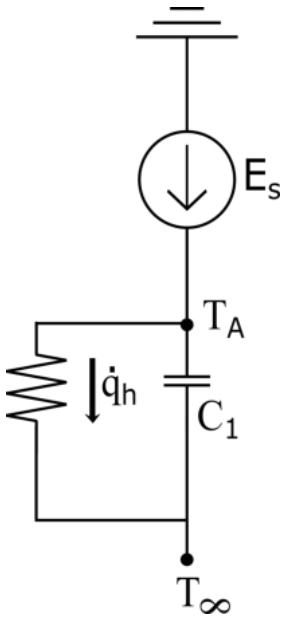

Figure 6: Thermal-electrical diagram for first-order model.

The Newton´s cooling law is:

$$\dot{q}_h = h \cdot A \cdot (T_A - T_\infty) \tag{11}$$

Then, substituting the Eq. (11) into Eq. (10) and developing the result according ours considerations it is obtained:

$$\frac{C_1}{h \cdot A} \cdot \frac{dT_A}{dt} + (1 + \frac{1}{h \cdot A \cdot R_1}) \cdot T_A - \frac{1}{h \cdot A} \cdot H_s = 0 \tag{12}$$

Where the term ($\frac{C_1}{h \cdot A}$) is the known thermal time constant (τ). The form of which is as follows:

$$a_2 \cdot y' + a_1 \cdot y + a_0 = 0 \tag{13}$$

Each coefficient accompanying the variable corresponds to those in Eq. (12), so they must be taken into account in the solution. Also, the b term in the following equation is related to the amplitude of the external heat source (E_s). This turns out to be a first order linear ordinary differential equation, the solution of which is:

$$T_A = b \cdot e^{(-a_1/a_2) \cdot t} - \frac{a_0}{a_1} \tag{14}$$

As mentioned in the section on the thermal time constant, this Eq. (14) can be divided into a heating and a cooling stage, thus obtaining two responses with corresponding time constants. Obviously, this depends on the external source, among other factors, so we will focus on the generic equation as such.

3. Overview of experimental procedure.

The way to relate the study of turbulence and heat transfer is for the thermistor to be excited by an external source that causes the same disturbances and uncertainties as the vortices in an air current. Thus, in order to identify the limitations to which these temperature sensors are subject, a device and an experiment are designed to study their behaviour. This test consists of placing two thermistors in a small tube so that each sensor measures a different temperature: static temperature (T_1) and stagnation temperature (T_{01}). This refers to the diagram presented in Fig. 3.
Finally, this device is placed inside an isolated tube through which an airstream circulates.
The morphology of the described device is schematically represented in the following image.

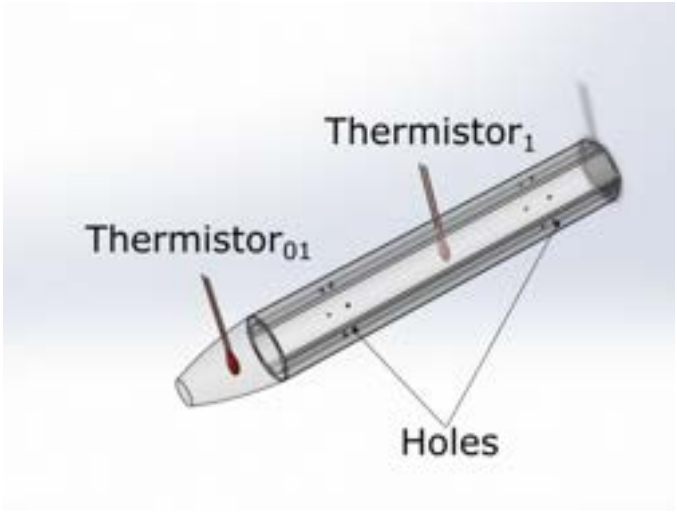

Figure 7: Sensor.

Figure 8: Sensor.

Fig. 8 below shows the actual assembly of the device:
Some parameters of the thermistor used in the experiment are shown in the Table 1 but, the most important one is the thermal time constant that will be compared with the numerical solution proposed.

The airstream is produced by fan controlled by a microcontroller. Inside of the tube there is the device with two thermistors NTC that read the different temperature changes (T_{01}) and (T_1). Also, there is an additional thermistor outside that reads atmosphere temperature but is not integrated in the system as its value is merely informative. These values, are reading using an integrated development environment. With this, it is possible to collect and show data comming from microcontroller.
Regarding to data acquisition, we have these devices:

- An adaptative stage of signal (Voltage divider): consists of $10k\Omega$ resistors and the power supply ensures a constant voltage of 5V.
- An analogical to digital converter of 16 bits (ADS1115 Texas Instruments): will allow a higher accuracy of

Table 1: Parameters of NTC thermistor used.

Parameter	Value
Resistance at 25 ºC	10.000Ω ± 1%
Temperature rating	-30º to 90 ºC
β (25º to 85ºC)	3.435 K nominal
Dissipation constant	0,7 mW/ºC nominal (Still air)
Thermal time constant	5 seconds nominal (air)

the temperature values read. It is also powered by the 5V power supply.

- A microcontroller ATmega328 (Atmel) implemented in an embebed system (Arduino): to prevent the microcontroller that records the data from crashing, another one is available to control the shutter. In turn, both are managed by an external application developed that allows real-time reading of the data.

Although, other devices are used in this experiment and keeping in mind all system described, Fig. 9 shows a schema of this:

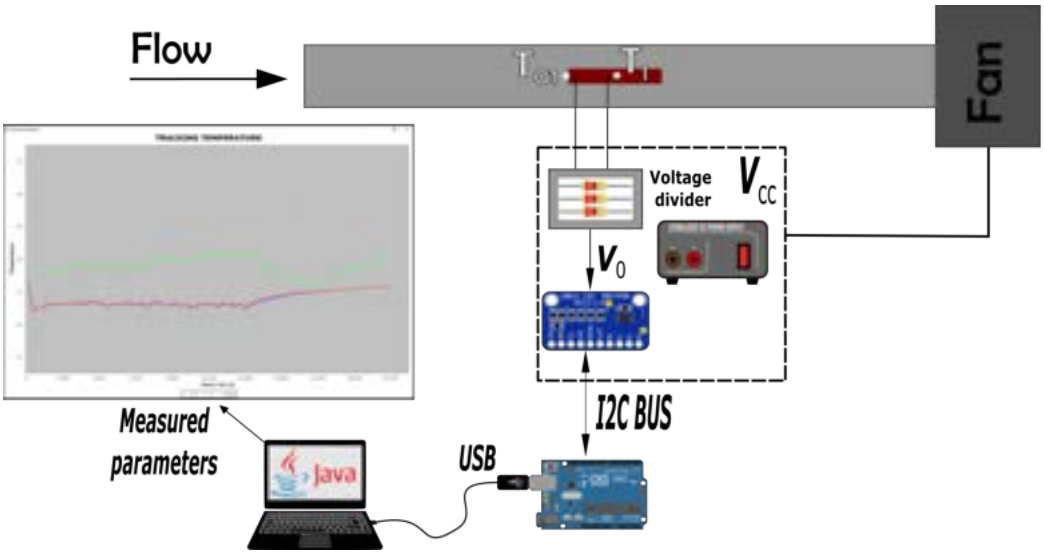

Figure 9: Acquisition and data capture for the experiment.

In Fig. 10, the response obtained during an experiment is shown. As can be seen, the temperature gradient value is proposed on the vertical axis and the test time on the horizontal axis. When the measurement is started, the fan is started and the evolution of the data is analysed in real time. This information is also stored for later study.

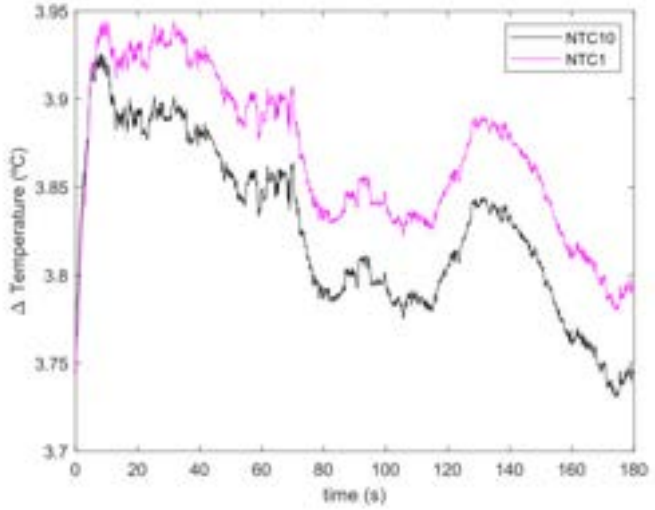

Figure 10: Response with tube experiment and two thermistors.

4. Results and discussion.

4.1. Response of thermistor in airstream

In this section, the results carried out in the tube with the device to measure temperatures will be presented. It should be noted that each test has a sample frequency of 10 data per second. The duration of the tests can be variable. This depends on the amount of data to be collected. Generally, however, tests last between 60 and 300 seconds.
For example, the two experiments shown below (Fig. 11 and Fig. 12) have a duration of 80 seconds. As soon as the temperature reading begins, the fan starts running and the data is recorded. In both tests, the magenta line corresponds to the static temperature (thermistor inside the device) and the black line to the stagnation temperature (thermistor at the tip of the device).

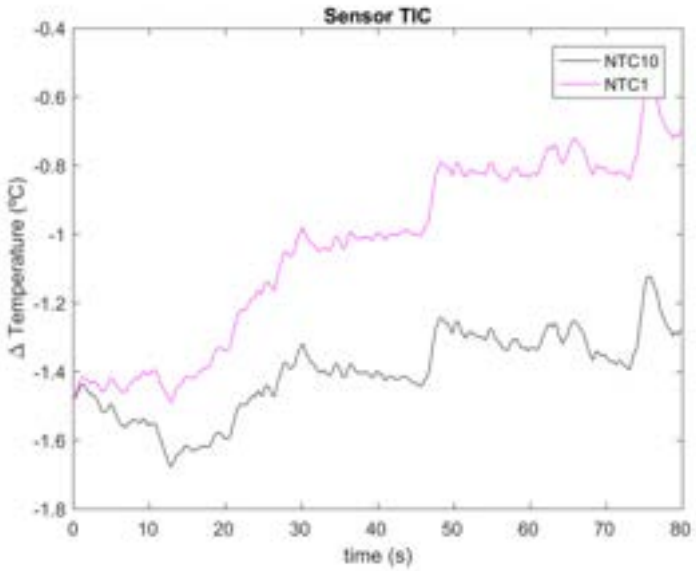

Figure 11: Response with tube experiment and two thermistors.

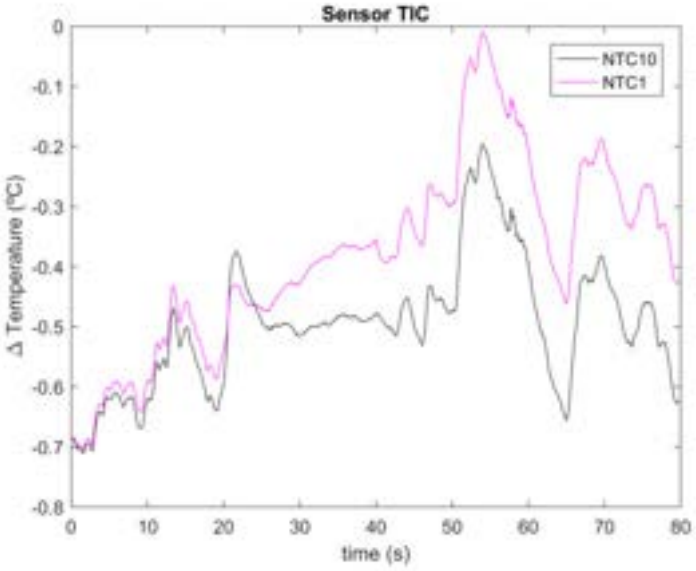

Figure 12: Response with tube experiment and two thermistors.

As can be seen in the previous graphs, the difference in temperature of both variables reaches maximums of 0.2 ºC. However, the most curious thing is the value that the stagnation temperature takes, when it is supposed to increase due to friction effects. This was later corroborated by a simple experiment that simulated the behaviour of the fluid inside the tube. This test consisted of exciting the isolated thermistor with an external heat source in a chamber in which two completely different fluids were introduced separately. This heat source allowed different excitation powers to be applied to the thermistor, thus contrasting the different media. Then, the typical response of the thermistor used to an external heat source that is applied for a certain time and then disappears is shown. It should be noted that these experiments are carried out in still fluids and under controlled conditions. Also, what is demonstrated is that the response of the sensor itself is simply reproducible from Eq. (14), as can be seen in the graph below.

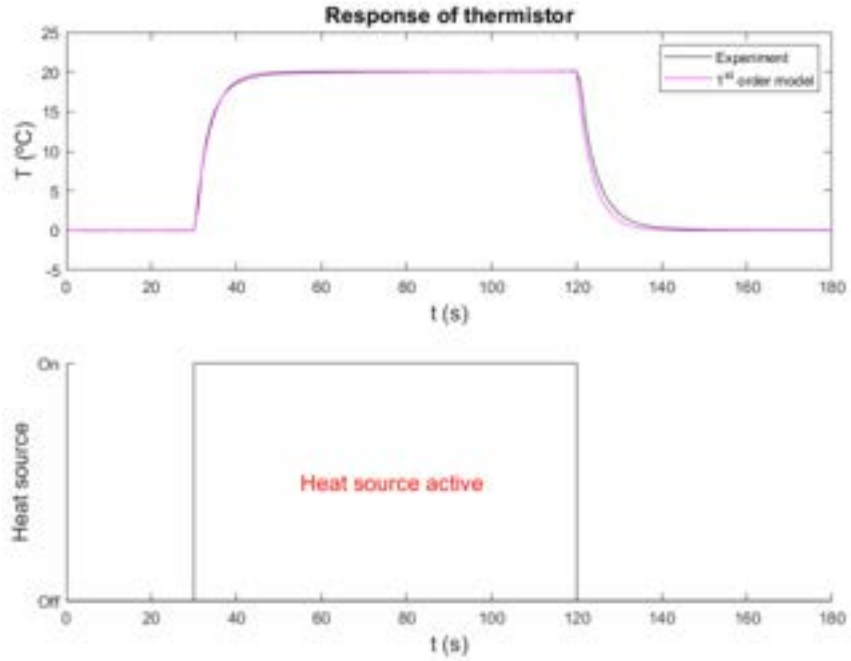

Figure 13: Response of thermistor during experiment using external heat source.

The following table shows the temperature gradient reached by the thermistor for each of the four powers during the tests with different fluids. Also, a quality estimator (QE) is shown to assess the accuracy with which

the first-order model is adapted to the response obtained. Fluid 1 has a lower heat transfer coefficient and after the tests a time constant of 3.57 s was obtained. For fluid 2, which has a higher heat transfer coefficient, the time constant was found to be 1.29 s.

Table 2: Temperature gradient results in different fluids and excitation powers.

	Fluid 1			Fluid 2		
Power	ΔT_1 ($^\circ C$)	STD_1	QE_1	ΔT_2 ($^\circ C$)	QE_2	STD_2
P_1	25,41	0,1	230,81	11,77	0,03	87,77
P_2	20,19	0,01	85,67	10,07	0,002	17,54
P_3	10,47	0,01	40,57	4,43	0,001	13,18
P_4	9,80	0,04	50,89	4,38	0,05	18,99

With all this, it is understood that there is an important fraction of heat flow that is lost through the cables and that is not analysed accordingly. Thus, from the first test in which the stagnation temperature and the static temperature were measured, results were obtained that suggested that certain phenomena related to the turbulent behaviour of the fluid were taking place and that heat flow through the cables was being generated.

4.2. Discussion.

Due to minimal surface of thermistors in a gaseous medium, there is a behaviour with a high dynamic responses. This high dynamic response of sensors proves to be a great advantage in several applications, in which temperature evolution measurements are sought with great precision in phenomena that occur in a short period of time, in which the temperature undergoes very abrupt variations. Also, due to the high transient response to which both thermistors are subjected in the temperature measurement during the experiment, it is unfeasible to obtain such behaviour by means of a first-order mathematical model. However, for applications where the measurements are more stable and are not constantly changing abruptly, such as Fig. 13, it is possible to resort to first-order mathematical models.

On the other hand, even if it is possible to find a model that fits the response obtained in the conditions of the tube experiments (Fig. 11 and Fig. 12), it must be stressed that there are other phenomena that are not considered. As mentioned above, the stagnation temperature will tend to increase its value due to the friction generated in the layers closest to the thermistor. But as can be seen, the opposite is true. This suggests that there is a fraction of energy that is flowing through the conductors and is inducing this contradictory behaviour. Therefore, it is necessary to have tools that allow us to discern the applications, models and sensors to be used in order to obtain more precise measurements.

5. Conclusions.

This article presents experiments carried out under specific conditions that have allowed conclusions to be drawn about first-order models and their accuracy in real applications.

Therefore, the existence of conduction phenomena through the cables is evident, which in certain applications introduce uncertainty in the measurements. Thus, all this leads us to consider that in order to use this type of sensors in temperature control systems, it is important to take into account the conditions of the fluid to be monitored. Thus, as mentioned, due to the high dynamic responses offered by these sensors, it is necessary to know the uncertainties introduced by boundary layer effects and vorticity. These phenomena can lead to errors in high-precision processes in terms of temperature knowledge, as we have seen.

However, not everything should be seen from a negative point of view, as this type of device could be used to determine the turbulence near the wall or to detect the boundary layer detachment zone in order to improve aerodynamics. Thermistors, knowing their influence, have an attractive application in this type of field due to their small size and the reduced instrumentation required. Therefore, the development of measuring devices that implement this type of sensors to study the conditions of a fluid is not ruled out. Likewise, the quantification of the energy lost through the cables could be a future motivation, as the introduction of tools would allow more detailed processes to be obtained.

Nomenclature

Letter symbols

- A area, m^2
- c_p specific heat at constant pressure, $J/(kgK)$
- h heat transfer coefficient, W/m^2K

$\dot{m}$ mass flow rate, kg/s

p pressure, N/m^2

$\dot{q}$ heat flow rate, J/s

T temperature, K

Greek symbols

Δ gradient

τ time constant

Subscripts and superscripts

h convection

∞ fluid

r radiation

s surface

sur surrounding

th thermistor

References

[1] Sekerka R. F. *Thermal physics. Thermodynamics and statistical mechanics for scientists and engineers.* Pittsburgh, USA: Carnegie Mellon University; 2015.

[2] Ross-Pinnock D., Maropoulos P. G. *Review of industrial temperature measurement technologies and research priorities for the thermal characterisation of the factories of the future.* Journal of engineering manufacture 2016; 230(5):793–806.

[3] Rishikesh G., Rakesh K. *Transient heat flux measurement analysis from platinum based thin film gauges in open and closed cavities.* Numerical heat transfer, Part A: Applications 2019; 76(7):576-592

[4] Darkhaneh H.E. *Measurement error caused by self-heating in NTC and PTC thermistors.* Texas, USA: Texas Instruments. Analog Design Journal; 2019.

[5] Antontsev S. N., Chipot M. *Analysis of blowup for the thermistor problem.* Siberian mathematical journal 1997; 38(5):827-841.

[6] Barabanova A. *The blowup of solution of a nonlocal thermistor problem.* Applied mathematics letters 1996; 9(1):59-63.

[7] Choi S.R., Kim D. *Real-time thermal characterization of 12 nl fluid samples in a microchannel.* Rev. Sci. Instrum 2008; 79 (6): 064901

[8] Liang X.M., Ding W., Chen H., Shu Z., Zhao G., Zhang H.F., Gao D. *Microfabricated thermal conductivity sensor: A high resolution tool for quantitative thermal property measurement of biomaterials and solutions.* Biomedical Microdevices 2011; 13(5): 923-928.

[9] Sanjeev K. M., Rakesh K. *Stagnation point transient heat flux measurement analysis from coaxial thermocouples.* Experimental Heat Transfer 2018; 31(5):405-424.

[10] Sanjeev K. M., Rakesh K. *Transient heat flux measurement analysis from coaxial thermocouples at convective based step heat load.* Numerical Heat Transfer 2019; 75(3):200-216.

[11] Pope S. B. *Turbulent flows.* New York, USA: Cambridge University Press; 2000.

[12] Tagawa M., Kato K., Ohta Y. *Response compensation of thermistors: Frequency response and identification of thermal time constant.* Review of scientific instruments 2003; 74(3):1350-1358.

[13] Cengel Y. A., Ghajar A. J. *Heat and mass transfer fundamentals and applications (5th edition).* New York, USA: McGraw-Hill Professional; 2014.

Predictive models for the "optimal" radius ratios in natural bi- and trifurcated vessels: beyond the Hess-Murray law

Enrico Sciubba
Università Niccolò Cusano – Roma, Italy
enrico.sciubba@unicusano.it

Abstract

Bifurcated structures are ubiquitous in nature, both in living and non-living systems. The modern approach to their physical modelling starts from the recognition that in plants and animals the substitution of (a portion of) a straight vessel length with a branched one serves a biological "goal" that requires some energy and material "expenditure". Such expenditure must be justified by a compensating gain for the resulting evolved structure. A great number of studies addressed this topic, mainly from a biomedical science perspective, but since all of them indicate a weak agreement with experimental data, it is useful to explore the matter in some more detail. The purpose of the vessels considered in this study is to "transport" material flows like sap, blood or air, and the striking geometrical similarity of the forked structures found in plants, circulatory systems, bronchial alveoli and river deltas suggests indeed the presence of a single underlying physical principle. Experimental evidence indicates that the topology of bifurcated blood, air and sap vessels (e.g., their "shape") is amazingly similar under quite different external constraints, and this might imply that the shape of a bifurcation is at least to some extent independent of the boundary conditions. Furthermore, it is unclear if and to what measure the functional advantage obtained by repeated bifurcations decreases with the number of splitting levels. This paper presents a critical review of the most popular physical model formulated for the description of bifurcated structures, the so-called Hess-Murray law ("H-M" in the following). It is first shown that, under a very restrictive set of assumptions, the H-M law can be obtained by the assumption of constant wall stress in the parent and daughter branches. Then both Hess' and Murray's original derivations are discussed from a physical point of view, and the extension of the rule to the case of non-symmetrical bi- and trifurcations is presented.
It is then argued that in real branched networks the actual optimality criteria (i.e., in an evolutionary sense the "driving force") may be quite different from the assumptions posited in the H-M law literature, which explains the weak predictive value of the law. Some adjustments to the model that include a resource-based cost/benefit of the formation of a bifurcation are presented and discussed.

Keywords: Bifurcated vessels; Branched Structures; Hess-Murray law; Entropy Generation Minimization; Constructal Theory

1. Introduction

1.1 The problem

Bifurcated structures in fluid carrying channels and vessels appear in tree roots and branches, leaf veins, circulatory systems in animals, air vessels in the respiratory systems, corals, river deltas… (Figure 1). At first sight, such structures display an amazing degree of geometric similarity, and understanding the underlying physics is important for three reasons: first, if the existence of a unifying physical principle can be convincingly identified, this knowledge may lead to a better comprehension of natural evolution. Second, linking the "shape" of these structures to their "function" would allow for better aimed interventions in the case of malfunctions (overflow and flooding of rivers and channels, poor tree health, poor soil exploitation, circulatory diseases…). Third, a clearer insight on the physics of natural bifurcations may lead to the formulation of more accurate and efficient design guidelines of artificial (manufactured) branched structures, for example, in pipelines, heat exchangers, biological implants etc.
It is therefore not surprising that a large number of studies have been devoted to this topic. Leaving aside engineering applications, which require a separate discussion and are subject to quite different external constraints, botanists and biologists have dedicated substantial time and resources to the search for a general model of bi-, tri- and polyfurcated fluid carrying vessels. A brief list of the main questions to be answered can be extracted from a careful consultation of the archival literature[1]:

a) Why do bifurcated structures appear in nature?
b) Why is the geometry of such structures apparently similar at all scales and in different instantiations?

[1] To the best of my knowledge, the first modern systematic inquiry into this matter was performed by Wilhelm Roux in his dissertation in 1878 [25]. The original text being not easily accessible, I had to rely on later citations.

c) How and to what measure is the shape of a bifurcation independent of the prevailing boundary conditions?
d) Does the functional advantage obtained by repeated bifurcations decrease with the number of splittings?

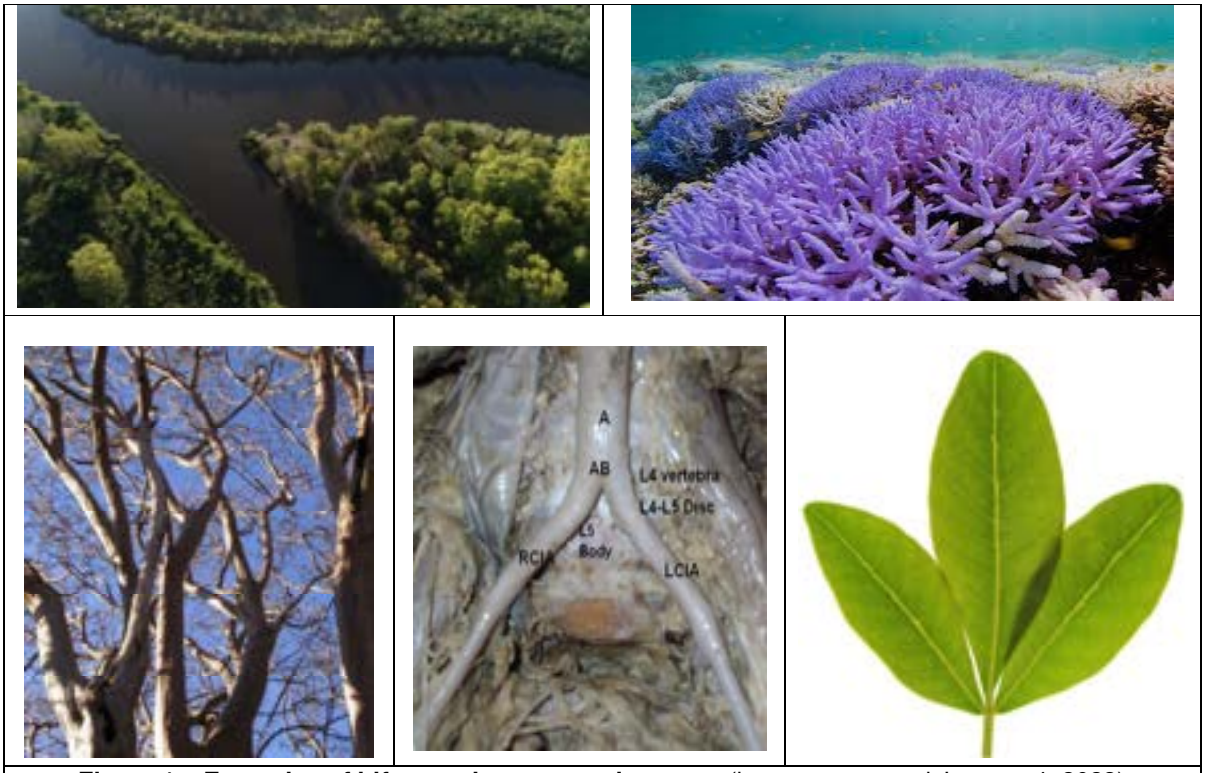

Figure 1 – Examples of bifurcated structures in nature (images accessed January 4, 2023)

A final answer to the above questions is yet to be found, and one of the goals of this paper is to clarify the current state of affairs and suggest possible paths to a solution.
To place this study in the correct perspective, it is useful to begin by examining the available empirical evidence collected over decades of valuable experimental campaigns. A summary of the knowledge that can be inferred from the large set of available data is the following:

1) Different types of branchings display an amazing degree of geometric similarity at large scales, but the exact geometric details (radius- and length ratio of daughter-to-parent branches, branching angle, complanarity) depend on the type of fluid being transported (newtonian or non-newtonian, pure substance or particle laden) [39,41], on the material and/or state of the channel walls (lignine, muscle fibers, gravel, sand…) [13,14,24,28,39,], and on the flow features (creeping, laminar or turbulent) [2,13,22,23,40,42];
2) Although a branched network resembles a fractal structure, there is no indication that the fractal exponent remains constant over successive branching levels [35];
3) While in plants the sap flow can be accurately modeled as stationary[2], in blood and air systems as well as in rivers the non-stationarity of the flow has a substantial influence on the geometry of the bifurcations [39,40].

1.2 – A very popular physical model: the Hess-Murray law

Over a century ago, the Swiss physiologist Walter Rudolf Hess formulated a model of blood flow in arterioles and capillaries that resulted in an allometric correlation between the radii of successive branchings in bi/trifurcated vessels: the original concept is presented and discussed in Hess' doctoral thesis published in a little known 1903 paper, with two further extended versions published (in german) in 1914 and 1917 [10,11]. Using a similar approach, the American physiologist Cecil Dunmore Murray "rediscovered" the same correlation in a 1926 article, and later refined and extended it in two other papers [16,17,18]. Since the

[2] Here and in the following, a significant distinction in the nomenclature must be made: while in blood- and air circulation systems one refers in fact to individual vessels (capillaries, veins, arteries etc.), in plants the "vessels" are either the mesoscale ducts of leaves and roots (the "veins") or the large scale twigs and branches. At the smallest xylem scale there is no bifurcation.

numerical result, i.e., the allometric rule, is the same, the law came to be referred to as "the Hess-Murray law".

The methods proposed by Hess and Murray are described in detail in sections 3 and 4 below: it is important to underline the novelty of both approaches, based on the assumption that the circulation of blood, lymph and air in living organisms is governed by a "work minimization" principle. The popularity of the H-M law is though not due to the "energy cost" methods they adopted (for a documented critique, see sections 3 and 4 below), but rather to the derivation of an "optimal branching ratio" $\delta = \frac{d_{i+1}}{d_i} = \frac{1}{\sqrt[3]{2}} = 0.7937$ between the diameters of two successive symmetrical branches. This "cubic root of 2" correlation underwent extensive theoretical and experimental reassessment in the second half of the 20th century, and the results indicate that while it is sufficiently accurate for the smallest vessels (capillaries), it fails for the larger ones (large veins and arteries); moreover, it does not apply to turbulent flows [42]. Recent comparisons with numerical investigations of branched flows led to similar conclusions [22,24,39,40].

In 1997 Bejan [4] published a very ingenious generalization of the H-M law: he reasoned that, if the law holds, then every bifurcated stream that carries a material or immaterial flow from one point (the *source*) to two others (the *sinks* or *end-users*) should -in an evolutionary sense- develop along a global structure exactly specified by the "cubic root of 2" rule. This intuition forms the basis for his Constructal Theory ("CT"), which has since seen a great number of applications in the most diverse fields (see also [5,6,15] for the Authors' own reassessment). Not by chance, the very name "constructal" was conceived to be an antonym of "fractal", to signify that real structures follow from goals and physical laws, in line with Hess' & Murray's teleology, rather than from abstract "shape factors" or Lyapunov exponents (borrowing Bejan's words: "*Nature is not fractal*" [4]). The goals are in turn determined by external influences related, in nature, to evolutionary pressures [5], and in engineering, to design specifications. In this sense, CT represents a "closed" scientific paradigm, not only *qualitative* but *quantitative*: it proposes a novel interpretation and classification of natural (abiotic and biological) structures and leads to measurable and repeatable design procedures for engineered artefacts. The entire body of its results depends though on the applicability of the H-M law, and more precisely on the general validity of the "cubic root of 2" correlation (or any other correlation of the form 2^{-n}).

The real legacy of the H-M law is not its (doubtful) universal accuracy, but rather its conceptual foundations: it states that biological organisms can be described by means of an allometric scaling arising from an "energy costing" approach. As noted in [36] and later by [5,27,31], this in turn implies the existence of a similar allometry between different species: if the relative sizes of the respective blood or sap vessels scale according to a 2^{-n} rule then, whatever the value of n, the average physical dimensions of the individual organism depend on the radius of the main branch, which in turn depends on the metabolic rate of the species.

On the engineering side, in spite of Sherman [36] argument that -if the hydraulic diameter d_h is substituted for d- the H-M law should also hold with minimal corrections for human artefacts (pipelines, fluid carrying networks, porous media), the matter is more complex, because heat exchangers and fluid networks are designed under several "non-natural" constraints, some of which derive from purely technical requirements (entry length in a HE, material compatibility, vessel wall mechanical resistance, etc.) and others are cost-related (minimal material costs, optimal thermal insulation, minimum pumping work, etc.). The analysis of the applicability of the H-M law to engineered structures is outside of the scope of the present study.

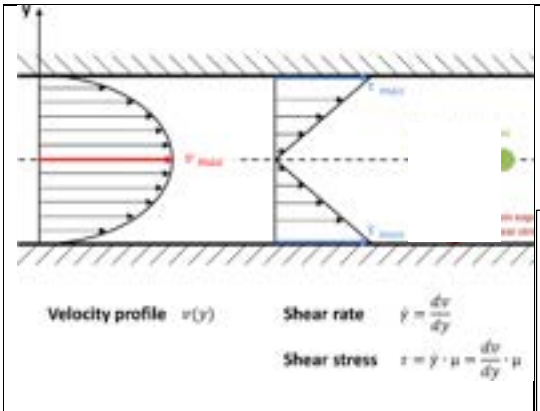

Figure 2 – Flow of a newtonian fluid in a circular channel: velocity and viscous stress profiles

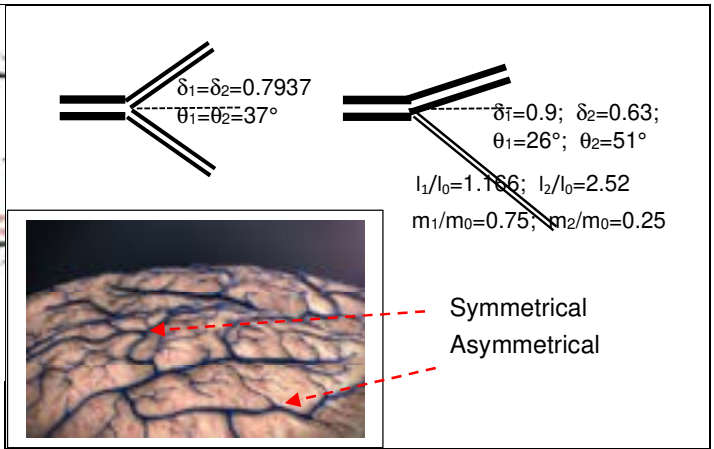

Figure 3 – Symmetric vs asymmetric branching under the constant viscous stress prescription

2- Young's Constant Wall Stress Law

2.1 -Theoretical model

It is interesting to remark that, as reported by Thomas Young in its Croonian lecture 1809 [44], presented well before Hess' study, an exact form of the radius ratio in branched tubes was already known to hydraulic engineers. This formula also reads $\delta = \frac{d_{i+1}}{d_i} = \frac{1}{\sqrt[3]{2}} = 0.7937$, but its derivation does not depend on the approximations introduced by Hess on the "regulatory power of the blood flow" nor on the inaccurate "metabolic cost of blood volume" calculated by Murray.

2.2 - The mathematical derivation

Consider the steady laminar and isothermal flow of a Newtonian fluid in a symmetrically branched circular channel (Figure 3, top left). Assuming that the flow can be described by Poiseuille formula and remains laminar in the daughter branches (i.e., neglecting the possible onset of turbulence at the junction), the wall stress calculated in the parent (ℓ_0) and daughter (ℓ_1, ℓ_2) branches takes the form:

$$\tau_w = \frac{4\nu m_j}{\pi r_j^3} \quad (1)$$

with *j=0* for the main and 1 and 2 for the splits. Let us impose the constancy of the wall stress throughout the bifurcation:

$$\tau_{w,0} = \frac{4\nu m_0}{\pi r_0^3} = \tau_{w,1} = \frac{4\nu m_1}{\pi r_1^3} = \tau_{w,2} = \frac{4\nu m_2}{\pi r_2^3} \quad (2)$$

If the split is symmetrical, then $m_1 = m_2 = m_0/2$, and we obtain:

$$\delta = \frac{r_1}{r_0} = \frac{r_2}{r_0} = \frac{1}{\sqrt[3]{2}} = 0.7937 \quad (3)$$

i.e., the same value prescribed by the H-M rule.

The validity of Eq. (3) rests of course upon the assumptions of steady Poiseuille flow, and therefore there is no reason for the exponent $n=-1/3$ to apply under turbulent- or non-stationary flow conditions. It is to be expected though that in leaf tubules, blood capillaries and in the smallest tubules of the respiratory tract, where diameters are well below 1 mm and the Reynolds number of the flow is very low, the above correlation should apply.

An interesting consequence of Eq. (3) can be derived if we prescribe the Δp in the main- and in the daughter branches to be the same. This implies:

$$\lambda = \frac{l_1}{l_0} = \frac{l_2}{l_0} = 2 \quad (4)$$

Eq. (4) would suggest that at each bifurcation the length of the daughter branches doubles, a condition not supported though by experimental evidence.

The above calculation can be adapted to non-symmetric branchings (Figure 3 top right). To close the calculation, we need to know the ratio of the mass flowrates through the daughter branches, $k_1 = m_1/m_0 = x$, $k_2 = m_2/m_0 = 1-x$. We obtain:

$$\delta_1 = \frac{r_1}{r_0} = x^{1/3}$$

$$\delta_2 = \frac{r_2}{r_0} = (1-x)^{1/3} \quad (5)$$

In this case the pressure drops through the daughter branches are different, unless one selects a proper ℓ_1/ℓ_2 ratio:

$$\Delta p_1 = \Delta p_2 \quad iff \quad \frac{l_1}{l_2} = \left(\frac{1-x}{x}\right)^2 \left(\frac{\delta_1}{\delta_2}\right)^4 \quad (6)$$

3 – Hess' original model

3.1 - Problem position

In 1903, in a preparatory paper for his M.D. thesis [10], the Swiss physiologist Walter Rudolf Hess proposed the existence of a physical "optimization criterion" that guides the branching of arterial vessels. This idea was also the topic of later work in his "Habilitation" thesis [11], but the 1903 work already contains -albeit in a convolute way and with some debatable assumptions- a complete derivation of his "cubic root of 2" law. Hess was clearly inspired by previous work by Roux [25] who postulated a "dynamic mechanical principle" to be the driver of vessel bifurcations in animal circulatory systems. Trying to interpret the large mass of experimental data presented by Roux, Hess starts by assuming that nature would adopt a "minimum resource consumption" criterion to build the human circulatory system and proceeds to calculate how this task can be attained ("*Wie kann die Aufgabe des Blutes mit dem kleinsten Kraftverbrauch erledigt werden*" [10], p.5). In spite of his convolute writing style, Hess' approach emerges clearly: the optimal radius of a vessel carrying a given volumetric blood flowrate is the one that minimizes a cost function given by the sum of the pumping work (inversely proportional to the fourth power of the radius) and the metabolic cost of the volume of the pumped blood (proportional to the square of the radius).

3.2 - The mathematical derivation

In modern terms, Hess' procedure can be reformulated as follows:

a) Assume the flow in arteries can be described by Poiseuille's law for steady laminar flow in circular vessels with rigid walls;

b) Calculate the pumping power in W/(meter of vessel) required of the heart to process a flowrate m [kg/s]:

$$P_{pump} = K_1 \frac{m^2}{r^4} \quad (7)$$

where K_1 is a constant that depends on the fluid viscosity and density;

c) Calculate the metabolic cost of the pumped blood, neglecting its thermal content:

$$C_{blood} = K_2 r^2 \quad (8)$$

Where C_{blood} is also in W/m of vessel and K_2 is a constant depending on the metabolic rate;

d) Find the optimal radius by solving the corresponding Lagrangian[3]:

$$\mathcal{L}_{Hess} = P_{pump} + C_{blood} = K_1 \frac{m^2}{r^4} + K_2 r^2 \quad (9)$$

Which results in:

$$r_{opt} = \left(\frac{2K_1}{K_2}\right)^{1/6} m^{1/3} = \kappa m^{1/3} \quad (10)$$

Where the constant κ depends on the fluid properties and on the metabolic rate. If a vessel bifurcates symmetrically (Figure 4), i.e., if $m_1=m_2=m_0/2$, the optimality can be extended to the daughter branches:

$$r_0 = \kappa m_0^{1/3}; \quad r_1 = r_2 = \kappa \left(\frac{m_0}{2}\right)^{1/3} \quad (11)$$

Whence

$$\delta = \frac{r_1}{r_0} = \frac{1}{\sqrt[3]{2}} \quad (12)$$

Throughout his papers Hess repeatedly stresses that he is aware that his result depends on two critical assumptions, namely Poiseuille flow and stationarity, and makes accurate reference to selected contemporary literature that reinforces his belief that a branching does not generate turbulence and that the low-frequency pulsations do not affect the flow in such a way as to invalidate Eq. (12).

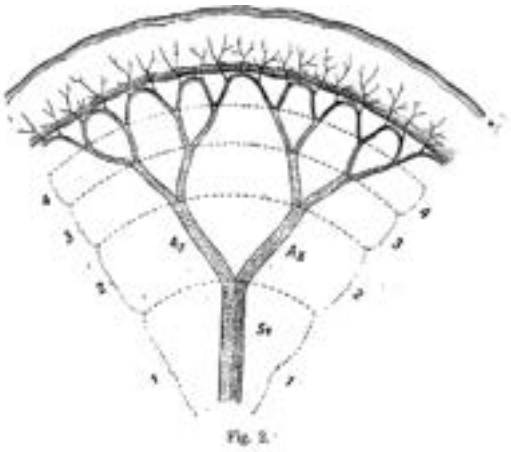

Figure 4 – Hess' original concept [11]

Figure 5 – Asymmetric trifurcation of a corkbark tree tip ($r_1=r_2\neq r_3$)

4 – MURRAY'S model

4.1 - Problem position

Between 1926 and 1927, Cecil B. Murray, an American physiologist, published a set of papers aimed at the identification of the most "economic" oxygen supply to the human limbs via blood transport through the vessels. He demonstrated that such an optimal value can be derived by minimizing a cost function consisting of two terms: the power needed to overcome friction and the "metabolic cost" of the blood flowing through the vessel. The premises are similar to those posited by Hess, but the calculation of the blood cost function is different. He, too, arrived at a "cubic root of 2" formula. Murray -as Hess- assumed the blood flow to be

[3] In fact, Hess only presents a graphical derivation, because the expression he derives for K_2 is not explicit in the variable "r", and thus he must use an approximation to make the dependence explicit

described by the stationary Poiseuille formula, and explicitly stated that his derivation ought to be considered a statistically valid theoretical guideline and that his model represents a "theoretical approximation" of the more complex physiology of blood transport. In his own words [16]: "*If we examine the arterial system bearing in mind the question of economy, we find that there are two main antagonistic factors. If the vessels are too small, the work required to drive the blood through them becomes too great; if the volume of the vessels is too large, the volume of blood, being equally large, becomes a burden to the whole body*". Murray was aware of Hess' previous work but maintained that his calculation of the blood cost was more accurate and based on the latest experimental results. Besides reformulating the theory, Murray also derived the "optimal angles" for a symmetric bifurcation using the minimum virtual work principle (Figures 6, 7).

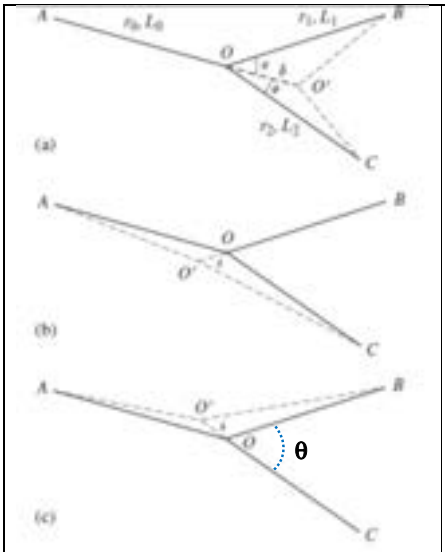

Figure 6 - Murray's derivation of the optimal branching angle [16]

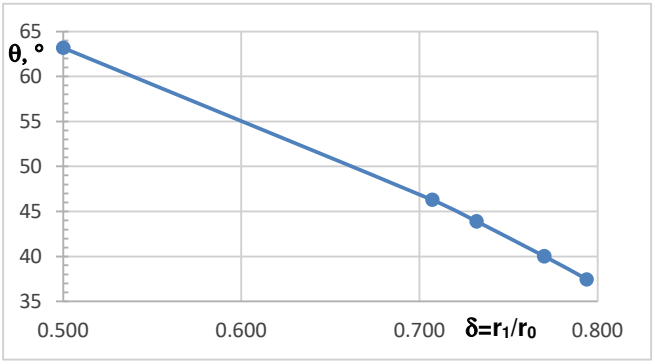

n	1.00	2.00	2.22	2.65	3.00
$\delta=r_1/r_0$	0.500	0.707	0.732	0.770	0.794
theta °	63	46	44	40	37
$\lambda=\ell_1/\ell_0$	0.25	1.00	1.15	1.41	1.59

Figure 7 – Branching angle θ as a f(δ) for symmetrical bifurcations. $\delta=2^{-1/n}$, $\theta=arcos(0.5/\delta^2)$

4.2 - The mathematical derivation

Proceeding along the same path previously proposed by Hess, Murray obtained an expression identical to Hess' for the power required to pump a given mass flowrate of blood in a straight vessel with rigid walls, Eq. (7): $P_{pump} = K_1 \frac{m^2}{r^4}$,

where K_1 is the same constant as in Hess' formulation.

He then proceeded to calculate the metabolic cost of the pumped blood:

$$C_{blood} = b\rho l\pi r^2 = K_3 r^2 \qquad (13)$$

Where b is the "cost of blood" calculated on the basis of the then available data on heart rates, and varies between 980 and 1980 W/m^3 according to the adopted calculation method. For the purpose of this paper, the accuracy of the value of b is though irrelevant.

The optimal radius is again obtained by solving the corresponding Lagrangian:

$$\mathcal{L}_{Hess} = P_{pump} + C_{blood} = K_1 \frac{m^2}{r^4} + K_3 r^2 \qquad (14)$$

Which results in:

$$r_{opt} = \left(\frac{4K_1}{K_3}\right)^{1/6} m^{1/3} = \xi m^{1/3} \qquad (15)$$

Where the constant ξ depends on the fluid properties and on the power absorbed by the heart. If a vessel bifurcates symmetrically (Figure 3, top left), i.e., if $m_1=m_2=m_0/2$, the optimality can be extended to the daughter branches and the "cubic root of 2" law $\delta = \frac{r_1}{r_0} = \frac{1}{\sqrt[3]{2}}$ is recovered.

In a second paper [17], Murray calculates the optimal branching angle by applying again the principle of minimum work: as shown in Figure 6, among the possible paths the branching angles that minimize the total work are given by:

$$cos\theta = \frac{r_0^4+r_1^4-r_2^4}{2r_0^2r_1^2}; \quad cos\varphi = \frac{r_0^4+r_2^4-r_1^4}{2r_0^2r_2^2} \qquad (16)$$

Now Murray argued that, since according to Eq. 10 the mass flow rate at optimal configuration is proportional to the cube of the radius, the correlation between the radii of the main- and the daughter branches is:

$$r_0^3 = r_1^3 + r_2^3 \qquad (17)$$

So that the final relationship between the splitting angles becomes:

$$\theta = arccos\left[\frac{r_0^4+r_1^4-\left(r_0^3-r_1^3\right)^{4/3}}{2r_0^2r_1^2}\right];\quad \varphi = arccos\left[\frac{r_0^4+r_2^4-\left(r_0^3-r_2^3\right)^{4/3}}{2r_0^2r_1^2}\right] \tag{18}$$

Introducing the optimal radius ratio δ (Eq. 12):

$$\theta = \varphi = arccos\left[\frac{1+\delta^4-\left(1-\delta^3\right)^{4/3}}{2\delta^2}\right] \sim 37° \tag{19}$$

The above result predicts that symmetrical branches should have a total branching angle ($\theta+\varphi$) of about 75°.
If the vessel trifurcates as shown in Figure 5, with two side daughter branches being symmetrical with equal radii $r_1=\gamma r_0$ and the third coaxial with the main and also of radius $r_2=r_1$, the optimal value of the radius ratio is $\gamma = \frac{1}{\sqrt[3]{3}} = 0.6934$ and Murray's optimization procedure provides:

$$\psi = arccos\left[\frac{r_0^2-\left(r_0^3-2r_1^3\right)^{2/3}}{2\gamma^2r_0^2}\right] \tag{20}$$

with the splitting angle ψ=57°.
Murray did not elaborate on the fact that Eqs. (16) & (20) retain their validity under <u>any</u> law of the type 2^{-n}. Figure 7 displays the branching angle θ as a function of the radius ratio δ for n=1, 2, 3 and two experimentally & numerically validated values, namely 2.22 and 2.45 [13,26,34,41,42].
Another consequence of the H-M law (or of any similar allometric correlation) is that the length of the branches may also be derived as a function of *n*: for example, imposing a constant pressure drop across all branches (i.e., $\Delta p_0=\Delta p_1=\Delta p_2$, not necessarily an "optimal" choice) one obtains

$$\lambda_1 = \frac{\ell_1}{\ell_0} = 2^{\left(2\frac{n-2}{n}\right)} \tag{21}$$

The λ_1 are also shown in Figure 7: in spite of their not being optimal in any sense, these values can be used as a yardstick for assessing field-measured values. In fact, the largest majority of field data report ℓ_1 values lower than 1, which indicates that the "constant Δp" is not a preferred configuration in nature.

5 – Limitations of the Hess-Murray Law

5.1 - Theoretical analysis

The applicability of the H-M law depends on several assumptions, the more stringent being:

a) *Validity of the Poiseuille flow*
While in plants the sap flow is so slow that it can be modelled as a creeping flow, in animals laminarity is the exception rather than the rule. Notice though that this fact *per se* does not affect the value of the branching ratio: the <u>necessary</u> condition for the H-M law to apply is that a phenomenon can be modeled as emerging from the combined influence of two competing "forces", one proportional to the square of the mass flowrate and to the inverse fourth power of the radius, and the other to the square of the radius.

b) *Validity of the steady state flow conditions*
This is a major simplification, and both experimental [12,20,21,34,45] and numerical [2,13,22,23,24,33,34,40] studies demonstrated that the inherent unsteadiness in blood vessels has a major impact on the exponent of the allometric correlation.

c) *Independence on the type of fluid*
Both sap and blood are non-Newtonian fluids, and experimental and numerical studies demonstrate that releasing the newtonianity condition results in a different value of the exponent *n* in Eq. (15).

d) *Validity of the assumption of rigid walls*
On this point one must differentiate between application of the law to plants and animals: in the former case, the lignino-cellulosic walls are for all practical purposes rigid, while in the latter the compliant muscle-structure of arteries and veins may even invalidate the non-slip condition.

Allometric branching models exist that are not derived from a Hess-Murray perspective (for details see [7,43]), but their treatment is outside of the scope of this paper.

5.2 – Comparison with experimental results

Given the convenience of a simple correlation like the H-M law, several experimental campaigns have been conducted over the years to verity its applicability, especially in biology. The verified experimental evidence may be summarized as follows:

a) As anticipated by Murray, both *in vitro* and *in vivo* tests convincingly demonstrate the validity of a H-M-like allometry in capillaries and arterioles, with exponent values in the range $2^{-0.16}$ through $2^{-0.43}$ [2,23,26,36,41]. In larger vessels (veins, arteries) a $2^{-0.47}$ value is more appropriate [26,41].

b) More importantly, several independent experiments on animal circulatory systems [12,45] conclude that radius-dependent *slenderness factors* appear to be correlated by a power law of the type $\ell/(2r)=\alpha r^n$, with $0.47<n<1.1$ and α a case-dependent function of r_0: this implies that the dimensionless splitting length $\lambda_0=\ell_0/L$ (see Figure 7) is also a relevant parameter.

c) Although, for the reasons discussed in the previous sections, the agreement is expected to be better in plants, independent studies report vessels ratios between 0.47 and 0.85 for both leaves and soft twigs [1,25]. Following Murray [19] and in spite of a critique by Savage [27], some Authors assume bough-to-trunk and twig-to-bough radius ratios to follow the "cubic root of 2" rule: as we shall see in section 6.4, it is possible to formulate a physical model for such a case also by assuming a volume conserving law that leads to an exponent $n=2$. Some Authors prefer to use a log/log fit for the branch lengths and the radius [12,20].
Referring the reader to [29,31] for a more detailed discussion, it is fair to conclude this analysis by saying that the Hess-Murray's law:

a) Has the great merit of introducing the idea that the growth of branches in a tree or in epithelial tissue is dictated by a "balance" of material and metabolic energy cost;
b) It is valid in a first approximation for all processes in which the two contrasting "forces" are friction and fluid volume;
c) Displays an acceptable agreement for small, rigid-walled vessels and laminar flow, but fails significantly to describe branching ratios observed in real structures for any other condition (larger vessels, compliant walls, non-newtonian fluid, turbulent flow).

6 - Models based on a different "cost" structure

All of the hitherto formulated alternative models maintain the physical approach suggested by Hess and Murray: the formation and operation of a branched configuration must serve some physiological goal and therefore it ought to "minimize" in some sense the resources invested by the system in generating the bifurcation. Adam [1] proposes some alternative cost functions, all of them confirming the "cubic root of 2" correlation but having different values for the constant ξ in the solution of the "optimal" radius (Eq. 15). The unsatisfactory agreement of the H-M law has stimulated further research in the topic, and it is instructive to examine some other Lagrangians that have been explicitly or implicitly proposed in relatively recent archival publications. In this section we shall discuss three alternative models based on the consideration that a bifurcation must be created with an investment of both material and energy.

6.1 – Minimal pumping power in a target volume

The simplest cost function considers only the "system operation cost", i.e., the pumping power required to overcome friction losses. Simply imposing minimum P_{pump} (Eq. 7) leads of course to the trivial and unphysical result $r\to\infty$. It is though interesting to investigate the existence of geometrically constrained values for the radius ratio and for the branching angle. Consider Figure 8: in real instantiations a branching takes place within a "volume" (here, area) defined by the origin "O" and the final points A and B, and if the splitting point moves along the parent branch, ℓ_0 varies and so does $\ell_1=\ell_2$ (if the branching is symmetrical). The Poiseuille pressure loss along the three vessels is:

$$\Delta p_0 = \frac{8\nu l_0 m_0}{\pi r_0^4}; \qquad \Delta p_1 = \Delta p_2 = \frac{4\nu l_0 m_0}{\pi r_1^4} \tag{22}$$

The corresponding pumping powers:

$$P_{pump,0} = q_0\Delta p_0 = \frac{8\nu l_0 m_0^2}{\pi\rho r_0^4}; \qquad P_{pump,1} = P_{pump,2} = q_1\Delta p_1 = \frac{2\nu l_1 m_0^2}{\pi\rho r_1^4} \tag{23}$$

The lengths ℓ_0 and ℓ_1 are subject to the constraints:

$$L = l_0 + l_1 cos\theta; \text{ or } \qquad \lambda_0 = 1 - \lambda_1 cos\theta \tag{24}$$

The ratio P_{bif}/P_0 is less than unity (i.e., it brings an advantage in terms of pumping power) only above a certain splitting angle of about 61°, i.e. for an exponent $n\cong 2$ and a radius ratio very close to $\frac{1}{\sqrt{2}} = 0.707$ (Figure 9). There is no minimum.
Notice that the application of Eq. (23) results in an implicit correlation between the radius ratio and the aspect ratio $a=H/L$ of the 2D domain defined by the branching, because the splitting lengths l_0 and l_1 depend on the aspect ratio and θ as per Eq. (24). This is a useful outcome, and shows that different values of the exponent n may accommodate more closely the deviations from the H-M law in real plants and blood vessels.

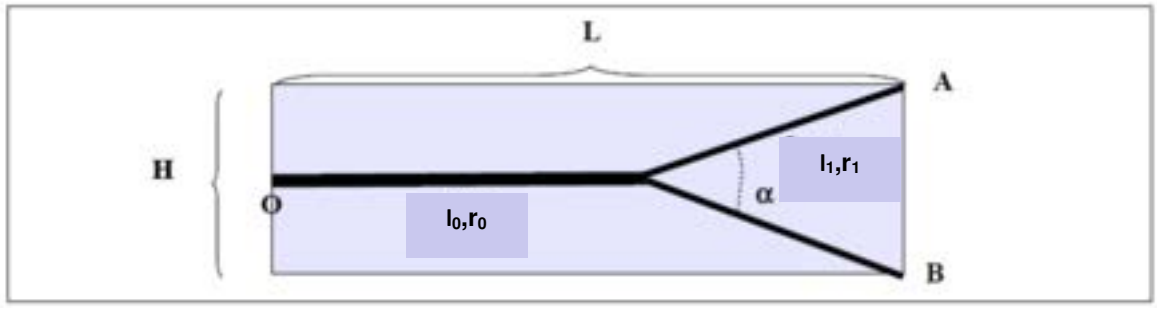

Figure 8 – Definition of the influence area of a bifurcation (adapted from [30])

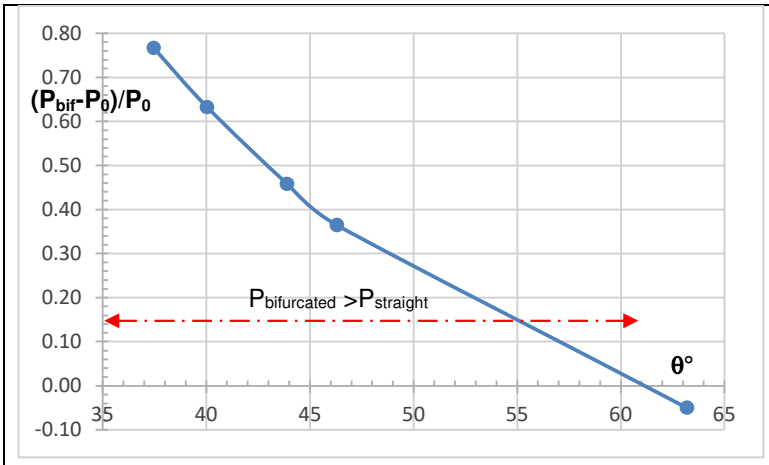

Figure 9 – Symmetric bifurcation: dimensionless pumping power vs. splitting angle θ

Figure 10 – Vessel vs. twig radius in a tree bifurcation

6.2 - Minimal entropy generation

Another very useful paradigm used to optimize bifurcated structures, pioneered by Bejan [3], is the Entropy Generation Minimization (EGM). True to its name, EGM is based on the idea that the "optimal" shape of a branched fluid-carrying conduit ought to minimize the total irreversibility occurring during its operational window (the lifetime of the vessel). EGM was formulated earlier than CT, is undoubtedly more comprehensive than the latter and -more important- it generates richer insight. Contrary to common belief, it can be proven that the two approaches do not consistently lead to the same results [30,31]. Since the flow of sap and blood can be assumed as isothermal and single phase, the only entropy generation is caused by friction, and the lagrangian becomes:

$$\mathcal{L}_{\dot{s}} = K_s \dot{s}_{visc} \tag{25}$$

It turns out that, since the rate of viscous entropy generation is directly proportional to the lost work due to friction, the solution to Eq. (25) leads to the same results as in section 6.1 [29].

6.3- Minimal pumping power and material formation cost

This model, formulated by researchers investigating tree growth, [8,9], is based on the premise that the growth of a bifurcation carries a cost equal to the biological production expenditure required of the tree to produce the volume of the material (lignine) of the new sap carrying vessels. This cost is assumed to be proportional to the Net Primary Production of the plant (NPP), a measure of the efficiency of the tree to transform its global resource input into "new wood" [20,21,37,38]. This expenditure must be added to that required to pump the sap. It is readily seen that the new volume is proportional to the square of the vessel radius, and thus the Lagrangian takes the same form as Hess' one, although with a different value for the constant K_5.

$$\mathcal{L}_{material} = K_1 \frac{m^2}{r^4} + K_5 r^2 \tag{26}$$

Thus, while the optimal radius that carries a given mass flow rate of sap is of course different than that predicted by the H-M law, still the radius ratio of the daughter branches to the parent one follows the cubic root of 2 rule, because the solution of (28) is again $r_{opt}^3 = \left(\frac{K_1}{K_5}\right)^{1/2} m$.

6.4- Minimal pumping power, material formation and fluid cost

It is useful to address the problem from a different viewpoint: it is correct that the system "resource expenditure" is proportional to the pumping power and to the material cost require for building the vessel's envelope, one ought to consider that the scope of circulating the nutrients is to allow the system to "grow". Therefore, there is another expense required, namely that of the generation and maintenance of the material that surrounds the vessel: in a tree, the twig, and in an animal system, the surrounding tissue. The additional cost is proportional to the metabolic rate required by this "growth", and it dictates the mass flowrate[4]. Denoting as R the radius of the twig or bough (or of the organic tissue surrounding a blood vessel), the mass flow of sap or blood depends on the growth rate, and at steady state can be expressed as:

$$m = K_3 R^2 \tag{27}$$

Where K_3 is a function of the metabolic rate of nutrients needed to build a cylinder of radius R and unit length. The Lagrangian becomes:

$$\mathcal{L}_{ex} = K_4 \frac{R^4}{r^4} + K_5 r^2 \tag{28}$$

With $K_4 = K_1 * K_3$. Experimental evidence shows that the volume per unit length of the two splits is equal to that of the root trunk[i5]:

$$V_{root} = V_{b1} + V_{b2} \tag{29}$$

i.e., that (Figure 10):

$$R_{root}^2 = R_{b1}^2 + R_{b2}^2 \tag{30}$$

And in a symmetric bifurcation:

$$\frac{R_{b1}}{R_{root}} = \frac{1}{\sqrt{2}} \tag{31}$$

The radius R of the twig or epithelial system is obviously much larger than the radius r of the xylems or of the capillaries, and thus the constant K_5 must also contain the number N of the vessels participating to the feeding of R, a constant not affected by the differentiation. Minimizing the Lagrangian leads to:

$$\delta = \frac{r_1}{r_0} = 2^{-2/3} = 0.63 \tag{32}$$

Since the correlation between θ and δ is derived on the basis of the minimization of virtual work, Murray's formula still applies, and for a symmetric bifurcation we obtain:

$$\theta = \arccos\left(\frac{1}{2\delta^2}\right) = \arccos\left(2^{-1/3}\right) = 37.5° \tag{33}$$

i.e., a value almost equal to that prescribed for a symmetric bifurcation before introducing the cubic correlation between the vessel radius and the mass flowrate (Eq. 19). Notice that in this type of model it is necessary to take into account the permeability of the vessel walls: a more detailed description is provided in [32].

7 - Conclusions

In spite of its being overcelebrated -especially in biosciences- the Hess-Murray law does not display a satisfactory agreement with experimental results. Furthermore, most of the assumptions on which the $n=3$ exponent has been derived are far from being realized in nature. Nevertheless, its fruitful legacy is the concept that th*e creation and maintenance of a bifurcation serves an evolutionary criterion of minimal energy cost*. The idea underlying the study discussed in this paper is that it is not the allometry itself, but the "cost/benefit" evaluation that is worthy of further analysis. In fact, a different model based on a different form of the Lagrangian "cost function" leads to a different "optimum" (or to no optimum altogether).

This suggests to extend the horizon of the investigation: in line of principle, it would be very satisfactory if the "construction" of a bifurcation could be derived by a single principle of minimization of the amount of resources needed to create and maintain the branched structure so that it serves the scope for which it was generated. The mass- and energy balances of a living system (be it a plant or an animal) depend on the amount of resources the system can avail itself of, and these "costs" include "nutrients", thermal and chemical flows, water and solar radiation. It is likely that the benefits could be expressed in terms of "more effective access to resources" or "higher productivity", and in such a perspective the most convenient quantification of both resource cost and evolutionary benefit is the equivalent amount of primary exergy resources consumed for each given "task". The resulting models become somewhat more involved and are left for a future study.

8 - References

[1] J.A.Adam, 2011: *Blood Vessel Branching: Beyond the Standard Calculus Problem*, Math. Magazine, 84,196–207

[4] The nutrients required by the maintenance and growth of the "surrounding tissue" diffuse through the selectively permeable blood vessel walls. In plants, leaf tubules display a sufficiently high permeability to distribute sap through the leaf body.

[5] This is called the "Da Vinci rule", because it was apparently stated for the first time in one of Leonardo's notebooks.

[2] A.A.Al-Shammari, E.A.Gaffney, S.Egginton, 2014: *Modelling capillary oxygen supply capacity in mixed muscles: capillary domains revisited*, J. Theor.Biology, 356, 47–61.

[3] A.Bejan, 1982: *Entropy Generation through Fluid and Heat Flow*, J. Wiley, NY.

[4] A.Bejan, 1997: *Constructal-theory network of conducting paths for cooling a heat generating volume*, Int. J. Heat Mass Transf., 40, 799–816.

[5] A.Bejan, 2017: *Evolution in thermodynamics*, Physics Reviews A, v.4

[6] A.Bejan, S.Lorente, 2011: *The constructal law and the evolution of design in nature*, Physics of Life Reviews, 8, n.3, 209-240

[7] V.V. Gafiychuk; I.A. Lubashevsky, 2001: *On the Principles of the Vascular Network Branching*, J. Theoretical Biology, v.212, n.1, 1–9

[8] K.Goodwin, C.M. Nelson, 2020: *Branching morphogenesis*, Development, n.147, dev184499, The Company of Biologists Pub. Ltd

[9] E.Hannezo et al., 2017: *A Unifying Theory of Branching Morphogenesis*, Cell, n.171, 242–255

[10] W.R.Hess, 1903: *Eine mechanisch bedingte Gesetzmäßigkeit im Bau des Blutgefäßsystems*, (A mechanically conditioned regularity in the structure of the blood vessel system), Arch. Entwicklungsmech. Org.,*16*, 632–641

[11] W.R.Hess, 1914: *Das Prinzip des kleinsten Kraftverbrauches im Dienste hämodynamischer Forschung* [Habilitation], (The principle of minimum power applied to blood dynamics studies). Veit. Arch. Anat. Physiol., Leipzig, 1–62

[12] W.Huang, R.T.Yen, M.Mclaurine, G.Bledsoe, 1985: *Morphometry of the human pulmonary vasculature*, J. Al. Physiology, 81, n.5, 2123–2133

[13] Y-L.Huo et al., 2012: *Which Diameter and Angle Rule Provides Optimal Flow Patterns in a Coronary Bifurcation?* , J. Biomech., v. 45 n.7, 1273–1279

[14] H.H.S.Lakshmanan et al., 2019: *Modeling the effect of blood vessel bifurcation ratio on occlusive thrombus formation*, Comp. Methods Biomech. Biomed. Eng. 22, n.11, 972–980.

[15] A.F.Miguel, 2016: *A study of entropy generation in tree-shaped flow structures*, Int. J. Heat & Mass Transf. 92, 349–359

[16] C.D.Murray, 1926a: *The physiological principle of minimum work applied to the angle of branching of arteries*, J. General Physiol., 20 July, 9, n.6, .835–841.

[17] C.D.Murray, 1926b: *The physiological principle of minimum work – I: the vascular system and the cost of blood volume*, Proc. Nat. Acad. Sci., 12, 207–214.

[18] C.D.Murray, 1926c: *The physiological principle of minimum work – II: oxygen exchange in capillaries*, Proc. Nat. Acad. Sci., 12, 299–304.

[19] C.D.Murray, 1927: *A relationship between circumference and weight in trees and its bearing on branching angles,* J. General Physiol., 20 May, 10, n.5, 725–729

[20] M.E.Olson, J.A.Rosel, 2012: *Vessel diameter–stem diameter scaling across woody angiosperms and the ecological causes of xylem vessel diameter variation*, New Phytologist, 197, 1204–1213

[21] J.W. Oyston, M.Hughes, S.Gerber, M.A.Wills, 2015: *Why should we investigate the morphological disparity of plant clades?*, Annals of Botany, 1-21

[22] M.U.Qureshi et al., 2014: *Numerical simulation of blood flow and pressure drop in the pulmonary arterial and venous circulation*, Biomech. Model Mechanobiol., n.13, 1137–1154.

[23] M.S.Razavi, E.Shirani, G.S.Kassab, 2018: *Scaling Laws of Flow Rate, Vessel Blood Volume, Lengths, and Transit Times With Number of Capillaries*, Front. Physiol., v.9, pap.n.581

[24] R. Revellin, F.Rousset, D.Baud, J.Bonjour, 2009: *Extension of Murray's law using a non-Newtonian model of blood,* Theoretical Biology and Medical Modelling, 6, 1-9

[25] W.Roux, 1878: *Über die Verzweigungen der Blutgefässe der Menschen: eine morphologische Studie* (On the branching of blood vessels in humans: a morphological study), Doctoral thesis, Jena; 1878. in W.Roux Gesammelte Abhandlungen über Entwicklungsmechanik der Organismen. V.1, I-XII, 1-76. Wilhelm Engelmann Verlag Leipzig, 1895

[26] A.G.Roy, M.J.Woldenberg, 1982: *A generalization of the optimal models of arterial branching*, Bull. Math. Biology, 44, n.3, 349–360.

[27] V.M.Savage, E.J.Deeds, W.Fontana, 2008: *Sizing Up Allometric Scaling Theory*. PLoS Comput Biol v.4, n.9

[28] A.W.Schoenenberger et al., 2012: *Deviation from Murray's law is associated with a higher degree of calcification in coronary bifurcations,* Atherosclerosis, 221(1):124-130

[29] E.Sciubba, 2010: *Entropy Generation Minima in Different Configurations of the Branching of a Fluid-Carrying Pipe in Laminar Isothermal Flow*, Entropy, 12, 1855-1866

[30] E.Sciubba, 2011: *Entropy Generation Minimization as a Design Tool. Part 1: Analysis of Different Configurations of Branched and Non-branched Laminar Isothermal Flow Through a Circular Pipe*, IJoT 13, 4 (7)

[31] E.Sciubba, 2016: *A Critical Reassessment of the Hess–Murray Law*, Entropy, 13, 283-300

[32] E.Sciubba, 2023: *Exergy cost analysis of bifurcated circular vessels with permeable walls: beyond the Hess-Murray law*, submitted to Bulletin of Mathematical Biology, 2023

[33] A.Serrenho, A.F. Miguel, 2013: *Assessing the influence of Hess-Murray Law on suspension flow through ramified structures*, Defect and Diffusion Forum, v.334-335, 322–328
[34] R.S.Seymour, Q-H.Hu, E.P.Snelling, 2020: *Blood flow rate and wall shear stress in seven major cephalic arteries of humans*, J. Anat. 236,522—530
[35] O.R.Shenker*, 1994: Fractal Geometry is not the Geometry of Nature*, Stud. Hist. Phil. Sri., v.*25,* n.*6,* 967-981
[36] T.F.Sherman, 1981: *On Connecting Large Vessels to Small: The Meaning of Murray's Law*, J. General. Physiol., 78, 431-453
[37] P.J.Schulte, J.R.Brooks, 2003: *Branch junctions and the flow of water through xylem in Douglas-fir and ponderosa pine stems*, J. Experimental Botany, v. 54, n. 387, 1597-1605
[38] D.Slater, R.S et al., 2014: *The anatomy and grain pattern in forks of hazel (Corylus avellana L.) and other tree species*, Trees, n.28, 1437–1448
[39] T.Sochi, 2013: Fluid Flow at Branching Junctions, Int.J. Fluid Mechanics Research, v.42,59-81
[40] B. Soni, A.F.Miguel, A.K.Nayak, 2021: *A critical reassessment of the Hess-Murray law under unsteady flow*, Proc. 12th Conf. on Dynamical Systems Applied to Biology and Natural Sciences, Virtual DSABNS, February 2-5, 2021, 201-202
[41] D.J.Taylor et.al., 2022: *Refining Our Understanding of the Flow Through Coronary Artery Branches; Revisiting Murray's Law in Human Epicardial Coronary Arteries*, Front. Physiol., 13, publ. online apr 4,2022
[42] H.B.M.Uylings, 1977: *Optimization of diameters and bifurcation angles in lung and vascular tree structures*, Bull. Math. Bio, 39, 509–520.
[43] G.B.West, J.H.Brown, 2005: *The origin of allometric scaling laws in biology from genomes to ecosystems: towards a quantitative unifying theory of biological structure and organization*, J. Exp. Biology, 208, 1575–1592.
[44] T.Young, 1809: *The Croonian Lecture: On the Functions of the Heart and Arteries,* Phil. Trans. R. Soc. London*,* 99, 1-31
[45] M.Zamir, S.M.Wrigley, B.L.Langille, 1983: *Arterial bifurcations in the cardiovascular system of a rat*, J. General Phys., 81, 325–335.

ULPGC
Universidad de
Las Palmas de
Gran Canaria

grres ULPGC
group for the research on renewable energy systems

D. Computational Thermo-Fluid Dynamics (CFD)

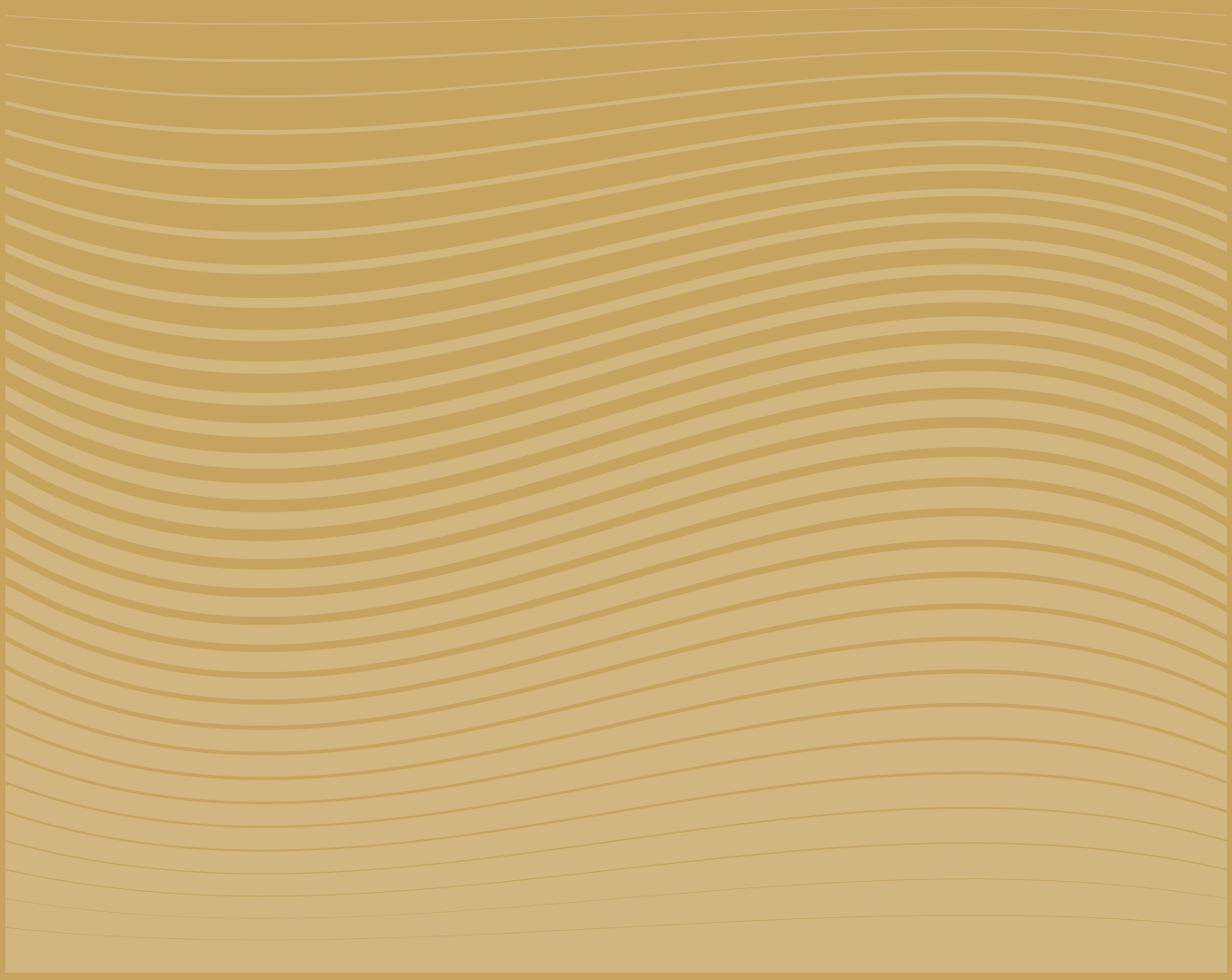

ECOS2023

PROCEEDINGS OF ECOS 2023 - THE 36TH INTERNATIONAL CONFERENCE ON
EFFICIENCY, **C**OST, **O**PTIMIZATION, **S**IMULATION AND ENVIRONMENTAL IMPACT OF ENERGY SYSTEMS
25-30 JUNE 2023, LAS PALMAS DE GRAN CANARIA, SPAIN

Preliminary design guidelines for a vortex-based energy harvester for water flows

Francesco De Vanna[a], Alberto Benato[b, (CA)], and Giovanna Cavazzini[c]

[a] Department of Industrial Engineering - University of Padova, Padova, Italy, francesco.devanna@unipd.it
[b] Department of Industrial Engineering - University of Padova, Padova, Italy, alberto.benato@unipd.it (CA)
[c] Department of Industrial Engineering - University of Padova, Padova, Italy, giovanna.cavazzini@unipd.it

Abstract:
The proposed study presents preliminary design guidelines for vortex-induced vibration energy harvesting devices. In particular, this study combines high-quality computational fluid dynamics techniques to systematically examine the oscillatory behaviour of flow-induced vibration cylinders in cross-flow configurations. Simple cylinders are examined and modelled in terms of masses, damping, and stiffness. The design maps are derived after a comprehensive validation of the numerical model. The maps link the most important flow characteristics at which the device should be installed to the foundational variables relevant to energy recovery and the most important flow properties on which the device must be installed. The results show that the lock-in conditions are achieved with a reduced velocity value of about 5. Additionally, the analysis revealed that the density ratio is a key design parameter, since the functional properties of the device are ensured only for modest values, roughly around 10. In essence, the results provide significant insights into the fluid mechanics of the system, direct indications of the nondimensional groups that regulate system physics, and practical tips for its design.

Keywords:
vortex-induced vibrations, energy harvesting, mini-hydro, virtual design.

1. Introduction

Since the beginning of civilisation, the harvesting of energy from waterways has played a fundamental role in the implementation of human society. In fact, water flows are generally easily accessible and provide a constant energy supply to help with several human activities. However, today, the scientific community recognises that the most profitable water resources for electricity generation have already been fully exploited with standard and well-established technologies. Therefore, novel and disruptive ideas are needed in the hydroelectric landscape. In particular, the mini-hydro aims to generate electricity from tiny/minimal water sources using innovative concepts. These prototypes are a long way different from canonical turbine/watermill plants, the latter requiring significant financial investments and long payback periods. Thus, in a world that is moving from fossil to renewable resources and from concentrate to distributed generation, mini- and microhydro technologies will play a crucial role, especially if the new devices/systems will generate electricity from untapped water flows in an appealing way for building, industrial, and tertiary sectors.

One of the most relevant innovations in this field is related to energy harvesters. Generally speaking, these devices consist of electrofluid-mechanical systems designed to convert the energy content of water flowing into pipes, canals, and conduits into electricity, mainly inducing a vibration on a bluff body linked to an electric generator. In this context, in-depth study and understanding of the Vortex-Induced Vibration (VIV) phenomenon become fundamental, especially concerning its application to energy harvesting systems. Therefore, several studies have made great progress in understanding the causes and characteristics of VIV. This need comes from the fact that vibrations induced by fluid flows on bluff bodies can be particularly dangerous in many engineering situations, such as projects that involve bridges, offshore structures, and cables, in particular if the lock-in state is reached. However, vibrations can also be seen as an energy source and can be used for energy production.

In particular, from the pioneering work of Goswami et al. [1], which presented the experimental results of the properties of the vortex-induced response of a spring-mounted circular cylinder in a low-speed wind tunnel, several other contributions appeared in the literature. Blackburn and Henderson [2], for instance, addressed the free vibration behaviour and wake models in vortex-induced and free oscillations through a numerical model, showing that the method is a valid alternative to experimental setups. Later on, Zhao et al. [3], investigated the steady and oscillatory flow of VIV systems by numerically solving the two-dimensional Reynolds-Averaged Navier-Stokes (RANS) equations. The main finding is that the combination of steady flow and oscillatory pattern widens the lock-in regime, achieving a twice broader lock-in regime concerning the pure steady or pure

oscillatory flow.

The works mentioned above can be considered to be the foundation of VIV fundamental physics, while the use of VIV systems to harvest energy became a hot research topic only in recent years. In particular, the idea at the base of energy harvesting with VIV systems refers to the combination of bluff bodies with piezoelectric generators or coil-magnet electromagnetic systems. In this regard, [4] found that the inviscid component of the fluid is responsible for the instability and that the viscous drag has a dual influence on energy harvesting. In particular, at a given flow speed, its dissipative action reduces the power output while leading to a sustained limit cycle of oscillations. Molino-Minero-Re et al. [5] examined the energy harvesting performance of different cylinder sizes. The results show that the frequency of oscillation decreases as the diameter of the cylinders increases, whereas the power supplied does not follow a clear trend. Also Abdelkefi et al. [6] focused on the motion of a rigid cylinder, providing a mathematical model that accounts for the coupled lifting force, the movement of the cylinder, and the harvested voltage, describing the lift with a modified van der Pol equation. As a result, the influence of the load resistance of the coupled circuit influences the onset synchronisation, shifting it to higher free-stream velocities. As Abdelkefi et al. [6] stated, Mehmood et al. [7] found the same results regarding the effects of the load of the coupled electromechanical circuit. Andrianne et al. [8] developed an energy harvester based on the phenomenon of wind galloping. More recently, Zhu et al. [9] introduced a new perspective in the field of energy harvesting research by proposing a particular configuration with a circular cylinder combined with a free-rotating pentagram impeller. Cylinder vibration and impeller rotation energy are harvested simultaneously. The result shows an efficiency of 22.6% and an expected power output of 885.53 W/m^3. Finally, Nitti et al. [10] studied the coupling mechanism between cross-flow translation and rotation, providing a single degree of freedom cylinder system. The research findings underlined that the rotation maintains the lock-in condition.

Despite the extensive numerical and experimental contributions inherent in the research and development of VIV devices, no investigations have provided detailed and precise design criteria that can be considered valid for maximising the exploitation of the water-fluid dynamics. In particular, literature contributions typically focus on specific configurations, frequently offering laboratory testing, with few hints about the influence of the flow field conditions on the choice of the design parameters such as mass and control circuit settings (i.e., stiffness and damping).

The present research investigates in detail the mutual relationship between fluid dynamics and body behaviour and attempts to offer design guidelines for a VIV energy harvester, with the aim of maximising the energy production by ensuring the lock-in condition. For this purpose, a database of configurations is considered and virtually analysed under different fluid-dynamic operating conditions using Computational Fluid Dynamics (CFD) tools. In this preliminary investigation, only a basic cross-flow cylinder arrangement is addressed, and the influence of the control system mass and stiffness on the device displacements depending on the flow characteristics is explored, the latter being unambiguously connected to electrical power generation.

The rest of the work is organised as follows. Section 2. describes the model and its validation procedure, while Section 3. presents the results of the analysis. Finally, Section 4. makes conclusive remarks.

2. Model description and validation

The configuration, investigated in this study, is represented by a cross-flow cylinder arrangement, whose behaviour under different water flow conditions was thoroughly analysed to establish the basis for an innovative design strategy aimed at maximising energy production. In this Section, the mathematical description of the mechanical model of the device is first presented. Then, the numerical CFD model and its validation are outlined.

2.1. Mechanical model description

The interaction between the flow stream and the cylinder displacement was modelled by a 2D model concerning an elastically mounted circular cylinder immersed in a cross-flow. The cylinder can undergo vertical displacement; therefore, the single degree-of-freedom system is governed by a forced second-order oscillator equation.

$$m\ddot{\tilde{y}} + c\dot{\tilde{y}} + k\tilde{y} = F_y \tag{1}$$

where F_y is the resulting lift force on the surface of the cylinder, m is the mass of the cylinder, while c and k are the damping and stiffness parameters, respectively. $\tilde{y}$, $\dot{\tilde{y}}$ and $\ddot{\tilde{y}}$ denote vertical dimensional movement, velocity, and acceleration. Since the aim of the study is to propose a design strategy not customised to specific conditions, Eq. (1) was transformed into an equivalent nondimensional formulation by casting $y = \tilde{y}/D$ and $t = \tilde{t}U_\infty/D$, being D the diameter of the cylinder, U_∞ the free stream speed of the flow and $\tilde{t}$ the dimensional time. Thus, the following equation holds:

$$\rho d\ddot{y} + \mu\dot{y} + \xi y = 2c_y \tag{2}$$

where $\rho = \rho_s/\rho_\infty$ is the solid-to-fluid density ratio, $d = A/D^2$ is a geometric parameter in which A is the cylinder area, $c_y = F_y/q_\infty$ is the lift coefficient, with $q_\infty = 1/2\rho_\infty U_\infty^2 D$ the free stream pressure load, while $\mu = c/(\rho_\infty U_\infty D)$ and $\xi = k/(\rho_\infty U_\infty^2)$ are the nondimensional damping and stiffness, respectively.

Equation (2) highlights the relevant design criteria for the system. In particular, body motion is affected by the density ratio (ρ), the geometrical characteristic of the body (d) and the nondimensional damping and stiffness (μ, ξ). However, it is also affected by the lift coefficient (c_y), which in turn depends on the interaction between the fluid motion and the cylinder itself. So, to establish the above-mentioned design parameters, it is necessary to define the fluid-dynamics around the cylinder, but this fluid-dynamics can be only determined once the geometry is defined.

To face this challenge by providing useful design guidelines, it is hence necessary to combine the mechanical model with a CFD 2D model, described in the next section, allowing one to determine the fluid-dynamics for a given geometry.

2.2. CFD simulation settings and model validation

To describe the dynamics of the system within a fluid force field, in this study, the numerical model of the cylinder was built in such a way that it can be free to move vertically. In particular, the ANSYS Fluent platform is used to fill the CFD database. The software, in particular, is specifically used to solve the fluid equation of motion, while Python scripts are employed to postprocess the results.

To analyse the behaviour of the cylinder under free flow conditions, the two-dimensional model consists of a rectangular box of size $(50 \times 30)D$, where D indicates the diameter of the cylinder, in which the cylinder is set at $15D$ from the inlet and is subtracted from the entire fluid domain using a Boolean operation to form a solid part (Figure 1).

Regarding the boundary conditions, the *velocity inlet*, which is a known parameter in the design procedure, is imposed on the left side of the domain to obtain a precomputed free stream Reynolds number, $Re = \rho_\infty u_\infty D/\mu_\infty$. A *wall-type* boundary is enforced at the edge of the cylinder, resulting in a non-slip condition for the velocity components. The upper and lower edges correspond to a *symmetry* condition, and the right domain side imposed a homogeneous pressure distribution according to the *pressure outlet* Fluent option.

The initial dynamics is predicted through *hybrid initialisation*, which implies the solution of simplified equations during ten iterations.

Regarding the pressure-velocity coupling algorithm, the recommendations of the ANSYS Fluent user guide have been followed, and the *PISO* algorithm is used. The method provides stable calculations despite a more significant time step and optimal under-relaxation factor for both momentum and pressure. Default options are used. The discretisation process of the spatial terms accounts for second-order upwind formulas.

The system dynamics is simulated according to a RANS approach in both steady and unsteady versions.

In order to identify the most appropriate numerical model to reproduce most of the critical flow properties of the investigated geometry, the turbulence model and the mesh refinement level are defined by comparison with experimental results and validated numerical results.

Regarding mesh size, three hybrid meshes with increasingly refined dimensions with a size of approximately 20k, 40k, and 90k elements are used. The grids will be referred to as coarse (C), medium (M), and fine (F). In all the three cases, the meshing process has been performed with the built-in meshing software available in ANSYS. A hybrid structured/unstructured approach is used to ensure a reasonable approximation near the cylinder wall region and, simultaneously, reduce the calculation time.

Figure 1 provides a mesh overview and some zooms around the cylinder region for the fine grid of 90k elements. In particular, structured cells are located in the near-wall area (Figure 1c) to capture velocity gradients in the boundary layers. Construction lines are also used to cluster most of the computational cells in the wake region and around the cylinder. The entire meshes are built on the basis of the maximum investigated Reynolds number, i.e. $Re = 10^6$, and keeping the wall Y plus distribution, $y_w^+ = \rho_w u_\tau y_w/\mu_w$, below the unit. This ensures that a sufficient number of cells are used to resolve the near-wall velocity gradients throughout the Reynolds spectrum. Note that ρ_w and μ_w are the wall fluid density and molecular viscosity, y_w is the first-off-the-wall cell distance, while $u_\tau = \sqrt{\tau_w/\rho_w}$ denotes the wall friction velocity, with $\tau_w = \mu_w \partial u_p/\partial y$ the wall shear stress.

Regarding turbulence models, three increasingly sophisticated models are considered: the one equation Spalart-Allmaras (SA) model by Spalart and Allmaras [11], the two equations k-ω Shear Stress Transport (SST) model by Menter [12] and the four equations Transition SST (TSST) model by Menter et al. [13]. The convergence of the flow under steady conditions was monitored, granting 10^{-6} residual drop tolerance of all flow parameters.

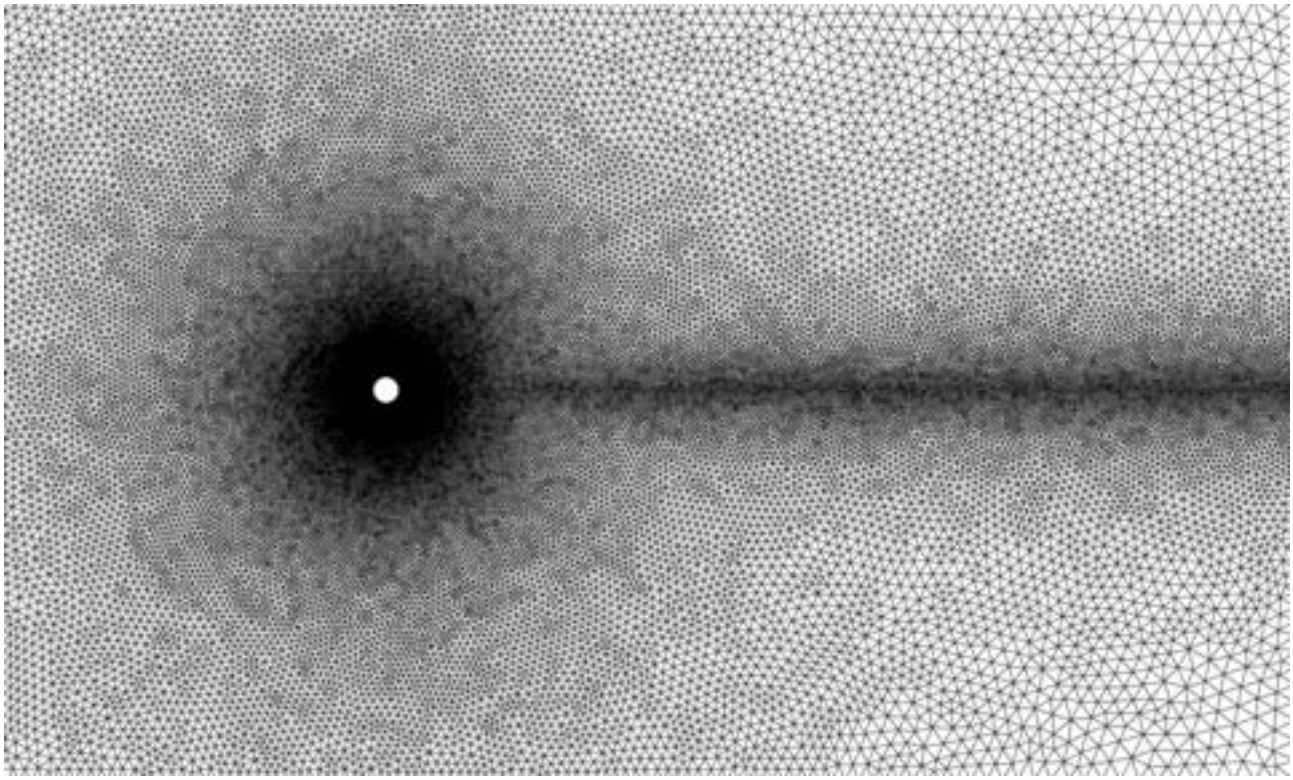

(a) Mesh overview

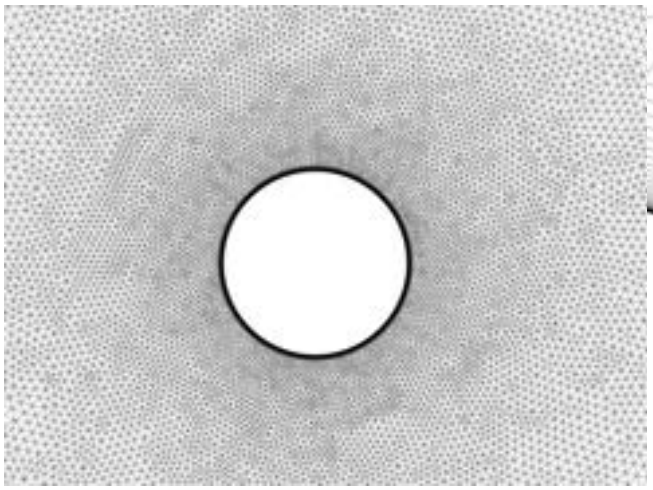

(b) Near cylinder details

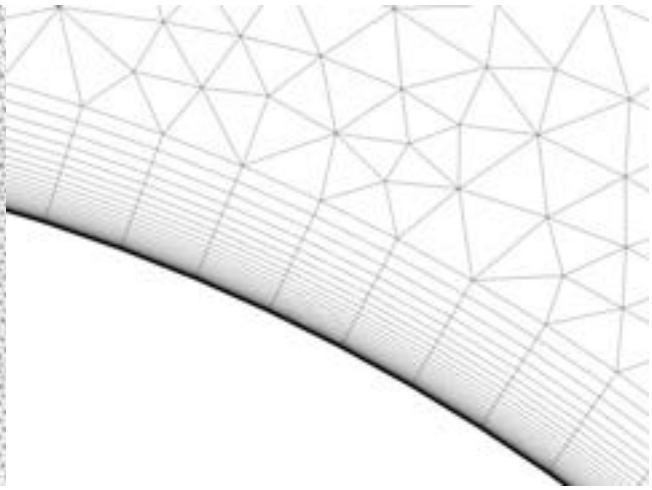

(c) Near wall details

Figure 1: Mesh overview (a) and details (b,c). The figures refers to the fine grid of 90k elements.

To define the most suitable numerical approach, according to the best CFD practises (see, e.g., [14]), the three sets of meshes and the three turbulence models are compared in terms of the cylinder drag coefficient, $C_D = D/q_\infty$, with the experimental results by Warschauer and Leene [15] and with the time average drag value of the unsteady RANS simulations by Ong and Wallace [16] (Figure 2). D denotes the drag force per unit length. In all cases, the Reynolds number of the flow is set to 10^6, which is the maximum Reynolds number that will be used in the following analyses.

As can be seen in Figure 2, the medium and fine arrangements yield little discrepancies, both in the steady- and time-averaged versions of the drag coefficient. A C_D error of around 5% is observed for steady setup, while a 0.4% mismatch is observed in medium arrangements combined with the k-ω SST model.

The results suggest that the medium mesh gives a good compromise between computational performance and accuracy, while adopting the fine mesh would increase the computational time of the simulation drastically, particularly with respect to the unsteady setup, without introducing appreciable accuracy effects.

To fully validate the numerical model, the proper resolution of the boundary layer gradients is also verified. In this regard, we focus on the y_w^+ distribution on the cylinder. Figure 3 shows the y_w^+ distribution as a function of

the angular cylinder coordinate, of the mesh refinement and the turbulence model.

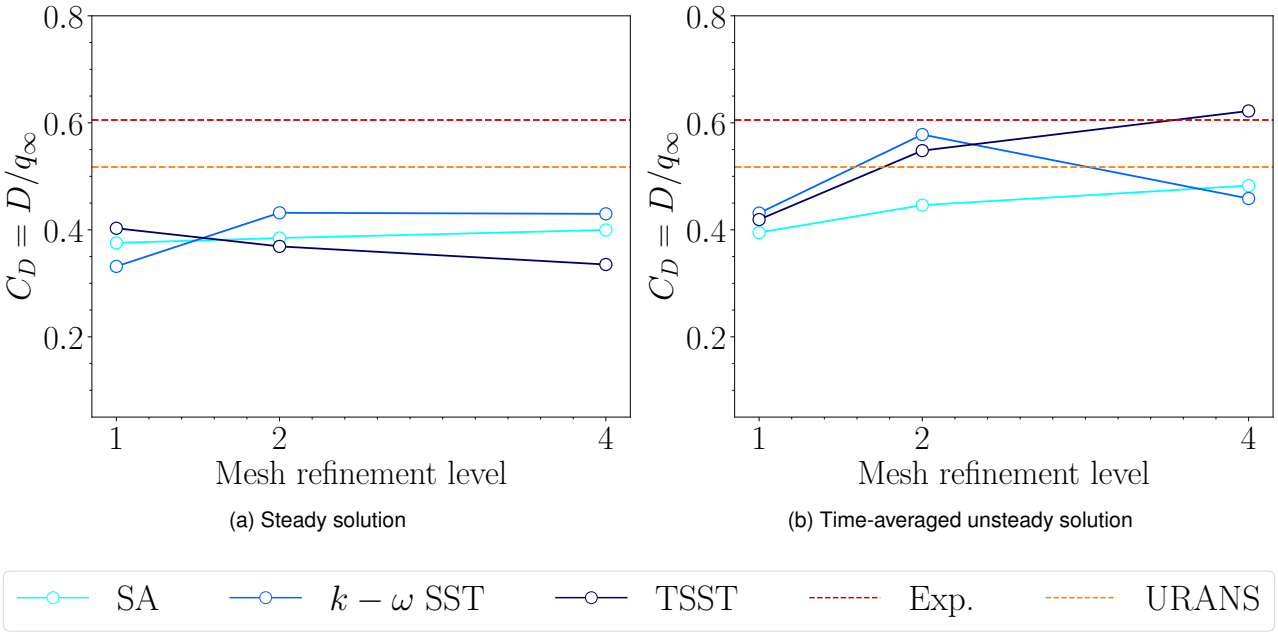

(a) Steady solution

(b) Time-averaged unsteady solution

Figure 2: Comparison between cylinder drag coefficient at Re=10^6 as a function of turbulence model and mesh refinement level. Results are compared with the time average drag value of the unsteady RANS simulations by Ong and Wallace [16] and the experimental results by Warschauer and Leene [15].

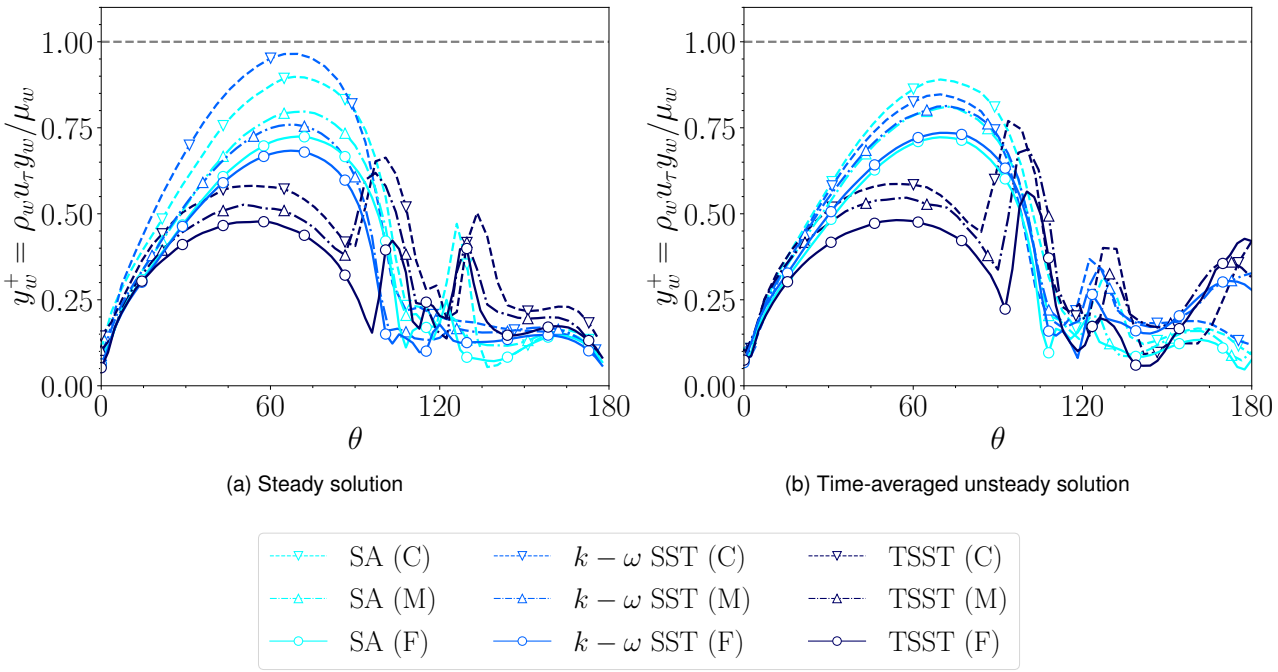

(a) Steady solution

(b) Time-averaged unsteady solution

Figure 3: y_w^+ distribution on the upper half of the cylinder as a function of the mesh refinement level and the turbulence model.

Both time-averaged unsteady case (Fig. 3a) and steady results are provided (Fig. 3b). Note that all the built meshes provide results close to the suggested threshold for wall-resolved RANS simulations, i.e., $y_w^+ \leq 1$, giving an average Y plus value around the cylinder from $y_w^+ = 0.46$ for the coarse mesh to $y_w^+ = 0.33$ for the fine setup. Thus, this result confirms that the proposed numerical model provides a good representation of

the velocity profiles near the cylinder surface. Discrepancies between distributions have to be ascribed to turbulence modeling only.

2.3. The database

VIV components can generate a significant amount of energy only when their fundamental frequency matches the natural frequency of the rigid system in a vacuum environment, a condition known as the lock-in state. To characterise the system the non-dimensional parameters are: *(i)* the Strouhal number associated with the body motion, $St_y = f_y D/U_\infty$, where f_y denotes the first harmonic frequency associated with the body motion in the flow, *(ii)* and the Strouhal number of the flow, $St_v = f_v D/U_\infty$, where f_v denotes the frequency associated with the vortex shedding. This system nondimensional dynamics is conveniently described as a function of the so-called reduced velocity, $U_r = U_\infty/(f_n D)$, representing the relationship between the convective time scale of the flow, U_∞/D, and the natural time scale of the motion of the body in a vacuum environment, $1/f_n$, being $f_n = 1/(2\pi)\sqrt{k/m}$ the natural frequency of the cylinder.

The lock-in state is achieved when $St_y \approx 1/U_r$. On the contrary, outside of the lock-in state, body movement tends to follow the vortex shedding frequency, that is, $St_y \approx St_v$.

According to Equation (2), the system dynamics depends on the design parameters but also on the fluid-body interaction, and hence, to choose the design parameters it is necessary to know beforehand the fluid-dynamic behaviour.

To solve this problem, a database of numerical CFD simulations is created, by determining the fluid-cylinder interaction for different values of the diameter of the cylinder D, of the density ratio, of the control stiffness, of the water velocity, and of the Reynolds number.

The resulting database was then organised as follows. Given a certain geometry, the dynamics of the system was parametrically organised to the density ratio and the nondimensional stiffness, setting for simplicity μ equal to zero. However, since ξ depends on the Reynolds regime of the flow, the results are given as a function of the following modified stiffness:

$$k^* = \frac{kD}{mg} \tag{3}$$

where mg is a reference force, with g denoting gravity acceleration. Obviously, ξ is linked to k^* as follows:

$$\xi = k^* \frac{mg}{\rho_\infty U_\infty^2 D} \tag{4}$$

These organised results will be presented in the following section together with an insight of the fluid dynamics in the lock-in state.

3. Results and discussion

3.1. The fluid mechanics of the system in the lock-in condition

As a first step, we analyse fluid mechanics of the system in lock-in condition. Figure 4 shows the non-dimensional vorticity contours as a function of the cylinder location in a lock-in state. The results refer to $Re = 4 \cdot 10^3$, $\rho = 10$ and $k^* = 6.5$. In particular, Fig. 4a shows the location of $y \simeq 0$ in a negative speed framework, $\dot{y} < 0$. Fig. 4b shows the cylinder flow field around its minimal excursion ($y \simeq y_{min}$, $\dot{y} \simeq 0$). Fig. 4c provides the location of the $y \simeq 0$ cylinder in a positive speed framework, $\dot{y} > 0$). Finally, Fig. 4d shows the flow field where the cylinder reaches the dead top location ($y \simeq y_{max}$, $\dot{y} \simeq 0$).

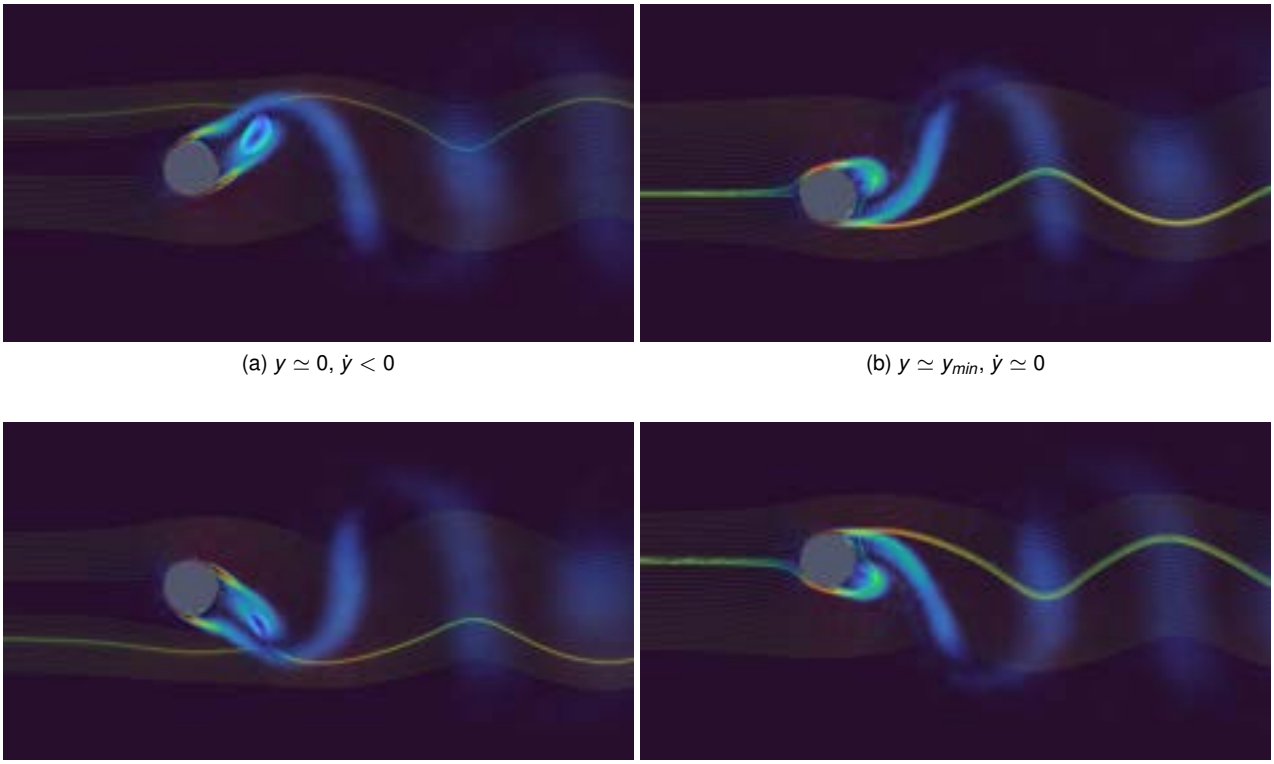

(a) $y \simeq 0$, $\dot{y} < 0$ (b) $y \simeq y_{min}$, $\dot{y} \simeq 0$

(c) $y \simeq 0$, $\dot{y} > 0$ (d) $y \simeq y_{max}$, $\dot{y} \simeq 0$

Figure 4: Instantaneus ω_z vorticity contours and pathlines in four dynamical locations of the cylinder. Present results refers to $Re = 4 \cdot 10^3$, $\rho = 10$ and $k^* = 6.5$.

According to Guilmineau and Queutey [17], the lock-in state is maintained by a vortex pattern near the tail of the cylinder. In particular, the main vortex of the cylinder determines the location of the lower pressure, the value of which is significantly related to the act of motion of the cylinder. The lower and upper dead locations (Fig. 4b and Fig. 4d) indicate that the vortex is quite close to the surface of the cylinder. This state significantly desymmetrises the force field surrounding the cylinder, which is pushed back to the side opposite the tail vortex. The states in which the cylinder passes through the zero displacement location (Figs. 4a and 4c), on the other hand, indicate how the main vortex detaches the surface, allowing the cylinder motion to reach maximum speed.

3.2. Design guidelines and energy production

This section aims to understand the interaction between the frequency of the body motion and the natural frequency of the cylinder when ρ and k^* change in light of the optimisation of the mechanics and fluid dynamics of the system. Indeed, as explained above, the lock-in state is not obvious as a priority, preventing the adoption of a simple and straightforward design procedure. Figure 5 shows the trend of the Strouhal number associated with body movement, St_y, as a function of the reduced speed, U_r, parametrically with respect to the density ratio (Fig. 5a), setting the modified stiffness at 6.5, and the modified stiffness (Fig. 5b), setting the density ratio at 10.

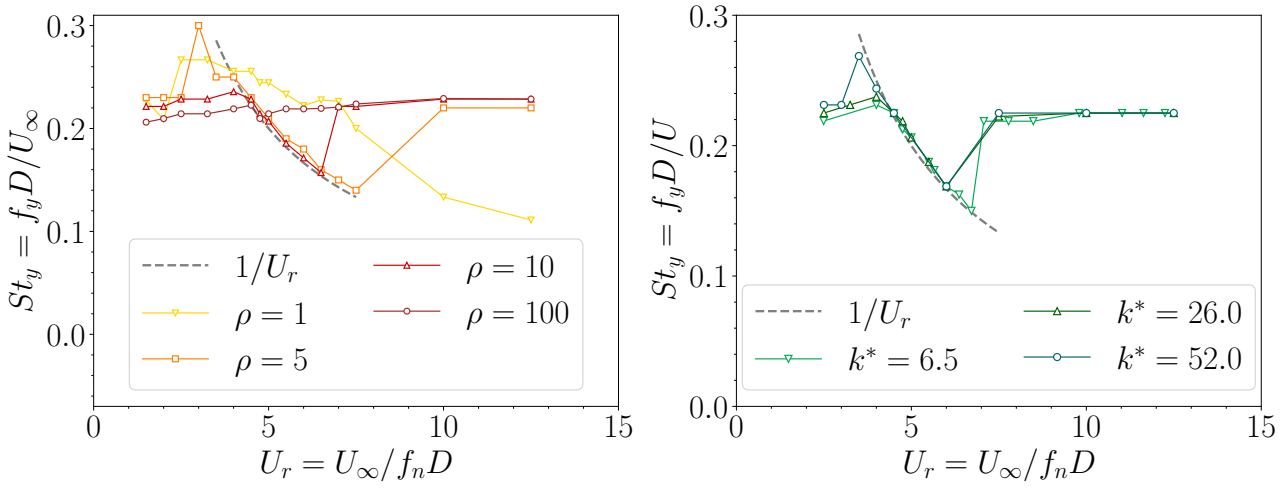

(a) Density ratio effect

(b) Reduced frequency effect

Figure 5: Strouhal number of the body motion as a function of the reduced velocity. Results are reported parametrically to (a) the solid-to-fluid density ratio, fixing $k^* = 6.5$ and (b) the reduced stiffness with $\rho = 10$.

As already explained above, the reduced speed U_r is an excellent self-similarity coordinate since it can be used to compare the convective time with the natural oscillation scale of the cylinder: for certain conditions, as the physical speed increases, a variation in ρ or k^* keeps the curves collapsing in the same intervals. Furthermore, such a representation is extremely useful, as it highlights the lock-in region (grey-shaded branch of the hyperbola in Figure 5).

In Figure 5a, the dynamics of the system is explored with a density ratio of $\rho = \{1, 10, 100\}^T$. The lock-in regime fails for both small and large density ratios. In particular, the $\rho = 1$ arrangement lacks a real lock-in state, and the system tends to a hyperbolic trend but with a systematic error; this indicates that the cylinder oscillates at a frequency primarily determined by the flow, and in general, it is difficult to control. Conversely, high density ratios make the lock-in area mostly disappear, collapsing in a narrow range of reduced speed values. As a result, it is evident that ρ must be kept within a reasonable range, restricting the choice of the VIV material in certain ranges of density, which can be optimised for the specific characteristic of the fluid flow.

In Figure 5b, the analysis is carried out by adjusting ρ to 10 and varying the reduced stiffness within the sample $k^* = \{6.5, 26, 52\}^T$. On the contrary to the density ratio, the stiffness variation preserves the lock-in regime, which always occurs in the same range of reduced velocity, suggesting the existence of an optimal value of the cylinder diameter depending on the fluid velocity.

After grasping the effect of density and stiffness on the lock-in condition, it is also interesting to analyse the system response in terms of displacement in this condition and outside. This analysis is of fundamental importance, as the nondimensional root mean square displacement of the cylinder, y_{rms}/D, is directly related to the amount of energy that the VIV system can extract from the flow.

Figure 6 shows the y_{rms}/D trend as a function of the reduced speed (Fig. 6a) and of the Reynolds number of the flow (Fig. 6b). Data are provided parametrically to the density ratio ρ, with a fixed reduced stiffness of $k^* = 6.5$.

All curves exhibit bumped-like behaviour, clustering non-trivial cylinder displacements in the $U_r = 3 \div 10$ range.

The reduced speed at which the highest displacement is centred is essentially independent of the density ratio and is limited to a band around $U_r \approx 5$, in agreement with the results presented in Figure 5a. On the other hand, the extension of the bump is heavily affected by ρ, and the lower ρ, the higher the operating range of the VIV device.

Analysing the simulation results as a function of the Reynolds number, significant insights can be derived in terms of the flow regime in which the device is supposed to be installed. In fact, as ρ increases, the peak of the displacement moves to a lower Reynolds regime. This is an important information at the design level since it highlights that the higher the device mass with respect to the flow, the lower the Reynolds number tolerated in the system.

In conclusion, the density ratio is a very tricky design parameter, since as ρ increases, the operational range of the lock-in state narrows dramatically, thus reducing the flexibility of the VIV device, but also requires higher Reynolds, which are not so easy to reach in the water flows targeted by the VIV device. Therefore, keeping ρ in

the range of 10 seems to represent a good compromise between flexibility and applicability, in the hypothesis of reduced stiffness of 6.5.

To verify the influence of reduced stiffness k^* on these conclusions, the results were analysed, fixing the density ratio equal to 10 and varying the reduced stiffness. Figure 7 shows the y_{rms}/D trend as a function of the reduced speed (Fig. 7a) and the Reynolds number of the flow (Fig. 7b).

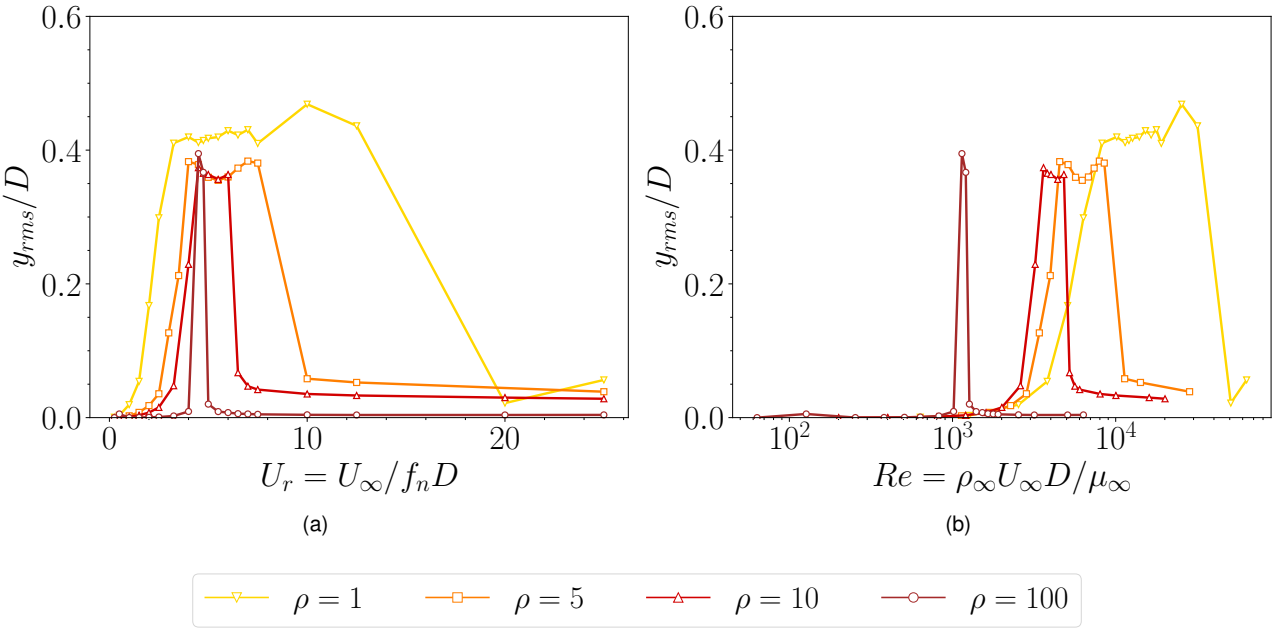

Figure 6: Density ratio effect on the non-dimensional root-mean-square cylinder displacement as a function of (a) the reduced velocity and (b) the flow Reynolds number. Present results are obtained with a reduced stiffness equal to k^* = 6.5.

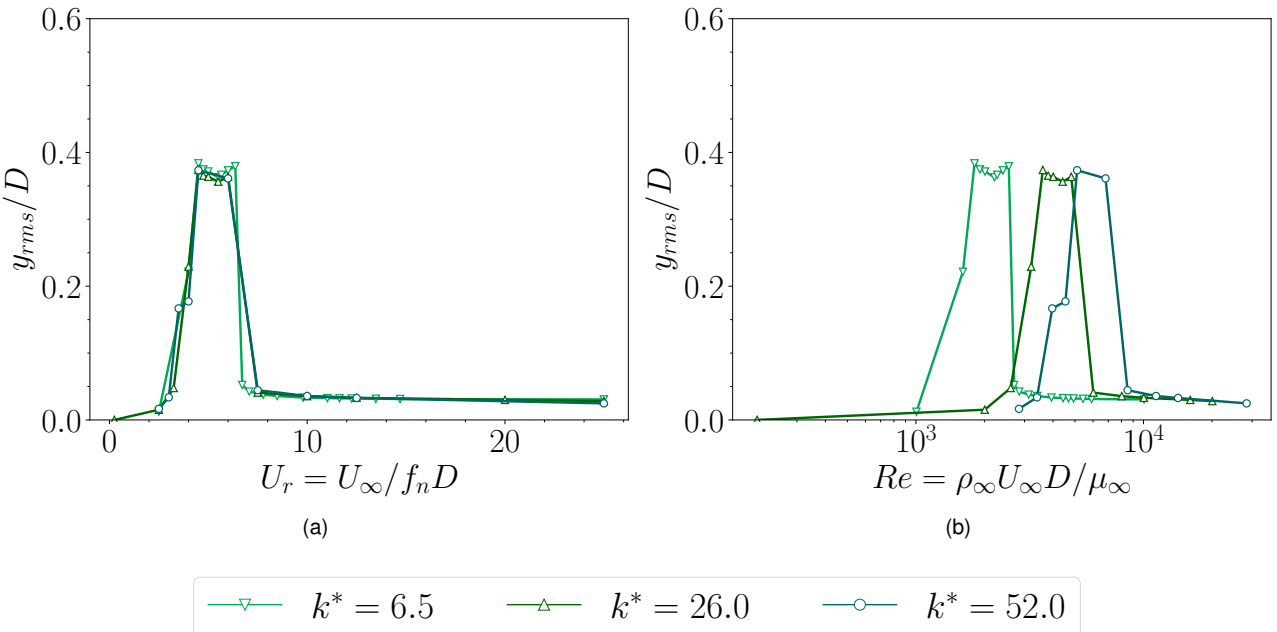

Figure 7: Reduced stiffness effect on the non-dimensional root-mean-square cylinder displacement as a function of (a) the reduced velocity and (b) the flow Reynolds number. Present results are obtained with a density ratio equal to ρ = 10.

It can be seen that the reduced stiffness keeps the displacement amplitude constant as a function of the Reynolds regime without narrowing or widening the lock-in region (Fig. 7b). Subsequently, in terms of reduced velocity (Fig. 7a), this causes the system lock-in in the same U_r range, clustered around 5. Therefore, another important design guideline for VIV devices can be deduced: controlling the stiffness of the system is the key to match the lock-in condition (and hence the maximum displacement) with the flow regime of the installation site.

Note that in the lock-in state, the cylinder oscillates with mean square displacements of $\approx 0.4D$ (Fig. 7); thus performing harmonic oscillations of amplitude $\approx 0.4\sqrt{(2)}D$. This result is independent of the Reynolds regime and of the mechanical characteristics of the system, which is a really interesting starting point for the preliminary design of the system.

Finally, it is also possible to estimate the mechanical power that can be extracted by the VIV device in the different configurations (reduced stiffness, density ratio, etc.). In particular, the non-dimensional mechanical power (power coefficient) is determined according to the following equation:

$$P^*_{rms} = \sqrt{\frac{1}{\Delta T}\int_{t+\Delta T}\left[\frac{\dot{y}(t)}{U_\infty}\frac{F_y(t)}{1/2\rho_\infty D U^2_\infty}\right]^2 dt} \tag{5}$$

where $F_y(t)$ and $\dot{y}(t)$ are the instantaneous lift force and cylinder velocity respectively.

Figure 8 shows the trend of the mechanical power coefficient, P^*_{rms}, as a function of the reduced speed and parametrically with the density ratio and the reduced-stiffness.

As shown in Figure 8, P^* is significant only in the lock-in area ($U_r \approx 5$) where values around 0.2 are reached. In particular, if the density ratio increases, the power coefficient decreases (Fig. 8a); while, as the modified stiffness varies, the power output remains practically constant.

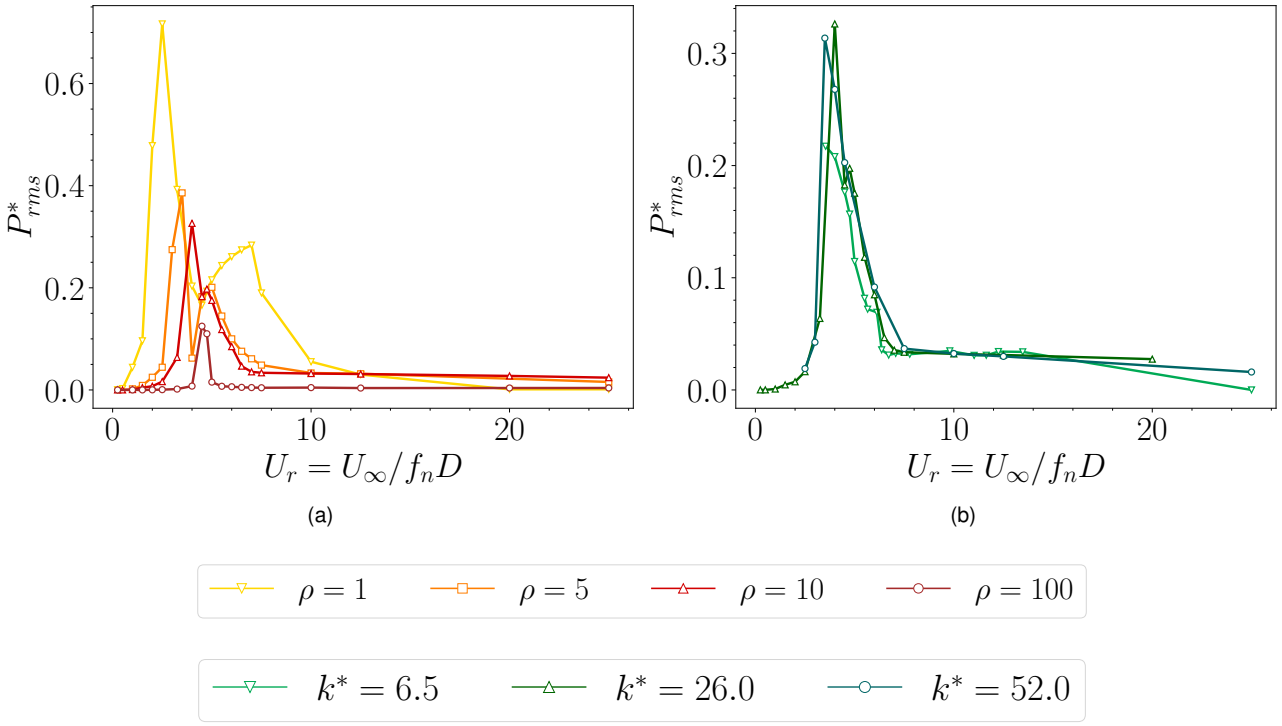

Figure 8: Non-dimensional power coefficient associated to the cylinder body motion as a function of the density ratio, ρ and the reduced stiffness, k^*.

4. Conclusions

The proposed investigation addresses the critical aspects of the design of VIV devices for energy harvesting, with the aim of providing some preliminary design guidelines and estimation of the mechanical power that can be extracted.

In particular, a simple cylinder configuration in cross-flow conditions is investigated and modelled in terms of mass, damping, and stiffness. This model was combined with a numerical CFD model to estimate the

fluid-body interaction. By means of these models, the system behaviour was investigated in several configurations, by parametrically varying the system fundamental mechanical properties (solid-to-fluid density ratio and stiffness of the control system), the cylinder geometry (diameter), and the flow regime in which it is immersed.

The resulting database was analysed to highlight the influence of the different parameters on the achievement of the lock-in conditions, which results to be achieved for a reduced velocity value of about 5.

The analysis also revealed that the density ratio is a key design parameter, since the functional properties of the VIV device are ensured only for modest values of it, roughly around 10. Smaller values of the density ratio make the system lose its ability to attain the lock-in state by creating a difficult-to-control oscillation pattern with optimal Reynolds values between 10^4 and 10^5. On the other hand, high density ratio values dramatically shrink the lock-in zone, limiting the flexibility of the VIV device to maintain lock-in conditions even in operating conditions close to the optimal one.

Concerning the stiffness effects, this well fits the system modulation, especially to match the maximum displacements on a specific Reynolds regime. In fact, if the density ratio is kept constant, the control system stiffness can retain the cylinder displacements and lock-in state at different Reynolds regimes.

Future analyses will investigate a broader spectrum of density ratios and reduced stiffness to build an extensive database in view of system sizing. The damping effect and other geometrical configurations will also be analysed to further investigate the VIV devices behaviour and their best design practises.

Acknowledgments

This study is founded by the European Union. The project has received funding from the European Climate, Infrastructure and Environment Executive Agency research and innovation programme under grant agreement number 101084362. However, the views and opinions expressed are those of the authors alone and do not necessarily reflect those of the European Union. Neither the European Union nor the granting authority can be held responsible for them. The authors also acknowledge the CINECA award under the ISCRA initiative, for the availability of high-performance computing resources with the project H-HOPE1 HP10CGZTU8.

Abbreviations

CFD Computational Fluid Dynamics

RANS Reynolds-Averaged Navier-Stokes

SA Spalart-Allmarass

SST Shear Stress Transport

TSST Transition Shear Stress Transport

VIV Vortex-Induced Vibration

References

[1] Indranil Goswami, Robert H Scanlan, and Nicholas P Jones. Vortex-induced vibration of circular cylinders. i: experimental data. *Journal of Engineering Mechanics*, 119(11):2270–2287, 1993. doi: https://doi.org/10.1061/(ASCE)0733-9399(1993)119:11(2270).

[2] Hugh Blackburn and Ron Henderson. Lock-in behavior in simulated vortex-induced vibration. *Experimental Thermal and Fluid Science*, 12(2):184–189, 1996. doi: https://doi.org/10.1016/0894-1777(95)00093-3.

[3] Ming Zhao, Kalyani Kaja, Yang Xiang, and Guirong Yan. Vortex-induced vibration (VIV) of a circular cylinder in combined steady and oscillatory flow. *Ocean Engineering*, 73:83–95, 2013. doi: https://doi.org/10.1016/j.oceaneng.2013.08.006.

[4] Kiran Singh, Sébastien Michelin, and Emmanuel De Langre. Energy harvesting from axial fluid-elastic instabilities of a cylinder. *Journal of Fluids and Structures*, 30:159–172, 2012. doi: https://doi.org/10.1016/j.jfluidstructs.2012.01.008.

[5] Erik Molino-Minero-Re, Montserrat Carbonell-Ventura, Carles Fisac-Fuentes, Antoni Mànuel-Làzaro, and Daniel Mihai Toma. Piezoelectric energy harvesting from induced vortex in water flow. In *2012 IEEE International Instrumentation and Measurement Technology Conference Proceedings*, pages 624–627. IEEE, 2012. doi: https://doi.org/10.1109/I2MTC.2012.6229686.

[6] A Abdelkefi, MR Hajj, and AH Nayfeh. Phenomena and modeling of piezoelectric energy harvesting from freely oscillating cylinders. *Nonlinear Dynamics*, 70(2):1377–1388, 2012. doi: https://doi.org/10.1007/s11071-012-0540-x.

[7] A Mehmood, A Abdelkefi, MR Hajj, AH Nayfeh, I Akhtar, and AO Nuhait. Piezoelectric energy harvesting from vortex-induced vibrations of circular cylinder. *Journal of Sound and Vibration*, 332(19):4656–4667, 2013. doi: https://doi.org/10.1016/j.jsv.2013.03.033.

[8] Thomas Andrianne, Renar P Aryoputro, Philippe Laurent, Gérald Colson, Xavier Amandolese, and Pascal Hémon. Energy harvesting from different aeroelastic instabilities of a square cylinder. *Journal of Wind Engineering and Industrial Aerodynamics*, 172:164–169, 2018. doi: https://doi.org/10.1016/j.jweia.2017.10.031.

[9] Hongjun Zhu, Ying Zhao, and Tongming Zhou. Cfd analysis of energy harvesting from flow induced vibration of a circular cylinder with an attached free-to-rotate pentagram impeller. *Applied energy*, 212:304–321, 2018. doi: https://doi.org/10.1016/j.apenergy.2017.12.059.

[10] A Nitti, G De Cillis, and MD de Tullio. Cross-flow oscillations of a circular cylinder with mechanically coupled rotation. *Journal of Fluid Mechanics*, 943, 2022. doi: https://doi.org/10.1017/jfm.2022.442.

[11] Philippe Spalart and Steven Allmaras. A one-equation turbulence model for aerodynamic flows. *AIAA*, 439, 01 1992. doi: 10.2514/6.1992-439.

[12] F. Menter. Two-equation eddy-viscosity turbulence models for engineering applications. *AIAA Journal*, 32:1598–1605, 01 1994. doi: https://doi.org/10.2514/3.12149.

[13] Florian Menter, RB Langtry, S. Likki, Y. Suzen, P. Huang, and S Völker. A correlation-based transition model using local variables-part I: model formulation. *Journal of Turbomachinery*, 128, 07 2006. doi: 10.1115/1.2184352.

[14] Francesco De Vanna, Danilo Bof, and Ernesto Benini. Multi-objective rans aerodynamic optimization of a hypersonic intake ramp at mach 5. *Energies*, 15(8):2811, 2022. doi: https://doi.org/10.3390/en15082811.

[15] K.A. Warschauer and J.A. Leene. Experiments on Mean and Fluctuating Pressures of Circular Cylinders at Cross Flow at Very High Reynolds Numbers. *Proceeding of International Conference on Wind Effects on Buildings and Structures*, pages 305–315, 1971.

[16] Lawrence Ong and J Wallace. The velocity field of the turbulent very near wake of a circular cylinder. *Experiments in fluids*, 20(6):441–453, 1996. doi: https://doi.org/10.1007/BF00189383.

[17] Emmanuel Guilmineau and P Queutey. A numerical simulation of vortex shedding from an oscillating circular cylinder. *Journal of Fluids and Structures*, 16(6):773–794, 2002. doi: https://doi.org/10.1006/jfls.2002.0449.

PROCEEDINGS OF ECOS 2023 - THE 36TH INTERNATIONAL CONFERENCE ON
EFFICIENCY, **C**OST, **O**PTIMIZATION, **S**IMULATION AND ENVIRONMENTAL IMPACT OF ENERGY SYSTEMS
25-30 JUNE 2023, LAS PALMAS DE GRAN CANARIA, SPAIN

CFD-driven optimization of a Venturi tube for wastewater treatment applications

Francesco De Vanna[a], Alberto Benato[b (CA)], Matteo Ballan[c] and Anna Stoppato[d]

[a] Department of Industrial Engineering - University of Padova, Padova, Italy, francesco.devanna@unipd.it
[b] Department of Industrial Engineering - University of Padova, Padova, Italy, alberto.benato@unipd.it (CA)
[c] Department of Industrial Engineering - University of Padova, Padova, Italy, matteo.ballan@studenti.unipd.it
[d] Department of Industrial Engineering - University of Padova, Padova, Italy, anna.stoppato@unipd.it

Abstract:

The paper presents a procedure for a systematic numerical optimisation of a Venturi tube for water treatment using cavitation conditions. The numerical method employs computational fluid dynamics techniques within a Reynolds-Averaged Navier-Stokes framework in conjunction with an optimisation procedure to improve a baseline Venturi configuration. To define the numerical model associated with the baseline solution, a reliable meshing method is given. The procedure evaluates various mesh sizes and turbulence closure to determine the ideal balance between processing time and accuracy. The model is then used as a starting point for an optimisation procedure. The optimised arrangement improves the mean vapour quality of the tube by approximately 130% compared to the original geometry.

Keywords:

Hydrodynamic cavitation; Venturi tube; CFD investigation; wastewater treatment.

1. Introduction

Hydrodynamic cavitation is a well-known phenomenon gaining prominence due to its use in various technical and chemical processes, such as emulsification, oxidation, nanomaterial production, and wastewater treatment. Hydrodynamic cavitation aims to induce cavitating microbubbles into the water flow, and the Venturi tube is a commonly adopted device for this purpose.

The Venturi tube is a simple device that consists of a converging section where the flow is accelerated, a throat zone where the pressure reaches its lowest value, and a diverging segment where the tube recovers the cross section of the pipe in which it is placed. If the ratio between the Venturi throat diameter and the diameter of the external pipe is small enough, the increase in velocity induced by section reduction can lead to cavitating conditions in the throat flow. When the static pressure falls below the vapour pressure, cavitation is defined as the development, growth, and collapse of microbubbles or vapour cavities in a liquid. Due to the adiabatic compression of the cavities, the collapse occurs at various points. Consequently, a substantial amount of energy is quickly released, generating a supercritical state with high temperature and pressure (5000 K and 500 bar) similar to those on the solar surface. These conditions accelerate chemical and physical transformations, which can be used for a variety of practical applications, including the destruction of chemical contaminants in water (Gogate et al. [1], Dular et al. [2], Sarc et al. [3], Biasiolo et al. [4]).

Carpenter et al. [5] sum up the theory of cavitation, focussing on the hotspots of collapsing cavities, and discuss the available approaches to generate the multiphase phenomena and the corresponding uses of the technology in different contexts. Researchers emphasised the importance of the specific geometric characteristics of the Venturi tube.

Using Computational Fluid Dynamics (CFD) techniques, Dastane et al. [6] numerically analysed the cavitating flow in a Venturi tube, comparing various mesh sizes and performing single- and multiphase simulations. They observed that the single-phase method underestimates the value of the input pressure. Bashir et al. [7] offer a CFD-based optimisation technique for the geometry of cavitating Venturi tubes. Using experimental tests and simulations, Li et al. [8] explored the impact of Venturi geometries on cavitation.

Despite the already published work, the prediction of cavitating flows using computational methods is still a critical issue, and only few results are available in the literature. In particular, the most advanced CFD strategies, such as Large-Eddy Simulations (LES) and Direct Numerical Simulations (DNS), can hardly be adopted in multiphase and complex flow conditions, such as those about a deep cavitating wall-bounded flow. Therefore, digital prototyping of such devices is still demanded by Reynolds-Averaged Navier-Stokes (RANS) based models, albeit with all the limitations that such strategy embeds.

The present work aims to determine the most critical parameters that influence the RANS CFD simulation results for flow cavitation inside Venturi tubes and to provide optimisation suggestions to enhance the Venturi baseline design. A RANS model has been built and used to predict the two-phase flow and to make a comparison between various model resolutions in terms of grid discretization level. The results indicate that high grid resolutions are required for numerically insensitive outcomes. Finally, the baseline model is used as a starting point for an optimisation procedure devoted to design a novel tube shape capable of improving steam generation.

The paper is organised as follows: Section 2. presents the numerical model and provides a description of the numerical settings. Section 3. summarises and discusses mesh sensitivity analysis with the aim of finding the optimal mesh size. Section 4. provides hints regarding the Latin Hypercube Sampling (LHS) method implemented to optimise the Venturi geometry and gives quantitative information concerning the characteristics of the tube shape. Finally, Section 5. gives the concluding remarks.

2. Computational setup

The development of a Venturi tube optimised configuration requires the development of a properly calibrated numerical model of the device. To this end, the University of Padova research group (Turbomachinery and Energy Systems - TES Group), after an in-depth review of the literature, has selected the baseline geometry of the Venturi tube (see De Vanna et al. [9]). The developed model reproduces the geometry proposed by Shi et al. [10]. The baseline geometry is used to (i) correctly set the numerical model, (ii) determine the most appropriate grid dimension, and (iii) choose the reliable turbulence model.

Figure 1 shows the shape of the baseline configuration, while Table 1 lists the dimensions of the Venturi tube. The device has a throat diameter (d) of 3.18 mm, while the diameter of the pipe (D) is equal to 12.7 mm. The converging angle slopes is of 19° while the diverging one is equal to 5°. The CFD model is extended by 30 and 80 mm before and after the L_1 and L_5 segments to achieve fully developed turbulent flow and prevent unphysical recirculations. The axial symmetry of the tube limits the task to a 2D domain. Ansys-Workbench 2020 R1 is used to build both geometry and grids, while Ansys-Fluent is used to solve the flow field [11].

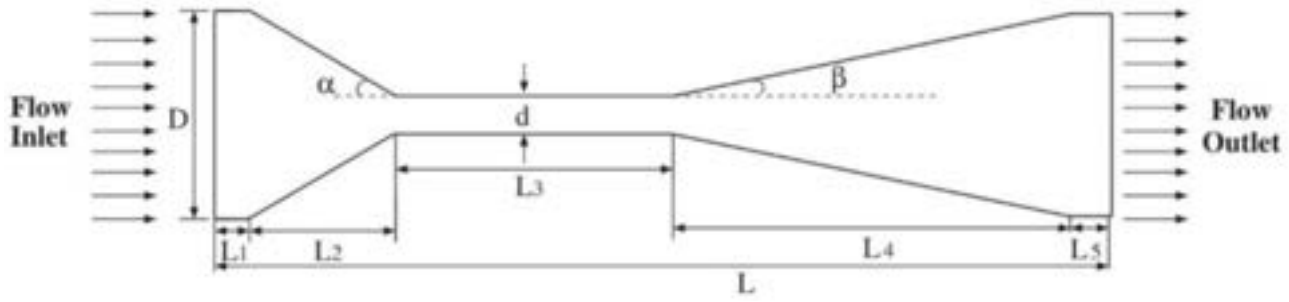

Figure 1: Schematic view of the Venturi tube geometry. Dimensions are listed in Table 1.

Table 1: Geometry characteristics of the baseline shape of the Venturi tube as given by Shi et al. [10].

D (mm)	d(mm)	L_1 (mm)	L_2 (mm)	L_3 (mm)	L_4(mm)	L_5 (mm)	α (°)	β (°)
12.7	3.18	6.00	14.0	20.0	54.0	6.00	19.0	5.00

Based on the experience of the research team in the field of CFD, three structured meshes of 100′000 (100k), 200′000 (200k) and 300′000 (300k) elements have been built and tested with the aim of finding the dimension of the grid that guarantees a good compromise between the accuracy of the results and the efficiency of the computation.

Adopting the internal software suites, each computational grid is quality validated to ensure a maximum skewness value below 0.22, an inflation growth rate between 1.05 and 1.20, and an orthogonality quality value above 0.99. Inflation is placed close to the walls to improve the resolution in the boundary layer and ensure that the wall Y plus (defined as $y^+ = y_w/\delta_\nu$, $\delta_\nu = \mu_w/(\rho_w u_\tau)$) values are accurate. δ_ν is the wall viscous length while ρ_w and μ_w are the fluid density and viscosity at the location of the wall, respectively. u_τ is the friction velocity, while y_w is the first-off-the-wall cell distance. Specifically, the objective is to address a y^+ value lower than 1. Table 2 reports the mean aspect ratio, the mean skewness and the mean orthogonal quality of the three developed meshes while Figure 2 shows an extent zoom of the 300k grid in the Venturi inflowing corner.

Table 2: Grid quality parameters.

Mesh	Mean aspect ratio	Mean Skewness	Mean Orthogonal quality
100k	4.194	$2.80 \cdot 10^{-2}$	0.996
200k	4.508	$2.73 \cdot 10^{-2}$	0.996
300k	6.091	$2.21 \cdot 10^{-2}$	0.997

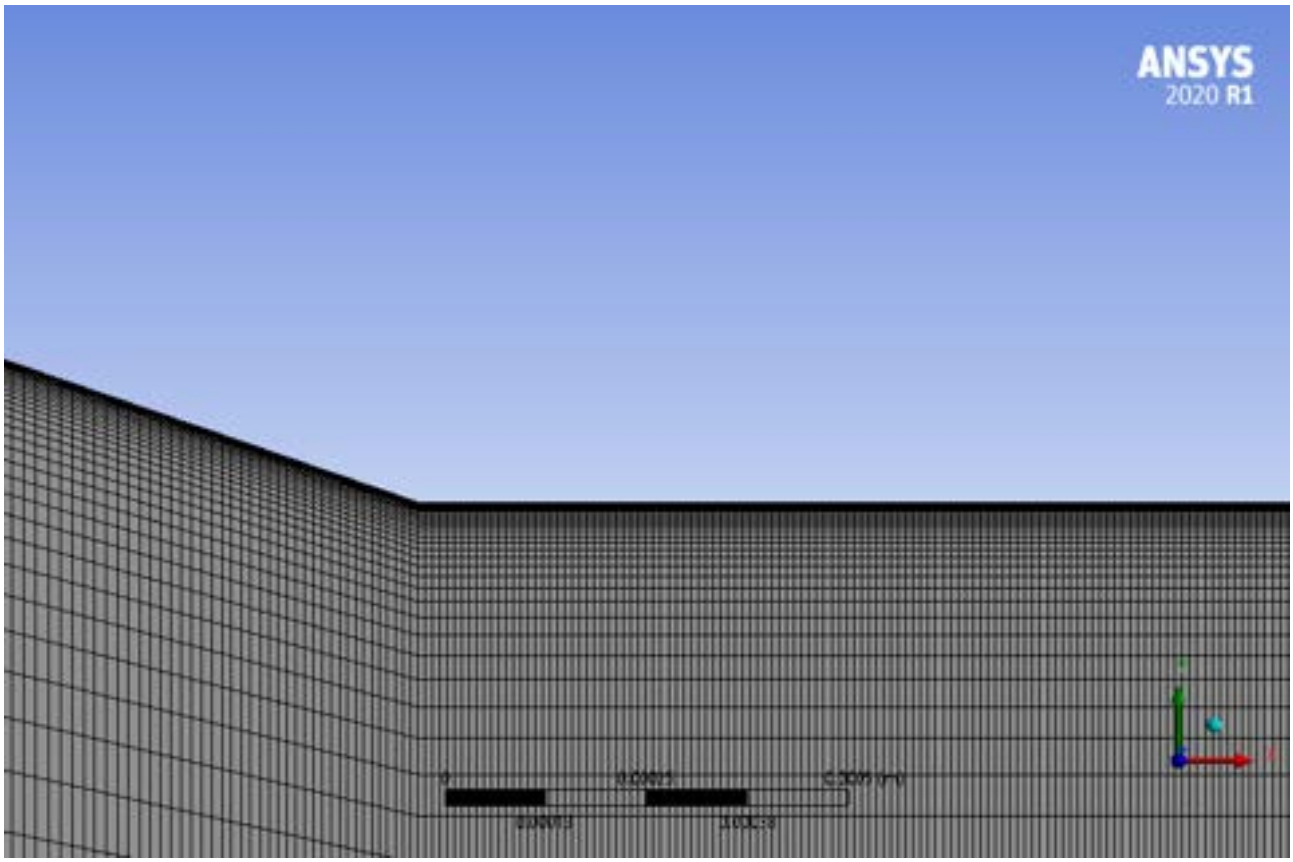

Figure 2: Detailed view of the 300k mesh in the inflowing Venturi corner.

The system's dynamics is simulated by finding solutions to an incompressible RANS system of equations in a steady-state framework. The flow field dynamics is solved using four different turbulence models. As said, the test of different turbolence models is used to find the best compromise between accuracy and calculation time.

The complexity of the model gradually increases from first to last: the one-equation Spalart-Allmaras (SA) model, the two-equations k-epsilon realisable model, the two-equations k-omega shear stress transport (SST) model, and the four-equation transition SST (TSST) model.

To solve the mass and momentum conservation equations related to the behaviour of the cavitating flow in the mixture model, the pressure-velocity coupled method is adopted. Thus, to satisfy the requirements of the coupling algorithms, the equations include implicit discretization of the pressure gradient terms and the mass flow.

To discretise the convective components in the transport equations for the vapour volume fraction, the Quadratic Upwind Interpolation for Convection Kinematics (QUICK) technique is used. The PREssure STaggering Option (PRESTO) method is adopted in the computation of the pressure. To discretize the convection terms that are included in the momentum equations, the second-order upwind technique is selected. Finally, the "water-vapor" mixture model is adopted to mimic two-phase cavitation flows for multiphase flow solutions. The phase transition is computed according to the Schnerr-Sauer cavitation model. As boundary conditions, the "pressure inlet" and "pressure outlet" conditions are enforced at the inflowing and outflowing edges, respectively; this means setting the total and static pressure. Additionally, "adiabatic no-slip wall" conditions are enforced at the Venturi internal surfaces. In the nameplate conditions, a condition that embeds cavitating events in the throat of the tube is set. This means an inlet total pressure, p°_{in}, of 180'000 Pa and a static pressure at the

outlet, p_{out}, of 101'325 Pa.

3. Baseline Venturi model validation procedure

The validation process of the developed model aims to define the most suitable turbolence model and grid size. First, mesh sensitivity analysis is performed with the total intake pressure set at its design value (180 kPa). The process follows CFD best practises according to De Vanna et al. [12]. Figure 3 provides the freestream-scaled axial velocity, u/u_∞, and pressure, p/p_∞, distributions along the throat-scaled axial coordinate, $x^* = x/d$, as a function of both the grid resolution and the turbulence model. As shown in Figure 3, results are clustered in a really narrow band, except for the results obtained with the SA model and in the coarser cases. Therefore, the comparison allows to certainly exclude the simplest turbulence model as well as the mesh with the lower resolution.

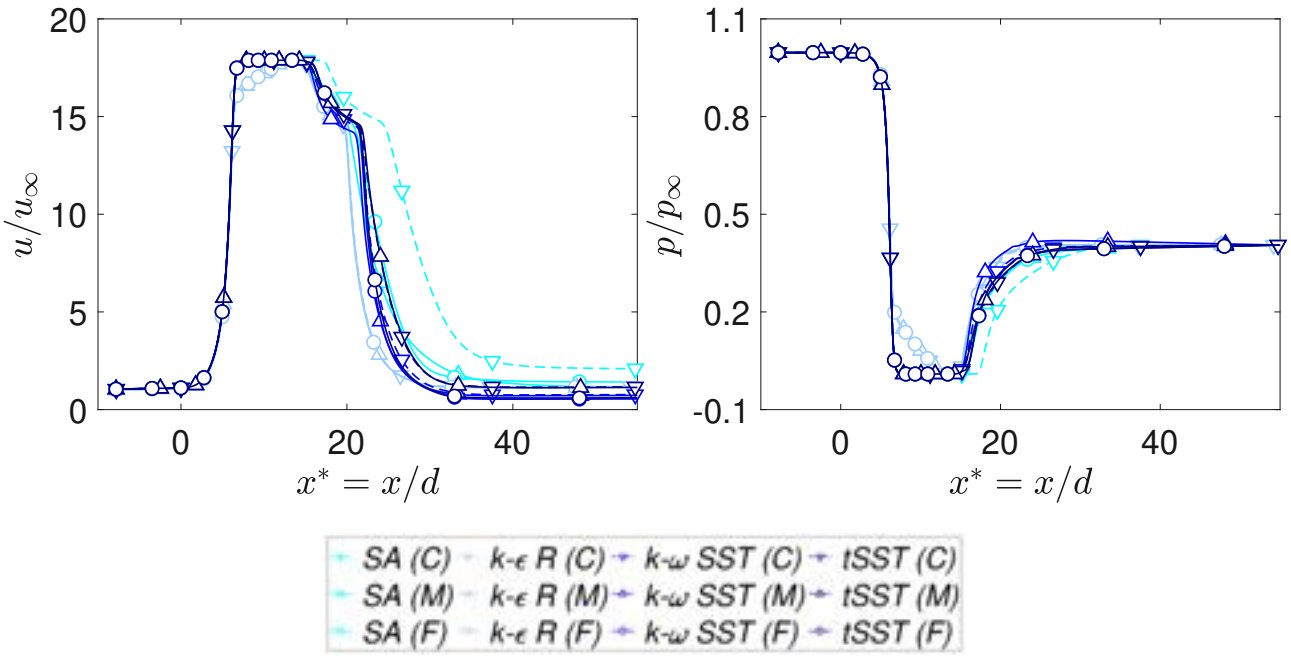

Figure 3: Axial velocity and pressure distributions as a function of the grid refinement and turbulence model. The lighter to darker tone of the colour refers to gradually more complex turbulence models, i.e. SA, $k-\epsilon$ realisable, $k-\omega$ SST and TSST, respectively.

The global parameters are compared to fine-tune the grid and assess the influence of the discretization level on the investigation results. Figure 4 depicts the non-dimensional Venturi pressure drop and the coarse-scaled drag force as a function of the grid resolution. The 100k element mesh somewhat underestimates the drop in pressure, but the model saturates the value after 200k grid refinements. Instead, the drag coefficient data are exactly matched as the grid size changes. This implies that an excessive number of mesh elements would be unreasonable, which would only result in stressing computer resources. Based on the evaluation of global parameters, the 200k configuration seems to be the ideal trade-off between numerical accuracy and computing load. Thus, the 200k mesh arrangement, combined with the k-omega SST, is selected and used for the upcoming analyses.

4. Latin Hypercube Sampling and optimisation results

In this work, the Latin Hypercube Sampling (LHS) technique is used to improve the design of the Venturi geometry regarding a priori specified goals. The LHS technique has been proposed by McKay et al. [13] as a sampling mechanism to fill a design variable space. The importance of sampling is derived from the need to correctly choose the input variables of a mathematical model that describes real occurrences, thus gathering the necessary information about the probability distribution of the output with the fewest number of inputs. Swiler et al. [14] define Latin Hypercube Sampling as a technique to examine the probability distribution of a multivariate function with k variables by selecting n different values for each variable. Using the equal probability reasoning, the values are selected by dividing each variable into n different pieces. As a result, after randomly selecting a value from each layer, the values collected for each variable are randomly paired, producing n evaluations of the input variables. Loh [15] provided a more detailed examination of the theoretical

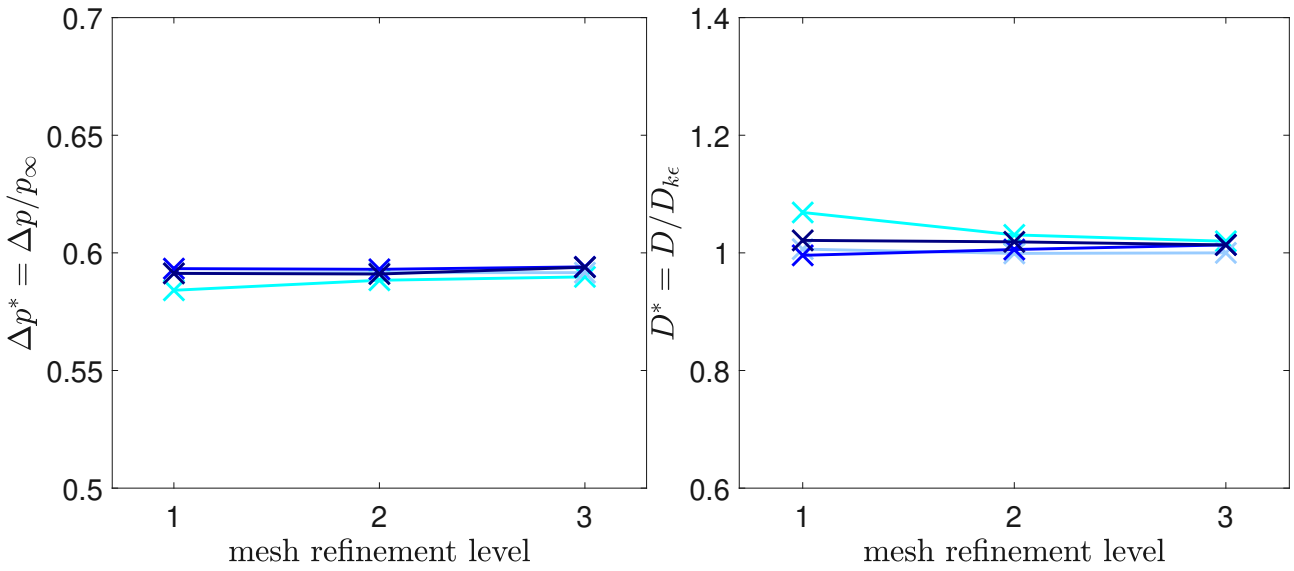

Figure 4: Model validation as a function of the grid refinement and turbulence model. From lighter to darker tones colours refer to gradually more complex turbulence models, i.e., SA, $k-\epsilon$ realisable, $k-\omega$ SST and TSST, respectively. The refinement level refers to the 100k, 200k, and 300k mesh, respectively.

background of the LHS approach, as well as the fundamental mathematical formulation of the method. As presented by Helton et al. [16], this technique has been widely used in complex system analyses, with its main characteristics highlighted, such as its simplicity and ability to result in more uniform stratification than other random sampling strategies, revealing to be a suitable method for selecting input variables or having a rough estimate of optimal locations. In this study, the Latin Hypercube Sampling technique is employed using the Matlab "lhsdesign" function, which generates an LHS matrix of size $k \times n$, where k and n are again variables and different values for each variable, respectively. In particular, each configuration generated by the LHS method consists of a variation of the baseline solution reconstructed through Beziér splines. The approach allows to obtain different Venturi tube geometries in terms of shape angles, inlet, throat, and discharge lengths, as well as it ensures a smooth profile of the tube.

To assess the performance of the geometric configurations of the Venturi tube in terms of the ability to generate cavitation events, each configuration has been assigned a performance parameter related to the generation of steam in the discharge portion of the pipe. Five stations (named *stat*1, *stat*2, *stat*3, *stat*4, *stat*5) are placed beside the tube discharging section to sample the radial distribution of the vapour quality. The average integral value of the steam quality, X_v, is derived for each distribution according to Equation 1:

$$X_v(x_i) = \frac{1}{R}\int_0^R X_v(x_i, r)dr, \quad i = 1, \dots, N_{stats} \tag{1}$$

where r and R denote the radial coordinate and the maximum radius associated with each station, respectively, while x_i are the axial coordinates of the samples. As a result, this value indicates how much steam is connected to each station. Finally, the five measurements associated with each station are averaged to provide a single performance parameter for each geometric arrangement, i.e.,

$$X_v = \frac{1}{N_{stats}}\sum_{i=1}^{N_{stats}} X_v(x_i) \tag{2}$$

When applied to the baseline Venturi's configuration, this method produces a performance metric of X_v = 0.1421. Instead, the LHS optimisation process produces a set of 12 configurations capable of greatly enhancing the performance inherent in steam generation compared to the baseline (see Table 3).

Table 3: Results of the optimisation analysis.

Configuration	Vapor performance index	Improvement [%]
baseline	0.1421	-
1	0.2688	89.11
2	0.2382	67.59
3	0.2825	98.75
4	0.1734	22.01
5	0.1933	36.02
6	**0.3321**	**133.7**
7	0.2138	50.40
8	0.1627	14.48
9	0.1455	2.38
10	0.2275	60.05
11	0.1931	35.88
12	0.1451	2.10

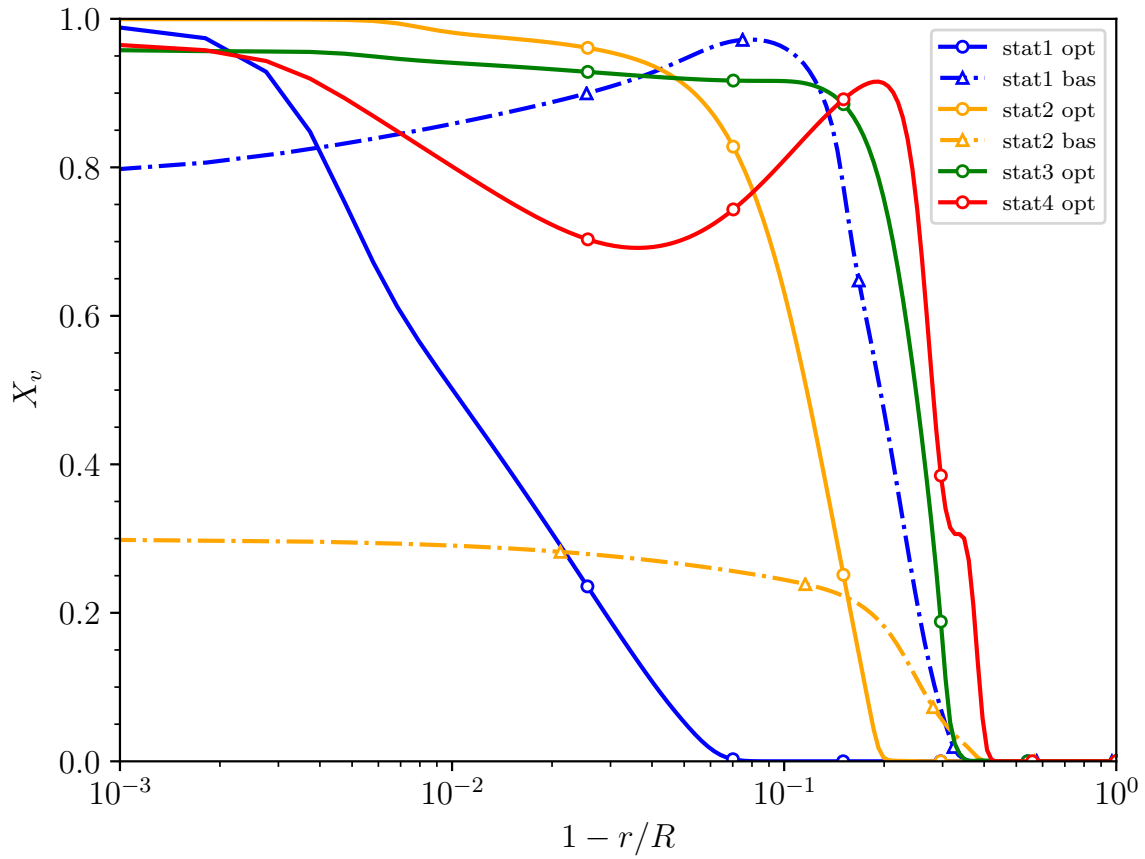

Figure 5: Baseline and optimal solutions comparison in terms of steam production distribution in the Venturi discharging sections.

Although all factors considered result in a significant boost in steam production performance, individual 6 is unquestionably the best. In fact, it is observed a 133% increase in the steam generation on average when compared to the baseline solution. Figure 5 compares the trend in steam quality at the five stations in configuration 6 with the same data acquired in the baseline situation. The solid curves represent the optimal case, while the dashed-dotted curves report the baseline solution. It can also be seen that the baseline configuration tends to cluster the vapour production in the early stations, with the first station having a clear advantage. Furthermore,

stations 1 and 2 of the baseline solution (in Figure 5 (named *stat*1 and *stat*2) concentrate the quality of the vapour along the wall of the pipe. Instead, the optimal solution not only improves the steam distribution in *stat*1 and *stat*2, but also generates a significant amount of steam in *stat*3 and *stat*4 (see Figure 5), whereas the baseline does not. For completeness, it is reasonable to claim that stations with a vapour quality less than 10^{-2} are not meaningful and, therefore, are not reported.

5. Conclusions

The proposed investigation examines a baseline and an improved Venturi tube geometry for applications involving hydrodynamic cavitation. After building the numerical model of the device, it is first calibrated as a function of grid resolution and turbulence model, with a focus on the independence of the results from mesh refinement. The baseline model is then used as the leading configuration in an LHS-based automatic optimisation process. Compared to the baseline configuration, the method can increase the steam production of the Venturi tube by almost 130%. In addition, the improved design concentrates steam production along the channel axis, while the baseline design directs steam production toward the wall. Therefore, the study demonstrates that by modifying the Venturi tube design, the hydrodynamic system performance can be improved. Without chemical components, solvents, and/or addition of man-made substances, the optimised geometry can be an economic solution to abate contaminants in water systems. In future studies, experimental campaigns will be conducted in both baseline and optimised configurations to validate numerical findings and/or design new, more efficient Venturi tube configurations. In addition to optimisation and numerical simulations, alternative configurations, including numerous Venturi tubes or asymmetrical nozzles, will be designed and tested.

Acknowledgments

The authors acknowledge Veritas S.p.A. and, particularly, Dr. Graziano Tassinato and Francesco Nisato for the fruitful discussions on Venturi systems for water treatment.

Abbreviations

CFD Computational Fluid Dynamics

DNS Direct Numerical Simulations

LES Large-Eddy Simulations

PRESTO PREssure STaggering Option

QUICK Quadratic Upwind Interpolation for Convection Kinematics

RANS Reynolds-Averaged Navier-Stokes

SA Spalart-Allmarass

SST Shear Stress Transport

TSST Transition Shear Stress Transport

Symbols

α Venturi converging angle, [°]

β Venturi diverging angle, [°]

d Venturi throat diameter, [m]

D Venturi pipe diameter, [m] / Drag force, [N]

δ_ν Viscous length, [m]

Δp Pressure drop, [Pa]

μ_w Wall viscosity, [Pa s]

p_{in}° Inflowing total pressure, [Pa]

p_{out} Outflowing static pressure, [Pa]

ρ_w Wall density, [$kg \cdot m^{-3}$]

u Axial mean velocity, $[m \cdot s^{-1}]$

u_∞ Freestream velocity, $[m \cdot s^{-1}]$

p_∞ Freestream pressure, $[Pa]$

u_τ Friction velocity, $[m \cdot s^{-1}]$

x^* Throat scaled axial coordinate

X_v Vapor quality

y^+ Inner scaled wall distance

References

[1] Gogate, P. R., & Kabadi, A. M. A review of applications of cavitation in biochemical engineering/biotechnology. Biochemical Engineering Journal (2009), 44(1), 60-72.

[2] Dular, M., Khlifa, I., Fuzier, S., Adama Maiga, M., & Coutier-Delgosha, O. Scale effect on unsteady cloud cavitation. Experiments in fluids (2012), 53, 1233-1250.

[3] Sarc, A., Kosel, J., Stopar, D., Oder, M., & Dular, M. . Removal of bacteria Legionella pneumophila, Escherichia coli, and Bacillus subtilis by (super) cavitation. Ultrasonics sonochemistry (2018), 42, 228-236.

[4] Biasiolo M., Ballarin M., Tassinato G., Stoppato A. &, Cavinato, C.. Semi-continuous Chlorella Vulgaris Cultivation Using Anaerobic Digestate Liquid Fraction Pre-treated by Ultrasonic Cavitation to Improve Carbon Dioxide Solubilization. Chemical Engineering Transactions (2022), 92, 151-156.

[5] Carpenter J., Badve M., Rajoriya S., George S., Saharan V.K., Pandit A.B. *Hydrodynamic cavitation: an emerging technology for the intensification of various chemical and physical processes in a chemical process industry.* Rev. Chem. Eng. (2017); 33: 433–468.

[6] Dastane G.G.,Thakkar H., Shah R., Perala S., Raut J., Pandit A.B. *Single and multiphase CFD simulations for designing cavitating venturi* Chemical Engineering Research and Design (2019); 149: 1-12.

[7] Bashir, T. A., Soni, A. G., Mahulkar, A. V., & Pandit, A. B. The CFD driven optimisation of a modified venturi for cavitational activity. The Canadian Journal of Chemical Engineering (2011), 89(6), 1366-1375.

[8] Li M., Bussonnière A., Bronson M., Zhenghe X., Liu Q. *Study of venturi tube geometry on the hydrodynamic cavitation for the generation of microbubbles* Miner. Eng. (2019); 132: 268–274.

[9] De Vanna F., Benato A., Scramoncin A. Stoppato A., *CFD modelling of a Venturi tube for wastewater treatment applications*. In: Elmegaard, B., Sciubba , E., Blanco-Marigorta , A. M., Jensen, J. K., Markussen, W. B., Meesenburg, W., Arjomand Kermani, N., Zhu, T., & Kofler, R., editors. ECOS 2022: Proceedings of the 35th International Conference on Efficiency, Cost, Optimization, Simulation, and Environmental Impact of Energy Systems; 2022 July 1-3; COPENHAGEN, DENMARK. Danmarks Tekniske Universitet (DTU).

[10] Shi, H., Li, M., Nikrityuk, P., Liu, Q. *Experimental and numerical study of cavitation flows in venturi tubes: From CFD to an empirical model*. Chemical Engineering Science (2019), 207, 672-687.

[11] Ansys. *FLUENT 12.0 Theory Guide.* Available at: `https://www.afs.enea.it/project/neptunius/docs/fluent/html/ug/node1.htm` [accessed 9.9.2021].

[12] De Vanna, F., Bof, D., & Benini, E. . Multi-objective RANS aerodynamic optimization of a hypersonic intake ramp at Mach 5. Energies (2022), 15(8), 2811.

[13] McKay, M. D., Beckman, R. J., & Conover, W. J. . A comparison of three methods for selecting values of input variables in the analysis of output from a computer code. Technometrics (2000), 42(1), 55-61.

[14] Swiler, L. P., & Wyss, G. D. (2004). A user's guide to Sandia's latin hypercube sampling software: LHS UNIX library/standalone version (No. SAND2004-2439). Sandia National Laboratories (SNL), Albuquerque, NM, and Livermore, CA (United States).

[15] Loh, W. L. On Latin hypercube sampling. The annals of statistics (1996), 24(5), 2058-2080.

[16] Helton, J. C., & Davis, F. J.. Latin hypercube sampling and the propagation of uncertainty in analyses of complex systems. Reliability Engineering & System Safety (2003), 81(1), 23-69.

Performance characterization of the proton exchange membrane fuel cell (PEMFC) using the Lattice Boltzmann Modeling (LBM)

Hossein Pourrahmani[a], Milad Hosseini[b], Majid Siavashi[c], Hamza Moussaoui[d], Isabel Vázquez-Fernández[e], Mardit Matian[f], and Jan Van herle[g]

[a] Group of Energy Materials, École Polytechnique Fédérale de Lausanne (EPFL), Sion 1951, Switzerland, hossein.pourrahmani@epfl.ch, CA
[b] Applied Multiphase Fluid Dynamics Laboratory, School of Mechanical Engineering, Iran University of Science and Technology (IUST), Tehran, Iran, mldhosseini73@gmail.com
[c] Applied Multiphase Fluid Dynamics Laboratory, School of Mechanical Engineering, Iran University of Science and Technology (IUST), Tehran, Iran, msiavashi@iust.ac.ir
[d] Group of Energy Materials, École Polytechnique Fédérale de Lausanne (EPFL), Sion 1951, Switzerland, hamza.moussaoui@epfl.ch
[e] EH group, Chemin de Vuarpillière 27, Nyon 1260, Switzerland, isabel.vazquez@ehgroup.ch
[f] EH group, Chemin de Vuarpillière 27, Nyon 1260, Switzerland, mardit.matian@ehgroup.ch
[g] Group of Energy Materials, École Polytechnique Fédérale de Lausanne (EPFL), Sion 1951, Switzerland, jan.vanherle@epfl.ch

Abstract:

Fuel cells have proved to be promising alternatives for Internal Combustion Engines (ICEs) with higher efficiency and lower harmful environmental impact. Among different types, Proton Exchange Membrane Fuel Cell (PEMFC) has proved to be the best option to reach zero adverse emissions at low temperatures, which enables the operation of the PEMFC for mobility applications. However, cost, durability, and thermal/water management should be further considered to better commercialize PEMFCs. Durability and water/thermal management of the PEMFC can be improved by increasing the liquid removal from the gas diffusion layers (GDL) inside each stack of the PEMFC. However, there are no efficient simulation methods to analyze water removal based on experimental efforts. The goal of this study is to use the Lattice Boltzmann Method (LBM) to precisely capture the characterization of the GDLs that have been scanned by the Computed Tomography (CT) scans. Once the three-dimensional CT scans of the GDL are performed, the segmentation and reconstruction will be made to provide the needed geometry for fluid flow simulation. The geometry will be then used to characterize the effective parameters of the thermal/water management of the PEMFC. This study can also be a valid reference for future computational fluid dynamic analyses in the GDL using the numerical modeling with the conservative equations or the Lattice Boltzmann modeling (LBM) with the kinetic and particle distribution equations.

Keywords:

Proton exchange membrane fuel cell (PEMFC); Gas Diffusion layer (GDL); Lattice Boltzmann Method (LBM); Computed Tomography (CT) scan.

1. Introduction

The harmful environmental impacts of fossil fuels and the low efficiency of combustion engines have motivated the decision-makers to find alternative fuels [1]. In this regard, methanol, ethanol, bio-fuels, ammonia, hydrogen, etc. have been suggested as possible candidates having advantages/disadvantages for each of them [2]. Among the mentioned alternative fuels, hydrogen has been suggested as the most promising option for a wider spectrum of usages [3]. This means that hydrogen production methodologies should be developed to provide the required demand of fuel for different industries [4].

As a promising technology to facilitate the transition from fossil fuels to hydrogen, fuel cells are proposed [5]. Among the introduced fuel cell variants, the Proton Exchange Membrane Fuel Cell (PEMFC) is considered the most commercialized and efficient type in low-temperature operations [6]. The basis of PEMFC's operation is to use hydrogen as fuel and produce water and electricity as outputs [7]. Although significant developments have been achieved to improve the performance of the PEMFCs, the main barriers toward further commercialization of the PEMFCs are water/thermal management, cost, and durability [8].

Considering the low-temperature operation of the PEMFCs, a concentrated effort should be made to keep the operating conditions such as humidity and temperature in the desired range to manage the highest lifetime [9]. The PEMFC is a composition of different layers, namely, membrane, Catalyst Layer (CL), Gas Diffusion Layer (GDL), Micro-Porous Layer (MPL), and Bipolar Plate (BP) [10]. The desired operating temperature range of the membrane should be around 65 to 85 degrees Celsius to prevent drying or flooding the cell in addition to a humid condition to prevent drying the membrane [11]. However, high humidity results in the formation of water droplets/columns in the GDL, which acts as a diffusing medium to split the hydrogen and a backing layer to support the CL [12]. To improve water management and reduce the water columns (breakthroughs) inside the GDL, the MPL is being used [13]. The remaining water droplets in the GDL and MPL result in filling the pores and difficulties in cold start, that is starting the PEMFC from sub-zero temperatures [14]. In addition to the usage of MPL, controlling the capillary pressure in those regions are proven efficient method to prevent the formation of breakthroughs [15]. To control the capillary pressure, the microstructure and the wettability of the porous regions can be modified [16]. In other words, water management and the formation of breakthroughs in the GDL can be improved by the changes in the microstructure of the GDL [17]. Although these concepts are supported by the I-V characteristic curves and the experimental setups, novel simulation methods based on experiments should be developed to facilitate the quantitative measurements of each GDL's breakthroughs.

Although experimental methods are unable to calculate the number of each GDL's breakthroughs, the computational fluid dynamic (CFD) is able to present quantitative amounts in different applications [18]. The significant developments of the CFD commercial softwares such as ANSYS, and COMSOL have enabled the researchers to have a better vision of the fluid flow inside the porous media [19]. However, these softwares are developed based on conservation equations such as mass, energy, and momentum. This means that this commercial softwares cannot be used to simulate the fluid flow inside the GDL/MPL since the dominating driving force in those regions is the capillary pressure [20]. In this regard, CFD models that are based on the kinetics of the particles, such as the Lattice Boltzmann Method (LBM), rather than the conservation equations should be used to characterize the fluid flow inside the GDL/MPL and to quantitatively measure the formation of the breakthroughs in these regions [21]. Although the structure of the GDL and MPL can be obtained using different prediction methods, the exact structure can be observed using novel microscopy and tomography techniques [22].

To obtain the exact structure of a porous region, it is common to either use Focused Ion Beam-Scanning Electron Microscopy (FIB-SEM) or Computational Tomography (CT) scans [23]. Although FIB-SEM is an efficient method to characterize the structure of the GDL/MPL, it is a destructive method and demands special procedures to embed the samples to minimize the destruction of the samples through microscope imaging [24]. Additionally, FIB-SEM imaging demands more operation time to detect the structure of the same porous regions in comparison to the CT scan. CT scans [25] are also non-destructive and they are the best options considering the thickness of the GDL which is approximately around 200 μm. FIB-SEM is capable of measuring up to the resolution of 3 *nm* while CT scans reach 1 μm. Concerning the mentioned information, the combination of CT scans, which produce the exact geometry of the GDL, accompanied by the LBM CFD simulation will enable the quantitative measurement of the amount of water breakthroughs inside the GDL.

This study aims to provide a methodology to calculate the amount of water breakthroughs in an arbitrary GDL. The suggested methodology is based on using CT scan imaging to segment and reconstruct the exact geometry of the GDL in the PEMFCs. The reconstruction of the GDL provides the exact geometry of the GDL to be used for CFD simulations. This study benefits from LBM concepts, which are based on the kinetics of the particles rather than conservation principles in the CFD commercial softwares. The novelty of this study is to perform the quantitative measurement and characterization of the breakthroughs inside an arbitrary GDL using the LBM and CT scans. The results of this study can be used as a reference methodology to analyze the characteristics of the GDL considering the water/thermal management.

2. Problem description

This study aims at providing a reference method to characterize the water management of GDLs in PEMFC applications. In this regard, an arbitrary GDL sample has been used followed by the required CT scan to obtain the precise geometry of the carbon fibers for simulation purposes.

Figure 1 (a) shows the whole domain of the considered GDL sample while Figure 1 (b) illustrates the carbon fibers with more details. The mentioned geometry in Figure 1 has been obtained using $\mu - CT$ scan imaging with the operating conditions indicated in Table 1. The size of the sample is $1.685 \times 1.464 \times 0.225$ (mm^3) and the image resolution is 1 μm. The segmentation and reconstruction of the images have been done using Dragonfly software, Version 2020.2 developed by Object Research Systems (ORS) Inc in Montreal (Canada).

Once the segmentation and reconstruction of the GDL images are done, the reconstructed model was used to perform the Lattice Boltzmann Method (LBM) simulation to analyze the water flow in the GDL. The required governing equations to develop the LBM simulation model are presented in Section 3.. The results of the LBM

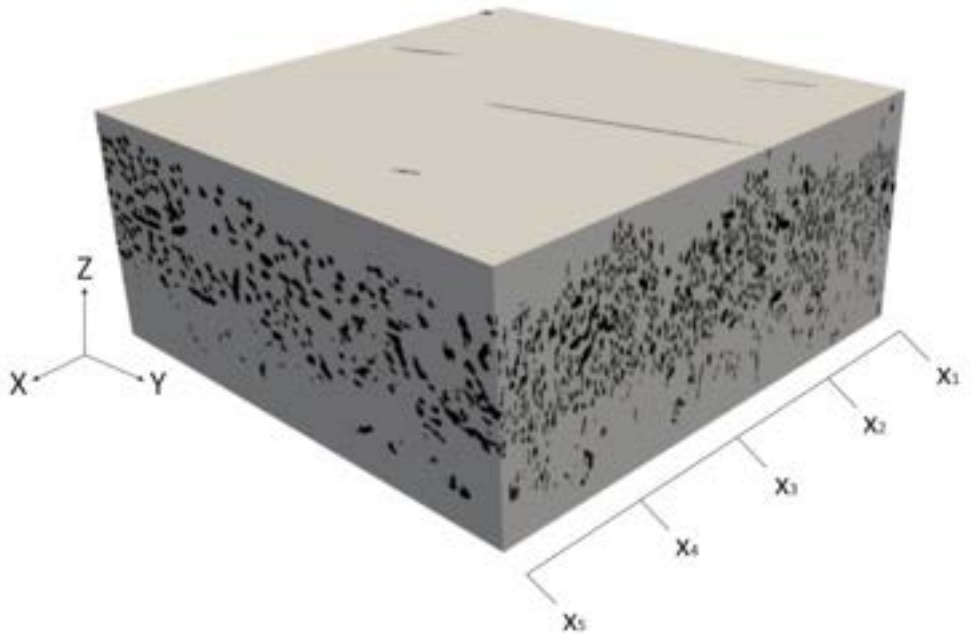

(a)

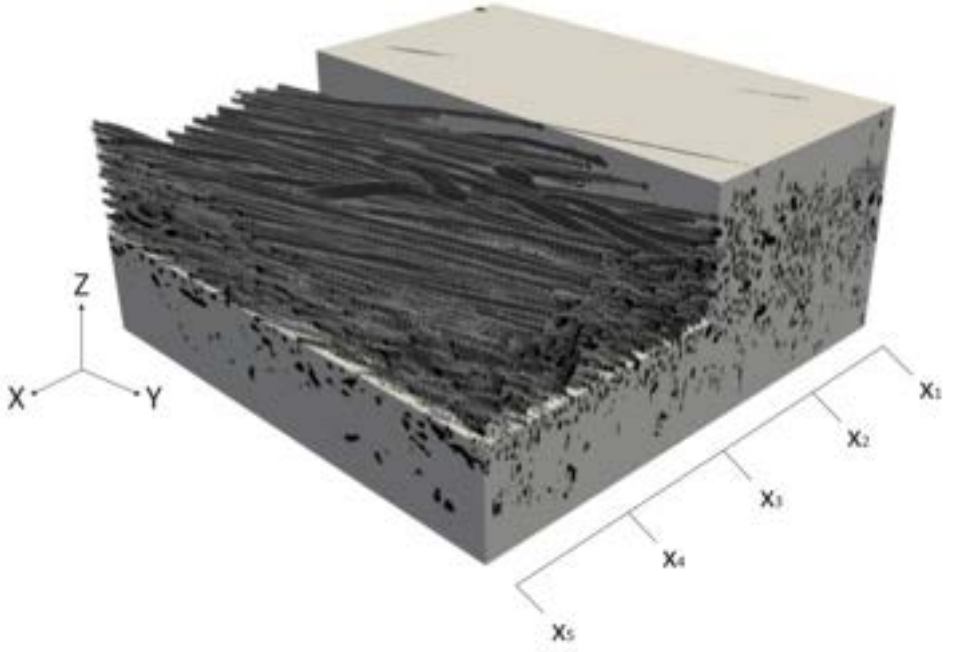

(b)

Figure 1: The schematic of the scanned, segmented, and reconstructed GDL to be analyzed using the LBM: (a) the whole considered region, (b) the clipped image to show the GDL inside the boundary condition.

simulation provide the three-dimensional flow distribution of the flow inside the GDL, hence the existence of breakthroughs (water columns) in the GDL can be predicted. It is believed that the formation of the water columns in the GDL is a form of degradation that fills the GDL pores and increases the possibility of remaining the water at sub-zero temperatures, leading to difficulties for the cold-start.

3. Governing equations

To implement the Multiple Relaxation-Time (MRT) model of the Lattice Boltzmann Method (LBM), the LBM can be developed based on the MRT collosion equation considering the force term as of Eq. 1 [26]:

Table 1: The operating conditions to perform the CT scans and the characteristics of the analyzed GDL sample

Parameter	Value	Parameter	Value
Acceleration voltage	40 kV	Averaging frames	10
Current	120 μA	Exposure time	500 ms
Image resolution	1 μm	Rotation step	0.22 degrees
Sample size (X-direction)	1.685 mm	Sample size (Y-direction)	1.464 mm
Sample size (Z-direction)	0.225 mm	Stage temperature	21 Celsius degrees
Voxel size (X-direction)	1685	Voxel size (Y-direction)	1464
Voxel size (Z-direction)	225		

$$f(x + e\Delta t, t + \Delta t) = f(x, t) - M^{-1}[SM(f^{eq}(x, t) - f(x, t)) + (I - \frac{1}{2}S)MF] \tag{1}$$

here, the density distribution function is shown with f (see Eq. 2 while Δt is the time step. M indicates the orthogonal matrix [27], which transfers the distribution functions and S is the diagonal matrix designed for D3Q19 as $S = \omega I$ [28]. As required in LBM, the discretized velocity is obtained using a D3Q19 lattice model, which is shown by e [29].

$$f_i^{eq}(\rho, u) = \rho w_i[1 + \frac{e_i.u}{c_s^2} + \frac{(e_i.u)^2}{2c_s^4} - \frac{u^2}{2c_s^2}] \tag{2}$$

where, F represents the body forces based on the Guo's model [30, 31]:

$$F_i = \omega_i(\frac{e_i - u}{c_s^2} + \frac{(e_i.u)e_i}{c_s^4}).F \tag{3}$$

The indicated sound speed, c_s in 3 is considered to be $\frac{1}{\sqrt{3}}$. Each velocity direction is attributed with a weighting factor of ω_i based on ref. [26]. The respective values of the density and velocity can be obtained in Eqs. 4 and 5:

$$\rho = \Sigma_i f_i \tag{4}$$

$$u = \frac{1}{\rho}\Sigma_i e_i f_i + \frac{F\Delta t}{2\rho} \tag{5}$$

3.1. The magic parameter

Although in the Single Relaxation Time (SRT) LBM, the impacts of magic parameter is negligible on the results due to not being a parameter of viscosity, the MRT-LBM model demands the determination of magic parameter. For instance, the magic parameter can be calculated using Eq. 6 for Two Relaxation Time (TRT) LBM model:

$$\Lambda = \Lambda^+\Lambda^- = (\frac{1}{\omega^+\Delta t} - \frac{1}{2})(\frac{1}{\omega^-\Delta t} - \frac{1}{2}) \tag{6}$$

where, ω^- can be selected arbitrary while ω^+ should be computed through Eq. 7:

$$\vartheta = c_s^2(\frac{1}{\omega^+} - \frac{1}{2}) \tag{7}$$

In the MRT model, multiple frequencies correspond to the relaxation times and can be divided into symmetric, Λ_j^+, and anti-symmetric, Λ_k^-, groups. The combination of the mentioned two groups creates a single magic parameter that modifies the simulation error as follows [32]:

$$\Lambda_{j,k} = \Lambda_j^+\Lambda_k^- j = e, \pi, \varepsilon, \vartheta k = q, m \tag{8}$$

$$\Lambda_{j,k} = [\Lambda_\vartheta^+\Lambda_q^-, \Lambda_e^+\Lambda_q^-, \Lambda_\varepsilon^+\Lambda_q^-, \Lambda_\pi^+\Lambda_q^-, \Lambda_\vartheta^+\Lambda_m^-, \Lambda_e^+\Lambda_m^-, \Lambda_\varepsilon^+\Lambda_m^-, \Lambda_\pi^+\Lambda_m^-] \tag{9}$$

Considering the 9, there are eight different magic parameters for the D3Q19 model. As all the magic parameters are considered identical, the presented MRT can be assumed as TRT model. Thus, the existing frequencies of the symmetric group ω^s can be considered equal to the calculated frequency from the viscosity as of Eq. 10:

$$\omega^s = \frac{1}{\frac{\vartheta}{c_s^2\Delta t} + \frac{1}{2}} \tag{10}$$

where, the superscript "*s*" indicates the existing frequencies of the symmetric part. the related superscript for the anti-symmetric part is "*as*" and the corresponding frequency can be calculated using Eq. 11:

$$\omega^{as} = \frac{4 - 2\omega^{s}}{(4\Lambda - 1)\omega^{s} + 2} \tag{11}$$

3.2. Mean velocity computation

Considering the Darcy model, the permeability tensor is defined as follows:

$$K_{ij} = \frac{\mu}{\Delta P_j}\bar{U}_i; i, j = 1, 2, 3 \tag{12}$$

here, ΔP_j is the pressure gradient in j-direction while $\bar{U}_i$ is the mean volumetric velocity in the i-direction as follows [33]:

$$\bar{U}_i = \frac{1}{V_t}\int_{\Omega} u_i d\Omega \tag{13}$$

where, V_t is the total volume of the sample while $d\Omega$ is the volumetric element in the pore domain. Using the trapezoidal discrete form, Eq. 14 can be solved as follows:

$$\bar{U}_x = \frac{\sum_k^{N_k}\sum_j^{N_j}\sum_i^{N_i} u_{x_{ijk}}}{N_i N_j N_k} \tag{14}$$

Accounting the form of Eq. 14, error will be produced, which can be controlled using the magic parameter, and by using high-order interpolations to solve the Eq. 13. The effective permeability can be presented as follows [34]:

$$K_{eff} = K_{ideal} + \frac{2}{3}\Lambda - \frac{1}{12} \tag{15}$$

where, K_{ideal} is the exact value of the permeability in the ideal boundary condition.

4. Results and discussion

In the first step, the GDL sample, shown in Figure 1, is scanned with $\mu - CT$ imaging to enable the segmentation and reconstruction of the sample for CFD analysis. Furthermore, the $\mu - CT$ imaging enables the calculation of the porosity and the mean pore diameter that can be needed for the LBM simulation. Using the Dragonfly software and after the reconstruction of the images, the respective values of the porosity and the mean pore diameter were calculated to be 0.8516 and 2.894 μm, respectively.

As mentioned in Section 3., there are three methods to use the LBM, Single-Relaxation Times (SRT), Two-Relaxation Times (TRT), or Multi-Relaxation Time (MRT). Among these methods, the MRT-LBM benefits from the highest accuracy and precision, hence this study has utilized this model to simulate the scanned GDL sample by the $\mu - CT$ imaging. Each of the Lattice vectors is located in the position of x and the time of t, which enables the transient simulation of the fluid flow inside the GDL. In this study, the D3Q19 discretization model has been used, that means each of the lattice vectors has 19 different components in the momentum space.

Accounting for the boundary conditions, the fluid flow is at low speeds (laminar flow) and Darcy conditions and the aim is to consider the capillary pressure as well. The implemented pressure gradient as the driving force for the fluid flow in the Z-direction, shown in Figure 1, is 0.1 $\frac{Pa}{m}$. The four surfaces of the GDL sample shown in Figure 1 parallel to the ZY and XZ planes are considered walls with no-slip boundary conditions.

A simplification has been made and pure water has been selected for the working fluid. In this regard, the kinematic viscosity of the fluid is 0.802 $\frac{mm^2}{s}$ while the fluid density is 995.7 $\frac{kg}{m^3}$. The maximum number of iterations for flow simulation is 80,000,000 while the Navier-Stokes relaxation time is 1. Additionally, the frequency that the convergence being checked is 0.5 s while the convergence criteria for the flow field is 10^{-4}. The inflation parameter regarding the LBM simulation, which considers the surface mesh before the visualization is 0.1.

Once the required parameters for the LBM simulation are provided, the fluid flow analysis is done. Figure 2 presents the results of the LBM simulation for the GDL sample shown in Figure 1. As can be seen, there are regions with higher velocities in the three-dimensional domain with red, yellow, and green colors. These regions are indicators of the possibilities for the formation of breakthroughs inside the GDL. Notably, the analyzed GDL by the $\mu - CT$ scan has not gone through aging and is a pristine sample. To have a better visualization of the breakthroughs inside the GDL, Figure 3 is provided, which illustrates the fluid flow inside the GDL considering

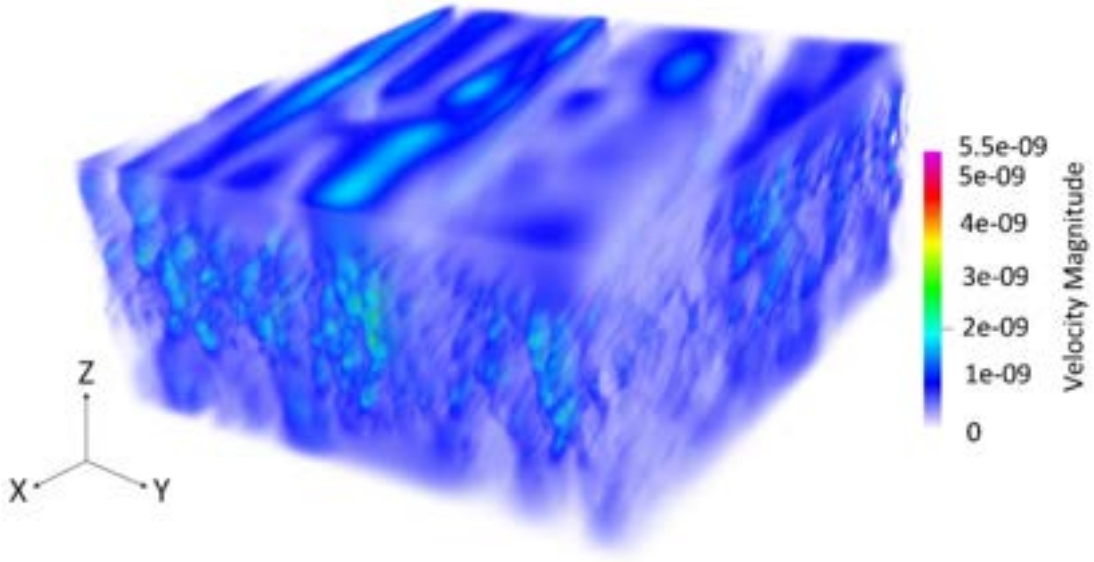

(a)

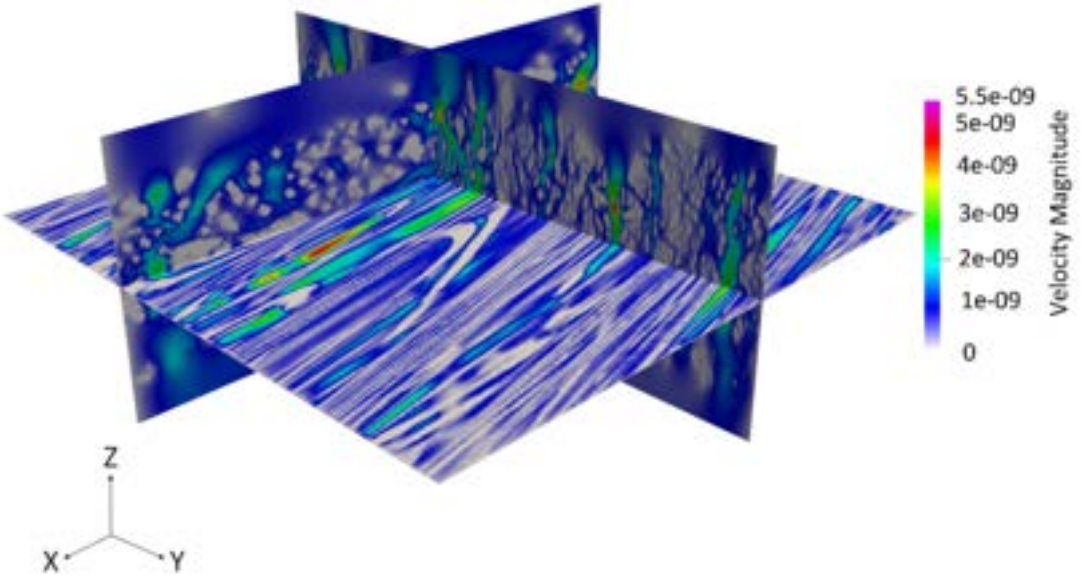

(b)

Figure 2: The three-dimensional results of the performed CFD analysis using the LBM method on the presented sample in Figure 1: (a) The three-dimensional changes in the velocity in the considered domain, (b) The changes in the velocity considering three different slices in the X-, Y-, and Z- directions.

the X_1, X_2, X_3, X_4, and X_5 slices shown in Figure 1. Specifically, in Figure 3(c) and 3(e), the breakthroughs can be seen, as the green regions (indicating the breakthrough) pass through the GDL carbon fibers. The GDL carbon fibers in Figure 3 are shown with while values since the velocity vectors are zero if there exist solid materials.

As Figure 2 illustrates, the visualization of the breakthroughs inside the GDL is not a straightforward procedure and better quantification measurements are required. In this regard, each voxel that has velocity values of more than 2×10^{-9} in the domain given by Figure 2 (a) is considered as a region of breakthrough. In this regard, 9.13% of the GDL porous region, which is illustrated in Figure 2(a), is consisted of the breakthroughs. This means that 50,675,060 voxels are labeled as breakthroughs inside the whole domain with 555,039,000 voxels. In other words, 0.051 mm^3 of the illustrated domain in Figure 1 is prone to create breakthroughs in the whole domain of 0.555 mm^3.

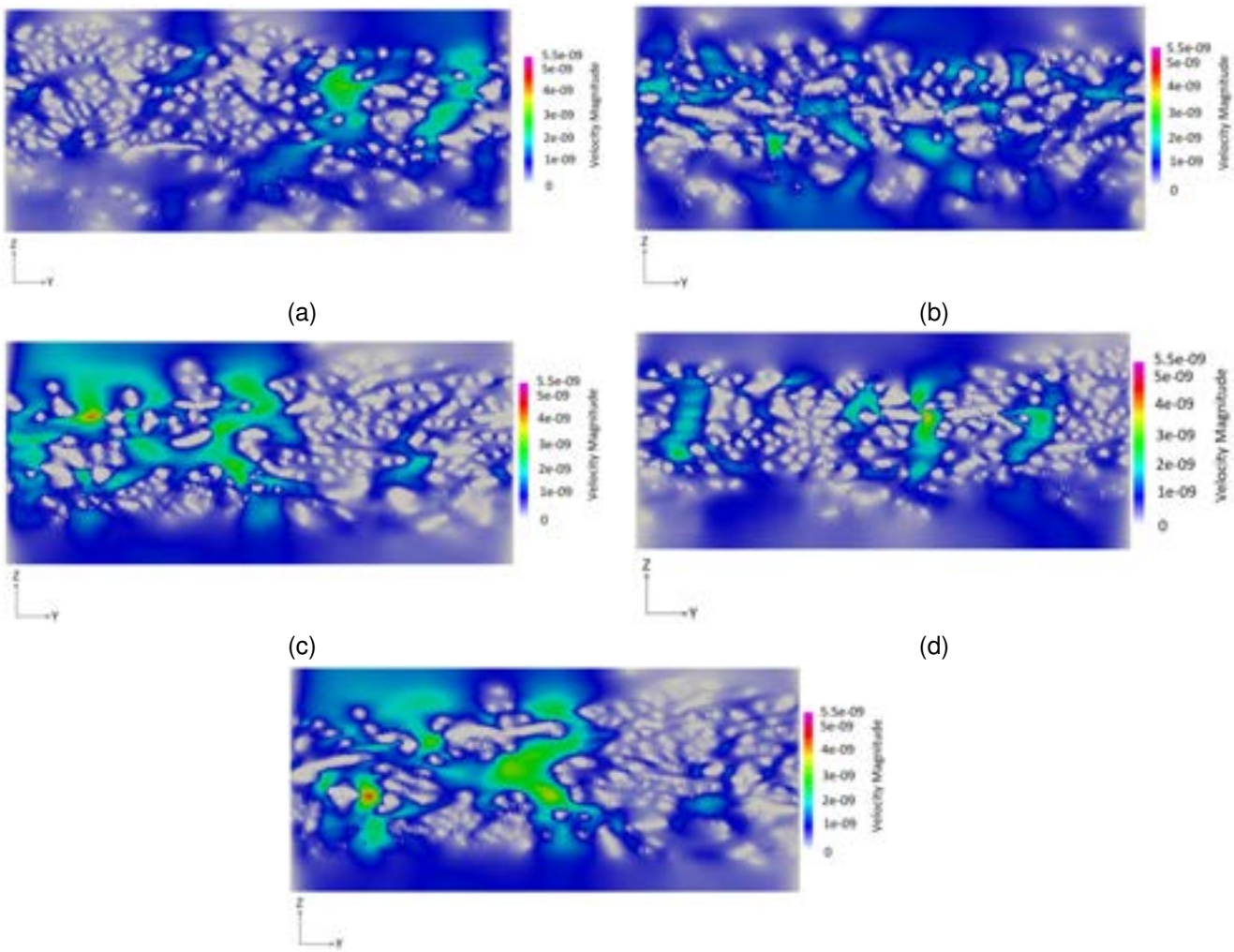

Figure 3: The two-dimensional velocity contours in the X-direction after performing the LBM simulations on the analyzed samples shown in Figure 1: (a) Slice X_1 depicted in Figure 1, (b) Slice X_2 depicted in Figure 1, (c) Slice X_3 depicted in Figure 1, (d) Slice X_4 depicted in Figure 1, (e) Slice X_5 depicted in Figure 1

5. Conclusion

This study could analyze the formation of the water columns inside the GDL of the PEMFC. The formation of water columns, which is also famous as breakthroughs, is known as a degradation phenomenon that fills the pores and leads to difficulties in starting the cell from sub-zero temperatures. As the driving force of the fluid flow in the GDL is the capillary pressure, the conventional conservation principles such as momentum, energy, and mass are not the governing equations, and methods based on the kinetics of the particles should be used. In this regard, LBM formulation, which is considered a powerful CFD methodology based on the kinetics of the particles to simulate the fluid flow at the interfaces between the gas/solid/liquid and at low-velocity conditions, has been used using the obtained $\mu - CT$ images of the GDL. $\mu - CT$ images could provide the exact geometry of the GDL followed by the porosity and the mean pore diameter that is required for the LBM simulation.

The results of the LBM simulation could provide the velocities of the water passing through the GDL. The illustrated contours visualized the locations of the breakthroughs followed by the corresponding voxels. To enable the quantitative measurement of the breakthroughs, the voxels with higher velocity values of 2×10^{-9} were considered to be a part of the breakthroughs in the domain. In this regard, it was calculated that 50,675,060 voxels are labeled as breakthroughs among the whole 555,039,000 voxels. In other words, considering the whole size of the domain, which is 0.555 mm^3, the created breakthrough is equal to 0.051 mm^3. The LBM simulation could also provide a quantitative percentage of 9.13% as the share of the breakthrough in the whole domain.

The output results of this study proved that the performance of the GDLs can be characterized without experimental testing and novel GDLs can be analyzed before assembly to reduce the costs and time. The current novelty of this study can be used in future studies to facilitate GDL characterization. Additionally, the following

topics can be accounted for future studies:

- This study only analyzed an arbitrary pristine GDL to analyze the possibility of the GDL characterization using the LBM simulation and CT scan imaging. It is suggested to consider aged or degraded samples of GDL and evaluate the impacts of different types of degradation phenomena on the amount of created breakthroughs.
- To facilitate the LBM simulations, simplifications were made and only pure water was considered as the fluid flow in the GDL. However, in reality, the fluid is either hydrogen or oxygen in a humid environment with the possibility of water formation.
- LBM simulation is also a powerful tool to analyze the droplet formation and movement in porous media, which is the exact electrochemical phenomenon inside the GDL. In this regard, further details can be added to this model to obtain the highest precision in the simulation results.

Acknowledgments

This project has received funding from the European Union's Horizon 2020 research and innovation program under the Marie Sklodowska-Curie grant agreement No. 754354.

The segmentation and reconstruction of the images have been done using the Dragonfly software, Version 2020.2 developed by Object Research Systems (ORS) Inc in Montreal, Canada. The required link to the company's website is: http://www.theobjects.com/dragonfly.

References

[1] H. Pourrahmani *et al.*, "Water management of the proton exchange membrane fuel cells: Optimizing the effect of microstructural properties on the gas diffusion layer liquid removal," *Energy*, vol. 256, p. 124712, 2022.

[2] H. Pourrahmani, M. Gay, A. Yavarinasab *et al.*, "Optimization and dynamic responses of an integrated fuel cell and battery system for an 800 kw ferry: A case study," *Energy Reports*, vol. 8, pp. 9757–9776, 2022.

[3] M. Gay, H. Pourrahmani *et al.*, "Fuel cell and battery technologies for a 800 kw ferry: Two optimized scenarios," *Science Talks*, vol. 3, p. 100039, 2022.

[4] V. Walter, L. Göransson, M. Taljegard, S. Öberg, and M. Odenberger, "Low-cost hydrogen in the future european electricity system–enabled by flexibility in time and space," *Applied Energy*, vol. 330, p. 120315, 2023.

[5] H. Pourrahmani, C. Xu, and J. Van herle, "Two novel cogeneration charging stations for electric vehicles: Energy, exergy, economic, environment, and dynamic characterizations," *Energy Conversion and Management*, vol. 271, p. 116314, 2022.

[6] H. Pourrahmani, A. Rajabi *et al.*, "A modified design of the gas flow channel geometry for the proton exchange membrane fuel cells: A three-dimensional simulation," *Science Talks*, vol. 3, 2022.

[7] H. Pourrahmani and J. Van herle, "Evaluation criterion of proton exchange membrane (ecpem) fuel cells considering inserted porous media inside the gas flow channel," *Applied Thermal Engineering*, vol. 203, p. 117952, 2022.

[8] Y. Wang, D. F. R. Diaz, K. S. Chen, Z. Wang, and X. C. Adroher, "Materials, technological status, and fundamentals of pem fuel cells–a review," *Materials today*, vol. 32, pp. 178–203, 2020.

[9] M. Raeesi, S. Changizian, P. Ahmadi, and A. Khoshnevisan, "Performance analysis of a degraded pem fuel cell stack for hydrogen passenger vehicles based on machine learning algorithms in real driving conditions," *Energy Conversion and Management*, vol. 248, p. 114793, 2021.

[10] K. Christmann, K. A. Friedrich, and N. Zamel, "Activation mechanisms in the catalyst coated membrane of pem fuel cells," *Progress in Energy and Combustion Science*, vol. 85, p. 100924, 2021.

[11] L. Xu, Z. Hu, C. Fang, J. Li, P. Hong, H. Jiang, D. Guo, and M. Ouyang, "Anode state observation of polymer electrolyte membrane fuel cell based on unscented kalman filter and relative humidity sensor before flooding," *Renewable Energy*, vol. 168, pp. 1294–1307, 2021.

[12] M. Mortazavi, A. D. Santamaria, V. Chauhan, J. Z. Benner, M. Heidari, and E. F. Médici, "Effect of pem fuel cell porous media compression on in-plane transport phenomena," *Journal of Power Sources Advances*, vol. 1, p. 100001, 2020.

[13] F. S. Nanadegani, E. N. Lay, and B. Sunden, "Effects of an mpl on water and thermal management in a pemfc," *International Journal of Energy Research*, vol. 43, no. 1, pp. 274–296, 2019.

[14] W. Pan, P. Li, Q. Gan, X. Chen, F. Wang, and G. Dai, "Thermal stability analysis of cold start processes in pem fuel cells," *Applied Energy*, vol. 261, p. 114430, 2020.

[15] D. Niblett, V. Niasar, S. Holmes, A. Mularczyk, J. Eller, R. Prosser, and M. Mamlouk, "Water cluster characteristics of fuel cell gas diffusion layers with artificial microporous layer crack dilation," *Journal of Power Sources*, vol. 555, p. 232383, 2023.

[16] H. Pourrahmani and J. Van herle, "The impacts of the gas diffusion layer contact angle on the water management of the proton exchange membrane fuel cells: Three-dimensional simulation and optimization," *International Journal of Energy Research*, vol. 46, no. 11, pp. 16 027–16 040, 2022.

[17] D. Zapardiel and P. A. García-Salaberri, "Modeling the interplay between water capillary transport and species diffusion in gas diffusion layers of proton exchange fuel cells using a hybrid computational fluid dynamics formulation," *Journal of Power Sources*, vol. 520, p. 230735, 2022.

[18] Y. Zhang, S. He, X. Jiang, M. Xiong, Y. Ye, and X. Yang, "Three-dimensional multi-phase simulation of proton exchange membrane fuel cell performance considering constriction straight channel," *Energy*, vol. 267, p. 126544, 2023.

[19] H. Pourrahmani, M. Moghimi, M. Siavashi, and M. Shirbani, "Sensitivity analysis and performance evaluation of the pemfc using wave-like porous ribs," *Applied Thermal Engineering*, vol. 150, pp. 433–444, 2019.

[20] Y. Wang, H. Xu, W. He, Y. Zhao, and X. Wang, "Lattice boltzmann simulation of the structural degradation of a gas diffusion layer for a proton exchange membrane fuel cell," *Journal of Power Sources*, vol. 556, p. 232452, 2023.

[21] P. Sarkezi-Selsky, H. Schmies, A. Kube, A. Latz, and T. Jahnke, "Lattice boltzmann simulation of liquid water transport in gas diffusion layers of proton exchange membrane fuel cells: Parametric studies on capillary hysteresis," *Journal of Power Sources*, vol. 535, p. 231381, 2022.

[22] H. Pourrahmani, M. Matian, and J. Van Herle, "Poisoning effects of cerium oxide (ceo2) on the performance of proton exchange membrane fuel cells (pemfcs)," *ChemEngineering*, vol. 6, no. 3, p. 36, 2022.

[23] E. Leonard, A. D. Shum, N. Danilovic, C. Capuano, K. E. Ayers, L. M. Pant, A. Z. Weber, X. Xiao, D. Y. Parkinson, and I. V. Zenyuk, "Interfacial analysis of a pem electrolyzer using x-ray computed tomography," *Sustainable Energy & Fuels*, vol. 4, no. 2, pp. 921–931, 2020.

[24] R. Moroni and S. Thiele, "Fib/sem tomography segmentation by optical flow estimation," *Ultramicroscopy*, vol. 219, p. 113090, 2020.

[25] P. Irmscher, D. Qui, H. Janßen, W. Lehnert, and D. Stolten, "Impact of gas diffusion layer mechanics on pem fuel cell performance," *International Journal of Hydrogen Energy*, vol. 44, no. 41, pp. 23 406–23 415, 2019.

[26] T. Krüger, H. Kusumaatmaja, A. Kuzmin, O. Shardt, G. Silva, and E. M. Viggen, "The lattice boltzmann method," *Springer International Publishing*, vol. 10, no. 978-3, pp. 4–15, 2017.

[27] D. d'Humières, "Multiple–relaxation–time lattice boltzmann models in three dimensions," *Philosophical Transactions of the Royal Society of London. Series A: Mathematical, Physical and Engineering Sciences*, vol. 360, no. 1792, pp. 437–451, 2002.

[28] I. Ginzburg, F. Verhaeghe, and D. d'Humieres, "Study of simple hydrodynamic solutions with the two-relaxation-times lattice boltzmann scheme," *Communications in computational physics*, vol. 3, no. 3, pp. 519–581, 2008.

[29] M. Hosseini, M. Siavashi, M. Shirbani, and M. M. Nezhad, "Reliability assessment of the lattice-boltzmann method for modeling and quantification of hydrological attributes of porous media from microtomography images," *Advances in Water Resources*, vol. 171, p. 104351, 2023.

[30] Z. Guo, C. Zheng, and B. Shi, "Discrete lattice effects on the forcing term in the lattice boltzmann method," *Physical review E*, vol. 65, no. 4, p. 046308, 2002.

[31] G. Silva and V. Semiao, “First-and second-order forcing expansions in a lattice boltzmann method reproducing isothermal hydrodynamics in artificial compressibility form,” *Journal of fluid mechanics*, vol. 698, pp. 282–303, 2012.

[32] S. Khirevich and T. W. Patzek, “Behavior of numerical error in pore-scale lattice boltzmann simulations with simple bounce-back rule: Analysis and highly accurate extrapolation,” *Physics of Fluids*, vol. 30, no. 9, p. 093604, 2018.

[33] B. P. Muljadi, M. J. Blunt, A. Q. Raeini, and B. Bijeljic, “The impact of porous media heterogeneity on non-darcy flow behaviour from pore-scale simulation,” *Advances in water resources*, vol. 95, pp. 329–340, 2016.

[34] L. Talon, D. Bauer, N. Gland, S. Youssef, H. Auradou, and I. Ginzburg, “Assessment of the two relaxation time lattice-boltzmann scheme to simulate stokes flow in porous media,” *Water Resources Research*, vol. 48, no. 4, 2012.

A Machine Learning-based Calibration of a 1D ejector model from CFD

Jan Van den Berghe[a,b], Jagadish Babu Vemula[b], Yann Bartosiewicz[b] and Miguel Alfonso Mendez[a]

[a] von Karman Institute for Fluid Dynamics (VKI),
Waterloosesteenweg 72, 1640 Sint-Genesius-Rode, Belgium, jan.vandenberghe@vki.ac.be, CA.
[b] Institute of Mechanics, Materials, and Civil Engineering (iMMC)
Université catholique de Louvain (UCLouvain), 1348 Louvain-la-Neuve, Belgium

Abstract:

Ejectors are devices that expand a primary flow through a nozzle to entrain and compress a secondary flow without moving parts. They can be modelled in 1D as two streams exchanging momentum. However, the engineering modelling of this exchange is based on closure parameters such as friction coefficients that must be calibrated against experimental or numerical data. This work proposes a general machine learning framework for calibrating engineering models governed by Ordinary Differential Equations (ODEs) and presents its application to the 1D modelling of an ejector. We combine a physics-separated approach with a physics-integrated approach, with the first acting as an initial guess for the second. The first approach calibrates shear and friction coefficients from their counterpart extracted via post-processing of an axisymmetric CFD simulation. The second consists of calibrating these coefficients from the prediction of physical quantities (pressures, temperatures, and cross-sections), thus making the training process aware of the ODEs driving the forecast.

Keywords:

1D ejector modelling, closure modelling, physics-constrained machine learning

1. Introduction

Ejectors are flow devices that expand a primary flow to entrain and compress a secondary flow into a mixing pipe. These 'compressors' have no moving parts and are thus robust and without limitations on the working fluid (gas, liquid, two-phase). Their applications include aeronautics, the chemical and processing industry, power generation and refrigeration [1].

Ejectors are commonly modelled with 0D lumped parameter formulations [2–6], meaning that conservation laws are expressed between key sections such as the throat and the exit of the primary nozzle, the constant area section of the mixing pipe and the exit of the diffuser. These models give fast predictions of the global performance in the form of mass flow rates but require calibration of several closure coefficients accounting for the isentropic efficiencies of key components. On the other hand, classic CFD provides detailed flow fields [7,8], but requires more computational time and effort for meshing and setting up the solver, which is generally too expensive at system scale. A compromise consists of 1D models, which discretize the flow field in the axial direction. The mixing pipe can be modelled with a single domain [9], or with two interacting domains [10–12]. These models still require calibration, for example, for modelling wall friction and shear. Nevertheless, they provide local information and resolve more physics related to entrainment than 0D models, at a fraction of the cost of 2D/3D CFD.

Closure relations mapping these closure coefficients to physical quantities (e.g., a friction coefficient which depends on the Reynolds number) could make these models self-standing and thus more useful in early design stages, but their derivation is particularly challenging. This work proposes a machine learning formalism to discover such closure relations from data. By training the model on reliable CFD data, the intricacies of the 2D flow field can be lumped into the closure coefficients of the lower dimensional 1D model to maximize the accuracy of these models. This data-driven approach has been successfully applied in other branches of fluid mechanics such as heat transfer or and turbulence modelling. These can be classified as physics-separated (as in [14]) or physics-integrated (as in [15, 16]) depending on whether the learning process is carried out on data extracted from a simulation or during a simulation. These approaches are briefly reviewed in the next section. None of these have been implemented for the calibration of ejector models.

In this work, we propose a general formulation for machine learning-based closure of a system of ordinary differential equations (ODEs), and we apply it to a 1D ejector model with two streams (1D-2s hereafter). The

general framework is presented in section 2. and its application on the ejector model in section 3.. The results are discussed in section 4., leading to the conclusions in section 5..

2. A general framework for machine learning-based calibration

We consider a physical problem governed by a system of ordinary differential equations (ODEs) in the state variables $\boldsymbol{u} \in \mathbb{R}^{n_u}$ and a set of parameters $\boldsymbol{p} \in \mathbb{R}^{n_p}$ to be linked to the state variables. In this work, we focus on boundary value problems in $x \in [0, L]$, and denote the sought-after closure relation as $\boldsymbol{p} = g(\boldsymbol{u}, x)$. Thus the closure problem can be written as

$$f\left(\boldsymbol{u}, \frac{d\boldsymbol{u}}{dx}, \frac{d^2\boldsymbol{u}}{dx^2}, ..., x, \boldsymbol{p} = g(\boldsymbol{u}, x)\right) = 0\,, \tag{1}$$

with boundary conditions $\boldsymbol{u}(0) = \boldsymbol{u}_L$ and $\boldsymbol{u}(L) = \boldsymbol{u}_R$. This framework is general enough to encompass many physical systems, from turbulence modelling [15–18] to general inverse modelling [13]. This work presents the first implementation of this framework for the closure of 1D ejector models.

The problem of finding the unknown function is generally a difficult variational problem. Machine learning offers an alternative approach by approximating the unknown function using a parametric model $\boldsymbol{p} = g(\boldsymbol{u}, x; \boldsymbol{w})$ which depends on a finite set of weights $\boldsymbol{w} \in \mathbb{R}^{n_w}$. This could range from a simple linear relation to artificial neural networks (ANNs), and the range of possible functions that the given model can represent defines the 'hypothesis set' in the machine learning formalism [21]. Following [19], the identification of the weights $\boldsymbol{w}$ can be carried out using physics-separated and physics-integrated approaches (see also [14], and [13, 15–18]).

The physics-separated approach is a classic supervised learning formulation which assumes that a set of instances $(\tilde{\boldsymbol{u}}_i, x_i)$ and the associated parameters $\tilde{\boldsymbol{p}}_i$ are available. Therefore, the optimal set of weights is the one that minimizes a cost function $J(\boldsymbol{w})$ such as, for example:

$$J_1(\boldsymbol{w}) = \sum_i \sum_r \frac{\left(\tilde{\boldsymbol{p}}_{i,r} - g(\boldsymbol{u}_{i,r}, x_i; \boldsymbol{w})\right)^2}{\tilde{\boldsymbol{p}}_{i,r}^2}\,, \tag{2}$$

where i is the index spanning the instances $\tilde{\boldsymbol{p}}_i$ at coordinates x_i and r is the index spanning the entries in each vector of parameters (i.e. the closure coefficients that make up $\boldsymbol{p}$).

This regression problem is shown schematically in block II of figure 1 and starts with an initial guess $\boldsymbol{w}_0$. The gradient of the cost function $d_{\boldsymbol{w}}J$ only requires the gradient of the parametric function $d_{\boldsymbol{w}}g$; this is easily available for usual machine learning models (e.g. using backpropagation in ANNs) hence classic gradient-base optimizer such as the BFGS algorithm [20] can be implemented efficiently. However, this approach requires that both the parameters $\tilde{\boldsymbol{p}}_i$ and the full states $\tilde{\boldsymbol{u}}_i$ can be extracted from a sufficiently rich dataset with sufficient accuracy (cf. block I in figure 1). This is rarely possible from experimental data. Moreover, the trained model g is unaware of the underlying physical problem in (1) since the model is never called during training.

The physics-integrated approach includes the physical problem in (1) during the learning process (cf. block III in figure 1). Note that both approaches are self-standing, but can be applied successively. The extraction of the model parameters from data is not required, and the training is based on some observation of the states and the prediction that the model f can achieve for a given set of weights $\boldsymbol{w}$. Considering the simplest case of full observation of the states $\tilde{\boldsymbol{u}}_i$ and denoting the solution of (1) as $\boldsymbol{u}_i(g(\boldsymbol{u}_i, x_i; \boldsymbol{w}))$ when the closure is achieved with the weights $\boldsymbol{w}$, the optimal set of weights minimizes a cost function of the form

$$J_2(\boldsymbol{w}) = \sum_i \sum_r \frac{\left(\tilde{\boldsymbol{u}}_{i,r} - \boldsymbol{u}_{i,r}(g(\boldsymbol{u}_{i,r}, x_i; \boldsymbol{w}))\right)^2}{\tilde{\boldsymbol{u}}_{i,r}^2} \tag{3}$$

where i is the index spanning the instances $\tilde{\boldsymbol{u}}_i$ at coordinates x_i and r is the index spanning the entries in each state vector (i.e. the variables considered for the cost function definition).

The relative error is preferred here due to the composite nature of common state vectors (e.g., pressures and temperatures). Using the chain rule, it is easy to see that in this formulation, the gradient of the cost function $d_w J$ requires the gradient of the problem solution with respect to the parameters and the gradient of the parameters with respect to the weights, i.e. $d_w J(\boldsymbol{u}(g(\boldsymbol{w}))) = d_u J d_p \boldsymbol{u} d_w g$. Computing this gradient symbolically is challenging and requires adjoint differentiation (cf. [13, 15–18]), but for a computationally inexpensive solver of f and a small number of parameters, a simple finite difference implementation is feasible. Besides avoiding the need for extracting the parameters $\tilde{\boldsymbol{p}}$ from data, this approach has the main merit of pairing the closure

with the solver with which it is later deployed. On the other hand, the model sensitivity to the parameters ($d_p\boldsymbol{u}$) strongly influences the cost function gradient and often results in more poorly behaved and multimodal cost functions.

In this work, we propose a combination of the two approaches, whereby the solution of a physics-separated approach is used as a starting point for a physics-integrated approach (hence successively following blocks I to III in figure 1). This offers an excellent balance between accuracy, robustness and computational cost.

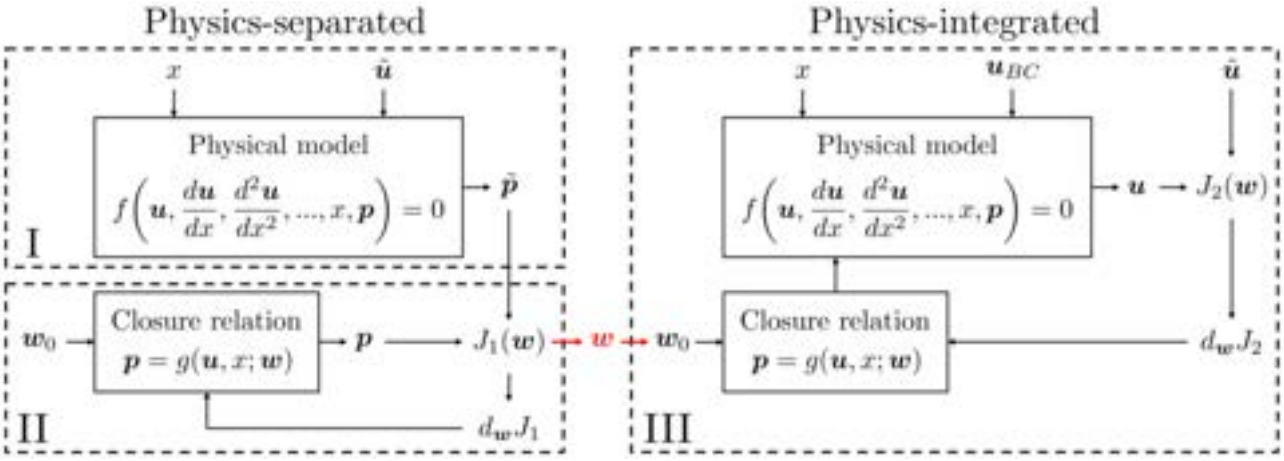

Figure 1: Schematic overview of the physics-separated and the physics-integrated approach for calibrating a physical model f through a closure relation g, given data $\tilde{\boldsymbol{u}}$. The physics-separated approach consists of (I) extracting the reference parameters $\tilde{\boldsymbol{p}}$ from data and (II) applying a classic supervised machine learning technique for regressing $\boldsymbol{p}$. The physics-integrated approach (III) includes the physical model in the training process and thus requires the sensitivity of the model with respect to its parameters $d_{\boldsymbol{p}}\boldsymbol{u}$. Both methods are self-standing, but this work proposes to apply them successively (I-III) as indicated in red.

3. Application to a 1D ejector model

The previously introduced model calibration framework is applied to the modelling of a supersonic ejector using a 1D and two streams formulation. The calibration is based on data from a 2D axisymmetric CFD simulation presented in [22]. This is briefly reviewed in section 3.1.. The model formulation is presented in section 3.2. while the procedure for the calibration is reported in section 3.3..

3.1. The CFD Dataset

We consider an ejector with a converging primary nozzle, operating with total pressures p_{tp} = 5 bar, p_{ts} = 1 bar and static back pressure p_b = 2.2 bar. Herein, the subscripts p and s are used for variables related to the primary and the secondary flows, respectively (see list of symbols at the end of the article). The total temperatures equal T_{tp} = T_{ts} = 293K. The numerical domain and a contour of the Mach number field are shown in figure 2. The primary jet is under-expanded due to the large pressure difference between the inlets, which leads to a shock train in the mixing pipe. This is evidenced by the dividing streamline as indicated by the full red line in figure 2. The ejector operates in off-design conditions, so the maximal flow rate is not reached, and the mixed flow remains subsonic. Consequently, no shock train is present in the diffuser as would be the case in on-design conditions [7]. Interested readers are referred to [22] for further numerical details and the validation against experiments.

The data assimilation in this work focuses on the mixing pipe since the primary and secondary inlets can be accurately described with classic quasi-1D flow theory. The mixing pipe features complex flow phenomena, mixing the two streams and shock trains interacting with shear layers. This portion of the ejector is the one where closure relations are required the most.

The first step in the data preparation consists of calculating the dividing streamline in the mixing pipe. This is defined as the line bounding the primary mass flow rate. Hinging on the axisymmetry of the problem, this is the radius r_{div} such that:

$$\dot{m}_p(x) = \int_0^{r_{div}} \rho(x,r)u(x,r)\, 2\pi r\, dr, \quad \text{and} \quad \dot{m}_s(x) = \int_{r_{div}}^{R} \rho(x,r)u(x,r)\, 2\pi r\, dr, \tag{4}$$

The dividing streamline is also used to average the relevant flow variable across the ejector's section, i.e.

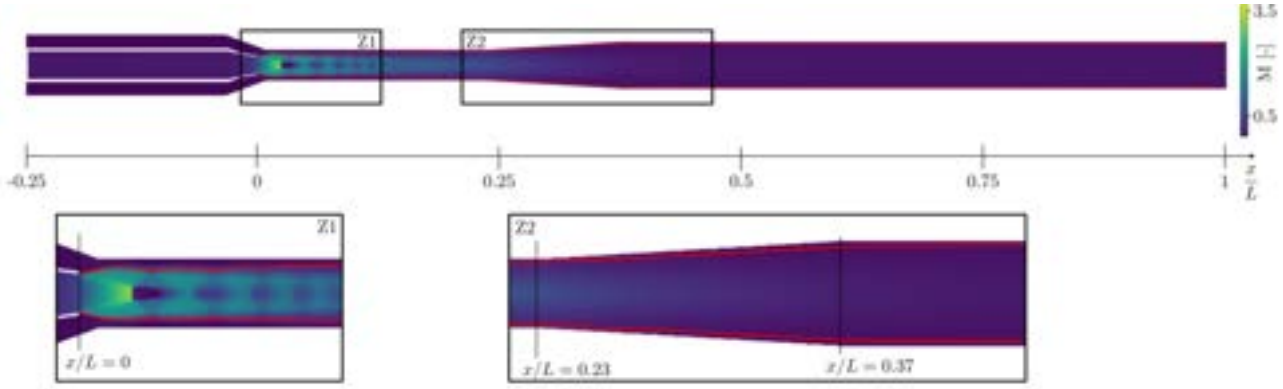

Figure 2: Mirrored Mach number field of an ejector operating in off-design conditions, obtained through classic axisymmetric CFD [22]. A shock train is present in the mixing pipe due to the different static pressures of both streams at the exit of the primary nozzle. The red line indicates the dividing streamline. The reference 1D data in the rest of the work is obtained through averaging over the resulting cross-sections with equations (5).

$$\hat{\rho}_{p,s}(x) = \frac{1}{A_{p,s}} \int_{A_{p,s}} \rho \, dA_{p,s}, \quad \hat{u}_{p,s}(x) = \frac{1}{\hat{\rho}_{p,s} A_{p,s}} \int_{A_{p,s}} \rho u \, dA_{p,s}, \quad \text{and} \quad \hat{e}_{t\,p,s}(x) = \frac{1}{\hat{\rho}_{p,s} A_{p,s}} \int_{A_{p,s}} \rho e_t \, dA_{p,s}, \tag{5}$$

where the hat $\hat{\cdot}$ denotes the cross-section averaged variables and the subscripts p, s denote the primary and the secondary stream. Therefore, the areas $A_{p,s}$ are the portion of the domain corresponding to $r \in [0, r_{div}]$ and $r \in [r_{div}, R]$ respectively. It is worth noticing that the specific choice of density average is arbitrary, but the other two equations enforce that the 1D variables keep the same mass flow rate and total internal energy as the CFD [23]. The final dataset consists of the cross-sections $A_{p,s}$ and the flow variables obtained with equation 5 at 1530 spatial coordinates x of the single CFD simulation shown in figure 2. Hence, the available data is locally rich, but limited to a single geometry and a single operating condition. Therefore, the resulting calibration in section 4. can not be expected to generalize to different operating conditions.

3.2. Model definition

The main idea of the 1D- two stream ejector model is to treat the inlets as 1D domains with the variable area along the axial coordinate x (as in the 1D modelling of nozzle flows). The mixing pipe is modelled as a 1D domain with 2 streams that exchange momentum through shear and with the wall. The division of the complete section between the two streams remains a degree of freedom, e.g., the same primary mass flow rate can pass through a narrow or a wide flow passage, with the secondary cross-section adapting accordingly. Therefore, the static pressure is assumed to be equal in both streams as an additional constraint. This set of equations is known as the compound flow theory, originally proposed by Bernstein [24] and adopted later in ejector modelling [6, 10, 23, 25]. The set of ODEs (1) consists of the following governing equations:

$$\frac{d_x p}{p} = \frac{1}{\beta}\left(d_x A + \frac{1}{2} f_{ps} l_{ps} \frac{\left(M_p^2 - M_s^2\right)^2}{M_p^2 M_s^2} - \frac{1}{2} f_w l_w \left(1 + (\gamma - 1) M_s^2\right)\right), \tag{6}$$

$$\frac{d_x p_{tp}}{p_{tp}} = -\frac{1}{2} \frac{f_{ps} l_{ps}}{A_p} \gamma \left(M_p^2 - M_s^2\right), \tag{7}$$

$$\frac{d_x p_{ts}}{p_{ts}} = \frac{1}{2} \frac{f_{ps} l_{ps}}{A_s} \gamma \left(M_p^2 - M_s^2\right) - \frac{1}{2} \frac{f_w l_w}{A_s} \gamma M_s^2, \tag{8}$$

$$\frac{d_x T_{tp}}{T_{tp}} = 0 \text{ and } \frac{d_x T_{ts}}{T_{ts}} = 0, \tag{9}$$

$$\frac{d_x A_p}{A_p} = \left(\frac{1 - M_p^2}{\gamma M_p^2}\right) \frac{d_x p}{p} + \frac{1}{2} \frac{f_{ps} l_{ps}}{A_p} \left(1 + (\gamma - 1) M_p^2\right) \left(1 - \frac{M_s^2}{M_p^2}\right), \tag{10}$$

$$\frac{d_x A_s}{A_s} = \left(\frac{1 - M_s^2}{\gamma M_s^2}\right) \frac{d_x p}{p} - \frac{1}{2} \frac{f_{ps} l_{ps}}{A_s} \left(1 + (\gamma - 1) M_s^2\right) \left(\frac{M_p^2}{M_s^2} - 1\right) + \frac{1}{2} \frac{f_w l_w}{A_s} \left(1 + (\gamma - 1) M_s^2\right), \tag{11}$$

where

$$\beta = A_p \frac{1 - M_p^2}{\gamma M_p^2} + A_s \frac{1 - M_s^2}{\gamma M_s^2}, \tag{12}$$

and with the constraint that $A_p + A_s = A$. It is worth noticing that eq. (6) implies that the static pressure is equal on both primary and secondary sides, i.e. $p_p = p_s = p$. The derivation of these equations from conservation principles is presented in appendix A. We refer to the list of symbols for the definition of all variables.

The two closure parameters to be identified in a data-driven model calibration are the shear coefficient f_{ps} between the streams and the wall friction coefficient f_w. These are linked to the shear forces acting on the perimeter of the primary cross-section (l_{ps}) and the wall's perimeter (l_w), respectively. Therefore, in the formalism introduced in section 2., these variables constitute the model parameters $\boldsymbol{p} = [f_{ps}, f_w]^T$ to be provided by the closure function g while the state variables are $\boldsymbol{u} = [p, p_{tp}, p_{ts}, T_{tp}, T_{ts}, A_p, A_s]^T$. The local Mach numbers can be computed from these variables (e.g. the static and total pressures) or the local densities using the ideal gas law. Note that the constraint on the cross-sections can be imposed by first calculating the gradient of the primary cross-section A_p and subtracting it from the gradient of the total cross-section.

It is worth stressing that the assumption of equal static pressure is problematic at the inlet of the mixing pipe because the primary flow is generally under-expanded (cf. figure 2). Therefore, the proposed model cannot be used from the exit of the primary nozzle ($x = 0$) unless a pressure equalization mechanism is introduced in the model. Alternatively, the areas for the primary and secondary flows must be provided at the inlet of the mixing channel: in this case, the pressures naturally equalize within a short distance from the inlet; this is akin to what happens through the shock cells in the CFD simulation. The development of the first approach is left to future work. In this work, we use the dividing streamline identified from the CFD up to the point where the pressures equalize, and downstream, we use the compound equations (6)-(12) (this is further discussed in Section 4.)

The research question addressed in this work is the feasibility of deriving the spatial distribution of shear and friction coefficients that makes the 1D model comply with the post-processed CFD data. Moreover, in this work, we do not (yet) link the closure parameters to the state, which is a more complex task and should be studied across a wide range of operating conditions. We focus on the parameters' spatial distributions and their derivation by implementing the physics-separated and physics-integrated approaches.

3.3. Calibration

Physics-separated approach

Following the framework in Section 2., the physics-separated approach consists of calculating the closure coefficients from the processed CFD data. To this end, equations (7) and (8) can be used to compute the 1D shear and friction coefficients (f_{ps} and f_w) if all the other terms are extracted from data via appropriate processing. These two equations give:

$$f_{ps} = -\frac{2A_p}{l_{ps}\gamma\left(M_p^2 - M_s^2\right)}\frac{d_x p_{tp}}{p_{tp}} \quad \text{and} \quad f_w = -\frac{2A_s}{l_w \gamma M_s^2}\left(\frac{d_x p_{ts}}{p_{ts}} - \frac{1}{2}\frac{f_{ps} l_{ps}}{A_s}\gamma\left(M_p^2 - M_s^2\right)\right). \tag{13}$$

Both definitions rely on the differentiation of pressure evolution, computed using finite differences on a smoothed version of the signal. The derivation was carried out with a second-order centred scheme, while the smoothing was carried out with a Savitzy-Golay filter with a second-order polynomial. The resulting closure coefficients are, therefore, functions of the spatial coordinate x and could be linked to the local value of the state variables $\boldsymbol{u}$, or local values of dimensionless numbers such as Reynolds and Mach numbers in each stream, or pressure and temperature ratios. However, this regression has a high risk of overfitting because the flow field (and thus the closure coefficients) can change drastically with the operating conditions. This challenging regression requires a large dataset and is foreseen for future work. This work focuses on a single off-design operating point, with regression as a function of the axial coordinate x. Practically, we minimize the cost function (2) separately for the shear and the wall friction coefficient with a parametric function g heuristically constructed after analyzing the data. The specific choice is provided in Section 4.1.. Note that we can split the regression in two smaller problems because the predicted closure coefficients $\boldsymbol{p}$ can be evaluated independently against their references $\tilde{\boldsymbol{p}}$.

Physics-integrated approach

The closure coefficients derived in the previous section are those that minimize the error in the definitions (13), but this does not guarantee that the model prediction is the most accurate. The complex interplay of this parameter with the other equations in the model (6)-(11) introduces additional sensitivities to the model prediction. The physics-integrated approach seeks to account for all of these using the cost function (3) to penalize model prediction (that indirectly depends *also* on the parameters). In the investigated calibration problem, the observed quantities included in the cost function are the pressures p_{tp} and p_{ts} and the cross-sections A_p and A_s. The static pressure p is not included because the shock trains make p_p and p_s oscillate. Since the 1D model can only reproduce the mean trends due to the assumption of equal static pressures, this oscillation could unfairly penalize the model prediction and produce local minima in the cost function landscape. Moreover, the total temperature is excluded because it is assumed to be constant in the mixing pipe and

thus does not contribute to accentuating the cost function gradient distribution along the spatial coordinate. Finally, an additional term is added at the exit ($x = L$) to penalize the potential error on the back pressure. This penalization helps enforce the boundary condition of the model. Therefore, the cost function (3) for this approach becomes

$$J_2(\boldsymbol{w}) = \sum_i \left[\frac{(\tilde{p}_{tp,i} - p_{tp,i}(g))^2}{(\tilde{p}_{tp,i})^2} + \frac{(\tilde{p}_{ts,i} - p_{ts,i}(g))^2}{(\tilde{p}_{ts,i})^2} + \frac{(\tilde{A}_{p,i} - A_{p,i}(g)^2}{(\tilde{A}_{p,i})^2} + \frac{(\tilde{A}_{s,i} - A_{s,i}(g))^2}{(\tilde{A}_{s,i})^2} \right] + \frac{\tilde{p}(L) - p(g, L)}{\tilde{p}(L)} \tag{14}$$

where the summation is carried out over the available instances (e.g. grid points in x), the functional dependency on g denotes the model prediction based on the closure g and the summation over the index r is made explicit over the four variables involved. We recall that the closure function depends on weights $\boldsymbol{w}$, i.e. $g := g(x, \boldsymbol{w})$. For a given guess of the weights, hence a given closure law $\boldsymbol{p} = g(x, \boldsymbol{w})$, the cost function $J_2(\boldsymbol{w})$ in (14) is computed by first solving numerically the set of equations in (6)-(11) using a shooting method.

4. Results

4.1. Physics-separated approach

Figure 3 shows the original and filtered 1D distributions of the total pressure in both streams from the post-processed CFD, from the exit of the primary nozzle at $x/L = 0$ to the exit of the numerical domain at $x/L = 1$ (cf. equations (5)). The total pressures equalize for $x/L > 0.4$, as a result of the mixing process and the growth of the shear layer separating the two streams. After this equalization, the two streams are fully mixed and indistinguishable, driven by a common total pressure and temperature. The zoom Z1 (shown on the right) displays a sharp drop in total pressure at $x/L = 0.025$. This corresponds to the Mach disk in figure 2. This is a 2D effect which can not be reproduced by the 1D model and is thus better filtered out before the data is used for calibration. The filtered signal thus 'averages' the shock train for the computation of the closure coefficients. The window length of the Savitzky-Golay filter has been tuned to this end.

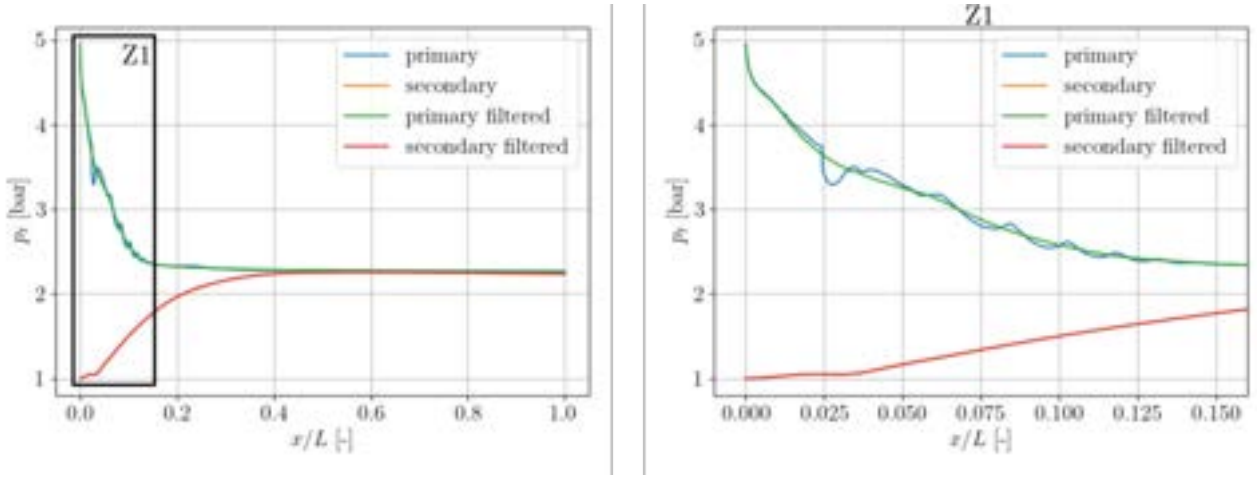

Figure 3: Filtering of the 1D total pressure field obtained through post-processing the CFD simulation in figure 2. The total pressures tend towards a common value as the primary and secondary streams exchange momentum. The shock train at the inlet of the mixing pipe strongly affects the primary total pressure, which is therefore filtered with a Savitzky-Golay filter before being differentiated (cf. equations (13)). The filtered secondary total pressure coincides with its raw counterpart since it is already quite smooth.

The shear and friction coefficients computed with equations (13) are shown in figures 4 and 5 respectively. The unfiltered coefficients show a sharp peak at the position of the Mach disk, as the primary total pressure changes suddenly at this point. This artefact is avoided through filtering. Still, both results indicate large coefficients at the inlet of the mixing pipe, especially in the wall friction f_w, which reaches an extreme value of 25 (with values expected to be of the order 0.01). A possible explanation could be the separation region behind the wall between the exit of the primary nozzle and the secondary inlet. This trailing edge is not sharp, so it is followed by a region of separated flow which slows down both the primary and the secondary stream through shear. This effect is locally quite strong for the primary flow due to a momentum deficit between the sonic flow and the stagnant flow in the bubble, hence a large value of the shear coefficient f_{ps}. However, this force is applied equally but with an opposite sign on the secondary flow, which therefore tends to *accelerate* rather than *decelerate*. In turn, a high wall friction coefficient is thus needed to overcome this numerical acceleration and still represent the actual friction forces on the secondary stream.

The peak at the inlet of the mixing domain shows an exponential decay, so an exponential function is chosen in the parametric closure function g for the calibration. Downstream, the evolution is rather flat, except for the oscillations induced by the shock train. Therefore, the closure function g is parametrized with a linear trend downstream. This leads to the following parametric function with 5 weights:

$$\begin{cases} y = w_1 + w_2 \exp(-w_3 x) & \text{if} x \leq w_0 \\ y = w_1 + w_2 \exp(-w_3 w_0) + w_4 x & \text{if} x > w_0 \end{cases} \tag{15}$$

This function is used for both closure coefficients, bringing the number of weights to 10. The mismatch with the post-processed coefficients is minimized using the summed squared error as a cost function and with the BFGS algorithm available in SciPy [20]. The gradient computation is performed with finite differences, which is affordable due to the low cost of the function to be called and the low number of weights. The resulting regression is shown alongside the raw and the filtered signals in figures 4 and 5.

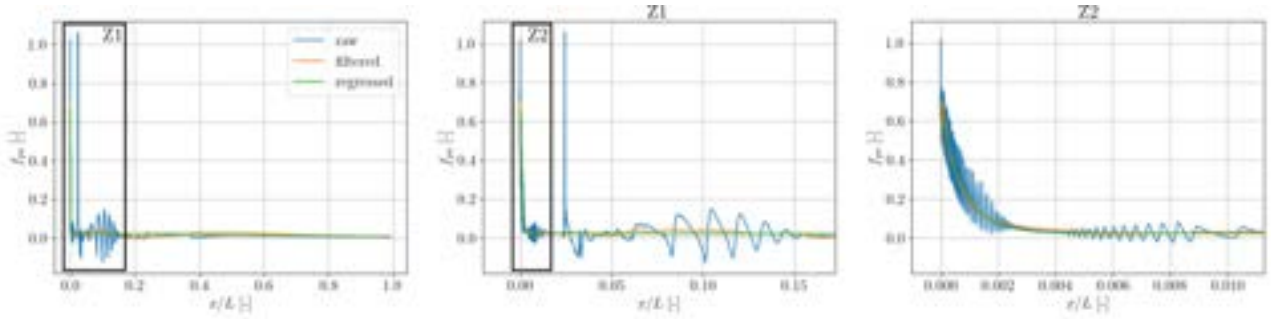

Figure 4: Shear coefficient calculated from the raw and filtered total pressure field from figure 3 with equation (13). The exponential decay at the inlet is attributed to a separation bubble at the exit of the primary nozzle. The calculation on the raw signal suffers from sharp gradients in the shock train and the Mach disk ($x/L = 0.025$). The physics-separated regression is carried out with equation (15) on the filtered shear coefficient f_{ps}.

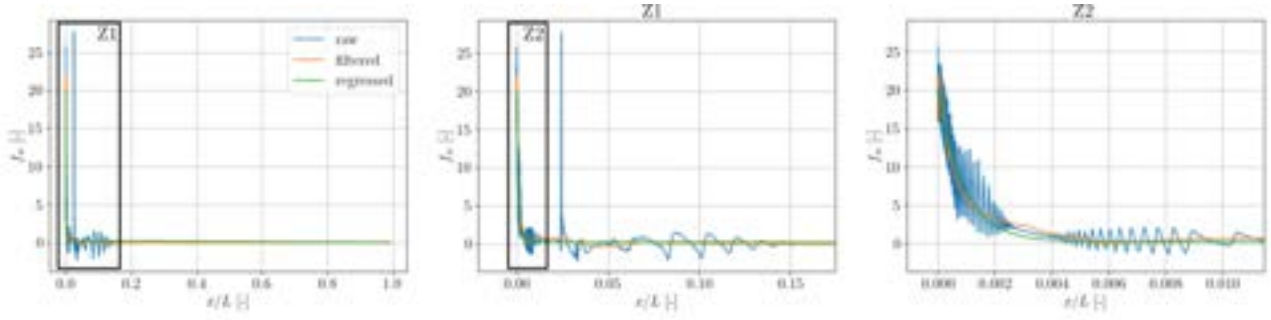

Figure 5: Wall friction coefficient calculated from the raw and filtered total pressure field from figure 3 with equation (13). The same trends are observed for the shear between the streams (cf. figure 4), so the same parametric function is used for the regression.

Next, we use the regressed closure relation to predict the flow field of the ejector with the 1D model. The resulting flow field compares well to the post-processed CFD (cf. figure 6). Upstream, the cross-section is imposed by the CFD, leading to a close match. Downstream, the unique pressure deviates from the values in the CFD due to the shock train (the primary stream is particularly affected). Nevertheless, the 1D model captures the global rising trend. This pressure increase arises from the momentum exchange between the two streams of the compound flow (cf. equation (6) with $\beta > 0$). The pressure rises more strongly in the diffuser from $x/L = 0.23$ and reaches a constant value where the streams reach the same total pressure. The constant total temperature in the 1D-2s model matches the post-processed CFD within 3 K. The deviation is attributed to the low enthalpy in the separation bubble at the exit of the primary nozzle, which influences the total temperature field downstream near the dividing streamline. The constant total temperature remains a good approximation for the bulk of the streams. Thermal mixing through different inlet temperatures is foreseen as a future extension of the 1D-2s model.

Despite the indirect penalization on the closure coefficients, an excellent match is obtained. The assumption of equal static pressure in both streams proves to be an acceptable assumption to close the system of equations (6)-(11) (at least in this off-design operating point). The match of the cross-sections between the 1D model and the CFD best validates the model. However, the 1D model shows a mismatch in back pressure (2.3 bar in the model and 2.2 bar in the CFD). The formulation with the ODEs always requires a shooting method to match a boundary condition at the exit of the domain ($x = L$), but none of the flow quantities is penalized in the physics-separated approach. Therefore, we apply the physics-integrated method in the next section to improve the prediction in the flow quantities both in the internal domain and the boundary condition for the static pressure.

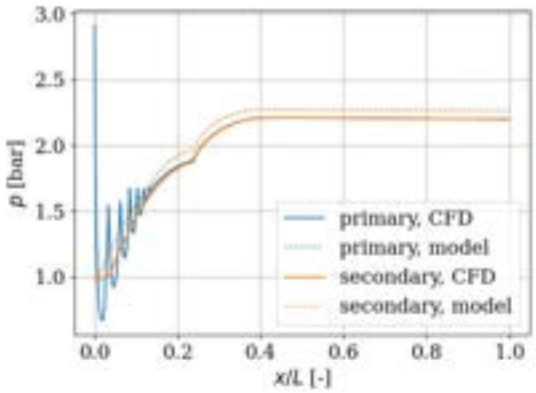

(a) Static pressure p

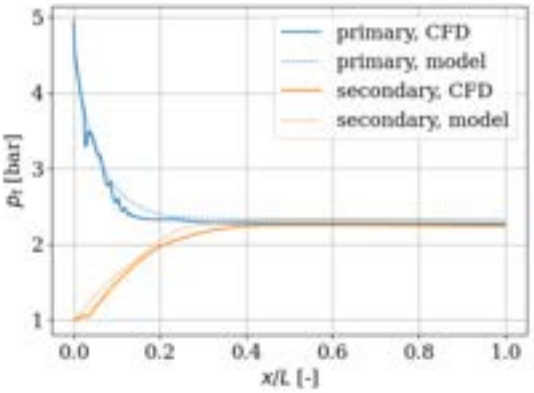

(b) Total pressure p_t

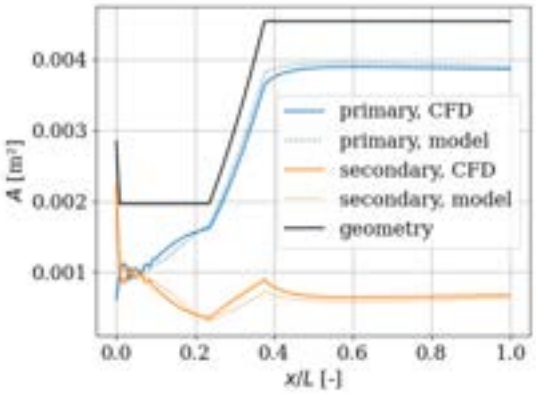

(c) Cross-section A

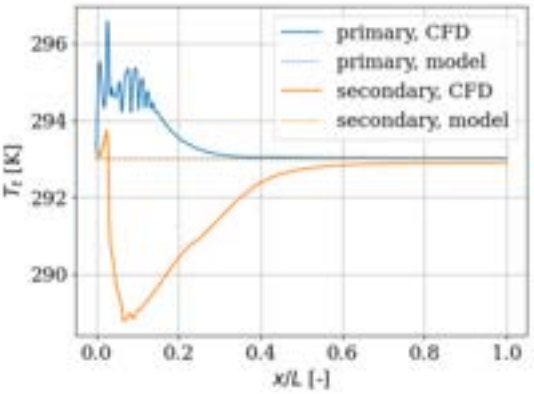

(d) Total temperature T_t

Figure 6: Model predictions with the regressed closure relation from the physics-separated approach (cf. figures 4 and 5). All variables match the post-processed 1D data quite well (the cost function (14) equals 0.0044). However, the boundary condition of the static pressure at the outlet is not met due to the indirect regression on the post-processed closure coefficients instead of on the physical quantities (cf. equations (2) and (14)).

4.2. Physics-integrated approach

The closure relation from the section above serves as an initial guess for the physics-integrated approach, where the prediction error on the physical quantities is minimized (including the back pressure as a boundary condition, cf. equation (14)). The resulting evolution of the shear and friction coefficients is shown in figure 7. The wall friction coefficient increased significantly, resulting in lower static pressure and a satisfied boundary condition (cf. figure 8a). An increased shear coefficient compensates for the corresponding loss in secondary total pressure. Finally, we note that the exponential decay between the inlet and $x/L = 0.01$ from figures 4 and 5 has sharpened, which results in a flat plateau in the coefficients in figure 7. This indicates the extreme values found with the physics-separated approach were not necessary.

The physics-integrated approach has decreased the value of the cost function (equation (14)) from 0.0044 with the initial guess from the physics-separated approach to 0.0036. This significant improvement can be appreciated visually by comparing figures 6 and 8. However, the integrated approach is less straightforward

a priori; one does not know which type of parametric function allows a close match. Additionally, initializing the weights is also non-trivial. For example, an excessive wall friction coefficient could decrease the static pressure enough to choke the flow and lead to problems in the integration of the system of ODEs (which becomes singular if $\beta = 0$). Therefore, the initialization through the physics-separated approach followed by fine-tuning with the physics-integrated proves an effective strategy for the model calibration, profiting from their complementary advantages.

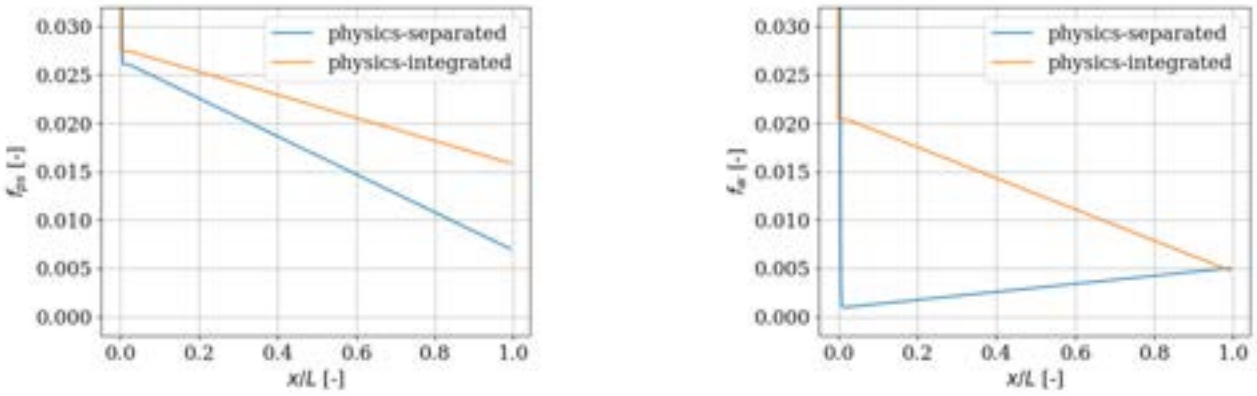

(a) Shear coefficient f_{ps}

(b) Wall friction coefficient f_w

Figure 7: Comparison of the regressed closure relations of the physics-separated and the physics-integrated approach. The first serves as initial guess for the latter method and is optimized to minimize cost function (14) (final value of 0.0036). A significant increase of the wall friction coefficient has allowed to decrease the static pressure in the mixing duct, leading to a satisfied boundary condition (cf. figure 8a).

5. Conclusion

This work proposes a general machine learning framework for calibrating physical models governed by a system of ODEs. We have explored a physics-separated approach, which consists of calculating the closure coefficients from higher resolution data (CFD) and then regressing the post-processed coefficients, and a physics-integrated approach, where the model is called upon during the optimization (training) phase to minimize the prediction error on the observed physical quantities. Both approaches have been applied successfully on a 1D ejector model to find the shear and wall friction coefficients as a function of the spatial coordinate.

The results show that a successive application of both approaches proves to be a convenient and robust method to calibrate the 1D model. The physics-separated approach guides the choice of the parametric function and provides a valid initial guess for the physics-integrated approach,. This then acts as a refinement tool to further minimize the prediction error by *directly* penalizing mispredictions in the state variables.

The proposed methodology is robust and flexible: it is compatible with state-of-the-art optimizers and leaves a free choice of the regressor. Any parametric tool fits the framework, ranging from linear regression to artificial neural networks. Furthermore, the method brings physical insight through closure relations for low-order but highly interpretable models. Finally, the framework can be categorized as physics-*constrained*, as opposed to physics-*informed*, machine learning since the conservation equations are always respected. From a more global perspective, splitting the problem in a set of physical equations f and closure relations g (cf. equation (1)) allows the continued use of dedicated solvers for the physical problem f, which are conservative and efficient, and simplifies the machine learning task by restricting its scope to the closure problem g. In this sense, the framework is an extension of neural ODEs, which solve the combined problem of f and g with neural networks without including prior physical knowledge. Consequently, less complex regressors may suffice for solving the problem, reducing the amount of required data or improving the performance on a fixed dataset.

Improvements are foreseen on two fronts. Firstly, the 1D ejector model is currently being extended to on-design operation with a pressure equalization mechanism to remove the requirement of imposing the cross-section from CFD at the inlet of the mixing pipe. Secondly, the adjoint method is being explored to handle closure laws requiring many weights (e.g., neural networks). Finally, the closure coefficients can be linked to the state variables rather than space coordinates to discover more universal closure relations for the 1D ejector model. This will require an extensive study on operating conditions and various geometries.

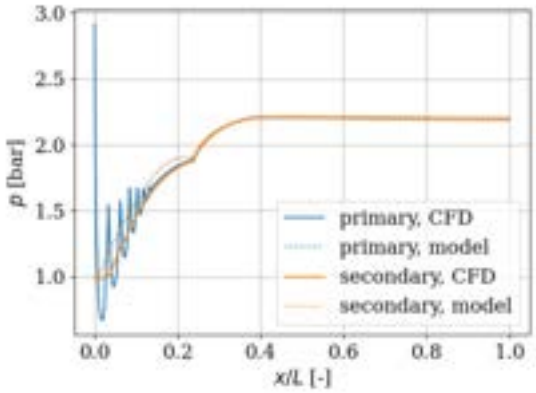

(a) Static pressure p

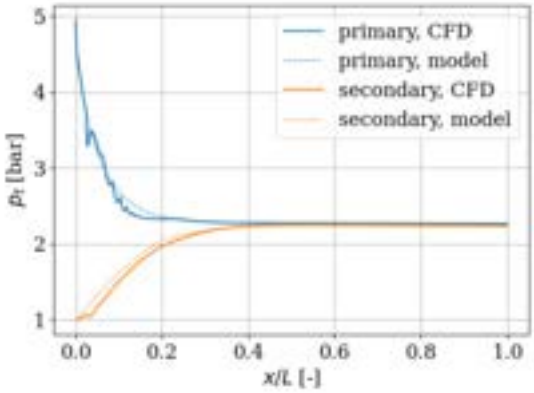

(b) Total pressure p_t

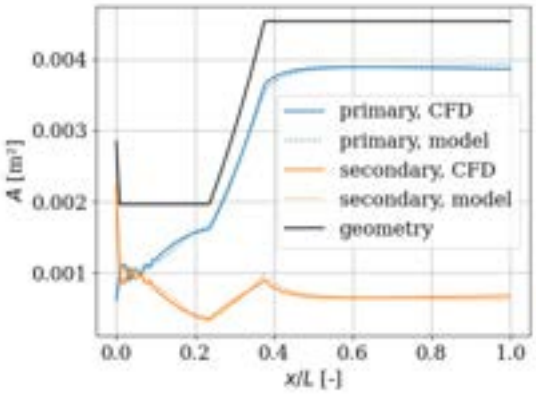

(c) Cross-section A

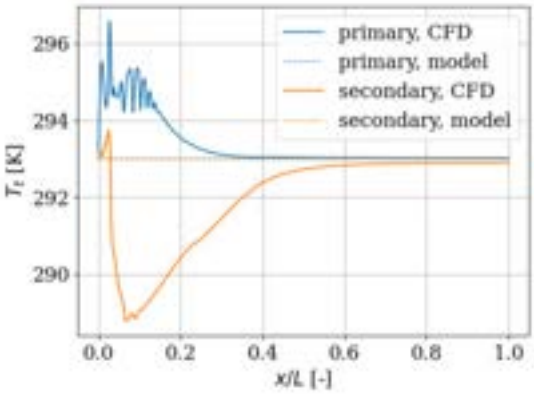

(d) Total temperature T_t

Figure 8: Model predictions with the regressed closure relation from the physics-integrated approach (cf. figure 7). The agreement improved compared to the physics-separated approach in figure 6 (the cost function (14) equals 0.0036). Moreover, the boundary condition of the static pressure at the outlet is now respected.

Acknowledgments

J. Van den Berghe is supported by a F.R.S.-FNRS FRIA grant. This project has received funding from the Clean Sky 2 Joint Undertaking (JU) under grant agreement No 101008100. The JU receives support from the European Union's Horizon 2020 research and innovation programme and the Clean Sky 2 JU members other than the Union.

Disclaimer: The contents presented in this article reflect only the author's point of view: the authors and Clean Sky JU are not responsible for any use that may be made of the information it contains.

Appendix A Derivation of the 1D ejector model from first principles

The base equations of the 1D model are the quasi-1D Euler equations with a force term F:

$$d_x(\rho_i A_i V_i) = 0; \quad d_x(\rho_i A_i V_i^2) = -A_i d_x p_i + F_i; \quad d_x(\rho_i A_i V_i h_{ti}) = 0 \tag{16}$$

where the index i denotes either the primary (p) or the secondary stream (s). The following equivalent system can be derived from these conservation equations (cf. [26] for a detailed derivation):

$$\frac{d_x p_i}{p_i} = \left[\frac{1+(\gamma-1)\,M_i^2}{1-M_i^2}\right]\frac{F_i}{A_i p_i} + \left[\frac{\gamma M_i^2}{1-M_i^2}\right]\frac{d_x A_i}{A_i}; \quad \frac{d_x p_{ti}}{p_{ti}} = \frac{F_i}{A_i p_i}; \quad \frac{d_x T_{ti}}{T_{ti}} = 0 \tag{17}$$

The wall friction force acts on the secondary stream and is defined through a classic friction coefficient:

$$F_w = -\frac{1}{2} f_w \rho_s v_s^2 = -\frac{1}{2} f_w \gamma p_s M_s^2 \tag{18}$$

The shear force is defined in a similar way and depends on the difference in dynamic pressure:

$$F_{ps} = \frac{1}{2} f_{ps} \left(\rho_p v_p^2 - \rho_s v_s^2 \right) = \frac{1}{2} f_{ps} \gamma p \left(M_p^2 - M_s^2 \right) \tag{19}$$

The primary and secondary forces are given by $F_p = -F_{ps}$ and $F_s = F_{ps} + F_w$. Combining the equations above results in equations (7) and (8). The equation for the static pressure results from the assumption of equal static pressure in both streams. The first step is to inverse equation (17) in terms of the area:

$$d_x A_i = \left[A_i \frac{1 - M_i^2}{\gamma M_i^2} \right] \frac{d_x p}{p} - \left[\frac{1 + (\gamma - 1) M_i^2}{\gamma M_i^2} \right] \frac{F_i}{p} \tag{20}$$

where the static pressure p lost the index because we assume $p_p = p_s$. Equations (10) and (11) for the gradient of the cross-sections follow from the equation above after filling in the forces. We sum the equation above for both streams and obtain the gradient of the known geometry $A = A_p + A_s$:

$$d_x A = \left[A_p \frac{1 - M_p^2}{\gamma M_p^2} + A_s \frac{1 - M_s^2}{\gamma M_s^2} \right] \frac{d_x p}{p} - \left[\frac{1 + (\gamma - 1) M_p^2}{\gamma M_p^2} \right] \frac{F_p}{p} - \left[\frac{1 + (\gamma - 1) M_s^2}{\gamma M_s^2} \right] \frac{F_s}{p} \tag{21}$$

The first term corresponds to the compound choking indicator β from equation (12). We reverse the equation above, to obtain the following expression of the pressure gradient:

$$\frac{d_x p}{p} = \frac{1}{\beta} \left(d_x A + \left[\frac{1 + (\gamma - 1) M_p^2}{\gamma M_p^2} \right] \frac{F_p}{p} + \left[\frac{1 + (\gamma - 1) M_s^2}{\gamma M_s^2} \right] \frac{F_s}{p} \right) \tag{22}$$

Equation (6) follows after filling in the forces and some simplifying operations.

Nomenclature

Letter symbols

e	specific internal energy, J/(kgK)
f_{ps}	shear coefficient, $-$
f_w	wall friction coefficient, $-$
l_{ps}	perimeter of the primary cross-section, m
l_w	perimeter of the wall, m
$\dot{m}$	mass flow rate, kg/s
p	pressure, Pa
r	radial coordinate, m
t	time, s
u	axial velocity, m/s
x	axial coordinate, m
A	cross-section, m^2
F	force per unit length, N/m
L	length of the ejector, m
M	Mach number, $-$
R	wall radius, m
T	temperature, K
$\boldsymbol{p}$	vector of closure parameters, $-$
$\boldsymbol{u}$	state vector, $-$
$\boldsymbol{w}$	weight vector, $-$

Greek symbols

β	compound choking indicator, m^2
γ	ratio of specific heat capacities (air: 1.4), $-$
ρ	density, kg/m^3

Subscripts and superscripts

$\hat{\cdot}$	cross-sectional average of a variable
$\tilde{\cdot}$	observation of a variable
b	back, outlet of the ejector
p	primary stream
s	secondary stream
t	total quantity (pressure, temperature, internal energy)

References

[1] Aidoun Z., Ameur K., Falsafioon M., Badache M., *Current advances in ejector modeling, experimentation and applications for refrigeration and heat pumps. Part 1: Single-phase ejectors*. Inventions 2019;4(1):15.

[2] Keenan J. H., Neumann E. P., *A Simple Air Ejector*. Journal of Applied Mechanics 1942;9(2):A75-A81.

[3] Munday J. T., Bagster D. F., *A New Ejector Theory Applied to Steam Jet Refrigeration*. Industrial & Engineering Chemistry Process Design and Development 1977;16(4):442-449.

[4] Eames I. W., Aphornratana S., Haider H., *A theoretical and experimental study of a small-scale steam jet refrigerator*. International journal of refrigeration 1995;18(6):378-386.

[5] Chen W., Liu M., Chong D., Yan J., Little A. B., Bartosiewicz Y., *A 1D model to predict ejector performance at critical and sub-critical operational regimes*. International Journal of Refrigeration 2013;36(6):1750-1761.

[6] Metsue A., Debroeyer R., Poncet S., Bartosiewicz Y., *An Improved Thermodynamic Model for Supersonic Real-Gas Ejectors using the Compound-Choking Theory*. Energy 2021;238:121856.

[7] Bartosiewicz Y., Aidoun Z., Desevaux P., Mercadier Y., *Numerical and experimental investigations on supersonic ejectors*. International Journal of Heat and Fluid Flow 2005;26(1):56-70.

[8] Hemidi A., Henry F., Leclaire S., Seynhaeve J., Bartosiewicz Y., *CFD analysis of a supersonic air ejector. Part I: Experimental validation of single-phase and two-phase operation*. Applied Thermal Engineering 2009;29(8):1523-1531.

[9] Van den Berghe J., Dias B. R. B., Bartosiewicz Y., Mendez M. A., *A 1D model for the unsteady gas dynamics of ejectors*. Energy 2023;267:126551.

[10] Clark L., *Application of compound flow analysis to supersonic ejector-mixer performance prediction*. In: 33rd Aerospace Sciences Meeting and Exhibit; 1995; 645.

[11] Banasiak K., Hafner A., *1D Computational model of a two-phase R744 ejector for expansion work recovery*. International Journal of Thermal Sciences 2011;50(11):2235-2247.

[12] del Valle J. G., Jabardo J. M. S., Ruiz F. C., Alonso J. S. J., *A one dimensional model for the determination of an ejector entrainment ratio*. International Journal of Refrigeration 2012;35(4):772-784.

[13] Berg J., Nyström K., *Neural network augmented inverse problems for PDEs*. arXiv preprint arXiv:1712.09685 2017.

[14] Parish E. J., Duraisamy K., *A paradigm for data-driven predictive modeling using field inversion and machine learning*. Journal of computational physics 2016;305:758-774.

[15] Holland J. R., Baeder J. D., Duraisamy K., *Field inversion and machine learning with embedded neural networks: Physics-consistent neural network training*. In: AIAA Aviation 2019 Forum; 2019.

[16] Sirignano J., MacArt J. F., Freund J. B., *DPM: A deep learning PDE augmentation method with application to large-eddy simulation*. Journal of Computational Physics 2020;423:109811.

[17] MacArt J. F., Sirignano J., Freund J. B., *Embedded training of neural-network subgrid-scale turbulence models*. Physical Review Fluids 2021;6(5):050502.

[18] Sirignano J., MacArt J., Spiliopoulos K., *PDE-constrained models with neural network terms: optimization and global convergence*. arXiv preprint arXiv:2105.08633 2021.

[19] Chang C., Dinh N. T., *Classification of machine learning frameworks for data-driven thermal fluid models*. International Journal of Thermal Sciences 2019;135:559-579.

[20] *scipy.optimize.minimize* Available at: `https://docs.scipy.org/doc/scipy/reference/generated/scipy.optimize.minimize.html` [accessed 7 March 2023].

[21] Mendez M. A., Dominique J., Fiore M., Pino F., Sperotto P., Van den Berghe J., *Challenges and Opportunities for Machine Learning in Fluid Mechanics*. In: Proceedings of the 19th International Topical Meeting on Nuclear Reactor Thermal Hydraulics (NURETH); 2022. Preprint at arXiv 2202.12577.

[22] Schillaci E., Oliet Casasayas C., Vemula J. B., Duponcheel M., Bartosiewicz Y., Planquart P., *Air Ejector Analysis in Normal and Abnormal Modes, Oriented to Control Purposes in Aircraft Systems*. In: 9th European Conference for Aeronautics and Space Sciences (EUCASS); 2022; European Conference for AeroSpace Sciences (EUCASS); 2022; 1-12.

[23] Lamberts O., Chatelain P., Bourgeois N., Bartosiewicz Y., *The compound-choking theory as an explanation of the entrainment limitation in supersonic ejectors*. Energy 2018;158:524-536.

[24] Bernstein A., Heiser W. H., Hevenor C., *Compound-compressible nozzle flow*. 1967.

[25] Croquer S., Fang Y., Metsue A., Bartosiewicz Y., Poncet S., *Compound-choking theory for supersonic ejectors working with real gas*. Energy 2021;227:120396.

[26] Shapiro, A. H., *Generalized one-dimensional continuous flow.*. In: The dynamics and thermodynamics of compressible fluid flow. New York: Ronald Press. 1953. p. 219-262.

PROCEEDINGS OF ECOS 2023 - THE 36TH INTERNATIONAL CONFERENCE ON
EFFICIENCY, **C**OST, **O**PTIMIZATION, **S**IMULATION AND ENVIRONMENTAL IMPACT OF ENERGY SYSTEMS
25-30 JUNE 2023, LAS PALMAS DE GRAN CANARIA, SPAIN

Contribution of Geometric Features on the Aeroacoustic Behaviour of a Slot Diffuser

Philipp Ostmann[a], Lisa Krüger[b], Martin Kremer[b] and Dirk Müller[b]

[a] Institute for Energy Efficient Buildings and Indoor Climate, Aachen, Germany, philipp.ostmann@eonerc.rwth-aachen.de, CA
[b] Institute for Energy Efficient Buildings and Indoor Climate, Aachen, Germany, ebc-office@eonerc.rwth-aachen.de

Abstract:
Sound generated by air diffusers is a factor that affects a productive working environment and therefore plays an important role in the operation of HVAC systems. A reliable prediction of sound sources and levels offers the potential to minimise noise emissions by modifying geometric features in the early design stage of air diffusers. The research field of aeroacoustics yielded many approaches to compute not only sound propagation but also sound generation in airflows. Based on the prominent Lighthill analogy the Curle analogy and Proudman analogy were developed. In this work, we investigate a commercially available slot diffuser. The airflow through the diffuser is calculated using steady-state simulations at diffuser outlet velocities of 4, 6 and 8 m/s, which corresponds to roughly 181, 267 and 351 m^3/h, respectively. To evaluate the influence of the solid surfaces we compute the emission according to Curle's analogy. We further use Proudman's analogy to assess the effect of the freestream. Based on the flow simulation geometric optimisations are proposed. By design, a steady-state simulation is not able to capture time-resolved phenomena, such as periodic vortex shedding. But since they are far less demanding in regards to computational resources, we can simulate a wider variety of flow conditions. By identifying the primary sound source regions we not only increase the awareness towards the impact of certain flow structures, such as large scale vortex systems, but also offer a first indicator of possible design optimisations. The computed flow field is to be validated with near-field Laser-Doppler-Anemometry (LDA) measurements.

Keywords:
Aeroacoustics, Slot Diffuser, Flow Simulation, Aeroacoustics Analogy.

1. Introduction

In addition to thermal comfort, the acoustic environment also affects the general perceived comfort in buildings. Since legislation and increasing public awareness require the ventilation of public buildings, the associated acoustic emissions are gaining importance. While ventilation noise is desirable to some degree to mask other noise sources, the ventilation system should generally be as quiet as possible. The components transmitting the ventilation noise into the occupied room are air diffusers.

Typical air diffusers can be divided into two common groups: swirl and slot diffusers. In this work, we focus on the investigation of a commercially available two-slot diffuser, which is shown in Figure 1. To gain insight on the flow field, we use a detailed flow simulation which provides us the strength of acoustic sources based on a steady-state solution.

In his PhD thesis Tautz [13] performed a detailed investigation of an automotive ventilation system. He was able to reproduce not only the acoustic spectrum but also the location of the acoustic sources. The computation however required significant computational ressources.

Ravichandran et al. [11] investigated a generic automotive diffuser with disturbed inflow conditions. They used detailed transient flow simulations to compute the acoustic emissions. Although not explicitely evaluated, the main features contributing to the acoustic emissions were the guiding flaps inside the diffuser.

Kusyumov et al. [7] succesfully applied a steady-state simulation to an isolated helicopter fuselage to predict broadband noise sources. Their case included Mach numbers greater than in our case, but it demonstrates the ability of Proudman's model to predict noise emissions.

For a generic slot diffuser we already showed, that the main acoustic sources are located near sharp edges [9]. Here a steady-state simulation indicated the same regions as a transient simulation. Therefore we deem it possible to identify the main noise source regions by steady-state simulations, if the spectral distribution of the noise is not of greater interest.

Although some researchers have adressed the acoustic emissions of air diffusers in the automotive sector, a

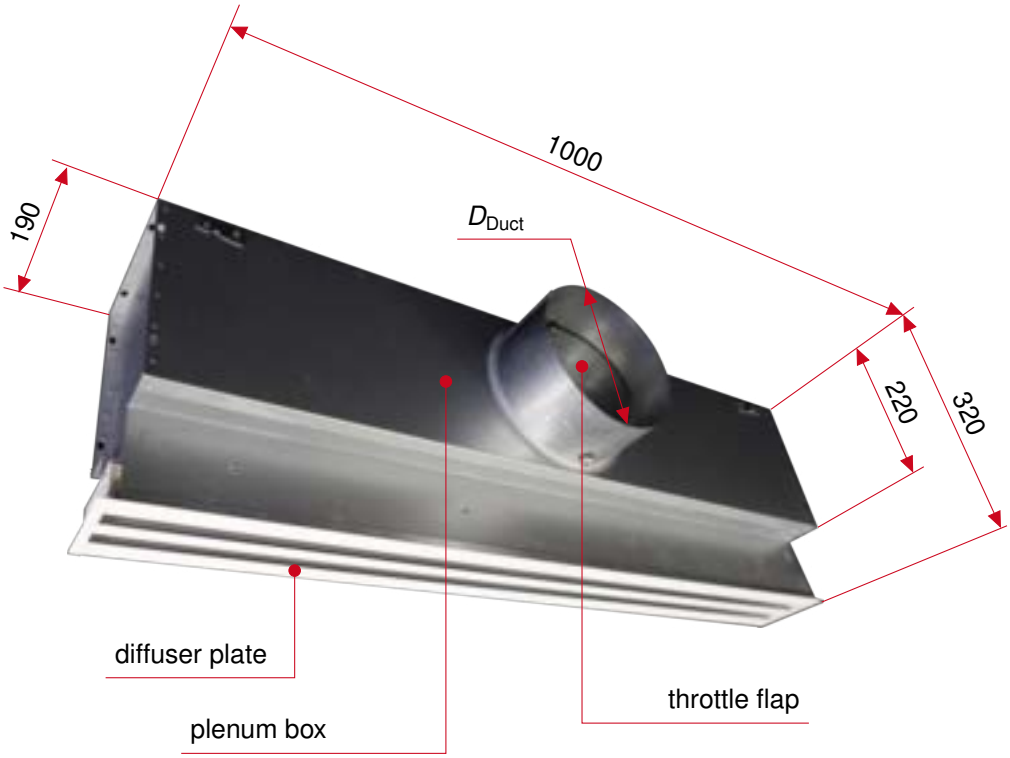

Figure 1: Picture of the investigated diffuser, dimensions given in mm

detailed investigation of the acoustic emissions of air diffusers applied in buildings have not been investigated. In this work we aim to investigate the acoustic behaviour of a slot diffuser while reducing the computational cost to locate the geometric features mainly responsible for the acoustic emission. A transient simulation offers a detailed investigation of acoustic phenomena (see [11, 13]). However the lower fidelity of a steady-state simulation is sufficient, if one is only interested in determining the main source locations (see [7, 9]).

2. Methodology

In this section we first describe the geometry of the slot diffuser and explain certain simplifications we made. We then explain the numerical and experimental setup, where the latter is needed to validate our simulations. We then present our method to rate the broadband noise emission. The slot diffuser is investigated at three diffuser outlet velocities $v_D = 4$, 6 and 8 m/s, which correspond to volume flow rates of $\dot{V} = 181$, 267 and 351 m^3/h. The diffuser outlet velocity is defined as the maximum occuring velocity within the diffuser.

2.1. Description of the geometry

Figure 1 shows the slot diffuser consisting of a circular connection duct with diameter D_{Duct}, that is connected to a plenum box. In order to limit the volume flow, an additional, perforated throttle flap is implemented in the connecting section between duct and plenum box. Preliminary simulations show, that the perforation has a negligible impact on the flow and aeroacoustic results, which is why we simplify the throttle flap by a solid round plate. The beams visible in Figure 2a, which are required to attach the diffuser plate to the plenum box, are also omitted to reduce the model size. Using the length of the plenum box l_{Plenum}, the diffuser plate features two rectangular slots with length $l_{Slot} = l_{Plenum}$ and width b_{Slot} (see Fig. 2c). Both slot channels are separated by a wall (see Fig. 2b), resulting in a total diffuser width of $b_{diffuser}$.

To alter the outlet flow pattern, both slots feature adjustable flaps, which are visible in Figure 2b. By changing the flap angle α_{Flap}, the exit flow angle can be varied between a ceiling-attached or ceiling-normal direction. In our study we only investigate the ceiling-attached case, since this is the most common setting. The geometric parameters are summarised in Table 1 and a detailed view of the simplified geometry used for the simulation is shown in Figure 2c.

2.2. Modelling of the flow and broadband noise

The slot diffuser is modelled in the commercially available software package STAR-CCM+ (17.06.008) from Siemens [12]. Although acoustic phenomena are by definition of transient nature, several models have been developed in the past to capture at least the acoustic sources from steady-state simulations. The use of

Table 1: Geometric parameters of the prepared slot diffuser

Parameter	Value	Unit	Description
D_{Duct}	198	mm	Connection duct diameter
l_{Slot}	997	mm	Length of the rectangular slots
b_{Slot}	20.5	mm	Width of one rectangular slot
α_{Flap}	43.5	°	Angle of the slot flaps

(a) View normal to the outlet of the diffuser

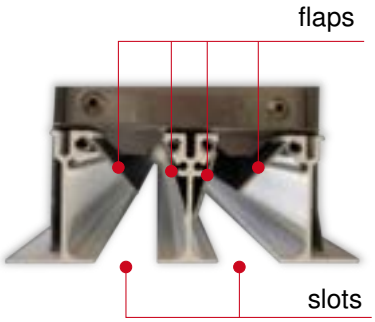

(b) Picture of the diffuser plate

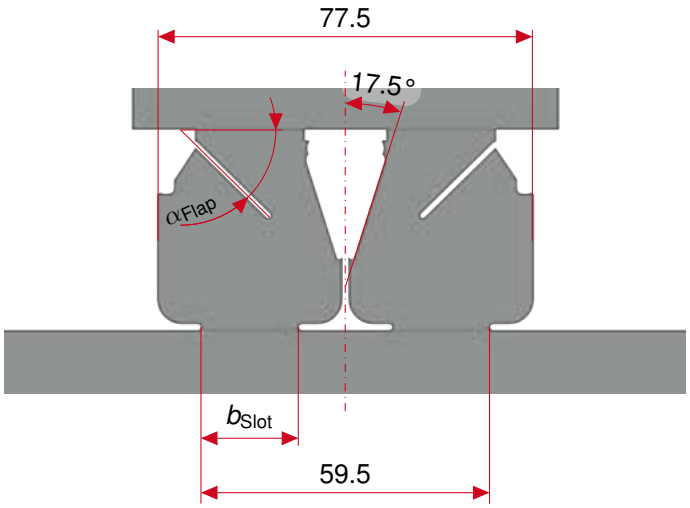

(c) Prepared geometry for the simulation model, dimensions in mm

Figure 2: Detail view of the diffuser outlet region

steady-state simulations offers significant savings in computational effort.

To accurately resolve all important geometric features, we employ an unstructured polyhedral mesh with a resolution up to $\Delta = 0.25\,\text{mm}$ near the curvatures of the flaps. Inside the plenum, the average resolution is kept close to $\Delta \approx 1.5\,\text{mm}$. We resolve the boundary layer with $n_{\text{Prism}} = 7$ prism layers with a total thickness of $\Delta_{\text{Prism}} = 2\,\text{mm}$ which results in $y^+ < 1$ in all important areas. To prevent steep gradients of mesh resolution, we set both the surface and the volumetric growth rate to 1.05. The total mesh size is $n_{\text{Cells}} \approx 61 \cdot 10^6$ cells. We use the same mesh for all simulations, since only the inlet mass flow changes.

We assume the air flow to be incompressible with a constant density ρ (see Tab. 2). The steady-state simulation is computed using a segregated flow solver. We use a pressure-velocity coupling scheme (SIMPLE), which is designated for incompressible flows [12]. In addition to incompressibility, we assume the air to be isothermal. As turbulence model we select the realizable $k-\varepsilon$ - model with all y+ wall treatment, since in our case it gives a more accurate solution of the ceiling-attached flow than e.g. the $k-\omega$ - model.

We define the inlet boundary condition with a constant mass flow condition $\dot{m} = \rho \cdot \dot{V}$ and low turbulence intensity v'/v (see Tab. 2). The diffuser is connected to a large volume which represents part of a room. While the ceiling is modelled as a no-slip wall, the other faces of the room are modelled as a pressure outlet with $p_{\text{out}} = 0\,\text{Pa}$.

Two broadband noise source models are used to calculate the aeroacoustic sources. The first model computes

broadband noise from dipole sources as a surface acoustic power P^{a}_{Curle}, which are most dominant in the vicinity of solid boundaries. It evaluates the turbulent boundary layer and was first developed by Curle [2, 3] based on the work of Lighthill [8].

$$P^{a}_{\text{Curle}} = \frac{1}{12\,\pi\overline{\rho}\overline{c}^{3}} \cdot 4\pi^{3}\,\overline{(u')^{2}}\,\left(p'_{\text{Wall}}\right)^{2} \tag{1}$$

The fluctuations $\overline{(u')^{2}}$ and p'_{Wall} can be further simplified according to Hinze [6, pp. 668-680]. The simplification yields expressions that only depend on the turbulent kinetic energy k and the wall shear stress τ_{Wall}.

$$\overline{(u')^{2}} = \frac{2}{3}\max\left(k;\ \frac{3.3\,\tau_{\text{Wall}}}{\overline{\rho}}\right) \qquad \left(p'_{\text{Wall}}\right)^{2} = \max\left(3\,\tau_{\text{Wall}};\ 0.7\,\overline{\rho}\cdot\frac{2}{3}k\right)$$

The second model was developed by Proudman [10] based on the work of Lighthill [8] and computes broadband noise from quadrupole sources originating from free stream turbulence as a volumetric acoustic power P^{a}_{Proudman}. Here u_{t} and L are the turbulent scales for the velocity and length.

$$P^{a}_{\text{Proudman}} = \alpha\rho\frac{\left(\overline{u_{\text{t}}}^{2}\right)^{4}}{c^{5}\,L} = \alpha\rho\frac{\overline{u_{\text{t}}}^{3}}{L}\frac{\overline{u_{\text{t}}}^{5}}{c^{5}} \qquad \text{with } u_{\text{t}} = \sqrt{\frac{2}{3}k} \tag{2}$$

Both models assume isotropic turbulence, which is consistent with turbulence modelling assumptions.

2.3. Laser-Doppler-Anemometry setup

We use a 3D-LDA system from *Dantec* that consists of a 2D *FiberFlow* and a 1D *FlowLite* probe. With proper arrangment both probes form a 3D-setup that allows us to measure all three velocity components. All optical measurements are performed in a separate chamber, which allows for a completely dark environment. The required volume flow $\dot{V}$ is delivered by a supply unit located outside of the chamber. We calculate the volume flow by measuring the pressure drop over an orifice. This method is calibrated by using a reference orifice as specified in DIN EN ISO 5167 - 2.

A schematic view of the setup in the chamber is given in Figure 3a. The diffuser is fed with air by utilising existing openings in the chamber walls to allow a connection to the supply unit. When feeding the required DEHS particles the chamber quickly fills up with fog, which renders the LDA system unable to produce good results. To mitigate this problem, we install a special exhaust system that provides an additional volume flow $\dot{V}_{\text{ex}} > 1200\,\text{m}^3/\text{h}$ to ventilate the whole chamber (depicted by → in Fig. 3a). The exhaust system draws air from the test hall environment outside the chamber through an opening in the chamber ceiling. It is then distributed using a suspended ceiling such that the exhaust volume flow is guided downwards along the chamber wall until it is captured by the exhaust hoods. We use 12 hoods that are evenly distributed around the diffuser frame. All hoods feed into a collection plenum below the frame from which an additional fan draws the exhaust volume flow. The exhaust system ensures, that the LDA probes have clear sight on the target location and no fog accumulates during the course of the whole measurement.

The 2D probe is connected to a laser which generates wavelengths of 488 nm (blue laser) and 514.5 nm (green laser), while the 1D probe utilises a laser with a wavelength of 532 nm (green laser). Each velocity component is recorded separately in non-coincident mode, since a measurement in coincident mode requires much more time to acquire a sufficient number of samples. We use beam expanders to allow the mounting of lenses with a focal length of $f_{\text{LDA}} = 500\,\text{mm}$. We attach the probes to a movable traverse system, which allows us to automatically measure a wide range of locations. Both probes are aligned along the z-direction of the diffuser with an angle of $\alpha_{\text{LDA}} = 15°$ and therefore enclose an angle of 30°. We further tilt the whole probe system by $\beta_{\text{LDA}} = 15°$ to allow for a measurement at $y = 0\,\text{mm}$. The diffuser coordinate system, that we use in this paper, is colored red in Figure 3b.

Table 2: Parameters of the flow and aeroacoustic models

Parameter	Value	Unit	Description
ρ	1.18415	$\text{kg}\,\text{m}^{-3}$	Density of the air
T	25	°C	Temperature of the air
v'/v	0.01	-	Inlet turbulence intensity
c	343	$\text{m}\,\text{s}^{-1}$	Speed of sound
$P_{\text{ac,ref}}$	$1 \cdot 10^{-12}$	W	Reference value of the acoustic power

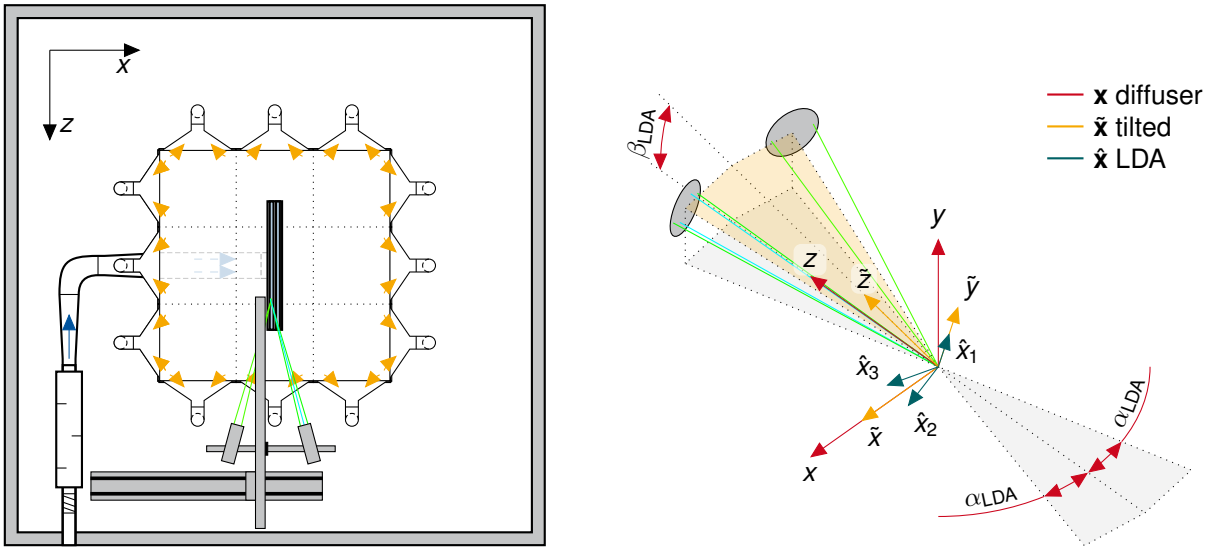

(a) Schematic of the LDA setup in the measurement chamber

(b) Sketch of the coordinate transformation

Figure 3: Setup of the LDA measurement and definition of the diffuser coordinate system

For each measured velocity component u_i, we acquire $N_i \geq 5000$ samples over a maximum duration of 5 min per evaluation point. The averages are calculated by using the arithmetic average, where $N_1 \neq N_2 \neq N_3$ due to non-coincident measurement.

$$\overline{u_i} = \frac{1}{N_i} \sum_{k=1}^{N_i} u_i(k) \tag{3}$$

To calculate the velocity components within the diffuser coordinate system $\mathbf{x} = (x, y, z)$, two transformations are required. A sketch of the coordinate transformations is given in Figure 3b. The first transformation $\mathbf{A}$ is used to translate the probe signals from their coordinate system $\hat{\mathbf{x}} = (\hat{x}_1, \hat{x}_2, \hat{x}_3)$ into a tilted, intermediate coordinate system $\tilde{\mathbf{x}} = (\tilde{x}, \tilde{y}, \tilde{z})$.

The blue laser (488 nm) is oriented vertically and measures u_1. Both green lasers (514.5 nm and 532 nm) are aligned horizontally and measure u_2 and u_3 respectively. We then apply another rotation transformation $\mathbf{B}$ about the $\tilde{x}$-axis to acquire the velocity components in the diffuser coordinate system.

$$\tilde{\mathbf{x}} = \mathbf{A} \cdot \hat{\mathbf{x}} \quad \text{, with } \mathbf{A} = \begin{bmatrix} 0 & \frac{1}{2\cos(\alpha_{\mathrm{LDA}})} & \frac{1}{2\cos(\alpha_{\mathrm{LDA}})} \\ 1 & 0 & 0 \\ 0 & -\frac{1}{2\sin(\alpha_{\mathrm{LDA}})} & \frac{1}{2\sin(\alpha_{\mathrm{LDA}})} \end{bmatrix} \tag{4}$$

$$\mathbf{x} = \mathbf{B} \cdot \tilde{\mathbf{x}} \quad \text{, with } \mathbf{B} = \begin{bmatrix} 1 & 0 & 0 \\ 0 & \cos(\beta_{\mathrm{LDA}}) & -\sin(\beta_{\mathrm{LDA}}) \\ 0 & \sin(\beta_{\mathrm{LDA}}) & \cos(\beta_{\mathrm{LDA}}) \end{bmatrix} \tag{5}$$

$$\mathbf{x} = \mathbf{B} \cdot \mathbf{A} \cdot \hat{\mathbf{x}} = \mathbf{C} \cdot \hat{\mathbf{x}} \tag{6}$$

We use the combined transformation matrix $\mathbf{C}$ to transform the velocity components and their respective variances.

2.4. Validation of the computed flow-field

To validate the flow field, the computed average velocity magnitude $\overline{|\mathbf{v}|}$ and the turbulent kinetic energy (TKE) k are compared with the LDA measurements. The steady-state simulation calculates time-averaged results only but directly reports the necessary values for $\overline{|\mathbf{v}|}$ and k.

In the case of the LDA measurements both values need to be computed from the recorded samples. For the velocity components, we can directly apply the coordinate transformation from equation 6 to the averaged probe signals $\overline{u}_{\mathrm{LDA}} = (\overline{u}_1, \overline{u}_2, \overline{u}_3)$.

$$\overline{\mathbf{v}} = \mathbf{C} \cdot \overline{u}_{\mathrm{LDA}} \tag{7}$$

Since we measure the variance of the velocity in the skewed LDA-coordinate system, we need to apply the transformation directly to the measured values. The transformation of the variances of u_i onto the x-direction

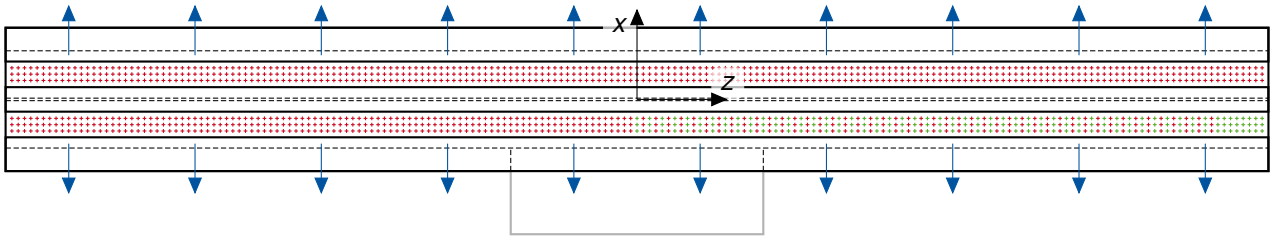

Figure 4: Evaluation points for the velocity field validation (green: LDA, red CFD)

is illustrated by equation 8, the other velocity components are treated similarly.

$$\overline{v_x'^2} = \left[\frac{1}{N_1}\sum_{i=1}^{N_1}\Big((u_1(i)-\overline{u_1})\cdot c_{11}\Big)^2\right] + \left[\frac{1}{N_2}\sum_{j=1}^{N_2}\Big((u_2(j)-\overline{u_2})\cdot c_{12}\Big)^2\right] + \left[\frac{1}{N_3}\sum_{k=1}^{N_3}\Big((u_3(k)-\overline{u_3})\cdot c_{13}\Big)^2\right] \tag{8}$$

Since the data rate for a full or semi-coincident measurement is too low, we are however not able to validate this approach yet. Finally, we use the transformed values to calculate the average velocity magnitude $\overline{|\mathbf{v}|}$ and TKE k according to equations 9 and 10.

$$\overline{|\mathbf{v}|} = \sqrt{\overline{v_x}^2 + \overline{v_y}^2 + \overline{v_z}^2} \tag{9}$$

$$k = \frac{1}{2}\left(\overline{v_x'^2} + \overline{v_y'^2} + \overline{v_z'^2}\right) \tag{10}$$

We validate the flow-field on the diffuser outlet plane at specific points on a x-z-plane at $y = 0\,\mathrm{mm}$. We spatially discretise the outlet section by $\Delta x = \Delta y = 5\,\mathrm{mm}$. The positioning of the validation points is displayed in Figure 4. Due to the limited spatial range of the LDA traverse system, we only measure points below $x < 0$ and above $z \geq 0$. We further reduce the number of points to be measured by downsampling the points towards the centre of the outlet and investigating only one slot. This is applicable as the flow field is symmetrical. Consequently, we measure the green points + with LDA. In the simulation, we additionally capture all red points +. In total, the outlet is discretised by 1194 points, of which 162 are measured with LDA.

The manufacturer's data sheet specifies certain operating points which are you used to validate the total-to-static pressure drop between the diffuser inlet $p_{\mathrm{tot,in}}$ and the ambient pressure in the chamber $p_{\mathrm{st,amb}}$. The inlet pressure is measured at the same section for the simulation and the experiment.

$$p_{\mathrm{tot,in}} = p_{\mathrm{st,in}} + \frac{\rho}{2}v^2 \tag{11}$$

$$\Delta p = p_{\mathrm{tot,in}} - p_{\mathrm{st,amb}} \tag{12}$$

Since the volume flow rates given in the data sheet do not match the simulated flow rates, the pressure drop is approximated.

$$\Delta p_{\xi,x} = \xi \cdot \dot{V}^x \tag{13}$$

$$\min \sum_{i=1}^{N}\left(\frac{\Delta p_{\mathrm{data}} - \Delta p_{\xi,x}}{\Delta p_{\mathrm{data}}}\right)^2 \tag{14}$$

The pressure loss coefficient ξ and the exponent x are calulated by using a regression model, which minimises the sum of the squared errors. Using $\xi = 4.18 \cdot 10^{-4}$ and $x = 1.91$, we can approximate the data sheet values with a maximum relative error of MAE = $4.195 \cdot 10^{-2}$. By using the approximated pressure $\Delta p_{\xi,x}$ we can assess the error of the flow model regarding the pressure losses at the respective volume flow $\dot{V}$.

$$\Delta p_{\mathrm{error}} = \frac{\Delta p_{\mathrm{sim}}(\dot{V}) - \Delta p_{\xi,x}(\dot{V})}{\Delta p_{\xi,x}(\dot{V})} \tag{15}$$

2.5. Evaluation of aeroacoustic broadband noise

To evaluate the total broadband noise predicted by both aeroacoustic broadband noise models, we integrate their respective acoustic power values. The Curle model predicts noise emitted from surfaces, which is why we integrate its power on representative boundary surfaces (see Fig. 5a). Since Proudman's model computes

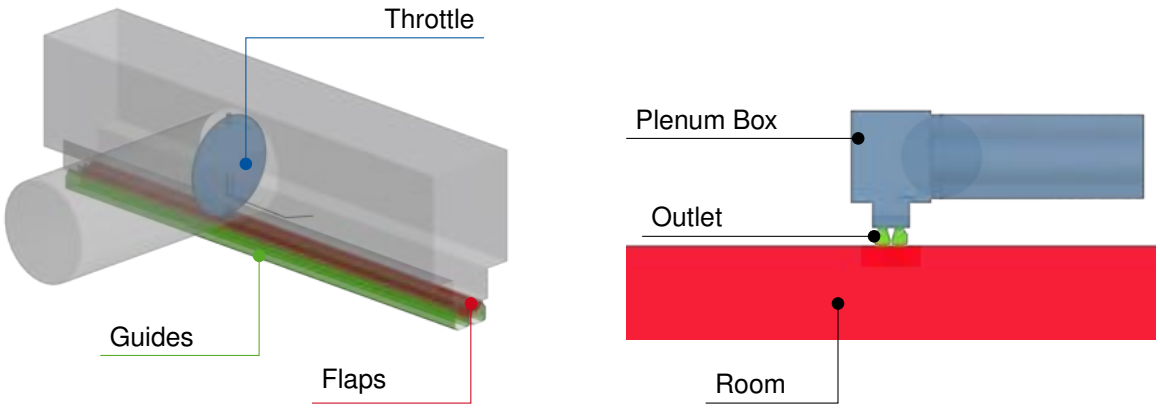

(a) Evaluation surfaces for the Curle calculation

(b) Evaluation volumes for the Proudman calculation

Figure 5: View on the surfaces and volumes used for the aeroacoustic broadband noise evaluation

a volumetric acoustic power, we apply a volume integral to specific subregions of interest (see Fig. 5b).

$$P_{\text{int,Curle}} = \int_S P^{\text{a}}_{\text{Curle}} \cdot ds \tag{16}$$

$$P_{\text{int,Proudman}} = \int_V P^{\text{a}}_{\text{Proudman}} \cdot dv \tag{17}$$

All integrated acoustic powers are then converted into the dB scale using the reference value $P_{\text{ac,ref}}$ (see Tab. 2).

$$P_{\text{ac,Curle/Proudman}} = 10 \cdot \log_{10}\left(\frac{P_{\text{int,Curle/Proudman}}}{P_{\text{ac,ref}}}\right) \tag{18}$$

By comparing the individual subsets, we can assign high noise emissions to individual geometric features. The selected subsets are shown in Figure 5. To evaluate the acoustic emissions from solid boundaries with Curle's model, we select three boundary subsets (see Fig. 5a). We further define three volumes in which we evalute the emissions from Proudman's model (see Fig. 5b). In both cases we also evaluate the overall emission from all boundaries (including the plenum box and the ceiling) and from the entire fluid region.

3. Results

We give a detailed discussion and validation of the results for the medium diffuser velocity $v_{\text{D}} = 6\,\text{m/s}$ which corresponds to a volume flow of $\dot{V} = 267\,\text{m}^3/\text{h}$.

3.1. Flow field validation

To validate the flow field we reduce the evaluation to the half of the lower slot ($x < 0, z > 0$) that was measured with LDA (see Sec. 2.3.). The sampled fields are shown in Figure 6 with their respective available spatial sampling resolution (see Sec. 2.4.).

By applying the sampling we calculate the computed average velocity to $|\overline{v}|_{\text{avg,CFD}} = 4.13\,\text{m/s}$, which is slightly higher than the measured value of $|\overline{v}|_{\text{avg,LDA}} = 3.80\,\text{m/s}$. The relative deviation of the average velocity is $|\overline{v}|_{\text{avg,CFD}}/|\overline{v}|_{\text{avg,LDA}} < 8\,\%$. The maximum values are $|\overline{v}|_{\text{max,CFD}} = 5.13\,\text{m/s}$ and $|\overline{v}|_{\text{max,LDA}} = 4.75\,\text{m/s}$ respectively. Although we set the same volume flow rates in both simulation and measurement, small leakages in the ducting system and non-airtight edges of the diffuser may have contributed to discrepancies between our computed and measured results. In addition to the influence of the inlet duct, the beams inside the diffuser plenum box (see Fig. 2a) cause significant distortions in the flow field. In the centre and near the edge the wake is clearly visible by considerably lower velocities. Since the beams are neglected in the simulation setup, this leads to a significant local deviation. We still consider the computed velocity field to be valid, given the fact, that the beams are neglected. The overall lower average velocity in the measurement is explained by leakages in the measurement setup.

The sampled measured and computed TKE distributions are shown in Figure 7. We observe considerably higher measured levels than in the simulation. Again the wake of the beams is clearly notable, but even in the area between the beams the measured TKE values are approximately doubled. By design the simulation assumes isotropic turbulence ($v_{\text{x}}'^2 = v_{\text{y}}'^2 = v_{\text{z}}'^2$). However, the measurements show a strong anisotropic

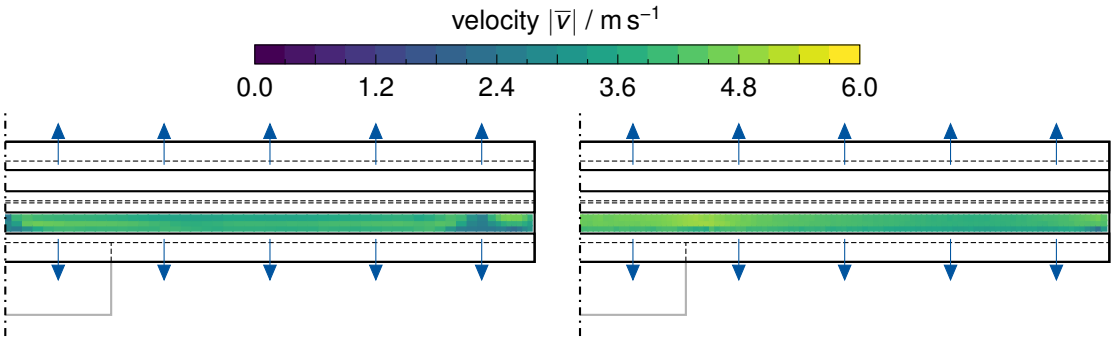

(a) Measured flow field

(b) Computed flow field

Figure 6: Velocity field

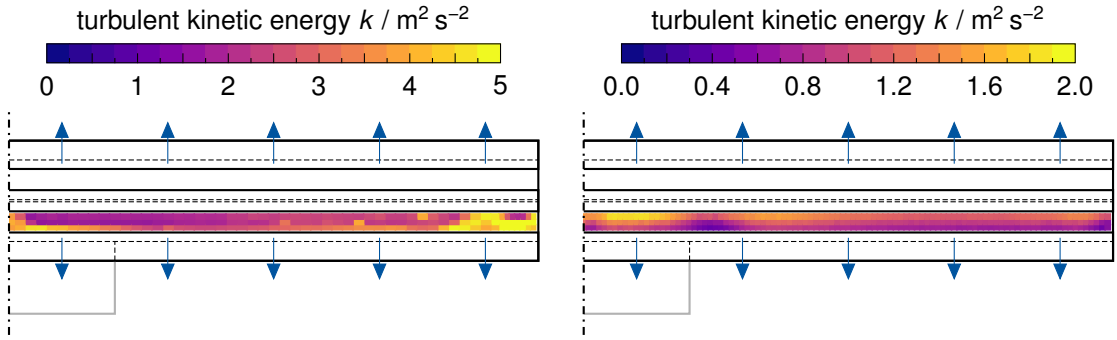

(a) Measured turbulent kinetic energy

(b) Computed turbulent kinetic energy

Figure 7: Turbulent kinetic energy

behaviour. In our case the variance in z-direction is almost an order of magnitude higher higher than in the other directions ($v_z'^2 \gg v_y'^2 > v_x'^2$). Overall, the measured kinetic energy is higher than in the simulation and the impact of the beam wakes prevent a proper validation of the turbulence.

As an additional metric, we also assess the pressure drop across the diffuser. In Figure 8 the pressure drop Δp is plotted against the volume flow $\dot{V}$. The solid lines indicate the regression model as explained in Section 2.4. and the points represent the individual values. The evaluation shows no significant difference between the measured and simulated pressure drop. Furthermore the regression model shows practically the same slope over the investigated volume flow range. Since the measured and computed pressure drop is practically equal, we only summarise the data sheet and the computed values in Table 3. The data sheet reports a higher pressure drop than measured and computed but also shows a comparable slope. Since the setup used by the manufacturer to assess the pressure drop is unknown, the slightly higher values might be due to other ambient air conditions or differences in the setup. We consider the pressure drop and therefore the wall shear stresses τ_{Wall} to be valid as well, because the pressure drop of our measurement and simulation match (see Fig. 8)

In conclusion, we deem our simulation to be valid in regards to the averaged velocity field and the overall pressure drop across the diffuser. We compute significantly lower turbulence levels. In large parts we account this to the assumption of isotropic turbulence by the $k-\varepsilon$ - model. Another factor might be, that we achieve higher turbulence intensities at the diffuser inlet in our measurements. Since the computation of Curle's model is mainly defined by the wall shear stress instead of the low turbulent kinetic energy in the boundary layer (see eq. 1), we deem it's results sufficiently accurate.

Figure 9 shows the computed flow field on two sections through the whole diffuser which originate at $(x, y, z) = (0, 0, 0)$. The flow exits the diffuser at an angle of $\approx 40°$ and attaches to the ceiling shortly after exit, as can be seen in Figure 9a. The maximum diffuser velocity of $v_D = 6\,\text{m/s}$ occurs in the vicinity of the flaps at $y \approx -15\,\text{mm}$. The velocity field shown in Figure 9b is inhomogeneous, although it is nearly symmetric along the x-axis. The maximum velocity at the outlet plane is lower than the diffuser velocity ($|\overline{v}|_{\text{max},y=0} = 5.24\,\text{m/s} < v_D$), which can be attributed to the larger cross-sectional area available for the flow. By averaging the velocity in the outlet section, we can calculate the relative average velocity, which is roughly constant across all investigated

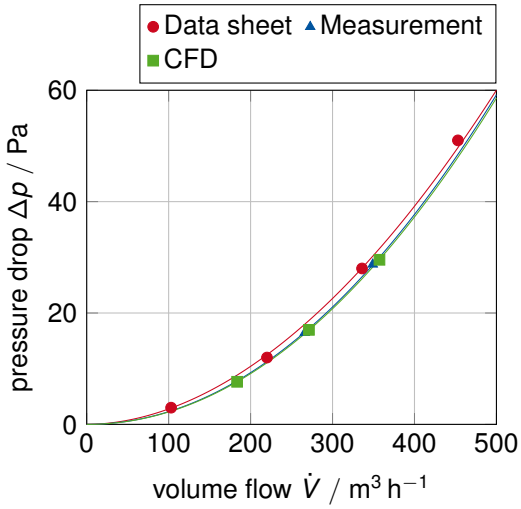

Figure 8: Validation of the pressure drop

Table 3: Overview of Δp_{error} values for the three computed volume flows

volume flow $\dot{V}$ m³/h	$\Delta p_{\xi,x}$ Pa	Δp_{sim} Pa	Δp_{error} %
184	8.8	7.6	−13.5
271	18.6	17.0	−9.0
357	31.6	29.6	−6.4

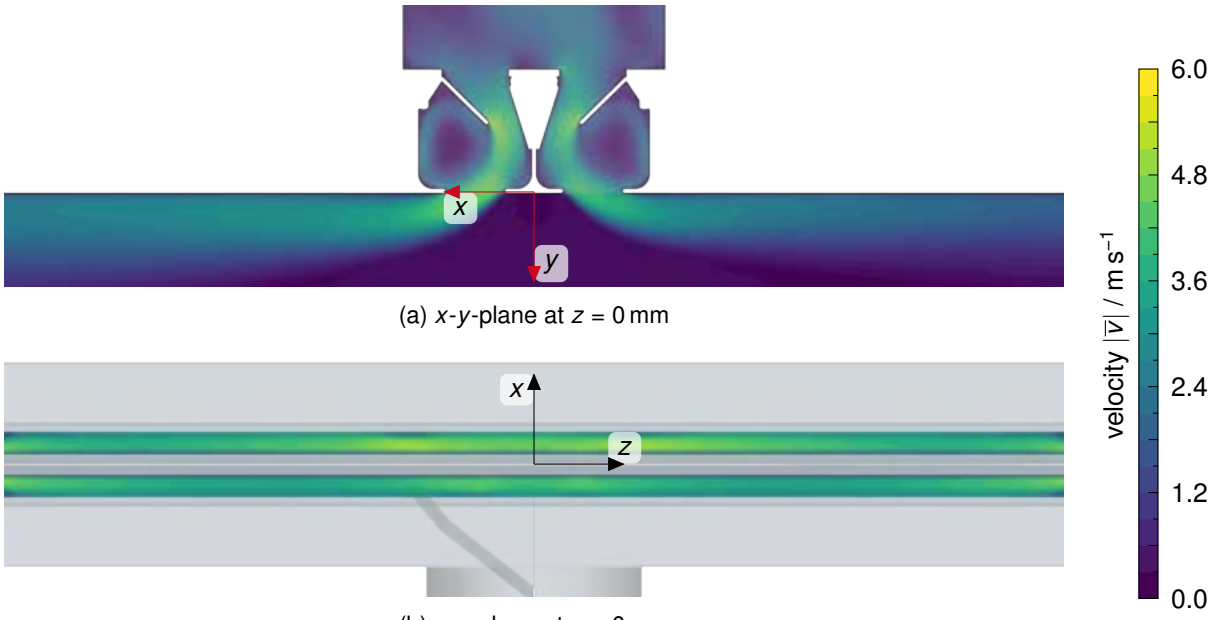

(a) x-y-plane at $z = 0\,\text{mm}$

(b) x-z-plane at $y = 0\,\text{mm}$

Figure 9: Computed velocity field for $v_{\text{D}} = 6\,\text{m/s}$

diffuser velocities.

$$\frac{|\overline{v}|_{\text{avg},y=0}}{v_{\text{D}}} = \frac{3.46\,\text{m/s}}{6\,\text{m/s}} = 0.58 \approx \text{const.} \tag{19}$$

Especially in the centre of the diffuser ($-150\,\text{mm} < z < 150\,\text{mm}$) the inflow duct has a great impact on the flow field. The areas where high velocities occur in the upper slot ($x > 0$) are further spread apart ($|z| \uparrow$). We do not observe the same spread distribution in the lower slot ($x < 0$), where multiple areas of roughly equal velocity are located near the centre and near the outer edges.

Figure 10 shows the distribution of the computed turbulent kinetic energy k. Figure 10a depicts a strong imbalance of the TKE between both slots. In the slot near the inflow duct significantly higher levels of turbulence occur. The TKE in the outlet section, shown in Figure 10b, reaches to a maximum of $k_{\text{max},y=0} = 2.11\,\text{m}^2/\text{s}^2$ with its average at $k_{\text{avg},y=0} = 1.06\,\text{m}^2/\text{s}^2$. The overall distribution is also nearly symmetric along the x-axis.

In both slots, the field smoothens towards the edges of the slots. Near the end of the slots ($|z| \gtrsim 470\,\text{mm}$) the influence of the wall becomes more prominent and causes another distortion of the flow field. In particular, we observe a sharp drop in velocity in the outer corners of the slots, which is accompanied by higher values of TKE.

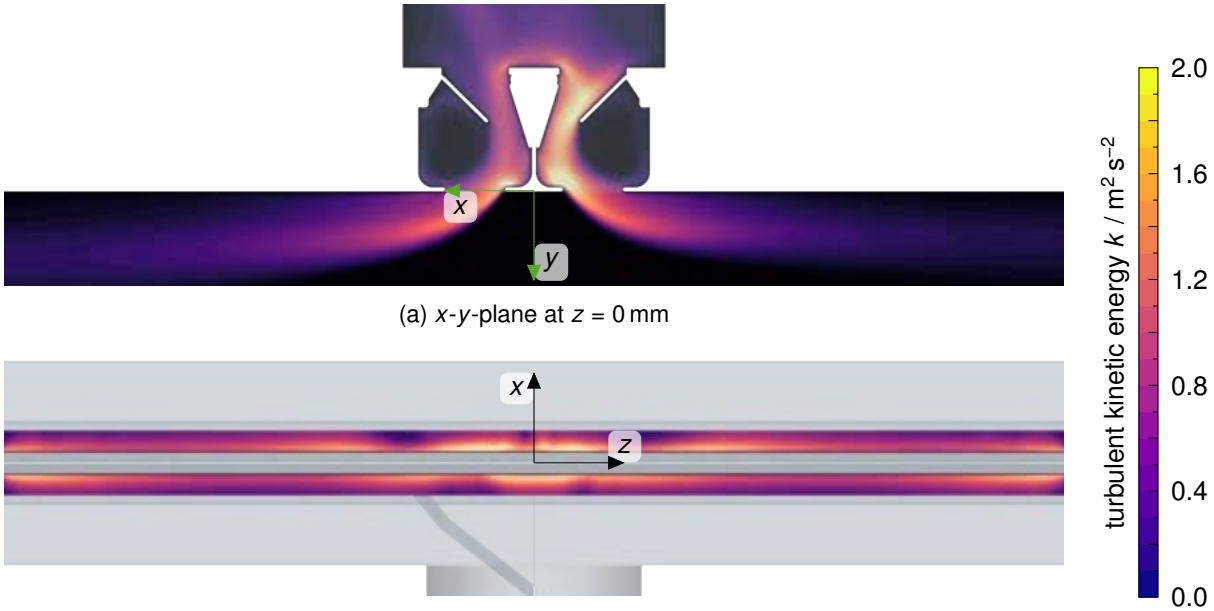

(a) x-y-plane at z = 0 mm

(b) x-z-plane at y = 0 mm

Figure 10: Computed distribution of the turbulent kinetic energy for v_D = 6 m/s

3.2. Broadband noise

In order to identify the regions where high levels are present and therefore identify the most noisy geometric features, we discuss the results of the two broadband noise source models. Figure 11 shows the distribution of the surface acoustic power which was computed with Curle's model. To allow for a better visualisation the model is clipped on a x-y-plane at z = 0 mm. Observing the diffuser from below (see Fig. 11a), different areas of high power levels are visible than from above (see Fig. 11b). The highest power levels are marked in the figures. Due to the dB-scale, it becomes clear that the edges contribute noise that is of several magnitudes stronger than the noise originating from the walls on the short edge (marked with 46 dB).

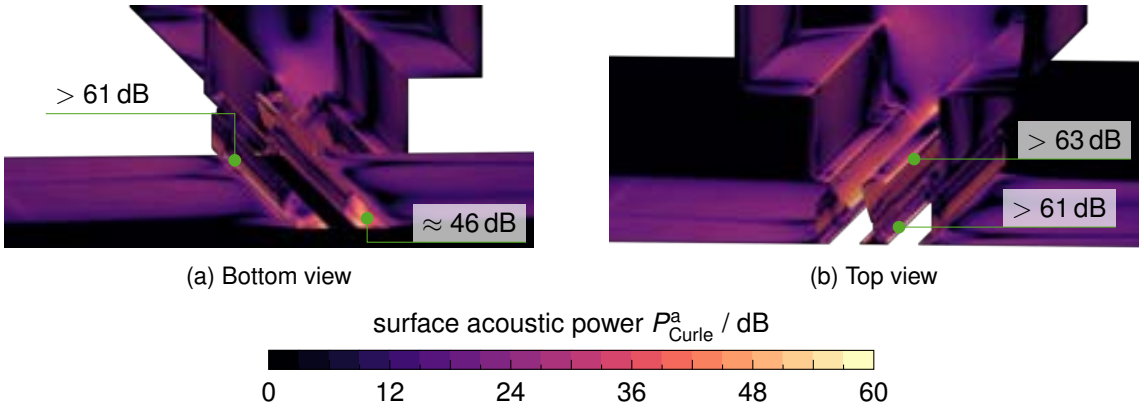

(a) Bottom view

(b) Top view

Figure 11: Distribution of surface acoustic power according to Curle's model for v_D = 6 m/s

Although Proudman's model depends primarily on the turbulent kinetic energy k, which is not fully valid in the simulations, we still give an impression of the according results in Figure 12. When comparing the distribution of the TKE and P^a_P, the relation becomes obvious. Even if we consider that our model presumably underpredicts the turbulence by a factor of $2-3$, the predicted noise levels according to Proudman's model would be of several magnitudes smaller than the levels predicted by Curle's model. Therefore the contribution of freestream turbulence to the overall noise emissions can be neglected.

Tables 4 and 5 list the integral values for both broadband noise models and all investigated velocities. Across all investigated diffuser velocities the general trends are the same, indicating that the influence of varying flow velocities mainly affects the overall level of emitted sound, rather than the aeroacoustic characteristics of the diffuser itself. Therefore, we again focus only on the medium velocity for a more detailed discussion.

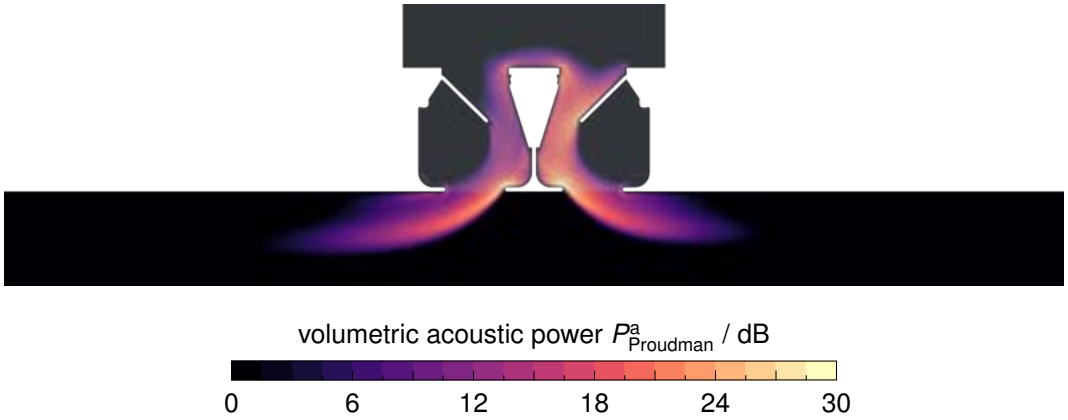

Figure 12: Distribution of volumetric acoustic power according to Proudman's model on a x-y-plane at $z = 0\,\mathrm{mm}$ for $v_D = 6\,\mathrm{m/s}$

Table 4: Aeroacoustic results for Curle's model

Boundary	$P_{ac,Curle}$ / dB		
	4 m/s	6 m/s	8 m/s
Throttle	23.28	40.20	52.08
Flaps	61.93	79.80	92.48
Guides	66.81	86.25	99.82
Total	73.50	92.29	105.47

Table 5: Aeroacoustic results for Proudman's model

Volume	$P_{ac,Proudman}$ / dB		
	4 m/s	6 m/s	8 m/s
Plenum Box	–82.08	–48.72	–26.69
Outlet	–65.37	–32.92	–11.02
Room	–68.16	–36.01	–12.63
Total	–58.72	–26.29	–3.79

As we could already observe from the surface distribution (see Fig. 11) the *Flaps* and *Guides* contribute the most to the overall noise emission. Although the *Throttle* also has considerable emissions, it is neglectable compared to the other two surface groups. As already said, the emissions predicted by Proudman's model are neglectable compared to Curle's noise emissions. However we can note, that the increase of $P_{ac,Proudman}$ with rising diffuser velocity is greater than $P_{ac,Curle}$. This aligns with literature ([3, 8, 10]), where the acoustic power is theoretically derived to be dependent on the Mach number $M = \frac{v_D}{c}$.

$$P^{a}_{Curle} \propto M^3 \tag{20}$$

$$P^{a}_{Proudman} \propto M^5 \tag{21}$$

As our results show, the geometric features mainly responsible for acoustic emissions, are the edges in the diffuser plate region. In order to significantly reduce the noise of this particular diffuser, we propose design changes to these edges. Possible alterations may depend on if an edge is of the type of a leading or a trailing edge. Other researches already developed many measures to improve the aeroacoustic behaviour of such edges, which is why we just give a few examples. Gruber et al. [4] and Clark et al. [1] investigated the impact of trailing edge serrations. To improve the behaviour of a leading edge, Hansen et al. [5] added sinusoidal tubercles.

4. Conclusion

In this study, we presented a flow simulation of a two-slot air diffuser to predict areas of high noise emission for three diffuser velocities. By conducting flow measurements with a 3D-LDA system, we successfully validated the flow simulation in regards to velocity field and pressure loss. The computed turbulent kinetic energy is not only lower than measured, but we also observed strong anisotropy in the measured turbulence. However, under the investigated flow conditions, the contribution of freestream turbulence to the noise emission can be neglected. Therefore, the presumably under-predicted TKE does not appear to be relevant to the overall results. This leads us to the conclusion, that our flow model allows an accurate prediction of the most relevant regions responsible for noise emission. The main contributors are edges located in areas of high flow velocity. Both leading and trailing type edges emit noise of roughly equal strength.

There are various measures that can be taken to reduce noise emissions attributed to flow edges, depending on whether the edge being considered is a leading or trailing edge. In further studies these measures can be analysed regarding their influence on the noise emissions.

Acknowledgments

This project was funded by the AiF (Arbeitsgemeinschaft industrieller Forschungsvereinigungen) and the German Federal Ministry for Economic Affairs and Climate Action (BMWK) based on a resolution of the German Bundestag (IGF No.: 21611 N/1).

The authors gratefully acknowledge the computing time provided to them at the NHR Center NHR4CES at RWTH Aachen University (project number p0020083). This is funded by the Federal Ministry of Education and Research, and the state governments participating on the basis of the resolutions of the GWK for national high performance computing at universities (www.nhr-verein.de/unsere-partner).

References

[1] Ian A. Clark, W. Nathan Alexander, S. Devenport, W. und Glegg, C. Jaworski, J. W. und Daly, and N. Peake. Bioinspired Trailing-Edge Noise Control. *AIAA Journal*, 55(3):740–754, 2017. ISSN 0001-1452. doi: 10.2514/1.J055243.

[2] N. Curle. The mechanics of edge-tones. *Proceedings of the Royal Society of London. Series A. Mathematical and Physical Sciences*, 216(1126):412–424, 1953. ISSN 0080-4630. doi: 10.1098/rspa.1953.0030.

[3] N. Curle. The influence of solid boundaries upon aerodynamic sound. *Proceedings of the Royal Society of London. Series A. Mathematical and Physical Sciences*, 231(1187):505–514, 1955. ISSN 0080-4630. doi: 10.1098/rspa.1955.0191.

[4] Mathieu Gruber, Phillip Joseph, and Tze Chong. On the mechanisms of serrated airfoil trailing edge noise reduction. In *17th AIAA/CEAS Aeroacoustics Conference (32nd AIAA Aeroacoustics Conference)*, Reston, Virigina, 2011. American Institute of Aeronautics and Astronautics. ISBN 978-1-60086-943-3. doi: 10.2514/6.2011-2781.

[5] Kristy L. Hansen, Richard M. Kelso, and Bassam B. Dally. Performance Variations of Leading-Edge Tubercles for Distinct Airfoil Profiles. *AIAA Journal*, 49(1):185–194, 2011. ISSN 0001-1452. doi: 10.2514/1.J050631.

[6] Julius Oscar Hinze. *Turbulence*. McGraw-Hill series in mechanical engineering. McGraw-Hill, New York, NY, 2. edition, 1975. ISBN 0070290377.

[7] A. N. Kusyumov, S. A. Mikhailov, L. I. Garipova, A. S. Batrakov, and G. Barakos. Distribution of acoustic power spectra for an isolated helicopter fuselage. *EPJ Web of Conferences*, 114, 2016. doi: 10.1051/epjconf/201611402062.

[8] M. J. Lighthill. On sound generated aerodynamically i. general theory. *Proceedings of the Royal Society of London. Series A. Mathematical and Physical Sciences*, 211(1107):564–587, 1952. ISSN 0080-4630. doi: 10.1098/rspa.1952.0060.

[9] Philipp Ostmann, Christian Bruchhaus, Martin Kremer, and Dirk Müller. Numerische untersuchung des aeroakustischen verhaltens eines generischen schlitzauslasses. In *Fortschritte der Akustik - DAGA 2022*, pages 875–878, 2022.

[10] I. Proudman. The generation of noise by isotropic turbulence. *Proceedings of the Royal Society of London. Series A. Mathematical and Physical Sciences*, 214(1116):119–132, 1952. ISSN 0080-4630. doi: 10.1098/rspa.1952.0154.

[11] Asvath Ravichandran, Andreas Logdesser, Nikolaus Peller, and Michael Manhart. Experimentelle und numerische untersuchung des effekts der zuströmbedingungen auf die schallabstrahlung eines generischen ausströmers. In *Fortschritte der Akustik - DAGA 2022*, pages 1250–1253, 2022.

[12] Siemens. *STAR-CCM+ v. 17.06.008 UserGuide*, 2022.

[13] Matthias Tautz. *Aeroacoustic Noise Prediction of Automotive HVAC Systems*. Dissertation, FAU University, Erlangen, 2019.

Urban wind potential analysis: Case study of wind turbines integrated into a building using on-site measurements and CFD modelling

Alexander Vallejo[a,b], Idalberto Herrera[b], Juan E. Castellanos[b], Carlos Pereyra[a,b] and Edwin Garabitos[a]

[a] Instituto Especializado de Estudios Superiores Loyola, San Cristóbal, Dominican Republic, avallejo@ipl.edu.do, CA
[b] Instituto Tecnológico de Santo Domingo, Santo Domingo, Dominican Republic

Abstract:

Energy solutions based in renewable energy sources are needed to overcome fossil fuel crisis due to supply uncertainties, increasing prices and climate changes. Innovative energy solutions for a sustainable and resilient energy system for the cities is required, special attention should also be paid greenhouse gases emissions. Wind energy systems integrated in to building in urban areas are a promising technological alternative. In this work an assessment of wind energy potential in a typical building in Santo Domingo, Dominican Republic was performed. The main idea is establish a methodology to explore how small wind turbines can be integrated in building to contribute to the energy sufficiency in urban areas. For this purpose, was developed a simple but robust framework to provide a city-environment assessment of the wind energy potential considering roof-mounted turbines. An especial distinction was made to capture the effect of the building geometry in the electricity generation using Computational Fluid Dynamic (CFD) modelling and the related in the energy production. The framework is based on seven main steps: (1) site selection, (2) resource prospecting/analysis including CFD, (3) turbine selection, (4) estimation of currently produced energy, (5) Environmental evaluation, (6) Resilience and Economic Analysis, and (7) System Installation. The urban wind energy potential was assessed considering one small two-blade Darrius H-type vertical axis wind turbines on the roofs of a 29 m high-rise buildings, yielding an annual energy production in the best site of about 1030 kWh with a potential CO_2 emission reduction of 0.64 Ton/yr. It was also found that the wind speed decrees significantly downstream the wind flow direction due to the building geometry, this means that the average speed could decrees in about 100% from the site of the wind flow incidence to the opposite, with the consequent impact in the energy generation.

Keywords:

Urban wind energy assessment; Distributed power system; Wind turbine; CFD.

1. Introduction

The world is undergoing an energy transition to limit climate change, the main base of such transition is accelerating the use of clean energy. Several of the United Nations Sustainable Development Goals until 2030 are set in this direction, especially Goal 7, which sets out the challenge of Affordable and Clean Energy for All [1]. For this purpose, it is necessary to reduce the costs of renewable energies and take full advantage of the potential of energy efficiency, digitalization, smart technologies and sustainable solutions for electrification [2]. This paper proposes the use of urban wind energy as one of the alternatives to decouple the necessary economic expansion from the intensive use of fossil fuels. The goal is to promote the idea of providing energy accessibility in a sustainable way for humanity, taking the Dominican Republic (DR) as a case study. In that way, the DR, in the frame of the Paris agreement has the commitment to reduce by 25% the estimated per capita emissions of 3.6 tCO_{2eq} by 2030, with respect to 2010 [3].

Due to the high population density in urban areas, both in emerging and developed countries, tailor-made energy solutions close to the area where demand is generated are required. Globally, consumption in buildings accounts for 30 % of primary energy consumption [4]. With the implementation of energy efficiency measures, savings about 20 – 40 % can be achieved. Small wind turbine (SWT) installations are expected to contribute to the energy transition towards low carbon and high efficiency services in cities [5]. Decentralized generation in urban environments is a possible solution, involving technologies such as solar PV and SWT [6]. In this direction, a full understanding of the renewable resources available in urban environments is needed. Tasneem et al. [7] argued that SWTs can be positioned in or around high-rise buildings, rail tracks, highways, and other

urban sites. The estimated energy of the wind in these places becomes very complicated due to it being aerodynamically irregular and heterogeneous. The obstacles, such as buildings, trees, and others have an influence on wind turbulence [8]. These obstacles significantly reduce the use of the resource through SWTs due to those extract momentum from the wind flow, causing a lower average wind speed [9]. Building shape, height, and separation between itself influence wind flow and direction due to the turbulence and surface roughness produced by them [7]. A proper wind speed assessment, wind selection and installation are the most challenging goals to address. Wind flow around a building is complex, since a separation zone results and vortices generated, however, the main region of interest is where there is an amplification of the flow [10].

For the studies in the urban environment of wind potential the progress of Computational Fluid Dynamic (CFD) scope is a corner stone. CFD can be efficiently integrated in the urban wind energy assessments methods. These studies are in principle dedicated to characterizing air flow through obstacles, such as building and trees in a volume of control. In an urban location the flow is considered as turbulent. In this way should be used the Favre-averaged Navier-Stokes equations with SOLIDWORKS Flow Simulation software to model turbulent flows in the urban environment [11], [12].

A two-equation standard model k-ε is involved in the flow simulations because of its robustness and simplicity, more advanced turbulence models could be employed, however the k-ε model is accurate enough for the purpose of this work. The propose of this study is develop existing methodologies for better prediction of wind behaviour in urban environment and predict the energy potential of small wind turbines in microgeneration.

This research, rather novel in the Caribbean region and especially in the DR, aims to contribute to the characterization of wind in urban environments for the proper assessment of the technology to be used. The wind characteristics and the orography (existing buildings, terrain, etc.) are crucial elements for the deployment of SWT in urban environment. Another expectation of this work is to influence the architecture and urban planning to facilitate the use of the wind resource in the future. This research focuses on the potential of urban building in the DR, Santo Domingo for urban wind energy deployment. One building is studied in detail using CFD analysis in order to achieve the best performance of the wind energy technology.

2. Methodology

The methodology presented in this research have the purpose to perform with adequate precision a characterization of the urban wind energy potential in the Caribbean area, especially in the DR. It is important to highlight the efforts made to combine the current state of the art in the subject and the data available in the context of the region. In the literature consulted, very few studies of urban wind potential in tropical areas have been identified [13], [14]. However, worldwide scale there are many of such studies, important contributions has been made by authors such as AL-Yahyai, Bekele and Rezaeiha [15]–[19]. So far, no consistent research on the potential of urban wind in Caribbean cities has been identified in the consulted literature. In that way, a methodology is proposed to analyse the energy potential of urban wind. This methodology adopts several steps from some existing ones and proposes to incorporate an environmental evaluation and a detailed CFD analysis integrated to Geographic Information Systems (GIS) and on-site measurements. This adding lead to a wider study, taking into account the need to reduce the CO_2 emissions, define best site to install the wind turbine and predict accurately enough the annual electricity generation. The methodology includes seven steps: (1) site selection, (2) resource prospecting/analysis including CFD, (3) turbine selection, (4) estimation of currently produced energy, and (5) Environmental evaluation, (6) Resilience and Economic Analysis, and (7) System Installation as shown synthetically in Figure 1. The last two steps of the methodology are the Resilience and Economic evaluation and the Detailed Engineering of the final project; both are beyond the scope of this work. The step from 1 to 7 presented in Figure 1 are described in the following sections.

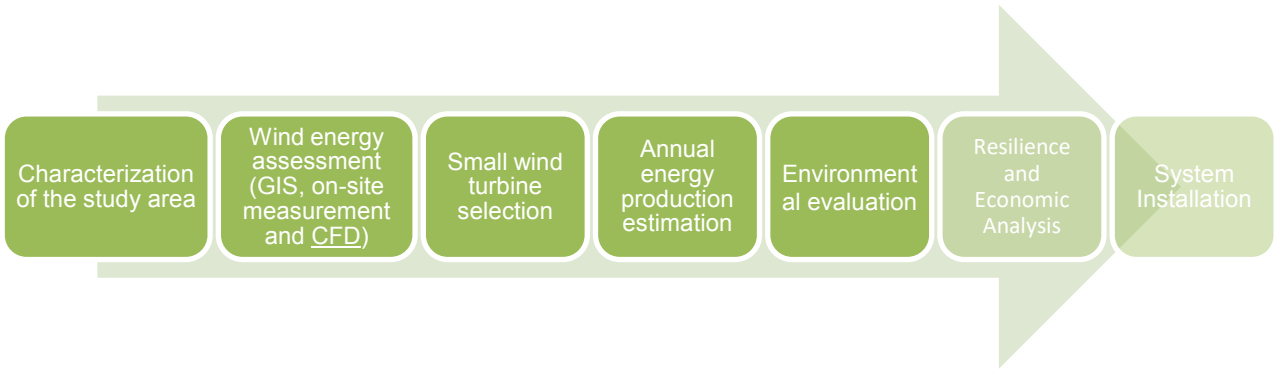

Figure 1. Schematic illustration of the steps of the proposed methodology.

2.1. Characterization of the study area

There is great potential in the use of urban wind for distributed electricity generation in densely populated urban areas [20], [21]. In these environments, small wind turbines (SWTs) can be conceived as building-

integrated from the design phase or installed on rooftops of existing buildings or surrounding areas. Distributed wind energy in cities has the advantage of its proximity to the point of electricity demand, which means reduced costs for high-voltage transmission lines as well as for the necessary devices of such a system [22].

Trees, buildings and other obstacles on the ground influence wind speed and turbulence, especially in sites with low wind speed and high turbulence levels [8]. This significantly reduces the resource utilisation using SWTs, obstacles extract wind flow momentum, resulting in lower average wind speed [9].

In order to identify potentially usable buildings for SWTs siting, parameters such as height, available roof area and structural integrity need to be assessed. A possible method for this purpose was identified in the work performed by Rezaeiha [18]. In this type of research, buildings in cities should identified and classified using GIS databases available on freely accessible websites, such as: [23]. These tools serve as a starting point to stratify buildings that meet the criteria for SWT installation. In this kind of research, in the case of Santo Domingo, buildings considered could be taken from the data base https://skyscraperpage.com/. In the case there is not existing database with information about the buildings an inspection must be carried out.

2.2. Wind energy assessment

In the literature several methods can be found for site-specific urban wind forecasting for energy purposes. The most commonly used methods are: on-site measurement, wind tunnel, numerical weather prediction, Computational Fluid Dynamic (CFD) and analytical methods [18], [24]–[28]. In any case, the main objective is to perform a wind characterization that includes the determination of parameters such as: average speed, direction, turbulence, energy density, etc. In this work, on-site measurements are used to evaluate the urban wind potential in the cities of Santo Domingo and, in DR. A brief description of this method is presented below.

2.2.1 On-site measurement

Wind speed and direction are the main parameters for the characterisation of the urban wind for energy purposes. The reference wind speed is established on the basis of measurements averaged every 10 minutes, according to the International Electrotechnical Commission standard. For the measurement of these parameters, an anemometer installed according to the aforementioned standard at the measurement site is needed [29]. In this study a data set collected from an anemometer installed in representative building in Santo Domingo were used.

Usually, the wind speed and direction are statistically processed and plotted on a polar diagram called a wind rose, where the radial axis indicates the magnitude and frequency of the wind, showing the prevailing wind direction. It can also be displayed in a Cartesian coordinate diagram [21], [30], [31].

The accumulated records of wind parameters allow the construction of probability functions and predict the energy potential. The Weibull, Rayleigh and Lognormal distributions are widely adopted to predict wind speed. The most widely used is the Weibull distribution because of its flexibility and simplicity. However, limitations have been observed in this function for average wind speed lower than 2 m/s or close to zero, in this speed range the density distribution estimation can be very inconsistent [17]. This limitation is not relevant to use this function evaluating the potential for SWT, because typically the cut-out speed of this machines is 2 m/s. In this work, the Rayleigh Distribution, a variant of the Weibull distribution with a form factor equal to 2 is adopted [29]. Weibull distribution $p(v)$ is the probability distribution function used to describe the distribution of wind speeds over time duration. The Weibull probability function is given by Eq. (1):

$$p(v) = \left(\frac{k}{c}\right) * \left(\frac{v}{c}\right)^{k-1} e^{-\left(\frac{v}{c}\right)^{k}}, \quad (1)$$

Where k is the shape factor, a parameter that controls the width of the distribution and c is the scale factor in m/s, this parameter controls the average wind speed and is defined in Eq. (2).

$$c = \frac{V_{avg}}{\sqrt{\pi}}, \quad (2)$$

Where: V_{avg}, is the average wind speed.

The parameters k and c can be estimated by several methods, being the method of maximum likelihood the most commonly used (Karthikeya et al., 2016; Islam et al., 2011).

Another important characteristic of the wind is the Turbulence Intensity (TI), it is defined as the ratio of standard deviation of fluctuating wind velocity to the mean wind speed, and it represents the intensity of wind velocity fluctuation. This index should be calculated at 15 m/s, as it is one of the characteristic parameters included in the classification (classes) of SWTs according to the International Electrotechnical Commission [29]. At presents four SWT classes has been defined, for all classed the turbulence intensity should be 0.18 or less, and for the "S" class, it should be determined according to the referred standard. A turbine should not be exposed to wind turbulence intensity higher than 25 %, so this parameter is essential for determining the installation of small wind turbines [8]. Small wind turbines must be able to respond to frequent urban wind fluctuations and the site and system characteristics [32]. According to the National Renewable Energy

Laboratory (NREL) of the United States, turbulence levels can be categorised as follows: low, if TI have values less than or equal to 10%; moderate, if TI have values between 10% to 25%; and high, if TI have values greater than 25% [33]. The TI calculation is given by Eq. (3).

$$TI = \frac{\sigma}{V_{avg}} \tag{3}$$

Where: σ is the 10-min standard deviation, V_{avg} is 10-min average wind speed.

2.2.2. Computational Fluid Dynamic

Computational Fluid Dynamic (CFD) is a numerical simulation technique to study the behaviour of wind flow in urban locations. This method has become widely used due to advances in number methods and computational resources [34]. The CDF models have the ability to calculate the aerodynamic components with the integration of the Navier-Stokes equations at the periphery of the turbine blades [32]. The CFD is an efficient alternative to characterize the turbulence in the wind in the building. The method has been improved in simplification, calculation model, mesh processing, setting of boundary conditions, equation solver, simulation tools and other aspects [8].

The biggest barrier to the acceptance of CFD results is related to the accuracy of the technique, the costs, and the skill of the user. Verification and valuation is required for the CDF simulation results. Typically, the validation of CFD studies for real urban areas are carried out with field measurement data (Experimental tests) and wind tunnel [13], [28], [32], [34].

According to Mittal et al. [28], the accuracy of the CFD simulation strongly depends on the selection of the turbulence model. The capacity of each turbulence model and its precision for different analysis resolutions are reported in the literature based on the experiences of the researchers. With this method, important findings have been obtained, such as: the recommendation to install small wind turbines 1.4 m above the roof of buildings and if they are horizontal axis wind turbines, that they be installed in the middle of the roof, as well as installing the turbine as high as possible in the windward direction [35].

The proposed methodology for the development building wind turbines projects in an urban environment based on CFD analysis was summarized in the in the Figure 1. This methodology lead to a better estimation and reduced the time, cost and risk of the feasibility studies in the development of such projects.

As mentioned in section 2.1 it is necessary to delimit the project location and the surrounding zone to study the feasibility of the project. It is important to develop a general view aided by the CFD simulation to predict the flow patterns of the wind stream in the urban complex. With the purpose of assess the performance of the small wind turbines on the roof of the building of interest for the CFD simulations. After the site is selected, a standard wind resource assessment is completed, by using statistical and historical field data to estimate the power output of SWTs. The next stage is the CFD-based assessment, which includes four steps: the modelling site assessment, the modelling building-structure study, the modelling SWT study, and the modelling structure-SWT study. In these steps, a CFD model of the site that includes the building and the surrounding areas, is elaborated, as well as a model of the building or structure suitable for CFD analysis. This analysis will allow selecting the type of turbine to install. After the SWTs selection a performance study using CFD analysis should be conducted. The results of this final analysis using the integrated method will define the viability of the project regarding technical performance. In this study is adopted SOLIDWORKS Flow Simulation to evaluate wind behaviour using CFD and applying finite volume analysis [36].

2.3. Selection of small turbines

SWTs are aerodynamic machines, used to convert wind energy into electricity. Electricity production is a function of air density, the sweep area of the turbine blades, and the speed cube [37]. There is a wide variety of designs and types of small wind turbines. Commonly, highly efficient developments are considerably influenced by criteria related to the operation and location of the machine. In the wind turbine industry, there are mainly two designs, horizontal axis wind turbines (HAWTs) and vertical axis wind turbines (VAWTs) [26], [35], [38].

HAWTs are generally installed in areas relatively separated from cities, and with considerable heights above ground level, according to local policies and regulations. These machines must always be oriented with the rotor perpendicular to the wind direction, which makes it unappropriated to be installed in places with frequent changes in wind direction or high turbulence [7], [10].

VAWTs can be classified into two main categories, Darrieus and Savonius rotor. Darrieus VAWTs are usually considered a lift rotor, since the torque is generated by the average lift force. On the other hand, Savonius rotors operate normally by the action of drag force. H-type rotor VAWTs are a combination of lift and drag forces. VAWTs are more used in urban environments because they are less vulnerable to changes in wind directions.

According to the International Electrotechnical Commission (IEC), SWTs are those with a capacity ≤ 50 kW and a rotor swept area ≤ 200 m^2 [29]. Different classifications, according to power, hub height, and swept exist in different countries. In this work we adopt IEC classification.

According to Rezaeiha [18], urban wind energy harvesting systems can be categorized as follow: (i) Stand-alone near building, (ii) Retrofitted to existing building, and (iii) Fully integrated into building architectural form. In this work it is considered appropriate to use a small two-blade Darrieus H-type vertical axis turbine (VAWT). This machine is 1 m in diameter and 5 m in height, with a sweeping area of 5 m^2. This SWTs were selected because a good performance at low speeds and turbulent environments, which is a condition that generally occurs in urban areas.

2.4. Annual energy production estimation

For the estimation of the annual energy production (AEP), the methodology proposed by Rezaeiha [18] is adopted. The equation to estimate the AEP is shown in Eq. (4):

$$AEP = 8760 * \int_0^\infty P\left(V_{avg}; c; k\right) * P(V)dv \quad (4)$$

Where: 8760 are the hours during a year, $P\left(V_{avg}; c; k\right) *$ is the probability of occurrence of a given speed based on the Weibull distribution, and $P\ (V)$ is the power produced by the wind turbine at that speed. The power extracted by the wind turbine is described according to Eq. (5):

$$P(V) = 0.5 * C_P * \rho * A * {V_{avg}}^3 \quad (5)$$

Where: A is rotor area, C_P is the power coefficient of the rotor, V_{avg} is the wind speed and ρ is the air density.

2.5. Environmental evaluation

To evaluate the potential environmental benefit from the installation of the SWTs an assessment of the avoided CO_2 emissions from replacing electricity generation from fossil fuels by electricity from SWTs can be carried out. Fossil fuels prevail in DR electricity sector, according to Guerrero-Liquet: oil (46.27%), natural gas (25.92%) and coal (14.03%), represented 86% of electricity generation in the country. Only 10% of electricity generation is produced from renewable sources, particularly hydropower (6.26%) and wind energy (1.90%) [39]. Is it important to highlight that Oil and coal are the higher CO_2 emitters. With data from the Coordinating Body of the National Interconnected Electrical System (OC-SENI) an estimation of the emission factors for these fuels has been done [40]. It was found that emissions factors expressed in $kgCO_2eq/kWh$ for oil and coal are about 0.75 and 0.98 respectively. On the other hand, according to the Standardized baselines set by the United Nations Framework Convention on Climate Change, the CO_2 emission factor for the SENI in DR applicable to wind and solar power generation project activities is 0.6216 $kgCO_2/kWh$. This standardized baseline will be adopted for calculations in this research [41]. Assuming the SWT electricity generation carbon free, the Avoided Emission (AE) in $kgCO_{2eq}$ can be calculated by multiplying the annual energy production (AEP) in kWh, by Emission Factor (EF) in $kgCO_{2eq}/kWh$, as shown in Eq. (6).

$$AE = AEP * EF \quad (6)$$

3. Case study, results, and discussion

This work has been developed to stablish a methodology to assess the urban wind energy potential in buildings for the Dominican Republic, as a first case study a representative building located in the Technological Institute of Santo Domingo (INTEC) has been taken. The most important findings are presented from a survey campaign carried out at INTEC located in Santo Domingo. Two anemometers were installed for data recording, which are identified with the following nomenclature: Anem1-INTEC and Anem2-INTEC. The Santo Domingo Institute of Technology (INTEC) is a private, non-profit, public service, Dominican higher education institution founded in 1972 by a group of academics committed to the social transformation of the country and the continuous promotion of the quality of education. It is located in the coordinate 18°29'16.81"N, 69°57'45.18"W. A detailed map of the INTEC campus is shown in Figure 2.

The Anem1-INTEC and Anem2-INTEC registered data during the period May-December and June-December 2017 respectively. The sensors were installed in building with 20 m height. A total of 208881 and 152816 records were taken from Anem1-INTEC and Anem2-INTEC, with an availability of 71% and 77% respectively. In 2017 the country was hit by several meteorological adverse events which affected the data collection. Figure 3 a) shows the behaviour of the monthly average wins speed. The mean speed for the periods was about 2.50 m/s at 20 m. At 40 m height the estimated average wind speed using the Hellmann exponential law and the logarithmic wind profile law was 3.05 m/s. The Hellmann exponential is the general methods for estimating wind speeds at higher hub heights from known wind speed at lower heights [30].

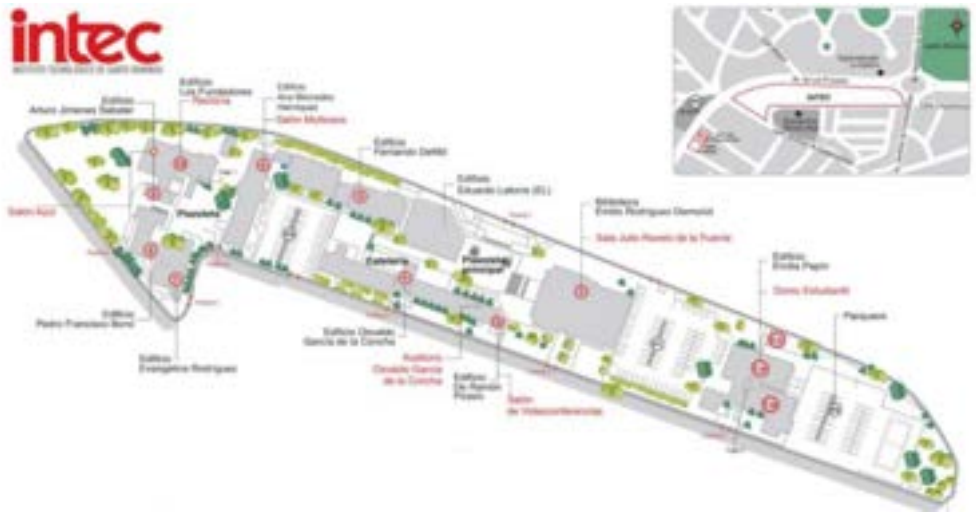

Figure 2. Detailed map of the INTEC campus.

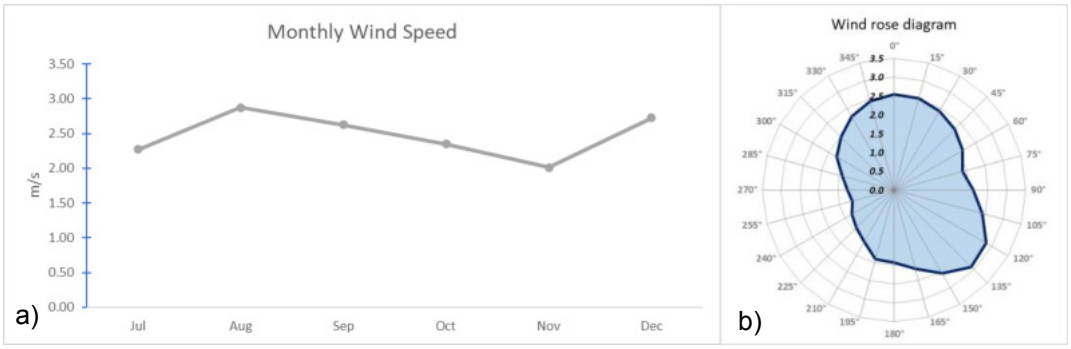

Figure 3. a) Average monthly wind speed, b) Period average wind rose.

Fig. 3b) shows the wind rose for the three sensors during the study period. The predominant wind direction is North-East, with a strong correlation with the data records of the meteorological services for both measurements sites [31]. The predominant wind direction with the highest intensity was registered from 15° respect to North.

Table 1 shows the hourly variation of wind speed (WS) for one day. Table 1 has a colour scale, where red represents unfavourable speeds and green favourable. Note that in the interval from 13:00 to 15:00 the highest energy potential occurs. This is very positive, since the energy consumption associated with air conditioning in this horary is considerable in tropical areas. Note that in Santo Domingo there are average wind speeds higher than 2 m/s during approximately 18h every day.

Table 1. Daily average variation of wind speed.

h	1	2	3	4	5	6	7	8	9	10	11	12	13	14	15	16	17	18	19	20	21	22	23	24
WS	2.00	1.98	1.92	1.91	1.88	1.90	2.06	2.49	2.80	2.90	2.97	3.13	3.21	3.42	3.29	3.07	2.92	2.68	2.54	2.36	2.27	2.14	2.10	2.07

From the minute-by-minute recordings, the average speed was calculated for 10-minute intervals. The most probable speed recorded were 2 m/s, 3 m/s and 4 m/s with probabilities of occurrence of 24.5%, 24% and 17.7% respectively. Figure 4 shows the Weibull distribution for the parameters given in Table 2. For a mean wind speed of 3.05 m/s the corresponding parameters for the Weibull distribution are 3.44 m/s and 2 for the share factor and scale factor, respectively. TI was categorised as moderate, high and low to 63%, 29% and 8%, respectively. This may be mainly associated with the terrain orography, deeming that these measurements were made in a building in an urban environment.

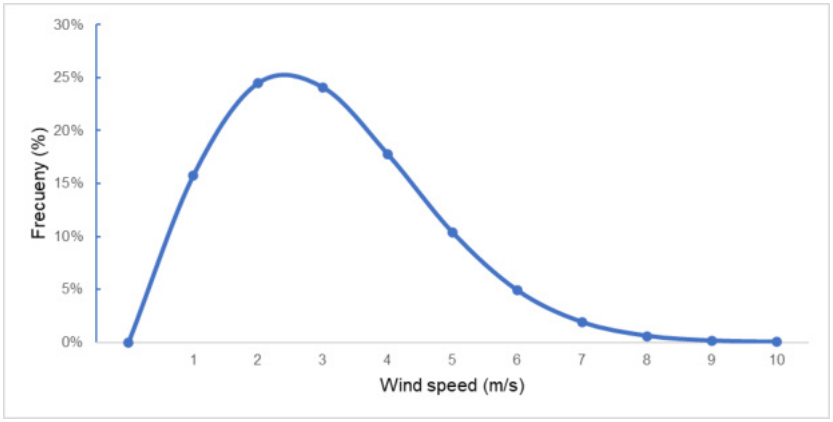

Figure 4. Weibull distribution.

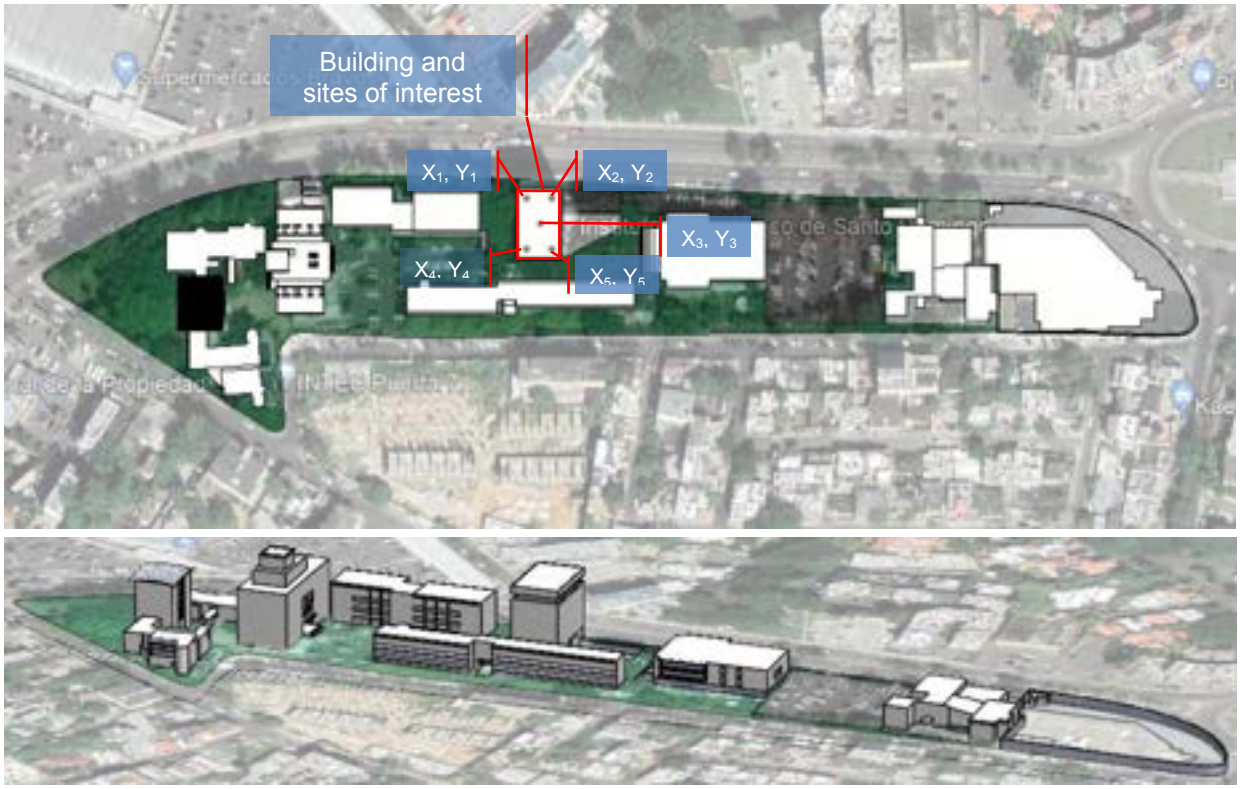

Figure 5. Physical model of the INTEC campus, building and sites of interest.

Table 2 Describes each one of the optimized initial conditions selected which correspond to the CFD simulations performed. The wall condition of 1,000,000 micrometres comes from “Guide to Meteorological Instruments and Methods of Observation”, where it is pointed out that the roughness of the terrain is classified by the class of the terrain. INTEC is surrounded by class 7 terrain, presenting large regular obstacles typical of the suburbs, assigning it a roughness height of 1 m. The decomposition of each velocity parameter is represented at the Table 3.

The configuration of the grid and the determination of the size of the refinement of the mesh states the precision of which the CFD simulation will be performed. For these CFD simulation, a global mesh structured are selected with a manual refinement definition of 249 cells per X, 100 cells per Y and 100 cells per Z. This global mesh refinement exceeds the number of cells assigned in all axis by the highest level of auto refinement with the sole porpoise of ensure precision at the areas of interest. This results in 2,643,484 cells that integrate the meshing of which 78,416 are in contact with solids. Additional to the mesh refinement a control plane tool was employed to increase the density of cells at the areas of interest.

Table 2. Optimized Initial and boundary conditions for the development of CFD simulations.

Analysis type	Fluid Type	Boundary Conditions	Initial and Environment Conditions	Mesh Configuration
Flow Type: External. Gravity force: 9.81 m/s^2.	Air with all its physical properties. Laminar and Turbulent Flow.	Roughness length: 1,000,000 µm.	a)Thermodynamic parameters: -Temperature 28°C=301K. -Atmospheric pressure:101325 Pa. b) Velocity parameters: Wind speed of air 1 m/s, 2 m/s, 3 m/s, 4 m/s, 5 m/s, 6, m/s 7 m/s, 8 m/s, at 15°. c) Turbulence parameters: - Turbulence length: 0.4003m - Turbulence intensity: 0.1%. d) Humidity parameters: -Average relative humidity of 80%.	Manual Mesh with 2,643,484 control volume cells.

Table 3. Wind Velocity vector decomposition.

Magnitude (m/s)	Angle (degrees)	Velocity in X (m/s)	Velocity Y (m/s)
1	15°	-0.965926	0.258819
2	15°	-1.93185	0.517638
3	15°	-2.89778	0.776457
4	15°	-3.86370	1.03528
5	15°	-4.82963	1.29410
6	15°	-5.79555	1.55291
7	15°	-6.76148	1.81173
8	15°	-7.72741	2.07055

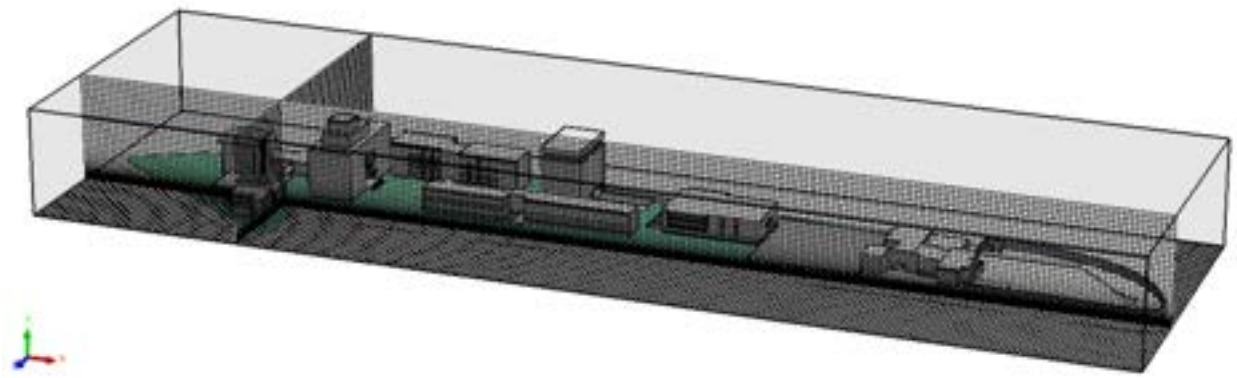

Figure 6. Dimetric view of the INTEC campus in SolidWorks Flow Simulation.

Figure 7 reveals the top view of velocity contour at 3 m/s at 15° of the INTEC was obtained by CFD simulations. Results shows how the wind is distributed across the campus and the high-speed zones over the tall buildings. The image below also reveals the possible positions to locate wind turbines over the EL building. Note in the Figure 7 how different is the wind speed in the different site of interest. From this observation can be deduced that energy generation of a wind turbine can be significantly different depending on the site of installation even over the same roof.

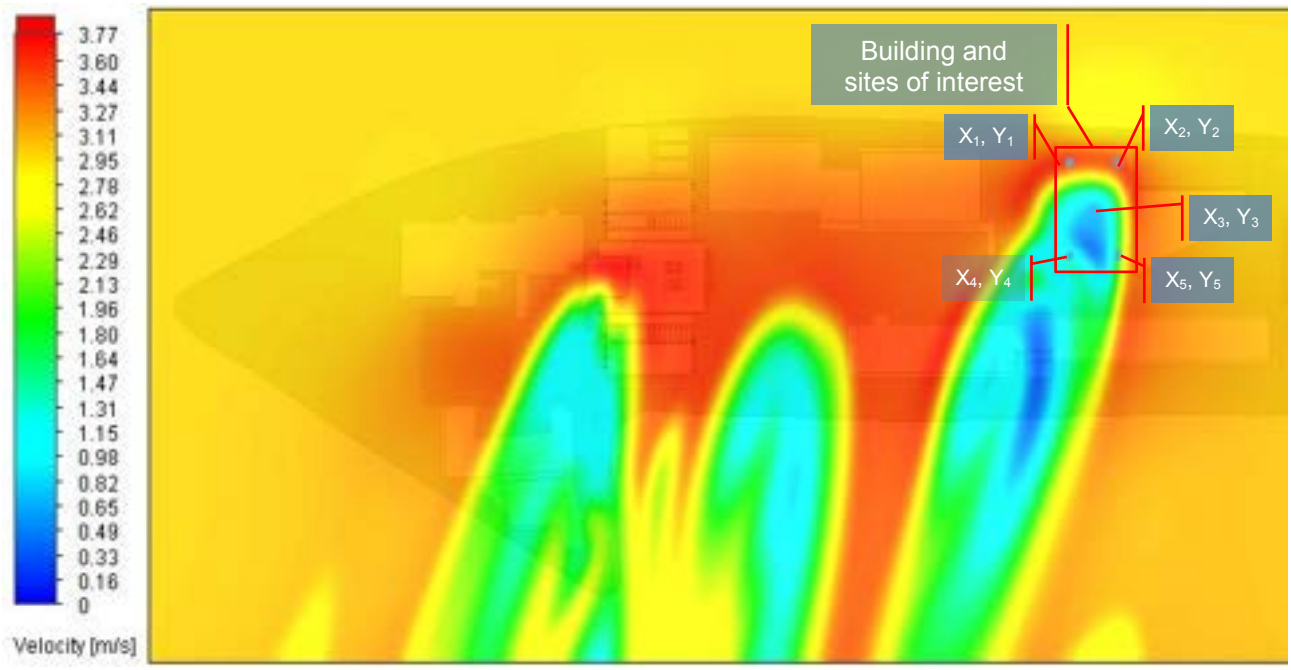

Figure 7. CFD simulation velocity contour at 34 m elevation, 3 m/s free stream flow.

The Table 4 summarise result of measurement analysis regarding the wind speed behaviour based on anemometers measurements collected near the building studied and wind behaviour analysed using CFD analysis.

Table 4. Wind speed information from anemometers and modelling results at sites of interest.

Free stream flow Wind speed (m/s)	Occurrence (hours)	Wind Speed at sites of interest from modelling (m/s)				
		X_1, Y_1	X_2, Y_2	X_3, Y_3	X_4, Y_4	X_5, Y_5
1	1380	1.1	1.1	0.1	0.4	0.3
2	2142	2.3	2.3	0.4	0.9	1.1
3	2106	3.5	3.5	0.6	1.2	1.8
4	1554	4.7	4.6	0.8	1.6	2.5
5	908	5.9	5.8	0.9	1.9	3.3
6	430	7.1	6.9	1.2	1.8	4.9
7	167	8.3	8.0	0.7	1.0	6.9
8	72	9.4	9.2	1.4	3.1	5.1

The Figure 8 shown how the wind speed may differ from one site to another even over the same roof.

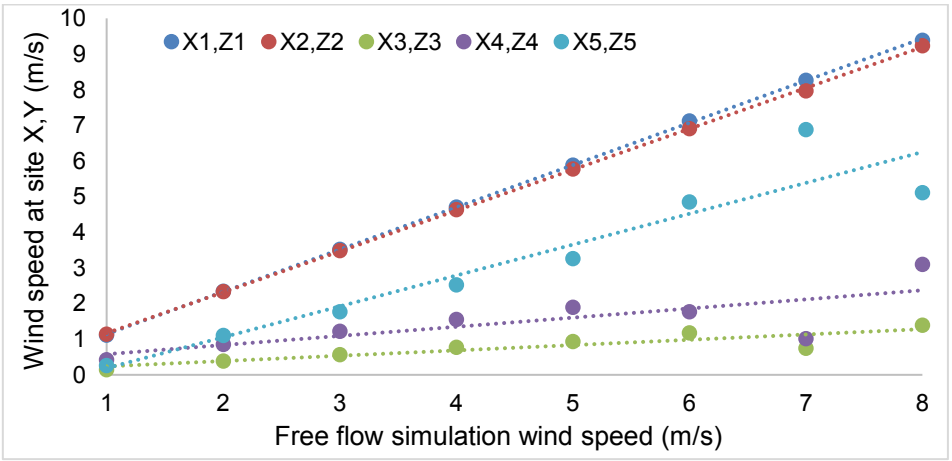

Figure 8. Wind speed at site vs. free flow simulation speed.

Given the wind characteristics described above, VAWT technology was chosen in this study, since this type of turbine have a good performance in urban locations with low wind speeds and high TI [18]. A turbine similar to the one selected by Rezaeiha in the wind potential studies in 12 cities in the Netherlands was selected [18]. The selected turbine is a Darrieus Type-H rotor with a rated power of 2.4 kW at a wind speed of 12.5 m/s and a swept area of 5 m^2. From the power curve of the Darrieus Type-H turbine, the energy produced during the year can be estimated as a function of wind speed regimes. The equation that best fit to the power curve for this machine was estimated using the potential regression method, with a correlation of $R^2 = 0.9944$, the function is given by Eq. (7):

$$y = 1.1501x^{3.0842} \quad (7)$$

Where: y, is the power delivered by the machine in Watt and x, is the wind speed in (m/s).

Table 5 shows the estimated annual power and energy generated for the given speed ranges of a VAWT installed at each sensor position, the energy that could potentially be generated at Anem2-INTEC position. Also, Table 5 shows the estimated annual power and energy generated for the given speed ranges of a VAWT installed at each sensor position, the energy that could potentially be generated at Anem2-INTEC position would be 1030 kWh/year.

Table 5. Power generation based on free stream speed and modelling results at sites of interest.

Speed (m/s)						Ocurr. (h/year)	Power (W)					
Free stream	X_1, Y_1	X_2, Y_2	X_3, Y_3	X_4, Y_4	X_5, Y_5		Free stream	X_1, Y_1	X_2, Y_2	X_3, Y_3	X_4, Y_4	X_5, Y_5
0	0	0	0	0	0	0	0	0	0	0	0	0
1	1.11	1.14	0.14	0.15	0.26	1,380	0	0	0	0	0	0
2	2.34	2.33	0.38	0.86	1.11	2,142	10	16	16	-	-	-
3	3.52	3.48	0.56	1.22	1.77	2,106	34	56	54	-	-	-
4	4.7	4.63	0.77	1.55	2.53	1,554	83	136	130	-	-	20
5	5.88	5.78	0.93	1.89	3.26	908	165	271	257	-	8	44
6	7.08	6.94	1.15	2.39	4.01	430	289	481	453	-	17	83
7	8.27	8.1	1.34	2.81	4.75	167	465	776	729	-	28	140
8	9.46	9.26	1.54	3.22	5.49	72	701	1175	1101	-	43	220

Table 6 shows the estimated annual energy generated for the given speed of a VAWT installed at each sensor position, the energy that could potentially be generated by one unit at X_1,Y_1 position would be 1,030 kWh/year. The avoided emissions CO_2 are also presented in Table 6.

Table 6. Power generation based on free stream speed and modelling results at sites of interest.

Parameters	Generated Energy (W-h/yr)					
	Free stream	X_1, Y_1	X_2, Y_2	X_3, Y_3	X_4, Y_4	X_5, Y_5
Annual energy per VAWT [kWh]	623	1,030	978	0	22	146
Avoided emissions CO_2 [kg/Year]	387	640	608	0	14	91
VAWTs	5	5	5	5	5	5
Total annual energy [kWh]	3,116	5,151	4,891	0	112	731
Total avoided emissions of CO_2 [kg/Year]	1,937	3,202	3,040	0	70	454

The Figure 9 is to illustrate how different can be the energy generation of a wind turbine depending on the site where this is installed even on the same roof. Based on the estimated annual energy production with an emission factor of 0.6216 TonCO_2/MWh, it can be determined that 0.640 tonnes of CO_2 emissions into the atmosphere per year could be avoided per SWT if it is located in the best site.

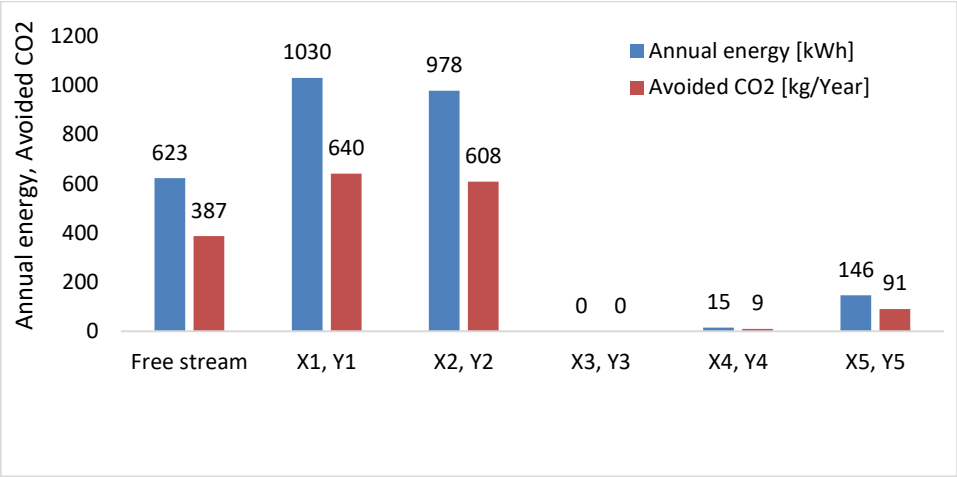

Figure 9. Annual energy generation and Avoided CO_2 emissions at site characterized by the anemometers and by CFD simulations.

4. Conclusions

This research is a starting point for assessing the urban wind potential for electricity generation in urban environment and contribute to the decarbonization of the Dominican Republic energy matrix. The wind generation potential in a typical building located in an urban area from Santo Domingo has been assessed. On-site measurement campaigns conducted at INTEC and simulation result analysis has been used.

The average wind speed in Anem1-INTEC, Anem2-INTEC was about 2.5 m/s respectively, which is considered a relatively low. At 40 m It was estimated an average wind speed of about 3.05 m/s. The prevailing wind direction with the highest intensity was recorded at 15° respect to North. The wind roses have good correlation with freely available GIS databases. Between 13:00h to 15:00h the higher wind intensity occurs.

A methodology was presented to estimate the wind potential in urban buildings taking into account the exact site of the SWT and the building geometry using, and integrated approach based on on-site measurements and CFD analysis. The selected turbine was VAWT Darrieus Type-H, with good performance at low speed and very turbulent environments. The estimated AEP for one turbine in best site was 1030 kWh/yr with a potential CO_2 emission reduction of 640 kg/yr. The site of the turbines even in the same roof is relevant for the energy generation, modelling results shown differences in the estimate energy generation from one corner of the roof to the opposite of 100%.

Future research should quantify 100% of the available potential in buildings with a detailed estimate of the number of buildings and the area available for VAWT installation. In addition, survey studies should be extended both spatially and temporally. Given the geographical position of the DR and its exposure to adverse meteorological events, a resilience and feasibility analysis will be performed for future urban wind potential analysis.

Acknowledgments

First author gratefully acknowledges the financial support by FONDO NACIONAL DE INNOVACIÓN Y DESARROLLO CIENTÍFICO Y TECNOLÓGICO, **Grant No. 2022-3C1-141**, through the Ministry of Higher Education, Science and Technology (MESCyT) from the Dominican Republic.

References

[1] "Objetivo 7: Energía asequible y No contaminante | PNUD," *UNDP*, Jun. 11, 2020. https://www.undp.org/content/undp/es/home/sustainable-development-goals/goal-7-affordable-and-clean-energy.html (accessed Jun. 11, 2020).

[2] "Global energy transformation: A roadmap to 2050 (2019 edition)," */publications/2019/Apr/Global-energy-transformation-A-roadmap-to-2050-2019Edition*, Mar. 15, 2020. /publications/2019/Apr/Global-energy-transformation-A-roadmap-to-2050-2019Edition (accessed Mar. 15, 2020).

[3] Á. Estévez Bourdierd, E. Peña Acosta, and I. Mattila, "Primer Informe Bienal de Actualización ('fBUR')," no. 1, p. 267, Feb. 2020.

[4] S. Chen, G. Zhang, X. Xia, S. Setunge, and L. Shi, "A review of internal and external influencing factors on energy efficiency design of buildings," *Energy Build.*, vol. 216, p. 109944, Jun. 2020, doi: 10.1016/j.enbuild.2020.109944.

[5] J. T. Millward-Hopkins, A. S. Tomlin, L. Ma, D. B. Ingham, and M. Pourkashanian, “Mapping the wind resource over UK cities,” *Renew. Energy*, vol. 55, pp. 202–211, Jul. 2013, doi: 10.1016/j.renene.2012.12.039.
[6] B. R. Karthikeya, P. S. Negi, and N. Srikanth, “Wind resource assessment for urban renewable energy application in Singapore,” *Renew. Energy*, vol. 87, pp. 403–414, Mar. 2016, doi: 10.1016/j.renene.2015.10.010.
[7] Z. Tasneem *et al.*, “An analytical review on the evaluation of wind resource and wind turbine for urban application: Prospect and challenges,” *Dev. Built Environ.*, vol. 4, p. 100033, Nov. 2020, doi: 10.1016/j.dibe.2020.100033.
[8] Q. Wang, J. Wang, Y. Hou, R. Yuan, K. Luo, and J. Fan, “Micrositing of roof mounting wind turbine in urban environment: CFD simulations and lidar measurements,” *Renew. Energy*, vol. 115, pp. 1118–1133, Jan. 2018, doi: 10.1016/j.renene.2017.09.045.
[9] J. Fields, F. Oteri, R. Preus, and I. Baring-Gould, “Deployment of Wind Turbines in the Built Environment: Risks, Lessons, and Recommended Practices,” NREL/TP--5000-65622, 1260340, Jun. 2016. doi: 10.2172/1260340.
[10] D. Micallef and G. Van Bussel, “A Review of Urban Wind Energy Research: Aerodynamics and Other Challenges,” *Energies*, vol. 11, no. 9, Art. no. 9, Sep. 2018, doi: 10.3390/en11092204.
[11] NASA, “Implementing Turbulence Models into the Compressible RANS Equations,” Apr. 03, 2023. https://turbmodels.larc.nasa.gov/implementrans.html (accessed Apr. 03, 2023).
[12] SOLIDWORKS, “Numerical Basis of CAD-Embedded CFD,” Apr. 03, 2023. https://www.solidworks.com/sw/docs/flow_basis_of_cad_embedded_cfd_whitepaper.pdf (accessed Apr. 03, 2023).
[13] Y. Toparlar, B. Blocken, B. Maiheu, and G. J. F. van Heijst, “A review on the CFD analysis of urban microclimate,” *Renew. Sustain. Energy Rev.*, vol. 80, pp. 1613–1640, Dec. 2017, doi: 10.1016/j.rser.2017.05.248.
[14] A. Vallejo-Díaz, I. Herrera-Moya, A. Fernández-Bonilla, and C. Pereyra-Mariñez, “Wind energy potential assessment of selected locations at two major cities in the Dominican Republic, toward energy matrix decarbonization, with resilience approach,” *Therm. Sci. Eng. Prog.*, vol. 32, p. 101313, Jul. 2022, doi: 10.1016/j.tsep.2022.101313.
[15] S. AL-Yahyai, Y. Charabi, A. Gastli, and S. Al-Alawi, “Assessment of wind energy potential locations in Oman using data from existing weather stations,” *Renew. Sustain. Energy Rev.*, vol. 14, no. 5, pp. 1428–1436, Jun. 2010, doi: 10.1016/j.rser.2010.01.008.
[16] G. Bekele and B. Palm, “Wind energy potential assessment at four typical locations in Ethiopia,” *Appl. Energy*, vol. 86, no. 3, pp. 388–396, Mar. 2009, doi: 10.1016/j.apenergy.2008.05.012.
[17] M. R. Islam, R. Saidur, and N. A. Rahim, “Assessment of wind energy potentiality at Kudat and Labuan, Malaysia using Weibull distribution function,” *Energy*, vol. 36, no. 2, pp. 985–992, Feb. 2011, doi: 10.1016/j.energy.2010.12.011.
[18] A. Rezaeiha, H. Montazeri, and B. Blocken, “A framework for preliminary large-scale urban wind energy potential assessment: Roof-mounted wind turbines,” *Energy Convers. Manag.*, vol. 214, p. 112770, Jun. 2020, doi: 10.1016/j.enconman.2020.112770.
[19] K. Sharma and M. R. Ahmed, “Wind energy resource assessment for the Fiji Islands: Kadavu Island and Suva Peninsula,” *Renew. Energy*, vol. 89, pp. 168–180, Apr. 2016, doi: 10.1016/j.renene.2015.12.014.
[20] T. Simões and A. Estanqueiro, “A new methodology for urban wind resource assessment,” *Renew. Energy*, vol. 89, pp. 598–605, 2016, doi: https://doi.org/10.1016/j.renene.2015.12.008.
[21] A.-S. Yang, Y.-M. Su, C.-Y. Wen, Y.-H. Juan, W.-S. Wang, and C.-H. Cheng, “Estimation of wind power generation in dense urban area,” *Appl. Energy*, vol. 171, pp. 213–230, Jun. 2016, doi: 10.1016/j.apenergy.2016.03.007.
[22] F. Toja-Silva, A. Colmenar-Santos, and M. Castro-Gil, “Urban wind energy exploitation systems: Behaviour under multidirectional flow conditions—Opportunities and challenges,” *Renew. Sustain. Energy Rev.*, vol. 24, pp. 364–378, Aug. 2013, doi: 10.1016/j.rser.2013.03.052.
[23] SkyscraperPage, “Database - SkyscraperPage.com,” *SkyscraperPage*, Jul. 01, 2023. https://skyscraperpage.com/cities/ (accessed May 02, 2021).
[24] A. Al-Quraan, T. Stathopoulos, and P. Pillay, “Comparison of wind tunnel and on site measurements for urban wind energy estimation of potential yield,” *J. Wind Eng. Ind. Aerodyn.*, vol. 158, pp. 1–10, Nov. 2016, doi: 10.1016/j.jweia.2016.08.011.
[25] F. C. Emejeamara, A. S. Tomlin, and J. T. Millward-Hopkins, “Urban wind: Characterisation of useful gust and energy capture,” *Renew. Energy*, vol. 81, pp. 162–172, Sep. 2015, doi: 10.1016/j.renene.2015.03.028.
[26] A. Gagliano, F. Nocera, F. Patania, and A. Capizzi, “Assessment of micro-wind turbines performance in the urban environments: an aided methodology through geographical information systems,” *Int. J. Energy Environ. Eng.*, vol. 4, no. 1, p. 43, Nov. 2013, doi: 10.1186/2251-6832-4-43.
[27] G. F. Garuma, “Review of urban surface parameterizations for numerical climate models,” *Urban Clim.*, vol. 24, pp. 830–851, Jun. 2018, doi: 10.1016/j.uclim.2017.10.006.

[28] H. Mittal, A. Sharma, and A. Gairola, “A review on the study of urban wind at the pedestrian level around buildings,” *J. Build. Eng.*, vol. 18, pp. 154–163, Jul. 2018, doi: 10.1016/j.jobe.2018.03.006.
[29] *IEC 61400-2:2013*. 2013. [Online]. Available: https://webstore.iec.ch/publication/5433
[30] E. Arteaga-López, C. Ángeles-Camacho, and F. Bañuelos-Ruedas, “Advanced methodology for feasibility studies on building-mounted wind turbines installation in urban environment: Applying CFD analysis,” *Energy*, vol. 167, pp. 181–188, 2019, doi: https://doi.org/10.1016/j.energy.2018.10.191.
[31] A. Vallejo, “Procedimiento para la Caracterización del Viento Urbano como Fuente Energética en la Ciudad de Santo Domingo,” Instituto Tecnológico de Santo Domingo, Santo Domingo, 2018.
[32] F. C. Emejeamara and A. S. Tomlin, “A method for estimating the potential power available to building mounted wind turbines within turbulent urban air flows,” *Renew. Energy*, vol. 153, pp. 787–800, Jun. 2020, doi: 10.1016/j.renene.2020.01.123.
[33] J. Blackledge, E. Coyle, D. Kearney, E. Murphy, and M.-J. R. Duartes, “Wind Resource in the Urban Environment,” *Forthcom. J. Appl. Res. Innov. Eng. Built Environ. 2013*, Jan. 2012, doi: 10.21427/D70P7R.
[34] A. Kc, J. Whale, and T. Urmee, “Urban wind conditions and small wind turbines in the built environment: A review,” *Renew. Energy*, vol. 131, pp. 268–283, Feb. 2019, doi: 10.1016/j.renene.2018.07.050.
[35] T. Stathopoulos *et al.*, “Urban wind energy: Some views on potential and challenges,” *J. Wind Eng. Ind. Aerodyn.*, vol. 179, pp. 146–157, Aug. 2018, doi: 10.1016/j.jweia.2018.05.018.
[36] SOLIDWORKS, “SOLIDWORKS Flow Simulation,” *SOLIDWORKS*, Apr. 03, 2323. https://www.solidworks.com/es/product/solidworks-flow-simulation (accessed Apr. 03, 2023).
[37] K. Dai, A. Bergot, C. Liang, W.-N. Xiang, and Z. Huang, “Environmental issues associated with wind energy – A review,” *Renew. Energy*, vol. 75, pp. 911–921, Mar. 2015, doi: 10.1016/j.renene.2014.10.074.
[38] I. Paraschivoiu, “Wind Turbine Design: With Emphasis on Darrieus Concept - Ion Paraschivoiu,” *Polytechnic International Press, Canada*, 2002. https://books.google.com.do/books?hl=es&lr=&id=sefVtnVgso0C&oi=fnd&pg=PR13&ots=HmDYuSgz1d&sig=8Ef1nSjDDSp1SDRWbmPZiX_F_Go&redir_esc=y#v=onepage&q&f=false (accessed Jul. 17, 2020).
[39] G. C. Guerrero-Liquet, J. M. Sánchez-Lozano, M. S. García-Cascales, M. T. Lamata, and J. L. Verdegay, “Decision-Making for Risk Management in Sustainable Renewable Energy Facilities: A Case Study in the Dominican Republic,” *Sustainability*, vol. 8, no. 5, Art. no. 5, May 2016, doi: 10.3390/su8050455.
[40] “OC,” Apr. 03, 2023. https://www.oc.do/ (accessed Apr. 03, 2022).
[41] UNFCCC, “Grid emission factor for the Dominican Republic (version 01.0),” Jan. 12, 2022. https://cdm.unfccc.int/methodologies/standard_base/2015/sb143.html (accessed May 15, 2021).

PROCEEDINGS OF ECOS 2023 - THE 36TH INTERNATIONAL CONFERENCE ON
EFFICIENCY, **C**OST, **O**PTIMIZATION, **S**IMULATION AND ENVIRONMENTAL IMPACT OF ENERGY SYSTEMS
25-30 JUNE, 2023, LAS PALMAS DE GRAN CANARIA, SPAIN

Numerical simulation on thermal management of concentrating photovoltaic-thermal module with confined jet impingement with Ag-ZnO hybrid nanofluids

Abhishek Gupta[a], Sandesh S. Chougule[b], Sandip K. Saha[c]

[a] Department of Mechanical Engineering, Indian Institute of Technology Bombay, India, 204100029@iitb.ac.in

[b] Clean Energy Processes (CEP) Laboratory, Department of Chemical Engineering, Imperial College London, London SW72AZ, United Kingdom, s.chougule@imperial.ac.uk

[c] Department of Mechanical Engineering, Indian Institute of Technology Bombay, India, sandip.saha@iitb.ac.in

Abstract:

The high concentration of solar light on photovoltaic cells leads to extremely high cell temperatures, leading to decreased cell efficiency. Appropriate cooling techniques need to be integrated to sustain the high rise in temperature and maintain a uniform temperature throughout the photovoltaic cell. This study focuses on the cooling of photovoltaic cells with a confined jet impingement cooling technique. The major objective is to improve cell efficiency using the confined jet impingement technique to avoid hotspots, thermal stress, and current mismatching problem. The channels are created on the backside of the photovoltaic cell such that the coolant strikes the cell at the center and leaves at the four corners of the cell. Water-based ZnO and Ag-ZnO hybrid nanofluids are used as a coolant because of their high thermal conductivity and heat transfer capacity. The results showed better cooling performance and improved cell efficiency of photovoltaic cells with nanofluids compared to water as a coolant. In addition, sufficient temperature uniformity is maintained within PV cells. The effect of the coolant mass flow rate and nanoparticle volume concentration is also studied. Results showed improved cell electrical efficiency at higher coolant mass flow rates and higher nanoparticle volume concentration.

Keywords:

Concentrated photovoltaic; Confined jet impingement; Efficiency; Energy; Nano-fluids

1. Introduction

Solar energy is considered a significant renewable energy source. The annual potential of solar energy is 1,575–49,837 exajoules (EJ), which is 1.8–58 times the estimated future world energy consumption of 860 EJ in 2040 [1,2]. Solar energy can be used by various technologies such as photovoltaic (PV) systems, concentrated PV systems, solar thermal collectors, *etc*. PV systems and solar thermal collectors can be combined to obtain electrical and thermal energy outputs. Photovoltaic thermal (PVT) systems improve solar cell conversion efficiency, expanding solar energy utilization. However, the flat plate PVT system generates heat at low temperatures, which restrains the use of these systems for some high-temperature applications. To overcome such problems, concentrated photovoltaic thermal (CPVT) systems are a better alternative.

Concentrated photovoltaic (CPV) systems utilize optics to concentrate sunlight onto PV cells. Therefore, CPV can replace the expensive PV cells with cheaper concentrator optics to enable harnessing the same amount of solar radiation but with fewer PV receivers. Despite several advantages of a CPV system over flat plates, CPV systems face many challenges. The main challenge is that the high concentration of solar light on photovoltaic cells leads to extremely high cell temperatures, resulting in decreased cell efficiency. A major portion of the available solar energy is converted to thermal energy, leading to problems such as hotspots, current mismatching, and thermal fatigue. It is essential to have a uniform PV cell temperature to avoid current mismatching and thermal stresses. To sustain the high rise in temperature and to maintain a uniform

temperature throughout the photovoltaic cell, appropriate cooling techniques are required to be integrated. Many cooling techniques, such as air-based cooling, liquid immersion, jet impingement, phase change material cooling, heat pipe, micro-channel cooling, and thermoelectric cooling, have been employed, which were reviewed in various literature [3]. Theristis et al. [4] reported that passive cooling is not enough to dissipate heat from the cell under high concentration ratios. Jet impingement is an appropriate cooling method for densely packed PV cells to achieve a uniform cell temperature [5]. Many researchers reviewed unconfined and confined jet impingement cooling systems for PV cells. Recent studies showed that the temperature of the PV cell can be reduced from 1360 °C to 65 °C for a concentration ratio of 1000 suns using confined jet impingement cooling with water at a mass flow rate of 50 g/min [6]. Javidan et al. [7] reported that temperature of the PV module decreased from 63.95 °C to 33.68 °C by using an optical set of parameters for jet impingement cooling. Bahaidarah et al. [8] reported a temperature decrease from 69.7 °C to 36.6 °C using an unconfined jet impingement cooling technique. Zubeer et al. [9] reported that the temperature of an uncooled PV system and a low-concentrated (1-3 suns) PV system was 57.5 °C and 64.1 °C, respectively, which decreased to 36.5 °C with water jet impingement cooling. Barrau et al. [10] studied the performance of hybrid jet impingement micro-channel cooling for densely packed PV cells, and calculated the heat transfer coefficient as a function of pressure drop, and compared the performance of hybrid cooling to micro-channel cooling alone. Markal et al. [11] performed experiments to investigate the effect of impinging air jets on the cooling of PV cells. It was found that the average surface temperature of the PV cell can be decreased by 61.5%, and the output power can be improved by 13.2%. Amanlou et al. [12] studied the effect of air diffuser geometry on the performance of low-concentrated PV systems. Also, the effect of air mass flow rates on concentrated PV cells' performance was studied. It is reported that by increasing the air mass flow rate from 0.0008 to 0.016 kg/s, the electrical, thermal, and overall efficiency of the PV cell was improved by 13.5, 22.75, and 22.41%, respectively. Singh et al. [13] performed numerical modelling and experimental study for performance improvement of PV modules with a hybrid cooling system with a thermoelectric cooler and phase change material. It was reported that TECs provide better cooling than PCMs under similar conditions as panel efficiency increases by 5.73%. It was observed that electrical efficiency shows a maximum increment of 19.4% with hybrid cooling. Sabry et al. [14] studied thermoelectric generator (TEG) cooling on concentrated PV systems. Compared to only a CPV cell on top of a heat sink, the generated power of the CPV/TEG hybrid system increased by 7.4%, 5.8%, and 3% corresponding to using the 30 × 30 mm^2, 40 × 40 mm^2 and the 62 × 62 mm^2 TEG modules, for which the number of junctions is 31, 127 and 49, respectively.

The aim is to design a highly efficient CPVT system with hybrid cooling, such as confined jet impingement and a thermoelectric generator. Although many researchers have worked on the performance of jet impingement cooling of microelectronics, very few studies are reported on confined jet impingement cooling of highly concentrated PV systems. Confined jet impingement cooling provides a better uniform PV cell temperature, eliminating thermal stresses and current mismatching. Most researchers use water as a cooling fluid for jet impingement cooling of PV cells. Nanofluids provide better cooling than water because of their higher thermal conductivity [15]. In this work, the performance improvement of a highly concentrated PV system under confined jet impingement with Ag-ZnO hybrid nanofluids as a coolant is studied. The effect of volume concentration of Ag-ZnO nanoparticles on CPV cell cooling and electrical efficiency is observed. Also, the effect of the mass flow rate of the Ag-ZnO hybrid nanofluid on the performance of confined jet impingement cooling of CPV cell is studied, and the performance of Ag-ZnO hybrid nanofluids is compared with water as a cooling fluid.

2. System description

2.1 System Geometry

The solar cell used in this analysis is a multi-junction solar cell with a reference cell efficiency of 40.3% at a reference temperature of 298 K. The dimension of the solar cell is 10 mm × 10 mm with 0.19 mm thickness. The solar cell is supported by a board structure which consists of a copper structure followed by a ceramic and copper board. The upper copper layer's dimensions are 24 mm × 19.5 mm with 0.25 mm thickness, followed by a 25.5 mm × 21 mm ceramic layer and a 25 mm × 20.5 mm copper layer with 0.32 mm and 0.25 mm thickness, respectively. An aluminium heat sink of 25.5 mm × 21 mm with 4 mm height is placed at the bottom of the structure. An inlet is placed at the center of the heat sink, and four outlets are placed at the four corners. The cooling fluid enters the center of the heat sink and exits through the four outlets at the corner.

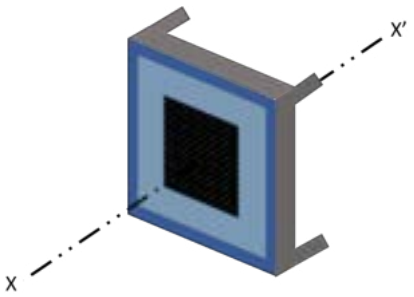

(a)

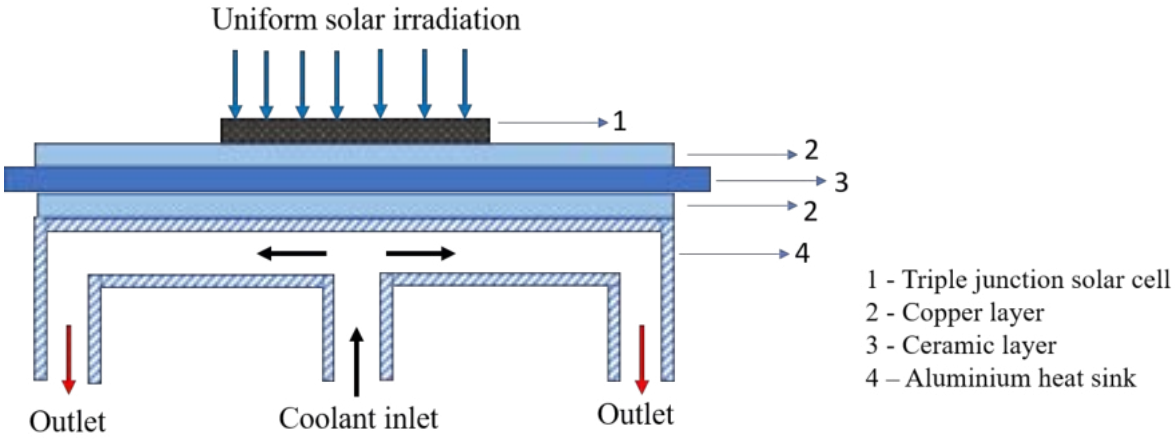

(b)

Figure 1. (a) Isometric view of the assembly (b) Solar cell layers and jet impingement channel configuration.

Table 1. Properties of solar cell layers and board structure

Solar cell layer	Thermal conductivity (k) (W/m.K)	Specific heat (C) (J/kg.K)	Density (ρ) (kg/m^3)	Emissivity (ε)
Germanium	60	320	5323	0.9
Copper-1	400	385	8700	0.05
Ceramic	30	900	3900	0.75
Copper-2	202.6	871	2719	0.9

2.2 Governing equations

For solar cell layers:

The heat conduction equation between the layers of the PV cell is as follows:

$$\nabla(k_i \nabla T_i) + q_i = 0 \quad (1)$$

where k_i represents the thermal conductivity of the ith layer.

Internal heat generation term is added for the germanium layer because heat is generated inside the germanium layer due to solar radiation absorption.

The heat generated in the germanium layer is calculated according to the following expression:

$$q_{Ge} = \frac{(1-\eta_{cell}).G.\alpha_{Ge}.A}{V} \quad (2)$$

where *G* is the net concentrated solar irradiation, *α* is the absorptivity of the germanium layer, and *A* and *V* are the surface area and volume of the germanium layer, respectively. η_{cell} is the cell's electrical efficiency.

The net concentrated solar irradiation is a function of the optical efficiency of the solar cell (η_{opt}) and the concentration ratio (CR) of the solar cell.

$$G = I.CR.\eta_{opt} \quad (3)$$

where *I* is the solar irradiation falling on the solar cell.

The electrical efficiency of the solar cell (η_{cell}) is a function of the operating temperature of the solar cell. As the temperature of the solar cell increases, the cell efficiency decreases. The term (1-η_{cell}) represents the portion of absorbed concentrated solar irradiance converted to heat. This heat has to be dissipated or absorbed by the coolants to keep the cell's temperature low. The solar cell's electrical efficiency is expressed in terms of the operating temperature of the cell by the following equation:

$$\eta_{cell} = \eta_{ref} - \beta_{thermal}(T_{cell} - T_{ref}) \quad (4)$$

where cell reference efficiency η_{ref} is taken as 40.3% at reference temperature T_{ref} = 298K and CR = 1000, and $\beta_{thermal}$ is the thermal coefficient and is equal to 0.047%.

For jet impingement:

Continuity equation:

$$\nabla.\left(\rho_f \vec{V}\right) = 0 \quad (5)$$

Momentum equation:

$$\vec{V}.\nabla\left(\rho_f \vec{V}\right) = -\nabla P + \nabla.(\mu_f \nabla \vec{V}) \quad (6)$$

Energy equation:

$$\vec{V}.\nabla\left(\rho_f C_f T\right) = \nabla.(k_f \nabla T) \quad (7)$$

where, ρ, μ and *k* are the density, viscosity, and thermal conductivity of the coolant fluid, respectively. $\vec{V}$ and *P* is the velocity and pressure, respectively.

2.3 Boundary conditions:

The top layer of the concentrated PV system is subjected to mixed convection radiation heat losses boundary conditions. All of the sides of the CPV system are given adiabatic boundary conditions. For the coolant, inlet jets are given uniform temperature and velocity normal to the inlet boundary conditions, and at the outlet, zero-gauge pressure boundary condition was given.

For the top layer of the germanium cell layer and copper layer:

$$-k_{Ge}\frac{\partial T_{Ge}}{\partial z} = q_{rad,Ge\to S} + q_{conv,Ge\to a} \quad (8)$$

$$-k_{cu}\frac{\partial T_{cu}}{\partial z} = q_{rad,cu\to S} + q_{conv,cu\to a} \quad (9)$$

where, $q_{rad,Ge\to S}$ is the radiative heat loss from the Germanium layer to the sky and $q_{conv,Ge\to a}$ is the convective heat loss from the germanium layer to the ambient.

The convective heat loss from the Germanium layer to the ambient can be calculated using the following correlations:

$$q_{conv,Ge\to a} = h_{conv,wind}(T_{Ge} - T_a) \quad (10)$$

$$h_{conv,wind} = 5.82 + 4.07V_{wind} \quad (11)$$

where T_a is the ambient temperature, T_{Ge} is the temperature of the Germanium cell, $h_{conv,wind}$ is the convective heat transfer coefficient, and V_{wind} is the wind velocity.

Radiation heat loss from the germanium layer to the sky can be calculated using the following expression:

$$q_{rad,Ge\to S} = \sigma\epsilon_{Ge}(T_{Ge}^4 - T_s^4) \quad (12)$$

$$T_s = 0.0522T_a^{1.5} \quad (13)$$

where ε_{Ge} is the emissivity of Germanium, T_s is the sky temperature in Kelvin, and T_a is the ambient temperature in Kelvin.

At the interfaces between all layers, thermally coupled boundary conditions are given. At the interface between the germanium layer and copper top layer, the thermally coupled boundary condition is given as follows:

$$-k_{Ge}\nabla T_{Ge} = -k_{cu}\nabla T_{cu} \quad (14)$$

$$T_{Ge} = T_{cu}$$

At the interface between the top copper layer and the ceramic layer:

$$-k_{cu}\nabla T_{cu} = -k_{ce}\nabla T_{ce} \quad (15)$$

$$T_{cu} = T_{ce}$$

At the interface between the ceramic layer and the bottom copper layer:

$$-k_{ce}\nabla T_{ce} = -k_{cu,b}\nabla T_{cu,b} \quad (16)$$

$$T_{ce} = T_{cu,b}$$

At the interface between the bottom copper layer and the heat sink top surface:

$$-k_{cu,b}\nabla T_{cu,b} = -k_{Al}\nabla T_{Al} \quad (17)$$

$$T_{cu,b} = T_{Al}$$

where T_{Ge}, T_{cu}, T_{ce}, $T_{cu,b}$, T_{Al} are the temperatures of the germanium cell layer, top copper layer, ceramic layer, bottom copper layer, and aluminium heat sink, respectively. k_{Ge}, k_{cu}, k_{ce}, $k_{cu,b}$, k_{Al} are the thermal conductivities of the germanium cell layer, top copper layer, ceramic layer, bottom copper layer, and aluminium layer, respectively.

For heat sink inlets and outlets:

At inlet: $V_f = V_{in}$ and T_{in} = 298K

At outlet: gauge pressure P_{out} = 0

All sides of the heat sink wall and the back side are adiabatic.

No slip boundary condition at the fluid-solid interface.

3. Results and discussion

3.1 Validation

The present numerical model is validated with Zahhad et al. [6]. The authors investigated the variation in cell temperature with a mass flow rate of cooling fluid and concentration ratio. The authors studied the variation in thermal stress along the center and diagonal lines of the cell. Zahhad et al. [6] used water as a cooling fluid. Figure 2 shows the variation in the temperature of the Germanium cell with respect to the inlet mass flow rate of the cooling fluid. It is observed that the cell temperature decreases with an increase in the coolant mass flow rate. The configuration with one inlet at the center is better than multiple inlet jets because of the absence of cross-flow. Therefore, the impingement zone develops without restrictions at the target surface of the impinging. A reasonable agreement is found between the present numerical model and the results by Zahhad et al. [6]. An average error of 1.68% and an average temperature difference of 1.33 K is found between the present numerical model and the results by Zahhad et al. [6].

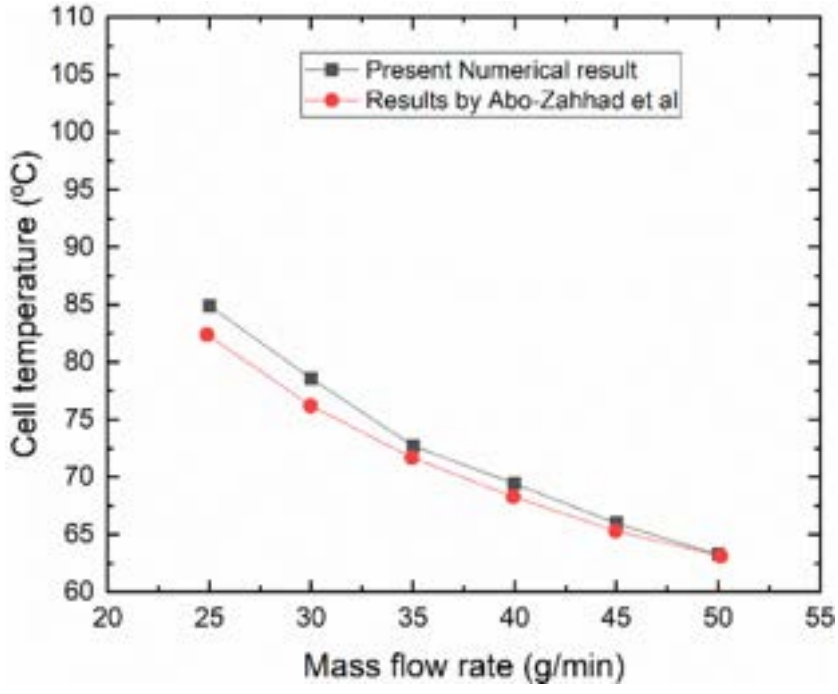

Figure 2. Validation of numerical model with Zahhad et al. [6].

The simulation is further performed for the same configuration with Ag-ZnO hybrid nanofluids as a cooling fluid. The thermophysical properties used for Ag-ZnO hybrid nanofluids are listed below [15] :

Table 2. Thermophysical properties of Ag-ZnO hybrid nanofluids

Volume concentration (%)	Density (kg/m^3)	Specific heat (J/kg-K)	Thermal conductivity ratio (K_{nf}/K_b)	Viscosity (Pa-s)
0.02	1000.932	4186.264	1.08	0.0031
0.04	1001.864	4185.527	1.145	0.0035
0.06	1002.796	4184.791	1.185	0.0042
0.08	1003.728	4184.054	1.25	0.0045
0.10	1004.66	4183.318	1.29	0.0052

Figure 3 shows the cell temperature at varying volume concentrations of Ag-ZnO nanoparticles at a mass flow rate of 25 g/min. The cell temperature decreases with an increase in the volume concentration of nanoparticles. This is because of the enhanced thermophysical properties of nanofluids at a higher volume concentration of nanoparticles. The thermal conductivity of nanofluids increases due to the Brownian motion of nanoparticles. Nanoparticles move through the liquid, and convection is induced due to the Brownian motion of nanoparticles. This leads to an increase in nanofluid thermal conductivity. Also, the ballistic phonon transport of nanoparticles helps increase the thermal conductivity of nanofluids. Due to the increase in the thermal conductivity of nanofluids, the amount of heat transferred from the bottom copper layer to the coolant increases.

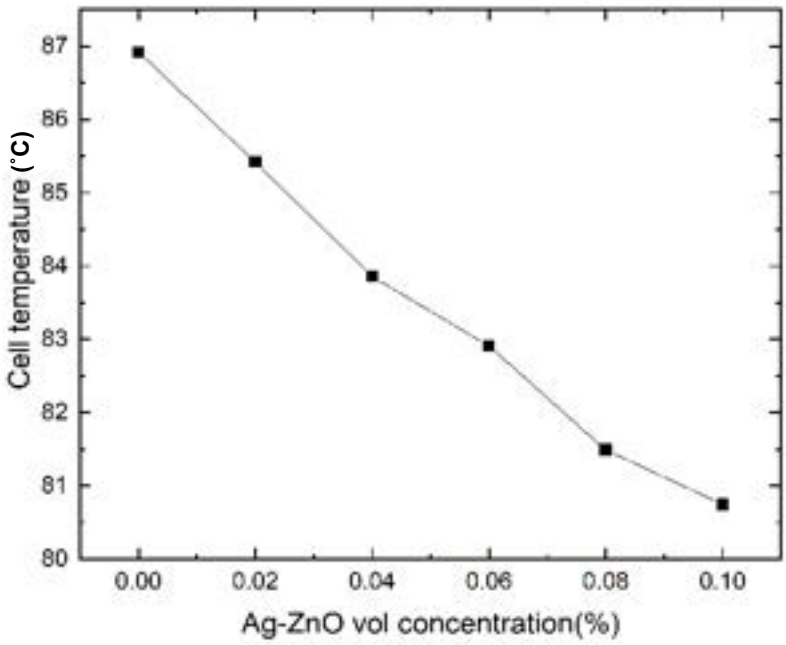

Figure 3. Variation in cell temperature with Ag-ZnO volume concentration.

Figure 4 shows the cell electrical efficiency with a varying volume concentration of Ag-ZnO nanoparticles at a mass flow rate of 25 g/min. It is evident that the electrical efficiency increases with increasing nanoparticle volume concentration. Since the cell temperature decreases with an increasing volume concentration of nanoparticles, the cell's electrical efficiency increases.

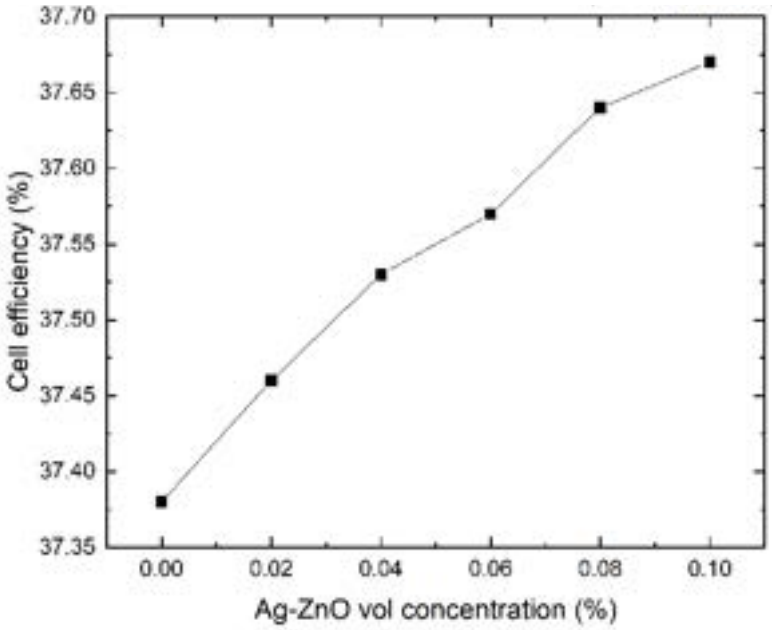

Figure 4. Variation in cell electrical efficiency with Ag-ZnO volume concentration.

Figure 5 shows the effect of the mass flow rate of Ag-ZnO nanofluids at 0.1% volume concentration on the average cell temperature and compares it with water as a coolant. The minimum mass flow rate is 25 g/min to avoid flow boiling. It is observed that Ag-ZnO hybrid nanofluids cool the cell better because of their enhanced thermophysical properties. Therefore, the cell's electrical efficiency will be higher with nanofluids as a cooling fluid.

Although cell temperature decreases at higher coolant mass flow rates, the pressure drop also increases with the increase in the coolant mass flow rate. The net power gained is affected by frictional pressure drops. To use waste heat from highly concentrated PV system applications, the coolant mass flow rate should be low.

Cell temperature variation on the cell surface is also evaluated. It is observed that the maximum temperature difference at the surface of the cell is 2.06 °C for a mass flow rate of 25 g/min at 0.1% volume concentration of Ag-ZnO nanoparticles. It shows that temperature uniformity can be achieved using a confined jet impingement cooling technique on the surface of the PV cell. This will eliminate the problems associated with thermal stresses and current mismatching.

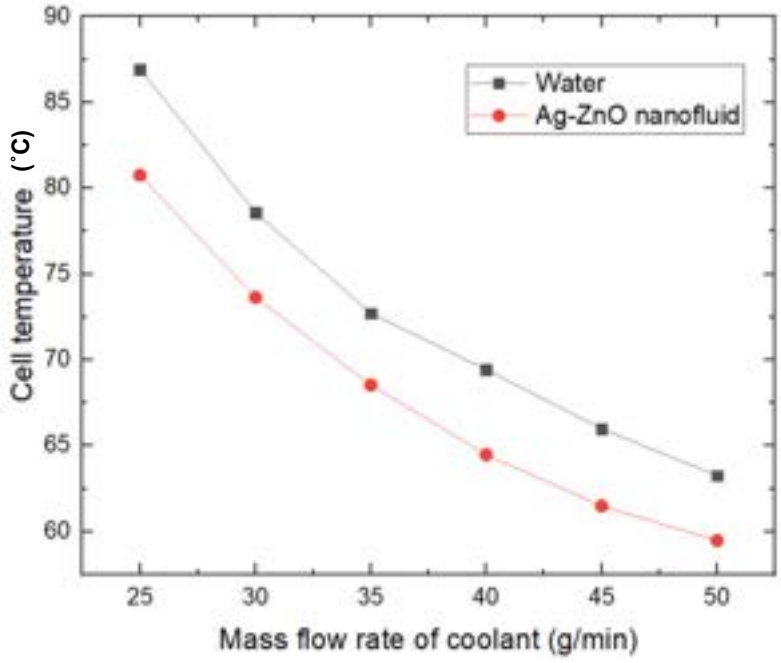

Figure 5. Variation in cell temperature with mass flow rate of coolant.

4. Conclusions

It is found that Ag-ZnO hybrid nanofluids can perform a better cooling of the cell than water because of the enhanced thermophysical properties of nanofluids. The thermal conductivity of nanofluids increases compared to base fluid, which increases heat transfer from the bottom copper layer to the coolant. The higher the nanoparticle volume concentration, the better the cooling effect. Also, nanofluids will increase cell electrical efficiency. It is observed that numerically there is only a slight increase in cell efficiency with nanofluids compared to water. Experiments with the proposed system will be performed in the future. Surely, the cooling of CPV cells and cell electrical efficiency will be improved in experimentation since the effect of Brownian motion and ballistic transport phonon of nanoparticles will be observed in experiments.

Nomenclature

A	area of the solar cell, m^2
CR	concentration ratio
G	concentrated solar irradiance, W/m^2
h	convective heat transfer coefficient, $W/(m^2\ K)$
I	direct normal irradiation, W/m^2
k	thermal conductivity, W/(m K)
L	length, m
$\dot{m}$	mass flow rate of coolant, kg/s
q	heat flux, W/m^2
T	temperature, ˚C
V	volume of solar cell, m^3
v	velocity, m/s
W	width, m

Greek symbols

μ	Viscosity, Pa s
α	absorptivity
$\beta_{thermal}$	solar cell temperature coefficient
Δ	difference
δ	thickness, m
η	efficiency, %
ρ	density, kg/m^3
σ	Stefan-Boltzmann constant, $5.67\times10^{-8}\ W/(m^2\ K^4)$

Subscripts and superscripts

a	ambient
b	base fluid
cell	for cell layer
conv	convection
cu	copper layer
f	fluid
Ge	germanium layer
in	inlet
nf	nanofluid
opt	optical
out	outlet
rad	radiation
ref	reference

Abbreviations

CPV	concentrated photovoltaic
CPVT	concentrated photovoltaic thermal
HCPV	high concentrated photovoltaic

PV photovoltaic

TEC Thermoelectric coolers

TEG Thermoelectric generator

References

1. World energy assessment. United Nations Development Programme; 2000.
2. International energy outlook 2016 with projections to 2040. U.S. Energy Information Administration; 2016.
3. Dwivedi P, Sudhakar K, Soni A, Solomin E, Kirpichnikova I. Advanced cooling techniques of P.V. modules: A state of art. Case Stud Therm Eng [Internet]. 2020;21(December 2019):100674. Available from: https://doi.org/10.1016/j.csite.2020.100674
4. Theristis M, O'Donovan TS. Electrical-thermal analysis of III-V triple-junction solar cells under variable spectra and ambient temperatures. Sol Energy [Internet]. 2015;118:533–46. Available from: http://dx.doi.org/10.1016/j.solener.2015.06.003
5. Royne A, Dey CJ. Design of a jet impingement cooling device for densely packed PV cells under high concentration. Sol Energy. 2007;81(8):1014–24.
6. Abo-Zahhad EM, Ookawara S, Radwan A, El-Shazly AH, ElKady MF. Thermal and structure analyses of high concentrator solar cell under confined jet impingement cooling. Energy Convers Manag [Internet]. 2018;176(September):39–54. Available from: https://doi.org/10.1016/j.enconman.2018.09.005
7. Javidan M, Moghadam AJ. Experimental investigation on thermal management of a photovoltaic module using water-jet impingement cooling. Energy Convers Manag. 2021;228(October 2020).
8. Bahaidarah HMS. Experimental performance evaluation and modeling of jet impingement cooling for thermal management of photovoltaics. Sol Energy [Internet]. 2016;135:605–17. Available from: http://dx.doi.org/10.1016/j.solener.2016.06.015
9. Zubeer SA, Ali OM. Experimental and numerical study of low concentration and water-cooling effect on PV module performance. Case Stud Therm Eng [Internet]. 2022;34(September 2021):102007. Available from: https://doi.org/10.1016/j.csite.2022.102007
10. Barrau J, Rosell J, Chemisana D, Tadrist L, Ibañez M. Effect of a hybrid jet impingement/micro-channel cooling device on the performance of densely packed PV cells under high concentration. Sol Energy. 2011;85(11):2655–65.
11. Markal B, Varol R. The Effect of Jet Impingement on the Performance of a Photovoltaic Module. 2019;4(1):647–50.
12. Amanlou Y, Tavakoli Hashjin T, Ghobadian B, Najafi G. Air cooling low concentrated photovoltaic/thermal (LCPV/T) solar collector to approach uniform temperature distribution on the PV plate. Appl Therm Eng. 2018;141(May):413–21.
13. Singh D, Chaubey H, Parvez Y, Monga A, Srivastava S. Performance improvement of solar PV module through hybrid cooling system with thermoelectric coolers and phase change material. Sol Energy [Internet]. 2022;241(June):538–52. Available from: https://doi.org/10.1016/j.solener.2022.06.028
14. Sabry M, Lashin A, Al Turkestani M. Experimental and simulation investigations of CPV/TEG hybrid system. J King Saud Univ - Sci [Internet]. 2021;33(2):101321. Available from: https://doi.org/10.1016/j.jksus.2020.101321
15. Barewar SD, Chougule SS, Jadhav J, Biswas S. Synthesis and thermo-physical properties of water-based novel Ag/ZnO hybrid nanofluids. J Therm Anal Calorim [Internet]. 2018;134(3):1493–504. Available from: https://doi.org/10.1007/s10973-018-7883-6

An industrial-scale cement rotary kiln CFD model to characterise altenative fuel combustion profiles.

Antonio Alcaide-Moreno[a], Miguel Ángel Castán-Lascorz[b] and Valter Tavares[c]

[a] Research Centre for Energy Resources and Consumption, Zaragoza, Spain, aalcaide@fcirce.es, CA
[b] Research Centre for Energy Resources and Consumption, Zaragoza, Spain, macastan@fcirce.es
[c] Secil-Outão, Setúbal, Portugal, valter.tavares@secil.pt

Abstract:

This work proposes a Computational Fluid Dynamics (CFD) model of a cement rotary kiln capable of reproducing some 3D effects which cannot be solved by simpler models. Specifically, flight behaviour and falling position of fuels particles are captured. Furthermore, detailed combustion chemistry (devolatilization, char combustion and moisture evaporation) is solved. The 64-meter-long kiln burns a blend of petcoke and Refuse Derived Fuel (RDF). Both were characterized and their properties introduced in the model. The clinker bed was simplified by fixing a temperature profile, a typical approach in literature. Different air excess numbers (λ) were simulated to assess the impact on flight of particles and combustion profiles. The resulting combustion profiles give a valuable input to simpler models in which a much larger and faster set of simulations can be performed, allowing kiln operators to run several different operational scenarios.

Keywords:

Cement kiln; CFD; Refuse-Derived-Fuel; Combustion.

1. Introduction

Cement production is a major source of environmental pollution due to high energy consumption and pollutant emissions [1-3]. To reduce its impact, studies have focused on using waste-derived fuels and biomass, as well as oxy-fuel and oxy-coal combustion technologies. CFD modelling has been used to investigate the co-combustion of different fuels in cement rotary kiln [1-8].

One study [1] found that annulus fuel feeding results in faster devolatilization and char combustion than central tube fuel feeding. Another study [2] aimed to reduce CO_2 emissions by optimizing the combustion process through co-combusting biomass with pulverized coal and showed that oxy-fuel combustion is promising for cement production and some studies [9-11] about oxy-coal combustion in cement rotary kilns revealed that increased combustion efficiency reduces fuel consumption [11] but may lead to a decrease in the calcination time of cement [10]. Also, the amount of NOx produced increases with increasing oxygen content in the primary air [10, 11].

Waste materials have also been used as alternative fuels in cement rotary kilns, due to the depletion of fossil fuels and an increase in their cost [4]. If thermochemical processes in clinker formation want to be modelled, a mathematical model is necessary to understand and quantify the different processes occurring inside clinker bed, particularly the homogeneous processes taking place in the freeboard of the bed of material being processed [3, 4, 6, 7]. The impact of coating layers on the clinker production process within a rotary kiln burning both coal and Refuse Derived Fuel (RDF) was investigated in one study [7], showing that a thin coating profile increases the gas phase temperature in the kiln (due to the insulation effect) reducing free lime content of the final clinker product. Study carried out in [6] showed that co-combustion of coal and RDF can lead to lower gas and clinker temperatures in the sintering zone, which can affect the clinker properties. Regarding RDF properties, [5] provided a careful characterization of its flight and combustion behaviour, useful for accurate computation of co-combustion with coal.

RETROFEED EU H2020 project main objective is to enable the use of an increasingly variable, bio-based and circular feedstock in process industries (in which a cement production industry is included) through the retrofitting of core equipment and the implementation of an advanced monitoring and control system and providing support to the plant operators by means of a Decision Support System (DSS) covering the

production chain. In this paper, we present the first part of the development of a cement rotary kiln model, comprising careful CFD setup and simulations of a co-firing of petroleum coke (petcoke) and RDF. Results are used to obtain characteristic combustion profiles of both fuels along the kiln, to feed a simpler 1-D model which can provide fast near real time results to the DSS.

2. Materials and methods

Figure 1 shows an overview of the modelled kiln.

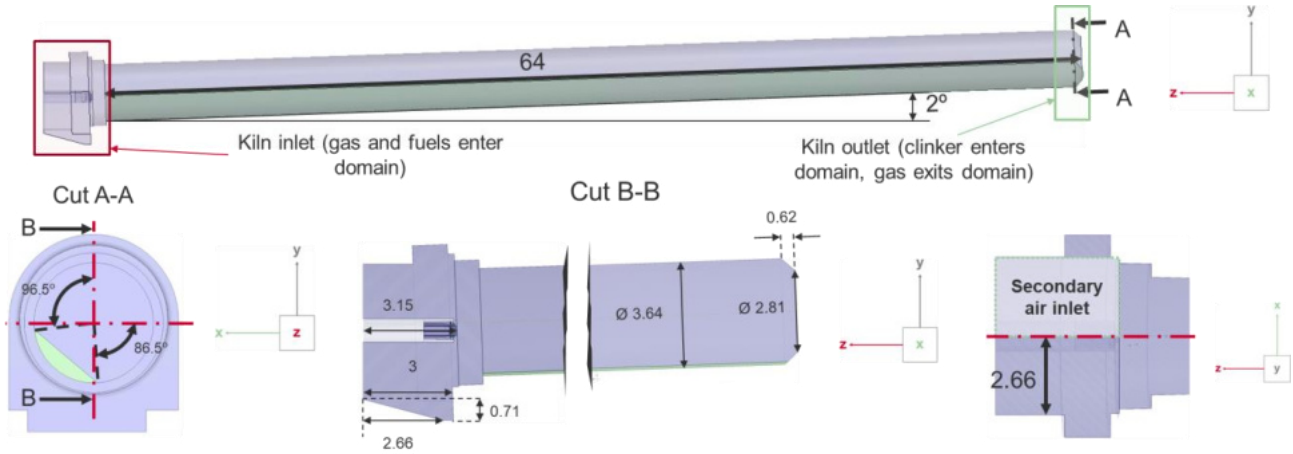

Figure 1. Modelled kiln overview and dimensions. All dimensions in meters. Kiln body is coloured in blue and actually modelled in simulations. Clinker bed is coloured in green, and it is shown only for visualization purposes, since it is not directly modelled in simulations.

2.1. Combustible characterization

In order to properly characterize the employed fuels in the modelled cement kiln, a combination of real measured and literature values was used. Petcoke and RDF are introduced by the burner.

2.1.1. Petcoke

Chemical information about petcoke is gathered in Table 1. For unmeasured values, a literature review was carried out. Properties were selected from the most similar fuel to the actually used. This was assessed by evaluating the Weighted Sum of Errors (WSE) according to Eq. (1), with all the x_i variables in unit basis (for heating values, $x_{i\ real}$ is set to one, given the importance of this term in fuel characterization). The references consulted are: [5, 7, 8, 12, 13, 14, 15, 16, 17].

$$WSE = \sum_{i=1}^{n} \left(\left| \frac{x_{i_{literature}} - x_{i_{real}}}{x_{i_{real}}} \right| \cdot x_{i_{real}} \right) \quad (1)$$

Table 1. Chemical characterisation of employed petcoke.

Parameter		Value	Unit	Source
Ultimate analysis (daf)	Carbon	85.20	%	Measured
	Hydrogen	4.04	%	Measured
	Nitrogen	1.05	%	Measured
	Oxygen	3.12	%	Measured
	Sulfur	6.59	%	Measured
Proximate analysis	Moisture	2.37	%	Measured
	Ash	0.78	%	Measured
	Volatiles	28.8	%	Normalized value of sample 9 from [13]
	Fixed carbon	68.05	%	Normalized value of sample 9 from [13]
LHV		34130	kJ/kg	Measured
Density		1423.5	Kg/m^3	Daqing petcoke from [14]
Specific heat		1000	J/(kg-K)	Average value from [18]

A granulometry analysis was also carried out, which was fitted to a Rosin-Rammler distribution. Results of granulometry are collected in Table 2, and Rosin-Rammler parameters in Table 5.

Table 2. Results from petcoke granulometry.

Diameter range (μm)	Mass fraction in range	Y_d: Mass fraction over diameter range
0.724 - 6.468	0.1	0.9
6.468 - 25.498	0.4	0.5
25.498 - 69.534	0.4	0.1
69.534 - 138.038	0.1	0

2.1.2.Refuse Derived Fuel (RDF)

Before introducing RDF into kiln burner, it passes through a sieve, in which particles with size over 30 mm are removed. After that, metals are also removed from the mix. From the received RDF from different suppliers all along 2020, a statistical analysis was performed to determine the typical share of components in demosite's RDF. Six samples from different suppliers were characterized, shown in Figure 2. It is noticeable the very different nature of each bucket content, confirming the heterogeneous nature of RDF fuels. As for the petcoke, data of RDF coming from demosite analysis is limited and needed to be completed with literature values. Specifically, moisture and ash content, low heating value, as well as elemental composition (ultimate analysis) is available for all the RDF received along 2019 and 2020. RDF received at demosite is divided into five main groups, gathered in Table 3. RDF/CDR is general mix of very different and heterogeneous residues. Plástico e borracha is composed of plastics and undetermined agglomerated particles, having a very high moisture content. Fluff are textiles from different sources. Materiais Impróprios p/Consumo are different residues with a similar aspect to fines as defined by [5]. They are present in demosites silos as a negligible fraction. RDF pellets are present as a low fraction in demosite silos.

From all the suppliers' lorries that arrived at demosite's facilities in 2020, the total quantity of RDF of the different groups described above is gathered in Table 3. The main difference between RDF and petcoke is about the heterogeneity of particles composing it. To properly characterize particles shape and size distribution of RDF is a very challenging task. Together with samples characterization, a literature review was done to fulfil this task. Following [5], it was found that a proper way for defining RDF particles is splitting them into five main groups of particles, namely 3D plastics, 2D foils, paper and cardboard (P&C), textiles and fines (which are unclassifiable particles smaller than ~2mm).

Table 3. RDF types received by demosite in 2020.

RDF type	Sample from Figure 2	Tons received in 2020	Mass fraction over total tons (%)
RDF/CDR	b), d) and g)	26897.4	80.7
Plástico e borracha	e)	902.2	2.7
Fluff	c) and f)	5044.9	15.1
Materiais Impróprios p/Consumo	-	27.3	0.1
RDF pellets	-	443.5	1.3

There is a need to know the quantity of each of the five groups defined by [5] in each of the RDF types from Figure 2, so a proper shape factor and size distribution can be applied to the developed model.

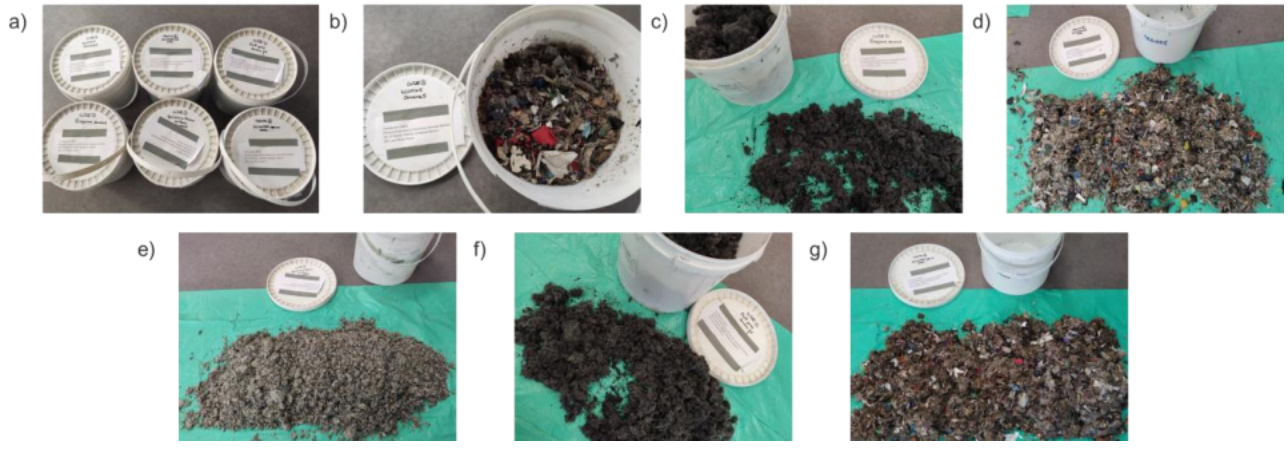

Figure 2. Samples of RDF obtained from different suppliers.

A sieve analysis was carried out for the three main components of RDF mix (RDF/CDR, Plástico e borracha and Fluff), which sum up a 98.6% of the total RDF used in demosite, removing previously particles with a dimension higher than 31.5 mm, which is the procedure followed in demosite. Seven sieves were used, with holes sizes of 100, 63, 45, 31.5, 16, 8 and 3.15 mm. Buckets b), e), d) and g) were sieved. Unfortunately, fluff buckets were not able to be sieved due to continuous sticking and very low density; in this case, size distribution from [5] was used. Results of the size distribution are shown in Table 4. Following the same procedure as for the petcoke, a Rosin-Rammler size distribution was obtained from the above results, obtaining the distribution parameters collected in Table 5 for each sample measured.

Table 4. Size distribution obtained from sieve analysis of RDF.

Sample from Figure 2	Type of RDF	Mass fraction (%) between sizes (mm)[1]			
		31.5-16	16-8	8-3.15	3.15-0
b)	RDF/CDR	66.7	12.4	11.8	9.1
e)	Plástico e borracha	8.4	81.4	6.7	3.5
d)	RDF/CDR	65.1	10.9	14.8	9.2
g)	RDF/CDR	77.3	8.0	8.9	4.8

[1]After removing all >31.5 mm particles and normalizing mass fractions

To properly model the chemical and combustion characteristics of RDF introduced in the developed model, it is still necessary to determine the quantity of each of the five groups given by [5]. Nevertheless, all RDF components were treated as only one, with average values of chemical parameters, due to the high computational cost of computing five different chemical species. A match between the RDF types provided to demosite and those used by [5] was done. By visual inspection, all the six samples were matched to one or various of the types of RDF reported by [5]. These matches are collected in Table 6. Percentages for RDF/CDR are the same as in RDF mixture used by [5], given the visual similarities of both mixtures.

Table 5. Rosin-Rammler distribution parameters of demosite's petcoke and RDF.

Fuel	Sample from Figure 2 (only RDF)	Diameter (μm) $\bar{d}$ (Mean)	Minimum	Maximum	n (size distribution parameter)
RDF	b)	26.0308	3.15	31.5	1.0492
	e)	12.2157	3.15	31.5	2.7679
	d)	25.9332	3.15	31.5	0.9894
	g)	28.0448	3.15	31.5	1.3136
	Fluff[1]	7.00	2.52	9.74	4.06
Petcoke	-	34.193	0.724	138.038	0.944

[1]Assumed as textiles. All data coming from [5].

Table 6. Equivalences between RDF used by demosite and the used by [5].

Demosite's RDF type	Sample from Figure 2	RDF component mass fraction (%) following [5]				
		3D plastics	2D foils	P&C	Textiles	Fines
RDF/CDR	b), d), g)	22	24	19	8	27
Plástico e borracha	e)	100[1]	0	0	0	0
Fluff	c), f)	0	0	0	100	0

[1]Despite this sample seemed to be mainly formed of fines particles, they were all agglomerated forming much larger particles that are alike 3D plastics in terms of geometry/shape.

Applying the mass fractions of Table 3 and Table 6, the resulting RDF mixture that was used in the models (only in terms of shape and physical composition; different chemical and combustion parameters are allowed to be introduced) is the shown on the right side of Figure 3. As for the petcoke, a literature review was carried out to obtain the RDF remaining properties that best fitted the ones used by demosite. It was determined that the main parameter for charaterisation of RDF combustion is moisture. Therefore, the following procedure was performed for selecting the RDF chemical properties to introduce in the models:

- A statistical analysis of all the received RDF samples in demosite during 2020 was carried out.
- To avoid abnormal values of moisture which are not representative of a typical RDF mixture, the three quartiles of the moisture content in RDF samples were obtained.

- Three samples of RDF were selected from the whole set: one sample with a slightly lower moisture than the first quartile one; another with a moisture almost equal to the median, and a third with a slightly higher moisture than the third quartile one.

The selected RDF samples chemical properties, as well as density, specific heat and LHV, are collected in Table 7. These will be named as RDF type 1, type 2 and type 3 in the rest of the paper.

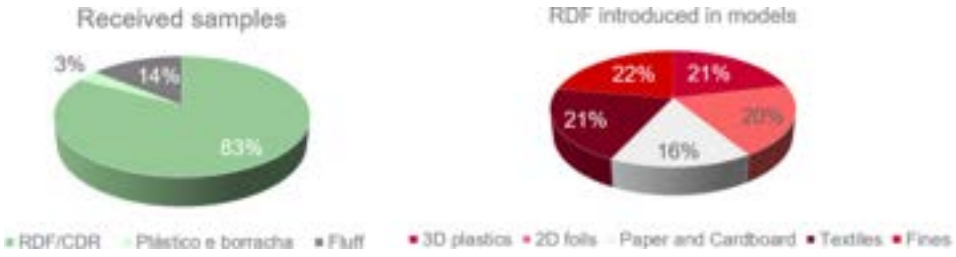

Figure 3. RDF share both in demosite's nomenclature and in reference [5] nomenclature.

Table 7. Chemical characterisation of selected RDF. Ultimate analysis basis: daf.

Parameter		Value 1	Value 2	Value 3	Unit	Source
Ultimate analysis (daf)	Carbon	75.5	49.6	57.00	%	Measured
	Hydrogen	6.67	6.17	7.23	%	Measured
	Nitrogen	1.45	1.45	1.45	%	Measured
	Oxygen	16.38	42.78	34.32	%	Measured
	Sulfur	0.00	0.00	0.00	%	Measured
	Moisture	8.58	14.82	21.06	%	Measured
Proximate analysis	Ash	6.20	210	15.20	%	Measured
	Volatiles	69.48	58.96	58.74	%	Measured
	Fixed carbon	15.74	5.22	5.00	%	Measured
LHV			28611	17345	18299	Measured
Density			852.73	852.73	852.73	Average value from [5]
Specific heat			1810	1810	1810	Average value from [5]

2.2. Simulation setup

A 3D CFD model was developed to capture the complex behaviour of fuel combustion, specifically its flight behaviour, to obtain burning profiles along its length. Three different mixes of fuels, each with two different air excess numbers (λ) were simulated. Geometry shown in Figure 1 was modelled in Ansys Fluent 2020R1. Clinker phase was not meshed nor directly simulated. Instead, it was set as a moving wall boundary condition with a fixed temperature profile. This approach has been also employed by [3]. Other researchers have used a heat flux boundary condition instead of temperature profile [6]. To avoid the prohibitive computational cost of simulating the whole burner together with the kiln cylinder, simulations of only the burner were performed, to obtain the velocity and turbulence profiles at burner outlet, to be used as boundary conditions of the whole kiln model.

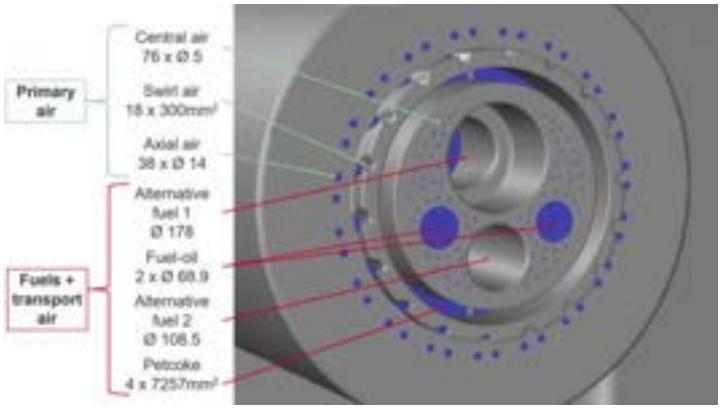

Figure 4. Modelled burner for CFD simulations.

Figure 4 shows the modelled burner. Central air holes were not meshed nor simulated, since they are so small that computational cost of a proper mesh is prohibitive. As the manufacturer of the burner ensures that 1% of flow goes through these holes, that condition was used for the whole kiln simulations. A set of

simulations of the burner alone were performed, to determine the mass flow share for each boundary. In total, five simulations were run, starting with a primary air input of 5 m/s air, and increasing in 5 by 5 steps up to 25 m/s. For all of them, the resulting mass flow share is the one collected in Table 8. Apart from that, it was also checked that, for all cases, the resulting air flow at the swirl outlet has a 0.86/1 relation in terms of tangential/axial flow direction.

Table 8. Mass flow share for each of the three primary air inlets in CFD model.

Boundary	Mass flow share (%)
Axial air inlet	63
Central air inlet	1
Swirl air inlet	36

Since primary air mass flow is fixed in the kiln to 2.83 kg/s, a simulation with the burner model was used to obtain the quantitative values of the k and ε parameters for the turbulence model in axial and swirl inlets, introduced as boundary conditions in the whole kiln model. The results are gathered in Table 9.

Table 9. Turbulence parameters for primary air inlets obtained from simulation with fixed primary air mass flow input.

Boundary	k (m^2/s^2)	ε (m^2/s^3)
Axial air inlet	132.3	896648
Swirl air inlet	243.2	1979220

Table 10 gathers some data about the resulting meshes. A detail of the whole kiln model mesh can be seen in Figure 5. Table 11 shows the type of each boundary of the kiln CFD model.

Table 10. Details of the meshes of CFD models.

Parameter	Burner model	Whole kiln model
Type of cells	Hexahedral	Hybrid polyhedral-hexahedral
Number of cells	2.99 M	2.29 M
Minimum orthogonal quality	0.10	0.27
Maximum aspect ratio	33.45	42.23

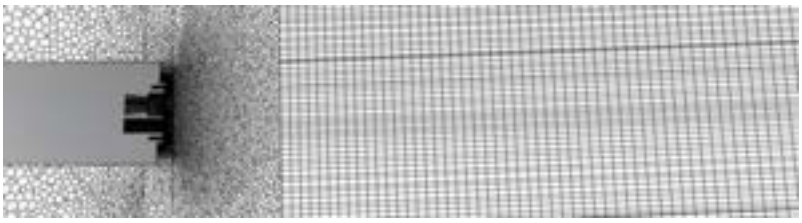

Figure 5. Example of mesh in axial cut plane of whole kiln mesh.

Table 11. Boundary types in CFD kiln model.

Boundary	Name in Figure 4 (only burner inlets)	Boundary
Axial air inlet	Axial air	Mass flow inlet
Central air inlet	Central air	Mass flow inlet
Swirl air inlet	Swirl air	Mass flow inlet
Petcoke inlet	Petcoke	Mass flow inlet
RDF inlet	Alternative fuel 1	Mass flow inlet
Secondary air inlet	-	Mass flow inlet
Outlet	-	Pressure outlet
Burner walls	-	Adiabatic wall
Clinker-gas contact interphase	-	Moving fixed-temperature wall

Details of boundary conditions are gathered in Appendix A: detailed boundary conditions in CFD simulations. Mass, momentum and energy were solved with a Reynolds Averaged Navier Stokes (RANS) approach. Turbulence was solved with the realizable κ–ε model with enhanced wall treatment [19]. Radiation is solved using the Discrete Ordinates model. Chemistry is solved with the species transport model, with one volatiles

species for petcoke and another for RDF. Turbulence-chemistry interaction was solved with the eddy-dissipation model [7]. Particles flight and combustion behaviour were solved with the Discrete Phase Model (DPM) ([3, 6, 7], and similar to the used in [8]). One injection for petcoke and five for RDF were used, with size distribution according to Table 5. Particles devolatilization and char combustion models parameters, as well as water droplet mass transfer model (drying of fuels) and parameters, are collected in Table 22. All values for petcoke and water are obtained from [20], whereas those for RDF come from [5].

Table 12. Combustion modelling parameters for discrete phase model in CFD simulations.

Parameter		Material		
		Petcoke particle	RDF particle	Water droplet
Vaporization temperature (K)		550	550	-
Devolatilization	Model	Single rate		-
	Preexponential factor (s^{-1})	9.59e+04	2.47e+06	-
	Activation energy (J/kgmol)	8.26e+07	1.065e+08	-
Combustion	Model	Kinetics/ diffusion limited		-
	Rate constant	5e-12	5e-12	-
	Preexponential factor (s^{-1})	0.01	0.00204	-
	Activation energy (J/kgmol)	1.05e+08	7.9423e+07	-
Thermolysis	Model	-	-	Single rate
	Preexponential factor (s^{-1})	-	-	5.13e+06
	Activation energy (J/kgmol)	-	-	8.79e+07

3. Results and discussion

One kiln operating point corresponding to typical values was simulated with values shown in Table 13.

Table 13. Common boundary conditions of inlets in CFD simulations.

Parameter	Value	Unit
Primary air flow (divided according to Table 8)	2.83	Kg/s
Petcoke transport air flow	1.17	Kg/s
RDF transport air flow	0.75	Kg/s
Petcoke particles flow	0.61	Kg/s
RDF particles flow (divided according to Figure 3)	1.94	Kg/s
Primary air temperature	49	ºC
Petcoke air and particles temperature	61	ºC
RDF air and particles temperature	34	ºC
Secondary air temperature	916	ºC

Two different excess air numbers were simulated for each RDF type, as shown in Table 14.

As a representative case, some detailed results of temperature and particle flight and reaction behaviour are shown from CFD simulation 1-1. Figure 6 shows the temperature contour of simulation 1-1. As can be seen, temperature increases due to combustion relatively far from burner, unlike traditional petcoke and low-share RDF quantities (such as those reported by [3] and [7]). This is due to the poor combustion quality of RDF, displacing the flame formation downwards. RDF's higher size and ash fraction compared to petcoke can explain this result. It can be also seen that temperature increase starts from the bottom of kiln (i.e., clinker surface), and shows a high peak of temperature in that zone. This is due to the flight of RDF particles (as will be seen in next figures): given their high size (thus, low burning rate) and non-spherical shape, they tend to

fall onto clinker surface instead of being blown away by air. This result is in agreement with the reported by [3, 6, 7]. After the first third of kiln length (~20m), flame profile widens and effectively heats homogeneously the whole domain.

Table 14. Performed CFD simulations boundary conditions.

Simulation	RDF type from Table 7	RDF power share (%)	λ
1-1	1	72.90	1.1
1-2	1	72.90	1.4
2-1	2	61.99	1.1
2-2	2	61.99	1.4
3-1	3	63.25	1.1
3-2	3	63.25	1.4

To explain the above results, Figure 7 shows the particle tracking of each type of particle introduced through the burner up to the half of kiln length. As it can be seen, only petcoke and fines (which are the smallest RDF particles) are blown by air throughout the kiln length. The rest of particles fall onto clinker bed soon, where they start to burn. Though fines are blown by air, they start burning in the same location than the rest of RDF particles. This is due to their low combustion quality (they need very high temperatures to start the reaction) in comparison with petcoke. The burning location of RDF particles explain the peak temperature found at clinker bed surface in Figure 6. These particles flight trajectories of RDF particles also found by [6].

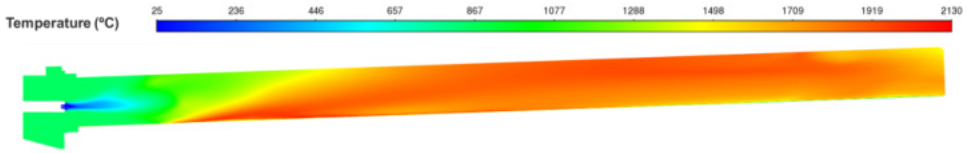

Figure 6. Temperature contours from CFD simulation in a longitudinal plane contour.

To obtain the combustion profiles from the simulations, the CFD domain was split into 64 axial slices, in which the integral of petcoke and RDF volatiles and burnout (char oxidation), as well as water evaporated from particles, was obtained. Results are shown in Figure 8.

Some general comments apply for all the simulations results:

- Petcoke devolatilization and fixed carbon burning show a well-shaped Gauss bell distribution.
- Dried water profiles show two humps. The first coincides with the higher petcoke volatiles and fixed carbon release; the second hump, higher than the first, takes place at around 10 meters, where high temperatures appear near clinker surface.
- Higher air excess show wider distributions, which reflect the higher drag force and flow speed suffered by particles, which tend to spread out their burning locations.
- Very low RDF char is burned in gas phase for all the simulated cases. This results in a burning after falling onto clinker surface, which CFD is unable to capture and has to be taken into account in some way if an accurate modelling is intended, as [3] and [6] affirm.

Something very noticeable is that, for RDF types 1 and 2, burning profiles are very similar regardless the excess air used; on the other hand, RDF type 3 shows large differences in petcoke combustion between the two air excesses simulated, but not on RDF combustion or evaporation. This may be due to the poor resolution of the discretization employed; a higher number of slices may provide less discrepancies between cases. It can be seen that the totality of petcoke combustible matter burns within gas phase in the first 10 meters of the kiln, confirming its very good burning behaviour with respect to RDF. An interesting result is that, in all the cases, RDF power is released earlier in the case with lower air excess, reflecting less drag force and speed of particles.

Another interesting result is that all RDF volatiles are released a bit later than half of the kiln (~40 m). All the RDF char that combusts in gas phase (which is very low in general) also does it mostly in the first 40 meters of the kiln. It can be also seen that, in all the cases, RDF volatiles start to be released earlier and end later in the case with λ=1.4 than in the case with λ=1.1. This may be due to the higher oxygen availability for RDF in the first part of the kiln in the case with λ=1.4, but less gas temperature is achieved (more mass of air is heated), so reaction is slower than in the case with λ=1.1. On the other hand, the opposite happens to RDF

char combustion. It starts later in the case with more excess air. A higher char combustion can be achieved in gas phase when increasing excess air number, particularly in the RDF type 3 case.

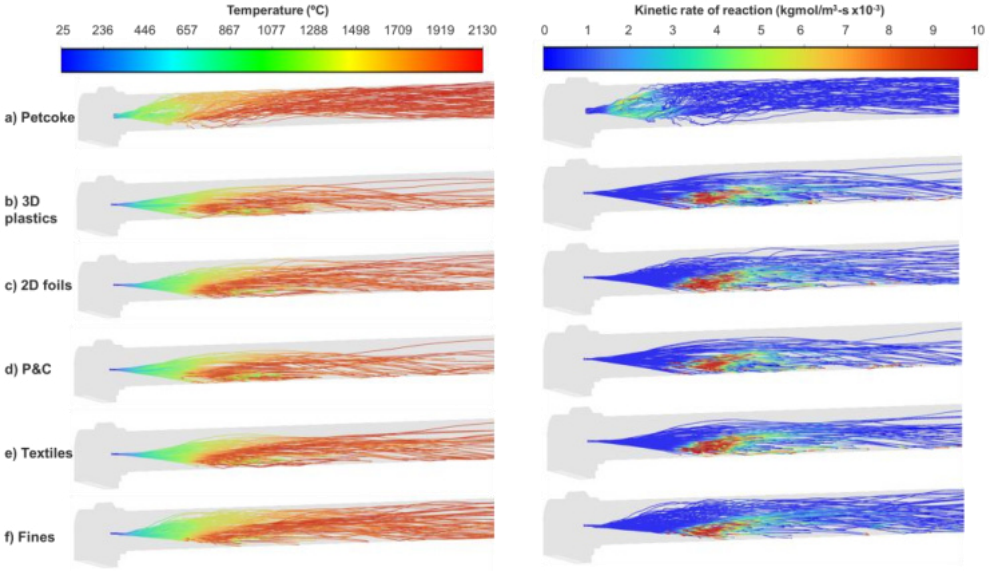

Figure 7. Trajectories coloured by temperature (left) and kinetic rate of reaction (right) of the different modelled particles within CFD, from simulation 1-1.

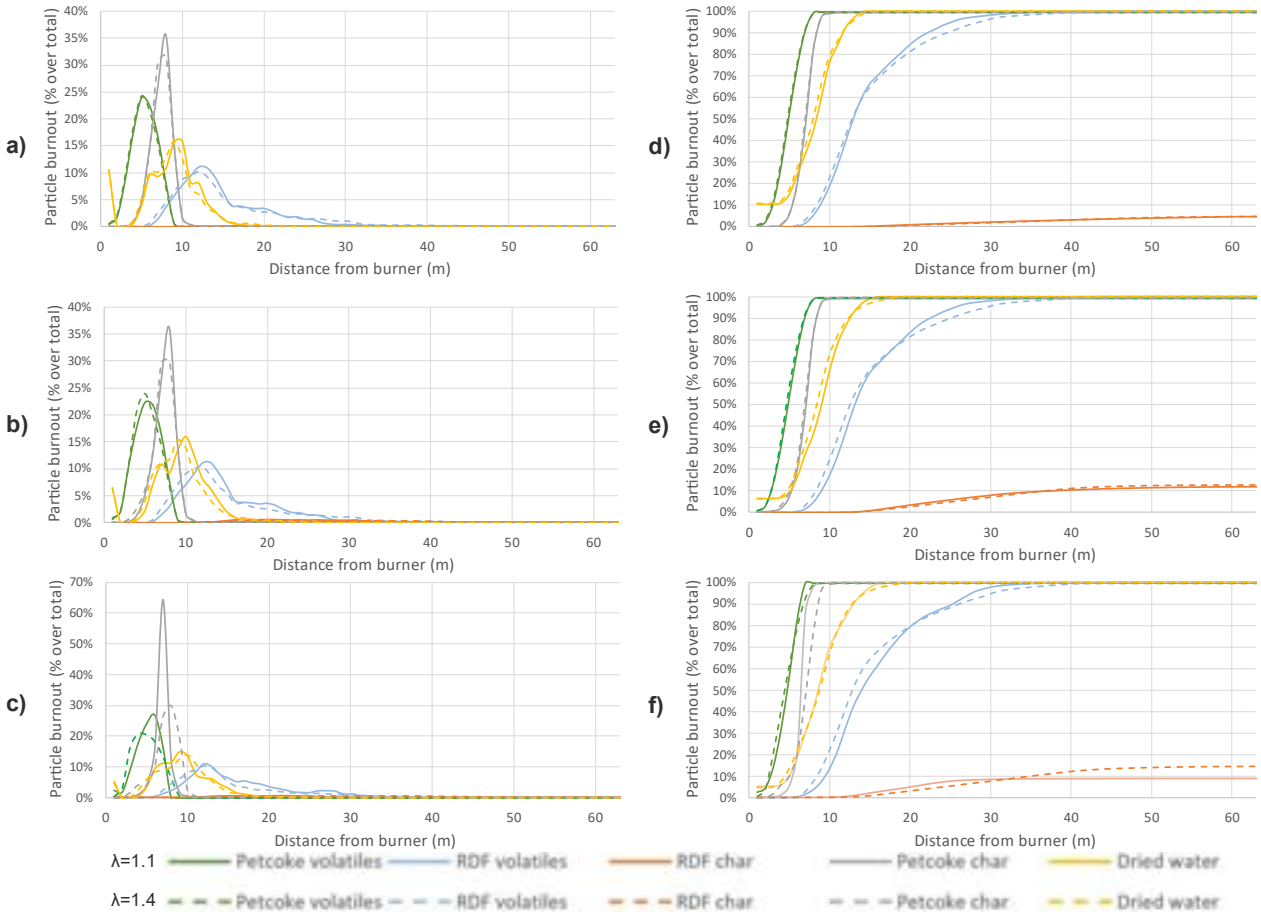

Figure 8. Burning and evaporation profiles from CFD simulations. Left: per slice profile. Right: histogram of profile. a), d) RDF type 1; b), e) RDF type 2; c), f) RDF type 3.

4. Conclusions

From the performed CFD study, some conclusions can be extracted:

- Combustion temperature increases far from the burner due to poor combustion quality of RDF, which displaces the flame formation downwards.
- Temperature increase starts from the bottom of kiln, with a high peak of temperature in that zone due to the flight of RDF particles falling onto clinker surface.
- Only petcoke and smallest RDF particles are blown by air throughout the kiln length, while the rest of particles fall onto clinker bed more or less soon, where they start to burn.
- Petcoke devolatilization and fixed carbon burning show a well-shaped Gauss bell distribution.
- Very low RDF char is burned in gas phase for all the simulated cases, resulting in burning after falling onto clinker surface.
- Burning profiles are very similar for RDF types 1 and 2 regardless of excess air used, while RDF type 3 shows large differences in petcoke combustion between two air excesses simulated.
- All petcoke combustible matter burns within gas phase in the first 10 meters of the kiln, confirming its very good burning behaviour with respect to RDF.
- All RDF volatiles are released a bit later than half of the kiln, and RDF char that combusts in gas phase also does it mostly in the first half of the kiln.
- RDF volatiles start to be released earlier and end later in the case with higher air excess.
- A higher char combustion can be achieved in gas phase when increasing excess air number, particularly in the RDF type 3 case.
- CFD seems to be a useful tool for understanding the combustion behaviour, as well as temperature profiles in the complex processes that take place inside a cement kiln which, in practice, cannot be measured in experiments due to high quantities of dust, kiln rotation and hard temperature conditions. This allows to understand and optimize their functioning.

5. Funding

This project received funding from the European Union's Horizon 2020 research and innovation programme under grant agreement No. 869939. https://retrofeed.eu/ (accessed on 11 March 2023).

References

[1] W. K. Hiromi Ariyaratne, A. Malagalage, M. C. Melaaen and L.-A. Tokheim, "CFD modelling of meat and bone meal combustion in a cement rotary kiln – Investigation of fuel particle size and fuel feeding position impacts," Chemical Engineering Science, vol. 123, no. 17, pp. 596-608, 2015.

[2] H. Mikulčić, D. Cerinski, J. Baleta and X. Wang, "Improving Pulverized Coal and Biomass Co-Combustion in a Cement Rotary Kiln by Computational Fluid Dynamics," Chemical Engineering & Technology, vol. 42, no. 12, pp. 2539-2545, 2019.

[3] B. Liedmann, S. Wirtz, V. Scherer and B. Krüger, "Numerical Study on the Influence of Operational Settings on Refuse Derived Fuel Co-firing in Cement Rotary Kilns," Energy Procedia, vol. 120, pp. 254-261, 2017.

[4] B.-J. R. M. Bisulandu and F. Marias, "Modeling of the Thermochemical Conversion of Biomass in Cement Rotary Kiln," Waste and Biomass Valorization, vol. 12, no. 2, pp. 1005-1024, 2021.

[5] B. Liedmann, W. Arnold, B. Krüger, A. Becker, S. Krusch, S. Wirtz and V. Scherer, "An approach to model the thermal conversion and flight behaviour of Refuse Derived Fuel," Fuel, vol. 200, pp. 252-271, 2017.

[6] C. Pieper, B. Liedmann, S. Wirtz, V. Scherer, N. Bodendiek and S. Schaefer, "Interaction of the combustion of refuse derived fuel with the clinker bed in rotary cement kilns: A numerical study," Fuel, no. 117048, 2020.

[7] C. Pieper, S. Wirtz, S. Schaefer and V. Scherer, "Numerical investigation of the impact of coating layers on RDF combustion and clinker properties in rotary cement kilns," Fuel, no. 283, 1 January 2021.

[8] M. Nakhaei, H. Wu, D. Grévain, L. Jensen, P. Glarborg and K. Dam-Johansen, "CPFD simulation of petcoke and SRF co–firing in a full–scale cement calciner," Fuel Processing Technology, no. 196, 2019.

[9] M. Ditaranto and J. Bakken, "Study of a full scale oxy-fuel cement rotary kiln," International Journal of Greenhouse Gas Control, vol. 83, pp. 166-175, 2019.

[10] Z. Ying, C. Lixin, L. Qiao, C. Guozan and Y. Xuchu, "Simulating the Process of Oxy-Fuel Combustion in the Sintering Zone of a Rotary Kiln to Predict Temperature, Burnout, Flame Parameters and the Yield of Nitrogen Oxides," Chemistry and Technology of Fuels and Oils, vol. 54, pp. 650-660, 2018.

[11] M. Wang, B. Liao, Y. Liu, S. Wang, S. Qing and A. Zhang, "Numerical simulation of oxy-coal combustion in a rotary cement kiln," Applied Thermal Engineering, vol. 103, pp. 491-500, 2016.

[12] G. Fuyan, L. Jianzhong, W. Chuancheng and Z. K. C. Junhu, “Effects of the physical and chemical properties of petroleum coke on its slurryability,” Petroleum Science, vol. 9, pp. 251-256, 2012.

[13] P. Ghetti, “DTG combustion behaviour of coal. Correlations with proximate and ultimate analysis data.,” Fuel, pp. 636-639, May 1986.

[14] Q. He, R. Wang, W. Wang, R. Xu and H. Baixing, “Effect of particle size distribution of petroleum coke on the properties of petroleum coke-oil slurry,” Fuel, no. 90, pp. 2896-2901, 2011.

[15] K. Jayaraman and I. Gokalp, “Gasification characteristics of petcoke and coal blended petcoke using thermogravimetry and mass spectrometry analysis,” Applied Thermal Engineering, vol. 80, pp. 10-19, 2015.

[16] J. Parikh, S. A. Channiwala and G. K. Ghosal, “A correlation for calculating HHV from proximate analysis of solid fuels,” Fuel, vol. 84, pp. 487-494, 2005.

[17] S. J. Yoon, Y.-C. Choi, S.-H. Lee and J.-G. Lee, “Thermogravimetric study of coal and petroleum coke for co-gasification,” Korean Journal of Chemical Engineering, vol. 24, pp. 512-517, 2007.

[18] M. Long, J. Sheng, T. Liu, D. Chen, Y. Yang, S. Gong and C. Chen, “Thermo-Physical Properties of Petroleum Coke during Calcining Graphitization Process,” in Drying, Roasting, and Calcining of Minerals, TMS (The Minerals, Metals & Materials Society), 2015, pp. 193-199.

[19] H. F. M. Elattar, Flame Simulation in Rotary Kilns Using Computational Fluid Dynamics (PhD thesis), Magdeburg: Otto Von Guericke Universität Magdeburg, 2011.

[20] M. N. Pedersen, Co-firing of Alternative Fuels in Cement Kiln Burners (PhD thesis), Technical University of Denmark, 2018.

[21] S. Chen, J. Wang and Q. Li, “Composite Design of Low Thermal Conductivity Mullite Brick for Application to Cement Kiln,” International Conference on Materials Applications and Engineering 2017 (ICMAE2017) , vol. 142, 2018.

[22] Y. A. Çengel and A. J. Ghajar, Heat and Mass Transfer. Fundamentals & Applications, New York, NY: McGraw-Hill Education, 2015.

[23] C. Lou, H.-C. Zhou, P.-F. Yu and Z.-W. Jiang, “Measurements of the flame emissivity and radiative properties of particulate medium in pulverized-coal-fired boiler furnaces by image processing of visible radiation,” Proceedings of the combustion institute, no. 31, pp. 2771-2778, 2007.

Appendix A: detailed boundary conditions in CFD simulations

Table A.1. Clinker-gas contact interphase boundary conditions.

Physics	Parameter	Value	Unit	Source
Momentum	Moving wall direction	From kiln outlet to kiln inlet	-	-
	Translational speed	0.02262	m/s	Calculation from raw meal input, kiln cross-sectional area and estimated kiln fill degree
Thermal	Condition	Fixed temperature, Eq. (A.2)	K	Curve fitting from demosite’s measurements in six different points of clinker surface
	Thermal conductivity	0.33	W/m-K	[6]
Radiation	Internal emissivity	0.8	-	[6]
DPM	Boundary condition	Trap	-	From observations

[1]x: axial direction of kiln cylinder, taking x=0 at the cylinder end near to kiln inlet

Applied fixed temperature profile is given by Eq. (A.2).

$$T(K) = 3.1822 \cdot 10^{-4}\, x^4 + 3.5854 \cdot 10^{-2}\, x^3 + 0.78137\, x^2 - 5.3164x + 1502.7 \qquad (A.2)$$

Table A.2. Kiln cylinder walls boundary conditions.

Physics	Parameter	Value	Unit	Source
Momentum	Wall motion	Stationary wall	-	-
Thermal	Condition	Convection	-	-
	Heat transfer coefficient	10	W/m2-	Typical value for natural convection

			K	
	Free Stream Temperature	27	ºC	Estimated mean temperature values along a year
	Wall thickness	0.2	m	Estimation from SECIL
	Wall density	2650	Kg/m3	[21]
Radiation	Wall specific heat	835	J/kg-K	Chrome brick, from [22] table A-8
DPM	Wall thermal conductivity	2.74	W/m-K	[21]

Table A.3. Burner and hood walls boundary conditions.

Physics	Parameter	Value	Unit	Source
Momentum	Wall motion	Stationary wall	-	-
Thermal	Condition	Heat flux	-	-
	Heat flux	0	W/m^2	Negligible participation in convection and radiation heat transfer
Radiation	Internal emissivity	0.6	-	Typical value for aluminium, from [22] table A-18
DPM	Boundary condition	Reflect	-	From observations

Table A.4. Thermophysical and radiation properties of materials employed in CFD simulations.

Material	Parameter	Value	Unit	Source
Gas mixture	Specific heat	Mixing law	-	[5]
	Thermal conductivity	Mass weighted mixing law	-	-
	Viscosity	Mass weighted mixing law	-	[5]
	Absorption coefficient	WSGGM method	-	[7], [5]
	Scattering coefficient	0.54	-	Derived from [23]
Petcoke particle	Emissivity	0.7	-	[23]
	Scattering coefficient	0.54	-	[23]
RDF particle	Emissivity	0.877	-	[5]
	Scattering coefficient	0.54	-	[23]

Optimization of a Horizontal Entrained Flow Plasma Gasification Test Rig through CFD-Simulation

Sebastian Bastek[a], Mariam Fahmy[a], Sebastian Wilhelm[a], Sebastian Fendt[a] and Hartmut Spliethoff[a]

[a] Chair of Energy Systems, Technical University of Munich, Garching, Germany,
sebastian.bastek@tum.de, CA

Abstract:

Plasma gasification is a promising method for the thermochemical conversion of biomass and wastes into high quality syngas with lower tar content and higher energy densities compared to conventional processes. This study aims to optimize a horizontal tubular entrained flow plasma gasification test rig which should produce plasma pyrolysis chars. Therefore, mixing of fuel particles in the plasma zone as indicated by the respective particle temperatures needs to be improved. For that a couple of configurations were investigated by a CFD simulation in Ansys Fluent: First, the plasma torch gas outlet diameter of 1mm was doubled to reduce plasma gas velocities. Then, several vertical fuel particle inlet tubes were integrated at different distances from the plasma torch nozzle (5, 15, 25 and 35mm) to insert fuel particles more directly into the plasma zone. The wider nozzle outlet diameter resulted in higher particle temperatures, lower velocities and better convergence. From the different particle tube configurations, the closest to the plasma inlet, resulted in the highest average particle temperatures, residence times and better distribution in the reactor than the other cases. It was subsequently concluded that the optimal configuration for enhanced particle heating and mixing shall be designed with a 2mm wide diameter and a 49mm long tube that is 5 mm away from the torch outlet.

Keywords:

CFD; Plasma gasification; Entrained flow gasification; Biomass.

1. Introduction

The demand for biomass as a renewable energy source for heat and energy production as well as a source of sustainable carbon for the chemicals and materials industry is expected to increase strongly over the next decades [1]. Therefore, conversion processes are needed which achieve high efficiencies in terms of their feedstock utilization. One approach for the conversion of biomass for the material use of its inherent carbon is gasification. Traditional gasification processes are often autothermal or require the combustion of part of the biomass feedstock to provide the energy required for the gasification and pyrolysis reactions. This leads to a loss of carbon in the form of CO_2 which should be avoided for maximum carbon conversion into syngas. A possible solution is the operation of the gasification process with plasma assistance. In this way, the energy for gasification and pyrolysis reactions is provided through electricity input and higher quality syngas at higher carbon efficiencies can be produced. One type of such gasifier which looks promising based on first process simulations in Aspen Plus is a plasma-assisted entrained flow gasifier for steam gasification of pulverized biomass input [2].

While there has been significant progress on understanding entrained flow gasification of pulverized fuels under conventional gasification conditions [3, 4], plasma gasification under entrained flow conditions has only seen very limited research activity so far. Vishwajeet et al [5] have examined the gasification of sewage sludge in plasma-assisted entrained flow gasification conditions using a nitrogen plasma torch in a vertical drop tube reactor. The focus was placed on achieving a proof of concept. Detailed reaction mechanisms such as, e.g., char burnout behaviour and char reactivity were not studied. As these characteristics are essential for modelling of plasma-assisted entrained flow gasification and, therefore, need to be in place for the simulation-based design of these gasifiers, research into char properties after plasma entrained flow conditions is necessary. For this purpose, the authors have designed a horizontal entrained flow plasma gasification test rig to produce plasma pyrolysis chars for examination in thermogravimetric analysers and characterization. The design of the test rig consists of a horizontal water-cooled tubular reactor with a concentrically positioned DC plasma torch as shown in Figure 1. Pulverized biomass is fed from the top via a ceramic tube into the plasma zone created by the plasma torch. After leaving the plasma zone, the produced char falls onto a solids extraction tool which can be removed from the tubular reactor after the experiments are finished. This makes it possible to study char characteristics of this char created under plasma entrained flow conditions.

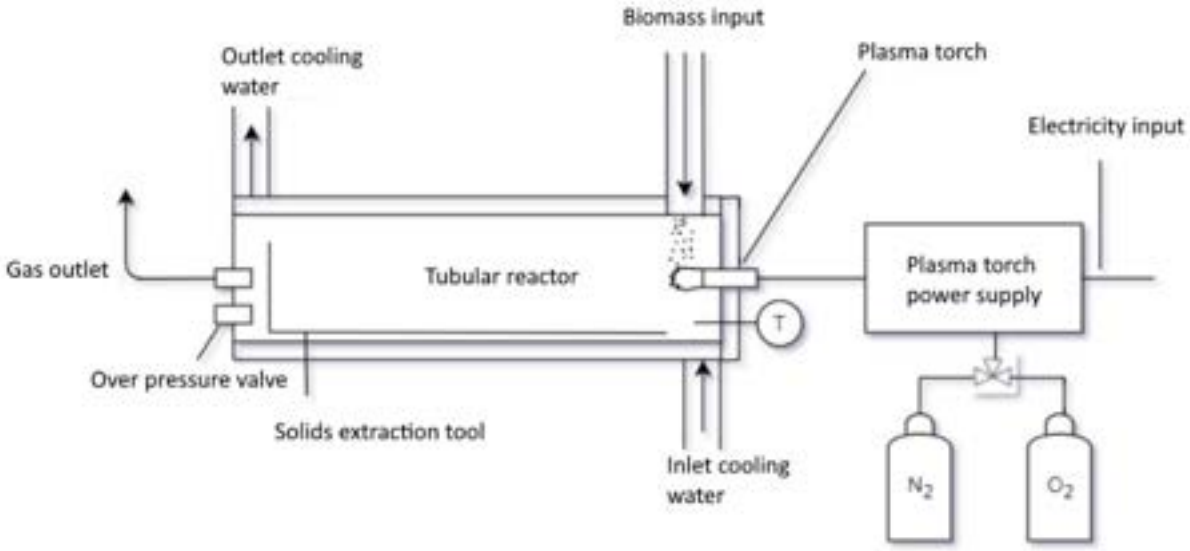

Figure 1. Schematic overview of the tubular plasma gasification test rig for biomass conversion into char under plasma-assisted entrained flow conditions.

In order to produce the highest quality plasma pyrolysis chars, the pulverized fuel needs to mix as well as possible with the plasma zone of the plasma torch resulting in very high heating rates and as high as possible particle temperatures. This leads to two research questions which this research aimed at through computational fluid dynamics simulation of the reactor setup: How can the reactor be modified to improve particle mixing and heating in the plasma zone? At which distance from the plasma inlet should particles be injected to maximize heat transfer to the fuel particles?

Therefore, this research not only helps optimizing the design of the plasma gasification test rig, it also adds to the existing literature on CFD for plasma gasification/pyrolysis because existing CFD research in this area has mainly focussed on fixed bed, downdraft or updraft plasma gasifiers instead of entrained flow reactor setups [6–9].

To answer the research questions, the following cases were simulated in Ansys Fluent:

- Case 0: **1 mm** plasma torch nozzle diameter, free vertical particle drop 40 mm from torch outlet
- Case 1: **2 mm** plasma torch nozzle diameter, free vertical particle drop 40 mm from torch outlet
- Case 2: 2 mm plasma torch nozzle diameter, vertical particle inlet tube **5 mm** from plasma torch outlet
- Case 3: 2 mm plasma torch nozzle diameter, vertical particle inlet tube **15 mm** from torch outlet
- Case 4: 2 mm plasma torch nozzle diameter, vertical particle inlet tube **25 mm** from torch outlet
- Case 5: 2 mm plasma torch nozzle diameter, vertical particle inlet tube **35 mm** from torch outlet

Section 2 presents an overview of the methodology behind the simulations for these cases. Section 3 details how the geometry for the model was generated and presents the mesh independence study. Section 4 goes into detail on the simulation results for the different cases by presenting the results and discussing them. Section 5 finishes with the conclusion and outlook into future research opportunities.

2. CFD modelling methodology

The CFD simulation of the reactor was performed using Ansys Fluent. The CFD model simulates the plasma gas, in this case air, as a single high temperature fluid neglecting species created by the plasma through ionization, dissociation, etc. The pulverized biomass particles, in this case torrefied wood particles, are simulated with the help of a discrete phase model with the Eulerian-Lagrangian approach [10]. Ionization and dissociation of air in the single fluid model is covered with the help of adjusted plasma air properties. Chemical reactions involving the torrefied wood particles have been neglected as the major focus of the created model is on assessing the mixing behaviour and heat transfer between the hot plasma gas zone and the particles.

2.1. Air plasma properties

The adjusted plasma air properties are retrieved from curve fits calculated by Gupta et al. [11] for a temperature range of 1,000-30,000 K. The study considers 11 species while neglecting real-gas interactions and radiation effects. The plasma torch manual [12] specifies the power range as well as the temperatures of the arc plasma. At an operating temperature of $T_P = \sim 17 \cdot 10^3\ K$, the gas composition varies drastically from undissociated air. Table 1 compares the mole fractions of species at temperatures lower than 1,000 K, 5,000 K and 17,000 K.

Table 1. Mole (X) and mass (w) fractions of air components at atmospheric pressure for different temperatures, adapted from [13].

		N_2	O_2	N	O	N^+	O^+	e^-
Temperature /K	M /g/mol	28.01	32.00	14.01	16.00	14.01	16.00	5.49e-4
<1,000	X	0.78	0.21					
	w	0.76	0.23					
5,000	X			0.23	0.08	0.29	0.08	0.03
	w			0.34	0.14	0.43	0.10	1.63e-6
17,000	X			0.09	0.03	0.35	0.09	0.45
	w			0.16	0.06	0.61	0.17	3.07e-5

As the mole fractions were read off a logarithmic diagram provided by Selle [13], the values remain somewhat inaccurate. This realization arose when later computing the ionization degree using three different equations from [14]:

$$\alpha_i = \frac{1-X_A}{1+X_A} = \frac{X_{A+}}{1-X_{A+}} = \frac{X_{e-}}{1-X_{e-}} \tag{1}$$

where x_A, x_{A+} and x_{e-} denote the molar fraction of (dissociated) neutral species, ionized species and electrons, respectively. This yields $\alpha_i \in [77\%, 83\%]$ and thus a maximum deviation of 5.9%, which was accepted for further calculations.

In the material dialogue box in Ansys Fluent, properties can be adapted in many ways: Aside from the defined gas models (ideal gas, real gas, kinetic theory...), there are user-defined options as well. To transfer the curves from Gupta et al. [11] to Fluent, two of those were tried out; the first being the piecewise polynomial and the second the user defined function (UDF). The UDF option resulted in a much less stable simulation, forcing the authors to go for the piecewise polynomial option for specific heat capacity, thermal conductivity, and viscosity. Since Gupta et al. [11] provide no graph for the density, it had to be computed.

2.2. Model choice and assumptions

As the pressure-based solver is more suited for thermochemical conversion (e.g., combustion, …) cases and offers many advantages over the density-based solver, it was chosen and combined with the energy and discrete phase models for all simulations of the plasma entrained flow gasification test rig. The flow was assumed to be steady while particles are unsteady by default. The model has also only been tested using inert wood particles, which by definition do not exchange mass with the gas and follow the laws of inert heating and cooling [15]. Since this mass exchange is the main source of energy and momentum transfer, the study deals with a one-way coupling case and so, no interaction with continuous phase was needed. Instead, the Discrete Random Walk Model was activated for all cases because it produces much more realistic tracks. As the turbulence at the wall boundary are of less interest, the k-ω-model and its related SST-models were excluded for this study. Instead, the standard k-ϵ-model was selected, for it is better at modelling the bulk phase than the former and simpler than the latter. This model choice is also supported by Bobzin et al. [16], who examine an argon arc plasma spray using Ansys-CFX and classify it as a "valid alternative". There, the k-ω-model yields fairly different profiles of the arc plasma than all other investigated models. As a simplification, radiation effects are not considered as the focus of this simulation is mainly on the mixing behaviour of fuel particles and plasma zone as indicated by particle temperatures.

2.3. Boundary conditions

This section explains which boundary conditions as well as particle variables were set for the simulations. An overview of all values can be found in Table 2, Table 3, and Table 4.

2.3.1. Inlet

To determine the mass flow rate, the energy equation (2) was applied to the plasma torch represented as an electric heater and subsequent nozzle as depicted in Figure 2:

$$\frac{d}{dt}(U + K + \phi) = \sum_j \dot{m}_j \left(h_j + k_j + \phi_j\right) + \sum_j \dot{Q}_j + \dot{W}_V + \dot{W}_S \tag{2}$$

where the upper case variables U, K and ϕ denote the internal, kinetic and potential energy, respectively, while the equivalent lower case letters signify their specific forms for the different components j. h_j represents the specific enthalpy of component j. Furthermore $\dot{m}$ stands for the mass flow rate, $\dot{Q}$ for the heat flux and $\dot{W}_V + \dot{W}_S$ (volume change and shaft work) for the technical work.

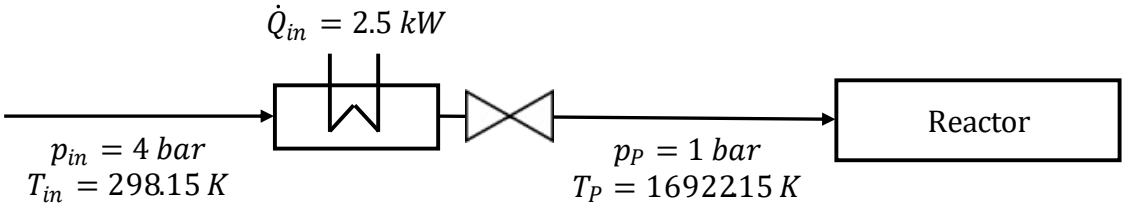

Figure 2. Simplified representation of plasma torch as thermodynamic process leading to plasma inlet: Temperature T and pressure p before (in) and after (P) power input $\dot{Q}_{in}$.

The subscripts in and P denote the states at the inlet of the heater and the outlet of the plasma torch, respectively. Compressed air enters at an operating pressure of $p_{in} = 4\,bar$ [12] and an assumed temperature of $T_{in} = 300K$. It then flows isobarically through the plasma torch that is connected to a power supply and is expanded after the plasma torch, which is illustrated as a nozzle in Figure 2. Through this abrupt (ideally isentropic) expansion, the pressure is reduced back to atmospheric pressure ($p_P \approx 1bar$). According to the torch manual [12], the plasma zone is expected to enter the reactor at a core temperature of $T_P = 16922.15K$. For the incoming specific enthalpy, Bernoulli's equation for compressible ideal gases was used without the kinetic term ($h_{in} = c_p \cdot T_{in} + p/p(T_{in})$) [17, 18] while the outgoing specific enthalpy h_P was taken from [11] for $T_P = 16922.15K$. The energy equation was then solved for the velocity at the outlet of the nozzle. To characterize the flow conditions, some dimensionless numbers were calculated: Reynolds number (Re), turbulence intensity (TI) and Mach number (Ma).

As the standard configuration of the plasma torch uses a very small outlet diameter of 1 mm which results in very high outlet velocities with Mach numbers >0.5, it was decided to modify plasma torch nozzle diameter from 1 mm (= case 0) to 2 mm (= case 1, reference case). For this reference case, plasma temperature increases slightly while Mach number and plasma gas velocity drastically decrease (see Table 2).

Table 2. Calculated plasma inlet conditions for varied plasma inlet diameters. For general boundary conditions and torrefied wood properties please refer to Table 3 and Table 4 respectively.

Case	0 (Smaller diameter)	1 (Reference)
d_P /[mm]	1.00	2.00
T_P /[K]	16922.15	17193.74
v_P /[m/s]	3561.33	917.65
$\dot{m}$ /[kg/s]	1.60E-2	1.60E-2
Ma /[-]	0.58	0.15
Re /[-]	7.53E+5	3.18E+5
TI /[%]	2.95	3.28

2.3.2. Gas outlet

As the gas outlet at the end of the reactor is a pressure outlet where internal and atmospheric pressures can be assumed to be roughly equal, the gauge pressure was set to zero and the backflow temperature to 360 K, which was the mass weighted average of total temperature at the outlet from an initial simulation. By also using the mass weighted average of velocity in z-direction at the outlet, the turbulence intensity was determined. The outlet variables are listed in Table 3 and were used for all cases.

2.3.3. Reactor wall

The wall thickness of the reactor's stainless steel wall was set to 2.5 mm [19] with a heat generation rate $\dot{Q}_{gen}$ of 0 W/m3. Since shell conduction treats the boundary as a thin wall [20] and disables the wall material specification, which is important for heat transfer phenomena, it was deactivated. It was assumed that the heat transfer rate from the cooling water to the reactor wall is much greater than that of air inside the reactor to the reactor wall. Thus, it was assumed that the wall temperature is constant at 293.15 K. The wall boundary conditions are summarized in Table 3.

Table 3. General boundary conditions.

	Plasma inlet	Particle inlet		Outlet		Reactor wall
d_P /[mm]	2.00	5.00	d_{out} /[mm]	26.00	d_{wall} /[mm]	25.00
T_P /[K]	17193.74	298.15	$T_{Backflow}$ /[K]	358.43	T_{wall} /[K]	293.15
$\dot{m}$ /[kg/s]	1.60E-2	2.34E-1	p_{gauge} /[Pa]	0	$\dot{Q}_{gen}$ /[W/m^3]	0
TI /[%]	3.28	2.50	TI /[%]	2.49	Shell cond.	no

2.3.4. Particle injections

The simulated torrefied wood particles have a density of $\rho = 700kg/m^3$, a lower heating value of $LHV = 19.855MJ/kg$ and a specific heat capacity of $C_p = 2310J/kgK$ based on previous lab analysis. The mass flow rate of the torrefied wood particles was determined by specifying that the plasma power should make up 50% of the lower heating value input of the wood particles. This is typically the maximum required plasma power input to operate under pure allothermal plasma gasification conditions for comparable feedstocks [2]. Based on this assumption, the mass flow of wood particles were calculated resulting in the values indicated in Table 3. The wood particles were assumed to have a particle size distribution as shown in Table 4.

Table 4. Torrefied wood injection settings for Discrete Random Walk Model.

Inert Wood Particles					
d_{min}	/[m]	9E-5	T_{BM}	/[K]	298.15
d_{max}	/[m]	1.1E-4	v_{BM}	/[m/s]	10.31
d_{mean}	/[m]	1E-4			

3. Geometry and mesh generation

The first step of the CFD simulation of the plasma entrained flow gasification test rig was to create a geometry and mesh which is mesh independent for an acceptable level of deviation from the benchmark mesh. The target was to accept a maximum deviation from the benchmark mesh of 10%. A lower deviation level is not required because the simulations serve the purpose of informing the optimization of the experimental set-up. Maximum accuracy is not necessary for this purpose.

3.1. Mesh

The reactor design as shown in Figure 1 was recreated using SpaceClaim. The first step was to simplify the constructed plasma-jet-tube configuration down to what is essential for Fluent calculations, so the cooling jacket, the tubular viewing window and all external components were neglected. Running the first few simulations showed that the posterior section of the 1.5 m long reactor had no influence on results and was hence cut off to reduce computational time.

To generate the mesh, several tubular bodies of influence (BoI) were defined for each section of the tube: Starting from the smallest grid cell size x_{min} at the plasma inlet, the mesh was gradually coarsened along the tube as demonstrated in Figure 3. Since the chosen mesh type is poly-hexcore, the octree meshing algorithm had to be taken into account when conducting the sensitivity study, so that they do not get set arbitrarily during meshing. Therefore, the target cell size x of each refinement level had to fulfil the relation:

$$x = x_{min} \cdot 2^t \tag{3}$$

where x_{min} denotes the smallest cell length (in this case: at the plasma zone refinement), and t the number of transition layers from x_{min} to x_{max}. The plasma zone's BoI includes the sharpest part of the plasma zone and is supported by a face of influence with the same cell size at the inlet boundary.

The starting point for x_{min} was inspired by Wilhelm [21], where a mesh refinement of 10 cells per diameter was used. The following relation has proven to be sufficiently accurate in his case:

$$d_c = \sqrt{\frac{A(d_c)}{A(d_i)}} \cdot d_i \tag{4}$$

For an inlet diameter of $d_i = 1mm$ and a cell diameter of $d_c = d_i/10$, the resulting minimum cell size was 0.1mm (case C). From there on, the other cell sizes were derived. Then x_{min} along with its other cell sizes were reduced to create the different cases for the mesh independence study as shown in Table 5.

3.2. Mesh independence study

After performing the simulations for the mesh independence study using the mesh parameters as detailed in the previous section, the velocity magnitude and total temperature were evaluated along the reactor length for each refinement level and compared to the most detailed reference case A. This yields the discrepancies plotted in Figure 4 along the significant part of reactor.

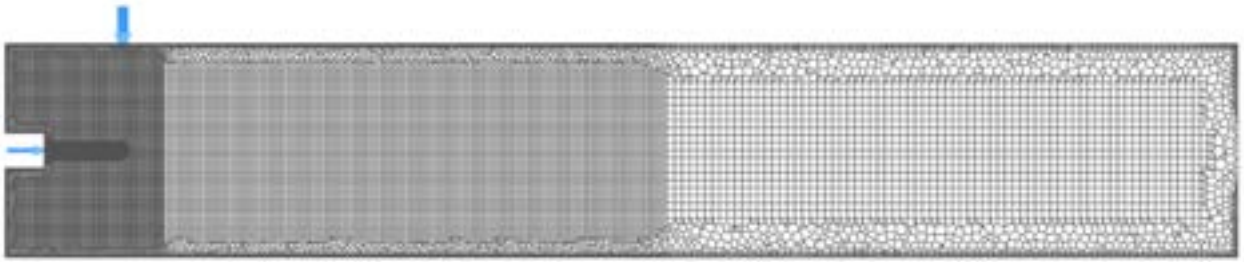

Figure 3. Poly-Hexcore mesh of reactor tube (coarsened to xmin = 0.12mm for visibility).

Table 5. Mesh independence study: Cell lengths x /[mm] for each body of influence of transition layer t.

BoI t	Plasma zone 0	Anterior 3	Middle 4	Posterior 5	Total cells
A	0.06	0.48	0.96	1.92	9,772,469
B	0.08	0.64	1.28	2.56	4,301,751
C	0.10	0.80	1.60	3.20	2,274,814
D	0.12	0.96	1.92	3.84	1,370,240

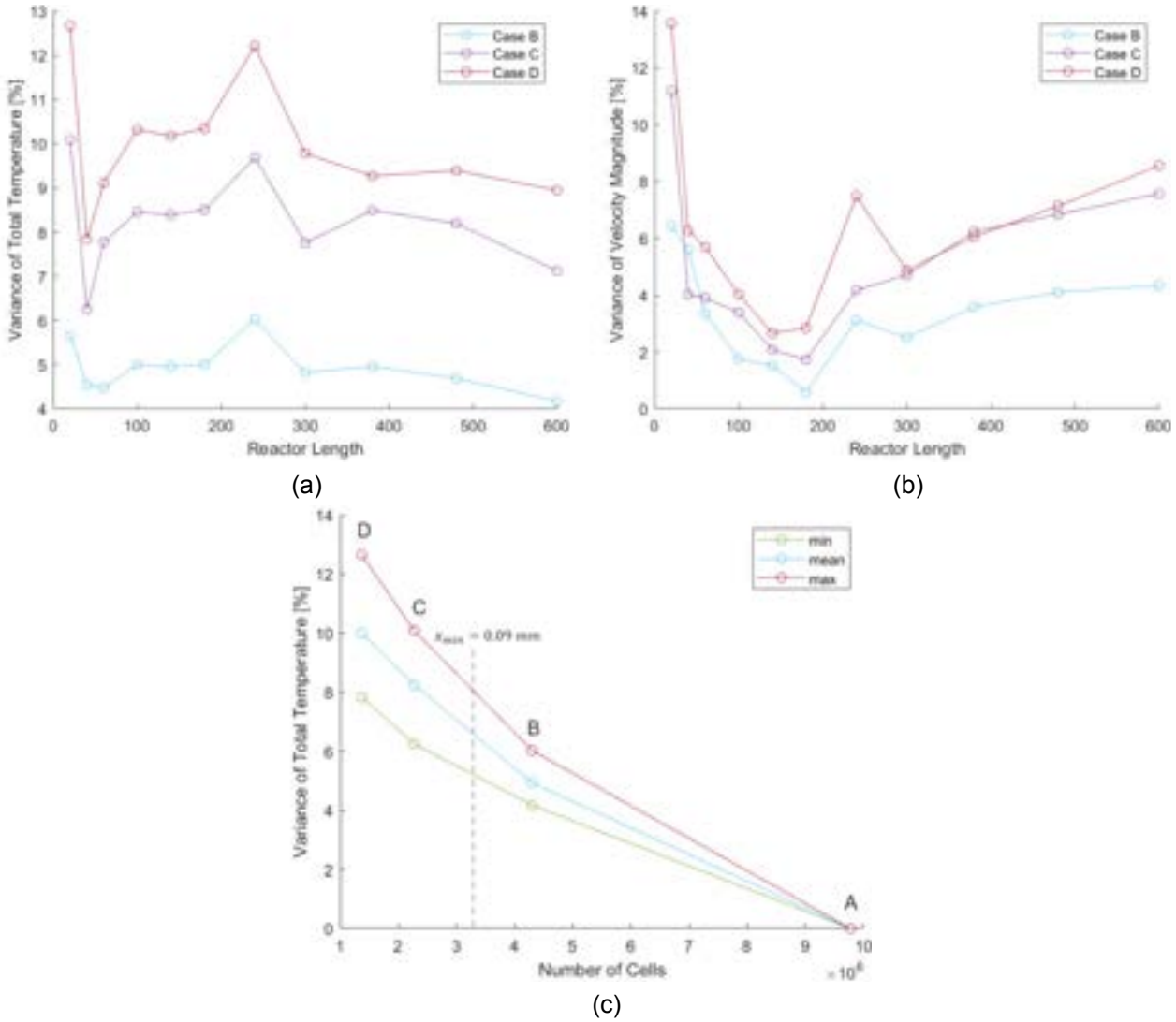

Figure 4. Mesh independence study for mesh cases A, B, C and D. (a) Total temperature error along the reactor length in mm for cases B, C and D relative to case A. (b) Velocity magnitude error along the reactor length in mm for cases B, C and D relative to case A. (c) Mean, minimum and maximum error of velocity magnitude along the reactor length as a function of the number of cells for meshes A, B, C and D.

Due to the high inlet velocity of the plasma gas and the sharp temperature gradients, one can see the highest variance at the inlet (20 mm from reactor inlet) and another peak in the middle. A possible explanation for the peak in the middle could be that the solution seems to start at the boundaries and spreads throughout the reactor with more iterations. As mass-weighted variables have not been tracked at each measurement point during the simulation, the properties at this position of the reactor might not have plateaued yet. Supporting this explanation is the fact that this peak is farther away from the outlet of the reactor's mesh (630 mm from reactor inlet) where the cell size is larger, so the converged solution is reached quicker. Also, the mass imbalance is comparatively higher at this position.

Because the velocity magnitude shows higher variability than the temperature, it has been chosen as the determining factor for the final mesh size; its minimum, maximum and mean values are plotted against the cell number in Figure 4 (c). Weighing computation expenses against solution accuracy led to the decision, that a refinement level of $x_{min} = 0.09\,mm$ should suffice to keep the maximum deviation from mesh A below 10%.

Based on this mesh independence study, a slightly modified final mesh B' was created using the mesh B as the basis. This resulted in the mesh data as shown in Table 6 and made it possible to reduce the required number of cells by ~28% compared to mesh B.

Table 6. Modified mesh refinements: Cell lengths x /[mm] for each body of influence of transition layer t.

BoI t	Plasma zone 0	Anterior 3	Middle 4	Posterior 5	Total cells /[%]
B	0.08	0.64	1.28	2.56	100
B'	0.09	0.72	1.44	2.88	71.80

4. Results and discussion

4.1. Cases overview

The first two cases, case 0 and case 1, which were assessed, only vary geometrically in terms of the outlet diameter of the plasma torch nozzle as shown in Table 2.

The other cases focus on the way in which the biomass particles are introduced to the plasma zone. Case 1, and also case 0, assume a simple opening at the top of the reactor's tube through which biomass particles can be sent into the reactor. To examine the direct effect of plasma on biomass particles, the particle inlet was brought closer to the plasma zone with the help of a vertical particle inlet tube, which was integrated at different distances from the plasma torch outlet for the cases 2 to 5. The job of the vertical particle inlet tube was to guide the biomass particles as close to the plasma zone as possible. Assuming the tube is made from high-temperature resistant ceramic material, its length l_{tube} was determined, so that it does not meet temperatures exceeding 1500 K. To obtain the plasma zone's temperature profile, the particle inlet was defined as a wall and its mass flow rate, turbulence intensity as well as hydraulic diameter were set to 0, so that the flow is not affected by cold incoming air. The injected particles were also defined as massless. The distance of the vertical particle inlet tubes from the plasma torch outlet was then varied along the 1500 K isotherm. The resulting inlet tube positions for the cases 2 to 5 and case 1 as the reference are listed in Table 7.

Table 7. Geometry parameters for varied particle inlet tube lengths l_{tube} and distance of the particle inlet tube from the plasma torch outlet s_{tube}. All remaining parameters are based on Table 3 and Table 4.

Cases		1 (reference)	2	3	4	5
l_{tube}	/[mm]	0.00	49.00	46.50	44.50	42.50
s_{tube}	/[mm]	40.00	5.00	15.00	25.00	35.00
$d_{part,in}$	/[mm]	5.00	5.00	5.00	5.00	5.00

4.2. Cases 0-1: Results of plasma torch outlet diameter variation

The main results for cases 0 and 1 consisting of average particle temperatures and respective residuals are presented in Figure 5.

Figure 5 (a) shows the average temperature of all particles in a selected time interval for both cases. In case 1, the plasma gas flows in at a velocity of $v_1 = 917.65 m/s$ and a temperature of $T_1 = 17193.74 K$ compared to $v_0 = 3561.33 m/s$ and $T_0 = 16922.15 K$ in the reference case. The conservation of energy explains this increase in temperature, which compensates the reduction in the kinetic term because of the lower plasma gas velocity. Consequently, particles reach average temperatures up to 2.1x higher in case 1 compared to case 0 ($T_{max,0} = 986.534 K$ and $T_{max,1} = 2092.61 K$). They also remain hotter as indicated by higher volume-averaged temperatures ($T_{V,0} = 513.64 K$ and $T_{V,1} = 703.45 K$). Therefore, case 1 performs better than case 0 at achieving a good mixing between biomass particles and the hot plasma gases in the plasma zone.

The residuals also indicate that convergence for case 0 is worse than convergence for case 1. Due to the increased mass flow rate and thereby also velocity gradient at the inlet, the solution does not converge as smoothly for case 0. Despite the enlargement of the plasma zone and anterior bodies of influence and using a finer mesh than the initial one (0.08 mm), the continuity remains above 10^{-3} for case 0 as shown in Figure 5 (b). Furthermore, the volume-averaged velocity oscillates around $v_{V,0} \approx 0.7m/s \pm 0.03m/s$ while temperature stagnates at $T_{V,0} \approx 520K$. This behaviour could be explained by one of three potential causes; the first one being the mesh, the second one under relaxation factors and the third being the complexity of the flow:

1. The mesh might still not be sufficiently fine in some areas of the reactor. The higher inlet velocity also leads to increased velocities in other parts of the reactor.
2. Under-relaxation factors (URFs) were varied differently for both cases, which could justify this behaviour.
3. Because of the complexity of the flow, a unique solution might simply not exist. As the solution of the flow is steady, it is very likely to have more than one solution for the same boundary conditions. This would justify why properties oscillate periodically between two possible states.

As case 1 performed better in terms of both the average particle temperatures, as a proxy of the quality of mixing between particles and plasma zone, and convergence, the worse convergence of case 0 was not further studied. Instead, it was decided, as already indicated in section 2.3.1 due to the lower plasma gas velocities, to continue with case 1 as the base case for the further improvement of the reactor.

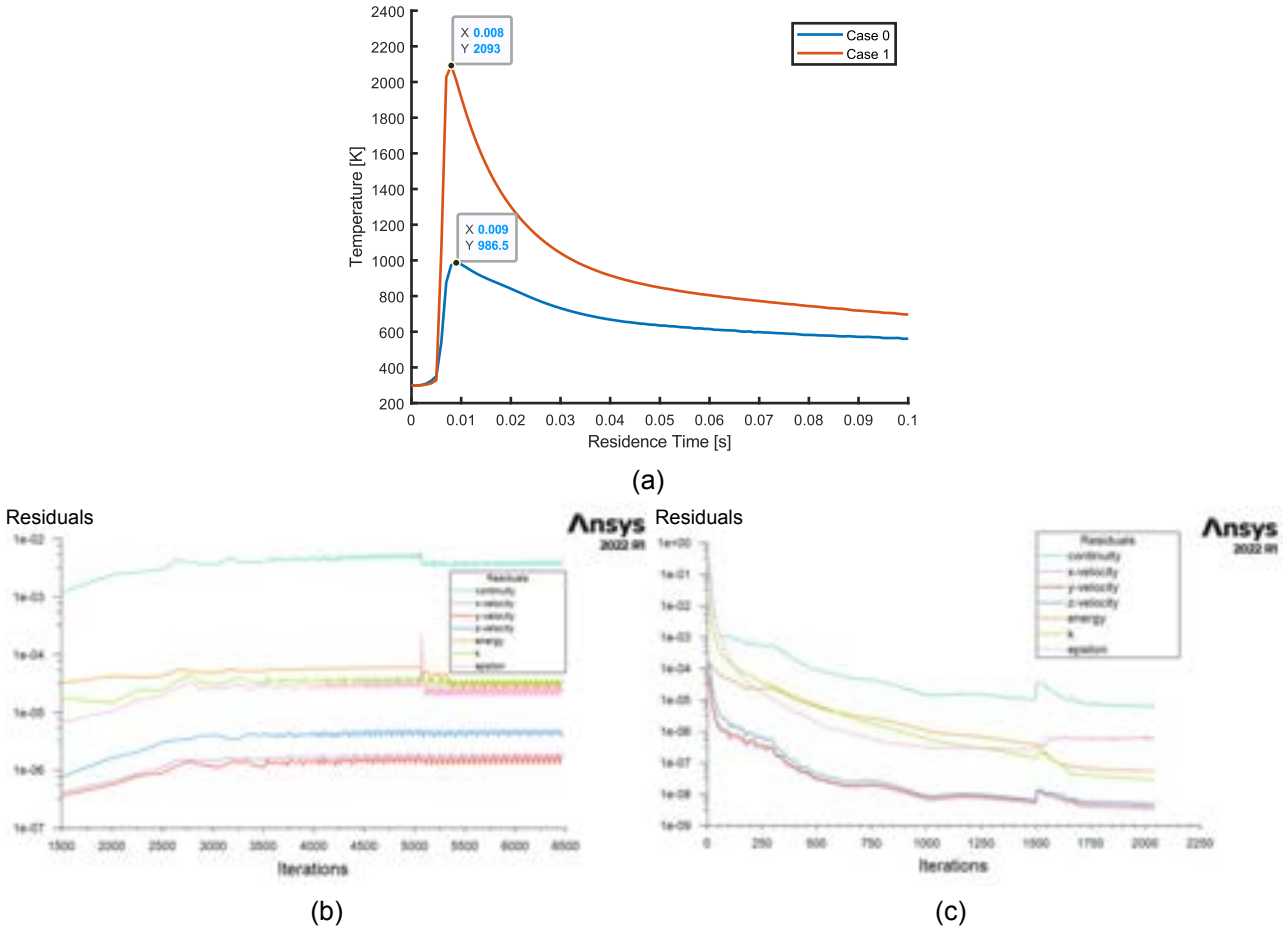

Figure 5. Comparison of residuals and average particle temperatures of cases 0 and 1. (a) Average particle temperatures over residence time for cases 0 and 1. (b) Residuals of case 0. (c) Residuals of case 1.

4.3. Cases 1-5: Results of variation of particle inlet tube's position

The intention behind varying the tube position is to find the configuration where particles reach the highest temperatures and maintain them for the longest period. Figure 6 shows the average particle temperatures plotted over the residence time. For each case, the mean value of all temperatures in a specified time interval were evaluated using Matlab and then plotted with the other cases. Figure 7 compares particle temperatures and their tracks for the different cases. The graphs of the two figures clearly indicate that cases 2 and 3 perform better in terms of maximum (average) temperature compared to the other cases which do not exceed 2200K. This is essentially a consequence of the extreme temperatures particles come in contact with in the core

plasma zone, which reach up to 15,000K and 7,500K, respectively. The higher deflection angle of the plasma zone might also improve the particle heating, as higher temperatures are shifted downwards towards the particle tracks and thus heat them longer. High collision velocities also cause particles to be distributed better in cases 2 compared to other cases. As previously established by Gupta et al. [11], the higher thermal conductivity at such temperatures is higher and therefore particle heating is improved even more significantly as shown in Figure 6 (a). The delayed peak in case 1 is due to the fact that particles have to travel longer from the top of the reactor before hitting the flame – while the residence time only starts counting in cases 2 to 5 when the particles exit the ceramic tube close to the plasma zone. The slight bump in cases 4 and 5 may be a consequence of high turbulence in that time interval, which could be deduced from the particle tracks. But it may also be a consequence of incomplete convergence.

When looking at the long-term particle temperatures in Figure 6 (b), case 5 surpasses the other cases, even if only slightly. Looking at the particle path lines, it gets clear that this is because particles fly back into the plasma region and are thereby reheated. However, particles in all cases do not maintain a high temperature after the sharp decline down from the peak. This goes back to the relatively low overall temperature of the gasifier. It shows that the particles are quenched rather fast upon leaving the plasma zone reaching temperatures <1000K within <<0.1s in all cases. This is beneficial for the production of plasma pyrolysis char as fast quenching would be helpful in preserving the change of the char properties caused by the plasma zone.

Based on Figure 6 and Figure 7, case 2 looks the most promising. It achieves both a very high peak temperature, indicating a good mixing of particles with the plasma zone, as well as comparatively fast quenching of the particle temperature after the plasma zone.

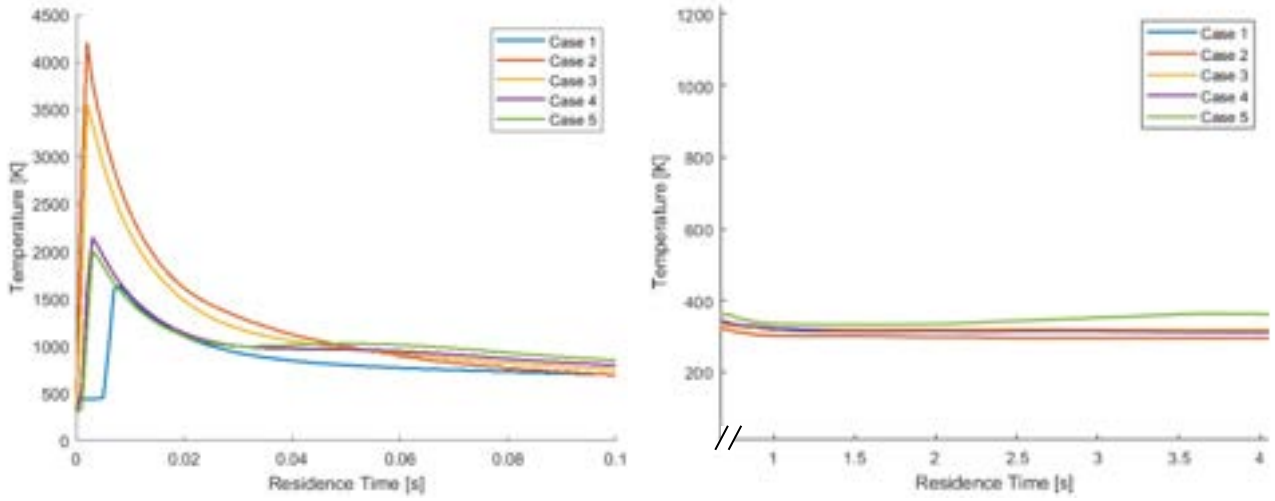

Figure 6. Average particle temperature distribution over residence time for cases 1-5. (a) Average particle temperature peaks during first 0.1 seconds of residence time. (b) Long-term average particle temperatures.

Based on the residuals for cases 2 to 5 in Figure 8 and those of case 1 in Figure 5, the convergence of cases 2, 4 and 5 are far less stable than cases 1 and 3. One reason is the change and increase in the plasma zone upon integration of the plasma tubes (cases 2-5). This means that the plasma zone BoI does not only need to be angled but enlarged as well. For case 2 the instability could be easily explained by the fact that the collision velocities of particles and plasma gas are significantly higher than in all other cases as the particle inlet tube in this case is closest to the plasma torch outlet. Even after modifying the plasma zone BoI in case 2, the residuals still oscillate, but around 10^{-4} to 10^{-3} instead of 10^{-2} before modification. The gradual decrease in the residuals around 2000 iterations (Figure 8 (a)) is a consequence of reduced under relaxation factors, which were improving the solution until approximately 2700 iterations.

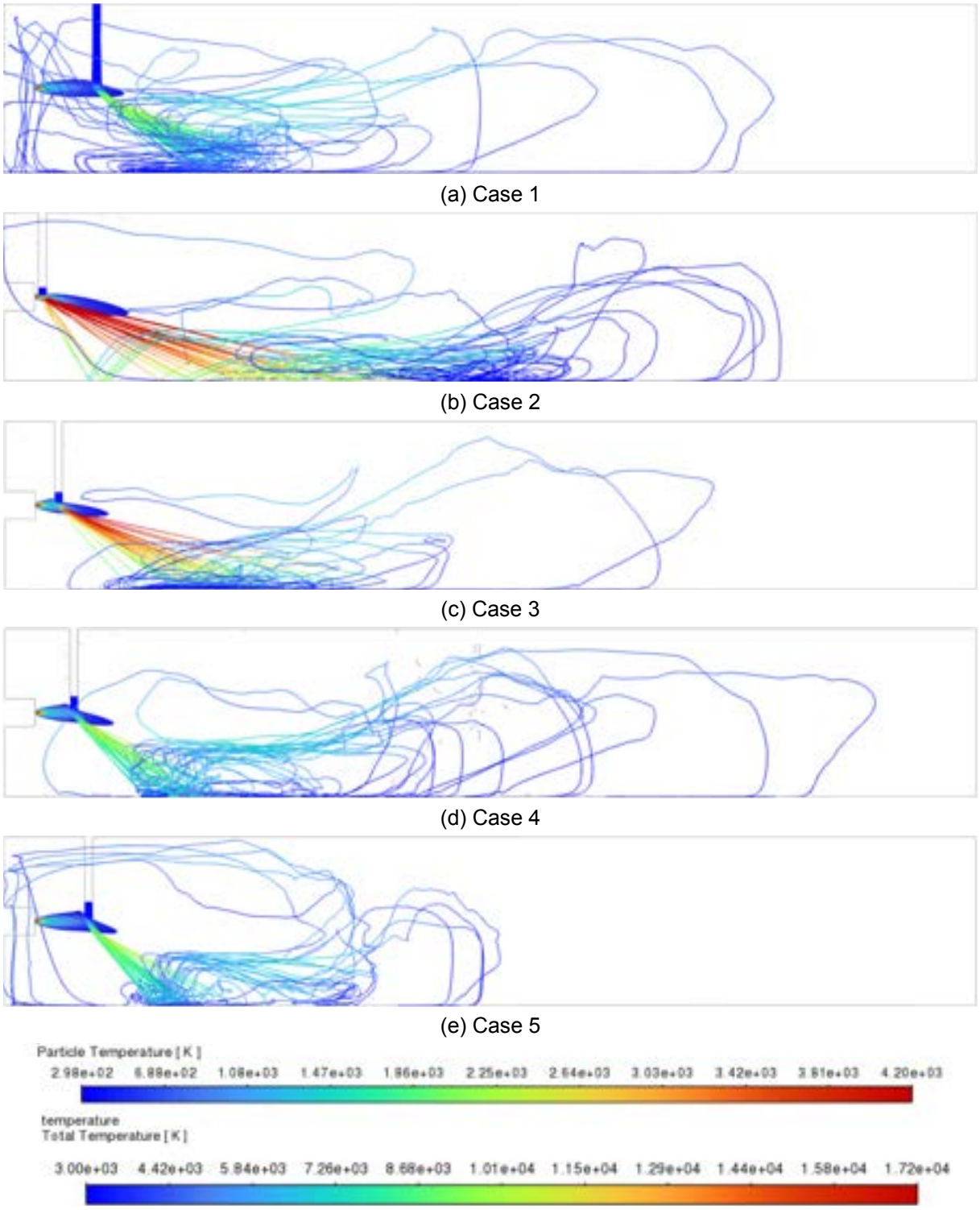

Figure 7. DC arc plasma zone temperature and (inert) torrefied wood particle streamlines coloured based on temperature for cases 1 to 5.

Same applies for cases 4 and 5, where volume-average-temperature and velocity are oscillating periodically around the same range that is computed by case 1. It is only in case 3 where both physical and numerical properties stagnate as shown in Figure 8 (b). Although the same case and data file was used for interpolation at the beginning, this case is far better converging than all three other cases.

However, since all cases oscillate periodically around 10^{-4} to 10^{-3}, the change in solution should not be significant. For example, in case 4: $v_{V,4} \approx 0.7m/s \pm 0.05m/s$ and $T_{V,4} \approx 700K \pm 5K$. The aim of these cases anyway is to reveal the trend of the best tube position for particle mixing and heating, which would not be heavily affected by oscillations at such a comparatively small magnitude. As long as the physical phenomena make sense, which they do in all of those cases, the result should be valid.

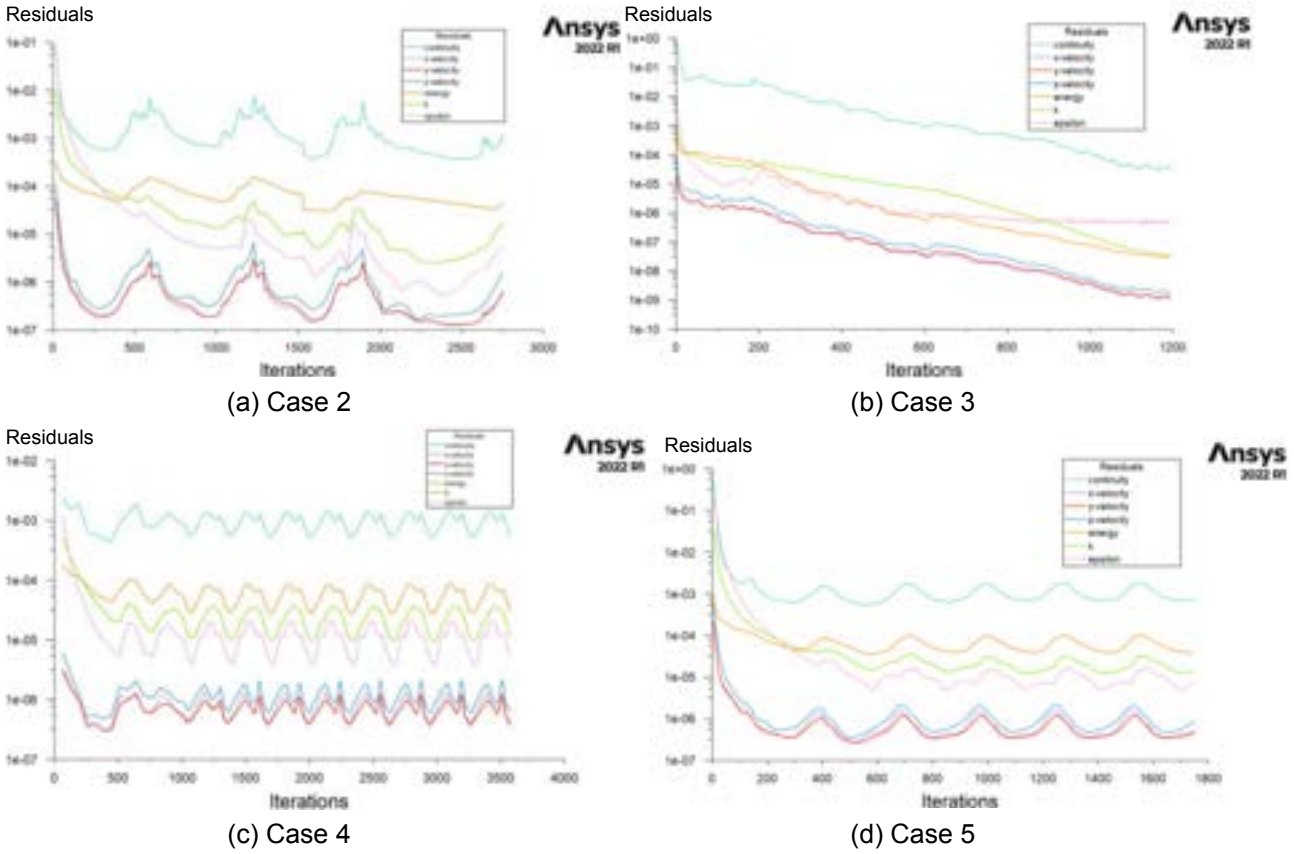

(a) Case 2 (b) Case 3

(c) Case 4 (d) Case 5

Figure 8. Residuals of cases 2-5 vs. number of iterations.

5. Conclusion

This work has investigated the flow characteristics of a DC air plasma torch in a horizontal tube reactor and investigated different optimization options to improve the interaction of biomass particles with the plasma zone. Plasma gas properties were modelled by integrating the adjusted plasma air properties provided by Gupta et al. [11]. Simplifying assumptions were made to ensure the feasibility of the CFD model – among others, neglecting chemical reactions, assuming a single fluid model and ignoring heat exchange by radiation. The different optimization options which were assessed focused on the one side on changing the plasma torch's outlet nozzle diameter to adjust plasma gas velocities and on the other side the integration of vertical biomass particle inlet tubes to better guide the fuel particles directly into the plasma zone (at distances 5, 15, 25 and 35 mm from the torch outlet along the isotherm of 1500 K). It can be concluded that the wider diameter offers not only better convergence, but much higher particle temperatures as well. From all conducted cases, the closest tube to the plasma inlet (case 2) leads to the highest particle temperatures. Cases 4 and 5 do not seem to offer a significant advantage over case 1 without a tube. All cases exhibit comparatively fast quenching (<<0.1s) of the particle temperatures after the plasma zone, which is beneficial for producing plasma pyrolysis char for further experimental analysis. In addition, all cases (except for case 5) show the same long-term cooling behaviour. The deciding factor for the best configuration to enhance particle heating is therefore only highest average temperatures, which was demonstrated in case 2 followed by case 3.

The created CFD simulation model is a good starting point for further research into modelling of plasma-assisted entrained flow gasification. In subsequent models, it would make sense to look into the option of changing the single fluid model to a more sophisticated plasma representation also accounting for dissociated and ionized, highly reactive species. For this, it would also be beneficial to integrate chemical reactions into the model as well as radiative heat transfer to better simulate the processes happening in the high temperature zones. In this regard, a combination with other existing CFD models for conventional entrained flow gasification such as the model developed by DeYoung [10] will be a suitable next step. In addition, experimental data will be necessary to inform the modelling and create kinetic models for the simulation of these plasma gasification processes. Experimental results from the modelled test rig can also be used to validate the simulative results.

Acknowledgments

This study was carried out in the framework of the EU Horizon 2020 project "TWIN-PEAKS" (project no.: 951308) funded by the European Union and the International Future Lab on Green Hydrogen Technologies "REDEFINE Hydrogen Economy (H2E)" (project no.: 01DD21005) sponsored by the Federal Ministry for Education and Research (Germany). The financial support is gratefully acknowledged.

Nomenclature

c	specific heat, J/(kg K)
d	diameter, mm
h	heat transfer coefficient, W/(m^2 K)
$\dot{m}$	mass flow rate, kg/s
p	pressure, Pa
t	transition layer
v	velocity, m/s
x	cell length, mm
A	area, m^2
BoI	Body of Influence
CFD	Computational Fluid Dynamics
DC	direct current
K	kinetic energy, kJ
LHV	lower heating value, MJ/kg
Ma	Mach number
Re	Reynolds number
TI	turbulence intensity
T	temperature, °C or K
UDF	user defined function
U	internal energy, kJ
W	work, kJ
α	ionization degree
ϕ	potential energy, kJ
ρ	density, kg/m^3

References

[1] M. Carus, F. Kähler, and O. Porc, *Global Carbon Demand for Chemicals and Derived Materials: Global Carbon Demand for Chemicals and Derived Materials in 2020 and Scenario for 2050 in million of embedded carbon.* [Online]. Available: https://renewable-carbon.eu/publications/product/global-carbon-demand-for-chemicals-and-derived-materials-png/ (accessed: Mar. 25 2023).

[2] S. Bastek, M. Kerschbaum, M. Dossow, S. Fendt, and H. Spliethoff, “Process Simulation of Plasma-Assisted Entrained Flow Gasification for Hydrogen-rich Syngas Production,” in *2022 International Freiberg Conference on Waste Gasification*, Freiberg, 2022.

[3] T. Netter, A. Geißler, and H. Spliethoff, “Determination of the Intrinsic Gasification Kinetics of a Bituminous Coal Including Product Gas Inhibition and Char Deactivation Under Entrained Flow Conditions,” *Journal of Energy Resources Technology*, vol. 142, no. 7, 2020, doi: 10.1115/1.4046142.

[4] T. Netter, S. Fendt, and H. Spliethoff, “A collection of model parameters describing the gasification behavior of different fuels under entrained flow conditions,” *Fuel*, vol. 296, p. 120536, 2021, doi: 10.1016/j.fuel.2021.120536.

[5] Vishwajeet *et al.,* “Entrained Flow Plasma Gasification of Sewage Sludge–Proof-of-Concept and Fate of Inorganics,” *Energies*, vol. 15, no. 5, p. 1948, 2022, doi: 10.3390/en15051948.

[6] M. Sakhraji, A. Ramos, E. Monteiro, K. Bouziane, and A. Rouboa, “Plasma gasification process using computational fluid dynamics modeling,” *Energy Reports*, vol. 8, pp. 1541–1549, 2022, doi: 10.1016/j.egyr.2022.08.069.

[7] S. Choi, “Numerical Simulation of Thermal Plasma Gasification Process,” *AMM*, 799-800, pp. 90–94, 2015, doi: 10.4028/www.scientific.net/AMM.799-800.90.

[8] F. Rojas-Perez, J. A. Castillo-Benavides, G. Richmond-Navarro, and E. Zamora, “CFD Modeling of Plasma Gasification Reactor for Municipal Solid Waste,” *IEEE Trans. Plasma Sci.*, vol. 46, no. 7, pp. 2435–2444, 2018, doi: 10.1109/TPS.2018.2844867.

[9] N. K. C. Qing, N. A. Samiran, and R. A. Rashid, “CFD Simulation Analysis of Sub-Component in Municipal Solid Waste Gasification Using Plasma Downdraft Technique,” *CFDL*, vol. 14, no. 8, pp. 63–70, 2022, doi: 10.37934/cfdl.14.8.6370.

[10] S. DeYoung, “Numerical simulation of entrained flow gasification with focus on char reaction kinetics,” Dissertation.

[11] R. Gupta, K.-P. Lee, R. Thompson, and J. Yos, *Calculations and curve fits of thermodynamic and transport properties for equilibrium air to 30000 K*: NASA, 1991.

[12] Parkside, *PLASMA CUTTER PPS 40 B2*.

[13] S. Selle, “Transportkoeffizienten ionisierter Spezies in reaktiven Strömungen,” PhD-thesis, Universität Heidelberg, Heidelberg, Deutschland, 2002.

[14] M. Capitelli, G. Colonna, and A. D’Angola, *Fundamental Aspects of Plasma Chemical Physics*. New York, NY: Springer New York, 2012.

[15] ANSYS Inc., *ANSYS FLUENT 12.0 Theory Guide.* [Online]. Available: https://www.afs.enea.it/project/neptunius/docs/fluent/html/th/main_pre.htm

[16] K. Bobzin, M. Öte, J. Schein, S. Zimmermann, K. Möhwald, and C. Lummer, “Modelling the Plasma Jet in Multi-Arc Plasma Spraying,” *J Therm Spray Tech*, vol. 25, no. 6, pp. 1111–1126, 2016, doi: 10.1007/s11666-016-0438-0.

[17] W. Polifke and F. Schilly, *Engineering Thermodynamics*.

[18] A. Sasoh, *Compressible Fluid Dynamics and Shock Waves*. Singapore: Springer Singapore, 2020.

[19] C. Kranig, “Auslegung und Konstruktion eines Plasmapyrolyseteststands,” Semesterarbeit, Technische Universität München, Deutschland, 2022.

[20] ANSYS Inc., *ANSYS FLUENT User’s Guide: 2022R1*.

[21] S. Wilhelm, “Stationary CFD Simulation of High Temperature Fuel Cell Stacks,” Master's thesis, Technische Universität München, Germany, 2020.

Improvement and optimization of the convective heat transfer in the polymer pipes with internal surface modifications

Piotr Łapka[a], Juliusz Wachnicki[b]

[a] Faculty of Power and Aeronautical Engineering, Warsaw University of Technology, Warsaw, Poland, e-mail: piotr.lapka@pw.edu.pl
[b] Faculty of Power and Aeronautical Engineering, Warsaw University of Technology, Warsaw, Poland, e-mail: juliusz.wachnicki.stud@pw.edu.pl

Abstract:
The objective of the work was to improve convective heat transfer intensity in the polymer pipes, e.g., made of high-density polyethylene or cross-linked polyethylene, by applying and optimizing internal pipe surface modifications in the form of small helical ribs. These helical ribs act as turbulence promoters and additionally induce angular velocity in the flowing medium, increasing the flow path length. Such pipes with the modified inner surface may be applied in the vertical and horizontal ground heat exchangers, which are one of the most expensive elements of ground-source heat pump systems. Improving heat transfer intensity between ground and working fluid in pipes may reduce the required number or length of boreholes and, therefore, decrease the overall installation costs of the heat pump system. This will allow more heat delivery to the working fluid per one running meter of the borehole. However, due to the increased turbulence in pipes with the modified internal surface, the pressure losses will also increase, which will increase the power consumed by the pump. Therefore, finding the balance between heat transfer gains and pumping losses is necessary. This paper further numerically analyzes previously selected modifications with rectangular and equilateral triangular cross-sections. Factors such as the height of ribs (vortex generators) and helix pitch were studied in terms of pressure drop and convective heat transfer intensity. Optimal geometrical parameters of ribs were found. Compared to the smooth pipes, optimized pipes with rectangular turbulators had Nusselt numbers 47-58% higher for the considered Reynolds number range, while pipes with triangular turbulators 21-42%. However, optimized pipes also had 92-126% and 31-39% higher pressure drops for rectangular and triangular turbulators, respectively, than the smooth pipe in the same Reynolds number range.

Keywords:
Convective heat transfer intensification; Ground heat exchanger; Numerical simulations; Internal surface modification; Polymer pipe.

1. Introduction

Recently, the share of renewable energy sources in total power and heat generation significantly increases as society focuses more and more on ecological and renewable energy sources. This is due to high greenhouse gas emissions by conventional power and heat sources, an increase in global warming, and high prices of fossil fuels. Renewable energy sources have been replacing fossil fuels-based power sources for years. The current social pressure and political decisions are speeding up this trend. In the European Union, the power sector must quickly adapt to the assumed emission targets by replacing coal-fired power plants, heating plants, and combined heat and power plants with new gas/hydrogen turbines, nuclear reactors, and renewable energy sources. However, in order to achieve the very ambitious climate neutrality targets established by the European Union, it is necessary to dynamically develop technologies allowing more efficient utilization of renewable power and heat sources. This should be done on a macro-scale (i.e., on the level of the power generation system) and on a micro-scale (i.e., on the local level by power and heat consumers). One of the solutions which can be applied on the micro-scale level is the application of heat pumps for space heating and domestic hot water production. Among them, ground-source heat pumps are characterized by the highest efficiency. Therefore, such heat pumps should especially be promoted.

Ground-source heat pumps are used to transfer the heat from the ground to the buildings. Their investment costs are usually higher than in the case of air-to-air or air-to-water heat pumps, but the exploitation costs are lower as they have a higher average coefficient of performance than other types of heat pumps. They work in

combination with the ground heat exchangers, one of the system's most expensive elements. The pipes for ground heat exchangers are usually made of polymers, e.g., high-density polyethylene (HDPE) or cross-linked polyethylene (PEX). One of the ways to decrease the overall cost of the ground-source heat pumps might be by increasing heat transfer intensity in the ground heat exchangers. This operation may reduce the required number or length of boreholes and, therefore, the system installation's overall costs. The higher effectiveness of ground heat exchangers can be achieved, e.g., by increasing the heat transfer rates inside pipes due to the introduction of modifications in the form of small helical ribs or fins on the internal surface of the pipes used in the ground heat exchanger. The purpose of the modifications on the pipe's internal surface is to increase the intensity of heat transfer between the soil and the working medium flowing through the pipe. The modifications act as turbulence promoters, increase flow turbulisation, force the formation of angular velocity in the flowing medium, and increase the flow path length. This will allow more heat delivery to the working fluid per one running meter of the borehole. However, due to the increased turbulence, the pressure losses will also rise in polymer pipes with internal surface modifications. That will increase power consumption by the pump, which circulates the working medium in the lower heat source. Therefore, the modifications allowing for the highest heat transfer intensity increase at the lowest pressure drop should be designed.

The studies on increasing heat pump systems efficiency were focused, among others, on improving the efficiency of the thermodynamic heat pump cycle itself [1], improving control systems and optimizing the heat pump system configuration and operation [2,3], or using hybrid heat pumps systems in combination with other systems [4-6]. There are only a few efforts to increase the heat transfer efficiency in the ground heat exchangers applied in the heat pump systems. The factors affecting vertical ground heat exchanger efficiency were summarised in [7]. The working fluid mass flow rate, thermal properties of the pipe material, thermal properties of the grout material and soil, soil density and moisture level in the ground, the geological structure of the earth crust in implementation location, groundwater presence, borehole diameter and depth, inlet and outlet pipe diameters, and the pipes' configuration (e.g., coaxial, single/double U-tube, spiral-tube, and multi-tube) are the ground heat exchanger parameters which have the greatest impacts on the efficiency of ground-source heat pump systems. Some of these parameters are related to the ground heat exchanger location and ground parameters. Therefore, the engineers have no influence on them. But there is a group of factors, e.g., the level of flow turbulization in the pipe, which may be modified and optimized to improve heat transfer rates in the ground heat exchanger.

The internal surface modifications, e.g., in the form of grooved, riffled, or corrugated surfaces, in pipes made of metals, were studied numerically and experimentally in many works [8-10]. However, this problem was not investigated thoroughly in the case of polymer pipes. There are only a few papers in which this problem was undertaken. The pressure drop in polyethylene (PE) pipes with internal micro-fins was numerically investigated in [11]. But the simulations were carried out for only one shape of internal micro-fins, and for pipe configurations and sections typical for vertical ground heat exchangers, i.e., entrance, U-turn, and downward sections, were considered. Łapka and Wachnicki [12] recently simulated fluid flow and heat transfer in PEX pipes with internal helical turbulence promoters in the configurations typical for ground heat exchangers. The internal pipe modifications were in the form of rectangles, trapezoids, triangles, and semicircles. They calculated the dependencies between the shape of the internal embossment and the Nusselt number (Nu) and pressure drop in relation to the smooth pipe.

This short state-of-the-art shows that there is a lack of knowledge related to the heat transfer intensity and pressure drop in the polymer pipes with internal modifications. Moreover, the polymer pipes' properties and manufacturing methods are significantly different from pipes made of metals. This means that the knowledge about heat transfer intensification in metal pipes cannot be directly applied in the case of plastic pipes. Therefore, this problem is further analyzed in this paper. Previous studies in [12] showed that heat transfer intensity in polymer pipes might be significantly improved, i.e., in the Reynolds number (Re) range of 3000-8000, depending on the shape of modification, the Nu rose up to 25% in relation to the smooth pipe. But the penalty was a significant increase in the pressure drop, which also depended on the modification shape. Among the studied shapes, Łapka and Wachnicki [12] choose the triangular vortex generators as having the most promising pressure drop and heat transfer characteristics. The second shape selected in this paper was rectangular due to its possible manufacturing easiness. However, Łapka and Wachnicki [12] emphasized that before considering these shapes in practical applications, they have to be optimized in terms of pressured drop and heat transfer intensity, i.e., by finding their optimal geometrical parameters. Therefore, the optimization problem of polymer pipes' internal modifications is undertaken in this paper.

The paper is organized as follows. At first, considered internal modifications of the polymer pipes are presented. Then, the simulation methodology is described. Next, selected shapes of turbulence promoters and the way of their optimization are described. After that, the results of the simulations are shown and discussed in terms of Nu and pressure drop characteristics, and then the work is concluded.

2. Considered pipe models and initial studies

In the previous work [12], six internal modifications were tested, i.e., their influence on the heat transfer intensity and pressure drop were evaluated in the Re range of 3000-8000 and in reference to the smooth pipe. The

considered pipes had an outer diameter of 32 mm. The minimum wall thickness was 2.9 mm, so the inner diameter of the reference smooth pipe and also the base of the modification was 26.2 mm. The internal surface modifications were based on extruding certain shapes along the helix. In [12], this helix had a pitch of 300 mm. The considered geometries are shown in Fig. 1. For all cases, the embossings were 1.4 mm high. The first case had modification prepared by embossing a rectangle 2.8 mm wide (Fig. 1a). The second one had the shape of a trapezoid with arms at an angle of 15° and the distance between the arms centers of 2.8 mm (Fig. 1b). In the third, the vortex generators were equilateral triangles (Fig. 1c). In the fourth, the vortex generators were semicircles with a radius of 1.4 mm (Fig. 1d). In the fifth and sixth (Fig. 1e and f), the turbulators had the shape of rectangular triangles with an angle at the base of 60°, and with the right angle located on the left- and right-hand side, respectively. Moreover, the reference pipe with a smooth surface was also prepared to obtain reference results.

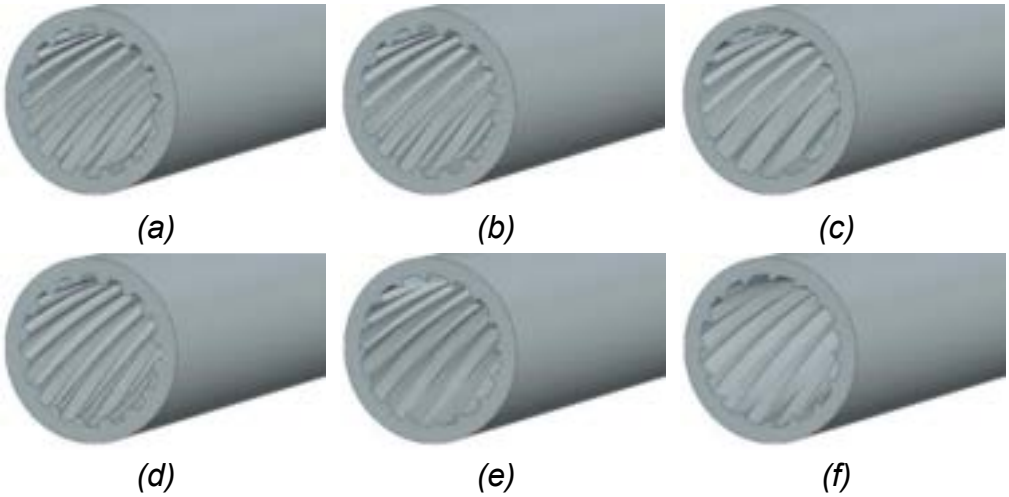

Figure 1. Shapes of turbulence promoters: a) rectangular, b) trapezoidal, c) equilateral triangle, d) semicircular, e) rectangular triangle with a right angle on the left-hand side, f) rectangular triangle with a right angle on the right-hand side.

The simulations conducted in [12] showed that triangular vortex generators had the most promising pressure drop and heat transfer characteristics. They had the lowest pressure drop increase compared to the reference pipe, i.e., they attained a pressure drop 95-125% higher than the reference pipe. The convective heat transfer was most intense for pipes with vortex generators in the shape of equilateral triangles. Moreover, the pipe with rectangle embossing performed well in terms of heat transfer intensity. In the whole considered Re range, these two types of modifications, i.e., equilateral triangle and rectangle, attained c.a. 21-23% higher Nu in relation to the smooth pipe. However, the pipe with rectangle modification had the most significant pressure drop increase, i.e., 170-190% in reference to the smooth pipe. Despite this, considering the results obtained in [12], and also manufacturing limitations, i.e., that modifications in the form of a right triangle might be difficult to manufacture and that the rectangular vortex promoters seem to be the easiest to manufacture, the optimization in terms of heat transfer and fluid flow characteristics was carried out for the embossing having shapes of a rectangle (Figure 1a) and equilateral triangle (Figure 1c). It is expected that further optimization of these geometries might significantly improve their heat transfer efficiency and reduce the pressure drop.

3. Optimization strategy

The vortex generators' optimization process was based on parameterizing some of their geometrical features (i.e., dimensions). The parameters for the optimization process were chosen so that it was possible to obtain great changes in the heat transfer and pressure drop characteristics in the pipe. The goal was to capture geometric features that can most significantly affect the pipes' heat transfer and fluid flow performances. For both selected models, the influence of the pitch of the helix was investigated. This parameter can potentially greatly impact variations in the pressure drop and heat transfer characteristics in the flow. In the base geometries, the pitch of the helix was set to 300 mm [12]. In this paper, additional calculations have been carried out for the pitch values of 150, 450, and 600 mm. The second examined parameter was the size of the turbulators, which was defined as their height. The turbulators were properly scaled to maintain the turbulence shape itself. The basic height of the vortex generators was 1.4 mm [12]. The current calculations have been performed for the following embossing heights: 0.6, 1, and 1.8 mm. Based on the optimization of these two parameters, pipe internal modifications that will potentially achieve the best heat transfer and pressure drop performances were selected. When creating optimized geometries, other geometrical parameters, e.g., the number of turbulators on the perimeter and the width of the embossing, were left unchanged. It was assessed that their influence is not as significant as the influence of helix pitch and embossing height.

4. Simulation methodology

4.1. Discretisation

The computational meshes were generated for the optimized models presented in Figures 1a and b. Due to the necessity for the correct prediction of convective heat transfer at the pipe's internal wall, very fine meshes in the wall region had to be generated. The goal was to create as structured meshes as possible. Therefore, the sweep method available in the software ANSYS Meshing was used for this purpose, together with significant mesh refining to the wall. The length of the division along the axis was 1 mm. Additionally, the mesh size at the pipe walls was set to 0.00005 m to keep $y+$ as low as possible for the whole considered Re range. These allowed for keeping the same meshes at the inlet and outlet from the computational domain (necessary due to the periodic flow assumption in the first phase of the solution) and obtaining a satisfactorily dense mesh close to the wall. The generated meshes consisted mainly of very good quality hexahedral elements. For a few geometries, triangular prism elements were also generated. An exemplary mesh for a pipe with a rectangular turbulator with a height of 1 mm is shown in Figure 2, while the parameters of the generated meshes are presented in Tables 1 and 2 for pipes with rectangular and triangular vortex generators, respectively.

The meshes' qualities shown in Tables 1 and 2 were within acceptable ranges. However, to obtain these parameters' values, the models with modified internal surfaces had to have a very large number of elements due to the necessity to resolve near-wall regions accurately (see fine mesh at pipe boundaries in Figure 2). Moreover, the aspect ratio was very high to keep a suitable value of $y+$ at the wall, i.e., the k-ω shear stress transport (SST) turbulence model was applied in numerical simulations and required $y+$ to close or be below 4-5.

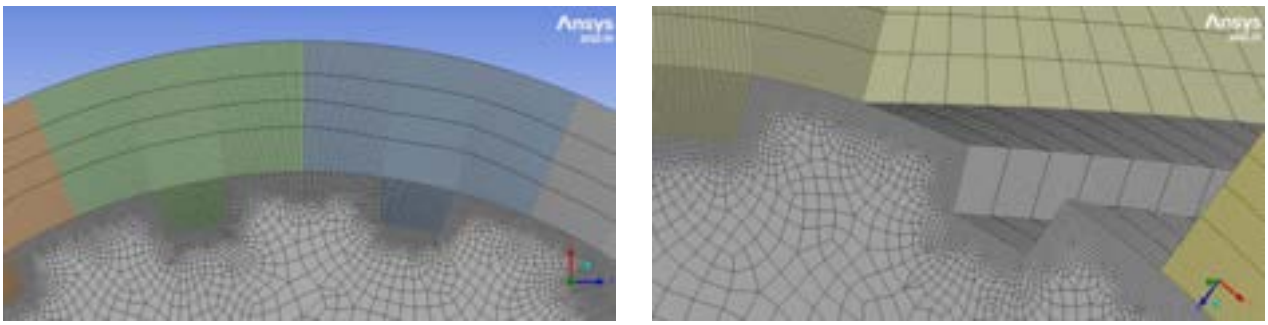

Figure 2. An exemplary mesh for a pipe with rectangular turbulators with a height of 1 mm.

Table 1. Parameters of meshes for pipes with rectangular turbulators.

Turbulator geometry	Number of elements	Max skewness	Max aspect ratio
Height = 0.6 mm	26 633 700	0.86	86.1
Height = 1.0 mm	32 958 900	0.86	84.7
Height = 1.4 mm (base pipe)	91 407 600	0.74	316.59
Height = 1.8 mm	52 866 000	0.86	76.7
Pitch = 150 mm	28 716 300	0.89	95.5
Pitch = 300 mm (base pipe)	91 407 600	0.74	316.59
Pitch = 450 mm	27 999 000	0.89	97.7
Pitch = 600 mm	30 336 360	0.87	240.4

Table 2. Parameters of meshes for pipes with triangular turbulators.

Turbulator geometry	Number of elements for single	Max skewness	Max aspect ratio
Height = 0.6 mm	26 028 900	0.89	285.7
Height = 1.0 mm	27 901 800	0.86	229.2
Height = 1.4 mm (base pipe)	117 933 300	0.74	198.51
Height = 1.8 mm	33 593 400	0.90	181.8
Pitch = 150 mm	28 716 300	0.89	204.9
Pitch = 300 mm (base pipe)	117 933 300	0.74	198.51
Pitch = 450 mm	19 101 600	0.88	230.6
Pitch = 600 mm	17 353 600	0.90	250.5

Compared to the calculations made in [12], the computational grids are characterized by much higher values of the aspect ratio parameter because longer pipes were simulated (0.3 m in [12] vs. 0.9 and 1.2 m in this work) to ensure thermally and hydrodynamically fully developed flow in the rear part of the pipe. This positively

affects the accuracy of calculations and mapping changes in thermal and flow parameters along the pipe axis (i.e., the fully developed flow was obtained). On the other hand, skewness has slightly increased. But elements with poorer skewness are mainly located in the solid region. Only the energy equation that accounts for heat conduction in solid elements is solved there, which solution is immune to poorer quality elements. In the fluid region, the maximum skewness never exceeds 0.72 in pipes with rectangular vortex generators and 0.81 with triangular vortex generators. The *y*+ values also slightly increased compared to the results from [12], ranging from 1 to 2 for the maximal considered Re of 8000. However, the SST *k*-ω model allows accurate calculations for *y*+ up to 4-5.

4.2. Solution strategy

In the beginning, it was necessary to consider the stabilization of the thermal boundary layer in the pipe. This was required to find heat transfer rates for fully developed flow in the rear part of the pipes, in which the calculation results were averaged. Therefore, it was necessary to determine the optimal length of the tested pipe sections. It turned out that very good results were obtained for a pipe with a length of 0.9 m for 150, 300, and 450 mm pitches and 1.2 m for a pitch of 600 mm. The results for averaging were picked from the pipe section of length between 0.8 and 0.9 m.

Performed initial verification for the model of smooth pipe using Nu number correlations showed that the differences between correlations and numerical results were in the range of 3-5% for considered Re values. This analysis proves the good accuracy of the developed model. Moreover, mesh sensitivity analyses were performed for the smooth pipe and selected pipes with ribs, i.e., refined meshes were generated with smaller elements close to the walls. For refined grids, the *y*+ was below 1. These simulations' results were compared with those obtained for meshes used in this paper. The relative differences in calculated Nu numbers between current and fine meshes were below 1%, which showed the grid size independence of the developed model. The model validation was not performed at the current state, but the experimental studies are ongoing.

The solution strategy was divided into two phases. In the first phase, the periodic fluid flow problem in pipes without heat transfer was considered to find hydrodynamically fully developed velocity and turbulence fields in the computational domains. The fluid flow in the pipes was solved using the *k*-ω SST turbulence model implemented in the commercial engineering software ANSYS Fluent. In the second phase, the energy equation was only solved based on the fluid velocity and turbulence fields in the pipes obtained in the previous phase, but the problem was not further assumed periodic. In this phase, the momentum and turbulence equations were not solved. This strategy allowed for simulations of short repeatable segments of the pipes. The heat transfer problem in the pipes was solved based on the hydrodynamically fully developed flow and turbulence fields. As fluid flow and heat transfer equations were decoupled (i.e., fluid properties were assumed temperature-independent), the applied solution strategy did not influence the accuracy of the results. But it significantly speeded up the simulations and reduced the required length of pipe necessary to be simulated to obtain developed flow and thermal profiles.

Table 3. Properties of PEX and 24% wt. ethylene glycol solution.

Property	PEX	Ethylene glycol solution
Density (kg/m^3)	940	1049.56
Specific heat (J/kg/K)	2302.3	3852.09
Thermal conductivity (W/m/K)	0.46	0.258
Dynamic viscosity (kg/m/s)	-	0.00387

Table 4. The hydraulic diameters, cross-sectional areas, and mass flow rates of the working medium for assumed pipes geometries.

Turbulator geometry	Hydraulic diameter (m·10^3)	Cross-sectional area (m^2·10^4)	Mass flow rate (kg/s)		
			Reynolds number		
			3000	5500	8000
Smooth pipe	26.20	5.350	0.233	0.427	0.622
Rectangular height 0.6 mm	22.09	5.179	0.265	0.487	0.708
Rectangular height 1.0 mm	19.91	5.048	0.287	0.527	0.767
Rectangular height 1.4 mm	16.63	4.929	0.336	0.616	0.896
Rectangular height 1.8 mm	14.41	4.640	0.365	0.669	0.974
Triangular height 0.6 mm	22.97	5.358	0.264	0.484	0.705
Triangular height 1.0 mm	21.08	5.299	0.285	0.523	0.760
Triangular height 1.4 mm	19.35	5.212	0.306	0.559	0.814
Triangular height 1.8 mm	18.61	5.096	0.325	0.596	0.868

4.3. Material properties

The pipes were assumed to be made of PEX, while the working medium was 24% wt. aqueous solution of ethylene glycol. Their properties assumed in the simulations are given in Table 3.

4.4. Boundary conditions

In the first phase of the calculations, a periodic boundary condition at the inlet and outlet from the pipe with a given mass flow rate was applied (see Table 4, which contains mass flow rates for different Re, hydraulic diameters, and cross-sectional areas of pipes). In each case, the hydraulic diameter-based Re values were assumed to be the same and equal to 3000, 5500, and 8000. These values corresponded to smooth pipe glycol velocities of 0.335, 0.614, and 0.893 m/s, respectively. However, differences in the values of hydraulic diameters caused the mass flow to vary for each pipe with different vortex generator shapes, as shown in Table 4. In the case of variable helix pitch, mass flow rates were the same for each helix pitch and corresponded to the values for the respective pipes with a height of the turbulators equal to 1.4 mm. In the case of the variable height of the turbulator, mass flow rates varied, as shown in Table 4. In the second phase of the calculations, the fixed glycol temperature of 275.15 K was set at the pipe's inlet and 323.15 K at the external pipe surface. The rest of the surfaces were assumed to be adiabatic. The pipe outer wall temperature was significantly higher than the usual ground temperature, i.e., 281.15 K. However, this boundary condition allowed for obtaining a measurable working fluid temperature increase along the pipe section. The results were read from the pipe section of length between 0.8 and 0.9 m. Obtaining larger temperature increases in the pipe also eliminated the impact of possible numerical errors.

5. Results

5.1. Parametric simulations

In [12], the results of pressure drops and temperature increase in the pipe, heat flux density on the pipe wall, and average Nu were presented. However, to determine the effectiveness of the tested pipes, it is enough to look at the pressure drops and Nu values. In order to show the performances of the modeled pipes, these parameters are shown relative to the smooth pipe in Figures 3 and 4.

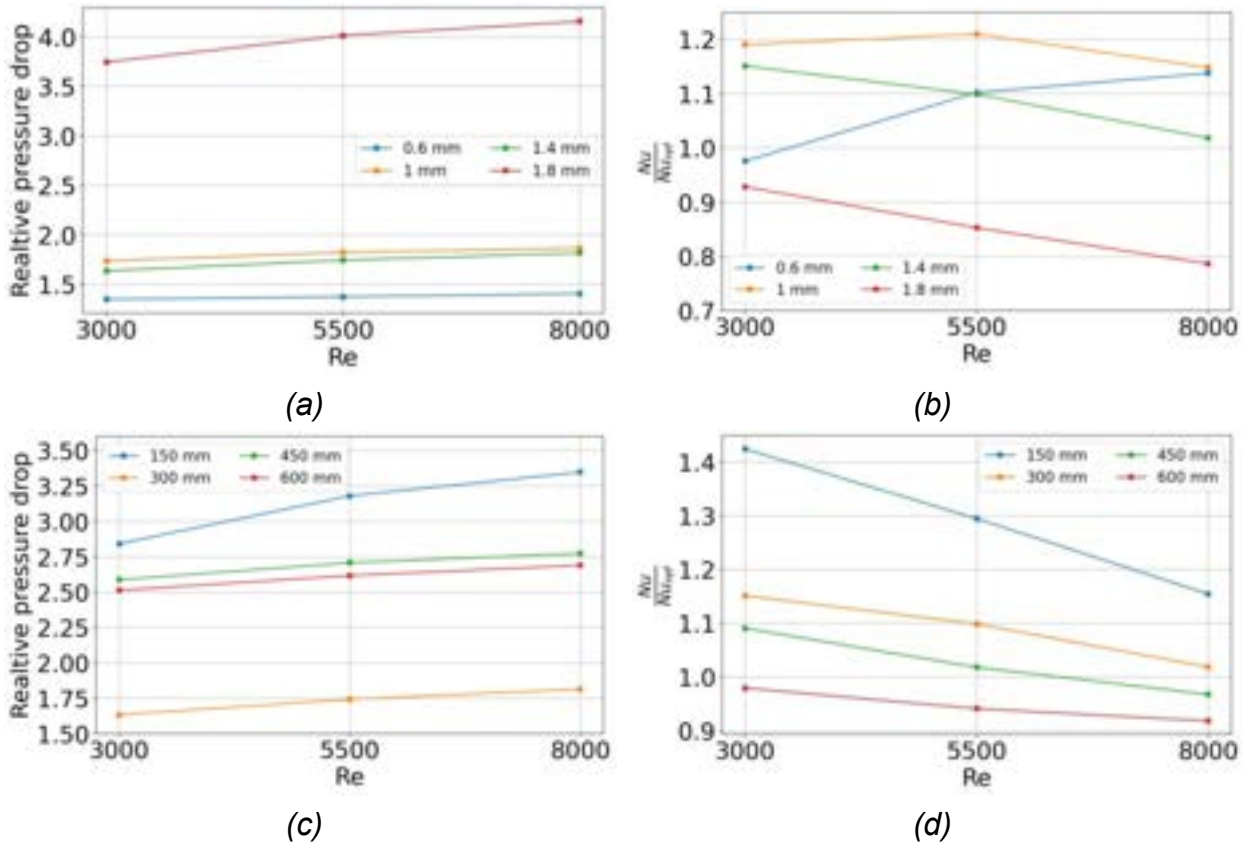

Figure 3. Parametrization analysis results for the model with rectangular turbulators: a) pressure drop depending on turbulator height, b) Nu depending on turbulator height, c) pressure drop depending on the pitch of the helix, d) Nu depending on the pitch of the helix.

In the first step, the pipes with rectangular turbulators were taken into account. Figure 3a shows that the size of the turbulators has a significant impact on the values of the obtained pressure drops. Generally, the larger

the turbulator, the greater the pressure drop. It can be seen that for turbulators with a height of 1.8 mm, the pressure drop is very large and is over 250-300% of the value for a smooth pipe. Thus, heights in the range of 0.6-1.4 mm, which are characterized by much lower pressure drop increase than the height of 1.8 mm, have the potential to improve the performance of the rectangular turbulators. For a height of 0.6 mm, the increase of the pressure drop is about 35-40%, while for 1 mm and 1.4 mm, the pressure drop rises by 60-80%. Figure 3b also shows that very large turbulators do not improve convective heat transfer. Pipes with heights of 0.6 mm and 1.4 mm achieve very different results depending on the Re. Pipes with vortex generators of a height of 1 mm turned out to be the best, characterized by an increase of the Nu in the range of 15-21% in the entire range of Re. Considering the pitch of the helix, it can be seen in Figure 3c that a pitch of 150 mm gives by far the greatest pressure drop, up to 230% more than for the smooth pipe. The pipe with a helix pitch of 300 mm turned out to be the best, which had the smallest increase in the pressure drop in the range of 60-85%. However, the results of the intensity of convective heat transfer indicate that the model with the smallest pitch of the helix gives the best results. It records an increase in the Nu by 15.5-43% compared to the smooth pipe. The model with a pitch of 300 mm already gives an increase of only 2-15%. The other two pipes perform worse both in terms of pressure drop and intensity of convective heat transfer than the base case. Based on these results, an optimized pipe was proposed. Its turbulators height is assumed to be 1 mm, and the pitch of the helix of 150 mm is selected.

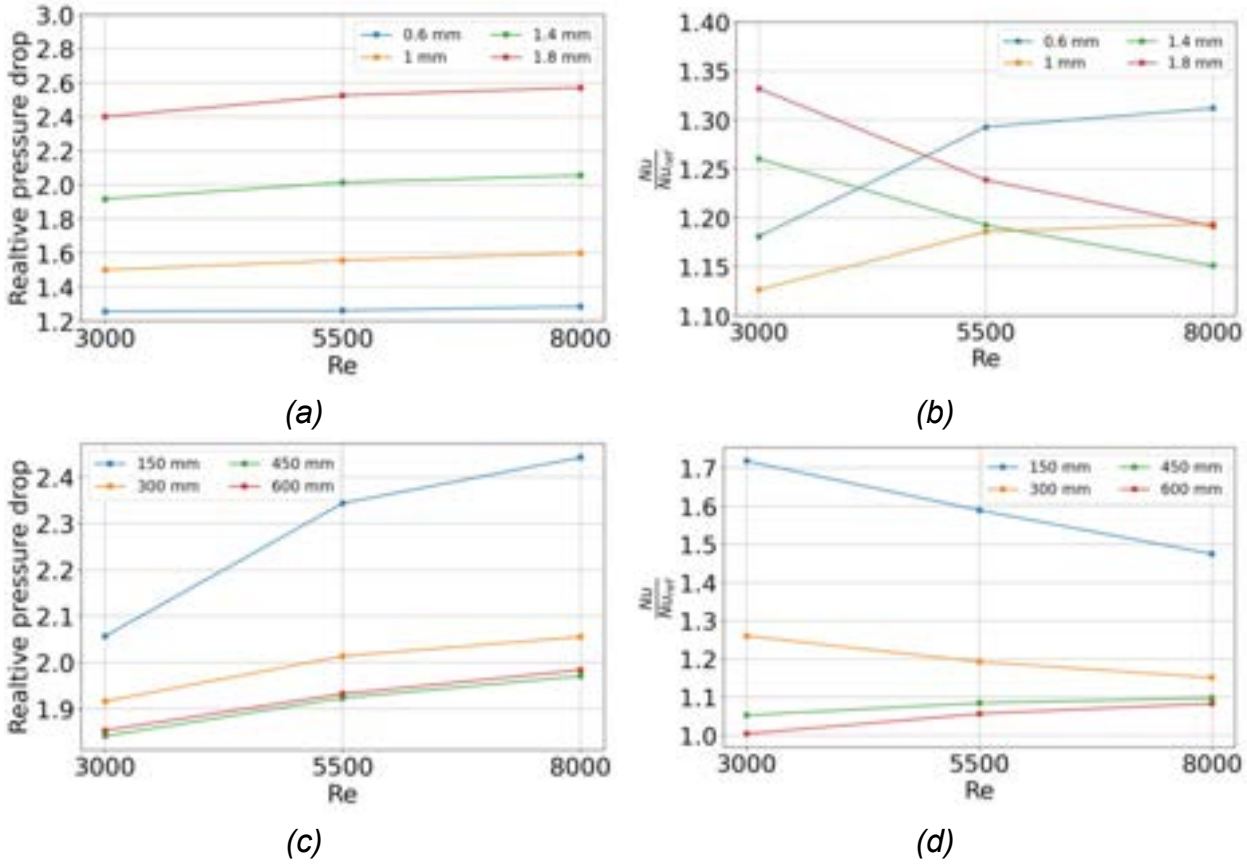

Figure 4. Parametrization analysis results for the model with triangular turbulators: a) pressure drop depending on turbulator height, b) Nu depending on turbulator height, c) pressure drop depending on the pitch of the helix, d) Nu depending on the pitch of the helix.

In the second step, the pipes with triangular turbulators were considered. Again, the increase in the size of the turbulators causes an increase in the pressure drop (Figure 4a), but this time the relationship is much more clear and linear. Of course, the best results are obtained for the pipe with 0.6 mm high turbulators, for which the increase is only 23%. For a height of 1 mm, it is already 50-60% depending on Re value. The thermal performance of all pipes is similar. The increase in the Nu is in the range of 12-33%. Larger turbulators (i.e., 1.4 and 1.8 mm) show better properties at lower Re numbers, while smaller turbulators (i.e., 0.6 and 1.0 mm) are more effective at higher Re. Considering the pitch of the helix, again, the pitch of 150 mm gives the greatest increase in pressure drop of 105-143% (Figure 4c) and the greatest increase in the Nu of 47-72% (Figure 4d). For other pipes, the increase in the pressure drop is significantly lower and amounts to 83-105%. But the increase in the Nu is also much smaller for these pipes and is in the range of 1-26%. Based on these results, the selected optimal pipe with triangular turbulators has a turbulators height of 0.6 mm and a helix pitch of 150 mm.

5.2. Optimized models

In this section, proposed optimized pipes are investigated. Information on computational meshes for optimized pipes is presented in Table 5, while mass flow rates for different Re, hydraulic diameters, and cross-sectional areas of these pipes are presented in Table 6.

Table 5. Parameters of meshes for optimized pipes.

Turbulator geometry	Number of elements	Max skewness	Max aspect ratio
Rectangular	24 056 100	0.86	277.58
Triangular	37 247 400	0.79	119.80

Table 6. The hydraulic diameters, cross-sectional areas, and mass flow rates of the working medium for optimized models.

Turbulator geometry	Hydraulic diameter ($m \cdot 10^3$)	Cross-sectional area ($m^2 \cdot 10^4$)	Mass flow rate (kg/s)		
			Reynolds number		
			3000	5500	8000
Rectangular	19.04	5.155	0.307	0.562	0.818
Triangular	22.97	5.358	0.264	0.484	0.705

The results obtained for the optimized pipes were compared with the base pipes calculated, among others, in [12]. Relative pressure drops and Nu were again compared in Figure 6.

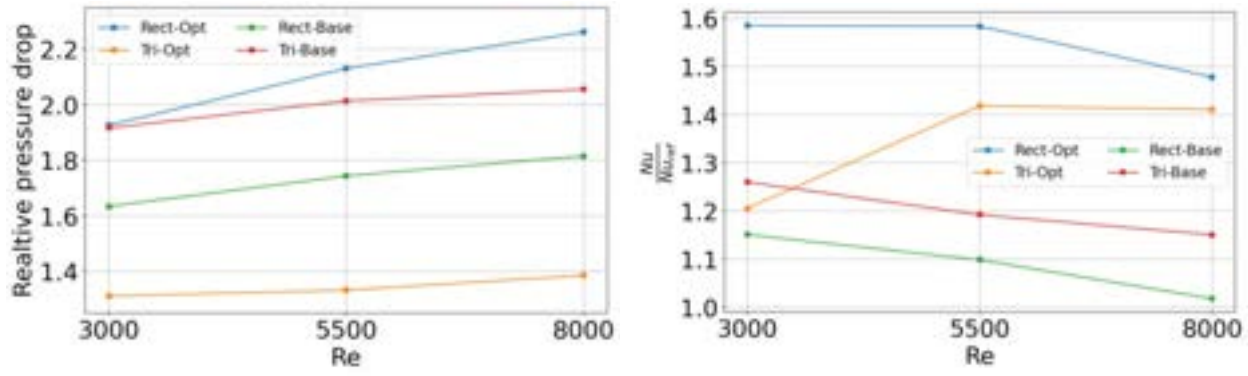

(a) *(b)*

Figure 5. Results for optimized models: a) pressure drop and b) Nu for different values of Re (Rect-Base – base pipe with rectangular turbulators, Rect-Opt – optimized pipe with rectangular turbulators, Tri-Base – base pipe with rectangular triangular, Tri-Opt – optimized pipe with rectangular triangular).

The optimized pipes have much better convective heat transfer performances. The increase in the Nu for the optimized pipe with rectangular turbulators is 47-58%, while for the pipe with triangular turbulators is 21-42%. For non-optimized pipes (base geometries), it was 2-15% and 15-26%, respectively. The average increments of the Nu for optimized pipes relative to the smooth ones are several times greater in both cases. The situation is different in the case of pressure drops, and the optimized model with rectangular turbulators has higher pressure drops. Optimized triangular turbulators are much better in this regard. For the pipe with triangular turbulators, a lower pressure drop was recorded for the considered Re range than for the base pipe, i.e., the relative pressure drop varied in the 31-39% range. For the optimized pipes with rectangular turbulators, the increase in pressure drop is 92-126%.

It should be noted that in these simulations, the Re was in the same range for all cases. This resulted in significantly higher glycol mass flow rates in modified pipes than the smooth ones, as modified pipes had lower cross-sectional area and lower hydraulic dimeters than the smooth pipe. For optimized pipes, the mass flow rates were higher, c.a. 32 and 13% for rectangular and triangular vortex promoters, respectively. Applying the same mass flow rates of the working medium in the smooth and modified pipes will result in a much lower pressure drop increase than shown in this work, while Nu will still be significantly higher. This shows that the practical implementation of pipes with turbulence promoters in ground heat exchangers may be profitable.

6. Conclusions

This paper presents numerical optimization of the geometry of turbulence promoters in polymeric-made pipes in terms of heat transfer and fluid flow performances. Two rib shapes, i.e., rectangular and triangular, were

selected based on the previous studies [12] as the most promising. Two geometrical parameters, i.e., vortex generators' height and pitch of the helix along which the ribs were extruded, were selected as variable parameters.

In the first step, a series of simulations were conducted for four ribs heights and four helix pitches. The results of these simulations allowed for finding the pressure drop and Nu characteristics for each pipe with internal surface modifications for Re in the range of 3000-8000. The results were analyzed, and optimal turbulators parameters were proposed based on that. For both rectangular and triangular vortex generators, their optimal height was selected to be 1 and 0.6 mm, respectively, while the pitch of the helix in both cases was chosen to be 150 mm.

In the second step, optimal turbulators' performances were compared to the initial (base) geometries. The optimized pipes have much better convective heat transfer performances. The increase in the Nu for the optimized pipe with rectangular vortex generators was 47-58% regarding the smooth pipe, while for the pipe with triangular modifications, it was 21-42%. These values, on average, are several times higher than for the initial turbulence promoters' geometries. However, for rectangular modifications, the pressure drops were higher than for base pipes and were in the range of 92-126%. Optimized triangular turbulators are much better in this regard. The triangular vortex promoters attained pressure drops in the 31-39% range, which was lower than for the base case.

In the performed analyses, the Re was in the same range for all simulated cases. This resulted in significantly higher glycol mass flow rates in modified pipes than the smooth ones. Applying the same mass flow rates of the working medium in the smooth and modified pipes will result in a much lower pressure drop increase than shown in this work for the fixed Re range, while Nu will still be significantly higher. This shows that the practical implementation of pipes with turbulence promoters in ground heat exchangers might be profitable.

Acknowledgments

The European Union supported this work within the European Regional Development Fund under project no. POIR.01.01.01-00-0188/2 "Development of innovative geothermal systems based on new probes with increased heat exchange efficiency applicable in vertical ground heat exchangers" granted by the National Centre for Research and Development (Poland).

References

[1] Ma G.-Y., Chai Q.-H., Characteristics of an improved heat-pump cycle for cold regions. Appl Energy 2004;77:235-47.

[2] Hart R., Price W., Improving ground-source heat pump efficiency: Optimizing pumping control and configuration of closed-loop heat pump systems in smaller commercial buildings. In Proc ACEEE Summer Study Energy Effic Build 2000;10:111-22.

[3] Park H., Lee J.S., Kim W., Kim Y., Performance optimization of a hybrid ground source heat pump with the parallel configuration of a ground heat exchanger and a supplemental heat rejecter in the cooling mode. Int J Refrig 2012;35:1537-46.

[4] Allaerts K., Al Koussa J., Desmedt J., Salenbien R., Improving the energy efficiency of ground-source heat pump systems in heating dominated school buildings: A case study in Belgium, Energy Build 2017;138:559-68.

[5] Liu Z., Li Y., Xu W., Yin H., Gao J., Jin G., Lun L., Jin G., Performance and feasibility study of hybrid ground source heat pump system assisted with cooling tower for one office building based on one Shanghai case. Energy 2019;173:28-37.

[6] Lee M., Lee D., Park M.H., Kang Y.T., Kim Y., Performance improvement of solar-assisted ground-source heat pumps with parallelly connected heat sources in heating-dominated areas. Energy 2022;2401:122807.

[7] Eswiasi A., Mukhopadhyaya P., Critical review on efficiency of ground heat exchangers in heat pump systems. Clean Technol 2020;2:204-24.

[8] Pethkool S., Eiamsa-ard S., Kwankaomeng S., Promvonge P., Turbulent heat transfer enhancement in a heat exchanger using helically corrugated tube. Int Commun Heat Mass Transf 2011:38;340-7.

[9] Liu J., Xie G., Simon T.S., Turbulent flow and heat transfer enhancement in rectangular channels with novel cylindrical grooves. J Heat Mass Transf 2015;81:563-77.

[10] Chen X., Han H., Lee K.-S., Li B., Zhang Y., Turbulent heat transfer enhancement in a heat exchanger using asymmetrical outward convex corrugated tubes. Nucl Eng Des 2019;350:78-89.

[11] Nowak A.J., Smolka J., Palacz M., Haida M., Wos J., CFD analysis of pressure drops within riffled pipes of vertical ground heat exchanger. In: Owen R., de Borst R., Reese J., Pearce C., editors. ECCM 6 and ECFD 7: Proceedings of the 6th European Conference on Computational Mechanics (Solids, Structures and Coupled Problems) and the 7th European Conference on Computational Fluid Dynamics; 2018 Jun

11-15; Glasgow, United Kingdom. International Center for Numerical Methods in Engineering CIMNE:4349-60.

[12] Łapka P., Wachnicki J., Analysis of possibilities of increasing convective heat transfer intensity in PEX pipes for applications in ground heat exchangers. CONV-22: Proceedings of CONV-22: International Symposium on Convective Heat and Mass Transfer; 2022 Jun 5-10; Izmir, Turkey. Begell House Digital Library:355-362.

Heat and Mass Transfer Analysis within a Disc-Shaped Fluidized Sorption Reactor

Marcin Sosnowski[a], Jaroslaw Krzywanski[b], Karolina Grabowska[c], Anna Zylka[d], Anna Kulakowska[e], Dorian Skrobek[f], Marcin Dyner[g], Waqar Muhammad Ashraf[h], Radomír Ščurek[i]

[a] *Jan Dlugosz University, Czestochowa, Poland, m.sosnowski@ujd.edu.pl, CA*
[b] *Jan Dlugosz University, Czestochowa, Poland, j.krzywanski@ujd.edu.pl*
[c] *Jan Dlugosz University, Czestochowa, Poland, k.grabowska@ujd.edu.pl*
[d] *Jan Dlugosz University, Czestochowa, Poland, a.zylka@ujd.edu.pl*
[e] *Jan Dlugosz University, Czestochowa, Poland, a.kulakowska@ujd.edu.pl*
[f] *Jan Dlugosz University, Czestochowa, Poland, d.skrobek@ujd.edu.pl*
[g] *Jan Dlugosz University, Czestochowa, Poland, m.dyner@ujd.edu.pl*
[h] *University College London, London, United Kingdom, waqar.ashraf.21@ucl.ac.uk*
[i] *VŠB - Technical University of Ostrava, Octrava, Czech Republic, radomir.scurek@vsb.cz*

Abstract:

The depletion of fossil fuels and increased greenhouse gas emissions are crucial factors forcing innovation in various branches of industry and life. In the 21st-century air conditioning is becoming a necessity in terms of well-being and health. Therefore, adsorption cooling technology constitutes a very promising alternative to energy-consuming and environmentally hazardous vapour compression chillers. The main challenge in the wider popularization of adsorption technology is the intensification of heat and mass transfer within the adsorption bed. Therefore, the paper presents different sorption reactor concepts aimed at solving the aforementioned issue. The main parameters influencing heat and mass transfer for each of the analyzed cases are calculated using the computational fluid dynamics code adapted to capture the specific phenomenon occurring in the adsorption bed. The developed numerical model is validated against the experimental data collected on the test stand dedicated to experimental research of innovative adsorption beds operating in various conditions. The results of numerical modelling with the use of the developed coupled CFD & DEM model concerning the adsorbent particles movement and variation in relative temperature of the adsorbent within the fluidization process are presented in the paper. The research allowed to define the design parameters of the adsorption bed that allow intensifying the heat and mass transfer in the adsorption reactor and, in consequence, significantly contribute to the development and popularization of the adsorption cooling technology.

Keywords:

Adsorption chiller; CFD & DEM coupling; Computational fluid dynamics; Discrete element modelling; Fluidization; Heat and mass transfer.

1. Introduction

1.1. Innovation for a sustainable future

The depletion of fossil fuels and the urgent need to reduce greenhouse gas emissions have forced various industries to innovate and develop sustainable alternatives. The major development activities are carried out in energy [1], transportation [2], agriculture [3], and construction industry [4] among which the energy industry is one of the largest contributors to greenhouse gas emissions and climate change. To reduce emissions, the industry has shifted toward renewable energy sources such as solar, wind, and geothermal power. In addition, innovations in energy storage technologies such as batteries and hydrogen fuel cells are also helping to make renewable energy more viable. According to the roadmap presented by the International Renewable Energy Agency [1], renewable energy technologies could provide 90% of the world's electricity by 2050, reducing greenhouse gas emissions by 60%. In addition, cooling systems are responsible for up to 26% of electricity consumption depending on the country [5], with more than 40% of energy consumption in the residential and service sector [6]. This leads directly to the occurrence of peak demand for electricity during the summer period

when the capacity of the power system is the lowest. Such a situation may result in local power deficits or even blackouts, examples of which have already appeared many times. Therefore, the energy industry has been exploring alternative and sustainable energy sources such as solar energy or wind energy but attempts have also been made to waste heat utilization. One of the technologies allowing to effectively utilize the low-grade waste heat for chill generation, seawater desalination or long-term heat storage is the adsorption technology.

1.2. Advantages and disadvantages of adsorption technology

Adsorption technology involves using solid adsorbents to capture and store or transform energy. The process involves the adsorption of a gas or vapour onto a solid surface, which releases heat energy. Several types of adsorbents can be used in adsorption technology, such as zeolites, activated carbons, and metal-organic frameworks (MOFs). Each type of adsorbent has unique properties that make it suitable for specific applications. Metal and carbon nanotube additives to adsorbent are capable to improve its thermal diffusivity and subsequently the overall performance of the process [9]. One of the advantages of adsorption technology is its ability to use low-grade waste heat sources, which are typically not viable for other heat recovery technologies. The recent interest in adsorption cooling technology results from the following benefits of adsorption chillers in comparison to conventional vapour-compression systems:

- powered with a renewable or waste heat source of temperature as low as 50°C [10], which directly leads to a reduction in CO_2 emissions and pollution [11],
- environmentally friendly due to the absence of hazardous and environmentally harmful refrigerants [12],
- capable to desalinate seawater [13],
- almost zero electricity consumption [14],
- no moving parts resulting in high reliability [15],
- quiet due to the absence of compressors and no vibration [16],
- simple control & maintenance [16].

But the widespread application of adsorption chillers is limited by the following shortcomings of adsorption cooling technology:

- low coefficient of performance [17],
- large weight & volume [15],
- intermittent cooling [18],
- high initial procurement cost [18],
- exploitation under vacuum conditions [19].

1.3. Adsorption chiller work cycle

The adsorption process in the chiller is used to transfer heat and produce cooling, with the refrigerant being adsorbed onto the surface of a solid adsorbent material [20]. The work cycle of an adsorption chiller typically involves several subsequent stages, including adsorption, refrigerant transfer, desorption, and refrigerant condensation.

1.3.1. Adsorption

In the adsorption stage, the adsorbent material is exposed to the refrigerant vapour and the refrigerant molecules are adsorbed onto the surface of the adsorbent. The adsorption process is driven by a heat source, which raises the temperature of the adsorbent and facilitates the adsorption of the refrigerant.

1.3.2. Refrigerant Transfer

Once the refrigerant is adsorbed onto the adsorbent material, the next stage of the cycle is the transfer of the refrigerant. This involves the movement of the refrigerant vapour from the adsorber to the evaporator.

1.3.3. Desorption

In the desorption stage, the temperature of the adsorbent is lowered. This causes the refrigerant molecules to be released from the surface of the adsorbent and return to the vapour phase. The desorption stage is the key to the cooling process as it releases the heat that was previously absorbed during the adsorption stage.

1.3.4. Refrigerant Condensation

The final stage of the work cycle is the condensation of the refrigerant vapour back into a liquid. This stage involves the use of a condenser, which is typically cooled using a cooling medium such as water. As the refrigerant vapour flows through the condenser, it gives up its heat to the cooling medium and condenses into a liquid, ready to repeat the cycle.

1.3.5. Thermodynamic cycle

The sorption reactor operates between the condenser/evaporator pressure and the minimum/maximum adsorbate concentration levels. The Clapeyron diagram depicted in Figure 1 illustrates the four ideal thermodynamic stages occurring in the bed i.e., isosteric preheating (1–2), isobaric desorption (2–3), isosteric precooling (3–4), and isobaric adsorption (4–1).

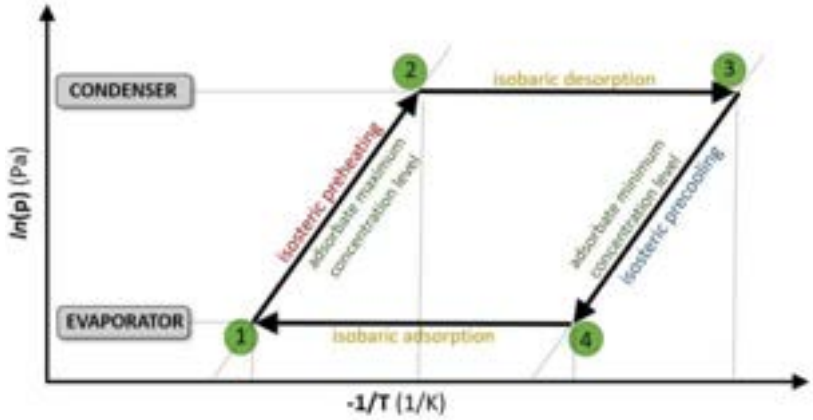

Figure 1. Clapeyron diagram of a basic adsorption chiller work cycle

1.4. Adsorption chiller construction

The operation of an adsorption chiller typically involves a closed-loop system, which includes an evaporator, an adsorber, a condenser, and a desorber as shown in Figure 2a. The refrigerant absorbs heat and evaporates in the evaporator, while it is adsorbed onto the surface of the adsorbent material in the adsorber. The refrigerant is cooled and condenses back into a liquid in the condenser and the desorber is where the refrigerant is desorbed from the adsorbent material, releasing the heat that was previously absorbed. Typically, the adsorber and desorber are combined into one sorption reactor to simplify the system and reduce its overall cost (Figure 2b). Moreover, at least two sorption reactors operating interchangeably are commonly used to assure constant delivery of cool (Figure 2c). The operation of an adsorption chiller is controlled with valves linking the above-mentioned parts of the system. Researchers have also proposed more sophisticated concepts: combined heating and cooling adsorption chiller [21], three-bed adsorption chiller [22] or re-heat two-stage adsorption chiller [23].

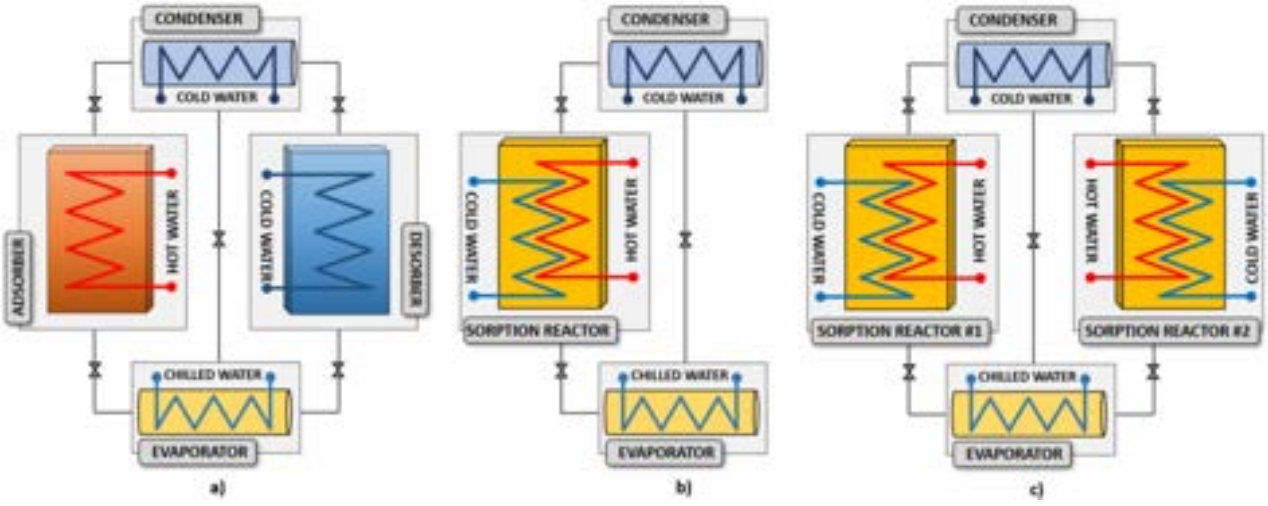

Figure 2. The schematic diagram of the adsorption chiller construction: a) basic concept, b) adsorber and desorber combined into a sorption reactor, c) two sorption reactors operating interchangeably.

1.5. Previous research

The effect of cooling temperature on the performance of a solar adsorption chiller with enhanced mass transfer was investigated in [24]. The authors proposed a new enhanced mass transfer mode with two condensers and a micro vacuum pump for decreasing the desorption pressure. The refrigerant vapour was condensed before being pumped into the receiver, which increased the density of the refrigerant and improved the mass flow

rate with the same pressure and working speed of the pump. The performance of the solar adsorption cooling system with the enhanced model was evaluated and compared with three different cooling temperatures. The results showed that reducing the cooling temperature can greatly improve the coefficient of performance (COP) under the mode of enhanced mass transfer.

The integrated adsorption-absorption system driven by transient heat sources for cooling and desalination was investigated in [25] and [26]. In the first case, the system operated with a relatively low exergy efficiency in the absorption cycle of up to 15.33%. The adsorption bottoming cycle successfully utilised the heat from the absorption subsystem at a relatively higher exergy efficiency of up to 42.69%. The execution of a transient heat source of sinusoidal waveform enhanced the water production by up to 30% and the cooling of absorption and adsorption subsystems by 24% and 15%, respectively. The performance of innovative combined absorption and adsorption cooling systems employing the same evaporating and condensing units was theoretically investigated in [26]. The performance of the proposed system was compared with a separated absorption and adsorption cooling system, combined absorption and adsorption cooling system employing the parallel operation mode, a conventional single-stage adsorption cooling cycle, and other integrated systems available in the literature.

Triply periodic minimal surface structures have been implemented in adsorber/desorber to improve the performance of adsorption cooling systems in [27]. The use of metal triply periodic minimal surface-based structures considerably increased the effective thermal conductivity of the porous media/metal composite due to its large surface area to porous media volume. A fully three-dimensional computational fluid dynamics model was constructed using ANSYS Fluent in the above-mentioned research. This research methodology was also applied in [28].

An experimental and analytical study on the application of adsorber plate heat exchangers in thermally driven chillers was carried out in [29]. The authors investigated the effect of both heat and mass transfer characteristic lengths of two different adsorber plate heat exchangers for application in an adsorption chiller on the adsorption and desorption kinetics. It turned out that the adsorption kinetics is mainly influenced by the mass transfer characteristic lengths, while the desorption kinetics is dominated by the heat transfer characteristic lengths of the adsorbent domain.

Apart from computational fluid dynamics, the artificial intelligence approach is also commonly used in the analysis of adsorption systems. Heat and mass transfer prediction in fluidized beds of cooling and desalination systems was researched in [30]. The developed model allowed the study of input parameters' effect on the outputs and optimize the operating strategy of the bed. Also, the cost of manufacturing adsorption chillers is described in the scientific literature [31] - at a maximum Coefficient of Performance of 1 and maximum Specific Cooling Power of 300 W/kg, the specific selling price of a Silica gel adsorption chiller is €1018 per kW of cooling power.

The effectiveness of adsorption technology in waste heat utilization has been proved in numerous research papers e.g. [32]. The authors conducted experimental and theoretical analyses on the effects of temperature, dew point, and the flow velocity of high-temperature moist air on the regeneration rate in the adsorption heat pump systems.

1.6. Motivation and novelty

Despite the presented numerous research activities aiming to improve the adsorption cooling technology, further research and development are needed to optimize it and make it more cost-effective for commercial applications. Therefore, this paper aims to propose the novel concept of using computational fluid dynamics (CFD) coupled with discrete element modelling (DEM) to analyse the benefits of using fluidization to improve heat and mass transfer within the adsorption bed. Such an approach has never been used before and reveals great potential for further improvement in optimizing the construction of adsorption reactors with numerical methods. It will deliver new knowledge, especially concerning the adsorbate velocity field within the sorption reactor at the operating conditions (absolute pressure below 3 kPa) and it will allow to design the reactor and control the process in a way that maximizes the heat and mass transfer within the whole volume of the adsorbent material.

2. Methods and research objects

As the heat and mass transfer in the sorption reactor are the main factors influencing the overall performance of the adsorption chiller, several design concepts of the reactor were analysed within the carried-out research. They are described in the following paragraphs with the newest concept of fluidized sorption reactor being the main focus of attention.

2.1. Honeycomb sorption reactor

The concept of a honeycomb sorption reactor depicted in Figure 3 was presented in detail in [33]. It contributed to the increased heat transfer surface area and simultaneously assured a compact and lightweight design of the chiller. The computational fluid dynamics analysis performed with the use of the developed endothermic desorption model incorporated into the ANSYS Fluent software allowed defining of the optimal design of the

investigated type of heat exchanger and its correlation with basic factors influencing the performance of the sorption reactor and its dimensions such as the gradient of heating/cooling water temperature, logarithmic mean temperature difference, heat exchanger mass to sorbent ratio, effective mass factor, heat transfer surface to sorbent mass ratio and solid volume fraction. Moreover, the spatial temperature distribution in the reactor as well as the influence of construction material on the above-mentioned factors were defined.

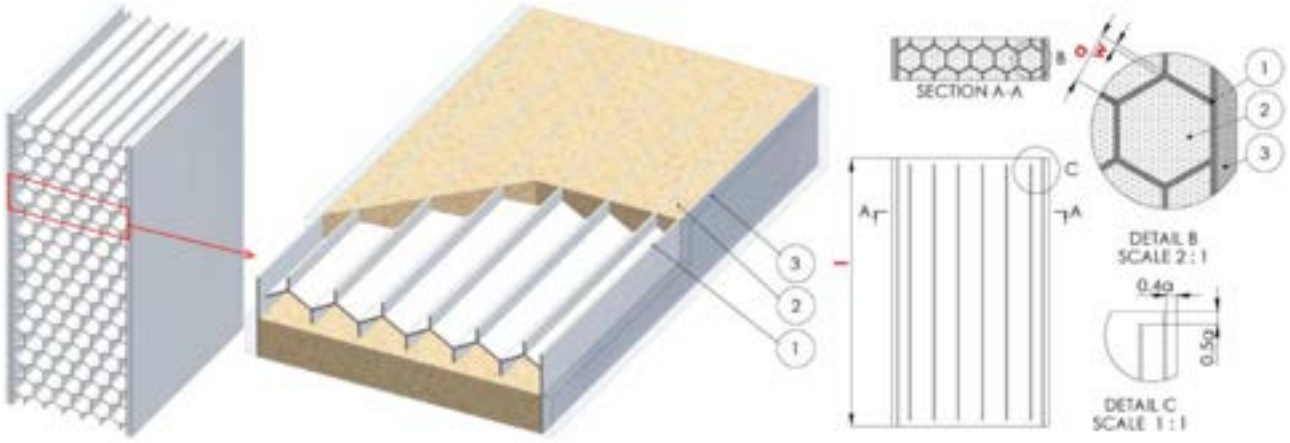

Figure 3. Concept of a honeycomb sorption bed [33], 1 – metal heat exchanger, 2 - sorbent, 3 – heating/cooling water collector

The commercial ANSYS Fluent tool dedicated to computational fluid dynamics was used in this research. However, it does not allow for sufficient consideration of the aspects related to heat and mass exchange during sorption processes. Therefore, the User-Defined Functions (UDF) capability was used to create the model of sorption processes, as it is necessary to take into account fluctuations in the local intensity of heat production or consumption during the exothermic adsorption or endothermic desorption process, respectively. The above-mentioned intensity of heat production or consumption in the sorption reactor depends directly on the local temperature of the sorbent. The mathematical dependence of the sorption intensity and the sorbent temperature was determined as a polynomial function of coefficients defined and validated during previous studies concerning heat transfer in the sorption beds [34].

2.2. Multi-disc sorption reactor

The innovative construction of a multi-disc sorption reactor depicted in Figure 4 was investigated and presented in detail in [35]. In contrast to the commonly applied designs, in a multi-disc reactor, the sorbent is placed in separate disc-shaped packets, and the cooling/heating water washes the packets of sorbet from the outside transferring heat. The adsorbate vapour flows through the fixing net into the sorbent packets penetrating them. The fixing net holds the granular sorbent inside the disc-shaped packets.

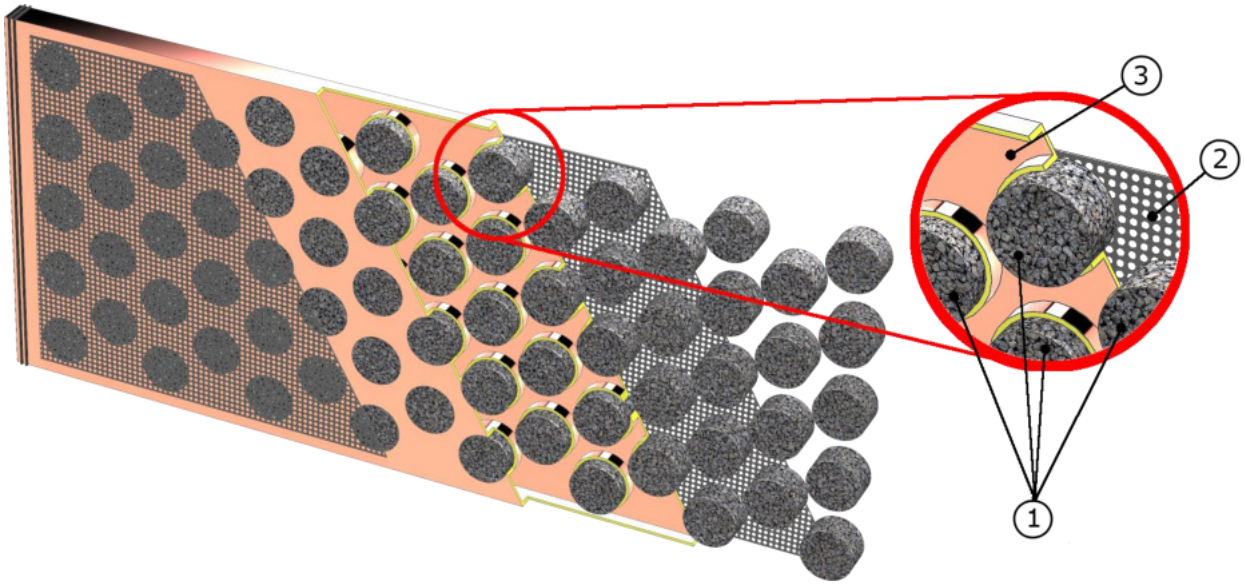

Figure 4. Section view of the investigated multi-disc sorption bed [35]: 1 - disc-shaped sorbent packets; 2 - fixing net; 3 - the main body of the sorption reactor

The proposed construction allowed to place the sorption reactor e.g. in the ceiling of the building or integrating it with solar panels to directly supply the reactor with the necessary heat. Such a solution allows to significantly expand the potential installation sites of the adsorption chillers and thus reduces the need to save a large space for the installation of the adsorption chiller – it is one of the main disadvantages of these devices. Another advantage of the proposed solution is its potential for scalability by adjusting the number of sorbent discs to the expected cooling capacity of the adsorption chiller or the possibility of installing two or more multi-disc sorption reactors with sorbent packages one above another with the space between them being a vapour collector [35].

2.3. Disc-shaped fluidized sorption reactor

The low coefficient of performance of the conventional fixed-bed adsorption chillers is one of their main disadvantages. It results from the low heat transfer in the sorbent beds. One of the well-known methods, allowing to improve the heat transfer coefficient between the porous material and the immersed heating surface is fluidization [36]. Therefore, based on the best practices and numerical models developed and validated within the research concerning honeycomb sorption reactor and multi-disc sorption reactor, the novel concept of a disc-shaped fluidized sorption reactor has been proposed to maximize the coefficient of performance of the adsorption chiller.

2.3.1. Experimental test stand

The experimental test stand was adapted to investigate the operation of the disc-shaped fluidized reactor and to deliver experimental data necessary to validate the developed numerical model of the sorption reactor described in paragraph 2.3.2. Coupled CFD & DEM.

The schematic diagram and the photograph of the experimental test stand are depicted in Figure 5. The test stand consists of a bottom tank operating as an evaporator and an upper tank equipped with an interchangeable sorption reactor. Both tanks are connected to the vacum pump and to each other via valves controlled individually by the data acquisition and control unit. Both tanks are equipped with electrical heating and an additional inlet/outlet to be supplied with liquid medium (water) for cooling or heating. Moreover, mass sensors, absolute and relative pressure sensors and temperature sensors are installed in both tanks. A detailed description of the experimental test stand is provided in [37].

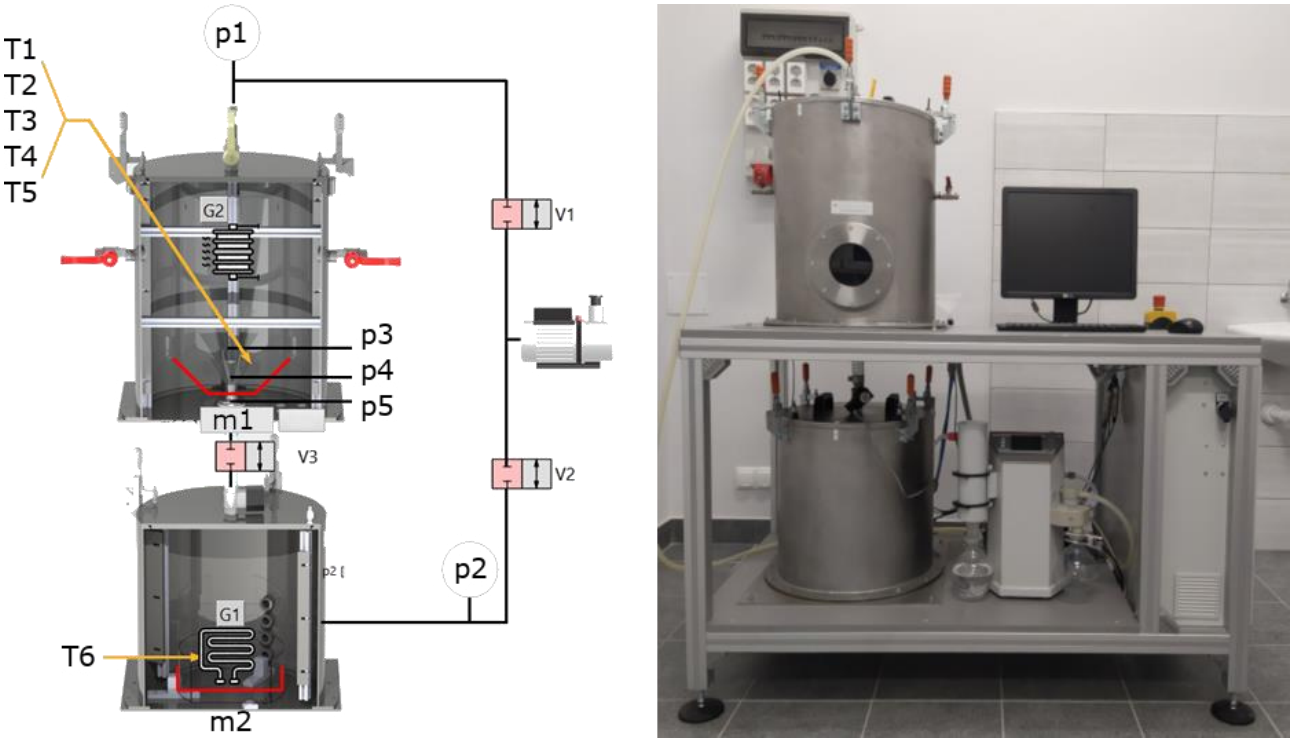

Figure 5. Experimental test stand: schematic diagram (left) and photograph (right)

The top tank can be equipped with different types of sorption reactors and for the purpose of the research the investigated disc-shaped fluidized reactor depicted in Figure 6 was installed in the test stand. The diameter of the reactor was 30 mm and the height of the adsorbent material bed was 30 mm at steady state. The spherical silica gel of 500 μm diameter and bulk density equal to 780 kg/m^3 was used as the adsorbent. The initial pressure in the top tank was 1500 Pa and 2500 Pa in the bottom tank resulting in the initial pressure difference of 1000 Pa. This pressure difference was the driving force of the fluidization process in the sorption reactor. The fluidization lasted until the equilibrium of pressure in both tanks which was 20 seconds.

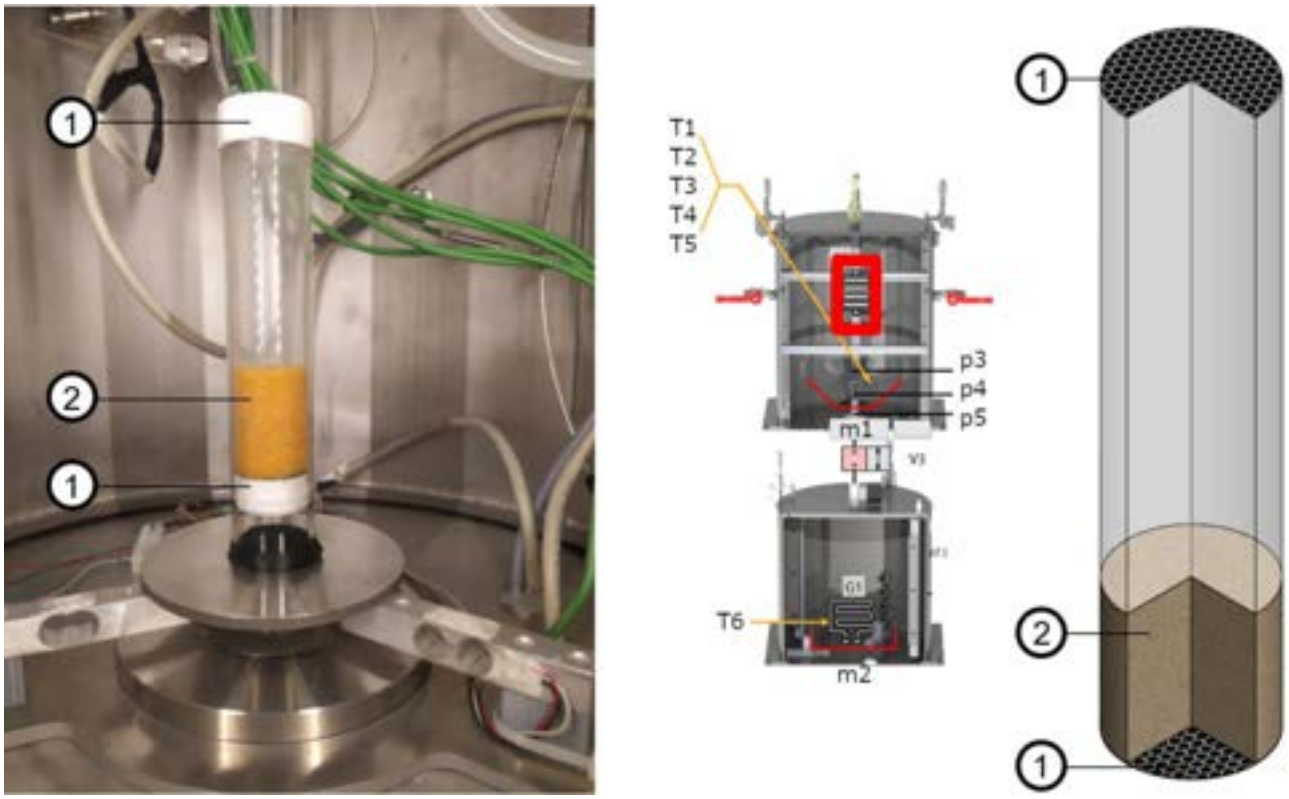

Figure 6. Disc-shaped fluidized sorption reactor: 1 – fixing net, 2 – silica gel

2.3.2. Coupled CFD & DEM

The detailed numerical analysis of the disc-shaped fluidized reactor is a challenging task due to the lack of suitable models. Therefore, the carried-out research aimed to develop a comprehensive model coupling the computational fluid dynamics code with the discrete element method. Such an approach is a promising alternative for modelling granular-fluid systems, expanding the range of coupled particle-fluid processes that can be managed with numerical simulations. Two-way coupling, in which the fluid flow affects the particle movement and the particle flow influences the continuous phase behaviour was applied within the research. Complex phenomena such as heat and mass transfer in a fluidized reactor can be handled with such configured tools after further expanding their standard capabilities with an adsorption/desorption model.

Therefore, the numerical research was divided into two stages: (1) adsorbent particles movement and heat transfer with wall-particle and particle-particle interactions, and (2) additional analysis with a user-defined function capable to take the heat and mass transfer resulting from the sorption processes into account. The results resented below are obtained within the first stage of the research.

The developed model was validated using the data registered on the experimental test stand presented in paragraph 2.3.1.

3. Results

The results of numerical modelling with the use of the developed coupled CFD & DEM model concerning the adsorbent particles movement and variation in relative temperature of the adsorbent within the fluidization process lasting 20 seconds are presented in Figure 7 for time step equal 1 s. The initial pressure difference equal to 1 kPa between the bottom tank (evaporator) and the upper tank induced the flow of the adsorbate (water vapour) directed towards the upper tank. Within the first second of the process, all the adsorbent particles were fluidized by the flow and approx. 40% of the total number of particles were suspended in the upper part of the reactor. The upper fixing net indicated in Figure 6 with the number (1) prevented the particles from being pushed out of the sorption reactor. These particles were suspended there until the ninth second of the process – at that time the pressure difference between the tanks was reduced, which induced a decrease in the adsorbate flow velocity. Therefore, the particles suspended in the upper part of the reactor began to move towards the bottom of the reactor where they were effectively fluidized and the heat transfer was intensified. This process lasted until the sixteenth second when the fluidization stopped due to the decrease of the flow velocity below the fluidization velocity. It can be seen that the heat transfer between the sixteenth and the twentieth second significantly decreased and occurred mostly only in the 10% of the particles located at the very bottom of the disc-shaped fluidized sorption reactor.

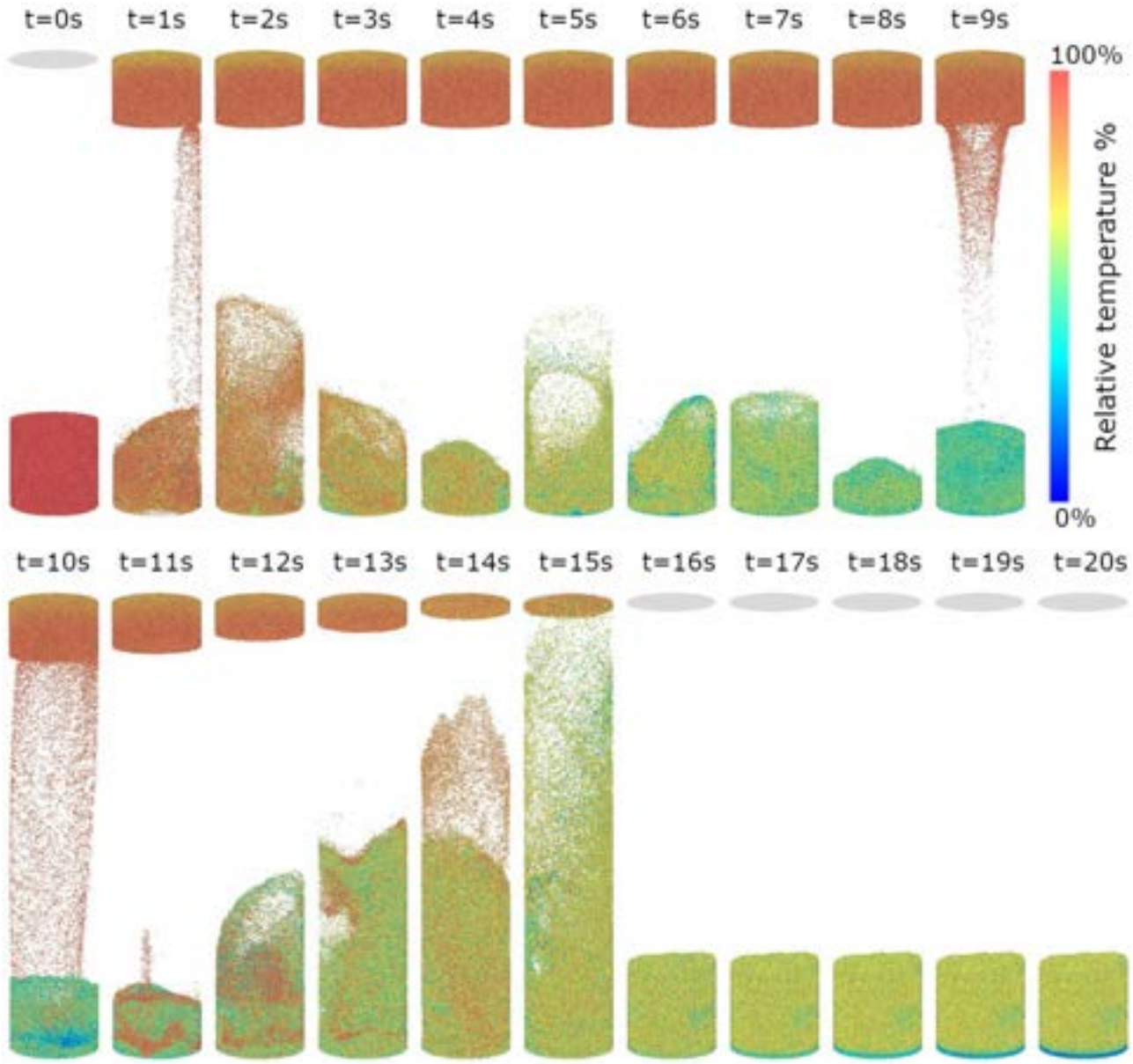

Figure 7. Adsorbent particles movement and variation in relative temperature of the adsorbent within the disc-shaped fluidized reactor for consecutive time steps.

4. Conclusions

The paper presents three concepts of sorption reactors dedicated to adsorption chillers with a special focus on the novel disc-shaped fluidized reactor. All the reactors are analysed with numerical methods. The new approach of coupled computational fluid dynamics and discrete element modelling was applied in the numerical analysis of the disc-shaped fluidized sorption reactor.

The developed numerical model was validated using the data obtained on the experimental test stand.

The results indicate that the coupled CFD & DEM modelling approach is a powerful and cost-effective research tool capable of effectively analysing complicated physical phenomena occurring in the proposed concept of a disc-shaped fluidized reactor. Such an approach has never been used before and reveals great potential for further improvement in optimizing the construction of adsorption reactors with numerical methods.

Further research is needed to extend the model with a user-defined function capable to take the heat and mass transfer resulting from the sorption processes into account. Moreover, the optimal pressure difference inducing the adsorbate flow has to be defined to intensify the heat and mass transfer within the process. The above-mentioned issues will be investigated and presented in the forthcoming papers.

Acknowledgements

This work was performed within project No. 2018/29/B/ST8/00442, “Research on sorption process intensification methods in modified construction of adsorbent beds” supported by the National Science Center, Poland. The support is gratefully acknowledged.

References

[1] Global Energy Transformation: A roadmap to 2050, International Renewable Energy Agency, Abu Dhabi, 2018.
[2] Global EV Outlook 2020, International Energy Agency, Paris, 2020.
[3] Regenerative Organic Agriculture and Climate Change: A Down-to-Earth Solution to Global Warming, Rodale Institute, Kutztown, 2014.
[4] Bringing Embodied Carbon Upfront: Coordinated Action for the Building and Construction Sector to Tackle Carbon Emissions, World Green Building Council, London, 2019.
[5] Quality report of European Union energy statistics, European Commission, 2017.
[6] R. Saidur, H.H. Masjuki, M.Y. Jamaluddin. "An application of energy and exergy analysis in residential sector of Malaysia". Energy Policy 2007; 35(2):1050-1063.
[7] Sztekler K, Kalawa W, Nowak W, Mika L, Grabowska K, Krzywanski J, et al. Performance evaluation of a single-stage two-bed adsorption chiller with desalination function. Journal of Energy Resources Technology. 2021;1–22.
[8] Sztekler K, Kalawa W, Nowak W, Stefański S, Mkia Ł, Siwek T, et al. Experimental study of two-bed adsorption chiller with desalination. In: , editor. ECOS 2019 - Proceedings of the 32nd International Conference on Efficiency, Cost, Optimization, Simulation and Environmental Impact of Energy Systems 2019. p. 3143–51.
[9] Kulakowska A, Pajdak A, Krzywanski J, Grabowska K, Zylka A, Sosnowski M, et al. Effect of Metal and Carbon Nanotube Additives on the Thermal Diffusivity of a Silica-Gel-Based Adsorption Bed. Energies [Internet]. 2020;13(6). Available from: https://www.mdpi.com/1996-1073/13/6/1391
[10] Hassan, H.; Mohamad, A.; Alyousef, Y.; Al-Ansary, H. A review on the equations of state for the working pairs used in adsorption cooling systems. Renewable and Sustainable Energy Reviews 2015, 45, 600–609.
[11] Pyrka, P. Modelowanie trójzłożowej chłodziarki adsorpcyjnej. Zeszyty Energetyczne 2014, 1, 205–216.
[12] Voyiatzis, E.; Stefanakis, N.; Palyvos, J.; Papadopoulos, A. Computational study of a novel continuous solar adsorption chiller: performance prediction and adsorbent selection. International journal of energy research 2007, 31, 931–946.
[13] Shahzad, M. W.; Ybyraiymkul, D.; Burhan, M.; Oh, S. J.; Ng, K. C. An innovative pressure swing adsorption cycle. AIP Conference Proceedings 2019, 2062, 020057.
[14] Sur, A.; Das, R. K. Review of technology used to improve heat and mass transfer characteristics of adsorption refrigeration system. International Journal of Air-Conditioning and Refrigeration 2016, 24, 1630003.
[15] White, J. Literature review on adsorption cooling systems. Latin American and Caribbean Journal of Engineering Education 2013.
[16] Sultana, T. Effect of overall thermal conductance with different mass allocation on a two stage adsorption chiller employing re-heat scheme. 2013.
[17] Grabowska, K.; Sosnowski, M.; Krzywanski, J.; Sztekler, K.; Kalawa, W.; Zylka, A.; Nowak, W. The Numerical Comparison of Heat Transfer in a Coated and Fixed Bed of an Adsorption Chiller. Journal of Thermal Science 2018, 27, 421–426.
[18] Kurniawan, A.; Rachmat, A.; others CFD Simulation of Silica Gel as an Adsorbent on Finned Tube Adsorbent Bed. In E3S Web of Conferences; 2018; Vol. 67, p. 01014.
[19] Elsheniti, M. B.; Hassab, M. A.; Attia, A.-E. Examination of effects of operating and geometric parameters on the performance of a two-bed adsorption chiller. Applied Thermal Engineering 2018.
[20] Sosnowski M. Experimental and numerical analysis of multi-disc heat exchanger efficiency in adsorption chillers powered with waste heat. Journal of Physics: Conference Series [Internet]. IOP Publishing; 2019;1398:012013.
[21] Krzywanski J, Sztekler K, Bugaj M, Kalawa W, Grabowska K, Chaja PR, et al. Adsorption chiller in a combined heating and cooling system: simulation and optimization by neural networks. Bulletin of the Polish Academy of Sciences: Technical Sciences. e137054–e137054.
[22] Krzywanski J, Grabowska K, Herman F, Pyrka P, Sosnowski M, Prauzner T, et al. Optimization of a three-bed adsorption chiller by genetic algorithms and neural networks. Energy Conversion and Management. Elsevier; 2017;153:313–22.
[23] Krzywanski J, Grabowska K, Sosnowski M, Zylka A, Sztekler K, Kalawa W, et al. Modeling of a re-heat two-stage adsorption chiller by AI approach. MATEC Web Conf. 2018;240:05014.

[24] Liang, J, Zhao, W, Wang, Y, Ji, X, Li, M. "Effect of cooling temperature on the performance of a solar adsorption chiller with the enhanced mass transfer". Applied Thermal Engineering 2023; 219.
[25] Mohammed, R, Radwan, A, Rezk, A, Olabi, A, Sharma, V, Kalam Hossain, A, Alaswad, A, Abdelkareem, M. "Energy and exergy study of the integrated adsorption-absorption system driven by transient heat sources for cooling and desalination". Energy Conversion and Management 2023; 277.
[26] Hassan, M, El-Sharkawy, I, Harby, K. "Study of an innovative combined absorption-adsorption cooling system employing the same evaporator and condenser". Case Studies in Thermal Engineering 2023; 42.
[27] Gado, M, Ookawara, S, Hassan, H. "Utilization of triply periodic minimal surfaces for performance enhancement of adsorption cooling systems: Computational fluid dynamics analysis". Energy Conversion and Management 2023; 277.
[28] Grabowska K, Sosnowski M, Krzywanski J, Sztekler K, Kalawa W, Zylka A, et al. Analysis of heat transfer in a coated bed of an adsorption chiller. MATEC Web Conf. 2018;240:01010.
[29] Mikhaeil, M, Gaderer, M, Dawoud, B. "On the application of adsorber plate heat exchangers in thermally driven chillers; An experimental and analytical study". Applied Thermal Engineering 2023; 220.
[30] Krzywanski, J, Skrobek, D, Zylka, A, Grabowska, K, Kulakowska, A, Sosnowski, M, Nowak, W, Blanco-Marigorta, A. "Heat and mass transfer prediction in fluidized beds of cooling and desalination systems by AI approach". Applied Thermal Engineering 2023; 225.
[31] AL-Hasni, S, Santori, G. "The cost of manufacturing adsorption chillers". Thermal Science and Engineering Progress 2023; 39.
[32] Wijayanta, A, Ooga, S, Hironaka, S, Xue, B, Fukai, J. "Waste heat for regeneration of a packed bed of zeolite particles". International Journal of Heat and Mass Transfer 2023; 203.
[33] Sosnowski M, Krzywanski J, Grabowska K, Makowska-Janusik M, Nowak W, Sztekler K, et al. Implementation of a honeycomb bed in an adsorption cooling technology. In: , editor. ECOS 2019 - Proceedings of the 32nd International Conference on Efficiency, Cost, Optimization, Simulation and Environmental Impact of Energy Systems. 2019. p. 2521–30.
[34] Grabowska K, Sosnowski M, Krzywanski J, Sztekler K, Kalawa W, Zylka A, et al. The Numerical Comparison of Heat Transfer in a Coated and Fixed Bed of an Adsorption Chiller. Journal of Thermal Science. 2018;27(5):421–6.
[35] Sosnowski, M. "Evaluation of Heat Transfer Performance of a Multi-Disc Sorption Bed Dedicated for Adsorption Cooling Technology". Energies 2019; 12(24).
[36] Krzywanski J, Grabowska K, Sosnowski M, Zylka A, Kulakowska A, Czakiert T, et al. Heat Transfer in Adsorption Chillers with Fluidized Beds of Silica Gel, Zeolite, and Carbon Nanotubes. Heat Transfer Engineering. Taylor & Francis; 2021;0(0):1–15.
[37] Grabowska K, Zylka A, Kulakowska A, Skrobek D, Krzywanski J, Sosnowski M, et al. Experimental Investigation of an Intensified Heat Transfer Adsorption Bed (IHTAB) Reactor Prototype. Materials. 2021;14(13).

Analysis of cyclone separator solutions depending on SEC outlet conditions in nCO2PP

Milad Amiri [1*], Pawel Ziolkowski[1], Kamil Stasiak[1], Dariusz Mikielewicz [1]

[1] Faculty of Mechanical Engineering and Ship Technology, Gdańsk University of Technology, ul. Gabriela Narutowicza 11/12, 80-233 Gdańsk, Poland

Corresponding Author:

milad.amiri@pg.edu.pl

Abstract

Utilization of spray ejector condenser in order to carry out direct-contact condensation of vapour with inert gas (CO_2) on a spray of subcooled liquid integrated with separator (to make pure CO_2) has been proposed for the task of condensation and CO_2 separation in the negative CO_2 emission gas power plant. Condensation and separation has a significant impact on the thermodynamic efficiency of the entire negative CO_2 emission gas power plant cycle. The study presents the accomplished analysis using the numerical model of cyclone separator cases with varying spray ejector condenser outlet conditions. The model incorporates the continuity and momentum equations to describe the phenomenon of separation. Here, transient, turbulent and three-dimensional separator is numerically modelled based on a control volume method in Fluent. The Reynolds Stress Model is also derived from Reynolds Averaged Navier-Stokes's solution. This model is adopted to numerically simulate turbulent flow in separators. In addition, the mixture model is applied for simulation of turbulent swirl two-phase flow in gas-liquid separator. To obtain a numerical model and optimize the purification of CO_2, firstly, different length of cone of cyclone separator should be investigated. Then, the numerical simulation on different value of volume fraction of two phase flow is conducted, and by applying 10% up to 20% of volume fraction for water liquid, the model is derived. Results show that as the liquid volume fraction decreases, the separation efficiency improves. The most optimal separation efficiency of 90.7% is achieved when the liquid volume fraction is at 10%. In addition, Increasing the length of the cone results in both higher efficiency and pressure drop. Specifically, when the length of the cone is increased from 128 mm to 528 mm, the efficiency and pressure drop increases by 4.2% and 194.14 (pa), respectively.

Keywords

CFD, Separator, Gas-liquid separation, Separation efficiency, Three-Dimensional

1. Introduction

Carbon dioxide is deemed to be a major contributor to global warming [1]. Given the substantial effect of CO_2 on climate change, various methods have been devised in recent years to manage carbon emissions, including CO_2 capture [2] and storage [3]. Generating electricity with negative CO_2 emissions is achievable through a new concept that involves oxy-combustion in a wet combustion chamber, followed by separation of water and CO_2 through a compact spray ejector condenser (SEC), and finally compression of the separated CO_2. The developed cycle of a negative CO_2 emission power plant includes some devices, out of which, spray ejector condenser as well as separator plays an indispensable role to make pure CO_2. Figure 1 depicts the process flow diagram (PFD) of the negative CO_2 emission gas power plant [4, 5]. As it can be seen in Fig.1b, separation unit consists of SEC and cyclone separator. The main task of SEC is to condense the water vapour from the exhaust gases while maintaining a compact system structure, so that it has two inlets (for suction fluid and motive fluid) and one outlet. At the SEC outlet, the water liquid and CO_2 are expected to enter the cyclone separator for purification of CO_2.

Cyclones are widely utilized in industries including mineral, chemical, environmental and petroleum engineering for separating gas from solids or liquids [6, 7]. The performance of a cyclone separator is influenced by various factors including its structure geometry and operational parameters [8]. Studies have also been investigated on the impact of a cone that is extended with a vertical tube on the efficiency of a cyclone separator [9, 10]. The effects of cone and cylinder length on separation efficiency and pressure drop have been investigated by Brar et al. [11] and Prasanna et al. [12].

In this paper, the SEC and cyclone separator are considered a novel separation process to purify CO2, which has not been extensively studied in previous literature. Therefore, a tangential-flow CO_2-water separator was designed to obtain the desired high-purity CO_2 flow for the Negative CO_2 Emission Gas Power Plant (nCO_2PP) [13]. To obtain a numerical model and optimize the performance of separator, firstly, the effect of cone size could be defined. Then, a suitable value of liquid volume fraction depending on conditions of spray ejector condenser can be obtained using separation efficiency, so that the numerical simulation on different value of volume fraction of water liquid is conducted, and by applying 10% up to 20% of volume fraction for water liquid, the model is derived.

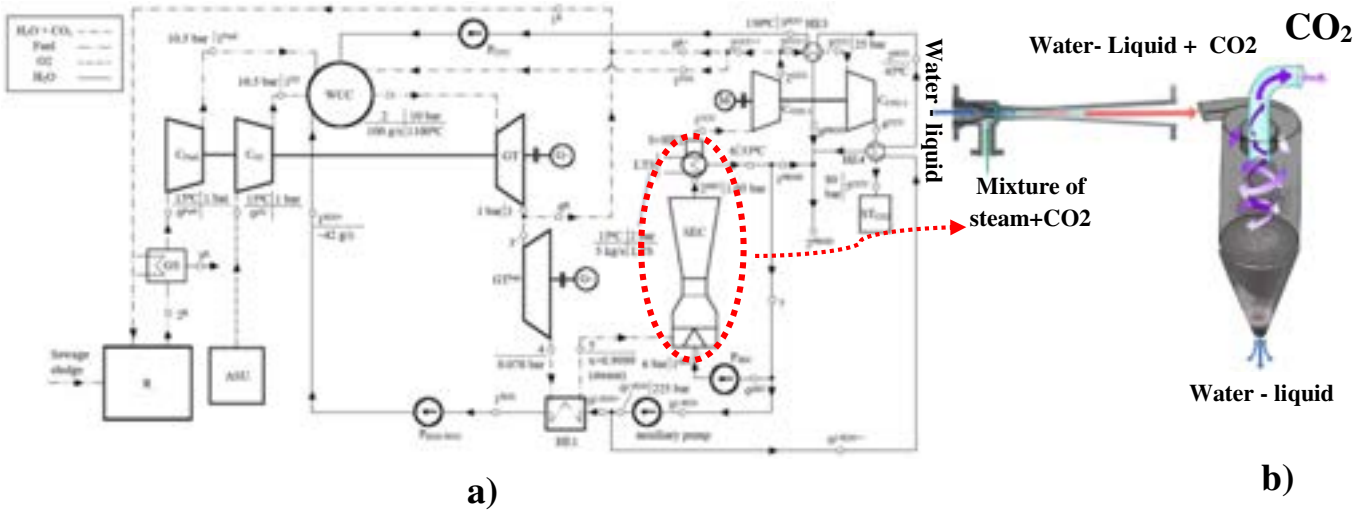

Figure. 1. a) Negative CO_2 emission gas power plant process flow diagram (PFD), b) Capturing CO_2 part consist of spray ejector condenser (SEC) and cyclone separator [4, 5]

2. Modeling

The effectiveness of a cyclone separator is influenced by various factors, and optimal separation efficiency and reduced pressure loss can only be achieved when the dimensions of its components are suited to the purpose. The tangential inlet type is widely adopted in industries and is considered mature with a simple structure typically consisting of a cylinder and cone section. Figure 2a shows the geometry of a three-dimensional tangential inlet cyclone separator. CO2-Water mixture enters the separator with high velocity in a tangential direction and rotates rapidly in the annular space between the exhaust pipe and cylinder. Under the influence of centrifugal force, the water droplets in the mixture are hurled to the wall and then fall down along the wall due to the gravity and momentum of the mixture. Afterward, they are discharged through the underflow outlet. The purified CO2 travels upward through the center and discharges through the exhaust pipe. The dimensions of three-dimensional tangential single inlet cyclone separator have been indicated in Fig 2b and table 1.

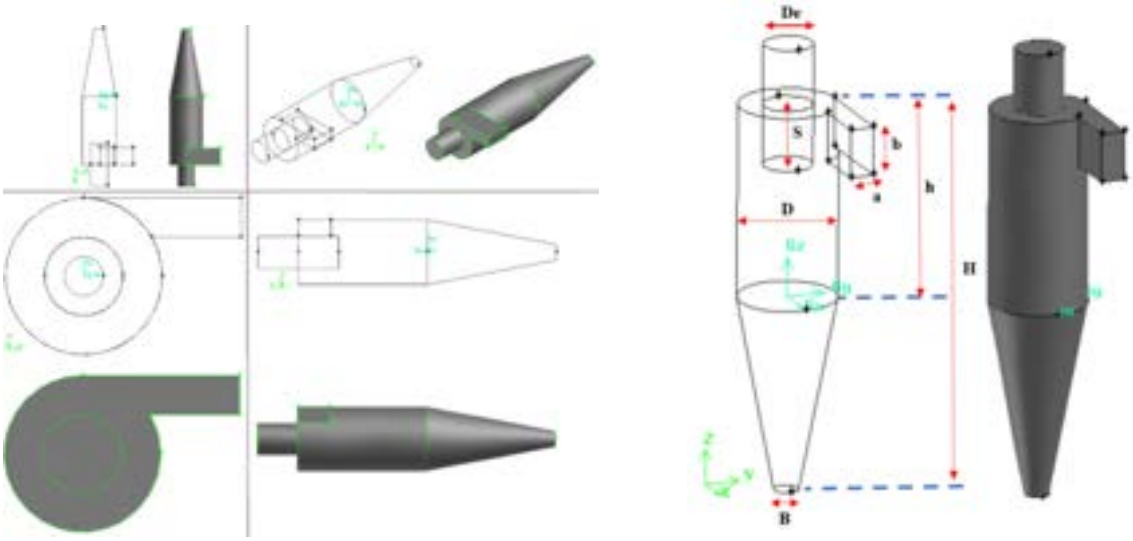

Figure. 2. a) Geometry of the cyclone separator seen from different views and b) its dimensions

Table 1. Dimensions of the cyclone (D = 0.2 m)

$\frac{a}{D}$	$\frac{b}{D}$	$\frac{De}{D}$	$\frac{S}{D}$	$\frac{h}{D}$	$\frac{H}{D}$	$\frac{B}{D}$
0.25	0.5	0.5	0.625	2	4	0.25

a) **b)**

2.1. Governing equations

In this study, we applied the mixture model, also known as the algebraic slip model, a simplified version of the Euler-Euler approach. This model is appropriate for bubbly, droplet, or particle-laden flows where the volume fraction of the dispersed phase is high enough (>10%), to ensure pronounced inter-particle collision. The mixture model allows fluid phases to flow at different velocities and permits fluid phases to penetrate each other, and enables the exchange of mass, momentum, and energy between fluid phases. The mixture model has also been used in CFD simulations of turbulent swirl two-phase flow in gas-liquid cyclone separators.

However, the calculation for the continuous and dispersed fluid phases is performed through the following methods: The Reynolds-averaged Navier-Stokes, continuity, and momentum equations are used to solve for the continuous phase.

$$\frac{\partial \rho}{\partial t} + \frac{\partial (\rho u_i)}{\partial x_i} = 0 \tag{1}$$

$$\frac{\partial (\rho u_i)}{\partial t} + \frac{\partial \left(\rho u_i u_j\right)}{\partial x_j} = \frac{\partial P}{\partial x} + \frac{\partial}{\partial x}\left(\mu \frac{\partial^2 u_i}{\partial x_j^2} + \frac{\partial^2 u_j}{\partial x_i^2} - \frac{2}{3}\delta_{ij}\frac{\partial u_k}{\partial x_k} + \frac{\partial}{\partial x_j}\right)\left(-\rho\overline{u_I u_J}\right) \tag{2}$$

$$\left(-\rho\overline{u_I u_J}\right) = \mu_t\left(\frac{\partial^2 u_i}{\partial x_j^2} + \frac{\partial^2 u_j}{\partial x_i^2}\right) - \frac{2}{3}\left(\rho k + \mu_t \frac{\partial u_k}{\partial x_k}\right)\delta_{ij} \tag{3}$$

The equation for the continuity of the mixture can be calculated as:

$$\frac{\partial (\rho_m)}{\partial t} + \frac{\partial (\rho_m u_m)}{\partial x_i} = 0 \tag{4}$$

Mixture momentum:

$$\frac{\partial (\rho_m u_{mi})}{\partial t} + \frac{\partial \left(\rho_m u_{mi} u_{mj}\right)}{\partial x_i} = \frac{\partial P}{\partial x_i} + \frac{\partial}{\partial x_j}\mu_m\left(\frac{\partial u_{mi}}{\partial x_j} + \frac{\partial u_{mj}}{\partial x_j}\right) + \rho g_i + \frac{\partial}{\partial x_i}\left(\sum_{q=1}^{n} \alpha_q \rho_q u_{dr,qi} u_{dr,qj}\right) \tag{5}$$

Where u_m is the mass-averaged velocity, ρ_m is the mixture density and μ_m is the viscosity of the mixture.

$$U_m = \frac{\sum_{q=1}^{n} \alpha_q \rho_q u_q}{\rho_m}\ ,\ \rho_m = \sum_{q=1}^{n} \alpha_q \rho_q\ ,\ \mu_m = \sum_{q=1}^{n} \alpha_q \mu_q \tag{6}$$

Where $u_{dr,q}$ represents the drift velocity for secondary, calculated as $u_{dr,q} = u_q - u_m$.

In the RSM with a time step of 0.001 (s), the equation for transport is formulated as follows.

$$\frac{\partial}{\partial t}\left(\rho\overline{u_i' u_j'}\right) + \frac{\partial}{\partial x_k}\left(\rho u_k \overline{u_i' u_j'}\right) = D_{ij} + P_{ij} + \Pi_{ij} + \varepsilon_{ij} + S \tag{7}$$

where the two terms on the left side represent the local time derivative of stress and the convective transport term, respectively. The five terms on the right side are:

The stress diffusion term: $D_{ij} = -\frac{\partial}{\partial x_k}\left[\rho\overline{u_i' u_j' u_k'} + \overline{(P' u_j')}\delta_{ik} + \overline{(P' u_i')}\delta_{jk} - \mu\left(\frac{\partial}{\partial x_k}\overline{u_i' u_j'}\right)\right]$ (8)

the shear production term: $P_{ij} = -\rho\left[\overline{u_i' u_k'}\frac{\partial u_j}{\partial x_k} + \overline{u_j' u_k'}\frac{\partial u_i}{\partial x_k}\right]$ (9)

The pressure-strain term: $\Pi_{ij} = \overline{p\left(\frac{\partial u_i'}{\partial x_j} + \frac{\partial u_j'}{\partial x_i}\right)}$ (10)

The dissipation term: $\varepsilon_{ij} = -2\mu\overline{\frac{\partial u_i'}{\partial x_k}\frac{\partial u_j'}{\partial x_k}}$ (11)

and the source term: S (12)

2.2. Numerical simulation and boundary conditions

As it mentioned the CO_2-water multiphase flow in the cyclone separator was accurately modeled using the multiphase mixture model in ANSYS Fluent 2021 R1. This was deemed necessary as the CO_2 and water phases are expected to have a strong interaction within the swirling environment of the cyclone separator. In the interpenetrating continuum, CO_2 was the primary (continuous) phase and water was the secondary (dispersed) phase and surface tension was considered. The SIMPLE algorithm was applied to establish the coupling between the pressure and velocity in the continuity and momentum equations. PRESTO scheme was considered for its superior performance in estimating high-speed swirling flows and flows in curved domains. The momentum, volume fraction, and kinetic energy equations were discretized using the QUICK method, which provides more accurate results for rotational swirling flows compared to first- and second-order schemes due to its higher-order discretization. The first-order discretization can result in higher error and unreliable results [14]. The boundary conditions are presented in Table 2.

Table 2. Boundary conditions

Boundary	Types
Inlet	Velocity inlet
Outlets	Outflow
Wall	No Slip wall

3. Evaluation of numerical model

The ANSYS Fluent 2021 R1 was used to evaluate the flow pattern of the studied cyclone separator. As a preliminary parameter, the separation efficiency was calculated, which was defined as follows:

$$\eta = \left(\frac{\dot{m}_{liquid\ at\ inlet} - \dot{m}_{liquid\ at\ gas\ outlet}}{\dot{m}_{liquid\ at\ inlet}}\right) \times 100 \tag{13}$$

Where $\dot{m}$ is the mass flow rate.

3.1 Grid Independence

The geometry and mesh of the cyclone separator created in Gambit 2.4.6 are shown in Fig. 3. To ensure accuracy in calculations, all edges were meshed in the created model. Following that, all the faces and volumes were meshed. For the purpose of meshing, the Tet/Hybrid elements and TGrid type were employed to create cells appropriate for the geometry involved in computational fluid dynamics (CFD) simulations. A high-quality mesh was crucial to avoid errors caused by numerical diffusion. Thus, mesh-independent solutions for the cyclone separator were verified using different grids. So, to examine the independence of the results from the grid size, the variation of tangential velocity and separation efficiency versus different nodes is shown in Fig 4. As it can be seen, the results of 40574 and 80974 grids are different from other grids (120654 and 160214). Even though the 120654 and 160214 consequences are approximately the same, in order to lower computational cost, the 120654 nodes have been opted.

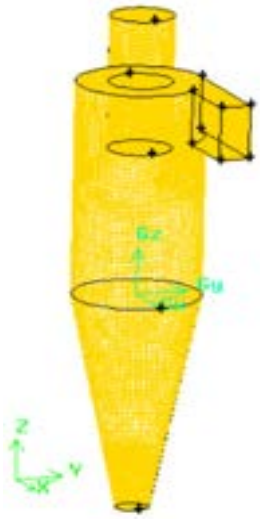

Figure. 3. Meshing of cyclone separator

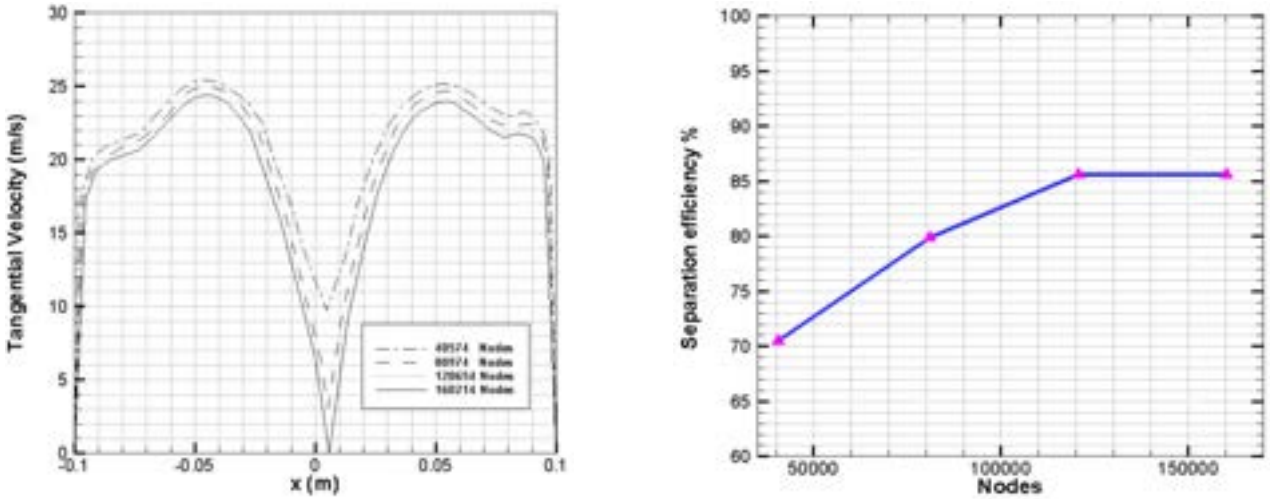

a) **b)**

Figure. 4. Grid independency for a) Tangential velocity and b) separation efficiency of single inlet cyclone at 2.8 ($\frac{kg}{s}$) when volume fraction of water is 10%

3.2 Model Validation

Figure 5. shows predicted variation of the Pressure drop, tangential velocity and separation efficiency in comparison to the results of Wang et al [15]. In their physical experiment, air was fed into the inlet of the cyclone, and its flow rate was monitored using a flowmeter. The velocity of both phases was set at 20 m/s. The outlet tube was open to the atmosphere and the gas pressure at the top of the vortex finder was maintained at 1 atm. The volume fraction of the second phase was 10%. The measurement of velocity and pressure in the gas field was performed using a five-hole probe, which comprised an adjustable frame and five pressure transducers. The voltage signals generated by the five pressure transducers on the five-hole probe were amplified after being placed in the gas flow field. The amplified voltage signals were collected by a data acquisition system equipped with a

microprocessor and a personal computer. As it can be seen in Fig 5. good agreement was achieved between the experimental and the numerical results data taken from the studies by Wang et al.

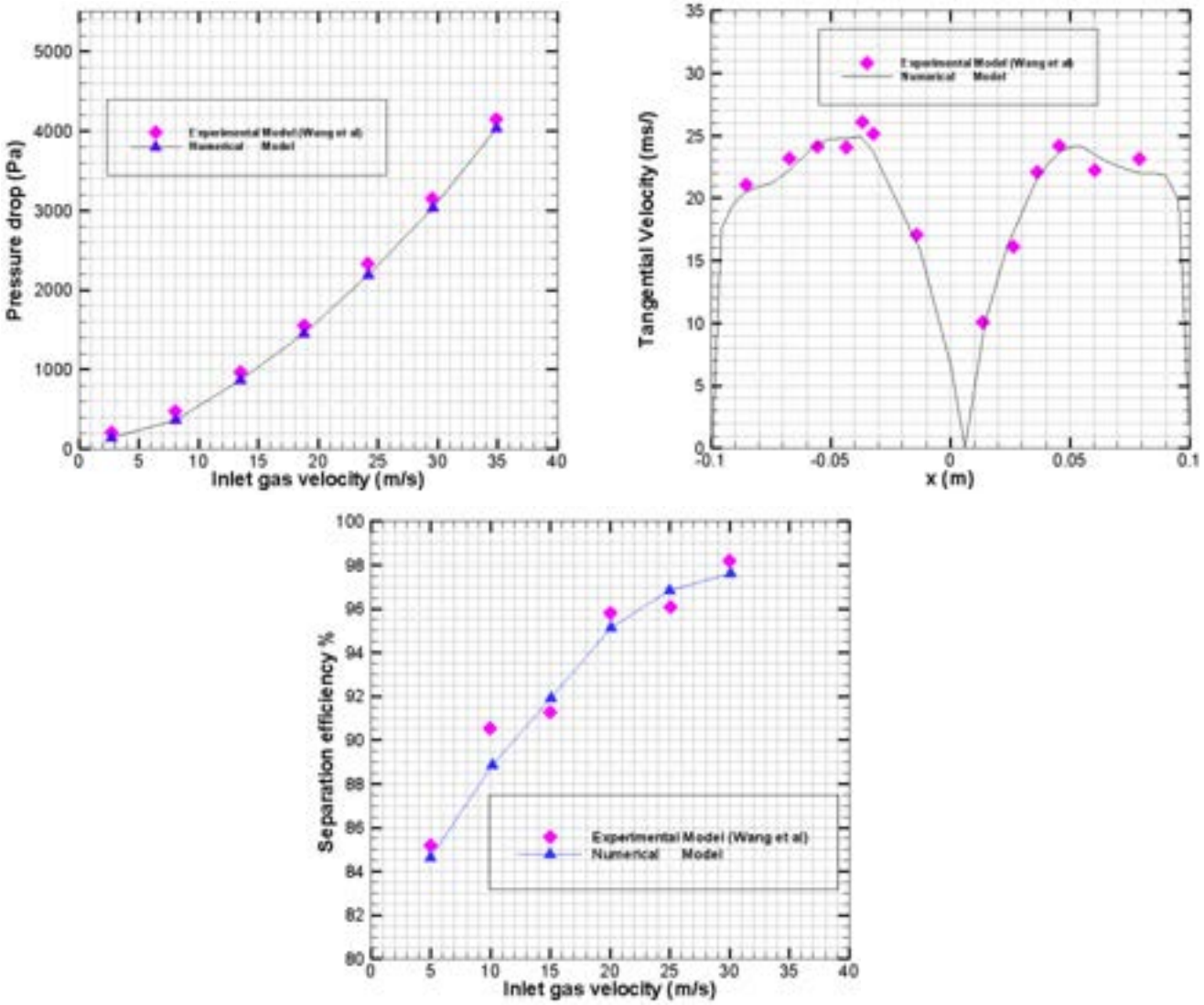

Figure. 5. Pressure drop, tangential velocity and separation efficiency comparison of experimental model (Wang et al) and current simulation

4. Results and discussion

4.1 Effect of cone size

The design and operation of a cyclone separator is crucial in determining the efficiency of particle separation in various industrial applications. One of the design parameters that affects the performance of the cyclone separator is the size of cone. Figure 6 depicts geometry and mesh of cyclones with different cone length. In this section, the effect of cone size (at constant total length of cyclone: 638 (mm)) on the efficiency and pressure drop of a cyclone

separator has been examined (Table.3). The results indicate that while the efficiency of the cyclone increases with a longer cone, there is also a corresponding increase in pressure drop

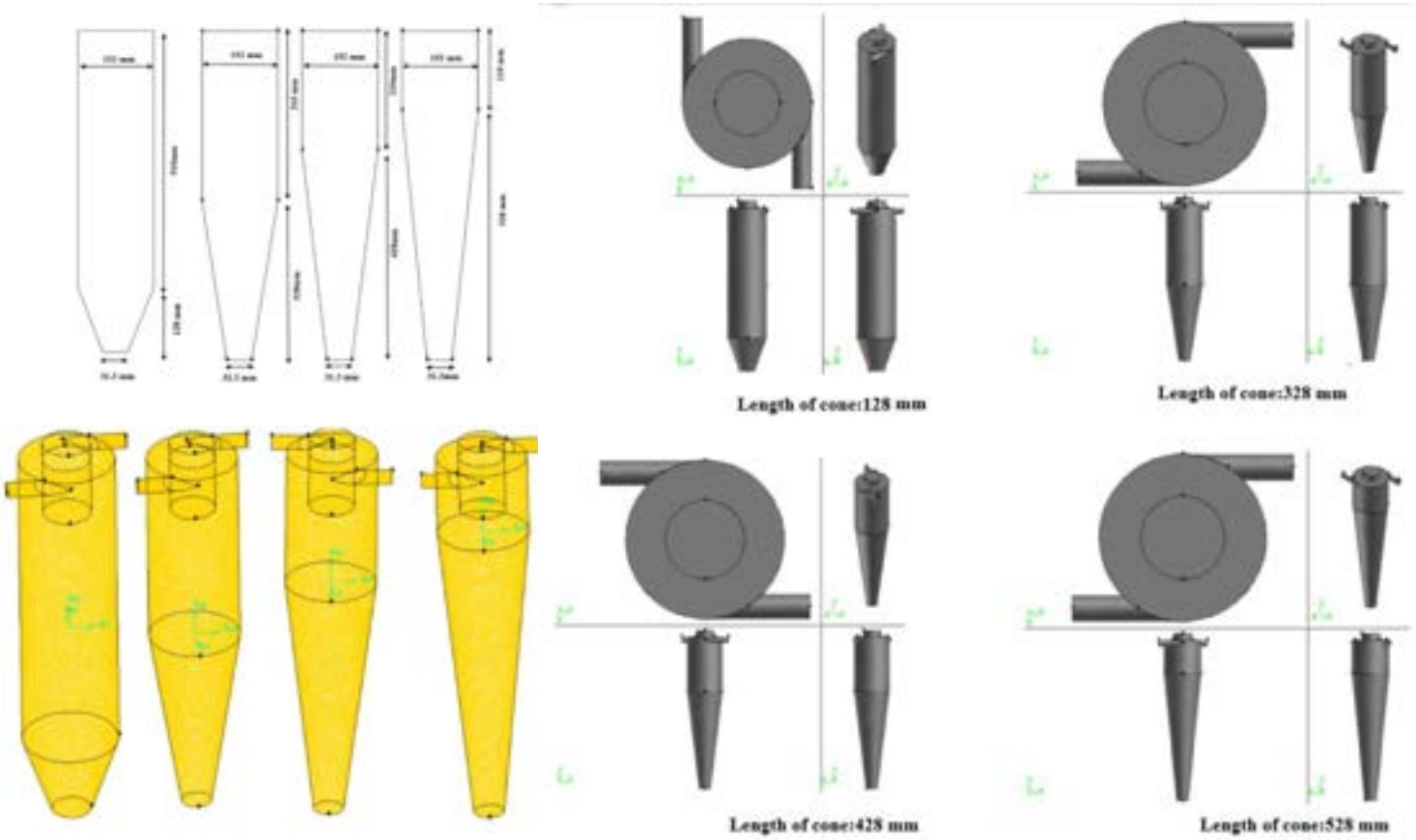

Figure.6. Geometry and mesh of cyclones with different cone length

Table 3. Mass flow rate of liquid phase at the inlet and gas outlet for different length of cone at 10% of liquid volume fraction and diameter of water droplet : 10 (μm)

Length of Cone (mm)	$\dot{m}_{liquid\ at\ inlet}$ (kg/s)	$\dot{m}_{liquid\ at\ gas\ outlet}$ (kg/s)	Efficiency %	Pressure drop (Pa)
128	0.43527386	0.14555562	66.5 %	514.62
328	0.43527386	0.136807	68.6 %	556.62
428	0.43527386	0.13143237	69.8 %	622.66
528	0.43527386	0.12750024	70.7 %	706.76

4.2 Efficiency of cyclone separator depending on SEC outlet conditions

When a saturated vapour contacts subcooled drops with a size larger than the critical value, the condensation occurs. Following our previous analytical model [16, 17], it is assumed that the inlet properties of the fluids are

supplied at a state denoted as "inlet" in Figure 7. To calculate the suction mass (m_g) and pressure at the beginning of the mixing zone, knowledge of the equations resulting from the flow in the inlet zone is required.

$$m_g = u_{gin}\rho_g A_{gin} = u_{g0}\rho_g(A_0 - A_l) \tag{14}$$

From Bernoulli equation:

$$p_{g,in} + \frac{1}{2}\cdot \rho_{g,0}u_{g,in}^2 = p_{g,0} + \frac{1}{2}\cdot \rho_{g,0}u_{g,0}^2 + \Delta p_{loss,1} \tag{15}$$

The suction pressure ($p_{g,1}$) generated by the liquid jet mixing with gases can be calculated by balancing the momentum between the pre-mixing section and the entrance to the mixing section, which corresponds to states 0 and 1.

$$p_{g,0}A_{g,0} + m_g u_{g,0} + p_l A_l + m_l u_l = p_{g,1}A_1 + (m_g + m_l)u_l \tag{16}$$

To obtain the values in state 2, the conservation equations for mass, energy, and momentum were applied simultaneously for the adiabatic process. When a non-condensable gas (CO_2) is present in the condensation space, it is necessary to analyse both heat and mass transfer. Based on the equations used in our previous analytical study [16, 17], condensation of vapour on subcooled droplet stream, heat balance of droplet stream and balance of mass and heat for vapour-gas mixture have been considered.

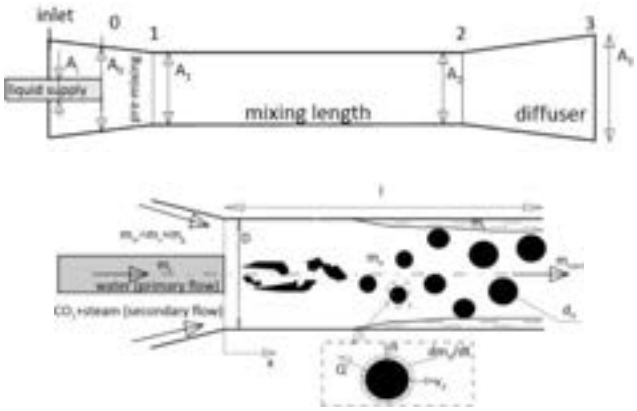

Figure. 7. Schematic of the spray ejector of condenser [16, 17]

4.2.1 Effect of volume fraction

As mentioned above, spray ejector condenser and cyclone separator have been used as a separation section of a negative CO_2 emission power plant in regard to making pure CO_2. Two choking phenomena exist in the ejector performance: one in the primary flow through the nozzle and the other in the entrained or suction flow (due to acceleration of the entrained flow from a stagnant state at the suction port to a supersonic flow in the mixing chamber). In addition, a jet coming out of the nozzle dissipates and breaks up into various-sized drops. The liquid stream breaks into droplets under the influence of waves formed on the surface of the stream due to instability. These waves cause a loss of stability and the formation of primary droplets. Secondary droplet breakup occurs under the influence of aerodynamic forces. Primary droplets are deformed and broken up by aerodynamic drag forces and surface tension forces.

So, according to aforementioned effects, volume fraction of water liquid will be different. This section presents the accomplished analysis using the numerical model of cyclone separator cases with varying SEC outlet conditions. To this end, 10%, 15% and 20% of volume fraction of water liquid have been considered. Figure 8 indicates the contour of volume fraction of water liquid for dual inlet cyclone at 2.8 ($\frac{kg}{s}$) inlet mass flow rate for 10%, 15% and 20% feed stream liquid volume fraction.

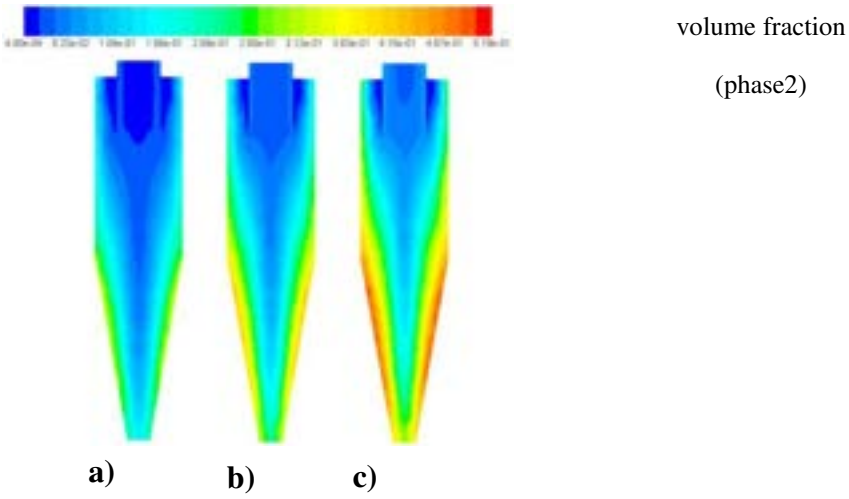

Figure. 8. The contours volume of liquid fraction for 2.8 ($\frac{kg}{s}$) inlet mass flow rate, at feed stream liquid volume fraction a) 10%, b) 15 % and c) 20%

To assess the impact of liquid volume fraction on the internal configuration separation performance, the separation efficiency was computed at various volume fractions using Equation 13, and the results were compared. The separation efficiencies, inlet and outlet liquid mass flow rates ($\dot{m}$) at the considered three liquid volume fractions are shown in Table 4. As seen in the table, separation efficiency increases with decreasing liquid volume fraction, so that the maximum separation efficiency has been obtained at 10% of liquid volume fraction and its value is 90.7%.

Table 4. Separation efficiency of dual inlet cyclone at different volume fraction of water liquid when diameter of water droplet is 10^{-5}

Liquid Volume Fraction	$\dot{m}_{liquid\ at\ inlet}$ (kg/s)	$\dot{m}_{liquid\ at\ gas\ outlet}$ (kg/s)	Separation efficiency, $\eta\%$
10 %	2.74649	0.254949	90.7 %
15 %	4.1197319	0.43964297	89.33 %
20 %	5.4929759	0.68230528	87.58 %

5. Conclusion

A numerical simulation was conducted to optimize the performance of a tangential-flow vanes CO_2-water separator design in Negative CO_2 Emission Power Plant (NCO_2PP) in regard to producing high-purity CO_2, using a transient RSM turbulent model and a three-dimensional model.

The key findings are summarized as follows:

- Increasing the cone length leads to elevated efficiency and pressure drop.
- The cone length is extended from 128 mm to 528 mm, the efficiency and pressure drop increase by 4.2% and 194.14 pa, respectively.
- Separation efficiency improves as the liquid volume fraction decreases, with the highest efficiency of 90.7% achieved at a liquid volume fraction of 10%.

For future research, the proposed model will be experimentally tested using single and multi-nozzle configurations to generate the motive fluid jets. Additionally, electro hydrodynamic (EHD) effects can be used to enhance heat transfer in direct contact condensation in spray ejector condensers. EHD is a process that involves the interaction between electric fields and fluid flow. In direct contact condensation, EHD can be used to create an electrostatic field that enhances the droplet size distribution, which leads to improved heat transfer. One way to implement EHD in spray ejector condensers is to use a corona discharge to create an electric field that attracts the charged droplets towards the condenser surface. This increases the surface area available for heat transfer and also increases the mass transfer rate between the droplets and the condenser surface. Another way to use EHD in spray ejector condensers is to apply a voltage to the ejector nozzle. This can cause the liquid droplets to break up into smaller droplets, which increases the surface area available for heat transfer and also enhances the mass transfer rate. So, it is aimed to impose EHD in spray ejector condenser which results in significant improvements in heat transfer efficiency and can also reduce the overall size of the condenser. Moreover, a quadruple inlet cyclone separator will be used to purify CO_2.

Acknowledgements

The research leading to these results has received funding from the Norway Grants 2014–2021 via the National Center for Research and Development. Article has been prepared within the frame of the project: “Negative CO2 emission gas power plant” - NOR/POLNORCCS/NEGATIVE-CO2- PP/0009/2019–00 which is co-financed by programme “Applied research” under the Norwegian Financial Mechanisms 2014–2021 POLNOR CCS 2019 - Development of CO2 capture solutions integrated in power and industry processes.

Nomenclature

Dj	diameter of jet, m	ρ	Density, (kg/m^3)
D_{ij}	stress diffusion term, kg/(ms^2)	ρ_m	mixture density, (kg/m^3)
D_0	diameter of mixing length, m	μ_m	viscosity of the mixture, kg/(ms)
d_d	diameter of droplet, m	Π_{ij}	pressure-strain term, kg/(ms^2)
l	mixing length, m	μ_l	dynamic viscosity, kg/(ms)
m_g	suction mass, kg/s		
n	total number of droplet	ε_{ij}	dissipation term, (kg/ms^3)
P	static Pressure, pa	η	separation efficiency, (%)
P_{ij}	shear production term, N/(m^3)	σ_l	surface tension, N/m
$p_{g,1}$	suction pressure, pa	$\Delta p_{loss,1}$	pressure drop, pa

Re	Reynolds number
S	source term
$\vec{u}$	velocity vector, m/s
$u_{dr,q}$	drift velocity for secondary,m/s
We	Weber number
Greek Symbols	
ρ_l	liquid density, kg/(m^3)

References:

[1] Pelletier C., Rogaume Y., Dieckhoff L., Bardeau G., Pons M-N., Dufour A. Effect of combustion technology and biogenic CO2 impact factor on global warming potential of wood-to-heat chains. Applied Energy. 2019;235:1381-8.
[2] Zhang Y., Gao Y., Louis B., Wang Q., Lin W. Fabrication of lithium silicates from zeolite for CO2 capture at high temperatures. Journal of energy chemistry. 2019;33:81-9.
[3] Lee E., Hornafius JS., Dean E., Kazemi H. Potential of Denver Basin oil fields to store CO2 and produce Bio-CO2-EOR oil. International Journal of Greenhouse Gas Control. 2019;81:137-56.
[4] Ziółkowski P., Madejski P., Amiri M., Kuś T., Stasiak K., Subramanian N., et al. Thermodynamic analysis of negative CO2 emission power plant using Aspen Plus, Aspen Hysys, and Ebsilon software. Energies. 2021;14(19):6304.
[5] Ziółkowski P., Stasiak K., Amiri M., Mikielewicz D. Negative carbon dioxide gas power plant integrated with gasification of sewage sludge. Energy. 2023;262:125496.
[6] Yang J., Liu C., Li S., Sun B., Xiao J., Jin Y. A new pressure drop model of gas–liquid cyclone with innovative operation mode. Chemical Engineering and Processing: Process Intensification. 2015;95:256-66.
[7] Safikhani H., Mehrabian P. Numerical study of flow field in new cyclone separators. Advanced Powder Technology. 2016;27(2):379-87.
[8] Han C., Hu Y., Li W., Bie Q. Gas-solid separation performance and structure optimization in 3D printed guide vane cyclone separator. Advanced Powder Technology. 2022;33(11):103815.
[9] Qian F., Zhang J., Zhang M. Effects of the prolonged vertical tube on the separation performance of a cyclone. Journal of hazardous materials. 2006;136(3):822-9.
[10] Kaya F., Karagoz I. Numerical investigation of performance characteristics of a cyclone prolonged with a dipleg. Chemical Engineering Journal. 2009;151(1-3):39-45.
[11] Brar LS., Sharma R., Elsayed K. The effect of the cyclone length on the performance of Stairmand high-efficiency cyclone. Powder Technology. 2015;286:668-77.
[12] Prasanna N., Subramanian K., Ajay S., Rajagopal T., Vigneshwaran V. CFD study on the performance of reducing pressure drop holes in cyclone separator. Materials Today: Proceedings. 2021;43:1960-8.
[13] Available from: https://nco2pp.mech.pg.gda.pl/pl.
[14] Utikar R., Darmawan N., Tade M., Li Q., Evans G., Glenny M., et al. Hydrodynamic simulation of cyclone separators. Computational fluid dynamics: InTech; 2010. p. 241-66.
[15] Wang B., Xu D., Chu K., Yu A. Numerical study of gas–solid flow in a cyclone separator. Applied Mathematical Modelling. 2006;30(11):1326-42.
[16] Mikielewicz D., Amiri M., Mikielewicz J. A Simple Analytical Model of Direct-Contact Condensation from Vapour-Inert Gas Mixture in a Spray Ejector Condenser. Available at SSRN 4147312.
[17] Mikielewicz D., Amiri M., Mikielewicz J. Direct-contact condensation from vapour-gas mixture in a spray ejector condenser for negative CO2 power plant. 2nd International Conference on Negative CO2 Emissions; 2022, Chalmers University of Technology, June 14-17.

Numerical Multiphase assessment of geometric key parameters in Venturi-type reactor for process intensification

Nicola Andreini[a], Guglielmo Vaccaro[a], Luca Socci[a],Adriano Milazzo[a]

[a] Department of industrial Engineer University of Florence, Florence, Italy.
Corresponding author: nicola.andreini@unifi.it

Abstract:
Hydrodynamics cavitation has the potential to significantly improve the efficiency and effectiveness of a wide range of industrial processes, including water treatment, chemical reactions, food processing, and biomass pretreatment. Cavitation can be used to replace traditional processing methods that are more energy-intensive or use harmful chemicals, which can help to increase the sustainability of industrial processes. Overall, using cavitation for process intensification can help improve efficiency, sustainability, and circularity in industry. One of the most used device that is easy to integrate with the production line is the cavitating Venturi reactor. In the present work, influence of the key geometric parameters such as the height and length of Venturi throat are evaluated to find the optimum reaction conditions enhancing cavitating treatment intensity and minimizing the pressure drop. The analysis has been conducted by varying the ratio of the throat section to the inlet section, keeping constant the cavitation number, to have cavitation dependent only on the geometry. A series of multiphase simulations have been performed using an open-source solver (OpenFOAM) that implements the Zwart-Gerber-Belamri cavitation model. The adopted modelling approach was the VOF (volume of fluid) mixture type coupled with the URANS (Unsteady Reynolds Averaged Navier Stokes) method, in which a komegaSST turbulence model has been applied. An FFT analysis was conducted to evaluate the cavitation regime. It was observed that by increasing the throat diameter, the frequency of the re-entrant jet mechanism decreases while the cavitation region extends. Finally the impact of pressure drop in various geometries was evaluated and compared with the CEP (cavitation efficiency parameter), a term developed to properly evaluate the efficiency of the cavitation phenomenon.

Keywords:
CFD, multiphase, cavitation, process intensification , energy saving.

1. Introduction

Hydrodynamic cavitation has gained a strong interest in recent years for its unique features, versatility, and effectiveness in many fields. Among them, it is possible to mention waste wastewater treatment and biofuel production [1]. In wastewater treatment, hydrodynamic cavitation represents a useful help to achieve high standards of depuration. Generally speaking, standard wastewater treatments aim to reduce the concentration of certain pollutants. Biological treatments are widely used, but they are not completely effective on constituents persistent to biodegradation, which undergo only minor structural changes in absence of additional treatments [2]. Moreover, the widespread diffusion of high-environment impact industrial processes, that produce new kinds of pollutants, has accentuated this fact [3]. So, in the context of wastewater treatments, there is a necessity to apply specific processes able to reduce the presence of these pollutants. In this sense, cavitation can be considered a very promising option, eventually coupled with advanced techniques (such as Advanced Oxidation Processes, AOP). Indeed, the so high values of pressure (up to a GigaPascal range) and temperature (in the order of 10 000 K) are suited for all the mechanisms of degradation of biological and chemical compounds [2]. In the hydrodynamic cavitation phenomenon applied to wastewater treatment, all consequences deriving from bubbles collapse are employed [4]: thermal, mechanical and chemical effects. The thermal effects include temperature gradient and temperature rise rate, which are beneficial to damage the structure of pathogens and to assist other removal mechanisms. The intensive mechanical effect breaks the outer structures of pathogens, inactivating them. The chemical effects are determined by the breaking of water molecules, leading to the formation of strongly oxidising radicals: hydroxyl OH and hydrogen peroxide -OH 2, which are highly effective on persistent pollutants. The real effectiveness of hydrodynamic cavitation on various species of water pollutants depends on the operating parameters and specific design of cavitating reactors [1], [3], [4]. Moreover, the combined use of hydrodynamic cavitation with other advanced oxidation processes has been proposed [3], [[5]. Regarding biofuels, hydrodynamic cavitation can be employed to enhance the production of biodiesel and bioethanol. In particular, bioethanol production is based on the availability of a

sugar matrix, that could derive from sugar/starch crops (1st generation bioethanol) or lignocellulosic plants (2nd generation). The latter has gained particular attention because it does not need dedicated crops. This process relies on some pretreatments aiming to change the supramolecular structure of biomass in which the cellulose, lignin and hemicellulose are closely interconnected to finally release free sugars making them available for the next transformation (fermentation, distillation, refining) [6], [7]. In this regard, hydrodynamic cavitation can be used as a pre-treatment for delignification, effectively and with energy savings compared to traditional technologies. Results obtained in several tests indicate that pre-treatment with hydrodynamic cavitation leads to excellent ethanol production yields and a high degree of ethanol purity [8] For extensive industrial uses, hydrodynamic cavitation (HC), produced by accelerated flow, is well suited [9].When compared to other generation techniques like optic, acoustic, and particle, HC has the benefits of good scalability, simplicity of manufacture, and a promising treatment outcome. The geometric design of the cavitating device has a significant impact on cavitation intensity like operating pressure, flow rate, etc. Numerous devices have been investigated as cavitating reactor for process intensification, including orifices, venturi, vortex diodes, etc. Even so, there are still gaps in the knowledge of cavitating flow through these devices, particularly the cavitating venturi, despite its simplicity and widespread use. The design methods for a cavitating reactor currently used are mostly empirical and have no optimization criteria that can increase the yield of the process to which cavitation is applied. Another gap in the literature is the lack of an unambiguous term for evaluating the efficiency of a cavitating device. Various methods, based on experiments, for assessing cavitation intensity have been proposed, for example, Dastane et al. [11] estimated the efficiency of the cavitation process by introducing a parameter called Cavitational Efficacy Ratio (CER), the ratio between pressure generated after cavity collapse and pressure losses. The collapse pressure reflects the greatest quantity of energy that a cavity can release when collapsing. Wu et al. [10] developed a formulation for the energy released during the cavitation phenomenon to quantify its intensity. Other works attempt to give a formulation for cavitation efficiency however for engineering purposes they are very complex and difficult to use on an industrial scale. From the aforementioned literature, it is clear that stronger cavitation causes higher effects on process intensification. This connection is straightforward and natural. In this paper, various key parameters are analyzed to evaluate which one is the best in terms of optimization of cavitation performance and pressure loss minimization. To evaluate the impact of the geometry, 2D axisymmetric simulations taken from the literature have been used. Next, a cavitation model based on the Rayleight-Plesset equations developed by Zwar-Belamri-Gerber [16] and a modification for turbulent viscosity proposed by Delgosha [19] was implemented in a multiphase solver available in OpenFOAM software. After validating the model on a literature test case taken from Stutz-Reboud [12], sensitivity analysis was performed on the cavitating device.

2. Numerical Model

To simulate the phenomenon of cavitation, an unsteady solver of the OpenFOAM has been adopted. The solver was modified appropriately to increase the accuracy of the results. The chosen solver is designed to simulate the phenomenon of cavitation for an incompressible, isothermal, and immiscible fluid. It adopts a VOF mixtures (Volume of fluid) approach with an interface capturing method proposed by Hirt and Nichols [14]in which a single set of governing equations is defined for the two liquid-vapour phases. The Reynolds-averaged Navier stokes equations in their unsteady formulation for Newtonian fluids have been considered, than the conservative equations of mass, momentum, and the transport equation for the volume fraction α, used to solve the interface between liquid and vapour, can be written as:

$$\frac{\partial \rho_m}{\partial t} + \nabla \cdot (\rho_m \mathbf{U}) = 0 \tag{1}$$

$$\frac{\partial (\rho_m U)}{\partial t} + \nabla \cdot (\rho_m \mathbf{U}\mathbf{U}) = -\nabla P + \nabla \cdot [\mu_{eff}(\nabla \mathbf{U} + (\nabla \mathbf{U})^T)] + f_\sigma + \rho_m g \tag{2}$$

$$\frac{\partial \alpha_v}{\partial t} + \nabla \cdot \mathbf{U} + \nabla \cdot [\mathbf{U}\mathbf{c}\alpha_v(1-\alpha_v)] = S_\alpha \tag{3}$$

Where μ_{eff} represents the sum of molecular viscosity and turbulent viscosity, S_α The term due to the amount of evaporation and condensation rates, f_σ is the surface tension force acting at the liquid-vapour interface while the third LHS term of the transport equation of volume fraction is called as artificial compression term, which is not zero only at the interface. This contribution is important because using a VOF approach with a purely convective α equation would lead to numerical diffusion and thus in a non-conservative interface. The generic fluid property is instead calculated as a weighted average over the volume fraction of the individual properties

of the two liquid-vapour phases. For the fluid was considered Newtonian although someone to be treated may exhibit different behavior because a general treatment has been conducted. The specific response of cavitating fluids, whether it leads to a suppression or enhancement of non-Newtonian behavior, depends on the rheological properties of the fluid, such as its viscosity, elasticity, yield stress, and the specific conditions of the cavitation process, including pressure, flow velocity, and geometry. The properties of the individual phases were calculated using REFPROP software and were considered constant, as in most of the work in the literature:

$$\phi_m = (1 - \alpha_v)\phi_l + \phi_v\alpha_v \tag{4}$$

To model the phase change effects due to the cavitation phenomenon, the Zwart-Gerber- Belamri (ZGB) [16] model based on the Rayleigh-Plesset equations has been implemented: it describes the behaviour of the single cavitation bubble in space and time. By simplifying the terms due to surface tension, the second-order derivatives, liquid viscosity, and non-condensable gas, the relationship between the change in the bubble radius and the pressure become:

$$\frac{dR}{dt} = \sqrt{\frac{2(P_v - P)}{3\rho_l}} \tag{5}$$

From this equation it is possible to express the evaporation and condensation rates and derive the source terms to be included in the transport equation [3]. Considering spherical bubbles of radius R_B , with a density per cell equal to n, it is possible to write:

$$\alpha_v = n(\frac{4}{3}\pi(R_B)^3) \tag{6}$$

From here, combining equations 6 and 5, after some mathematical steps it is possible to derive the formulation of the sink terms of evaporation and condensation proposed by [16]:

$$\dot{S}_\alpha = \begin{cases} F_v \frac{3r_{nuc}(1-\alpha_v)\rho_v}{R_B}\sqrt{\frac{2}{3}\frac{P_{sat}-P}{\rho_l}} & \text{if } P < P_{sat} \\ F_{\text{cond}} \frac{3r_v\alpha_v}{R_B}\sqrt{\frac{2}{3}\frac{P-P_{sat}}{\rho_l}} & \text{if } P > P_{sat} \end{cases} \tag{7}$$

where $r_{nuc} = 5x10^{-4}$ is the nucleation site volume fraction, $R_B = 10^{-6}[m]$ nucleation site radius and $F_v = 50$, $F_{cond} = 0.01$ empirical calibration constants. These model parameters were set as proposed by ZBG. For turbulence modelling, a k-omega SST (Shear Stress Transport) was proposed by Menter [17]. As suggested by the work of Chebli, Delgosha et Al. [13] modification for turbulent viscosity was added in order to simulate unsteady behaviour of cavitating flow [Equation 8,9]. The model uses two transport equations: one for the turbulent kinetic energy k and another for the specific dissipation rate of turbulent kinetic energy omega. The k equation accounts for the production and dissipation of turbulence, while the omega equation accounts for the transport and destruction of turbulence. The SST model uses a blending function for a smooth transition between a near wall low-Reynolds number model and a far field high-Reynolds number model. Other turbulence models, such as the Reynolds Stress Model or the Large Eddy Simulation, may also be appropriate for certain cavitation applications.

$$\mu_t = f(\rho)a_1\frac{k}{\max(a_1\omega, b_1F_{23}\mathbf{S})} \tag{8}$$

$$f(\rho) = \frac{\rho_v + \alpha_l^n(\rho_l - \rho_v)}{\rho_v + \alpha_l(\rho_l - \rho_v)} \tag{9}$$

A wall-resolved approach was chosen for the wall boundary layer. For this reason, the grid was built to have a Y^+ less than 5, as is usually done in the literature. Regarding unsteady cavitation flows, it has been observed in the literature that standard turbulence models cannot correctly predict the oscillatory behaviour of the flow. The turbulent viscosity is a key parameter in turbulence models that describes the rate at which turbulent energy is dissipated into heat. In cavitating flows, the presence of vapour bubbles can cause significant changes in the

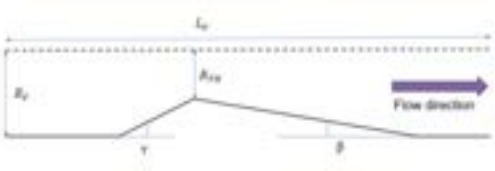

Figure 1: schematic view of nozzle geometry where L_V = 340mm is the lenght of entire domain, R_{TH} and L_{TH} = 10mm are the radius and lenght of the throath, R_V = 50mm radius of the channel and γ = 22.5°- β = 6° are the convergent and divergent angle.

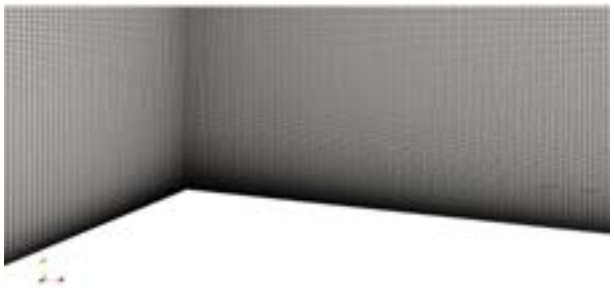

Figure 2: View of 2D axisymmetric computational mesh in which the grid thickening in the near-wall and cavitation region can be observed.

turbulent viscosity due to the highly compressible nature of the vapour phase. As is reported in the literature turbulent viscosity is overestimated in the cavitation region, since most turbulent models are not sensitive to phase change. This causes an inhibition of the phenomenon of cavitating bubble cluster shedding that affects the correct numerical prediction. For this reason, a correcting function [eq 9] developed by Delgosha [19], a modification to standard turbulence models that aims to account for the effects of cavitation on the turbulent viscosity, was implemented. The value of n is fixed to 10 as suggested by Delgosha et al. [19]

3. Geometry and numerical setup

For sensitivity analysis on the influence of throat cross-section on the phenomenon of cavitation, a Venturi-type reactor studied by Long et al. [15] was taken as a test case. The chosen geometry is shown in [Figure 1]. To prevent the length of the throat from having an impact in the simulations, we decided to remove it and use a sharp edge. As pointed out by the work of Ulla et al. [18] , the absence of the throat section, increases cavitation length. The domain for the simulation was realized by an axisymmetric structured 2D mesh shown in the figure 2 , consisting of about 100k hexahedral elements. In the regions near the wall, the mesh was refined and a wall resolved approach was adopted. For numerical simulations, 4 geometries were chosen in which the convergent and divergent ramp angles were kept constant and the throat height was varied: 5-10-15-20 mm. Boundary conditions represent a crucial aspect for simulations of cavitation phenomena since the development of the cavitation generates numerous pressure oscillations that spread within the channel, both upstream and downstream. For this reason to avoid pressure fluctuations and possible spurious solutions, two stitches were added, one downstream and one upstream of the venturi nozzle. The following boundary condition is used: an imposed velocity at the inlet equal to 0.89 m/s (in agreement with experimental data where the reference flow rate was imposed equal to 1.74 L/s), a static pressure set at the outlet equal to 200k Pa that was selected to reproduce the pressure value at the inlet measured from experimental data. One of the most widely used dimensionless parameters to study cavitation phenomena is the cavitation number, which takes into account the pressure drop in the fluid and the kinetic energy of the fluid, which are the two main factors that influence the behaviour of cavitation, and is defined as:

$$\sigma = \frac{P_{out} - P_{sat}}{\frac{1}{2}\rho U_{TH}^2} \tag{10}$$

where P_{out} represents the pressure imposed at the outlet, P_{sat} the fluid saturation pressure calculated at a temperature of 19°, U_{TH} the average velocity in the throat section. To evaluate the effects of throat diameter on the development of the cavitation region, which is a useful effect for process intensification, and to study the

Table 1: list of numerical models and schemes

Parameter/variable/name	*Model/Scheme*
Multiphase model	Eulerian–Eulerian VOF
Volume fraction	parameters Implicit scheme
Viscous model	$k-\omega SST$
Cavitation model	Zwart-Gerber- Belamri
ThermoPhisical Properties	constant
Spatial discretization-Gradient	Gauss linear
Spatial discretization-Momentum	Second order upwind
Spatial discretization-Volume fraction	Gauss VanLeer
Spatial discretization-Turbulent kinetic energy	Second order upwind
Spatial discretization-Specific dissipation rate	Second order upwind
Transient formulation	Second Order Backward

behaviour of pressure drop, 4 geometries were created. For the generation of the geometries, the convergent and divergent ramp angles were kept constant, while for the boundary conditions, both the outlet pressure and the throat velocity were kept constant by varying the inlet velocity to obtain the same cavitation number value (shown in table 2). A second-order numerical schemes for both time and other variables has been used, and in addition, the PIMPLE algorithm was used for solving governing equations, while the MULES algorithm (semi-implicit and second order in time) was used to ensure that the volume fraction (alpha) remains between strict bounds of 0 and 1. Regarding computational settings, we chose a time step $TS = 10^{-7}[s]$ to ensure a $CFL < 0.7$.

Table 2: Values used for sensitivity analysis on the influence of throat section in the cavitation process

$D_{TH}(mm)$	$U_{in}(m/s)$,	σ
5	0.223	0.8
10	0.89	0.8
15	2	0.8
20	3.55	0.8

4. Result

4.1. Re-entrant jet mechanism

the unsteady phenomena governing cavitation are mainly two:

- Shock front mechanism in which a shock front is formed in a certain region of the cavitation zone and moving upstream causes vapour condensation.
- Re-entrant jet mechanism is a pressure driven mechanism in which a vortex causes the detachment of a cavitating cluster that is carried downstream by the flow.

For all simulations, we observe that only the re-entrant jet mechanism is present. To investigate the influence of geometry in terms of re-entrant jet mechanism and shedding frequency, virtual probes are located on the axis in the control section near the inlet. In figures 3 and 4 show the dynamics of the re-entrant jet mechanism and the pressure signal obtained from the simulation of the Venturi device having a throat diameter of 10 mm. From point A to point E the cavitation zone grows until the re-entrant jet is created and cavitating cell detachment occurs. Subsequently attached sheet cavity decrease until disappears (point H). Starting from here we have three pressure spikes related to points (G to I), where the cavity breakoff takes place. This is the first cycle of the cavity shedding mechanism. After that, at point (L) the appearance of a new cavitating region, marking the beginning of the secondary cycle with pressure peaks less intense than in the first cycle happens. Once the cavity that was generated in the first cycle collapses the shedding phenomenon ends (Q) and the pressure values return to those of state A.

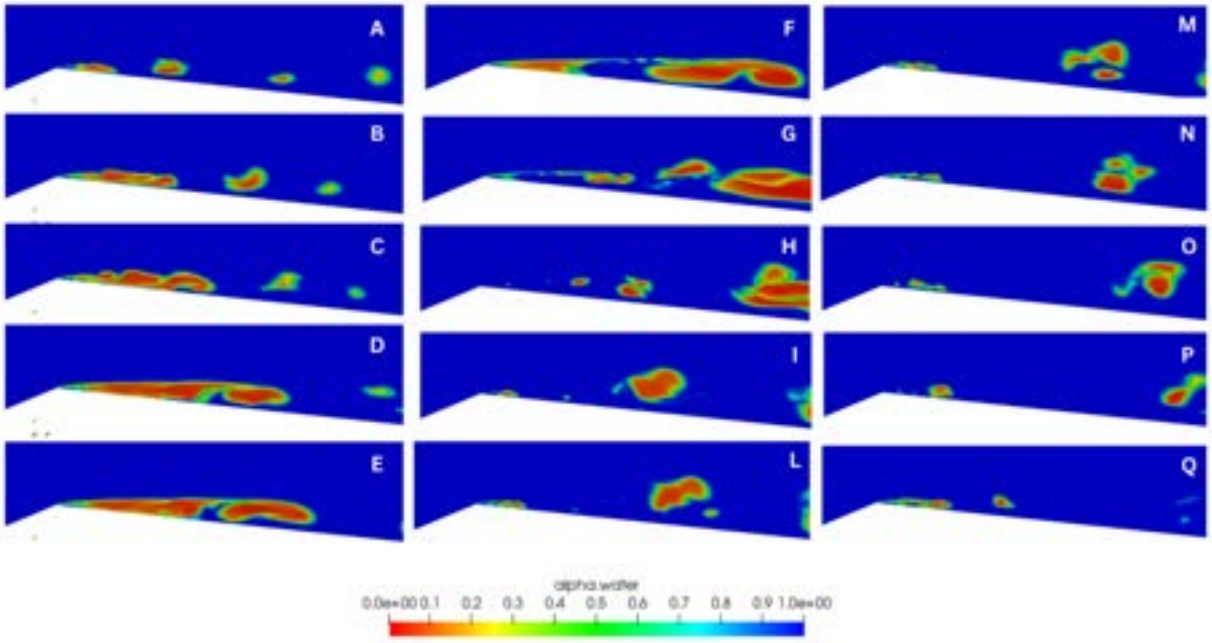

Figure 3: Re-entrant jet cycles in a Venturi device with D_{TH} = 10mm. From point A to H the first cycle of the re-entrant jet mechanism, characterized by an extended cavitation region, is shown. From I to L can be notices the second cycle in which the extension of cavity is smaller that the first.

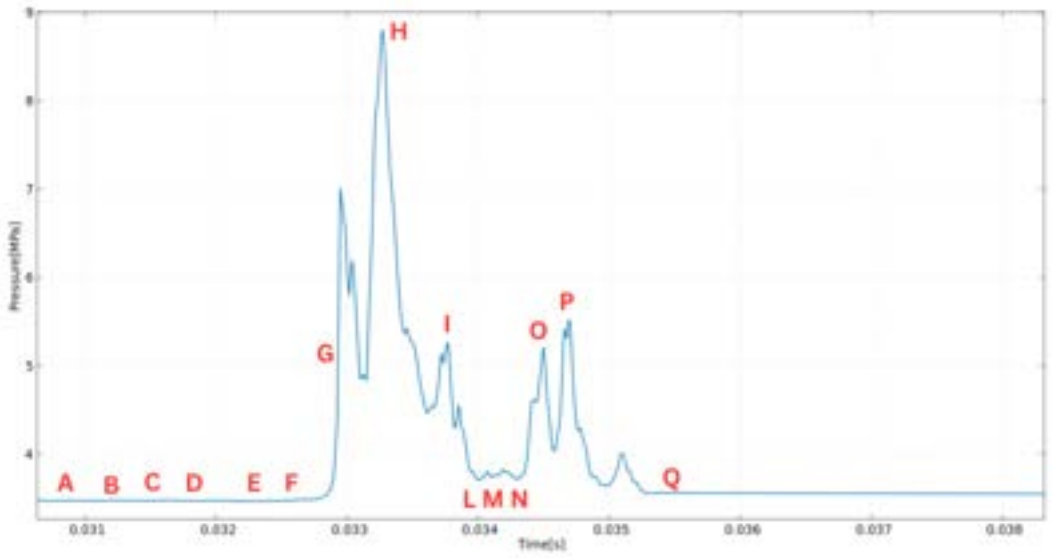

Figure 4: Pressure behaviour calculated at the inlet section in a Venturi device with D_{TH} = 10mm

Using the FFT fast Fourier transform 5, it was possible to analyze the characteristic frequencies of the re-entrant jet phenomenon of the four simulated geometries. At smaller throat cross sections, the frequency of the system increases while the pressure peaks associated with the breakoff of the cavities decrease. As reported in a later section, this behaviour is associated with the formation of a cavities in the first shedding cycle. Downstream of the throat, the pressure recovery is more gradual for larger diameters, this causes the life of the cavitating cells to increase (the collapse position is moved downstream), this lead to dwindle of frequency. The oscillation period increases. Geometries with larger throat cross sections showed higher oscillation, both in terms of frequency and flow rate. This is something to investigate as it could be an undesirable effect for the system in which the cavitating device will be installed.

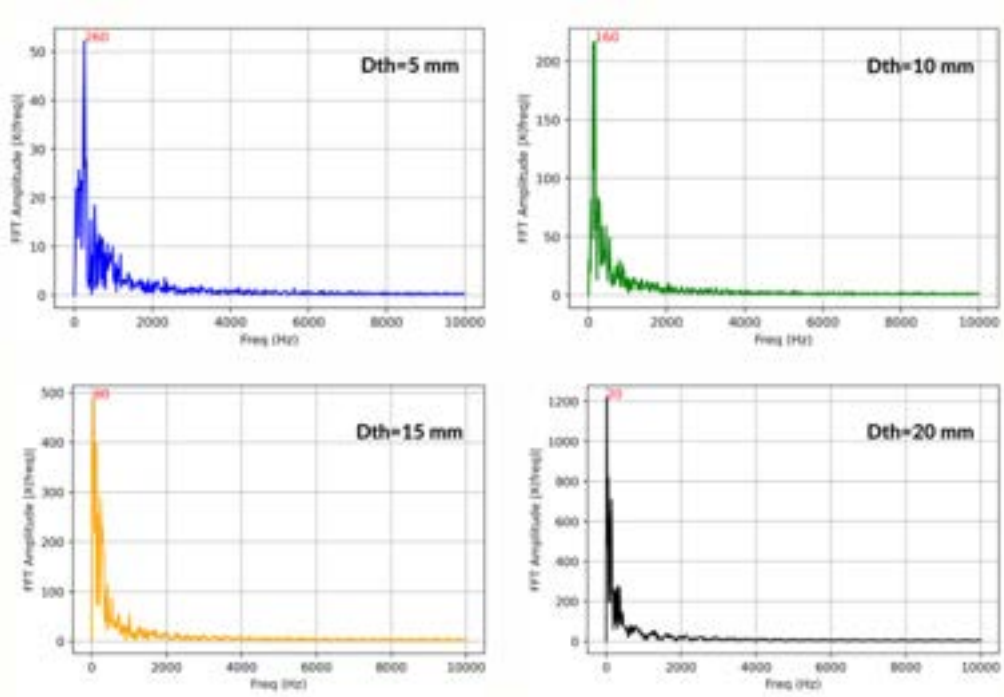

Figure 5: Result from FFT analysis, the number in red represents the frequency of the system .

4.2. Evaluation of overall cavitation efficiency

From the simulations obtained, it was possible to calculate parameters related to cavitation efficiency (length of cavitation, the value of volume fraction at certain stations and amplitude of the cavitating region) and parameters related to pressure drop with which an optimized geometry could be chosen. For this purpose, it has been developed a term called cavitation efficiency parameter (CEP) for evaluating cavitation efficiency that takes into account the average volume occupied by cavities:

$$CEP = \frac{\sum_{i=0}^{n}[V_i \alpha_{Vi}]}{\pi D_{in} \frac{D_{TH}^2}{4}} \tag{11}$$

where V_i is the volume of i-th cell , α_{Vi} is the value of vapour volume fraction in the i-th cell, n is the number of cells, while D_{TH} is the throat diameter. The ratio represents a weighted average over the volume fraction of the cavitating volume and a cylinder having diameter equal to D_{TH} and height equal to the channel's diameter D_{in}. To calculate CEP a python code that takes as input the results obtained from the simulations and returns the value of CEP was developed. This parameter is very fast and simple to be obtained and can be easily integrated into the design process of the cavitating device. Then the value of pressure losses over the entire nozzle was calculated, defined as:

$$K = \frac{\Delta P}{\frac{1}{2}\rho U_{TH}^2} \tag{12}$$

where ΔP is the difference between total pressure at the inlet and outlet while U_{TH} is the throat velocity. These two parameters were used to compare the various simulations and estimate the influence of the throat section on the cavitation process. Time average Volume fraction fields are shown in figure 6 for the four geometries. It can be seen that as the diameter increases, the cavitation region becomes larger. The lengths of the average cavitating region for the various geometries are given in Table 3 while the plot of K and CEP are shown in fig. 7. From the results obtained, it can be seen that at the same cavitation number both losses and CEP have a favourable trend for larger diameters. The best configuration seems to be that for DTH = 20mm in which the cavitation volume increases while the losses decrease as the main flow has less blocking effect due to the cavitating region.

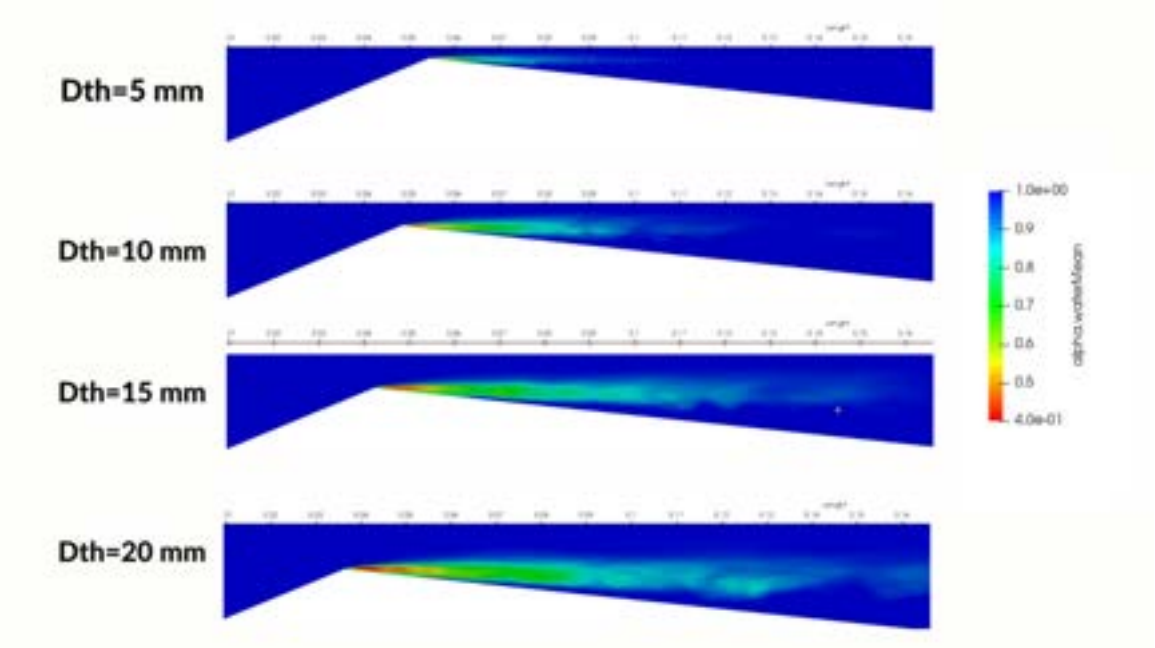

Figure 6: Time average liquid volume fraction for simulated geometry.

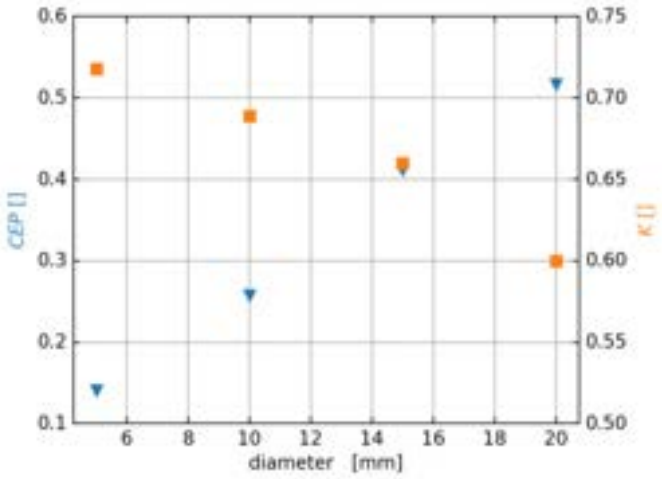

Figure 7: The graph shows the trend of K losses and CEP as a function of throat diameter.

4.3. Effect of throat length in cavitating flow dynamics

This section analyzes the differences in terms of the dynamics of the cavitation phenomenon between a sharp-edged geometry and a geometry in which there is a throat section of length L_{TH}. It has been decided to consider the geometry with D_{TH} = 10mm and L_{TH} = 10mm. Once the simulations were finished, it was possible to evaluate the differences between the two geometries using the FFT and calculating both the K losses and the cavitating efficiency parameter. The presence of the throat region causes the emergence of a quasi-stable sheet cavity region, which causes a clear decrease in the oscillation period. In terms of frequency, we have a reduction from 160 Hz for the sharp-edged to 40 Hz for the geometry in which the throat region is present. While the amplitude related to the pressure spike remains almost the same (Figure 9). Regarding the velocity field, the presence of two recirculation zones located at the beginning of the throat section and at the beginning of the diverging ramp is observed in figure 10. The instabilities that are generated at the sheet cavity interface, tend to energize the flow in the second recirculation zone. This results in an inhibition of the cavitation phenomenon which is therefore less intense than having a sharp-edged throat. The performance for process intensification values of CEP = 0.17 while the losses give a value of K = 0.58. Compared with the values found for the sharp-edged geometry, it is observed that CEP decreases given the smaller extent of the cavitation region. Pressure losses, directly related to the extent of the cavitation region where the largest contributions of pressure degradation are shown, also decreasing from 0.689 to 0.58.

Table 3: Lenght of cavitation region measured from the throat to the point of maximum abscissa with liquid volume fraction equal to 0.95.

$D_{TH}(mm)$	$L_{cav}(mm)$
5	23
10	46
15	79
20	97

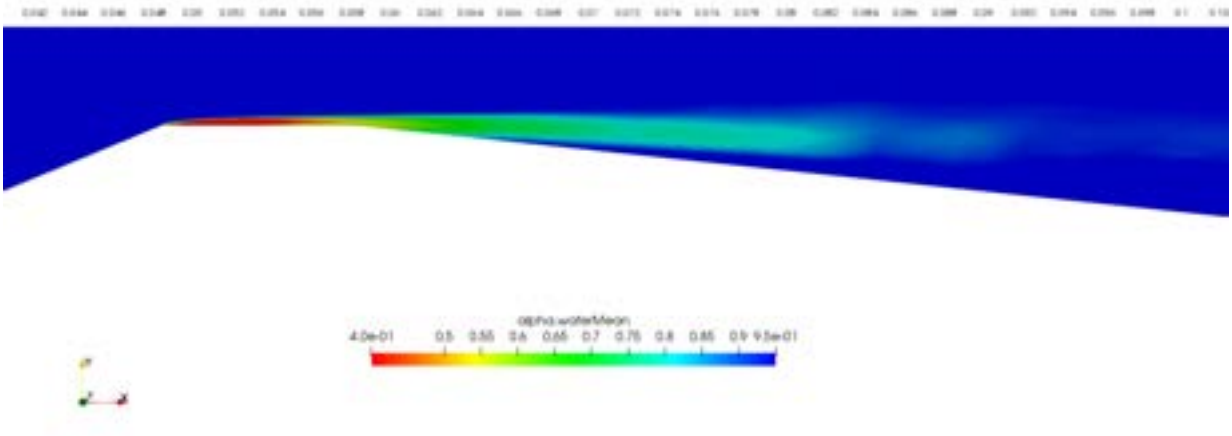

Figure 8: Average volume fraction of geometry with cavitating lenght of 10 mm, in the throat section there is presence of quasi stable sheet cavity.

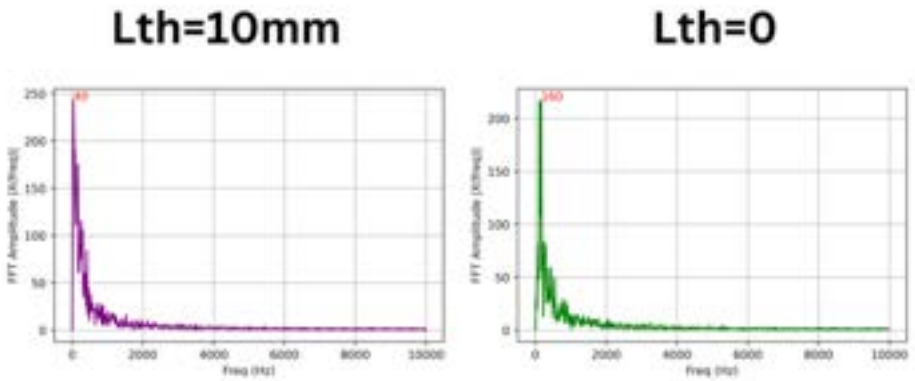

Figure 9: FFT Fast Fourier Transform for evaluate the effect of throat lenght in cavitation dynamics behaviour.

5. Conclusion

In this paper, the influence of the throat section on the cavitation process for process intensification was investigated. It is understood that the unsteady process of cavitation is very complex and it depends on many factors. Using an FFT analysis it was possible to study the phenomenon of the re-entrant jet mechanism and

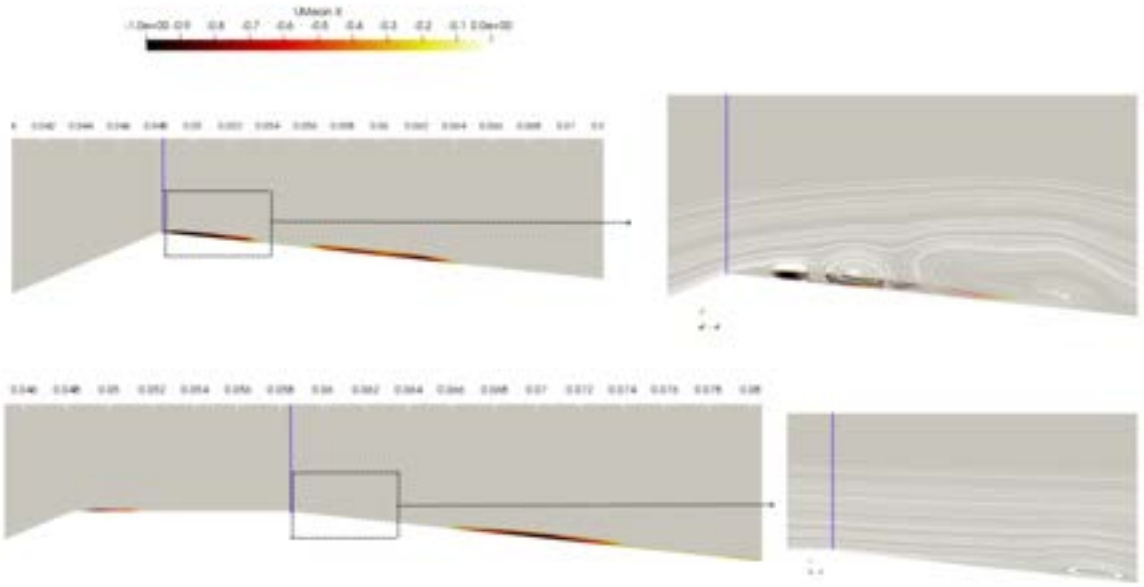

Figure 10: Average velocity field in which are compared the recirculation zone, the purple line represent the downstream throat section. On the left the streamline of the flow are plotted.

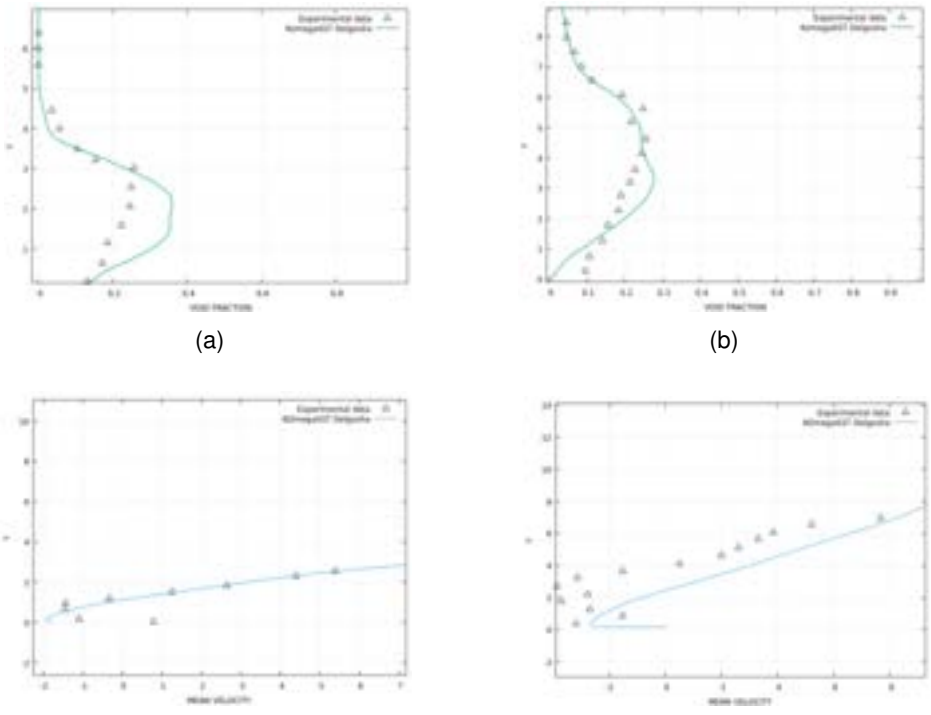

(a) (b)

(c) (d)

Figure 11: Stutz Reboud test case [12]: a comparison between experimental data across the cavity at the station 1 and 2 and time-avarage numerical simulation. on the top a) b) show the mean volume fraction profile while on the bottom c) d) show the mean velocity field.

was found that an increase in throat section leads to a decrease in the oscillation frequency of cavities while a decrease in throat leads to a reduction in cavitation region extension. Despite the simplicity of the venturi device, there is no parameter to evaluate the effectiveness of the reactor for process intensification. For this reason, a specific term was developed to evaluate cavitation efficiency that was compared to the pressure drop within the cavitating device. Further experimental or numerical studies, are needed to determine the effect of varying the pressure at the outlet and keeping the same mass flow rate on the cavitation behaviour (at

a constant cavitation number). This forms the scope of future work.

Appendix A Model Validation

One of the critical aspects of cavitation models is to obtain reliable and accurate results. This is because especially empirical models or those based on Rayleigh-Plesset equations need a careful calibration process from the point of view of the numerical schemes and simulation settigs. from the point of view of the numerical schemes. For this work, since we do not have experimental data of the momentum field and volume fraction trend for the chosen geometry, we considered one of the most widely used test cases in the literature (Stutz and Reboud [12]) [12]) that offers experimental data on both the velocity field and volume fraction profile in the cavitation zone. Numerical settings are the same as those mentioned in the numerical setup section while a mesh of 100K hexahedral elements was made for the geometry. From the comparisons with the experimental data shown in graph 11, it can be seen that there is good agreement with the volume fraction and velocity profiles calculated with the developed model. The only differences are found at the first station where the mean value of volume fraction is overestimated, showing an inaccuracy in simulating the sheet cavitation region. While at the second station it is noticeable that the velocity profile calculated with cfd tends to underestimate the recirculation region. This is due to the URANS model used, in fact such models fail to totally capture adverse pressure gradients. A more detailed study of the velocity profile can be done using high fidelity approaches to evaluate the interaction between cavitating flow and turbulence. Comparison with experimental data showed how there is an error of about 4 percent in the calculation of cavitation length (48mm with numerics and 50 mm from experiment). For these reasons, the model was considered as validated.

Nomenclature

- D Diameter [m]
- f_σ surface tension [N/m]
- K Pressure losses
- k Turbulent kinetic energy [J/Kg]
- L Lenght [m]
- L_V total Venturi's Lenght [m]
- P pressure [Pa]
- R_B bubble radius [m]
- R_V Channel radius[m]
- S_α evaporation/condensation source term [kg/m^4]
- V volume [m^3]
- t time [s]
- T temperature, [°C]
- U velocity [m/s]

Greek symbols

- α volume fraction
- β divergent angle [DEG]
- γ convergent angle [DEG]
- ω specific dissipation rate [1/s]
- μ_{eff} effective viscosity [Ns]
- ρ density [kg/m^3]
- ϕ generic function

Subscripts and superscripts

in	inlet section
m	mixture
out	outlet section
sat	saturation
TH	Throat
v	vapour
w	water

References

[1] . Wang, H. Su, and B. Zhang, *'Hydrodynamic cavitation as a promising route for wastewater treatment – A review', Chemical Engineering Journal, vol. 412, p. 128685, May 2021, doi: 10.1016/j.cej.2021.128685.*

[2] . Dular et al., *'Use of hydrodynamic cavitation in (waste) water treatment', Ultrasonics Sonochemistry, vol. 29, pp. 577–588, Mar. 2016*

[3] R. Darandale, M. V. Jadhav, A. R. Warade, and V. S. Hakke, *'Hydrodynamic cavitation a novel approach in wastewater treatment: A review', Materials Today: Proceedings, p. S2214785322074478, Dec. 2022.*

[4] Y. Song, R. Hou, W. Zhang, and J. Liu, *'Hydrodynamic cavitation as an efficient water treatment method for various sewage:- A review', Water Science and Technology, vol. 86, no. 2, pp. 302–320, Jul. 2022*

[5] B. Wang et al., *'Hydrodynamic cavitation and its application in water treatment combined with ozonation: A review', Journal of Industrial and Engineering Chemistry, vol. 114, pp. 33–51, Oct. 2022*

[6] F. Verdini, E. Calcio Gaudino, G. Grillo, S. Tabasso, and G. Cravotto, *'Cellulose Recovery from Agri-Food Residues by Effective Cavitational Treatments', Applied Sciences, vol. 11, no. 10, p. 4693, May 2021*

[7] Sun et al., *'Recent advances in hydrodynamic cavitation-based pretreatments of lignocellulosic biomass for valorization', Bioresource Technology, vol. 345, p. 126251, Feb. 2022*

[8] Kim, I. Lee, S. H. Jeon, T. Hwang, and J.-I. Han, *'Hydrodynamic cavitation as a novel pretreatment approach for bioethanol production from reed', Bioresource Technology, vol. 192, pp. 335–339, Sep. 2015.*

[9] Ivakumar, Manickam, Siah Ying Tang, and Khang Wei Tan.*S "Cavitation technology–a greener processing technique for the generation of pharmaceutical nanoemulsions." Ultrasonics sonochemistry 2014.*

[10] Wu, Pengfei, Lixin Bai, and Weijun Lin. *On the definition of cavitation intensity. Ultrasonics Sonochemistry.*

[11] Dastane, Gaurav G., et al. *Single and multiphase CFD simulations for designing cavitating venturi. Chemical Engineering Research and Design 149 (2019): 1-12.*

[12] Stutz, B., and J. L. Reboud. *Experiments on unsteady cavitation. Experiments in fluids 22.3 (1997): 191-198.*

[13] Chebli, R., B. Audebert, G. Zhang, and O. Coutier-Delgosha. *Influence of the turbulence modeling on the simulation of unsteady cavitating flows. Computers Fluids 221 (2021): 104898.*

[14] Hirt, C.W.; Nichols, B.D. *Volume of fluid (VOF) method for the Dynamics of Free Boundaries. J. Comput. Phys. 1981, 39, 201–225.*

[15] Long, Xinping, et al. *"Experimental investigation of the global cavitation dynamic behavior in a venturi tube with special emphasis on the cavity length variation." International Journal of Multiphase Flow.*

[16] Zwart, Philip J and Gerber, Andrew G and Belamri, Thabet and others - *Two-phase flow model for predicting cavitation dynamics , Fifth international conference on multiphase flow, Yokohama 2004*.

[17] F.R. Menter, R. Langtry, and S. Volker. *Transition Modelling for General Purpose CFD Codes. Flow, Turbulence and Combustion 2006*.

[18] Ullas, P. K., Dhiman Chatterjee, and S. Vengadesan. *"Experimental study on the effect of throat length in the dynamics of internal unsteady cavitating flow." Physics of Fluids 35.2 (2023): 023332.*

[19] Coutier-Delgosha, Olivier and Fortes-Patella, Regiane and Reboud, Jean-Luc *Evaluation of the turbulence model influence on the numerical simulations of unsteady cavitation - J. Fluids Eng. 2003*.

Numerical Investigation of Performance of a Disc Shaped Branched Heat Exchanger

Cihan Sezer[a], Kenan Kaya[b], Mahdi Tabatabaei Malazi[c], Enrico Sciubba[d], Roberto Capata[e], and Hasan Alpay Heperkan[f]

[a] *Istanbul Aydin University, Istanbul, Turkey, cihansezer@aydin.edu.tr*
[b] *Istanbul Aydin University, Istanbul, Turkey, kenankaya@aydin.edu.tr, CA*
[c] *Istanbul Aydin University, Istanbul, Turkey, mahditabatabaei@aydin.edu.tr*
[d] *Sapienza University of Rome, Rome, Italy, enrico.sciubba@gmail.com*
[e] *Sapienza University of Rome, Rome, Italy, roberto.capata@uniroma1.it*
[f] *Istanbul Aydin University, Istanbul, Turkey, hasanheperkan@aydin.edu.tr*

Abstract:

This study investigates the heat transfer performance of a disc-shaped branched heat exchanger numerically. The numerical calculations have been conducted using the commercial computational fluid dynamics solver *ANSYS Fluent*, while three laminar and three turbulent cases are considered with Reynolds numbers of 100, 200 and 400 for the former; and 3000, 4000 and 6000 for the latter. Turbulence closure is achieved by employing the k-eps Realizable turbulence model, which uses Boussinesq approximation to model the eddy viscosity. The working fluid is water. Constant heat flux is applied at the bottom wall of the heat exchanger. The numerical method is validated by a previous experimental study. The heat transfer performance of the heat exchanger is evaluated by monitoring the temperatures at the outlet section, as well as the volume-averaged temperature of the solid part. It is observed that values of the heat transfer coefficient for the turbulent cases are much greater than that of the laminar case, whereas it is directly proportional with the Reynolds number, in general.

Keywords:

Disc shaped heat exchanger, Electronic device cooling, Computational fluid dynamics

1. Introduction

The purpose of this study is to carry on with the determination of the most effective configuration for a branching heat exchanger that uses water as the coolant fluid and implement any necessary improvements.

Capata and Gagliardi [1] investigated the performance of branched heat exchangers working with organic fluids. An automotive refrigerant called glycol was used in experiments at two different concentrations (50 and 100 %). An organic fluid has also been employed and examined for heat transmission. After completing all the tests, the numerous dimensionless parameters that characterize the heat exchange have been determined, and a comparison analysis has been performed, in order to determine and suggest the optimal configuration for the branched heat exchanger.

Reis [2] investigated constructal theory and its applications to a variety of domains, including engineering, natural living and inanimate systems, social structure, and economics. A constructal approach offers an integrated structure to guide the creation of flow architectures in systems with fluid flow. The relationship between of constructal law and the thermodynamic optimization strategy for minimizing entropy generation is described. The constructal law is an independent principle separate from the Second Law of Thermodynamics. In addition, the relationship between the constructal law and other fundamental concepts, including the Second Law, the principle of least action, and the principles of symmetry and invariance, is discussed.

Capata and Beyene [3] investigated three distinct compact branched heat exchangers by assessing the thermal efficiency and pressure drop of each device. A performance comparison of several refrigerant fluids improves the generality of the understanding of phenomena. To provide an average constant flow speed throughout the exchanger, the channels in the first arrangement have been built with different inner diameters. In the second, a constant flow Reynolds number has been maintained inside the channels. According to Bejan Constructal Theory, the final configuration is constructed using the constructal diameter variation. The results of multiple comparative tests have been assessed to find the ideal exchanger for each refrigerant based on the gathered data.

Asgari et al [4] considered the simulation of phase change material solidification in a heat exchanger with branch-shaped fins. The thermal conductivity of phase change materials is studied in relation to the impacts of branch-shaped fins with varying thicknesses and lengths. The results demonstrated that fins considerably

accelerate the solidification process, and simulation efficiency is maximized when thin, branch-shaped fins and nanoparticles with a volume fraction of 0.04 are utilized simultaneously.

Zhu and Jing [5] examined a numerical analysis of the thermal and melting performance of a horizontal latent heat storage unit with tree-like convergent fins. The paper presents a horizontal LHS unit embedded with branched tree-like convergent fins (BTCF) and statistically explores the influences of various geometric and structural characteristics of the BTCF. The results demonstrate that increasing N, m, and α values can efficiently enhance heat transfer between the fin and phase change material (PCM), speed up PCM melting, and increase energy storage.

Huang et al [6] studied the heat transfer improvement of a latent heat storage unit using gradient tree-shaped fins, both experimentally and numerically. They examine two new LHS units with tree-shaped uniforms and gradient fins. The results indicate that tree-shaped fins promote heat diffusion from point to area, hence breaking the heat transport hysteresis in conventional LHS units and speeding the melting/solidification rate.

2. Numerical Method

This study investigates heat transfer characteristics in a disc shaped heat exchanger (Disc HEx), numerically. Steady, three-dimensional, and incompressible problem is modelled using commercial computational fluid dynamics (CFD) solver, *ANSYS Fluent*. Water as a heat transfer fluid for this study, enters disc heat exchanger through inlet section at temperature of 308 K with diameter of 22 mm which is located on the top of the disc heat exchanger. Diameter of branches are 5.9 mm, 2.9 mm, and 1.48 mm, respectively. Twelve outlets are located on sides of the disc and applied pressure outlet boundary condition, where static pressure is adjusted at zero gauge. Constant heat flux of 28294.212 W/m^2 is applied to the bottom of the disc for all cases. All surfaces of heat exchanger, except bottom surface where heat flux is applied, is considered adiabatic. Physical properties of water those of density, specific heat, heat conductivity and dynamic viscosity are assumed to be constant. Geometry description, branch definitions and boundary conditions are presented in Fig. 1 and Table 1.

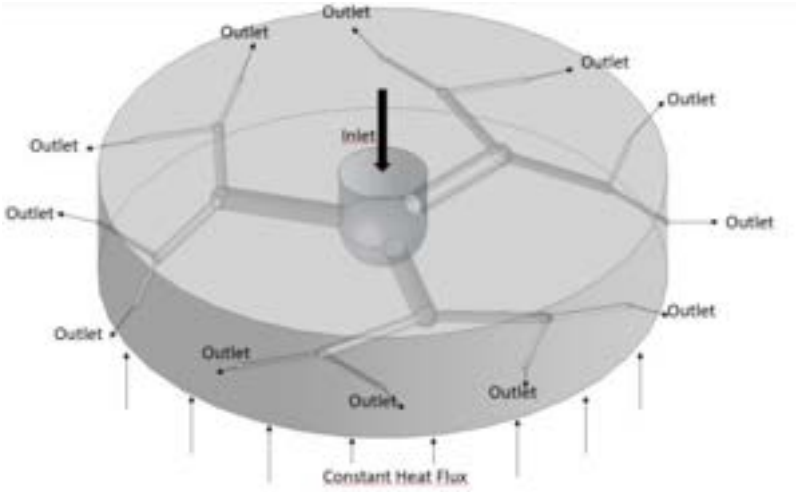

(a)

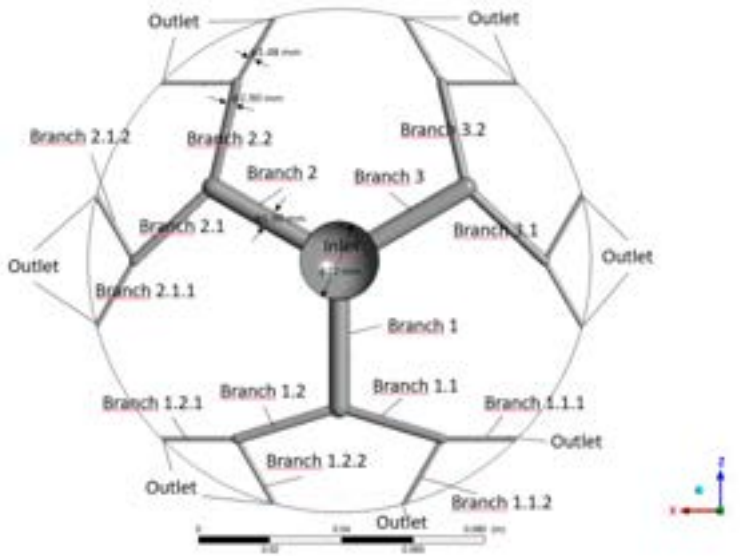

(b)

Figure 1. *Geometry description and boundary conditions,* ***(a)*** *isometric view,* ***(b)*** *top view*

An unstructured mesh with approximately 3.5 million elements is generated for numerical calculations (Fig. 2). Reynolds number is calculated considering inlet diameter and inlet velocity (Eq. 1). In numerical calculations, three laminar cases with Reynolds number of 100, 200 and 400, and three turbulent cases with Reynolds number of 3000, 4000 and 6000 are considered, respectively. For turbulent cases, k-ε Realizable turbulence model with Enhanced Wall Treatment is employed. Coupled algorithm is utilized for pressure-velocity coupling.

$$Re = \frac{\rho V_o D_o}{\mu} \tag{1}$$

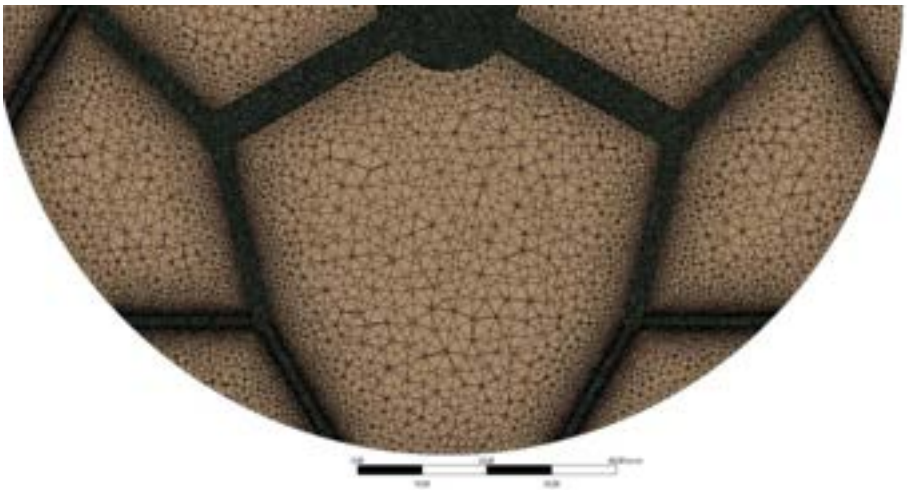

Figure 2. *The numerical grid used in this study*

Logarithmic mean temperature difference (ΔT_{lm}) is calculated according to Eq (2):

$$\Delta T_{lm} = \frac{\left(T_{wall,in} - T_{in}\right) - \left(T_{wall,out} - T_{out}\right)}{\ln \frac{\left(T_{wall,in} - T_{in}\right)}{\left(T_{wall,out} - T_{out}\right)}} \tag{2}$$

Where, T_{in} and T_{out} refer to inlet and outlet temperatures of certain branch, while $T_{wall,in}$ and $T_{wall,out}$ refer to solid temperature near inlet and outlet sections. Heat flux is calculated through the following equation:

$$q = \frac{\dot{m} c_p (T_{out} - T_{in})}{A_s} \tag{3}$$

In Eq (3), A_s is heat transfer area, while $\dot{m}$ and c_p are mass flow rate and specific heat. While mass flow rate is variable depending to Reynolds number, specific heat is assumed to be constant and 4182 J/kg K. Eventually, mean Nusselt number throughout each branch is calculated with Eq (4):

$$Nu_{m,i} = \frac{q D_i}{k\, \Delta T_{lm}} \tag{4}$$

Area-weighted average Nusselt number throughout whole disc for each case is calculated by Eq (5):

$$Nu_{m,ave} = \frac{\sum (A_s\, x\, Nu_{m,i})}{\sum A_s} \tag{5}$$

3. Results and Discussion

This study is validated with a previous experimental work of Capata and Gagliardi [1]. Solution parameters used in the previous experimental work are employed in numerical calculations, and obtained results are compared. Validation parameters are given in Table 1, and compared results are presented in Table 2. Results of the numerical and experimental studies agree very well, while the absolute percentage error in the estimated values of temperature is 1.35 % for volume-averaged temperature of the heat exchanger, T_{solid}, whereas error is less than 0.5% for outlet fluid temperatures, T_{out}. Thus, the numerical model is validated to be used for further investigating heat transfer characteristics of the disc-shaped heat exchanger.

Table 1. Solution parameters

Refrigerant	Inlet velocity [m/s]	Reynolds number	Inlet Temperature [K]
Water	0.253	3267	304
	0.505	6534	309
	1.263	16336	312

Table 2. Comparison of experimental and numerical results

$T_{solid, exp}$ [K]	$T_{solid, num}$ [K]	Error %	$T_{out, exp}$ [K]	$T_{out, num}$ [K]	Error %
320.00	320.84	0.26	309.50	308.97	-0.17
318.80	320.26	0.46	311.3	311.31	0.003
315.00	319.25	1.35	312.80	312.81	0.003

Figure 3 illustrates the temperature distribution on the horizontal mid-plane of the heat exchanger. Accordingly, cooling effect increases with Reynolds number, while the maximum temperature decreases. It is also observed that fluid temperature increases with each branching. This increase in temperature can be attributed to the vortex formation in the junctions due to the impingement of fluid on the junction wall, as is seen in Fig. 4. Apparently, this is the primary factor increasing the heat transfer rate from solid walls to the fluid for all cases. Also, streamlines shown in Fig.4 indicate that higher values of velocity are observed in Branch 1.1.1 than those in Branch 1.1.2, since Branch 1.1.1 deviates from Branch 1.1 with a smaller angle than Branch 1.1.2 does. Temperature contours on the branch walls for Re=200 and 3000 (Fig. 5) are in accordance with those shown in Figs. 3b and 3d, where the wall temperature drops gradually as the fluid travels through the branches.

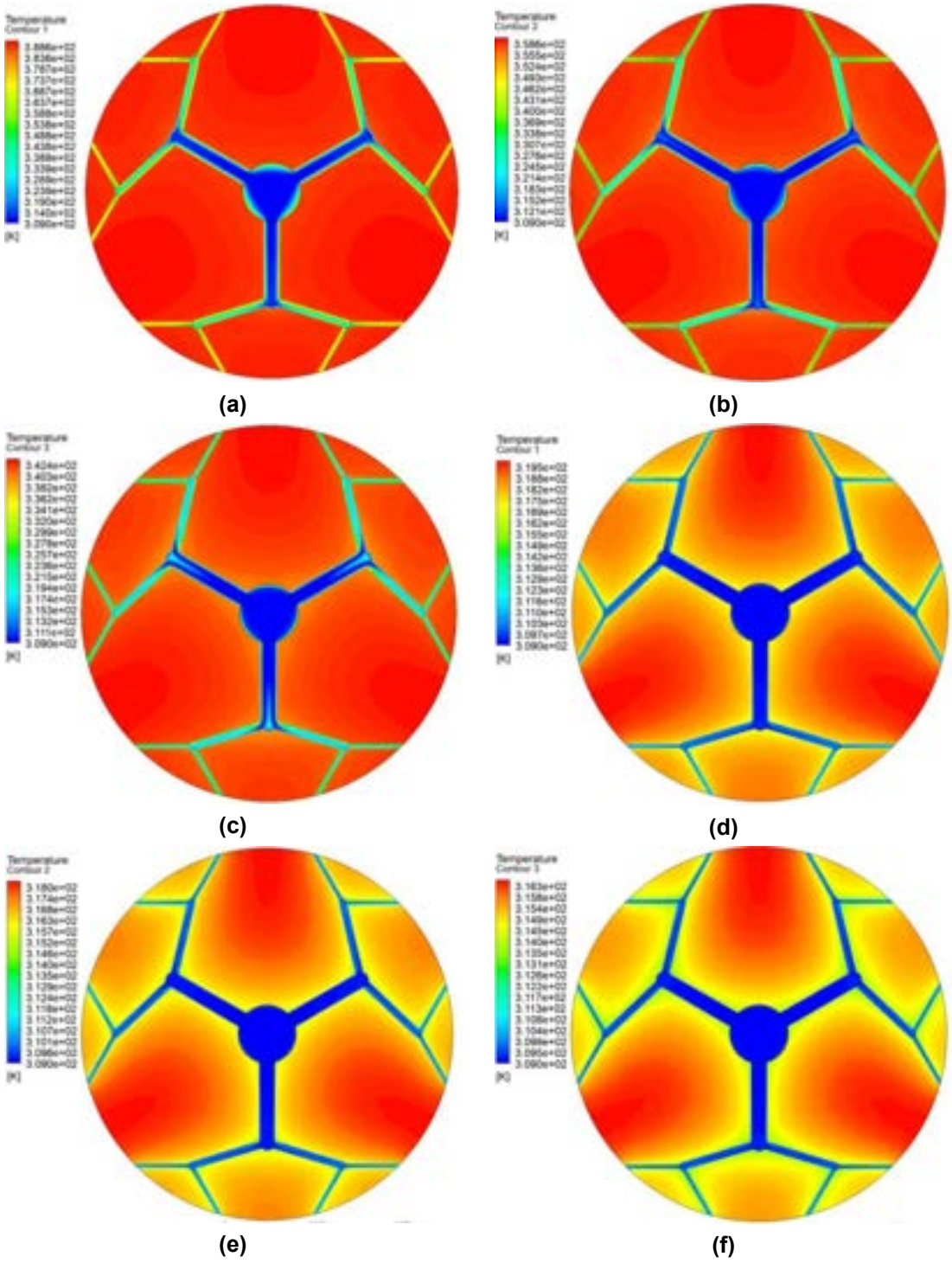

Figure 3. *Temperature distribution on mid-plane of the disc heat exchanger for* ***(a)*** *Re=100,* ***(b)*** *Re=200,* ***(c)*** *Re=400,* ***(d)*** *Re=3000,* ***(e)*** *Re=4000,* ***(f)*** *Re=6000.*

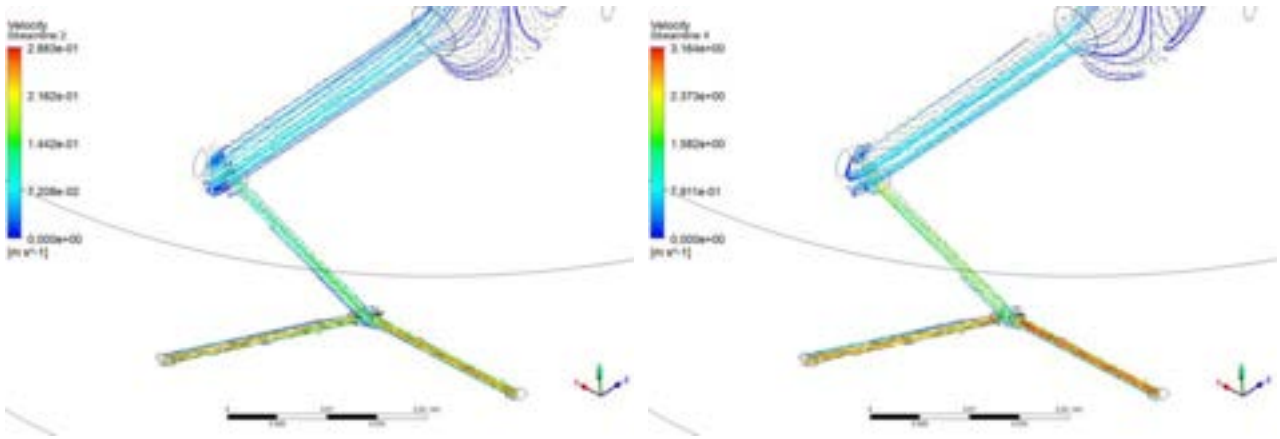

(a) **(b)**

Figure 4. *Streamlines and velocity vectors through branches for* ***(a)*** *Re=200 and* ***(b)*** *Re=3000*

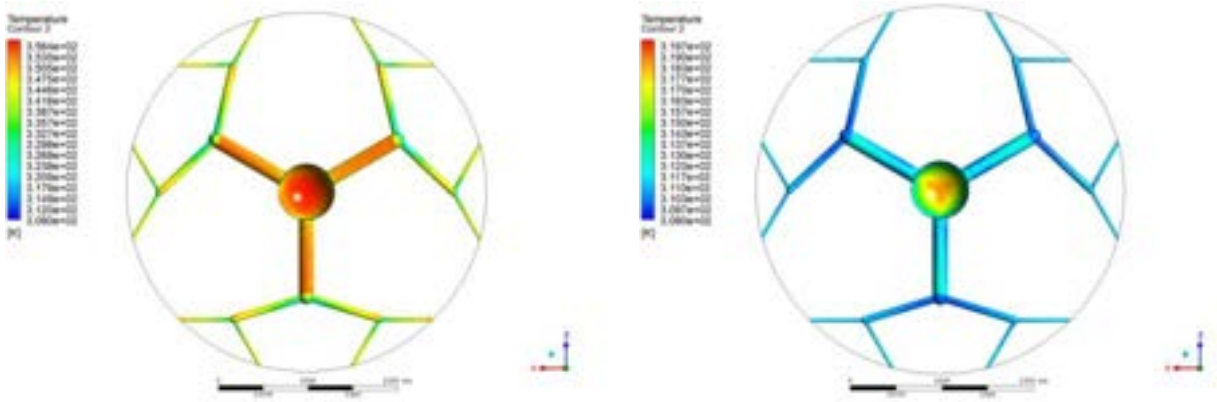

(a) **(b)**

Figure 5. *Temperature contours of the solid walls of the branches for* ***(a)*** *Re=200 and* ***(b)*** *Re=3000*

Variation of calculated mean Nusselt number with branching is presented in Fig. 6 for each Reynolds number. It is interesting to note that mean Nusselt number in Branch 1.1.2 is higher than that in Branch 1.1.1 in case of laminar flow, while it is the other way around for turbulent cases (Fig. 6). One reason for such a difference might be the difference in temperature distribution as seen in Fig. 7. A horseshoe-like temperature profile is evident throughout the branches which is thought to be caused by the vortices generated at the junctions due to the impingement.

Figure 8 shows variation in area-weighted average Nusselt number ($Nu_{m,ave}$) for the whole disc heat exchanger with Reynolds number. Accordingly, there is a linear variation in Nusselt number which can be expressed by Eq. (6) with a normalized root-mean-square error (NRMSE) less than 2%:

$$Nu_{m,ave} = 0.216Re + 7.205 \quad (6)$$

Variation in average fluid outlet temperature and volume-averaged solid temperature of the heat exchanger is presented in Fig. 9. Both the average fluid temperature at outlet and volume-averaged solid temperature exhibits an exponential variation with the Reynolds number. It should be noted that in high Re number limit the average outlet temperature approaches the inlet fluid temperature, i. e. 308 K.

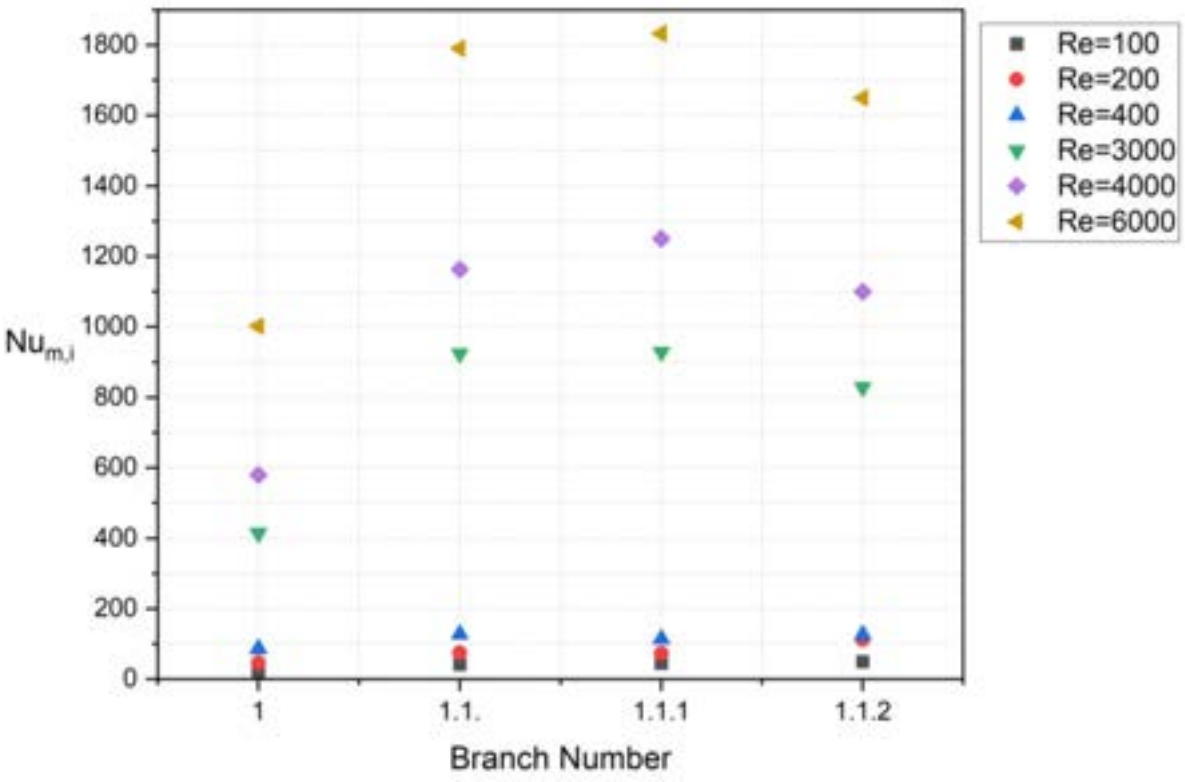

Figure 6. *Variation of mean Nusselt number with branching*

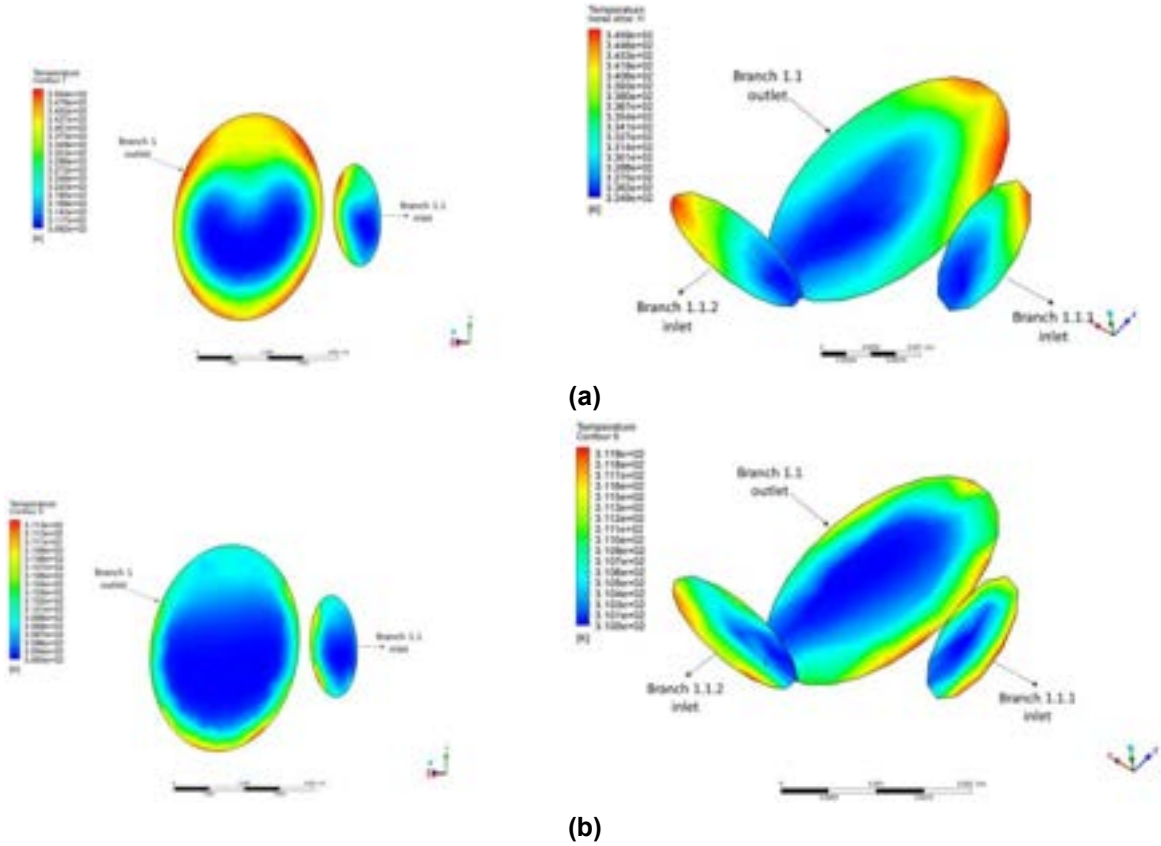

Figure 7. *Temperature contours on inlet and outlet planes of branches for* ***(a)*** *Re=200 and* ***(b)*** *Re=3000*

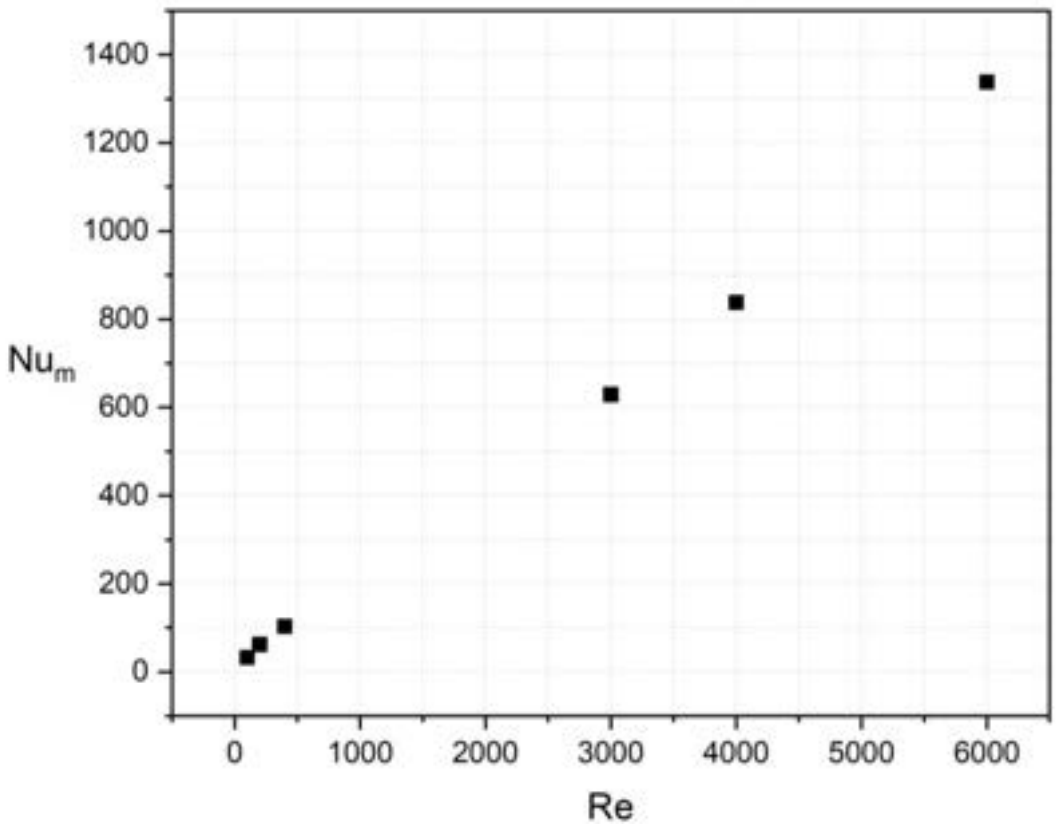

Figure 8. *Variation in area weighted average Nusselt number for the whole disc heat exchanger with Reynolds number*

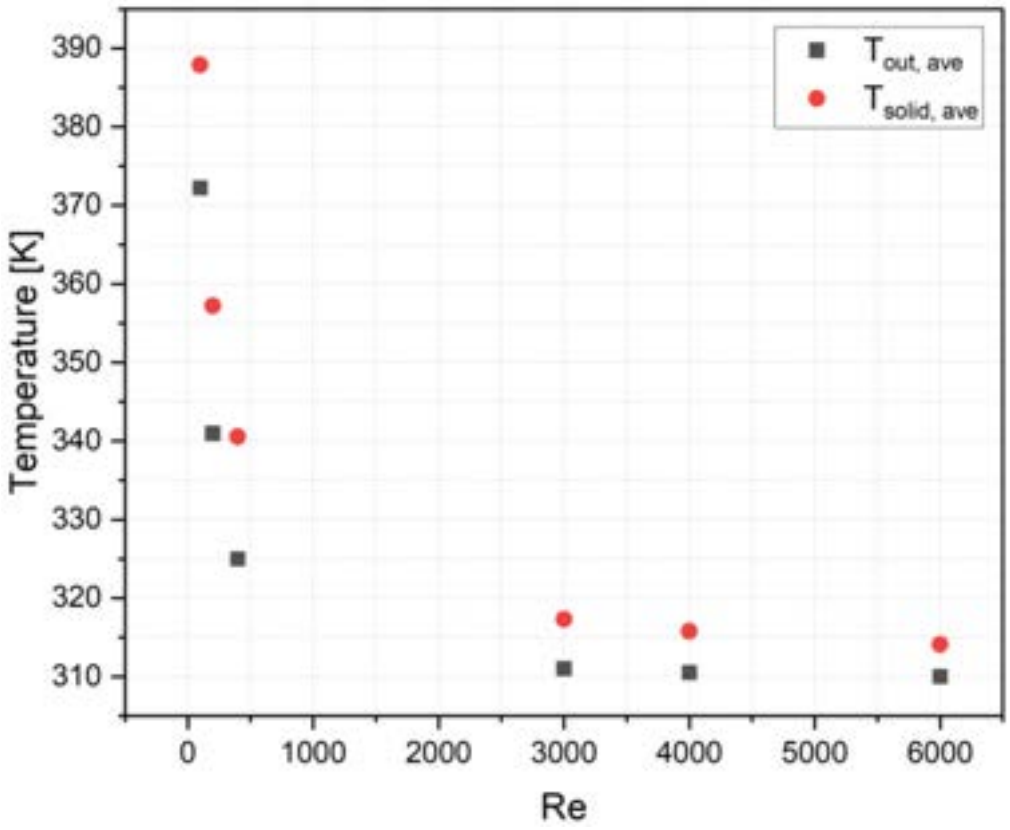

Figure 9. *Variation in average fluid outlet temperature and volume-averaged solid temperature with Reynolds number*

4. Conclusion

In this study, heat transfer characteristics of a disc-shaped branched heat exchanger is investigated for laminar and turbulent cases for Reynolds numbers of Re = 100, 200, 400, 3000, 4000 and 6000. The flow pattern and its effect on the heat transfer coefficient is discussed. According to the numerical results, mean Nusselt number for a given branch and the whole disc increases with the Reynolds number. The variation of the average Nusselt number for the whole disc with the Reynolds number is almost linear, a first order polynomial expression is offered which yields the average Nusselt number corresponding to a given Reynolds number with a maximum normalized root mean square error of less than 2%, for $100 \leq Re \leq 6000$. Extremely high values for volume-averaged solid temperatures are calculated for cases of relatively lower Reynolds number, which may exceed the design temperatures of device to be cooled. On the contrary, volume-averaged solid temperature of the heat exchanger approaches the inlet temperature of the coolant at high Reynolds numbers.

It is observed that the most significant factor affecting heat transfer coefficient of the disc-shaped heat exchanger is fluid impingement on the walls in junctions. This implies that a design allowing more effective impingement may provide higher heat transfer characteristics. However, although pressure losses are not considered in this study, a trade-off should be made between pressure loss and increase in heat transfer coefficient.

Nomenclature

A_s *surface area* m^2

c_p *specific heat, J/(kg K)*

D *diameter m*

k *heat conductivity W/(m K)*

$\dot{m}$ *mass flow rate, kg/s*

Nu_m *average Nusselt number*

T_{in} *inlet temperature K*

T_{out} *outlet temperature K*

$T_{out,ave}$ *average outlet temperature K*

$T_{solid,ave}$ *volume-averaged solid temperature K*

$T_{wall,in}$ *solid temperature near inlet K*

$T_{wall,out}$ *solid temperature near outlet K*

ΔT_{lm} *logaritmic mean temperature difference K*

q *heat flux* W/m^2

V *velocity m/s*

ρ *density* kg/m^3

μ *dynamic viscosity kg/(m s)*

References

[1] Capata, R., Gagliardi L., Experimental investigation on the Reynolds dependence of the performance of branched heat exchangers working with organic fluids. Int. J. Heat Mass Transf. 2019; 140: 129-138.

[2] Reis, A. H., Constructal theory: from engineering to physics, and how flow systems develop shape and structure. Appl. Mech. Rev. 2006; 59(5): 269–282.

[3] Capata, R., Beyene, A., Experimental evaluation of three different configurations of constructal disc-shaped heat exchangers. Int. J. Heat Mass Transf. 2017; 115: 92–101.

[4] Asgari, M., Javidan, M., Nozari, M., Asgari, A., Ganji, D.D., Simulation of solidification process of phase change materials in a heat exchanger using branch-shaped fins. Case Studies in Thermal Engineering. 2021; 25: 100835.

[5] Zhu, R., Jing, D., Numerical study on thermal and melting performances of a horizontal latent heat storage unit with branched tree-like convergent fins. Journal of Energy Storage. 2023, 62: 106889.

[6] Huang, Y., Cao, D., Sun, D., Liu, X., Experimental and numerical studies on the heat transfer improvement of a latent heat storage unit using gradient tree-shaped fins. Int. J. Heat Mass Transf. 2022; 182: 121920.

ULPGC
Universidad de
Las Palmas de
Gran Canaria

grres ULPGC
group for the research on renewable energy systems

E. Power generation and Combined Heat and Power (CHP) plants

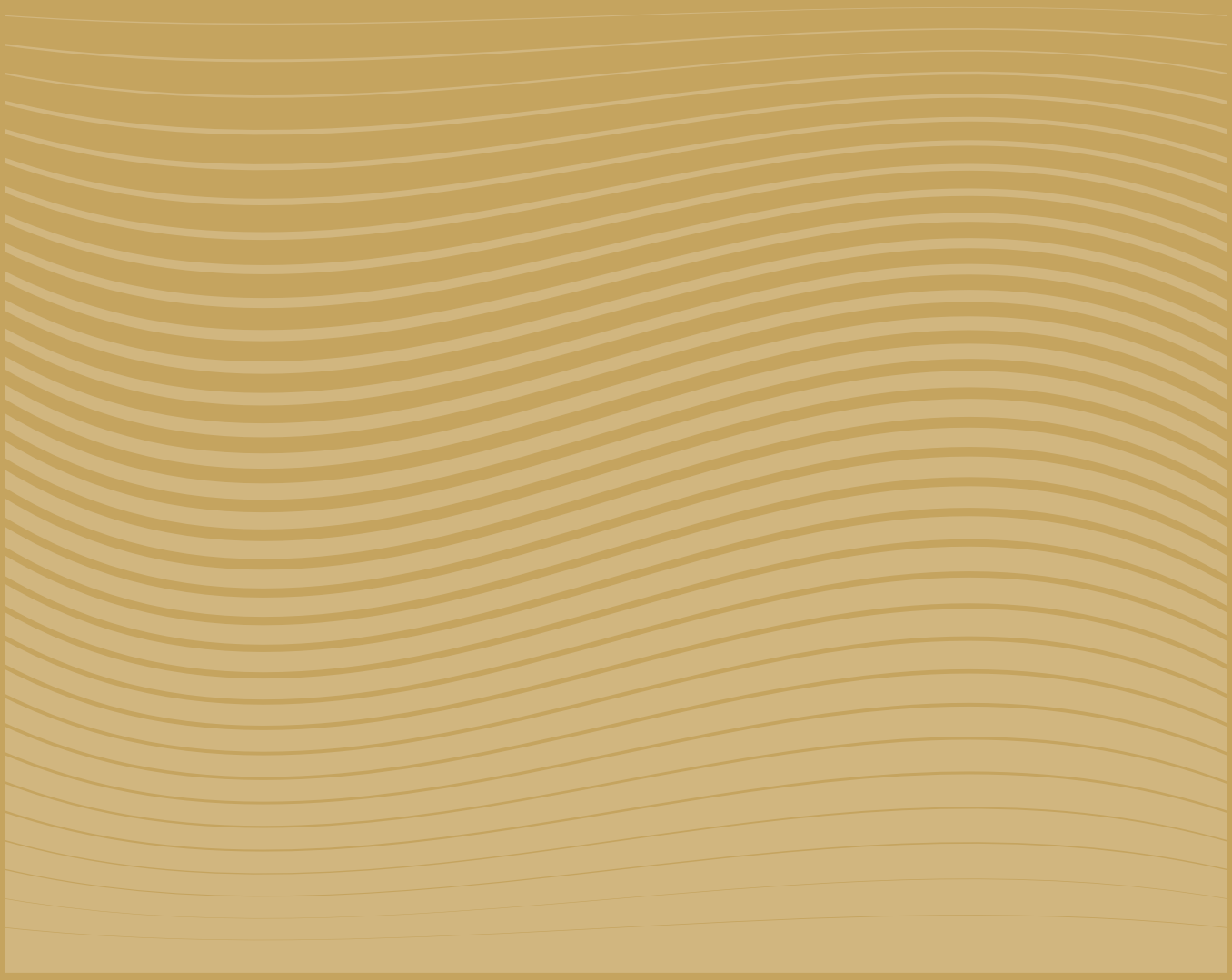

ECOS2023

Analytical study of the waste heat in a Hygroscopic Cycle with high lithium bromide concentration for energy use

Roberto Martínez-Pérez[a], Andrés Meana-Fernández[a], Juan Manuel González-Caballín[a], Alessia Manfredi[b], Francisco Javier Rubio-Serrano[c] and Antonio José Gutiérrez-Trashorras[a]

[a] Department of Energy - University of Oviedo, Gijón, Spain, martinezroberto@uniovi.es (CA), andresmf@uniovi.es, gonzalezsjuan@uniovi.es, gutierrezantonio@uniovi.es
[b] Department of Industrial Engineering - University of Padua, Padua, Italy, alessia.manfredi.1@phd.unipd.it
[c] Imasa Technologies S.L.U. (Imatech), Madrid, Spain, fj.rubio@imasatechnologies.com

Abstract:

The current world energy context requires solutions to reduce energy demand and increase the energy efficiency of thermal power plants, which typically release heat into the ambient without a further useful purpose. Climate change, leading to higher temperatures and water scarcity, may make difficult heat rejection processes in power cycles. Hygroscopic Cycle Technology can become a relevant technology due to the increase in the cooling reflux temperature thanks to the incorporation of hygroscopic salts. This work analyzes the possibility of using the waste heat rejected from the cycle cooling reflux by developing a thermodynamic model with a lithium bromide-water (LiBr-H_2O) mixture as the working fluid. The model, validated with experimental tests performed at a pilot plant, was used to optimize cycle operating conditions regarding waste heat recovery potential without substantially decreasing the cycle efficiency. The increase in LiBr mass concentration led to higher cooling reflux temperatures, allowing for easier heat rejection and an increase in enthalpy and the cooling reflux mass flow rate. The effect of condensing pressure was found to have a relatively low impact on the mass flow rate and the potential heat recovery per unit mass flow. An exergy analysis revealed a decrease in potential physical exergy recovery as LiBr concentration increases. Concentrations between 30 and 50% seem the most suitable ones for maximizing the power output of the cycle, while maintaining a high enough heat recovery potential, with values of 0.6 kJ/kg for the optimum concentration of 45%. Finally, prospective uses for the waste heat are proposed, considering that current applications of the technology rely on the use of biomass fuels from olive oil production waste.

Keywords:

Cycle Optimization; Hygroscopic Cycle Technology; Thermodynamic Modelling; Waste Heat Recovery Potential.

1. Introduction

Current environmental conditions and resource depletion trends are a worldwide challenge. In this context, electricity and heat generation represent the primary source of CO_2 emissions, reaching an all-time high of 14.6 Gt in 2022 [1]. Furthermore, electrical generation accounted for approximately 20% of global final energy consumption in 2021, with renewables contributing in 28% [2]. Moreover, the increasing electrification of the energy system and the growing population result in scenarios with significant increments in energy demand [2], requiring greater power generation capacities [3] while aiming for decarbonization and energy transition [4]. For this purpose, the Paris Agreement [5] aims for net-zero emissions by 2050 to prevent further rising of ambient temperatures and freshwater scarcity. In this sense, power generation, accounting for around 15% of freshwater withdrawal [6], plays a vital role, as the supply shortfall is expected to reach 40% by 2030 [7], while water consumption in the energy sector is predicted to rise 50% [8]. In this regard, energy supply reliability may be affected by droughts, as water stress hinders thermodynamic power cycles, which are key for the generation mix. Recent water shortage episodes have led to shutdowns and output disruptions. For instance, in France, the Chooz nuclear power plant was interrupted for two months in 2020 [2]. It is also estimated that India lost 14 TWh of thermal power generation in 2016 due to water shortfall [9]. In addition, rising ambient temperatures also lead to lower efficiencies of condensing and cooling systems, resulting in thermal processes being unable to respect discharge water temperature regulations. Lack of freshwater resources may also become problematic, with more significant desalination needs leading to greater energy demand. Hence, the viability of thermodynamic power cycles depends strongly on developing water-smart processes with

advanced cooling systems [8]. Ultimately, economic dependence on energy [10] and primary sources implies profound strategic and social implications. In this sense, stress over resources affects energy security [11], not only in reliability, stability and availability terms but also in affordability, with electricity rate increments [12], jeopardizing proper development of manufacturing industries, services and commodities. In this regard, worldwide policies are gradually turning towards sustainability through non-linear production and consumption models. Subsequently, circular economy [13] stands as the economic paradigm to minimize waste and pollution by extending the life cycle of products through reusing and recycling strategies in order to protect natural assets while ensuring secure and affordable energy supplies.

As per the state of the art, thermal efficiency and saving upgrade research has been intensely focused on recovering waste heat. Early analysis evaluated the introduction of regenerative-reheat processes within the Rankine cycle showing thermal efficiency increments of up to 14% [14]. Moreover, Tuantuan et al. [15] proposed a method for re-heat and regeneration stages optimization. Additional Rankine process stages have been further evaluated. In [16], the impact of close Feed-Water Heaters (FHWs) on the efficiency of a 200 MWe power plant was performed, resulting in a maximum efficiency enhancement of 10%. External source heat integration for water pre-heating has also been considered in the literature. Hu et al. [17] introduced the concept of Solar Aided Power Generation (SAPG) by replacing turbine steam bleed-offs for FWHs in regenerative Rankine with solar thermal energy. Prosin et al. [18] proposed a thermal power plant configuration in which secondary air flux was to be heated by solar thermal energy. Furthermore, Nsanzubuhoro et al. [19] considered geothermal energy as Low-Pressure Feed-Water Heaters (LPFHs) source. Solar thermal energy inclusion has been further evaluated. In this sense, Li et al. [20] examine the performance of Rankine cycles with a solar double re-heat system, observing a significant reduction in fuel consumption.

As energy demand grows, development has focused on cycles capable of operating with low-grade heat sources, which were technically unfeasible with previous systems [21]. In this regard, the Organic Rankine Cycle (ORC), Goswami Cycle (GC) and Kalina Cycle (KC) represent the most notorious power generation systems developed to work with low-grade temperature inputs [22], such as geothermal, solar thermal, waste heat and biomass combustion, by basing their operation on working fluids with boiling points lower than pure water. To date, most of the research efforts have concentrated on ORC, as it presents higher efficiency levels than those of GC and KC, which, although normally ranging between 10% and 18%, can reach peaks of up to 30% depending on the cycle parameters [22]. Moreover, ORC is generally more cost-effective due to its lower complexity and, consequently, lower capital and maintenance costs [23]. Additionally, ORCs can be easily adapted to a wide range of heat sources [24] and working fluids [25] while offering greater reliability due to its deeper study. Instead of rejecting heat into the environment, Combined Heat and Power (CHP) systems pose as an alternative for taking advantage of waste heat from power generation processes for practical applications, increasing thermal efficiency. As an example, Ballzus et al. [26] presented the Hellisheiði geothermal plant, which produces electricity (303 MWe) and hot water (133 MWt) for district heating [27] by harnessing thermal energy from the turbine exhaust steam.

Prevailing energy challenges require bold technical improvements in thermodynamic power systems to guarantee supply. In this context, the Hygroscopic Cycle Technology (HCT) [28], first developed in 2010 by Imatech, opens new prospects toward long-term power generation sustainability, posing as a Rankine cycle enhancement regarding efficiency, condensing and cooling terms. For this purpose, HCT operates with mixtures of water and hygroscopic compounds [29] as the working fluid, enabling to condensate turbine exhaust steam through absorption phenomena. As a result, HCT can optimize overall performance by working at lower condensing pressures for a given condensing temperature, effectively increasing the electrical power output of the cycle. Furthermore, absorption through hygroscopic compounds displays higher condensing temperatures [30], enabling the adoption of dry-cooling systems. In this sense, HCT can reject heat more efficiently, allowing the cycle to operate at high ambient temperatures, even over 45 ºC. Dry mode refrigeration advantages further expand as HCT is able to fully decouple power generation from water withdrawal, consequently expanding power plant availability while eliminating steam emissions. Low-concentration HCT has already been developed at an industrial scale. For example, HCT was implemented in Vetejar 12.5 MWe biomass power plant [31], successfully extending availability as the cycle was decoupled from disadvantageous climate conditions due to high external temperatures and water scarcity. Findings showed a 100% cooling water savings of 229,200 m^3/year, an additional 75 MWh/month power generation and a 150 MWh/month reduction of self-consumption due to high-efficiency dry-coolers. Other cases [28] like Baena 25 MWe biomass power plant and Industrias Doy 4.5 MWe cogeneration facilities emphasize the potential of HCT as it can be adapted [32] to any power generation range.

Despite the above improvements, HCT is subject to further enhancement, especially considering thermodynamic power cycles adaptation requirements toward circular economy principles and, subsequently, environmental protection [33]. In this sense, thermal efficiency improvement within HCT becomes relevant, especially with high hygroscopic concentrations where the thermal grade of the condensate flux is greater.

Currently, there are no HCT plants with implemented waste heat recovery systems. In this context, the work presented in this manuscript aims to evaluate the potential for waste heat recovery in high-concentration lithium bromide HCT (HC-HCT). With this objective, a thermodynamic model for evaluating the potential of waste heat recovery has been developed and validated with experimental tests. The final objective is to optimize operating conditions of the cycle regarding waste heat recovery potential without substantially decreasing the cycle efficiency. In addition, prospective uses for the waste heat are proposed, considering that current applications of HCT rely on the use of biomass fuels from olive oil production waste.

2. Methodology

To fulfill the objectives of this study, experimental tests were performed in the HCT pilot plant developed by Imatech in Gijón (Spain) to characterize the thermodynamic conditions at the condensing and cooling systems with high hygroscopic concentration. Then, the results were used to validate an analytical model capable of estimating the potential for the recovery of HCT waste heat.

2.1. Experimental methodology

The HCT pilot plant developed by Imatech in Gijón (Spain), used for performing the experimental tests of this work, is presented in Figure 1. In this work, the hygroscopic salt used is lithium bromide (LiBr) due to its several advantages: LiBr is highly hygroscopic but easily desorbed from water, non-flammable, non-toxic and chemically stable at typical cycle operating conditions.

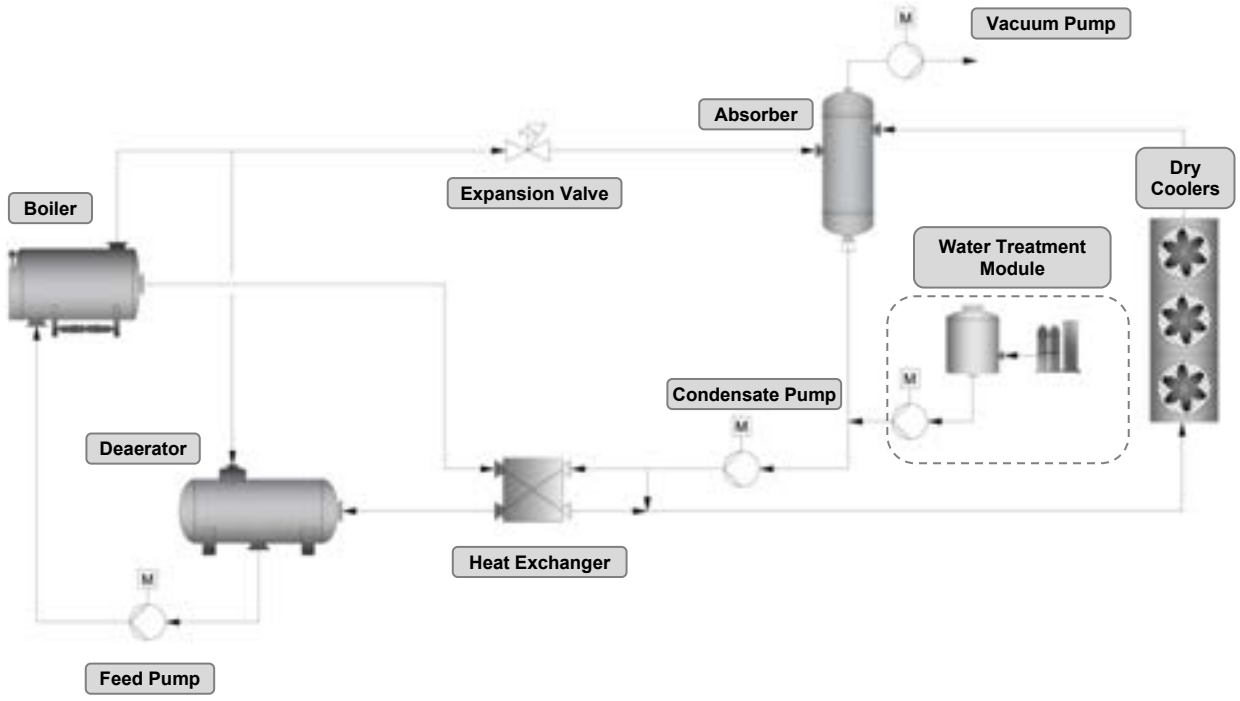

Figure 1. Operation process of HCT pilot plant.

The pilot plant is able to reproduce HCT power plant conditions by generating 100 kg/s of superheated steam at 14 bar and a maximum temperature of 200ºC. This steam is then led to an expansion valve that simulates the behavior of a 30 kW turbine-generator. The valve outlet steam then flows to the absorber, the key component of the HCT. In the absorber, the steam is condensed by absorbing a high-concentrated LiBr/H_2O cooling reflux coming from the dry cooling system that enters the absorber through nozzles to increase contact surface. Condensing pressure is controlled using a vacuum pump. The condensate then leaves the absorber, is pumped by the condensate pump and is separated into two flows: one continues to the boiler, while the other one is recirculated towards the dry coolers, releasing heat from the cycle, to be later reinjected into the absorber to provide the required salts for absorption to take place. A closed heat exchanger is used to recover thermal energy from boiler blowdowns to pre-heat the condensate water, which is then sent to a deaerator before entering the boiler, where LiBr salts are desorbed and purged. LiBr-H_2O mixtures are prepared and controlled via a 2 m^3 atmospheric tank and a demineralizing water module. Concentration values are derived from electrical conductivity measurements from samples taken from cycle purges.

The instrumentation used for performing the experiments is collected in Table 1. Data were collected using a Supervisory Control and Data Acquisition (SCADA) system developed by Siemens (SIMATIC S7, maximum uncertainty 0.004%).

Table 1. HCT pilot plant instrumentation.

Parameter	Instrument	Accuracy
Temperature	Endress+Haussser TR-61 platinum resistances PT100 RTD	± 0.1 °C
Absolute pressure	Aplisens PCE-28	± 0.5 %
Mass flow	Khrone OPTISWIRL-5080	± 0.5 %
Electrical conductivity	HANNA HI 98188-02	± 2.0 %

The parameters set for the different tests are collected in Table 2.

Table 2. HCT pilot plant working parameters.

Parameter	Value
Steam mass flow ($\dot{m}_S$)	100 kg/h
Steam temperature (T_S)	170 ºC
Condensing pressure (P_C)	3, 5, 7, 10, 15 kPa
LiBr concentration at the condensate (C_C)	45 %
Ambient temperature (T_C)	15 ºC
Temperature drop at dry coolers (ΔT_{DC})	7 ºC

2.2. Analytical model

2.2.1. Description of the model

Engineering Equation Software (EES, version V10.833-3D) [34] was used to develop a thermodynamic model of the condensing and cooling process of the HC-HCT, as represented in the scheme of Figure 2. The range of condensing pressure (P_C) studied was from 1 to 20 kPa.

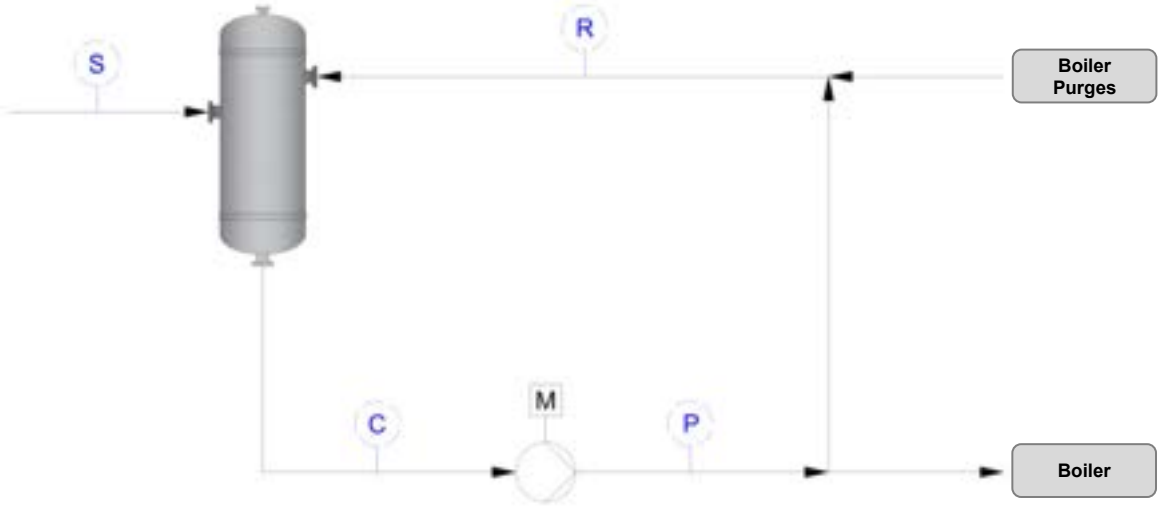

Figure 2. HCT condensing and cooling process model detail.

The following assumptions were considered to develop the model: kinetic and potential energy changes are negligible; the condensate pump only compensates for pressure losses in the pipes and equipment, which are perfectly insulated; and, since the cycle is closed, only the physical exergy is considered to estimate waste heat potential. The condensing process in the absorber is described by the mass, concentration and energy balances in Eqs. (1-3):

$$\dot{m}_S + \dot{m}_R = \dot{m}_C \quad (1)$$

$$\dot{m}_S \cdot C_S + \dot{m}_R \cdot C_R = \dot{m}_C \cdot C_C \quad (2)$$

$$\dot{m}_S \cdot h_s + \dot{m}_R \cdot h_R - \dot{Q}_D = \dot{m}_C \cdot h_C \quad (3)$$

The thermal power from the heat of dilution ($\dot{Q}_D$) depends on the difference between the concentration of the condensate (C_C) and reflux (C_R) streams. In this case, the correlations proposed by Yuan and Herold [35] were

implemented into the model. The LiBr concentration at the turbine outlet (C_S) was set to zero, being pure steam. The thermodynamic state at the condensate pump outlet was obtained from the isentropic efficiency of the pump (η_{CP}), considered 50%, according to industrial values from small centrifugal pumps [36]. Eqs. (4) and (5) determine the pump outlet properties:

$$\dot{m}_C = \dot{m}_P \tag{4}$$

$$\eta_{CP} = \frac{h_{Ps} - h_C}{h_P - h_C} \tag{5}$$

Once the energy analysis of the condensing and cooling process was finished, the physical exergy recovery potential (ex_{RCVY}) from the cycle cooling process was estimated with Eq. (6) as the difference between the physical exergy per unit mass of the flow before (ex_P) and after (ex_R) the heat rejection process, calculated with Eq. (7) [37]:

$$ex_{RCVY} = ex_P - ex_R \tag{6}$$

$$ex_i = (h_i - h_\infty) - T_\infty(s_i - s_\infty) \tag{7}$$

The reference environment or dead state for the exergy calculations was defined accordingly to the methodology proposed in [38]. The dead state temperature was set as the mean ambient temperature during the experimental tests, T_∞=15 ºC. The overall mass and volume of the cycle are constant, so no pressure equilibrium can be achieved with the exterior. Hence, the dead state pressure was set to the condensing pressure. The composition of the dead state was calculated at chemical equilibrium within the cycle, with the chemical potential of water in the LiBr-H_2O solution matching the Gibbs free energy of the water vapor, resulting in 0% of LiBr mass concentration for all the considered pressure values (over 1 kPa).

Finally, the heat per unit mass of cooling reflux rejected to the environment was corrected with the Carnot factor to study the influence of ambient temperature in the process, defined as:

$$\theta_{CP} = 1 - \frac{T_\infty}{T_{HR}} \tag{8}$$

With the temperature at which the fluid rejects heat (T_{HR}) calculated as the logarithmic mean between the temperatures of the condensate pump outlet (T_P) and the cooling reflux (T_R) [27]:

$$T_{HR} = 1 - \frac{T_P - T_R}{log\left(\frac{T_P}{T_R}\right)} \tag{9}$$

2.2.2. Experimental validation

Figure 3a shows the condensate and cooling reflux mass flow rates calculated by the model alongside the experimental measured values for 45% LiBr concentration. It may be appreciated that the developed models are able to follow the tendency of the experimental results, with a slight underprediction in the mass flow rates that increases with the condensing pressure up to a maximum error of 3%.

Regarding the prediction of enthalpy values, Figure 3b depicts the contrast of the model with experimental results. The tendency of the evolution of enthalpy values with the condensing pressure is adequately followed by the model, with average errors of 5%. Therefore, the developed model may be considered as suitable for the analysis of the thermodynamic processes of the cycle under study.

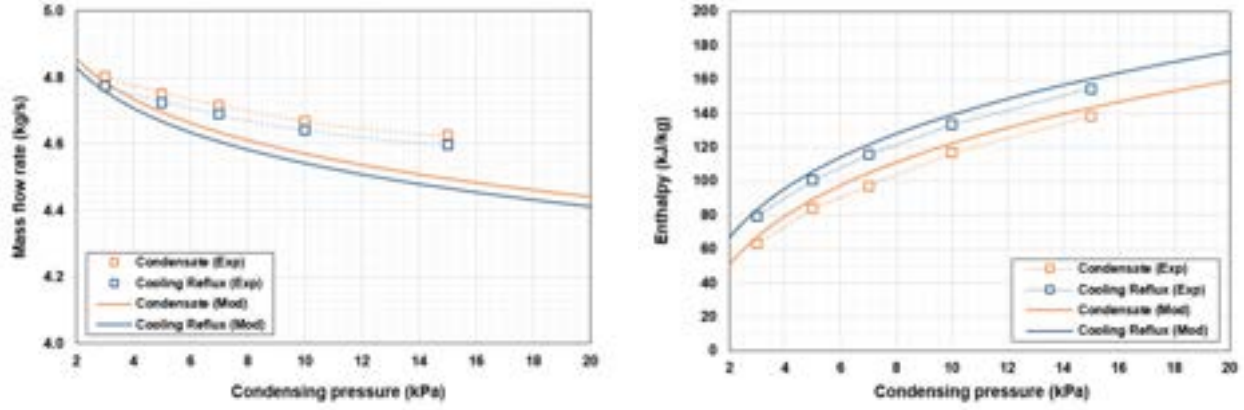

a) Mass flow rate vs condensing pressure

b) Enthalpy vs condensing pressure

Figure 3. Experimental validation of the model

3. Results

Firstly, the results of the thermodynamic parametric analysis of the model are presented. Then, the selection of the most suitable operating conditions for the cycle are discussed and potential applications for the recovery of heat waste form the cycle are presented.

3.1. Thermodynamic parametric analysis

Figure 4 shows the evolution of the condensate temperature as a function of the LiBr concentration of the reflux and the condensing pressure. It may be observed that the increase in concentration leads to higher temperatures, with a slower increasing rate up to 30% LiBr concentration.

Above this concentration value, the slope of the temperature curves becomes much greater. The increase in pressure has an additional effect of increasing condensing temperature. The increase of the condensate temperature may be linked to higher temperature differences with the environment and thus an easier heat rejection from the cycle and possibly easier use of that waste energy. Nevertheless, it must be considered that, if the turbine power is kept constant and the heat rejected increases, more fuel consumption at the boiler will be required. Paralelly, if the heat input at the boiler is kept constant and the heat rejected increases, there will be less power delivered by the turbine and the cycle efficiency will decrease.

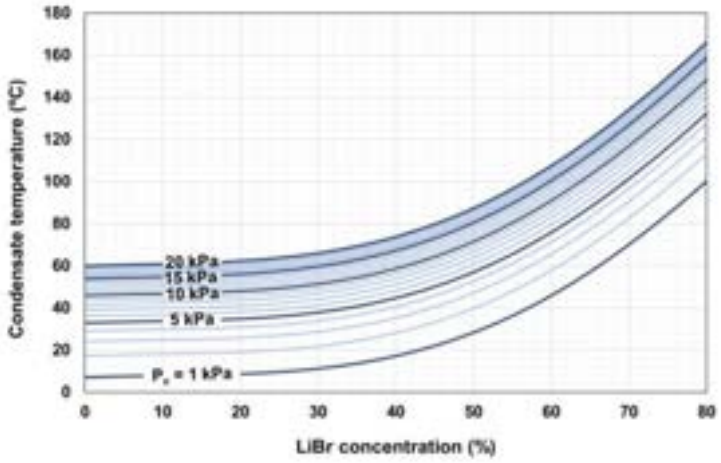

Figure 4. Condensate temperature as a function of LiBr concentration and condensing pressure

The results from the change of enthalpy with respect to LiBr concentration and condensing pressure are shown in Figure 5. A minimum for all curves may be found around 45% LiBr concentration, hinting to the selection of this concentration to minimize the enthalpy difference at the turbine and thus maximize the power delivered by the cycle. With concentration values up from this point, the condensate enthalpy increases very quickly, discouraging too high concentration values for the optimal performance of the turbine. Regarding the condensing pressure, it should be kept as lower as possible if the aim is to maximize cycle efficiency.

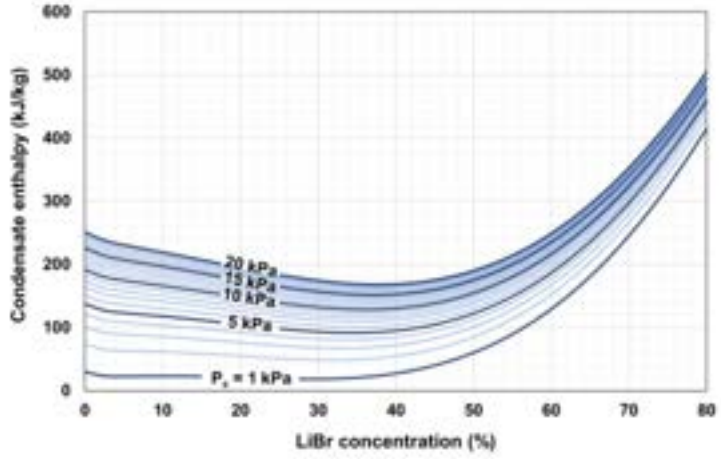

Figure 5. Condensate enthalpy as a function of LiBr concentration and condensing pressure

The cooling reflux mass flow rate shows an increasing trend with the increase of LiBr concentration, as shown in Figure 6. The effect of pressure in the ranges studied does not have a determining effect, becoming more important at intermediate LiBr concentration values. Nevertheless, for the sake of clarity, the results of all the pressure values studied have been averaged and represented as intervals with a 95% confidence level. It may be observed that the cooling reflux mass flow rate increases with the concentration, requiring a higher working fluid consumption and potentially leading to higher pumping requirements and pressure losses in the circuit. It seems sensible to keep the values of LiBr concentration below 50%, to avoid the steeper increase in the mass flow rate that comes with the increase of concentration.

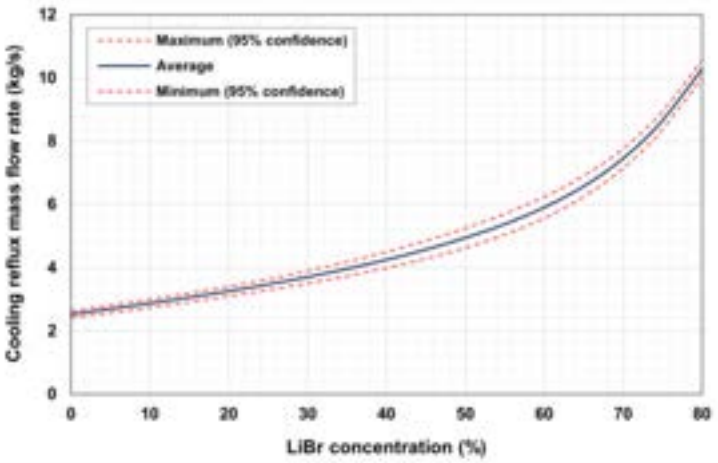

Figure 6. Average cooling reflux mass flow rate as a function of LiBr concentration

Regarding the heat recovery potential per unit mass of the cooling reflux, Figure 7 shows the results from the energy balance. Again, the effect of the pressure only becomes noticeable for intermediate LiBr concentration values, but it is minimal compared with the effect of LiBr concentration, so the values have been averaged and represented again as intervals with a 95% confidence level. A decreasing trend in the heat per unit mass is observed as the LiBr concentration increases, probably due to the increasing mass flows in the cycle. From these results, it seems sensible to try to maximize the heat per unit mass and avoid too high LiBr concentration values, which results in a lower energy density for potential applications.

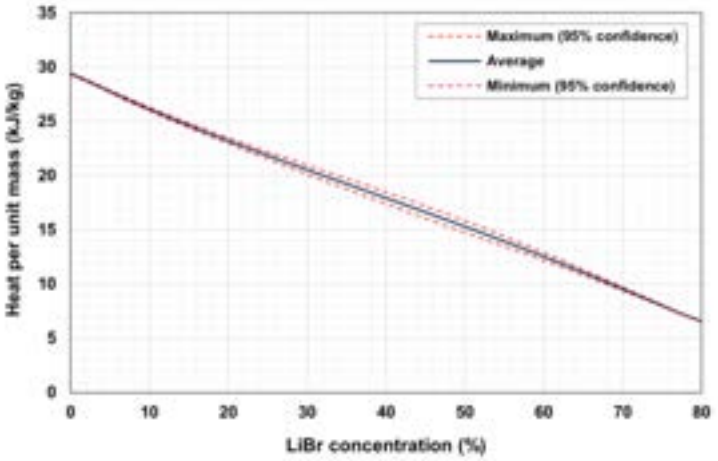

Figure 7. Heat recovery potential per unit mass of cooling reflux as a function of LiBr concentration

Finally, to evaluate the feasibility of the heat recovery process itself, the results from the physical exergy recovery potential per unit mass of cooling reflux mass flow, considering the dead state from the experimental conditions, are presented in Figure 8. In this case, the role of the condensing pressure cannot be overlooked, with higher condensing pressures leading to higher exergy recovery potentials. For the lowest condensing pressures, below 2 kPa, physical exergy increases with the increase in concentration. The negative values of potential recovery at these pressure conditions may be ascribed to the fact that the temperatures at the absorber would become lower than the dead state temperature. In addition, these lower pressures require higher-performance vacuum pumps, so there is no apparent reason to work at these operating conditions.

On the other hand, the global trend with the increase of LiBr concentration is the decrease of the potential specific exergy recovery. This decrease becomes more apparent for LiBr concentrations above 50%,

discouraging again the use of too high concentration values. The region between 30 and 40% shows a relatively smooth decrease with the increase in concentration, with similar potential recovery values. This advantage could be exploited for the stable operation of the heat recovery system.

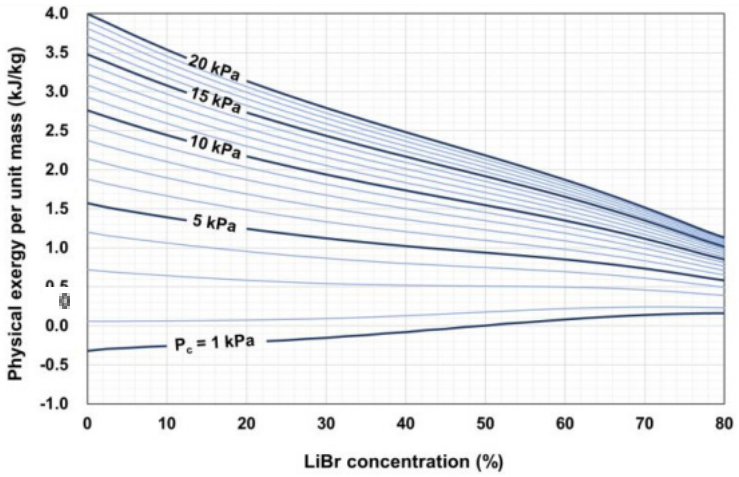

Figure 8. Physical exergy recovery potential per unit mass as a function of LiBr concentration

In summary, gathering all the results from the parametric analysis, it may be proposed to use concentrations of LiBr around 45% to maximize the enthalpy difference at the turbine. The exergy analysis has revealed that, at the dead state conditions of the experiment, the physical exergy recovery potential per unit mass of cooling reflux decreases sharply for values above 60%. On the other hand, concentration values lower than 30% may not achieve cooling reflux temperatures high enough for cycle heat rejection.

Regarding pressure values, selecting 5 kPa as the condensing operating pressure has several advantages. It increases the pressure difference at the turbine with respect to higher operating pressures, resulting in a higher turbine power output and in cooling reflux temperatures high enough to release heat from the cycle. In addition, it does not result in a significant effect regarding the cycle mass flow rates or the actual energy recovery potential per unit mass of cooling reflux. Apart from requiring higher-performance vacuum pumps, lower pressures are not justified in terms of the exergy analysis, while an operating pressure of 5 kPa has been verified in actual power plant operation.

3.2. Potential applications of waste heat recovery

After selecting a pressure of 5 kPa as the condensing pressure and 45% as the LiBr concentration for cycle waste heat recovery, the effect of the ambient temperature in the heat recovery potential per cooling reflux unit mass is depicted in Figure 9, to evaluate possible applications for the recovered waste heat.

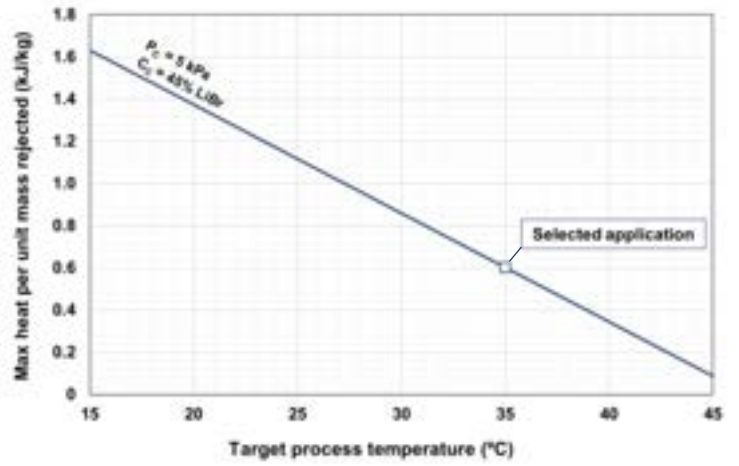

Figure 9. Heat recovery potential per cooling reflux unit mass vs ambient temperature.

Although desirable, it is not possible to reach conditions for pyrolysis (250ºC) or alperujo drying (100ºC) to treat the biomass and use it in the cycle boiler [39]. Nevertheless, there is enough potential for developing anaerobic mesophilic processes at 35ºC for biogas production [40] or compost for agriculture [41] with a

potential heat recovery of 0.6017 kJ/kg of cooling reflux. Considering typical industrial cooling reflux values of around 6000 t/h in HCT cycles, the potential heat that could be delivered to the biodigesters is in the range of 1 MW.

4. Conclusions

The current world energy context requires solutions to reduce energy demand and increase the energy efficiency of power plants. Thermal power plants typically release heat into the ambient without a further useful purpose. Climate change, leading to higher temperatures and water scarcity, may difficult heat rejection processes in power cycles. HCT can become a relevant technology due to the increase in the temperatures in the cooling reflux produced by the incorporation of hygroscopic salts, such as LiBr. In this work, it has been possible to analyze the possibility of using the waste heat rejected from the cooling reflux of the HCT by developing a thermodynamic model in EES and validating it with experimental tests. The main conclusions obtained are collected in the following paragraphs.

Firstly, the results from the thermodynamic parametrical analysis have revealed that the increase of LiBr leads to higher temperatures in the cooling reflux. This may be linked to easier heat rejection to the environment and thus an easier use of that waste energy, but the effect on the power delivered by the cycle and its thermal efficiency must also be considered. Regarding the enthalpy at the absorber outlet, a minimum value, linked to higher cycle power output values, was found to be around 45% LiBr concentration. With the increase of LiBr concentration up from this point, this enthalpy and the cooling reflux mass flow rate showed a steep increase trend. As these higher mass flow rates lead to higher pumping requirements and pressure losses in the pipes and equipment, values of LiBr concentration over 60% are strongly discouraged. On the other hand, the effect of condensing pressure was relatively small to the effect of LiBr concentration in both the mass flow of the cooling reflux and the heat recovery potential per unit mass of the cooling reflux. The increase of LiBr concentration was also linked to a decreasing trend in the heat recovery potential per unit mass and a lower energy density for potential applications.

The exergy analysis of the cooling process revealed a decrease in the potential physical exergy recovery with the increase of LiBr concentration, becoming more apparent with concentrations above 50%. Considering all the results obtained from this work, concentrations of LiBr around 45% seem the most suitable ones for maximizing the power output of the cycle, always working in the range between 30 and 50%. Regarding pressure values, 5 kPa of condensing pressure seems promising, finding a compromise between the pressure difference at the turbine and temperature high enough for heat rejection in the cooling reflux.

Finally, the results of evaluating the cycle with 45% LiBr concentration and a condensing pressure of 5 kPa for different ambient temperatures resulted in the identification of potential applications for the cycle. Sadly, pyrolysis or alperujo drying temperatures cannot be reached with this cycle configuration, preventing the use of this heat to treat olive residue as fuel in the biomass boiler of the circuit. Nevertheless, there is enough potential for developing anaerobic mesophilic processes at 35ºC for the production of biogas or compost for agriculture, with a potential heat recovery of 0.6017 kJ/kg of cooling reflux.

Acknowledgments

This work has been supported by the project *"Improvement of energy performance of the Hygroscopic Cycle for power production"* - PID2019-108325RB-I00/AEI/10.13039/501100011033 from the Agencia Estatal de Investigación - Ministerio de Ciencia e Innovación, Spain; and the *"Severo Ochoa"* grant program for training in research and teaching of the Principality of Asturias - Spain (BP20-176). The authors also want to acknowledge the contribution of the Spanish company Imasa Technologies S.L.U. (Imatech), owner of the Hygroscopic cycle pilot plant, as well as the support from the University Institute of Industrial Technology of Asturias (IUTA), financed by Gijón City Council, Spain. The help provided by Dr. María Rosario López is also highly appreciated.

Nomenclature

C	mass concentration, %
ex	physical exergy per unit mass, kJ/kg
h	enthalpy per unit mas, kJ/kg
$\dot{m}$	mass flow rate, kg/s
P	absolute pressure, kPa
Q	heat, kW
T	Temperature, ºC

Greek symbols

η	efficiency, %
θ	Carnot factor, %

Subscripts and superscripts

C	condensate
CP	Condensate pump
DC	dry cooler
HR	recovery heat
P	condensate pump outlet
R	cooling reflux
$RCVY$	recovery
S	steam
∞	dead state

References

[1] International Energy Agency (IEA), “CO2 Emissions in 2022,” 2022. Accessed: Mar. 01, 2023. [Online]. Available: https://www.iea.org/reports/co2-emissions-in-2022

[2] International Energy Agency (IEA), “World Energy Outlook 2022,” 2022. Accessed: Mar. 01, 2023. [Online]. Available: https://www.iea.org/reports/world-energy-outlook-2022

[3] BP plc, “Statistical Review of World Energy 2021,” 2021. Accessed: Mar. 01, 2023. [Online]. Available: https://www.bp.com/en/global/corporate/energy-economics/energy-outlook.html

[4] International Energy Agency, “Net Zero by 2050 - A Roadmap for the Global Energy Sector,” 2021. Accessed: Mar. 01, 2023. [Online]. Available: https://www.iea.org/reports/net-zero-by-2050

[5] United Nations (U.N.), “Conference of the Parties, Adoption of the Paris Agreement.” United Nations (U.N.), 2015. Accessed: Mar. 01, 2023. [Online]. Available: https://treaties.un.org/Pages/ViewDetails.aspx?src=IND&mtdsg_no=XXVII-7-d&chapter=27&clang=_en

[6] J. C. Terrapon-Pfaff, W. Ortiz, P. Viebahn, E. Kynast, and M. Flörke, “Water Demand Scenarios for Electricity Generation at the Global and Regional Levels,” *Water (Switzerland)*, vol. 12, no. 9, Sep. 2020, doi: 10.3390/w12092482.

[7] United Nations Environmental Program (UNEP), *Options for Decoupling Economic Growth from Water Use and Water Pollution*. 2016. Accessed: Mar. 01, 2023. [Online]. Available: https://wedocs.unep.org/handle/20.500.11822/7539;jsessionid=E1936BD6383E87C738483E8B592A8DF3

[8] International Energy Agency (IEA), “If The Energy Sector Is To Tackle Climate Change, It Must Also Think About Water,” 2020. Accessed: Mar. 01, 2023. [Online]. Available: https://www.iea.org/commentaries/if-the-energy-sector-is-to-tackle-climate-change-it-must-also-think-about-water

[9] T. Luo, D. Krishnan, and S. Sen, “Parched Power: Water Demands, Risks, and Opportunities for India’s Power Sector,” 2018.

[10] G. K. Sarangi, A. Mishra, Y. Chang, and F. Taghizadeh-Hesary, “Indian electricity sector, energy security and sustainability: An empirical assessment,” *Energy Policy*, vol. 135, Dec. 2019, doi: 10.1016/j.enpol.2019.110964.

[11] C. J. Axon and R. C. Darton, “Sustainability and risk – a review of energy security,” *Sustainable Production and Consumption*, vol. 27. Elsevier B.V., pp. 1195–1204, Jul. 01, 2021. doi: 10.1016/j.spc.2021.01.018.

[12] Internationa Energy Agency (IEA), “Electricity Market Report - July 2022,” 2022. Accessed: Mar. 01, 2023. [Online]. Available: https://www.iea.org/reports/electricity-market-report-july-2022

[13] P. Ekins, T. Domenech, P. Drummond, R. Bleischwitz, N. Hughes, and L. Lotti, “The Circular Economy: What, Why, How and Where,” 2019. Accessed: Mar. 01, 2023. [Online]. Available: https://discovery.ucl.ac.uk/id/eprint/10093965/1/Ekins-2019-Circular-Economy-What-Why-How-Where.pdf

[14] M. A. Habib and S. M. Zubair, “Second-Law-Based Thermodynamic Analysis OF Regenerative-Reheat Rrankine-Cycle Power Plants,” *Energy*, vol. 17, no. 3, pp. 295–301, 1992, doi: https://doi.org/10.1016/0360-5442(92)90057-7.

[15] T. Xin, C. Xu, and Y. Yang, “A general and simple method for evaluating the performance of the modified steam Rankine cycle: Thermal cycle splitting analytical method,” *Energy Convers Manag*, vol. 210, Apr. 2020, doi: 10.1016/j.enconman.2020.112712.

[16] S. O. Oyedepo *et al.*, “Thermodynamics analysis and performance optimization of a re-heat – Regenerative steam turbine power plant with feed water heaters,” *Fuel*, vol. 280, Nov. 2020, doi: 10.1016/j.fuel.2020.118577.

[17] E. Hu, Y. P. Yang, A. Nishimura, F. Yilmaz, and A. Kouzani, “Solar thermal aided power generation,” *Appl Energy*, vol. 87, no. 9, pp. 2881–2885, 2010, doi: 10.1016/j.apenergy.2009.10.025.

[18] T. Prosin, T. Pryor, C. Creagh, L. Amsbeck, and R. Buck, “Hybrid Solar and Coal-fired Steam Power Plant with Air Pre-heating Using a Centrifugal Solid Particle Receiver,” in *Energy Procedia*, May 2015, vol. 69, pp. 1371–1381. doi: 10.1016/j.egypro.2015.03.134.

[19] C. N. Nsanzubuhoro, T. Bello-Ochende, and A. G. Malan, “Second law analysis of a fossil-geothermal hybrid power plant with thermodynamic optimization of geothermal preheater,” *Heat Transfer*, vol. 49, no. 7, pp. 3997–4018, Nov. 2020, doi: 10.1002/htj.21692.

[20] J. Li *et al.*, “Safety and thermal efficiency performance assessment of solar aided coal-fired power plant based on turbine steam double re-heat,” *Energy*, vol. 226, Jul. 2021, doi: 10.1016/j.energy.2021.120277.

[21] J. Ling-Chin, H. Bao, Z. Ma, W. Taylor, and A. Paul Roskilly, “State-of-the-Art Technologies on Low-Grade Heat Recovery and Utilization in Industry,” in *Energy Conversion - Current Technologies and Future Trends*, IntechOpen, 2019. doi: 10.5772/intechopen.78701.

[22] Y. Lan, S. Wang, J. Lu, H. Zhai, and L. Mu, “Comparative analysis of organic rankine cycle, Kalina cycle and thermoelectric generator to recover waste heat based on energy, exergy, economic and environmental analysis method,” *Energy Convers Manag*, vol. 273, Dec. 2022, doi: 10.1016/j.enconman.2022.116401.

[23] U. Larsen, F. Haglind, and O. Sigthorsson, “A comparison of advanced heat recovery power cycles in a combined cycle for large ships,” in *Proceedings of ECOS 2013 - The 26th International Conference on Efficiency, Cost, Optimization, Simulation and Environmental Impact of Energy Systems*, 2013.

[24] M. N. Karimi, A. Dutta, A. Kaushik, H. Bansal, and S. Z. Haque, “A Review of Organic Rankine, Kalina and Goswami Cycle,” *International Journal of Engineering Technology, Management and Applied Sciences*, vol. 3, 2015, [Online]. Available: https://www.researchgate.net/publication/283302991

[25] H. Chen, D. Y. Goswami, and E. K. Stefanakos, “A review of thermodynamic cycles and working fluids for the conversion of low-grade heat,” *Renewable and Sustainable Energy Reviews*, vol. 14, no. 9, pp. 3059–3067, 2010, doi: 10.1016/j.rser.2010.07.006.

[26] C. Ballzus, H. Frimannson, G. I. Gunnarsson, and I. Hrolfsson, “The Geothermal Power Plant at Nesjavellir, Iceland,” in *World Geothermal Congress*, 2000.

[27] V. Colucci, G. Manfrida, B. Mendecka, L. Talluri, and C. Zuffi, “LCA and Exergo-Environmental Evaluation of a Combined Heat and Power Double-Flash Geothermal Power Plant,” *Sustainability (Switzerland)*, vol. 13, no. 4, pp. 1–23, Feb. 2021, doi: 10.3390/su13041935.

[28] Imasa Technologies S.L.U. (Imatec), “Hygroscopic Cycle.” https://imasatechnologies.com/tecnologia-hct/ (accessed Mar. 01, 2023).

[29] F. J. Rubio-Serrano, F. Soto-Pérez, and A. J. Gutiérrez-Trashorras, “Experimental study on the influence of the saline concentration in the electrical performance of a Hygroscopic cycle,” *Appl Therm Eng*, vol. 165, Jan. 2020, doi: 10.1016/j.applthermaleng.2019.114588.

[30] F. J. Rubio-Serrano, F. Soto-Pérez, and A. J. Gutiérrez-Trashorras, “Influence of cooling temperature increase in a hygroscopic cycle on the performance of the cooling equipment,” *Energy Convers Manag*, vol. 200, Nov. 2019, doi: 10.1016/j.enconman.2019.112080.

[31] F. J. Rubio-Serrano, A. J. Gutiérrez-Trashorras, F. Soto-Pérez, E. Álvarez-Álvarez, and E. Blanco-Marigorta, “Advantages of Incorporating Hygroscopic Cycle Technology to a 12.5-MW Biomass Power Plant,” *Appl Therm Eng*, vol. 131, pp. 320–327, Feb. 2018, doi: 10.1016/j.applthermaleng.2017.12.027.

[32] A. Meana-Fernández, B. Peris-Pérez, A. J. Gutiérrez-Trashorras, S. Rodríguez-Artime, J. C. Ríos-Fernández, and J. M. González-Caballín, “Optimization of the propulsion plant of a Liquefied Natural Gas transport ship,” *Energy Convers Manag*, vol. 224, Nov. 2020, doi: 10.1016/j.enconman.2020.113398.

[33] A. Meana-Fernández, J. M. González-Caballín, R. Martínez-Pérez, F. J. Rubio-Serrano, and A. J. Gutiérrez-Trashorras, “Power Plant Cycles: Evolution towards More Sustainable and Environmentally Friendly Technologies,” *Energies*, vol. 15, no. 23. MDPI, Dec. 01, 2022. doi: 10.3390/en15238982.

[34] F-Chart, “EES - Engineering Equation Solver. Version: V10.833-3D.” [Online]. Available: https://fchartsoftware.com/ees/

[35] Z. Yuan and K. E. Herold, “Thermodynamic properties of aqueous lithium bromide using a multiproperty free energy correlation,” *HVAC and R Research*, vol. 11, no. 3, pp. 377–393, 2005, doi: 10.1080/10789669.2005.10391144.

[36] Bombas Grundfos España S.A., “Centrifugal Pumps.” https://www.grundfos.com/es (accessed Mar. 01, 2023).

[37] M. Shamoushaki, D. Fiaschi, G. Manfrida, and L. Talluri, “Energy, exergy, economic and environmental (4E) analyses of a geothermal power plant with NCGs reinjection,” *Energy*, vol. 244, Apr. 2022, doi: 10.1016/j.energy.2021.122678.

[38] A. M. Blanco-Marigorta and J. D. Marcos, “Key issues on the exergetic analysis of H2O/LiBr absorption cooling systems,” *Case Studies in Thermal Engineering*, vol. 28, Dec. 2021, doi: 10.1016/j.csite.2021.101568.

[39] R. Arjona, A. García, and P. Ollero, “The drying of alpeorujo, a waste product of the olive oil mill industry,” *J Food Eng*, vol. 41, pp. 229–234, 1999, doi: 10.1016/S0260-8774(99)00104-1.

[40] M. Orive, B. Iñarra, M. Cebrián, and J. Zufía, “New integrated polyphenols recovery and anaerobic digestion of alpeorujo,” in *3rd Edition of the International Conference on Wastes: Solutions, Treatments and Opportunities*, 2015. doi: 10.13140/RG.2.1.2059.3125.

[41] J. A. Alburquerque, J. Gonzálvez, D. García, and J. Cegarra, “Composting of a solid olive-mill by-product (‘alperujo’) and the potential of the resulting compost for cultivating pepper under commercial conditions,” *Waste Management*, vol. 26, no. 6, pp. 620–626, 2006, doi: 10.1016/j.wasman.2005.04.008.

Integration of solar field into a combined cycle power plant for fuel saving in insular subtropical climates

Adham M Abdelhalim[a], Andrés Meana-Fernández[b], Ines Suarez-Ramon[c]

[a] Mechanical Engineering Department, College of Engineering and Technology, Arab Academy for Science, Technology and Maritime Transport, Alexandria, Egypt, adhammuhamed90@aast.edu
[b,c] Thermal Machines and Engines Area, Department of Energy, University of Oviedo, Gijon, Spain, [b]andresmf@uniovi.es (CA), [c]ines@uniovi.es

Abstract:
The harmful environmental effects of fossil fuels and the variability in their prices are shifting attention away from conventional combined cycle power plants. Supply issues in islands are also a problem to be considered. The objective of this work is to evaluate the feasibility of integrating solar energy into a combined cycle power plant for fuel saving in insular subtropical climates. With this aim, a case study comprising a 93 MW combined cycle in Las Palmas de Gran Canaria (Spain) and the integration of solar energy in the gas upper cycle has been presented and analyzed with a thermodynamic model. The effects of incorporating solar heat before and after the cycle compressor were assessed, finding that injecting 35 MW of solar heat before the compressor resulted in savings of 49% of the original fuel consumption and an increase of 2% in the global cycle efficiency, but at the expense of reducing the net power delivered by 47%. On the other hand, incorporating the solar heat after the compression process resulted in an overall 16.2% increase in the cycle efficiency, while delivering the same net power as the original cycle and reducing fuel consumption in 22%. With the increase in the amount of solar heat added to the cycle, the difference between both options became greater, with the best option being injecting solar heat after the compressor. Estimations of the economic and environmental effects of the most suitable option are provided, resulting in potential overall savings of 7.14 million Euro per year and a yearly potential of 13.75 Mkg of CO_2 emissions avoided. The results of this work are expected to contribute to improve energy supply problems by using a renewable energy source and reduce fuel imports, providing more energy stability and security to the inhabitants of islands with similar climates as Las Palmas.

Keywords:
Integrated solar combined cycle power plants (ISCCs), fuel saving, insular subtropical climate, dynamic analysis, and CO_2 emission.

1. Introduction

Nowadays, there is almost no debate on the damaging effects that global reliance on fossil fuels holds for the future of the world. Fossil fuels (e.g., coal, natural gas, and oil), apart from being finite, entail several harmful effects in the environment, especially with CO_2 emissions increasing at an alarming rate. Over the past 12 years, global CO_2 emissions from energy combustion and industrial processes have increased by 4.2 Gt CO_2, to a value of 36.8 Gt CO_2 in 2022 [1]. CO_2 emissions from natural gas combustion increased by more than 215 Mt CO_2 in 2021, to reach an all-time high of 7.35 Gt CO_2, representing 22% of the total CO_2 emissions. On the other hand, the use of renewable energy sources increased by 3% in 2020, with a prime 7% growth in renewable electricity generation. Global renewable electricity generation increased from 27% in 2019 to 29% in 2020, reaching 30% in 2021 [1]. In this context, solar energy technologies represent one of the most mature options, with its share increasing from 1.08% in 2015 to 3.74% in 2022 [2].

Integrated solar combined cycle power plants (ISCCs) are one of the most promising solar hybrid configurations for power plants. ISCCs are composed of a concentrated solar power plant (CSP) and a natural gas-fired combined cycle (NGCC). The CSP plant is normally used either to produce additional steam for the combined cycle steam turbine [3, 4], or to preheat the compressed air in the gas turbine before entering the combustion chamber [5]. It has been estimated that the CSP contribution to global energy supply may reach 3-3.6% by 2030 and 8-11.8% by 2050 [6], alongside a drop in CSP costs to $0.05/kWh by 2050. Four main technologies exist for concentrating solar power in the CSP: parabolic trough collectors, solar tower, solar dish, and linear Fresnel systems, with parabolic trough collectors (PTC) being the most mature technology. These collectors, with high thermal efficiency, high performance systems, light structures, and low-cost technology,

can deliver up to 400 ºC. This temperature is generally high enough for most of industrial heating processes and applications. In addition, this technology is also suitable for low-temperature industrial applications, such as desalination and sterilization processes.

1.1. Solar integration in combined power plants and research question

The first solar plant using parabolic trough technology was built in 1913 in Maadi, Cairo, Egypt. It was built for the purpose of power generation for pumping water for irrigation [7,8]. The technology of the ISCC system was proposed by Luz Solar International [9]. During 1980s, nine solar electric generating systems (SEGS) with a total capacity of 356 MW were installed in California desert, United States, where solar collectors capture and concentrate sunlight to heat a synthetic oil (Therminol), which then heats water to generate steam [10]. SEGS became one of the most important projects that paved the way for executing subsequent similar works. In 2000, the Global Environment Facility (GEF), an organization that supports developing countries' work to address the world's most pressing environmental issues, embraced the idea of encouraging the erection of ISCC power plants in developing countries with high solar irradiation, allocating up to $50 million for the construction of four ISCCs in the Middle East. This led to an increase in the interest in CSP technologies, especially in PTCs [11]. Consequently, wide research has been performed on this technology. Some works focus on studying system integration schemes between the PTC and the combined cycle, while others analyze the static or dynamic performance of the ISCC under different conditions. In 1997, the first technical and economic analysis of the ISCC was performed in Tunisia, where the authors clarify that ISCC system is more profitable than SEGS [12]. The performance of ISCC, SEGS and Combined Cycle (CC) power plants was studied, using IPSEpro and GateCycle software [13]. After comparing the three systems, they stated that ISCC technology had the best efficiency.

In 2013, the dynamic performance of a solar Rankine cycle and ISCC was compared with the solar thermoelectric components library in TRNSYS [14]. The results showed that ISCC had higher solar-to-electric efficiency values than the solar Rankine cycle. It was also found that using solar tower technology improved annual solar-to-electric efficiency by 21.8% with respect to PTC. One year later, ISCC and the conventional CC were compared, finding many advantages with ISCC, such as peak time efficiency and less carbon dioxide emissions [15]. Several configurations of solar integration with conventional CC plants were discussed later [16]. Results show that lower stack temperatures may be achieved, allowing for a better thermal match in the heat recovery steam generator (HRSG), so more feedwater may be circulated in the cycle. In 2018, ISCC power plant was compared with a thermal storage system and a conventional CC in thermo-economic and environmental terms, using a TRNSYS dynamic simulation [17]. Overall electrical efficiency improved by 1% compared to the conventional CC. A MATLAB dynamic model for the Hassi R'mel ISCC power plant in Algeria was validated under off-design conditions, finding that some factors could affect strongly the ISCC performance, such as wind speed and direct normal irradiance (DNI) [18]. In 2021, a dynamic model was developed of an ISCC power plant in Kuraymat, Egypt, using APROS software to evaluate the ISCC performance, limitations, and capabilities, validating the results with actual operational data [19]. The model was able to reproduce most of the operating parameters, such as pressure, temperature, mass flow rates and output power. An economic and performance assessment of the ISCC-PTC system in Hassi R'mel (Algeria), coupled with a new thermal storage system was performed [20]. Results revealed that a better grid stability was reached, increasing solar energy conversion and overall performance. The net solar thermal energy conversion ratio and the energy efficiency reached 14 and 56.06%, with natural gas consumption savings representing around $30 million. Finally, in 2022, different basic ISCC system models were compared with SEGS and gas turbine combined cycles (GTCC), presenting a method for assessing ISCC systems with different integration modes and solar operating temperatures [21]. Different integration points in the steam and gas cycles, as well as two working modes, "power boosting" and "fuel saving" were discussed. For the "power boosting" mode, solar energy is injected into the steam bottom cycle to heat up the gas turbine exhaust, the live steam, the reheated steam, or the feedwater. The main idea is to keep fuel consumption constant, while the output power increases as a consequence of the increase in the steam flowrate (mas flowrate boosting) or the enthalpy increase (parameter boosting). On the other hand, the "fuel saving mode" injects the solar energy in the upper Brayton cycle, heating the compressed air before entering the combustion chamber. This leads to a decrease in the fuel mass flowrate, leaving unaffected the operating conditions in the gas turbine and thus the bottom steam cycle.

The objective of this work is to evaluate the feasibility of integrating solar energy into a combined cycle power plant for fuel saving in insular subtropical climates and estimate its effect on the energy efficiency of the cycle, fuel saving, and possible economic savings and reduction of CO_2 emissions. With this aim, a case study comprising a combined cycle in the Canary Islands (Spain) and the integration of solar energy in the gas upper cycle has been developed and analyzed with a thermodynamic model. The results are expected to contribute to improve energy supply problems by using a renewable energy source and thus reducing fuel imports, providing more energy stability and security to the island inhabitants. After briefly reviewing the energy context in the Canary Islands, the methodology followed in this work is detailed. Then, the results are discussed, and finally the main conclusions of this work are presented.

2. Case study

The geographical nature of islands enforces them to have isolated energy systems unless a connection between their electricity power grid and another grid beyond its shores is developed. This entails a series of economic and environmental difficulties. Islands are highly dependent on imported fossil fuel, leading to high costs of fuel transportation, energy supply insecurity and higher electricity prices [22]. However, renewable energy resources (solar, wind & ocean waves) often exist in abundance in islands.

2.1. The energy context in the Canary Islands

The Canary Islands are a group of seven Spanish islands that are located off the African west coast. Around 84.2% of their energy demand was supplied from non-renewable energy sources in 2022, as shown in Figure 1. Combined cycle power plants have the highest share, 44.5%, while renewable energy resources contribute only with 15.8% [23]. Figure 2 shows the solar thermal capacity installed on each island, alongside the occupied area by thermal installations. The total thermal capacity of the archipelago is 88.7 MW, being Gran Canaria Island the highest contributor, with 38.7% of the total solar thermal energy installed in the Canary.

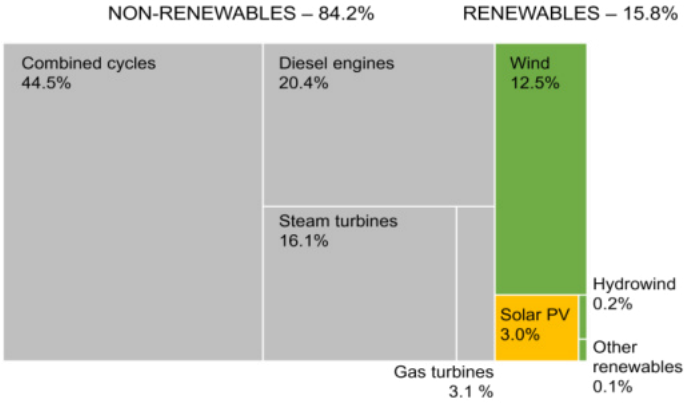

Figure 1. Canary Island electricity distribution in 2022 (Data source: [23]).

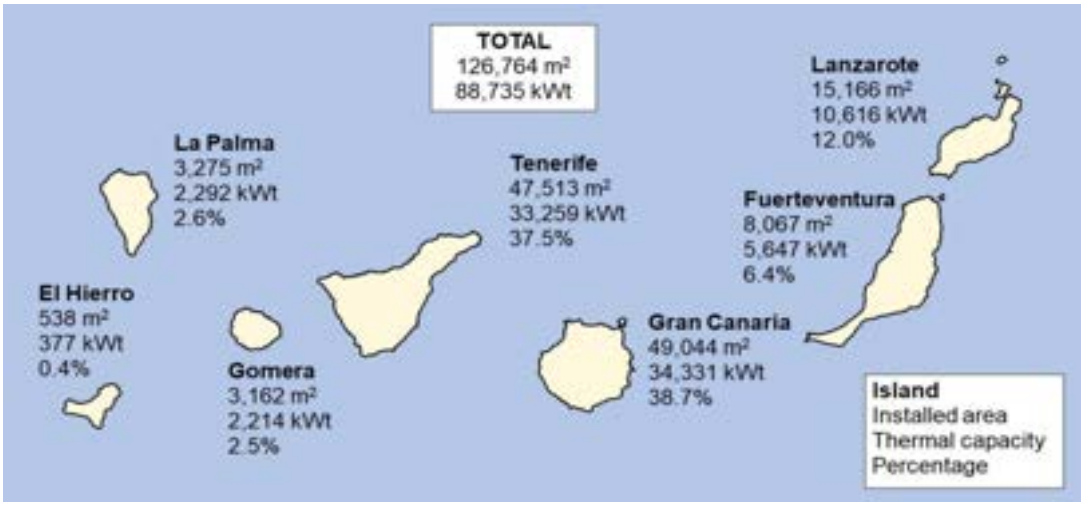

Figure 2. Installed solar thermal capacity in the Canary Islands on Dec 31st, 2021 (Data source: [24]).

The details of the energy system of the Canary Islands are collected in Table 1 [24]. The highest renewable energy sources (RES) share may be found in the island El Hierro, with 66.8%; however, this represents only 0.4% of the whole archipelago generation. The lowest RES capacity is found in La Gomera island, with only 0.4 MW. In this context, the study presented in this work may contribute to improve the energy supply network in the Canary Islands with a proposal based on renewable energy sources to integrate solar energy into existing combined cycles, providing more energy security to the islands.

2.2. ISCC in Las Palmas de Gran Canaria

The basic combined cycle power plant consists of an upper gas cycle, a bottom steam cycle, and a Heat Recovery Steam Generator (HRSG). The main characteristics of the CC, based on the power plant from Egyptian Petrochemical Company [25], with a thermal efficiency of 57.8% are shown in Table 2. In this work, two possibilities (Figures 3 &4) for the integration of the solar field within the CC, both working on a fuel saving scheme, have been studied and compared:

- Case A: solar field is integrated to preheat ambient air before the compressor inlet.
- Case B: solar field is integrated to heat up compressed air, before the combustion chamber inlet.

Table 1. Overview of the power system of the Canary Islands [24]

	Tenerife	Gran Canaria	Lanzarote	Fuerteventura	La Palma	La Gomera	El Hierro	Total
Total Generation (MWh)	3,710,951	3,581,933	906,078	716,839	281,016	76,850	62,430	9,336,098
Thermal Generation (MWh)	3,014,854 (81.2%)	3,028,053 (84.5%)	826,454 (91.2%)	636,732 (88.8%)	251,935 (89.7%)	76,696 (99.8%)	20,738 (33.2%)	7,855,463 (84.1%)
RES Generation (MWh)	696,097 (18.8%)	553,880 (18.8%)	79,623 (8.8%)	80,108 (11.2%)	29,081 (10.3%)	154 (0.2%)	41,692 (66.8%)	1,480,635 (15.9%)
Total Installed Capacity (MW)	1428.5	1228.4	266.8	229.8	118.4	21.6	37.8	3331.3
Thermal Capacity (MW)	1111.6 (77.58%)	1024.1 (83.4%)	232.4 (87.12%)	187 (81.4%)	105.3 (89%)	21.2 (98.1%)	14.9 (39.4%)	2696.5 (80.9%)
RES Capacity (MW)	316.9 (22.2%)	204.3 (16.6%)	34.4 (12.9%)	42.8 (18.6%)	13.1 (11%)	0.4 (1.9%)	22.9 (60.6%)	634.8 (19.1%)
CO_2 Emissions (tCO_2)	2,119,442	2,065,132	549,592	482,643	171,820	52,844	14,268	5,451,691

Table 2. Technical data for the combined cycle power plant [25]

Gas cycle	**Compressor**	
	Inlet Ambient temperature (ºC)	24
	Inlet pressure (bar)	1
	Isentropic efficiency (%)	97.5
	Combustion chamber	
	Inlet pressure (bar)	15.7
	Inlet temperature (ºC)	379
	Turbine	
	Inlet temperature (ºC)	1174
	Exhaust temperature (ºC)	549
	Exhaust mass flow rate (kg/s)	174.7
	Isentropic efficiency (%)	84.7
Steam cycle	Inlet steam pressure (bar)	43
	LP evaporator pressure (bar)	2.4
	Condenser pressure (bar)	0.08
	Inlet steam temperature (ºC)	452
	Pinch temperature (ºC)	18.3
	Economizer outlet temperature (ºC)	228
	Approach temperature (ºC)	26.7
	LP evaporator mass flow rate (kg/s)	5
	HP evaporator mass flow rate (kg/s)	25
Combined cycle	Total power output (MW)	93
	Cycle efficiency (%)	57.8

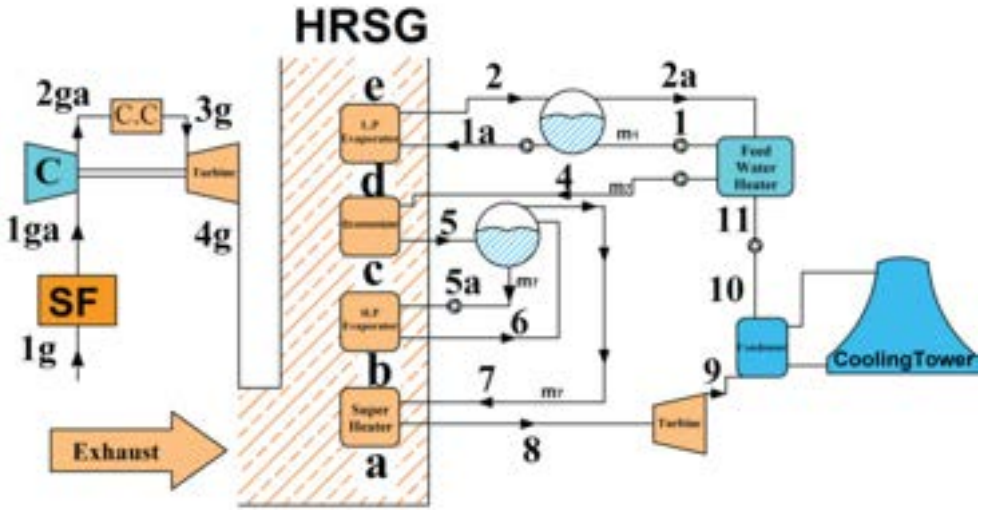

Figure 3. Case A: solar field integrated before gas cycle compressor.

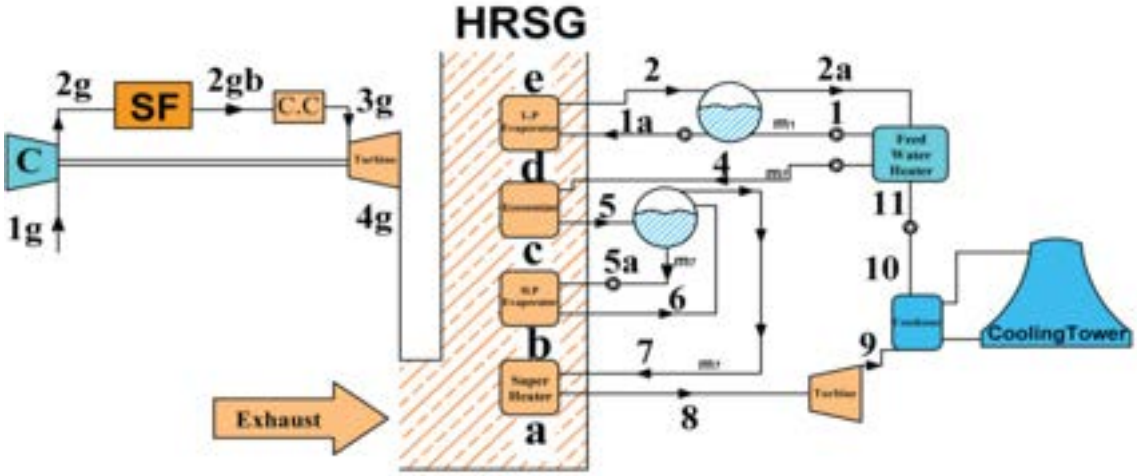

Figure 4. Case B: solar field integrated after gas cycle compressor.

3. Methodology

To fulfill the objectives of the study, a thermodynamic model has been developed in MATLAB with the Ideal Air code and the X Steam toolbox to obtain air and water properties for the upper gas and bottom steam cycles. The sequence of the methodology has been summarized in Figure 5, whereas the main thermodynamic equations used are discussed in the following subsections. A system of thermodynamic equations based on mass and energy balances in the cycle was solved, with the aim of calculating thermodynamic states, net power, efficiency, and air and fuel mass flows for the original CC and the two ISCC cases, allowing to estimate the amount of fuel saved, as well as economic savings and the reduction in CO_2 emissions. The values of solar heat integrated ranged from 0 to 35 MW. Pressure drop in the cycle was not considered, as well as the effect of inlet conditions in the isentropic efficiency of the compressor.

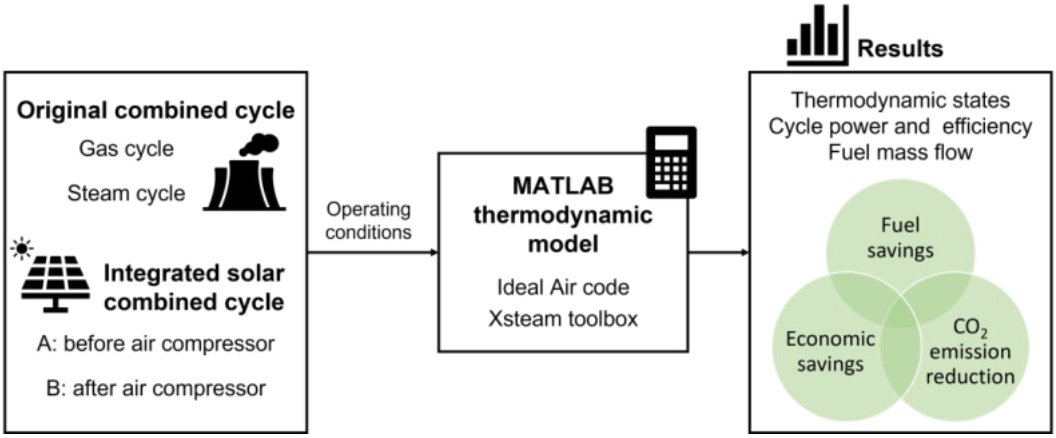

Figure 5. Methodology followed in this work.

3.1 Thermodynamic model of the original combined cycle

The upper gas cycle of the CC consists of three main components: compressor, combustion chamber and gas turbine. Ambient air (1g) is compressed to a higher pressure and temperature (2g). Then, it enters the combustion chamber, where fuel is added and burnt. The resulting high temperature gases (3g) enter the turbine and are expanded to ambient pressure (4g), producing useful work. Finally, exhaust gases are sent to the HRSG. The power of the gas turbine and compressor, the heat supplied in the combustion chamber and the net power of the gas cycle are calculated using the following equations:

$$\dot{W}_{GT} = \dot{m}_g \cdot (h_{3g} - h_{4g}) \quad (1)$$

$$\dot{W}_{comp} = \dot{m}_a \cdot (h_{2g} - h_{1g}) \quad (2)$$

$$\dot{Q}_{cc} = \dot{m}_f \cdot LHV = \dot{m}_g h_{3_g} - \dot{m}_a h_{2g} \quad (3)$$

$$\dot{W}_{G_{net}} = \dot{W}_{GT} - \dot{W}_{comp} \quad (4)$$

The bottom steam cycle of the CC comprises a steam turbine, a condenser, and a preheater. The steam that powers the cycle is generated in the HRSG with heat from the gas turbine exhaust gases. Energy balances in the HRSG yield the following equations (please refer to Figures 3-4 for the labels of thermodynamic states):

$$\dot{m}_g \cdot (h_a - h_b) = \dot{m}_7 \cdot (h_8 - h_7) \quad (5)$$

$$\dot{m}_g \cdot (h_b - h_c) = \dot{m}_7 \cdot (h_6 - h_{5a}) \quad (6)$$

$$\dot{m}_g \cdot (h_c - h_d) = \dot{m}_7 \cdot (h_5 - h_4) \quad (7)$$

$$\dot{m}_g \cdot (h_d - h_e) = \dot{m}_1 \cdot (h_2 - h_{1a}) \quad (8)$$

The steam turbine power is calculated as:

$$\dot{W}_{ST} = \dot{m}_7 \cdot (h_8 - h_9) \quad (9)$$

Hence, the total net power and efficiency of the CC power plant may be obtained as:

$$\dot{W}_{Total} = \dot{W}_{G_{net}} + \dot{W}_{ST} \quad (10)$$

$$\eta_{CC} = \frac{\dot{W}_{G_{net}} + \dot{W}_{ST}}{\dot{Q}_{cc}} \quad (11)$$

3.2 Thermodynamic model of the integrated solar combined cycle

The solar field has been integrated into the upper gas cycle, either to preheat ambient air before compression (case A), or to heat up compressed air before it enters the combustion chamber (case B). Gas turbine operating conditions (mass flow, inlet and outlet temperatures) are kept constant, so the steam cycle is virtually the same as the original one. In case A, the solar field generates a temperature rise before the compressor:

$$\dot{Q}_{Solar} = \dot{m}_{a_{new}} \cdot (h_{1gnew} - h_{1g}) \quad (12)$$

And the compressor power becomes:

$$\dot{W}_{comp_a} = \dot{m}_{a_{new}} \cdot (h_{2gnew} - h_{1gnew}) \quad (13)$$

On the other hand, in case B, heat is added after the compression process, leaving the compressor unaffected:

$$\dot{Q}_{Solar} = \dot{m}_{a_{new}} \cdot (h_{2gnew} - h_{2g}) \quad (14)$$

In both cases, the mass and energy balances in the combustion chamber are affected:

$$\dot{m}_g = \dot{m}_{a_{new}} + \dot{m}_{f_{new}} \quad (15)$$

$$\dot{Q}_{cc,new} = \dot{m}_{f_{new}} \cdot LHV = \dot{m}_g h_{3_g} - \dot{m}_{a_{new}} h_{2g_{new}} \quad (16)$$

And the total net power and cycle efficiency are modified accordingly, following Equations 10 and 11.

3.3 Estimation of economic and environmental effects of solar integration

Considering a natural gas price of 0.131 €/kWh [26], an estimation of the economic savings related to the amount of fuel saved may be performed using the following equation:

$$\text{Savings}_f = (\dot{m}_f - \dot{m}_{f_{new}}) \cdot LHV \cdot C_f \cdot \Delta t = \dot{m}_{f_{saved}} \cdot LHV \cdot C_f \cdot \Delta t \quad (17)$$

In addition, the introduction of solar energy reduces fuel combustion in the gas combustion chamber, leading to a reduction in CO_2 emissions. This reduction may be estimated from the lower heating value of natural gas (47,000 kJ/kg) [27] and the emission factor that relates natural gas and CO_2, 0.252 kg/kWh [28]:

$$\text{Savings}_{CO_2} = \dot{m}_{f_{saved}} \cdot LHV \cdot EF_{NG \rightarrow CO_2} \cdot \Delta t \quad (18)$$

4. Results

The results of the model show that the integration of solar heat into the combined cycle power plant results in a decrease in the fuel flow rate in cases A and B, with the air to fuel ration increasing accordingly. Table 4 collects the results from the three studied cycles when 35 MW of solar heat are added to the cycle.

Table 4. Original CC vs ISCC with 35 MW solar heat

Mass flow rates	**Original CC**	**ISCC (case A)**	**ISCC (case B)**
Air to fuel ratio	*50*	*99*	*64*
Turbine gas flow rate (kg/s)	*174.7*		
Air flow rate (kg/s)	*171.27*	*172.9*	*172.02*
Fuel flow rate (kg/s)	*3.42*	*1.74*	*2.67*
Fuel saving (%)	*--*	*49*	*21.83*
Operating temperatures	***Original CC***	***ISCC (case A)***	***ISCC (case B)***
Compressor inlet (ºC)	*24*	*223.6*	*24*
Combustion chamber inlet (ºC)	*379*	*785*	*565*
Gas turbine inlet (ºC)	*1174*		
Gas turbine outlet (ºC)	*549*		
Solar heat integration	***Original CC***	***ISCC (case A)***	***ISCC (case B)***
Integrated solar heat (MW)	*--*	*35*	
Cycle efficiency	***Original CC***	***ISCC (case A)***	***ISCC (case B)***
Gas turbine cycle (%)	*39.84*	*25.2*	*51*
Combined cycle (%)	*57.8*	*60.4*	*73.9*
Cycle power breakdown	***Original CC***	***ISCC (case A)***	***ISCC (case B)***
Compressor (kW)	*62,450*	*106,601*	*62,450*
Gas turbine (kW)	*126,727*	*126,727*	*126,727*
Gas cycle (kW)	*64,277*	*20,722*	*64,277*
Steam cycle (kW)	*28,810*	*28,810*	*28,810*
Total net power (kW)	*93,000*	*49,087*	*93,000*
Specific work per unit fuel mass flow (kJ/kg)	*27,193*	*28,211*	*34,831*
CO_2 emissions saving (kg CO_2/kWh)	*-*	*0.0572*	*0.0166*

Option A results in a higher amount of fuel saving, 49%, whereas option B saves around 22%. However, the compressor power required increases by 70% with option A. Considering the changes in energy efficiency, option A results in a drop in the efficiency of the gas cycle of around 14.5%, although a slight increase in the overall combined cycle of around 2% is achieved, due to the reduction of heat supplied to the combustion chamber. Option B achieves the maximum cycle efficiency increase, around 11% for the gas cycle, leading to a 16.2% increase in the efficiency of the combined cycle. Therefore, option B seems the most beneficial option, delivering the same net power to the net with a substantial reduction on fuel consumption. The specific work per unit fuel mass flow rate reflects the superiority of case B over case A as 34,831 kJ could be delivered for each kg of fuel, while only 28,211 kJ for case A. CO_2 emissions avoided per net energy production is computed, where it is found that CO_2 emissions could be saved at a rate of 0.0572 and 0.0166 kg/kWh for case A and case B respectively.

Figure 6 shows the evolution of the cycle efficiency for the ISCC options studied as a function of the integrated solar heat, from 0 to 35 MW. It may be observed that integration of solar heat always results in better cycle efficiencies if it is done as proposed in option B, with the gap between options B and A increasing with further addition of solar heat. On the other hand, considering the fuel mass flow rates, depicted in Figure 7, and the reduction with respect to the original CC, shown in Figure 8, option A is the one that achieves the highest reduction in fuel consumption. From the original consumption of 3.42 kg/s, option A may save around 49% of the original fuel consumption if 35 MW of solar heat are added to the cycle, whereas option B can only reach around 21% savings. Nevertheless, it must not be forgotten that, although option A increases the cycle efficiency and reduces fuel consumption, the total net power delivered by the cycle is decreased with the integration of solar heat, as a consequence of the increase on the compressor power. Therefore, its use is not recommended. Option B does not have that disadvantage, as the integration of solar heat is performed after the compression stage. In addition, cycle efficiency increases more than with option A. Consequently, option B is the most adequate for integrating solar heat into the upper gas cycle of a CC.

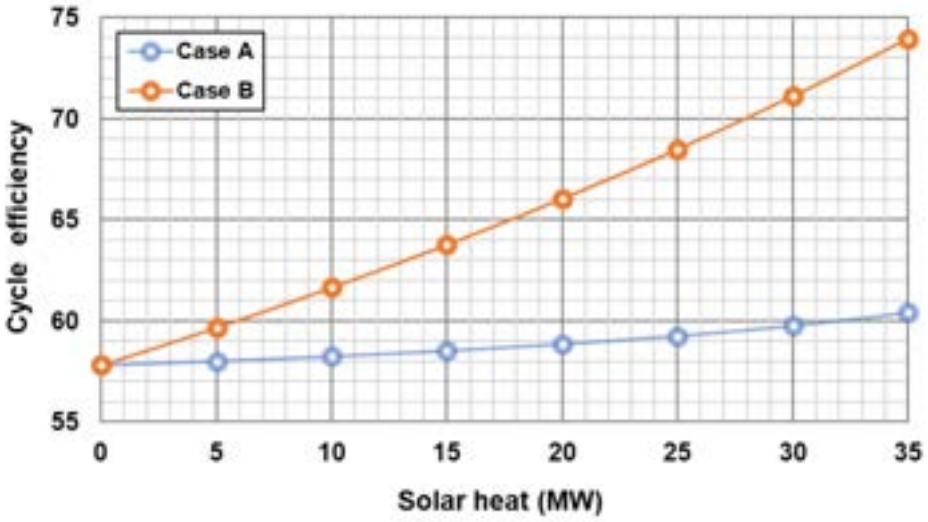

Figure 6: Combined cycle efficiency as a function of solar heat integrated into the cycle.

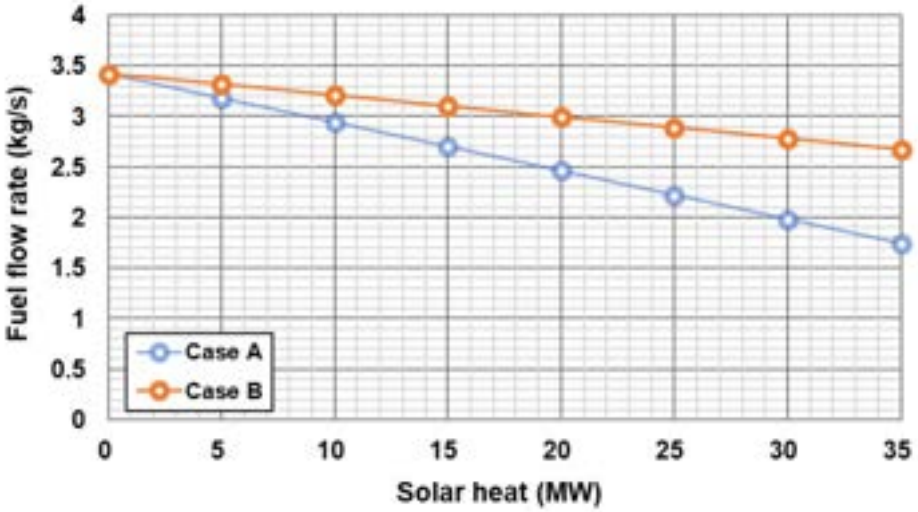

Figure 7: Fuel mass flow rate as a function of solar heat integrated into the cycle.

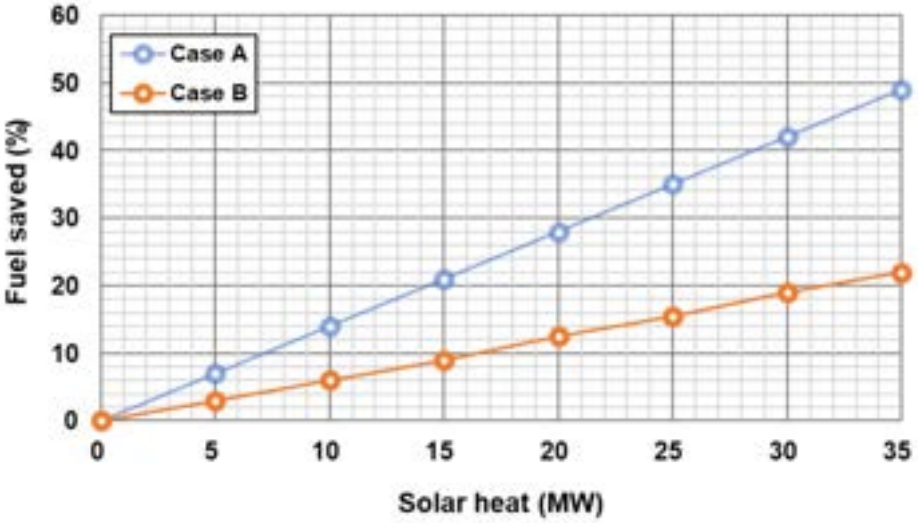

Figure 8: Fuel savings (%) as a function of solar heat integrated into the cycle.

Once it was been verified that option B is the most suitable one, in order to provide an estimation of the economic and environmental effects of solar heat integration, values from average solar irradiation in Las Palmas de Gran Canaria were considered. Figure 9 shows the monthly average daily global irradiation in Las Palmas, alongside the average heat power that could be provided by a 300,000 m^2 solar collector [29]. Maximum values of solar power are found in July, with 30,448 kW, while the minimum average solar heat is 15,597 kW, in December.

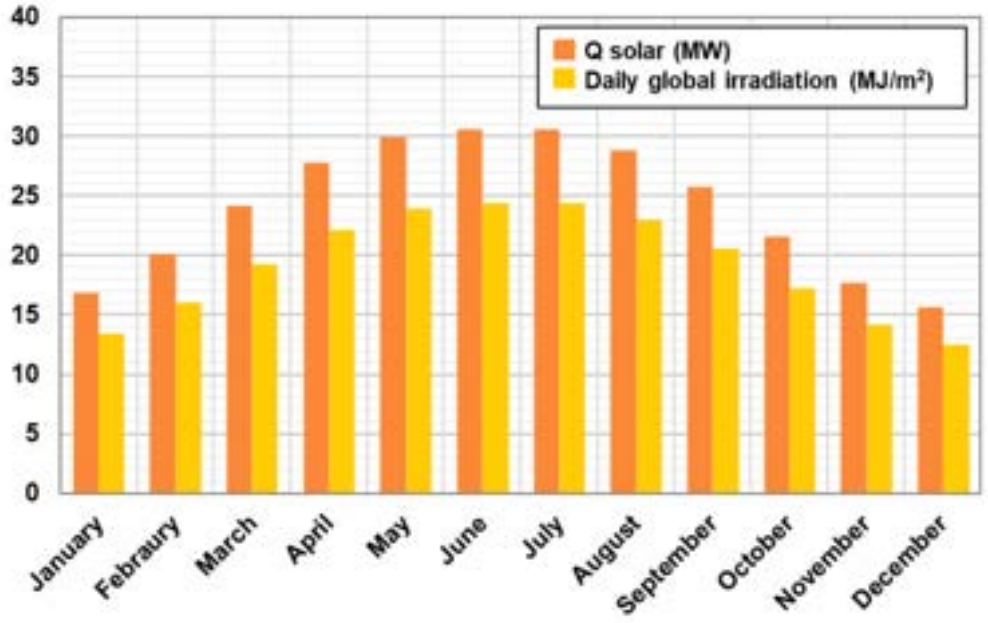

Figure 9: Monthly average daily global irradiation and solar heat power potential for a 300,000 m^2 collector in Las Palmas de Gran Canaria [29].

After the data from the solar heat power potential provided by the collector are introduced into the thermodynamic model of option B for the ISSC, the reduction in the fuel mass flow was calculated and translated into an estimation of the economic savings and reduction in CO_2 emissions. The results reveal a direct proportionality relation between the introduced solar heat power and the amount of fuel that may be saved. As shown in Figure 10, the highest savings may be achieved in July, of around 0.75 M€, while the lowest savings are reached in December, of around 0.38 M€. In all, if option B is integrated into the combined cycle, potential yearly savings of around 7.14 M€ might be achieved.

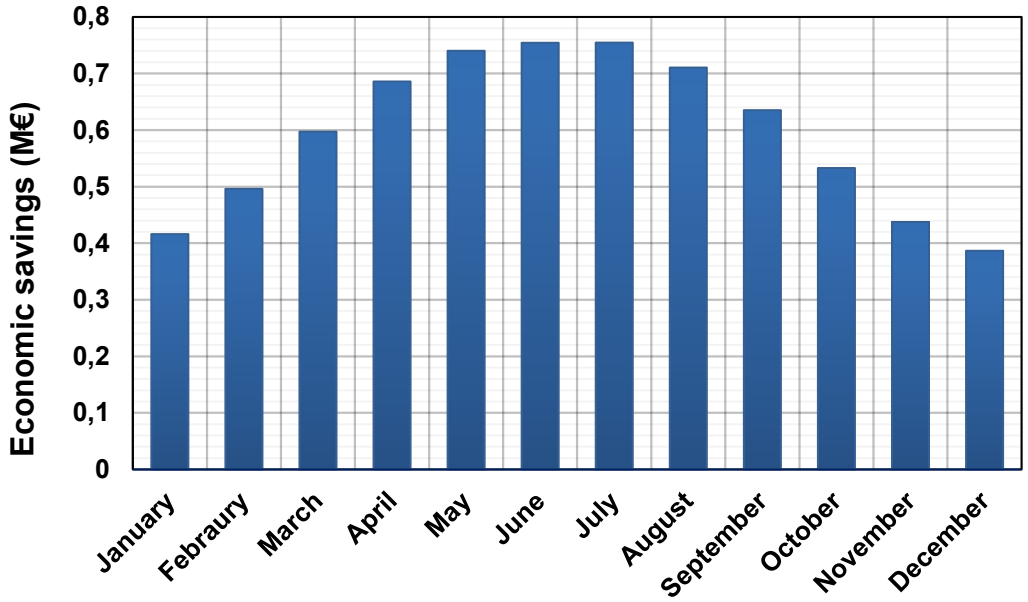

Figure 10: Monthly potential economic savings (M€) related to fuel consumption reduction.

Regarding the CO_2 emissions avoided by the integration of option B into the combined cycle, depicted in Figure 11, a direct proportionality with solar irradiance is found as well. Maximum values of potential reduction of emissions are found in July, of around 1.45 Mkg, whereas lowest values are found in December, of around 0.74 Mkg. In the aggregate, it has been estimated that incorporating option B into the combined cycle might lead to a total potential of reduction in CO_2 emissions of 13.75 Mkg per year.

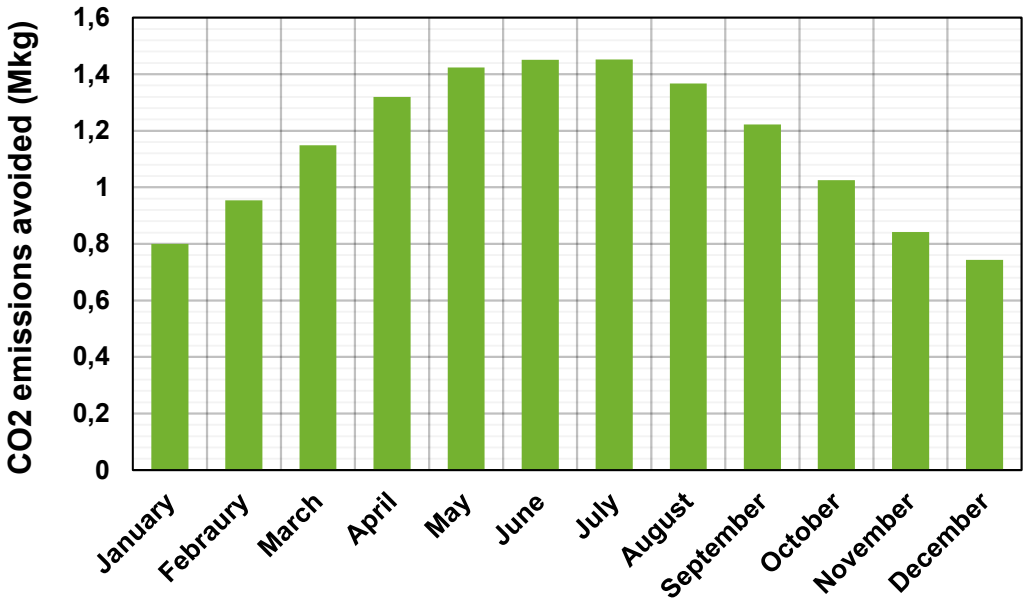

Figure 11: Monthly potential CO_2 emissions avoided (Mkg) related to fuel consumption reduction.

5. Conclusion

The overview of the power generation system in the Canary Islands reveals the important effect of renewable energy resources (especially, solar energy) to provide stability and reinforcement for power generation in thermal plants. The results from this work, which aims to evaluate the feasibility of integrating solar energy into a combined cycle power plant for fuel saving in insular subtropical climates, may contribute to improve the energy supply network in the Canary Islands, providing more energy security to the islands and reducing fuel imports. A thermodynamic model for solar heat integration into the upper gas cycle of the combined cycle was developed, studying the effects of injecting the solar heat before (case A) and after (case B) the compressor, before the combustion chamber.

It was found that the highest amount of fuel saved, 49% when injecting 35 MW of solar heat, was achieved when injecting the solar heat before the compressor (option A). However, this option resulted in a substantial increase of the compressor work due to the higher temperatures at the compressor inlet, reducing the net power of the cycle, although a global efficiency increase of around 2% was achieved. On the other hand, integrating the solar heat after the compressor (option B) had a very positive effect, with an overall 16.2% increase in the combined cycle efficiency when 35 MW of solar heat were introduced before the combustion chamber and. This option, in addition, can deliver the same net power with a substantial reduction of 22% in fuel consumption. The gap between the combined cycle efficiencies of both integration options became larger with the increase in the injected heat, with option B outperforming option A. Consequently, it may be argued that the most adequate for integrating solar heat into the upper gas cycle of a CC is right after the compressor and before the combustion chamber.

Combining the results from the energy analysis with the monthly solar irradiation distribution in Las Palmas de Gran Canaria and considering a solar collector of 300,000 m^2, it was possible to obtain an estimate of the economic savings and reduction in CO_2 emissions with the introduction of the solar field before the gas cycle combustion chamber. Oscillating between a minimum value of around 0.38 M€ in December and a maximum of 0.75 M€ in July, the integration of the proposed option may lead to potential savings of 7.14 M€ per year. Considering the CO_2 emissions potentially avoided with to the proposed solar heat integration, between 0.74 Mkg in December and 1.45 Mkg in July, it has been estimated that incorporating option B into the combined cycle might lead to a total potential of reduction in CO_2 emissions of 13.75 Mkg per year.

To conclude with, the integration of solar heat into a combined natural gas-fired cycle before the combustion chamber seems to be a very beneficial option for insular systems with solar irradiance values similar to Las Palmas de Gran Canaria. Substantial increases in the cycle efficiency, high potential economic savings, and a high reduction in potential CO_2 emissions are to be expected. Future works may focus on developing an exergoeconomic and environmental analysis of the studied alternatives, as well the study of other possible integration options of solar heat into the combined cycle.

Nomenclature

CC	Combined cycle
C_f	Fuel cost (€/kWh)
CSP	Concentrated solar power
DNI	Direct Normal Irradiance
$EF_{NG \to CO_2}$	Emission factor of natural gas (kg CO_2/kWh)
GEF	Global Environment Facility
GTCC	Gas turbine combined cycle
h_i	Specific enthalpy at state i (kJ/kg)
HRSG	Heat Recovery Steam Generator
ISCC	Integrated solar combined cycle power plant
LHV	Lower heating value (kJ/kg)
Mtoe	Million tonnes of oil equivalent
$\dot{m}_i$	Mass flow of fluid i (kg/s)
NGCC	Natural gas-fired combined cycle
PTC	Parabolic trough collectors
$\dot{Q}_i$	Heat transfer rate exchanged by component i (kW)
RES	Renewable energy sources
SEGS	Solar electric generating system
$\dot{W}_i$	Power of component i (kW)

Greek symbols

Δt	Time period (month)
η	Cycle efficiency

Subscripts

a	Air, case “A”
b	Case “B”
cc	Combustion chamber
CC	Combined cycle
$comp$	Compressor
f	Fuel
g	Gas
G	Gas cycle
GT	Gas turbine
new	New value (after solar integration)
ST	Steam turbine

References

[1] International energy agency (IEA), Global energy review 2021 <https://www.iea.org/>

[2] Our world in data, project of the Global change data lab (GCDL), <https://ourworldindata.org/>

[3] Bakos, G. C., and D. Parsa. "Technoeconomic assessment of an integrated solar combined cycle power plant in Greece using line-focus parabolic trough collectors." Renewable energy 60 (2013): 598-603.

[4] Behar, Omar, et al. "Instantaneous performance of the first integrated solar combined cycle system in Algeria." Energy Procedia 6 (2011): 185-193.

[5] Amelio, Mario, et al. "An evaluation of the performance of an integrated solar combined cycle plant provided with air-linear parabolic collectors." Energy 69 (2014): 742-748.

[6] Kabir, Ehsanul, et al. "Solar energy: Potential and future prospects." Renewable and Sustainable Energy Reviews 82 (2018): 894-900.

[7] Duffie, John A., William A. Beckman, and W. M. Worek. "Solar engineering of thermal processes." (1994): 67-68.

[8] Raafat, Samir W. Maadi 1904-1962: Society and history in a Cairo suburb. Palm Press, 1994.

[9] TB, Johansson, et al. Renewable Energy-Sources for Fuels and Electricity. 1993.

[10] Pilkington, S. "Solar International." Status Report on Solar Trough Power Plants, Pilkington Solar International GmbH, Germany (1996).

[11] The World Bank. Implementation Completion and Results Report (TF-91289) on A Grand in The Amount of US $49.80 Million to the Arab Republic of Egypt for the Kureimat Solar Thermal Hybrid Project; The World Bank: Washington, DC, USA, 2012.

[12] Allani, Yassine, Daniel Favrat, and M. R. Von Spakovsky. "CO2 mitigation through the use of hybrid solar-combined cycles." Energy conversion and management 38 (1997): S661-S667.

[13] Dersch, Jürgen, et al. "Trough integration into power plants—a study on the performance and economy of integrated solar combined cycle systems." Energy 29.5-6 (2004): 947-959.

[14] Franchini, Giuseppe, et al. "A comparative study between parabolic trough and solar tower technologies in Solar Rankine Cycle and Integrated Solar Combined Cycle plants." Solar Energy 98 (2013): 302-314.

[15] Antonanzas, J., et al. "Potential solar thermal integration in Spanish combined cycle gas turbines." Renewable and Sustainable Energy Reviews 37 (2014): 36-46.

[16] Li, Yuanyuan, and Yongping Yang. "Thermodynamic analysis of a novel integrated solar combined cycle." Applied energy 122 (2014): 133-142.

[17] Calise, Francesco, et al. "Thermoeconomic analysis of an integrated solar combined cycle power plant." Energy Conversion and Management 171 (2018): 1038-1051.

[18] Abdelhafidi, Nedjma, İbrahim Halil Yılmaz, and Nour El Islam Bachari. "An innovative dynamic model for an integrated solar combined cycle power plant under off-design conditions." Energy Conversion and Management 220 (2020): 113066.

[19] Temraz, Ayman, et al. "Development and Validation of a Dynamic Simulation Model for an Integrated Solar Combined Cycle Power Plant." Energies 14.11 (2021): 3304.

[20] Benabdellah, Hamza Moussa, and Adel Ghenaiet. "Energy, exergy, and economic analysis of an integrated solar combined cycle power plant." Engineering Reports 3.11 (2021): e12404.

[21] Zhang, Zuxian, et al. "General performance evaluation method of integrated solar combined cycle (ISCC) system." Energy 240 (2022): 122472.

[22] Lee, Taedong, Mark B. Glick, and Jae-Hyup Lee. "Island energy transition: Assessing Hawaii's multi-level, policy-driven approach." Renewable and Sustainable Energy Reviews 118 (2020): 109500.

[23] Daily characteristics of the Canary Islands' electricity system. Available at:
<https://www.ree.es/en/balance-diario/canarias/2022/03/31>

[24] Canary Islands energy yearbook 2020. Available at:
https://www.gobiernodecanarias.org/energia/publicaciones/

[25] Egyptian Petrochemicals Company (egy-petrochem.com)

[26] Energy price data and fuel price forecasts. Available at:
<https://www.globalpetrolprices.com/>

[27] World Nuclear Association – Heat values of various fuels. Available at:
<https://world-nuclear.org/information-library/facts-and-figures/heat-values-of-various-fuels.aspx>

[28] "Recognized Document of the Regulation of Thermal Installations in Buildings (RITE)" Joint resolution of the Ministries of Industry, Energy and Tourism, and the Ministry of Public Works. Available at: <https://energia.gob.es/desarrollo/EficienciaEnergetica/RITE/Reconocidos/Reconocidos/Otros%20documentos/Factores_emision_CO2.pdf>

[29] Technical guide to solar thermal energy provided by The Institute for Energy Diversification and Saving (IDAE) and the Solar Thermal Industry Association (ASIT), organizations affiliated with the European Union. Available at:
<https://www.idae.es/publicaciones/guia-tecnica-de-energia-solar-termica>

First experimental results of a new free liquid piston Ericsson engine

Ryma Chouder[a], Max Ndamé Ngangué[b], Pascal Stouffs[c] and Azzedine Benabdesselam[d]

[a] Universite de Pau et des Pays de l'Adour, E2S UPPA, LaTEP, Pau, France, rchouder@univ-pau.fr
[b] Laboratoire de Technologie et de Sciences Appliquées, IUT de l'Université de Douala, Cameroun, maxndame@yahoo.fr
[c] Universite de Pau et des Pays de l'Adour, E2S UPPA, LaTEP, Pau, France, pascal.stouffs@univ-pau.fr, Corresponding Author
[d] Laboratoire des Transports Polyphasiques et Milieux Poreux (LTPMP), FGPGM, USTHB, Algiers, Algeria, benabdesselam2000@yahoo.com

Abstract:

A new Ericsson free-liquid-piston engine (FLPEE) configuration was previously presented. This consists of a U-shaped tube filled with water in its lower part, and whose two branches are closed by cylinder heads fitted with valves. The space between the surface of the liquid and the cylinder head of one of the branches constitutes the compression space, while this same space constitutes the expansion space in the other branch. The configuration studied operates in an open cycle. This system is able to produce compressed air which can be expanded in an external device to produce mechanical energy. This FLPEE is thought to be suited for the conversion of thermal energy such as solar energy, biomass or flue gases. In this communication, the experimental bench is presented in detail. In particular, the valve control system of the compression and expansion spaces, the various sensors and the data acquisition system are described. Various experimental results are presented, notably in the form of (p, V) indicator diagrams of the compression and expansion cylinders. These results confirm what the theoretical modelling had predicted, namely that it is possible to obtain a set of values of the operational parameters of the system leading to a stable operation of the free-piston system.

Keywords:

Free piston engine; Ericsson engine; Liquid piston, Experimental results.

1. Introduction

External heat engines such as Stirling or Ericsson engines [1] are proving to be a relevant technological solution for the valorisation of thermal energy such as solar energy, the energetic valorisation of hot gaseous effluents or the combustion of biomass, in order to produce low power mechanical or electrical energy. A major advantage of Ericsson engines over Stirling engines is that the heat exchangers are not dead volumes and can therefore be sized solely on heat transfer considerations [2]. This is particularly interesting in the case of hot sources with relatively low temperature or low transfer coefficient, such as flue gases. However, with regard to Ericsson engines, despite their interest and numerous theoretical developments [3-7], there is still little experimental work.

Liquid piston machines are particularly interesting because they ensure a perfect seal between the piston and the cylinder, while drastically reducing frictional forces. In addition, they can considerably improve heat transfer with the working fluid, for example to approach isothermal compression [8-10].

Free piston engines do not require a crank-connecting rod arrangement to transform reciprocating motion into rotary motion. Mechanical losses are therefore lower and the cost of the engine is reduced [11]. There are free piston internal combustion engines [12-15] or free piston Stirling engines [16-18] and free liquid piston Stirling engines, also known as Fluidyne. These engines, developed for pumping applications, have a poor efficiency [19-20].

In this paper, a totally new engine configuration combining the advantages of Ericsson engines, liquid piston machines and free piston engines is studied [21]. Dynamic simulation results of this engine have shown that it is possible to design a free liquid piston Ericsson engine (FLPEE) which, combined with a judicious choice of operational parameters, allows stable operation with interesting energy performance [22]. In particular, the FLPEE has a much better energy performance than the Fluidyne, which is the most similar configuration.

An experimental bench is being developed to validate the theoretical results. This bench is described and the first results are presented.

2. The test bench

2.1. The configuration under consideration

The configuration studied (Figure 1) consists of a U-shaped tube filled with water in its lower part, and whose two branches are closed by cylinder head fitted with valves.

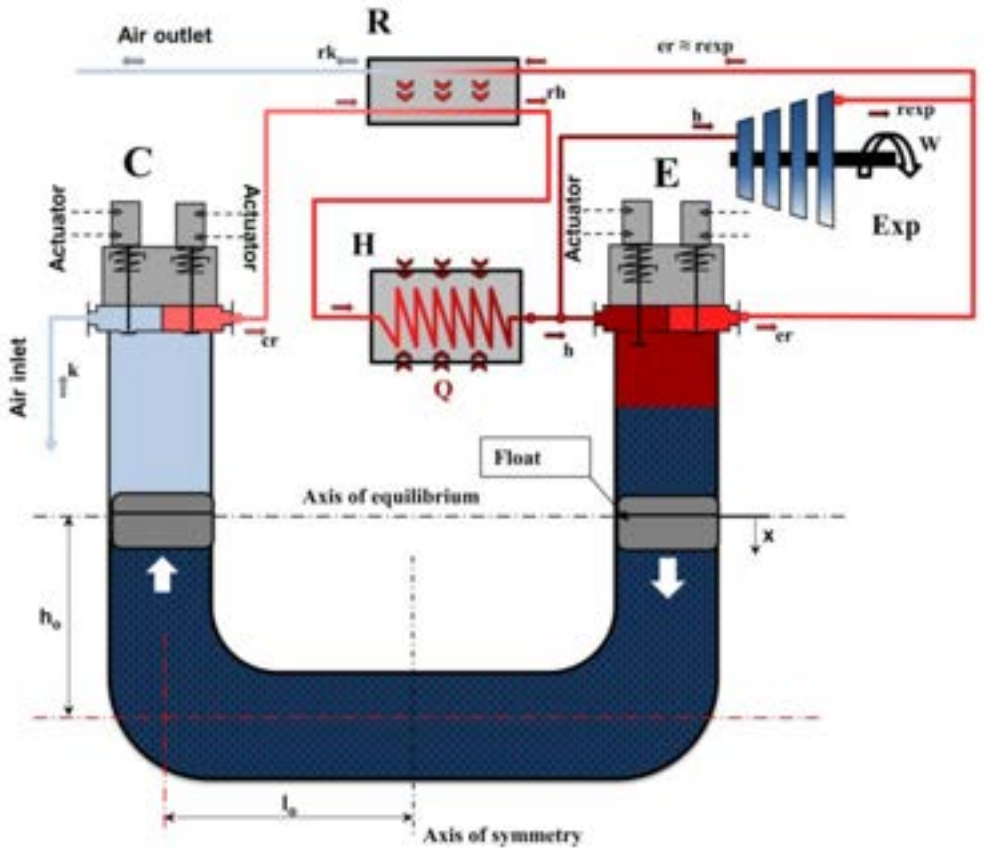

Figure 1. Schematic diagram of the free liquid piston Ericsson engine.

The space between the liquid surface and the cylinder head of one branch is the compression space C, while the same space is the expansion space E in the other branch. The configuration studied operates in an open cycle, with atmospheric air entering the compression space, being compressed by the liquid piston, then discharged to a heat recovery exchanger R and a heater H (hot source of the cycle) before being introduced into the expansion space E. The hot air expanded by the descent of the liquid piston is then discharged to the other branch of the heat recovery exchanger R, during the ascent of the liquid piston. In the case of the configuration studied, only a part of the air mass flow discharged by the compression space is introduced into the expansion space, the mass flow introduced being such that the expansion work exactly compensates for the compression work. In this configuration, the liquid piston and the compression and expansion spaces it defines are similar to a 'free piston gas generator', like the gas generator of the PESCARA engine [23-24]. The compressed air mass flow not admitted to the expansion space can be used as such, at the outlet of the compression space, the system being then a thermal compressor, or be taken after passing through the heat recovery R and heater H exchangers and be expanded in a machine operating in parallel to the liquid piston expansion space, if the objective is to produce mechanical energy (Figure 1).

2.2. The experimental set-up

Figure 2 shows the schematic diagram of the test bench, while figure 3 shows an overview of the experimental set-up. In order for the system to be tested in 'motored engine' mode, the device (Figure 2) is supplied with compressed air from the lab network (1). The compressed air from the external air compressor first passes through a pressure regulator (2) which allows the bench supply pressure to be adjusted, and then passes through a safety valve (3) which limits the downstream pressure to 3 bar, in order to avoid any risk of bursting the Pyrex tube (11). The valve (4) allows the compressed air in the test rig to be drained. A T-connection allows the expansion cylinder to be supplied from both the external compressor and the compression chamber of the liquid piston engine.

When the valves (1) and (5) are open, the compressed air from the external compressor pressurises the entire high-pressure branch of the device, including the two buffer tanks (8) and (15). The pressure line of the compression cylinder is pressurised and the engine can be started by opening the inlet valve of the expansion cylinder and introducing external compressed air.

When the valve (5) is closed, no more compressed air is introduced from the external compressor. A fluidic circuit is established which allows the bench to operate in "engine mode", i.e. the compressed air leaving the compression cylinder is divided into two flows: one part passes into the cold buffer (8), then through the heating cartridge (14) and the hot buffer tank (15) to be admitted into the expansion cylinder (11), and the other part passes into a back-pressure regulator (7) which makes it possible to keep the upstream pressure constant. The flow of air delivered by this back-pressure regulator can be measured by the float flow meter (6). This measurement allows the available air flow to be assessed for practical applications of the engine, such as the production of compressed air or mechanical power by adding an external expander.

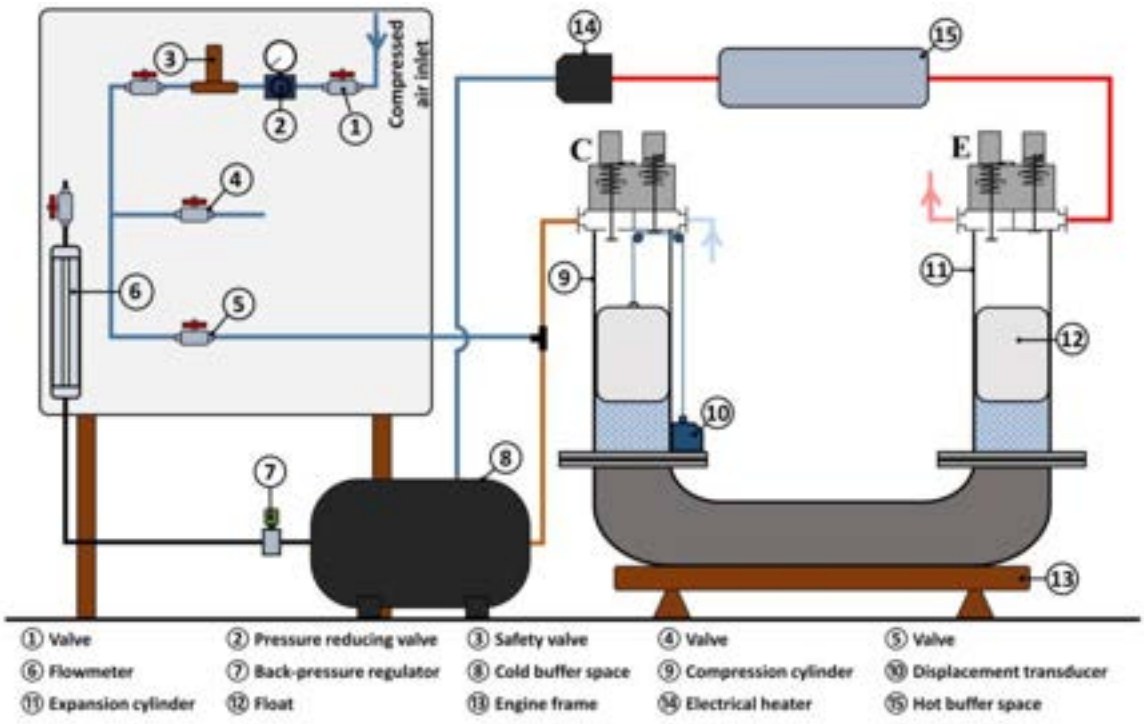

Figure 2. Schematic diagram of the test bench.

The lower part of the liquid piston system is made from commercial high-strength PN 10 pressure PVC pipe. The compression cylinder is made of stainless steel, while the expansion cylinder is made of Pyrex pipe with an external diameter of 180 mm, thickness of 8 mm, length of 500 mm. Two floats, with an external diameter of 156 mm and a length of 250 mm, are inserted in the cylinders. The length of the floats has been chosen to be at least equal to the maximum amplitude of movement of the liquid piston, so that water never licks portions of the wall of the expansion cylinder that would have been in contact with hot air. This reduces the evaporation of water from the liquid piston, as the nominal temperature of introduction of air into the expansion cylinder is 360°C.

Commercial YAMAHA XT500 motorbike engine heads are used to close the compression and expansion cylinders. The valves in these heads are operated by Festo 3/2-way quick-acting 1/4" valves, model MHE4-MS1H3/2G14K, and single-acting pneumatic cylinders, model AEN-40-8APA-S6, also from Festo. These valves are supplied with compressed air from the external air compressor.

The compressed air is heated before it enters the expansion workspace by an electric heating cartridge (item (14) in Figure 2), Osram Sylvania model SureHeat JET 074719, with a maximum power of 8 kW. A control box allows the supply temperature of the expansion cylinder to be set.

The test bench is equipped with K-type thermocouple temperature sensors with a measuring uncertainty of ± 1.5 °C, Keller-Druk PR23S and 23SY pressure sensors which have been calibrated beforehand and have a measuring uncertainty of ± 0.025 bar, and a micro-Epsilon WDS-300-P60-SR-I displacement sensor with a measuring uncertainty of ±0.25 %. This sensor (item (10) in Figure 2) is connected by a pulley system to the float of the compression cylinder. The measurement of the instantaneous pressure in each compression and expansion space is obtained by means of pressure sensors connected to the original location of the spark plugs in the cylinder heads. The sensors are connected to a National Instrument NI cDAQ 9172 modular

chassis data logger controlled by Labview. The sampling rate is 1 kHz. A control box operates the solenoid valves on the valve cylinders based on a comparison between the setpoints and the float position measured by the taut wire sensor.

Figure 3. Overview of the experimental set-up.

3. First experimental results

The first tests did not allow the system to operate autonomously [25], for reasons that will be explained later. The results presented here are therefore all related to a 'motored engine' mode, i.e. with consumption of compressed air from the network. In addition, according to the theoretical results, the displacement amplitude of the free liquid piston increases with the intake pressure of the expansion cylinder. However, in its current version, the amplitude is limited by the length of the tubes and the length of the floats. Therefore, the tests that have been carried out are limited to low pressure ratios. On the other hand, the frequency also depends on the inlet pressure of the expansion cylinder. Experience shows that above a frequency of about 3 Hz, the liquid-air interface no longer behaves satisfactorily. Due to its inertia, the float 'lifts off' from the liquid column and the interface breaks up into a multitude of droplets. For these reasons, the tests are limited to an absolute pressure of 1.6 bar at the inlet of the expansion cylinder.

3.1. Valves setting

The position of the liquid piston is denoted by x. The position $x = 0$ corresponds to the lowest bottom dead centre possible in the expansion cylinder (float on the bottom stop of the cylinder) and the highest top dead centre (TDC) possible in the compression cylinder (float in contact with the top stop of the cylinder). The position $x = 0.3$ m corresponds to the lowest bottom dead centre (BDC) possible in the compression cylinder (float on the bottom stop of the cylinder) and the highest top dead centre possible in the expansion cylinder (float in contact with the top stop of the cylinder).

The compression cylinder valves are supposed to simulate automatic valves, whereas the expansion cylinder valves are actuated valves whose opening and closing are governed by the values of the position of the liquid piston and its direction of movement.

The valves are actuated as follows:

- The inlet valve of the compression cylinder is open when the liquid piston moves downward and the in-cylinder pressure is lower than the atmospheric pressure.
- The outlet valve of the compression cylinder is open when the liquid piston moves upward and the in-cylinder pressure is higher than the pressure in the exhaust pipe.
- The inlet valve of the expansion cylinder is open when the liquid piston moves upward and $x >$ IVO or when the liquid piston moves downward and $x >$ IVC.
- The exhaust valve of the expansion cylinder is open when the liquid piston moves downward and $x <$ EVO or when the liquid piston moves upward and $x >$ IVC.

Figure 4 presents the valves setting of the expansion cylinder. Unless otherwise specified, the results presented here correspond to the following expansion cylinder valves setting:

- IVO = 0.16 m
- IVC = 0.1 m
- EVO = 0.03 m
- EVC = 0.16 m

Theoretically, with this valves setting, there should be an expansion process of the working fluid, since all valves are closed when the liquid piston moves downward from IVC = 0.1 m to EVO = 0.03 m, but there should be no re-compression of the dead space volume since the inlet valve opens at the same time as the exhaust valve closes: EVC = IVO.

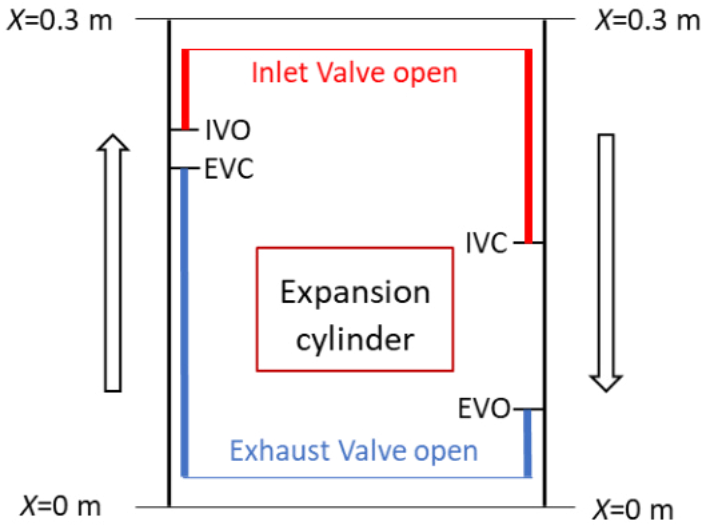

Figure 4. Valves setting for the expansion cylinder.

3.2. Cold tests

3.2.1. Frequency and stroke

Figure 5 shows the theoretical and experimental liquid piston displacement as a function of time, for a test duration of 20 s with a time step of 10^{-3} s. The expansion cylinder inlet pressure is set to 1.3 bar. There is good agreement between the theoretical and experimental data, both in term of frequency (about 2.2 Hz for the experimental and theoretical results) and stroke (about 124 mm for the theoretical results and 105 mm for the experimental ones, that is less than half the maximum possible travel between the stops).

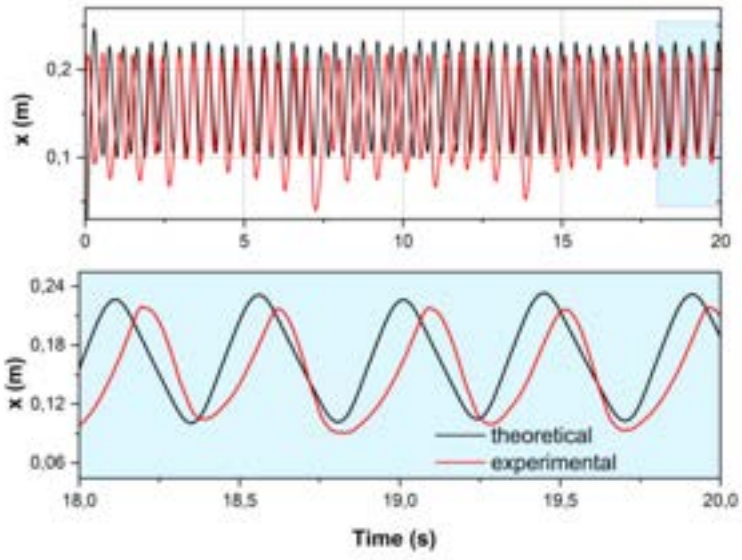

Figure 5. Liquid piston displacement as a function of time.

Figure 6 presents the frequency and the stroke as a function of the expansion cylinder inlet pressure. As the modelling has shown, it is not possible to vary the expansion cylinder inlet pressure without adjusting the valves setting. The experimental results shown in figure 6 are obtained by varying the pressure of the air admitted into the expansion cylinder from 1.15 to 1.5 bar. For the theoretical results, the model has been re-run, with the experimentally imposed pressure and valves setting, to allow comparison between the experimental and theoretical data. It can be seen that the theoretical frequency and stroke increases nearly linearly with the expansion cylinder inlet pressure. The experimental values are in fairly good agreement with the theoretical values, and the differences can be attributed largely to the fact that the experimental instantaneous pressure in the expansion cylinder is far from the theoretical pressure, due to pressure losses in the intake line, as will be shown below. The same applies to the compression cylinder, where the exhaust valve generates large pressure losses.

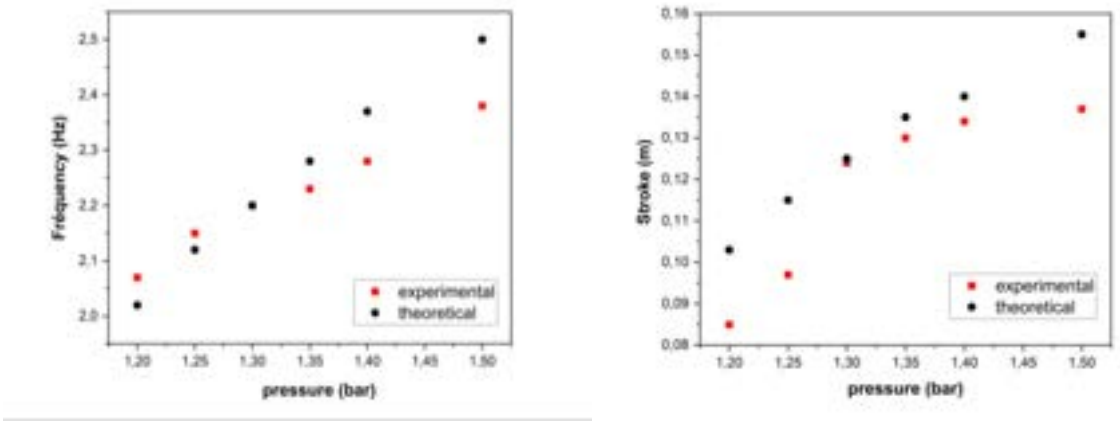

Figure 6. Frequency and stroke as a function of the expansion cylinder inlet pressure.

3.2.2. Instantaneous pressures

Figure 7 presents the instantaneous pressures measured at the expansion cylinder inlet (*p_admE*), in the compression cylinder (*p_C*), at the compression cylinder outlet (*p_echC*), in the expansion cylinder (*p_E*) and at the heater cartridge inlet (*p_Cart*), as a function of time for different expansion cylinder inlet pressures.

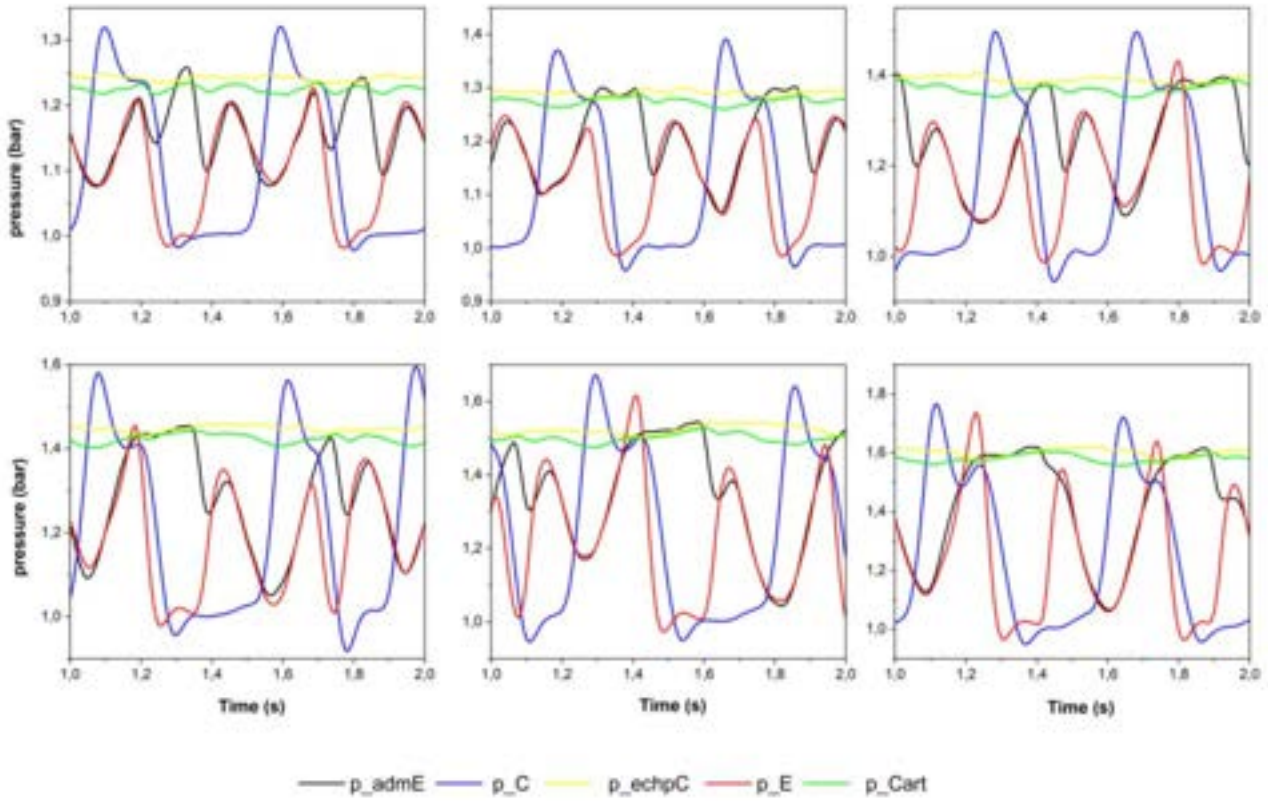

Figure 7. Instantaneous pressures as a function of time for different expansion cylinder inlet pressures.

It can be seen in Figure 7 that the pressures at the inlet of the heater cartridge *p_Cart* and at the outlet of the compression cylinder *p_echC* are almost constant, and almost identical, the pressure at the inlet of the

cartridge being slightly lower due to the greater pressure drop in the connecting pipe. In contrast, the expansion cylinder inlet pressure *p_admE*, which is supposed to be constant in the model, varies greatly when the inlet valve opens and closes. This is due to the high pressure drop generated by the pipe that connects the hot buffer tank to the expansion cylinder head. This line 'deflates' when the inlet valve opens and 're-inflates' to the cartridge inlet pressure when the inlet valve closes. The higher the pressure imposed by the compressed air in the high-pressure branch, the more pronounced this phenomenon becomes. This high pressure drop is the main reason why the engine has not yet been able to operate autonomously, without energy supply from the compressed air network. During the opening phases of the expansion cylinder intake valve, the pressure *p_E* in the cylinder is almost identical to the pressure in the intake pipe *p_admE*, proving that the pressure losses in the intake valve are negligible. However, these pressures are far from being equal to the constant pressure *p_Cart* as assumed in the model.

As far as the compression cylinder is concerned, it can be seen that when the free liquid piston moves up towards its top dead centre, the pressure in the cylinder *p_C* exceeds the pressure in the exhaust pipe *p_echpC* even though the exhaust valve is open, which indicates that the pressure losses generated by this valve are too high under these operating conditions.

3.2.3. In-cylinder pressures

Figure 8 presents the liquid piston displacement, the state of the valves (1 = open, 0 = closed) and pressure in the expansion cylinder as a function of time. For the valves setting considered, it can be seen that there is a time lag between the closing of the intake valve and the moment when the piston reaches its bottom dead centre. This should lead to an expansion of the fluid in the cylinder, which does not seem to be systematically observed. Similarly, it is also observed that the pressure in the cylinder increases when the liquid piston rises, while the exhaust valve is open, which seems to indicate that the exhaust valve generates significant pressure losses.

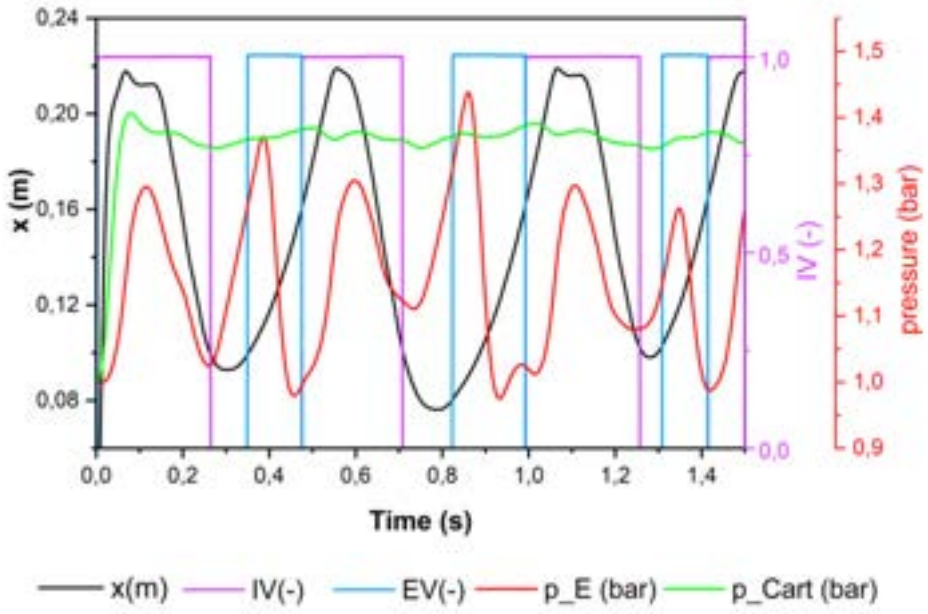

Figure 8. Liquid piston displacement, state of the valves and pressure in the expansion cylinder.

Figure 9 compares the experimental and theoretical pressure evolutions in the compression cylinder (Figure 9 (a)) and in the expansion cylinder (Figure 9 (b)). For the compression cylinder, it can be seen that the experimental pressure is slightly higher than the simulation pressure during the discharge phase, with a peak that is due to pressure drops around the exhaust valve. For the expansion cylinder (Figure 9 (b)), the theoretical results predict isobaric inlet, then isentropic expansion, followed by isobaric outlet and finally isentropic dead volume recompression. As mentioned earlier, the evolution of the experimental pressure *p_E* is significantly different, due to the pressure losses in the inlet line and in the valves, and the time needed for the complete opening and closing of these valves. Despite these problems, it can be seen that the theoretical cycle time corresponds to the experimental cycle time.

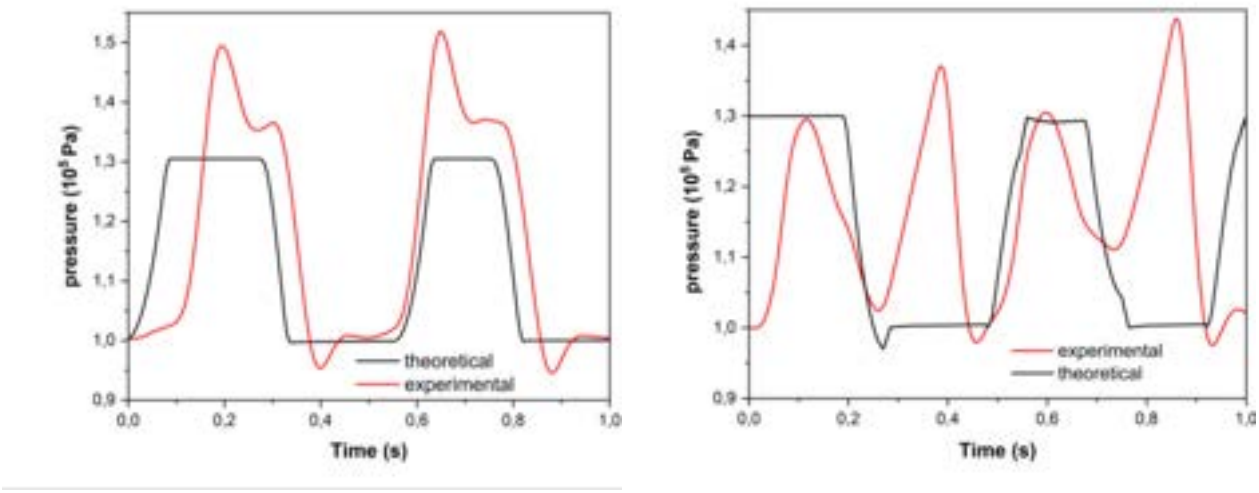

Figure 9. Instantaneous pressure in the compression cylinder (a) and the expansion cylinder (b).

3.2.4. Indicator diagrams

Figure 10 presents the (*p, V*) indicator diagram for the compression (blue) and expansion (red) cylinder. The area included in the closed curve of the (*p, V*) diagram corresponds to the work of the pressure forces on the liquid piston. A clockwise loop corresponds to a negative work, meaning that the working fluid produces mechanical work on the liquid piston, while a counter-clockwise loop corresponds to a positive work, meaning that the working fluid receives mechanical work from the liquid piston. Obviously, the two diagrams do not resemble the theoretical diagrams composed of almost isobaric and isentropic transformations. Normally, the compression cylinder indicator diagram should be a single counter-clockwise loop and the expansion cylinder indicator diagram should be an identical but clockwise loop.

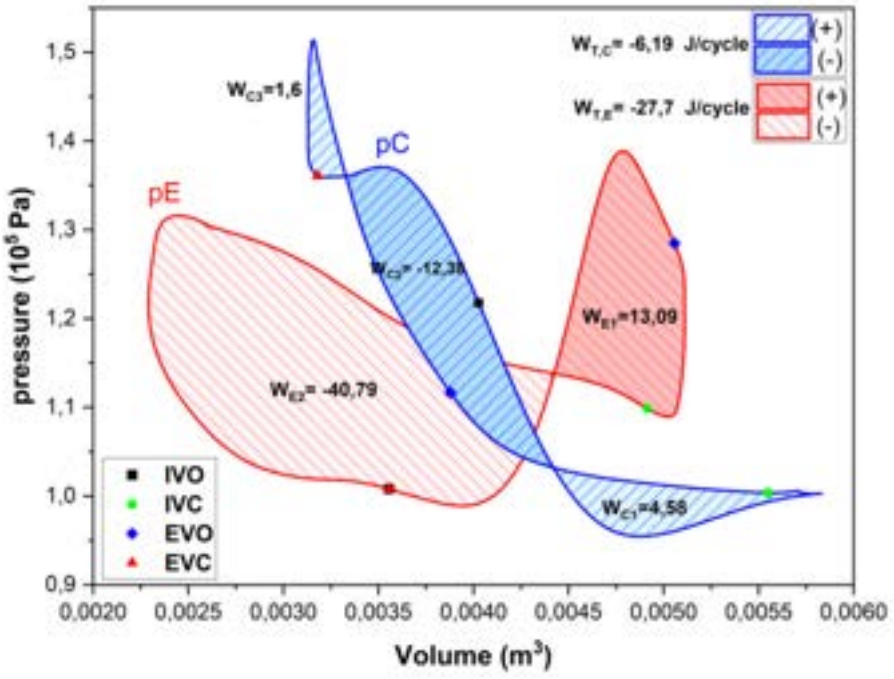

Figure 10. Compression (blue) and expansion (red) cylinder indicator diagram.

Experimentally, it can be seen that the working fluid in the compression cylinder globally gives up work to the liquid piston and the working fluid in the expansion cylinder receives mechanical work from the liquid piston during some phases of the cycle, around the BDC. There are many reasons for this.

As far as the expansion cylinder is concerned, at the moment when, simultaneously, the exhaust valve closes and the intake valve opens, the pressure *p_E* does indeed increase dramatically but with some delay, meaning that the inlet valve does not open instantaneously. But as the piston descends from its TDC towards its BDC, the pressure *p_E*, which should theoretically remain constant at its maximum value, decreases due to pressure losses in the intake line as mentioned above. When the intake valve closes, there should be an isentropic expansion of the fluid. However, the experimental pressure increases. This is due to the fact that the inlet valve

does not close instantaneously, meaning that compressed air goes on entering the expansion cylinder after the EVC point indicated on the red loop of figure 10. The liquid piston being nearly at rest around the BDC, the pressure increases dramatically. Similarly, when the exhaust valve opens around the BDC, the pressure *p_E* does not drop immediately to the value of atmospheric pressure, as would be expected in the theoretical cycle, but instead begins to rise and then gradually falls. This phenomenon is attributable firstly to the time required for the discharge valve to open fully, as it does not open completely instantaneously at the time shown in the diagrams, and secondly to the pressure drop generated by this valve.

As far as the compression cylinder is concerned, it can be assumed that the exhaust valve does not close instantaneously at the EVC point shown in the diagrams in figure 10. Compressed air would therefore enter the compression cylinder even as the liquid piston begins its stroke towards its BDC, leading to a cycle producing mechanical work instead of a cycle receiving mechanical work. In the case where there is no back pressure at the exit of the compression space (figure 11), the discharge of the compressed air is done towards the atmosphere. In figure 11, it can be seen that the indicator diagram (*p, V*) of the compression cylinder rotates counter-clockwise, which means that mechanical work is absorbed by the working fluid, and the expansion cylinder rotates clockwise, which means that mechanical work is supplied by the working fluid. However, despite the early opening of the compression cylinder exhaust valve, the pressure drops around this valve are significant, as the discharge is at a pressure *p_C* much higher than atmospheric pressure, especially when the piston has a high speed, around its mid-stroke. It can be seen that as the piston approaches its top dead centre, the pressure drop decreases and the pressure *p_C* falls towards atmospheric pressure. The mechanical work supplied by the expansion cylinder is more than twice as great as that absorbed by the compressor and the net work is 16.4 J/cycle at a pressure of just over 1.2 bar. The indicator diagrams of figure 11 confirms what the modelling has predicted, that is the possibility to design a free liquid piston Ericsson engine. Indeed the inertia of the liquid piston allows to achieve the compression of the air in the compression cylinder even when the pressure in the compression is higher than the one in the expansion cylinder, the liquid piston moving against the pressure forces.

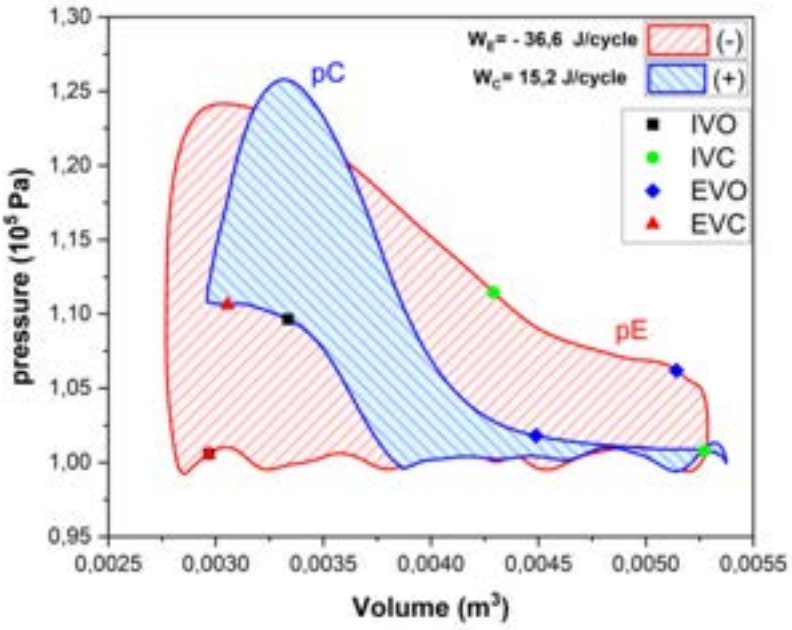

Figure 11. Compression (blue) and expansion (red) cylinder indicator diagram without back-pressure at the compression cylinder outlet.

Finally, it should be mentioned that, although the volumes swept by the liquid piston are obviously identical in the compression and expansion cylinders, the indicator diagrams in figure 10 and figure 11 show that there may be a very slight imbalance between the 2 branches of the liquid piston. The average volume of the compression cylinder is slightly higher than the average volume of the expansion cylinder, which means that the average height of the water in the E-arm of the engine is slightly higher than the average height in the C-arm.

3.3. Hot tests

Different tests were carried out at hot temperatures, up to 200°C.

The results of the experimental tests showed that the temperature does not affect the frequency or the stroke of the free liquid piston, as shown in figure 12, which represents the temporal evolution of the liquid piston displacement for different air inlet temperatures in the expansion cylinder, at the same inlet pressure of 1.3 bar. It can be seen that for the different temperature levels, the amplitude is almost the same. If, for example, we take the displacement for a temperature of 20°C and 190°C, we notice that it is almost the same stroke that is covered by the liquid piston, with the same cycle frequency, as predicted by the theoretical model.

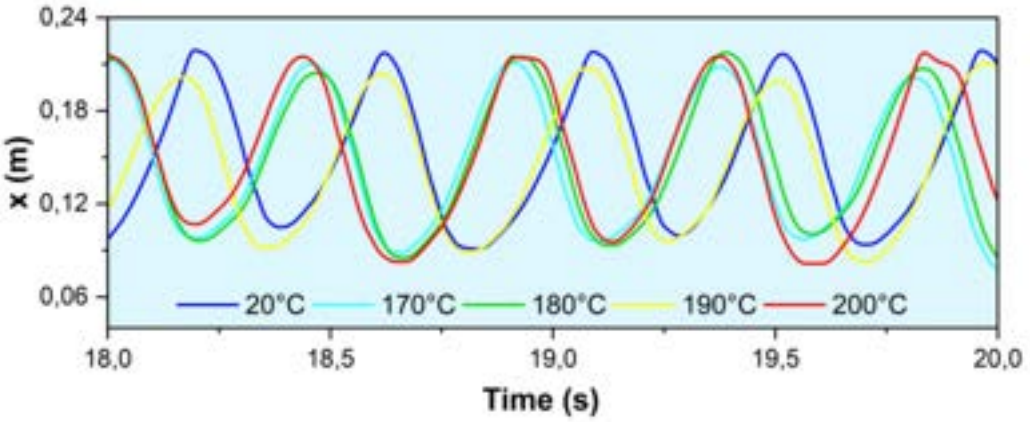

Figure 12. Liquid piston displacement for different inlet temperatures of the expansion cylinder.

The hot tests were carried out in a completely satisfactory manner, without any technical problems. At most, some fogging was observed on the wall of the Pyrex tube, due to the weak evaporation-condensation phenomena of the water in the liquid piston at high temperatures of the air admitted into the expansion cylinder.

4. Conclusion

The results of tests carried out on an original configuration of the Ericsson free liquid piston engine were presented. In its current configuration, the test bench did not allow for 'engine' operation. Tests in 'motored engine' mode using an external compressed air supply showed that it is possible to obtain stable engine operation, provided that the operational parameters (supply pressure, valve opening/closing settings) are carefully chosen. The oscillation frequency of the free piston and its stroke are in good agreement with the results of the theoretical model. The hot tests also demonstrated the good operation of the engine at high temperatures without encountering any technical problems. The examination of the experimental results highlighted the improvements to be made to the test bench.

Nomenclature

IV	state of the inlet valve of the expansion cylinder
IVC	inlet valve closure
IVO	inlet valve opening
EV	state of the exhaust valve of the expansion cylinder
EVC	exhaust valve closure
EVO	exhaust valve opening
p_admE	instantaneous pressure at the inlet of the expansion cylinder, bar
p_C	instantaneous pressure in the compression cylinder, bar
p_Cart	instantaneous pressure at the electrical heater inlet, bar
p_E	instantaneous pressure in the expansion cylinder, bar
p_echpC	instantaneous pressure at the outlet of the compression cylinder, bar
x	liquid piston instantaneous position, m

Subscripts and superscripts

C	compression space
E	expansion space
H	heater
R	heat recovery exchanger
T	external expander

References

[1] Finkelstein T., Organ A. J., Air engines, London: Professional Engineering Publishing Ltd (2001).

[2] Ndamé Ngangué M., Stouffs P., Dynamic simulation of an original Joule cycle liquid pistons hot air Ericsson engine, Energy, 190 (2020), 116293.

[3] Bell M. A., Partridge T., Thermodynamic design of a reciprocating Joule cycle engine, Proc Instn Mech Engrs Part A J Power Energy (2003), vol. 217, pp. 239–246.

[4] Moss R. W., Roskilly A. P., Nanda S. K., Reciprocating Joule-cycle engine for domestic CHP systems, Appl. Energy (2005), vol. 85, pp. 169–185.

[5] Stanciu D., Bădescu V., Solar-driven Joule cycle reciprocating Ericsson engines for small scale applications. From improper operation to high performance, Energy Convers. Manag. (2017), vol. 135, pp. 101–116, doi: 10.1016/j.enconman.2016.12.070.

[6] Komninos N. P., Rogdakis E. D., Design considerations for an Ericsson engine equipped with high-performance gas-to-gas compact heat exchanger: A numerical study, Appl. Therm. Eng. (2018), vol. 133, pp. 749–763, doi: 10.1016/j.applthermaleng.2018.01.078.

[7] Creyx M., Delacourt E., Morin C., Desmet B., Peultier P., Energetic optimization of the performances of a hot air engine for micro-CHP systems working with a Joule or an Ericsson cycle, Energy (2013), vol. 49, no. 1, pp. 229–239, 2013, doi: 10.1016/j.energy.2012.10.061.

[8] Van De Ven R. J. D., Li P. Y., Liquid piston gas compression, Appl. Energy (2009), 86, 2183–2191, doi: 10.1016/j.apenergy.2008.12.001.

[9] Patil V. C., Acharya P., Ro P. I., Experimental investigation of heat transfer in liquid piston compressor, Appl. Therm. Eng. (2018), vol. 146, pp. 169–179, doi: 10.1016/j.applthermaleng.2018.09.121.

[10] Kumar N., Hofacker M., Barth E., Design and Control of a Free-Liquid-Piston Engine Compressor for Compact Robot Power, Vanderbilt Undergrad. Res. J. (2013), vol. 9, pp. 0–6, doi: 10.15695/vurj.v9i0.3796.

[11] Mikalsen R., A. P. Roskilly A. P., A review of free-piston engine history and applications, Appl. Therm. Eng. (2007), 27, 2339–2352, doi: 10.1016/j.applthermaleng.2007.03.015.

[12] Johnson T. A., Leick M. T., Moses R. W., Experimental Evaluation of a Prototype Free Piston Engine - Linear Alternator (FPLA) System, SAE Technical Paper (2016), doi: 10.4271/2016-01-0677.

[13] Xu Z., Chang S., Prototype testing and analysis of a novel internal combustion linear generator integrated power system, Appl. Energy (2010) vol. 87, no. 4, pp. 1342–1348, doi: 10.1016/j.apenergy.2009.08.027.

[14] Jia B., Wu D., Smallbone A., Lawrence C., Paul A., Design, modelling and validation of a linear Joule Engine generator designed for renewable energy sources, Energy Convers. Manag. (2018), vol. 165, pp. 25–34, doi: 10.1016/j.enconman.2018.03.050.

[15] Wang J., Feng H., Zhang Z., Wu L., Yang F., Development of a coupling model and parametric analysis of an opposed free-piston engine linear generator, Appl. Therm. Eng. (2023) vol. 219, doi: 10.1016/j.applthermaleng.2022.119205.

[16] Li H. et al., Development of a Performance Analysis Model for Free-Piston Stirling Power Convertor in Space Nuclear Reactor Power Systems, Energies (2022), vol. 15, no. 3, p. 915, doi: 10.3390/en15030915.

[17] Jiang Z., Yu G., Zhu S., Dai W., Luo E., Advances on a free-piston Stirling engine-based micro-combined heat and power system, Appl. Therm. Eng. (2022), vol. 217, doi: https://doi.org/10.1016/j.applthermaleng.2022.119187.

[18] Zare S.,Tavakolpour‐Saleh A., Free piston Stirling engines: A review, Int. J. Energy Res.(2020), vol. 44, no. 7, pp. 5039‐5070, doi: 10.1002/er.4533.

[19] West C. D., Liquid Piston Stirling Engines, (1983) Van Nostrand Reinhood Company Inc.

[20] Romanelli A., The Fluidyne engine, Am. J. Phys. (2019), vol. 87, no. 1, pp. 33–37, doi: 10.1119/1.5078518.

[21] Chouder R., Stouffs P., Benabdesselam A., Etude d'une nouvelle configuration de moteur Ericsson à piston liquide libre, Actes du Congrès de la Société Française de Thermique (2022), 52.

[22] Chouder R., Benabdesselam A., Stouffs P., Modeling results of a new high performance free liquid piston engine, Energy (2023), 125960, doi:10.1016/j.energy.2022.125960

[23] Pescara R. P., Motor compressor apparatus, Patent N° 1 657 641 (1928).

[24] Pescara C., Générateurs à pistons libres Pescara, Rev. Tech. de l'association des ingénieurs de l'Ecole Breguet, 69 (1963).

[25] Chouder R., Ndamé Nguangué M., Stouffs P., Benabdesselam A., Moteur Ericsson à piston liquide libre : premiers résultats expérimentaux, accepted for presentation, Congrès de la Société Française de Thermique, (2023).

Energy analysis of a hybrid top/bottoming ORC-based CHP configuration for residential applications

João S. Pereira* and José B. Ribeiro

Univ Coimbra, ADAI, Department of Mechanical Engineering, Coimbra Portugal,
joao.pereira@dem.uc.pt

Abstract:

The development of ORC-based micro-CHP systems to retrofit the current combi-boilers is receiving noticeable attention from research centres and companies due to the huge dimension of the potential market. Recognizing the importance that the evaporator has on the technological/ commercial success of these systems, and instead of avoiding the problem through the adoption of alternative restricting solutions (i.e.: indirect vaporization process), it seems reasonable to face the challenges associated with the development of a specifically designed ORC-evaporator capable to directly use the high-temperature combustion gases to perform the vaporization of the working fluid. In an attempt to overcome those challenges, that are believed to be preventing the widespread use of these systems, this paper presents and discusses some of its main design principles. From those principles emerged a hybrid (top/bottoming) CHP configuration in which the thermal energy is produced stepwise: firstly in the ORC condenser and then in a post-heater, that is integrated into the ORC-evaporator. A model of this configuration was developed to determine the fraction of the CHP water heating process performed in the post-heater that maximizes the primary energy savings and ORC net power output for a wide range of CHP operating conditions. When compared to a standard CHP configuration, this solution show benefits for the greater part of those conditions. Besides the performance benefits shown and solving the safety issue posed by the ORC-evaporator requirements, this configuration has an additional positive side effect: the decrease of the combustion gases' temperature before they reach the organic fluid heat-exchanger section in the ORC-evaporator that leads to a reduction of the risk its thermal degradation.

Keywords:

Organic Rankine Cycle, Hybrid CHP configuration, ORC-evaporator, Direct vaporization arrangement.

1. Introduction

The combined production of heat and power (CHP) is one of the major alternatives to traditional energy production systems in terms of energy savings and environmental conservation [1–3]. The most promising target for the micro-CHP systems lies in the residential sector given the huge dimension of the market [4,5]. At this scale, and for solutions attempting to retrofit the wall-mounted combi-boilers that are currently applied in residential dwellings, where the noise, vibrations, weight, dimension and reliability are crucial features, the Organic Rankine Cycle (ORC) based technology appears to be the most promising [6,7]. Even if it may seem surprising, in its basic configuration and from a thermodynamic point of view, an ORC is almost identical to a reverse refrigeration cycle in which the throttling valve is replaced by a pump, the condenser works as an evaporator, the compressor works as an expander and the evaporator as a condenser. From a technological point of view, the ORC-based micro-CHP system may share with the refrigeration devices their main component, the compressor (converted to an expander in the micro-CHP [8,9], while the pump and the condenser are off-the-shelf components of, e.g., coffee machines and HVAC systems, respectively [10]. This share of technology presents obvious benefits from the point of view of reliability, maintenance and cost that, partially due to the existence of alternative moving parts in Stirling Cycle and spark-ignited internal combustion systems, are envisaged to present less noise, vibrations and maintenance requirements [11,12].

Among the ORC-based micro-CHP main components, the evaporator is the only one that, due to its specificities (e.g. working with a vaporizing fluid at relatively high pressures, typically above 10 bar), cannot be found directly on the market or easily adapted from a mass production part of other appliances and needs to be specially designed and analyzed [13]. To partially avoid this question, the overwhelming majority of manufacturers and research centres choose to perform indirect vaporization of the working fluid. In those cases, an intermediate circuit with thermal oil, or slightly pressurized water, is commonly used to transfer the

energy from the high-temperature combustion gases to the organic fluid, being its vaporization performed in a plate-type heat exchanger [14,15]. In this way, it is not only possible to reduce the pressure but also to ensure the existence of a continuous liquid phase in the heat exchanger that is directly exposed to the high-temperature combustion gases, from which a significant reduction in the design requirements is obtained. Moreover, such a solution is expected to perform better control of the temperature of the working fluid vaporization process that can reduce the risk of its thermal degradation [16,17]. In comparison with direct vaporization, in which the phase change of the organic fluid occurs in the part of the evaporator directly exposed to the combustion gases, the aforementioned CHP configuration demands the inclusion of, at least, an additional heat-exchanger, a circulating pump, an expansion vessel, and the necessary tubes and accessories from which an increase of the system dimension and thermal inertial are expected. As an obvious consequence, such micro-CHP strongly reduces its ability to face the intermittence of the hot-water demands, with multiple short-time requests, that characterize one of the operation modes of the boilers [18].

Recognizing the importance that the evaporator has on the technological success of ORC-based micro-CHP systems, and instead of avoiding the problem through the adoption of restricting solutions (indirect vaporization [13]), it seems reasonable to face the challenges associated with the development of a specifically designed ORC-evaporator capable to directly use the combustion gases to perform the vaporization of the working fluid [19,20]. In an attempt to overcome those challenges and fulfil this technological gap, that is believed to be preventing the widespread use of these systems, this paper presents a solution for such evaporators. This solution leads to a hybrid (topping/ bottoming) CHP configuration in which the useful thermal energy is produced stepwise, firstly in the ORC condenser and then in a post-heater directly with hot combustion gases [21]. The benefits arising from its use, in what refers to the primary energy savings, cycle efficiency, net power output and risk of the organic fluid thermal degradation, are illustrated and discussed as a function of several CHP operating (design) conditions.

2. Direct vaporization ORC-evaporator

The gas burner with the characteristics required for the ORC-evaporator was promptly found in the market and is shown in Figure 1-a. Contrarily, the heat exchanger needs to be specifically designed. A schematic representation of its configuration can be seen in Figure 1-b. In this, the hot combustion gases flow around the tubes of the heat exchanger, within which is the organic fluid, in what can be described as a mixed counter flow/cross-flow arrangement. The use of high-temperature insulation material sleeves (presented in brown in Figure 1-b) prevents the energy transfer along the radial direction from the central combustion chamber to the helical coils to keep the counter-flow arrangement nature. Besides the mentioned characteristics, this configuration contains a water-cooled baffled sleeve to be used as a cold surrounding of the gas-burner head to ensure its proper and safe operation. In this, the water flows through the sleeve after being pre-heated in the ORC condenser, reducing the organic fluid condensing temperature in this component, which is beneficial for the cycle efficiency. In addition, this baffle sleeve can also reduce the risk of organic fluid thermal degradation because it decreases the combustion gases' temperature before they reach the ORC heat-exchanger part.

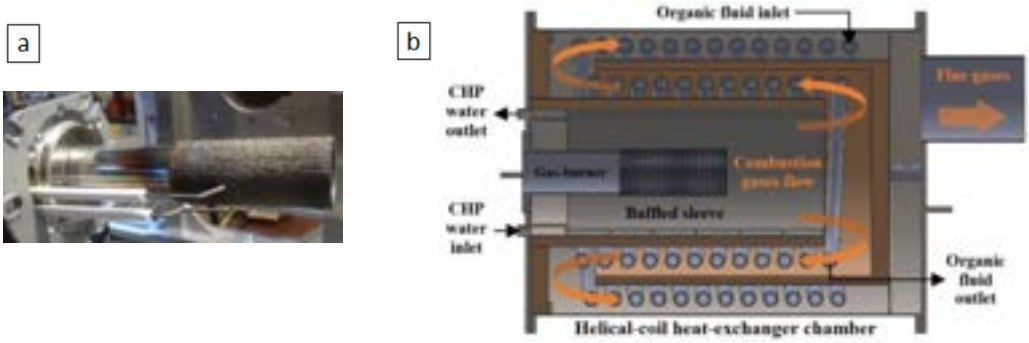

Figure 1: Photograph of the premix gas-burner head with the ignition spark and flame detector rod (a) and the schematic representation of the ORC-evaporator design with the water baffled sleeve (b).

3. Hybrid ORC-based CHP configuration

The schematic configuration of the micro-CHP system, derived from the integration of the newly designed ORC-evaporator, is shown in Figure 2. This can be described as a hybrid (topping/bottoming) CHP configuration [21] since the useful thermal energy is transferred to the water stepwise - before and after the production of work in the prime mover (expander).

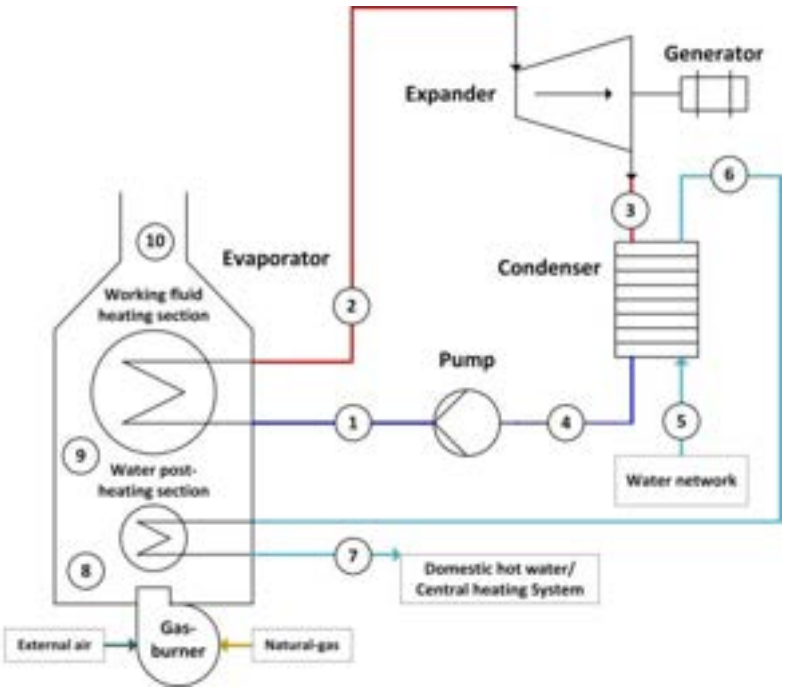

Figure 2: Schematic diagram of the hybrid CHP configuration with the new ORC-evaporator

The T-s diagrams of the hybrid and a standard ORC-based CHP configuration, including the combustion gases and water streams, can be found in Figure 3 using the organic fluid r245fa. For the same CHP outlet water temperature, the condensing pressure (and the temperature) of the ORC in this hybrid configuration may be significantly lower. The well-known advantages of such a decrease in the condensing pressure are an increase in the ORC specific power (net power per unit of working fluid mass flow rate) and an increase in the cycle efficiency. However, these advantages need to be considered against an inevitable reduction of the ORC working fluid mass flow rate that can partially, or totally, hinder them.

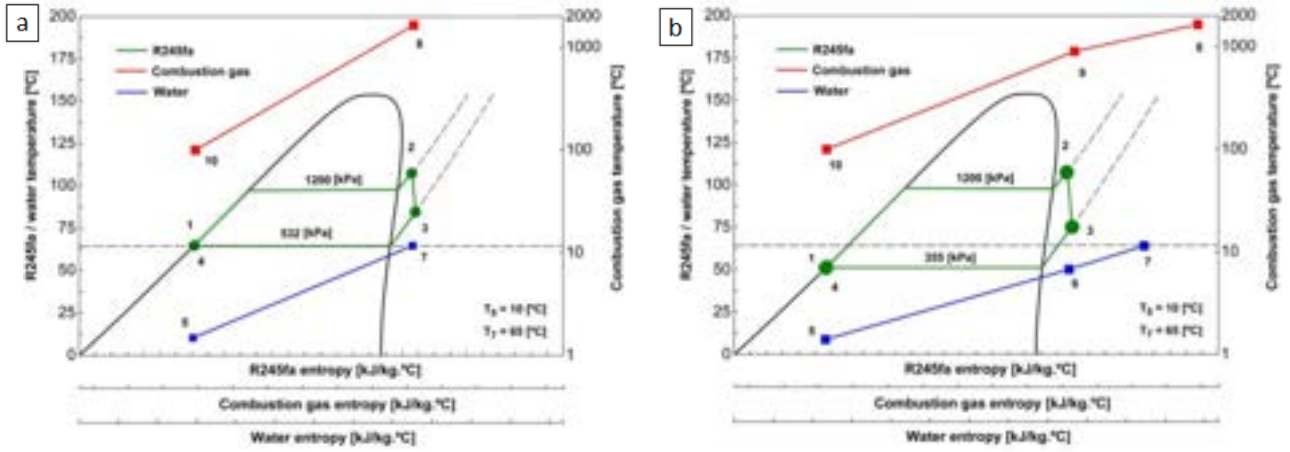

Figure 3: T-s diagrams of R245fa ORC-based CHP configurations: a) standard and b) hybrid

In this configuration, the amount of energy transferred to the water in the post-heating section is an additional design parameter that needs to be analyzed. This parameter can be defined by equation (1) where θ can be seen as the fraction of the water heating process that is done in the water post-heating section of the ORC-evaporator. To perform such analysis, a physical model, where all the main ORC components are considered working on their nominal conditions, was developed using Matlab® and REFPROP thermodynamic database [22]. The model assumes no heat or pressure losses as well as neglects the electro-mechanical inefficiencies for both the pump and expander generator.

$$\theta = \frac{T_7 - T_6}{T_7 - T_5} \times 100 \qquad (1)$$

The input parameters of this model, with the values used or the intervals within they are allowed to vary (in case of a parametric analysis), are listed in Table 1. Within the list of the input parameters is the water post-heating fraction (θ), defined by equation (1), which can be seen as the fraction of the water heating process that is done in the ORC-evaporator water post-heating section. A value of $\theta = 0\%$ refers to a standard CHP system in which all the water heating process occurs in the ORC condenser, while a value of $\theta = 100\%$ refers to a situation in which there is no cogeneration, or the ORC system is not working.

Table 1. Input parameters of the CHP physical model (based on [21]).

Model parameter	Symbol	Units	Value
Working fluid	-	-	R245fa
Expander isentropic efficiency	η_T	%	0,75
Pump isentropic efficiency	η_P	%	0,5
Condenser efficiency	η_{CHE}	%	0,98
Evaporator efficiency	η_{EHE}	%	0,9
Maximum ORC pressure	p_{max}	kPa	1200
Working fluid superheating degree	ΔT_2	^oC	10
Water pressure	p_w	kPa	300
CHP inlet water temperature	T_5	^oC	10 [a]
CHP outlet water temperature	T_7	^oC	65 [a]
Water post-heating fraction	θ	%	$[0, 50]$
End-user thermal power demand	Q_w	kW	25
Atmospheric pressure	p_{atm}	kPa	101,325
Combustion gases adiabatic flame temperature	T_{flame}	^oC	1540 [b]
Combustion gases' mass flow rate	$\dot{m}_{cg}$	kg/s	0,0137 [b]
Combustion products' mass fraction	m'_{cg_j} [c]	kg_j/kg_{fuel} [c]	[b, d]

[a] Isolated values were used to simulate a specific CHP operating condition (in accordance with the standard [23]) while the intervals were used to perform a system's parametric analysis. [b] The presented values were obtained for the complete combustion of natural gas with 30% of the excess air (according to the gas-burner manufacturer recommendation as shown in section 2.3). [c] $j = \{CO_2;\ H_2O;\ O_2;\ N_2\}$. [d] $\{m'_{cg,CO_2} = 0{,}123;\ m'_{cg,H_2O} = 0{,}093\ ; m'_{cg,N_2} = 0{,}734; m'_{cg,O_2} = 0{,}051\}$.

The way how the properties of the working fluid, the water or the combustion gases are evaluated at each of the CHP key points is presented in Table 2. To avoid problems related to the pinch-point in the ORC-condenser, the model assumes that the condensing temperature is limited (inferiorly) by the water temperature at the ORC-condenser exit (see Table 2 where, for point 3, at the expander exit, the pressure is equal to the saturation value defined by the water temperature at the condenser exit, point 6). The knowledge of the enthalpy at those key points allows solving the energy balance equations as they are shown, for each of the CHP main components, in Table 3 from which the CHP behaviour can be inferred and the usual performance indicators can be obtained.

Table 2. Evaluation of the thermodynamic properties at different CHP key points.

# [a]	$p\ [kPa]$	T [°C]	$h\ [kJ/kg]$	$s\ [kJ/kg]$	State [b]
1s [c]	$p_{1i} = p_{max}$	-	$h_{1i} = h(p_{1i}, s_{1i})$	$s_{1i} = s_4$	–
1	$p_1 = p_{max}$	$T_1 = T(p_1, h_1)$	$h_1 = h_4 + \left({}^{h_{1i} - h_4}/_{\eta_P}\right)$	$s_1 = s(T_1, h_1)$	CL
2	$p_2 = p_{max}$	$T_2 = T_{sat}(p_2) + \Delta T_2$	$h_2 = h(T_2, p_2)$	$s_2 = s(T_2, p_2)$	SH
3s [c]	$p_{3i} = p_3$	-	$h_{3i} = h(p_{3i}, s_{3i})$	$s_{3i} = s_2$	–
3	$p_3 = p_{sat}(T_6)$	$T_3 = T(p_3, h_3)$	$h_3 = h_2 - \eta_T \times (h_2 - h_{3i})$	$s_3 = s(h_3, p_3)$	SH
4	$p_4 = p_3$	$T_4 = T(p_4, x_4)$	$h_4 = h(T_4, p_4)$	$s_4 = s(T_4, x_4)$	SL
5	$p_5 = p_w$	T_5	$h_5 = h(T_5, p_5)$	–	–
6	$p_6 = p_w$	$T_6 = T_7 - \theta \times (T_7 - T_5)$	$h_6 = h(T_6, p_6)$	–	–
7	$p_7 = p_w$	T_7	$h_7 = h(T_7, p_7)$	–	–
8	$p_8 = p_{atm}$	$T_8 = T_{flame}$	$h_8 = h(T_8, p_8)$	–	–
9	$p_9 = p_{atm}$	$T_9 = T(p_9, h_9)$	$h_9 = h_8 - \dot{Q}_{w_{PH}}/\dot{m}_{cg}$	–	–
10	$p_{10} = p_{atm}$	$T_{10} = T(p_{10}, h_{10})$	$h_{10} = h_9 - \dot{Q}_{in}/\dot{m}_{cg}$	–	–

[a] In accordance with Figure 2. [b] CL – Compressed liquid; SL - Saturated liquid; SH – Superheated vapour. [c] Correspond to an intermediate calculation for the isentropic thermodynamic condition.

Table 3. Power balance equations of the CHP system.

CHP component [a]	Stream	Power balance
Pump	ORC working fluid	$\dot{W}_{in} = \dot{m}_f \times (h_1 - h_4)$
Working fluid heating section (ORC-evaporator)	ORC working fluid	$\dot{Q}_{in} = \dot{m}_f \times (h_2 - h_1)$
	Combustion gases	$\dot{Q}_{cg_f} = \left(\dot{m}_{cg} \times (h_9 - h_{10})\right)/\eta_{EHE}$
Water post-heating section (ORC-evaporator)	Water	$\dot{Q}_{w_{PH}} = \dot{m}_w \times (h_7 - h_6)$
	Combustion gases	$\dot{Q}_{cg_{PH}} = \left(\dot{m}_{cg} \times (h_8 - h_9)\right)/\eta_{EHE}$
Expander	ORC working fluid	$\dot{W}_{out} = \dot{m}_f \times (h_2 - h_3)$
Condenser	ORC working fluid	$\dot{Q}_{out} = \dot{Q}_{w_{CHE}}/\eta_{CHE}$
	Water	$\dot{Q}_{w_{CHE}} = \dot{m}_w \times (h_6 - h_5)$
Hybrid CHP system	Natural gas/air mixture	$\dot{Q}_{CHP} = \dot{Q}_{cg_f} + \dot{Q}_{cg_{PH}}$
	Water	$\dot{m}_w = \dot{Q}_w/(h_7 - h_5)$
	ORC working fluid	$\dot{m}_f = \dot{Q}_{out}/(h_3 - h_4)$

[a] In accordance with Figure 2.

Among these indicators are the ORC efficiency (η_{ORC}), defined as shown in equation (2), the ORC net power output ($\dot{W}_{net}$), see equation (3), and the Primary Energy Savings (PES), as defined by the EU directive [24], that can be calculated using equation (4). In this, η_{REF_H} and η_{REF_E} are the harmonized efficiency reference value for separate production of heat (for the purpose of this paper was assumed 0,9 considering that the thermal energy produced is in the form of hot water from a natural-gas boiler manufactured before 2016 [25]) and the harmonized efficiency reference value for separate production of electricity (for this paper was assumed 0,445, considering that the electrical energy is produced in a natural-gas fueled power plant built before 2012 and an aggregated correction factor that includes the climatic specificities and the grid losses for low-voltage level end-users [25]). The values of η_{CHP_H} and η_{CHP_E}, that represents the thermal and electrical efficiencies of the CHP systems, respectively, are calculated by equation (5). Besides that, two non-dimensional parameters, the $rPES$ and the $r\dot{W}_{net}$, that relate the values obtained for the hybrid configuration (CHP system with $\theta \neq 0\%$) with those obtained for the standard configuration (CHP system with $\theta = 0\%$), see equation (6), and the reduction of the combustion gases temperature associated with the energy transfer in the water post-heating section of the ORC-evaporator ($T_8 - T_9$), are also retrieved from the model.

$$\eta_{ORC} = \frac{\dot{W}_{out} - \dot{W}_{in}}{\dot{Q}_{in}} \times 100 \quad (2)$$

$$\dot{W}_{net} = \dot{W}_{out} - \dot{W}_{in} \quad (3)$$

$$PES = \left(1 - \left(\frac{1}{\left(\frac{\eta_{CHP_H}}{\eta_{REF_H}} + \frac{\eta_{CHP_E}}{\eta_{REF_E}}\right)}\right)\right) \times 100 \quad (4)$$

$$\eta_{CHP_H} = \frac{\dot{Q}_{wPH} + \dot{Q}_{wCHE}}{\dot{Q}_{CHP}}, \qquad \eta_{CHP_E} = \frac{\dot{W}_{out} - \dot{W}_{in}}{\dot{Q}_{CHP}} \quad (5)$$

$$rPES = \frac{PES\ (\theta)}{PES\ (\theta = 0)}, \qquad r\dot{W}_{net} = \frac{\dot{W}_{net}(\theta)}{\dot{W}_{net}(\theta = 0)} \quad (6)$$

4. Model results

The variation's effect of θ over the net specific work, the efficiency (η_{ORC}) and the organic fluid mass flow rate ($\dot{m}_f$) is shown in Figure 4-a. As expected, mainly due to the increase of the pressure difference in the working fluid when passing through the expander, the net specific work and the efficiency increased with θ. However, since an increasing part of the water heating process is shifted from the ORC condenser to the post-heating section, an inevitable reduction of the working fluid mass flow rate is observed. The non-despicable result of these antagonistic variations is presented in Figure 4-b, where the values of the primary energy savings (PES) and the ORC net power output ($\dot{W}_{net}$) are shown as a function of θ. The maximum positive variations of PES and $\dot{W}_{net}$ are 23% and 7% for values of θ equal to 33% and 21%, respectively. The shifting of part of the water heating process from the ORC condenser to the post-heating section of the ORC-evaporator allows for solving a safety issue that will permit the adoption of a compact ORC-evaporator design and also induces positive effects in the CHP performance increasing not only the efficiency (an increase of PES) and economic (an increase of $\dot{W}_{net}$) figures in comparison with the standard configuration (for which $\theta = 0\%$).

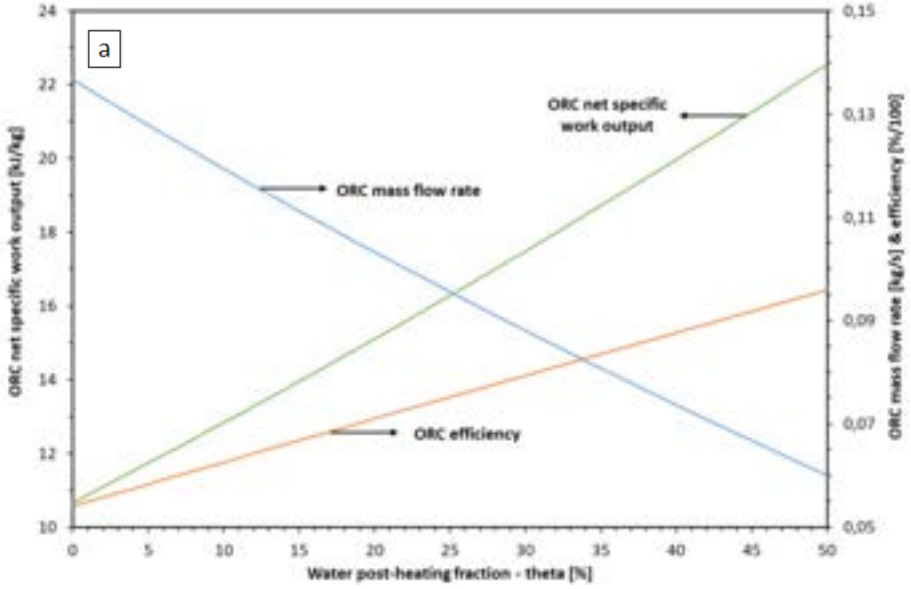

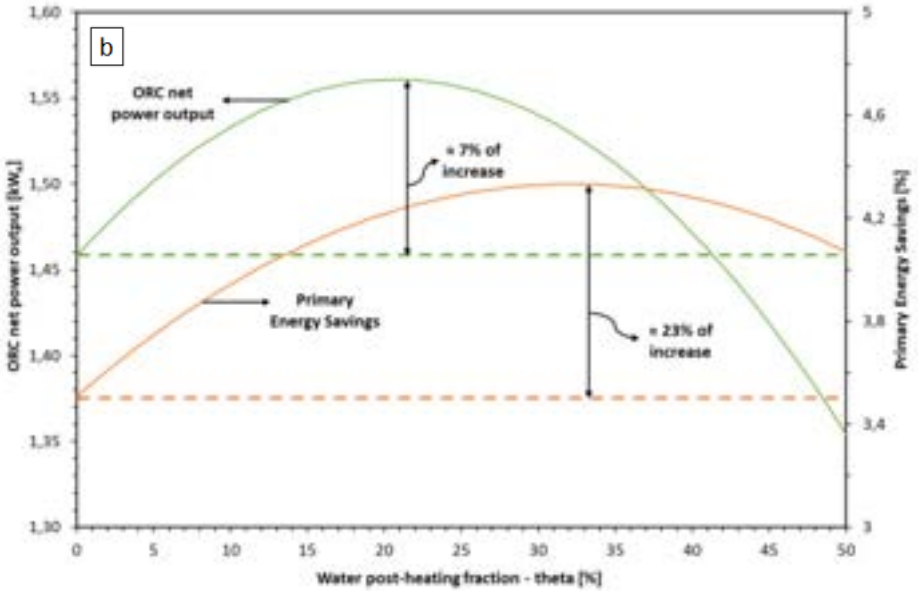

Figure 4: a) ORC net specific work, $\dot{m}_f$ and η_{ORC} as function of θ, b) PES and $\dot{W}_{net}$ as function of θ.

Moreover, the proposed hybrid configuration presents an additional advantage of reducing the risk of organic fluid thermal degradation that arises from a significant temperature reduction of the combustion gases on their passage through the water post-heating section of the ORC-evaporator. The temperature reduction for the value of θ that maximizes PES is about 420 ºC and for the value of θ that maximizes $\dot{W}_{net}$ is about 260 ºC. It is also important to mention that this value can be increased without any efficiency or net power output losses regarding the standard CHP configuration ($\theta = 0\%$) to more than 500 ºC if θ is increased to around 41%, as shown in Figure 5.

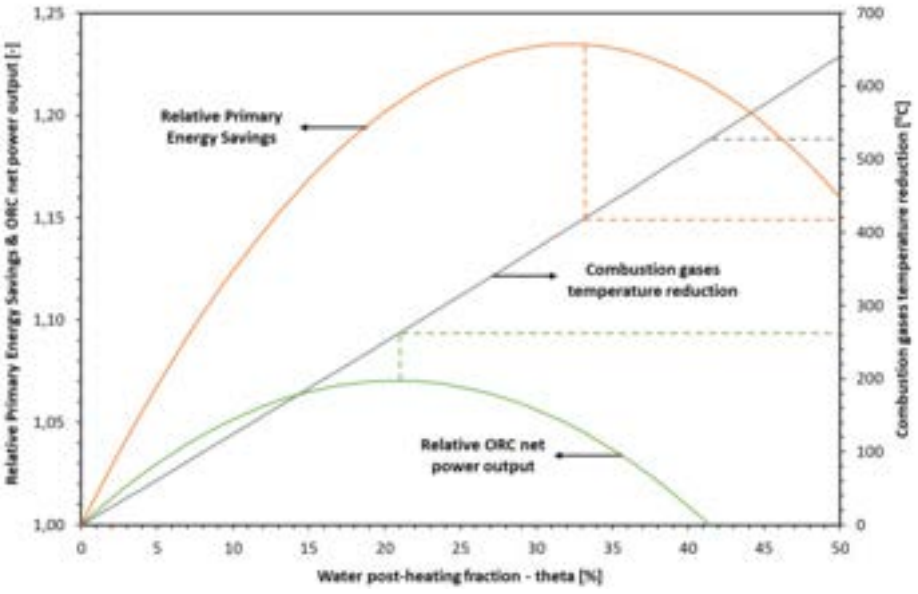

Figure 5: Relative value of $PES\ /\ \dot{W}_{net}$ and combustion gases temperature reduction as a function of θ.

5. Conclusion

The development of ORC-based micro-CHP systems aiming to retrofit the current combi-boilers demands small dimensions, high efficiency and high turn-down ratio evaporators. To achieve such requirements, the design principles of those ORC-evaporators should include: i) direct vaporization, ii) counter-flow arrangement and iii) pre-mixed gas burners. A solution for an ORC-evaporator accomplishing these specifications was presented. That solution showed the need for a cold surrounding on the gas-burner head. This last design principle led to the development of an ORC-evaporator where part of the energy contained in the combustion gases is transferred to the water before they reach the ORC working fluid heat exchanger. The integration of such ORC-evaporator in the CHP system gave origin to a hybrid configuration in which the useful thermal energy transferred to the water is done stepwise: firstly, in the ORC-condenser and then in

the water post-heating section of the ORC-evaporator. Such configuration, since it reduces the average temperature at the ORC-condenser, increases the cycle efficiency and the net specific work mainly because it increases the pressure ratio of the ORC cycle. Even taking into consideration the negative effect of the associated working fluid mass flow rate reduction, for a significant part of the CHP typical operating conditions, an increase of the primary energy savings by 23% and of the ORC net power output by 7% for values of θ equal to 33% and 21%, respectively, are shown for one of the most characteristic CHP operating condition (T_5 = 10 ºC, T_7 = 65 ºC). Furthermore, and for the same operating condition, the temperature reduction of the combustion gases in the water post-heating section of the ORC-evaporator can be as high as 520 ºC without no losses in the primary energy savings or the ORC net power output. This temperature reduction can help prevent, in a significant way, the occurrence of one of the major concerns associated with the direct vaporization of the ORC working fluid: the risk of thermal degradation. Therefore, the fraction of the CHP water heating process performed in the post-heater becomes a new design parameter that needs to be considered not only for the ORC-evaporator but for all of the CHP components which must be accordingly selected or designed.

The integration of part of the CHP water heating process in the ORC-evaporator led to a hybrid (topping/bottoming) configuration that not only solves a safety issue related to the gas-burner head overheating but also brings several (non-despicable) performance benefits and important reliability improvements for systems attempting to retrofit the current combi-boilers. Besides, this hybrid configuration applies to all the situations where the difference between the temperature of hot and cold sources is smaller as when water from non-pressurized biomass (or other fuels) boilers is used to power those CHP systems.

Nomenclature

h	Enthalpy, kJ/kg	EHE	ORC-Evaporator
θ	Tetha, %	f	ORC working fluid
η	Efficiency, %	flame	Combustion flame conditions
$\dot{m}$	Mass flow rate, kg/s	fuel	Related to the fuel used
$\dot{Q}$	Thermal power, kW	H	Thermal reference
$\dot{W}$	ORC power output, kW_e	*s*	Isentropic
m'	Mass fraction, kg_i/kg_{fuel}	in	Inlet conditions
PES	Primary Energy Savings, %	max	Maximum value
T	Temperature, ℃	Net	Net value
p	Pressure, kPa	ORC	Organic Rankine cycle system
$r\dot{W}_{net}$	Relative ORC net power output -	out	Outlet conditions
$rPES$	Relative Primary Energy Savings, -	P	ORC-Pump
s	Entropy, $kJ/(kg.℃)$	PH	Post heater
x	Quality, -	REF	Reference value
$\Delta T2$	Superheating temperature, ℃	T	ORC-Expander
		w	End-user water circuit
Subscripts and superscripts			
$\{1 \dots 10\}$	CHP locations	***Acronym***	
atm	Atmospheric conditions	CHP	Combined heat and power
cg	Combustion gases	EU	European Union
CHE	ORC-Condenser	GHG	Greenhouse gases
CHP	Combined heat and power system	HVAC	Heating, ventilation and air conditioning
E	Electrical reference	ORC	Organic Rankine Cycle

References

[1] M. Bianchi, L. Branchini, A. De Pascale, A. Peretto, Application of environmental performance assessment of CHP systems with local and global approaches, Appl. Energy. 130 (2014) 774–782. https://doi.org/10.1016/j.apenergy.2014.04.017.

[2] Y. kuang Chen, I.G. Jensen, J.G. Kirkerud, T.F. Bolkesjø, Impact of fossil-free decentralized heating on northern European renewable energy deployment and the power system, Energy. 219 (2021) 119576. https://doi.org/10.1016/j.energy.2020.119576.

[3] International Energy Agency, Global CHP/DHC Data - Current Baseline, (n.d.). https://www.iea.org/chp/data/globalchpdhcdata-currentbaseline/ (accessed October 26, 2018).

[4] CODE 2 - Cogeneration Observatory and Dissemination Europe, Micro-CHP potential analysis - European level report, (2014). http://www.code2-project.eu/wp-content/uploads/D2.5-2014-12-micro-CHP-potential-analysis_final1.pdf.

[5] S. Pezzutto, S. Croce, S. Zambotti, L. Kranzl, A. Novelli, P. Zambelli, Assessment of the space heating and domestic hot water market in Europe—open data and results, Energies. 12 (2019). https://doi.org/10.3390/en12091760.

[6] B. Peris, J. Navarro-Esbrí, F. Molés, A. Mota-Babiloni, Experimental study of an ORC (organic Rankine cycle) for low grade waste heat recovery in a ceramic industry, Energy. 85 (2015) 534–542. https://doi.org/10.1016/j.energy.2015.03.065.

[7] E. Galloni, G. Fontana, S. Staccone, Design and experimental analysis of a mini ORC (organic Rankine cycle) power plant based on R245fa working fluid, Energy. 90 (2015) 768–775. https://doi.org/10.1016/j.energy.2015.07.104.

[8] M. Cambi, R. Tascioni, L. Cioccolanti, E. Bocci, Converting a commercial scroll compressor into an expander: Experimental and analytical performance evaluation, Energy Procedia. 129 (2017) 363–370. https://doi.org/10.1016/j.egypro.2017.09.234.

[9] S. Declaye, S. Quoilin, L. Guillaume, V. Lemort, Experimental study on an open-drive scroll expander integrated into an ORC (Organic Rankine Cycle) system with R245fa as working fluid, Energy. 55 (2013) 173–183. https://doi.org/10.1016/j.energy.2013.04.003.

[10] S. Quoilin, V. Lemort, J. Lebrun, Experimental study and modeling of an Organic Rankine Cycle using scroll expander, Appl. Energy. 87 (2010) 1260–1268. https://doi.org/10.1016/j.apenergy.2009.06.026.

[11] A. Algieri, P. Morrone, Energetic analysis of biomass-fired ORC systems for micro-scale combined heat and power (CHP) generation. A possible application to the Italian residential sector, Appl. Therm. Eng. 71 (2014) 751–759. https://doi.org/10.1016/j.applthermaleng.2013.11.024.

[12] R. Bracco, D. Micheli, R. Petrella, M. Reini, R. Taccani, G. Toniato, Micro-Organic Rankine Cycle systems for domestic cogeneration, Elsevier Ltd, 2016. https://doi.org/10.1016/B978-0-08-100510-1.00018-1.

[13] J.S. Pereira, J.B. Ribeiro, R. Mendes, G.C. Vaz, J.C. André, Development of a direct concept helical-coil evaporator for an ORC based micro-CHP system, Energy Procedia. 129 (2017) 474–478. https://doi.org/10.1016/j.egypro.2017.09.162.

[14] J.S. Pereira, J.B. Ribeiro, R. Mendes, G.C. Vaz, J.C. André, ORC based micro-cogeneration systems for residential application – A state of the art review and current challenges, Renew. Sustain. Energy Rev. 92 (2018) 728–743. https://doi.org/10.1016/j.rser.2018.04.039.

[15] M. Farrokhi, S.H. Noie, A.A. Akbarzadeh, Preliminary experimental investigation of a natural gas-fired ORC-based micro-CHP system for residential buildings, Appl. Therm. Eng. 69 (2014) 221–229. https://doi.org/10.1016/j.applthermaleng.2013.11.060.

[16] X. Dai, L. Shi, Q. An, W. Qian, Thermal stability of some hydrofluorocarbons as supercritical ORCs working fluids, Appl. Therm. Eng. 128 (2018) 1095–1101. https://doi.org/10.1016/j.applthermaleng.2017.09.046.

[17] C.M. Invernizzi, D. Bonalumi, Thermal stability of organic fluids for Organic Rankine Cycle systems, Elsevier Ltd, 2016. https://doi.org/10.1016/B978-0-08-100510-1.00005-3.

[18] M.O. Bamgbopa, E. Uzgoren, Quasi-dynamic model for an organic Rankine cycle, Energy Convers. Manag. 72 (2013) 117–124. https://doi.org/10.1016/j.enconman.2013.01.040.

[19] J.S. Pereira, J. Almeida, J.C. André, R. Mendes, J.B. Ribeiro, Modelling and experimental validation of the heat-transfer processes of a direct vaporization micro-scale ORC-evaporator for thermal degradation risk assessment, Energy Convers. Manag. 238 (2021) 114130. https://doi.org/10.1016/j.enconman.2021.114130.

[20] J.S. Pereira, M. Santos, R. Mendes, J.C. André, J.B. Ribeiro, Thermal degradation assessment study of a direct vaporization ORC based micro-CHP system under close-to-real operating conditions, Appl. Therm. Eng. 214 (2022). https://doi.org/10.1016/j.applthermaleng.2022.118878.

[21] J.S. Pereira, J.B. Ribeiro, R. Mendes, J.C. André, Analysis of a hybrid (topping / bottoming) ORC based CHP configuration integrating a new evaporator design concept for residential applications, Appl. Therm. Eng. 160 (2019) 113984. https://doi.org/10.1016/j.applthermaleng.2019.113984.

[22] M.O. Lemmon, E.W., Huber, M.L., McLinden, NIST Reference Fluid Thermodynamic and Transport Properties (REFPROP) - Version 9.1, Natl. Inst. Stand. Technol. (2013).

[23] European Committee for Standardization, EN 13203: Gas-fired domestic appliances producing hot water, 2016.

[24] European Parliament, European Council, Directive 2012/27/EU, Off. J. Eur. Union. L315/1 (2012) 1–56. https://doi.org/10.3000/19770677.L_2012.315.eng.

[25] European Commision, COMMISSION DELEGATED REGULATION (EU) 2015/2402 of 12 October 2015 reviewing harmonised efficiency reference values for separate production of electricity and heat in application of Directive 2012/27/EU of the European Parliament and of the Council and rep, Off. J. Eur. Union. L 333/54 (2015) 54–61.

ACKNOWLEDGEMENTs

In association with the authors' host institutions, this research was also supported by the Energy for Sustainability Initiative (EfS) and, by the Portuguese Recovery and Resilience Plan (PRR) and Next Generation European Funds EU through the project AM2R with the reference 7253 under the title AM2R - Agenda Mobilizadora para a inovação empresarial do setor das Duas Rodas. The financial support is gratefully acknowledged.

ORC design optimization method for offshore applications in part load conditions

Rafael Silverio Barbosa[a], Jurandir Itizo Yanagihara[b]

[a] Department of Mechanical Engineering, Polytechnic School of University of São Paulo, São Paulo, Brazil, rafael.s.barbosa@usp.br
[b] Department of Mechanical Engineering, Polytechnic School of University of São Paulo, São Paulo, Brazil, jiy@usp.br

Abstract:
Current environmental goals to reduce greenhouse gas emissions impose a challenging thermal design scenario for power generation equipment in oil platforms. The low thermal efficiency seen in gas turbines and the large amount of wasted heat at plant systems are elements that need to be addressed in the next few years. In this context, the application of organic Rankine cycles (ORC) in oil platforms has been studied. However, given the intrinsic characteristics of the power plant and processing systems onboard, the ORC design must consider not only the thermal aspects, but also the operational conditions. In this paper, an ORC design methodology based on a fuzzy and particle swarm-based optimization algorithm (HORCAT) is proposed, where the design variables are the geometric parameters of the equipment and the organic working fluid. In addition, the generated designs are evaluated under part load conditions. Aiming at the simultaneous maximization of the ORC electrical power output and the minimization of the equipment volume, this method is applied for the ORC design for waste heat recovery from the exhaust gas of a GE LM2500+ gas turbine, whose model was calibrated accordingly with the performance of an equipment operating in an FPSO at the Brazilian Pre-salt. The results were evaluated from two perspectives: at a suboptimal condition and considering a highly optimized Pareto front. Although the former returned configurations that led to a maximum power output of 4.1 MW, 4 different working fluids and a large overall volume of the equipment, some solutions were not valid under partial loads. The results of the latter, all operating with toluene, were robust under part loads. Although the maximum electric power output was of 1.97 MW, all results remained valid and its thermal efficiency was not lower than 24% for all cases.

Keywords:
organic Rankine cycles, multi-objective optimization, particle swarm optimization, thermal design.

1. Introduction

The low thermal efficiency of power systems operating on oil platforms is a well-known challenge that has been evaluated over the years [1] [2]. Although this concern has been studied from a technical and economical perspective, today the solution of this problem has become mandatory, given its social and environmental impacts [3].

Taking into account the variety of equipment and thermal systems operating on the platforms, there are multiple sources of losses and, in addition, multiple options to increase the efficiency. From a detailed exergetic model of a North Sea platform, [4] identified the main sources of exergy destruction, being the loss at the gas turbine the most prominent, contributing with almost 50% of the total exergy destruction of the platform. The work of [5] presented the measurement of efficiencies at the main subsystems of four platforms operating in the North and Norwegian Seas. In addition, options for design and waste heat recovery were evaluated. The authors identified low thermal efficiencies in gas turbines, primarily due to their operation at partial loads. The authors also investigated WHR systems to be applied to the platform equipment studied, including an LM-2500 power plant. With focus given on the compression systems, the work of [6] presents a detailed review on the exergy destruction in a FPSO operating in Brazil. The study shows that the compressor system rearrangement could lead up to a reduction of 39% in the power consumption.

Therefore, gas turbines operating at oil platforms power plants offer an excellent opportunity to increase efficiency [7], given their typical operation at part loads and the massive exergy destruction seen in exhaust gases. Although heat recovery from these gases is an evident option for efficiency increase, the space for implementing the typical solutions such as HRSGs is extremely limited in platforms.

In this scenario, ORCs can be a preferable option, due to their smaller footprint and high flexibility in terms of design and working fluids. Reckoning with the need to increase the efficiency and reduce the footprint of the

power plant, multi-objective optimization techniques have been applied to the design of the system. Having as reference the power plant in a FPSO operating at Santos Basin, Brazil, [8] apply ORCs for the heat recovery of gas turbines. By using a model of the power plant and applying a genetic algorithm for optimization, the results obtained show that it would be possible to operate with only two gas turbines (instead of the original three) and achieve a maximum thermal efficiency of 47.3%. In their work, [9] developed a complete design methodology for ORCs for gas turbine WHR , taking into consideration its dynamic behavior and a multi-objective optimization is applied to generate potential designs. Also using multi-objective optimization, [10] used a combine heat a power unit at a platform operating in the Norwegian Sea for WHR at the gas turbines exhaust.

Considering the challenges in designing and applying ORC to real-life offshore conditions, this paper presents a new ORC design methodology based on a multi-objective optimization performed by a fuzzy-PSO algorithm. The algorithm is applied for the ORC design and waste heat recovery from a GE LM2500+ gas turbine with the typical configuration found in Brazilian FPSOs. Furthermore, the analysis is made by considering not only the gas turbine full load condition, but also its part load operation.

2. Methodology

2.1. Overview

Since the methodology presented here was implemented in an ORC design computational system, it is important, firstly, to present and discuss its overall design process, which is shown in Figure 1. Initially, the parameters for the analysis are defined, including:

- The conditions of the heat source: if the data come from a model of data is read; if it operates at part or full load.
- The optimization constraints and limits for the optimized parameters.
- The optimization system parameters: number of iterations, population size, and particle swarm constants (initial values).

In the case presented in this work, the heat source model simulates a GE LM2500+ gas turbine, taking into account data from a real life equipment used for power generation in an FPSO [11]. Therefore, once the data from the heat source are available, the optimization system – HORCAT[1] – runs the design. The ORC model acts as an objective function that calculates the cycle thermal performance and returns the heat exchanger volume and the Rankine cycle electric power as outputs. Once the ORC design data have been defined, the proposed designs are evaluated and compared, given the part load data from the heat source. In the next subsections, HORCAT and the ORC model will be discussed in detail. In the case here studied, the ORC recovers heat from a single gas turbine.

Figure 1: Overall process of optimization and calculation for the ORC design.

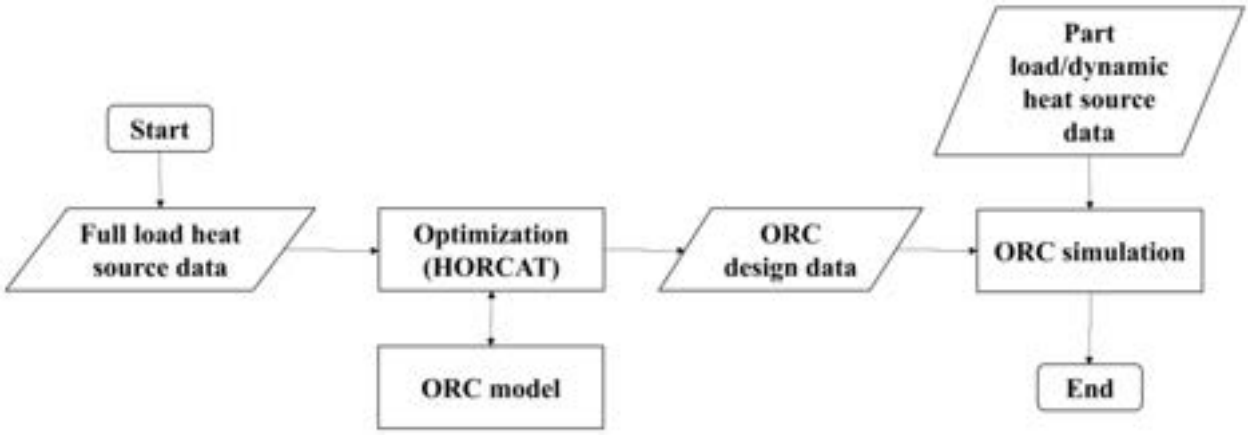

The system was fully implemented in Python and the thermal properties are calculated using the CoolProp library [12].

The approach presented here is novel due to the application of a tailor-made optimization methodology for thermal systems. Notably, the use of part-load conditions to validate the optimization results, i.e., the proposed designs, is a new approach for the selection of ORC plants to be applied offshore.

[1] HORCAT - Hunting ORCs with *Asa-de-Telha*: *asa-de-telha* is the name in Portuguese for the Harris's hawk, a very common hawk in Brazil, which has the unusual characteristic of hunting in cooperative packs.

The approach here presented is novel due to the application of such optimization methodology and a tailor-made algorithm to thermal systems. Most conspicuously, the use of the part load conditions to validate the optimization results (i.e., the proposed designs) is a new approach for the selection of ORC plants to be applied offshore.

2.2. The optimization algorithm: HORCAT

The optimization-based design method applied to complex models such as the ORC model described in this work demands an algorithm that can deal with a highly nonlinear objective function, from which it is impossible to calculate its Jacobian or Hessian matrices and whose domain cannot be properly defined. This is a situation where heuristic optimization methods are typically employed [13]. Most specifically, due to its lightweight calculations and suitability to complex systems [14], the particle swarm method [15] is used as the core of HORCAT.

Two swarms (packs) are used, one for each objective to be evaluated, which means that, given the vector of objective functions, each pack optimizes a single function f_i, being

$$f(\overline{x}) = [f_1(\overline{x}), f_2(\overline{x}), \ldots, f_n(\overline{x})], \tag{1}$$

and

$$\overline{x} = [x_1, x_2, \ldots, x_m], \tag{2}$$

is the design vector.

Moreover, each pack cooperates in the global search by sharing the same results of "Elite" (Pareto optimal set) that, at the end of the search, comprise the Pareto front. In the specific case of the ORC design, two objective functions are calculated: the global equipment volume and the electric power output from the steam turbine, hence,

$$f(\overline{x}) = \left[Vol(\overline{x}), \dot{W}_{ST}(\overline{x})\right] \tag{3}$$

and

$$\overline{x} = [\text{fluid}, A_{ST}, p_{10}, L_{OTB}, A_C]. \tag{4}$$

Initially, Elite is defined as a matrix containing the best results,

$$\overline{E} = \begin{bmatrix} Vol_{1,1} & \dot{W}_{ST1,2} \\ Vol_{2,1} & \dot{W}_{ST2,2} \\ \vdots & \vdots \\ Vol_{m,1} & \dot{W}_{STm,2} \end{bmatrix}, \tag{5}$$

each result (f_k) from an evaluated design (an element of the pack, $\overline{x}_k$) is compared with each element of Elite. If f_k Pareto dominates any element of $\overline{E}$, this specific element is replaced by f_k elements, i.e., given

$$f(\overline{x}_k) = \left[Vol(\overline{x}_k), \dot{W}_{ST}(\overline{x}_k)\right], \tag{6}$$

if $Vol(\overline{x}_k) < \overline{E}(j,1)$ and $\dot{W}_{ST}(\overline{x}_k) > \overline{E}(j,2)$, then $\overline{E}(j,1) = Vol(\overline{x}_k)$ and $\overline{E}(j,2) = \dot{W}_{ST}(\overline{x}_k)$.

To prevent the results of the packs to stop converging to the best solutions, a Fuzzy Logic System (FLS) is coupled to the optimization loop. The aim is to dynamically change the PSO parameters (ω, c_1 and c_2) used to calculate the velocity of the particles, as shown in equation (7). This adjustment allows for a better balance between the particle best and the global best since it is fitted accordingly with the results already found.

$$v_i(t+1) = \omega v_i(t) + c_1 r_1 (\pi_i(t) - x_i(t)) + c_2 r_2 (\pi_G - x_i(t)). \tag{7}$$

If no change in the Elite is observed after a certain number of iterations, even with the action of the FLS, the entire population is replaced. Figure 2 presents an overview of HORCAT's components and its functional behavior.

Figure 2: HORCAT's optimization flowchart.

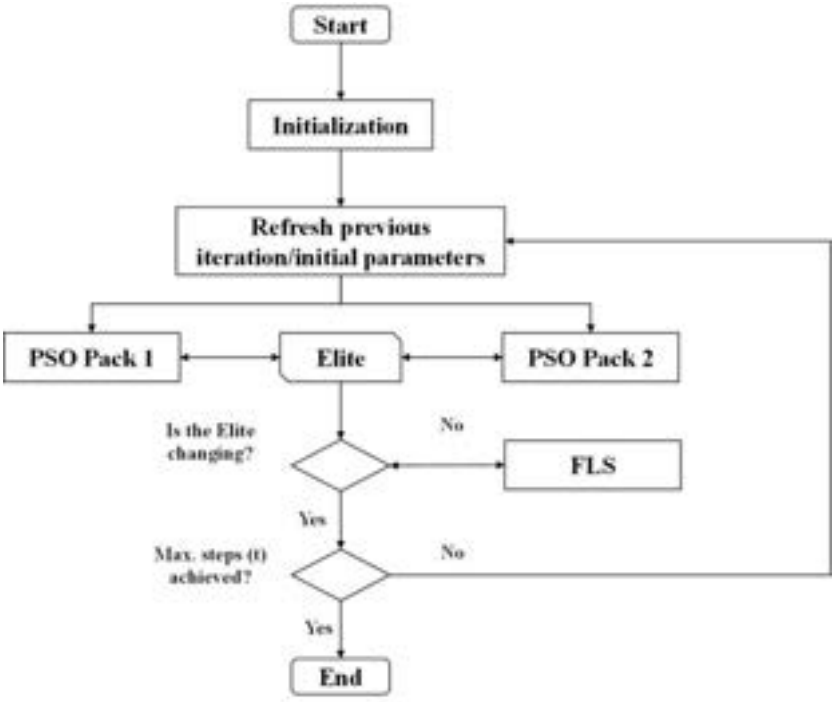

Figure 3: ORC equipment arrangement.

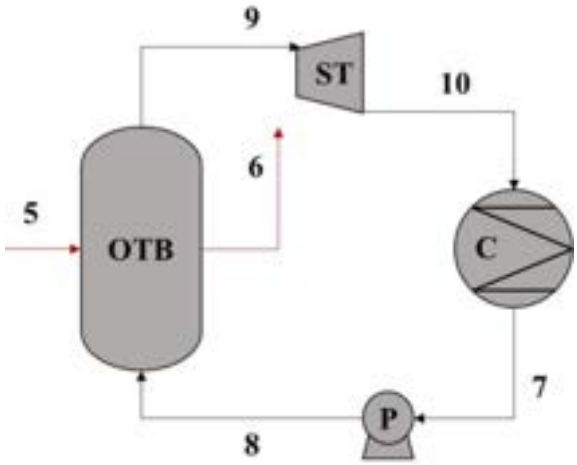

2.3. The ORC model

Given the design variables generated by HORCAT, the ORC thermal performance is calculated for each individual in the pack. The ORC arrangement is composed by an once-through boiler, a steam turbine, a condenser, and a pump, as presented in Figure 3. In general, mass and energy conservation equations are applied to each of these components. Constitutive equations are applied as discussed below.

The steam turbine model is based on the choked-nozzle model proposed by [16], where the mass flow rate at the inlet is given by,

$$\dot{m} = \rho_T a_T A_{ST}. \tag{8}$$

The electric power output and the isentropic efficiency are given by equations 9 and 10.

$$\dot{W_{ST}} = \dot{m}(h_9 - h_{10})\eta_M \tag{9}$$

$$\eta_{ST} = \frac{h_9 - h_{10}}{h_9 - h_{10s}} \tag{10}$$

The OTB model considers a two-step calculation. First, the NTU model is applied for the thermal calculation. The shell-and-tube heat exchanger design methodology presented by [17] and [18] is then applied to calculate the geometric parameters of the once-through boiler.

For a heat exchanger composed of finned tubes and in cross flow, the overall heat transfer coefficient and the effectiveness are calculated by [19]:

$$U_{global} = \beta \dot{m}_5^{\alpha}, \tag{11}$$

$$\varepsilon = 1 - exp\left\{\left(\frac{NTU^{0.22}}{C_r}\right)\left[-1 + exp\left(-C_r NTU^{0.78}\right)\right]\right\}, \tag{12}$$

where,

$$NTU = \frac{U_{global} A_{OTB}}{C_{min}} \tag{13}$$

and,

$$C_r = \frac{C_{min}}{C_{max}}. \tag{14}$$

Therefore, the energy balance is given by:

$$\dot{Q}_{max} = C_{min}\left(T_5 - T_8\right), \tag{15}$$

$$\dot{Q}_{OTB} = \varepsilon \dot{Q}_{max}. \tag{16}$$

For the pump, a simple fixed efficiency model is adopted, and for the condenser, a constant shell temperature model is applied.

3. Results and discussion

3.1. HORCAT validation

HORCAT was implemented following a novel approach in terms of methodology and application. Hence, before applying the algorithm to a thermal optimization and design problem, it was necessary to validate its robustness and suitability for the optimization of complex objective functions. Therefore, objective functions given in the literature to test multi-objective optimization algorithms were used, allowing the evaluation of the algorithm effectiveness when dealing with highly nonlinear conditions and non-continuous domains. Then, two test functions were applied: the (A) Binh & Korn function [20]; and (B) the Zitzler τ_1 function [21]. For the latter, the reference results were taken from Maghawry et al. [22].

Figure 4 shows the optimization results , given in terms of Pareto fronts for both functions. It is important to mention that HORCAT discards similar designs, which leads to sparse Pareto fronts, but actual unique solutions. For both cases, HORCAT optimized results were similar (or even better) than the references given in literature. From the results obtained, it could be seen that the algorithm provides an effective optimization and is comparable with other algorithms given in the literature.

3.2. ORC design at full load

To generate ORC designs considering the gas turbine full load condition, the HORCAT setup considered two packs of 100 individuals. Two scenarios of results are shown in Figure 5: (A) after 3 iterations and (B) after 30 iterations.

In scenario (A), 10 valid designs were generated and, of a total of 18 organic fluids available for selection, only 4 resulted in the valid ORC designs. In this suboptimal condition, a wide ORC electrical power range (1.2 - 4.1 MW) can be seen, however, with large and unfeasible equipment volumes. There is a sensitive change in these conditions in scenario (B), where the effects of Pareto domination can be seen after several iterations and a higher power/volume ratio is obtained. In scenario (A), only toluene results as a valid design working

Figure 4: HORCAT validation against test functions.

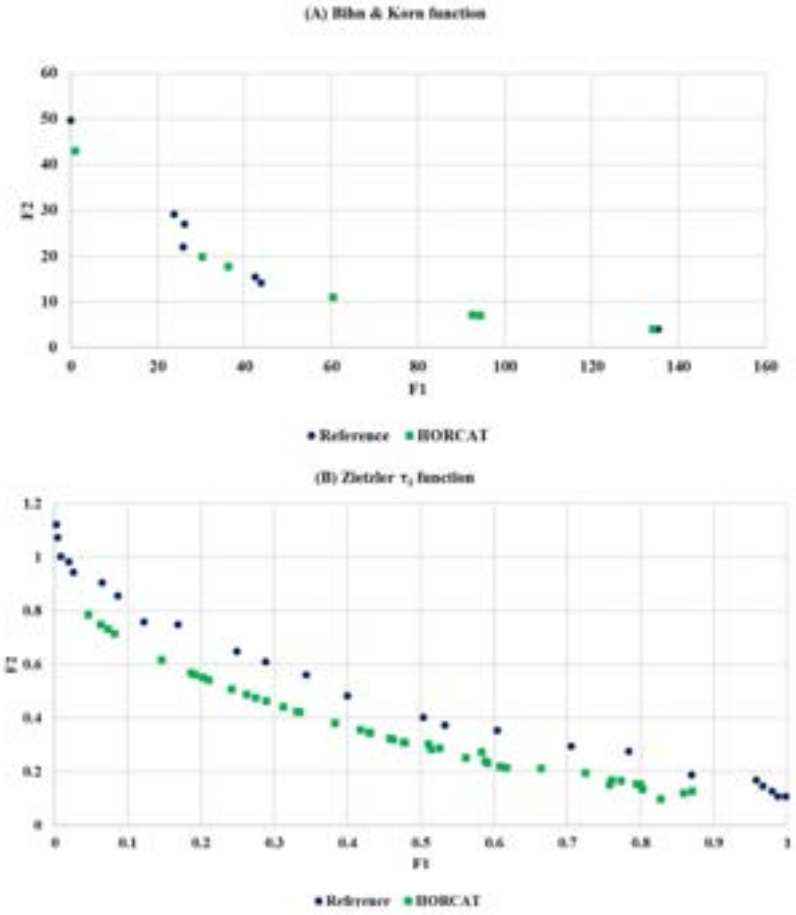

fluid. In scenario (B), 16 valid designs were generated, with an ORC electric power range from 489 kW to 1.97 MW, which can lead to an increase of more than 8% in the power output when considering the gas turbine and the ORC combined. Furthermore, the Rankine cycle thermal efficiency of these valid designs is in the range 27-29%. The effect of Pareto dominance is evident when comparing scenarios (A) and (B). First, the lower number of valid designs in scenario (A) is a consequence of insufficient iterations so that the HORCAT packs were still unable to find a broader number of solutions that makes sense in terms of thermodynamic validity. As the number of iterations increases, more solutions are found in scenario (B). These solutions Pareto-dominate those found in scenario (A) and, additionally, there is a clear and expected migration of the Pareto front to the bottom (lower equipment volume) and to the right (lower power output) .

3.3. Comparative analysis of part load and design conditions

To test the ORC designs generated in scenarios (A) and (B) in load conditions typically found in FPSOs, the proposed solutions were simulated under part load conditions (50 and 75%) of the gas turbine. Figure 6 presents the Pareto fronts for scenario (A). Under part load conditions, the valid designs dropped from 10 to 8 cases, since the ORCs operating with n-dodecane were not able to operate at lower temperatures and remain thermodynamically feasible, given the geometry of the components that were designed for the full-load condition.

Regarding thermal efficiency, as seen in Figure 7, there is a significant drop under part loads for all fluids, with toluene having the lowest variation. It is important to highlight the case 5 as one example where the full load condition could not bring about a better solution. Although it presents the higher efficiency at full load, it also has the second worst performance at 50% load.

Comparative analysis considering part loads applied for scenario (B) returned more stable conditions compared to scenario (A). The number of solutions found after 30 iterations at full load did not drop under part load conditions, which can be explained by two factors: the highly optimized solutions and the suitability of toluene under such conditions. Figure 8 shows the Pareto fronts for each condition.

Moreover, as seen in Figure 9, the thermal efficiencies found for all cases remain high even under partial loads.

Figure 5: Optimization results for the ORC design considering only the gas turbine at full load. Scenario (A) is given after 3 iterations (valid designs for 4 working fluids) and scenario (B) after 30 iterations (only toluene resulting as working fluid).

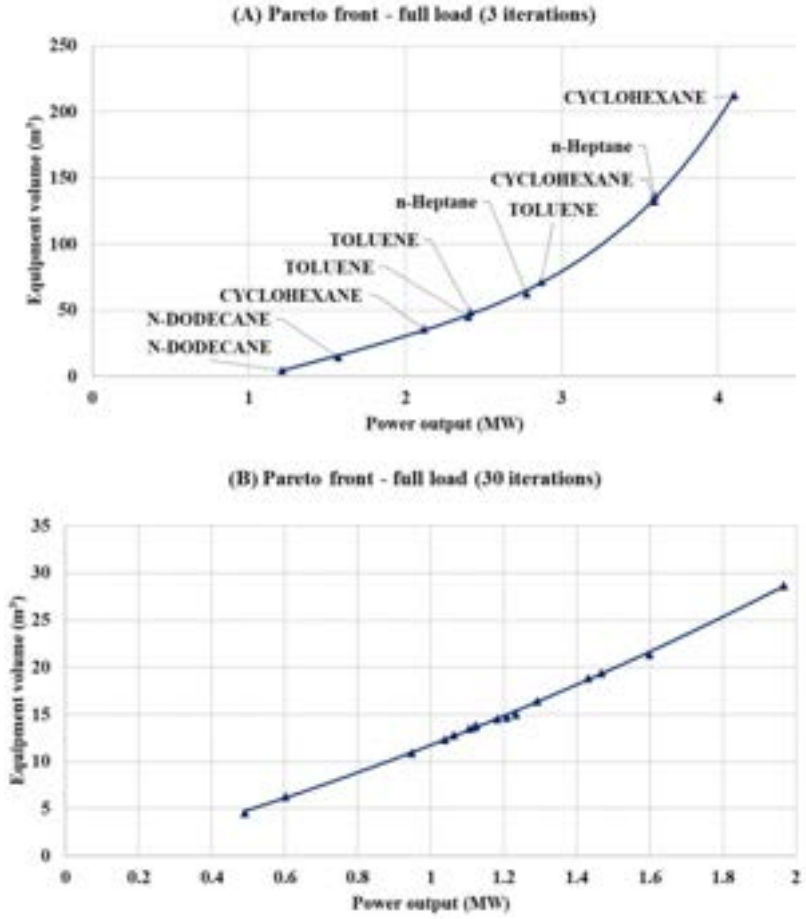

Figure 6: Pareto fronts for the scenario (A) proposed designs under the gas turbine loads of 50%, 75% and 100%.

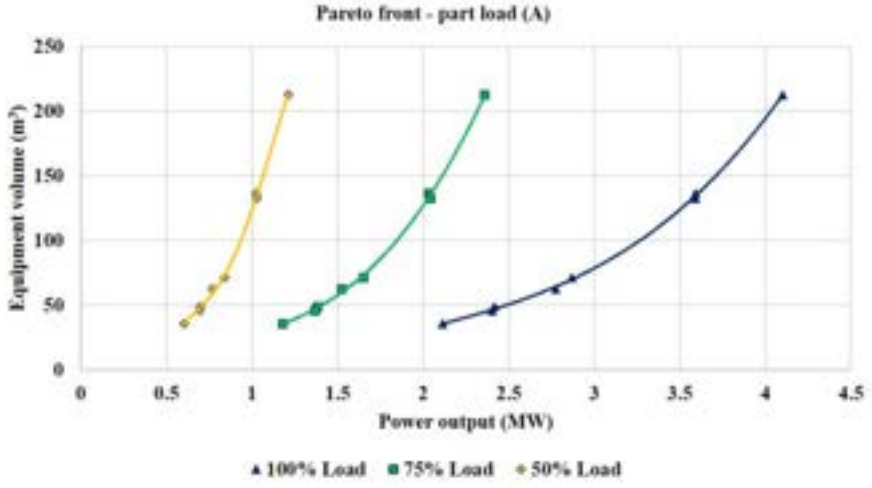

4. Conclusion

This work presented a new ORC design methodology for waste heat recovery application, which applies a fuzzy-PSO algorithm to find valid designs through a multi-objective optimization. HORCAT, the optimization algorithm, was validated against literature benchmark functions and was able to deal with the specific characteristics of the ORC model to be optimized.

Figure 7: Thermal efficiencies for each valid design under part load conditions - scenario (A).

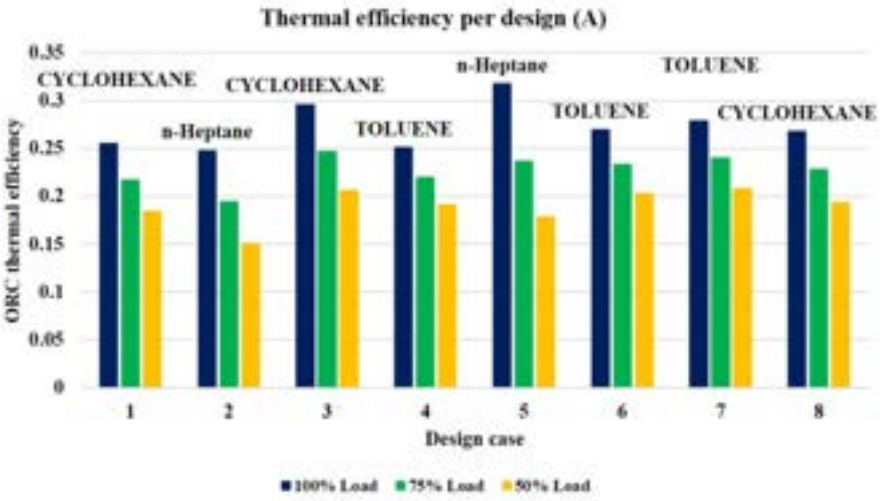

Figure 8: Pareto fronts for the scenario (B) proposed designs under the gas turbine loads of 50%, 75% and 100%.

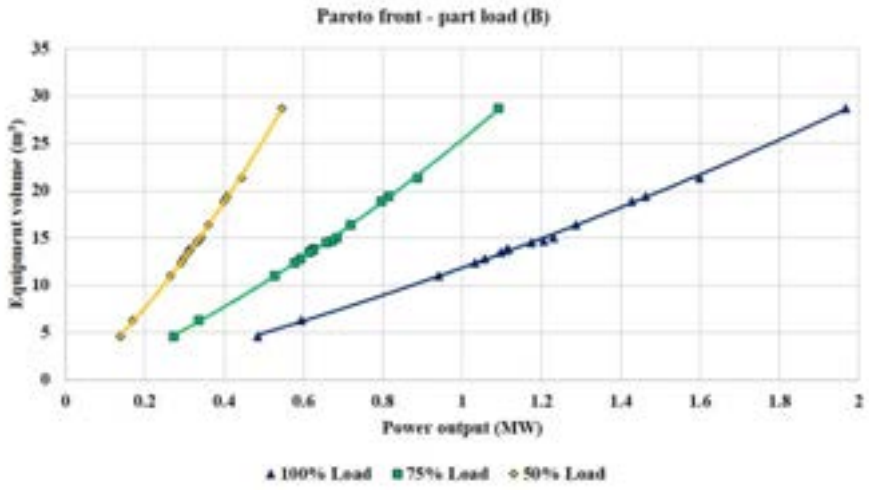

Figure 9: Thermal efficiencies for each valid design at part load conditions - scenario (B).

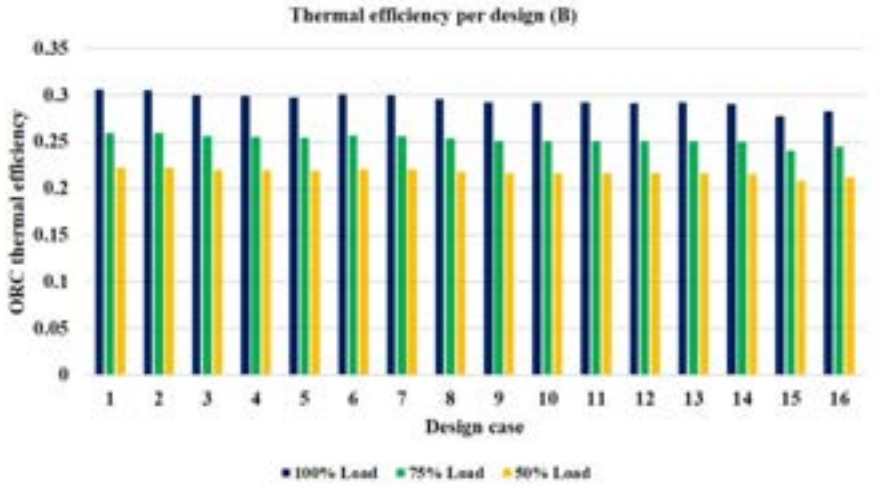

HORCAT was employed to provide optimized ORC designs for waste heat recovery from the exhaust gas of a gas turbine operating at an FPSO - using a single gas turbine coupled to a single Rankine cycle. To evaluate

the effect of suboptimal solutions on the thermal performance and, additionally, to analyze the impact of the part load operation of the given designs, the results were evaluated considering two scenarios: (A) after three iterations and (B) after 30 iterations.

In scenario (A), the results show that feasible ORC solutions decrease from 10 to 8 valid designs, when considering, respectively, the gas turbine at full and at partial loads. At full load, there were ORC designs providing up to 4.1 MW of electric power, however with an overall equipment volume that could make it impossible to be applied in FPSOs.

All the scenario (B) solutions were feasible at full and partial loads, showing that free optimization led to robust ORC designs. The electric power range of the solutions at full load for this scenario was from 489 kW to 1.97 MW, with a thermal efficiency range from 20 to 30%. Moreover, even at partial loads, the efficiency could be kept above 24% for all casess.

Finally, as verified in scenario (A), the analysis performed led to the conclusion that the full-load based design can provide unfeasible ORC solutions to oil rigs, most specifically because gas turbines at these facilities operate at part and unsteady load conditions. The approach proposed in this work shows that the optimal design needs also to consider both the near-optimal conditions and also part load scenarios in order to address the correct operational conditions at the platform.

Nomenclature

Abbreviations:

FPSO Float Production Storage and Offloading

HORCAT Hunting ORCs with *Asa-de-Telha*

HRSG Heat Recovery Steam Generator

ORC Organic Rankine Cycle

WHR Waste Heat Recovery

Symbols:

a speed of sound (m/s)

A area (m^2)

c particle swarm acceleration parameter

C heat capacity (J/K)

E Elite

f generic function

h specific enthalpy (J/kg)

L heat exchanger tube length (m)

$\dot{m}$ mass flow rate (kg/s)

NTU number of transfer units

p pressure (Pa)

$\dot{Q}$ heat transfer rate (W)

r random number

t time (s)

T temperature (K)

U global heat transfer coefficient (W/m^2K)

v particle velocity

Vol volume(m^3)

$\dot{W}$ power (W)

x generic variable

Greek symbols:

α constant

β constant

ε effectiveness

η efficiency

π particle swarm pack best solution found

ρ density (kg/m_3)

ω particle swarm inertia weight parameter

Lowercase:

G global

i generic index

M mechanical

OTB once-through boiler

r rate

s isentropic

ST steam turbine

T total

References

[1] Oliveira Junior S., Van Hombeeck M. *Exergy analysis of petroleum separation processes in offshore platforms*. *Energy Conversion and Management* v.38 n.15. 1997. p. 1577–1584

[2] Allahyarzadeh-Bidgoli A., Salviano L., Dezan D., Oliveira Junior S., Yanagihara J. I. *Energy optimization of an FPSO operating in the Brazilian pre-salt region*. *Energy*, 2018.

[3] International Energy Agency. *Net Zero by 2050 - A Roadmap for the Global Energy Sector*. 2021.

[4] Nguyen T. V., Pierobon L., Elmegaard B., Haglind F., Breuhaus P., Voldsund M. *Exergetic assessment of energy systems on North Sea oil and gas platforms*. *Energy* v.62. 2013. p. 23–36.

[5] Nguyen T.V., Voldsund M., Breuhaus P., Elmegaard B. *Energy efficiency measures for offshore oil and gas platforms*. *Energy* 04 2016.

[6] Cruz M., Araujo O., de Medeiros J. *Exergy comparison of single-shaft and multiple-paralleled compressor schemes in offshore processing of CO2-rich natural gas*. *Journal of Natural Gas Science and Engineering*, v.81, 2020.

[7] Pierobon L., Nguyen T. V., Larsen U., Haglind F., Elmegaard B. *Multi-objective optimization of organic rankine cycles for waste heat recovery: Application in an offshore platform*. *Energy* v.58. 2013. p. 538–549.

[8] Reis M., Guillen J., Gallo W. *Off-design performance analysis and optimization of the power production by an organic rankine cycle coupled with a gas turbine in an offshore oil platform*. *Energy Conversion and Management* v.196. 2019. p. 1037–1050.

[9] Pierobon L., Casati E., Casella F., Haglind F., Colonna P. *Design methodology for flexible energy conversion systems accounting for dynamic performance*. *Energy* v.68. 2014. p. 667–67.

[10] Kazemiani-Najafabadi P., Amiri Rad E. *Multi-objective optimization of a novel offshore CHP plant based on a 3E analysis*. *Energy* v.224. 2021.

[11] Barbosa, R. S., Yanagihara, J. I. *Performance simulation of an aeroderivative gas turbine operating at a Brazilian FPSO*. In: *Proceedings of ECOS 2021 - The 34th International Conference on Efficiency, Cost, Optimization, Simulation and Environmental Impact of Energy Systems*. 2021.

[12] Bell I. H., Wronski J., Quoilin S.; Lemort V. *Pure and pseudo-pure fluid thermophysical property evaluation and the open-source thermophysical property library CoolProp*. *Industrial Engineering Chemistry Research*, v.53, n.6. 2014. p. 2498–2508.

[13] Colaço M., Dulikravich G. *A survey of basic deterministic, heuristic, and hybrid methods for single-objective optimization and response surface generation*. In: Orlande H. R. B. , Fudym O., Maillet D., Cotta R. M., editors. Thermal Measurements and Inverse Techniques. Rio de Janeiro, Brazil. CRC Press. 2009. p. 355–405.

[14] Esmin A. A., Coelho R. A., Matwin, S. *A review on particle swarm optimization algorithm and its variants to clustering high-dimensional data*. *Artif. Intell. Rev.*, Kluwer Academic Publishers, USA, v.44, n.1, 2015. p. 23–45.

[15] Kennedy J., Eberhart R. *Particle swarm optimization*. In: *Proceedings of ICNN'95 - International Conference on Neural Networks*. 1995. v.4 p. 1942–1948.

[16] Casella F., Mathijssen T., Colonna P., van Buijtenen J. *Dynamic modeling of organic rankine cycle power systems*. *Journal of Engineering for Gas Turbines and Power*, v.135, n.4, 03. 2013.

[17] Sinnott R. *Chapter 12 - Heat-transfer equipment*. In: Sinnott R. (Ed.). Coulson and Richardson's Chemical Engineering. Second edition. Amsterdam: Pergamon 1993.p. 565–702. ISBN 978-0-08-041865-0.

[18] Kakaç S., Liu H., Pramuanjaroenkij A. *Heat Exchangers: Selection, Rating, and Thermal Design, Second Edition*. Taylor & Francis, 2002. ISBN 9780849309021.

[19] Ordys A., Pike A., Johnson M., Katebi R., Grimble M. *Modelling and Simulation of Power Generation Plants*. Springer. 1994. ISBN 978-1-4471-2114-5.

[20] Binh T.T., Korn U. *An evolution strategy for the multiobjective optimization*. In: CITESEER. *Pro. 2nd Int. Conf. Genetic Algorithms*. 1996. p. 23–28.

[21] Zitzler E., Deb K., Thiele L. *Comparison of multiobjective evolutionary algorithms: Empirical results*. *Evolutionary computation* MIT Press v.8 n.2. 2000. p.173–195.

[22] Maghawry A., Hodhod R., Omar Y., Kholief M. *An approach for optimizing multi-objective problems using hybrid genetic algorithms*. *Soft Computing* Springer v.25 n.1. .2021. p. 389–405

PROCEEDINGS OF ECOS 2023 - THE 36TH INTERNATIONAL CONFERENCE ON
EFFICIENCY, **C**OST, **O**PTIMIZATION, **S**IMULATION AND ENVIRONMENTAL IMPACT OF ENERGY SYSTEMS
25-30 JUNE, 2023, LAS PALMAS DE GRAN CANARIA, SPAIN

Energy system optimization towards a fossil-free power plant portfolio

Duk Yong Kwon[a], Mathias Hofmann[b]

[a] Vattenfall Wärme Berlin AG & Technische Universität Berlin, Berlin, Germany, dukyongdaniel.kwon@vattenfall.de
[b] Technische Universität Berlin, Berlin, Germany, hofmann@iet.tu-berlin.de, CA

Abstract:
To decarbonize our energy system, appropriate technology options must be established and applied at the right site. The investment decisions required for this are usually conducted based on techno-economic portfolio optimization. The presented research aims to optimize an energy system configuration for a district heating network of a global city located in Central Europe. The objective is to evaluate different configurations and determine the optimal combination for a fossil-free supply system. The energy system model is based on real district heating network data, including hydraulic restrictions, combined heat and power plants, heat-only boilers, heat storage, power-to-heat technologies, and fuel input options. Time series are heat demand, weather conditions, and exchange prices. Furthermore, investment costs and operating and maintenance costs are taken into account. Aristopy, a free and open-source Python-based framework, has been used to implement mixed-integer linear programming, which is solved by the state-of-the-art algorithm Gurobi. The model includes a time series aggregation to achieve accuracy and appropriate computation time. Multiple scenarios with different input data evaluate the robustness of each configuration. By assessing these configurations, the optimal system design is selected. The model succeeded in determining an optimal portfolio configuration and its operation. Simplification through time series aggregation has shown that the computation time can be shortened while providing the necessary accuracy. The scenario analysis shows the impact of the different input parameters and assumptions on portfolio planning. The presented methodology improves portfolio planning and operation of a real-world energy system. Simultaneously, license costs can be saved.

Keywords:
Energy System, Optimization, Decarbonization, District Heating, Python-Based Framework, Time Series Aggregation, Portfolio Planning, Fossil-Free, Renewable Energy

1. Introduction

The uncertainty and volatility of energy prices and fuel supplies have increased dramatically in recent developments within the energy market. This dynamic progress is also reflected in recent political and societal developments. The regulatory framework is an additional driver which impacts the operation and investments of power and heat generation units. The importance of scenario analysis is increasing due to the additional uncertainty. Optimization models are needed to find robust portfolios and analyze the impact of specific parameters. Within the presented research, the city, the district heating system, and the generation units under investigation are called by anonymous names.

In general, there are numerous research papers on energy system analysis, both on the level of methodological development and on the level of application-oriented research. Due to many works, only a relevant selection of overviews of the current state of research is compiled. DeCarolis et al. [1] conduct an extensive literature review to formalize best energy system optimization modeling practices. Kotzur et al. [2] note that many complexity drivers could be avoided a priori with a tailored model design. They review systematic complexity reduction methods for energy system optimization models and develop a guide for system modelers encountering computational limitations. Wirtz et al. [3] perform a comparison of different combinations of energy system model features: Piece-wise linear investment curves, multiple component resolution, minimum part-load limitations, part-load efficiencies, and start-up costs.

Decomposition approaches and approaches for optimization under uncertainty have also been proposed recently for energy system modeling. Wirtz et al. [4] present a Dantzig–Wolfe approach to decompose a mixed-integer linear program into multiple subproblems and a master problem. A realistic case study based on a district heating system was considered. They demonstrated that the proposed decomposition approach yields the same results attained by the original, not decomposed problem while achieving gains in scalability and computational times. Göke et al. [5] applied Benders decomposition to two-stage stochastic problems for energy planning with

multiple climatic years. With their approach they slightly increase solve time of the master-problem, but greatly reduce the number of iterations. Yue et al. [6] have identified four prevailing uncertainty approaches applied to energy system optimization models: Monte Carlo analysis, stochastic programming, robust optimization, and modeling to generate alternatives. They provided a critical appraisal of the use of these methods.

Studies focusing on the local district heating portfolio and dispatch optimization were published in the past. Jüdes et al. [7] and Christidis et al. [8] investigated the contribution of heat storage for the district heating network using large-scale optimization models developed and solved within the General Algebraic Modeling System (GAMS). The advantage of pressurized short-term heat storage for operating a district heating network was investigated by Hofmann et al. [9]. Gonzalez-Salazar et al. [10] present a district heating network portfolio optimization. Due to computation time restrictions, they use a merit order model instead of mixed-integer linear programming. Concerning the local portfolio of the city under investigation, it is clear that comprehensive portfolio analyses require further methodological development in model reduction while maintaining the same quality of results.

This research analyzes the energy system's behavior depending on the changing energy market scenarios. The purpose is to find a suitable optimization method with an appropriate computational load and framework to analyze different scenarios concerning the district heating grid and the future portfolio. Based on different input scenarios, portfolio options are presented, which can support investment planning.

The article is structured as follows: The next section summarizes the methods and tools applied here. The system analysis presents the technology options, input data, and boundary conditions taken into account. The portfolio optimization and sensitivity analysis results are discussed in Section 4., followed by the conclusions.

2. Methodology

2.1. Energy System Optimization

The current energy market is more volatile than ever, and the urge to transform the current energy system into a more climate-friendly portfolio is at its highest peak. Due to these reasons, it has become even more difficult for most energy suppliers to determine the future energy system configuration that fulfills economic and environmental objectives. Energy system optimization is an essential tool to address this challenge.

There are various approaches for energy system optimization depending on the question to be answered within the decision process. In all cases, the goal is to determine a set of decision variables so that the value of the objective function is maximized or minimized while fulfilling all constraints. The optimization objective can be the dispatch of individual generation units or a system configuration optimization where the entire grid is considered over the given period.

An overview of the available functionality and the specific advantages and disadvantages of the energy system modeling frameworks and open models are presented on the websites of the Open Energy Platform [11] or the Openmod Initiative [12]. Both platforms aim to actively exchange and initiate relevant energy system modeling topics, approaches, and data. Since the field of the energy system modeling is broadly diversified, and each tool has individual strengths and weaknesses, the community helps to enhance the quality and efficiency. In addition to those platforms, Groissböck [13] presents a general assessment of open-source energy system modeling.

This research uses the Python-based, objective-oriented framework Aristopy, which was developed under the research project "MINLP-Optimization of Design and Operation of Complex Energy Systems" and is presented in the following section.

2.2. Aristopy

Aristopy[1] is a free and open-source Python-based framework for the optimization of energy systems. In contrast to other frameworks, aristopy allows integrated time series aggregation methods that can be used directly within the model, see section 2.3. Aristopy uses the algebraic modeling language of Pyomo [14, 15]. The user can formulate individual restrictions and constraint which adapts to multiple programs such as LP, MILP, or MINLP. Various solvers can be utilized. For this research, the optimization problem has been solved using Gurobi [16]. For visualization of results, aristopy uses Plotter[2].

In aristopy, an optimization model is set up by creating the class EnergySystem. Within the class, five pre-defined components (Source, Sink, Conversion, Bus, Storage) can be used to describe different characteristics and behaviors of the energy system parts. All inputs and outputs of components are connected with a class Flow, which contains all variables and ensures energy transport. Figure 1 shows a simple illustration of an example energy system and the dependency of each component.

The Source component contains only one output, which provides fuel in the example. With the help of a Flow component, the fuel is transported to the Conversion component, where fuel is converted into thermal and

[1] https://aristopy.readthedocs.io/en/latest/
[2] https://pypi.org/project/plotter/

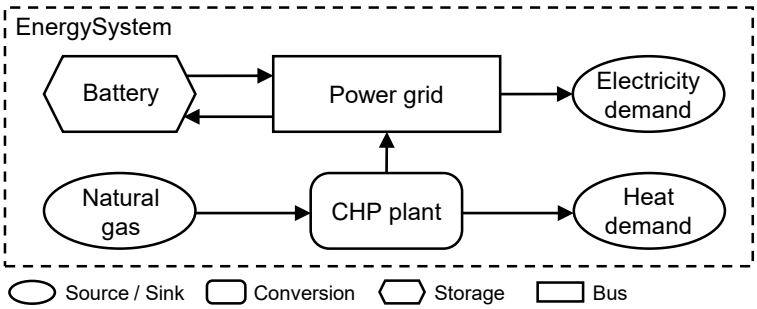

Figure 1: Simple example of generic model building using the class EnergySystem and the elementary component classes Source, Sink, Conversion, Bus, and Storage in the Python library aristopy. Translated adoption with permission from [17].

electrical energy. The energy flows are transported to a Bus component, where different streams of the same energy are gathered and transported to a Sink component. The Sink component, e.g., heat demand in the example, is the inverted component of Source. A Storage component (either battery or heat storage) can be added to the energy system, allowing more system flexibility. The storage can be directly integrated into the overall system or an individual grid by creating multiple Bus components.

Aristopy contains a particular class of photovoltaic or solar thermal collectors. An existing method from the Python library pvlib [18] is used for this. Furthermore, the built-in functions of add_variable, add_constraint, and add_objective_function_contribution are provided to add additional variables, constraints, and objective functions to the optimization model.

2.3. Time Series Aggregation

One of the biggest hurdles for an energy system optimization is the need to optimize numerous scenarios of possible future developments and the needed calculation time or computational capacity. Time series aggregation methods have been introduced for energy system optimization to reduce model complexity. Reviews are presented by Hoffmann et al. [19] and Teichgräber et al. [20]. This thesis uses the Python-based Time Series Aggregation Module (tsam) [21].

The concept of time series aggregation is to reduce an extensive and detailed data set into a representation with fewer time steps, ideally without loss of information by aggregating repetitive patterns. An appropriate method can reduce CPU and RAM requirements and make processing and analyzing extensive time series data sets efficient.

There are several time series aggregation methods. The most common is reducing the resolution by grouping the data into larger time intervals, from hourly time steps to days, weeks, or months. This method is called downsampling, which usually leads to underestimating the original times series' variances and the maximum and minimum values.

Besides the downsampling method, there is the segmentation method. It is a more complex but accurate method of aggregating time steps with similar characteristics to create an artificial time series replicating the original times series. There are different aggregation methods with their advantages and disadvantages. When this approach was introduced for energy system optimization, the heuristic method, where one representative day per month is selected, was a standard application. In the meantime, systematic aggregation methods are introduced, in which the time series is divided into particular periods of defined length and assigned to a cluster based on their similarity. The Euclidean distance function, see Eq. (1), is used to measure similarity. The equation is formulated for a one-dimensional distance where p and q represent two points on the real line.

$$d(p, q) = |p - q| \tag{1}$$

Three main methods exist to aggregate time series into groups with a single representative period. The most commonly used clustering method is the k-means algorithm. It belongs to the family of non-hierarchical cluster analysis methods where k random centroids are created in the feature space. All data points are assigned to the nearest centroid using the Euclidean distance function, which provides an initial cluster solution. Every data point is attached to one cluster, and the centroids are updated by finding the empirical mean of the features across all data points attached to that cluster. When the centroids are updated, the algorithm repeats the assignment of each data point to the next nearest (updated) centroid. The critical feature of a k-means algorithm is that the final centroids are not actual data points but a calculated mean of data points within that cluster.

Another algorithm called k-medoids chooses the final centroids from the actual data points, thereby allowing for greater interpretability of the cluster centers than in k-means. The "Partitioning Around Medoids" (PAM)

algorithm finalizes the point as a new centroid from the existing data points with a minimum loss. Besides k-means and k-medoid, there is the hierarchical clustering algorithm. In hierarchical clustering, each data point is grouped into a cluster tree by treating all data points as a separate cluster. When all data points are determined as individual clusters, the algorithm identifies two clusters that are closest together. Those two clusters will be merged into one cluster. As a result of this iterative process, all clusters are merged.

Since peak periods are not representative of a whole group or cluster of periods, the methods introduced for time series aggregation have the disadvantage of potentially cutting off so-called peak periods. An accurate energy system design must be able to meet all requirements. There are different approaches for identifying and mapping the extreme points. The append method adds the extreme periods as additional representative periods to the other representative periods. In contrast, the additional-cluster-center method sets the peak period as an additional new cluster center. The replace-representative-period method integrates the extreme value where the peak period is assigned as the new representative of the cluster.

For the analysis, it is essential to set the correct number of representative data points the user gives. Depending on the number of representative data points, the results can differ. Additionally, choosing the period length and the number of time steps per representative period is essential for the time series aggregation. Different energy systems behave individually depending on the preset of representative clusters. Usually, the aggregated time series are modeled individually, where the connection and correlation between those periods are not modeled accordingly. It can impact the integrated storage system, so it is suggested to choose more extended periods to model the impact of storage.

3. System Analysis

Figure 2 represents the example energy system generated for this research. The considered optimization problem represents an energy system where the coal capacities have been phased-out. By taking out the coal-firing capacities and providing each production site with various potential technology options, the solver can optimize the optimal portfolio configuration for the system and each production site.

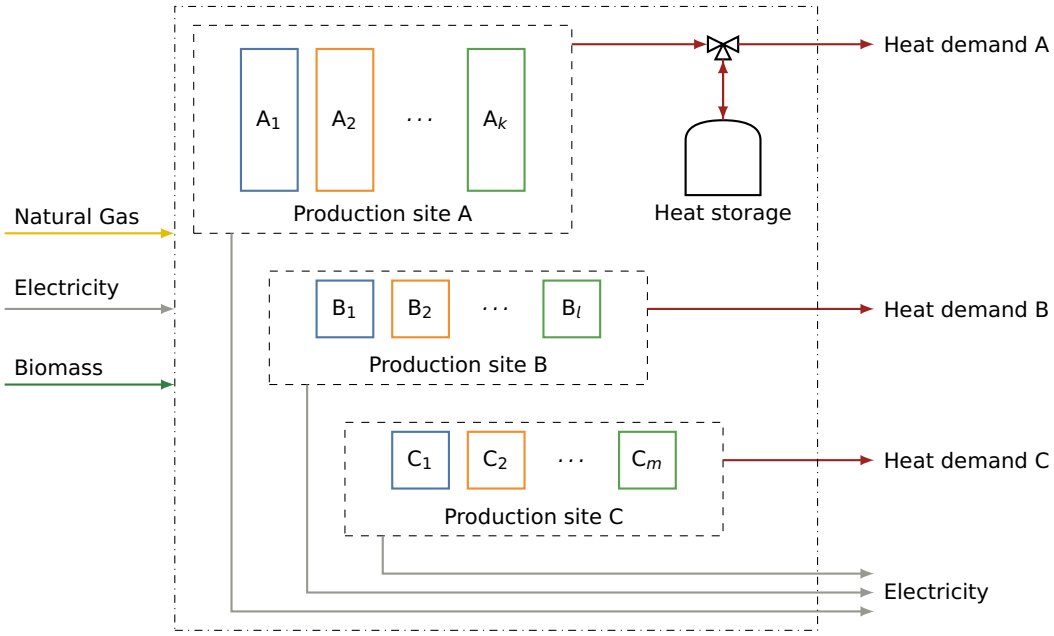

Figure 2: Simplified district heating system. Colors indicating recent and potential technology options at the sites.

As Figure 2 shows, the model is given with the possible fuel inputs, potential technology options, and the heat demand which must be met for each time step. The model considers portfolio options under various scenarios to find the most suitable and beneficial technology option for each site. The electrical grid is not given as a demand but as a market where the generation units can either sell or buy. The district heating grid can be divided into multiple sub-grids considering the geographical condition. Each generation site is assigned to a specific sub-grid to avoid significant heat losses and bottlenecks. The possibility of transferring heat from one sub-grid to nearby sub-grids is also modeled. Even though, it is physically possible to transport to the furthest sub-gird, it is very unusual considering the grid efficiency. Even when primary capacity fails, the heat-reserve boilers compensate for the capacity instead of transporting it from other sub-grids. The heat-reserve boilers are not set as a variable in this thesis but as given plants with extremely high operating costs.

The objective for the optimization is to maximize the net present value (NPV), see Eq. (2). The net present value measures the financial profitability of the portfolio. Equation (2) determines the difference between all revenues and expenses over the economic life of the investment.

$$\max NPV = -I + S + C \cdot k^{\mathrm{AF}} \tag{2}$$

In this equation, all expenses and revenues arising from the investment are discounted throughout the investment. As part of the input assumptions, various model parameters have been pre-determined.

All technology options are modeled with a fuel equation with technology-specific coefficients k_i and time-depending variables (Fuel rate $\dot{F}$, Electric power $\dot{W}_{\mathrm{el}}$, and heat rate $\dot{Q}_{\mathrm{th}}$); and if necessary (combined technology) with an additional $\dot{W}_{\mathrm{el}}$, $\dot{Q}_{\mathrm{th}}$-function.

$$\dot{F}_{\mathrm{f}} = \begin{cases} k_1 \cdot \dot{Q}_{\mathrm{th}} & \text{Heat pumps or heat-only boilers, } f = \{\text{Electricity, Bioenergy, } CH_4\} \\ (k_1 + k_2)^{-1} \left(\dot{W}_{\mathrm{el}} + \dot{Q}_{\mathrm{th}} \right) & \text{Gas turbines w/ or w/o heat-recovery boiler, } f = \{CH_4, H_2\} \\ k_1 \left(\dot{W}_{\mathrm{el}} + k_2 \cdot \dot{Q}_{\mathrm{th}} \right) + k_3 \cdot Y & \text{Combined heat and power plants, } f = \{CH_4, H_2\} \text{ and } Y = \{0, 1\} \end{cases} \tag{3}$$

Fundamental model parameters are given in Table 1. The complete model with all equations and specifications can be obtained from the authors. Note that due to corporate confidentiality, actual values can not be given.

Table 1: Fundamental model parameters and maximum heat rate per unit of the technology options

Parameter	Symbol	Unit	Value
Number of production sites	N	[–]	5
Economic lifetime	t	a	15
Future technology options (Abbreviation)	$\dot{Q}_{\mathrm{max}}$ [MW]		
Natural gas heat-only boiler (GHOB)			40
Combined cycle gas turbine (CCGT)			230
Gas turbine (GT)			120
Bioenergy heat-only boiler (BIOB)			100
River heat pump (HP)			50
Geothermal heat pump (GEOT)			50
E-Boiler (EB)			40

4. Results

4.1. Portfolio Optimization with time aggregation

As mentioned in the previous section, the total solution time increases with the additional complexity of the optimization problem. However, it is essential to analyze various scenarios with different assumptions to find the most robust portfolio for the future. With an average optimization duration of 5 to 6 hours for an optimization period of 15 years, the effort to investigate and analyze multiple scenarios is too high. The time series aggregation algorithm has been implemented to simplify this process and aim for similar results. For the analysis, different types of algorithms were used to analyze the impact of the aggregation methods. For the consistency of the result analysis, a similar scenario has been selected to compare different algorithms.

First, multiple combinations of representative periods and period lengths have been analyzed. Table 2 shows the average configuration variance with different representative periods and period lengths. The variance represents the percent difference compared to the original scenario result, optimized with hourly input data. The first column, Cluster Period, represents the combination selected for the optimization. The first number indicates the number of representative periods from the input data of 15 years and hourly resolution. The second number indicates the length of each period, represented as hours in full resolution. For the analysis, 18 representative periods and length variations have been optimized with the k-mean algorithm. The variance from the reference scenario has been filtered after technology types. As assumed, the number of representative periods and the length of the period drives the total solution time. The longer the period, the more optimized time steps, which leads to a longer solution time. Table 2 also shows that each technology option behaves differently depending on the variation of the cluster period. A significant variance can be seen for the gas heat-boiler option. The gas boilers have been utilized in the full hourly resolution, especially for peak shaving. By aggregating the time series, those continuous peaks of the heat demands have been relatively neglected, which makes the investment in gas boilers unnecessary. The analysis of the hourly resolution result is that the operation periods

of gas boilers are limited, but it is still economical to have the gas boiler as peak demand cover when the electricity generation is not beneficial for the operator.

Compared to the heat-only generation, the co-generation units show relatively low variance. Even though the solver could invest in the GT, which is also an option, the preferred investment is the CCGT technology. The CCGT has the lowest variance since the flexibility of such technology is higher and adaptable for almost any input assumptions. In the hourly resolution result of the original scenario, bio boilers were not preferred since the period where the bioenergy is more favorable compared to other technology options was significantly low. This relativity is underestimated by aggregating the time series, which leads to the solver investing in bioenergy-based heat generation units. Similar to the solution time, the impact of the number of periods and period lengths for the P2H technology is undoubtedly visible. Since the P2H technology is strongly dependent on the EEX price, which varies hourly in this energy system, the impact is significant. The more time steps are considered in the energy system, the more the error of over-investing or under-investing in P2H technology will decrease. As the analysis shows, the suitable representative periods are between 12 and 18 days concerning the accuracy of the configuration and the optimization duration. For the length of the period, the length of between 24 and 72-time steps is enough to expect a sufficient optimization result.

Table 2: Variance per technology and solve time for different representative periods and period lengths

Cluster Period	GHOB [%]	CCGT [%]	GT [%]	BIOB [%]	HP [%]	GEOT [%]	EB [%]	Solve time [s]
4_24	−179.38	14.46	9.79	3.91	25	0	73	7
4_72	−142.55	4.95	56.68	0	25	0	73.17	8
4_168	−136.92	0	61.52	0	25	0	61.3	16
8_24	−178.73	15.62	39.22	35.52	25	0	72.5	9
8_72	−172.38	0.18	34.23	0	25.34	0	71.67	16
8_168	−165.68	0	62.37	19.67	25	0	63.6	30
12_24	−187.73	6.85	75	55.86	25	0	72.48	11
12_72	−178.11	0	60	21.52	25	0	65.12	24
12_168	−178.1	0	42.41	8.85	25	0	52.57	39
18_24	−182.1	0	58.8	20	0.65	0	27.93	15
18_72	−188.88	0	71.03	22.23	5.76	0	65.57	30
18_168	−175.25	0	54.73	24.32	25	0	50.25	67
24_24	−250.28	0	64.37	23.37	3.43	0	44.16	18
24_72	−192.95	0	69.45	25.05	5.05	0	66.92	44
24_168	−178.40	0	50.72	21.91	12.33	0	50	91
72_24	−158.05	0	48.21	0	1.46	0	19.83	53
72_72	−165.93	0	57.52	19	2.09	0	27.31	114
72_168	−172.96	0	42.84	7.04	5.782	0	32.12	397

The results also showed that the capacitive variance differs depending on the technology and fuel type, but it still proves that the behaviors of the overall configuration are complementary. Interestingly, the natural gas-based technologies were relatively over or underestimated, even up to 100% underestimation. The overestimation and underestimation of different technologies also highly depended on the input scenarios, emphasizing the importance of input assumptions. The time series aggregation fulfills its requirement to assess numerous scenarios and various input assumptions. It is essential to acknowledge that optimization results for future configuration planning should be assessed in comparison and not as a stand-alone result. Due to the highly unpredictable and incalculable forecast data, the optimization serves the purpose of observing different behaviors of the technology, which can support a robust portfolio configuration.

Figure 3 compares *NPV* and *CAPEX* results for different time series aggregation algorithms. The k-medoids aggregation algorithm is excluded from this analysis due to the high aggregation time and computational load. With the given input assumptions, the solver could not build and aggregate the time series of 15 years with the k-medoids algorithms. However, the following section includes the k-medoids algorithm for shorter time series. As expected, the averaging algorithm is the most distanced result from the reference scenario. The relativeness of different input assumptions is neglected by averaging 140 256 time series into dramatically lower resolution, making the result not comparable with the reference scenario.

Figure 4 shows the variance of each aggregated optimization result filtered by technology options. Like the financial result, the k-medoids algorithm demonstrates each technology's least capacitive difference. It is

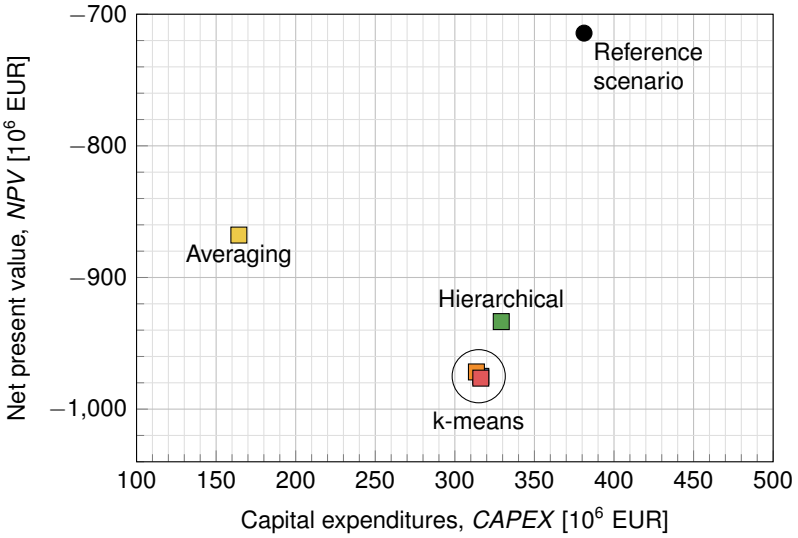

Figure 3: Net present value and capital expenditures for different time series aggregation methods

recognizable that the averaging method overestimates the capacities for each technology option and that the hierarchical method underestimates the capacity of heat pump technologies. The hierarchical algorithm ranked the heat pump technology lower than the other algorithms and assessed the gas turbine higher. The simplification of the input assumptions by the hierarchical algorithm is stronger than the other algorithms. Technologies with volatile dependencies can be underestimated in this algorithm, which makes it more difficult for technologies such as heat pumps or E-boilers to set the suitable representative period due to more unexpected developments. The capacitative overestimated technology options directly or indirectly depend on the most volatile input assumption. Even though the input energy of a geothermal plant depends on the power price, the constant heat source can level out the difference, elevating the value as a promising technology. The difficulty to optimize and the most discrepancy are shown for the gas-fired heat-only-boilers dispatched for the peak shaving. The number of representative periods is insufficient to express each peak demand, leading to higher variance in the GHOB result.

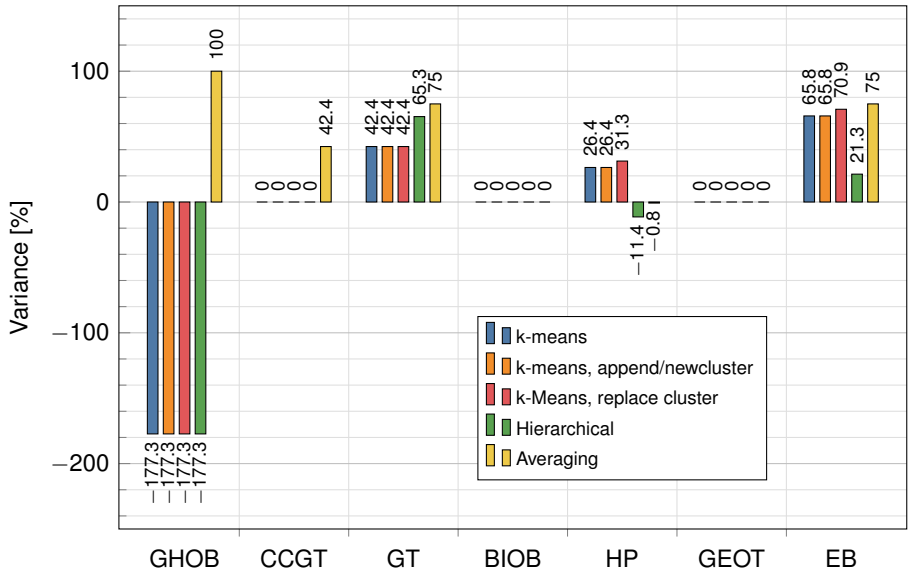

Figure 4: Variance comparison by cluster algorithm and capacity of technology

Overall, using the k-means or hierarchical algorithm as a clustering method is favorable for reducing the optimization problem's computational load. Keeping in mind that depending on the algorithm and the technology option, the particular capacitative result might be overestimated or underestimated. To reduce the computational load and shorten the optimization duration, the time series aggregation methods with appropriate periods can give sufficient indications for each portfolio configuration.

4.2. Sensitivity Analysis

Multiple activities exist to decarbonize gas-based power plants to realize a continuous hydrogen supply in the current gas grid. With enough supply for the required sectors, hydrogen will be the fastest way to decarbonize the gas-fired processes in Germany. Considering the significant increase of renewables in power generation, the potential of inland green hydrogen is considerable. This sensitivity analysis assumes that there will be enough hydrogen from 2040 onwards for the energy sector in Germany. Furthermore, green hydrogen combustion is counted as fossil-free fuel input, excluding the CO_2 certificate fee. For this analysis, the gas price ends in 2040 and is replaced by the hydrogen price from 2040 onwards. It assumes that there will be no natural gas in the grid from 2040, and the existing grid will be operated 100% with hydrogen. Besides the hydrogen price, all other input assumptions are equal to the original scenarios.

Figures 5a and 5b show the fuel mix of the portfolio for the H_2-integrated scenario and the original scenario. The apparent difference is the investment in bio boiler in the hydrogen integrated scenario. The share of gas/H_2-plants decreased, and the additional bio boiler and P2H plant compensated for the gap. The significant decrease in gas/H_2-based heat generation is recognizable from 2040. Due to the amortization of a plant, the bio boiler is invested from the beginning of the period. However, the high hydrogen price compensation can be seen by the increased heat generation of P2H and bio boiler from 2040. Even though hydrogen combustion relieves the CO_2 certificate fee, the hydrogen price is still too high to compete against power-based or bio-energy-based technologies.

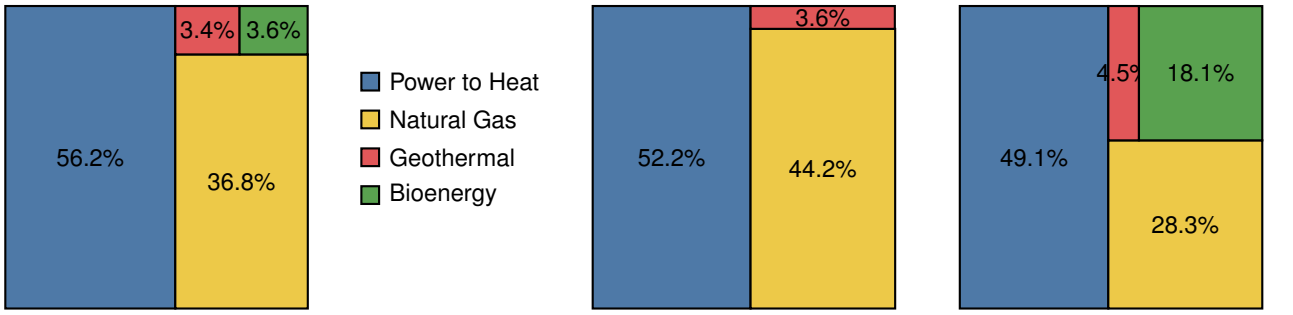

(a) H_2-integrated reference case

(b) Reference case

(c) H_2-integrated reference case (hiearchical aggregation)

Figure 5: Scenario results showing fuel mix

Figure 5c shows the H_2 sensitivity analysis results compared to the aggregated results. As a result of the main portfolio optimization, the hierarchical algorithm was chosen for the sensitivity analysis. The results represent a higher variance of bioenergy and P2H share of total installed capacities. The higher flexibility of P2H technologies is preferable when the depths of the EEX price development are low. Increasing gas prices and switch to expensive hydrogen prices encourages the model for more investment in P2H technologies, and the increase in the CO_2 price also encourages investment in bio boilers despite the higher investment costs. Especially the discrepancy in bioenergy share is higher than in other fuel types. The main reason behind this result is the transition from natural gas to hydrogen. The non-aggregated scenario considers the yearly development and transition of fuel switch, making the natural gas capacities very attractive before the transition. However, the aggregated scenario emphasizes the higher price of hydrogen in the later years, which reduces the natural gas / H2-based assets and increases the alternatives.

5. Conclusion

Within this contribution, a simplified district heating system has been modeled as a case study with the Python-based optimization framework aristopy. The objective was to optimize the future district heating portfolio configuration and assess various impact parameters influencing the composition and operation of the portfolio. Additionally, the work analyzes the impact of the time series aggregation methods on portfolio planning to simplify and accelerate the comparison of different scenarios.

Potential technologies were analyzed to close the capacitative gap resulting from the coal phase-out. The existing district heating systems and recently commissioned power plants have been modeled with the optimization framework aristopy. Different technology options were implemented for each generation site for the future scenario comparison, considering the geographical and technological feasibility. The model identifies the main drivers for an advantageous portfolio configuration by comparing various scenarios with different input assumptions.

This contribution also showed that the right time series aggregation method could reduce the computational load and produce viable optimization results for portfolio planning. From the total optimization time of 3 to 8 hours for 15 years of considered time horizons, the time series aggregation could reduce the time to under 60 seconds with manageable optimization results. Comparing different clustering algorithms and representative periods, the hierarchical algorithm showed the most promising optimization results with a significantly shorter solution time. For clustering time series of 15 years, 12 to 18 representative periods with 24 period lengths were sufficient to indicate the configuration well.

An improvement potential is the time determination of the investment or refurbishment. The decommissioning process of existing coal-fired power plants is a long-term process, and decommissioning or refurbishing existing gas units into H_2-firing plants will also take time. By integrating the time factor as a variable for the investment, the optimized time for the construction and commissioning phase can be estimated considering the transformation plan of the portfolio. In addition to the time determination, various factors, such as government support schemes, change with a fixed factor over time. These factors are primarily key factors derived from the regulatory framework. Certain subsidies are given by the full-load operation hours, or efficiency goals reached every year. By aggregating the input assumptions, it is impossible to consider such subsidy types and goals, which depend on the generation unit's operation. Such considerations can improve portfolio planning but require detailed and accurate forecast data. The value of such optimization can be enhanced by integrating multi-objective or multicriteria optimization of an energy system. With more ambitious climate goals, the regulations for the energy sector will be stricter and more demanding. This means the government will require specific key indicators from the energy utilities. Key indicators such as primary energy factor, yearly renewable share in the system, or specific greenhouse gas emissions can influence the dispatch of each generation unit. The current aristopy framework allows the user to adjust the objective function, but each optimization problem must have only one objective function. By integrating multi-objective optimization, the user can plan a portfolio configuration that satisfies different regulatory requirements and maximizes the financial value of the portfolio. The downside of such optimization is the computational load. A multi-objective optimization comes with an exponentially higher computational load and solution time due to the multidimensional variables. However, when comparing various scenarios and the impact of the input assumptions, the additional computational load could be compensated by various methods, such as time series aggregation. When multi-objective optimization with an appropriate solution time and assessable granularity is possible, it can enormously enhance the planning of a portfolio configuration.

CRediT author statement

Duk Yong Kwon: Methodology, Software, Validation, Formal analysis, Investigation, Data Curation, Writing - Original Draft, Writing - Review & Editing **Mathias Hofmann:** Conceptualization, Methodology, Validation, Resources, Writing - Original Draft, Writing - Review & Editing, Visualization, Supervision

Nomenclature

Abbreviations

BIOB Bioenergy heat-only-boiler

CCGT Combined cycle gas turbine

CHP Combined heat and power

CPU Central processing unit

EB E-Boiler

EEX European Energy Exchange

GAMS General Algebraic Modeling System

GEOT Geothermal heat pump

GHOB Natural gas heat-only-boiler

GT Gas turbine

HP River heat pump

LP Linear programming

MILP Mixed-integer linear programming

MINLP Mixed-integer nonlinear programming

P2H Power-to-heat

RAM Random-access memory

Letter symbols

C Costs, €

$CAPEX$ Capital expenditure, €

d Euclidean distance function, –

$\dot{F}$ Fuel rate, MW

I Investment, €

k Present value of annuity factor, –

k_i Technology specific coefficient, –

NPV Net present value, €

p Point p ,–

q Point q, –

$\dot{Q}$ Heat rate, MW

S Subsidy, €

t Economic lifetime, a

$\dot{W}$ Work rate, MW

Y Binary variable, –

Subscripts and superscripts

el Electric

f Fuel type

max Maximum

th Thermal

References

[1] J. DeCarolis et al. “Formalizing best practice for energy system optimization modelling”. In: *Appl. Energy* 194 (2017), pp. 184–198. DOI: 10.1016/j.apenergy.2017.03.001.

[2] L. Kotzur et al. “A modeler’s guide to handle complexity in energy systems optimization”. In: *Adv. Appl. Energy* 4 (2021), p. 100063. DOI: 10.1016/j.adapen.2021.100063.

[3] M. Wirtz, M. Hahn, T. Schreiber, and D. Müller. “Design optimization of multi-energy systems using mixed-integer linear programming: Which model complexity and level of detail is sufficient?” In: *Energy Convers. Manag.* 240 (2021), p. 114249. DOI: 10.1016/j.enconman.2021.114249.

[4] M. Wirtz, M. Heleno, A. Moreira, T. Schreiber, and D. Müller. “5th generation district heating and cooling network planning: A Dantzig–Wolfe decomposition approach”. In: *Energy Convers. Manag.* 276 (2023), p. 116593. DOI: 10.1016/j.enconman.2022.116593.

[5] L. Göke, M. Kendziorski, and F. Schmidt. *Planning macro-energy systems with multiple climatic years – A quadratic trust-region approach for Benders decomposition*. 2022. DOI: 10.48550/ARXIV.2208.07078.

[6] X. Yue, S. Pye, J. DeCarolis, F. G. Li, F. Rogan, and B. Ó. Gallachóir. “A review of approaches to uncertainty assessment in energy system optimization models”. In: *Energy Strategy Rev.* 21 (2018), pp. 204–217. DOI: 10.1016/j.esr.2018.06.003.

[7] M. Jüdes, A. Christidis, C. Koch, L. Pottel, and G. Tsatsaronis. “Combined optimization of the operation of existing power plants with the design and operation of heat storage systems for a large district heating network”. In: *Proceedings of ECOS*. Foz do Iguaçu, Paraná, Brazil, 2009, pp. 1–10.

[8] A. Christidis, C. Koch, L. Pottel, and G. Tsatsaronis. “The contribution of heat storage to the profitable operation of combined heat and power plants in liberalized electricity markets”. In: *Energy* 41 (2012), pp. 75–82. DOI: 10.1016/j.energy.2011.06.048.

[9] M. Hofmann, A. Christidis, J. Schneider, and G. Tsatsaronis. “Optimierung eines Energiesystems mit Kraft-Wärme-Kopplungsanlagen und Kurzzeit-Wärmespeichern”. In: *VDI Expertenforum – Energieeffizienz in den Städten und der Industrie von morgen*. Ed. by R. McKenna and W. Fichtner. in German. Karlsruhe, 2011, pp. 43–59. DOI: 10.5445/KSP/1000023676.

[10] M. Gonzalez-Salazar, J. Klossek, P. Dubucq, and T. Punde. “Portfolio optimization in district heating: Merit order or mixed integer linear programming?” In: *Energy* 265 (2023), p. 126277. DOI: 10.1016/j.energy.2022.126277.

[11] Open Energy Platform. *Framework Factsheets*. Retrieved: Feb 23rd, 2023. Version 2023. URL: https://openenergy-platform.org/factsheets/frameworks/.

[12] Openmod Initiative. *Open Models*. Retrieved: Mar 21st, 2023. Version Mar 17th, 2023. URL: https://wiki.openmod-initiative.org/wiki/Open_Models.

[13] M. Groissböck. “Are open source energy system optimization tools mature enough for serious use?” In: *Renew. Sust. Energ. Rev.* 102 (2019), pp. 234–248. DOI: 10.1016/j.rser.2018.11.020.

[14] M. L. Bynum et al. *Pyomo–optimization modeling in python*. Third. Cham, Switzerland: Springer, 2021. DOI: 10.1007/978-3-030-68928-5.

[15] W. E. Hart, J.-P. Watson, and D. L. Woodruff. “Pyomo: modeling and solving mathematical programs in Python”. In: *Math. Prog. Comp.* 3 (2011), pp. 219–260. DOI: 10.1007/s12532-011-0026-8.

[16] Gurobi Optimization, LLC. *Gurobi Optimizer Reference Manual*. 2023. URL: https://www.gurobi.com.

[17] S. Bruche. “Optimierung der Konfigurationen von Fernwärmeversorgungsanlagen unter Berücksichtigung der Einsatzpläne”. in German. Ph.D. thesis. Technische Universtät Berlin, Germany, 2021. DOI: 10.14279/depositonce-12574.

[18] W. F. Holmgren, C. W. Hansen, and M. A. Mikofski. “pvlib python: a python package for modeling solar energy systems”. In: *J. Open Source Softw.* 3 (2018), p. 884. DOI: 10.21105/joss.00884.

[19] M. Hoffmann, L. Kotzur, D. Stolten, and M. Robinius. “A Review on Time Series Aggregation Methods for Energy System Models”. In: *Energies* 13 (2020), p. 641. DOI: 10.3390/en13030641.

[20] H. Teichgraeber and A. R. Brandt. “Time-series aggregation for the optimization of energy systems: Goals, challenges, approaches, and opportunities”. In: *Renew. Sust. Energ. Rev.* 157 (2022), p. 111984. DOI: 10.1016/j.rser.2021.111984.

[21] Forschungszentrum Jülich. *Time Series Aggregation Module (tsam)*. Retrieved: Feb 23rd, 2023. Version 2.2.2. URL: https://github.com/FZJ-IEK3-VSA/tsam.

Dynamic modelling of ORC system for vessel waste heat recovery

Georgios Verykokkos[a], Efstratios Varvagiannis[b], Konstantinos Braimakis[c] and Sotirios Karellas[d]

[a] National Technical University of Athens, Athens, Greece, george_verykokkos@mail.ntua.gr
[b] National Technical University of Athens, Athens, Greece, svarv@mail.ntua.gr
[c] National Technical University of Athens, Athens, Greece, mpraim@central.ntua.gr
[d] National Technical University of Athens, Athens, Greece, sotokar@mail.ntua.gr

Abstract:

The present study presents the dynamic modelling in Dymola software of a vessel waste heat recovery Organic Rankine Cycle-ORC operating with R1233zd(E) that functions as a topping cycle of a cascade prototype also involving an Ejector Vapor Compression Cycle-EVCC as a bottoming cycle developed in the framework of the ZHENIT project. The ORC is designed to have a nominal thermal input of about 95 kW_{th} and is driven by Therminol VP1 oil at inlet and outlet temperatures of 150 ºC and 130 ºC while it includes two operating modes: 1) electricity-only, in which a recuperator is used and the condensation temperature is low and 2) combined heat and power (CHP), in which the recuperator is bypassed and the condensation temperature is raised to produce hot water. At the system design point, the evaporation temperature is 120 ºC, the condensation temperature 30ºC and 50ºC for electricity-only mode and CHP mode respectively, the superheating degree at expander inlet 10 K and the subcooling degree at condenser outlet 5 K. The system dynamic behavior is investigated considering a pump and expander reduction speed from 100% to 80% of the nominal. According to the results, the system has a fast response to the aforementioned disturbances.

Keywords:

Combined heat and power; Dynamic modelling; ECOS Conference; Electricity production; Organic Rankine cycle; Waste heat recovery.

1. Introduction

1.1. Basics of dynamic modelling

Organic Rankine Cycle (ORC) plays an important role in decarbonisation, especially in the field of waste heat recovery (WHR) in shipping, due to its effectiveness for the conversion of medium and high temperature waste heat into power [1]. ORC is an attractive WHR technology owing to its high reliability and simple design [2]. Because vessel engines operate extensively under variable loads, their waste heat has an intensely fluctuating profile (temperatures, flow rates), which poses technical challenges in the design and operation of ORC systems [3-4]. Therefore, dynamic modelling of ORC systems is necessary to predict their behavior and implement the essential control strategies for effective waste heat utilization, since dynamic models are able to trace the variation of the system operating parameters and detect critical points and outranges. In general, the dynamic behavior of a system including mechanical, electrical, fluid, thermal etc., can be described by a set of transient differential equations (ODE or PDE). The basic concepts that have to be known in dynamic modelling include system inertia, initial conditions, input stimulus variable and time constant [5].

1.2. Organic Rankine Cycles' dynamic operation

Dynamic behavior of ORCs is of interest during their start-up and shut-down and while their operating conditions are varied to respond to fluctuating boundary conditions (heat source, heat sink) to ensure their safe and efficient operation. The main investigated factors include [6]:

- the total system response time, overshoots, and identification of limitations and outranges
- recognition of the start-up and shut-down operation mode
- the part-load capability of the system

A prototype of the ORC system which is presented in this study is going to be developed in the context of the ZHENIT project, focusing on vessel engine WHR at different temperature levels to provide various on-board services. The present work presents the preliminary dynamic modelling of the prototype based on two operating modes: 1) electricity-only 2) Combined heat and power (CHP).

2. Methodology

2.1. System description

The prototype which is going to be developed within the ZHENIT project consists of a cascade ORC (topping cycle) integrated with an ejector-vapor compression cycle (bottoming cycle), utilizing heat sources of temperature levels ranging from 60 ºC (jacket cooling water) to 150 ºC (engine flue gas) for the production of electricity, heating and cooling. A micro-scale prototype (10 kW_e) will be constructed and demonstrated at lab-scale, along with other alternative proposed WHR solutions.

In the present study, only the topping cycle (ORC) of the aforementioned cascade system is presented, which operates under two modes: electricity-only and CHP mode and is driven by Therminol VP1 oil at a temperature of 150ºC. The two modes are simulated through Dymola software [7]. The layout of the system is illustrated in **Figure. *1***.

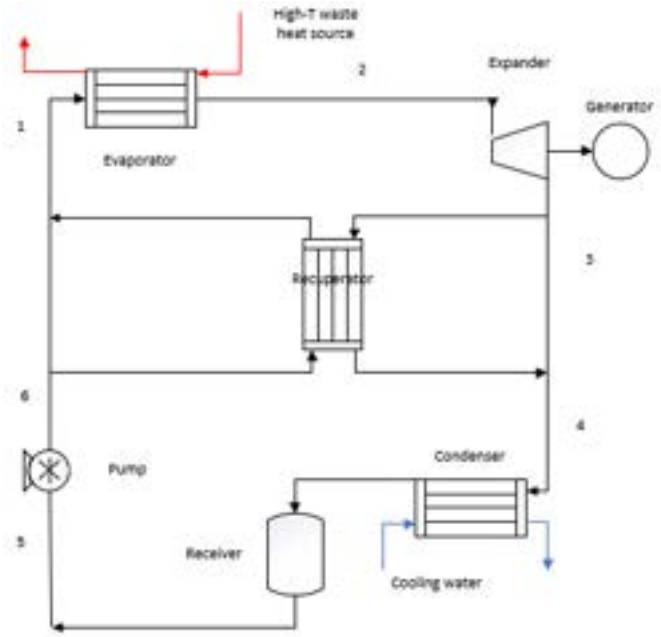

Figure. 1. ORC layout (2 first operating modes)

After a parametric study between three hydrofluoroolefins (HFOs), R1233zd(E) was proven to be the most suitable working fluid, considering its low environmental impact [low global warming potential (GWP) and ozone depletion potential (ODP)], following the regulations of Montreal [8] and Kyoto [9] protocol, as well as the F-gases regulations [10]. What is more, R1233zd(E) has no flammability, according to ASHRAE safety classification and relatively higher critical temperature, leading to higher cycle efficiency. The values of R1233zd(E) properties are mentioned in **Table 1**.

Table 1. R1233zd(E) properties

Working fluid	T_{crit} (°C)	p_{crit} (bar)	ODP	GWP	ASHRAE safety group
R1233zd(E) (ORC)	165.5	35.7	0	1	A1

2.2. System operating parameters and design point

The design point of the system was determined through a steady-state modelling methodology that is not elaborated in the present study. The values of the design point parameters are shown in **Table *2*Error! Reference source not found.**. In brief, the waste heat stream is Therminol VP1, which enters and exits the evaporator at 150 ºC and 130 ºC, respectively. The evaporation temperature (T_{evap}) for both modes was considered 120 ºC, while the condensation temperature (T_{cnd}) is 30 ºC in electricity-only mode (Mode 1) and 50 ºC in CHP mode (Mode 2).

The net electrical power output of the ORC ($P_{el,net}$) is defined as the gross electrical output of the expander ($P_{el,exp}$) minus the electrical power consumed by the pump ($P_{el,pump}$) and is given by the Eq. (1), considering also the expander-generator electromechanical efficiency ($\eta_{em,exp\text{-}G}$) and the pump motor efficiency ($\eta_{M,pump}$). The numeric subscripts (e.g. 2, 3) correspond to the points of the system layout in **Figure. *1***.

$$P_{el,net} = P_{el,exp} - P_{el,pump} = \dot{m}_{wf} \cdot \left(\eta_{em,exp-G} \cdot (h_2 - h_3) - \frac{(h_6 - h_5)}{\eta_{M,pump}} \right) \quad (1)$$

Table 2. ORC prototype design-point parameters

	Mode 1 (electricity-only)	Mode 2 (CHP)
Heat source mass flow rate (kg/s)	2.5 kg/s	
Heat source inlet temperature (℃)	150	
Heat source outlet temperature (℃)	130	
Expander isentropic efficiency	0.70	
ORC pump isentropic efficiency	0.65	
Expander-generator electromechanical efficiency	0.92	
ORC pump motor efficiency	0.95	
Superheating degree at expander inlet (K)	10	
Subcooling degree at condenser outlet (K)	5	
ORC working fluid	R1233zd(E)	
ORC evaporation temperature (℃)	120	
ORC condensation temperature (℃)	30	50
Cold stream temp. rise in recuperator (K)	20	-
Electrical power output (kW_e)	11.35	8.06
Heating output (kW_{th})	-	85.5
ORC electrical efficiency (%)	12.84	10.01

The heat input to the cycle ($\dot{Q}_{evap,ORC}$), is calculated according to Eq. (2), where $\dot{m}_{wh}$, $h_{wh,in}$ and $h_{wh,out}$ are the waste heat stream 's mass flow rate and enthalpies at the inlet and outlet of the evaporator respectively.

$$\dot{Q}_{evap,ORC} = \dot{m}_{wf}(h_2 - h_1) = \dot{m}_{wh}(h_{wh,in} - h_{wh,out}) \quad (2)$$

2.3. ORC dynamic modelling in component level

To develop a robust and concurrently a relatively fast dynamic model it is imperative to choose the proper components, correct initial conditions and to consider appropriate simplifying assumptions for the overall model. For instance, there are various types, sizes and modelling approaches for the heat exchangers, pumps, expanders etc. Consequently, in this point the types and the approaches of the models that were used in the model are described briefly.

2.3.1. Heat exchangers

The system heat exchangers (evaporator, condenser, recuperator) were modelled using the finite volume method, according to the available models that are included in the Thermocycle library [11]. In this method, the flow length of the heat exchanger is discretized into n equal volumes (cells), in which the equations of mass and energy conservation are applied.

The properties of the fluid for each volume can be calculated either at the mean states of the two nodes ("central scheme"), or it can be assumed that the properties of the fluid for each volume are equal to the properties of the fluid leaving the volume ("upwind scheme"). If the fluid flows only in one direction, the upwind scheme is more robust. The central scheme is more computationally intensive than the upwind scheme, but it deals better with discontinuities in the case of flow reversal. For the heat exchangers of the present study the upwind scheme was implemented. The properties of the fluid at the cell boundaries are represented by the symbol "*" in **Figure. 2**. The area of cell, volume of cell, temperature and enthalpy at each node are given by the following equations [Eq. (3), Eq. (4)] [12]:

$$A_i = \frac{A}{n}; \qquad V_i = \frac{V}{n}; \qquad i = 1,2,3,\dots,n \quad (3)$$

$$T_i = \frac{T_{i+1}^* + T_i^*}{2}; \qquad h_i = \frac{h_{i+1}^* + h_i^*}{2}; \qquad i = 1,2,3,\dots,n \quad (4)$$

The mass balance and the energy balance for each side and cell of the heat exchanger are given by Eq. (5) and Eq. (6) respectively:

$$\frac{d\dot{m}_i}{dt} = \dot{m}_i^* - \dot{m}_{i-1}^* \quad (5)$$

$$\frac{d\mathrm{U}_i}{dt} = (\dot{m}_{i-1}^* \mathrm{h}_{i-1}^* - \dot{m}_i^* \mathrm{h}_i^*) + \dot{Q}_i \quad (6)$$

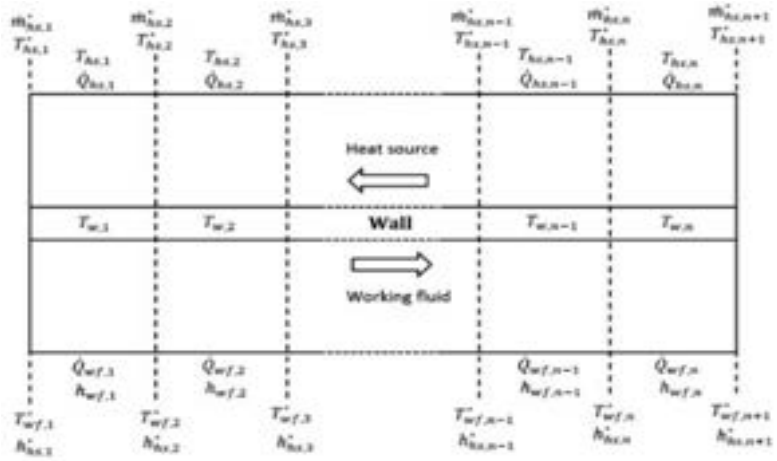

Figure. 2. Finite volume modelling approach of the heat exchangers [13]

Furthermore, for the modelling of the heat exchangers the following assumptions are considered:

- One-dimension fluid flow in the heat exchangers
- Constant heat flow per area unit and linear allocation of specific enthalpy in every control volume
- Negligible gravity forces in the fluid flow
- Negligible pressure drops in the heat exchangers and the pipes

2.3.2. Expander

For the dynamic modelling of the system a volumetric screw expander is used. The dynamics of the expander and the pump are very fast compared to those of the heat exchangers and are modelled at steady-state. Neglecting the heat loss, a volumetric expander can be modelled by its isentropic efficiency and filling factor, given by Eq. (7) and Eq. (8) respectively:

$$\eta_{exp,is} = \frac{\dot{W}_{exp}}{\dot{m}_{wf}(h_{exp,in} - h_{exp,out,is})} \tag{7}$$

$$ff = \frac{\dot{m}_{wf}}{\rho_{exp,in} V_{sw} N_{exp}} \tag{8}$$

The work output of the expander is given by Eq. (9):

$$\dot{W}_{exp} = \dot{m}_{wf}(h_{exp,in} - h_{exp,out}) \tag{9}$$

Expander boundary conditions are pressure and enthalpy at the inlet and pressure at outlet. In addition, the inlet and outlet are considered adiabatic.

Through the work of the expander, the net electrical power output and the waste heat energy as defined in Eq. (1) and Eq. (2) respectively, the ORC electrical efficiency is calculated and given by Eq. (10):

$$\eta_{el,ORC} = \frac{P_{el,net}}{\dot{Q}_{evap,ORC}} \tag{10}$$

2.3.3. Pump

Similarly, the dynamic response of the working fluid pump is very fast compared to that of the system heat exchangers. Hence, the pump is modelled by a steady-state lumped parameter model. In the present dynamic system, a centrifugal pump is used, whose role is to maintain the pressure and the mass flowrate of the working fluid. Usually for this type of pump the volume flow rate is a function of both the head and the rotational speed. However, in this model there is also the ability to define the mass flow as an input parameter. As a result, the pump power consumption and outlet temperature are calculated by the following equations [Eq. (11), Eq. (12)]:

$$P_{pump} = \frac{\dot{m}_{pump}(p_{out,pump} - p_{in,pump})}{\rho \eta_{is,pump}} \tag{11}$$

$$T_{out,pump} = T_{in,pump} + \frac{(1-\eta_{is,pump}) P_{pump}}{\dot{m}_{pump} C_{pump}} \tag{12}$$

2.3.4. Tank

A tank in an ORC system operates as a buffer storage for the working fluid to provide fluid or accumulate it during the transition phase of the system (start-up, part-load operation or shut-down). To calculate the working

fluid properties, the mass balance [Eq. (13)] and energy balance [Eq. (14)] are applied in the tank, while the tank level is calculated by Eq. (15), where V_0 is the initial total fluid volume in the tank.

$$\frac{d\dot{m}_f}{dt} = \dot{m}_{f,in} - \dot{m}_{f,out} \tag{13}$$

$$\frac{\mathrm{d(E)}}{dt} = \dot{m}_{in}h_{in} - \dot{m}_{out}h_{out} \tag{14}$$

$$H_{tank} = \frac{V}{V_0} \tag{15}$$

2.4. ORC system modelling

Based on the modelling of each individual component, the overall ORC system was modelled in Dymola through the Modelica language [14], as indicated in **Figure. 4** for Mode 1 and in **Figure. 3** for Mode 2.

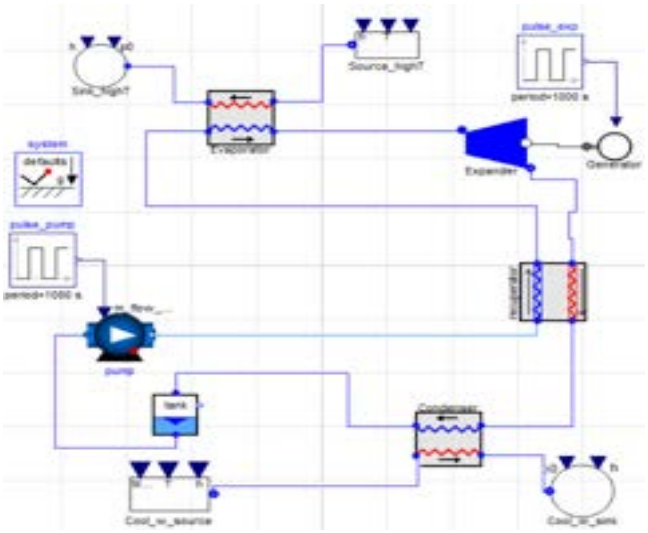

Figure. 4. Dymola ORC system layout (mode1)

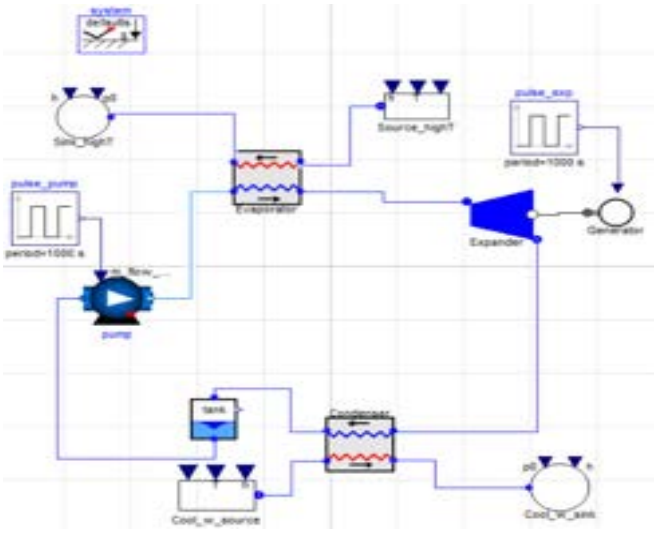

Figure. 3. Dymola ORC system layout (mode2)

During the modelling, the pressure drops of the pipes are omitted. Additionally, the system begins in steady-state (to avoid any discontinuities and consequent errors during the start-up) using initial conditions and then comes to a new steady-state after internal disturbances have been applied (heat transfer, mass flow etc). After that, a specific disturbance is imposed and the system results in a new steady-state. Two different scenarios regarding the type of the implemented disturbance are investigated, with alteration of the mass flow rate of the pump and change of the rotational speed of the expander. When the imposed disturbance ceases, the system returns to the initial steady-state. After a relevant investigation, it was inferred that a time period of 1000 s is well enough for the system to establish the steady-state. Thus, 1000 s is the time period that each disturbance lasts during the simulations.

3. Results and discussion

3.1. Initial conditions for the system

As mentioned before, the initial conditions of the system are selected so that the system reaches initially the steady-state at the design point. The two following scenarios are investigated for each mode:

Scenario 1: part-load operation of the system, reducing the pump mass flow rate at the 80 % of the nominal point and then bringing it back to the initial value

Scenario 2: part-load operation of the system, reducing the rotational speed of the expander at the 80 % of the nominal point and then bringing it back to the initial value

The initial conditions that have been defined for the system, after a relevant parametric analysis are presented in the **Table *3***.

For the simulations of Scenario 1 for both modes the pump mass flow rate is 0.435 kg/s for the first 1000 s, then it is reduced at 0.385 kg/s for the next 1000 s and finally it increases again at its initial value for the last 1000 s.

Likewise, for the simulations of Scenario 2 for both modes the rotational speed of the expander is 2400 rpm for the first 1000 s, then it is reduced at 1950 rpm for the next 1000 s and eventually it increases again at its initial value for the last 1000 s.

Table 3. Initial input conditions of the system

	Mode 1 (electricity-only)	Mode 2 (CHP)
Heat source mass flow rate (kg/s)	2.5	
Heat source inlet temperature (℃)	150	
Heat source outlet temperature (℃)	130	
Nominal working fluid mass flow rate (kg/s)	0.435	
Working fluid outlet temperature from the evaporator (℃)	130	
Working fluid outlet temperature from the condenser (℃)	25	45
Recuperator cold stream temperature rise (K)	20	-
Cooling water mass flow rate (kg/s)	3.94	3.94
Cooling water temperature inlet in condenser (℃)	15	25

Each simulation run is conducted for 3000 s with a time step of 6 s for each iteration and a tolerance of 0.0001 for the convergence of each iteration. Also, a noticeable feature is that it needs almost 170 s and 63 s in real time for the systems of Mode 1 and Mode 2 respectively to converge during the simulation.

3.2. Mode 1 results

To begin with, an important characteristic of the system is the temperature of the working fluid at the evaporator outlet, as, along with the pressure, it can be used for determining the superheating degree. The variation of this parameter for the scenarios of Mode 1 is depicted in **Figure. *5***. As it is illustrated in this diagram, initially the evaporator outlet temperature is 130 ºC for both scenarios, corresponding to the design parameter (120 ºC and 10 ºC superheating). During the disturbance, in the first scenario the examined temperature is increased, because, although the heat recovered from the heat source remains approximately the same [slightly lower due to reduction of the evaporator heat transfer coefficient (U)], the working fluid mass flow rate decreases and thus more energy is absorbed per working fluid unit mass. Furthermore, the fluctuation of the working fluid pressure in the evaporator is shown in **Figure. *6***. At the design point, the evaporator pressure is 15.7 bar, equal to the design evaporation pressure. On the contrary, when the disturbance occurs, in Scenario 1 the evaporator pressure decreases, as less working fluid mass passes through the expander, which has the same rotational speed. Thus, less pressure is required at the inlet of the expander in order for the working fluid to enter the expander. In the second scenario, in which the rotational speed of the expander is decreased, the evaporator outlet temperature is reduced. Inside the evaporator there is a constant volume of working fluid and while its density rises due to the pressure increase, there is more working fluid mass accumulated in the evaporator. The accumulated working fluid absorbs more thermal energy resulting in the reduction of the evaporator outlet temperature. Regarding the pressure, in Scenario 2 it increases, since the lower speed of the expander does not facilitate the passage of the working fluid, whose mass flow rate is imposed by the pump and remains constant. Hence, it needs to increase the pressure difference in the expander through higher pressure at its inlet. Furthermore, it is remarkable that in Scenario 2, although the pressure and subsequently the evaporation temperature rise, there is some liquid formed at the evaporator outlet reducing the temperature of the working fluid at the vapor saturation temperature (there is no superheating).

It is notable that the hypothesis of constant heat flow along the heat exchanger, which is implemented during the modelling of the heat exchangers, is validated by the fact that the inlet and outlet temperatures of the heat source are 150 and 130 ºC, while the evaporation temperature is 120 ºC. Thus, at the evaporator inlet and outlet there is an alteration of the temperature difference of the same order of magnitude. The impact of this hypothesis on the results is the easier convergence of the total system and the smooth temperature increase along the heat exchanger. What is more, as it is also shown in the following figure, the system response during the implemented disturbances is rapid, as the system reaches a new steady state quite fast.

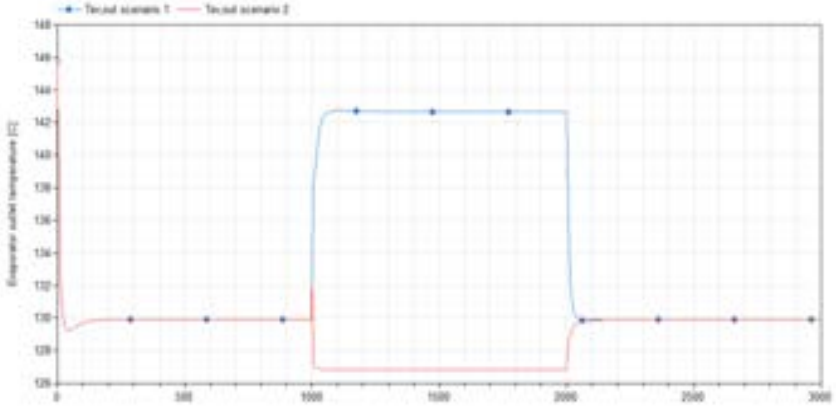

Figure. 5. Evaporator outlet R1233zd(E) temperature for scenarios 1 & 2 (Mode 1)

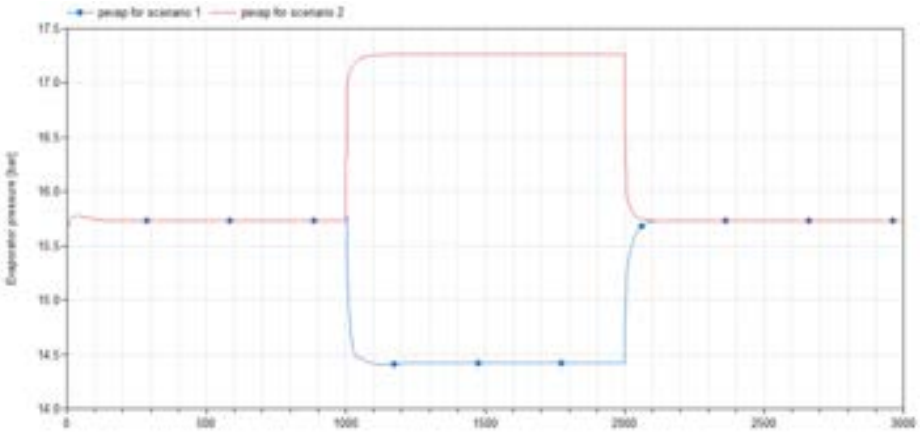

Figure. 6. Evaporator working fluid pressure for Mode 1

In **Figure. 7**, the inlet and outlet temperatures of the cold stream of the recuperator are shown. At the design point the temperature rise of the cold stream is indeed 20 K equal to the design parameter, while during the imposed disturbance, the system reaches fast to a new steady state. In Scenario 1 the cold stream temperature rise in the recuperator increases, while in Scenario 2 the respective value decreases. The heat transfer in the recuperator is described by Eq. (16).:

$$\dot{Q} = \dot{m}_{wf} c_p \Delta T \tag{16}$$

As a result, when the mass flow rate of the working fluid declines in Scenario 1 and the temperature of the fluid at the expander inlet rises, the thermal heat rate is increased. In this way, the temperature difference of the cold stream is increased so as to counterbalance the reduction of the mass flow rate. On the contrary, in Scenario 2, in which the rotational speed of the expander and its inlet temperature decline, the outlet temperature of the expander is also reduced, resulting in lower heat rate transferred to the cold stream. Thus, because the mass flow rate remains constant, the cold stream temperature difference decreases.

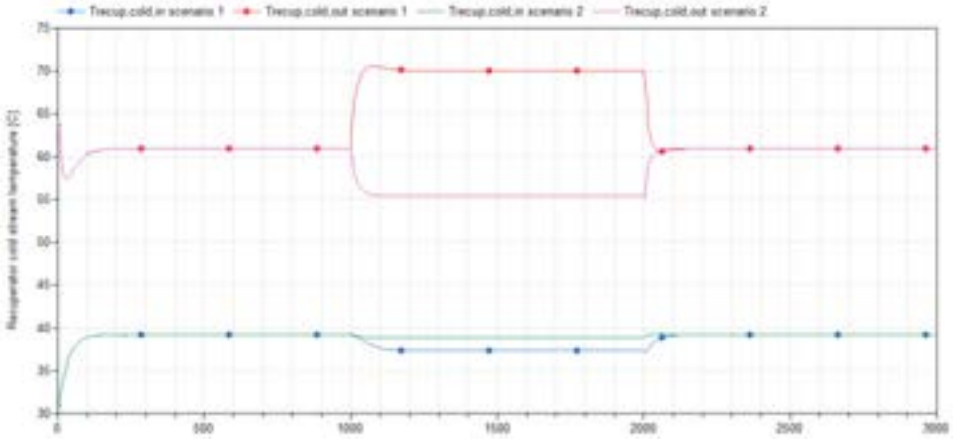

Figure. 7. Recuperator cold stream temperatures for scenarios 1 & 2 of Mode 1

The following diagrams demonstrate the working fluid temperature at the condenser outlet (**Figure. *8***) and the condenser pressure (**Figure. *9***) for the system of Mode 1 and the scenarios 1 and 2 respectively. As it is illustrated in the relevant diagram, during the dynamic modelling the working fluid temperature at the condenser outlet and at the design point, as well as the condensation temperature, is approximately 37 ºC, namely 7 ºC higher than the respective design point value. Similarly, the condenser pressure at the design point is 1.96 bar, higher than the design point condensation pressure. These significant differences are justified by the high complexity of the overall system and the fact that the design parameters of the heat exchangers, the expander and the pump have not been taken into account in the thermodynamic design of the system. In Scenario 1, the condenser outlet temperature of the working fluid and its pressure are reduced. This is due to the fact that the working fluid mass flow rate is decreased, while the cooling water mass flow rate and inlet temperature remain constant. Consequently, the working fluid is cooled in higher degree (lower outlet temperature and condenser pressure). In Scenario 2, the condenser outlet temperature and pressure remain stable, since the mass flow rate of the working fluid does not change and only the recuperator is affected by the reduced temperature at the expander outlet.

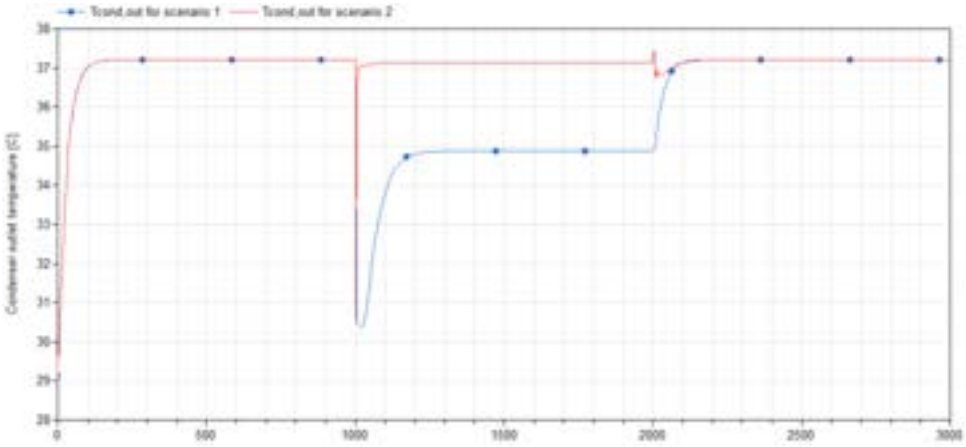

Figure. 8. Condenser outlet R1233zd(E) temperature for scenarios 1 & 2 (Mode 1)

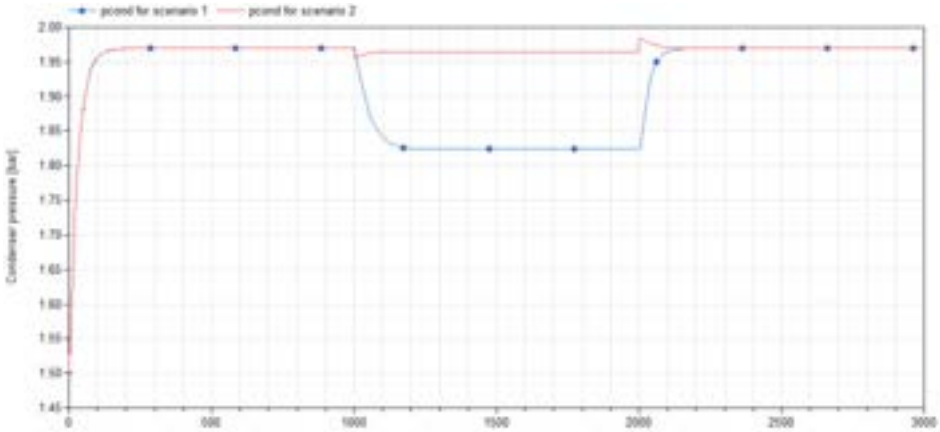

Figure. 9. Condenser working fluid pressure for Mode 1

As it is described in **Figure. *10***, the net electrical power output of the system for both scenarios at the design point is approximately 11280 W, almost equal as the design parameter of 11.35 kW (0.6 % lower). When the disturbance is imposed, in both scenarios the electrical power output is reduced because of the reduction of the working fluid mass flow rate (and lower expander inlet pressure and pressure difference as indicated before) and the rotational speed of the expander (lower evaporator outlet temperature and no superheating at expander inlet) respectively.

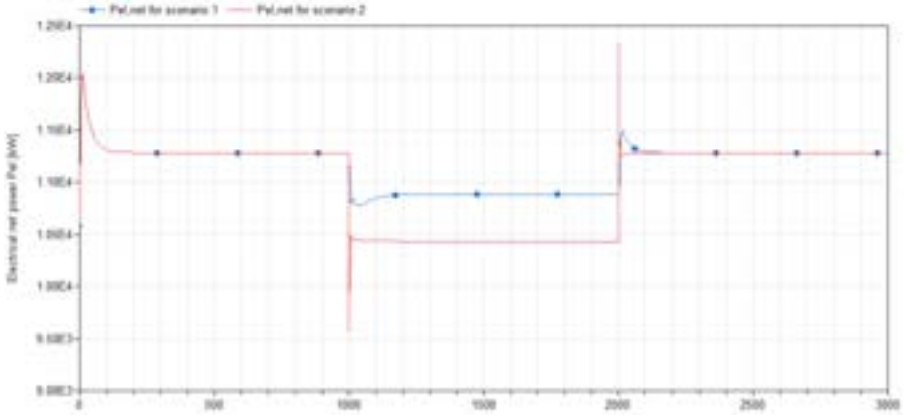

Figure. 10. System electrical net power (Mode 1)

It is worth pointing out that the heat source transfers 92.66 kW to the evaporator of the system at the design point. Therefore, the electrical efficiency of the system at the design point, according to Eq. (1), is 12.17 %, declining in 11.87 % and 11.40 %, due to the net electrical power output reduction, as long as the external disturbance lasts in Scenario 1 and 2 respectively. Moreover, as it is demonstrated from the diagrams of she system parameters for Mode 1, the system needs approximately 300 s in simulation time, to reach a new steady-state after an alteration in its parameters.

3.3. Mode 2 results

The temperature of the working fluid at the evaporator outlet for both scenarios of Mode 2 is demonstrated in **Figure. *11***, while the evaporator pressure for the correspondent cases is illustrated in **Figure. *12***. During the imposed disturbance, in the first scenario the examined temperature is increased, whereas in the second scenario the outlet temperature from the evaporator declines, following the trend of Mode 1 for similar reasons. At the design point the pressure is almost 15.7 bar, equal to the evaporation pressure. At the Scenario 1, the pressure of R1233zd(E) is reduced, as well as its mass flow rate, while lower expander rotational speed leads to the increase of the evaporator pressure in Scenario 2, for the same causes as in Mode 1.

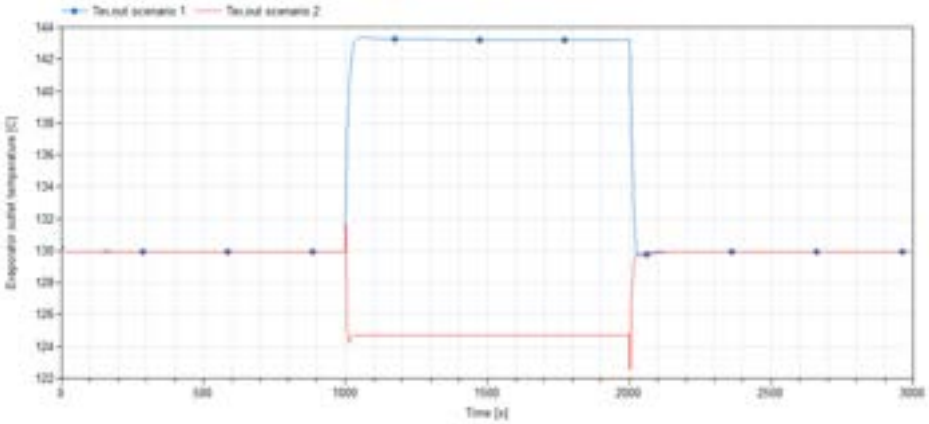

Figure. 11. Evaporator outlet R1233zd(E) temperature for scenarios 1 & 2 (Mode 2)

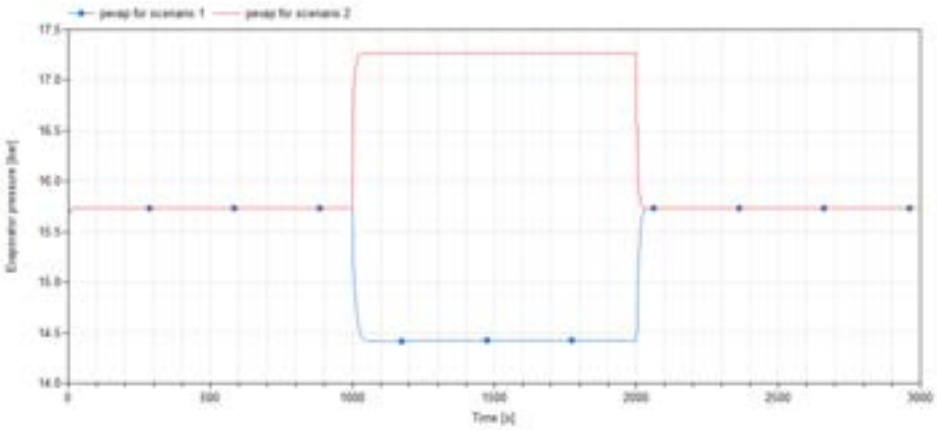

Figure. 12. Evaporator working fluid pressure for Mode 2

Moving to the condenser analysis, at the design point the working fluid outlet temperature (**Figure. *13***) is slightly lower than 50 ºC, which is the condensation temperature. In other words, R1233zd(E) exits the condenser lightly subcooled, being close to the saturation curve, but in the one-phase region along the whole simulation. During the disturbance, in Scenario 1 the temperature of the fluid after the condenser is lower for the same reason as it happens in the evaporator, while in Scenario 2, due to lower expander speed, the temperature at the expander outlet is lower, as mentioned above. Hence, because the cooling water parameters remain unchanged, the working fluid is cooled in a higher degree.

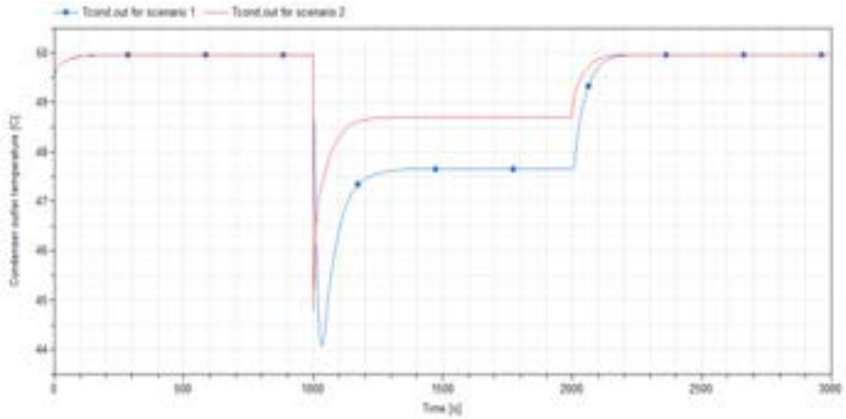

Figure. 13. Condenser outlet R1233zd(E) temperature for scenarios 1 & 2 (Mode 2)

Figure. *14* illustrates the condenser working fluid pressure, whose value at the design point is 2.93 bar just like the design parameter. During the disturbance, the pressure declines similarly to the working fluid temperature at the outlet of the condenser.

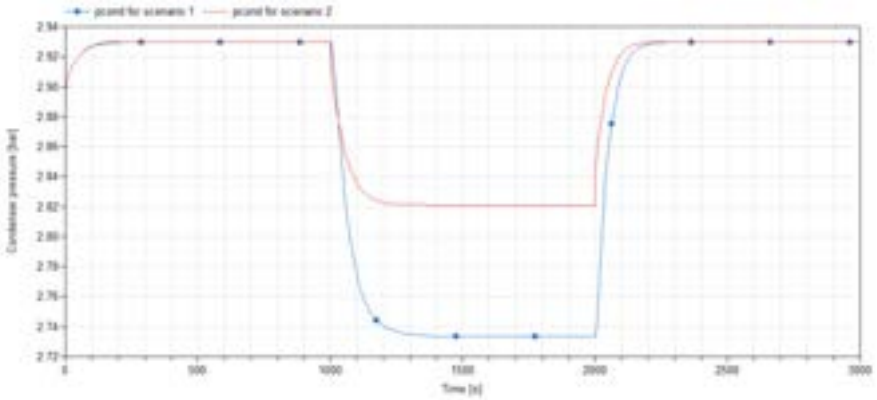

Figure. 14. Condenser working fluid pressure for Mode 2

Afterwards, in **Figure. *15*** the net electrical power output of the system is demonstrated. At the design point, the electrical net power is almost 7800 W, approximately 2.5 % lower than its design value. This deviation is owed to the fact that the design parameters of the system components have not been taken into account in the thermodynamic design, as well as because of the fact that R1233zd(E) was inserted in Dymola via CoolProp [15], which also contain some slight errors regarding its thermodynamic properties. In scenarios 1 and 2, the net power is reduced due to similar causes as in Mode 1.

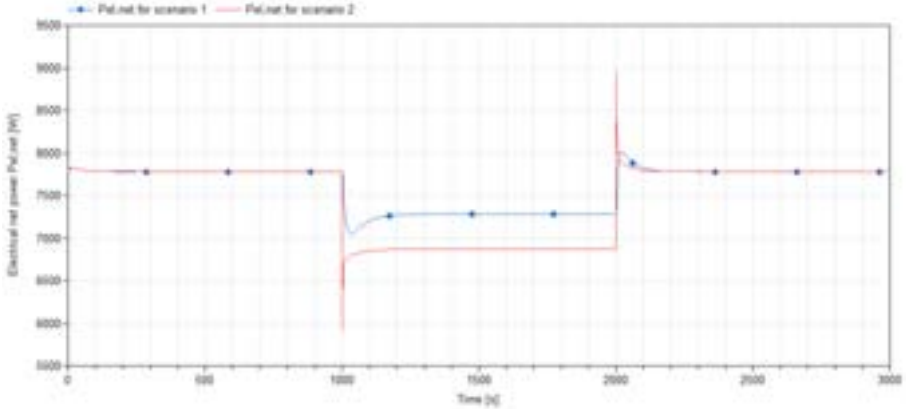

Figure. 15. System electrical net power (Mode 2)

It is notable that the heating output of the system of Mode 2 at the design point is 92.6 kW (higher than the design point value) decreasing in 89.44 kW and 87.03 kW in Scenario 1 and 2 respectively, while the heat source transfers 99.81 kW to the evaporator of the system at the design point. Therefore, the electrical efficiency of the system at the design point is 7.8 %, declining in 7.6 % and 7.4 % during the external disturbance in Scenario 1 and 2 respectively. The electrical efficiency arised from the dynamic modelling is lower than the design point ‘s one. The difference is owed to the same reasons as the deviation of the net electrical power. These are also the causes of the increased heating output of the system of Mode 2, which contribute to the reduced electrical efficiency.

4. Conclusions

The present study analysed the dynamic modelling of a vessel engine waste heat recovery Organic Rankine Cycle (ORC) system, which makes up the topping of a cascade ORC combined with an ejector vapor-cooling compression cycle (EVCC) and operates in two different modes: 1) electricity-only and 2) combined heat and power (CHP) via heat recovery by the ORC condenser. In the beginning, the basic concepts of dynamic modelling were mentioned briefly and the ORC system was described, as well as its main features and design point operating parameters. Furthermore, the modelling elements and methods at system component level were defined, whereas the total ORC system in Dymola and its simulations’ characteristics were highlighted. Eventually, after the presentation of the simulation results for the two modes and two different scenarios [1) reducing the pump mass flow rate at 80% of the nominal one and 2) decreasing the expander rotational speed at the 80% of the nominal one], it was demonstrated that the system, regarding most of its parameters’ values, during its steady-state at the design point parameters matches the values of the off design, resulting in net electrical power output up to 11.28 kW (Mode 1) with electrical efficiency of up to 12.17 % (Mode 1). What is

more, the system 's response to the disturbances ranges from 250 up to 300 s, whereas some slight deviations from the design point are owed to the fact that the design parameters of the system components have not been considered in its thermodynamic design.

Acknowledgment

This study has been performed within the context of the ZHENIT project, funded by the European Union's Horizon Europe research and innovation program, under grant agreement No. 101056801

Nomenclature

Abbreviations

WHR Waste heat recovery
ORC Organic Rankine cycle
LTES Latent thermal energy storage
ODE Ordinary differential equations
PDE Partial differential equations
CHP Combined heat and power
HFO Hydrofluoroolefin
GWP Global warming potential
ODP Ozone depletion potential
FMI Functional mock-up interface
EVCC *Ejector vapor cooling cycle*

Symbols:

T temperature, ºC
p pressure, bar
HT high temperature
n number
A area, m^2
V volume, m^3
h enthalpy, J/kg
$\dot{m}$ mass flow rate, kg/s
$\dot{Q}$ heat transfer rate, W
Ui internal energy, J
$\dot{W}$ work, W
ff filling factor
N rotational speed, rpm
P power, W
C specific heat capacity, J/(kgK)
U heat transfer coefficient, $W/(m^2K)$

Greek symbols

η efficiency
ρ density, kg/m^3
ΔT temperature difference

Subscripts and superscripts

$crit$ critical
$evap$ evaporation
cnd condensation
wf working fluid
em electromechanical
el electrical

exp	expander
$pump$	pump
M	motor
wh	waste heat
in	inlet
out	outlet
i	index
hs	heat source
w	water
sw	swept volume
is	isentropic
0	initial value
ev	evaporator
$cond$	condenser

References

[1] Zhai H., An Q., Shi L., Lemort V., Quoilin S., Categorization and analysis of heat sources for organic Rankine cycle systems. Renewable and Sustainable Energy Reviews 2016; 64: pp. 790-805

[2] Li Z., Yu X., Lei W., Jiang R., Yu X.., Huang R., Wu J., Comparative investigations of basic ORC and cascaded LTES-ORC under transient heat sources. Applied Thermal Engineering 2022; 207

[3] Li Z., Lu Y., Huang R., Chang J., Yu X., Jiang R., Yu X., Roskilly A.P., Applications and technological challenges for heat recovery, storage and utilisation with latent thermal energy storage. Applied Energy 2021; 283

[4] Da Lio L., Manente G., Lazzaretto A., A mean-line model to predict the design efficiency of radial inflow turbines in organic Rankine cycle (ORC) systems. Applied Energy 2017; 205: pp. 187-209

[5] Assadi M., Barzi Y. M., Organic Rankine Cycle Technology for Heat Recovery, 2018, Chapter 6: Dynamic Modeling of ORC Power Plants

[6] Braden Lee T., Dynamic simulation and experimental validation of an Organic Rankine Cycle model, [PhD Thesis, School of Mechanical and Mining Engineering, The University of Queensland], 2016

[7] Dassault Systemes, Dymola systems engineering, Multi-engineering modelling and simulation based on modelica and FMI – Available at:< https://www.3ds.com/products-services/catia/products/dymola/> [accessed 12.3.2023]

[8] European Parliament, Regulation (EC) No 2037/2000 of the European Parliament and of the Council of 29 June 2000 on substances that deplete the ozone layer. 2000, Council of the European Union

[9] United Nations, Kyoto Protocol. 1997: Kyoto, Japan

[10] European Parliament, Regulation (EU) No 517/2017 of the European Parliament and of the Council of 16 April 2014 on fluorinated greenhouse gases and repealing Regulation (EC) No 842/2006. 2014, Council of the European Union.

[11] Quoilin S., Desideri A., Wronski J., Bell I. H., Thermocycle library – Available at:< http://thermocycle.squoilin.eu/download/thermocycle-library/> [accessed 12.3.2023]

[12] Imran M., Pili R., Usman M., Haglind F., Dynamic modeling and control strategies of organic Rankine cycle systems: Methods and challenges, 2020, Applied Energy 276

[13] Xu B, Rathod D, Kulkarni S, Yebi A, Filipi Z, Onori S, et al., Transient dynamic modeling and validation of an organic Rankine cycle waste heat recovery system for heavy duty diesel engine applications. Applied Energy 2017; 205:260–7

[14] Modelica Association, Modelica language – Available at:< https://modelica.org/modelicalanguage.html> [accessed 12.3.2023]

[15] Bell I. H., Wronski, J., Quoilin S., Lemort V., Pure and Pseudo-pure Fluid Thermophysical Property Evaluation and the Open-Source Thermophysical Property Library CoolProp, Industrial & Engineering Chemistry Research 2014,53:2498-2508 – Available at:<http://www.coolprop.org/> [accessed 13.3.2023]

Analysis of an electrical energy production system from solar energy using a microscale CSP and ORC

Márcio Santos[a], Bernardo Almeida[b], Jorge André[c], Ricardo Mendes[d] and José B. Ribeiro[e]

[a] University of Coimbra, ADAI-LAETA, Coimbra, Portugal, marcio.santos@dem.uc.pt,
[b] University of Coimbra, ADAI-LAETA, Coimbra, Portugal, bernardo.almeida@dem.uc.pt,
[c] University of Coimbra, ADAI-LAETA, Coimbra, Portugal, jorge.andre@dem.uc.pt,
[d] University of Coimbra, ADAI-LAETA, Coimbra, Portugal, ricardo.mendes@dem.uc.pt,
[e] University of Coimbra, ADAI-LAETA, Coimbra, Portugal, jose.baranda@dem.uc.pt

Abstract:

Topics such as climate change and global warming that the world has been experiencing are increasingly a cause for alarm and concern which means that several goals must be achieved to avoid irreversible damages to the environment that interfere with its stability. For that aim, it is crucial to reduce emissions by discontinuing the use of fossil fuels, as an energy source to produce electricity, and replacing it with renewable energies. For a 100% renewable energy transition it is necessary to ensure dispatchability, flexibility, safety, and reliability of the electrical distribution grid. The main goal of this study is to evaluate the potential of a small-scale system using solar energy captured by Concentrated Solar Power (CSP) technology to produce electricity through an Organic Rankine Cycle (ORC). The System Advisor Model (SAM), one of the main tools for evaluating renewable energy projects, was used for system analysis. The CSP system implemented has gross installed power of 50kW$_e$ with 6 hours of Thermal Energy Storage (TES), whose main results are: production of 145529 kWh in the first year of operation, $559416.06 total investment cost and a Levelized Cost of Electricity (LCOE) of $0.3009/kWh. From the analysis of the results obtained, it can be seen the effect of economies of scale reflected in the LCOE value, which an expected consequence of scale reduction.

Keywords:

Concentrated Solar Power; Dispatchability; Organic Rankine Cycle; Renewables; Small-scale.

1. Introduction

The development of the humanity and society has brought, inherently, an energy dependence that is so naturally present in our daily life, almost like something previously acquired, that if for some reason there is a failure in the electricity distribution grid, there is no redundant system until that same failure is solved. This dependence coupled with the progressive increase in energy needs due, in part, to population growth and improvement in living standards, has led to an increase in the implementation of conventional electricity generation systems based on fossil fuels, resulting in increased greenhouse gas (GHG) emissions.

Topics such as climate change and global warming have emerged more frequently, more prominent and alarming, as they can result in irreversible damage to the environment. The use of renewable energy cannot be seen as a mere investment, but rather as a civil obligation, which implies a change of mindset to achieve carbon neutrality, a zero balance between GHG emissions and carbon retention. Knowing that this is a global problem with increasing emphasis among various organizations, several targets have been imposed and sanctions are applied to those who do not comply with them. For that aim, the member states of the European Union (EU) have stipulated and agreed to carry out, through the Paris Agreement (2015), three main goals [1] : limit the global average temperature rise below 2ºC compared to pre-industrial levels and pursuing efforts to keep it below 1.5ºC; increase the capacity to adapt to the impacts of climate change and foster climate resilience; make financial flows consistent with a pathway towards climate resilient and low-carbon development. Among the goals presented, the first is the most important since it could prevent irreversible damage to the environment that could put the population at risk.

In 2016, Portugal committed to ensuring carbon neutrality by the end of 2050 and developed the Roadmap for Carbon Neutrality (RNC2050) [1], which presents the main vectors of decarbonization and the path to follow for emission reduction, in conjunction with National Energy-Climate Plan (PNEC) [2], the main energy and climate policy instrument for the decade 2021-2030.

As can be seen from Figure 1, Portugal showed a growth in GHG emissions from 1990 until 2005, when it reached a peak, with a significant decrease from then on, in line with the targets for carbon neutrality. In 2017, there was a sharp increase in emissions related to the forest fires that occurred that year. An analysis of the evolution without considering emissions from Land Use, Land-Use Change and Forestry (LULUCF) shows a global trend of reducing GHG emissions.

Figure. 1. Evolution of Portugal's GHG emissions [3].

The electricity production sector, which will be target of analysis in this study, is one of the most potential for reducing emissions. The goal that Portugal has in this sector is clear, total decarbonization by 2050. The main drivers for decarbonisation in this sector are the transition from conventional electricity generation systems based on the use of fossil fuels to renewable energy systems, the discontinuation of use of coal by 2030 (already achieved) and natural gas by 2040, the development of new technologies that enable energy storage and ensure greater intelligence and flexibility of electrical distribution grid [1].

Investing in carbon neutrality will result in savings importing fossil fuels with a reduction in dependence on foreign countries. This result is of extreme importance for Portugal economy, as the acquisition of these fuels from other countries represents one of the main expenses. On the other hand, it would somehow attenuate fluctuations in the price of energy as it would be produced nationally, reducing the dependence on the availability of fossil fuels and external requirements or impositions.

In 2020, Portugal was the 11th country in the EU with the most energy dependence, with a value of 65.8%, while the European average was at 58%. The 8.4% decrease between 2020 and 2019 has three main causes: breakdown in energy consumption due to the COVID-19 pandemic; cessation of imports of coal for electricity production; increased production of energy from renewable sources at residential level [4]. The breakdown in consumption due to the pandemic leads the value of energy dependence in 2020 is not taken as a benchmark, since it is "artificially" low. The Figure 2 show the energy dependence in Portugal from 2000 until 2020, the latest data available.

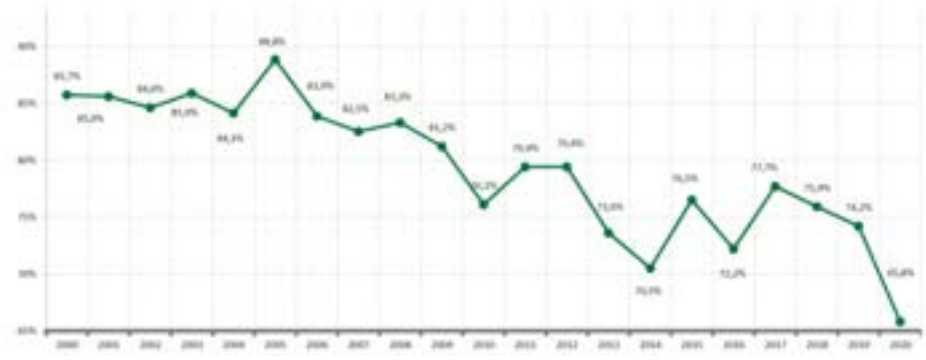

Figure. 2. Evolution of Portugal's energy dependence [4].

In recent years there have been large investments in photovoltaic (PV) and wind technology, but since their production is highly variable and depends on the availability of the resource, problems arise in terms of the dispatchability and stability of the electricity distribution network. As the goal is to ensure that 100% of the energy produced by 2050 comes from renewable resources, there will be a need to invest in other technologies that allow for some gap between the availability of the renewables and the production of electricity.

Following the development and investment in non-dispatchable electricity production technologies such as photovoltaic and wind, arises the need to create means of storage that allow a gap between renewable resource availability and electricity production. CSP technology emerges as one of the potential solutions to

ensure this gap. Its main advantage is the possibility of incorporating a TES system whose associated costs, as well as storage efficiency and environmental impact, make the technology favourable when compared to battery storage systems. Large-scale systems are well-known and mature but requires a very significant geographical area and a transport costs and losses due to a central electric production. Micro and mini-scale CSP – ORC systems integrated with TES can overcome the geographical limitation in a decentralized production.

1.1. Solar energy as a renewable resource

Solar energy is one of the most abundant renewable resources. Only 47% of the available solar energy reaches the Earth's surface (31% directly and the remaining 16% diffuse, through dust, water vapor and other molecules), with the remainder 53% of energy being divided into: 15% absorbed in the troposphere, 23% reflected by clouds, 7% reflected by the soil, 2% absorbed by the stratosphere and 6% of radiation diffused by the atmosphere, which does not reach the surface [5].

In Portugal, the implementation of renewable resources as a way of producing electricity has verified 3 main waves, each of which is represented by the development, growth and deployment of a given technology. The 80s and 90s were represented by the exploitation of water energy as a strong bet on electricity production, however, from the 2000s there is an increase in the use of wind energy and more recently the solar resource with a great potential for exploration and development [6].

The electricity consumption in Portugal has, in the last 10 years, an average value of 50 TWh/year, but only 2% of the total electricity production is made from solar energy [7], which reveals a fairly reduced value in relation to the potentiality it presents, however this technology is relatively recent when compared to the production systems from water and wind energy, which have a higher degree of maturity [8].

In assessing the potential of a zone for solar energy exploitation, radiation is the most important factor, being divided as: Direct Normal Irradiance (DNI), Diffuse Horizontal Irradiance (DHI) and Global Horizontal Irradiance (GHI).

Among several parameters, the one that has the greatest influence on the decision on the potential of a region to implement a Concentrated Solar Power (CSP) system is the DNI, which are considered more interesting and economically more viable when the value of the average DNI is equal to or greater than 2000 kWh/m^2.year [8,9]. Besides that, it is necessary to consider factors such as the level of nebulosity and dust since it decreases the fraction of available DNI.

Portugal is one of the countries in Europe with the highest availability of solar radiation, which, despite having a large variability in the distribution of the DNI, presents an annual average value across the national territory of 1800 kWh/m^2 [8], reaching 2200 kWh/m^2 in certain regions, with a number of annual hours of sun from 2200 to 3100 hours, which is much higher than the values of 1200 to 1700 hours presented by Germany [11], or 1750 hours of European average [12]. This makes Portugal one of the European countries with the greatest potential for exploiting this resource for national energy production. According to the study conducted in [9], CSP technology presents, in Portugal, the greatest potential among all renewable energies, namely: hydraulic, geothermal, biomass, wind, photovoltaic and waves / tide.

The DNI distribution in Europe and Portugal is presented in Figure 3.

(a) (b)

Figure. 3. DNI distribution in Europe (a) and Portugal (b) [11].

2. Concentrated Solar Power - CSP

The principle of operation of the CSP technology, presented in Figure 4, is based on the generation of electricity through a heat machine involving the concentration of solar radiation. Unlike PV technology that makes use of GHI, CSP technology only takes advantage of the DNI fraction of the radiation that, through solar concentrators, causes it to focus on a receiver, heating a Heat Transfer Fluid (HTF), thereby transforming solar radiation into thermal energy. The concentration of radiation makes it possible for the HTF to reach quite high temperatures, and this thermal energy can be used to produce electricity through a heat machine, usually with a turbine associated with a generator. on the other hand, to be stored to create a gap between solar radiation and electricity production, the concept of dispatchability.

The existence of Thermal Energy Storage (TES) allows thermal energy to be stored, creating a gap between solar radiation and electricity production, the concept of dispatchability. This makes it possible to create a more stable power distribution network, since most of the power generation systems are non-dispatchable, they produce and introduce electricity into the grid only when the primary resource is available. This inherent feature of CSP systems is one of its main advantages.

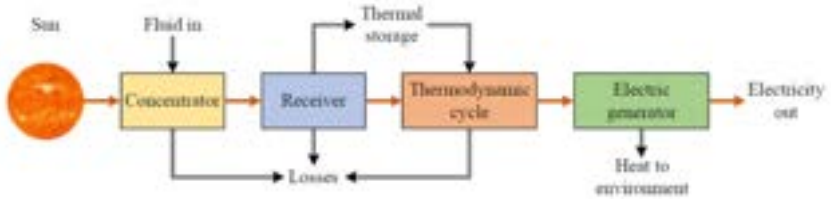

Figure. 4. Principle scheme of a CSP system [8].

2.1. CSP technologies

The aim of the solar field is to concentrate solar radiation in a receiver, converting it into thermal energy. The concentration of radiation causes the absorbed radiative density to be higher than that on the Earth's surface, so that, high temperatures are reached to operate a heat machine. The CSP technologies can be classified according to Figure 5. Despite having the same goal, they have forms and characteristics that distinguish them and that cause their application to be differentiated.

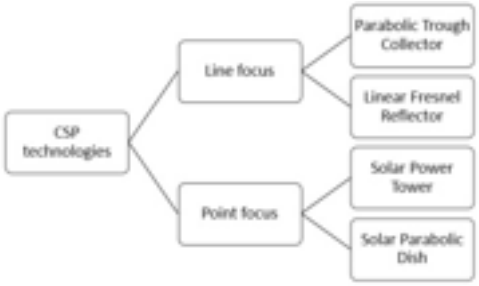

Figure. 5. Classification of CSP technologies

The aforementioned technologies are illustrated in Figure 6. A tracking system is implemented with the aim of making greater use of solar radiation, so that it constantly focuses the radiation on the receiver as the sun moves. Linear focus systems use single-axis tracking systems, while point focus systems are implemented with two-axis tracing systems. The orientation of the collectors is usually made in the longitudinal north-south direction with tracking east-west, as they ensure a greater amount of energy absorbed.

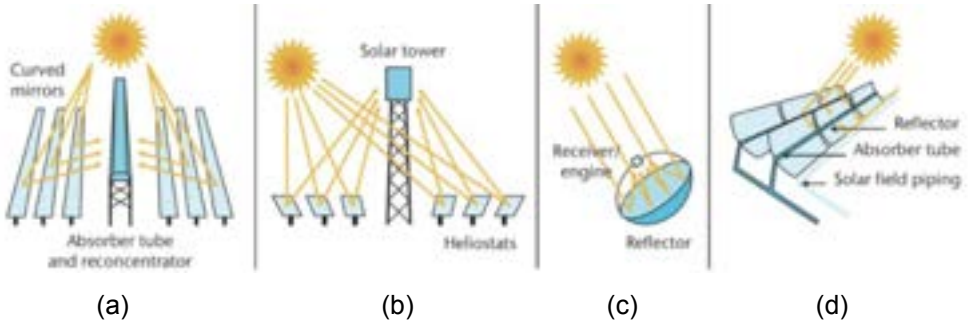

Figure. 6. Configuration of CSP different technologies: Linear Fresnel Reflector (LFR) (a); Solar Power Tower (SPT) (b); Solar Parabolic Dish (SPD) (c); Parabolic Trough Collector (PTC) (d) [12].

3. Thermal Energy Storage - TES

The production of electricity from renewable energies is not deterministic due to the variation of the natural resources' availability, as well as variation in electricity consumption demand. Given the intermittent availability, variability and limitation of certain natural resources, the existence of storage means becomes crucial to compete with the dispatchability that fossil-based electricity production systems offer, which has led to the development of different forms of energy storage, making them efficient and sustainable [13]. In general, the TES allows, not only the temporary storage of thermal energy for subsequent use of that same energy, compensating the intermittency of the solar resource or ensuring the dispatchability of the system, but also gives it thermal inertia, ensuring a greater stability of operation. Some of the advantages of its use are: increase the capacity factor (CF), ratio between actual energy produced during a certain period and maximum theoretical production in the same period, by 20-25%, without TES, up to 60-85% with TES; reduce the operation of the power cycle at partial load; and adjust production for peak hours [14].

3.1. Application of TES to CSP systems

The TES system can be classified, according to Figure 7, in Sensible Heat Storage, Latent Heat Storage and Chemical Energy Storage. The TES system can be characterized according to the following characteristics: capacity, charge and discharge power, efficiency, storage time, charge and discharge time and cost [13].

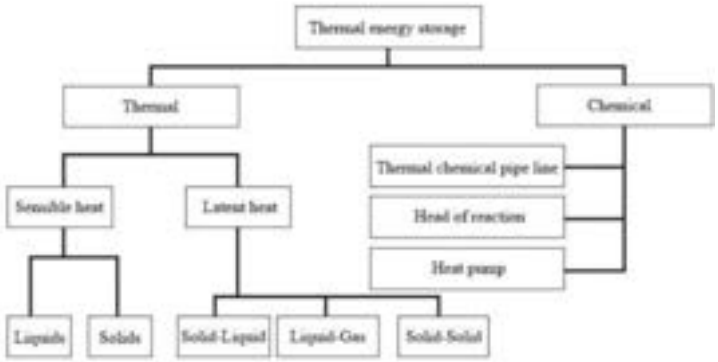

Figure. 7. Types of TES [13].

The development and choice of the TES system to be implemented requires knowledge of the heat flows between HTF and TES during the charge process and between TES and the heat machine in the discharge process [13]. Most CSP systems feature two types of TES configurations: two tanks and a single tank.

In the two-tank system the HTF is stored in two tanks with different temperatures, one of high temperature and another of low temperature, referred to as hot tank and cold tank, respectively. This type of TES can also be divided in direct, where the solar field HTF itself is used as a storage fluid, and indirect systems, where the HTF is different from the storage fluid, which requires the use of a heat exchanger that promotes energy exchange between the two fluids, as illustrated in Figure 8.

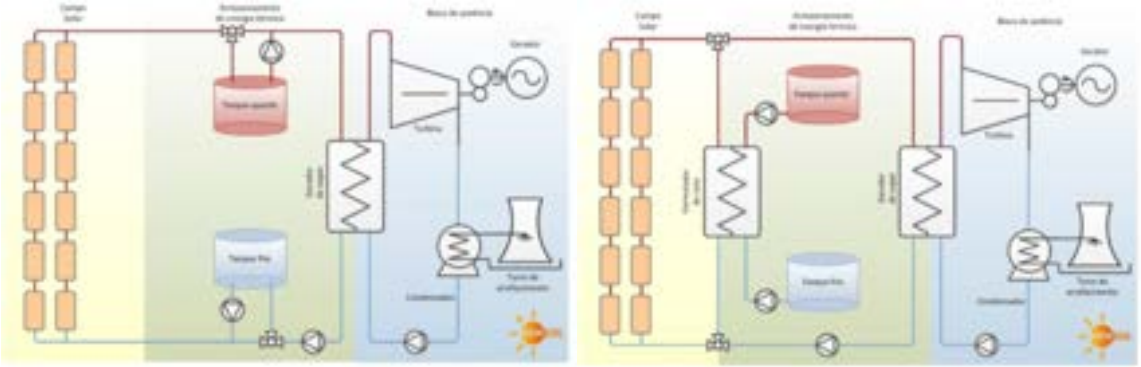

(a) (b)

Figure. 8. Configuration of a two-tank direct (a) and two-tank indirect (b) storage system [15].

In single tank storage systems is typically used thermocline technology, presented in Figure 9. The storage medium can be the HTF itself or be a solid medium, such as rock or silica. In the first case, the hot HTF remains at the top of the tank while the cold is at the bottom, with a dividing line called the thermocline gradient. The distribution of temperatures is guaranteed by the difference in material density at different temperatures. In the

second case, in the charging process, the hot solar field HTF enters the upper zone of the tank and goes out in the lower zone of low temperature, adding thermal energy to the solid medium, and the opposite happens in the discharge process [13]. This type of storage is suitable for small-scale applications as it allows a cost reduction compared to a two-tank system [16].

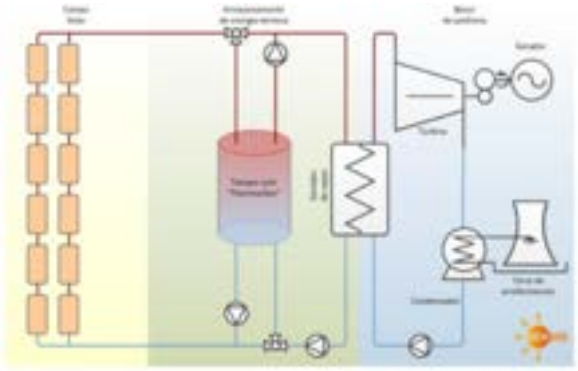

Figure. 9. Single-tank storage system [15].

4. Heat Transfer Fluid - HTF

The HTF is one of the key components of a CSP system with direct influence on its performance and efficiency [17]. According to Benoit et al. [18], the HTF should be compatible with the materials used and the storage medium and be able to operate in the required temperature range, receive and transfer heat easily and circulate well in confined spaces. Given the high amounts of HTF required in the system, since it can be used as a receiver and storage medium, it is necessary to minimize its cost while increasing performance [17]. In addition to having direct influence on overall system efficiency, the choice of the HTF determines the type of TES and the power cycle to be implemented, as well as the performance it can achieve [19]. Table 1 lists the main properties to be considered when choosing the HTF and its influence on the system.

Table 1. Influence of the HTF properties on the CSP system, adapted from [14]

Property	Related to
Solidification temperature	Minimum operation temperature
	Thermal protection needs
Thermal stability limit	Maximum operation temperature
Heat capacity	TES capacity
Viscosity	HTF pumping
Density	TES volume
Thermal conductivity	Heat transfer
	Heat exchanger

Improvement in the thermal properties of HTF is one of the most effective ways to improve the efficiency of CSP systems, as improvements in physical system have little potential since thermal losses are reduced [20]. The range of operating temperatures set by the HTF, and its thermal stability are the limiting factors in the overall system performance. The most used HTFs are water, gases, thermal oils, and molten salts.

5. Analysis of a small scale CSP system through the System Advisor Model (SAM)

CSP systems modelling is quite complex due to existing time fluctuations, resulting in transient effects on the system, unlike conventional power generation systems that operate much of the time at nominal conditions under a predominantly stationary regime [21].

The System Advisor Model (SAM) is a program developed by the National Renewable Energy Laboratory (NREL) from funding from the U.S. Department of Energy and is presented as: “free techno-economic software model that facilitates decision-making for people in the renewable energy industry”, namely, solar, water, wind, geothermal and biomass energy [22]. SAM is based on several series of the Transient System Simulation Program (TRNSYS) model that uses the program interface inputs as data to make the annual simulation with hourly system resolution.

SAM is currently one of the most widely used software for the techno-economic analysis of CSP systems worldwide. One of the main benefits of using SAM, in addition to the high reliability of results, is the possibility of making probabilistic, stochastic, and parametric analyses, with special emphasis on the latter, since it allows to make the optimization of the systems based on the change of certain parameters.

5.1. Implementation of the system in SAM

For the simulation of a model in SAM it is necessary, firstly, to choose the systems model and then the economic model that is intended to be used to carry out the analysis.

Due to the power cycle type being implemented and since it is the most mature technology and one of the most developed models in SAM, it was chosen the PTC system. Within the PTC option, the SAM have two distinct models: physical and empirical. The empirical model is based on correlations derived from data analysis obtained in systems already implemented, mainly from the Solar Energy Generating Systems (SEGS) in the United States of America, which makes the analysis of systems with distinct conditions more controversial and uncertain. On the other hand, the physical system uses concepts of heat transfer, thermodynamics, and fluid mechanics to characterize the system [23], so that, it was the model considered.

The economic model chosen was the Levelized Cost of Electricity (LCOE) Calculator, suitable for preliminary analysis of project feasibility, that is calculated using the Fixed Charge Rate method.

After base simulation, an optimization of the CSP system can be done. It involves choosing several parameters that result in a minimum LCOE value. If, on the one hand, the increase in the solar field area increases the electricity production, reducing the LCOE, on the other hand, in periods when the power cycle operates at maximum capacity and the TES is at maximum, the waste of energy increases, as well as the costs of installation, operation and maintenance. There is a turning point where the benefits of electricity production are overtaken by the remaining costs.

The system's layout to be implemented in SAM is presented in Figure 10.

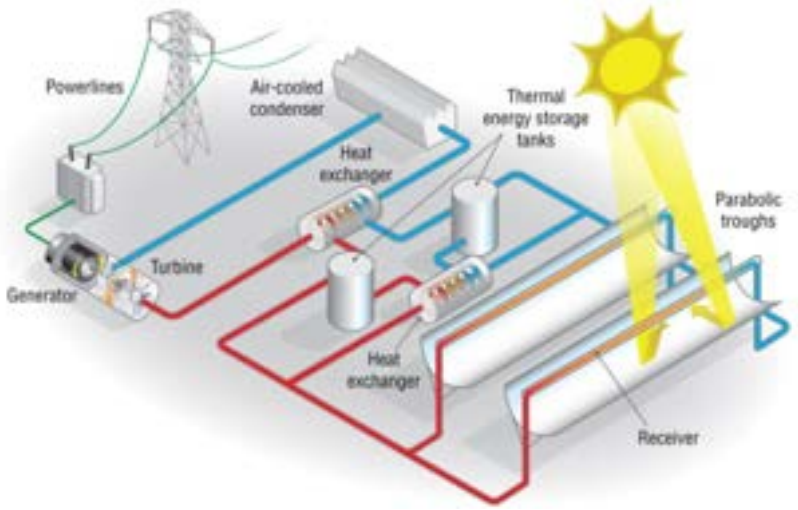

Figure. 10. Configuration of a CSP with PTC technology and a two-tank indirect TES [24].

5.1.1. Location and Resource

The SAM uses weather data from the National Solar Resource Data Base (NSRDB) developed by NREL.

Based on the levels of radiation that are potentially most viable for the implementation of a CSP system presented earlier, average values of DNI above 2000 kWh/m^2/year or 5.5 kWh/m^2/day, the region of Faro was chosen for the analysis of the system, since it is in the south of Portugal that is the region with the highest potential to implement CSP systems, exceeding the values presented above. The main values taken from the database with applicability in CSP systems are: DNI, average temperature and average wind speed and the values referring to Faro are 5.56 kWh/m^2/day, 18.5 ºC and 4.0 m/s, respectively.

5.1.2. System Design

The main system design parameters that determine the nominal capacity of the system are related with solar field, power cycle and TES, as presented in Table 2. Regarding the solar field, two crucial factor needs to be set: Solar Multiple (SM), design DNI.

The SM consists of the multiple of the area of the solar field required to operate the power cycle at its nominal capacity, in other words, a SM=1 represents the opening area of collectors that, when exposed to the design DNI, generates the exact thermal energy needed to operate the power cycle at nominal capacity.

The design DNI value is used to calculate the opening area of the solar collectors, which allows the power cycle to operate at the nominal capacity. Since the DNI varies over the course of the day and year, it is necessary to set a fixed value for the size of the solar field, knowing that its value depends on the geographical location and its value should be close, but lower, to the maximum value of annual DNI.

Table 2. Main system design parameters for SAM simulation [24].

Solar field	
Solar Multiple	2
Design point DNI	800 W/m^2
HTF	Pressurized water
Solar field inlet/outlet HTF temperature	100-150ºC
Power Cycle	
Design turbine gross output	50 kW_e
Estimated gross to net conversion factor	0.9
Cycle thermal efficiency	0.15
Thermal Energy Storage	
Hours of storage at design point	6 hours

5.1.3. Power cycle

The CSP system that comes implemented in SAM by default is the conventional Rankine cycle. SAM allows to use a custom power cycle, called User-Defined Power Cycle (UDPC), that uses data from a certain range of operating conditions to make a regression model. The performance of an ORC was modelled using actual operating data. The UDPC requires, as independent variables, the HTF temperature, HTF mass flow, and ambient temperature and, as dependent variables, gross electrical power generated and the thermal power entering the cycle.

5.1.4. Thermal Storage

The TES sizing is made based on the number of hours of storage of thermal energy that allow the power cycle to operate at the defined nominal power. In small-scale systems, the use of the thermocline tank has great potential, as it reduces costs and has high performance. According to Rodriguez et al. [16], the use of thermocline can represent a 33% reduction in TES costs when compared with a two-tank system with the same thermal storage capacity. SAM only allows to set two tanks direct and indirect storage system configurations, so that it was not possible to use thermocline in the simulation. The main parameters for TES are summarized in Table 3.

Table 3. Main parameters for TES system implementation [24].

Parameter	Value
TES type	Two-tank indirect storage system
TES fluid	Therminol VP-1
Hours of storage at design point	6h
TES thermal capacity	2 MWh_t
TES volume	109.04 m^3

5.1.5. Financial Parameters

The choice of the economic model, LCOE Calculator, leads to the need to introduce the relative installation costs as well as the fixed and variable operating costs. The relative installation costs were calculated through Power Purchase Agreement (PPA) economic model given that it allows to detail each of the system costs. The values used for installation costs are the values that SAM presents by default since they are an estimate of the NREL that best represents the typical costs of a CSP system. All standard values were kept except the cost of the power cycle which was adjusted to \$1000/kW_e to best represent the ORC under study. In Figure 11 the cost to install the CSP system is presented, where it is possible to verify that the solar field and TES system are the main costs, with shares of 31,5% and 22,2%, respectively.

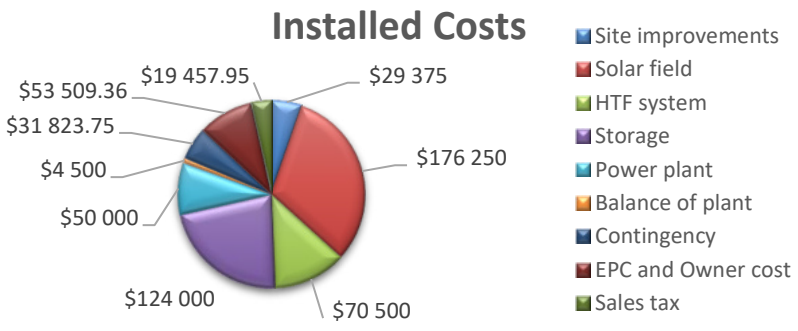

Figure. 11. CSP system installation costs [24].

5.2. Results

SAM offers several options that allow the analysis of the obtained data. The main results of the simulation are summarized in the Table 4 and a heat map is presented in the Figure 12. The implemented model has an annual electricity output of 145529 kWh for the gross installed power of 50 kW_e, which reveals a relative output of 3234 kWh/kW. The capacity factor of 36.9% is representative of the dispatchability that the system offers. The economic indicator obtained is the LCOE with a value of $0.3009/kWh which, when compared to the benchmark costs in the literature, $0.10-$0.20/kWh for large scale systems [8], is evident the effect of economies of scale of CSP systems.

Table 4. Main results of SAM simulation [24].

Metric	Value
Annual Net Electrical Energy Production	145,529 kWh-e
Annual Freeze Protection	618 kWh-e
Annual TES Freeze Protection	0 kWh-e
Annual Field Freeze Protection	618 kWh-e
Capacity factor	36.9%
Power cycle gross electrical output	163,673 kWh-e
First year kWh/kW	3,234 -
Gross-to-net conversion	88.9 %
Annual Water Usage	52 m^3
LCOE Levelized cost of energy	30.09 ¢/kWh

The heat map shows the system's electricity output over the first year of operation, which allows to identify the TES influence on the overall system performance. The period where the largest continuity of production occurs is between the 70th and 260th days of the year, between March and September, as expected. It is possible to verify the non-linear form as the system begins to operate in the early hours of the morning, which is in accordance with the relative movement of the sun during the year. Similarly, although the TES does not allow to see it, the system would also present a rounded shape in the afternoon. There are periods when the system presents negative power values, which is explained by the power required for the system to operate exceeds the power produced, such as the consumption of circulation pumps or tracking system.

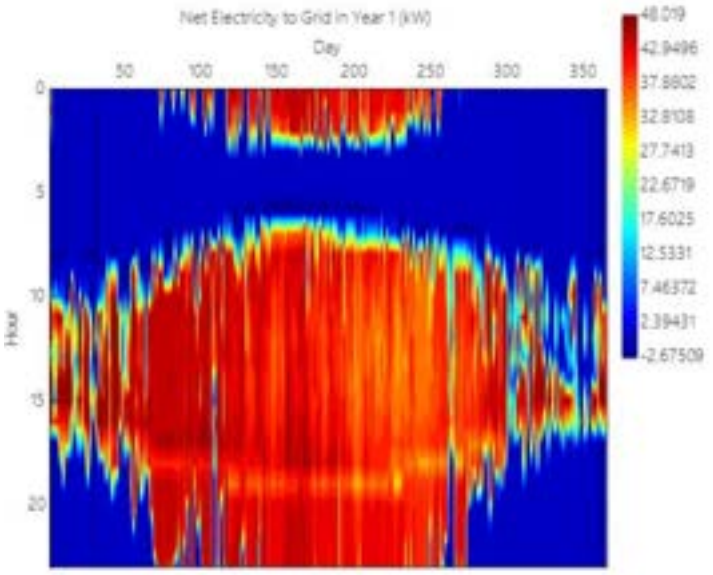

Figure. 12. Heat map of the system's electricity production in the first year of operation [24].

A comparison between the typical operation of the system on a winter day compared to a summer day is presented in Figure 13 and Figure 14, respectively. It is possible to verify that on winter days the system rarely operates at the design point as the available DNI is quite small and heavily affected by weather. All the energy that is captured in the solar field is used for power generation, there is no TES charging. On the other hand, in a typical summer day, a large amount of DNI is available which leads the system to a more stable operation at nominal capacity with great use of TES. The profile of the DNI on June 21 is perfect, which indicates that during that day the radiation does not face any obstacles to its passage, such as clouds.

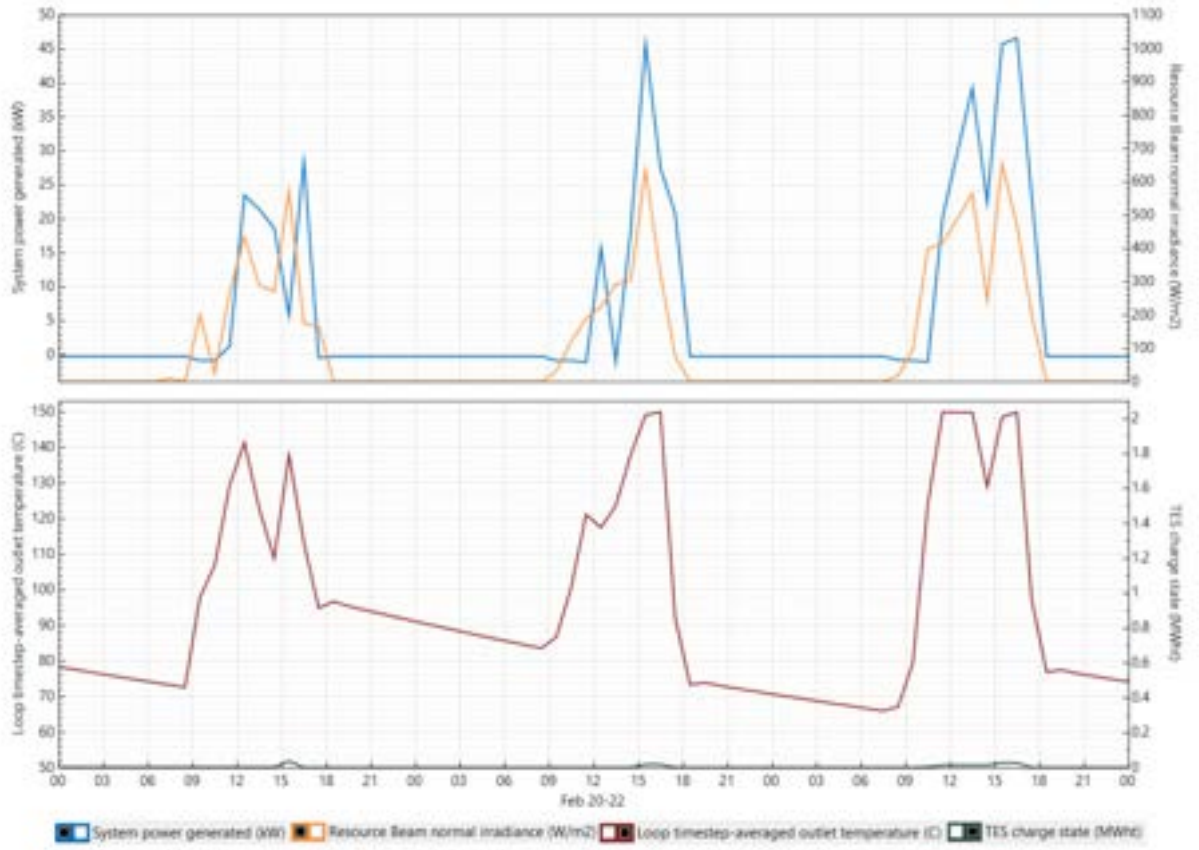

Figure. 13. System operation on a typical winter day [24].

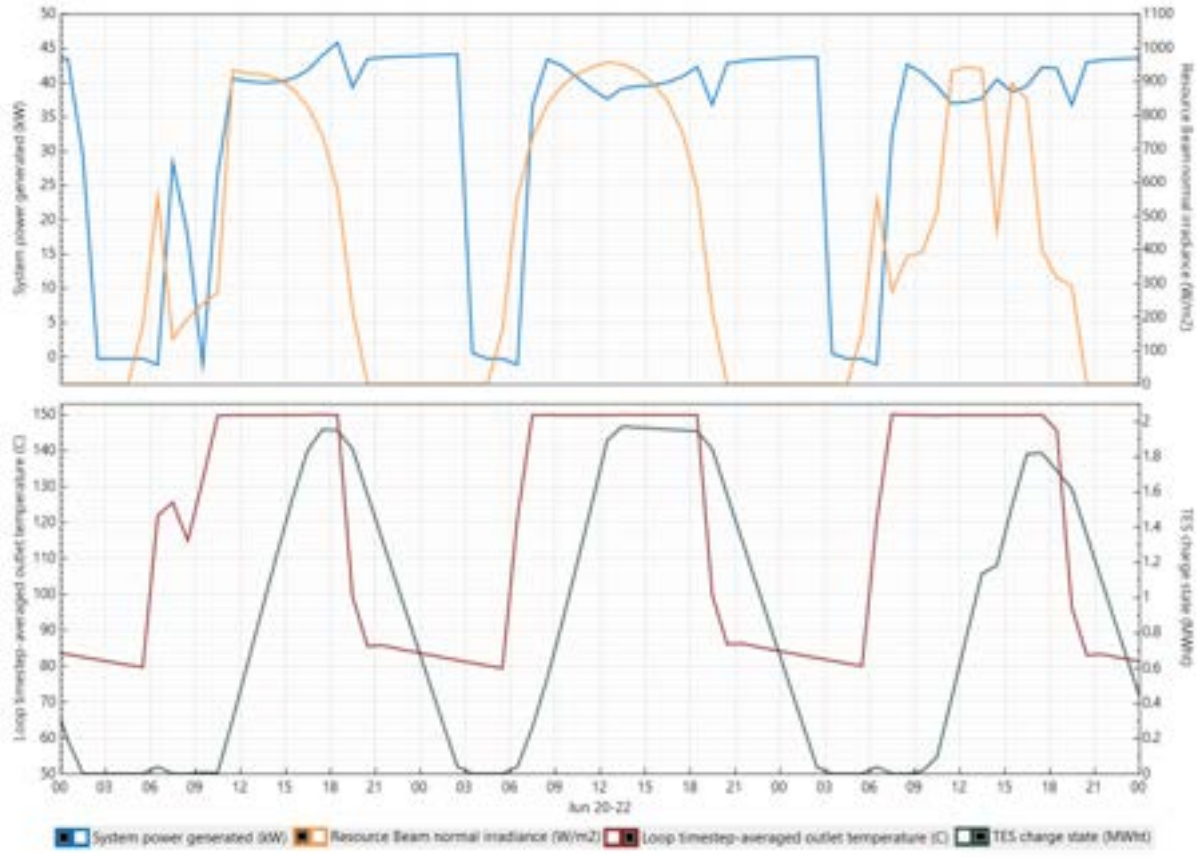

Figure. 14. System operation on a typical summer day [24].

Figure 15 presents the monthly production of energy throughout the year, where it is possible to prove that most of the production takes place between March and September. That profile results from the climate discrepancy between the seasons of the year in Portugal.

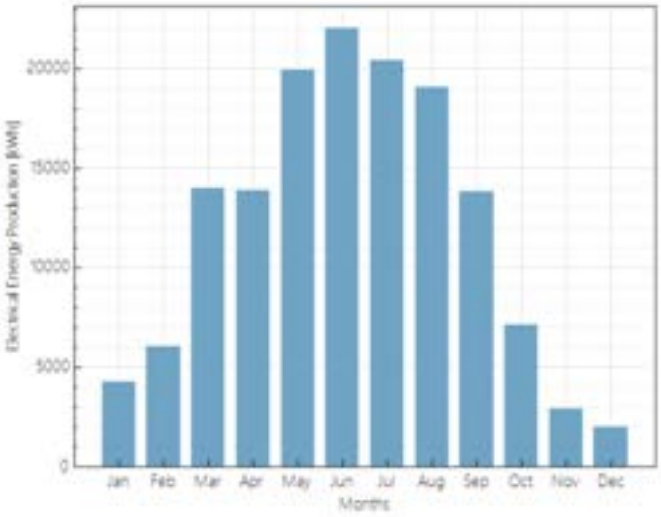

Figure. 15. Monthly electricity production in the first year of operation [24].

6. Conclusion

The shift in energy paradigm to reduce GHG emissions brings with it the need to replace the use of fossil fuels with renewable energies. In the power generation system, the transition to 100% renewable has some challenges to ensure the safety, reliability and dispatchability of the power grid. Following the development and investment in non-dispatchable electricity production technologies such as hydropower, wind, and PV, arises the need to create means of storage that allow a gap between renewable resource availability and electricity production.

CSP technology emerges as one of the potential solutions to ensure this gap. Its main advantage is the possibility of incorporating a TES system whose associated costs, as well as storage efficiency and environmental impact, make the technology favourable when compared to battery storage systems.

SAM is one of the leading tools for the techno-economic analysis of renewable energy systems, but its use for small-scale CSP systems analysis has proved challenging. Despite this, it was possible to implement a small-scale CSP case study that enabled the integration of an ORC actual data. The main results are: annual electricity production (145529 kWh), system cost ($559416.06), capacity factor (36.9%) and LCOE ($0.3009/kWh).

Even though SAM has several options that allow to create models with different characteristics and functions, it was found that it is not fully adapted for systems with such a small scale.

Acknowledgments

This work is funded by National Funds through the PRR – Plano de Recuperação e Resiliencia and European Funds through the Next Generation EU, under the scope of the project Polisport – Agenda AMR2 in copromotion with SRAMPORT.

References

[1] “ROTEIRO PARA A NEUTRALIDADE CARBÓNICA 2050 (RNC2050),” 2019.

[2] Direção Geral de Energia e Geologia, Agência Portuguesa do Ambiente, ADENE, and LNEG, “PLANO NACIONAL ENERGIA-CLIMA,” 2019.

[3] “Emissões GEE | Agência Portuguesa do Ambiente.” https://apambiente.pt/clima/emissoes-gee (accessed Mar. 14, 2023).

[4] Observatório de Energia, DGEG, and ADENE, “Energia em Números - Edição 2022,” 2022.

[5] J. J. C. S. Santos, J. C. E. Palacio, A. M. M. Reyes, M. Carvalho, A. J. R. Freire, and M. A. Barone, “Concentrating Solar Power,” in *Advances in Renewable Energies and Power Technologies*, vol. 1, Elsevier, 2018, pp. 373–402. doi: 10.1016/B978-0-12-812959-3.00012-5.

[6] “ENERGIA EM PORTUGAL - Principais Números,” 2020. Accessed: May 03, 2022. [Online]. Available: www.dgeg.gov.pt

[7] LNEG, “Fórum Energias Renováveis em Portugal 2020,” Jul. 2020.

[8] S. Tabassum *et al.*, “Solar Energy in the United States: Development, Challenges and Future Prospects,” *Energies (Basel)*, vol. 14, no. 23, Dec. 2021, doi: 10.3390/en14238142.

[9] M. T. Islam, N. Huda, A. B. Abdullah, and R. Saidur, “A comprehensive review of state-of-the-art concentrating solar power (CSP) technologies: Current status and research trends,” *Renewable and Sustainable Energy Reviews*, vol. 91. Elsevier Ltd, pp. 987–1018, Aug. 01, 2018. doi: 10.1016/j.rser.2018.04.097.

[10] A. Alami Merrouni, R. Conceição, A. Mouaky, H. G. Silva, and A. Ghennioui, “CSP performance and yield analysis including soiling measurements for Morocco and Portugal,” *Renew Energy*, vol. 162, pp. 1777–1792, Dec. 2020, doi: 10.1016/j.renene.2020.10.014.

[11] “Weather data and software for solar power investments | Solargis.” https://solargis.com/ (accessed Sep. 16, 2022).

[12] Newsol, “Energia Solar de Concentração (CSP Concentrated Solar Power).” http://www.newsol.uevora.pt/pt-pt/tecnologia-csp/ (accessed May 11, 2022).

[13] I. Sarbu and C. Sebarchievici, “A Comprehensive Review of Thermal Energy Storage,” *Sustainability* , vol. 10, no. 1, Jan. 2018, doi: 10.3390/su10010191.

[14] A. Bonk, S. Sau, N. Uranga, M. Hernaiz, and T. Bauer, “Advanced heat transfer fluids for direct molten salt line-focusing CSP plants,” *Prog Energy Combust Sci*, vol. 67, pp. 69–87, Jul. 2018, doi: 10.1016/j.pecs.2018.02.002.

[15] Newsol, “Armazenamento de Energia Térmica (TES Thermal Energy Storage).” http://www.newsol.uevora.pt/pt-pt/tecnologia-tes/ (accessed Jul. 05, 2022).

[16] J. M. Rodríguez, D. Sánchez, G. S. Martínez, E. G. Bennouna, and B. Ikken, “Techno-economic assessment of thermal energy storage solutions for a 1 MWe CSP-ORC power plant,” *Solar Energy*, vol. 140, pp. 206–218, Dec. 2016, doi: 10.1016/j.solener.2016.11.007.

[17] K. Vignarooban, X. Xu, A. Arvay, K. Hsu, and A. M. Kannan, “Heat transfer fluids for concentrating solar power systems - A review,” *Appl Energy*, vol. 146, pp. 383–396, May 2015, doi: 10.1016/j.apenergy.2015.01.125.

[18] H. Benoit, L. Spreafico, D. Gauthier, and G. Flamant, “Review of heat transfer fluids in tube-receivers used in concentrating solar thermal systems: Properties and heat transfer coefficients,” *Renewable and Sustainable Energy Reviews*, vol. 55, pp. 298–315, Mar. 2016, doi: 10.1016/j.rser.2015.10.059.

[19] W. Fuqiang, C. Ziming, T. Jianyu, Y. Yuan, S. Yong, and L. Linhua, “Progress in concentrated solar power technology with parabolic trough collector system: A comprehensive review,” *Renewable and Sustainable Energy Reviews*, vol. 79, pp. 1314–1328, 2017, doi: 10.1016/j.rser.2017.05.174.

[20] Y. Krishna, M. Faizal, R. Saidur, K. C. Ng, and N. Aslfattahi, “State-of-the-art heat transfer fluids for parabolic trough collector,” *Int J Heat Mass Transf*, vol. 152, May 2020, doi: 10.1016/j.ijheatmasstransfer.2020.119541.

[21] M. J. Wagner and P. Gilman, “Technical Manual for the SAM Physical Trough Model,” 2011. [Online]. Available: http://www.osti.gov/bridge

[22] “Home - System Advisor Model - SAM.” https://sam.nrel.gov/ (accessed Aug. 09, 2022).

[23] R. Soria, “INTRODUÇÃO AO USO DE FERRAMENTA SAM.”

[24] CO. National Renewable Energy Laboratory. Golden, “System Advisor Model Version 2022.5.5 (SAM 2022.5.5).” https://sam.nrel.gov .

Thermodynamic and economic performance of novel organic cycle designs powered by low-temperature waste heat

Panagiotis Lykas[a], Christina Antonopoulou[a], Apostolos Gkountas[b], Konstantinos Atsonios[a], Grigorios Itskos[a], Nikolaos Nikolopoulos[a], Panagiotis Grammelis[a], Dimitrios Manolakos[c] and Panteleimon Bakalis[b]

[a] Centre of Research and Technology Hellas, Chemical Process Engineering Research Institute, Athens, Greece, p.lykas@certh.gr, antonopoulou@certh.gr, atsonios@certh.gr CA, itskos@certh.gr, n.nikolopoulos@certh.gr, grammelis@certh.gr
[b] Psyctotherm, R&D Department, Piraeus, Greece, agountas@psyctotherm.gr, pbakalis@psyctotherm.gr
[c] Agricultural University of Athens, Department of Natural Resources and Agricultural Engineering, Athens, Greece, dman@aua.gr

Abstract:
Waste heat recovery is one of the alternative energy sources that have been investigated by scientists in recent decades to address ongoing environmental problems, such as global warming. The organic Rankine cycle is a promising waste heat recovery technology to exploit industrial waste heat, even at low-temperature levels (<100^{o}C), for electricity production. The proposed study presents and compares two innovative organic cycle designs feeding with the same available heat source. The first cycle includes a nearly isothermal expander, where a small fraction of the supplied waste heat is continuously provided to the expander, aiming to approach a quasi-isothermal process instead of an adiabatic one, avoiding the temperature decrease due to the expansion process. The result is an increase in the cycle's thermal efficiency and greater power output production compared to the adiabatic expansion process. The second configuration is called the trilateral flash cycle, where the working fluid does not reach the saturated vapor state during heating at the heat recovery system, while it expands into the two-phase region of the fluid. The aforementioned cycles are investigated parametrically in terms of thermodynamics with a low-temperature heat source (80-100^{o}C) for different organic working fluids, such as the R1234ze(E), R1234yf, R1233zd(E), and R134a. Parametric studies are carried out through Aspen Plus software, while a techno-economic comparison of the organic cycle designs is conducted based on Aspen Process Economic Analyzer and literature data. According to the final results, R1233zd(E) seems to be the most proper working fluid thermodynamically, while the organic Rankine cycle with nearly isothermal expansion achieves higher values of both electrical and exergy efficiencies, reaching the maximum values of 10.51%, and 52.27%, respectively. In terms of finance, both cycles achieve similar payback period values, reaching the value of 1.56 years in the case of the trilateral flash cycle and assuming 8,000 operating hours per year. Finally, for the trilateral flash cycle, lower net present value levels of about 30% compared to the corresponding values for the other cycle, are determined despite its lower installation cost.

Keywords:
Trilateral Flash Cycle, ORC, isothermal expander, thermodynamic analysis, cost analysis, low-grade WHR.

1. Introduction

In recent decades, the increasing energy demand, economic, and population growth, as well as the high penetration of fossil fuels into the energy sector have led to significant environmental problems, such as air pollution, and global warming. Thus, the international community and scientists worldwide have promoted the utilization of alternative energy sources, such as the recovery of waste heat. In the industrial sector, considerable amounts of heat in various temperature levels depending on the processes, are rejected to the ambient, which can be recovered and further exploited to produce electricity or heating [1]. One of the most commercially available low-grade waste heat recovery technologies is the Organic Rankine Cycle (ORC). This cycle has a similar structure to the water-steam Rankine cycle but employs organic fluids with low saturation temperature levels. Thus, ORC can exploit low-temperature heat sources, even below 100^{o}C to produce electricity, while this kind of installation is highly reliable and easy to maintain [2].

Many researchers around the globe have focused on the performance of ORC modules. Indicatively, Eyerer et al. [3] analyzed experimentally the utilization of substances with low Global Warming Potential (GWP), such as R1233zd(E) and R1224yd(Z), instead of conventional fluids, such as R245fa. According to the final results, the maximum power output was achieved, when R245fa was used, which was 9%, and 12% higher than that of R1233zd(E), and R1224yd(Z), respectively. However, in the case of using the eco-friendly medium R1233zd(E), the thermal efficiency was enhanced by 2% compared to the other two fluid options. In the past few decades, the integration of the nearly isothermal expansion process in the ORC has been investigated. During the expansion process, heat is transferred to the organic medium maintaining the temperature at a higher level, compared to the conventional adiabatic process. Thus, the power output and thermal efficiency are expected to be enhanced [4]. Indicatively, Ziviani et al. [5] studied an ORC unit with liquid-flooded expansion and internal regeneration for different working media. In that case, a secondary fluid was ejected at the expander inlet being in thermal equilibrium with the organic fluid, to limit the temperature reduction due to the expansion procedure. So, the net electricity production and cycle efficiency could be increased by 20%, reaching up to 50% of the Carnot efficiency. Moreover, Kosowski and Piwowarski [6] performed the thermodynamic analysis of both a conventional ORC and an ORC with the ideal isothermal process. The incorporation of the isothermal process led to an increased cycle efficiency of up to 12% when the organic fluid reached the saturated vapor state, and up to 7% when the organic fluid reached the superheated vapor state.

In addition, another design has also gained attention and is called Trilateral Flash Cycle (TFC), which is a cycle similar to ORC. In TFC application, the working fluid reaches the saturated liquid state without evaporation and expands into the two-phase region. More specifically, Iqbal et al. [7] investigated in terms of energy a TFC system in comparison with a conventional ORC, considering a low-temperature heat source, up to 100^{o}C. According to this study, TFC could produce at least 50% further useful electricity compared to the conventional ORC for the same heat source and heat sink conditions. Ajimotokan [8] analyzed energetically and exergetically four TFC configurations, i.e. the simple TFC, the recuperated TFC, the reheat TFC, and the regenerative TFC. The results indicated that the aforementioned cycles could achieve thermal efficiencies of 21.97%, 23.91%, 22.07%, and 22.9%, respectively if the highest temperature of the cycle was equal to 473 K, and n-pentane was utilized as the working medium.

In parallel, many publications are concentrated on the comparison of different cycle designs. First, Zhar et al. [9] studied thermodynamically and economically three ORC configurations, i.e. the basic ORC, the reheat ORC, and the regenerative ORC, for different working fluids. According to the final outcomes, the regenerative ORC performed better energetically and exergetically, as the energy efficiency was enhanced by 13%, and the exergy destruction was reduced by 44%, contrasted to the basic ORC installation. From an economic point of view, all the configurations achieved similar payback periods and levelized cost of energy values. Furthermore, Kanno and Shikazono [10] carried out a thermodynamic comparison between a Rankine cycle, a TFC, and a supercritical cycle, taking into consideration different working media. Two different heat source cases were examined i.e. exhaust gas at a temperature level of about 400^{o}C, and hot water at a temperature level of about 80^{o}C. Assuming the 80^{o}C hot water as the heat source, the maximum exergy efficiency was determined based on the sink temperature for the TFC unit, using hydro-fluorocarbon refrigerants. Finally, for the 400^{o}C exhaust gas case, the ethanol supercritical cycle achieved the highest sink-temperature-based exergy efficiency.

According to the previous literature review, scientists are interested in the investigation of innovative organic cycle designs, such as the ORC with nearly isothermal expansion (ORC-NIE) or the TFC. Nevertheless, most of the aforementioned studies focus on a single design or compare these designs with other ones. There is a lack of research articles that compare these two configurations in terms of energy, exergy, and economics. So, the present work investigates the thermodynamic performance of both ORC-NIE and TFC, taking into account different working fluids. The heat source of both cycles is hot water with a temperature of up to 100^{o}C. Additionally, the two cycles are analyzed financially. The thermodynamic simulations are carried out in Aspen Plus software, while the cost estimation analysis is based on Aspen Process Economic Analyzer, and data from the literature studies [11,12].

2. Organic cycle designs' fundamentals

2.1. Organic Rankine cycle with nearly isothermal expansion

The proposed configuration includes the basic ORC devices, i.e. the pump, the heat recovery system, and the condenser. It is assumed that the organic fluid exits the heat recovery system as superheated steam, with a superheating level of 10 K. The subcooling level at the condenser is considered at 2 K. Additionally, the innovative element of this design, which is the incorporation of the nearly isothermal expansion process, has been decided to be modeled as a two-stage expansion, with intermediate additional heat input (Q_{heater}). It is also assumed that the fluid exits the first stage at an intermediate pressure level, then is heated up reaching the same temperature level as the one of the superheated steam at the heat recovery system outlet, and, finally, expands up to the condenser saturation pressure in the second stage. The intermediate pressure level (P_{med}) is defined taking into account the high (P_{high}) and the low-pressure level (P_{low}) as [13]:

$$P_{med} = \sqrt{P_{high} \cdot P_{low}}, \quad (1)$$

The ORC high pressure (P_{high}) is determined by taking into consideration a temperature difference of 10 K between the heat source inlet temperature ($T_{w,in}$) and the fluid temperature at the outlet of the heat recovery system. The main outputs of the ORC-NIE, which are the net electricity production ($P_{el,net,ORC\text{-}NIE}$), the electrical efficiency ($\eta_{el,ORC\text{-}NIE}$), and the exergy efficiency ($\eta_{ex,ORC\text{-}NIE}$), are described by the following expressions:

$$P_{el,net,ORC-NIE} = P_{el,exp,ORC-NIE} - P_{el,pump,ORC-NIE}, \quad (2)$$

$$\eta_{el,ORC-NIE} = \frac{P_{el,net,ORC-NIE}}{Q_{HRS,ORC-NIE}+Q_{heater}}, \quad (3)$$

$$\eta_{ex,ORC-NIE} = \frac{P_{el,net,ORC-NIE}}{E_{HRS,ORC-NIE}+E_{heater}}, \quad (4)$$

The exergy rate (E) due to a heat rate (Q) at a temperature level of (T), considering the reference temperature (T_0) of 25°C (298.15 K) can be defined as [14]:

$$E = Q \cdot \left(1 - \frac{T_0}{T}\right), \quad (5)$$

The model of the ORC-NIE in Aspen Plus is depicted in Figure 1.

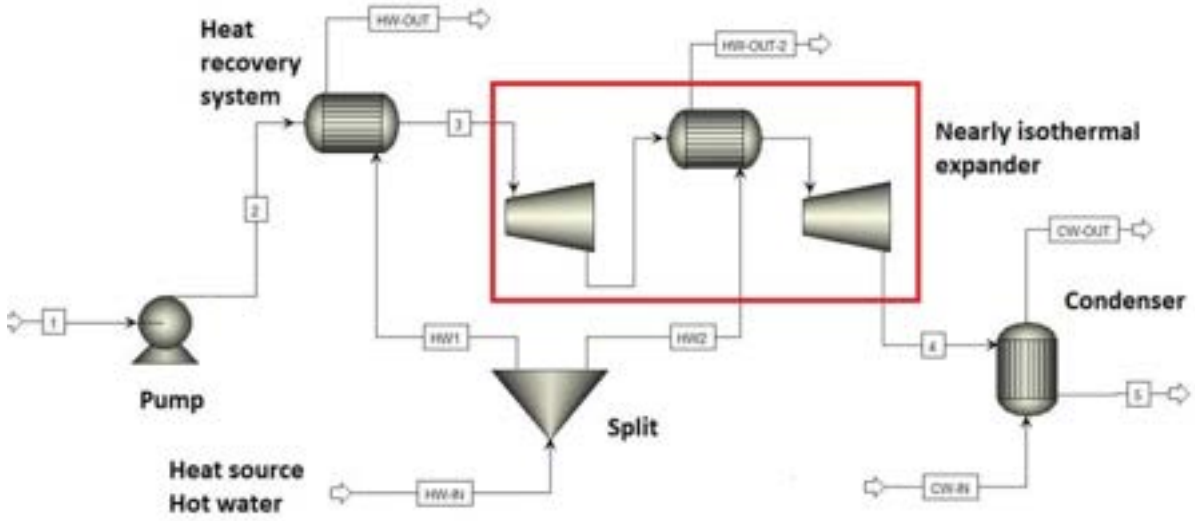

Figure. 1. Model of the ORC-NIE in Aspen Plus.

2.2. Trilateral flash cycle

The other examined design includes all the basic ORC devices, i.e. the pump, the heat recovery system, the expander, and the condenser. The main difference between the basic ORC module and the proposed one (TFC) is that the working medium exits the heat recovery system in the state of saturated liquid, without any evaporation or superheating. Subsequently, the fluid expands into the two-phase region of the substance. Additionally, the subcooling level at the condenser is considered at 2 K. The ORC high pressure (P_{high}) is determined by taking into consideration a temperature difference of 10 K between the heat source inlet temperature ($T_{w,in}$) and the fluid temperature at the outlet of the heat recovery system. The main outputs of the TFC, which are the net electricity production ($P_{el,net,TFC}$), the electrical efficiency ($\eta_{el,TFC}$), and the exergy efficiency ($\eta_{ex,TFC}$), are described by the following equations:

$$P_{el,net,TFC} = P_{el,exp,TFC} - P_{el,pump,TFC}, \quad (6)$$

$$\eta_{el,TFC} = \frac{P_{el,net,TFC}}{Q_{HRS,TFC}}, \quad (7)$$

$$\eta_{ex,TFC} = \frac{P_{el,net,TFC}}{E_{HRS,TFC}}, \quad (8)$$

The model of the TFC in Aspen Plus is depicted in Figure 2.

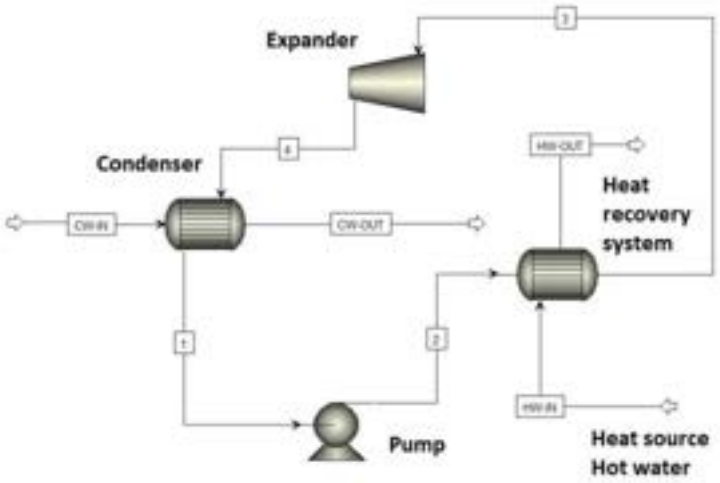

Figure. 2. Model of the TFC in Aspen Plus.

2.3. Techno-economic analysis

First, the investment cost (*IC*) of each cycle is defined taking into account the values that come from Aspen Process Economic Analyzer, and the literature studies [11,12]. In addition, the annual cash flow (*CF*) is defined considering the annual inflows and outflows. The annual inflows are consisted of the revenues from electricity selling, while the annual outflows include the operation & maintenance costs ($K_{O\&M}$). Taking into account the annual electricity production in kWh (Y_{el}), the operating hours per year (*hours*), and the electricity selling price in €/kWh (K_{el}), the annual cashflow is described by the following expression:

$$CF = Y_{el} \cdot K_{el} - K_{O\&M} = P_{el,net} \cdot hours \cdot K_{el} - K_{O\&M} \quad (9)$$

Then, the major financial indexes are defined. First, the payback period (*PBP*) is calculated as:

$$PBP = \frac{ln\left(\frac{CF}{CF - IC \cdot i}\right)}{ln\,(1+i)} \quad (10)$$

The net present value (*NPV*) is calculated as:

$$NPV = -IC + CF \cdot \frac{(1+i)^N - 1}{i \cdot (1+i)^N} \quad (11)$$

The aforementioned financial parameters are presented in Table 1.

Table 1. Parameters of financial analysis

Parameters	Values
Electricity selling price (K_{el})	0.2 €/kWh
Project lifetime (*N*)	20 years
Discount factor (*i*)	4%
Operation & maintenance cost ($K_{O\&M}$)	2% of the investment cost

2.4. Simulation methodology

First, the aforementioned cycles are studied parametrically in terms of thermodynamics in steady-state conditions through the developed models in Aspen Plus. More specifically, three main parameters are examined, the heat source inlet temperature ($T_{w,in}$), which strongly affects the cycle's high pressure (P_{high}), the condenser saturation temperature (T_{cond}), which strongly affects the cycle's low pressure (P_{low}), and the expander isentropic efficiency ($\eta_{is,exp}$). These values vary into a specific range to investigate their influence on the energetic and exergetic performance of the system. The heat source inlet temperature ($T_{w,in}$) ranges from 80 to 100°C, with a default value of 100°C, the condenser saturation temperature (T_{cond}), ranges from 10 to 40 °C, with a default value of 30°C, and the expander isentropic efficiency ($\eta_{is,exp}$) ranges from 0.4 to 0.8, with a default value of 0.7. Other parameters that remain constant during this analysis for both cycles are presented in Table 2. In parallel, the systems' operation is also examined for four different working fluids, which are depicted in Table 3. REFPROP is utilized as a proper method for refrigerants' properties [15]. Three of them (R1234ze(E), R1234yf, R1233zd(E)) are eco-friendly media with low GWP values, while R134a is a conventional refrigerant with a high level of GWP. All these fluids have zero Ozone Depletion Potential (ODP) and are selected as they have a critical temperature close to the examined heat source temperature levels. Then, the 2 designs are investigated financially. For this study, different values of

operating hours per year are assumed. All the defined thermodynamic and financial indexes (η_{en}, η_{ex}, *PBP, NPV*) are used to compare the aforementioned two cycles and specify the most techno-economically viable one when the two cycles are fed with the same heat source. Finally, it is important to mention that the two cycles are decided to be compared for similar heat input rates. That's why, a constant temperature difference of 20K and a constant flow rate is considered for the hot water stream.

Table 2. Constant parameters of both cycles.

Parameters	Values
Pump isentropic efficiency	0.7
Pump driver efficiency	0.93
Expander mechanical efficiency	0.95
Heat source (hot water) volume flow rate	75.5 m^3/h
Heat source (hot water) pressure	3 bar
Heat source (hot water) temperature difference	20 K

Table 3. Examined working fluids [14,16].

Working fluid	Flammability & Toxicity	P_{crit} (bar)	T_{crit} (°C)	ODP	GWP
R1234ze(E)	No	36.35	109.26	0	7
R1234yf	No	33.82	94.70	0	4
R1233zd(E)	No	36.24	166.45	0	4.5
R134a	No	40.56	101.03	0	1320

3. Results and discussion

3.1. Thermodynamic analysis

In this section, the results of the thermodynamic analysis are presented. More specifically, the influence of the three aforementioned parameters, i.e. the heat source inlet temperature the condenser saturation temperature, and the expander isentropic efficiency, on the electrical and exergy efficiency of both cycles for different organic working media, is examined.

Figures 3 and 4 indicate that both electrical and exergy efficiencies increase with increasing heat source inlet temperature for both cycles and all working fluids. The maximum achieved electrical and exergy efficiencies of the ORC-NIE are equal to 7.7% and 38.32% respectively, while the same values for TFC are found at 5.19%, and 25.82% respectively when the heat source inlet temperature is equal to 100°C and R1233zd(E) is used as the fluid.

On the other hand, the electrical and exergy efficiencies have a decreasing rate depending on the condenser saturation temperature for both cycles and all fluids, as shown in Figures 5 and 6. The lower the condenser saturation temperature, the lower the cycle's low pressure, so the cycle's useful work increases. The maximum electrical efficiency of the ORC-NIE and the TFC is calculated at 10.51% and 7.46%, respectively, for a condenser saturation temperature of 10°C and R1233zd(E) as the working medium. At the same temperature and for the same fluid, the exergy performance reaches the value of 52.27%, for the case of ORC-NIE, and 37.11%, for the case of TFC.

Moreover, the electrical and exergy efficiencies increase when the expander isentropic efficiency increases for both cycles and all the fluids, as it is illustrated in Figures 7 and 8. When the isentropic efficiency increases, the process is getting closer to the ideal isentropic one, leading to higher power output. The maximum determined electrical and exergy efficiencies of the ORC-NIE are equal to 8.79% and 43.72% respectively, while for TFC these values are defined at 6.08% and 30.26% respectively when the expander isentropic efficiency is equal to 0.8 and R1233zd(E) is the fluid used.

Consequently, according to Figures 3-8, in all cases, the electrical and exergy efficiencies of the ORC-NIE are higher compared to the corresponding values of TFC, as the energy content of the fluid at the expander inlet is greater for the case of the ORC-NIE, leading to higher power output. Furthermore, the most efficient fluid in terms of energy and exergy performance is R1233zd(E) for both cycles. At this point, it is important to mention that the influence of the working fluid type on the expander isentropic efficiency is not taken into account. It is assumed that the entire range of isentropic efficiency from 0.4 to 0.8 can be achieved utilizing all the examined working media.

The maximum achieved value of ORC-NIE electrical efficiency, which is equal to 10.51%, is similar to the corresponding optimized value calculated in the study [5]. For a heat source temperature of 100°C, the optimum efficiency was found at 9.6%. Moreover, according to one study [10], the TFC electrical efficiency reached the value of 7.4 %, when the heat source temperature was equal to 80°C. In the present study, the maximum defined level of TFC electrical efficiency is equal to 7.46%, which is close to the value in the literature.

The main thermodynamic results for both cycles at the default scenario conditions (heat source inlet temperature, the condenser saturation temperature, and the expander isentropic efficiency equal to 100°C, 30°C, and 0.7, respectively) and R1233zd(E) as the working fluid, including the main results of the heat exchangers, are presented in Table 4. The TFC condenser requires greater surface area as the condenser load is larger in this case compared to the case of ORC-NIE. Additionally, for the ORC-NIE a greater exchange area at the heat recovery system is needed to be installed, as in this case, three processes are taking place, which are the preheating, the evaporation, and the superheating of the working medium. On the other hand, TFC requires a heat recovery system with a smaller area, because the fluid reaches the state of saturated liquid.

In addition, the Sankey diagrams for the default case of each cycle are illustrated in Figures 9 and 10. It is important to mention that the available heat source load has been defined taking into account the temperature difference between the heat source inlet temperature and the reference (ambient) temperature. According to the Sankey diagrams, the pump and the condenser loads of TFC are greater than the ones of ORC-NIE, leading to poorer exploitation of the available heat source. In addition, a temperature-specific entropy (T-s) chart for both cycles is depicted in Figure 11. According to this diagram, it is obvious that the enclosed surface of the ORC-NIE, which represents the cycle's useful output, is larger compared to the case of TFC. Taking all of the above into consideration, the ORC-NIE is the most proper choice in terms of thermodynamics for low-grade heat sources.

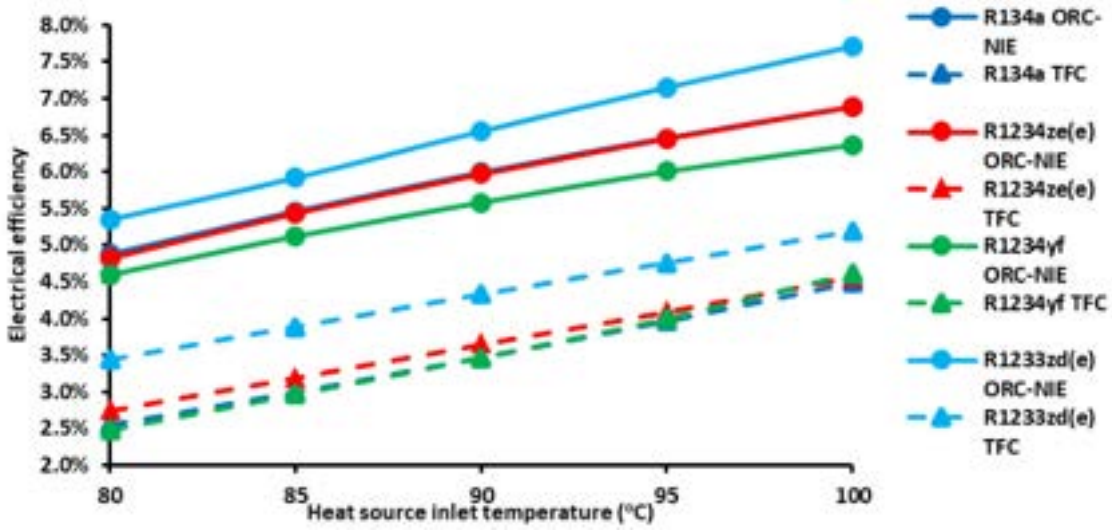

Figure. 3. Electrical efficiency depending on the heat source inlet temperature for both cycles and different organic working fluids.

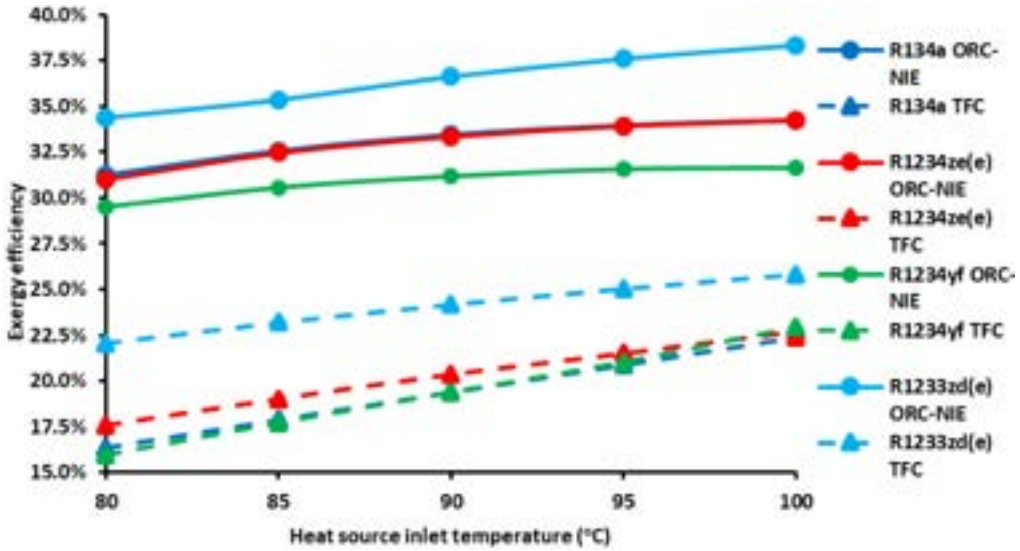

Figure. 4. Exergy efficiency depending on the heat source inlet temperature for both cycles and different organic working fluids.

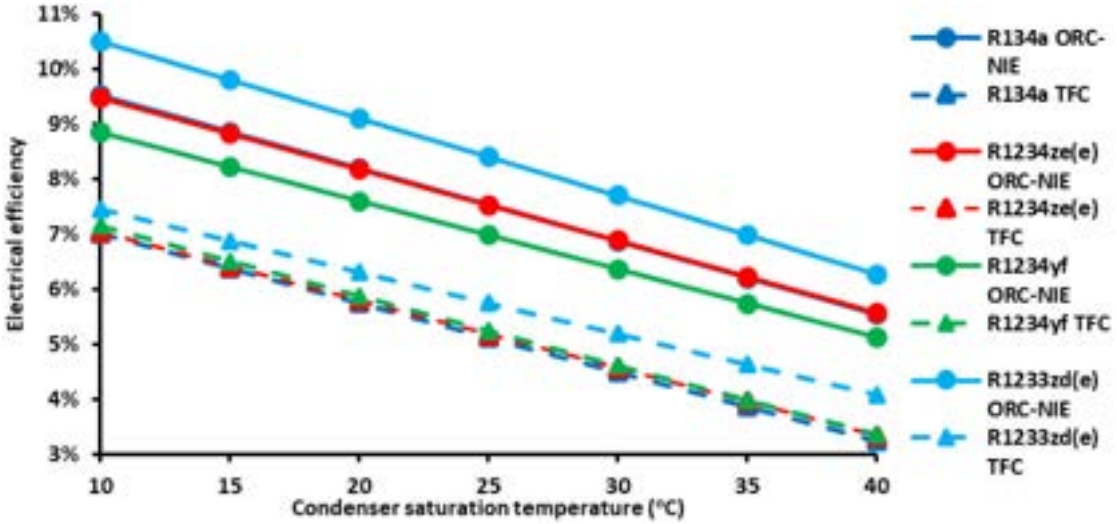

Figure. 5. Electrical efficiency depending on the condenser saturation temperature for both cycles and different organic working fluids.

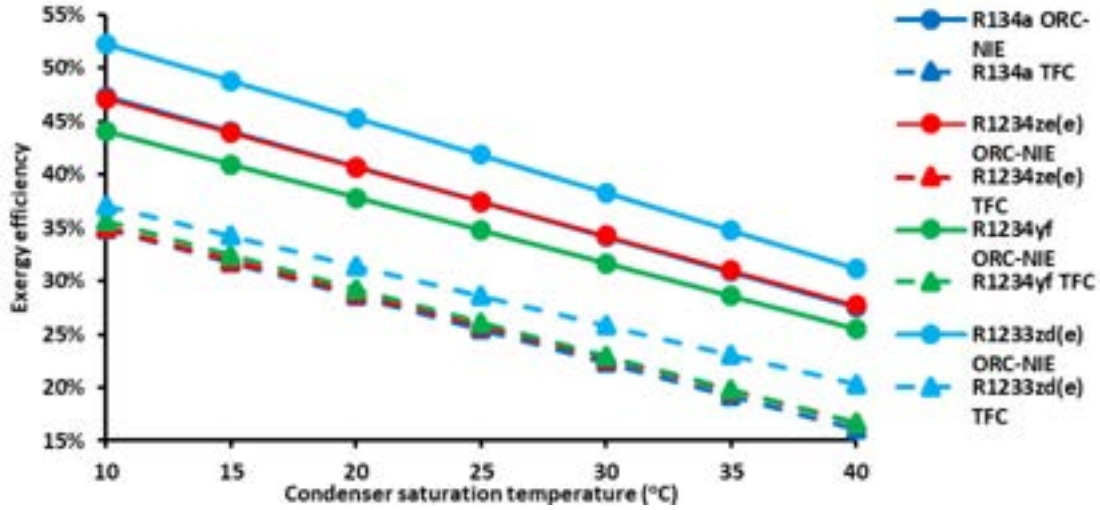

Figure. 6. Exergy efficiency depending on the condenser saturation temperature for both cycles and different organic working fluids.

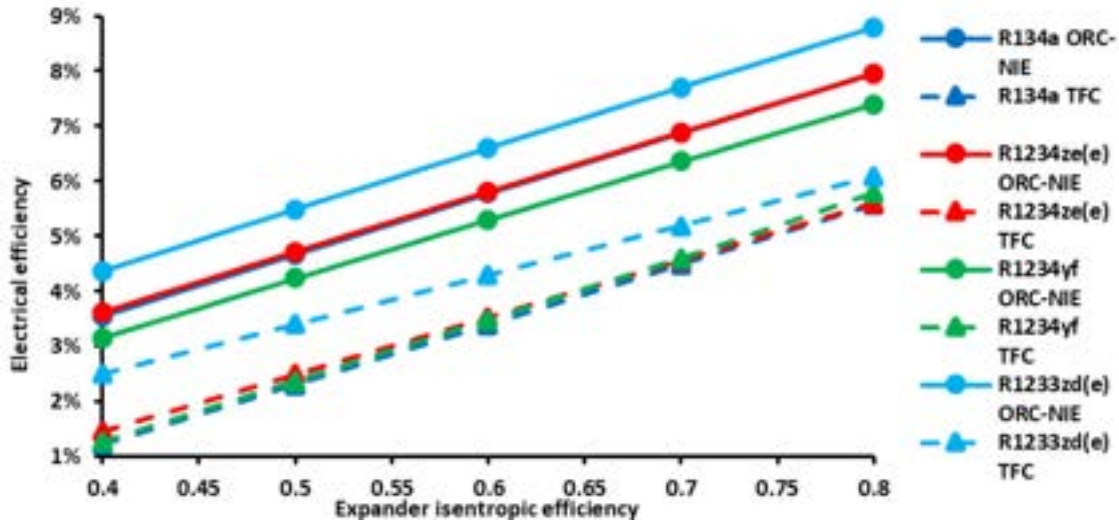

Figure. 7. Electrical efficiency depending on the expander isentropic efficiency for both cycles and different organic working fluids.

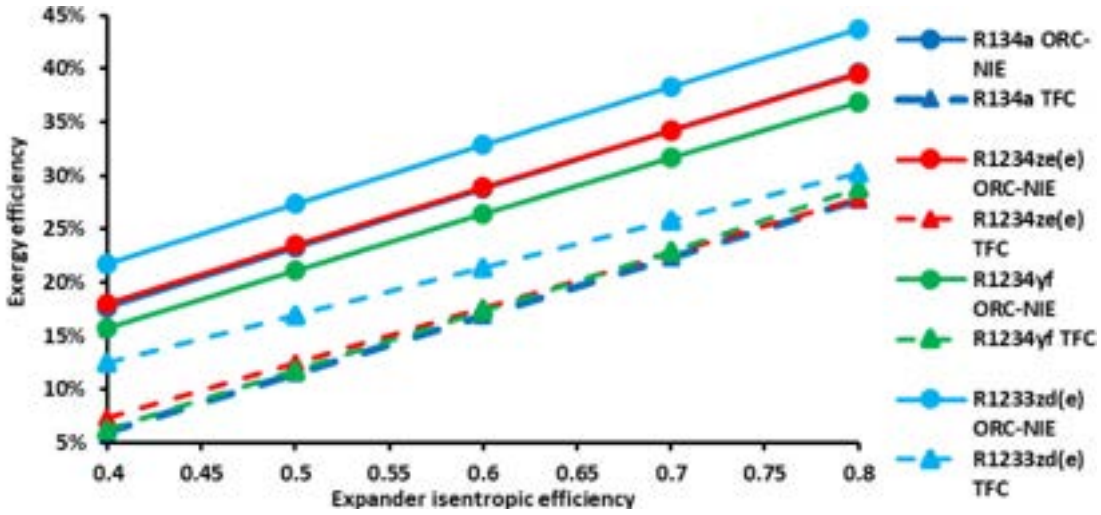

Figure. 8. Exergy efficiency depending on the expander isentropic efficiency for both cycles and different organic working fluids.

Table 4. Main thermodynamic results of both cycles at the default scenario (R1233zd(E) as working fluid).

Outputs	Values for ORC-NIE	Values for TFC
Condenser area	210.2 m^2	261.4 m^2
Condenser UA	178.7 kW/K	222.2 kW/K
Heat recovery system area	143.7 m^2	78.5 m^2
Heat recovery system UA	122.2 kW/K	66.7 kW/K
Additional heater area	14.7 m^2	-
Additional heater UA	12.5 kW/K	-
Low pressure	1.55 bar	1.55 bar
High pressure	6.58 bar	8.33 bar
Refrigerant mass flow rate	6.7 kg/s	21.4 kg/s
Total heat input	1686.2 kW	1690.5 kW
Pump electricity consumption	4.15 kW	17.77 kW
Expander electricity production	134.05 kW	105.53 kW
Net electricity production	129.9 kW	87.76 kW
Electrical efficiency	7.70%	5.19%
Exergy efficiency	38.32%	25.82%

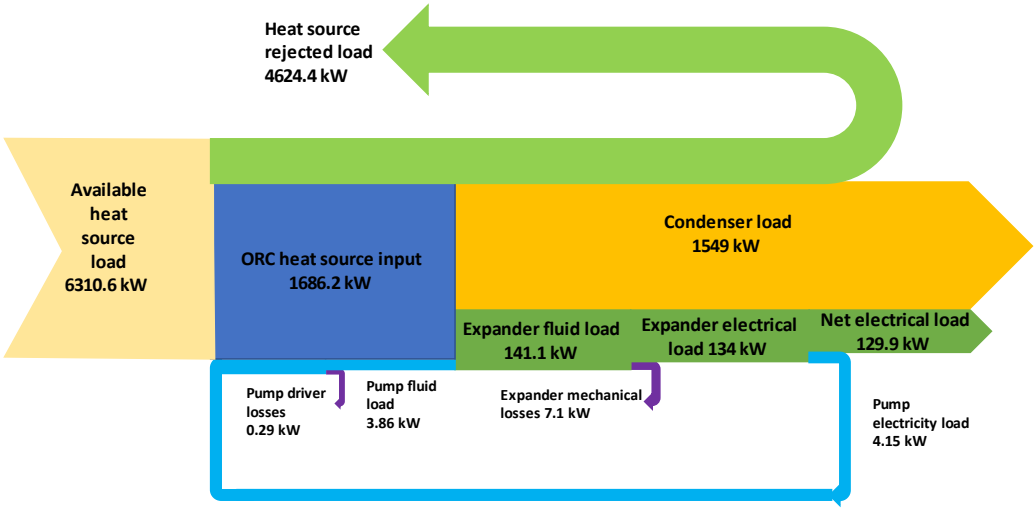

Figure. 9. Sankey diagram for the default scenario (R1233zd(E) as working fluid) of the ORC-NIE.

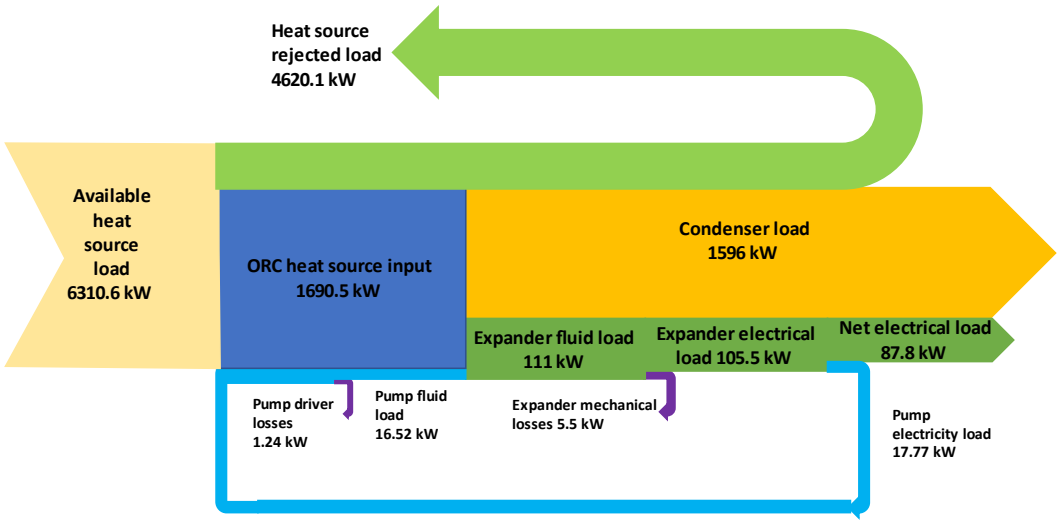

Figure. 10. Sankey diagram for the default scenario (R1233zd(E) as working fluid) of the TFC.

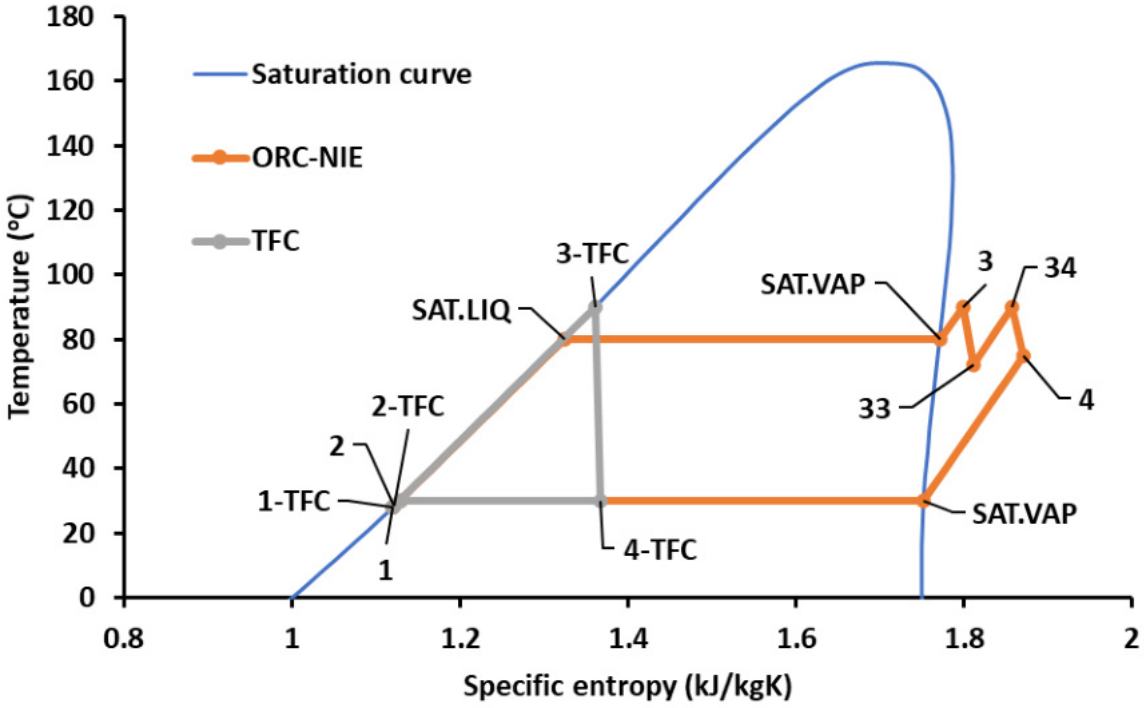

Figure. 11. Temperature-specific entropy (T-s) diagram for the default scenario (R1233zd(E) as working fluid) of the two examined cycles.

3.2. Techno-economic analysis

In this section, the results of the techno-economic study are presented, which have been calculated taking into account R1233zd(E) as working fluid and the thermodynamic results of the default scenario, from the previous section. As it is shown in Table 5, the investment cost of the ORC-NIE is greater compared to the corresponding value of the TFC. It is considered a reasonable result, as the higher electricity production requires a larger expander size. Additionally, the ORC-NIE requires heaters with larger heat-exchanging areas, as shown in Table 4. The greater size of these components strongly affects the investment cost, leading to a significant increase. Additionally, the ORC-NIE achieves greater values of NPV for all the examined operating hours. NPV is equal to 299 k€ in the case of 2,000 operating hours per year, and 2,417 k€ for 8,000 operating hours. However, for the TFC, slightly lower values of PBP are calculated, which are determined from 1.56 years for 8,000 operating hours per year up to 7.68 years when the operating hours are equal to 2,000. Consequently, the TFC is more economically viable in terms of initial cost and achieves slightly lower PBP, but in terms of NPV, the ORC-NIE performs better financially. For the case of 8,000

operating hours per year, the main techno-economic results are presented in Table 5. The financial indexes for both cycles and different operating hours per year are shown in Figure 12.

Table 5. Results of techno-economic analysis

Costs	Values for ORC-NIE	Values for TFC
Investment cost	320,300 €	202,000 €
Investment cost per kW_{el}	2,466 €/kW_{el}	2,300 €/kW_{el}
Annual electricity production (8,000 operating hours)	1,039.1 MWh	702.1 MWh
Annual cash flow (8,000 operating hours)	201.4 k€	136.4 k€
Net present value (8,000 operating hours)	2,417 k€	1,651 k€
Payback period (8,000 operating hours)	1.68	1.56

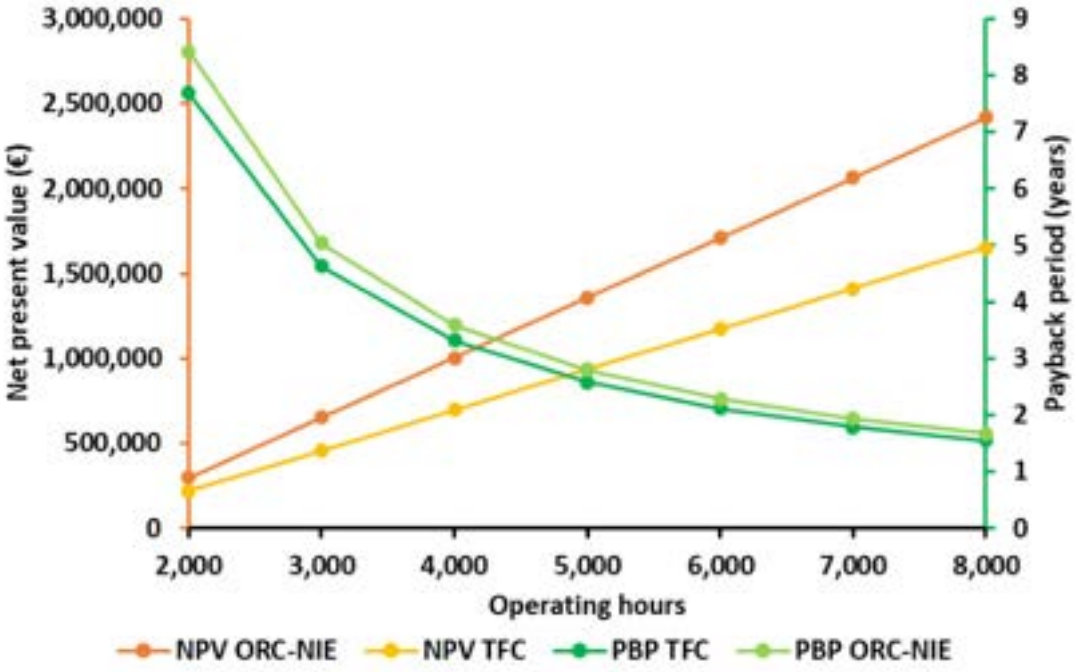

Figure. 12. Net present value and payback period for both cycles and different operating hours per year.

4. Conclusions

The present paper focuses on thermodynamic and techno-economic analysis and comparison of two organic cycle designs that are capable of operating at low-grade heat sources. For the comparison, the same available heat source conditions are assumed. The first one is similar to the ORC, but the expansion process approaches the isothermal conditions, and the second one is the TFC. The main conclusions are summarized below:

- R1233zd(E) seems to be the most proper organic working medium for both cycles in terms of thermodynamics.
- Both electrical and exergy efficiencies are enhanced with the increase of the heat source inlet temperature, and the expander isentropic efficiency while having a decreasing rate when the condenser saturation temperature increases.
- For the ORC-NIE, higher levels of electrical and exergy efficiencies are determined. The maximum achieved values are 10.51%, and 52.27%, respectively.
- For the case of TFC, lower investment costs and slightly lower payback period values are defined. The payback period can reach the value of 1.56 years when the annual operating hours are equal to 8,000.
- The ORC-NIE performs better in terms of net present value levels. On the other hand, TFC achieves net present values which are about 30% lower compared to the corresponding values of ORC-NIE.

The present work can be extended in the future, considering other organic cycle configurations, such as the recuperative ORC, and performing transient simulations.

Acknowledgments

This research has been co-financed by the European Regional Development Fund of the European Union and Greek national funds through the Operational Program Competitiveness, Entrepreneurship, and Innovation, under the call RESEARCH – CREATE – INNOVATE (project code: T2EΔK-00351). Moreover, this study has received funding from the European Union's Horizon Europe research and innovation program under grant agreement No 101058453 (FLEXIndustries - Digitally-enabled FLEXible Industries for reliable energy grids under high penetration of Variable Renewable Energy Sources (VRES)).

Nomenclature

CF	Cash Flow, €
E	exergy rate, kW
GWP	Global Warming Potential, -
i	Discount factor, %
IC	Investment Cost, €
K	Cost, €
N	Project lifetime, years
NPV	Net Present Value, €
ODP	Ozone Depletion Potential, -
P	pressure, bar
PBP	Payback Period, years
P_{el}	electrical load, kW
Q	heat rate, kW
T	temperature, °C or K
UA	Heat transfer coefficient, kW/K

Greek symbols

η	efficiency

Subscripts and superscripts

0	reference
cond	condenser
crit	critical
el	electrical
ex	exergy
exp	expander
heater	heater
high	high
HRS	heat recovery system
in	inlet
is	isentropic
low	low
med	intermediate
net	net
O&M	Operation and maintenance
ORC-NIE	Organic Rankine Cycle with nearly isothermal expansion
pump	pump
TFC	Trilateral Flash Cycle
w	water

References

[1] Inayat A., Current progress of process integration for waste heat recovery in steel and iron industries. Fuel 2023;338:127237.

[2] Bao J., Zhao L., A review of working fluid and expander selections for organic Rankine cycle, Renewable and Sustainable Energy Reviews 2013;24:325–342.

[3] Eyerer S., Dawo F., Kaindl J., Wieland C., Spliethoff H., Experimental investigation of modern ORC working fluids R1224yd(Z) and R1233zd(E) as replacements for R245fa, Applied Energy 2019;240:946–963.

[4] Igobo O., Davie P., Review of low-temperature vapour power cycle engines with quasi-isothermal expansion, Energy 2014;70:22-34.

[5] Ziviani D., Groll E., Braun J., De Paepe M., Broek M., Analysis of an organic Rankine cycle with liquid-flooded expansion and internal regeneration (ORCLFE), Energy 2018;144:1092-1106.

[6] Kosowski K., Piwowarski M., Subcritical Thermodynamic Cycles with Organic Medium and Isothermal Expansion, Energies 2020;13:4340.

[7] Iqbal M., Rana S., Ahmadi M., Date A., Akbarzadeh A., Trilateral Flash Cycle (TFC): a promising thermodynamic cycle for low grade heat to power generation.

[8] Ajimotokan H., Efficiency analysis of trilateral-cycle power systems for waste heat recovery-to-power generation, J. Cent. South Univ. 2016;23:3160−3170.

[9] Zhar R., Allouhi A., Jamil A., Lahrech K., A comparative study and sensitivity analysis of different ORC configurations for waste heat recovery, Case Studies in Thermal Engineering 2021;28:101608.

[10] Kanno H., Shikazono N., Thermodynamic simulations of rankine, trilateral and supercritical cycles for hot water and exhaust gas heat recovery, Mechanical Engineering Journal 2014;1(5):1-15.

[11] Bellos E., Vellios L., Theodosiou I., Tzivanidis C., Investigation of a solar-biomass polygeneration system, Energy Conversion and Management 2018;173:283-295.

[12] Iqbal M., Rana S., Ahmadi M., Date A., Akbarzadeh A., Experimental study on the prospect of low-temperature heat to power generation using Trilateral Flash Cycle (TFC), Applied Thermal Engineering 2020;172:115139.

[13] Willis R., Pollman A., Gannon A., Hernandez A., Modeling of a Building Scale Liquid Air Energy Storage and Expansion System with ASPEN HYSYS. The 3rd IEEE ICDCM: Proceedings of the International Conference on DC Microgrids; 2019 May 20-23; Kunibiki Messe, Japan.

[14] Antonopoulou C., Atsonios K., Grammelis P., Manolakos D., Skiadopoulos A., Bakalis P., Thermodynamic analysis on trilateral flash cycle (TFC) for low grade heat to power generation using different working fluids. ORC Munich 2021: Proceedings of 6th International Seminar on ORC power systems; 2021 October 11-13; Munich, Germany.

[15] NIST Reference Fluid Thermodynamic and Transport Properties Database (REFPROP).

[16] Abbas W., Vrabec J., Cascaded dual-loop organic Rankine cycle with alkanes and low global warming potential refrigerants as working fluids, Energy Conversion and Management 2021;249:114843.

PROCEEDINGS OF ECOS 2023 - THE 36TH INTERNATIONAL CONFERENCE ON
EFFICIENCY, COST, OPTIMIZATION, SIMULATION AND ENVIRONMENTAL IMPACT OF ENERGY SYSTEMS
25-30 JUNE, 2023, LAS PALMAS DE GRAN CANARIA, SPAIN

Exergoeconomic Analysis of a Solar Powered ORC using Zeotropic Mixtures for Combined Heat & Power Generation

C. Wolf[a], *E. Rothuizen*[b], *T. Ommen*[c]

[a] *Sensible Energy A/S, cmw@sensibleenergy.dk, CA*
[b] *Sensible Energy A/S, edr@sensibleenergy.dk*
[c] *Sensible Energy A/S, tso@sensibleenergy.dk*

Abstract:

As a part of the transition of the energy system towards renewables, new technologies and combinations of technologies are emerging. These include utilization of medium temperature industrial processes or availability of surplus heat from renewables. For these applications, organic Rankine cycles may be cost efficient solutions, if both expander work and condenser heat may be utilized as valuable products. In this study, a solar powered organic Rankine cycle using a zeotropic mixture is investigated from a design perspective. Both an Exergy and Exergoeconomic analysis were conducted. The investigated unit is capable of co-producing approximately 30 kW electricity and 160 kW district heating with a exergetic efficiency of > 60 %. The unit is able to compete with existing renewable power generating systems in terms of specific cost of electricity.

Keywords:

Exergy, Exergoeconomic Analysis, Organic Rankine Cycle, Zeotropic Mixtures, District Heating.

1. Introduction

The climate crisis is the defining crisis of our time, and the escalation has been substantial in the last decade. The global threat is substantial and we as a society have the possibility of changing our current heading [1, 2]. In the last decade, the focus on finding new solutions to slow down or reverse our impact on the climate has been growing. This is also due to the heightened commitment from many governing bodies to pass laws and set goals that push the transition towards a carbon-neutral society. The European Union has published the Strategic Energy Technology Plan (SET-plan) which highlights 10 innovations and reaches areas that boost the progress to reach the goals set by the European Union [3]. The overall goal set by the European Union is to reduce the total emissions by 40 % between 1990 and 2030 [4]. In Denmark, the ambitions have been set high and goals of reducing the total emission by 70 % by 2030 and achieving net zero emissions by 2050 have been established by the Danish government. These goals will be achieved by increasing the supply of renewable energies and through energy optimisation. This will be guaranteed by investing in programmes such as the EUDP programme which focuses on research, development and demonstration (R&D) of new technologies related to renewable energy [5–7].

Due to their flexibility, safety, and low maintenance, ORC's appears to be a promising technology. They have favourable characteristics to exploit waste heat or low-temperature heat sources stemming i.e. from power-to-X or pyrolysis plants for conversion into work or electricity [8–10]. The combinations of heat source and ORC are many. However, in recent years extensive research has been carried out investigating solar-powered ORC systems. The use of solar irradiation as the driving force of the ORC shows great promise as a renewable energy technology due to the high compatibility between the achievable temperature of the solar collector matches well with the working temperature of the ORC cycle [8, 11, 12]. The Parabolic Trough Collector (PTC) is the most mature solar concentrating technology and is typically chosen due to their reasonable cost and relatively high efficiency. Furthermore, they perform well in lower solar resources and/or more cloudy climates [11–13].

The investigation of working fluids for ORC systems is covered in great length in literature where many have applied exergy analysis while fewer have performed an exergoeconomic analysis. The performance and economics of an ORC system are tightly linked to the working fluid. A higher efficiency may be achieved by choosing the correct working fluid, even with less expensive components [9, 14]. Many studies also consider the use of fluid mixtures as the working fluid. The great interest in fluid mixtures for use in power cycles stems from the possibility to reduce the irreversibility during a two-phase heat transfer process by utilizing the temperature glide of the working fluid mixture [14]. Rayegan and Tao [15] developed a methodology specifically for the selection of working fluids for solar-driven ORC systems. The method based the selection of working on several different parameters such as the molecular components of the fluids, temperature-entropy diagram and effects on the thermal and exergy efficiency. Tchanche et al. [9] investigated the performance of a low-temperature solar ORC based on thermodynamic criteria such as working pressure, mass and

volume flow of different working fluids. Isentropic working fluids proved favourable such as butane and n-pentane. R152a, R600a, R600 and R290 also resulted in attractive performances. Habka and Ajib [16] investigated the performance of zeotropic mixtures in a small solar-driven ORC for combined heat and power. They further compared the mixture with pure fluids. The results showed that the mixture R409A outperformed the pure fluid R134a and R245fa, and could reduce the production cost of the energy unit to 16.20%. In a similar study done by Wang and Zhao [17], a low-temperature solar-driven ORC using both pure fluid and zeotropic mixtures is investigated. They also introduced an internal heat exchanger (IHEX) to the ORC. The IHEX improves the overall efficiency of the cycle. They found that when superheating the zeotropic mixtures and introducing the IHEX, a significant increase in thermal efficiencies can be gained. Garg et al. [18] investigated hydrocarbons mixed with carbon dioxide for flammability suppression of the hydrocarbons in a medium-temperature concentrated solar-powered ORC. Their study showed that extending the heat recovery in the IHEX into the two-phase region resulted in higher efficiency and is advantageous. However, at the same time, an exergy analysis showed that irreversibility in the IHEX was caused by the shifting of the pinch point towards the warm end of the IHEX. With a mixture of propane and CO_2 a real cycle efficiency of 15–18% was achieved at a source temperature of 573 K.

Ashouri et al. [19] performed an exergo-economic analysis and optimization of a double pressure ORC with a solar collector and storage tank. Results show that system can reach the efficiency of 22.7%. The exergoeconomic analysis revealed that the solar collector has the highest $\dot{Z} + \dot{C}_D$ due to both high exergy destruction and high investment costs of the collector. Following the collector, the storage tank, condenser, turbine, recuperator and evaporators had the highest destruction. Le et al. [20] carried out similar thermodynamic and economic optimization of a subcritical ORC (Organic Rankine Cycle) using a pure (n-pentane and R245fa) or a zeotropic mixture working fluid (mixtures of the two). In the study, a maximization of exergy efficiency and minimization of the LCOE (Levelized Cost of Electricity) was found which showed that the n-pentane-based ORC showed the highest maximized exergy efficiency of 53.2% and the lowest minimized LCOE of 0.0863 $/kWh. Regarding ORCs using zeotropic working fluids, 0.05 and 0.1 R245fa mass fraction mixtures present comparable economic features and thermodynamic performances to the system using n-pentane at minimum LCOE.

In this study, a solar-powered ORC with a storage tank will be investigated. The sytem is designed to have a 200 kW heat input which is converted into 30 kW of electricity and 160 kW of district heating. The system is constrained to off-the-shelf components. The system will be evaluated based on thermodynamic performance, exergetic performance and exergoeconomic performance. Furthermore, three different working fluids will be investigated, one pure fluid and two mixtures. By conducting the various analysis, options for improvement of the design should be identified and ranked in terms of priority. The analysis differentiates from available literature as it focusses on medium scale (e.g. 100-1000 kW thermal) ORC systems to be coupled to solar thermal collectors, with the aim to supply both electricity and district heating. As the system is synthesized by off-the-shelf components, exergoeconomic analysis was used to differentiate the value of various improvement possibilities. The design of the system is part of a EUDP-project abbreviated Fullspec, which stands for full spectrum solar power.

2. Methods

This section covers the theory and working principles of the system and the methods used for performing an exergy analysis and exergoeconomic analysis.

2.1. System Description

The system investigated in this study is illustrated in Fig 1. The system can be dived into three main loops: 1) Solar loop, 2) ORC loop and 3) District Heating loop. The solar loop consists of the PTC field and storage tank. In the solar loop, a thermal oil is used as heat transfer fluid. In the analysis it is assumed that the thermal oil is heated to 250 °C in the PTC field and transferred to a stratified storage tank. The thermal oil is then used as a heat source for the ORC loop by transferring heat in the evaporator. The thermal oil used in the solar loop is Gobaltherm® Omnisol.

The ORC loop is a standard ORC configuration with an IHEX and a liquid receiver. Here the liquid working fluid from the receiver is pressurized through the ORC pump. In the IHEX heat is recovered to preheat the working fluid from state 2 to 3. The working fluid is evaporated in the evaporator and then expanded through the expander resulting in the production of electricity. Lastly, the working fluid condenses in the condenser, transferring heat to the DH water and hereby heating it.

Three different working fluids are investigated. The different working fluids in three cases are 1) pure iso-pentane, 2) iso-pentane/CO_2 (0.99/0.01) and 3) iso-pentane/undecane/CO_2 (0.89/0.10/0.01). Here all ratios are given regarding mass basis. This numbering of cases will be used onwards. Case 1 might be viewed as the base case. The two mixtures additionally investigated are due to a desire to 1) avoid vacuum with in the system when the system is offline, and 2) maintain or increase performance compared to case 1.

2.2. Thermodynamic Model

The modelling of the system was done using Engineering Equation Solver (EES) [21] where all thermodynamic properties were determined using REFPROP [22]. All parameters used for the modelling of the system is presented in Table 1. The system was modelled in a steady state where mass and energy balances were applied to control volumes for each

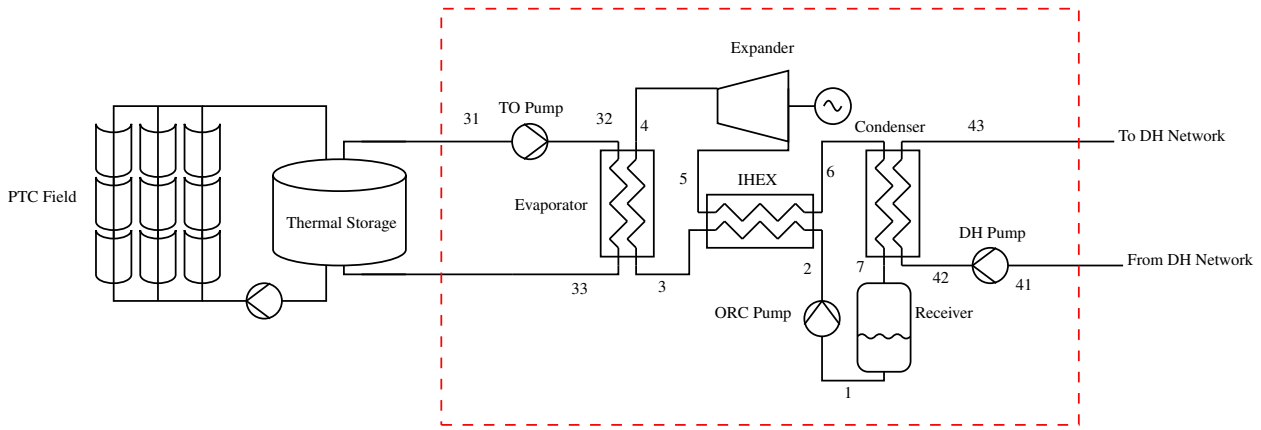

Figure 1: Schematic of the PTC powered ORC. The red dashed line mark the boundaries of the system investigated.

component using the general forms given in (1). Here, $\dot{m}$ is the mass flow rate, $\dot{Q}$ is the heat transfer rate across the control volume boundary, $\dot{W}$ is energy transfer by work, and h is enthalpy. The subscripts i and o denotes inlet and outlet streams, respectively.

$$0 = \sum_i \dot{m}_i - \sum_o \dot{m}_o \qquad \text{and} \qquad 0 = \dot{Q} - \dot{W} + \sum_i \dot{m}_i h_i - \sum_o \dot{m}_o h_o \tag{1}$$

Heat loss to the surroundings was neglected. However, the model did accounts for the pressure loss in the pipes and heat exchanger. The pressure loss through the heat exchanger is based on values from obtained heat exchanger manufactures. The pressure loss through the pipes is determined by the energy equation for pipe flows in (2) where the difference in velocity and height is neglected.

$$\Delta p = \frac{1}{2}\rho u^2 \left(f_f \frac{L}{D} + \sum K \right) \tag{2}$$

The power consumption of the pumps and gross power output of the expander are both determined using their respective isentropic efficiency, η_{pump} and η_{exp}.

The net electrical power output of the system is defined as the gross electricity production where the required electricity of the all pump are subtracted.

$$\dot{W}_{\text{net}} = \eta_{\text{gen}} \dot{W}_{\text{exp}} - \dot{W}_{\text{ORC,pump}} - \dot{W}_{\text{TO,pump}} - \dot{W}_{\text{DH,pump}} \tag{3}$$

The work required by the thermal oil pump accounts for the pressure loss through evaporator and pipes back and forth to the thermal storage.Similar, the worked required by the district heating pump accounts for the pressure loss through the condenser and the pipes connecting to the district heating network. The district heating pump does not take into account the loss through the overall district heating network.

The electric net efficiency of the system is defined as

$$\eta_{net,el} = \frac{\dot{W}_{net}}{\dot{Q}_{evap}} \tag{4}$$

The UA-value of each heat exchanger is determined based on a discretisation of the overall heat transfer in the heat exchangers. For each control volume, the following is applied assuming the cold side of the heat exchanger:

$$\dot{Q}_n = \dot{m}_{n,c} \left(h_{n,o,c} - h_{n,i,c} \right) \tag{5}$$

$$\dot{Q}_n = UA_n \Delta T_{\text{lmtd},n} \tag{6}$$

The overall UA is then determined by

$$UA = \sum_{j=1}^{n} UA_j \tag{7}$$

2.3. Exergy Analysis

To perform exergy analysis and exergoeconomic, the exergy destruction rate ($\dot{E}_{\text{D},k}$) for each component k was determined, using the theory described in [23].

Table 1: System parameters used in the present study

Parameter		Value	Parameter		Value
Thermal Oil Loop			*ORC Loop*		
TO inlet temperature	T_{31}	250 °C	Evaporator heat input	$\dot{Q}_{\text{evap}}$	200 kW
TO outlet temperature	T_{33}	200 °C	Expander inlet temperature	T_4	225 °C
TO inlet pressure	p_{31}	500 kPa	Expander isentropic efficiency	η_{exp}	225 °C
District Heating Loop			Expander inlet pressure	p_4	3000 kPa
DH outlet temperature	T_{43}	70 °C	Pinch temperature in IHEX and condenser	ΔT_{pinch}	5 K
DH inlet temperature	T_{41}	40 °C	Expander generator efficiency	η_{gen}	0.98
DH inlet pressure	p_{41}	500 kPa	Condenser outlet quality	x_7	0
Overall					
Pump isentropic efficiency	η_{pump}	0.7			

In this study, only the physical part of the exergy is accounted as no changes in chemical composition occurs due to the implied steady state assumption, the system being a closed cycle and no splitting of streams with respect to the working fluid. The physical exergy is determined from (8) where the difference in velocity and elevation has been neglected.

$$e^{\text{PH}} = (h - h_0) - T_0(s - s_0) \tag{8}$$

For the exergy analysis, the fuel and product for each component were used to evaluate the performance of each individual component and the entire system. The general definitions of fuel and product are given by Bejan, Tsatsaronis, and Moran [23] and are presented in Table 2 for relevant components.

From the exergy rate of fuel and product, two exergy destruction ratios and the exergetic efficiency:

$$y^*_{D,k} = \frac{\dot{E}_D}{\dot{E}_{D,\text{tot}}} \qquad \text{and} \qquad \epsilon_k = \frac{\dot{E}_P}{\dot{E}_F} \tag{9}$$

Here y_D is the exergy destruction with a component with respect to the overall fuel input, y^*_D is the exergy destruction with a component with respect to the overall exergy destruction in the system and ϵ is the exergertic efficiency.

2.4. Exergoeconomic Analysis

The exergoeconomic analysis is, as the name implies, the combination of exergy analysis and the economics regarding the system. Prices for components within the ORC for all three cases along with the price for solar collectors, storage and district heating connection are based on offers collected from suppliers. Prices will not be presented due to confidentiality. Furthermore, price for each component with the ORC are adjusted such that the sum of prices of components matches with the actual retail price of the ORC unit. The actual retail price is based on a fixed percentage of profit desired for the sale of a ORC-unit. Parameters used for the exergoeconomic analysis is presented in Table 4. The exergoeconomic analysis is based upon the cost balances known from conventional economic analysis. In conventional economical analysis, the cost balance will typically be formulated for an entire system, whereas in the exergoeconomic analysis, they will be formulated for each component. The cost balance for the k'th component is given by

$$\dot{C}_{P,k} = \dot{C}_{F,k} + \dot{Z}^{\text{CI}}_k + \dot{Z}^{\text{OM}}_k \tag{10}$$

where $\dot{C}_{P,k}$ is the cost rate associated with the product, $\dot{C}_{F,k}$ is the cost rate associated with the fuel, $\dot{Z}^{\text{CI}}_k$ is the cost rate associated with the capital investment and $\dot{Z}^{\text{OM}}_k$ is the cost rate associated with operation and maintenance (O&M). The capital investment and O&M were be combined to $\dot{Z}_k = \dot{Z}^{\text{CI}}_k + \dot{Z}^{\text{OM}}_k$. The cost balance states that the cost rate associated

Table 2: Fuel and product definitions for various components. Subscripts c and h refers to the hot and cold stream in a heat exchanger

Parameter	Pumps	Expander	Heat Exchanger
Product, $\dot{E}_P$	$\dot{E}_o - \dot{E}_i$	$\dot{W}$	$\dot{E}_{o,c} - \dot{E}_{i,c}$
Fuel, $\dot{E}_F$	$\dot{W}$	$\dot{E}_i - \dot{E}_o$	$\dot{E}_{i,h} - \dot{E}_{o,h}$

with the product must be equal to all expenditures used to generate the product. Similar to the definitions of fuel and products presented in Table 2, definitions of the cost rate associated fuel and product is also created. Furthermore, auxiliary equation are needed. Both are presented in Table 3. The cost rate associated with capital investment of the component is determined based on the lifetime of the component and the yearly operational hours which yields in

$$\dot{Z}_k^{\mathrm{CI}} = \frac{CI_k}{t_{\mathrm{OP}} Y_k} \tag{11}$$

where Y is the expected lifetime of the component in years, t_{OP} is the yearly operation of the system in seconds. Furthermore, the cost rate associated with O&M of each component is assumed to be 5% of the capital investment for the given component and is then determined from the yearly operation.

$$\dot{Z}_k^{\mathrm{OM}} = \frac{0.05 CI_k}{t_{\mathrm{OP}}} \tag{12}$$

2.5. Exergoeconomic Performance Parameters

Based on the thermoeconomic properties previously introduced, several performance parameters were defined. The three employed performance parameters are 1) the cost of exergy destruction, $\dot{C}_{D,k}$, 2) the relative cost difference, r_k and 3) the exergoeconomic factor, f_k.

The cost of exergy destruction does not directly show itself from the cost balance previously presented. However, from the exergy balance and cost balance, one will be able to obtain the cost of exergy destruction of the k'th component, which describes as

$$\dot{C}_{D,k} = c_{F,k} \dot{E}_{D,k} \qquad \text{or} \qquad \dot{C}_{D,k} = c_{P,k} \dot{E}_{D,k} \tag{13}$$

As seen the cost of exergy destruction may be defined in two different ways. The first definition assumes that the rate of product ($\dot{E}_{P,k}$) is fixed and that the unit cost of fuel ($c_{F,k}$) is independent of the exergy destruction. The second definition assumes that the rate of fuel ($\dot{E}_{F,k}$) is fixed and that the unit cost of the product($c_{P,k}$) is independent of the exergy destruction. In general, the first definition gives a lower estimate and the second definition gives a higher estimate with the actual value of $\dot{C}_{D,k}$ being in-between.

The relative cost difference r_k for the k'th component is defined by

$$r_k = \frac{c_{P,k} - c_{F,k}}{c_{F,k}} \tag{14}$$

The relative cost difference displays the relative increase in average cost per exergy unit between product and fuel. The relative cost difference also highlights whether the increase in the cost of the product stems from the price of fuel or the price associated with capital investment and O&M for the component.

Lastly, the exergoeconomic factor is defined for k'th components as

$$f_k = \frac{\dot{Z}_k}{\dot{Z}_k + c_{F,k} \dot{E}_{D,k}} \tag{15}$$

The exergoeconomic factor expresses a ratio which enables one to highlight whether the increase in cost rate from fuel to product stems from non-exergy-related cost or not. In the denominator of (15) $\dot{Z}_k$ is associated with non-exergy-related cost and $c_{F,k}\left(\dot{E}_{D,k} + \dot{E}_{L,k}\right)$ is associated exergy-related cost. A low value of the exergoeconomic factor for a component indicates that the increase in cost is due to high exergy destruction within the component and vice versa. Often the value of the exergoeconomic factor varies dependent of the component type. For compressors or turbines, the value is typically between 0.35 and 0.75, heat exchanger typically have a value below 0.55 and pumps tend to have a value above 0.7.

Table 3: Cost of fuel and product definitions for various components. Subscripts c and h refers to the hot and cold stream in a heat exchanger

Parameter	Pumps	Expander	Heat Exchanger
Product, $\dot{C}_P$	$\dot{C}_o - \dot{C}_i$	$\dot{C}_w$	$\dot{C}_{o,c} - \dot{C}_{i,c}$
Fuel, $\dot{C}_F$	$\dot{C}_w$	$\dot{C}_i - \dot{C}_o$	$\dot{C}_{i,h} - \dot{C}_{o,h}$
Auxiliary equation	None	$c_i = c_o$	$c_{i,h} = c_{o,h}$

2.6. Levelised Cost of Electricity

The levelised cost of electricity (LCOE) is a measurement that enables one to assess and compare alternative methods of energy production. The LCOE of an energy-generating system should be seen as the average total investement and O&M cost of the system per unit of total electricity generated over an assumed lifetime. Alternatively, the LCOE can be seen as the average minimum price at which the electricity generated by the system is required to be sold to break even with the total costs of building and operating the system over its lifetime [24]. The overall assumptions used for the calculation of LCOE is presented in Table 4. The LCOE is determined by

$$\text{LCOE} = \frac{\sum_{y=1}^{Y} \frac{CI_y + O\&M_y}{(1+r_r)^y}}{\sum_{y=1}^{Y} \frac{W_y}{(1+r_r)^y}} \tag{16}$$

where CI is the capital investment per year, O&M is the cost of the operational and maintenance per year, W is the electricity production per year and r_r is the discount rate. No fuel term is used as the solar input is assumed to be free of charge. The value of O&M in year 1 is estimated as 5% of the investment cost of entire system, equal to the definition used in the exergoeconomic analysis. After year 1 the cost of O&M increases with r_{OM} percent per year. This yields in

$$O\&M_y = O\&M_1 \, (1 + r_{\text{OM}})^y \quad \text{for} \quad y > 1 \tag{17}$$

The yearly production of electricity is determined by

$$W_y = \dot{W}_{net} t_{\text{OP}} \quad \text{for} \quad y = 1, 2 \ldots Y \tag{18}$$

3. Results and Discussion

A comparison between the different cases has been carried out and the main thermodynamic findings are presented in Table 5. The overall electrical efficiency of the system is greatest for the third case, followed by case 1 with the second highest. This relates to the output of the expander. As the inlet conditions of the expander are equal for all three cases, outlet conditions determine the possible output of the expander. Here lower outlet pressure contributes to more power output. This also means that one should strive to find working fluids that allow for a lower condensation pressure. On the other hand, case 2 has the greatest overall efficiency due to a higher district heating output. However, as electrical efficiency is valued highest, Case 3 is promising as the electrical efficiency of the system increases compared to case 1 while avoiding vacuum in a non-operational state. The gained efficiency does come at a price as the sizing of heat exchangers is influenced by the choice of the working fluid. Compared to case 1, the UA-values of the condenser and IHEX in case 3 are $\approx 38\,\%$ and $\approx 127\,\%$ greater, respectively. One of the reasons that increases in UA-values are observed for mixtures is the temperature glide occurring in the condensation phase which affects the temperature differences. This is quite evident when comparing the process in the condenser for cases 1 and 3. As seen Fig 2, a larger temperature difference can be clearly seen the in the condenser (state 6-7) for case 1 to case 3 and even though $\dot{Q}_{\text{cond}}$ is smaller than in case, the UA-value needed is still greater. The temperature glide of the mixtures and the desired $\Delta T_{\text{pinch}} = 5[\text{K}]$ in the condenser and IHEX further results in condensation starting in the IHEX. This means that two-phase flow will exit the IHEX and enter the condenser. Especially in case 3, where a large portion of the process is in the two-phase region. These conditions should be taken into account when building the system as it might lead to maldistribution in the condenser.

Table 4: Economical parameters used for the exergoeconomic analysis and determination of LCOE. All components are assumed to have equal expected lifetime.

Parameter		Value
Expected lifetime	Y	20 years
Discount rate	r_r	5%
Yearly increase of O&M	r_{OM}	0.25%
Yearly operation	t_{OP}	6000 hours

Table 5: Thermodynamic performance parameters

Case	η_{net} [-]	$\dot{W}_{\text{net}}$ [kW]	$\dot{Q}_{\text{cond}}$ [kW]	$\dot{Q}_{\text{IHEX}}$ [kW]	p_{cond} [kPa]	UA_{cond} [kW K^{-1}]	UA_{evap} [kW K^{-1}]	UA_{IHEX} [kW K^{-1}]
1	0.1295	25.90	172.3	123.8	395.6	11.71	5.204	9.592
2	0.1273	25.47	172.8	146.6	413.0	12.51	4.961	11.56
3	0.1418	28.37	169.7	187.1	345.0	16.84	5.905	21.90

3.1. Exergy Analysis

The results of the exergy analysis are presented in Table 6. There are four major components that stand for 98 % of all the exergy destruction in the system and they are the heat exchanger and expander. This also shows that the pumps are almost neglectable. Based on the analysis, the expander is in all three cases the component associated with the largest amount of exergy destruction, followed by the evaporator, condenser, IHEX and pumps. The expander stands for 37 % to 43 % of the overall exergy destruction. The high exergy destruction in all three is related to the relatively low isentropic efficiency of the expander. The expander also has the lowest exergetic efficiency of major components. This combination of high exergy destruction and low exergetic efficiency could suggest that the expander would be the first component to optimize in order to reduce the exergy destruction.

The large amount of exergy destruction within the evaporator is mostly due to the specification of the system, where thermal oil must return at 200 °C. This creates large temperature differences throughout the heat exchanger. A lower outlet temperature could be considered with the goal of reducing exergy destruction as the evaporator is a heat exchanger with the greatest amount of exergy destruction.

It is quite interesting to note that case 3 has the highest exergetic efficiency for all heat exchangers. This also highlights the benefits of utilizing the temperature glide which allows lower temperature differences and therefore, lower exergy destruction. The mixture of case 3 has a quite significant temperature glide, as seen from Fig 2. The effects of the temperature glide are particularly clear in the condenser where both case 2 and 3 have lower exergy destruction and higher exergetic efficiency compared to case 1. However, for case 2 the benefit of the mixture is only present in the condenser as lower exergetic efficiencies are seen in the evaporator and IHEX compared to case 1.

When investigating the overall performance of the system, case 3 has the best performance of the three cases with a system exergetic efficiency of 64.1 % and a total exergy destruction of 35 kW. Case 2 results in the lowest thermal efficiency of the 3 cases. However, opting for case 2 to obey the no-vacuum criteria will only result in a 1.0 % decrease in exergetic performance while opting for case 3 will result in a 4.4 % increase in exergetic performance. As expected a small difference is observed in the overall performance, due to the two cases being almost identical.

3.2. Exergoeconomic Analysis

The main findings of the exergoeconomic analysis is presented in Table 7. The exergoeconomic parameters will be evaluated based on the procedure suggested by [23]. Here the analysis starts by investigating the value of $\dot{Z} + \dot{C}_D$ and ranking the components based on their value. This couple with firstly evaluating the value of r and secondly, evaluating

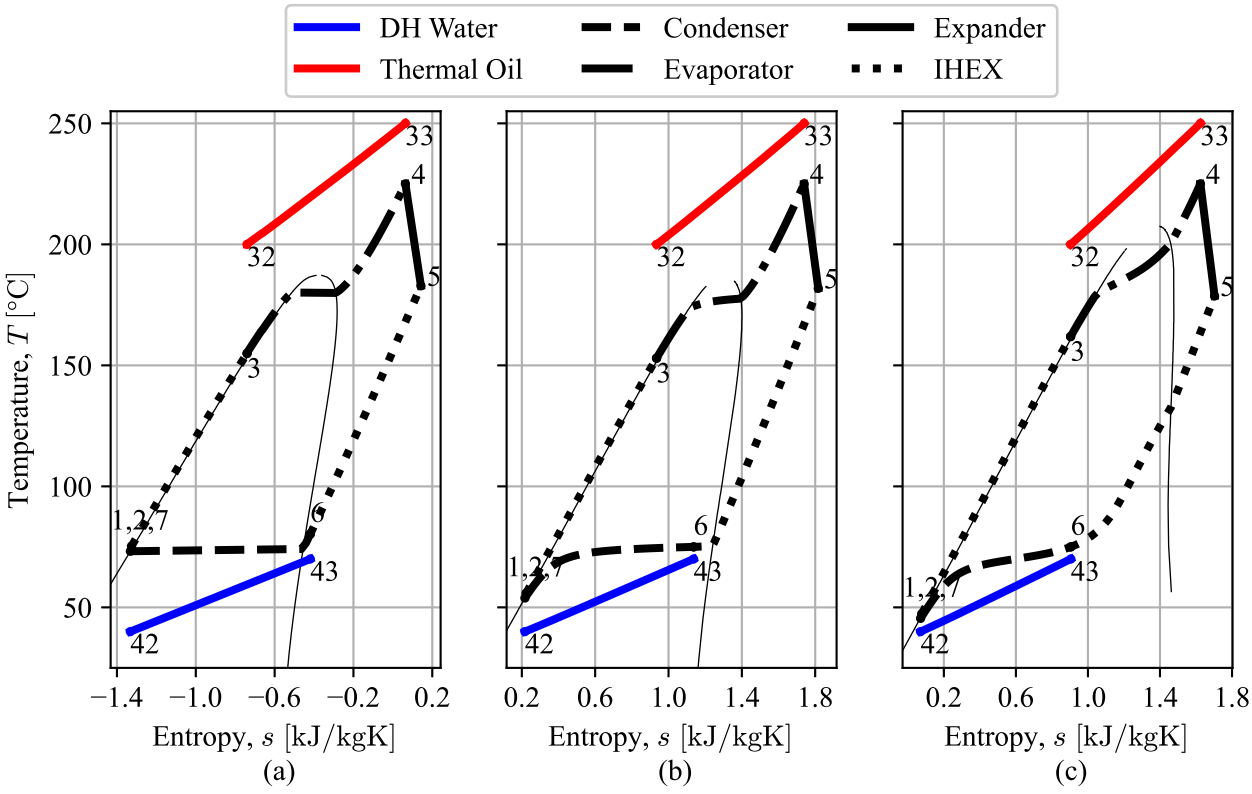

Figure 2: T,s-diagram for (a): Case 1, (b): Case 2 and (c): Case 3. It should be noted DH water and Thermal oil is used for visualisation and entropy is only for the working fluid

the value of f.

The expander is in all three cases the component with the greatest value of $\dot{Z} + \dot{C}_D$ and the value is more than 3 times greater than that of other components. However, this is expected as the expander is the most expensive component of all, coupled with having the highest exergy destruction. This indication suggests that the expander would be the first component where design changes or choice of expander type should be considered. For the rest of the components, the

Table 6: Fuel, Product and Exergy destruction

Case	ORC Pump	IHEX	Evaporator	Expander	Condenser	TO Pump	DH Pump
			Fuel, $\dot{E}_F$ [kW]				
1	3.636	37.448	86.716	43.412	31.896	0.183	0.014
2	3.482	41.723	86.683	42.553	30.882	0.161	0.013
3	3.808	51.806	86.683	47.369	28.345	0.161	0.013
			Product, $\dot{E}_P$ [kW]				
1	2.749	33.612	76.395	29.737	23.527	0.154	0.010
2	2.582	36.742	75.834	29.132	23.600	0.135	0.002
3	2.797	46.939	77.783	32.361	23.180	0.135	0.002
			Destruction, $\dot{E}_D$ [kW]				
1	0.887	3.836	10.321	13.675	8.369	0.029	0.004
2	0.900	4.981	10.849	13.421	7.282	0.026	0.011
3	1.011	4.867	8.900	15.007	5.164	0.026	0.011
			Exergetic Efficiency, ϵ [-]				
1	0.756	0.898	0.881	0.685	0.738	0.840	0.729
2	0.741	0.881	0.875	0.685	0.764	0.840	0.172
3	0.735	0.906	0.897	0.683	0.818	0.840	0.172
			Exergy Destruction Ratio, y^*_D [-]				
1	0.024	0.103	0.278	0.368	0.225	0.001	0.000
2	0.024	0.133	0.290	0.358	0.194	0.001	0.000
3	0.029	0.139	0.254	0.429	0.148	0.001	0.000
	Total Exergy Destruction, $\dot{E}_{D,\text{tot}}$ [kW]			System Exergetic Efficiency, ϵ_{tot} [-]			
1		37.122			0.614		
2		37.469			0.608		
3		34.985			0.641		

Table 7: Exergoeconomic Perfomance Parameters

Case	ORC Pump	IHEX	Evaporator	Expander	Condenser	TO Pump	DH Pump
			$(\dot{Z} + \dot{C}_D) \cdot 10^{-3}$ [DKK/s]				
1	1.68	0.66	0.78	5.70	1.27	0.43	0.42
2	1.72	0.88	0.81	5.73	1.17	0.43	1.78
3	1.76	1.12	0.66	6.00	0.89	0.43	1.78
			Relative Cost Difference, r [-]				
1	1.99	0.17	0.15	1.30	0.39	10.11	132.27
2	2.08	0.20	0.15	1.30	0.37	11.20	557.03
3	2.01	0.20	0.12	1.21	0.30	11.55	599.53
			Exergoeconomic Factor, f [-]				
1	0.84	0.34	0.08	0.65	0.10	0.98	1.00
2	0.83	0.33	0.05	0.65	0.16	0.98	0.99
3	0.82	0.49	0.08	0.62	0.26	0.98	0.99

three cases differ with regards to the ranking of highest to the lowest value of $\dot{Z} + \dot{C}_D$.

When further investigating the relative cost difference, r, for the expander, a value above 1 can be observed. This indicates that a majority of the increase in the cost of the product stems from the price of the capital investment and O&M, rather than the price of the fuel. The same conclusion can be made for all pumps. Especially for thermal oil pump and district heating pump, the value of r is very high. On the contrary, the increase in the cost of the product for all heat exchangers stems from the price of the fuel rather than capital investment and O&M. The fact that all the more mechanically complicated component have a higher value of r, is as expected due to the much higher price of components such as turbo machinery and pump compared to heat exchangers. Furthermore, components which do add much thermodynamic value to the system also then to have high values of r. This is seen from both the thermal oil and district heat pump. The pump does not have to overcome high pressure differences and should mainly ensure flow, hereby having close to zero exergy destruction associated with these components. Therefore, a high value of r is inevitable.

Last, the exergoeconomic factor, f, is investigated. This factor should ideally be 0.5, meaning that the cost is evenly distributed between the cost of capital investment and O&M and the cost of exergy destruction. However, the value tends to depend on the type of component. The exergoeconomic factor for the pumps and expander for all cases is above 0.5. Therefore, it could be cost-effective to decrease the capital investment of these components at the expense of their efficiency. Especially, the values for the pumps as their values are quite close to 1. The value of the expander may be over 0.5 but as the value for an expander is between 0.35 and 0.75, a value of 0.65 is quite acceptable. Therefore, the expander may not be the right component to optimize as few economical benefits would stem from it. As expected, it would be beneficial to increase the capital investment for both the evaporator and condenser as most of the cost is associated with the cost of exergy destruction. Especially, the evaporator which also relates to the high exergy destruction and the boundary conditions set for the system. The value of f for the IHEX is greater compared to the evaporator and condenser. In case 1 and 2, a greater investment could be beneficial but the IHEX in case 3 is very close to the optimum of 0.5.

When comparing the exergy analysis and the exergoeconomic analysis, similar conclusions may be drawn for some components, whereas conflicting conclusions can be drawn from others. The pumps in the system would not harm the exergy efficiency of the system greatly if the pumps were downgraded to cheaper models with lower efficiencies due to their low contribution to the overall exergy destruction. In most cases, both the exergy and exergoeconomic analysis indicates that more could be invested in the heat exchangers which would reduced to exergy destruction and benefit the system. Here the exception is the IHEX in case 3 as the exergoeconomic factor is 0.49. The expander is a component that stands out in all cases as the exergy analysis would suggest improving it as it is the greatest contributor to the exergy destruction of the system. However, it would not be cost effective to improve the expander as shown by the exergoeconomic analysis.

3.3. Levelised Cost of Electricity

Lastly, LCOE may also be used to compare the three systems. The LCOE is presented in Table 8. Here the lowest value of LCOE is found for case 3 with a value of 0.87 DKK/kWh and 1.69 DKK/kWh. Even though, the ORC-unit is more expensive in case 3 compared to case 1 because of the larger heat exchangers needed, the increased performance of the system results in a lower LCOE. Compared to another renewable technology photovoltaics (PV), the LCOE for case 3 is slightly above the LCOE for PV but within the price range of PV systems with battery storage when looking at the ORC-unit isolated. However, when including the solar collectors and storage, the price slightly exceeds to LCOE of PV with battery storage. However, the ORC benefits from producing district heating as well. Therefore, an additional source of income will also be associated with the ORC system.

Table 8: LCOE for all three cases. LCOE are given for the ORC-unit isolated and including the solar field and storage

Parameter	Case 1	Case 2	Case 3
$LCOE_{\text{ORC}}$ [DKK/kWh]	0.89	0.92	0.87
$LCOE_{\text{ORC+Solar}}$ [DKK/kWh]	1.79	1.84	1.69

4. Conclusion

The current study investigates a 200 kW heat input solar driven ORC-unit based on thermodynamic, exergetic and exergoeconomic performance. The study has been investigating three different ORC working fluids, one pure fluid and 2 mixtures. The mixtures are chosen to ensure an offline pressure of 1 atm Iso-pentane is the pure fluid and the two mixture are iso-pentane/CO_2 (0.99/0.01) and iso-pentane/undecane/CO_2 (0.89/0.1/0.01). The greatest electrical net efficiency of the ORC was found for the last mixture at 14.18 % which is a 9.5 % improvement compared to the pure fluid. The first mixture performed worst with an efficiency of 12.73 %. The improvement from pure fluid to second mixture does require greater heat exchangers compared due the temperature glide of the mixture ensuring lower temperature differences. Similar, results are seen from the exergy analysis. Here the second mixture has the smallest overall exergy destruction 34.96

kW and the highest exergetic efficiency of 64 % due to the utilization of the temperature glide. The expander was in all three cases the component with the largest amount of exergy destruction.

The exergoeconomic factor of the exergoeconomic analysis highlighted the pumps in the system as the components where capital investment should be greatly reduced as it would benefit the overall system economically. For all three cases, the analysis suggested that a greater investment for both the condenser and evaporator could be made improving the components and hereby being both exergetic and economically beneficial. The exergoeconomic analysis illustrated IHEX and expander are two components that are close their optimal operational state with regard to capital investment and thermodynamic efficiency. Even though, the expander is associated with the greatest amount of exergy destruction, no economical benefits will be the result of improving the component.

With the current layout and specific choice of components, the ORC unit isolated will be able to produce electricity at LCOE of 0.87 DKK/kWh which is within the range of PV systems with battery storage but the LCOE of 1.69 DKK/kWh for combined system with the ORC unit, solar field and storage slightly exceeds that of PV systems with battery storage. However, this is without accounting for the extra revenue generated by the district heat.

Nomenclature

Roman Letters

$\dot{C}$	Cost rate [DKK/s]
c	Average cost per unit of exergy [DKK/kJ]
D	Diameter [m]
$\dot{E}$	Exergy flow rate [kW]
f	Exergoeconomic factor [−]
f_f	Friction Factor [−]
h	Specific enthalpy [kJ/kg]
K	Minor Losses [−]
L	Length [m]
$\dot{m}$	Mass flow rate [kg/s]
p	Pressure [kPa]
$\dot{Q}$	Heat transfer rate [kW]
r	Relative Cost Difference [−]
r_r	Discount rate [−]
$\dot{S}$	Entropy flow rate [kJ/(Ks)]
T	Temperature [°C]
t	Time [s]
u	Velocity [m/s]
$\dot{W}$	Power [kW]
Y	Lifetime [year]
y^*	Exergy desctruction ratio [−]
$\dot{Z}$	Non-exergy related cost rate [DKK/s]

Greek Letters

η	Efficiency [−]
ν	Kinematic viscosity [m^2/s]
ρ	Density [kg/m^3]

Subscripts

k	Component
0	Reference state
[1;43]	State points
c	Cold Side
D	Destruction
F	Fuel
gen	generation
h	Hot Side
i	inlet
L	Loss
o	Outlet
P	Product
pinch	Pinch point
s	Isentropic
tot	Total system
y	Year

Superscripts

CI	Capital Investment
OM	Operation & Maintenace
OP	Operational
PH	Physical

Acronyms

DH	District heating
IHEX	Internal heat exchanger
LCOE	Levelized cost of electricity
O&M	Operation and Maintenance
ORC	Organic Rankine Cycle
PTC	Parabolic Trough Collector
TO	Thermal Oil

References

[1] United Nations. *The Climate Crisis – A Race We Can Win*. https://www.un.org/en/un75/climate-crisis-race-we-can-win. Accessed on 31-01-2023. 2020.

[2] Mohammad Bahrami et al. "Low global warming potential (GWP) working fluids (WFs) for Organic Rankine Cycle (ORC) applications". In: *Energy Reports* 8 (2022), pp. 2976–2988. ISSN: 2352-4847. DOI: https://doi.org/10.1016/j.egyr.2022.01.222. URL: https://www.sciencedirect.com/science/article/pii/S2352484722002220.

[3] European Commision. *Strategic Energy Technology Plan*. https://energy.ec.europa.eu/topics/research-and-technology/strategic-energy-technology-plan_en. Accessed on 10-12-2022. 2019.

[4] Danish Energy Agency. *Danish Climate Policies*. https://ens.dk/en/our-responsibilities/energy-climate-politics/danish-climate-policies. Accessed on 30-01-2023. 2019.

[5] Energy Danish Ministry of Climate and Utilities. *Denmark's Integrated National Energy and Climate Plan*. https://kefm.dk/media/7095/denmarks-national-energy-and-climate-plan.pdf. Accessed on 14-12-2022. 2019.

[6] Danish Government. *Denmark can do more II [Danmark kan mere II]*. https://www.regeringen.dk/media/11205/danmark-kan-mere-iidocx.pdf. Accessed on 25-09-2022. 2022.

[7] Danish Heat Association. *About Us*. Available at: https://www.danskfjernvarme.dk/sitetools/english/about-us [accessed 25-02-2021].

[8] Kyoung Hoon Kim and Chul Ho Han. "A review on solar collector and solar organic rankine cycle (ORC) systems". In: *Journal of Automation and Control Engineering* 3.1 (2015).

[9] Bertrand Fankam Tchanche et al. "Fluid selection for a low-temperature solar organic Rankine cycle". In: *Applied Thermal Engineering* 29.11 (2009), pp. 2468–2476. ISSN: 1359-4311. DOI: https://doi.org/10.1016/j.applthermaleng.2008.12.025. URL: https://www.sciencedirect.com/science/article/pii/S1359431108004900.

[10] Zhiqi Wang et al. "Fluid selection and advanced exergy analysis of dual-loop ORC using zeotropic mixture". In: *Applied Thermal Engineering* 185 (2021), p. 116423. ISSN: 1359-4311. DOI: https://doi.org/10.1016/j.applthermaleng.2020.116423. URL: https://www.sciencedirect.com/science/article/pii/S1359431120339016.

[11] Fahad A. Al-Sulaiman. "Exergy analysis of parabolic trough solar collectors integrated with combined steam and organic Rankine cycles". In: *Energy Conversion and Management* 77 (2014), pp. 441–449. ISSN: 0196-8904. DOI: https://doi.org/10.1016/j.enconman.2013.10.013. URL: https://www.sciencedirect.com/science/article/pii/S019689041300633X.

[12] Reyhaneh Loni et al. "A review of solar-driven organic Rankine cycles: Recent challenges and future outlook". In: *Renewable and Sustainable Energy Reviews* 150 (2021), p. 111410. ISSN: 1364-0321. DOI: https://doi.org/10.1016/j.rser.2021.111410. URL: https://www.sciencedirect.com/science/article/pii/S1364032121006948.

[13] James Freeman et al. "Working fluid selection and electrical performance optimisation of a domestic solar-ORC combined heat and power system for year-round operation in the UK". In: *Applied Energy* 186 (2017). Sustainable Thermal Energy Management (SusTEM2015), pp. 291–303. ISSN: 0306-2619. DOI: https://doi.org/10.1016/j.apenergy.2016.04.041. URL: https://www.sciencedirect.com/science/article/pii/S0306261916304949.

[14] Anish Modi and Fredrik Haglind. "A review of recent research on the use of zeotropic mixtures in power generation systems". In: *Energy Conversion and Management* 138 (2017), pp. 603–626. ISSN: 0196-8904. DOI: https://doi.org/10.1016/j.enconman.2017.02.032. URL: https://www.sciencedirect.com/science/article/pii/S0196890417301383.

[15] R. Rayegan and Y.X. Tao. "A procedure to select working fluids for Solar Organic Rankine Cycles (ORCs)". In: *Renewable Energy* 36.2 (2011), pp. 659–670. ISSN: 0960-1481. DOI: https://doi.org/10.1016/j.renene.2010.07.010. URL: https://www.sciencedirect.com/science/article/pii/S0960148110003344.

[16] Muhsen Habka and Salman Ajib. "Performance estimation of mixtures in solar Organic Rankine Cycle with two mini cogeneration options for improvement purpose". In: *Sustainable Energy Technologies and Assessments* 16 (2016), pp. 174–189. ISSN: 2213-1388. DOI: https://doi.org/10.1016/j.seta.2016.06.002. URL: https://www.sciencedirect.com/science/article/pii/S2213138816300327.

[17] X.D. Wang and L. Zhao. "Analysis of zeotropic mixtures used in low-temperature solar Rankine cycles for power generation". In: *Solar Energy* 83.5 (2009), pp. 605–613. ISSN: 0038-092X. DOI: https://doi.org/10.1016/j.solener.2008.10.006. URL: https://www.sciencedirect.com/science/article/pii/S0038092X08002764.

[18] Pardeep Garg et al. "Evaluation of carbon dioxide blends with isopentane and propane as working fluids for organic Rankine cycles". In: *Applied Thermal Engineering* 52.2 (2013), pp. 439–448. ISSN: 1359-4311. DOI: https://doi.org/10.1016/j.applthermaleng.2012.11.032. URL: https://www.sciencedirect.com/science/article/pii/S1359431112007843.

[19] Milad Ashouri et al. “Exergy and exergo-economic analysis and optimization of a solar double pressure organic Rankine cycle”. In: *Thermal Science and Engineering Progress* 6 (2018), pp. 72–86. ISSN: 2451-9049. DOI: https://doi.org/10.1016/j.tsep.2017.10.002. URL: https://www.sciencedirect.com/science/article/pii/S2451904917301981.

[20] Van Long Le et al. “Thermodynamic and economic optimizations of a waste heat to power plant driven by a subcritical ORC (Organic Rankine Cycle) using pure or zeotropic working fluid”. In: *Energy* 78 (2014), pp. 622–638. ISSN: 0360-5442. DOI: https://doi.org/10.1016/j.energy.2014.10.051. URL: https://www.sciencedirect.com/science/article/pii/S0360544214012018.

[21] S.A. Klein. *EES: Engineering Equation Solver*. https://fchartsoftware.com/. Version V10.836-3D. 2020.

[22] E. W. Lemmon et al. *NIST Standard Reference Database 23: Reference Fluid Thermodynamic and Transport Properties-REFPROP, Version 10.0, National Institute of Standards and Technology*. 2018. DOI: https://doi.org/10.18434/T4/1502528. URL: https://www.nist.gov/srd/refprop.

[23] Adrian Bejan et al. *Thermal Design & Optimization*. John Wiley & Sons, Inc., 1996.

[24] CFI. *Levelized Cost of Energy (LCOE)*. https://corporatefinanceinstitute.com/resources/valuation/levelized-cost-of-energy-lcoe/. Accessed on 05-02-2023. 2023.

Energy, exergy, exergoeconomic, and exergoenvironmental study of an innovative solar-wind-biomass driven polygeneration system for power, heat and ammonia production

Mohammad Hassan Khoshgoftarmanesh[a], Soheil Davadgaran[b], Seyed Alireza Mousavi Rabeti[c], Ana M Blanco-Marigorta[d]

[a] Energy, Environment and Biological Systems Research Lab (EEBRlab), Division of Thermal Sciences and Energy Systems, Department of Mechanical Engineering, Faculty of Technology & Engineering, University of Qom, Qom, Iran, m.khoshgoftar@qom.ac.ir, mh.khoshgoftar@gmail.com,
[b] Energy, Environment and Biological Systems Research Lab (EEBRlab), Division of Thermal Sciences and Energy Systems, Department of Mechanical Engineering, Faculty of Technology & Engineering, University of Qom, Qom, Iran, sohildavadgaran@gmail.com,
[c] Energy, Environment and Biological Systems Research Lab (EEBRlab), Division of Thermal Sciences and Energy Systems, Department of Mechanical Engineering, Faculty of Technology & Engineering, University of Qom, Qom, Iran, mousavi.sayed20@gmail.com,
[d] Department of Process Engineering, Universidad de las Palmas de Gran Canaria, Las Palmas de Gran Canaria, Country, anamaria.blanco@ulpgc.es

Abstract:

Global warming has increased the use of renewable energy in energy systems. In this regard, the present work presents an innovative polygeneration system to produce power, ammonia, and process steam using solar, biomass, wind, and geothermal energies. By using a solar-syngas hybrid boiler, steam has been created in two high-pressure (HP) and low-pressure (LP) levels, and the HP steam is used for the gasification process. Syngas produced from biomass gasification process produces ammonia with the nitrogen obtained from an air separation unit by going through water gas shifting and carbon capture processes. Power consumption in the mentioned sections is produced by wind turbines. A Brayton cycle with ammonia and hydrogen hybrid fuel has been used to produce power and heat. The integration of supercritical CO_2 and organic Rankine cycles with the hot flue gas output from the Brayton cycle has reduced heat losses and increased power generation. The presented renewable system has been analysed from the point of view of energy, exergy, exergeoeconomic, and exergoenvironmental (4E) methods. The overall results indicate that the total energy and exergy efficiencies are 31.33% and 38.53%, respectively. Also, the cost rate and environmental impacts of the whole system are calculated as 3222.35 $/h and 53.16 Pts/h, respectively. Meanwhile, the levelized cost and environmental impacts of electricity are equal to 0.18 $/kWh and 0.003 Pts/kWh, and the presented system is capable of producing 297.86 ton/day of ammonia.

Keywords:

Ammonia synthesis; Solar and biomass; Wind energy; Geothermal; Polygeneration.

1. Introduction

In the field of energy, there are various crises that indicate the importance of using renewable resources as a sustainable solution for energy production. These crises include rising prices of fossil fuels, decreasing levels of oil production, increasing air pollution, and the effects of desertification and global warming. In addition to the existing crises in the field of energy, energy production is also facing environmental crises. The use of fossil fuels leads to an increase in greenhouse gases and climate change, which has serious effects on life globally. Also, the use of fossil fuels causes air pollution and an increase in respiratory-related diseases. Biofuel production has been considered as a sustainable solution for energy production due to its biological properties. Biofuel is obtained from renewable sources such as plants, agricultural waste, and other organic materials and reduces greenhouse gases and air pollution [1]. In 2020, more than 80% of the installed power capacity worldwide was supplied by renewable sources [2]. This percentage will likely increase due to the increasing growth of the renewable industry.

One of the famous examples of biofuels is ammonia. Ammonia is one of the most widely used chemicals in the world. Ammonia synthesis from natural gas reforming [3], or ammonia production with syngas is one of its production methods [4]. Recently, the idea of creating an alternative fuel for fossil fuels has arisen, hydrogen can be converted into ammonia and then ammonia can be used as a fuel [5]. In addition, producing ammonia and replacing it with fossil fuels has advantages, including reducing air pollution and generating energy [6]. Furthermore, considering that hydrogen is not easily accessible and its storage is not necessarily easy, producing ammonia from hydrogen as an alternative approach has many advantages. In this regard, Aziz et al [7]. showed in their research that ammonia can be used in internal combustion engines, combustion for gas turbines, and direct ammonia fuel cells due to its high efficiency. Also, Lamb et al [8]. proposed hydrogen storage by ammonia production as a suitable way to transport and store it. Tinoco Caicedo et al [9]. conducted a study using biofuels in tri-generation systems to meet the energy demands of an instant coffee plant located in Guayaquil, Ecuador. The results show an increase in exergy efficiency from 51.9% to 84.5%

The use of renewable energies such as wind, solar, geothermal, and biomass is highly justifiable due to the countless benefits they have in the fields of energy, economy, health, and the environment [10]. Although each of the renewable energies individually creates many possibilities for us, the integration of these energies can significantly improve efficiency and reduce energy production costs [11]. Mousavi Rabati et al [12]. have proposed an integrated multi-generation system based on renewable energy sources such as solar and biomass for the production of power, heat, freshwater, and hydrogen. Their analysis results show that for Municipal Solid Waste (MSW) fuel, the overall energy and exergy efficiencies of the multi-generation system are 39% and 32.01%, respectively. The flexibility of renewable energy systems allows us to have the most efficient energy production systems in any condition. Borhanazad et al [13]. showed the potential of using wind, solar, and water energy well for two states in Malaysia to provide electricity. In these two states, due to the high potential of solar radiation, they can produce 3182 kW and 6317 kW through 18 and 22 sites, respectively. During their research in Europe and Latin America, Bersalli et al [14]. observed the positive impact of using renewable energy sources on reducing the economic costs of energy production. Khani et al [15]. demonstrated a multi-technology solar-based energy production system, which integrates gas and steam turbine cycles, organic Rankine cycle (ORC), and carbon dioxide capture, Humidification-dehumidification (HDH), showing that electricity production can be increased from 37.3% (in winter) to 59.41% (in summer) by integrating solar energy.

There are different solutions for integrating energy systems, for example, cogeneration and polygeneration systems can be used [16]. The Brayton cycle is one of the processes in cogeneration, in which electricity and heat are produced using a fuel such as ammonia. The goal of using renewable fuels is to reduce the environmental impact of using fossil fuels [17]. Also, the Supercritical CO_2 (S-CO_2) cycle is a power generation technology in which supercritical carbon dioxide is used as the working fluid in a closed-loop system. The supercritical carbon dioxide cycle offers several advantages over traditional steam-based cycles in energy systems, such as higher efficiency, lower footprint, lower capital costs, and lower greenhouse gas emissions [18]. The economic and environmental characteristics of a multi-generation system are very important. Multi-generation production systems can be used in various industries, such as freshwater production [16]. Diyoke and Ngwaka [19], integrated a gasifier, a syngas electric motor, connected to an absorption refrigeration system, and a wind turbine generator. They observed that the overall energy efficiency and exergy efficiency were 0.48 and 0.25, respectively, and major exergy destruction of about 95% for this system in this system, wastes are first collected and separated, and then sent to processes for energy production [20].

Despite extensive research in the field of renewable energy systems, the dependence of these systems on fossil fuels is still felt to create stability. Therefore, presenting a system that is entirely based on renewable energies requires further research. In this regard, the present work focuses on utilizing solar, biomass, and wind energies to produce ammonia as an alternative fuel for energy systems. The ammonia produced as a biofuel is then used in the Brayton cycle to generate sustainable power. The integration of S-CO_2 cycles and ORC in this system has increased power production and improved the efficiency of the studied system. Finally, by conducting energy, exergy, economic, and environmental analyses for the studied system, the feasibility of operating such a system has been examined in more detail. A series of innovations carried out in the present work are as follows:

- Ammonia production has been done using the integration of solar, wind, and biomass energies.
- The gas turbine cycle with a combined fuel of ammonia and hydrogen has been analyzed.
- The integration of S-CO_2 and ORC with the Brayton cycle based on ammonia has been investigated.
- Machine learning has been used to analyze and model parts in the processing unit.

2. System description

In this work, a polygeneration system based on solar, wind, geothermal, and biomass renewable energy is proposed to produce ammonia, power, and heat (process steam). This system has been analyzed for the city of Tehran in Iran. Tehran is located at 51° 6' to 51° 38' east longitude and 35° 34' to 35° 51' north latitude. The solar irradiance in Tehran is about 1800 to 2200 kilowatt-hours per square meter per year. The average wind speed in this city is around 4.5 meters per second [21], and the geothermal source in Tehran can provide heat up to 110 degrees Celsius for the energy systems. Also, the biomass used in the system is municipal solid waste (MSW), and its annual production in Tehran is around two million tons on average. The designed system consists of sections for ammonia synthesis, CO_2 capture, water gas shift (WGS), gasification process, ORC (R123), S-CO_2 cycle, and Brighton cycle. Their explanations are given below. Based on Figure (1), which illustrates the schematic of the designed system, it can be stated that after the water makeup, steam is produced at two pressure levels, LP and HP, from a hybrid solar-syngas boiler using syngas as fuel. The produced LP steam is used as a process steam, while the HP steam is fed into the gasification reactor for the production of synthesis gas using the air-steam gasification agent. The chemical reaction that occurs in the gasifier is as follows:

$$CH_\alpha O_\beta N_z + wH_2O + m(O_2 + 3.76N_2) \rightarrow x_1H_2 + x_2CO + x_3CO_2 + x_4H_2O + x_5CH_4, \quad (1)$$

In the boiler, water is initially preheated by the heat of the syngas outlet from the gasifier and the heat resulting from its combustion in the boiler, and exits the system from the stream (4) and by solar energy, it loses its latent energy and enters the boiler and the LP steam leaves the stream (8). In the same way, another part enters and leaves the boiler with a higher pressure (HP) to enter the gasifier and produce syngas. The use of solar energy has been used as an aid to produce steam in the boiler. The second section of the syngas stream, which is the stream (21), enters the WGS stage to convert the CO in the syngas to CO_2. Its reaction is reported in relation (2):

$$CO + H_2O \leftrightarrow CO_2 + H_2, \quad (2)$$

The final synthetic gas, devoid of CO, is directed into a CO_2 capture process. Using an air separator unit (ASU), nitrogen is added to the exhaust gas from the CO_2 capture to produce ammonia with higher and more suitable efficiency, and gas rich in nitrogen and hydrogen enters the ammonia synthesis stage. In this section, the ammonia reaction takes place through two converters with a conversion efficiency of 25%, operating at a temperature and pressure of 350 ℃ and 30 bar, respectively [4, 22]. The ammonia reaction is as follows:

$$N_2 + 3H_2 \leftrightarrow 2NH_3, \quad (3)$$

The produced ammonia with a purity of 99% is removed from the separator, and a part of it is stored while the other part is used to maximize the use of the system designed for burning in the Brayton cycle, which is coupled with a PEM electrolyzer (PEMEC) to provide hydrogen for the combustion chamber. Hydrogen is added to ammonia to increase the fuel's calorific value. It is also noteworthy that the power required for the operation of the PEMEC and ASU in the CO_2 capture section is supplied by renewable wind energy through wind turbines. The wind turbine used is LTW77 and has a capacity of 1MW [23]. The required heat for the S-CO_2 cycle and ORC is supplied from the exhaust temperature of the gas turbine, which is high to reduce losses, recover heat, and generate power. The working fluid used in the Rankine cycle is R123, which utilizes geothermal energy to change the phase of the output water stream (55). Assumptions used in the proposed system:

- The system has been studied in a steady state, and kinetic and potential energies in all flows have been neglected.
- There is enough time to carry out the gasification reaction, so this equilibrium process is carried out
- Gasification pressure is considered constant.
- The production of tar and char in gasification has been disregarded.
- Heat losses in all heat exchangers have been disregarded.
- The temperature and working pressure of WGS reactors are 450 ℃ and 14.4 bar, respectively, and their fractional conversion is 88.2 [22].
- Ambient temperature and pressure are considered to be 25 ℃ and 1.01 bar, respectively.
- The collectors used are PTC and their model is ET100 [24].
- The temperature and pressure are assumed to be constant in the PEMEC, equal to 80 ℃ and 1 bar, respectively [25].
- The production of nitrogen oxides, sulfur, chlorides, etc. in the syngas products has been disregarded.

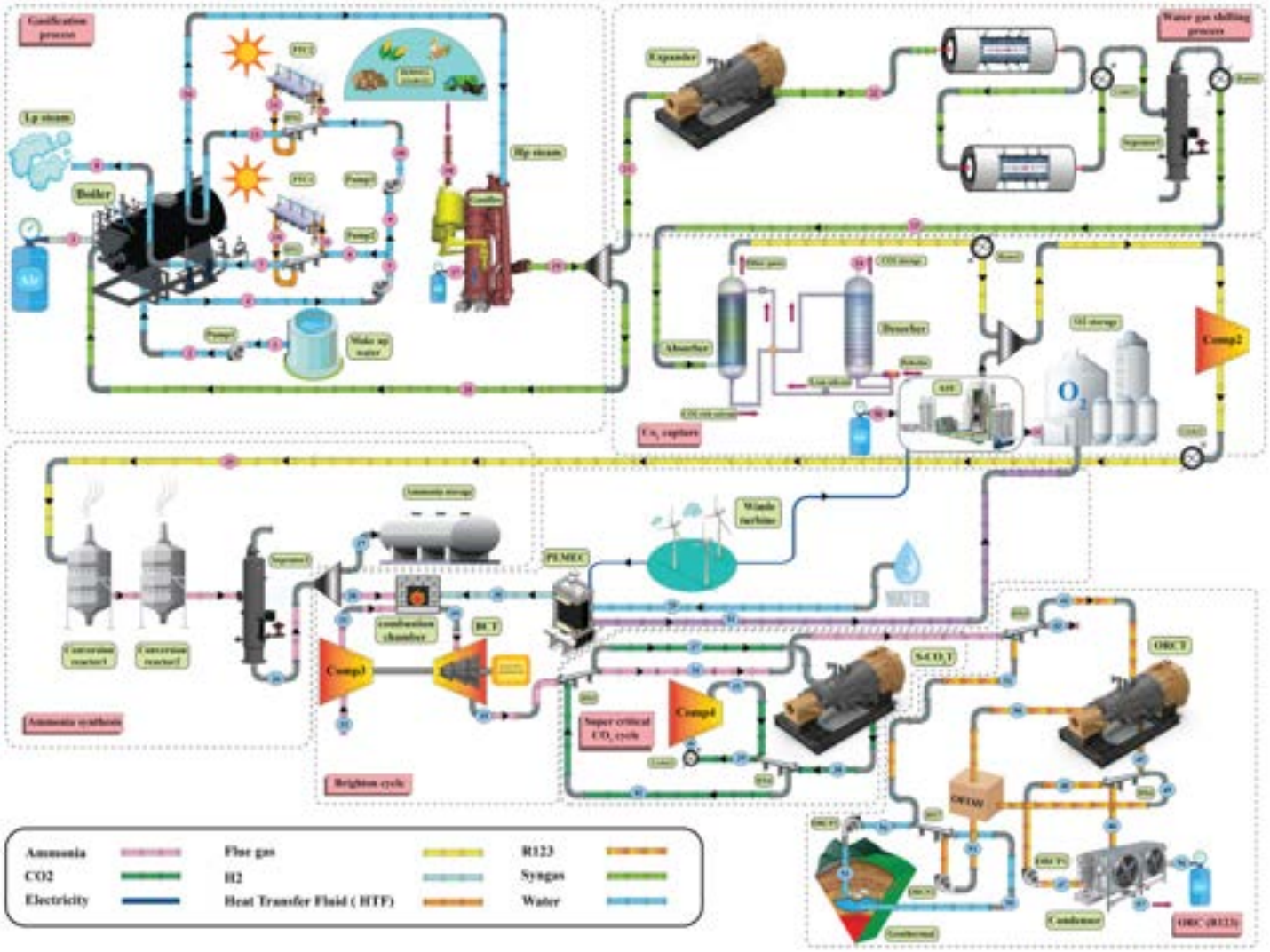

Figure. 1. Schematic of polygeneration system based on solar, wind, geothermal, and biomass renewable energy to produce ammonia, power, and heat

3. Governing equations

To calculate the heat and power exchanged by an energy system in a steady state, the mass and energy balances can be calculated based on the first law of thermodynamics, and the equations are as follows [26]:

$$Q - W = -\sum_{i=1}^{n} m_{out}\left(h + \frac{V^2}{2} + gz\right)_{out} - \sum_{i=1}^{n} m_{in}\left(h + \frac{V^2}{2} + gz\right)_{in}, \quad (4)$$

$$\sum_{i=1}^{n} m_{out} = \sum_{i=1}^{n} m_{in}, \quad (5)$$

In equation (4), Q is the heat transfer rate, W is the power transfer rate, and m_{in} and m_{out} are the input and output mass flow rates. Also, each input and output flow has parameters g gravity, h specific enthalpy, v velocity, and z height. It should be noted that in flows where the potential and kinetic energy values are negligible, these terms are disregarded. However, for inflows such as the inflow and outflow of wind turbines where the kinetic energy is important, this term is included. By using the conventional principle of state and knowing two independent thermodynamic variables, it is possible to calculate other thermodynamic variables. Writing the energy and mass balance for all equipment is not enough because these equations consider the system in a closed state and only check the input and output flows to this system. If necessary, to investigate mass transfer, heat transfer, and other important parameters in equipment, additional equations must be involved for each piece of equipment. For example, in PTC, energy transfer is not the only issue and the required collector surface is also important, so it is necessary to use heat transfer equations to calculate it. Also, in a gasification reactor, it is necessary to balance the molar flow rates based on equilibrium constants to calculate the molar coefficients on the reactant side. For process systems such as ASU and ammonia production, writing the energy and mass balance and modeling these systems is very complicated. The equipment in these systems all have equations related to energy and mass balance, and each piece of equipment can also be divided into several sub-systems. As there are feedback currents in these systems, modeling them, like other components of the system, will be very time-consuming and complex. Therefore, machine learning or faster alternative methods are suggested for these systems. In the present work on the gasification system, ASU, and ammonia production, machine learning has been used, and the equations governing these systems have been extracted. The equations are extracted by simulating or modeling each of the mentioned systems in software. For ASU, it was simulated in Aspen Plus software according to the reference [27]. For ammonia production, it was simulated in Aspen Hysys software based on the reference [22]. For gasification, modeling was performed using MATLAB software based on the article by Sirinivas et al [28]. After that, the validation was done and the data bank was formed by repeated calculations to extract comprehensive relationships by Python software. For analyzing and investigating other equipment such as PEMEC, equations from the reference [25] have been utilized. For wind turbines, references [23, 29] were employed. For PTC, references [24, 30] were used, and for gasification, reference [28] was employed. In the current work, exergy analysis, exergoeconomic analysis, and exergoenvironmental analysis have been utilized for a more precise investigation and better evaluation of the system. The analysis of entropy production, irreversibility, and measurement of energy system deviations in ideal operational conditions can be easily achieved by employing the second law of thermodynamics to more accurately investigate and evaluate the energy systems. Equation (6) shows the exergy balance [31]:

$$Ex_Q + \sum_i m_i ex_i = \sum_e m_e ex_e + Ex_w + Ex_D, \quad (6)$$

Where Ex_Q, Ex_w, Ex_D, ex_i, and ex_e correspond to the exergy caused by heat transfer, exergy caused by power transfer, exergy destruction, and exergy caused by mass flow rates of the inlet and outlet streams, respectively. Other necessary equations for this analysis are mentioned in reference [31].

Exergoeconomic and exergoenvironmental analyzes have been reviewed to check the economic and environmental performance of the system, and its balance is as follows [32]:

$$C_Q + \sum_{in}(c.Ex)_{out} + Z_k = C_w + \sum_{out}(c.Ex)_{out}, \quad (7)$$

$$B_Q + \sum_{in}(b.Ex)_{out} + Y_k = B_w + \sum_{out}(b.Ex)_{out}, \quad (8)$$

Z_k, b, c, and Y_k respectively represent the investment cost of each piece of equipment, environmental impacts of the flow, flow cost, and environmental impacts of each piece of equipment over its lifetime. Other necessary equations have been mentioned in reference [32]. The constants used in this study are: an interest rate of 10%, a maintenance factor of 1.06, and a 20-year lifespan for the power plant and operating hours considered are 3500 hours for PTC, 6000 hours for wind, and 8000 hours for other equipment [32]. In addition, references [12, 32] have been used for capital investment cost and equipment weights in economic and environmental calculations. Environmental analysis using LCA. LCA, as a technique, searches, evaluates, and examines the environmental impacts of a product or equipment from manufacturing, transportation, use, disposal, and important environmental impact aspects are analyzed.

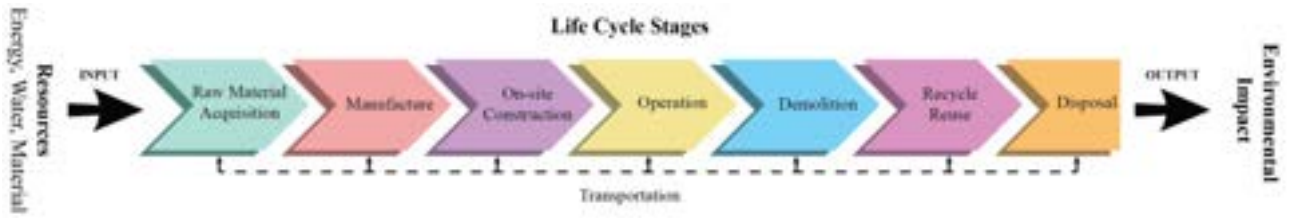

Figure. 2. Life cycle Assessment stages [33]

4. Results

Figure (3) shows the results of the energy analysis of the proposed system in a block form. In this figure, it is possible to observe the relationship between the different parts of the proposed system and the exchanged energies within the system.

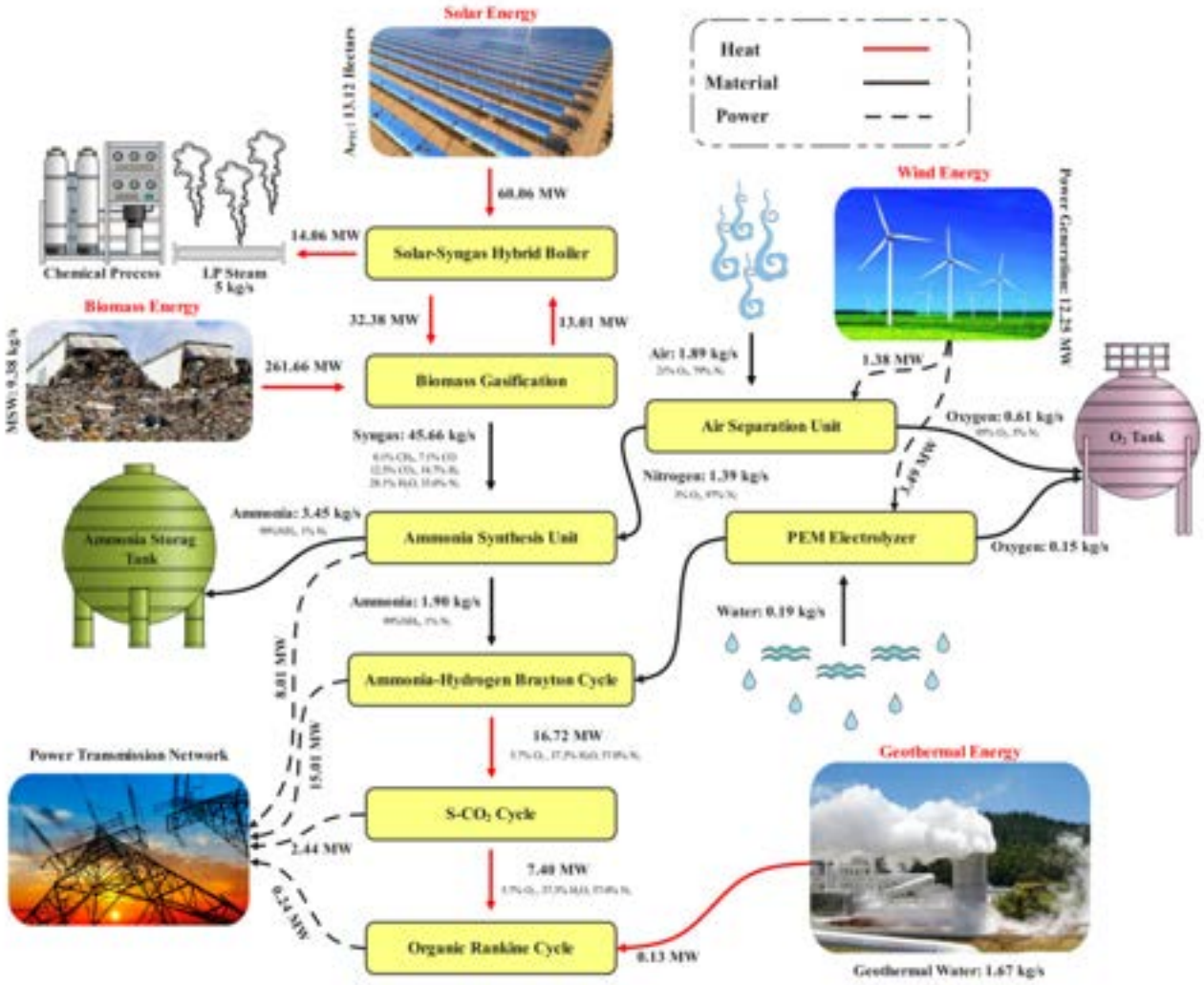

Figure. 3. The block diagram of the proposed system.

For a more detailed analysis of the proposed system, energy, exergy, economic and environmental analyzes have been performed on the system and its results have been discussed. The highest exergy efficiency is related to the expander equipment for power generation from syngas. The lowest exergy efficiency is related to the wind turbine farm. The highest investment costs in the studied system are related to the solar farm with a cost of 0.46 $/s and the wind farm with a cost of 0.22 $/s, respectively. The highest environmental impacts have been caused by the S-CO_2 turbine, and it is necessary to modify this equipment to reduce the environmental impacts. According to Table (1) which shows the 4E results on the proposed system, it can be stated that the Net power generation, Total exergy destruction, Overall polygeneration exergy efficiency, Total cost rate of polygeneration system, and Total environmental impact rate of polygeneration system are 17.93

(MW), 553.31 (MW), 38.53 (%), 3222.35 ($/h), and 53.16 (Pts/kWh), respectively. The pie diagrams in Figures (1a), (1b), (1c) represent exergy destruction, cost destruction, and environmental impact destruction of the system, respectively. It is clear that the ASU is more destructive in terms of exergy destruction, cost destruction, and environmental impact compared to other parts of the system. One reason for this is that the system involves deep cooling processes which require high energy consumption. Therefore, the exergy destruction, cost destruction, and environmental impact of this unit are very high, and corrective measures need to be taken to improve the system. The ammonia production unit has high exergy destruction after ASU due to high energy consumption and high losses. It is necessary to recover these losses in the system to reduce exergy destruction. In the gasification unit, because many chemical reactions occur and the production of entropy is high, its exergy destruction is also significant. The use of solar energy for the boiler has reduced the environmental impact of the equipment, but on the other hand, it has increased the cost of destruction of this equipment. The reason for the significant amount of exergy destruction, cost, and environmental impact in the Brayton cycle is the presence of chemical reactions and the release of a large amount of energy in the combustion chamber. Improvements must be made in the direction of improving this system. Wind turbines have a noticeable level of exergy destruction, but it is well observed that in Figures (1b) and (1c), the destruction cost and destruction environmental impact of this unit is minimized as much as possible. This shows that wind farm can be very effective in reducing costs and environmental impacts.

Table 1. overall result of 4E analysis of the proposed system.

Parameters	**value**
Net power generation (MW)	17.93
Net ammonia flow rate production (ton/day)	297.86
Mass flow rate of LP steam generation (kg/s)	5
Mass flow rate of oxygen generation (ton/day)	52.30
Overall polygeneration energy efficiency (%)	31.33
Total exergy destruction (MW)	553.31
Overall polygeneration exergy efficiency (%)	38.53
Total cost rate of polygeneration system ($/h)	3222.35
Total environmental impact rate of polygeneration system (Pts/h)	53.16
Levelized cost of electricity ($/kWh)	0.18
Levelized environmental impact of electricity (Pts/kWh)	0.003
MSW mass flow rate consumption (kg/s)	9.38
Geothermal mass flow rate consumption (kg/s)	1.67
Number of wind turbines (model: LTW77)	35
Area of PTC (model: ET-100) in the solar field (Hectares)	13.12

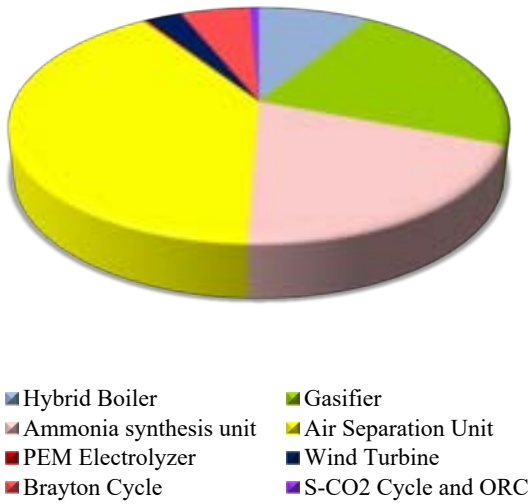

(a)

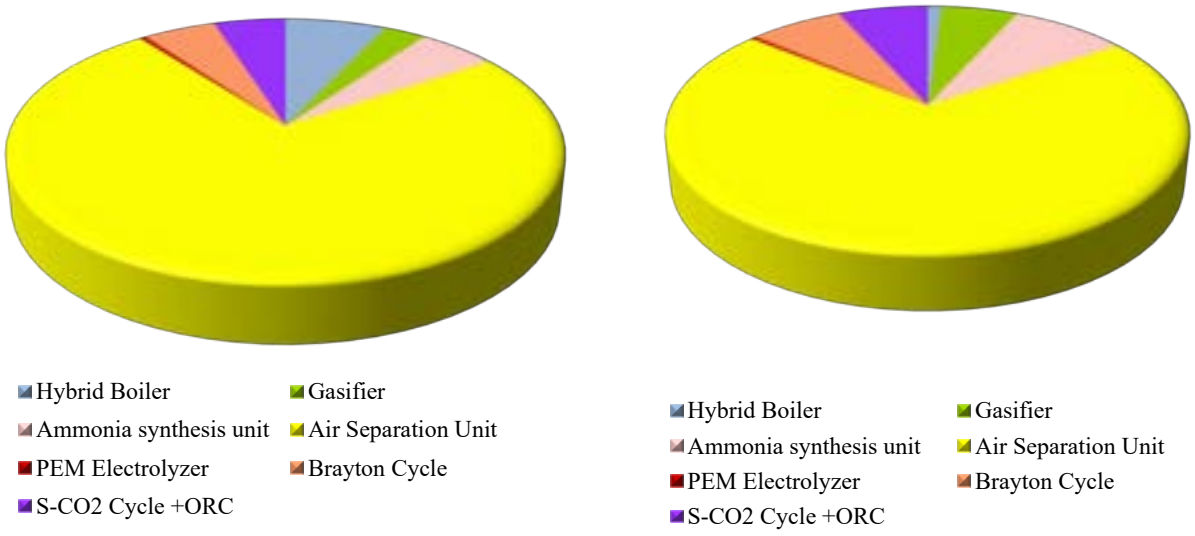

(c) (b)

Figure. 4. (a) Exergy Destruction, (b) cost destruction, and (c) environmental impact destruction Contributions of all parts in the proposed polygeneration system

5. Validation

The thermodynamic validation of the proposed system, which includes the Brayton cycle, S-CO_2 cycle, ORC, ammonia production, PEMEC, PTC, wind turbine, and gasification sections, has been verified by credible articles. It should be noted that the cases of PEMEC and gasification have been validated in the work of Mousavi Rabeti et al [12]. and PTC has also been validated in the research conducted by Khoshgoftar Manesh et al [30]., who are among the authors of this study. It has been refrained from including them due to limitations in this section. In addition, the cases of the S-CO_2 cycle, ORC, Brayton cycle, and wind turbine have been validated by modeling in MATLAB software, and their results have been validated with the articles of [23, 34-36]. Ammonia production has been simulated in Hysis software and validated with the article by Ishaq et al [22]. The performed validations have been compared with articles and their results have the least errors, so the performed validation is correct. The average validation error has been reported to be below 5%.

6. Conclusions

This article has presented a new polygeneration system with the driver of solar-biomass-wind-geothermal energy to produce power, heat (steam), and ammonia for the city of Tehran in Iran. MSW gasification has been used for ammonia synthesis. A part of produced ammonia along with hydrogen has also been used as biofuel to produce electricity in Brayton, supercritical CO_2, and organic Rankine cycles. Modeling of the proposed system has been done using energy, exergy, exergeoeconomic, and exergoenvironmental (4E) analyses. The general results of polygeneration system modeling show that this system has an average energy and exergy efficiency of 31.33% and 38.53%. The results of the economic and environmental analysis show that the overall cost rate and environmental impacts rate of the entire system are 3222.35 $/h and 53.16 Pts/h, respectively. Other main results are as follows:

- Production of ammonia and process steam is equal to 297.86 ton/day and 5 kg/s, respectively.
- Using biomass and solar energy to produce products in the proposed system is more than other energies.
- The most destruction of exergy, destruction of costs, and destruction of environmental impacts is related to the air separation unit.
- The highest investment cost is related to the solar and wind field sectors.

In the end, this system can be integrated with other energy systems, such as a variety of thermal desalination systems, in order to have more flexibility in producing products while having low environmental impacts. Conducting more investigations including dynamic analysis and optimization can better evaluate the performance of such a system.

Acknowledgments

This research has been co-funded by ERDF funds, INTERREG MAC 2014-2020 programme, within the ACLIEMAC project (MAC2/3.5b/380). No funding sources had any influence on study design, collection, analysis, or interpretation of data, manuscript preparation, or the decision to submit for publication.

References

[1] Joshi, G., Pandey, J. K., Rana, S., & Rawat, D. S. Challenges and opportunities for the application of biofuel. Renewable and Sustainable Energy Reviews 2017; 79, 850-866.

[2] Murdock, H. E., Gibb, D., André, T., Sawin, J. L., Brown, A., Ranalder, L., & Brumer, L. Renewables 2021-global status report; 2021.

[3] Boyano, A., Blanco-Marigorta, A. M., Morosuk, T., & Tsatsaronis, G. Exergoenvironmental analysis of a steam methane reforming process for hydrogen production. Energy 2011; 36(4), 2202-2214.

[4] Ishaq, H., & Dincer, I. Investigation and optimization of a new hybrid natural gas reforming system for cascaded hydrogen, ammonia and methanol synthesis. Computers & Chemical Engineering 2021; 148, 107234.

[5] Dincer, I., Erdemir, D., Aydin, M. I., Karasu, H., & Vezina, G. Ammonia production. In Ammonia Energy Technologies.Cham: Springer International Publishing; 2023.

[6] Wan, Z., Tao, Y., Shao, J., Zhang, Y., & You, H. Ammonia as an effective hydrogen carrier and a clean fuel for solid oxide fuel cells. Energy Conversion and Management 2021; 228, 113729.

[7] Aziz, M., Wijayanta, A. T., & Nandiyanto, A. B. D. Ammonia as effective hydrogen storage: A review on production, storage and utilization. Energies 2020; 13(12), 3062.

[8] Lamb, K. E., Dolan, M. D., & Kennedy, D. F. Ammonia for hydrogen storage; A review of catalytic ammonia decomposition and hydrogen separation and purification. International Journal of Hydrogen Energy 2019; 44(7), 3580-3593.

[9] Tinoco Caicedo, D. L., Santos Torres, M., Mero-Benavides, M., Patiño Lopez, O., Lozano Medina, A., & Blanco Marigorta, A. M. Simulation and Exergoeconomic Analysis of a Trigeneration System Based on Biofuels from Spent Coffee Grounds. Energies 2023; 16(4), 1816.

[10] Patel, M. R. Wind and solar power systems: design, analysis, and operation. CRC press; 2005.

[11] Farret, F. A., & Simões, M. G. Integration of renewable sources of energy. John Wiley & Sons; 2017.

[12] Rabeti, S. M., Manesh, M. K., & Amidpour, M. Techno-economic and environmental assessment of a novel polygeneration system based on integration of biomass air-steam gasification and solar parabolic trough collector. Sustainable Energy Technologies and Assessments 2023; 56, 103030.

[13] Borhanazad, H., Mekhilef, S., Saidur, R., & Boroumandjazi, G. Potential application of renewable energy for rural electrification in Malaysia. Renewable energy 2013; 59, 210-219.

[14] Bersalli, G., Menanteau, P., & El-Methni, J. Renewable energy policy effectiveness: A panel data analysis across Europe and Latin America. Renewable and Sustainable Energy Reviews 2020; 133, 110351.

[15] Khani, N., Manesh, M. H. K., & Onishi, V. C. 6E analyses of a new solar energy-driven polygeneration system integrating CO2 capture, organic Rankine cycle, and humidification-dehumidification desalination. Journal of Cleaner Production 2022; 379, 134478.

[16] Manesh, M. H. K., & Amidpour, M. Cogeneration and Polygeneration Systems. Academic Press; 2020.

[17] Valera-Medina, A., Morris, S., Runyon, J., Pugh, D. G., Marsh, R., Beasley, P., & Hughes, T. Ammonia, methane and hydrogen for gas turbines. Energy Procedia 2015; 75, 118-123.

[18] Crespi, F., Gavagnin, G., Sánchez, D., & Martínez, G. S. Supercritical carbon dioxide cycles for power generation: A review. Applied energy 2017; 195, 152-183.

[19] Diyoke, C., & Ngwaka, U. Thermodynamic analysis of a hybrid wind turbine and biomass gasifier for energy supply in a rural off-grid region of Nigeria. Energy Sources, Part A: Recovery, Utilization, and Environmental Effects 2021; 1-19.

[20] Rajput, V. D., Yadav, A. N., Jatav, H. S., Singh, S. K., & Minkina, T. Sustainable Management and Utilization of Sewage Sludge. Springer International Publishing; 2022.

[21] Alamdari, P., Nematollahi, O., & Mirhosseini, M. Assessment of wind energy in Iran: A review. Renewable and Sustainable Energy Reviews 2012; 16(1), 836-860.

[22] Ishaq, H., & Dincer, I. Development and multi-objective optimization of a newly proposed industrial heat recovery based cascaded hydrogen and ammonia synthesis system. Science of The Total Environment 2020; 743, 140671.

[23] Makkeh, S. A., Ahmadi, A., Esmaeilion, F., & Ehyaei, M. A. Energy, exergy and exergoeconomic optimization of a cogeneration system integrated with parabolic trough collector-wind turbine with desalination. Journal of Cleaner Production 2020; 273, 123122.

[24] Tzivanidis, C., Bellos, E., & Antonopoulos, K. A. Energetic and financial investigation of a stand-alone solar-thermal Organic Rankine Cycle power plant. Energy conversion and management 2016; 126, 421-433.

[25] Ahmadi, P., Dincer, I., & Rosen, M. A. Energy and exergy analyses of hydrogen production via solar-boosted ocean thermal energy conversion and PEM electrolysis. International Journal of Hydrogen Energy 2013; 38(4), 1795-1805.

[26] Cengel, Y. A., Boles, M. A., & Kanoğlu, M. Thermodynamics: an engineering approach New York: McGraw-hill; 2011.

[27] Dash, S. M. Study of Cryogenic Cycles with Aspen-Hysys Simulations (Doctoral dissertation); 2009.

[28] Srinivas, T., Gupta, A. V. S. S. K. S., & Reddy, B. V. Thermodynamic equilibrium model and exergy analysis of a biomass gasifier. Journal of energy resources technology 2009; 131(3).

[29] Rokni, M. M. Power to hydrogen through polygeneration systems based on solid oxide cell systems. Energies 2019; 12(24), 4793.

[30] Manesh, M. K., Rabeti, S. M., Nourpour, M., & Said, Z. J. S. E. T. Energy, exergy, exergoeconomic, and exergoenvironmental analysis of an innovative solar-geothermal-gas driven polygeneration system for combined power, hydrogen, hot water, and freshwater production. Sustainable Energy Technologies and Assessments 2022; 51, 101861.

[31] Dincer, I., Rosen, M. A., & Ahmadi, P. Optimization of energy systems. John Wiley & Sons; 2017.

[32] Cavalcanti, E. J. C. Exergoeconomic and exergoenvironmental analyses of an integrated solar combined cycle system. Renewable and Sustainable Energy Reviews 2017; 67, 507-519.

[33] Chau, C. K., Leung, T. M., & Ng, W. Y. A review on life cycle assessment, life cycle energy assessment and life cycle carbon emissions assessment on buildings. Applied energy 2015; 143, 395-413.

[34] Kim, M. S., Ahn, Y., Kim, B., & Lee, J. I. Study on the supercritical CO2 power cycles for landfill gas firing gas turbine bottoming cycle. Energy 2016; 111, 893-909.

[35] Yari, M. Exergetic analysis of various types of geothermal power plants. Renewable energy 2010; 35(1), 112-121.

[36] Ezzat, M. F., & Dincer, I. Energy and exergy analyses of a novel ammonia combined power plant operating with gas turbine and solid oxide fuel cell systems. Energy 2020; 194, 116750.

Experimental investigation of a Solid Oxide Fuel Cell (SOFC) used in residential cogeneration applications

Nicolas Paulus[a] and Vincent Lemort[b]

[a] *University of Liège, Thermodynamics Laboratory, Liège, Belgium, nicolas.paulus@uliege.be, CA*
[b] *University of Liège, Thermodynamics Laboratory, Liège, Belgium, vincent.lemort@uliege.be*

Abstract:

The much-needed energy transition brings special focus on fuel cell micro-combined Heat and Power (mCHP) systems for residential uses, one of which is a Solid Oxide Fuel Cell (SOFC), fed by natural gas, designed to provide continuously 1.5 kW_{el} with an associated amazingly high expected Low heating Value (LHV) electrical efficiency of 60%. Fortunately, this power output can be modulated as desired down to 500 W_{el}. With this machine, heat can also be recovered to partially contribute to the heat demand of the household. One main advantage of this appliance is that the heat recovery system is designed to be purely optional and it can be shut down, removed or added as desired, even if the machine is running. The machine is driven and completely monitored by the manufacturer remotely.
This system has been installed in a laboratory environment and has been specifically instrumented in order to evaluate its performance at thermal loads (according to the electrical output power controlled remotely by the manufacturer). In this paper, focus is brought on the resulting thermal output and efficiencies, both thermal and electrical, which have also been modelled with great goodness of fit. With several electrical power outputs between the 500-1500 W_{el} range, this study shows total High Heating Value (HHV) total efficiencies up to 88-89% at minimal return temperatures (around 20°C) in the heat recovery circuit. Maximum LHV electrical efficiency has been found to be equal to 57% at nominal output power (regardless of the thermal loads), which is close to the manufacturer's target of 60%.

Keywords:

Experimental, Fuel cell, Micro-CHP, Efficiency, Model, Part-load

1. Introduction

In its latest Sixth Assessment Report in 2022, the Intergovernmental Panel on Climate Change (IPCC) has reported a maximum carbon budget of 890 $GtCO_2$ that humanity can emit from January 1st 2020 in order for global warming to likely remain under the +2°C widely acknowledged limit compared to preindustrial temperature levels [1]. Even at residential scales, this much-needed decarbonation brings focus on cleaner power sources such as fuel cells combined heat and power (CHP) systems [2, 3, 4].

One system, already commercialized and tested in inhabited dwellings in field-test applications [5], is a Solid Oxide Fuel Cell (SOFC) fed by natural gas, designed to provide 1.5 kW_{el} of nominal output power with an amazingly high announced Low heating Value (LHV) electrical efficiency of 60%, along with a heat recovery of 0.6 kW_{th} representing a LHV thermal efficiency up to 25%. The output power can be modulated down remotely (by the manufacturer, upon the owner's request) as wanted in the 0.5 - 1.5 W_{el} range, affecting those announced efficiencies, but it is not advised to completely shut it down. Indeed, the thermal cycles that would be induced would imply too intense temperature gradients, which are known to contribute to degradation by opening micro-cracks and delaminations (failure mode for which materials fracture into layers) [6]. It is known that start-up and shut-down procedures require appropriate control to ensure fuel cell durability [7] and it is believed that in this case, this is the reason why start-up operations have been reported in the user manual to last up to 30 hours.

The purpose of this paper is to report the laboratory test campaigns that have been conducted in the facilities of the University of Liege on this SOFC system. This study aims to verify the electrical and thermal efficiencies announced at nominal output power, as well as to investigate how part-load operations affect them, which have not been extensively studied in literature with commercialized mCHP fuel cells. In addition, a wide range of operating temperatures for the heat recovery system of the SOFC have been tested and reported in this paper. The novelty of this work also lies in the performance models that have been computed from the experimental results and that can be easily integrated in building simulation tools.

2. Description of the system and the test bench

Discarding its chimney, the system has approximately the same size as a dishwasher, as it can be seen in Figure 1. Its internal schematics has not been disclosed but has been discussed in a previous publication [5], based on observations of the system and cogeneration SOFC literature. Amongst other particularities, the reforming process of the inlet natural gas (into hydrogen) is not only internal, i.e. directly onto the stack, at the anode (allowed with high operating temperatures occurring with that fuel cell technology [8]), but it also uses an external steam reformer upstream of the stack (called 'pre-former' [5]).

Figure 1. Tested mCHP SOFC in ULiege laboratory facilities

The test bench, presented in Figure 2, has been described in a previous publication [9]. It has been designed to control the heat recovery flow rate, through a variable speed circulator, and the operating temperatures, through a high-capacity cooling heat exchanger bypassed by a thermostatic three-way valve [9].

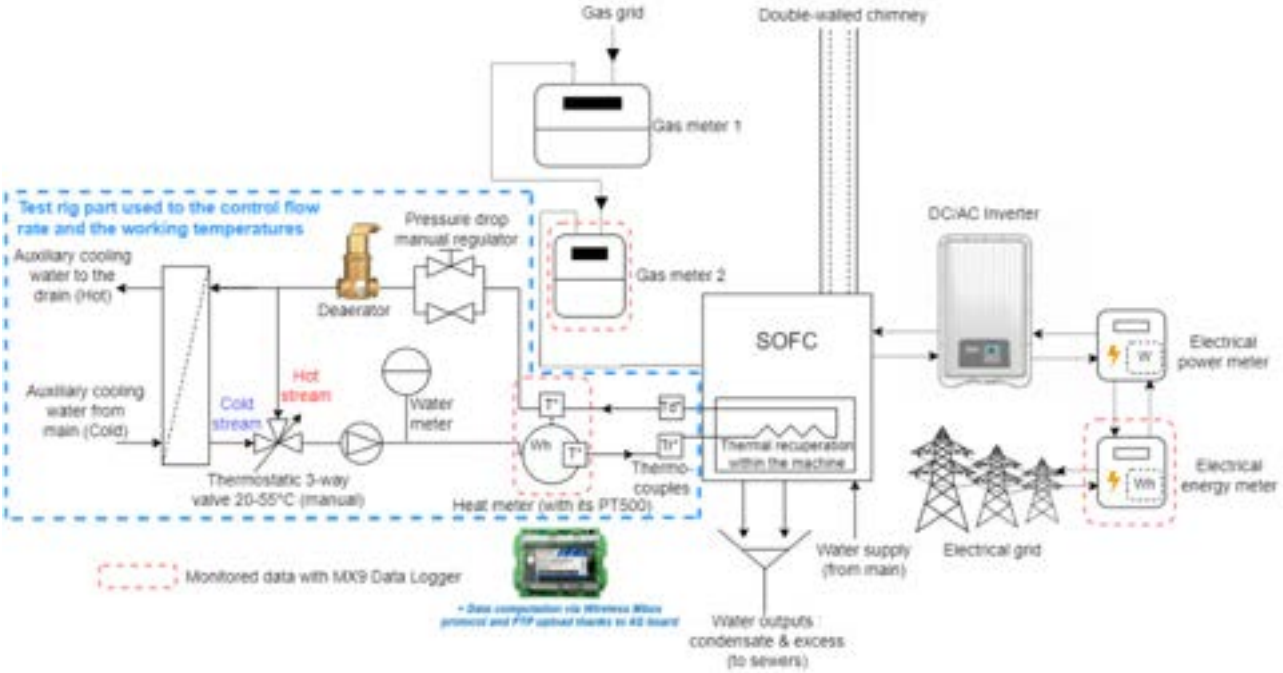

Figure 2. Schematics of the SOFC test bench described in this paper

2.1 Measurement devices

The test bench has also been designed to offer redundancy of the sensors required to compute electrical and thermal efficiencies: gas, electrical and heat meters (consisting of flow rate meters and temperature probes) have indeed all been doubled with field-test monitoring sensors connected to a Wireless M-bus (Meter-bus) data-logger [10]. It is worth mentioning that the same Wireless M-bus sensors have been implemented in a parallel field-test study on the same mCHP SOFC [5]. Therefore, the purpose of adding the same sensors as in the field-test study was to correlate the measurements and subsequently validate the field-test measurements. Main sensors used in the test bench for efficiency computation are shown in Figure 3 and Figure 4. Their references, accuracy and resolution have been reported in Table 1.

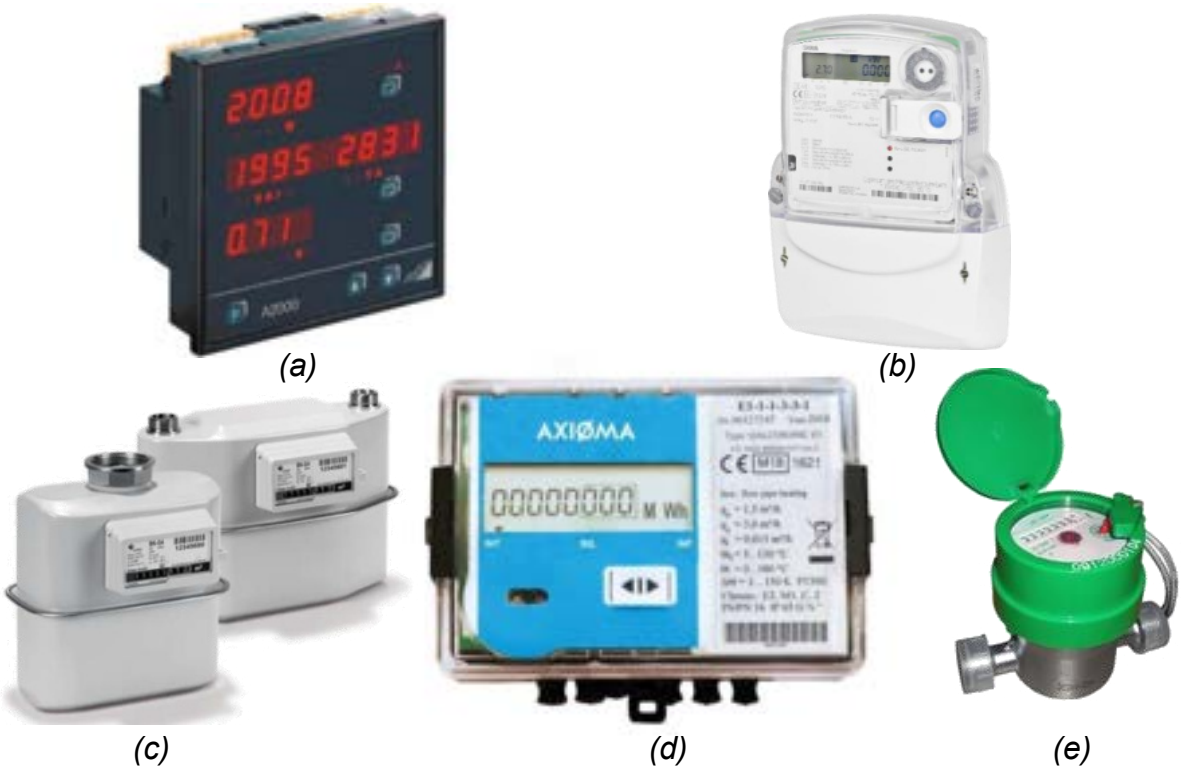

Figure 3. Metering sensors used on the test bench: a) electrical power, electrical energy meter, c) gas meters, d) heat recovery meter (that computes supply and return temperatures as well as the flow rate).

Table 1. Specifications of the main sensors used to compute efficiency laboratory results

Sensors	Reference	Resolution	Accuracy
Recovery heat rate (and flow rate)	Qalcosonic E1 Qn2,5 qi=0.025m³/h | L=130mm	1 W_{th}* 1 L/h*	<5% Accuracy Class 2 [11]
Paired [12] depart and return temperature (PT500)***	Qalcosonic E1 Qn2,5 qi=0.025m³/h | L=130mm	0,1 K*	<0,04 K at 293 K [13] <0,04 K at 333 K [13]
Recovery heat volumetric water meter***	DHV1300	0.1 L	<2% (datasheet)
Paired [12] depart and return temperature***	'type T' thermocouples	Analog signal	±1 K [14]
Electrical power	A2000	1 W_{el}	<0.5% (datasheet)
Electrical energy counter	Iskrameco MT174	10 Wh*	< 1% Accuracy Class 1 [15]
Gas volume counter	BK-G4T DN25 Qmax 6 m³/h	10 L*	<0.5% (datasheet)

** Data logger included* *** Assumed from Class B* [13]*, highest tolerance figure for most common PT500*
**** For redundancy of the heat rate calculation*

The field-test electricity meter is a Iskraemeco MT174, shown in Figure 3(b). It computes two indexes of electrical energy (for production and consumption). Electrical power is not directly provided and must

be established by taking the derivative of the energy index. The electrical power meter, which is shown in Figure 3(a), is an A2000 bidirectional electrical power meter that shows both the net electrical power consumed and generated.

It is important to mention that the generated power exported to the grid is reduced by the power consumed by the operation of the SOFC itself. In electrical production mode (which occurs for all the test conducted in the laboratory), no electrical consumption is measured: the system provides for its own auxiliaries, except for the circulator of the (optional) heat recovery circuit, that is external to the SOFC and could be sized and chosen independently.

The field-test heat meter sensor is a Qalcosonic E1, shown in Figure 3(d). It is preferably placed on the return line (as close as possible to the heating appliance to reduce the impact of thermal losses). It is composed of flow rate ultrasonic sensor combined with two PT-500 temperature probes to implement power calculations according to the first thermodynamics principle. One of those probes is included in the main body part of the sensor (where the flow rate measurement occurs) whereas the other probe has to be mounted in separate valve body (to place on the depart line as close as possible to the heating appliance). A commented photograph of this separate temperature probe assembly is presented in Figure 4(a).

The Qalcosonic sensor also provides the flow rate and temperature it measures. It also computes an energy index (by integration of the power measurement).

The heat meter is correlated to a specific combination of independent water flow rate and temperature measurements. On the one hand, 'type-T' thermocouples are placed in specifically manufactured immersion sleeves, as shown in Figure 4(b). Those are located at the recovery circuit return and depart (close to the PT-500 probes of the Qualcosonic E1 heat meter). The thermocouples are insulated after installation to ensure that the collected data to avoid the influence of radiation or convection with other sources. On the other hand, the water flow rate of the heat recovering circuit is also measured thanks to a DHV 1300 water meter, shown in Figure 3(e). It computes the volume of water that is passing through the sensor (thanks to the displacement of a rotating piston). It provides 10 pulses every litre so a frequency meter can be implemented to generate an analog signal. A specific calibration process allows for converting its frequency signal into the desired flow rate measurement.

Both gas metering diaphragm sensors reported in the test bench are BKG4T (temperature compensation implemented). They are shown in Figure 3(c).

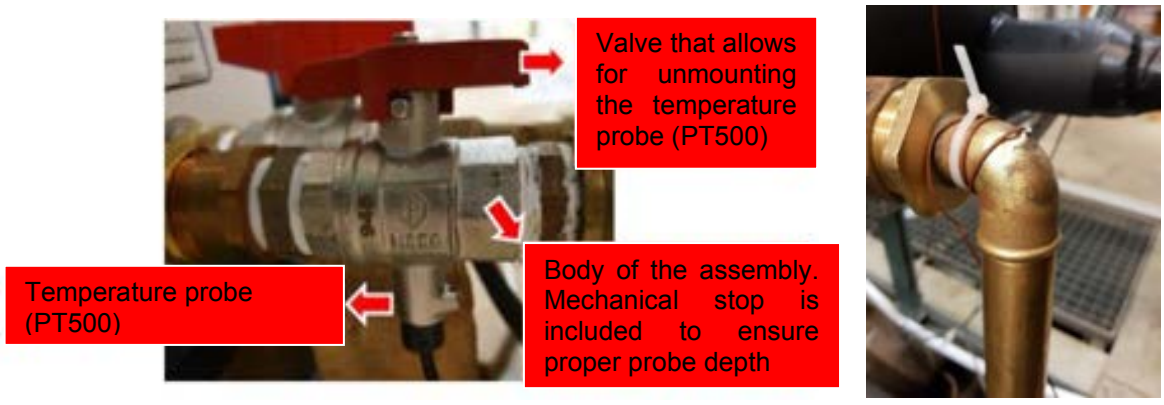

Figure 4. Temperature measurements required to establish the heat recovery rate: a) separate PT-500 probe assembly required for the Qualcosonic E1 heat meter, b) thermocouple elbow immersion sleeve associated with the DHV1300 water meter.

2.2 Testing procedure

As explained, one purpose of the laboratory test campaigns is to evaluate the heat recovery performance according to the electrical power output of the SOFC (set remotely by the manufacturer and measured in the test bench). The heat recovery performance is studied related to the working temperature levels (it suffices to only control and measure the return temperature) and related to the heat recovery flow rate (also controlled and measured).

It has been chosen to discretize the net electrical output range into three: nominal (maximum) power (1500 W), minimal power (500 W) and an intermediate power setting (1000 W).

The flow rate range is also discretized into three. The chosen discretized flow rates are about 230 L/h, about 160 L/h and about 90 L/h. They correspond to the three positions of the chosen manual variable-speed circulator ('Yonos Para 15/6' by Wilo) and therefore cover its whole operating range.

The minimal return temperature that could be obtained depends on the auxiliary heat exchanger efficiency (and the temperature of the water mains which it is supplied from). At the time of the test campaign (September 2021), it was not possible to go lower than about 18°C. Maximum temperature of the return line is obtained by bypassing the auxiliary heat exchanger completely and depends on the thermal losses of all the heat recovery circuit to the air of the room (that can be considered at a constant temperature and humidity). At the time of the test campaigns, it was difficult to obtain return temperature higher than 47°C (corresponding to about 50°C of depart/supply temperature), especially for low output power setting (and therefore low heat recovery capacity). Beyond those extremes, it was then chosen to conduct the tests with 8 additional intermediate temperature levels: each temperature step is about 3 or 4 K.

For each tested operating conditions, one has waited at least 15 minutes to ensure for the system to be considered at steady-state.

2.3 Equivalent energy contained in the consumed gas

It is worth mentioning that all the laboratory tests were conducted in three separate days over two weeks in September 2021, allowing the electrical power output to be changed in between.

Natural gas consumed on the test bench comes from the grid. Its HHV has been provided hourly by the gas provider and the daily average values have been reported in Table 2.

Table 2. Average HHV and LHV figures on the day of the test sequence

AC Electrical power output of the test sequences	HHV (given by the gas provider)	LHV (assuming HHV/LHV ratio of 1.1085 [16])
1500 W_{el}	11,5762 kWh/m³	10,4431 kWh/m³
1000 W_{el}	11,5885 kWh/m³	10,4542 kWh/m³
500 W_{el}	11,6133 kWh/m³	10,4766 kWh/m³

It must be stated that the HHV figures of Table 2 have been measured by the gas provider in reference conditions (1 atm and 0°C), which are different from the gas delivery conditions. Therefore, the metered gas volume must be corrected to be applied to those HHV or LHV figures, following the method described in a previous publication [17]. Since the atmospheric pressure was not measured at the laboratory facility, it has been computed considering an assumed pressure at sea level of 101325 Pa and an ambient temperature of 15°C (see reference [17] for explanatory details).

The uncertainty levels of the HHV-LHV figures of Table 2 have not been given by the gas provider. Therefore, since the laboratory facility is receiving type 'H' natural gas ('rich' gas, as opposed to 'lean' gas, called type 'L' gas), the uncertainty level of those heating values can be assumed equal to ±234 Wh/m³, i.e. the same uncertainty level considered in the already referenced field-test study [5] for the site that also receives type 'H' gas.

3. Results

It is worth mentioning that the measured output power fluctuated in a range of only ± 3 W around the power output setting set remotely by the manufacturer (i.e. ± 0.6% in the worst case), not affected by the working temperature of the heat recovery system (nor its flow rate). Similarly, the gas consumption was observed to be very stable according to the output power setting and therefore not to depend on neither the temperature nor the flow rate of the heat recovery system. Indeed, it was observed to vary at worst in the ± 0.5% range. Those fluctuating ranges are even in the same order as the accuracy of the corresponding sensors, as shown in Table 1. Therefore, it has been established that electrical efficiency (not considering the power consumption of the circulator of the heat recovery system) also only depends on the output power setting (and is not affected by the state of the heat recovery system). Since the state of the heat recovery system affects the temperature of the flue gases, which heat up the incoming air required for the fuel cell reaction through the double-walled chimney (Figure 2), it could have indeed been imagined that it might have affected the electrical efficiency of the stack. However, it is not the case and one can assume that the internal heat management of the system is robust enough so the state of the heat recovery circuit only impacts the thermal efficiency of the system.

Indeed, only the thermal efficiency has significantly varied in all the laboratory test campaigns. So, the system's thermal efficiency dependency related to working temperature and flow rate of the heat recovery circuit is presented in Figure 5, Figure 6 and Figure 7, according to the electrical power output setting (respectively 1500 W_{el}, 1000 W_{el} and 500 W_{el}).

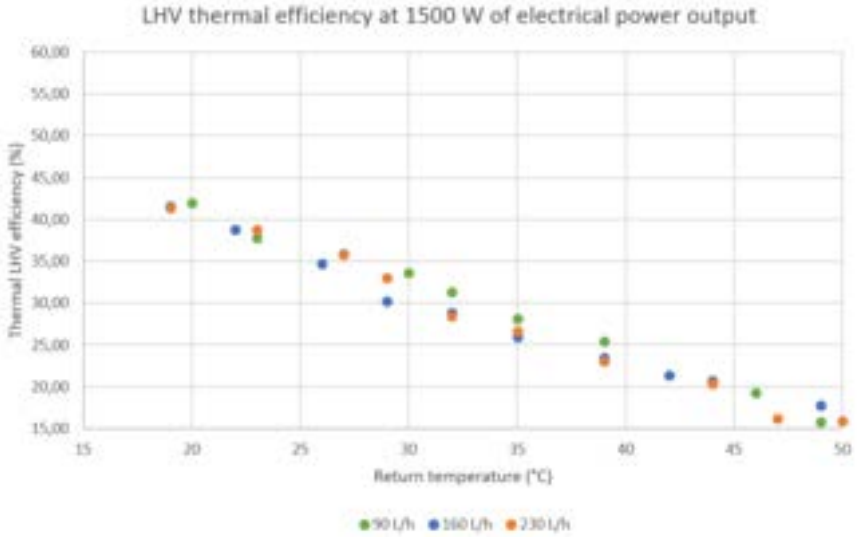

Figure 5. LHV thermal efficiency of the SOFC related to working temperature (and water flow rate) at 1500 W of power output. LHV electrical efficiency has been found constant and equal to about 57%.

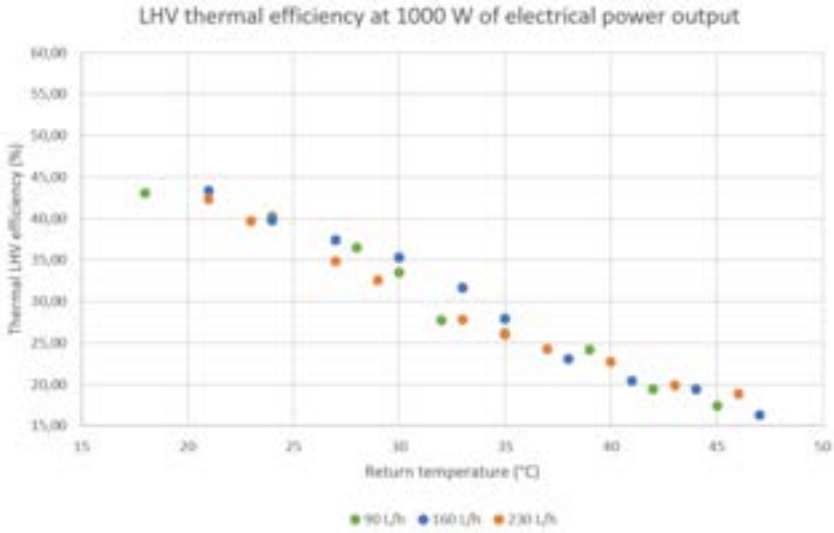

Figure 6. LHV thermal efficiency of the SOFC related to working temperature (and water flow rate) at 1000 W of power output. LHV electrical efficiency has been found constant and equal to about 55%.

It is clear that the flow rate, in the tested range, has no significant influence on thermal efficiency. On the contrary, the efficiency decrease according to increased working temperatures is always noticeable and quite linear. It even increases (exponentially) as the electrical output power setting is lowered. Indeed, over similar tested working temperature ranges (of about 30°C each time), at 1500 W, the decrease in thermal efficiency is about 26 percentage points; at 1000 W, it is about 28 percentage points and at 500 W, it is about 35 percentage points. This exponential trend can be explained by the exponential relation between thermal efficiency and electrical output power, observable in Figure 8, which highlights efficiency results according to the power output setting. It also compares directly the results gathered in this particular experimental study with the one previously published by the manufacturer [18] (all obtained at a return temperature of 30°C). It is worth mentioning that those previous results have been presented in 2011 and might be relevant for a previous version of the system.

As shown in Figure 8, total LHV efficiency is always about or above 80%. Figure 8 also shows that the laboratory efficiency variations between nominal electrical output power and 1000 W of output power is

not significant. On the other hand, working at minimal power brings significant total efficiency decrease (explained by the 17 percentage points decrease in electrical efficiency, which is not balanced by the slightly higher thermal efficiency). It is quite trivial that partial load functioning leads to lower electrical and total efficiencies (mainly due to higher heat losses than at design operating conditions because the internal temperature must be kept constant [19]). Therefore, it is also quite normal that, as electrical efficiency increases, thermal efficiency decreases. This has been verified in literature for many CHP systems [20], as demonstrated with Figure 11, for which the experimental results of the BlueGen system reported in Figure 8 have been added for comparison.

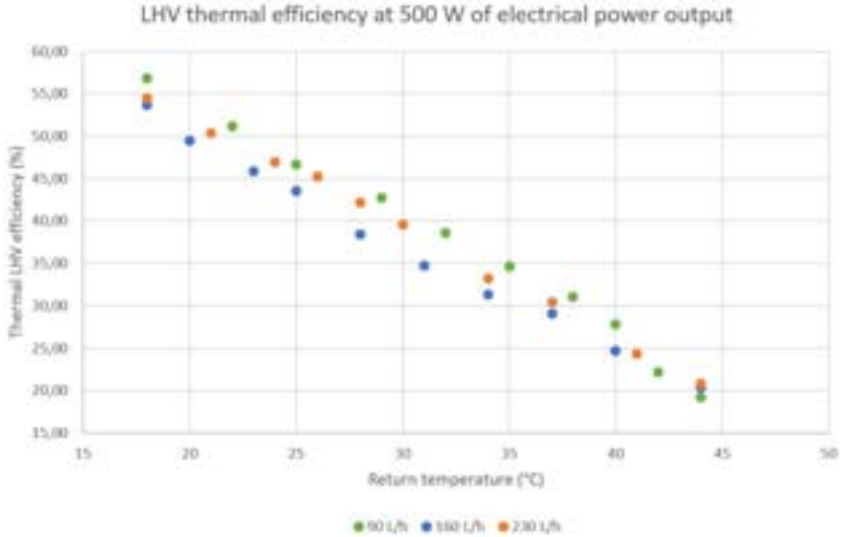

Figure 7. LHV thermal efficiency of the SOFC related to working temperature (and water flow rate) at 500 W of power output. LHV electrical efficiency has been found constant and equal to about 40%.

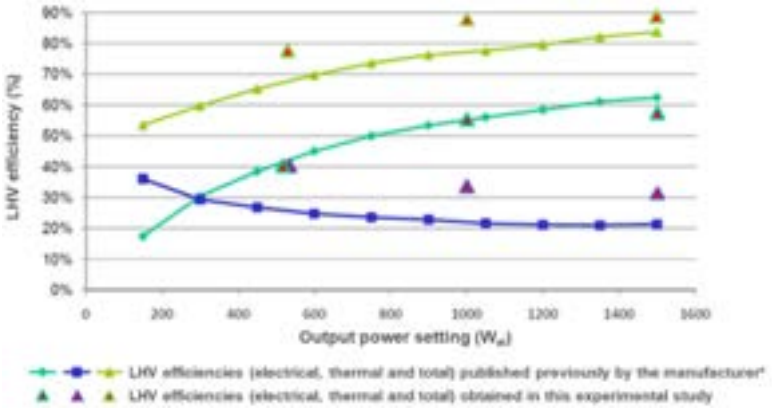

**Reference :* [16]

Figure 8. LHV efficiency results obtained in this laboratory study superposed on reproduced ones previously published by the manufacturer [18] (all obtained with a return temperature of 30°C). System's version in the results published by the manufacturer has not been disclosed, neither as the way efficiencies have been measured or computed (which might explain the few differences).

4. Performance models

Based on those results, the system has been modelled in two main steps with the Matlab software, starting with the thermal efficiency and finishing with the electrical efficiency.

As stated, the thermal efficiency of the system does not depend on the water flow rate of the heat recovery circuit. Therefore, the only influencing parameters for the thermal efficiency are the electrical output power $\dot{W}_{el}$ and the working temperature of the heat recovery circuit (which influence has been studied through its return temperature T_R). The resulting LHV thermal efficiency model (with its tremendous goodness of fit) is presented in Figure 9. It consists of a polynomial regression of the second order on both axes of all the results presented in Figure 5, Figure 6 and Figure 7, independently of the water flow rate of the heat recovery circuit. Between electrical power output $\dot{W}_{el}$ of 500 and 1500 W_{el}, this LHV thermal efficiency $\eta_{th,model}$ model is defined by Equation (1), whose parameters are

provided in Table 3. Equation (1) has been nondimensionalized in Equation (2). Equation (2) is therefore expressed in terms of load factor λ, i.e. the nondimensionalized ratio between the electrical output power and the nominal power, equal to 1500 W_{el} in this case ($\lambda = \dot{W}_{el}/1500W_{el}$).

$$\eta_{th,model}(\%) = f(\dot{W}_{el}, T_R) = p_{00} + p_{10}\dot{W}_{el} + p_{01}T_R + p_{20}{\dot{W}_{el}}^2 + p_{11}\dot{W}_{el}T_R + p_{02}{T_R}^2 \quad (1)$$

$$\eta_{th,model}(\%) = f(\lambda, T_R) = p_{00} + 1500p_{10}\lambda + p_{01}T_R + 1500^2p_{20}\lambda^2 + 1500p_{11}\lambda T_R + p_{02}{T_R}^2 \quad (2)$$

Table 3. Parameters of the LHV thermal efficiency model of the SOFC of Equation (1) and Equation (2), valid between electrical power output $\dot{W}_{el}$ of 500 W_{el} and 1500 W_{el}

Thermal LHV efficiency model parameters	p_{00}	p_{10}	p_{01}	p_{20}	p_{11}	p_{02}
Values	97.52	-0.03938	-1.699	9.855e-6	4.257e-4	3.249e-3

It must be stressed that this thermal efficiency model is valid on the tested heat recovery water flow rate. It is likely that higher heat recovery flow rate will not affect the model (because efficiency of the thermal exchange within the system seems to have reached its maximum asymptote). However, extremely low heat recovery flow rate will trivially reduce the efficiency of the exchange within the machine. It would therefore be considered as good practice to ensure at least 90 L/h of water flow rate in the recovery heat circuit (or to ensure that lower flow rates will not affect the thermal efficiency of this system). The model is likely to be valid in real applications since 90 L/h of water flow rate has been obtained at the 'lowest position' of the variable speed circulator used in the test bench (see Figure 2). Lower water flow rates could only occur with unlikely great pressure losses on the heat recovery circuit.

It is worth mentioning that goodness of fit can indeed be studied easily with the Matlab software thanks to RMSE and R-square values. The following explanations have been provided by the Matlab Software support regarding those fitting variables :

- R-square: This statistic measures how successful the fit is in explaining the variation of the data. Put another way, R-square is the square of the correlation between the response values and the predicted response values. R-square can take on any value between 0 and 1, with a value closer to 1 indicating that a greater proportion of variance is accounted for by the model.
- RMSE: This statistic is an estimate of the standard deviation of the random component in the data. RMSE value closer to 0 indicates a fit that is more useful for prediction.

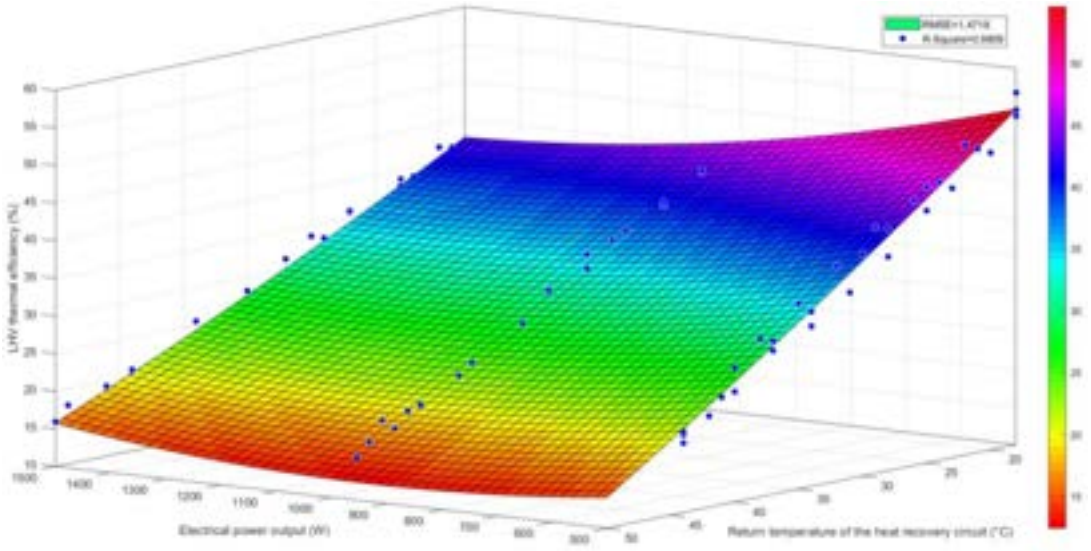

Figure 9. Model of the laboratory BlueGen LHV thermal efficiency according to return temperature of the heat recovery circuit and electrical output power

Modelling the LHV electrical efficiency is simpler as it does not depend on the return temperature of the heat recovery circuit (nor on its flow rate, as it was already the case with the thermal efficiency).

Again, the Matlab software has been used on all the results presented in Figure 5, Figure 6 and Figure 7. The resulting model is defined by the exponential Equation (3), which has been nondimensionalized in Equation (4). Equation (4) is therefore expressed in terms of load factor λ, i.e. the ratio between the electrical output power and the nominal power, equal to 1500 W_{el} in this case ($\lambda = \dot{W}_{el}/1500W_{el}$). Model parameters and goodness of fit indicators are given in Table 4.

$$\eta_{el,model}(\%) = f(\dot{W}_{el}) = a \times \dot{W}_{el}{}^{b} + c \quad (3)$$

$$\eta_{el,model}(\%) = f(\lambda) = a \times 1500\lambda^{b} + c \quad (4)$$

Table 4. Parameters and goodness of fit indicators of the LHV electrical efficiency model of the SOFC of Equation (3) and Equation (4)

Electrical LHV efficiency model parameters	a	b	c	RMSE	R-Square
Values	-7.491e8	-2.82	57.64	0.1687	0.9996

5. Discussion

5.1 Comparison with previously published results

LHV electrical efficiency at nominal power is about 3 percentage points behind the manufacturer target (one has obtained 57% experimentally and not 60% as stated in the Introduction) and this could be explained by the intrinsic statistical difference between production units and/or simply by the natural ageing of the stack (as shown in Figure 10). At lower electrical power (1000 W and 500 W), the laboratory electrical efficiency results seem to be relevant with the 2011 results of Figure 8 [18]. On the other hand, it seems that heat recovery has been significantly improved since the earlier manufacturer's publication in 2011, probably achieved with the use of an internal recovery heat exchanger of larger size.

By deduction of Figure 5, the 25% LHV thermal efficiency announced by the manufacturer (as stated in the Introduction) is relevant with a return temperature of 40°C, which is sufficient in some DHW production applications as well as if the SOFC was directly connected to high-temperature terminal units (in older dwellings, for example). This SOFC mCHP performance has been compared with other well-known cogeneration technologies in Figure 11 [20]. It confirms that fuel cells (especially SOFC's) allow for achieving much higher electrical efficiencies than other technologies.

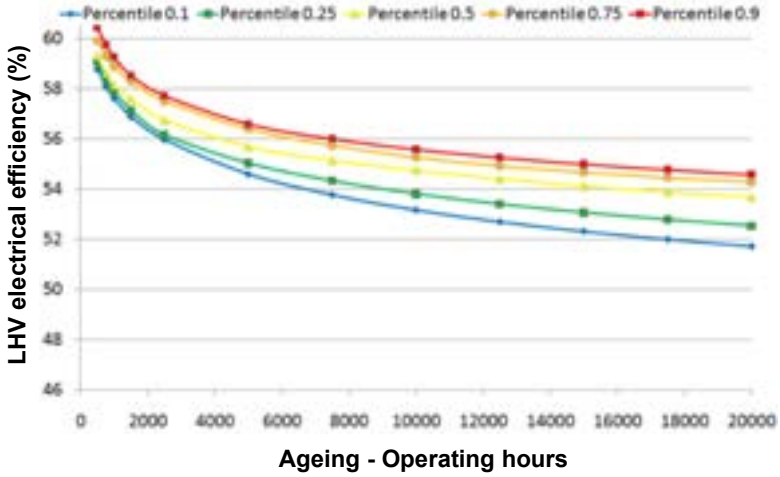

Figure 10. Statistical analysis of production systems back in 2011 [18] expressed in terms of LHV electrical efficiency decay over time at nominal output power (1500 W_{el}). System's version in the results published by the manufacturer has not been disclosed. Reproduced from reference with the addition of this study's laboratory results.

5.2 External weather conditions

At the time, it was decided not to monitor the external temperature and humidity during the test campaigns. Looking at the outcomes published in this paper, there are no unexpected results that are significant enough to be related to any weather variation that has occurred during the test campaigns. Therefore, with such a SOFC system, with tremendously high internal temperatures around 800°C [21], it could be considered that moderate external temperature and humidity variations (typical of Western Europe's climate) have no significant influence on the efficiencies of the system. It is worth mentioning that there were also neither any significant influence of external weather conditions that could have been inferred from the field-test study previously published about that particular SOFC system [5].

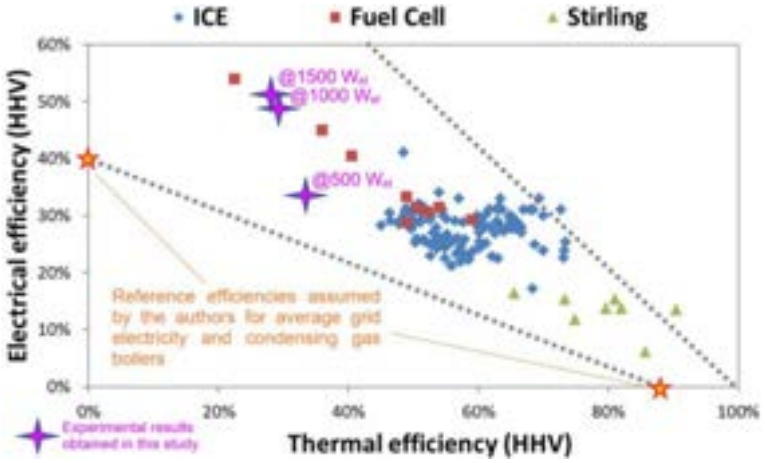

Figure 11. Market study on reported efficiencies for three different groups of micro-CHPs: Internal Combustion Engines (ICE), Fuel Cell based micro-CHPs and CHP based on Stirling principle. The efficiencies are put in perspective with a line (lower dotted one) representing the reference conventional power that the micro-CHPs must beat (i.e. the average grid efficiency for electrical generation and the gas condensing boiler for heat production). Average efficiency of the grid electrical mix is considered to be at 40 % HHV (as comparison, the one of UK in 2013 was about 38.6% LHV, i.e. 34.8% HHV [22]). Reference thermal efficiency of condensing gas boiler is considered to be at 90% HHV (as comparison, yearly HHV efficiency figure of field-tested gas condensing boiler have been reported in the 82-89% range [23] whereas the Walloon energy regulator in Belgium has stated, based upon field-test studies, that reference state-of-the-art gas condensing boilers have efficiencies of 90% LHV, i.e. 81.2 % HHV [24]). The maximum physically possible upper limit corresponding to total HHV efficiency of 100% is represented by the upper dotted line. Reproduced and adapted from reference [20]. The experimental results of this SOFC system at 30°C of return temperature reported in Figure 8 according to the output power setting have been added considering a 1.1085 HHV to LHV ratio [16]. The efficiency results over the upper line (total efficiency results over 100% HHV) are most likely due to measurement uncertainty, especially regarding how the HHV is accounted for [17].

5.3 Water consumption (and evacuation)

As explained in the field-test study previously published about that particular SOFC [5], the system consumes water (discontinuously, a few times a day) from the mains in order to (filter and) store water that could later on help provide steam for methane reforming purposes. Even though a water meter was placed on the test bench (at the water mains connection), in such steady-state tests, the water consumption can hardly be related to the operating conditions as water withdrawals are only executed periodically (a few times a day). Indeed, generally, no water consumption was observable while conducting the test procedure for one particular set of operating conditions. For example, water withdrawal occurred a couple hours later, while the test campaign was finished or while conducting the test for other operating conditions.

However, from 20th September 2021 to 16th February 2022, the SOFC was turned on in the laboratory facilities and has provided (continuously, mostly at its nominal power output) 5048 kWh_{el} of electrical energy and 1434 kWh_{th} of heat. During that time, the system consumed 6274 L of water from the grid. This accounts for a water consumption of 1.24 L/kWh_{el}. This figure can be considered as in the upper range related to this SOFC system because, in the laboratory facilities, the heat recovery circuit was turned off most of the time (except during the three days of the actual test campaigns). Therefore, the return temperature was generally not cooled down and water in the flue gases was less likely to condensate and be fed back to the internal tank, which would have reduced the water consumption from the mains [5].

As shown in Figure 2, the system has two water outlets to the sewers (that have not been instrumented as water evacuations are quite sporadic). The first outlet evacuates brine water from a reverse osmosis filter [25] that cleans the water supply (from the mains) and feeds an internal tank (with cleaned water required for steam reforming processes of the inlet fuel, that is subsequently processed by the fuel cell stack) [5]. With such a two-chamber filter (separated with a filtering membrane), the water impurities concentration in the periodical inlet water volume becomes too high compared to the pressure used for the reverse osmosis. Thus, the remaining inlet water (with high levels of impurities) has to be thrown

away for another periodical grid fresh water inlet to take place (and to be submitted to the reverse osmosis filter). The more water is consumed from the grid, the more brine water will be evacuated.

As mentioned here above, flue gases are ideally cooled down by the optional heat recovery circuit and the condensates, which are not required to be processed in the reverse osmosis filter, are recovered and fed to the internal water tank [5]. However, this latter might be full so a second water outlet to evacuate its potential excess has been implemented [5].

Thus, enabling the heat recovery circuit and allowing for more processed water recovery (from the flue gases) will increase the probability of water excess in the internal tank (and water evacuation from the second outlet), but it will more importantly reduce water consumption from the grid and the resulting brine water evacuation (from the first outlet).

6. Conclusion

Electrical and thermal performance (efficiencies) models of the studied SOFC mCHP system are demonstrating great goodness of fit. Its electrical power output is tremendously stable and corresponds quite accurately to the output power setting as well as to the performance announced by the manufacturer (especially considering ageing). Along with the stable gas consumption, this leads to very stable electrical efficiencies. The electrical efficiency (and power output) is not altered at all by changes in working temperature of the heat recovery circuit (nor by potential change in heat recovery flow rate). In the tested range (corresponding to the range of a variable speed regular space heating circulator), thermal efficiency is almost not altered by the heat recovery flow rate.

Thermal efficiency is affected by the working temperature of the heat recovery circuit quite linearly and it decreases as working temperature increases. The slope of that linear decrease increases exponentially as electrical power output decreases. Indeed, at nominal electrical power output (1500 W), the thermal efficiency increase between about 50°C and 20°C of return temperature is about 26 percentage points. And, over a similar temperature range at minimal electrical output power (500 W), the thermal efficiency decrease reaches 35 percentage points. At nominal electrical power output (1500 W), highest LHV thermal efficiency is about 42% whereas it increases up to about 55% at minimal electrical power output (500 W).

The efficiency results at 1000 W of electrical power output are really close to the one obtained at 1500 W of electrical power output (for both electrical and total efficiency). However, lowering the electrical power output down to 500 W mainly reduces the electrical efficiency, which is not balanced by the increase of the thermal efficiency, meaning that the total efficiency still decreases compared to higher power output settings. Total LHV efficiency is indeed about 78% at 500 W of electrical power output whereas it comes close to 90 % at 1000 W and 1500 W of electrical power output.

The LHV thermal efficiency of 25% at nominal electrical output power of 1500 W announced by the manufacturer seems to correspond to a return of 40°C, which is relevant for many residential DHW applications. This corresponds to about 600 W of heat recovered. Residential DHW represents thus a suitable way of recovering the heat provided with the system. As explained, lowering the return temperature (without significantly reduce the heat recovery flow rate below the operating range of the variable speed circulator that has been used) would even increase the amount of heat recovered (and the thermal efficiency of the system) but at temperature lower than 40°C, it would no longer be convenient for DHW production.

Compared with CHP literature, this SOFC technology demonstrates quite high electrical efficiencies and satisfactory thermal efficiencies. In fact, no commercialized CHP system exhibiting higher electrical efficiencies than this system have been found by the authors of this paper.

Nomenclature

mCHP Micro-Combined Heat and Power

DHW Domestic Hot Water

HHV (LHW) High (Low) Heating Value

SOFC Solid Oxide Fuel Cell

References

[1] N. Paulus, “Confronting Nationally Determined Contributions to IPPC’s +2°C Carbon Budgets through the Analyses of France and Wallonia Climate Policies,” *Journal of Ecological Engineering,* vol. 24, no. 6, 2023.

[2] N. Q. Minh and Y. Shirley Meng, “Future energy, fuel cells, and solid-oxide fuel-cell technology,” *MRS Bulletin,* vol. 44, no. 9, 2019.

[3] N. Paulus, C. Davila and V. Lemort, “Field-test economic and ecological performance of Proton Exchange Membrane Fuel Cells (PEMFC) used in micro-combined heat and power residential applications (micro-CHP),” *Proceedings of the 35th International Conference On Efficiency, Cost, Optimization, Simulation and Environmental Impact of Energy Systems (ECOS 2022),* 2022.

[4] N. Paulus, C. Davila and V. Lemort, “Grid-impact factors of field-tested residential Proton Exchange Membrane Fuel Cell systems,” in *Proceedings of the 14th REHVA HVAC World Congress (CLIMA 2022)*, Rotterdam, 2022.

[5] N. Paulus and V. Lemort, “Field-test performance of Solid Oxide Fuel Cells (SOFC) for residential cogeneration applications,” *Proceedings of the 7th International High Performance Buildings Conference at Purdue (Herrick 2022),* 2022.

[6] C. Dikwal, W. Bujalski and K. Kendall, “The effect of temperature gradients on thermal cycling and isothermal ageing of micro-tubular solid oxide fuel cells,” *Journal of Power Sources,* vol. 193, no. 1, 2009.

[7] A. Nakajo *et al* “Mechanical reliability and durability of SOFC stacks. Part II,” *International Journal of Hydrogen Energy,* vol. 37, no. 11, 2012.

[8] P. Aguiar, D. Chadwick and L. Kershenbaum, “Modelling of an indirect internal reforming solid oxide fuel cell,” *Chemical Engineering Science,* vol. 57, no. 10, 2002.

[9] N. Paulus and V. Lemort, “Simplified test bench for experimental investigations of space heating appliances,” *Proceedings of 8th Conference of the Sustainable Solutions for Energy and Environment (EENVIRO 2022),* 2022.

[10] EN13757-4, *Communication systems for meters and remote reading of meters - Part 4: Wireless meter readout (Radio meter reading for operation in SRD bands),* European Commission, 2013.

[11] OIML R 75-, *Heat meters. Part 1: General requirements*, 2002.

[12] E. Tegeler, D. Heyer and B. R. L. Siebert, “Uncertainty of the Calibration of Paired Temperature Sensors for Heat Meters,” *International Journal of Thermophysics,* vol. 29, no. 3, 2008.

[13] IEC 60751, *Industrial platinum resistance thermometers and platinum temperature sensors,* International Electrotechnical Commission, 2022.

[14] K. Lombardi, V. Ugursal and I. Beausoleil-Morrison, “Proposed improvements to a model for characterizing the electrical and thermal energy performance of Stirling engine micro-cogeneration devices based upon experimental observations,,” *Applied Energy,* vol. 87, no. 10, 2010.

[15] IEC 62053-21, *Electricity metering equipment (a.c.) – Particular requirements. Part 21 : Static meters for active energy (classes 1 and 2),* International Electrotechnical Commission, 2003.

[16] I. Daoud, “Installer une Cogénération dans votre Etablissement,” Ministère de la Région wallonne. Direction Générale des Technologies, de la Recherche et de l'Energie (GGTRE), 2003.

[17] N. Paulus and V. Lemort, “Establishing the energy content of natural gas residential consumption : example with Belgian field-test applications,” *Proceedings of 8th Conference of the Sustainable Solutions for Energy and Environment (EENVIRO 2022),* 2022.

[18] K. Föger, “Ceramic Fuel Cells Residential Generator BlueGen - Ultra-efficient distributed power generation in Smart Grid Environment,” in *IGRC 2011 Proceedings*, Seoul, 2011.

[19] V. Liso *et al*, “Performance comparison between partial oxidation and methane steam reforming processes for solid oxide fuel cell (SOFC) micro combined heat and power (CHP) system,” *Energy,* vol. 36, no. 7, 2011.

[20] I. Verhaert *et al*, “Performance evaluation of different micro-CHP configurations in real life conditions and the influence of part load behaviour,” *E3S Web of Conferences (CLIMA 2019 Congress),* vol. 111, no. 01084, 2019.

[21] R. Payne, J. Love and M. Kah, “Generating Electricity at 60% Electrical Efficiency from 1 - 2 kWe SOFC products,” *ECS Transactions,* vol. 25, no. 2, 2009.

[22] I. Staffell, “Zero carbon infinite COP heat from fuel cell CHP,” *Applied Energy,* vol. 147, 2015.

[23] I. Staffell *et al*, “UK microgeneration. Part II: technology overviews,” *Proceedings of the Institution of Civil Engineers - Energy,* vol. 163, no. 4, 2010.

[24] CWaPE, “Décision CD-5j18-CWaPE relative à "la définition des rendements annuels d'exploitation des installations modernes de référence, ...",” CWaPE, 2005.

[25] C. Fritzmann *et al*, “State-of-the-art of reverse osmosis desalination,” *Desalination,* vol. 216, no. 1-3, 2007.

ULPGC
Universidad de
Las Palmas de
Gran Canaria

grres ULPGC
group for the research on renewable energy systems

F. Refrigeration and heat pumps

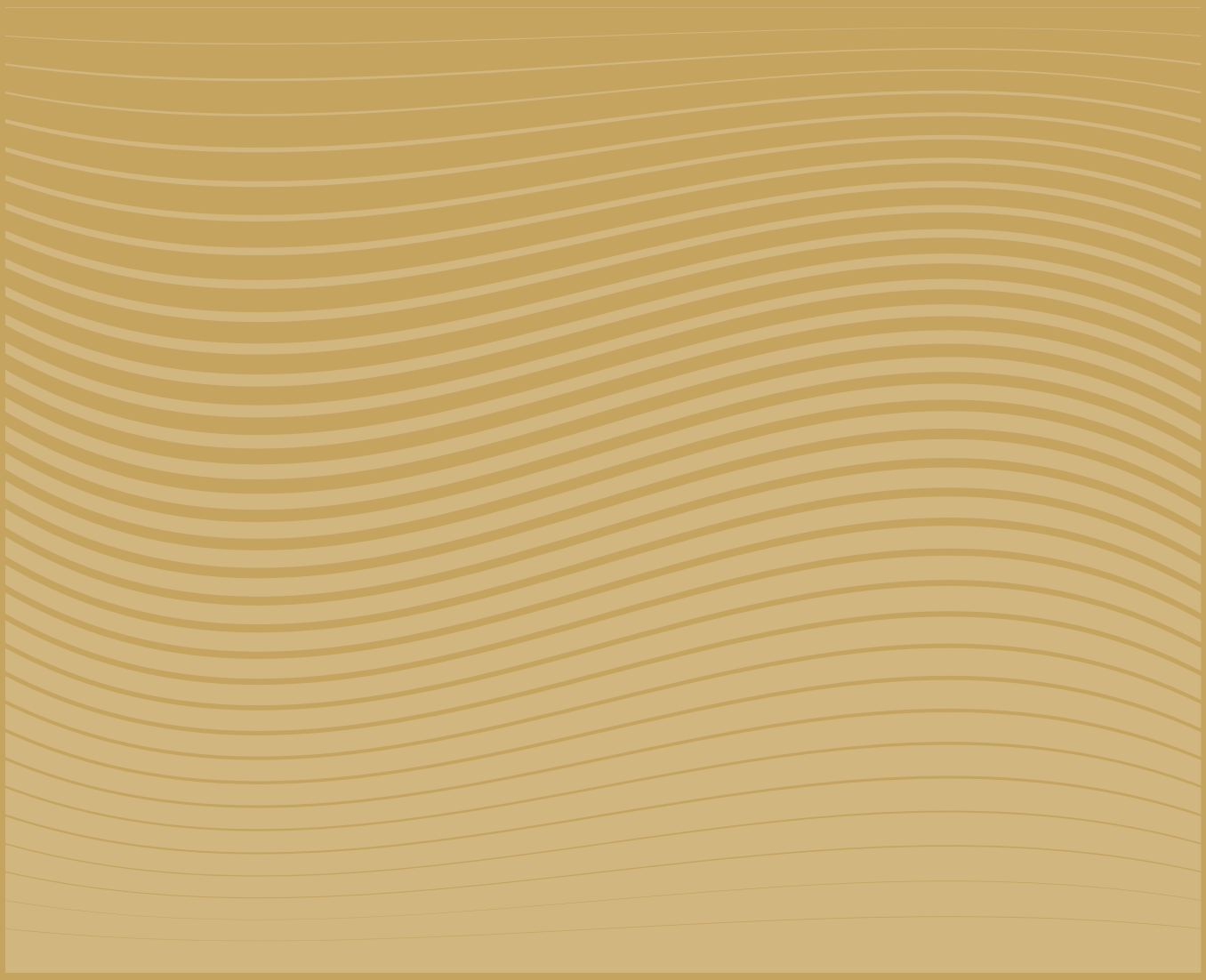

ECOS2023

How to Choose the Best Refrigerant in Heat Pumps from an Ecologic Perspective? Analyzing the Influence of the Evaluation Method

Christoph Höges[a,*], Lennard Wissing[a], Christian Vering[a] and Dirk Müller[a]

[a] Institute for Energy Efficient Buildings and Indoor Climate, Aachen, Germany
** CA, christoph.hoeges@eonerc.rwth-aachen.de*

Abstract:

Heat pumps are one of the key technologies to reduce CO_2-emissions and reach a net zero building stock. However, heat pumps still induce CO_2-emissions, which split up into direct and indirect emissions. Direct emissions result from leakages on site and indirect emissions mainly relate to the power consumption. In particular, the refrigerant choice influences both direct emissions due to its global warming potential, and indirect emissions due to the efficiency of the heat pump. Thus, the refrigerant choice is crucial to minimize the overall emissions of heat pumps. When selecting a proper refrigerant, several evaluation methods exist in the state of the art. In this work, we analyze the influence of the evaluation method on optimal fluid selection. Four methods are employed: Efficiency-based method using the seasonal coefficient of performance (*SCOP*), Total Equivalent Warming Impact (*TEWI*), Life Cycle Climate Performance (*LCCP*), and Life Cycle Assessment (LCA). The study includes ten refrigerants. For method comparison, the study includes refrigerants with either a high GWP or an ODP greater zero also to account for the sensitivity with respect to the evaluation method. The investigation shows only minor differences between the studied refrigerants when comparing the results of *SCOP*, *TEWI* and *LCCP*. The refrigerant ranking is not influenced by the assessment method. Main reason is the high share of the indirect emissions and thus, the dependency on *SCOP*. Using the LCA, the main difference occurs for refrigerants with an ODP. Using current regulations (zero ODP, GWP < 150), we conclude, *SCOP* comparison is a sufficient evaluation criterion when selecting refrigerants.

Keywords:

Fluid selection; TEWI; LCCP; LCA; low-GWP refrigerants.

1. Introduction

In the context of climate change, global greenhouse gas (GHG) emissions have to be reduced in all sectors. In the building sector, the provision of heating and cooling in the building sector is responsible for approximately 19 % of global CO_2-emissions [1]. To achieve the goal of a CO_2-neutral building stock, heat pumps are considered a key technology to replace conventional technologies. Typically, heat pumps use electricity to upgrade ambient heat and thus provide useful heat for heating purposes. Thereby, the emissions of heat pumps are divided into indirect and direct emissions [2]. Indirect emissions are related to the energy demand to operate the system. Most heat pumps use mechanical energy to lift the temperature level and match heat supply and demand. In Germany, the necessary energy is mostly provided by power plants that emit CO_2 and thus, leads to emissions not at the place of the heat pump but at the power plant. For a user-specific heating demand, the emissions depend on electric power demand and thus, on the cycle efficiency of the heat pump. Direct emission originates to refrigerant leakages on site. All currently used refrigerant have a non-zero global warming potential (GWP). Therefore, their leakage supports the greenhouse effect. The main contributor to direct emissions is the used refrigerant, its charge, and its respective GWP. To reduce the overall emissions of heat pumps, direct and indirect emissions need to be reduced.

Besides the GWP, the overall cycle efficiency depends on the choice of refrigerant [3]. Thus, selecting a proper working fluid is crucial regarding low emissions. The refrigerants, however, are subject to increasingly strict political regulations that lead to maximum allowed limits for the GWP, refrigerant charges, and include bans on specified characteristics of refrigerants [4]. In search for possible alternatives that satisfy the political restrictions, the current research focuses on natural refrigerants and hydrofluoroolefins (HFO) since both have near zero GWP values [5–8]. However, selecting the optimal refrigerant is complex and depends on many boundary conditions. Thus, evaluation criteria exist comparing and evaluating refrigerants. In addition

to conventional energetic assessment metrics like seasonal coefficient of performance (*SCOP*), multiple evaluation methods estimate the environmental impact at different levels of complexity: The *Total Equivalent Warming Impact* (*TEWI*) [9], the *Life Cycle Climate Performance* (*LCCP*) [10] and the *Life Cycle Assessment* (LCA) [11]. However, to the authors' knowledge it is unknown how different ecologic evaluation methods influence the results regarding the refrigerant selection and whether the high complexity of the evaluation is necessary within the selection process. Thus, this work aims to analyze the influence of the evaluation method on the optimal refrigerant selection. In the evaluation, the *SCOP*, the *TEWI*, *LCCP*, and LCA are evaluated for ten refrigerants. The refrigerants are mainly low-GWP refrigerants, e.g. propane (R290). Additionally, conventional refrigerants such as R410A, R134a and R404A are included as well as R22, which has an ozone depletion potential (ODP) to include multiple environmental aspects and derive general conclusions.

The paper is structured as follows: Sections 2 describes and discusses the simulation model. We investigate three refrigerant cycle flowsheets since the flowsheet strongly influences the energetic performance of refrigerants. Additionally, the calculation methods of the assessment criteria are presented. Section 3 shows the results and highlights the differences of each evaluation method. Section 4 discusses the impact of the evaluation method on refrigerant selection and Section 5 draws the overall conclusions and give a suggestion for future work.

2. Method

This section describes the overall method and assessment criteria. Section 2.1 presents the heat pump modeling approach. Section 2.2 shows the evaluation of the energetic assessment criteria of the seasonal coefficient of performance. Sections 2.3 to 2.5 describe the evaluation of the ecologic criteria *TEWI*, *LCCP* and LCA. Finally, section 2.6 shows the selected parameter and the case study.

2.1. Heat pump modeling approach

In the present investigation, we evaluate three heat pump cycle configurations. For each cycle configuration a thermodynamically consistent modeling approach is used. A short description of the selected approach is presented. A detailed description is given in [12]. The modeling approach follows an optimization procedure using the *Python* scipy package [13]. Equation (1) shows its formulation.

$$\begin{aligned} &\max_{\vec{x}} COP(\vec{x}) \\ &s.t.\ \ g\left(\vec{x},\vec{\theta}\right) \geq 0 \\ &\qquad \vec{x}_{\min} \leq \vec{x} \leq \vec{x}_{\max} \end{aligned} \tag{1}$$

In the optimization, the coefficient of performance (*COP*) is maximized by adjusting the process parameters $\vec{x}$. The process parameters depend on the individual cycle configuration and are presented below. For each process parameter, the optimization considers box-bounds. Additionally, the optimization is subject to inequality constraints $g\left(\vec{x},\vec{\theta}\right)$. The inequality constraints depend on the process parameters $\vec{x}$ and on the temperatures of heat sink and source. The constraints ensure a physical and technical feasible operation and include (1) wet compressor prohibition, (2) subcritical operation and (3) minimal approach temperatures for all heat exchangers to satisfy the 2nd law of thermodynamics. The heat exchanger modeling uses a minimum approach temperature $\Delta T_{\min} = 2$ K. The expansion valves are assumed isenthalpic. Losses due to friction in the pipes, pressure losses, and heat losses to the surroundings are neglected.

For the compressor, a loss-based compressor model of a reciprocating compressor is used to evaluate refrigerant and operating point dependent isentropic and volumetric compressor efficiencies [14]. The model includes multiple loss mechanisms within a compressor and combines them to a single definition of the compressor efficiency. Thereby, losses due to friction of the piston, flow losses at the compressor valves, electrical losses of the inverter, and heat losses to the environment are included. Additionally, the model scales all effects for a predefined heat flow rate in the condenser. In this work, we consider a 10 kW heat pump for a residential building at the design point -10 °C ambient air temperature and a sink temperature of 55 °C. Thus, the size of the calculated heat pump does not vary between fluids, and a general comparison is possible. A fluid-dependent and operating point-dependent calculation is crucial since the compressor is the component with the highest irreversibilities in the cycle, and an inaccurate calculation can lead to significant differences between the fluids [15].

To account for the influence of the cycle configuration, the study includes three different flowsheets. All models are implemented in *Python* and use *REFPROP* version 10.0 [16] to calculate the fluid properties of all refrigerants. **Figure 1** shows the flowsheets.

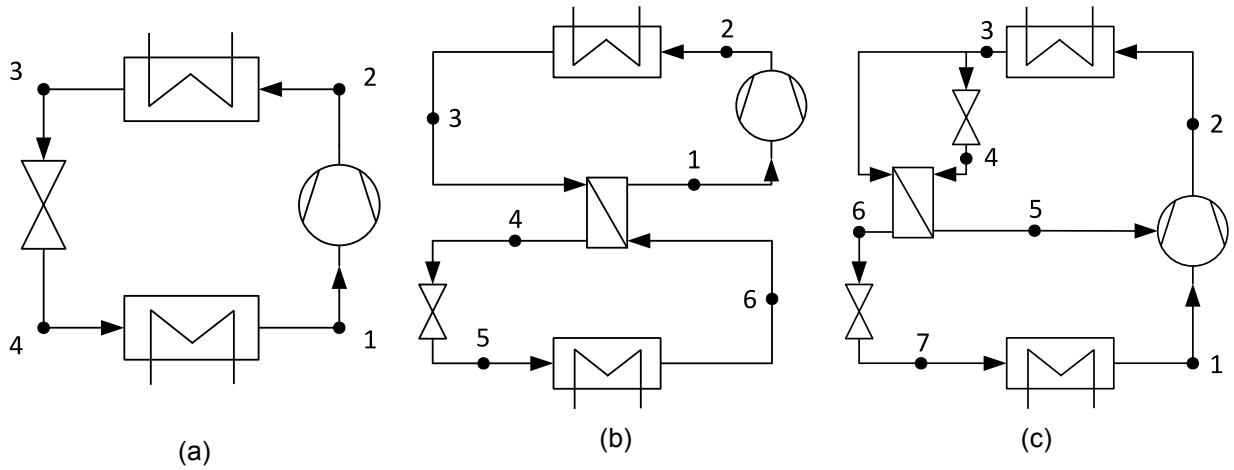

Figure 1: Selected heat pump cycle configurations for the case study.

The simple flowsheet (**Figure 1**a) consists of the four basic components. During the cycle calculation, the optimizer adjusts four optimization variables that specify the simple cycle. Equation (2) shows the optimization variables for the simple cycle.

$$\vec{x}_{\text{simple}} = \vec{x}_{\text{ihx}} = [p_{\text{eva}};\ p_{\text{con}};\ \Delta T_{\text{SH}};\ \Delta T_{\text{SC}}]^T \tag{2}$$

Thereby, the amount of superheating at the compressor inlet ΔT_{SH}, the amount of subcooling at the condenser outlet ΔT_{SC}, the evaporation pressure p_{eva} and the condensation pressure p_{con} are optimized. For each parameter set, the cycle efficiency *COP* is evaluated by equation (3).

$$COP_{\text{simple}} = \frac{\dot{Q}_{\text{con}}}{P_{\text{el}}} = \frac{h_2 - h_3}{h_2 - h_1} \tag{3}$$

The second flowsheet uses an internal heat exchanger (**Figure 1**b). The amount of superheating is shifted from the evaporator to the internal heat exchanger, recuperating heat from the high-pressure side. Thus, the evaporator outlet is saturated vapor. Within the used modeling approach, the internal heat exchanger provides heat for the necessary amount of superheating only and the calculation of the efficiency *COP* in the ihx-cycle is similar to the simple cycle stated in equation (3).

The third cycle uses vapor injection to increase the overall cycle performance (**Figure 1**c). For the vapor injection (vi), a two-stage compression model is used. After the first stage, a partial mass flow rate $\dot{m}_{\text{inj}}$ (state 5) is injected into the compressor. The injected mass flow rate arises from the expansion of a partial mass flow after the condenser to an intermediate pressure level and the heat transfer within the economizer (state 5). Due to the vapor injection, the cycle includes two additional degrees of freedom: (1) The intermediate pressure p_{int} of states 4 and 5 and (2) the injection ratio *y*, which is the ratio of injected vapor $\dot{m}_{\text{inj}}$, and total mass flow rate in the condenser $\dot{m}_{\text{con}}$.

$$y = \frac{\dot{m}_{\text{inj}}}{\dot{m}_{\text{con}}} \tag{4}$$

$$\vec{x}_{\text{vi}} = [p_{\text{eva}};\ p_{\text{con}};\ \Delta T_{\text{SH}};\ \Delta T_{\text{SC}};\ p_{\text{int}};\ y]^T \tag{5}$$

The injected mass flow rate at state 5 is assumed saturated vapor. Due to the two-step compression and vapor injection into the compression chamber, the cycle efficiency calculation is more complex than the simple heat pump cycle. Equation (6) shows the definition of the *COP* for the vi cycle.

$$COP_{\text{vi}} = \frac{h_2 - h_3}{(1-y)\cdot \Delta h_{\text{com,step,1}} + \Delta h_{\text{com,step,2}}} \tag{6}$$

Thereby, $\Delta h_{\text{com,step}\,i}$ is the specific enthalpy difference due to the compression in step *i*. Since the mass flow within the evaporator and thus, the first compression step only includes a partial mass flow rate.

2.2. Seasonal coefficient of performance

To evaluate the annual energy consumption of a single-family house, we evaluate the seasonal coefficient of performance (*SCOP*). In this work, a weighting approach is used that divides a whole test reference year (TRY) into representative clusters. Here, we use the *k-medoids* clustering method [17] and a TRY of the city Aachen in Germany provided by the German Weather Service. A building energy model from the *AixLib* Modelica library calculates the heating demand of a defined operating point [18]. The building has a heating

demand of 9.7 kW at nominal ambient air temperature. Equation (7) shows the resulting formula of the *SCOP*.

$$SCOP = \frac{\sum_i \dot{Q}_{\mathrm{heating},i} \cdot \omega_i}{\sum_j \frac{\dot{Q}_{\mathrm{heating},j}}{COP_j} \cdot \omega_j} \tag{7}$$

Here, the indices *i* and *j* indicate the selected cluster, ω_i is the weight of the cluster in hours, $\dot{Q}_{\mathrm{heating},i}$ is heating demand of the building and thus, the condenser heat flow rate of the heat pump and *COP* is the evaluated *COP* for the defined flowsheet at the operating point of the cluster.

The temperatures of the source and sink, describing the operating point of the heat pump, are derived from the ambient air temperature given by cluster *i*. Additionally, a heat curve of a radiator system is coupled, using a nominal design temperature of 55/45 (supply temperature in °C / return temperature in °C), which is a common heating system in the German building stock. Thus, the heat pump operates at different working and load conditions.

The annual electricity demand $W_{\mathrm{el,annual}}$ can be calculated using equation (8).

$$W_{\mathrm{el,annual}} = \sum_j \frac{\dot{Q}_{\mathrm{heating},j}}{COP_j} \cdot \omega_j \tag{8}$$

2.3. Total Equivalent Warming Impact

In addition to the energy evaluation, selected refrigerants and flowsheets are evaluated with regards to their environmental impact. Different approaches exist in the literature for this purpose. A comparatively simple estimation allows the calculation of the *Total Equivalent Warming Impact* (*TEWI*). The *GWP* evaluates refrigerants in terms of their direct emissions to the environment. This value indicates the global warming potential of the refrigerant, but does not take into account the actual amount of refrigerant released into the environment in case of leakage. In addition to the GHG emissions from refrigerant leakage, the *TEWI* also takes into account the GHG emissions from the electricity used to operate the heat pump. Thus, the *TEWI* considers direct and indirect emissions [9]:

$$TEWI = GWP \cdot m_{\mathrm{ref}} \cdot (L_{\mathrm{annual}} \cdot n + EOL) + (W_{\mathrm{el,annual}} \cdot EM_{\mathrm{GWP}} \cdot n) \tag{9}$$

Where L_{annual} is the annual refrigerant leakage, m_{ref} is the refrigerant mass, *n* is the system lifetime, *EOL* is the end of life refrigerant leakage, $W_{\mathrm{el,annual}}$ is the annual electricity demand, and EM_{GWP} is the CO_2-emission factor of the electricity grid. The *TEWI* provides an approximation of the actual CO_2-emissions caused by a heat pump. However, this assessment method only covers the use phase and neglects further climate-relevant life cycle phases.

2.4. Life Cycle Climate Performance

To include further life cycle phase, an extension to the *TEWI* is the *Life Cycle Climate Performance* (*LCCP*). Compared to the *TEWI*, the *LCCP* includes further sources of equivalent GHG emissions. Like the *TEWI*, this is composed of direct (equation (11)) and indirect emissions (equation (12)) [19, 20].

$$LCCP = LCCP_{\mathrm{DE}} + LCCP_{\mathrm{IE}} \tag{10}$$

$$LCCP_{\mathrm{DE}} = m_{\mathrm{ref}} \cdot (n \cdot L_{\mathrm{annual}} + EOL) \cdot (GWP + Adp.GWP) \tag{11}$$

$$LCCP_{\mathrm{IE}} = n \cdot W_{\mathrm{el,annual}} \cdot EM_{\mathrm{GWP}} + \sum_{i=1}^{n} \left(m_{\mathrm{new},i} \cdot MM_i\right) + \sum_{j=1}^{m} \left(m_{\mathrm{rec},j} \cdot RM_j\right) + m_{\mathrm{ref}} \cdot (1 + n \cdot L_{\mathrm{annual}}) \cdot RFM + m_{\mathrm{ref}} \cdot (1 - EOL) \cdot RFD \tag{12}$$

Here the additional variables stand for:

- *Adp.GWP*: *GWP* of the atmospheric decomposition products
- m_{new}: mass of the new material of the heat pump unit
- m_{rec}: mass of recycled material of the heat pump unit
- *MM*: emissions per kg of virgin material of the heat pump unit
- *RM*: emissions per kg of recycled material of the heat pump unit
- *RFM*: emissions from the production of the refrigerant
- *RFD*: Emissions from disposal of the refrigerant

The metric follows the so-called cradle-to-grave approach so that GHG emissions are captured regarding the entire life cycle. In addition to the GHG emissions captured by the *TEWI*, GHG emissions from energy contained in product materials and for refrigerant production, and disposal are also included. The additional parameters introduced in the *LCCP* supplement the *TEWI*, but account for only a small proportion in the overall analysis. However, *TEWI* and *LCCP* use equivalent GHG emissions and do not account for further assessment criteria that might be of importance to avoid misleading the fluid choice.

2.5. Life Cycle Assessment

The Life Cycle Assessment (LCA) includes all life cycle stages of a heat pump and introduces several assessment metrics. To utilize this method, first the overall goal of the assessment must be defined. In this case, the goal is the environmental evaluation of heat pumps and refrigerants in a single-family house in Germany. The LCA aims to investigate the influence of the refrigerant on environmental impact caused during the life cycle of a heat pump. Thereby, the environmental impact is divided into different environmental categories.

This work investigates the life cycle of an air-to-water heat pump (cf. section 2.1 and 2.6). The investigation focuses on the production of refrigerants and heat pump, the operation of the heat pump and the disposal (including a possible recycling). The function of the air-to-water heat pump is to provide space heating and domestic hot water over an observation period of 20 years, matching the heat pump's lifetime (cf. **Table 3**).

This study comprises four main environmental impact categories: global warming (GW), ozone depletion (OD), Photochemical Ozone Formation (POF) and Acidification (A). Overall, their normalized values (normalized by the maximum of each category) are weighted (cf. **Table 1**) and summed to one single LCA-value.

Table 1: Weighting factors for each environmental impact within the LCA.

Environmental impact	Weights in %
Global Warming (GW)	40
Ozone Depletion (OD)	30
Photochemical Ozone Formation (POF)	15
Acidification (A)	15

Since this work aims to compare multiple evaluation methods using the same overall technology, in this case the heat pump, these are the main environmental impact categories. In case different technologies should be compared, however, further impact categories are necessary to provide a full LCA and, thus, a proper ecologic comparison.

2.6 Case study

Within the present case study, we consider ten refrigerants of different fluid groups (hydrocarbons, hydrofluoroolefins, hydrofluorocarbons and chlorofluorocarbons) to account for several effects when evaluating the ecologic parameters. **Table 2** presents the selected refrigerants and their fluid properties.

Table 2: Properties of the investigated refrigerants [16, 21].

Refrigerants	Safety	GWP	Adp. GWP	ODP	T_{crit} in °C	ΔT_{g} in K
R436A	A3	3	0	0	115.89	7.2
R32	A2L	675	0	0	78.11	0
R1270	A3	2	0	0	91.06	0
R290	A3	3	0	0	96.74	0
R22	A1	1760	0	0.055	96.15	0
R410A	A1	1920	0	0	71.34	0.1
R454C	A2L	146	0	0	85.67	7.5
R134a	A1	1300	1.6	0	101.06	0
R404A	A1	3940	0	0	72.12	0.4
R1234yf	A2L	4	3.3	0	94.70	0

In addition to the refrigerant properties, further parameters for the ecologic assessment are necessary. Thus, **Table 3** provides an overview of the constant parameters.

Table 3: Parameters for ecologic assessment. [2]

Parameter	Value
Temperature difference of source	5 K
Lifetime of heat pump (*n*)	20 a
Annual leakage rate (L_{annual})	2 %
Refrigerant mass (m_{ref})	2.5 kg
End of life leakage (*EOL*)	20 %
Heat pump mass (simple cycle)	150 kg

Due to missing data within the literature, the emissions due to the disposal of the refrigerants (*RFD*) are neglected, which is a similar approach to Wan et al. [20] and Yang et al. [2]. For the emissions due to refrigerant production (*RFM*), values of Hwang et al. [10] are used.

The heat pump itself has an assumed constant mass of 150 kg for all refrigerants. However, additional mass is added for the ihx and the vi cycle due to additional piping and further components (e.g. internal heat exchanger). The mass of the basic configuration (simple cycle) of the heat pump is split into four main materials: steel, aluminum, copper, and plastic. **Table 4** shows their share of the total heat pump mass in the basic configuration, their recycling material percentage, and their emissions during production. The additional mass for the more complex cycle configurations consists of copper (piping) and steel (heat exchanger) only.

Table 4: Share of materials with in the heat pump and their individual emissions during production [2, 10].

Material	Share of heat pump in %	Recycling percentage in %	Emissions virgin materials in $kg_{CO2\text{-}eq}/kg$	Emissions recycled materials in $kg_{CO2\text{-}eq}/kg$
Steel	46	29	1.8	0.54
Aluminum	12	67	12.6	0.63
Copper	16	40	3.0	2.46
Plastic	23	7	2.8	0.12

Lastly, equation (13) defines the specific grid emissions for the main investigation. The curve was derived by using the specific emissions of the German grid of the last ten years and predict the general trend for the next 20 years.

$$EM_{\mathrm{grid}} = 405 \cdot 0.9542^{year} \text{ in } g_{CO2}/kWh_{el} \tag{13}$$

In the equation, *year* represents the current lifetime of the heat pump starting with one. Besides equation (13), two constant values are used for section 3.5 to analyze the sensitivity of the results in section 3.2 to 3.4. Here, zero emissions and 50 g/kWh are selected to account for a grid that has no emissions at all and a grid that uses only solar generated power.

3. Results

The following section presents the results of the conducted case study (cf. section 2.6). Section 3.1 shows the results of the energetic assessment for all three investigated flowsheets. Afterwards, sections 3.2 to 3.4 show the results for the ecologic assessments using the energetic assessment of the ihx flowsheet. Finally, a sensitivity analysis is conducted to evaluate the influence of specific parameters on the ecologic assessment results.

3.1. *SCOP*

Figure 2 shows the results of the energetic assessment using the seasonal coefficient of performance (*SCOP*) of all three mentioned flowsheets using the boundary conditions stated in section 2.6.

For the simple cycle (grey bars), the pure fluid R32 shows the highest efficiencies with 3.82, whereas R1234yf shows the lowest efficiencies with 3.29. Besides R1234yf, the pure refrigerants show significantly higher efficiencies than the investigated mixtures. For the flowsheet with vapor injection (vi – blue bars) the absolute values for the efficiencies increase. Overall, the efficiencies increase by a mean value of approximately 6 %. The improvements mainly result from reduced throttling losses since only a partial mass flow rate must overcome the whole pressure difference. Additionally, the mean temperature in the condenser is reduced, leading to reduced losses due to heat transfer in the condenser.

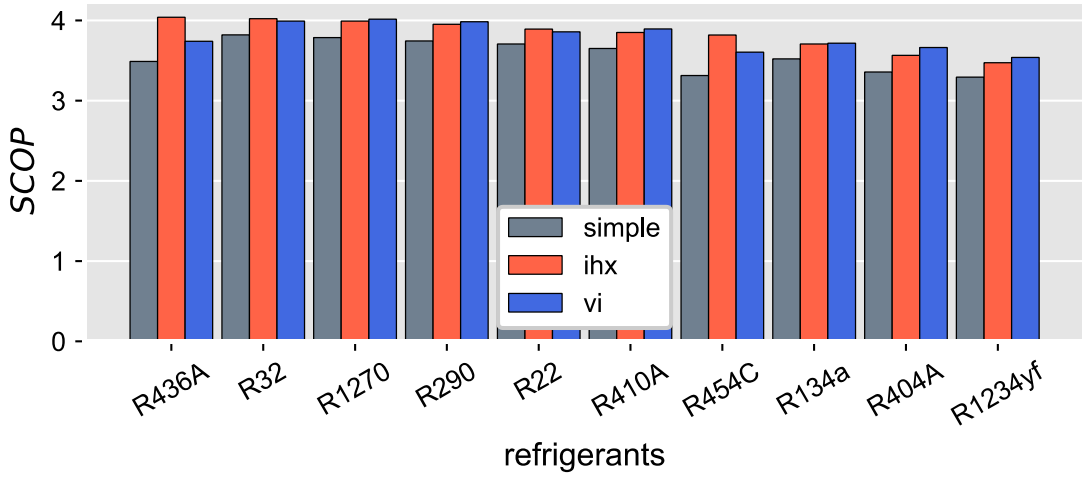

Figure 2: *SCOP* evaluation for the selected refrigerants within all three investigated cycle configurations. The refrigerants are sorted by their highest value in the ihx cycle.

In the vi cycle, the mixtures (e.g., R454C) show higher improvements (approx. 8 %) compared to the pure fluids (4 %). Nevertheless, the overall refrigerant ranking does not vary. Thus, R32 still shows the highest efficiency in the vapor injection cycle.

The ihx cycle (red bars) lead to the overall highest *SCOP* value. Additionally, the ranking of the refrigerants changes. Compared to the simple and vi flowsheet, R436A shows the highest efficiency of 4.04. Overall, the improvements range from approx. 16 % (R436A) to 5 % (R22) with much higher values for the zeotropic mixtures (e.g., R454C and R436A). Main reason for the higher improvements of zeotropic mixtures is the temperature glide (cf. **Table 2**) in combination with an internal heat exchanger. In the simple and vi flowsheet, the pinch point in the evaporator is located at the refrigerant outlet due to the amount of super heating necessary for a safe heat pump operation. Thus, the temperature glide of the zeotropic mixtures leads to a decrease in the mean temperature during heat transfer, increasing heat transfer losses and thus, lowering the efficiency. In the ihx flowsheet, however, the amount of superheating is shifted into the internal heat exchanger. Thus, the pinch point shifts to the evaporator inlet resulting in higher evaporation pressures and overall, higher efficiencies. For zeotropic mixtures, the increase in pressure can exceed the improvements of pure refrigerants due to the temperature glide, especially if the temperature glide matches the temperature difference of the heat source. Therefore, the observed improvements are higher for zeotropic mixtures following findings within the literature [12].

Since the highest differences occur when using the ihx cycle due to the utilization of the temperature glide of zeotropic mixtures, *SCOP* values of the ihx cycle are used in the following ecologic assessments to exploit the full potential of fluid choice. Additionally, the refrigerants will be sorted by their energetic ranking in the ihx cycle, starting with R436A with the highest *SCOP* and ending with R1234yf with the lowest.

3.2. *TEWI*

Figure 3 shows the results for the *TEWI* evaluation of the mentioned refrigerants separated by their cause. For the operational evaluation, the results of the *SCOP* using the ihx cycle are selected.

Similar to the energetic evaluation, R436A shows the best performance and leads to the lowest emissions with overall 18.950 kg_{CO2eq} emissions during the heat pump's lifetime. Additionally, the main contributor to the *TEWI* are the emissions related to the energy demand and thus, are proportional to the *SCOP* (cf. section 3.1). For the low-GWP (<150) refrigerants, the share of the emissions due to energy demand is 99 % and higher, proving that the direct emissions are negligible. For refrigerant with high GWP (e.g. R404A with a GWP of 3.940), the share is 75 %. Due to the high influence of the emissions due to the energy demand and thus, the influence of the indirect emissions due to the power generation in Germany, the additional categories do not lead to changes in the refrigerant ranking regarding the optimal refrigerant choice. Considering the ban on high-GWP refrigerants, the *TEWI* evaluation shows similar results compared to the assessment of the energetic efficiency *SCOP*. Thus, the *SCOP* is sufficient when selecting a refrigerant compared to the *TEWI* evaluation in case low-GWP refrigerants are studied that satisfy current regulations.

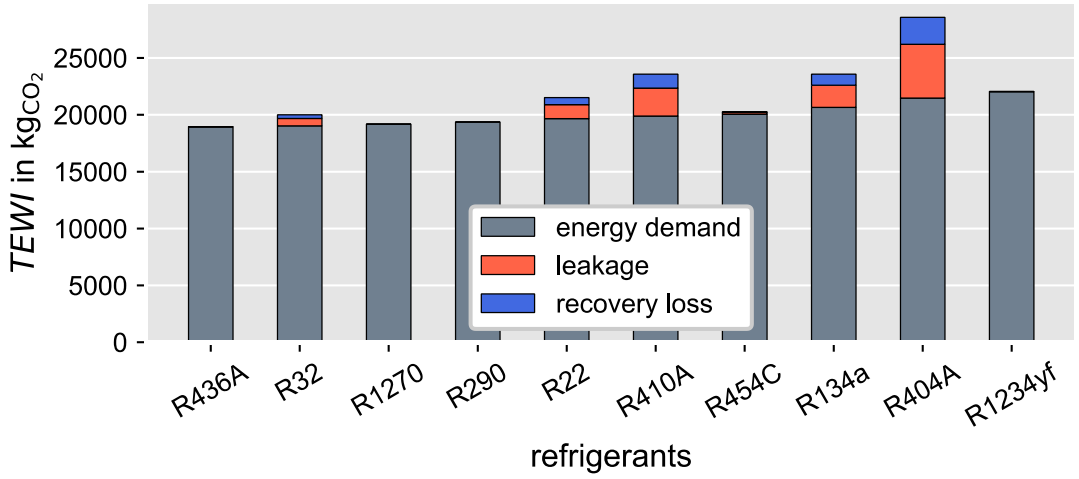

Figure 3: *TEWI* values for the investigated refrigerants. The value is split into each share regarding the emissions related to energy demand, leakage and recovery losses. The refrigerants are sorted by their *SCOP* value within the ihx cycle.

3.3. *LCCP*

Figure 4 shows the results of the *LCCP* evaluation. The results are divided into their individual categories and compared to the *TEWI* (cf. section 3.2).

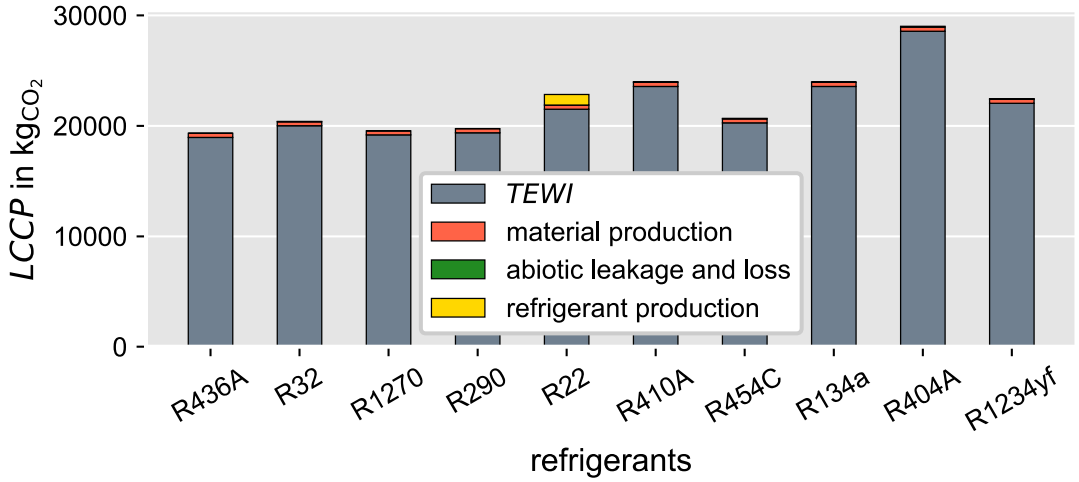

Figure 4: *LCCP* values for the investigated refrigerants. The bars show the share of the *TEWI* and the additional factors within the *LCCP* analysis. The refrigerants are sorted by their *SCOP* value within the ihx cycle.

Compared to the *TEWI*, the *LCCP* accounts for the CO_2-equivalent emissions of the lifecycle *cradle to grave*. However, the main differences between the *TEWI* assessment (grey bars) and the *LCCP* occurs for R22 since the production of R22 and the chemical reactions required have a high energy consumption as well as byproducts with high GWP values. The production of the materials of the heat pump shows only a minor influence on the *LCCP* of a heat pump with a defined refrigerant. Additionally, the composition and weight of a heat pump do not vary between the refrigerants in the current modeling approach leading to identical values. However, the differences in materials due to a refrigerant change and possible bigger components (e.g., larger heat transfer area) is negligible since the influence of the materials of a 150 kg heat pump is already below 1 % of the total emissions. Therefore, a significant influence regarding the CO_2-emissions is unlikely.

Overall, the *LCCP* results are similar to the *TEWI* and *SCOP* results especially for the low-GWP refrigerants. Thus, the more complex evaluation method is not required during a low-GWP refrigerant comparison. Additionally, the figure shows the results for the ihx cycle only. However, the total ecologic assessment conducted for this paper included the evaluation of all three flowsheets. The comparison of the selected

flowsheets leads to the conclusion that the emissions due to additional components within the heat pump are negligible, if improvements in the energy efficiency occur. Thus, more complex flowsheet are always beneficial from a CO_2-emission related point of view as long as the *SCOP* improves.

Besides the CO_2-emissions, the construction and operation of a heat pump influences further environmental impact categories. Thus, the following section presents the results of the LCA, which accounts for multiple environmental impacts.

3.4. LCA

Figure 5 shows the results of the LCA analysis. The LCA value of a refrigerant is the sum of all normalized values in the individual environmental impact category multiplied with the weights in **Table 1**.

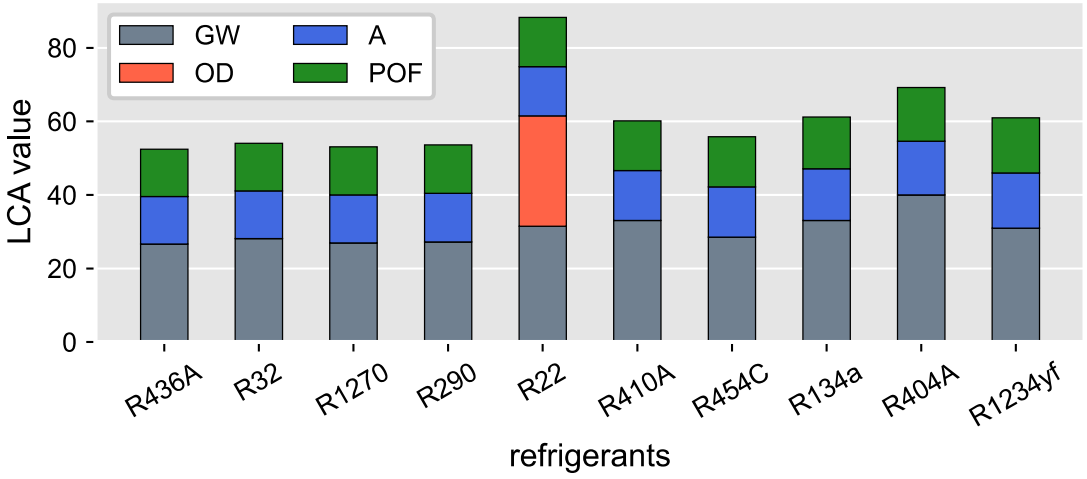

Figure 5: LCA values for the investigated refrigerants. GW: global warming, A: acidification, OD: ozone depletion, POF: photochemical ozone formation.

The most apparent difference compared to the previous results is the huge discrepancy between R22 and the other refrigerants due to the ozone depletion bar (OD – red). Since all other refrigerants have an ODP of zero the differences are to be expected and within the current regulation. Regarding the other impacts, no huge differences occur between the refrigerants. R436A still shows the lowest overall environmental impact and thus, is still favorable. The photochemical ozone formation (POF) and the acidification (A) of the refrigerants are mainly related to the power generation. Thus, the influence of the *SCOP* increases further.

To demonstrate the overall influence of the *SCOP* and the dependency of the environmental assessment criteria, **Figure 6** shows the normalized environmental functions (*TEWI*, *LCCP*, LCA) and the *SCOP*. Additionally, linear functions are included within the figure to show the overall trend.

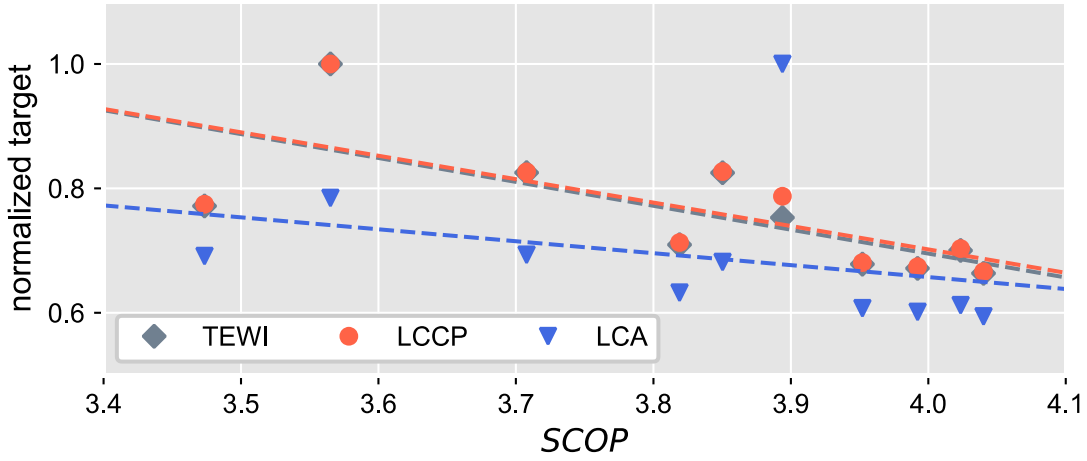

Figure 6: Correlation between the *SCOP* and the ecologic assessment parameters *TEWI*, *LCCP* and LCA. The ecologic parameters are normalized using the maximum value of the present investigation.

The figure shows that the ecologic assessment criteria strongly depend on the *SCOP* and follow a linear curve. The highest differences occur for R22 in the LCA assessment since R22 has an ODP, which is not assessed within the *SCOP* and the energy demand related emissions. Nevertheless, all three linear regression curves offer a good fit for low-GWP and zero ODP refrigerants. Hence, using the *SCOP* offers an accurate assessment criterion when selecting a refrigerant under current regulations (ODP = 0 and GWP < 150).

Table 5 summarizes the results of a refrigerant selection in dependency of the investigated targets. The best performing refrigerant does not vary when the target function is adjusted. However, the ranking of the other refrigerants is offset.

Table 5: Overview of the refrigerant ranking in dependency of the target function.

	SCOP		***TEWI***		***LCCP***		**LCA**	
Ranking	Ref.	$\Delta SCOP$	Ref.	$\Delta TEWI$	Ref.	$\Delta LCCP$	Ref.	ΔLCA
1	R436A	0 %	R436A	0 %	R436A	0 %	R436A	0 %
2	R32	-0,4 %	R1270	1,2 %	R1270	1,2 %	R1270	1,2 %
3	R1270	-1,2 %	R290	2,2 %	R290	2,2 %	R290	2,2 %
4	R290	-2,2 %	R32	5,5 %	R32	5,6 %	R32	3,0 %
5	R22	-3,6 %	R454C	6,9 %	R454C	7,0 %	R454C	6,4 %
6	R410A	-4,7 %	R22	13,5 %	R1234yf	16,3 %	R410A	14,7 %
7	R454C	-5,5 %	R1234yf	16,3 %	R22	18,2 %	R1234yf	16,3 %
8	R134a	-8,2 %	R410A	24,4 %	R410A	24,1 %	R134a	16,6 %
9	R404A	-11,8 %	R134a	24,4 %	R134a	24,1 %	R404A	32,0 %
10	R1234yf	-14,0 %	R404A	50,7 %	R404A	50,1 %	R22	68,3 %

Since the energy demand related emissions strongly depend on the emissions during the power generation, the influence of the emissions factor is evaluated in the following section.

3.5. Influence of the power related emissions

The results of the ecologic assessment show that the environmental impact of a heat pump is mainly influenced by the energy demand. Thus, in the following the influence of the specific emissions related to the power generation is evaluated. Since the energy demand dominates the emissions due to the production and disposal of the heat pump for the German grid emissions (with average values of approx. 290 g/kWh – cf. equation (13)), **Figure 7** shows the influence of lower specific emissions on the *LCCP*.

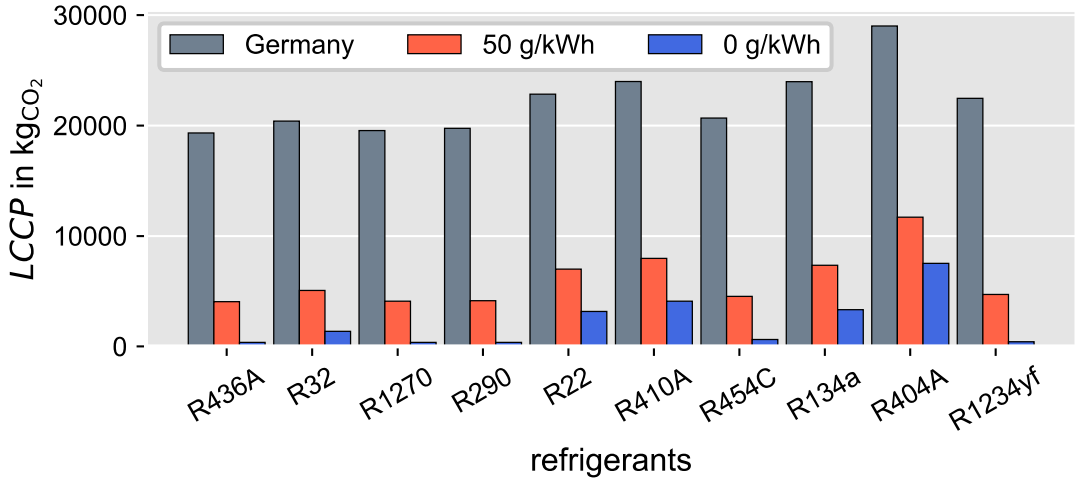

Figure 7: *LCCP* values for all investigated refrigerants using different specific grid emissions. The refrigerants are sorted by their *SCOP* value within the ihx cycle.

The grey bars show the results mentioned in section 3.3. When using a lower power with a lower specific emission ratio which results from the usage of only solar power (red bars – 50 g/kWh), the lifecycle related emissions decrease significantly due to the high influence of the energy related emissions. For most refrigerants, the decrease is similar to the reduction in grid related emissions (approx. 80 %). However, the best performing refrigerant does not change since R436A has a single digit GWP value (3) and the emissions related to material productions are similar for all refrigerants. Thus, the ranking does not change and, the *SCOP* has significant influence on the ranking due to the low GWP of most refrigerants.

Reducing the emissions to a net zero (blue) bars, the dependency on the *SCOP* is lost since no emissions occur due to the energy demand. Thus, the GWP is the main influencing parameter. However, current regulations demand low-GWP refrigerants leading to quite low emission rates. Due to the low energy related emissions, the impact on the environmental impact category of climate change is close to zero whereby other environmental impact categories become more dominant – e.g., material and water usage. Thus, for a zero-emission grid, ecologic assessment criteria based on CO_2 emissions only are insufficient. Nevertheless, there is no country currently with a net zero power grid. Therefore, the authors suggest that the *SCOP* is a sufficient evaluation category when selecting low-GWP refrigerants for a heat pump application.

4. Discussion

The investigations in section 3 show that a correlation between the environmental impact of a heat pump and its individual *SCOP* exists. Thus, the authors conclude that the *SCOP* is a sufficient evaluation criterion when comparing different refrigerants and heat pump systems for residential applications using current regulations regarding a low-GWP (<150) and a zero ODP. Since most electric grids over the globe have emissions higher than 100 g_{CO2}/kWh, which also will not change significantly within the upcoming decade, the described trend will be similar soon. Additionally, the effect increases for electric grids that have higher significantly emission rates than the mentioned 100 g_{CO2}/kWh, reducing the influence of leakages and production even further. Even for lower values (cf. section 3.5), the energy related emissions are more significant still compared to production and leakage related emissions. On top of that, a zero-emission electric grid does not imply that the systems efficiency (*SCOP*) can be neglected since lower efficiencies lead to higher power demand and thus, bigger infrastructure, which once again leads to emissions and the usage of other resources.

Besides the impact on global warming, there are further environmental impact categories of a heat pump, e.g., the mention resource usage. Within the conducted LCA, four out of 16 commonly used environmental categories were used and weighted individually. The results strongly depend on the selected weighting factors and thus, should be investigated further. Additionally, future studies should include further categories to assess the whole impact on the environment. Nevertheless, the selected categories show the strong impact of the *SCOP*.

In this regard, future investigations should include the analysis of more complex flowsheets that improve the cycle efficiency. The present study shows that the impact of the additionally components due to the more complex flowsheet is negligible as long as the cycle efficiency increases. However, additional target functions such as costs must be included in future analysis to assess the energy efficiency, environmental impact, and the economic aspects for a feasible transition towards a net-zero building sector.

Overall, the refrigerant R436A, which is a zeotropic mixture of propane (R290) and isobutane (R600a) shows the best ecologic performance when using a flowsheet with an internal heat exchanger. Additionally, the hydrocarbons R290 and R1270 lead to high efficiencies and thus, low environmental impacts. Furthermore, hydrofluoroolefins (HFO) show lower efficiencies than the hydrocarbons leading to a bigger environmental impact. Additionally, most HFOs lead to the formation of trifluoroacetic acid (TFA) when leaked into the atmosphere. The impact of TFA on the overall lifecycle performance was neglected within the study due to insufficient data. Thus, the actual ecologic performance of HFO will decrease when TFA formation is included in the lifecycle. Thus, the authors conclude that hydrocarbons pave the way towards long-term environmentally friendly solutions in residential heat pumps. Due to their high flammability (A3), however, additional safety measures must be implemented that might worsen the overall ecologic performance. The influence of the additional factors should be investigated in future studies.

5. Conclusions

In the present paper, the influence of the evaluation method with focus on ecologic assessment criteria on the selection of a refrigerant for heat pump systems is investigated. We apply four evaluation methods (*SCOP*, *TEWI*, *LCCP* and LCA) and study ten refrigerants, ranging from high to low-GWP refrigerants. The investigation shows that the main influence on the ecologic performance of a heat pump in a residential building in Germany is the energy demand and the related emissions. Thus, the *SCOP* is the key metric that is sufficient for the ecologic assessment. The key findings of the investigations are:

1. Since *TEWI* and *LCCP* assess CO_2-equivalent emissions only, they strongly depend on the energy demand related emissions and thus, the *SCOP*.
2. When using low-GWP and zero ODP refrigerants, the *SCOP* is a sufficient assessment criterion when selection a refrigerant for a heat pump application.
3. Adjustments in the cycle configuration or the selected flowsheet that improve the *SCOP* are recommended since the overall emissions of the heat pump can be reduced. This effect is valid for specific power grid emissions of 50 g_{CO2}/kWh and higher.
4. The hydrocarbon zeotropic mixture R436A shows the overall best performance in combination with an internal heat exchanger flowsheet.
5. Further research regarding the influence of TFA and a more detailed LCA are necessary to validate all findings of the present work and over a proper comparison to other technologies, e.g., hydrogen related systems.

Acknowledgments

We gratefully acknowledge the financial support by the German Federal Ministry for Economic Affairs and Climate Action (BMWK), promotional reference 03EN4011.

References

[1] O. Lucon *et al.,* “Buildings,” *Climate Change 2014: Mitigation of Climate Change. Contribution of Working Group III to the Fifth Assessment Report of the Intergovernmental Panel on Climate Change*, 2014.

[2] C. Yang, S. Seo, N. Takata, K. Thu, and T. Miyazaki, “The life cycle climate performance evaluation of low-GWP refrigerants for domestic heat pumps,” *International Journal of Refrigeration*, vol. 121, pp. 33–42, 2021, doi: 10.1016/j.ijrefrig.2020.09.020.

[3] M. O. McLinden, J. S. Brown, R. Brignoli, A. F. Kazakov, and P. A. Domanski, “Limited options for low-global-warming-potential refrigerants,” *Nat Commun*, vol. 8, no. 1, p. 14476, 2017, doi: 10.1038/ncomms14476.

[4] M. W. Roberts, “Finishing the job: The Montreal Protocol moves to phase down hydrofluorocarbons,” *RECIEL*, vol. 26, no. 3, pp. 220–230, 2017, doi: 10.1111/reel.12225.

[5] M. O. McLinden, C. J. Seeton, and A. Pearson, “New refrigerants and system configurations for vapor-compression refrigeration,” *Science (New York, N.Y.)*, vol. 370, no. 6518, pp. 791–796, 2020, doi: 10.1126/science.abe3692.

[6] V. Nair, “HFO refrigerants: a review of its present status and future prospects,” *International Journal of Refrigeration*, 2020, doi: 10.1016/j.ijrefrig.2020.10.039.

[7] Z. Li, H. Jiang, X. Chen, and K. Liang, “Comparative study on energy efficiency of low GWP refrigerants in domestic refrigerators with capacity modulation,” *Energy and Buildings*, vol. 192, pp. 93–100, 2019, doi: 10.1016/j.enbuild.2019.03.031.

[8] C. Höges, V. Venzik, C. Vering, and D. Müller, “Bewertung alternativer Arbeitsmittel für Wärmepumpen im Gebäudesektor,” (in de), *Forsch Ingenieurwes*, pp. 1–12, 2022, doi: 10.1007/s10010-022-00584-0.

[9] S. K. Fischer, “Total equivalent warming impact: a measure of the global warming impact of CFC alternatives in refrigerating equipment,” *International Journal of Refrigeration*, vol. 16, no. 6, pp. 423–428, 1993, doi: 10.1016/0140-7007(93)90059-H.

[10] Y. Hwang, C. I. Ferreira, and S. Troch, *Guideline for Life Cycle Climate Performance 2015.* [Online]. Available: https://iifiir.org/en/fridoc/guideline-for-life-cycle-climate-performance-lccp-calculation-tool-145241 (accessed: Jan. 24 2023).

[11] A. C. Violante, F. Donato, G. Guidi, and M. Proposito, “Comparative life cycle assessment of the ground source heat pump vs air source heat pump,” *Renewable Energy*, 2022, doi: 10.1016/j.renene.2022.02.075.

[12] C. Höges, D. Roskosch, J. Brach, C. Vering, V. Venzik, and D. Müller, “Investigation of the Interactions between Refrigerant, Flowsheet, and Compressor in Residential Heat Pumps,” *Energy Technol.*, p. 2201295, 2023, doi: 10.1002/ente.202201295.

[13] P. Virtanen *et al.,* “SciPy 1.0: fundamental algorithms for scientific computing in Python,” *Nature methods*, vol. 17, no. 3, pp. 261–272, 2020, doi: 10.1038/s41592-019-0686-2.

[14] D. Roskosch, C. Arpagaus, S. Bertsch, and A. Bardow, “Compressor design vs. refrigerants properties: What is the main influence on compressor efficiency?,” *26th International Compressor Engineering Conference at Purdue, July 10-14*, 2022.

[15] V. Venzik, D. Roskosch, and B. Atakan, “Propene/isobutane mixtures in heat pumps: An experimental investigation,” *International Journal of Refrigeration*, vol. 76, pp. 84–96, 2017, doi: 10.1016/j.ijrefrig.2017.01.027.
[16] E. W. Lemmon, I. H. Bell, M. L. Huber, and M. O. McLinden, “NIST Standard Reference Database 23: Reference Fluid Thermodynamic and Transport Properties-REFPROP, Version 10.0, National Institute of Standards and Technology,” 2018, doi: 10.18434/T4/1502528.
[17] H.-S. Park and C.-H. Jun, “A simple and fast algorithm for K-medoids clustering,” *Expert Systems with Applications*, vol. 36, no. 2, pp. 3336–3341, 2009, doi: 10.1016/j.eswa.2008.01.039.
[18] D. Müller, M. Lauster, A. Constantin, M. Fuchs, and P. Remmen, “AixLib – An Open-Source Modelica Library within the IEA-EBC Annex 60 Framework,” *Proceedings of the CESBP Central European Symposium on Building Physics and BauSIM 2016*, pp. 3–9, 2016.
[19] H. Lee, S. Troch, Y. Hwang, and R. Radermacher, “LCCP evaluation on various vapor compression cycle options and low GWP refrigerants,” *International Journal of Refrigeration*, vol. 70, pp. 128–137, 2016, doi: 10.1016/j.ijrefrig.2016.07.003.
[20] H. Wan, T. Cao, Y. Hwang, S. O. Andersen, and S. Chin, “A Comprehensive Review of Life Cycle Climate Performance (LCCP) for Air Conditioning Systems,” *International Journal of Refrigeration*, 2021, doi: 10.1016/j.ijrefrig.2021.06.026.
[21] F. Ceglia, E. Marrasso, C. Roselli, and M. Sasso, “An innovative environmental parameter: Expanded Total Equivalent Warming Impact,” *International Journal of Refrigeration*, 2021, doi: 10.1016/j.ijrefrig.2021.08.019.

Fault Detection and Diagnosis by Machine Learning Methods in Air-to-Water Heat Pumps: Evaluation of Evaporator Fouling

Sebastian Borges*[a], Lasse Jöhnk[a], Tim Klebig[a], Christian Vering[a], Dirk Müller[a]

[a]Institute for Energy Efficient Buildings and Indoor Climate, Aachen, Germany
**sebastian.borges@eonerc.rwth-aachen.de, CA*

Abstract:

Heat pumps have emerged as key technology to pave the way for a sustainable heat supply in buildings. However, the ongoing shortage of trained experts counteracts the current heat pump trend. Increasing the capacity of experts, services like Fault Detection and Diagnosis (FDD) can support the identification of malfunctions and integration of methods for predictive maintenance. The primary objective of FDD is to detect faults, diagnose their causes, and possibly enable correction to prevent efficiency losses as well as system damage or downtime. This involves a comparison between a fault-free reference case and the real system. In research, machine-learning methods like Artificial Neural Networks (ANN) show the capability to learn the behavior of fault-free systems. In practice, however, the implementation of ANN is limited due to missing data in operation for training. Therefore, it is common to utilize physically simulated data for pre-training.

One way to achieve high efficiency in heat pumps is to maximize heat transfer in the evaporator. Fouling within this component therefore leads to significant performance degradation and reduced system lifespan. As a result, this work introduces and evaluates an extendable FDD method for evaporator fouling in air-to-water heat pumps. To detect evaporator fouling during operation using an ANN, a transient model of a refrigerant cycle provides the training data. Based on literature, the fouling effect is emulated afterwards, serving the data for the reference system considering faulty operation. Applying the present concept, we reveal a reduction in *COP* due to evaporator fouling of approximately 3 % over a whole year, while our fault detection methodology detects 55.65 % of the faults within the given heat pump model. Overall, this study provides insights into the performance of FDD methods for evaporator fouling in air-to-water heat pumps, which can help to improve the efficiency and reliability within the system lifespan. The results of this study demonstrate that the concept of FDD offers the potential to be applied in practice, and proposes recommendations for future perspectives about ANN within FDD in heat pump systems.

Keywords:

Operational Optimization, Digital Twins, Data-Driven Modeling and Simulation, Artificial Neural Networks

1. Introduction

As part of the agreements of the Paris Climate Convention, a sharp decrease in greenhouse gas emissions is enforced [31]. This also affects the building sector. One of the objectives of the German government is to achieve a nearly climate-neutral building stock by 2045 and thus a sustainable energy supply for the building sector [32].

Most renewable energy is available as electric energy, which can only be converted into commonly used forms such as methane with significant energy losses. Thus, sector coupling by electrification seems to be essential for decarbonization in the building sector. Heat pumps represent a key technology in this field and offer a good possibility to replace fossil fuel-based heat production with electric power [33]. Due to a limited availability as well as high demand for renewable energies, a reduction of primary energy consumption through increased efficiency is also necessary for the success of the energy transition. [35]

The heat pump efficiency is thereby strongly dependent on a fault-free operation of the system. The rising challenges such as the ongoing lack of technicians, the gas crisis or the increasing demand due to the decision of the *Heat Pump Summit 2022* in Germany carries the risk that the vast number of new installations and maintenance of heat pumps cannot be handled. The consequences are, that specialized companies will be overwhelmed, system efficiency decreases and comfort is reduced. [4] [36]

A promising approach to face these challenges is the integration of Fault Detection and Diagnosis (FDD) methods. The development in technology and sensor devices provides a basis for embedding continuous system monitoring and thus implementing such algorithms [6]. FDD is about detection and identification of the reduced functionality or performance within a component at an early stage, as well as localization and determination of the causes [10]. In technical systems, the goal of Fault Detection and diagnosis (FDD) is to guarantee the quality, safety, and efficiency of operation. One way to achieve this is the automated detection of faults in operation, so the fault can subsequently be resolved rapidly [1]. Thus the integration has the potential to minimize system installation/control errors, detect performance degradation during operation, avoid unnecessary visual inspections and component replacement as well as reduce maintenance costs and downtime [37]. Madani et al. [37] furthermore states that already small modifications in heat pump systems can reduce size and costs caused by the fault. Their suggested framework *Smart Fault Detection and Diagnosis* (SFDD) system is capable of Detection and Diagnosis of possible faults in installation and operation phases in order to reduce maintenance costs and system down time.

FDD is a well-established research field with broad utilization. These fields include, for example, the aviation, automotive, chemical, and power plant industries. In contrast, FDD is still in an early stage for the building sector. This can also be seen in the lack of consistent terminology. [2] [28]

Isermann [29] differentiates the following notions in the context of FDD:

- **Fault Detection** - Determination of faults in a system and the time of their detection.
- **Fault Isolation** - Determination of the type, location and time of detection of a fault via evaluation of its symptoms; follows after Fault Detection.
- **Fault Identification** - Determination of the impact and evolution of a fault over time.
- **Fault Diagnosis** - Determination of the type, impact, location, and time of detection of a fault via evaluation of its symptoms; follows after Fault Detection and includes Fault Detection, Fault Isolation, and Fault Identification.

A considerable amount of FDD methods have been developed for building energy systems in the last decades, such as for air handling units, chillers, or HVAC system levels [9]. Only a small part of FDD methods relates to heat pump systems. Bellanco et al. [11] have summarized several common faults and their effects on system performance from literature for different types of heat pumps; some of them are stated in Table 1. Particles or impurities such as rust can lead to clogging or deposits in the filter, affecting the refrigerant mass flow. Consequently, the superheat increases and the cooling capacity decreases in cooling mode [13]. However, this effect is negligible for moderate fault level, when using units with thermostatic expansion valves [13]. This also applies to refrigerant undercharge, which represents a fault of the design phase [40]. The effect on system performance like *COP* due to refrigerant overcharge, though, seems to be more significant [41]. [14] and [30] refer that refrigerant leakage, which occurs especially due to broken valves on the suction and discharge line of the compressor, can negatively affect the *COP* of vapor compression systems in particular [11]. According to Kocyigit et al. of [12], fouling of the outdoor unit (e.g. by fallen leaves) has a major influence on the *COP* in cooling mode for air-to-air systems. Primarily caused by an increased thermal resistance at the fin heat exchangers due to fouling as well as a decrease of the external air flow rate, whereby the former shows a more significant impact on the *COP*. While the emulation of common faults for experimental validation such as refrigerant leakage [15] or liquid line restriction [39] are complex studies in some cases, fouling is frequently conducted in the literature by simply blocking the area of the heat exchanger with paper or cardboard [15] [16] [39]. Therefore the present work focuses on evaporator fouling.

Table 1. Common faults in heat pump systems [11].

Faults type	System	Effect	Reference
Outdoor unit fouling (FO)	Air-to-Air (cooling mode)	*COP* decreases 9 % Capacity decreases 14 %	[12]
Indoor unit fouling (FI)	Air-to-Air (heating mode)	*COP* remains	[39]
Valve leakage (VL)	Air-to-Air (heating mode)	*COP* decreases 4.4 %	[39]
Ref. overcharge (RO)	Air-to-Water (heating mode)	*COP* decreases 3.4 %	[38]
Ref. undercharge (RU)	Air-to-Water (heating mode)	*COP* decreases 1.2 %	[38]
Liquid line restriction (LL)	Air-to-Air (heating mode)	*COP* and Capacity remains	[12]

Typically, FDD methods are integrated as follows: The calculations of a simulation model representing the fault-free state of the device are compared to the behavior of the system in which a fault has been injected [17]. There are two modeling techniques in order to represent the fault-free behavior. First-principle models are (partly) based on physical knowledge of underlying physical phenomena to describe the system. Unfortunately equations describing real systems are complex and usually difficult to solve. For this reason, data-driven models are attracting more and more attention [17], using experimental or simulative data to learn the relationship between the inputs and outputs of the system to build both linear and nonlinear models. Apart from established methods like Support Vector Machine (SVM) [18] or Partial Least Squares (PLS) [19], Artificial Neural Networks (ANN) [7] [8] revealed comparatively better results [sources]. [6]

Few references dealt with the study of air-to-water heat pump systems in heating mode, although this is one of the most common heat pump systems in the building sector with further increasing interest in the future [3]. To bridge this research gap, this paper proposes the development of FDD for air-source heat pumps. For implementation, we include an ANN-model that simulates the fault-free operation of the plant and calculates the *COP* (Section 2). The actual fault is then injected in a further (physical) simulation for simplicity reasons and compared with the *COP* of the fault-free calculation. Based on the deviation between the two simulation models, a methodology for Fault Detection in case of evaporator fouling is developed (Section 3), and the results are presented (Section 4). Finally, the main conclusions are given in Section 5.

2. Methodology

The methodology used within this paper for FDD can be isolated based on Figure 1 (red section). Here, Melgaard et al. [20] aggregated from [23] a generic framework for engineering systems. In a first step, the real system or device is monitored metrologically to detect any abnormal conditions. The data is subsequently analyzed and evaluated in the process of Fault Detection (FD), Fault Isolation (FDD), and Fault Identification (FDD). In case a fault is detected, a notification is provided (FD). The FDD also provides information about the location, time and length of the fault occurrence as well as the fault's level. In a final step, the fault is evaluated in terms of the level and significance of its impact on system performance (e.g. costs, energy consumption and other performance indicators). The Fault Evaluation allows to make a decision about the further procedure and handling of the fault inside the fault tolerant control. [23] Within the scope of this work, as first step, fault detection (FD) without further evaluation is carried out (red section), which serves as a basis for future developments.

2.1 Modeling

An essential part of FDD is typically a model, which in case of data-driven based methods can represent either a classifier or a regressor. Classification methods described for example in [9] provide a simple approach to detect and diagnose faults. However, a major disadvantage of this technique is the necessity of large labeled datasets (subdivided into faulty and fault-free modes) for the training procedure. This means the fault behavior must be emulated experimentally, which may cause high costs and efforts. Regression-based methods as used in [24] compare a simulated variable (obtained e.g. from a trained ANN) with the measured variable of the real system in order to detect and/or diagnose a fault by comparing both. Therefore, the model learns in a preceding training process the fault-free behavior of the system with measured features, which are ideally not affected by the fault itself. Thus, only fault-free operation must be modeled, which is why this approach is addressed within this work (section 3).

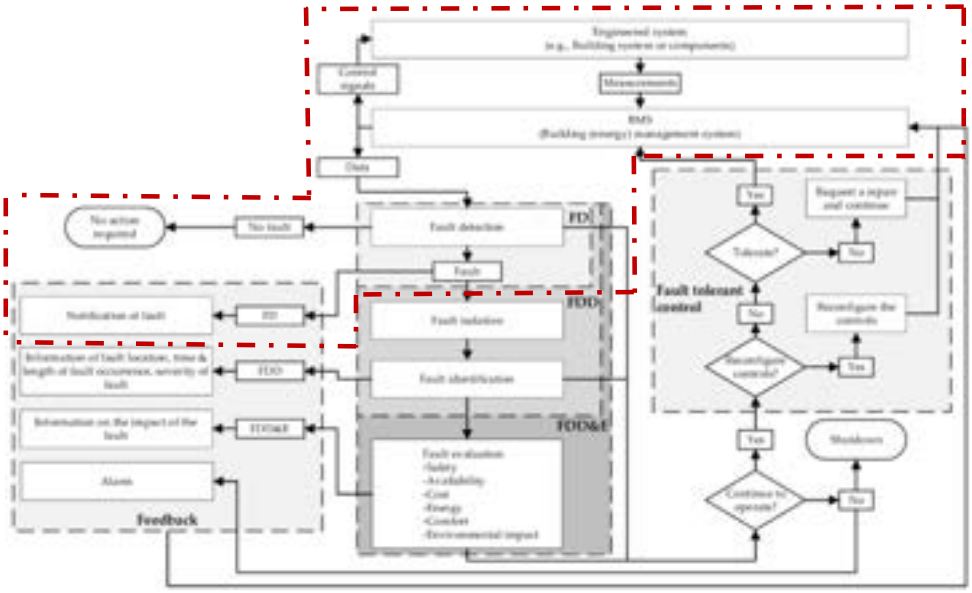

Figure 1: Generic FDD framework for building energy systems according to [20]. The marked red section describes the scope within this work.

2.2 Notification of faulty operation

A further important aspect is the implementation of a subsequent method, which detects the fault as reliably as possible depending on the described comparison between the real system and the ANN. Keliris et al. [21] introduced a simple threshold-based approach using the residual of the real and simulated system (Figure 2). Essential and subject of current research is the selection of a proper threshold for the residual from which a fault is detected. This strongly depends on the model, the real system and the use case. Within this work, the threshold is subsequently adjusted according to the fault level (section 4).

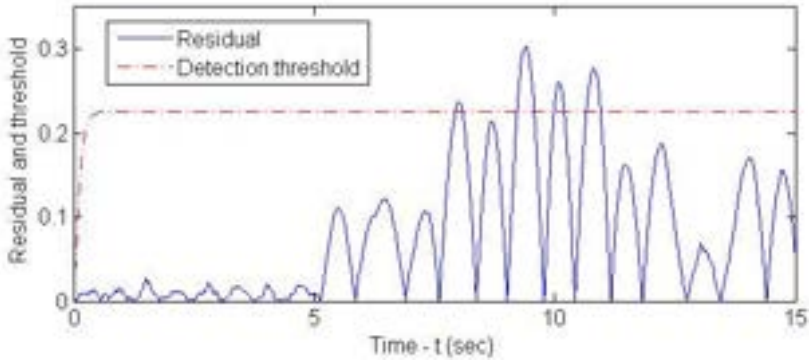

Figure 2: Example of a threshold-based method for a Fault Detection and Diagnosis using the residual [21].

2.3 Evaluation of FDD method

To evaluate the proposed FDD method, the literature suggests a classification into the following parameters, as shown in Table 2. The False Alarm Rate (FA) may be the most serious for FDD, since it could be trigger service being done on a properly working system. Although the algorithm or protocol does not trigger any unintended operations by services in the case of Missed Detection Rate (MD), the failed fault detection can lead to further subsequent faults and performance degradation in the long term. [22]

Yuill et al. [22] also take into account the fault intensity when evaluating the algorithm or protocol. The key parameters within this paper are the FA and MD parameters. However, this is because the intensity of the fault is not considered and the FDD focuses solely on the fault of the evaporator fouling. A Missed Diagnosis can thus be excluded as well as No Response.

Table 2: Evaluation parameter of FDD methods [22].

Parameter	Declaration
False Alarm Rate (FA)	Algorithm returns fault notification during fault-free operation.
False Negative Rate or Missed Detection Rate (MD)	Algorithm fails to detect faulty operation.
No Response (NR)	No response from algorithm.
Missed Diagnosis Rate (MDI)	Algorithm diagnosed wrong fault.

3. Modeling of Artificial Neural Network and reference system

The literature shows great potential for the using ANN, especially for fault detection in complex HVAC systems, improving the results compared to other data-driven methods [25]. The ANN in the context of this work is intended to represent the fault-free state of the system, the dataset used for training and the reference case as well as the hyperstructure of the model is explained below. The investigation period covers one year with an hourly resolution.

3.1 Simulated reference system

In order to consider the effect of the air flow rate on the evaporator capacity, this paper uses the TiL-Suite [34] to model the heat pump. This allows a detailed and transient simulation of the refrigerant cycle. The heat exchanger in the evaporator is designed as fin tubes in crossflow mode and is based on the finite volume approach. We use a simple refrigeration cycle and the medium is propane. The *COP* is then obtained from an energy balance of the evaporator, condenser and compressor. This model is applied in section 3.2 in order to train a fault-free ANN.

To simulate evaporator fouling, the external air flow rate in the evaporator needs to be decreased. In this paper, a gradual reduction of the fan speed is implemented using tangens hyperbolicus (Eq. 1), motivated by [26]. n_{fan} is the fan speed with its maximum value of 15 Hz, t the time and t_{half} the time at half a year in hours. The assumption in this context is that fault-free operation correlates to a fan speed of 15 Hz (Figure 9).

$$n_{\mathrm{fan}}(t) = 15Hz - 7.5Hz \cdot tanh\left(\frac{\pi}{2} \cdot \frac{t}{t_{\mathrm{half}}}\right) \quad (1)$$

3.2 ANN model for fault-free operation

The selected hyperstructure of the ANN is shown in Figure 3 and will be used within this work to represent the fault-free mode of the reference heat pump. The structure is a result of a predefined hyperparameter optimization beforehand and consists of two hidden layers and a total of 176 neurons to calculate the *COP* ("signal"). The input variables ("features") represent compressor speed n_{comp}, discharge temperature T_{dis} from the compressor and refrigerant mass flow $\dot{m}_{\mathrm{ref}}$. The feature selection is a result of an optimization using ADDMo [27], a tool developed by the Institute for Energy Efficient Buildings and Indoor Climate at RWTH Aachen University. This tool automatically calculates the correlation of different features to the signal based on the Pearson correlation coefficient.

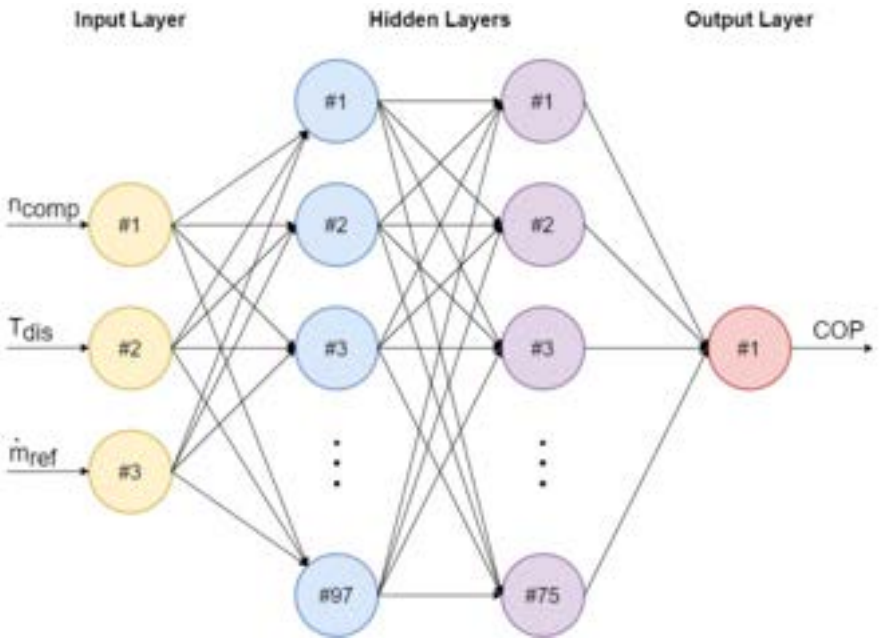

Figure 3: ANN hyperstructure used within this work for calculation of *COP* in fault-free operation. The model's features are the compressor speed, the discharge temperature of the compressor, and the refrigerant mass flow rate.

4. Results

In this section, the fault detection results obtained from the described methodology (section 2) using simulated data (section 3.1) and the ANN model for training and testing (section 3.2) are presented and discussed afterwards.

4.1 Validation of *COP* model

In order to train an ANN for fault-free operation, the relevant simulation data for one year is presented below for validation. For simplification, we assume an operation of the heat pump over the whole year. The data are subsequently shuffled to obtain a heterogeneous and randomly spread data set for the training of the ANN. The result is shown in Figure 4; the *COP* ranges between about 3.5 and 6.

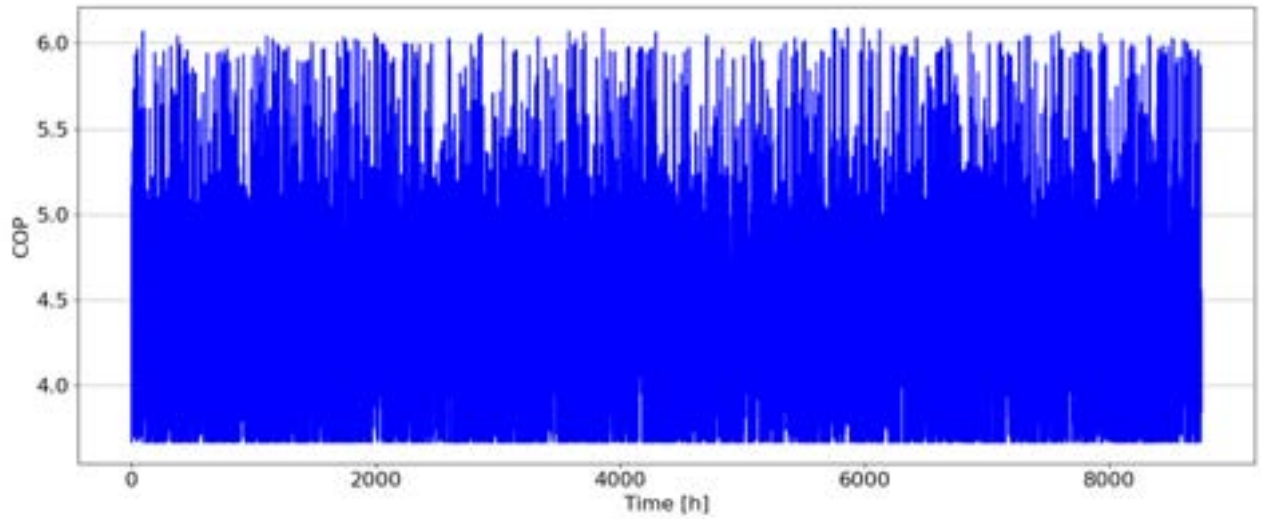

Figure 4: Shuffled dataset of *COP* within the yearly simulation and an hourly resolution.

Figure 5 provides a part of Figure 4, which is used for training (400 hours) and testing (100 hours). This corresponds to a 75 to 25 % split. The majority of the data points are below a *COP* of 5, similar to Figure 4. In addition, Figure 6 shows the test data set used to validate the ANN based on *COP* comparisons to the reference model. The result is an RMSE of about 0.03 for mapping fault-free operation by the ANN.

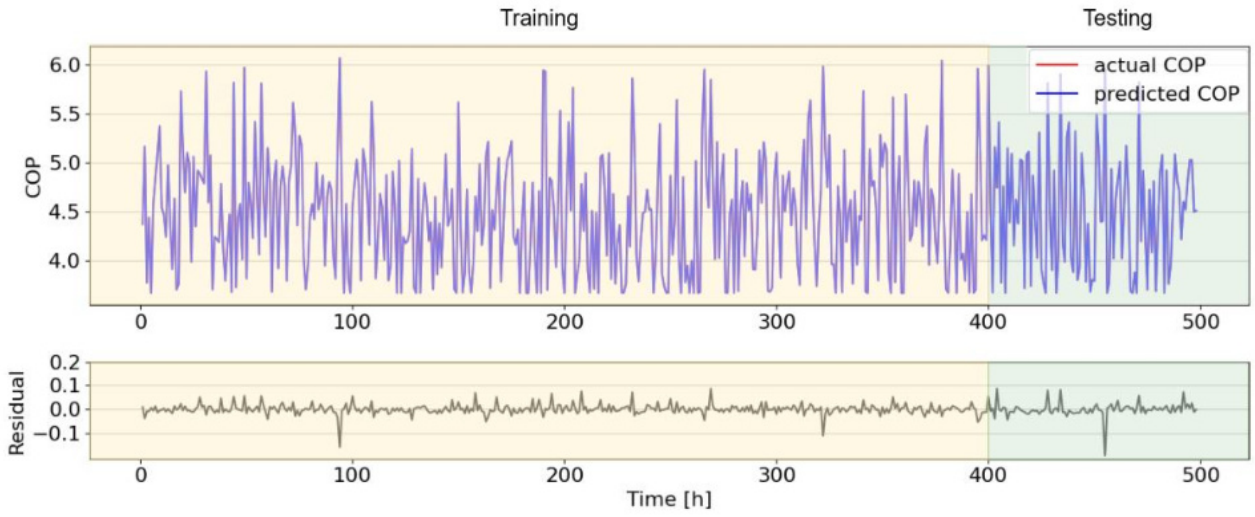

Figure 5: Shuffled dataset of Training and Testing period for ANN Validation.

In Figure 7 we compare the predicted *COP* from ANN and the reference system from the simulation with TiL-Suite (section 3.1) in fault-free operation combined with the residual of both. An RMSE of 0.023 is obtained, hence the ANN seems to be able to model the *COP* quite well. The residual is significantly higher in the summer period compared to winter. This might be due to the composition of the training data set (Figure 5), where the amount of data coming from the winter period is higher, even after shuffling the data. This can be observed as well in the histogram of Figure 8.

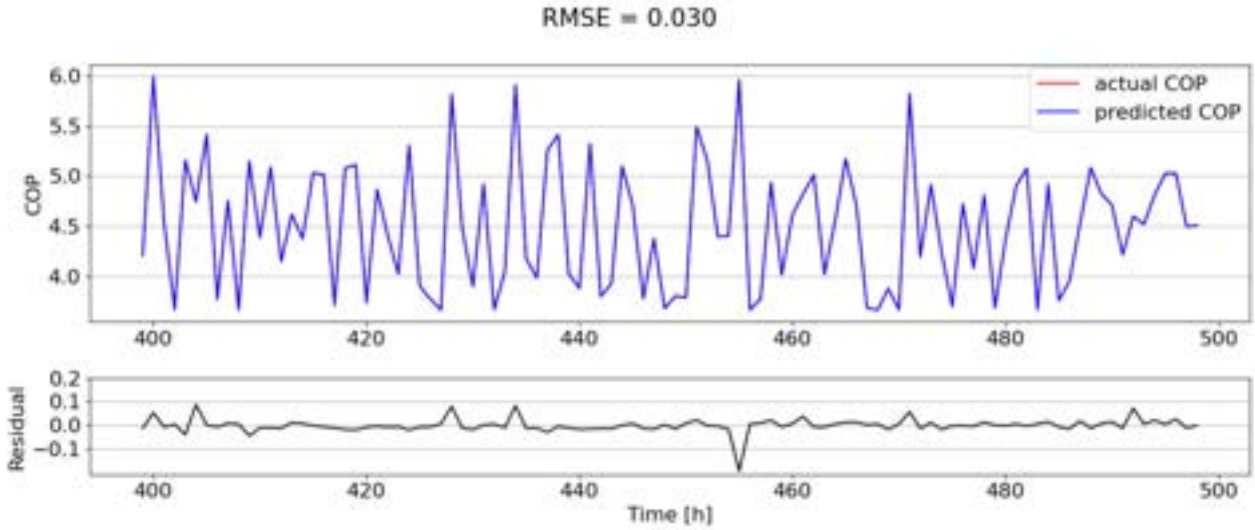

Figure 6: Testing period for ANN Validation from Figure 5.

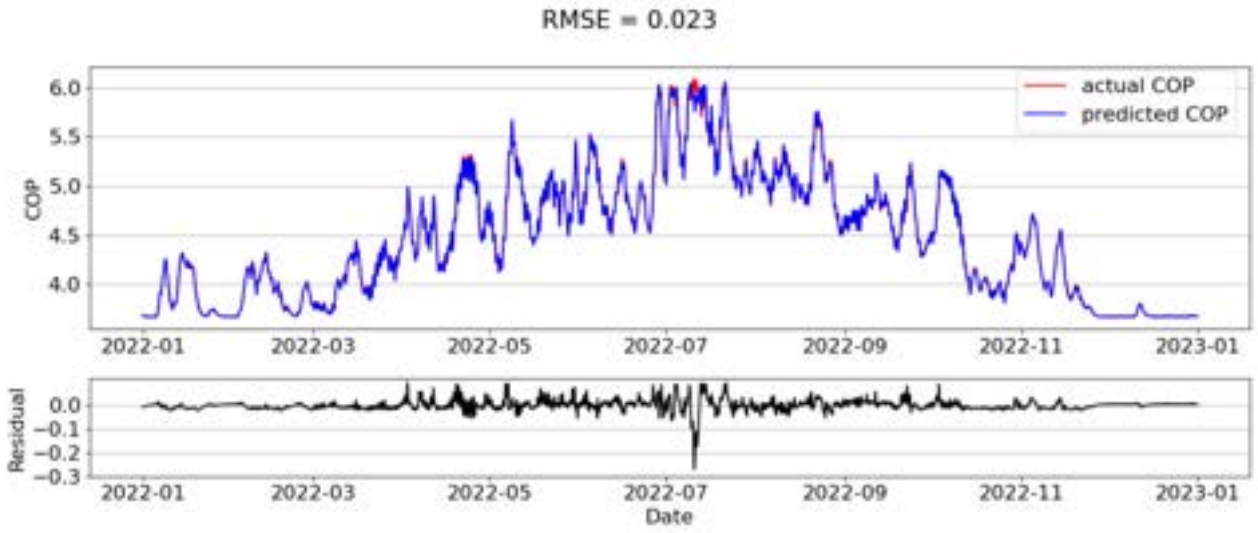

Figure 7: Above: Predicted *COP* with ANN (blue) and *COP* of reference system (red) within the study period. Below: Residual of predicted and actual *COP*.

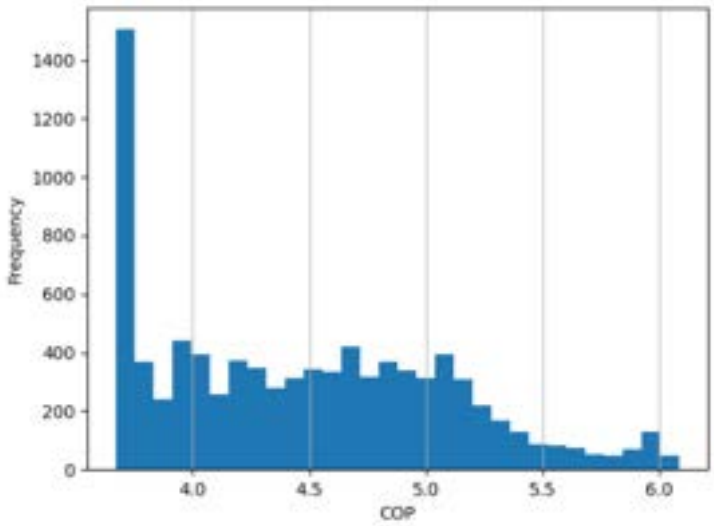

Figure 8: Histogram of occurred *COP*s in the Simulation.

4.2 Model tests for Fault detection

In Figure 9, we again show the *COP* of prediction from ANN and the reference system (with injected fault) from the simulation with TiL-Suite (section 3.1) combined with the residual of both. The green plot demonstrates the fault intensity, which increases according to equation 1 from 0 to 100 %. The maximum fault indication is limited to a reduction of the fan speed by 50 %. The residual increases significantly from April and hence a fault intensity of around 70 % (fan speed accordingly corresponds to 10.5 Hz) on average. It can be observed that the residual increases from April and thus an error intensity of around 70 % (fan speed thus corresponds to 10.5 Hz) on average. The *COP* does not seem to be affected significantly at lower fault intensities. This seems to be partly due to the problem described in section 4.1 above, where the ANN is generally poorer at representing the *COP* in the summer periods, but an increased residual compared to Figure 7 can be detected clearly as well.

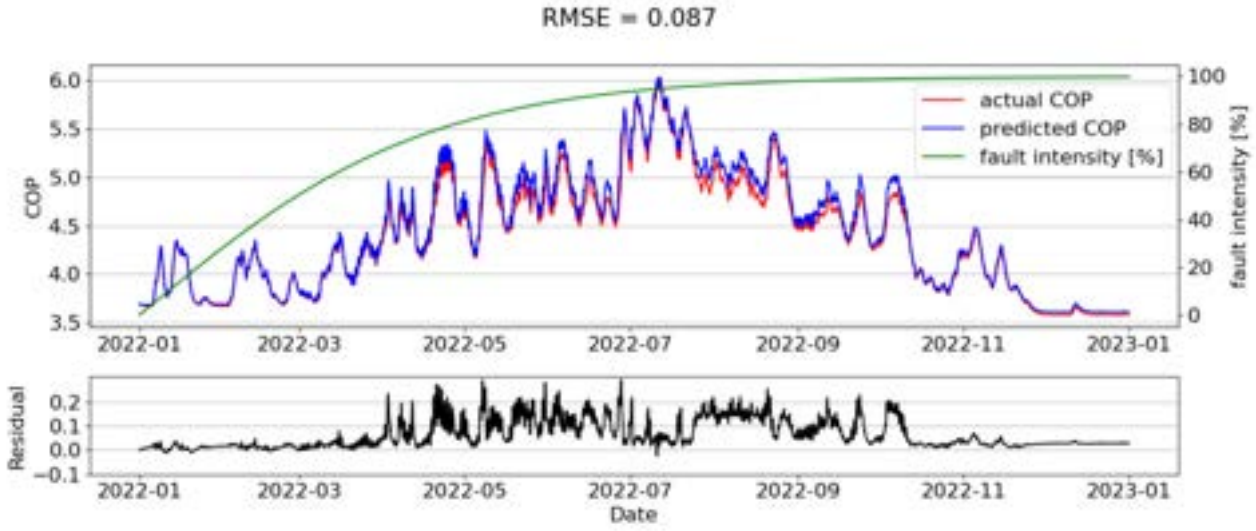

Figure 9: Above: Predicted *COP* with ANN (blue) and *COP* of reference system (red) within the study period including the fault injection. The fault intensity is shown in green. Below: Residual of predicted and actual *COP*.

Based on the results shown in Figure 7 and Figure 9, the threshold value, which serves the basis for fault notification, is defined to be a residual of 0.05. Exceeding this value leads to a notification and in this case to a MD of 44.35 % and FA of 1.35 % (Evaluation is carried out starting from a fault intensity of 70 %).

4.3 Limitations of the work

Within the scope of this work, all results were obtained from simulation data in order to emulate the effect of evaporator fouling. The associated model has not yet been completely validated, but has been compared with similar results from the literature. Hence, a validation based on real experiments, focusing the effect of evaporator fouling, is necessary in the future. For evaluation the threshold value (Section 4.2) has a significant impact on both the MD and the FA. The divergence in model accuracy between the winter and summer periods of the ANN leads to a significant increase in MD starting from early October. A further decreasing of the threshold may help here, but leads to an increase of FA, thus a pareto-optimization is necessary. Thus, this work has demonstrated the importance of training data selection for data-driven model performance. For future work, we expect better accuracy of the fault detection results by using a confidence interval instead of a threshold approach. Moreover, a valid benchmark for the evaluation of FDD methods by e.g. MD and FA is missing in the literature so far and needs to be elaborated.

5. Conclusion

This paper provides a first proof of concept for FDD using Artificial Neural Networks (ANN) to detect any abnormal behavior like evaporator fouling in air-to-water heat pumps early on. The early detection of faults like evaporator fouling is essential in maintaining the efficiency and performance of air-to-water heat pumps. Fouling causes a decrease in heat transfer, which reduces the system efficiency and increases energy consumption. Fault detection enables the scheduling of maintenance before significant performance degradation or system downtime occurs. For this purpose, an ANN is trained to predict the *COP* representing the fault-free operation of an annual simulation. The training data is obtained based on a transient simulation of a refrigerant cycle from the TiL-Suite, which also represents the reference system for fault injection. By gradually reducing the fan speed in the model, the heat transfer within the evaporator is decreased, thus emulating the fouling effect. Subsequently, using the residual of the ANN and the reference model, the deviation of *COP* correlates to the fault and a notification is provided based on a predefined threshold value. This way we are able to detect 55.65 % of all occurring faults and a false alarm is raised only in 1.35 % of the cases.

In future work, instead of using simulation data, we intend to apply experimental data to monitor and detect the effect of fouling and other faults more accurately. Furthermore, we will extend the fault notification method by including a confidence interval and further examine the selection and effect of training data to the ANN. Another crucial aspect in this paper is that a reduction of *COP* is no indication for a specific type of fault. Thus, a key for further development towards fault diagnosis in the future will be the identification of decoupled features which indicate specific fault characteristics or at least isolate potential fault types.

Acknowledgments

We gratefully acknowledge the financial support by the German Federal Ministry for Economic Affairs and Climate Action (BMWK), promotional reference 03EN1022B. We also thank our partners, TU Dresden, Viessmann and Glen Dimplex Deutschland GmbH for their good cooperation in this project.

References

- **Journals**:

[1] Shi Z., O'Brien W., Development and implementation of automated fault detection and diagnostics for building systems: A review. Automation in Construction 2019; 104:215–229. DOI: 10.1016/j.autcon.2019.04.002. URL https://linkinghub.elsevier.com/retrieve/pii/S0926580518312354

[2] Melgaard S. P., Andersen K. H., Marszal-Pomianowska A., Rasmus L. J., Heiselberg P. K., Fault Detection and Diagnosis Encyclopedia for Building Systems: A Systematic Review. Energies 2022, 15(12):4366, January 2022. DOI: 10.3390/en15124366. URL https://www.mdpi.com/1996-1073/15/12/4366

[3] Rosenow, J., Gibb, D., Nowak, T., & Lowes, R., Heating up the global heat pump market. Nature Energy 2022, 7(10), 901-904.

[4] Li Y., O'Neill Z., A critical review of fault modeling of HVAC systems in buildings. Building Simulation 2018, 11(5):953–975. DOI:10.1007/s12273-018-0458-4. URL https://doi.org/10.1007/s12273-018-0458-4

[5] Madani H., The Common and Costly Faults in Heat Pump Systems. Energy Procedia 2014, 61:1803–1806. DOI: 10.1016/j.egypro.2014.12.217. URL https://linkinghub.elsevier.com/retrieve/pii/S1876610214032469

[6] Song Y., Rolando D., Avellaneda J. M., Zucker G., Madani H., Data-driven soft sensors targeting heat pump systems. Energy Conversion and Management 2023, 279 (2023): 116769. DOI: 10.1016/j.enconman.2023.116769. URL https://doi.org/10.1016/j.enconman.2023.116769

[7] Varlamis I., Sardianos C., Chronis C., Dimitrakopoulos G., Himeur Y., Alsalemi A., et al., Smart fusion of sensor data and human feedback for personalized energy-saving recommendations. Appl Energy 2022, 305:117775.

[8] Fan Y., Tao B., Zheng Y., Jang S-S., A data-driven soft sensor based on multilayer perceptron neural network with a double LASSO approach. IEEE Trans Instrum Meas 2019, 69(7):3972–9.

[9] Zhao, Y., Li Tingting, Thang X., Zhang C., Artificial intelligence-based fault detection and diagnosis methods for building energy systems: Advantages, challenges and the future. Renewable and Sustainable Energy Reviews 2019, 109: p. 85-101.

[10] Aguilera, J. J, et al. A review of common faults in large-scale heat pumps. Renewable and Sustainable Energy Reviews 2022, 168: 112826.

[11] Bellanco, I., et al., A review of the fault behavior of heat pumps and measurements, detection and diagnosis methods including virtual sensors. Journal of Building Engineering 2021, 39: 102254.

[12] Kocyigit N., Bulgurcu H., Lin C. X., Fault diagnosis of a vapor compression refrigeration system with hermetic reciprocating compressor based on p-h diagram, Energy Econ, 2014. 45 44–54, https://doi.org/10.1016/j.ijrefrig.2014.05.027

[13] Mehrabi M., Yuill D., Generalized effects of faults on normalized performance variables of air conditioners and heat pumps, Int. J. Refrig. 85, 2018. 409–430, https://doi.org/10.1016/j.ijrefrig.2017.10.017

[14] Breuker M.S., Braun J.E., Common faults and their impacts for rooftop air conditioners, HVAC R Res. 4, 1998. 303–318, https://doi.org/10.1080/10789669.1998.10391406

[15] Li H., Braun J.E., A methodology for diagnosing multiple-simultaneous faults in rooftop air conditioners, HVAC R Res. 13, 2004. 369–395.

[16] Armstrong P.R., Laughman C.R., Leeb S.B., Norford L.K., Detection of rooftop cooling unit faults based on electrical measurements, HVAC R Res. 12, 2006 151–175, https://doi.org/10.1080/10789669.2006.10391172

[17] Rogers, A. P., F. Guo, and B. P. Rasmussen, A review of fault detection and diagnosis methods for residential air conditioning systems, Building and Environment, 2019. 161: 106236.

[18] Herceg S., Andrijić Ž.U., Bolf N., Development of soft sensors for isomerization process based on support vector machine regression and dynamic polynomial models, 2019. Chem. Eng. Res. Des.,149:95–103. https://doi.org/10.1016/j.cherd.2019.06.034

[19] Zheng J., Song Z., Semisupervised learning for probabilistic partial least squares regression model and soft sensor application, 2018. J. Process Control, 64:123–31.

[20] Melgaard S.P., Andersen K.H., Marszal-Pomianowska A, Jensen R.L., Heiselberg P.K., Fault Detection and Diagnosis Encyclopedia for Building Systems: A Systematic Review. Energies, 2022. 15(12):4366. https://doi.org/10.3390/en15124366

[21] Keliris C., Polycarpou M., Parisini T., A Distributed Fault Detection Filtering Approach for a Class of Interconnected Continuous-Time Nonlinear Systems, 2013. IEEE Transactions on Automatic Control. 58. 2032–2047. DOI: 10.1109/TAC.2013.2253231

[22] Yuill D. P., Braun J. E., Evaluating the performance of fault detection and diagnostics protocols applied to air-cooled unitary air-conditioning equipment, 2013. HVAC&R Research. 7. 882-891. DOI: 10.1080/10789669.2013.808135

[23] Katipamula S., Brambley M., Review Article: Methods for Fault Detection, Diagnostics, and Prognostics for Building Systems—A Review, Part I, 2005. HVAC&R Research. 11. 3-25. DOI: 10.1080/10789669.2005.10391123

[24] Mavromatidis G., Acha S., Shah N., Diagnostic tools of energy performance for supermarkets using Artificial Neural Network algorithms, Energy Build, 2013. 62:304–14 URL https://doi.org/10.1016/j.enbuild.2013.03.020

[25] Nelson W., Culp C., Machine Learning Methods for Automated Fault Detection and Diagnostics in Building Systems—A Review. Energies, 2022. 15(15):5534. DOI: 10.3390/en15155534. URL https://www.mdpi.com/1996-1073/15/15/5534

[26] M. S. Abd-Elhady, Malayeri M.R., Asymptotic characteristics of particulate deposit formation in exhaust gas recirculation (EGR) coolers, 2013. Applied Thermal Engineering 60.1-2: 96-104. URL http://dx.doi.org/10.1016/j.applthermaleng.2013.06.038

[27] Rätz M. et al., Automated data-driven modeling of building energy systems via machine learning algorithms, 2019. Energy & Buildings. 202. URL https://doi.org/10.1016/j.enbuild.2019.109384

- **Chapter in a book**:

[28] Gertler J., Fault Detection and Diagnosis. In Baillieul J. and Samad T., editors. Encyclopedia of Systems and Control, Springer, London, 2015. p. 417–422. DOI: 10.1007/978-1-4471-5058-9_223. URL https://doi.org/10.1007/978-1-4471-5058-9_223

[29] Isermann R., Terminology in fault detection and diagnosis. In Rolf Isermann, editor. Combustion Engine Diagnosis: Model-based Condition Monitoring of Gasoline and Diesel Engines and their Components, ATZ/MTZ-Fachbuch, p. 295–297. DOI:10.1007/978-3-662-49467-7_9. URL https://doi.org/10.1007/978-3-662-49467-7_9

[30] Du Z., Domanski P.A., Payne W.V., Effect of common faults on the performance of different types of vapor compression systems, Appl. Therm. Eng., 2016. 98 61–72, https://doi.org/10.1016/j.applthermaleng.2015.11.108

- **Web references:**

[31] Vereinte Nationen. Übereinkommen von Paris, December 2015. Available at: https://www.bmz.de/de/service/lexikon/klimaabkommen-von-paris-14602 [accessed 10.03.2023]

[32] Presse und Informationsamt der Bundesregierung. Generationenvertrag für das Klima, 2022. Available at: https://www.bundesregierung.de/breg-de/themen/klimaschutz/klimaschutzgesetz-2021-1913672 [accessed 10.03.2023]

[33] Umwelt Bundesamt. Umgebungswärme und Wärmepumpen, 2022. Available at: https://www.umweltbundesamt.de/themen/klima-energie/erneuerbare-energien/umgebungswaerme-waermepumpen [accessed 10.03.2023]

[34] TLK-Thermo GmbH. TIL Suite Softwarepaket zur Simulation thermischer Systeme. Available at: https://www.tlk-thermo.com/index.php/de/til-suite [accessed 10.03.2023]

- **Books and other monographs:**

[35] Quaschning V., Quaschning C., Energierevolution jetzt! Mobilität, Wohnen, grüner Strom und Wasserstoff: Was führt uns aus der Klimakrise - und was nicht? Hanser, München, 2022.

- **Conference Papers**:

[36] Roth, Kurt W., Westphalen D., Llana P., Feng M., The energy impact of faults in US commercial buildings. International Refrigeration and Air Conditioning 2004.

[37] Madani H. et al., Smart Fault Detection and Diagnosis for Heat Pump Systems, Refrigeration Science and Technology 2016, 3703-3710.

[38] Noel D., Riviere P., Marchio D., Non-Intrusive Performance Assessment Method For Heat Pumps : Experimental Validation And Robustness Evaluation Facing Faults, in: 17 Th, Int. Refrig. Air Cond. Conf. 2018.

[39] Ho Yoon S., Vance Payne W., Domanski P.A., Residential heat pump heating performance with single faults imposed. http://docs.lib.purdue.edu/iracc/1107, Int. Refrig. Air Cond. Conf. 2010.

[40] Mehrabi M., Yuill D., Normalized effect of condenser fouling and refrigerant charge on performance of vapor compression air conditioning systems, Int. Compress. Eng. Refrig. Air Cond. High Perform. Build. Conf. 2016.

[41] Noel, D., Teuillieres, Riviere P., Cauret O., Marchio D., Experimental Characterization of Fault Impacts on the Functioning Variables of an Inverter Driven Heat Pump, 2018.

Transient analysis and control of a Brayton heat pump during start-up

Matteo Pettinari[a], Guido Francesco Frate[a], A. Phong Tran[b], Johannes Oehler[b], Panagiotis Stathopoulos[b], and Lorenzo Ferrari[a]

*[a] University of Pisa, Department of Energy, Systems, Territory and Construction Engineering, Pisa, Italy, matteo.pettinari@phd.unipi.it, guido.frate@unipi.it, lorenzo.ferrari@unipi.it (**CA**)*
[b] German Aerospace Center (DLR), Institute of Low-Carbon Industrial Processes, Cottbus, Brandenburg, Germany, Anh.Tran@dlr.de, Johannes.Oehler@dlr.de, Panagiotis.Stathopoulos@dlr.de

Abstract:

High-temperature heat pumps represent a valuable technology to decrease fossil fuel consumption in industry, as they can use renewable electricity to cover a given heat demand. Conventional heat pumps provide heat at temperatures around a maximum of 80 °C. Nowadays, heat production up to 150 °C can be achieved with high-temperature heat pumps. For higher temperatures between 150 °C and 250 °C, specialized designs, such as Brayton heat pumps, are required. This paper aims to investigate the transient response of the DLR's CoBra prototype, an innovative Brayton-cycle heat pump intended to provide heat above 250 °C and currently under commissioning at the DLR facility in Cottbus, Germany. First, a comprehensive transient thermodynamic model of the system is developed, accounting for heat exchangers and piping thermal inertia. Furthermore, a control logic is presented that ensures safe operation throughout off-design conditions and start-up manoeuvres. In particular, several control parameters are considered to avoid potential operational issues, such as critical temperature gradients, compressor surge, and critical mechanical vibration phenomena due to resonance. The performed simulations aim to reduce start-up time and energy consumed during start-up. Results show that with the help of the described controller, the system can reach design operation via a transient trajectory safely and quickly. Therefore, the capability of the CoBra prototype to flexibly supply high-temperature heat is demonstrated.

Keywords:

High-Temperature Heat Pump; Process Heat; Reverse Brayton Cycle; Transient Modelling; Closed Cycle Control.

1. Introduction

Heat provision accounts for over 50 % of the final energy consumption, with about 25 % for domestic purposes and space heating and 25 % for industrial processes [1]. For industrial processes, the great majority of this energy demand is met by fossil fuels. High-temperature heat pumps represent one of the most efficient options to abate emissions in this sector, as such technology may use renewable electricity to recover heat from low-temperature sources. To date, the market for industrial high-temperature heat pumps offers machines with up to 150 °C heat delivery temperature and COP values up to 5 [2–4]. Primarily fields of applications comprise the food, chemical, paper, and textile industries. Nevertheless, recent studies reported that a significant heat demand at higher temperatures currently exists in Europe [5,6], suggesting it could be addressed through heat pumps in the case higher sink heat temperatures are achieved.

Nowadays, heat pump development is limited by economic and technical barriers [2,4,7]. Economic barriers primarily consist of the long payback periods and the high ratio of electricity to gas costs. Conversely, the technical ones are related to the limited heat sink temperature and the lack of eco-compatible refrigerants performing well and safely at higher temperatures. In their investigation on the heat pumps potential for high-temperature process heat supply, Zühlsdorf et al. [3] suggest that with the proper technology, for instance, by adopting equipment already available within the oil and gas industry, sink temperatures of up to at least 280 °C can be met with heat pumps, both from a technical and economic perspective. Therefore, their scope of applications in the industry may extend.

Most heat pumps are based on the thermodynamic Rankine cycle [2]. However, other cycles can be advantageous depending on the temperature profile or the plant where they are used. In their analysis of different industrial heat consumers, Gai et al. [8] found that sometimes the transcritical, Brayton or Rankine cycle is optimal depending on the process under consideration. In particular, Brayton-based heat pumps may

offer more versatility in design and operability when processes characterized by large temperature glides are considered, as they use single-phase operating fluid and exchange sensible heat with the temperature sink and source [3]. Nevertheless, such systems generally offer a more straightforward construction than the Rankine or hybrid ones and also allow for partial power recovery leveraging turbo expanders. Possible processes include the food industry, with the heating of thermal oil or frying needed, hot air processes like baking or drying, paper and pulp and chemical industries but also thermal energy storage systems where Brayton heat pumps offer the advantage of supplying very high temperatures and also sub-ambient cold temperatures [9,10]. However, systems must be developed, built, and integrated into the relevant industries. Furthermore, they should be compact and provide flexibility in operation to replace or supplement current state-of-the-art gas boilers in brownfield applications. Hence, new concepts should allow for quick start-up times and load changes, ideally at high efficiencies, whilst ensuring safe operation.

To date, few Brayton-based prototypes have been proposed and developed for industrial applications [11–13], whilst most of the research focused on the energy storage field, where several projects and developers are already present on the market [14,15]. Although several research may be found in the literature discussing the cycle optimization or analysing the system behaviour in design conditions, only a few works analyse the dynamic behaviour of such plants, especially when critical operations such as start-ups are considered. In this regard, Frate et al. [16] analyzed the dynamics of a Brayron PTES during warm start-up and off-design operations. Despite not optimizing the gas turbine speed ramp for quick start-ups, a start-up time of around 30 min was reported. Smith et al. [17] presented the design of a laboratory scale pumped thermal electricity storage demonstration plant in order to test the control strategies and demonstrate the system operability and criticalities. Start-up times of around 1.38 h and 2 h were reported depending on the compressor recycle valve opening. Furthermore, Oehler et al. [12] developed and analyzed a control strategy to safely perform a cold start-up of an air-based Brayton heat pump for industrial purposes. A start-up time of more than 2.5 h and a turbine bypass valve was used to avoid compressor surge. However, the control inputs used to drive such maneuver were not designed to optimize the start-up of the system. Faster start-ups are then possible.

To further investigate in this regard, the present work analyses the transient capabilities of the Brayton heat pump proposed in [12] while undergoing a cold start-up manoeuvre. A closed-loop control system is developed and presented in the following to determine whether the system can achieve faster start-up times safely. Results aim to provide useful insights into the system's behaviour and limitations and help design an optimised procedure for quick start-ups.

2. Prototype overview

The CoBra (Cottbus Brayton Cycle) heat pump is currently under development by the German Aerospace Center (DLR) in Cottbus. Figure 1 shows the schematic and thermodynamic cycle of the heat pump.

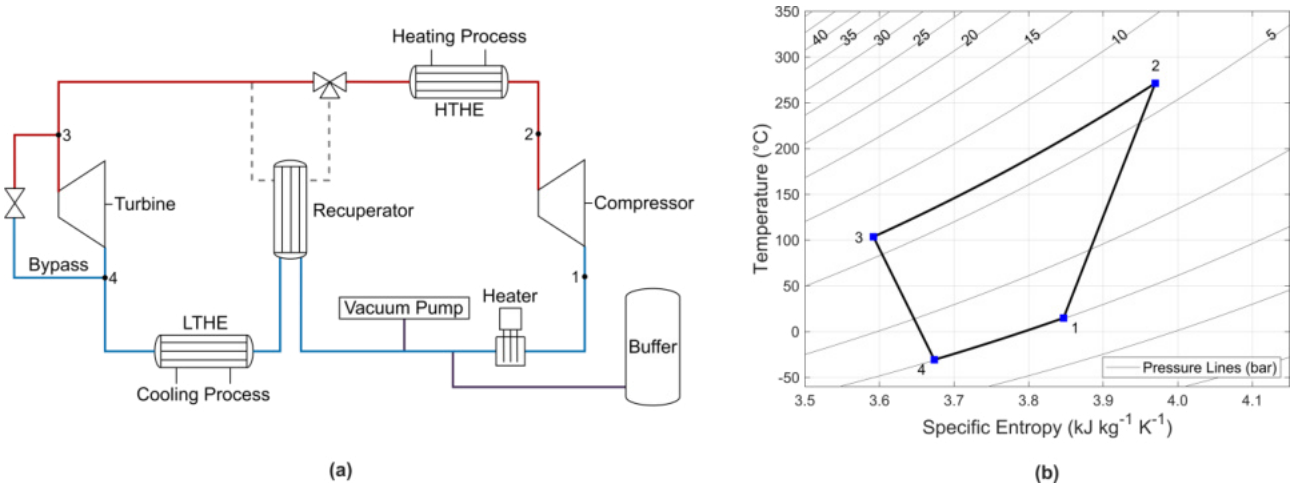

Figure. 1. CoBra heat pump: (a) system layout; (b) T-s diagram.

As a closed-loop Brayton cycle heat pump, the CoBra features a three-stage turbo compressor with pressure ratios of up to 7. The compressor raises the pressure and temperature of the working gas, which is primarily dry air but can also use other media such as argon or CO_2. With the available pressure ratios, the heat pump can achieve heat sink temperatures of 250 °C and more. After rejecting heat to a high-temperature heat sink (e.g. industrial process heat or thermal energy storage), the gas is expanded using an axial two-stage turbine, which recovers power and cools the gas to sub-ambient temperatures. A turbine bypass valve can be opened to increase the mass flow rate in the heat pump, thereby stabilizing the compressor flow. In the low-temperature heat exchanger, the gas absorbs heat from a heat source before returning to the

compressor. An internal recuperator may leverage the remaining temperature difference between the heat exchanger outlet flows to raise the temperature at the compressor inlet. All three heat exchangers are shell-and-tube heat exchangers. The heat pump cycle is nearly hermetically sealed, thus enabling load variation via injection or air removal. Using valves and pressurized buffer storages, the system pressures and, consequently, the load can be controlled [11].

3. Dynamic modelling methodology

A transient model of the CoBra heat pump was developed through the Simulink® environment of Matlab® R2022b [18]. In particular, the Simscape™ libraries were used as they provide built-in models for all the main components constituting the plant. As for the system fluid, dry air was considered and treated as real gas. Its thermophysical properties were retrieved through RefProp [19].

3.1 Turbomachinery

The compressor and turbine were modelled from a system level by using custom components available in Simscape™. The mathematical model of each element comprises continuity equations, such as mass and energy balances. In particular, mass is conserved such that:

$$\dot{m}_{in} + \dot{m}_{out} = 0, \tag{1}$$

where $\dot{m}_i$ are the inlet and outlet mass flow rates, respectively. In a similar fashion, energy balance is computed as:

$$\dot{\Phi}_{in} + \dot{\Phi}_{out} + \dot{W}_{fluid} = 0, \tag{2}$$

where $\dot{\Phi}_i$ are the inlet and outlet energy fow rates, and $\dot{W}_{fluid}$ is the power delivered to/done by the operating fluid (e.g., $\dot{W}_{fluid} = |\dot{W}_{fluid}|$ in case of a compressor, and $\dot{W}_{fluid} = -|\dot{W}_{fluid}|$ in case of a turbine), defined as:

$$\dot{W}_{fluid} = \dot{m}_{in} \frac{\Delta h_{is}}{\eta_{is}}, \tag{3}$$

where $\dot{m}_{in}$ is the inflow mass flow rate, Δh_{is} is the specific enthalpy isentropic variation, and η_{is} is the turbomachine isentropic efficiency. Compressor and turbine mechanical powers are respectively computed according to Eq. (4) and Eq. (5):

$$\dot{W}_c = \frac{\dot{W}_{fluid}}{\eta_m}, \tag{4}$$

$$\dot{W}_t = \eta_m \dot{W}_{fluid}, \tag{5}$$

where η_m is the turbomachine mechanical efficiency. As for the design and off-design modelling, performance maps were used, therefore establishing the relationship between the machines inlet conditions (e.g., mass flow rate, temperature, and pressure) and quantities such as pressure ratio and isentropic efficiency. Figure 2 reports the performance maps considered in this work. Corrected parameters, defined as in Eq. (6), were used to account for variations at the machine inlet:

$$\begin{cases} \dot{m}_{corr} = \dfrac{\sqrt{T_{in}/T_0}}{p_{in}/p_0} \\ n_{corr} = \dfrac{n}{\sqrt{T_{in}/T_0}} \end{cases}, \tag{6}$$

where $p_0 = 101325$ Pa and $T_0 = 288.15$ K. Furthermore, turbomachines were assumed adiabatic with neglibile volume. Their thermal dynamic was therefore neglected. Conversely, inertial effects were considered by accounting for the compressor, turbine, motor, generator, and transmission moments of inertia. Inertial torques were therefore computed as:

$$\tau = J\dot{\omega}, \tag{7}$$

where J is the moment of inertia of the component, whilst $\dot{\omega}$ is its angular acceleration. Finally, coupling between compressor and motor, as well as turbine and generator, was assumed ideal. Hence, gearboxes losses due to backlash and friction were neglected.

3.2. Heat exchangers

Similarly to the turbomachinery, the shell-and-tube heat exchangers were modelled through Simscape™ Fluids library components. Heat exchangers were assumed adiabatic with and a fixed-volume construction to capture variations in fluid mass flow rates due to compressibility. Therefore, mass is conserved along the tube/shell side of the exchanger such that:

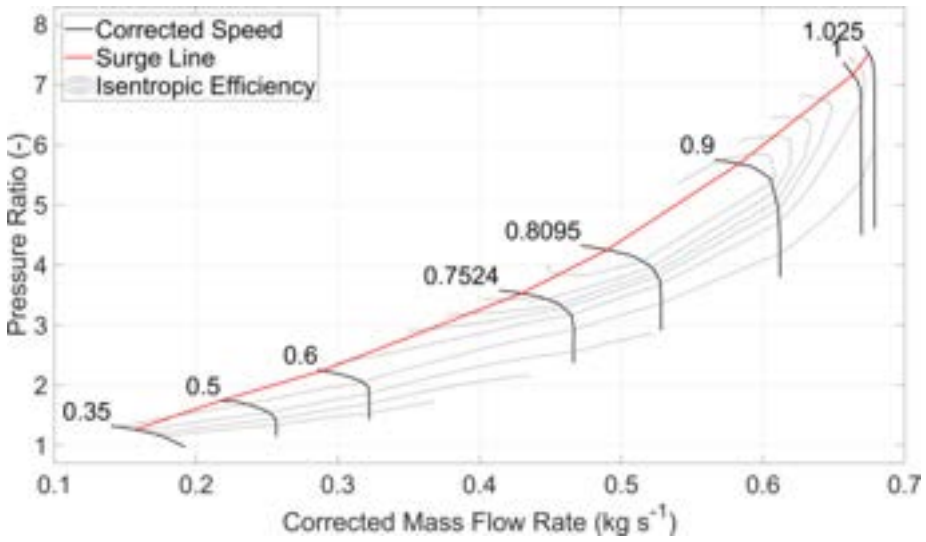

Figure. 2. Compressor map.

$$\left[\left(\left(\frac{\partial \rho}{\partial \mathrm{p}}\right)_u \frac{d\mathrm{p}_I}{d\mathrm{t}} + \left(\frac{\partial \rho}{\partial \mathrm{u}}\right)_p \frac{d\mathrm{u}}{d\mathrm{t}}\right] \mathrm{V} = \dot{\mathrm{m}}_{\mathrm{in}} + \dot{\mathrm{m}}_{\mathrm{out}}, \tag{8}$$

where $\dot{\mathrm{m}}_{\mathrm{i}}$ are the mass flow rates at the inlet/outlet of the tube or shell side, whilst ρ, p_I, u, and V are the gas mass density, pressure, specific internal energy, and volume, respectively. Pressure losses were modelled as:

$$\Delta \mathrm{p} = \left(\frac{\rho_{\mathrm{nom}}}{\rho}\right)\left(\frac{\dot{\mathrm{m}}^2}{\dot{\mathrm{m}}_{\mathrm{nom}}{}^2}\right)\Delta \mathrm{p}_{\mathrm{nom}}, \tag{9}$$

where the subscript $_{\mathrm{nom}}$ refers to the thermophysical quantities evaluated when the system operates at nominal conditions. Furthermore, energy is conserved such that:

$$\left[\left(\left(\frac{\partial \mathrm{U}}{\partial p}\right)_{\mathrm{T,V}} \frac{d\mathrm{p_I}}{d\mathrm{t}} + \left(\frac{\partial \mathrm{U}}{\partial \mathrm{T}}\right)_{\mathrm{p,V}} \frac{d\mathrm{T_I}}{d\mathrm{t}}\right] = \dot{\Phi}_{\mathrm{in}} + \dot{\Phi}_{\mathrm{out}} + \dot{\mathrm{Q}}, \tag{10}$$

where $\dot{\Phi}_{\mathrm{i}}$ are the energy flow rates at the tube or inlet/outlet, $\dot{\mathrm{Q}}$ is the heat transfer rate exchanged between the two fluids, and $\mathrm{p_I}$, $\mathrm{T_I}$, and U are the pressure, temperature and internal energy of the gas volume, respectively.

As for the heat transfer through the heat exchanger, it was determined according to the ε-NTU method. At each simulation step, the number of transfer units (NTU) was therefore computed as:

$$\mathrm{NTU} = \frac{1}{\mathrm{C_{min}R_{overall}}}, \tag{11}$$

where $\mathrm{C_{min}} = \min\left(\mathrm{c_{p,tube}}\dot{\mathrm{m}}_{\mathrm{tube}}; \mathrm{c_{p,shell}}\dot{\mathrm{m}}_{\mathrm{shell}}\right)$, whilst $\mathrm{R_{overall}}$ is the overall thermal resistance defined as:

$$\mathrm{R_{overall}} = \frac{1}{\alpha_{\mathrm{tube}}\mathrm{A_{tube}}} + \mathrm{R_{foul,tube}} + \mathrm{R_{wall}} + \mathrm{R_{foul,shell}} + \frac{1}{\alpha_{\mathrm{shell}}\mathrm{A_{shell}}}, \tag{12}$$

where α_{i} are the convective heat transfer coefficients of the fluids flowing within the tube/shell, $\mathrm{A_i}$ are the aggregate heat transfer surface areas, $\mathrm{R_{foul,i}}$ are the fouling resistances, and $\mathrm{R_{wall}}$ is the wall interface thermal resistance. The heat exchanger effectiveness was then computed as a function of the NTU value through correlations based on the heat exchanger type [20].

In order to capture the thermal transient due to the heat exchangers mass, the wall thermal mass was defined as:

$$\mathrm{C_{wall}} = \mathrm{c_{p,wall}}\mathrm{M_{wall}}, \tag{13}$$

where $\mathrm{c_{p,wall}}$ is the wall specific heat, and $\mathrm{M_{wall}}$ is its inertial mass. Therefore, the heat transfer rate exchanged across the heat exchanger was determined according to:

$$\dot{\mathrm{Q}}_{\mathrm{tube}} = \varepsilon\dot{\mathrm{Q}}_{\mathrm{max}} + \mathrm{C_{wall,tube}}\dot{\mathrm{T}}_{\mathrm{wall,tube}}, \tag{14}$$

$$\dot{\mathrm{Q}}_{\mathrm{shell}} = \varepsilon\dot{\mathrm{Q}}_{\mathrm{max}} - \mathrm{C_{wall,shell}}\dot{\mathrm{T}}_{\mathrm{wall,shell}}, \tag{15}$$

where $C_{wall,i} = \frac{C_{wall}}{2}$ is the thermal capacity evenly divided between the two sides of the heat exchanger, $\dot{T}_{wall,i}$ is the rate of change in temperature in the wall half (positive if the temperature increases, negative when it drops), and $\dot{Q}_{max}$ is the ideal heat transfer rate. Finally, to improve simulation accuracy, each heat exchanger was modelled as a series of ten components characterized by the mathematical model described above. Hence, nominal gas volumes, heat transfer surface areas, as well as pressure losses have been evenly distributed among the elements.

3.3. Piping

As piping represents a non-negligible fraction of the gas volume of the system volume, it was considered and distributed throughout the model according to the actual plant layout. Similarly to the heat exchangers, pipe components conserve energy as in Eq. (10), whilst mass is conserved such that:

$$\left[\left(\left(\frac{\partial M}{\partial p}\right)_{T,V}\frac{dp_I}{dt} + \left(\frac{\partial M}{\partial T}\right)_{p,V}\frac{dT_I}{dt}\right]\right. = \dot{m}_{in} + \dot{m}_{out}. \quad (16)$$

Momentum balance was determined by assuming the pipe in half. Hence, the momentum flux and the viscous friction of each half were computed as:

$$p_i - p_I = \left(\frac{\dot{m}_i}{S}\right)^2\left(\frac{1}{\rho_i} - \frac{1}{\rho_I}\right) + \Delta p_{iI}, \quad (17)$$

where the subscripts $_i$ and $_I$ refer to the pipe inlet/outlet and gas volume nodes, respectively, S is the pipe cross-sectional area, and Δp_{iI} are the pressure losses due to viscous friction, computed accordingly to the flow regime. As for the heat transfer occurring throughout the pipe, it was modelled as:

$$\dot{Q} = \dot{Q}_{conv} + \dot{Q}_{cond}, \quad (18)$$

where $\dot{Q}_{conv}$ is the convective heat transfer between the pipe wall and the gas volume, whilst $\dot{Q}_{cond}$ denotes the heat transfer within the pipe material. By assuming an exponential distribution along the pipe, the convective heat transfer was computed as:

$$\dot{Q}_{conv} = \left|\dot{m}_{avg}\right| c_{p,avg}\left(1 - \exp\left(-\frac{\alpha_{avg} A}{\left|\dot{m}_{avg}\right| c_{p,avg}}\right)\right)(T_{wall} - T_{in}) + -\frac{k_I A}{d_h}(T_{wall} - T_i), \quad (19)$$

where $\dot{m}_{avg}$ is the average mass flow, $c_{p,avg}$ is the specific heat evaluated at the average gas temperature, α_{avg} is the convective coefficient computed by considering the gas thermal conductivity at average temperature (k_{avg}), A is the pipe surface area, d_h is hydraulic diameter, and T_{wall}, T_i, T_{in} are the wall, gas volume, and inlet mass flow rate temperatures, respectively. Finally, the heat transfer due to the conduction within the pipe metal was computed as:

$$\dot{Q}_{cond} = 2\pi k_{mat} L\left[\frac{(T_{mat} - T_{in})}{\ln\left(\frac{d_{avg}}{d_{in}}\right)} + \frac{(T_{out} - T_{mat})}{\ln\left(\frac{d_{out}}{d_{avg}}\right)}\right] + c_{mat} M_{mat} \dot{T}_{mat}, \quad (20)$$

where L is the pipe length, k_{mat}, c_{mat}, M_{mat}, $\dot{T}_{mat}$ are the thermal conductivity, specific heat, inertial mass, and temperature of the pipe material, d_i are the pipe inner, mean, and outer diameters, and T_i are the respective metal temperatures.

3.4. Valves and other equipment

The transient model also accounted for the ancillary equipment reported in Figure 1a. Hence, valves were modelled as adiabatic variable restrictions with negligible volume. In particular, the three-way valve was modelled through two inversely linked valves, such that opening one valve results in the closing of the other. Furthermore, valve geometry was characterized based on manufacturer data, and a linear flow characteristic was considered. As for the heater, only pressure drops were accounted for and modelled as in Eq. (9).

3.5. Controls

Two independent control loops were implemented to simulate the system in transient conditions, namely:

- anti-surge controller;
- temperature controller.

The anti-surge controller was designed to prevent the compressor from operating within critical regions in proximity to the surge line. With reference to Figure 1a, compressor surge was avoided by manipulating the turbine bypass opening, thus increasing the primary mass flow rate. The valve opening was regulated by a

variable-gain PI feedback controller based on the surge margin error. In the present work, the surge margin was defined as:

$$\mathrm{SM} = \left(\frac{\mathrm{PR_{surge}}}{\mathrm{PR_{op}}} - 1\right)_{\dot{m}_c}, \tag{21}$$

where $\mathrm{PR_{op}}$ is the actual pressure ratio, while $\mathrm{PR_{surge}}$ is the surge line pressure ratio evaluated at the same reduced flow. Controller gains were determined to provide a pure proportional action at high errors to ensure a prompt response in case of critical operating conditions. An integral control action was gradually added at low errors for setpoint tracking.

On the other hand, the temperature controller varies the compressor shaft speed in order to control the compressor outlet temperature. As discussed in [12], the control requirements were set as follows:

temperature slopes of no more than 2 K/min to avoid critical thermal stresses at the heat exchangers;

fast crossing of critical low speeds to avoid resonance effects of the compressor shaft.

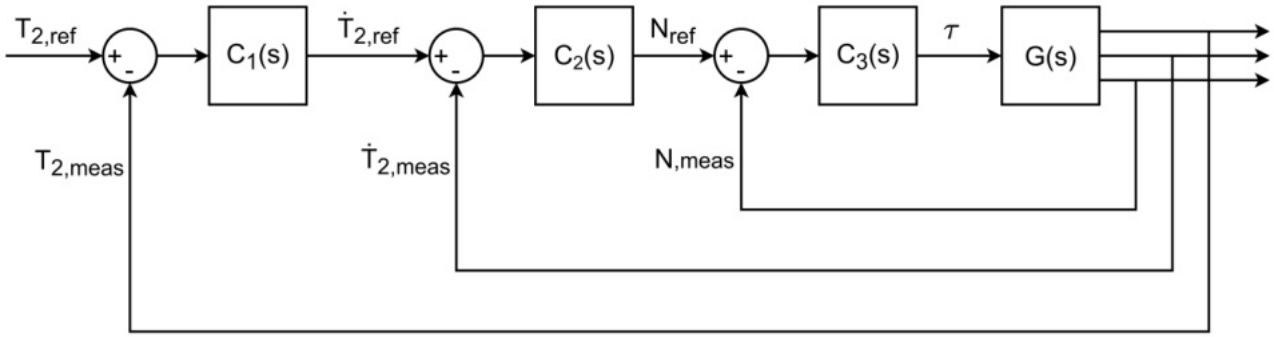

Figure. 3. Simplified temperature control schematic.

A cascade control architecture, made of three nested loops, was found suitable for the given requirements. The compressor outlet temperature was chosen as the primary controlled variable, as measuring the temperature inside the heat exchanger is a non-trivial task. As shown in Figure 3, the outer regulator uses the temperature error to determine a setpoint for the compressor outlet temperature slope. Here, the slope setpoint is limited to a maximum value of 2 K/min. Subsequently, the intermediate control loop processes the temperature slope setpoint and compares it with the actual measurement/estimation to provide a motor speed setpoint. Similar to the outer loop, the speed setpoint is limited to values within the compressor's operating range. Finally, an inner loop determines the motor torque based on the difference between the reference and measured motor speed.

It is worth mentioning that sensor and controller dynamics are negligible as they are faster than the ones characterizing the system under analysis. Nevertheless, standard anti-windup techniques were employed to manage the undesired effects related to the interaction between the controllers' integral actions and the saturations characterizing the physical system and the control schemes.

3.6. Transient simulation

The model outlined in the previous sections was used to investigate the system's transient behaviour during the start-up, aiming at determining the characteristic time and the significant criticalities that occur while performing such a manoeuvre.

At first, a cold start-up manoeuvre was simulated while imposing a maximum temperature slope of 2 K/min. The start-up time was assumed to be when the system provides heat at a temperature with an absolute error of less than one degree with respect to the design value. Secondly, a sensitivity analysis was performed by varying the maximum allowed slope in the 2−50 K/min range to investigate how the start-up time of the system is affected by the temperature slope limit.

Each simulation scenario was initialized through the same initial conditions. In particular, initial conditions were computed such that the system had enough mass to reach nominal conditions at the end of the start-up. Therefore, the initial system pressure was assumed to be almost 2 bar, whilst the initial fluid and metal temperatures were set between 15−20 °C. Mass flow rates on the secondary side of the cycle heat source and sink heat exchangers were considered constant throughout the simulation and were already at their nominal values. The turbine and generator were supposed to rotate at their respective design speeds. Conversely, the motor and compressor were assumed to rotate very slowly (~3 % of the nominal speed) to avoid numerical instability during the transient initialization of the model. Finally, control actuators such as the heater and the recuperation valve three-way were not considered during the start-up manoeuvre. In particular, the three-way valve was set such that the primary mass flow exiting the high-temperature heat

exchanger went directly to the turbine inlet. Therefore, the recuperator was disabled and a non-regenerated configuration of the plant was assumed.

4. Results and discussion

4.1. Cold start-up

During the cold start-up, the system goes from steady conditions to nominal ones based on the control inputs determined by the temperature and anti-surge regulators. Control input and outputs are reported in Figure 4.

At the beginning of the simulation, the system is at an ambient temperature at a pressure of 2 bar. As the compressor rotates at low speeds, corrected flow is negligible. The surge margin is less than 10% (e.g., minimum allowable value), and the bypass valve is fully open due to the anti-surge controller action (Figure 4a). Moreover, as the compressor outlet temperature is lower than 271 °C (e.g., the desired setpoint), the temperature controller causes the motor/compressor to accelerate (Figure 4b). Consequently, the compressor outlet temperature increases, as reported in Figure 5a, whilst the turbine inlet temperature remains constant as heat is absorbed by the high-temperature heat exchanger. Since the bypass is fully open, part of the primary mass flow does is not expanded by the turbine, and only a minor temperature drop

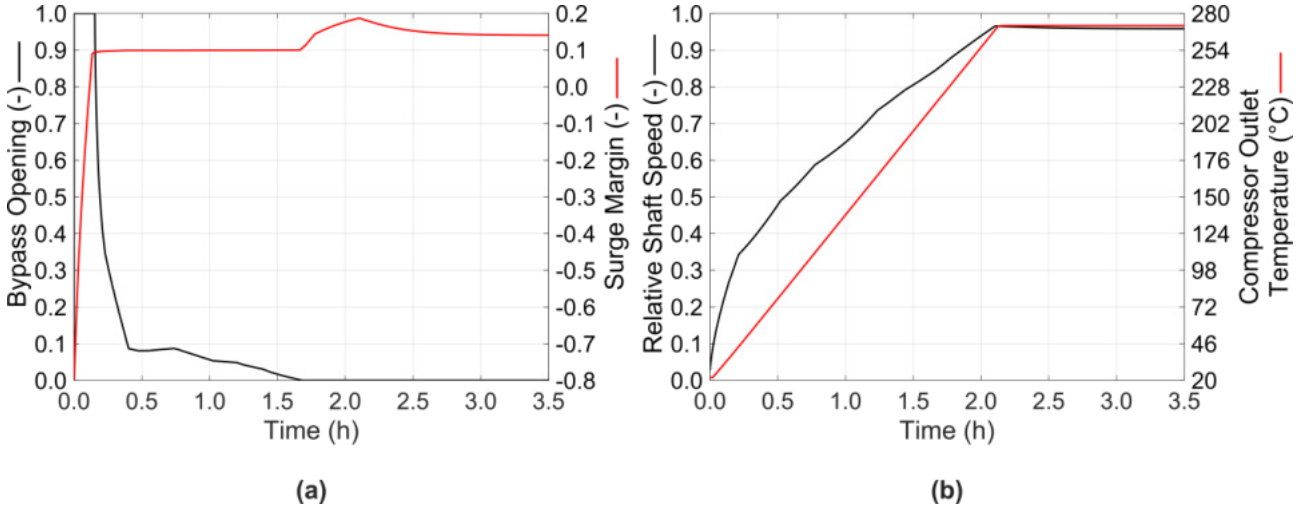

Figure. 4. Control signals (in blue) against controlled variables (orange): (a) surge margin controller ($SM_{ref} = 10\%$); (b) compressor outlet temperature controller ($T_{2,ref} = 271°C$).

occurs through the valve. The system operates in the abovementioned configuration for almost ten minutes. In such a period, the compressor keeps accelerating, increasing its outlet temperature and reducing the surge margin. As a result, the operating point slowly moves toward higher speeds and efficiencies on the right of the compressor map at an almost constant pressure ratio (Figure 6).

At t = 9 min, the surge margin becomes greater or equal to the minimum allowable limit. Since the compressor keeps accelerating, the anti-surge regulator gradually closes the bypass valve to maintain the setpoint surge margin. In more detail, the bypass valve goes from 100% open down to around 10 % open at t = 23 min, and it is fully closed after t = 1.67 h, as shown in Figure 4a. Due to the bypass closure, part of the primary mass flow expands through the turbine, and consequently, the temperature at the turbine outlet starts to decrease (Figure 5a). Also, the pressure ratio progressively increases because of the higher rotational speed (Figure 5b). As a result, the operating point moves toward higher speeds and efficiencies parallel to the surge line.

At t = 1.67 h, the anti-surge controller fully closes the bypass valve as the system operates safely away from the surge line. On the other hand, slightly after two hours, the compressor outlet temperature reaches the design value, and the temperature regulator stops accelerating the compressor. The system operates close to the design conditions at this point, providing a heat flow rate of 115 kW at around 262 °C. From here to the end of the simulation, the temperature controller provides only minor adjustments. In particular, the motor/compressor speed slightly decreases as a consequence of the stabilization of the system temperatures, which is not instantaneous due to the thermal inertia of the system (e.g., T_3, T_4 and T_{wall}). This can also be observed in Figure 6, where the compressor operating point remains almost in the same position on the map, experiencing only a minor displacement toward higher efficiencies and pressure ratios as the temperatures settle.

It is worth noting that, during the transient, the compressor outlet temperature increases at a constant slope, which is maintained below the maximum allowable value by the temperature controller. Limiting the compressor outlet temperature helps contain the temperature gradients within the heat exchangers. For

instance, by looking at Figure 5a, it can be observed that the metal temperature at the high-temperature heat exchanger inflow shows a similar trend after a delay of almost 12 min caused by the thermal mass of the piping and the first element of the heat exchanger. A significant delay can also be noted in the turbine inlet temperature as it increases only after 40 min with respect to the compressor outlet temperature. Here, the delay magnitude is higher as it accounts for the thermal inertia of the complete high-temperature heat exchanger and the piping connecting the heat exchanger with the expander. Furthermore, as the temperature slope is determined based on the capability of the heat exchangers to sustain thermal stresses, it can be stated that their design represents a critical constraint for quick plant start-up.

It can be further noted that the motor/compressor speed increases quickly, especially at the lower values, ensuring the compressor never operates at critical speeds for an extended amount of time, thus avoiding potential deleterious effects related to compressor shaft vibrations. Moreover, the motor/compressor acceleration is continuously modulated as a reaction to the bypass valve closure, thereby denoting interaction and the goodness of the developed control system.

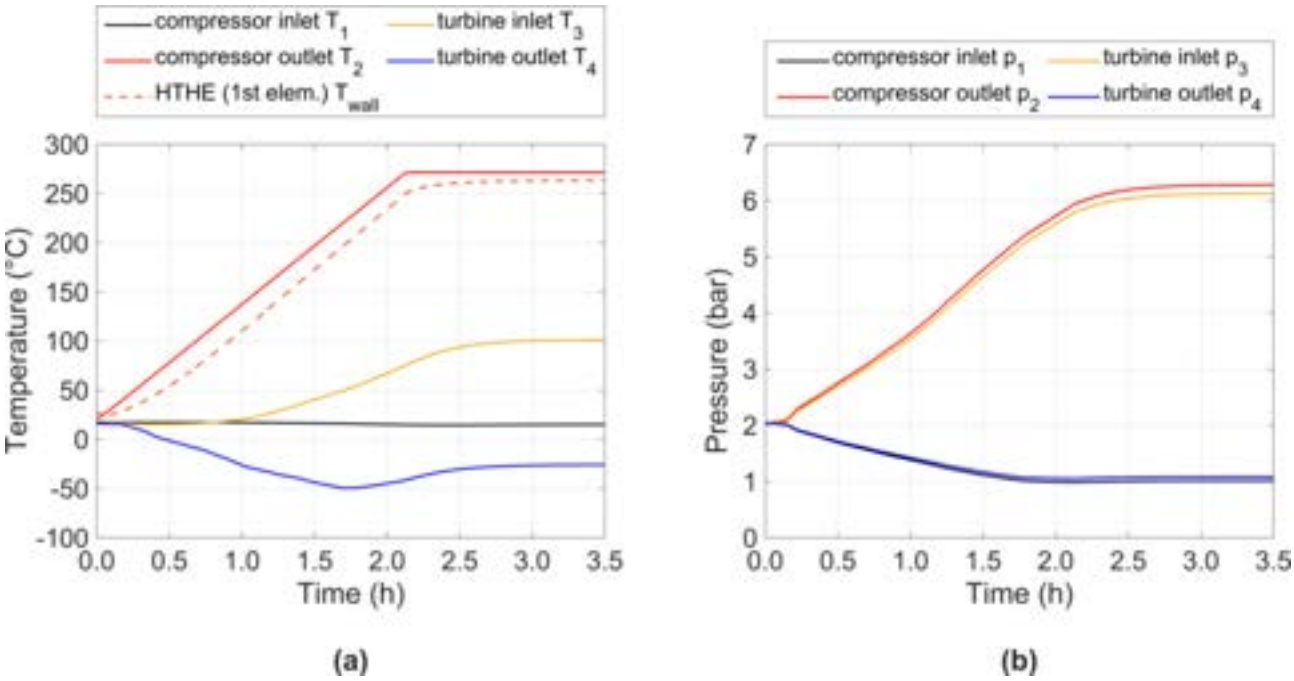

Figure. 5. System transient response during a cold start-up: (a) cycles temperatures and HTHE first element average wall temperature; (b) cycle pressures.

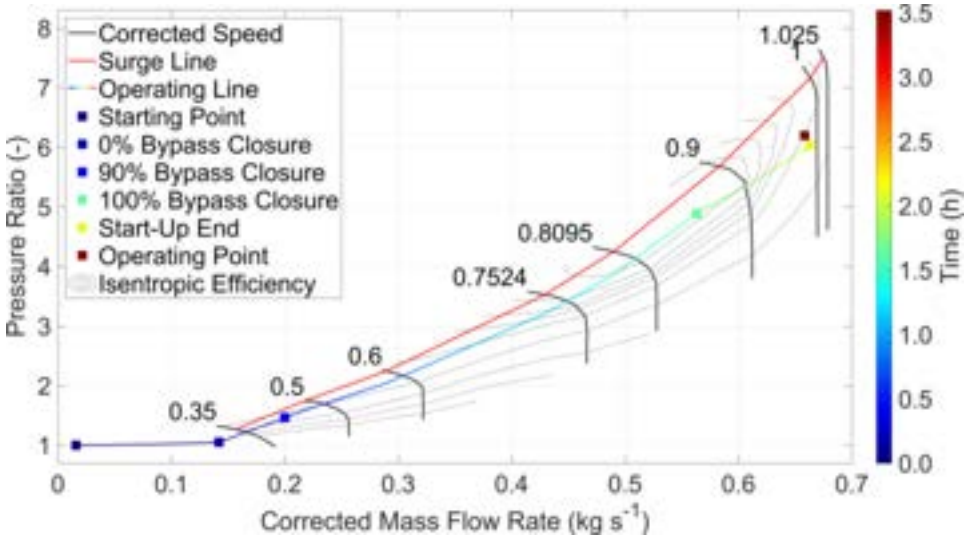

Figure. 6. Compressor operating line during the start-up.

4.2. Sensitivity analysis

The previous section showed that the thermal stresses sustainable by the heat exchangers mainly constrain the start-up time of the system. Hence, a sensitivity analysis was performed to further investigate such a relationship. The system's start-up was simulated by varying the maximum allowable slope at the compressor outlet temperature in the 5−50 K/min range with a 5 K/min step. Each simulation was initialized as discussed in Section 3.6. Results are summarized in Figure 7, which reports the start-up times and system power consumption as a function of the maximum allowable slope of the compressor outlet temperature.

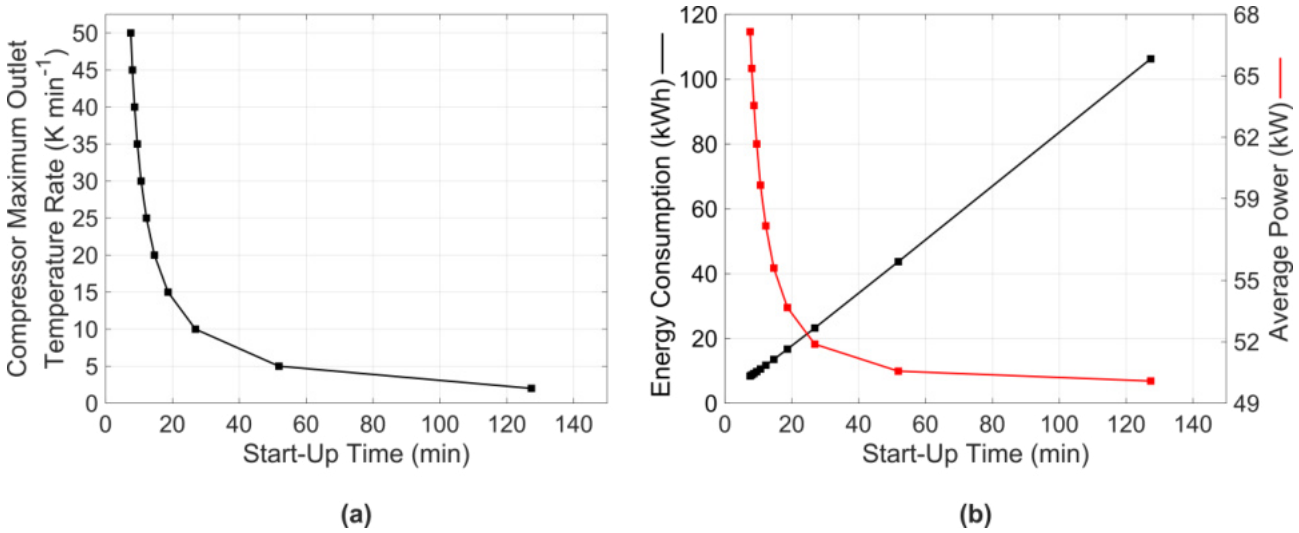

Figure. 7. Sensitivity to the maximum compressor outlet temperature rate: (a) start-up time; (b) energy consumption and average absorbed power during the start-up.

It can be observed that start-up time significantly reduces as the slope constraint is relaxed (Figure 7a). For instance, allowing for a temperature slope of 5 K/min leads to a start-up time of around 52 min (e.g., 60 % reduction), whilst in case of a slope of 10 K/min, the start-up time drops to 27 min (e.g., 80 % reduction), providing more flexibility of use in real applications. From there on, minor advantages are shown for higher temperature slopes. However, it is worth noting that such temperature slopes would require suitably designed heat exchangers, potentially increasing the capital cost of the plant and thus making it less appealing from an economic perspective. It can also be noticed that the system's energy consumption decreases almost linearly with the start-up time reduction (Figure 7b). Therefore, higher temperature slopes lead to lower energy consumption. On the other hand, less conservative slopes cause higher average power absorbed by the system increases, with a trend similar to the one reported in Figure 7a.

Apart from the considerations discussed above, shortening the start-up may lead to new technical challenges to be addressed. For instance, Figure 8 reports the cycle temperatures trend for a maximum temperature slope of 2, 10, and 15 K/min while performing the start-up.

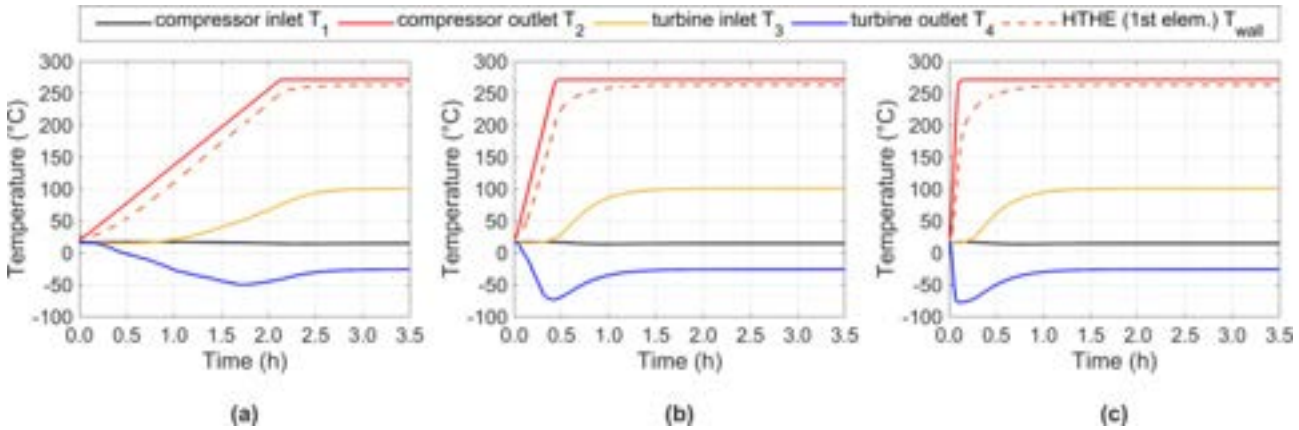

Figure. 8. Cycle and HTHE tube inlet temperatures for different values of temperature rate constraint at the compressor outlet: (a) $\dot{T}_2 = 2$ K min^{-1}; (b) $\dot{T}_2 = 10$ K min^{-1}; (c) $\dot{T}_2 = 50$ K min^{-1}.

It can be observed that higher allowable slopes lead to faster accelerations of the compressor, causing a quicker increase in both mass flow rate and pressure ratio. During rapid acceleration manoeuvres, the target pressure ratio and the bypass valve closing are reached before the metal temperatures in the high-temperature heat exchanger have settled. This leads to low turbine inlet temperatures and, consequently, turbine outlet temperatures of below −50 °C. As these low temperatures may lead to icing at the turbine outlet, further solutions are needed to handle these problems. A possible workaround may involve regulating the turbine shaft speed to operate with lower isentropic efficiencies, thereby mitigating the low outlet temperatures. However, at this stage of the work, it is not yet clear whether their adoption may affect the final start-up time of the plant. Therefore, further investigations must be conducted in this regard.

5. Conclusions

This paper investigates the transient behaviour of the DLR's CoBra heat pump during a cold start-up, assessing the time needed to reach design conditions and studying potential criticalities while performing such a manoeuvre. To this extent, a thermodynamic model of the system, comprehensive of mechanical, thermal and volume dynamics, was developed based on actual data characterizing the prototype. In addition, a control strategy was designed to automatically drive the compressor whilst ensuring the safe operation of the plant.

Results show the time needed to perform a cold start-up is around 2 hours when a maximum temperature slope is limited to 2 K/min to prevent thermal stresses at the heat exchangers. As expected, mechanical and pressure transient effects showed to be negligible when compared to the thermal dynamics characterizing the heat exchangers and piping. In particular, the heat exchangers showed delays of around 40 min.

Further analysis showed faster start-ups are possible in the case of less conservative temperature slopes. For instance, by increasing the maximum allowable slope to 5 or 10 K/min through adopting more advanced heat exchangers, the start-up time decreases to 52 and 27 min (e.g., start-ups shorter by more than 50 % and 80 % compared to a slope limit of 2 K/min). However, it was observed that quicker start-ups might lead to undesired effects at the turbine, as the outlet temperatures go below −70 °C during the transient, potentially causing icing. Further work is then required to assess the magnitude of these issues and to investigate whether possible solutions may negatively affect the start-up time of the plant, therefore nullifying the economic effort of using more sophisticated heat exchangers.

Finally, it is worth mentioning that the considered Brayton heat pump showed a start-up time consistent with the ones reported for a similar cycle specifically designed for energy-storage purposes [17], where start-up times in the 1.38−2 h range have been reported depending on the opening the compressor recycle valve opening. Here, differences in the results may be due to the different designs of the components, operating modes, temperature levels, and heat exchangers' size or technology, as the system are meant for different purposes. Although the comparison may suggest the validity of the proposed analysis, the proposed results should be confirmed through experimental data. Therefore, future work must be conducted in this direction in order to validate and further improve the developed transient model of the Brayton heat pump.

Acknowledgments

This research has received financial contribution from the Italian Operative National Plan (Piano Operativo Nazionale, PON) in the framework of the project Ricerca e Innovazione 2014−2020 (PON R&I) – Azioni IV.4 e IV.5 "Dottorati di ricerca su tematiche dell'innovazione e green" (DM MUR 1061/2022) e IV.6 "Contratti di ricerca su tematiche dell'innovazione e green" (DM MUR 1062/2022)

Nomenclature

Abbreviations:

CoBra	Cottbus Brayton cycle heat pump
NTU	Number of Transfer Unit
HTHE	High-Temperature Heat Exchanger
LTHE	Low-Temperature Heat Exchanger

Letter symbols:

$\dot{m}$	mass flow rate, kg/s
T	temperature, °C
p	pressure, Pa
V	volume, m^3
h	specific enthalpy, J/kg
u	specific internal energy, J/kg
U	internal energy, J

$\dot{W}$	power, W
n	rotational shaft speed, rad/s
J	moment of inertia, kg/m^2
$\dot{M}$	mass accumulation, kg/s
$\dot{Q}$	heat transfer rate, W
C	heat capacity rate, W/K
c	specific heat, J/(kg K)
R	thermal resistance, K/W
A	heat transfer surface area, m^2
S	cross-sectional area, m^2
k	thermal conductivity, W/(m K)
d	diameter, m

Greek symbols

η	efficiency
$\dot{\Phi}$	energy flow rate, W
τ	torque, N m
$\dot{\omega}$	component rotational acceleration, rad/s^2
ρ	mass density, kg/m^3
α	convective heat transfer coefficient, W/(m^2 K)
ε	effectiveness

Subscripts and superscripts

0	reference state
$1,2,3,..$	cycle points
i	*i*-th element
p	at constant pressure
u	at constant specific internal energy
T	at constant temperature
V	at constant volume
in	inlet/inner
out	oulet/outer
is	isentropic
$fluid$	fluid
$corr$	corrected
I	internal/gas volume
$overall$	overall
$foul$	fouling
hot	hot fluis/side
$cold$	cold fluid/side
$wall$	wall
rel	relative
h	hydraulic
$conv$	convective
$cond$	conductive
avg	average
mat	material

References

[1] IEA, 2022, *Heating*, IEA, Paris.

[2] Arpagaus, C., Bless, F., Uhlmann, M., Schiffmann, J., and Bertsch, S. S., 2018, “High Temperature Heat Pumps: Market Overview, State of the Art, Research Status, Refrigerants, and Application Potentials,” Energy, **152**, pp. 985–1010. https://doi.org/10.1016/j.energy.2018.03.166
[3] Zühlsdorf, B., Bühler, F., Bantle, M., and Elmegaard, B., 2019, “Analysis of Technologies and Potentials for Heat Pump-Based Process Heat Supply above 150 °C,” Energy Conversion and Management: X, **2**, p. 100011. https://doi.org/10.1016/j.ecmx.2019.100011
[4] Jesper, M., Schlosser, F., Pag, F., Walmsley, T. G., Schmitt, B., and Vajen, K., 2021, “Large-Scale Heat Pumps: Uptake and Performance Modelling of Market-Available Devices,” Renewable and Sustainable Energy Reviews, **137**, p. 110646. https://doi.org/10.1016/j.rser.2020.110646
[5] Naegler, T., Simon, S., Klein, M., and Gils, H. C., 2015, “Quantification of the European Industrial Heat Demand by Branch and Temperature Level: Quantification of European Industrial Heat Demand,” Int. J. Energy Res., 39(15), pp. 2019–2030. https://doi.org/10.1002/er.3436
[6] Rehfeldt, M., Fleiter, T., and Toro, F., 2018, “A Bottom-up Estimation of the Heating and Cooling Demand in European Industry,” Energy Efficiency, 11(5), pp. 1057–1082. https://doi.org/10.1007/s12053-017-9571-y
[7] Thekdi, A., and Nimbalkar, S. U., 2015, *Industrial Waste Heat Recovery - Potential Applications, Available Technologies and Crosscutting R&D Opportunities*, ORNL/TM--2014/622, 1185778.
[8] Gai, L., Varbanov, P. S., Walmsley, T. G., and Klemeš, J. J., 2020, “Critical Analysis of Process Integration Options for Joule-Cycle and Conventional Heat Pumps,” Energies, **13**(3), p. 635. https://doi.org/10.3390/en13030635
[9] Angelino, G., and Invernizzi, C., 1995, “Prospects for Real-Gas Reversed Brayton Cycle Heat Pumps,” International Journal of Refrigeration, **18**(4), pp. 272–280. https://doi.org/10.1016/0140-7007(95)00005-V
[10] 2021, *Thermal, Mechanical, and Hybrid Chemical Energy Storage Systems*, Elsevier.
[11] Oehler, J., Gollasch, J., Tran, A. P., and Nicke, E., 2020, “Part Load Capability of a High Temperature Heat Pump with Reversed Brayton Cycle,” 13th IEA Heat Pump Conference, Jeju, Korea, p. 12.
[12] Oehler, J, Tran, AP, & Stathopoulos, P. "Simulation of a Safe Start-Up Maneuver for a Brayton Heat Pump." *Proceedings of the ASME Turbo Expo 2022: Turbomachinery Technical Conference and Exposition*. *Volume 4: Cycle Innovations; Cycle Innovations: Energy Storage*. Rotterdam, Netherlands. June 13–17, 2022. V004T06A003. ASME. https://doi.org/10.1115/GT2022-79399
[13] Längauer, A., Adler, B., and Rakusch, C., 2020, “Test Results of a Rotation Heat Pump and Further Developments.” 13th IEA Heat Pump Conference, Jeju, Korea
[14] https://www.maltainc.com/. (last accessed 15-05-2023)
[15] https://www.echogen.com/. (last accessed 15-05-2023)
[16] Frate, GF, Pettinari, M, Di Pino Incognito, E, Costanzi, R, & Ferrari, L. "Dynamic Modelling of a Brayton PTES System." *Proceedings of the ASME Turbo Expo 2022: Turbomachinery Technical Conference and Exposition*. *Volume 4: Cycle Innovations; Cycle Innovations: Energy Storage*. Rotterdam, Netherlands. June 13–17, 2022. V004T07A013. ASME. https://doi.org/10.1115/GT2022-83445
[17] Smith, NR, Tom, B, Rimpel, A, Just, J, Marshall, M, Khawly, G, Revak, T, & Hoopes, K. "The Design of a Small-Scale Pumped Heat Energy Storage System for the Demonstration of Controls and Operability." *Proceedings of the ASME Turbo Expo 2022: Turbomachinery Technical Conference and Exposition*. *Volume 4: Cycle Innovations; Cycle Innovations: Energy Storage*. Rotterdam, Netherlands. June 13–17, 2022. V004T07A012. ASME. https://doi.org/10.1115/GT2022-83424
[18] The MathWorks Inc., 2022, “MATLAB Version: 9.13.0 (R2022b).”
[19] Lemmon, E. W., Bell, I. H., Huber, M. L., and McLinden, M. O., 2018, “NIST Standard Reference Database 23: Reference Fluid Thermodynamic and Transport Properties-REFPROP, Version 10.0, National Institute of Standards and Technology.”
[20] Holman, J. P., 2002, *Heat Transfer*, McGraw-Hill, New York, NY.

PROCEEDINGS OF ECOS 2023 - THE 36TH INTERNATIONAL CONFERENCE ON
EFFICIENCY, **C**OST, **O**PTIMIZATION, **S**IMULATION AND ENVIRONMENTAL IMPACT OF ENERGY SYSTEMS
25-30 JUNE 2023, LAS PALMAS DE GRAN CANARIA, SPAIN

Investigation of a Heat Pump using Two-phase Refrigerant Compression

Nicolas Leclercq[a], Javier Vega[a], Vincent Lemort[a]

[a] *University of Liège, Energy Systems Research Unit, 4000 Liège, Belgium, N.Leclercq@ULiege.be*

Abstract:

Two-phase compression in volumetric machines shows several advantages: sealing effects brought by the liquid blocking the gap between two working chambers and it allows to get closer to an isothermal process, reducing the thermal stress on moving parts and minimizing compressor work. However, such compression also comes with some disadvantages: the mechanical reliability of the machine is questioned due to the presence of liquid during the compression, moreover, literature has shown that compressing in the two-phase region usually tends to decrease the isentropic efficiency of the machine.

The irreversibility creation in cycles such as ORC's or vapor compression cycles comes from two sources: the deviation of compression/expansion processes from internally reversible processes and the temperature difference between the hot/cold sources/sinks and the working fluid along heat exchanges (external irreversibility). Therefore, two-phase refrigerant compression/expansion can be integrated to pursue a beneficial trade-off between internal and external irreversibility, searching to increase the performance of the cycle by allowing to match as close as possible the temperature profile of the hot/cold sources/sinks. This paper presents an investigation on vapor compression heat pump cycles where the pressure increase is performed by a two-phase compressor. To this aim, a validated semi-empirical model of a scroll compressor tested with two-phase refrigerant is integrated into the cycle model. Moreover, a moving boundary model is used to model the cycle heat exchangers. The overall model is used to investigate the performance of the heat pump cycle and to quantify both internal and external irreversibility. The results show that the exergy destruction rate of the compressor at low vapor qualities are too high to be counterbalanced by the optimal heat exchange in the condenser. Therefore, the maximum coeffient of performance (COP) is located at saturated vapor compressor inlet condition. Nevertheless, the analysis is strongly dependent on the compressor used and a more optimized compressor for the application could enhance the heat pump COP at low qualities.

Keywords:

Two-phase compression, Heat Pump, Performance analysis, Exergetic analysis

1. Introduction

1.1. Two phase compression/expansion: state of the art

Two-phase compressions and expansions can be categorized in two parts: on one hand, two different fluids can be used (e.g., air and water mixture or refrigerant oil mixture), on the other hand, the state of one single fluid can be located under the saturation bell resulting in the presence of a liquid phase and a vapor phase. In the former case, experimental studies have started in the nineteen fifties, where the use of oil to lubricate air screw compressors and expanders was necessary to expand machines lifetime. In the latter case, the first studies can be found in the nineteen seventies where the expansion of flashing liquid and expansion of refrigerant started to gain interest for better machine performance and reliability purposes.

Two-phase expansion/compression have many advantages, in addition to the sealing effects brought by the liquid blocking the gap between two working chambers, it also allows to get closer to an isothermal process, reducing the thermal stress on the moving parts [1]. Nevertheless, some disadvantages can also be found: the increase of the pressure losses in suction/discharge ports due to either the reduction of the speed of sound or the increase of the density but also the loss of mechanical efficiency resulting from the higher viscosity of the liquid phase in contact with the moving parts [8].

Nevertheless, the use of two-phase compression/expansion could bring some innovations to conventional thermal systems. For instance, the Trilateral Flash Cycle shows better power outputs than classical Organic Rankine Cycles or flash steam systems resulting in a reduced system cost (in $/kW) [9]. Despite the potential of two-phase expansion for power generation, it has not been applied on an industrial scale yet, with only a few experimental studies published in the literature. The innovative cycle currently being developed in the REGEN-BY-2 European project (Horizon 2020) is also making use of two-phase refrigerant to operate [3]. In [10], the

investigation of a two-phase compression in a heat pump is conducted numerically using wet fluids and non-azeotropic mixtures with high vapor qualities, and the results show a better COP when no superheat occurs in the cycle.

1.2. Objectives of the paper

In most of the studies where two-phase compression/expansion is used, the performances of the cycles are better than in classical cycles where a superheated state is reached before the compression or the expansion. However, the numerical results obtained strongly rely on the performance of the compression/expansion machine used in the cycle. Using internally reversible processes or not taking into account the increase of irreversibilities in the two-phase region is not always a valid assumption. For these reasons, the present study will numerically assess the performance of a heat pump using an experimentally investigated two-phase compressor. To this aim, experimental data from a commercial compressor tested with two-phase refrigerant flows are used to validate a compressor semi-empirical model. This model is embedded in a heat pump model, making use of a moving boundary model to simulate the heat exchangers. The irreversibility creation in the heat pump comes from two sources: the deviation of compression process from internally reversible processes and the temperature difference between the heat source/sink and the working fluid along heat exchanges (external irreversibility). Therefore, the integration of two-phase refrigerant compression in the heat pump allows to follow a trade-off between internal and external irreversibility and can, in some cases, increase the performance of the cycles by allowing to better match the temperature profile of the heat source/sink.

The investigated heat pump is a theoretical water-water heat pump providing hot water (50°C) with a heat sink power of 5 kW. It uses a high temperature lift (from 15°C to 50°C) from a 15 °C heat source. It uses the refrigerant R1233zd(E) as the working fluid. A diagram of the heat pump can be found in Fig. 1. The evolution of the Coefficient of Performance (COP) of the heat pump will be investigated with a varying vapor quality up to superheated states. An example of Temperature-Entropy and Pressure-Enthalpy diagrams can be found in Figs. 2 and 3. The conventional cycle using a superheat (10 K) at the compressor inlet is the cycle 1-2-3-4 while the cycle 1′-2′-3-4 makes use of a low inlet quality compression and cycle 1″-2″-3-4 a medium inlet quality compression.

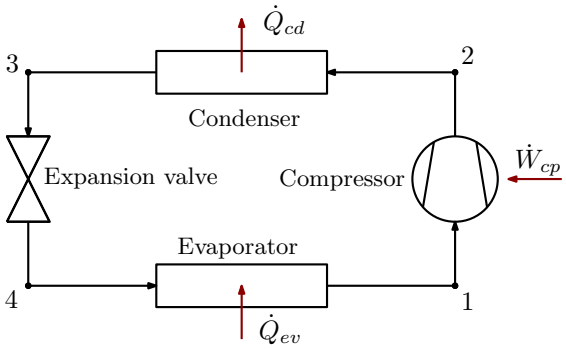

Figure 1: Heat pump cycle.

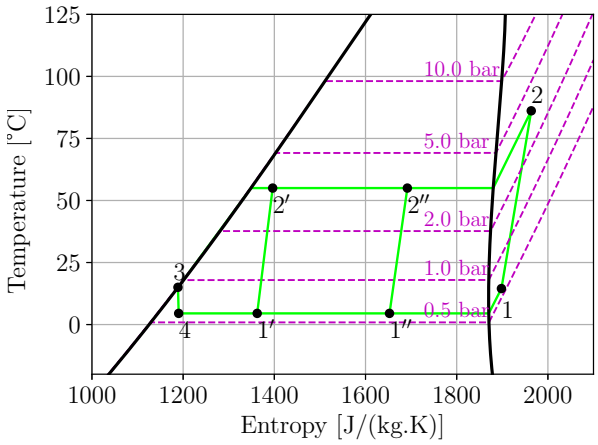

Figure 2: Temperature-entropy diagram of the heat pump cycle with different inlet qualities.

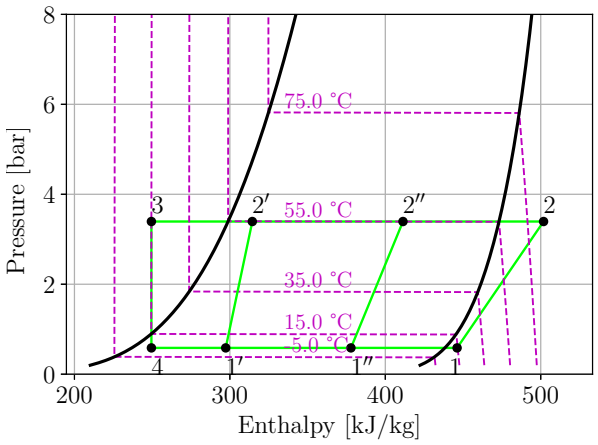

Figure 3: Pressure-enthalpy diagram of the heat pump cycle with different inlet qualities.

2. Modeling of the heat pump cycle

As previously said, the heat pump is modeled using a semi-empirical model for the compressor and a moving boundary heat exchanger model for the condenser and the evaporator. As presented in Fig. 4, the inputs of the model are the condenser inlet/outlet water temperature ($T_{w,su,cd}$, $T_{w,ex,cd}$) as well as its heat transfer rate ($\dot{Q}_{cd}$), the inlet vapor quality or superheating of the compressor ($Q_{su,cp}$ or SH) and the evaporator water inlet temperature ($T_{w,su,ev}$) and mass flow rate ($\dot{m}_{w,ev}$).

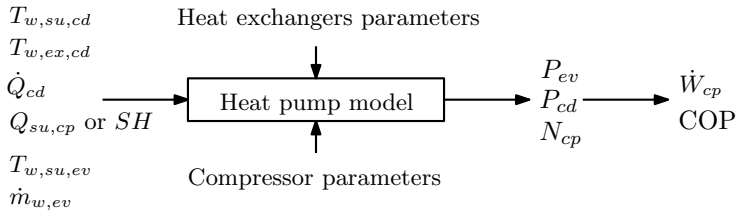

Figure 4: Model of the heat pump.

The model is then applying energy balances on the condenser and the cycle to find the evaporation pressure and the speed of the compressor giving the right working fluid mass flow rate. The condensation pressure could physically be fixed by the charge of refrigerant of the cycle, however, due to convergence problems, it has been decided to fix the condensation pressure with the condenser outlet temperature considering a pinch point of 5 K as can be seen in Fig. 15. Eventually, after fixing both level of pressure and the compressor speed, the compressor power consumption is determined and the COP can be calculated using 1. Obviously, the aforementioned procedure is an iterative process.

$$COP = \frac{\dot{Q}_{cd}}{\dot{W}_{cp}} \tag{1}$$

2.1. Compressor modeling

2.1.1. Experimental results

The compressor performance can be characterized using its volumetric and isentropic efficiencies. They can respectively be defined using the two following equations:

$$\varepsilon_v = \frac{\dot{m}_{tot}}{N_{cp} V_{disp} \rho_{su,cp}} \tag{2}$$

$$\varepsilon_s = \frac{\dot{m}_{tot}(h_{ex,cp,is} - h_{su,cp})}{\dot{W}_{shaft,cp}} \tag{3}$$

where $h_{ex,cp,is}$ is the isentropic compression exhaust enthalpy of the compressor. In particular, the isentropic efficiency (3) is used to characterize the irreversility creation of the compressor. In the case of an adiabatic and reversible evolution, the isentropic efficiency would be equal to one.

The variation of volumetric and isentropic efficiencies of the compressor with a varying pressure ratio and inlet vapor quality can respectively be found in Figs. 5 and 6, for a fixed inlet pressure, Oil Circulation Ratio (OCR) and speed. Those maps direclty comes from the experimental data used to calibrate the semi-emprical compressor model. The decrease of isentropic efficieny (thereby corresponding to an increase of irreversibilies) can clearly be observed, especially for high pressure ratios where the inlet-outlet volume ratio is getting furthest from the built-in volume ratio of the compressor. More information about the isentropic efficiency interpretation can be found in [6]. A similar behavior can be observed for the volumetric efficiency, although a sealing effect can be observed at low qualities and low pressure ratios.

2.1.2. Semi-empirical model

The scroll compressor model is a semi-empirical model inspired by [7]. The behavior of the compressor model relies on a set of physically-meaningful semi-empirical parameters to fit the experimentally tested compressor performances. The diagram of the semi-empirical model can be found in Fig. 7

This model considers a fictious isothermal envelope interacting with the fluid for supply and discharge heat transfer, taking the power losses of the compression process and rejecting ambient heat losses. It decomposes the fluid transformation inside the compressor in the following steps:

- $su \rightarrow su, 1$: isobaric heat transfer from the hot isothermal envelope to the working fluid.

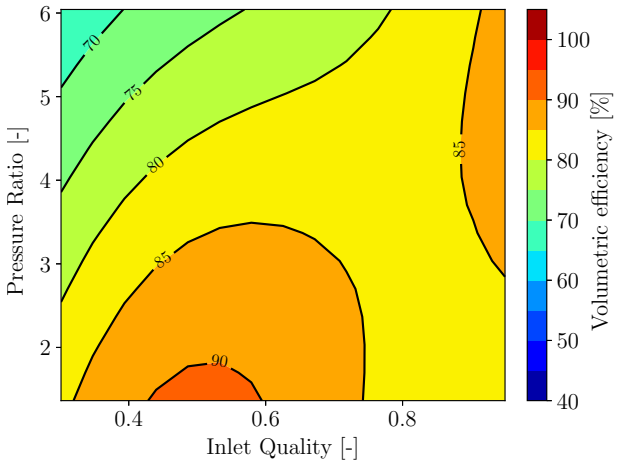

Figure 5: Evolution of the volumetric efficiency with the inlet quality and the pressure ratio for an inlet pressure of 1.5 bar, an OCR of 5% and a compressor speed of 4000 RPM.

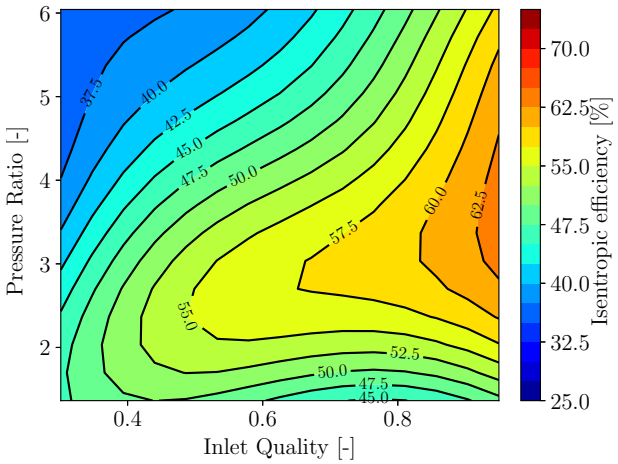

Figure 6: Evolution of the isentropic efficiency with the inlet quality and the pressure ratio for an inlet pressure of 1.5 bar, an OCR of 5% and a compressor speed of 4000 RPM.

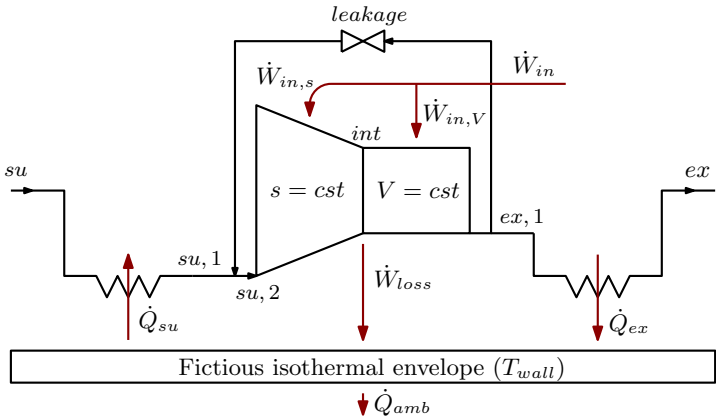

Figure 7: Model of the heat pump.

- $su, 1 \rightarrow su, 2$: energy balance due to the leakage flow adding to the compressor upstream flow
- $su, 2 \rightarrow int$: adiabatic and reversible (isentropic) compression. First part of the compression imposed by the built-in volume ratio of the compressor r_v and consuming a power $\dot{W}_{in,s}$.
- $int \rightarrow ex, 1$: constant volume compression to account for under/over compression losses. Second part of the compression consuming/producing a power $\dot{W}_{in,V}$.
- $ex, 1 \rightarrow su, 1$: leakage flow defined with an adiabatic pressure drop through a convergent nozzle.
- $ex, 1 \rightarrow ex$: isobaric heat transfer from the hot working fluid to the isothermal envelope.

The model uses 6 semi-empirical parameters. Among them, 3 are used for the supply, exhaust and ambient heat transfers, respectively, $AU_{su,ref}$, $AU_{ex,ref}$, AU_{amb}. Two other parameters are used for the friction losses characterization $\dot{W}_{loss,ref}$ and α_{loss}. The last parameter A_{leak} is used for the characterization of the leakage flow. The subscript *ref* stands for the reference, On the heat and mechanical power transfer side, the following definitions are set:

- $\dot{Q}_{su} = \varepsilon(AU_{su,ref}, \dot{C}_{wf})\dot{C}_{wf}\left(\frac{\dot{m}}{\dot{m}_{ref}}\right)^{0.8}(T_{wall} - T_{su})$: heat transfer from the hot isothermal envelope to the working fluid. ε is the heat exchanger efficiency computed using the Number of Transfer Units (NTU) method and $\dot{C}_{mix}$ is the heat capacity rate of the mixture flow.
- $\dot{Q}_{ex} = \varepsilon(AU_{ex,ref}, \dot{C}_{wf})\dot{C}_{wf}\left(\frac{\dot{m}}{\dot{m}_{ref}}\right)^{0.8}(T_{ex,1} - T_{wall})$: heat transfer from the working fluid to the isothermal envelope.

- $\dot{Q}_{amb} = AU_{amb}(T_{amb} - T_{wall})$: ambient heat transfer from the isothermal envelope.
- $\dot{W}_{in,s} = \dot{m}(h_{int} - h_{su,2})$: isentropic compression power.
- $\dot{W}_{in,V} = \dot{V}_{int}(P_{ex,1} - P_{int})$: constant volume compression power consumption.
- $\dot{W}_{loss} = \dot{W}_{loss,ref}\left(\frac{N}{N_{ref}}\right)^2 + \alpha_{loss}\dot{W}_{in}$: friction power loss of the compressor.

The calculation of properties considers the oil fraction in the whole working fluid path. Thereby, every enthalpy, entropy, density calculated takes into account the oil fraction similarly to what is used in [11]. Let X be a property of a pure fluid, the mixture property calculated would use the following equation:

$$X_{mix} = QX_{r,vap}(P,T) + z_o X_o(T) + (1 - Q - z_o)X^{\sigma}_{r,liq}(T) \tag{4}$$

where the subscripts r refers to pure refrigerant properties, *vap* and *liq* respectively refer to the vapor and the liquid phases, o stands for the oil and σ refers to a saturated property. The vapor quality Q, defined as vapor mass divided by the total mass, is linked with the oil fraction z_o using the Raoult law solubility equation. As can be noticed, 4 assumes that the oil only stands in the liquid phase.

The model takes five inputs: the compressor speed (N), the oil circulation ratio (OCR, z_o), the inlet pressure (P_{su}), pressure ratio (r_p) and the inlet quality (Q). It gives as outputs the mass flow rate and the power consumption at the shaft.

2.1.3. Model validation

As already mentioned, the compressor semi-empirical model is validated against experimental data. The experimental data comes from a commercial compressor with a displacement volume of 86 cm^3 and a built-in volume ratio of 2.3, tested with two-phase conditions on 110 operating points. The model validation is performed with the shaft power consumption and the mass flow rate, as those are the two relevant variables used in the heat pump model. The validations with regards to the shaft power and the mass flow rate can be found in Figs. 8 and 9.

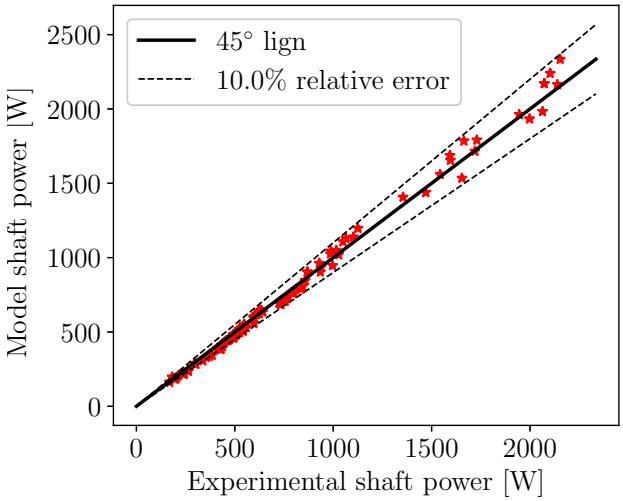

Figure 8: Shaft power prediction of the compressor model versus experimental data.

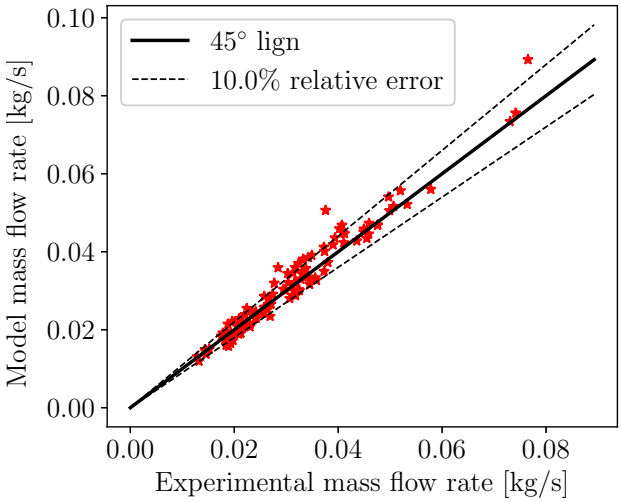

Figure 9: Mass flow rate prediction of the compressor model versus experimental data.

As can be observed in Figs. 8 and 9, the power predictions remain within the range of 10% of relative error with regards to the experimental power while the mass flow rate prediction is less precise, in particular, three points are going way outside the 10% relative error range. Nevertheless, the mean relative errors of the whole set of data are equal to 4.46% for the power and 6.47% for the mass flow rates.

Finally, the tuned parameters as well as the characteristics of the tested compressor can be found in Table 1. It can be noticed that the inlet and outlet heat transfer coefficients are abnormally high compared to what can be found in the litterature (between 1 and 10 W/K). On one hand, it can be explained by the two-phase conditions that increases the heat transfer coefficient. On the other hand, it could be explained by the lack of a suction pressure loss model. In particular, the model increases the inlet heat transfer to the fluid to increase its vapor quality to get lower mass flow rate, and adding an inlet pressure loss would have the same effect. However, the

inlet pressure losses were not added because of a convergence problem. Therefore, even though the semi-empirical parameters seems to predict with a relatively good accuracy the performance of the compressor, their physical meaning can not be trusted in every aspect.

Table 1: Parameters of the compressor semi-empircal model.

Parameter	Value	Unit
$AU_{su,ref}$	72.73	W/K
$AU_{ex,ref}$	46.47	W/K
AU_{amb}	2	W/K
$\dot{W}_{loss,ref}$	75.19	W
α_{loss}	0.0848	-
A_{leak}	$3.84 \cdot 10^{-7}$	m^2
V_{disp}	86	cm^3
r_v	2.3	-

2.2. Heat exchanger modeling

The heat exchanger model used for both the condenser and the evaporator is a moving boundary model inspired from [2], it has been selected for its ability to get the temperature evolutions of both fluids inside the heat exchangers. It calculates the maximum heat rate that can be transferred based on an internal and an external pinching analysis. Then, the heat exchanger is divided into a given number of cells having a fixed power transferred and two boundaries representing the saturated liquid and vapor points are are moving to define cells with subcooled liquid, two-phase fluid and superheated vapor. The log mean temperature difference is then solved on every cell to get the outlet and inlet temperatures on both primary and secondary fluid sides (refrigerant and water). The calculation of the heat transfer coefficients in each cell is different in two-phase regime and single-phase regime. For the two-phase regime, the evaporative and condensation heat transfer coefficients are respectively calculated using the Han boiling and condensing correlations in plate heat exchangers, while for single-phase regimes, the Gnielinski pipe heat transfer correlation is used. More information about these correlations can be found in [5].

The heat exchanger used for the present analysis is a plate heat exchanger and the same heat exchanger is used for both evaporator and condenser. The plate heat exchanger characteristics used can be found in Table 2, they are based on a real heat exchanger, oversized with regards to the application.

Table 2: Parameters of the plate heat exchanger used.

Parameter	Value	Unit
Surface exchange area	5.04	m^2
Number of plates	88	-
Cross section area	$2.1 \cdot 10^4$	m^2
Dimensions (H×L×l)	524×117×232	mm

2.3. Model limitations

The results of the heat pump model presented obviously have some limitations, although the main component, i.e., the compressor, is modeled based on experimental data. These limitations can be listed as follows:

- The compressor model is taking the OCR (z_{oil}) into account, it has therefore been tested with oil and the compressor performances shown in the subsequent section depend on this OCR. However, the heat exchanger model does not take the oil into account in the heat transfer coefficient correlations. Therefore, the oil will not be considered in the heat pump model. To make the conversion between the mixture vapor quality and the pure refrigerant vapor quality and vice versa, the following equation is used for the enthalpy conversion:

$$h_{r,pure}(P) = \frac{h_{mix}(T,P) - z_{oil} h_{oil}(T)}{1 - z_{oil}} \tag{5}$$

  A slight temperature change is therefore observed when doing the conversion. Moreover, only the refrigerant mass flow rate coming from the compressor model has been taken into account, this refrigerant mass flow rate is expressed as follows:

$$\dot{m}_r = \dot{m}_{mix}(1 - z_{oil}) \tag{6}$$

This theoretical separation is not feasible in reality, as the mechanical separation of the oil and liquid refrigerant is impossible to carry out. Nevertheless, this assumption should have a negative impact on the heat pump performance, as the oil compression work is taken into account in the compressor power. However, lower heat exchange coefficients could counterbalance this effect if the oil was circulated inside the cycle. In every simulation run, a OCR of 5% has been considered.

- The second model limitation comes from the compressor model simulated range that goes out of its testing range. In particular, the inlet pressure testing range lies in [0.8 - 2.3] bar, and the model inlet pressure goes down to 0.7 bar. This low pressure is necessary as the refrigerant used has a boiling point of 17 °C and the water of the heat source has a temperature of 15 °C. Thus, it is impossible to know if the compressor performance is well predicted or not. Nevertheless, the inlet pressure usually does not have a strong influence on the compressor isentropic and volumetric efficiencies.

  The two aforementionned reasons justify the need for a model instead of interpolations of experimental data for the compressor mass flow rate and power predictions.

- The last limitation is the fact that the model is using fixed-design components. For performance comparison, it is not always accurate to compare different conditions with the same designs, as, sometimes, the results are design-dependent. This is why the heat exchanger have been oversized, as the techno-economic aspect is not investigated in this paper. Moreover, the data to fit the compressor model comes from the testing of a commercial compressor, which has not been specifically designed for two-phase flows.

3. Heat pump performance analysis

3.1. Exergetic analysis

As stated by the second law of thermodynamics, the performance of a heat pump are limited by the efficiency of the reverse Carnot cycle. The performance gap between the ideal heat pump cycle and the real cycle can be evaluated using an exergy analysis, where the heat pump irreversibility creation can be assessed analytically. Exergy can be defined as the maximum work recoverable from a process with regards to a reference temperature and pressure. For reversible processes, the exergy is conserved, while when irreversibilites occur, a part of the exergy is destroyed. The exergy analysis allows to evaluate irreversibility losses in each component in the heat pump, the best performance of the heat pump will therefore correspond to the minimal total exergy destruction. The exergy of a point in the cycle can be seen as a thermodynamic property, defined as:

$$e = (h - h_0) - T_0(s - s_0) \tag{7}$$

where h_0, T_0 and s_0 are respectively the reference values of enthalpy, temperature and entropy. Similarly to the heat pump exergetic analysis performed in [4], the exergy destruction rate in each component of the cycle can be evaluated using the following equations:

$$\dot{E}_{D,cp} = \dot{W}_{cp} - \dot{m}\left[(h_{ex,cp} - h_{su,cp}) - T_0(s_{ex,cp} - s_{su,cp})\right] \tag{8}$$

$$\dot{E}_{D,cd} = \dot{m}\left[(h_{su,cd} - h_{ex,cd}) - T_0(s_{su,cd} - s_{ex,cd})\right] - \dot{Q}_{cd}\left(1 - \frac{T_0}{\overline{T}_{w,cd}}\right) \tag{9}$$

$$\dot{E}_{D,valve} = \dot{m}\left[-T_0(s_{su,valve} - s_{ex,valve})\right] \tag{10}$$

$$\dot{E}_{D,ev} = \dot{Q}_{ev}\left(1 - \frac{T_0}{\overline{T}_{w,ev}}\right) - \dot{m}[(h_{ex,ev} - h_{su,ev}) - T_0(s_{ex,ev} - s_{su,ev})] \tag{11}$$

where the temperatures of the heat sink $\overline{T}_{w,cd}$ and the heat source $\overline{T}_{w,ev}$ are calculated using a logarithmic mean (isentropic mean), with:

$$\overline{T}_{source} = \frac{T_{w,su} - T_{w,ex}}{\ln\left(\frac{T_{w,su}}{T_{w,ex}}\right)} \tag{12}$$

As already stated in the previous section, the irreversibility creation in the compressor mainly comes from the heat transfer and the pressure losses. Moreover, the mechanisms in contact, such as the scroll and the bearings, creates friction which is also a source of irreversibility. The tendency observed is a drop in isentropic efficiency, i.e. an increase of irreversibility creation when decreasing the inlet quality.

Regarding the heat exchangers, the irreversibility creation primarily comes from the temperature difference standing between the working fluid and the secondary fluid. Pressure losses can also create irreversibilities

in the heat exchangers, however, they have not been taken into account in the present analysis. By going from a superheated state to a two-phase state down to a low vapor quality at the compressor inlet, the outlet quality of the compressor is also going to decrease, allowing to better match the temperature profile of the heat sink, which reduces exergy destruction. The objective of the analysis is therefore to optimize the system with regards to the inlet quality of the compressor to minimize the total exergy destruction.

3.2. Results

As already stated, the studied model is a water-water heat pump model. To match the profile of the subcooling at the end of the condenser, the condenser supply water temperature is the same as the heat source temperature, i.e., 15 °C, and the exhaust available water temperature is 50 °C, resulting in a temperature lift of 35 K. The condenser thermal capacity, input of the model, is varied in order to investigate the influence of the design (compressor, heat exchanger) on the heat pump performance. Varying the nominal point by keeping the same design is actually equivalent to a variation of design for a constant nominal point. As a reminder, the inlet quality of the compressor is varying and the model adapts the evaporation pressure and the compressor speed, directly impacting the working fluid flow rate, to keep a constant water exhaust temperature and condenser capacity. The evaporator water mass flow rate has been fixed to 0.3 kg/s to avoid evaporator exergy destruction and to focus the analysis on the compressor-condenser exergy destruction trade-off.

The evolution of the COP with the compressor inlet condition can be found in Fig. 10. The corresponding compressor speeds and pressure ratios (the evaporation pressure being an output of the model) can be found in Fig. 11. The COP evolution tendency is clear, the maximum of the COP stands near the saturated vapor point. Furthermore, for a high condenser capacity, the performance seems to follow a plateau between an inlet quality of 0.6 and 1, on the contrary to a low condenser heat transfer rate where the COP sees a consequent drop at low qualities. For a high condenser capacity, the speed of the compressor is higher, which increases its isentropic efficiency at low qualites. Regarding the evolution of the pressure ratio, it seems that higher pressure ratios are needed when having a superheated inlet state, simply because the water supply temperature is fixed and must be higher than the compressor inlet temperature.

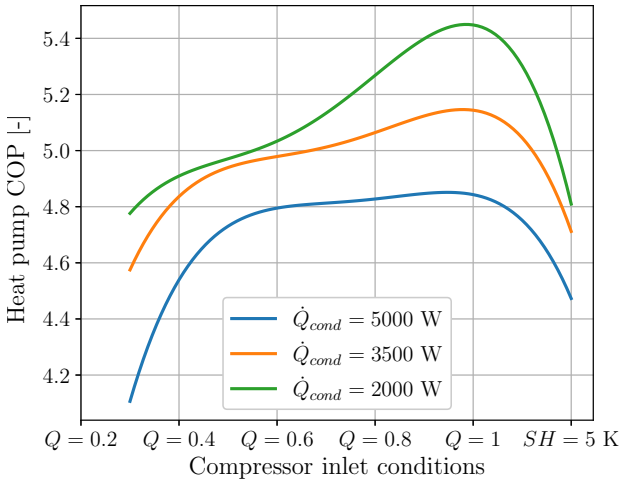

Figure 10: Heat pump COP for a varying compressor inlet condition for three different condenser powers.

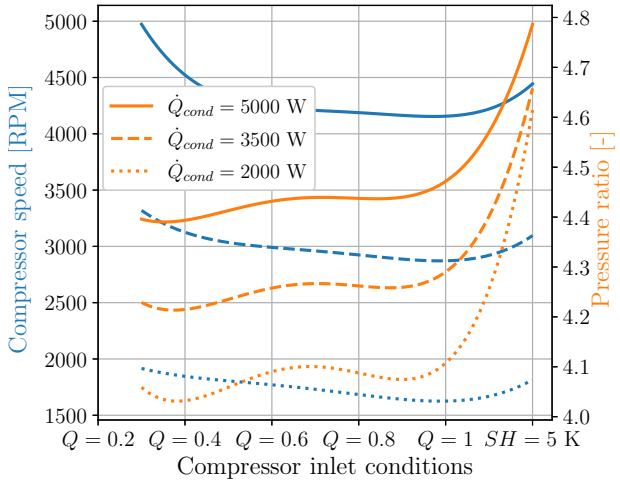

Figure 11: Compressor speed and pressure ratio for a varying compressor inlet condition.

The exergy destruction rate of each component for a 5000 W and a 2000 W condenser capacity can respectively be found in Fig. 12 and 13. In both cases, the exergy destruction of the evaporator and the valve are negligible, and the trade-off is well focused on the compressor and the condenser. When starting from a low vapor quality, the compressor exergy destruction rate is the highest, and it reaches a maximum at a vapor quality of 1 to eventually re-increase due to the increase of pressure ratios for superheated inlet states. Regarding the condenser curve, it is clearly lower for low vapor qualities, due to the better match with the condenser water curve, and increases when increasing the vapor qualities. The total exergy destruction is perfectly matching the tendency of the COP in Fig. 10, the COP maximum corresponds to the total exergy destruction minimum. Furthermore, Figs. 14 and 15 show the evolutions of the water temperature inside the condenser and the evaporator, respectively for a 0.3 quality and a 5K superheated inlet point. The temperature difference inside the evaporator can clearly justify the low exergy destruction rate in this heat exchanger. The same conclusion can be drawn on the condenser, where the exergy destruction rate is lower for the low quality compressor inlet condition due to the proximity between the temperature curves.

Finally, it seems that for both condenser capacities, the compressor exergy destruction rate variations with the

inlet conditions will always remain higher than the condenser exergy destruction rate variations. Therefore, the total exergy destruction rate tendancy is following the shape of the compressor exergy destruction rate. The present analysis is therefore very sensitive to the compressor performance. Hence, the compressor design has a strong influence on the results, and the current commercial compressor may not be the best candidate to be used with two-phase refrigerant flow. A compressor with a higher built-in volume ratio could better fit for the presented model as its performance would be better for higher pressure ratios. It should also be noted that reducing the water condenser outlet temperature could reduce the pressure ratio and enhance the heat pump performance.

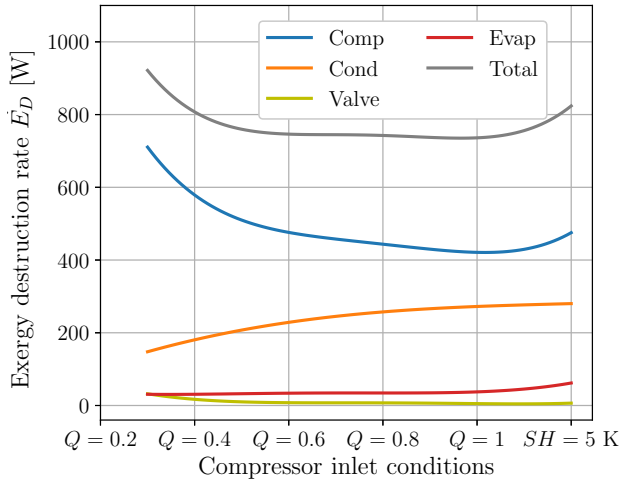

Figure 12: Exergy destruction rate of each heat pump component for a condenser power of 5000 W.

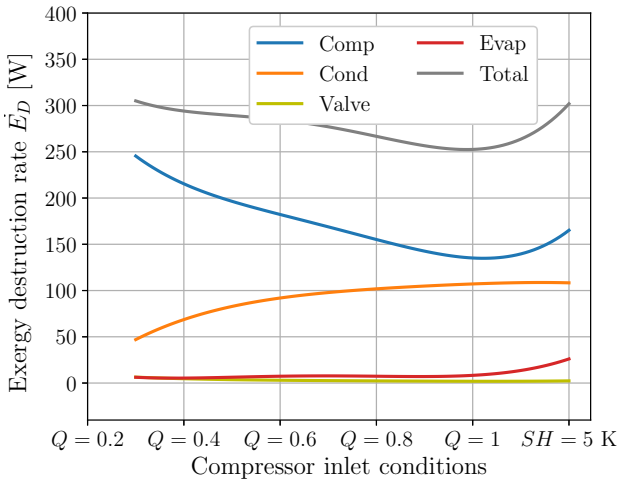

Figure 13: Exergy destruction rate of each heat pump component for a condenser power of 2000 W.

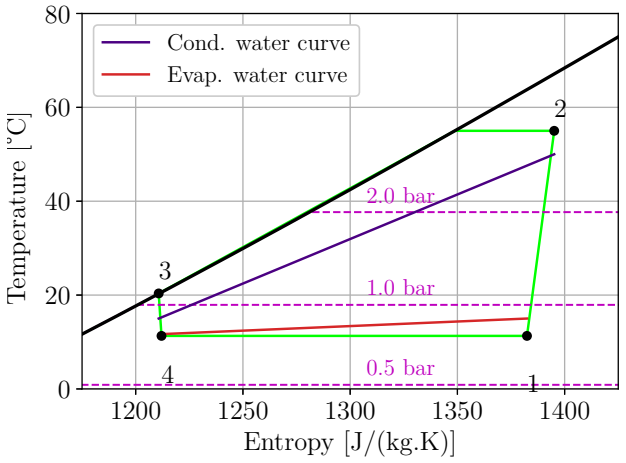

Figure 14: Temperature-entropy diagram of the heat pump with a condenser power of 5000 W and a compressor inlet quality of 0.3.

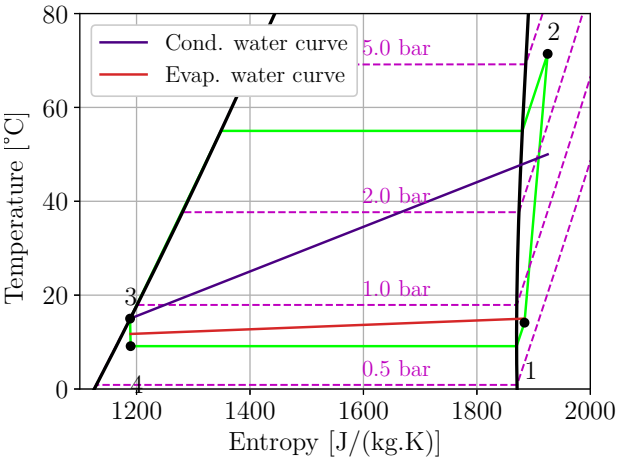

Figure 15: Temperature-entropy diagram of the heat pump with a condenser power of 5000 W and a compressor inlet superheat of 5 K.

4. Conclusions

The current study presents an investigation on a fixed-design water-water high temperature lift heat pump making use of two-phase compression. The objectives of the investigation is the heat pump performance assessment under varying compressor inlet conditions with two-phase refrigerant vapor qualitites as low as 0.3, up vapor with 5 K of superheat. To that end, the heat pump system has been described by coupling a validated scroll compressor semi-empirical model with moving boundaries heat exchanger models.

The model predicts good system efficiency. The performances of the heat pump at different operating conditions are governed by a trade-off between heat exchange and compressor irreversibilities. On one hand, when a low inlet vapor quality is used, the condenser temperature profiles of both fluid (refrigerant R1233zd(E) and water) are getting closer, reducing the irreversibilities. On the other hand, the compressor irreversibility

creation is increased when decreasing the inlet quality.

The heat pump model has been tested with a temperature lift of 35 K, from a water condenser inlet temperature of 15 °C to 50 °C and condenser capacities from 2 kW to 5 kW. The results have shown a maximum in the COP curve around a compressor inlet quality of 1. The compressor being the most important source of exergy desctruction, the trade-off could not find better performance at low inlet qualities because the exergy destruction rate of the compressor is too high. Finally, it is important to highlight that the results are very design-sensitive, and the use of a more optimized compressor for two-phase refrigerant flows could enhance the performance of the heat pump and the trade-off could find a lower optimal inlet quality. This potential scenario is the object of future research, as another compressor, specifically designed for two-phase flows with a higher built-in volume ratio is going to be experimentally tested. The integration of the new two-phase compressor performance will allow to see if the trade-off conclusion can be changed.

Aknowledgement

The project source of the results presented in this paper has received funding from the European Union's Horizon 2020 research and innovation programme under grant agreement N° 851541.

Nomenclature

Letter symbols

$\dot{Q}$	heat transfer rate, W
Q	vapor quality, –
SH	superheat, K
T	temperature, °C
$\dot{m}$	mass flow rate, kg/s
P	pressure, Pa
$\dot{W}$	power, W
COP	coefficient of performance, –
$\dot{C}$	heat capacity rate, W/K
N	rotation speed, RPM
$\dot{E}$	exergy transfer rate, W
V	volume, m^3
h	enthalpy, J/kg
s	entropy, J/(kgK)
e	exergy, J/kg
AU	heat transfer coefficient, W/K
OCR	oil circulation ratio, –

Greek symbols

ε	efficiency
ρ	density

Subscripts and superscripts

cd	condenser
ev	evaporator
cp	compressor
w	water
su	supply
ex	exhaust
v	volumetric
s	isentropic
tot	total
mix	mixture
$disp$	displacement
V	constant volume
ref	reference
amb	ambient
r	refrigerant
vap	vapor
liq	liquid
o	oil
D	destruction
σ	saturation

References

[1] Bell, I. H., Lemort, V., Groll, E. A., Braun, J. E., King, G. B., and Horton, W. T. Liquid-flooded compression and expansion in scroll machines - part i: Model development. *International Journal of Refrigeration 35* (11 2012), 1878–1889.

[2] Bell, I. H., Quoilin, S., Georges, E., Braun, J. E., Groll, E. A., Horton, W. T., and Lemort, V. A generalized moving-boundary algorithm to predict the heat transfer rate of counterflow heat exchangers for any phase configuration. *Applied Thermal Engineering 79* (3 2015), 192–201.

[3] Briola, S., Gabbrielli, R., Baccioli, A., Fino, A., and Bischi, A. Thermo-economic analysis of a novel trigeneration cycle enabled by two-phase machines. *Energy 227* (7 2021).

[4] Byrne, P., and Ghoubali, R. Exergy analysis of heat pumps for simultaneous heating and cooling. *Applied Thermal Engineering 149* (2 2019), 414–424.

[5] Dickes, R. Charge-sensitive methods for the off-design performance characterization of organic rankine cycle (orc) power systems, 2019.

[6] Leclercq, N., and Lemort, V. Modeling and simulation of a two-phase scroll compressor. International Compressor Engineering Conference 2022.

[7] Lemort, V., Quoilin, S., Cuevas, C., and Lebrun, J. Testing and modeling a scroll expander integrated into an organic rankine cycle. *Applied Thermal Engineering 29* (10 2009), 3094–3102.

[8] Nikolov, A., and Brümmer, A. Analysis of indicator diagrams of a water injected twin-shaft screw-type expander. International Compressor Engineering Conference.

[9] Smith, I., Stosic, N., and Aldis, C. Trilatekal flash cycle system a high efficiency power plant for liquid resources. Proceedings World Geothermal Congress 1995.

[10] Vorster, P., and Meyer, J. Wet compression versus dry compression in heat pumps working with pure refrigerants or non-azeotropic binary mixtures for different heating applications. *International Journal of Refrigeration 23* (6 2000), 292–311.

[11] Youbi-Idrissi, M., and Bonjour, J. The effect of oil in refrigeration: Current research issues and critical review of thermodynamic aspects, 3 2008.

The impact of controller settings in heat pumps: Numerical findings and experimental verification

Stephan Göbel[a], Kevin Waiz[a], Christian Vering[a] and Dirk Müller[a]

[a] RWTH Aachen University, Institute for Energy Efficient Buildings and Indoor Climate, Aachen, Germany, stephan.goebel@eonerc.rwth-aachen.de

Abstract:

In residential buildings, the efficiency of heat pump systems (HPS) significantly depends on the HPS design and operation. In particular, HPS controllers often use ambient temperature-dependent heating curves for operation. The resulting supply temperature serves as the reference variable for the internal controller, which is used to manipulate the compressor speed. Typically, the internal controller has constant parameters for the PI controller, hysteresis, and operational time. While buildings have a highly dynamic, time-variant demand, these dynamics are rarely considered in controller development.

This work investigates internal control parameters' sensitivity to the overall HPS efficiency in annual, dynamic simulations and experiments. To consider different supply temperatures, two buildings with underfloor heating and radiators serve as case studies. Based on a validated simulation model, the one-factor-at-a-time sensitivity analysis method determines the controller's influence on the seasonal coefficient of performance (SCOP). Hardware-in-the-loop experiments are conducted for representative periods extracted from annual simulation results for experimental verification.

The results for the building with underfloor heating and radiators prove that the control parameter influences the SCOP up to 18.5 % and 4.2 %, respectively. In particular, different control parameters for the optimal operation were determined for both case studies, challenging the constant settings used in the state-of-the-art. In addition, we observe a significant increase of 300 % in the avoidable compressor starts in experiments due to poor parameter settings. To ensure maximum efficiency of HPS and significantly reduce the number of compressor starts in any residential building, we recommend integrating adaptive setting of control parameters into the HPS controller.

Keywords:

Sensitivity analysis, hardware-in-the-loop, heating curve, Modelica, inverter-driven, PID, hysteresis.

1. Introduction

Electrically-driven heat pump systems (HPS) are the most efficient solution for the defossilation of the building sector. Since emissions are mainly related to electricity consumption [1], HPS efficiency greatly impacts consumption reduction and thus on emissions.

Besides the refrigerant cycle design which is tailored to operate under dedicated temperature levels (design condition), the HPS controller influences the efficiency in off-design conditions. The controller aims to set the HPS thermal output to the building's heat demand by adjusting the compressor speed. Typically, the control loop begins with a weather compensation heating curve calculating the required supply temperature to reach the heating demand (part I). While On-Off HPS uses a hysteresis controller, inverter-driven HPS also uses a PID controller to realize the link between the set supply temperature and the compressor speed (part II).

Thermodynamic Carnot efficiency strongly depends on the source and supply temperature spread. Aiming for an efficient part I control loop means decreasing the supply temperature as low as possible with a well-designed heating curve or higher control strategies, e.g., model predictive control (MPC). The literature provides different solutions for the part I control loop [2]–[4]. This work focuses on part II of the control loop and uses a heating curve that fits the building load for each case study.

Part II of the control loop translates the set supply temperature value into a compressor speed. This part of the control loop is an internal variable to avoid compressor damage. To the best of the author's knowledge, the literature only provides a few studies about the influence of the part II control loop on the heat pump's efficiency. Uhlmann et al. [5] show in experimental and simulative studies that the loss of efficiency caused by the startup and shutdown processes is less than 2% if a continuous minimum running time of 15 minutes can be ensured. A related study [2] suggests that a compressor running time of at least 20 minutes is required to avoid degradation effects or startup losses. The study shows that the unit control and the system's thermal inertia strongly influence the heat pump's energy losses. Thus, the configuration of the hysteresis control strongly

influences the cycling behavior. Dongellini et al. [6] simulate the dynamic performance of three types of heat pumps (single-stage, multi-stage, and inverter-controlled). The results indicate that the efficiency losses during the heat pump startup process significantly impact the overall system efficiency, especially for single-stage units. In this case, the reduction in SCOP is up to 12%. Xu et al. [7] study focuses on inverter-controlled heat pumps, in particular, the hysteresis parameter of the control. In order to improve the dynamic performance under frequent partial load conditions, a control concept with variable hysteresis of the supply temperature was proposed, in which the lower threshold value increases piecewise with increasing outside air temperature. All the studies mentioned use the manufacturer's inverter control settings, i.e., the PID controller parameters remain unchanged. However, to the best of the author's knowledge, the sensitivity of PID parameters on the efficiency of inverter-controlled heat pumps is not discussed in the literature. Furthermore, the influence of the heat pump's operational behavior is only discussed in the context of efficiency but not on the degradation.

This paper closes the identified research gaps in a simulative and experimental case study:

- To access all parameters of the heat pump's control loop, we conduct measurement campaigns with a fully-controllable heat pump test bench [8].
- To integrate degradation into the evaluation process, we use the number of startups per hour as a key performance indicator (KPI).
- To prove the sensitivity of PID controller parameters, we develop a heat pump controller, which we use in a simulative and experimental case study.
- To verify our simulative results, we use the hardware-in-the-loop approach by coupling a heat pump test bench to a developed heat pump controller and a virtual building.

The paper is divided into five sections:

- Section 2 shows the simulative and experimental setup.
- Section 3 describes the results of the case studies.
- Section 4 discusses the results by underlining the influence of the control loop part II on the efficiency
- Section 5 concludes all findings and gives recommendations for future work.

2. Method

To investigate the sensitivity of the PID controller's parameters and the hysteresis bandwidth to the heat pump process, we develop a simulation model that comprehensively analyzes and evaluates the part II control concept. Subsequently, we use sections of the recorded measurement data in an experimental setup to verify the obtained results on a real heat pump. This section starts with an overview of the simulation models, followed by the experimental setup description, and ends with the introduction of the simulative and experimental case study.

2.1 Building Energy System Simulation

For the adequate execution of a parameter study, we develop a simulation model that computes the conditions of the system in a meaningful way and outputs system variables in a comprehensible and plausible manner. For this purpose, the simulation model of the building energy system (BES), which forms the basis for the parameter study, is presented in Figure 1, including the associated submodels. We develop the BES in Modelica using the Dymola [9] environment. The individual models are generally based on the *BESMod* library [10]. The library draws on *AixLib* [11], *BuildingSystems* [12] and *IBPSA* (basic library of the previous archives) [13].

Figure 1 shows the BES model, which consists of the submodels weather, user, transfer, building, control, generation, and distribution. The latter three together form the sub-model of hydraulics. The weather submodel is based on meteorological data recorded and published by the German Weather Service (DWD) at hourly intervals for a specific region within Germany during a representative year [14]. Concerning an appropriate computational time compared to the effort, we use a reduced building model as a heat sink. We reparametrize the basic model using the TeaserTool [15]. It allows building construction based on information about the net area, number, and height of floors, year of construction, and intended use of the building. The heating load calculated according to EN 12831 is 6596.21 W, and the volume of the heating zone is 325.0 m^3 with a net area of 130.0 m^2.

On the user side, we assume constant behavior to avoid the superposition of effects. For the same reason, we also neglect any internal gains. Therefore, the room's setpoint temperature is constant at 20 °C for each room, regardless of the time of year or day. We consider two systems for the hydraulic heating network within the scope of the analysis. Thermal energy distribution and transfer are accomplished by underfloor heating (UFH) or a radiator. We adopt the models from the *BESMod* library for this purpose. Both models have a throttle and a bypass valve, the latter to decouple the hydraulic cycle and thus protect the system from a sharp rise in the heating water pressure.

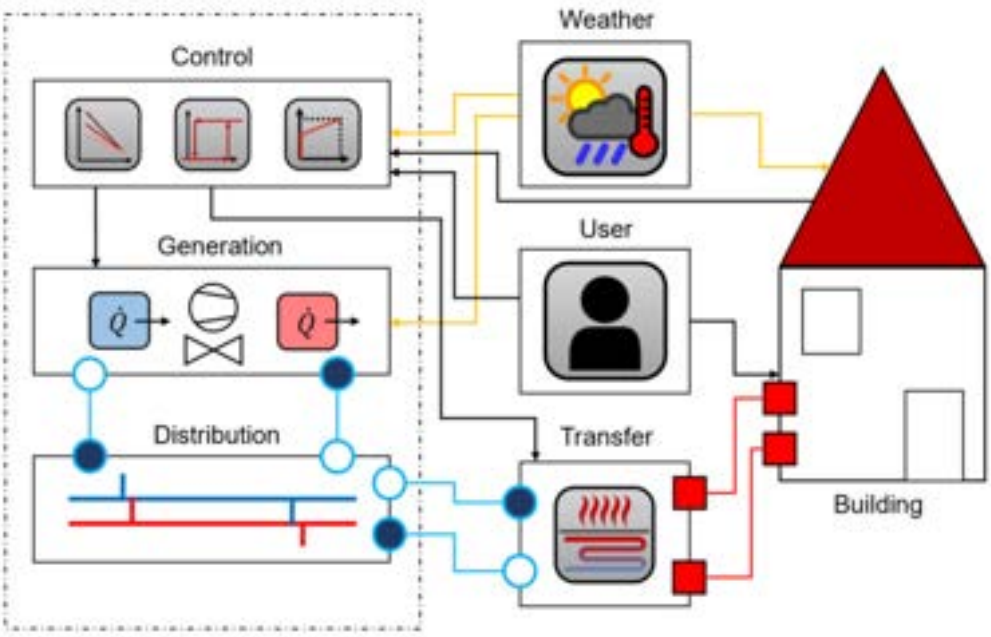

Figure 1: Simulation structure of the building energy system - With fluid flows in blue, heat flows in red, weather data in yellow and data transfer in black as connecting elements [10].

We have mapped the adapted control of the system in the *MonovalentOptihorst* model. In addition to the hysteresis-based heating curve controller, it also contains the integration of safety functions. With the help of the room temperature set by the user $T_{set,Room}$, and the current outdoor temperature T_{amb}, the heating curve specifies the required supply temperature T_{set}. The downstream hysteresis controller uses the difference between T_{set} and T_{sup} and determines whether the heat pump sets its operating mode to On or Off. If the supply temperature exceeds the set temperature by half of the set bandwidth of the hysteresis, the heat pump is switched off until it reaches the lower limit (T_{set} - $Hys/2$). This on/off-signal and T_{set} are then used via the PI controller to set the compressor speed n_{set} is output. The *SecurityControl* [16] model of *AixLib* then checks compliance with the safety functions and operating limits. In addition to the minimum runtime and resting time, these also include the maximum number of start operations per hour. Triggering the safety functions causes the heat pump to shut down or to continue running, depending on which safety function takes effect. For example, compliance with the minimum running time requires the machine to continue running to prevent damage, even though a signal from the PI control wants to switch it off.

The simulation model of the heat pump corresponds to the *HeatPumpAndHeatingRod* model of *BESMod.* We use a black-box model, which specifies the required electrical power P_{el} and the resulting heating power $\dot{Q}_{\mathrm{Con}}$ as a function of the supply temperature, the inlet temperature of the evaporator, and the compressor speed. When the compressor is switched on, it immediately requires electrical power. The problem of the missing dynamics of the model in relation to the provision of the heat is mitigated by the interposition of a PT3 element. Through the PT3 element, we can implement an artificial inertia, resulting in a delay of the effective heat flow analogously to the real system. The duration of the delay can be determined by the setting of a constant parameter, which corresponds to a cut-off frequency. [16]

To integrate the established model's dynamic processes within the heat exchangers and the mentioned cut-off frequency, we conduct experimental tests on a real heat pump to calibrate the model with the measured data. We calibrate the adjusted heat pump model using the fully-controllable heat pump test bench, which is also used in the experimental case study. Basically, calibration refers to the variation of model parameters so that the difference between simulated and measured values is as small as possible. Therefore, we use parameters of the condenser, such as the heat transfer coefficients or the condenser volume, and the cut-off frequency to match simulated and measured values. The program AixCaliBuHA [17] is used to calibrate the system. It allows the automatic calibration of dynamic buildings and heating systems using the Python-Dymola interface.

The different operating conditions associated with the inverter technology, as a result of the variably adjustable compressor speed, necessitate the inclusion of dynamic factors in the calibration. For example, several different temperatures are set for the source and sink in succession during the temperatures are set for the source and sink to compensate for the resulting transient and departure processes. For the calibration process, we record the temperatures T_{amb}, T_{sup} and T_{ret}, the mass flow in the condenser, the electrical power of the compressor P_{el} as well as the speed of the compressor. Here, P_{el} and T_{sup} correspond to the target variables of the calibration. The four remaining quantities are used as real input for the simulation. The temporal

resolution of the data intervals is one second, and the period of consideration is 8800 s. As a basis for evaluation, we use a normalized weighted error measure (NRMSE), which gives equal and scale-independent weight to both target variables.

The corresponding curves of the simulated and measured quantities for the minimum NRMSE are visualized in Figure 2. It can be seen that especially the supply temperature is sufficiently modeled. Quantitatively, this can also be confirmed with an NRMSE of less than one percent. The higher NRMSE for the electrical power of 2.37% is due to inaccuracies between 8000 - 8800 s. The noticeably broader curve section of the magnitude in this interval can be derived from perceived speed oscillations while recording the experimental measurement data. Overall, we achieve a final NRMSE of 1.658%. This can be considered a positive result; other works obtained results in a comparable range [16], [18].

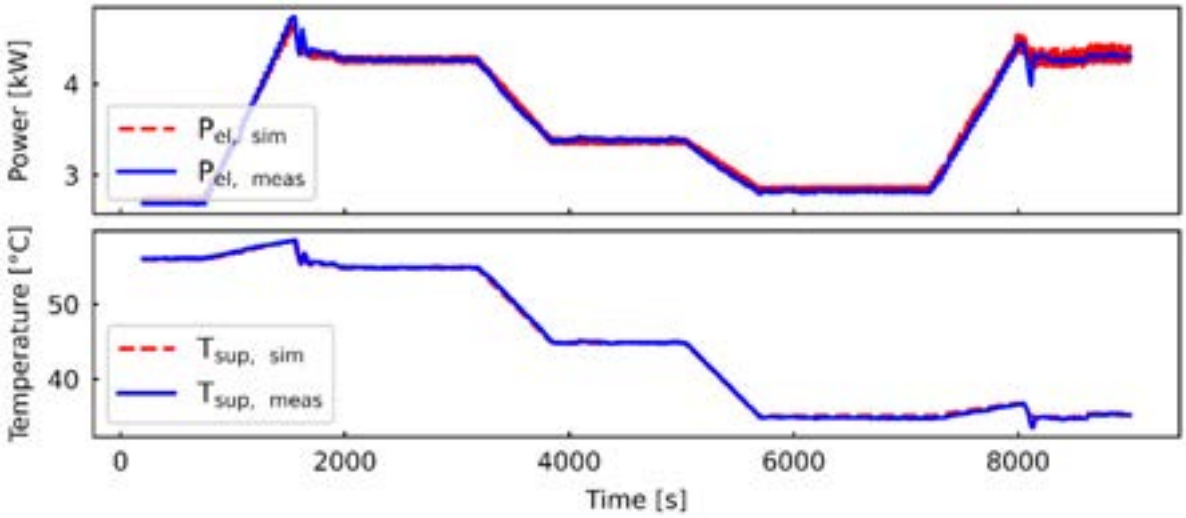

Figure 2: Visualization of the measured target variables $P_{el,meas}$, $T_{sup,meas}$ and the corresponding simulation variables $P_{el,sim}$, $T_{sup,sim}$.

2.2 Experimental setup

We validate all our findings in this work with experiments using the hardware-in-the-loop (HiL) approach and a fully-controllable heat pump test bench. The HiL approach connects virtual buildings to the heat pump by emulating the weather conditions and the thermal heat flows. Figure 3 shows the schematic overview of the experimental setup. The system consists of an air-to-water heat pump test bench in split design, which is fully controllable, test benches emulating the boundary conditions (climatic chamber and hydraulic test bench), simulation models for the building and the heat pump controller, and the cloud-based data infrastructure (MQTT-Broker and InfluxDB tick-stack). The used HiL approach and the corresponding test benches are well described in the literature [19], [20]. In this study, we use a self-developed heat pump test bench where we can freely control the compressor speed. The heat pump test bench has its own PLC, which gets the current set compressor speed via MQTT. Only necessary safety controllers (e.g., superheat) are part of the heat pump test bench. Further details about the test bench and its internal control can be found in the literature [8].

With the help of our method, it is possible to change between a pure simulation model and a HiL experiment without significant effort. Only the submodels of heat generation and distribution are swapped to communication models. Measured values (e.g., supply temperature) are subscribed from the test bench, and relevant values for the heat pump (e.g., return temperature) are published to the test bench.

We develop and calibrate our building energy system simulation models with the experimental setup to perform verified annual simulations and experimental results.

2.3 Annual and daily simulative case study

We use the one-factor-at-a-time (OFAT) method [21] for the annual and daily horizons parameter study. Here a single parameter is varied while the remaining ones assume constant reference values. The advantage of the OFAT method is that overlaps and synergies can be excluded by varying a single parameter. Thus we can relate system changes to modifying the input variable.

In the preliminary state of the parameter study, the framework conditions of the analysis must be defined. Table 1 shows the value ranges of the control parameters, the reference values, the safety functions' values, and the other models' relevant values. The control parameters consist of the proportionality factor K_P, the integral time T_N and the hysteresis bandwidth *Hys*. In the annual simulation studies, the proportionality factor K_P and the integral time T_N varies from 0.00001 to 20 and from 10 s to 50000 s, respectively, on a logarithmic

scale. We set the corresponding reference values to 0.5 and to 1000 s. Performing the OFAT method with the chosen parameter variation results in 42 simulations for each system. Thus, we perform a total of 82 annual simulations.

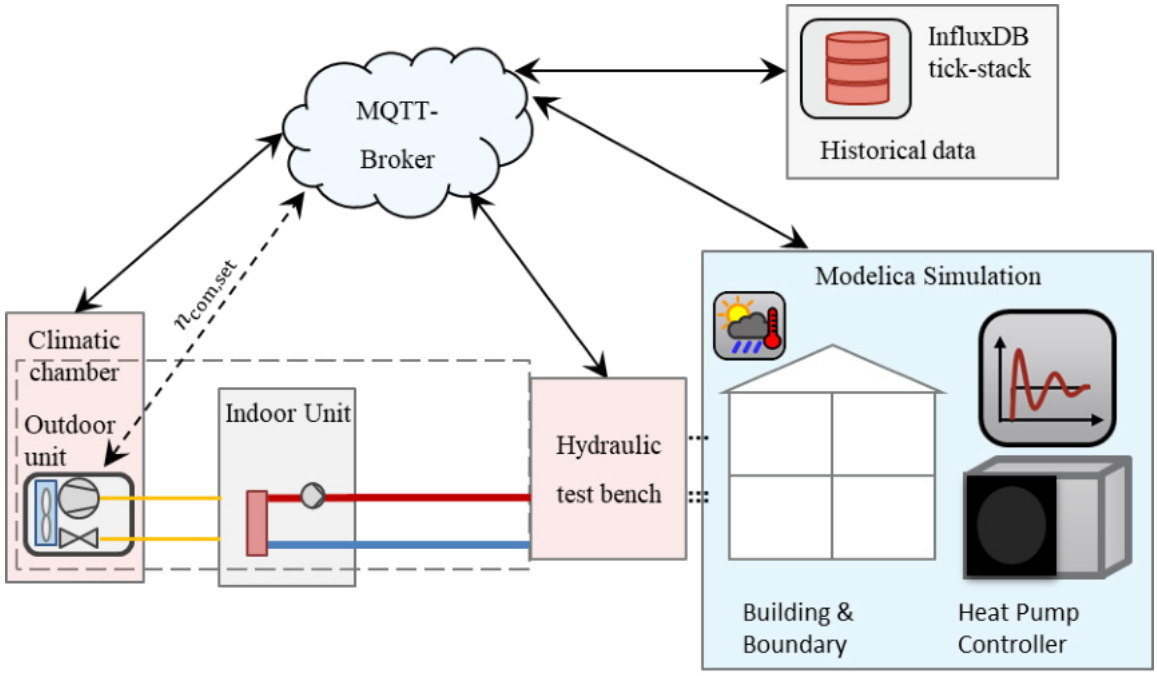

Figure 3: Schematic overview of HiL setup: heat pump test bench (indoor unit and outdoor unit), climatic chamber, hydraulic test bench, simulation model, InfluxDB tick-stack, and MQTT Broker

The safety parameters allow the heat pump to run a maximum of 10 times per hour for a minimum running time of 180 s. The resting time after shutdown has to be a minimum of 180 s. In addition, the maximum supply temperature is set to 70 °C. The presented simulation model with the underfloor system has a nominal supply temperature of 40 °C and a nominal mass flow of 0.315 kg/s. The system with radiators uses a nominal supply temperature of 55 °C with a nominal mass flow of 0.197 kg/s.

A detailed look into the operation behavior is realized with representative days. Thus, the interaction of the outdoor temperature and the solar irradiation with the variation of the control parameters can be considered in a bundled way. The outdoor temperatures of the three used representative days can be seen in Figure 4. The days correspond to representative periods calculated using the k-medoids clustering [22] and cover three different temperature levels.

Table 1: Value ranges, step sizes, and reference values of the controlled variables, the safety functions, and operating variables of both transfer systems.

Control parameter	Min. value	Max. value	Step size	Reference value
Proportionality factor K_p	0.00001	20	Log	0.5
Integral time T_N	10 s	50000 s	Log	1000 s
Hysteresis bandwidth	1 K	12 K	1 K	8 K
Safety parameter	Value	Transfer parameter	Value	
Max. runs per hour	10	UFH - nominal supply temperature	40 °C	
Min. run time	180 s	UFH – mass flow	0.315 kg/s	
Min. rest time	180 s	Rad. - nominal supply temperature	55 °C	
Max. supply temperature	70 °C	Rad. – mass flow	0.197 kg/s	

2.4 Experimental case study

Test runs under real conditions are necessary to validate the results obtained. Since field tests in real buildings are costly and time-consuming, we perform HiL experiments to emulate almost field behavior.

We conduct three experiments for the underfloor and radiator system. We vary the hysteresis bandwidth for each system from a low level over the reference level to a high level. The goal of the experiments is to validate the method and underline that the developed controller leads to the same operation behavior for the simulation model and the heat pump test bench.

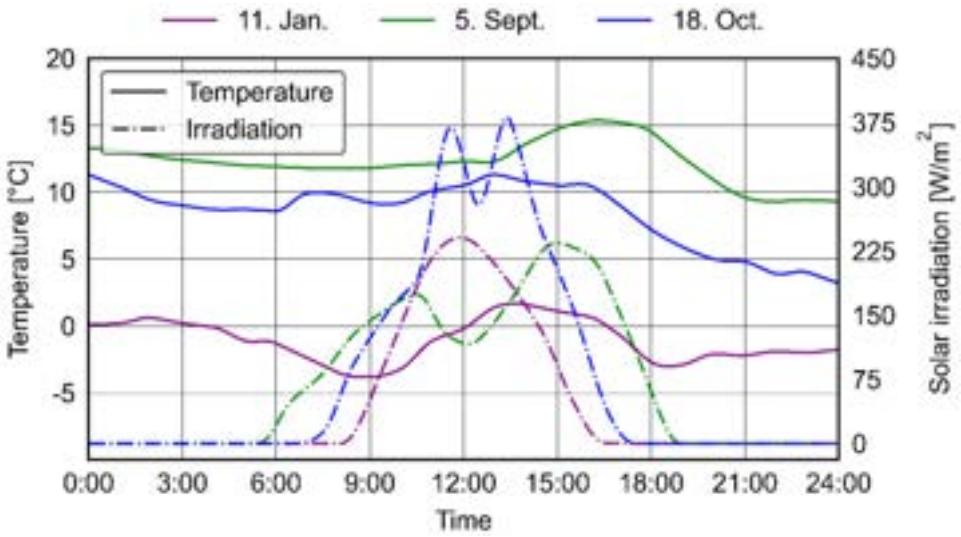

Figure 4: Outdoor temperature and solar irradiation for the reference days in Potsdam in 2015.

3. Results

This section starts with the sensitivity analysis results, which are mainly simulative performed and ends with the validation with the help of experimental results.

3.1 Simulative case study: sensitivity analysis

In order to visualize the effect of control parameters, it can be seen from Figure 5 to what extent different parameter values influence the number of daily on/off cycles. As shown in Figure 5 (a) for using a UFH, the number of cycles for a hysteresis bandwidth of 2 K below a temperature of 10 °C is increased in contrast to the use of a bandwidth of 10 K. Thereby, the number of cycles for a bandwidth of 2 K often reaches its maximum of 240 cycles per day. Notably, for a bandwidth of 10 K, the number of cycles initially increases at -5 °C before decreasing again from a temperature of 10 °C. A similar picture is also provided using K_p= 0.00001, shown in Figure 5 (b). Again, the daily cycles decrease for temperatures above 10 °C. Analogous to UFH, the radiator increases cycles for a decreased bandwidth. According to Figure 5 (c), we can identify a trend for the use of a bandwidth of 2 K and 10 K, according to which the number of cycles decreases with a rising outdoor temperature and the number of cycles increases with smaller hysteresis. Only using low proportionality factors ensures that the cycles decrease for outdoor temperatures below 5 °C, so the scatter plots of UFH and radiator show comparable results.

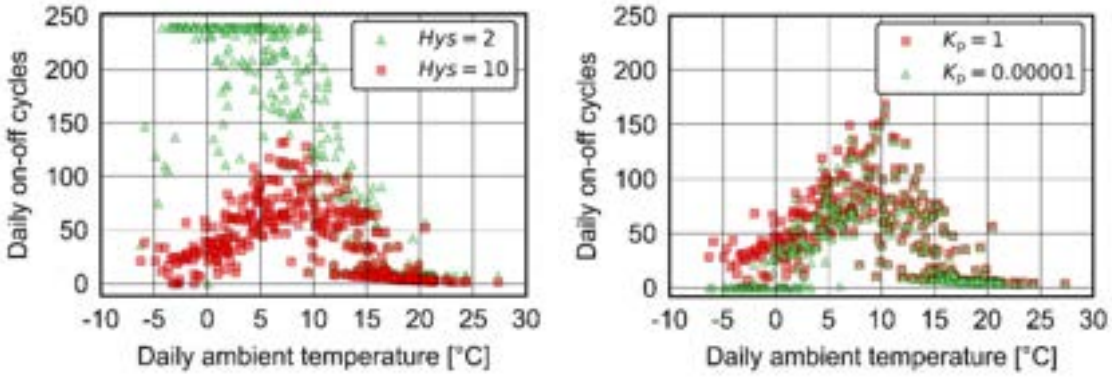

(a) UFH – Hysteresis

(b) UFH – Proportionality factor

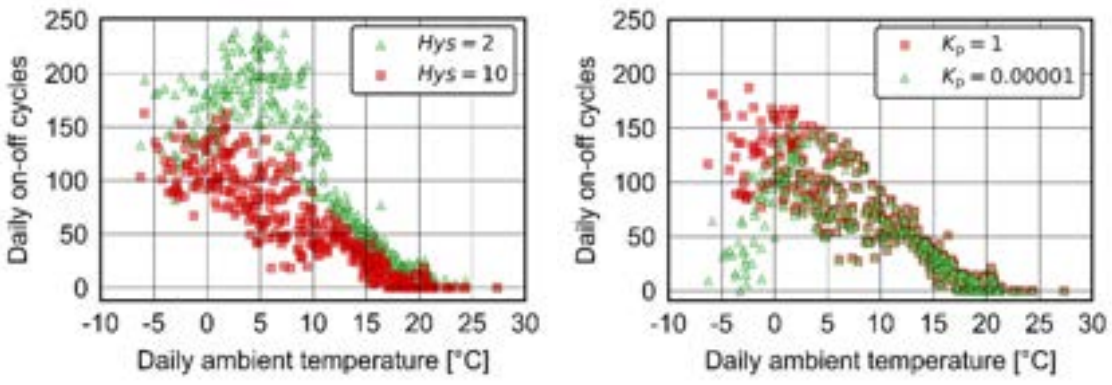

(c) Radiator – Hysteresis (d) Radiator – Proportionality factor

Figure 5: Representation of the annual simulation's daily on/off cycles when using UFH (a,b) or radiator (c,d) as a function of the ambient temperature.

Figure 6 (a,c) shows that the Kp and TN boundary values represent the SCOP's respective minima and maxima. The variation's optimum reset time is at T_N = 50,000, with a value of 3.2. Whereas an increase of K_p continuously decreases the system efficiency, we observe an efficiency drop for T_N = 50 - 150. The SCOP decreases to a value of up to 2.70, corresponding to a relative change concerning the maximum efficiency of 15.6 %. We detect that the efficiency initially increases with a rising hysteresis bandwidth before continuously decreasing from a value of three Kelvin (Figure 6 (e)). Here, a SCOP maximum of 3.25 (3 K) contrasts with a minimum of 3.14 (12 K). The relative change is 3.6 %.

For the radiator as a heat sink, analogous to using UFH, we notice that the boundary values for K_p and T_N represent the maxima and minima. Again, K_p = 0.00001 and T_N = 50,000 s correspond to the highest SCOP parameters (cf. Figure 6 (b,d)). Their use implies a SCOP of 2.60 and 2.58, with the resulting relative efficiency differences of 3% and 3.9%, respectively. For the integral time variation, a noticeable reduction of the SCOP to 2.48 is shown only for T_N = 10.

For the proportionality factor, we observe that its increase means an increase in the cycles by up to 25 %. The hysteresis bandwidth's variation yields a maximum SCOP of 2.58 for a bandwidth of 12 K. Despite an increasing number of cycles with decreasing bandwidth, we cannot detect a significant change in efficiency (cf. Figure 6 (f)). The number of cycles increases by almost 250 %, while the SCOP varies only within a range of 2 %.

An overview of the obtained results of the most efficient parameter values for the considered periods is given in Table 2. It contains the SCOP, the relative change of the SCOP from the minimum to the maximum value (ΔSCOP), and the number of cycles per control variable and period. The associated results for the variation of the proportionality factor for both transfer systems show that the maximum values are different not only for the representative days but also for the same day for different transfer systems. Except for a proportionality factor of 0.00001 for the annual simulation, none of the best values for a given reference day are the same. For example, a value of 0.0001 for the UFH is compared to 0.1 for the radiator on 10/18. We recognize that the number of cycles increases with the average day temperature for the UFH system. At the same time, the SCOP rises with an increasing temperature for both transfer systems to a maximum of 3.77 and 3.02, respectively.

It is noticeable that proportionality between the number of cycles and the efficiency can only be determined to a limited extent. For the variation of K_p and T_N when using a radiator, the increasing number of cycles from reference day 01/11 to 10/18 inevitably increases efficiency due to the higher temperature level. However, comparing the various results of the control variables for a given day shows that more cycles do not necessarily result in lower efficiency. For example, we observe that for the under-floor heating on 10/18, the SCOP maximum of the hysteresis with a value of 3.51 at 156 cycles is higher than the respective maximums of the other two control variables, although their cycle numbers are lower (107).

Considering the ΔSCOP according to Table 2, we notice that the variation of T_N causes a high deviation, equivalent to a high sensitivity. Thus, we observe a deviation of 46.3 % for reference day 01/11 when UFH is used. The hysteresis variation also shows a high value of 27.3 % compared to the deviation of the remaining variables.

The collected consideration of the results finally show that the integral time T_N has the most significant sensitivity overall. As a variation result, it causes a deviation of 18.5 % (UFH) and 4.2 % (Radiator) from the lowest to the highest SCOP within the annual simulation and also shows the largest percentage on average for the reference days. Only when the radiator is used the hysteresis causes a significantly higher sensitivity

of 18.2 % and 11.0 %, respectively, for reference days 10/18 and 05/09. The various proportionality factors result in a deviation for the UFH and the radiator of 7.4 % and 3.2 %, respectively. Hysteresis has the lowest influence in annual simulation, with a difference of 3.2 % and 1.7 %, respectively.

Table 2: SCOP, relative change of SCOP from minimum to maximum value (ΔSCOP) and absolute number of cycles for a parameter variation of Kp ,TN and the hysteresis bandwidth for reference days and an annual simulation (AS). Listed are the highest values determined based on SCOP.

Reference days/ Annual simulation	Underfloor heating				Radiator			
	11.01	18.10	05.09	AS	11.01	18.10	05.09	AS
K_p - Value	**0.00001**	**0.0001**	**0.05**	**0.00001**	**0.01**	**0.1**	**0.75**	**0.00001**
SCOP	3.14	3.44	3.77	3.32	2.27	2.95	3.02	2.60
ΔSCOP / %	8.40	7.10	5.00	7.40	9.10	5.40	5.60	3.20
Cycles per day	25	107	130	39	113	120	63	57
T_N - Value	**50000**	**35000**	**1500**	**50000**	**50000**	**20000**	**100**	**50000**
SCOP	3.00	3.44	3.78	3.30	2.26	2.95	3.03	2.58
ΔSCOP / %	46.30	14.30	8.10	18.50	9.70	8.40	8.60	4.20
Cycles per day	25	107	130	41.77	113	120	63	59.26
Hysteresis bandwidth	**5 K**	**4 K**	**9 K**	**3 K**	**12 K**	**12 K**	**11 K**	**12 K**
SCOP	2.93	3.51	3.80	3.25	2.24	3.05	3.12	2.59
ΔSCOP / %	27.30	4.50	5.80	3.20	3.20	18.20	11.00	1.70
Cycles per day	38	156	121	122.93	126	78	54	49.98

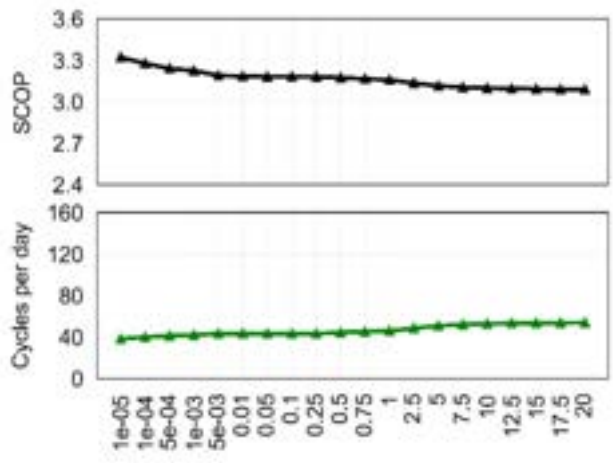

(a) UFH – Proportionality factor K_{p} [-]

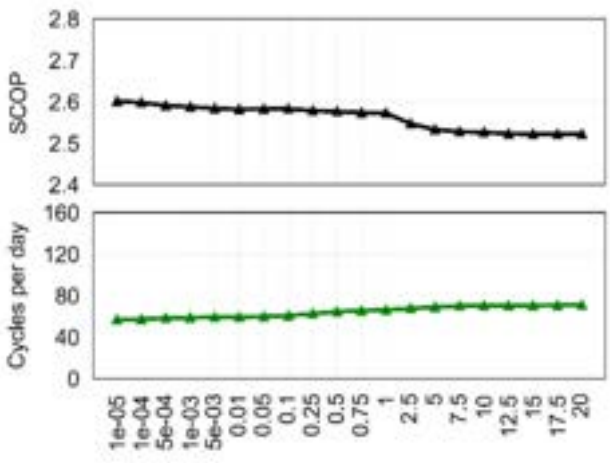

(b) Radiator – Proportionality factor K_{p} [-]

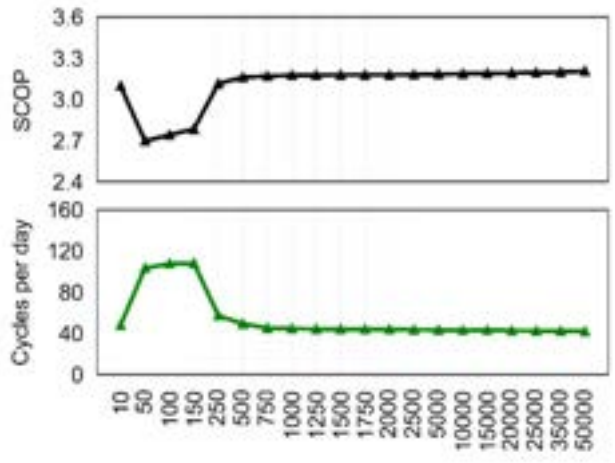

(c) UFH – Integral time T_{N} $[s]$

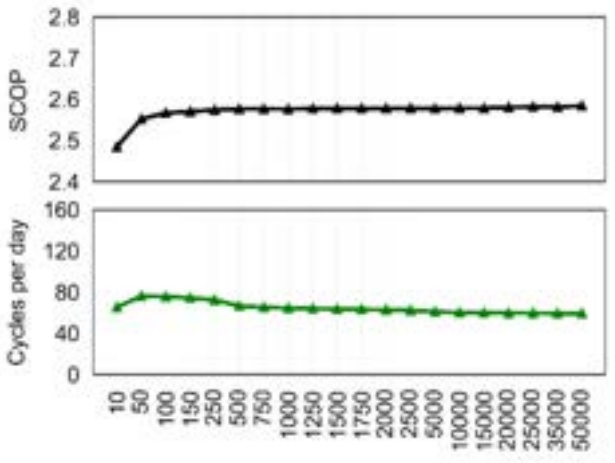

(d) Radiator – Integral time T_{N} $[s]$

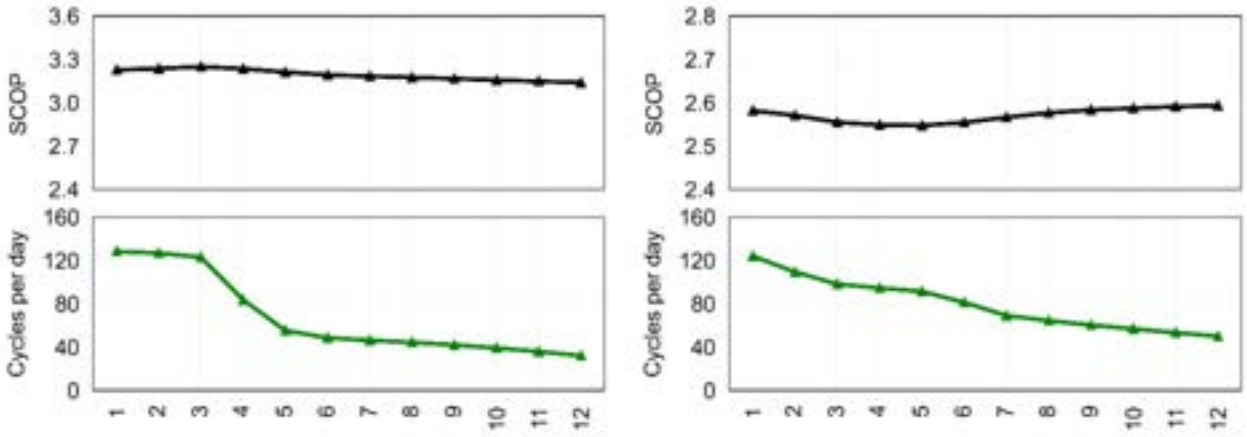

(e) UFH – Hysteresis

(f) Radiator – Hysteresis

Figure 6: Comparison of the SCOP and the cycles per day for the annual simulation with different parameter values for the UFH (left) and the radiator (right).

3.2 Experimental case study: validation experiments

The conducted experiments underline the essential findings and trends. First, the developed controller results in equal operation behavior. Figure 7 compares the heat pump's supply and return temperature between the simulation (red) and the experiment (blue). The one-hour experiment begins with the start of the heat pump. After approximately 20 minutes, the experiment and the simulation resulted in similar behavior. The negligible error of under 0.2 K between simulation and experiments underlines the accurate simulation model and validates its application.

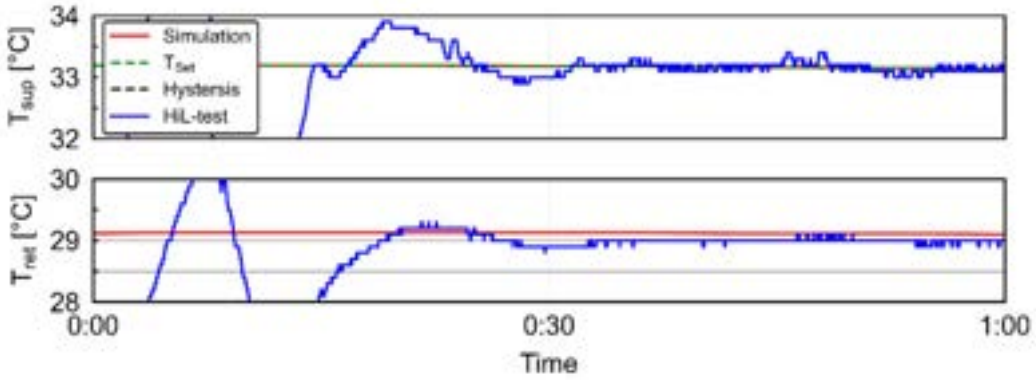

Figure 7: Comparison of supply temperature T_{sup}, and return temperature T_{ret} of the UFH system between simulation (red) and experiment (blue) for $Hys = 8\ \mathrm{K}$ on reference day 01/11.

Nevertheless, we also observe differences between simulation and experiment. Figure 8 compares supply and return temperatures between the simulation (red) and the experiment for the same day but with a lower hysteresis bandwidth of 2 K. The experiment the general operation behavior with many startups within one hour but at different temperature levels. The differences arise from an inaccurate mapping of the model's startup process and additional inertias on the test stand, such as leads, that were not part of the calibration process. In general, the successfully performed experiments show the applicability of the method and the possibility of fast model validation.

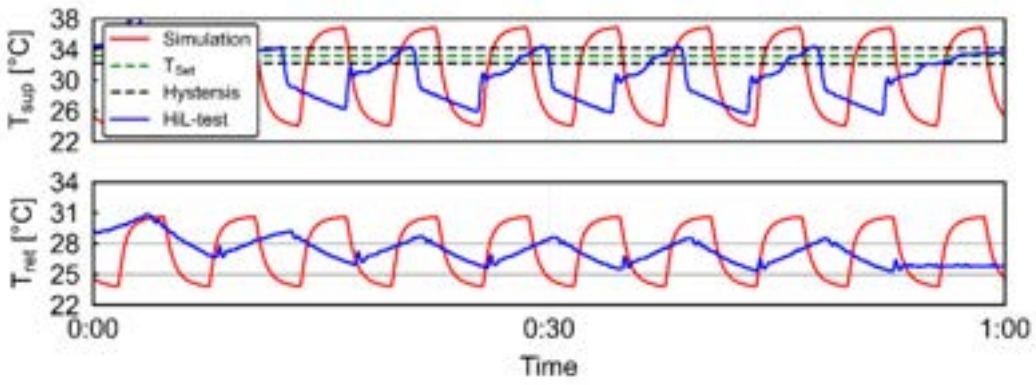

Figure 8: Comparison of supply temperature T_{sup}, and return temperature T_{ret} of the UFH system between simulation (red) and experiment (blue) for $Hys = 2$ K on reference day 01/11

4. Discussion

The following section discusses the obtained results in the context of the literature and is divided into four sections. While many studies discuss the heat pump's operation behavior only in the context of efficiency, we suggest considering the influence on the heat pump's service life (1). Furthermore, we observed discrete operating changes during periods with high solar irradiation (2) and due to bad hysteresis parametrization (3). Control parameters are also sensitive to the transfer system and boundary condition (4).

Typically, in the literature, system operation is only discussed concerning efficiency. Nevertheless, in this context, attention must be paid to assessing the system's service life due to the increased compressor starts. The service life is influenced by the number of operating hours and the frequency of the starting processes. For example, Perrin [22] found that a 12% increase in cycles can reduce compressor life by up to 15%. Therefore, overall consideration of the cycles is imperative for a comprehensive analysis.

The interplay between transfer mass flow and solar irradiation significantly influences the cyclic behavior of the system. From the analysis of the daily simulations, we found that for both transfer systems, there are significant amplitudes of the supply temperature in the midday hours compared to the morning and evening hours. The reason for this is the lack of a buffer tank, which significantly changes the inertia of the sink and solar irradiation. Lower heat output is required when solar irradiation heats the building midday. However, the heating curve only depends on the outdoor temperature, and the solar irradiance is not considered to determine the reference variable T_{set}. The result is that the overflow valve trips as a result of the rising pressure, thus reducing the transfer mass flow to a minimum. This causes high amplitudes of the supply temperature due to that low mass flow. Such cycles result in the system overshooting continuously due to the high control deviation. Because the cooling process is delayed due to the high amplitudes, fewer cycles can be observed overall if this operating state continues for longer. A cycles comparison of the radiator with the aid of Table 2 shows that this issue explains that the number of cycles is almost halved from reference day 10/18 to day 09/05. Accordingly, solar irradiation can result in a tipping point from which the heat pump operating switches from continuous to cycling behavior.

The interaction of the control variables, particularly the hysteresis, with the starting process, can also be regarded as a tipping point which we observe in the validation experiments using the real heat pump. For example, a hysteresis bandwidth of 6 K results in cyclic behavior, while a hysteresis bandwidth of 8 K results in continuous operation. Here, the startup process leads to a supply temperature that slightly exceeds the hysteresis's upper limit and thus maintains the cyclic state. Accordingly, there are threshold values which, as a result of the compressor starting process, mean different characteristics of the operation if they are under or exceeded. However, these threshold values differ between simulation and experiment since the starting process is not accurately modeled.

From the findings of Section 3 and Table 2, we can conclude that both the parameters by themselves in their variation influence the efficiency, and also, the transfer systems show different deviations concerning a SCOP maximum for the same day. Therefore, it is possible to adjust the controller to the building to increase efficiency. Furthermore, since differences in the SCOP-maximum parameter values for the different representative days can be found, the control should be adapted to the ambient conditions. One option for this is the adaptation of the control variables depending on the season or, ideally, based on weather forecasts for the following days.

Conclusion

This work contributes to the defossilation of the building sector by indicating the sensitivity of HPS controller settings on the efficiency and the service life of heat pump systems. In this paper, we develop a simulation model for Building Energy Systems applicable to purely simulation studies and hardware-in-the-loop experiments. The performed sensitivity analysis is based on 82 annual simulations considering various parameters for the proportional factor, the integral time, and the hysteresis bandwidth. We validate the trend of the annual results in further measurement campaigns with a fully-controllable heat pump test bench. The results show the impact of the controller settings on the heat pump's efficiency and operating behavior. Therefore, we analyze the daily heat pump's startups besides the SCOP. We show that the controller parameters influence the SCOP up to 18.5 %, and bad settings can increase the number of compressor starts up to 300 %. Furthermore, the results show discrete steps and nonlinear efficiency values over various parameters, which results from tipping points from which the heat pump operating switches from continuous to cycling behavior.

We will integrate the heat pump's starting process into the simulation model to increase the model's accuracy in future work. Further controller comparisons with the help of the experimental setup will support the efficient development of future systems. Dedicated studies should analyze the influence of the transfer system in more detail by focusing on the system's inertia.

Acknowledgments

We gratefully acknowledge the financial support by the German Federal Ministry for Economic Affairs and Climate Action (BMWK), promotional reference 03EN1022B and 03ET1595A.

not in the reviewed version

Nomenclature

Acronym

BES	building energy system
HIL	Hardware-in-the-loop
HPS	heat pump system
KPI	key performance indicator
MPC	model predictive control
OFAT	one-factor-at-a-time
UFH	underfloor heating

Variables:

Hys	hysteresis bandwidth, K
K_p	proportionality factor
$\dot{m}$	mass flow rate, kg/s
n	rotational speed, 1/s
P	power, W
$SCOP$	seasonal coefficient of performance
T	temperature, °C/K
T_n	integral time

Greek symbols

η	efficiency
φ	maintenance factor

Subscripts and superscripts

amb	ambient
el	electric
ret	return
sup	supply

References

[1] C. Vering, D. Schwarz, P. Stefaniak, V. Venzik, and D. Müller, ‘Kältemittel in Wärmepumpen für die Gebäudeheizung: Ökologische Auswirkungen im gesamten Lebenszyklus’, *Chemie Ingenieur Technik*, vol. 94, no. 4, pp. 542–554, Apr. 2022, doi: 10.1002/cite.202100016.

[2] P. Stoffel, L. Maier, A. Kümpel, T. Schreiber, and D. Müller, ‘Evaluation of Advanced Control Strategies for Building Energy Systems’, Social Science Research Network, Rochester, NY, SSRN Scholarly Paper 4251878, Oct. 2022. Accessed: Oct. 23, 2022. [Online]. Available: https://papers.ssrn.com/abstract=4251878

[3] S. Göbel, C. Vering, and D. Müller, 'Experimental Investigation of Rule-Based Control Strategies for Hybrid Heat Pump Systems Using the Smart Grid Ready Interface', in *PROCEEDINGS OF ECOS 2022*, Kopenhagen, 2022.

[4] J. Drgoňa *et al.*, 'All you need to know about model predictive control for buildings', *Annual Reviews in Control*, Sep. 2020, doi: 10.1016/j.arcontrol.2020.09.001.

[5] M. Uhlmann and S. S. Bertsch, 'Theoretical and experimental investigation of startup and shutdown behavior of residential heat pumps', *International Journal of Refrigeration*, vol. 35, no. 8, pp. 2138–2149, Dec. 2012, doi: 10.1016/j.ijrefrig.2012.08.008.

[6] M. Dongellini and G. L. Morini, 'On-off cycling losses of reversible air-to-water heat pump systems as a function of the unit power modulation capacity', *Energy Conversion and Management*, vol. 196, pp. 966–978, 2019, doi: 10.1016/j.enconman.2019.06.022.

[7] Z. Xu *et al.*, 'Field experimental investigation on partial-load dynamic performance with variable hysteresis control of air-to-water heat pump (AWHP) system', *Applied Thermal Engineering*, vol. 182, p. 116072, 2021, doi: 10.1016/j. applthermaleng.2020.116072.

[8] S. Göbel, T. Fiedler, J. Klingebiel, C. Vering, and D. Müller, 'Development and experimental validation of model-based superheat control strategies for air-to-water heat pumps.' International Institute of Refrigeration (IIR). doi: 10.18462/IIR.GL2022.0143.

[9] Dymola, 'Dymola - Dynamic Modeling Laboratory Full User Manual', 2021.

[10] F. Wüllhorst, L. Maier, D. Jansen, L. Kühn, and Hering, D., and Müller, D., ‘BESMOD – A Modelica Library for Providing Building Energy System Modules’, *THE AMERICAN MODELICA 2022 CONFERENCE*, vol. 2022, pp. 9–19, 2022, doi: 10.3384/ECP211869.

[11] EBC, *AixLib: A Modelica model library for building performance simulations*. 2018. [Online]. Available: https://github.com/RWTH-EBC/AixLib

[12] C. Nytsch-Geusen, J. Huber, M. Ljubijankic, and J. Rädler, ‘Modelica BuildingSystems − eine Modellbibliothek zur Simulation komplexer energietechnischer Gebäudesysteme’, *Bauphysik*, vol. 35, no. 1, Art. no. 1, Feb. 2013, doi: 10.1002/bapi.201310045.

[13] International Building Performance Simulation Association (IBPSA), 'Modelica IBPSA Library'. https://github.com/ibpsa/modelica-ibpsa

[14] D. Wetterdienst, ‘Deutscher Wetterdinest’, 2021. [Online]. Available: https://www.dwd.de/DE/Home/home_node.html

[15] P. Remmen, M. Lauster, M. Mans, M. Fuchs, T. Osterhage, and D. Müller, 'TEASER: an open tool for urban energy modelling of building stocks', *Journal of Building Performance Simulation*, vol. 11, no. 1, Art. no. 1, Jan. 2018, doi: 10.1080/19401493.2017.1283539.

[16] F. Wüllhorst, ‘Implementierung eines Grey-Box-Wärmepumpenmodells in Modelica mit Fokus auf sicherheitsrelevante Regeleinrichtungen’, Bachelorarbeit, 2018.

[17] F. Wüllhorst, T. Storek, P. Mehrfeld, and D. Müller, 'AixCaliBuHA: Automated calibration of building and HVAC systems', *Journal of Open Source Software*, vol. 7, no. 72, p. 3861, 2022, doi: 10.21105/joss.03861.

[18] M. Steinbach, ‘Erstellung und Analyse energetischer Gebäudesimulationen mit Fokus auf kalibrierte Modelle von hybriden Wärmepumpensystemen’. RWTH Aachen University, E.ON Energy Research Center, Institute for Energy Efficient Buildings and Indoor Climate, Jul. 2018.

[19] M. J. Nürenberg, P. Mehrfeld, K. Huchtemann, and D. Müller, 'Hardware-in-the-Loop test bench setup and its application to determine seasonal performance of heat pump systems', 12th IEA Heat Pump Conference 2017, Rotterdam (Netherlands), 15 May 2017 - 18 May 2017, 2017. [Online]. Available: http://publications.rwth-aachen.de/record/712437

[20] P. Mehrfeld *et al.*, 'Dynamic evaluations of heat pump and micro combined heat and power systems using the hardware-in-the-loop approach', *Journal of Building Engineering*, vol. 28, p. 101032, Mar. 2020, doi: 10.1016/j.jobe.2019.101032.

[21] V. Czitrom, 'One-Factor-at-a-Time versus Designed Experiments', *The American Statistician*, vol. 53, no. 2, p. 126, 1999, doi: 10.2307/2685731.

[22] K. Huchtemann, H. Engel, P. Mehrfeld, M. Nürenberg, and D. Müller, 'Testing method for evaluation of a realistic seasonal performance ofheat pump heating systems: Determination of typical days', in *CLIMA 2016 - proceedings of the 12th REHVA World Congress // CLIMA 2016*, P. K. Heiselberg, Ed., [Aalborg: University, 2016.

The general exergy method of heating/cooling technology design for optimization

Malick Kane[a], Daniel Favrat[b]

*[a] HES-SO//FR, University of Applied Science in Fribourg, Mechanical Engineering Department (ENERGY institute), Fribourg, Switzerland, malick.kane@hefr.ch, **CA***
[b] EPFL, Ecole Polytechnique Fédérale de Lausanne, Switzerland, daniel.favrat@epfl.ch

Abstract:

A general exergy based-design method for optimization of heat pump/refrigeration systems is proposed. It is based on a concept of overall temperature level of a flow-energy, to propose a general expression of overall exergy efficiency and losses of any heat pump/refrigeration cycle. Explicit and general relations of exergy efficiency and coefficient of performances are given to evaluate de performance of such cycles regarding the selection of working fluids, the characteristic of equipment (pinches on evaporators and condensers, performance characteristics of compressors and expansion valve) and the design methods for optimization.

Rigorously we introduce the overall and complete exergy efficiency for the most general cases where two energy services are provided, like producing simultaneously refrigeration and heating services or when the cycle is located in a temperature domain far from the atmospheric temperature. This complete exergy efficiency is determined by considering losses in the various components of the cycle and permits to analyse the various cases of heat pump systems including frigopump and thermopump with or without cogeneration systems. Such a method will facilitate the use of exergy theory in a way to highlight the existing link and relationship between energy and exergy losses of heat pump systems. Results of using such a method will be shown for simple and advanced cycles. Results show that the coefficient of performance of a heat pump/refrigeration installation does not necessarily depend on the reference atmospheric temperature but only on the intrinsic parameters relating to the choice of cycle, the operating conditions and the components of the machine. These parameters are obviously chosen according to the temperature levels of the available sources.

Keywords:

Thermodynamics; Exergy losses; Exergy efficiency; Effectiveness; design and optimisation method

1. Introduction

"Pumping" heat from a lower temperature to an upper temperature can be done by using a vapor compression heat pump/refrigeration cycle most commonly used in heating and cooling applications. It consists of a process for which refrigerant vapor is compressed in the compressor and then used to the condenser where it is first cooled or desuperheated and then condensed and finally slightly subcooled. The saturated or slightly subcooled refrigerant is then expanded in a valve then evaporated in an evaporator and the cycle begins again. Whether operating in frigopump mode (providing cooling services while dissipating energy to the environment), in thermopump mode (providing heating service to customers while capturing energy from environment) or in cogeneration mode (providing heating and cooling simultaneously) the process is accompanied with different losses, resulting from various irreversibilities that occurred on their components. Generally, different approaches to assess exergy performances of such heating/cooling systems can be distinguished and applied at different levels [1, 2]:

- The method of calculating the exergy efficiency by quantitatively evaluating the global exergy losses $\dot{L}$ on the basis of internal/external losses [3, 4] (exergy losses $\dot{L}_D$ called also exergy destruction inside the strictly defined system and external exergy losses $\dot{L}_E$ or exergy destroyed between the system and the atmosphere) or on the basis of an exergy balance carried out on the boundary of the system extended to the atmosphere in order to internalize and attribute all losses to the system [1, 5]. Such a method is useful to compare different options or configurations of systems providing the same service (of heating and cooling);
- The assessment made on the basis of an exergy balance carried out on each of the components in the whole system in order to identify and locate the major losses. Borel & Favrat [5] subdivide $\dot{L}$ into:

$$\dot{L} = \dot{L}_r + \dot{L}_t$$

Where $\dot{L}_r$ includes the dissipation exergy losses (pressure losses and friction) inside the system and $\dot{L}_t$ includes the heat transfer exergy losses. The performance of a system is then characterised by calculating exergy losses of various components and/or subsystems.

In this article, we use the approach of components/subsystems level analysis to propose a **general exergy based-design method for optimization** of heat pump/refrigeration systems. Such method makes it possible to identify and locate the major losses in the whole system in order to take optimization measures and to determine the exergy efficiency characteristics of any heat pump system. New method [6] using explicit and general relations of exergy efficiency and coefficient of performances will be given to evaluate de performance of such cycles regarding the selection of working fluids and the characteristic of equipment (pinches on evaporators and condensers, performance characteristics of compressors and expansion valve).

Simplified effectiveness (or COP-coefficient of performance) models of heat-pumps/refrigeration cycles using perfect gases on the compressor and/or equation-fit models have been proposed in many studies. [7] performed models to calculate the COP by using a theoretical Lorentz efficiency multiplied by a constant exergy efficiency (of around 40% for boosters HP and 50% for the centralized HP). [8] gives a review of recent development in variable refrigerant flow (VRF) systems with models ranging from detailed physics-based models to equation-fit models. [9] proposed a modular simplified model using perfect gas in compression for a fast multi-year simulation. [10] performed a detailed simulation model based-exergy performance characteristics of heat-pumps and applied by in [11] to simulate different configurations of network integration where the performances in term of exergy efficiency on the substation are determined in function of the temperature of the network and the differential temperature on the primary network.

This detailed process exergy-based design model uses real working fluids with the possibility of evaluating the exergy efficiency in function of all key parameters that influence the system. This method allows to give precise recommendations on the optimization of a real process in operation or on the decision support for the conception or the design of a heating or cooling system.

2. The general exergy model of heat pump cycles

2.1. The concept of overall temperature for the calculation of flow-exergy

A fluid stream carrying a flow-energy ($\dot{Y} = \dot{M}\,\Delta h$) at constant pressure ($P$) between two states (1 and 2) can be characterized by its overall temperature level ($\bar{T}$) or logarithmic mean temperature. This temperature value is calculated on the basis of Gibbs equation of enthalpy variation ($dh = Tds + vdP$), for which we can thus write $vdP = 0$ and the integration will give a perfect relationship between enthalpy/entropy variations:

$$\frac{h_2 - h_1}{\bar{T}} = s_2 - s_1 \tag{1}$$

$$\bar{T} = (T_2 - T_1) \,/\, ln\left(\frac{T_2}{T_1}\right) \tag{2}$$

The logarithmic mean value of two different quantities is well known in Physics as well as in Thermodynamics, especially the calculation of a heat exchanger area with the method of mean temperature differences (heat transfer between fluids at constant pressure and without phase change. Considering Eq. (1) and the definition of co-enthalpy variation ($\Delta k = \Delta h - T_a \Delta s$) of the stream, the corresponding flow-exergy ($\dot{E}_y$) could then be given by the following equation:

$$\dot{E}_y = \dot{M}\,\Delta k = \left(1 - \frac{T_a}{\bar{T}}\right) \cdot \dot{Y} \qquad with \quad P = cste \tag{3}$$

This concept of logarithmic mean temperature (called here overall temperature) has been used and applied by various authors [12, 13] for the modelling of a stream flow-exergy. Indeed, a fluid stream can be seen as a succession of matter carrying exergy (co-enthalpy) at a temperature level $\bar{T}$. The latter is simply given by the variation of enthalpy of the fluid to the entropy variation (($\bar{T} = \Delta h / \Delta s$). The exergy losses associated to the flow-energy is given as:

$$\dot{L} = \dot{M}\, T_a\, (s_2 - s_1) = \dot{M}\, \frac{T_a}{\bar{T}} (h_2 - h_1) \tag{4}$$

In the case of a phase change fluid in evolution at constant pressure, Eq. (3) is still valid and the process is subdivided in different phases e.g. superheating, bi-phasic and subcooling phases. The expression given in Eq. (1) becomes:

$$\frac{h_2 - h_1}{\bar{T}} = (s_2 - s_l) + \left(s_l - s_g\right) + \left(s_g - s_1\right) \tag{5}$$

Where s_l and s_g represent respectively the liquid and gas saturated entropy.

2.2. Energy/exergy balances of a standard cycle

The vapor compression heat pump or refrigeration cycle that we considered (Figure 1-a) is so far an open system comprising a compressor, a condenser, an expansion valve and an evaporator, with various streams and with the following hypotheses: kinetic and potential energies neglected, heat devaluation in the condenser and in the evaporator but no dissipation in the heat exchangers (heat transfer processes occurring at constant pressures) and adiabatic compression and expansion with dissipation in the compressor and in the valve. Figure 1-b shows a T-s diagram of the refrigerant working fluid.

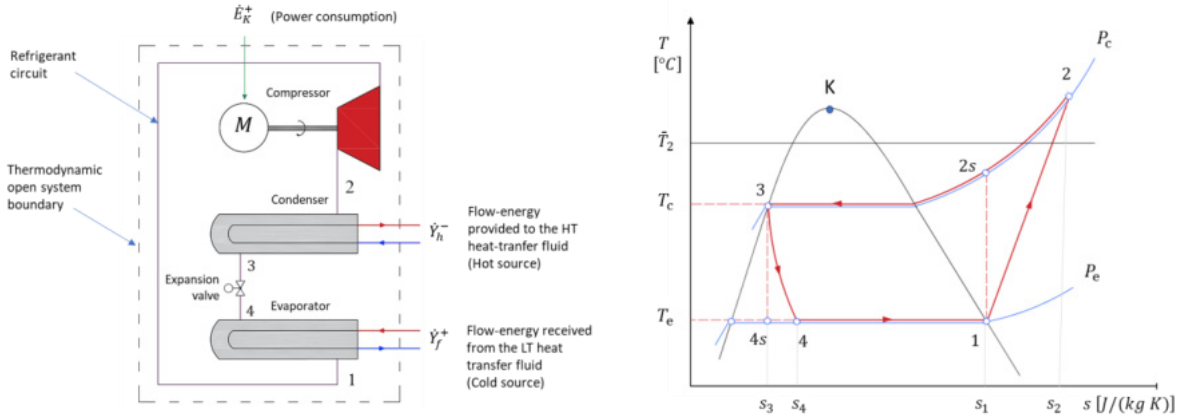

Figure. 1. Heating/cooling processes through a heat pump/refrigeration cycle
a) Schematic diagram, b) T-s diagram

The hot source is constituted by the HT heat transfer circuit in the condenser and the cold source is constituted by the LT heating circuit in the evaporator. The transformation (or flow) energy ($\dot{Y}_f^+$) received by the system from the cold source at a given temperature level ($\bar{T}_f$) is transferred through the heat pump/refrigeration system to the hot source ($\dot{Y}_h^-$) at a higher temperature level ($\bar{T}_h$). This is possible by consuming mechanical or electrical energy ($\dot{E}_K^+$) in the compressor. Note that the terms **hot** and **cold** here used to qualify the sources refer only to the temperature level of these sources. Not then to be confused with the **hot** and **cold streams** defined for heat exchangers where the cold stream is that of the flow to be heated by increasing its enthalpy level and the hot stream is that of the flow to be cooled by decreasing its enthalpy level. Thus,

- For the condenser, the hot stream is represented by the condensing refrigerant circuit at constant pressure (P_c) from state 2 to state 3. The overall temperature level of the stream is here noted ($\bar{T}_c$). The cold stream is represented by the HT heat transfer circuit heated in the condenser and supplying energy ($\dot{Y}_h^-$) to the hot source;
- For the evaporator, the hot stream is represented by the LT heat transfer circuit cooled in the evaporator and receiving energy ($\dot{Y}_f^+$) from the cold source. The cold stream is represented by the evaporating refrigerant circuit at constant pressure (P_c) from state 4 to state 1 ($\dot{Y}_e^-$).

These condensing or evaporating streams at constant pressure can be represented in the diagram T-s by their corresponding overall temperature values (or logarithmic mean temperature values at constant pressure), like $\bar{T}_c$ for the condenser and $\bar{T}_e$ for the evaporator. Figure 2 illustrates an example of this type of diagram with the advantage of showing the average pinches on heat exchangers characterizing the heat devaluation and the variations of entropies characterizing the dissipations in the compressor and the valve.

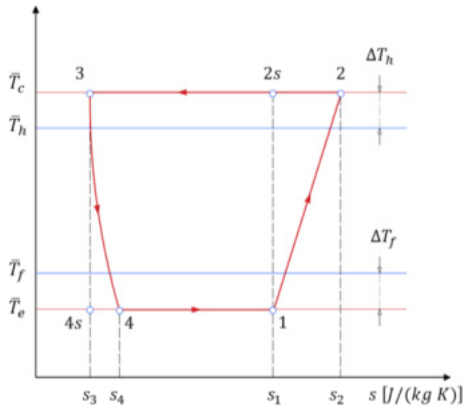

Figure. 2.: T-s diagram of a standard heat pump/refrigeration cycle

For adiabatic components with steady state open operation and based on the energy balance equation (Eq. xx), we can give the following relations:

$$\dot{Y}_h^- = \dot{Y}_c^+ = \dot{M}\,(h_2 - h_3) \qquad \dot{Y}_f^+ = \dot{Y}_e^- = \dot{M}\,(h_1 - h_4) \tag{5}$$

$$\dot{E}_K^+ = \dot{Y}_h^- - \dot{Y}_f^+ = \dot{M}\,(h_2 - h_1) \tag{6}$$

2.3. Overall exergy efficiency and losses of the cycle

From the general expressions given in [6], the overall exergy efficiency of a vapor compression heat pump/refrigeration system can be given as a function of the temperature levels of the hot ($\bar{T}_h$) and cold ($\bar{T}$) sources:

$$\eta = 1 - T_a \left(\frac{\varepsilon_h}{\bar{T}_h} - \frac{\varepsilon_f}{\bar{T}_f}\right) \qquad with \qquad \varepsilon_h = \varepsilon_f + 1 \tag{7}$$

Where $\varepsilon_h = \dot{Y}_h^- / \dot{E}_K^+$ and $\varepsilon_f = \dot{Y}_f^+ / \dot{E}_K^+$ respectively represent the effectiveness (or coefficient of performance) for heating and cooling. Considering that the mass flow rate of refrigerant ($\dot{M}$) is the same throughout the different component of the standard cycle, we can here work with energy/exergy quantities per unit of mass of refrigerant. Effectiveness for heating and cooling can then be done by using the specific energies of cooling ($y_h^- = h_1 - h_4$), of heating ($y_f^+ = h_2 - h_3$) and of power consumption ($e_K^+ = h_2 - h_3$):

$$\varepsilon_h = \frac{h_2 - h_3}{e_K^+} \qquad \varepsilon_f = \frac{h_1 - h_4}{e_K^+} \tag{8}$$

From Eq. (7), we found the well-known and particular relationships between the overall exergy efficiency of a heat pump cycle, the coefficient of performance (effectiveness) and the ideal effectiveness based on the Carnot factor :

For a thermopump ($\bar{T}_f = T_a$):

$$\eta_h = \varepsilon_h \left(1 - \frac{T_a}{\bar{T}_h}\right) \qquad COP_h = \eta_h \cdot \frac{\bar{T}_h}{\bar{T}_h - T_a} \tag{9}$$

For a frigopump ($\bar{T}_h = T_a$):

$$\eta_f = \varepsilon_f \left(\frac{T_a}{\bar{T}_f} - 1\right) \qquad COP_f = \eta_f \cdot \frac{\bar{T}_f}{T_a - \bar{T}_f} \tag{10}$$

Considering that the mass flow rate of refrigerant ($\dot{M}$) is the same throughout the different component of the standard cycle, we can here work with energy/exergy quantities per unit of mass of refrigerant. Equations Eq. 5.12 can then be done by using the specific energies of cooling ($h_1 - h_4$), of heating ($h_2 - h_3$) and/or of power consumption ($e_K^+ = h_2 - h_3$). These values can directly be read in the P-h diagram of the cycle.

$$\varepsilon_h = \frac{h_2 - h_3}{e_K^+} \qquad \varepsilon_f = \frac{h_1 - h_4}{e_K^+} \tag{11}$$

Based on Eq. (7) and Eq. (8), Exergy losses per unit of mass (l_G) of the **complete heat pump or refrigeration system** are then:

$$l_G = (1 - \eta) \cdot e_K^+ = \frac{T_a}{\bar{T}_h}\,(h_2 - h_3) - \frac{T_a}{\bar{T}_f}\,(h_1 - h_4) \tag{12}$$

Two components of exergy losses can be distinguished: exergy losses that are rather related to both the temperature level of the hot source ($\bar{T}_h$) and the specific energy of heating ($h_2 - h_3$) and exergy losses that are related to the temperature level of the cold source ($\bar{T}_f$) and the specific energy of cooling ($h_1 - h_4$). The temperature levels of the sources therefore play an important role in the assessment of the overall exergy losses or irreversibilities in heat pumps. The exergy losses do decrease with the temperature level of the hot source while they increase with the temperature level of the cold source.

Such global exergy efficiency and losses given by Eq. (7) and Eq. (12) are very useful for comparing the performance of different options or configurations of heat pump systems but are not explicit enough to provide more specific recommendations on the optimization of the cycle and more particularly on the design and operation of the components but also on the choice and characteristics of the refrigerant.

2.4. Detailed exergy assessment of the heat pump cycle

Not that, the exergy losses by dissipation in the compressor and in the valve enter into the expression of the global exergy loss (Eq. 12) through the enthalpy values of h_2 and h_4. If the isentropic efficiency of the compressor (η_{Ks}) decreases, h_2 increases and so does the compressor dissipation loss. If the pressure at the condenser (P_c) increases, h_4 increases and so does the loss in the valve. In general, the temperature level of a source is initially a known parameter based on the need of heating ($\overline{T}_h$) or of cooling ($\overline{T}_f$). Thus, improving the performance of a heatpump/refrigeration cycle (COP) shall involve improving its overall exergy efficiency by minimizing exergy dissipation ($\dot{L}_r$) and devaluation ($\dot{L}_t$) losses in the system.

Let us now determine the expression of exergy efficiency and losses by carrying out a detailed exergy assessment of losses in various components of the system (compressor, condenser, evaporator, valve). The global exergy losses ($\dot{L}_G$) here can be calculated by separating the dissipation exergy losses in the compressor and in the expansion valve ($\dot{L}_r = \dot{L}_K + \dot{L}_V$) and the devaluation (or heat transfer) exergy losses in the condenser and in the evaporator ($\dot{L}_t = \dot{L}_C + \dot{L}_E$). Then, the exergy efficiency of the cycle can be developed in function of these losses (dissipation and devaluation) per unit of power:

$$\eta = \ 1 - \left(\frac{\dot{L}_r}{\dot{E}_K^+}\right) - \left(\frac{\dot{L}_t}{\dot{E}_K^+}\right) \tag{13}$$

Let us then quantify these specific losses per unit of power.

Modelling dissipation exergy losses (compressor and valve)

Exergy losses in the compressor ($\dot{L}_K$):

For a compressor, adiabatic compression is aimed at, i.e. with perfect thermal insulation from the external environment to obtain the best exergy efficiency. In order to determine the compressor dissipation exergy losses $\dot{L}_K = \dot{M}\, T_a(s_2 - s_1)$ we first need to determine the variation of entropy in compression. According to Eq. (1) and to the fact that $s_1 = s_{2s}$ (Figure 2), the difference in entropy of the compression ($s_2 - s_1$) can also be determined in function of the overall discharge temperature ($\overline{T}_d$), when considering the refrigerant stream at constant pressure P_c from state 2 to state 2s (i.e., $vdP = 0$). The following equations can thus be defined:

$$s_2 - s_1 = \frac{h_2 - h_{2s}}{\overline{T}_d} = \frac{1 - \eta_{Ks}}{\overline{T}_d}\,(h_2 - h_1) \tag{14}$$

$$\overline{T}_d = (T_2 - T_{2s}) \,/\, ln\left(\frac{T_2}{T_{2s}}\right) \tag{15}$$

Where η_{Ks} represents the isentropic efficiency of the compression and $1 - \eta_{Ks} = (h_2 - h_{2s})/(h_2 - h_1)$ represents the part of dissipation losses in the compression. The variations in the kinetic and potential energies of the fluid are neglected in relation to the work energy consumed by the compressor. We can finally express the dissipation exergy losses in the compressor by the following simple relation:

$$\dot{L}_K = \dot{M}\,\frac{T_a}{\overline{T}_d}\,(1 - \eta_{Ks})(h_2 - h_1) \tag{16}$$

The power consumption is:

$$\dot{E}_K^+ = \dot{M}\left(\frac{\Delta h_{Ks}}{\eta_{Ks}}\right) \qquad with \quad \Delta h_{Ks} = h_{2s} - h_1 \tag{17}$$

Exergy losses in the expansion valve ($\dot{L}_V$):

In the case of the **adiabatic expansion** in a valve, i.e., with perfect thermal insulation thus avoiding external heat losses, the enthalpy variation of the fluid is equal to zero (isenthalpic expansion, $h_3 = h_4$). According to Eq. (4) and to the fact that $s_3 = s_{4s}$ (Figure 2), the difference in entropy of the compression ($s_4 - s_3$) can also be determined in function of the evaporation temperature ($\overline{T}_e$), when considering the evaporating pressure P_e from state 4s to state 4 (i.e., $vdP = 0$). The following equation can thus be defined:

$$\dot{L}_V = \dot{M}\, T_a(s_4 - s_3) = -\dot{M}\,\frac{T_a}{T_e}\,\Delta h_{Ks} \qquad with \quad \Delta h_{Vs} = h_{4s} - h_3 \tag{18}$$

From these Eq. (16), Eq. (17) and Eq. (18), we can deduce the specific dissipation losses as a function of the isentropic efficiency, a ratio of isentropic enthalpy variations between the valve and the compressor (here called isentropic expansion/compression ratio) and the overall discharge temperature level of the fluid at the outlet of the compressor:

$$\frac{\dot{L}_r}{\dot{E}_K^+} = \frac{T_a}{\overline{T}_d}(1-\eta_{Ks}) + \frac{T_a}{T_e}\left(\frac{-\Delta h_{Vs}}{\Delta h_{Ks}}\right)\cdot\eta_{Ks} \tag{19}$$

Such expression of dissipation exergy losses per unit of power can be given by the following simple equation:

$$\frac{\dot{L}_r}{\dot{E}_K^+} = \frac{T_a}{\overline{T}_d}(1-\eta_{Gs}) \tag{20}$$

Where we introduce a cycle global isentropic efficiency (η_{Gs}) which takes into account the total dissipation losses or irreversibilities in the compressor and in the expansion valve and therefore is intrinsic to the heatpump cycle:

$$\eta_{Gs} = \eta_{Ks}\left[1-\left(\frac{-\Delta h_{Vs}/T_e}{\Delta h_{Ks}/\overline{T}_d}\right)\right] \tag{21}$$

This relationship Eq. (20) clearly expresses the link between the exergy losses, the fluid temperature level (via the overall discharge temperature ($\overline{T}_d$) at the outlet of the compressor) and the dissipation losses in the whole cycle ($1-\eta_{Gs}$). For the same percentage of dissipation losses in the cycle ($1-\eta_{Gs}$), the dissipation exergy losses are lower the higher the discharge temperature level of the compressor ($\overline{T}_d$). The fluid temperature level plays an important role in the exergy assessment.

Modelling heat transfer exergy losses (condenser and evaporator)

From the general expressions given in [Kane, ecos 2023], the devaluation exergy losses on heat exchangers can be given as a function of the temperature levels of the streams.

Exergy losses in a condenser:

$$\dot{L}_C = \dot{M}\left[T_a\left(\frac{1}{\overline{T}_h}-\frac{1}{\overline{T}_c}\right)\right](h_2-h_3) \tag{22}$$

Exergy losses in an evaporator:

$$\dot{L}_E = \dot{M}\left[T_a\left(\frac{1}{\overline{T}_e}-\frac{1}{\overline{T}_f}\right)\right](h_1-h_4) \tag{23}$$

By combining equations Eq. (22), Eq. (23) and Eq. (8), we can determine the specific devaluation losses as a function of the effectiveness for heating and cooling and the overall temperature levels of the streams:

$$\frac{\dot{L}_t}{\dot{E}_K^+} = T_a\left[\left(\frac{1}{\overline{T}_h}-\frac{1}{\overline{T}_c}\right)\cdot\varepsilon_h + \left(\frac{1}{\overline{T}_e}-\frac{1}{\overline{T}_f}\right)\cdot\varepsilon_f\right] \tag{24}$$

Or then:

$$\frac{\dot{L}_t}{\dot{E}_K^+} = T_a\left[\frac{\varepsilon_h}{\overline{T}_h}\frac{\Delta T_h}{\overline{T}_c} + \frac{\varepsilon_f}{\overline{T}_f}\frac{\Delta T_f}{\overline{T}_e}\right] \tag{25}$$

The exergy losses by internal heat devaluation on the heat exchangers (condenser and evaporator) increase not only with the pinch differential temperatures of the hot (ΔT_h) and cold (ΔT_f) sources but are lower the higher the source temperature levels. The temperature therefore plays an important role in the assessment of the overall exergy losses or irreversibilities.

Let us know express the exergy efficiencies and effectiveness of a heatpump/refrigeration system explicitly in terms of all key parameters influencing the performance of the cycle: the overall discharge temperature level ($\overline{T}_d$) characterizes the type of the working fluid, the global isentropic efficiency (η_{Gs}) characterizes the losses by dissipation in the cycle and the pinch differential temperatures in the hot (ΔT_h) and cold (ΔT_f) sources characterize devaluation losses by heat transfer in the condenser and the evaporator.

2.5. Explicit relations between exergy efficiency and effectiveness

By developing the expression given in Eq. (24), the exergy loss by devaluation in a heat pump/refrigeration cycle can also be determined by the following relation:

$$\frac{\dot{L}_t}{\dot{E}_K^+} = T_a \left[\left(\frac{\varepsilon_h}{\bar{T}_h} - \frac{\varepsilon_f}{\bar{T}_f} \right) - \left(\frac{\varepsilon_h}{\bar{T}_c} - \frac{\varepsilon_f}{e_f} \right) \varepsilon_f \right] \tag{26}$$

Considering the general expression of exergy efficiency given by Eq. (7), we can deduct from Eq. (24) the expression of the system's devaluation exergy losses:

$$\frac{\dot{L}_t}{\dot{E}_K^+} = 1 - \eta - T_a \left(\frac{\varepsilon_h}{\bar{T}_c} - \frac{\varepsilon_f}{\bar{T}_f} \right) \tag{27}$$

By replacing equations Eq. (20) and Eq. (27) in Eq. (13) and by considering the general equation of overall exergy efficiency (Eq. 7), we found a simple expression between the effectiveness for heating ε_h) and cooling (ε_f), the overall temperature levels of the fluid in the evaporator (T_e), the condenser ($\bar{T}_c$) and the compressor ($\bar{T}_d$) and the global isentropic efficiency (η_{Gs}) defined above:

$$\frac{\varepsilon_h}{\bar{T}_c} - \frac{\varepsilon_f}{\bar{T}_e} = \frac{1 - \eta_{Gs}}{\bar{T}_d} \tag{28}$$

Such an expression Eq. (28) shows that the quantity or ratio $(1 - \eta_{Gs})/\bar{T}_d$ is in fact a decisive parameter for calculating the effectiveness (or coefficient of performance) of the cycle as a function of the evaporation and condensation temperature levels of the fluid. Considering the egality $\varepsilon_h = \varepsilon_f + 1$, we can finally deduce the following explicit expressions of effectiveness:

$$\varepsilon_h = \eta_{0h} \cdot \frac{\bar{T}_c}{\bar{T}_c - \bar{T}_e} \qquad with \qquad \eta_{0h} = 1 - \frac{\bar{T}_e}{\bar{T}_d}(1 - \eta_{Gs}) \tag{29}$$

$$\varepsilon_f = \eta_{0f} \cdot \frac{\bar{T}_e}{\bar{T}_c - \bar{T}_e} \qquad with \qquad \eta_{0f} = 1 - \frac{\bar{T}_c}{\bar{T}_d}(1 - \eta_{Gs}) \tag{30}$$

Where η_{0h} and η_{0f} correspond respectively to the exergy dissipation efficiency for the heating and the cooling application.

These expressions are similar to Eq. (9) and Eq. (10) for the coefficient of heating (COP_h) and for cooling (COP_f) given in function of the exergy efficiency for heating (η_h) and cooling (η_f) and the Carnot factors related to the temperature levels of the sources. The performances of a heat pump/refrigeration cycle are better than if it operates at higher temperatures. Dissipation exergy efficiency equal to unit ($\eta_{0h} = \eta_{0f} = 1$) corresponds to losses that are represented only by the internal heat transfer devaluation on heat exchangers. The final expressions for the exergy efficiency of a heat pump/refrigeration cycle are then determined by combining the equations of effectiveness for heating Eq. (9) and Eq. (29) and for cooling Eq. (10) and Eq. (30) and then become:

$$\eta_h = \eta_{0h} \cdot \frac{1 - \bar{T}_f/\bar{T}_h}{1 - \bar{T}_e/\bar{T}_c} \tag{31}$$

$$\eta_f = \eta_{0f} \cdot \frac{\bar{T}_h/\bar{T}_f - 1}{\bar{T}_c/\bar{T}_e - 1} \tag{32}$$

Where: $\bar{T}_c = \bar{T}_h + \Delta\bar{T}_h$ and $\bar{T}_e = \bar{T}_f - \Delta\bar{T}_f$ according to the diagram given in Figure 2.

These expressions Eq. (31) and Eq. (32) of exergy efficiency are explicit as a function of the various parameters that define the qualities that a heat pump/refrigeration cycle must have, namely: the temperature levels of the hot ($\bar{T}_h$) and cold ($\bar{T}_f$) sources, the pinch temperature difference characterizing the condenser (ΔT_h) and the evaporator (ΔT_f), the overall discharge temperature level of the compressor here expressing the type of the working fluid ($\bar{T}_d$) and the global isentropic efficiency (η_{Gs}) that expresses the dissipations in the compressor and the expansion valve.

3. Results and discussion

3.1. The exergy-based design method for optimization

As already shown for the detailed exergy model above, the coefficient of performance of a standard heating (ε_h) or cooling (ε_f) heat pump cycle is determined by the explicit relations of the equations Eq. (29) and Eq. (30). The terms η_{0h} and η_{0f} are exergy efficiencies defined with respect to ideal Carnot efficiency expressed here as a function of the difference ($\Delta\bar{T} = \bar{T}_c - \bar{T}_e$) of condensation ($\bar{T}_c$) and evaporation temperature levels ($\bar{T}_e$). Indeed, it can be shown that there is a simple relationship between these two exergy efficiency values by considering their expressions given in Eq. (29) and Eq. (30):

$$\eta_{0h} - \eta_{0f} = \frac{\Delta\bar{T}}{\bar{T}_d} \cdot (1 - \eta_{Gs}) \tag{33}$$

Based on this formulation of Eq. (33), we express what we already knew in practice or from the theory of exergy, that the best heat pump or refrigeration cycles are those which will:

- Reduce the difference in temperature levels of the refrigerant cycle ($\Delta\bar{T}$);
- Minimize the dissipations at the level of the expansion valve and the compressor ($1 - \eta_{Gs}$)
- Use a fluid with a higher discharge temperature at the compressor ($\bar{T}_d$) from the point of view of exergy analysis

For known evaporation and condensation temperature levels, these exergy dissipation efficiencies are fully determined if one knows the **overall isentropic efficiency** (η_{Gs}) and the compressor outlet **discharge temperature** ($\bar{T}_d$). The advantage is that they only depend on the parameters intrinsic to the refrigerant circuit. Knowing their values makes it possible to determine the cycle coefficient of performance in function of the evaporation and condensation temperature levels. Figure 3 shows an example of a refrigerant-ammonia ($R717$) with different temperature conditions (evaporation and condensation), the corresponding overall isentropic efficiencies and discharge temperatures. Knowing the temperature of evaporation ($T_e = -10°C$) and condensation ($T_c = 40°C$) streams for the heat pump, the overall isentropic efficiency can be determined, in the order of $\eta_{Gs} \cong 65\%$. The corresponding coefficient of performances based on Eq. (29) and Eq. (30) are in the order of $\varepsilon_h \cong 4.3$ for heating and $\varepsilon_f \cong 3.3$ for cooling.

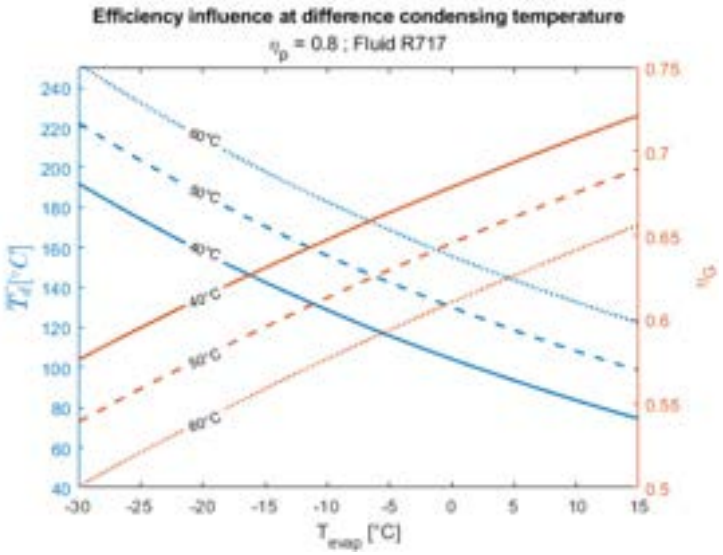

Figure. 3.: The effect of the evaporation temperature on the global dissipation efficiency of a heat pump cycle with parametric curves corresponding to the condensing temperature

Note that these quantities are a function of other parameters and are also dependent on each other:

- The difference in temperature levels of the cycle ($\Delta\bar{T}$) depends on the temperatures of the sources and the pinches at the evaporator and condenser and it is also influenced by the discharge temperature of the compressor;
- The overall isentropic efficiency of the cycle (η_{Gs}) defined above is also a function of the various characteristic parameters of the valve ($-\Delta h_{Vs}/\Delta h_{Ks}$), of the compressor ($\eta_{Ks}$) and of the refrigerant

fluid ($\bar{T}_d$). Figure 31 allows to highlight a dimensionless parameter enabling a fluid to be chosen if the operating conditions of evaporation and condensation and the isentropic efficiency of the compressor are known;

- Since the isentropic efficiency of the compressor is also not constant, it can be a function of various parameters including, for example, the built-in volume ratio (VR_i) and the compression ratio ($\pi_K = PR$) for volumetric compressors.

The thermodynamic optimization of the cycle based on the exergy criterion given by the Eq. (33) therefore makes it possible to obtain a better compromise between these different parameters. Different actions are mentioned theoretically in the literature or actually carried out in practice to improve the coefficient of performance of heat pump or refrigeration cycles and whose results find their explanation based on this analysis of the Eq. (33).

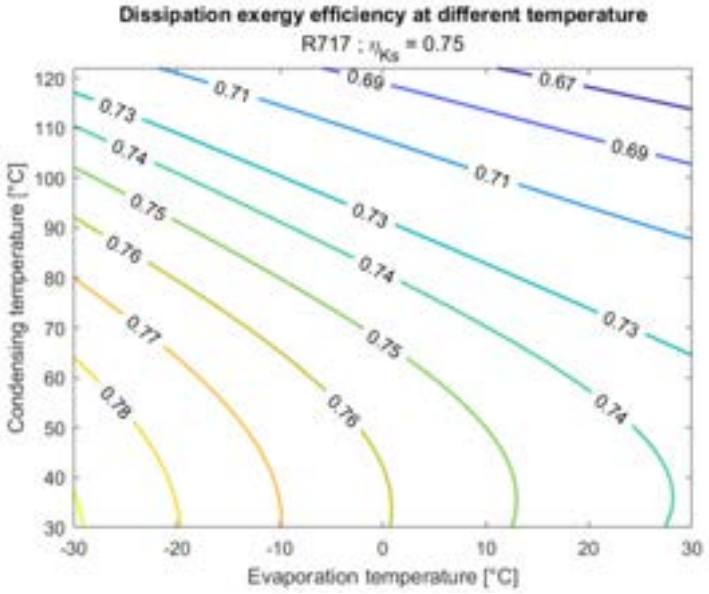

Figure. 4.: Dissipation exergy efficiency for heating in function of the condensing and evaporation temperatures

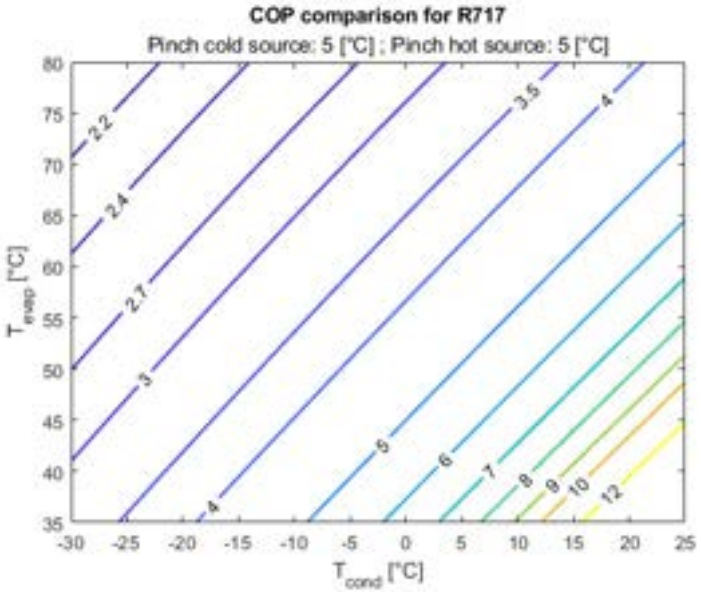

Figure. 5.: Coefficient of performance of heating, R717

These expressions and curves clearly show that the coefficient of performance of a heat pump/refrigeration installation does not necessarily depend on the reference atmospheric temperature but only on the intrinsic

parameters relating to the choice of cycle, the operating conditions and the components of the machine. These parameters are obviously chosen according to the temperature levels of the available sources.

3.2. A dimensionless parameter to select the right working fluid

For the same evaporation and condensation temperatures, the specific power per unit of temperature of discharge compression ($\Delta h_{Ks}/\bar{T}_d$) is a decisive parameter for the selection of the working fluid for the compressor. On the other hand, for the valve, it is the isentropic expansion/compression ratio ($-\Delta h_{Vs}/\Delta h_{Ks}$) which is the determining parameter for the choice of fluid. Figure 6a and 6b show the variation of those parameters for various working fluids.

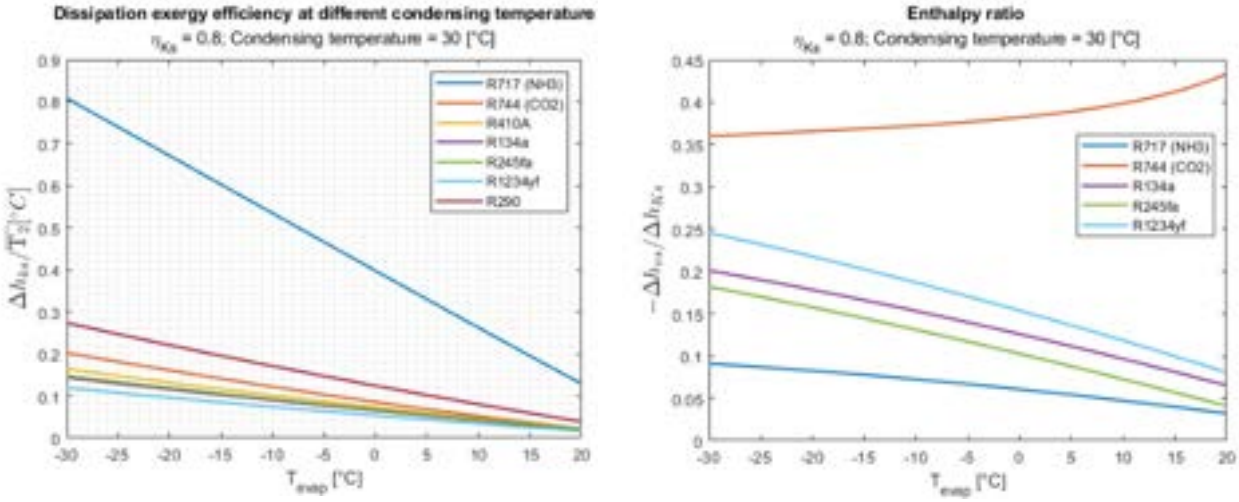

a) Specific power per unit of temperature b) Isentropic expansion/compression ratio

Figure. 6. Heat pump/refrigeration cycle with various working fluids

Refrigerants with the highest discharge temperature at the compressor e.g. with low molar mass refrigerants like ammonia also have the highest specific compression power per unit of discharge temperature ($\Delta h_{Ks}/\bar{T}_d$). The isentropic expansion/compression ratio ($-\Delta h_{Vs}/\Delta h_{Ks}$) is higher for CO2 than for other refrigerants.

An isentropic efficiency of $\eta_{Ks} = 80\%$ is considered for comparison. If this isentropic efficiency of the compressor decreases, the overall discharge temperature ($\bar{T}_d$) increases and so does the global dissipation loss (η_{Gs}). If the temperature at the evaporator (T_e) decreases, the loss in the valve increases too and so does the global dissipation loss (η_{Gs}). We identify an explicit dimensionless dissipation factor as a new criterion for estimating the exergy performance of the heatpump/refrigeration system:

$$a_s = \frac{-\Delta h_{Vs}/T_e}{\Delta h_{Ks}/\bar{T}_d} = \frac{1}{\eta_{Ks}} \cdot \left(\frac{\Delta s_V}{\Delta s_K}\right) \tag{34}$$

For same operating conditions of the cycle (evaporation and condensation temperatures), this dimensionless dissipation factor could be used as a good characteristic parameter to select the right working fluid. To illustrate this, we can visualize the effect of such a factor on the global isentropic efficiency (η_{Gs}) and for various refrigerants (Figure 7) and for different temperature levels (Figures 8).

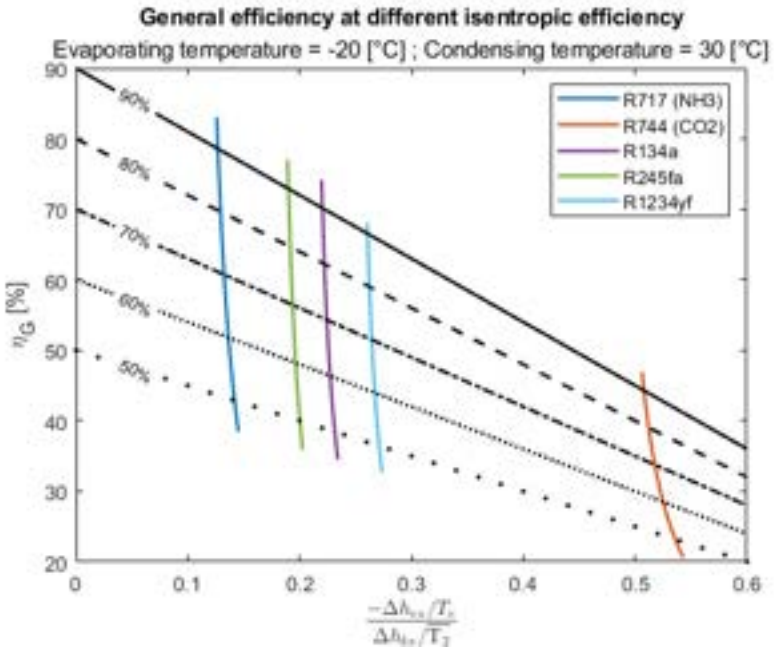

Figure. 7. Global isentropic efficiency in function of the dimensionless dissipation factor of a heatpump cycle and for various refrigerants (single stage cycle)

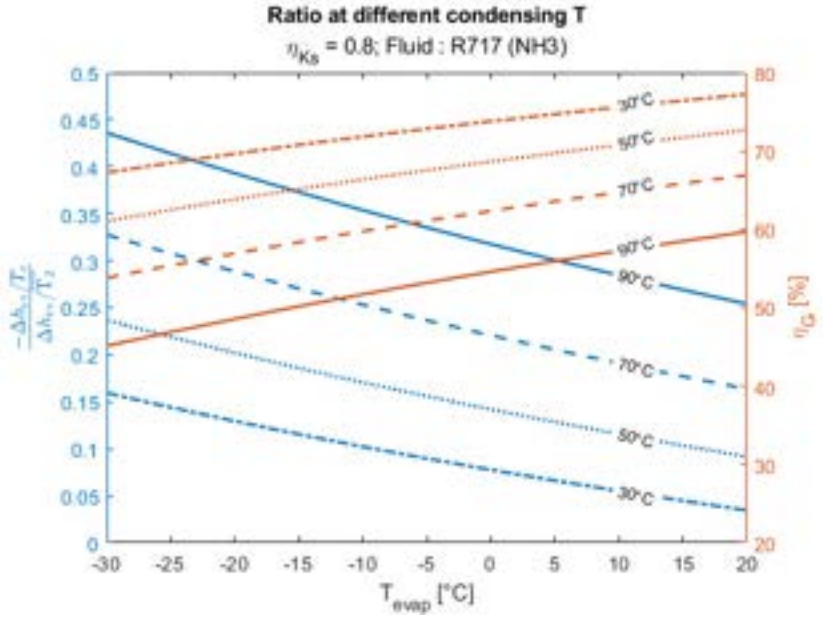

Figure. 8. Global isentropic efficiency in function of the dimensionless dissipation factor of a standard cycle working with R717-ammonia for different temperature levels

4. Conclusion

A **general exergy based-design method for optimization** of heat pump/refrigeration systems is proposed. It is based on a concept of overall temperature level of a flow-energy, to first propose a general expression of overall exergy efficiency and losses of any heat pump/refrigeration cycle.

Rigorously we introduced an overall and complete exergy efficiency for the most general cases where two energy services are provided, like producing simultaneously refrigeration and heating services or when the cycle is located in a temperature domain far from the atmospheric temperature. This complete exergy efficiency is determined by considering losses in the various components of the cycle and allows to analyse the various cases of heat pump systems including frigopump and thermopump with or without cogeneration systems. Main results of such a study are:

- Developing explicit and general relations of exergy efficiency and coefficient of performances of vapor compression heat pump/refrigeration systems. This allows to evaluate de performance of such cycles

regarding the selection of working fluids and the characteristic of equipment (pinches on evaporators and condensers, performance characteristics of compressors and expansion valve);

- Providing an explicit dimensionless dissipation factor as a new criterion for estimating the exergy performance of a heatpump/refrigeration system. For same operating conditions of the cycle (evaporation and condensation temperatures), this dimensionless dissipation factor could be used as a good characteristic parameter to select the right working fluid with the definition of a global isentropic efficiency given in a function of the various characteristic parameters of the valve, the compressor and the heat exchangers;
- Developing a new exergy-based method for the design and optimization of heat pump/refrigeration systems. Such a method has the advantage of facilitating the use of exergy theory in a way to highlight the existing link and relationship between energy and exergy losses of heat pump systems.

Nomenclature

Roman symbols

E work energy, exergy, J
k co-enthalpy, J
L global exergy losses, J
$\dot{M}$ mass flow rate, kg/s
Q heat energy, J
Y flow or transformation energy, J
T temperature, K
U utility, energy service, J

Greek symbols

η exergy efficiency
ε effectiveness, coefficient of performance

Subscripts and superscripts

a ambient, atmosphere
C condenser
E evaporator
f cooling service
h heating service
K compressor
V Expansion valve

References

[1] Favrat D., Kane M., Clear paths to teach exergy. Proc. of ECOS2023

[2] Kane M., Favrat D., New approach for a general expression of effectiveness. Proc. of ECOS2023

[3] Bejan, A., Tsatsaronis, G., Moran, M.J., (1995). Thermal Design and Optimization. John Wiley & Sons

[4] Moran M.J., Shapiro H.N., Boettner D.D, Bailey M.B. (2018). Fundamentals of engineering thermodynamics. Wiley 9th edition 2018

[5] Borel, L., Favrat, D., (2010). Thermodynamics and energy systems analysis. EPFL Press

[6] Kane M., Favrat D., New approach for a general expression of effectiveness. Proc. of ECOS2023

[7] AlbergØstergaard P., Andersen A., (2016). Booster heat pumps and central heat pumps in district heating, Applied Energy 2016;184:1374-1388

[8] Lin, X., Lee, H. Hwang, Y., & Radermacher, R., (2015). A review of recent development in variable refrigerant flow systems. Science and Technology for the Built Environment, 21(7), 917-933

[9] Mbaye A., Cimmino M., (2022). Comparison of a Variable Refrigerant Flow Heat Pump Model in Cooling Mode to Data from ASHRAE. Building Performance Analysis Conference and SimBuild and IBPSA-USA, pp366-372.

[10] Rime S., Kane M., Wyler S., (2020). Alternative solutions fort he optimal integration of decentralized heat-pumps in district heating/cooling networks. Proc. Of ECOS2020

[11] Adihou Y. (2022). Modélisation et optimisation exergétique des réseaux thermiques basse température. Thèse Doctorat USMB

[12] Neveu, P. 2002, Apports de la thermodynamique pour la conception et l'intégration des procédés., habilitation à diriger des recherches, Université de Perpignan. 31, 121, 257

[13] Canivet, Y. 2017, Analyse Entropique et Exergétique des Systèmes Énergétiques par des Représentations Géométriques., Thèse doctorat d'Energétique, Université Paris Nanterre., pp388

Multi-objective optimization of a solar-assisted ground-source CO_2 heat pump system for space and water heating using the Taguchi method and utility concept

Thor Alexis Sazon[a], Qian Zhang[a], and Homam Nikpey[a]

[a] University of Stavanger, Stavanger, Norway, thor.a.sazon@uis.no

Abstract:

This work deals with the optimization of a solar-assisted ground-source CO_2 heat pump system using the Taguchi method and the utility concept. Nine control factors were investigated, including the Borehole Heat Exchanger (BHE) length, BHE spacing, BHE number, solar collector (SC) area, tank thermal energy storage volume, BHE-SC mass flow rate, space heating return temperature, heat pump high-side pressure, and heat pump's output temperature. The seasonal performance factor (SPF), levelized cost of heating (LCOH), and the estimated maximum annual ground temperature change (GTC) were chosen as the response factors to evaluate system performance. The system model was developed using Modelica and 27 simulation runs were implemented according to the L_{27} (9^3) Taguchi orthogonal array. Single objective optimizations were first performed using the Taguchi method to determine the parameter combinations that would optimize the SPF, LCOH, and GTC, separately. After that, multi-objective optimization was performed using the combined Taguchi method-utility concept to determine the control factor combination that would give the optimal overall performance when all response factors are considered simultaneously and given equal importance. Single objective optimizations show that the SPF, LCOH, and GTC are individually most sensitive to the target output temperature of the heat pump, the BHE length, and the SC area, respectively. Optimizing the response factors individually resulted in an SPF of 4.2, an LCOH of 0.122 USD/kWh, and a GTC of 100.24%. Multi-objective optimization resulted in a control factor combination that gave an SPF of 3.58, LCOH of 0.165 USD/kWh, and GTC of 100.03%. When optimized, this system exhibited a performance that is almost comparable to that of conventional systems.

Keywords:

Trans-critical CO_2 heat pump; Borehole heat exchanger; Solar thermal; Modelica; Space and water heating; Taguchi method; Utility concept.

1. Introduction

Recent occurrences that have impacted energy security and affordability have provided significant momentum for a transition away from fossil-fuel-based heating. However, much is still to be done since fossil fuels still meet over 60% of the heating energy demand [1].

Heat pumps (HPs) are recognized by the European Union as a key technology for replacing existing gas boilers and reducing the reliance on Russian natural gas [2]. They can facilitate the utilization of low-grade energy to replace the traditional building energy supply with renewable sources and reduce the consumption of high-grade energy, such as electricity and fuels. However, most HPs currently operate using Hydrofluorocarbons (HFCs) as the working fluid [3]. HFCs replaced the once widely-used ozone-depleting Hydrochlorofluorocarbons (HCFCs) and Chlorofluorocarbons (CFCs) because they exhibited similarly good performance, efficiency, low toxicity, and non-flammability. Unfortunately, they are very strong greenhouse gases, some of which are around a thousand times more potent that CO_2 [4]. Recent initiatives, like the EU's F-gases regulation (EC517/2014) and the Kigali amendment to the Montreal Protocol, suggest that HFC production and utilization will be phased down in the coming years [5,6].

The use of natural working fluids has gained more attention recently because they offer a long-term solution to the problems posed by conventional working fluids. Much interest has been given to CO_2 (R744) due to its zero ozone depletion potential, low GWP, non-toxicity, non-flammability, superior thermodynamic properties, and affordability [7]. Lorentzen first proposed the modern use of CO_2 in a trans-critical HP cycle [8]. So far, it has been commercially applied in different sectors, like combined cooling, heating, ventilation, and air conditioning in supermarkets [9], water heating [10], and automotive air conditioning [11].

Air source heat pumps (ASHPs) account for the majority of global sales (60% in 2021) [2]. However, they have the problem of poor low-temperature heating performance and frosting of the heat exchanger [12].

Ground source heat pumps (GSHPs) are considered more efficient for indoor climate control applications since they use the heat from the ground, which remains at a nearly constant temperature. There are already some studies that have investigated the performance of CO_2 GSHPs [13–16].

Some of the challenges of using a GSHP are: (1) its higher installation cost relative to ASHPs due to the need to drill boreholes and install Borehole Heat Exchangers (BHEs) and (2) the difficulty of operating a single-source HP system continuously and efficiently [12]. One way to overcome these is to add another heat source, such as solar collectors (SCs), to allow for shorter BHEs and more operational options.

There are only very few studies that tackled SAGSHPs that use CO_2 as the working fluid. Kim et al. [17] performed simulations that showed how the various operating parameters could affect the performance of a residential solar-assisted ground-source CO_2 heat pump (CO_2 SAGSHP). They showed that the performance of a CO_2 HP can be improved by using solar and geothermal heat sources and it could supply sufficient heat to the space during winter. Choi et al. [18] performed simulations to compare an R22 and a CO_2 SAGSHP. They found that the R22 SAGSHP had a more stable performance and exhibited a higher heating capacity. Both studies considered relatively low temperatures since their systems were only designed for space heating (SH).

Optimizing the design and operation of SAGSHP systems is necessary to maximize its benefits, considering its high initial cost. However, these are quite complex systems, and optimizing them concerning multiple performance indicators would require a heavy simulation workload.

The Taguchi method [19] is an approach that could be employed to reduce the simulation runs needed to optimize systems. It makes use of an orthogonal array (OA) experimental design with a single analysis of variance and utilizes the signal-to-noise (S/N) ratio to assess parameter settings that minimize the sensitivity of system performance to sources of variations. However, the Taguchi method focuses on the optimization of one performance indicator at a time. To optimize systems while simultaneously considering multiple performance indicators, some studies combined the Taguchi method with the utility concept [20]. Some studies on manufacturing and quality engineering have integrated it with the Taguchi method to handle muti-response optimization problems [21,22]. Some studies have applied the Taguchi method with the utility concept on GSHP systems [23–27].

Verma and Murugesan [28] applied the Taguchi method and the utility concept on a conventional SAGSHP system to optimize the BHE length and the SC area for optimum performance. This paper employs the same concept but with a trans-critical CO_2 heat pump instead of a typical sub-critical vapor compression HFC heat pump. The optimization of a CO_2 SAGSHP for simultaneous space and water heating was performed. Different design and operating parameters were optimized using the Taguchi method and the utility concept, considering the seasonal performance factor (SPF), levelized cost of heating (LCOH), and the estimated maximum ground temperature change (GTC) in a year as response factors.

2. System description

The thermal energy system model in this study was developed using Modelica [29] through the Dymola v2021x [30] environment. It includes a CO_2 HP, SCs, BHEs, and tank thermal energy storage (TTES). The CO_2 HP was modeled using the Thermal Systems library v1.6.1 [31] and then calibrated with experimental data; the BHEs were modeled using a modified version of the MoBTES library v2.0 [32]; the SCs and TTES were both modeled with the Buildings library v9.0.0 [33]. Modelica Standard Library (MSL) v4.0.0 was used here.

2.1. The CO_2 solar-assisted ground source heat pump system model

Figure. 1 shows the schematic of the Modelica model of the whole thermal system in this work while the models of the different system components are given in Figure. 2. Verification of the validity of a system model is best done by calibrating it against data from a real-world installation of the exact system. However, since neither the facility nor data is available to the researchers, the system model was built using component models that have been validated or calibrated individually.

The SCs and the BHEs, connected in series, provide the heat input to the CO_2 HP. This configuration was chosen to allow the storage of excess solar energy in the ground. Different studies [34,35] have shown that this configuration results in better performance. When solar irradiation is available, the SC heats the cold water-side fluid coming from the evaporator of the heat pump. The solar-heated fluid is then directed to the BHEs, where it either extracts or injects energy, depending on its temperature relative to the ground. After passing through the BHEs, the fluid then goes to the evaporator of the CO_2 HP.

A controller that varies the rotational speed of the HP's compressor is used to set the temperature of the hot fluid coming from the CO_2 HP. Another controller sets the flow from the bottom of the TTES to ensure that the temperature there does not go below 50°C. This ensures that the temperature in the DHW distribution system is kept higher than the proliferation temperature of Legionella (20 - 45°C) [36]. The used colder fluid

coming from SH, water heating, and from the bottom of the TTES gets recirculated, mixed, and then reheated in the system. The temperature of the fluid after being used for DHW production was set at 10°C since the city water was assumed to be at 7°C. Although not explicitly modeled here, this assumes that the heat exchange process to supply the heat needed for DHW production occurred at a 3°C pinch temperature. The SH return temperature is varied as one of the control factors. The weather of Bergen, Norway, obtained from the EnergyPlus database [37], was used in this work and the demand side was represented by one year of measured hourly thermal demand data.

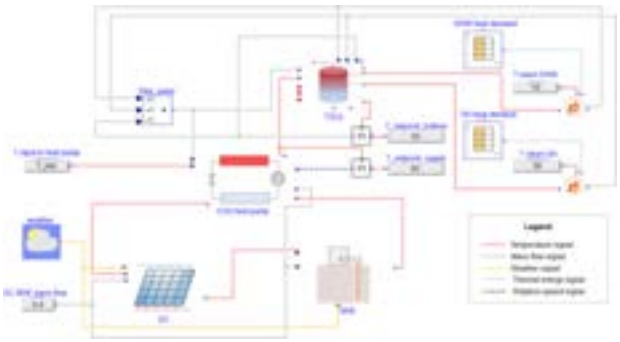

Figure. 1. The CO_2 SAGSHP system model.

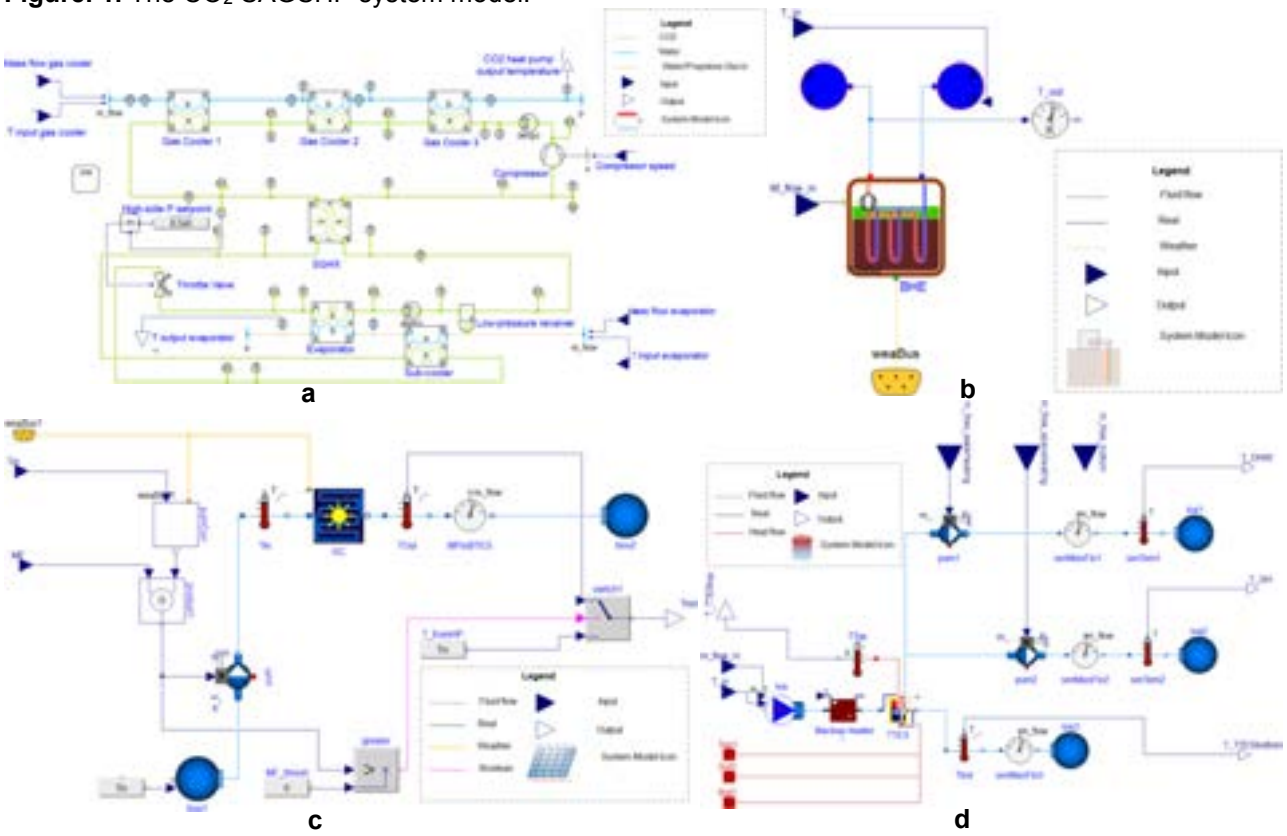

Figure. 2. Component models: (a) CO_2 HP, (b) BHE, (c) SC, (d) TTES.

2.2.1. The CO_2 heat pump model

The CO_2 HP (Figure. 2a), modeled after a 6.5-kW prototype unit [38,39], consists of counter-flow tripartite gas coolers, an evaporator, a compressor, a throttle valve, a suction gas heat exchanger (SGHX), a sub-cooler, and a low-pressure receiver. The throttle valve and the low-pressure receiver function together to control the high-side pressure of the HP [38]. The CO_2 HP model was developed using basic components, such as heat exchangers, valves, and compressors. Thus, it required calibration.

Measured data at the design condition at 85 bars were used to calibrate the model. Available information [38] was used to set the values of some parameters, including the tube diameters of all the tube-in-tube heat exchangers, as well as their weights, material of construction, and length; the size of the low-pressure receiver; and the compressor displacement and operating range. During the calibration, the values of the heat transfer coefficients of every heat exchanger and the efficiencies of the compressor were adjusted until

the model could simulate measured test data (Table 1). The model was calibrated against the data for the high-side pressure P_{GC} = 85 bars, while the other measured data were used to test the calibrated model. Calibration and test errors were obtained by comparing the measured and simulated COPs. The error generated by the calibrated model increases when it is used to simulate the off-design lower high-side pressure. This can be partly attributed to the choice of using a simplified compressor model that assumes constant efficiencies.

Table 1. Calibration of the CO_2 HP unit at ~60°C GC3 output temperature, ~35/30°C GC2 input/output temperature (GC refers the gas coolers; T_E is the evaporator temperature in the CO_2 loop).

Data type	P_{GC} (MPa)	T_E (°C)	Q_{GC1} (W)	Q_{GC2} (W)	Q_{GC3} (W)	Power (W)	Tin/out_{CO2_GC} (°C)	M_{CO2} (kg/s)	COP	Error
Measured*	8.5	-5.1	1608	2942	2357	1775	86.40/9.80	1.441	3.89	-0.26%
Calibrated	8.5	-5.1	1534	2934	2242	1730	86.56/9.80	1.449	3.88	
Measured*	8.98	-5	1550	2596	2801	1878	90.60/8.50	1.442	3.70	1.89%
Simulated	8.98	-5	1480	2637	2594	1779	90.76/8.17	1.417	3.77	
Measured	8.03	-5.1	1674	2728	1828	1699	81.60/18.00	1.440	3.67	4.90%
Simulated	8.03	-5.1	1707	2981	1907	1715	83.82/15.41	1.500	3.85	

*Design conditions

2.2.2. The borehole heat exchanger model

The BHE model (Figure. 2b) was developed using the MoBTES library [32]. MoBTES was originally developed under MSL v3.4, but in this work, it was revised to function with MSL v4.0. The parameters assumed for the BHE are given in Table 2. The ground was assumed to have the characteristics of Slate, one of the common rock types in some parts of Norway [40] while the thermal gradient was assumed to be 0.0125 K/m, similar to that of some wells drilled in Bergen, Norway [41].

Table 2. Summary of BHE parameters.

BHE parameter	Value
Geothermal gradient (K/m)	0.0125
Ground density (kg/m^3)	2760
Ground specific heat (J/kg-K)	920
Ground thermal conductivity (W/m-K)	2.1
BHE type	Single U
Borehole diameter (m)	0.15
Tube inner diameter (m)	0.034
Tube thickness (m)	0.003
Tube thermal conductivity (W/m-K)	0.4
Shank spacing (m)	0.08
Grout density (kg/m^3)	1900
Grout thermal capacity (J/kg-K)	1300
Grout thermal conductivity (W/m-K)	1.5

2.2.3. The solar thermal model

The solar thermal component model (Figure. 2c) was developed using the Buildings library v9.0.0 [33]. The main components used here are the solar pump controller and the SCs. The solar pump controller dictates whether the pump to the SCs is active or inactive depending on the value of the incident solar radiation. The pump is activated when the incident solar radiation is higher than the critical radiation, as defined by [42]:

$$G_{TC} = (F_R U_L (T_{in} - T_{ENV}))/(F_R(\tau\alpha)), \quad (1)$$

where G_{TC} is the critical solar radiation, $F_R U_L$ is the heat loss coefficient, T_{in} is the inlet temperature, T_{ENV} is the ambient temperature, and $F_R(\tau\alpha)$ is the maximum efficiency. When the incident solar radiation is lower than G_{TC}, the fluid bypasses the SCs. The solar collector was modeled according to the EN12975 [43] test data for a glazed flat-plate solar collector WTS-F1-K1/K2 from Max Weishaupt GmbH [44] (Table 3).

Table 3. Summary of SC parameters following the EN 12975 test standard

SC parameter	Value
Area/collector (m^2)	2.32
Dry weight (kg)	42
Fluid volume (m^3)	0.0023
Pressure drop during test conditions (Pa)	100
Mass flow per unit collector area (kg/s-m^2)	0.02
Maximum efficiency	0.802
Heat loss coefficient	3.601
Temperature dependence of heat loss	0.014
Incidence angle modifier	0.97

Nominal solar irradiance in ratings data (W/m^2)	1000
Nominal temperature difference in ratings data (K)	20

2.2.4. The tank thermal energy storage model

The TTES component (Figure. 2d) was also developed using the Buildings library. It uses the stratified storage tank model, which implements several volumes that exchange heat between themselves and with the ambient via conduction. Each volume contains a fluid port that may be used to inject or withdraw water to or from the tank. After passing through a backup heater, hot fluid from the heat pump is injected into the top layer. Relatively cold fluid is drawn from the bottom to manage the temperature inside the tank. Hot water from the top layer and the middle layer are withdrawn to provide the energy required for water heating and SH, respectively.

2.2.5. The thermal demand

Hourly demand data for SH and DHW production from a school in Stavanger, Norway was utilized as the reference of the demand input to this model. The choice of using heat demand and weather data from two different cities was due to data availability. Nonetheless, Stavanger and Bergen are two cities close to one another that have relatively similar climate conditions. The capacity of the system model in this study is limited to ~6.5 - 7 kW since the data used to calibrate the CO_2 heat pump is from a 6.5 - 7kW prototype unit. The demand data from the school is much higher than this so it was normalized, by dividing all data by the measured maximum demand, and then multiplied to 3 kW and 3.5 kW for SH and water heating, respectively (Figure. 3). Peak demands, which comprise less than 1% of the total demand data, were also filtered out for simplicity.

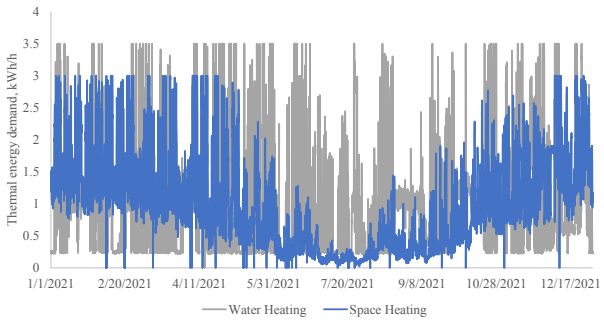

Figure. 3. The thermal energy demand.

3. Methods

The Taguchi method was implemented to determine the runs needed to be simulated, determine the parameters that significantly affect system performance, and determine how to optimize the system concerning individual performance indicators. Multi-objective optimization was then performed by combining the utility concept with the Taguchi method.

3.1. Taguchi method

The Taguchi method is a technique that applies the standard OA to determine the optimal number and set-up of the necessary trial runs for optimization. This allows the determination of the best level of each parameter (control factor) to optimize a given response factor. The first step in this method is the determination of the response factors, the objective functions, the parameters to be considered, and their corresponding levels. In this work, the response factors include the SPF, LCOH, and estimated maximum GTC. The objective is to keep the SPF and GTC high while keeping the LCOH low. Based on the number of control parameters and levels, the OA would be selected. The OA specifies the optimum number of trial runs needed to get maximum information about the system. The minimum number of trial runs to be conducted can be determined by:

$$N_{Taguchi} = 1 + NV(J-1). \quad (2)$$

Where $N_{Taguchi}$ is the minimum number of trial runs, NV is the number of variables, and J is the number of levels. Analysis of the results entails the calculation of the S/N ratio for each run and the analysis of variance (ANOVA). The S/N ratio is a measure of robustness, which is used to identify parameters that reduce process or product variability by minimizing the effects of uncontrollable factors. The S/N ratio of the SPF and GTC were calculated using the higher the better concept (Eq. 3), while the S/N ratio of the LCOH was calculated using the lower the better concept (Eq. 4).

$$Higher\ the\ better\ \frac{S}{N} = -10\ log_{10}\frac{1}{n}\sum_{i=1}^{n}\frac{1}{y_i^2} \quad (3)$$

$$Lower\ the\ better\ \frac{S}{N} = -10\ log_{10}\frac{1}{n}\sum_{i=1}^{n}y_i^2 \quad (4)$$

Where y_i is the raw response factor. ANOVA was used to determine the relative importance of the control factors by computing the percentage contribution of each parameter to the overall response. The degree of freedom (df), the sum of squares (SS), mean squares (MS), significance, and percentage of contribution were all calculated in the analysis.

3.2. The response and control factors

There are 9 control parameters considered, each having 3 levels (Table 4). Given this, an OA with 27 trial runs L_{27} was utilized. A full factorial combination will require 19683 experiments (3^9), which would be too time-consuming and complex. Applying the OA will give the same quality of information with just 27 runs. The BHE length, BHE number, SC area, and TTES volume were chosen since they are known to have a direct relationship with the cost of the system. The BHE spacing was included since it is a way to diffuse the thermal imbalance induced by the system to the ground [25]. The SC-BHE mass flow, CO_2 HP high-side pressure, and HP output temperature were chosen since they are parameters that could easily be controlled. The SH return temperature was included to represent the effects of the efficiency of the distribution system.

Table 4. Control factors investigated and their levels.

Parameter	Label	Level		
		1	2	3
BHE length (m)	A	50	100	150
BHE spacing (m)	B	3	5	7
BHE number	C	4	5	6
SC area (m^2) (number of collectors)	D	6.96 (3)	13.92 (6)	20.88 (9)
TTES volume (m^3)	E	0.5	1	2
SC-BHE mass flow* (kg/s)	F	0.2	0.4	0.8
SH return Temperature (°C)	G	20	30	35
CO_2 HP high-side pressure (MPa)	H	8.5	9.0	10
CO_2 HP output temperature** (°C)	I	60	65	70

*the flow rate of the fluid circulating through the SC, BHE, and the evaporator's waterside
**the temperature of the water as it comes out of the water side of the gas cooler

The values of the different levels of the parameters were determined by running trial simulation runs, some initial sizing calculations, and some operational considerations to ensure that the system would be able to provide the thermal energy demand while keeping the performance at reasonable levels.

The response factors considered in this work are the SPF, LCOH, and GTC. The SPF was calculated by dividing the total energy delivered by the system to the demand for a year by the total energy utilized to run it. The system spends energy to run the compressors and the circulation pumps. The LCOH was calculated by dividing the total cost of the system by its total energy production throughout its lifetime. Note that the electricity cost from 1 year of simulating the operation of the system was assumed to be the cost of the yearly operation. The assumptions used for cost calculations are summarized in Table 5. The GTC was obtained from the BHE model, which gives out the average ground temperature as it is utilized as a heat source or heat sink. The GTC is calculated by dividing the ground temperature after one year of simulation by the initial ground temperature (GTC > 100%: temperature in the ground went up; GTC < 100%: the ground temperature went down). Changes to the GTC were kept minimal, but a higher-the-better concept was applied since the system was designed for heating purposes. SPF, LCOH, and GTC values that are more representative of the long-term performance of the system could be obtained if the model was run for more years. However, because of the relatively big computational load, the simulations were limited to one year only. Trial runs show that the SPF and LCOH do not vary so much. However, the GTC was seen as highest for the first year and substantially declines in the succeeding years, assuming the yearly weather and demand remain similar. Hence, the GTC calculated in this study was assumed to represent the maximum expected temperature decline throughout the lifetime of the system.

Table 5. Summary of parameters used for cost calculations.

Parameter	Value	Reference/Notes
Cost of flat plate SC (EUR/m^2)	632.5	Average of SC costs in [45]
Cost of BHE (EUR/m)	65	[46]
Cost of TTES (EUR/m^3)	1150	Average cost of 0.8 – 2 m^3 TTES [47]
CO_2 Heat pump compressor cost (RMB)	$17547W^{0.4488}$	W is the rated compressor power [48]
CO_2 Heat pump gas cooler cost (RMB)	$1874.4A^{0.9835}$	A is heat exchanger area [48]
CO_2 Heat pump evaporator cost (RMB)	$331.7A^{0.9390}$	A is heat exchanger area [48]
Lifetime of the system (years)	25	[46]
Weighted Average Cost of Capital (WACC)	2%	Weighted Average Cost of Capital (WACC) HP [49]
Exchange rate (USD/EUR)	1/1.01	Exchange rate in Sept. 2022
Exchange rate (USD/RMB)	0.14/1	Exchange rate in Sept. 2022
Exchange rate (NOK/USD)	1/0.0975	Exchange rate in Sept. 2022
Electricity cost (NOK/kWh)	2.4415	Average electricity price in Norway in 2022 [50]

3.3. The utility concept

The utility concept was used to perform multi-response optimization by combining the individual values of the response factors (SPF, LCOH, and GTC) into one unified index called utility [20]. The overall utility function can be expressed as the utility of every performance indicator. Assuming that the performance indicators are independent of one another, the overall utility can be calculated as the sum of individual utilities. Prioritization of the effect of a response factor on the overall utility can be done by introducing a weighting coefficient w_j (Equation 5).

$$U(y_1, y_2, \dots, y_n) = \sum_{j=1}^{n} w_j U_j(y_j) \quad (5)$$

In the utility concept, a preference scale must be set up to represent the lowest and the highest performance. As in previous studies that used the utility concept in thermal energy systems [24–26,28], this study employs a minimum preference number of 0 and a maximum of 9. In a logarithmic scale, the preference number is represented by the formula below so that it has a value of 9 at the optimal level of a performance indicator.

$$U_j(y_j) = P_j = A_j \log \frac{y_j}{y'_j} \;\; with \;\; A_j = \frac{9}{\log \frac{y*}{y'_j}} \quad (6)$$

Where y'_j is the minimum acceptable value of a performance indicator and y* is the optimal value of the performance indicator. The overall utility is then calculated by:

$$U = \sum_{j=1}^{n} w_j P_j. \quad (7)$$

4. Results and discussions

The main objective of the study is to optimize a CO_2 SAGSHP system considering 3 performance indicators: SPF, LCOH, and GTC. Taguchi method was performed first to optimize the systems with regard to each performance indicator individually. Afterward, a combination of the Taguchi method and the utility concept was implemented to perform multi-objective optimization, assuming that all response factors are equally important.

4.1. Taguchi method – the orthogonal array and the S/N ratios

Following the Taguchi design concept, an L_{27} orthogonal array was chosen. Each trial run was performed according to the combination of parameters determined by this array to get the values of the response factors and the S/N ratios (Table 6). The S/N ratio values for the SPF and GTC were calculated using the higher-the-better concept while those for LCOH were calculated with the lower-the-better concept. The S/N ratios were then averaged in consideration of the different levels of each control factor (Figure. 4).

Table 6. The Taguchi L_{27} (3^9) standard orthogonal array and the experimental plan.

Trial No.	A	B	C	D	E	F	G	H	I	Response Factors			S/N ratios		
										SPF	LCOH (USD/kWh)	GTC (%)	SPF	TAC	GTC
1	1	1	1	1	1	1	1	1	1	3.52	0.131	99.3208	10.93	17.67	-0.0592
2	1	1	1	1	2	2	2	2	2	3.12	0.141	99.3329	9.88	17.02	-0.0581
3	1	1	1	1	3	3	3	3	3	2.81	0.152	99.329	8.96	16.36	-0.0585
4	1	2	2	2	1	1	1	2	2	3.44	0.154	99.8624	10.73	16.23	-0.012
5	1	2	2	2	2	2	2	3	3	3.15	0.162	99.856	9.95	15.81	-0.0125
6	1	2	2	2	3	3	3	1	1	2.58	0.182	99.8545	8.23	14.81	-0.0126
7	1	3	3	3	1	1	1	3	3	3.36	0.178	100.0275	10.52	15.01	0.0024
8	1	3	3	3	2	2	2	1	1	3.19	0.183	100.0203	10.07	14.75	0.0018
9	1	3	3	3	3	3	3	2	2	2.45	0.208	100.0196	7.78	13.62	0.0017
10	2	1	2	3	1	2	3	1	2	2.6	0.236	99.9384	8.31	12.56	-0.0054
11	2	1	2	3	2	3	1	2	3	2.48	0.241	99.9021	7.88	12.35	-0.0085
12	2	1	2	3	3	1	2	3	1	3.41	0.217	99.9313	10.65	13.26	-0.006
13	2	2	3	1	1	2	3	2	3	2.68	0.226	99.8583	8.56	12.91	-0.0123
14	2	2	3	1	2	3	1	3	1	3.37	0.209	99.833	10.54	13.6	-0.0145
15	2	2	3	1	3	1	2	1	2	2.85	0.225	99.8597	9.1	12.95	-0.0122
16	2	3	1	2	1	2	3	3	1	3.24	0.186	99.9441	10.22	14.63	-0.0049
17	2	3	1	2	2	3	1	1	2	2.72	0.202	99.9427	8.69	13.9	-0.005
18	2	3	1	2	3	1	2	2	3	2.83	0.201	99.959	9.04	13.94	-0.0036
19	3	1	3	2	1	3	2	1	3	2.22	0.313	99.8968	6.92	10.08	-0.009
20	3	1	3	2	2	1	3	2	1	3.38	0.278	99.8915	10.57	11.12	-0.0094
21	3	1	3	2	3	2	1	3	2	3.53	0.276	99.8694	10.95	11.2	-0.0113
22	3	2	1	3	1	3	2	2	1	2.89	0.245	99.9751	9.23	12.21	-0.0022
23	3	2	1	3	2	1	3	3	2	3.24	0.236	99.9989	10.22	12.53	-0.0001
24	3	2	1	3	3	2	1	1	3	2.65	0.256	99.9986	8.46	11.83	-0.0001
25	3	3	2	1	1	3	2	3	2	3.17	0.239	99.9221	10.01	12.42	-0.0068
26	3	3	2	1	2	1	3	1	3	2.35	0.268	99.9424	7.42	11.44	-0.005
27	3	3	2	1	3	2	1	2	1	3.92	0.23	99.9128	11.86	12.75	-0.0076

The combination of the levels that give the highest average S/N represents the optimal setup. Thus, the combination of control factors that gave the optimum SPF is A1B3C1D1E1F1G1H3I1. The effect of a certain control factor on the response factor could be inferred from the difference between the highest and the

lowest value of the S/N ratio. It could be seen that the SPF is most responsive to HP output temperature (I) and least sensitive to the TTES volume (E). Higher SPFs are expected when the target output temperature of the HP (I) is set low because less energy is needed by the compressor to reach a lower output temperature for a given high-side pressure. However, this is limited by the minimum temperature requirements of the DHW and SH distribution systems. Applying the determined control factor combination in simulation resulted in an optimal SPF of 4.2.

The combination of control factors that would give the optimum LCOH is A1B2C1D1E1F1G1H3I1. This resulted in an optimal LCOH of 0.122 USD/kWh, which is comparable to the LCOH of some conventional solar thermal combi HP systems [51]. As expected, optimizing the LCOH requires the reduction of capital and operation expenses, like using shorter and fewer BHEs (C), a smaller SC area (D), a smaller tank (E), a smaller pumping requirement (F), and a lower HP output temperature (I).

For GTC, the optimum parameter combination is A3B3C3D3E1F1G3H1I3. This resulted in an optimal GTC of 100.24%. The GTC is most responsive to the BHE spacing (B) and SC area (D). This means that the reduction of the temperature in the ground could be reduced by increasing the spacing between the BHEs or increasing the solar input to the system. Large solar input could even increase ground temperature, which could be beneficial to the system to some extent. Drilling deeper and more boreholes could also help, albeit would entail higher costs.

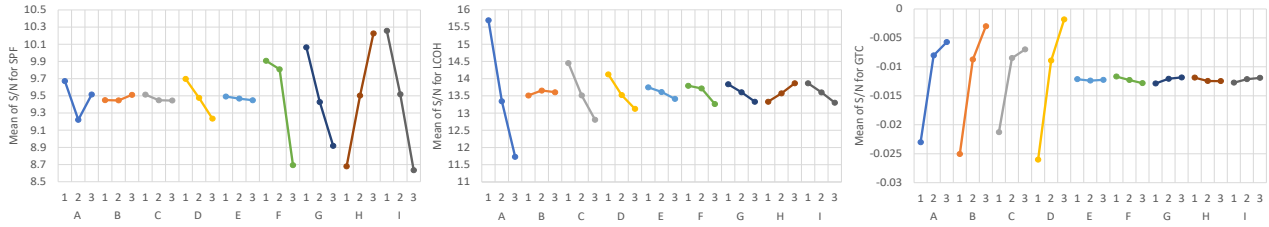

Figure. 4. The Taguchi average S/N ratio for each control parameter for every response factor.

4.2. Taguchi method – ANOVA analysis

ANOVA was used to estimate the relative significance of each parameter in terms of percentage contribution to the overall response (Table 7). The significance denotes which control factors could induce statistically significant effects on the response factor at different confidence levels. As shown, the SPF was most sensitive to the target output temperature of the HP. It is also noticeably more responsive to the operating parameters (F-I) than the design parameters (A-E). The LCOH is most sensitive to the BHE length (A) and number (C) since the BHE is the most expensive component of the system. This shows the influence of capital expenses. Almost all control parameters considered induced statistically significant changes to the LCOH. In contrast to the SPF, the GTC is mostly affected by the design parameters (A-D). The SC area (D) and BHE spacing (B) are shown to be the main contributors to the GTC.

Table 7. The results of the ANOVA for each response factor.

	df	SS	MS	F	Pr(>F)	Significance	Contribution	SS	MS	F	Pr(>F)	Significance	Contribution	SS	MS	F	Pr(>F)	Significance	Contribution
				SPF						**LCOH**						**GTC**			
A	2	0.942	0.471	1.817	0.224		2.43%	71.590	35.795	1673.636	0.000	***	75.83%	0.002	0.001	1586.000	0.000	***	20.19%
B	2	0.024	0.012	0.046	0.955		0.06%	0.095	0.048	2.221	0.171		0.10%	0.002	0.001	2357.000	0.000	***	30.00%
C	2	0.027	0.014	0.053	0.949		0.07%	12.285	6.142	287.189	0.000	***	13.01%	0.001	0.001	1112.000	0.000	***	14.15%
D	2	0.963	0.482	1.859	0.217		2.49%	4.564	2.282	106.707	0.000	***	4.83%	0.003	0.001	2786.000	0.000	***	35.46%
E	2	0.009	0.004	0.017	0.983		0.02%	0.513	0.256	11.988	0.004	**	0.54%	0.000	0.000	0.000	0.756		0.00%
F	2	8.183	4.091	15.791	0.002	**	21.13%	1.482	0.741	34.639	0.000	***	1.57%	0.000	0.000	6.000	0.024	*	0.08%
G	2	5.935	2.967	11.453	0.004	**	15.33%	1.156	0.578	27.013	0.000	***	1.22%	0.000	0.000	5.000	0.030	*	0.06%
H	2	10.776	5.388	20.795	0.001	***	27.83%	1.301	0.650	30.413	0.000	***	1.38%	0.000	0.000	2.000	0.170		0.03%
I	2	11.864	5.932	22.895	0.000	***	30.64%	1.430	0.715	33.419	0.000	***	1.51%	0.000	0.000	3.000	0.082	.	0.04%
Residual Error	8	2.073	0.259					0.171	0.021			***		0.000	0.000				

Significance codes: 0 '***' 0.001 '**' 0.01 '*' 0.05 '.'

4.3. Utility-Taguchi – S/N ratios

The utility index for each trial run for every response factor was calculated assuming that all response factors have equal weights (Table 8). The utility index is a number between 0 to 9 that represents the performance of the system (closer to 9 = better performance). The corresponding S/N ratios of the global utility indices were next calculated using the higher-the-better concept. The average S/N ratios are plotted in Figure. 5.

Taking note of the highest S/N ratio for each control parameter gives an optimal parameter combination of A1B3C2D3E2F1G1H3I1. This combination gives the best overall performance of the system. This results in

a global utility index of 6.77 (SPF of 3.58, an LCOH of 0.165 USD/kWh, and a GTC of 100.03%). Compared to a SAGSHP system that uses a conventional working fluid, this optimized system exhibited a slightly lower SPF ($SPF_{conventional}$ = 3.89) [52] and comparable LCOH ($LCOH_{conventional}$ = 0.043 – 0.206 USD/kWh) [51], and GTC (<1°C increase) [52]. Although relatively good performance has been observed, other system or component changes can be explored to further improve its overall performance.

Table 8. The utility indices and their S/N ratios

Trial	SPF utility	LCOH utility	GTC utility	Global utility	S/N ratio global utility
1	6.76	8.41	0.15	5.11	14.16
2	5.32	7.77	0.27	4.45	12.97
3	4.07	7.13	0.23	3.81	11.62
4	6.47	7.00	5.36	6.28	15.96
5	5.42	6.59	5.29	5.77	15.22
6	3.07	5.61	5.28	4.65	13.36
7	6.19	5.81	6.94	6.31	16.00
8	5.58	5.55	6.87	6.00	15.56
9	2.47	4.45	6.86	4.59	13.24
10	3.18	3.40	6.08	4.22	12.51
11	2.60	3.20	5.74	3.85	11.70
12	6.37	4.09	6.02	5.49	14.79
13	3.53	3.75	5.32	4.20	12.47
14	6.23	4.43	5.07	5.24	14.39
15	4.26	3.79	5.33	4.46	12.99
16	5.79	5.43	6.14	5.79	15.25
17	3.70	4.72	6.12	4.85	13.71
18	4.18	4.75	6.28	5.07	14.10
19	1.30	0.98	5.69	2.65	8.47
20	6.26	2.00	5.63	4.63	13.31
21	6.78	2.07	5.42	4.76	13.55
22	4.44	3.06	6.44	4.65	13.34
23	5.78	3.38	6.66	5.27	14.44
24	3.40	2.69	6.66	4.25	12.56
25	5.50	3.27	5.93	4.90	13.81
26	1.97	2.30	6.12	3.47	10.80
27	8.02	3.59	5.84	5.82	15.29

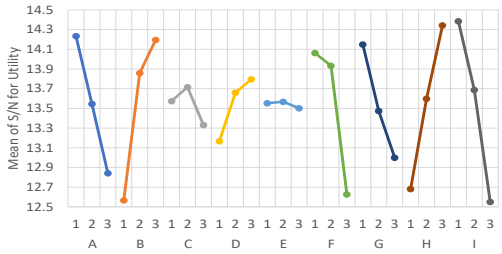

Figure. 5. The Taguchi average S/N ratio for each control parameter for every response factor.

4.4. Utility-Taguchi – ANOVA

As shown in Table 9, the utility index of a CO_2 SAGSHP is most sensitive to the BHE length (A) and least sensitive to the TTES size (E). Relatively significant contributions can also be seen from the output temperature of the HP (I), BHE spacing (B), high-side pressure of the HP (H), and mass flow rate of the fluid circulating through the BHE and SC (F).

Table 9. The results of the ANOVA for the utility index

	df	SS	MS	F	Pr(>F)	Significance	Contribution
			Utility Index				
A	2	25.138	12.569	22.415	0.001	***	22.64%
B	2	18.275	9.138	16.295	0.002	**	16.46%
C	2	2.969	1.485	2.647	0.131		2.67%
D	2	5.879	2.940	5.242	0.035	*	5.30%
E	2	0.053	0.027	0.047	0.954		0.05%
F	2	15.744	7.872	14.038	0.002	**	14.18%
G	2	7.082	3.541	6.315	0.023	*	6.38%
H	2	17.244	8.622	15.376	0.002	**	15.53%
I	2	18.634	9.317	16.615	0.001	***	16.78%
Residual Error	8	4.486	0.561				

Significance codes: 0 '***' 0.001 '**' 0.01 '*' 0.05 '.'

5. Conclusion

A SAGSHP system that utilizes CO_2 as a working fluid was modelled and then optimized in this study using the Taguchi method and the utility concept. The system was first optimized with regards to the SPF, LCOH, and GTC individually using the Taguchi method. Then a combination of the Taguchi method and the utility concept was then applied to perform multi-response optimization, considering the overall performance of the system if the SPF, LCOH, and GTC were deemed of equal importance.

The different combinations of control parameters that optimize the SPF, LCOH, and GTC individually, are A1B3C1D1E1F1G1H3I1, A1B2C1D1E1F1G1H3I1, and A3B3C3D3E1F1G3H1I3, respectively. Applying these set-ups to the model results in an optimal SPF of 4.2, LCOH of 0.122 USD/kWh, and GTC of 100.24%. According to the ANOVA results, the most influential control factors are the HP's target output temperature, the BHE length, and the SC area for the SPF, LCOH, and GTC, respectively.

Combining the Taguchi method with the utility concept allows multi-objective optimization to determine the parameter set-up that will give the optimal overall performance, considering all response factors are weighed equally. By this, the parameter combination that gave the optimal utility index is A1B3C2D3E2F1G1H3I1. This resulted in a 3.58 SPF, a 0.165 USD/kWh LCOH, and a 100.03% GTC. Compared to a SAGSHP system that uses a conventional working fluid, this optimized system exhibited a slightly lower SPF but comparable LCOH. Although relatively good performance has been observed, other system or component changes can be explored to further improve its overall performance. For instance, other system configurations could be examined.

Nomenclature

$\mathrm{F_R U_L}$	heat loss coefficient, W/(m² K)	NV	number of variables
$\mathrm{F_R}(\tau\alpha)$	maximum efficiency of the solar collector	T_{ENV}	ambient temperature, K
G_{TC}	critical solar irradiation, W/m²	T_{in}	inlet temperature, K
J	number of levels	U	overall utility index
$N_{Taguchi}$	minimum number of Taguchi trial run		

Subscripts and superscripts

C	compressor	DHW	domestic hot water
$CO2$	CO_2 working fluid	E	evaporator
$CO2\_GC$	CO_2 through the gas coolers	GC	gas cooler

References

[1] IEA, "Heating," 2022. Accessed: Feb. 03, 2023. [Online]. Available: https://www.iea.org/reports/heating

[2] IEA, "Heat Pumps," 2022. Accessed: Feb. 03, 2023. [Online]. Available: https://www.iea.org/reports/heat-pumps

[3] BSRIA Ltd., "BSRIA's view on refrigerant trends in AC and Heat Pump segments," Jan. 2020. Accessed: Nov. 14, 2022. [Online]. Available: https://www.bsria.com/uk/news/article/bsrias_view_on_refrigerant_trends_in_ac_and_heat_pump_segments/

[4] K. Onno, "Report Annex 46 HPT-AN46-04: Refrigerants for Heat Pump Water Heaters," Heat Pump Centre c/o RISE – Research Institutes of Sweden, Borås, Dec. 2019. Accessed: Oct. 12, 2022. [Online]. Available: https://heatpumpingtechnologies.org/annex46/wp-content/uploads/sites/53/2020/10/hpt-an46-04-task-1-refrigerants-for-heat-pump-water-heaters-1.pdf

[5] "EU legislation to control F-gases," Jan. 2015. Accessed: Apr. 01, 2022. [Online]. Available: https://ec.europa.eu/clima/eu-action/fluorinated-greenhouse-gases/eu-legislation-control-f-gases_en

[6] United Nations, "The Kigali Amendment (2016): The amendment to the Montreal Protocol agreed by the Twenty-Eighth Meeting of the Parties (Kigali, 10-15 October 2016) | Ozone Secretariat," Oct. 2016. Accessed: Mar. 18, 2021. [Online]. Available: https://ozone.unep.org/treaties/montreal-protocol/amendments/kigali-amendment-2016-amendment-montreal-protocol-agreed

[7] J. Wang, M. Belusko, M. Evans, M. Liu, C. Zhao, and F. Bruno, "A comprehensive review and analysis on CO2 heat pump water heaters," *Energy Conversion and Management: X*, vol. 15, p. 100277, Aug. 2022, doi: 10.1016/j.ecmx.2022.100277.

[8] G. Lorentzen, "Trans-critical vapour compression cycle device," WO1990007683A1, Jul. 12, 1990 Accessed: Feb. 17, 2021. [Online]. Available: https://patents.google.com/patent/WO1990007683A1/en

[9] A. Hafner *et al.*, "Efficient and integrated energy systems for supermarkets," *11th IIR Gustav Lorentzen Conference on Natural Refrigerants: Natural Refrigerants and Environmental Protection, GL 2014*, pp. 311–319, Jan. 2014.

[10] K. Hashimoto, “Technology and Market Development of CO2 Heat Pump Water Heaters (ECO CUTE) in Japan,” IEA Heat Pump Centre Newsletter, 2006. Accessed: Feb. 28, 2023. [Online]. Available: http://waterheatertimer.org/pdf/Market-develop-CO2.pdf
[11] AutomotiveTechinfo, “CO2 as a Refrigerant is Happening,” Jun. 2021. Accessed: Feb. 28, 2023. [Online]. Available: https://automotivetechinfo.com/wp-content/uploads/2021/06/CO2-as-a-Refrigerant-is-Happening.pdf
[12] Z. Han, C. Bai, X. Ma, B. Li, and H. Hu, “Study on the performance of solar-assisted transcritical CO2 heat pump system with phase change energy storage suitable for rural houses,” *Solar Energy*, vol. 174, pp. 45–54, Nov. 2018, doi: 10.1016/j.solener.2018.09.001.
[13] W. Wu, H. M. Skye, and J. J. Dyreby, “Modeling and experiments for a CO2 ground-source heat pump with subcritical and transcritical operation,” *Energy Conversion and Management*, vol. 243, p. 114420, Sep. 2021, doi: 10.1016/j.enconman.2021.114420.
[14] Y.-J. Kim and K.-S. Chang, “Development of a thermodynamic performance-analysis program for CO2 geothermal heat pump system,” *Journal of Industrial and Engineering Chemistry*, vol. 19, no. 6, pp. 1827–1837, Nov. 2013, doi: 10.1016/j.jiec.2013.02.028.
[15] Z. Jin, T. M. Eikevik, P. Nekså, and A. Hafner, “Investigation on CO2 hybrid ground-coupled heat pumping system under warm climate,” *International Journal of Refrigeration*, vol. 62, pp. 145–152, Oct. 2015, doi: 10.1016/j.ijrefrig.2015.10.005.
[16] Z. Jin, T. M. Eikevik, P. Nekså, A. Hafner, and R. Wang, “Annual energy performance of R744 and R410A heat pumping systems,” *Applied Thermal Engineering*, vol. 117, pp. 568–576, May 2017, doi: 10.1016/j.applthermaleng.2017.02.072.
[17] W. Kim, J. Choi, and H. Cho, “Performance analysis of hybrid solar-geothermal CO2 heat pump system for residential heating,” *Renewable Energy*, vol. 50, pp. 596–604, Feb. 2013, doi: 10.1016/j.renene.2012.07.020.
[18] J. Choi, B. Kang, and H. Cho, “Performance comparison between R22 and R744 solar-geothermal hybrid heat pumps according to heat source conditions,” *Renewable Energy*, vol. 71, pp. 414–424, Nov. 2014, doi: 10.1016/j.renene.2014.05.057.
[19] G. Taguchi, *Introduction to Quality Engineering: Designing Quality Into Products and Processes*. Asian Productivity Organization, 1986.
[20] P. Karande, S. K. Gauri, and S. Chakraborty, “Applications of utility concept and desirability function for materials selection,” *Materials & Design*, vol. 45, pp. 349–358, Mar. 2013, doi: 10.1016/j.matdes.2012.08.067.
[21] P. Kumar, P. B. Barua, and J. L. Gaindhar, “Quality optimization (multi-characteristics) through Taguchi’s technique and utility concept,” *Quality and Reliability Engineering International*, vol. 16, no. 6, pp. 475–485, 2000, doi: 10.1002/1099-1638(200011/12)16:6<475::AID-QRE342>3.0.CO;2-0.
[22] T. Goyal, R. S. Walia, and T. S. Sidhu, “Multi-response optimization of low-pressure cold-sprayed coatings through Taguchi method and utility concept,” *Int J Adv Manuf Technol*, vol. 64, no. 5, pp. 903–914, Feb. 2013, doi: 10.1007/s00170-012-4049-8.
[23] S. Kumar and K. Murugesan, “Optimization of geothermal interaction of a double U-tube borehole heat exchanger for space heating and cooling applications using Taguchi method and utility concept,” *Geothermics*, vol. 83, p. 101723, Jan. 2020, doi: 10.1016/j.geothermics.2019.101723.
[24] N. Pandey, K. Murugesan, and H. R. Thomas, “Optimization of ground heat exchangers for space heating and cooling applications using Taguchi method and utility concept,” *Applied Energy*, vol. 190, pp. 421–438, Mar. 2017, doi: 10.1016/j.apenergy.2016.12.154.
[25] Y. Xie, P. Hu, F. Lei, N. Zhu, and L. Xing, “Parameters optimization of ground source heat pump system combined energy consumption and economic analysis using Taguchi method,” in *Proceedings of the IGSHPA Research Track 2018*, International Ground Source Heat Pump Association, Sep. 2018, pp. 1–15. doi: 10.22488/okstate.18.000047.
[26] T. Sivasakthivel, K. Murugesan, and H. R. Thomas, “Optimization of operating parameters of ground source heat pump system for space heating and cooling by Taguchi method and utility concept,” *Applied Energy*, vol. 116, pp. 76–85, Mar. 2014, doi: 10.1016/j.apenergy.2013.10.065.
[27] T. Sivasakthivel, K. Murugesan, and P. K. Sahoo, “Optimization of ground heat exchanger parameters of ground source heat pump system for space heating applications,” *Energy*, vol. 78, pp. 573–586, Dec. 2014, doi: 10.1016/j.energy.2014.10.045.
[28] V. Verma and K. Murugesan, “Optimization of solar assisted ground source heat pump system for space heating application by Taguchi method and utility concept,” *Energy and Buildings*, vol. 82, pp. 296–309, Oct. 2014, doi: 10.1016/j.enbuild.2014.07.029.
[29] Modelica Association, “Modelica Language,” 2021. https://modelica.org/modelicalanguage.html (accessed Sep. 02, 2021).
[30] Dassault Systèmes, “Dymola,” 2022. https://www.3ds.com/products-services/catia/products/dymola/ (accessed May 23, 2022).

[31] Claytex Technia Company, “Thermal Systems Library & TIL Suite.” 2022. Accessed: May 23, 2022. [Online]. Available: https://www.claytex.com/products/dymola/model-libraries/thermal-systems-library/
[32] J. Formhals, H. Hemmatabady, B. Welsch, D. O. Schulte, and I. Sass, “A Modelica Toolbox for the Simulation of Borehole Thermal Energy Storage Systems,” *Energies*, vol. 13, no. 9, Art. no. 9, Jan. 2020, doi: 10.3390/en13092327.
[33] Lawrence Berkeley National Laboratory, “Modelica Buildings library.” Berkley, May 31, 2022. Accessed: Oct. 17, 2022. [Online]. Available: https://simulationresearch.lbl.gov/modelica/index.html
[34] L. Dai, S. Li, L. DuanMu, X. Li, Y. Shang, and M. Dong, “Experimental performance analysis of a solar assisted ground source heat pump system under different heating operation modes,” *Applied Thermal Engineering*, vol. 75, pp. 325–333, Jan. 2015, doi: 10.1016/j.applthermaleng.2014.09.061.
[35] S. H. Razavi, R. Ahmadi, and A. Zahedi, “Modeling, simulation and dynamic control of solar assisted ground source heat pump to provide heating load and DHW,” *Applied Thermal Engineering*, vol. 129, pp. 127–144, Jan. 2018, doi: 10.1016/j.applthermaleng.2017.10.003.
[36] Health and Safety Executive UK, “Managing legionella in hot and cold water systems,” 2022. https://www.hse.gov.uk/healthservices/legionella.htm (accessed Nov. 14, 2022).
[37] ASHRAE, “EnergyPlus Weather Data (Bergen).” 2001. Accessed: Oct. 17, 2022. [Online]. Available: Deutsches Institut für Normung
[38] J. Stene, “Residential CO2 Heat Pump System for Combined Space Heating and Hot Water Heating,” Fakultet for ingeniørvitenskap og teknologi, 2004. Accessed: May 23, 2022. [Online]. Available: https://ntnuopen.ntnu.no/ntnu-xmlui/handle/11250/233381
[39] J. Stene, “Residential CO2 heat pump system for combined space heating and hot water heating,” *International Journal of Refrigeration*, vol. 28, no. 8, pp. 1259–1265, Dec. 2005, doi: 10.1016/j.ijrefrig.2005.07.006.
[40] J. Stene, “Ground-source heat pump systems in Norway IEA HPP Annex 29 (2004-2006),” Norway, NEI-NO--0706407, 2007. [Online]. Available: https://inis.iaea.org/search/search.aspx?orig_q=RN:38097084
[41] K. Midttømme, “Geothermal Energy in Norway and Hordaland,” Bergen Energy Lab, 06 2017. [Online]. Available: https://www.uib.no/en/energy/108628/kirsti-midtt%C3%B8mme-geothermal-energy-norway-and-hordaland
[42] J. A. Duffie and W. A. Beckman, *Solar Engineering of Thermal Processes*, 4th ed. New Jersey: John Wiley & Sons, Inc., 2013. [Online]. Available: https://onlinelibrary.wiley.com/doi/pdf/10.1002/9781118671603.fmatter
[43] Deutsches Institut für Normung, “DIN EN 12975-1:2011-01 Thermal solar systems and components - Solar collectors - part 1: General requirements.” Jan. 2011.
[44] TUV Rheinland DIN CERTCO, “DIN CERTCO - Registration Number 011-7S094 F: Summary of EN 12975 Test Results.” 2014. Accessed: Oct. 18, 2022. [Online]. Available: https://www.dincertco.tuv.com/registrations/60064975?locale=en
[45] R. Valančius, A. Jurelionis, R. Jonynas, V. Katinas, and E. Perednis, “Analysis of Medium-Scale Solar Thermal Systems and Their Potential in Lithuania,” *Energies*, vol. 8, no. 6, Art. no. 6, Jun. 2015, doi: 10.3390/en8065725.
[46] B. Badenes, M. Á. Mateo Pla, T. Magraner, J. Soriano, and J. F. Urchueguía, “Theoretical and Experimental Cost–Benefit Assessment of Borehole Heat Exchangers (BHEs) According to Working Fluid Flow Rate,” *Energies*, vol. 13, no. 18, Art. no. 18, Jan. 2020, doi: 10.3390/en13184925.
[47] F. Mauthner and S. Herkel, *IEA SHC Task52 - Deliverable C1: Classification and benchmarking of solar thermal systems in urban environments*. 2017. doi: 10.13140/RG.2.2.31437.28648.
[48] Y. Wang, S. Zong, Y. Song, F. Cao, Y. He, and Q. Gao, “Experimental and techno-economic analysis of transcritical CO2 heat pump water heater with fin-and-tube and microchannel heat exchanger,” *Applied Thermal Engineering*, vol. 199, p. 117606, Nov. 2021, doi: 10.1016/j.applthermaleng.2021.117606.
[49] Quintel, “Cost of capital | Energy Transition Model,” 2023. https://docs.energytransitionmodel.com/main/cost-wacc/ (accessed Feb. 17, 2023).
[50] Statistics Norway, “09387: Electricity price, grid rent and taxes for households, by contents and quarter. Statbank Norway,” *SSB*, 2023. https://www.ssb.no/en/system/ (accessed Feb. 17, 2023).
[51] IEA, “Levelized cost of heating (LCOH) for consumers, for selected space and water heating technologies and countries,” *IEA*, 2022. https://www.iea.org/data-and-statistics/charts/levelized-cost-of-heating-lcoh-for-consumers-for-selected-space-and-water-heating-technologies-and-countries (accessed Feb. 23, 2023).
[52] C. Xi, L. Lin, and Y. Hongxing, “Long term operation of a solar assisted ground coupled heat pump system for space heating and domestic hot water,” *Energy and Buildings*, vol. 43, no. 8, pp. 1835–1844, Aug. 2011, doi: 10.1016/j.enbuild.2011.03.033.

Exergy-based sizing of a R290 air-to-water reversible heat pump for space heating and cooling purposes

Volodymyr Voloshchuk[a], Paride Gullo[b], Oleksandr Stepanets[c] and Eugene Nikiforovich[d]

[a] National Technical University of Ukraine "Igor Sikorsky Kyiv Polytechnic Institute", Kyiv, Ukraine, vl.volodya@gmail.com
[b] University of Southern Denmark (SDU), Department of Mechanical and Electrical Engineering, Sønderborg, Denmark, parigul@sdu.dk
[c] National Technical University of Ukraine "Igor Sikorsky Kyiv Polytechnic Institute", Kyiv, Ukraine, stepanets.av@gmail.com
[d] National Technical University of Ukraine "Igor Sikorsky Kyiv Polytechnic Institute", Kyiv, Ukraine, eugnik@gmail.com

Abstract:

This works aims at evaluating the impact of different ratios of heating design loads to cooling ones on the thermodynamic efficiency of a R290 air-to-water reversible heat pump with the aid of an exergy analysis. The potential improvements of the investigated solution were also assessed. The heat pump was sized for a two-pipe fan-coil system designed with supply/return water temperatures of 45/40 °C in winter and 7/12 °C in summer. The outdoor air was cooled from -7 ℃ to -12 ℃ in heating mode and heated from 30 ℃ up to 35 ℃ in cooling mode, respectively. The heating loads were varied in a range from 8 kW to 13 kW, whereas the cooling loads were ranged between 6 kW and 15 kW, respectively.

The results obtained showed that heat exchanger sizing plays a significant impact on the distribution of exergy destruction within the system components. As the system was sized based on the cooling load, the air-based heat exchanger was found to be oversized and the water-based heat exchanger was observed to be undersized for covering the heating loads and vice versa. It was also found that for the ratios of heating design loads and cooling ones less than 1.2 the system should be sized based on the cooling design loads. In this case lower system exergy destruction could be obtained. Furthermore, in this case the thermodynamic improvement of the air-based heat exchanger, the water-based heat exchanger and the compressor had approximately the same potential of increasing the efficiency of the system. As the ratios of heating design loads and cooling ones were higher than 1.2, the heating load should have been used for sizing the system components due to higher thermodynamic efficiency of the system compared to the previous case and technical possibilities to be operated. Removing the avoidable irreversibilities within the air-based heat exchanger offered the biggest decrease of the exergy destruction within the system.

Keywords:

Exergetic analysis; Exergy destruction; Heat pump; Propane; Thermodynamic enhancement.

1. Introduction

Today a large offer of reversible heat pumps with investment costs comparable to those of non-reversible units is available. These solutions are one of the most widely used heating, ventilation and air conditioning (HVAC) technologies in Europe. About 70 % of air-conditioned office buildings are cooled down by reversible heat pumps [1]. Such units have the ability to provide low carbon heating and cooling and great thermal comfort levels through one distribution system (assuming the emitter is capable of providing both modes).

During the last decades the research has demonstrated the impact of refrigerants on ozone depletion and global warming. So, the implementation of highly thermodynamically efficient heat pumps relying on very low global warming potential (GWP) refrigerants is compulsory.

The authors of [2] dealt with a numerical analysis of a reversible air-source heat pump incorporated into the HVAC system of a typical office building. The results obtained showed that energy performance of the system strongly depended on the of the unbalance indicator, estimated as the ratio of cooling loads to heating ones of the building, and of the overall index of heat pump oversizing/downsizing with respect to the design loads of the building.

In [3] the simulation model of an air-to-water R410A based reversible heat pump was developed to simulate its performance at off design conditions. The annual efficiency of the system was found to be able to be maximized by changing temperature, flow rate of air and water and refrigerant mass flow rate.

The relationship between air-to-water heat pump performance using R410A and the Italian building heating and cooling loads was numerically investigated by Madonna et al. [4]. The authors observed that the reversible heat pump oversizing can cause an excessive on/off cycling and an efficiency reduction (up to 25 %).

Most of current heat pumps use hydrofluorocarbons (HFCs), which have a massive GWP. Therefore, in the last decade several studies have been devoted to investigate environmentally friendlier alternatives, e.g. hydrofluoroolefins (HFOs) [5] and hydrocarbons (HFC) [6]. However, the recent environmental concerns on HFOs are promoting the adoption of natural refrigerants. In addition, [6] observed that R290 is a better substitute for R134a than R600a for residential heat pump water heaters.

From the review made above, it is possible to conclude that the reversible heat pump sizing strongly affects energy efficiency of such systems. Most of the investigations has been based on analyses focusing on conventional objective variables and conventional energy assessments. However, application of exergy analysis would provide better insight into possibilities to reveal the location, the magnitude and the sources of thermodynamic inefficiencies within the system. Advanced exergy analysis additionally considers thermodynamic interactions among components and the real potential for the system improving. Investigations of reversible heat pumps with ultra-low GWP refrigerants are also of high interest. Thus, the goal of this work is to bridge this knowledge gap by applying the exergy methodology for sizing an air-to-water reversible heat pump with propane and evaluating the real potential for its thermodynamic improvement.

2. Materials and Methods

2.1. Conventional Exergy Analysis

In the conventional exergetic evaluation of the k-th component of the investigated system, the following equations were used [7]:

- Gouy–Stodola theorem

$$\dot{E}_{D,k} = T_0 \dot{S}_{gen,k}, \qquad (1)$$

where $\dot{E}_{D,k}$ is exergy destruction rate within the k-th component, T_0 is temperature of the reference environment and $\dot{S}_{gen,k}$ is the entropy generation owing to internal irreversibilities;

- the exergy balance for the k-th component

$$\dot{E}_{F,k} = \dot{E}_{P,k} + \dot{E}_{D,k}, \qquad (2)$$

where $\dot{E}_{F,k}$ and $\dot{E}_{P,k}$ are exergy rates associated with fuel and product of the component, respectively.

2.2. Evaluation of Removable Exergy Destruction

Since evaluating removable parts of exergy destruction occurring in each system component was within the scope of the work the method presented in [8] was applied. According to this method, the avoidable exergy destruction rate ($\dot{E}_{D,k}^{AV,INT}$), which is internally caused, can be computed as the difference between the total exergy destruction of the investigated component ($\dot{E}_{D,k}$), i.e., calculated under real operation conditions, and its exergy destruction ($\dot{E}_{D,k}^{MIN,k}$) evaluated under conditions at which its irreversibilities are reduced by improving its efficiency while accounting for the fact that the remaining components are operating under real conditions:

$$\dot{E}_{D,k}^{AV,INT} = \dot{E}_{D,k} - \dot{E}_{D,k}^{MIN,k}. \qquad (3)$$

The avoidable exergy destruction within the k-th component, which is caused by the avoidable irreversibilities occurring within the r-th component (i.e., externally caused) ($\dot{E}_{D,k}^{AV,EXT,r}$), can be computed by subtracting the exergy destruction rate ($\dot{E}_{D,k}^{MIN,r}$) within the k-th component under the conditions at which the r-th component operates with reduced irreversibilities and the remaining components are operated under their real conditions from the exergy destruction rate ($\dot{E}_{D,k}$) occurring within the k-th component under its real operation conditions:

$$\dot{E}_{D,k}^{AV,EXT,r} = \dot{E}_{D,k} - \dot{E}_{D,k}^{MIN,r}. \qquad (4)$$

The importance of the components from the thermodynamic viewpoint and priorities for improving the k-th components were identified on the basis of the sum of the internally caused avoidable exergy destruction ($\dot{E}_{D,k}^{AV,INT}$) and the externally caused avoidable exergy destruction within the remaining components ($\dot{E}_{D,r}^{AV,EXT,k}$)

$$\dot{E}_{D,k}^{AV,\Sigma,INT,EXT} = \dot{E}_{D,k}^{AV,INT} + \sum_{\substack{r=1 \\ r\neq k}}^{n-1} \dot{E}_{D,r}^{AV,EXT,k} . \qquad (5)$$

2.2. Case Study

The investigated heat pump system was considered to be able to be reversed by means of a refrigerant change-over, which reverses the flow passage into the two exchangers (Figure 1). In cooling mode, the air-based heat exchanger (outside heat exchanger) worked as condenser, rejecting heat into the outdoor air, while the water-based heat exchanger (inside heat exchanger) worked as an evaporator, absorbing heat from the two-pipe water distribution system. In heating mode, the air exchanger worked as an evaporator, absorbing heat from outdoor air, while the water exchanger worked as a condenser, transferring heat into the same distribution system. It was assumed that the cold-emission terminal units were adapted for hot emission at low temperatures.

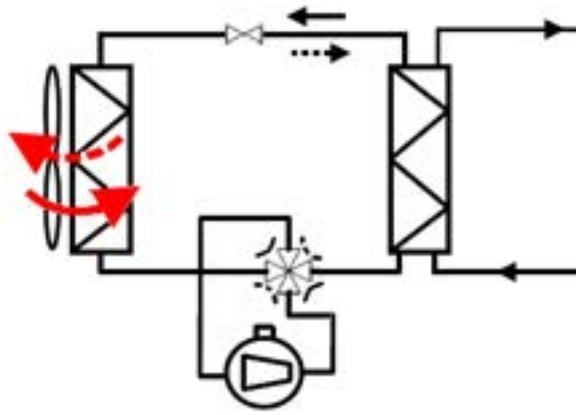

Figure. 1. Investigated reversible air-to-water unit connected to a two-pipe distribution system.

In heating mode the outside air was assumed to be cooled in the air-based heat exchanger from −7 °C down to −12 °C and the water was assumed to be heated in the condenser (water-based heat exchanger) from 40 °C up to 45 °C. In cooling mode the outside air was assumed to be heated in the outside heat exchanger (condenser) from 30 °C up to 35 °C and the chilled water was assumed to be cooled in the inside heat exchanger (evaporator) from 12 °C down to 7 °C. The pinch-point temperature in the outside and inside heat exchangers were taken as 12 K and 5 K, respectively. The pressure drop of the working fluids in the pipes and components was neglected.

In the design mode, which was used for sizing system, the following assumption were made:

- the evaporation temperature of R290 was calculated as the difference between the temperature of the secondary working fluid (air for heating mode and chilled water for cooling mode, respectively) at the evaporator outlet and the pinch point temperature difference in the evaporator (12 K or 5 K, respectively);
- the temperature of R290 at the compressor inlet was increased by 5 K due to superheating within the evaporator;
- the condensation temperature of R290 was calculated by adding the value of the pinch point temperature of the condenser (5 K or 12 K, respectively) to the temperature of the secondary working fluid (heated water or outside air, respectively) at the condenser outlet.

The specific power required by compressor was estimated from the following equation [3], [9]

$$l_{CM} = \frac{\left(h_{CM,in} - h_{CM,out}\right)}{\eta_{is}}, \qquad (6)$$

where η_{is} is the compressor's isentropic efficiency, and $h_{CM,in}$ and $h_{CM,out}$ are the specific enthalpies at the inlet and outlet of the compressor, respectively.

Specific enthalpy at the compressor outlet after real compression was calculated as

$$h_{CM,out} = h_{CM,in} + \frac{h_{CM,out,is} - h_{CM,in}}{\eta_{is}}, \qquad (7)$$

where $h_{CM,out,is}$ is the specific enthalpy at the compressor outlet after isentropic compression.

The volumetric (η_{vol}) and isentropic (η_{is}) efficiencies of the compressor were calculated using Pierre's correlations for "good" reciprocating compressors [10] following the methodology used in [11], [12]:

$$\eta_{vol} = k_1 \cdot \left(1 + k_s \cdot \frac{t_{CM,in} - 18}{100}\right) \cdot exp\left(k_2 \cdot \frac{p_{CM,in}}{p_{CM,out}}\right); \qquad (8)$$

$$\frac{\eta_{vol}}{\eta_{is}} = \left(1 + k_e \cdot \frac{t_{CM,in} - 18}{100}\right) \cdot exp\left(a \cdot \frac{T_1}{T_2} + b\right), \qquad (9)$$

where $t_{CM,in}$ is the refrigerant temperature at the compressor inlet, $p_{CM,in}/p_{CM,out}$ is the pressure ratio, T_1/T_2 is the ratio of the condensation and evaporation absolute temperatures (in Kelvin) corresponding to the discharge and the suction compressor pressures. The remaining symbols - k_1, k_s, k_2, k_e, a and b - are constants equal to 1.04, 0.15, −0.07, −0.1, −2.40, and 2.88, respectively.

The expansion valve was modelled as an isenthalpic component

$$h_{EXV,in} = h_{EXV,out}, \qquad (10)$$

where $h_{EXV,in}$, $h_{EXV,out}$ are the specific enthalpies at the inlet and outlet of the expansion valve, respectively.

Mass flow rate of R290 under design conditions in heating mode was calculated as

$$\dot{m}_{wf} = \frac{\dot{Q}_{Heat}^{Design}}{h_{CD,in} - h_{CD,out}}, \qquad (11)$$

where $\dot{Q}_{Heat}^{Design}$ is the heating load of the system at the design conditions, $h_{CD,in}$ is the specific enthalpy of the refrigerant at the condenser inlet (i.e. at the compressor outlet) and $h_{CD,out}$ is the specific enthalpy of the refrigerant at the condenser outlet.

And consequently, the heat transfer rate in the evaporator was calculated as

$$\dot{Q}_{EV} = \dot{m}_{wf}\left(h_{EV,out} - h_{EV,in}\right), \qquad (12)$$

where $h_{EV,out}$ and $h_{EV,in}$ are the specific enthalpies of R290 at the evaporator's outlet and inlet, respectively.

In cooling mode the mass flow rate of R290 was calculated by the following equation

$$\dot{m}_{wf} = \frac{\dot{Q}_{Cool}^{Design}}{h_{EV,out} - h_{EV,in}}, \qquad (13)$$

where $\dot{Q}_{Cool}^{Design}$ is the cooling load of the system at the design conditions, $h_{EV,out}$ is the specific enthalpy of the refrigerant at the evaporator outlet (at the compressor inlet) and $h_{EV,in}$ is the specific enthalpy of the refrigerant at the evaporator inlet (at the expansion valve outlet).

Hence, the heat transfer rate of the condenser was found as

$$\dot{Q}_{CD} = \dot{m}_{wf}\left(h_{CD,in} - h_{CD,out}\right). \qquad (14)$$

The power required by compressor was evaluated as

$$\dot{W}_{CM} = \dot{m}_{wf}\left(h_{CM,out} - h_{CM,in}\right). \qquad (15)$$

The compressor swept volume ($\dot{V}_s$) was estimated using the following equation

$$\dot{V}_s = \frac{\dot{m}_{wf}\upsilon_{CM,in}}{N\eta_{vol}}. \qquad (16)$$

where N is the compressor rotational speed, η_{vol} is the compressor's volumetric efficiency and $\upsilon_{CM,in}$ is the specific volume of R290 at the suction line of the compressor.

Mass flow rates of the secondary fluids through the heat exchangers were governed by the energy rate balance equations

$$\dot{m}_{air(water)} = \frac{\dot{Q}_{EV}}{\left(h_{air(water),in} - h_{air(water),out}\right)}; \qquad (17)$$

$$\dot{m}_{water(air)} = \frac{\dot{Q}_{CD}}{\left(h_{water(air),out} - h_{water(air),in}\right)}; \qquad (18)$$

where h_{air} and h_{water} are the specific enthalpies of the air and water at inlet (in) and outlet (out), respectively.

The condenser was divided into two main sections: the de-superheating region and the phase change region. The subcooled zone was neglected. The evaporator consisted of an evaporation region and a superheating one. The heat transfer rate within these sections was evaluated using the logarithmic mean temperature difference approach [3], [9]

$$\dot{Q} = U \cdot A \cdot LMTD, \qquad (19)$$

where $\dot{Q}$ is the heat transfer rate, U is the overall heat transfer coefficient, A is the heat transfer area of the considered section and $LMTD$ is the logarithmic mean temperature difference defined by the following equation

$$LMTD = \frac{\Delta T_2 - \Delta T_1}{ln\left(\frac{\Delta T_2}{\Delta T_1}\right)}, \qquad (20)$$

where ΔT_1 and ΔT_2 are temperature differences between the working fluids on the hot and cold sides at each end of the considered section.

For the air-based heat exchanger (finned-tube heat exchanger), the following expression for the overall heat transfer coefficient referring to secondary fluid heat transfer surface was applied

$$U = \left(\frac{1}{\alpha_{air}} + \frac{1}{\alpha_{wf}} \cdot \frac{A_{air}}{A_{wf}}\right)^{-1}, \qquad (21)$$

where A_{air} and A_{wf} are the heat transfer areas on the air and the refrigerant side, respectively, and α_{air} and α_{wf} are the corresponding heat transfer coefficients, respectively.

The plate heat exchanger was designed as the inside unit.

The data presented in [13], [14], [15] were generalized and used for calculation of the overall heat transfer coefficients within the specified condenser and evaporator regions.

The temperature and absolute pressure of the outside air were used to ascertain the thermodynamic properties at the evaporator inlet for heating mode and at the condenser inlet for cooling mode, respectively.

The thermo-physical properties of all the working fluids were evaluated via CoolProp [16]. The simulations were performed through MATLAB software package.

The same procedure was applied for the design of the system and estimation of internally and externally caused exergy destruction with pinch point temperatures in the air-based heat exchanger and the water-based heat exchanger equal to 6 K and 2 K, respectively and increased efficiency of the compressor by 10 % compared to real designed conditions.

After finding geometric parameters of the system, the operating characteristics were calculated for off-design conditions. During the off-design operations in heating mode, the water temperatures at the inlet and outlet of the water-based heat exchanger were equal to 40 °C and 45 °C, respectively. During cooling mode at the off-

design conditions, the water temperatures at the water-based heat exchanger's outlet and inlet were equal to 7 °C and 12 °C, respectively. Then, the mathematical approach suggested in [17] was adopted to assess the thermodynamic parameters of the investigated heat pumps under off-design conditions in both cooling and heating modes. During these calculations the mass flow rate of the working fluid was governed by the Eq. (16). Eq. (19) was used for the evaluation of either the heat transfer rates or the temperatures within considered heat transfer section.

As the main focus of this work is on the implementation of an exergetic evaluation, the overall heat transfer coefficients were considered as constant under off-design modes and equal to the ones estimated for the design mode.

The off-designed modes were estimated under real operation conditions and under conditions conducive to the evaluation of the removable exergy destruction.

Exergetic analysis was performed based on the selection of the ambient (outdoor) air parameters as the reference ones [18].

3. Results and Discussion

Heat transfer areas of the air- and water-based heat exchangers, which were required for covering heating or cooling loads by the inside heat exchanger, are presented in Figure 1. It could be observed that in general for covering cooling loads the air-based heat exchanger was found to be larger and the water-based heat exchanger was found to be smaller compared to the required heat transfer areas for covering the same heating loads with the same pinch point temperature. Also, the value of oversizing or undersizing depended on the ratios between heating and cooling loads ($\dot{Q}_{Heat}/\dot{Q}_{Cool}$), which then was found to affect the irreversibilities within the components.

For example, if the system had been sized with the specified pinch point temperature within heat exchangers on the base of heating design loads equal to 12 kW the area of the outside heat exchanger should have been 7.7 m^2 and the area of the inside heat exchanger should have been 2.2 m^2. However, for providing the same cooling load with the same pinch point temperature the heat transfer area of the outside and inside heat exchangers should have been 18.4 m^2 and 1.3 m^2, respectively. Thus, the system designed in this way would have had undersized area of the air-based heat exchanger for operation with 12 kW cooling load, which should have been compensated with larger temperature difference, leading to increased irreversibilities within the outside heat exchanger, expansion valve and compressor. On the other hand, the water-based heat exchanger of the system would have had oversized area for covering 12 kW cooling demand, which would have provided lower temperature difference within the heat exchanger and thus decreased irreversibilities within this component, expansion valve and compressor. The higher the ratios of heating demand to cooling one ($\dot{Q}_{Heat}/\dot{Q}_{Cool}$) for the system designed on the base of heating loads, the better agreement between the designed and required areas of the air-based heat exchanger and larger oversizing of the designed areas of water-based heat exchanger for covering cooling loads.

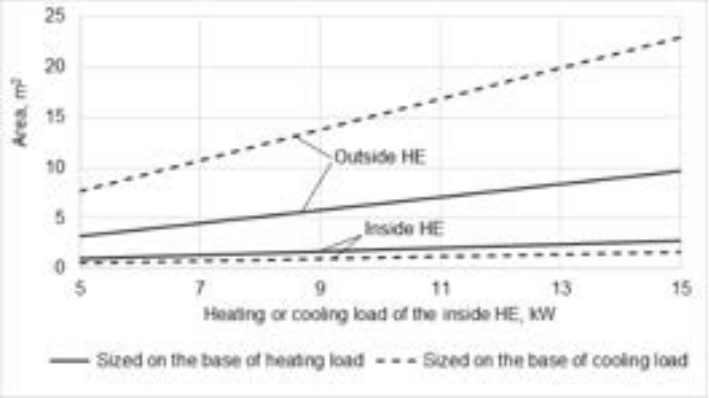

Figure. 2. Needed heat transfer areas for the air- and water-based heat exchangers required for covering the heating or cooling loads of the water-based heat exchanger.

If the system had been sized using a cooling design load of 10 kW, the areas of the outside and inside heat exchangers would have been equal to 15.3 m^2 and 1.1 m^2, respectively, and appropriate exergy destruction would have been obtained. In case of providing 10kW of heating load, due to oversized area of the air-based heat exchanger and undersized area of the water-based heat exchanger, this system would demonstrate other values of exergy destruction. For higher ratios $\dot{Q}_{Heat}/\dot{Q}_{Cool}$ of the system designed on the base of the cooling loads the degree of difference between the designed areas of the air-based heat exchanger and the needed

ones for covering heating loads would have been smaller. However, undersizing the water-based heat exchanger for covering heating loads would have been bigger.

The distribution of the exergy destruction rates in the components of the investigated system sized on the base of the heating design load with different ratios between heating and cooling loads ($\dot{Q}_{Heat}/\dot{Q}_{Cool}$) is shown in Figure 3. It could be seen that when the designed system was operated for covering cooling loads (empty circles in Figure 3a) at the ratios of heating loads to cooling ones ranging from 0.65 to 1.4 the air-based heat exchanger had much larger exergy destruction rates compared to the mode operated for covering heating loads (filled circles in Figure 3,a). This could be obtained due to undersized area of the outside heat exchanger, which was explained with the above suggestions (see Figure 2).

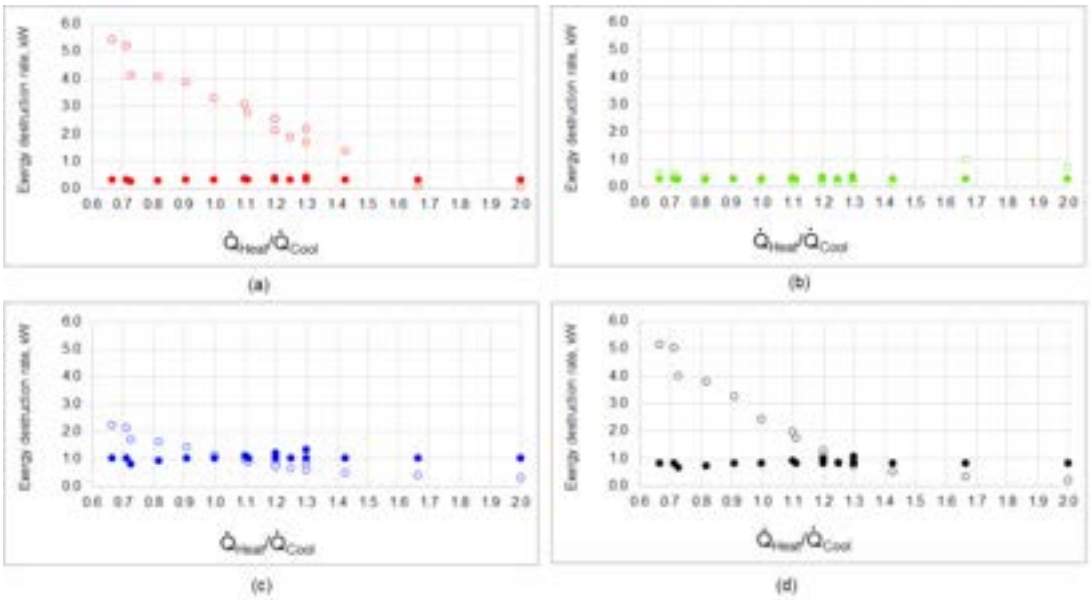

Figure. 3. Exergy destruction rates in the components of the system sized on the base of heating design loads with different ratios to heating loads and cooling ones: a) outside heat exchanger, b) inside heat exchanger, c) compressor, d) expansion valve, filled circles – operated for covering heating load, empty circles - operated for covering cooling load.

Oversized areas of the water-based heat exchanger did not change substantially exergy destruction rates within the inside heat exchanger operated for covering cooling loads (see Figure 3b).

At the ratios of heating loads and cooling ones ranging from 0.65 to 1.4 temperature differences in the air-based heat exchanger was increased. As a result, it provided higher pressure ratios in the compressor and the expansion valve. The exergy destruction within these components was incresed (empty circles in Figure 3c and Figure 3d) in comparison to heating modes (filled circles in Figure 3c and Figure 3d).

If the system had been sized on the base of the cooling design loads (Figure 4) it could not have been operated for the values of $\dot{Q}_{Heat}/\dot{Q}_{Cool}$ higher than 1.3 due to technological limitations. Similarly to the previous scenario, in case of sizing system based on cooling design loads the outside heat exchanger would have been oversized for covering heating loads, resulting in decreased exergy destruction rates (filled circles in Figure 4a) within this component compared to the cooling modes (empty circles in Figure 4a). For $\dot{Q}_{Heat}/\dot{Q}_{Cool}$ values higher than 0.8, in case of the use of an undersized water-based heat exchanger during heating modes, the exergy destruction rates would have been higher (filled circles in Figure 4b) than during cooling modes (empty circles in Figure 4b). As it was said above, oversized and undersized areas led to a decrease and an increase of temperature driving force for heat transfer (temperature differences) and pressure ratios, respectively. As a result, exergy destruction rates within compressor and expansion valve in heating mode (filled circles in Figure 4c and Figure 4d) were found to be larger than during cooling modes (empty circles in Figure 4c and Figure 4d).

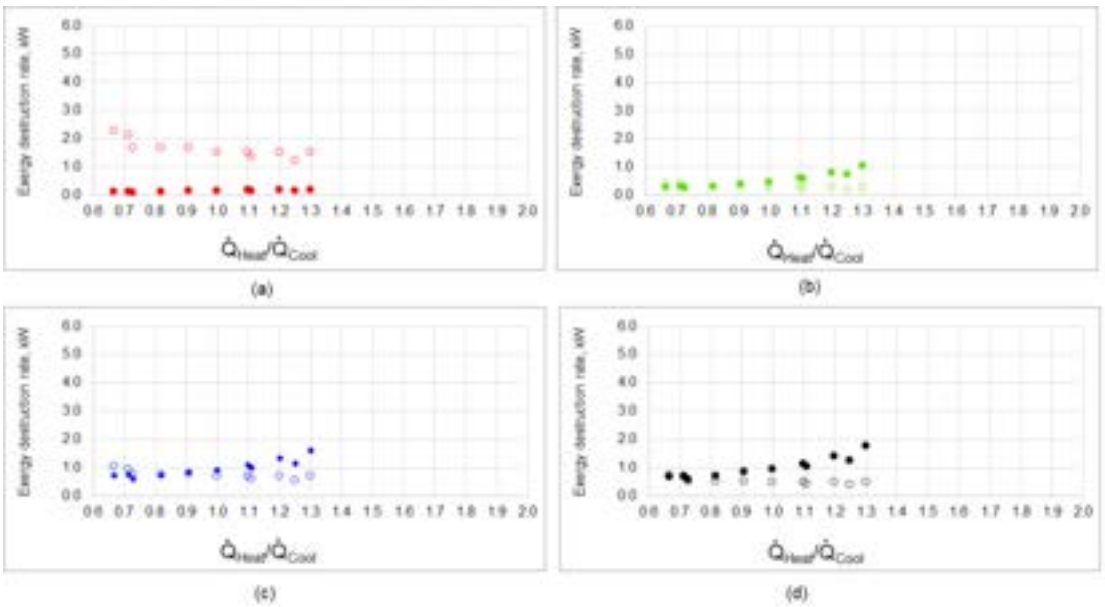

Figure. 4. Exergy destruction rates in the components of the system sized on the base of cooling design loads with different ratios of heating loads and cooling ones: a) outside heat exchanger, b) inside heat exchanger, c) compressor, d) expansion valve, filled circles – operated for covering heating load, empty circles - operated for covering cooling load.

The values of the total exergy destruction rates in the system with different ratios of heating loads and cooling ones are shown in Figure 5.

It was found that for the ratios of heating loads and cooling ones within the range 0.65 to 1.2 the system should have been sized based on the cooling loads. For such design lower total exergy destruction within the system could have been obtained (from 4.5 kW to 6.5 kW) compared to the system sized on the base of heating loads, which demonstrated higher total exergy destruction (from 12.0 kW to 6.5 kW).

As the ratios of heating design loads and cooling ones were higher than 1.2, the heating design load should have been used for sizing the system components. Under such design conditions thermodynamic efficiency of the system was substantially decreased.

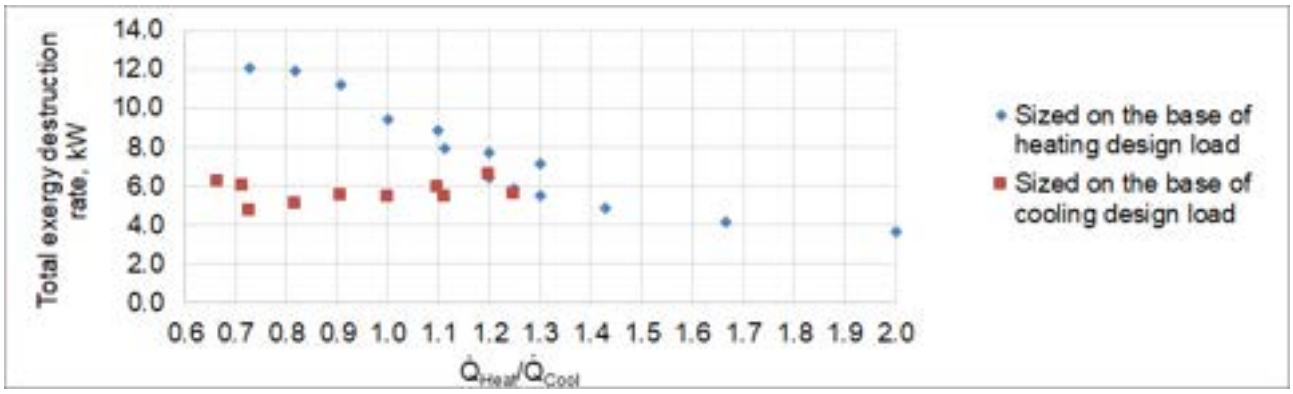

Figure. 5. Total exergy destruction rates in the system with different ratios between heating and cooling loads.

The values of the removable and internally caused exergy destruction rate within the k-th component ($\dot{E}_{D,k}^{AV,INT}$) and that of the removable and externally caused exergy destruction rate within the remaining components caused by the k-th component ($\dot{E}_{D,r}^{AV,EXT,k}$) for the system designed on the base of heating load are presented in Figure 6. The system was operated for covering 10 kW and 7 kW of heating and cooling loads, respectively.

It was observed from Figure 7 that 0.44 kW of removable exergy destruction rate in the compressor could be reduced by improving this component. Another smaller part of removable exergy destruction rate in the compressor was caused by the irreversibilities that occurred in the remaining components: inside heat exchanger (i.e. 0.07 kW) and outside heat exchanger (0.29 kW). Also, 0.11 kW of removable exergy destruction rate within the inside heat exchanger could be reduced by decreasing the irreversibilities within this component. Another part of removable exergy destruction rate within the water-based heat exchanger

(0.06 kW) could be eliminated by improving the remaining components (i.e. compressor and air-based heat exchanger). The results obtained from the proposed methodology indicated that the internally caused and removable exergy destruction rate in the expansion valve was zero. This means that the exergy destruction rate within this component could be reduced through the enhancement in the remaining components. The inside heat exchanger was found to be responsible for 0.12 kW of exergy destruction rate, which could be removed within the expansion valve. In addition, 0.38 kW of removable exergy destruction rate within the expansion valve were caused by irreversibilities within outside heat exchanger. Furthermore, 0.04 kW of removable exergy destruction rate within the expansion valve depended on irreversibilities taking place in the compressor. According to the results presented in Figure 6 the largest value of exergy destruction rate, which could be removed in the air-based heat exchanger, was internally caused (0.62 kW). Furthermore, 0.12 kW and 0.05 kW of avoidable exergy destruction within the outside heat exchanger depended on irreversibilities taking place in the compressor and the inside unit, respectively.

Therefore, according to the results obtained the highest priority for improvement of the considered system had to be given to the air-based heat exchanger. This was due to the fact that the sum of the internally caused and the externally caused exergy destruction rates, which could be avoided within the investigated heat pump with the help of improving this component, was the highest one and equal to 1.32 kW (i.e. 58 %) (Figure 6). Secondly, the investigator needed to focus on the compressor, being accountable for 0.63 kW (i.e. 27 %) of avoidable exergy destruction within the evaluated system. Thirdly, the water-based heat exchanger enhancement was found to lead to a potential decrease of 0.35 kW (i.e. 15 %) of exergy destruction.

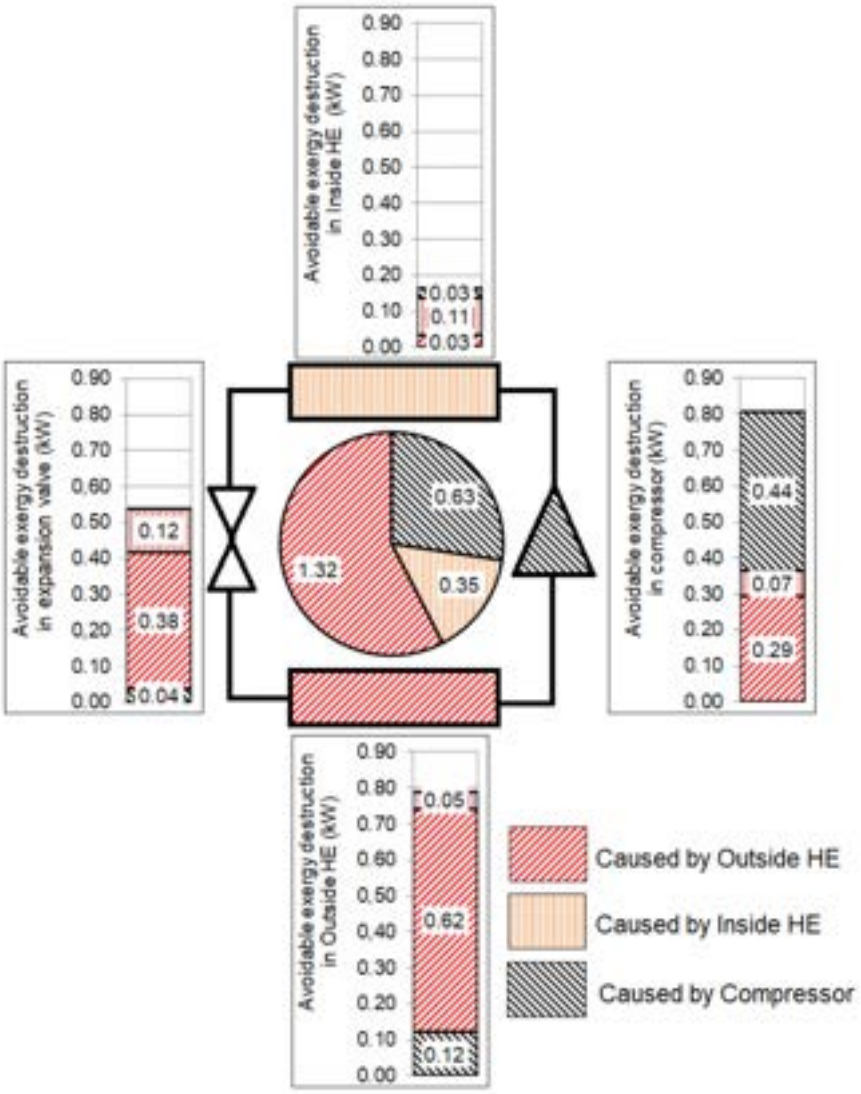

Figure. 6. Values of the internally caused and externally caused avoidable exergy destruction rates (kW) in the components of the R290 air-to-water reversible heat pump designed on the base of heating load and operated for covering 10kW and 7kW of heating and cooling loads, respectively.

Compared to the results obtained from the previous case, slightly different values of the avoidable exergy destruction were evaluated within the studied system designed on the base of cooling load (see Figure 7). The

system was operated for covering 8kW and 11kW of heating and cooling loads. The major differences were found to be associated with the avoidable parts of exergy destruction caused by the outside heat exchanger.

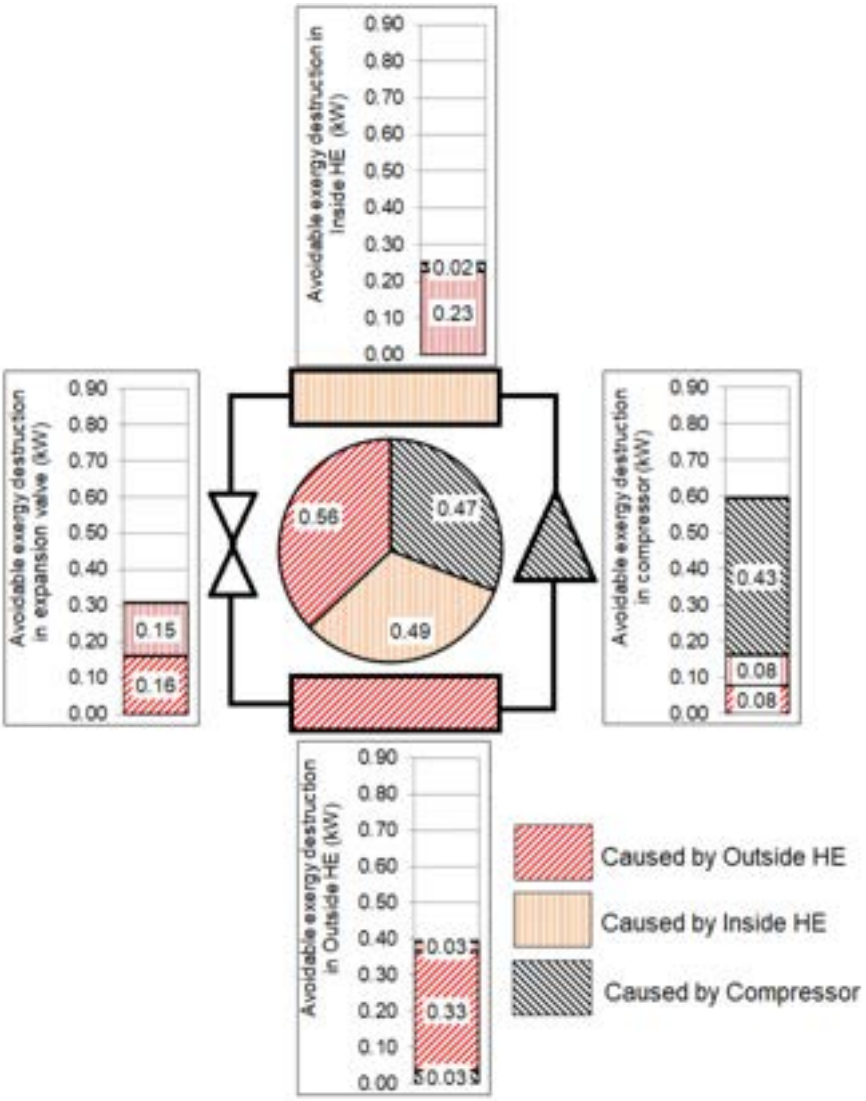

Figure. 7 Values of the internally caused and externally caused avoidable exergy destruction rates (kW) in the components of the R290 air-to-water reversible heat pump designed on the base of cooling load and operated for covering 8 kW and 11 kW of heating and cooling loads, respectively.

The impact of irreversibilities within the outside heat exchanger was decreased. As a result, the outcomes obtained showed that the outside, inside heat exchanger and the compressor had almost the same priority for improvement. The air-based heat exchanger revealed 0.56 kW avoidable exergy destruction within the system. Also, the water-based heat exchanger offered the potential to reduce 0.49 kW of exergy destruction rate. Also, the compressor enhancement was found to lead to a potential decrease of 0.47 kW of exergy destruction within the investigated system.

Conclusions

An exergy-based analysis has been carried out to evaluate the impact of different ratios between heating and cooling loads on the thermodynamic efficiency of a reversible air-to-water system with propane for providing heating and cooling needs. The following major findings have been found:

- For the system sized using heating design loads undersizing and oversizing areas of the air-based and water-based heat exchangers were obtained, respectively, for covering the same cooling loads with the same pinch-point temperature differences and vice versa;
- Such disagreement of designed and required heat transfer areas affect the distribution of irreversibilities within the components of the system significantly, mainly depending on the ratios between heating and cooling loads and the way of system design (based on heating or cooling load);
- It has been found that for the ratios of heating loads and cooling ones within the range from 0.65 to 1.2 the system should be sized based on the cooling loads. For such design approach lower total

exergy destruction within the system could be obtained compared to the system sized on the base of heating loads. As the ratios of heating loads and cooling ones are higher than 1.2, the heating design load should be used for sizing system components. This is because the system designed on the base of cooling load could not be operated for covering heating needs due to technological limitations.

- For the system sized on the base of heating loads removing the avoidable irreversibilities within the air-based heat exchanger offer the biggest decrease of the exergy destruction within the system;
- thermodynamic improvement of the air-based, water-based heat exchanger and the compressor have approximately the same potential for increasing efficiency of the system designed on the base of cooling loads.

Acknowledgments

This research was funded by Ministry of Education and Science of Ukraine, grant number 0122U001750.

Nomenclature

A heat transfer area (m^2)

$\dot{E}$ exergy rate (W)

$\dot{Q}$ heat transfer rate (W)

h specific enthalpy (J/kg)

k_1, k_s, k_2, k_e, a and b Pierre's correlations constants

$\dot{m}$ mass flow rate (kg s^{-1})

N rotational speed (s^{-1})

P absolute pressure (Pa)

s specific entropy (J/(kg·K))

T temperature (K)

U overall heat transfer coefficient (W m^{-2} K^{-1})

V volume (m^3)

υ specific volume (m^3/kg)

$\dot{W}$ shaft power required by compressor (W)

GWP global warming potential

HFC hydrofluorocarbon

HFO hydrofluoroolefin

HVAC heating, ventilation, and air-conditioning

$LMTD$ logarithmic mean temperature difference (K)

Subscripts and superscripts

air air

CD condenser

CM compressor

D destruction

EXT external

EXV expansion valve

EV evaporator

F fuel

gen generation

INT, int internal

is isentropic

in inlet

k k-th component

MIN minimum

out outlet

P product

r r-th component

ref refrigerant

s swept

vol volumetric

water water

wf working fluid

0 reference state

Greek symbols

α convection heat transfer coefficient (W m^{-2} K^{-1})

η efficiency (-)

References

1. Stabat, P.; Marchio, D. Opportunities for Reversible Chillers in Office Buildings in Europe. *Build. Simul.* **2009**, *2*, 95–108, doi:10.1007/S12273-009-9207-z.
2. Dongellini, M.; Naldi, C.; Morini, G.L. Sizing Effects on the Energy Performance of Reversible Air-Source Heat Pumps for Office Buildings. *Applied Thermal Engineering* **2017**, *114*, 1073–1081, doi:10.1016/j.applthermaleng.2016.12.010.
3. Kinab, E.; Marchio, D.; Rivière, P.; Zoughaib, A. Reversible Heat Pump Model for Seasonal Performance Optimization. *Energy and Buildings* **2010**, *42*, 2269–2280, doi:10.1016/j.enbuild.2010.07.007.
4. Madonna, F.; Bazzocchi, F. Annual Performances of Reversible Air-to-Water Heat Pumps in Small Residential Buildings. *Energy and Buildings* **2013**, *65*, 299–309, doi:10.1016/j.enbuild.2013.06.016.
5. Nawaz, K.; Shen, B.; Elatar, A.; Baxter, V.; Abdelaziz, O. R1234yf and R1234ze(E) as Low-GWP Refrigerants for Residential Heat Pump Water Heaters. *International Journal of Refrigeration* **2017**, *82*, 348–365, doi:10.1016/j.ijrefrig.2017.06.031.
6. Nawaz, K.; Shen, B.; Elatar, A.; Baxter, V.; Abdelaziz, O. R290 (Propane) and R600a (Isobutane) as Natural Refrigerants for Residential Heat Pump Water Heaters. *Applied Thermal Engineering* **2017**, *127*, 870–883, doi:10.1016/j.applthermaleng.2017.08.080.
7. Bejan, A.; Tsatsaronis, G.; Moran, M.J. *Thermal Design and Optimization*; Wiley: New York, 1996; ISBN 978-0-471-58467-4.
8. Voloshchuk, V.; Gullo, P.; Nikiforovich, E. A New Approach for Estimation of Avoidable Exergy Destruction: A Case Study of a Heat Pump Unit. *In Proceedings of the 34th International Conference on Efficency, Cost, Optimization, Simulation and Envi-ronmental Impact of Energy Systems (ECOS'21),* **2021**, 1369–1377.
9. Sanaye, S.; Chahartaghi, M.; Asgari, H. Dynamic Modeling of Gas Engine Driven Heat Pump System in Cooling Mode. *Energy* **2013**, *55*, 195–208, doi:10.1016/j.energy.2013.03.074.
10. Granryd E.; Ekroth I.; Lundqvist P.; Melinder A.; Palm B.; Rohlin P. *Refrigeration Engineering*; K. Tek. Högskolan, 1999;
11. Mateu-Royo, C.; Sawalha, S.; Mota-Babiloni, A.; Navarro-Esbrí, J. High Temperature Heat Pump Integration into District Heating Network. *Energy Conversion and Management* **2020**, *210*, 112719, doi:10.1016/j.enconman.2020.112719.
12. Mateu-Royo, C.; Navarro-Esbrí, J.; Mota-Babiloni, A.; Amat-Albuixech, M.; Molés, F. Thermodynamic Analysis of Low GWP Alternatives to HFC-245fa in High-Temperature Heat Pumps: HCFO-1224yd(Z), HCFO-1233zd(E) and HFO-1336mzz(Z). *Applied Thermal Engineering* **2019**, *152*, 762–777, doi:10.1016/j.applthermaleng.2019.02.047.
13. Botticella, F.; Viscito, L. Seasonal Performance Analysis of a Residential Heat Pump Using Different Fluids with Low Environmental Impact. *Energy Procedia* **2015**, *82*, 878–885, doi:10.1016/j.egypro.2015.11.832.
14. Longo, G.A. Heat Transfer and Pressure Drop during Hydrocarbon Refrigerant Condensation inside a Brazed Plate Heat Exchanger. *International Journal of Refrigeration* **2010**, *33*, 944–953, doi:10.1016/j.ijrefrig.2010.02.007.
15. Amalfi, R.L.; Vakili-Farahani, F.; Thome, J.R. Flow Boiling and Frictional Pressure Gradients in Plate Heat Exchangers. Part 1: Review and Experimental Database. *International Journal of Refrigeration* **2016**, *61*, 166–184, doi:10.1016/j.ijrefrig.2015.07.010.
16. Bell, I.H.; Wronski, J.; Quoilin, S.; Lemort, V. Pure and Pseudo-Pure Fluid Thermophysical Property Evaluation and the Open-Source Thermophysical Property Library CoolProp. *Ind. Eng. Chem. Res.* **2014**, *53*, 2498–2508, doi:10.1021/ie4033999.
17. Herbas, T.B.; Berlinck, E.C.; Uriu, C.A.T.; Marques, R.P.; Parise, J.A.R. Steady-State Simulation of Vapour-Compression Heat Pumps. *Int. J. Energy Res.* **1993**, *17*, 801–816, doi:10.1002/er.4440170903.
18. *Exergy Assessment Guidebook for the Built Environment: ECBCS Annex 49 - Low Exergy Systems for High-Performance Buildings and Communities*; Torío, H., Fraunhofer-Institut für Bauphysik, Eds.; Fraunhofer Verlag: Stuttgart, 2011; ISBN 978-3-8396-0239-3.

A high-fidelity simulation model for the precise characterization of a solar air-cooled ammonia-water absorption chiller at part load operation

María Esther Palacios-Lorenzo[a], José Daniel Marcos[a]

[a]*Dept. of Energy Engineering, UNED, Madrid, Spain, epalacios@ind.uned.es*

Abstract:

A differential mathematical model has been developed for the simulation of the ammonia-water absorption refrigeration system ROBUR®, model ACF60-00 LB. The model, with modular structure, contains the governing equations based on mass, species, and energy, implemented for the main system components. The model captures both thermal and mass resistance in the mass and transfer processes that simultaneously occur in the system. A calculation procedure is presented to evaluate the performance of the cooling system under off-design conditions, when driven by hot water temperature ranging between 160 and 210 ºC. Performance of the system when the ambient temperature is up to 40ºC has been analysed, assumed that the pumped solution flow rate kept constant, and the high-pressure level may be used as a control strategy. Results show that, at ambient temperature of 40ºC, the cooling capacity of the is restricted by the size of the air-coolant absorber if the feed hot water temperature is 210ºC. However, difficulties in condenser operation reduce the cooling capacity of the system when the temperature of the feed water drops to 160ºC. In addition, at ambient temperature of 40ºC and feed water temperature of 210ºC, geometry restriction due to the rectifier and the solution-cooled absorber results in COP increase. In such working conditions, the refrigeration system operates at its maximum high-pressure level.

Keywords:

Thermodynamics; ammonia-water; hot climate; absorption; GAX; ASTEP

1. Introduction

The world's population is expected to reach 9,7 billion people in 2050 [1]. Population growth beside economic development and changing consumption pattern will be followed of a notable increase in energy and water consumption. Therefore, there is a greater concern to reduce the environmental impact of energy and to optimize the efficient use of water. Currently, there is a great deal of interest in absorption systems because of their environmentally friendly technology. Absorption systems can help to reduce CO_2 emissions, slowing global warming and biodiversity loss. One of the main advantages of absorption systems is the possibility of using both waste heat from industrial processes and solar energy as a power source. In addition, absorption systems when air-cooled have no water consumption.

In this framework, the European ASTEP project has, among other main goals, to demonstrate the feasibility of the application of solar thermal energy to partially cover the cooling demands at an industrial site. Specifically, one of the tasks is partially satisfy the MANDREKAS dairy company cooling demand, at 5ºC, at different operating conditions, such as feed hot water temperature and outdoor temperature. Feed hot water temperature is supplied by a patented solar concentrator (sun dial).

The ammonia-water mixture is particularly suitable for generating chilled water at sub-zero temperatures in air-cooled systems. The most relevant drawback of the ammonia-water mixture, which determines the operation of the absorption systems, is that the vapor pressure of the water is not negligible as compared to the vapor pressure of the ammonia. As a result, the refrigerant always contains a small amount of water. The presence of water in the evaporator significantly deteriorates the performance and the efficiency of the system. The water content in the refrigerant can be reduced by using a distillation column [2]-[3], a condensation rectifier [5]. The efficiency of the system may be improved when the absorption system operates according to a GAX cycle. The key problem in the GAX cycle is the heat transfer between the absorber and the generator [6].

In the present analysis, a differential mathematical model with modular structure has been developed. The model implemented is based on the equations developed by Colburn and Drew for the condensation of a binary vapor mixture with a miscible condensate, [7]. The model includes the mass transfer resistance in both the liquid and vapor phases, which is dominant in the mass transfer processes occurring in an absorber system

[8]. The discretized and modular character of the model together with the consideration of mass transfer resistances gives it a high reliability. The model studies the performance and efficiency of the ammonia-water absorption refrigeration system ROBUR®, model ACF60-00 LB, at part load operation, focusing on the operating condition in hot climate when driven with hot water at high and low temperature. Limitations in the operation of the chiller to ambient temperature beyond 40ºC are analysed.

2. Methodology

2.1 System description

To study the performance of the single effect air-cooled ammonia/water absorption chiller, a mathematical model has been implemented in Engineering Equation Solver Software, on the bases of mass, species and energy conservation balances. The material thermal properties have been evaluated from [9]. Figure 1 shows a schematic diagram of the chiller. The geometry of the different devices of which the chiller consists, are detailed in Table 1. The distillation column includes a rectifying section and a stripping section, located respectively, above and below of the column feed entry point. A rectifier completes the purification system to achieve vapor refrigerant with a high grade of purity. The lack of appreciable benefits that the rectifying section entails, beside the decrease of COP associated with the use of coupled fluid-cooled rectifier [2]-[3] justifies considering the purifying system to consist of a distillation column fed from above (only with striping section) helped by a concentrated solution-cooled rectifier to obtain refrigerant vapor of the required purity. This assumption is corroborated by the schematic diagram of the ROBUR [10]-[11]. An solution-cooled absorber operates as regenerative generator absorption heat chiller, GAX [12]. The chiller includes three restrictors. Restrictors 2 and 3 allow to reestablish the low-pressure level at the inlet of the solution pump. In this study, it is assumed that restrictor 1 allows regulate both high- and low-pressure levels to optimize the chiller performance.

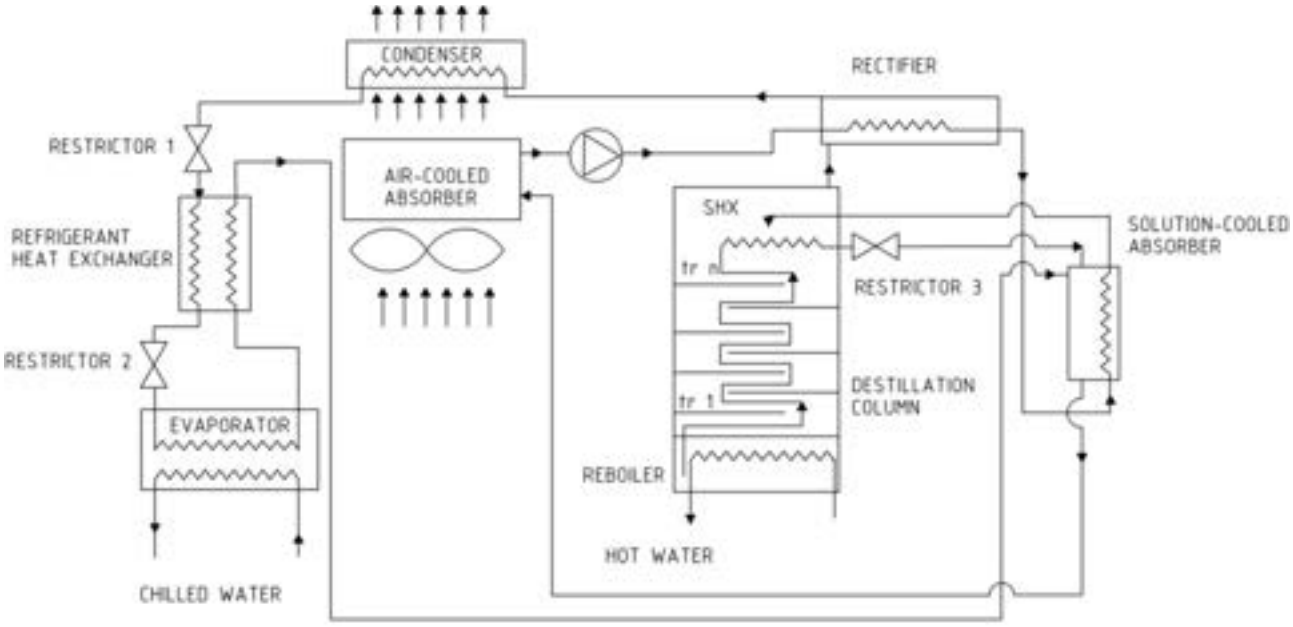

Figure. 1: Schematic diagram of the ammonia-water absorption chiller ROBUR model ACF60-00 LB

The coupling between the absorption and desorption processes is achieved in the solution-cooled absorber (CABS), which operates, on the one hand, thanks to the temperature reduction that occurs in the lean solution flow that leaves the desorber as it passes through the distillation tower (DC), the solution heat exchanger (SHX) and the solution valve (SV), to finally enter the CABS. On the other hand, the rich solution leaving the absorber increases significantly in temperature as it passes through the solution cooled rectifier (CR), until it reaches values close to the dew point temperature of the steam leaving the distillation tower to the rectifier. Therefore, the performance of the absorption system according to a GAX cycle depends on the heat recovery efficiency in DC, SHX and CR.

Condenser, air-cooled absorber, and evaporator tubes are described by its inner diameter, D_i, and thickness, e. The number of tubes is fixed for condenser and absorber, while the tubes length for these devices are obtained in the design process. Conversely, the evaporator tubes length, L, is fixed, while the number of baffles

for the chilled water passage is obtained in the design process. In addition, the refrigerant quality at the exit of evaporator is fixed at 0,96 to limit the temperature glide. It is assumed that both solution-cooled absorber and the solution-cooled rectifier consist of a helical tube. Vapor mass fraction at the rectifier outlet, efficiency of the solution-cooled absorber and the number of turns for both the rectifier and the air-cooled absorber are determined by an iterative process. Nevertheless, while the number of turns remain invariable once are determined, both vapor mass fraction at the rectifier outlet and efficiency of the solution-cooled absorber is determined according to the operational conditions of the chiller. Refrigeration heat exchanger is modeled assuming that its efficiency is 0,9.

The distillation column geometry is defined by its inner diameter D_i, hole diameter, d_h=0,00381 m, tray thickness, e_{tray}, tray spacing, S_t, weir length, l_w, hole pitch, s_h=3 d_h, weir height, h_w. and two relationships, f_1 and f_2 [13], being A_t=π/4 D_i^2, A_d, and A_a=A_t-2A_d, the column area, the downcomer area and the active area, respectively. e_w refers to the weight of the liquid entrainment per unit weight of vapor flowing in the distillation column. The reboiler is assumed to be a cylinder equipped externally with annular fins, with the hot water in cross flow over the cylinder, through the resulting fined annuli passage. The geometry of the finned external surface for condenser, absorber and reboiler annuli, determined by its thickness, t_m, and pitch, s, of their fins are shown in table 1.

Table 1. Chiller geometry.

Condenser/air-cooled absorber		Rectifier/solution cooled absorber		Evaporator	
D_i [m]	0.02	D_{to} [m]	0.075	D_i [m]	0.015
t_m [m]	0.0002	D_{ti} [m]	0.045	e [mm]	0.002
s [m]	0.003	D_{wi} [m]	0.0065	s [m]	1.15(D_i+e)
e [m]	0.002	*e [m]*	0.002	N_{tube}	35
N_{tube}	2			$D_{i,shell}$ [m]	(N_{tube} +1) s
				L [m]	1.1

Reboiler		Distillation column	
h_f [m]	0,63	D_i [m]	0.075
t_m [m]	0,0004	A_d [m^2]	0.12 A_t
s [m]	0,003	S_t [m]	0.15
		h_w [m]	0.1 S_t
		e_{tray} [m]	0.003
		A_d/A_t	$f_1(l_w/D_i)$
		A_h/A_a	$f_2(d_h/s_h)$

2.2. Mathematical models

Mathematical models have been developed for each of the key devices that make up the absorption machine [11]. Such models provide the flow, temperature, concentration of liquid and vapor phases throughout the length of these devices. The following assumptions have been considered:

- Processes are in steady-state
- Heat losses to the ambient are neglected
- Flow is one-dimensional
- Heat and mass transfer is in radial direction of the tube

- Pressure in distillation column, rectifier, solution-cooled absorber, air-cooled absorber, evaporator and condenser is constant

2.2.1 Distillation column

It is assumed that the rectifying section of the distillation column is avoided in the model, due to is low efficiency [3]. Vapor generated in a lower tray interacts with the liquid solution from the upper tray increasing its ammonia content. Simultaneously, the liquid solution coming from the reboiler dissimilates its temperature on its way to the heat exchanger, located at the top of the tower, by interacting with the liquid coming down from the successive trays. For simplicity, the interaction between the liquid coming from the reboiler and the steam generated in each of the trays is disregarded. The ammonia molar fraction of the vapor leaving the i-tray, $\bar{x}_{v,i}$, is obtained calculating the Murphree vapor plate efficiency, e_M. In that way,

$$\bar{x}_{v,i} = \bar{x}_{v,i-1}(1 - e_M) + e_M \bar{x}_{v\,e,i}, \tag{1}$$

where $\bar{x}_{v\,e,i}$, refer to the molar fraction of the vapor leaving the i-tray at thermodynamic equilibrium. The Murphree vapor plate efficiency is obtained as

$$e_M = 6.8 \left(N_{R_e} N_{S_c}\right)^{0.1} \left(N_{D_g} N_{S_c}\right)^{0.115}, \tag{2}$$

here N_{R_e}, N_{S_c}, N_{D_g} are dimensionless groups depending on some thermodynamic properties of the liquid (σ_L, μ_L, ρ_L, D_{kl}, evaluated with the Wilke-Chang expression [13], vapor velocity and geometrical characteristics of the column (fractional free area, A_h/A_t, and weir height, h_w). The effect of the liquid entrainment in the Murphree vapor plate efficiency has also been considered by using the Fair method [13]. The reboiler Murphree efficiency is assumed to be 1. The vapor purification process is eventually completed by partial condensation in the liquid-cooled rectifier. Reboiler is considered as an additional tray. Conservation equations for mass, species and energy in a generic tray are expressed as

$$\dot{m}_{L,F} + \dot{m}_{L,i+1} + \dot{m}_{V,i-1} = \dot{m}_{L,i-1} + \dot{m}_{V,i+1}, \tag{3}$$

$$x_F \dot{m}_{L,F} + x_{L,i+1}\dot{m}_{L,i+1} + x_{V,i-1}\dot{m}_{V,i-1} = x_{L,i-1}\dot{m}_{L,i-1} + x_{V,i+1}\dot{m}_{V,i+1}, \tag{4}$$

$$h_{L,F}\dot{m}_{L,F} + \tilde{h}_{L,i+1}\dot{m}_{L,i+1} + h_{V,i-1}\dot{m}_{V,i-1} + \dot{Q}_{reb} = \tilde{h}_{L,i-1}\dot{m}_{L,i-1} + h_{V,i+1}\dot{m}_{V,i+1}, \tag{5}$$

$$h_{L,i+1}\dot{m}_{L,i+1} + h_{dP,i}\,\dot{m}_{dP} = \tilde{h}_{L,i+1}\dot{m}_{L,i+1} + h_{dP,i+1}\dot{m}_{dP}, \tag{6}$$

$$\left(h_{dP,i} - h_{dP,i+1}\right)\dot{m}_{dP} = \pi D_{wo} e_{tray} h_{t,dP} \frac{(T_{dP\,i} - T_{w0}) - (T_{dP\,i+1} - T_{w0})}{ln\left(\frac{T_{dP\,i} - T_{w0}}{T_{dP\,i+1} - T_{w0}}\right)} \tag{7}$$

where *F* refers to the feed flow, applicable in the feed tray. $\dot{Q}_{reb}$ refers to heat flux supplied by the hot water supply, applicable in the bottom tray. Eq (7) models the heat transfer process that takes place between the dilute solution and the concentrated solution in the gap between consecutive trays. $h_{t,dP}$ refers to the heat transfer coefficient between the dilute solution and the tube wall.

2.2.2 Air-cooled absorber, solution cooled absorber and rectifier

Bulk temperature of the liquid phase, T_{bL}, is obtained by means of mass, species and energy balance at the vapor and liquid interface. Namely, mass balance at interface, which states than the mass transfer between the vapor and the liquid phases must be equal, can be expressed as Eq. (8), where a film model is used. Eq. (9) is obtained stating a balance energy at the liquid vapor interface [7]

$$f_1(T_i, z) = 0, \tag{8}$$

$$f_2(T_i, z) = 0, \tag{9}$$

In these equations, *z* refers to the ratio of ammonia to total molar flux through the interface and T_i is the temperature interface. An iterative process leaves to calculate total and partial mass fluxes transferred through the interface, $\dot{m}$, $\dot{m}_{NH3}$ and $\dot{m}_{H2O}$. New vapor condition is calculated from mass and energy balance in the bulk vapor phase based on the differential control volume, which stablish that

$$d\dot{m}_v = -\dot{m}, \tag{10}$$

$$d(x_{vb}\dot{m}_v) = -\dot{m}_{NH3}, \quad (11)$$

$$d(h_{vb}\dot{m}_v) = -\left(\dot{m}_{NH3} \cdot h_{v,NH3} + \dot{m}_{H2O} \cdot h_{v,H2O} + \dot{q}_{v,i}\right), \quad (12)$$

Similarly, flow rate, temperature and composition of the liquid phase at the exit of the control volume may be obtained with mass balance in the bulk liquid, which states that

$$d\dot{m}_l = \dot{m}, \quad (13)$$

$$d(x_{lb}\dot{m}_l) = \dot{m}_{NH3}, \quad (14)$$

$$d(h_{lb}\dot{m}_l) = -d(h_{vb}\dot{m}_v) - \dot{q}_{cf,i}, \quad (15)$$

The pumped mass flow rate is assumed to be constant, equal to 0,045 kg/s.

2.2.3 Evaporator and condenser

Bulk temperature of the biphasic phase is obtained by means of energy balance

$$h_i\dot{m}_i + h_{cf,i}\dot{m}_{cf} = h_{i+1}\dot{m}_{i+1} + h_{cf,i+1}\dot{m}_{cf}, \quad (16)$$

2.2.4 Reboiler

The energy balance is expressed as

$$h_{L\,2}\dot{m}_{L\,2} + h_{cf,reb\ in}\dot{m}_{cf,reb\ in} = h_{L,1}\dot{m}_{L,1} + h_{cf,reb\ out}\dot{m}_{cf,reb\ out}, \quad (17)$$

where subscripts *L1* and *L2* refers, respectively, to the liquid coming out to the tray 1 and 2 of the distillation column

2.2.5 Heat flux in condenser, air-cooled absorber and reboiler

These devices are externally finned. The heat flux transferred between the coolant and the bulk solution of the discrete element *i*, $\dot{q}_{cf,i}$, is evaluated as

$$\dot{q}_{cf,i} = UA_{cf,i} \cdot DTLM_i, \quad (18)$$

where $UA_{cf,i}$ is the thermal conductance referred to the element outer finned surface, $A_{cf,i}$, defined as

$$\frac{1}{UA_{cf,i}} = \frac{1}{h_{Lw}A_{L,i}} + \frac{1}{\eta \cdot h_{cf}A_{cf,i}} + \frac{D_i}{2\,k_w A_{L,i}} ln\left(\frac{D_{w0}}{D_{wi}}\right), \quad (19)$$

$DTLM_i$ is the logarithm mean temperature difference, calculated as

$$DTLM_i = \frac{(T_L - T_{cf\,i}) - (T_L - T_{cf\,i+1})}{ln\left(\frac{T_L - T_{cf\,i}}{T_L - T_{cf\,i+1}}\right)}, \quad (20)$$

η is the overall outer surface efficiency, evaluated as $\eta = 1 - A_{f,i}/A_{cf,i}\left(1 - \eta_f\right)$, where $\eta_f$is the fin efficiency and $A_{f,i}$ is the element fin area. In case of the reboiler, only one discrete volume has been considered. The cooling air-facing velocity is fixed at 1,25 m/s

2.2.6 Heat flux in rectifier, solution-cooled absorber and evaporator

The heat flux transferred between the coolant and the bulk solution of the discrete element *i* is evaluated as

$$\dot{q}_{cf,i} = \frac{A_{cf,i}(T_{w0} - T_{cf,i})}{\frac{1}{h_{cf}} + \frac{ln(D_{wo}/D_{wi})}{2k_{w/D_{wi}}}}, \quad (21)$$

where T_{w0} is the temperature of the outer wall of the tube

2.3. Heat and mass transfer coefficients

In the reboiler, the heat transport coefficient between the finned tube wall and the coolant is obtained from [15] and the heat transfer coefficient in the solution side is calculated from Táboas et al. [16], to consider the mass

transfer resistance though the liquid-vapor interface at solution side. The correlation proposed by Klimenko [17] is used between the biphasic refrigerant and the tube surface. In the evaporator, the heat transport coefficient between the tube wall and the coolant is obtained following the procedure described in [18] for the shell-side heat transfer in baffled shell-and-tube heat exchangers. In the condenser and in the absorber, the heat transfer coefficient between the liquid and the tube surface is calculated from the film wise condensation theory in a horizontal tube. In laminar regime, the heat transfer coefficient is obtained from the Nusselt equation for a smooth film [18] ignoring the vapor shear stress effect. The increase in heat transfer due to the waviness of the film flow is considered with the Kutateladze and Gogonin equation [18]. In turbulent regime, the Yüksel and Müller equation [18] has been used to calculate the heat transfer coefficient. Corrections proposed by Numrich equations [18] have been applied to consider the effect of the shear stress at the condensate film surface, both in laminar and turbulent regime. The heat transport coefficient between the solid surface and the coolant for absorber and condenser has been evaluated by [18]. In the absorber, the heat transfer coefficient between the liquid and the liquid vapor interface is assumed to be equal to the heat transfer coefficient between the liquid and the tube wall. The heat transfer coefficient in the refrigerant vapor phase is obtained from Gnielinski [18]. The mass transfer coefficient is calculated by means of the Chilton and Colburn analogy [18] from the heat transfer coefficient.

2.4. Solution method

An iterative process has been implemented to integrate each device that make up the absorption chiller and, thus, to determine the performance of the chiller. It is assumed that the following parameters have fixed values: geometry of the refrigeration system, detailed in Table 1, mass fraction of the solution filled, x_0, quality of the refrigerant at the evaporator outlet, $Q_{evap\ out}$, mass flow rate of the pumped solution, $\dot{m}_{dR}$, air-facing velocity, v_a, and mass flow rate of feed hot water,. Both $N_{turns,\ rect}$ and $N_{turns,\ cabs}$ are fixed values, which must be determined to satisfy all operating conditions. In addition, the mass flow rate of the chilled water, $\dot{m}_{cf,evap}$, may be altered, according to the manufacturer data.

For every operating condition of the absorption system, determined by the ambient temperature and the temperature of the hot water supply, the magnitudes that must be calculated are: the loss of pressure in the valve 1, that participates in determining P_H, and P_L, and thus, the minimum interface area of the condenser and of the air-cooled absorber, x_{ref}, which allows the coupling of the rectifier, eff_{cabs}, which allows the coupling of the solution-cooled absorber, and $\dot{m}_{cf,evap}$, which allows the coupling of the evaporator. The calculation procedure is summarized below.

1. Guess the number of the turns of the rectifier, $N_{turns,\ rect}$
2. Guess the number of the turns of the solution-cooled absorber, $N_{turns,\ cabs}$
3. Guess the los of pressure in valve 1, ΔP_{valv1}
4. Calculate the high-pressure level, P_H, given by ΔP_{valv1} added to the condensation pressure of the saturated refrigerant at ambient temperature
5. Guess the refrigerant mass fraction, x_{ref},
6. Guess the low-pressure level, P_L
7. Guess the refrigerant mass flow rate $\dot{m}_{ref}$
8. Calculate the circulation ratio f given by $\dot{m}_{ref}/\dot{m}_{dR}$
9. Calculate the mass fraction of the dilute solution, x_{dP}, given by $\left(f \cdot x_0 - x_{ref}\right)/(f-1)$
10. Calculate the mass fraction of the concentrate solution, x_{dR}, given by $(1-1/f)x_{dP} + x_{ref}/f$
11. Calculate the dilute solution flow rate, $\dot{m}_{dP}$, given by $\dot{m}_{dR} - \dot{m}_{ref}$
12. Calculate the reboil heat flux, $\dot{Q}_{reb}$, the mass fraction, mass flow rate and specific enthalpy of the vapor flow coming out of the upper tray of the distillation column and the temperature of the liquid flow from the reboiler, given by Eqs (1)-(7)
13. Guess the temperature of the solution at the pump outlet, $T_{pump\ out}$
14. Guess the efficience of the solution-cooled absorber, eff_{cabs}
15. Guess the reflux ratio and the mass fraction and temperature of the condensate at the rectifier outlet, T_R and x_R, respectively
16. Check $\dot{Q}_{reb}$ using Eqs (18)-(20). If verified, go to step 17. Otherwise, guess a new value of $\dot{m}_{ref}$ and go to step 8
17. Check the interface area of the evaporator using Eqs (16) and (21). If verified, go to step 17. Otherwise:
    - guess a new value of $\dot{m}_{cf,evap}$, and go to step 17, or
    - guess a new value of P_L and go to step 12

18. Check the reflux ratio and the temperature and mass fraction of the condensate at the rectifier outlet using Eqs (8)-(15). If verified, go to step 19. Otherwise, guess new values of reflux ratio, T_R and x_R and go to step 16
19. Check the number of turns of the rectifier, $N_{turns,\ rect}$ using Eqs (8)-(15) and Eq. (21). If verify, go to step 20. Otherwise, guess a new value of x_{ref} and go to step 9
20. Calculate the refrigerant mass flow rate absorbed in the solution-cooled absorber, $\Delta\dot{m}_{ref,cabs}$, using Eqs (8)-(15) and Eq. (21).
21. Check the number of the solution-cooled absorber, $N_{turns,\ cabs}$, using Eqs (8)-(15) and Eq. (21). Check eff_{cabs}. If verified, go to step 22. Otherwise, guess a new of eff_{cabs} and go to step 15
22. Calculate the interface area of the air-cooled absorber, A_{abs}, using Eqs. (8)-(15) and Eqs. (18)-(20). If the resulting frontal area is greater that of the comercial chiller, guess a new value for ΔP_{valv1} and go to steep 4
23. Check $T_{pump\ out}$. If verified, go to step 24. Otherwise, guess a new value of $T_{pump\ out}$ and go to step 16
24. Calculate the interface area of the condenser using Eqs. (8)-(16) and (18)-(20). If the interface area is greater that a certain máximum value, guess a new value for ΔP_{valv1} and go to steep 4

Table 2 shows input and output parameters of each device to carry out the described iterative process.

Table 2. Iterative process. Input and output parameters.

Distillation column		reboiler		Evaporator	
input	output	input	output	input	output
$\dot{m}_{dR}$, $\dot{m}_{ref}$ x_{dR}, x_{ref}	$x_{v\ upper}$, $\dot{m}_{v,upper}$ $h_{v,upper}$	$\dot{Q}_{reb}$ $\dot{m}_{cf\ reb}$ $T_{cf\ reb\ in}$	$\dot{m}_{ref}$ $\dot{Q}_{evap}$ COP	x_{ref}, $Q_{evap,\ out}$, $\dot{Q}_{evap}$ P_L	$L_{eff,\ evap}$
x_R, T_R, $T_{pump,\ out}$ Reflux ratio	$\dot{Q}_{reb}$	$x_{v\ bottom}$, $x_{L\ 2}$ $\dot{m}_{L,2}$		$\dot{m}_{cf\ evap}$ $T_{cf\ evap\ out}$	
ΔP_{valv1}, P_L	$h_{dP\ cabs\ in}$	ΔP_{valv1}		$\dot{m}_{ref}$	

rectifier		Solution-cooled absorber		Air-cooled absorber		Condenser	
input	output	input	output	input	output	input	output
$x_{,ref}$ ΔP_{valv1}	$N_{turns,\ rect}$	$x_{m,ref}$, P_L, ΔP_{valv1}	$\Delta\dot{m}_{ref,cabs}$	v_{air}, T_{amb}	$T_{pump,\ out}$	v_{air}, $T_{cf\ out\ abs,m}$	$L_{eff\ cond}$
$T_{pump\ out}$, $h_{v\ cond\ in}$	x_R, T_R, x_{ref}, $T_{cf\ out}$ $h_{v\ top}$	$T_{ref\ cabs\ in}$, $T_{dP,\ cabs\ in}$, $T_{cf\ cabs\ in}$	$N_{turns,\ cabs}$	$\dot{m}_{ref,abs}$, $x_{ref\ „cabs\ out}$ $\dot{m}_{L„abs,in}$, $x_{L\ cabs\ out}$	$L_{eff\ abs}$	ΔP_{valv1} $h_{v\ cond\ in}$	
x_{dR}, $x_{v\ top}$	Reflux ratio	$x_{dP,}$ eff_{cabs}		$T_{L„abs,in}$, $x_{L\ cabs\ out}$		$\dot{m}_{ref}$, x_{ref}	
$\dot{m}_{ref}$, $\dot{m}_{dR}$	$\dot{m}_{v,top}$	$\dot{m}_{dP}$, $\dot{m}_{dR}$	$x_{L\ cabs\ out}$	P_L			

2.4.1. Mathematical model validation

Model has been validated with the data supplied by the manufacturer. Figure 2 compares measured (manufacturer data) and predicted (model), provided that the loss of pressure in valve 1 to be the suitable.

The agreement is fair in the whole range of ambient temperature and of hot feed water analysed. Nevertheless, the validity range of the implemented model cannot be extended to ambient temperatures above 40ºC, as explained below.

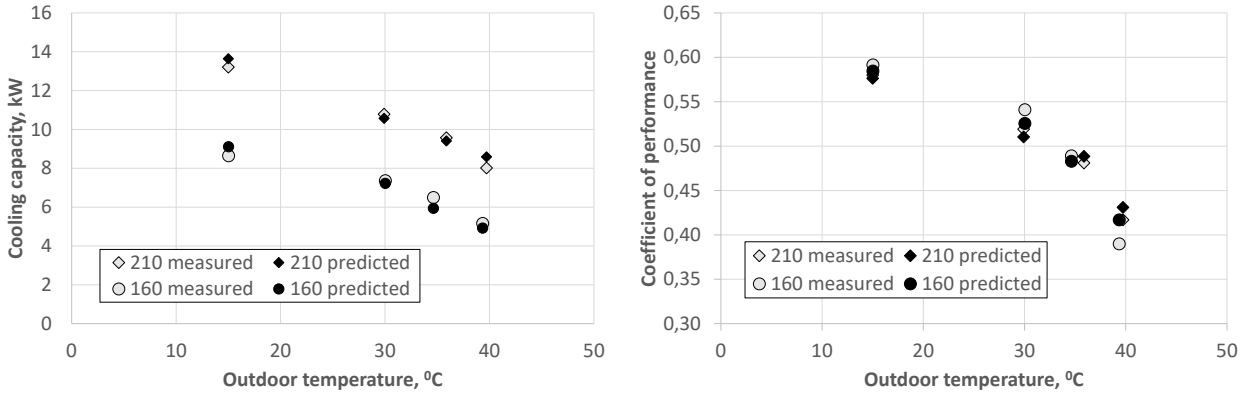

Figure. 2. Measured and predicted values for the performance of the ammonia-water chiller: a) cooling capacity, b) coefficient of performance.

3. Results

Figure 3 depicts shows the effect of the loss of pressure in valve 1 on the high-pressure levels at each operating condition, determined by the feed water temperature and the ambient temperature, ºC. It is observed that, for a certain value of ΔP_{valv1}, P_H increases with ambient temperature as the refrigerant condensing pressure increases. P_H also increases with hot water supply temperature as the mass fraction of the dilute solution decreases.

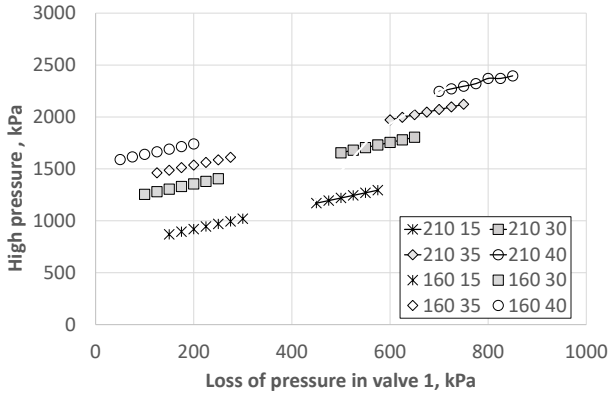

Figure. 3. High-pressure level in the ammonia-water absorption system. Box: feed hot water temperature and ambient temperature, ºC

Figure 4 shows the evolution of the logarithmic mean temperature difference in the condenser, $LMDT_{cond}$, when varying ΔP_{valv1}. The results shows that $LMDT_{cond}$ increases notably when ΔP_{valv1} increases, due to P_H rise. The ambient temperature has also influence on the $LMDT_{cond}$. This is because the condensing pressure of the refrigerant decreases.

It is concluded that the operational limit of an absorption system operating at high ambient temperature and low feed water temperature is established by the size of the air-cooled condenser.

Figure 5 left illustrates the evolution of the low-pressure level, P_L. Results shows that, in all operating conditions, P_L decreases as the ambient temperature drops. This is because P_L is eventually determined by thermal resistance between the refrigerant vapor being absorbed and the coolant-air at the outlet of the air-cooled absorber. Results also show that P_L increases as the temperature of the feed hot water decreases. This is attributable to the influence exerted by the refrigerant mass flow rate, $\dot{m}_{ref}$, as it is explained below.

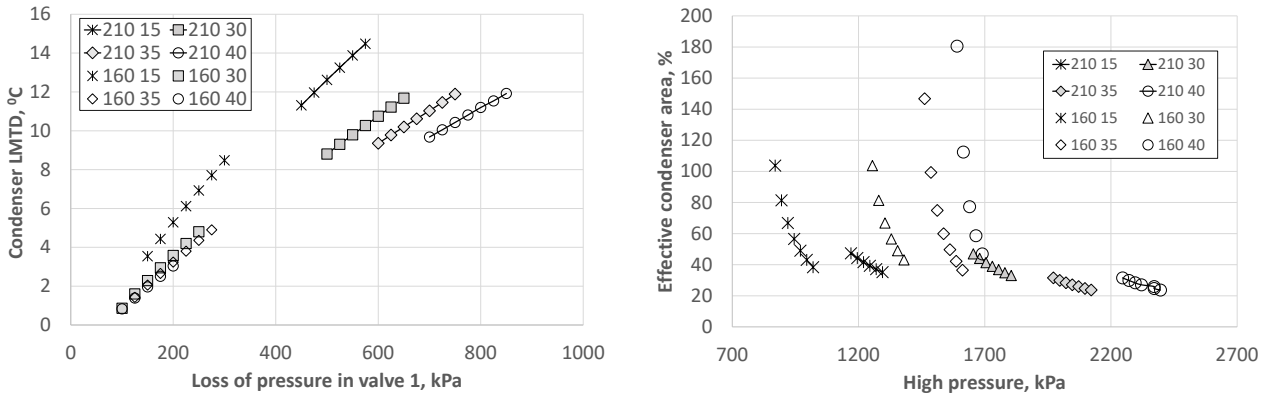

Figure. 4. Condenser: a) logarithmic mean temperature difference, b) Minimum required transfer area, expressed as a percentage of its geometric area. Box: feed hot water temperature and ambient temperature, ºC

Figure 6 left shows the evolution of the cooling capacity, that is, of the refrigerant mass flow rate, with the operating conditions. Figure 6 right illustrates the influence of the temperature of the feed hot water on the logarithmic mean temperature difference of the evaporator, $LMTD_{evap}$. When comparing results in Figure 5 and Figure 6, it can be observed that evaporator coupling results in P_L reduction and $LMTD_{evap}$ increase when $\dot{m}_{ref}$ increases. However, when the temperature of the hot water is 210º C, $LMTD_{evap}$ experiences a slight increase instead when $\dot{m}_{ref}$ is incremented. This is due to, at 210ºC, the rectifier coupling entails refrigerant mass fraction increases as the ambient temperature does, as will see later, what favours $LMTD_{evap}$ increase.

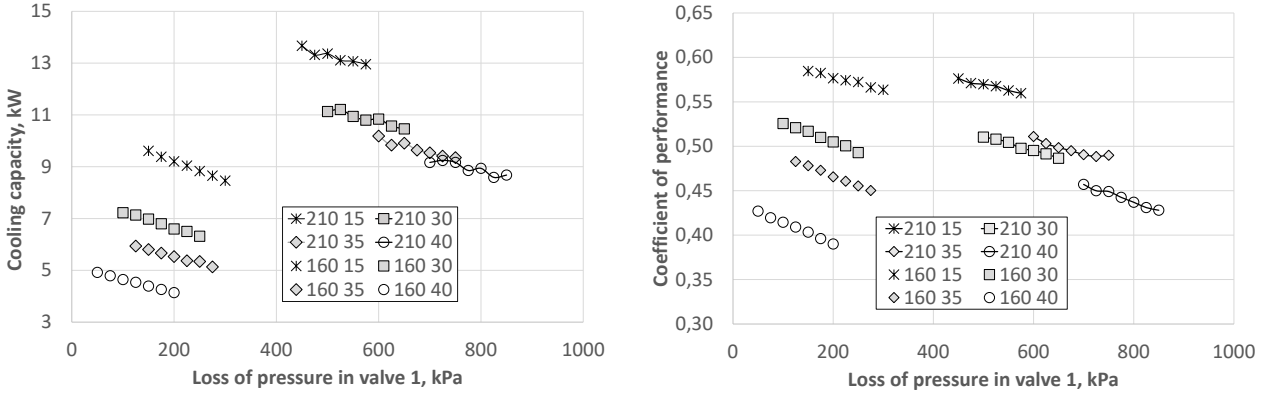

Figure. 5. a) Cooling capacity of the ammonia-water absorption system. b) Coefficient of performance. Box: feed hot water temperature and ambient temperature, ºC.

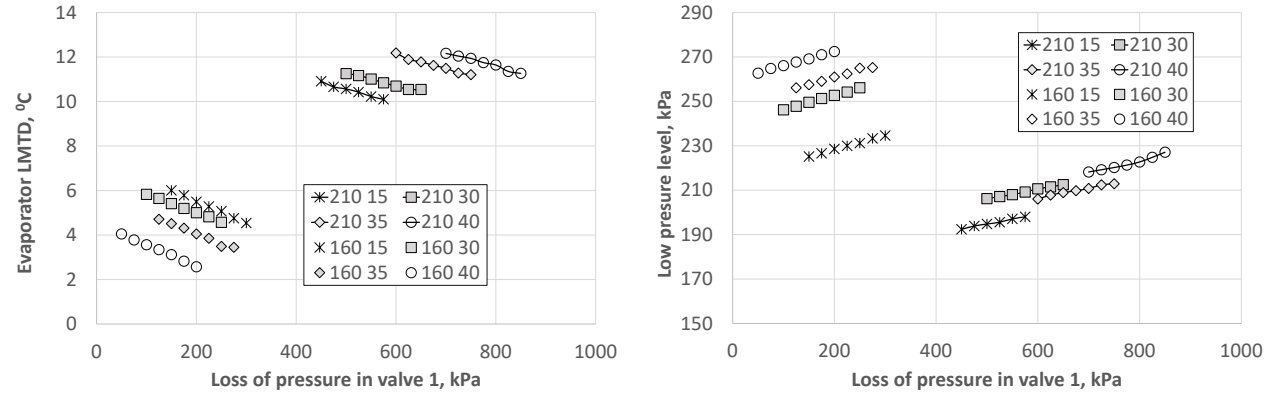

Figure. 6. a) Logarithmic mean temperature difference of the evaporator. b) Low-pressure level. Box: feed hot water temperature and ambient temperature, ºC.

Figure 7 left illustrates the evolution of the effectiveness of the solution-cooled absorber, eff_{cabs}, and the refrigerant mass fraction that allows the coupling of the rectifier and of the solution-cooled absorber. Results

show that eff_{cabs} decreases as the ambient temperature increase when the temperature of the feed hot water is 210ºC. Hence, the temperature of the concentrated solution flow at the CABS outlet reduces, what favours the absorption system to operate as a GAX cycle, even when the ambient temperature is high. In addition, results shows that x_{ref} increases as the ambient temperature increases when the temperature of the feed hot water is 210ºC. This behaviour, particularly noteworthy when the ambient temperature approach to 40ºC, favours COP when the ambient temperature is high.

Figure 7 right shows the influence of the feed water temperature on the minimum area required by the air-cooled absorber, A_{abs}, normalized with the geometric area of the air-cooled absorber. Results show that A_{abs} increases when the temperature of the feed hot water increases. In fact, set the feed water temperature, P_L must be larger than a certain value, which increases as the ambient temperature increases, to assure that A_{abs} remains below the geometric area of the air-cooled absorber. Results show that A_{abs} quickly dismisses when P_L increases. In this sense, since P_L increase as ΔP_{valv1} does, high values of ΔP_{valv1} are preferred when the ambient temperature is high to assure a high cooling capacity. However, reached the maximum value of P_H, a higher ambient temperature entails a reduction of $\dot{m}_{ref}$. Otherwise, $\dot{m}_{ref}$ cannot be absorbed in its entirety.

It is remarkable that, despite the feed water temperature is 210ºC, A_{abs} keeps far from its geometric value when the ambient temperature is 15ºC as compared with that obtained at 30ºC. This behaviour is due to PL is quite similar for both ambient temperatures.

It is concluded that the operational limit of an absorption system operating at high ambient temperature and high feed water temperature is established by the size of the air-cooled absorber.

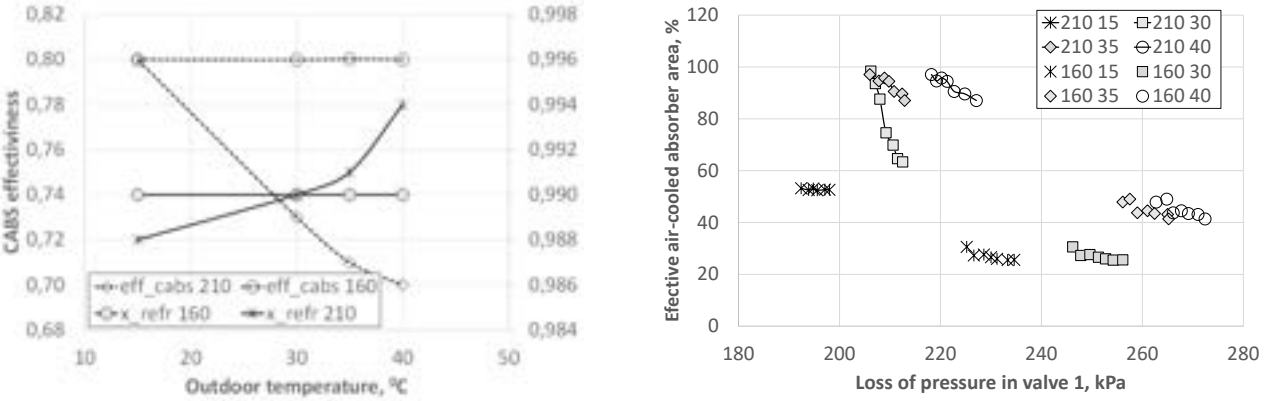

Figure. 7. a) Effectiveness of the solution-cooled absorber. Refrigerant mass fraction. Box: Feed hot water temperature, ºC, b) Minimum required transfer area of the air-cooled absorber, expressed as a percentage of the geometry area

4. Conclusions

In this studio, a detailed analysis of the heat and mass transfer processes that take place in an air-cooled ammonia-water system that operates according to a GAX cycle. The goal is to achieve a detailed inside of the refrigeration system when operates at part load, particularly in hot climates. With that objective, a mathematical model has been developed. The model captures both thermal and mass resistance in the mass and transfer processes that simultaneously occur in the system. The discretized character of the model, with modular structure, together with the consideration of mass transfer resistances gives it a high reliability. The model has been validated with the data of the absorption system manufactured by ROBUR®, model ACF60-00 LB, provided by the manufacturer.

A calculation procedure is presented to evaluate the performance of the cooling system under off-design conditions, when driven by hot water temperature in the range from 160 and 210 ºC and operating in ambient temperature from 15 to 40ºC. It has been assumed that the pumped solution flow rate keeps constant, and the high-pressure level may be used as a control strategy.

Limitations in the operation of the chiller to ambient temperature beyond 40ºC are analysed. Results show that, at high ambient temperature, the cooling capacity of the system when the hot water temperature is 210 ºC is restricted by the size of the air-coolant absorber. On the other hand, difficulties in condenser operation reduce the cooling capacity of the system at high ambient temperature when the feed hot water temperature is 160ºC. At high ambient temperature and high feed hot water temperature, geometry restrictions due to rectifier and to solution-cooled absorber results in high COP, what favours the system operation. However, at such operating condition, the refrigeration system demand for the maximum high-pressure level. Such COP improvement is due to the refrigerant mass fraction increase and efficiency solution-cooled absorber decrease.

Acknowledgement

This work has been developed in the frame of the ASTEP project, funded by the European Union's Horizon 2020 research and innovation program under grant agreement No 884411 and the ACES2030-CM project, funded by the Regional Research and Development in Technology Program 2018 (ref. P2018/EMT-4319)

Nomenclature

Abbreviations

Symbols:

A	area transfer
A_a	active area of the tray, m
A_d	downcomer area
A_h	hole area of the tray, m
A_h/A_t	fractional free area
A_n	net open liquid area of one tray
A_t	tower cross-section area, m^2
CABS	solution-cooled absorber
D_w	wall diameter, m
DLK	diffusivity of the liquid light key
d_h	hole diameter of the tray in the distillation column
e	wall thickness, m
e_{tray}	tray spacing in the distillation column, m
e_M	Murphree vapor plate efficiency
e_w	weight of the liquid entrainment per unit weight of vapor flowing in the distillation column
f	circulation ratio, $\dot{m}_{dR}/\dot{m}_{ref}$
FA	fractional free area
G	superficial mass vapor velocity based on the cross-sectional area of the column
h	reboiler length, m
h	specific enthalpy, kJ/kg
h	heat transfer coefficient
h_f	fin length, m
h_m	mass transfer coefficient
h_w	weir length in the distillation column
l_w	hole pitch of the tray in the distillation column
$\dot{m}$	mass flux
N_{D_g}	dimensionless group, $\sigma_L/\rho_L U_v$
N_{S_c}	dimensionless group, $\mu_L/\rho_L D_{LK}$
N_{R_e}	dimensionless group, $h_w G/\mu_L FA$
P	pressure, kPa
$\dot{Q}$	heat flux
RECT	solution-cooled rectifier
RHX	refrigerant heat exchanger
s	fin pitch, m
S_t	weir length, m
SHX	solution heat exchanger
T	temperature, ºC
t_m	fin thickness, m
V	velocity
x	mass fraction
z	ammonia to molar flux ratio across the vapor-liquid interface

Greek symbols

μ	viscosity, kg/m-s
ρ	density, kg/m^3
σ	surface tension, N/m

Subscripts and superscripts

abs	air-cooled absorber
air	coolant air
cabs	solution-cooled absorber
cond	air-cooled condenser

cf	coupling fluid
dP	dilute solution in ammonia
dR	concentrate solution in ammonia
e	at thermodynamic equilibrium
evap	evaporator
H_2O	water content
H	high level
i	inner
i	interface
L	liquid
L	low level
F	feed of the column distillation
NH_3	ammonia content
o	outer
reb	reboiler
rect	solution-cooled rectifier
ref	refrigerant
V	vapor
¯	molar basis

References

[1] UN United Nations. World Population Prospects — Population Division. Available online: https://population.un.org/wpp/ (accessed on 10 January 2023).

[2] Fernández-Seara J., Sieres J., Vázquez M., Distillation column configurations in ammonia-water absorption chiller refrigeration systems. Int. J. Refrigeration 2003; 26: 28-34

[3] Fernández-Seara J., Sieres J., Vázquez M., Simultaneous heat and mass transfer of packed distillation for ammonia-water absorption refrigeration systems. Int J. Thermal Sciences 2002; 41: 927-935

[4] Fernández-Seara J., Sieres J., Rodríguez C., Vázquez M., Ammonia–water absorption in vertical tubular absorbers. Int J. Thermal Sciences, 2005; 44: 277-288

[5] Fernández-Seara J., Sieres J., Vázquez M., Heat and mass transfer analysis of a helical coil rectifier in an ammonia–water absorption system. Int J. Thermal Sciences 2003; 42: 783-794

[6] Wu S., Eames I.W., Innovations in vapor-absorption cycles. Applied energy 2000, 66: 251-266

[7] Sieres, J., Fernández-Seara J., Modelling of simultaneous heat and mass transfer processes in ammonia-water absorption systems from general correlations. Heat Mass Transfer 2007; 44: 113-123

[8] Killion J.D., Garimella S., A critical review of models of coupled heat and mass transfer in falling-film absorption. Int. J. Refrigeration 2001: 755-797

[9] Ibrahim O.M., Klein S.A., Thermodynamics properties of ammonia-water mixtures. ASHRAE Transaction: Symposia, 1993; CH-93-21-2: 1495-1502

[10] Pereira, J.J., Cabral C.A., Almir C., Batista J., Ochoa A.A., Charamba J.C, Energetic analysis of a commercial absorption refrigeration unit using an ammonia-water mixture. Acta Scientiarum, Technology 2017; 39: 439-448

[11] Klein S.A., A model of the steady-State performance of an absorption heat pump. NBSIR,1982:82-2606

[12] Ng K.C., Tu K., Chua H.T., Gordon J.M., Kashiwagi T., Akisawa A, .Saha B.B, Thermodynamical Analysis of absorption chillers: internal dissipation and process average temperature. Applied Thermal Engineering, 1998; 18: 671-682

[13] Coker A. K., Ludwing's Applied process design for chemical and petrochemical plants. Elsevier, 4th edition; 2010.

[14] Herold K.E., Radermacher R., Klein S.A., Absorption chillers and heat pumps, CRC Press, 2nd edition; 2016.

[15] Kay W.M., A.L. London Compact heat exchangers, McGrawHill, 3rd edition; 1984.

[16] Táboas, F., Vallès M., Bourouis M., Coronas A., Pool boiling of ammonia/water and its pure components: comparison of experimental data in the literature with the predictions of standard. Int. J. Refrigeration 2007; 30: 778-788.

[17] Mills A.F., Transferencia de Calor, McGrawHill, 1st edition; 1999.

[18] VDI Wärmeatlas, VDI Heat Atlas, Springer, 2nd edition, 2010.

PROCEEDINGS OF ECOS 2023 - THE 36TH INTERNATIONAL CONFERENCE ON
EFFICIENCY, **C**OST, **O**PTIMIZATION, **S**IMULATION AND ENVIRONMENTAL IMPACT OF ENERGY SYSTEMS
25-30 JUNE, 2023, LAS PALMAS DE GRAN CANARIA, SPAIN

Thermodynamic investigation and design of a multi-generation ORC-ejector cooling cycle heat pump for vessel waste heat recovery

Konstantinos Braimakis[a], Christos Xynos[b], and Sotirios Karellas[c]

[a] National Technical University of Athens, Athens, Greece, mpraim@central.ntua.gr
[b] National Technical University of Athens, Athens, Greece, christos_xynos@mail.ntua.gr
[c] National Technical University of Athens, Athens, Greece, sotokar@mail.ntua.gr

Abstract:
The present study presents the thermodynamic design of a vessel waste heat recovery prototype based on a cascade Organic Rankine Cycle (ORC) and an ejector cooling-vapor compression cycle (EVCC) in the context of the ZHENIT project. The system can be driven by high-temperature (>120 °C) and a low-temperature (<80 °C) waste heat and features 3 main operating modes: 1) electricity-only, 2) combined heat and power (CHP) via heat recovery from the ORC condenser and 3) combined cooling and power (CCP) from the simultaneous operation of the ORC and EVCC. Waste heat is supplied to the ORC (topping cycle), while heat recovered during the desuperheating is used for driving the EVCC (bottoming cycle). A series of parametric analyses were carried out to investigate the influence of key design parameters (working fluids and maximum ORC and EVCC temperatures, recuperator temperature rise, condensation temperature, compressor pressure ratio) on the performance of the prototype and select its design point. R1233zd(E) and R1234ze were found to be the best-performing fluids in the ORC and EVCC, respectively. Furthermore, the selected design ORC evaporation temperature is 120 °C, the condensation temperature (CHP mode) is 50 °C, while the EVCC generator evaporation temperature and compressor pressure ratio (CCP mode) are equal to 52 °C and 0.84, respectively. Under the above conditions, the prototype ORC electric efficiency is up to 12.62% (electricity-only mode), while the overall electrical and CCP efficiency (CCP) are 10.29% and 14.96%, respectively. Finally, the electrical COP of the EVCC is 7.62.

Keywords: Thermodynamics; ORC; ejector cooling; waste heat; CHP; CCHP; trigeneration.

1. Introduction

The Organic Rankine Cycle (ORC) is a widely considered technology for electricity production from low-temperature heat sources such as solar, biomass, geothermal and waste heat from industrial processes as well as exhaust gases and hot jacket cooling water of internal combustion engines of stationary and mobile applications, such as maritime vessels [1, 2]. Especially in the maritime industry, large amounts of fossil fuels are annually consumed for ship propulsion, cargo operations and electricity production. Therefore, there is an abundance in waste heat that could be exploited by ORC systems [3] in the form of engine and genset exhaust gases, compressed air intercoolers and jacket water cooler with typical temperatures from 60°C to 250°C [4].

Vessel energy demand is not limited to electrical energy but also includes heating and cooling. The combination of ORCs with thermally activated cooling systems can also contribute to covering these demands. In the literature, cascade configurations of ORCs and sorption cooling technologies have been considered to this end, especially, absorption [5] and adsorption [6] chillers. In such configurations, low-temperature heat is recovered from the ORC desuperheater or condenser and is used for driving the chiller. An alternative thermally activated cooling technology is based on the ejector cooling cycle (ECC), which is typically considered for use in solar thermal applications (solar cooling) [7]. The operating principle of ECCs is similar to that of conventional vapor compression cycles (VCCs), however, it involves the substitution of the mechanical compressor with an ejector device that thermally compresses the low-pressure vapor exiting the cooling evaporator utilizing a high-pressure stream generated through the exploitation of waste heat.

Notably, ejectors of ECCs can be easily integrated with conventional electricity-driven vapor compression cycles (VCCs) to improve their performance and improve their reliability and flexibility. The aforementioned concept is the basis of the prototype to be developed in the ZHENIT project, which is based on an innovative ejector-vapor compression cooling cycle (EVCC). In particular, the prototype will be based on a cascade layout, with an ORC as a topping cycle and an EVCC as a bottoming cycle. The ORC will be driven by waste heat, while the EVCC will be driven by heat recovered from the ORC desuperheater.

The present work presents the preliminary thermodynamic design process and results of the prototype based on three operating modes: 1) electricity-only, 2) CHP and 3) CCP. For the design, a series of parametric investigations were carried out to select the most appropriate working fluids and investigate the impact of different key design parameters on its performance.

2. Methodology

2.1. System description

The ZHENIT ORC-EVCC prototype is designed for vessel engine waste heat recovery at temperature levels ranging from 60°C (jacket engine cooling water) to 150°C (engine exhaust gases) for electricity, heating and cooling production. Within the project, a micro-scale (10 kW_e) prototype will be developed and demonstrated at lab-scale, along with the alternative vessel waste heat recovery solutions that are part of the ZHENIT solutions.

In the present study, a high-T waste heat source consisting of Therminol VP1 oil [8] at a mass flow rate of 2.5 kg/s with inlet/outlet temperatures of 150 °C /130°C, is considered. Meanwhile, a low-T waste heat source is additionally considered, consisting of hot water at inlet/outlet temperatures of 60°C /52°C with a mass flow rate of 0.4 kg/s.

The layout of the prototype is pictured in ***Figure. 1***. The ORC is the topping cycle and is driven by the high-T and (provisionally) low-T waste heat sources. Heat may be recovered during the desuperheating of the ORC working fluid in a heat exchanger (Generator) and used for driving the EVCC, which is the bottoming cycle. The EVCC is based on integrating an ejector into a conventional VCC. Compared to a VCC, the compression process of the low-pressure working fluid exiting the cooling evaporator is accomplished not only by a mechanical compressor but also by an ejector. More specifically, in the ejector, the working fluid leaving the compressor is further compressed as it is entrained by and mixed with high-pressure vapor produced in the Generator. As a result, the electricity consumption compared to a conventional VCC can be potentially reduced.

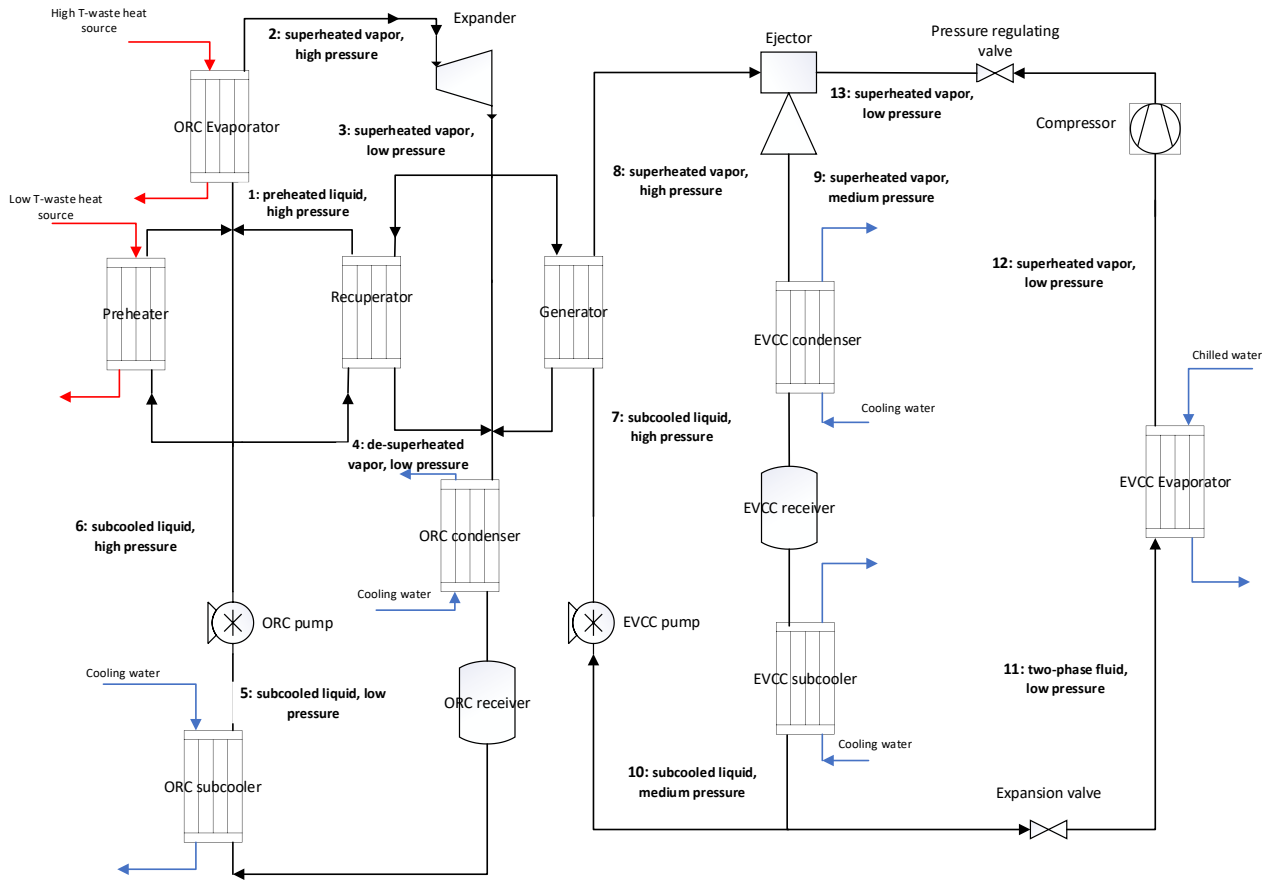

Figure. 1. Waste heat recovery ORC-EVCC layout

2.2. Operating modes

The prototype can operate in three different modes:

Mode 1 – Electricity-only: In this Mode, the EVCC is not operational and no cooling is produced. The ORC is driven exclusively by high-T waste heat. Furthermore, a recuperator is used to increase its efficiency.

Mode 2 – Combined heat and power (CHP): As in the previous case, the EVCC is not operational and the ORC is driven only by high-T waste heat. However, in this mode, the recuperator is bypassed and the condensation pressure of the ORC is increased to produce hot water at 45 °C.

Mode 3 – Electricity and cooling (CCP): In this Mode, both the ORC and EVCC are operational. The ORC may be driven by both a high-T and a low-T waste heat source. After exiting the expander, the ORC working fluid is desuperheated in the Generator, in which the EVCC working fluid evaporates on the cold side of the heat exchanger. Cooling (chilled water at 10 °C) is produced in the EVCC evaporator. The low-pressure working fluid exiting the cooling EVCC evaporator is compressed in the compressor and enters the low-pressure port of the ejector. Meanwhile, the high-pressure vapor exiting Generator enters the high-pressure port of the ejector. In the ejector, the two flows are mixed. The resulting mixed flow exits the ejector at an intermediate pressure and is driven to the EVCC condenser, where it is condensed by cooling water.

2.3. Working fluids

The investigated ORC and EVCC working fluids and their properties are summarized in **Table *1***. A set of hydrofluoroolefins (HFOs), namely R1233zd(E), R1234ze and R1234yf, were considered because of their low environmental impact (low global warming and ozone depletion potential (ODP), being compliant with the regulations imposed by the Montreal [9] and Kyoto Protocols [10], as well as the F-gases regulations [11]. Furthermore, these fluids have either no (R1233zd(E)) or low flammability according to the ASHRAE safety classification. For the ORC, R1233zd(E) and R1234ze were considered, owing to their relatively higher critical temperatures, resulting in improved cycle efficiencies. For the EVCC, R1233zd(E) was not considered because of its significantly lower evaporation pressure, which is below the atmospheric and may cause issues because of air leakage into the refrigerant circuit.

Table 1. Investigated working fluids and their properties

Working fluid	T_{crit} (°C)	p_{crit} (bar)	ODP	GWP	ASHRAE safety group
R1233zd(E) (ORC)	165.5	35.7	0	1	A1
R1234ze (ORC& EVCC)	109.4	33.4	0	6	A2L
R1234yf (EVCC)	94.7	33.8	0	4	A2L

2.4. Design

The modeling of ORC and ECC/VCC systems has been extensively investigated in the relevant literature [7]. Therefore, in the present work, only the most significant modeling aspects which are relevant to the particular investigated prototype are presented.

All modeling assumptions are summarized in ***Table 2***. The thermophysical properties of the heat source stream, working fluids and cooling water are calculated with REFPROP [12]. Two ORC evaporation temperatures are investigated, equal to 90 and 120 °C. Although higher ORC evaporation temperatures would potentially result in improved efficiencies, a maximum upper bound of 120 °C was considered because of technological limitations (material limitations and limitations of built-in volume ratios) of volumetric expansion machines (scroll and screw expanders) at the targeted scale of the prototype (around 10 kW_e) and technical challenges of testing higher temperature heat sources (above 140 °C) at lab scale. A condensation temperature (T_{cond}) of 30÷65 °C is assumed for the ORC (depending on whether only electricity or heating is also produced) and 30 °C for the EVCC. The subcooling degree in both condensers is 5 K to prevent pump cavitation problems, while the superheating degree at the ORC evaporator and EVCC generator is 10 K. Finally, the evaporation temperature in the EVCC evaporator is 5 °C while the working fluid leaves it superheated by 5 K. Additional modeling assumptions are included in the table. For some parameters, ranges are provided instead of particular values. This is because, for these parameters, parametric investigations are carried out (presented in Section 3).

Table 2 General modeling assumptions

Parameter	Value
High-T waste heat source	
HT source mass flow rate	2.5 kg/s
HT source inlet temperature	150°C
HT source outlet temperature	130°C
Low-T waste heat source	
LT source mass flow rate	0.4 kg/s
LT source inlet temperature	60°C
LT source outlet temperature	52°C
ORC	
Expander isentropic efficiency	0.70
ORC pump isentropic efficiency	0.65

Expander-generator electromechanical efficiency	0.92
ORC pump motor efficiency	0.95
Pinch point in Generator (ORC desuperheater)	5 K
Superheating degree at expander inlet	10 K
Condensation temperature	30 °C (Mode 1), 50÷65 °C (Mode 2)
Subcooling degree at condenser outlet	5 K
Recuperator cold stream temperature rise	10÷20 °C (Mode 1), 0 K (Mode 2 and Mode 3)
Evaporation temperature	70÷120 °C
EVCC	
EVCC pump isentropic efficiency	0.65
EVCC pump motor efficiency	0.95
EVCC compressor isentropic efficiency	0.65
Compressor-motor electromechanical efficiency	0.95
Superheating degree at ejector inlet	10 K
Evaporation temperature (EVCC cooling evaporator)	5 °C
Superheating degree at EVCC cooling evaporator outlet	5 K
Condensation temperature	30 °C
Subcooling degree at condenser outlet	5 K
Compressor pressure ratio (Eq. 9)	0.70÷0.98
Generator evaporation temperature	46÷60 °C
EVCC working fluid mass flow rate in generator	calculated to satisfy pinch point in Generator
Primary flow isentropic efficiency	0.95
Secondary flow isentropic efficiency	0.65
Ejector throat and constant area section cross-flow areas	calculated from ejector model
entrainment ratio	calculated from ejector model

The mass flow of the ORC working fluid ($\dot{m}_{ORC}$) is calculated from the energy balance equation in the ORC evaporator, based on the mass flow rate ($\dot{m}_{wh,HT}$) and enthalpy of the high-T waste heat stream at its inlet ($h_{wh,in}$) and outlet ($h_{wh,out}$):

$$\dot{Q}_{evap,ORC} = \dot{m}_{ORC}(h_2 - h_1) = \dot{m}_{wh,HT}(h_{wh,in} - h_{wh,out}) \quad (1)$$

In Mode 3, the enthalpy of the ORC working fluid at the preheater outlet is determined from the energy balance equation of this heat exchanger based on the mass flow rate ($\dot{m}_{wh,LT}$) and inlet ($h_{wh,in}$) and outlet ($h_{wh,out}$) enthalpy of the low-T waste heat stream in the heat exchanger:

$$\dot{Q}_{pre,ORC} = \dot{m}_{wh,LT}\left(h_{wh,in} - h_{wh,out}\right) = \dot{m}_{ORC}(h_1 - h_6) \quad (2)$$

The net electric power output of the ORC ($P_{e,ORC}$) is equal to the gross electrical power of the expander ($P_{e,exp}$) minus the electrical power consumed by the ORC pump ($P_{e,pump,ORC}$):

$$P_{e,ORC} = P_{e,exp} - P_{e,pump,ORC} = \dot{m}_{ORC}\left(\eta_{em,exp-G}(h_2 - h_3) - \frac{(h_6 - h_5)}{\eta_{M,pump}}\right) \quad (3)$$

These are calculated also considering the ORC expander-generator electromechanical efficiency ($\eta_{em,exp-G}$) and ORC pump motor efficiency ($\eta_{M,pump,ORC}$).

In Mode 2, useful heat is recovered from the ORC condenser ($\dot{Q}_{heat}$), calculated according to the following equation:

$$\dot{Q}_{heat} = \dot{m}_{ORC}(h_4 - h_5) \quad (4)$$

The EVCC is designed considering the thermal input provided to the cycle from the desuperheating of the ORC working fluid in Generator 1 in Mode 3. More specifically, for each EVCC generator evaporation temperature, the mass flow rate of the EVCC primary flow at the ejector inlet ($\dot{m}_p$), along with the state of the ORC working fluid at the Generator outlet are iteratively calculated to achieve the desired 5 K pinch point in this heat exchanger (Table 2), according to the energy balance equation:

$$\dot{Q}_{gen} = \dot{m}_{ORC}(h_3 - h_4) = \dot{m}_p(h_2 - h_1) \quad (5)$$

A critical operational parameter of the EVCC is the mass flow rate of the secondary flow entrained in the ejector ($\dot{m}_s$), which affects the cooling output of the system. For its calculation, a modified ejector design model based on the 1-D model by Huang [13] is applied. The details of the aforementioned model can be found in the

original publication by Huang [13]. The inputs to this model are: 1) the primary flow thermodynamic state (pressure and temperature), 2) the primary flow mass flow rate, 3) the secondary flow state (pressure and temperature) and 4) the backpressure of the ejector (imposed and equal to the EVCC condensation pressure).

The outputs of the model are the main ejector dimensions, namely the converging-diverging nozzle throat and outlet cross-sectional areas, the mixing section cross-sectional area as well as the diffuser outlet cross-sectional area, as well as the secondary flow mass flow rate of the ejector. The ratio of the secondary and primary mass flow rate of the ejector is defined as the ejector entrainment ratio (ω):

$$\omega = \frac{\dot{m}_s}{\dot{m}_p} \tag{6}$$

Higher entrainment ratios indicate that the ejector operates more efficiently, since more low-pressure vapor is entrained for the same amount of high-pressure vapor supplied to the ejector.

An important design parameter of the EVCC is the compressor pressure ratio (not to be confused with the common compressor pressure ratio definition), which is defined according to the following equation:

$$p_{r,comp} = \frac{p_{13} - p_{12}}{p_9 - p_{12}} \tag{7}$$

The compressor pressure ratio as it is defined in the present study is the ratio of the pressure increase of the secondary flow achieved by the compressor divided by the pressure difference of the EVCC working fluid in the condenser and cooling evaporator. It can theoretically vary from a minimum of 0 (the whole compression is achieved by the ejector and no compressor is used) to a maximum of 1 (the whole compression is achieved by the compressor and no ejector is used).

In addition to the mass flow rate of the secondary flow, an additional output of the ejector model is the state of the mixed flow at the ejector outlet.

The cooling produced in the EVCC evaporator ($\dot{Q}_{cool}$) is calculated from the equation:

$$\dot{Q}_{cool} = \dot{m}_s(h_6 - h_5) \tag{8}$$

The power consumption of the EVCC ($P_{e,EVCC}$) is equal to the power consumption of the compressor ($P_{e,comp}$) plus the power consumed by the EVCC pump ($P_{e,pump,EVCC}$):

$$P_{e,EVCC} = P_{e,comp} + P_{e,pump,EVCC} = \frac{\dot{m}_s(h_{13} - h_{12})}{\eta_{em,comp-M}} + \frac{\dot{m}_p(h_7 - h_{10})}{\eta_{M,pump,EVCC}} \tag{9}$$

For their calculation, the compressor electromechanical efficiency ($\eta_{em,comp-M}$) and the EVCC pump motor efficiency ($\eta_{M,pump,EVCC}$) are considered.

The total net power produced by the whole ORC-EVCC system ($P_{e,tot}$) in Mode 3 is equal to the net power produced by the ORC electrical generator minus the power consumption of the EVCC:

$$P_{e,tot} = P_{e,ORC} - P_{e,EVCC} \tag{10}$$

2.5. Performance assessment indexes

The electrical efficiency of the ORC is defined as follows:

$$\eta_{e,ORC} = \frac{P_{e,net,ORC}}{\dot{Q}_{evap,ORC} + \dot{Q}_{pre,ORC}} \tag{11}$$

The electrical COP of the EVCC is defined according to the following equation:

$$COP_e = \frac{\dot{Q}_{cool}}{P_{e,EVCC}} \tag{12}$$

The overall electrical efficiency of the ORC-EVCC in Mode 3 is defined as follows:

$$\eta_{e,tot} = \frac{P_{e,tot}}{\dot{Q}_{evap,ORC} + \dot{Q}_{pre,ORC}} \tag{13}$$

The combined cooling and power overall efficiency in Mode 3 is defined as follows:

$$\eta_{CCP} = \frac{P_{e,tot} + \dot{Q}_{cool}}{\dot{Q}_{evap,ORC} + \dot{Q}_{pre,ORC}} \quad (14)$$

3. Results and discussion

3.1. Parametric investigations

The design of the prototype is based on the selection of several parameters, some of the most significant being the following: 1) working fluid in ORC, 2) working fluid in EVCC, 3) ORC evaporation temperature, 4) EVCC generator evaporation temperature, 5) compressor pressure ratio (as defined in Eq. 7). The selection of these parameters is subject to thermodynamic (waste heat temperature, efficiencies) and technical constraints (equipment components). As a first step in the design process, a series of parametric investigations are carried out to examine their influence on the performance of the prototype. In the following investigations, while these parameters are varied, all other design parameters are kept constant, equal to the values summarized in ***Table 2***.

The ORC electrical efficiency variation as a function of the recuperator cold stream temperature rise for different ORC evaporation temperatures for Mode 1 (electricity-only) is presented in ***Figure. 2***. As expected, the highest evaporation temperature of 120 °C results in the highest efficiency. Because low evaporation temperatures are considered in the ORC, the possible cold stream temperature rise in the recuperator is relatively low, thus the efficiency improvement potential is very small. A maximum efficiency of 12% is achieved with R1233zd(E) for an evaporation temperature of 120 °C when the temperature rise is 20 K. For R1234ze(E), the maximum electrical efficiency is 8.86% when the evaporation temperature is 120 °C and the temperature rise in the recuperator is 14 K. Note that because of the significantly lower critical temperature of R1234ze(E) compared to R1233zd(E), the cycle's maximum operation temperature is lower, thus less heat can be recovered in the recuperator, and the cold stream temperature rise is limited .

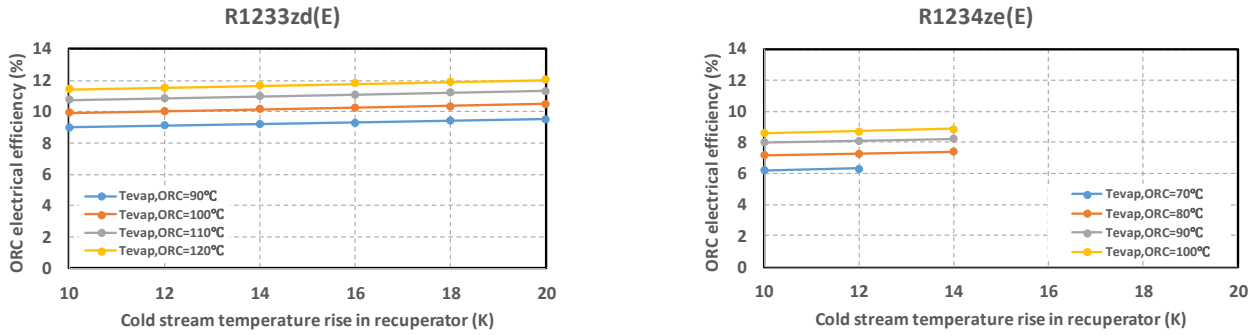

Figure. 2. ORC electrical efficiency as a function of the cold stream temperature rise in the recuperator for different ORC evaporation temperatures in Mode 1 (Electricity-only, T_{cond}=30 °C)

The ORC electrical efficiency as a function of the ORC condensation temperature for different evaporation temperatures in Mode 2 (CHP) is depicted in ***Figure. 3***. As expected, increasing the condensation temperature results in a significant, linear decline in electrical efficiency, since useful heat is produced to the detriment of electrical power. Therefore, the ORC condensation temperature must be selected to have an intermediate value in order to produce hot water at a sufficiently hight temperature as well as securing the highest possible ORC electric efficiency .

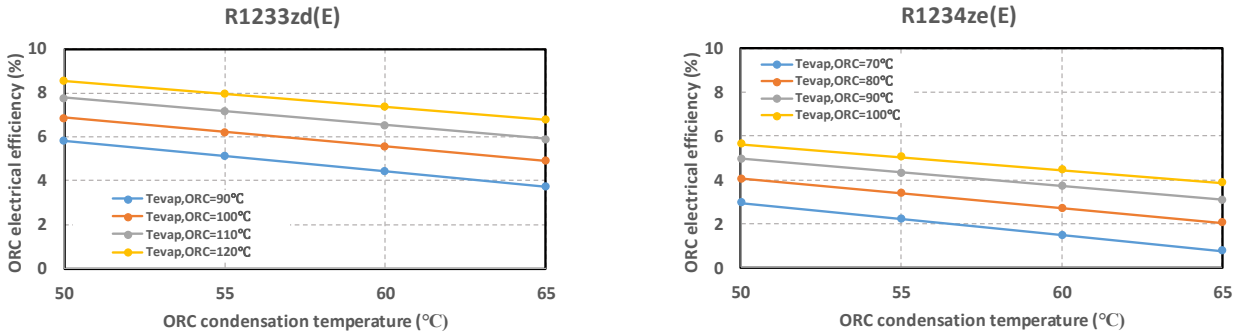

Figure. 3. ORC electrical efficiency as a function of the ORC condensation temperature for different ORC evaporation temperatures in Mode 2 (CHP)

The ejector entrainment ratio as a function of the compressor pressure ratio for different EVCC generator evaporation temperatures is illustrated in ***Figure. 4***.

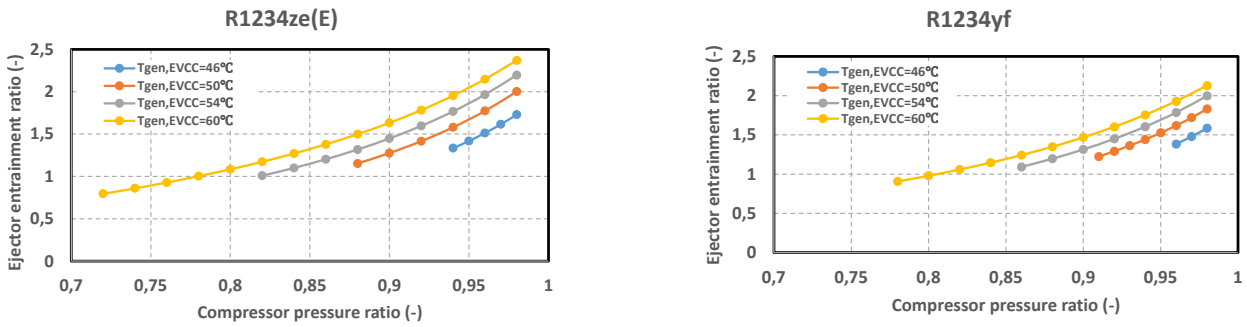

Figure. 4. Ejector entrainment ratio as a function of the compressor ratio for different EVCC generator evaporation temperatures

Higher compressor pressure ratios result in higher ejector entrainment ratios since the secondary flow enters the low-pressure port at a higher pressure and is more easily entrained by the primary flow. Furthermore, higher EVCC generator evaporation temperatures also result in increased entrainment ratios. This is because as the pressure of the primary flow is increased, it can more easily entrain low-pressure vapor. It can be observed that for each EVCC generator evaporation temperature, there is a minimum compressor pressure ratio which is necessary for the ejector to be able to operate. This is because, for lower pressure ratios, the primary flow can't entrain any low-pressure vapor exiting the cooling evaporator. The minimum required pressure ratio is positively correlated with the primary flow pressure (and hence the EVCC generator pressure). Notably, for an EVCC generator evaporation temperature of 46 °C, the compressor pressure ratio must be at least equal to approximately 0.94 (R1234ze) and 0.96 (R1234yf) for the ejector to be able to operate. On the other hand, if the EVCC generator evaporation temperature is increased to 60 °C, the compressor pressure ratio may be reduced to as low as 0.72 (R1234ze) and 0.76 (R1234yf).

If the compressor pressure ratio is higher than 0.9, essentially the whole compression is carried out by the compressor, which greatly assists the primary flow in entraining low-pressure vapor, reading to entrainment ratios above 1.5. Note that the ejector entrainment ratio is independent of the ORC evaporation temperature.

The EVCC electrical COP as a function of the compressor pressure ratio for different EVCC generator evaporation temperatures is illustrated in ***Figure. 5***. On the same diagrams, the electrical COP of a conventional VCC operating within the same cooling evaporation and condensation temperatures (see ***Table 2***) is illustrated (straight line).

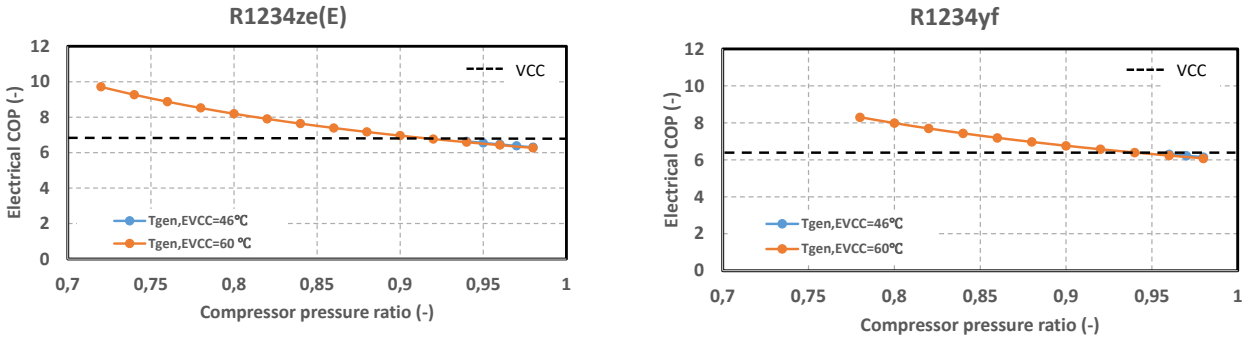

Figure. 5. Electrical COP of EVCC as a function of the compressor pressure ratio for different EVCC generator evaporation temperatures in Mode 3 (CCP)

As the pressure ratio increases, both the cooling output and the electrical consumption of the compressor increase. However, the increase in the compressor electricity consumption is more significant, and thus the electrical COP ultimately declines. Notably, for pressure ratios above approximately 0.95, the electrical COP of the EVCC is lower than that of a conventional VCC. In this case, the secondary's stream pressure rise through the ejector is significantly low, thus the whole cycle is operating practically as a VCC. However, due to the existence of EVCC pump the electrical power required is slightly higher compared to VCC, thus the electrical COP takes lower values. Although lower compressor pressure ratios result in higher electrical COP values, they are also associated with lower ejector entrainment ratios and cooling output. Therefore, the compressor ratio should be selected to ensure 1) a higher electrical COP than that of a conventional VCC and 2) a sufficiently high cooling production for a particular application, and 3) it should be sufficiently high to enable the ejector operation.

Note that the EVCC generator evaporation temperature does not affect the electrical COP. As the generator evaporation temperature is increased, the primary flow mass flow rate in the generator is decreased because the heat recovered from the ORC is reduced (this happens because the pinch point in the EVCC generator is located at the end of preheating and the start of boiling for the EVCC working fluid, thus increasing the EVCC generator saturation temperature results in less heat being recovered from the ORC working fluid), while the enthalpy difference of the EVCC working fluid in the heat exchanger is increased (Eq. 5). Although the entrainment ratio of the ejector is increased, the secondary flow mass flow rate is reduced, because the reduction of the primary flow mass flow rate is more significant. Consequently, increasing the EVCC generator evaporation temperature only leads to lower secondary flow mass flow rates, equally resulting in both lower compressor power consumption and cooling output for a given thermal input to the EVCC, affecting in the same way both the numerator and denominator of the electrical COP (Eq. 12). Considering the above, the EVCC generator evaporation temperature should be kept as low as possible so that more heat is recovered from the ORC, but at the same time the ejector is capable of operating at low compressor pressure ratios (that also lead to better electrical COP).

The overall electrical efficiency of the ORC-EVCC as a function of the compressor pressure ratio for different EVCC generator evaporation temperatures and ORC evaporation temperatures in Mode 3 is illustrated in ***Figure. 6***. For the results presented in both of these diagrams, the ORC working fluid is assumed to be R1233zd(E).

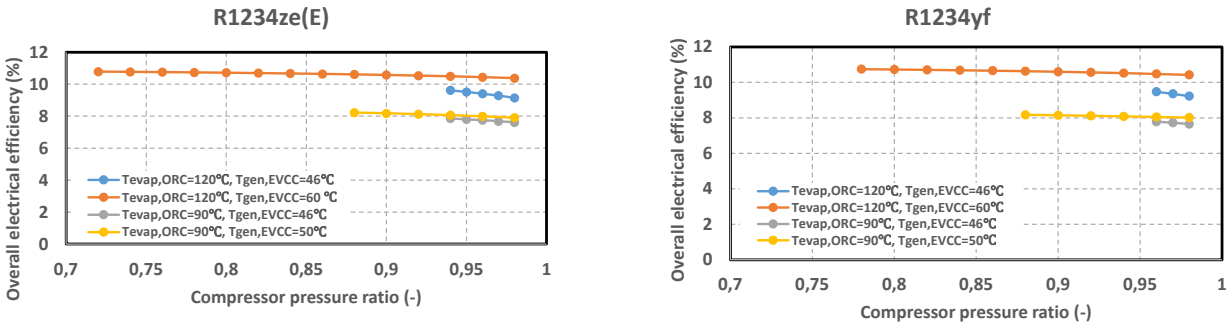

Figure. 6. Overall electrical efficiency of ORC-EVCC as a function of the compressor pressure ratio for different EVCC generator evaporation temperatures and ORC evaporation temperatures in Mode 3 (CCP)

Higher overall efficiencies are observed for the highest ORC evaporation temperature of 120 °C because of the significantly higher power output of the ORC. Furthermore, the overall electrical efficiency is increased for higher EVCC generator evaporation temperatures, since these lead to lower compressor power consumption (as described previously). Finally, for higher compressor ratios, more electric power is required to drive the compressor, thus the net electric power output (and overall electrical efficiency) is decreased. Regardless, the impact of the compressor pressure ratio on the overall electric efficiency is not significant. Therefore, to maximize the overall electric efficiency, both the ORC evaporation and EVCC generator evaporation temperatures must be as high as necessary.

The overall combined electrical and cooling efficiency of the ORC-EVCC as a function of the compressor pressure ratio for different EVCC generator evaporation temperatures and ORC evaporation temperatures is illustrated in ***Figure. 7***.

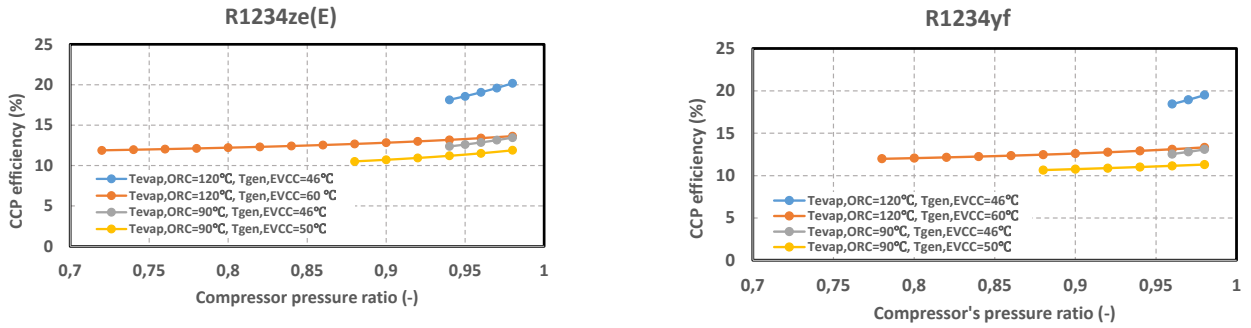

Figure. 7. Combined cooling and power efficiency of ORC-EVCC as a function of the compressor pressure ratio for different EVCC generator evaporation temperatures and ORC evaporation temperatures in Mode 3 (CCP)

The variation of the CCP efficiency depends on the combined variation of the net power output and the cooling output of the system. The highest CCP efficiency is observed for the ORC evaporation temperature of 120 °C,

for which the net power output is significantly high. The influence of the EVCC generator evaporation temperature on the CCP efficiency is not completely straightforward, since, as was mentioned previously, increasing the EVCC generator evaporation temperature results in both lower cooling output and also compressor power consumption. However, because the cooling output reduction is more significant, the CCP efficiency is reduced.

3.2. Design point selection

Based on the results presented in the previous section, R1233zd(E) and R1234ze show the best performance in the ORC and EVCC, respectively, as they result in higher power and cooling output. Therefore, these working fluids were selected to be used in the prototype. Moreover, higher ORC evaporation temperatures are favorable as they result in higher ORC electrical efficiencies and allow for more heat to be recovered by the EVCC, thus also leading to higher electrical COP values. Therefore, the highest possible ORC evaporation temperature (120 °C) is selected for the design of the prototype. Regarding the cold stream temperature rise in the recuperator, the maximum possible value of 20 K is selected, owing to its positive influence on the ORC electric efficiency in Mode 1. Regarding Mode 2, a condensation temperature of 50 °C is selected for the ORC, since it is sufficient for the production of hot water without severely penalizing the electrical efficiency. The final set of variables to be selected include the EVCC generator evaporation temperature and compressor pressure ratio. Based on the parametric investigations that were presented in the previous section, an ECC generator evaporation temperature of 52 °C and compressor pressure ratio of 0.84 represent a good compromise between a sufficiently high electrical COP and cooling output for the EVCC in Mode 3. The system design variables along with the system operating parameters in the three operating modes are summarized in **Table 3**.

Table 3 Design point operating parameters

	Mode 1 (Electricity-only)	**Mode 2 (CHP)**	**Mode 3 (CCP)**
ORC working fluid		R1233zd(E)	
ECC working fluid		R1234ze	
ORC evaporation temperature (°C)		120	
ORC condensation temperature (°C)	30	50	30
Cold stream temp. rise in recuperator (°C)	20	0	0
ECC generator evaporation temperature (°C)	-	-	52
Compressor pressure ratio (-)	-	-	0.84
Electric power output (kW_e)	11.35	8.06	10.57
Cooling output (kW_c)	-	-	4.80
Heating output (kW_{th})	-	85.5	-
ORC electrical efficiency (%)	12.84	10.01	12.62
CHP efficiency (%)	-	-	14.96
Electrical COP (-)	-	-	7.69
Overall electrical efficiency (%)	12.04	8.55	10.29
CCP efficiency (%)	-	-	14.96

4. Conclusions

The present study presented the thermodynamic design of a vessel engine waste heat recovery prototype based on a cascade Organic Rankine Cycle (ORC) and an ejector cooling-vapor compression cycle (EVCC) considering three operating modes: 1) electricity-only, 2) combined heat and power (CHP) via heat recovery from the ORC condenser and 3) combined power and cooling (CCP) from the simultaneous operation of the ORC and EVCC. To determine the preliminary design point, a series of parametric analyses were carried out to investigate the influence of key design parameters on the performance of the prototype and select its design point. R1233zd(E) and R1234ze were selected as the working fluids in the ORC and EVCC, respectively, as they led to the highest electrical efficiency and electrical COP in the two cycles. Furthermore, the selected design ORC evaporation temperature is 120 °C, which can lead to high ORC electrical efficiencies of up to 12.62% in electricity-only mode. The most suitable condensation temperature of the ORC in CHP mode was found to be 50 °C since it can allow the production of hot water at a sufficiently high temperature without penalizing the power output of the ORC. Regarding the design of the EVCC, higher EVCC generator evaporation temperatures do not influence the electrical COP but result in lower cooling outputs. Meanwhile, increasing the compressor pressure ratio has a negative impact on the electrical COP but leads to higher

cooling output. Therefore, an EVCC generator evaporation temperature of 52 °C was selected, as it allows the operation of the ejector at a compressor pressure ratio of 0.84, which results in good electrical COP and substantial cooling output. Under the above conditions, the prototype ORC electric efficiency is up to 12.62% (electricity-only mode), while the overall electrical and CCP efficiency (CCP) are 10.29% and 14.96%, respectively. Finally, the electrical COP of the EVCC is 7.62, being superior to that of a conventional vapor compression cycle.

Acknowledgment

This study has been performed within the framework of the ZHENIT project, funded by the European Union's Horizon Europe research and innovation program, under grant agreement No. 101056801

Nomenclature

Abbreviations

CCP	combined cooling power
EVCC	ejector vapor compression cooling cycle
GWP	global warming potential
HFO	hydrofluoroolefin
ODP	ozone depletion potential
ORC	organic Rankine cycle

Variables

COP	coefficient of performance (-)
h	mass enthalpy, kJ/kg
$\dot{m}$	mass flow rate, kg/s
P	power, kW
p	pressure, bar
$\dot{Q}$	heat duty, kW
T	temperature, °C

Greek symbols

η	efficiency (-)
ω	entrainment ratio (ejector)

Subscripts and superscripts

CCP	combined cooling and power
$cond$	condenser
$cool$	cooling
$crit$	critical
e	electric
$evap$	evaporator
exp	expander
G	generator (electric)
gen	generator (heat exchanger)
in	inlet
m	mechanical
M	motor
net	net
out	outlet
p	primary flow (ejector)
pre	preheater

$pump$ pump

s secondary flow (ejector)

tot total

wh waste heat

References

1. Konstantinos Braimakis, A.M., Antonios Charalampidis, Sotirios Karellas, *Exergetic performance of CO2 and ultra-low GWP refrigerant mixtures as working fluids in ORC for waste heat recovery.* Elsevier, 2020(Energy): p. 23.
2. Konstantinos Braimakis, M.P., Dieter Brüggemann, Sotirios Karellas, Kyriakos Panopoulos, *Low grade waste heat recovery with subcritical and supercritical Organic Rankine Cycle based on natural refrigerants and their binary mixtures.* Elsevier, 2015(Energy): p. 13.
3. Olgun Konur, O.Y., S. Aykut Korkmaz, C. Ozgur Colpan, Omur Y. Saatcioglu, *Thermal design and analysis of an organic rankine cycle system utilizing the main engine and cargo oil pump turbine based waste heats in a large tanker ship.* Elsevier, 2022(Journal of Cleaner Production): p. 18.
4. George Kosmadakis, P.N., *Reversible high-temperature heat pump/ORC for waste heat recovery in various ships: A techno-economic assessment* Elsevier, 2022(Energy): p. 12.
5. Farhad Salek, A.N.M., Mohammad Mahdi Naserian, *Thermodynamic analysis of diesel engine coupled with ORC and absorption refrigeration cycle.* Elsevier, 2017(Energy Conversion and Management): p. 7.
6. Tryfon C. Roumpedakis, T.C., Evropi Monokrousou, Konstantinos Braimakis, Sotirios Karellas, *Integrated ORC-Adsorption cycle: A first and second law analysis of potential configurations.* Elsevier, 2019(Energy): p. 13.
7. Braimakis, K., *Solar ejector cooling systems: A review.* Renewable Energy, 2021. **164**: p. 566-602.
8. Eastman, *Therminal VP1 - Heat transfer fluid*.
9. European Parliament, *Regulation (EC) No 2037/2000 of the European Parliament and of the Council of 29 June 2000 on substances that deplete the ozone layer*. 2000, Council of the European Union.
10. United Nations, *Kyoto Protocol*. 1997: Kyoto, Japan.
11. European Parliament, *Regulation (EU) No 517/2017 of the European Parliament and of the Council of 16 April 2014 on fluorinated greenhouse gases and repealing Regulation (EC) No 842/2006*. 2014, Council of the European Union.
12. National Institute of Standards and Technology, *REFPROP NIST Standard Reference Database 23*.
13. Huang, B.J., et al., *A 1-D analysis of ejector performance.* International Journal of Refrigeration, 1999. **22**(5): p. 354-364.

Efficient Integration of advanced absorption heat pumps and chillers in District Heating and Cooling networks

Joan Carles Bruno, Addarda Irsyad Usman

Universitat Rovira i Virgili, Dept. of Mechanical Engineering, CREVER-Research Group on applied Thermal Engineering, Tarragona, Spain, juancarlos.bruno@urv.cat, CA

Abstract:

The design and analysis of District Heating and Cooling (DHC) networks using local renewable energy sources such as thermal energy from solar collectors is one of the most interesting tools to fight against greenhouse gas emissions. The development and viability of these networks will be facilitated by the parallel development of new highly efficient absorption systems to efficiently produce not only chilled water but also heating and/or cooling and working as booster absorption heat pumps for the fifth generation of DHC networks using very low temperatures. These new absorption units are already commercialized and ready to be integrated as central units or distributed as substations with other energy conversion technologies. The new absorption systems considered include the following: a) double-lift chillers to improve the recovery of waste heat by producing a very high temperature glide in the driving heat, b) double-lift absorption units, or very low-temperature driven systems. This paper examines the technical assessment of solar thermal based cooling networks using advanced absorption chillers and taking as a reference conventional DHC networks. The indicators used include the saving in energy and greenhouse gas emissions and a prospect of the economic benefit. The results show the role that the new advanced absorption chillers could play for the development of future net zero-emissions DHC networks.

Keywords:

Absorption chillers and Heat pumps; Thermal solar energy; District networks; Energy integration.

1. Introduction and objectives

There is a great interest to fulfil the increasing energy demand for refrigeration and air conditioning using renewable energies. Encouraged by the Renewable Energy Directive (EU) 2018/2001 [1], it is projected that by 2030, 40% of heating and cooling sector in Europe will come from renewable energy sources. If we compared this goal with the current situation, there is still a long way for renewable heating and cooling to fulfil the projected vision of the directive. One of the technological options could be the development of large-scale solar cooling plants to benefit from the scale economic factor in conjunction with the use of advanced absorption chillers.

In the project Task 55 of the International Energy Agency [2] (IEA SHC, 2016-20) was conducted a comprehensive study on the modelling, analysis, and real case study survey for the integration of large solar heating and cooling systems into District Heating and Cooling (DHC) Networks. The main conclusion was that in the selected case studies mainly in Denmark and Austria the main solar technologies used Flat Plate collectors and hot water as working fluid, and only a few of them used parabolic collectors. Using renewable energies for air conditioning applications, the preferred working fluid for absorption chillers is Water/LiBr instead of Ammonia/water because of its higher efficiency, although direct fired units using ammonia/water of could be considered for certain small capacity applications such as when air heat rejection is needed.

The objective of this paper is to provide a brief review of novel features incorporated in the current absorption chillers and their integration into DHC networks. It is presented a preliminary assessment of technologies using low-temperature flat plate solar collectors and the current state-of-the-art hot water driven absorption chillers in comparison with alternative and much more extended compression chillers using electricity grid. The idea is to compare different thermal solar cooling technologies by measuring its performance using key parameters with respect to an equivalent electric compression chiller but not to design cooling alternatives for a certain specific case study.

This paper is organized as follows. After the introduction to justify the research interest and to set the objectives in the second section are presented the current trends in the technology of absorption heat pumps and chillers followed in section 3 with a short review of how these units could be integrated in District networks. Finally, in

section 4 and 5 is presented a modelling and analysis to compare the performance of selected hot water driven absorption chillers being the conclusions summarized in section 6.

2. High efficiency absorption heat pumps and chillers

Some of the main new features related with the current high-efficiency absorption chillers could be classified as:

1. Improvement on the system components and internal arrangements such as:

    1.1. Double section components. This two-step evaporator and absorber technology has two pressure levels but the overall pressure is reduced. The absorption process is also divided in two steps reducing the solution concentration values but increasing the overall concentration different between the rich and poor solution [3]. This arrangement enhances absorption of the refrigerant into the concentrated solution, making the unit more efficient and reliable than conventional absorption chillers. The result is that quite simple cycles such as single effect units can reach COP values higher than 0.8 or up to 1.48 for double-effect steam driven configuration, the highest of its class. Moreover, the cost of the chiller benefits of lower solution concentrations due to the cost of the LiBr.

    1.2. Falling-film generator design provides superior heat transfer compared to a conventional flooded generator. This design also reduces the required amount of solution to be circulated, decreasing start-up time from a cold start [3].

    1.3. Internal heat recovery of the absorption heat. In this case one of the two absorber steps uses part of the absorption heat to reduce the demand for cooling water. This feature is really not new in the absorption field and was proposed in the past but only for ammonia/water systems [4].

    1.4. Some manufacturers produce water/LiBr absorption chillers that use refrigerant mixed with water and lithium bromide solution, so that they can decrease the evaporative temperature of refrigerant to 0℃ or less [5]. Delivering brine at temperatures down to -7℃, which is applicable not only to comfort cooling but also to phase change cold storage with its corresponding volume savings and provide below zero process cooling. Other chiller versions are prepared for onboard ship operation recovering hot water and waste steam from engines to produce cooling using sea water as heat rejection fluid.

2. Improvement of the thermal cooling cycles by the incorporation of additional components in multiple stages arrangements. The result is the development of new chiller types beyond the traditional single and double effect cycles:

    2.1. Single-effect double-lift absorption chillers. This configuration concept was proposed in the literature [6] and now implemented commercially and consist of a three-level pressure cycle (fig. 1) with a high temperature glide of the heat source that enables a higher heat input and consequently a higher cooling capacity for a given heat source. This thermally driven cycle uses the source heat in three generators (high-temperature generator, low-temperature generator and auxiliary generator) to lower temperature more efficiently than a conventional single-effect cycle. Several manufacturers offer this cycle configuration very suitable for district cooling systems that could benefit from its low return temperatures.

    2.2. Half effect absorption chillers use two water/LiBr solution circuits with the aim to recover very low temperature heat sources of about 70ºC to produce cooling. The COP is much lower than single effect cycles but could be an ideal solution for some specific cases such as geothermal energy sources or for the use of waste heat from low temperature fuel cells or electrolyzers.

    2.3. Triple effect absorption chillers are high-temperature chillers that claim a COP as high as 1.8 [7]. The high temperatures to drive double or triple effect chillers using fuel-fired units, steam, pressurized hot water or exhaust gas and certain specific manufacturing limitations, reduce the range of application of these type of chillers to medium or large size applications (starting at a few hundreds of kilowatts). Due to the materials used (stainless steel) and flow circulation, the rate of corrosion is negligible even for triple effect cycles that include also online concentration measurement [7]. Moreover, the variable frequency drives on solution pumps helps to improve the COP during part loads. The stainless-steel plate type solution heat exchangers also helps to increase the COP by offering maximum internal heat recovery.

3. New cycle arrangements to cover applications not fully available commercially until the last years:

3.1. Heat pumps of Type I driven by high-temperature heat to work as amplifiers from low temperature sources close to ambient temperature to medium temperature. The heat source can be steam, hot water, exhaust gas, fuel, geothermal energy, or any combination of these heat sources.

3.2. Heat pumps of Type II known also as heat transformers driven by medium-temperature than in part is degraded to ambient temperature and the other part upgraded to produce high-temperature hot water or steam.

3.3. Simultaneous production of heating and cooling using high-temperature driven systems such as waste steam or direct-fired units. In some case also multi-energy systems recovering hot water and exhaust gases simultaneously to produce cooling and hot water.

3.4. Reversible operation systems to provide cooling in summer and heating in winter or domestic hot water along the year. One of the weaknesses of absorption systems is the lack of reversibility so they operate only during certain periods of the year. However, using certain flow configurations [8] is possible to use the evaporator to increase the temperature glide of the heat-driving source and increase the temperature of the heat rejected at the condenser/absorber for useful heat applications.

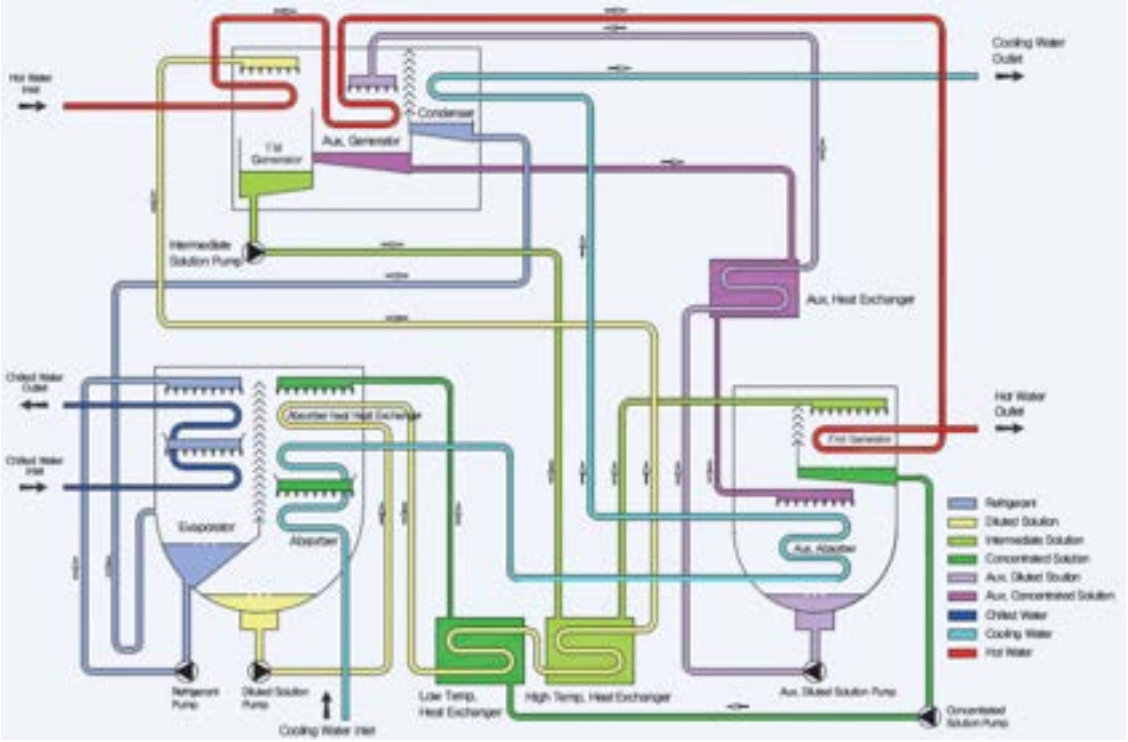

Figure 1. Single-effect Double Lift hot water driven absorption chiller (World Energy 2ABH). Source: [5].

3. Integration of absorption systems in DHC networks

District energy systems have been successfully implemented in many countries around the world and will play an important role in future sustainable cities. The current heating network technology, usually classified as 3rd generation district heating uses hot water between 70-100ºC. But other lower temperature networks are in development in order to reduce heat losses because of its lower operation temperature, the 4th generation working at around 55ºC and even a 5th generation using temperatures around the ambient temperature. The integration of compression heat pumps for their integration in this kind of networks has been started to be studied in the literature [9, 10] but not yet using absorption heat pumps. Nevertheless, the use of absorption systems in District heating networks has been used quite extensively to produce cooling using heat from a heating network [11]. One almost unexplored application is the use of absorption heat pumps and chillers as substations close to each user using smaller capacity units [8]. In that case, the absorption unit could also be configurated to provide heating and cooling in a reversible way (fig. 2) as shown in Ayou et al. [8].

The integration of some of the new advanced low-temperature absorption chillers mentioned in section 2 will be studied here for its integration in District cooling networks. The modelling for a preliminary assessment of these chillers for that kind of applications is given in the next section.

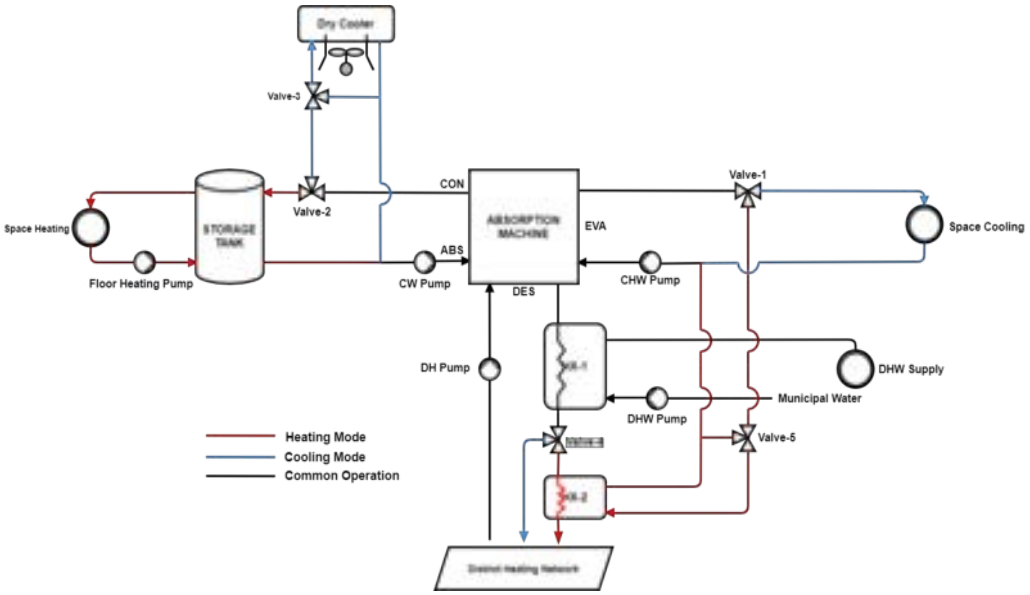

Figure 2. Connection as substation of district heating driven absorption heat pump for space heating and cooling. Source: [8].

4. Modelling of absorption chillers for District Solar Cooling

The electric efficiency factor for the rejection of heat at the condenser for compression chillers and condenser and absorber for absorption chillers is defined as:

$$f_{rej} = \frac{E_{rej}}{Q_{rej}} \tag{1}$$

The solar thermal collector efficiency is modelled using equation (2). The solar collector's area can be also calculated using this same equation.

$$\eta = \frac{Q_D}{I\,A_c} = c_0 - c_1 x - c_2\, I\, x^2 \tag{2}$$

Where x is given by:

$$x = \frac{(T_{av} - T_a)}{I} \tag{3}$$

The rejection of heat is higher for absorption chillers than in compression chillers. The additional heat that has to be rejected with respect to an electric chiller can be computed as:

$$\Delta Q_{rej} = Q_{rej,TDC} - Q_{rej,EC} = Q_D \cdot (1 + COP_{TDC}) - \dot{W}_e \cdot (1 + COP_{EC}) \tag{4}$$

The pump work required to provide the specified hot water flow rate to drive the absorption chiller has been estimated as:

$$\dot{E}_{sol} = \frac{\dot{V} \cdot \Delta P}{\mu_{pump}} \tag{5}$$

The internal electrical efficiency factor for the absorption chiller is defined as the ratio between the electricity consumed internally by the absorption chiller per unit of cooling capacity:

$$f_{el,int} = \frac{E_{TDC}}{Q_c} \tag{6}$$

Similarly, the electrical efficiency factor for the solar plant can be defined as:

$$f_{el,int} = \frac{E_{sol}}{Q_D} \tag{7}$$

Absorption systems are usually known by being bulky and heavy. To compare these characteristics among the considered chillers, it is defined the cooling density per unit of volume and weight as follows:

$$C_v = \frac{Q_c}{V_{chiller}} \quad (8)$$

$$C_w = \frac{Q_c}{W_{chiller}} \quad (9)$$

Thus, the total electricity consumption to run the absorption chiller will be mainly given by the electricity to run the absorption chiller itself, the electricity to be used for the additional heat rejected with respect to the electric chiller and the electricity used in the solar plant to pump the hot water from the solar collectors to the absorption chiller:

$$E_{tot} = E_{TDC} + E_{rej} + E_{sol} \quad (10)$$

The electricity to drive the compression chiller of reference can be easily estimated from its COP and used to compute the electricity savings provided by the absorption chiller:

$$\Delta E = \frac{E_{EC} - E_{tot}}{E_{EC}} \cdot 100\ \% \quad (11)$$

The saving in emissions is deduced from the considered emissions associated with the electricity mix. With respect to the economics comparison, the Levelized Cost of Cooling (LCOC) is selected to compare the three selected low-temperature absorption chillers. This LCOC is calculated using the following definitions and equations.

$$LCOC = \frac{I \cdot CRF + I \cdot f_{O\&M} \cdot n \cdot CRF}{Q_c \cdot N} \quad (12)$$

Where:

$$CRF = \frac{i}{1-(1+i)^{-n}} \quad (13)$$

5. Preliminary analysis of high-efficiency low-temperature absorption chillers

The most common Solar District Cooling networks consist of Flat plate collectors and hot water driven chillers. Even that parabolic solar collectors producing directly steam could be an option to produce high COP cooling using double-effect chillers, it would be difficult to justify its selection unless process steam could be required in the case studying specific small industrial applications.

The main objective of the present analysis is to compare the performance of three different types of absorption chillers using as a reference an electric compression chiller and the simple model described in the previous section 4. The selected chillers are: High-efficiency Single-effect (SE chiller), Single-effect Double-Lift (SE DL chiller) and Half-effect (HE chiller). The main technical data for these chillers is given in Tables 1, 2 and 3. These data is taken from the public catalogue data provided by the Korean company World Energy Co. Ltd [5]. The selected thermal solar collector is a large size double glazed flat plate collector used for District Heating applications manufactured by GreenOneTec. Table 4 shows technical data of these solar collectors and additional information used for the energy, environmental and economic assessment.

The results of the economic and environmental analysis are summarized in Table 5. At a first glance, the low driving temperature as the main advantage of the HE Chiller is not enough to produce an improvement in the solar collector efficiency that could compensate its lower COP. Therefore, it would not be a good idea to use an HE chiller in large scale solar cooling plants. Instead, the HE chiller is clearly a good candidate to be used as bottoming cycle of another cycle such as other higher driving temperature absorption chiller or Organic Rankine Cycle or any other cycle producing an outlet stream of at least 70ºC or used in smaller scale thermal solar plants working at those temperatures.

The main benefit provided by the SE DL chiller is the high temperature difference of the driving hot water. As a result, the hot water flowrate is reduced for a given cooling capacity. Two advantages are derived from this feature: the power required to pump the hot water is considerably reduced and the average temperature of the solar collector is also lower increasing the collector efficiency both with respect to the high efficiency SE chiller. The results show that even with a lower COP than the SE chiller the energy and emissions savings with respect to the compression chiller are similar (Table 5). However, the increased temperature glide is not enough to compensate for the lower COP and the economic indicators are favourable to the SE chiller (Table 6).

The SE chiller is simpler, thus it is not surprising that for the same capacity the other units are larger and more heavy as it is shown using the cooling density parameter (Table 5) and exhibits also the lowest internal electricity consumption. The increase of rejected heat in comparison with a compression chiller of similar size is also the lowest for the case of the SE chiller. Even that the solar collector efficiency is the worst, the required

size of the solar plant is the smallest. It is also true that for the case of an specific application, the heat at the outlet would not return to the solar collector plant but integrated into other applications such as the production of heating of domestic hot water because of its still high temperature, 80ºC. From the economics, the SE chiller is the one that exhibits the lowest Capex and best LCOC. Considering a CAPEX for the compression chiller of 250 €/kW and an average electricity cost of 30 c€/kWh, the payback for a solar thermal plant driven high-efficiency single-effect chiller would be slightly below 5 years.

Table 1. Technical data of the single-effect hot water driven absorption chiller.

Characteristics		Unit	Data
Cooling Capacity		kW	1055
Chilled Water	Inlet Temp	^{0}C	12
	Outlet Temp	^{0}C	7
	Flow Rate	m^3/h	181.4
Cooling Water	Inlet Temp	^{0}C	30
	Outlet Temp	^{0}C	35
	Flow Rate	m^3/h	401.4
Hot Water	Inlet Temp	^{0}C	95
	Outlet Temp	^{0}C	80
	Flow Rate	t/h	73.3
	Flow Rate	m^3/h	76.2
Electricity		kW	2.4
COP			0.825
Volume (LxWxH)		m	4.86x1.451x2.736
Weight in operation		kg	10100

Table 2. Technical data of the single-effect double-lift hot water driven absorption chiller.

Characteristics		Unit	Data
Cooling Capacity		kW	1055
Chilled Water	Inlet Temp	^{0}C	13
	Outlet Temp	^{0}C	8
	Flow Rate	m^3/h	181
Cooling Water	Inlet Temp	^{0}C	31
	Outlet Temp	^{0}C	36.5
	Flow Rate	m^3/h	400
Hot Water	Inlet Temp	^{0}C	95
	Outlet Temp	^{0}C	55
	Flow Rate	t/h	32.3
	Flow Rate	m^3/h	33.6
Electricity		kW	3.1
COP			0.702
Volume (LxWxH)		m	4.96x1.966x2.845
Weight in operation		kg	15300

Table 3. Technical data of the half-effect hot water absorption chiller.

Characteristics		Unit	Data
Cooling Capacity		kW	1055
Chilled Water	Inlet Temp	^{0}C	13
	Outlet Temp	^{0}C	8
	Flow Rate	m^3/h	181
Cooling Water	Inlet Temp	^{0}C	31
	Outlet Temp	^{0}C	36
	Flow Rate	m^3/h	622
Hot Water	Inlet Temp	^{0}C	70
	Outlet Temp	^{0}C	60
	Flow Rate	t/h	220
	Flow Rate	m^3/h	225
Electricity		kW	3.9
COP			0.412
Volume (LxWxH)		m	5.266x2.36x2.853
Weight in operation		kg	15700

Table 4. Additional information for the energy, environmental and economic assessment.

Characteristics		Unit	Data
Ambient conditions	Temperature	^{0}C	25
	Solar Radiation		36.5
Compression Chiller	COP		5
Emissions	Grid CO_{2eq} emissions	kg/kWh	0.14
Solar collector	Coef. C_0		0.814
	Coef. C_1		2.102
	Coef. C_2		0.016
Economic data	Cost solar district heating	€/m^2	500
	Cost SE Chiller	€/kW	400
	Cost Comp. Chiller	€/kW	250
	Main. & Oper. cost		0.02
	Operation time	h/year	3000
	Plant life time	year	25
	Interest rate		0.07

Table 5. Energy and environmental results.

Characteristics	Unit	SE	SE DL	HE
Cooling density by volume	kW/m^3	54.7	38	29,8
Cooling density by weight	kW/kg	0.104	0,069	0.067
Heat input (Q_D)	kW	1278	1502	2557
Increase heat rejected	kW	1067	1291	2346
Elec. solar plant	kW	24.2	10.7	71.4
Elec. chiller	kW	2.4	3.1	3.9
Elec. add. rejection system	kW	32	38.7	70.4
Total elec. consumption	kW	58.6	52.5	145.7
Elec. savings	kW	152	159	65
Elec. savings	%	72.2	75.1	30.9
Average solar collector temp.	ºC	87.5	75	65
Efficiency of solar collector	%	49.1	57.2	63.1
Required solar col. area	m^2	1045	1432	2690
Solar plant Elec. Eff. Factor		0.0189	0.0071	0.0279
Chiller Elec. Eff. Factor		0.0023	0.0029	0.0037
Rejec. Syst. Elec. Eff. Factor		0.03	0.03	0.03
Emissions saving	kg/h	21	22	9

Table 6. Economic results.

Characteristics	Unit	SE	SE DL	HE
Solar plant cost	€	522700	715900	1345000
Chiller cost	€	422000	464200	464200
Total cost	€	944700	1180100	1809200
LCOC	€/MWh	38.4	48.0	73.6

6. Conclusions

The integration of the most efficient low-temperature absorption chillers is essential for the deployment of District heating and cooling renewable networks and particularly using thermal solar cooling to contribute to the abatement of greenhouse emissions. Many new features have been added to absorption systems beyond the typical single or double effect configurations. The result are higher efficiencies and a broader field of applications not only restricted to cooling but also different types of heat pumps and combined cooling and heating applications.

To compete with traditional compression electric chillers characterized for a continuous decrease in cost, the simple flat plate collectors driving low-temperature absorption chillers could be an interesting alternative. Due to the low driving temperature required by half effect absorption cycles, they provide the best collectors efficiency, but this is not enough to compensate its lower efficiency. Single effect double lift chillers have a very interesting low electricity consumption because of its characteristic high temperature glide of the driving heat. Nevertheless, the highly efficient single effect cycle incorporating the latest advance cycle improvements provide a good energy efficiency and the lowest levelized cost for the produced cooling. It is true also that despite this preliminary comparison among available low-temperature hot water alternatives, the real selection should be made for specific applications.

Acknowledgments

The funding provided by the research project RAHP (PID2020-119004RB-C21) from the Ministry of Science and Innovation of Spain is highly appreciated.

References

[1] Renewable Energy Directive (EU) 2018/2001 - Available at: <https://energy.ec.europa.eu/topics/renewable-energy/renewable-energy-directive-targets-and-rules_en> [accessed 15.3.2022].

[2] Int. Energy Agency – Solar Heating and Cooling Task 55 - Available at: <https://task55.iea-shc.org/> [accessed 15.3.2022].

[3] York (Johnson Controls – Hitachi Air Conditioning) - Available at: <https://www.york.com/commercial-equipment/chilled-water-systems/absorption-chillers>

[4] Herold KE., Radermacher R., Klein SA., Absorption chillers and Heat Pumps, CRC Press, 1996.

[5] World energy absorption systems - Available at: < http://worldenergy.co.kr/en/catalogue-2/>

[6] Schweigler C., Hellmann HM., Preissner M., Demmel S., Ziegler F., Operation and performance of a 350 kW (100 RT) Single-Effect/Double-Lift Absorption Chiller in a District Heating network", AsHRAE Transactions 104 (1), 1420, 1998.

[7] Thermax – Available at:<https://www.thermaxglobal.com/tripple-effect-chiller/> [accessed 15.3.2022].

[8] Ayou DS., Wardhana, MFV., Coronas, A., Performance analysis of a reversible water/LiBr absorption heat pump connected to district heating network in warm and cold climates, Energy, 268, 126679, 2023.

[9] von Rhein J., Henze G.P., Long N., Fu Y., Development of a topology analysis tool for fifth-generation district heating and cooling networks, Energy Conversion and Management,196, 705-716, 2019.

[10] Barco-Burgos J., Bruno J.C., Eicker U., Saldaña-Robles A.L., Alcántar-Camarena V., Review on the integration of high-temperature heat pumps in district heating and cooling networks, Energy, 239, 122378, 2022.

[11] Conte B., Bruno JC., Coronas A., Optimal cooling load sharing strategies for different types of absorption chillers in trigeneration plants, Energies, 9, 8, 573, 2016.

[12] GreenOneTec - Available at: <https://www.greenonetec.com/en/units/oem-collector/>

Experimental setup design for multi-purpose Ranque-Hilsch vortex tube investigation

Wojciech Kostowski[a], Paweł Bargiel[b] , Marcel Barzantny[c], Daniel Adamecki[d] , Michał Majchrzyk[e], Barbara Mendecka[f], and Erwin Maciak[g]

[a] Silesian University of Technology, Gliwice, Poland, wojciech.kostowski@polsl.pl , CA
[b] MESco sp. z o.o., Bytom, Poland, pbargiel@mesco.com.pl
[c] Silesian University of Technology, Gliwice, Poland, marcbar945@student.polsl.pl
[d] Silesian University of Technology, Gliwice, Poland, daniel.adamecki@polsl.pl
[e] Silesian University of Technology, Gliwice, Poland, michal.majchrzyk@polsl.pl
[f] Niccolò Cusano University, Rome, Italy, barbara.mendecka@unicusano.it
[g] Silesian University of Technology, Gliwice, Poland, erwin.maciak@polsl.pl

Abstract:

The paper presents design considerations for experimental investigation of the Ranque-Hilsch vortex tube effect (VT). The research aims to find physical mechanisms governing the thermal and mass separation of non-homogenous gases entering the VT. Also, an approach to study phase-change phenomena inside the VT will be undertaken to evaluate the applicability of the VT in refrigeration systems. For this purpose, it is essential to have a mutually validated experimental setup and numerical model.

The 1st generation test rig was based on a VT of 36 mm inner diameter and up to 1.62 m length. With inlet air supply at 3 bar abs, it was possible to achieve outlet temperature values from 0.1 C at the cold side to 42.3 C at the hot side, and the maximum air flow was 123 kg/h.

The 2nd generation should be reduced in size for two reasons. First, lighter and heavier gases (helium, carbon dioxide) will be supplied from pressurized cylinders and mixed with air or nitrogen. The flow rate should be minimized to enable a continuous operation from the pressurized cylinders. Second, to apply higher inlet pressure, it is required to reduce the flow channels to maintain the gas flow below the technical limit of about 60...100 kg/h.

The proposed test rig configuration is based on two supply options. In the first option, pure gases can be supplied from batteries (bundles) of pressurized cylinders, and then mixed to achieve the desired composition. The second option can be obtained by connecting the test installation to an air compressor, which is more suitable for test operation or for multiple-parameter measurements required to obtain boundary conditions for numerical modelling. Moreover, the test rig will be extended to include a multi-phase flow unit with a liquid dosing and separation equipment.

Keywords:

Ranque-Hilsch effect; Vortex Tube; Measurements; Gas flow; Mass separation.

1. Introduction

Ranque-Hilsch vortex tubes (RHVTs) is a device that allows separation of a pressurized and highly turbulent inlet stream into two distinct outlet streams of lower pressure and varying temperatures. Temperature and mass separation effects are unique and potentially useful phenomena occurring in RHVTs. The effect was discovered by Ranque [1] and then investigated by Hilsch [2], which is commemorated by the scientific community by the use of these surnames to denote both the effect and the device.

The effect of the inlet pressure on the temperature difference was observed and studied by Martynovskii and Alekseev. They observed that the temperature difference increases with the inlet flow pressure [3]. According to Crocker et al. [4], temperature increase at the hot side can be as high as 120 K. On the other hand, the temperature drop on the cold side is said to be up to 50 K with respect to the inlet temperature [5].

Significant number of papers has been published on temperature separation in RHTVs, contributing to our understanding of temperature separation phenomena occurring in vortex tubes (VTs). The current state of knowledge aimed to explain the phenomena occurring in VTs was presented by Xue et al. [6]. It was confirmed that when studying temperature separation in a RHTV, various factors such as pressure gradient, viscosity, secondary flow structure in the tube [7], and acoustic flow [8] should be considered. Furthermore, none of the above factors proved to be the real reason for the energy separation in his RHVT due to the complexity of the

flow structure in the pipe. The various and sometimes conflicting conclusions of the investigation suggested the need for deeper and more thorough experimental and theoretical research work to better understand the complex processes inside the tube.

Regarding the mass separation phenomena in RHTVs, the reduced number of publications, with respect to the temperature separation can be found in literature. Most of studies focused on the VT application using compressed air. However, hydrocarbon processing (such as natural gas) is an example where knowledge of gas species distribution is important to keep dew point and hydrate formation conditions under control [9–11]. Practical applications for LPG processing have recently been reported by Majidi et al. [12]. Several experimental studies have been carried out by various investigators to investigate the potential for gas species separation in Ranque-Hilsch counter-flow vortex tubes. As one example, Yun et al. [13] performed an industry-oriented experimental study for CO2 separation from its mixture with air, observing the importance of the inlet pressure and the cold mass fraction. However, no qualitative conclusions leading to the explanation of the physical mechanisms were given.

The availability of such decoupling mechanisms presents a valid opportunity to integrate RHVT into various design systems to improve overall system efficiency. The potential areas of application are very wide and include, for example, improving the performance of refrigeration circuits [14, 15] or separating gas network zones with different hydrogen contents. Although a wide range of applications for RHVT can be presented [16-18], the mechanism of temperature and mass separation still lacks a fundamental scientific explanation [19, 20] as well as proper design of RHVT as a functional part of the system.

The current paper presents the initial part of a new research project, dedicated to the understanding and to possible applications of the highly interesting and still not fully explained Ranque-Hilsch phenomenon.

1.1. The ATHLETE project

The aim of the project is to carry out fundamental experimental and numerical research to improve the understanding of the Ranque-Hilsch phenomenon in a vortex tube (VT), comprising the thermal, mass and phase separation, and to demonstrate the potential of applicability in the most promising engineering areas of refrigeration and gas separation.

The project contains experimental and numerical research, and investigation on gas mixtures will be preceded by a fundamental research on pure compounds. The project will be concluded by a thermodynamic study of RHVT-based systems.

The main questions to be answered are:

1. does the difference in gas density cause a systematic mass stratification?

2. can the stratification mechanisms be confirmed by numerical modelling and flow visualization?

3. can the stratification mechanisms contribute to the performance of selected energy/process systems?

The specific project objectives comprise: O1: to build a functional CFD model of RHVT validated by experiments, O2: to elaborate a 0D (functional) representation of RHVT, O3: to demonstrate the benefits of integrating an optimized RHVT into energy systems using two specific case studies. Accordingly, five work packages (WPs) are proposed. Work packages WP1 and WP3 are related with experimental research for pure fluids and gas mixtures, respectively. Similarly, packages 2 and 4 aim to mirror the experimental results using a numerical model, which is supposed to provide a more detailed information on the flow structure. WP5 is aimed at a demonstration of benefits of the RHVT in two selected technical systems:

1.R744 (CO2)-based refrigeration cycle with an integrated RHVT;

2. Pressure let-down station for hydrogen rich natural gas, equipped with RHVT for separation of network zones of different hydrogen content.

1.2. Aim and novelty of work

The aim of this paper is to present the project development starting from the previous work of two team members, and then to explain the design of the experimental test rig which will be used to carry out the WP1 and WP3. Moreover, some technical issues influencing the experimental set-up and some modifications in the assumed plan of experiments are presented.

The novelty of work is related to the investigation of mass separation in the vortex tube, carried out within the ongoing ATHLETE project. Moreover, a detailed presentation of the test rig design, along with scale evaluation based on gas dynamics equation and preliminary measurements represents an original contribution as well.

2. First generation test installation

2.1. Installation layout and measurement methodology

The first generation test rig was built in the Laboratory of High Temperature Processes at the Silesian University of Technology. It was partially adapted from the previous test installation for the natural gas industry,

therefore, one flow measurement unit was composed of a distribution-type turbine flow meter Elster G65 with an integrated RTD Pt100 temperature sensor and an electronic volume corrector with built-in pressure transducer (0...600 kPa). A scheme and a photograph of the installation is presented in Fig. 1.

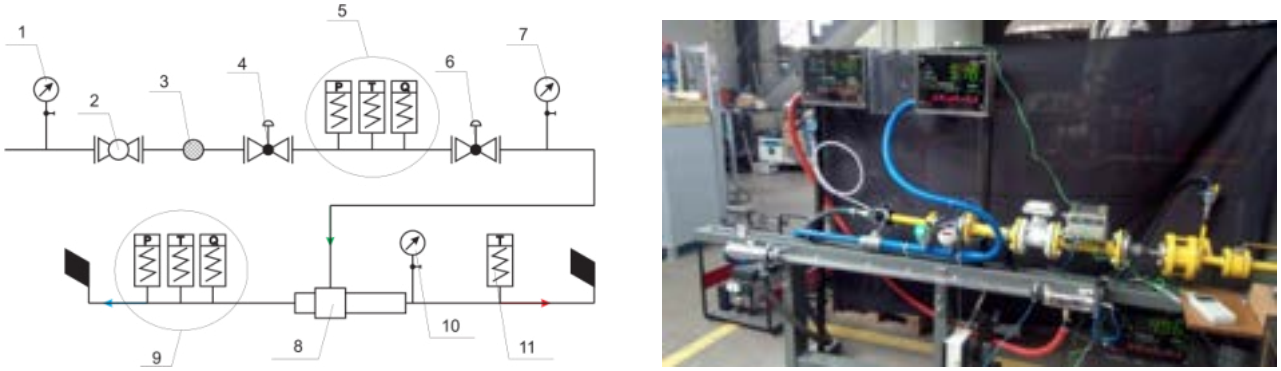

***Figure 1**. Experimental setup of the 1st generation installation. 1, 7, 10: Manometers, 2. Inlet valve, 3. Filter, 4. Pressure regulator, 5, 9 Pressure, temperature and volumetric flow measurement, 6. Fine pressure regulator, 8. Vortex tube, 11: Temperature measurement.*

The vortex tube was designed by the team member Paweł Bargiel and manufactured by an external company. The main purpose of the designed experimental rig was to use it for the validation of the numerical approach, based on which the original analytical description of the VT was proposed.

The inner VT diameter was 36.0 mm. The construction was based on a set of 2 identical nozzles tangentially located to the core part of the tube. Each nozzle had a dimension of 4.4 × 7.2 (channel height × channel width) and they were positioned in parallel. The set of nozzles was integrated with an orifice of a constant diameter equal to 13 mm.

The main set of measurements was performed for the maximum inlet pressure possible to maintain at the vortex tube inlet, i.e. about 360 kPa abs. It was found that lower values of inlet pressure decreased the thermal effect. For the maximum pressure, two key variables were modified:

a) The Length/Diameter ratio L/D, ranging from 15 to 45. This parameter was modified by replacing the core part of the tube.
b) The cold mass fraction (CMF), ranging approx. from 0 to 0.9. This value, representing the ratio of the mass flow rate at the cold outlet to the total inlet flow, was modified by adjusting the conical valve located at the ‘hot’ outlet of the VT.

2.2. Selected results

Fig. 2 Presents the total (inlet) mass flow rate of air flowing into the vortex tube in terms of the length/diameter ratio and in terms of the cold mass fraction.

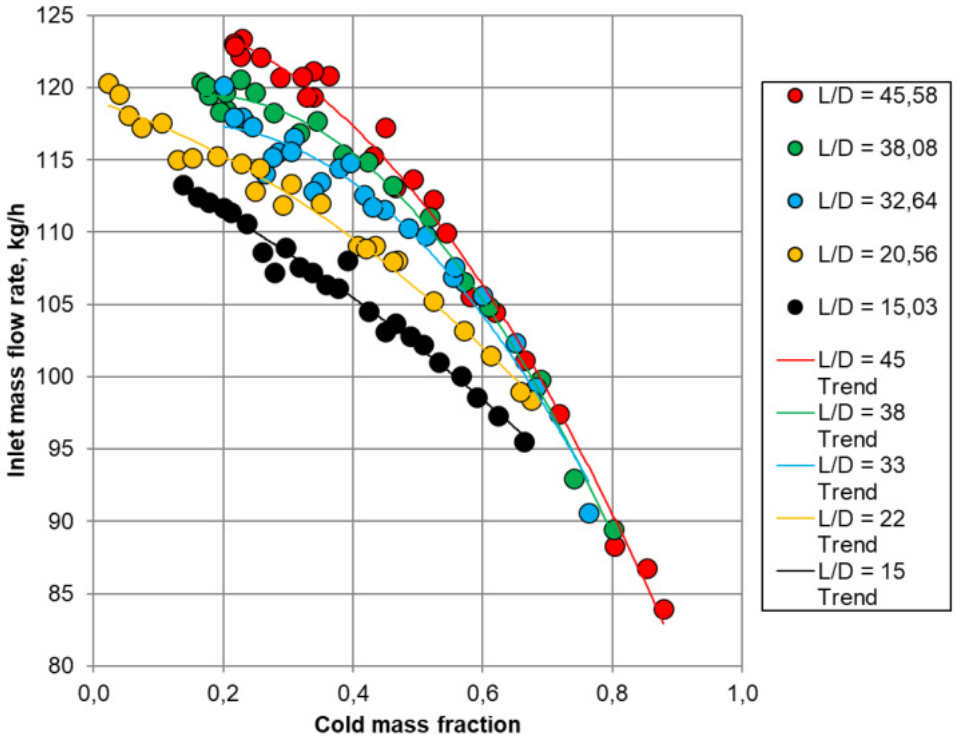

***Figure 2**. Total (inlet) mass flow rate of air through the vortex tube, inner diameter 36.0 mm; average inlet parameters: 363.5 kPa, 24.0°C.*

It can be seen that for the investigated design of the vortex tube, the total mass flow rate decreases with the cold mass fraction. However, from the point of view of the ATHLETE project, to properly design the new test installation it is essential to register the scale of the mass flow rate. In this case, inlet pressure of approx. 3.6 bar abs generates a flow exceeding 100 kg/h.

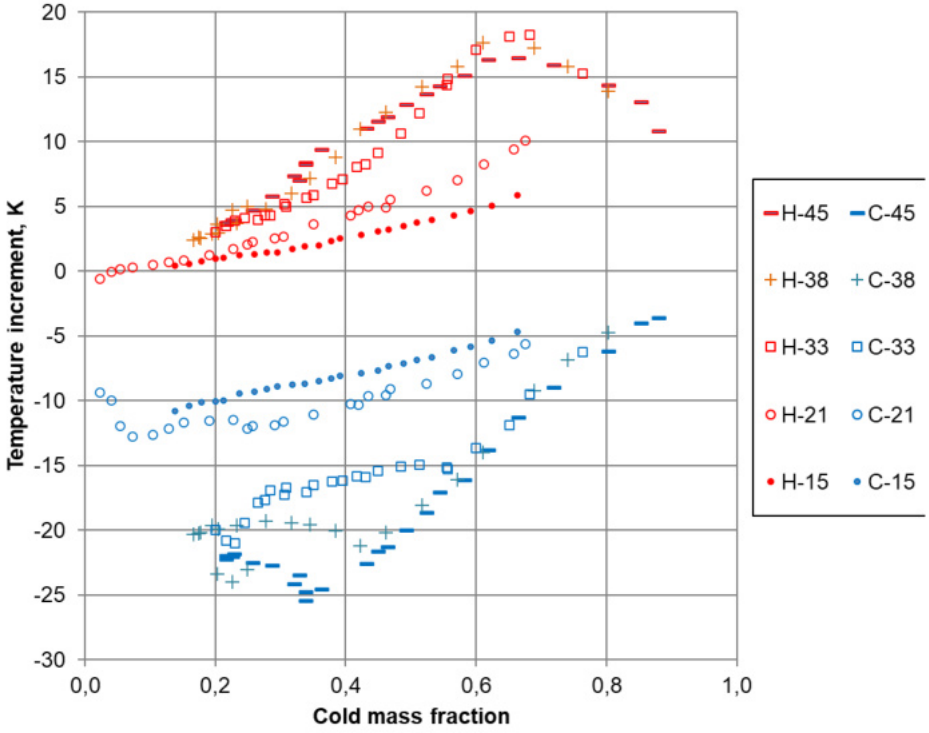

***Figure 3**. Thermal separation obtained in the 1st generation test rig with compressed air in terms of the Length/Diameter L/D ratio. Exact L/D values are given in Fig. 2. Pipe diameter (inner): 36 mm.*

Figure 3 presents the thermal performance of the studied vortex tube in terms of the length/diameter ratio. It can be observed that the increased L/D ratio improves the Ranque-Hilsch effect, however, there is no strict regularity for L/D > 33. Also, one cannot define a specific cold mass fraction corresponding to the maximum R-H effect. Maximum temperature drop at the cold outlet occurs for CMF = 0.3...0.4, while the maximum increment at the hot outlet corresponds to CMF = 0.6...0.7. For shorter vortex tubes (L/D = 15 and 21) no function maxima can be identified. Compared to similar reported studies [21], the function dependency for the hot outlet temperature in terms of the CMF is similar; different results are obtained for the cold outlet temperature. Here, a minimum value is obtained for most L/D ratios at CMF below 0.4, while Behera et al. [21] failed to obtain a minimum value as they only considered CMF ranging from 0.4 to 1.

Some more results of this work, including the numerical modelling, are shown by Bargiel et al. [22].

3. Second generation test installation

The first generation installation (related with a PhD programme) was designed to study the vortex tube operation using compressed air. To develop the idea according to the ATHLETE project assumptions, it is required to increase the scope of measurements which can be carried out at the experimental test rig. The most important modification is the adaptation to operation with compressed gases from gas cylinders, which in turn entails the reduction of the vortex tube size.

3.1. Preliminary assumptions

The initial concept of the ATHLETE research installation was based on the research questions formulated in the project application. The proposed scheme of the test rig is presented in Fig. 4.

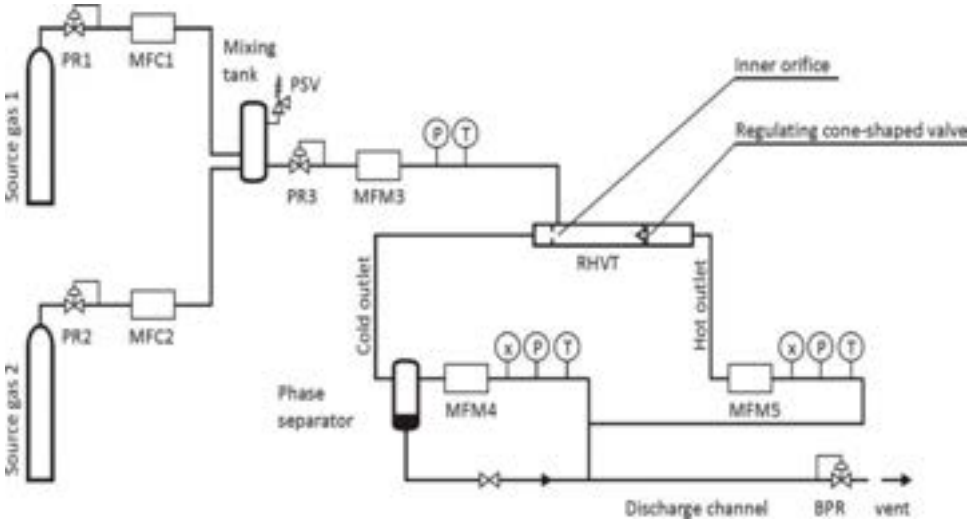

***Figure 4**. The initial concept of the ATHLETE project experimental set-up. {B]PR – [back] pressure regulators, MFC/MFM - mass flow controller/meter, p, T, x – measurement of pressure, temperature, concentration, PSV – pressure safety valve.*

In this configuration, it is possible to mix two source gases by means of two mass flow controllers supplying a specific quantity of gas to a mixing tank. Next, pressurized medium is supplied to the vortex tube, and its pressure is precisely adjusted in the regulator PR3. The discharge side of the VT is pressurized, its pressure is controlled by a back pressure regulator. This enables operation with carbon dioxide decompressed from supercritical conditions of approx. 140 bar to a back pressure of approx. 40 bar. Liquid phase of CO2 is collected in a phase separator. The objective of this set-up is to investigate the mechanism of phase separation in the vortex tube.

3.2. Simplified flow model and preparatory measurements

To evaluate the mass flow rate of a compressed gas flowing through a vortex tube of given dimensions, it was proposed to combine a simple analytical approach with some preparatory measurements.

Within the analytical approach, the flow through a vortex tube was approximated by a flow through a set of two consecutive nozzles (Fig. 5):

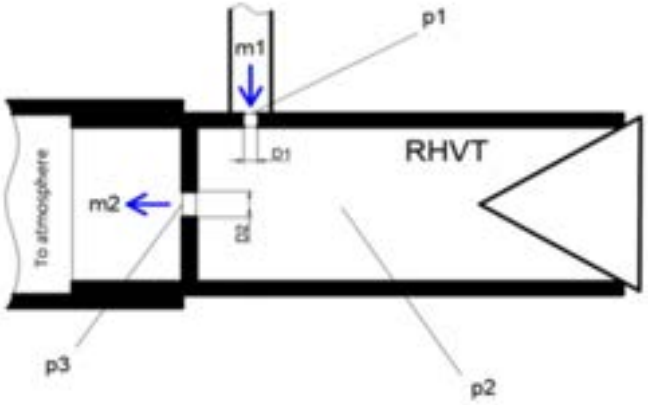

***Figure 5**. Simplified flow model for the estimation of the RHVT mass flow rate*

For the purpose of scale determination, it can be assumed that the hot outlet is completely closed. Results from the 1st generation installation show that, despite the increment in the total outlet cross section, opening the cone-shaped outlet valve does not cause any increment of the total inlet flow[1]. Accordingly, in the simplified model, mass flow rate through the inlet nozzles equals the flow rate through the orifice, provided that steady state is achieved.

For each nozzle, the outet-to-inlet pressure ratio $p_{\mathrm{out}}/p_{\mathrm{in}}$, henceforth denoted by β, generates a mass flow rate $\dot{m}$, which can be calculated as:

$$\dot{m} = C_D A \psi_s \sqrt{\frac{p_{\mathrm{in}}}{R T_{\mathrm{in}}}} \tag{1}$$

where C_D is the discharge coefficient (ideal nozzle = 1), A is the cross section area, R is the gas constant, and p_{in} , T_{in} are total (stagnation) inlet parameters. The flow coefficient ψ_s depends on the pressure ratio β, and it also determines the flow condition at the nozzle exit section (subsonic/sonic):

$$\psi_s = \begin{cases} \sqrt{\dfrac{2\kappa}{\kappa-1}\left(\beta^{\frac{2}{\kappa}} - \beta^{\frac{\kappa+1}{\kappa}}\right)}, & \text{if } \beta > \beta_{\mathrm{crit}} \\ \sqrt{\kappa\left(\dfrac{2}{\kappa+1}\right)^{\frac{\kappa+1}{\kappa-1}}}, & \text{if } \beta \le \beta_{\mathrm{crit}} \end{cases} \tag{2}$$

The critical value of the pressure ratio for the ideal gas model is:

$$\beta_{\mathrm{crit}} = \left(\frac{2}{\kappa+1}\right)^{\frac{\kappa}{\kappa-1}} \tag{3}$$

This value ranges 0.48 to 0.54 depending on the isentropic exponent κ. Accordingly, if the nozzle inlet pressure is approx. 2 times higher than the outlet pressure, sonic flow is achieved. The derivation of ideal and real gas nozzle equations was presented i.a. by Rist [23].

In the studied case, two nozzles are connected in series. The first nozzle has p_1 as inlet, and the unknown value of p_2 as outlet pressure. The second nozzle has p_2 as inlet, $p_3 \cong p_{\mathrm{atmosphere}}$ as outlet pressure. The model has a set of simplifications:

- Ideal gas model is used (acceptable for p < 4 bar);
- Stagnation parameters are approximated by static parameters;
- Outlet pressure is approximated by atmospheric pressure;
- The impact of the orifice geometry on the critical pressure value is neglected.

All these simplifications are attributed to the discharge coefficient C_D (which now includes flow contraction, the velocity coefficient and the above listed assumptions).

[1] This is an interesting paradox still to be investigated.

By setting the requirement of flow continuity $\dot{m}_{1-2} = \dot{m}_{2-3}$, the unknown internal pressure p_2 and the equalized flow rate $\dot{m}$ can be found within a simple numerical procedure.

The theoretically obtained value of the flow rate has been compared with the measured values for a commercially available small-scale vortex tube (Fig. 6). This VT is equipped with a suction chamber and a set of 6 identical nozzles. Each nozzle has a dimension of 0.9 × 3.1 mm (channel width × channel depth along the main VT axis). The set of nozzles is integrated with a divergent orifice with the smallest diameter of 4.7 mm.

a) b)

Figure 6*. a) A commercially available small-scale vortex tube used for system downscaling b) Set of nozzles in the commercially available vortex tube*

The commercially available small-scale vortex tube has been installed in the 1st generation test rig, however, due to the different scale of the object, only the inlet mass flow rate was measured. The objective of measurements was to define the range of mass flow rate which is critical for the selection of all process equipment, in particular the most expensive elements (flow meters, mass flow controllers and pressure regulators).

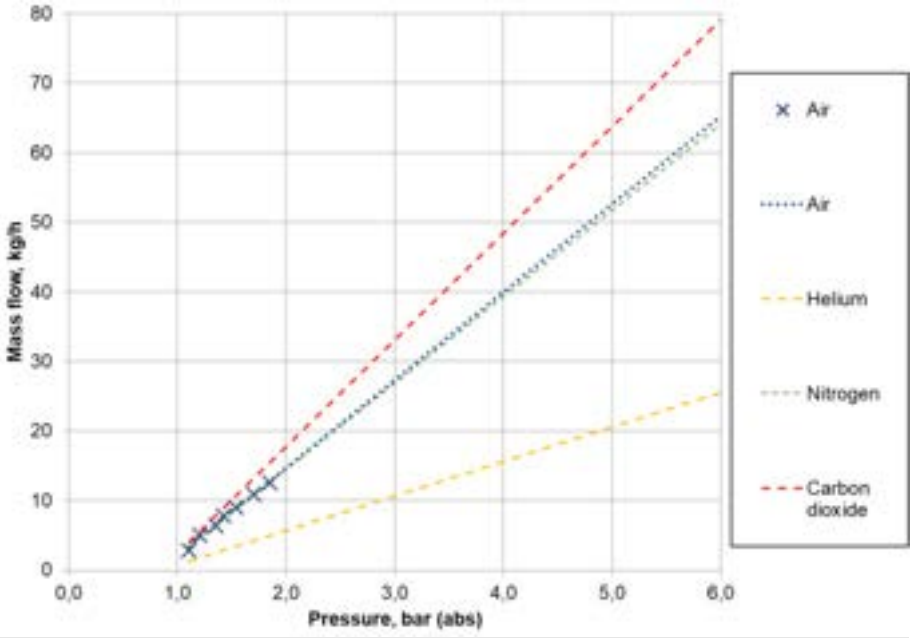

Figure 7*. System scale evaluation based on air flow under variable inlet pressure. Points represent the measured values. Dashed lines represent an extrapolation to higher pressure values and a flow estimation for other gases using the calibrated analytical model.*

The measured values have been compared with the simple analytical model (Eq. (1)-(3)). Assuming that the discharge coefficient for the inlet nozzles is 0.98, the discharge coefficient for the orifice 0.854 provides the

equality of the measured value and the calculated value. Accordingly, the simplified model is calibrated enough to be useful for the prediction of the flow range and the selection of process equipment. Values for other gases and for higher pressure have been calculated from the model, and the results are depicted in Fig. 7.

It can be concluded that if the designed vortex tube is kept at a similar scale, the range of flow 0...100 kg/s should be sufficient to analyze the flow of all technical gases foreseen in the project. Moreover, it was decided that heavier and lighter gases will be supplied at a maximum mass fraction of 10%, which should be sufficient to observe their possible stratification in the vortex tube.

3.3. Technical questions for the 2nd generation test installation

The conceptual design of the installation, depicted in Fig. 4, does not reveal technical details related to flow parameters. The selection of equipment and the estimation of the project budget was based on a single round of commercial requests which were sent to manufacturers of metering equipment, pressure regulators and tanks and to the suppliers of pressurized gases.

Within the first part of the project, a detailed, second round of commercial request was launched, followed by a series of meetings. In this way, the general idea was subject to verification with market reality, additionally suffering from consecutive global events, but most importantly, it was confronted with technical details. Several major conclusions could be drawn from this work are:

1. It is currently not possible to supply supercritical carbon dioxide from gas cylinders. Theoretically, the pressure of any gas in a cylinder can reach 300 bar or more, however, major suppliers of technical gases limit their offer here to a 2-phase fluid, with the saturation pressure resulting from ambient temperature (e.g. 57.3 bar @20°C);
2. Creating a closed-loop CO_2 system is technically possible, but it exceeds the budget of the current project. Also, there is no sufficient knowledge on how the vortex tube would operate and which part of the agent would condense. Accordingly, this idea represents an interesting field of future research.
3. It is essential to keep the topic of phase change inside the vortex tube within the scope of the project. To investigate a two-phase flow, an alternative strategy is required.
4. It was proposed to investigate the two-phase flow by dosing some liquid (e.g. water or ethyl alcohol) to the saturation level at the VT inlet, and then by measuring the liquefied quantity at VT outlet(s). A corresponding experimental installation is currently under design.
5. Using carbon dioxide as a heavy gas component is still possible and it enables to evaluate species separation (e.g. CO_2 from N_2). However, the CO_2 flow rate is technically limited by the evaporation rate in a gas cylinder, which is about 1 Nm^3/h. To ensure higher flow of CO2, a bundle of cylinders is needed.

The design of the experimental installation is presented in the subsequent section. The section of humidification and liquid separation is not included at this stage.

3.4. Current design of the installation

The key elements of the proposed installation are shown in Fig. 8.

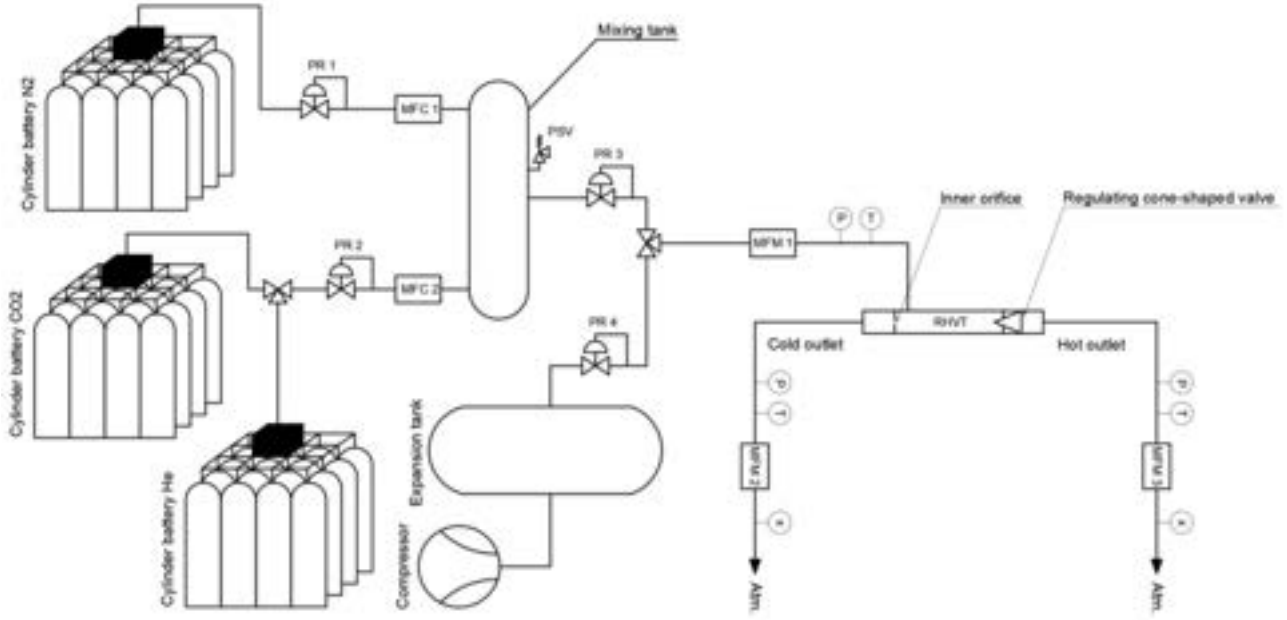

Figure 8. *The proposed test rig configuration for WP1 and WP3 measurements. Symbols are the same as in Fig. 4.*

The research installation is adapted to the supply of various gases. The first supply path leads from cylinder batteries (bundles), whereas the basic gas is nitrogen, obtain from a battery of 16 cylinders. Nitrogen can be mixed either with carbon dioxide CO_2 (a heavier gas CO2), or helium He (a lighter gas). Pressure of gases leaving the tank batteries is regulated by regulators PR1 and PR2. Next, a precisely determined mass of each gas is supplied to a mixing tank via mass flow controllers MFC1 and MFC2. The tank is protected by a pressure safety valve PSV. Currently, tank pressure of 16 bar is considered.

Next, the mixed gas leaves the tank and its pressure is adjusted again by a regulator PR3. The gas mixture passes through the mass flow meter MFM1. Here, a thermal flow meter with adjustable gas composition was selected. Once the gas pressure and temperature are measured, it enters the vortex tube and then leaves it through the hot and the cold outlet. Then, thermal parameters and mass flow rates are measured again by the same type of equipment. Finally, gas composition is measured at both ends. A dedicated gas composition measurement system will be developed based on commercially available calibrated gas sensors.

Another path for supplying the pressurised gas is obtained if an air compressor is used. In this case, compressed air passes through a tank and a local installation (this part of equipment was used in the 1st generation research). A newly adapted regulator PR4 will be installed for the reduced flow rate and increased pressure, compared with the 1st generation set-up.

The compressed air supply line is essential for multiple-parameter testing, where the use of pure gases is too expensive. Experimental results obtained with compressed air will be supplied as boundary conditions to multi-scenario numerical modelling. Only a reduced set of parameters obtained from the numerical modelling will be used for experimental work with pure gases.

4. Conclusions and further work

Results obtained from the 1st generation experimental set-up have been used to evaluate the scale of the system for the 2nd generation. In general, it is possible to maintain the previous maximum range of the mass flow rate at 100 kg/h maximum, however, the reduction of the vortex tube size enables the project team to work with higher supply pressures, reaching 6-10 bar depending on the final scale of the vortex tube.

The first stage of the project related with the detailed technical design of the experimental test installation revealed a series of problems, mostly related with the availability of pressurized carbon dioxide. To keep the desired flow capacity, it was decided to use bundles (batteries) of cylinders with pressurized gases instead of a single container, and to apply pressure regulators of higher capacity than that of standard cylinder regulators.

The current work within the project is performed in parallel in three areas:

1. Construction of an own vortex tube and its numerical model (twin); the construction is kept as simple as possible to enable an exact representation within the numerical model;
2. Completion of the experimental test rig, some elements (flow meters, temperature and pressure sensors, regulator PR4) have been purchased, other elements (mass flow controllers, pressure regulators PR1-PR3, tank) are at the selection stage and will be purchased in the upcoming weeks;
3. Design of the liquid phase dosing and separation system: this part of project is being carried out with a wider engagement of students within a dedicated Project-Based-Learning scheme, within a small grant obtained from the University.

Future work comprises advanced multi-scenario numerical modelling and optimization of the vortex tube, as well as elaboration of the gas composition measurement system and at attempt to flow visualisation.

The project team expects to obtain interesting and novel results, in particular in the topic of mass and phase separation, which is scarcely reported in subject literature.

Acknowledgments

This work was funded by the National Centre of Science, Poland (*Narodowe Centrum Nauki*) within the ATHLETE project entitled *Investigation of mass, thermal and phase separation in the Ranque Hilsch Vortex Tube: from fundamentals to technological concepts in energy and process engineering*, Grant No. UMO-2021/43/B/ST8/03320 which is carried out in co-operation of the Silesian University of Technology, Poland with Niccolò Cusano University, Italy).

Nomenclature

A area, m^2

C_D discharge coefficient

$\dot{m}$ mass flow rate, kg/s

p pressure, Pa

R gas constant, J/(kg K)

T temperature, K

Greek symbols

β pressure ratio

κ isentropic exponent

ψ_s nozzle flow coefficient

Subscripts

$()_{\mathrm{crit}}$ critical

$()_{\mathrm{D}}$ discharge

$()_{\mathrm{in}}$ inlet

$()_{\mathrm{out}}$ outlet

$()_{\mathrm{s}}$ isentropic

References

[1] G. Ranque Experiences sur la détente giratoire avec productions simultanées d'un échappement d'air chaud et d'un échappement d'air froid J. Phys 8 (1933): 112-114.

[2] R. Hilsch The use of the expansion of gases in a centrifugal field as cooling process Review of Scientific Instruments 18.2 (1947): 108-113.

[3] V. S. Martynovskii and V. P. Alekseev Investigation of the vortex thermal separation effect for gases and vapors Soviet Physics-Technical Physics 1.10 (1956): 2233-2243.

[4] A. M. Crocker, S. M. White and F. Bremer Jr. Experimental results of a vortex tube air separator for advanced space transportation AIAA 4451 (2003): 20-23.

[5] B. K. Ahlborn and J. M. Gordon The vortex tube as a classic thermodynamic refrigeration cycle Journal of applied physics 88.6 (2000): 3645-3653

[6] Y. Xue et al. A critical review of temperature separation in a vortex tube Experimental Thermal and Fluid Science 34.8 (2010): 1367-1374

[7] Ahlborn, B., and Groves, S., 1997. "Secondary flow in a vortex tube". Fluid Dynamics Research, 21(2), p. 73

[8] Kurosaka, M., 1982. "Acoustic streaming in swirling flow and the Ranque-Hilsch (vortex-tube) effect". Journal of Fluid Mechanics, 124, pp. 139–172

[9] A. D. Gutak Experimental investigation and industrial application of Ranque-Hilsch vortex tube International Journal of Refrigeration 49 (2015): 93-98

[10] N. V. Poshernev and I. L. Khodorkov. Natural-gas tests on a conical vortex tube (CVT) with external cooling Chemical and Petroleum Engineering 40.3 (2004): 212-217

[11] V.L. Bondarenko, Y. M. Simonenko, and D. P. Tishko. Generation of Cold and Heat in Vortex Tubes during Pressure Reduction of Natural Gas. Chemical and Petroleum Engineering 56, 272–279 (2020)

[12] D. Majidi, H. Alighardashi, F. Farhadi, LPG mass separation by vortex tube cascade and its economics, Applied Thermal Engineering, 148 (2019): 1139-1147

[13] Jinwon Yun, Younghyeon Kim, Sangseok Yu, Feasibility study of carbon dioxide separation from gas mixture by vortex tube, International Journal of Heat and Mass Transfer, Volume 126, Part A, 2018, Pages 353-361

[14] Christensen, K., Heiredal, M., Kauffeld, M., and Schneider, P., 2001. "Energy savings in refrigeration by means of a new expansion device. report of energy research programme". Journal(1223/99), p. 0006

[15] Li, D., Back, J., Groll, E., and Lawless, P., 2000. "Thermodynamic analysis of vortex tube and work output expansion devices for the co2 trans-critical cycle". In Proceedings of the Fourth IIR-Gustav Lorentzen Conference on Natural Working Fluids at Purdue, Lafayette, IN, USA, pp. 25–28

[16] Bakhsheshi, M. F., Keenliside, L., and Lee, T.-Y., 2016. "Rapid and selective brain cooling method using vortex tube: a feasibility study". The American journal of emergency medicine, 34(5), pp. 887–894

[17] Khodorkov, I., Poshernev, N., and Zhidkov, M., 2003. "The vortex tube—a universal device for heating, cooling, cleaning, and drying gases and separating gas mixtures". Chemical and petroleum Engineering, 39(7-8), pp. 409–415.

[18] Chiappini, D., Mendecka, B., and Bella, G., 2021. "Sizing and optimization of a vortex tube for electric vehicle hvac purposes". In 15th International Conference on Engines & Vehicles, SAE International

[19] M. Attalla et al. An experimental study of nozzle number on Ranque Hilsch counter-flow vortex tube Experimental Thermal and Fluid Science 82 (2017): 381-389

[20] S. E. Rafiee and M. M. Sadeghiazad Three-dimensional numerical investigation of the separation process in a vortex tube at different operating conditions Journal of Marine Science and Application 15.2 (2016): 157-165

[21] Behera U. et al. CFD analysis and experimental investigations towards optimizing the parameters of Ranque-Hilsch vortex tube. International Journal of Heat and Mass Transfer 48 (2005) 1961-1973.

[22] Bargiel P. et al. Vortex Tube Operational Temperature Regime. ASME Journal of Energy Resources Technology. 142 (2020) / 082001-1

[23] Rist D. Dynamik realer Gase – Grundlagen, Berechnungen und Daten für Thermogasdynamik, Strömungstechnik und Gastechnik. Berlin-Heidelberg, Germany: Springer-Verlag; 1996. (in German).

Thermodynamic analysis of a high-temperature heat pump using low GWP natural working fluids for upgrading district heating to process heating

Mohsen Sadeghi[a], Tage Petersen[b], Zhenyu Yang[c], Benjamin Zühlsdorf[d], Kim Stenholdt Madsen[e] and Ahmad Arabkoohsar[f]

[a] AAU Energy, Aalborg University, Esbjerg, Denmark, msad@energy.aau.dk
[b] Energy and Climate, Danish Technological Institute, Aarhus, Denmark, tagp@teknologisk.dk
[c] AAU Energy, Aalborg University, Esbjerg, Denmark, yang@energy.aau.dk
[d] Energy and Climate, Danish Technological Institute, Aarhus, Denmark , bez@teknologisk.dk
[e]DIN Forsyning A/S, Esbjerg, Denmark, ksm@dinforsyning.dk
[f]AAU Energy, Aalborg University, Esbjerg, Denmark

Abstract:
High-temperature heat pump (HTHP) is a promising technology for decarbonization of process heating through electrification and energy efficiency. Exploiting the potentials requires a simultaneous optimization of the cycle layout and the working fluid. This paper proposes an efficient cascade HTHP and optimizes its thermodynamic performance. Using steam for high-temperature loop and use of alternative hydrocarbons for low-temperature loop are examined. On the application level, district heating is considered as a heat source and evaluated for different supply temperatures, including 80 °C, 70 °C and 40 °C.
The results reveal that pentane with highest critical temperature among the suggested hydrocarbons, shows the best energy performance to be paired with steam in the proposed cascade HTHP system. However, concerning the hydrocarbon compressor volumetric heating capacity (VHC) and safety issues, butane is an excellent candidate. In addition, when the heat available in the main transmission lines of district heating unit is considered as the source cooled from 80 °C down 70 °C, the highest value of coefficient of performance (COP) is achieved as 2.74 for the sink condensation temperature of 160 °C.

Keywords:
High-temperature heat pump, Low GWP working fluids, Steam, Hydrocarbons, District heating.

1. Introduction

High-temperature heat pump (HTHP) technology using renewable electricity is a promising solution to decarbonize the industrial process heat supply; which is mainly based on fossil fuels and contributes with 36.8 % to the CO_2 emissions in industry [1]. In this regard, optimizing the performance of the HTHP systems concerning various configurations and working fluids is a vital issue.

Chen et al. [2] investigated performance of an improved vapor injected cascade heat pump system for high-temperature applications, from the viewpoints of thermodynamics and exergoeconomics. Considering zero Ozone Depletion Potential (OPD) and low Global Warming Potential (GWP) as the main environmental criteria, they examined the use of R1233zd(E), R1336mzz(Z) and R245fa in the high-temperature loop and R1234yf, R290 and R134a through the low-temperature loop, meeting the required target temperatures. The highest coefficient of performance (COP) value of 2.3, when the evaporation and condensation temperatures are 10 °C and 100 °C, respectively, was achieved.

Performance of simple vapor compression HTHP system with condensation temperature up to 125 °C using low GWP working fluids of R1234ze(E) and R1234ze(Z) was compared by Fukuda et al. [3]. It was discussed when the condensation temperature is about 20 °C below the corresponding working fluid critical point, the COP is maximized, which is higher also for R1234ze(Z). In another study by Kondou et al. [4], again R1234ze(Z) showed promising performance among other low GWP refrigerants such as R1234ze(E), R717 and R365mfc for high-temperature applications of heat pumps up to 160 °C. In addition, performance of dual pressure condensation HTHP using 10 different working fluids including R600a, R1234ze(Z), R1224yd(Z), R245fa, R1233zd(E), R245ca, R601a, R1336mzz(Z), R365mfc and Isohexane was carried out and compared to the single-stage, two-stage and cascade systems, by Dai et al. [5]. It was revealed that the system using R1234ze(Z) shows the highest COP of 4.16, which is about 9 % higher than that of the conventional HTHP configurations.

In a semi-empirical work by Mateu-Royo et al. [6], they demonstrated that in a HTHP system covering the wide range of sink temperatures of 110- 140 °C, using HCFO-R1224yd(Z) shows promising performance from the energy efficiency and environmental perspectives and could be replaced with R245fa.

R1233zd(E) also was introduced as promising working fluid in heat pumps with high-temperature applications by Arpagaus et al. [7] and Frate et al. [8]. Mateu-Royo et al. [9] focused on the effects on the heat pump performance of superheating degree in an internal heat exchanger. They concluded that using HCFO-R1233zd(E), HFO-R1336mzz(Z) and HCFO-R1224yd(Z) instead of R245fa leads to an improvement of 27%, 21% and 17% in COP, respectively. In similar study, Mateu-Royo et al. [10] conducted experimental study of HTHP system to upgrade the heat from 60 °C to 80 °C to the temperature of 90 °C to 140 °C. Performance of the system was compared using different refrigerants such as R245fa, R1224yd(Z), R1233zd(E), and R1336mzz(Z). They reported that under the same operating condition, using R1336mzz(Z) leads to higher COP values and reduction in CO_2 emissions up to 57 %, compared to a natural gas boiler.

However, through another work, Mateu-Royo et al. [11] showed that using pentane as a hydrocarbon working fluid in heat pumps with condensation temperature up to 150 °C leads to higher COPs than for using R1233zd(E), R1336mzz(Z) and R245fa. Following the promising performance of using hydrocarbon refrigerants, a comprehensive study on the performance prediction of water source HTHP system screening various working fluids were performed by Yan et al. [12]. The results revealed that butane as hydrocarbon working fluid with a low GWP value, also shows a better performance than HFCs and HFOs. In addition, Mota-Babiloni et al. [13] reported that in a cascade HTHP system, butane and pentane are the best choices for the low-temperature and high-temperature loops, respectively. A 20 kW capacity cascade heat pump using such hydrocarbons as propane and butane in the low and high-temperature cycles, respectively, was investigated by Bamigbetan et al. [14]. It was revealed that recovering waste heat at 30 °C, the heating COP could reach 3.1 for the temperature lift of above 70 °C. Bai et al. [15] also reported that R600 (butane), R1224yd(Z), R1234ze(Z) and R1233zd(E) show high COPs and smaller compressor sizes in high-temperature applications of heat pumps.

However, despite the promising performance of heat pumps for high-temperature applications using hydrocarbons such as butane and pentane and also hydrofluoroolefins in particular R1234ze(Z), R1233zd(E) and R1336mzz(Z), steam as zero GWP working fluid showed a better performance with higher COP through the study conducted by Wu et al. [16]. Steam also was successfully used and recommended by Zühlsdorf et al. [17] in a cascade multi-stage HTHP system for steam generation and process heat supply up to 280 °C.

On the other, based on the recent reports, more than 6000 district heating networks operate in Europe and supply 11 % to 12 % of the total domestic heat demand [18]. District heating systems can be categorized in five generations, as summarized in Table 1 [18,19].

Table 1. Different district heating networks and their characteristics [18].

DH Network	Operating temperature	Main drawback
1G	120 °C to 200 °C	High implementation and maintenance costs and huge amount of thermal losses up to 30 %.
2G	120 °C to 160 °C	
3G	70 °C to 100 °C	
4G	35 °C to 70 °C	Emergent technologies and high electricity and HP costs.
5G	10 °C to 35 °C	

As briefly discussed in Table 1, due to the inefficient distribution processes for 1G and 2G DH networks, 4G and 5G DH systems are the most considered and dominant DH generations. They do not suffer from large thermal losses and as results sharp thermal stresses as well as high pressure drops in the pipelines [18]. In addition, comparing the traditional heating systems based on natural gas boiler, the CO_2 emissions could decrease up to 45%, which allies with the decarbonization of the heating sector, as well [18]. Regarding the promising environmental performance of new generation DH networks and their temperature range of operation, heat pumps (HP) can be effectively integrated with them to decarbonize the district heat sector.

Using R245fa and R134fa, thermodynamic and economic analyses of booster heat pump in low-temperature district heating was carried out by Roh et al. [20]. It was concluded that the economic feasibility of using heat pumps in the DH networks strongly is affected by the electricity and district heat prices. The optimum combination of booster heat pumps in a very low-temperature district heating was performed and compared with low-temperature district heating by Ommen et al. [21]. They reported that using central heat pump, the performance of the system is improved up to 12 %. Combining a ground source central heat pump and local boosters, Yang et al. [22] proposed and analyzed a system for domestic hot water production. According to the exergy analysis results, the low-temperature district heating operating at 55 °C showed higher efficiency

than high-temperature DH at 70 °C. Use of modern heat pumps in the existing district heating networks was investigated by Kontu et al. [23]. Possibility of utilization of various heat sources in the HP-boosted DH networks was introduced as one of the main advantages. However, it was outlined that using heat pumps in DH networks is very sensitive to the heat source and electricity prices.

Various scenarios on the integration of heat pumps with district heating concerning heat pumps location, connection and operations mode was studied by Sayegh et al. [24]. They reported that, higher share of heat pumps in district heating networks yields less emissions, and environmental impacts. Pieper et al. [25] evaluated integrating three different heat sources of groundwater, seawater and air with heat pumps to supply district heating. They reported that the most appropriate heat source to be integrated by heat pump is changed seasonally and using multi-source heat leads to the maximum COP. In addition, Arabkoohsar et al. [26] proposed a new generation of district heating system using booster heat pumps and triple pipes. They reported that the new system shows a better energy efficiency, especially during winter days.

In all aforementioned studies, the district heating was considered as the sink and the heat pump was supposed to supply or boost the required heat for the DH network. However, referring to Table 1, 4G DH networks, which provide heat up to 70 °C, can be considered as heat source for heat pumps, to supply heat for medium or high-temperature process applications. The main benefit of this integration is that the district heat is always available as a source. In this regard, the present study aims to evaluate the performance of a cascade heat pump system integrated with district heat. In addition, on the HTHP system configuration level, reviewing the literature outlines those hydrocarbons such as butane and pentane as natural working fluids shows competitive performance with synthetic hydrofluoroolefins. However, using steam could lead to higher COPs in the high-temperature applications. Since, considering the special environmental characteristics of steam (zero ODP and zero GWP), it turns into a very interesting choice, as the working fluid in HTHP systems. However, for industrial applications with high-temperature lifts, using single-stage steam heat pump brings about some serious challenges, in particular high superheating degrees at the compressor discharge. Therefore, this work also aims to address these challenges and then find solutions through proposing efficient system design and choosing appropriate natural low GWP working fluids.

2. System description and modelling

Selecting the optimal cycle layout and working fluid for a given application must consider a variety of thermodynamic and technical parameters, such as temperatures, pressures, and main operating parameters for the equipment. Steam is found to be an optimal working fluid for applications above around 100 °C, due to the high required volume flow rates, high pressure ratios and high superheating during compression for lower temperatures, as depicted in Figure 1. Therefore, a cascade system is suggested, consisting of a single-stage bottom cycle using a hydrocarbon and a steam compression as top-cycle.

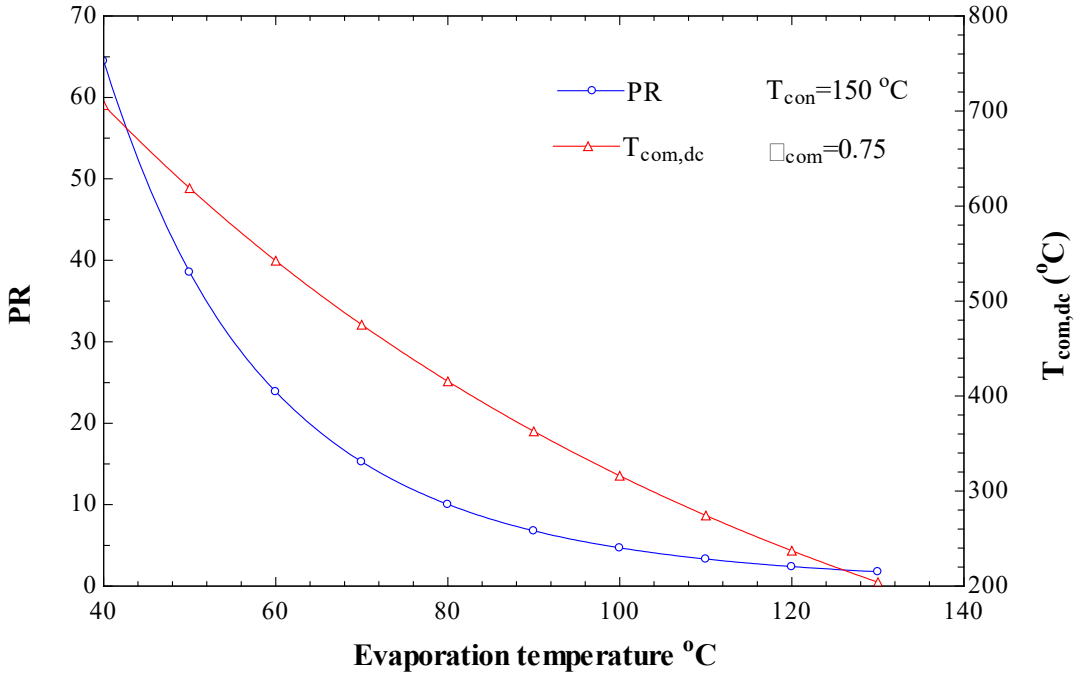

Figure 1. Steam compressor pressure ratio (PR) and discharge temperature ($T_{com,dc}$) of varying evaporation temperatures and a fixed condensation temperature

A schematic of the proposed cascade heat pump system is presented in Figure 2. In the proposed HP system, the high-temperature loop is not closed and steam as non-flammable and non-toxic fluid could be directly delivered to the sink after discharging from the compressor. The steam is generated through the steam generator, which receives thermal energy from the bottoming cycle. In the bottoming cycle, the working fluid absorbs heat in the evaporator and then is superheated through the internal heat exchanger. Then passing through the compressor, the pressurized hot stream cools down through the condenser and is throttled in the expansion valve.

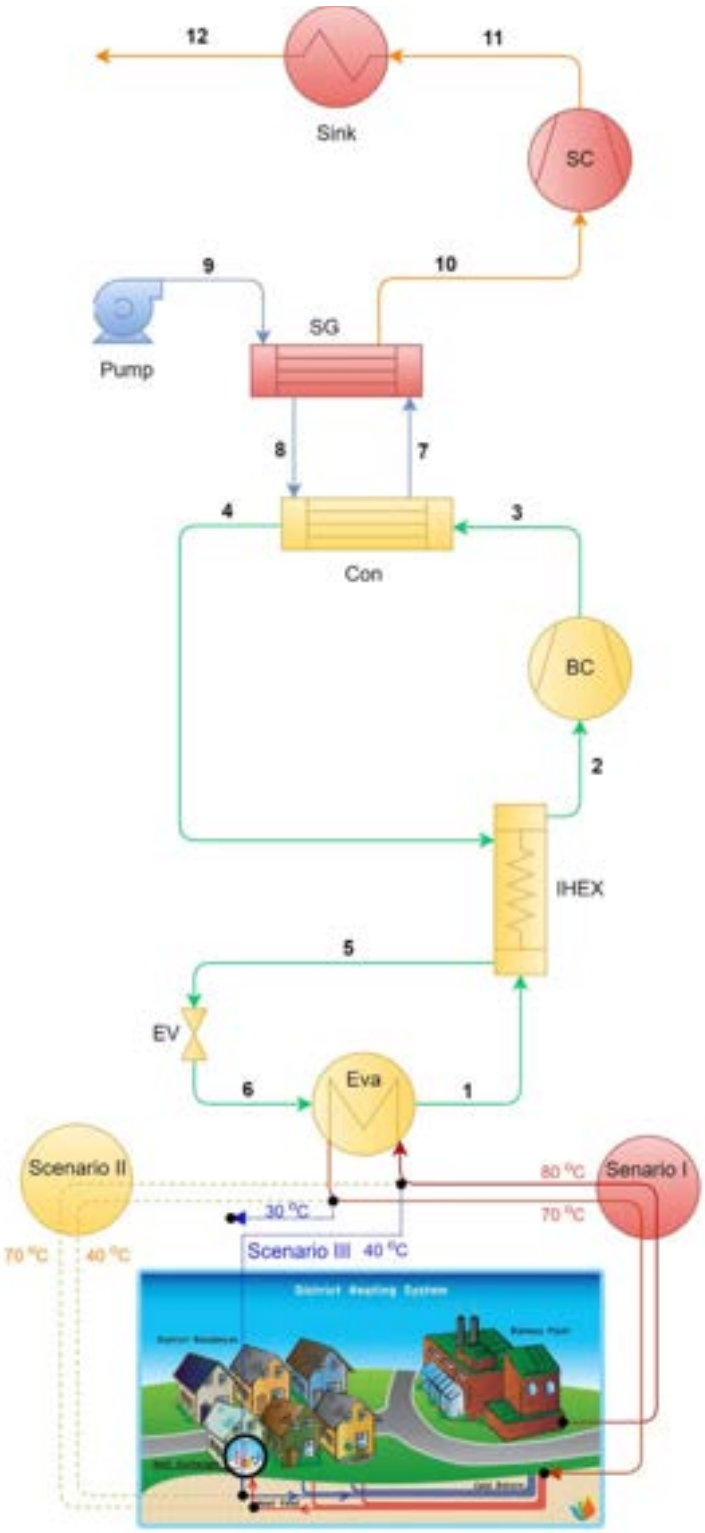

Figure 2. Proposed cascade high-temperature heat pump system (red and yellow lines: heat source, blue lines: water, green lines: alternative hydrocarbons, orange lines: steam)

For the low-temperature cycle, hydrocarbons with high enough critical temperatures above 130 °C are considered as the low GWP natural working fluids. The selected working fluids and their properties are listed in Table 2.

Table 2. Properties of the selected working fluids for the cascade HTHP system [1].

Working fluid	Safety group	ODP	GWP	P_{cri} (bar)	T_{cri} (°C)	Auto-ignition temperature (°C)
Steam (R718)	A1	0	0	220.6	374	-
Pentane (R601)	A3	0	5	33.64	196.6	260
Isopentane (R601a)	A3	0	5	33.7	187.2	420
Butane (R600)	A3	0	4	37.96	152	405
Isobutane (R600a)	A3	0	4	36.4	134.7	460

In addition, as illustrated in Figure 2, the HTHP system uses the heat available from district heating as the source through three different scenarios, which is explained in detail in Table 3.

Table 3. Three different scenarios for integrating the heat pump system with district heating.

Scenario	$T_{source,in}$ (°C)	$T_{source,out}$ (°C)	T_{eva} (°C)	Description	Connection
I	80	70	65	High-quality and expensive heat source	Main transmission line from biomass plant
II	70	40	35	Moderate heat source	DH Distribution lines
II	40	30	25	Cheapest heat source but low-quality	DH Return lines

Using Engineering Equation Solver (EES) and based on the input data given in Table 4, thermodynamic steady state model has been implemented using a control volume approach with energy and mass balances for each control volume. The heat exchangers are modelled with a defined minimum pinch point temperature difference and the compressor is based on an isentropic efficiency.

Table 4. The input data for modelling the HTHP system

Parameter	Value
Sink condensation temperature, T_{12}	160 °C
Superheating degree in IHEX, T_2-T_1	10 K
Pinch point temperature difference in HEXs except IHEX	5 K
Intermediate water circuit temperature difference, T_7-T_8	5 K
Feed water temperature, T_9	105 °C
Cascade temperature, T_{10}	105 °C (1.21 bar)
Compressors isentropic efficiency, η_{is}	75 %

Considering that high-temperature superheated steam is completely condensed through the sink, and is subcooled up to the feedwater temperature (105 °C), the COP and VHC of the compressors are defined, as follows:

$$COP = \dot{Q}_{sink}/(\dot{W}_{BC} + \dot{W}_{SC}) \quad (1)$$

$$VHC_{SC} = \dot{Q}_{sink}/\dot{V}_{10} \quad (2)$$

$$VHC_{BC} = \dot{Q}_{con}/\dot{V}_{2} \quad (3)$$

Here, $\dot{Q}_{sink}, \dot{W}_{BC}$ *and* $\dot{W}_{SC}$ are the heat transfer rate delivered to the sink and power consumption of the hydrocarbon and steam compressors, respectively.

3. Results and discussion

The HTHP system has been simulated for the three scenarios with 4 different refrigerants in the bottom cycle. The COP of the HTHP system is depicted in Figure 3. Referring to this figure, the HTHP system gets higher COPs, when is integrated with district heating based on scenario I. This is because; considering the 5 K pinch point temperature difference in the evaporator, it could operate at 65 °C under scenario I, which is much higher than 35 °C and 25 °C in scenarios II and III, respectively. Therefore, the temperature lift of the cascade HTHP system in scenario I is lower than that of the other scenarios, which leads to a significant reduction in the pressure ratio and power consumption of the compressors as shown in Figures 4 and 5, respectively.

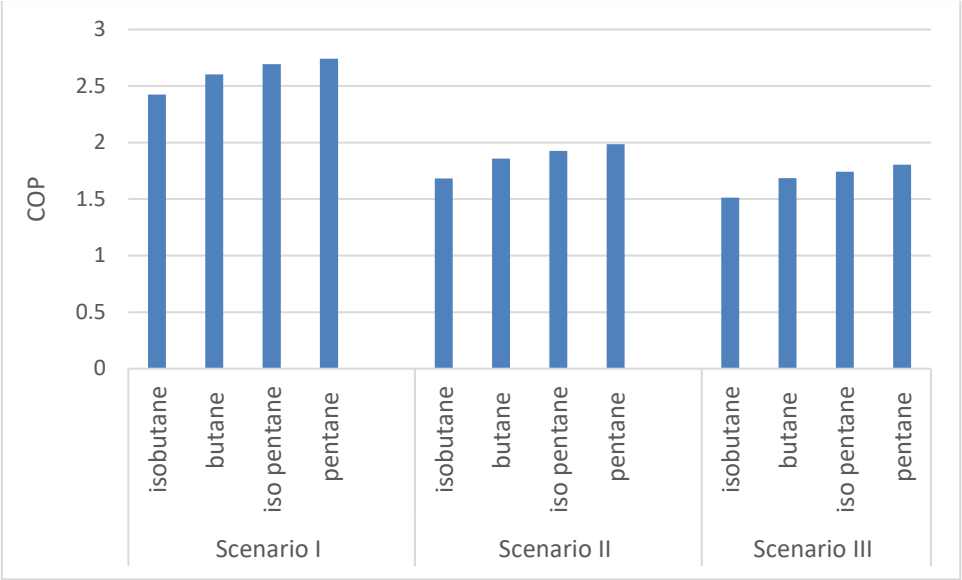

Figure 3. COP of the HTHP system using various hydrocarbons in the low-temperature loop based on the three different scenarios

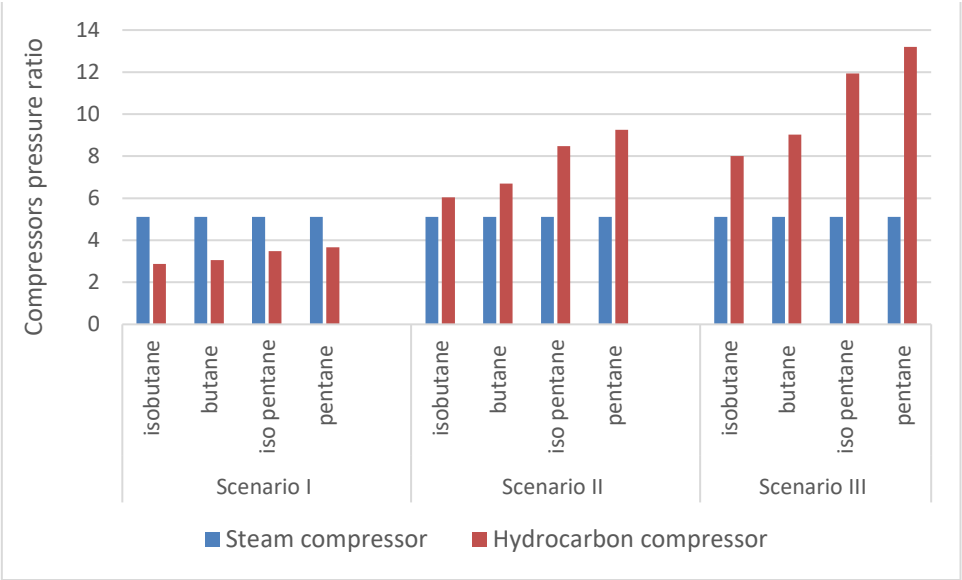

Figure 4. Pressure ratio of the compressors using various hydrocarbons in the low-temperature loop based on the three different scenarios

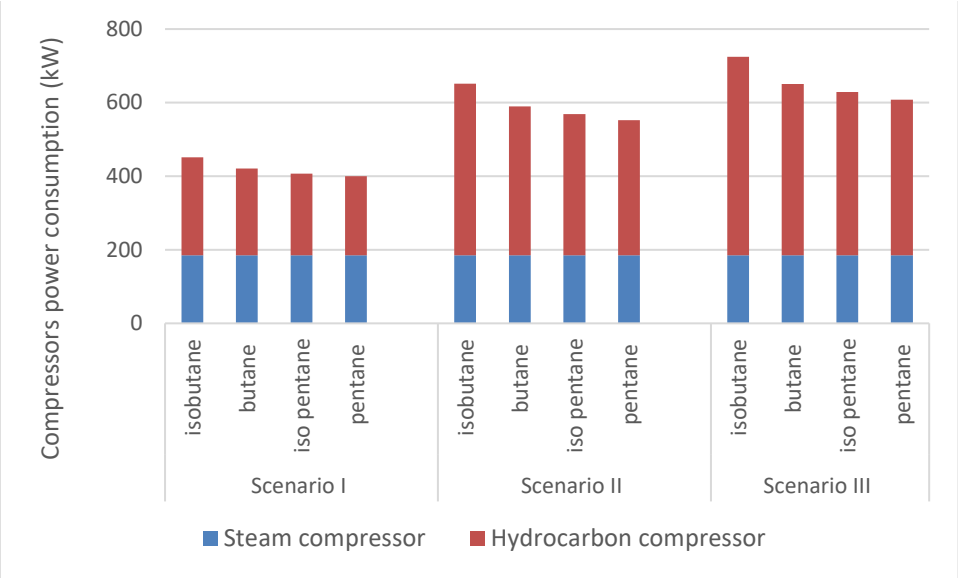

Figure 5. Power consumption of the compressors using various hydrocarbons in the low-temperature loop based on the three different scenarios

Referring to Figures 4 and 5, the pressure ratio and power consumption of the steam compressor in all the cases does not change (5.1 and 185 kW, respectively). This is due to the constant evaporation pressure of the steam generator.

However, referring to Figure 4, in all the scenarios, pentane compressor shows higher pressure ratios, which is mainly due to the higher critical temperature of pentane compared to the other hydrocarbons. Though, thanks to the relatively smaller mass flow rate of pentane through the compressor, the hydrocarbon compressor consumes less power in the case of using pentane, as depicted in Figure 5.

In conclusion, the HTHP system achieves the highest COP of 2.74, when is integrated with district heating based on scenario I and uses pentane as the working fluid in the low-temperature loop, as shown in Figure 3. Therefore, from the energy point of view, pentane is the best candidate to be used as the working fluid in the bottoming loop.

However, Figure 6 shows that pentane has a higher specific volume compared to the other hydrocarbons, meaning that the volumetric flow rate of pentane in the compressor suction is larger, requiring a bigger hydrocarbon compressor. Thus, from the viewpoint of sizing, butane is introduced as a good candidate with almost twice VHC compared to pentane, just in the expense of about 5 % reduction in the HTHP COP. In addition, using butane could be safer, as well, due to its higher auto-ignition temperature compared to pentane (405 °C Vs 260 °C).

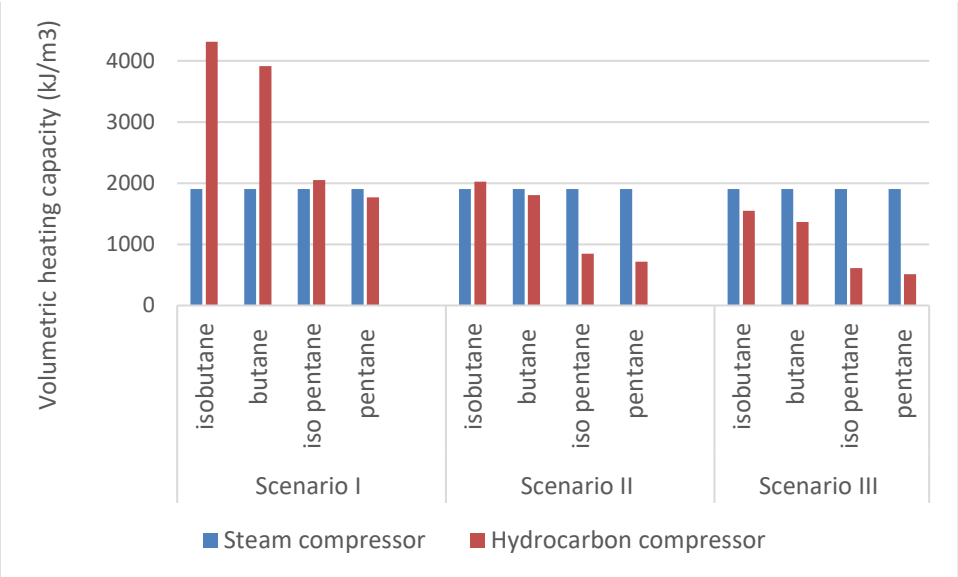

Figure 6. VHC of the compressors using various hydrocarbons in the low-temperature loop based on the three different scenarios

Moreover, as shown, in Figure 6, the steam compressor VHC is a constant value in all the cases, due to the unchanged operating condition of that.

All in all, depending on the objective function, either maximizing the COP or minimizing the sizing and auto-ignition risk, pentane and butane are recommended, respectively, as the low-temperature loop working fluids to reach out a promising HTHP system performance.

However, in all the twelve case studies, the steam compressor discharge temperature is a high value. In this regard, some technology improvements e.g. water injection and re-designing the system could enhance the COP, as well.

4. Conclusions

Thermodynamic analysis of a cascade high-temperature heat pump using steam in the high-temperature loop and low GWP hydrocarbons including isobutane, butane, isopentane and pentane in the low-temperature loop, was carried out. The importance and advantages of using steam as well as the necessity of using cascade layout was discussed. On the application level, there different scenarios for integrating the proposed HTHP system with a district heating unit were studied and compared, in terms of the COP, pressure ratio, power consumption and VHC of the compressors. The most significant results of the present study are summarized, as follows:

- Integrating the HTHP system with district heating based on scenario I- which suggests the use of district heat available in the main transmission line at 80 °C cooled down 70 °C - leads to the higher COP values compared to the other scenarios.
- Among the suggested hydrocarbons, pentane shows the most promising performance from the energy perspective, leading to high COP values.
- The highest COP value of 2.74 is achieved for the case based on scenario I and using pentane as the low-temperature loop working fluid.
- Concerning the hydrocarbon compressor sizing criterion, butane is introduced as a good candidate; with VHC value of about two times more than that of pentane, in the expense of just about 5 % reduction in the HTHP COP.
- Considering the high auto-ignition temperature of butane, it is also suggested for the high-risk applications.
- Regarding the high discharge temperature of the steam compressor, technology improvements e.g. water injection or proposing more effective layouts are recommended for the future works.

Acknowledgments

This research project is financially funded by EUDP (Energy Technology Development and Demonstration) under the project title: “Demonstrating high-temperature heat pumps at different integration levels” with the grant number 64021-7018. The support is gratefully acknowledged.

Nomenclature

Symbols

P Pressure, bar

T Temperature, K

$\dot{V}$ Volumetric flow rate, m^3/s

$\dot{W}$ Power, kW

Abbreviations

BC Butane compressor

Com Compressor

Con Condenser
COP Cofficient of perfromance
EV Expansion valve
Eva Evaporator
HEX Heat exchnager
IHEX Internal heat exchanger
PR Pressure ratio
SC Steam compressor
SG Steam generator
VHC Volumetric heating capacity, kJ/m3

Subscripts
cri Critical point
dc Discharge
is Isentropic

Greek symbols
ε Effectivness
η Efficiency

References

[1] K.M. Adamson, T.G. Walmsley, J.K. Carson, Q. Chen, F. Schlosser, L. Kong, D.J. Cleland, High-temperature and transcritical heat pump cycles and advancements: A review, Renew. Sustain. Energy Rev. 167 (2022). https://doi.org/10.1016/J.RSER.2022.112798.

[2] J. Chen, Q. Chen, X. Qin, D. Wang, Energy, exergy, economic and environmental analyses and optimization of a novel vapor injection autocascade heat pump for high-temperature water heating, Energy Convers. Manag. 267 (2022) 115909. https://doi.org/10.1016/J.ENCONMAN.2022.115909.

[3] S. Fukuda, C. Kondou, N. Takata, S. Koyama, Low GWP refrigerants R1234ze(E) and R1234ze(Z) for high temperature heat pumps, Int. J. Refrig. 40 (2014) 161–173. https://doi.org/10.1016/J.IJREFRIG.2013.10.014.

[4] C. Kondou, S. Koyama, Thermodynamic assessment of high-temperature heat pumps using Low-GWP HFO refrigerants for heat recovery, Int. J. Refrig. 53 (2015) 126–141. https://doi.org/10.1016/J.IJREFRIG.2014.09.018.

[5] B. Dai, X. Liu, S. Liu, Y. Zhang, D. Zhong, Y. Feng, V. Nian, Y. Hao, Dual-pressure condensation high temperature heat pump system for waste heat recovery: Energetic and exergetic assessment, Energy Convers. Manag. 218 (2020) 112997. https://doi.org/10.1016/J.ENCONMAN.2020.112997.

[6] C. Mateu-Royo, A. Mota-Babiloni, J. Navarro-Esbrí, Semi-empirical and environmental assessment of the low GWP refrigerant HCFO-1224yd(Z) to replace HFC-245fa in high temperature heat pumps, Int. J. Refrig. 127 (2021) 120–127. https://doi.org/10.1016/J.IJREFRIG.2021.02.018.

[7] C. Arpagaus, S.S. Bertsch, Experimental results of HFO/HCFO refrigerants in a laboratory scale HTHP with up to 150 °C supply temperature, (n.d.).

[8] G.F. Frate, L. Ferrari, U. Desideri, Analysis of suitability ranges of high temperature heat pump working fluids, Appl. Therm. Eng. 150 (2019) 628–640. https://doi.org/10.1016/J.APPLTHERMALENG.2019.01.034.

[9] C. Mateu-Royo, J. Navarro-Esbrí, A. Mota-Babiloni, M. Amat-Albuixech, F. Molés, Thermodynamic analysis of low GWP alternatives to HFC-245fa in high-temperature heat pumps: HCFO-1224yd(Z), HCFO-1233zd(E) and HFO-1336mzz(Z), Appl. Therm. Eng. 152 (2019) 762–777. https://doi.org/10.1016/J.APPLTHERMALENG.2019.02.047.

[10] C. Mateu-Royo, J. Navarro-Esbrí, A. Mota-Babiloni, F. Molés, M. Amat-Albuixech, Experimental exergy and energy analysis of a novel high-temperature heat pump with scroll compressor for waste heat recovery, Appl. Energy. 253 (2019) 113504. https://doi.org/10.1016/J.APENERGY.2019.113504.

[11] C. Mateu-Royo, J. Navarro-Esbrí, A. Mota-Babiloni, M. Amat-Albuixech, F. Molés, Theoretical evaluation of different high-temperature heat pump configurations for low-grade waste heat recovery,

Int. J. Refrig. 90 (2018) 229–237. https://doi.org/10.1016/J.IJREFRIG.2018.04.017.

[12] H. Yan, L. Ding, B. Sheng, X. Dong, Y. Zhao, Q. Zhong, W. Gong, M. Gong, H. Guo, J. Shen, Performance prediction of HFC, HC, HFO and HCFO working fluids for high temperature water source heat pumps, Appl. Therm. Eng. 185 (2021) 116324. https://doi.org/10.1016/J.APPLTHERMALENG.2020.116324.

[13] A. Mota-Babiloni, C. Mateu-Royo, J. Navarro-Esbrí, F. Molés, M. Amat-Albuixech, Á. Barragán-Cervera, Optimisation of high-temperature heat pump cascades with internal heat exchangers using refrigerants with low global warming potential, Energy. 165 (2018) 1248–1258. https://doi.org/10.1016/J.ENERGY.2018.09.188.

[14] O. Bamigbetan, T.M. Eikevik, P. Nekså, M. Bantle, C. Schlemminger, The development of a hydrocarbon high temperature heat pump for waste heat recovery, Energy. 173 (2019) 1141–1153. https://doi.org/10.1016/J.ENERGY.2019.02.159.

[15] T. Bai, G. Yan, J. Yu, Thermodynamic assessment of a condenser outlet split ejector-based high temperature heat pump cycle using various low GWP refrigerants, Energy. 179 (2019) 850–862. https://doi.org/10.1016/J.ENERGY.2019.04.191.

[16] D. Wu, B. Hu, R.Z. Wang, H. Fan, R. Wang, The performance comparison of high temperature heat pump among R718 and other refrigerants, Renew. Energy. 154 (2020) 715–722. https://doi.org/10.1016/J.RENENE.2020.03.034.

[17] B. Zühlsdorf, F. Bühler, M. Bantle, B. Elmegaard, Analysis of technologies and potentials for heat pump-based process heat supply above 150 °C, Energy Convers. Manag. X. 2 (2019) 100011. https://doi.org/10.1016/J.ECMX.2019.100011.

[18] J. Barco-Burgos, J.C. Bruno, U. Eicker, A.L. Saldaña-Robles, V. Alcántar-Camarena, Review on the integration of high-temperature heat pumps in district heating and cooling networks, Energy. 239 (2022) 122378. https://doi.org/10.1016/J.ENERGY.2021.122378.

[19] S. Buffa, M. Cozzini, M. D'Antoni, M. Baratieri, R. Fedrizzi, 5th generation district heating and cooling systems: A review of existing cases in Europe, Renew. Sustain. Energy Rev. 104 (2019) 504–522. https://doi.org/10.1016/J.RSER.2018.12.059.

[20] C.W. Roh, G. Lee, Y.-J. Baik, M. Kim, H. Shin, B. Lee, J. Cho, Thermodynamic performance and economic feasibility of booster heat pumps in low-temperature district heating, (2017).

[21] T. Ommen, J.E. Thorsen, W.B. Markussen, B. Elmegaard, Performance of ultra low temperature district heating systems with utility plant and booster heat pumps, Energy. 137 (2017) 544–555. https://doi.org/10.1016/J.ENERGY.2017.05.165.

[22] X. Yang, S. Svendsen, Ultra-low temperature district heating system with central heat pump and local boosters for low-heat-density area: Analyses on a real case in Denmark, Energy. 159 (2018) 243–251. https://doi.org/10.1016/J.ENERGY.2018.06.068.

[23] K. Kontu, S. Rinne, S. Junnila, Introducing modern heat pumps to existing district heating systems – Global lessons from viable decarbonizing of district heating in Finland, Energy. 166 (2019) 862–870. https://doi.org/10.1016/J.ENERGY.2018.10.077.

[24] M.A. Sayegh, P. Jadwiszczak, B.P. Axcell, E. Niemierka, K. Bryś, H. Jouhara, Heat pump placement, connection and operational modes in European district heating, Energy Build. 166 (2018) 122–144. https://doi.org/10.1016/J.ENBUILD.2018.02.006.

[25] H. Pieper, T. Ommen, B. Elmegaard, W. Brix Markussen, Assessment of a combination of three heat sources for heat pumps to supply district heating, Energy. 176 (2019) 156–170. https://doi.org/10.1016/J.ENERGY.2019.03.165.

[26] A. Arabkoohsar, A.S. Alsagri, A new generation of district heating system with neighborhood-scale heat pumps and advanced pipes, a solution for future renewable-based energy systems, Energy. 193 (2020) 116781. https://doi.org/10.1016/J.ENERGY.2019.116781.

PROCEEDINGS OF ECOS 2023 - THE 36TH INTERNATIONAL CONFERENCE ON
EFFICIENCY, **C**OST, **O**PTIMIZATION, **S**IMULATION AND ENVIRONMENTAL IMPACT OF ENERGY SYSTEMS
25-30 JUNE 2023, LAS PALMAS DE GRAN CANARIA, SPAIN

Heat pump systems with photovoltaics: Influence of the control strategy on the optimal design

Fabian Wüllhorst[a], Jonas Reuter-Schniete[a], Laura Maier[a], Dominik Hering[a] and Dirk Müller[a]

[a] RWTH Aachen University, E.ON Energy Research Center, Institute for Energy Efficient Buildings and Indoor Climate, Aachen, Germany, fabian.wuellhorst@eonerc.rwth-aachen.de

Abstract:

Electrifying the heat supply of buildings is key to mitigate climate change. Inhere, photovoltaic and heat pump systems are promising technologies. Studies indicate that an increase in self-consumption is economically beneficial. Coupling photovoltaic with heat pump systems enables the aspired increase of self-consumption, especially in combination with thermal energy storages. The coupling of the systems is influenced by the control strategies, for which rule-based and model predictive-based approaches exist. Research finds that optimal control methods heavily depend on the system design and vice versa. Contrary to these interdependencies, current design guidelines neglect a possible influence of photovoltaics on the design of the heat pump system.

To analyze a possible influence on the optimal heat pump system design, we apply nonlinear, dynamic simulation-based optimization to find the optimal design of the heat pump system for three different cases: no photovoltaic, no supervisory control, and a state-of-the-art supervisory control. The model consists of the whole building energy system, including the building envelope, radiators, a heat pump, a photovoltaic, and a grid connection. The dynamic simulation covers a whole year. To obtain generalizable results, we conduct optimizations for varying boundary conditions, including changes in weather and photovoltaic roof area.

Consistent over all boundary conditions, results indicate that cost optimal heat pump system design does not change for current price assumptions. However, maximizing the thermal energy storage is vital to obtain maximal costs savings compared to the case with no photovoltaic system. Thus, for different price assumptions, the optimal design will change.

Keywords:

Simulation-based Optimization, Rule-based Control, Dynamic Simulation, Modelica, Design of Experiments

1. Introduction

The residential building sector accounts for 25 % of Germany's CO_2 emissions [1]. To reduce these CO_2 emissions, electrification of the residential building heating sector is vital. Inhere, heat pumps (HPs) and photovoltaic systems (PVs) are essential technologies [2–5].
Heat pumps are able to provide space heating (SH) and domestic hot water (DHW) using electrical energy. Besides refrigerant leakage, operational emissions depend on the emission factor of the used electrical energy [5].
PVs generate generate emission-free electricity during operation. Typically, a higher self-consumption leads to faster pay-off rates. Combining heat pumps and PV, synergies arise. While the heat pump can utilize the emission-free electricity, the self-consumption and, thus, viability of PV increases as well [2, 3]. However, this effect is impeded by asynchronous supply and demand of residential buildings on a daily and seasonal timescale. At daytime, the PV generates more electricity due to solar radiation; simultaneously, the heat pump requires less, as the heat demand decreases. In summer, the PV generates overall more electricity; but the heat pump, if only used for heating, requires electricity only for DHW applications.

Several storage technologies are suitable to overcome this issue. Battery storages enable a shift of emissions-free PV-generated electricity to more useful times, while thermal energy storages shift the heat pump operation to more useful times. As a storage medium, water or the building's mass may be used. In residential heat pump systems, water-based thermal energy storages are already used for several reasons: Storing DHW [6], buffering defrost cycles [5], limiting on/off cycling at part load [6], or acting as a hydraulic separator to enable different mass flow rates [7]. Hence, using the existing water-based storages is a viable option compared to the capital-cost-intensive invest into a battery [2, 3, 8].

Minimizing costs and emissions requires optimizing the design and control of the heat pump, the PV, and the thermal energy storage. Researchers use advanced design and control methods to achieve optimality, such

as supervisory model predictive control (MPC) [9] or simulation-based optimization of heat pump systems [5]. However, these advanced methods are not state-of-the-art [10, 11]. In practice, rule-based design and control methods are applied [4,6,12]. With an expected service-life of around 20 years [12], each suboptimal design of a building energy system today impedes the climate goals of Germany for 2045 [13]. Additionally, the market share of heat pumps in the German building stock is only 5 % [14]. To enable a fast ramp-up of heat pump systems in the building stock, practitioners require simple rules for design. For control, manufacturers will presumably not open up the internal control interfaces to external energy management systems. In Germany, a heat pump is considered Smart-Grid-Ready (SG-Ready), if it allows four modes: (1) block the heat pump, (2) normal operation, (3) turn-on request, and (4) turn-on command [15]. The latter two may increase setpoints in the local control of the heat pump and, hence, indirectly the compressor frequency [16]. Hence, current state-of-the-art heat pumps only support mode-based supervisory controls. Resulting, this contribution focuses on ready-to-use, rule-based design and control methods for heat pump systems with photovoltaic.

In the following, we review contributions regarding (1) rule-based design approaches and (2) rule-based control approaches. In this review, we focus on heat pump systems with PV using thermal energy storages.

1.1. Rule-based design approaches

Research contributions highlight the importance of a correct heat pump and thermal energy storage size [2, 5, 10, 17]. As central guideline in the European Union, the EN 15450 provides rules for sizing heat pump systems based on the bivalence temperature T_{Biv}, the heat demand at nominal outdoor air temperature, and further assumptions for space heating as well as DHW usage [6]. German guidelines follow similar approaches relying on the bivalence temperature for design [12]. The bivalence temperature affects the sizing of the heat pump and, thus, invest and operational costs. Furthermore, the space heating storage is sized with a factor depending on the heat demand $V_{\dot{Q}_{\mathrm{Bui}}}$ between 12 and 35 l kW^{-1}. Despite the influence of T_{Biv} and $V_{\dot{Q}_{\mathrm{Bui}}}$ on the design, current guidelines require both T_{Biv} and $V_{\dot{Q}_{\mathrm{Bui}}}$ as an input [6, 12]. Recommendations depending on the boundary conditions, like weather or building envelope, are not given. Additionally, a potential influence of PV on the rule-based design is neglected.

In research, several contributions aim at an optimized design of heat pump systems. They highlight that the operational phase determines the optimal design. Consequently, they perform annual simulations and integrated design and control optimizations. While heat pump and storage sizes are varied, the influence of PV is not assessed. [5, 10, 17]
Designing heat pump systems with PV, Kemmler and Thomas [2] vary heat pump and storage sizes for different buildings and technologies, always considering PV and an MPC. However, MPC is not yet state-of-the-art. Huang el al. [18] perform a design optimization for a system containing PV, heat pump, thermal energy storage, and electric vehicles using simulation-based generated load profiles as an input. This impedes the control analysis and a possible influence on the optimal design. For PV-thermal systems, Miglioli et al. [19] state optimal design heavily depends on the boundary conditions. They advise to size the heat pump independent from the PV-thermal sizing, as summer operation is dominant for the optimal sizing of solar-based technologies.

Overall, contributions either do or do not consider PV for the optimal design of the heat pump system. A direct comparison between using PV and using no PV in optimal design is only given by Fischer et al. [20]. They analyse the impact of PV on the optimal heat pump system design using mixed-integer linear programming. Varying boundary conditions, they find that the heat pump size does not change with PV. Moreover, the thermal energy storage size changes only slightly. Therefore, they follow that current guidelines are sufficient. However, they assumed optimal control and simplified component models, highlighting the need for detailed simulations in their outlook.

1.2. Rule-based control approaches

Fischer et al. [4] compare control approaches for heat pump systems with PV. Both predictive and non-predictive controls are considered. While predictive controls are more efficient, current state-of-the-art heat pump rely on non-predictive, rule-based approaches. However, the non-predictive, rule-based controls applied in [4] or [21] use the compressor frequency as an actuator, which is not state-of-the-art.

Rule-based supervisory controls using setpoint changes follow the same principle: If enough PV surplus is present, thermal storage setpoints are increased - either by a fixed temperature difference, or to a maximal value [3, 4, 8, 21]. Both Haller et al. [8] and Pinamonti et al. [3] first increase DHW setpoints and later space heating setpoints. Pinamonti et al. [3] go further and activate the building inertia as well.

In general, the optimal values for these controls depend on the design of the system [4, 22]. For instance, different contributions find that increasing the storage volume is not necessary to achieve an increase self-consumption with good control values [8,21]. However, these results depend on price assumptions and storage

insulation levels.

1.3. Research questions

The review on rule-based design and control approaches shows their mutual dependence. However, it is not apparent to what extent PV and the use of a state-of-the-art supervisory control may influence the optimal design of the heat pump system [2–5, 8, 10, 18, 19, 21].

Therefore, we conduct an analysis by means of detailed annual simulation-based optimization aiming to answer two questions:

1. *Does the existence of PV affect the optimal design of residential, retrofit heat pump systems?*
2. *Does the usage of a state-of-the-art, rule-based control for PV surplus affect the optimal design of residential, retrofit heat pump systems?*

To answer these questions, the remainder of the contribution is structured as follows: Section 2 presents the simulation model, rule-based control approach, and the study design to analyse the influence of PV on the design. In Section 3, we analyse the results. Section 4 presents limitations and implications of this contribution. In Section 5, we summarize the findings and highlight future research prospectives.

2. Methods

2.1. System model

As motivated in Section 1, we focus on retrofit residential buildings in the German building stock. Following current guidelines [6], a typical building energy system consists of: A heat pump and heating rod (HR) connected in series; a space heating storage connected in parallel; a separate DHW storage with an internal heat exchanger connected in parallel; radiators to transfer heat to the rooms; analogue thermostatic valves which control the volume flow through each radiator to ensure thermal comfort; and rule-based controllers.

We model this system using the open-source Modelica library BESMod [23]. In here, components, control, and building envelope are modelled in a dynamic, nonlinear fashion:

- **Heat Pump**: Air-to-water heat pump with Propane as refrigerant [24, 25].
- **Heating Rod**: Ideal heater with a constant efficiency of 97 % [5, 25].
- **PV**: Model from [26] based on manufacturer data [27] with 133 $\mathrm{Wp/m^2}$ maximum power peak (MPP) per area.
- **DHW storage**: Indirect heat exchanger and a constant volume of 125 l [6, 25].
- **Space heating storage**: Directly charged storage with a volume depending on $V_{\dot{Q}_{\mathrm{Bui}}}$ [6].
- **Radiators**: Model according to EN 442 [25, 28] with a nominal supply temperature of 55 °C.
- **Building envelope**: The reduced order approach from the AixLib [25] is used, which is coupled to TEASER [29].

In the following, we highlight the control approach of the building energy system. As in literature, we separate the control into two layers: supervisory and local control.

2.1.1. Supervisory control

Rule-based, non-predictive supervisory control approaches in literature follow the basic principle of [3, 30]. As we analyse a retrofit building with low mass and radiator transfer system, only overheating of the DHW and space heating storage are considered.
Figure 1 depicts the implemented control logic. The electrical surplus power, $P_{\mathrm{el,Sur}}$, acts as an input. The electrical subsystem calculates the surplus based on current PV generation and all electrical power demands of the heat pump system.
Then, a hysteresis checks if the current surplus exceeds the upper hysteresis limit $P_{\mathrm{el,Hys}}$. The lower hysteresis limit is 0 W. Current research uses the minimal electrical power of the heat pump, $P_{\mathrm{el,HP,Min}}$ as a value for $P_{\mathrm{el,Hys}}$ [21]. At the same time, [4] highlights that the control strategy and component sizing is strongly interconnected. As $P_{\mathrm{el,Hys}}$ essentially defines the number of times the supervisory control overrides the local control, we vary the value as a fraction $f_{\mathrm{HP,PV}}$ based on the heat pumps nominal electrical power $P_{\mathrm{el,HP,Nom}}$, which is given in datasheets at rated conditions A2W35:

$$P_{\mathrm{el,Hys}} = f_{\mathrm{HP,PV}} \cdot P_{\mathrm{el,HP,Nom}} \tag{1}$$

If surplus exceeds the threshold, the control increases the DHW storage setpoint to $T_{\text{set,DHW,PV}}$. If the measured DHW storage temperature from the uppermost layer $T_{\text{mea,DHW}}$ exceeds this setpoint, the control increases the space heating storage setpoint by $\Delta T_{\text{SH,PV}}$. Using a winter mode from September until April, space heating is never affected during summer period.

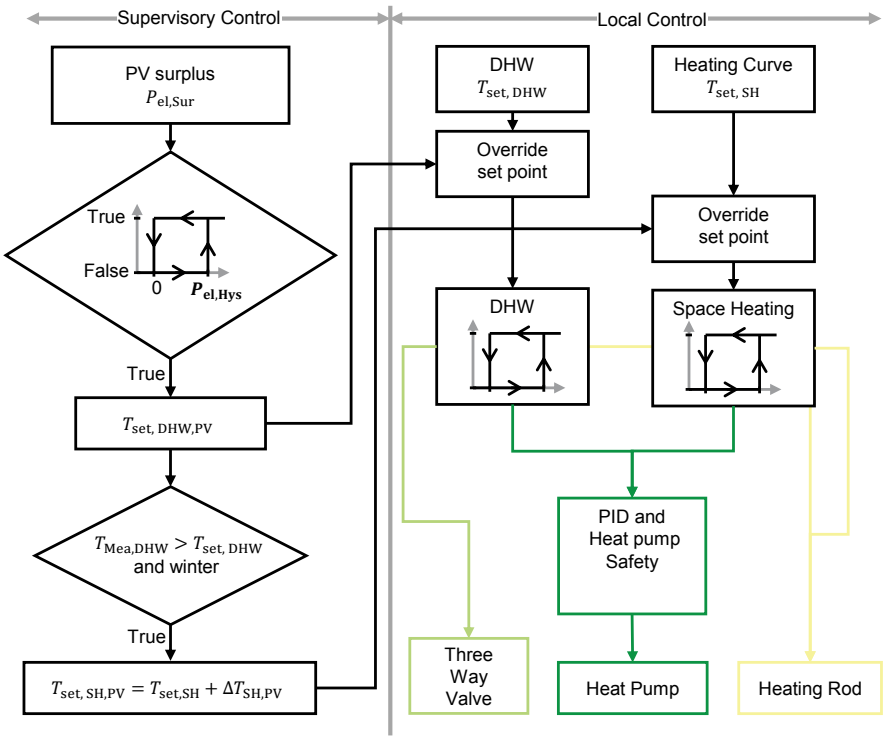

Figure 1: Rule-based supervisory and local control logic following the approaches in [3,30,31]. Colors indicate the flow of the lines.

The supervisory control only changes the setpoints of the local control. Three parameters may be changed: $f_{\text{HP,PV}}$, $T_{\text{Set,DHW,PV}}$, and $\Delta T_{\text{SH,PV}}$. We performed a separate control optimization for a single guideline-based design using the same model. Here, the values $T_{\text{Set,DHW,PV}}$ =60 °C and $\Delta T_{\text{SH,PV}}$ =15 K are pareto-optimal for relevant objectives (cf. Section 2.2.3.). The detailed analysis of this control optimization exceeds the scope of this contribution. It is noteworthy that 60 °C is also the maximal value used by [21].
As the parameter $f_{\text{HP,PV}}$ dictates to what extent surplus may be used, we include this parameter in a design and control optimization (cf. Section 2.2.2.).

2.1.2. Local control

A local controller actuates the different components based on these setpoints.
The local control follows the approach in [31] and is depicted in the right part of Figure 1. Two hystereses decide whether the heat pump and heating rod turn on or off for space heating and DHW. DHW has priority over space heating. For the heating rod control, the time-based approach from [5] is used. If the lower hysteresis limit is violated for more than 30 minutes, the control activates the heating rod. A PI controller actuates the heat pumps compressor frequency based on the set and measured values in the system. Moreover, a safety controller ensures minimal runtime, off-time, and limits the maximal number of starts per hour to three [24].

2.2. Study design

The research question's answers depend on uncertain economic parameters (i.e., electricity tariffs) and involves multiple relevant objectives, for instance, costs, emissions, efficiency or self-consumption. To evaluate multiple scenarios and objectives, we use a full-factorial design of experiments to evaluate every possible combination of discrete optimization variables [32]. Factors of the full-factorial design are different boundary conditions (cf. Section 2.2.1.) and optimization variables (cf. Section 2.2.2.). Section 2.2.3. highlights relevant objectives for our analysis.

Using discrete variables leaves untapped potential. For instance, a 9.48 kW heat pump could be the global optimum; whereas the discrete choice for a 10 kW heat pump is only near-optimal. However, manufacturers only offer discrete component sizes anyway. Thus, insights on whether these discrete choices change is

sufficient to answer the question if the optimal design changes. If the continuous optimum is of interest, a surrogate-based optimization approach can be applied to efficiently search for it [33].

2.2.1. Boundary conditions

The boundary conditions may influence the findings in this contribution. To limit the complexity of the study, we only vary certain boundary conditions. In the following, we motivate our choices.

Weather

The system design according to guidlines [6, 34] depends on the nominal outdoor air temperature $T_{\mathrm{Oda,Nom}}$, which is defined by the buildings's location [35]. Additionally, the solar radiation at different locations may influence the design of a heat pump system with PV. Thus, we define three weather cases: cold, average, and warm. We extract these cases from the German guideline DIN 4710 [36], which seperates Germany into 15 climatic regions. For weather data, the test reference year *average* is selected for each location provided by Germany's Meteorological Services [37].
Using this data, we calculate $T_{\mathrm{Oda,Nom}}$, the minimal temperature $T_{\mathrm{Oda,Min}}$, the mean temperature $T_{\mathrm{Oda,Mean}}$, and the sum of direct and diffuse radiation on a horizontal plane H_{Glo}. Based on the values, we select the coldest (Fichtelberg), warmest (Bremerhaven), and average (Bad Marienberg) region based on $T_{\mathrm{Oda,Nom}}$. Table 1 lists all four relevant characteristics for the three regions. With cumulative global radiation between 931.59 kW h m^{-2} in Hamburg and 1123.95 kW h m^{-2} in Weihenstephan, the selected locations represent a typical range of global radiation in Germany.

Table 1: Values for relevant characteristics of climatic regions in Germany.

Region	$T_{\mathrm{Oda,Mean}}$ in °C	$T_{\mathrm{Oda,Nom}}$ in °C	$T_{\mathrm{Oda,Min}}$ in °C	H_{Glo} in kWh/m^{2}a
Bremerhaven	9.8	-7.8	-10.2	1023.8
Bad Marienberg	7.8	-11.0	-17.6	955.8
Fichtelberg	3.4	-16.1	-18.4	984.2

Building Envelope

For the building envelope, we select a non-renovated building from the construction period 1983 with a net-floor-area of 156.25 m^2 from the German TABULA standard [38]. Using TEASER, the envelope model is generated [29].

The roof has a total area of 72.9 m^2 and two sides, each with a tilt of 35°. One half is south-facing, the other half north-facing. As south-facing installations are a common recommendation, we focus on this orientation [39]. Using 100 % of the south-facing roof, the MPP equals 4.8 kW.

User

Besides weather and building envelope, user profiles may influence the optimal design of the system. At the same time, user profiles are inherently uncertain and stochastic. To neglect a possible influence of stochastic profiles, we assume deterministic profiles based on guidelines.
For DHW, Profile M according to European Union Regulation 811/2013 [40] is used.
For internal gains, standard profiles from TEASER are used [29]. However, we neglect the influence of internal gains on the electricity demand. All available PV electricity may be used for the heat pump system. This either represents a tenant-landlord scenario or a best-case scenario, where homeowners adjust their appliances usage in favour of the heat pump. While the latter is not realistic, it maximizes the possible influence of PV on the heat pump system, and, thus, its optimal design.

2.2.2. Design and control optimization

Table 2 lists the factors and levels of the integrated design and control optimization. Following findings in recent literature, we use 1 K levels for the bivalence temperature, as this parameter has the highest influence on efficiency, cost, and emissions [5, 17].
Aside from the aforementioned factors, we enable and disable the supervisory control. Combined with the roof area usage factors, this leads to three cases which we use to analyse the influence of PV and the control strategy on the optimal design of the heat pump system:

1. *No PV*: Reference case with no PV and no supervisory control
2. *No Control*: PV but no supervisory control
3. *Control*: PV and a rule-based supervisory control

Case 2 applies when components of different manufacturers are used which are not able to communicate with a supervisory control.

Overall, 2640 annual simulations are run, with an average computation time of 15 min[1].

Table 2: Full-factorial design for the design and control optimization

Factor	Values	Number of levels
Weather	Fichtelberg, Bad Marienberg, Bremerhaven	3
Roof area usage	0 %, 50 %, 100 %	3
Supervisory Control	Disabled, Enabled	2
$f_{\mathrm{HP,PV}}$	10 % to 100 %	4
T_{Biv}	$-16\,^{\circ}\mathrm{C}$ to $5\,^{\circ}\mathrm{C}$	20
$v_{\dot{Q}_{\mathrm{Bui}}}$	$5\,\mathrm{l\,kW^{-1}}$ to $100\,\mathrm{l\,kW^{-1}}$	4

2.2.3. Objectives

As the invest decision of a homeowner may depend on more than one objective, we analyse the optimal design with regard to multiple objectives.

Besides costs and efficiency, the self-consumption rate and the self-sufficiency degree are often used as characteristic values for the evaluation of systems with PV [30].
Emissions are not analysed in detail within this contribution. However, the full-factorial design enables a post-analysis of further objectives.

Economics

The cost functions for annuity of the heat pump system follow [10, 41]. Inhere, invest, operation, and maintenance costs are considered.
As we want to analyse a possible change in the heat pump system design if PV is used, we explicitly neglect the investment in PV. In reality, the economic viability of PV depends on the self-consumption rate, which is influenced by household appliances. As we neglect those, assessing economic viability of PV is not within the scope of this contribution.

Further, we assume current electricity tariffs from Germany, with 36.06 $\mathrm{ct_{EUR}/kWh}$ for electricity consumption and 8.2 $\mathrm{ct_{EUR}/kWh}$ for feed-in.

Efficiency

The seasonal coefficient of performance $SCOP_{\mathrm{Sys}}$ indicates the annual efficiency of the heat pump system. To incorporate the whole system, we define the $SCOP_{\mathrm{Sys}}$ according to an energy balance around the building energy system:

$$SCOP_{\mathrm{Sys}} = \frac{\int_{0a}^{1a} (\dot{Q}_{\mathrm{SH}}(\tau) + \dot{Q}_{\mathrm{DHW}}(\tau)) d\tau}{\int_{0a}^{1a} (P_{\mathrm{el,HP}}(\tau) + P_{\mathrm{el,HR}}(\tau)) d\tau} \tag{2}$$

Inhere, $\dot{Q}_{\mathrm{SH}}$ is the building's space heating demand, $\dot{Q}_{\mathrm{DHW}}$ is the DHW's demand, as well as $P_{\mathrm{el,HP}}$ and $P_{\mathrm{el,HR}}$ the heat pump's and heating rod's electrical power consumption, respectively.

Self consumption rate

The ratio of directly used PV electricity $W_{\mathrm{el,PV,use}}$ and the generated PV electricity $W_{\mathrm{el,PV}}$ defines the self consumption rate SCR [39]:

$$SCR = \frac{W_{\mathrm{el,PV,use}}}{W_{\mathrm{el,PV}}} \tag{3}$$

In literature, the SCR is commonly used to evaluate design and control approaches for PV systems [3, 4, 8].

Self-sufficiency degree

The ratio of directly used PV electricity $W_{\mathrm{el,PV,use}}$ to the total electricity demand defines the self-sufficiency degree SSD [39]:

$$SSD = \frac{W_{\mathrm{el,PV,use}}}{W_{\mathrm{el,tot}}} = \frac{W_{\mathrm{el,PV,use}}}{W_{\mathrm{el,PV,use}} + W_{\mathrm{el,Grid}}} \tag{4}$$

[1] Intel(R) Xeon(R) CPU E5-1650 v3 @3.50GHz, 32 GB DDR3 RAM, 64 bit, SSD hard drive

3. Results

We separate the results of the design and control optimization into two cases. First, we analyse if the existence of PV changes the optimal design. Second, we highlight the influence of the design on the optimal control parameters.

3.1. Influence of PV on the heat pump system design

Figure 2 illustrates three cases for the medium weather case and a south-facing PV installation with 100 % roof area usage. For all other cases, the absolute values change, but the relative deviations are comparable. Thus, we focus on this case for our analysis.

First, the optimal design does not change; neither when using no supervisory control, nor when using a supervisory control. Second, the relative objective space, i.e. the gradients, does not change between the cases. This observation holds for all simulated boundary conditions. Thus, for the current price assumptions (cf. Section 2.2.3.), PV does not influence the optimal design of the heat pump system.

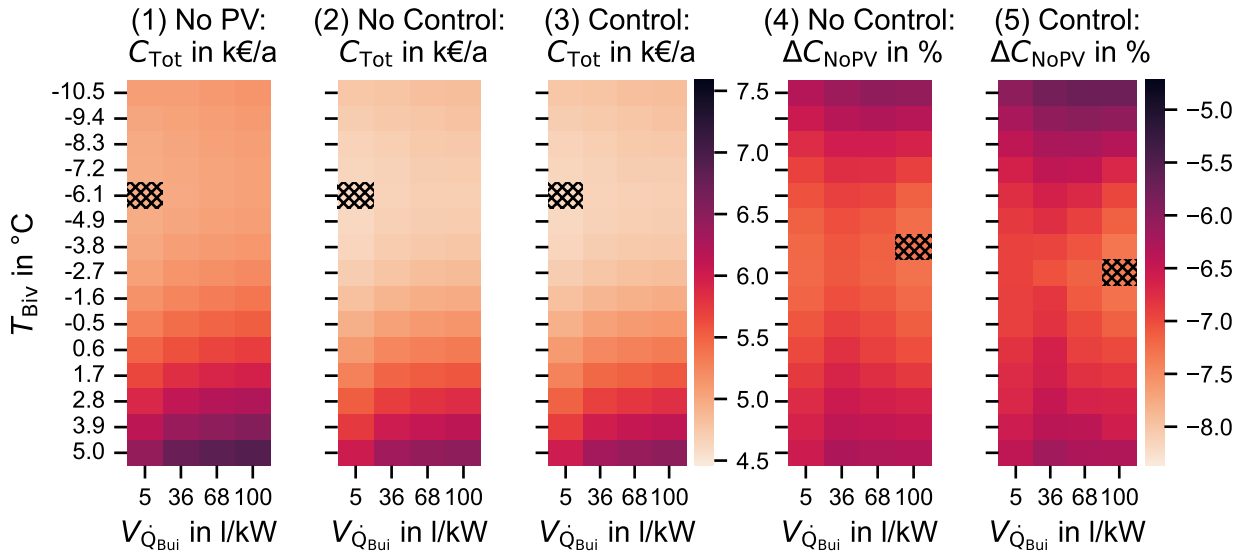

Figure 2: Optimal total costs over T_{Biv} and $V_{\dot{Q}_{Bui}}$ for the three cases (1) *No PV*, (2) *No Control*, and (3) *Control*. Furthermore, the percentage change in total costs compared to case *No Pv* ΔC_{NoPV} for the cases (4) *No Control*, and (5) *Control* is depicted. Results are for location Bad Marienberg and a south-facing PV installation with 100 % roof area usage. The hatched cell indicates the optimal design.

Looking at further differences in the objective space, Figure 2 also depicts the change in total costs compared to the case *No PV*. For these boundary conditions, the case *No Control* yields cost reductions between 5.8 % and 7 %, while the case *Control* obtains cost reductions between 5.7 % and 7.3 %. Over all boundary conditions, the case *No Control* obtains cost reductions between 5.3 % and 7.7 %, while the case *Control* obtains cost reductions between 2.6 % and 7.9 %. With 0.3 % additional cost reduction, case *Control* is only slightly better than case *No Control* for the highest cost reduction. At the same time, case *Control* achieves lower cost reductions in some cases compared to case *No Control*.

Consistent over boundary conditions, the highest cost reductions are achieved with smaller heat pumps and larger thermal energy storages compared to the economic optimum.

Figure 3 illustrates four important metrics to explain why the optimal design changes. Inhere, the self-sufficiency degree *SSD* closely resembles the cost reductions. Essentially, the *SSD* is a superposition of the self-consumption rate *SCR* and the system efficiency $SCOP_{Sys}$.

First, the *SCR* increases with bigger thermal energy storages and smaller heat pumps. Bigger thermal energy storages enable a better exploitation of surplus electricity. Smaller heat pumps lead to higher times of heating rod usage t_{HR} and, thus, an increased electricity demand. This increased electricity demand increases the chance of PV electricity being used and, therefore, the *SCR*.

Second, the $SCOP_{Sys}$ decreases with smaller heat pumps and increases slightly for bigger storages, as the local control requires the heating rod less frequently. For small storages and monovalent heat pumps, the $SCOP_{Sys}$ decreases slightly. Suboptimal PID-values lead to this decrease.

The results in this section hold for the optimal control value $f_{PV,HP}$. The following section analyses how the optimal values of $f_{PV,HP}$ change with the design.

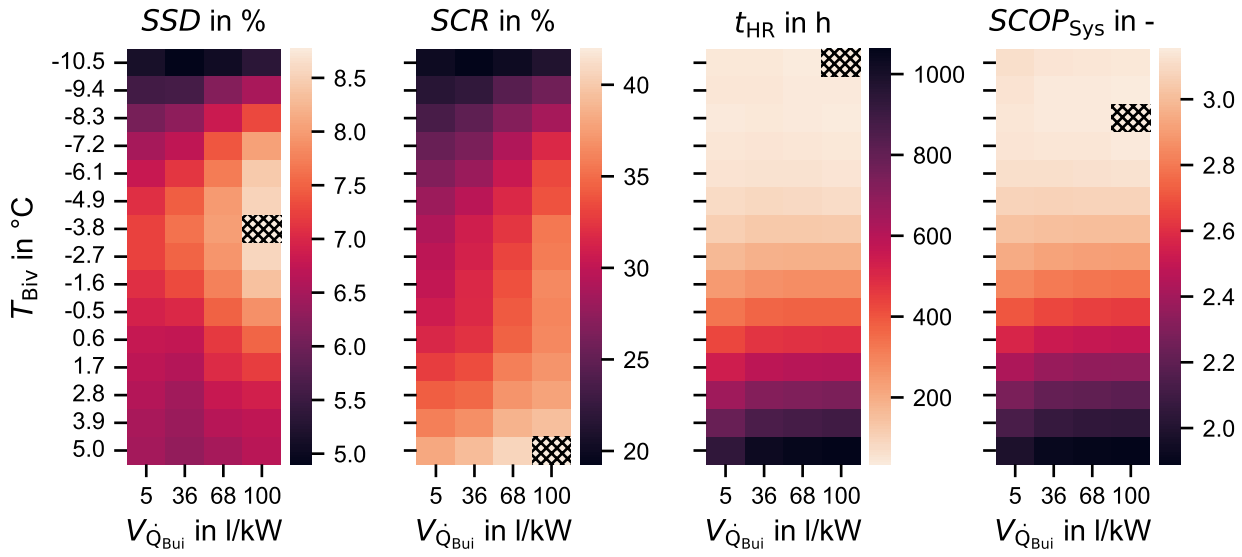

Figure 3: Optimal values for the *SSD*, *SCR*, heating rod on-time t_{HR}, and $SCOP_{Sys}$ over T_{Biv} and $V_{\dot{Q}_{Bui}}$ in case *Control*. The results hold for location Bad Marienberg and a south-facing PV installation with 100 % roof area usage. The hatched cell indicates the optimal design.

3.2. Influence of the design on the optimal control

The control parameter $f_{HP,PV}$ defines the threshold to increase setpoints and, thus, use surplus electricity. Figure 4 illustrates the optimal settings for $f_{HP,PV}$ depending on different designs of heat pump and storage, as well as relevant objectives. For cases with multiple optima, especially for monovalent designs (minimal T_{Biv}), the maximal value of $f_{HP,PV}$ is used.
Looking at total costs, settings equal or greater than 40 % are optimal. For bivalence temperatures around $-6\,°C$, the lowest values of 40 % are optimal for larger storages. This design is concurrent with the highest cost reduction through the control. Thus, to achieve the highest cost reduction, the supervisory control needs to be included into the optimization problem.
Focusing on the efficiency, maximal values of $f_{HP,PV}$ maximize the $SCOP_{Sys}$. Only for the smallest heat pump, where the efficiency is already low, smaller values of $f_{HP,PV}$ are advisable. Looking further at *SSD* and *SCR*, minimizing $f_{HP,PV}$ is advisable. These findings hold for different boundary conditions considered in this study.

4. Discussion

Before discussing the implication of our results, we highlight limitations in the methods applied.

4.1. Limitations

The results show that the applied rule-based control is better or worse for different designs compared to using no control. Overall, not more than 0.3 % of costs are additionally saved due to the supervisory control. We optimized the set-temperatures in a separate study and the threshold in our design and control optimization. Including the set-temperatures may yield further saving potential. However, as the separate operational optimization is conducted for designs close to the optimal design, we do not expect the optimal design to change. In contrast to [3], we do not consider space cooling. Further, we study colder climates and buildings with a DHW share of only 5 % to 8 %. As Fischer et al. [21] point out, DHW is the dominating factor for PV. Our study confirms these results. Fischer et al. study a DHW share of 16 % [21], Pinamonti et al. of 23 % up to 48 % [3]. While investigating higher DHW shares might benefit the supervisory control, it does not affect the optimal rule-based design according to current guidelines [6]. In here, the DHW storage volume is fixed by demand. However, future studies should check if an optional over-sizing factor could be introduced to guidelines to increase self-sufficiency for heat pump systems with PV.
Furthermore, the rule-based control in current research are either based on digital thermostats or the ability to control the compressor frequency. Especially the latter is not given for the current SG-Ready label. Thus, we follow that the rule-based control is plausible for current state-of-the-art retrofit systems in Germany.

A further limitation in the methodology is the assumption that PV is only used for the electricity demand of the heat pump system. In reality, household appliances decrease the PV surplus. This further minimizes the chance of the heat pump system to use cheap PV electricity. While not relevant to our research questions

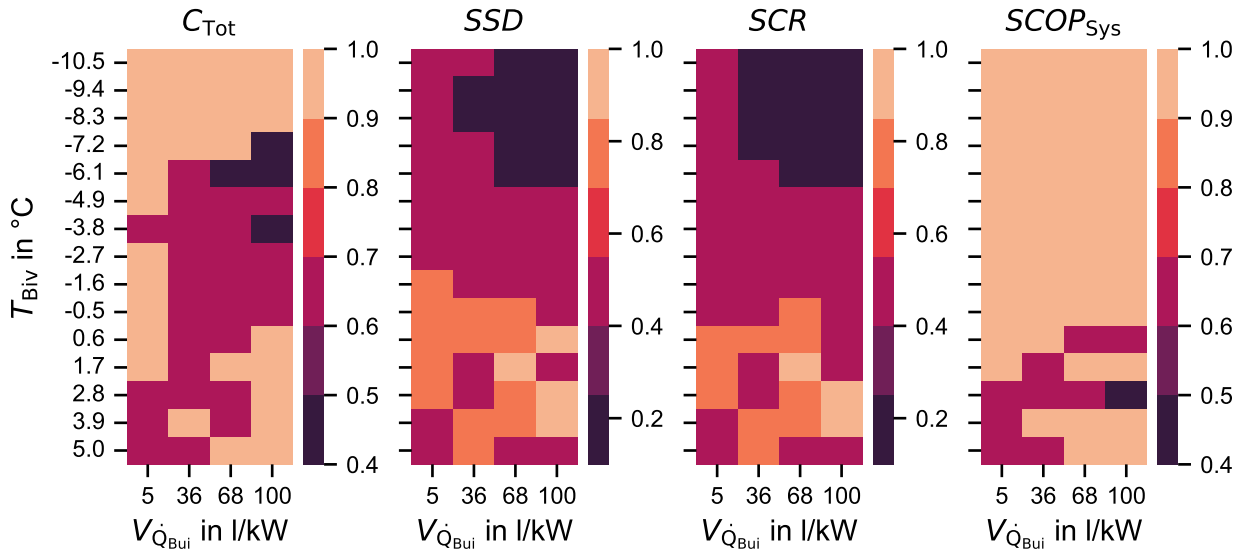

Figure 4: Optimal control values for $f_{HP,PV}$ with regard to the optimal objective values given in Figure 2 and Figure 3. Values are given over T_{Biv} and $V_{\dot{Q}_{Bui}}$ and hold for location Bad Marienberg with a south-facing PV installation and 100 % roof area usage.

regarding the change in optimal design, realistic internal gain profiles should be used if an optimal design for a specific case is required.

Our results are consistent for varying weather data and PV areas. However, other boundary conditions such as the ratio of roof area to heating demand may influence the results. For our cases, PV surplus is mostly available during spring, summer, and autumn. For better-insulated buildings with a larger roof, the surplus usage and, thus, the optimal design may change. The same holds true for the orientation of PV. West- or east-facing installations with different tilts could benefit PV surplus during heating season. Last, the usage of a battery or dynamic energy tariffs could impact the heat pump and thermal energy storage design.

Aside from control and boundary conditions, only some components of the dynamic simulation model are empirically validated [24]. The others follow white-box model approaches or are verified using comparative validation [25]. As the thermal energy storage enables the efficient exploitation of PV surplus, experimental validation should be carried out.

4.2. Implications

Keeping the limitations of this study in mind, three implications for current practice arise.

First, optimal design of the heat pump does not change when using PV with no or ineffective supervisory controls. While minor changes in T_{Biv} occur depending on the price assumptions, heat pumps are only available in discrete steps anyway.

Second, for current price assumptions, the optimal design of the storage does not change. However, to maximize PV usage, the thermal energy storage should be maximized. This contradicts the optimal design without PV, where the economic optimum is always at minimal storage volumes. However, other factors, such as defrost or utility blocking times may require the need of a larger thermal energy storage for space heating. Thus, simply minimizing the storage volume is not advisable when combining PV with heat pumps. Third, the four discrete options of the SG-Ready-Label do not enable a substantial increase of self-sufficiency. Hence, different interfaces for supervisory controls, such as the compressor speed, should be opened for external access.

5. Conclusion

This contribution analyses the influence of PV on the optimal design of heat pump systems for retrofit buildings using state-of-the-art rule-based controls. Applying annual simulation-based optimization of design and control using detailed Modelica models, we highlight findings and implications for practice and research:

1. At least in retrofit, PV does not influence the optimal heat pump size for the used rule-based controls. For current practice, neglecting PV is a valid assumption in current guidelines [6]. However, advanced control strategies could change the optimal design in future systems.

2. PV does not affect the cost-optimal thermal energy storage size. However, optimal storage sizes change

when changing price scenarios or objective functions. Thus, PV should be considered when sizing the thermal energy storage. The same could apply for the DHW storage, as DHW enables an efficient PV usage during summer.

3. Future studies should incorporate additional boundary conditions and technologies. Different DHW profiles, internal gains, or PV installations may impact the influence of PV on the optimal design.

4. Future research should develop simplified design rules - both for rule-based controls and system design. First, assessing advanced approaches as in [4] for different designs is advisable. Afterwards, design-independent rules should be extracted to enable a fast and optimal planning of building energy systems.

6. Acknowledgments

We gratefully acknowledge the financial support by the Ministry of Economic Affairs, Industry, Climate Action and Energy of the state of North Rhine-Westphalia within the research project PractiCon.

Nomenclature

Symbols

T	Temperature, °C
ΔT	Temperature difference, K
$V_{\dot{Q}_{Bui}}$	Volume per heat demand, $\mathrm{l\,kW^{-1}}$
f	factor, –
P_{el}	Electrical Power, W
W_{el}	Electrical Energy, W
$W_{el,PV,use}$	Self-used electrical energy, W
$W_{el,Grid}$	Electrical energy taken from grid, W
C_{Tot}	Total costs, €/a
$\dot{Q}$	Heat flow rate, W
t	Time period, –
H_{Glo}	Global horizontal diffuse and direct radiation, $\mathrm{kWh/m^2a}$
SCR	Self-consumption level, %
SSD	Self-sufficiency degree, %
$SCOP_{Sys}$	Seasonal coefficient of performance for whole system, –

Subscripts and superscripts

HR	Heating rod
HP	Heat pump
PV	Photovoltaic
SH	Space Heating
MPP	Maximum Peak Power
MPC	Model Predictive Control
Bui	Building
Oda	Outdoor air
DHW	Domestic Hot Water
tot	total
SG	Smart-Grid
Sur	Surplus
Hys	Hystereses
Nom	Nominal
Mea	Measured
set	setpoint

References

[1] Wilke S. Kohlendioxid-Emissionen im Bedarfsfeld ,,Wohnen“ [Text]. Umweltbundesamt; 2016. https://www.umweltbundesamt.de/daten/private-haushalte-konsum/wohnen/kohlendioxid-emissionen-im-bedarfsfeld-wohnen.

[2] Kemmler T, Thomas B. Design of Heat-Pump Systems for Single- and Multi-Family Houses Using a Heuristic Scheduling for the Optimization of PV Self-Consumption. Energies. 2020 Mar;13(5):1118.

[3] Pinamonti M, Prada A, Baggio P. Rule-Based Control Strategy to Increase Photovoltaic Self-Consumption of a Modulating Heat Pump Using Water Storages and Building Mass Activation. Energies. 2020 Jan;13(23):6282.

[4] Fischer D, Bernhardt J, Madani H, Wittwer C. Comparison of Control Approaches for Variable Speed Air Source Heat Pumps Considering Time Variable Electricity Prices and PV. Applied Energy. 2017 Oct;204:93-105.

[5] Vering C, Wüllhorst F, Mehrfeld P, Müller D. Towards an Integrated Design of Heat Pump Systems: Application of Process Intensification Using Two-Stage Optimization. Energy Conversion and Management. 2021 Dec;250:114888.

[6] EN 15450:2007-12. Heating Systems in Buildings - Design of Heat Pump Heating Systems; German Version EN 15450:2007; Dezemebr 2007.

[7] Floss A, Hofmann S. Optimized Integration of Storage Tanks in Heat Pump Systems and Adapted Control Strategies. Energy and Buildings. 2015 Aug;100:10-5.

[8] Haller M, Battaglia M, Haberl R, Reber A, Bamberger E, Borner M. Steigerung Des PV-Eigenverbrauchs Durch Intelligente Wärmepumpen. 23 Tagung des BFE-Forschungsprogramms "Wärmepumpen und Kälte". 2017.

[9] Drgoňa J, Arroyo J, Cupeiro Figueroa I, Blum D, Arendt K, Kim D, et al. All You Need to Know about Model Predictive Control for Buildings. Annual Reviews in Control. 2020 Sep.

[10] Vering C, Maier L, Breuer K, Krützfeldt H, Streblow R, Müller D. Evaluating Heat Pump System Design Methods towards a Sustainable Heat Supply in Residential Buildings. Applied Energy. 2022 Feb;308:118204.

[11] Killian M, Kozek M. Ten Questions Concerning Model Predictive Control for Energy Efficient Buildings. Building and Environment. 2016 Aug;105:403-12.

[12] Association of German Engineers. VDI 4645: Heating Plants with Heat Pumps in Single-Family and Multi-Family Houses - Planning, Construction, Operation. 4645. Beuth Verlag GmbH; 2018.

[13] Bundesregierung. Klimaschutzgesetz: Klimaneutralität bis 2045 — Bundesregierung; 2022.

[14] Bundesverband der Deutschen Heizungsindustrie. Gesamtbestand Zentrale Wärmeerzeuger 2019; 2020.

[15] Bundesverband Wärmepumpe e V . SG Ready-Label; 2023. https://www.waermepumpe.de/normen-technik/sg-ready/.

[16] Danny Günther, Jeannette Wapler, Robert Langner. WPSMART IM BESTAND – Felduntersuchung Optimal Abgestimmter Wärmepumpenheizungssysteme in Bestandsgebäuden Beim Betrieb Im Konventionellen Sowie Im Intelligenten Stromnetz (Smart Grid). Fraunhofer-Institut für Solare Energiesysteme ISE. 2020 Jul.

[17] Dongellini M, Naldi C, Morini GL. Influence of Sizing Strategy and Control Rules on the Energy Saving Potential of Heat Pump Hybrid Systems in a Residential Building. Energy Conversion and Management. 2021 May;235:114022.

[18] Huang P, Lovati M, Zhang X, Bales C, Hallbeck S, Becker A, et al. Transforming a Residential Building Cluster into Electricity Prosumers in Sweden: Optimal Design of a Coupled PV-heat Pump-Thermal Storage-Electric Vehicle System. Applied Energy. 2019 Dec;255:113864.

[19] Miglioli A, Aste N, Del Pero C, Leonforte F. Photovoltaic-Thermal Solar-Assisted Heat Pump Systems for Building Applications: Integration and Design Methods. Energy and Built Environment. 2023 Feb;4(1):39-56.

[20] Fischer D, Lindberg K, Madani H, Wittwer C. Impact of PV and Variable Prices on Optimal System Sizing for Heat Pumps and Thermal Storage. Energy and Buildings. 2016 Jul;128.

[21] Fischer D, Rautenberg F, Wirtz T, Wille-Haussmann B, Madani H. Smart Meter Enabled Control for Variable Speed Heat Pumps to Increase PV Self-Consumption. In: International Congress on Refrigeration. vol. 24. Yokohama; 2015. p. 8.

[22] Williams CJC, Binder JO, Kelm T. Demand Side Management through Heat Pumps, Thermal Storage and Battery Storage to Increase Local Self-Consumption and Grid Compatibility of PV Systems. In: 2012 3rd IEEE PES Innovative Smart Grid Technologies Europe (ISGT Europe); 2012. p. 1-6.

[23] Wüllhorst F, Maier L, Jansen D, Kühn L, Hering D, Müller D. BESMod - A Modelica Library Providing Building Energy System Modules. In: American Modelica Conference 2022. Dallas; 2022. p. 10.

[24] Wüllhorst F, Jansen DP, Mehrfeld P, Müller D. A Modular Model of Reversible Heat Pumps and Chillers for System Applications. In: Doi:10.3384/Ecp21181561. 14th Modelica Conference 2021, Linköping (Sweden), 20 Sep 2021 - 24 Sep 2021; 2021. p. 8.

[25] Müller D, Lauster M, Constantin A, Fuchs M, Remmen P. AixLib – An Open-Source Modelica Library within the IEA-EBC Annex 60 Framework. In: BauSIM 2016. Dresden; 2016. p. 8.

[26] Maier L, Kratz M, Vering C, Mehrfeld P, Müller D. Open-Source Photovoltaic Model for Early Building Planning Processes: Modeling, Application and Validation. In: 17th International IBPSA Conference, September 1th to 3th 2021, Bruges, Belgium. vol. 17. IBPSA; 2021. p. 2315-6.

[27] Schüco International KG. Schüco Photovoltaikmodule Der SME-1 Serie; 2022.

[28] EN 442-2:2014. Radiators and Convectors - Part 2: Test Methods and Rating. Bruxelles, Belgium: CEN; 2014.

[29] Remmen P, Lauster M, Mans M, Fuchs M, Osterhage T, Müller D. TEASER: An Open Tool for Urban Energy Modelling of Building Stocks. Journal of Building Performance Simulation. 2018 Jan;11(1):84-98.

[30] Haller M, SPF LF, Battaglia M, Haberl R, Reber A, Bamberger E. Steigerung Des Photovoltaik-Eigenverbrauchs Durch Intelligente Wärmepumpen. Tagung des BFE-Forschungsprogramms Wärmepumpen und Kälte, June 14th. 2017.

[31] Wüllhorst F, Vering C, Maier L, Müller D. Integration of Back-Up Heaters in Retrofit Heat Pump Systems: Which to Choose, Where to Place, and How to Control? Energies. 2022 Jan;15(19):7134.

[32] Antony J. Design of Experiments for Engineers and Scientists. 2nd ed. Elsevier Insights. London: Elsevier; 2014.

[33] Akhtar T, Shoemaker CA. Multi Objective Optimization of Computationally Expensive Multi-Modal Functions with RBF Surrogates and Multi-Rule Selection. Journal of Global Optimization. 2016 Jan;64(1):17-32.

[34] Verein Deutscher Ingenieure e V (Hrsg). VDI 4645: Heizungsanlagen Mit Wärmepumpen in Ein- Und Mehrfamilienhäusern Planung, Errichtung, Betrieb. Beuth Verlag; 2018.

[35] DIN EN 12831-1. Energetische Bewertung von Gebäuden – Verfahren Zur Berechnung Der Norm-Heizlast – Teil 1: Raumheizlast, Modul M3-3. Beuth Verlag; 2017.

[36] DIN 4710. Statistiken meteorologischer Daten zur Berechnung des Energiebedarfs von heiz- und raumlufttechnischen Anlagen in Deutschland. Beuth Verlag; 2003.

[37] German Meteorological Service. Handbuch: Ortsgenaue Testreferenzjahre von Deutschland Für Mittlere, Extreme Und Zukünftige Witterungsverhältnisse; 2017.

[38] Loga T, Stein B, Diefenbach N, Born R, und Umwelt IW, editors. Deutsche Wohngebäudetypologie: beispielhafte Maßnahmen zur Verbesserung der Energieeffizienz von typischen Wohngebäuden ; erarbeitet im Rahmen der EU-Projekte TABULA. 2nd ed. Darmstadt: IWU; 2015.

[39] Wesselak V, Voswinckel S. Photovoltaikanlagen. In: Wesselak V, Voswinckel S, editors. Photovoltaik – Wie Sonne zu Strom wird. Technik im Fokus. Berlin, Heidelberg: Springer; 2016. p. 63-116.

[40] Eurpäische Union. Delegierte Verordnung (EU) Nr. 811/2013 Der Kommission; 2013.

[41] Association of German Engineers. VDI 2067: Economic efficiency of building installations: Fundamentals and economic calculation. Beuth Verlag; 2012.

Identifying techno-economic improvements for a steam generating heat pump with exergy-based costs minimization

Brendon de Raad[a], Marit van Lieshout[b], Lydia Stougie[c], Andrea Ramirez[d]

[a] Rotterdam University of Applied Sciences, Rotterdam & Delft University of Technology, Delft, Netherlands, B.W.de.Raad@HR.nl, CA
[b] Rotterdam University of Applied Sciences, Rotterdam, Netherlands, M.van.Lieshout@HR.nl
[c] Delft University of Technology, Delft, Netherlands, L.Stougie@TUDelft.nl
[d] Delft University of Technology, Delft, Netherlands, C.A.RamirezRamirez@TUDelft.nl

Abstract:

Steam generating heat pumps show great potential for reducing carbon emissions in the industrial sector. However, predicting their performance is challenging as the exergy destruction of e.g., compressors and expansion valves increases with the temperature lift and condenser temperature. With over seventy design improvements mentioned in the literature, selecting the most effective design improvements is crucial. In this study, energy and exergy-based methods were compared in their ability to identify design improvements for a single stage subcritical heat pump to produce steam from hot condensate. The energy-based method suggested the addition of a sequential compressor with an intermediate cooler; however, this design did not improve the heat pump's techno-economic performance. The suggestion of adding either an internal heat exchanger or a flash vessel by exergy-based methods did lead in both cases to improved techno-economic performance. The internal heat exchanger performed best and increased the coefficient of performance from 2.3 to 2.8 and reduced operational costs by 0.8 M€ after 5 years of operation. Additionally, the initial investment decreased by 135 k€, and the total costs of operation decreased from 10.3 M€ to 8.7 M€. These findings show that exergy-based methods are the way forward in identifying effective design improvements for steam generating heat pumps.

Keywords:

High-temperature heat pump, Steam generation, Exergy-based costs minimization, Techno-economic analysis, advanced heat pump configuration

1. Introduction

1.1. Steam generating heat pumps

Heat pumps are being widely considered as a crucial technology for reducing carbon emissions in the industrial sector by 2030, and steam generation heat pumps (SGHPs) are a notable example. By converting renewable electricity into heat, SGHPs can effectively contribute to the sector's CO_2-reduction goals. These heat pumps have the potential to decrease energy consumption in the European industrial sector by almost 30%, as they can supply heat at a temperature of up to 300 °C [1]. SGHPs have three major advantages over other high temperature heat pumps: 1. they have a low installation costs factor because they can be connected to existing steam networks, 2. they have a good heat transfer coefficient compared to other working media (organic vapours), and 3. they are easier to control compared to hot water systems [2].

A large temperature lift is required to produce steam from waste heat. The typically used subcritical single stage heat pump, also known as simple cycle heat pump, becomes uneconomical at temperature lifts exceeding 50°C [3] due to increased inefficiencies in the compressor and expansion valve [4]. Advanced heat pump configurations, on the other hand, are an economically viable alternative at these large temperature lifts [3]. The coefficient of performance (COP), which is the key technical performance indicator of heat pumps, reflects this increase in techno-economic viability. By advancing the simple cycle through intermediate cooling in the compressor, for example, the heat pump's COP can be increased. Advanced configurations can have a COP up to three times that of the simple cycle at the same temperature difference [5]. Many researchers have explored the performance and techno-economic potential of advanced heat pump configurations, including Arpagaus [6, 7], Schlosser [5], and Adamson [8]. These studies have identified over seventy different configurations that can help improve upon the simple cycle's performance.

However, it is important to note that selecting an advanced heat pump configuration based solely on its listed performance in a different technical context can be ill-advised, as a heat pump's performance is highly sensitive to its technical surroundings. An example of the sensitivity of a heat pump's performance to its technical surroundings is demonstrated by Bless et al. [2], who found that the COP of high-temperature heat pump configurations for steam generation appeared comparable at first, but differed by almost two times when applied to the same case. This highlights the need for caution when selecting advanced heat pump configurations based solely on listed performance in a different technical context.

While there are over seventy possibilities for optimizing the simple heat pump configuration, currently, there is no systematic method for determining the optimal improvements. In other words, there is no established approach for selecting the most effective configuration for a specific application. This presents a challenge for researchers and engineers who seek to develop more efficient heat pump systems, as trial-and-error is currently the only means of determining which advanced heat pump configurations will perform optimally in a given context. It is, therefore, needed to develop a systematic method for selecting the most efficient and effective heat pump configurations for specific applications.

1.2. Economics and exergy analysis of high temperature heat pumps

Arpagaus [6, 7], Schlosser [5], and Adamson [8] have identified various advanced heat pump configurations that aim to minimize irreversibilities resulting from non-ideal pressure changes and heat exchange. These modifications involve adding expanders, compressors, flash vessels, open connections, heat exchangers, or switching the working fluid. The reduction of irreversibilities results in less work being required by the compressor and therefore a higher COP. Simple cycle heat pumps typically operate at about 50% of their ideal COP, due to these irreversibilities. Hence, they require twice the amount of shaft work to drive the compressor compared to the ideal operation [9]. Exergy analysis is a technique that helps to identify where irreversibilities occur. Opposite to energy, exergy is not a conserved measure. Hence, an exergy balance needs to account for exergy loss to the environment or loss to irreversibilities. The latter is known as exergy destruction.

Bergamini et al. [10] used exergy analysis to study the exergy destruction in a high temperature single-stage ammonia heat pump that produced heat at 140°C from an isothermal 30°C source. They found that the exergy destruction of the heat pump’s components increased at different rates and that exergy destruction in the expansion valves was the most sensitive to the temperature lift, whereas its initial contribution to the total exergy destruction was limited. Hence, the dominant source of exergy destruction in the heat pump varied among components as the temperature lift was increased. Hu et al. [11] found similar results when assessing a heat pump that produced pressurized water at 120 °C from a heat source ranging from 50 to 90 °C. They concluded that there is a strong correlation between exergy loss in the heat pump and the temperature lift, while exergy destruction in the evaporator and the condenser remained relatively constant.

Moran et al. [12] combined exergy with economic analysis to help decision makers in identifying how much an additional component would increase both the technical and economic performance. Wang et al. [13], for instance, applied the exergoeconomic principle of exergy loss per total capital investment to compare the performance of mechanically and thermally driven heat pumps. Their analysis shows that exergy loss per capital investment as a function of temperature lift differs between mechanically and thermally driven heat pumps. Based on this distinction, they formulated a guide map to aid in the selection of the technologies. In a follow-up study, Wang et al. [14] used the same principles when evaluating the performance of a transcritical heat pump cycle for hot water production and increased the heat pump’s cost rate by 17%.

Hence, exergy-based economic analysis has emerged as a valuable tool for enhancing the techno-economic performance of heat pumps. However, its application to high temperature heat pumps has been limited. Moreso, to the author’s knowledge, no known cases exist where exergy-based economic analysis has been applied to a SGHP despite the challenges in selecting design changes and their significant potential for improvements.

1.3. Objective

Assessing the performance of advanced heat pump configurations is challenging due to their substantial dependence on the temperature of the heat source and sink. This is especially true for steam generating heat pumps, where the exergy destruction of pressure equipment increases with the temperature lift and condenser temperature. To address this issue, this paper employs exergy-based economic analysis to identify techno-economic improvements to a steam generating heat pump and compares the results with an energy-based method. The objective of this paper is to illustrate how exergy-based economic analysis can be used to identify techno-economic improvements to a steam generating heat pump and show how the results differ from an energy-based method.

2. Method

The method section is built up out of three sections. The first section goes into the general description of the followed approach. The underlying thermodynamic analysis is explained in section 2.2 and the costs calculations in 2.3.

2.1. Identification of techno-economic improvements

Advancements to a simple cycle heat pump configuration to produce steam were explored by using a four-step method: 1. setting costs targets, 2. performing energy, economic, and exergy analysis (3E-analysis), 3. assigning costs to exergy losses, and 4. assessment of design changes.

Step No. 1: To set cost targets, the performance of an ideal (i.e., lossless) heat pump was compared to an electric boiler. This comparison is common in industry because both are a way to industrial electrification. The heat pump was defined to be economically viable when the total costs of ownership (TCO) after five years of full-time operation (8000 h) were lower than that of an e-boiler. The cost of electricity was taken to be 0.041 €/kWh [15] based on the expected average electricity costs between 2022 and 2030 in the Netherlands for large consumers. The required capital investment for an e-boiler of the required size was based on a capital costs price of 165 €/kW [15]. For both the e-boiler and the heat pump an installation costs factor of 3 was used to convert bare unit costs to installed costs. Based on the TCO of an e-boiler and the operational costs of an ideal heat pump, the maximal capital investment for a heat pump was calculated.

The next step was initiated when the capital costs price of the heat pump was at the high end of typical heat pump cost price ranges (100-1000 €/kW) [16].

Step No. 2: An energy, economic, and exergy (3-E) analysis was applied to a heat pump. The thermodynamic states of the heat pump were fixed by the outlet conditions of both the evaporator and the condenser. For both heat exchangers the pinch point temperature difference was set to 5 K with respect to the heat source and sink and conditions are assumed to be saturated [17]. When subcooling and super heating are considered using an internal heat exchanger, the amount of heat transferred was limited by the temperature at the outlet of the compressor to below 175 °C to limit the degradation of compressor lubricants and seals [3]. In the assessment, the exergy value of heat was omitted when assessing heat exchangers, as an exergy balance was made over both sides. The compressor's isentropic efficiency was stated to be 70% and its mechanical efficiency was 85%. The costs of the bare units, e.g., the heat exchangers, were based on their duty and cost functions. The bare unit costs were indexed to December 2022 with the Chemical Engineering Price Index (CEPI) [18] and converted into total costs of installation (TCI) using an installation factor to account for the cost of integrating the unit, contingencies, and other fees.

Step No. 3: Exergy-aided cost minimization was applied and the exergy losses were translated into additional operational costs [19]. Since the operational costs of a heat pump consist mainly of electricity consumption by the compressor, the amount of work required to compensate for the exergy destruction of a component can be translated to additional operational costs with the help of electricity costs and the number of operational hours.

Step No. 4: advancements to the evaluated heat pump cycles were made. The component whose performance caused the largest increase in operational costs was selected to be changed. This change was realized by adding one of the standard cycle's components; i.e., a compressor, an expansion valve, an internal heat exchanger, an ejector, a closed economiser, a flash tank, a desuperheater, a cascade condenser, or an expander. The selection among these components was based on the origin of the exergy destruction and the estimated costs of the design change. This was also done based on an energy analysis to benchmark the results of the exergy analysis. Once selected, a 3-E evaluation was done on the advanced configuration. The resulting component, together with the changes in exergy destruction, were used to evaluate the techno-economic validity of the change in the design. The performance of the advanced heat pump should have exceeded that of the e-boiler and the previously evaluated heat pump configurations. This performance is defined based on four performance indicators: 1. the total costs of ownership, 2. the initial investment, 3. the coefficient of performance, and 4. the total exergy destruction. Of these, the first two indicate the economic viability, whereas the third and fourth give insight into the technical and environmental performance of the proposed configuration, respectively.

To illustrate the application of the method, it was applied to a case study where 10 tonnes per hour (t/h) of 2 bar(a) pressure steam is produced from a water condensate steam of 50 kg/s and an initial temperature of 80 °C. This case study was selected for its common appearance in different industries like chemical, paper, and food production. All configurations were modelled using refrigerant R-1234ze(Z) due to its high critical point, low GDP and ODP [11].

2.2. Thermodynamic analysis

2.2.1. Energy balance

The basis of the energy balance was a consistent mass balance. For the simple cycle, the mass flow rate of the refrigerant (m_r) was defined by the heat transferred required in the condenser (Q_{cd}), the enthalpy after compression, and after condensation, as shown in Eq. (1):

$$Q_{cd} = m_r(h_{cd,in} - h_{cd,out}) \quad (1)$$

The refrigerant exited the condenser as a saturated liquid. All open systems were assumed to operate in a steady state and did not accumulate mass. This also holds in the case of a (flash) vessel, where an enthalpy balance defined the quality of the vapour and hence the mass ratio of its outgoing streams, and thereby the mass ratio between the top and bottom cycle.

Work added to the system (W_c) by the compressor based on the isentropic enthalpy difference (Δh_{is}) between the pressure stages and an isentropic efficiency (η_{is}) of 70%, as indicated in Eq. (2):

$$W_c = \frac{m_r \Delta h_{is}}{\eta_{is}} \quad (2)$$

The required amount of work by the compressor's drive (W_D) was based on a correction for electrical, volumetric, and mechanical losses based on overall motor efficiency (η_m) of 85%, as shown in Eq. (3):

$$W_D = \frac{W_c}{\eta_m} \quad (3)$$

The intermediate pressure (p_i) is corrected by 0.35 bar when multiple pressure stages are considered based on the work by Mateu-Royo et al. (2018), see Eq. (4):

$$p_i = \sqrt{p_1 p_2} + 0.35 \quad (4)$$

where p_1 and p_2 are the pressures before and after the compressor, respectively. Pressure relief in expansion valves is considered isenthalpic. Other forms of pressure loss are neglected, as well as heat losses. The coefficient of performance (COP) of the heat pump was based on the heat delivered at the condenser and the work required by the compressor's drive, as shown in Eq. (5):

$$COP_{hp} = Q_{cd}/W_D \quad (5)$$

The energy balance of the heat pump was closed by defining the required thermal duty of the evaporator as the difference between the duties of the condenser and the compressor.

2.2.2. Exergy balance

The influx of exergy (Ex_{in}) equals the outflux of exergy (Ex_{out}) plus exergy losses. The loss of exergy is the sum of internal exergy destruction (Ex_{des}) and transfer of exergy to external sources [20]. Since heat loss to the environment was neglected and all heat transferred from the heat pump to the environment is valuable, the exergy balance simplifies to Eq. (6):

$$Ex_{des} = \Sigma Ex_{in} - \Sigma Ex_{out} \quad (6)$$

Exergy destruction will be zero in the case of an ideal operation. In that case, the exergy flowing into the system in the form of heat at the evaporator and work by the compressor is equivalent to the exergy of the outflow of heat at the condenser. The exergy value of the streams is defined by the enthalpy (H) and entropy (S) of the stream shown in Eq. (7) [21]:

$$Ex = H - H_0 - T_0(S - S_0) \quad (7)$$

Where subscript "0" denoted the reference state at T_0 = 298,15 K and p_0 = 101325 Pa. Substituting Eq. (7) in Eq. (6) and accounting for the exergy value of heat: $Q(1 - T_0/T)$ at a thermodynamic mean temperature and that of work: W, results in Eq. (8):

$$Ex_{des} = \left(1 - \frac{T_0}{T}\right) Q + W - [H_2 - H_1 - T_0(S_2 - S_1)] \quad (8)$$

Exergy destruction due to mechanical losses in the drive was taken as equivalent to the loss of work during transfer.

2.3. Costs equations

The total cost of ownership and the total capital investment are taken as the key performance indicators for the economic evaluations. These costs are based on the indexed bare unit costs of the components, the cost

of installation, and operation. The bare unit costs ($C_{0,p}$) required for the heat pump's components were based on the costs function provided by Zuhlsdorf et al. (2019), which is presented in Eq (9):

$$\log(C_{0,p}) = k_1 + k_2 \log x + k_3 (\log x)^2 \quad (9)$$

where "x" is the scaling parameter of a certain technology and "k_i" is a calibrated value. Table 1. shows the used values adapted from Zuhlsdorf et al., [17].

Table 1. Parameters for estimation of component capital costs according to Zuhlsdorf et al., [17]

Component	Scaling Parameter X	Range	k_1	k_2	k_3	f_{cepi}	f_{bm}
Centrifugal compressor	Fluid power	450 - 3000 kW	2.2897	1.13604	-0.1027	2.3749	2.8
Drive	Shaft power	75 - 2600 kW	1.9560	1.7142	-0.2282	2.3749	1.5
Plain vessel	Volume	1 – 800 m^3	3.5970	0.2163	0.0934	2.0793	3.0
Shell & tube heat exch.	Area	10 – 900 m^2	3.2476	0.2264	0.0953	2.0793	3.2
Radial turbine	Fluid power	100 – 1500 kW	2.2476	1.4965	-0.1618	2.3749	3.5

These values were homogenized into the equivalent costs of the components for December 2022 with f_{cepi} based on the Chemical Engineering Price Index (CEPI) [18]. Bare module costs were converted into total capital investment (TCI) using the installation costs factor (f_{IF}), as shown in Eq. (10):

$$TCI_p = C_{0,p} f_{cepi} f_{IF} \quad (10)$$

For the centrifugal compressor and its drive, Eq. (4) was used as input for the scaling parameter by either including or excluding η_m, respectively. The resulting costs were benchmarked to the costs data provided in the DACE-booklet [22] and found to be plausible. In case multiple compressors were used, their scaling parameters were combined to account for the economics of scale. Their respective costs were based on the ratio between the scaling factor of the individual component and the scaling factor of the combined components. The volume of a vessel was based on being able to supply the outlet streams for 10 minutes without an influx of new refrigerant. The heat exchanging area (A) of the heat exchangers was calculated using Eq. (11):

$$Q_{hx} = U \cdot A \cdot \Delta T_{lm} \quad (11)$$

where "U" is the heat transfer coefficient and ΔT_{lm} is the logarithmic mean temperature difference between the hot and cold streams. A heat transfer coefficient of 1000 W/m^{2}K is used for heat transfer between a liquid and an evaporating liquid and 1250 W/m^{2}K was used when both sides were changing phases [17]. The total costs of the installation were equal to the sum of all the TCI of the components. This value is expressed as a factor of the condenser duty for benchmarking purposes.

The operational costs of the heat pump were defined to be equivalent to the electricity consumption by the compressor. Hence, the amount of work required to compensate for the exergy destruction of a component was translated to costs (c_i) by using electricity costs (c_{el}), and the number of operational hours in a certain period (t), as indicated in Eq. (12):

$$C_i = Ex_{des,i} \cdot c_{el} \cdot t \quad (12)$$

herein, the payback time of the process change should be less than five years of full-time operation or 40,000 hours. The costs resulting from non-ideal operation of the components were listed in descending order.

3. Results

Exergy-based cost minimization is used to advance the design of the heat pump. The performance of an ideal heat pump is compared to that of an e-boiler to indicate whether a heat pump would be an economically viable alternative. Thereafter, the performance of a single stage subcritical heat pump, a simple cycle, is assessed. Alterations to this base design are suggested based on its energetic and exergetic performance. The techno-economic performance of these advanced designs is thereafter compared.

3.1. Costs targets for a steam generating heat pump

To identify the techno-economic best heat pump configuration, an exploration of its technical surroundings and technical competitor, of the e-boiler was carried out. Producing 10 t/h of 2.0 bar(a) steam with an e-boiler required 6.5 MW of electricity. Based on the assumed bare unit costs of 165 €/kW and an installation factor of 3 this resulted in the costs as listed in Table 2. The total costs of ownership of the heat pump must be below that of the e-boiler to be competitive. In an ideal operation, this heat pump required 1.0 MW to operate, or 1.7 M€. Hence, the total installed costs must be below 12.3 M€, or 625 €/kW$_{th}$, which seemed

plausible based on the benchmarked 100-1000 €/kW_{th} [22]. The heat pump would then operate with a COP of 6.38 and reduce electricity consumption by 85%.

Table 2. Costs comparison of an ideal e-boiler with an ideal heat pump based on 5 years of operation, 8000 h/year, and an electricity price of 0.041 €/kWh – iterated values in italic

Unit	Supplied power [MW_{th}]	Required power [MW_e]	Specific costs [€/kW_x]	Bare unit costs [M€]	Total installed costs [M€]	Operational costs [M€]	Total costs of ownership [M€]
e-boiler	6.5	6.5	165	1.1	3.2	10.8	14.1
Heat pump	6.5	1.0	<625	<4.1	<12.3	<1.7	<14.1

3.2. Energy, Exergy, and Economic (3-E) performance assessment of a simple heat pump

The layout of a simple, single stage subcritical, heat pump thermodynamically consists of an evaporator, compressor, condenser, and expansion valve. The results of the 3E analysis of this cycle are presented in Table 3. These results show that the compressor's drive is the largest energy consumer. The electric drive of the compressor required 2.9 MW, and the COP was therefore 2.3. Hence, 1.9 MW is required to compensate for exergy destruction compared to the ideal heat pump. No costs were assigned to the expansion valve as the required capital investment was two orders of magnitude less than the other components. The compressor and its electric drive cost 3.2 M€ and made up for more than 70% of the total installed costs. Total costs of ownership (TCO) of 9.2 M€ were based on the electricity consumption of the drive and the total installed costs. The economic performance of the simple heat pump is a cost competitive option to the e-boiler, with a bare module cost of 234 €/kW.

The energy analysis presented in Table 3 highlights that work is solely required by the compressor and its driver. Consequently, enhancing the compressor's efficiency emerges as a viable solution based on the energy analysis. However, when subjected to exergy analysis, it is revealed that the expansion valve is responsible for the majority of exergy destruction, accounting for 689 kW (or 37% of total exergy destroyed) and incurring operational losses of over 1.1 M€. In addition, both the compressor and its drive account for 53% of the total 1848 kW destroyed. As a result, modifying the process to utilize the work potential before the expansion valve, and thereby reduce work requirement, is viewed as a promising avenue for improving the cycle based on the exergy analysis.

Table 3. 3E-evaluation of a simple cycle heat pump based on 5 years of operation, 8000 h/year, and an electricity price of 0.041 €/kWh.

Component	Heat transfer [MW]	Required power [MW]	Exergy destruction [kW]	Operational losses [k€]	Scaling factor [X]	Indexed bare unit costs [k€]	TCI [k€]	TCO [M€]
Evaporator	4.1	0.0	95	156	278	161	514	
Compressor	0.0	2.4	545	894	2,448	724	2,028	
Drive	0.0	2.9	432	708	2,880	412	1,153	
Condenser	6.6	0.0	87	142	1,054	248	792	
Exp. Valve	0.0	0.0	689	1,131				
Total			1,848	3,031		1,544	4,488	9,2

3.3. Improving the heat pump configuration

Increasing the efficiency of the compressor, as suggested by the energy-analysis, was pursued in advanced configuration No. 1 (Figure 1.A.), which depicts the common [4, 8] configuration of sequential compression with intermediate cooling to improve upon the compressor's efficiency. Utilization of the exergy before the expansion valve, as suggested by the exergy analysis, was pursued with advanced configurations No. 2 (Figure 1.B.) and No. 3 (Figure 1.C.). The aim of advanced configuration No. 2 is to use the exergy available before the expansion valve to reduce work requirements by the compressor with the help of an internal heat exchanger (IHX), also known as a closed economizer. Various authors cite this option as an interesting configuration due to its low equipment costs [23]. Advanced configuration No. 3 was designed to utilize the exergy before the expansion valve and to increase the compressor's efficiency by reducing the temperature of the pressure gas after the first compressor and utilizing the exergy available after the condenser [24]. All three configurations are well-established in current practices and have a relatively high performance [8].

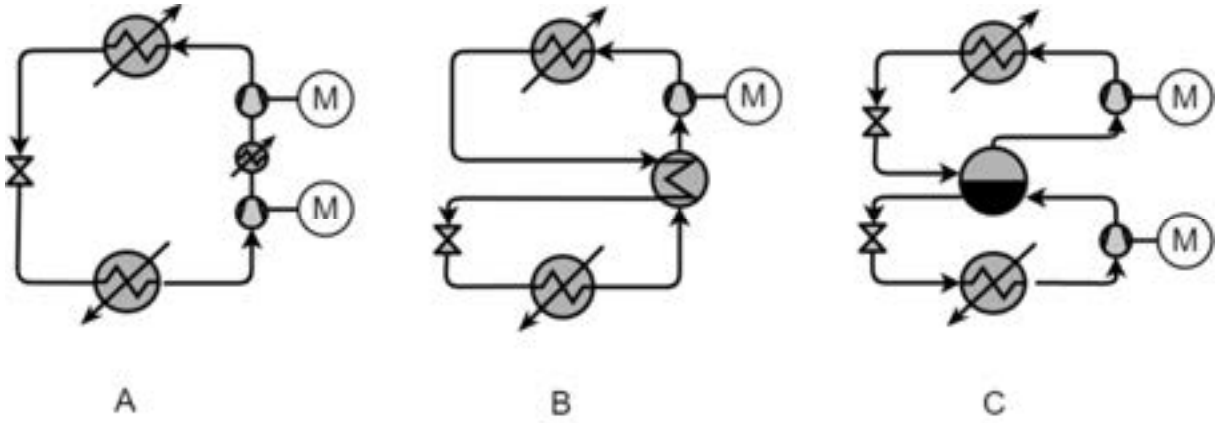

Figure. 1. Overview of advanced configurations. A) Advanced configuration No. 1: the reference simple cycle updated with an additional compressor and intermediate intercooler, B) Advanced configuration No. 2: the reference simple cycle updated with an internal heat exchanger (IHX), and C) Advanced configuration No. 3: the reference simple cycle updated with an open economizer.

3.3.1. Advanced configuration No. 1: Two stage compression with intermediate intercooling

The introduction of a second compression stage with an intermediate cooling step reduced the COP from 2.3 to 2.2, as work requirements by the driver increased to a total of 2.6 MW (Table 4.). Exergy losses are dominated by the expansion valve at 641 kW, or 32%. However, combined losses in both compressors and drives account for 1,042 of the total 2,016 kW exergy destroyed, or 53%. Though the specific work requirements by the compressor were slightly reduced by the intermediate cooling step, these gains are negated by the required increase in refrigerant mass flow to meet the energy demand in the condenser. This is partially a result of not being able to utilize the apparent heat in the intercooler due to its relatively low temperature of 92 – 89 °C and an initial sink temperature of 80 °C with an advised minimal temperature difference of at least 5 K [17]. Due to the higher work requirements and the additional investment, the total cost of ownership of this configuration is higher than that of the simple cycle. The total installed costs of the configuration are 5.3 M€, with a TCO of 10.3 M€, or 255 €/kW as a bare module.

Table 4. 3E-evaluation of advanced heat pump configuration No. 1 with two compression stages and intermediate cooling based on 5 years of operation, 8000 h/year, and an electricity price of 0.041 €/kWh.

Component	Heat transfer [MW]	Required power [MW]	Exergy destruction [kW]	Operational losses [k€]	Scaling factor [X]	Indexed bare unit costs [k€]	TCI [k€]	TCO [M€]
Evaporator	4.3	0.0	174	286	282	161	516	
Compressor 1	0.0	1.4	343	563	1,392	397	1,112	
Drive 1	0.0	1.6	246	403	1,637	223	625	
intercooler	0.3	0.0	55	90	102	121	388	
Compressor 2	0.0	1.2	264	433	1,183	338	946	
Drive 2	0.0	1.4	209	342	1,392	190	946	
Condenser	6.6	0.0	84	138	1,054	248	792	
Exp. Valve	0.0	0.0	641	1,052				
Total			2,016	3,307		1,678	5,325	10.3

3.3.2. Advanced configuration No. 2: Internal heat exchanger

The addition of an internal heat exchanger (IHX) is a viable option to significantly increase the overall performance of the heat pump, leading to a reduction in the total costs of ownership (TCO) by 0.5 M€ in comparison to the simple cycle. Although the installation of the IHX increases the initial installed costs by 0.5 M€, the reduction in the size of the compressor and electric drive results in savings of 135 k€ in installed costs and a reduction of 0.8 M€ in operational costs after 5 years (Table 4.). The total cost of ownership for the heat pump with the IHX is 8.7 M€ or 249 €/kW as a bare module.

The lower operational cost is primarily attributed to the increase in the COP to 2.8 from 2.3, resulting from the addition of the IHX. This decrease in the work required by the drive from 0.6 MW to 2.3 MW is the main reason behind the increase in the COP. The total exergy destruction was reduced by 490 kW to 1,358 kW, with the compressor contributing the most to the total exergy destruction at 379 kW (28%), followed by its

driver at 351 kW (25%), and the condenser at 476 kW (22%). The exergy destruction became evenly distributed among the components with the introduction of the IHX. The increase in exergy in the evaporator is due to the higher COP, requiring more energy from the sink and a temperature drop from 55 to 54 °C of the source. The exergy destruction in the condenser significantly increases due to its high inlet temperature, which is increased by superheating the suction gas before the compressor with the IHX. The introduction of the IHX led to an exergy destruction of 64 kW.

Table 5. 3E-evaluation of advanced heat pump configuration No. 2 with an internal heat exchanger based on 5 years of operation, 8000 h/year, and an electricity price of 0.041 €/kWh.

Component	Heat transfer [MW]	Required power [MW]	Exergy destruction [kW]	Operational losses [k€]	Scaling factor [X]	Indexed bare unit costs [k€]	TCI [k€]	TCO [M€]
Evaporator	4.6	0.0	195	319	288	162	520	
Compressor	0.0	2.0	379	621	1,991	682	1,909	
Drive	0.0	2.3	351	576	2,342	406	1,137	
IHX	2.3	0.0	64	105	185	143	456	
Condenser	6.6	0.0	290	476	1,054	248	792	
Exp. Valve	0.0	0.0	79	130				
Total			1,358	2,227		1,640	4,814	8.7

3.3.3. Advanced configuration No. 3: Two stage heat pump with open economizer

The addition of an open economizer splits work requirements over two compressors with a combined duty of 2 MW, or 2.4 MW at the electric drive. Hence, the required 6.6 MW at the condenser can be delivered with a COP of 2.8. Exergy destruction is evenly distributed among the components. The second stage compressor was the main source of exergy destruction at 269 kW (19% of total exergy destroyed), followed by its drive at 212 kW (15%) and the expansion valve directly after the condenser at 207 kW (15%). Together with the first stage and their drives, the compressors accounted for 60% of total exergy destruction, compared to 21% of both expansion valves, with a total of 1,4 MW destroyed. The exergy destruction in the evaporated increased by 100 kW as more heat is transferred. The intermediate cooling in the vessel slightly reduced exergy destruction in the condenser compared to the simple cycle. The vessel itself also has a negligible amount of exergy destruction, when considering heat transfer between the top and bottom cycle. Exergy destruction in the expansion valves went from 689 kW in the simple cycle to 294 kW for both valves. As a result, total exergy destruction was reduced by 445 kW. The reduced size of the compressors and electric drive reduced investment costs by 43 k€. However, the installation of the vessel requires an additional 0.55 M€. The TCO is 8.8 M€, or 255 €/kW as a bare module. Hence, the initial investment increases compared to the simple cycle, but the increased efficiency mitigates the impact of operational costs and reduced the TCO by 0.4 M€ during the five years.

Table 6. 3E-evaluation of advanced heat pump configuration No. 3 with an open economizer and two stage compression based on 5 years of operation, 8000 h/year, and an electricity price of 0.041 €/kWh.

Component	Heat transfer [MW]	Work transfer [MW]	Exergy destruction [kW]	Operational losses [k€]	Scaling factor [X]	Indexed bare unit costs [k€]	TCI [k€]	TCO [M€]
Evaporator	4.5	0	192	314	287	162	519	
Compressor 1.	0	0.8	204	335	826	279	781	
Driver 1.	0	1.0	146	239	972	165	463	
Vessel	5.4	0	1	2	690	183	548	
Compressor 2.	0	1.2	269	442	1,207	407	1,140	
Driver 2.	0	1.4	213	349	1,420	241	676	
Condenser	6.6	0	84	138	1,054	248	792	
Exp. Valve 1.	0	0	207	339		2		
Exp. Valve 2.	0	0	87.4	143		162		
Total			1,403	2,301		1,685	4,919	8.8

4. Discussion

The central question of this study was whether an exergy-based economic analysis provides a solid basis for identifying improvements to a heat pump's configuration. This question is answered by first evaluating the quality of the output and thereafter discussing the usability of the method.

4.1. Quality of output

The approach described in this paper yields outputs in two phases. Firstly, the feasibility of an ideal heat pump is compared to an e-boiler based on the findings of section 3.1. The second phase involves modifying the heat pump's configuration to improve its techno-economic performance, based on the results of sections 3.2 and 3.3. It is worth noting that advanced configuration No. 1 is not included in this evaluation, as it was the outcome of design changes stemming from an energy analysis.

The first phase provides a broad indication of the feasibility of a heat pump compared to an e-boiler. The simplicity of this approach makes it inherently vulnerable to the quality of the data input. For example, changes in the installation costs factor or the costs of electricity are likely to move the solution in a certain direction. A “plug-and-play” e-boiler design is likely to reduce the installation costs factor, which will result in the capital costs being a smaller percentage of the TCO, and a lower TCO overall. Changes in the electricity price can have a similar impact on the decision between an e-boiler and a heat pump, as an e-boiler uses more electricity. The easiness of the approach makes it a valuable tool for a first assessment and conducting a sensitivity analysis will aid in exploring tipping points in the decision-making process. Moreover, additional considerations like the size of the grid connection and the dynamic behavior of both systems should be considered when comparing these techniques.

The second phase explored the advancement of the simple cycle heat pump configuration. This option is already an economically interesting alternative based on its COP of 2.3 and a bare unit cost of 234 €/kW compared to a COP >1 and a bare unit cost of 165 €/kW for the e-boiler. The TCO of the simple cycle is 9.2 M€ after 5 years of full-time operation, which is significantly less than the 14.1 M€ of the e-boiler. The expansion valve is the largest single source of exergy destruction in the simple cycle, as it accounts for 37% of the total exergy destruction. This is in line with the findings of Bergamini [10] and Hu [11]. Moreso the COP of 2.3 compared to the listed COP of 1.7 to 2.3 when transferring heat at 60 to 100 °C to a heat sink of 140 °C by Adamson et al. [8]. However, when considering the compressor (29%) and its drive (23%) as a single operational unit, they become the dominant source of exergy destruction at a combined 53%, on a total exergy destruction of 1,85 MW. Exergy destruction by the compressor’s drive is quite significant, despite its efficiency of 85%. This impact can be explained by the high exergy-value of the drive’s energy, work. The drive’s losses are entirely dependent on its duty and electric, volumetric, and mechanical efficiency. Hence, after the duty is reduced by advancing the cycle, this destruction could be reduced by more advanced mechanical equipment.

The addition of the internal heat exchanger reduced the amount of work that must be delivered to the compressor compared to the simple heat pump and increased the COP from 2.3 to 2.8. This is 22% larger than the 2.3 reported by Adamson et al. [8] at the same temperature lift with the same working media. This difference is the result of the 20 °C higher condenser temperature in the case of Adamson’s findings. This highlights the sensitivity of a heat pump's techno-economic performance to the temperature of the heat source and sink.

Advancing the simple cycle heat pump with an internal heat exchanger seems to be the preferred route compared to the open economizer, as it has similar operational (and emission) savings at a lower cost. This is in part due to the high efficiency with which the IHX can utilize the work potential compared to the vessel and the lower unit costs. This outcome is the opposite of what is expected based on the commonly found link between higher exergy efficiency and capital costs, as mentioned by Rosen and Dincer [25]. One possible explanation for this discrepancy is that the use of a constant compressor efficiency in the analysis does not account for the volumetric efficiency gains offered by the open economizer. Overall, the analysis highlights the importance of considering a detailed unit operation when evaluating the performance and economic feasibility of heat pump configurations.

4.2. Usability of exergy-based costs minimization

The starting point of this study was that a framework is needed that aids in identifying advanced configurations that improve the techno-economic performance of a considered heat pump and help decision-makers in their quest to identify techno-economically feasible options. The proposed approach helps visualize where losses manifest together with their accompanying costs. This is different from an energy analysis, which will only be able to account for the costs of the operation of the drives and the profits from supplying heat to the condenser. Advanced configuration No. 1., where an additional compression stage and intermediate cooling are added to the simple cycle design, is a logical result of energy analysis, as it uses a common strategy to improve upon the efficiency of the compressor. However, the changes did not increase techno-economic performance in this case study. Moreso, it reduced the COP by 0.1, increased exergy destruction by 168 kW, increased the total capital investment by 837 k€, and increased the total cost of operation by 1.1 M€. Hence, reducing the overall performance of the simple cycle heat pump. Another route based on the outcomes of an energy analysis would be to buy a more efficient compressor and drive. For these upgrades to be economically competitive with the second advanced configuration with the internal heat exchanger, the overall motor efficiency must increase from 85% to 95% and the isentropic efficiency from 70% to 85%, whilst the cost increase of the compressor increases is limited to 13%.

In contrast, both design changes based on exergy analysis improved the techno-economic performance of the simple cycle heat pump. However, both advanced options still had an exergy destruction of 1.4 MW. The degree to which this can be reduced is currently unknown.

5. Conclusions and recommendations

Exergy based economic analysis can be used to identify techno-economic improvements to a steam generating heat pump. Not only was the method able to quickly assess the boundaries to its economic performance compared to other technologies (e.g., an e-boiler), but also improved on the technical performance of a single stage subcritical heat pump layout, whereas suggestions by an energy analysis were not.

The exergy-based costs minimization method identified the expansion valve as the source of most operational costs, as it accounts 37% of the total exergy destruction. However, the compressor and its drive combined contributed 53%. The work potential available before the expansion valve can be used to improve on the compressor efficiency by either a closed or an open economizer. The closed economizer, or internal heat exchanger, increased the heat pump's COP from 2.3 to 2.8 at the cost of an additional investment of 0.5 M€. This additional investment reduces the total costs of ownership by 0.6 M€ after five years of operation. The open economizer also increased the COP from 2.3 to 2.8 and required an additional investment of 0.5 M€. The total costs of ownership are reduced by 0.4 M€ after five years of operation. The approach thus succeeded in identifying techno-economically beneficial process changes and helped to produce two options that both increased the technical and economic performance of the heat pump, whereas the energy-based approach did not.

However, the exergy-based approach only pinpoints the exergy destruction that could be utilized. It is not able to identify how much the exergy destruction could be reduced. A variation of exergy analysis link *Advanced exergy analysis* as proposed by Tsatsaronis [20] may aid in this process. Moreover, the method does not suggest the technology that should be selected. Hence an extension of the framework is needed in which a strong link is made between the techno-economic performance gains of an additional component and the operational context of the heat pump. The same holds for a link to other working media, where a link between the gradient of the isentropic curves and exergy destruction is a likely candidate based on the presented results (i.e., the two stage compressor with intermediate cooling requiring more work). Lastly, it is recommended to use a more detailed thermodynamic analysis of the operational units to provide a fair basis for the comparison of added components. The assumption of a constant isentropic efficiency is likely to skew the presented results.

Acknowledgments

This research publication is partly financially funded by the Dutch Government office for Enterprising (RVO) within the framework of the Mission-driven Research, development, and innovation funds (MOOI) under the project title: "THIO – The Heat is On" under the lead of the Dutch Institute for Sustainable Process industry (ISPT).

Nomenclature

A	heat exchanger area (m2)
C	costs (€)
COP	Coefficient of Performance
Ex	Exergy [kJ/kg]
f	factor (-)
h	enthalpy [kJ/kg]
IHX	internal heat exchanger
K	Costs factor (-)
m	mass flow rate [kg/s]
q	heat transfer rate [kW]
S	Entropy [kJ/kgK]
T	Temperature [K]
t	time (s)
TCI	Total capital investment (€)
TCO	Total costs of ownership (€)
U	heat transfer coefficient [W/m2K]
W	Work/power [kW]

Subscripts & superscripts

0,p	bare unit value of component "p"
c	compressor
cd	condenser
CEPI	Chemical Engineering Plant Costs Index
d	drive
des	destruction
el	electricity
evap	evaporator
hp	heat pump
hx	heat exchanger
i	intermediate
if	installation factor
in	influx
is	isentropic
lm	logarithmic mean
m	mechanical

X	scaling factor	*out*	outflux
Greek symbols		*r*	refrigerant
η	efficiency		
Δ	difference		

References

[1] Marina A., et al., An estimation of the European industrial heat pump market potential. Renewable and Sustainable Energy Reviews, 2021. 139: p. 110545.

[2] Bless F., et al., Theoretical analysis of steam generation methods-Energy, CO2 emission, and cost analysis. Energy, 2017. 129: p. 114-121.

[3] Mateu-Royo C., et al., Advanced high temperature heat pump configurations using low GWP refrigerants for industrial waste heat recovery: A comprehensive study. Energy conversion and management, 2021. 229: p. 113752.

[4] Cao X.Q., et al., Performance analysis of different high-temperature heat pump systems for low-grade waste heat recovery. Applied Thermal Engineering, 2014. 71(1): p. 291-300.

[5] Schlosser F., et al., Large-scale heat pumps: Applications, performance, economic feasibility and industrial integration. Renewable and Sustainable Energy Reviews, 2020. 133: p. 110219.

[6] Arpagaus C., et al., Multi-temperature heat pumps: A literature review. International Journal of Refrigeration, 2016. 69: p. 437-465.

[7] Arpagaus C., et al., High temperature heat pumps: Market overview, state of the art, research status, refrigerants, and application potentials. Energy, 2018. 152: p. 985-1010.

[8] Adamson K.M., et al., High-temperature and transcritical heat pump cycles and advancements: A review. Renewable and Sustainable Energy Reviews, 2022. 167: p. 112798.

[9] Oluleye G., et al., Evaluating the potential of process sites for waste heat recovery. Applied Energy, 2016. 161: p. 627-646.

[10] Bergamini R., Jensen J.K., and Elmegaard B., Thermodynamic competitiveness of high temperature vapor compression heat pumps for boiler substitution. Energy, 2019. 182: p. 110-121.

[11] Hu P., et al., Energy and exergy analysis of a ground source heat pump system for a public building in Wuhan, China under different control strategies. Energy and Buildings, 2017. 152: p. 301-312.

[12] Moran M.J., Fundamentals of exergy analysis and exergy-aided thermal systems design. Thermodynamic optimization of complex energy systems, 1999: p. 73-92.

[13] Wang M., et al., Exergoeconomic performance comparison, selection and integration of industrial heat pumps for low grade waste heat recovery. Energy Conversion and Management, 2020. 207: p. 112532.

[14] Wang Y., Yin Y., and Cao F., Comprehensive evaluation of the transcritical CO2 ejector-expansion heat pump water heater. International Journal of Refrigeration, 2023. 145: p. 276-289.

[15] Planbureau voor de Leefomgeving, Klimaat-en Energieverkenning 2022. 2022.

[16] Zuhlsdorf B., Task 1: Technologies – State of the art and ongoing developments for systems and components, in About High Temperature Heat Pumps. 20, International Energy Agency: https://heatpumpingtechnologies.org/annex58/task1/.

[17] Zühlsdorf B., et al., Analysis of technologies and potentials for heat pump-based process heat supply above 150 C. Energy Conversion and Management: X, 2019. 2: p. 100011.

[18] Statistics U.S.B.o.L. Databases, Tables & Calculators by Subject - Inflation & Prices. 2022 [cited 2023 21/02/2023]; Available from: https://www.bls.gov/data/.

[19] Tsatsaronis G. and Moran M.J., Exergy-aided cost minimization. Energy Conversion and Management, 1997. 38(15-17): p. 1535-1542.

[20] Tsatsaronis G., Recent developments in exergy analysis and exergoeconomics. International Journal of Exergy, 2008. 5(5-6): p. 489-499.

[21] Moran M. and Sciubba E., Exergy analysis: principles and practice. 1994.

[22] DACE Cost Engineers, DACE Price Booklet Vol. 33. 2021.

[23] Kosmadakis G., et al., Techno-economic analysis of high-temperature heat pumps with low-global warming potential refrigerants for upgrading waste heat up to 150° C. Energy Conversion and Management, 2020. 226: p. 113488.

[24] Mateu-Royo C., et al., Experimental exergy and energy analysis of a novel high-temperature heat pump with scroll compressor for waste heat recovery. Applied Energy, 2019. 253: p. 113504.

[25] Rosen M. and Dincer I., Exergy–cost–energy–mass analysis of thermal systems and processes. Energy Conversion and Management, 2003. 44(10): p. 1633-1651.

[26]
1. Marina, A., et al., *An estimation of the European industrial heat pump market potential.* Renewable and Sustainable Energy Reviews, 2021. **139**: p. 110545.
2. Bless, F., et al., *Theoretical analysis of steam generation methods-Energy, CO2 emission, and cost analysis.* Energy, 2017. **129**: p. 114-121.
3. Mateu-Royo, C., et al., *Advanced high temperature heat pump configurations using low GWP refrigerants for industrial waste heat recovery: A comprehensive study.* Energy conversion and management, 2021. **229**: p. 113752.
4. Cao, X.-Q., et al., *Performance analysis of different high-temperature heat pump systems for low-grade waste heat recovery.* Applied Thermal Engineering, 2014. **71**(1): p. 291-300.
5. Schlosser, F., et al., *Large-scale heat pumps: Applications, performance, economic feasibility and industrial integration.* Renewable and Sustainable Energy Reviews, 2020. **133**: p. 110219.
6. Arpagaus, C., et al., *Multi-temperature heat pumps: A literature review.* International Journal of Refrigeration, 2016. **69**: p. 437-465.
7. Arpagaus, C., et al., *High temperature heat pumps: Market overview, state of the art, research status, refrigerants, and application potentials.* Energy, 2018. **152**: p. 985-1010.
8. Adamson, K.-M., et al., *High-temperature and transcritical heat pump cycles and advancements: A review.* Renewable and Sustainable Energy Reviews, 2022. **167**: p. 112798.
9. Oluleye, G., et al., *Evaluating the potential of process sites for waste heat recovery.* Applied Energy, 2016. **161**: p. 627-646.
10. Bergamini, R., J.K. Jensen, and B. Elmegaard, *Thermodynamic competitiveness of high temperature vapor compression heat pumps for boiler substitution.* Energy, 2019. **182**: p. 110-121.
11. Hu, P., et al., *Energy and exergy analysis of a ground source heat pump system for a public building in Wuhan, China under different control strategies.* Energy and Buildings, 2017. **152**: p. 301-312.
12. Moran, M.J., *Fundamentals of exergy analysis and exergy-aided thermal systems design.* Thermodynamic optimization of complex energy systems, 1999: p. 73-92.
13. Wang, M., et al., *Exergoeconomic performance comparison, selection and integration of industrial heat pumps for low grade waste heat recovery.* Energy Conversion and Management, 2020. **207**: p. 112532.
14. Wang, Y., Y. Yin, and F. Cao, *Comprehensive evaluation of the transcritical CO2 ejector-expansion heat pump water heater.* International Journal of Refrigeration, 2023. **145**: p. 276-289.
15. voor de Leefomgeving, P.P., *Klimaat-en Energieverkenning 2022.* 2022.
16. Zuhlsdorf, B., *Task 1: Technologies – State of the art and ongoing developments for systems and components*, in *About High Temperature Heat Pumps*. 20, International Energy Agency: https://heatpumpingtechnologies.org/annex58/task1/.
17. Zühlsdorf, B., et al., *Analysis of technologies and potentials for heat pump-based process heat supply above 150 C.* Energy Conversion and Management: X, 2019. **2**: p. 100011.
18. Statistics, U.S.B.o.L. *Databases, Tables & Calculators by Subject - Inflation & Prices*. 2022 [cited 2023 21/02/2023]; Available from: https://www.bls.gov/data/.
19. Tsatsaronis, G. and M.J. Moran, *Exergy-aided cost minimization.* Energy Conversion and Management, 1997. **38**(15-17): p. 1535-1542.
20. Tsatsaronis, G., *Recent developments in exergy analysis and exergoeconomics.* International Journal of Exergy, 2008. **5**(5-6): p. 489-499.
21. Moran, M. and E. Sciubba, *Exergy analysis: principles and practice.* 1994.
22. Engineers, D.A.o.C., *DACE Price Booklet* Vol. 33. 2021.
23. Kosmadakis, G., et al., *Techno-economic analysis of high-temperature heat pumps with low-global warming potential refrigerants for upgrading waste heat up to 150° C.* Energy Conversion and Management, 2020. **226**: p. 113488.
24. Mateu-Royo, C., et al., *Experimental exergy and energy analysis of a novel high-temperature heat pump with scroll compressor for waste heat recovery.* Applied Energy, 2019. **253**: p. 113504.
25. Rosen, M. and I. Dincer, *Exergy–cost–energy–mass analysis of thermal systems and processes.* Energy Conversion and Management, 2003. **44**(10): p. 1633-1651.

[27]

PROCEEDINGS OF ECOS 2023 - THE 36TH INTERNATIONAL CONFERENCE ON
EFFICIENCY, **C**OST, **O**PTIMIZATION, **S**IMULATION AND ENVIRONMENTAL IMPACT OF ENERGY SYSTEMS
25-30 JUNE, 2023, LAS PALMAS DE GRAN CANARIA, SPAIN

Data-driven Modelling of Supermarket Refrigeration Systems for Model Predictive Control Applications

Max Bird[a], Salvador Acha[b], Emilio José Sarabia Escriva[c] and Nilay Shah[d]

[a] *Imperial College London, United Kingdom, max.bird16@imperial.ac.uk, CA*
[b] *Imperial College London, United Kingdom, salvador.acha@imperial.ac.uk*
[c] *Universitat Politècnica de València, Spain, emsaes@upv.edu.es*
[d] *Imperial College London, United Kingdom, n.shah@imperial.ac.uk*

Abstract:

With uncertainty in energy markets, and the effects of climate change looming, reducing energy use and operational cost of existing building systems is more important than ever. To this end, this paper presents a grey-box modelling approach to characterise the behaviour of chilled and frozen and coldrooms using basic system specifications and measured data. An overall energy balance is used to devise a discrete state space model for each cabinet, characterised by unknown empirical parameters relating to heat capacity and heat transfer properties. Historical system data from a UK supermarket are used in combination with a genetic algorithm optimisation to determine the optimal empirical parameters for 10 display cases and 10 coldrooms. The resulting cabinet temperature predictions have a good level of accuracy, achieving a root-mean squared error (RMSE) of 0.37℃ to 0.98℃. Overall this data-driven approach is effective and efficient in modelling refrigeration systems, and can be easily generalised to any system where historical data is available. Finally, the use of the proposed approach in cost minimisation or demand response application is presented.

Keywords:

Supermarket, Refrigeration, Genetic Algorithm, Model Predictive Control, Demand Response

1. Introduction

Commercial refrigeration systems are highly energy intensive and can be responsible for up to 40-60% of a supermarket's overall electricity use [1]. As such, there is clear motivation to reduce energy use and operating costs of such systems through smart control applications. At a high level these control schemes aim to utilise the thermal capacity of refrigerated foodstuffs to shift cooling requirements to low-price or low overall grid demand periods based typically on real-time energy prices to minimise operating costs [2], [3] or demand-side response scenarios [4], [5] to alleviate periods of high grid demand. Such control methods often require simulation models in order to test and calibrate the proposed approach ahead of real-world deployment, which motivates a better understanding of the data requirements and best practices for developing such a model.

A popular refrigeration modelling approach is discussed in [6], which presents 3 separate sub-models to characterise the performance of the chilled cabinets, suction manifold and condenser. A grey-box approach is used to devise the fundamental mass and energy balances across the sub-systems, for which empirical constants are then fit using historical data via an iterative prediction-error minimization (PEM) method. Optimal empirical parameters and temperature fitting results are presented for 7 chilled cabinets, but deliberately excludes behaviour during defrost periods and doesn't consider frozen cabinets. This limits the application of the method to control of real-world systems. An alternative grey-box modelling approach is presented in [7], which uses a state-space model derived from thermodynamic heat and mass balances of individual cabinets and evaporators. Model parameters were estimated using a maximum likelihood estimation approach, based on 2.5 years of minutely telemetry from 6 chilled and 4 frozen units. The approaches lumps the cabinet air and food temperatures together, preventing individual tracking of food temperature which is a key variable to monitor in control applications.

This paper demonstrates a grey-box modelling approach to model temperature dynamics in commercial chilled and frozen cabinets. This is achieved using a genetic algorithm to fit unknown physical parameters for individual cabinets, demonstrated using a UK supermarket as a case study. The method improves over existing literature by modelling temperature dynamics during defrost cycles, as well as explicitly accounting for electric defrost elements present in frozen units.

2. Case Study

2.1. System Description

This paper uses two identical R744 CO_2 booster refrigeration systems installed in a UK food retail store as a case study, shown in Figure 1. Each refrigeration loop services roughly 50% of the cabinets and coldrooms in the store, as detailed in Table 1. They are designed to operate in both the subcritical and transcritical regions depending on the ambient temperatures, but typically they operate subcritically [8]. The flash tank feeds saturated liquid refrigerant to the medium temperature (MT) evaporators in the refrigeration cabinets and coldrooms, as well as feeding the low temperature (LT) evaporators in the frozen cabinets and coldrooms. ”Cabinets” refer to display cases which hold the chilled or frozen food on the shop floor, while ”coldrooms” refer to large rooms in the back of house area which hold additional chilled or frozen stock. Expansion valves are present in each individual cabinet or coldroom, which are locally controlled to maintain the specific cabinet temperature setpoint. A superheat control also operates on the cabinet valves to ensure the refrigerant leaving the evaporators and entering the compressors is only in the gas phase. The LT evaporator outlet feeds directly into the low pressure (LP) compressor bank, and then the MT evaporator outlet mixes with this LP compressor outlet before entering the high pressure (HP) compressor bank. The LP compressor bank is comprised of three 2ESL-4k Bitzer compressors and the HP bank uses six 4FTC-20k Bitzer compressors, one of which has a variable speed drive. The HP compressor outlet then passes through a series of plate heat exchangers which facilitates heat recovery from the refrigeration system into the primary side of the ground-source heat pump (GSHP) which provides heating and hot water services for the building. Refrigerant then enters the gas cooler to remove the remaining heat, the outlet of which feeds the refrigerant flash tank.

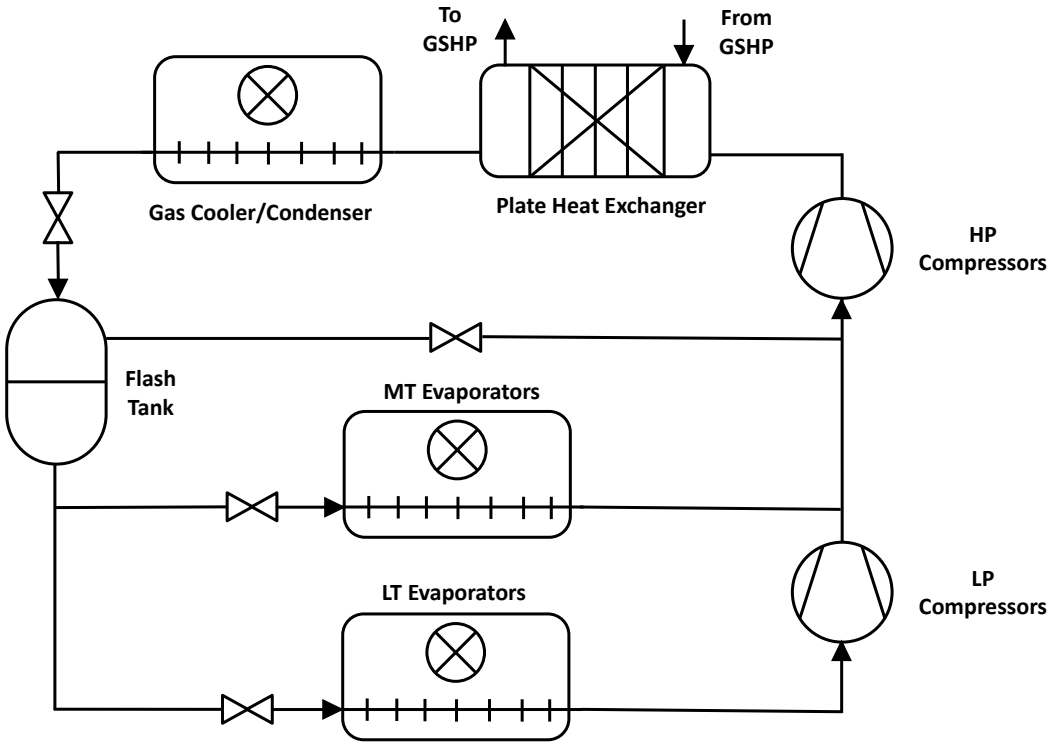

Figure 1: Schematic of typical CO_2 booster refrigeration system.

Due to the subzero refrigerant temperatures required to absorb sufficient heat from the cabinet air, moisture in the air will condense and then freeze over the evaporator. Over time this ice layer can build up and prevent sufficient circulation of the cabinet air which dramatically reduces the available cooling capacity. To prevent this, regular defrost cycles are run in both the LT and MT evaporators. For MT evaporators, an off-cycle defrost is used meaning the refrigerant valve is fully shut for 15-30 minutes, which warms the cabinet and melts the ice, and in LT evaporators an additional heating element is used to actively melt the ice. The operating power of the heating element can be found in the system specification documents for each cabinet. This study is based on data from 10 cabinets (5 chilled, 5 frozen) and 10 coldrooms (5 chilled, 5 frozen) chosen across the two refrigeration systems present in this store.

Fixture	Setpoint [℃]	Refrigeration Load* [kW]	Defrost Power [kW]	System 1 Count	System 2 Count
Fridge Cabinet	1 - 4	2.1 - 7.7	-	36	39
Frozen Cabinet	-20	1.0 - 2.6	5.0 - 21.0	11	12
Fridge Coldroom	1	6.2 - 6.7	-	5	4
Frozen Coldroom	-21	2.6	5.0 - 8.0	3	3

Table 1: Cabinet specifications for each refrigeration system. *Under 25℃ and 60% RH.

2.2. Operating Behaviour

To showcase the operating behaviour of the chilled and frozen cabinets, 12 hours of telemetry data are presented for each cabinet type in Figure 2. All system data are collected using a cloud-based monitoring platform, presented in more detail in [9]. As seen in this plot, the cabinet air temperature is maintained at the setpoint using a local PI controller which manipulates the opening degree (OD) of the expansion valve to provide the required cooling duty. During the off-cycle defrost periods (highlighted in blue) expansion valves fully shut which raises the cabinet air temperature and melts any ice build up. Immediately following the end of the defrost, the valve opens to pull the cabinet temperature back down to setpoint. Frozen cabinet telemetry looks similar but has some notable differences. Firstly, they operate using hysteresis control on the expansion valve, which opens and closes the valve as the cabinet air temperature breaches upper or lower temperature bounds. This control approach is more suitable for frozen cabinets as they use case doors which maintain air temperature much more steadily compared to doorless chilled cabinets. The lack of doors also causes chilled cabinets to need more frequent defrosts compared to frozen units, due to increased ingress of warm, humid air from the shop floor.

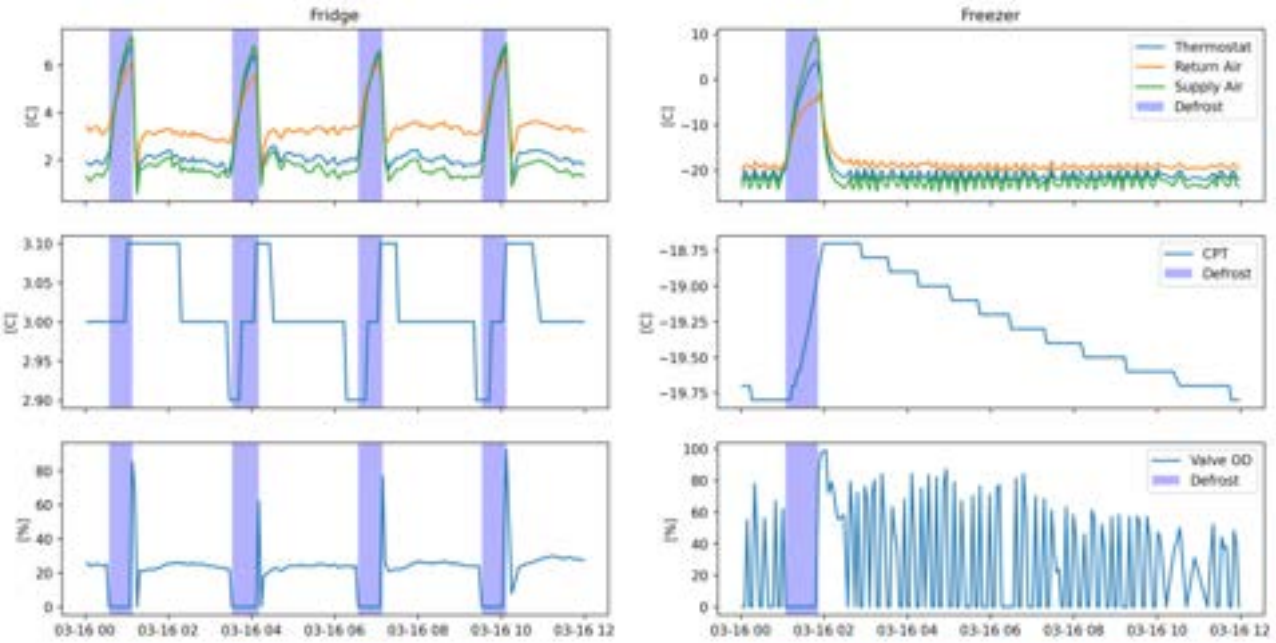

Figure 2: Cabinet telemetry for a chilled cabinet (left) and frozen cabinet (right).

In addition to cabinet air temperature and valve OD sensors, the calculated product temperature (CPT), also referred to as food temperature, in each cabinet is estimated using a proprietary algorithm provided by a resource data management (RDM) panel which monitors and collects data from the local cabinet controllers. As seen in Figure 2, the CPT in chilled cabinets only changes by 0.2℃ during an off-cycle defrost, but can change by up 1℃ during a frozen cabinet defrost due to the additional electric heating element in the evaporator.

3. Modelling

3.1. Cabinet Temperature

The proposed cabinet temperature model is adapted from a popular approach seen in [6], based on an energy balance over an individual cabinet. In cabinets, heat is transferred from the food items to the cabinet air,

$\dot{Q}_{foods/c}$, as well as from the internal building to the cabinet air, $\dot{Q}_{load}$. Heat is then exchanged between the cabinet air and the evaporator, $\dot{Q}_e$. This paper improves upon previous approaches by including the additional term, $\dot{Q}_D$, to account for the heat added by the electrical defrost element present in the evaporators of most frozen units. For all chilled and frozen cabinets, the cabinet air temperature, T_c, and internal building temperature, T_{indoor}, are directly measured using temperature sensors and the calculated product temperature (CPT), T_{food}, is estimated using the previously discussed approach. Assuming purely conductive heat transfer, the energy balance on this system can be written as

$$MCp_{food}\frac{dT_{food}}{dt} = -\dot{Q}_{food/c} \tag{1}$$

$$MCp_c\frac{dT_c}{dt} = \dot{Q}_{load} + \dot{Q}_{food/c} + \dot{Q}_D - \dot{Q}_e \tag{2}$$

$$\dot{Q}_{food/c} = UA_{food}\,(T_{food} - T_c) \tag{3}$$

$$\dot{Q}_{load} = UA_{load}\,(T_{indoor} - T_c) \tag{4}$$

where MCp_{food} and MCp_c are the product of mass and specific heat capacity for the food and cabinet air respectively, and UA_{food} and UA_{load} are the heat transfer coefficients between the cabinet air and the food and store air respectively. The cooling duty of the evaporator can then be written as

$$\dot{Q}_e = \beta\, OD \tag{5}$$

$$\beta = K_v\,(h_{oe} - h_{ie})\,\sqrt{\rho_{suc}\,(P_{rec} - P_{suc})} \tag{6}$$

where OD is the opening degree of the expansion valve, K_v is a valve specific constant, ρ_{suc} is the density of the refrigerant on the suction side, P_{suc} and P_{rec} are the suction and receiver pressures, and h_{oe} and h_{ie} are the specific refrigerant enthalpies at the inlet and outlet of the evaporator respectively. Under normal operation, compressor controllers aim to keep the operating pressures and temperatures of the refrigerant constant at specific points in the cycle, allowing the combination of these parameters into one constant β.

From this point, the above system (1)-(6) can be rearranged and expressed as an LTI state space model.

$$\begin{cases} \dot{\boldsymbol{x}} = A\boldsymbol{x} + B\boldsymbol{u} \\ \boldsymbol{y} = C\boldsymbol{x} \end{cases} \tag{7}$$

with the state values, $\boldsymbol{x} = [T_{food},\, T_c]^T$, controls and disturbances, $\boldsymbol{u} = \left[OD,\, \dot{Q}_D,\, T_{indoor}\right]^T$, and model parameters

$$A = \begin{bmatrix} \frac{-UA_{f/c}}{MCp_f} & \frac{UA_{f/c}}{MCp_f} \\ \frac{UA_{f/c}}{MCp_f} & \frac{-UA_{load}-UA_{f/c}}{MCp_c} \end{bmatrix}, \qquad B = \begin{bmatrix} 0 & 0 & 0 \\ \frac{-\beta}{MCp_c} & \frac{1}{MCp_c} & \frac{UA_{load}}{MCp_c} \end{bmatrix}, \qquad C = \begin{bmatrix} 1 & 1 \end{bmatrix} \tag{8}$$

In order to fit model parameters from historical data, the continuous state space model (7), should be discretised using the sampling time of the sensors.

$$\begin{cases} \dot{\boldsymbol{x}}\,[k+1] = A_d\boldsymbol{x}\,[k] + B_d\boldsymbol{u}\,[k] \\ \boldsymbol{y}\,[k] = C_d\boldsymbol{x}\,[k] \end{cases} \tag{9}$$

3.2. Parameter Estimation

The required input data, namely T_{food}, T_c, T_{indoor} and OD are collected for a range of chilled and frozen cabinets from the case study system. An additional binary variable is collected from the cabinet controllers which shows when the cabinet is in defrost mode to allow calculation of $\dot{Q}_D$ using the rated defrost power discussed previously. Raw telemetry is collected at irregular 2-3 minute intervals and resampled to 1 minute intervals using linear interpolation to better capture the dynamics of the system. One day of data from 10/03/2023 is used for each cabinet to show the flexibility of the method using even just a small sample of N total data points. The system (7) - (9) is expressed using the *StateSpace* function within the *scipy*.*signal* package in Python [10]. This system is then wrapped within a genetic algorithm (GA) optimisation which finds the optimal empirical parameters MCp_{food}, MCp_c, UA_{food}, UA_{load} and β, by using measured system states, $\boldsymbol{x}$ and measured control and disturbances $\boldsymbol{u}$ to estimate the system states in the next timestep $\hat{\boldsymbol{x}}[k+1]$ and compare these to the measured system states $\boldsymbol{x}[k+1]$. This multi-objective optimisation is formulated as

$$\min_{\boldsymbol{Z}} \left(RMSE_c, RMSE_{food}\right) \tag{10}$$

$$RMSE_i = \sqrt{\frac{1}{N}\sum^{N}\left(\hat{T}_i - T_i\right)^2} \tag{11}$$

subject to constraints

$$\begin{cases} \boldsymbol{Z} = [MCp_{food}, MCp_c, UA_{food}, UA_{load}, \beta] \\ \boldsymbol{Z} \geq [0, 0, 0, 0, 10^3] \\ \boldsymbol{Z} \leq [10^9, 10^6, 10^4, 10^4, 10^4] \end{cases} \tag{12}$$

In this paper we utlilise the Python optimisation package *Pymoo* [11] and their implementation of a Non-dominated Sorting Genetic Algorithm (NSGA-II) [12]. Each generation has a population of 100, and the optimisation terminates after 100 generations, and all other GA parameters are left at their default values.

4. Results

The optimal empirical parameters for the chilled and frozen cabinets are shown in Table 1, with *MCp* values given in [J/K], *UA* values in [W/K], β in [W/OD%] and *RMSE* in [K]. For each cabinet, the GA fitting process took at most 2 minutes to complete on a desktop PC with a Ryzen 5 3600 6-core CPU. On average the chilled cabinets have a satisfactory fit, with an RMSE of 0.56℃ and 0.13℃ for cabinet air and food temperature predictions respectively, while frozen cabinets are slightly higher at 0.89℃ and 0.17 ℃ respectively. Chilled cabinets also have higher UA_{load} values, ranging from 42-82 W/K compared to only 1-4 W/K for the frozen cabinets, and higher β values, 3,769 - 6,450 W/OD% compared to 1,000 - 1,576 W/OD% for frozen cabinets. Both of these differences are due to chilled cabinets not having doors, causing a larger heat transfer from the building air to the cabinet air, and consequently requiring a larger evaporator cooling duty to keep the food at setpoint.

	Chilled Cabinets					Frozen Cabinets				
Cabinet ID	1	2	3	4	5	6	7	8	9	10
MCp_{food} ($\times 10^6$)	942.5	222.5	865.8	138.0	951.0	10.7	13.2	577.4	6.3	36.0
MCp_c ($\times 10^5$)	3.2	1.6	2.5	2.2	1.7	2.0	2.1	1.9	1.5	1.8
UA_{load}	82	64	42	60	63	4	3	2	3	1
UA_{food}	391	254	301	222	100	174	189	191	134	194
β ($\times 10^3$)	5738	3796	6450	6308	4673	1576	1050	1000	1050	1032
$RMSE_c$	0.46	0.37	0.68	0.56	0.72	0.98	0.87	0.84	0.89	0.87
$RMSE_{food}$	0.13	0.11	0.15	0.09	0.17	0.18	0.19	0.11	0.18	0.18

Table 2: Empirical parameters and RMSE values for the chilled and frozen cabinets.

Figure 3 shows 24 hours of cabinet air and food temperature predictions from the training sample compared with measured values for the two best chilled and frozen cabinets. Air temperature predictions are generally

good, fitting well the temperature spikes due to defrost, but struggling sometimes to predict the smaller, higher frequency temperature variations when the cabinet is at setpoint. This is particularly noticeable in the frozen cabinet which use hysteresis control to maintain the air temperature within a bound around the setpoint.

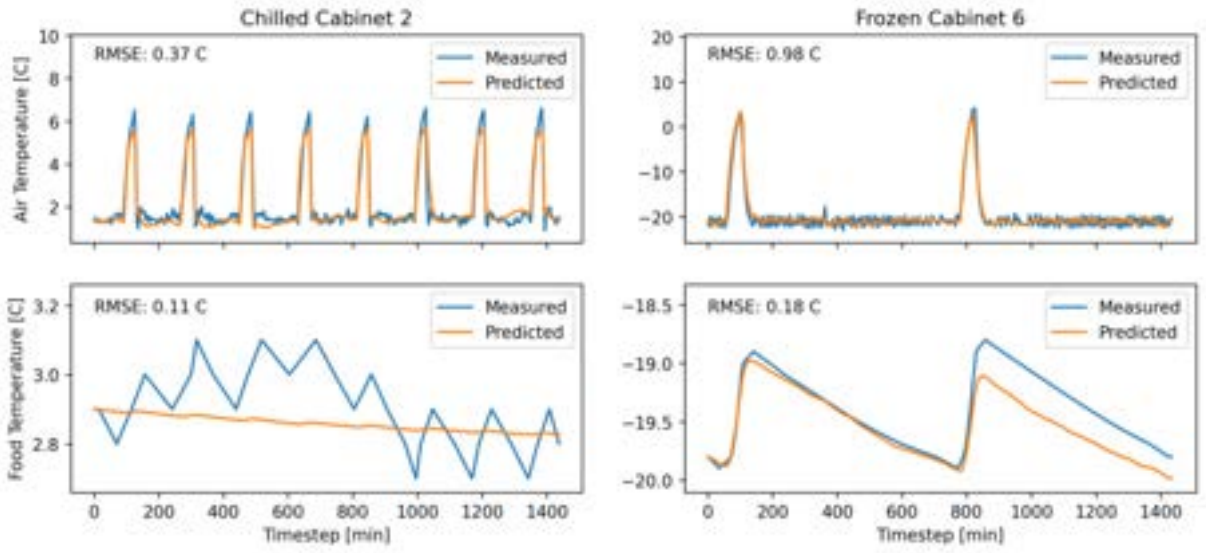

Figure 3: Cabinet temperature predictions based on optimal GA fitting.

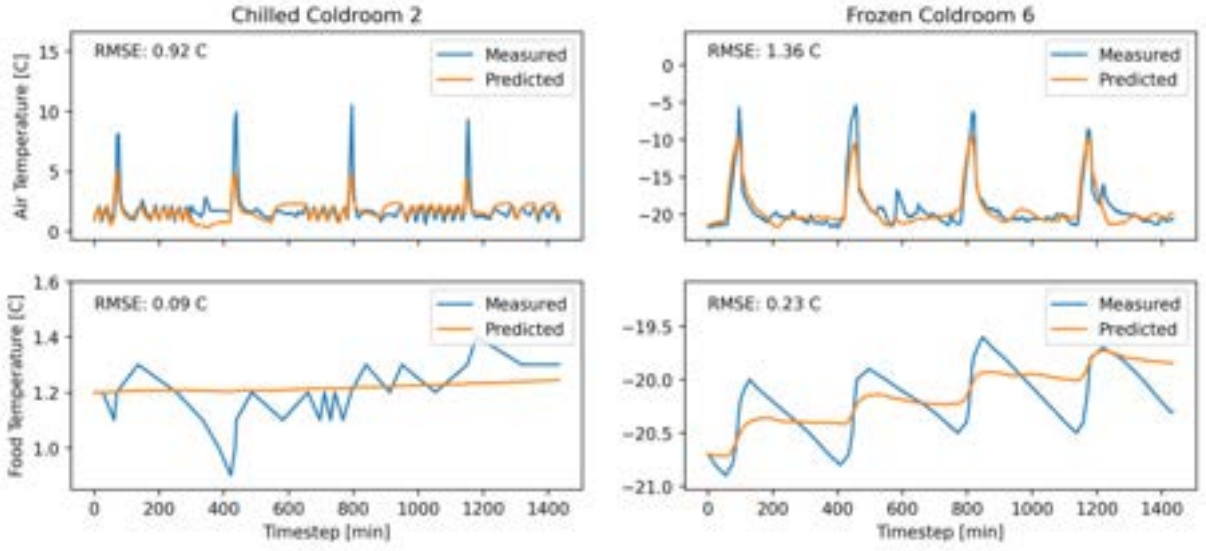

Figure 4: Coldroom temperature predictions based on optimal GA fitting.

Food temperature predictions are less reliable, particularly for the chilled cabinets. Over most of these cabinets the food temperature predictions fail to pick up any of the observed changes in food temperature due to defrost, instead just predicting a constant value which is on average correct. In addition, the food temperature in the chilled cabinets only changes by a maximum of 0.3℃ during a defrost, which is small temperature change for this model to account for, especially compared to the air temperature which varies by around 5℃. Empirical parameters for the 5 chilled and 5 frozen coldrooms analysed can be found in Table 3, and temperature predictions compared to measured values are shown in Figure 4. The air temperature predictions are not as accurate compared to the chilled and frozen cabinets, especially during the defrost periods, achieving an average RMSE of 0.61℃ and 0.16℃ for cabinet air and food temperature predictions respectively for chilled coldrooms, which increases to 2.74℃ and 0.37℃ for frozen coldrooms. This could be due to uneven temperature distribution in coldrooms, which are much larger than cabinets, and so this effect is not by the individual air temperature sensors.

	Chilled Coldrooms					Frozen Coldrooms				
Coldroom ID	1	2	3	4	5	6	7	8	9	10
MCp_{food} ($\times 10^6$)	22.0	799.7	318.6	998.9	997.9	413.0	5.5	15.1	5.2	9.4
MCp_c ($\times 10^5$)	2.3	2.2	10.0	10.0	9.6	0.8	2.7	0.4	0.5	3.0
UA_{load}	15	25	102	111	196	5	27	6	8	75
UA_{food}	241	339	3831	4501	8775	54	178	34	31	251
β ($\times 10^3$)	1000	1002	1706	2964	1054	1000	2631	1811	1355	6121
$RMSE_c$	0.67	0.92	0.29	0.27	0.91	3.07	1.36	3.60	2.73	2.96
$RMSE_{food}$	0.08	0.09	0.14	0.18	0.30	0.26	0.23	0.56	0.31	0.50

Table 3: Empirical parameters and RMSE values for chilled and frozen coldrooms.

5. Application Example

In advanced control applications, simulation models are often required to test and refine the chosen approach prior to real-world implementation. A schematic demonstrating an example framework for a supervisory model predictive control (MPC) approach applied to a refrigeration system can be seen in Figure 5. The MPC scheme will have a user-defined objective function, which is typically minimising operational cost subject to variable electricity prices, or tracking a reference power consumption sent from the grid for demand-response applications. In either case, the key control variable is the optimal temperature setpoint, T^*_{sp}, which can be forwarded to the local cabinet controllers to enact the required expansion valve position OD. The devised cabinet models can then be used to simulate the resulting cabinet and food temperature changes. An equivalent modelling and control approach has been demonstrated for a commercial HVAC system in the UK and simulations show the ability to reduce operational costs while adhering to user specified constraints [9].

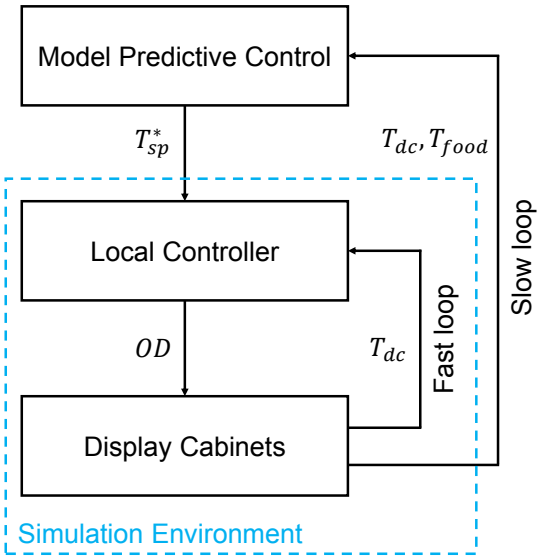

Figure 5: Example supervisory MPC application using refrigeration cabinet model.

The proposed cabinet modelling approach is well suited to these control applications for a number of reasons. Firstly, a large number individual cabinet models can be fit offline with low computational overhead, allowing a user to easily simulate a entire supermarket refrigeration system. Additionally, the modelling approach shows satisfactory modelling accuracy when trained on only a small snapshot of 24 hours of data. Finally, once the optimal empirical parameters are known, the cabinet models are a simple system of linear equations providing a fast, efficient method to test any proposed control approach.

6. Conclusion

This paper presents a data-driven modelling approach to simulate the behaviour of chilled and frozen cabinets and coldrooms, using a UK supermarket as a case study. Individual units are modelled using a discrete LTI state space model, based on an overall system energy balance, for which empirical parameters are determined using a genetic algorithm fitting approach. The proposed approach is demonstrated using 24 hours

of historical data from 10 display cabinets and 10 coldrooms, and shows satisfactory performance across the range of cabinets tested. Finally, a high-level example application of the proposed modelling approach to a supervisory, model predictive control scheme was discussed. Future work should look to better understand the food temperature dynamics, perhaps using temperature probes instead of an estimated CPT value, as this is the most important variable to track in control applications.

Acknowledgments

This research was supported by funds provided via the Imperial College London – Sainsbury's Supermarkets Ltd. Partnership.

Bibliography

[1] Maria Kolokotroni, Zoi Mylona, Judith Evans, et al. "Supermarket Energy Use in the UK". In: *Energy Procedia* 161 (2019). Proceedings of the 2nd International Conference on Sustainable Energy and Resource Use in Food Chains including Workshop on Energy Recovery Conversion and Management;ICSEF 2018, 17 – 19 October 2018, Paphos, Cyprus, pp. 325–332. ISSN: 1876-6102. DOI: https://doi.org/10.1016/j.egypro.2019.02.108. URL: https://www.sciencedirect.com/science/article/pii/S1876610219311907.

[2] Seyed Ehsan Shafiei, Jakob Stoustrup, and Henrik Rasmussen. "A supervisory control approach in economic MPC design for refrigeration systems". In: IEEE Computer Society, 2013, pp. 1565–1570. ISBN: 9783033039629. DOI: 10.23919/ecc.2013.6669413.

[3] "Flexible and cost efficient power consumption using economic MPC a supermarket refrigeration benchmark". In: Institute of Electrical and Electronics Engineers Inc., 2011, pp. 848–854. ISBN: 9781612848006. DOI: 10.1109/CDC.2011.6161162.

[4] Seyed Ehsan Shafiei, Jakob Stoustrup, and Henrik Rasmussen. "Model predictive control for flexible power consumption of large-scale refrigeration systems". In: Institute of Electrical and Electronics Engineers Inc., 2014, pp. 412–417. ISBN: 9781479932726. DOI: 10.1109/ACC.2014.6858921.

[5] Rasmus Pedersen, John Schwensen, Benjamin Biegel, et al. "Aggregation and Control of Supermarket Refrigeration Systems in a Smart Grid". In: *IFAC Proceedings Volumes* 47 (3 2014), pp. 9942–9949. ISSN: 14746670. DOI: 10.3182/20140824-6-ZA-1003.00268.

[6] S. Ehsan Shafiei, Henrik Rasmussen, and Jakob Stoustrup. "Modeling supermarket refrigeration systems for demand-side management". In: *Energies* 6.2 (2013). Cited by: 43; All Open Access, Gold Open Access, Green Open Access, pp. 900–920. DOI: 10.3390/en6020900.

[7] K. Leerbeck, P. Bacher, C. Heerup, et al. "Grey box modeling of supermarket refrigeration cabinets". In: *Energy and AI* 11 (Jan. 2023). ISSN: 26665468. DOI: 10.1016/j.egyai.2022.100211.

[8] Emilio José Sarabia Escriva, Salvador Acha, Niccolo Le Brun, et al. "Modelling of a real CO2 booster installation and evaluation of control strategies for heat recovery applications in supermarkets". In: *International Journal of Refrigeration* 107 (Nov. 2019), pp. 288–300. ISSN: 01407007. DOI: 10.1016/j.ijrefrig.2019.08.005.

[9] Max Bird, Camille Daveau, Edward O'Dwyer, et al. "Real-world implementation and cost of a cloud-based MPC retrofit for HVAC control systems in commercial buildings". In: *Energy and Buildings* (June 2022), p. 112269. ISSN: 03787788. DOI: 10.1016/j.enbuild.2022.112269.

[10] Pauli Virtanen, Ralf Gommers, Travis E. Oliphant, et al. "SciPy 1.0: Fundamental Algorithms for Scientific Computing in Python". In: *Nature Methods* 17 (2020), pp. 261–272. DOI: 10.1038/s41592-019-0686-2.

[11] J. Blank and K. Deb. "pymoo: Multi-Objective Optimization in Python". In: *IEEE Access* 8 (2020), pp. 89497–89509.

[12] K. Deb, A. Pratap, S. Agarwal, et al. "A fast and elitist multiobjective genetic algorithm: NSGA-II". In: *IEEE Transactions on Evolutionary Computation* 6.2 (2002), pp. 182–197. DOI: 10.1109/4235.996017.

Review of Business Models for Industrial Heat Pumps

Cordin Arpagaus[a], Sidharth Paranjape[a], Stefan Nertinger[b], Rigo Tietz[b] and Stefan S. Bertsch[a]

Eastern Switzerland University of Applied Sciences
[a] Institute for Energy Systems (IES), Werdenbergstrasse 4, CH-9471 Buchs,
cordin.arpagaus@ost.ch, Tel. +41 58 257 34 94
[b] Institute for Strategy and Marketing (ISM), Rosenbergstrasse 59, CH-9001 St. Gallen

Abstract:

The heat pump market is experiencing remarkable growth and rapidly expanding in various sectors. Industrial heat pumps are an emerging technology for electrifying and decarbonizing the heat supply, such as hot water, hot air, and steam. However, integrating industrial heat pumps into business models is not yet common. As a result, little research has been conducted linking business model frameworks to the rapidly evolving heat pump sector. Besides, there are challenges in the transition from fossil fuel heating to electrical-driven heat pumps, including unfavorable electricity-to-gas price ratios, regulatory issues, alternative heating technologies, low maturity of services, the requirement for tailor-made designs, more complex integration principles, simultaneous need for excess heat, and higher CAPEX (compared to fossil or electric boilers). This study reviews business models for industrial heat pumps based on scientific literature and interview results with manufacturers as part of the EU Horizon project PUSH2HEAT. The goal is to explore innovative business models that could emerge from industrial heat pumps based on the changing framework conditions. First, the status of business models is reviewed to identify gaps in the academic literature. Next, ideation inputs are considered from case studies on high-temperature heat pumps, analogies to other markets such as domestic heat pumps, large-scale heat pumps for district heating networks, waste heat recovery, combined heat and power generation, as well as lessons from other innovative business models in the energy sector (e.g., energy contracting, heat as a service). Then, various players in the value chain (e.g., planners, manufacturers, integrators, installers, service providers, etc.), their capabilities, and the added value will be analyzed. Finally, a short list of business models will serve as a basis for decision-making for existing players, such as utilities and new companies considering entering the heat market.

Keywords:

Heat pumps; industry; innovative business models; value-chain.

1. Introduction to industrial heat pumps

Industrial heat pumps (HP) will play an important role in decarbonizing process heat and improving the energy efficiency of industrial processes in the future while driving the shift from fossil fuels to renewable electricity as an energy source [1], [2]. There are more and more suppliers of industrial heat pumps, as summarized in the IEA Annex 58 project [3], [4]. Four types of heat pump technologies are most relevant for industrial applications:

- standard heat pumps with supply temperature < 80 °C,
- high-temperature heat pumps (HTHP) with supply temperature > 100 °C,
- steam-generating HP with mechanical vapor compression (MVR) and supply temperature < 200 °C,
- heat transformers with supply temperature < 300 °C [5].

These heat pump technologies cover heat capacities ranging from about 100 kW to 10 MW [4]. In most cases, the heat source is excess heat from the processes with a typical temperature level of 30 °C to 80 °C, while some are also used to provide cooling simultaneously.

Examples of existing and potential industries using industrial HPs include the food, paper, chemical, and refinery industries, where processes such as drying, pasteurization, sterilization, evaporation, and distillation can be made more energy-efficient [2].

An estimate of the European industrial HP market potential showed that the cumulative heating capacity of industrial HPs in EU28 is about 23 GW, consisting of 4’174 heat pump units that could cover 178 TWh/a of process heat demand up to 200 °C [6]. Standard HPs could meet 50% of the cumulative heating capacity of the total market with heating capacities up to 10 MW; for above 10 MW, tailormade HP solutions are required.

In general, the ongoing energy transformation and the growth of renewable energies are changing the structure and value creation of the energy industry, enabling new business models that can be classified according to customer proximity [7]. In particular, there is a need for new business models for industrial heat pump market players (e.g., heat pump manufacturers, energy service companies ESCOs [8]) to strengthen market acceptance and faster market uptake.

This study aims to identify innovative business models to drive the market introduction of industrial heat pumps. Because there are limited sources of business models for industrial heat pumps so far, the current state of business models for large-scale heat pumps for district heating networks and domestic use is first analyzed to identify gaps in the scientific literature. Then, business models from empirical interviews from the perspective of manufacturers of high-temperature heat pumps are evaluated based on the value chain. Next, a short list of business models is summarized to serve as a basis for decision-making when entering the industrial heat pump market. Finally, the study should help motivate existing companies in the value chain and start-ups to develop new business models for commercializing industrial heat pumps.

2. Business model development

2.1. The “magic triangle”

At its core, a business model describes the rationale of how an organization creates, delivers, and captures value [9]. Value creation describes what benefits are created by the company, and value capture explains how the company can generate revenue from the offered benefits. To assist companies in designing business models, researchers and practitioners have developed tools and procedures to facilitate development. A simple way to describe business models is the "magic triangle," which consists of four essential dimensions – WHO, WHAT, HOW, and VALUE (see Figure 2).

The "magic triangle" was developed at the University of St. Gallen (HSG) by Prof. Gassmann and team [10]–[12]. Briefly, the triangle aims to clarify the logic behind a business model by answering 4 questions (i.e., dimensions) about a business model:

1. WHO is your target customer? (Customer segment)
2. WHAT do you offer to the customer? (Value proposition)
3. HOW is the value proposition created? (Value chain)
4. How is VALUE achieved? (Revenue or profit mechanism)

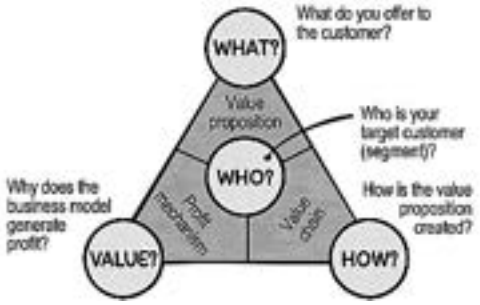

Figure. 1. Business model definition – the “magic triangle” (Adapted from [10]–[12])

The “magic triangle” is a qualitative representation to support companies in (re)designing their business model. The different dimensions can be further elaborated. By answering the 4 interrelated questions, a company's business model becomes more tangible.

- **WHO** - Each business model serves a specific group of customers. Defining the target customer is the first dimension in designing a new business model. Therefore, it should answer the question, "Who is the target customer?"
- **WHAT** - The second dimension describes what is offered to the target customer or the customer’s value. This term is commonly referred to as the value proposition. It can be defined as a holistic view of a company's bundle of products and services that are of value to the customer.
- **HOW** - The third dimension describes how to build and disseminate the value proposition. To do this, a company masters multiple processes and activities, along with the resources and capabilities involved and the value chain behind creating that value.
- **VALUE** - The fourth dimension explains why the business model is financially sustainable and thus refers to the revenue model. Essentially, it combines aspects such as the cost structure and the profit mechanism applied and refers to the elementary question of any business, namely, how to make money from the business.

For a given technology, e.g., an industrial heat pump, the question is how to use it profitably. Depending on the business model, different actors can play the central role. It is, therefore, worth considering from whose perspective the business model is viewed. This study focuses on industrial heat pump manufacturers.

2.2. The "business model canvas" framework

This study also uses the "business model canvas" framework to describe innovative business models [9], [13], [14]. Business model canvas provides a common language for representing, evaluating, and changing key aspects of complex business models.

As shown in Table 1, the business model canvas contains nine elements arranged in a structured format. The nine interdependent building blocks are (1) customer segments, (2) value proposition, (3) customer relationships, (4) customer channel, (5) revenue streams, (6) key activities, (7) key resources, (8) key partners, and (9) cost structure. Applying the business canvas methodology involves answering a series of key questions in a particular sequence (see numbering (1) to (9) in Table 1). In this study, a business model canvas is developed from the perspective of industrial heat pump manufacturers.

Table 1. The Business Model Canvas framework, the mapping phases in development (numbering from 1 to 9), and the key questions (Adapted from [9], [13], [14])

(8) Key partners	**(7) Key resources**	**(2) Value proposition**	**(1) Customer segments**
Who can help you? • Who are our key partners? • Who are our key suppliers? • Which key resources are we acquiring from partners? • Which key activities do partners perform?	What do you need? • What key resources do these business activities require?	What do you do? • What value do we deliver to the customer? • Which customer's problems are we helping to solve? • Which customer needs are we satisfying?	Whom do you help? • For whom are we creating value? • Who are our most important customers
(9) Cost structure	**(6) Key activities**	**(4) Customer channel**	**(3) Customer relationships**
What will it cost? • What are the most important costs inherent in our business model? • Which key resources are the most expensive? • Which key activities are the most expensive?	How do you do it? • What key activities do our value propositions, distribution channels, customer relationships, and revenue streams require?	How do you reach them? • Through which channels do our customer segments want to be reached?	How do you interact? • What type of relationship does each of our customer segments expect us to establish and maintain with them?
		(5) Revenue streams	
		What will it generate? • For what value are our customers willing to pay?	

3. Business models of heat pumps for district heating and domestic use

Before focusing on industrial heat pumps, this section briefly overviews published work on business models with heat pumps for district heating and domestic use. Table 2 summarizes the studies.

Various studies exist on the utilization of heat pumps for district heating networks in different European countries (e.g., Denmark [15], Austria [16], and Sweden [14]). A quick starting point for business model theory and contract theory concerning district heating can be found in the ReUseHeat report [17]. Their conclusions on urban waste heat recovery investments with a payoff of 15 years and more could apply to their respective regions. However, general conclusions should be made with caution.

Østergaard et al. (2019) [15] conducted a business analysis of heat pumps for small district heating systems combined with heat storage on Samsø island in Denmark. Simulations showed that heat pumps and heat storage are useful for fluctuating renewable energy in part-load operation but are not economically competitive with straw-fired boilers. However, this conclusion may not be entirely applicable outside of Denmark.

Terreros et al. (2020) [16] explored different potentials of heat pumps in rural district heating networks in Austria. Through simulations, it was found that the optimal bidding strategy for the heat pump is to buy 50% of the electricity on the day-ahead spot market and to offer 50% of the capacity for negative balancing energy for the automatic frequency restoration reserve, as this allows a significant reduction of the heat generation costs. The optimal operating strategy reduced heat generation costs by up to 17.7% for use cases with flue gas as a heat source for the heat pump and up to 27.5% for cases with sewage water. In addition, the results showed that variations in biomass price and call probabilities could significantly affect heat pump profitability.

In Sweden, Lygnerud et al. (2021) [14] applied the business model canvas concept to map the required change in the district heating networks to generate cost and emission savings by integrating small-scale heat pumps in buildings. The authors showed that by combining efficient small heat pumps in district heating networks with optimal control, maximum cost savings of 33% and CO_2 emission savings of 75% could be achieved. However, challenges exist due to the tendency of Swedish district heating companies to view heat pumps as competition.

Vivian et al. (2018) [18] studied the economic performance of a low-temperature district heating system below 45 °C. They used booster heat pumps in customers' substations to provide the temperature required for space heating and domestic hot water. Two types of business models were considered a district heating utility responsible only for heat recovery and distribution and a utility that also invests in heat pumps and electricity. At the same time, the user pays for the delivered heat. The economic analysis showed that the system with booster heat pumps is already competitive with single gas boilers for multi-family buildings, provided a local low-temperature heat source with minor marginal costs can be used.

Heat pump flexibility can play a major role in enabling a transition towards a renewable heat and electricity sector. In this context, Fischer et al. (2017) [19] analyzed different business models that could arise from using the flexibility of domestic heat pumps in a smart grid context. Results showed that due to high-end customer prices, grid fees and complicated market requirements, less integrated business models were more attractive than the direct use of heat pump flexibility on the reserve or spot market or the provision of balancing energy. However, additional revenues could be generated by using heat pump flexibility, such as providing a secondary reserve or balancing energy.

Lyon et al. (2021) [20] considered the challenge of retrofitting existing residential buildings in Europe, where heat pumps struggle to compete against traditional heating systems. The alternative business model “heat as service” (HaaS) proposition was investigated, which involves a residential building occupier signing a contract for heating provision and heating equipment for a fixed monthly fee rather than purchasing the heat pump equipment. It was concluded that the HaaS business model could be a critical step for overcoming the end-user barriers for heat pumps, i.e., high upfront costs, risk of high running costs and lack of trust in the technology. The potential of HaaS has also been explored as a route to decarbonize the domestic heat supply in Scotland [21] to increase the uptake of low-carbon heat, improve the energy efficiency of people’s homes, and reduce fuel poverty.

Table 2. Studies on business models with heat pumps for district heating applications and domestic use

Paper	Description	Business model
Østergaard et al. (2019) [15]	• Heat pumps and heat storage combination for small district heating system in Denmark covering fluctuating renewables	• Simulations of optimal business economic design • No business model was discussed
Terreros et al. (2020) [16]	• Heat pumps in rural district heating networks in Austria • Flue gas and sewage water as heat sources	• Electricity market options • Costs savings by optimal bidding strategy (day-ahead & balancing market)
Lygnerud et al. (2021) [14]	• Combination of small-scale heat pumps in district heating networks in Sweden	• Efficiency gains impacting cost and CO_2 emissions (business model canvas method used for business model mapping)
Vivian et al. (2018) [18]	• Booster heat pumps with low-temperature district heating network (15 to 45 °C) • System is economically competitive to gas boilers • Utility investing in heat pumps and electricity	• District heating utility responsible only for heat recovery and distribution • Customer pays for heat delivered
Fischer et al. (2017) [19]	• Flexibility of residential heat pumps in a smart grid context	• Provision of the secondary reserve or balancing energy (business model canvas established for various business cases)
Lyon et al. (2021)[20]	• Retrofit existing residential buildings with heat pumps • Increasing trust in heat pump technology • Reduction of risk of high running costs	• Heat as a Service • Contract for the heating provision • No high upfront costs
Fleck et al. (2021) [21]	• Decarbonization of domestic heat in Scotland • Increase the uptake of low-carbon heat, improve the energy efficiency of homes, and reduce fuel poverty	• Heat as a Service
Britton et al. (2021) [22]	• Heat pumps for cooling or keeping temperatures in the UK domestic market	• Heat as a Service • Consumer pays for produced heat, annual service fee, initial installation

HaaS business models have also been reviewed in the UK domestic market by Britton et al. (2021) [22]. Recommendations for policy and research were made based on insights from facilitated group discussions with key stakeholders and experiences from HaaS trials in the UK. Based on the findings, policy and research recommendations were proposed to better understand the role of HaaS business models in decarbonization.

Skovshoved & Sandqvist (2017) [23] discussed HaaS from a more academic perspective and aimed to identify value propositions for heat pumps in Sweden. The same study also described a business model in Denmark by Best Green, where end users pay an annual service fee and initial installation costs for the heat generated by the heat pump. However, the heat pump is purchased and owned by the service provider.

Further studies published on business models in the heat and energy sector with heat pumps include:

- solar heat pump water heaters [24],
- solar thermal air conditioners [25],
- district energy providers [13],
- perspective of the electrical grid operator [26],
- urban waste heat recovery [17],
- combining district heating and heat pumps in buildings [27],
- heat pump retrofits in metro Vancouver [28],
- small-scale heat energy production in Finland [29], and
- heat purchase agreements [30].

4. Business models specific to industrial heat pumps

To the best of the authors' knowledge, no free literature is available on business models specifically for industrial heat pumps. Therefore, interviews with manufacturers of industrial high-temperature heat pumps (i.e., SPH, Enertime, BSNOVA, and QPinch) with reciprocating and turbo compressors, absorption and thermochemical technology were conducted as part of the EU Horizon project PUSH2HEAT [31].

The following section summarizes the empirical findings from initial interviews with the heat pump manufacturers and ongoing studies. The interviews were conducted in a structured manner using a questionnaire. The aim was to gain a deeper understanding of the topic, identify innovative business models, and draw parallels between the general answers of the manufacturers. The "magic triangle" and the "business model canvas" framework were used to describe and visualize the business models.

4.1. Business models and value chain of industrial heat pumps

Figure 2 illustrates the main activities in the value chain of the industrial heat pump market ranging from research and development (R&D), manufacturing, consulting, design, distribution, installation, and commissioning to after-sales (maintenance, service), energy data management (EDM) and trading of heat (e.g., with heat storage and back-up systems) or CO_2 certificates on the energy markets. Innovative approaches to business models can be mapped along the value chain. As customer integration increases, so does the degree of collaboration with the customer and involvement in the value chain.

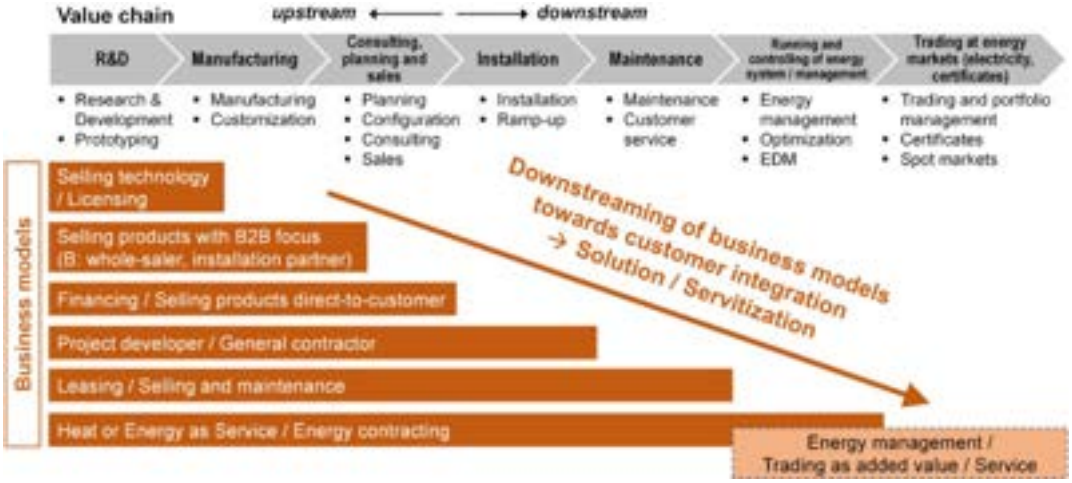

Figure. 2. Business models and value chain of industrial heat pumps (Source: PUSH2HEAT project)

Figure 3 shows three basic types of companies within the value chain, which differentiate by a targeted selection of core activities (indicated by arrows in different colors). A distinction is made between integrator, specialist, and solution provider. The integrator offers everything from a single source and masters the entire value chain in depth. The specialist supplies specific parts of the value chain and benefits from economies of scale, achieving quality advantages and flexibility. Finally, the solution provider (or orchestrator) can select the best from all specialists and thus offer the customer the most suitable solution.

Figure. 3. Basic types of companies within the value chain (integrator, specialist, and solution provider)

Table 3. List of likely business models from the perspective of a manufacturer of industrial heat pumps

Business model	Value proposition (WHAT)	Revenues (VALUE)	Key activities (HOW)
Licensing of heat pump technology	• Subcontractor using HP technology for own production • Users: Local partner	• Licensing fees from subcontractor (recurring), e.g., depending on units	• Licensing agreement • Trustworthy subcontractor
Selling heat pump technology (IP)	• Buyer receives state-of-the-art technology without any R&D risks	• One-time sales	• Technology readiness • IP purchase contract
Selling heat pump products with a B2B focus (B: wholesaler, project developer, installation/sales partners)	• Local partner (distributor) as a one-stop shop for user customer	• Income and profits from sales	• Trustworthy sales partner/dealer network
Selling heat pump products Direct2Customer	• Customization One-Stop shop: installed pump (Financing as added service)	• Earnings from sales and installation • Customer loyalty/customer data • Provisions from a financing partner	• Sales • Installation resources
Project developer / General contractor	• "One-stop-shop" solution from idea to operating system	• Fixed income for the successful project (in-time, in-budget)	• Coordination of entities/partners • Sales resources • Resources for installation and planning
Leasing / Selling and maintenance	• Low capital spending • All services included • Service level agreed	• Fixed earnings over the project duration • Provisions from financing/leasing partner or earnings in case of self-financing	• Service level and leasing agreements • Resources for installation, planning, maintenance
Energy contracting	• Guaranteed efficiency performance (energy, costs, CO_2, white certificates, etc.) • Monetization of efficiency increase (achieve financial benefit)	• Fixed, recurring earnings • Further revenues arising from efficiency surpluses	• Risk management and assessment of projects and contracts
Heat as a Service (HaaS)	• Heat for a fixed price over the contract duration	• Fixed, recurring earnings	• Financial resources
Energy as a Service (EaaS) (Running the whole energy infrastructure of a customer)	• Energy for a fixed price over the contract duration	• Fixed, recurring earnings	• Construction and provider of a heat pump in own response
Trading and profiting on arbitrage: • Energy markets (e.g., spot markets EPEX/EEX), • Selling Carbon certificates (CO_2-ETS, CO_2-voluntary like VCS, Gold • Electricity (renewables) - Efficiency (White like ESC, EEC)	• Earnings from certificates	• Service fees, provisions from sales of certificates • Energy management fees	• Trading capabilities • Energy management capabilities
Energy consulting and management	• Energy management competence	• Consulting fees • Energy management service fees	• Energy management and consulting capabilities

Table 3 summarizes the list of likely business models from the perspective of an industrial heat pump manufacturer and describes the business models based on value propositions, revenue streams and key activities (according to the “magic triangle”). The list of business models is intended to serve as a common basis for further discussion and is, therefore, neither very detailed nor conclusive or complete. The target customers are industrial companies (i.e., end users of the pulp, paper, food, and oil industry) that need to decarbonize their heat supply in the wake of climate targets. A brief description of each likely business model for industrial heat pump manufacturers follows.

4.2. Licensing of heat pump technology

When licensing a heat pump technology or parts of the technology, a subcontractor uses the technology to produce heat pumps. The heat pump manufacturer receives recurring license fees from the subcontractor, e.g., depending on the number of sold units. The business model requires a license agreement and a trustworthy subcontractor. For example, licensing can be interesting for a European heat pump manufacturer to reach certain markets (e.g., USA, China).

4.3. Selling heat pump technology (IP)

When selling a heat pump technology's intellectual property (IP), the buyer receives the most advanced technology without R&D risks. For the technology provider, it is a one-time sale based on an IP purchase agreement and the provision of the technology according to a defined technology readiness level (TRL).

4.4. Selling heat pump products with Business2Business (B2B) focus

When selling heat pump products over B2B (B: wholesaler, project developer, installation partners), the local partner is a one-stop shop for customers. Revenues are generated from the sale of heat pump products. Important is a trustworthy distribution partner and distributor network.

4.5. Selling heat pump products Direct2Customer

The heat pump products are sold directly to end customers by salesforce, and technicians or subcontractors carry out the installation. This is today's traditional and most common business model for industrial heat pump manufacturers. It leaves the customer with most of the risks (i.e., financial and technical). For a "new" technology like HTHP, this generates extra risk for the customer. In comparison, this risk is quite low for refrigeration systems due to long market experience. In most cases, key aspects are maintenance and service by third-party companies. Certain heat pump manufacturers are developing modular heat pumps to offer customized solutions. Here, the aim is to offer a package (i.e., package supplier). Some compressor manufacturers sell their products directly to heat pump manufacturers as subcontractors.

4.6. Project developer / General contractor

A project developer/general contractor acts as a one-stop shop and offers the heat pump solution from concept to commissioning. This provides a fixed income for the successful project (in-time, in-budget). The business model requires coordination of units/partners, sales resources, and resources for installation and planning.

4.7. Leasing / Selling and maintenance

Leasing (including maintenance) promises low investment costs, and all services are included depending on the agreed service level. Service level and leasing agreements and installation, planning, and maintenance resources are required. This generates fixed income over the project duration. Heat pump manufacturers might find this business model interesting but require a financial partner with know-how.

4.8. Energy contracting

Energy contracting is a comprehensive energy service normally provided by an energy service company (ESCO) [22]. The flexible operation of utility processes holds great potential and creates opportunities for third-party involvement. Examples include outsourcing activities by industry towards ESCOs, especially for technologies used in utility processes. Energy contracting guarantees performance in terms of efficiency (e.g., energy, cost, CO_2, white certificates, etc.). Efficiency improvements allow for fixed, recurring revenues. Additional revenues result from efficiency surpluses. Risk management and evaluation of projects and contracts are required.

4.9. Trading and arbitrage profits

As a complementary revenue stream, an industrial company may install a heat pump for its processes and use unused capacity for trading/arbitrage. Participation in trading on the energy markets (e.g., spot markets on the European Power Exchange (EPEX), European Energy Exchange (EEX)) and sales of carbon certificates in the emissions trading scheme (CO2-ETS, CO_2-voluntary such as Verified Carbon Standard (VCS, Gold) enable revenue from certificates using heat flexibility [32]. Revenue arises from service fees,

provisions from certificate sales, and energy management fees. Key activities include trading capabilities and energy management capabilities.

4.10. Heat as a Service (HaaS)

An increasingly popular business model for industrial heat pumps is heat as a service (HaaS) [20]–[23], [33]. Instead of a company investing directly in a new heat pump, HaaS allows a third party (e.g., service provider, ESCO) to bear the capital costs and guarantee the availability and performance of the heat pump system during the contract period. The ESCO designs, builds, owns, operates, maintains, and finances the heat pump system [33]. In addition, the ESCO can achieve better economies of scale and potentially receive volume discounts by buying several heat pumps. Delta-EE Ltd. estimated that the number of customers currently using a HaaS-type business model is in the low 1,000s across Europe in the domestic sector [20].

Among others, the Danish Energy Agency introduced a subsidy program to encourage direct heat pump uptake in oil-heated homes in areas where district heating is not available [20]. Under this business model, the company that buys HaaS essentially pays an upfront cost for the installation of the heat pump, a fixed price per kWh of heat delivered and a fixed annual fee to the service provider to pay for the cost of the heat pump, installation, and any maintenance costs. Depending on their business model, energy service providers are free to adjust each of these three factors. The minimum contract period is typically 10 years [20]. In another example, Fleck et al. (2021) [21] described the potential of HaaS as a way to decarbonize residential heat supply in Scotland.

4.11. Energy as a Service (EaaS)

Beyond HaaS, there are also further developments possible, such as Comfort as a Service, Cooling as a Service [34], Temperature as a Service, or more general Energy as a Service (EaaS) [35]. The EaaS market is flourishing and is expected to be worth over 140 billion by 2027 [36].

Figure 4 shows an example of an EaaS concept from ANEO Industry AS (Norway) [37] for high-temperature heat pumps to generate steam between 100 °C and 150 °C (1 to 5 bar(a)). With its sustainable EaaS platform, ANEO reduces fossil emissions and energy consumption in the process industry and increases energy efficiency. ANEO's services include engineering, installation, operation, and maintenance of industrial heat pumps from the initial case study to the system’s life cycle.

Figure. 4. Example of an Energy as a Service (EaaS) concept from ANEO Industry AS (Norway) [37] for high-temperature steam-producing heat pumps. Currently, ANEO’s EaaS is more a HaaS, but the intention is to supply electricity within the same framework.

Like HaaS, the basic idea of EaaS is to take financial and technical risks (i.e., investment, operation, and maintenance) of the heat pump system out of the scope and liability of the end customer, meaning that the investment risk, financial risk, and operational risk are placed in the scope and liability of a service provider. The EaaS provider purchases the heat pump system under a contractual agreement with a technology partner and certain performance guarantees, such as operability, availability, capacity, etc., with penalties for non-performance.

Energy is guaranteed at a fixed price during the contract period (e.g., service agreement). This results in fixed, recurring revenue while profit for the EaaS provider is generated over the life cycle of the heat pump system (typically 10 years) and covers management, administration, risk mitigation, etc., in addition to profit margin. Depending on the project's location, investors in EaaS agreements can benefit from predictable cash flow, CO2 tax credits, and renewable energy certificate revenue. The EaaS business model allows the customer to focus its capital and resources on its core business.

5. Business model building blocks of a heat pump manufacturer

Finally, Table 4 attempts to compile various business model building blocks from an industrial heat pump manufacturer's perspective based on the interview responses. This overview represents a snapshot and needs to be refined in further studies to identify the relevant building blocks for each business case.

Table 4. Business model building blocks from the perspective of an industrial heat pump manufacturer

(8) Key partners	(7) Key resources	(2) Value proposition	(1) Customer segments
• Heat pump producer • Suppliers of key components (e.g., compressor, heat exchanger, valves, control system, etc.) • Distribution partners like OEM integrators to expand the network • Demo customers for on-site visits • Regional, national, and European public institutions for the promotion • Private and public investment funds and banks for financing projects • Technical consultants and process integration experts • Universities and research partners	• Know-how about heat pump design and compressor integration • Intellectual property • Supply chain management for key components • Proof-of-concept and demonstration projects • Sales with a large industry network • Dedicated sales force • Technical resources for after-sales service and maintenance	• Sustainable process heat supply • Reductions in energy consumption, energy costs, and CO_2 emissions (i.e., carbon-free on-site heat source) as a contribution to carbon neutral/net zero strategies • Saving fossil fuels • Integration into existing industrial processes • Training the customer regarding heat pump technology (how it works and what benefits it can bring)	• Various energy-intensive industries (e.g., food & beverage, paper, chemical, oil) • Sugar mills, distilleries, petrochemical plants, paper mills, gypsum, ceramics, etc. • Steam and drying processes • Energy service suppliers (ESCOs) and providers of district heating networks; infrastructure providers for large industry parks • B2B resellers, wholesalers, project developers, and utilities
(9) Cost structure	**(6) Key activities**	**(4) Customer channel**	**(3) Customer relationships**
• Investment costs for equipment and technical works (i.e., construction, mechanics, electrification, electricity grid, etc.) • Operating costs (i.e., electricity consumption during lifetime) • Maintenance costs (i.e., annual inspections, spare parts) • Subsidy programs	• Development of high-quality heat pump technology (TRL9) • Demo units • Standardization and modularization • Sales and marketing activities • Hiring and training new competent employees	• Direct sales • Sales through distribution partners • Reference customers (i.e., pilot projects)	• Direct sales of equipment to end users or integrators • Direct sales of turnkey projects (100% one-stop-shop) • Sale of heat pump products through partners • Special leveraged tenders (e.g., waste heat recovery, virtual power plants)
		(5) Revenue streams	
		• Direct sales of heat pump equipment (hardware) • Installation and commissioning • Maintenance and service contracts (EaaS) • Subsidies and incentives • Licensing/IP fees	

5.1. Customer segments

As heat pump technology is a cross-sectional technology, the end users of industrial heat pumps can be found in various process industries. Most requests come from the food and beverage industry, followed by the paper and chemical industries. End users own energy-intensive industrial plants such as sugar mills, distilleries, petrochemical plants, paper mills, gypsum, ceramics, etc. The focus is on processing heat supply through steam and drying processes. Process integration is often performed confidentially within an industrial company. Developing specific industry solutions to take advantage of the multiplication potential is possible. Customers can also be B2B resellers, wholesalers, project developers, utilities, and energy service companies (ESCOs) focused on plant operations (facility management).

5.2. Value proposition

The main added value to customers by industrial heat pumps is the conversion of several industrial sectors to a sustainable process heat supply and significant reductions in energy consumption and CO_2 emissions (i.e., carbon-free on-site heat source). This enables:

- Reduction of energy consumption and energy costs (i.e., operating costs)
- Increasing the share of renewable energies
- Reduction of greenhouse gas emissions (CO_2, carbon emissions, carbon neutrality)
- Saving of fossil fuels (e.g., independence from gas imports)
- Reducing dependency on energy markets and their volatility (level of energy autarky)
- Increasing the use of energy from excess heat sources
- Profits from trading on the spot market

Training the customer about how a heat pump works and what benefits it can bring is also a value proposition. The heat pump manufacturers assist potential customers in the selection, purchase and integration process and provide customers with a lower-cost alternative (life cycle costs) compared to competing or existing heating technologies such as gas boilers or biomass. At the same time, technical innovation will stimulate the creation of numerous jobs and significantly contribute to the economy's growth.

5.3. Customer relationships

Building trust, good sales and customer support, and a good network in the industry are crucial for establishing successful customer relationships. In service concepts, a distinction is made between long-term and short-term customer relationships. In the eyes of the customers, individual and customized solutions are important.

5.4. Customer channels

The customer relationship can take place through various channels:

- Direct sales of heat pumps to end users
- Direct sales of heat pumps to integrators
- Direct sales of turnkey projects (100% one-stop-store) to end users
- Sales of heat pump products through partners
- Special tenders with leverage effect (e.g., waste heat recovery)

As a confidence-building measure, demo sites of industrial heat pumps for on-site visits are important.

5.5. Revenue streams

The current revenue streams come mainly from direct heat pump equipment (hardware) sales to customers or integrators and a little from installation and commissioning. This means turnkey projects will be sold directly to end customers (100% one-stop-shop). In the future, revenue will also be generated from the sale of maintenance and service contracts. Energy as a Service is a very interesting business model (e.g., lease-like contracts with fixed lease rates and residual purchase value at the end of the contract). Important sources of revenue are also local, national, and European subsidies and incentives.

5.6. Key activities

Because industrial high-temperature heat pumps are a relatively new technology, the development (R&D) of a stable, high-quality product is a top priority. Some heat pump manufacturers need more operational experience (i.e., operating hours) to increase the technology readiness level from TRL7 to TRL9. A goal is also to build standardization and modularization into the product line. In sales, high growth and demand for heat pump products are expected in the coming years. At the moment, sales activities are reactive rather than active. Nevertheless, numerous discussions are being held with customers in various countries, particularly Europe, to sell the technology throughout Europe. Depending on the order situation, project planning is a key activity for which additional employees must be hired. Project execution also expects a strong increase in personnel for the delivery, installation, and commissioning of the heat pump products. The biggest challenge will probably be finding enough competent employees and training them quickly and properly.

5.7. Key resources

The most important resources are internal know-how about heat pump design and the integration of compressors into a heat pump circuit, which may be based on intellectual property. Supply chain management for key components is important for delivery capability (i.e., enabling short delivery times). Proof-of-concept and demonstration projects are important to customers. Internally, marketing and sales with a large industry network are advantageous. A balance is needed between new human resources for marketing (e.g., dedicated sales force) and technical resources for after-sales service and maintenance.

5.8. Key partners

Important partners for a heat pump manufacturer are subcontractors and equipment suppliers for the core components such as compressors, heat exchangers, valves, control systems, etc. For commercialization, some heat pump manufacturers act as original equipment manufacturers (OEM). They actively work with distribution partners in selected countries to expand their sales network by integrating heat pump products into their portfolio. It is also crucial to have companies as demo customers that operate the first units to gain operational experience (i.e., running hours). For example, demo units are returned to the heat pump manufacturer after 6 to 12 months to check for wear.

Furthermore, there is the possibility of inviting end customers for an on-site visit to see the demonstration units in operation to build trust in the market (i.e., seeing is believing). Finally, important partners are also:

- Regional, national, and European public institutions for promotion,
- Private and public investment funds and banks for financing projects,
- Technical consultants and experts for knowledge transfer, and
- Universities and research partners for further development of the heat pump technology (e.g., cooperations with other technology providers).

5.9. Cost structure

The costs arising from the sale of industrial heat pumps and services are mainly investment costs for equipment and technical work (i.e., construction, mechanics, electrification, electricity grid, etc.), but also operating costs (i.e., electricity consumption during lifetime) and maintenance costs (i.e., annual inspections, spare parts). In some cases, subsidy programs are used to pre-finance project development.

6. Conclusions

Industrial heat pumps are on the rise for the electrification of process heat in industry and are an important cross-cutting technology for the transition to renewable energies. Accordingly, the market will experience increased competition in the coming years, pushing industrial heat pump manufacturers to develop new business models. This review has shown that business models for industrial heat pumps are overall insufficiently described and that a scientific research gap exists. Initial findings could be summarized based on empirical responses from interviews with manufacturers and literature research analyses.

The most widespread business model appears to be the Direct2Customer, which primarily involves project development and directly selling heat pumps to end customers. Revenues from installation and commissioning and future services from maintenance and servicing supplement this. However, each heat pump technology (e.g., vapor compression, MVR, absorption, thermochemical heat pump) requires its own business model evaluation using the proposed model building blocks. The highly customer-integrated business models such as Energy-as-a-Service (EaaS) and especially Heat-as-a-Service (HaaS) are opening new market opportunities for industrial heat pumps. However, none of the heat pump manufacturers interviewed has yet implemented HaaS in connection with industrial heat pumps. So far, only individual energy service companies (ESCO) now offer EaaS business models for industrial heat pumps.

As an outlook, an attempt could be made to quantify the effectiveness and impact of the different business models, e.g., on marginal prices, consumer behavior or societal acceptance. Further interviews with industry partners in the industrial heat pump value chain need to be conducted for a more detailed investigation of customer needs and business models. A PESTEL analysis with political, economic, social, technological, environmental, and legal influencing factors will be realized within the PUSH2HEAT project.

Further research could examine the structure of business relationships between the organizations involved in manufacturing, distributing, and using industrial heat pumps. Such an ecosystem-level analysis can identify ways to better align the respective business models to accelerate the adoption of heat pumps by industrial customers and ensure high-quality installations.

Acknowledgments

This study is part of the EU-funded Horizon Europe project PUSH2HEAT (Pushing forward the market potential and business models of waste heat valorization by full-scale demonstration of next-gen heat upgrade technologies in various industrial contexts, Grant Agreement No. 101069689) (www.push2heat.eu). In addition, the authors gratefully acknowledge the Swiss Federal Office of Energy (SFOE) for the financial support of the SWEET project DeCarbCH (DeCarbonisation of Cooling and Heating in Switzerland) (www.sweet-decarb.ch) and the project Annex 58 HTHP-CH (Contract number SI/502336-01). Finally, the authors acknowledge Dr. Matthias Speich from ZHAW School of Engineering (Switzerland), Dr. Michael Bantle from ANEO Industry (Norway), and Jan Haraldsen from EPCON Evaporation Technology AS (Norway) for reviewing the final manuscript. The authors bear sole responsibility for the conclusions and the results.

References

[1] R. De Boer *et al.*, “Strengthening Industrial Heat Pump Innovation, Decarbonizing Industrial Heat, White Paper,” 2020. [Online]. Available: https://www.ost.ch/fileadmin/dateiliste/3_forschung_dienstleistung/institute/ies/projekte/projekte_tes/91_sccer-eip/2020-07-10_whitepaper_ihp_-a4_small.pdf

[2] C. Arpagaus, F. Bless, M. Uhlmann, J. Schiffmann, and S. S. Bertsch, “High temperature heat pumps: Market overview, state of the art, research status, refrigerants, and application potentials,” *Energy*, vol. 152, pp. 985–1010, Jun. 2018, doi: 10.1016/j.energy.2018.03.166.

[3] IEA HPT, “Annex 58 High-Temperature Heat Pumps,” 2021. https://heatpumpingtechnologies.org/annex58

[4] C. Arpagaus *et al.*, “Integration of High-Temperature Heat Pumps in Swiss Industrial Processes (HTHP-CH),” in *14th IEA Heat Pump Conference, 15-18 May 2023, Chicago, Illinois*, 2023, pp. 1–12. [Online]. Available: https://whttps//www.hpc2023.org/wp-content/uploads/gravity_forms/3-7075ba8a16c5f78b321724d090fb2a34/2023/05/0494_HPC2023_Full_Paper_Arpagaus_v02.pdf

[5] F. Bless, C. Arpagaus, M. Speich, and S. Bertsch, “Electrification of Heat Generation in Industry: State of Technologies, Integration Examples, and Integration Barriers,” in *Young Energy Researchers Conference 2022 Electrification, 5. April 2022, Wels, Austria*, 2022, pp. 1–14.

[6] A. Marina, S. Spoelstra, H. A. Zondag, and A. K. Wemmers, “An estimation of the European industrial heat pump market potential,” *Renew. Sustain. Energy Rev.*, vol. 139, p. 110545, 2021, doi: 10.1016/j.rser.2020.110545.

[7] J. Giehl, H. Göcke, B. Grosse, J. Kochems, and J. Müller-Kirchenbauer, “Survey and classification of business models for the energy transformation,” *Energies*, vol. 13, no. 11, pp. 1–17, 2020, doi: 10.3390/en13112981.

[8] EHPA, “Shifting paradigms with heat pumps: new business models, EHPA Online Webinar Series 2021,” 2021. https://www.youtube.com/watch?v=qbbG446VwrM

[9] A. Osterwalder and Y. Pigneur, *Business Model Generation*. John Wiley & Sons, Inc., 2010.

[10] O. Gassmann and K. Frankenberger, “Geschäftsmodelle entwickeln: Von der Kunst zum Handwerk,” in *Geschäftsmodellinnovationen*, Wiesbaden: Springer Fachmedien Wiesbaden, 2016, pp. 17–33. doi: 10.1007/978-3-658-08623-7_1.

[11] O. Gassmann, K. Frankenberger, and M. Choudury, *Geschäftsmodelle entwickeln: 55+ innovative Konzepte mit dem St. Galler Business Model Navigator*. München: Carl Hanser Verlag GmbH, 2016.

[12] O. Gassmann, K. Frankenberger, and M. Csik, “The St . Gallen Business Model Navigator,” *Int. J. Prod. Dev.*, vol. 18, no. 3, pp. 249–273, 2013.

[13] T. Crosbie, M. Short, M. Dawood, and U. Shvadron, “Specific business models for demo cases, Deliverable 2.2, IDEAS project, Teesside University,” 2014. https://www.researchgate.net/publication/269631950%0ASpecific

[14] K. Lygnerud, J. Ottosson, J. Kensby, and L. Johansson, “Business models combining heat pumps and district heating in buildings generate cost and emission savings,” *Energy*, vol. 234, p. 121202, Nov. 2021, doi: 10.1016/j.energy.2021.121202.

[15] P. A. Østergaard, J. Jantzen, H. M. Marczinkowski, and M. Kristensen, “Business and socioeconomic assessment of introducing heat pumps with heat storage in small-scale district heating systems,” *Renew. Energy*, vol. 139, pp. 904–914, Aug. 2019, doi: 10.1016/j.renene.2019.02.140.

[16] O. Terreros *et al.*, “Electricity market options for heat pumps in rural district heating networks in Austria,” *Energy*, vol. 196, p. 116875, 2020, doi: 10.1016/j.energy.2019.116875.

[17] ReUseHeat, “Efficient contractual forms and business models for urban waste heat recovery,” 2019. https://www.reuseheat.eu/wp-content/uploads/2021/03/D2.3-UPDATED_20210223.pdf

[18] J. Vivian, G. Emmi, A. Zarrella, X. Jobard, D. Pietruschka, and M. De Carli, “Evaluating the cost of heat for end users in ultra low temperature district heating networks with booster heat pumps,” *Energy*, vol. 153, pp. 788–800, Jun. 2018, doi: 10.1016/j.energy.2018.04.081.

[19] D. Fischer, M.-A. Triebel, T. Erge, and R. Hollinger, “Business Models Using the Flexibility of Heat Pumps - A Discourse,” *12th IEA Heat pump Conf. Rotterdam, May 14-17, 2017*, pp. 1–11, 2017.

[20] C. Lyon, L. Sugden, and R. Pieterse, “Disruption to heat business models: from shifting boxes to selling comfort,” in *13th IEA Heat Pump Conference, April 26-29, 2021 Jeju, Korea*, 2021, pp. 891–900. [Online]. Available: https://heatpumpingtechnologies.org/publications/disruption-to-heat-business-models-from-shifting-boxes-to-selling-comfort-13th-iea-heat-pump-conference-jeju-korea/

[21] R. Fleck, A. Annam, E. Hunt, and M. Lipson, “The potential of Heat as a Service as a route to decarbonisation for Scotland,” no. January, 2021, doi: http://dx.doi.org/10.7488/era/809.

[22] J. Britton, A. M. Minas, A. C. Marques, and Z. Pourmirza, “Exploring the potential of heat as a service in decarbonization: Evidence needs and research gaps,” *Energy Sources, Part B Econ. Planning, Policy*, vol. 16, no. 11–12, pp. 999–1015, Dec. 2021, doi: 10.1080/15567249.2021.1873460.

[23] S. Skovshoved and I. Sandqvist, “Customer Value Driven Service Innovation: Identifying service opportunities in the residential heating market based on customers’ value preferences, Master Thesis, Linköping University, Sweden,” 2017. http://liu.diva-portal.org/smash/record.jsf?pid=diva2%3A1112376&dswid=552

[24] Z. Li, L. Ma, Z. Li, and W. Ni, “Multi-energy cooperative utilization business models: A case study of the solar-heat pump water heater,” *Renew. Sustain. Energy Rev.*, vol. 108, no. April, pp. 392–397, Jul. 2019, doi: 10.1016/j.rser.2019.04.015.

[25] A. R. Kalair, S. Dilshad, N. Abas, M. Seyedmahmoudian, A. Stojcevski, and K. Koh, “Application of Business Model Canvas for Solar Thermal Air Conditioners,” *Front. Energy Res.*, vol. 9, no. July, pp. 1–23, Jul. 2021, doi: 10.3389/fenrg.2021.671973.

[26] J. Zapata Riveros, M. Speich, M. West, and S. Ulli-Beer, “Combining Business Model Innovation and Model-Based Analysis to Tackle the Deep Uncertainty of Societal Transitions—A Case Study on Industrial Electrification and Power Grid Management,” *Sustainability*, vol. 13, no. 13, p. 7264, Jun. 2021, doi: 10.3390/su13137264.

[27] J. Ottosson, L. Johansson, J. Kensby, K. Lygnerud, J. Nilsson, and A. Nilsson, “Business models for combining district heating and heat pumps in buildings, Report 2020:679,” 2020. www.energiforsk.se

[28] A. Nelson, “Business Model Innovation to Support Heat Pump Retrofits in Metro Vancouver,” no. August, p. 43, 2019, [Online]. Available: https://sustain.ubc.ca/sites/default/files/2019-13_Business Model Innovation to Support Heat Pump Retrofits_Nelson_0.pdf%0Afiles/1401/Nelson - Business Model Innovation to Support Heat Pump Ret.pdf

[29] L. Okkonen and N. Suhonen, “Business models of heat entrepreneurship in Finland,” *Energy Policy*, vol. 38, no. 7, pp. 3443–3452, Jul. 2010, doi: 10.1016/j.enpol.2010.02.018.

[30] K. J. Kircher and K. M. Zhang, “Heat purchase agreements could lower barriers to heat pump adoption,” *Appl. Energy*, vol. 286, no. January, p. 116489, Mar. 2021, doi: 10.1016/j.apenergy.2021.116489.

[31] Push2Heat, “PUSH2HEAT: Pushing forward the market potential of heat upgrade technologies,” 2023. https://www.ehpa.org/press_releases/push2heat-pushing-forward-the-market-potential-of-heat-upgrade-technologies/

[32] J. Tan, Q. Wu, and M. Zhang, “Strategic investment for district heating systems participating in energy and reserve markets using heat flexibility,” *Int. J. Electr. Power Energy Syst.*, vol. 137, no. December 2021, p. 107819, May 2022, doi: 10.1016/j.ijepes.2021.107819.

[33] WBCSD, “Industrial Heat Pumps: It’s time to go electric,” 2022. https://www.wbcsd.org/contentwbc/download/14846/211001/1

[34] BASE, “Market Transformation: Servitisation of Cooling Industry, Basel Agency for Sustainable Energy,” 2023. https://energy-base.org/projects/cooling-as-a-service-initiative/

[35] M. Singh, J. Jiao, M. Klobasa, and R. Frietsch, “Servitization of Energy Sector: Emerging Service Business Models and Startup’s Participation,” *Energies*, vol. 15, no. 7, p. 2705, Apr. 2022, doi: 10.3390/en15072705.

[36] Mordor Intelligence, “Energy as a Service Market - Growth, Trends, COVID-19 Impact, and Forecasts (2023 - 2028),” 2023. https://www.mordorintelligence.com/industry-reports/energy-as-a-service-market#:~:text=Market Overview,as-a-service market

[37] ANEO, “Our Service Platform: Energy as a Service,” 2023. https://www.aneo.com/tjenester/industry/english/serviceplatform/

ULPGC
Universidad de
Las Palmas de
Gran Canaria

grres ULPGC
group for the research on renewable energy systems

G. Fuels, combustion & gasification. Fuel cells. Hydrogen use in energy systems

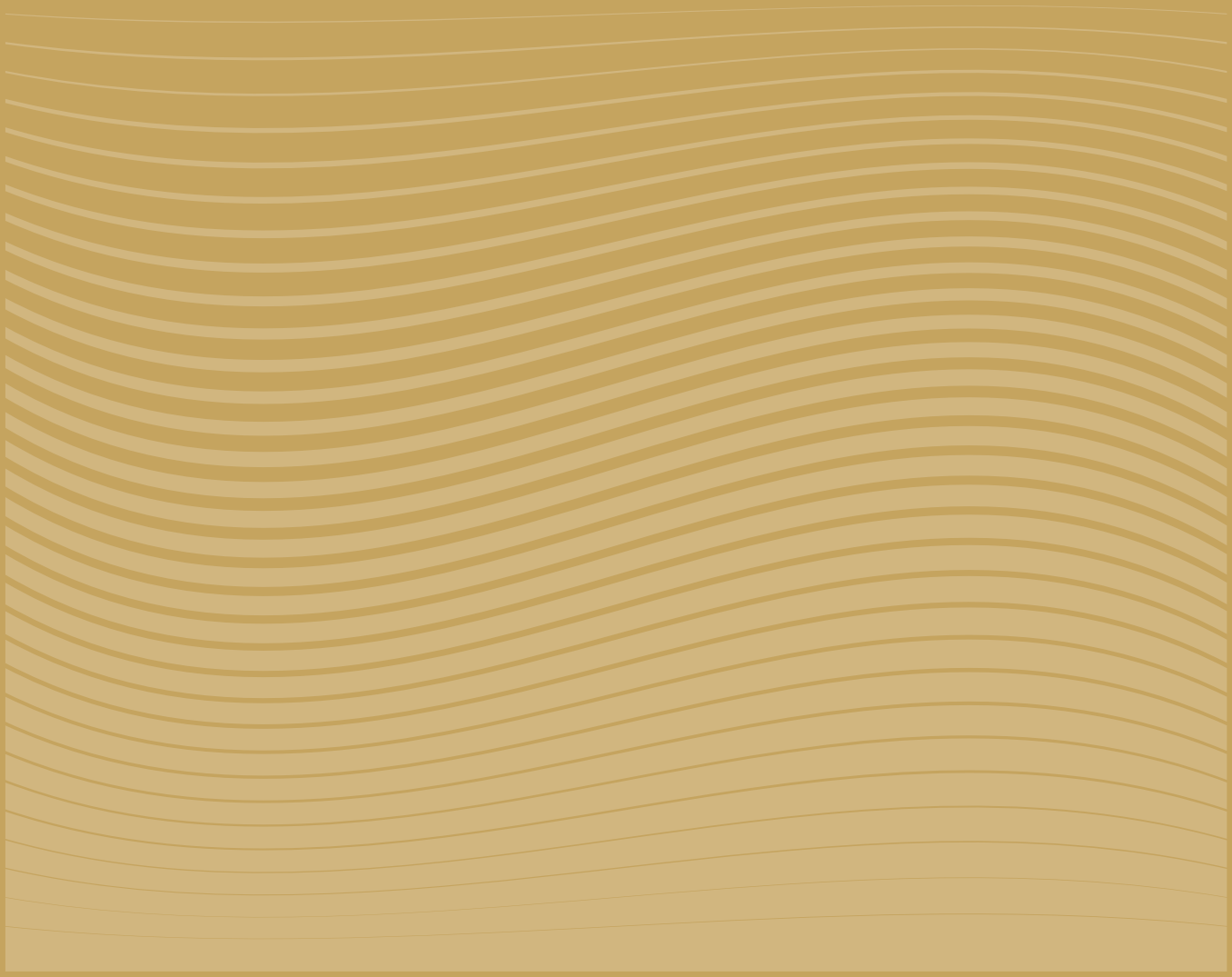

ECOS2023

GreenH2CM. Fuel cell-based hybrid powertrain research and testing laboratory for maritime and aeronautical environments

Antonio Villalba-Herreros[a], Rafael d'Amore-Domenech[b], Vladimir L. Meca[c], David Gómez-García[d], Emilio Navarro[e] and Teresa J. Leo[f]

[a] Universidad Politécnica de Madrid, Madrid, Spain, antonio.villalba@upm.es
[b] Universidad Politécnica de Madrid, Madrid, Spain, r.damore@upm.es
[c] Universidad Politécnica de Madrid, Madrid, Spain, vl.meca@upm.es
[d] Universidad Politécnica de Madrid, Madrid, Spain, david.gomez.garcia@alumnos.upm.es
[e] Universidad Politécnica de Madrid, Madrid, Spain, emilio.navarro@upm.es
[f] Universidad Politécnica de Madrid, Madrid, Spain, teresa.leo.mena@upm.es, CA

Abstract:

Power trains based on fuel cells hybridized with any secondary power sources provide similar effectiveness levels than current powertrains based on internal combustion engines but achieve better efficiency values and have the potential to be free of harmful emissions. However, the development of these powertrains is still in its childhood and research efforts must be reinforced, especially in marine and aeronautical applications. One part of the project GreenH2CM will provide a valuate tool that will support the research in this area. In the frame of the GreenH2CM Activity Line "Uses of hydrogen in heavy transport, aviation and maritime sectors", the research group PiCoHiMA from the Universidad Politécnica de Madrid (Spain) is developing a Laboratory for testing fuel cell integrations for marine and aeronautical applications. The resulting installation will allow to test fuel cell stacks with powers up to 300 kW and the simulation of hybridized secondary power sources as batteries or capacitors. The laboratory will not only allow to monitor and control the critical parameters of the stack under study to simulate adequate environmental conditions, besides, a 6-freedom degrees hexapod will allow to simulate the movements of the platform to study its impact.

Keywords:

Hydrogen; PEM fuel cell; propulsion; test bench; marine; aeronautical.

1. Introduction

Although green hydrogen is a versatile energy carrier that will play a key role in meeting the decarbonisation targets to which Spain has committed, a major R&D&I effort is still needed for it to be considered as an economically viable alternative.

The project that is presented here, "Strategic Positioning of the Community of Madrid in Green Hydrogen and Fuel Cell R&D&I GreenH2CM", is being developed by several national and regional research institutions and is funded by the Ministerio de Ciencia e Innovación de España (Spanish Ministry of Science and Innovation) MCIN/AEI/10.13039/501100011033, by "NextGeneration EU/PRTR", and by the Regional Government of Madrid, in the frame of the Complementary Plans. GreenH2CM project pursues three general objectives in the field of Hydrogen and Fuel Cells:

- To structure and coordinate the R&D&I capacities of the Madrid Region, among themselves and with other Spanish Regions with common interests, around the green hydrogen value chain and its application by means of: (i) optimisation of the connection between renewable electricity generators and electrolysers, (ii) innovative high temperature hydrogen production techniques with reversible operation capability, (iii) optimisation of fuel cell integration and (iv) safe combustion techniques of hydrogen and its mixtures for use in the industrial, residential and transport sectors. These innovative concepts will allow the necessary progress in reducing the production costs of green hydrogen so that it can reach the market.
- To collaborate in defining the Madrid Region strategic lines of work on new concepts of green hydrogen production and fuel cell applications that generate industrial and economic value and act as an instrument to position the Madrid Region at national and European level in the development of these technologies. It also aims to establish alliances and cooperation agreements on renewable energies,

green hydrogen and fuel cells and to promote technological surveillance and competitive intelligence to identify new work niches in this area.

- To educate and train researchers, through the recruitment of research personnel at different stages of their training, and to generate human capacities for the development of a national industry covering the entire value chain around green hydrogen and fuel cells.

Therefore, this R&D will complement and help support national industry in the development of innovative electrolyser concepts with higher efficiency, longer life and lower cost, as well as other hydrogen generating systems from concentrated solar energy; integration of fuel cells in transport (air, maritime, rail and road), industry and building applications and the development of new combustion devices and/or the adaptation of existing ones to move towards decarbonisation and climate neutrality.

The GreenH2CM Project addresses the development of five main lines of action (LIA), out of the 13 lines included in the Green Energy and Hydrogen programme of Complementary Plans:

- LIA1: Low temperature green hydrogen generation from renewable energy.
- LIA3: High-temperature hydrogen generation from renewable energy and waste heat utilisation.
- LIA7: Uses of hydrogen in heavy transport, aviation and maritime sectors.
- LIA8: Uses of hydrogen in the industrial combustion sector.
- LIA11: Techno-economic studies and market launch of utility models. Dissemination, education and training activities for new researchers.

2. Uses of hydrogen in heavy transport, aviation and maritime sectors (LIA7) in GreenH2CM

Since the beginning, mankind has need for mobility. Means of transport have evolved looking for higher speed, safety, and more power and efficiency. This evolution has been always supported by scientific and technical developments allowing the transition from human or animal power to steam, from steam to oil and, more recently, from oil to electrochemical energy stored in batteries and alternative fuels to look for more environmentally friendly solutions. In this sense, hydrogen and fuel cells are a promising technology for the mobility of the future that should make it possible to decarbonise those transport segments in which electrification does not provide a competitive solution compared to conventional combustion technologies. The aim of LIA7 is to investigate and develop advanced technological solutions for the integration and optimal operation of hydrogen-based systems for heavy, air and maritime transport applications.

The overall objective of Line of Action 7 (LIA7), *Uses of hydrogen in heavy transport, aviation and maritime sectors*, of the GreenH2CM project is to:

- Design, build and operate a facility for the testing of fuel cell integrated power trains in the maritime and aviation sectors.

In general terms, this line of action includes: a) Development of technology to improve the reliability of the energy and degradation models of fuel cells to optimise their subsequent sizing and operation in hydrogen-based vehicles. b) Development of advanced methodologies to optimise the sizing of hybrid traction solutions (fuel cells with batteries) and their configuration and thermal management. c) Generation of innovative solutions for the intelligent management of hydrogen-based vehicles, ships and aircraft to optimise their operation throughout their useful life.

The *expected results* are summarized as follows:

- Training to develop detailed dynamic models of the tested power generation system and its components for real-time simulation and/or digital twin applications;
- Implementation of a power distribution system that will connect the primary and secondary sources (fuel cell, battery and supercapacitor) to the load, which will reproduce the power operating profile under test;
- Development and qualification of the heat exchangers necessary to perform proper thermal management of a fuel cell-based power generation system on board a commercial aircraft;
- Prototype demonstrator of a hydrogen fuel cell hybrid vehicle, operational and functional in the field of heavy road, port and/or airport transport;
- Fuel cell testing capability with impurity measurements in the gas streams under various operating conditions.

The main work involved in this LIA7 of GreenH2CM is the development of a laboratory for the testing of powertrains in the maritime and aviation sectors. It is described in Section 3.

3. Laboratory for testing fuel cell integrations for marine and aeronautical applications

In order to be able to carry out research, training and provide services to private companies, it is necessary to develop the design, construction and commissioning of a facility to test fuel cell integration in power trains for marine and aeronautical applications. Figure 1 shows the preliminary design of the facility.

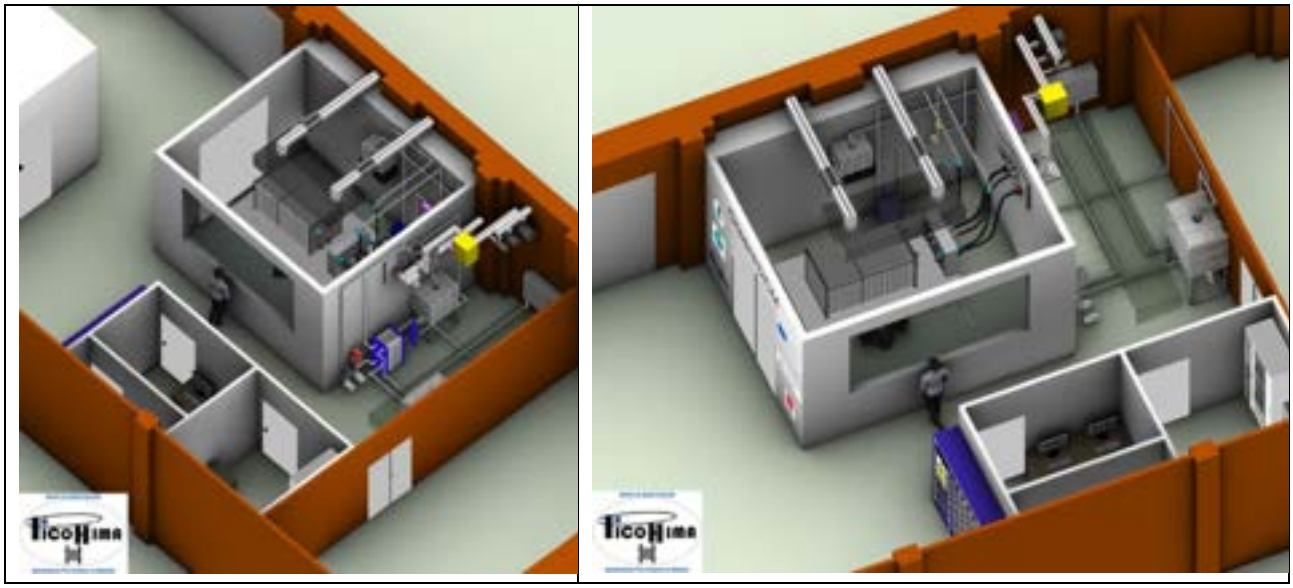

Figure 1. Two views of the preliminary design of the Laboratory for testing fuel cell integrations for marine and aeronautical applications in the frame of the GreenH2CM project.

The tasks planned to achieve this facility are as follows:

- Detailed design of the test facility.
- Selection of components and services for the test facility.
- Procurement of components and services for the test facility.
- Construction of the test facility.
- Configuration, testing and commissioning of test facility systems.
- Operational tests with real operating profiles of a fuel cell and battery integration, with and without movements.

In addition to this, it is planned to develop: a Doctoral thesis on the subject, dissemination activities and establish company-university agreements.

The resulting installation will allow to test fuel cell stacks with powers up to 300 kW and the simulation of hybridized secondary power sources as batteries or capacitors. The laboratory will not only allow to monitor and control the critical parameters of the stack under study to simulate adequate environmental conditions, but a 6-freedom degrees hexapod will allow to simulate the movements of the platform to study its impact.

This facility will be located at the Escuela Técnica Superior de Ingenieros Navales (Technical School of Naval Architects and Marine Engineers) of the Universidad Politécnica de Madrid (Spain) and will be under the management of the PiCoHiMA Research Group [1]. This Laboratory is an important asset that will offer valuable services to both the academy and the private sector. This facility can be integrated into large projects, allowing fuel cell solutions to be tested not only at a laboratory scale but also at a near-market scale, ensuring the quality of the final product at a critical stage of its development where such tools are scarce. This is an advantage for companies and research institutions in ensuring the reliability of their developments.

4. Conclusions

GreenH2CM is an important project that poses the basis for the development of critical knowledge and facilities around hydrogen technologies in the Madrid Region also structuring and coordinating the R&D&I capabilities in this Region.

Among the five Lines of Action covered by this project, the Line of Action 7 “Uses of hydrogen in heavy transport, aviation and maritime sectors” stands out.

The purpose of this Action Line to research and develop advanced technological solutions for the integration of hydrogen-based systems for heavy transport, aviation and maritime applications is reflected in its main objective, i.e. the design, construction and operation of a facility for the testing of fuel cell integrated power trains in the maritime and aeronautical sectors.

The resulting installation will allow to test fuel cell stacks with powers up to 300 kW and the simulation of hybridized secondary power sources such as batteries or capacitors, including the impact on the fuel cell stack of the movements induced by a 6-freedom degrees hexapod that simulates the movements of the platform where the stack is embarked.

This laboratory is an important asset that will provide valuable services to both academia and the private sector, facilitating the testing of fuel cell systems not only at laboratory scale but also at near market scale, ensuring the quality of the final product at a critical stage.

Acknowledgments

This work has been carried out thanks to the Project GreenH2CM funded by MCIN/AEI/10.13039/501100011033, by “NextGenerationEU/PRTR” and the Regional Government of Madrid and to the Grant PID2021-124263OB-I00 funded by MCIN/AEI/10.13039/501100011033 and by “ERDF a way of making Europe”.

References

[1] (https://blogs.upm.es/picohima/).

Development of Electrodes for fuel cells Pt-free load

Elena Posada[a], Oscar Santiago[b], Vladimir L. Meca[c], Teresa J. Leo[d], Isabel Carrillo[e], Eva Chinarro[f]

[a] Dept. Arquitectura, Construcción y Sistemas Oceánicos y Navales, ETSI Navales, Universidad Politécnica de Madrid, Avda. Memoria 4, 28040 – Madrid, Spain, elena.posada@upm.es
[b] University of Bremen, Bremen, Germany, santiago@uni-bremen.de
[c]Dept. Arquitectura, Construcción y Sistemas Oceánicos y Navales, ETSI Navales, Universidad Politécnica de Madrid, Avda. Memoria 4, 28040 – Madrid, Spain, vl.meca@upm.es
[d]Dept. Arquitectura, Construcción y Sistemas Oceánicos y Navales, ETSI Navales, Universidad Politécnica de Madrid, Avda. Memoria 4, 28040 – Madrid, Spain, teresa.leo.mena@upm.es, CA
[e]Dept. Ingeniería Mecánica, Química y Diseño Industrial, ETSIDI, Universidad Politécnica de Madrid (UPM), Ronda de Valencia 3, 28012 – Madrid, Spain, Isabel.carrillo@upm.es
[f]Instituto de Cerámica y Vidrio del CSIC (ICV-CSIC), C/Kelsen 5, 28049 – Madrid, Spain, martin@icv.csic.es

Abstract:

Direct methanol fuel cells, DMFCs, have a great interest due to their applications in the development of devices for portable energy applications due to their ability to produce electricity using methanol as fuel. These systems are environmentally friendly. Nevertheless, the methanol crossover from the anode to the cathode through the electrolytic membrane, the poisoning of the catalyst and the cost of these systems are some of the problems. One of the responsible of the high cost of these systems is the use of platinum, Pt, for the development of the electrodes.

The objective of this work is to develop catalysts Pt-free. Materials based on FeCo solid solutions are synthesized by the combustion method and characterized for their further application as anode catalysts in DMFC. In addition, a post-treatment in reactive environments has been carried out the aim of improving the metal solution. The prepared materials have been morphological, structural and electrochemically characterized to test their activity towards methanol oxidation. Further, the catalytic layer composition has been designed to prepare electrodes by spray, in such a way that the slurry can be homogeneously sprayable on the surface of the carbon paper gas diffusion layer. The catalyst and electrodes have been studied to know if they are good candidates as anode of DMFCs, and to modify the synthesis and/or the different processes to improve their activity.

Keywords:

DMFC; electrocatalyst; Pt free; catalytic layer; combustion synthesis.

1. Introduction

The development of the society has increased the consumption of energy. The high cost of energy, the lack of resources and the pollution among others, make urgently to seek and develop new and renewable energies [1,2]. Fuel cells, which convert chemical energy into electrical energy via electrochemical reactions on the electrode surface are a promising alternative and clean energy resource [3-5]**.**

Direct methanol fuel cells, DMFCs, have a great interest due to their high energy density, high conversion efficiency, low operating temperatures, low emissions of toxic substances [4] and also to their applications in the development of devices for portable energy applications [6-8]. Moreover, these systems are environmentally friendly, have easy operation and simple construction [4,9]. However, the crossover of methanol from the anode to the cathode through the electrolytic membrane, sluggish oxidation kinetics and the durability and deteriorating catalyst performance are some factors which have restricted the commercialization of DMFC tools [1]. Another problem is the high cost of the catalysts due to the use of Nobel metals like platinum. Consequently, it is necessary to reduce the cost of fuel cell catalyst and enhance their lifespan.

As catalysts in DMFC are commonly supported on conductive and porous membranes being this another important fact. It is well known that supported metal catalysts show improved stability and higher activity compared to unsupported bulk metal catalysts. Surface area, porosity, electrical conductivity, electrochemical stability, and surface functional groups characterise a support [5,10]. In this sense, carbon materials have been used as catalyst support due to remarkable properties, such as good electronic conductivity, better stability and environment friendliness. There are several materials such as mesoporous carbon, carbon black, carbon quantum dots, carbon nanotubes, carbon nanofibre, graphene and other carbon forms such as carbon nanosheet, nanohorns, nanosphere as electrocatalyst support have been reported [11].

In order to diminish or avoid the use of platinum in fuel cells several low-platinum catalyst, Pt-C or free Pt catalyst have been developed including Pt-based alloying, Pt-based nanostructure design and supports-enhanced methods [10,12-17]. Alloying Pt with more abundant and cheaper 3d-transition metals (such as Fe, Co, Cu, Ni) is considered as a facile strategy for heightening the electrochemical properties of [18-20].

Combustion synthesis is an effective, low-cost method for production catalysts and nanocarries by solid state and solution combustion [21,22]. The exothermicity of the redox chemical reaction is used to produce the material. Depending on the nature of reactants different methods has been developed [22].

The objective of this work is to develop catalysts Pt-free. Materials based on FeCo solid solutions are synthesized by the combustion method and characterized for their further application as anode catalysts in DMFC. Further, the catalytic layer composition has been designed to prepare electrodes by spray, in such a way that the slurry can be homogeneously sprayable on the surface of the carbon paper gas diffusion layer. The prepared materials have been morphological, structural and electrochemically characterized to teste their activity towards methanol oxidation.

2. Experimental

2.1. Sample preparation by combustion method

To prepare the catalysts have been used are used iron (II) nitrate and cobalt and cobalt (II) nitrate as precursors. Urea has been chosen as fuel to maintain or modify the balance of valences. To obtain different local conditions during combustion different amounts of fuel have been employed. The nominal compositions formulated for the catalysts are Fe_xCo_{1-x} (x=0, 0.25, 0.5, 0.75, 1).

2.2. Structural and morphological characterization

The structural identification was performed by XRD with a Bruker to D8 Advance (CuKα radiation, 30 mA, 50kV). For composition determination was used EVA Application V6.0 program with PDF-2 Database sets 1-46.

2.3. Electrochemical measurements

Catalytic activity of the prepared powders towards methanol oxidation reaction was analysed by CV in a three-electrode cell (CE: Pt sheet, RE: Ag/AgCl and the material ink onto a glassy carbon tip as WE), at 25ºC. Using $HClO_4$ 0.1M + CH_3OH 0.5M as electrolyte. All data are collected in a I-V curve by AUTOLAB PGSTAT302N, firstly the samples have been activated, and measurements have been recorded at 50 mV/s from -0.1 to 1.3 V vs Ag/AgCl.

3. Results and discussion

Combustion synthesis exhibit four more or less rapid stages depending on raw materials (Fig. 1). The ignition temperature achieved allows obtaining, in a short time, the crystalline phases of the nanopowder material with porous structure. That phenomenon accelerates the kinetic reaction that is why this is the stage that controls the global process.

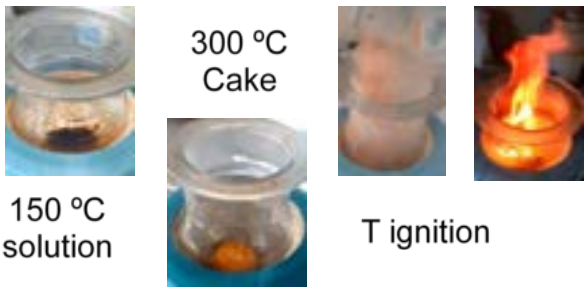

Figure 1. Scheme of urea synthesis processes.

Figure 2 shows that a mixture of oxides is obtained directly from the combustion with stoichiometric urea, observing small amounts of mixed oxides of iron and cobalt when different proportions of them are used to prepare the distinct nominal compositions.

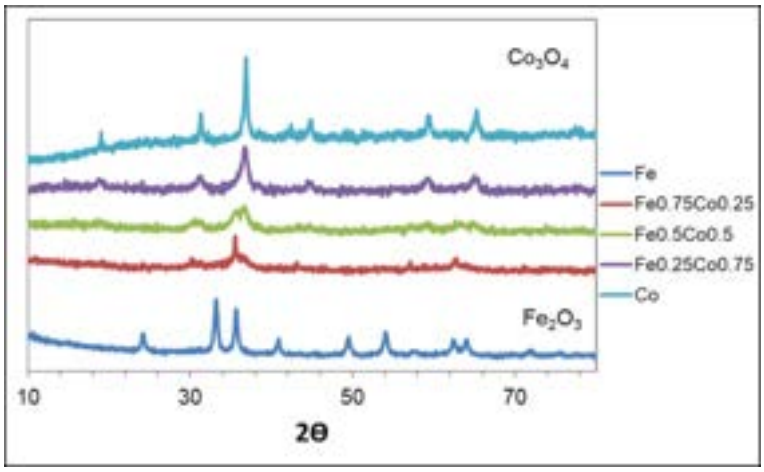

Figure 2. XRD of FexCo1-x (x=0, 0.25, 0.5, 0.75, 1) prepared by combustion synthesis with stoichiometric urea.

While in Fig. 3 it can be seen how the variation in the proportion of fuel makes it go from having Co_3O_4 to obtaining CoO.

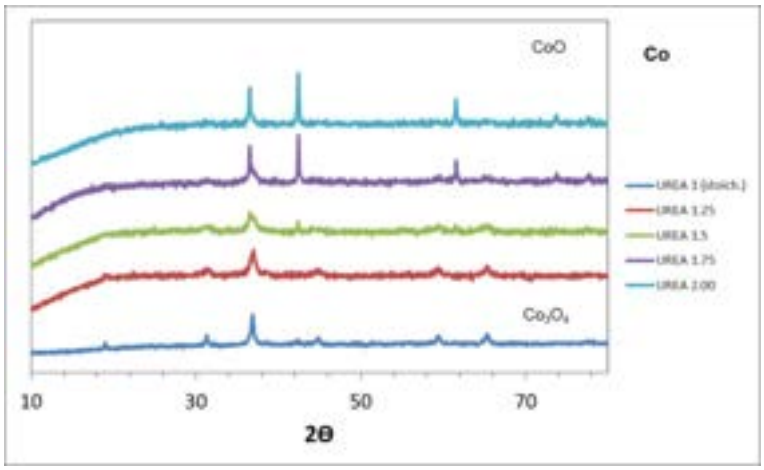

Figure 3. XRD of FexCo1-x (x=0) prepared by combustion synthesis with different ratios of urea.

By varying the stoichiometry of urea, in the case of x=0.25, 0.5, 0.75, the concentration of the mixed oxides of iron and cobalt increases.

Regarding the preliminary electrochemical measurements carried out, it has been observed that when iron or cobalt oxide is found alone there is no activity against methanol oxidation. But this activity begins to appear, although slightly, as the iron-cobalt mixture appears in the catalyst formulation.

4. Conclusions

The ignition stage of the combustion synthesis determines the final crystallographic and morphological properties of the powders due to the number of gases released in that condition and both the atmosphere and the local synthesis temperature. The combustion method has been studied tailoring the properties of the final product based on the raw mixture used. It has been proven that final features and electrochemical behaviour is different, mainly due to the different crystalline phases achieved in the synthesis.

The higher electrochemical activity is related to the crystal structure, the microstructure and morphology of the material. And these differences are directly related with time of reaction, local temperature and oxygen partial pressure reached.

Acknowledgments

This work has been carried out thanks to the Project GreenH2CM funded by MCIN/AEI/10.13039/501100011033, by “NextGeneration EU/PRTR” and the Regional Government of Madrid and to the Grant PID2021-124263OB-I00 funded by MCIN/AEI/10.13039/501100011033 and by “ERDF a way of making Europe.

References

[1] Bai Y., Ye N., Jiang Z., Zhang R., Fang T. Enhancing the activity and stability by coupling Ni-M bimetals and TaN for methanol oxidation reaction in alkaline media, Fuel 2023;341(1):127758-https://doi.org/10.1016/j.fuel.2023.127758 -71

[2] Luo Z., Lim S., Tian Z., Shang J., Lai L., Macdonald B., et al. Pyridinic N doped graphene: Synthesis, electronic structure, and electrocatalytic property. J. Mat. Chem. 2011;21:8038–8044. doi: https://doi.org/10.1039/c1jm10845j

[3] Wang B., Chang T.Y, Jiang Z.; Wei K.J., Fang T., Component controlled synthesis of bimetallic PdCu nanoparticles supported on reduced graphene oxide for dehydrogenation of dodecahydro-N-ethylcarbazole. Appl. Catal. B 2019;251:261-272 https://doi.org/10.1016/j.apcatb.2019.03.071

[4] Xiang Y., Xaho J., Quin L., Zhang X., W-Y, Tang X., Xu Y. Preparation of Pd/ZnO/Ni hierarchical porous array film with enhanced electrocatalytic activity for methanol oxidation, Int. J. Hydrogen Energy 2021;46(71): 35397-407. https://doi.org/10.1016/j.ijhydene.2021.08.079

[5] Sharma S., Pollet BG., Support materials for PEMFC and DMFC electrocatalysts—A review, J. Pwer Sources 2012; 208:96-119. https://doi.org/10.1016/j.jpowsour.2012.02.011

[6] Dyer C.K., J. Fuel cells for portable applications. Power Source 2002;10681-2):31-34. https://doi.org/10.1016/S0378-7753(01)01069-2

[7] Zuo Y., Sheng W., Tao W., Li Z., Direct methanol fuel cells system–A review of dual-role electrocatalysts for oxygen reduction and methanol oxidation, J. Mater. Sci. Technol. 2022;114:29–41. https://doi.org/10.1016/j.jmst.2021.10.031

[8] M.S. Alias, S.K. Kamarudin, A.M. Zainoodin, M.S. Masdar, Active direct methanol fuel cell: An overview, Int. J. of Hydrogen Energy 2020;45(38):19620-41. https://doi.org/10.1016/j.ijhydene.2020.04.202

[9] Shrivastava N.K., Thombre S.B., Chadge S.B. Liquid feed passive direct methanol fuel cell: challenges and recent advances. Ionics 2016;22:1-23. https://doi.org/10.1007/s11581-015-1589-6

[10] Jha N., Leela Mohana Reddy A., Shaijumon M.M., Rajalakshmi N., Ramaprabhu S. Pt–Ru/multi-walled carbon nanotubes as electrocatalysts for direct methanol fuel cell. Int. J. Hydrogen Energy 2008;33:427-433 https://doi.org/10.1016/j.ijhydene.2007.07.064

[11] B. Baruah, P. Deb, Performance and application of carbon-based electrocatalysts in direct methanol fuel cell. Mat. Advances 202;16:5344-64 https://doi.org/10.1039/D1MA00503K

[12] Wang J., Sun H-B, Adil Shah S., Liu C., Zhang G-Y, Li Z., Zhang Q-F, Han M., Palladium nanoparticles supported by three-dimensional freestanding electrodes for high-performance methanol electro-oxidation, Int J Hydrogen Energy 2020;45(19);11089-96. https://doi.org/10.1016/j.ijhydene.2020.02.046

[13] GlüSen A., Dionigi F., Paciok P., Heggen M., MüLler M., Gan L., et al. Dealloyed PtNi-core–shell nanocatalysts enable significant lowering of Pt electrode content in direct methanol fuel cells. ACS Catal. 2019;9:3764–72. https://doi.org/10.1021/acscatal.8b04883

[14] Sheikhi S., Jalali F., Remarkable electrocatalytic activity of Ni-nanoparticles on MOF-derived ZrO2-porous carbon/reduced graphene oxide towards methanol oxidation. Int. J. Hydrogen Energy 2021;46(18):10723-38. https://doi.org/10.17632/8j2b6xw5k9.1

[15] Nguyen V.Y., Kim H., Lee D. Enhanced methanol oxidation using porous Pd/Cdot nanocomposite synthesized with controlled morphology, Inorganic Chemistry Communications 2023;151:110548-55 https://doi.org/10.1016/j.inoche.2023.110548

[16] C. Quin, S. Tian, W. Wang, Z-J. Jiang, Z. Jiang, Advances in platinum-based and platinum-free oxygen reduction reaction catalysts for cathodes in direct methanol fuel cells, Front. Chem. 10 (2022) https://doi.org/10.3389/fchem.2022.1073566

[17] S Luo, R Wang, P Hei, L Gao, J Yang, T Jiao Self-assembled Ni2P nanosheet-implanted reduced graphene oxide composite as highly efficient electrocatalyst for oxygen evolution reaction. Colloids and Surfaces A: Physicochemical and Engineering Aspects; 2021. 612.

https://doi.org/10.1016/j.colsurfa.2020.125992

[18] Chen, Y., Chen, J., Zhang, J., Luo, Y., Zhang, C., Xue, Y., et al. (2021). Assist more Pt-O bonds of Pt/MoO3-CNT as a highly efficient and stable electrocatalyst for methanol oxidation and oxygen reduction reaction. J. Alloys Compd. 873, 159827. https://doi.org/10.1016/j.jallcom.2021.159827

[19] Zhu H., Zhang S., Guo S., Su D., Sun S. Synthetic control of FePtM nanorods (M = Cu, Ni) to enhance the oxygen reduction reaction J. Am. Chem. Soc. 2013;135(19):7130-7133 https://doi.org/10.1021/ja403041g

[20] Li X., Liu Y., Zhu J., Tsiakaras P.; Shen P.K. , Enhanced oxygen reduction and methanol oxidation reaction over self-assembled Pt-M (M = Co, Ni) nanoflowers J. Colloid Interf. Sci. 2022:607:1411-1423 https://doi.org/10.1016/j.jcis.2021.09.060

[21] Aruna S.T., Mukasyan A.S. Combustion synthesis and nanomaterials, Curr. Opin. Solid State Mater. Sci. 2008;12(3–4):44-50. https://doi.org/10.1016/j.cossms.2008.12.002

[22] Patil K.C., Aruna S.T., Mimani T., Combustion synthesis: an update, Curr. Opin. Solid State Mater. Sci. 2002;6:507-12. https://doi.org/10.1016/S1359-0286(02)00123-7

PROCEEDINGS OF ECOS 2023 - THE 36TH INTERNATIONAL CONFERENCE ON
EFFICIENCY, **C**OST, **O**PTIMIZATION, **S**IMULATION AND ENVIRONMENTAL IMPACT OF ENERGY SYSTEMS
25-30 JUNE 2023, LAS PALMAS DE GRAN CANARIA, SPAIN

Real-time data assimilation for the thermodynamic modeling of a cryogenic fuel tank

Pedro Afonso Marques[a,b], Samuel Ahizi[b], Miguel Alfonso Mendez[b]

[a] von Karman Institute for Fluid Dynamics, Sint-Genesius-Rhode, Belgium, pedro.marques@vki.ac.be, CA Transfers, Interfaces & Processes (TIPs) laboratory, Université libre de Bruxelles, Brussels, Belgium
[b] von Karman Institute for Fluid Dynamics, Sint-Genesius-Rhode, Belgium,

Abstract:
The current energy crisis has accelerated the interest in sustainable energy sources and cryogenic propellants, liquid hydrogen (LH_2) or liquefied natural gas (LNG). The thermal management of these systems requires advanced control strategies to minimize the boil-off losses produced by heat leakages and sloshing-enhanced heat and mass transfer. This work presents a data-assimilation approach to calibrate a 0D thermodynamic model for cryogenic fuel tanks from data collected in real time from multiple tanks. The proposed approach combines ideas from traditional data assimilation with multi-environment reinforcement learning, where an agent's training (i.e., model assimilation) is carried out simultaneously on multiple systems (environments). The real-time assimilation uses a mini-batch version of the well-known Limited-memory Broyden–Fletcher–Goldfarb–Shanno with bounds (L-BFGS-B) and adjoint-based gradient computation for solving the underlying optimization problem. The approach is tested on synthetic datasets simulating multiple tanks undergoing different operation phases (pressurization, hold, long-term storage and sloshing). We present the general closure problem for the tank's thermodynamics and the multi-environment assimilation framework. The results show that the simultaneous sampling from multiple environments and loading scenarios significantly accelerates the assimilation. Moreover, it is shown that the time scale for the training process is shorter than the relevant time scales of the tank's thermodynamics. This opens the path towards model predictive control based on data-driven engineering models.

Keywords:
Thermodynamics; Cryogenics; Sloshing; Modeling; Machine learning; Data assimilation.

1. Introduction

Cryogenic fuels such as liquid hydrogen (LH_2) or liquefied natural gas (LNG) are managed and stored at extremely low temperatures (typically $\approx$-170 °C for LNG and $\approx$-250 °C LH_2). LH_2 has been mainly used in rocket engines [1] but is now actively explored as alternatives to fossil fuels in many applications, including naval [2] and aeronautical [3] industries. The need for cryogenic temperatures stems from the need to maximize the fuel density without resorting to extreme operating pressures ($>$ 300 bars for gaseous H_2) [4]. In addition, the higher thrust-to-weight ratio compared to classical propulsive solutions [4] and the absence of pollutant emission make LH_2 a promising energy carrier for a carbon-neutral future [3, 5]. LNG is not entirely emission-free but can still bridge the gap between traditional fossil fuels and a fully renewable energy system [3].

Nevertheless, storage at cryogenic temperatures requires a complex thermal management system, which poses significant challenges to any application requiring long holding times, from marine to aeronautical, from ground transportation to deep space exploration. No insulating system can entirely prevent heat exchanges with the surroundings. Thus some of the fuel unavoidably evaporates over time and increases the tank pressure [6]. Additional challenges are faced in tanks installed on vehicles, as the external accelerations induce sloshing. Sloshing, defined as the movement of the free liquid surface, can (suddenly) increase heat and mass transfer rates between the liquid and ullage gasses and thus produce significant variations of the tank's pressure [7, 8].

This work proposes a data assimilation framework for identifying closure laws in a 0D thermodynamic model from real-time measurements of pressure, temperature, and liquid level in cryogenic tanks. The underlying optimization problem is efficiently solved via gradient-based optimization using the L-BFGS-B (Limited-memory Broyden–Fletcher–Goldfarb–Shanno with bounds) algorithm [9] coupled with the adjoint method [10] for evaluating the cost function gradient. The main novelty in our approach lies in the simultaneous assimilation of observations from multiple fuel tanks (i.e., multiple environments) undergoing distinct thermodynamic evolution in potentially widely different operating conditions.

The proposed approach takes inspiration from multi-agent reinforcement learning (MARL) [11]. MARL is a subfield of reinforcement learning where multiple agents learn to interact with each other and with the environment

to maximize a global reward. This is an active area of research with many open questions and challenges [12] on handling communication and coordination between agents and learning effective policies in large-scale multi-agent systems. Nevertheless, we believe that the potential impact of this concept in data assimilation is enormous and worth investigating. This work moves the first steps towards its application to the problem of data-driven calibration of thermodynamic models for cryogenic tanks. Leveraging synthetic data, we aim to quantify the performance of the model's calibration as the number of *environments* increases, using a single *agent* to learn the closure terms. As a complementary investigation, the single-environment scenario is also investigated to assess the impact of noise on the training data and the uniqueness of the solution.

This article is structured as follows. Section 2. outlines the physical modeling of the cryogenic fuel tank implemented in this work. The real-time data assimilation and inverse method strategies are outlined in Section 3.. Furthermore, this section also describes how the synthetic test cases were generated. Lastly, Section 4. overviews the results of the model calibration in single-environment and multi-environment conditions. Concluding remarks and future outlook are discussed in Section 5..

2. Thermodynamic modeling

The cryogenic propellant tank considered in this work is a single-species system composed of a liquid and its vapor enclosed in an insulated tank Fig. 1 provides a schematic of the problem with the relevant parameters involved. Subscripts l, v, and w are used to distinguish variables related to the liquid, the vapor, and the wall, respectively. The gas-liquid interface separating vapor and liquid is treated as an infinitesimally thin region where heat and mass transfer occurs. The system exchanges heat and mass, both on the liquid and the vapor side, during various operations (e.g., pressurization, venting, filling). The reader is referred to the list of symbols at the end of the article for the nomenclature.

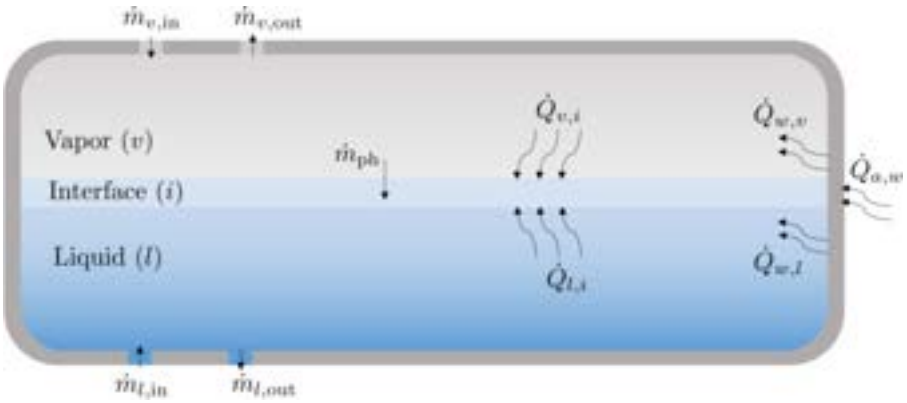

Figure 1: Schematic of the cryogenic fuel tank and its subsystems: vapor (v), liquid (l), and insulating walls (w). The heat and mass exchanges between these control volumes are expressed through the $\dot{m}$ and $\dot{Q}$ fluxes.

The 0D thermodynamic model used in the assimilation expresses the conservation of mass and energy applied to three control volumes: the liquid, the vapor, and the solid. Considering mass-averaged thermodynamic properties, these balances result in a system of ordinary differential equations (ODEs), which must be closed with empirical relations for the heat and mass transfer rates. Finding closure from sampled data is the objective of the assimilation.

The mass conservation between the liquid and the vapor is given by

$$\frac{dm_v}{dt} = \sum \dot{m}_{v,\text{in}} - \sum \dot{m}_{v,\text{out}} - \dot{m}_{\text{ph}} \quad ; \quad \frac{dm_l}{dt} = \sum \dot{m}_{l,\text{in}} - \sum \dot{m}_{l,\text{out}} + \dot{m}_{\text{ph}} \,, \tag{1}$$

where $\dot{m}_{\text{ph}} = \dot{m}_{\text{cond}} - \dot{m}_{\text{evap}}$ is the net mass flux through the interface, accounting for the balance of condensation and evaporation. The mass conservation in the vapor and liquid phases give

$$\frac{dU_v}{dt} = \sum \dot{m}_{v,\text{in}} \hbar_{v,\text{in}} - \sum \dot{m}_{v,\text{out}} \hbar_{v,\text{out}} - \dot{m}_{\text{ph}} \hbar_{v,\text{sat}} - \dot{Q}_{v,i} + \dot{Q}_{w,v} + \dot{W}_v \tag{2}$$

$$\frac{dU_l}{dt} = \sum \dot{m}_{l,\text{in}} \hbar_{l,\text{in}} - \sum \dot{m}_{l,\text{out}} \hbar_{l,\text{out}} + \dot{m}_{\text{ph}} \hbar_{v,\text{sat}} - \dot{Q}_{l,i} + \dot{Q}_{w,l} + \dot{W}_l, \tag{3}$$

where U_v and U_l are the internal energies of the vapor and liquid phases, $\dot{Q}$ denotes the general heat flux, $\hbar$ is the specific enthalpy, and $\dot{W} = -pdV/dt$ is the expansion/compression work due to changes in filling level.

The model closure is required to link the heat transfer rates at the interface. Assuming that the heat transfer occurs at much larger time scales than the interface dynamics, we consider quasi-steady formulation and use Newton's cooling law for the closure relation:

$$\dot{Q}_{v,i} = A_i h_{v,i}(T_v - T_i) \;\; ; \;\; \dot{Q}_{w,v} = A_{w,v} h_{w,v}(T_w - T_v) \;\; ; \;\; \dot{Q}_{l,i} = A_i h_{l,i}(T_l - T_i) \;\; ; \;\; \dot{Q}_{w,l} = A_{w,l} h_{w,l}(T_w - T_l), \tag{4}$$

where $h_{v,i}$, $h_{l,i}$, $h_{w,v}$, $h_{w,l}$ are the heat transfer coefficients, A_i is the gas-liquid interface area, $A_{w,v}$ and $A_{w,l}$ are the surface exchange areas between the walls-vapor and walls-liquid phases. The heat transfer coefficients are unknown and must be identified from the data. The interface temperature in (4) is assumed to be the saturation temperature evaluated at vapor pressure p_v; hence the energy balance at the interface provides the mass flux due to phase change as $\dot{m}_{\text{ph}} = (\dot{Q}_{l,i} - \dot{Q}_{v,i})/\mathcal{L}_v$, with $\mathcal{L}_v$ the latent heat of vaporization.

Concerning the exchange areas in (4), we do not account for the time variation of A_i (due to, e.g., sloshing), and take it as the tank's cross-section when the tank is half-filled. On the other hand, given the tank's geometry, the areas $A_{w,v}$ and $A_{w,l}$ are updated at each time step depending on the liquid level. This can be computed from the liquid and vapor masses and their properties. In particular, treating the liquid phase as incompressible (as in [13]), its density is solely a function of temperature $\rho_l(p, T) \approx \rho(T)$, hence

$$\frac{dV_l}{dt} = -\frac{dV_v}{dt}. \approx \frac{1}{\rho_l}\frac{dm_l}{dt} - \frac{m_l}{c_{p,l}\rho_l^2}\left(\frac{d\rho_l}{dT}\right)_p \frac{du_l}{dt}, \tag{5}$$

where c_p is the specific heat at constant pressure, ρ is the density, and $u = U/m$ is the specific internal energy. Finally, in the 0D formulation, the insulating walls are treated as a single control volume which can exchange heat with the vapor and liquid phases, as well as with the external environment at ambient conditions. For a single control volume with mass-averaged properties, the internal energy of the walls is described through

$$\frac{dU_w}{dt} = \dot{Q}_{a,w} - \dot{Q}_{w,v} - \dot{Q}_{w,l} \tag{6}$$

where $\dot{Q}_{a,w}$ is the heat entering the tank from the environment. This term could be computed from existing literature correlations [14], but in this work, this is taken as a user-defined function that depends on the specific scenario experienced by the tank (described in the following section). It is worth noticing that (6) can be written as a function of the mass-averaged solid temperature by introducing $dU_w = m_w c_w dT_w$.

Finally, all thermodynamic properties (c_p, ρ), as well as the link between internal energies, temperatures and pressures, were evaluated using the CoolProp package [15] in Python. This library implements pure fluid equations of state and transport properties using the Helmholtz energy formulations.

To conclude this section, we note that the thermodynamic model is constituted of equations (1)-(6) and can be cast in the form of a parametric initial value problem:

$$\begin{cases} \dfrac{d\mathbf{x}}{dt} = \mathbf{f}(\mathbf{x}, t; \boldsymbol{\theta}) \\ \mathbf{x}(0) = \mathbf{x}_0 \end{cases} \tag{7}$$

where $\mathbf{x} = [m_v, m_l, u_v, u_l, T_w, V_v, V_l] \in \mathbb{R}^7$ is the state vector (composed by the masses, volumes and internal energies of each control volume), describing the thermodynamic condition of the system at time-instant t, $\mathbf{x}_0 \in \mathbb{R}^7$ is the (known) initial condition and $\boldsymbol{\theta} \in \mathbb{R}^p$ is the vector of unknown parameters. These identify a function mapping the state vector to the heat transfer coefficients in (4) as further detailed in Section 3.1..

3. Real-time data assimilation framework

We describe the generation of the synthetic database in section 3.1. and the multi-environment real-time assimilation approach in section 3.2..

3.1. Synthetic database generation

Borrowing from the reinforcement learning terminology, the assimilation is carried out by an *agent* interacting with an *environment* to achieve a goal. In our context, the *agent* is a function that must predict the closure parameters (heat transfer coefficients) with the goal of having the model prediction as close as possible to the available data. In our context, the *environment* definition requires defining (1) the geometry of the fuel tanks, (2) the working fluid, (3) the initial conditions of the system, (4) the temporal evolution of the heat transfer coefficients (unknown to the agent), and (5) the sequence of operations applied to the tank. These are summarised in Fig. 2.

The proposed multi-environment formulation involves learning the *same* closure law from multiple environments. In this work, we consider multiple cryogenic fuel tanks, partly filled with LH_2. The environment parameters in terms of dimensions and initial conditions are presented in Table 4 in Appendix A. Tank 1 is the

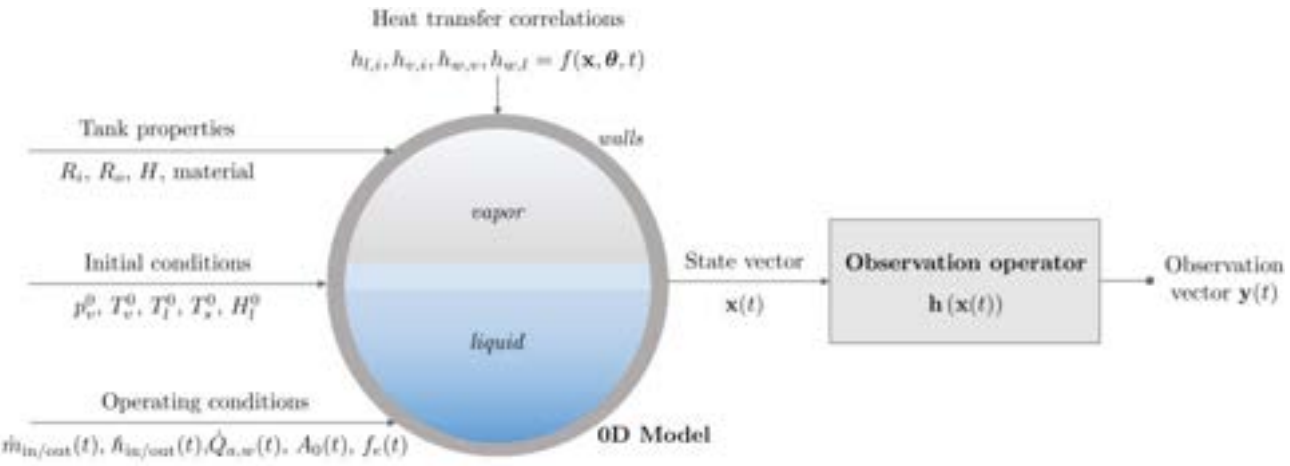

Figure 2: Schematic of the parameters required to define an environment for the data assimilation of the 0D thermodynamic model of the cryogenic tank. Interaction with the environment produces the observation vector $\mathbf{y}(t)$ simulating measurements from the tank.

reference case used to assess the single-environment performance of the assimilation framework (Section 4.1.). The remaining tanks are added to the analysis of the multi-environment scenario (Section 4.2.).

In all environments, the heat transfer coefficients in (4) were modeled as

$$h_{v,i} = \frac{k_v}{R}\left(\theta_0 \mathrm{Re}_{s,v}^{0.69}\mathrm{Pr}_v^{1/3} + \theta_1 \mathrm{Ra}_v^{0.15}\right) \;;\; h_{l,i} = \frac{k_l}{R}\left(\theta_2 \mathrm{Re}_{s,l}^{0.69}\mathrm{Pr}_v^{1/3} + \theta_3 \mathrm{Ra}_l^{0.15}\right) \;;\; h_{w,v} = \theta_4 h_{v,i} \;;\; h_{w,l} = \theta_5 h_{l,i} \tag{8}$$

where Re_s is the Reynolds number due to sloshing, $\mathrm{Pr} = \nu/\alpha$ is the Prandtl number, Ra is the Rayleigh number, and $\theta_0 - \theta_5$ are the set of parameters governing the heat and mass transfer evolution in the tank.

The dimensionless numbers in (8) are defined as

$$\mathrm{Re}_s = \frac{f_e}{f_{11}}\left(\frac{b}{R}\right)^2 \frac{\left(gR^3\right)^{1/2}}{\nu}\sqrt{1.841} \quad ; \quad \mathrm{Ra} = \frac{g\beta\Delta T R^3}{\nu\alpha} \tag{9}$$

where f_e is the frequency of the forcing motion acting on the tank, f_{11} is the natural frequency of the tank [1], b is the maximum expected wave-height during sloshing, which is a function of the forcing amplitude A_0 [8], R is the tank's radius, ν is the kinematic viscosity, g is the gravitational acceleration, β is the volumetric thermal expansion coefficient, and α is thermal diffusivity.

The $h_{l,i}$ and $h_{v,i}$ coefficients simultaneously account for forced convection through the Reynolds and Prandtl numbers, as well as buoyancy-driven fluxes through the Rayleigh number. All synthetic test cases were generated using the set of parameters $\boldsymbol{\theta} = [\theta_0, \theta_1 \ldots]$ presented in Table 3 in Appendix A. These were tuned to roughly portray the experimental pressure and temperature reported in [7, 16].

Assuming that the functional relations in (8) are prescribed beforehand, the scope of data assimilation consists in identifying the parameters $\boldsymbol{\theta}$ from multiple environments. A general formulation of the problem could be based on general parametric models (e.g. using radial basis functions expansions or artificial neural networks) to learn the closure laws. These are currently being explored and will be presented in future work.

The interaction between the agent and the environment is carried out by monitoring some observations of the system, here denoted as $\mathbf{y}(t) = \mathbf{h}(\mathbf{x}(t))$, with $\mathbf{h}(\cdot)$ the observation function simulating a measurement process. The observations considered in this work are the vapor pressure $p_v(t)$, the mass-averaged vapor $T_v(t)$, liquid $T_l(t)$, and wall $T_w(t)$ temperatures, and the fill-level $H_l(t)$. These quantities were retrieved from the state vector. Hence the observation function is $\mathbf{h}(\cdot) : \mathbb{R}^7 \to \mathbb{R}^5$.

3.2. Real-time inverse method for multiple environments

Identifying the parameters $\boldsymbol{\theta}$ requires solving an optimization problem. The optimal parameters are those that minimize a cost function $\mathcal{J}(\boldsymbol{\theta})$ measuring the discrepancy between model prediction and data across all the available environments. Denoting as $\mathbf{x}_{\{j\}}(t)$ the time evolution of the thermodynamic state in the j^{th} environment and as $\mathbf{y}_{\{j\}}(t)$ the evolution of the corresponding observations, the cost function considered in this work is

$$\mathcal{J}(\boldsymbol{\theta}) = \frac{1}{N}\sum_{j=1}^{N}\int_{t_i}^{t_i+T} g(\mathbf{y}_{\{j\}}, \mathbf{x}_{\{j\}}, t; \boldsymbol{\theta})dt = \frac{1}{2N}\sum_{j=1}^{N}\int_{t_i}^{t_i+T}\left(\mathbf{y}_{\{j\}}(t) - \mathbf{h}(\mathbf{x}_{\{j\}}(t))\right)^T \mathbf{R}_{\{j\}}^{-1}\left(\mathbf{y}_{\{j\}}(t) - \mathbf{h}(\mathbf{x}_{\{j\}}(t))\right) dt \tag{10}$$

where N is the number of environments, T is the observation time and $\mathbf{R}_{\{j\}}$ is the covariance matrix accounting for measurement noise. Since the assimilation seeks to learn the full set of parameters from all environments, the proposed formulation is a multiple-environment but single-agent framework, as opposed to a multi-agent formulation in which different agents could be assigned to learn different coefficients in the same environment.

In this work, the function $\mathcal{J}(\boldsymbol{\theta})$ is minimized through gradient-based optimization using the L-BFGS-B optimizer [9] coupled with the adjoint method [10] to compute the gradient $\nabla_{\boldsymbol{\theta}}\mathcal{J}$. The adjoint method allows computing this gradient without computing the sensitivity of the state with respect to the closure parameters, i.e. $d\boldsymbol{x}/d\boldsymbol{\theta}$.

The gradient is computed by relying on the augmented Lagrangian function $\mathcal{L}(\boldsymbol{\theta})$

$$\mathcal{L}(\boldsymbol{\theta}) = \mathcal{J}(\boldsymbol{\theta}) + \sum_{j=1}^{N} \left(\int_{t_i}^{t_i+T} \left(\mathbf{f}(\mathbf{x}_{\{j\}}, t; \boldsymbol{\theta}) - \frac{d\mathbf{x}_{\{j\}}}{dt} \right) \boldsymbol{\lambda}_{\{j\}}(t)^T dt \right) \tag{11}$$

where the (row) vector $\boldsymbol{\lambda}_{\{j\}}(t) \in \mathbb{R}^7$ is the vector of adjoint variables for each environment. The cost function (10) and the augmented cost function (11) are equivalent because the additional term is identically null for any finite choice of the variable $\boldsymbol{\lambda}_{\{j\}}$ (by definition of the underlying dynamics in (7)). Therefore, it is possible to make the gradient computation of both cost functions independent of the sensitivities if the adjoint variables are taken as the solution of the following terminal value problem [17]:

$$\begin{cases} \dfrac{d\boldsymbol{\lambda}_{\{j\}}}{dt} = -\left(\dfrac{\partial g}{\partial \mathbf{x}}\right)_{\{j\}} - \boldsymbol{\lambda}_{\{j\}}(t) \left(\dfrac{\partial \mathbf{f}}{\partial \mathbf{x}}\right)_{\{j\}} \\ \boldsymbol{\lambda}_{\{j\}}(T) = 0 \end{cases} \tag{12}$$

This is a linear system of equations that must be integrated backward in time to solve for $\boldsymbol{\lambda}_{\{j\}}$. The gradient can then be computed as

$$\nabla_{\boldsymbol{\theta}}\mathcal{J}(\boldsymbol{\theta}) = \sum_{j=1}^{N} \left(\int_{t_j}^{t_j+T} \left(\frac{\partial g}{\partial \boldsymbol{\theta}}\right)_{\{j\}} + \boldsymbol{\lambda}_{\{j\}}(t) \left(\frac{\partial \mathbf{f}}{\partial \boldsymbol{\theta}}\right)_{\{j\}} dt + \boldsymbol{\lambda}_{\{j\}}(0) \frac{d\mathbf{x}_{\{j\}}}{d\boldsymbol{\theta}}(0) \right) \tag{13}$$

where $d\mathbf{x}_{\{j\}}/d\boldsymbol{\theta}(0)$ is known from the initial conditions of each environment (tank). Thus, in the adjoint-based approach, the gradient of the loss function is evaluated by solving two systems of equations for each environment in the ensemble (i.e., one forward pass to obtain $\mathbf{x}_{\{j\}}(t)$, and one backward pass to obtain $\boldsymbol{\lambda}_{\{j\}}(t)$).

The vector of parameters is iteratively updated throughout the optimization loop as

$$\boldsymbol{\theta}^{(k+1)} = \boldsymbol{\theta}^{(k)} - \mathbf{B}^{(k)} \nabla_{\boldsymbol{\theta}}\mathcal{J}(\boldsymbol{\theta}^{(k)}) \text{ for } k \in [0, 1 \dots n_k] \tag{14}$$

where the superscript $^{(k)}$ indicates the iteration counter, and $\mathbf{B}$ is the approximation of the Hessian matrix inverse according to [9]. The gradient computation in (13) and the updates in (14) define two-time scales of the assimilation problem. The first scale is the observation time T, linked to the rate at which new information is collected. The second is the learning time scale implicitly defined by the number of optimization iterations n_k carried out before an update on the gradient is requested (or is available). The first time scale defines the rate at which the cost function changes because of the dynamics of the system and the potential occurrence of unseen scenarios. The second time scale defines the rate at which the optimizer travels along the parameter space before the cost function changes.

The optimal setting of these scales poses a fundamental question on the impact of the observation time T in relation to the observed scenarios and the quality of the gradient computation: one might ask, for example, whether the observation time should be long enough to observe at least two or three pressurizations or sloshing events. This work investigates the impact of this parameter by making it vary from T = 10 min until T = 60 min, with the five environments observing different scenarios and different combinations of events.

4. Results and discussion

We split the presentation of results and the discussion into a section dedicated to the performance of a single environment (Section 4.1.) and a section dedicated to multiple environments (Section 4.2.).

4.1. Single-environment performance

We first describe the investigated scenario in 4.1.1.. Section 4.1.2. studies the impact of measurement noise in the collected data for different observation times T. Finally, section 4.1.3. reports on the impact of mini-batching the assimilation using only a portion of the data.

4.1.1. Test case description

We consider the environment denoted as 'case 1' in Table 4. Figure 3 illustrates the loading and operation scenario of the tank in an observation of 1 hour. The first row of plots illustrates the time evolution of the ullage gas pressure (on the left), and the mass averaged temperatures of the vapor, the liquid and the solid volumes (on the right). The second row plots the time amplitude (left) and the frequency (right) of sinusoidal sloshing events. The third row plots the mass inflow/outflow of vapor (left) and liquid (right) as a function of time. Finally, the last row shows the heat flux exchanged through the walls (left) and the liquid level (right).

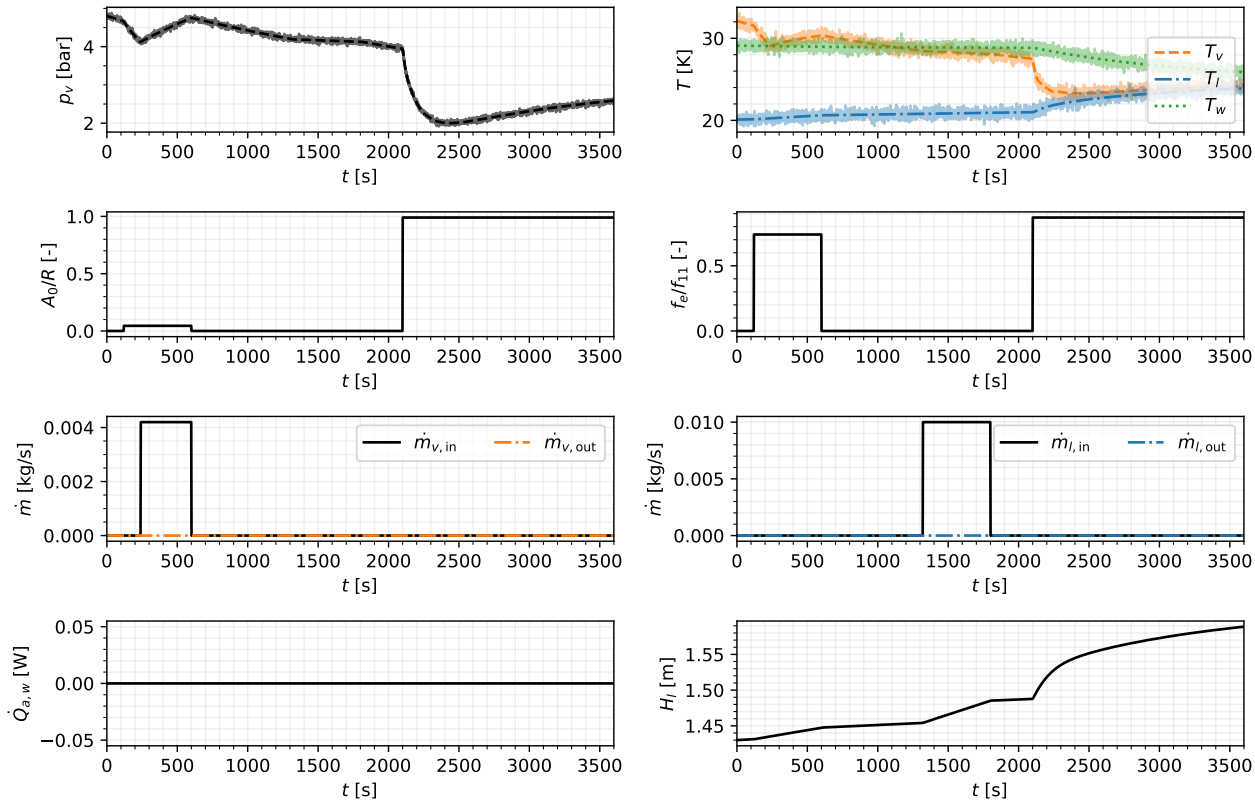

Figure 3: Synthetic data generated for Tank 1 (see Table 4) used to evaluate the single-environment performance. The components of the observation vector are displayed alongside the injected/removed mass fluxes, the non-dimensional excitation conditions, and the external heat flux.

A detailed overview of these graphs helps understand the complexity of the system control problem. In the presented scenario, the tank is undisturbed in the first 2 minutes. Then, a moderate sloshing event occurs with a dimensionless amplitude of $A_0/R = 0.045$ and dimensionless frequency $f_e/f_{11} = 0.8$ (see definitions of sloshing conditions in (9)). This triggers a visible pressure drop. To counter-balance this, at time $t = 4$ minutes, hydrogen vapor at 40 K and 2 bar is injected in the ullage at a rate of 4.2 g/s for 6 minutes. This allows the tank to recover 4.8 bar pressure at 10 minutes when the sloshing event ends. From $t = 10$ to $t = 22$ minutes, the tank is again undisturbed but the temperature difference between the wall, the gas, and the liquid results in the warming of the liquid and the cooling of the vapor. This slightly reduces the pressure in the ullage. Finally, between $t = 22$ and $t = 30$ minutes, liquid at 22 K is injected into the system at a rate of 0.01 kg/s. This reduces the ullage volume, resulting in a moderate compression that arrests the decreasing trend. Finally, at $t = 35$ minutes, a violent sloshing event occurs and continues until the end of the observation. This results in a violent pressure drop due to the significant condensation (see liquid level evolution), followed by a moderate pressure rise due to heat exchanges with the (now) warmer walls. Throughout this test, no heat exchange is assumed to occur from the environment.

4.1.2. Impact of noise in the observation data

We here consider three scenarios in terms of measurement noise in the collected observations; these are termed (1) 'clean' (2) 'low-noise', and (3) 'high-noise'. No noise is present in the first, while Gaussian noise (with zero average) is added in the other two. In (2), the noise's standard deviation is 2 kPa on the pressure, 0.2 K on the temperature, and 0.5 mm on the fill level. In (3), these values are doubled.

We considered various observation windows T of the environment described in the previous section for the

three scenarios. Figure 4 shows the results of the real-time data assimilation applied to the 'clean' data for T = 10, 20, and 30 minutes. The thick solid lines indicate observations from the virtual experiment, whereas the thin dashed lines indicate the predictions given by data assimilation. The columns of the figure show the tank pressure, vapor temperature, and liquid temperature as the observation time increases.

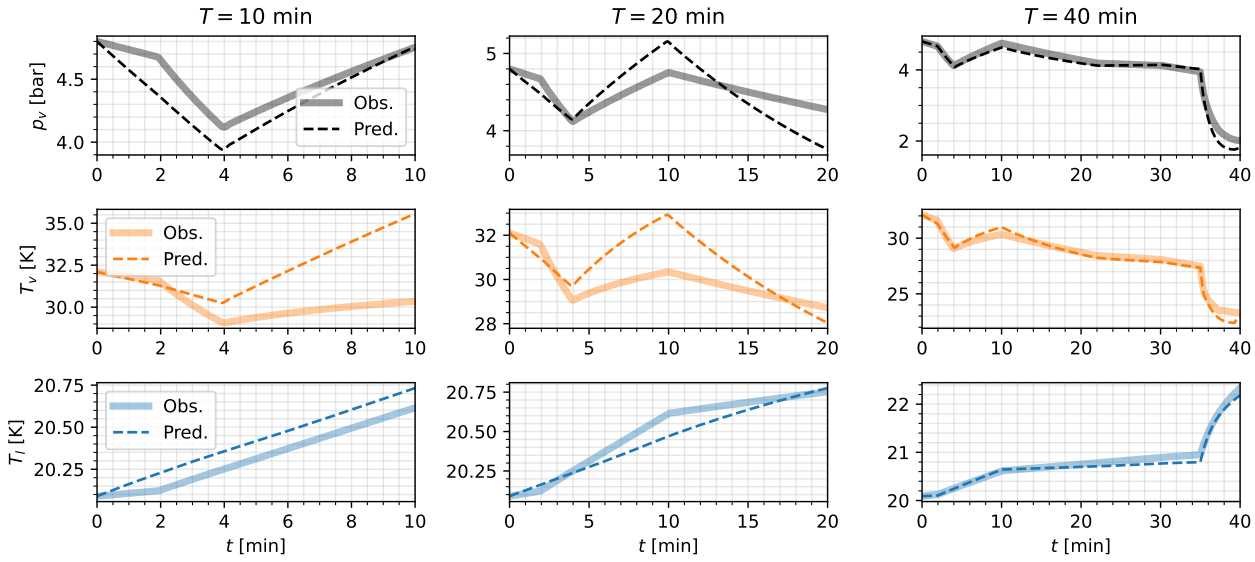

Figure 4: Model predictions and observation data extracted from the test described in Section 4.1.1. for 10, 20 and 40 minutes of observation.

Interestingly, the assimilation produces excellent matching between the model and observation if the observation time is sufficiently long. In the virtual experiment analyzed, this is of the order of T = 40 min, i.e., enough to see all the events in the environment (sloshing, filling on the vapor and the liquid side).

The analysis of the noise impact is thus completed in Fig. 5, which presents the minimum of $\mathcal{J}$ (on the left) and the l_2 relative error norm of $\boldsymbol{\theta}$ (on the right) as a function of the observation time, for the three tested scenarios as a function of the observation time. When noise is added, the minimal cost function is expected to be larger in the presence of noise since the underlying model filters it out from the data. Nevertheless, these results show that the noisy cases consistently produced smaller values of $\mathcal{J}$ when the full observation is used. Surprisingly, the measurement noise helps the optimization avoid local minima, and the parameters identified in the assimilation are more accurate (right plot in Fig. 5) and learned with shorter observation times. Interestingly, in all cases, the learning of the parameters saturates for $T > 40$ min.

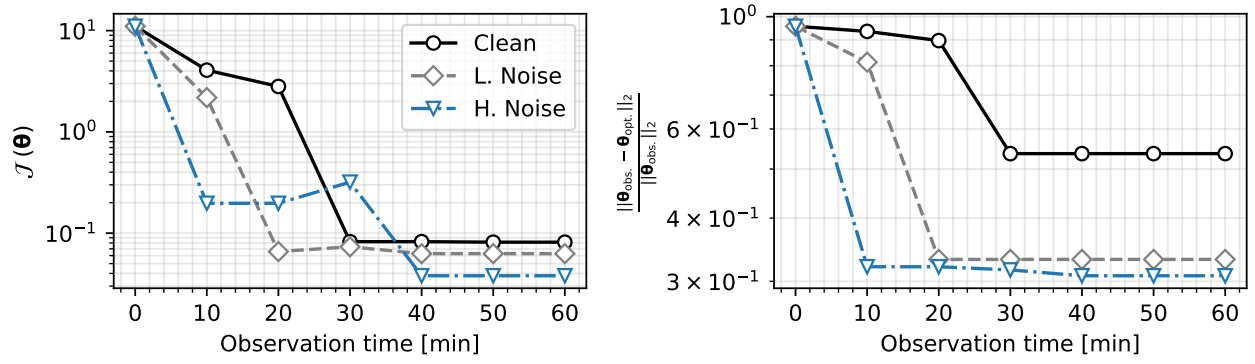

Figure 5: Performance of the data assimilation framework applied to one environment for different noise levels in the data. Left: minimum of the cost function as a function of the observation time. Right: l_2 relative error norm associated with $\boldsymbol{\theta}$.

We close this analysis by comparing the retrieved parameters from the assimilation and those used to generate the data; these are reported in the next section and presented alongside the impact of data batching for the gradient computation.

4.1.3. Impact of approximating the gradient of the cost function via mini-batches

The mini-batch sampling [18] is a classic approach to escape local minima and limit memory requirements in the gradient descent method. The idea consists in computing the cost function gradient using a randomly chosen subset of the observation data; this produces an approximation of the gradient $\nabla_\theta \mathcal{J}$ that might point away from local minima.

The use of mini-batch strategies on quasi-Newton methods, such as the L-BFGS-B technique used in this work, is the subject of active research (see [19]). Nevertheless, in this work, we explored its impact on the 'high-noise' configuration from the previous subsection. We test the assimilation using 80%, 50%, 20% and 5% of the observed data to evaluate $\nabla_\theta \mathcal{J}$. To account for the stochasticity of the process, the assimilation is repeated one hundred times in each case and the results are averaged. The average behavior of the cost function evolution and the convergence of the parameters are shown in Fig. 6. Remarkably, the additional stochasticity of the minibatch selection further improves the result of the assimilation in both aspects. Interestingly, the relative error is nearly identical when sampling 80%, 50%, and 5% of the training data, whereas for the 20% bath size the error is reduced by roughly 6%. The cost function, on the other hand, is slightly higher.

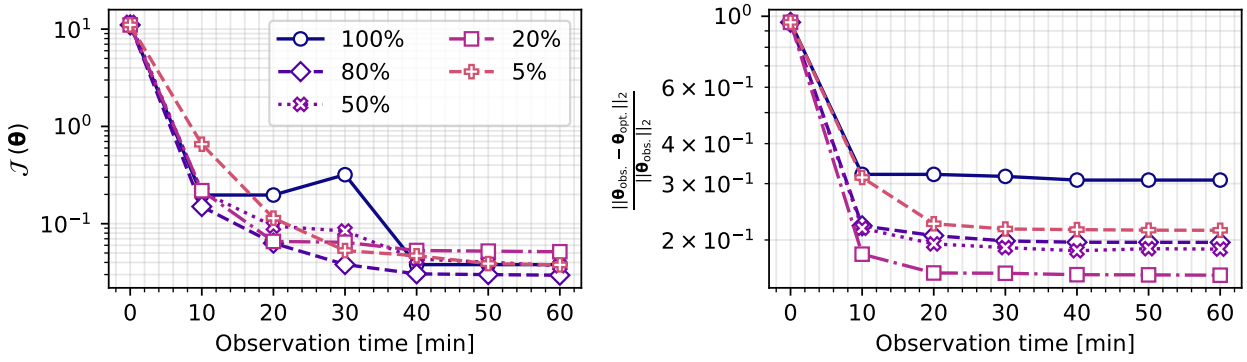

Figure 6: Performance of the data assimilation framework applied to one environment. Left: minimum of the cost function as a function of the observation time. Right: l_2 relative error norm associated with θ.

Finally, we compare the parameters obtained in the assimilation for different mini-batch sizes in table 1. For each coefficient, the table collects the average and the standard deviation (over 100 repetitions of assimilation). The reference coefficients used to generate the synthetic data are shown in the last row of the table. These results confirm that the best match of θ was achieved when 20% of the training data was sampled at each gradient computation, even though this case reported the highest cost function evaluation on average.

Table 1: Mean coefficients obtained during the model training, alongside their respective standard deviation. The cases in which $\nabla_\theta \mathcal{J}$ was approximated via mini-batches were repeated 100 times.

Data sampled	min $\mathcal{J}$	θ_0	θ_1	θ_2	θ_3	θ_4	θ_5
100%	3.8e-2	98.3	17.2	65.2	1.21	8.91	11.6
80%	2.7e-2	134.1 ± 14.6	10.7 ± 2.4	51.6 ± 4.7	1.9 ± 0.2	34.9 ± 37.5	10.1 ± 0.4
50%	2.8e-2	128.3 ± 16.4	11.1 ± 2.9	50.9 ± 3.8	1.9 ± 0.3	28.8 ± 32.0	10.2 ± 0.7
20%	3.4e-2	134.5 ± 16.3	10.0 ± 3.6	49.6 ± 5.5	2.0 ± 0.3	18.1 ± 19.2	10.0 ± 0.6
5%	3.0e-2	120.0 ± 23.8	12.8 ± 4.2	53.3 ± 7.2	1.8 ± 0.4	18.7 ± 16.6	10.0 ± 0.6
Reference	-	140.0	10.0	50.0	2.00	20.0	10.0

The table shows that the standard deviation for each component of θ increases as the batch size decreases. This is attributed to less accurate gradient evaluation during the parameter updates. The only outlier to this trend is θ_4, which shows the opposite behavior. However, this is characterized by a significantly larger standard deviation. This parameter is associated with the heat transfer coefficient $h_{w,v}$, governing the heat exchanges between the vapor and the insulating walls, which appears to have a minor impact on the system's dynamics. Thus, given the insensitivity of the model to this parameter, the assimilation cannot determine its true value from the observed data.

In summary, these results showcased that sampling portions of the training data during the optimization can improve the assimilation results. Furthermore, this sampling provides an approximation of $\nabla_\theta \mathcal{J}$, which allows for a broader exploration of the parameter space, yielding better predictions for θ, even if the value of the cost

function is not significantly affected (on average). For the current training data set, the best compromise was obtained by sampling 20% of the input data.

4.2. Multi-environment performance

We here extend the previous analysis to the case of multiple environments characterised by vastly different geometries, sloshing profiles, thermal loading and inflow/outflow control actions.

The first environment is the tank described in Section 4.1.1. while the geometrical parameters, and initial conditions for the others are summarised in Table 4 in Appendix A. All environments are observed for the same T = 60min, but their thermodynamic evolutions differ by imposing different sequences of filling, pressurization, venting, sloshing, and external heating.

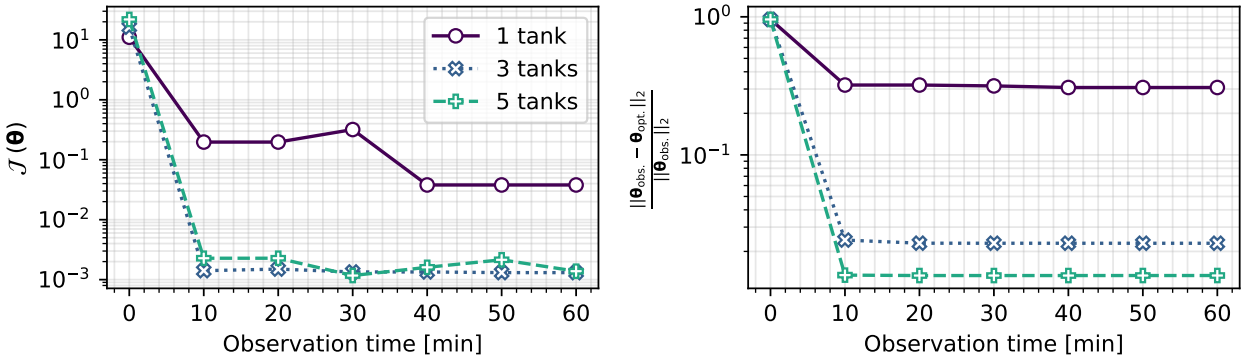

Figure 7: Performance of the data assimilation framework applied to multiple environments. Left: minimum of the cost function as a function of the observation time. Right: l_2 relative error norm associated with $\boldsymbol{\theta}$.

The multi-environment framework requires solving for N forward and backward passes for every parameter update. However, these evaluations could be performed in parallel to improve runtimes and could be batched also across multiple environments. We repeat the same analysis as in the previous section, applying high noise to the observed data and using a batch of 20% of the observation points to update $\boldsymbol{\theta}$ during the optimization loop. The results for $N = 1, 3, 5$ environments are shown in Fig. 7.

The increase in the learning convergence as the number of environments increases is evident, as the cost function drops by one order of magnitude compared to the single-environment scenario for an observation time of T =10 min. The increase in performance between 3 to 5 environments is much less significant, hinting that saturation with respect to the number of environments is to be expected.

Table 2: Mean coefficients obtained during the model training, alongside their respective standard deviation for the multi-environment network. The assimilation of each case was repeated 10 times.

No. of tanks	min $\mathcal{J}$	θ_0	θ_1	θ_2	θ_3	θ_4	θ_5
1	3.8e-2	134.5 ± 16.3	10.0 ± 3.6	49.6 ± 5.5	2.0 ± 0.3	18.1 ± 19.2	10.0 ± 0.6
3	3.9e-3	137.3 ± 19.9	10.6 ± 4.0	49.8 ± 0.7	2.0 ± 0.1	21.3 ± 22.8	10.0 ± 0.1
5	6.9e-3	138.7 ± 32.8	10.2 ± 3.4	50.0 ± 4.8	2.0 ± 1.3	19.3 ± 2.2	10.0 ± 10.7
Reference	-	140.0	10.0	50.0	2.00	20.0	10.0

Like in the previous section, Table 7 collects the average and standard deviation of the identified parameters over 100 realizations in the case of multiple environments. The accuracy in the detection is comparable, although the standard deviation grows for some coefficients (e.g. θ_4 and θ_5). This might be due to the relative importance of these terms with respect to the various scenarios considered: θ_0 strongly influences the model performance in the presence of sloshing, but the relative importance of sloshing events over the five scenarios is reduced with respect to the first environment as other physical mechanisms are more present.

5. Conclusions

We presented a multi-environment real-time data assimilation framework for the data-driven thermodynamic modeling of cryogenic fuel tanks.

The implemented approach sets up an optimization problem in which the error between system observations and model predictions must be minimized by acting on closure parameters. The model is based on a lumped

formulation of mass and energy balances for each of the system's control volumes (i.e., the vapor, liquid, and solid walls), and the optimization is carried out by combining a quasi-Newton approach with the adjoint-based evaluation of the cost function gradients.

The training data is collected by multiple environments, i.e. different tanks undergoing various operating conditions (e.g., sloshing, filling, etc.). To provide the first proof of concept of the proposed framework, synthetic data generated through the model was used as a reference for the learning algorithm. The heat transfer closure relations in this model depend on six closure coefficients. The assimilation algorithm aimed to identify these from noisy pressure and temperature observations, which simulate measurements sampled from multiple fuel tanks.

Various tests were performed for the data assimilation applied to a single environment: we assessed the impact of measurement noise on the training data and the effect of 'mini-batches' in the gradient computation alongside the duration of an observation within which the assimilation is carried out. Remarkably, it was found that measurement noise improves the data assimilation, allowing for better identifying the underlying coefficients in shorter observation times. Similarly, an optimal batch size of 20% of the available data produced systematic improvements in the assimilation convergence. Finally, further improvements in the assimilation were achieved in a multi-environment scenario considering three or five tanks undergoing widely different loads and control scenarios.

To conclude, this work provides a solid proof of concept for applying a multi-environment data assimilation framework for the data-driven calibration of thermodynamic models of cryogenic tanks, potentially enabling model predictive control in thermal management systems. In the era of the fourth industrial revolution, where intelligent sensors are becoming widely available, the perspective of deploying the proposed multi-environment assimilation to a large fleet of heavily instrumented tanks appears particularly promising.

Acknowledgments

This work has been funded by the Flemish Agentschap Innoveren & Ondernemen in the framework of the cSBO project HBC.2021.0680 "Clean Hydrogen Propulsion for Ships (CHyPS)". Pedro Marques is supported by the FRIA grant 40009348 from the 'Fonds de la Recherche Scientifique (F.R.S. -FNRS)'.

Appendix A Details of the multi-environment framework

Table 3 shows the vector of parameters used to close the heat transfer correlations. In addition, Table 4 summarises the geometric parameters and initial conditions associated with each fuel tank.

Table 3: Coefficients associated with the heat transfer coefficients in (8) used to produce the synthetic test cases. Each column pair indicates the c_i coefficients linked to the heat transfer term in the header.

Coef.	θ_0	θ_1	θ_2	θ_3	θ_4	θ_5
Value	140	10	50	2	20	10

Table 4: Geometrical parameters and initial conditions associated with each fuel tank. All tanks were filled with liquid hydrogen and were treated as upright cylinders.

Tank	Geometry			Initial conditions					Wall properties
case	R_i [m]	R_o [m]	H [m]	p_v^0 [bar]	T_v^0 [K]	T_l^0 [K]	T_w^0 [K]	H_l^0 [m]	$m_w c_w$ [MJ/K]
1	0.9	1.00	2.2	4.80	32.1	20.1	29.1	1.43	2.44
2	2.7	2.90	14	3.10	30.1	20.1	25	6.16	91.4
3	1.4	1.50	6.2	4.40	30.1	20.1	28.1	4.03	10.5
4	0.4	0.50	1.2	0.94	20.1	20.1	21.1	0.43	0.10
5	1.0	1.05	2.1	0.94	20.1	20.1	22.1	1.56	0.63

Nomenclature

Letter symbols

A area, m^2

A_0 forcing amplitude, m

b maximum wave amplitude, m

$\mathbf{B}$ approximated Hessian inverse

C specific heat, $\mathrm{J}/(\mathrm{kgK})$

f frequency, Hz

g gravity, m/s^2

g integrand of the objective function

H height, m

h heat transfer coefficient, $\mathrm{W}/(\mathrm{m}^2\mathrm{K})$

$\hbar$ mass-specific enthalpy, J/kg

$\mathcal{J}$ cost function, $[-]$

$\mathcal{L}$ Lagrangian function, $[-]$

$\mathcal{L}_v$ latent heat of vaporisation, J/kg

m mass, kg

$\dot{m}$ mass flow rate, kg/s

$\dot{Q}$ heat transfer rate, W

R radius, m

T temperature, K

t time, s

U internal energy, J

u mass-specific internal energy, J/kg

V volume, m^3

$\dot{W}$ work, W

$\mathbf{y}$ observation vector

Greek symbols

α thermal diffusivity, m^2/s

β volumetric thermal expansion coefficient, K^{-1}

$\boldsymbol{\theta}$ vector of parameters

$\boldsymbol{\lambda}$ adjoint variable

$\boldsymbol{\nu}$ kinematic viscosity, m^2/s

$\boldsymbol{\rho}$ mass-specific density, kg/m^3

Subscripts and superscripts

a ambient

i interface

l liquid

$\{j\}$ environment counter

(k) iteration counter

ph phase change

v vapor

w walls

References

[1] Abramson H. N., Dodge F. T., Bauer H. F., Brooks G. W., Chu W., Dalzell J. F., Kana D. D., Reynolds W. C., Satterlee H. M., Silverman S. *The Dynamic Behavior of Liquids in Moving Containers*. Washington DC, USA: National Aeronautics and Space Administration, NASA SP 106, Scientific and Technical Information Division; 1966.

[2] Grotle E. L., Æsøy, V., *Dynamic modeling of the thermal response enhanced by sloshing in marine LNG fuel tanks*. Applied Thermal Engineering 2018;135:512-520.

[3] Michael B., Wietschel M., *The Future of Hydrogen—Opportunities and Challenges*. International Journal of Hydrogen Energy 2009;34:615-627. 10.1016/j.ijhydene.2008.11.014.

[4] Swinerd G., Stark J., *Propulsion systems*. In: Fortescue P., Swinerd G., Stark J., editors. Spacecraft Systems Engineering. West Sussex, England: Wiley. 2003. p. 169-210.

[5] Janic M., *The potential of liquid hydrogen for the future 'carbon-neutral' air transport system*. Transportation Research Part D: Transport and EnvironmentTransportation Research Part D: Transport and Environment 2008;13(7):512-520. doi.org/10.1016/j.trd.2008.07.005

[6] Petitpas G., *Boil-off losses along LH2 pathway.* United States: Lawrence Livermore National Lab. (LLNL), USDOE National Nuclear Security Administration (NNSA); 2018 April, Technical Report No.: 1466121.

[7] Arndt T. *Sloshing of Cryogenic Liquids in a Cylindrical Tank under normal Gravity Conditions [dissertation]* Bremen, Germany: Universitat Bremen; 2011.

[8] Ludwig C., Dreyer M.E., Hopfinger E.J., *Pressure variations in a cryogenic liquid storage tank subjected to periodic excitations*. International Journal of Heat and Mass Transfer 2013. 66. 223-234. doi.org/10.1016/j.ijheatmasstransfer.2013.06.072.

[9] Byrd R., Lu P., Nocedal J., Zhu C., *A Limited Memory Algorithm for Bound Constrained Optimization*. SIAM Journal on Scientific Computing 2003;16. doi.org/10.1137/0916069.

[10] Granzow G. D., *A tutorial on adjoint methods and their use for data assimilation in glaciology*. Journal of Glaciology 2014;60(221):440-446. doi.org/10.3189/2014JoG13J205.

[11] Zhang K., Yang Z., Başar T., *Multi-Agent Reinforcement Learning: A Selective Overview of Theories and Algorithms*. In: Vamvoudakis K., Wan Y., Lewis F., Cansever D., editors. Handbook of Reinforcement Learning and Control. Springer International Publishing. 2021. p. 321-374. doi.org/10.1007/978-3-030-60990-0_12

[12] Buşoniu L., Babuška R., De Schutter B., *Multi-Agent Reinforcement Learning: An Overview*. In: Srinivasan D., Jain L., editors. Innovations in Multi-Agent Systems and Applications - 1. Berlin, Heidelberg: Springer Berlin Heidelberg. 2010. p. 183-221. doi.org/10.1007/978-3-642-14435-6_7

[13] Foreest A., *Modeling of cryogenic sloshing including heat and mass transfer [dissertation]* Bremen, Germany: Universitat Bremen; 2010. 10.2514/6.2010-6891.

[14] Bergman T., Lavine A., Incropera F., DeWitt D., *Fundamentals of Heat and Mass Transfer*. Hoboken, New Jersey. Wiley. 2007.

[15] Bell I. H., Wronski J., Quoilin S., Lemort V., *Pure and Pseudo-pure Fluid Thermophysical Property Evaluation and the Open-Source Thermophysical Property Library CoolProp*. Industrial & Engineering Chemistry Research 2014. 53. 2498–2508. doi.org/10.1021/ie4033999.

[16] Moran M., McNelis N., Kudlac M., Haberbusch M., Satornino G., *Experimental results of hydrogen slosh in a 62 cubic foot (1750 liter) tank.* 30th Joint Propulsion Conference and Exhibit 1994. doi.org/10.2514/6.1994-3259.

[17] Navon I. M., *ractical and theoretical aspects of adjoint parameter estimation and identifiability in meteorology and oceanography*. Dynamics of Atmospheres and Oceans 1998;27(1):55-55-79. doi.org/10.1016/S0377-0265(97)00032-8.

[18] Li M., Zhang T., Chen Y., Smola A. J., *Efficient Mini-Batch Training for Stochastic Optimization.* Association for Computing Machinery 2014;661-670. doi.org/10.1145/2623330.2623612.

[19] Bollapragada R., Mudigere D., Nocedal J., Shi H., Tang P., *A Progressive Batching L-BFGS Method for Machine Learning.* 2018.

Experimental model of a hydrogen fuel cell using graphene pads as heat spreaders

Álvaro García-Martínez[a], Aitor Fernández-Jiménez[b], Eduardo Álvarez-Álvarez[c], Eduardo Blanco-Marigorta[d] and María José Suárez-López[e]

[a] Departamento de Energía, Universidad de Oviedo, C/Wifredo Ricart s/n, Gijón, Asturias (España), 33203, garciaalvaro@uniovi.es
[b] fernandezaitor@uniovi.es,
[c] edualvarez@uniovi.es
[d] eblanco@uniovi.es
[e] suarezlmaria@uniovi.es

Abstract:

The implementation of new low-carbon technologies for electricity generation and storage will involve the use of new resources such as hydrogen. In this sense, the use of hydrogen fuel cells will make it possible to store and transport energy for subsequent use by industry or other consumption. However, these devices generate large amounts of heat, which reduces their electrical efficiency. For this reason, recent studies have focused on the use of carbon allotropes, such as graphene, as heat sinks. This work presents a reduced model of a hydrogen fuel cell with graphene sheets, which has been subjected to several experimental tests, varying its heating and cooling conditions. Thus, the main objective of the experiment was to find out how the graphene sheets behave under different heat gradients and to assess their suitability as a heat sink. Specifically, temperature values, gradients and heat maps have been obtained in the different cells that make up the experimental prototype. In this way, the high performance of graphene as a heat sink in hydrogen fuel cells has been confirmed.

Keywords:

Heat dissipation; graphene; hydrogen fuel cells; experimental test rig.

1. Introduction

Hydrogen, the most abundant chemical element in nature, is a low-carbon resource whose only emission when burned is water vapour. This inert gas has been used in industry since the beginning of the 20th century and today, thanks to the stabilisation of its volatility, it has begun to be used in the automotive and aerospace industries [1]. The main advantage of this fuel is that it does not emit polluting gases to atmosphere. It is this last characteristic that has recently attracted increasing interest. In fact, the World Hydrogen Council (WHC) estimates that by 2030 the energy generated by the use of this green fuel will reach 3000 TWh/year [2].

Hydrogen energy is stored using electrochemical devices called fuel cells, where chemical energy is converted directly into electricity. The fuel (hydrogen) and comburent (oxygen) undergo a chemical exchange to produce water and electricity in the form of direct current and heat [3]. There are several types of hydrogen fuel cells, depending on the type of electrolyte used, which determines the type of chemical reactions that take place in the cell (see Table 1).

Table 1. Classification of hydrogen cells according to electrolyte type [3].

Fuel cell	Proton Exchange Membrane Fuel Cell (PEMFC)	Phosphoric Acid Fuel Cell (PAFC)	Molten Carbonate Fuel Cell (MCFC)	Solid Oxide Fuel Cell (SOFC)
Electrolyte	Solid polymer	Phosphoric acid	Molten carbonates	Solid polymer
Operating temperature (ºC)	60 – 80	200 – 250	600 – 700	50 – 120
Power range (kW)	5 – 250	5 – 150	100 – 2000	5
Advantages	Low temperature	Accept impure H_2	Cogeneration	No fuel reforming required
Applications	Transport	Electricity generation	Electricity generation	Electricity generation
Efficiency	34%	38%	48%	47%

These devices have among their characteristics the need to operate in an optimum temperature range to achieve high performance and minimise their degradation [4]. Specifically, the most common ways of removing excess heat inside hydrogen cells are free convection, condensers, heat sinks and cooling plates [5]. Heat dissipation by convection is therefore the simplest system, since all that is done is to add fins to the cell interfaces and leave them in contact with air, so it is only feasible at low temperatures [6]. Dissipation by condensers or cooling plates involves much more complex designs and the incorporation of devices that force the movement of a fluid (water or air) to force this dissipation, so they are used in batteries with high temperature ranges [7]. Finally, the use of heatsinks is based on the concept of thermal conductivity to transport heat to a cold source (passive or active). This implies the use of different materials that have adequate thermal conductivity behaviour (K in W/mK) [8].

In the specific case of heatsinks, the material from which they are made is particularly important, as it will transfer heat more or less efficiently depending on its thermal conductivity. In addition, other properties such as anisotropy, size, aspect ratio or the orientation of its atomic structure are key to ensuring proper heat exchange [9]. Up to now, the main materials used to dissipate heat in hydrogen fuel cells have been steel, aluminium and copper, the latter being the most suitable but also the most expensive [10]. However, the use of new polymers and carbon-derived materials (allotropes) is taking over much of the research into heat dissipation in hydrogen fuel cells.

The most important compound of carbon allotropes is graphene, since it is the basic element from which other materials such as graphite, fullerenes or carbon nanotubes (CNTs) are obtained. On the one hand, the main properties of these compounds are a well-defined atomic structure [11], high thermal conductivity (≈ 2000 W/mK), low coefficient of thermal expansion, strong mechanical and chemical resistance and anisotropy [12]. On the other hand, they have the disadvantage of being technically difficult to produce, and their high price undermines their competitiveness compared to other common materials. In fact, these materials have only been studied using advanced numerical models and, after sintering in the laboratory, they have been thermally characterised [13].

For example, in the research by Bahru et al…, a study is carried out using different techniques to characterise graphene, determining some thermal parameters according to the manufacturing method used (thickness, K or thermal resistance) for its subsequent use as a heat dissipating material in fuel cells [14]. In addition, the paper by Sun et al. carried out a numerical simulation of the heat transfer phenomena that occur in high-power LED light emitters, complementing the study with experimental tests based on thermography [11]. Finally, the article by Suzsko et al. presents a numerical analysis of the anisotropy of graphene for its use as a dissipator in high-efficiency microprocessors and its comparison with other materials [15].

In this sense, the present paper carries out an experimental study on the use of graphene sheets for heat dissipation inside a hydrogen fuel cell. For this purpose, a reduced scale model of a hydrogen fuel cell has been designed and fabricated, which has been subjected to a series of experimental tests simulating the heat exchange processes that occur during the operation of the cell. In each of the tests, temperature, gradient and heat map values were obtained to study the behaviour of graphene as a heat spreader.

2. Materials and methods

2.1. Experimental model

To study the thermal conductivity of graphene as a heat spreader, a reduced model of a hydrogen cell was designed, manufactured and studied in different experimental tests. In addition, to know its behaviour under different operating conditions, three different cases were simulated: Case 1, 2 and 3 (see Figure 1). In cases 1 and 2, passive cooling is used since the fins (case 1) and the graphene solid (case 2) are in exclusive contact with air. In case 3, however, both the fins and the graphene solid are in direct contact with a liquid cooling unit (active cooling).

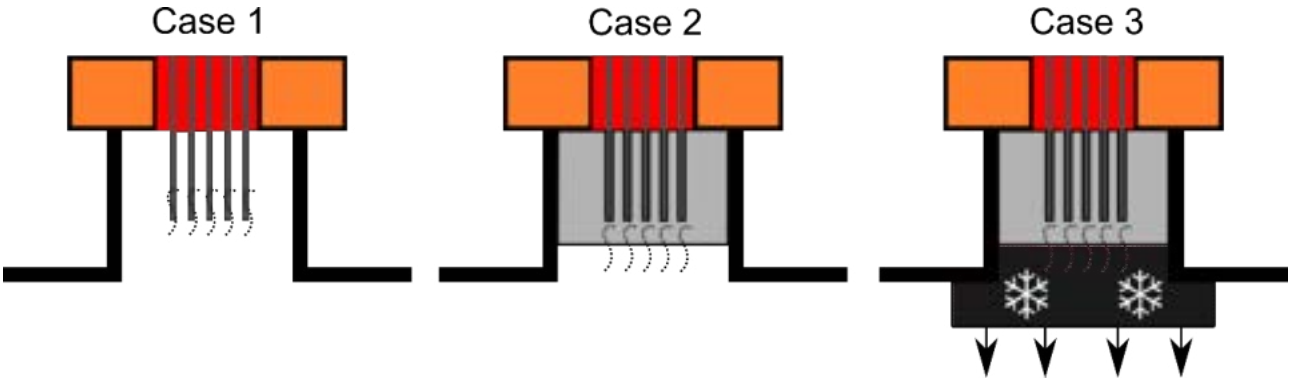

Figure 1. Geometry of the different cases implemented.

In all three cases, the functional scheme of the experimental model was the same. Specifically, the battery is made up of 5 identical cells placed one after the other. Each cell contains a heating pad with a maximum power of 5 W and a size of 100x50 mm, powered by a DC power supply. This makes it possible to control the operating temperature range of the system. This pad is flanked on both sides by a thermal interface with a conductivity of 3 W/mK to ensure heat transfer between cells. In turn, between two successive cells, a 0.5 mm thick graphene sheet measuring 120x50 mm has been placed to channel the heat flow towards some external fins where the cooling (passive or active) will take place. Finally, the whole system is supported by a 20 mm thick wooden case and a clamping system that ensures suitable contact between all the layers. Figure 2 shows a photograph of the implemented scale model and the location of the temperature sensors in each layer.

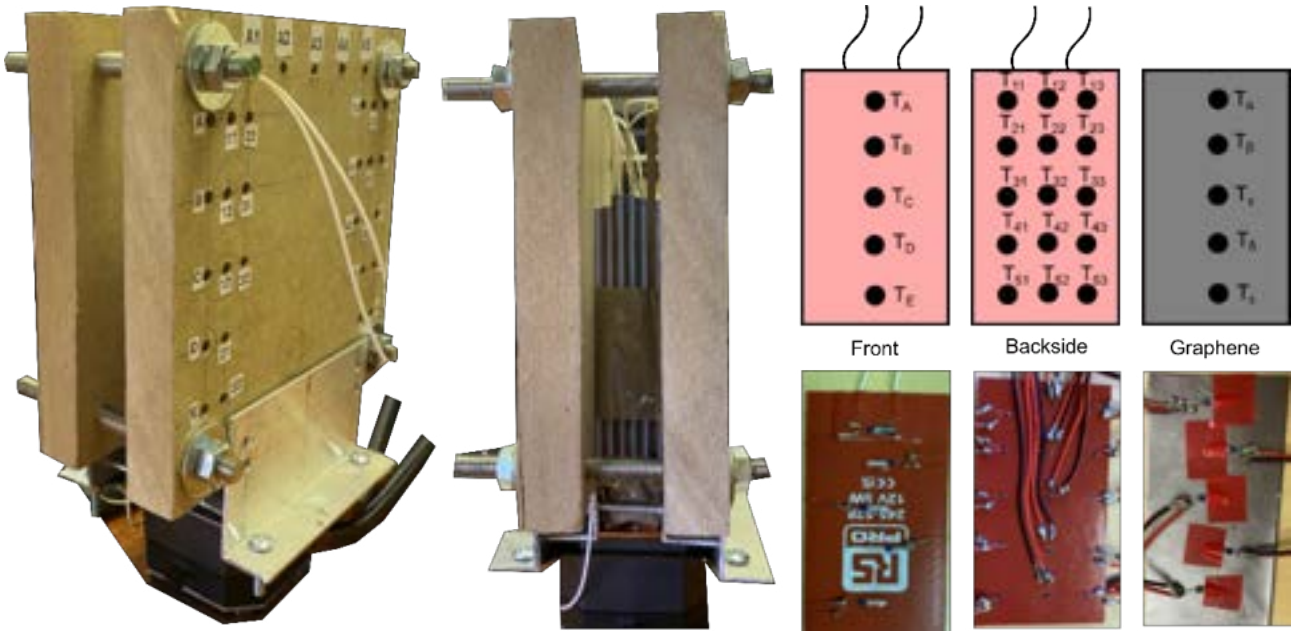

Figure 2. Photograph of the reduced experimental model and location of temperature sensors on each sheet of the fuel cell.

The parameter used for the study was temperature, using resistance thermometers according to the required accuracy of measurement. These sensors were only placed in the central cell of the reduced model because it was considered that this is the section where the greatest amount of heat is generated and therefore the study will be more interesting. Thus, as shown in Figure 3, fifteen temperature sensors were placed in an array on the back (T_{ij} ... $T_{(i+4,j+2)}$) and five temperature sensors on the front (T_A ... T_E) of the heating pad. In this way, the first ones make it possible to obtain a map of the heat distribution over the entire surface where the heat is generated, while the second ones were placed along the centre line to obtain the temperature gradient in the heating pad. In addition, five temperature sensors were placed along the axis of the graphene sheet (T_α ... T_ϵ) and one additional temperature sensor in the lamellar area (T_{flap}). In this way it was possible to obtain the temperature gradients in the carbon allotrope. Finally, it should be noted that several temperature sensors resistors were also used to obtain the temperature in other parts of the model: the contact zone between the graphene and the cooling unit (T_{con}), and two to obtain the ambient temperature on the surface of the case (T_m) and in the room (T_{amb}).

The temperature data are recorded using a data acquisition unit (model DAQ970A) for subsequent analysis. In addition, the cooling unit used (model iCUE H150i ProXT) can be controlled by computer, allowing the heat dissipation of the experimental model to be varied. All the tests were carried out in the maximum heat extraction mode. The experimental test rig used is shown in the following photograph (see Figure 3).

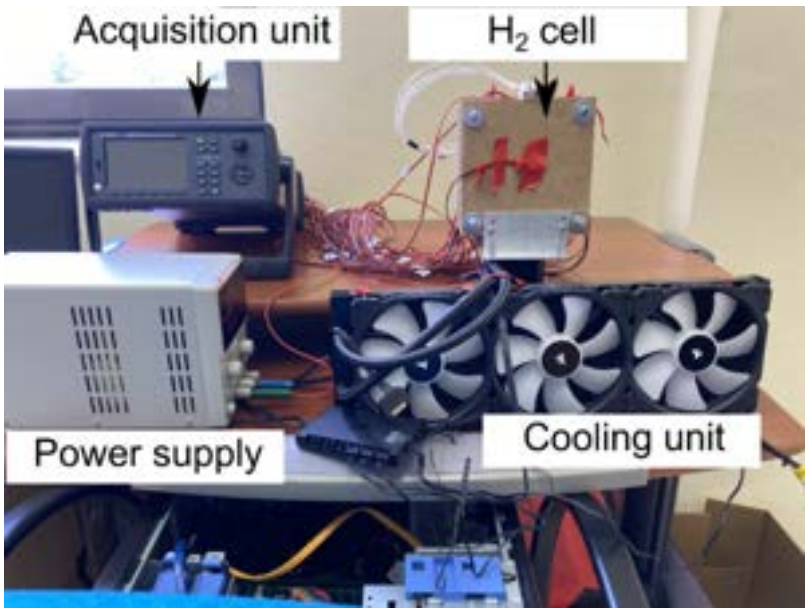

Figure 3. Experimental test rig designed and used for experimental tests.

To minimise the influence of external effects on the experiment, a constant temperature of 23°C was maintained in the room through the use of an air-conditioning unit. In addition, the prototype has been protected from solar radiation due to the use of opaque curtains that prevent the penetration of the sun's rays into the interior of the room. Finally, it should be noted that the effect of artificial convection was not considered relevant during the tests, since the air-conditioning unit kept the temperature values constant.

3. Results and analysis

For each of the cases implemented, tests were carried out focusing on the behaviour of the graphene sheet, while at the same time confirming the correct functioning of the heating pad. In this way, it was possible to obtain the temperature variation over time, the temperature gradient along the central part of the graphene sheet and the thermal maps in both materials.

The test consisted of switching on each of the heating pads with a power of 1 W, producing a heating phase of the stack for 40 minutes. This simulates the heat that would be generated inside the battery during operation. After this time, the power supply is switched off and the cooling phase begins. In cases 1 and 2 the cooling was passive (natural convection), while in case 3 the cooling unit remained on throughout the test (heating-cooling phases). The tests were repeated twice, obtaining consistent and reproducible results.

In case 1, the curves of the temperature variation with time during the whole duration of the test and the variation of the temperature gradient along the length of the sheet at the moment t = 40 min were obtained (see Figure 4).

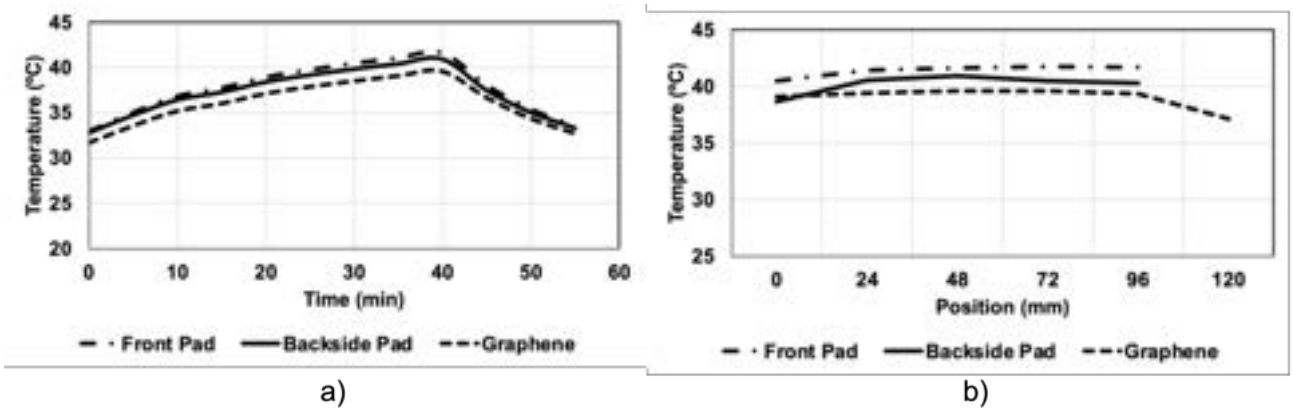

Figure 4. a) Temperature variation throughout the test and b) temperature gradient along the central section of the pad and graphene at t=40 min. Case 1.

For case 2, the same curves have also been obtained (see Figure 5).

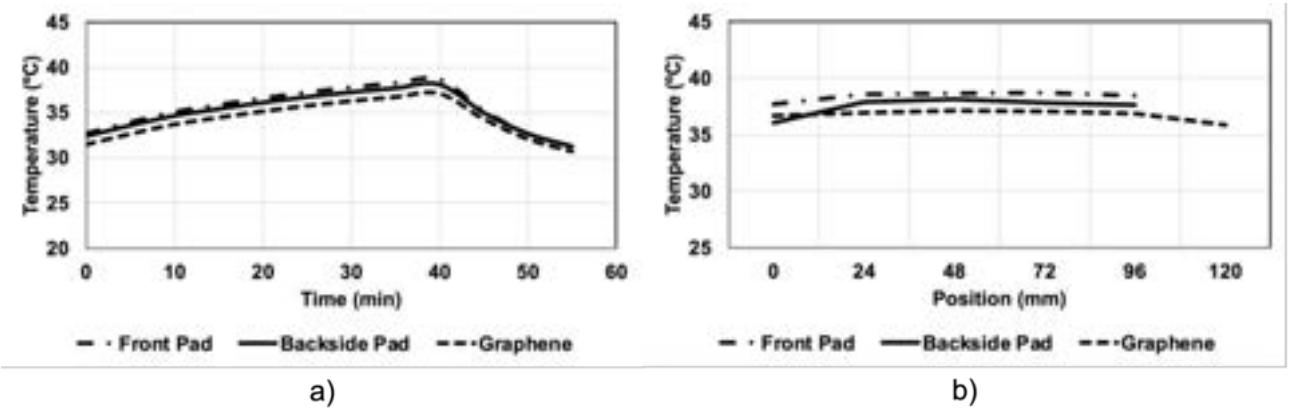

Figure 5. a) Temperature variation along the whole test and b) temperature gradient along the central part of the pad and graphene at t=40 min. Case 2.

Finally, Figure 6 shows the same graphs as above but for case 3.

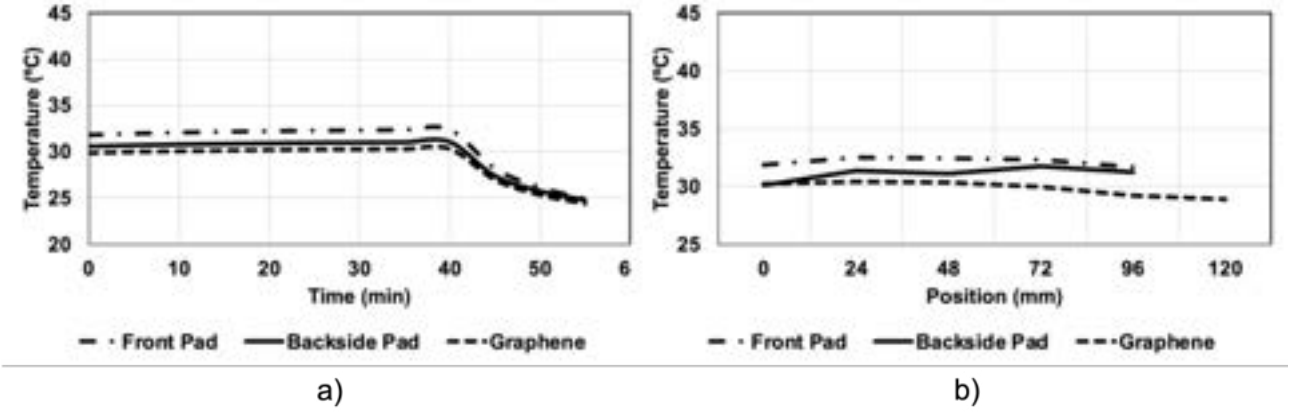

Figure 6. a) Temperature variation during the test and b) temperature gradient along the middle part of the pad and graphene at t=40 min. Case 3.

Note that in all cases both the back and the inside of the pad reach a higher temperature than the graphene sheet, which corresponds to reality as it is the heat source. Furthermore, looking at the temperature gradients, the pad still reaches a higher temperature than the graphene. It should be noted that the line representing the graphene sheet reaches up to 120 mm, since this position corresponds to the fins or the contact with the cooling unit, depending on the case considered. These results confirm that the equipment worked correctly in the three experimental cases considered. In addition, Figure 7 shows the heat maps obtained in the back of the heating pad in cases 1, 2 and 3.

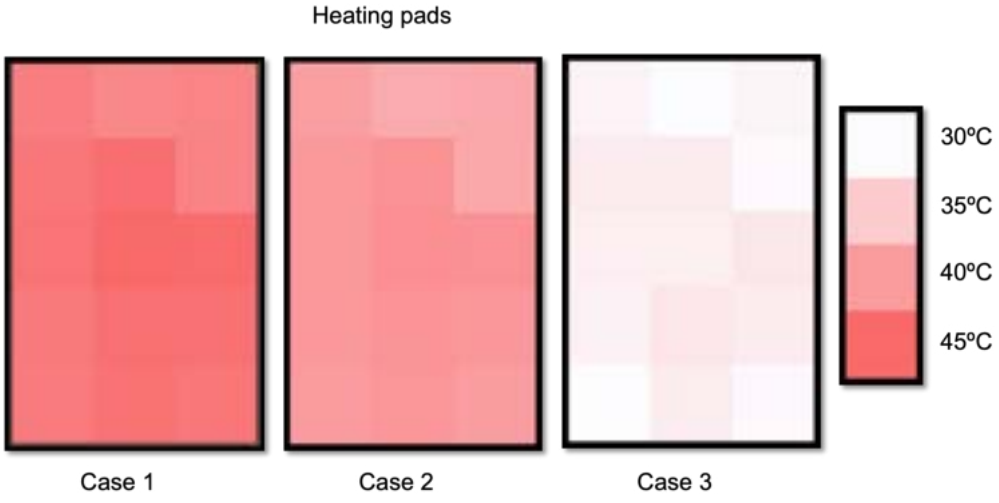

Figure 7. Heat maps for all three cases on the backside of the heating pad.

It can be seen that, in all cases, the temperature differences are less than 275,15 ºK, so it can be considered that the entire surface of the heating pad has a homogeneous behavior, confirming its correct functioning. Focusing on the graphene sheet, Figure 8 shows a comparison of the three experimentally studied cases.

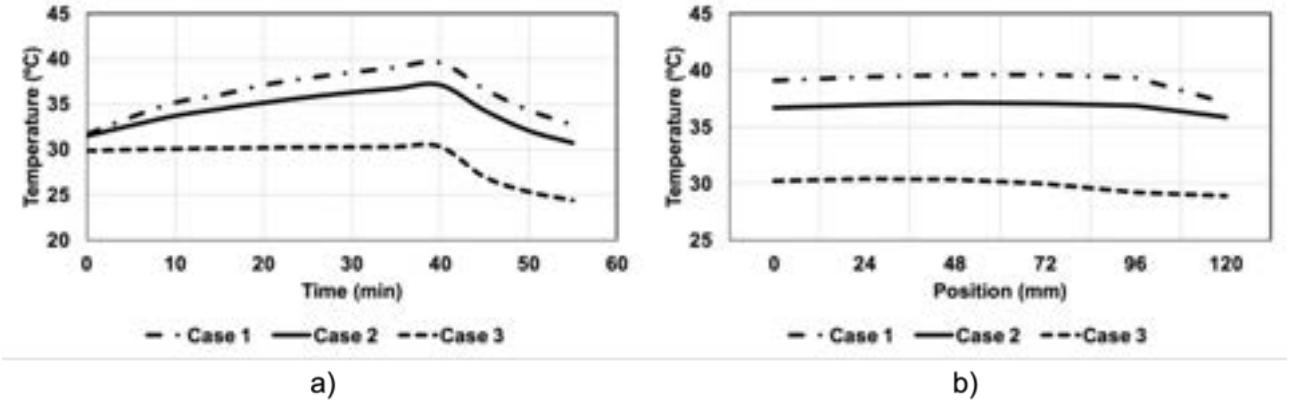

Figure 8. Comparison between the three cases considered: a) temperature variation in the graphene during the test and b) temperature gradient along the graphene sheet at t=40 min.

On the one hand, looking at Figure 8a, we can see that in the passive cooling cases, the graphene gradually increases its temperature until, at t=40 min, it abruptly starts its cooling phase. However, in case 3, since the cooling unit is on throughout the test, we can see how the graphene maintains a constant temperature during the heating phase, thanks to its thermal homogeneity properties. Then, from t=40 min, its temperature drops abruptly as the cooling unit actively removes the heat.

On the other hand, in Figure 8b, the temperature gradients in the central part of the graphene sheet show a negative slope to the left, i.e. the heat extraction is at the 120 mm position. Moreover, this slope is weak due to the latent isotropy in the graphene, which acts as a suitable heat sink.

4. Conclusions

The development of new low-carbon technologies for electricity generation and the construction of devices that allow more effective energy storage will be key to addressing future energy scenarios. In this sense, hydrogen-based technology will play a fundamental role through the development and implementation of batteries that allow safe and effective energy storage. However, these devices generate large amounts of heat, which significantly reduces their efficiency. To improve the efficiency of these devices, carbon allotropes such as graphene have recently been used. One of the many properties of these materials is their high thermal conductivity, which makes them ideal for use as heat sinks. Recent research has been based on the in-depth characterisation of this new material from a technical point of view, achieving in some cases conductivity values close to 6000 W/mK.

This publication shows an investigation through the construction of a reduced hydrogen cell model to study how graphene works as a heat sink in these devices. Specifically, three different cases were carried out in which the cooling conditions (passive and active) were varied. In this way, the aim is to verify that graphene can be used as a thermal conductor, allowing optimal heat extraction inside hydrogen cells. To this end, the temperature variation at different points of a graphene sheet under heating and cooling conditions was studied. In addition, the temperature gradients and their variation with the position in the material sheet itself have been calculated by studying the thermal slopes. In both cases, it has been confirmed that the heat dissipation takes place towards the location of the fins and the cooling unit, thus presenting a suitable thermal homogeneity.

In particular, graphene performs very well as a heat spreader, with temperature differences of less than 2ºC achieved along the entire length of the sheet. Moreover, when the same graphene surfaces are used to dissipate heat to the outside (cases 1 and 2), the temperature does not increase by more than 15ºC with respect to the ambient temperature. Finally, if a sufficiently powerful active cooling unit is used, the temperatures inside the cell are only 3ºC higher than the ambient temperature.

From the results obtained, it was found that the high thermal conductivity of the graphene allows efficient heat extraction to the cooling points. In addition, the graphene sheet has a very homogeneous behaviour, so that its entire surface reaches practically the same temperature, which translates into efficient heat transport.

Future work will validate a numerical model based on CFD, which will allow the simulation of passive and active cooling conditions, so that it will be possible to vary the heat extraction scenarios. It will also be possible to test other materials used as heat sinks, such as aluminium or copper. It is also planned to repeat the experimental tests but with different materials and compare the results with those presented in this article.

Acknowledgments

This work was carried out in the framework of Next Generation Heat Sink Design Project (Reference AYUD/2021/57485), funded by Principality of Asturias through FICYT and co-funded by ERDF. Also, the authors would like to thank the company The Next Pangea for their participation and collaboration.

References

[1] S. P. Yu *et al.*, "Integration of low-pressure hydrogen storage cylinder and automatic controller for carbon deposit removal in car engine," *Int J Hydrogen Energy*, vol. 41, no. 46, pp. 21795–21801, Dec. 2016, doi: 10.1016/J.IJHYDENE.2016.07.191.

[2] IEA, "The Future of Hydrogen – Analysis - IEA," 2021. https://www.iea.org/reports/the-future-of-hydrogen (accessed Mar. 09, 2021).

[3] S. Mekhilef, R. Saidur, and A. Safari, "Comparative study of different fuel cell technologies," *Renewable and Sustainable Energy Reviews*, vol. 16, no. 1, pp. 981–989, Jan. 2012, doi: 10.1016/J.RSER.2011.09.020.

[4] R. A. Felseghi, E. Carcadea, M. S. Raboaca, C. N. Trufin, and C. Filote, "Hydrogen Fuel Cell Technology for the Sustainable Future of Stationary Applications," *Energies 2019, Vol. 12, Page 4593*, vol. 12, no. 23, p. 4593, Dec. 2019, doi: 10.3390/EN12234593.

[5] "Fuel Cell Heat Management." https://www.fuelcellstore.com/blog-section/fuel-cell-heat-transfer-management (accessed Feb. 23, 2023).

[6] M. D. Mat and K. Aldas, "Application of a two-phase flow model for natural convection in an electrochemical cell," *Int J Hydrogen Energy*, vol. 30, no. 4, pp. 411–420, Mar. 2005, doi: 10.1016/J.IJHYDENE.2004.04.002.

[7] J. Choi, Y.-H. Kim, Y. Lee, K.-J. Lee, and Y. Kim, "Mechanical Science and Technology Numerical analysis on the performance of cooling plates in a PEFC," *Journal of Mechanical Science and Technology*, vol. 22, pp. 1417–1425, 2008, doi: 10.1007/s12206-008-0409-6.

[8] D. Hu, J. Liu, F. Yi, Q. Yang, and J. Zhou, "Enhancing heat dissipation to improve efficiency of two-stage electric air compressor for fuel cell vehicle," *Energy Convers Manag*, vol. 251, p. 115007, Jan. 2022, doi: 10.1016/J.ENCONMAN.2021.115007.

[9] L. Fan, Z. Tu, and S. H. Chan, "Recent development of hydrogen and fuel cell technologies: A review," *Energy Reports*, vol. 7, pp. 8421–8446, Nov. 2021, doi: 10.1016/J.EGYR.2021.08.003.

[10] L. Vasiliev and L. Vassiliev Jr, "Heat Pipes in Fuel Cell Technology," *Proceedings of the NATO Advanced Study Institute on Mini-Micro Fuel Cells-Fundamental and applications*, 2007. https://www.researchgate.net/publication/271074215_Heat_Pipes_in_Fuel_Cell_Technology (accessed Feb. 23, 2023).

[11] Q. Sun, J. Liu, Y. Peng, A. Wang, Z. Wu, and M. Chen, "Effective heat dissipation of high-power LEDs through creation of three-dimensional ceramic substrate with kaolin/graphene suspension," *J Alloys Compd*, vol. 817, p. 152779, Mar. 2020, doi: 10.1016/J.JALLCOM.2019.152779.

[12] A. A. Balandin, "Thermal Properties of Graphene, Carbon Nanotubes and Nanostructured Carbon Materials," California, US: National Library of Medicine, 2011.

[13] Y. Zhang *et al.*, "Recent advanced thermal interfacial materials: A review of conducting mechanisms and parameters of carbon materials," *Carbon N Y*, vol. 142, pp. 445–460, Feb. 2019, doi: 10.1016/J.CARBON.2018.10.077.

[14] R. Bahru *et al.*, "Allotrope carbon materials in thermal interface materials and fuel cell applications: A review," *Int J Energy Res*, vol. 44, no. 4, pp. 2471–2498, Mar. 2020, doi: 10.1002/ER.5077.

[15] A. Suszko and M. S. El-Genk, "Thermally anisotropic composite heat spreaders for enhanced thermal management of high-performance microprocessors," *International Journal of Thermal Sciences*, vol. 100, pp. 213–228, Feb. 2016, doi: 10.1016/J.IJTHERMALSCI.2015.09.018.

PROCEEDINGS OF ECOS 2023 - THE 36TH INTERNATIONAL CONFERENCE ON
EFFICIENCY, **C**OST, **O**PTIMIZATION, **S**IMULATION AND ENVIRONMENTAL IMPACT OF ENERGY SYSTEMS
25-30 JUNE, 2023, LAS PALMAS DE GRAN CANARIA, SPAIN

The implications of the basic materials industry electrification on the cost of hydrogen

Alla Toktarova[a], Lisa Göransson[a] and Filip Johnsson[a]

[a] Department of Space, Earth and Environment, Energy Technology, Chalmers University of Technology, Gothenburg, Sweden,
alla.toktarova@chalmers.se,
lisa.göransson@chalmers.se,
filip.johmsson@chalmers.se

Abstract:

This work applies techno-economic optimisation modelling to investigate how electrification of the basic material industry (ammonia, cement, plastics, and steel) impacts hydrogen production costs when considering flexibility options for the electrified industry. The context of the work is a zero-carbon emissions energy system of the EU, including future electricity demands from transport, heat, and industry.

The modelling results show that in the future electricity system, the lowest hydrogen production cost is the outcome of the production with full flexibility, i.e., the flexibility of time and location, and flexibility of CO_2 utilisation. Among the flexibility options, flexibility in time, i.e., the ability to follow electricity price variations, gives the largest reduction in hydrogen production costs in comparison to the scenarios without industrial flexibility options. With flexibility in location, it is possible to utilise solar power sites and remote areas for wind sites to satisfy electricity demand from industry. The difference in hydrogen production cost between scenarios with different combinations of flexibility options decreases with the size of the hydrogen demand. The decreased value of industrial flexibility when electricity demand from industry grows is due to the reduced access to sites with good conditions for VRE and some regions invest in nuclear power which benefits less from the industrial flexibility options. Still, even with the electrification of all ammonia, cement, steel and plastics production in the EU, there remains a value in industrial flexibility options.

Keywords:

Electrification; Industry; Electricity Systems Modelling; Storage; Flexibility; Hydrogen; Renewables.

1. Introduction

In the coming decades, as efforts to meet climate targets intensify, the demand for hydrogen within Europe is expected to significantly increase [1]. Hydrogen has the potential to play a crucial role in eliminating carbon dioxide emissions in the industry and transport sectors [2].

The production of basic materials (ammonia, cement, steel, and plastics) accounts for 70% of European industrial CO_2 emissions (2020), including energy and process-related emissions [3]. The basic materials industry faces two main challenges in achieving carbon neutrality: providing high-temperature heat without carbon emissions, and mitigating process emissions. The decreasing costs and low-carbon environmental impacts of wind and solar power, along with the potential to utilize low-cost electricity for flexible consumers, have made direct and indirect (through hydrogen) electrification a key pathway towards electrification of the basic materials industry [4]. Consequently, there are several ongoing projects related to hydrogen deployment in the basic material industries [5,6].

To implement and utilize hydrogen effectively for emissions reduction, it is crucial to study and analyse the cost of hydrogen. Calculating the cost of hydrogen produced through electrolysis commonly involves using the levelized cost of electricity (LCOE) from wind or solar power, combined with an assumed cost and capacity factor for the electrolyser [7]. In the method of calculating the cost of hydrogen using LCOE is assumed that hydrogen is always available at a certain cost, independently of when and how much hydrogen is required. In addition, the possibility of hydrogen production which follows the electricity price variations using hydrogen storage is not considered. An average annual cost for hydrogen can be a useful benchmark when comparing different energy systems in terms of the role that hydrogen can play and at what cost. However, consideration of the operational flexibility of hydrogen production (including both investments in over-capacity and storage) is an important factor when designing new industries that plan to use hydrogen in their processes.

Walter et al. [8] have shown the impacts of the hydrogen demand (varying it from 0 TWh_{H2} to 2,500 TWh_{H2} in steps of 500 TWh_{H2}) on the future European zero-emission electricity system, taking into consideration

flexibility in time (hydrogen storage and investments in overcapacity of hydrogen-consuming industries) and location. They find that the scenarios implementing flexibility options (flexibility in time (by means of both overcapacity and storage), and in location) for the electrolyser have the lowest production costs. However, the location of future industrial plants (including commodities trade) was not analysed in the above works.

By implementing a techno-economic optimisation model of the European electricity system, Öberg et al. [9] have shown that flexible operation of the electrolyser, i.e., the ability to follow electricity price variation due to overcapacity of the electrolyser and hydrogen storage capacities, have significant impacts on the cost of hydrogen. Unlike Walter et al., Öberg et al. considered hydrogen demand connected to its usage, i.e., they consider additional hydrogen demand from transport and industries (ammonia, cement, and plastics). They conclude that the characteristics of the hydrogen demand also impact hydrogen production costs. Flexible operation of industry (i.e., overcapacity is available) can reduce the cost of hydrogen production by up to 35% compared to constant operation of the industrial units. However, the model developed by Öberg et al. does not account for the additional cost for overcapacity of industrial units and storage of the products or intermediate products.

The studies from [8,9] have also shown that flexibility in the time of the electrolyser can have a major influence on the hydrogen production cost. The impacts of industrial electrification on process design (investments in industrial overcapacity and available commodities storage options) are not studied in the previous works.

Therefore, the aim of this work is to further improve the understanding of the electrification of industries (ammonia, cement, plastics, and steel) impacts on the hydrogen production cost in systems with high shares of VRE taking into consideration industrial flexibility options (flexibility in relation to time, location and CO_2 utilisation). We address the following research questions:

- How the potential future electricity demands from industries that have different types and levels of flexibility influence the cost of hydrogen?
- How does electrification of industry influence a cost-efficient spatial distribution of new locations of electrified industrial plants?

1.1. Electrification of industry

Table 1 lists the assumptions made on electrification options for the basic materials industry, including annual direct electricity and hydrogen demands. Direct electrification refers to the direct use of electricity as an input (plasma rotary kiln, EAF, electrified heat of steam cracker). Indirect electrification is the production of hydrogen and hydrogen-rich fuels and feedstocks from electrolysis.

Table 1. Annual assumed electricity demand for the basic materials industries.

Industry	Electrification option	Basic materials production in the EU[a], Mt	Annual direct electricity demand, TWh	Annual hydrogen demand, TWh_{el}	References
Ammonia	Power-to-ammonia	21	20	185	[10,11]
Cement	Plasma	133	174	-	[12,13]
Steel	H-DR	115	95	279	[14–16]
Plastics	Thermochemical recycling	38	349	436[b]	[17,18]

[a] The geographical scope corresponds to the area of the EU (excluding Cyprus and Malta), UK, Norway and Switzerland subdivided into 22 regions corresponding to major bottlenecks in the transmission grid. These investigated regions are: Northern Sweden (SE_N), Southern Sweden (SE_S), Northern Germany (DE_N), Southern Germany (DE_S), Estonia, Latvia and Lithuania (BAL), Northern Poland (PO_N), Southern Poland (PO_S), Ireland (IE_T), Norway (NO_T), Portugal and Western Spain (IB_W), Eastern Spain (IB_E), Northern France (FR_N), Southern France (FR_S), Switzerland and Northern Italy (ALP_W), Southern Italy (IT_S), Austria, Czech Republic and Slovakia (ATCZSK), Croatia, Slovakia (Slovak Republic) and Hungary (CRSIHU), Romania, Bulgaria and Greece (ROBGGR), Belgium, Netherlands and Luxembourg (BENELUX), Finland (FI_T), Scotland (UK_N) and Southern UK (UK_S).

[b] Depends on CO_2 utilization, i.e., the CO_2 emissions that arise from the process can be captured and converted to olefins through a synthesis process, or they can be captured and stored.

1.2. Process description – electrified ammonia production

The electrified ammonia production is the most hydrogen intensive commodity produced by basic materials industries investigated in this study, with an average hydrogen intensity of 8.6 MWh_{el} per 1 t of ammonia (cf. Table 1).

Figure 1 shows that the electrified ammonia production process includes electrolysis for H_2 production, an air separation unit (ASU) for nitrogen production and the ammonia synthesis via the Haber-Bosch (HB) process.

An ASU uses a cryogenic distillation process to separate ambient air into nitrogen, oxygen, and argon. All products can be stored in storage tanks [19]. The inlet air compressor is the main electricity consumer of an ASU [20]. The Haber-Bosch process combines hydrogen and nitrogen under high pressure and temperature. The HB process is normally optimized for continuous mass production, however, reconfiguration for dynamic production is possible [11]. The total electricity consumption of the ammonia production process, including electricity for hydrogen is 9.6 MWh/tNH_3.

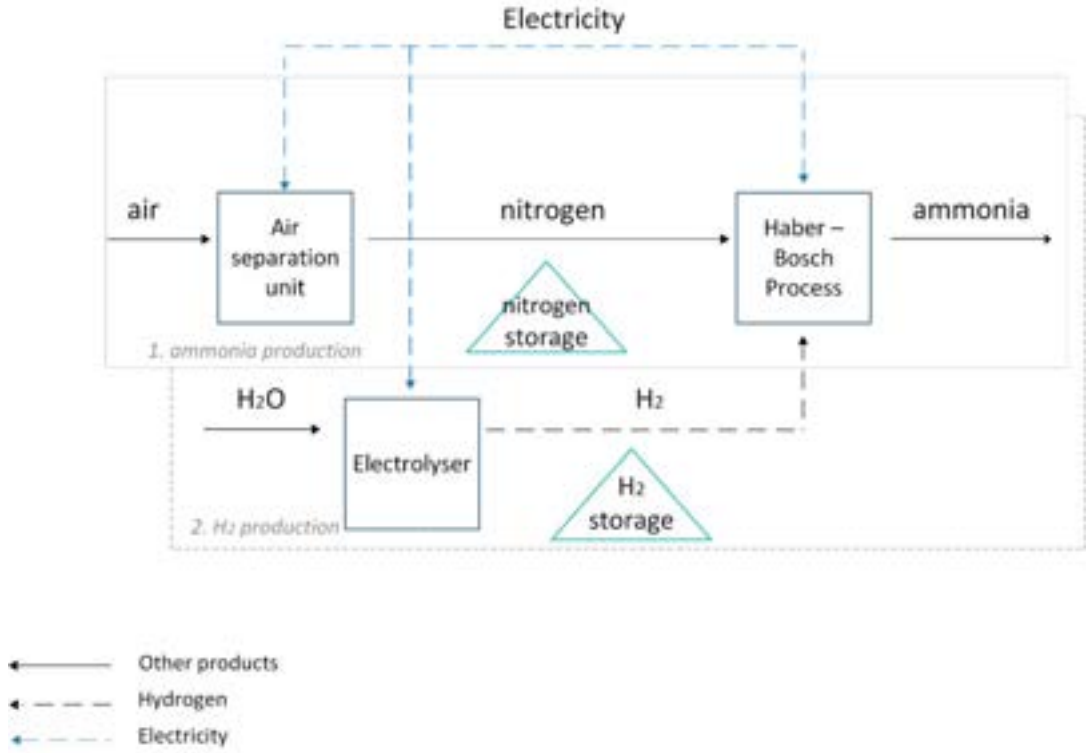

Figure. 1. Schematic representation of the electrified ammonia production process.

A detailed description of the electrification options (cf. Table. 1.) assumed for the basic materials industry investigated in this work is given in [21].

1.3. Industrial flexibility options

Three types of flexibility for the electrified industry were considered in this work: flexibility in relation to time, location, and CO_2 utilisation.

The ability of the industrial unit to vary the output within the load ranges, i.e., operational flexibility, is defined as flexibility in time. The lack of flexibility in time gives the capacity utilisation rate of 100%, i.e., there is no investment in overcapacity and storage. With flexibility in time, storage of commodities (e.g., hydrogen, hot-briquetted iron, nitrogen, and methanol) allows for rescheduling electricity consumption to periods with lower cost when available.

The electrification of the basic materials industry can significantly change cost structures of industrial production and with them the most cost-effective geographic location for production. The optimal location for production may shift from being close to demand and/or raw material supply centres to places where zero-emissions electricity is readily available at low cost, or where there are favourable conditions for CCS [22]. Flexibility in location is defined by the ability to export commodities. With flexibility in location, it is possible to locate new industrial units into regions without existing basic materials industries, increase capacity and/or production in the regions with existing industry, and separate parts of the existing supply chain. Distance-dependent transport costs for commodities are assumed, i.e., we consider the transport distance between regions and the amount of transported commodity. To represent some of the material and immaterial values in the current industrial sites, i.e., regions with existing industries, we apply an investment penalty for investments in new production sites for regions without existing industries: a 50% increase in investment cost—compared to investments in existing sites—for units producing commodities in regions without existing production of that basic material.

For some basic materials, such as plastics, electrification is not enough to eliminate production CO_2 emissions. Here, we assume that for plastics the process-related CO_2 can be captured and converted to olefins through

a synthesis process (CCU mode) and/or captured and stored (CCS mode). The term flexibility in CO_2 utilisation refers to the ability of production units to vary between CCU and CCS.

2. Method

To investigate how the potential future electricity demands from industries that have different types and levels of flexibility influence the cost of hydrogen in EU we deploy the cost-minimising electricity system investment model ENODE (Figure 2). The wide range of the electricity generation technologies considered in the model, including storage and transmission technologies. The model accounts for the economic and technical properties of the technologies, including start-up cost, start-up time and minimum load level of thermal generation. In terms of energy storage technologies, investments in lithium-ion batteries and H_2 storage are possible.

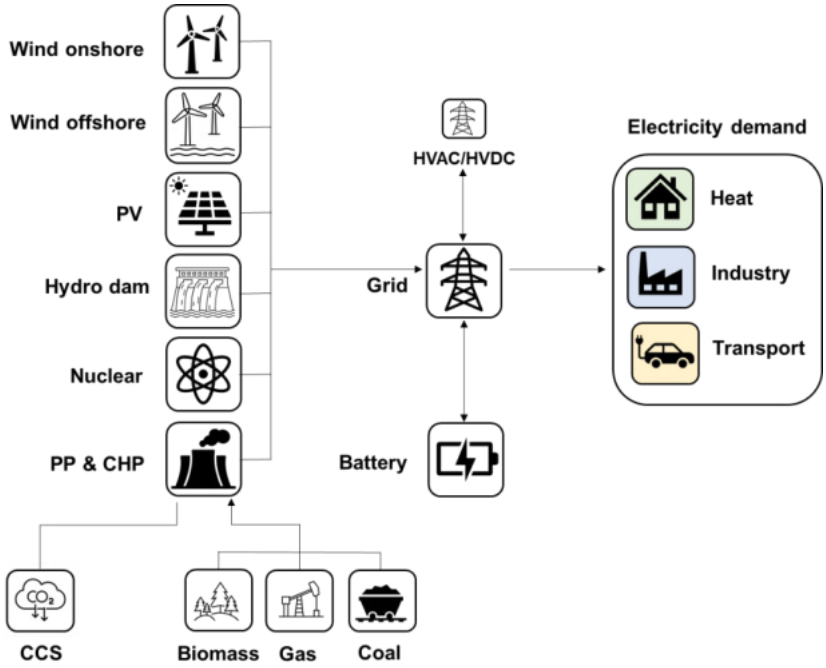

Figure. 2. Schematic representation of ENODE model.

ENODE was designed by Göransson et al. [23] to investigate the interactions between VRE and thermal generation technologies. Our version minimises the cost for investments in and operation of the electricity system and electrified industry, while meeting the demands for electricity and commodities. The objective function is expressed as:

$$min: C^{tot} = \sum_{r\in R} \sum_{p\in P\setminus P^{transm}} i_{p,r}(C_p^{inv} + C_p^{O\&M,fix}) + \sum_{t\in T} C_{p,t}^{run} g_{p,t,r} + \sum_{r_2\in R\setminus r} \sum_{p\in P^{transm}} C_{p,r,r_2}^{inv} i_{p,r,r_2} + \sum_{p\in P^{ind}\cup P^{transm}} \sum_{t\in T} C_{r,r_2}^{transp} e_{p,t,r,r_2}^{pos} + \sum_{p\in P^{plastic}} \sum_{t\in T} C^{st} b_{p,t}^{CCS} \quad (1)$$

where P is the set of all technologies, T is the set of time-steps, and R is the set of the regions. The annualized investment costs, the fixed operational and maintenance costs and the running costs per technology p at time-step t are denoted C_p^{inv}, $C_p^{O\&M,fix}$, and $C_{p,t}^{run}$, respectively. The variable $i_{p,r}$ is the capacity investment per technology p installed in region r, and $g_{p,t,r}$ is the generation of electricity and production of commodities per time-step t and region r, respectively. For the product trade that is transmitted/produced by technologies P^{transm} (the subset of P for transmission lines) and P^{ind} (the subset of P for commodity production units) between regions r and r_2 at per time-step t, the costs C_{r,r_2}^{transp} are considered. The CO_2 emissions $b_{p,t}$ from technology $P^{plastic}$ at time-step t are captured and stored at cost C^{st}.

Equation (2) represents the H_2 balance. Hydrogen is produced in the electrolyser and used to satisfy demand from basic materials industries. Hydrogen can be traded via a pipeline network.

$$g_{P^{Electrolyser},t,r}\eta_p + \sum_{p\in P^{H_2}} z_{p,t,r}^{dis} \geq \sum_{p\in P^{ind}} g_{p,t,r}\, a_p + \sum_{p\in P^{H_2}} z_{p,t,r}^{ch}$$

$$\forall t \in T, \forall r \in R \quad (2)$$

where a_p is the coefficient applied to relate commodities (ammonia, cement, steel, and plastics) production to H_2 demand for technology $p \in P^{ind}$. The efficiency of electrolyser is written as η_p.

The cost of electricity and hydrogen for the basic material industries is calculated according to Eq. (3),

$$C_i = \frac{\sum_t C_{t,i}^{maginal} g_t}{\sum_t g_t} \quad (3)$$

where the marginal cost $(C_{t,i}^{maginal})$ of electricity or hydrogen (i) per time-step (t) is weighted by the amount of electricity or hydrogen demanded by commodities production units (g_t) in each time-step. The marginal cost of electricity is taken as a proxy for the electricity price and is a result of the modelling, i.e., the marginal value from Eq. (1). The marginal cost of hydrogen is the marginal value of Eq. (2). The marginal value reflects the cost to supply one additional unit of electricity or hydrogen to the energy system.

The ENODE model is a green-field model, in which a new system is designed from scratch. A full mathematical description of the original eNODE model is given in [8].

2.1. Electricity demand

In the ENODE model, the electricity demand is classified into four categories: present demand used as a base level for the hourly demand profile and new electricity demand from transport, heat, and industry. The present electricity demand is determined on annual electricity consumption levels of the European countries obtained from Eurostat [24] and is subject to an hourly demand profile obtained from ENTSO-E [25]. The electricity demands from transport and heat are exogenously added to the present electricity demand. The electricity demand from heat is the electricity required to replace individual natural gas-based heating for decentralised heat pumps in Germany and the UK [26]. The electricity demand from the transport sector is modelled based on [27]. Full electrification of the passenger car fleet and partial (60 %) electrification of the heavy-duty vehicle fleet is considered in this model. The annual demand for commodities production (cf. Table 1) is given exogenously while the hourly electricity demand from basic materials industry is endogenous, thus investments in units producing commodities as well as the dispatch of these units are a result of the optimisation. The current production of commodities in the investigated regions is used as the regional demand for commodities in all scenarios to reflect the connection of the basic materials industry to the location of other industries.

2.2. Scenarios description

Figure 3 shows that the scenarios in this work vary in the type of industry that is electrified (ammonia, cement, steel, plastics) and the flexibility options that can be applied (flexibility in time and location and flexibility in CO_2 utilisation, the square under the parameter name indicates "yes" if included). The electrified ammonia industry is used as the reference industry to investigate how the electrification of industries impacts hydrogen production costs, since ammonia production is the most-hydrogen-intensive industry and has the highest operational flexibility among all the industries investigated in this study. The names of the scenarios with all flexibility options start with *Flex*; with limited flexibility in time - *Inflex_time*; with limited flexibility in location - *Inflex_location*; and with both limited flexibility in time and location – *Inflex_time_location*.

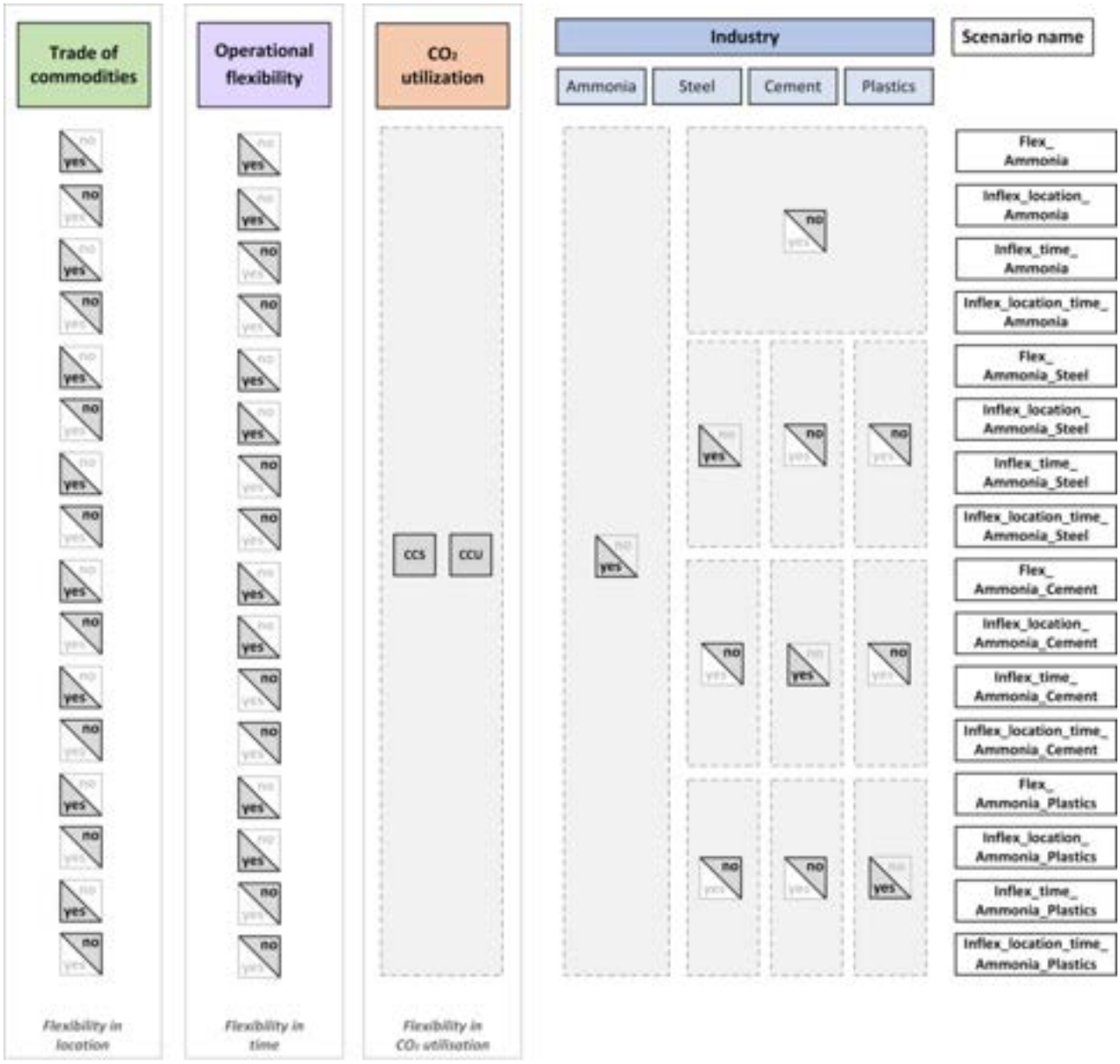

Figure. 3. Schematic overview of the parameters that define the investigated scenarios.

3. Results

The result presentation is divided into the following two parts: how electrified basic materials industries influence the production cost of hydrogen for the investigated scenarios (Section 3.1) and the location and production levels of the electrified industrial unit (for the example of direct reduction shaft furnace (DR shaft)) for the investigated scenarios (Section 3.2).

3.1. Hydrogen production cost

Figure 4 shows the break-down of the hydrogen production cost per MWh for the scenarios in which: only the ammonia industry is electrified; the ammonia and steel industries are electrified; and all the investigated industries (i.e., ammonia, cement, steel, and plastics) are electrified. The model results for the scenarios with electrified ammonia and cement industries, as well as with electrified ammonia and plastics industries are given in Figure A.1, Appendix A. Hydrogen production cost includes the annualized investment cost, the fixed O&M costs, the electricity cost, and hydrogen transportation costs for the investigated scenarios.

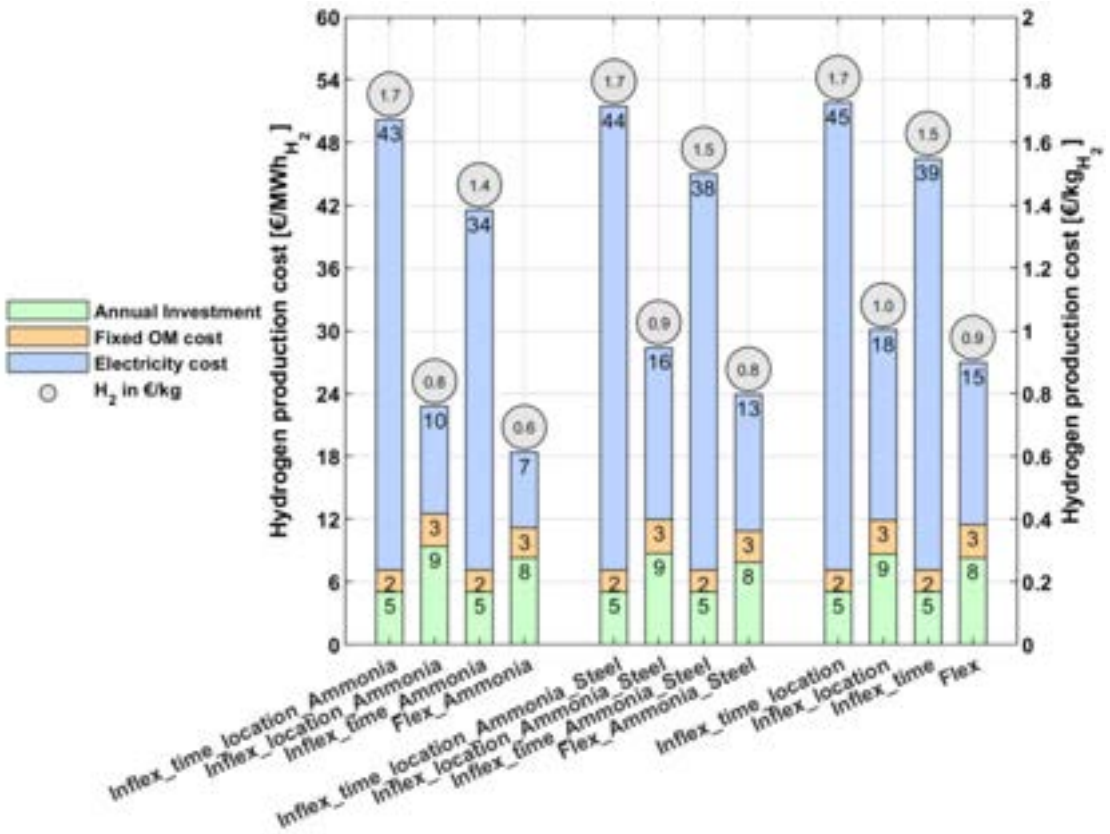

Figure. 4. The hydrogen production cost obtained from the modelling for the scenarios in which only the ammonia industry is electrified, scenarios in which the ammonia and steel industries are electrified, and scenarios in which all industries are electrified (i.e., ammonia, cement, steel, and plastics) are electrified. The scenarios with all flexibility options begin with *Flex*. Scenarios with limited flexibility in time or location are denoted by *Inflex_time* or *Inflex_location*, respectively. Scenarios with limited flexibility in both time and location are titled with *Inflex_time_location*.

The modelled costs given in Figure 4 yield a hydrogen production cost that ranges from 18 to 44 €/MWh$_{h2}$ (corresponding to 0.6–1.7 €/kg of hydrogen) for the investigated scenarios. The relatively low hydrogen cost obtained in this work is due to the ability of the electrolyser to follow electricity price variations. The range of hydrogen costs projected by the IEA is 1.1–4.0 €/kg of hydrogen. The electricity cost constitutes 55% of the total hydrogen production cost obtained from the IEA, if in regions with good access to renewable energy, the cost of electricity (mainly from solar power) for hydrogen production is 14 €/MWh and that the electrolyser operates for 2,600 full-load hours. According to the IEA projections, by Year 2030 the electrolyser investments cost will have decreased to 300–500 €/kW compared to the current levels (1,400–1,770 €/kW), due to the scaling up of electrolyser capacity [28]. Because of the falling costs for electrolysers, BloombergNEF [29]projects that renewable hydrogen could be produced for 0.6–1.4 €/kg in most parts of the world before Year 2050. The current work and other projections [8,9]suggest that two important factors are crucial to decreasing the cost of producing hydrogen: the flexible consumption by the electrolysers of the electricity supplied from VRE; and the scaling up of the electrolyser capacity.

The modelling results show that in the future European electricity system, the lowest cost for hydrogen production arises from production with full flexibility, i.e., flexibility in both time and location, and flexibility of CO_2 utilisation. The limitation of the flexibility in time for the industrial units has a stronger impact on the hydrogen production cost compared with the scenarios in which the flexibility in location is limited. For scenarios with limited flexibility in time, the hydrogen cost increases by 100%, and for scenarios with limited flexibility in location the hydrogen cost increases by 20%, as compared with the scenarios in which all flexibility options are available.

The hydrogen production cost is affected by not only industrial flexibility options but also by commodity demands. The low-medium operational flexibility of plasma kilns makes it challenging to follow electricity price variations. Nonetheless, the electrification of both the ammonia and cement industries, when at least one flexibility option is available, leads to a 1%–4% increase in the hydrogen cost compared to electrifying only the ammonia industry. In contrast, electrification of the ammonia and steel industries results in an 8%–23% increase in the hydrogen cost, and electrification of ammonia and plastics production processes leads to a 2%–17% increase in the hydrogen cost. The lower increase in hydrogen cost when the ammonia and cement

industries are electrified, as compared to the scenario where the ammonia industry is electrified along with steel and plastics production, is attributed to the low total electricity demand from cement production driven by the demand for cement. In other words, the lower hydrogen cost increase can be attributed to the fact that the cement industry requires less electricity in total (under the given assumptions regarding the cement demand) than the steel and plastics industries.

Among the scenarios in which only two industries are electrified, the highest cost for hydrogen production arises when the ammonia and steel industries are electrified. The high electricity demand driven by the steel demand reduces access to sites with good conditions for VRE. Thus, the number of high electricity price events increases, and this diminishes the value of the operational flexibility of the steel production units.

When electrifying the plastics and ammonia industries, flexibility in CO_2 utilisation compensates for the limited flexibility in time. Thus, the ability to switch between CO_2 utilisation modes (i.e., between CCU and CCS) allows the industrial units to avoid the consumption of electricity during high-cost events, which also implies increased costs for feedstock and CCS.

3.2. Locations and sizes of industrial units

Figure 5 presents the location and size of the DR shaft furnace capacity (in ktonnes) for two scenarios (*Flex* and *Flex_Ammonia_Steel*) in which the industrial units have full flexibility. In the *Flex* scenario, all the investigated industries are electrified, while in the *Flex_Ammonia_Steel* scenario, only the ammonia and steel industries are electrified.

Figure 5 shows that electrification of only the ammonia and steel industries, as applied in the *Flex_Ammonia_Steel* scenario, leads to the clustering of the DR shaft furnace capacity around countries that have good conditions for VRE and low-cost access to iron ore, such as FR_N. The electrification of the ammonia, cement, steel, and plastics industries (*Flex* scenario) results in investments, and investments in DR shaft furnace capacity increase in the regions that have existing steel production in UK_S, SE_N and FI_T, as compared with the *Flex_Ammonia_Steel* scenario.

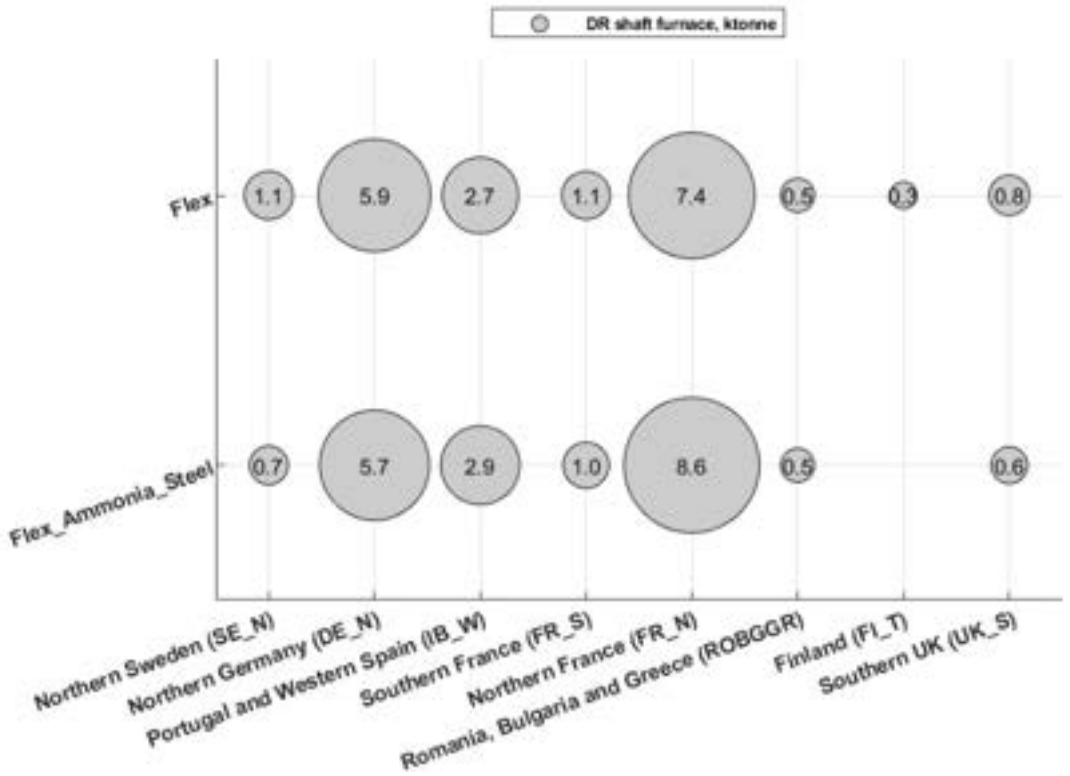

Figure. 5. The modelling results for the regional allocations of the steel production capacities in terms of the DR shaft furnace (in ktonnes) for the *Flex_Ammonia_Steel* and *Flex* scenarios.

The effects of electrification, such as the cost of hydrogen production for the industry, may vary depending on whether one or multiple sectors are electrified simultaneously. Investment decisions regarding industrial units, such as those in over-capacity and storage to take advantage of electricity price variations, which are made by the "first" industry that electrifies its production could impact the investment decisions of subsequent industries. Furthermore, the benefits of the industrial flexibility options provided by electrification might lessen as more industries electrify their production processes. Thus, further analysis is needed to understand the different stages of the industrial transition toward electrification.

4. Conclusions

This work applied a techno-economic optimisation model to analyse and discuss how electrification of energy-intensive basic materials industry impact hydrogen production cost, considering industrial flexibility options. The model is developed for a zero-carbon emissions electricity system of the EU that considers the current electricity demand as well as future demands from the transport, heat, and industrial sectors

The modelled costs yield a hydrogen production cost that ranges from 18 to 44 €/MWh$_{h2}$ (corresponding to 0.6 – 1.7 €/kg of hydrogen) for the investigated scenarios. Full flexibility (flexibility with regards to time and location, and flexibility of CO_2 utilisation) of the energy-intensive basic materials industry yields in the lowest hydrogen production cost.

The results indicate that in a future electricity system with more fluctuating electricity prices (in comparison to today's price fluctuations), the production of the basic materials which follows electricity variations gives lower hydrogen production cost, as compared to the scenarios with the optimised geographical location of industries. The electricity price following production would require investment in over-capacity of industrial units (i.e., electrolyser) and commodities storages (i.e., hydrogen).

In the scenarios with flexibility in location which are defined by the ability to export commodities, the basic materials industry capacity and/or production increase in the regions with existing industry and access to low-cost electricity. As a result, it is possible to utilise solar power sites and remote areas for wind power generation sites to satisfy the hydrogen demand from industry.

Finally, the modelling results indicate that as the demand for hydrogen increases, the difference in hydrogen production cost between scenarios with different combinations of flexibility options decreases. The decreased value of industrial flexibility when the electricity demand from industry grows is due to the reduced access to sites with good conditions for VRE and the fact that some regions invest in nuclear power, which benefits less from the industrial flexibility options.

Acknowledgments

This work was financed by the Mistra Carbon Exit and Mistra Electrification research programmes with additional support from the Chalmers Area of Advance.

Appendix A - Model

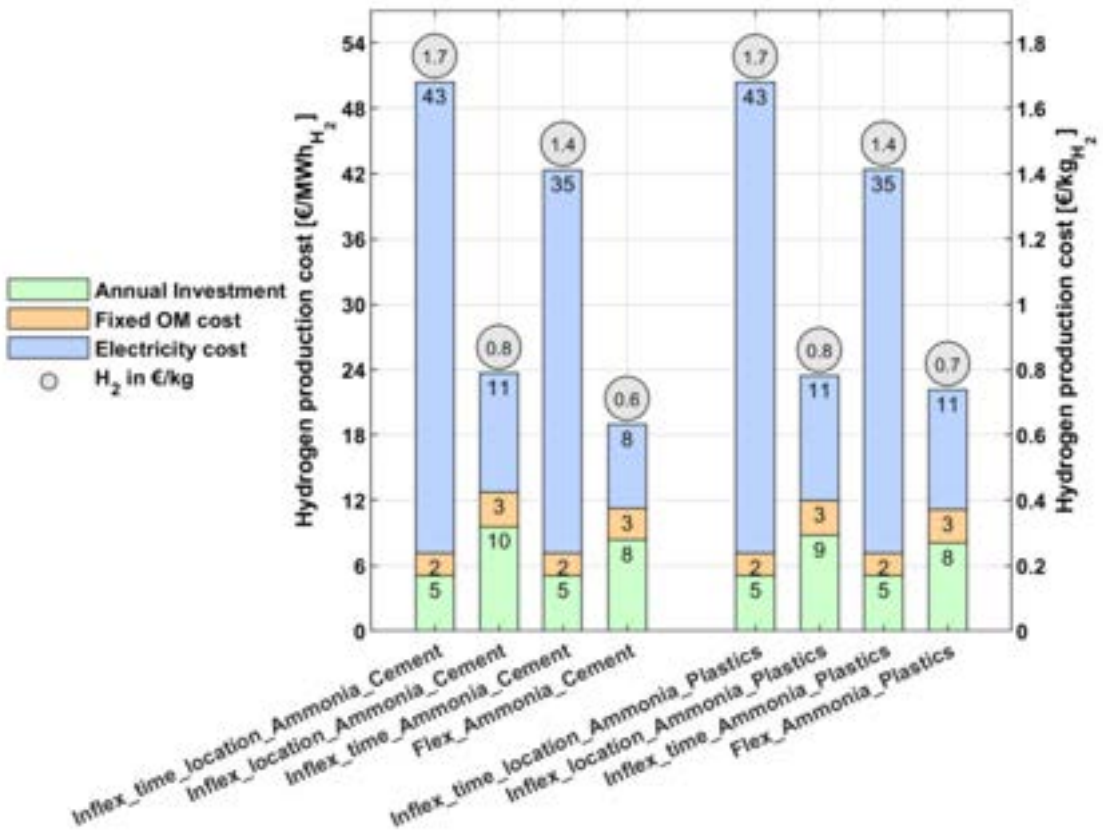

Figure. A.1. The hydrogen production cost obtained from the modelling for scenarios with electrified ammonia and cement industries and for scenarios with electrified ammonia and plastics industries. Hydrogen production cost includes the annualized investment cost, fixed O&M costs, electricity cost, and hydrogen transportation costs for the investigated scenarios. This study uses an electrolyser investment cost of 550 €/kW$_{el}$ [30].

References

[1] Fuel Cells and Hydrogen Joint Undertaking (FCH). Hydrogen Roadmap Europe. 2019.

[2] EC. A hydrogen strategy for a climate-neutral Europe 2020.

[3] IEA. Industry 2023 – Available at: https://www.iea.org/reports/industry [accessed 31.3.2023].

[4] IRENA. Renewable Power Generation Costs in 2020. Abu Dhabi: 2021.

[5] HYBRIT. SSAB, LKAB and Vattenfall first in the world with hydrogen-reduced sponge iron 2021 – Available at: https://www.hybritdevelopment.se/en/hybrit-ssab-lkab-and-vattenfall-first-in-the-world-with-hydrogen-reduced-sponge-iron/ [accessed 3.4.2023].

[6] Eurofer. Low-CO2 emissions projects - Detailed map and pathways 2022 – Available at: https://www.eurofer.eu/issues/climate-and-energy/maps-of-key-low-carbon-steel-projects/ [accessed 30.3.2023].

[7] Longden T, Beck FJ, Jotzo F, Andrews R, Prasad M. 'Clean'hydrogen?–Comparing the emissions and costs of fossil fuel versus renewable electricity based hydrogen. Appl Energy 2022;306:118145.

[8] Walter V, Göransson L, Taljegard M, Öberg S, Odenberger M. Low-cost hydrogen in the future European electricity system–Enabled by flexibility in time and space. Appl Energy 2023;330:120315.

[9] Öberg S, Odenberger M, Johnsson F. The cost dynamics of hydrogen supply in future energy systems–A techno-economic study. Appl Energy 2022;328:120233.

[10] Ausfelder F, Herrmann EO, Gonzalez LFL. Perspective Europe 2030 Technology Options for CO2—Emission Reduction of Hydrogen Feedstock in Ammonia Production. Frankfurt Am Main DECHEMA Gesellschaft Für Chem Tech Und Biotechnol 2022.

[11] Ikäheimo J, Kiviluoma J, Weiss R, Holttinen H. Power-to-ammonia in future North European 100% renewable power and heat system. Int J Hydrogen Energy 2018;43:17295–308.

[12] Wilhelmsson B, Kollberg C, Larsson J, Eriksson J, Eriksson M. CemZero–A feasibility study evaluating ways to reach sustainable cement production via the use of electricity. Vattenfall Cem 2018.

[13] de Vet J-M, Pauer A, Merkus E, Baker P, Gonzalez-Martinez AR, Kiss-Galfalvi T, et al. Competitiveness of the European Cement and Lime Sectors. WIFO Stud 2018.

[14] Eurofer. European steel in figures 2022, 2022 – Available at: https://www.eurofer.eu/assets/publications/brochures-booklets-and-factsheets/european-steel-in-figures-2022/European-Steel-in-Figures-2022-v2.pdf [accessed 28.3.2023].

[15] Vogl V, Åhman M, Nilsson LJ. Assessment of hydrogen direct reduction for fossil-free steelmaking. J Clean Prod 2018;203:736–45. https://doi.org/10.1016/j.jclepro.2018.08.279.

[16] Fischedick M, Marzinkowski J, Winzer P, Weigel M. Techno-economic evaluation of innovative steel production technologies. J Clean Prod 2014;84:563–80. https://doi.org/10.1016/j.jclepro.2014.05.063.

[17] PlasticsEurope E. Plastics—The Facts 2020. An Analysis of European Plastics Production, Demand and Waste Data. Brussels, Belgium: 2020.

[18] Thunman H, Vilches TB, Seemann M, Maric J, Vela IC, Pissot S, et al. Circular use of plastics-transformation of existing petrochemical clusters into thermochemical recycling plants with 100% plastics recovery. Sustain Mater Technol 2019;22:e00124.

[19] Mitra S, Grossmann IE, Pinto JM, Arora N. Optimal production planning under time-sensitive electricity prices for continuous power-intensive processes. Comput Chem Eng 2012;38:171–84.

[20] Johansson T. Integrated scheduling and control of an air separation unit subject to time-varying electricity prices. Master's Thesis, KTH R Inst Technol 2015.

[21] Toktarova A, Göranssona L, Johnssona F. Electrification of the energy-intensive basic materials industry – Implications for the European electricity system. Submitted to Renew Sustain Energy Rev 2023.

[22] Bataille C, Nilsson LJ, Jotzo F. Industry in a net-zero emissions world: new mitigation pathways, new supply chains, modelling needs and policy implications. Energy Clim Chang 2021;2:100059.

[23] Göransson L, Goop J, Odenberger M, Johnsson F. Impact of thermal plant cycling on the cost-optimal composition of a regional electricity generation system. Appl Energy 2017;197:230–40. https://doi.org/10.1016/j.apenergy.2017.04.018.

[24] Eurostat. Supply, transformation and consumption of electricity 2022 – Available at: https://ec.europa.eu/eurostat/databrowser/view/nrg_cb_e/default/table?lang=en [accessed 28.2.2022].

[25] ENTSO-E. Hourly Load Values for a Specific Country for a Specific Month (in MW) 2017 – Available at: https://www.entsoe.eu/data/power-stats/hourly_load/ h [accessed 28.12.2021].

[26] Göransson L, Lehtveer M, Nyholm E, Taljegard M, Walter V. The benefit of collaboration in the North European electricity system transition—System and sector perspectives. Energies 2019;12. https://doi.org/10.3390/en12244648.

[27] Taljegard M, Walter V, Göransson L, Odenberger M, Johnsson F. Impact of electric vehicles on the cost-competitiveness of generation and storage technologies in the electricity system. Environ Res Lett 2019;14:124087.

[28] IEA IEA. Global Hydrogen Review 2022. Paris: 2022.

[29] Bloomberg NEF. Hydrogen Economy Outlook. 2020.

[30] Danish Energy Agency. Technology data. 2021.

Developing a Novel and Integrated Datacenter Concept Design Based on Hydrogen Production

Ali Khosravi[a], Mohammad Malekan[b]

[a] *Centre for Industrial Mechanics, Department of Mechanical and Electrical Engineering, University of Southern Denmark, 6400 Sønderborg, Denmark, alkh@sdu.dk*
[b] *Centre for Industrial Mechanics, Department of Mechanical and Electrical Engineering, University of Southern Denmark, 6400 Sønderborg, Denmark, malekan@sdu.dk*

Abstract

Over the past few decades, data centers have made significant strides in enhancing their sustainability practices. These efforts range from minimizing power usage effectiveness (PUE) and carbon usage effectiveness (CUE) to enhancing water usage effectiveness (WUE). However, it's time for the data center industry to take a groundbreaking step forward. By effectively managing waste heat, data centers can become energy providers, boosting their profitability, and improving their energy reuse effectiveness (ERE) metrics. In this paper, we explore the crucial role of efficient heat management in optimizing the performance of an electrolyzer and maximizing the production of green hydrogen. Specifically, we focus on the importance of maintaining the stack temperature of the electrolyzer within a specific range to ensure maximum efficiency. We then propose a novel and integrated design concept for data centers that combines hydrogen production with district heating. An electrolyzer can be connected to both the data center and district heating systems, enabling the heat management system of the data center (e.g., heat pump) for powering the electrolyzer. Additionally, district heating can be utilized for thermal management of the electrolyzer, further improving the overall efficiency of the system. Additionally, the waste heat produced during the electrolysis process can be harnessed and employed to supplement the district heating system. This symbiotic relationship between the two systems results in a reduction in carbon emissions and improved energy efficiency. Our paper examines the technical feasibility of this proposed system and highlights the potential benefits for data centers and district heating systems.

Keywords:

Datacenter; Hydrogen production; Waste heat recovery; District heating; Green transition

1. Introduction

Data centers are essential for the modern digital economy, enabling the storage, processing, and transmission of vast amounts of data [1]. However, data centers have become a significant contributor to global energy consumption and carbon emissions, which has led to a growing focus on sustainability in the industry [2]. In recent years, data centers have made significant strides in improving their energy and water usage effectiveness, but there is still untapped potential for waste heat recovery to generate energy and improve their environmental metrics [3]. The energy consumption of data centers (DCs) has significantly expanded in response to the expansion of the information technology industry, which in 2019 used around 3% of the world's electricity supply [4]. The consumption is growing at a pace of 15-20% annually [5]. The electricity needed to run cooling systems accounts for around 40% of the power utilized by DCs [6]. On the one hand, the usage of high-grade electrical energy to fulfill the low-grade cooling DC requirements results in a considerable energy loss of energy flow in DCs [7]. On the other hand, the electric refrigeration systems in DCs often discharge a significant quantity of waste heat to the external environment, which results in urban heat islands [8]. Therefore, it is necessary to enhance the DC energy systems' structure and thermodynamic energy efficiency. If significant quantities of low- and medium-grade waste heat could be efficiently recovered and used for things like building heating, water heating, and refrigeration, DCs may be regarded as energy producers [9]. As a result, data centers (DCs) could fully embrace the concept of prosumers, who simultaneously act as producers and consumers, and surpass the current energy efficiency optimization model, which only considers the consumer perspective. Apart from utilizing waste heat across the system, a DC energy system can be tailored

to the overall energy system, an integrated energy system, or a systematic approach to the energy network. With the expected growth in demand for data-based services and the accompanying power consumption, data centers are seeking cost-effective, sustainable, and dependable ways to power their operations. Hydrogen and fuel cells are viable options that could fulfill these requirements and integrate with a variety of potential benefits.

What is the need for a new design in data centers? There are multiple factors that could drive a departure from the conventional data center design. Data centers have significant power and space requirements, which necessitate considering regional factors such as land and labor costs, access to affordable power, and business-friendly governmental policies when selecting their locations. Stricter air permitting regulations for diesel backup generators in certain regions could reinforce the case for integrating hydrogen and fuel cells. Furthermore, some companies have established corporate strategies to increase their reliance on non-carbon or green fuels, with a few already transitioning to 100% renewables and other co-locators following suit. This provides further rationale for using green hydrogen or locating data centers near wind or other renewable power sources [10].

The literature on sustainable data centers has focused on reducing energy and water consumption, improving energy efficiency, and exploring renewable energy sources. Grange et al. [11] developed an algorithm for scheduling the data center by renewable energy. Their results showed a reduction of brown energy consumption up to 49%. According to Khosravi et al. [12], an ejector heat pump was designed to recover waste heat from a data center for use in a low temperature district heating network in Finland. The study revealed that the use of a water-water heat pump is a viable method for recovering waste heat from data centers. Iverson et al. [13] focused on the design of hybrid renewable energy systems (HRES) for data center applications, leveraging hydrogen storage technology. The aim of their research was to develop an optimal design for HRES that would effectively meet the energy demands of data centers, while minimizing energy costs and reducing the environmental impact of the system.

While these studies provide valuable insights into the potential for waste heat recovery in data centers, there is a need for more research on the specific technical and economic aspects of integrating hydrogen generation into data center infrastructure. This paper aims to contribute to this literature by proposing a novel and integrated data center concept design based on hydrogen production and conducting an analysis to determine its feasibility and potential. This paper proposes a novel approach to data center sustainability, in which waste heat is captured and reused to generate hydrogen fuel. By integrating an electrolyzer into the data center infrastructure, waste heat can be converted into a valuable energy source that can be used for district heating or as an ancillary service. This approach not only increases the overall profitability of data centers but also improves their environmental metrics by enhancing their energy reuse effectiveness. The proposed approach has the potential to transform the data center industry by making waste heat recovery a viable and profitable solution to energy generation. The approach not only improves the sustainability of data centers but also positions them as energy suppliers, which could have far-reaching implications for the broader energy industry. Overall, this paper contributes to the ongoing conversation on data center sustainability by proposing a novel and integrated design that has the potential to enhance both the environmental and economic performance of data centers.

2. Case study

Data centers are characterized by their use of air cooling, the most widely used technique in the sector, to provide low temperature, high capacity, and reliable heat. About 40% of the power utilized by DCs goes to power cooling systems. However, the electric refrigeration systems in DCs often release a significant amount of waste heat into the environment. The current Danfoss design for the data center at Nordborg is depicted in Figure 1. This system uses air cooled system to cool the data center. Danfoss is seeking for an alternate system because the current system is no longer providing economic benefits.

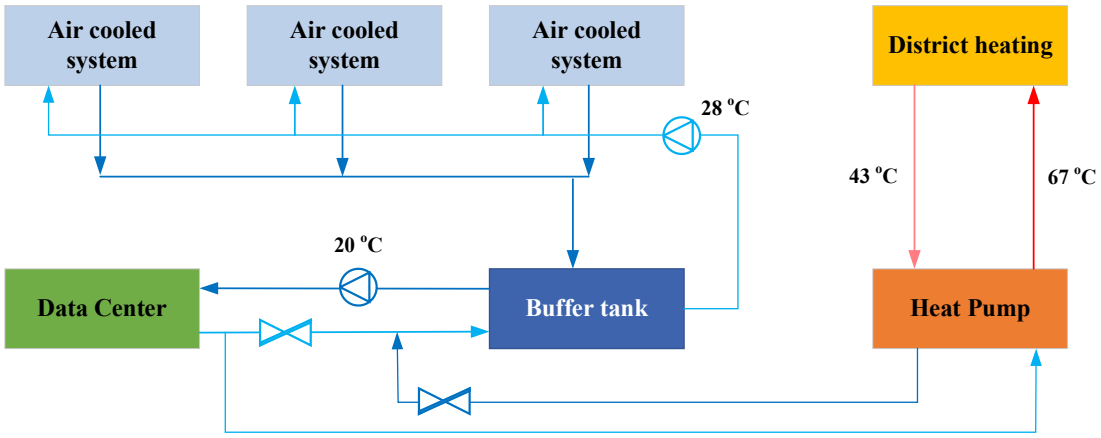

Figure 1. *Danfoss Nordborg data center, the current design.*

3. Material and methods

3.1 The proposed system

The system proposed in this paper incorporates an alkaline electrolyzer into a district heating system, heat pump layout, and data center, with the goal of optimizing the efficiency and sustainability of energy production. As shown in Figure 2, temperature control is a crucial factor in achieving optimal performance of the electrolyzer. To achieve this, the fourth generation of district heating networks is proposed for use with this technology, with the possibility of using the district heating for heat management of the electrolyzer. The heat pump is also an essential component for providing cooling for the data center and can be utilized for heat management of the electrolyzer. The heat pump has an electricity input of 174 kW and is capable of generating 824 kW of heat output and 650 kW of cooling output. The alkaline electrolyzer has a capacity of 2 MWe and produces 16.3 kg/h of hydrogen.

The system is powered by electricity from the NordPool electricity spot market, which is used to meet the electricity demand of the data center, which is 10,932,821 kWh as well as electricity demand for heat pump and electrolyzer. Additionally, the cooling demand of the data center is 3,000,000 kWh. To manage the thermal energy generated by the system, heat storage with a capacity of 6952 kWh and cooling storage with a capacity of 1158 kWh are included in the system design.

Furthermore, the electrolyzer is connected to the district heating network, allowing for the waste heat produced during the electrolysis process to be harnessed and employed to supplement the district heating system. The district heating system can be utilized as a free source for heat management of the electrolyzer. The system model proposed in this paper consists of an electrochemical model, a thermal model, and a model of the cooling system. The electrochemical model simulates the relationship between current and voltage for various operating temperatures and pressures, describing the kinetics of the reactions that take place and providing details required for precisely modeling the creation of heat inside the alkaline electrolyzer. The system proposed in this paper provides valuable insights into the potential for integrated energy systems to improve the sustainability and efficiency of energy production. Further research and development in this area may lead to the widespread implementation of similar systems, resulting in significant improvements in sustainability and energy efficiency.

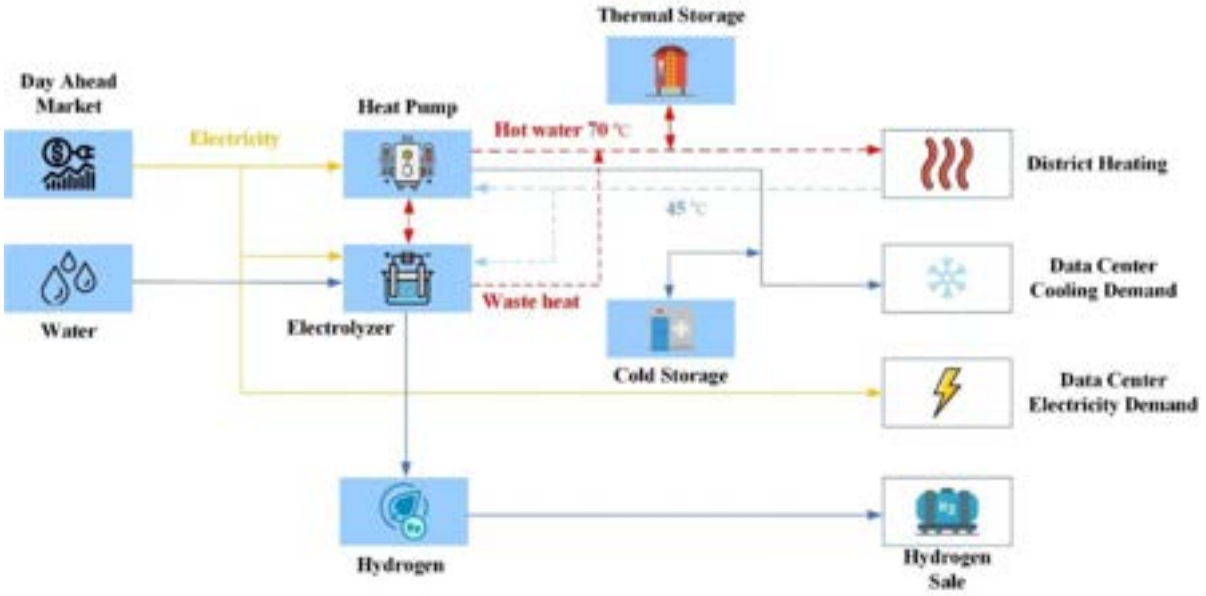

Figure 2. *Data center incorporated with alkaline electrolyzer.*

3.2 Electrolyzer Model

The following is a description of a mathematical model designed for a high-pressure alkaline water electrolyzer. The model is constructed by integrating fundamental principles of thermodynamics, heat transfer theory, and empirical electrochemical relationships. Additionally, the model includes a dynamic thermal component. The electrochemical model is based on a temperature dependent current-voltage curve at a specific pressure, as well as a Faraday efficiency relation that is not influenced by temperature or pressure.

The process of breaking down water into hydrogen and oxygen can be accomplished through the use of direct current (DC) passed between two electrodes that are separated by an aqueous electrolyte with strong ionic conductivity. The overall reaction for the separation of water can be expressed as:

$$H_2O(l) + \text{electrical energy} \rightarrow H_2(g) + \frac{1}{2}O_2(g) \quad (1)$$

For the reaction to take place, a minimum electric voltage must be applied to the two electrodes. This minimum voltage, also known as the reversible voltage, can be calculated using the Gibbs energy for water splitting. Alkaline electrolyzers typically use aqueous potassium hydroxide (KOH) as the electrolyte, with the potassium ion (K^+) and hydroxide ion (OH^-) facilitating ionic transport. The anodic and cathodic reactions that occur in this system can be described as follows:

$$\text{Anode: } 2OH^-(aq) \rightarrow \frac{1}{2}O_2(g) + H_2O(l) + 2e^- \quad (2)$$

$$\text{Cathode: } 2H_2O(l) + 2e^- \rightarrow H_2(g) + 2OH^-(aq) \quad (3)$$

In an alkaline solution, the electrodes must possess properties such as resistance to corrosion, good electrical conductivity, and catalytic activity, as well as structural integrity, while the diaphragm should have low electrical resistance. This can be achieved by using anodes made of materials such as nickel, cobalt, and iron (Ni, Co, Fe), cathodes with a platinum-activated carbon catalyst on a nickel base (Ni, C-Pt), and diaphragms made of nickel oxide (NiO).

3.2.1 Thermodynamic Model

Thermodynamics serves as a framework to describe reaction equilibrium and thermal effects in electrochemical reactors and provides a basis for defining driving forces for transport phenomena in electrolytes. Additionally, it aids in describing the properties of electrolyte solutions. The thermodynamics of the low-temperature hydrogen-oxygen electrochemical reactions utilized in the electrolyzer model are described below.

Assumptions can be made about the water splitting reaction: (a) hydrogen and oxygen are ideal gases, (b) water is an incompressible fluid, and (c) the gas and liquid phases are separate. Based on these assumptions, changes in enthalpy (ΔH), entropy (ΔS), and Gibbs energy (ΔG) of the water splitting reaction can be calculated with respect to pure hydrogen (H_2), oxygen (O_2), and water (H_2O) at standard temperature and pressure (25°C

and 1 bar). The total change in enthalpy for water splitting is the enthalpy difference between the products (H_2 and O_2) and the reactants (H_2O), and the same applies for the total change in entropy. The expression for the change in Gibbs energy is as follows [14]:

$$\Delta G = \Delta H - T\Delta S \tag{4}$$

In electrochemical processes, the splitting of water requires a significant amount of energy due to its positive change in Gibbs energy. At standard conditions (25°C and 1 bar), the standard Gibbs energy for water splitting is 237 kJ/mol, indicating that the reaction is non-spontaneous. However, Faraday's law states that the electrical energy required to split water is directly proportional to the chemical conversion rate in molar quantities. Therefore, the reversible cell voltage or *emf* for a reversible electrochemical process can be calculated using the change in Gibbs energy. This information is crucial when designing and optimizing electrochemical processes for the production of hydrogen and oxygen from water. The reversible cell voltage, also known as the electromotive force (*emf*) of a reversible electrochemical process, can be expressed as:

$$U_{rev} = \frac{\Delta G}{zF} \tag{5}$$

The expression relating the thermoneutral cell voltage to the total energy demand (ΔH) is:

$$U_{tn} = \frac{\Delta H}{zF} \tag{6}$$

3.2.2 Electrochemical model

Empirical current-voltage (I-U) relationships can be utilized to model the electrode kinetics of an electrolyzer cell. There are multiple suggested empirical I-U models for electrolyzers. In this study, the I-U curve utilized has a fundamental form that is dependent on the temperature, and can be expressed as:

$$U = U_{rev} + \frac{r}{A}I + s\,log\left(\frac{t}{A}I + 1\right) \tag{7}$$

The Faraday efficiency, also known as the current efficiency, is the ratio between the actual and theoretical maximum amount of hydrogen produced in an electrolyzer. The efficiency is affected by parasitic current losses along the gas ducts, which increase with decreasing current densities due to an increasing share of electrolyte and lower electrical resistance. The parasitic current is linearly proportional to the cell potential, which means that the fraction of parasitic currents to total current increases with decreasing current densities. An increase in temperature results in lower resistance, higher parasitic current losses, and lower Faraday efficiencies. Understanding the Faraday efficiency is essential for optimizing the performance and efficiency of an electrolyzer.

$$\eta_F = \frac{(I/A)^2}{f_1 + (I/A)^2} f_2 \tag{8}$$

Faraday's law states that the production rate of hydrogen in an electrolyzer cell is directly proportional to the transfer rate of electrons at the electrodes, which is equivalent to the electrical current flowing through the external circuit. Therefore, the total rate of hydrogen production in an electrolyzer, which comprises multiple cells connected in series, can be mathematically represented as:

$$\dot{n}_{H_2} = \eta_F \frac{n_c I}{zF} \tag{9}$$

The rate of oxygen production can be determined straightforwardly using stoichiometry, as shown in Eq. 11, which is expressed on a molar basis as:

$$\dot{n}_{H_2O} = \dot{n}_{H_2} = 2\dot{n}_{O_2} \tag{10}$$

The primary source of heat generation in an electrolyzer is attributed to electrical inefficiencies. The efficiency of energy conversion can be determined by utilizing the thermoneutral voltage (Equation 3) and the cell voltage (Equation 4), and is expressed mathematically as:

$$\eta_e = \frac{U_{tn}}{U} \tag{11}$$

3.2.3 Thermal Model

To determine the temperature of the electrolyte in an electrolyzer, a simple or complex thermal model can be employed depending on the required level of accuracy. If a lumped thermal capacitance model is assumed, the overall thermal energy balance can be expressed as a linear, non-homogeneous, first-order differential equation. This model enables the calculation of the stack temperature and analytically solves for the temperature distribution [14]:

$$C_t \frac{dT}{dt} = \dot{Q}_{gen} - \dot{Q}_{loss} - \dot{Q}_{cool} \tag{12}$$

$$\dot{Q}_{gen} = \eta_c (U - U_{tn}) I = n_c U I (1 - \eta_e) \tag{13}$$

$$\dot{Q}_{cool} = C_{cw}\left(T_{cw,i} - T_{cw,o}\right) = U A_{HX} LMTD \tag{14}$$

4. Results and Discussion

The figure presented in this section, Figure 3, depicts the behavior of the cell voltage (V) of an alkaline electrolyzer as a function of current density (mA/cm^2). The results demonstrate that as the current density is increased, the cell voltage also increases, starting from 0 and reaching 1.88 V. Interestingly, after a current density of 300 (mA/cm^2), the cell voltage becomes nearly constant and remains horizontal. This suggests that the performance of the electrolyzer plateaus at higher current densities and that further increases in current density may not result in a significant improvement in performance. This finding is significant because it indicates the importance of careful selection of current density to achieve optimal performance of the electrolyzer for hydrogen production. By identifying the point of plateau in cell voltage, it is possible to determine the maximum current density that can be used for efficient and sustainable hydrogen production. Overall, the results presented in Figure 2 provide valuable insights into the behavior of the cell voltage of an alkaline electrolyzer as a function of current density. These insights are important for optimizing the performance of the electrolyzer and achieving maximum efficiency in hydrogen production.

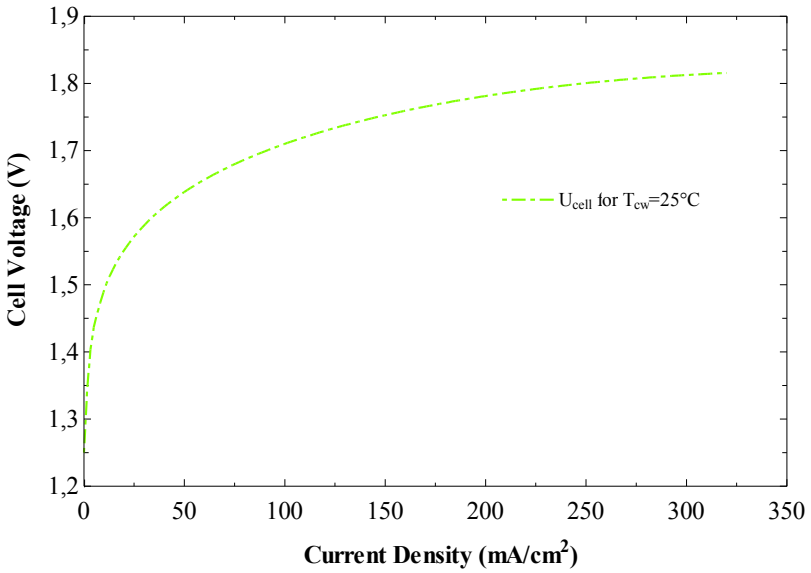

Figure 3. *Relationship between Cell Voltage and Current Density at 25℃ Cooling Water Temperature.*

Figure 4 presents the results of an investigation into the effects of current density and cooling water temperature on the temperature of an electrolyzer. The figure clearly shows that as the current density increases, the temperature of the electrolyzer also increases. Similarly, an increase in cooling water temperature results in a corresponding increase in the electrolyzer temperature. These findings highlight the importance of careful temperature management in optimizing the performance of the electrolyzer. If the electrolyzer temperature becomes too high, it can lead to reduced efficiency and potentially cause damage to the system. The results presented in Figure 4 have significant implications for the design and operation of electrolyzers. Specifically, they suggest that careful consideration must be given to the impact of both current density and cooling water temperature on the temperature of the electrolyzer. The analysis also shows that the use of district heating return water, which typically has a temperature of 43-45 ℃, could potentially be used

to manage the temperature of the electrolyzer and maintain it at the desired value. Overall, the results presented in Figure 4 provide valuable insights into the factors that influence the performance of electrolyzers and offer guidance for their design and operation.

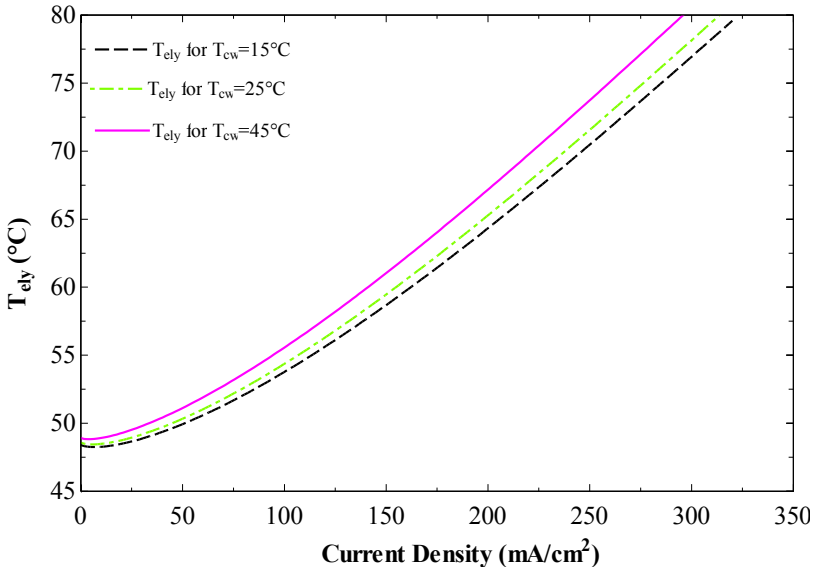

Figure 4. *Relationship between Current Density and Electrolyzer Temperature for Different Cooling Water Temperatures.*

Figure 5 illustrates the relationship between current density and the efficiency of hydrogen production in an alkaline electrolyzer. The figure indicates that as the current density increases from 0 to approximately 50 (mA/cm^2), the efficiency of hydrogen production increases from 0 to 80%. This finding highlights the potential for significant improvements in the efficiency of hydrogen production by increasing the current density. However, the results also show that beyond a current density of 50 (mA/cm^2), the efficiency of hydrogen production becomes almost constant, suggesting that further increases in current density may not result in a significant improvement in efficiency. These findings are significant for the optimization of electrolyzer performance in hydrogen production, as they emphasize the importance of carefully selecting the appropriate current density to achieve maximum efficiency. The results presented in Figure 5 offer valuable insights into the relationship between current density and the efficiency of hydrogen production in an alkaline electrolyzer and can inform the design and operation of electrolyzers for sustainable and efficient hydrogen production. Overall, Figure 5 provides important information for researchers and engineers working in the field of hydrogen production and underscores the potential for further advances in this critical area.

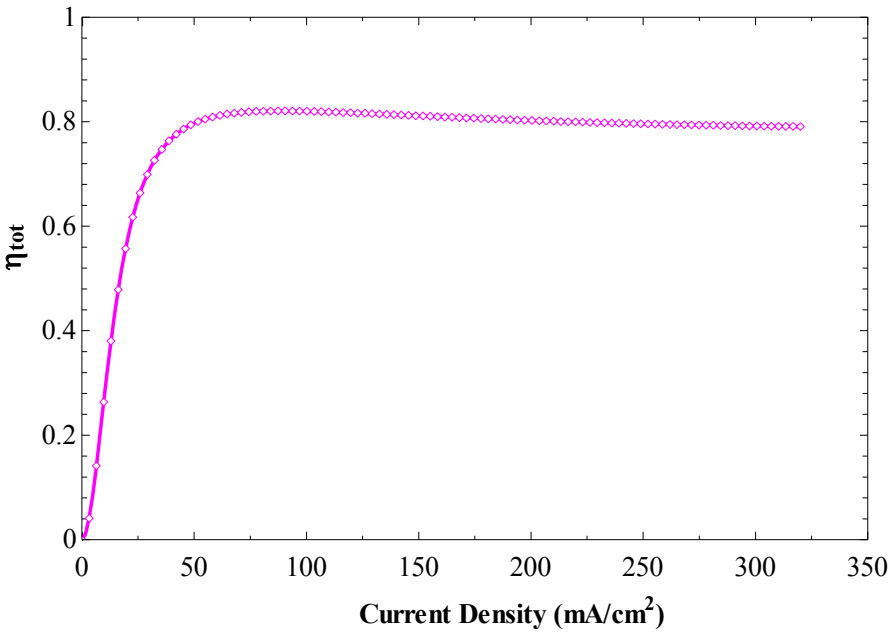

Figure 5. *Impact of Current Density on the Efficiency of Hydrogen Production.*

Figure 6 presents the results of an investigation into the impact of cooling temperature on the efficiency of hydrogen production in an electrolyzer (A), as well as its effect on electrolyzer temperature (B). The figure demonstrates that increasing the cooling temperature results in an increase in the efficiency of the electrolyzer, which in turn leads to an increase in the efficiency of hydrogen production. This finding is significant because it highlights the importance of careful temperature control for optimizing the performance of electrolyzers for hydrogen production. By maintaining an appropriate cooling temperature, it may be possible to improve the efficiency of the electrolyzer and increase the overall efficiency of hydrogen production. The results presented in Figure 6 provide valuable insights into the factors that influence the efficiency of hydrogen production in an electrolyzer and suggest that the use of district heating could potentially be used to manage the temperature of the electrolyzer and maintain it at an optimal value. In summary, the findings presented in Figure 6 demonstrate the importance of temperature control in the optimization of electrolyzer performance for hydrogen production.

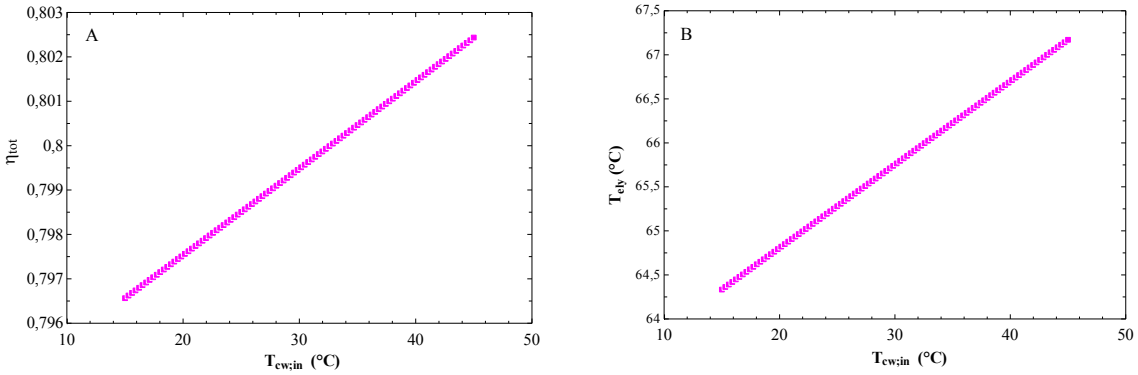

Figure 6. *(A) The effect of cooling water temperature over the efficiency of hydrogen production, (B) the effect of cooling water temperature over the electrolyzer temperature.*

Figure 7 presents an overview of the heat generation by a heat pump and electrolyzer, as well as the heat demand of a district heating system. The figure highlights that the demand for district heating in the summer months is significantly lower than in the winter months. This finding is important because it underscores the need to carefully consider the demand for waste heat when connecting an electrolyzer to a district heating network. In particular, it is crucial to ensure that there is sufficient demand for the waste heat generated by the electrolyzer in order to avoid potential inefficiencies or even system failures. The results presented in Figure 7 suggest that the design of the heat management system for an electrolyzer should consider the seasonal variation in district heating demand. If there is always sufficient district heating demand, then there may be no concerns about delivering the waste heat generated by the electrolyzer. However, if there is a significant

imbalance between the heat generation and demand, then it may be necessary to explore other strategies for managing the waste heat, such as storage or alternative uses. Overall, Figure 7 provides important insights into the relationship between heat generation, demand, and waste heat management in the context of an electrolyzer connected to a district heating network. The results offer guidance for the design and operation of electrolyzers and can inform decision-making related to the integration of these systems with district heating networks. In this case the operation of electrolyzer is 73% and heat pump 90%.

Figure 8 illustrates the operation of thermal energy storage (TES) in the context of a district heating system. During periods of excess heat production, such as in the summer months when demand for district heating is low, the excess heat can be stored in the hot water tank. The TES system can then release the stored heat during periods of high demand.

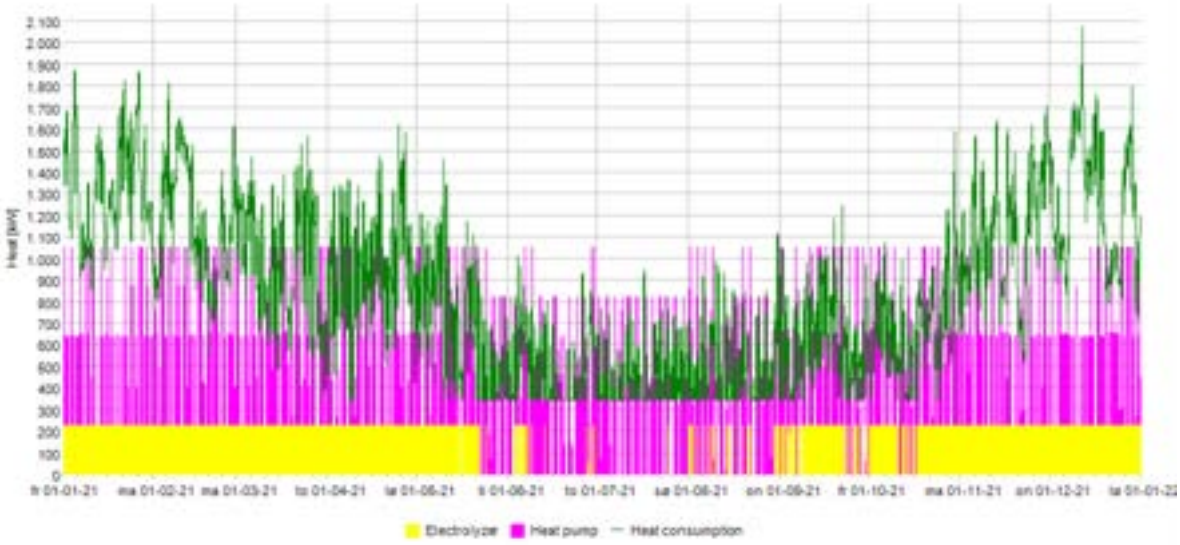

Figure 7. *Heat generation by heat pump and electrolyzer and heat demand of district heating.*

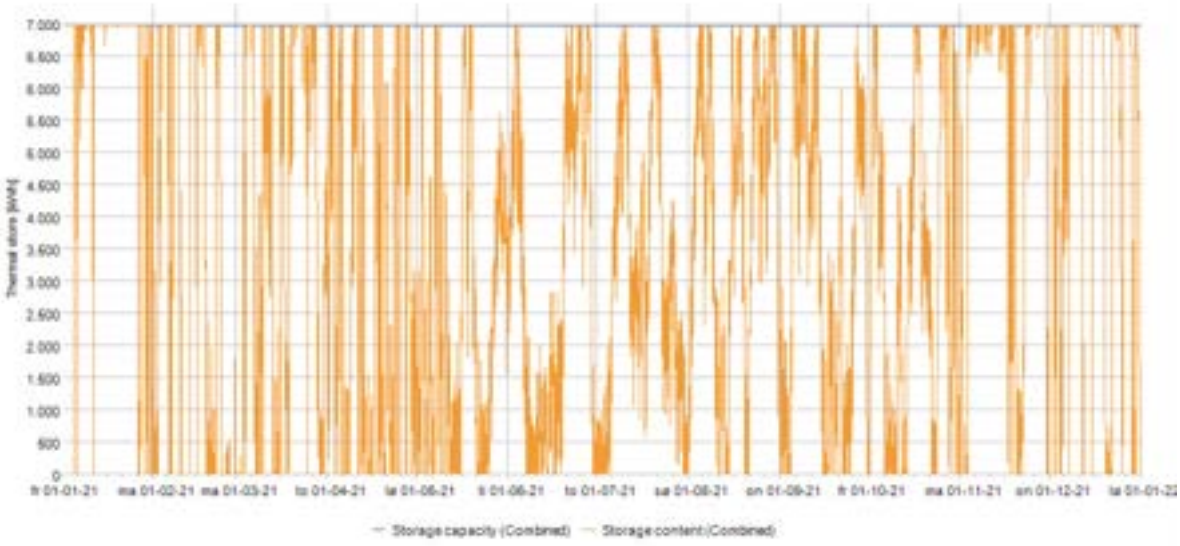

Figure 8. *The operation of thermal energy storage.*

Figure 9 presents the pattern of electricity consumption for a data center, heat pump, and electrolyzer over the course of one year. The figure provides valuable insights into the electricity consumption patterns of these systems and highlights the potential for optimization and efficiency improvements.

***Figure 9**. Electricity consumption of heat pump, electrolyzer and data center.*

5. Conclusion

In conclusion, this paper has explored the crucial role of efficient heat management in optimizing the performance of alkaline electrolyzer and maximizing the production of green hydrogen. Specifically, the importance of current density and cooling temperature on the efficiency of the electrolyzer for hydrogen production has been demonstrated. The paper also proposed a novel and integrated design concept for data centers that combines hydrogen production with district heating, enabling waste heat to be harnessed and employed to supplement the district heating system. The results of this study showed that increasing the current density and cooling temperature can lead to significant improvements in the efficiency of hydrogen production, while careful temperature control is important for optimizing the performance of electrolyzers. Furthermore, by integrating hydrogen production with district heating, the waste heat produced during the electrolysis process can be harnessed and employed to supplement the district heating system, resulting in a reduction in carbon emissions and improved energy efficiency.

The technical and economic feasibility of the proposed system was examined, highlighting the potential benefits for data centers and district heating systems. The results suggest that the proposed system has the potential to improve the sustainability and efficiency of energy systems, contributing to the development of more environmentally friendly and economically viable solutions for energy production. Overall, this paper provides valuable insights into the future of sustainable energy systems and the potential for data centers to play a crucial role in this transition. Further research and development in this area may lead to the widespread implementation of integrated energy systems, resulting in significant improvements in sustainability and energy efficiency.

References

[1] P. Huang *et al.*, “A review of data centers as prosumers in district energy systems: Renewable energy integration and waste heat reuse for district heating,” *Appl Energy*, vol. 258, p. 114109, Jan. 2020, doi: 10.1016/J.APENERGY.2019.114109.

[2] C. Koronen, M. Åhman, and L. J. Nilsson, “Data centres in future European energy systems—energy efficiency, integration and policy,” *Energy Effic*, vol. 13, no. 1, pp. 129–144, Jan. 2020, doi: 10.1007/S12053-019-09833-8/TABLES/1.

[3] S. Kwon, “Ensuring renewable energy utilization with quality of service guarantee for energy-efficient data center operations,” *Appl Energy*, vol. 276, p. 115424, Oct. 2020, doi: 10.1016/J.APENERGY.2020.115424.

[4] J. G. Koomey, “Growth in data center electricity use 2005 to 2010,” 2011. Accessed: Aug. 15, 2022. [Online]. Available: http://www.koomey.comhttp://www.analyticspress.com/datacenters.html

[5] Z. Ding, Y. Cao, L. Xie, Y. Lu, and P. Wang, "Integrated Stochastic Energy Management for Data Center Microgrid Considering Waste Heat Recovery," in *IEEE Transactions on Industry Applications*, May 2019, vol. 55, no. 3, pp. 2198–2207. doi: 10.1109/TIA.2018.2890789.

[6] A. Habibi Khalaj and S. K. Halgamuge, "A Review on efficient thermal management of air- and liquid-cooled data centers: From chip to the cooling system," *Applied Energy*, vol. 205. Elsevier Ltd, pp. 1165–1188, Nov. 01, 2017. doi: 10.1016/j.apenergy.2017.08.037.

[7] R. Gupta, S. Asgari, H. Moazamigoodarzi, S. Pal, and I. K. Puri, "Cooling architecture selection for air-cooled Data Centers by minimizing exergy destruction," *Energy*, vol. 201, p. 117625, Jun. 2020, doi: 10.1016/j.energy.2020.117625.

[8] P. Huang *et al.*, "A review of data centers as prosumers in district energy systems: Renewable energy integration and waste heat reuse for district heating," *Applied Energy*, vol. 258. Elsevier Ltd, p. 114109, Jan. 15, 2020. doi: 10.1016/j.apenergy.2019.114109.

[9] A. M. Haywood, J. Sherbeck, P. Phelan, G. Varsamopoulos, and S. K. S. Gupta, "The relationship among CPU utilization, temperature, and thermal power for waste heat utilization," *Energy Convers Manag*, vol. 95, pp. 297–303, May 2015, doi: 10.1016/j.enconman.2015.01.088.

[10] D. Turek and P. Radgen, "Optimized data center site selection—mesoclimatic effects on data center energy consumption and costs," *Energy Effic*, vol. 14, no. 3, pp. 1–14, Mar. 2021, doi: 10.1007/S12053-021-09947-Y/TABLES/1.

[11] L. Grange, G. da Costa, and P. Stolf, "Green IT scheduling for data center powered with renewable energy," *Future Generation Computer Systems*, vol. 86, pp. 99–120, Sep. 2018, doi: 10.1016/J.FUTURE.2018.03.049.

[12] A. Khosravi, T. Laukkanen, V. Vuorinen, and S. Syri, "Waste heat recovery from a data centre and 5G smart poles for low-temperature district heating network," *Energy*, vol. 218, p. 119468, Mar. 2021, doi: 10.1016/j.energy.2020.119468.

[13] Z. Iverson, A. Achuthan, P. Marzocca, and D. Aidun, "Optimal design of hybrid renewable energy systems (HRES) using hydrogen storage technology for data center applications," *Renew Energy*, vol. 52, pp. 79–87, Apr. 2013, doi: 10.1016/J.RENENE.2012.10.038.

[14] Ø. Ulleberg, "Modeling of advanced alkaline electrolyzers: a system simulation approach," *Int J Hydrogen Energy*, vol. 28, no. 1, pp. 21–33, Jan. 2003, doi: 10.1016/S0360-3199(02)00033-2.

Pollutant testing (NOx, SO_2 and CO) of commercialized micro-combined heat and power (mCHP) fuel cells

Nicolas Paulus[a], Dávila Camila[b] and Vincent Lemort[c]

[a] *University of Liège, Thermodynamics Laboratory, Liège, Belgium, nicolas.paulus@uliege.be, CA*
[b] *University of Liège, Thermodynamics Laboratory, Liège, Belgium, cdavila@uliege.be*
[c] *University of Liège, Thermodynamics Laboratory, Liège, Belgium, vincent.lemort@uliege.be*

Abstract:

Energy transition currently brings focus on fuel cell micro-combined heat and power (mCHP) systems for residential uses. The two main technologies already commercialized are the Proton Exchange Membrane Fuel Cells (PEMFCs) and Solid Oxide Fuel Cells (SOFCs). The pollutant emissions of one system of each technology have been tested with portable probes both in laboratory and field-test configurations. In this paper, the nitrogen oxides (NOx), sulphur dioxide (SO_2) and carbon monoxide (CO) emission levels are compared to other combustion technologies such as a recent Euro 6 diesel automotive vehicle and a classical gas condensing boiler. At last, a method of converting the concentration of pollutants (in ppm) measured by the sensors into pollutant intensity per unit of energy (in g/kWh) is documented and reported. This allows for comparing the pollutant emissions levels with relevant literature, especially other studies conducted with other measuring sensors.
Both tested residential fuel cell technologies fed by natural gas can be considered clean in terms of SO_2 and NOx emissions. The CO emissions can be considered quite low for the tested SOFC and even nil for the tested PEMFC. The biggest issue of natural gas fuel cell technologies still lies in the carbon dioxide (CO_2) emissions associated with the fossil fuel they consume.

Keywords:

SO_2; Fuel cell; mCHP, NOx, pollutant emissions; CO.

1. Introduction

In its latest Sixth Assessment Report in April 2022, the Intergovernmental Panel on Climate Change has reported a maximum carbon budget of 890 $GtCO_2$ that humanity can emit from January 1st 2020 in order for global warming to likely remain under the +2 °C widely acknowledged limit compared to preindustrial temperature levels [1]. Even at residential scales, this much-needed GreenHouse Gases (GHG) mitigation brings focus on cleaner power sources and on combined heat and power (CHP) systems, such as fuel cells [2]. The two primary technologies that have already been commercialized are the Proton Exchange Membrane Fuel Cells (PEMFCs) and the Solid Oxide Fuel Cells (SOFCs), which are compared in Table 1. GHG emissions (in terms of CO_2 or CO_{2eq}) of such systems have already been addressed [3, 4] but another key element in assessing the environmental impacts of those technologies lies in the other common air pollutants : the emissions of nitrogen oxides (NOx), sulphur dioxide (SO_2), and carbon monoxide (CO).

The novelty of this study lies within the evaluation of SO_2, NOx and CO emissions of fuel cell technologies commercialized for residential applications in both laboratory and field-test configurations (in real dwellings in Belgium). This has been performed on several machines of different ages, for one PEMFC-based and one SOFC-based technology, thanks to a combustion analyser portable meter. This study compares the emission levels of those pollutants measured for the studied fuel cell systems with other combustion technologies, such as a recent Euro 6 diesel automotive vehicle and classical gas condensing boilers. To facilitate comparison with relevant literature, a method of converting the concentration of pollutants (measured in ppm) detected by the sensors into pollutant intensity per unit of energy (in g/kWh) has been documented and reported, which has never been the case in an academic paper to the knowledge of the authors. This approach enables the assessment of pollutant

emissions levels across different studies, including those conducted using alternative measuring sensors.

Table 1. Comparison between PEMFCs and SOFCs. Reproduced and adapted from reference [9].

Fuel cell type & Charge carrier	Typical electrolyte	Major contaminants	Stack operating temperature (°C)	Specific advantages	Specific disadvantages	LHV Electrical efficiency (%)
PEMFC & H^+	Solid Nafion®, a polymer	Carbon monoxide (CO) [a] Hydrogen sulfide (H_2S) [a]	60–80 (only low-temperature PEMFC are currently commercialized [5])	Highly modular for most applications High power density Compact structure Rapid start-up due to low temperature operation Excellent dynamic response	Complex water and thermal management [a] Low-grade heat High sensitivity to contaminants [d] Expensive catalyst Expensive Nafion® membrane [6]	40-60 (with H_2) (Max 38.5 with CH_4 as some fuel needs to be burned to provide heat to a methane reformer [7])
SOFC & O^{2-}	Solid yttria-stabilized zirconia, i.e. YSZ, a ceramic	Sulfides	800-1000	High electrical efficiencies High-grade heat High tolerance to contaminants Possibility of internal reforming Fuel flexibility Inexpensive catalyst Simpler water management (SOFC can work at a perfect drying state [8])	Slow start-up Low power density Strict material requirements High thermal stresses Sealing issues Durability issues High manufacturing costs	55-65 (with H_2) (Max 60% with CH_4 [5], i.e. still high thanks to the SOFC fuel flexibility)

[a] Contaminants, thermal and water management of PEMFC stacks have been discussed more deeply in a previous work [10].

2. Material and methods

2.1 Tested systems

2.1.1 PEMFC hybridized to a gas condensing boiler

The PEMFC is not a standalone unit. It is hybridized to a gas condensing boiler and to a Domestic Hot Water (DHW) tank. It is fed by natural gas and is designed to cover all the heat demands, including DHW, of residential houses and to participate locally in the electrical production. This particular system exists in several versions all based upon the same PEMFC module of nominal constant power of 0.75kW$_{el}$ (and 1.1kW$_{th}$) and the same 220L DHW tank. The only module that may vary is the gas boiler that is supposed to ensure peak heat demands. Indeed, it exists in four rated power versions from 11.4 to 30.8kW$_{th}$, depending on thermal needs [11]. The heat rate output of the field-test system considered in this study is rated to 24.5 kW$_{th}$ and is located in Huy, in Belgium. System's architecture is presented in Figure 1 (which does not show the double walled chimney used for both the air inlet and flue gases exhaust [12]) and main datasheet characteristics are presented in Table 2.

Table 2. PEMFC gas boiler hybrid expected targets (data published by manufacturer) [11].

Datasheet figures	Values
Maximum electrical production a year	6200kWh$_{el}$
Fuel cell rated electrical and thermal power as defined by EN 50465 [2]	0.75kW$_{el}$ & 1.1kW$_{th}$
Electrical fuel cell efficiency	37% (LHV)
Max global Fuel cell efficiency	92% (LHV)
Max boiler efficiency (at rated power) [a]	108.6% (LHV)
NOx, class 6 [13]	7.2 mg/kWh
Size without chimney (Hight x Width x Depth)	1800 mm x 595 mm x 600 mm

[a] Considering High Heating Value (HHV) to Low Heating Value (LHV) ratio of 1.1085 [14]

The complete system behaviour is heat driven. Its PEMFC has not been designed to be driven by the electrical demand and it is preferable that it runs as long as possible. It includes a methane reforming apparatus to feed the fuel cell stack with clean hydrogen and requires an automated fuel cell shutdown recovery procedure of 2.5 hours at least every two days to handle some reversible ageing processes

[10]. For further information, this system has been quite exhaustively studied in other publications [2, 4, 10, 15, 16, 17].

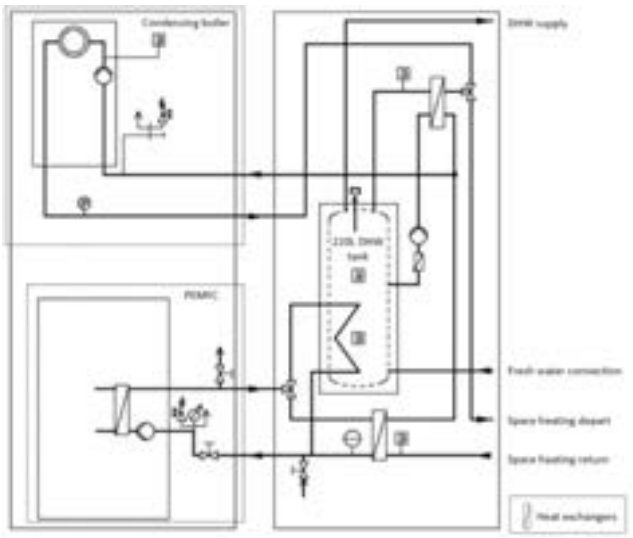

Figure 1. PEMFC system's architecture, including two heat exchangers, several 3-way valves, several circulators, the gas condensing boiler and the DHW tank.

2.1.2 SOFC

The studied SOFC is also fed by natural gas. It is designed to provide 1.5 kW_{el} of nominal output power with a high announced LHV electrical efficiency of 60%, along with a heat recovery of 0.6 kW_{th} representing a LHV thermal efficiency up to 25%. The output power can be modulated down remotely (by the manufacturer, upon the owner's request) as wanted in the 0.5 - 1.5 W_{el} range, affecting those announced efficiencies. It is not advised to completely shut it down because thermal cycles affect its durability and because start-up operations are long and have been reported in the user manual to last up to 30 hours [18] .

Discarding its chimney, the system has approximately the same size as a dishwasher, as it can be seen in Figure 2. Its internal schematics has not been disclosed but has been discussed in a previous publication [3], based on observations of the system and cogeneration SOFC literature. Amongst other particularities, the reforming process of the inlet natural gas (into hydrogen) is not only internal, i.e. directly onto the stack, at the anode (allowed with high operating temperatures occurring with that fuel cell technology [19]), but it also uses an external steam reformer upstream of the stack (called 'pre-former' [3]). The system is reported by the manufacturer as belonging to class 6 in terms of NOx [13] but the exact emission levels have not been quantified in the datasheet.

Figure 2. Tested mCHP SOFC in the laboratory facilities of the University of Liege

2.1.3 Gas condensing boiler

The tested mural gas condensing boiler dates from 2005 and is quite classical. Its identification name is 'Buderus Logamax plus GB142-45' and it can provide up to 45 kW_{th} (that can be modulated down to 30%). It is able to provide heat to an optional DHW tank but cannot provide instantaneous DHW directly

as it has only one hydraulic inlet/outlet (for close circuit water). The emissions of CO and NOx are reported by the manufacturer respectively to 15 mg/kWh and 20 mg/kWh.

2.1.4 Euro 6 diesel vehicle

The tested vehicle is a 4-year BMW X1 sDrive18d that is proper maintenance and had 111210 kilometers on the odometer at the moment of the test. Its four-stroke engine has four cylinders and represents a displacement of 1995cm³. Net power is 100 kW at 4000 rpm. The certificate of conformity presents average emissions on the New European Driving Cycle (NEDC) for CO and NOx respectively of 86.8 mg/km and 19.2 mg/km. Maximum Real Driving Emissions (RDE) NOx emissions are reported to be equal to 168 mg/km. Considering an effective consumption of 6L per 100 km (according to the dashboard of the vehicle), considering a diesel LHV of 43.51 MJ/kg and a density of 827 kg/m³ [20], those emissions correspond respectively to 145 mg/kWh (average CO emissions on the NEDC), 32 mg/kWh (average NOx emissions on the NEDC) and 280 mg/kWh (maximum Real Driving Emissions NOx). They are relative to the diesel LHV input to the engine.

2.2 Measurement device

To perform the pollutants emissions analyses of the tested systems, the same portable combustion analyser meter has been used. It is called 'Multizyzer STx' and is shown in Figure 3 whereas its specifications are shown in Table 3.

It measures CO, NO, NO_2 and SO_2 in ppm, whereas O_2 and CO_2 concentration levels are expressed in percentage (by volume). Carbon monoxide sensors have generally a significant cross-sensitivity to hydrogen, meaning that the real carbon monoxide concentration can be overestimated if hydrogen is present as well in the tested gas sample [21]. Therefore, as presented in Table 3, the 'Multizyzer STx' combustion analyser portable meter has implemented a hydrogen compensation for its carbon monoxide measurements.

Figure 3. 'Multizyzer STx' combustion analyser portable meter

Table 3. Specifications of the 'Multizyzer STx' combustion analyser portable meter

Sensor	Range	Accuracy	Resolution
NO	0 - 5000 ppm	± 5 ppm (< 50 ppm) ± 5% reading (> 50 ppm)	1 ppm
NO_2	0 - 500 ppm	± 10 ppm (< 50 ppm) ± 10% reading (> 50 ppm)	1 ppm
SO_2	0 - 5000 ppm	± 10 ppm (< 200 ppm) ± 5% reading (> 200 ppm)	1 ppm
CO (hydrogen compensated)	0 - 10000 ppm	± 5 ppm (< 50 ppm) ± 5% reading (> 50 ppm)	1 ppm
O_2	0 - 21 % vol.	± 0,2% vol.	0,1% vol.
CO_2 (calculated from O_2 level)	0 % vol. up to $(CO_2)_N$ which depends on fuel type, see Equation (1)	± 0,2% vol.	0,1% vol.
Gas temperature	0 - 1150 °C	± 1 °C (0 - 300°C) ± 1% reading (> 300°C)	0,1 °C

2.3 Conversion ppm to mg/kWh

Literature on space heating appliances pollution levels is quite rare and pollutant emissions are regularly reported in terms of concentration (in ppm [22]) or in terms of intensity (in mg/kWh [23]). However, it is quite rare for both information to be provided. In this case, the pollutant emissions measurements are provided by the metering device in ppm (see Table *3*) whereas, for comparison purposes, it would be more meaningful to express them in terms of mg/kWh, as reproduced in Table 4, which reports from literature the NOx emission levels of several space heating appliances. In addition, as it has been seen in *Section 2.1 - Tested systems*, the datasheets of the tested space heating appliances only express the emissions in terms of mg/kWh. Therefore, to use those figures as references for this study, measured emissions must be converted from ppm to mg/kWh.

For natural gas appliances, this can be performed for carbon monoxide emissions thanks to Equation (*1*) [13]:

$$CO_{(mg/kWh)} = 1.074 \times CO_{(ppm)} \times \frac{(CO_2)_N}{(CO_2)_M} \quad (1)$$

Where $CO_{(mg/kWh)}$ is the carbon monoxide emissions level per unit of energy (kWh) that must be established for the studied combustion test, $CO_{(ppm)}$ is the measured carbon monoxide concentration at the exhaust of the system during the combustion test (in ppm), $(CO_2)_M$ is the measured carbon dioxide concentration at the exhaust of the system during the combustion test (in %) and $(CO_2)_N$ is the maximum carbon dioxide concentration of the dry, air-free combustion products (in %), which depends only on the natural gas type that is fed to the studied system during the combustion. $(CO_2)_N$ is equal to 11.7% for G20 natural gas and 11.5% for G25 natural gas [13].

Indeed, in Belgium [24] (as in France or Germany [25]), natural gas comes from different sources, which implies different gas compositions and different HHV, which leads to the appellations 'lean' and 'rich' gas, respectively for the natural gas source providing the lower and the higher HHV [26]. Lean gas is also called 'L-gas' [27], 'type L' gas [24] or G25 [25] whereas rich gas is also called 'H-gas' [27], 'type H' gas [24] or G20 [25]. The type of gas provided on the grid only depends on the localization of the delivery point but lean gas deliveries are supposed to be progressively replaced (in Belgium) by 2030 by rich gas deliveries [27].

As reported in the previous section, $(CO_2)_M$ and $CO_{(ppm)}$ are provided by the meter used in this study. Also, in Equation (*1*), the 1.074 constant is the unit conversion coefficient related to CO emissions from natural gas appliances [28].

Table 4. Combustion only and Life Cycle Assessment (LCA) NOx emission level reported from Energie+ [23] (website developed by the University of Louvain-la-Neuve and the Energy department of the Walloon Region, in Belgium)

Space-heating appliance	NOx range (source from 1998 : Electrabel-SPE – combustion only) mg/kWh$_{LHV}$	NOx (source from 2007 : Fondation Rurale de Wallonie - combustion only) mg/kWh$_{th}$	NOx (source accessed in 2007: Gemis 4.5 - complete LCA cycle) mg/kWh$_{th}$
Old oil-fired boiler	up to 200	Unavailable	Unavailable
Non-Low NOx oil-fired boiler	150 – 180	144	244
Low NOx oil-fired boiler	90 – 120	Unavailable	Unavailable
Old gas boiler	150 – 200	Unavailable	Unavailable
Atmospheric gas boiler	100 – 180	Unavailable	Unavailable
Modulating gas condensing boiler	20 – 90	144	140
Old log wood boiler	Unavailable	180	Unavailable
Modern log wood boiler	Unavailable	151	235
Wood chip boiler (wood chips)	Unavailable	162	Unavailable
Condensing wood boiler (pellets)	Unavailable	Unavailable	344

Similarly, ppm to mg/kWh conversion for NOx emissions of natural gas appliances is obtained thanks to Equation (*2*) :

$$NOx_{(mg/kWh)} = \frac{\left(C_g \times NOx_{(ppm)} \times \frac{(CO_2)_N}{(CO_2)_M}\right) - 0.85(20 - T_m) + \frac{0.34(h_{m-10})}{1-0.02(h_{m-10})}}{\left(1 + \frac{0.02(h_{m-10})}{1-0.02(h_{m-10})}\right)} \quad (2)$$

Where $NOx_{(mg/kWh)}$ is the nitrogen oxide emissions level per unit of energy (kWh) that must be established for the studied combustion test; C_g is the unit conversion coefficient related to NOx emissions from natural gas appliances [29] and is equal to 1.764 for G20 (rich gas) or 1.767 for G25 (lean gas) [13]; $NOx_{(ppm)}$ is the sum of the measured nitrogen dioxide and nitric oxide concentrations at the exhaust of the system during the combustion test (in ppm); $(CO_2)_N$ and $(CO_2)_M$ have already been described for Equation (*1*); T_m is the temperature of the outdoor air used for the combustion (in °C); h_m is the absolute humidity of the outdoor air used for the combustion (in g of water per kg of dry air). h_m is the only variable of Equation (2) that is not provided by the combustion analyser meter (see Table 3). By assimilating inlet air to humid air of relative humidity between 40 and 80%, at atmospheric pressure and at the T_m temperature, h_m can be approximated with the Engineering Equation Solver (EES) software. It is worth mentioning for Equation (*2*) that the allowable ranges for T_m, h_m $NOx_{(mg/kWh)}$ and are respectively 15 - 25 °C and 5 - 15 g of water per kg of dry air, and 50-300 mg/kWh. However, industrial partners in this project advise to use Equation (*2*) anyway even if some parameters are out of those ranges.

The European standard from which Equation (*1*) and Equation (*2*) are deduced [13] unfortunately does not provide any information about SO_2 emissions conversion. Fortunately, another reference [30] provided Equation (3), which has been reported to be relevant not only for SO_2 but also for CO and NOx emissions, giving similar conversion results respectively to Equation (*1*) and Equation (*2*) (in its allowable range).

$$PEI_{(mg/kWh)} = F \times PEC_{(ppm)} \times \frac{20.9}{20.9-(O_2)_M} \quad (3)$$

Where $PEI_{(mg/kWh)}$ is the pollutant emissions intensity, i.e. the emission level per unit of energy (kWh) that must be established for the studied combustion test, F is an emission rate conversion factor that depends on the pollutant (and the type of fuel) and that is given in Table 5, $PEC_{(ppm)}$ is the measured pollutant emissions concentration at the exhaust of the system during the combustion test (in ppm) and $(O_2)_M$ is the measured oxygen concentration at the exhaust of the system during the combustion test (in %). Equation (3) has the particularity to consider O_2 concentration (in %) in the exhaust whereas Equation (*1*) and Equation (*2*) lies on CO_2 concentration (in %).

Similar conversion equations for diesel engine have not been reported in this paper but can also be found in literature [31].

Table 5. Natural gas F coefficients for Equation (3) depending on the pollutant type [30]

Pollutant	F mg/(kWh-ppm)
CO	0.974313
NOx	1.608389
SO_2	2.242466

3. Testing procedure and results

The end of the probe of the 'Multizyzer STx' must be placed at the centre of the exhaust gas chimney (or tailpipe) and the probe axis can either be oriented in the perpendicular plane of this chimney (or tailpipe) or parallel to it (if the measurements are conducted at the exit of the chimney/tailpipe). The probe disposes of a conical adjustable mechanical stop to ensure the correct probe depth to the centre of the chimney (see Figure 3).

The studied PEMFC system, which is composed of a PEMFC stack hybridized to a gas condensing boiler (see *Section 2.1 - Tested systems*), has the advantage of being equipped by design with a small, sealable access hole fitted with a cap directly at the exhaust of the system (in the first 5 cm of the chimney). There is thus no need with the PEMFC system to place the combustion analyser meter at the exit of the chimney, which access is very often difficult and potentially risky if it figures on the roof of the building. However, some measurements have still been taken at the exit of the chimney for comparison purposes (with the probe fully inserted in the chimney). Indeed, temperature (which varies all along the double walled chimney that cools down the flue gases and heats up the inlet air from outdoors) is not only known to influence the NO_x formation but also the NO-NO_2 equilibrium. This is especially the case in the near-post-flame zone [32] (close to the outlet of the system), but also in the atmosphere in the presence of Volatile Organic Compounds (close to the exit of the chimney) [33], which can be co-emitted in hydrocarbons combustion [32]. The PEMFC hybrid system was tested in two separate modes : with only the PEMFC turned on and with only the gas condensing boiler turned

on. This system, installed in 2019, was tested in a field-test application (in a real house) in Huy (in Belgium). At the moment of the tests, the whole machine has been functioning for about 15000 hours but its integrated fuel cell has only been producing electricity for about 5500 hours. It is worth mentioning that another machine of this system, which was perfectly new, was tested in a laboratory environment (see Figure 4).

The studied SOFC system does not involve any hole in its chimney by design. However, since one machine of this system was tested in laboratory facilities, a hole was manufactured at a chimney height of 50 cm (above the system flue gases outlet). For one pollutant test campaign (at full rated electrical power output, i.e. 1500 W_{el}), the combustion analyser meter was also placed at the exit of the chimney (and fully inserted in it) since this campaign was performed on another machine (with the same reference) in a field-test application in Riemst (Belgium). At the moment of the pollutant measurements, this machine, installed in 2017, has already been functioning for about 45000 hours. For the other two pollutant test campaign (conducted at minimum and intermediate electrical power output, i.e. 500 W_{el} and 1000 W_{el}), this SOFC mCHP system was tested in laboratory facilities and the return temperature of the heat recovery circuit could be controlled [18] (which affects the exhaust gas temperature). At the moment of the pollutant measurements, this other machine, installed in 2021, has already been functioning for about 6000 hours.

As mentioned in *Section 2.1 - Tested systems*, another classical gas condensing boiler has been tested (only at the exit of its chimney, with the probe fully inserted in it). This system was tested in a field-test application in Riemst (Belgium).

At last, the Euro 6 diesel vehicle was tested at the exit of both of its tailpipes. The probe of the sensor could be oriented parallel to the tailpipe so it has either been fully inserted in the tailpipe (about 35 cm before its exit) or only inserted over about 15 cm. The purpose was to see the changes in the exhaust gas temperature and their impact on the pollutant measurements. It is worth mentioning that the car engine was tested at idle (±850 rpm) and at 1500 rpm but the clutche was always disengaged.

All the tests include a purge with clean air before starting the test. It is indeed a mandatory step requested by the 'Multizyzer STx' combustion analyser meter. At last, the sample time was always one second.

All the tests have other specificities in the way they have been conducted and those are reported accordingly in Table 6 along with the pollutant emissions results.

In addition, a graphical example of the type of the PEMFC only startup phase is given in Figure 4. In that test, no NOx nor SO_2 could be measured. Startup phase (duration between the machine startup with a thermal demand and the moment when the fuel cell starts producing electricity) takes about 7 min whereas the total duration to reach steady-state is about 15-20 min (gradually from 0 W_{el} to its nominal output power of 750 W_{el}). A CO peak of about 2 minutes, with a maximum at 55 ppm, can be noticed at the beginning of the power and heat generation phase, probably due to transient behaviours of the internal reformer required for this PEMFC fed by natural gas [10]. The stepped behaviour of the CO_2 percentage measurement is explained by the resolution of the sensor and the fact that it is not directly measured but established by the combustion analyser from O_2 measurements (Table 3). The CO_2 peak is probably an outlier as it could not be explained.

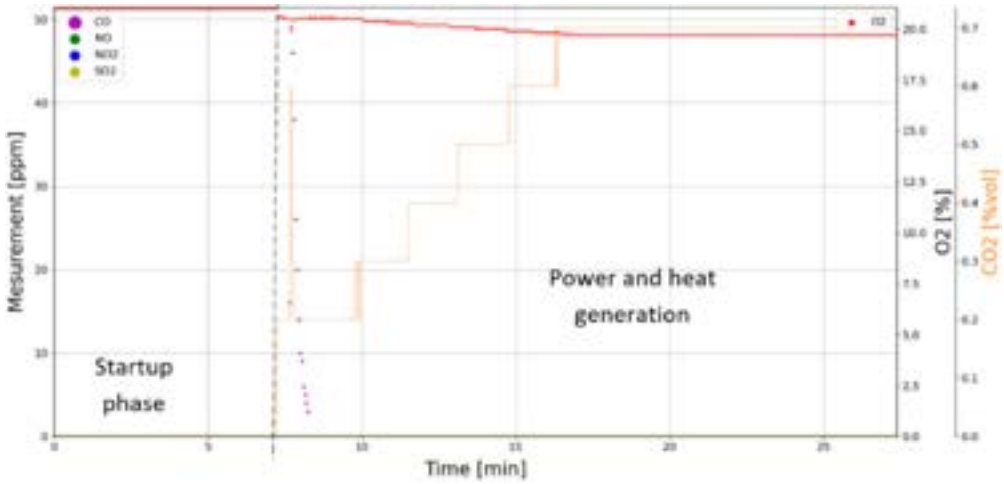

Figure 4. Pollutant measurements of the fuel cell (only) startup phase of the PEMFC-gas condensing boiler hybrid system (performed in a laboratory environment).

Table 6. Pollutant emissions measurements results (in all tests, the sensor indicated 0 ppm of SO_2 emissions).

Test and conditions	NO [a]	NO_2 [a]	CO [a]	Remarks
PEMFC hybrid system (**PEMFC only mode**) Measured on the field-test site in Huy without control on the return temperature (or on the exhaust gas temperature)	0	0	- Startup : short peak up to 55 ppm for 2 min (in total). Also measured in the laboratory (Figure 4). - Steady state : 0 but an unexplainable short peak similar to FC startup has been measured while the PEMFC was running	- Boiler turned down by closing the radiator valves in the house - No difference in the pollutant measurement between the exit of the chimney (on the roof) and the exit of the system
PEMFC hybrid system (**condensing gas boiler only mode**) Measured on the field-test site in Huy without control on the return temperature (or on the exhaust gas temperature)	- Startup : peak up to 7 ppm for 5 min (in total) - Steady state : 0	- Startup : 3 ppm - Steady state : 3 ppm, i.e. 6.7 mg/kWh	- Startup : short peak up to 80 ppm for 30 sec (in total) - Steady state : 30 ppm, i.e. 40.7 mg/kWh	- Boiler turned on by opening the radiator valves in the house and setting a high temperature setpoint on the thermostat (the PEMFC happened to be turned off, probably conducting a regeneration procedure [10])
SOFC – 500 and 1000 W_{el} output Tested in laboratory with different heat recovery temperatures, i.e. different exhaust gases temperature (from 45°C to 25°C)	0	0	5 ppm (at 500 W_{el}), i.e. 28.3 mg/kWh 11 ppm (at 1000 W_{el}), i.e. 41.5 mg/kWh	- Return temperature of the heat recovery circuit has no influence on the pollutant measurements - Only steady state data (the system in supposed to be turned on continuously and the startup test was not conducted)
SOFC - 1500 W_{el} output Measured on the field-test site in Riemst with only one heat recovery temperature corresponding to 60°C of exhaust gases temperature	0	0	8 ppm, i.e. 17.0 mg/kWh	- Same reference but a different system as the previous row) - Only steady state data (the system in supposed to be turned on continuously and the startup test was not conducted)
Classical gas condensing boiler - high DHW load (exhaust gases temperature of about 65°C at the exit of the chimney) Measured on the field-test site in Riemst	- Startup : peak up to 8 ppm for 2 min (in total) - Steady state : 5 ppm, i.e. 10.1 mg/kWh	- Startup : peak up to 4 ppm for 2,5 min (in total) - Steady state : 2 ppm, i.e. 4.1 mg/kWh	- Startup : peak up to 50 ppm for 2 min (in total) - Steady state : 10 ppm, i.e. 12.3 mg/kWh	- No remark
Classical gas condensing boiler - low temperature space heating load (exhaust gases temperature of about 30°C at the exit of the chimney) Measured on the field-test site in Riemst	- Startup : Untested - Steady state : 0 ppm	- Startup : Untested - Steady state : 0 ppm	- Startup : Untested - Steady state : 8 ppm, i.e. 10.7 mg/kWh	- No remark
Euro 6 Diesel Engine at idle, i.e. ±850 rpm (car in neutral)	- Startup : continuous increase for about 20 min up to 60 ppm - Steady state : 55 ppm, i.e. 238 mg/kWh [31]	0	- Startup : rapid increase for about 3 min to the 200-300 ppm range - Steady state : 200-300 ppm, i.e. 800-1200 mg/kWh [31]	- The probe must be fully inserted in the tailpipe to record pollutant emissions - There is no difference between the left and right tailpipes
Euro 6 Diesel Engine at 1500 rpm	- Startup : unavailable (engine already warmed up) Steady state : 40 ppm, i.e. 173 mg/kWh [31]	0	- Startup : unavailable (engine already warmed up) Steady state : 850 ppm, i.e. 3430 mg/kWh [31]	- The probe must be fully inserted in the tailpipe to record pollutant emissions - There is no difference between the left and right tailpipes

[a] Equation (3) has been used to convert ppm measurement into mg/kWh for steady-state measurements only (of natural gas appliances). The similar conversion law for diesel engines comes from literature [31]. Peaks and start-ups have highly transient dynamic behaviours both on the pollutant concentration and the O_2 percentage signal, making the ppm to mg/kWh conversion hazardous.

4. Discussion and conclusion

None of the tested systems (PEMFC, SOFC, gas condensing boilers and Euro 6 diesel engine) showed any SO_2 emissions. This is either an indication of an issue with the SO_2 sensor or it proves the efficiency of the desulphurization treatment implemented in the natural gas process before it enters the grid [10]. Regarding the diesel vehicle, the lack of SO_2 emissions could be explained by the oxidation of SO_2 into SO_3 in the selective catalytic converter used in the exhaust of the engine to reduce NOx emissions [34].

Both fuel cell systems (PEMFC and SOFC) do not show any NOx emissions even if they involve reforming processes [3, 10]. Oppositely NOx emissions of gas boilers (in steady state) were measured between 3 and 7 ppm, which is rather low. Using Equation (3) and thus considering the O_2 percentage measurement (not shown in Table 6), those figures can be converted in the 6.7-14.2 mg/kWh range, which is slightly better than literature provided (see Table 4). The lower part of that range, i.e. 6.7 mg/kWh, corresponds to the gas boiler of the PEMFC hybrid system, and it is indeed under the 7.2 mg/kWh figure announced by the manufacturer. For the other classical gas condensing boiler, it is also under the announced value of 20 mg/kWh (see *Section 2.1 - Tested systems*). In comparison, the diesel Euro 6 engine showed NOx concentration of 55 ppm in neutral and 40 ppm at 1500 rpm (without any load since the clutch was not engaged). Considering another conversion equation from ppm to mg/kWh provided by literature relevant for diesel engines [31] (Equation (3) and the coefficients of Table 5 being only relevant with natural gas appliances) and a molar mass of NO of 30, these NOx emission concentrations corresponds to the 173-238 mg/kWh range, i.e. under but close to the maximum NOx Real Driving Emissions announced at about 280 mg/kWh, assuming an average consumption of 6L per 100 km (see *Section 2.1 - Tested systems*). It also approximately corresponds to the emissions of an old oil-fired boiler (Table 4).

For all tested systems, the NO_2 emissions are either nil or quite low compared to NO emissions, which was expected as NO has been reported to be the predominant nitrogen oxide emitted by combustion devices [32].

There were no CO emissions regarding the steady state operating conditions of the PEMFC (other than an explicable peak that is similar to the transient CO peak that occurs at the PEMFC startup). This was expected since CO is a major pollutant of PEMFC stacks and since it has been reported that the system is equipped with a CO removing apparatus in the fuel (natural gas) processing system (prior to the stack) [10]. Transient CO peaks are surely not caused by the fuel cell stack but by the fuel processor of the PEMFC system (when the reforming processes start and is not yet at its steady state temperature levels, impeding the CO remover to operate efficiently). During these transients for which CO can occur, the PEMFC stack must surely be bypassed [10]. Also, it has been reported that the PEMFC system involves an afterburner for reforming purposes (because methane reforming requires temperatures much higher than the one occurring in the PEMFC stack) [10]. In addition to burning the stack exhaust gases when the PEMFC is running (the anode exhaust still contains used hydrogen and the cathode contains air at a higher temperature that the ambient air), this afterburner also requires a direct feed from the natural gas supply to ensure enough heat for the reforming processes [10]. The inexplicable CO peak while the PEMFC was running is likely to be related to this afterburner (after the stack) and it can be assumed that no CO has gone through the PEMFC stack. Oppositely, the SOFC system (two machines tested) showed slight CO emissions (5 ppm, 11 ppm and 8 ppm respectively at 500 W_{el}, 1000 W_{el} and 1500 W_{el} of power output) with no dependence on the thermal output or on the exhaust gases temperature (driven by the return temperature of the heat recovery system). Through Equation (*3*), these CO concentrations respectively correspond to 28.3 mg/kWh, 41.5 mg/kWh and 17.0 mg/kWh. It is worth mentioning that the PEMFC system was only tested in field-test real applications so the return temperature (and the exhaust gas temperature) could not be controlled, although it is not believed to affect the pollutant emissions in steady state (which were nil).

CO emissions peak (between 50 and 60 ppm) at gas condensing boilers startup is probably due to the momentary incomplete combustion in this highly transient starting process. In steady-state, the tested machines showed 8 to 30 ppm of CO emissions, corresponding to 10.7 mg/kWh to 40.7 mg/kWh using Equation (*3*) (very similar to the SOFC CO emissions range). The gas condensing boilers were tested in field-test applications so the return temperature (and therefore the exhaust gases temperature) could not be controlled. Regarding the diesel engine, the steady state CO emissions were much higher, between 200 and 300 ppm at idle and up to 850 ppm at 1500 rpm. Equation (*3*) and the coefficients of Table 5 can only be used with natural gas. Therefore, another conversion law has been found in literature [31], leading to the 800-1200 mg/kWh range at idle and to about 3430 mg/kWh for the 1500 rpm test. Those levels of CO emissions are far greater than the one announced on the certificate of

conformity for the average NEDC (calculated in this work to about 145 mg/kWh, as seen in *Section 2.1 - Tested systems*). This is another proof of the inadequacy of the NEDC to account for pollutant emissions [35] but it also should be reminded that maintaining the engine at 1500 rpm while keeping the vehicle stationary is also not a representative test of real driving conditions (although it provides interesting results for comparisons).

As a final conclusion, both tested residential fuel cell technologies fed by natural gas can be considered clean in terms of SO_2 and NOx emissions. The CO emissions can be considered quite low for the tested SOFC and even nil for the tested PEMFC. Those statements apply even with machines that have already been running for up to 45000 hours. Therefore, the biggest issue of natural gas fuel cell technologies still lies in the CO_2 emissions associated with the fossil fuel they consume.

Nomenclature

(m)CHP (Micro-)Combined Heat and Power

DHW Domestic Hot Water

GHG GreenHouse Gases

HHV (LHV) High (Low) Heating Value

LCA Life Cycle Assessment

NEDC New European Driving Cycle

PEMFC Proton Exchange Membrane Fuel Cell

SOFC Solid Oxide Fuel Cell

References

[1] N. Paulus, “Confronting Nationally Determined Contributions to IPPC’s +2°C Carbon Budgets through the Analyses of France and Wallonia Climate Policies,” *Journal of Ecological Engineering,* vol. 24, no. 6, 2023.

[2] C. Davila, N. Paulus and V. Lemort, “Experimental investigation of a Micro-CHP unit driven by natural gas for residential buildings,” in *Proceedings of the 19th International Refrigeration and Air Conditioning Conference (Herrick 2022)*, 2022.

[3] N. Paulus and V. Lemort, “Field-test performance of Solid Oxide Fuel Cells (SOFC) for residential cogeneration applications,” *Proceedings of the 7th International High Performance Buildings Conference at Purdue (Herrick 2022),* 2022.

[4] N. Paulus, C. Davila and V. Lemort, “Field-test economic and ecological performance of Proton Exchange Membrane Fuel Cells (PEMFC) used in residential micro-combined heat and power applications (micro-CHP),” in *Proceedings of the 35th International Conference On Efficiency, Cost, Optimization, Simulation and Environmental Impact of Energy Systems (ECOS 2022)*, 2022.

[5] E. Energy, “D1.7 - Summary report on specifications for newest model deployment in PACE,” 2021.

[6] J. O. Park, S.-G. Hong and Q. Li, “Design and Optimization of HT-PEMFC MEAs,” in *High Temperature Polymer Electrolyte Membrane Fuel Cells: Approaches, Status, and Perspectives*, Springer International Publishing, 2016, p. 331–352.

[7] A. Perna and M. Minutillo, “Chapter 9 - Residential cogeneration and trigeneration with fuel cells,” in *Current Trends and Future Developments on (Bio-) Membranes*, Elsevier, 2020, pp. 197-239.

[8] T.-L. Wen *et al*, “Material research for planar SOFC stack,” *Solid State Ionics,* vol. 148, no. 3, 2002.

[9] O. Z. Sharaf and M. F. Orhan, “An overview of fuel cell technology: Fundamentals and applications,” *Renewable and Sustainable Energy Reviews,* vol. 32, 2014.

[10] N. Paulus and V. Lemort, “Investigation of degradation mechanisms and corresponding recovery procedures of a field-tested residential cogeneration Polymer Electrolyte Membrane fuel cell,” To be submitted.

[11] Viessmann, *Vitovalor PT2 - Notice pour étude, DOC N° 5790433 BE,* 2021.

[12] K. Lichtenegger, B. Hebenstreit, C. Pointner, C. Schmidl and E. Höftberger, “The role of leak air in a double-wall chimney,” *Heat Mass Transfer,* vol. 51, no. 6, 2015.

[13] EN15502-1, *Gas-fired heating boilers - Part 1: General requirements and tests*, 2021.

[14] I. Daoud, “Installer une Cogénération dans votre Etablissement,” Ministère de la Région wallonne. Direction Générale des Technologies, de la Recherche et de l'Energie (GGTRE), 2003.

[15] N. Paulus and V. Lemort, “Field-test performance models of a residential micro-cogeneration system based on a proton exchange membrane fuel cell and a gas condensing boiler,” *Energy Conversion and Management,* vol. Under Review, 2023.

[16] N. Paulus, C. Davila and V. Lemort, “Grid-impact factors of field-tested residential Proton Exchange Membrane Fuel Cell systems,” in *Proceedings of the 14th REHVA HVAC World Congress (CLIMA 2022)*, 2022.

[17] N. Paulus and V. Lemort, “Correlation between field-test and laboratory results for a Proton Exchange Membrane Fuel Cell (PEMFC) used as a residential cogeneration system,” *Proceedings of the 30e Congrès de la Société Française de Thermique (SFT 2022),* 2022.

[18] N. Paulus and L. Lemort, “Experimental investigation of a Solid Oxide Fuel Cell (SOFC) used in residential cogeneration applications,” *Proceedings of the 36th International Conference On Efficiency, Cost, Optimization, Simulation and Environmental Impact of Energy Systems (ECOS 2023),* 2023.

[19] P. Aguiar, D. Chadwick and L. Kershenbaum, “Modelling of an indirect internal reforming solid oxide fuel cell,” *Chemical Engineering Science,* vol. 57, no. 10, 2002.

[20] M. Parravicini, C. Barro and K. Boulouchos, “Compensation for the differences in LHV of diesel-OME blends by using injector nozzles with different number of holes: Emissions and combustion,” *Fuel,* vol. 259, 2020.

[21] J. Hall, P. Hooker and K. Jeffrey, “Gas detection of hydrogen/natural gas blends in the gas industry,” *International Journal of Hydrogen Energy,* vol. 46, no. 23, 2021.

[22] R. McDonald, “Evaluation of Gas, Oil and Wood Pellet Fueled Residential Heating System Emissions Characteristics,” Brookhaven National Laboratory, New York, 2009.

[23] Energie+, “Emissions de polluants liée à la consommation énergétique,” 2007. [Online]. Available: https://energieplus-lesite.be/theories/consommation-energetique/les-emissions-de-polluants-liee-a-la-consommation-energetique/. [Accessed 15 05 2023].

[24] N. Paulus and V. Lemort, “Establishing the energy content of natural gas residential consumption : example with Belgian field-test applications,” *Proceedings of 8th Conference of the Sustainable Solutions for Energy and Environment (EENVIRO 2022),* 2022.

[25] TNO Industrie en Techniek, “Biogas composition and engine performance, including database and biogas property model,” BiogasMax, 2008.

[26] D. Haeseldonckx and W. D’haeseleer, “The use of the natural-gas pipeline infrastructure for hydrogen transport in a changing market structure,” *International Journal of Hydrogen Energy,* vol. 32, no. 10-11, 2007.

[27] (F)1736, “Study on the cost-effectiveness of natural gas (CNG or compressed natural gas) used as fuel in cars,” CREG, 2018.

[28] P. Zlateva, N. Penkova and K. Krumov, “Analysis of combustion efficiency at boilers operating on different fuels,” *Proceedings of the 7th International Conference on Energy Efficiency and Agricultural Engineering (EE&AE 2020),* 2020.

[29] D.-T. Bălănescu and V.-M. Homutescu, “Experimental Study on the Combustion System Optimization in the Case of a 36 kW Condensing Boiler,” *Procedia Engineering,* vol. 181, 2017.

[30] TSI Incorporated, “Combustion Analyses Basics - An Overview of Measurements, Methods and Calculations Used in Combustion Analysis,” P/N 2980175 Rev. B, Shoreview, United States, 2004.

[31] T. Pilusa, M. Mollagee and E. Muzenda, “Reduction of Vehicle Exhaust Emissions from Diesel Engines Using the Whale Concept Filter,” *Aerosol and Air Quality Research,* vol. 12, no. 5, 2012.

[32] C. T. Bowman, “Kinetics of pollutant formation and destruction in combustion,” *Progress in Energy and Combustion Science,* vol. 1, no. 1, 1975.

[33] P. N. Cheremisinoff and R. A. Young, Air pollution control and design handbook. Part II, New York, United States: Marcel Dekker, 1977, pp. 672-673.

[34] J. Wade and R. Farrauto, “12 - Controlling emissions of pollutants in urban areas,” in *Metropolitan Sustainability*, Cambridge, United Kingdom, Woodhead Publishing, 2012, pp. 260-291.

[35] J. Pavlovic *et al*, “The Impact of WLTP on the Official Fuel Consumption and Electric Range of Plug-in Hybrid Electric Vehicles in Europe,” *Proceedings of the 13th International Conference on Engines & Vehicles (ICEV 2015),* 2015.

Anode flow field design effect on direct methanol fuel cells

Vladimir L. Meca[a] , Oscar Santiago[b], Elena Posada[c], Rafael d'Amore-Domenech[d], Antonio Villalba-Herreros[e] and Teresa J. Leo[f]

[a] Universidad Politécnica de Madrid, Madrid, Spain, vl.meca@upm.es, CA
[b] University of Bremen, Bremen, Germany, santiago@uni-bremen.de
[c] Universidad Politécnica de Madrid, Madrid, Spain, elena.posada@upm.es
[d] Universidad Politécnica de Madrid, Madrid, Spain, r.damore@upm.es
[e] Universidad Politécnica de Madrid, Madrid, Spain, antonio.villalba@upm.es
[f] Universidad Politécnica de Madrid, Madrid, Spain, teresa.leo.mena@upm.es

Abstract:
Within the last years, there has been an increasing interest in the use of alternative fuels, among others, methanol. This fuel is liquid at ambient temperature and pressure and can be obtained through a synthesis process from hydrogen and captured CO_2, becoming e-methanol. Direct methanol fuel cells (DMFC) are devices that use this fuel in liquid form, without a reforming step, to produce electricity. These fuel cells have few moving parts and are used in portable electronic devices and electric vehicles. However, DMFC have efficiencies around 32 % and its commercial application is limited at present. Besides, advances need to be made to solve problems such as methanol crossover, sluggish methanol oxidation reaction and demand of noble metal for fabrication of these fuel cells. In this work, the effect of the depth of an anode serpentine flow field design on the performance of a direct methanol fuel cell is investigated experimentally. Stainless steel plates (SS316L) with single serpentine flow fields of different depths are designed, fabricated and tested. The study is conducted with these plates forming a single cell of 16 cm^2 of active membrane area. The aim of this work is to study the effect of the anode channel depth on the performance of a DMFC, analysing the influence of this parameter on the power density of this device and the methanol crossover that takes place during its operation. When the channel depth decrease from 1.5 mm to 0.5 mm, can be observed a power density increment of 18.86 %. However, the decrease of the channel depth resulted in an increase of the limiting methanol crossover current density by 28.75 %.

Keywords:
Methanol; fuel cell; anode flow field design; single serpentine flow field.

1. Introduction

Fuel cells are electrochemical devices that convert the chemical energy from a fuel and oxidant directly into electrical energy and heat. Theoretically, this way of obtaining electrical energy has higher efficiency as compared to internal combustion engines [1]. Fuel cells have the capability of supplying energy meanwhile the corresponding reactants are fed, and they are very versatile and scalable. Therefore they are a good alternative to traditional energy devices such as Li-ion batteries, having an enormous growth potential [1]–[3]. Considering the type of electrolyte used, there is a wide variety of fuel cell types. One of the most popular choices for renewable and sustainable energy conversion devices is the Proton Exchange Membrane Fuel Cell (PEMFC) [2]. This type of fuel cell is popular due to its high-power output, high efficiency, high specific energy, cleanliness, low operating temperature (below 100ºC), quick start-up times, longer life span and quiet operation [4],[5]. The main feature of the PEMFC is the electrolyte used, a proton conductive polymer membrane whose main function is the transport of protons from the anode to the cathode. Meanwhile, this membrane avoids the transport of electrons or reactants [5],[6]. PEMFC can use different fuels, being hydrogen the most studied, but its properties imply some drawbacks that make difficult their commercialization at this moment [3],[7]. Hydrogen has high flammability and a low volumetric energy density (hydrogen volumetric energy density in liquid state is 10.1 MJ/L, and compressed at 70 MPa is 5.6 MJ/L, while the volumetric energy density of natural gas is 22.2 MJ/L) [8]–[10]. This leads to the use of high-pressure technologies (like bulky pressure tanks or compressors) or/and very low temperature technologies for its handling, storage and

distribution [8]. These particularities represent a technological challenge at this moment. Nevertheless, the use of liquid fuels at room temperature, like methanol or ethanol, requires a notably easier storage and refuelling systems, because liquid fuels can be operated at standard temperatures and pressure [3],[9].

Direct methanol fuel cells (DMFC) use methanol as fuel, which offers advantages compared to hydrogen fuel cells, as a cheaper refuelling system, as methanol is easy to handle at standard temperatures and pressures derived from its liquid state [3],[11]–[13]. DMFCs are especially effective at delivering electricity for portable electronic devices and other mobile applications. [9],[13],[14].

DMFCs are fuel cells of PEMFC type and essentially consist of a membrane-electrode assembly (MEA), composed by two electrodes (anode and cathode) separated by an electrolyte (usually a polymeric membrane) [13]. The MEA is sandwiched between two bipolar plates (BPs) which have channels to distribute the fuel and oxidant through the gas diffusion layer [12],[13].

In DMFCs, methanol is oxidized at the anode yielding protons, electrons and CO_2. The protons are transported to the cathode, through the membrane, while the electrons are transported via an external circuit to the cathode. On the cathode the electrons and protons react with oxygen to produce water. By-products from both reactions, methanol oxidation and oxygen reduction, CO_2 and water are formed on anode and cathode respectively, and they are evacuated by BPs [3],[12],[13],[15]. The reactions are:

Anode: $\mathrm{CH_3OH} + \mathrm{H_2O} \rightarrow \mathrm{CO_2} + 6\mathrm{H^+} + 6\mathrm{e^-}$ (R1)

Cathode: $\frac{3}{2}\mathrm{O_2} + 6\mathrm{e^-} + 6\mathrm{H^+} \rightarrow 3\mathrm{H_2O}$ (R2)

Overall: $\mathrm{CH_3OH} + \frac{3}{2}\mathrm{O_2} \rightarrow \mathrm{CO_2} + 3\mathrm{H_2O}$ (R3)

The efficiency of fuel cells is determined by many variables, including operational parameters, such as cell operating temperature, mass transport, flow rates and other physical components of the cell like the membrane electrode assembly (MEA) as well as the BPs [4], [16].

BPs have fundamental roles that affect the performance of the fuel cell. Their design determines water management for the DMFC, preventing the flooding of the cathode. Also, BPs provides structural support for the thin and mechanical weak MEAs, facilitating heat and electrical conductivity, and mass transport (reactants and by-products). In fact, the geometry of BP channels helps the entry and distribution of the reactants onto the active surface of the cell, the gas diffusion layer, and the evacuation of the by-products. In addition, the geometry of BP channels influences the crossover process. Experimental results show that single serpentine flow fields present low pressure drops between the inlet and the outlet of the channel, which effectively removes products and prevents blockages of the flow field [11],[17].

The objective of this work is to determine the influence of channel depth on the electrochemical performance of a DMFC and crossover produced during the operation of this device. For that purpose, three different anode channel depths (0.5, 1.0 and 1.5 mm) have been studied. Channels depth affects the mass transport, fluid velocity and the fraction of the two phases (gas and liquid phase) thus affecting the cell performance [14]. In this work, a series of experiments was designed to obtain the polarization curves and measure the limiting methanol crossover current density for each depth.

2. Methodology

This section outlines the methodology used to determine the impact of the anode channel depth on the performance of a DMFC. The parameters of the anode channel configuration, as well as the material of the single cell plates, are set except for the depth.

As previously stated, BPs have fundamental roles on cell performance, as supply reactants, remove reaction products, act as current collectors and facilitate thermal management and structural support [4]. Having those fundamental roles in mind, the material used in this work for bipolar plates is stainless steel 316L (SS316L). As metallic material, SS316L has good mechanical resistance, high electrical conductivity, it is easily machinable [19] and it has good characteristics over a prolonged period of time [20]. Stainless steel is also capable of self-passivating, which allows a significant reduction of corrosive rate, however, it results in a notable increase in interfacial contact resistance with other elements such as gas diffusion layer in the case of fuel cells [21].

The DMFC single cell used this work (Figure 1A) is composed by two plates of stainless steel 316L (anode and cathode plates), two gaskets which prevent the electrical contact between the plates and avoid fluid leaks, and a MEA. The MEA is composed by a Nafion membrane, sandwiched between two layers of commercial electrodes.

Figure 1B shows the front view of the flow field plate used in this work, depicting stainless steel plates for the anode flow field. These plates feature single-channel serpentines measuring 1 mm of channel width. The channel depths studied include 0.5, 1.0 and 1.5 mm. As introduced before, according to literature the single-channel serpentine configuration prevents the blockage of the channel, allows the effective removal of products, suitable two-phase mass transport and appropriate flow behind the ribs [22], and facilitates a uniform reactant distribution [23]. For all these reasons single-serpentine flow field is the flow pattern more commonly used at present. However, this flow pattern presents significant concentration gradient between the inlet and the outlet [23].

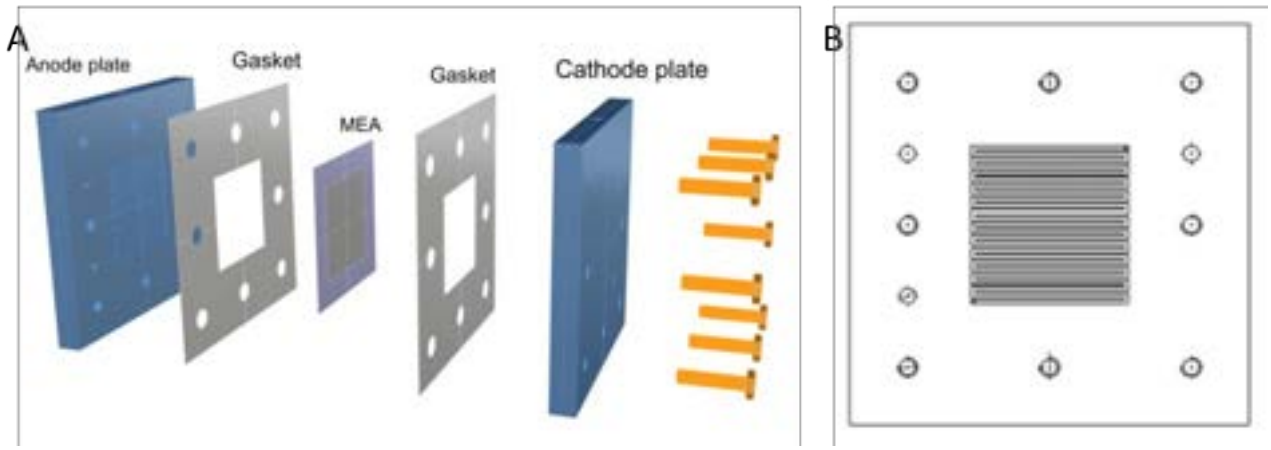

Figure 1. A- Exploded view of the designed and fabricated in-house DMFC single cell used in this work. B- Front-view projection of the flow field design of the anode plate studied.

The performance of the DMFC is also affected by the direction of the supply of the reactant, as this direction is related to the uniformity of the reactant distribution and temperature over the cell [24]. The methanol solution inside the anode is supplied bottom-up, against gravity. In this way, the formed gaseous CO_2 would be swept by the methanol solution, following the natural pressure gradient for easier evacuation [25]. Analogously, the oxidant, oxygen, is supplied from the top inlet of the cell to ease the evacuation of the liquid water produced in the cathode, to prevent the cathode channels from flooding [24].

The design parameters of the anode and cathode plates, used with the aim of determining the effect of the depth channel on the cell performance, are summarized in Table 1.

Table 1. Parameters of the anode channels studied in this work.

Parameter	BP1	BP2	BP3
Depth of anode channels, mm	0.5	1.0	1.5
Depth of cathode channels, mm	0.5	0.5	0.5
Material of the bipolar plates	SS316L	SS316L	SS316L
Number of channels	25	25	25
Width of the channel, mm	1.0	1.0	1.0
Open Ratio	0.624	0.624	0.624
Contact surface treatment	N3	N3	N3

The fuel and oxidant flow rates are set to obtain excess supply of the reactants avoiding possible mass transfer losses. The parameters used in this work are summarized in Table 2.

Table 2. Parameters used during the experimental tests developed in this work.

Parameter	Value
Temperature, °C	60
Methanol concentration, mol/l	1
Methanol flow rate, ml/min	3
Methanol supplier	Panreac AppliedChem (99.9%)
Oxygen flow rate, ml/min	110
Oxygen pressure, MPa	0.1
Anode catalyst	Pt/Ru
Anode catalyst charge, mg/cm^2	3
Anode commercial reference	BC-H225-10F
Anode supplier	Quintech
Cathode catalyst	Pt
Cathode catalyst charge, mg/cm^2	1
Cathode commercial reference	BC-M100-30F
Cathode supplier	Quintech

3. Results and discussion

Figure 2 shows the polarisation and power density curves obtained for each of the anode channel depths studied.

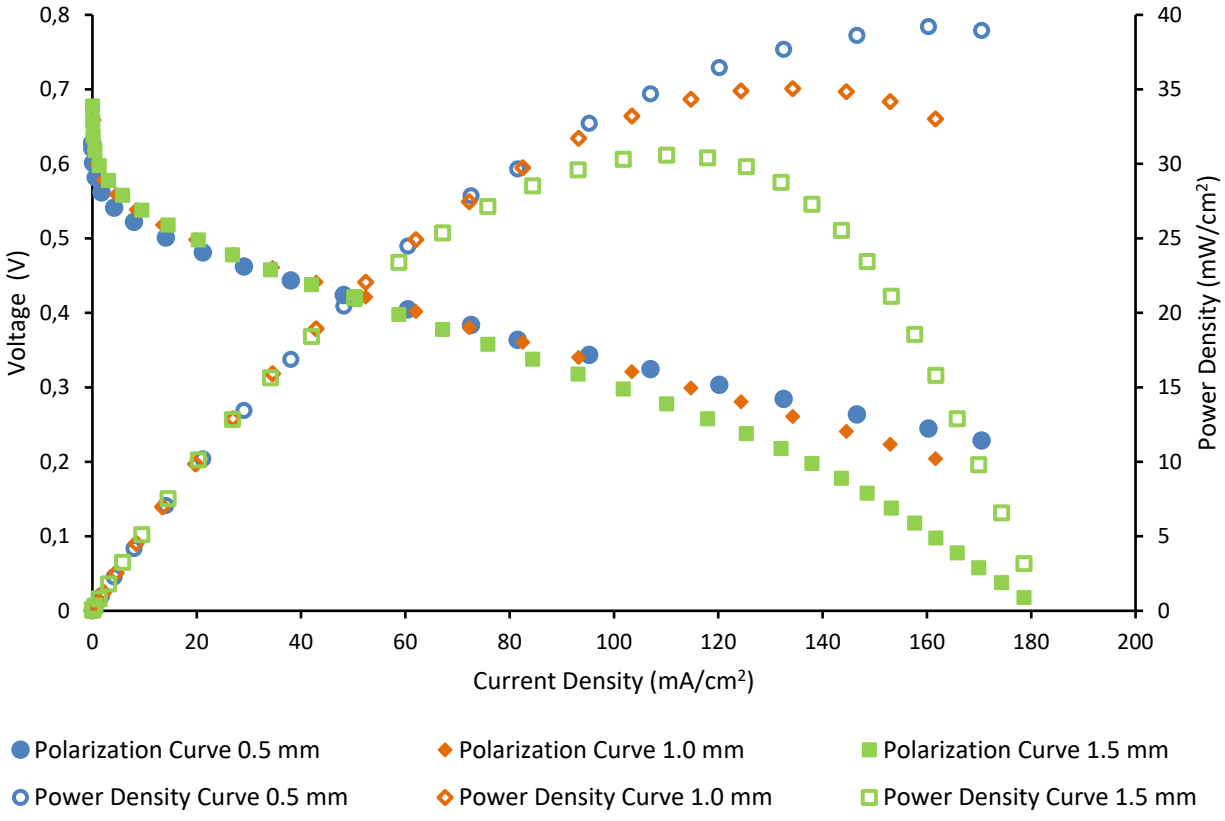

Figure 2. Polarization and power density curves of the DMFC single cell with anode channel depths of 0.5 mm, 1.0 mm and 1.5 mm, results obtained at a temperature of 60 ºC, cathode pressure 1 bar, oxygen flow rate of 110 ml/min, a methanol concentration of 1 M and methanol flow rate of 3 ml/min.

The results suggest that, for a given operating condition, a decrease in the anode channel depth leads to an improvement in the DMFC performance, contrary to the conclusions of the work of Chen et al. for a DMFC stack [14], as a reduction in the depth of the anode channels of the stack does not cause significant changes in the analysed stack performance. This may mean that the performance of the channel configuration in a single cell and a stack could not have a directly proportional relationship, so smaller improvements can be observed when working with a stack.

Furthermore, during the tests for obtaining polarization curves using the anode channel depth of 1.5 mm it was observed an accumulation of CO_2 in the anode channel. Results suggest that difficulties on CO_2 removal can affect the DMFC performance producing a decrease in peak power density.

In Figure 2 it can be observed that the peak power density increases from 32.76 mW/cm^2 with 1.5 mm of depth to 38.94 mW/cm^2 with 0.5 mm of depth. However, it should be noted that reducing the depth of the flow channel results in increased pressure drops along the channel [27]. This, in turn, increases the power required for pumping the methanol solution. Consequently, the overall efficiency of a DMFC system may decline. Furthermore, a higher pressure drop could cause a portion of the methanol solution to bypass the flow channel and instead flow directly through the diffusion layer. Also, a lower channel depth than the 0.5 mm tested could produce a worst performance due to factors including methanol crossover and the void fraction of CO_2 [27]. For these reasons, future research should examine the trade-off between the advantages and disadvantages arising from the alteration in channel depth for a DMFC stack and its auxiliary systems.

Figure 3 shows the impact of channel depth on limiting crossover current density. Methanol crossover causes electrode depolarization, mixed potential, resulting in an open-circuit voltage below 0.8V. Besides it consumes some reactant at the cathode, so it produces intermediates of the reaction, like carbon monoxide, that poisons the cathode catalyst and generates water accumulation on the cathode. Consequently, the crossover current density cause the reduction of fuel cell performance [26],[15].

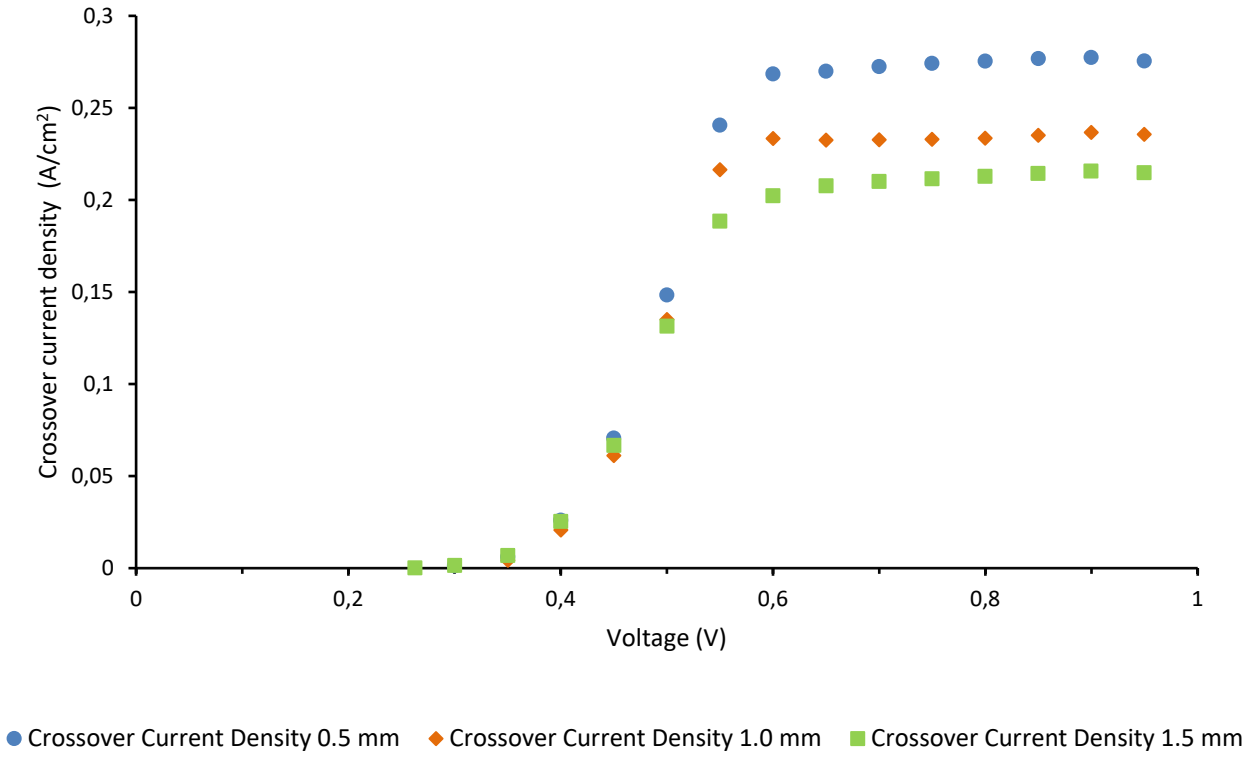

Figure 3. Crossover current density of the DMFC with bipolar plate with 0.5 mm, 1.0 mm and 1.5 mm of channel depth, results obtained at a temperature of 60 ºC, cathode pressure 1 bar, nitrogen flow rate of 110 ml/min, a methanol concentration of 1 M and methanol flow rate of 3 ml/min.

The graph presented in Figure 3 illustrates the relationship between the applied potential and the current density generated by the oxidation of methanol as it passes through the assembly. The maximum current density observed for each MEA represents its respective limiting crossover current density. Minimizing methanol crossover through the membrane is crucial for enhancing both fuel utilization and the potential at the cathode in DMFC operations [28]. Regarding this matter, Figure 3 demonstrates that deeper channels feature superior properties in preventing methanol crossover compared to shallower channels. This is evident from its slightly lower limiting methanol current density. As a result, the DMFC with the 1.5 mm channel displays the lowest limiting crossover current density value (215 mA/cm^2), which is significantly lower than that of 1 mm (236 mA/cm^2) and 0.5 mm (277 mA/cm^2).

Comparing the results shown in Figures 2 and 3, it can be concluded that despite producing a higher crossover, a shallower channel depth seems to give better results when analysing the power density of the studied single cell.

4. Conclusions

The effect of the anode channel depth on the DMFC performance has been investigated experimentally. The results show that an anode channel depth of 0.5 mm provides a higher peak power density than 1.0 mm and 1.5 mm channels depths, obtaining an increase of 18.86 % in peak power density with respect to the deepest channel. It has also been found that gas bubbles, formed during the reaction on the anode, can generate a decrease in the cell performance when the channel depth increases. These results suggest that shallower channels improve CO_2 removal and consequently cell performance. However, changes in the anode channel depth also have an influence on the limiting crossover current density obtained, as measurements of this parameter with 0.5 mm channel depth show an increase of 28.75% over those obtained with 1.5 mm channel depth.

Future studies should be carried out to analyse the effect of anode channel depth in combination with other parameters, like temperature, methanol concentration and oxygen flow rate, to improve the performance of DMFC.

Acknowledgments

This work has been carried out thanks to the Project GreenH2CM funded by MCIN/AEI/10.13039/501100011033, by “NextGenerationEU/PRTR” and the Regional Government of Madrid and to the Grant PID2021-124263OB-I00 funded by MCIN/AEI/10.13039/501100011033 and by “ERDF a way of making Europe”.

References

[1] Abdelkareem M. A., Elsaid K., Wilberforce T., Kamil M., Sayed E. T., and Olabi A. Environmental aspects of fuel cells: A review, Science of The Total Environment, 2021;752: 141803.

[2] Majlan E. H., Rohendi D., Daud W. R. W., Husaini T., and Haque M. A., Electrode for proton exchange membrane fuel cells: A review. Renewable and Sustainable Energy Reviews 2018;89:117–134.

[3] Alias M. S., Kamarudin S. K., Zainoodin A. M., and Masdar M. S., Active direct methanol fuel cell: An overview, Int J Hydrogen Energy 2020; 45(38): 19620–19641.

[4] Wilberforce T. El Hassan Z, Ogungbemi E., Ijaodola O., Khatib F.N., Durrant A. Thomson J., Baroutaji A., Olabi A.G.., A comprehensive study of the effect of bipolar plate (BP) geometry design on the performance of proton exchange membrane (PEM) fuel cells. Renewable and Sustainable EnergyReviews 2019; 111: 236–260.

[5] Tellez-Cruz M. M., Escorihuela J., Solorza-Feria O., and Compañ V., Proton Exchange Membrane Fuel Cells (PEMFCs): Advances and Challenges. Polymers (Basel) 2021; 13(18):3064.

[6] Jamil A. et al., Current status and future perspectives of proton exchange membranes for hydrogen fuel cells. Chemosphere 2022;303: 135204..

[7] Wang Y., Ruiz Diaz D. F., Chen K. S., Wang Z., and Adroher X. C., Materials, technological status, and fundamentals of PEM fuel cells – A review. Materials Today 2020;32: 178–203.

[8] Jena P., Materials for hydrogen storage: Past, present, and future. Journal of Physical Chemistry Letters 2011; 2(3):206–211.

[9] Charoen K. Prpainainar C., Sureeyatanapas P., Suwannaphisit T., Wongamornpitak K., Kongkachuichay P., Holmes S.M., Prapainainar P., Application of response surface methodology to optimize direct alcohol fuel cell power density for greener energy production. J Clean Prod 2017;142:1309–1320.

[10] Mazloomi K. and Gomes C., Hydrogen as an energy carrier: Prospects and challenges. Renewable and Sustainable Energy Reviews 2012; 16:3024–3033.

[11] Kianimanesh A., Yu B., Yang Q., Freiheit T., Xue D., and Park S. S., Investigation of bipolar plate geometry on direct methanol fuel cell performance. Int J Hydrogen Energy 2012; 37(23):18403–18411.

[12] Kamarudin S.K., Achmad F., Daud W.R.W., Overview on the application of direct methanol fuel cell (DMFC) for portable electronic devices. Int J Hydrogen Energy 2009;34:6902–6916.

[13] Goor M., Menkin S., and Peled E., High power direct methanol fuel cell for mobility and portable applications. Int J Hydrogen Energy 2019;44(5):3138–3143

[14] Chen C. Y., Shiu J. Y., and Lee Y. S., Development of a small DMFC bipolar plate stack for portable applications. J Power Sources2006;159(2):1042–1047

[15] Ahmed M. and Dincer I., A review on methanol crossover in direct methanol fuel cells: challenges and achievements. Int J Energy Res 2011;35(14): 1213–1228

[16] Vuppala R. K. S. S., Chedir B. A., Jiang L., Chen L., Aziz M., and Sasmito A. P., Optimization of Membrane Electrode Assembly of PEM Fuel Cell by Response Surface Method. Molecules 2019; 24(17):3097

[17] Aricò A. S., Cretì P., Baglio V., Modica E., and Antonucci V., Influence of flow field design on the performance of a direct methanol fuel cell. J Power Sources 2000; 91(2):202–209

[18] Yang H., Zhao T. S., and Ye Q., Addition of non-reacting gases to the anode flow field of DMFCs leading to improved performance. Electrochem commun 2004;6(11):1098–1103.

[19] Song Y. Zhang C., Ling C.Y., Han M., Yong R.Y., Sun D., Chen J.,, Review on current research of materials, fabrication and application for bipolar plate in proton exchange membrane fuel cell. Int J Hydrogen Energy 2020;45(54):29832–29847.

[20] Scott K., Argyropoulos P., Yiannopoulos P. and Taama W. M., Electrochemical and gas evolution characteristics of direct methanol fuel cells with stainless steel mesh flow beds. Journal of Applied Electrochemical 2001; 31: 823–832.

[21] Tawfik H., Hung Y. and Mahajan D., Metal bipolar plates for PEM fuel cell-A review. J Power Sources 2007; 163(2):755–767.

[22] Yang H. and Zhao T. S., Effect of anode flow field design on the performance of liquid feed direct methanol fuel cells. Electrochim Acta 2005; 50(16–17): 3243–3252.

[23] Rahimi-Esbo M., Ranjbar A. A., Ramiar A., Alizadeh E., and Aghaee M., Improving PEM fuel cell performance and effective water removal by using a novel gas flow field. Int J Hydrogen Energy 2016; 41(4): 3023–3037.

[24] Kim D., Lee J., Lim T. H., Oh I. H., and Ha H. Y., Operational characteristics of a 50 W DMFC stack. J Power Sources 2006; 155(2): 203–212.

[25] Yang H., Zhao T. S., and Ye Q., Pressure drop behavior in the anode flow field of liquid feed direct methanol fuel cells. J Power Sources 2005;142(1–2):117–124.

[26] Qi Z. and Kaufman A., Open circuit voltage and methanol crossover in DMFCs. J Power Sources 2002;110(1):177-185.

[27] Kumaresan T., Palaniswamy K., Fly A., Sundaram S., Studies on anode mass composition and cathode flow field design for small-scale to large-scale direct methanol fuel cell stack systems. AIP Advances 2022; 12: 125316.

[28] Ranjani M., Jin Yoo D. and Gnana Kumar, G., Sulfonated Fe_3O_4@SiO_2 nanorods incorporated sPVdF nanocomposite membranes for DMFC applications. Journal of Membrane Science 2018, 555, 497-506.

Dynamic modeling of a power-to-gas system for green methane production from wind energy

Valeria Pignataro[a], Angelica Liponi[a], Eleonora Bargiacchi[b] and Lorenzo Ferrari[a]

[a] University of Pisa, Department of Energy, Systems, Territory and Construction Engineering, Pisa, Italy
*valeria.pignataro@phd.unipi.it, angelica.liponi@phd.unipi.it, lorenzo.ferrari@unipi.it (**CA**)*
[b] Systems Analysis Unit, IMDEA Energy, 28935, Móstoles, Spain
eleonora.bargiacchi@imdea.org

Abstract:

Despite the impact of global warming on the living conditions of the Earth, fossil fuels still dominate the global energy scenario. The precariousness of our energy system requires the use of more reliable and less polluting energy sources, but a greater penetration of intermittent renewables implies the need for large-scale flexible energy storage. This need, combined with the growing interest in the use of hydrogen in mobility and industry, makes the prospect of including this energy vector in our daily lives tangible. However, the problems related to the development of dedicated infrastructures make its positioning on the market complex. In a transition phase, power-to-gas systems constitute an emerging solution that allows the use of existing structures for natural gas and, at the same time, solves the problem of hydrogen storage. In this study, a power-to-gas system producing synthetic methane from wind energy was modelled. Management strategies for both the electrolysis system and the hydrogen storage tank were tested to assess the flexibility and versatility of the system. Particular attention was dedicated to the analysis of the impact of the storage on the mitigation of the operating condition fluctuation of the methanation unit. Results of the simulations showed similar performances of the four electrolyzers and a limited number of methanation unit shutdowns. Nevertheless, the annual utilization factor of the subsystems was low, and this suggests a further investigation of the subsystems' sizing. Overall, the effectiveness of the management strategies developed for the power-to-methane system makes the proposed model a good instrument to be used for further analysis and evaluations.

Keywords:

Dynamic operations; Hydrogen; Modeling; Management strategies; Methane; Power-to-Gas.

1. Introduction

Decarbonizing the world's energy system requires the use of green and renewable energy sources (RES). However, a high penetration of renewable sources in the global energy mix creates additional challenges related to the more complex management of energy flows and the difficulty of synchronizing energy demand and production. This problem can be solved using energy storage systems. In this context, hydrogen has been identified as a sustainable energy vector for electricity and heat generation; nevertheless, today 96% of the produced hydrogen is obtained from fossil fuels and only 3.9% comes from electrolysis [1] due to the elevated costs associated with its entire supply chain.

Although some hydrogen production technologies (e.g.: alkaline electrolysis) alternative to fossil fuel-based ones are already mature, the lack of dedicated infrastructures makes the introduction of hydrogen in the market difficult [2]. Using hydrogen for the synthesis of various hydrocarbons, including methane [3,4], could be considered a promising solution to foster hydrogen economy while using the existing infrastructure. Lewandowska-Bernat & Desideri [4] identify various opportunities for the power-to-methane systems (both in off-grid and on-grid systems) that are considered promising for the development of more efficient and flexible energy systems, the reduction of polluting emissions, and the increase of sustainability in sectors such as industry and mobility. After a comparison among short-term storage systems, Belderbos et al. [5] conclude that power-to-fuel systems can play a significant role in scenarios with a high share of renewable energy. In particular, they analyze four case studies each of which characterized by a different type of RES (onshore wind, offshore wind or solar). Their study illustrates the different trends of methane production and how power-to-gas systems play a more important role when the renewable energy production profile has a seasonal trend. Furthermore, Walker et al. [6] identify power-to-fuel as an attractive solution to implement, especially for seasonal storage.

Some issues arise and should be considered when electrolysis systems are directly coupled with variable RES. In particular, alkaline electrolyzers have some limitations on the lower operating load because of safety reasons, and they can generally operate in a range of 20-100% of the nominal power [7].The variability of these sources might affect the system operation by causing frequent shutdowns, part-load and dynamic operation. However, frequent shutdowns can speed up the stack degradation and should be limited. In addition, the intermittent RES availability causes a low number of annual equivalent operating hours that negatively affects the specific production cost of hydrogen. Several studies investigated techno-economic aspects of electrolysis systems coupled with RES. Liponi et al. [8] investigate the effect of the electrolyzer size on the levelized cost of hydrogen in the case of PV-electrolyzer coupling. The choice of the electrolyzer size should be a trade-off between the maximization of hydrogen production and the needs of limiting shutdowns and having sufficiently high electrolyzer utilization factors to minimize the specific production costs. The possibility of adopting an electric storage [9] and/or grid-electricity support [10] to mitigate wind variability has also been investigated. On one side, by allowing grid support, the electrolyzer operation can be more continuous and annual operating hours are increased, resulting in a reduction of specific production costs. However, on the other side, if the electricity grid is not completely decarbonized, CO_2 emissions are associated with hydrogen production. In another study [11] Liponi et al. perform a techno-economic comparison of different configurations of an electrolysis system consisting of multiple electrolysis units that can operate separately for hydrogen production from wind sources.

In this study, an electrolysis system composed by several separated units is adopted and a management strategy is implemented to limit the number of electrolyzers shutdowns.

Several models for power-to-gas systems were proposed in the literature. In particular, Baccioli et al. [12] analyze the costs associated with the production and sale of liquefied methane and oxygen from a power-to-gas plant associated with a CO_2 source from a geothermal plant. This study reveals that using hydrogen storage does not increase the cost-effectiveness of the plant, while "only small storage systems will be needed for managing the different dynamic behavior of the components" [12]. Gorre et al. also published two studies in this subject [13,14]. In the first study, they observe that the production costs of methane in a power-to-gas system can be reduced by releasing the operation of electrolyzer and methanation unit by using an intermediate storage system. They also assert the importance of optimizing the size of the methanation unit. In the second study, they underline the importance of using an intermediate storage to decouple the electrolysis system and the methanation unit, but also the need to optimize its size to reduce production costs, depending on the operation strategy and the case study.

In a 2009 study [15] Frate et al. investigate the use of electric storage systems to counter the problem of wind power fluctuations in small-sized wind farms. In particular, they study the effectiveness of Li-Ion batteries and flywheels in managing the rates of power output from a wind turbine. Nevertheless, the impact of the management strategy of hydrogen and electricity surplus on the mitigation of the operating condition fluctuation of the methanation unit have not been deeply investigated.

In the present work, a mathematical model to simulate the operation of a power-to-gas system with wind-energy source is proposed. The problems related to the variability of the energy source will be addressed by developing a management strategy for both the electrolysis system and the hydrogen storage tank, in order to limit the number of shutdowns (and consequently the equipment degradation) and, at the same time, to exploit to the maximum the electricity produced by the wind farm.

2. Modeling

A schematic representation of the power-to-gas system modelled in this study is given in Figure 1. The first step is the production of hydrogen (and oxygen) through an electrolysis system (composed of four alkaline electrolyzers of equal nominal power) powered by a dedicated wind farm. The produced hydrogen is partly sent to the methanation unit and partly injected in a storage system before the methanation unit. The conversion of hydrogen and CO_2 to methane takes place in a catalytic methanation reactor. The main components of the system are modelled (wind farm, electrolyzers, and methanation unit) as described below.

2.1. Alkaline electrolyzer

Several models for the simulation of the operation of an alkaline electrolyzer are provided in literature. The foundations of “semi-empirical” alkaline electrolyzers models are built by Ulleberg [16], whose model is based on a combination of fundamental thermodynamics, heat transfer theory and empirical electrochemical relationships. An extension of this model is proposed in the study of Amores et al. [17] in which the effect of electrolyte concentration and cell architecture is also studied. Sánchez et al. published two other relevant studies on this subject [18,19] in which a semi-empirical mathematical model based on the polarization curve and the Faraday efficiency in dependence of pressure, temperature and current density is proposed. Dièguez et al [20] develop a thermal modeling of the electrolyzer focusing on coupling the stack with a renewable energy source.

Whereas the above-mentioned studies use a simplified lumped parameter configuration for the description of the electrolyzer, in which stack, gas-liquid separators and heat exchangers are treated as a single component,

in this study a more detailed modelling is performed, paying greater attention to individual elements and control systems. The baseline study used is from Sakas et al. [21], in which a model based on energy and mass balances with adjustable parameters with a zero-dimensional approach is proposed.

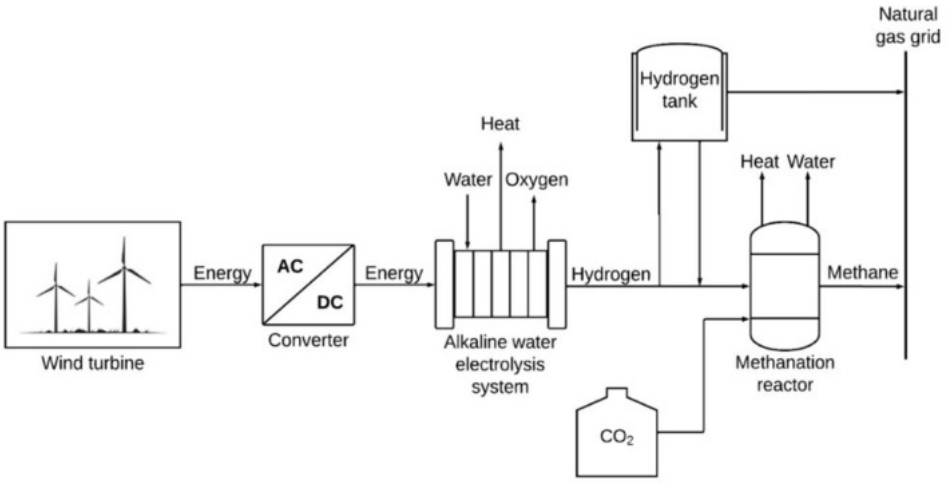

Figure 1. Schematic representation of the power-to-gas system.

Electric current powers the stack for the production of gaseous hydrogen and oxygen. At the stack outlet, a mixture of electrolyte (25wt% KOH) and hydrogen on one side, and oxygen on the other side, are sent to the horizontal gas-liquid separators. Hydrogen and oxygen are removed from the separator, while the electrolyte mixture is sent to the mixer where it is mixed with the make-up water. The oxygen leaving the separator is just flushed from the process, while the produced hydrogen is sent to the methanation unit (see Figure 2).

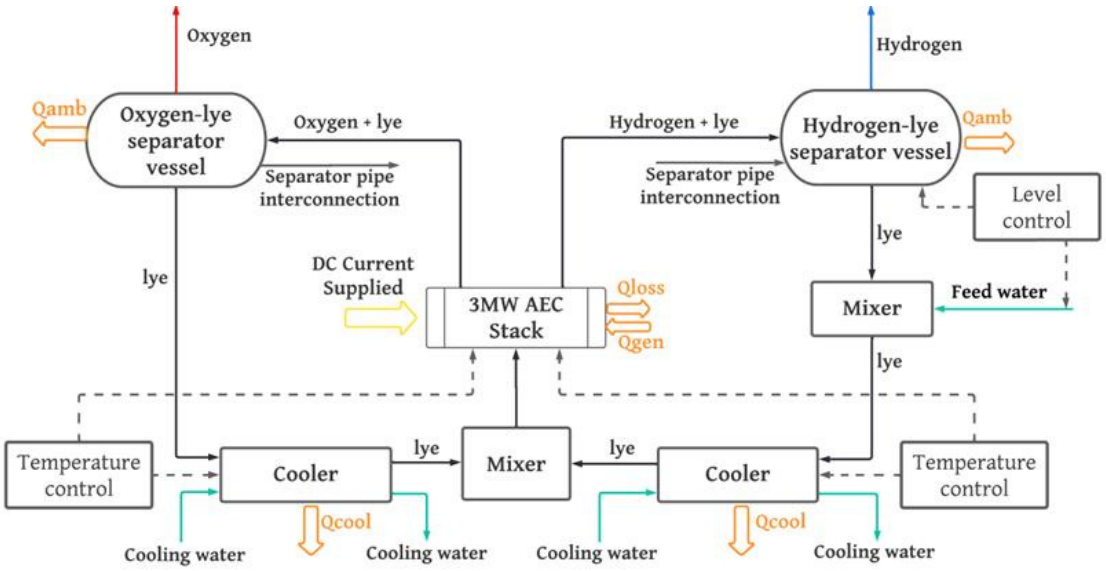

Figure 2. Alkaline water electrolyzer plant process diagram.

The stack is modeled in Matlab assuming the parameters listed in Table 1.

Table 1. Stack model parameters [21]

Parameter	Unit	Value
Number of cells	-	326
Cell lateral area	m^2	2.66
Cell block diameter	m	1.84
Free cell volume	m^3	0.027
Distance between bipolar plates	m	0.01
Stack length	m	5.85

A thermal model and an electrochemical model are used to calculate the production of hydrogen, the trend of flow rates, temperatures, energy losses, cell voltage and cell current.

2.1.1. Electrochemical model

The cell voltage is calculated as the sum of the reversible potential and overvoltage terms:

$$E_{cell} = E_{rev} + E_{act} + E_{ohm} + E_{conc} \quad (1)$$

The reversible potential is the minimum voltage necessary for the water splitting reaction to take place and depends on the temperature and pressure according to Nerst equation. Overvoltage are expressed through semi-empirical expressions as a function of temperature and current density [21].

The polarization curve is defined as a function of the cell current, which is calculated through Newton's iterative method using the parameters adopted by Sakas et al. [21] for a 3 MW alkaline electrolyzer.

2.1.2. Thermal model

The stack temperature of an alkaline electrolyzer is one of the parameters that most affects its performance. In this paper, internal temperature gradients in the stack are assumed spatially uniform, according to Sakas et al.'s lumped thermal capacitance model [21].

The overall thermal energy balance is expressed by:

$$C_{stack} \cdot \frac{dT_{stack}}{dt} = Q_{gen} - Q_{loss} + \dot{m}_{lye,stackin} \cdot \bar{c}_{p,lye} \cdot T_{stackin,cooled} - \left(\dot{m}_{lye} + \dot{m}_{cons,wat}\right) \cdot \bar{c}_{p,lye} \cdot T_{stack} \quad (2)$$

The term on the left in Equation (2) represents the rate of change of the electrolyzer temperature over time, while Q_{gen} is the heat generated inside the stack, Q_{loss} is the total heat loss to the ambient and the other two terms are the enthalpy flows of the incoming and outgoing electrolyte mixture from the stack.

Since the flow rates of hydrogen and oxygen are very low compared to the flow rate of the electrolytic mixture circulating in the system (0.0138 kg/s, 0.12 kg/s and 19.68 kg/s respectively at nominal conditions), they can be neglected in the energy balances.

The hydrogen and oxygen produced by the electrolysis process exit from the stack in the form of a mixture of gas and electrolytic solution, therefore it is necessary to separate them from liquid phase through two horizontal gas-liquid separator vessels. In the present study, for simplicity, the separation efficiency is considered unitary.

To prevent gas-liquid separators from excessively emptying or filling, an on/off control of their liquid level is applied to the water make-up pump to keep the separators' level within a certain range (0.4 m – 0.6 m) for the entire duration of the simulation.

After gas separation, the electrolytic mixture enters the mixer where the consumed water is refilled. Although mixing with low temperature water (15°C) results in a lowering of the temperature of the electrolyte mixture, this is not enough to reach the target temperature of the stack. Therefore, a cooling system with a temperature control is required. The regulation has the aim to keep the stack temperature always near the target value (70°C).

The efficiency of the electrolyzer was defined as:

$$\eta_{ele} = \frac{\dot{m}_{H_2} \cdot LHV_{H_2}}{P_{stack}} \quad (3)$$

2.1.3. Operation at nominal conditions

The simulation is performed using a 5-minute time discretization. By simulating the operation of a single electrolyzer fed with nominal power, the results obtained were very close to those obtained in the reference study [21], whose model was validated. In Table 2, the main operating parameters of the electrolyzer are given.

2.2. Hydrogen storage tank

The storage system was considered an ideal component, and it was modeled as a variable volume at constant pressure (16 bar). Its storage capacity is 4,434 Nm^3 of hydrogen, corresponding to the amount of hydrogen required by the methanation unit to operate continuously for two-and-a-half hours at nominal conditions. The State of Charge (SOC) of the tank is defined as:

$$SOC(t) = \frac{V_{H_2,tank}(t-1)}{V_{H_2,tank,cap}} \quad (4)$$

Where $V_{H2,tank}(t-1)$ is the hydrogen volume content inside the tank at the timestep "t-1" and $V_{H2,tank,cap}$ is the storage capacity of the tank.

2.3. Methanation unit

The methanation unit is modelled in Matlab without going into the thermodynamic details of its operation. The model provides the methane flow rate on the basis of the produced hydrogen according to stoichiometry.

The methanation unit is assumed to operate in a range of 40-100% of the nominal flow rate, without major changes in the quality of the produced gas, with a maximum load change rate of ±10%/min [13]. Since the electricity input might fluctuate strongly and electrolyzers and the methanation unit work at different loads, it is necessary to decouple the two components. For this purpose, a hydrogen storage tank is installed between the electrolyzer and the methanation unit, and it is modeled as an ideal component. In this study, the methanation unit, the electrolysis system and the storage system are considered at the same pressure (16 bar), but compressing the hydrogen after the electrolysis system could significantly decrease storage volume. The methane flow rate is retrieved from the methanation efficiency according to the Eq. (5).

$$\eta_{\mathrm{met}} = \frac{\mathrm{LHV}_{\mathrm{CH_4}} \cdot \dot{m}_{\mathrm{CH_4}}}{\mathrm{LHV}_{\mathrm{H_2},} \cdot \dot{m}_{\mathrm{H_2,in}}} \cdot 100 \quad (5)$$

Table 2. Alkaline electrolyzer operating parameters at nominal conditions.

Parameter	Unit	Value
Stack target temperature	°C	70
Ambient temperature	°C	25
Stack nominal power	MW	3
System efficiency	%	92
Average electrolyzer efficiency	%	60
Stack pressure	bar	16
Faraday efficiency	%	86
Water consumption	kg/s	0.125
Hydrogen production	Nm^3/h	554
Oxygen production	Nm^3/h	277
Specific energy consumption	kWh/Nm^3	4.45

Table 3. Methanation unit operating parameters.

Parameter	Unit	Value
mol H_2 : mol CO_2	-	4:1
Pressure	bar	16
Methanation efficiency at nominal conditions	%	80 [13]
Load of methanation	%	40 – 100 [13]
Load change rate of methanation	%/min	± 10 [13]
Nominal hydrogen molar flow	Nm^3/h	1,773

3. Management algorithms

3.1. Electrolysis system

The power generated by the wind farm is sent to an electrolysis system composed of four alkaline electrolyzers, each of which has a nominal power of 3 MW. During the simulations, due to the variability of the renewable source, the wind farm rarely produces its nominal power. For this reason, a management algorithm is developed to ensure that the four electrolyzers have similar operating conditions and, at the same time, a limited number of shutdowns.

Three operating states are defined: on, off and standby. The management algorithm ensures the electrolysis system to work always within its operative range (20-100% of its nominal power). Based on the input power, which is fairly divided among the operating machines, the electrolyzers state is established at each timestep according to the following parameters:

- the state of the electrolyzer at the previous timestep.
- the equivalent operating hours.
- the duration of the off and the standby states.

The aim of the management algorithm is to ensure that the four electrolyzers have averagely similar performances in terms of number of shutdowns, equivalent operating hours and hydrogen production.

3.2. Methanation unit and hydrogen storage system

The hydrogen flow rate feeding the methanation unit is often different than the nominal flow rate depending on the power supplied by the wind farm. In particular, if the inlet hydrogen flow rate from the electrolysis system

exceeds the value of methanation unit nominal feed flow rate, the methanation unit works at maximum load, and the storage tank provides the missing amount of hydrogen (Figure 3, timesteps "i+1"). On the other hand, if the produced hydrogen is lower than the minimum flow rate of methanation, the methanation unit is set to its minimum load, and the storage tank stores the surplus hydrogen (Figure 3, timesteps "i-1"). When the electrolysis system has greater load change rates than those tolerable by the methanation unit, the storage system acts as a "ramps mitigator" (Figure 3, timestep "i+2"). When the methanation unit operates within the load range, it does not only convert into methane the produced hydrogen flow from the electrolysis system, but the hydrogen feed flow rate could be increased or decreased (if SOC > SOC_{target} or SOC < SOC_{target} respectively). The SOC_{target} is set to 50%.

Then, when the methanation unit operates within the load range, the inlet flow rate is calculated as:

$$\dot{m}_{met}(t) = \dot{m}_{ele}(t) + \dot{m}_{SOC}(t) \quad (6)$$

Where $\dot{m}_{SOC}(t)$ depends on the SOC at the timestep "t-1".

The storage system, therefore, has the function of absorbing the off-range hydrogen production peaks, keeping the ramps within the constraints imposed to the load change rate of methanation, and methane production support.

Depending on the size of the methanation unit, during the simulations the electrolysis system could produce a certain amount hydrogen which cannot be converted into methane. However, the storage tank can store hydrogen until it reaches the full status, after which the surplus hydrogen can no longer be stored. In this case, we could have hydrogen losses.

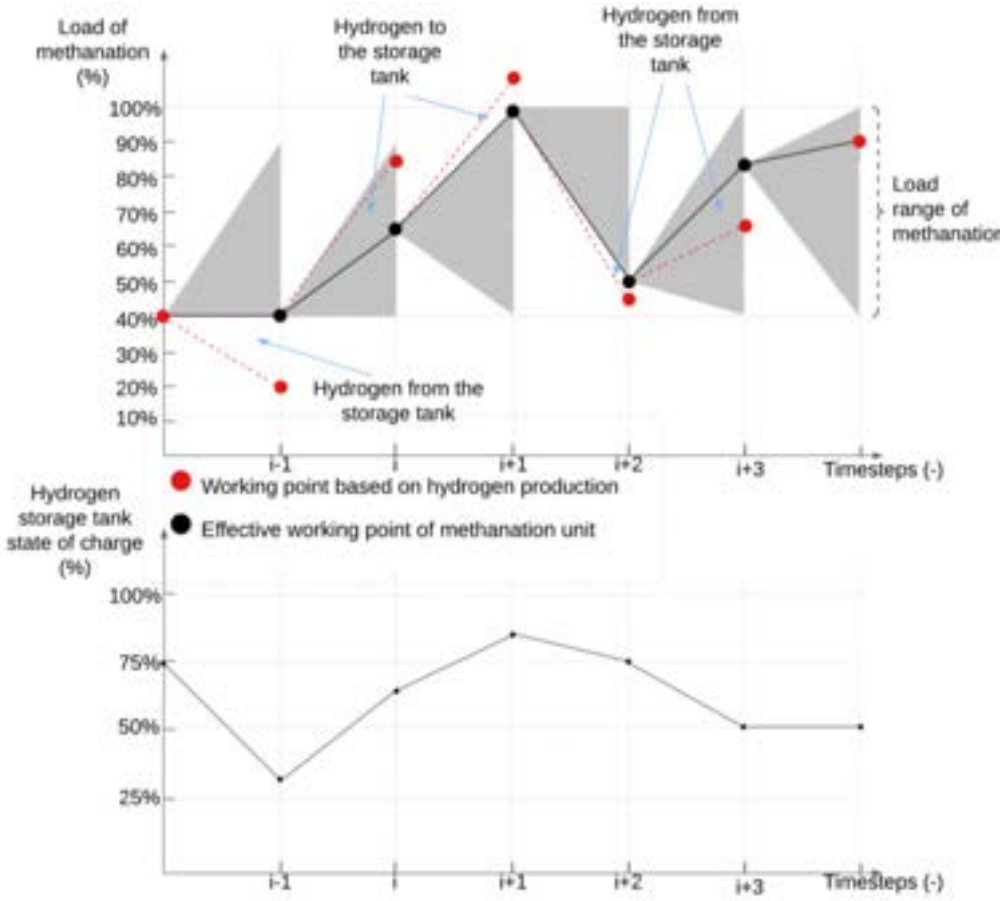

Figure 3. Example of operating of the methanation unit management strategy. The grey area represents the permissible operating points of the methanation unit at each timestep [15].

In order to avoid excessive shutdowns, a minimum SOC is imposed to allow the methanation unit to extract the required hydrogen from the storage tank to ensure operation at the minimum load. This constraint is needed only if the methanation unit was in the "off" state at the previous timestep. In fact, especially during less windy seasons, the hydrogen production is not enough to ensure the operation at minimum load. Therefore, allowing an uncontrolled adsorption of hydrogen from the tank would cause excessive on/off cycles of the methanation unit, since the low hydrogen production and the low SOC of the tank are not able to support continuous operation. Setting a minimum SOC (SOC_{min} = 50%) to be achieved to withdraw from the hydrogen storage tank

allows it to reach the conditions for supporting the methanation unit for a certain period, limiting its shutdowns and, consequently, its degradation.

4. Results and discussion

In a first phase, simulations of the single electrolyzer operation powered by a 3 MW wind farm were carried out on four typical days characterizing the seasonal trend of the wind: December 21, September 25, March 22, June 21 (solstices and equinoxes, or, when the wind data for those specific days seemed to have an untypical trend, days close to solstices and equinoxes). Figure 4 and Figure 5 show the performance of the cooling system and the separators level control system, respectively. During windy days (December 21 and September 25) the cooling system was in the “on” state for almost all the day. This happens because a greater windiness results in a most intensive use of the electrolyzer and then in a greater heat generation.

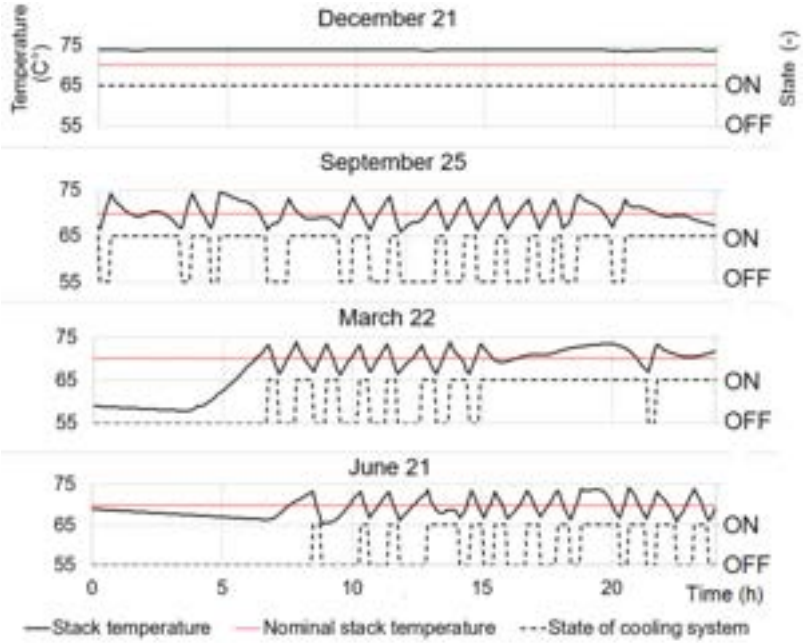

Figure 4. Performance of the cooling system during four seasonal characteristic days.

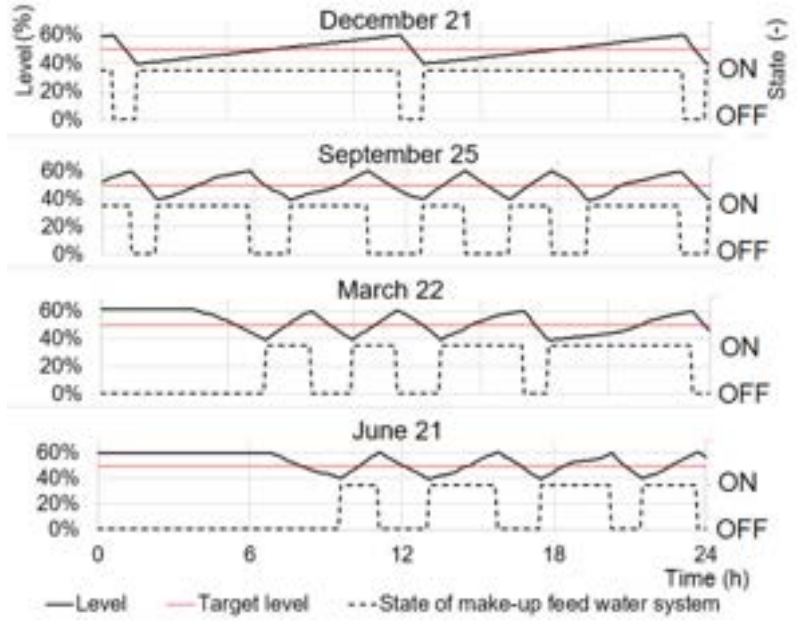

Figure 5. Performances of the separators level control system during four seasonal characteristic days.

Similarly, the separators level control system showed a longer working time of the make-up feed water system in winter and autumn (Figure 5). However, both the stack temperature and the separators level were always within the required range (70 ± 5°C and 50 ± 10% of the separator height, respectively), which is a sign that the applied control systems ensure the desired management of the alkaline electrolyzer.

Figure 6 shows the power distribution between the four electrolyzers of the electrolysis system during a daily simulation (September 25). The sizing of the electrolyzers was such as to ensure the utilization of all the renewable power and, on the other hand, the respect of the constraints imposed to the electrolyzers.

The four electrolyzers exhibited different performances in terms of hydrogen production, number of shutdowns and utilization factor (Table 5). However, the duration of a daily simulation is not enough to observe the efficacy of the proposed management algorithm.

Regarding to the whole power-to-gas system, Figure 7 shows the operation of the management algorithm for the methanation unit and hydrogen storage during a two-days simulation. Until 4 pm of the first day the the SOC of the hydrogen storage tank was under 50%; then, a certain share of the produced hydrogen incoming from the electrolysis system was used to fill the storage tank, while the remaining flow rate was sent to the methanation unit to be converted in methane.

Table 4. Performances of the alkaline electrolyzer for four seasonal typical days.

Day	Feed water system at the "on" state (%)	Stack average temperature (°C)	Average efficiency (%)	Cooling system at the "on" state (%)	Hydrogen production (Nm^3)	Utilization factor (%)
21-Dec	100	73.9	60	89	13,316	100
25-Sep	64	70.0	62	63	9,380	69
22-Mar	52	68.0	62	52	7,964	59
21-Jun	33	69.2	63	38	5,569	42

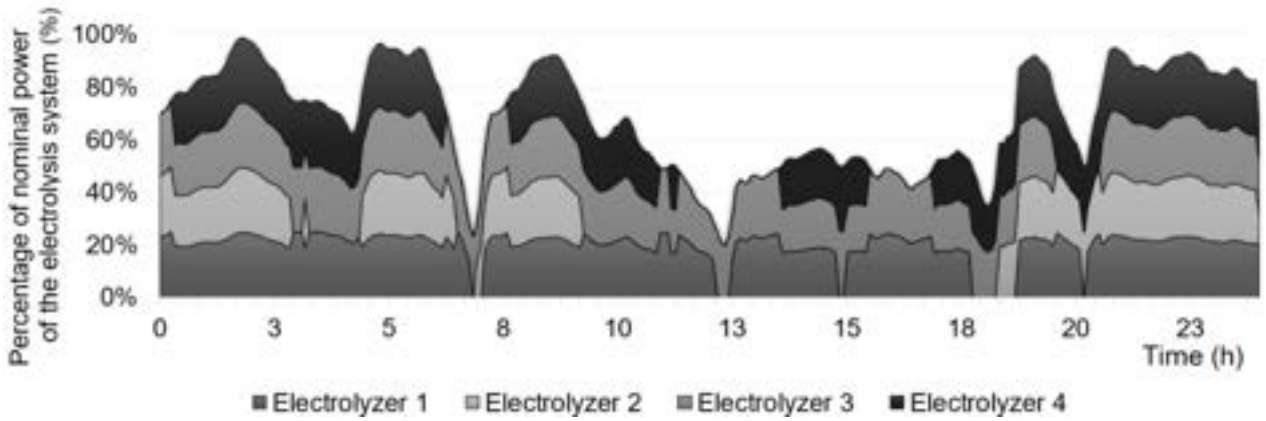

Figure 6. Power distribution between the four electrolyzers during a daily simulation.

From 4 pm of the first day the SOC of the hydrogen storage tank was over 50%; in particular, approximately from 8:30 pm to 10 pm of the first day and 2:30 am to 5 am of the second day the produced hydrogen and a certain share from the storage tank are sent to the methanation unit. During the remaining period, the produced hydrogen was out of the constraints of the methanation unit; in fact, the methanation unit was set to the maximum load or switched off, and the surplus hydrogen was stored up to the filling limit of the storage tank.

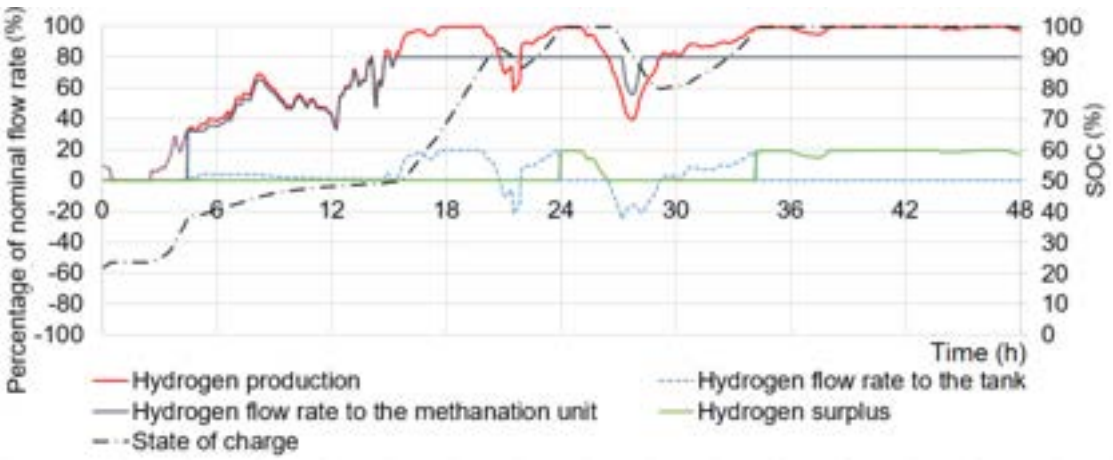

Figure 7. Performance of the management strategy for the methanation unit and hydrogen storage during a two-days simulation.

Table 5. Performances of the four electrolyzers in a daily simulation.

Electrolyzer	Efficiency (%)	Hydrogen production (Nm^3)	Utilization factor (%)	Number of shutdowns (-)	Oxygen production (Nm^3)	Water consumption (kg)	Average tack temperature (°C)	Maximum duration of the off period (h)
1	60	10,619	80	1	5,283	8,532	70.5	0.5
2	60	6,388	48	2	3,171	5,133	67.9	8.6
3	60	10,993	82	1	5,470	8,833	70.1	0.5
4	60	8,716	65	3	4,333	7,003	69.6	1.8
Electrolysis system	-	36,716	-	-	18,258	29,500	-	-

In Figure 8 the characteristic variable trends of the power-to-gas system during four seasonal characteristic days are shown. The hydrogen flow rates and the methane production were expressed as percentages of the nominal hydrogen production of the electrolysis system ($\dot{V}_{H_2,nom,ES} = 2{,}216\,Nm^3/h$) and the nominal production of the methanation unit ($\dot{V}_{CH_4,nom} = 439\,Nm^3/h$), respectively.
The methane production and the utilization factors for the methanation unit and the storage tank for four seasonal typical days are given in Table 6.

Table 6. Methane production and utilization factors for the methanation unit and the hydrogen storage system for four seasonal typical days.

Day	Methane production (Nm^3)	Storage utilization factor (%)	Methanation unit utilization factor (%)	Surplus hydrogen (Nm^3)	Number of shutdowns (-)	Average load (%)
21-Dec	10,538	80	100	10,539	0	100
25-Sep	8,831	45	84	0	0	84
22-mar	6,952	43	66	76	1	66
21-Jun	5,014	26	48	0	1	47

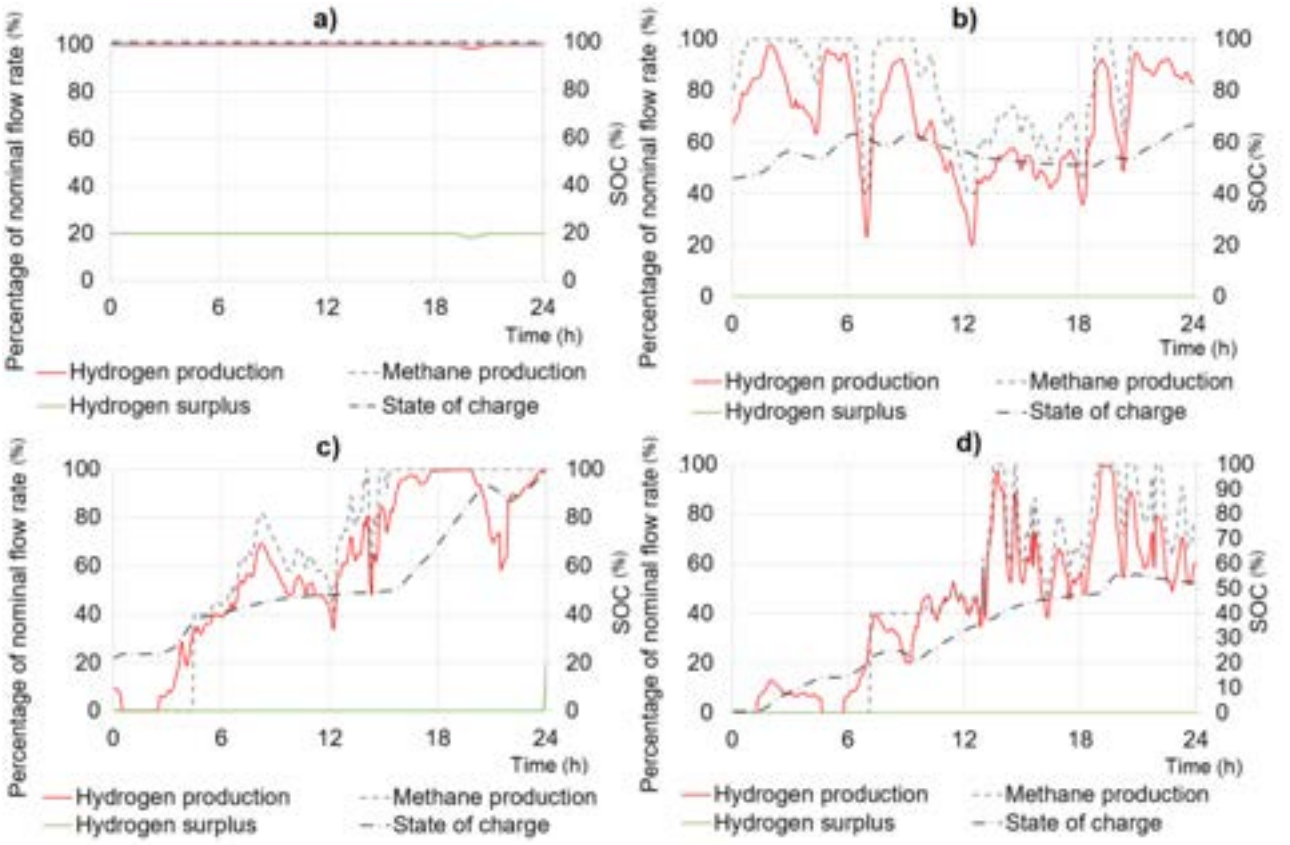

Figure 8. Performances of the power-to-gas system during four seasonal characteristic days: a) December 21; b) September 25; c) March 22; d) June 21.

Similarly to the electrolysis system, the results for the daily performances of the power-to-gas system showed a seasonal trend with a higher methane production in the windiest season, from which derives a most intensive use of the methanation unit.

During the summer, the SOC of the hydrogen storage tank was very low. This is due to the poorer wind conditions typical of this season, which makes the methanation unit work at relatively low load, even below the minimum limit value. In this condition, the methanation unit needs the support of the storage tank to be able to continue to work at his minimum load. When the storage tank is empty, it can no longer support the methanation unit. This could result in frequent shutdowns and a non-continuous operation ot the methanation unit.

On the other hand, on windy days the methanation unit worked at higher average loads, and, in some period, also exceeding the upper limit value. When the methanation unit is set to the nominal working point, and the storage tank SOC is 100%, a certain share of the produced hydrogen can't be converted in methane or stored. This condition mainly occurred during the winter, when the highest share of surplus hydrogen can be detected.

Table 7. Performances of the four electrolyzers at the end of a one-year simulation.

Electrolyzer	Efficiency (%)	Hydrogen production (Nm^3)	Utilization factor (%)	Number of shutdowns (-)	Water consumption (kg)	Stack temperature (°C)	Maximum duration of the off period (h)
1	61	1,597,493	33	537	1,283,546	66.5	62
2	61	1,598,248	33	548	1,284,152	66.3	62
3	61	1,595,090	33	541	1,281,615	66.2	64
4	61	1,597,295	33	546	1,283,387	66.6	56
Electrolysis system	-	6,388,126	-	-	5,132,700	-	-

In a second phase of this study an annual simulation on the power-to-gas system was carried on. Contrary to what results of the daily simulations suggested, the electrolyzers exhibited similar behavior and comparable performances in terms of all the observed variables on a yearly basis.In Table 8 and Table 9 the performance of the methanation unit and the hydrogen storage tank at the end of the one-year simulation are shown. Only the 2.4% of the produced hydrogen was in surplus. In addition, the management strategy effectively minimized the number of shutdowns.The use of an hydrogen storage, in fact, decreased the annual number of methanation-unit shutdowns from 1,006 within a year to only 301. Also, the imposed value of the SOC_{min} was essential to achieve this purpose. Indeed, without this constraint the annual number of methanation-unit shutdowns have been 5,950.

Nevertheless, the utilization factor of the subsystems at the end of the simulation was low, and this suggests that the sizing may not be optimal.

Table 8. Performances of the methanation unit at the end of a one-year simulation.

Methane production (Nm^3)	Surplus hydrogen (Nm^3)	Utilization factor (%)	Number of shutdowns (-)	Maximum duration of the OFF period (h)	Percentage of time in the ON state (%)	Percentage of time at the minimum load (%)	Percentage of time at the maximum load (%)
1,542,389	154,949	40	301	114	63	37	23

Overall, the management strategies performed both for the electrolysis system and for the methanation unit adequately managed to operate the power-to-fuel system minimizing the yearly surplus of hydrogen while ensuring a limited number of shutdowns that would otherwise increase the system degradation.

Table 9. Performances of the storage tank in a one-year simulation.

Percentage of time that SOC < SOC_{target} (%)	Utilization factor (%)
77	34

5. Summary and conclusions

In this study, a mathematical model of a power-to-methane system has been developed. An electrolysis system composed of four alkaline electrolyzers, each of which has a nominal power of 3 MW, is powered by a wind

farm with a nominal power of 12 MW. A hydrogen storage tank was designed for two-and-a-half hours of independent operation of the methanation unit, which nominal production of the methane is 438 Nm^3/h.

A management strategy of the electrolysis system, hydrogen storage and methanation unit to limit fluctuating and discontinuous operation of both the electrolysis system and the methanation unit was adopted. The management strategy of the electrolysis system was conceived to averagely ensure similar operating conditions of the four electrolyzers. The management strategy proposed for the methanation unit and the hydrogen storage tank effectively kept the operation of the methanation unit within the imposed constraints, and, at the same time, ensured a limited number of shutdowns while minimizing the surplus of hydrogen.

The simulated results over four seasonal typical days revealed a more intensive use of the electrolyzers, the methanation unit and the storage tank in windy seasons; however, the on/off control systems developed for the stack temperature and the separators level kept both the variables within the established range.

In addition only the 2.4% of the hydrogen producing during the year was in surplus and the number of shutdowns of the methanation unit turned out to be drastically reduced then without any storage tank (from 1,006 to 301). Nevertheless, the utilization factor of the subsystems at the end of the simulation was low (40% for the methanation unit and 34% for the storage system), and this suggests to explore different sizes of the subsystems. A sensitivity analysis should be carried out to determine the optimal value of the parameters (SOC_{min} and SOC_{target}) impacting the management strategy and the optimal size of the subsystems.

In addition, the influence of different management strategies on the operation of the power-to-methane system could be investigated in future studies.

Nomenclature

RES renewable energy sources

SOC state of charge

LHV Lower heating value, J/kg

Symbols

C thermal capacity, J/K

$\bar{c}_p$ average specific heat at constant pressure, J/(kgK)

E voltage, V

I current intensity, A

$\dot{m}$ mass flow rate, kg/s

n number, -

p pressure, bar

P power, W

Q heat flow, W/s

T temperature, °C

$\dot{V}$ volumetric flow rate, m3/s

Greek symbol

η efficiency, %

Subscripts

act activation

amb ambient environment

cap capacity

cooled at the heat exchanger outlet

cons consumed at the stack

ele electrolyzer

ES electrolysis system

Far faraday

gen generated inside of the stack

in at the methanation unit inlet

loss losses

nom nominal value

ohm ohmic

rev reversible

sys system

stack within the stack

stackin at the stack inlet

target target value

tn thermoneutral

wat water

References

Journals

[1] Suleman F, Dincer I, Agelin-Chaab M. Environmental impact assessment and comparison of some hydrogen production options. Int J Hydrogen Energy 2015;40:6976–87. https://doi.org/10.1016/j.ijhydene.2015.03.123.

[2] Schiebahn S, Grube T, Robinius M, Tietze V, Kumar B, Stolten D. Power to gas: Technological overview, systems analysis and economic assessment for a case study in Germany. Int J Hydrogen Energy 2015;40:4285–94. https://doi.org/10.1016/j.ijhydene.2015.01.123.

[3] Gahleitner G. Hydrogen from renewable electricity: An international review of power-to-gas pilot plants for stationary applications. Int J Hydrogen Energy 2013;38:2039–61. https://doi.org/10.1016/j.ijhydene.2012.12.010.

[4] Lewandowska-Bernat A, Desideri U. Opportunities of Power-to-Gas technology. Energy Procedia, vol. 105, Elsevier Ltd; 2017, p. 4569–74. https://doi.org/10.1016/j.egypro.2017.03.982.

[6] Walker SB, Mukherjee U, Fowler M, Elkamel A. Benchmarking and selection of Power-to-Gas utilizing electrolytic hydrogen as an energy storage alternative. Int J Hydrogen Energy 2016;41:7717–31. https://doi.org/10.1016/j.ijhydene.2015.09.008.

[7] Götz M, Lefebvre J, Mörs F, McDaniel Koch A, Graf F, Bajohr S, et al. Renewable Power-to-Gas: A technological and economic review. Renew Energy 2016;85:1371–90. https://doi.org/10.1016/j.renene.2015.07.066.

[10] Liponi A, Frate GF, Baccioli A, Ferrari L, Desideri U. Impact of wind speed distribution and management strategy on hydrogen production from wind energy. Energy 2022;256. https://doi.org/10.1016/j.energy.2022.124636.

[11] Liponi A, Baccioli A, Ferrari L. Feasibility analysis of green hydrogen production from wind. Int J Hydrogen Energy 2023.

[12] Baccioli A, Bargiacchi E, Barsali S, Ciambellotti A, Fioriti D, Giglioli R, et al. Cost effective power-to-X plant using carbon dioxide from a geothermal plant to increase renewable energy penetration. Energy Convers Manag 2020;226. https://doi.org/10.1016/j.enconman.2020.113494.

[13] Gorre J, Ortloff F, van Leeuwen C. Production costs for synthetic methane in 2030 and 2050 of an optimized Power-to-Gas plant with intermediate hydrogen storage. Appl Energy 2019;253. https://doi.org/10.1016/j.apenergy.2019.113594.

[14] Gorre J, Ruoss F, Karjunen H, Schaffert J, Tynjälä T. Cost benefits of optimizing hydrogen storage and methanation capacities for Power-to-Gas plants in dynamic operation. Appl Energy 2020;257. https://doi.org/10.1016/j.apenergy.2019.113967.

[15] Frate GF, Cherubini P, Tacconelli C, Micangeli A, Ferrari L, Desideri U. Ramp rate abatement for wind power plants: A techno-economic analysis. Appl Energy 2019;254. https://doi.org/10.1016/j.apenergy.2019.113600.

[16] Ulleberg I. Modeling of advanced alkaline electrolyzers: a system simulation approach. Int J Hydrogen Energy, vol. 28, 2003, p. 21-3. https://doi.org/10.1016/S0360-3199(02)00033-2.

[17] Amores E, Rodríguez J, Carreras C. Influence of operation parameters in the modeling of alkaline water electrolyzers for hydrogen production. Int J Hydrogen Energy, vol. 39, Elsevier Ltd; 2014, p. 13063–78. https://doi.org/10.1016/j.ijhydene.2014.07.001.

[18] Sánchez M, Amores E, Abad D, Clemente-Jul C, Rodríguez L. Development and Experimental Validation of a Model to Simulate an Alkaline Electrolysis System for Production of Hydrogen Powered by Renewable Energy Sources. Smart Innovation, Systems and Technologies, vol. 150, Springer Science and Business Media Deutschland GmbH; 2019, p. 358–68. https://doi.org/10.1007/978-3-030-22964-1_40.

[19] Sánchez M, Amores E, Rodríguez L, Clemente-Jul C. Semi-empirical model and experimental validation for the performance evaluation of a 15 kW alkaline water electrolyzer. Int J Hydrogen Energy 2018;43:20332–45. https://doi.org/10.1016/j.ijhydene.2018.09.029.

[20] Diéguez PM, Ursúa A, Sanchis P, Sopena C, Guelbenzu E, Gandía LM. Thermal performance of a commercial alkaline water electrolyzer: Experimental study and mathematical modeling. Int J Hydrogen Energy 2008;33:7338–54. https://doi.org/10.1016/j.ijhydene.2008.09.051.

[21] Sakas G, Ibáñez-Rioja A, Ruuskanen V, Kosonen A, Ahola J, Bergmann O. Dynamic energy and mass balance model for an industrial alkaline water electrolyzer plant process. Int J Hydrogen Energy 2022;47:4328–45. https://doi.org/10.1016/j.ijhydene.2021.11.126.

Conference papers

[5] Belderbos A, Delarue E, D'haeseleer W. Possible role of power-to-gas in future energy systems. International Conference on the European Energy Market, EEM, vol. 2015- August, IEEE Computer Society; 2015. https://doi.org/10.1109/EEM.2015.7216744.

[8] Liponi A, Baccioli A, Ferrari L, Desideri U. Techno-economic analysis of hydrogen production from PV plants. E3S Web of Conferences, vol. 334, EDP Sciences; 2022. https://doi.org/10.1051/e3sconf/202233401001.

[9] Liponi A, Frate GF, Baccioli A, Ferrari L, Desideri U. Green hydrogen from wind energy: mitigation of operating point fluctuations. In proceedings of the 34th International Conference On Efficiency, Cost, Optimization, Simulation and Environmental Impact of Energy Systems, ECOS 2021, June 27-July 2, 2021, Taormina, Italy.

PROCEEDINGS OF ECOS 2023 - THE 36TH INTERNATIONAL CONFERENCE ON
EFFICIENCY, **C**OST, **O**PTIMIZATION, **S**IMULATION AND ENVIRONMENTAL IMPACT OF ENERGY SYSTEMS
25-30 JUNE 2023, LAS PALMAS DE GRAN CANARIA, SPAIN

A numerical analysis of transport phenomena in a banded solid oxide fuel cell stack

Karol Śreniawski[a], Marcin Możdzierz[b], Grzegorz Brus[c], Janusz S. Szmyd[d]

[a] AGH University of Science and Technology, Krakow, Poland, sreniawski@agh.edu.pl
[b] AGH University of Science and Technology, Krakow, Poland, marcinm@agh.edu.pl
[c] AGH University of Science and Technology, Krakow, Poland, brus@agh.edu.pl
[d] AGH University of Science and Technology, Krakow, Poland, janusz.szmyd@agh.edu.pl

Abstract:
Solid oxide fuel cells (SOFCs) are being recognized as one of the promising energy conversion technologies. To study SOFCs systems operation, numerical modeling is a helpful tool, which allows one to understand and improve their operation. Moreover, a crucial feature of numerical modeling is the opportunity to reduce economical and time cost in prototyping methodology. In this work, a banded SOFC stack, which includes six 12 mm x 12 mm cells, connected in series, applied on a single electrolyte support, is studied numerically, using the finite-volume method. A mathematical model, which includes the heat, mass and electron/ion transport phenomena, was provided. To validate the model, a comparison of electrical characteristics obtained from the numerical and experimental study was performed. To inspect the possibilities of applying geometrical improvements to the existing prototype design, different versions of fuel and air channels were numerically modeled and inspected, including the option of extending the system into two or more stacks, connected by a shared fuel channel of two adjacent stacks. Moreover, the influence of the electrolyte thickness was tested. The proposed design modifications enhance the system by reducing the volume of the stack and improving the electric performance compared to the existing prototype design. The numerical model can be used to test further design modifications to the stack, including performance analysis by changing the operating parameters of the system and applying new materials.

Keywords:
Banded SOFC stack, Hydrogen Use in Energy Systems, Numerical Analysis, Solid Oxide Fuel Cell, Transport Phenomena.

1. Introduction

The use of hydrogen in energy systems is one of the promising and ecologically friendly ways to develop the energy and transport industry. To efficiently convert the chemical energy of hydrogen directly into electrical energy, fuel cells are often utilized. Solid Oxide Fuel Cells (SOFCs) are one of the most efficient fuel cells, with a low manufacturing price compared to other types of fuel cells and a wide range of systems power scale, recognized as the most advanced power generation systems, characterized by the highest thermal efficiency [1]. The prototyping of SOFCs is a highly complex process that involves many costs and time consumption. To reduce these factors, numerical modeling is often used.

Numerical modeling of Solid Oxide Fuel Cells is being recognized as a highly complex but helpful tool in order to better understand the operation and phenomena occurring inside the stack. Many different tools are used for the numerical modeling of SOFCs, while ANSYS Fluent forms one of the most popular and widely used [2]. Three-dimensional numerical modeling of SOFCs is often applied to simulate single-cell operation [3–6], as well as entire stacks [7–9]. 3D SOFC stack simulation was performed successfully by Wei et al. [7], using numerical modeling to study a novel stack arrangement and verify the new shape of the flow channel. The model allowed to observe the thermal stresses in the stack, as well as conduct a transport phenomena verification. To verify the results of the study, a comparison with the results found in the literature was presented. Wei et al. [7] has presented the geometry of the anode-supported planar SOFC stack, which consists of square cells connected electronically using metal interconnectors with ribs, which contribute fuel and air channels. The analyzed geometry of cells is conventional in SOFC systems, also in commercial usage. A proposed multistacking method introduces the original shape of interconnectors. Another interesting approach to the numerical modeling of the SOFC stack was demonstrated by Dong et al. [8]. An anode-supported, five planar, rounded cells stack was modeled. The cells were connected into a stack using nickel and crofer meshes, closed between the outer plates and separators, sealed with mica and the separators. Again, the alignment of cells is one on another. Dong et al. [8] presented the study of the flow uniformity and transport processes inside the stack. The research was also focused on the temperature distribution and electron transport. The

results were compared to the experimental study to demonstrate the correctness of the numerical model. The influence of system size and stack design in terms of flow arrangement was also examined by Pirasaci [9]. Research included the verification of the model by comparing with the results found in the literature. The commercial CFD package, ANSYS Fluent was used in order to simulate the behavior of different design options and study the influence of implemented modifications on the performance of the stack. The analyzed stack geometry is conventional and widely used in commercial systems with rectangular cells closed between metal interconnectors.

Solid Oxide Fuel Cells could also operate using alternative fuels, such as hydrocarbons, ammonia, and carbon monoxide. Due to the high temperature operation, the resistance to impurities in the fuel is elevated [13]. To better understand the processes during operation with alternative fuels, the numerical simulation of single cell SOFCs is also widely used [5, 6].

As shown in the literature review, most research focus on conventional stack designs with one on another single cells arrangement, connected using metal interconnectors in different shapes. When comparing our stack design with common SOFC stacks, the originality is clearly visible. Separate electrodes banded on a single electrolyte contribute the novel and original stack arrangement in SOFC systems subject. Moreover, the presented stack banded on the single electrolyte could significantly increase the output voltage, even in small-size systems. The studied design, introduced in [10], also consists of unusual flow channels and electrical connections. Because this paper discusses the impact of channel geometry on the transport phenomena within the recently proposed banded solid oxide fuel cell stack, the electrical connections were simplified. This study focuses on possible improvements in geometry and stack arrangement options. The developed computational fluid dynamic simulation considers momentum, heat, mass, electron and ion transport phenomena.

2. Geometry description

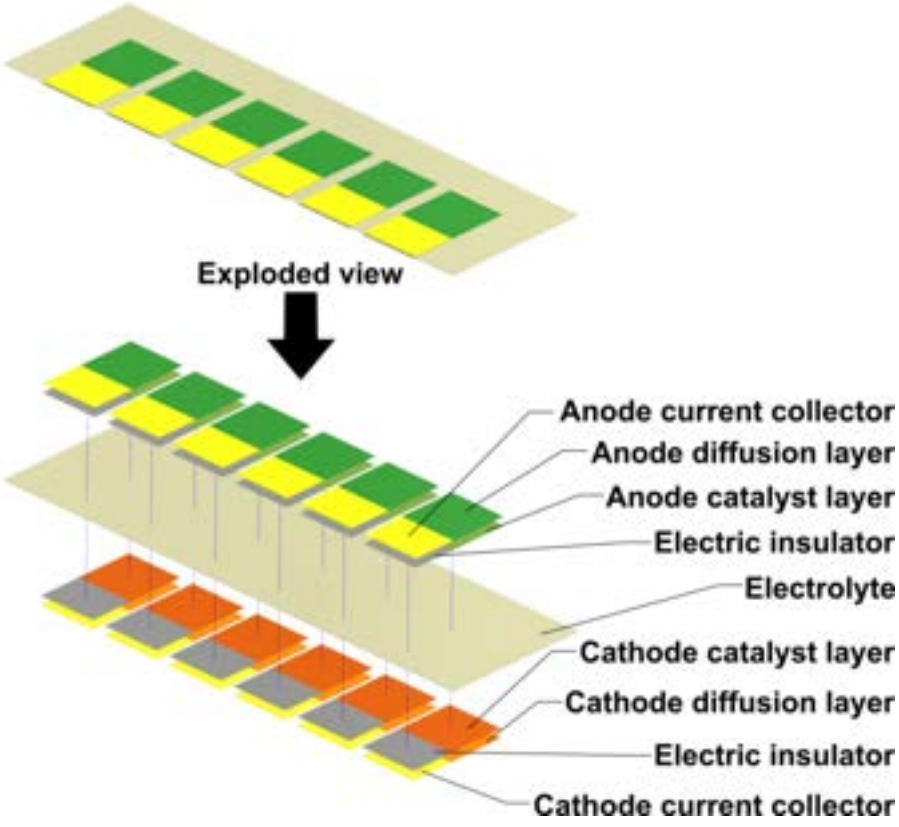

Figure 1: Investigated SOFC stack design with exploded view.

The studied SOFC stack is a novel, patented design [10], which prototype was successfully built and tested [11]. For further development of the stack, a numerical modeling method is used. To prepare a 3-dimensional (3D) numerical model, a computational domain has to be created. Using Autodesk Inventor software, a stack CAD model was created. The stack model, shown in Fig. 1, is composed of six pairs of 12 mm x 12 mm x 0.1 mm electrodes, banded on a single 105 mm x 30 mm x 0.3 mm electrolyte support. Electrolyte support provides high strength and durability of the stack, while maintaining a low production cost [12]. In this paper, the electrolyte of 0.1 mm of thickness is also investigated. The electrodes are divided into two bodies, contributing

catalyst and diffusion layers, as needed for numerical simulation. To simplify the geometry, current collectors are modeled as non-porous solid bodies with side contact to electrodes. Between the electrolyte and the current collectors, electric insulators were applied. Fig. 1 presents the stack assembly, and also to better visualize the model, an exploded view with descriptions was provided.

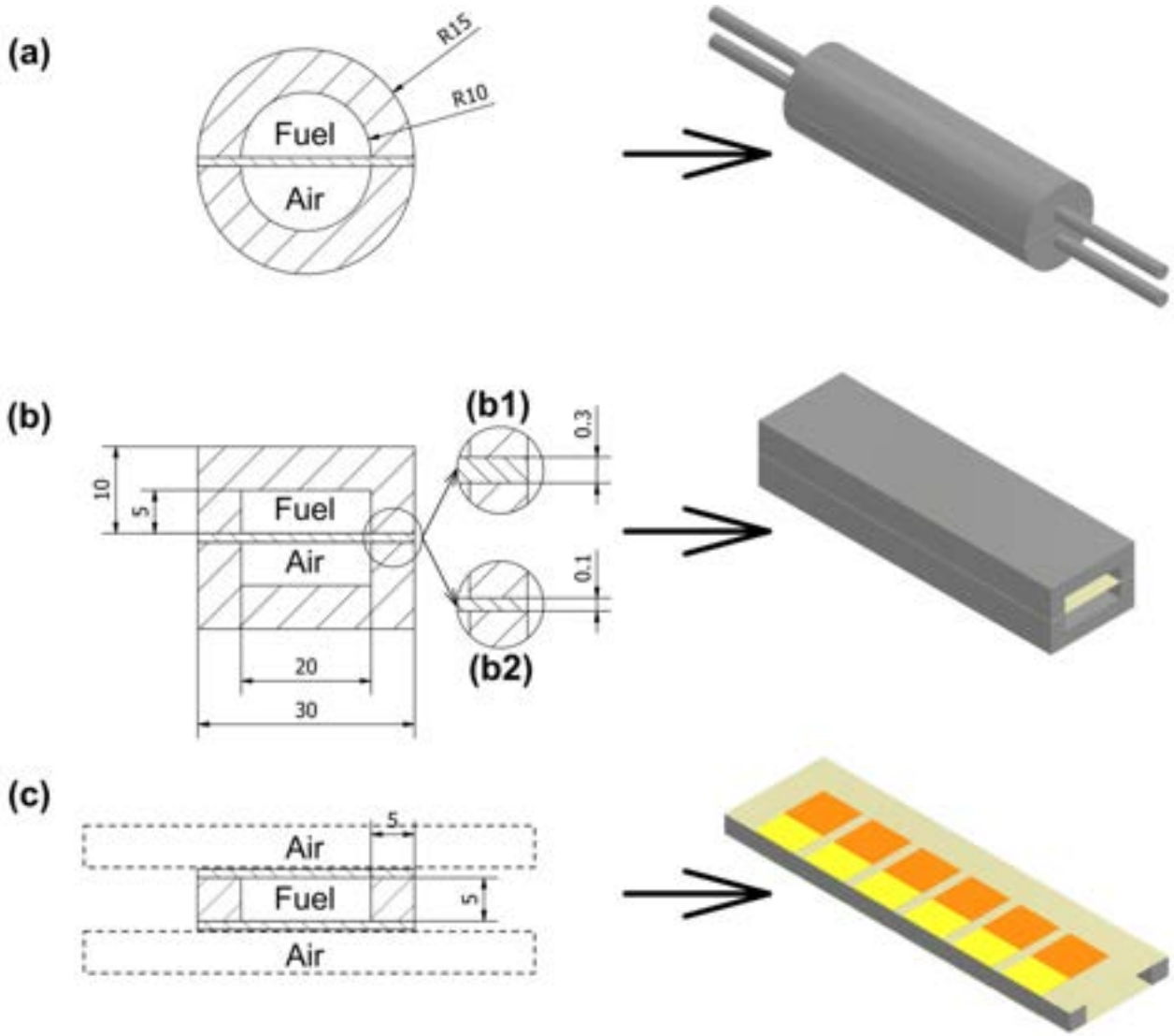

Figure 2: Stack configuration options with schematic cross-sections. Stack supported on 0.3 mm of electrolyte thickness, closed in half-tubular covers, marked (a). The stack with rectangular covers marked (b) comes in two versions: 0.3 mm of electrolyte thickness, marked as (b1), and 0.1 mm of electrolyte thickness, marked (b2). Multi-stack composition with 0.1 mm of electrolyte thickness, marked as (c).

The initial prototype design of the stack includes two ceramic covers, which contribute gases supply elements. During the investigation, a different covers shape and stack arrangement was provided, as shown in Fig. 2, which is divided into three sections. In the (a) section of Fig. 2, the electrolyte support of 0.3 mm of thickness, with deposited cells and the applied current collectors, is enclosed by two half-tubular covers, which state the fuel and air channels, as in the initial design. The (b) section of Fig. 2 presents a rectangular shape of the covers, which was modeled to reduce the stack volume and simultaneously increase the volumetric power density. Moreover, the (b) section was divided into two options. The section marked (b1) is the (b) design supported on 0.3 mm electrolyte, while (b2) is the (b) design supported on 0.1 mm electrolyte. In Fig. 2, the (c) section provides a new idea of extending the system into two or more stacks. By combining two stacks, of which anodes are targeted face to face, a fuel channel is created, while cathodes facing the outer sides could be supplied in the air without an air channel, using a fan. This case consists of two stacks supported on 0.1 mm of electrolyte thickness. This design allows to reduce the volume of the stack even more, and theoretically double the power. To better illustrate each design, schematic cross sections and 3D models were included, respectively. The cross sections demonstrate the arrangement of the stack(s) and covers that

determine the gases paths. This paper also includes a numerical verification of the influence of electrolyte thickness on stack performance, by comparing designs (b1) and (b2).

3. Mathematical model

The mathematical model contains a description of transport phenomena, using a set of partial differential equations. To simplify the model and focus on the demanded areas of physics, a few assumptions were contributed. The model assumes steady state behavior of the operation, the incompressible characteristics of fluids. The energy dissipation and gravitation were ignored. Flow in fluid and porous areas is described as laminar, and all fluids are treated as Newtonian ones.

Steady-state mass conservation equation is used to describe the mass transport in fluid and porous areas, written as follows [8]:

$$\vec{\nabla} \cdot \left(\rho\varepsilon\vec{v}\right) = S_{\mathrm{p}}, \tag{1}$$

where S_{p} (kg m^{-3} s^{-1}) represents the source term of mass, as a result of reactants consumed and produced in electrodes through the electrochemical reactions in SOFC. In areas other than porous anodes and cathodes $S_{\mathrm{p}} = 0$ and $\varepsilon = 1$ (-), which is the porosity rate. In the fluid areas, an equation that describes the conservation of momentum is solved as follows [8]:

$$\vec{\nabla} \cdot \left(\rho\vec{v}\vec{v}\right) = -\vec{\nabla}p + \vec{\nabla}\bar{\bar{\tau}} + \vec{S}, \tag{2}$$

where $\vec{S}$ (kg m^{-2} s^{-2}) is the source term, that describes the viscous and inertial pressure drop.

In porous and fluid areas, the species conservation equation describes the components of the gas mixture, given as follows [8]:

$$\vec{\nabla} \cdot \left(\rho\varepsilon\vec{v}Y_i\right) = -\vec{\nabla} \cdot \vec{J}_{i,\mathrm{eff}} + S_i, \tag{3}$$

where S_i (kg m^{-3} s^{-1}) represents the source and sink terms of species rates, written as follows [8]:

$$S_{\mathrm{O_2}} = -\frac{j}{4F}M_{\mathrm{O_2}}, \tag{4a}$$

$$S_{\mathrm{H_2}} = -\frac{j}{2F}M_{\mathrm{H_2}}, \tag{4b}$$

$$S_{\mathrm{H_2O}} = \frac{j}{2F}M_{\mathrm{H_2O}}. \tag{4c}$$

The electrons and ions transport potential equations, are given as [3]:

$$\vec{\nabla} \cdot \left(\sigma_{\mathrm{el}}\vec{\nabla}\phi_{\mathrm{el}}\right) + j = 0, \tag{5a}$$

$$\vec{\nabla} \cdot \left(\sigma_{\mathrm{ion}}\vec{\nabla}\phi_{\mathrm{ion}}\right) + j = 0, \tag{5b}$$

where j (A m^{-3}), the volumetric transfer current density, for the electrons transport on the anode side $j = -j_{\mathrm{an}}$ and on the cathode side $j = +j_{\mathrm{cat}}$, and for the ions transport $j = +j_{\mathrm{an}}$ and $j = -j_{\mathrm{cat}}$. The volumetric transfer current density j is described by the Butler-Volmer equation, written for the anode and the cathode side as follows [3]:

$$j_{\mathrm{an}} = \left(\zeta_{\mathrm{TPB}}i_{\mathrm{an}}^{\mathrm{eq}}\right)\left(\frac{X_{\mathrm{H_2}}}{X_{\mathrm{H_2,ref}}}\right)^{\gamma_{\mathrm{an}}}\left(e^{\alpha_{\mathrm{an}}^{\mathrm{a}}F\eta_{\mathrm{an}}/(RT)} - e^{-\alpha_{\mathrm{an}}^{\mathrm{c}}F\eta_{\mathrm{an}}/(RT)}\right), \tag{6a}$$

$$j_{\mathrm{cat}} = \left(\zeta_{\mathrm{DPB}}i_{\mathrm{cat}}^{\mathrm{eq}}\right)\left(\frac{X_{\mathrm{O_2}}}{X_{\mathrm{O_2,ref}}}\right)^{\gamma_{\mathrm{cat}}}\left(e^{-\alpha_{\mathrm{cat}}^{\mathrm{c}}F\eta_{\mathrm{cat}}/(RT)} - e^{\alpha_{\mathrm{cat}}^{\mathrm{a}}F\eta_{\mathrm{cat}}/(RT)}\right). \tag{6b}$$

The local surface overpotential η (V), for the anode and cathode side is given in the following form [3]:

$$\eta_{\mathrm{an}} = \phi_{\mathrm{el}} - \phi_{\mathrm{ion}}, \tag{7a}$$

$$\eta_{\mathrm{cat}} = \phi_{\mathrm{el}} - \phi_{\mathrm{ion}} - \phi_{\mathrm{OCV}}, \tag{7b}$$

where ϕ_{OCV} (V) represents the open-circuit voltage.

The heat transport in solid zones is described as the steady-state energy equation, written in the following form [8]:

$$\vec{\nabla} \cdot \left(\varepsilon\vec{v}\rho h\right) = \vec{\nabla} \cdot \left(\left(\varepsilon k_{\mathrm{eff}} + (1-\varepsilon)\,k_{\mathrm{s}}\right)\vec{\nabla}T - \sum_i h_i\vec{J}_i\right) + S_{\mathrm{h}}, \tag{8}$$

where S_h ($W\,m^{-3}$) is the total heat source. The heat source in the catalyst layers of electrodes and the electrolyte and is calculated as follows [8]:

$$S_h = -\frac{jh_{react}}{2F} + j\eta + \frac{i^2}{\sigma}. \tag{9}$$

In fluid zones, the steady-state energy equation is given in the following form [8]:

$$\vec{\nabla} \cdot \left(\vec{v}\rho h\right) = \vec{\nabla} \cdot \left(k_{eff}\vec{\nabla}T - \sum_i h_i \vec{J}_i\right). \tag{10}$$

4. Numerical analysis

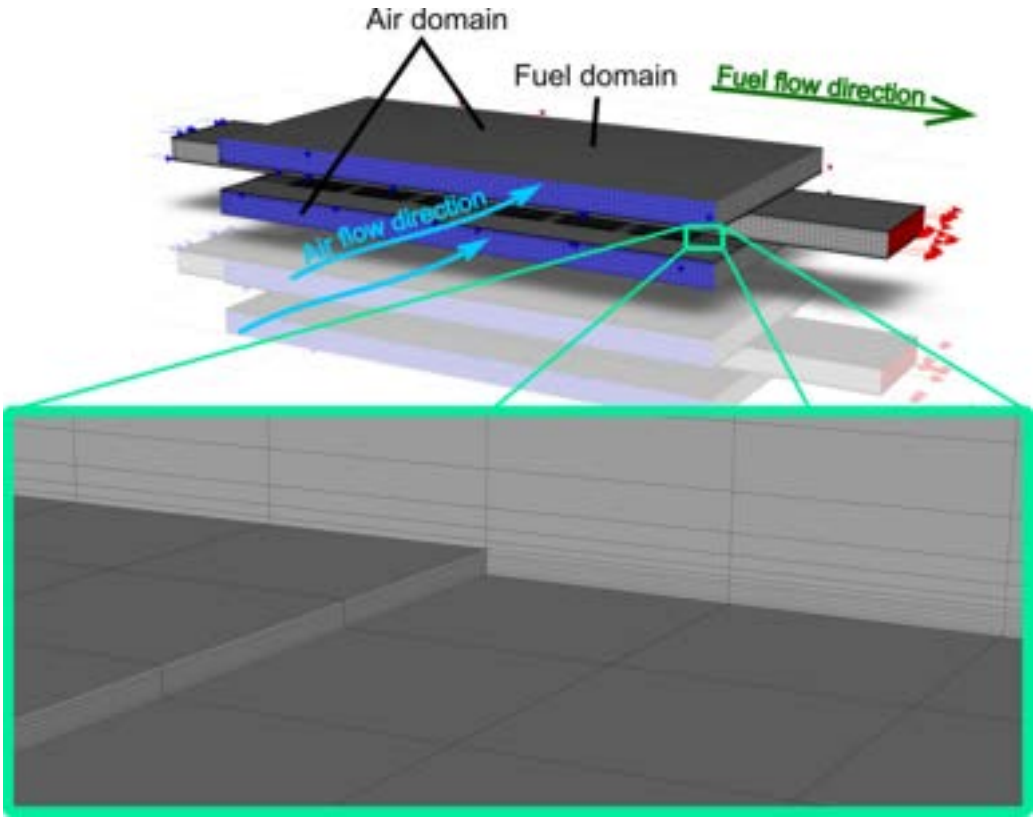

Figure 3: Visualization of computational mesh of multi-stack design with detailed view.

After the described mathematical model was determined, a series of 3D numerical simulations was performed using the finite-volume method. For the finite-volume method, a computational mesh must be made. To build the mesh of each design described in Section 2., the 3D models were modified to include bodies that represent the paths of the gases. To reduce the number of mesh elements, ceramic covers were removed from the geometries and replaced by the boundary conditions, which represent the behavior of the furnace maintaining constant temperature. Each mesh was created as a compromise between quality and the number of elements, which determined resolution, accuracy, and computational time. The mesh sensitivity study was performed for four different mesh sizes for the initial design marked as (a) in Fig. 2, starting from the number of elements of $1.6 \cdot 10^5$, through $6 \cdot 10^5$, $1.1 \cdot 10^6$ on $4 \cdot 10^6$ of the mesh elements ending. The measured time per iteration was: 1.05 s, 2.14 s; 3.68 s; 17.45 s, respectively. Since the mass conservation for each case remained values under 10^{-8} $kg\,s^{-1}$, and the electric characteristics did not change, the chosen mesh was the $1.1 \cdot 10^6$ of the elements one. As a result of the large difference in scale between the thin layers of the stack area and the gases domains, a smooth transition of element sizing was applied. Each mesh was built using hexahedral elements. The main mesh element was determined as a 1 mm x 1 mm x 1 mm cube. In the stack area, elements are flattened up to 0.01 mm to retain a minimum of three layers per body in the thickness direction, to then inflate smoothly in the gases areas to main dimensions. In Fig. 3, a computational mesh of multi-stack design, shown in Fig. 2(c), is illustrated, including the detailed view in the zoom box, which shows the inflation of elements thickness in the area of the solid and fluid zones contact. Other designs computational meshes are consistent with the illustrated one.

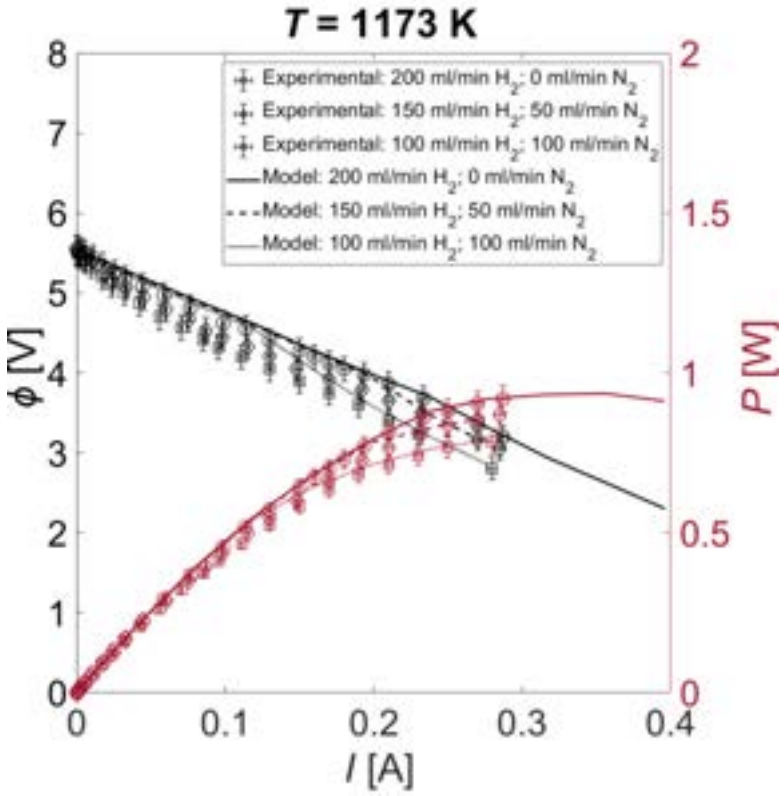

Figure 4: Comparison of current-voltage and current-power characteristics of initial design ((a) in Fig. 2), obtained from numerical analysis and experimental study [11]. Flow rates fitted to tested ones.

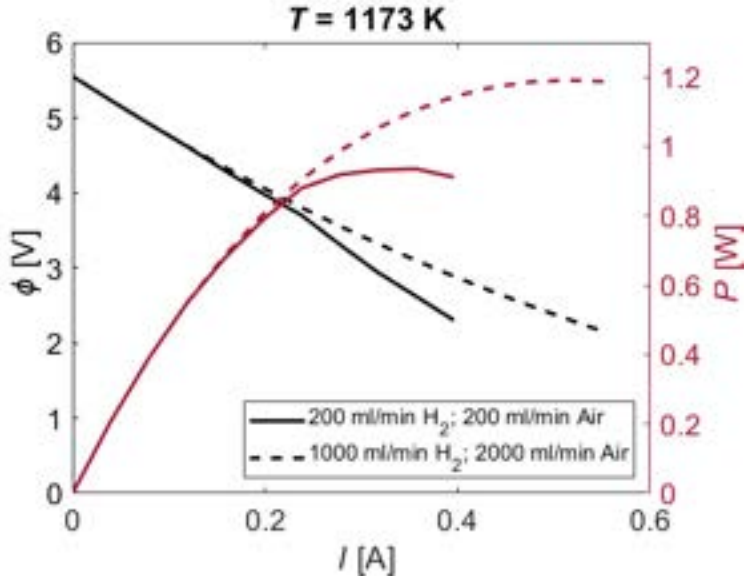

Figure 5: Comparison of current-voltage and current-power characteristics of initial design ((a) in Fig. 2) for different flow rates.

To make an accurate comparison of each investigated design, boundary conditions were retained in all simulations, as well as electrochemical, material, and operating parameters determined for the initial design. To simulate the behavior of the furnace interior and substitute the ceramic covers, constant temperature and zero species flux boundary conditions at the outer walls of the fluid domains were established. On the outer walls of the solids, no current leakage was allowed, except current collectors taps. At the current collectors tap walls, on the anodes side, a zero potential is forced, on the cathode side, a current flux was established. The constant current load simulates the in-series connection of the stack to build up the potential value. Constant velocity, temperature, and gas composition boundary conditions were formed at the inlets of flow channels. A

Table 1: Operating parameters applied for all stack configuration options comparison.

Parameter	Value (Unit)
Inlets/furnace temperature	1173 (K)
Air flow rate	2 (L/min)
Hydrogen flow rate	1 (L/min)

constant atmospheric pressure and furnace temperature were applied to the channels outlets.

The numerical modeling was conducted using the SIMPLE scheme with the Richie-Chow distance-based flux type. Different spatial discretization methods were used to compute each parameter. Green-Gauss Node-Based method was used to calculate gradient, pressure was computed using Second Order spatial discretization method. Density, momentum, energy, species, and potential equations were computed using First-Order Upwind spatial discretization.

In order to conduct a comparison of each design shown in Fig. 2, a series of simulations were performed. To obtain current-voltage and current-power characteristics, an electric load in the form of a constant current was applied to the cathodes current collectors in the value from zero until the power drop. To validate the model, a comparison of electrical characteristics, obtained from the numerical simulation and the experimental study [11], was presented in Fig. 4. The operating parameters of the simulations were fitted to the parameters used during the experimental study. The experimental points with error bars included are presented in the form of circles, triangles and deltiods. The numerical analysis results are presented as solid, dashed, and dotted lines. The numerical model introduced in this paper allows to simulate highly predictable characteristics, which is confirmed in the comparison contained in Fig. 4. During the analysis, the lack of fuel and air was clearly visible, so the decision to increase the flow rates was made. The hydrogen flow rate was increased ten times and the air flow rate twenty times. The comparison of electrical characteristics obtained during numerical analysis, for flow rates tested during the experimental study and increased as mentioned above, is presented in Fig. 5. The solid lines represent the characteristics for flow rates as experimentally tested, and the dashed lines represent the characteristics for increased flow rates. It clearly revealed the gain in power in the value of 27.4 percent, from $P = 0.935$ W at a current of $I = 0.356$ A up to $P = 1.191$ W at $I = 0.515$ A. In order to conduct a reasonable comparison of each presented in Fig. 2 design, including the multistack design that consists of twelve cells, the increased flow rates remained constant for the whole further study. The operating parameters for the study of different designs, applied for all cases, are presented in Table 1.

To clarify the comparison of the performance of each design, four different graphs were shown in Fig. 6. For reference, the marks (a), (b1), (b2), and (c) are consistent with the geometries shown in Fig. 2. The first graph of Fig. 6 illustrates the current-voltage and current-power characteristics of case (a) and (b1), so the comparison of half-tubular and rectangular covers, with the electrolyte of 0.3 mm of thickness. The second graph presents the comparison of the characteristics of the initial case (a) and the design with rectangular shape of covers with reduced electrolyte thickness up to 0.1 mm (b2). The third plot presents a comparison of the performance of the initial case (a) and the multi-stack design (b), which consists of 12 cells. To better illustrate the performance comparison of four cases (a), (b1), (b2) and (c), a bar plot of the peak power density, located at the bottom of Fig. 6, was presented. Between the (a) and (b1) cases, the difference is almost unrecognizable, flattening the channels by changing the shape to rectangular resulted in the power drop from 1.19 W (a) to 1.16 W (b1). Reducing the electrolyte thickness resulted in an increase in the performance, as expected, due to an enhancement of electrolyte ionic conductivity. The power of case (b2) reaches 1.46 W. Multistack design (c) is clearly the most powerful arrangement option, power reaches the value of 2.87 W, but the power density is slightly lower than the case (b2). Furthermore, in the (c) case, a concentration loss at the characteristics is clearly visible, which could mean insufficient hydrogen supply, due to doubling of the number of cells, which could be a reason for the drop in power density. Moreover, at this it is worth to underline that the multi-stack design (c) volume is still reduced compared to the initial design (a), so the volumetric power density, which considers whole system volume, would increase.

Comparison of the temperature distribution, shown in Fig. 7, was presented to compare the inspected geometries in terms of heat transfer. The (a), (b1), (b2) and (c) design marks are consistent with geometries shown in Fig. 2. The temperature scale for each case was set as a global range to visualize the differences between cases. The initial design (a), as well as designs (b1) and (b2), are co-flow arranged, flow direction from left to right. The multistack design cross-flow is shown in Fig. 3 (fuel flow according to x-axis, air flow opposite to the z-axis). The distributions illustrated in Fig. 7, are shown in the form of semi-transparent shadow, where the minimum value is fully transparent and the maximum value is opaque. Each distribution was presented for the peak power point, determined during the study of electric characteristics. The temperature distribution does not change meaningfully between (a) and (b1), for both cases, peak power retains the same value of

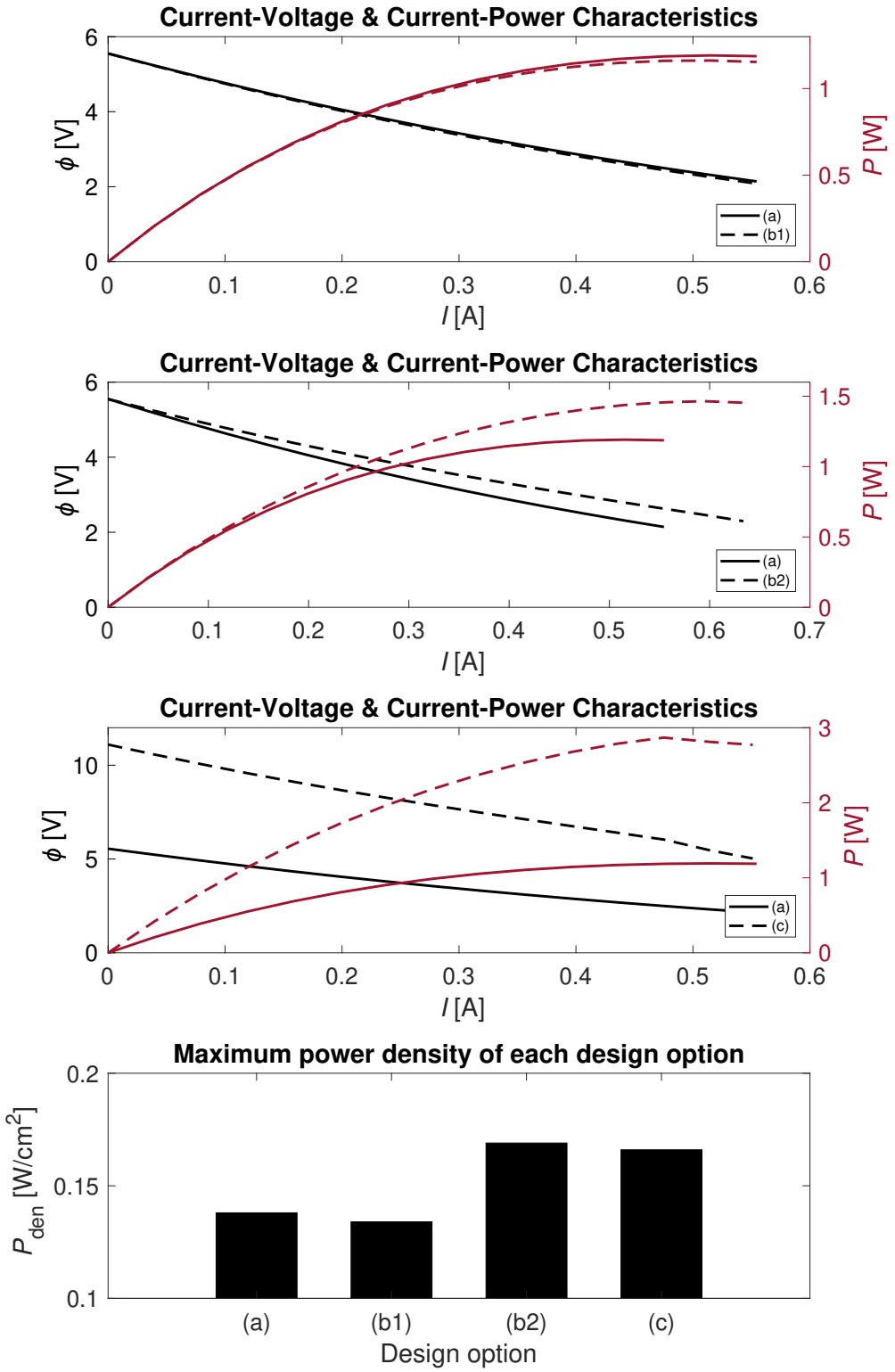

Figure 6: Comparison of current-voltage and current-power characteristics of four different designs, with a bar plot illustrating power density peak of each. Design marks (a), (b1), (b2) and (c) are consistent with geometries shown in Fig. 2.

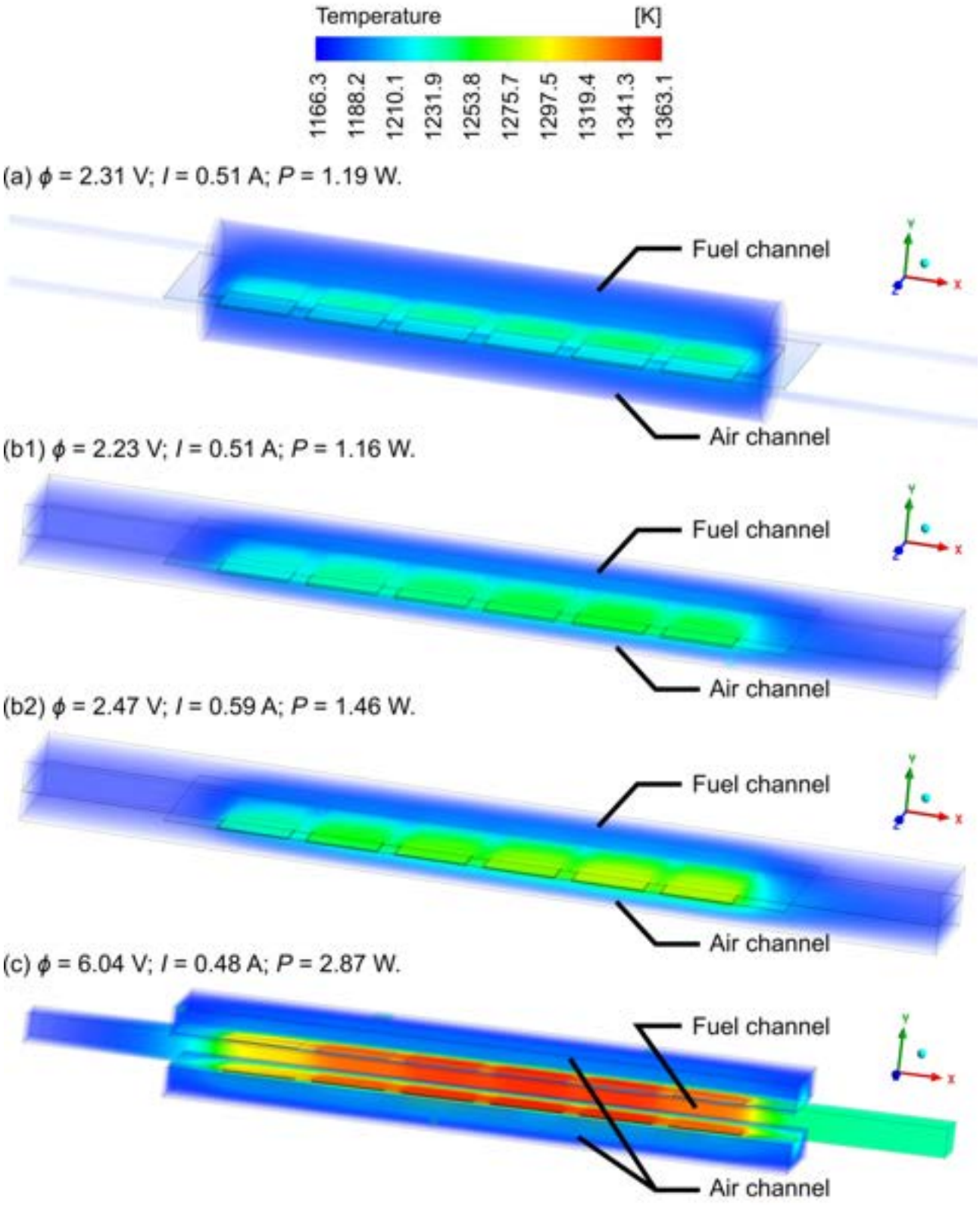

Figure 7: The temperature distribution comparison of peak power point of each inspected geometry. Design marks (a), (b1), (b2) and (c) are consistent with geometries shown in Fig. 2. The cases (a), (b1) and (b2) are co-flow formed, flow direction determines the x-axis. The (c) case cross-flow was shown in Fig. 3. Distribution in the form of semi-transparent shadow (min. value - transparent, max. value - opaque).

current. After implementing a thinner electrolyte (b2), the increase in current allowed the power peak to rise. Due to a higher load, a significant temperature increase occurs. The analysis of the multi-stack design reveals a major temperature increase in the fuel channel, between two sets of anodes. The interaction between both

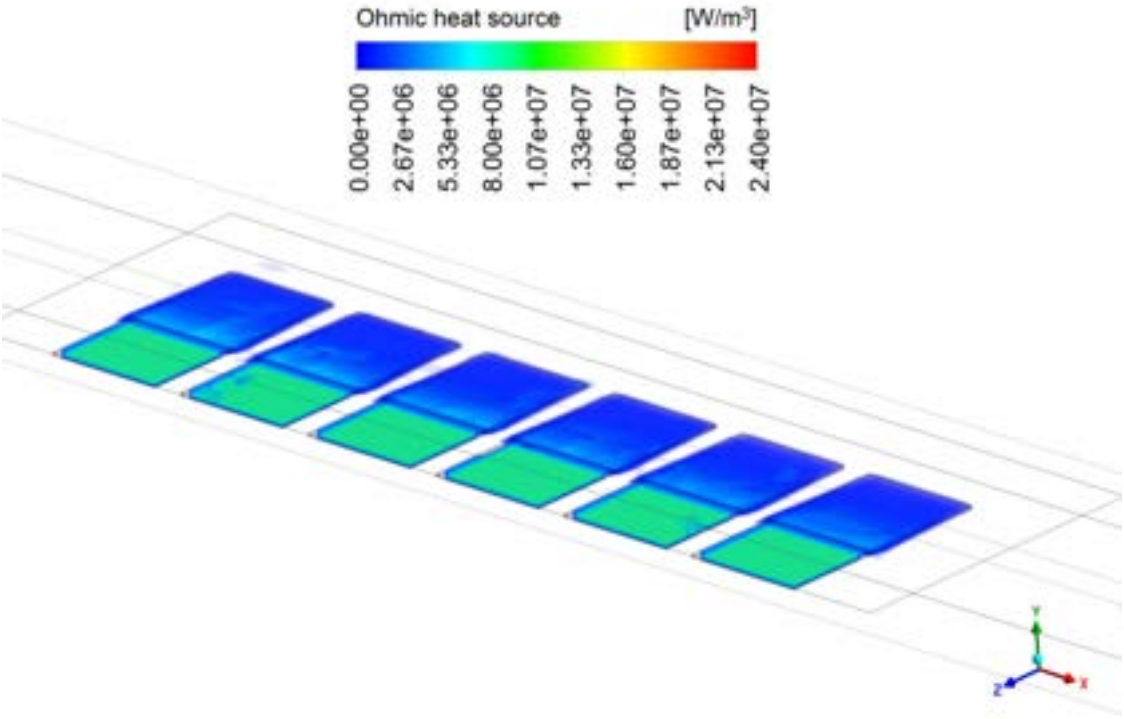

Figure 8: Ohmic heat source distribution in porous electrodes and current collectors, in the form of semi-transparent shadow (min. value - transparent, max. value - opaque). Design (b2), as shown in Fig. 2. Isometric view from the anode side. The flow direction determines the *x*-axis.

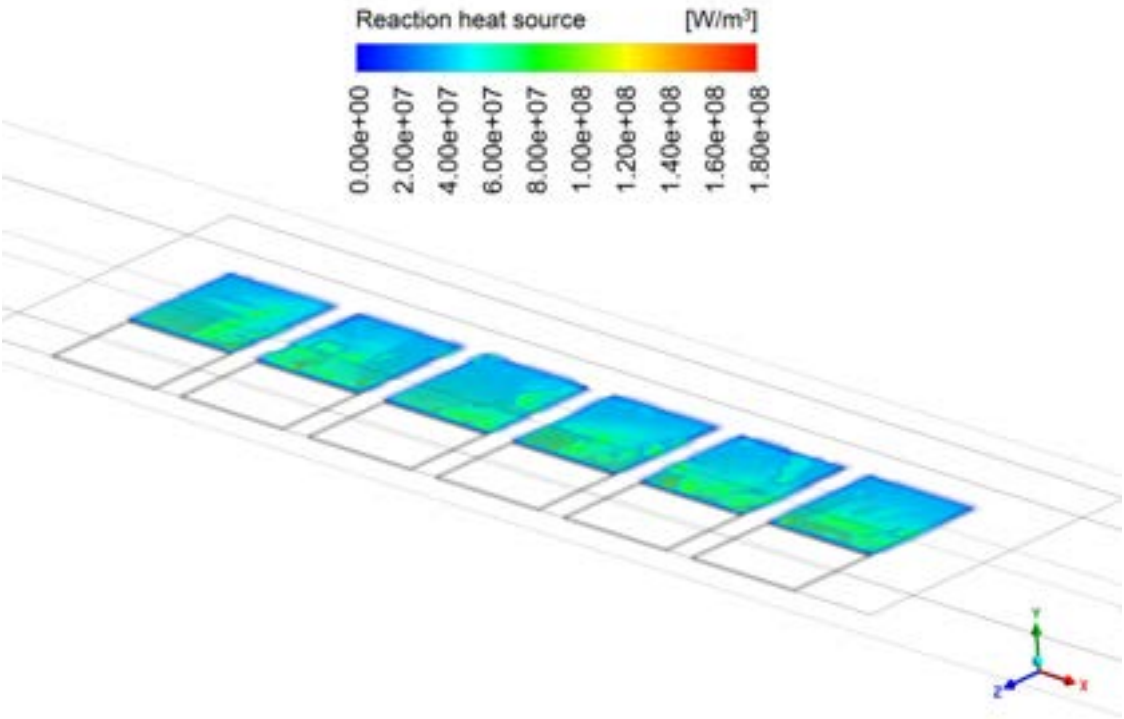

Figure 9: Reaction heat source distribution in porous electrodes, in the form of semi-transparent shadow (min. value - transparent, max. value - opaque). Design (b2), as shown in Fig. 2. Isometric view from the anode side. The flow direction determines the *x*-axis.

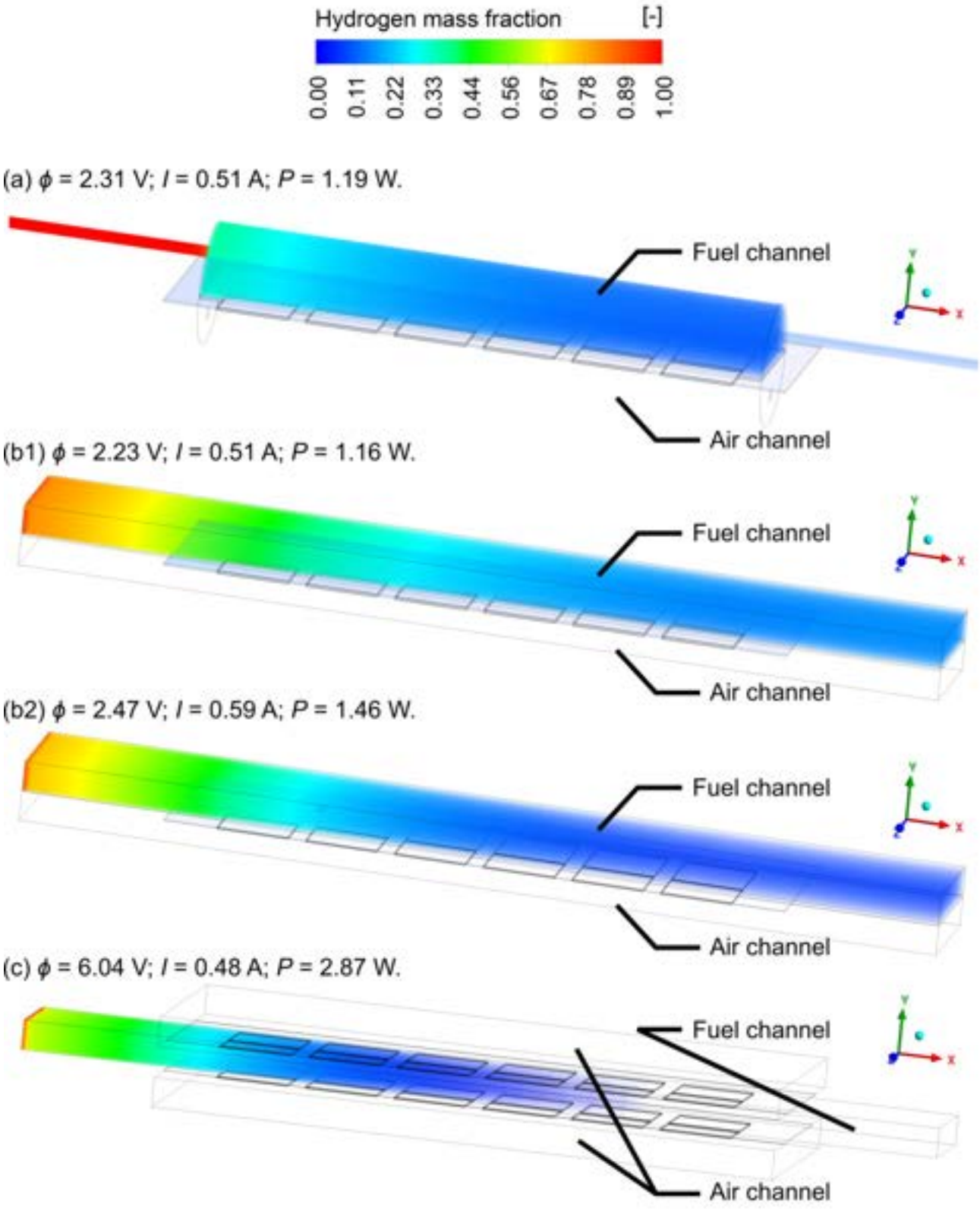

Figure 10: The hydrogen mass fraction distribution comparison of peak power point of each inspected geometry. Design marks (a), (b1), (b2) and (c) are consistent with geometries shown in Fig. 2. The cases (a), (b1) and (b2) are co-flow formed, flow direction determines the x-axis. The (c) case cross-flow was shown in Fig. 3. Distribution in the form of semi-transparent shadow (min. value - transparent, max. value - opaque).

stacks in the form of the generated, due to the electrochemical reaction and electrons/ions transport, heat, is clearly visible in the temperature distribution. From the outside, the constant temperature boundary condition cools the neighboring areas. The distribution analysis suggests that a multi-stack prototype could remain op-

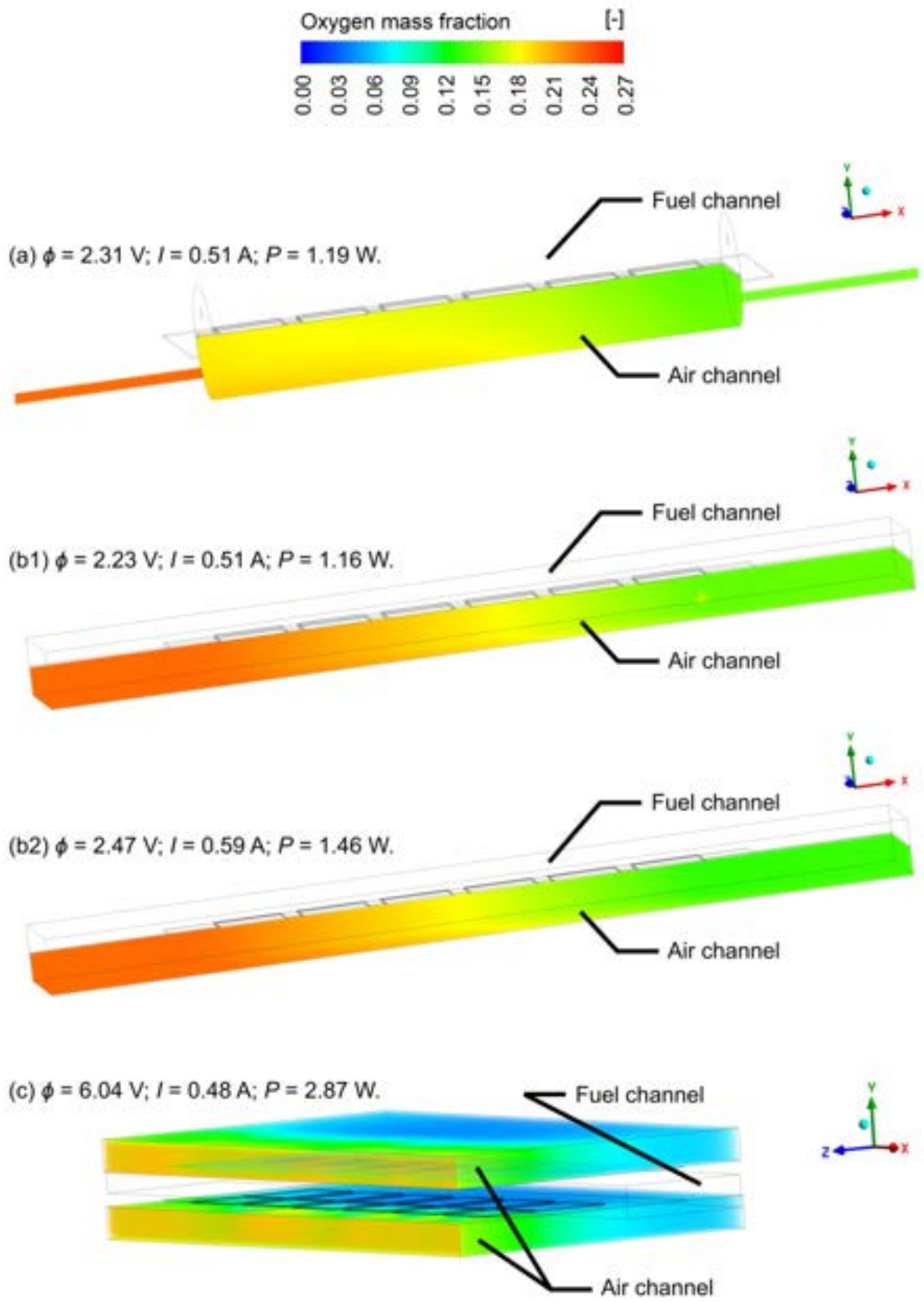

Figure 11: The oxygen mass fraction distribution comparison of peak power point of each inspected geometry. Design marks (a), (b1), (b2) and (c) are consistent with geometries shown in Fig. 2. The cases (a), (b1) and (b2) are co-flow formed, flow direction determines the *x*-axis. The (c) case cross-flow was shown in Fig. 3. Distribution in the form of semi-transparent shadow (min. value - transparent, max. value - opaque).

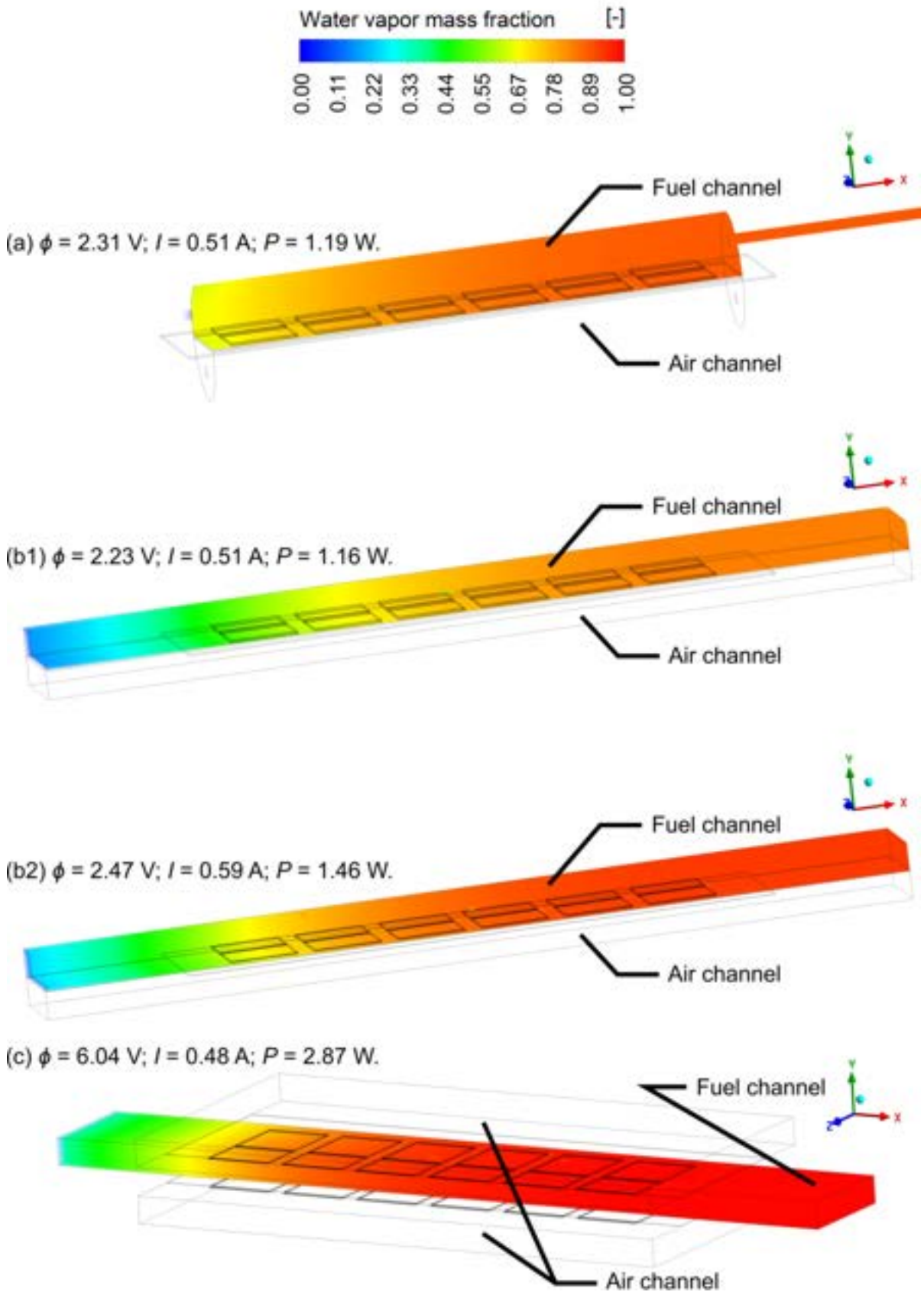

Figure 12: The water vapor mass fraction distribution comparison of peak power point of each inspected geometry. Design marks (a), (b1), (b2) and (c) are consistent with geometries shown in Fig. 2. The cases (a), (b1) and (b2) are co-flow formed, flow direction determines the x-axis. The (c) case cross-flow was shown in Fig. 3. Distribution in the form of semi-transparent shadow (min. value - transparent, max. value - opaque).

erating temperature with low input of furnace heating. The heat sources distributions are presented in Fig. 8 and Fig. 9, for ohmic and reaction heat sources, respectively. The distributions are illustrated in the form of semi-transparent shadow, similar to a temperature distribution. The case chosen to illustrate the heat sources is the (c) design (as shown in Fig. 2), due to the highest power density, as shown in Fig. 6. The flow direction is in accordance with the x-axis. The range of values is global, so the maximum visible value is the highest observed. As illustrated, the greatest impact on temperature rise has the reaction heat source, shown in Fig. 8, where the values remain an order of magnitude higher compared to the ohmic heat source, shown in Fig. 9.

The distributions of the mass fractions of hydrogen in the fuel channel, oxygen in the air channel, and water vapor in the fuel channel are illustrated in Fig. 10, Fig. 11 and Fig. 12, respectively. The distributions are presented in the form of semi-transparent shadow, where minimum values are fully transparent, and maximum values are opaque. The (a), (b1), (b2) and (c) design marks are consistent with geometries shown in Fig. 2. The scales for each case were set as global ranges to visualize the differences between cases. The initial design (a), and the designs (b1) and (b2) are co-flow arranged, flow direction in accordance with the x-axis. The multi-stack design cross-flow is illustrated in Fig. 3, where fuel flows according to x-axis and air in the opposite way to the z-axis. The distribution of the hydrogen mass fraction reveals the proper reaction of the model, while the comparison of (a) design and (b1) design does not give clear changes, between (b1) and (b2), the influence of changing the electrolyte thickness and simultaneously increasing the power, presents a visible difference. The case (b2) compared to (b1) utilizes much more fuel compared to the case (b1). In the (c) case, the fuel supply is utilized in full measure, so it is expected that the power density was lower than in (b2) due to the lack of fuel, especially counting the higher operating temperature in (c), which should result in higher performance. The high level of concentration loss in the (c) case is also visible in Fig. 6. The current load value in (c) case is also lower at the power peak point than in (b2), so the increase in fuel supply should yield in performance increase, and allow to apply load similar to (b2). The oxygen mass fraction illustrates the assumed surplus of air flow rate in all studied cases. The difference between the (a), (b1), and (b2) cases is subtle, the main difference is visible in the (c) case, due to doubling of cells amount, but still remaining some margin of oxygen. The water vapor mass fraction distribution also presents the proper operation of the model. After the oxygen and hydrogen are consumed, steam is produced and gradually fulfills the fuel channels. The steam mass fraction in cases (a) and (b1) remains at a similar level. After the increase in load and power gain, due to the decrease in the thickness of the electrolyte in case (b2), hydrogen and oxygen are consumed in greater amounts and the increase in steam generation is clearly visible. In the (c) case, the multistack generates the steam the most heavily and the value of steam mass fraction remains high since the first cells, while in the last cells area the water vapor fulfills the channel entirely.

5. Conclusions

This paper has provided an important analysis, in terms of further prototyping, of the novel banded SOFC stack. Four different geometries were designed as CAD models to include the influence of the configuration of the stack system on the performance. Also, different electrolyte thickness values were modeled. The computational mesh of each design was established to provide a domain for the finite-volume computation method. The mesh size was a result of the mesh sensitivity study to complete the requirements of high precision of the solution, high resolution, and reasonable computational time. As presented, the meshes were formed to fulfill the mentioned requirements, by forcing the elements dimensions changes in crucial areas. To understand the conducted research, a mathematical model was described, including implementing the model into the numerical analysis.

The main goal of this research was to inspect the performance changes. To validate the model for different gas flow rates, a comparison of electrical characteristics obtained from numerical analysis with experimental study results was performed and revealed the high level of predictability of the model. In order to obtain a proper comparison of different designs, including changes in the air and fuel channels, the electrolyte thickness, and the method of multistacking, the flow rates were set to higher value to maintain a surplus. To illustrate the results of the comparison, current-voltage and current-power characteristics were studied. Each design presented a response to applied modifications. The whole process of modification, from initial single stack with half-tubular covers design, to the final multi-stack design resulted in the performance increase of 141.2 %, from 1.19 W up to 2.87 W, while maintaining a comparable volume of the system. The multi-stack design proved to be the right way of extending the stack design into a bigger system. An arrangement of joining two stacks to one fuel channel, established partially by the stacks themselves, in terms of extending the system size, can double the power of the system without increasing the volume. Moreover, realizing the air supply as the side fan could significantly simplify the initial design. Temperature distribution analysis revealed another advantage of multistacking method as proposed. The neighboring stacks heat up each other, which in the prototype scale, could allow to minimize furnace input, and in the commercial scale, could enforce cooling the system, by fitting the gases flow rates. The full analysis of transport phenomena was performed including heat, mass, and electron transport. The results of hydrogen distribution exposed the lack of fuel in the multistack design, so the

final gain in power could be even higher than presented. The influence of load on transport phenomena was illustrated and inspected. In comparison of the studied stack with conventional, commercial-like designs the power density is not impressive, the highest power density value obtained during this study was 0.17 $\mathrm{W\,cm^{-2}}$, while it is common to reach values over 0.5 $\mathrm{W\,cm^{-2}}$ [9], so there is much space for further improvements.

In the future, the developed simulation can be used to analyze electrolyte and electrodes geometry and current collectors arrangement, allowing the construction of new and improved stack versions. Moreover, after contributing a new method of extending the single-stack system into a multistack, an analysis of the extended-scale fuel supply system in terms of fluid mechanics can be conducted. The model can also be used to analyze the influence of materials improvements by conducting material and electrochemical parametric studies, such as the impact of the electrolyte conductivity on performance, since it is considered as one of the most important parameters for this kind of stack.

Acknowledgments

The present research was supported by the Polish National Agency for Academic Exchange (NAWA), within the Strategic Partnerships Programme, Project No. BPI/PST/2021/1/00023. The numerical results were obtained by computational power financially supported by AGH University of Krakow (Grant AGH No. 16.16.210.476).

Nomenclature

Letter symbols

F	Faraday constant, ($9.65 \times 10^7\,\mathrm{C\,mol^{-1}}$)
h	specific enthalpy, ($\mathrm{J\,kg^{-1}}$)
h_{react}	enthalpy change, ($\mathrm{J\,mol^{-1}}$)
I	current, (A)
$i_{\mathrm{an}}^{\mathrm{eq}}$	anode equilibrium exchange current, ($\mathrm{A\,m^{-1}}$)
$i_{\mathrm{cat}}^{\mathrm{eq}}$	cathode equilibrium exchange current, ($\mathrm{A\,m^{-2}}$)
i	current density flux, ($\mathrm{A\,m^{-2}}$)
j	volumetric transfer current density, ($\mathrm{A\,m^{-3}}$)
$\vec{J}_i$	diffusion flux, ($\mathrm{kg\,m^{-2}\,s^{-1}}$)
k	thermal conductivity, ($\mathrm{W\,m^{-1}\,K^{-1}}$)
M	molar mass, ($\mathrm{kg\,mol^{-1}}$)
p	static pressure, (Pa)
P	power, (W)
P_{den}	power density, ($\mathrm{W\,cm^{-2}}$)
R	universal gas constant, ($8.314\,\mathrm{J\,K^{-1}\,mol^{-1}}$)
$\vec{S}$	source/sink term of momentum, ($\mathrm{kg\,m^{-2}\,s^{-2}}$)
S_h	source/sink term of heat, ($\mathrm{W\,m^{-3}}$)
S_i	source/sink term of species rates, ($\mathrm{kg\,m^{-3}\,s^{-1}}$)
S_p	source/sink term of mass, ($\mathrm{kg\,m^{-3}\,s^{-1}}$)
T	temperature, (K)
$\vec{v}$	velocity vector, ($\mathrm{m\,s^{-1}}$)
X_i	local species concentration, ($\mathrm{kmol\,m^{-3}}$)
Y_i	species mass fraction, (-)

Greek symbols

- α transfer coefficient, (-)
- γ concentration dependence, (-)
- ε porosity rate, (-)
- ζ_{TPB} triple phase boundary length density, ($\mathrm{m\,m^{-3}}$)
- ζ_{DBP} double phase boundary length density, ($\mathrm{m^2\,m^{-3}}$)
- η local surface overpotential, (V)
- ρ density, ($\mathrm{kg\,m^{-3}}$)
- σ conductivity, ($\mathrm{S\,m^{-1}}$)
- $\bar{\bar{\tau}}$ stress tensor, (Pa)
- ϕ potential, (V)

Subscripts and superscripts

- a anodic
- an anode
- c cathodic
- cat cathode
- den density
- DPB double phase boundary
- eff effective value
- el electronic
- eq equilibrium
- *i* reaction component
- ion ionic
- ref reference value
- s solid
- react reaction
- TPB triple phase boundary

Abbreviations

- 3D three-dimensional
- CAD computer aided design
- CFD computational fluid dynamics
- OCV open circuit voltage
- SOFC solid oxide fuel cell

References

[1] Buchaniec S., Sciazko A., Mozdzierz M., Brus G. *A Novel Approach to the Optimization of a Solid Oxide Fuel Cell Anode Using Evolutionary Alghorithms*. IEEE Access 2019;7:34361-34372.

[2] Ghorbani B., Vijayaraghavan K. *A review study on software-based modeling of hydrogen-fueled solid oxide fuel cells*. International Journal of Hydrogen Energy 2019;44:13700-13727.

[3] Mozdzierz M., Berent K., Kimijima S., Szmyd J.S., Brus G. *A Multiscale Approach to the Numerical Simulation of the Solid Oxide Fuel Cell*. Catalysts 2019;9/253.

[4] Pianko-Oprych P., Zinko T. *Simulation of the steady-state behaviour of a new design of a single planar Solid Oxide Fuel Cell*. Polish Journal of Chemical Technology 2016;1:64-71.

[5] Pianko-Oprych P., Zinko T. *Computational fluid dynamics calcultion of a planar solid oxide fuel cell design running on syngas*. Chemical and Process Engineering 2017;38:513-521.

[6] Chalusiak M., Wrobel M., Mozdzierz M., Berent K., Szmyd J.S., Kimijima S., Brus G. *A numerical analysis of unsteady transport phenomena in a Direct Internal Reforming Solid Oxide Fuel Cell*. International Journal of Heat and Mass Transfer 2019;131:1032-1051.

[7] Wei S.S., Wang T.H., Wu J.S. *Numerical modeling of interconnect flow channel design and thermal stress analysis of a planar anode-supported solid oxide fuel cell stack*. Energy 2014;69:553-561.

[8] Dong S.-K., Jung W.-N., Rashid K., Kashimoto A. *Design and numerical analysis of a planar anode-supported SOFC stack*. Renewable Energy 2016;94:637-650.

[9] Pirasaci T. *Non-uniform, multi-stack solid oxide fuel cell (SOFC) system design for small system size and high efficiency*. Journal of Power Sources 2019;426:135-142.

[10] Brus G. *High-Temperature Solid Oxide Fuel Cell Stack* International Claim no. H01M 8/2432 (2016.01), H01M 8/2475 (2016.01).

[11] Chalusiak M. *Development of solid oxide fuel cell manufacturing methodology using 3D printing technique.* PhD dissertation. Krakow, Poland: AGH University of Science and Technology; 2023.

[12] Mukerjee S., Leah R., Selby M., Stevenson G., Brandon N. P. *Chapter 9 - Life and Reliability of Solid Oxide Fuel Cell-Based Products: A Review*. In: Brandon N. P., Ruiz-Tjero E., Boldrin P. editors. Solid Oxide Fuel Cell Lifetime and Reliability. London, UK: Academic Press. 2017. p. 173-191.

[13] Prokop T.A., Berent K., Iwai H., Szmyd J.S. *A Three-Dimensional Numerical Assessment of Heterogeneity Impact on a Solid Oxide Fuel Cell's Anode Performance*. Catalysts 2018;8:503.

PROCEEDINGS OF ECOS 2023 - THE 36TH INTERNATIONAL CONFERENCE ON
EFFICIENCY, **C**OST, **O**PTIMIZATION, **S**IMULATION AND ENVIRONMENTAL IMPACT OF ENERGY SYSTEMS
25-30 JUNE 2023, LAS PALMAS DE GRAN CANARIA, SPAIN

Energy System Analysis of the Power Sector Flexibility via Hydrogen Utilisation

Andreas Hanel[a,*], Rasmus Schamper[a], Marcel Dossow[a], Sebastian Fendt[a] and Hartmut Spliethoff[a]

[a] *Technical University of Munich, Chair of Energy Systems, Garching, Germany*
[*] *andreas.hanel@tum.de, CA*

Abstract:
According to regulations from the EU Commission, investments in nuclear energy and fossil gas are considered sustainable. These new EU taxonomies, which are intended to provide financial markets with guidance on climate and environmentally friendly investments, actually exclude conventional fossil power- and heat plants. However, the reinterpretation of natural gas as a transitional energy until 2035 allows the construction of new gas-fired power plants. As a limiting factor, an increasing share of low-emission gases have to be used, primarily green hydrogen. In the future, fuel cell power plants could serve as an alternative to such new H_2-ready gas power plants. High-temperature solid oxide fuel cells can not only use fossil methane-containing natural gas and/or hydrogen efficiently, but can also be used reversibly for electrolysis and thus provides flexibility to the power grid. This study uses energy system optimization to analyse the behaviour of both technologies, H_2-ready gas turbines and fuel cell power plants. Across three scenarios, fuel cells are used to provide baseload and flexibility especially in periods of low wind and solar irradiation, whereas hydrogen gas turbines appear last in the order of operation. However, short-term flexibility is provided by battery storage, e.g. by using existing battery capacities from electric vehicles. As Germany has a lower potential for local hydrogen production in an international comparison, significant quantities of hydrogen will only be produced in Germany if import possibilities are strongly limited and technology costs decrease at the same time.

Keywords:
Energy system simulation, Hydrogen, rSOC, sector coupling.

1. Introduction

The decision to make the European energy system, or rather the entire European economic area, climate-neutral by 2050 at the latest is associated with high costs, especially in a short-term period. These costs can lead to a competitive disadvantage for the involved economies. In order to partially compensate for this, the European Commission has introduced regulations, e.g. the European Union (EU) taxonomy. The aim of the taxonomy is a clear definition or classification of sustainable (”green”) economic activities. In this context, the European Commission has agreed that the energy transition to a fully defossilised system can only succeed over a transition period in which fossil feedstocks continue to be used. These transitional technologies, in particular conventional natural gas (NG) and nuclear power plants, are initially intended to replace plants with higher specific emissions such as coal-fired power plants. Later on, these power plants are converted to be emission-free. [1]

Focusing on the German energy system, due to the nuclear phase-out, only NG power plants are affected. In recent system studies, it is usually assumed that centralised large-scale power plants will play an important role in energy supply both during the energy transition and in the long-term [2]. Thus, it is assumed that NG-fired power plants will initially replace coal and nuclear power plants in terms of supply security and flexibility. Subsequently, a fuel switch is expected beginning in 2040, whereby both hydrogen-fuelled gas turbines and synthetic natural gas (SNG) are mentioned. However, while these studies assume that the corresponding technology will be available at the respective time, hydrogen gas turbines are not yet state of the art. For this reason, the technical association of energy plant operators (vgbe energy e.V.) has published a position paper and a fact sheet [3] on the topic of *H_2-Readiness* of gas turbines. This includes the definition that *H_2-Readiness* only applies if a gas turbine can be used with 100 % hydrogen or can be upgraded to this in the future. Finally, it is stated that the necessary regulations are still missing at EU level. Thus, it can be concluded that the final boundary conditions for hydrogen utilisation have not yet been finalised. As policy makers often use energy system studies as part of the decision process, extensive research regarding hydrogen and other synthetic energy carrier utilisation is needed [4]. Reviewing existing literature, Yue et al. conclude the not cost-competitiveness is one of the major reasons for the slow increase in hydrogen utilisation worldwide [5].

They also note that a lack of system integration, e.g. as a planning model, could be a reason why policy makers hesitate to further promote the development of a hydrogen economy. Looking more detailed into existing literature, Ball et al., e.g., modelled the German energy system including a high spatial resolution to discuss the possibility of a German hydrogen economy, focusing on the infrastructure demand and impact on greenhouse gas emissions [6]. Here, hydrogen is not only seen as an alternative to fossil fuels, but also as a storage and flexibility option in fully renewable energy systems. However, the expected hydrogen demands and feedstock costs are outdated due to developments in the energy market in recent years. Robinius et al. discuss the possibilities of power-to-gas as a network expansion alternative [7]. It is shown that there are scenarios in which the use of electrolysers is more reasonable than the expansion of the power grid. Especially when considering both the possibility of selling hydrogen and the saved costs for laying new transmission lines. Li and Mulder evaluated the impact of hydrogen on the electricity and hydrogen market from an more economic point of view [8]. They show that especially in combination with the volatility of renewable power generation power-to-hydrogen brings huge economic advantages. However, they also state the importance of greenhouse gas emission reduction targets, as steam methane reforming still is the cheapest way to produce hydrogen. He et al. published a more detailed study of the complex interactions of sector-coupled systems considering hydrogen as a decarbonisation option on a northern american example [9]. In summary, the concept of sector coupling itself reduces total system costs. For example, since the round-trip efficiency of electricity-to-hydrogen-to-electricity is still low, using hydrogen in other sectors such as transportation reduces losses. They were also able to show that as the demand for hydrogen increases, the specific cost of flexibility decreases. However, the assessment lacks the inclusion of industrial and heating demand. In an extensive review on sector coupling Ramsebner et al. conclude, that there will always be the competition between the higher efficiency of direct electrification versus long-term storage capabilities of power-to-gas applications [10]. As there are many different system-wide effects, no specific predictions can be made. Especially since regional climate goals and policies can strongly influence the final technology deployment. Nevertheless, as some applications are not able to be electrified, there will be a non-neglectable share of hydrogen-based applications.

The use of hydrogen as a flexibility and storage option for the power sector has not been consensually agreed on. It strongly depends on the chosen scenario and assumptions regarding technological and economic parameters. The invention of innovative technologies, such as solid oxide cells (SOCs) with their ability to be operated reversibly for both hydrogen and electricity generation, adds further degrees of freedom to the decision-making process. In this study the utilisation of hydrogen as flexibility option in the electricity sector is evaluated. Therefore, both fuel cell and gas turbine based pathways are benchmarked alongside battery storage as main flexibility option (Figure 1). Due to the great influence of sector coupling on the use and the specific costs of hydrogen, a highly coupled energy system model is used. The German energy system embedded in an abstracted, interconnected European system serves as an example. The focus is on the application of the used technologies, as well as the interactions between different sectors. Therefore, different scenarios are considered and individual system parameters are evaluated. The assessment is related to the EU taxonomy rules, although the latest updates to the regulation regarding temporal and geographical correlation and additionality as defined in [11] are not considered.

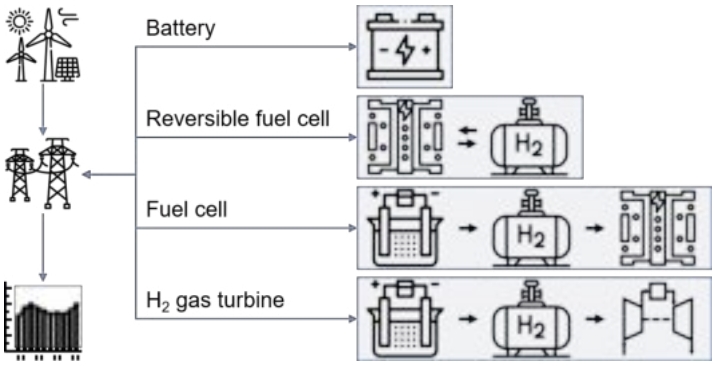

Figure 1: Overview of the considered hydrogen utilisation pathways, including separated hydrogen generation and consumption and the utilisation of reversible technologies.

2. State of the Art and Methods

2.1. Political Boundary Conditions and Current Situation

The use of hydrogen as a sustainable energy carrier is primarily based on the climate protection goals of the German government. The latest amendments to the climate protection law mandate that Germany should be

climate-neutral by 2045. This necessarily includes the replacement of fossil energy carriers with sustainable ones. This cost-intensive undertaking is also supported by the EU. Here, several regulations for the member states of the EU have been adopted, which are intended to provide security in financial planning. This includes, for example, the EU taxonomy, which defines whether an investment is beneficial for climate protection and in terms of sustainability. To qualify as a sustainable investment under the new rules, several technical screening criteria must be met [1]. In the case of power generation from fossil gases, a distinction is made between two groups. Plants with life cycle emissions of 100 $g_{CO2e}\,kWh^{-1}{}_{el}$ or less will be considered sustainable without any further conditions. In addition, there is the possibility to also fall under the label of sustainability for plants that receive their permit to operate by 2030. To do so, a set of criteria must be met, two of which are directly related to the use of hydrogen. For example, specific emissions must initially only comply with a limit of 270 $g_{CO2e}\,kWh^{-1}{}_{el}$. However, it must be ensured that by 2035 the plants are capable of running entirely on low-carbon fuels. In this context, the results of a UNECE[1] study can be used, in which the life cycle emissions of several power generating technologies are calculated [12]. Here, natural gas based combined cycle power plants without carbon capture and storage have emissions of 403-513 $g_{CO2e}\,kWh^{-1}{}_{el}$ and with carbon capture and storage 92-220 $g_{CO2e}\,kWh^{-1}{}_{el}$. Considering only the stoichiometric combustion of natural gas the emissions under assumption of a combined cycle plant efficiency of 63 % are already higher than 315 $g_{CO2}\,kWh^{-1}{}_{el}$ (see Figure 2). Using an Aspen Plus simulation, Figure 2 also shows the correlation of the specific direct CO_2 emissions with increasing hydrogen admixture. To comply with the limit value of 270 $g_{CO2e}\,kWh^{-1}{}_{el}$, at least 36.1 vol.-% hydrogen would be required, and for 100 $g_{CO2e}\,kWh^{-1}{}_{el}$ even more than 87.7 vol.-% hydrogen.

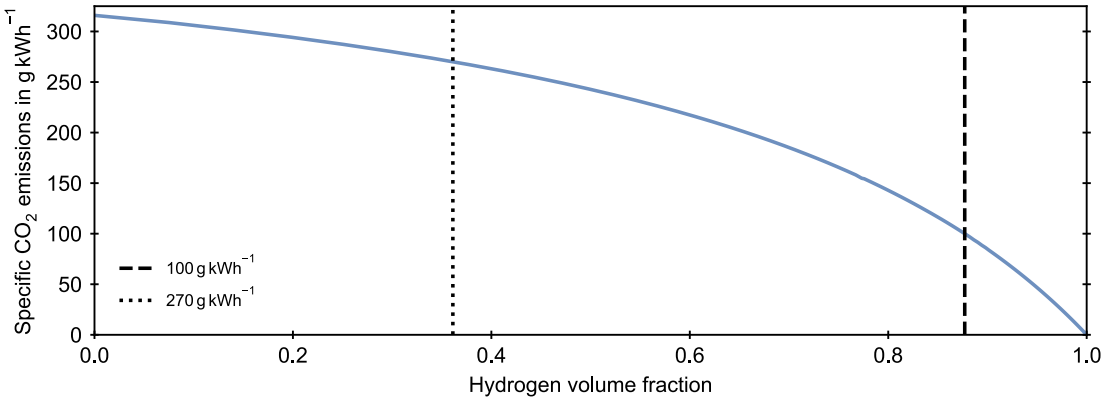

Figure 2: Specific CO_2 emissions of the stoichiometric combustion of a hydrogen-methane mixture with a varying hydrogen fraction.

2.2. Hydrogen Technologies

The aim of the study is to evaluate the flexibility supply via hydrogen in comparison to battery technologies. In the following, the technological and economic parameters of the hydrogen technologies are presented. On the side of battery technology, it is assumed that by 2045 the goals of the German government regarding the expansion of e-mobility and the large-scale application of bidirectional charging (vehicle to grid (V2G)) will have been implemented.

2.2.1. Hydrogen Supply

The supply of green hydrogen in context of this work is realised exclusively via water electrolysis. Both local production within the German energy system and import are allowed. The generation itself can take place via the three technologies alkaline electrolysis (AEL), polymer electrolyte membrane electrolysis (PEMEL) and solid oxide electrolysis (SOEL). The technological and economic parameters are based on literature values for all technologies. As several detailed studies and reviews on each of the technologies, as well as comparative work, are already available, a detailed description is not provided. For more detailed information, the authors refer to the existing literature such as [13, 14]. A summary of the parameters used and the corresponding references are given in Table 1. The import of hydrogen is again divided into two segments. First, the import via sea route is possible. Based on [15, 16], it is assumed that the import of hydrogen based on renewable power from Saudi Arabia will be possible for a cost of 2.4-3.1 $\$\,kg_{H2}{}^{-1}$ or 5.2 $€\,kg_{H2}{}^{-1}$ respectively. In addition, hydrogen pipelines can be used to import from sun-rich countries in the EU. For this purpose, the energy system model has the possibility to expand renewables in Italy or Spain in combination with electrolyser capacities to supply hydrogen to the German subsystem[2].

[1] United Nations Economic Commission for Europe

[2] For example the decision to extend the pipeline from the *H2Med* project to Germany.

2.2.2. Techno-Economic Parameters of Hydrogen Gas Turbines and rSOC

Hydrogen Gas Turbine

When assessing the hydrogen compatibility of gas turbines (GTs), it is necessary to distinguish between two types of combustion methods. Initially, gas turbines utilised a simple diffusion mechanic to burn fuel, which is a robust process. Indeed diffusion-style are already capable of burning pure hydrogen, but comes with the downside of higher NO_x emissions and lower efficiency. To reduce emissions, gas turbine manufacturers introduced a lean-premixed combustion process in the 1980s, for which fuel and air is mixed in a lean ratio before introduced into the combustion chamber. Since then, basically all heavy-duty gas turbines incorporate some form of premixing fuel and air. While the NO_x emissions can be significantly lowered using lean-premixed combustion, the stable operational range of these gas turbines is narrow, making them susceptible for any type of disturbances, like a fuel switch from natural gas to hydrogen, which has fundamentally different combustion characteristics, especially regarding flame temperature, flame speed, volumetric heating value and quenching distance. [17, 18]

The most challenging problem during the combustion of lean-premixed gas is the occurrence of flame flashbacks. Due to the combustibility of the fuel-air mixture, flames in premixed gas turbines can shift from the combustion chamber upstream to the fuel injection nozzles, damaging the turbine hardware. Fuelling hydrogen increases the risk of flame flashback as the higher flame speed of hydrogen more often fulfills the prerequisite of the local flame speed being higher than the local fuel-mixture flow velocity. Additionally, hydrogen has a shorter autoignition delay time. The autoignition delay time corresponds to the time interval for a reactive mixture to react without an ignition source. If this time interval is shorter than the fuel–air mixing residence time in the non-combustion zone, autoignition can occur and lead to local flame holding or further flashbacks. [19]

Another concern are thermoacoustic instabilities, which describe an unwanted feedback loop of combustion fluctuations leading to an unstable heat release and thus pressure oscillations which can excite natural acoustic modes of the combustor, intensify and cause more combustion fluctuations closing the loop. Consequences can reach from affected plant efficiency to damaged hardware. While not being an inherent consequence of fuelling hydrogen, thermoacoustic instabilities are a concern when switching to hydrogen in gas turbines former designed for fuelling natural gas and may prevent an easy retrofit. [20]

Lastly, the higher flame temperature of hydrogen and the increased heat input due to the larger water content in the hot gases have higher demands on materials used for turbine parts like heat shielding or turbine blades. The increased thermal stress will lead to a degradation of parts. Also, effects like hydrogen embrittlement and hot corrosion must be considered. [21]

While there will likely be technical solutions for all of the aforementioned issues, it becomes clear that hydrogen can not simple be burned in today's gas power plants. Yet there are no reports of successfully operating a premixed heavy-duty gas turbine with pure hydrogen. However, for state-of-the-art turbines like the Ansaldo GT36 up to 70 % hydrogen by volume are available for operation. [22]

SOFC and rSOC

SOCs are solid-state electrochemical devices which can either be configured as fuel cell (solid oxide fuel cell (SOFC)) producing electricity directly from oxidizing a fuel or, if configured as electrolyser cell (SOEL), produce hydrogen through water electrolysis. The reactions in a solid oxide cell are reversible, if a solid cell is configured to work alternating as a fuel cell and a electrolyser, it is called reversible solid oxide cell (rSOC) (see Figure 3). SOCs are made of four main components: the anode and cathode (defined in fuel cell-direction), named fuel and oxygen electrode to avoid confusion when the cell operation is reversed, the solid electrolyte layer and the interconnector. [23]

SOCs recently received increased attention due to advantages over other fuel cell/electrolyser technologies. First, the efficiency in both operation modes are the highest reported with over 65 % for SOFCs and over 80 % for SOELs [14]. Second, the aforementioned reversibility, which allow for a high utilization of rSOCs. Third, SOCs can utilize different fuels, like hydrogen, methane or ammonia, making them deployable for a wide range of applications. Fourth, due to their simple layer structure, the currently favoured design, they are predestinated for mass manufacturing and are scalable to any capacity. Additionally, no rare materials like iridium are used in SOCs. While research focuses on finding improved materials, currently mostly Ni-based alloys and yttria-stabilized zirconia (YSZ) are utilised. [24]

Drawbacks of SOCs are the current high investment costs which belong to the highest among all fuel cell/electrolyzer technologies and reported degradation issues. However, the high costs are predicted to decline from todays $>2000\,€\,kW_{el}{}^{-1}$ to less than $800\,€\,kW_{el}{}^{-1}$ in 2045 due to economics of scale (see Table 1). The lifetime is being constantly improved through better material choices and operating modes, like the reversible operation. An example for the improved durability is a long-term test of an SOFC in Jülich, which was shut down after 100,000 h of operation without major power degradation. [25]

Depending on the costs of imported hydrogen, rSOC are an attractive technology to provide flexible power gen-

eration to a future energy system as they have a natural investment advantage over an alternative combination of electrolysers and hydrogen gas turbines. They are considered a viable long-term energy storage technology and could improve the integration of renewable energy sources by utilising surplus electricity production for electrolysis.

Currently, SOCs are entering an early commercial phase with several manufacturers announcing investments to scale up their production in the gigawatt range. While this developments mainly relate to SOEC production, exemplary pilot-projects for dedicated rSOC are a 140 kW_{SOEC}/50 kW_{SOFC} installation in 2016 [26] and a 80 kW_{SOEC}/15 kW_{SOFC} in 2018. [27]

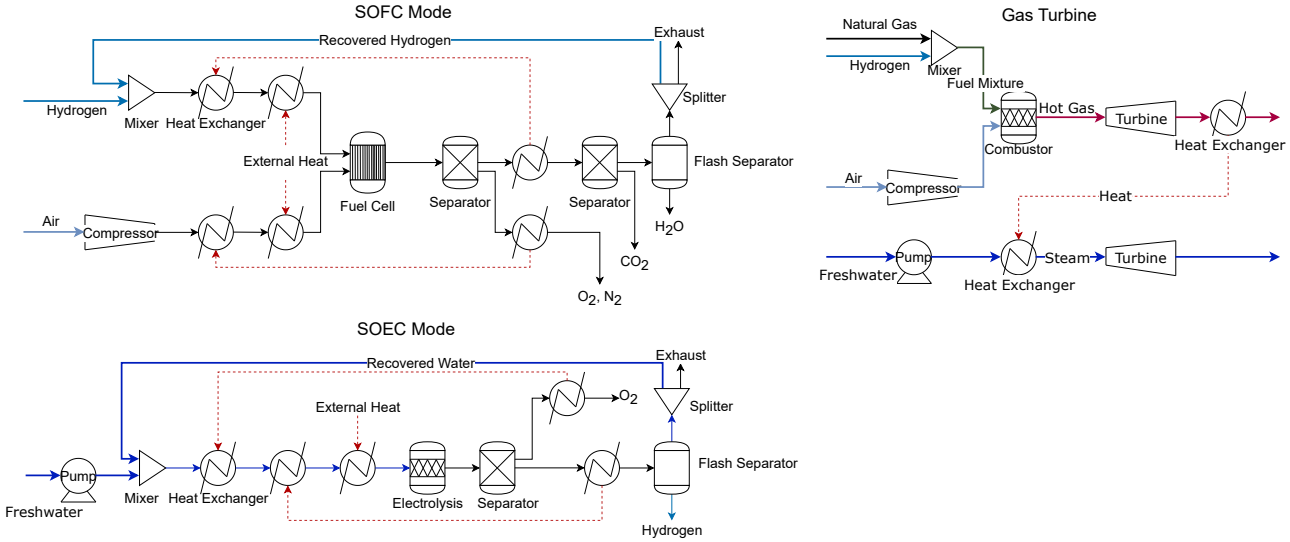

Figure 3: Process flow-sheets of SOC in fuel cell and electrolysis mode (left) and of a combined cycle gas turbine (right).

Cost estimations

Table 1 summarises the key parameters of the hydrogen technologies, where in case of H_2 gas turbines a CCGT is assumed. Included are the efficiency, expected lifetime, as well as the fixed and variable costs. Since the energy system model considers a whole year for each scenario, the costs must be scaled to the annual costs. For this purpose, the annuity method is used.

Table 1: Summary of the hydrogen technologies including technological and economic parameters.

Technology	TRL	Efficiency	Lifetime	CAPEX	OPEX	Reference
Hydrogen CCGT	6-8	0.630	45 a	920 € kW_{el}^{-1}	18 € kW_{el}^{-1} a^{-1}	o.a.[a]
SOFC	5-7	0.699	30 a	640 € kW_{el}^{-1}	51 € kW_{el}^{-1} a^{-1}	o.a.[a]
rSOC	3-6	-	30 a	704 € kW_{el}^{-1}	56 € kW_{el}^{-1} a^{-1}	o.a.[a]
SOEL	5-7	0.800	30 a	640 € kW_{H2}^{-1}	51 € kW_{H2}^{-1} a^{-1}	[13, 14, 29]
PEMEL	7-8	0.590	30 a	300 € kW_{H2}^{-1}	12 € kW_{H2}^{-1} a^{-1}	[13, 14, 29]
AEL	9	0.757	30 a	460 € kW_{H2}^{-1}	18 € kW_{H2}^{-1} a^{-1}	[13, 14, 29]

[a] Own assumption based on Aspen Plus process simulations and [13, 14, 28, 29]

2.3. Energy System Model Framework

The energy system model used is based on the framework ”OpTUMus”, which is described in detail by the authors in [30]. The energy system model is a linear optimization problem, which is solved with IBM ILOG CPLEX 22.10.0 using a barrier optimization algorithm. The temporal resolution for each optimisation problem corresponds to one year in one-hour steps. The model itself is constructed as a *nodes and edges* model. *Nodes* represent different forms of energy or energy carriers such as electricity, hydrogen or natural gas. According to Equation 1 in each time-step t energy and material balances must be conserved for all nodes n.

$$P_{demand}[n][t] + P_{out}[n][t] = P_{in}[n][t] \quad (1)$$

Edges, on the other hand, describe all possible transformation paths and thus all technologies for energy conversion and transport. This includes the efficiency of energy transportation or transformation from node n to m in each time step t (Equation 2). A simplified example is shown in Figure 4a.

$$P_{in}[n][t] = a_{mn} \cdot P_{in}[m][t] + b_{mn} \tag{2}$$

The model contains an abstract digital twin of the German energy system. This includes the electricity and heating sector as well as the supply of mobility and the supply of energy and a selection of basic chemicals to industrial applications. The German energy system is divided into four regions (Figure 4b) in order to be able to map the local potentials of renewable energies, energy demands and transport limitations. Furthermore, the model includes Germany's direct neighbors as well as Norway, Sweden, the United Kingdom, Spain and Italy, each reduced to the electricity sector. A graphical summary of the regions considered is given in Figure 4c. In order to enable the import of synthetic energy carriers from the southern European regions, electrolysers and pipelines can be built.

On the demand side of the German energy system model, the four sectors

(1) electricity (2) heat (3) mobility (4) industry

are considered. Here, it is important to note that the electricity sector includes all power demands consisting of conventional demands as well as electricity for heating, transport and industry. Each of the demand segments is based on a separate model, which determines the hourly demand for electricity. The material demands for basic chemicals and fuels (methanol (MeOH), SNG, Fischer-Tropsch (FT)-fuels, ammonia (NH_3), hydrogen (H_2)) are also calculated specifically for the respective applications and transferred to the model as a summed demand time series. The same accounts for the heating demand both in domestic and industrial applications. The overall demands are divided into the four regions using statistical methods. Each region is optimised by itself, having the possibility to interact with all neighboring regions. Additionally, the northern and southern Germany regions are allowed to built direct connections for both power and hydrogen transportation. In the same manner, Spain and Italy are connected to the southern German region via the possibility of an hydrogen pipeline. Finally, northern Germany has the option to import hydrogen by ship. The demand side models are adopted from previously by the authors published works [31–33] and therefore are not further discussed. However, an overview of the included technologies and the respective demand side connections are summarised in the appendix in Table 5.

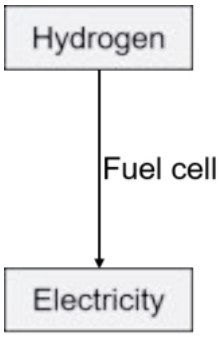

(a) Simplified Scheme of an *edge-node* based energy system model.

(b) Geographical resolution of the model of the German energy system.

(c) Overview of the considered Subsystems of the European energy system model.

Figure 4: Overview of the energy system model basic structure (a), the spatial resolution of the German subsystem (b) and the considered countries of the European energy system model (c).

2.4. Scenario Definition

Various scenarios are important in energy system optimisation to assess the robustness and flexibility of energy systems under different conditions, to identify potential risks and opportunities, and to inform decision-makers for long-term planning and policy development. In context of this work, a variation of hydrogen connected parameters is performed, to identify the influences of the energy system behaviour. Therefore, the parameters hydrogen demand, hydrogen import costs and the technology cost developments are chosen. In a base case scenario, most parameters of the entire model are set to the mean expected values found in literature. Two additional scenarios are defined, one with a higher hydrogen demand (H2-high) and one with a lower

penetration of hydrogen and a restricted availability, e.g. reduced pipeline availability, (H2-restr.). At the same time it is assumed, that a higher hydrogen demand correlates with lower specific technology costs and vice versa. Additionally, the overall end-use energy demand stays constant over the different scenarios. Therefore, a higher hydrogen demand is connected to a lower direct electrification. A summary of the scenarios and the respective parameter variation is given in Table 2.

Table 2: Scenario definition with the respective parameter variation.

Scenario	H_2 demand[a]	H_2 import[b]	Tech. costs[c]	Comment
BC	113 TWh a^{-1}	2.4 € kg_{H2}^{-1}	-	-
H2-high	172 TWh a^{-1}	2.1 € kg_{H2}^{-1}	-15 %	Electrification ↓, H_2-tech. costs ↓
H2-restr.	113 TWh a^{-1}	5.2 € kg_{H2}^{-1}	-25 %	H_2 availability ↓, H_2-tech. costs ↓

[a] Only predefined hydrogen demand. Not included are demands for power generation and for further synthesis.

[b] Import via ship from MENA region.

[c] Own assumption; Relative cost reduction for PEMEL, AEL, SOEL, SOFC and rSOC

3. Results

The energy system is largely based on electrical energy. As expected, most of this is provided by wind turbines and photovoltaics, as summarised in Table 3. The contribution of biomass via biogas and combined heat and power is also not to be neglected, whereas plants with higher complexity as polygeneration plants are only used in the restricted scenario. In addition to battery storage or V2G, both conventional gas turbines and hydrogen-based technologies are used to cover the flexibility demand. A summary of the amount of energy provided per technology is given in Table 3. In all scenarios the biomass potential of Germany, which summarises to around 420 TWh a^{-1} for all regions, is fully utilised. Large shares are needed for the heat supply and as carbon source for synthesising chemicals and fuels. This indicates the rising demand for carbon sources in future energy systems. Since this model only allows biomass as a sustainable feedstock, potentials from the use of residues and waste materials - as required in a circular economy - are neglected. In particular, technologies such as polygeneration plants will also be used in the future to exploit residues such as plastic waste and municipal solid waste as input for the synthesis of high-value products or for the efficient supply of flexibility to the electricity and heat sectors. However, doubling the sustainable feedstock potential could reduce the total system costs by 10 %[3], by using the same boundary conditions as in the base case scenario.

Table 3: Summary of the power generation in Germany without storage technologies or grid as comparison between the scenarios BC, H2-high and H2-restr.

	Biomass[a]	GT	H2GT	Hydro	PV	WOFF	WON	SOFC	PolyGen
BC in TWh	86.7	16.0	22.0	12.5	326.8	137.0	224.0	70.5	0.0
H2-high in TWh	85.1	5.5	25.0	13.2	284.9	91.0	225.3	128.0	0.0
H2-restr. in TWh	84.8	35.2	8.2	13.1	415.9	136.6	224.9	7.0	0.9

[a] Sum of all biomass based power plants and CHPs.

As can be seen in Table 4, in the base case scenario hydrogen is exclusively imported. As electricity prices are most of the time (90 %) higher than the import costs of hydrogen, hydrogen production in Germany is not viable under the given boundary conditions. The electricity and hydrogen prices are calculated as shadow prices, which is not directly comparable to the pricing on the stock exchange. In this case, they can rather be interpreted as the hourly system costs for one additional unit of electricity or hydrogen. Summarised, the hydrogen demand is covered mainly by pipeline import from Spain (66 %) and import via ship (30 %). From a system perspective, the mean electricity supply costs 64.06 € MWh^{-1} and the mean hydrogen supply costs 44.95 € MWh^{-1} in the base case scenario. In a restricted overarching system, both electricity and hydrogen prices rise. In the H2restr. scenario, in more than 20 % of the time hydrogen production in Germany becomes more viable than import. While the average electricity costs increase only slightly, the average hydrogen supply costs increase by almost 25 %, with significantly higher extremes in times of low renewable availability. Here, in some hours of the year, even hydrogen production from biomass becomes economical.

Figure 5 gives an overview of the time-resolved utilisation of flexible power in the described energy system, aggregated for all four regions in the base case scenario. As no electrolysis is operated only battery storage

[3] The number is based on a separate optimization in which the identical system but with twice the sustainable feedstock input potential was calculated.

Table 4: Summary of the hydrogen supply in Germany as comparison between the scenarios BC, H2-high and H2-restr.

	AEL	PEMEL	SOEL	rSOC	ES	IT	Ship
BC in TWh	0.0	0.0	0.0	0.0	176.2	9.6	80.8
H2-high in TWh	0.0	0.0	0.0	0.0	173.5	32.6	202.9
H2-restr. in TWh	0.0	0.0	77.9	0.0	18.1	16.0	36.9

via V2G is used to cover peaks in renewable power generation. Battery storage systems are particularly useful for short-term electricity generation. The available capacity of battery electric vehicles ultimately leads to a factor of 10 greater utilised power of V2G compared to SOFC and H2GT. However, the total amount of energy provided, 94.4 TWh, is comparable to the sum the power generation by fuel cells and gas turbines.

Due to the higher efficiency of the SOFC, fuell cells are used preferably to gas turbines. The load curve in Figure 5 shows that the fuel cells are used to provide the base load in both summer and winter, with a higher share in winter. Particularly during periods of low wind in winter, the fuel cells are operated at full load for several days, as shown in Figure 5 (top left and top right). The fluctuation in the utilisation is greater in summer, which, as can be seen in Figure 5 (top center), falls on the daily rhythm of PV electricity generation and thus behaves comparably to the load peaks of battery storage. Hydrogen gas turbines, in contrast, are used as the last flexibility provider. Particularly in the winter months, some periods can be identified in which gas turbines are operated at full load. However, during the rest of the year, hydrogen gas turbines are only used to cover peak loads for a few hours. The infrastructure of the hydrogen supply via ship combined with the storability of synthesis products as well as the sector coupling effect of hydrogen lead to no further[4] demand of hydrogen storage facilities.

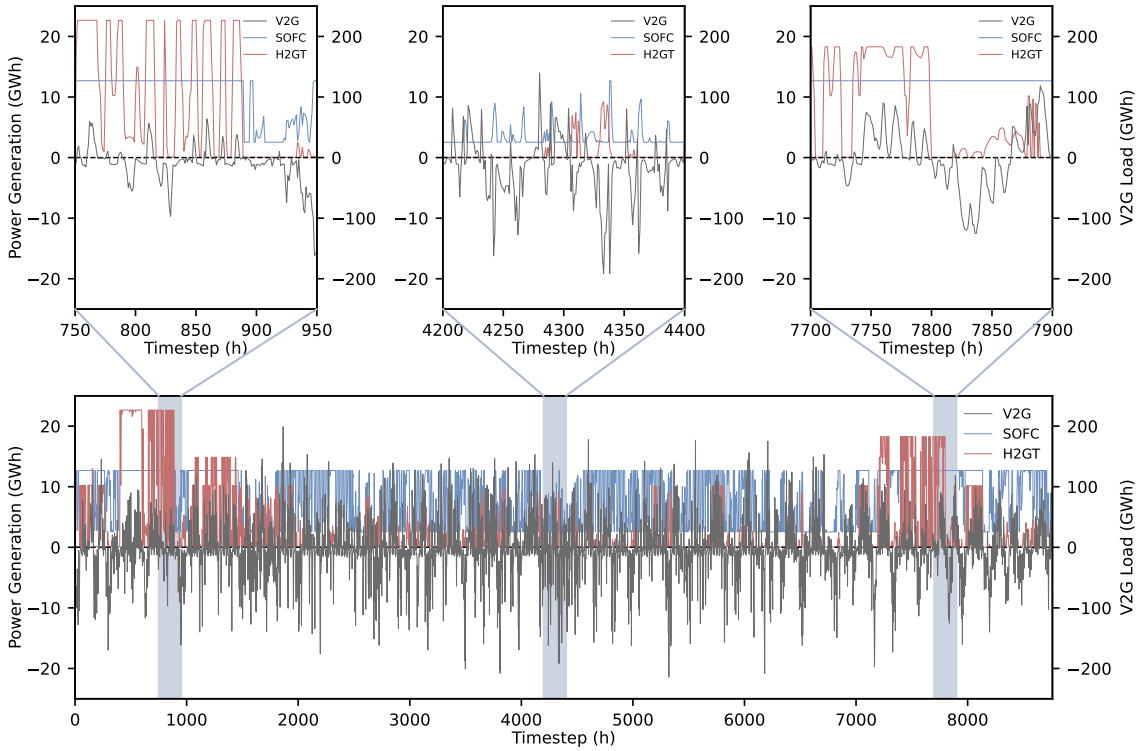

Figure 5: Timeline of the base case power generation via SOFC and hydrogen gas turbines and the utilisation of vehicle-to-grid (V2G) battery storage with additional cut outs for specific time periods.

A more detailed evaluation of the application of hydrogen as a feed-in fuel for electricity generation is shown in the residual load curves of the three scenarios in Figure 6. In the BC scenario and the case of significantly higher hydrogen penetration (Figure 6 left and centre), it can be seen that due to the significantly larger scaled hydrogen production worldwide, on-site generation in Germany is not economical. In contrast, in the restricted scenario (Figure 6 right), electrolysers are operated almost throughout the year. In the case of high residual

[4]Beyond the storage capacity of the ship discharge stations and the storage capacity of the grid.

load, hydrogen serves to provide base load in all cases, whereby a flexible behaviour with short load cycles can be observed except for a few hours. As the residual load decreases, the demand for electricity generation from hydrogen also decreases and fuel cells and hydrogen gas turbines are only required for flexible power. In case of negative residual load, hydrogen is continuously produced in the restricted scenario, whereby high fluctuation can also be seen here.

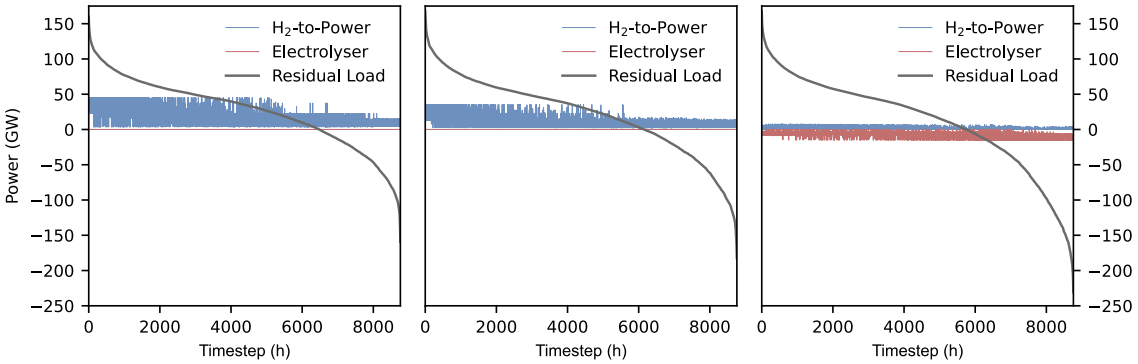

Figure 6: Residual load curve of the H2-high scenario (left), BC scenario (mid) and H2-restr. scenario (right) including the electrolysis and hydrogen based power generation.

4. Conclusion and Outlook

In this work the potential of hydrogen-fuelled gas turbines and solid oxide cells (SOCs) as solutions for providing flexibility in the future electricity grid is evaluated. The study reviews recent publications on both technologies, focusing on the engineering challenges that need to be overcome. Two simplified process simulations ware used to estimate future performance capabilities, and a cost estimation was conducted for both systems.

The analysis finds that both technologies are capable of providing flexible power output in future energy systems with high shares of renewable energy sources. While gas turbines benefit from higher technology maturity and availability, SOCs are more efficient and could act as energy storage due to their reversibility (rSOC), making them a potentially more economical option when considering the whole power-to-gas-to-power chain. However, both technologies still need to overcome significant engineering challenges, such as flashback avoidance in hydrogen gas turbines and better electrolyte and oxygen electrode materials in rSOCs. Cost-wise, gas turbines are currently favored over rSOCs, but rSOCs have the potential to decline in costs as mass manufacturing comes into play.

Energy system modeling shows that if SOCs become economically viable, they could make large scale usage of hydrogen turbines obsolete. Additionally, the results suggest that as long as the electricity supply costs stays to high, electrolysis is not cost-competitive compared to hydrogen import. However, if conservative estimates of future rSOC costs prove correct, the benefits of combining an efficient electrolyser and fuel cell in a single device could make up for the higher costs. Both gas turbines and fuel cells based on SOCs are viable options for providing flexible power output in future energy systems with high shares of renewable energy sources. The choice between these technologies will depend on their respective costs, efficiency, and performance capabilities, as well as the specific requirements of the energy system in question. Both technologies can reduce the overall system costs due to a lower demand of renewable power generation capacities.

However, further model development is needed for a broader discussion of the utilisation of hydrogen in energy systems. On the one hand, the carbon supply for the synthesis of fuels and chemicals could be identified as a limiting factor. Limiting the usability of biomass to what is currently assumed to be sustainable potential by using it to provide heat and electricity and as a carbon source leads to competitive behavior. The utilisation of residues should also be taken into account in order not to impose restrictive boundary conditions on the system. Furthermore, the largest influencing variables could not be clearly determined, which makes the use of a sensitivity analysis indispensable.

Acknowledgments

This study was carried out in the framework of the projects VERENA (project no.: 03EE5044B) sponsored by the Federal Ministry for Economic Affairs and Climate Action (Germany) and GOLD (grant no.: 101006873) as part of the European Union's Horizon 2020 Research and Innovation Program. The financial support is gratefully acknowledged.

Nomenclature

AEL	alkaline electrolysis	**NG**	conventional natural gas	**SOC**	solid oxide cell
EU	European Union	**NH_3**	ammonia	**SOEL**	solid oxide electrolysis
FT	Fischer-Tropsch	**PEMEL**	polymer electrolyte membrane electrolysis	**SOFC**	solid oxide fuel cell
GT	gas turbine			**V2G**	vehicle to grid
H_2	hydrogen	**rSOC**	reversible solid oxide cell	**WOFF**	Offshore wind turbines
MeOH	methanol	**SNG**	synthetic natural gas	**WON**	Onshore wind turbines

Appendix A Energy System Model Technology Portfolio

Table 5: Summary of the considered technology portfolio per region and temporal availability, as well as the associated demand and limitations.

technology	regions	time span	associated demand	limitations
power generation				
photovoltaic	DE, EU[a]	today-2045	electricity	local solar irradiation
onshore wind	DE, EU[a]	today-2045	electricity	local wind potential
offshore wind	DE, EU[a]	today-2045	electricity	local wind potential
biomass plants	DE, EU[a]	today-2045	electricity	local biomass potential
hydro power	DE, EU[a]	today-2045	electricity	today's capacities
CCGT	DE, EU[a]	today-2045	electricity	-
nuclear plant	EU[a]	today-2045	electricity	-
coal power plant	DE, EU[a]	today-2030	electricity	-
battery storage[b]	DE, EU[a]	today-2045	electricity	-
pumped hydro	DE, EU[a]	today-2045	electricity	today's capacities
power grid	DE, EU[a]	today-2045	electricity	-
building-specific heat supply				
heat pump	DE	today-2045	domestic heating	predefined demand[c]
heating rod	DE	today-2045	domestic/process heating	predefined demand[c]
biomass boiler	DE	today-2045	process heating	predefined demand[c]
gas boiler	DE	today-2045	process heating	predefined demand[c]
grid-connected heat supply				
heat pump	DE	today-2045	domestic heating	predefined demand[c]
heating rod	DE	today-2045	domestic heating	predefined demand[c]
biomass CHP	DE	today-2045	domestic heating	predefined demand[c]
gas CHP	DE	today-2045	domestic heating	predefined demand[c]
geothermal energy	DE	today-2045	domestic heating	predefined demand[c]
base chemicals and energy carriers				
electrolysis	DE, ES, IT	today-2045	H_2	-
power-to-x	DE	today-2045	MeOH, SNG, NH_3, FT-fuels	CO_2 point sources[d]
biomass-to-x	DE	today-2045	H_2, MeOH, SNG, NH_3, FT-fuels	local biomass potential
polygeneration[e]	DE	today-2045	H_2, MeOH, SNG, NH_3, FT-fuels, electricity	local biomass potential
hydrogen import	DE	today-2045	H_2	-
hydrogen pipelines	DE, ES, IT	today-2045	H_2	-

[a] If applicable in specific region.

[b] Implemented as bi-directional battery electrical vehicle storage: .

[c] The demand is calculated by an GIS based analysis in [31].

[d] If applicable to specific technology. This includes cement plants and fossil gas power plants.

[e] Polygeneration of synthetic energy carriers and electricity from biogenic feedstock.

References

[1] European Commission (07-15-2022): *Commission Delegated Regulation (EU) 2022/1214*. In: Official Journal of the European Union. https://eur-lex.europa.eu last accessed 02-13-2023.

[2] Hanel, Andreas and Fendt, Sebastian and Spliethoff, Hartmut (2022): *Operation of Conventional Power Plants During the German Energy Transition: A Mini Review*. In: Front. Energy Res. 10, 907251. doi:10.3389/fenrg.2022.907251.

[3] Ehret, Armin and Freimark, Manfred and Gampe, Uwe and Walter, Jens (2023): *vgbe Positionspapier. Factsheet H2-Readiness für Gasturbinenanlagen*. https://www.vgbe.energy/ last accessed: 02-08-2023

[4] Hanel, Andreas and Fendt, Sebastian and Spliethoff, Hartmut (2022): *Kampf der Studien - Ein Update*. doi:10.13140/RG.2.2.26608.12803.

[5] Yue, Meiling and Lambert, Hugo and Pahon, Elodie and Roche, Robin and Jemei, Samir and Hissel, Daniel (2021): *Hydrogen energy systems: A critical review of technologies, applications, trends and challenges*. In: Renewable and Sustainable Energy Reviews 146, S. 111180. doi:10.1016/j.rser.2021.111180.

[6] Ball, M. and Wietschel, M. and Rentz, O. (2007): *Integration of a hydrogen economy into the German energy system: an optimising modelling approach*. In: International Journal of Hydrogen Energy 32 (10-11), p. 1355–1368. doi:10.1016/j.ijhydene.2006.10.016.

[7] Robinius, Martin and Raje, Tanmay and Nykamp, Stefan and Rott, Tobias and Müller, Martin and Grube, Thomas et al. (2018): *Power-to-Gas: Electrolyzers as an alternative to network expansion – An example from a distribution system operator*. In: Applied Energy 210, S. 182–197. doi:10.1016/j.apenergy.2017.10.117.

[8] Li, Xinyu and Mulder, Machiel (2021): *Value of power-to-gas as a flexibility option in integrated electricity and hydrogen markets*. In: Applied Energy 304, S. 117863. doi:10.1016/j.apenergy.2021.117863.

[9] He, Guannan and Mallapragada, Dharik S. and Bose, Abhishek and Heuberger-Austin, Clara F. and Gençer, Emre (2021): *Sector coupling via hydrogen to lower the cost of energy system decarbonization*. In: Energy Environ. Sci. 14 (9), S. 4635–4646. doi:10.1039/d1ee00627d.

[10] Ramsebner, Jasmine and Haas, Reinhard and Ajanovic, Amela and Wietschel, Martin (2021): *The sector coupling concept: A critical review*. In: WIREs Energy Environ. 10 (4). doi:10.1002/wene.396.

[11] European Commission (02-10-2023): *Commission Delegated Regulation (EU) 2023/1087*. In: Official Journal of the European Union. https://energy.ec.europa.eu last accessed 03-13-2023.

[12] United Nations Economic Commission for Europe (2022): *Carbon Neutrality in the UNECE Region. Integrated Life-cycle Assessment of Electricity Sources*. https://unece.org last accessed 02-15-2023.

[13] Patonia, Aliaksei and Poudineh, Rahmatallah (2022): *Cost-competitive green hydrogen: how to lower the cost of electrolysers?* In: The Oxford Institute for Energy Studies (OIES paper EL, 47). https://www.oxfordenergy.org last accessed: 02-15-2023.

[14] Buttler, Alexander and Spliethoff, Hartmut (2018): *Current status of water electrolysis for energy storage, grid balancing and sector coupling via power-to-gas and power-to-liquids: A review*. In: Renewable and Sustainable Energy Reviews 82, S. 2440–2454. doi:10.1016/j.rser.2017.09.003.

[15] Brändle, Gregor and Schönfisch, Max and Schulte, Simon (2020): *Estimating Long-Term Global Supply Costs for Low-Carbon Hydrogen*. https://www.ewi.uni-koeln.de last accessed: 02-22-2023.

[16] Wietfeld, Axel and Krieg, Dennis and Hajjar, Thomas and Mitra, Sumit and Meier, Rebecca (2021): *Competitiveness of green hydrogen import pathways for Germany in 2025*. https://emvg.energie-und-management.de last accessed: 02-22-2023.

[17] Gazzani, M. and Chiesa, P. and Martelli, E. and Sigali, S. and Brunetti, I. (2014): *Using hydrogen as gas turbine fuel: premixed versus diffusive flame combustors*. Journal of engineering for gas turbines and power, 136(5). doi:10.1115/1.4026085.

[18] Noble, D. and Wu, D. and Emerson, B. and Sheppard, S. and Lieuwen, T. and Angello, L. (2021): *Assessment of current capabilities and near-term availability of hydrogen-fired gas turbines considering a low-carbon future*. Journal of Engineering for Gas Turbines and Power, 143(4). doi:10.1115/1.4049346.

[19] Benim, A. C. and Syed, K. J. (2014): *Flashback mechanisms in lean premixed gas turbine combustion*. Academic press. doi:10.1016/C2013-0-18847-2.

[20] Beita, J. and Talibi, M. and Sadasivuni, S. and Balachandran, R. (2021): *Thermoacoustic instability considerations for high hydrogen combustion in lean premixed gas turbine combustors: a review*. Hydrogen, 2(1), 33-57. doi:10.3390/hydrogen2010003.

[21] Stefan, E. and Talic, B. and Larring, Y. and Gruber, A. and Peters, T. A. (2022): *Materials challenges in hydrogen-fuelled gas turbines*. International Materials Reviews, 67(5), 461-486. doi:10.1080/09506608.2021.1981706.

[22] Bothien, M. R. and Ciani, A. and Wood, J. P. and Fruechtel, G. (2019): *Toward decarbonized power generation with gas turbines by using sequential combustion for burning hydrogen*. Journal of Engineering for Gas Turbines and Power, 141(12), 121013. doi:10.1115/1.4045256.

[23] Mogensen, M. B. and Chen, M. and Frandsen, H. L. and Graves, C. and Hansen, J. B. and Hansen, K. V. and Sun, X. (2019): *Reversible solid-oxide cells for clean and sustainable energy*. Clean Energy, 3(3), 175-201. doi:10.1093/ce/zkz023.

[24] Mogensen, M. B. (2020): *Materials for reversible solid oxide cells*. Current Opinion in Electrochemistry, 21, 265-273. doi:10.1016/j.coelec.2020.03.014.

[25] Menzler, N. H. and Sebold, D. and Zischke, S. (2019): *SOC degradation: long-term and small-scale effects*. ECS Transactions, 91(1), 719. doi:10.1149/09101.0719ecst.

[26] Sunfire (2016): *Sunfire supplies Boeing with world's largest commercial reversible electrolysis (RSOC) system*. https://www.sunfire.de last accessed: 03-14-2023.

[27] Elcogen (2018): *Reversible Solid oxide cell technology as a power storing solution for renewable energy (Italy)*. https://elcogen.com last accessed: 03-14-2023.

[28] Vimmerstedt, Laura; Stehly, Tyler; Akar, Sertac; Sekar, Ashok; Mirletz, Brian; Stright, Dana et al. (2022): *2022 Annual Technology Baseline (ATB) Cost and Performance Data for Electricity Generation Technologies*. doi:10.25984/1871952

[29] Böhm, Hans; Zauner, Andreas; Goers, Sebastian; Tichler, Robert; Kroon, Pieter (2018): *Innovative large-scale energy storage technologies and Power-to-Gas concepts after optimization. Report on experience curves and economies of scale.* https://www.storeandgo.info last accessed: 03-09-2023.

[30] Miehling, Sebastian and Lambert, Jerry and Hanel, Andreas and Fendt, Sebastian and Herrmann, Stephan and Spliethoff, Hartmut (2023): *Energy System Optimization using (Mixed Integer) Linear Programming*. In: MethodsX. (submitted).

[31] Miehling*, Sebastian and Schweiger*, Benedikt and Wedel, Wolf and Hanel, Andreas and Spliethoff, Hartmut and Schweiger, Jakob et al. (2021): *100% erneuerbare Energien für Bayern. Potenziale und Strukturen einer Vollversorgung in den Sektoren Strom, Wärme und Mobilität*. doi:10.13140/RG.2.2.25341.081660.

[32] Hanel, Andreas and Seibold, Antonia and Fendt, Sebastian and Spliethoff, Hartmut (2021): *Impact of Power-to-X on Energy Systems as a Key Technology to Defossilization*. In: 34th International Conference on Efficiency, Cost, Optimization, Simulation and Environmental Impact of Energy Systems (ECOS 2021). S. 289–298. doi:10.52202/062738-0026.

[33] Hanel, Andreas and Dossow, Marcel and Fendt, Sebastian and Spliethoff, Hartmut (2022): *Optimized Use of Polygeneration Plants in a Highly Coupled Energy System Model*. In: 35th International Conference on Efficiency, Cost, Optimization, Simulation and Environmental Impact of Energy Systems (ECOS 2022).

3D CFD simulation of water droplet dynamics on a fuel cell Gas Diffusion Layer by considering a realistic woven structure

C. Antetomaso[a], S. S. Merola[b], A. Irimescu[c], B. M. Vaglieco[d], S. Di Micco[e] and E. Jannelli[f]

[a] CNR-STEMS, Naples, Italy, christian.antetomaso@stems.cnr.it
[a] University of Naples "Parthenope", Naples, Italy, christian.antetomaso001@studenti.uniparthenope.it
[b] CNR-STEMS, Naples, Italy, simonasilvia.merola@stems.cnr.it
[c] CNR-STEMS, Naples, Italy, adrian.irimescu@stems.cnr.it
[d] CNR-STEMS, Naples, Italy, biancamaria.vaglieco@stems.cnr.it
[e] University of Naples "Parthenope", Naples, Italy, simona.dimicco@studenti.uniparthenope.it
[f] University of Naples "Parthenope", Naples, Italy, elio.jannelli@uniparthenope.it

Abstract:

Proton exchange membrane fuel cells have been identified as suitable for vehicle implementation. As for all fuel cell types, thermal management is a critical issue: the redox reactions taking place in the membrane electrode assembly generate water; a humid membrane is able to enhance transport phenomena, but too much water could flood the pathways of reactant gases. Recently, interest has grown with respect to the properties of the gas diffusion layer of membranes: its fibres pattern can critically affect water removal rates. Computation fluid dynamics represents a powerful tool that can be used for understanding the key design factors of fuel cell components to improve the overall performance. Specifically, in the case of the diffusion layer, 3D simulation can investigate droplet dynamics and define the optimized surface structure for water management. In this paper, optical data and numerical results were combined to characterize the behaviour (oscillation, detachment, etc) of a couple of droplets on the woven gas diffusion layer with a structure retrieved by using an approach typical of the textile industry. High-spatial resolution imaging allowed the evaluation of warp/weft size; these parameters were used for building the 3D mesh for simulations based on the Volume of fluid method. The dynamics of droplets, with diameters ranging from 200 to 600 µm, were investigated under the effect of a constant 10 m/s airflow for different gas diffusion layer geometries. In addition, the cases of the droplet pairs, deposited at different reciprocal distances, were studied by using the same methodological approach. Results demonstrated the impact of layer structure on the results obtained through simulations; moreover, an optimised design can contribute to control water removal and minimise flooding effects.

Keywords:

3D CFD, optical visualization, water dynamics, gas diffusion layer

1. Introduction

Among the numerous types of fuel cells, Proton Exchange Membrane (PEM) Fuel Cells (FCs) have gained a lot of interest in automotive industries due to the absence of pollutant emissions from the end gases pipeline and its low operative temperature. PEM FC is an established and reliable technology, but it still presents unresolved issues. Among them, water management is one of the most critical, given the need to humidify the membrane and the simultaneous risk of flooding the reactant pathways toward the catalyst layer.

In the last decade, research activities regarding water dynamics in PEM FCs were mainly focused on the design and characteristics of bipolar plates [1]: fabrication methods and innovative materials, suitable coatings and efficient channel design to simultaneously improve reactants diffusion and water removal rate. Those were the routes to further develop PEM FCs. Only recently, the design of properties of cloth Gas Diffusion Layer (GDL) have been considered more carefully [2], with the aim of improving water management by means of a potentially controlled droplet adhesion on the surface, while also studying flow through GDL. In this regard, efforts were mainly directed toward a deep comprehension on how the number and the pores dimension [3], fibers radius and distribution [4], porosity and permeability [5-6] and interface between GDL

and Catalyst Layer (CL) [7-8] can improve the FCs overall performances: optimization of the design of this layer is fundamental since GDL serves both as pathway for reactant gases and escape route for the forming water. However, as water emerge from GDL, is also important to boost its removal rate. Thus, starting from the well-known concept that the GDL wettability and surface roughness affect water dynamics [9-10], specific solutions such as GDL perforation [11] characteristics have been studied to enhance the drainage of the water from the electrode to the gas channel and to reduce the risk of flooding. As concern the numerical simulation of water detachment/rolling/sliding, both the lattice Boltzmann and the Volume Of Fluid (VOF) methods have been widely used to investigate droplet behaviour on the GDL with different channel geometry. A common assumption made in these models is to consider a smooth GDL surface [12-13], but recently authors started to investigate the role that microgeometry may play in membrane optimal design. Hou et. Al [14] used the lattice Boltzmann method to simulate droplet motion on a realistic GDL, confirming that a smooth surface led to faster water removal. Liu et al. [15] performed a 3D VOF assuming different patterns for the GDL: it was still an impermeable and hydrophobic surface, but they used a striped, dotted and waved surface to study the effects of GDL's microstructure and optimize the shape parameters of those "disturbances". Anyanwu et al. [16] compared the liquid water transport in wave-like channels for smooth and rough GDL. They substantially demonstrated that smaller fiber diameters and more ordered and uniform microstructure reduced the flooding of flow channels by favouring water removal. Wang et al. [10] performed molecular simulation of a droplet and proposed to improve water removal capacity by controlling superficial roughness of the GDL. Gao et. Al [4] focused their effort on reconstructing a realistic microgeometry for the outer layer of the Membrane Electrode Assembly (MEA) and evaluated the fluid flow through it. The nature of the woven structure allowed them to define a primitive cell: the interlaced GDL was represented by serial repetition of this primitive element.

Currently, few research efforts have combined experimental results and simulation analysis related to the droplet movement on a real GDL surface. In this paper, optical data and numerical results were combined to characterize the behaviour (oscillation, detachment, etc) of droplets on the woven GDL with a structure retrieved by using a typical approach of the textile industry. High-spatial resolution imaging allowed the evaluation of warp/weft size; these parameters were used for building the 3D mesh for CFD simulations based on the VOF method. The single droplets and pairs, with diameters ranging from 200 to 600 μm, were deposited at different reciprocal distances and their dynamics were studied under the effect of a constant 10 m/s airflow. Results obtained by simulations with different microstructure geometries were compared. In particular, a completely smooth surface and a hybrid one between the previous two were generated.

2. Experimental setup

Water dynamics were studied on the carbon cloth GDL of a Celtec®-P1000 membrane electrode assembly (MEA) with an active area of 45 cm^2 (6.72 by 6.72 cm). In order to support the CFD simulations, optical methodologies were applied to determine the structure of the GDL and the static contact angles of deposited water droplets. The GDL texture and profile were visualised by means of an 8-LED ring crown illuminator mounted on a 1280x720 digital microscope (Technaxx TX-158). This was equipped with a 1000x digital zoom system that permitted to range the spatial resolution up to 5.8 μm/pixel in full chip configuration. In Fig.1a-b, the texture with woven fibres is clearly distinguishable. Following an approach derived from the textile industry [17-18], a custom routine for image processing was developed by using NI Vision [19]; it allowed delineating the GDL geometrical cross-section (Fig.1c).

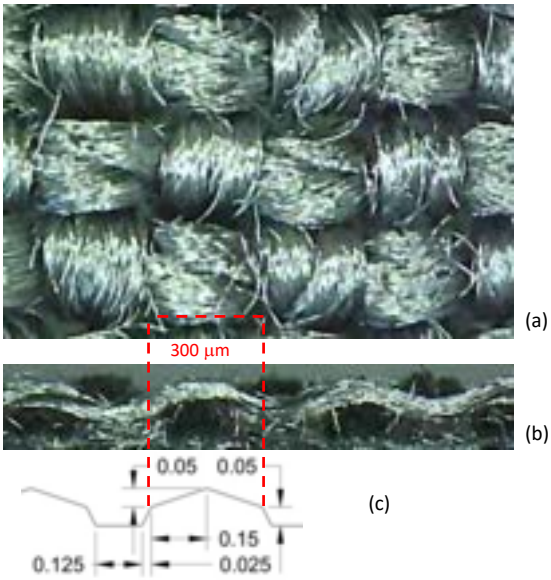

Figure. 1. GDL carbon cloth texture: (a) experimentally visualised surface and (b) profile; (c) geometrical profile used for CFD simulations (units are expressed in µm).

The GDL surface was mapped in 25 regions of interest 1x1 cm in size (Fig. 2a). On each region, a stainless-steel needle of a high-precision medical device (NIPRO) was used for depositing several droplets with a minimum diameter of 400 µm (due to the internal dimension of the capillary) [19-20]. With the digital visualization set-up described previously, droplet morphology was evaluated in terms of diameter and static contact angle. The occurrence distribution related to 115 droplets (Fig. 2b) demonstrated that the most probable contact angle (CA) for droplet in the 400-800 µm size range was 123±2 deg. This value agreed with those considered by other researchers for woven GDL surfaces [21]. The measured contact angles were practically constant, as shown in Fig. 3 that reports the average values measured for 9 classes of droplet diameters (from 400 µm to 800 µm step 50 µm). Consequently, 123 deg was used as boundary condition for the wettability parameter in the CFD simulations.

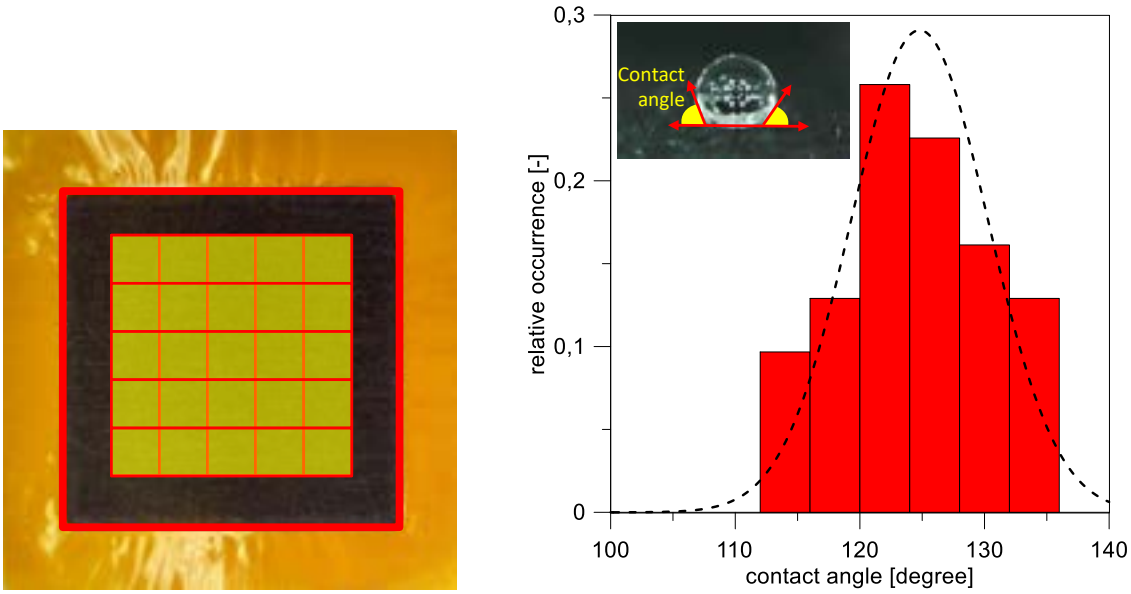

Figure. 2. (a) MEA with 25 regions of interest highlighted on GDL surface for optical investigations and (b) occurrence distribution of droplet contact angles.

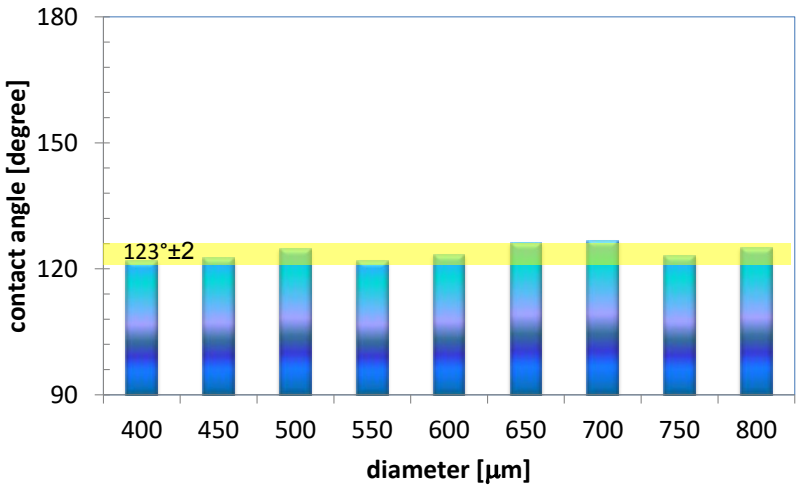

Figure. 3. Average contact angle of 9 classes of droplet diameter.

Droplet dynamics were investigated by using a 512x512 CMOS camera (5000fps in full chip configuration) coupled with a 25 mm objective. The setup allowed to achieve a spatial resolution of 55 µm/pixel. The exposure time was fixed in order to detect 1000 images per second; the setting represented a good compromise between luminosity and temporal resolution. Another image processing procedure developed

using NI Vision 2020 was applied for assessing the instantaneous contour and the centre of mass of the droplets. For dynamic conditions, 10m/s airflow was provided by a fan positioned at 50 mm from the region of droplet deposition; local air velocity was measured with an accuracy of 0.1 m/s by using a hot-film probe.

Optical investigations were performed in open-channel conditions. Since the air-flow rate and static wettability were fixed, the surface roughness was the only parameter that influenced the dynamic wettability and the adhesive force at the liquid-solid interface. In real-working configuration, humidity of the reactant gas should be considered when evaluating the removal efficacy of droplets from the GDL and flow channel. This is due to the fact that phase change phenomena and modifications in surface tension could occur. Nevertheless, this study mainly focused on the effects of airflow and GDL roughness on droplet removal; the effects of reactant gas humidity was out of the scope of the present work, but will be considered in future investigations.

3. Methodology

3.1. GDLs design

Taking into account the GDL's microstructural characteristics determined by optical methodologies, CREO Parametric 8.0 was used to design the 3D profile. The optical analysis was able to recover the two key parameters to reconstruct a realistic geometry: the height and length of the sinusoidal waves that interlaces on the surface. These dimensions, together with the width of the weft, were used to trace four sweep trajectories for a trapezoidal profile. The four surfaces were then merged and trimmed to obtain a squared elemental region. The latter could be used in the "Serial Repetition" CREO function to create a surface of the desired dimensions. Figure 4 shows the generation process and the obtained elemental region. Two more GDL surfaces were generated: a completely smooth and a hybrid solution one. The generation of the latter follow the same methodology showed in Figure 4, but amplitude and length were set equal to 0.075 mm and 0.4 mm respectively.

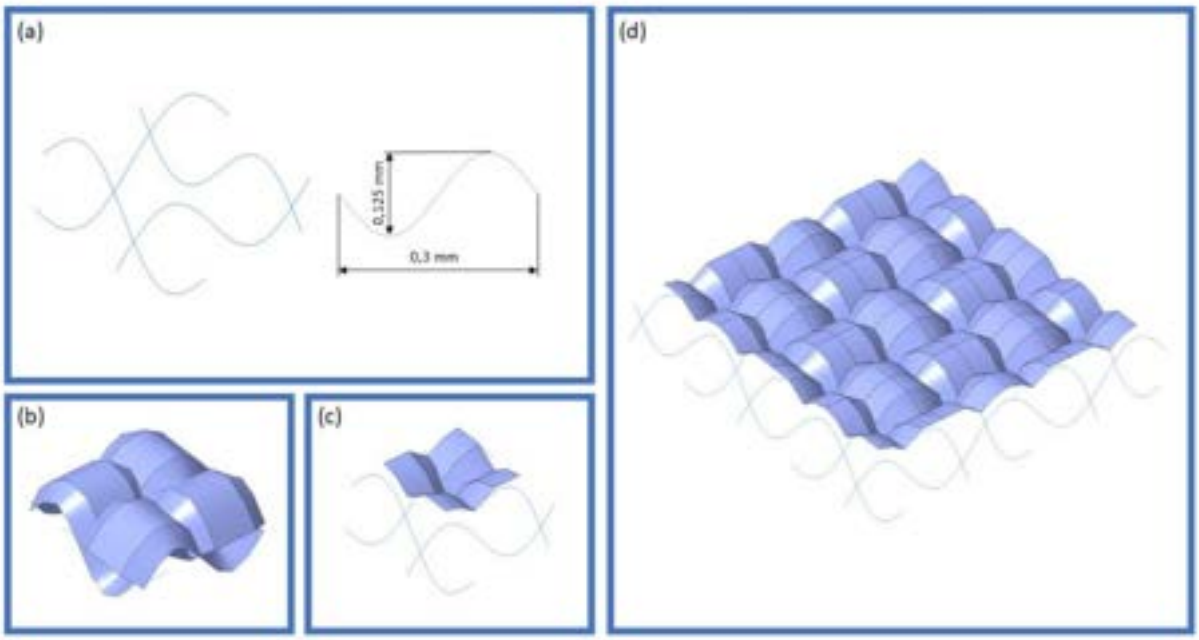

Figure. 4. Steps followed in generating the realistic GDL: (a) definition of 4 sinusoidal waves and their dimensions; (b) sweep of a trapezoidal profile on the defined trajectories; (c) surface trimming and identification of elemental regions; (d) serial repetition of elemental regions.

3.2. Governing equations

The VOF is one of the most used methods to simulate multiphase flow and it is the one adopted in this paper. The main characteristic of this method is that it assigns a numerical value to each cell. This index α_q represent the fraction of secondary phase presents in the cell; in particular:

- $\alpha_q = 0$, the cell contains pure primary phase,

- $\alpha_q = 1$, the cell contains pure secondary phase,
- $0 < \alpha_q < 1$, the cell contains a mixture of the two phases,

given that:

$$\sum_{q=1}^{n} \alpha_q = 1 \quad (1)$$

For every cell, with n equals to the number of phases in the flow. Considering two phases (air and liquid water), viscosity μ and density ρ are evaluated through a weighted mean as shown in Formula (2) and (3).

$$\rho = (1 - \alpha) \cdot \rho_1 + \alpha \cdot \rho_2 \quad (2)$$

$$\mu = (1 - \alpha) \cdot \mu_1 + \alpha \cdot \mu_2 \quad (3)$$

Mass conservation is expressed as:

$$\frac{\partial \rho}{\partial t} + \nabla(\rho \cdot \overline{v}) = 0 \quad (4)$$

A single momentum equation is solved through the domain:

$$\frac{\partial}{\partial t}(\rho \cdot \overline{v}) + \nabla(\rho \cdot \overline{v} \cdot \overline{v}) = -\nabla p + \nabla\left[\mu\left(\nabla\overline{v} + \nabla\overline{v}^T\right)\right] + \rho \cdot \overline{g} + \overline{F} \quad (5)$$

The Continuum Surface Force (CSF) model for a two-phase flow can be simplified as:

$$\overline{F} = \sigma \cdot \frac{\rho \cdot k \cdot \nabla\alpha}{\frac{1}{2} \cdot (\rho_1 + \rho_2)} \quad (6)$$

where σ and k are surface tension coefficient and surface curvature of the interface respectively.

3.3. Domain definition and simulation setup

The elemental square previously defined was used to model one of the surfaces of a 1x1x4.8 mm box and to obtain the simulation domain. The modified surface would represent the hydrophobic and impermeable GDL, whilst the others would represent the velocity inlet, pressure outlet and channel walls. The base dimension of the cell was set to 0.02 mm. A three layers inflation was added on the GDL.

Simulations were performed with Ansys Fluent 2022 R1. The whole domain was initialized as still air, then a water droplet was deposited on the GDL surface at 1 mm distance from the velocity inlet. Droplets ranged from 200 to 600 μm. From 0 to 1 ms of simulation, the inlet would be set to 0 m/s to allow the droplet to properly set on the surface. Thereafter a constant airflow of 10 m/s started to push the droplet. The flow was assumed to be laminar. Surface tension coefficient between water and air was set to 0.072 N/m and wall adhesion model was enabled.

The pressure-based solver was used for transient 3D simulation. Pressure-Implicit with Splitting of Operators (PISO) algorithm was selected for pressure-velocity coupling. PREssure STaggering Option (PRESTO!), Second Order Upwind and Geo-Reconstruct schemes were used respectively for pressure, momentum and volume fraction. Adaptive multiphase specific time step was adopted to improve solution stability. Simulated time was set to 25 ms.

4. Results and discussions

The typical liquid drainage process inside a GDL flow channel includes droplets emerging, growing, detachment, and removal. After the detachment, the airflow drives the liquid droplet out of the channel and another droplet emerges from the GDL pore simultaneously [13]. Water removal is mainly realized according three modes of movement: rolling, lifting, and break-up [22]. Studies demonstrated that the occurrence of each mode was influenced by the airflow rate, while no definitive results on the effects of surface roughness were discussed [23]. The first case in which it is possible to immediately identify the importance of a realistic interlaced GDL surface is the one that features 300 μm droplet diameter. Figure 5 clearly shows how the droplets on the realistic and hybrid surface were able to reach the exit of the closed channel, but with a significant time difference with respect to the flat design.

Dimensions of pores between warp and weft yarns of GDL texture comparable with the droplet diameter led to a longer detachment phase and slower movement towards the outlet. Figure 6 shows that at increasing droplet size the GDL microstructure decreased its influence on the water removal process; 600 μm droplets moved out the channel domain almost simultaneously for the realistic and hybrid case. For a more detailed characterization of droplet dynamics, high-speed visualization was applied for diameters of 600±20 μm as

estimated in static conditions. Fig.7a reports several selected frames of a 50ms sequence recorded for a 605 μm droplet. In agreement with the literature [24], after liquid deposition (#1) switching-on the fan determined around 1 second of droplet contour oscillations (as shown in frames #2-#3) due the balance between detaching and retention forces [25-26]. This occurred until a critical local velocity was reached; then the droplet started to move in the direction of the air-flow (#4) and reached the limit of the optical region in about 6 ms. It should be noted that the droplet motion was characterised by rolling rather than sliding. Thus the assumption to fix the GDL wettability without differentiating between advancing and receding angles resulted reasonable.

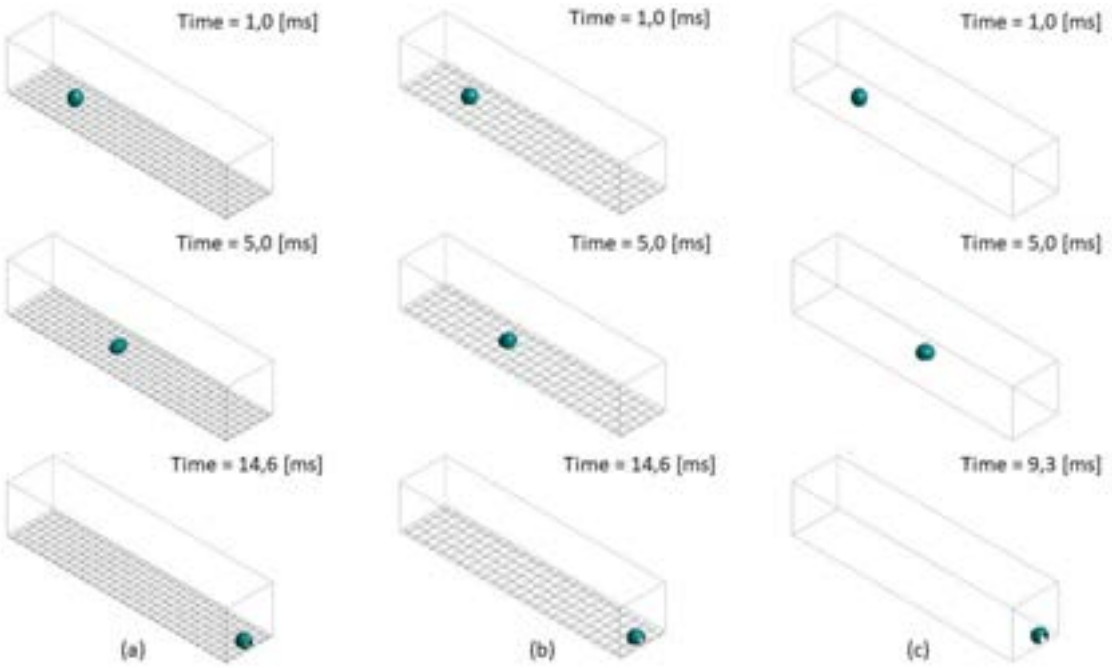

Figure. 5. Water fraction isosurface (equal to 0.8) for different GDLs for a 300 μm droplet. (a) Realistic GDL, (b) Hybrid GDL, (c) Flat channel surface.

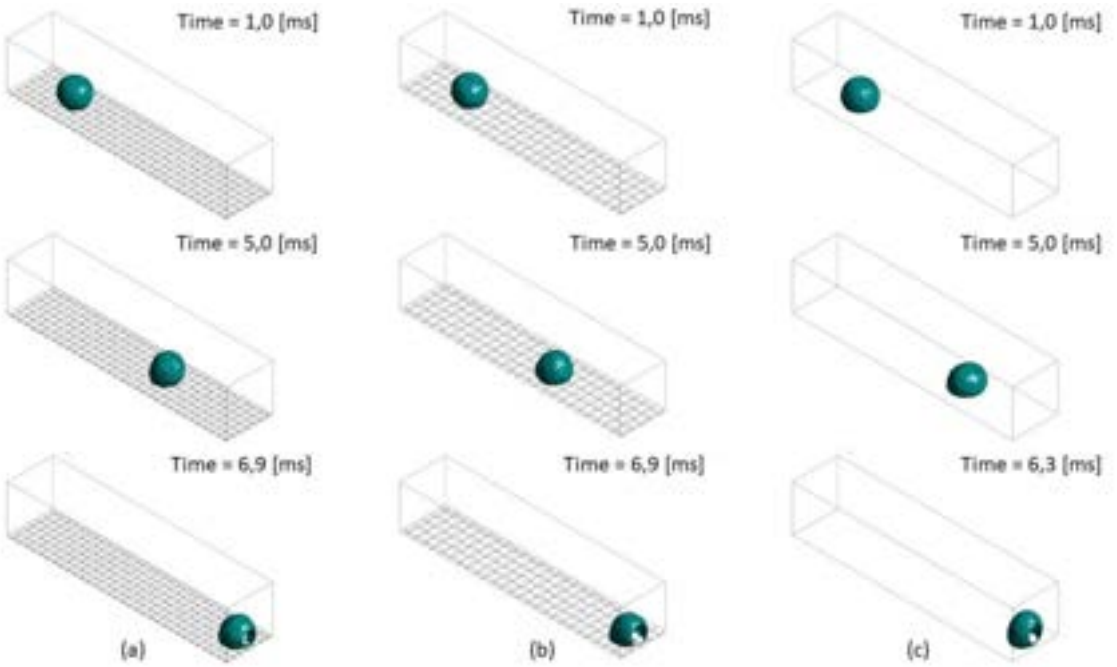

Figure. 6. Water fraction isosurface (equal to 0.8) for different GDLs for a 600 μm droplet. (a) Realistic GDL, (b) Hybrid GDL, (c) Flat channel surface.

The optical data were used for validating the simulation results; Fig.7b shows the comparison between the temporal evolution of the distance from the deposition point along the air-flow direction of a 600 μm droplet. The experimental results show the average value of the luminous center of mass calculated based on 15 sequences. The error bars correspond to the standard deviation. The agreement between simulation and experiments is very good; the discrepancy observed after 5 ms was due to the open channel condition of the optical tests that determined lower pressure forces on the droplet and thus lower acceleration. Nonetheless, it can be stated that model validation is satisfactory.

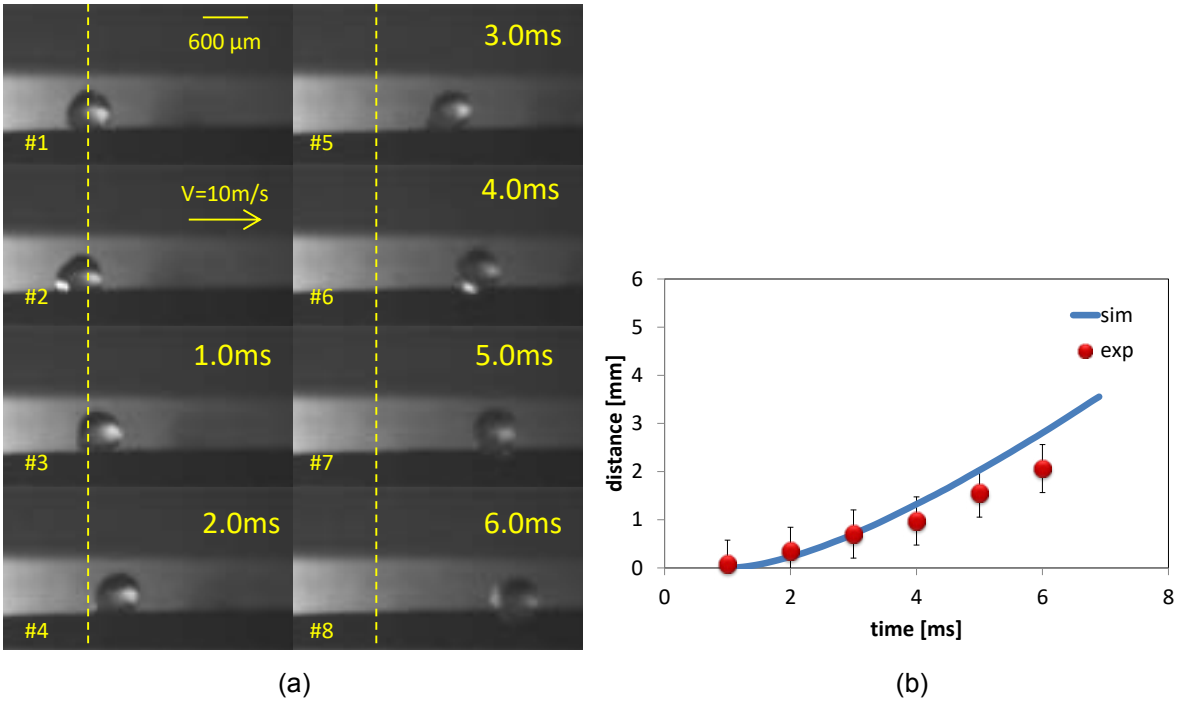

(a) (b)

Figure. 7. Visualization of the droplet motion on the GDL (a) and comparison with simulation results (b).

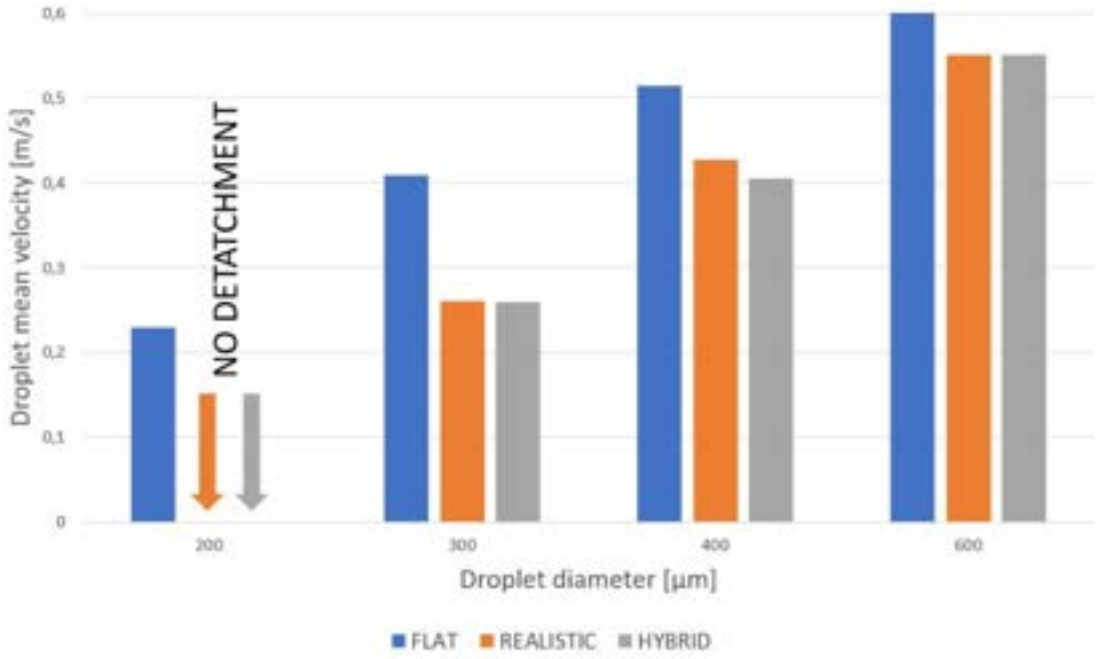

Figure. 8. Comparison of droplet mean velocity for all dimensions and cases analysed.

Fig.8 shows the mean droplet velocity for all the analyzed cases. Once again, the graph remarks that the importance of GDL microstructure is noticeably higher for smaller dimension, when droplet and pores have comparable sizes. However, even in the 600 µm case the droplet mean velocity is around 8% lower for the realistic and hybrid case, so still a significant amount.

Initial water removal time was defined as the instant in which the droplet as a whole surpassed a plane perpendicular to the airflow and passing through the middle of the drop when it is deposited. Figure 9 shows simulations results. For sure the flat surface is the one that led to faster removal since there are no obstacles in the way of the droplet. On the other hand, the pores of the realistic and hybrid surfaces offer a certain resistance to the initial rolling of the droplet. Moreover, even though the hybrid case has a lower sinusoidal amplitude and a higher wavelength and thus should be more similar to the flat one, it seems to offer more initial resistance. This outcome is linked to the fact that it also has a bigger wet area with respect to the realistic surface, increasing the adhesive force. These results agree with literature [14-15] that found that the GDL microstructure can slow down the droplet motion compared to the smooth surface simplification.

It worth noting that for both Fig. 8 and Fig. 9 the leftmost column reports a “no detachment” condition for the 200 µm case, since the droplet get stuck in membrane pores. This is a critical condition for the FC operation, since those droplets decrease overall efficiency by:

- blocking reactants flux towards the CL causing flooding and thus cell starvation.
- shielding the incoming airflow, thus reducing water removal rate for downstream drops; as distance increases, airflow reattach to GDL and this effect is reduced.

Water keeps on forming in the CL and the droplet will reach critical dimension and finally be removed. In this sense, the design of GDL superficial microgeometry determines critical detachment diameter.

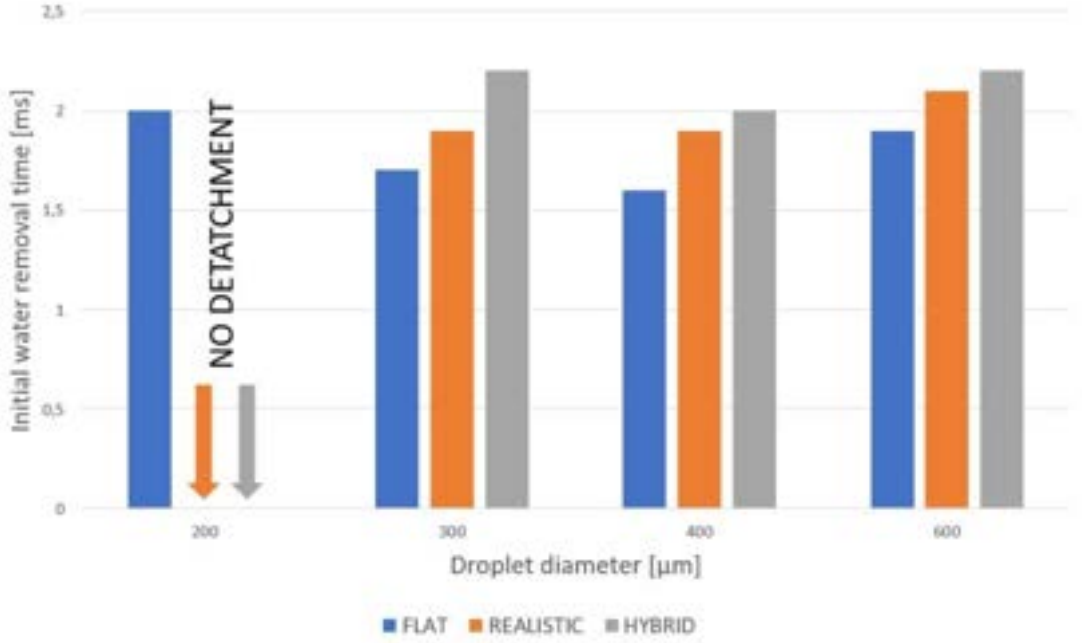

Figure. 9. Confront on droplet initial water removal time for all dimensions and cases analysed

The following step was to investigate how a second droplet could influence the behaviour of the first one. With this purpose, another set of simulation was prepared: a 300 µm droplet was deposited in the same position of the single case (1 mm from the inlet, middle of the channel), and a second one was initialized further in the channel, at a distance that depended on GDL microgeometry. For the real and the hybrid case, the second droplet was deposited in the fourth pore after the first droplet. Figure 10 graphically shows the used principle. For the flat case the used distance was the mean of the distances for the two other cases.

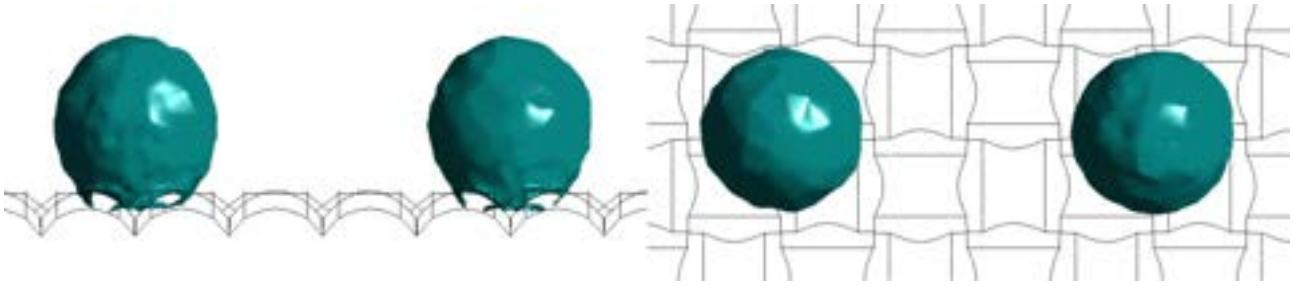

Figure. 10. Reciprocal positioning of the two droplets on the GDL

Simulated droplets at different time steps are shown in Figure 11. Once again, the effect of microgeometry design is highlighted by the difference in flat-realistic cases and realistic-hybrid one. As already seen for the single droplet case, the flat surface offers minimal resistance to the rolling of the pair, however the first droplet partially shield the second one from the incoming airflow, thus it moves at an higher speed. Moreover, the lower the distance between the two droplets, the higher seems to become the speed difference. A parametrization of droplet pair diameters and distances could be of interest for future study. As concern the realistic case, a similar behaviour was observed, but the mean velocities are lower and the initial detachment phase is longer. The comparison of realistic and hybrid case remarked the importance of GDL microstructure: in the hybrid case the second droplet was stuck in position due to the shielding of the first one and the higher wet area with respect to the realistic one. The hybrid GDL showed the highest exit time for this set of simulations.

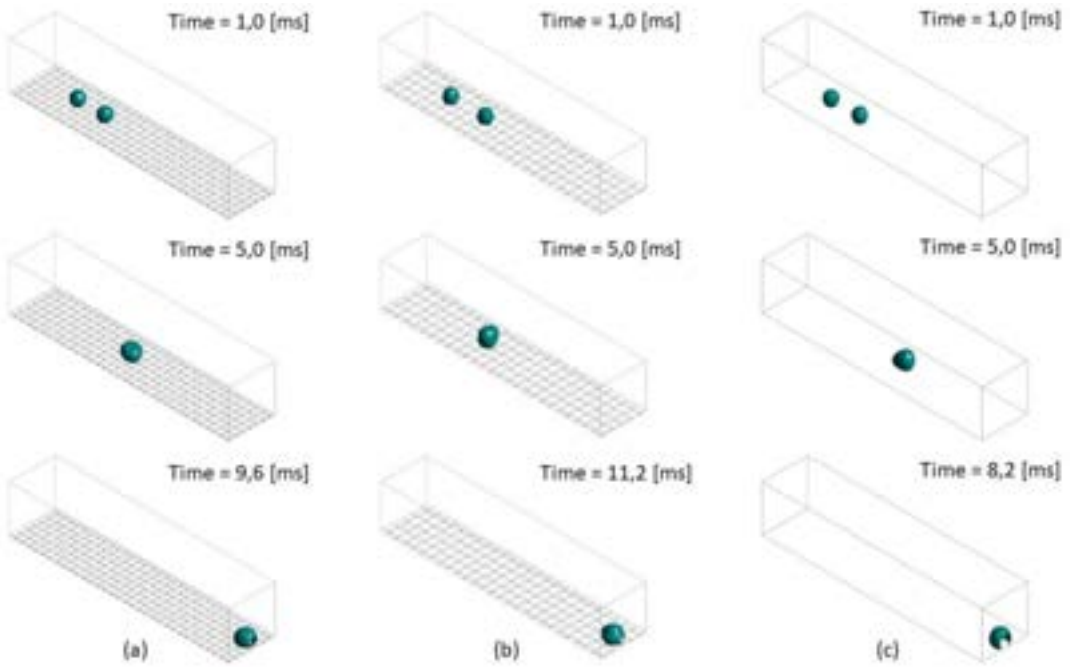

Figure. 11. Water fraction isosurface (equal to 0.8) for different GDLs for the 300-300 μm droplets pair. (a) Realistic GDL, (b) Hybrid GDL, (c) flat GDL

5. Conclusions

PEM FCs represent a decisive step in the direction of a cleaner mobility, but it is a device still far from optimal operation conditions. Experimental and simulation studies are fundamental to fully develop the technology, and in realizing models able to reproduce the actual behaviour of a cell it is important not to over-model a phenomenon. The surface microgeometry of a fuel cell is often deemed as negligible in channel flow simulations. The aim of this study has been to evaluate the importance of this microgeometry and to state if it should be taken into consideration when accounting for water removal rate of a cell.

The main results of this study can be summarized as follow:

- The importance of pores on the surfaces rises as smaller droplets are considered. Starting from the same initial and boundary conditions, the 200 μm droplet on the flat surface was able to reach the outlet, whilst for the others GDLs the drop was stuck in the pore. The influence of the surface is lower for bigger droplet, however even for the 600 μm droplet the mean velocity difference is around 8%.
- The microstructure also affects the initial water removal time of the droplet. The flat surface is the one that shows lower removal time, whilst the other two structures seem to slow down this phenomenon due to the presence of pores that work as obstacles for the droplet. In particular, the hybrid case is the slowest one, due to the fact that it has a bigger wet area with respect to the realistic surface, increasing the adhesive force.
- Simulations showed the influence of a second droplet deposition on different GDLs. Flat surface offers the highest water removal rate, while realistic and hybrid cases shows a behaviour linked to microgeometry design. In particular, due to the partial shielding effect and the higher wet area of the hybrid surface, the second droplet resulted stuck in the pore until it merged with the first one.

Next steps of the reported activity are planned for further improving the water dynamic modelling and evaluate the weight of commonly used approximations on predictive simulations. Specifically, the GDL intrusion in the gas channel and surface deformation near the channel ribs due to the clamping pressure of the cell will be estimated for a more realistic design. Moreover, the reactant gas humidity in closed channel configurations will be considered in the model. These parametric studies are on-going to further shed light on the possibility of a design for promoting controlled water removal mechanisms.

Acronyms

CA	Contact angle
CL	Catalyst Layer
CSF	Continuum Surface Force
FC	Fuel Cell

GDL	Gas Diffusion Layer
MEA	Membrane Electrode Assembly
PEM	Proton Exchange Membrane
VOF	Volume Of Fluid

References

[1] Y. Song, C. Zhang, C. Y. Ling, M. Han, R. Y. Yong, D. Sun, J. Chen, Review on current research of materials, fabrication and application for bipolar plate in proton exchange membrane fuel cell. *International Journal of Hydrogen Energy*, 2020, *45*(54), 29832-29847, https://doi.org/10.1016/j.ijhydene.2019.07.231

[2] G. Athanasaki, A. Jayakumar, A. M. Kannan, Gas diffusion layers for PEM fuel cells: Materials, properties and manufacturing–A review. *International Journal of Hydrogen Energy*, 2022, *48*(6), 2294-2313, https://doi.org/10.1016/j.ijhydene.2022.10.058

[3] J. Cho, H. Oh, J. Park, K. Min, E. Lee, J. Y. Jyoung, Study on the performance of a proton exchange membrane fuel cell related to the structure design of a gas diffusion layer substrate. *International journal of hydrogen energy*, 2014, *39*(1), 495-504, http://dx.doi.org/10.1016/j.ijhydene.2013.10.057

[4] Y. Gao, T. Jin, X. Wu, Stochastic 3D carbon cloth GDL reconstruction and transport prediction. *Energies*, 2020, *13*(3), 572, https://doi.org/10.3390/en13030572

[5] B. P. Abraham, K. K. Murugavel, Influence of catalyst layer and gas diffusion layer porosity in proton exchange membrane fuel cell performance. *Electrochimica Acta*, 2021, *389*, https://doi.org/10.1016/j.electacta.2021.138793

[6] H. Pourrahmani, J. Van herle, Water management of the proton exchange membrane fuel cells: Optimizing the effect of microstructural properties on the gas diffusion layer liquid removal. *Energy*, 2020, *256*, 124712, https://doi.org/10.1016/j.energy.2022.124712

[7] Y. Hiramitsu, K. Kobayashi, M. Hori, Gas diffusion layer design focusing on the structure of the contact face with catalyst layer against water flooding in polymer electrolyte fuel cell. *Journal of Power Sources*, 2010, *195*(22), 7559-7567, https://doi.org/10.1016/j.jpowsour.2010.05.067

[8] L. Guo, L. Chen, R. Zhang, M. Peng, W. Q. Tao, Pore-scale simulation of two-phase flow and oxygen reactive transport in gas diffusion layer of proton exchange membrane fuel cells: Effects of nonuniform wettability and porosity. *Energy*, 2022, *253*, 124101, https://doi.org/10.1016/j.energy.2022.124101

[9] Y. Wang, T. Liu, H. Sun, M. Yao, S. Liu, Y. Qin, X. Wang, Droplet dynamic behaviors on gas diffusion layer surface of various wettabilities in a PEMFC gas flow channel. *International Journal of Green Energy*, 2021, *18*(13), 1369-1382, https://doi.org/10.1080/15435075.2021.1904940

[10] X. L. Wang, W. K. Wang, Z. G. Qu, G. F. Ren, H. C. Wang, Surface roughness dominated wettability of carbon fiber in gas diffusion layer materials revealed by molecular dynamics simulations. *International Journal of Hydrogen Energy*, 2021, *46*(52), 26489-26498, https://doi.org/10.1016/j.ijhydene.2021.05.121

[11] D. Gerteisen, T. Heilmann, C. Ziegler, Enhancing liquid water transport by laser perforation of a GDL in a PEM fuel cell. *Journal of Power Sources*, 2008, *177*(2), 348-354, https://doi.org/10.1016/j.jpowsour.2007.11.080

[12] M. Andersson, A. Mularczyk, A. Lamibrac, S. B. Beale, J. Eller, W. Lehnert, F. N. Büchi, Modeling and synchrotron imaging of droplet detachment in gas channels of polymer electrolyte fuel cells. *Journal of power sources*, 2018, *404*, 159-171, https://doi.org/10.1016/j.jpowsour.2018.10.021

[13] R. Chen, Y. Qin, S. Ma, Q. Du, Numerical simulation of liquid water emerging and transport in the flow channel of PEMFC using the volume of fluid method. *International Journal of Hydrogen Energy*, 2020, *45*(54), 29861-29873, https://doi.org/10.1016/j.ijhydene.2019.07.169

[14] Y. Hou, H. Deng, N. Zamel, Q. Du, K. Jiao, 3D lattice Boltzmann modeling of droplet motion in PEM fuel cell channel with realistic GDL microstructure and fluid properties. *International Journal of Hydrogen Energy*, 2020, *45*(22), 12476-12488, https://doi.org/10.1016/j.ijhydene.2020.02.155

[15] S. Liu, L. Zhang, Z. Wang, R. Li, Influence of the surface microstructure of the fuel cell gas diffusion layer on the removal of liquid water. *International Journal of Hydrogen Energy*, 2021, *46*(62), 31764-31777, https://doi.org/10.1016/j.ijhydene.2021.07.051

[16] I. S. Anyanwu, Z. Niu, D. Jiao, A. U. H. Najmi, Z. Liu, K. Jiao, Liquid water transport behavior at GDL-channel interface of a wave-like channel. *Energies*, 2020, *13*(11), 2726, https://doi.org/10.3390/en13112726

[17] M. M. B. Hasan, A. Calvimontes, A. Synytska, V. Dutschk, Effects of topographic structure on wettability of differently woven fabrics. *Textile Research Journal*, 2008, *78*(11), 996-1003, https://doi.org/10.5772/10477

[18] A. Calvimontes, V. Dutschk, M. Stamm, Advances in topographic characterization of textile materials. *Textile research journal*, 2010,*80*(11), 1004-1015, https://doi.org/10.1177/0040517509348331

[19] C. Antetomaso, A. Irimescu, S. S. Merola, B. M. Vaglieco, S. Di Micco, E. Jannelli, G. Scarpati, E. Simeoni, CFD simulation of water droplet adhesion on the GDL of a low temperature PEM FC in air cross-flow conditions. ATI 2022 proceeding, 2022 Sep 12-14, published in *Journal of Physics: Conference Series*, 2385(1), 12074, https://doi.org/10.1088/1742-6596/2385/1/012074

[20] C. Antetomaso, S. S. Merola, A. Irimescu, B. M. Vaglieco, S. Di Micco, E. Jannelli, G. Scarpati, E. Simeoni, CFD simulation of the interaction between water droplets on the GDL of a low temperature PEM FC in conditions of air cross-flow, EAEC 2022 proceeding, 2022 Oct 26-28.

[21] Y. D. Wang, Q. Meyer, K. Tang, J. E. McClure, R. T. White, S. T. Kelly, M. M. Crawford, F. Iacoviello, D. J. L. Brett, P. R. Shearing, P. Mostaghimi, C. Zhao, R. T. Armstrong, Large-scale physically accurate modelling of real proton exchange membrane fuel cell with deep learning. Nature Communications, 2023, 14(1), 745. https://doi.org/10.1038/s41467-023-35973-8

[22] S. Xu, P. Liao, D. Yang, Z. Li, B. Li, P. Ming, X. Zhou, Liquid water transport in gas flow channels of PEMFCs: A review on numerical simulations and visualization experiments. *International Journal of Hydrogen Energy*, 2023, 48(27), 10118-10143, https://doi.org/10.1016/j.ijhydene.2022.12.140

[23] M. Li, Y. Li, Y. Qin, Y. Yin, J. Zhang, Z. Che, Water droplet detachment characteristics on surfaces of gas diffusion layers in PEMFCs. *International Journal of Hydrogen Energy*, 2022, *47*(18), 10341-10351, https://doi.org/10.1016/j.ijhydene.2022.01.077

[24] S. Burgmann, M. Dues, B. Barwari, J. Steinbock, L. Büttner, J. Czarske, U. Janoske, Flow measurements in the wake of an adhering and oscillating droplet using laser-Doppler velocity profile sensor. *Experiments in Fluids*, 2021, *62*, 1-16, https://doi.org/10.1007/s00348-021-03148-0

[25] A. Esposito, A. D. Montello, Y. G. Guezennec, C. Pianese, Experimental investigation of water droplet–air flow interaction in a non-reacting PEM fuel cell channel. *Journal of Power Sources*, 2010, *195*(9), 2691-2699, https://doi.org/10.1016/j.jpowsour.2009.11.078

[26] S. Burgmann, V. Krämer, M. Rohde, M. Dues, U. Janoske, Inner and outer flow of an adhering droplet in shear flow. *International Journal of Multiphase Flow*, 2022, *153*, 104140, https://doi.org/10.1016/j.ijmultiphaseflow.2022.104140

Partial load and transient operation of methane synthesis reactors using sorption-enhanced catalysis

Andrea Barbaresi[a], Florian Kiefer[b], Mirko Morini[a], Panayotis Dimopoulos Eggenschwiler[b] and Agostino Gambarotta[a]

[a] University of Parma, Parco Area delle Scienze 181/A, Parma, 43124, Italy
*andrea.barbaresi@unipr.it **CA**, mirko.morini@unipr.it, agostino.gambarotta@unipr.it*
[b] Empa, Ueberlandstrasse 129, Duebendorf, 8600, Switzerland
florian.kiefer@empa.ch, panayotis.dimopoulos@empa.ch

Abstract:
Sustainable synthetic carbon-based fuels can play a crucial role in the sectors of transportation, heating, and power, which can be challenging to electrify. Many of these synthetic fuels are based on green hydrogen produced by electrolysis. Due to difficulties in the handling and storage of hydrogen, an interesting solution is to convert it into hydrocarbons such as methane, with the advantage of using a well-established infrastructure and having the drop-in capability to substitute fossil natural gas.
In the presented study, the partial load and the transient behavior of a sorption-enhanced catalytic reactor for methane synthesis is analyzed. This kind of reactor can achieve high conversion through adsorption of product water. Its performance is defined and compared to that of a simulated conventional fixed-bed catalytic reactor without sorption-enhancement. In particular, the focus is on investigating the response to partial loads and load transients. These operating conditions are typically met when the hydrogen production system is directly coupled with fluctuating renewable electricity production, and storage is minimized. The results show an excellent partial load behavior, and, unlike traditional reactors, sorption-enhanced catalysis did not show ignition problems.
This article points out the strength of sorption-enhanced catalysis applied to the process of carbon dioxide methanation in transient and partial load operations both from the point of view of synthesized fuel quality and operation stability.

Keywords:
CO_2 methanation; Sorption-enhanced reactor; Synthetic fuels; Transient operation.

1. Introduction

Nowadays, carbon-neutral fuels are considered as an interesting solution for the energy transition in hard-to-abate sectors. An example is the synthesis of methane from hydrogen and carbon dioxide as a substitute for natural gas.
Methane production is carried out through the Sabatier process, which is characterized by the following reaction [1]:

$$\mathrm{CO_2} + 4\mathrm{H_2} \leftrightharpoons \mathrm{CH_4} + 2\mathrm{H_2O}, \qquad \Delta H_r^0 = -165\ \mathrm{kJ\ mol^{-1}} \tag{R1}$$

This strongly exothermic reaction can take place using heterogeneous catalysis in fixed-bed reactors. The relevance of this system can be deduced since it has been investigated in many experimental studies [2].
If the hydrogen feeding the process is produced via electrolysis from a fluctuating renewable energy supply, its availability would be discontinuous, and this leads to the need for the storage of either electrical energy or hydrogen. In both cases, high storage costs [1] lead to the need to reduce the battery capacity or the volume and the number of hydrogen tanks as much as possible. For this purpose, the synthesis reactor must be able to withstand continuously changing operating conditions. Therefore, an analysis of the behavior of methane production systems with regard to transient and partial load conditions has been developed by the authors and is presented in this paper.
Investigations of the performance of catalytic reactors for methane synthesis at dynamic load conditions reported in the literature are mainly focused on the thermal stability of the system [3,4]. This is due to the fact that too high temperatures could lead to deactivation and degradation of the catalyst while too low

temperatures could lead to failures in igniting the reaction [5]. Moreover, a decrease in reaction yield at transient and high load conditions is usually highlighted [6].
Many efforts have been made in the scientific community to deal with these problems, and various methods have been used to this end. Fischer et al. [7] and Bremer et al. [8] chose to use an adaptive temperature of the coolant, the former at the design stage and the latter by adopting a steady state “multiplicity” control strategy.
Another option available for managing the temperature distribution is the use of a reactor with recirculation, as investigated in Refs. [9–11]. The recirculation ratio was identified as an additional degree of freedom for thermal control.
With specific reference to the reactor, different approaches, mainly concerning temperature control, were evaluated. Stiegler et al. [6] experimentally analyzed the behavior of a rack-type reactor with a high thermal conductivity metal structure. Sun and Simakov [12] simulated a reactor internally cooled by molten salts and Kreitz et al. [13] numerically studied a microstructured fixed-bed reactor with a periodically oscillating feed composition. Another proposed approach is to dilute the catalyst with an inert material, which was done by means of simulation by Fache et al. [14] and both experimentally and numerically by Herrmann et al. [15].
In order to address these challenges while preserving high product quality, there are grounds for deepening the sorption-enhanced catalysis [16].
Therefore, in this study, the behavior of a methanation reactor of the sorption-enhanced type at an unsteady operating condition is investigated and presented. In order to do so, the reactor was tested experimentally at partial load conditions (i.e. partial inlet flow rates) and during transients (i.e. with single-step or multiple-step changes in inlet flow rates). In addition, a model of a catalytic methanation reactor without sorption-enhancement was set up and its results were compared with the measured data.

1.1. Sorption-enhanced CO_2 methanation

In the literature, sorption-enhanced methane synthesis reactors have been reported to achieve very high conversion yields through the removal of water (which is one of the two reaction products) due to in-situ adsorption [16]. Generally, the catalyst bed is composed of a bi-functional material with catalytic and adsorption properties. An important difference with respect to systems without sorption-enhancement is the way in which the reaction takes place. As shown by Borgschulte et al. in [17], sorption-enhanced methanation reactors differ from conventional plug flow reactors in that there is a moving coupled reaction and adsorption front. The propagation velocity of the reaction front (which separates the water saturated section of the reactor from the unsaturated one) depends on the adsorption capacity of the bed and the amount of water that is produced and adsorbed. The greater the amount of water that will interact with a section of the bed, the sooner it will be saturated and the faster the reaction front will move on [18]. From an engineering point of view, this means that a reactor saturated with water must be regenerated. Consequently, at least two reactors operating alternately are needed for continuous methane production.
As regards chemical kinetics, it should be noted that the removal of water leads to a significant increase in the partial pressure of the reactants and especially a decrease in water partial pressure, which leads to improved reaction rates.
In the zone of the reaction front, additional heat is released due to the adsorption process [19] which further promotes the conversion. The water adsorption capacity is inversely proportional to the temperature and directly proportional to the pressure. This behavior leads to a self-stabilizing effect since the greater the amount of adsorbed water, the greater the heat released, but if the temperature rises the bed will be saturated faster and the front will proceed [18].

2. Materials and methods

2.1. Experimental setup

The experimental apparatus involved a fixed-bed oil-cooled catalytic reactor consisting of four reactors arranged in parallel (Fig. 1). The bed consisted of pellets of adsorbent material impregnated with catalyst. In more detail, it was constituted by zeolite 13X pellets with a diameter of 1.6 mm to 2.6 mm impregnated with 5 % nickel on a mass basis [18]. In the inlet sectors of the reactors, these pellets were mixed with aluminum beads to improve heat transfer in that zone and partially absorb the released heat. This approach was used to deal with the problem of the continuous heat release in the inlet sector as reported by Kiefer et al. [18].
Each of the four reactors contained a pellet bed with a height of 1 m and a diameter of 32 mm. The reactors were cooled by thermal oil flowing into an external jacket in each reactor tube. The temperature was adjusted and kept constant with a PID controller (Julabo HT60 thermostat).

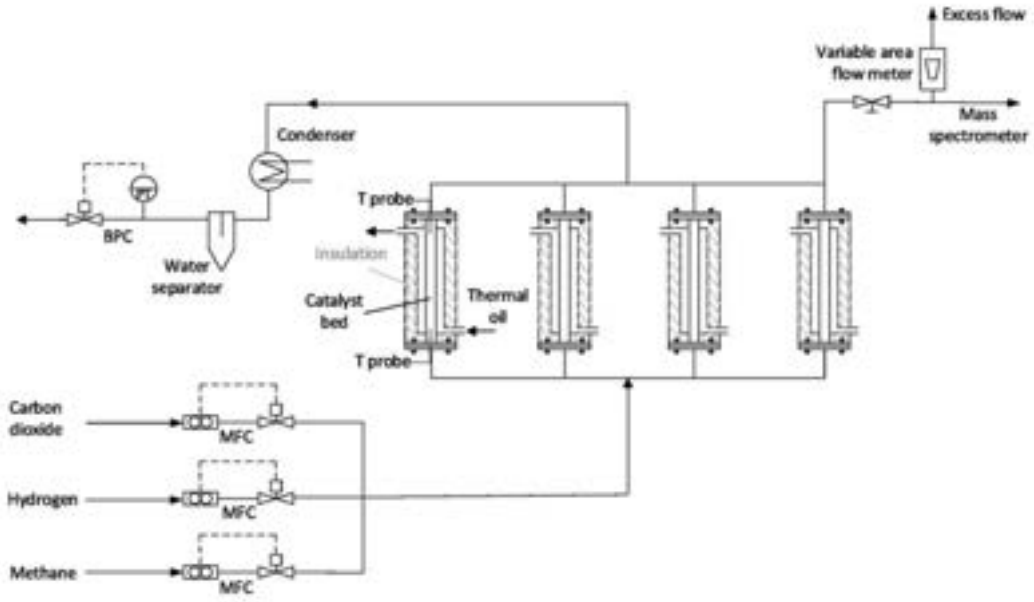

Figure 1. Schematic representation of the sorption-enhanced methanation test rig.

At the inlet and outlet sectors of each reactor duct the temperatures were measured by thermocouples (Type K class A, 1.5 mm jacket diameter) with a sampling period of 2 s. The inlet gas flow was controlled by means of mass flow controllers (MFC, Bronkhorst EL-FLOW Prestige) while the pressure was regulated through a back pressure controller (BPC, Bronkhorst EL-PRESS) located downstream of the reactor.
A sample of the produced syngas mixture was taken at the outlet of one of the four reactors and then directed to a mass spectrometer (Hiden Analytical RGA) to measure the mole fractions of the different gaseous species.

2.2. Testing procedure

Before each experiment, the reactors were heated to the operating temperature of 300 °C via the thermal oil and were purged with a stream of inert gas (i.e. nitrogen). After reaching the desired temperature, the reactors were purged with methane and the absolute pressure was increased to an operating point of 10 bar. Once stable conditions were reached, the reaction was started by flushing a defined mixture of the reactants. A carbon dioxide mole flux of 0.4 mol m^{-2} s^{-1} was set as the reference condition. The reactant ratio, for the full and the partial load tests, was then tuned to be close to stoichiometric conditions with a minimal excess of H_2 to overcome the inaccuracy of the control instrumentation. A small percentage of hydrogen was considered acceptable assuming that the produced syngas would be fed into the natural gas pipeline infrastructures.
The reaction phase of an experiment was terminated when the temperature values measured at the reactor outlet showed that the front had reached the end of the reactor. Afterwards, the reactor drying phase was initiated and the bed was purged with hydrogen to reach the initial state as regards the water content.
The partial load behavior of the system was investigated at loads of 25 %, 50 % and 75 % of the reference inlet mole flow of carbon dioxide.
The reaction time is inversely proportional to the load since the less the water is produced, the longer it takes to saturate the bed. In each case, the reaction time was not fixed a priori but it was determined through temperature and product gas measurements. On this basis, the step variations defined to characterize the considered transients were included in these time frames.

2.3. Mathematical model

A dynamic model based on Ref. [20] and implemented in Matlab®/Simulink® for catalytic methane synthesis reactors was used as a reference for reactors without sorption-enhancement.
The model was based on the equations of chemical kinetics of the process and on mass and energy balances. A one-dimensional approach has been used, discretizing the reactor bed with cylindrical sections in series assuming homogeneous properties of the gas mixture in each of them. While the gas flow is assumed as one-dimensional, the heat exchange with the coolant is estimated with reference to the cylindrical wall surface of each section. Changes in pressure, temperature and mole composition are calculated for each section using the aforementioned equations, written in differential form and solved using the stiff solver ode15s.
The kinetic model considered the Sabatier reaction (R1), methanation of carbon monoxide (R2), and reverse water gas shift (R3) [1]:

$$\mathrm{CO} + 3\mathrm{H_2} \leftrightharpoons \mathrm{CH_4} + \mathrm{H_2O}, \qquad \Delta H_r^0 = -206\ \mathrm{kJ\ mol^{-1}} \tag{R2}$$

$$\mathrm{CO_2} + \mathrm{H_2} \leftrightharpoons \mathrm{CO} + \mathrm{H_2O}, \qquad \Delta H_r^0 = +41\ \mathrm{kJ\ mol^{-1}} \tag{R3}$$

Reaction rates were modelled as proposed by Xu and Froment [21], using the following equations:

$$r_{R1} = \frac{k_{R1}}{p_{H_2}^{3.5}}\left(p_{CH_4}p_{H_2O}^2 - \frac{p_{H_2}^4 p_{CO_2}}{K_{R1}}\right)/(DEN)^2 \quad (1)$$

$$r_{R2} = \frac{k_{R2}}{p_{H_2}^{2.5}}\left(p_{CH_4}p_{H_2O} - \frac{p_{H_2}^3 p_{CO}}{K_{R2}}\right)/(DEN)^2 \quad (2)$$

$$r_{R3} = \frac{k_{R3}}{p_{H_2}}\left(p_{CO}p_{H_2O} - \frac{p_{H_2}p_{CO_2}}{K_{R3}}\right)/(DEN)^2 \quad (3)$$

$$DEN = 1 + A_{CO}p_{CO} + A_{H_2}p_{H_2} + A_{CH_4}p_{CH_4} + A_{H_2O}p_{H_2O}/p_{H_2}, \quad (4)$$

where k, K, and A are terms of the Arrhenius-type temperature functions.
The pressure drop in the reactor was calculated using the Ergun correlation [22].
Regarding heat exchange, the model of heat and mass transfer in packed beds with fluid flow, as described by Tsotsas in [23], was taken as the reference.
The radial heat flux has been estimated using the global heat transfer coefficient, evaluating the transfer coefficient at the reactor inner wall (α_w) as follows:

$$Nu_w = \alpha_w \frac{d}{\lambda_f} \quad (5)$$

$$Nu_w = \left(1.3 + \frac{5}{D/d}\right)\frac{\lambda_{bed}}{\lambda_f} + 0.19\, Re^{0.75} Pr^{1/3} \quad (6)$$

The characteristic length of the Reynolds number is, in this case, equal to the pellet diameter.
Fluid properties were calculated according to Ref. [24]. In particular, for the calculation of the thermal conductivity, the correlation of Mason and Saxena was used, while for the viscosity, the correlation of Wilke was applied.

3. Results and discussion

As a reference for partial load and transient experiments, a single experiment is analyzed to illustrate the operation of a sorption-enhanced catalytic reactor. To this extent, Fig. 2 shows plots of changes in the outlet mole fractions of the most relevant gases in the mixture and the temperatures measured respectively in the inlet and outlet sectors of the reactor. This experiment has been carried out with a CO_2 set flux of 0.3 mol m^{-2} s^{-1} and a CO_2/H_2 ratio as determined in the sorption-enhanced reaction experiments (see Table 1). The data reported ranges from the test initial condition (i.e. when no water is adsorbed in the bed) to the final condition (i.e. when the bed is completely saturated with water and the conversion process stops).
In Fig. 2 (a) the composition of the gas mixture at the reactor outlet is reported. The methane content at the beginning refers to the gas initially contained in the reactor after increasing the pressure of the system (see Section 2.2). The decline in CH_4 content corresponds to the point when the produced methane reached the reactor outlet.
It should be noted that when the first synthesized methane reached the reactor outlet, its mole fraction undergoes a slight downward peak. This is due to an overshooting of the hydrogen flow rate at the time when the reactant input was set through the flow controllers.
The decrease in methane mole fraction at the end of the test corresponds to the moment when the sorption front reached the outlet, which means that a mixture of reactants and products arrived at the outlet due to the lack of water removal capability (i.e. there is not sufficient sorption-enhancement taking place anymore). In the last part of the measuring period, the behavior of the reactor clearly shows that the synthesis phase has ended (usually in real operations the reaction is stopped, and the bed drying phase starts before reaching that point).
During the sorption-enhanced phase, the content of carbon dioxide was always below 1 %. Moreover, ethane and propane were measured below 0.5 % and water below 0.2 % as adjusted during the regeneration phase.
The temperatures shown in Fig. 2 (b) follow a trend determined by the displacement of the reaction front and the heat removal from the catalyst bed. Considering the temperature changes measured in the inlet sector of the reactor, it can be concluded that the peak is due to the front traveling through the temperature sensor at that point. Afterwards, in the inlet sector of the bed, the reaction takes place without sorption-enhancement because it is completely saturated with water. The heat released due to the exothermic reaction causes the temperature to stabilize at a value higher than that of the coolant.
The maximum temperature in the inlet sector is lower than that measured close to the outlet due to the mixing of the catalyst bed with aluminum beads.

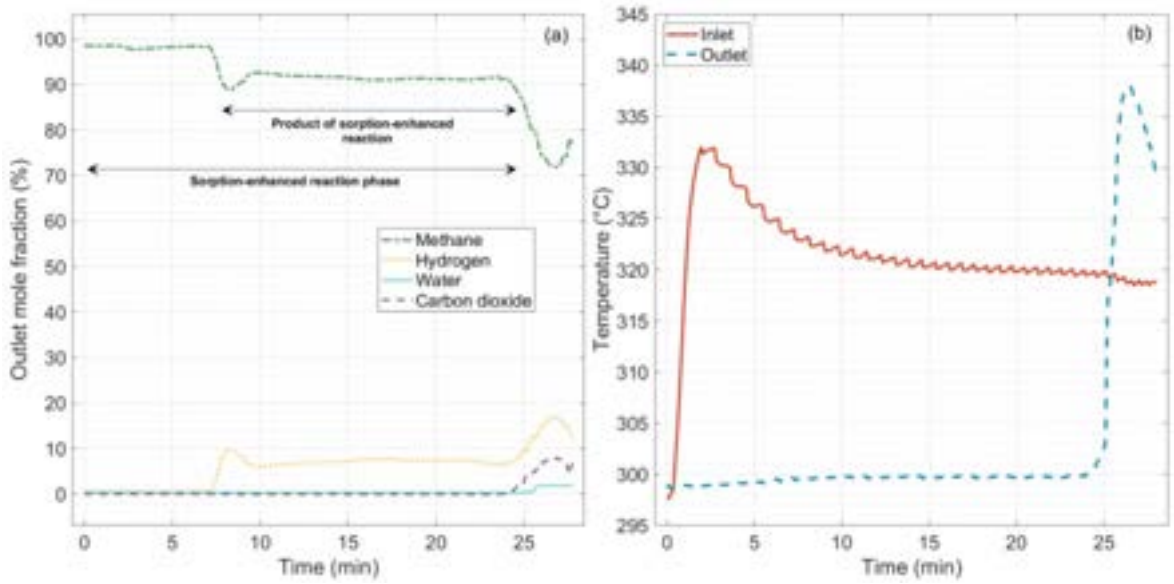

Figure 2. Outlet mole fractions measured by the mass spectrometer (a) and temperatures measured in the inlet and outlet sectors of the reactor (b) using a constant CO_2 set flux of 0.3 mol m^{-2} s^{-1}, and reaction absolute pressure of 10 bar.

Furthermore, a comparison of the behavior of the methanation reactors with and without sorption-enhancement that demonstrates the underlying differences of the two systems is shown.
For this purpose, Fig. 3. shows the simulated steady state temperature profile along the reactor axis of a conventional fixed-bed catalytic reactor considering the bed geometry and the operating conditions as introduced above for the sorption-enhanced case. More specifically, a CO_2 flux of 0.3 mol m^{-2} s^{-1}, a CO_2/H_2 ratio as determined in the sorption-enhanced reaction experiments (see Table 1), an initial reactor temperature and temperature control setpoint of 300 °C, and a reaction absolute pressure of 10 bar. Since a discretized lumped parameter approach was used, the profile is depicted by steps.
In the conventional reactor, the temperature profile reaches a steady state as shown in Fig. 3 (it should be considered that the section where maximum temperature is reached depends on the value of the inlet reactant flow rate). In contrast to this behavior, considering Fig. 2 (b), it can be noted that the temperature peak for sorption-enhanced systems is not static, but moves through the reactor together with the reaction front.
In the following, the partial load (Section 3.1) and transient operation of the system (Section 3.2) are presented, while in Section 3.3 the thermal behavior will be discussed.

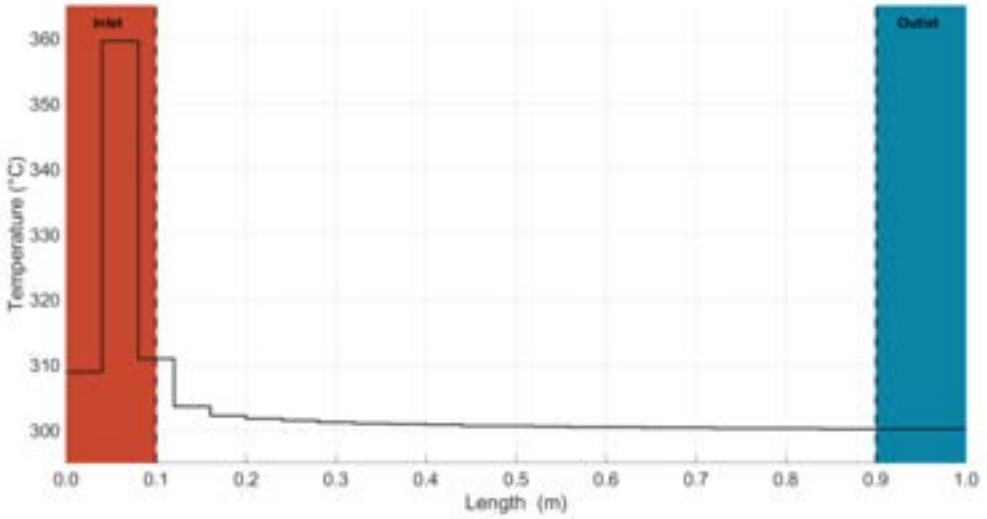

Figure 3. Temperature profile along the length of a simulated non-sorption-enhanced reactor with a constant CO_2 flux of 0.3 mol m^{-2} s^{-1}, an initial reactor temperature of 300 °C, and a reaction absolute pressure of 10 bar.

3.1. Partial load behavior

The reactor system was analyzed at partial load conditions by repeating the above-introduced experiment (i.e. 75 % of the reference load) at inlet flow rates of 25 %, 50 %, and 100 % of the reference load.
Table 1 presents the carbon dioxide conversion determined from the measured outlet gas composition. For the sake of comparison, the results are presented for a simulated conventional reactor, an equilibrium conversion calculation at a temperature of 300 °C and the measurements on the sorption-enhanced reactor.
The carbon dioxide conversion was calculated by means of the following equation:

$$Conv_{\mathrm{CO_2}} = 1 - x_{outlet\ \mathrm{CO_2}} / x_{inlet\ \mathrm{CO_2}} \quad (7)$$

The measured mole fraction was averaged over the timespan marked in Fig. 2 (a) as "product of sorption-enhanced reaction".
For the simulations and the calculation of equilibrium conversion, the actual flux determined from the experiments was used.
The simulation results for the conventional reactor show a decreasing conversion with increasing load, i.e. increasing inlet mole flux. This is due to a decreased residence time.
Compared to the equilibrium calculations, the gap between the equilibrium conversion and the simulated conversion in the reactor increases with the load. The changes in equilibrium conversion given in the table are due to the changes in the inlet stoichiometry determined for the different load conditions. In contrast to the conventional reactor, the CO_2 conversion determined for the sorption-enhanced reactor experiments does not show a dependency on the load. The conversion is significantly higher than the equilibrium conversion for all cases. This goes hand in hand with the above-introduced shift in the chemical equilibrium through water removal.
In addition to the CO_2 conversion given in Table 1, Table 2 shows the outlet CH_4 content for the simulation of the conventional reactor, the equilibrium value, and the average values measured for the sorption-enhanced reaction. This is the measurement relevant for the application of the product, e.g. feeding into a gas grid. The CH_4 mole fraction of the simulation and that of the calculation for the equilibrium were considered on a dry basis.
In addition, for further considerations on sorption-enhanced reactor measurements, the standard deviation of the averaged data is also presented.
The results for the simulated conventional reactor are in line with the trend observed for the CO_2 conversion. The theoretical maximum CH_4 content given by the equilibrium shows the strong influence of the non-stoichiometric reactant ratio, especially at low partial load. The CH_4 content in the product measured for the sorption-enhanced reactor shows a dependency on the stoichiometry. The quality of the product is limited by the accuracy of the initial mixing and not by the conversion. Furthermore, the low values of the standard deviation of the measured data imply that production is highly stable.
Another major characteristic of the sorption-enhanced reactor system is the duration of the production phase. With the aim of exploring this aspect, Fig. 4 shows the duration at the partial load conditions measured from the start of the feed supply until detecting an increase in CO_2 mole fraction at the reactor outlet above 1 %.

Table 1. Partial load CO_2 conversion with the corresponding inlet mole fluxes.

Inlet mole flux (mol m^{-2} s^{-1})	Reactant ratio (-)	$Conv_{\mathrm{CO_2}}$ (-)		
CO_2	H_2/CO_2	Conventional reactor simulation	Equilibrium* at 300 °C and 10 bar	Sorption-enhanced reactor measurements
0.1	4.18	0.9622	0.9985	0.9998
0.2	4.14	0.9187	0.9960	0.9998
0.3	4.09	0.8864	0.9902	0.9997
0.4	4.09	0.8657	0.9892	0.9999

** Calculations performed using Cantera [25].*

Table 2. Partial load CH_4 outlet content with the corresponding inlet mole fluxes.

Inlet mole flux (mol m^{-2} s^{-1})	Reactant ratio (-)	Outlet CH_4 mole fraction (%)		
CO_2	H_2/CO_2	Conventional reactor simulation	Equilibrium* at 300 °C and 10 bar	Sorption-enhanced reactor measurements
0.1	4.18	82.965	84.116	84.548 (std: 0.625)
0.2	4.14	73.682	87.053	88.063 (std: 0.454)
0.3	4.09	67.476	89.097	91.565 (std: 0.435)
0.4	4.09	63.852	89.269	92.364 (std: 0.460)

** Calculations performed using Cantera [25].*

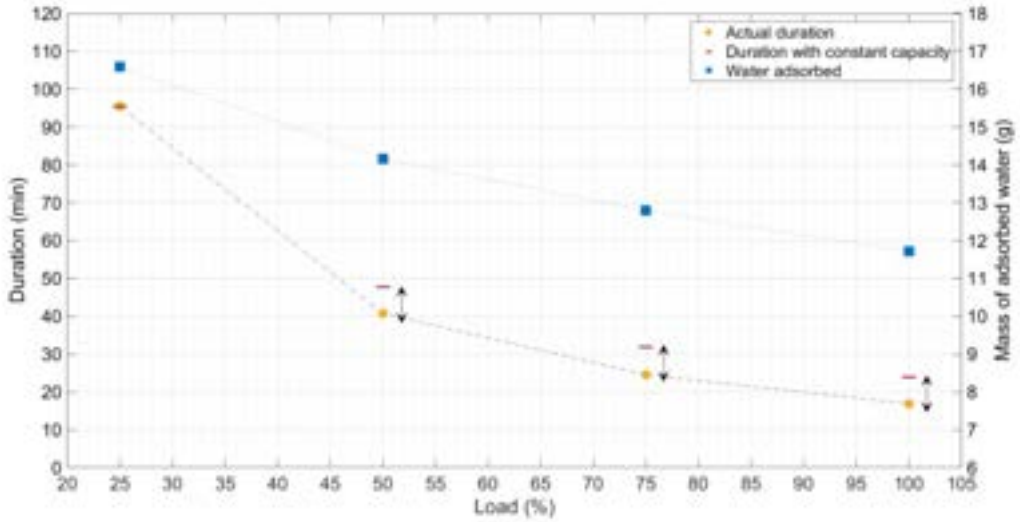

Figure 4. Actual durations of the production phase and calculated durations in the case of constant adsorption capacity at different partial loads with the mass of adsorbed water under the same conditions.

In addition, to the measured durations, those that would have been encountered if the adsorption capacity were constant and equal to that found at the lowest load are included in the figure. Furthermore, on the secondary vertical axis, the amount of water adsorbed at the corresponding conditions is presented. The water adsorbed (and consequently the adsorption capacity of the reactor) was estimated by multiplying the duration by the water production calculated from the conversion of the inlet CO_2 flow rate.
In an ideal system, the water adsorption capacity would be constant for the different load conditions. In Fig. 4, however, a decline in this capacity with increasing load can be seen. The measured durations of sorption-enhanced reactions are slightly shorter as the adsorption capacity decreases.
This behavior goes hand in hand with observations reported in Ref. [18], where it was contributed to increased bed temperatures and less distinct reaction fronts caused by kinetic limitations. This is an important aspect to consider when designing similar systems.

3.2. Transient response

The sorption-enhanced reactor system was assessed to load changes by investigating the system response to single and multiple subsequent steps in the feed flow rate. For the single step, the system was operated at 100 % of the load for 6 min, then the load was reduced to 25 % for 6 min and increased again to 100 % afterwards. Figure 5 (a) shows the outlet mole fraction of the species measured in the gas mixture at the outlet with reference to the single step case. As a multiple step case, the procedure was repeated with three steps lasting 3 min each as shown in Fig. 5 (b). Figures 5 (c) and 5 (d) show the respective feed flow rates as set by means of the mass flow controllers.
Figure 5 (a) presents the same characteristic features of methane synthesis that were evaluated in Fig. 2 with respect to the steady state case. In addition, it can be seen that the downward spike in methane fraction relates to the time when the step was imposed by decreasing the inlet flux. The same general behavior can be seen in Fig. 5 (b).
As the transition between one load to the other occurs, the methane content gradually changes to the levels obtained when the steady state is reached in the partial load tests. In fact, as presented in Table 2, the outlet methane mole fraction value changes for different tests at partial load.
The spikes in the hydrogen fraction are related to the change in the H_2/CO_2 ratio used in the corresponding partial load conditions. When considering the carbon dioxide outlet fraction, it can be argued that the steps have no impact on CO_2 conversion.

3.3. Effect on temperature

As a final analysis, the maximum temperature values measured during the different load and transient conditions are analyzed. These temperatures correspond to the peaks of the front measured in the reactor inlet and outlet sectors. In this regard, Table 3 shows that the variation of these peaks is limited for the different load conditions. The values measured at the inlet are lower than those at the outlet because, as mentioned earlier, in the first section of the reactor the catalyst was mixed with aluminum beads.

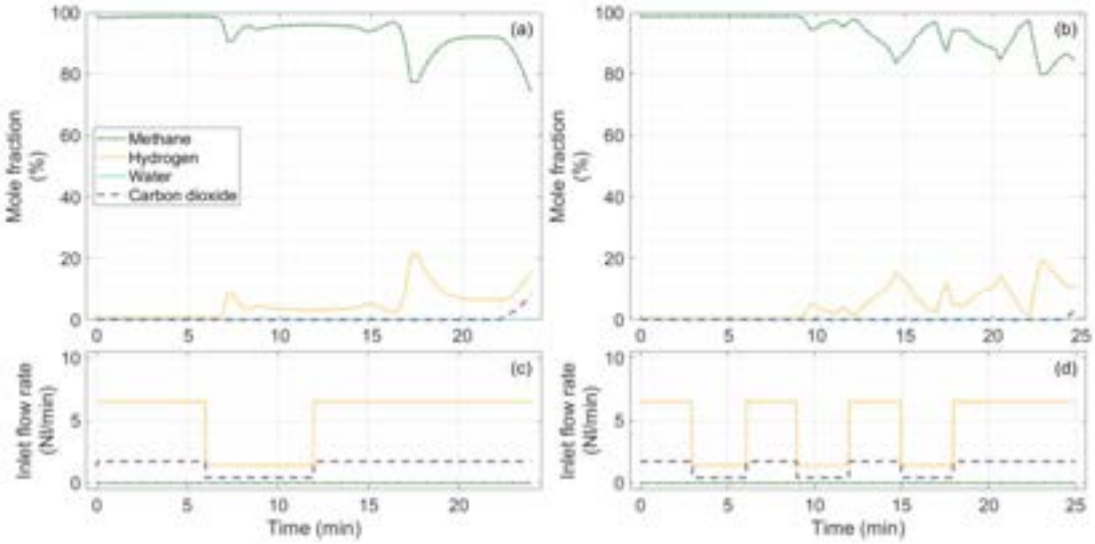

Figure 5. Outlet mole fraction as measured by the mass spectrometer in the case of single step input (a) and multiple step input (b); inlet flow rate of reactants in the case of single step input (c) and multiple step input (d).

Table 3. Maximum temperatures observed in the cases analyzed.

Partial load/step response	Maximum temperature measured at the inlet sector (°C)	Maximum temperature measured at the outlet sector (°C)
25 % load	323.5	333.8
50 % load	328.3	338.1
75 % load	332.0	338.0
100 % load	331.7	340.8
Single step	326.2	339.4
Multiple step	323.4	339.5

The location where the front is present at any given time experiences maximum conversion and concurrently maximum heat release due to both the exothermic nature of the reaction and that of the adsorption process. The local increase in temperature improves the chemical kinetics of the reaction and increases the conversion of the reactants to the products. The faster the water is produced, the more rapidly the bed will be saturated and consequently the front will move along the reactor axis. Since the temperature peak is not static, the system is able to handle the problem of hot-spot formation. This is not the case in conventional fixed-bed catalytic methanation reactors where, as explained when discussing Fig. 2, the temperature peak at a given flow remains steady.

4. Conclusion

In the perspective of sustainable fuel production from renewable sources, an investigation of methane production at transient and partial load conditions was presented. The potential of sorption-enhanced catalysis applied to the methanation of carbon dioxide has been analyzed for its potential of having high conversions at flexible operation conditions.

To this extent, the behavior of an oil-cooled fixed-bed methanation reactor with a bi-functional catalyst has been experimentally tested and compared to a dynamic model of a fixed-bed reactor without sorption-enhancement.

Partial load conditions were tested in terms of varying reactant flow rates. Furthermore, transient load changes were investigated by evaluating the response to abrupt changes from a partial load to another. These responses were evaluated considering conversion and thermal stability, which is the main issue discussed in the literature for conventional catalytic reactor systems.

The results show exceptional thermal stability of the system in response to transients, despite the exothermic nature of both the methanation reaction and the adsorption phenomenon. The system is able to autonomously manage the temperature so that deactivation of the catalyst by thermal degradation is avoided. Nonetheless, the sorption-enhanced catalyst allows for full conversion without ignition problems.

From the point of view of product quality, the sorption-enhanced reactor shows an excellent CO_2 conversion above 99.97 % independent of the load. In contrast, the simulation results for a conventional catalytic reactor of the same size show a CO_2 conversion ranging from 96.2 % to 86.7 %, which decreases as the feed flow rate increases. Sorption-enhanced reactors achieve higher CO_2 conversions than those calculated for an

equilibrium reactor, due to the continuous water removal. The conventional reactors simulated in this study approach the theoretical equilibrium conversion for low flow rates.
Another characteristic of the sorption-enhanced reaction is the existence of a coupled reaction and adsorption front moving through the reactor. The duration of a sorption-enhanced reaction phase is determined by the water adsorption capacity of the catalyst bed at the given conditions. Consequently, decreasing the load leads to slower movement of the front through the reactor. It was observed that the adsorption capacity of the reactor slightly decreases with the increasing load, which was attributed to transport limitations in the reactor bed. Nonetheless, this allowed the system to operate at low partial loads.
The investigations of step responses to analyze the transient behavior showed that there is no influence on the CO_2 conversion, which stays constantly high throughout the sorption-enhanced production phase, even for abrupt load changes. This is beneficial considering the direct coupling with the fluctuating supply of reactants. The characteristics identified help to design power-to-gas systems and to minimize electricity or gas storage as the system can be operated at very low partial loads during phases with a low wind speed or solar irradiation.
Based on these results, this paper shows the excellent performance of sorption-enhanced catalysis during transient operations or at partial load conditions in the perspective of coupling methane synthesis with renewable energy sources.

Acknowledgments

This work has been co-funded by a grant of European Union - PON Ricerca e Innovazione 2014-2020.

Nomenclature

A_j adsorption constant for species j

d pellet diameter, m

D reactor diameter, m

ΔH_r^0 standard reaction enthalpy, kJ/mol

k_i rate coefficient of reaction i, kmol/(kg_{cat} h bar)

K_i equilibrium constant of reaction i

Nu Nusselt number

p_j partial pressure of the species j, bar

Pr Prandtl number

r_i rate of reaction i, kmol/(kg_{cat} h)

Re Reynolds number

x_j Mole fraction of species j

Greek symbols

α heat transfer coefficient, W/(m^2 K)

λ thermal conductivity, W/(m K)

Subscripts and superscripts

f fluid

w wall

References

[1] Götz M., Lefebvre J., Mörs F., McDaniel Koch A., Graf F., Bajohr S, et al., Renewable Power-to-Gas: A technological and economic review. Renewable Energy. 2016;85:1371–90.

[2] Barbaresi A., Morini M., Gambarotta A., Review on the Status of the Research on Power-to-Gas Experimental Activities. Energies. 2022;15(16), 5942.

[3] Herrmann F., Grünewald M., Meijer T., Gardemann U., Feierabend L., Riese J., Operating window and flexibility of a lab-scale methanation plant. Chemical Engineering Science. 2022 Jun;254:117632.

[4] Fischer K.L., Langer M.R., Freund H., Dynamic Carbon Dioxide Methanation in a Wall-Cooled Fixed Bed Reactor: Comparative Evaluation of Reactor Models. Industrial & Engineering Chemistry Research. 2019 Sep 23;58(42):19406–20.

[5] Try R., Bengaouer A., Baurens P., Jallut C., Dynamic modeling and simulations of the behavior of a fixed-bed reactor-exchanger used for CO2 methanation. AIChE Journal. 2017 Sep 5;64(2):468–80.

[6] Stiegler T., Meltzer K., Tremel A., Baldauf M., Wasserscheid P., Albert J., Development of a Structured Reactor System for CO_2 Methanation under Dynamic Operating Conditions. Energy Technology. 2019 May 6;7(6):1900047.

[7] Fischer K., Freund H., On the optimal design of load flexible fixed bed reactors: Integration of dynamics into the design problem. Chemical Engineering Journal. 2020 Aug 1;393:124722–2.

[8] Bremer J., Sundmacher K., Operation range extension via hot-spot control for catalytic CO_2 methanation reactors. Reaction Chemistry and Engineering. 2019 May 28;4(6):1019–37.

[9] Matthischke S., Roensch S., Güttel R., Start-up Time and Load Range for the Methanation of Carbon Dioxide in a Fixed-Bed Recycle Reactor. Industrial & Engineering Chemistry Research. 2018 Apr 16;57(18):6391–400.

[10] Matthischke S., Krüger R., Rönsch S., Güttel R., Unsteady-state methanation of carbon dioxide in a fixed-bed recycle reactor — Experimental results for transient flow rate ramps. Fuel Processing Technology. 2016 Dec;153:87–93.

[11] Theurich S., Rönsch S., Güttel R., Transient Flow Rate Ramps for Methanation of Carbon Dioxide in an Adiabatic Fixed-Bed Recycle Reactor. Energy Technology. 2019 Nov 13;8(3):1901116.

[12] Sun D., Simakov D.S., Thermal management of a Sabatier reactor for CO_2 conversion into CH_4: Simulation-based analysis. Journal of CO_2 Utilization. 2017 Oct;21:368–82.

[13] Kreitz B., Wehinger G.D., Turek T., Dynamic simulation of the CO_2 methanation in a micro-structured fixed-bed reactor. Chemical Engineering Science. 2019 Feb;195:541–52.

[14] Fache A., Marias F., Guerré V., Palmade S., Optimization of fixed-bed methanation reactors: Safe and efficient operation under transient and steady-state conditions. Chemical Engineering Science. 2018 Dec;192:1124–37.

[15] Herrmann F., Grünewald M., Meijer T., Ulrich G., Riese J., Performance of a Laboratory-Scale Methanation Plant with Catalyst Dilution under Dynamic Operating Conditions. Industrial & Engineering Chemistry Research. 2022 Jun 30;61(27):9644–57.

[16] Borgschulte A., Gallandat N., Probst B., Suter R., Callini E., Ferri D., et al., Sorption enhanced CO_2 methanation. Physical Chemistry Chemical Physics. 2013;15(24):9620.

[17] Borgschulte A., Delmelle R., Duarte R.B., Heel A., Boillat P., Lehmann E., Water distribution in a sorption enhanced methanation reactor by time resolved neutron imaging. Physical Chemistry Chemical Physics. 2016 Jun 29;18(26):17217–23.

[18] Kiefer F., Nikolic M., Borgschulte A., Dimopoulos Eggenschwiler P., Sorption-enhanced methane synthesis in fixed-bed reactors. Chemical Engineering Journal. 2022 Dec;449:137872.

[19] Do D.D., Adsorption analysis: equilibria and kinetics. London: Imperial College Press; 1998.

[20] Bremer J., Rätze K.H., Sundmacher K., CO_2 methanation: Optimal start-up control of a fixed-bed reactor for power-to-gas applications. AIChE Journal. 2016 Sep 23;63(1):23–31.

[21] Xu J., Froment G.F., Methane steam reforming, methanation and water-gas shift: I. Intrinsic kinetics. AIChE Journal. 1989 Jan;35(1):88–96.

[22] Ergun S., Orning A.A., Fluid Flow through Randomly Packed Columns and Fluidized Beds. Industrial & Engineering Chemistry. 1949 Jun;41(6):1179–84.

[23] Tsotsas E., M7 Heat and Mass Transfer in Packed Beds with Fluid Flow. In: VDI Heat Atlas. 2010.

[24] Poling B.E., Prausnitz J.M., O'Connell J.P., Properties of Gases and Liquids, Fifth Edition. New York, N.Y.: Mcgraw-Hill Education; 2020.

[25] Goodwin D., Speth R., Moffat H., Cantera: An Object-oriented Software Toolkit for Chemical Kinetics, Thermodynamics, and Transport Processes. 2018 Aug 24.

Multi-criteria optimization of hydrogen energy supply chains considering economic and environmental impacts: theoretical case study in the context of Balearic Islands

Florent Montignac[a], Maria-Candelaria Arpajou[b], Diego Larrahondo Chavez[c] and Alain Ruby[d]

[a] Univ. Grenoble Alpes, CEA, Liten, DTCH, 38000 Grenoble, France
florent.montignac@cea.fr, CA
[b] Univ. Grenoble Alpes, CEA, Liten, DTCH, 38000 Grenoble, France
maria.arpajou@cea.fr
[c] Univ. Grenoble Alpes, CEA, Liten, DTCH, 38000 Grenoble, France
diego.larrahondochavez@cea.fr
[d] Univ. Grenoble Alpes, CEA, Liten, DTCH, 38000 Grenoble, France
alain.ruby@cea.fr

Abstract:

Hydrogen production through water electrolysis can play a role in the decarbonisation of energy systems when powered by electricity obtained from low carbon energy sources. The decision of deploying hydrogen technologies at a large scale in the future implies to get a comprehensive overview of the benefits and drawbacks on a variety of impacts compared to other alternative energy supply scenarios. The aim of this study was to perform a dynamic techno-economic and environmental impact assessment of renewable-based hydrogen supply chains relying on some of the characteristics of the GreenHysland EU deployment project in Mallorca (Spain). In this paper the optimization of the design and operation conditions of two hydrogen transport modes (trucks and pipeline) has been addressed for the supply of hydrogen to fuel cell buses and considering the possibility of injecting hydrogen into the natural gas grid. These hydrogen chains were assessed using PERSEE dynamic optimization tool developed at CEA relying on a Mixed Integer Linear Programming approach. A front of optimal solutions has been obtained considering both economic (Net Present Value) and environmental (cumulated equivalent carbon dioxide emissions) optimization criteria. Finally this study emphasizes the potential interest of such dynamic optimization approach to support impact assessment in pre-design phases of hydrogen projects complying with current and future greenhouse gases savings assessment methodologies defined at European level (e.g. RED II and related Delegated Acts) and corresponding green or low carbon hydrogen certification processes. This initial work opens the way to several perspectives for improvement in order to increase the robustness of these energy chain comparisons including sensitivity studies and the consideration of a broader set of environmental impact categories. These improvements are being reviewed by the research team and will help achieve a more complete analysis of the impacts of potential large-scale hydrogen deployment scenarios in the future energy mix of the Balearic Islands.

Keywords:

GreenHysland; Hydrogen; Supply chains; Optimization; Environmental impacts; Scenarios; PERSEE.

1. Introduction

1.1. Context: the GreenHysland EU project

The study presented in this paper has been performed in the frame of the GreenHysland EU project. This five years project (2021-2025) aims to deploy a fully functioning hydrogen (H_2) ecosystem on the island of Mallorca (Spain), turning the island into the first H_2 hub in Southern Europe [1]. The project comprises:

- The development of hydrogen production, transport and distribution infrastructure (green hydrogen production plant, hydrogen truck trailers, deployment of a hydrogen pipeline and hydrogen refuelling station)

- The demonstration of three types of end-use applications (hydrogen vans and buses, stationary fuel cells and hydrogen injection into the natural gas grid).

In addition to the technical aspects, the project also addresses the analysis of the economic, environmental and social impacts of the potential larger scale deployment of hydrogen as an energy carrier in the Balearic Islands. Part of these studies relies on dynamic simulation and optimization of current and future energy chains. Therefore, in the present paper, a methodology for a first analysis of hydrogen supply scenarios in the Balearic Islands is addressed considering economic and environmental evaluation criteria.

1.2. Topic of the paper

1.2.1. Disclaimer

The study presented in this article contributes to the development of appropriate methodologies for impact analysis activities planned within GreenHysland project. The authors do not pretend to provide here an evaluation of economic or environmental performance of the project in itself. The case study detailed in this paper consists in a theoretical evaluation of an energy system inspired by some of the technical characteristics of the project. This theoretical evaluation aims at illustrating a multi-criteria optimization methodology based on dynamic simulation. This study does not refer to potential hydrogen upscaling scenarios within the Balearic Islands

1.2.2. General objectives

The main goals of this study are:

- To illustrate how a multi-criteria optimization approach based on dynamic modelling can help assessing hydrogen supply chains from an economic and environmental impacts perspective;
- To provide insights about the most influencing components regarding cost and environmental emissions breakdown of these hydrogen chains.

We consider a theoretical case study relying on some of the characteristics of the GreenHysland project. This case study (described in Section 2) consists in a hydrogen energy chain comprising a 7.5 MW electrolyzer connected to a local PV plant and to the local electrical grid. The end-use applications consist in five hydrogen fuel cell buses and a flexible hydrogen injection into the natural gas grid. Two hydrogen transport modes are considered (truck trailers and pipeline) for connecting production and end-use applications separated by a distance of 30 km.

The main originality of the work relies in the simultaneous optimization of economic and environmental criteria considering all types of emissions (direct from fuel consumption, indirect from electricity consumption, and indirect from equipment manufacturing) within a dynamic optimization approach.

1.3. Background about optimization of hydrogen energy chains

1.3.1 Evaluating the carbon content of hydrogen

Hydrogen as an energy carrier is widely considered as one of the technologies that could help decarbonizing several energy demand sectors. However, this statement depends on the direct and indirect environmental impacts generated from the primary energy from which hydrogen is produced as well as life cycle impacts of the newly developed technologies over the whole hydrogen supply chains. As an example, water electrolysis is often considered as an environmental-friendly method for hydrogen production. However even though hydrogen produced by electrolysis tends to minimize environmental impact, the impact is not zero since electricity production involves environmental footprints as well as electrolysis and associated processes such as water treatment and desalination [2].

Hence several initiatives are being undertaken at National, European and International levels in order to support ramping-up of clean hydrogen market and related industry in the next years and decades by setting new rules and certification processes. The new version of the European Renewable Energy Directive commonly referred as RED II (2018) defines the global rules and targets for increasing deployment of renewable energies across European Union. Complementary to this directive, a specific Delegated Act recently published (February 2023) establishes a “Union methodology setting out detailed rules for the production of renewable liquid and gaseous transport fuels of non-biological origin” (RFNBO). These rules refer to consideration of additionally (new dedicated renewable power plants associated with hydrogen production plant), temporal correlation (from calendar month basis to hourly correlation basis) and geographical correlation (notion of bidding zone). Another Delegated Act establishes the minimum threshold for greenhouse gas emissions savings of RFNBO fuels at -70% compared to reference process. Complementary to the RED II directive and Delegated Acts, several initiatives (such as CertifHy, IPHE or GH2 standard) have been launched in order to define green or low-carbon hydrogen certification process). For instance, the so-called GH2 standard has been established by the Green Hydrogen Organization which refers to "near-zero greenhouse gas emissions". This standard requires green hydrogen projects to operate at a level of emissions less than or equal to 1 $kgCO_{2\text{-}eq}$ per kgH_2, taken as an average over a 12-month period [3]. However, GH2 considers emissions only during hydrogen production, without evaluating them in later stages of the process,

such as in hydrogen transportation, end-use applications, and so on. Therefore, if a study scope includes transportation, the expected emissions might be higher than 1 $kgCO_{2\text{-}eq}$ per kgH_2.

Hence, hydrogen stakeholders may be facing a new challenge regarding the appropriate and optimized size and operation of hydrogen equipment to fulfill the GHG requirements while maximizing the profitability of the production plants. Multi-criteria optimization techniques relying on dynamic simulation could help addressing this issue and then providing support to investment decision and daily operation of hydrogen plants. The next sections provide some background information about optimization approaches (section 1.3.2), multi-objective optimization (section 1.3.3) and environmental information in energy system optimization tools (section 1.3.4). Finally, section 1.3.5 presents the PERSEE optimization tool that has been used in the frame of this study.

1.3.2 Optimization approaches

Despite the various benefits resulting from renewable energy and hydrogen production, there are still new issues to overcome, such as system losses caused by inadequate operation, sizing or selection of location and sizing of systems [4]. By including optimization techniques, the design and operation of energy systems can be addressed, resulting in more efficient and cost-effective scenarios [5].

Numerous optimization techniques have been implemented in this area, and one of the most widely used is mixed integer linear programming (MILP) [6]. The main advantage of a MILP Solver method is the accuracy of the solution. If the problem is well defined, the solution found with the use of MILP Solver is the global optimal solution of the problem. The other advantage is that the optimal dispatch is found without the need to adjust the operating strategy of the units [7].

1.3.3 Multi-objective optimization methodology

Energy system optimization inherently involves multiple and conflicting objectives. As way of example, the most efficient energy processes are not necessarily the most economical ones, or a system with low $CO_{2\text{-}eq}$ emissions can suppose high investment costs. Therefore, energy system optimization is much more realistic and reliable if different evaluation aspects, such as cost, technical and environmental concerns, are explicitly taken into account. This can be accomplished by giving them an explicit role as objective functions, rather than aggregating them into a single economic indicator objective function [8]. Thus, the problem of optimizing energy systems can be addressed with a multi-objective approach, where the solution vector is not determined by a single technical solution, but by a set of optima. The optimal solution points form what is commonly referred to as a non-dominated set or Pareto optimum. For each of the Pareto arrangements, improving one objective without worsening another is not possible. For the calculation of the Pareto front, the epsilon-constraint method is widely used, especially for cases where there are two objectives. This is due to the fact that it provides high reliability of the results within brief computational time [9].

1.3.4 Environmental information in energy system optimization

Optimization techniques are used in various simulation software packages to plan energy systems. These pieces of software have been developed not only to evaluate the technical and economic potential of energy systems, but also to simplify the design and operation process of systems that include renewable sources maximizing, at the same time, their profitability [10]. Even though the use of software programs seeks to maximize the use of renewable energies and thus, minimize the environmental impact, most of them do not include environmental impact as a decision variable [11]. Moreover when environmental information is considered the impact related to equipment manufacturing is often excluded from the analysis perimeter.

In order to obtain and include environmental information in an optimization problem, a Life Cycle Analysis (LCA) of all components of the energy system must be performed. LCA is a standardized methodology developed to assess the environmental impacts of a product, a process or even a system [12]. Despite the fact that different LCA software have been developed over the past two decades, the research community has always developed its own software implementations that could be adapted and extended to build advanced, non-standard LCA models. As a way of example, Brightway version 2 has been developed since 2012 as an open source Python-based LCA framework, and has been widely used throughout the research community [13]. This software has been chosen for this study due to its flexibility for building parametrized environmental impact models (see Section 2.4.2).

1.3.5 PERSEE optimization tool

The technical and economic study presented in this paper is carried out with PERSEE software developed at CEA by members of LSET laboratory in Grenoble, France. PERSEE is a tool for optimizing the sizing and management of multivector energy systems, based on MILP formulation [14]. The software allows the modeling and multi-objective optimization of energy systems, such as industrial processes or energy production facilities. Two approaches can be implemented. If the size or production capacity of an existing facility is already known, optimization is performed to optimally extrapolate its performance over several years of operation. Conversely, if the facility size or production capacity is an unknown variable, it is optimized in order to determine the system optimal management. Whatever the case, from all the information entered by

the user, PERSEE creates a system of equations containing the objective function and all the constraints of the problem. Subsequently, this system of equations is solved using a commercial solver, such as Cplex.

As regards the multi-optimization criteria, PERSEE software works with the Net Present Value (NPV) and the cumulated greenhouse gases emissions over the entire industrial project lifetime. In order to build the front of optimal solutions, the epsilon-constraint method is currently implemented. Once the environmental, technical and economic constraints are set, the optimization is spread over a period of one year, with a specific time step, for example, one hour. Then PERSEE has to meet the imposed constraints maximizing the NPV and/or minimizing $CO_{2\text{-eq}}$ emissions.

2. Case study

2.1. System description

As it was mentioned before, the study presented in this paper is based on the GreenHysland hydrogen hub. Some of the characteristics of the GreenHysland project are used as a reference situation from where several scenarios are created. In this section, the overall flowsheet of the theoretical case study is described. Figure 1 shows a schematic representation of the case study general architecture.

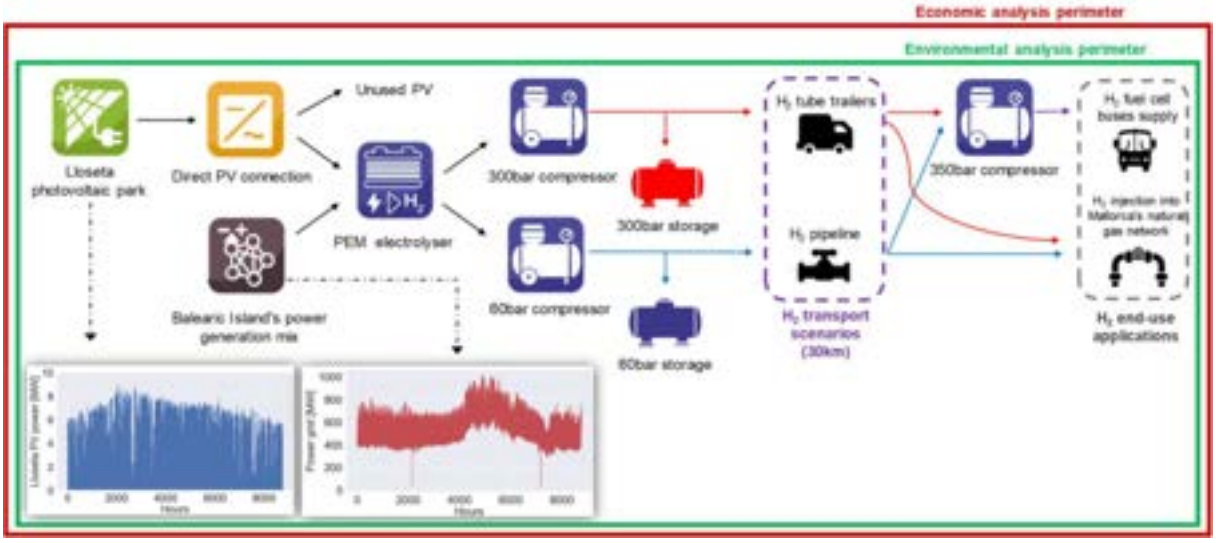

Figure. 1. Illustration of the considered hydrogen supply chains and applications.

As it can be seen in Figure 1, hydrogen is produced via water electrolysis. The green hydrogen production facility is placed in the municipality of Lloseta, at almost 30 km northeast from the capital city Palma de Mallorca. The electrolyzer plant mainly includes a 7.5 MW Proton Exchange Membrane (PEM) electrolyzer, compressors, and on-site hydrogen storages to allow desynchronizing hydrogen production and demand. Regarding energy sources, the electrolyzer is coupled to the electricity generation of a photovoltaic park located also in the municipality of Lloseta. This solar farm has a generation capacity of 8.56 MWp [1]. Additional power can be obtained from the Islands' electricity power grid.

Once produced, we assume that the hydrogen is compressed and subsequently transported to Palma de Mallorca to supply two applications: public transport mobility (hydrogen buses) and hydrogen injection into the Mallorca's gas grid.

- In the first end-use application, hydrogen is used as a fuel for a fleet of five fuel cell buses. As the buses refuelling station is placed in Palma de Mallorca, hydrogen must be transported 30 km from Lloseta municipality to the capital city. Each bus has five 350bar hydrogen tanks of 312 liters each, which makes 1,560 liters in total. We assume that this volume is equivalent to a usable capacity of 37.5 kg of hydrogen. It is supposed that all buses are refuelled once a day, hence ~70 tons of hydrogen are needed in a complete year corresponding to an average flowrate demand of 8 kg/h.
- For the second end-use application, green hydrogen is injected into the Mallorca's natural gas network. The injection point is supposed to be also in the capital city, therefore, 30 km hydrogen transport has to be considered. In this case, we consider a maximal allowable hydrogen injection flow rate of 4% of the natural gas volumetric flow.

For both applications, two hydrogen transport modes are considered: truck trailers and hydrogen pipeline.

2.2. Perimeter of economic and environmental evaluations

The environmental impact considered in this study is limited to greenhouse gases (GHG) emissions. As shown in Figure 1 the environmental analysis perimeter comprises the whole direct and indirect emissions of the

hydrogen supply chains. The cumulated emissions E_{GHG} ($kgCO_{2\text{-eq}}$) are calculated considering direct emissions $DE_{t,i}$ during each hour t over year i (e.g. from diesel combustion in truck trailers), indirect emissions $IEG_{t,i}$ related to grid electricity consumption, indirect product emissions IPE_{el} related to manufacturing of element el of the energy system (also referred as "capex-related emissions") and avoided emissions $AE_{t,i}$ related to substitution of diesel in buses by hydrogen and substitution of natural gas in the grid by hydrogen (this study only compares the avoided emissions in terms of fuel substitution and not the technological equipment involved in the fuel substitution; it is beyond the scope of the study to compare impacts of manufacturing of diesel buses and hydrogen buses). Equation (1) presents the calculation of the cumulated emissions considering a project lifetime of Y years, an annual operating time H of 8760 hours, a number of N elements and annual hydrogen production $M_{H2,i}$ (kgH_2). Then the specific emissions e_{GHG} ($kgCO_{2\text{-eq}}/kgH_2$) are obtained by dividing the cumulated emissions E_{GHG} by the cumulated hydrogen production M_{H2} (kgH_2) over the a Y years.

$$E_{GHG} = \sum_{i=1}^{\mathrm{Y}} \left[\sum_{t=1}^{H} DE_{t,i} + \sum_{t=1}^{H} IEG_{t,i} + \sum_{el=1}^{N} IPE_{el} - \sum_{t=1}^{H} AE_{t,i} \right] \quad (1)$$

As shown in Figure 1 the same perimeter has been considered for the economic analysis. PERSEE minimizes the total cost function $f(x)$ presented in Eq. (2) which is the opposite of the Net Present Value. This equation shows that the cost of each element el of the energy system is computed considering specific capital expenditures CA (€ per unit size) and size S (in the present study, only the sizes of 60bar and 300bar stationary hydrogen storage systems are optimized) as well as yearly operational expenses comprising direct operation and maintenance costs OP (€/year), energy buying costs BC (computed from hourly grid electricity price data in our case) and selling price SP (hydrogen prices for mobility application and gas grid injection application). These operational expenses are computed considering hourly dynamic flux over each year of operation.

$$f(x) = \sum_{el=1}^{N} \left[CA * S + \sum_{i=1}^{\mathrm{Y}} \frac{OP + BC * Flux * Dt - SP * Flux * Dt}{(1+k)^i} \right] \quad (2)$$

2.3. Optimization approach

2.3.1 Scenarios

In the present study a multi-criteria optimization of three hydrogen supply scenarios is addressed:

- [Truck scenario]: We assume that tube trailers are used to transport hydrogen from Lloseta photovoltaic plant to Palma de Mallorca, where the applications of mobility and injection into the natural gas grid are placed. In this case, it is assumed that all hydrogen produced by the PEM electrolyzer is transported by trucks. Here, 2 trucks are used to supply hydrogen to the refuelling station, whereas other 4 are involved in potential hydrogen injection into the natural gas grid. These numbers of trucks have been pre-determined based on electrolyzer maximal flowrate, hydrogen demand and unitary truck capacity ensuring, therefore, permanent availability of transport capacity at production site.
- [Pipeline scenario 1]: A pipeline is used for the transport of hydrogen from Lloseta to Palma.
- [Pipeline scenario 2]: In this scenario, the pipeline capacity is supposed to be oversized by a factor of 10 in order to cover an increase in the hydrogen production capacity of the production plant, compared to the initial value (135 kg/h). Therefore, the capital cost and embedded Greenhouse Gases (GHG) emissions of the pipeline are adjusted, being divided by 10.

2.3.2 Optimization variables

Table 1 provides an overview of the optimization variables considered in this study.

Table 1. Optimization variables

Type of optimization variables	Variables	Units
Size of components	300bar stationary storage capacity (Truck scenario)	kg
	60bar stationary storage capacity (Pipeline scenarios)	kg
Power or mass flow management (dynamic optimization of operation)	PV electricity consumption	MW
	PV electricity injection to electrical grid	MW
	Grid electricity consumption	MW
	PEM electrolyzer production	kg/h
	H_2 injection in NG grid at 4%vol max	kg/h

2.3.3 Multi-criteria optimization method

The optimization of the energy system is performed by using the economic objective function and restrictions on total $CO_{2\text{-eq}}$ emissions. In order to build the Pareto front, two mono-objective optimizations are performed. In the first one, NPV is maximized without applying any $CO_{2\text{-eq}}$ emissions restrictions. In the second one, $CO_{2\text{-eq}}$ emissions are minimized. This allows to obtain the extreme points of the Pareto front. Afterwards, the internal points in the front are determined by selecting 10 equidistant $CO_{2\text{-eq}}$ emissions values between the two extreme points (highest and lowest $CO_{2\text{-eq}}$ emissions cases). Each of them is fixed as a $CO_{2\text{-eq}}$ emissions constraint in subsequent mono-objective optimization problems, where the NPV is maximized. This means that 10 NPV optimization runs are generated for each hydrogen transport scenario, in which a restriction value of maximum $CO_{2\text{-eq}}$ emissions is set.

2.3.4 Project lifetime and discount rate

We assume a project lifetime of 20 years. However, as it is explained in the following section, data series are based only on information of the year 2019. For this reason, each time series is replicated over the years in order to guarantee the optimization over the 20-years period. The Net Present Value optimization is performed considering a discount rate of 7%.

2.4. Data sources and assumptions

A summary of all numerical assumptions is given in Appendix of this paper. In the following paragraphs, we provide more details about the sources and construction of input temporal data and environmental data.

2.4.1 Temporal data

The Table 2 provides the list of temporal data used in the present study.

Table 2. Input temporal data considered in the study

Type of temporal data	Units	Sources and characteristics
PV production	MW	PVGIS platform (Lloseta location)
Grid electricity price and emissions	€/MWh & $CO_{2\text{-eq}}$/MWh	UIB personal communication and additional calculations related to emissions from HVDC mainland connexion
Maximal allowable hydrogen injection	kg/h	4%vol of natural gas (NG) consumption NG consumption approximated from electrical production
Hydrogen demand for fuel cell buses	kg/h	Considered constant 8kg/h

Data of the hourly power generation mix and its $CO_{2\text{-eq}}$ emissions in 2019, as well as the hourly electricity spot price in 2019 in the Balearic Islands were provided by the Industrial Engineering Department of the University of the Balearic Islands. Even though data series from 2020 and 2021 were also available, they were not considered in the present study given that both 2020 and 2021 were atypical years due to the COVID-19 pandemic. As it was mentioned before, hydrogen demand for the mobility application is fixed at 8 kg/h. This constant value might not be representative of the real hourly hydrogen demand profile due to the fact that demand can vary, for instance, from summer to winter when the amount of tourists visiting the Islands is considerably lower. However this value represents a fixed constraint which forces the system to produce hydrogen to supply the demand. Thanks to this constraint, in the optimization problem there is at least one constant hydrogen demand to fulfil. In the case of hydrogen demand for injection into the natural gas network, a maximum constraint of 4% in volume of the existing natural gas flow is considered. As no information regarding real consumption of natural gas could be found, a roughly estimation is performed. It is supposed that all the natural gas sent to the Island is used exclusively for power generation. Figure 2 represents the maximum hydrogen mass flow that can be injected in to the natural gas grid.

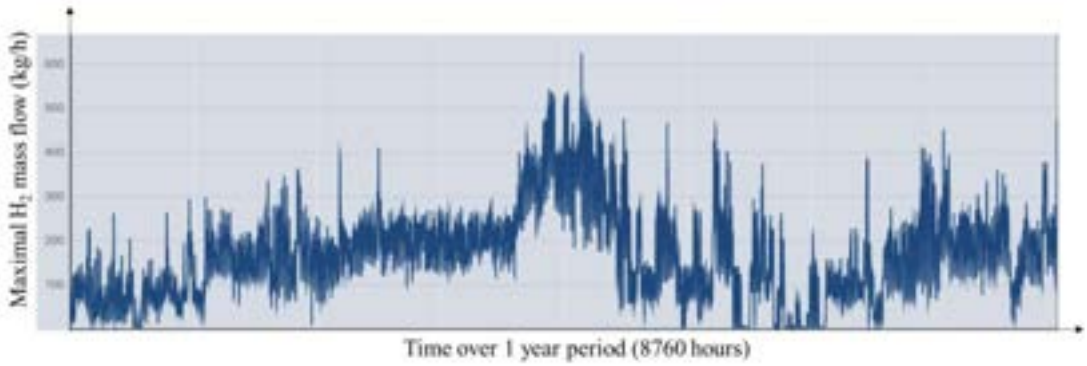

Figure. 2. Illustration of the yearly maximal hydrogen mass flowrate injection considering a limit of 4%vol of hydrogen in natural gas.

2.4.2 Environmental data

In order to obtain the results of the direct and indirect emissions of the different components of the system, it is necessary to define the boundaries and the impact categories. In this case, only the end-of-life stage of the components is not considered. In addition, the environmental impact category selected for the Life Cycle Impact Assessment (LCIA) is the Global warming potential of the EV3.0 method. Ecoinvent 3.8 database [15,16] is used for the selection of the activities for the diverse components. It is important to highlight that when selecting the Ecoinvent activities, a geographic prioritization is established. For this study, priority is given to Spain data in the database. If there is no Spain reference, European data (RER) is selected and, if the latter is not available, "global" (GLO) and "rest of the world" (RoW) data is chosen. In the next paragraphs a description of the environmental aspects of some elements of the system is presented (all other input data are available in the Appendix).

2.4.2.1 Compressor

In the case of the compressor, in order to obtain the $CO_{2\text{-eq}}$ emissions values, the study published by Ghandehariun and Kumar [17] is used. Since the assumptions between the literature and the studied system are different, particularly the system capacity, the exponential rule in Eq. (3) is applied for the calculation of energy and material inputs. In this way, the mass of the components and the energy required for compressor manufacturing are adapted to the system size, based on the study reported by Lee et al. [18].

$$\mathrm{m}_{1,\mathrm{BOP}} = \mathrm{m}_{2,\mathrm{BOP}} \times \left(\frac{\mathrm{P}_1}{\mathrm{P}_2}\right)^{\mathrm{f}} \quad (3)$$

Where m is the mass (or energy input), P the system capacity and f the scale factor.

This equation is used for the different components of the Balance of Plant (BOP) for electrolyzers. However, information must be adjusted in such a way that it can be added to the MILP optimization problem. Therefore, the value of the environmental impact, expressed in $kgCO_{2\text{-eq}}$, has been calculated for different compressor capacities and a linear regression was made resulting in the linear function expressed in Eq. (4) where $IPE_{compressor}$ refers to indirect production emissions ($kgCO_{2\text{-eq}}$) of compressor manufacturing and $P_{compressor}$ refers to compressor electrical power (MW).

$$IPE_{compressor} = 258027 * P_{compressor} + 24217 \quad (4)$$

2.4.2.2 Hydrogen Storages and Pipeline transportation

Equations 5, 6 and 7 provide the considered linear functions for calculating indirect product emissions $IPE_{product}$ ($kgCO_{2\text{-eq}}$) related to the manufacturing of type I tank for 60bar storage, type II tank for 300bar storage and hydrogen pipeline respectively. Variables $C_{storage60bar}$ and $C_{storage300bar}$ refer to storage capacity (kgH_2) and variable $L_{pipeline}$ refers to the length of the pipeline (km). Numerical coefficients are based on data from Ecoinvent [15,16] and [19] from which a dedicated environmental model has been built.

$$IPE_{storage60bar} = 310 * C_{storage60bar} \quad (5)$$

$$IPE_{storage300bar} = 350 * C_{storage300bar} \quad (6)$$

$$IPE_{pipeline} = 80000 * L_{pipeline} \quad (7)$$

2.4.2.3 PEM Electrolyzer

The PEM electrolyzer inventories used in this study are updated from the study published by Sharma et al. [20]. $CO_{2\text{-eq}}$ emissions for the production phase of the PEM system have been calculated for 10 system capacities, since some components of the PEM do not increase in a linear way. The information obtained must be adjusted so that it can be added to the MILP optimization problem. Therefore, a linear adjustment is made for the system, giving as a result the linear function shown in Eq. (8) where $IPE_{electrolyzer}$ refers to indirect production emissions ($kgCO_{2\text{-eq}}$) of electrolyzer manufacturing and $P_{electrolyzer}$ refers to electrolyzer electrical power (MW).

$$IPE_{electrolyzer} = 261351 * P_{electrolyzer} + 45156 \quad (8)$$

2.4.2.4 Mallorca Grid Data

Since the objective of the study is to optimize the hydrogen production, including the environmental impact, $CO_{2\text{-eq}}$ emissions of the Balearic Islands' electricity grid is required. Different sources such as Ecoinvent [15, 16] provide an average value of $CO_{2\text{-eq}}$ emissions resulting from the overall Spain electricity grid. Other

sources, such as ENTSOE [21] and REE [22] give hourly, monthly and yearly average values of $CO_{2\text{-eq}}$ emissions. However, this data correspond to the $CO_{2\text{-eq}}$ emissions of the energy generation mix in the Balearic Islands, without taking into account the energy import from Spain Mainland. Therefore, in order to know the $CO_{2\text{-eq}}$ emissions of the electricity consumed in the Balearic Islands, emissions from energy imports need to be taken into account.

For this purpose, ENTSOE and REE emission data of power generation in Spain Mainland were weighted, averaged and added to the $CO_{2\text{-eq}}$ emissions database provided by the Industrial Engineering Department of the University of the Balearic Islands. An emission factor of 590 $kgCO_{2\text{-eq}}$/MWh was obtained for our reference year 2019. In addition, we considered a reduction of carbon intensity of the electrical grid based on the scenario proposed by the Ministry for Ecological Transition and the Demographic Challenge of the Balearic Islands [23] and assuming an emission factor below 160 $kgCO_{2\text{-eq}}$/MWh for year 2039. This hypothesis implies a Balearic generation mix composed of 65% renewables and 35% of energy imports from the Peninsula. Thus, a reduction coefficient was implemented in PERSEE in order to take into account this decrease in grid $CO_{2\text{-eq}}$ emissions over the supposed 20 years of the project.

3. Optimization results & Discussion

3.1. Pareto Front

As it was explained in the section 2.2, a Pareto front is generated for each hydrogen transport scenario. Figure 3a shows the NPV and cumulated emissions over the 20 years project time. It can be noted that, as avoided $CO_{2\text{-eq}}$ emissions are being considered, the three scenarios present negative values of $CO_{2\text{-eq}}$, when the emissions are being exclusively optimized. We observe that all scenarios adopt negative values of NPV, meaning that the system is not economically profitable when environmental aspects are being exclusively optimized given our set of assumptions (see Appendix). Besides, in terms of emissions, tube trailer (truck) scenario and pipeline scenario do not considerably differ. In other words, for this study case, these two means of H_2 transportation produce similar amount of $CO_{2\text{-eq}}$ emissions. However, in economic terms, they present great differences, being the scenario of pipeline with reduced CAPEX the most profitable.

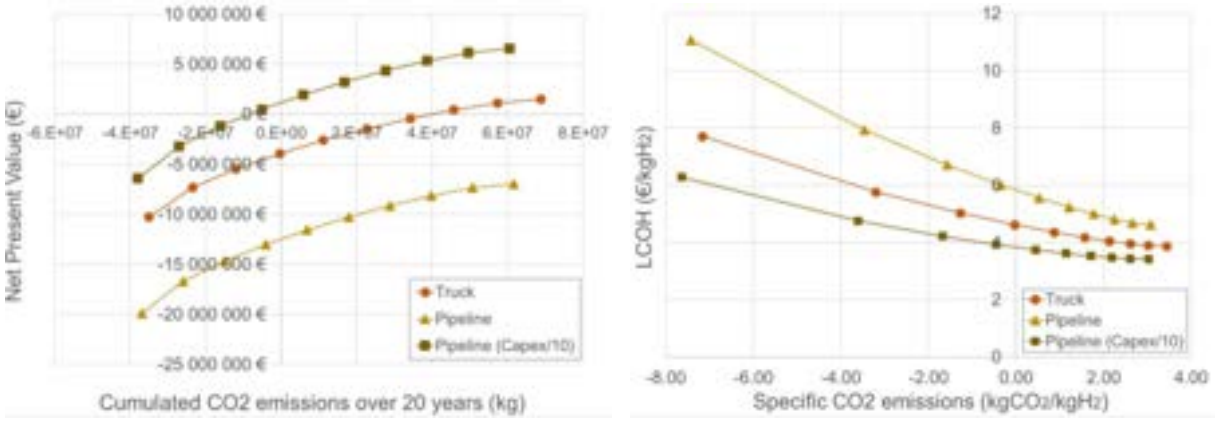

(a) *(b)*

Figure. 3. a) Pareto Front obtained for each of the three scenarios, b) Levelized Cost of Hydrogen compared with Specific $CO_{2\text{-eq}}$ emissions.

Figure 3b illustrates the Levelized Cost of Hydrogen and the specific emissions, expressed in kilograms of $CO_{2\text{-eq}}$ per kilogram of hydrogen. It can be seen from the Figure that, when the NPV is being exclusively optimized, the pipeline with reduced CAPEX scenario presents the lowest LCOH value, accounting for ~3.4€/kgH_2. It is then followed by the tube trailer scenario (~3.9€/kgH_2) and the original pipeline scenario (~4.6€/kgH_2). For each scenario, the reported LCOH values determine the minimum H_2 averaged sell price from which the system is profitable. In addition, the specific emissions give hint of which group of solutions generates a reduction in current emissions. This implies that the solutions with positive specific emission values lead to higher overall emissions. Therefore, the solutions considered as more sustainable would be the ones that present negative values of specific emissions despite higher cost.

3.2. Cost and emissions structure

In the present section, the cost and emissions breakdown analysis of the projects is performed. Figure 4a depicts the components relative contribution to the cost, while Figure 4b shows their relative contribution to the emissions.

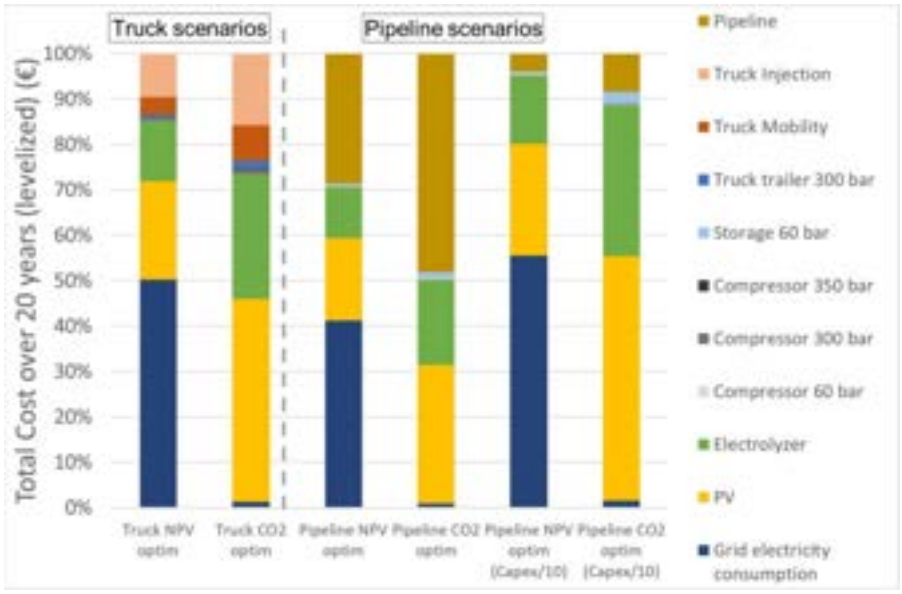

(a)

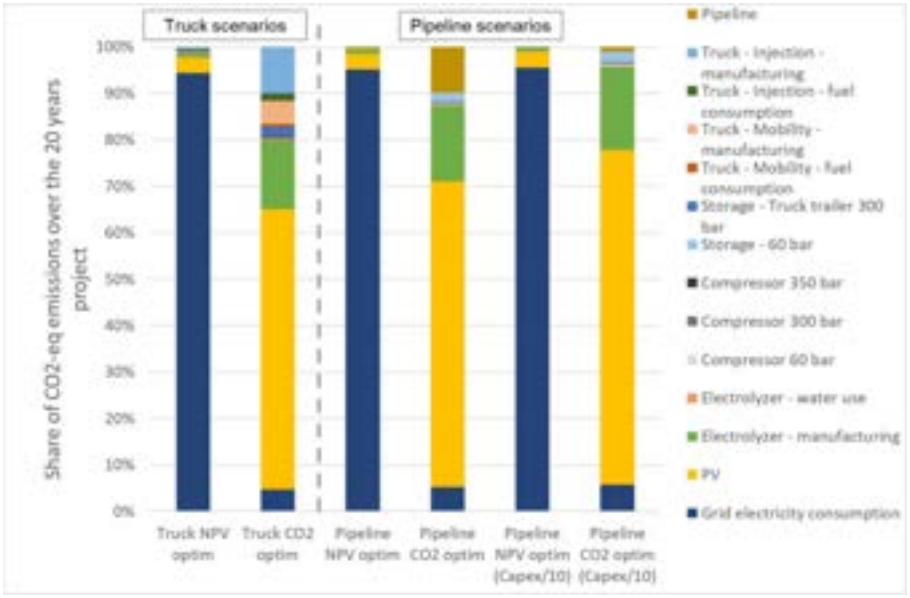

(b)

Figure. 4. Structure of each scenario considering: a) relative cost, b) relative emissions

For the NPV optimization cases, it can be observed that the electrical grid is responsible for the highest percentage of costs and $CO_{2\text{-eq}}$ emissions. This proves that, in this case, energy extraction from the grid takes the highest shares. For the $CO_{2\text{-eq}}$ optimization cases it can be seen that the photovoltaic farm is responsible for most of the costs and emissions. In this optimization case, the use of the grid is minimized in order to reduce overall $CO_{2\text{-eq}}$ emissions. Even though an emission reduction factor is assigned to the energy extracted from the grid, it seems that, environmentally speaking, it is better to reduce energy grid extraction anyway.

Finally, considering that the size of the components such as the photovoltaic farm, the electrolyzer, the compressors and the gas transport medium are fixed, the variations of the cost breakdown between the solutions are mainly due to the use of the electrical grid. In the set of solutions where emissions are exclusively optimized, the generation behavior of the electrolyzer follows the trend of the PV production, as it avoids the use of the grid. However, the hours of use of the electrolyzer are considerably reduced, generating an economically oversized system.

4. Conclusions and perspectives

In this paper a multi-criteria optimization approach based on dynamic modelling has been implemented for evaluating the economic performance and greenhouse gases emissions of a PV based hydrogen energy chain.

We considered a theoretical case study relying on some of the characteristics of the GreenHysland EU project deployed in Mallorca, Spain. This case study consisted in a hydrogen energy chain comprising a 7.5 MW electrolyzer connected to a local PV plant and to the local electrical grid. The end-use applications consisted in mandatory refuelling of five hydrogen fuel cell buses and a flexible hydrogen injection into the natural gas grid up to 4%$_{vol}$. Hydrogen truck trailers and hydrogen pipeline were both considered for connecting production and end-use applications. The optimization was conducted over 20 years plant lifetime and considering one year of data at a timestep of one hour. The two optimization criteria were the Net Present Value and the cumulated greenhouse gases emissions including direct (fuel combustion), indirect (capex-related and from grid electricity) and avoided emissions (substitution of diesel buses and natural gas).

Several fronts of non-dominated solutions were obtained using the epsilon-constraint method. These fronts show that the cumulated greenhouse gases emissions could become negative mainly due to the greenhouse gas emission savings from substitution of natural gas by hydrogen in the natural gas grid. The structure of costs and emissions was also analysed. It was shown that when maximizing the Net Present Value, the grid electricity consumption takes the greatest share of cost breakdown and $CO_{2\text{-eq}}$ emissions for all scenarios, as the optimizer tends to maximize the utilization rate of the electrolyzer for minimizing the costs.

On the contrary, when the cumulated $CO_{2\text{-eq}}$ emissions are being minimized, the optimizer prefers using direct production from the local PV plant, which in turns reduces the utilization rate of the electrolyzer and increases the costs. Hence, in this case the cost associated with photovoltaic power production represents the highest proportion in the cost structure (except in high capex pipeline scenario were pipeline becomes the highest cost factor). In terms of emissions, the photovoltaic production involves the biggest contribution for all scenarios. However, the optimal solution shows that share of embedded emissions from “other than Solar” elements (electrolyzer, pipeline, compressors, storages, truck trailers) is not negligible, representing between 25% and 35% of the emissions breakdown.

Hence, this study emphasizes the potential interest of such dynamic multi-criteria optimization approach to support impact assessment in pre-design phases of hydrogen projects complying with current and future GHG savings assessment methodologies defined at European level (RED II and related Delegated Acts) as well as green or low carbon hydrogen certification processes. By year 2030 the evolution of EU regulation towards mandatory hourly temporal correlation between renewable production and hydrogen production may increase the need of relevant dynamic multi-criteria optimization approaches.

Several perspectives can be envisaged for increasing the robustness of these approaches. In terms of environmental inventory information, a comprehensive study of the waste management of the system should be carried out, i.e. the end-of-life analysis of all components. Besides, in the LCA section, several other impact categories, such as water consumption and land use, could be added to the optimization problem. Future studies should focus on how to perform a complete environmental optimization study, considering several environmental indicators as objective functions. Finding the optimal solution in an optimization problem involving more than two objectives constitutes a challenge in terms of resolution time and appropriate algorithms should be investigated to reach this objective. Uncertainties regarding all types of inputs should also be included and handled in energy system optimization problems. Including them would ensure the derivation of more robust conclusions useful for investment decision-making process and daily optimal operation. However, such methods and tools do not substitute to stakeholders investment decisions which may depend on additional local and global considerations such as regulation, market readiness, business model, social acceptance or political support.

Acknowledgments

The authors acknowledge specially the University of Balearic Islands, in particular Dr. Vincent Canals for his highly valuable inputs. The authors thank the GreenHysland EU project. This project has received funding from the Fuel Cells and Hydrogen 2 Joint Undertaking (now Clean Hydrogen Partnership) under Grant Agreement No 101007201. This Joint Undertaking receives support from the European Union’s Horizon 2020 Research and Innovation programme, Hydrogen Europe and Hydrogen Europe Research. The content of this publication reflects only the authors' view and the JU is not responsible for any use that may be made of the information it contains.

Appendix

Table 3. Technical, economic and environmental assumptions considered.

Component	Parameters	Units	Data	References
Lloseta PV park	Installed peak power	MWp	8.56	[1]
	Solar production	MW/MWp	PV production time series. Lloseta location	[24]
	CAPEX	EUR/kWp	1,000	Assumption
	OPEX	EUR/kWp	1% of investments costs	Assumption

	Embedded emissions[1]	$kgCO_{2\text{-eq}}/MWh$	26	[25]
Balearic islands power mix	Power production	MW	Hourly power time series.	[26]
	Extraction price	EUR/MWh	Hourly energy sport price time series.	[26]
	Grid emissions	$kgCO_{2\text{-eq}}/MWh$	Hourly $CO_{2\text{-eq}}$ emissions time series.	[26]
PV connection	Efficiency	%	84.2	[27]
PEM Electrolyzer	Nominal power	MW	7.5[2]	[1]
	H_2 mass flow rate	kg/h	135[3]	[28]
	Efficiency	%	61.7	[28]
	Lifetime	years	20	Assumption
	CAPEX	EUR/MW	500,000	[29]
	OPEX	EUR/MW	1.8% of investments costs	[29]
	Emissions for water use	$kgCO_{2\text{-eq}}/kgH_2$	0.0044	[15,16]
	Embedded emissions	$kgCO_{2\text{-eq}}$	261351 x $P_{electrolyzer}$+ 45156	[6]
300bar compressor	Inlet H_2 pressure	bar	30	Assumption
	Outlet H_2 pressure	bar	300	Assumption
	H_2 mass flow rate	kg/h	135[4]	Assumption
	Embedded emissions	$kgCO_{2\text{-eq}}$	258027 x $P_{compressor}$ + 24217	Assumption
	CAPEX	EUR/MW	700,000	[29]
	OPEX	EUR/MW	7% of investments costs	[29]
60bar compressor	Inlet H_2 pressure	bar	30	Assumption
	Outlet H_2 pressure	bar	60	Assumption
	H_2 mass flow rate	kg/h	135[4]	Assumption
	Embedded emissions	$kgCO_{2\text{-eq}}$	258027 x $P_{compressor}$ + 24217	Assumption
	CAPEX	EUR/MW	700,000	[29]
	OPEX	EUR/MW	7% of investments costs	[29]
300bar storage tank	Storage capacity	kgH_2	**Optimized**	-
	Embedded emissions	$kgCO_{2\text{-eq}}/kgH_2$	350 (type II H_2 storage tank)	[19]
	CAPEX	EUR/kgH_2	550	[29]
	OPEX	EUR/kgH_2	0% of investments costs	Assumption
60bar storage tank	Storage capacity	kgH_2	**Optimized**	-
	Embedded emissions	$kgCO_{2\text{-eq}}/kgH_2$	310 (type I H_2 storage tank)	[19]
	CAPEX	EUR/kgH_2	550	[29]
	OPEX	EUR/kgH_2	0% of investments costs	Assumption
Tube trailers for mobility and H_2 injection	Distance	km	30[5]	-
	Fuel consumption	Kg_{diesel}/km	0.4	Assumption
	Max speed	km/h	60	Assumption
	Total capacity	KgH_2	462	Assumption
	Usable capacity	kgH_2	370[6]	-
	$CO_{2\text{-eq}}$ (fuel use)	$kgCO_{2\text{-eq}}/km$	0.79[7]	[15,16,30,31]
	Embedded emissions	$kgCO_{2\text{-eq}}/kgH_2$	350	[15,16,19]
	CAPEX	EUR/kgH_2[8]	550[9]	[29]
	OPEX	EUR/kgH_2[8]	0.153[10]	Assumption
H_2 pipeline	H_2 max mass flow rate	kg/h	1350 (Scenario 1); 135[4] (Pipeline Scenario 2)	Assumption
	Efficiency	%	100[11]	Assumption
	Embedded emissions	$kgCO_{2\text{-eq}}/km$	80,000	[15,16]
	$CAPEX_a$[12]	EUR/km	1,000,000	[32]
	$CAPEX_b$[13]	EUR/km	500,000	[32]
	OPEX	EUR/km	0% of investments costs	Assumption
350bar compressor	Inlet H_2 pressure	bar	60	Assumption
	Outlet H_2 pressure	bar	350	[1]
	H_2 mass flow rate	kg/h	8	Assumption
	Embedded emissions	$kgCO_{2\text{-eq}}$	258027 x $P_{compressor}$ + 24217	Assumption
	CAPEX	EUR/MW	700,000	[29]
	OPEX	EUR/MW	7% of investments costs	[29]
H_2 demand for buses	H_2 fixed flow rate	kg/h	8	Assumption
	Avoided $CO_{2\text{-eq}}$	$kgCO_{2\text{-eq}}/km$	1.222[14]	[15,16]
	H_2 sell price	EUR/kgH_2	4	Assumption

[1] Refers to $CO_{2\text{-eq}}$ emissions
[2] Three 2.5 PEM electrolyzers.
[3] Hydrogen production: 1080 kgH_2/day, which is 45 kgH_2/h. Considering three 2.5 MW electrolyzers, this gives 135 kgH_2/h.
[4] Based on the three-electrolyzer production.
[5] Lloseta – Palma de Mallorca distance
[6] Assuming a discharge equilibrium pressure of 60bar, hence usable capacity of 300bar trailer assumed at 80% of total capacity
[7] Two were considered for H2 transportation (while one refuels, the other delivers). Calculation:

$$0.3\ \frac{\mathrm{L_{diesel}}}{\mathrm{km}}\mathrm{x}0.85\frac{\mathrm{kg_{diesel}}}{\mathrm{L_{diesel}}}\mathrm{x}1.55\frac{\mathrm{kg_{CO2}}}{\mathrm{kg_{diesel}}}x2 = 0.79\frac{\mathrm{kg_{CO2}}}{\mathrm{km}}$$

[8] EUR per transported H_2
[9] The value of the investments costs of a H2 storage tank is used for estimating the investments costs of H_2 tube trailers.
[10] Calculation :

$$0.4\frac{\mathrm{kg_{diesel}}}{\mathrm{km}}\mathrm{x}\frac{1}{0.85}\frac{\mathrm{L_{diesel}}}{\mathrm{kg_{diesel}}}\mathrm{x}2\frac{\mathrm{EUR}}{\mathrm{L_{diesel}}} = 0.94\frac{\mathrm{EUR}}{\mathrm{km}} \rightarrow 0.94\frac{\mathrm{EUR}}{\mathrm{km}}\mathrm{x}60\mathrm{km} = 56.47\mathrm{EUR} \rightarrow \frac{56.47\mathrm{EUR}}{370\ \mathrm{kg_{H2}}} = 0.153\frac{\mathrm{EUR}}{\mathrm{kg_{H2}}}$$

[11] No head losses are considered for the pipeline
[12] Amortized in 20 years
[13] Amortized in 40 years
[14] $CO_{2\text{-eq}}$ emissions of a diesel bus

H_2 demand	Max H_2 flow rate	kg/h	Timeserie	[1]
NG grid injection	Avoided $CO_{2\text{-eq}}$	$kgCO_{2\text{-eq}}/kgH_2$	8.43[15]	[15,16]
	H_2 sell price	EUR/kgH_2	4	Assumption (same price as mobility)

Nomenclature

BOP	Balance of Plant
CEA	Commissariat à l'Energie Atomique et aux énergies alternatives
$CO_{2\text{-eq}}$	Carbon dioxide equivalent
EU	European Union
GHG	Greenhouse gases
H_2	Hydrogen
HVDC	High Voltage Direct Current
LCA	Life Cycle Assessment
LCI	Life Cycle Inventory
LCIA	Life Cycle Impact Assessment
LCOH	Levelized Cost of Hydrogen
MILP	Mixed Integer Linear Programming
NG	Natural gas
NPV	Net Present Value, €
PEM	Proton Exchange Membrane
PV	Photovoltaic
RED	Renewable Energies Directive
UIB	Universitat de les Illes Balears

References

[1] GreenHysland project. – Available at:<https://greenhysland.eu/> [accessed 15.03.2023].

[2] A. Valente, D. Iribarren, and J. Dufour, "Life cycle assessment of hydrogen energy systems: a review of methodological choices," *The International Journal of Life Cycle Assessment*, vol. 22, no. 3, pp. 346–363, 2017.

[3] T. G. H. Organisation, "The Green Hydrogen Standard," 2022, [Online]. Available: https://gh2.org/our-initiatives/gh2-green-hydrogen-standard

[4] E. Iturriaga, Á. Campos-Celador, J. Terés-Zubiaga, U. Aldasoro, and M. Álvarez-Sanz, "A MILP optimization method for energy renovation of residential urban areas: Towards Zero Energy Districts," *Sustainable Cities and Society*, vol. 68, p. 102787, 2021.

[5] O. Hafez and K. Bhattacharya, "Optimal planning and design of a renewable energy based supply system for microgrids," *Renewable Energy*, vol. 45, pp. 7–15, 2012.

[6] E. Cuisinier, C. Bourasseau, A. Ruby, P. Lemaire, and B. Penz, "Techno-economic planning of local energy systems through optimization models: a survey of current methods," *International Journal of Energy Research*, vol. 45, no. 4, pp. 4888–4931, 2021.

[7] C. Haikarainen, F. Pettersson, and H. Saxen, "An MILP model for distributed energy system optimization," *Chemical Engineering Transactions*, vol. 35, pp. 295–300, 2013.

[8] H. Ren, W. Zhou, K. Nakagami, W. Gao, and Q. Wu, "Multi-objective optimization for the operation of distributed energy systems considering economic and environmental aspects," *Applied Energy*, vol. 87, no. 12, pp. 3642–3651, Dec. 2010, doi: 10.1016/j.apenergy.2010.06.013.

[9] P. J. Copado-Méndez, C. Pozo, G. Guillén-Gosálbez, and L. Jiménez, "Enhancing the ϵ-constraint method through the use of objective reduction and random sequences: Application to environmental problems," *Computers & Chemical Engineering*, vol. 87, pp. 36–48, Apr. 2016, doi: 10.1016/j.compchemeng.2015.12.016.

[10] S. Sinha and S. S. Chandel, "Review of software tools for hybrid renewable energy systems," *Renewable and Sustainable Energy Reviews*, vol. 32, pp. 192–205, 2014, doi: https://doi.org/10.1016/j.rser.2014.01.035.

[15] Natural gas emission factor times LHV_{H2}

[11] H. Sharma, É. Monnier, G. Mandil, P. Zwolinski, and S. Colasson, “Comparison of environmental assessment methodology in Hybrid energy system simulation software,” *Procedia CIRP*, vol. 80, pp. 221–227, 2019.

[12] I. O. for Standardization (ISO), “ISO 14040: 2006 Environmental Management–Life Cycle Assessment–Principles and Framework (2).” International Organization for Standardization Geneva, 2006.

[13] B. Steubing, D. de Koning, A. Haas, and C. L. Mutel, “The Activity Browser—An open source LCA software building on top of the brightway framework,” *Software Impacts*, vol. 3, p. 100012, 2020.

[14] É. Cuisinier, P. Lemaire, B. Penz, A. Ruby, and C. Bourasseau, “New rolling horizon optimization approaches to balance short-term and long-term decisions: An application to energy planning,” *Energy*, vol. 245, p. 122773, Apr. 2022, doi: 10.1016/j.energy.2021.122773.

[15] G. Wernet, C. Bauer, B. Steubing, J. Reinhard, E. Moreno-Ruiz, and B. Weidema, “The ecoinvent database version 3 (part I): overview and methodology,” *The International Journal of Life Cycle Assessment*, vol. 21, no. 9, pp. 1218–1230, 2016.

[16] B. Steubing, G. Wernet, J. Reinhard, C. Bauer, and E. Moreno-Ruiz, “The ecoinvent database version 3 (part II): analyzing LCA results and comparison to version 2,” *The International Journal of Life Cycle Assessment*, vol. 21, no. 9, pp. 1269–1281, 2016.

[17] S. Ghandehariun and A. Kumar, “Life cycle assessment of wind-based hydrogen production in Western Canada,” *International Journal of Hydrogen Energy*, vol. 41, no. 22, pp. 9696–9704, Jun. 2016, doi: 10.1016/j.ijhydene.2016.04.077.

[18] Y. D. Lee, K. Y. Ahn, T. Morosuk, and G. Tsatsaronis, “Environmental impact assessment of a solid-oxide fuel-cell-based combined-heat-and-power-generation system,” *Energy*, vol. 79, pp. 455–466, 2015.

[19] H. W. Langmi, N. Engelbrecht, P. M. Modisha, and D. Bessarabov, “Chapter 13 - Hydrogen storage,” in *Electrochemical Power Sources: Fundamentals, Systems, and Applications*, T. Smolinka and J. Garche, Eds. Elsevier, 2022, pp. 455–486. doi: 10.1016/B978-0-12-819424-9.00006-9.

[20] H. Sharma, G. Mandil, É. Monnier, E. Cor, and P. Zwolinski, “Sizing a hybrid hydrogen production plant including life cycle assessment indicators by combining NSGA-III and principal component analysis (PCA),” *Energy Conversion and Management: X*, vol. 18, p. 100361, Apr. 2023, doi: 10.1016/j.ecmx.2023.100361.

[21] A. ENTSO-E, “ENTSO-E transparency platform,” *URL https://transparency. entsoe. eu*, 2017.

[22] Red Eléctrica de España (REE), “REData API,” *https://www.ree.es/es/apidatos*, 2022.

[23] Ministerio Para la Transición Ecológica y el Reto Demográfico, “Plan Nacional Integrado de Energía y Clima (PNIEC) 2021–2030,” 2019.

[24] JRC Photovoltaic Geographical Information System (PVGIS) - European Commission. Available at: < https://re.jrc.ec.europa.eu/pvg_tools/en/> [accessed 02.02.2023].

[25] Live 24/7 CO_2 emissions of electricity consumption. - Available at:< https://app.electricitymaps.com/zone/ES>[accessed 02.02.2023].

[26] Industrial Engineering Department, University of the Balearic Islands. Hourly datasheet from 2019.

[27] Tecnicos consultores. Parque solar fotovoltaico Lloseta: Proyecto: Power to Green Hydrogen. Balearic Islands, Spain. - Available at: https://www.caib.es/sites/normativaindustria/f/282195 [accessed 05.02.2023].

[28] *HyLYZER® WATER ELECTROLYZERS datasheet.* - *Available* at < https://mart.cummins.com/imagelibrary/data/assetfiles/0070330.pdf >. [accessed 05.01.2023].

[29] FCH 2 JU - MAWP Key Performance Indicators (KPIs). Available at: < https://www.clean-hydrogen.europa.eu/knowledge-management/strategy-map-and-key-performance-indicators/fch-2-ju-mawp-key-performance-indicators-kpis_en> [05.03.2023].

[30] International Council of Clean Transportation. Fuel Consumption Testing of Tractor-Trailers in The European Union and the United States. - Available at <https://theicct.org/wp-content/uploads/2021/06/EU_HDV_Testing_BriefingPaper_20180515a.pdf> [accessed 10.03.2023].

[31] Speight, J.G, 2-Production, properties and environmental impacts of hydrocarbon fuel conversion. In: Advances in Clean hydrocarbon Fuel Processing. United States: Woodhead Publishing Series in Energy. 2011.p.54-82.

[32] IEA, The Future of Hydrogen. Paris, France. 2019 Jun. Report prepared by the IEA for the G20.

Exergoeconomic Model of a PEM Fuel Cell

Abdelnasir Omran[a], José Sodré[b]

[a] Aston University, Birmingham, UK, omrana@aston.ac.uk
[b] Aston University, Birmingham, UK, j.sodre@aston.ac.uk

Abstract:

This paper presents an exergoeconomic model of a proton-exchange membrane (PEM) fuel cell stack. The model was calibrated using data from experiments performed in a 1.2 kW PEM fuel cell with varying load, operated at steady state. The exergy analysis was performed with fuel cell operation in the air stoichiometry range between 2 to 4. The results showed the system exergy efficiency varied from 26% to 39%, while the energy efficiency ranged between 37% and 56%. This range is slightly above the fuel cell data sheet from the manufacturer, which declares a rated energy efficiency of 48%. High pressure, temperature and cell voltage give better exergy efficiency. Variation of system temperature showed no significant impact on the exergy cost, as the PEM fuel cell operates at relatively low temperature in its load range not exceeding 174°C. The exergy cost of the system can be improved by adopting any combination of higher operating pressure, inlet air stoichiometry or cell voltage, which demonstrates a significant improvement in the exergy cost. By reducing the hydrogen cost from 6.7 $/kg to 1.9 $/kg, a 15 $/GJ decrease in exergy cost can be achieved.

Keywords:

Fuel Cells; Hydrogen; Mathematical Modelling; Numerical Simulation; Exergoeconomic Analysis.

1. Introduction

The importance of using clean fuels is acknowledged by the need to reduce emissions caused by fossil fuels. The current geopolitics in Europe and the energy crisis related to it made the demand for renewable energy even more appealing. In this respect, hydrogen-fed energy systems such as proton-exchange membrane (PEM) fuel cells can positively affect the future energy sector [1]. PEM fuel cells is a promising renewable power generation system that solves some of the existing and future energy shortages [2]. Low or zero emissions is the main advantage of PEM fuel cells as they convert chemical energy directly into electricity by combining hydrogen with oxygen from the air without combustion thus providing higher thermodynamic efficiency than heat engines and turbines.

After decades of research and development, practical PEM fuel cell systems became available and are expected to attract a growing share of automotive and electricity markets as costs decrease to competitive levels. Low-temperature PEM fuel cells can be used for aeroplanes, trains and passenger vehicles. PEM fuel cells use an electrolyte to conduct hydrogen ions from the anode to the cathode. The electrolyte is, in most cases, composed of a solid polymer film consisted of a form of acidified Nafion membrane. The membrane is treated on both sides with highly dispersed metal alloy particles, mainly platinum or platinum alloys, that are effective catalysts. Hydrogen is supplied to the anode side of the fuel cell where, due to the impact of the catalyst, hydrogen atoms discharge electrons and turn into hydrogen ions (protons). The electrons move in the form of an electric current that can be utilised before it returns to the cathode, where oxygen is fed from the ambient air. The protons disperse across the membrane to the cathode, where the hydrogen atom is re-joined and reacted with oxygen to produce water, thus completing the overall process [3].

Two primary performance analyses are usually applied: energy-based analysis and exergy-based analysis. Several authors [4-6] emphasise that the energy-based analysis can be misleading because it does not identify deviations from ideal situations. In contrast, the exergy of an energy form or substance is a measure of its usefulness, quality, or potential to cause change. However, a better understanding of exergy and the insights it can provide into the efficiency, environmental impact and sustainability of energy systems are required for researchers working in energy systems and the environment. Further, as energy policies play an increasingly important role in addressing sustainability issues and a broad range of local, regional and global environmental concerns, policymakers must also appreciate the exergy concept and its ties to these concerns.

During the past decade, the need to understand the connections between exergy and energy, sustainable development and environmental impact has become increasingly significant. Indeed, the universe's energy content is constant, just as its mass content is. On the other hand, exergy is not conserved; once the exergy is wasted, it can never be recovered. When energy is used for heating homes or public places, it is not destroyed but merely converted to a less proper form, a form of less exergy. The exergy of a system can be

defined as its work potential compared to an exergy reference environment. The work potential is intimately related to the maximum work obtainable when the analysed system interacts with the reference environment and simultaneously reaches equilibrium. The term exergy is also related to the thermodynamical availability of a system [7]. The exergy analysis complements the energy analysis and allows including the effect of the temperature level at which the analysis is being carried out [8].

The concept of exergy has also been explored in the area of fuel cells [9]. A thermodynamic and exergoeconomic assessment of the PEM Fuel Cell system was conducted at steady-state operation conditions [10]. The study found that, by increasing the current density, power density, exergy destruction rate, hydrogen consumption and the cost rate of power generation increases. An exergy analysis was carried out on a hybrid system consisting of 64 photovoltaic modules, a 5.5 kW fuel cell and an electrolyser [11]. The study concluded that the average annual exergy efficiency of the fuel cell is 32.8%.

Energy and exergy analyses were performed for a 1.2 kW Nexa PEM Fuel Cell unit in a solar-based hydrogen production system [12]. The study used a model and experimental setup of the system with different operating conditions and found that the increase in current density reduces the energy and exergy efficiencies by 14%. Varying pressure, temperature and anode stoichiometry, the research concluded that the energy and exergy efficiencies respectively increased by 23% and 15% when the pressure was increased, and by 17% and 14% while increasing the anode stoichiometry. Unlike pressure and anode stoichiometry, increasing the temperature has not affected the efficiency level. Exergy analyses were conducted on 10 kW [13] and 1.2 kW [14] PEM fuel cells, respectively, to observe the effect of the operating temperature, cell voltage, air stoichiometry and pressure on the efficiency. The studies concluded that the air stoichiometry should be less than 4, otherwise the membrane will dry out at a high temperature and the relative humidity level in the product air will not be maintained.

The economics of producing electricity from a PEM fuel cell was examined under various conditions [15], investigating the possibility of using a fuel cell vehicle to generate power while parking outside houses or offices. The study found that, for California, USA, net savings could be reached if the fuel cell costs are about $6000 for a 5 kW home system ($1200/kW) with favourable natural gas costs of $6/GJ at residences.

Cogeneration using PEM and other potential fuel cell types was investigated, using both exergy and energy analyses [16]. The research found that exergy analysis is more rational and meaningful as it considers the equivalent work potentials of the thermal and electrical energy products. The study added that energy analyses often present misleadingly optimistic views of performance. The feasibility of fuel cells in cogeneration applications was studied concentrating on both engineering and economic viewpoints [17], using an optimisation approach through a numerical study. The investigation concluded that, in terms of plant capacity, economics, and energy savings, fuel cell cogeneration is better than conventional gas engine cogeneration.

In this work, a MATLAB model was developed to provide an exergoeconomic analysis of a 1.2 kW Nexa™ PEM fuel cell module at variable operating mass flow rates, pressure, temperature, cell voltage and air stoichiometry. The model calculates the fuel and product exergy and the cost rates associated with these energies. Further details are given in the following sections.

2. Exergy and exergoeconomic analysis of the PEM fuel cell

The exergy efficiency of the PEM fuel cell, defined as the ratio between the fuel cell power output and maximum possible work output [18], is carried out by applying the second law of thermodynamics to the control volume shown by Fig. 1. By adding the cost, capital investment, operations, and maintenance cost, the exergoeconomic analysis is also performed. The exergoeconomic analysis is defined by the ratio of the difference between the exegetic cost rate (cost per unit time) of the streams entering and exiting the PEM fuel cell plus the capital investment, operation and maintenance cost of the PEM fuel cell to the electrical power output. The analyses consider all inlet hydrogen is consumed in the reaction, therefore the excess H_2 is zero.

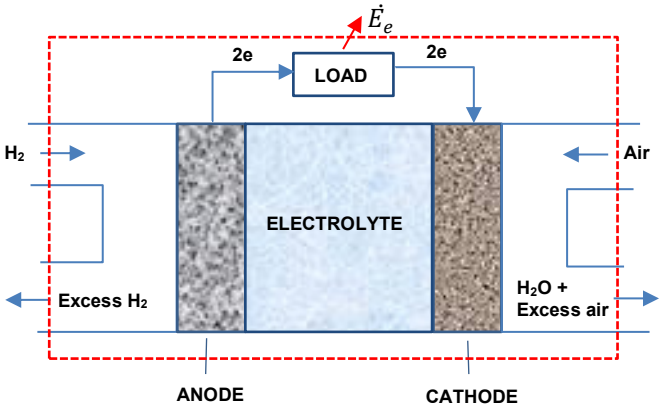

Figure 1. PEM fuel cell schematics.

2.1. Exergy analysis

The fuel cell efficiency (η) is calculated by the ratio of the electrical power output ($\dot{E}_e$) and the differences between the reactant and the product exergies [13]:

$$\eta = \frac{Electrical\ output}{(Total\ exergy)_R - (Total\ exergy)_P} = \frac{\dot{E}_e}{\left(\dot{E}x_{air,R} + \dot{E}x_{H_2,R}\right) - \left(\dot{E}x_{air,P} + \dot{E}x_{H_2O,P}\right)} \quad (1)$$

Where *R*, *P* and $\dot{E}x$ are reactants, products, and the total exergy, respectively. Kinetic and potential energy effects are neglected in the cell reactions.

The electrical power output is the sum of the auxiliary load ($\dot{E}_{aux}$) and the external load from reactant consumption ($\dot{E}_{ext}$), calculated by:

$$\dot{E}_e = \dot{E}_{aux} + \dot{E}_{ext} = I_{fc} \cdot V_{fc} \quad (2)$$

where I_{fc} and V_{fc} are the fuel cell stack current and voltage, respectively.

The external load ($\dot{E}_{ext}$) is the product of the measured current (I_m) and voltage (V_m):

$$\dot{E}_{ext} = I_m \cdot V_m \quad (3)$$

The auxiliary load is determined by the difference between the electrical power output and the external load.

The fuel cell current is calculated by:

$$I_{fc} = \frac{\mathrm{n}_{H_2} \cdot F \cdot \dot{m}_{H_2}}{N} \quad (4)$$

where n_{H_2} is the number of moles of hydrogen consumed per mol of oxidant in the reaction, taken as 2, F is Faraday's constant (96,485 C/mol), $\dot{m}_{H_2}$ is hydrogen mass flow rate, and N is the number of cells in the stack. The total exergy transfer per unit mass (ex) of products and reactants includes both chemical (ex_{CH}) and physical exergies (ex_{PH}) [13]:

$$ex = ex_{CH} + ex_{PH} \quad (5)$$

The physical exergy combines the pressure and temperature of both reactants and products. It can be distinguished as the maximum beneficial work attained by passing the unit of mass of an element from the generic state (T, P) to the environmental state (T_0, P_0). The general expression of the physical exergy is [13]:

$$ex_{PH} = (h - h_0) - T_0(s - S_0) \quad (6)$$

Where h and s are the specific enthalpy and entropy at the actual temperature and pressure condition (T, p), and h_o and s_o are the specific enthalpy and entropy at the standard condition of T_o = 298 K and p_o = 1 atm. The physical exergy of an ideal gas with constant specific heat c_p and specific heat ratio k is written as [13]:

$$ex_{PH} = c_p T_0 \left[\frac{T}{T_0} - 1 - ln\left(\frac{T}{T_0}\right) + ln\left(\frac{p}{p_0}\right)^{\frac{k-1}{k}}\right] \quad (7)$$

The chemical exergy is the attainment of a maximum quantity of valuable work by assigning a system in equilibrium with the environment using T_0 and P_0, calculated by [13]:

$$ex_{CH} = \sum x_n ex_{CH,n} + RT_0 \sum x_n ln x_n \quad (8)$$

where x_n, ex_{CH}^n are the respective mole fraction and chemical exergy of each component (n).

The total exergy $\dot{E}x$ of products (*P*) and reactants (*R*) are calculated by the following equations [13]:

$$\dot{E}x_{H_2,R} = \dot{m}_{H_2,R} ex_{H_2,R} = \dot{m}_{H_2,R}(ex_{CH} + ex_{PH})_{H_2,R} \quad (9)$$

$$\dot{E}x_{air,R} = \dot{m}_{air,R} ex_{airR} = \dot{m}_{air,R}(ex_{CH} + ex_{PH})_{air,R} \quad (10)$$

$$\dot{E}x_{H_2O,P} = \dot{m}_{H_2O,P} ex_{H_2O,P} = \dot{m}_{H_2O,P}\ (ex_{CH} + ex_{PH})_{H_2O,P} \quad (11)$$

$$\dot{E}x_{air,P} = \dot{m}_{air,P} ex_{airP} = \dot{m}_{air,P}(ex_{CH} + ex_{PH})_{air,P} \quad (12)$$

The chemical and physical exergies, efficiency and mass flow rates are calculated at temperature (T/T_0) and pressure (p/p_0) ratios from 0.94 to 1.2 and 7.40 to 4.88, respectively, which are performing temperature and pressure varieties distinctive for PEM fuel cells [13]. The voltage used in the calculations varies are 0.001 V and 0.79 V at air stoichiometry (λ) between 12.0 and 2.0 to examine its effect on efficiency.

2.2. Exergoeconomic analysis

The exergoeconomic analysis considers the exergy cost (c) of all reactants and products of the electrochemical process at several operating conditions, such as cell voltage, inlet air stoichiometry, temperature and pressure. The cost balance of the PEM fuel cell is given by [18]:

$$c_{H_2O}\dot{X}_{H_2O,P} + c_{air}\dot{X}_{air,P} + c_E\dot{E}_e = c_{air}\dot{X}_{air,R} + c_{H_2}\dot{X}_{H_2,R} + c_{FC,I} \quad (13)$$

Rearranging Eq. (13) for the exergetic power cost (c_E) to find the exergy cost [18]:

$$c_E = \frac{c_{air}\dot{X}_{air,R} + c_{H_2}\dot{X}_{H_2,R} - c_{H_2O}\dot{X}_{H_2O,P} - c_{air}\dot{X}_{air,P} + c_{FC,I}}{\dot{E}_e} \quad (14)$$

The total fuel cell investment cost ($c_{FC,I}$) is given by summation of the fuel cell stack capital cost ($c_{FC,C}$) and the cost rate of operation and maintenance (c_{OM}) [18]:

$$c_{FC,I} = c_{FC,C} + c_{OM} \quad (15)$$

The fuel cell investment cost can be calculated in terms of the power output ($\dot{E}_e$), capacity factor (CF) , i.e., the projected functioning rate, and the annual capital cost (ACC) [18]:

$$c_{FC,I} = \frac{ACC \cdot \dot{E}_e}{CF \cdot 8760(h/year) \cdot 3600(s/h)} \quad (16)$$

Taking the projected functioning rate CF as 90%, the annual capital cost, ACC, can be calculated in terms of the fuel cell stack capital cost and the capital recovery factor (CRF), which can be considered based on the equivalent annual cost over the number of years (n_y) of a specified venture at an annual interest rate (i_r) [18]:

$$ACC = c_{FC,C} \cdot CRF \quad (17)$$

The capital recovery factor can be calculated through the following equation [18]:

$$CRF = \frac{i_r(1+i_r)^{n_y}}{(1+i_r)^{n_y} - 1} \quad (18)$$

Where (i_r) has been chosen to be 10% and (n_y) is five years [18]. CRF is calculated as 0.264/year. The fuel cell capital cost, $c_{FC,C}$, is calculated based on the annual average cost for mass production as 2500 $/kW of power output [19]. The PEM fuel cell parameters and the related costs are shown by Table 1 [15,18,20-22]. Considering the annual operation and maintenance cost (C_{OM}) of 300 $/kW [15], the cost rate of operation and maintenance, c_{OM}, can be calculated as follow [18]:

$$c_{OM} = \frac{C_{OM} \cdot \dot{E}_e}{8760(h/year) \cdot 3600(s/h)} \quad (19)$$

Table 1. Baseline properties of PEM fuel cell for exergoeconomic evaluation.

PARAMETER	VALUE
Standard conditions	298 K, 1 atm
Electrical energy output	1.2 kW
Air stoichiometry	3
Hydrogen cost	10 $/kg
Water cost	1 $/m^3
Air cost (O_2)	0.011 $/kg
Fuel cell cost (capital cost)	2500 $/kW
The capacity factor of the fuel cell	0.9
Fuel cell lifetime	5 years
Average annual interest rate	10%
Annual operation and maintenance cost	300 $/kW yr

3. Experimental setup

Both the exergy and exergoeconomic analyses use data from experiments performed in a Ballard Nexa model fuel cell stack system consisting of 47 cells capable of generating 1.2 kW DC power output with 48% efficiency at 65°C. Each cell produces 1.0 V and 0.6 V at open-circuit and maximum current output, respectively. The stack voltage is 43 V and 26 V at no load and full load, respectively. The fuel is 99.99% hydrogen, maintained by the control system at 0.3 bar. The reactant oxygen comes from the ambient air, which pressure is maintained at 0.1 bar and humidified by a built-in humidifier. The area of the cells is 120 cm^2. The fuel cell stack specifications are shown by Tab. 2.

Table 2. Fuel cell stack specifications.

DOMAIN	PARAMETER	VALUE
Performance	Rated power	1.2kW
	Dissipated heat at rated power	1.6kW
	Idle/full voltage at rated power	43 V / 26 V DC
	Operating voltage rate	22 V to 50 V
	Input voltage allowable	18 V to 30 V
	Current at rated power	46 A DC
	Number of cells	47
	Lifetime	1,500 hours
Reactant	Hydrogen (dry)	99.99%,
	Pressure range of hydrogen	0.7 to 17 bar
	Hydrogen consumption	<18.5 L/min
	Process Air	≤ 90 L/min
	Air pressure	atm
Operating environment	Ambient temperature	(3°C to 40°C)
	Maximum stack temperature	65°C
	Humidity	5% to 95%
Product	Pure water (vapour and liquid)	0.870 L/h
Physical	L x W x H	56 x 25 x 33 cm
	System mass	13 kg

4. Results and discussion

The results presented in this section were obtained considering fuel cell operation along 5 years (Tab. 1) without the need of replacement, corresponding to 39,420 h of operation according to Eq. (16). This is based on a previous report that the polymer membrane of a PEM fuel cell can exceed 40,000 h of operation at harsh conditions [22]. Thus, the manufacturer's declaration of 1,500 h lifetime (Tab. 2) and the need of capital reinvestment each time this limit was reached along the evaluation period have not been part of the calculation.

4.1. Exergy analysis

Figure 2 illustrates the energy and exergy efficiencies of the system. While the exergy efficiency was calculated using Eq. (1), the energy efficiency was determined by the ratio of the fuel cell electrical power output and the inlet hydrogen energy content given by the product of hydrogen high heating value and its mass flow rate. It can be observed that both the energy and exergy of the fuel cell system decrease as the current density increases. The energy efficiency varies between 37 to 56% and the exergy efficiency ranges from 26 to 39% as the current density is changed from 0.02 to 0.37 A/cm^2. This behaviour is due to the increase of reactant air and decrease of hydrogen pressure with increasing current density (Fig. 3). The maximum energy efficiency here found is 9% lower compared with the fuel cell manufacturer datasheet, while the exergy efficiency is 3% lower compared to values reported by other authors [23]. The ambient air conditions may have been determinant to the discrepancies.

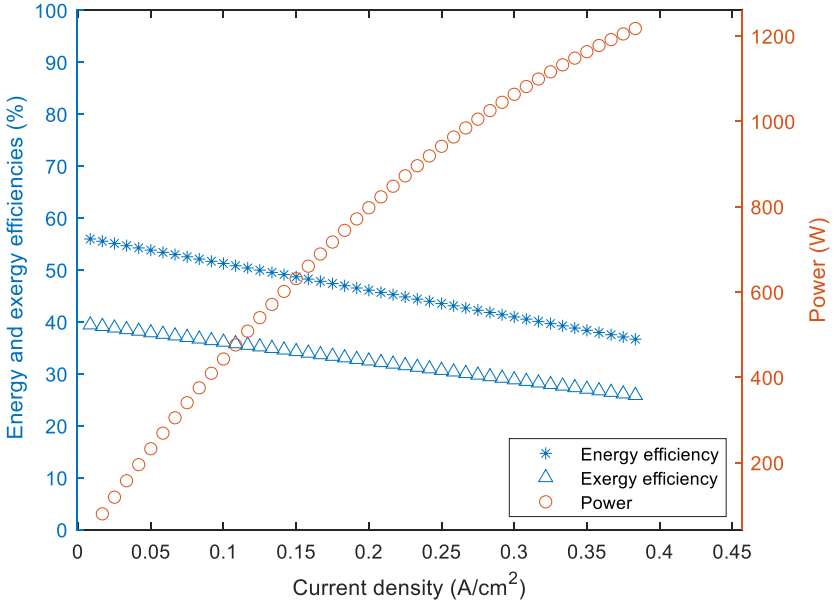

Figure 2. Variation of fuel cell output power, energy and exergy efficiencies with current density.

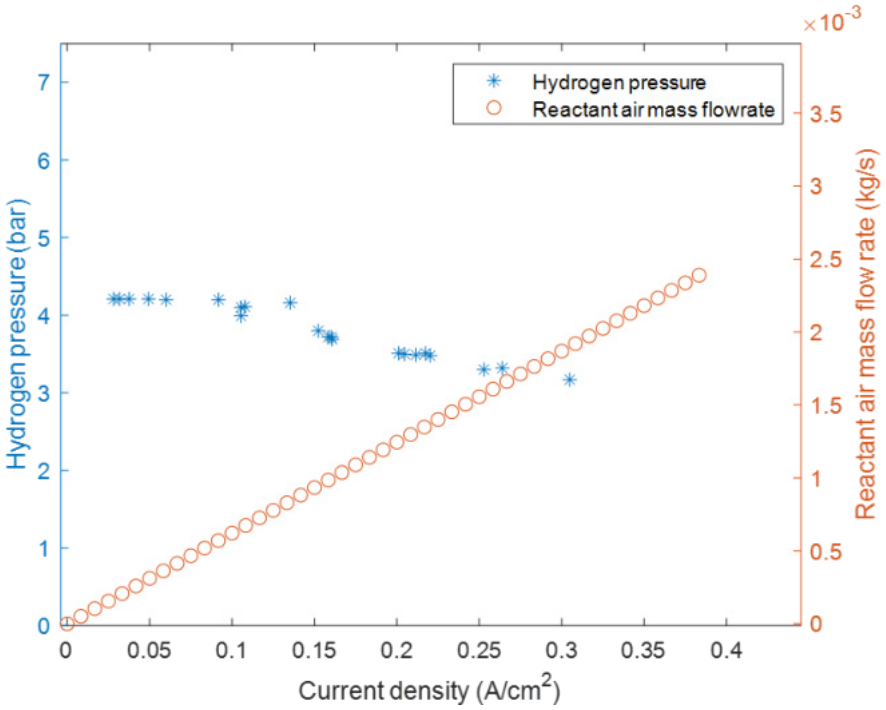

Figure 3. Variation of fuel cell hydrogen pressure and inlet air mass flow rate with current density.

Figures 4 and 5 show that the physical exergy of the flow stream through the fuel cell increase with both temperature and pressure ratios, though with different patterns. Higher temperature ratios intensify the growth of the physical exergy (Fig. 4), while, with increasing pressure ratio, the growth of physical exergy tends to be less intense (Fig. 5). Higher temperatures increase the diffusivity of the reactants and improve ionic conduction of the membrane, but they also lead to greater evaporation of water and, therefore, drying of the membrane and reduced conductivity [24]. The fuel cell system here considered has a humidity exchanger, therefore water vapour in the reactant gases balances the drying effect of temperature. On the other hand, increasing pressure benefits performance as this increases the diffusivity of the reactant gases, facilitating mass transport to the electrodes. The fuel cell humidity exchanger minimises the diffusion of product water into the membrane by the pressure gradient towards the anode, as the product water is used to humidify the inlet air.

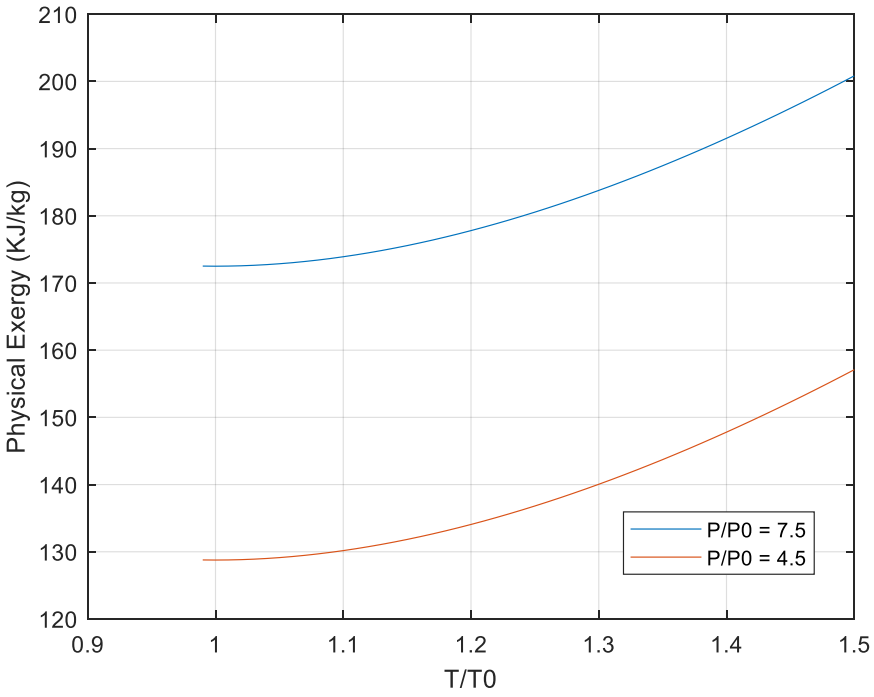

Figure 4. Variation of fuel cell physical exergy with temperature ratio.

The physical exergy of product water is shown by Figs. 6 and 7, as it varies with temperature ratio and pressure ratio, respectively. The increase of product water helps the reactant air to attain an ideal temperature without the need to operate at low pressure as it is heated when flowing through the compressor, thus evaporating the water to be used by the humidifier. The absence of an internal humidifier could lead to nonattractive options such as lowering the temperature, which increases losses, lowering air flowrate and hence the air stoichiometry, which would reduce the cathode performance, or increasing pressure, which would increase the auxiliary power to run the compressor [25]. Furthermore, the humidification of reactants favours the conduction of hydrogen ions in the membrane. Water content dramatically influences the membrane conductivity, and it is vital to transport the reactants and the reaction kinetics in the electrode. If water diffusion between the cathode and membrane is insufficient to keep the membrane hydrated, the ohmic losses in the membrane at high current density can cause a significant fraction of the cell voltage loss. Consequently, to minimise ohmic losses, the hydrogen flow must also be humidified [26].

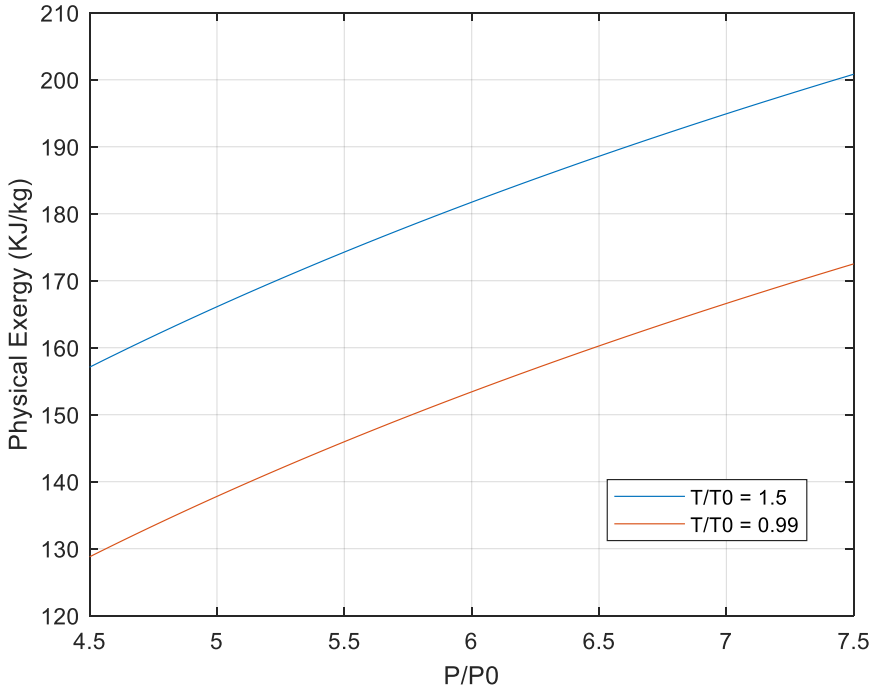

Figure 5. Variation of fuel cell physical exergy with pressure ratio.

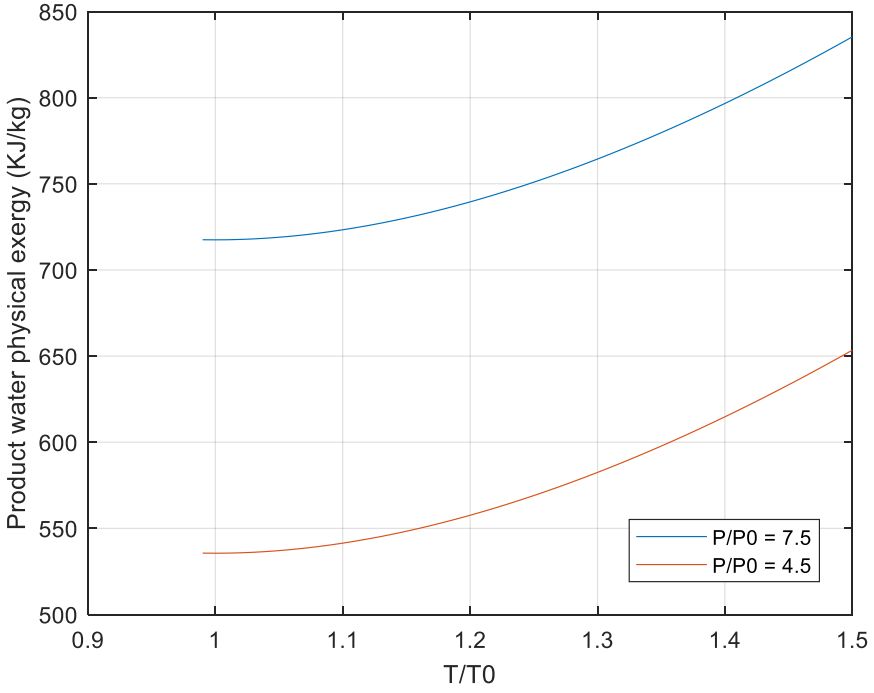

Figure 6. Variation of product water physical exergy with temperature ratio.

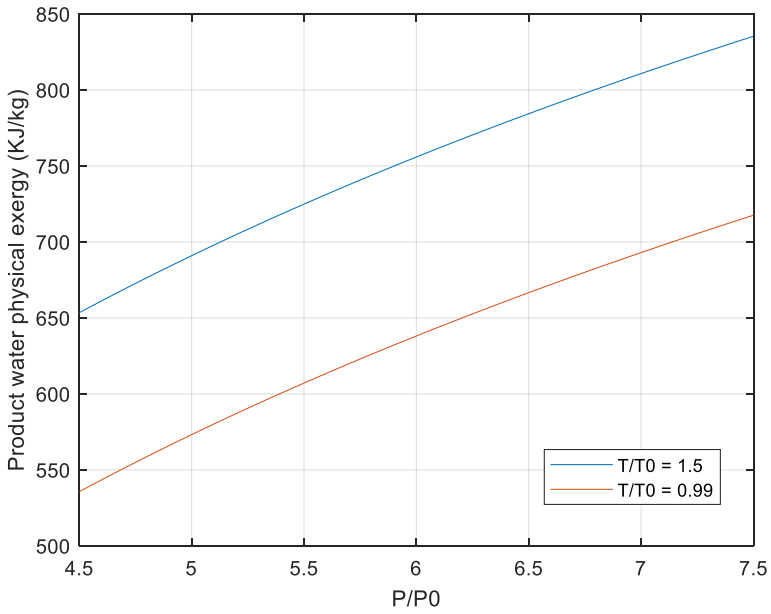

Figure 7. Variation of product water physical exergy with pressure ratio.

4.2. Exergoeconomic analysis

The exergoeconomic analysis considers the exergy cost of all reactants and products for the electrochemical process in the system at various operating conditions, such as temperature, pressure, cell voltage and inlet air stoichiometry (λ). The analysis was performed for cell operation from 0.55 V to 0.85 V, air stoichiometry ranging between 2 and 4, pressure ratio from 4.5 to 7.5, and temperature ratio ranging from 0.99 and 1.5. The capital recovery factor CRF was calculated by Eq. (18) as 0.244 per year. The fuel cell cost could range from as high as 9000 \$/kW to as low as 300 \$/kW for mass production, from which an average value of 2500 \$/kW of power output was used in this analysis. The exergy cost of the fuel cell system is not significantly affected by temperature and pressure variation, as shown by Fig. 8, staying in the range of 115.46 ± 0.01 \$/GJ.

Since hydrogen costs are expected to decrease dramatically over the next decade due to production, distribution, equipment and component manufacturing scale up, the estimated hydrogen price in 2030 was assumed to be 1.9 \$/kg to build the results of Fig. 9, representing a drop of 71.6% to the current hydrogen price of 6.7 \$/kg used in the exergy cost analysis of Fig. 8 [27]. The predicted hydrogen price will reduce the exergy cost by about 14.3 \$/GJ, corresponding to a relative decrease of 12.4% compared with today's price. These results reveal a long way to go to decrease hydrogen price in order to obtain a significant improvement on the fuel cell exergy cost. Anticipated lowering of capital cost due to production of electrodes, membranes and catalyst layers at a mass scale may further reduce the fuel cell exergy cost [28,29].

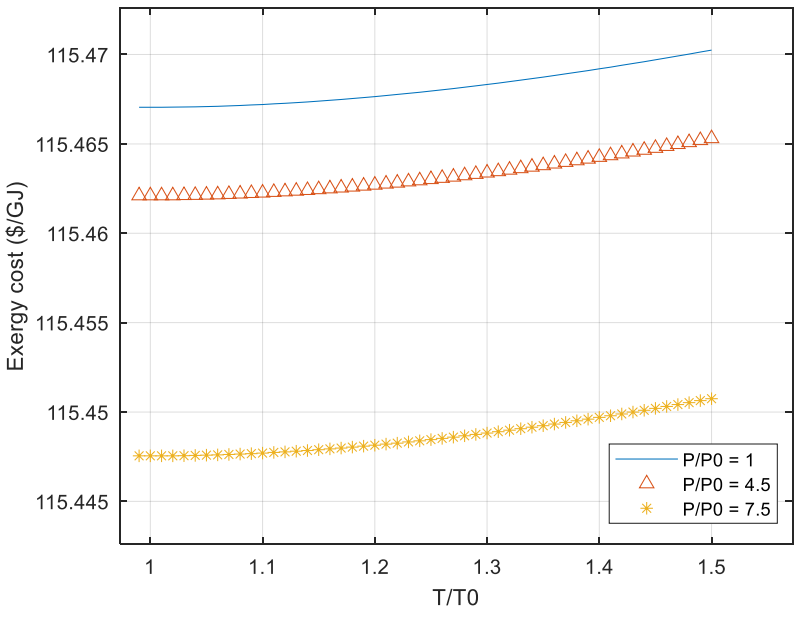

Figure 8. Variation of fuel cell exergy cost with temperature and pressure ratios, at current hydrogen cost.

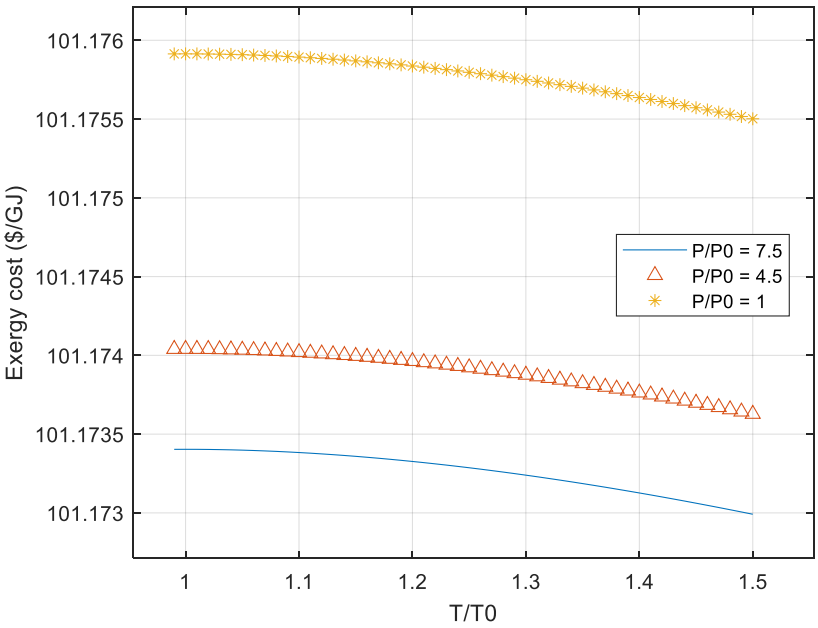

Figure 9. Variation of fuel cell exergy cost with temperature and pressure ratios, at estimated 2030 hydrogen cost.

An improvement of 35 $/GJ can be achieved by operating at a higher stoichiometric ratio (λ = 4) rather than using the recommended ratio of λ = 3, as shown by Fig. 10. In opposition, a similar increase of exergy cost will occur if operating at the lower stoichiometric ratio of λ = 2. However, one should be extremely careful in setting up the air stoichiometry higher than the recommended range because, at high fuel cell operating temperature and air stoichiometry, the relative humidity of the product air will be lowered. Hence, a higher risk of the cells dehydrating could occur, causing a sharp decrease in the system's efficiency [25,30].

The fuel cell system voltage can also play a key role in its exergy cost, as Fig. 11 shows. The cost can be lowered from 115.5 $/GJ to 108.40 $/GJ if the cell voltage is increased from 0.56 V to 0.6 V. The lower the cell voltage, the higher will be the mass flow rates required for reactants and the products to operate the system to produce the desired power output thus leading to lower exergetic efficiency and higher exergy cost. Changes in the exergy cost of the fuel cell system from various operating temperatures are negligible (see Fig. 8), as opposed to the effect of various cell voltages. However, it should be noted that PEM fuel cells are regarded as a low-temperature systems (up to 65°C) in comparison with other fuel cell types such as solid oxide fuel cells or molten carbonate fuel cells. For these fuel cells, the operating temperatures should play a more significant role to exergy efficiency and costs [25].

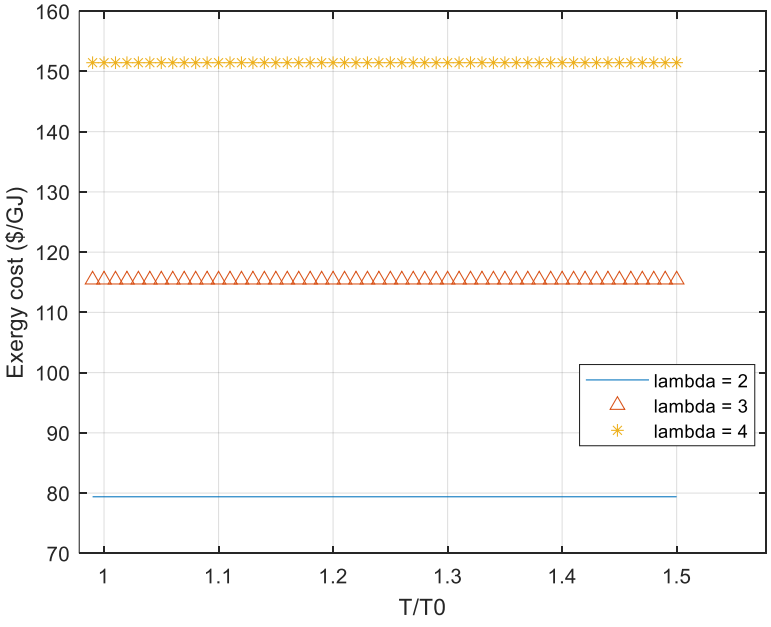

Figure 10. Variation of exergy cost with temperature and air/fuel stoichiometric ratios (V= 0.56 V, P/P_0 = 1).

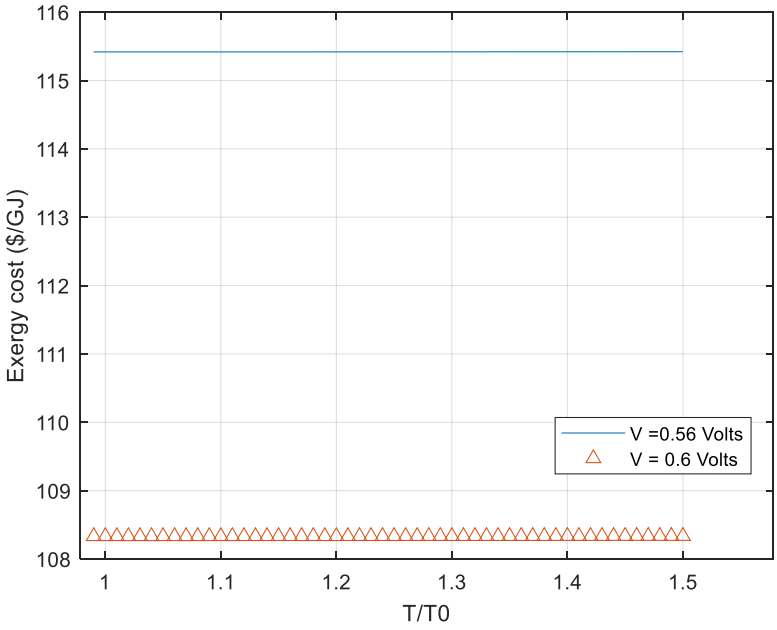

Figure 11. Variation of exergy cost with temperature ratio and voltage (λ = 3, and P/P_0 = 1).

5. Conclusion

This work revealed that the PEM fuel cell and product water physical exergies can be improved with increased operating temperature and pressure. However, operation at high temperatures is limited by excessive water evaporation with consequent drying of the membrane and, thus, reduced conductivity, while operation at increased pressure will require higher power demand by the compressor. High product water exergy benefits membrane conductivity and cathode performance as water evaporated during the air compression process can be used to humidify the membrane and enhance its conductivity. The operating temperature and pressure had negligible effect on the exergy cost, but it can significantly be affected by hydrogen price, air/fuel stoichiometry and operating voltage. An estimated reduction of just over 70% on the hydrogen price by 2030 will produce a decrease of the exergy cost by about 12%. Increasing the air stoichiometry by a third of its recommended value can reduce the exergy cost by 30%, but there are imposed limitations on this strategy by the risk of cell dehydration causing loss of efficiency. Operating voltage increase by 7% can produce a reduction of exergy cost by a similar rate. As overall recommendation, the fuel cell exergy cost can noticeably be improved by adopting a combination of higher inlet air stoichiometry and cell voltage, while more emphatic enhancement will be achieved by lowering the capital cost, annual operation and maintenance cost and hydrogen price.

Nomenclature

ACC	annual capital cost, US$
c	cost, US$
CF	capacity factor, dimensionless
CRF	capital recovery factor, dimensionless
$\dot{E}_{aux}$	auxiliary load, kW
$\dot{E}_e$	electrical power output, kW
$\dot{E}_{ext}$	external load from reactant consumption, kW
ex	total exergy transfer per unit mass, kW/kg
ex_{CH}	chemical exergy per unit mass, kW/kg
ex_{PH}	physical exergy per unit mass, kW/kg
$\dot{E}x$	exergy, kW
F	Faraday's constant (96,485 C/mol)
h	specific enthalpy, kJ/kg
i_r	annual interest rate, dimensionless
I_{fc}	fuel cell stack current, A
I_m	measured current, A
$\dot{m}_{H_2}$	hydrogen mass flow rate, kg/s
n_{H_2}	number of moles of hydrogen consumed per mol of oxidant in the reaction, mol
n_y	number of years, dimensionless
N	number of cells in the stack, dimensionless

P pressure, kPa
s specific entropy, kJ/kg.K
T temperature, K
V_{fc} fuel cell stack voltage, V
V_m measured voltage, V
x_n mole fraction of component n, dimensionless

Greek symbols

η fuel cell efficiency, %

Subscripts and superscripts

0 standard condition (1atm, 298 K)
air air
C capital
E exergy
FC fuel cell
H_2 hydrogen
H_2O water
I investment
n component in the reaction
OM operation and maintenance
P products
R reactants

References

[1] Hosseinpour J., Sadeghi M., Chitsaz A., Ranjbar F., Rosen M. A., Exergy assessment and optimization of a cogeneration system based on a solid oxide fuel cell integrated with a Stirling engine. Energy Convers Manag 2017;143:448–58.

[2] Alaswad A., Omran A., Sodre J. R., Wilberforce T., Pignatelli G., Dassisti M., Baroutaji A., Olabi A. G., Technical and commercial challenges of proton-exchange membrane (PEM) fuel cells. Energies 2020;14:144.

[3] Gencoglu M. T., Ural, Z., Design of a PEM fuel cell system for residential application. Int J Hydrogen Energy 2009;34(12):5242–8.

[4] Rosen M. A., Dincer I., Exergy as the confluence of energy, environment and sustainable development. Exergy, An International Journal 2001;1(1):3–13.

[5] Rosen M., Clarifying thermodynamic efficiencies and losses via exergy, Exergy, An International Journal 2002;2:3–5.

[6] Marmolejo-Correa D., Gundersen T., A new efficiency parameter for exergy analysis in low temperature processes. International Journal of Exergy 2015;17(2):135–70.

[7] Som S. K., Datta A., Thermodynamic irreversibilities and exergy balance in combustion processes. Prog Energy Combust Sci 2008;34(3):351–76.

[8] Taniguchi H., Mouri K., Nakahara T., Arai N., Exergy analysis on combustion and energy conversion processes. Energy 2005;30:111–7.

[9] Song S., Douvartzides S., Tsiakaras P., Exergy analysis of an ethanol fuelled proton exchange membrane (PEM) fuel cell system for automobile applications. Journal of Power Sources 2005;145:502–14.

[10] Chitsaz A., Haghghi M. A., Hosseinpour J., Thermodynamic and exergoeconomic analyses of a proton exchange membrane fuel cell (PEMFC) system and the feasibility evaluation of integrating with a proton exchange membrane electrolyzer (PEME). Energy Convers Manag 2019;186:487–99.

[11] Shaygan M., Ehyaei M. A., Ahmadi A., Assad M. E. H., Silveira J. L., Energy, exergy, advanced exergy and economic analyses of hybrid polymer electrolyte membrane (PEM) fuel cell and photovoltaic cells to produce hydrogen and electricity. J Clean Prod 2019;234:1082–93.

[12] Yilanci A., Dincer I., Ozturka H. K., Performance analysis of a PEM fuel cell unit in a solar-hydrogen system. Int J Hydrogen Energy 2008;33(24):7538–52.

[13] Kazim A., Exergy analysis of a PEM fuel cell at variable operating conditions. Energy Convers Manag 2004;45(11–12):1949–61.

[14] Sevjidsuren G., Uyanga E., Bumaa B., Temujin E., Altantsog P., Sang D., Exergy analysis of 1.2 kW NexaTM fuel cell module. Clean Energy for Better Environment 2012;3–18.

[15] Lipman T. E., Edwards J. L., Kammen D. M., Fuel cell system economics: comparing the costs of generating power with stationary and motor vehicle PEM fuel cell systems. Energy Policy 2004;32(1):101–25.

[16] Rosen M. A., Scott D. S., A thermodynamic investigation of the potential for cogeneration for fuel cells. Int J Hydrogen Energy 1988;13(12):775–82.

[17] Matsumoto Y., Yokoyama R., Ito K., Engineering-economic optimization of a fuel cell cogeneration plant. J Eng Gas Turbine Power 1994;116(1):8–14.

[18] Kazim A., Exergoeconomic analysis of a PEM fuel cell at various operating conditions. Energy Convers Manag 2005;46(7–8):1073–81.

[19] Fuel Cell Guide - Fuel Cell Costs – Available at: http://www.fuelcell.co.uk/fuel-cell-costs/.

[20] Bejan A., Tsatsaronis G., Moran M. J., Exergy analysis. In: Thermal design and optimization. Wiley. 1996. p. 113–65.

[21] Chen H., Pei P., Song M., Lifetime prediction and the economic lifetime of proton exchange membrane fuel cells. Appl Energy 2015;142:154-163.

[22] Barbir F., Gómez T., Efficiency and economics of proton exchange membrane (PEM) fuels cells, Int J Hydrogen Energy 1996;21(10):891-901.

[23] Sevjidsuren G., Uyanga E., Bumaa B., Temujin E., Altantsog P., Sang D., Exergy analysis of 1.2 kW NexaTM fuel cell module. Clean Energy for Better Environment 2012; 3–18.

[24] Chan S. H., Goh S. K., Jiang S., A mathematical model of polymer electrolyte fuel cell with anode CO kinetics, Electrochim Acta 2003;48:1905–19.

[25] Larminie J., Dicks A., Fuel Cell Systems Explained. Wiley; 2003.

[26] Nguyen T. v., White R. E., A water and heat management model for proton‐exchange‐membrane fuel cells, J Electrochem Soc 1993;140(8):2178–86.

[27] Sonal P., How much will hydrogen-based power cost? – Available at: https://www.powermag.com/how-much-will-hydrogen-based-power-cost/ [accessed 14.9.2022].

[28] Dewald U., Truffer B., Market formation in technological innovation systems-diffusion of photovoltaic applications in Germany. Ind Innov 2011;18(3):285–300.

[29] Staffell I., Scamman D., Abad A. V., Balcombe P., Dodds P. E., Ekins P., Shahd N., Ward K. R., The role of hydrogen and fuel cells in the global energy system. Energy and Environmental Science 2019;12(2).

[30] Büchi F. N., Srinivasan S., Operating proton exchange membrane fuel cells without external humidification of the reactant gases: Fundamental aspects. J Electrochem Soc 1997;144(8):2767–72.

Alkaline electrolysis for green hydrogen production: techno-economic analysis of temperature influence and control

Lingkang Jin[a], Rafael Nogueira Nakashima[b], Gabriele Comodi[c] and Henrik Lund Frandsen[d]

[a] Department of Industrial Engineering and Mathematical Sciences (DIISM), Università Politecnica delle Marche, Ancona, Italy, l.jin@pm.univpm.it, CA
[b] Department of Energy Conversion and Storage, Technical University of Denmark (DTU), Building 310, Fysikvej, DK-2800 Lyngby, Denmark, rafnn@dtu.dk ,
[c] Department of Industrial Engineering and Mathematical Sciences (DIISM), Università Politecnica delle Marche, Ancona, Italy, g.comodi@staff.univpm.it ,
[d] Department of Energy Conversion and Storage, Technical University of Denmark (DTU), Building 310, Fysikvej, DK-2800 Lyngby, Denmark, hlfr@dtu.dk

Abstract:

To mitigate climate change, a stronger reliance on renewable energy sources is foreseen, and Power-to-Hydrogen systems can be adopted to minimize curtailment losses derived from the intermittent nature of wind and solar power. Among different alternatives, alkaline water electrolysis is the most mature process for hydrogen production using sustainable electricity as its main energy source. The mathematical modelling of the alkaline electrolysis process is a crucial tool to improve green hydrogen production, energy conversion efficiency, sizing (model-based design) and thermal energy management. Although several studies have investigated alkaline electrolysis modelling, these analyses often neglect property variations along the stack area and its economic implications. In this work, the need for increasing the modelling complexity in system models by introducing a one-dimensional model of the alkaline electrolyzer cell/stack is investigated. With this, several operation parameter variations can be modelled, and among these, the internal temperature variation plays a crucial role in both technical and economic aspects. Results show that efficiency could vary between 58-70% while the Levelized cost of hydrogen is within the range of 1.3-1.6 €/kg, when various inlet-outlet temperature differences are considered. Furthermore, from both technical and economic aspects, the optimal temperature control of alkaline electrolysis is to maintain a very low-temperature difference (~1°C), from inlet to outlet, controllable with the alteration of the electrolyte flow rate.

Keywords:

Power-to-Hydrogen, Alkaline electrolysis, Temperature control, Levelized cost of hydrogen, Hydrogen production.

1. Introduction

The mitigation of the effects of climate change can be achieved through the integration of renewable energy sources into the electricity grid. However, the intermittent nature of these sources necessitates the use of storage and management mechanisms. One solution is the implementation of Power-to-X technologies, which involve the conversion of excess renewable electricity into other forms of energy that can be stored and utilized when needed. This facilitates the integration of intermittent renewable energy sources into the grid and supports the transition to a low-carbon energy system.

Water electrolysis can be divided into categories based on operating temperature: low-temperature electrolysis, working below 120°C, and high-temperature electrolysis. Among these technologies, alkaline water electrolysis, which utilizes a liquid electrolyte and Nickel-based catalysts, is the most mature and economically viable solution. However, it has lower efficiency and a limited current density range, as well as a constrained dynamic operating range [1].

Experimental investigation and modeling are essential tools for understanding the water electrolysis process. Based on the assumptions adopted, models can be classified as either data-driven or physical ones. Data-driven models rely on the mathematical treatment of experimental data and their parameters do not have a physical meaning, while pure physical models are based on the underlying physics of the electrolysis process

and all parameters have physical meanings. These models can be used to expand understanding of hydrogen production, energy conversion efficiency, sizing, thermal energy management and optimization.

The most known data-driven alkaline water electrolysis model is developed by Ulleberg [2], where the polarization curve, i.e., variation of voltage due to the current density through the alkaline cell, is modelled through six parameters. Several other researchers carried on this pathway, indeed Busquet et al. [3] carried on with the same approach using four parameters, while Ursua et al. [4] developed a sixteen parameters-based model. Since parameters are evaluated through experimental data, they can vary significantly even due to a slight variation of input data. Furthermore, more are parameters to be assessed, and more experimental variations are needed to generate unique data points. Indeed, with Ulleberg's model [2], the curve fitting requires following a seven-step procedure. Not to mention that these parameters do not have a physical meaning, thus is arduous to have a range estimation of these numbers.

As regards physical models, Hammoudi et al. [5] employed a multi-physical approach using Matlab Simulink® to carry out the physical model, considering both geometry and operating condition influence. They subsequently expanded this approach by coupling MATLAB-Simulink-SimPowerSystems®, validated using a Hydrogen Research Institute electrolyzer [6]. Such models can consider many aspects of the electrolysis process, however, but a high number of unknown physical parameters are needed, which are not easily achievable.

Both approaches have their opportunities and limitations, indeed, are applied to different cases of applications. Where at the system level. Fast and repeatable iterations, for a different set of operating conditions, are required, hence the data-driven models, once characterized are the most suitable ones; conversely, as for stack-level design, physical models are most suitable.

The temperature highly influences the operating conditions of the alkaline electrolyzers. To maintain it within the opportune range, several techniques can be used to control it. One approach is to use the water flow rate within the liquid electrolyte to maintain the desired temperature, such that the heat generated by the cell is efficiently dissipated or absorbed. When considering the techno-economic performance of an alkaline electrolysis system, it is crucial to carefully analyze the impact of temperature on the overall efficiency and cost of the system. For instance, Jang et al. [7] have built a model assessing electrolyte flow rate, needed as a temperature control measure, using a polynomial correlation, proposed by the same authors, based on temperature and current density, analyzing effects at various temperature differences, between inlet and outlet, of 1-3-5-10°C.

This work aims to cover the research knowledge gap by understanding the temperature dependencies of the alkaline electrolyzer system, solving the temperature evolution along the cells, and hence within the electrolyzer, based on a validated zero-dimensional/lumped model, extended to a one-dimensional model solving for mass and energy conservation, obtaining the electrolyte flow rate information by the physical meaning of the water electrolysis process, allowing to unlock the assessment of system performance at any temperature difference.

The main contributions of this work are the following:

- Propose and validate, with literature data, a semi-empirical alkaline water electrolysis model with four parameters, which can be applied to different types of electrolyzers.
- Formulation of a one-dimensional water electrolysis model, based on the physical process, solving ordinary differential equations. Which can assess the evolution of all operating parameters, such as temperature and pressure, illustrating its comparison with other dimensions models.
- Techno-economic assessment of the temperature control, by the sense of heating mass (electrolyte flow rate) variation, at a continuous range of gap temperatures.

The paper is structured as follows: Section 2 describes the methodology adopted in this work, highlighting the proposed semi-empirical model, validated and extended to a one-dimensional model, while Section 3 describes the results obtained and finally the conclusion of the work is reported in Section 4.

2. Methods

In this section, firstly a novel data-driven model, for Potassium Hydroxide (KOH) electrolyte-based alkaline electrolysis modelling, is proposed. Secondly, the model has been fitted with empirical data provided by literature, where four distinct datasets have been tested; Furthermore, the extension into the one-dimensional model, solving ordinary differential equations of mass, and energy balancing, has been discussed, concluding finally the indicators adopted for the technical and economic comparison of the work.

2.1. Alkaline electrolyzer modelling

Despite different assumptions and refinements present in alkaline electrolyzer modelling, they share the same goal, which is to describe accurately the polarization curve, indeed it is the curve which underlines the voltage (V_{cell}) variation due to the fluctuations of the current density (j), and it can be described with the following equation:

$$V_{cell} = V_{rev} + \eta_{act} + \eta_{ohm} + \eta_{bubble} \quad (1)$$

Where the V_{cell} is the voltage of a single electrolysis cell, V_{rev} is the reversible voltage i.e. the minimum electrical potential to have the electrolysis process going, η_{ohm} the ohmic overvoltage comprising both electrolyte and electrodes overpotential, η_{act} the activation overpotential of both electrodes and finally η_{bubble} is the overpotential, caused by bubble formation from liquid electrolyte.

Each term of the equation (1). can be modelled in different ways, based on the approach and researchers' decisions. It was found that almost all commercial alkaline electrolyzers adopt bipolar electrical configuration, meaning the cells are electrically connected in series since it allows to have higher utilization of the cell area, as reported in [8], therefore the whole electrolyzer has the same current of the cell level, while the overall voltage of the stack is the sum of all the cell's voltages. Furthermore, the polarization curve provides insights into hydrogen production as well as conversion efficiency.

The proposed model describes the polarization curve as follows:

$$V = V_{rev} + \left(\frac{1}{\alpha}\right)\frac{RT}{2F} ln\left(\frac{j}{j_0}\right) + j \cdot \left(\frac{\delta_{el}}{\sigma_{el}}\right) \quad (2)$$

$$j_0 = B \cdot \exp\left(-\frac{E_a}{RT}\right); \ln(j_0) = \ln(B) + \left(-\frac{E_a}{R}\right) \cdot \frac{1}{T} \quad (3)$$

Where V_{rev} can be assessed using the Nernst equation, which changes based on electrolyzer operating conditions, as reported in [9]. While for σ_{el}, using KOH electrolyte, is assessed through the empirical equation investigated by experiments performed by Gilliam et al.[10], and finally j_0, exchange current densities for both electrodes can be described through the Arrhenius equation.

Thus, four parameters remain to be estimated through the alkaline electrolyzer operating data. They are respectively: α, $\ln(B)$, $\left(\frac{E_a}{R}\right)$ and δ_{el}. Furthermore, several simplifications have been made to obtain a simple and versatile for different types of electrolyzers. Indeed, (i) both electrodes' activation overpotentials are grouped with a single Tafel equation, (ii) both diaphragm and electrolyte ohmic overpotential are grouped, due to the lack of information on the diaphragm material composition and experimental correlation, and finally (iii) the bubble formation overpotential, since its effects on activation overpotential are reduced the activation area and changes in electrolyte ionic conductivity, both effects are implicitly taken into account thanks to the parameter-estimation, through the electrolyzer operating data.

2.1.1. Model validation

The proposed model is further tested and validated, using the experiments presented in the literature by different researchers, to represent different types of alkaline electrolyzers with different set-ups of operating conditions. Such operating conditions are namely i) temperature, ii) KOH concentration, and iii) pressure. Additionally, the model's robustness, i.e. its ability to have reasonable accuracy, dealing with the minimum quantity of the data available, has been also tested.

The procedure of calibration of the model, based on the type of the electrolyzer with its results, is illustrated in Figure 1, which can be divided into 3 phases:

- Experimental data processing, ensuring at least 6 data points are present, ensuring a good accuracy of the model. If more data is available, they can be also included, however, not all available data should be used, to prevent the over-fitting problem.
- The pre-processed data is then inserted into a curve-fitting framework, commonly used ones are Matlab and Python adopting the proposed model, assessing 4 calibrating parameters ($\delta_{el}, \alpha, \ln(B), -E_a/R$),
- As a consequence of the previous step, the model is now defined, and as such, polarization curves at temperatures, different from the ones used to calibrate the parameters can be obtained and used as validation data.

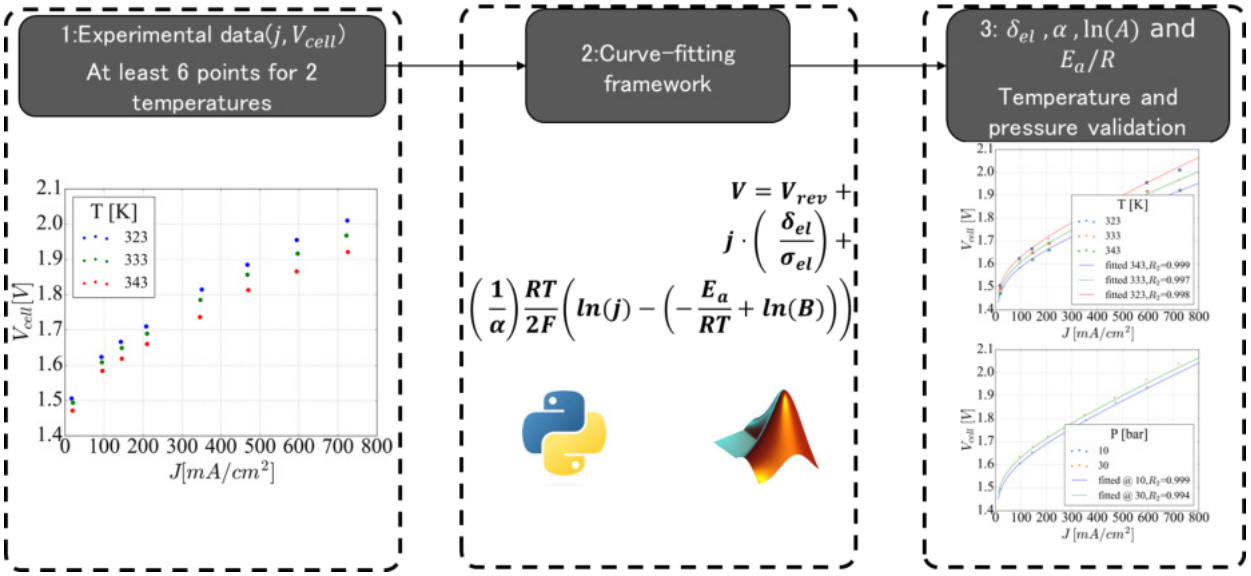

Figure 1. Parameters estimation procedure. Divided into three phases: 1) collection of experimental data at different temperatures, 2) parameter estimation and 3) temperature and pressure influence validation.

2.1.2. Extension of lumped model: one-dimensional model

The proposed model, describing the water electrolysis at the single cell level, can be called a zero-dimensional model/lumped model, in the sense that it assesses the performance of the cell with only a single set of operating conditions, meaning no variation of i) temperature ii) pressure and iii) KOH concentration along e.g. the flow direction and the temperature is considered.

It is possible to extend the lumped model to a half-dimensional model, where two sets of operating conditions are considered, namely inlet and outlet ones. However, this approach has an evident drawback, which is the need for information in advance about the outlet conditions, which is not always available, but can be assumed through e.g. a linear variation of parameters along the stack e.g. current density.

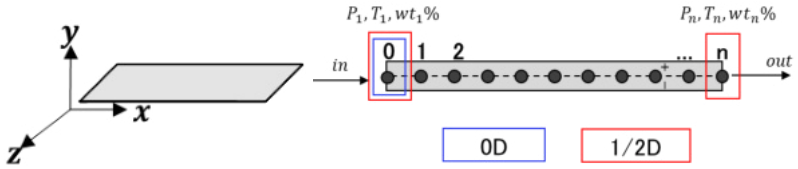

Figure 2. Alkaline electrolysis cell models. With the x-axis as the flow direction.

Therefore, in this study, such a model is further extended into a one-dimensional model, obtaining a complete cell performance evaluation (Figure 2), as an extension of zero-dimensional and half-dimensional ones, which can be applied also to stack-level once defined the electrolyzers cells interconnection, that for this study, bipolar configuration, i.e. cells electrically connected in series, is adopted, as illustrated by Figure 3.

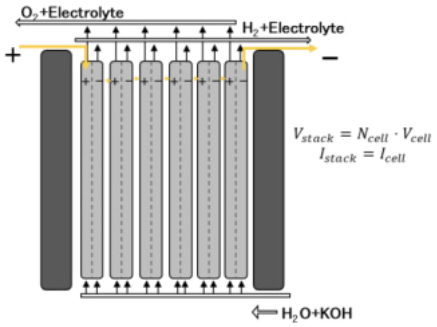

Figure 3. Alkaline electrolyzer bipolar configuration 1D model.

As a modeling assumption, it is considered that all properties vary only along the flow direction, which is the x axis, ignoring their contribution in other axes, in other meaning:

$$\frac{d\Gamma}{dy} = 0; \frac{d\Gamma}{dz} = 0 \tag{4}$$

Where Γ represents a generic physical property. The one-dimensional model proposed uses discrete element modeling, solving differential equations, wherein each element (i), molar flow rate ($\dot{n}_{H2}$), and temperature (T) are solved:

$$\frac{d\dot{n}_{H2}}{dx} = \frac{J_i}{2F} \cdot \Delta \tag{5}$$

$$\frac{dT}{dx} = \frac{(V - V_{th}) \cdot J_i}{\dot{n}_e \cdot Cp_e + \dot{n}_{H2} \cdot Cp_{H2} + \dot{n}_{O2} \cdot Cp_{O2}} \cdot \Delta \tag{6}$$

$$i = 0,1,2,3 \dots n; \Delta = \text{const} \tag{7}$$

While different parameters are defined in the nomenclature at the end of the paper, such equations represent the molar mass, and energy balance along the x-axis, where Δ represents the cell width (cell dimension in z-axis), which is constant. While for the standard chemical species, their thermodynamical properties, like specific heat (Cp) can be consulted or calculated using the well-known empirical equations from the database of NASA [11]. The electrolyte, composed of water and a certain mass fraction of KOH, its thermal properties can be assessed using empirical formulas reported in the [12], obtained as results of experiments, where for this study, Zaytsev empirical relationship has been used [13]:

$$Cp_{el} = k_1 + k_2 \ln\left(\frac{T_{\circ C}}{100}\right) + (k_3 + k_4 \cdot wt + 8 \cdot T_{\circ C}) \cdot wt \tag{8}$$

With the obtained Cp_e is expressed in [J/kg K], to converted into [J/mol K] using the following equation:

$$Cp_{e,mol} = Cp_e \cdot M_e \tag{9}$$

$$\sum \frac{wt_i}{M_i} = \frac{1}{M_{tot}} \sum \frac{n_i}{n_{tot}} \cdot \frac{M_i}{M_i}; M_{tot} = \frac{1}{\sum \frac{wt_i}{M_i}}; \; M_e = \frac{1}{\frac{wt}{M_{KOH}} + \frac{(1-wt)}{M_{H2O}}} \tag{10}$$

$$wt = \frac{m_{KOH}}{m_{KOH} + m_{H2O}} \tag{11}$$

The flowchart of the proposed 0D model, extension to the 1D cell model, and finally into the 1D stack model, is illustrated in Figure 4.

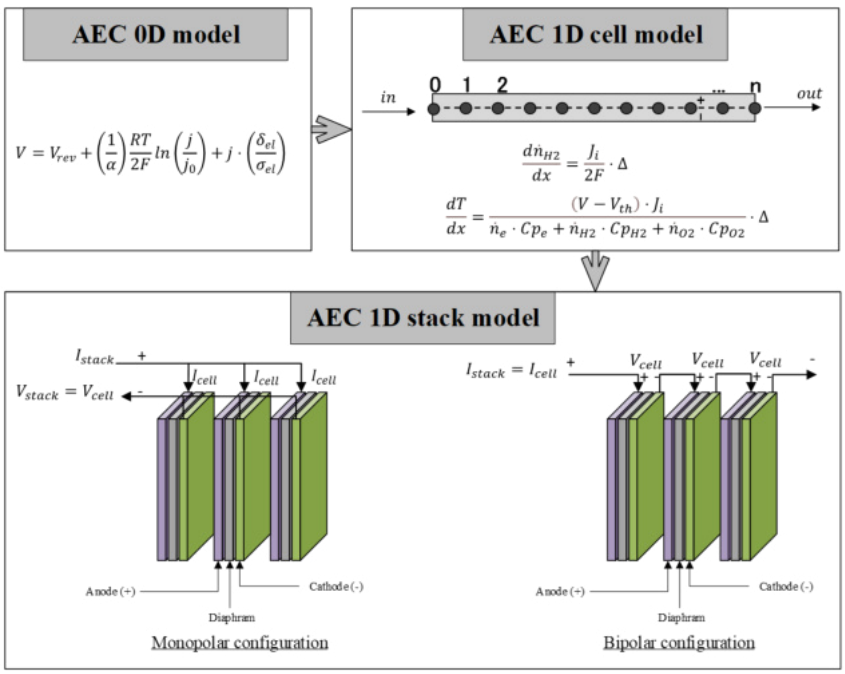

Figure 4. Alkaline 1D stack model flowchart. Starting with the single cell 0D model, extended to 1D cell model, solving mass and thermal balance, and finally 1D stack model, based on the electrical configuration among cells.

2.2. Technical and economic comparison

To have an overview of different models' comparison, in terms of both technical and economic perspectives, the assumption of having inlet and outlet temperature is the same for all models, whereas the 0D model considers only the inlet temperature.

$$\text{0D: } T_{inlet}; J = J_{inlet} = f(T_{inlet}, V, wt, p) \tag{12}$$

$$\text{1/2D: } T_{\text{inlet}}, T_{outlet}; J = J_{avg} = \frac{J_{inlet} + J_{outlet}}{2} \tag{13}$$

$$\text{1D: } T_i; i = 0, \dots n; J = J_{avg} = \frac{\int J_{i} \cdot dx}{n \cdot \Delta X} \tag{14}$$

$$Area = x \cdot width; x = 0, 1 \cdot \Delta x \dots, n \cdot \Delta x \tag{15}$$

Furthermore, for the technical comparison among different models, since the temperature-controlling components are included in this analysis, namely heat exchangers and pumps, the interconnection of these parts with the electrolyzer is described in Figure 5. Where heat exchangers, have the objective to cool the outlet electrolyte, warmed up by the inefficiencies, down to the inlet setting temperature. While temperature control can be done by controlling the flow rate of the inlet water, as described in equation (6) and equation (8) the increase of the water flow rate can lower the temperature gap, hence increasing the cell's overall working efficiency, however, with an expense of a higher required power for the electrolyte circulation. The pressure gap is assumed to be equal to 1 bar for the sake of simplicity.

The system integration between alkaline electrolyzer and other components of the plant is illustrated through the flow diagram reported in Figure 5, despite having multiple components present in the plant, not all of them have been modelled in the present study, as they are out of the scope of the objective.

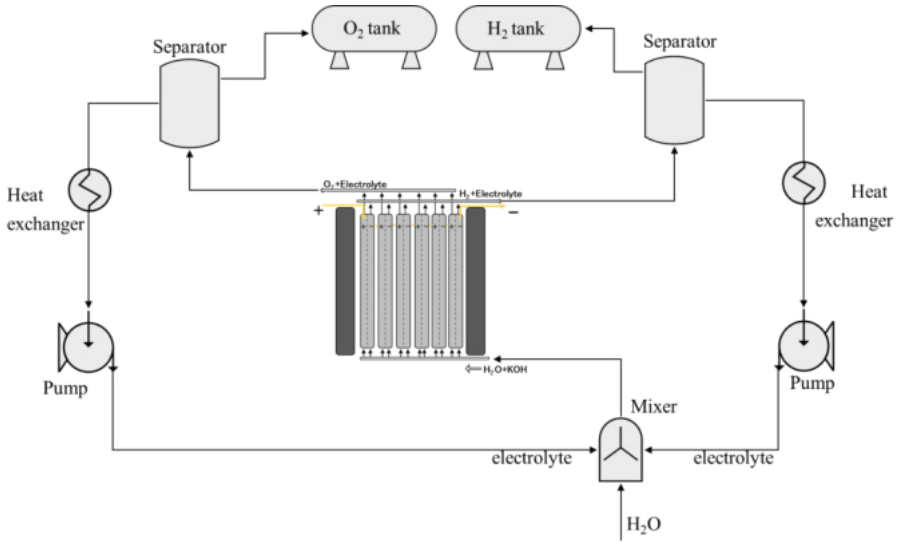

Figure 5. Systems connections. Illustrating auxiliary systems to be coupled with electrolyzer stack.

Indeed, the components that accounted for the evaluation of the temperature control, besides the electrolyzer stack itself, are water pumps and heat exchangers, where their characteristics, used for this work, are reported in Table 1.

Table 1. Model parameters.

Pheobus electrolyzer		Reference
Cell area (m2)	0.25	[2]
#n cells	21	[2]
Operating pressure (bar)	7	[2]
Nominal power (kW)	26	[2]
Unitary cost (€/kW)	830	[14]
Stack lifetime (years)	10	[14]
Water pump		
Efficiency	0.7	[14]
Input power	$P = \eta_{pump} \cdot \Delta P \cdot Q_e$	[-]

Pressure Gap	1 bar	[-]
Cost	60 €/(kg/s)	[14]
Heat exchanger		
Cost (€)	$C = C_1 \left(\frac{A_{HEX}}{0.093}\right)^{0.78}$	[14]
C_1	110 €/m^2	[14]
U (W/m2 K)	700	[14]
ΔT_{HEX} (K)	5	[-]
A_{HEX} (m2)	$A_{HEX} = \frac{\dot{n}_{H2O} \cdot M_{H2O} \cdot Cp_{H2O} \cdot \Delta T_{H2O}}{U \cdot \Delta T_{HEX}}$	[-]
Lifetime (years)	15	[14]
Levelized Cost of Electricity		
€/MWh	20-60	[14]

As evaluation indicators, exploiting the temperature effects, system-level efficiency, and levelized cost of the produced hydrogen are adopted to assess the temperature influence. And these indicators assessment criteria are reported in the following equations:

$$\eta_{tot} = \frac{N_{cell} \cdot \dot{n}_{H2_{cell}} \cdot LHV_{H2}}{P_{el} + P_{pump}} \quad (16)$$

$$LCOH = \frac{CAPEX_{el,a} + CAPEX_{HEX,a} + CAPEX_{WP,a} \cdot + LCOE \cdot E_{elc}}{m_{H2}} \quad (17)$$

Where all investment costs ($CAPEX$), that depend on the nominal size of the technology, are actualized while E_{el} is the electrical energy consumed to produce the m_{H2}.

3. Results & discussions

Different types of results are reported in this section, firstly the results regarding the validation of the novel are illustrated, to be followed with the comparison of different dimensionality of the model, and finally the technical andeconomic analysis of the temperature control effects, are discussed.

3.1. Ability for the model to fit data

The proposed model proved its validity and robustness; indeed, the results show that only six data points, three data points for each, and two temperatures are needed, to capture the temperature and the current density dependency. Of course, the parameters are strictly dependent on the data points used to estimate them, however, the difference is not significant, and they are listed in Table 2.

Table 2. Parameters for the datasets analyzed.

	Experiments conditions		**Calibrated parameters**				
	p	T	wt	δ_{el}	α	$-E_a/R$	ln(B)
Units	$[bar]$	$[°C]$	$[-]$	$[cm]$	$[-]$	$[K]$	$\left[\ln\left(\frac{mA}{cm^2}\right)\right]$
Sakas [15]	16	59.6-61.15-70	0.25	0.3914	0.1253	-6330	13.11
Ulleberg [2]	7	30-40-50-60-70-80	0.30	0.6637	0.1726	-5331	9.184
Sanchez [16]	7	55-65-75	0.35	0.5711	0.1181	-3592	4.768
Groot [17]	30	50-60-70	0.28	0.2716	0.2764	-3906	3.864

During the parameter estimation process, the dataset is split into two separate datasets. Namely train and test datasets, to prove the model's robustness. Indeed, the training dataset, i.e. the data used to find parameters, is randomly selected, with the only constraint that they need to be at least six data points, from at least two different operating temperatures. The results of the estimation, illustrating the model's wide applicability, are reported in Figure 6.

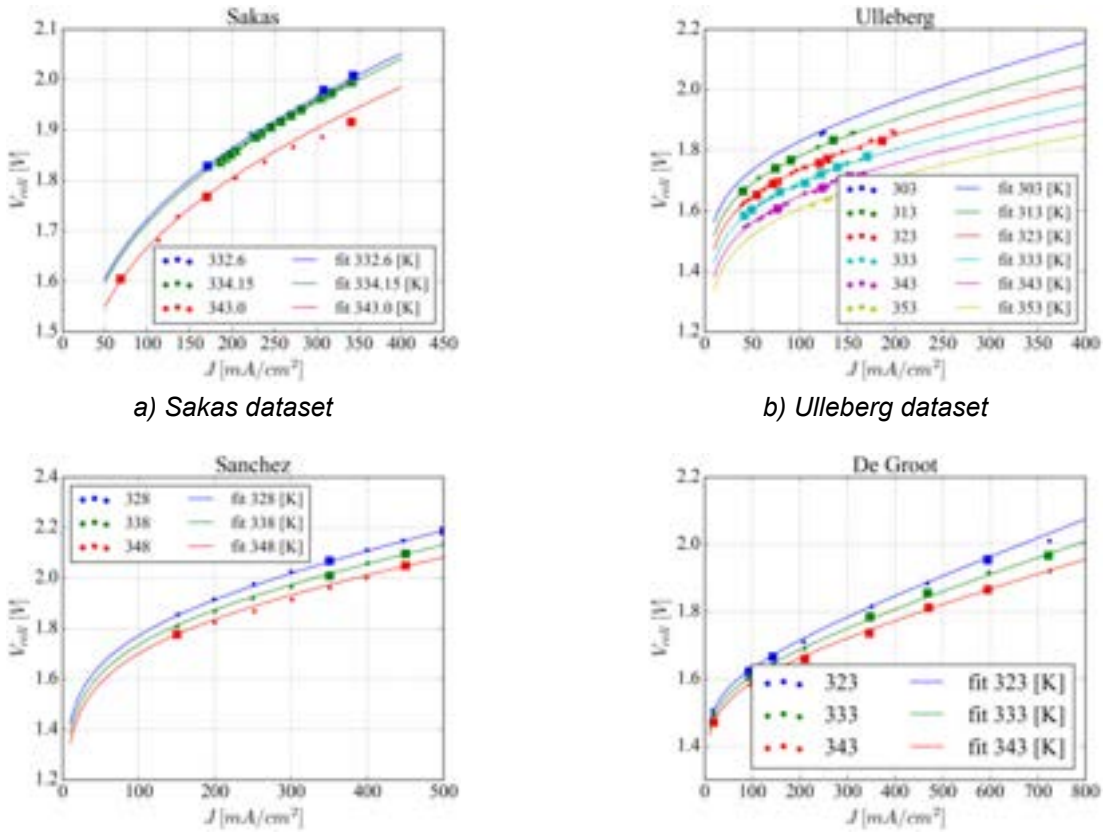

a) Sakas dataset

b) Ulleberg dataset

c) Sanchez dataset

d)De *Groot* dataset

Figure 6. Parameter estimation and validation with temperature variation. Where squared-dotted data are from the training dataset while the circle ones are from the test dataset.

Whereas the temperature dependence is explicitly highlighted, in activation overpotential, other operating conditions influence, namely KOH weight concentration and pressure are implicitly considered, through the ohmic overpotential and reversible voltage, respectively.

3.1. Accuracy of model dimensionality

The one-dimensional model is controlled by voltage; hence the voltage is an input parameter of the model. Whereas the current density, thus also the hydrogen production is an output data from the model.

The benefit of having a one-dimensional model resides in the possibility to perform analysis at different temperatures, between the inlet and outlet of the cell. Indeed, Figure 7 is reported the results of the 1D model for a 0.30x0.30 m cell, working at 1.8V, with an outlet temperature fixed at 80 °C with different gap temperatures, namely 1-2-10 °C.

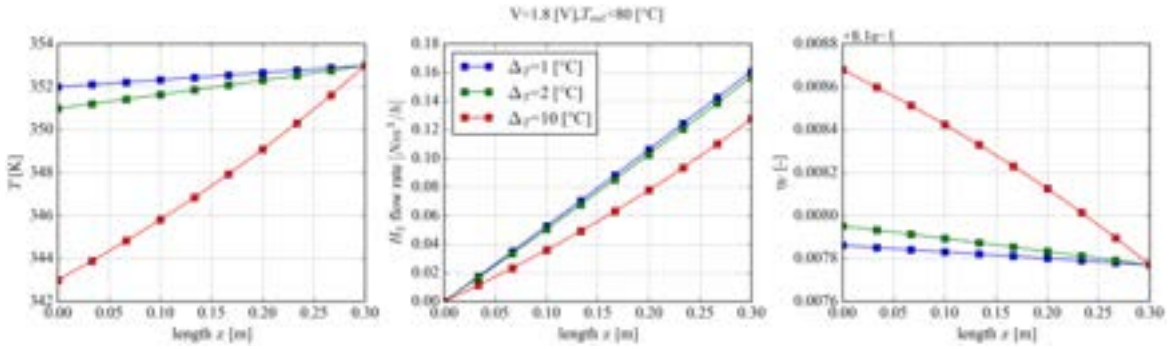

Figure 7. 1D model at 1-2-10 °C temperature difference. Illustrating namely i) temperature, ii) hydrogen production and iii) voltage efficiency along the cell. Where the outlet temperature is kept constant. Despite having a higher temperature difference achieves a higher efficiency, the produced hydrogen flow is lower.

A comparison of the different dimensionality of the model is illustrated in Figure 8. The 1D model is used as a reference, as this is considered the most accurate. The current density at a fixed potential of 1.8 V is compared. This is done at different flow rates of the electrolyte through the stack for cooling, resulting in different temperature increases over the stack.
The comparison shows that the 0D model is always underestimating the current density and thus the hydrogen production rate. The 1/2D model, in contrast, is overestimating the two. Furthermore, with an operating temperature of 80°C (353 K) and voltage of 1.8 V, considering the one-dimensional model as the benchmark, with a gap temperature of 5°C between the inlet and outlet, while the half-dimensional model's deviation is almost neglectable (0.75%), the zero-dimensional model has a significant deviation, underrating about 11% the hydrogen production.

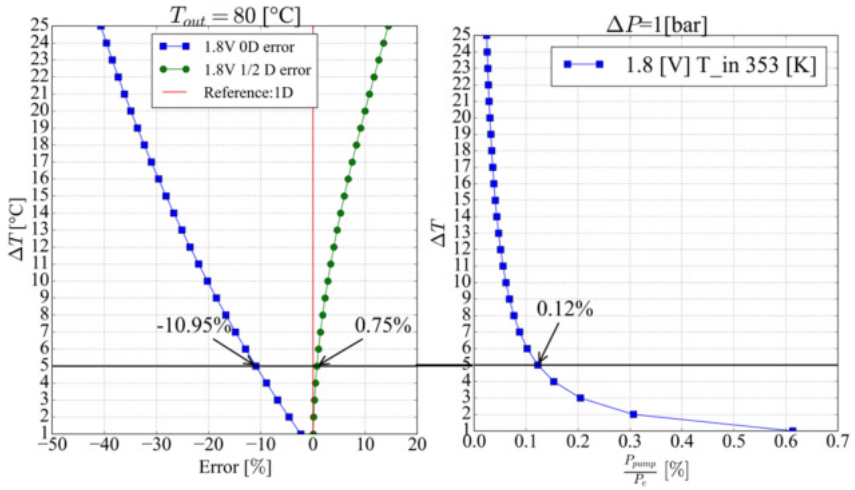

Figure 8. Models' comparison at different temperature increase over the stack. Where error is the difference between the models' average current density, compared with the 1D model's average current density, in percentage.

Regarding temperature effects, with a temperature increase, between the inlet and outlet of the electrolyzer stack, larger than 1°C, the overall efficiency (defined in equation (16)) remains almost constant at a value of 0.69 (Figure 9); and since the model is fixing voltage as input, results are implying that, after such threshold, the influence of the water pump energy consumption, which depends on the water flow rate, required to control the operating temperature, is almost neglectable, compared to the energy absorbed by the electrolyzer.

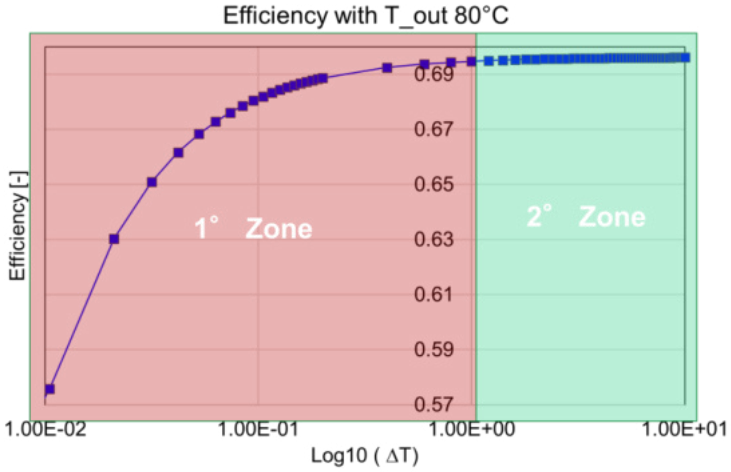

Figure 9. Influence of temperature difference (inlet to outlet) in system efficiency. Where the outlet temperature is set as 80°C.

As for the economic aspect, as illustrated in Figure 10, there's a clear zone (2° zone), where the LCOH stays at its minimum level, indeed, such range is around the gap temperature of 1°C, independently from the LCOE adopted, however, with a slope of LCOH (defined in equation (17)) decrease/increase different in two cases. However, the LCOH are higher in the other two zones (1° zone and 3° zone), due to different reasons, while for the 1° zone, the cause is the high operational cost due to the water pump energy absorption, for the 3°

zone instead, is due to a drop in current density, indeed with a higher gap temperature, the overall hydrogen production, results to be lower and lower.

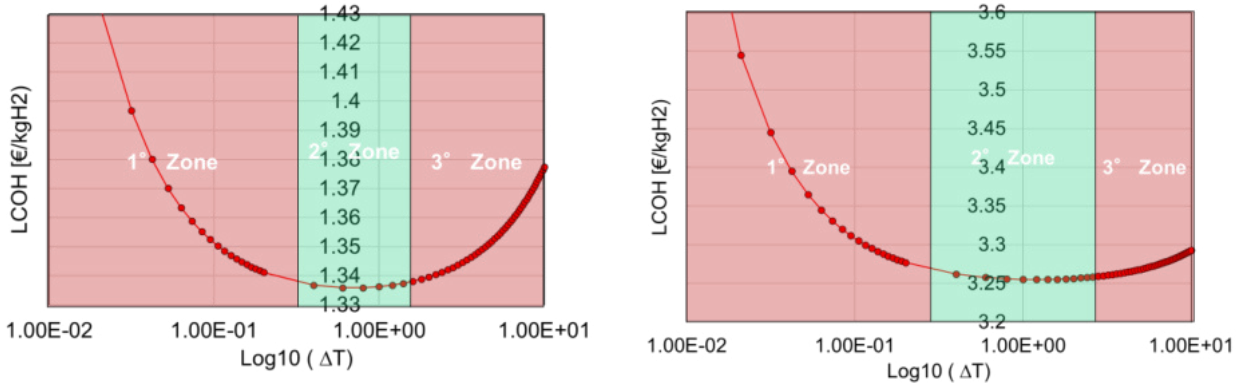

a) LCOH with minimum LCOE *b) LCOH with maximum LCOE*

Figure 10. Influence of temperature difference (inlet to outlet) in the levelized cost of hydrogen. Where the outlet temperature is set as 80°C

There are several limitations of the proposed model. It does not consider the faraday efficiency, because of the lack of an aligned approach to it in literature, furthermore, the water vapor formation has not been properly addressed. Nevertheless, since the objective of the work is to assess the temperature influence and its control, such limitations would not change the discussed results, yet they can certainly be subject to further investigation.

4. Conclusion

In this study, the assessment of the alkaline operating temperature effects and its control, from both technical and economic aspects, has been carried out.

To seize these quantities of the electrolysis process, a novel alkaline cell model is proposed. The model was fitted to various data from the literature and shown to provide good fits for all the considered measurements. The model included only four parameters, which are a combination of the physical parameters as well as empirical parameters describing certain physical phenomena.

Furthermore, after validating the proposed cell model, it has been extended to one-dimensional modelling, based on the finite element approach, including the mass and energy balance, which provides the evolution of different operating parameters along the cell, such as temperature. To understand the impact of model accuracy on system models, a comparison of different model refinements was conducted, i.e. a 0D, 1/2D and a 1D model. The 0D model is significantly underestimating the hydrogen production (-11%), while the 1/2D model has a slight overestimation (+0.75%), as compared to the more accurate 1D model.

Furthermore, the effect of electrolyte rate on the overall efficiency was investigated - both technically and economically. There are clear benefits of increasing the flow rate of the electrolyte to keep temperature increase over the stack close to 1°C.

The efficiency with increasing flow rates will go down, however, remains constant if the temperature increase is kept above 1°C. Economically there is an optimum flow rate, where losses from the pumping of electrolytes and losses in the stack due to higher resistance at lower temperatures are balanced.

Although the global trend of the LCOH does not change, with different values of LCOE (20-60 €/MWh), its value is quite different, where for 20 €/MWh, it can be 1.33-1.43 €/$kg_{H2,}$ alternately, 3.25-3.6 €/kg_{H2} for 60 €/MWh.

Nomenclature

$\dot{n}$	Molar flow rate, mol/s
LHV	Low heating value, J/mol
A	Area, m^2
B	Arrenhius constant, mA/cm^2
$CAPEX$	Capital Expenditure, €
E	Energy, kWh
F	Faraday constant, 96500 C/mol
H	Enthalpy, J/mol

I	Current, A
$LCOE$	Levelized Cost of Energy, €/kWh
$LCOH$	Levelized Cost of Hydrogen, €/kg
M	Molarity of the solution, mol/l
N	Number,-
P	Power, W
R	Universal gas constant, 8.314462618 J/mol K
T	Temperature, K
U	Heat transfer coefficient, W/m^2 K
V	Voltage, V
a	Water activity, -
j	Current density, A/m^2
m	mass, kg
n	Number of elements,-
p	Pressure, bar
v	Velocity, m/s
wt	Weight concentration, [0.0 - 1.0]

Greek symbols

α	Charge transfer coefficient, -
δ	Reaction distance, cm
η	Overpotential, V
σ	Ionic conductivity, S/cm
Δ	Cell width, m
Γ	Generic property, -

Subscripts and superscripts

$\%$	Percentage
H_2O	Water
$°C$	Celsius
$H2$	Hydrogen
HEX	Heat exchanger
KOH	Potassium Hydroxide
$O2$	Oxygen
X,a	Actualized cost of X technology
act	Activation
$bubble$	Bubbles
$cell$	Single cell
d	Diaphragm
el	Electrolyte/Electrolyzer
elc	Electricity
$inlet$	Cell inlet
ohm	Ohmic
$outlet$	Cell outlet
$pump$	Water pump
rev	Reversible
th	Thermo-neutral
v	Vapor

References

[1] Grigoriev SA, Fateev VN, Bessarabov DG, Millet P. Current status, research trends, and challenges in water electrolysis science and technology. Int J Hydrogen Energy 2020;45:26036–58. https://doi.org/10.1016/j.ijhydene.2020.03.109.

[2] Ulleberg Ø. Modeling of advanced alkaline electrolyzers: a system simulation approach. Int J Hydrogen Energy 2003;28:21–33. https://doi.org/10.1016/S0360-3199(02)00033-2.

[3] Busquet S, Hubert CE, Labbé J, Mayer D, Metkemeijer R. A new approach to empirical electrical modelling of a fuel cell, an electrolyser or a regenerative fuel cell. J Power Sources 2004;134:41–8. https://doi.org/10.1016/j.jpowsour.2004.02.018.

[4] Ursúa A, Sanchis P. Static-dynamic modelling of the electrical behaviour of a commercial advanced alkaline water electrolyser. Int J Hydrogen Energy 2012;37:18598–614. https://doi.org/10.1016/j.ijhydene.2012.09.125..

[5] Hammoudi M, Henao C, Agbossou K, Dubé Y, Doumbia ML. New multi-physics approach for modelling and design of alkaline electrolyzers. Int J Hydrogen Energy 2012;37:13895–913. https://doi.org/10.1016/j.ijhydene.2012.07.015.

[6] Henao C, Agbossou K, Hammoudi M, Dubé Y, Cardenas A. Simulation tool based on a physics model and an electrical analogy for an alkaline electrolyser. J Power Sources 2014;250:58–67. https://doi.org/10.1016/j.jpowsour.2013.10.086.

[7] Jang D, Choi W, Cho HS, Cho WC, Kim CH, Kang S. Numerical modeling and analysis of the temperature effect on the performance of an alkaline water electrolysis system. J Power Sources 2021;506. https://doi.org/10.1016/j.jpowsour.2021.230106.

[8] Ursúa A, Gandía LM, Sanchis P. Hydrogen production from water electrolysis: Current status and future trends. Proceedings of the IEEE, vol. 100, Institute of Electrical and Electronics Engineers Inc.; 2012, p. 410–26. https://doi.org/10.1109/JPROC.2011.2156750.

[9] Olivier P, Bourasseau C, Bouamama PB. Low-temperature electrolysis system modelling: A review. Renewable and Sustainable Energy Reviews 2017;78:280–300. https://doi.org/10.1016/J.RSER.2017.03.099.

[10] Gilliam RJ, Graydon JW, Kirk DW, Thorpe SJ. A review of specific conductivities of potassium hydroxide solutions for various concentrations and temperatures. Int J Hydrogen Energy 2007;32:359–64. https://doi.org/10.1016/J.IJHYDENE.2006.10.062.

[11] Mcbride BJ, Zehe MJ, Gordon S. NASA Glenn Coefficients for Calculating Thermodynamic Properties of Individual Species. 2002.

[12] le Bideau D, Mandin P, Benbouzid M, Kim M, Sellier M. Review of necessary thermophysical properties and their sensivities with temperature and electrolyte mass fractions for alkaline water electrolysis multiphysics modelling. Int J Hydrogen Energy 2019;44:4553–69. https://doi.org/10.1016/J.IJHYDENE.2018.12.222

[13] Zaĭtsev ID, Aseev GG. Properties of Aqueous Solutions of Electrolytes. Undefined 1992;30:30-4415-30–4415. https://doi.org/10.5860/CHOICE.30-4415.

[14] Nami H, Rizvandi OB, Chatzichristodoulou C, Hendriksen PV, Frandsen HL. Techno-economic analysis of current and emerging electrolysis technologies for green hydrogen production. Energy Convers Manag 2022;269:116162. https://doi.org/10.1016/J.ENCONMAN.2022.116162.

[15] Sakas G, Ibáñez-Rioja A, Ruuskanen V, Kosonen A, Ahola J, Bergmann O. Dynamic energy and mass balance model for an industrial alkaline water electrolyzer plant process. Int J Hydrogen Energy 2022;47:4328–45. https://doi.org/10.1016/J.IJHYDENE.2021.11.126.

[16] Sánchez M, Amores E, Rodríguez L, Clemente-Jul C. Semi-empirical model and experimental validation for the performance evaluation of a 15 kW alkaline water electrolyzer. Int J Hydrogen Energy 2018;43:20332–45. https://doi.org/10.1016/j.ijhydene.2018.09.029

[17] de Groot MT, Kraakman J, Garcia Barros RL. Optimal operating parameters for advanced alkaline water electrolysis. Int J Hydrogen Energy 2022. https://doi.org/10.1016/j.ijhydene.2022.08.075

Application of genetic algorithms to the design and dimensioning of maritime hybrid power plants fueled by alternative fuels

Álvaro Benet[a], Antonio Villalba-Herreros[a,b], Óscar Santiago[a,b] and Teresa J. Leo[a,b]

a Universidad Politécnica de Madrid, Madrid, Spain,
b Grupo de Investigación UPM Pilas de Combustible, Tecnología del Hidrógeno y Motores Alternativos (PICOHIMA), Madrid, Spain, teresa.leo.mena@upm.es,

Abstract:

The combination of emerging technologies such as fuel cells with well-known internal combustion engines, gas turbines and/or batteries is expected to enhance the efficiency of the resulting hybridized power plants compared to conventional ones installed onboard ships. Besides, the use of alternative fuels such as hydrogen, methanol or ammonia to power ships will allow to reduce the carbon footprint of vessels. However, hybridization and the use of alternative fuels imply that several variables such as efficiency, reliability, flexibility, space requirements, mass, investment costs or maintenance costs need to be taken into account simultaneously. To approach these designs Genetic Algorithms can be helpful. Genetic Algorithms are a powerful tool for solving a wide range of optimization problems in which several variables play a key role on the performance of the solution demanding a trade-off solution that also considers conflictive phenomena between these variables. In this work, the application of Genetic Algorithms to the design of hybridized marine power plants aiming to find compromised solutions is described. The outcome of these applications will help in the decision-making process to select the different components within the power plant, as well as the dimensioning of their capacities to get the most suitable design in accordance with a defined set of requirements that must be met.

Keywords:

Multi-objective optimization; Genetic algorithm; Hybrid power plant; Alternative fuels; Maritime.

1 Introduction

Multi-objective optimization problems (MOPs) arise frequently in engineering applications where several objectives need to be optimized simultaneously. In such cases, optimization algorithms are commonly used to solve that MOPs due to their ability to handle multiple criteria and objectives and search for the solution space efficiently. In the present work, the methodology for the application of an optimization algorithm on the design of a marine hybrid power plant is presented. This methodology will allow to create a tool to help in the decision-making process of the different power generation components of a marine hybrid power plant.

In Section 2, a brief review about the state-of-the-art of multi-objective optimization algorithms applied to power plant generation problems is presented. Non-Dominated Genetic Algorithm II (NSGA-II), Particle Swarm Optimization (PSO) and Strength Pareto Evolutionary Algorithm II (SPEA II) are found among the most used algorithms used for power plant generation problems. Economics, emissions and efficiency are found as the main objective functions defined.

The combination of emerging technologies such as fuel cells with well-known internal combustion engines, gas turbines and/or batteries is expected to enhance the efficiency of the resulting hybridized power plants compared to conventional ones installed onboard ships. Besides, the use of alternative fuels such as hydrogen, methanol or ammonia to power ships will allow to reduce the carbon footprint of vessels. However, hybridization and the use of alternative fuels imply that several variables such as efficiency, reliability, flexibility, space requirements, mass, investment costs or maintenance costs need to be taken into account simultaneously. All this results in a problem with multiple inputs, multiple variables well as multiple goals to fulfil simultaneously. Multi-objective algorithms are a powerful tool to cope with this problem. Nevertheless, a case-specific methodology adapted to the problematic of a modern marine hybrid power plant from needs to be developed to allow the use of multi-objective algorithms. In Section 3, this methodology is explained. Key aspects and future works to the methodology are discussed in Section 4.

2 Multi-objective optimization algorithms

Multi-objective optimization problems arise frequently in engineering applications where several objectives need to be optimized simultaneously. Applied to power generation plant problems, Non-Dominated Genetic Algorithm II (NSGA-II), Particle Swarm Optimization (PSO) and Strength Pareto Evolutionary Algorithm II (SPEA II) have been found to be widely used in the literature. This Section presents a brief review of these algorithms for such applications. Table 1, compares briefly the main features of these algorithms.

NSGA-II

Non-dominated Sorting Genetic Algorithm II (NSGA-II) is a powerful multi-objective optimization algorithm that is widely used in engineering and scientific applications. It is a variation of the NSGA algorithm, which is based on the concept of non-dominated sorting, where solutions in the population are classified into different "fronts" based on their dominance relationship with other solutions. NSGA-II builds on this concept by introducing several improvements that allow it to search for optimal solutions more efficiently and effectively. One of the key enhancements is the use of a crowding distance metric to maintain diversity in the population. This metric is used to encourage the selection of solutions that are spread out in the objective space, rather than focusing on a single region.

Another important improvement of NSGA-II is the use of an elitist selection mechanism. This ensures that the best solutions in the population are preserved from one generation to the next, which helps to prevent the loss of good solutions during the search process. NSGA-II also employs tournament selection, which involves selecting individuals for reproduction based on their dominance and crowding distance values. The algorithm uses binary tournament selection in the early generations to encourage diversity, and switches to crowding tournament selection in later generations to promote convergence towards the Pareto-optimal front.

Mayer et al. use NSGA-II in a multi-objective optimization problem of a household with renewable energy supply in which the net present cost and environmental footprint are the objective functions chosen to search for the Pareto-front solutions [1]. The results prove multi-objective optimization to be satisfactory to investigate trade-offs solution between two conflicting objective functions.

Similarly, Oyekale et al. develop a thermo-economic optimization of a solar organic Rankine cycle power plant with the NSGA-II. The Pareto-front is obtained with the objective functions of biomass mass flow rate and investment cost rate [2].

NSGA-II is also the algorithm chosen by Bolbot et al. for the optimization of a cruise ship power plant considering as objective functions the Life Cycle Cost and lifetime CO2 emissions [3]. The optimization has taken into account existing and future SOx and NOx IMO regulations, which were used as constraints in the optimization process. The algorithm has proved to succeed in finding an optimal solution that meets with these regulations.

Villalba-Herreros et al. make use of the NSGA-II in a multi-objective optimization of a power plant based on Direct Methanol Fuel Cells (DMFCs) with a CO2 capture system to power an Autonomous Underwater Vehicle (AUV) [4].

PSO

Particle Swarm Optimization (PSO) is a nature-inspired metaheuristic optimization algorithm that is widely used to solve complex optimization problems. The algorithm is based on the movement of particles in a multidimensional search space, which is designed to explore the space and find the best solution. In PSO, a population of particles represents candidate solutions, and the movement of the particles is influenced by their own best position (i.e., personal best) and the best position found by the swarm (i.e., global best). Each particle adjusts its position and velocity based on its own experience and the experience of the swarm, using a set of mathematical equations that determine the direction and speed of movement. This process is repeated over multiple iterations until a stopping criterion is met or the best solution is found.

One of the advantages of PSO is its simplicity and ease of implementation. The algorithm has a small number of parameters, which makes it easy to use and adjust for different optimization problems. PSO is also computationally efficient and can handle large and complex optimization problems, as it can quickly converge to a good solution with a small number of function evaluations. Additionally, PSO can handle both continuous and discrete optimization problems, and can be easily extended to handle multi-objective optimization problems. Despite its advantages, PSO can suffer from premature convergence and a lack of diversity in the population, which can result in suboptimal solutions. To mitigate these issues, various variants of PSO have been proposed, such as adaptive PSO, hybrid PSO, and cooperative PSO.

Vijayakumar et al. propose the use of a modified PSO algorithm in [5], in a load distribution optimization to find the lowest electric power generation cost. The results were compared with genetic algorithms and conventional PSO algorithms, offering the modified PSO the lowest electric power generation cost among them.

Azaza et al. use the PSO in a Multi-objective optimization of a hybrid micro-grid system composed of photovoltaic panels, wind turbines, diesel generators and battery storage [6]. The objective functions set were reliability, Cost of electricity (COE) and the renewable factor to minimise the use of the diesel generator.

SPEA II

Strength Pareto Evolutionary Algorithm II (SPEA II) is a multi-objective optimization genetic algorithm that uses a fitness function to evaluate the quality of solutions in the population. The fitness function considers both the solution's objective values and its distance to other solutions in the population. Solutions with high fitness are selected for the next generation, and the process is repeated to obtain a set of non-dominated solutions. SPEA II has been applied to various engineering problems, including transportation planning, manufacturing, and structural optimization. However, SPEA II can be computationally expensive for problems with a large population size.

This algorithm is used by Mehrdad et al. in [7] for the optimization of organic Rankine cycle used in a power plant. The objective functions used in the Pareto-front are the Levelized Energy Cost (LEC) and the exergy efficiency.

Dufo-López et al. make use of SPEA II in [8], where this algorithm is applied for the optimization of stand-alone photovoltaic, wind and diesel systems with battery storage. The objective functions are

the Levelized Cost of Energy and the equivalent CO2 life cycle emissions. The results of the optimization allowed to dimension and select the power generation devices for the plant, as well as discard others.

Table 1. Comparison features between NSGA-II, PSO and SPEA II.

Features	NSGA-II	PSO	SPEA II
Type of algorithm	Genetic	Stochastic	Genetic
Multi-objective	Yes	Not by default	Yes
Search space technique	Non-dominated sorting / crowding distance	Swarm of particles	Strength metric
Optimization criteria	Pareto dominance	Fitness function	Strength and distribution
Convergence criteria	Quality measure convergence	Fitness function convergence	Limit of space distance
Robustness	High	Lower	Higher
Computational demand	High	Light	Medium
Discontinuous functions	Yes	Struggle	Yes
Weakness	Computationally demanding	Discontinuous functions	Requires large population to maintain diversity
References	[1-4]	[5-6]	[7-8]

In summary, three different types of optimization techniques have been shown in the present Section and references of all of them related to power generation/distribution problems have been briefly explained. As can be observed, regardless of the method used, in all cases the economics are one of the objective functions of the Pareto-front. The second objective function is related either to the efficiency of the system or the emissions produced.

3 Methodology

The main focus of the investigation outlined in this work is shown in Figure 1. The figure shows the main overview of the algorithm methodology. In the following Sections 3.1 to 3.5 the steps of this workflow are explained.

3.1 Input data - Operational profile and fuels

The initial conditions that are the basis of the optimization process are given by the operational profile of the vessel and the fuels used.

The operational profile is broken down into endurance of the vessel, electrical demand and heat demand.

The electrical demand considered is defined as the sum of the propulsion power in a vessel with electric propulsion, and the auxiliary power demand of the vessel. This auxiliary power initially does not consider the electrical demand needed to make the power plant operational, that is, the power of the balance of the plant (BoP) as it depends on the size of the power plant itself. The BoP is sized in an iterative process further explained in Section 3.2.

The selection of one, two, three, four or all the fuels to be considered during the optimization process will depend on the specific case to which the methodology presented in this work is applied.

Regarding the fuels used onboard, five alternative fuels are considered: liquid hydrogen (LH2), methanol (MeOH), ammonia (NH3), liquid natural gas (LNG) and biofuels.

The different power plant components will be dimensioned according to the required demands as explained in Section 3.2.

Lastly, the endurance input is fed directly to the mathematical modelling of the algorithm as explained in Section 3.2.

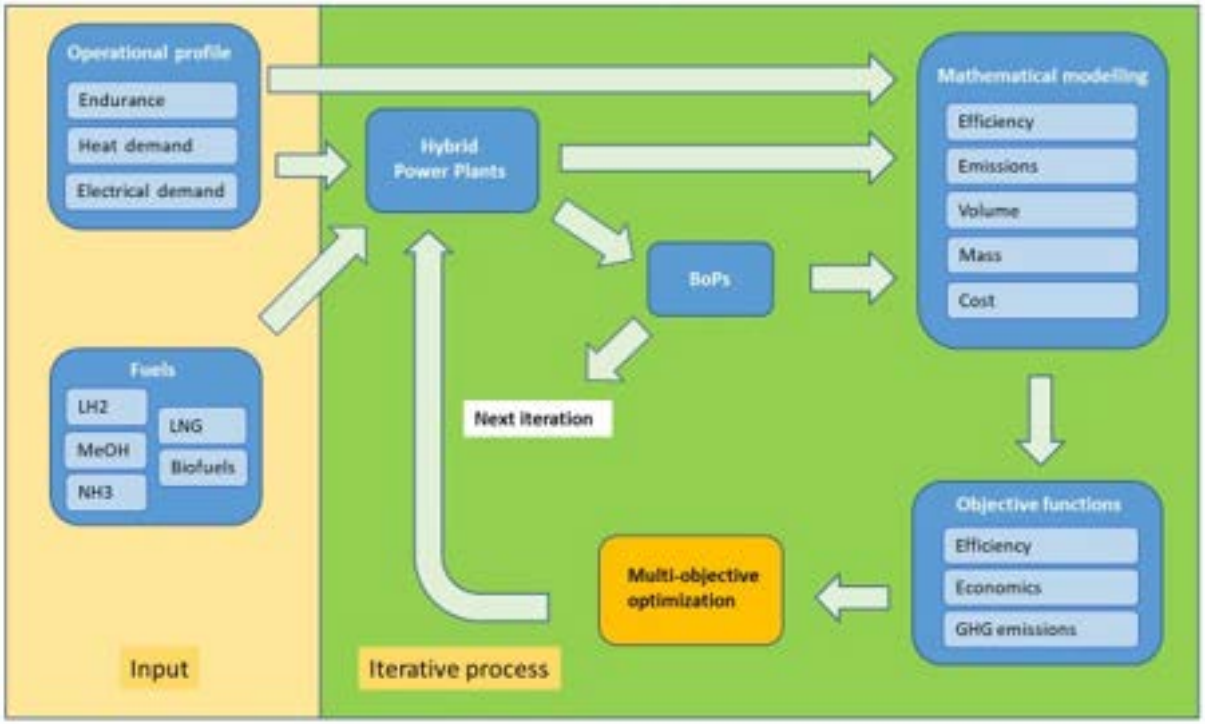

Figure 1. Methodology diagram of the multi-objective algorithm.

3.2 Hybrid Power Plants

The input parameters defined in Section 3.1 are introduced into the iterative process shown in Figure 2.

Electrical and heat demands of the operational profile as well as the fuels selected are used to establish an initial dimensioning of the power generation devices of the hybrid power plants.

During the first iteration, the population of hybrid power plants is created randomly, varying the power capacity of the different power generation devices.

The power plant components of the marine hybrid power plants are:

- PEM Fuel Cells (electricity generation)
- Generator sets (electricity generation)
- Battery energy storage (electricity storage/generation)
- Boiler (heat generation)
- Heat recovery systems (heat generation)

The set of hybrid power plants obtained in this step form the population that is subjected to the optimization process in the algorithm. In this respect it will be assumed that each individual of the population will make use of only one of the fuels. This is an extended practice in the maritime industry (although the use of two different fuels onboard a ship is also common) in order to minimize the amount of equipment needed to make the power plant functional.

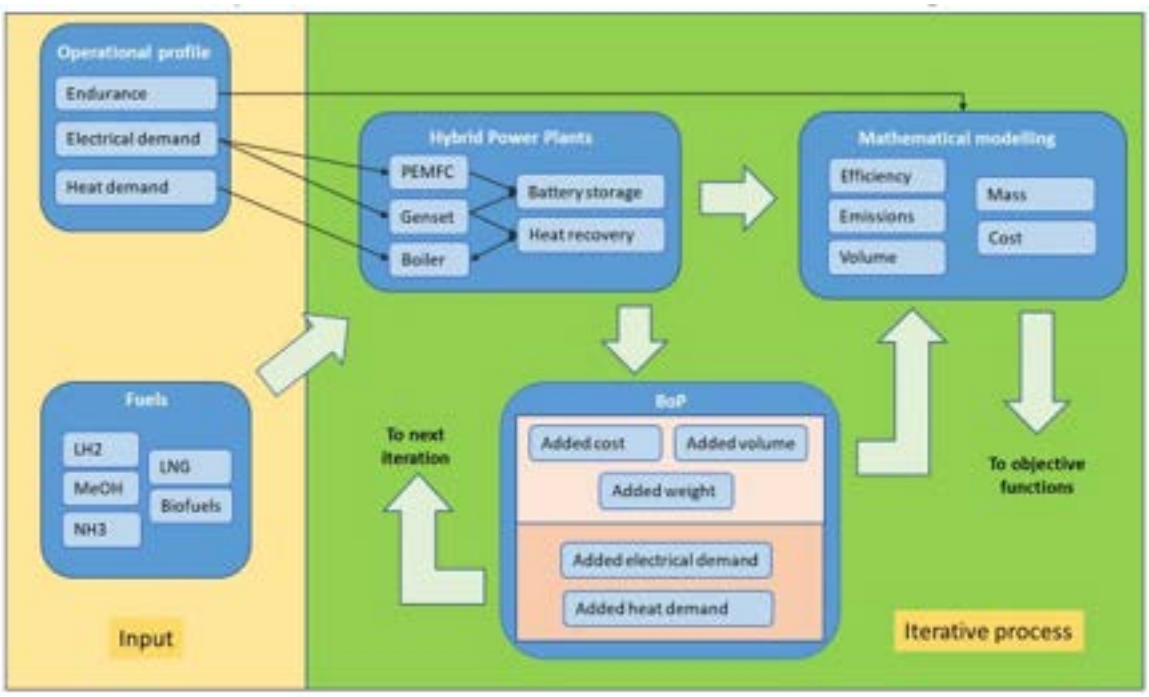

Figure 2. Workflow diagram of the mathematical modelling.

3.3 Mathematical modelling of hybrid power plants

Each individual of the hybrid power plants will have its own configuration of fuel, PEM Fuel Cells, generator sets, battery storage, boiler and heat recovery systems. For each individual, the mathematical model is the step in which the performance of the plant is assessed. Efficiency, emissions, volume required on board, mass and cost of the plant are calculated in this step.

The endurance of the vessel is also introduced at this step. Once the efficiency of the hybrid power plant is known, it will be possible to assess the volume of the fuel storage as well as its mass contributions.

3.3.1 Mathematical modelling of the balance of plants (BoPs)

Simultaneously to the mathematical modelling of the hybrid power plant individuals, the balance of plant (BoP) is also assessed. BoP is an important component of a marine power plant that refers to all of the auxiliary systems and equipment required to support the power generation process. It involves a wide range of systems and equipment, such as the electrical grid connection, transformers, control systems, fuel supply systems, reformers, exhaust systems, lube oil systems, compressed air or refrigeration systems.

Combining different power generation and power storage devices in a hybrid power plant needs to take into account that there will be interfaces and share of equipment between them, thus affecting the BoP. Such combination is taken into account in the BoP in order to create a model that considers the integration of different power plant devices.

The calculation of the BoP for each individual will allow to estimate the additional contributions of electrical demand, heat demand, cost, volume required onboard the vessel and mass.

As mentioned in Section 3.1, added electrical demand and heat demand will be used in the next iteration process to dimension the next generation of hybrid power plants. This will allow to estimate future individuals of hybrid power plants taking into account these contributions, so that after a few generations the additional electrical and heat demands will tend to zero.

Added cost, volume and mass parameters are combined with the contributions of these parameters calculated for the hybrid power plants in the mathematical model.

3.4 Objective functions

In Section 2, works found in the literature regarding multi-objective optimization cases applied to the dimensioning of hybrid power plants have been analysed. The analysis has shown that the objective functions selected to carry out the multi-objective optimizations are in most cases focused on costs combined with efficiency or greenhouse gas emissions. These objective functions entail the search of trade-off solutions in which a Pareto-Front is obtained in the multi-objective optimization process. This is one of the key elements that is seek in the present work, as the aim of the methodology proposed is to help during the decision-making of the optimum hybrid power plant. A range of hybrid power plants forming a Pareto-Front will give the end-user the possibility to take a decision based on a set of criteria that have opposite impacts.

In Figure 3 it is shown the workflow of how the parameters calculated in the mathematical model are distributed into the objective functions.

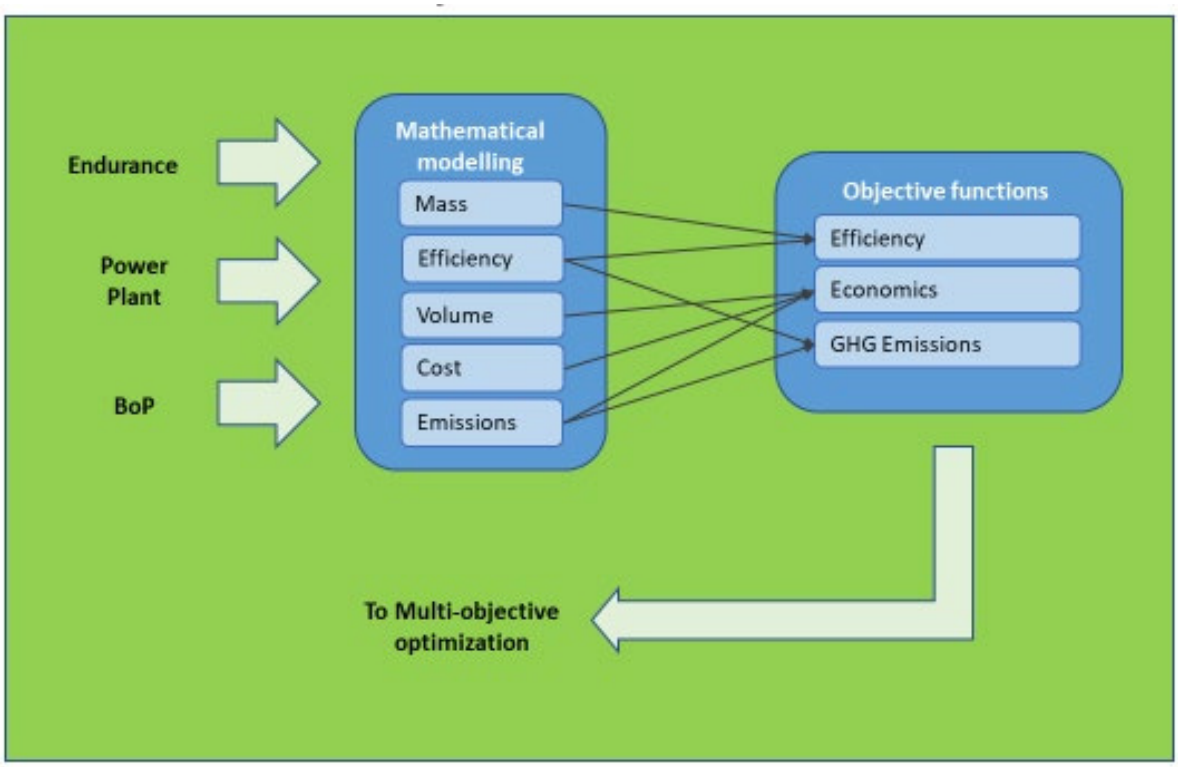

Figure 3. Workflow from mathematical modelling to objective functions.

3.4.1 Efficiency

The objective function of efficiency allows to give information of the performance of the hybrid power plant. Besides, it is a parameter that will not be subject to considerable changes in mid or long-term perspectives. Even though devices like the PEM Fuel Cells are emerging technologies in the maritime, efforts on their development are being focused on reducing their investment cost through the use of new materials. Therefore, this objective function will have the quality of a stability with high reliability.

3.4.2 Economics

The objective function of the economics has contributions from three different parameters of the mathematical model: costs, volume and emissions.

As it is reasonable, the costs of the hybrid power plant obtained in the mathematical model, which are calculated in capital expenses (CAPEX) and operational expenses (OPEX) of the plant, contribute greatly to this objective function.

The volume of the hybrid power plant, and the volume on the vessel required to store the fuel, can affect, depending on the type of vessel, to other spaces such as cargo, that would report a benefit otherwise. Therefore, the volume parameter calculated in the mathematical model can also influence the objective function of economics.

The emissions, which depending on the power generation device, can be composed of greenhouse gases and others such as NOx, SOx or PM, can be subject to penalties from the international regulatory organizations. Therefore, this is also taken into account in this objective function.

3.4.3 GHG Emissions

The purpose of objective function of greenhouse gas emissions is to be evaluate and compare the environmental impact of the hybrid power plants. Taking the operational profile of the vessel allows to calculate the mass of CO2 emitted to the atmosphere during in a specific amount of time. For each hybrid power plant analysed, this mass will be calculated and serve as basis of this objective function.

3.5 Multi-objective optimization and iteration

The multi-objective optimization is performed with the three objective functions defined in Section 3.4, economics, efficiency and GHG emissions. As a result of the optimization, a set of new hybrid power plants are obtained and introduced into the next iteration. The added electrical demand and added heat demand are introduced also in the next iteration, as explained in Section3.2, and their values will tend to stabilize as the number of iterations increase. The workflow of this step is shown in Figure 4.

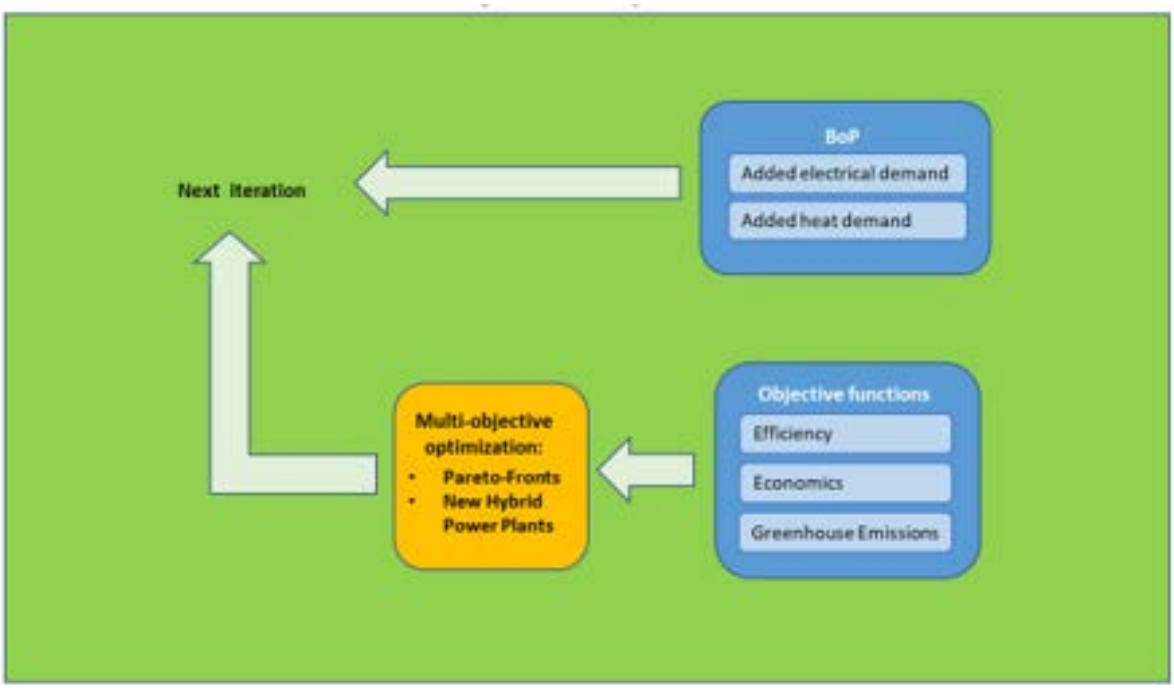

Figure 4. Workflow of multi-objective optimization.

The Pareto-Front generated in the optimization process will be based on the three objective functions defined. To take into account the three objective functions simultaneously, the Pareto-Front is represented in a 3-dimensional graph.

4 Discussion

In the present work a methodology to optimize maritime hybrid power plants fuelled with alternative fuels has been presented. In Section 2, the results of a search of optimization algorithms used in the literature applied to cases of dimensioning hybrid power plants are presented. Three optimization algorithms (NSGA-II, PSO and SPEA-II) have been found with positive results throughout the cases applied. Among the cases found in the literature, two objective functions are normally used in the

optimization process, from a group of three, efficiency, economics and GHG emissions. Pareto-Fronts of two objective functions are therefore the outcome of these works. The authors find that the three objective functions mentioned are of high relevance in the decision-making process of dimensioning a maritime hybrid power plant. For this reason, it has been decided that the methodology proposed in Section 3 makes use of the three objective functions simultaneously. Pareto-fronts are therefore represented in 3-dimensional graphs, with each x-y-z axis associated to each of the objective functions.

Hybrid power plants require to integrate different power generation devices working together in harmony. In order to achieve this integration, the auxiliary systems to make the hybrid power plant operational, known as the balance of plant (BoP), have a higher level of complexity compared to power plants with single power generation devices. For this reason, in the methodology proposed in Section 3, the BoP has been given significant relevance and importance within the algorithm. For each hybrid power plant, its BoP will have its specific needs, which results in specific mass of the equipment, volume required on board, costs, but also electrical power demand and heat demand. The workflow of the BoP is shown in Figure 2. As the BoP is based on the information of the hybrid power plant, the added electrical demand and heat demand are no longer considered in the current iteration step, otherwise this would affect the dimensioning of the hybrid power plant that has been already stablished. Therefore, added electrical demand and heat demand are introduced in the next iteration of the algorithm. As the number of iterations increase, the hybrid power plants tend to be dimensioned matching the needs of the BoP. Therefore, the added electrical demand and heat demand of the BoP will tend to zero as the iterations grow.

As explained in Section 3.1, one part of input data to be applied to the algorithm comes from the operational profile of a vessel with electric propulsion. Electrical power demand and heat demand are used to dimension initially the hybrid power plants. To do so, the reference points from which these demands are considered have to be common for all types of hybrid plants., e.g., the ship propeller, that has a mechanical demand to be moved, has a prime mover that is an electric motor, this electric motor has an electrical demand to move the propeller that can be common for any given hybrid power plant considered in this work. Future works that could include mechanical propulsion of the vessel would need to take this into account.

5 Conclusions

The emerging technologies that are being implemented in the maritime field regarding the use of alternative fuel devices such as PEM Fuel Cells have a direct impact on the power plants of vessels. The combination of different power generation devices entails a level of hybridization of power plants that requires a higher complexity to make the hybridized power plant to function in harmony. To solve this problem, a methodology for a multi-objective optimization process that will help during the decision-making process of the power plant has been proposed. The main conclusions obtained from are summarized below:

- The methodology proposed is able to integrate the different power generation devices through specific balance of plant oriented to each hybrid power plant considered.
- Three objective functions (efficiency, economics and GHG emissions) have been defined. The objective functions will allow to create a 3-dimensional Pareto-Front to assist the user on the decision-making process of the optimum hybrid power plant.
- The point of reference from the electrical demand and heat demand given by the operational profile of the vessel needs to be common for all hybrid power plants.

Acknowledgements

This work has been carried out thanks to the Project GreenH2CM funded by MCIN/AEI/10.13039/501100011033, by “NextGenerationEU/PRTR” and the Regional Government of Madrid and to the Grant PID2021-124263OB-I00 funded by MCIN/AEI/10.13039/501100011033 and by “ERDF a way of making Europe”.

References

[1] M. J. Mayer, A. Szilágyi, and G. Gróf, “Environmental and economic multi-objective optimization of a household level hybrid renewable energy system by genetic algorithm,” Appl Energy, vol. 269, p. 115058, 2020, doi: https://doi.org/10.1016/j.apenergy.2020.115058.

[2] J. Oyekale, M. Petrollese, and G. Cau, “Multi-objective thermo-economic optimization of biomass retrofit for an existing solar organic Rankine cycle power plant based on NSGA-II,” Energy Reports, vol. 6, pp. 136–145, 2020, doi: https://doi.org/10.1016/j.egyr.2019.10.032.

[3] V. Bolbot, N. L. Trivyza, G. Theotokatos, E. Boulougouris, A. Rentizelas, and D. Vassalos, “Cruise ships power plant optimisation and comparative analysis,” Energy, vol. 196, p. 117061, 2020, doi: https://doi.org/10.1016/j.energy.2020.117061.

[4] A. Villalba-Herreros, Ó. Santiago, L. Magistri, and T. J. Leo, “Autonomous Underwater Vehicle Powered by Direct Methanol Fuel Cell-Based Power Plants: A Quick Preliminary Design Model,” Applied Sciences, vol. 10, no. 21. 2020. doi: 10.3390/app10217687.

[5] T. Vijayakumar and V. R, “Efficient Energy Load Distribution Model using Modified Particle Swarm Optimization Algorithm,” Journal of Artificial Intelligence and Capsule Networks, vol. 2, pp. 226–231, Feb. 2021, doi: 10.36548/jaicn.2020.4.005.

[6] M. Azaza and F. Wallin, “Multi objective particle swarm optimization of hybrid micro-grid system: A case study in Sweden,” Energy, vol. 123, pp. 108–118, 2017, doi: https://doi.org/10.1016/j.energy.2017.01.149.

[7] S. Mehrdad, R. Dadsetani, A. Amiriyoon, A. S. Leon, M. Reza Safaei, and M. Goodarzi, “Exergo-Economic Optimization of Organic Rankine Cycle for Saving of Thermal Energy in a Sample Power Plant by Using of Strength Pareto Evolutionary Algorithm II,” Processes, vol. 8, no. 3. 2020. doi: 10.3390/pr8030264.

[8] R. Dufo-López et al., “Multi-objective optimization minimizing cost and life cycle emissions of stand-alone PV–wind–diesel systems with batteries storage,” Appl Energy, vol. 88, no. 11, pp. 4033–4041, 2011, doi: https://doi.org/10.1016/j.apenergy.2011.04.019.

Development of a numerical optimization model for sizing hydrogen refuelling stations: application to a case study

Ana Cristina Ferreira[a], José Paulo Ferreira[b], Senhorinha Teixeira[c], Luís Barreiros Martins[d] and José Carlos Teixeira[e]

[a]MEtRICs and ALGORITMI, University of Minho, Guimarães, Portugal; COMEGI, Universidade Lusíada, Portugal, acferreira@dps.uminho.pt (CA)
[b]MEtRICs, University of Minho, Guimarães, Portugal, a85354@alunos.uminho.pt
[c]ALGORITMI, University of Minho, Guimarães, Portugal, st@dps.uminho.pt
[d]MEtRICs, University of Minho, Guimarães, Portugal, lmartins@dem.uminho.pt
[e]MEtRICs, University of Minho, Guimarães, Portugal, jt@dem.uminho.pt

Abstract:
Interest in hydrogen as a transportation fuel is growing. Fuel cell electric vehicles fed by hydrogen are expected to play a key role in the decarbonization of the transportation sector. Its impact will depend upon the existence of reliable and cost-effective fuelling stations. Numerical simulation allows sizing hydrogen refuelling on-site stations in order to identify the most cost-effective solution for a specific utilization pattern. This study aims to define a numerical optimization model for a hydrogen refuelling station to supply both light and heavy vehicles. The objective function is to minimize the total storage volume, taking into account the number of vehicles to be refuelled. The pressure at each storage skid is considered a decision variable, as well as the hydrogen mass that is provided at each vehicle filling. The model considers the hydrogen properties and the physical constraints to size the station prior to its construction. Additionally, a cost analysis based on the capital expenditure concept was developed. The hydrogen refuelling station must be able to supply 300 kg/day of hydrogen. The station includes four main systems: the hydrogen production equipment, an electrolyzer, and a system that can store hydrogen to feed the compression cascade. The station should be able to fill 10 heavy vehicles at 350 bar (H35), considering 2 skid pressure levels and a supplied mass of 30 kg and 30 light vehicles at 700 bar (H70), considering 3 skid pressure levels, dispensing 4.2 kg of hydrogen each. At all vehicle fillings, a pressure differential of 50 bar between the high-pressure skid and the vehicle tank is mandatory so the refuelling can be validated. The results show that it is possible to refuel 10 heavy vehicles considering a total storage volume of 36.9 m^3, whereas, for light vehicles, it is possible to refuel 30 vehicles with a total volume of 22.9 m^3. Based on capital expenditure, the most representative capital costs are the production equipment (30%), high-pressure storage unit (20%) and the hydrogen compression system (18%).

Keywords:
Hydrogen; H_2 Refuelling protocols; Light and heavy vehicles; Numerical Optimization; CAPEX.

1. Introduction

Hydrogen as an energy carrier is currently seen as one of the most favourable ways to accelerate the decarbonization of various industrial sectors and vehicular mobility [1]. According to Perna et al [2], currently, there are approximately 200 hydrogen refuelling stations, mostly located in Japan, Germany, and USA. Yet, more than 5000 new stations are planned to be constructed by 2030.
Hydrogen-based refuelling stations comprise mainly four main steps, namely, production, storage, safety and utilization [3]. The selection of hydrogen production via requires considerable resources and their use, technological availability, efficiency, costs, environmental impacts and system integration options [4]. After production, the hydrogen needs to be stored [5]. According to the literature [4–9], storage and transport are the most difficult phases of the hydrogen supply chain. In order to use hydrogen as fuel, its physical state has to be altered in order to improve its density. Being hydrogen an energy vector that can be produced in a clean and environmentally friendly way, this gas is generally stored for local consumption or for transportation to the point of final consumption [3]. Either way, each solution must be studied individually in order to meet the specific needs. According to Demir and Dincer [8], identifying cost-effective pathways for supplying hydrogen remains an appealing prospect.

Refuelling gaseous hydrogen is a process that comprises two main ways: either the hydrogen is directly compressed in a tank using a compressor or the hydrogen is moved from a tank with higher pressure to the target tank at lower pressure [10]. In the context of vehicle refuelling stations, the storage of hydrogen in a gaseous state remains the most viable option [11]. Compressed hydrogen is a highly efficient methodology for hydrogen storage, but it requires the use of high-pressure systems. This represents an important issue because the energy density of the gas varies with the pressure inside the container. The fatigue caused by the repetitive cycles of high to low pressure, as well as, the inherent risks in having a pressurized gas are a key aspect in sizing the storage system [6,9,12].

For vehicular applications, it is required to have high-density storage systems, low weight and low cost, that are suitable for the hydrogen delivery system. High-pressure hydrogen storage technology is usually applied at hydrogen refuelling stations and hydrogen vehicles. The majority of refuelling stations require most of the following components: (i) hydrogen production equipment with a purification unit to secure that hydrogen purity meets the standards for supplying fuel cells; (ii) hydrogen compression system for high-pressure storage inside the station's main tanks; (iii) hydrogen storage tanks for either compressed gas or liquid hydrogen; (iv) equipment able to regulate pressure to 350 bar or 700 bar during the refuelling procedure; (v) a cooling unit to reduce hydrogen gas temperature down to − 40 °C to guarantee that during fast refills the vehicle's hydrogen tank does not exceed 85 °C, mostly to ensure the station safety; (vi) dispensers used to fill the vehicles tanks from the station's compressed storage containers; (vii) electrical and mechanical equipment such as valves, piping, pressure relief valves and hydrogen sensors [13].

Refuelling stations are categorized into off-site hydrogen stations and on-site infrastructures. The first type includes all the stations where hydrogen is delivered from a central production plant, being transported through pipelines or by heavy-duty trucks where hydrogen is stored in tube trailers as compressed gas [14]. For on-site stations, the hydrogen used to refuel the vehicles is generated locally. This represents a technical limitation because the station efficiency depends on the output quantity of the hydrogen generators, which typically ranges from 100 kg/day to 1000 kg/day. From an economic perspective, on-site hydrogen refuelling stations have a significantly higher capital investment cost due to the hydrogen production components, especially, on-site water electrolysis production. According to Perna et al [2], the investment cost of on-site stations may represent a capital cost 1.5 times higher than similar off-site stations with the same capacity.

Several authors are focused on studying the technical aspects of refuelling station operation. Miguel et al [15] showed with their experimental studies that the maximum gas temperature reached at the end of the filling increases linearly with the increase of the initial temperature while the temperature increase and the state of charge decreases linearly with increasing initial temperature. Zhao et al. [16] have developed numerical simulations, to identify the temperature increase within the hydrogen vehicle tank during the refuelling process at 350 bar (i.e., the so called H35 refuelling at 35 MPa). A similar study was performed by Wang et al [17] for fast filling at 700 bar (i.e., the so called H70 refuelling at 70 MPa). Maus et al [18] investigated the filling procedure taking into account tank systems with different storage volumes, from 2 kg to 10 kg hydrogen.

Some studies have been presented in the literature regarding the modelling of hydrogen refuelling station. These are mostly focused on thermodynamic models based on on-site electrolysis looking for energy-efficient station configurations, off-site production systems and respective delivery supply chain, and the definition of refuelling network location with or without production method [1,19–21]. However, these studies do not apply optimization algorithms in the design of the station operating conditions. Moreover, the focus is on finding the most economical design and not purely on energy efficiency. Also, it is important to notice that the current network park of refuelling stations for hydrogen vehicles is in its early stages. Thus, the refuelling infrastructure must be cost-effective in order to achieve successful market growth. The present work aims to contribute to the appeal of new mobility solutions.

The main purpose of this paper is to define a numerical optimization model for a hydrogen refuelling station for light and heavy vehicles. The station should include a hydrogen production unit, an electrolyzer and a system able to store hydrogen at high-pressure to later feed the compression cascade. The model considers the hydrogen properties and the physical constrain to size a hydrogen refuelling station, prior to its construction. It was defined as the objective function the minimization of the total storage volume, taking into account the expected number of vehicles to be fuelled.

2. Vehicle hydrogen refuelling

The process of vehicle refuelling with compressed hydrogen is subjected to control requirements in order to ensure that the vehicle tank is within a specified operating condition defined by an upper limit on pressure, and an upper and lower limit on temperature [19]. Thus, refuelling protocols have been established to define specific conditions for sizing hydrogen refuelling stations. In this section, SAE supply protocols are presented and discussed in order to understand the main constraints in the design of hydrogen refuelling stations.

2.1. Refuelling protocols

The hydrogen filling of light and heavy vehicles has been studied, improved, simulated and standardized by the Society of Automotive Engineers (SAE) since 2010. The purpose of defining these refuelling protocols is to ensure that this process is safe and that it maximizes supply performance. The first refuelling protocol, TIR J2601, was published in 2010, defining the standard for light-duty gaseous hydrogen surface vehicles [22].

Afterwards, in 2014 after a period of development with simulations and field tests, new versions were published: “J2601-2 – Refuelling Protocol for Gaseous Hydrogen Powered Heavy Duty Vehicles” and “J2601-3 – Refuelling Protocol for Gaseous Hydrogen Powered Industrial Trucks”. More recently, in 2020, a new version of TIR J2601 allowed modifying the protocols to facilitate the supply of H70 (hydrogen at 70 MPa for light cars) in tanks with a capacity of over 10 kg of hydrogen. Figure 1 presents the evolution of SAE supply protocols over the years [23].

This protocol determines the conditions under which the vehicle storage tank and dispenser should operate. The dispenser is connected to a high-pressure storage unit that ensures the pressure range required for refuelling. The supply pressure depends on three factors, namely, the ambient temperature, the precooling temperature of the hydrogen in the dispenser, the vehicle's tank volume and the respective initial pressure. During the refuelling process, the initial tank pressure should be 5 bar and the vehicle's Nominal Working Pressure (NPW) is defined as 35 MPa for heavy vehicles and 70 MPa for light vehicles). The mass flow rate of hydrogen to be supplied cannot exceed 60 g/s. Also, the hydrogen temperature limits vary between - 40 ºC and 85 ºC [22,24].

As stated, the NPW for light and heavy vehicles is different. For light vehicles, it is necessary to increase the pressure at which the gas is stored in order to increase the mass available in the system. As compression increases the temperature, when refuelling light vehicles, it is necessary to include a chiller in the station so the maximum admissible temperature in the tank at a pressure of 700 bar is not exceeded. In contrast to light vehicles, heavy vehicles have tanks with higher storage capacity, allowing these vehicles to be refilled with 35 kg of hydrogen at 35 MPa [22].

Thus, the expected performance for the protocol aims to guarantee a refuelling with a duration in the range of 3 minutes at a station, capable of pre-cooling the hydrogen to - 40 ºC. These conditions allow reaching a state of supply between 90 and 100% of the vehicle's capacity for NPW conditions and considering an ambient temperature of 15 ºC [19].

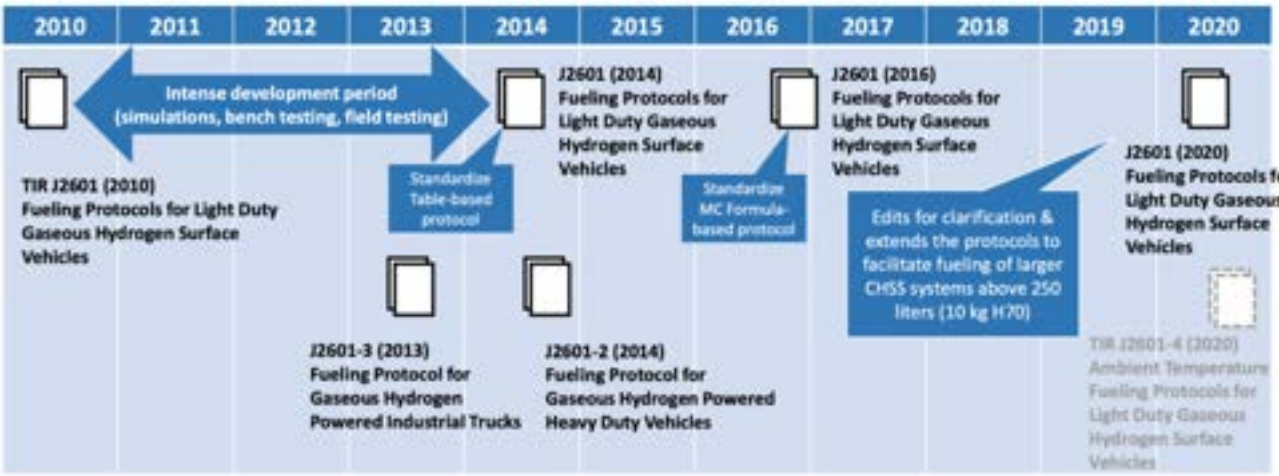

Figure. 1. Identification of SAE supply protocols between 2010 and 2020. The protocol J2601 determines the conditions under which the vehicle storage system and dispenser should operate. Adapted from [24].

The SAE J2601 protocol includes three main phases: (1) startup point; (2) refuelling phase; and (3) refuelling termination. In the first stage, it is ensured a secure connection between the dispenser nozzle and the vehicle. As soon as the connection is established, a signal is sent to verify that there is no error in the connection. Then, a pressure signal is sent to the tank to set the initial refuelling pressure and the second one to detect possible leaks and estimate the tank volume (estimated with an error of +/- 15%). During this phase, the hydrogen mass transfer limit to the tank is 200 g. Knowing the ambient temperature, the initial tank pressure, the refuelling temperature and the dispenser condition (hot or cold), the Average Pressure Ramp Rate (APRR) corresponding to the measured data is selected and the refuelling pressure condition is calculated. The initial phase is concluded when the mass of hydrogen begins to be transferred into the vehicle's tank. This is followed by the second phase, the main refuelling, in which the pre-cooling temperature is monitored during the refuelling and according to the calculated APRR. The temperature of the hydrogen when filling a tank needs to be monitored to ensure the safety of the process and to avoid overheating.

The validation of this process is based on the guarantee that the pre-cooling temperature is achieved. Otherwise, a process called Fallback Pressure Ramp Ratio (FPRR) is initiated and a new APRR is calculated. From the moment the refuelling process starts, the station controls the pressures at which the dispenser is delivering hydrogen. When the pressure in the dispenser reaches the limit established as the termination pressure, the refuelling process is complete [25].

Two main methods are used to implement SAE J2601 protocol: the LookUp Table method and the MC Formula. The LookUp Table method controls the evolution of the hydrogen pressure during the refuelling process based on the pressure and temperature in the vehicle's tank. It uses standardized table values, that specify pressure increases taking into account: vehicle tank capacity; type of refuelling system; hydrogen temperature when refuelling (T40, T30 and T20, i.e., the refuelling temperature of – 40 ºC, – 30 ºC, – 20 ºC, respectively); refuelling pressure (H35 or H70); type of vehicle-station interface and the hydrogen temperature at the dispenser outlet [22,26].

The method is based on the three identified phases of SAE J2601 protocol through the calculation of an APRR for a specific condition of ambient temperature and initial tank pressure.

The MC Formula is an alternative method based on a version of Honda's MC method that consists of analytical calculations. It uses thermodynamic properties to dynamically determine the APRR that controls the refuelling flow [10]. The MC formula can be illustrated in Figure 2, where all the parameters are presented. This method is defined for SAE J2601 boundary conditions and the APRR is adjusted according to the temperature measured at the dispenser outlet. It uses empirical equations whose coefficients are determined through the initial tank pressure, ambient temperature and tank capacity, constantly calculating the filling pressure throughout the filling.

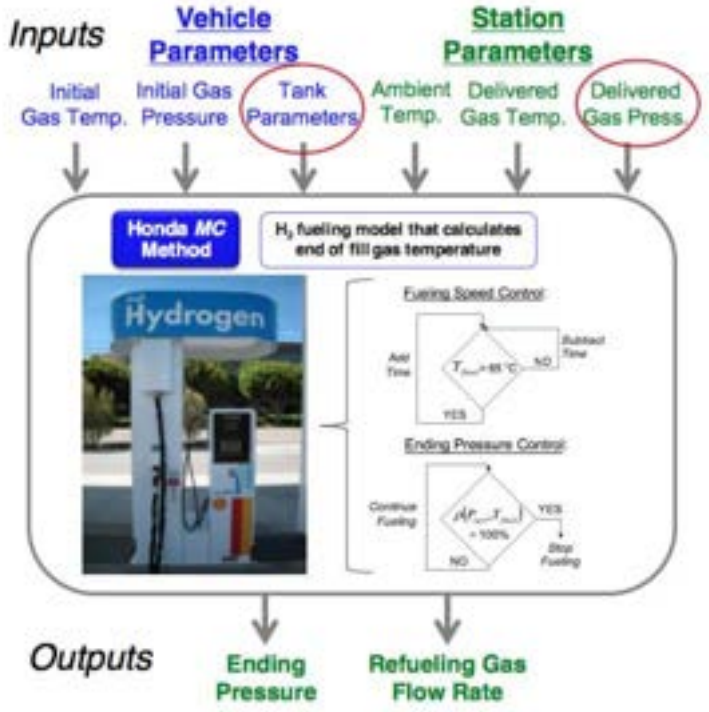

Figure. 2. Diagram control for MC formula method implementation considering the SAE J2601 protocol requirements. Adapted from [10,22].

Similarly to the LookUp Table method, the MC Formula is based in three phases. In the refuelling phase, the formula MC measures and actively uses the precooling temperature in the dispenser to calculate the hydrogen Mass Average Temperature (MAT) and the mass average enthalpy used to decide the APRR and termination pressure during the refuelling [27,28]. The refuelling process is controlled by both APRR and target pressure. The APRR is calculated based on the mass flow rate and pre-cooling temperature measured at the dispenser outlet. The actual pre-cooling temperature at the dispenser is calculated, as well as, the time defined as the total period needed to fill the vehicle tank, varying from a minimum to a maximum pressure [22]. The MC Formula method uses a MAT based on the pre-cooling temperature measured after thirty second (MAT30) to control the process until the transition pressure is reached. It is important to mention that both LookUp Table and MC formula methos apply the same boundary conditions and both collect information from the station to complete the refuelling safely.

2.2. Hydrogen Refuelling Constraints

As previously stated, the hydrogen refuelling station needs a hydrogen production equipment, a system able to store hydrogen to later feed the compression system, a chiller and a dispenser. Thus, the refuelling station operation is based on six main steps [20]:

- Step 1 – Hydrogen in gaseous state is produced through the water electrolysis in the electrolyzer which is stored at low pressure;
- Step 2 – A buffer is used to storage the hydrogen at low pressure to accumulate the required mass of hydrogen to start the compression;
- Step 3 – Hydrogen is admitted into the compression unit, able to pressurize the gas up to 10 times higher than the inlet condition;
- Step 4 – Hydrogen is stored at high pressure in containers after its compression in the gas cascade system;
- Step 5 (mandatory only for H70) – A chiller is used for hydrogen cooling till it reaches the required temperature;
- Step 6 – Hydrogen is filled through a dispenser connected to the vehicle's nozzle.

One of the main operational constraints of a refuelling stations is related with the hydrogen compression. Hydrogen rapid compression leads to the temperature increase inside the tank which, in case of an exaggerated increase, can compromise the complete refuelling station [9]. As previously mentioned, to prevent this event, the maximum temperature limit inside the tank was set at 85 ºC. In addition to safety considerations, this limitation is imposed because the density of the gas changes with the temperature, and, consequently, the existing mass inside the tank decreases with the temperature, affecting the State of Charge (SOC). A SOC close to 100% means that the refuelling allowed filling the tank with the highest mass capacity of hydrogen possible, maximizing the vehicle's autonomy. The technological solution to control this problem is cooling of hydrogen, incorporating a chiller in the refuelling system [10].

As the chiller represents an additional investment cost, the hydrogen refuelling mass flow rates must first be set, which should be lower than 60 grams of hydrogen per second for H70 and 120 grams of hydrogen per second for H35 (SAE J2601).

Regarding safety, ISO 19880 [29] defines some conditions that must be fulfilled so the refuelling station could operate. The refuelling stations must be designed to minimize gas leaks during station operation. Closing valves should be incorporated to minimize the risks in the event of a hydrogen leak. Regarding storage, containers must be equipped with valves activated by pressure or temperature. All materials must be compatible with hydrogen at the operating temperatures and pressures. Materials should be selected according to ISO 15916, ISO 11114 and ISO 16573.

3. Refuelling station modelling

The aim of this study is to define a mathematical model for the design of a hydrogen refuelling station for light and heavy vehicles. Thus, a case study was defined to model a real problem regarding the refuelling requirements for H35 and H70 and considering tangible operational parameters explained in this section.

3.1. Description of refuelling station

The refuelling station under modelling (Figure 3) must be able to supply 300 kg of hydrogen per day. The system needs to include the production equipment, an electrolyser, which feeds a low-pressure storage buffer tank at 35 bar. The compressors aim to raise the pressure to a maximum of 500 bar and store the hydrogen in high-pressure containers arranged in a cascade system, in order to minimize their energy consumption. The hydrogen is stored in skids with several containers connected to a certain pressure. Note that a pressure cascade storage system is considered in order to prevent multiple fatigue cycles that the skid containers are subjected from successive hydrogen filling processes. For cascade storage system, when the fuelling is initiated, the hydrogen pressure in the vehicle tank is compared with the tank pressure value, level by level till the final pressure and mass are reached. When the refuelling process is complete, the storage is refilled, starting by the lowest pressure level [12,19].

The mass of hydrogen is supplied through a dispenser from the high-pressure storage system, depending on the pressure level. A very important requirement that defines a large part of the problem is related to the need in guaranteeing a pressure differential of 50 bar between the vehicle tank and the stored hydrogen so the refuelling process can be validated.

In the case of refuelling heavy vehicles (buses), hydrogen is supplied directly from storage unit at 500 bar to the dispenser. In case of refuelling light vehicles, hydrogen stored at 500 bar is compressed to a second storing level, till reaching a pressure of 900 bar. Thus, to proper sizing the refuelling station, it is necessary to stablish the number of vehicles to fill, calculate the required mass of hydrogen, define the number of pressure levels and minimum hydrogen volumes to store at each pressure level. For this study it was assumed that the refuelling station should be able to:

1. Supply 10 heavy vehicles at 350 bar (H35), considering 2 skid pressure levels. This solution allows refuelling hydrogen at a maximum of 120 g/s, in order to comply with the maximum required refuelling time of 15 minutes. It is assumed that a mass of 30 kg is supplied by the dispenser. It is also assumed that the vehicle arrives at the station with the minimum hydrogen mass of 6 kg at 50 bar.
2. Supply 30 light vehicles at 700 bar (H70), considering 3 skid pressure levels. During the refuelling process is theoretically expected to dispense 4.2 kg.

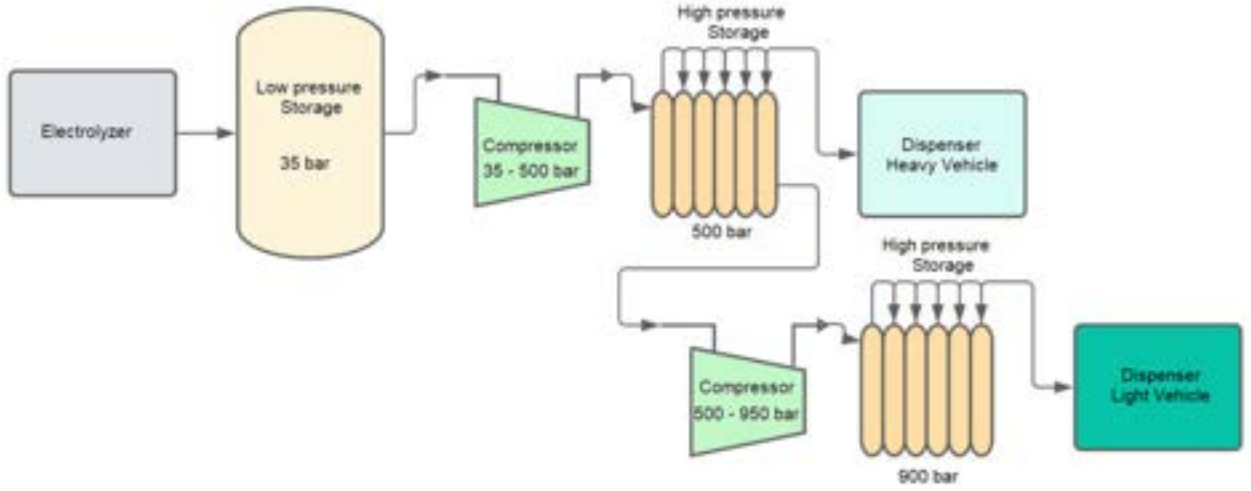

Figure. 3. Schematic representation of the hydrogen refuelling station considering the compression levels and the low and high-pressure storage.

3.2. Mathematical modelling

The model formulation includes the definition of the objective function, decision variables and physical constraints, for which an optimization algorithm is applied in order to disclose the best solution domain. Thus, at each complete simulation, the implemented model runs, iteratively, all the routines of the physical model [30].

3.2.1. Objective function

The mathematical model for storage sizing and refuelling is based on several physical variables, such as the storage volume (v), the pressure at which the hydrogen is stored (p) and the mass of hydrogen filled (m).

The objective function of the mathematical model is to minimize the total volume of high-pressure storage, whereas, the volume can be calculated through the hydrogen density. Thus, the objective function is defined by equation (1).

$$\begin{aligned} &min \quad v \\ &where \quad v = \frac{m}{Fp^2 + Gp + H} \end{aligned} \tag{1}$$

In equation (1), terms F, G and H correspond to the coefficients from the function of the density variation of hydrogen. The determination of these coefficients is based on the numerical approximation through *Polyfit* routine at Matlab®, considering reference discrete values that relates the density of hydrogen with the pressure for an operating temperature of 25ºC. The 2nd degree polynomial is presented in equation (2).

$$\frac{m}{v} = -2.55\times10^{-2}\,p^2 + 7.39\times10^{-2}\,p + 3.64\times10^{-1} \quad [\mathrm{kg/\,m^3}] \tag{2}$$

3.2.2. Decision variables and constraints

Defining the decision variables is in fact one of the hardest and/or most crucial steps in formulating an optimization problem. Three types of physical quantities were defined as explicit decision variables for the numerical model. For all of them upper and lower bounds were set in order to establish the operational relationships. The bounds in the variables guarantee that the optimum solution is within the technical operating capability. One of the main decision variables is the pressure at which the hydrogen is stored in the high-pressure system. The lower and upper pressure limits for each skid level are based on values that take into account the components to be used in the station and its operating requirements. Table 1 presents the pressures limits for both light and heavy refuelling models. For both H35 and H70 refuelling, it is defined a minimum pressure of 100 bar on skid 1. The lower pressure limit at each skid corresponds to the maximum value obtained by the optimization model at the previous skid pressure level. Thus, the hydrogen pressure at skid 1 ($p_{H35,1}$ and $p_{H70,1}$) varies between 100 and 375 bar.

The pressure in the skid 2 ($p_{H35,2}$ and $p_{H70,2}$) cannot exceed a maximum pressure of 500 bar. For H70 refuelling, a third skid level was considered ($p_{H70,3}$), establishing an upper limit of 900 bar.

Table 1. Lower and upper limits for skid pressure

Type of vehicle	Skid level	Variables and respective limits [bar]	
Heavy vehicles (H35)	Skid 1	$100 \leq p_{H35,1} < 375$	(3)
	Skid 2	$p_{H35,max,1} \leq p_{H35,2} \leq 500$	(4)
Light vehicles (H70)	Skid 1	$100 \leq p_{H70,1} < 375$	(5)
	Skid 2	$p_{H70,max,1} \leq p_{H70,2} < 500$	(6)
	Skid 3	$p_{H70,max,2} \leq p_{H70,3} \leq 900$	(7)

The second decision variable is the volume of hydrogen stored at each skid level, $v_{H35,1}, v_{H35,2}$ for H35 refuelling and $v_{H70,1}, v_{H70,2}, v_{H70,3}$ in the case of H70 refuelling. Due to operational considerations, it was set that the volume stored at high-ranked skids with pressure levels (see equation (8) and equation (9)).

$$v_{H35,1} \leq v_{H35,2} \quad [\mathrm{m}^3] \tag{8}$$

$$v_{H70,1} \leq v_{H70,2} \leq v_{H70,3} \quad [\mathrm{m}^3] \tag{9}$$

The third decision variable is the mass of hydrogen transferred from the skid to the vehicle during the refuelling ($m_{H_2 out,x}$). At each filling, there is a quantity of mass provided by the skid, depending on the final mass that is required to complete each refuelling. Yet, the mass that is supplied in the first H35 filling by the first pressure level must be lower or equal to 30 kg (equation (10)).

$$m_{H_2 out,1} \leq 30 \quad [\mathrm{kg}] \tag{10}$$

For all refuelling processes, the pressure drop of 50 bar between the station skid and the vehicle tank must be guaranteed (equation (11)).

$$p_{skid} - p_{\text{vehicle tank}} \geq 50 \quad [\mathrm{bar}] \tag{11}$$

3.2.3. Optimization method

In order to implement the optimization problem, the *MS Excel® Solver* was used, considering the Generalized Reduced Gradient (GRG) method. This popular optimization method is able to solve nonlinear optimization problems, only requiring that the objective function is differentiable. This method allows to solve the nonlinear problem dealing with active inequalities. The variables are separated into a set of basic (dependent) variables and non-basic (independent) variables. Then, the reduced gradient is computed in order to find the minimum in the search direction. This process is repeated until the convergence is obtained.
The used solver includes a multi start method that can improve the prospects of finding a globally optimal solution for an optimization problem [31,32].

4. Results and discussion

After defining the decision variables, their maximum and minimum limits, as well as the problem constraints, the mathematical model was programmed and the results obtained are presented in this section. The simulation results are depicted for heavy and light vehicles. The optimal values of pressure at each storage skid, the skid storage volumes and the hydrogen mass that is provided at each fuelling are presented considering the minimum storage capacity required.

4.1. Refuelling of heavy vehicles

The value of the objective function - minimize the total storage volume – corresponded to a storage volume of 36.90 m^3, being obtained a volume of 10.58 m^3 in the first skid and 26.32 m^3 in the second skid. The total stored volume can be considered high, since it represents a large volume to physically store, assuming normal conditions of pressure and temperature.

According to the results (Table 2), the pressures in the high-pressure storage system fulfil the functional requirements defined by equations (3) and (4). The pressure in the first skid does not exceed 375 bar and in the second level does not exceed 500 bar.

Table 2. Optimal solution for heavy vehicles refuelling (H35)

Parameter	Variable	Value
Volume [m^3]	Total volume, v	36.90
	Skid 1, $v_{H35,1}$	10.58
	Skid 2, $v_{H35,2}$	26.32
Pressure [bar]	Skid 1, $p_{H35,1}$	128.6
	Skid 2, $p_{H35,2}$	395.6

Figure 4 presents the mass of hydrogen dispensed at each skid ($m_{H_2\,out,x}$). As the number of fillings increase, the mass of hydrogen to be dispensed from the skid 1 decreases. This decrease is compensated by the raising mass provided skid 2. By the end of the 6th refuelling, it is observed that the mass provided by both skids is similar. This outcome is related to the fact that the initial pressure at which the hydrogen is stored in the skid 1 is very close to the supply pressure, which means that the useful mass in that first level is smaller than the useful mass available in the second. Also, it is shown that the first refuelling provides a mass lower than the required 30 kg.

Figure 5 shows the pressure drop between the heavy vehicle tank and the storage containers. It appears that the pressure decreases as fillings are accomplished, since the decrease in the usable available mass of hydrogen results in a decrease of the pressure in storage.

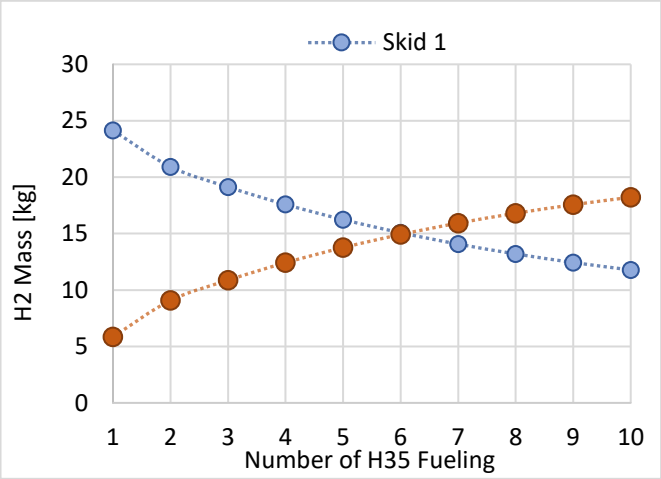

Figure. 4. Mass of hydrogen dispensed at each skid level for H35 refuelling.

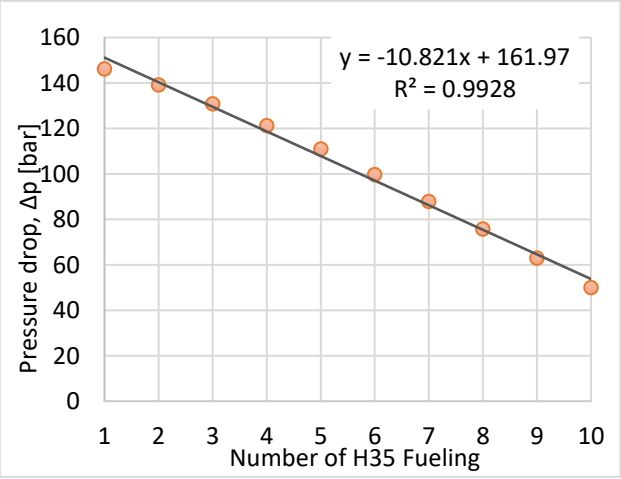

Figure. 5. Evolution of pressure drop between the station skid and the vehicle tank for H35 refuelling.

4.2. Refuelling of light vehicles

Regarding the light vehicles, the results for the total storage volume and the respective skid values are presented in Table 3. The total volume corresponded to 22.89 m^3, being obtained an equal volume of 7.63 m^3 for all 3 skids. Taking into account the number of vehicles to be fuelled and the pressure required by the system, these values are acceptable and allow all vehicles to be filled with the expected 4.70 kg of hydrogen. Thus, in order to respect all problem constraints, it is necessary a 5 hours period to fuel the 30 light vehicles.

The pressure in skid 1 and skid 2 corresponds to the lower limit established as the boundary condition, a value of 100 bar and 375 bar, respectively. In the skid 3, the pressure reaches the value of 750 bar. The value of the maximum pressure of the storage system is, in theory, the most limiting input parameter, but also the most important one in the sizing of the filling station. It is estimated that changing this input will cause sudden changes in the total volume required for hydrogen storage. Consequently, larger volumes of storage required imply a greater initial investment in the construction of the station.

Table 3. Optimal solution for light vehicles refuelling (H70)

Parameter	Variable	Value
Volume [m^3]	Total volume, v	22. 9
	Skid 1, $v_{H70,1}$	7.63
	Skid 2, $v_{H70,2}$	7.63
	Skid 3, $v_{H70,3}$	7.63
Pressure [bar]	Skid 1, $p_{H70,1}$	100
	Skid 2, $p_{H70,2}$	375
	Skid 3, $p_{H70,3}$	750

Figure 6 presents the mass of hydrogen dispensed at each skid ($m_{H_2\,out,x}$) considering the refuelling time. Equally to the results obtained for heavy vehicles, as the number of fillings increase, the mass of hydrogen to be dispensed from the skid 1 decreases. This decrease is compensated by the raising mass provided by both skid 2 and skid 3. In the skid 3, where the hydrogen storage pressure is higher than the final pressure in the vehicle tank ($p_{\text{vehicle tank}} = 671.4\ \text{bar}$), the results show that in the last hour of refuelling, almost 50% of the total mass of the vehicle's tank comes from the skid 3, taking into account that the two skids lose their ability to respond as fillings occur. Figure 7 shows the pressure drop between the light vehicle tank and the storage containers. As the refuelling is completed, the pressure differential decreases.

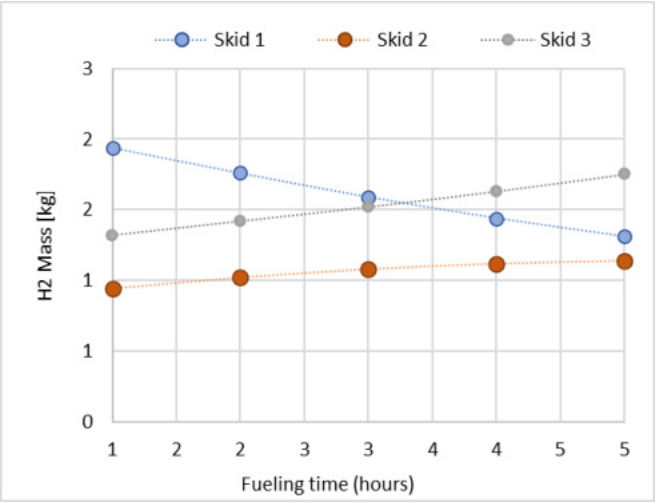

Figure. 6. Mass of hydrogen dispensed at each skid level for H70 refuelling.

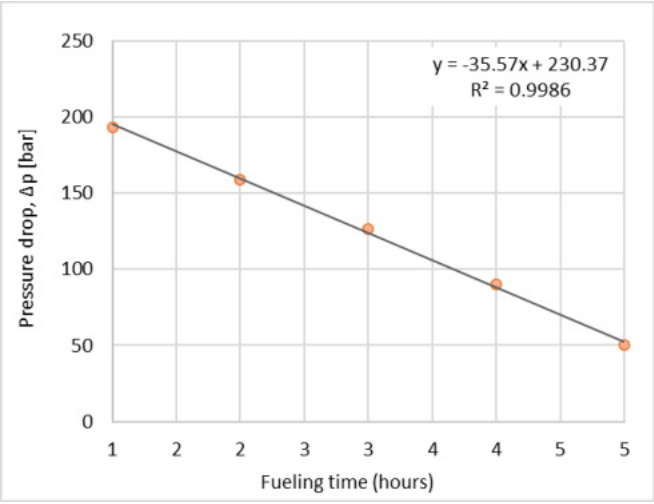

Figure. 7. Evolution of pressure drop between the station skid and the vehicle tank for H70 refuelling.

4.3. CAPEX determination

The costs of a hydrogen refuelling station depend on the characteristics of the equipment and components. Considering the components that the hydrogen refuelling station, the total investment cost can be determined by market sourcing of components with the characteristics closest to those obtained from the optimal solution. When determining the total capital costs, in addition to all the components already identified, it is necessary to calculate all accessories and labour costs.

The CAPital EXpenditure – CAPEX – is the total amount invested in the project [33]. Considering the data collected from the market, it was possible to estimate the relative weight of each component of the hydrogen refuelling station. Based in Figure 8, the highest percentages are represented by the cost of production equipment (30%), high-pressure storage unit (20%) and the hydrogen compression system (18%).

When sizing a hydrogen refuelling station, the electrolyzer and the compressors are components with more standardized working characteristics and their capital costs do not vary significantly with the increase in installed capacity. However, high-pressure storage unit cost depends on the capacity required for a given filling frequency, which in turn depends on the total volume and daily hydrogen requirements. The analysis also shows that the hydrogen dispenser only represents 7% of the total capital costs.

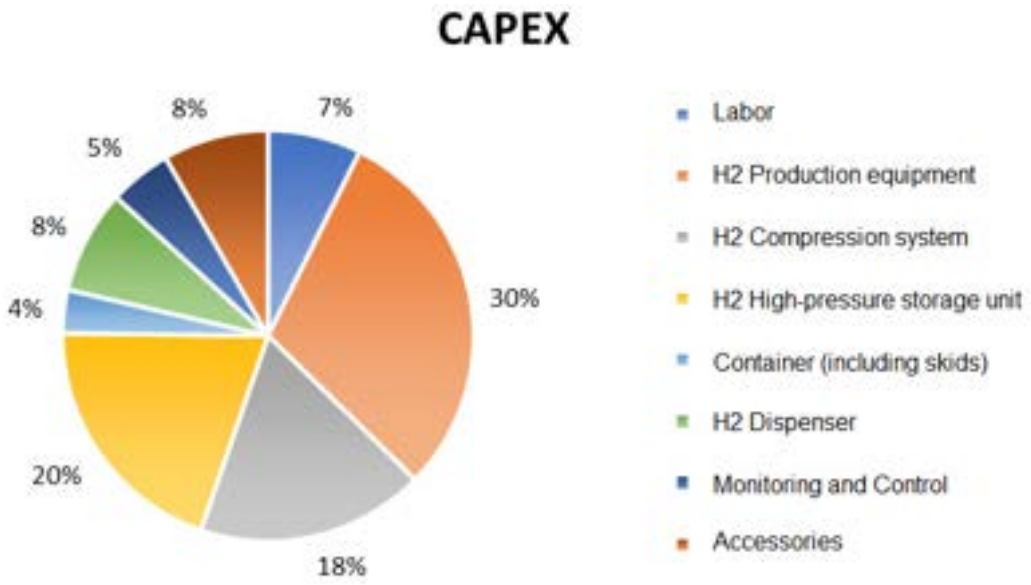

Figure. 8. CAPEX for the hydrogen refuelling station considering the commercial options for the optimal solution disclosed by the numerical model.

5. Conclusions

This paper aims to define a numerical optimization model for a hydrogen refuelling station to supply both light and heavy vehicles. The objective function is to minimize the total storage volume, taking into account the number of vehicles to be refuelled. The process of vehicle refuelling with compressed hydrogen was subjected to control requirements to ensure that the vehicle tank is within a specified operating condition defined by an upper limit on pressure, and an upper and lower limit on temperature. The

The refuelling station was defined considering the electrolyzer, a low-pressure storage buffer, the compressors aim to raise the pressure and the hydrogen high-pressure containers arranged in a cascade system in order to minimize their energy consumption. The hydrogen is stored in skids with several containers connected to a certain pressure. The station should be able to supply light and heavy (buses) vehicles. Thus, theoretically, the on-site infrastructure, 10 heavy vehicles at 350 bar and 30 light vehicles at 700 bar should be supplied. For H35 fuelling, 2 skid pressure levels were considered, allowing two fillings per hour. In this case, it is assumed that a mass of 30 kg is supplied by the dispenser. The compression cascade for light vehicles considers 3 skid pressure levels and is expected to dispense 4.2 kg. The objective function is to minimize the total storage volume required. As decision variables, the pressure at each storage skid is considered, as well as the hydrogen mass dispensed to the vehicle tank. One of the most important constraints is the pressure differential of 50 bar between the high-pressure skid and the vehicle tank that should be guaranteed at all vehicle fillings, so the refuelling can be validated. The requirements regarding the refuelling process in order to prevent over-heating and over-filling significantly influence hydrogen refuelling station design and have a strong impact on its performance.

Thus, the hydrogen filling of light and heavy vehicles has been studied and standardized by SAE through the implementation of fuelling protocols. According to the SAE J2601 protocol, the mass flow rate of hydrogen to be supplied cannot exceed 60 g/s. Also, the hydrogen temperature limits vary between - 40 ºC and 85 ºC.

Also, fast refuelling of hydrogen is constrained by the thermodynamic properties of hydrogen under compression. The optimization results show that is possible to refuel 10 heavy vehicles considering a total storage volume of 36.9 m^3, whereas, for light vehicles, it is possible to refuel 30 vehicles with a total volume of 22.9 m^3. Based on CAPEX, the most representative capital costs are: the production equipment (30%), high-pressure storage unit (20%) and the hydrogen compression system (18%).
In conclusion, the skid pressure, the useful mass of hydrogen and the storage volume are the most important parameters in the design of hydrogen refuelling station. Their variation can cause drastic changes in the capital investment cost to construct the station. As future work, it is proposed the development of a techno-economic model, considering the integration of costs in the process of optimizing the design of the on-site hydrogen refuelling station.

Acknowledgments

This work was supported by FCT - Portuguese foundation for science and technology through the R&D Units Project Scope UIDP/04077/2020 (METRICS) and R&D Unit Project Scope UIDB/00319/2020 (ALGORITMI).

References

[1] S.M. Riedl, Development of a Hydrogen Refueling Station Design Tool, Int. J. Hydrogen Energy. 45 (2020) 1–9. https://doi.org/10.1016/j.ijhydene.2019.09.234.

[2] A. Perna, M. Minutillo, S. Di Micco, E. Jannelli, Design and Costs Analysis of Hydrogen Refuelling Stations Based on Different Hydrogen Sources and Plant Configurations, Energies. 15 (2022) 541. https://doi.org/10.3390/en15020541.

[3] F. Dawood, M. Anda, G.M. Shafiullah, Hydrogen production for energy: An overview, Int. J. Hydrogen Energy. 45 (2020) 3847–3869. https://doi.org/10.1016/j.ijhydene.2019.12.059.

[4] T. Sinigaglia, F. Lewiski, M. Eduardo, S. Martins, J. Cezar, M. Siluk, Production, storage, fuel stations of hydrogen and its utilization in automotive applications: a review, Int. J. Hydrogen Energy. 42 (2017) 24597–24611. https://doi.org/10.1016/j.ijhydene.2017.08.063.

[5] G. He, D.S. Mallapragada, A. Bose, C.F. Heuberger, E. Gencer, Hydrogen Supply Chain Planning With Flexible Transmission and Storage Scheduling, IEEE Trans. Sustain. Energy. 12 (2021) 1730–1740. https://doi.org/10.1109/TSTE.2021.3064015.

[6] A.M. Abdalla, S. Hossain, O.B. Nisfindy, A.T. Azad, M. Dawood, A.K. Azad, Hydrogen production, storage, transportation and key challenges with applications: A review, Energy Convers. Manag. 165 (2018) 602–627. https://doi.org/10.1016/j.enconman.2018.03.088.

[7] D. Apostolou, G. Xydis, A literature review on hydrogen refuelling stations and infrastructure. Current status and future prospects, Renew. Sustain. Energy Rev. 113 (2019) 109292. https://doi.org/10.1016/j.rser.2019.109292.

[8] M.E. Demir, I. Dincer, Cost assessment and evaluation of various hydrogen delivery scenarios, Int. J. Hydrogen Energy. 43 (2018) 10420–10430. https://doi.org/10.1016/j.ijhydene.2017.08.002.

[9] R. Tarkowski, Underground hydrogen storage: Characteristics and prospects, Renew. Sustain. Energy Rev. 105 (2019) 86–94. https://doi.org/10.1016/j.rser.2019.01.051.

[10] C.-G. Chochlidakis, E.D. Rothuizen, Overall efficiency comparison between the fueling methods of SAEJ2601 using dynamic simulations, Int. J. Hydrogen Energy. 45 (2020) 11842–11854. https://doi.org/10.1016/j.ijhydene.2020.02.068.

[11] J.A. Riera, R.M. Lima, O.M. Knio, A review of hydrogen production and supply chain modeling and optimization, Int. J. Hydrogen Energy. (2023). https://doi.org/10.1016/j.ijhydene.2022.12.242.

[12] J. Andersson, S. Grönkvist, Large-scale storage of hydrogen, Int. J. Hydrogen Energy. 44 (2019) 11901–11919. https://doi.org/10.1016/j.ijhydene.2019.03.063.

[13] N. Miguel, B. Acosta, D. Baraldi, R. Melideo, R. Ortiz Cebolla, P. Moretto, The role of initial tank temperature on refuelling of on-board hydrogen tanks, Int. J. Hydrogen Energy. 41 (2016) 8606–8615. https://doi.org/10.1016/j.ijhydene.2016.03.158.

[14] M. Muratori, B. Bush, C. Hunter, M. Melaina, Modeling Hydrogen Refueling Infrastructure to Support Passenger Vehicles, Energies. 11 (2018) 1171. https://doi.org/10.3390/en11051171.

[15] N. de Miguel, B. Acosta, D. Baraldi, R. Melideo, R. Ortiz Cebolla, P. Moretto, The role of initial tank temperature on refuelling of on-board hydrogen tanks, Int. J. Hydrogen Energy. 41 (2016) 8606–8615. https://doi.org/10.1016/j.ijhydene.2016.03.158.

[16] L. Zhao, Y. Liu, J. Yang, Y. Zhao, J. Zheng, H. Bie, X. Liu, Numerical simulation of temperature rise within hydrogen vehicle cylinder during refueling, Int. J. Hydrogen Energy. 35 (2010) 8092–8100. https://doi.org/10.1016/j.ijhydene.2010.01.027.

[17] L. Wang, C. Zheng, R. Li, B. Chen, Z. Wei, Numerical analysis of temperature rise within 70 MPa composite hydrogen vehicle cylinder during fast refueling, J. Cent. South Univ. 21 (2014) 2772–2778. https://doi.org/10.1007/s11771-014-2240-9.

[18] S. Maus, J. Hapke, C.N. Ranong, E. Wüchner, G. Friedlmeier, D. Wenger, Filling procedure for vehicles with compressed hydrogen tanks, Int. J. Hydrogen Energy. 33 (2008) 4612–4621. https://doi.org/10.1016/j.ijhydene.2008.06.052.

[19] T. Bourgeois, T. Brachmann, F. Barth, F. Ammouri, D. Baraldi, D. Melideo, B. Acosta-Iborra, D. Zaepffel, D. Saury, D. Lemonnier, Optimization of hydrogen vehicle refuelling requirements, Int. J. Hydrogen Energy. 42 (2017) 13789–13809. https://doi.org/10.1016/j.ijhydene.2017.01.165.

[20] R.-H. Lin, Z.-Z. Ye, B.-D. Wu, A review of hydrogen station location models, Int. J. Hydrogen Energy. 45 (2020) 20176–20183. https://doi.org/10.1016/j.ijhydene.2019.12.035.

[21] N. Schmitz, L. Sankowski, F. Kaiser, C. Schwotzer, T. Echterhof, H. Pfeifer, Towards CO2-neutral process heat generation for continuous reheating furnaces in steel hot rolling mills – A case study, Energy. 224 (2021) 120155. https://doi.org/10.1016/j.energy.2021.120155.

[22] K. Reddi, A. Elgowainy, N. Rustagi, E. Gupta, Impact of hydrogen SAE J2601 fueling methods on fueling time of light-duty fuel cell electric vehicles, Int. J. Hydrogen Energy. 42 (2017) 16675–16685. https://doi.org/10.1016/j.ijhydene.2017.04.233.

[23] J. Cheng, J. Xiao, P. Bénard, R. Chahine, Estimation of Final Hydrogen Temperatures During Refueling 35 MPa and 70 MPa Tanks, Energy Procedia. 105 (2017) 1363–1369. https://doi.org/10.1016/j.egypro.2017.03.505.

[24] Society of Automotive Engineers (SAE), Fueling protocols for light duty gaseous hydrogen surface vehicles - standard J2601, (2014).

[25] J. Xiao, P. Bénard, R. Chahine, Estimation of final hydrogen temperature from refueling parameters, Int. J. Hydrogen Energy. 42 (2017) 7521–7528. https://doi.org/10.1016/j.ijhydene.2016.05.213.

[26] T. Bourgeois, F. Ammouri, M. Weber, C. Knapik, Evaluating the temperature inside a tank during a filling with highly-pressurized gas, Int. J. Hydrogen Energy. 40 (2015) 11748–11755. https://doi.org/10.1016/j.ijhydene.2015.01.096.

[27] R. Harty, S. Mathison, N. Gupta, Improving hydrogen tank refueling performance through the use of an advanced fueling algorithm-the MC method, in: Proc. Natl. Hydrog. Assoc. Conf., 2010.

[28] S. Mathison, R. Harty, J. Cohen, N. Gupta, H. Soto, Application of MC Method-Based H2 Fueling, in: SAE 2012 World Congr. Exhib., SAE Technical Papers, 2012: pp. 1–12. https://doi.org/10.4271/2012-01-1223.

[29] ISO International Standard Organization, ISO 19880-1 - Gaseous Hydrogen - Fuelling Stations, (2020).

[30] A.C. Ferreira, M.L. Nunes, J.C.F. Teixeira, L.A.S.B. Martins, S.F.C.F. Teixeira, S.A. Nebra, Design of a solar dish Stirling cogeneration system: Application of a multi-objective optimization approach, Appl. Therm. Eng. 123 (2017) 646–657. https://doi.org/10.1016/j.applthermaleng.2017.05.127.

[31] R.M. Lewis, A. Shepherd, V. Torczon, Implementing Generating Set Search Methods for Linearly Constrained Minimization, SIAM J. Sci. Comput. 29 (2007) 2507–2530. https://doi.org/10.1137/050635432.

[32] A.C.M. Ferreira, A.M.A.C. Rocha, S.F.C.F. Teixeira, M.L. Nunes, L.B. Martins, On Solving the Profit Maximization of Small Cogeneration Systems, in: B.M. et al. (Eds.) (Ed.), ICCSA 2012 - 12th Int. Conf. Comput. Sci. Its Appl. - Lect. Notes Comput. Sci. J., Springer-Verlag Berlin Heidelberg 2012, 2012: pp. 147–158. https://doi.org/10.1007/978-3-642-31137-6_11.

[33] A.H. Reksten, M.S. Thomassen, S. Møller-Holst, K. Sundseth, Projecting the future cost of PEM and alkaline water electrolysers; a CAPEX model including electrolyser plant size and technology development, Int. J. Hydrogen Energy. 47 (2022) 38106–38113. https://doi.org/10.1016/j.ijhydene.2022.08.306.

Effects of the use of 100% Biodiesel (B100) obtained from used vegetable oils on the consumption, emissions, and performance of vehicles and equipment.

Diogo Silva[a,b], Nuno Clara[a,b], João Fonseca Pereira[a,b], Paulo Carvalho[a,b], and Luis Serrano[a,b]

[a] Polytechnic of Leiria, Leiria, Portugal, luis.serrano@ipleiria.pt
[b] ADAI – University of Coimbra, Coimbra, Portugal

Abstract:

The transportation sector is one that has had more hurdle conversion to renewable energy sources. The purpose of this research is to determine whether a renewable source of energy like 100% biodiesel (B100) could be used in the vehicles and equipment of a fleet that supports an air force squadron instead of conventional diesel fuel. To accomplish this, a selection of vehicles and machinery was examined for three months while the working procedure remained as usual, and then introduce a change in the fuel type, using biodiesel considering the same monitoring process during a similar period. This made it possible to compare any modifications that might have been made to fuel consumption, performance, emissions, maintenance, and reliability. The findings demonstrated that, with an average increase of less than 5%, using biodiesel does not result in a noticeable rise in fuel consumption. Additionally, there is a slight decline in the power that is available from the engine, however at less severe levels than anticipated. Depending on the engine, and the operation mode, there are a variety of emission-related scenarios, but overall, NOx and CO_2 emissions were reduced. Additionally, it was confirmed that there were no important concerns with the operation of the machinery or vehicles; the only issue of notice was the requirement to anticipate the replacement of a few fuel filters.

Keywords:

Biodiesel; Internal Combustion Engines; Vehicles; Energy; Sustainability.

1. Introduction

Biofuels, such as biodiesel, contribute very little to the accumulation of greenhouse gas emissions. Biodiesel is a versatile fuel that may be combined with diesel in 7% (B7) mixes, like the mixture provided in 2022 in all fuel stations in Portugal, and potentially in 20% or even 100% blends, known as B20 and B100 respectively.

The conversion of biomass feedstocks into biofuels is a low-impact process. The usage of biofuels as transportation fuels can help to reduce atmospheric CO_2 by using this renewable fuel instead of diesel in different ways: it prevents the some of the emissions associated with diesel engines, it allows the CO_2 content of fossil fuels to remain stored and give a mechanism for absorbing CO_2 through the growth of fresh biomass for fuels.

Biofuels are the most advantageous solution for decreasing greenhouse gases from the transportation sector since they are compatible with the natural carbon cycle and can be used in vehicles actual technology. Increased use of biomass would hasten the deposition of fossil fuels and reduce greenhouse gas emissions in transport sector.

1.1. Research question

The use of biodiesel in actual vehicles is a possibility and some authors present that has a real path to reduce greenhouse gas emissions and the fossil fuel transport sector dependence.

The real-world exhaust emissions and fuel consumption of on-road diesel vehicles was an issue that deserves a particular attention. Two light-duty diesel trucks and two heavy-duty diesel trucks were fuelled by waste cooking oil biodiesel blends, considering four mixed fuels with blend ratios of 0% (neat diesel), 5% (B5), 20% (B20), and 100% (B100) (biodiesel in traditional fossil diesel). The results show that the total fuel consumption (biodiesel + traditional fossil diesel) did not clearly decrease, but blending biodiesel into traditional fossil diesel

could clearly decreased the consumption of traditional fossil diesel, reduce the countries' dependence on oil imports. The CO, HC, and PM emissions for all of the tested vehicles decreased with increasing biodiesel content in the blend, and the NO_X emissions also showed a decrease with increasing biodiesel content in the blend, not for all, but for most vehicles in this study [1].

Other research [2] examined several biofuels blends on a 2019 performance diesel EURO VI heavy-duty truck, with the objective of preparing a fuel consumption measurement and a performance analysis, an experimental procedure was developed based on the homologation cycles and processes of heavy-duty truck on a chassis bench roll, testing the following samples: B7, B15, B100 and a HVO15.

The powertrain performance results reveal that the fuel which presented higher power values was the HVO15, followed by B7, B15 and B100. With B100, the maximum power output decreases 4,5%, compared to B7. On fuel consumption, the smaller results were obtained for B7 and B15, without reasonable differences, followed by B100 and then HVO15. With B100, the fuel consumption increases 9%, compared to B7. To evaluate the fuel economy performance of neat biodiesel compared to fossil diesel on a real road use, three buses on their daily utilization were analysed. In this experiment, the biodiesel buses had an increase on fuel consumption about 4,5%.

1.2. Objective of the work

The use of biodiesel has been analyzed in different laboratory studies, with different levels of incorporation of biodiesel in commercial diesel, either using engine test bench or using chassis dynamometers. There are also some works that consider the use of biodiesel blends in vehicles in road use, analysing the effects that blending small amounts such as 15, 20, or 30% biodiesel have on the use of these vehicles.

This study attempted to employ a more severe change, such as switching from commercial diesel to a wholly renewable fuel, i.e., 100% biodiesel, in a wide range of vehicles and equipment in real-world use, over an extended length of time. This allows to understand what changes occur as a result of this fuel change in conditions as close to reality as possible, allowing to effectively evaluate the environmental impacts, energy, and performance of using this fuel in vehicles, as well as analyse the potential effects on the reliability and maintenance of these vehicles.

2. Experimental Methodology

As mentioned earlier, the study was divided into three types of tests: fuel consumption, emissions, and bench testing. Therefore, this chapter will be subdivided into each of the tests performed. However, firstly, we will discuss some important properties of diesel fuel for this study.

2.1. Fuel Properties

The fuels considered in this study are quite similar, however they have significant differences that could explain some discrepancies in engine and fuel injection system behaviour. A quick description of the engine's most influential characteristics is presented.

Density relates the mass of the fuel to the volume it occupies. Therefore, the higher the density, the greater the mass in the same volume, and consequently, the greater the energy. Thus, since fuel is quantified by volume, higher density results in greater fuel economy. Biodiesel has a density between 873 and 883 kg/m^3, while petroleum diesel has a density between 820-845 kg/m^3. These values are for a temperature of 15°C [3,4].

Viscosity is a measure of a fluid's resistance to flow. If the viscosity is high, the injection cone decreases and concentrates on a narrower and more concentrated jet, resulting in poor atomization. Poor atomization leads to poor engine performance. Additionally, the greater resistance to fluid movement creates greater difficulty in operating the fuel pump. According to the European standard EN14214:2008, diesel viscosity at 40°C must be between 3.5 and 5 mm^2/s. The viscosity of biodiesel is approximately 4 to 5 mm^2/s under the same conditions. In very cold temperatures, the increased viscosity can compromise proper fuel circulation, resulting in starting and initial engine operation problems [3].

Calorific Value is defined as the amount of energy available per unit mass, during the combustion process in which the reactants are at 25°C and the products cool to the same 25°C. Generally, two values are defined as "higher" and "lower", HHV and LHV, depending on the physical state of water in the products, liquid or vapor, respectively. In the context of internal combustion engines, LHV is usually used. The Lower Heating Value (LHV) of diesel has a range of values that varies between 42.9 and 43.3 MJ/kg. The calorific value of diesel is about 10 to 14% higher than that of biodiesel [5].

Cetane Number Indicates the ease with which the fuel enters in self-ignition. The higher this value, the easier and faster the fuel will ignite when injected. This characteristic is critical in compression ignition engines, as it is essential that the fuel quickly self-ignite after injection. In the previously mentioned standard (EN14214:2008), a minimum value of 51 is defined for the cetane number. The cetane number of biodiesel depends on the base raw material used to form the fuel, however, a large percentage of them remain above this mentioned limit [1].

The equivalent amount of oxygen content present in the fuel is one of the most altered characteristics of the mineral and renewable fuels. In petroleum-based fuel, this content is zero, whereas in biofuel, it can have a value between 10 and 12% oxygen [6].

Oxidative stability is closely related to the Iodine value, as it reflects the tendency of a fuel to react with other substances. Therefore, oxidation stability decreases with an increase in the Iodine value. The value of this parameter varies depending on the composition and storage of the fuel. Biodiesel, due to its chemical unsaturation, becomes more susceptible to deterioration, which can have various implications such as an increase in fuel viscosity and acidity, the development of contaminations, and the formation of insoluble products, which can damage the engine or compromise its performance [7].

The Cold Filter Plugging Point (CFPP) indicates the minimum temperature at which significant crystal formation does not occur, in other words, the minimum temperature at which the fuel is liquid enough to be filterable under certain conditions. As previously mentioned, this property complements the pour point and cloud point.

To determine the CFPP value, a certain volume of fuel is subjected to a rapid and constant cooling process and, by vacuum action, forced to pass through a filter. The value is fixed at the minimum temperature that allows this filtration within a stipulated time interval. Naturally, all these parameters and equipment are standardized to develop a universal test and enable comparison between fuels. The required CFPP values vary depending on the climatic conditions of the country or region where the fuel operates.

Biodiesel shows a significantly higher tendency than diesel to form crystals at low temperatures, acquiring higher CFPP values. This can be problematic in colder climates, as previously mentioned, since the presence of crystals in the fuel causes clogging of filters, the injection system, and consequently affects the performance of the engine. The solution may be to include additives in the fuel that counteract this tendency or reduce the percentage of biodiesel in the fuel blend [7].

In summary, Table 1 presents the characteristics of the two fuels considered in this work and it reveals a comparison between biodiesel and petroleum diesel for the previously mentioned parameters, indicating the typical changes introduced by B100 relative to B7.

Table 1. Indicative comparison of fuel B100 relative to B7.

Proprieties	**B7**	**B100**	Comparison with petroleum diesel (B7)
Density (kg/m^3, at 15ºC)	843,3	881,7	↑
Viscosity (mm^2/s, at 40ºC)	3*	4,6*	↓
Calorific Value (MJ/kg)	42,62*	37,21*	↓
Cetane Number	52,5*	56,2*	↑
Oxygen content (%)	0	10-12	↑
CFPP (ºC)	-15	-1	↓

2.2. Fuel consumption test

To carry out this type of test, initially, equipment and vehicles were selected for study, with the primary objective of avoiding any situation that could compromise the normal operation of the fleet.

Analysing the series of vehicles under study, it is visible that there is a great variety of typologies, from light to heavy-vehicles, both for goods and passengers, and even tanker trucks. The great variety previously mentioned is also noticeable in the engine displacement of the engines under study, where the smallest has a total displacement of 1868 cm^3, and the largest has a total displacement of 12760 cm^3. All are diesel cycle, and operate at 4 strokes, varying between 4, 6 and 8 cylinders. These characteristics can be seen as an advantage in carrying out this study. However, the vehicles do not have the most current injection and exhaust gas treatment systems, since the newest vehicle has 18 years old, and the oldest has 42 years old. In summary, the influence of ZeroDiesel was analysed in 14 vehicles.

Analysing the series of equipment used in the study, it is evident that there is a wide range of typologies with engines ranging in displacement from 916 cm^3 to 9050 cm^3. All of them are Diesel cycle, operate in 4-stroke, varying between 3, 4, and 6 cylinders, with both in-line and V configurations, except for one equipment that operates in 2-stroke. These characteristics can be seen as an asset in conducting this study. The influence of the use of ZeroDiesel was analysed in 8 pieces of equipment.

After the selection of vehicles and equipment, there was a period of monitoring the kilometres and litters of commercial diesel fuel (B7) consumed by the vehicles and monitoring the corresponding operating hours of the equipment with the litters of diesel fuel consumed. The monitoring was scheduled to start on January 31,

2022, and end on March 21, 2022, however, this period was extended until April 28. After this period, the same monitoring occurred but with ZeroDiesel (B100). It began after the end of B7 use and extended until August 8. The counting of hours or kilometres travelled, and fuel consumed was considered for both periods allowing to have the comparative information of

2.3. Emissions testing

The main objective of this type of test is to evaluate the influence of fuel types (B7 and B100) on pollutant and CO_2 emissions. For this purpose, two representative vehicles and two ground support equipment were selected from the analysed fleet. The operating regimes were also representative of the normal operation of each vehicle and equipment, with tests performed with the engine cold (immediately after starting) and at normal operating temperature. However, no load was imposed on the engine during the vehicle tests, deviating from normal operation.

The measurement of emitted gases was carried out with the TESTO brand equipment, model 350 XL. The analyser unit includes several gas sensors, allowing for the measurement of the concentration of CO, CO_2, NO, NO_2, SO_2, H_2S, or C_XH_Y, among others. The range extension allows measurements to be made without restrictions, even when there are high gas concentrations. To protect the sensor technology, the range extension (dilution) is automatically activated when unexpectedly high gas concentrations are detected. Of all the substances that can be measured, the acquisition of data on the concentration values of O_2, CO, NO_X, CO_2, C_XH_Y, and also the lambda factor and the temperature of the exhaust gases was considered most important. The last two parameters were only used to ensure that the regimes considered with B7 and B100 were identical. The lambda value and hydrocarbon emissions could not be considered for the study because the measuring equipment had an anomaly that prevented the presentation of these parameters. Two sets of data were collected: one when the vehicles and equipment had been operating for more than a month with B7 and another when they had been operating for more than a month with B100.

2.4. Power and Consumption Test – WLTP

The main objective of these tests is to accurately evaluate the fuel consumption and performance of a vehicle using B7 and B100. Both tests are carried out on a roller dynamometer. For the power test, three tests are performed to obtain data from both the dynamometer and the vehicle via OBD. Afterwards, an arithmetic mean is calculated for the acquired torque and power values, provided there are no incongruent values. The present study aims to perform a comparative analysis of the engine performance results when using B7 and B100 fuel.

The dynamometer used in this study is the MAHA LPS 3000, a brake-type roller test bench based on the principle of eddy currents. This equipment enables testing of various situations, such as instant maximum power, power at pre-defined rotation speeds, and simulation of loads (constant traction, constant speed, etc.). Furthermore, it is possible to measure vehicles with 2 or 4-wheel drive, with a maximum permissible power per axle of 257 kW and 522 kW respectively, for a maximum speed of 260 km/h.

To evaluate the power of the vehicle, it is accelerated to maximum rotation speed, covering the range of engine rotation speeds in a controlled manner by the dynamometer (roller bench). This control is continuously performed throughout the engine's rotation range (continuous test). Alternatively, it can be performed discretely at pre-defined rotation points, which are established to allow for a more effective comparison between different tests (discrete test).

To obtain the desired results (engine power and torque), the dynamometer measures the power at the wheel, to which the power losses in the transmission (resistive power) obtained in the deceleration process are added. After obtaining these two parameters, the value of the engine power is obtained, which is already corrected based on environmental conditions, assuming the designation of "Norm power". Through this power value, dividing by the corresponding rotation, the value of the engine torque is obtained. The correction selected is according to the standard also used by the manufacturer when announcing the engine characteristics. In this study, continuous and discrete performance tests were performed.

In the case of fuel consumption evaluation, the test performed follows the standardized WLTP cycle, considering its use on a roller bench. For this test, a series of sensors are added to monitor the vehicle's fuel consumption, such as a flow meter (to obtain volume flow) and a scale, to obtain mass flow. The cycle is divided into 4 phases, one called "low" with an average speed of 18.9 km/h, a medium with an average speed of 39.8 km/h, a high with an average speed of 56 km/h, and an extra-high with an average speed of 92.9 km/h, with a total cycle duration of approximately 30 minutes. Data acquisition was performed at a frequency of 5 Hz. To ensure data synchronization, data processing was based on the definition of the initial point of the test, for which the average fuel mass present on the scale was considered over a period of 2 seconds, 5 seconds before the vehicle's movement began. Similarly, the transition point between each stage was the average of the mass measured on the scale for a period of 2 seconds, 5 seconds after the cessation of the vehicle's wheel movement.

As previously mentioned for the power test, in each WLTP cycle, 3 tests are performed, and the arithmetic mean of the results obtained in these tests is then considered. Similarly, to the previous procedure, a comparative analysis was intended to be carried out regarding the use of the two fuels in the same vehicle, so

the entire procedure was repeated considering a first test in which the vehicle was fuelled with B7 fuel, and then a second test was performed fuelling the vehicle with B100 fuel. The vehicle chosen for the study was a passenger car of the Citroën Berlingo make/model equipped with a direct injection engine with a displacement of 1900 cm^3.

3. Results and Discussion

Similarly, to the presentation of the experimental procedure, this chapter of results discussion will be divided into 3 subheadings, one for each test previously mentioned.

3.1. Fuel consumption test

To obtain the average fuel consumption values, the averaging of consumption for each refuelling was considered, assuming that all kilometres travelled (or hours of operation) were performed with the corresponding fuel of that refuelling. This assumption is not entirely valid, however, the fluctuations in the obtained averages are compensated by the multiple refuelling's existing in each equipment or vehicle, since the final average was considered as the average of each refuelling. In a careful analysis of the averages of each refuelling, if they presented values that were very discrepant from expected, they would not be considered for analysis. Therefore, the average consumption was calculated for each fuel and the percentage difference between them. The results obtained are presented in Table 2 for equipment and in Table 3 for vehicles. The same results are also presented in the following Figure 1 and Figure 2 for fuel consumption and percentage difference for equipment and vehicles, respectively.

Table 2. Indicative comparison of fuel B100 relative to B7.

Equipment	B7 Fuel consumption (l/h)	B100 Fuel consumption (l/h)	Difference
EE01	4,62	4,28	-7,25%
EE03	1,18	0,98	-16,95%

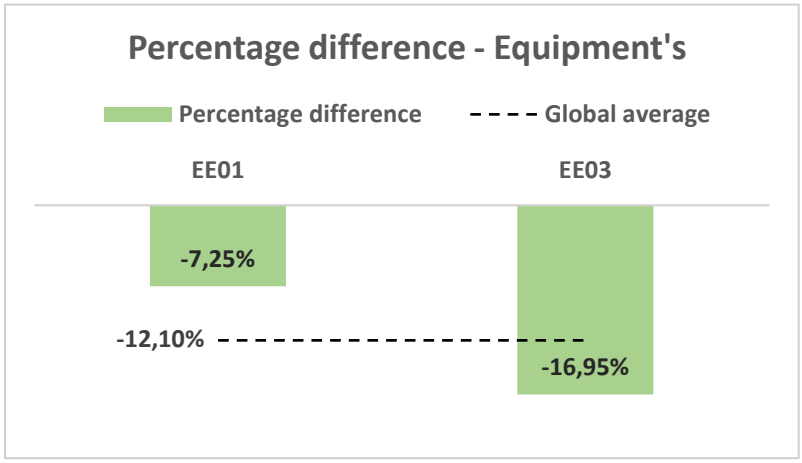

Figure. 1. Difference percentage in fuel consumption of the equipment.

Initially, it is noticeable that results for all vehicles and equipment under study are not presented. This is due to the lack of refuelling data for a particular type of fuel under study. It should be noted that for equipment EE01, there is no certainty in the results presented since only data from one refuelling for both fuels was available. Similarly, for vehicles AM05 and AMV12, the average consumption presented for fuel B7 is based on only one refuelling.

From the analysis of the results obtained, it is not possible to prove an increase or a decrease in fuel consumption when using biodiesel. For example, there is an increase in consumption of vehicle AMV03 in the order of 15% (corresponding to 1L/100km) and a decrease in consumption of vehicle AMV13 of about 13% (corresponding to 2L/100km). This difference in consumption can be justified, not due to differences in the chemical properties of the fuel but rather due to uncertainties in the obtained data, since there are several variables not controlled, such as different routes and drivers, which lead to different consumption rates, which is normal and corresponds to the operation of these vehicles even when fuelled with the same fuel. Additionally, since the consumption of vehicles is based on the distance travelled, it is not possible to determine whether they were stationary, consuming fuel without covering any distance. This aspect is particularly critical, for

example, in tanker trucks, where the pumps that transfer the fuel are operated by the vehicle's engine. Therefore, it is not possible to directly correlate an increase in fuel consumption when using B100, in the order of magnitude of the difference in calorific value between this and B7, as would be expected. Overall, in vehicles, the use of biodiesel increased consumption by 1.36%, while in equipment, there was an average decrease of 12.10%.

Table 3. Fuel consumption for each vehicle for both studied fuels and their respective percentage difference.

Vehicle	B7 Fuel consumption (l/h)	B100 Fuel consumption (l/h)	Difference
AM01	4,94	5,30	7,24%
AM02	7,37	8,04	9,10%
AM03	6,33	7,27	14,91%
AM04	8,31	7,84	-5,69%
AM05	10,89	10,64	-2,28%
AM06	10,27	10,94	6,54%
AM07	13,37	12,59	-5,78%
AM08	8,74	8,98	2,77%
AM09	75,62	80,48	6,42%
AM10	83,41	86,07	3,19%
AM11	17,65	17,64	-0,02%
AM12	10,90	10,24	-6,08%
AM13	17,41	15,20	-12,69%

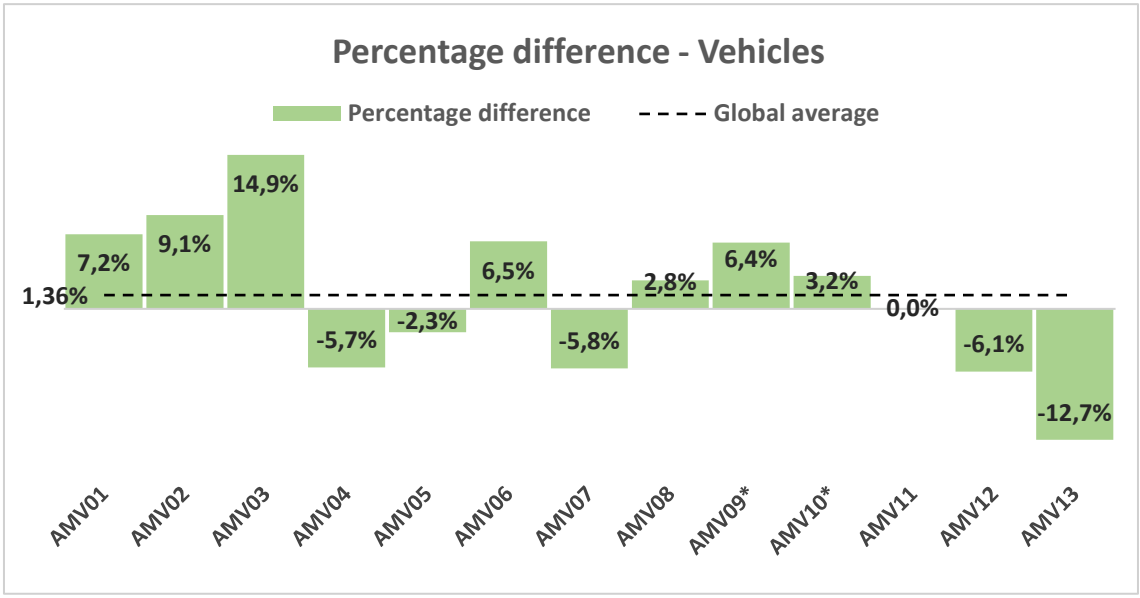

Figure. 2. Percentage difference in fuel consumption per vehicle.

3.2. Emissions testing

Analysing now the results obtained for emissions, Table 4 and Table 5 present respectively the vehicles and equipment results, with the representative operating conditions of their normal operation, the percentage differences in emissions between B100 and B7 with the overall average by chemical substance. It should be noted that, in the equipment, all tests were carried out considering their normal operating temperature.

The cases where the value presented is negative, for example, it indicates that after using B100 fuel, there was a decrease in the emission of the chemical substance being analysed, like it is clearer in the figure 3.

Table 4. Percentage difference in vehicle emissions.

Vehicle	Engine speed	O_2	CO	NO_x	CO_2
AM09	Hot Idle	0,24%	42,29%	-10,48%	-2,91%
AM09	1300 RPM (Hot)	0,79%	14,91%	-8,21%	-7,94%
AM09	1800 RPM (Hot)	0,79%	3,55%	-5,88%	-6,12%
AM11	Cold Idle	1,53%	59,81%	-63,32%	-7,28%
AM11	Hot Idle	-0,13%	201,02%	-49,03%	1,00%
AM11	2000 RPM (Hot)	-1,09%	12,70%	-28,33%	6,79%
AM11	3000 RPM (Hot)	-2,86%	1,36%	-16,16%	14,01%
Global Average		-0,06%	32,86%	-34,81%	0,37%

Table 5. Percentage difference in equipment's emissions.

Equipment	Engine speed	O_2	CO	NO_x	CO_2
EE03	Idle	-0,27%	51,68%	-4,06%	1,20%
EE03	Under Load	-1,12%	36,16%	0,67%	3,16%
EE04	Idle	-0,16%	-16,22%	7,49%	0,71%
EE04	1700 RPM	-0,88%	0,00%	12,03%	1,65%
EE04	2400 RPM	-3,77%	22,41%	1,27%	6,06%
Global Average		-1,12%	26,57%	5,78%	3,01%

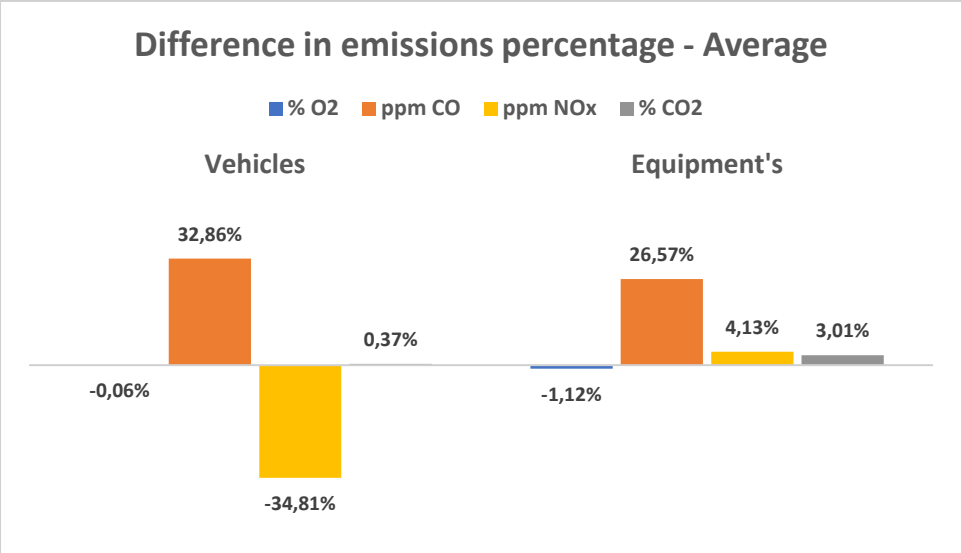

Figure. 3. Differences in global average, for both fuels, by chemical species.

3.2.1. Oxygen (O_2)

The changes obtained in oxygen (O_2) emissions were insignificant, demonstrated by the difference in the global average of -0.06% in vehicles and -1.12% in equipment, so it was considered an unchanged parameter when using biodiesel. The differences presented may be related to inaccuracies in the measurement device, meteorological differences, among others. When using B100, an increase in the emission of this compound derived from the higher percentage of O_2 present in the fuel would be expected, however, this was not observed.

3.2.2. Carbon monoxide (CO)

An increase in carbon monoxide (CO) emissions was observed in all regimes studied, except for one measurement at idle for the EE04 equipment, which is visible by analysing the difference in the global average, both for vehicles and equipment. The increase in the emission of this substance was more significant at idle with a warm engine, since it is mainly formed in rich mixing zones. Therefore, the increase in its concentration when using B100 can be explained by the higher viscosity of this fuel, which hinders atomization and subsequent combustion. This greater difficulty in atomization is more prevalent at idle due to the lower injection pressure associated with this regime. Although the values presented have a very significant percentage increase (on the order of 200%, for example), the emission of CO in diesel engines is not noticeable, as they always operate on lean mixtures, since the concentration values of this substance are quite low. Therefore, it is natural and expected that the percentage differences present more significant values.

3.2.3. Nitrogen oxides (NO_X)

Overall, there was a decrease in nitrogen oxides (NO_X) in all regimes, except for equipment EE04, where the emission of these substances increased. This is visible by analysing the difference in the global average in vehicles, which decreased by 34.81%, contrary to what happened in the equipment (which increased by 5.78%), solely provided by the aforementioned equipment. An explanation for the decrease in the emission of this substance, given that in the case of vehicles the tests were performed without load, is the lower temperature reached when the vehicle operates with biodiesel due to the lower calorific value of this fuel. Therefore, since temperature is the most important factor in NO_X emissions, a decrease in this chemical substance would be expected. In situations where the engine was tested under load, there may be greater emissions of this substance due to the greater amount of oxygen in the combustion, derived from the biodiesel itself. It should be noted that if the vehicles or equipment had gas treatment systems, the emission of this compound would be more controlled.

3.2.4. Carbon dioxide (CO_2)

It is not possible to correlate the presence of CO_2 emissions with the use of biodiesel in all equipment and vehicles. While there was a decrease in emissions for AMV09, the emission of this substance either slightly increased or stabilized in the other machines. CO_2 emissions are directly related to fuel consumption. As it was not unequivocally found that there was an increase in fuel consumption, only slight fluctuations in the emission of this compound would be expected for the various vehicles and equipment. Overall, there was a very slight increase in carbon dioxide emissions with the use of biodiesel, at 0.37% for vehicles and 3.01% for equipment.

3.3. Power and Consumption Test – WLTP

The power tests obtained are represented in the following Figure 4, where the power and torque developed as a function of rotation speed are visible for the two fuels under study.

The percentage difference between the values obtained for power is presented also in the same Figure 4. In this case, when the value presented is positive, it translates to a higher power obtained when the vehicle was operating with B100 compared to when it was operating with B7.

From the analysis of both graphs, it is visible that the differences obtained between the use of B7 and B100 are minimal. A decrease in power, in the order of magnitude of the difference in the calorific value of the fuel, i.e. 10%, could be expected, which could be attenuated by the greater volumetric mass of the fuel. However, this was not the case, and there was even an improvement in the delivered power at high speeds, after 4000 RPM. A slight decrease in the developed power occurred at low and medium speeds, which was less noticeable between 1500 and 2500 RPM. The increase in power at high rotation speeds would not be expected and may be related to some measurement problem, fundamentally in the final part of the test where the transition from measuring the power at the wheel to measuring the transmission losses occurs. The average numerical results for maximum power and torque are presented in the following Table 6. Therefore, the following percentage differences are obtained, visible in the same Table 6. If the presented value is negative, for example, it indicates that there was a decrease in this parameter after the use of B100 fuel.

Analysing the numerical results, it is visible that, contrary to expectations, an increase in the engine's delivered power occurs when using biodiesel. This may be related to some intervention that the vehicle has undergone or the alteration of any mechanical component that affects the maximum power delivered by the engine, mainly in high speed. A decrease of approximately 10%, corresponding to the difference in the calorific value of the fuels, would be expected when using biodiesel. On the other hand, the maximum torque obtained when using B100 decreased and was reached earlier.
Examining the results corresponding to the WLTP test, Table 7 presents the values of the average fuel mass flows obtained for each speed profile for each of the analysed fuels and also the results considering the percentage difference.

From the analysis of the results, it is possible to observe an increase in the average fuel mass flow for B100 in all speed profiles considered from 1% to 5%. This difference has a greater impact in the low-speed profile, decreasing with increasing speed, with a slight increase in the high-speed profile. The increase in fuel consumption can be explained by the lower calorific value present in biodiesel. However, since the result is shown on a mass basis, it makes sense to also analyse consumption on a volumetric basis, as is typically considered in vehicle usage. The average fuel consumption obtained, considering a typical volumetric mass for B7 of 839.8 kg/m^3 and for B100 of 881.7 kg/m^3, is visible in Table 8 and graphically in Figure 5.

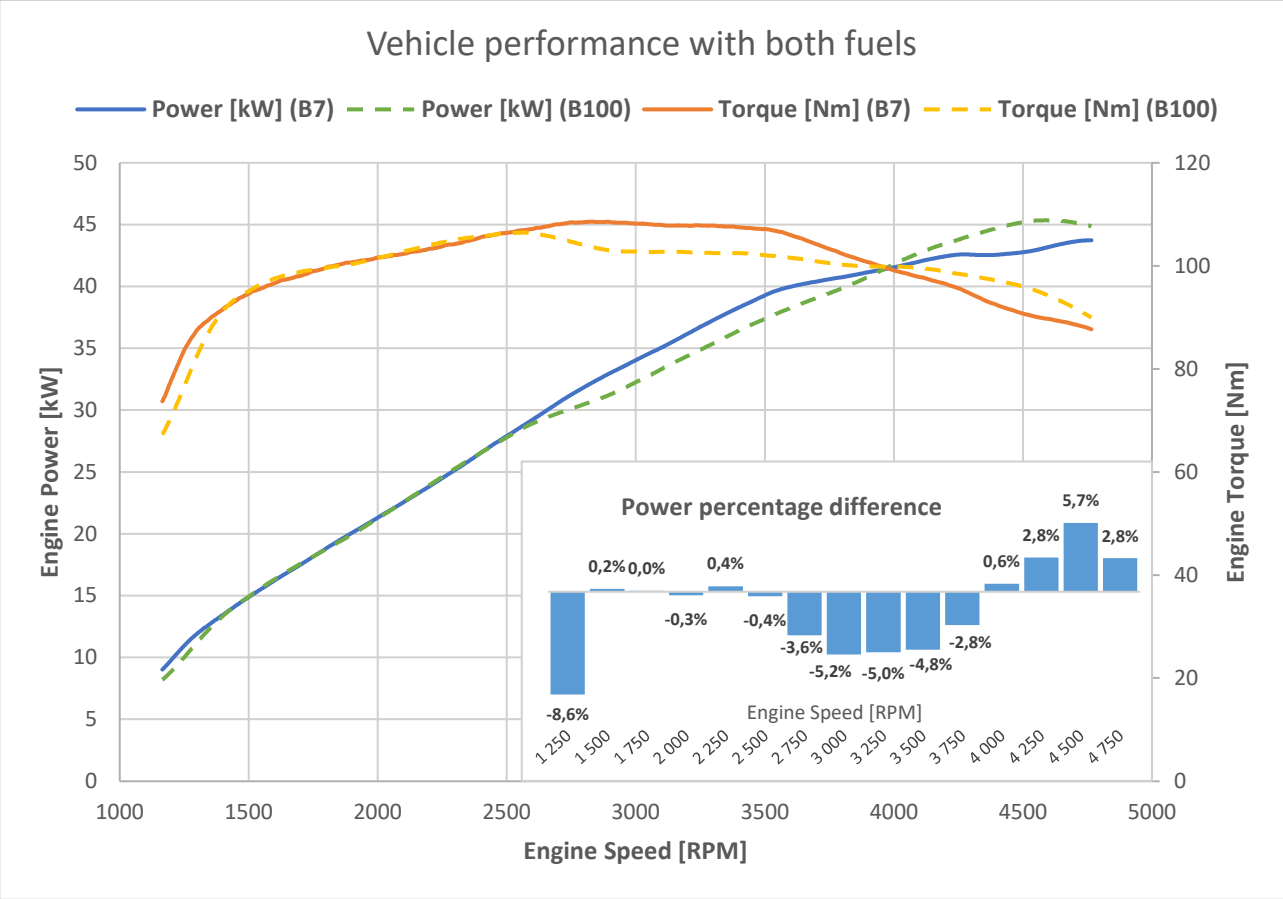

Figure. 4. Power and torque chart, and power percentual difference obtained between both fuels.

Table 6. Percentage difference and Maximum power and torque obtained.

Parameter	B7	B100	Unit	Percentage difference [%]
Standard power	43,8	45,4	kW	3,8
Engine power	44	45,2	kW	2,7
Wheel power	29,8	33,2	kW	12,6
Resistive power	14,1	11,6	kW	-18,2
@	4760	4590	rpm	-3,5
Standard torque	108,7	106,5	Nm	-2,0
@	2870	2600	rpm	-10,6

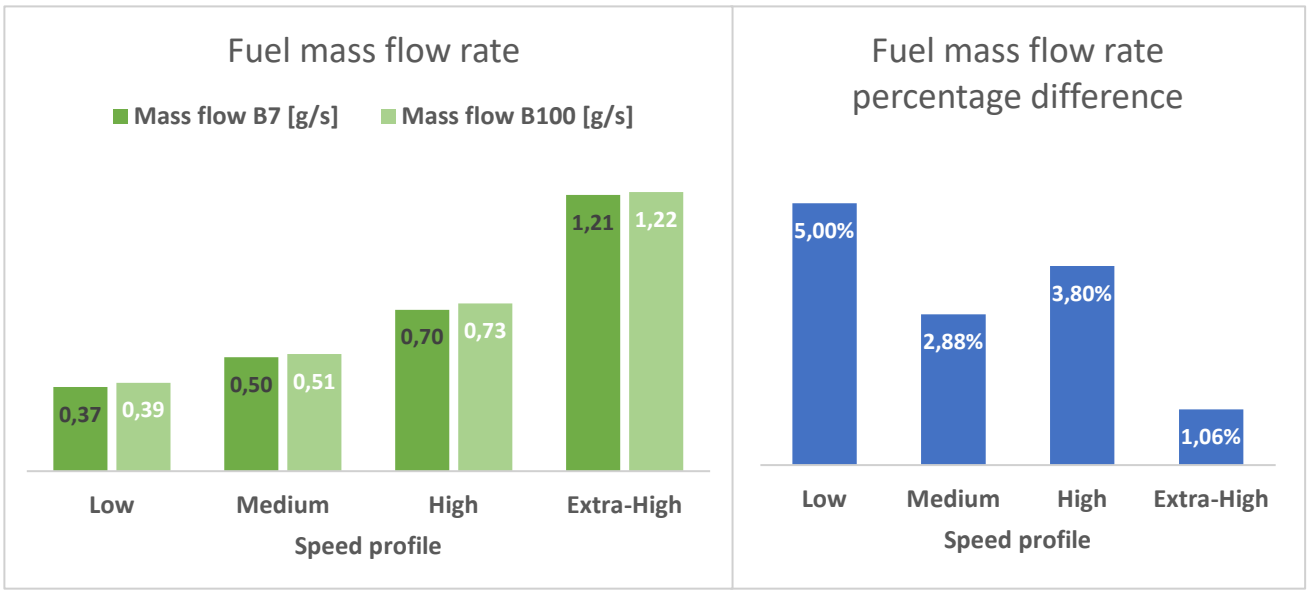

Figure. 5. Mass flow rates of fuel and percentual differences obtained in the WLTP test, for B7 and B100.

Table 7. Mass flows and percentage differences obtained in the WLTP test, for B7 and B100.

Speed profile	Mass flow B7 [g/s]	Mass flow B100 [g/s]	Percentage difference
Low	0,367	0,386	5,00%
Medium	0,497	0,511	2,88%
High	0,705	0,732	3,80%
Extra-High	1,206	1,219	1,06%

Table 8. Fuel consumptions and percentage differences obtained in the WLTP test, for B7 and B100.

Speed profile	Average consumption [l/100km] - B7	Average consumption [l/100km] - B100	Average consumption [l/100km]
Low	7,426	7,336	-1,21%
Medium	6,234	6,104	-2,08%
High	5,836	5,687	-2,54%
Extra-High	6,567	6,441	-1,93%

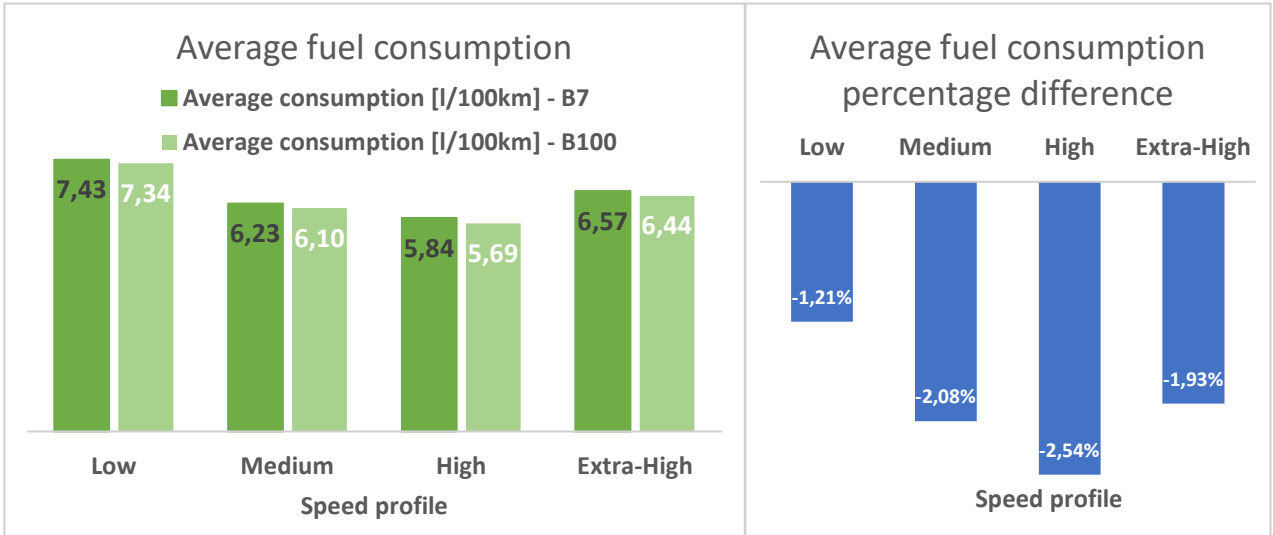

Figure. 7. Fuel mass flows and differences percent obtained in fuel consumption for WLTP test, with B7 and B100.

4. Conclusion

Just like the body of the work, the conclusions that can be drawn from this work can be grouped by the typology of the tests used:

4.1. Fuel consumption test

From the analysis of the results, it can be concluded that the use of biodiesel does not necessarily increase fuel consumption, as there were vehicles that showed increases and others that showed decreases. These fluctuations occur not only due to differences in fuel properties but also due to natural causes associated with the use of vehicles by different drivers on different routes, among other factors, which implies a fluctuation in vehicle consumption. Overall, there was a very slight increase of about 1% in the vehicles analysed. In the equipment, there was even a decrease in fuel consumption. This is not only due to differences in fuel properties but perhaps more to the different modes of operation to which they may have been subjected. Overall, in the equipment, there was a decrease in consumption of about 12% when B100 was used.

4.2. Emissions test

Analysing the exhaust gas emissions, it is evident that, in vehicles, the use of biodiesel causes an average increase in CO emissions (32.86%) and a decrease in NOx (34.81%), while there was virtually no change in O2 and CO_2. The increase in CO is not critical in diesel engines since they always operate in a lean mixture. The decrease in NOx is beneficial because it is one of the most critical pollutants associated with the use of diesel engines. For the equipment, globally, the same as in vehicles occurred, except for NOx emissions, which increased by about 6%, although this increase was only observed in one of the two pieces of equipment considered in this study. In both cases, there was no significant increase in CO_2 emissions, so it is possible to conclude that, by using biodiesel, there will be a decrease in emissions of this substance when considering the entire life cycle given the renewable nature of this fuel.

4.3. Power and Consumption Test – WLTP

Analysing the differences in power output by the vehicle under study when using biodiesel, there is no decrease in the vehicle's performance, with even a slight increase in the maximum power output by the engine. This may be related to some intervention that the vehicle has undergone or alteration of a critical component that affects the maximum power reached at higher engine rotation. Nevertheless, in a typical case, there would not be a significant decrease in the power output by the engine.

For the power bench consumption tests (WLTP), there is a visible increase in the mass fuel consumption in all speed profiles, between 1 and 5%. Even so, this value was lower than expected, which would be around 10%. Analysing the average volumetric consumption per distance travelled (l/100km), there is a slight decrease, around 2%. This is explained by the higher density of biodiesel.

Acknowledgments

The authors would like to acknowledge the major Rui Cotovio and his team that give an important and decisive contribution for this work. Authors also would like to express their acknowledgement to PRIO Energy who made this research possible.

Nomenclature

$\dot{m}$ mass flow rate, kg/s

LHV Lower Heating Value

HHV Higher Heating Value

CO2 carbon dioxide

CO carbon monoxide

NOx nitrogen oxides

HC hydrocarbons

B7 fuel mixture of 7% biodiesel in diesel

B100 fuel containing only biodiesel

O2 Oxygen

PM particle matter

WLTP World Light-duty Test Procedure

References

[1] Shen X., Shi J., Cao X., Zhang X., Zhanga W., Wua H. e Yao Z., “Real-world exhaust emissions and fuel consumption for diesel vehicles,” Atmospheric Environment, 2018, pp. 249-257.

[2] Serrano L., Pereira N. e Carvalho P. M. C., “Comparative Performance and Efficiency of EURO VI Heavy-Duty Engines Fueled by Biodiesel, HVO and Diesel,” Proceedings of the 1st International Conference on Water Energy Food and Sustainability, 2021, pp. 271-279.

[3] Serrano L. M. V., Análise comparativa do desempenho de motores de combustão interna quando utilizam biocombustíveis [dissertation]. Coimbra, Portugal: Faculdade de ciências e tecnologia da universidade de Coimbra; 2012.

[4] Prio, “Ficha Técnica - Gasóleo Aditivado,” Gafanha da Nazaré, 2017.

[5] Heywood J. B., Internal Combustion Engine Fundamentals, Singapore: McGraw-Hill, 1988.

[6] Ozsezen A. N., Canakci M., “Determination of performance and combustion characteristics of a diesel engine fueled with canola and waste palm oil methyl esters,” *Energy Conversion and Management*, January 2011, vol. 52, pp. 108-116.

[7] Santana B. J. R., Utilização de misturas com baixo teor de Biodiesel [dissertation]. Leiria, Portugal: Instituto Politécnico de Leiria; Setembro 2020.

Syngas-fed cogeneration for the tertiary sector: lessons learned from the Synbiose project

Andrea Borghi[a], Nicola Casari[b], Agostino Gambarotta[c], Edoardo Micconi[a], Mirko Morini[c], Michele Pinelli[b] and Alessio Suman[b]

[a] Siram Veolia, Milan, Italy, andrea.borghi@veolia.com edoardo.micconi@veolia.com
[b] University of Ferrara, Ferrara, Italy, nicola.casari@unife.it michele.pinelli@unife.it alessio.suman@unife.it
[c] University of Parma, Parma, Italy, agostino.gambarotta@unipr.it mirko.morini@unipr.it ***CA***

Abstract:

Within the strategies for sustainable transition and decarbonization, biomass gasification represents an interesting solution to yield renewable fuels that can be used in internal combustion plants for power and combined heat and power (CHP) generation. The use of syngas instead of original biomasses allows industrial internal combustion engines to achieve higher conversion efficiencies and lower pollutant emissions. However, limited experience on real operative plants has led to a lower diffusion of the technology than expected.

To investigate the real behavior of a gasifier fed with lignocellulosic woodchips and coupled with a CHP engine, a commercial-grade system has been installed in the Science and Technologies Campus of the University of Parma. The aim of the research project Synbiose was to gain a better understanding of the processes to enhance the application of small-scale gasification and CHP plants in the tertiary sector. Operating parameters of the system – properly instrumented – have been monitored to analyze its performance and to improve its maintainability. In order to investigate the effects of woodchips from different tree species on system performance, a second smaller plant was built and has been used for a specific experimental activity.

An extended modelling study has been developed to enhance the comprehension of the gasification process and of the plant operation. A hybrid thermochemical model has been used for the simulation of the gasification process, while a lumped parameter dynamic model and multiphase CFD simulations have been applied and integrated to analyze the operation of the whole plant.

The aim of the paper is to summarize the results of these research activities highlighting the issues that arose during the project with specific reference to the implemented solutions.

Keywords:
Biomass; Cogeneration; Experimentation; Gasification; Simulation.

1. Introduction

Renewable energy sources play a key role in the sustainable transition and decarbonization of the power system. Together with solar and wind technologies (which are typically non-programmable), biomasses represent an interesting way to exploit the use of renewable energy without having relevant storage issues.

Currently, biomasses are used for direct combustion in combined heat and power (CHP) steam plants (i.e. wooden biomass direct combustion, giving rise to noteworthy issues of pollutant formation), or they are converted into so-called biogas through anaerobic fermentation that can be used as fuel for CHP plants based on internal combustion engines or micro-gas turbines. In both cases the size and flexibility of the comprehensive conversion and generation plants hinder their applications in the tertiary sector (e.g. hospitals, university campuses).

Within this context, the gasification process of wooden biomasses is an interesting alternative allowing for the production of a gaseous fuel (syngas) that can be properly cleaned and used for CHP generation. Moreover, the use of thermochemical conversion and of internal combustion engines allows for smaller and more flexible plants, which can use locally available solid biomasses more efficiently.

However, the lack of field testing knowledge on these plants (with particular reference to operation and maintenance issues and to syngas production and cleaning technologies) still seems to limit their use in real applications. In the current Italian context, almost no small-size syngas-fed operating CHP plants can be found on which adequate operating experience has been acquired to evaluate their performance and reliability.

To overcome this issue, the Synbiose project has been started with the aim of enhancing the theoretical and experimental comprehension of small-scale gasification-CHP plants to allow for their wider application in the tertiary sector. The project lasted from February 2017 to May 2021 and involved the installation, instrumentation, testing and modelling of a commercial-grade plant based on a gasifier fed with lignocellulosic woodchips. The project partners were Siram S.p.A., the Center for Energy and Environment-CIDEA of the University of Parma, and the Department of Engineering of the University of Ferrara. The plant is installed in the Campus of the University of Parma and is directly connected to the local electrical grid and to the district heating network (fed by natural gas boilers) which fulfil the demands of the Campus buildings (with a total peak heating power demand of 16 MW).

Many examples can be found in the literature regarding the optimization of the gasification process [1] and its modelling [2, 3] or regarding experimental tests [4]. There are very few examples related to applications in an operating environment [5, 6] and none with an experimental and numerical approach.

1.1. Aim of the paper

The aim of this paper is to give a concise presentation of the outcomes of the activities of the 51-month project and to present a summary of the main lessons that have been learned from the experience gained. The main goal of the project was to bring the gasification technology to a sufficient level of maturity to be able to represent a viable technical solution for its application in the tertiary sector. To achieve this goal, the partners were involved in experimental and computational research which are summarized in the following sections. In particular, Section 2 presents the two plants that have been installed at the Campus and their measurement and acquisition systems.

The first plant is characterized by an installed nominal electrical power of 125 kW and it was used for long run testing to evaluate the reliability of the technology. The second, with an installed electrical nominal power of 25 kW, was instead used to evaluate the fuel flexibility of the technology by testing its operation with different tree species. The results of these experimental activities are summarized in Section 3.

Beside the experimental activity, the project also dealt with the development of the mathematical models of the process, of the whole plant and of its components. Section 4 briefly shows the mathematical model of the gasification process and its validation, the dynamic model of the whole syngas cleaning line and the CFD analyses that have been performed on relevant components.

Finally, some conclusions have been made in Section 5, wrapping up the whole project, and providing useful hints for those who will try to replicate the experience.

2. The plants

The experimental equipment used in the project consists of two biomass-fueled syngas cogeneration plants (Figure 1). The sizes of these two plants, in terms of electrical power output, are 125 kW and 25 kW, respectively. Both plants are located at a dedicated facility in the Science and Technologies Campus of the University of Parma.

2.1. The 125-kW plant

The plant consists of biomass storage, i.e. wood chips, which is fed by means of an auger system into a storage chamber that can guarantee an operating autonomy of the plant of approximately 3 to 4 days at maximum power. Downstream of this biomass storage site is a vibrating screener, consisting of opposing grates that allow the wood chips to be sieved in order to remove the finest fractions. These fine fractions would cause occlusions inside the gasification reactor, affecting the empty/full ratio and limiting the passage of the syngas, which would therefore not be able to flow properly inside the reactor.

The feeding of biomass into the reactor is not continuous, but is regulated by a rotating blade sensor which, once the wood chip level decreases, activates an auger system that transfers the wood chips from a hopper downstream of the vibrating screener to the gasifier. The inlet to the gasifier is regulated by two valves that open alternatively, introducing a finite amount of wood chips, so as to minimize unwanted air inlets at the top of the reactor, since the reactor operates at lower barometric pressure conditions in the range of - (3÷8) mbar gauge pressure. The gasification reactor is of the fixed-bed downdraft type, with an hourglass shape. The biomass is fed into the upper part and, as it descends into the gasifier, undergoes the reactions of drying, pyrolysis, combustion, and gasification.

In the restriction zone (i.e. the throat), air is supplied through the nozzles located on the reactor circumference, driven by a fan. Locally, exothermic combustion reactions take place (although the reactor works with a lack of oxygen compared to the stoichiometric quantity), which sustain the other endothermic reactions taking place in the gasifier. All reactions take place because the system is kept under negative gauge pressure due to the suction of the internal combustion engine. By means of this pressure, the syngas, at a temperature of approximately 750 °C, is forced to pass through a grate in the lower part of the gasifier, which prevents the passage of the coarser pieces of char or wood chips, and then the syngas passes through an air-syngas countercurrent exchanger that preheats the reaction air.

Figure. 1. The two plants in the Synbiose area of the thermal power plant of the Campus in Parma.

The gas is then filtered through ceramic fiber filter elements (alumina silicate wool) at a temperature of approximately 600 °C. This filtration stage separates the carbon particles and char that the syngas has dragged along with it in its flow. Downstream of this filter, the gas passes through a so-called check filter, consisting of a very fine metal grid. Within this filter, a differential pressure sensor detects the fouling on the metal grid and, if a ceramic filter element has broken, it interrupts the engine operation by sending the gas to the flaring to preserve the integrity of the engine. Downstream of this element is a water-syngas heat exchanger, of the shell-and-tube type, which allows the syngas to cool down to approximately 110 °C, dropping below the dew temperature of certain classes of tar, which, as they condense, can thus be removed from the gas stream and removed from the exchanger via a double valve system.

Approximately 20 kW of heat output can be recovered from this heat exchanger. After this element, the syngas is fed into a metal filter that separates a final portion of tar (consisting of elements with a lower molecular weight than those removed previously) by coalescence and also a portion of the moisture present in the syngas. At this point, the syngas is fed into an aspirated internal combustion engine to produce electricity and heat. Under optimal conditions, up to 125 kW of electrical power and 200 kW of thermal power can be recovered from the cooling of the engine and combustion gasses. The combustion gasses then pass through a trivalent catalytic converter before being emitted into the atmosphere. A dedicated dry cooler is used to dispose of the heat output in the event of no demand from the user. Both electrical and thermal power are fed to the electricity and district heating networks that supply the University Campus, respectively.

The plant was entirely equipped with measuring instruments (Figure 2). The measured data was acquired on a quarter-hourly basis. Pressure and temperature sensors were placed upstream and downstream of each component. All temperature sensors are RTD PT100 type except for the K-type thermocouple installed for the syngas at the outlet of the gasifier (where temperatures at start-up can exceed 1100 °C). Type J thermocouples were installed up to the point downstream of the main filter, again due to the high temperatures. The pressure sensors, connected to the process via a steel capillary that protects the instrument from high syngas temperatures, are of the capacitive type with a ceramic membrane and have an operating range of (- 400 ÷ 400) mbar.

An air flow meter is placed upstream of the fan feeding air into the gasifier. Two flow meters and two temperature sensors are placed on the hot water circuits recovered on the water-syngas exchanger and on the internal combustion engine in order to measure the thermal energy exchanged.

There are also temperature sensors inside the reactor (at the top and in the central part near the nozzles) and a negative gauge pressure sensor placed at the top of the reactor. In addition, there is a differential pressure sensor located across the ceramic filter elements to assess their state of fouling and to provide periodic cleaning by means of compressed air supplied in the counterflow.

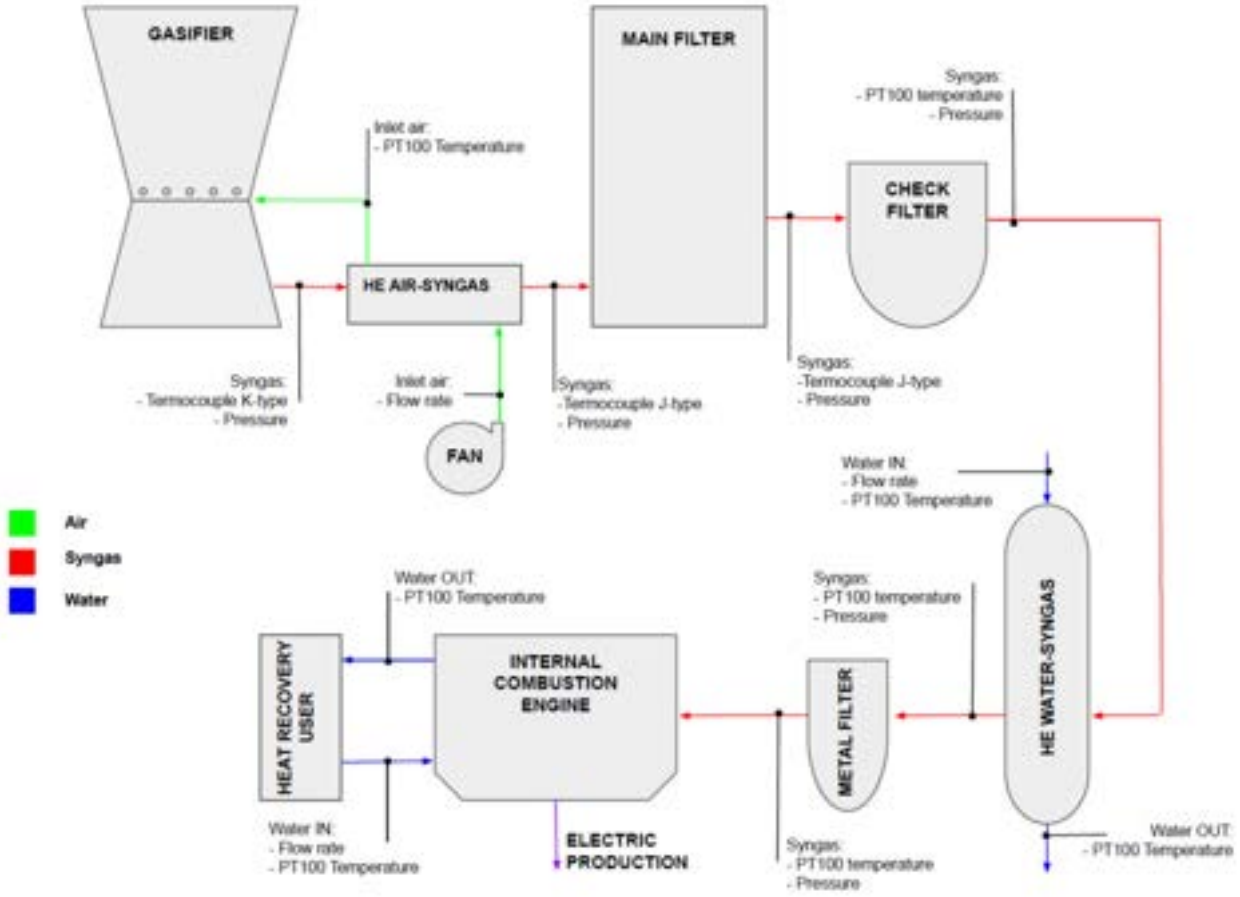

Figure. 2. A schematic representation of the measurement points on the 125-kW plant.

Since the syngas, rich in impurities, would have compromised any measuring instrument fitted to the line, the syngas flow rate was estimated by means of an energy balance on the syngas-air exchanger. Ambient temperature and pressure sensors were installed to characterize the ambient atmosphere.

2.2. The 25-kW plant

Due to its smaller size and easier maintenance, a smaller plant than the previous one was used for the experimental characterization of different wood species. This plant consists of a hopper in which approximately 0,33 m^3 of biomass is stored, which is then fed to a downdraft reactor. At the base of this reactor is a grate shaker system that removes the thicker flakes of char and favors the advancement of the biomass. The syngas thus produced is then further purified of carbon particles first through a cyclone, then cooled through a syngas-water tube bundle exchanger and subsequently, at lower temperatures, filtered in a fabric bag filter. Before being fed into the aspirated internal combustion engine, the air-syngas mixture is filtered through a paper filter.

For the sampling of the syngas required to perform characterization analyses, a suitable sampling valve is placed downstream of the bag filter.

3. The experimental campaign

The two plants presented in Section 2 were used for the experimental campaign. In particular, the 125-kW plant was operated in long run sessions with the aim to monitor the performances of each component and to improve its availability that was limited by its heavy maintenance needs. The 25-kW plant instead was used to test wood chips from different tree species in order to evaluate the quality of the syngas produced.

3.1. Long run sessions

The 125-kW plant was monitored during its operation while feeding the electrical and district heating networks of the Campus. The electrical power output was generally kept within the range (90÷100) kW. The measurements were collected every 15 minutes and stored for elaboration. In Fig. 3a, for example, the evolution of the absolute pressure at the filters is shown for one day. The oscillations are due to the deposit of dust cake on the ceramic candles of the main filter and their jet-pulse cleaning.

Since it was not possible to directly measure the mass flow rate of the syngas, this needed to be estimated indirectly. It was decided to use the energy balance at the air-syngas heat exchanger, since the air mass flow rate, the air inlet and outlet temperature, and the syngas inlet and outlet temperature are measured.

$$\dot{m}_{syn} = \frac{\dot{m}_{air} c_{p,air} (T_{air,out} - T_{air,in})}{c_{p,syn} (T_{syn,in} - T_{syn,out})} \quad (1)$$

The resulting mass flow rate ranged between (0.06÷0.10) kg/s and its evolution for one day is reported in Fig. 3b, confirming that the oscillations in pressure at the check filter were not due to a variation in mass flow rate.

The data gathered from the experiment have been used to train and validate the models presented in Paragraphs 4.2 and 4.3 and to evaluate health indices regarding the different components (e.g. pressure loss coefficient on filters and pipes, as shown in Fig. 4 for the ceramic candles).

3.2. Syngas characterization

The 25-kW plant was used to test 8 different tree species dried both naturally and artificially. The wood chips were sampled before the test. Then the elemental analysis and the evaluation of the ash content, of the moisture, and of the lower heating value on a dry basis were performed. The result of this characterization is reported in Table 1.

The test was then performed by feeding the 25-kW plant and keeping it at a constant electrical power output (i.e. 7.5 kW) until a steady state was reached. The syngas was then sampled with a Tedlar bag and analyzed through gas chromatography–mass spectrometry. Table 2 presents the results in terms of mass fraction of carbon monoxide, hydrogen, methane, carbon dioxide, hydrogen sulfide, oxygen, and nitrogen in the anhydrous syngas. Moreover, the water and tar content and the lower heating value is reported.

It can be noted that the data do not show any significative correlation between the characteristics of the biomass and those of the produced syngas.

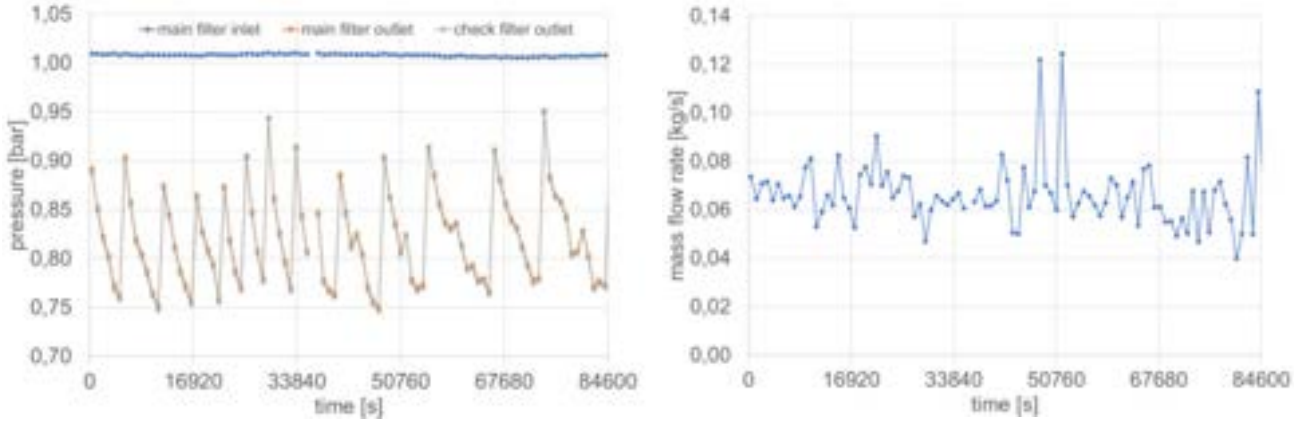

(a) (b)

Figure. 3. Evolution of pressures (a) and syngas mass flow rate (b) in a sampled day.

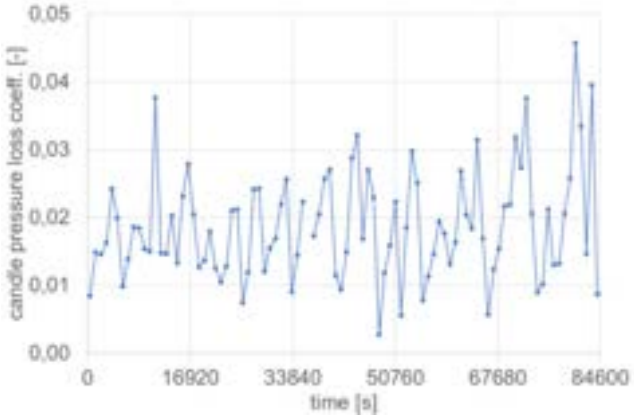

Figure. 4. Evaluation of the pressure loss coefficient on the ceramic candle in the main filter.

Table 1. Results of the wood chip characterization.

Tree species	Drying	C	H	O	N	S	Ash	Moisture	LHV
		%	%	%	%	%	%	%	kJ/kg
Chestnut	Natural	46,5	2,6	49,7	0,4	0,4	0,5	22,0	17350
Cherry	Natural	N/A	N/A	N/A	N/A	N/A	N/A	N/A	N/A
Beech	Natural	45,8	5,7	46,9	0,7	0,1	0,8	8,7	17740
Walnut	Natural	45,0	0,6	53,0	0,3	0,1	1,1	31,0	18100
Pine	Natural	N/A	N/A	N/A	N/A	N/A	N/A	N/A	N/A
Poplar	Natural	44,7	5,7	48,3	0,1	0,1	1,0	16,0	17730
Black locust	Natural	48,0	3,6	46,9	0,2	0,1	1,2	18,0	11080
Durmast	Natural	43,9	5,0	48,0	0,4	0,1	2,7	18,0	N/A
Chestnut	Artificial	47,8	5,9	45,2	0,4	0,1	0,7	2,5	16370
Cherry	Artificial	47,1	6,1	46,0	0,1	0,1	0,6	1,1	15473
Beech	Artificial	39,2	5,0	54,7	0,2	0,1	0,8	5,1	16710
Walnut	Artificial	42,6	5,4	50,7	0,1	0,2	1,1	7,5	16128
Pine	Artificial	44,3	5,3	50,3	0,0	0,1	< 0,5	6,5	18290
Poplar	Artificial	47,5	5,6	45,0	0,2	0,2	1,5	0,9	N/A
Black locust	Artificial	46,4	5,8	46,2	0,7	0,1	0,7	< 1,0	N/A
Durmast	Artificial	44,6	5,8	46,7	0,6	0,1	2,2	< 1,0	16570

Table 2. Results of the syngas characterization.

Tree species	Drying	CO	H_2	CH_4	CO_2	H_2S	O_2	N_2	H_2O	Tar	LHV
		%	%	%	%	%	%	%	g/Nm^3	mg/Nm^3	MJ/Sm^3
Chestnut	Natural	18,6	27,5	2,8	12,8	0,6	1,1	36,4	19,6	4457	6,41
Cherry	Natural	N/A	N/A	N/A	N/A	N/A	N/A	N/A	N/A	N/A	N/A
Beech	Natural	14,6	24,1	3,3	10,7	0,7	2,7	42,8	42,9	37717	7,13
Walnut	Natural	15,3	29,6	2,9	15,0	0,3	0,5	36,4	53,5	1793,1	6,23
Pine	Natural	N/A	N/A	N/A	N/A	N/A	N/A	N/A	N/A	N/A	N/A
Poplar	Natural	15,0	25,4	2,6	11,7	0,1	3,1	41,8	31,5	17310	5,83
Black locust	Natural	20,6	21,4	3,0	14,2	0,1	0,8	39,8	35,3	5678	6,55
Durmast	Natural	17,5	23,8	3,1	11,8	0,3	2,3	41,2	28,2	2271	5,58
Chestnut	Artificial	17,8	29,3	3,5	14,2	0,4	1,8	33,0	63,8	841	6,31
Cherry	Artificial	18,6	24,1	2,7	17,3	0,6	1,0	35,7	29,9	2713	5,61
Beech	Artificial	19,7	27,4	3,6	16,1	0,8	1,4	31,0	62,9	9922	6,52
Walnut	Artificial	19,7	22,2	2,8	11,4	0,3	2,6	41,1	36,8	2241	5,57
Pine	Artificial	20,1	24,0	4,0	16,9	0,7	1,5	32,8	66,0	11524	6,21
Poplar	Artificial	24,3	24,0	3,1	8,0	0,1	1,8	38,7	37,4	5447	6,41
Black locust	Artificial	18,0	26,4	3,5	17,6	0,9	1,1	32,3	61,6	7151	6,45
Durmast	Artificial	18,6	28,2	3,4	14,4	0,4	1,6	32,5	64,5	37298	7,67

4. The simulation campaign

4.1. Gasification process

A model for the simulation of the gasification process that takes place in a fixed-bed downdraft gasifier was developed and implemented in Scilab. The model combines a lumped parameter stoichiometric equilibrium model for the pyrolysis and oxidation zones with a one-dimensional kinetic model for the reduction zone.

In particular, the former takes into consideration two reactions, i.e. water gas shift (R1) and char methanation (R2), which are assumed to be at the equilibrium. The molar fraction of each species at the outlet of the pyrolysis and oxidation zones are constrained by the mass balances of each element (i.e. C, H, O) and by the ratio given by the equilibrium constants (Eq. 2):

$$CO + H_2O \leftrightarrow CO_2 + H_2 \quad \text{(R1)}$$

$$C + 2H_2 \leftrightarrow CH_4, \quad \text{(R2)}$$

$$K = \frac{\prod_{products} x_p^{sp}}{\prod_{reactants} x_r^{sr}} \quad (2)$$

The value of the equilibrium constant for each reaction is calculated through Eq. 3, where the temperature is determined by means of the energy balance in the pyrolysis and oxidation zones.

$$K = e^{-\frac{\Delta G^0}{RT}} \quad (3)$$

The kinetic model for the reduction zone, takes into consideration four reactions.

$$C + CO_2 \leftrightarrow 2CO \quad \text{(R3)}$$

$$C + H_2O \leftrightarrow CO + H_2 \quad \text{(R4)}$$

$$C + 2H_2 \leftrightarrow CH_4 \quad \text{(R5)}$$

$$CH_4 + H_2O \leftrightarrow CO + 3H_2 \quad \text{(R6)}$$

The rate of each reaction is evaluated through Eq. 4, where the equilibrium constant is calculated as seen before with Eq. 3 and the energy balance, for each control volume into which the reduction cone is divided. The net formation/destruction rate of each species is calculated considering all the reactions in which the species participates.

$$r = C_{\mathrm{RF}} A e^{-\frac{E}{RT}} \left(\prod_{reactants} x_r^{s_r} - \frac{\prod_{products} x_p^{s_p}}{K} \right) \quad (4)$$

The model is validated by applying it to a literature test case [7]. The main input data are reported in Table 3, and the output data in Table 4. It can be noticed that the results are satisfactory for the species (H_2 and CO) responsible for the lower heating value of the syngas.

4.2. System simulations

A comprehensive 0D lumped parameter dynamic model was developed for the simulation of the whole system (i.e. gasifier, syngas cleaning line and engine) and it was implemented in Matlab®/Simulink® by assembling component models. The model is based on the energy and mass balances for each component. Some of the components are considered as capacities (in green in Fig. 5a) and the balances are implemented with integral equations allowing for mass and energy storage. On the other hand, there are the resistances (in orange) with the balances implemented with algebraic equations. Particular care has been devoted to syngas conductivity, density, specific heat capacities and viscosity calculation. The model is able to simulate the behavior of the system both under stationary and transient conditions (e.g. the pressures before and after cleaning are shown in Fig. 5b). The most significant results are presented in [8, 9], showing that the model is a valuable tool for the diagnosis of the syngas cleaning line.

Table 3. Input of the gasification model for the validation [7].

Power	Fixed Carbon	Volatile Matter	Ash	C	H	O	S	N	Moisture	Biomass mass flow rate	Air to fuel ratio
[kW]				[g/100 g dry basis]						[g/s]	[g air/g biomass]
4										8,1	1,37
6										10,2	1,48
8	16,51	79,84	3,65	45,19	5,74	44,92	0,44	0,06	7,02	12,1	1,63
10										12,4	1,69
12										12,9	1,79

Table 4. Output of the gasification model and comparison with experimental data from the literature [7].

	Simulation					Experimental					Error (Sim. - Exp.)				
Power	H_2	CO	CO_2	CH_4	N_2	H_2	CO	CO_2	CH_4	N_2	H_2	CO	CO_2	CH_4	N_2
[kW]	[%mol/mol]					[%mol/mol]					[%mol/mol]				
4	18,9	17,4	13,8	0,1	49,8	15,4	17,3	6,9	3,4	56,9	3,5	0.1	6,9	-3,3	-7,1
6	17,1	17,4	13,5	0,0	52,0	15,3	17,2	7,0	3,4	57,2	1,8	0,2	6,5	-3,2	-5,2
8	15,2	17,3	13,2	0,0	54,3	15,1	17,0	7,2	3,0	57,8	0,1	0,2	6,1	-3,0	-3,5
10	14,7	17,2	13,1	0,0	55,0	14,9	17,0	7,2	2,8	58,1	-0,2	0,3	5,9	-2,8	-3,1
12	13,9	17,2	13,0	0,0	55,9	14,8	16,9	7,3	2,8	58,3	-0,9	0,3	5,7	-2,8	-2,4

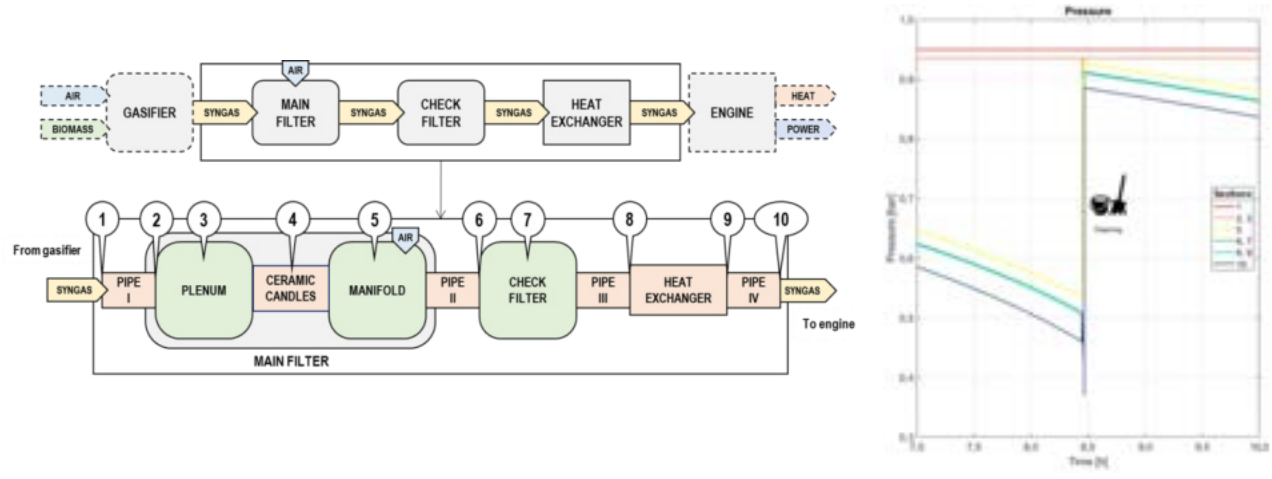

(a) (b)

Figure. 5. A schematic representation of the model (a) and the evolution of the simulated pressure when cleaning occurs (b) [9].

4.3. Component CFD simulations

An integrated 0D-3D approach is a methodology which combines a simplified thermodynamic 0D lumped parameters model (such as the one presented in Paragraph 4.2) with 3D CFD simulations. The 0D model is then able to describe the entire process by integrating information obtained by a detailed 3D CFD simulation of the individual components (such as performance maps, pressure drops, etc.). This information may be unknown or can be known with high uncertainty (for instance, from empirical correlation) and, thus, this procedure consents to obtain the set-up coefficients of the 0D models. Moreover, by means of the CFD simulation, it is possible to study the behavior of the specific components in detail in order to debug design weakness and optimize their operation. In a more sophisticated approach, then, the 0D and 3D models can actively interact as follows: the 0D model calculates the thermodynamic quantities and flow rates in the characterizing sections; it supplies them to the 3D models as the boundary conditions on which to carry out the simulation and to return the performance of the components to the 0D model; then the 0D model recalculates the thermodynamic quantities and flow rates through the balance sheets. This methodology offers a series of advantages, combining the speed and robustness of the 0D simulation model of the system with the complexity and accuracy of the 3D numerical fluid dynamics simulation. The most relevant results related to three of the most relevant components of the 125-kW plant (see Fig. 2) were the following:

- the gasifier, where the focus was on the inside (consequent to gasification reactions) and outside (consequent to the coupling with the environment) fluid dynamics and heat exchange processes;
- the syngas feeding duct, where the focus was on the fouling phenomena and on the consequences of the residual tar carried by the syngas;
- the water-syngas heat exchanger, where the focus was on both of the above topics, i.e. the internal and external fluid dynamics and heat exchange processes, and the fouling issues due to the cooling of the syngas through the heat exchanger.

4.3.1. Gasifier

The downdraft gasifier was simulated by means of the two commercial finite volume CFD codes of the ANSYS platform. The preliminary results obtained with FLUENT are reported in [10]. Subsequently, by acquiring the real geometry with a reverse engineering CAD-based methodology which make use of a 7-axis laser scanner, it was possible to verify that the gasifier worked as a “quasi-throatless” downdraft principle, and it was also possible to simulate the actual geometry by means of CFX. An interesting result is reported in Fig. 6, in which it is possible to appraise the influence of the grate on the internal temperature from a distribution point of view. Even though there is a restriction, the grate shifts the operation of the gasifier from throated to throatless. This can be seen from the variation of the temperature profile near the restriction which shifts from a typical throated profile (blue line) to a typical throatless profile (red line), as seen in [11]. Moreover, the influence of the grate can also be seen from a quantitative point of view, i.e. the calculated average temperature of the exhaust gases passes from 1148 °C (without grate) to 839 °C (with grate). It is also interesting to notice that the CFD calculation is in agreement with the experimental results T_{syn} = 750 °C (about 10 %).

4.3.2. Syngas feeding duct

The syngas feeding duct was simulated by means of the open-source finite volume CFD code OpenFOAM. In [12], the numerical methodology developed based on a mesh-morphing algorithm is presented. The analysis made it possible to estimate the amount, rate, and area of tar deposition on the duct, which was simulated as a mixture of 5 tar classes characterized by different concentration and dew points. In Fig. 7a, by comparing a take-over on a section of the actual duct and the numerical result in terms of deposition (grey area) in the same section, it can be noticed how the numerical simulation was able to capture the shape and amount of deposition. Subsequently, the same methodology was used to estimate the increase in duct pressure drop caused by the growth of the deposit over time (Fig. 7b). In this manner, the pressure drop in the duct module of the 0D model can be updated during the life of the plant.

4.3.3. Water-Syngas heat exchanger

The Water-Syngas heat exchanger geometry was also acquired on the real plant by means of reverse engineering methodology. The geometry (which is a vertical shell-and-tube heat exchanger) was then simulated by means of ANSYS CFX in clean and degraded conditions, the latter obtained by generating a modified domain according to on-field inspection of the device after several operating hours. The implanted faults were fouling (50 % area reduction of 21 tubes) and clogging (38 % of tubes fully blocked by tar solidification) [13]. The analysis showed how fouled and clogged conditions caused a decrease in heat exchanger effectiveness, an increase in pressure drop and a decrease in the capability of the heat exchanger to condense tar and separate it from the gas stream (which is the second most important function of the heat exchanger). The outcome of the simulation was also to characterize the performance of the heat exchanger which was not provided by the manufacturer since the heat exchanger was designed ad hoc and built on site. This characterization was used to feed the 0D model, as described below.

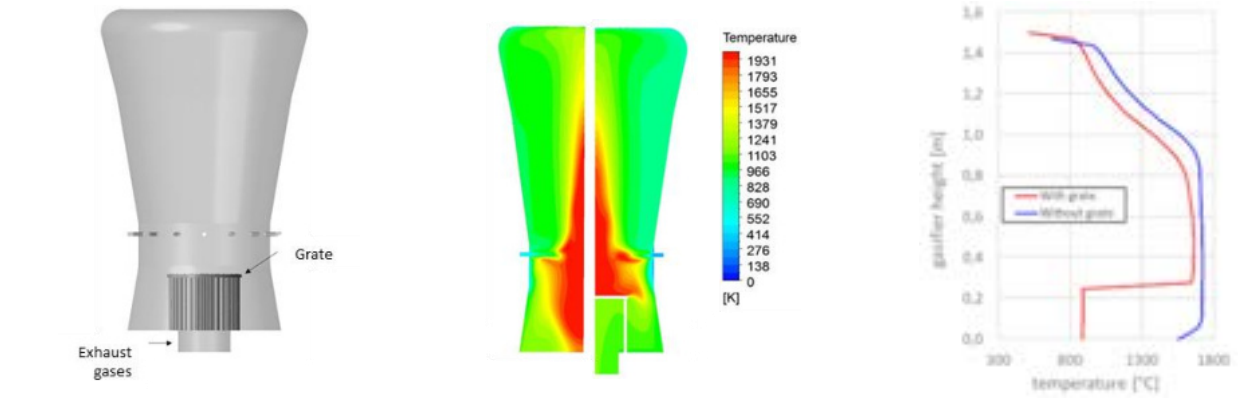

(a) (b) (c)

Figure. 6. Gasifier geometry (a), temperature distribution without grate on the left and with grate on the right (b) and temperature profile (c).

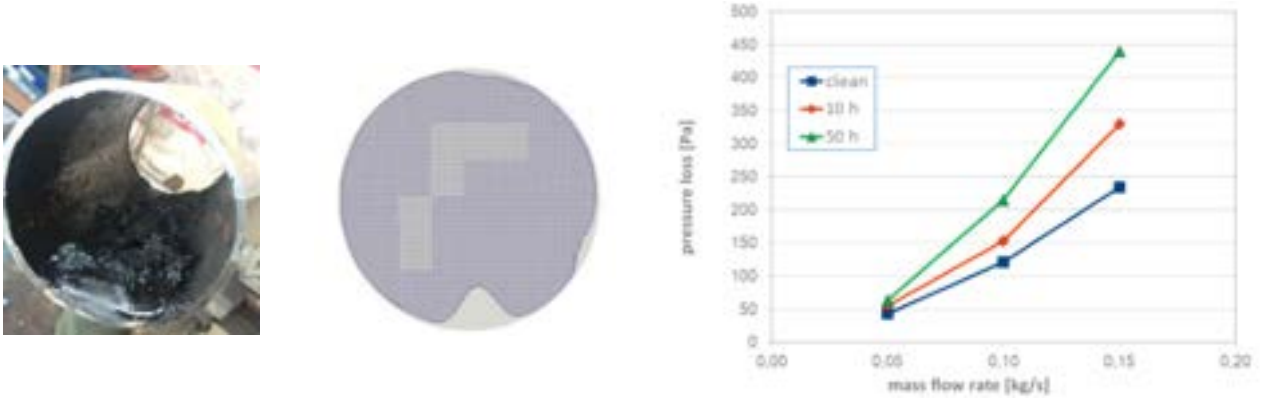

(a) (b) (c)

Figure. 7. Actual tar deposit (a), numerical tar deposit (b) and pressure drop curves as a function of elapsed time (c).

4.4. 0D-3D model integration

As depicted in Fig 8., by taking advantage of the CFD characterization described above, the 0D model can be fed by the obtained numerical 3D results to make the plant simulation more realistic. In the Figure, the interaction between the syngas feeding duct numerical 3D simulation and the 0D model are outlined.

5. Discussion

The project promoted the penetration of a renewable source technology, which is efficient as it is cogenerative, into a portion of the market (the tertiary sector) which is currently almost exclusively the domain of photovoltaic technology. Another impact on the national power system is the reductions in both climate-altering emissions (reduction in carbon dioxide emissions as renewable and cogeneration source technology) and pollutant emissions (by using biomass-derived fuels in internal combustion engines there is a reduction in pollutant emissions compared to direct biomass combustion). By experimenting with the potential expansion of the use of virgin and residual biomass blend technology, the research program has enabled the expansion of the technology to the use of residual biomass resulting in the increased sustainability of the supply chain. Finally, it should be emphasized that the diffusion of a technology such as the one being tested allows for an increase in the share of electricity produced from renewable sources without affecting the stability of the electricity grid as the technology is programmable. These benefits for the grid are amplified by the fact that it is a distributed generation technology with simultaneous self-consumption. Therefore there is no significant power transmission and it consequently decongests the grid.

After more than five thousand hours' monitoring the 125-kW plant, it can be stated that this kind of plant, although functioning from a technical point of view, has not yet reached a technological maturity allowing it to be operated continuously without continuous close monitoring. It require costly and constant maintenance, with many variables that can affect the performance of the system, beginning with the quality of the wood chips.

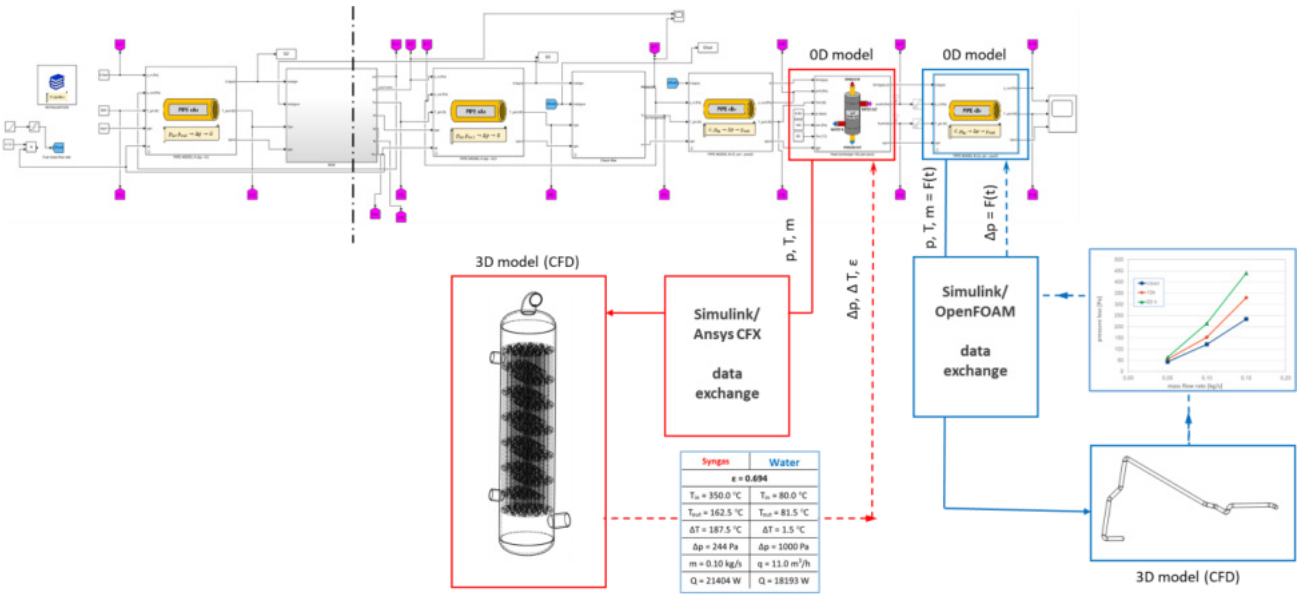

Figure. 8. 0D-3D methodology concept: interaction between the heat exchanger and syngas feeding duct 3D model results and the 0D lumped parameter model.

Since the raw material is inhomogeneous by nature, it is impossible to find standard operating conditions, as would be the case for a natural gas-fired plant. In addition, tar deposition creates major problems that require constant maintenance and cleaning. The cleanliness of the syngas, in terms of tar content, therefore, remains the point on which to focus research in order to make the plants more manageable.

It would be interesting to be able to feed the plants with residual biomass instead of virgin wood chips, e.g. those recovered from agricultural or forestry activities, to lower the cost of the feedstock. From an economic point of view, in fact, such plants can only be sustained in a context where there are incentives for the sale of energy.

5.1. Implemented plant improvements

Following an initial phase in which the plants were operated as delivered by the manufacturers, the following improvements were implemented:

- Substitution of the flaring torch with one more suitable for syngas, which has large passage sections, especially on the flame arrestor, to limit pressure drops because of tar condensation on this component. Moreover, to process syngas, a centrifugal fan with backward-curved blades and wide clearance between the case and rotor was adopted, so that any tar deposits would not compromise the functionality of the machine. Finally, the torch, compared to what was originally planned, was supplemented with support gas, to facilitate the ignition of the gas when it was still poor in the initial ignition phases, which also helped to limit the fouling of the torch itself;
- Insertion of a calm chamber upstream of the flare fan to limit the dust processed by the fan;
- Insertion of a metal filter upstream of the engine, to limit the presence of tar in the combustion chamber. Tar, if not burnt inside the engine cylinders, can condense as a result of low temperatures after mixing with air, creating a sticky layer that compromises engine functionality. A high molecular weight tar class condenses in the syngas-water exchanger; due to temperatures above around 105 °C, light-weight tar and water content do not condense in the heat exchanger. This metal filter, which operates at lower temperatures, allows the condensation of the moisture component and, by coalescence, the removal of a further proportion of the tar. This filter consists of a packed metal fiber. It preserves the life of the engine which, in the overall balance of the system, is a delicate and expensive component.

5.2. Designed improvements

Other solutions have been designed to further improve the plant, but they have not yet been implemented:

- Insertion of a cyclone between the gasifier and the main filter. By adopting this solution, it would be possible to eliminate an initial portion of carbon residues and thus relieve the ceramic filters of some of the fine dust. In this way, the frequency of pulsejet cleaning with compressed air would decrease, thus guaranteeing fewer interruptions to production and increasing the life of the filters. These filters tend to become fragile and break as a result of pulsejet cleaning; the cost of these components is not negligible and the intervention of stopping to replace them is rather onerous, so limiting the frequency of these occurrences would bring a significant benefit.

- Increasing the size of the filter case, by adding additional filter elements, would bring a benefit in terms of the quality of the syngas fed to the engine.
- It could be useful to include an ash/char removal system from the bottom of the gasifier, as is already present in the filter case, so that the frequency with which reactor cleaning is carried out can be reduced. In fact, this operation, carried out every 250 hours at the same time as the maintenance of the internal combustion engine, takes a long time (usually a couple of days) so that the system can cool down and be accessible by the operators. Doing so would also improve the general cleanliness, positively affecting the operational stability of the entire system.
- Following the CFD study, it was shown that the heat exchanger is not optimized and only condenses the tar in the last section of the tube bundle. Optimizing its fluid dynamics or simply adopting a longer heat exchanger could allow even more tar to be removed and feed a cleaner syngas to the engine.
- Increasing the cross-section of the piping, in addition to reducing pressure drops in general, could make it possible to reduce the frequency of any maintenance work, which entails disassembling the piping to remove any solidified tar that is obstructing the syngas passage.
- The flame arrestor serving the safety flare has very small gas passage sections and is extremely sensitive to the presence of tar. The deposition of tar on it leads to its complete obstruction with consequent problems for the functionality of the flare and safety problems in general, since the gas cannot find an outlet to the outside. The adoption of a hydraulic guard system, while bringing with it the burden of disposing of contaminated process water, would solve the problem of the fouling of the arrestor, which could be removed, itself representing an anti-backfire system. This would feed filtered syngas to the flare from the hydraulic stop, improving its performance.

Acknowledgments

The work was carried out within the framework of the research project ”SYNBIOSE - Gassificazione di biomasse lignocellulosiche in sistemi di cogenerazione di piccola taglia (<200 kW) per applicazioni nel settore terziario” (CUP G96G16000800003) funded by ”Cassa per i servizi energetici e ambientali” within the call ”Bando di gara per progetti di ricerca di cui all’art. 10, comma 2, lettera b) del decreto 26/1/2000, previsti dal Piano triennale 2012–2014 della ricerca di sistema elettrico nazionale e dal Piano operativo annuale 2013.”

Nomenclature

A	pre-exponential factor, s^{-1}
c	specific heat, J/(kg K)
C_{RF}	char reactivity factor [14]
G	Gibbs free energy, J/mol
K	equilibrium constant
LHV	lower heating value, kJ/kg or MJ/Sm^3
$\dot{m}$	mass flow rate, kg/s
R	gas constant, J/(mol K)
r	reaction rate, s^{-1}
s	stoichiometric coefficient
T	temperature, °C or K
x	molar fraction

Subscripts and superscripts

air	air
in	inlet
out	outlet
p	product
r	reactant
syn	syngas

References

[1] Ahmad, A. A., Zawawi, N. A., Kasim, F. H., Inayat, A., & Khasri, A., Assessing the gasification performance of biomass: A review on biomass gasification process conditions, optimization and economic evaluation. Renewable and Sustainable Energy Reviews 2016;53:1333-1347.

[2] Azzone, E., Morini, M., Pinelli, M., Development of an equilibrium model for the simulation of thermochemical gasification and application to agricultural residues. Renewable energy 2012;46:248-254.

[3] Gambarotta, A., Morini, M., Zubani, A., A non-stoichiometric equilibrium model for the simulation of the biomass gasification process. Applied Energy 2018;227:119-127.

[4] Havilah, P. R., Sharma, A. K., Govindasamy, G., Matsakas, L., & Patel, A., Biomass Gasification in Downdraft Gasifiers: A Technical Review on Production, Up-Gradation and Application of Synthesis Gas. Energies 2022;15(11):3938.

[5] Patuzzi, F., Prando, D., Vakalis, S., Rizzo, A. M., Chiaramonti, D., Tirler, W., Mimmo, T., Gasparella, A., Baratieri, M., Small-scale biomass gasification CHP systems: Comparative performance assessment and monitoring experiences in South Tyrol (Italy), Energy 2016;112:285-293.

[6] Stamponi, E., Giorgini, F., Cotana, F., Moretti, E., Preliminary assessment of a microgrid integrated with a biomass gasification CHP system for a production facility in Central Italy, E3S Web of Conferences 2021;238:01012.

[7] Mazhkoo, S., Dadfar, H., HajiHashemi, M., Pourali, O., A comprehensive experimental and modeling investigation of walnut shell gasification process in a pilot-scale downdraft gasifier integrated with an internal combustion engine, Energy Conversion and Management 2021;231:113836.

[8] Gambarotta, A., Manganelli, M., Morini, M., A model for filter diagnostics in a syngas-fed CHP plant. Energy Procedia 2018;148:400-407.

[9] Gambarotta, A., Manganelli, M., Morini, M., A model for the simulation of the gas cleaning system in a syngas-fed CHP plant. AIP Conference Proceedings 2019;2191(1):020084.

[10] Vulpio, A., Casari, N., Morini, M., Pinelli, M., Suman, A., Numerical investigation of a wood-chip downdraft gasifier. E3S Web of Conferences 2019;113:01002.

[11] Basu, P., Biomass Gasification, Pyrolysis and Torrefaction (Third Edition), Academic Press; 2018.

[12] Casari, N., Pinelli, M., Suman, A., Candido, A., Morini, M., Deposition of syngas tar in fuel supplying duct of a biomass gasifier: a numerical study. Fuel 2020;273:117579.

[13] Aldi, N., Casari, N., Pinelli, M., Suman, A., Vulpio, A., Performance Degradation of a Shell-and-Tube Heat Exchanger due to Tar Deposition. Energies 2022;15(4):1490.

[14] Sharma, A. K., Equilibrium and kinetic modeling of char reduction reactions in a downdraft biomass gasifier: A comparison. Solar energy 2008;82(10):918-928.

Process simulation of fuel production through integration of high-temperature co-electrolysis in a Biomass-to-Liquid process

Benjamin Steinrücken[a], Marcel Dossow[a], Maximilian Schmid[a], Maximilian Hauck[a], Sebastian Fendt[a], Florian Kerscher[a] and Hartmut Spliethoff[a]

[a] Chair of Energy Systems, Technical University of Munich, Munich, Germany,
benjamin.steinruecken@tum.de

Abstract:

To reduce greenhouse gas emissions in the aviation sector, the development of so-called sustainable aviation fuel (SAF) is indispensable. SAF can be produced via different synthesis routes and has identical properties to fossil-based conventional aviation fuel. Based on the results of previous research, a process pathway to produce SAF via a Biomass-to-Liquid (BtL) concept using entrained flow gasification and Fischer-Tropsch synthesis is simulatively investigated. To optimize overall process efficiency, high-temperature co-electrolysis can be integrated into the process chain resulting in a Power-and-Biomass-to-Liquid (PBtL) approach. Co-electrolysis makes it possible to split carbon dioxide as well as water electrochemically in a single apparatus and to produce synthesis gas with the required properties for Fischer-Tropsch synthesis. A detailed 0D Python model of a reversible solid oxide cell (rSOC) was developed at the Chair of Energy Systems to calculate the steady-state fuel cell and electrolysis operation based on a defined input parameter set. The validation using measured and literature data shows that the current density-cell voltage behaviour can be reproduced with an average relative error of less than 5%. Based on the existing BtL process, two concepts for the integration of co-electrolysis are identified and the 0D rSOC model is integrated into the Aspen Plus® flowsheet simulation. The newly developed process options are compared with alternative PBtL process variants showing that an identical product yield and carbon efficiency is achieved in different configurations and that electrical power demand can be significantly reduced by integrating co-electrolysis.

Keywords:

Power-and-Biomass-to Liquid; rSOC; Sustainable Aviation Fuels; co-electrolysis.

1. Introduction

To defossilize the aviation sector sustainable ‘‘drop-in’’ fuels are the only realistic strategy. These so-called sustainable aviation fuels (SAF) can be produced via the biomass-to-liquid (BtL) route. Using lignocellulosic biomass such as carbon-neutral biomass residues as feedstock, the thermochemical BtL route is based on combining high TRL gasification technology with Fischer–Tropsch synthesis (FTS). However, such processes typically result in low system performance because the carbon efficiency η_c of the overall process is limited [1]. The main reason for this is the low H/C ratio in the raw biomass resulting in the necessity of carbon removal from the syngas after gasification to reach a molar H_2/CO ratio of about 2 suitable for FTS.

Electrification of the BtL route can help to overcome the overall η_c limitation of the BtL pathway. Indirectly or directly electrifying the BtL process, results in a hybrid process which not only aims at increasing the processes product yield PY per input biomass, but also presents a way to defossilize the energy intensive sectors such as aviation or maritime transport. Such Hybrid Power-and-Biomass-to-Liquid (PBtL) systems thus enable higher η_c than BtL routes at lower electrolysis requirements than pure Power-to-Liquid (PtL) alternatives. Additionally, the energy efficiency of the such a process is greater than that of the pure biomass-based ones, while being less sensitive on the electricity price than PtL processes.

In indirect electrification, providing additional H_2 from water electrolysis powered by renewable electricity makes it possible to overcome the η_c limitation of conventional BtL processes. This concept not only allows overall η_c close to 100% but also enables complete utilization of the electrolysis products as O_2 produced in electrolysis can be used for gasification [2]. Several studies exist on this indirect PBtL approach [3–9] .

In direct electrification, electricity can be used within one of the BtL process steps itself for supplying energy to the process. One promising option for direct electrification of the BtL process is the use of high-temperature co-electrolysis in the form of solid oxide electrolysis (SOEL). In co-electrolysis H_2O and CO_2 are split into H_2, CO and O_2 in one single step. This enables the targeted production of synthesis gas, which is

why co-electrolysis is an alternative for the WGS reactor used in the existing BtL process or the separate production of green hydrogen in the indirect PBtL approach. The integration of a SOEL into the process is facilitated by the fact that reforming reactions are catalysed internally due to the electrode materials [10]. Consequently, the purity requirements for the fuel gas are low compared to other electrolysis processes and an in-cell conversion of low hydrocarbons is possible.

There are few published studies that consider integration between gasification and co-electrolysis and even fewer that include FTS as the fuel synthesis step. Integrating co-electrolysis into a BtL process the SOEL can be in parallel to the BtL process chain, using a CO_2 stream separated from the syngas for example during acid gas removal. Samavati et al. investigated a such a PBtL process option using entrained flow gasification (EFG) coupled with co-electrolysis with FTS [11] and Zhang et al. compared a different PBtL concepts using either SOEL in co-electrolysis mode or hydrogen addition from SOEL featuring an EFG and producing SNG, MeOH, DME or SAF via FTS [5]. Using a CO_2 streams separated from the main syngas stream results in an increased partial pressure of the reactants and the total volume flow through the electrolysis can be reduced resulting in economic savings. The resulting process variants allow for increased PY and energy efficiency compared to pure BtL processes. A similar approach is taken in Nielsen et al. [12]. Here, the SOEL is integrated into a BtL process with FTS, using the volatile products from the FTS reactor as the inlet stream [12]. When compared with process variants in which H_2 is added to the process by water electrolysis, the power requirement of the process can be reduced as a result of co-electrolysis and increased energy efficiency can be achieved [12].

The main objective of this work is to demonstrate to what extent the integration of co-electrolysis is a way to efficiently electrify the BtL pathway. To this end, the operating mode of a SOEL is first modelled in Python and then integrated into the BtL Aspen Plus® process simulation using suitable integration concepts. The process variants are then evaluated and compared to those of Dossow et al. 2021 [8]. Apart from the evaluation of the integration concepts developed within the scope of this work, further development possibilities for the individual SOEL integration options are also shown in the following.

2. Fundamentals

2.1. Reference (P)BtL Process Description

The PBtL model framework into which the 0D rSOC model is integrated is based on the work of Dossow et al. [8] with their PBtL pathway serving as a reference case and is shown in Figure 1. The pretreatment of the lignocellulosic feedstock consists of a dryer and the dried biomass stream is fed to a torrefaction reactor. The solid so-called torrcoal produced has a high energy density and is ground in a downstream mill to a defined particle size of less than 300 µm [8]. To produce synthesis gas with a low methane and tar content from the torrcoal, an oxygen-blown EFG is used in the PBtL process. In addition to the thermodynamic modelling approach for CO, CO_2, H_2O, H_2 and CH_4, the formation of N-, S- and Cl-containing compounds is also modelled, assuming a carbon conversion of 99% [8]. In addition to the solid torrcoal, the gaseous by-product streams from the torrefaction reactor and the light-ends from FTS are fed to the gasifier [8].

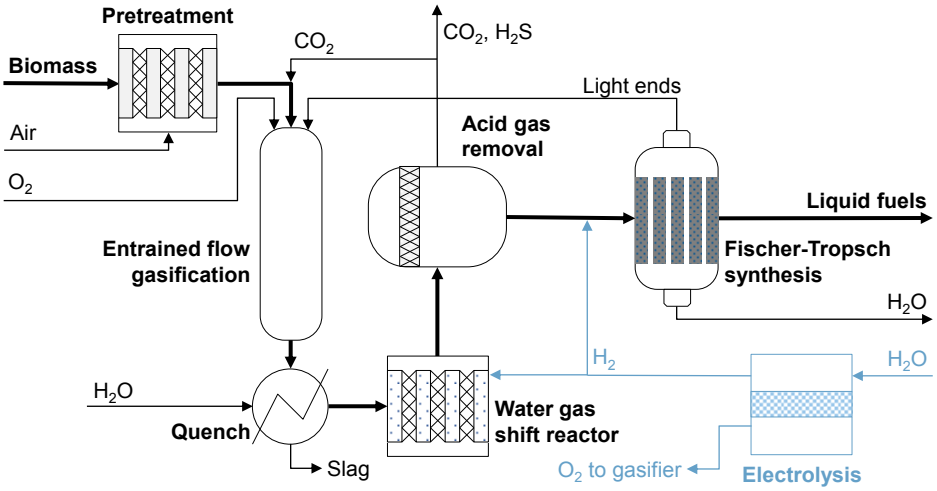

Figure 1. Schematic representation of the (P)BtL concept to produce SAF by Dossow et al. [8].

After EFG, slag and particles are removed, and the gas is abruptly cooled down by a water quench. Since halogen- and sulphur-containing impurities can lead to fouling in subsequent process steps or act as catalyst poisons, HCL is separated to a defined concentration by a chemically reactive filter system [8]. One of the key process parameters is the H_2/CO ratio of the synthesis gas. Typically, H_2/CO is below 1 directly after gasification and must be increased to a value of about 2 for the FTS. For this purpose, a sour WGS reactor

is used in the BtL process. It is assumed that the WGS reactor is operated isobarically and that the formation of H_2S and NH_3 is also catalysed in the reactor. The gas is then fed into an adsorption process that enables the separation of sulphur-containing components at high temperatures. The adsorbent used is ZnO, which is converted to zinc sulphide (ZnS) by a heterogeneous reaction. CO_2 is also removed from the synthesis gas in a downstream purification step. This is realised with the aid of a pressure swing adsorption (PSA) process, which is modelled in simplified form in the overall process. The products released in the process are removed from the process or, in the case of CO_2, partially used for pneumatic transport in the gasifier [8].

The synthesis gas prepared in the previous process steps is reacted in an FTS reactor at 230 °C and 20 bar using a cobalt-based catalyst. At the outlet of the reactor, the product stream is separated into a gaseous, an aqueous and an organic phase. The latter represents the crude fuel, which can be upgraded to SAF by a refinery process. The gas stream, which mainly contains unreacted synthesis gas and short-chain hydrocarbons, is fed into the FTS inlet stream or to the EFG via various recirculation routes. This can further increase overall η_c and PY [8]. The FTS reactor is modelled as a continuously operated stirred tank representing a slurry bed reactor. The reaction kinetics and product distribution are modelled using a macrokinetic model which is implemented as an object-oriented Python model using a FORTRAN subroutine that enables the exchange of calculation results between the two simulation environments [8].

In addition to the BtL process described above, Dossow et al. investigate different PBtL process variants. Here, an electrolyzer unit is integrated into the existing process and water is split into H_2 and O_2 which is then fed to the process. The electrolysers are assumed to be simplified stoichiometric reactors, with the product streams separated by a downstream separator [8]. An overview of the different PBtL process variants is provided in Table 1. Though the reference study contains both, PEMEL and SOEL, for comparison reasons in the following, only SOEL cases are considered.

Table 1. Indirect (P)BtL reference processes according to [8].

Process case	Description of the process modification
BtL case	Air separation is used to supply O_2 to the EFG. No electrolysis is used.
PBtL case 1	O_2 for the gasification is supplied from electrolysis instead of an air separation unit. The produced H_2 is fed partly to the WGS to adjust the H_2/CO ratio and partly to FTS.
PBtL case 2	No WGS to reduce complexity. H_2 is added to FTS to reach the desired H_2/CO ratio.
PBtL case 3	rWGS is used to convert CO_2 for maximum η_c H_2 is fed to FTS.

2.2. Solid oxide electrolysis (SOEL)

To substitute the WGS, a fuel electrode supported solid oxide electrolyser is chosen. A simplified model of the cell consists out of the supporting substrate layer, the electrolyte and the two electrode layers as shown in Figure 2.

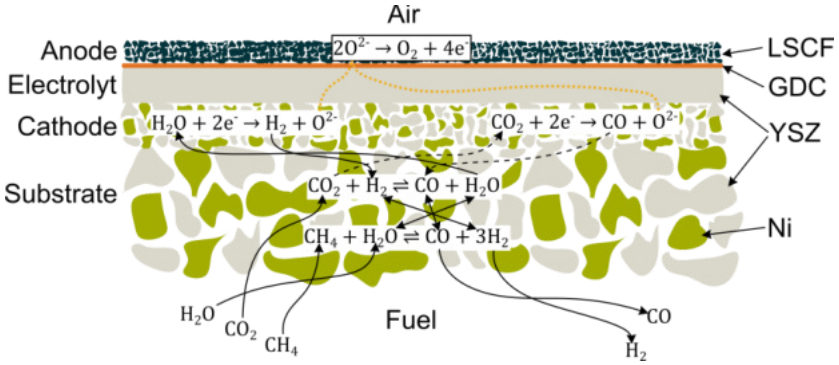

Figure 2. Schematic cross section of a solid oxide electrolysis with an internal reforming fuel.

The YSZ electrolyte is an O^{2-}-Ion conductor. The ions are created via the electrochemical reaction eq. 1 and eq. 2 under the consumption of electrons. These reactions are taking place at the triple phase boundaries where electrons from the electrically conducting nickel, Ions from the YSZ and gas from the porous layers meet.

$$H_2O + 2e^- \rightarrow H_2 + O^{2-} \quad (1)$$

$$CO_2 + 2e^- \rightarrow CO + O^{2-} \quad (2)$$

The simultaneous reduction of H_2O and CO_2 is referred to as co-electrolysis and, due to the catalysed side reactions, is based on a complex reaction network that has not yet been conclusively researched. Due to the high operating temperatures and the use of nickel, reforming and conversion reactions are catalysed on the surface of the fuel electrode in addition to the electrochemical reactions. The reaction equations for the steam reforming of methane eq. 3 and the reversed WGS reaction eq. 4 are given below, which take place when CH_4 or CO-containing fuel gas is fed to the fuel electrode. [13]

$$\mathrm{CH_4 + H_2O \rightleftharpoons CO + 3\,H_2} \qquad \Delta_R\overline{H}^0 = 206\,\frac{\mathrm{kJ}}{\mathrm{mol}} \tag{3}$$

$$\mathrm{CO_2 + H_2 \rightleftharpoons CO + H_2O} \qquad \Delta_R\overline{H}^0 = 41\,\frac{\mathrm{kJ}}{\mathrm{mol}} \tag{4}$$

These reactions take place in the substrate layer as well as in the fuel electrode layer. In addition to the already listed reaction equations, different pathways for the formation of CH_4 [14] or the separation of elemental carbon [15,16] are discussed in the literature. The extent to which the individual reactions are involved in the overall mechanism depends on the pressure and temperature as well as the process and material parameters due to the position of the reaction equilibrium [16–18]. To increase the efficiency of the SOEL, the O_2 generated on the anode side is discharged via a purge gas [16].

2.3. Electrochemical Model

The performance of the SOEL is calculated by subtracting the losses from the thermodynamically reversible cell voltage V_{Gibbs} calculated via eq. 6 by the global Gibbs Enthalpy difference of the reactions and the operational current J.

$$V_{Gibbs} = \frac{|\Delta G|}{J} \tag{5}$$

The global Gibbs enthalpy difference is calculated from the inlet and outlet streams via eq. 6.

$$\Delta\dot{G} = \dot{G}_{fuel,in} + \dot{G}_{oxy,in} - \dot{G}_{fuel,out} - \dot{G}_{oxy,out} \tag{6}$$

The operational voltage V_{op} of the electrolyser is calculated via eq. 7, by subtraction of the different loss mechanisms from the reversible cell voltage.

$$V_{op} = V_{gibbs} - \eta_{\mathrm{act}} - \eta_{ohm} - \eta_{diff} \tag{7}$$

The different loss mechanisms are included via over potentials: The activation over potential η_{act} is induced by the activation energy required for the electrochemical reaction. It is modelled with the Butler-Volmer formulation with a hyperbolic sine approach for fuel and oxygen electrode. The ohmic over potential η_{ohm} is induced by the temperature-dependent ohmic resistance of the electrolyte concerning the ion conduction and the constant contact resistance of the cell. The diffusion over potential η_{diff} models the loss mechanisms induced by the diffusion processes from the bulk phase to the electro-chemical reaction sites at the triple phase boundaries. These are modelled via Knudsen and binary diffusion for the fuel and the oxygen site. The bulk concentration is estimated via the mean over inlet and outlet concentrations with an inclusion of Methane and carbon monoxide for the hydrogen concentration. A complete description of the model used can be found in [19]. This recently updated model has been used in this work [20].

3. 0D rSOC Python Model

To meet the requirements of an open-source software solution with an simple syntax and object oriented paradigm, python coupled with Cantera is utilized for the thermodynamic equilibrium calculations. SOEL is still in the research and development phase (TRL<8), which is why the study results on co-electrolysis available in the literature are based on simulations or laboratory measurements on single cells or small stacks. In addition to the further development of the cell materials, the generation of synthesis gas is also the focus of research. The setting of the syngas parameters that is used to fuel the SOEL depends primarily on the composition of the inlet current and the location of the equilibrium of the WGS reaction. In addition, the current density has an influence on how much CO is formed.

3.1. SOEL Model

The calculation process of the SOEL model is shown in Figure 3: Both inlet gas streams are defined via their temperature, pressure, gas composition and flow rate. At the oxygen site, the temperature is increased to the operational temperature, the oxygen flow through the O^{2-}-Ions is added and in the last step the temperature is changed to the outlet temperature. At the fuel side after the temperature increase to operational temperature, an isothermal Gibbs reactor is positioned. Afterwards, the steam recycle stream is added and the electrochemical water splitting reaction takes place. The generated oxygen stream is removed and the chemical Gibbs equilibrium is formed. Afterwards, a portion of the stream is separated and recycled. In the last step, the temperature of the stream is changed to the outlet temperature. The steam recycle is required

to take the constantly ongoing water gas shift reactions in the cell into account. The positions of the Gibbs enthalpy for calculation of the global Gibbs enthalpy difference via eq. 5 are respectively marked.

To calculate the diffusion over potential, the partial pressures in the bulk phase are required. The inlet and outlet compositions x are used at the respective positions in the figure. For the over potential, the mean value between inlet and outlet is used. For the hydrogen diffusion, methane and CO are due to the water gas shift reaction and methane reforming considered as well.

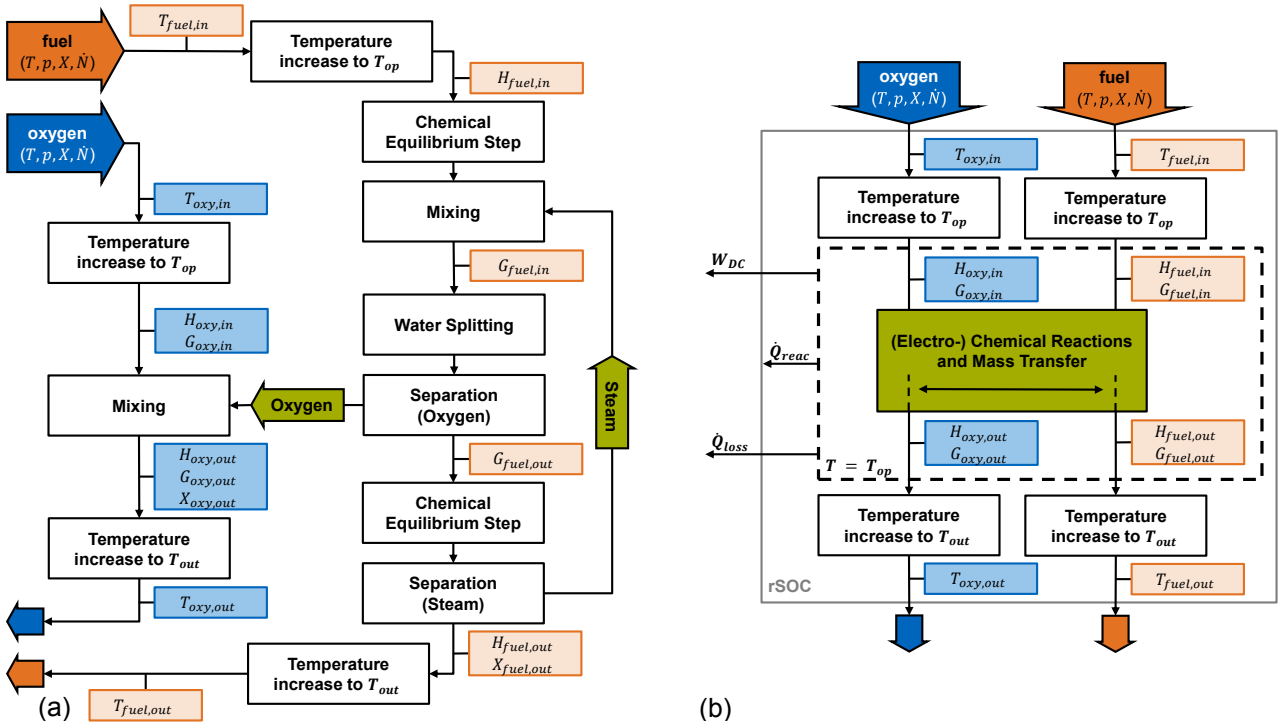

Figure 3. Calculation procedures of the SOEL model (a) and the energy balance (b).

All processes inside the SOEL model are isotherm at the operational temperature. Therefore, the energy balance is formulated via eq. 8.

$$\dot{Q}_R = \Delta\dot{H}_{oxy} + \Delta\dot{H}_{fuel} - W_{DC} - \dot{Q}_{loss} \tag{8}$$

The enthalpy difference of the inlet and outlet streams over the cell model, as well as the electrical power W_{DC}, heat losses $\dot{Q}_{loss}$ and the heat of reaction $\dot{Q}_R$ are considered. The positions for the enthalpy calculations of the streams are added into Figure 3.

3.2. Validation of the Python rSOC model

As described in [20], the parameters for the electrolyte activation energy and the electrolyte preexponential factor from [19] were optimized to fit experimental data. To validate the performance of the SOEL model for electrolysis and co-electrolysis operation experimental data is used [21]. The simulated data is compared to the experimental results for two different gas compositions in Figure 4.a). Gas composition A is a 50/50 H_2O/H_2, composition B is 25/25/25/25 $H_2/H_2O/CO/CO_2$. Both experiments were conducted at 770 °C.

The mean relative error of the SOEL mode is for the H_2/H_2O system 1.2 ± 1.2 % and for the co-Electrolysis operation with Gas B 0.5 ± 0.3 %. The accuracy of the model is reduced at higher current densities due to the increased influence of the diffusion losses. Due the usage of the mean concentrations over inlet and outlet for the bulk concentrations, nonlinear effects at low concentrations are not included. Besides the validated electrochemical performance of the cell, the fuel gas outlet composition of the electrolysis is crucial for a process integration. Hence, the outlet compositions for a relevant gas composition are validated as well, utilizing the experimental data from Schäfer et al. [15]. The model outlet concentrations are validated for an operation at 800 °C in a 10/60/30 $H_2/H_2O/CO_2$ gas composition. The comparison between the model and the experimental results by Schäfer are shown in Figure 4.b). For all gas species, an absolute error of the mole fraction of equal or below 0.02 is achieved. The accuracy of the model is high, expect for the methane concentration at high current densities. This relative high methane concentration at high current densities is discussed in Schäfer et al. [15], and is possible based on side reactions at the electrode. This phenomenon is still part of ongoing research.

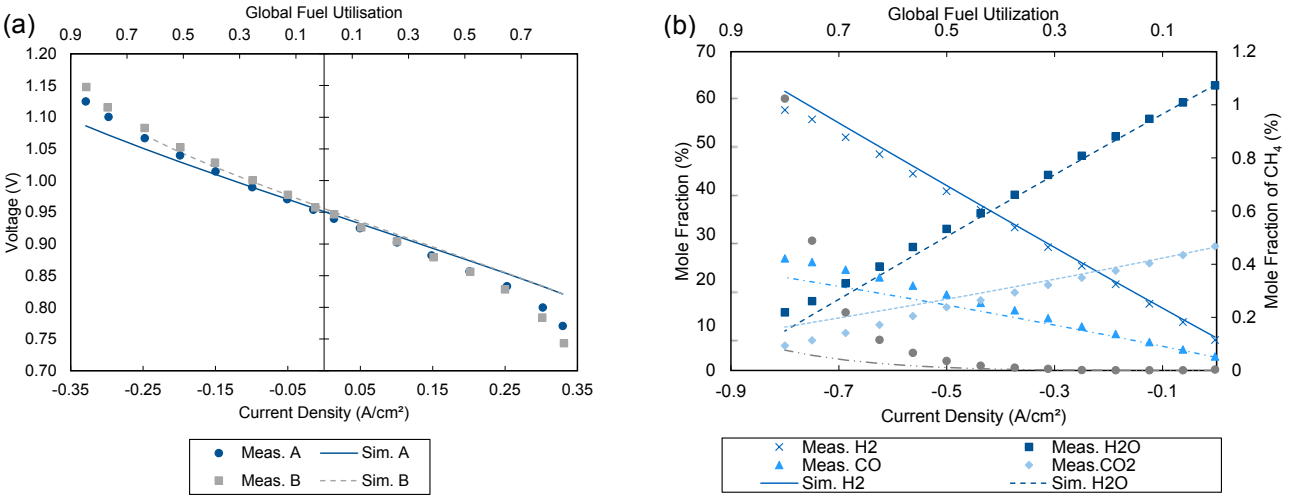

Figure 4. Validation of model performance with different fuels with experimental data [21] (a) and validation of the exhaust gas fractions in electrolysis mode with experimental data [15] (b).

4. PBtL Process Model using co-Electrolysis

The central objective of integrating co-electrolysis into the BtL process is to optimize and maximize the process in terms of PY, η_c, costs incurred and energy efficiency. For this purpose, the 0D rSOC model is integrated into the Aspen Plus® framework. Optimal points of integration of co-electrolysis into the BtL process are identified and suitable operational conditions are selected. To compare the different PBtL process options, a biomass inlet flow of 200 MW_{LHV} is assumed for all cases.

4.1. Integration of SOEL into PBtL Framework

The coupling between Python, FORTRAN and Aspen Plus® follows the procedure described in [8] as shown in Figure 5.a) For the integration of the rSOC into Aspen Plus®, a User2 model is used, as shown in Figure 5.b). This allows user-defined modelling of basic operations for any number of entry and exit streams. In addition to the material streams representing the entering and exiting fuel and O_2 streams, heat and work streams are also linked to the User2 block. Q-RSOC, Q-LOSS representing the heat of reaction and the heat losses that occur, and W-DC representing the required DC power, are calculated based on the energy balance solved within Aspen Plus®.

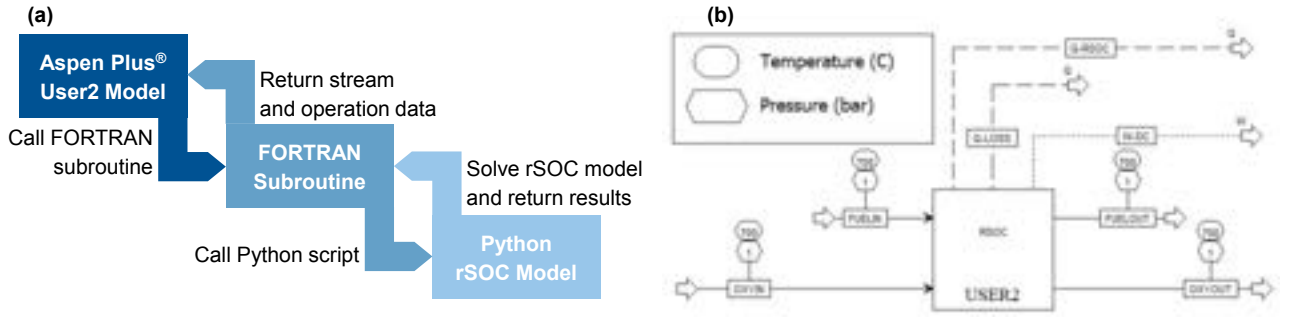

Figure 5. a) 0D rSOC Python model implementation in Aspen Plus® by using FORTRAN subroutine, b) Integration of subroutine into Aspen Plus® using USER2 model.

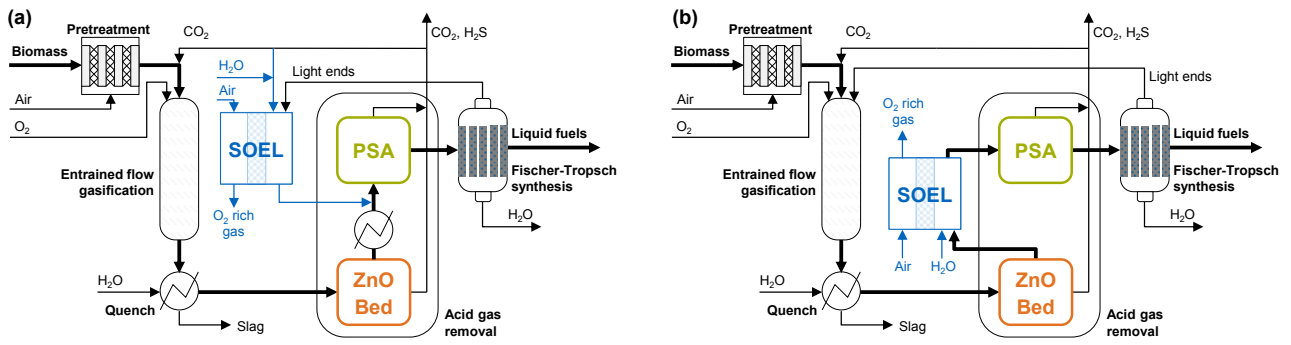

Figure 6. Process model for case I (a) and case II (b).

The SOEL makes it possible to produce H_2, O_2 and CO in one process step and to produce synthesis gas with defined properties. Thus, SOEL co-electrolysis offers an alternative to the WGS reactor as well as the additional feed of electrolytic H_2 as done in the reference PBtL process. For the PBtL concepts developed in this work, both, WGS and water electrolysis, can be dispensed. By removing the WGS reactor, the H_2/CO ratio of the synthesis gas required for the FTS must be adjusted with the help of co-electrolysis. The possible integration options are limited by catalyst poison and particle impurities in the raw syngas stream after gasification. If the SOEL is to be integrated into the main syngas stream, it must be located downstream of the ZnO bed and upstream of the CO_2 stream separation. At this point, the synthesis gas contains primarily H_2, CO, H_2O and CO_2 components. The catalyst poisons are removed down to very low concentrations <1 ppm. The corresponding process position is shown in Figure 6.a) and will be referred to as PBtL case I) in the following.

The SOEL makes it possible to produce H_2, O_2 and CO in one process step and to produce synthesis gas with defined properties. Thus, SOEL co-electrolysis offers an alternative to the WGS reactor as well as the additional feed of electrolytic H_2 as done in the reference PBtL process. For the PBtL concepts developed in this work, both, WGS and water electrolysis, can be dispensed. By removing the WGS reactor, the H_2/CO ratio of the synthesis gas required for the FTS must be adjusted with the help of co-electrolysis. The possible integration options are limited by catalyst poison and particle impurities in the raw syngas stream after gasification. If the SOEL is to be integrated into the main syngas stream, it must be located downstream of the ZnO bed and upstream of the CO_2 stream separation. At this point, the synthesis gas contains primarily H_2, CO, H_2O and CO_2 components. The catalyst poisons are removed down to very low concentrations <1 ppm. The corresponding process position is shown in Figure 6.a) and will be referred to as PBtL case I) in the following.

A second integration option is the insertion of a SOEL into the gaseous recycle stream of the FTS as shown in Figure 6.b). The FTS light ends primarily consist of unreacted H_2 and CO, as well as CH_4 and short-chain hydrocarbons, which can be converted to synthesis gas by the internally catalysed reforming reactions inside the SOEL. Since the corresponding material stream exits directly from the FTS reactor, the concentration limits for possible catalyst poisons are always met due to the upstream EFG. In this approach which locates the SOEL in parallel to the main syngas stream, the CO_2 contained in the main syngas stream after ZnO bed and SOEL is removed using a PSA. While part of the separated CO_2 is used as a carrier gas for the torrefied biomass at the gasifier section, the remaining CO_2 is recycled to the inlet fuel gas stream of the SOEL. This can increase η_c and PY. This PBtL case II) is similar to the approach of [12] for the integration of co-electrolysis into a BtL process with FTS. However, in the present work, as described at the beginning, the SOEL is used to adjust the H_2/CO ratio and, in contrast to [12], no additional WGS reactor is used.

4.2. Operational conditions of the SOEL

The SOEL are operated at atmospheric pressure and 800 °C. The active cell area and fuel utilisation are variable and defined in the simulation. The molar gas fractions are given in Table 2. The H_2S and HCl fractions are below ppm and thereby meet the quality requirements for the SOEL. Case II has non neglectable fraction of higher hydrocarbons in the range of C_2-C_4 from the FTS light end. Therefore, the risk of carbon formation for in case II is discussed in section 5.3.

Table 2. SOEL inlet gas fractions.

	H_2	H_2O	CO	CO_2	CH_4	C_{2-4}^{-}	$C_{2-4}^{=}$	HCl	H_2S
Case I	0.411	0.134	0.196	0.250	$8.69 \cdot 10^{-4}$	0.0	0.0	$8.30 \cdot 10^{-15}$	$8.08 \cdot 10^{-9}$
Case II	0.420	$1.72 \cdot 10^{-3}$	0.234	0.032	0.154	0.027	0.017	$1.90 \cdot 10^{-15}$	$9.25 \cdot 10^{-10}$

5. Results and Discussion

The PBtL cases I) and II) using co-electrolysis are evaluated in terms of operating parameters and possible heat integration. In addition, the occurrence of impurities and catalyst poisons as well as the formation of elemental carbon is considered.

The reference parameter used here is the syncrude produced in FTS, which is liquid at standard conditions (25 °C and 1 atm) and consists of a mixture of linear, saturated, and unsaturated hydrocarbons (mainly C5+). In addition to absolute parameters, such as the electrical power requirement or the raw syncrude or *fuel* mass flow produced, the focus of process development is on maximizing $PY = \dot{m}_{fuel} \cdot \dot{m}_{biomass,dry}^{-1}$, $\eta_c = \dot{m}_{C,fuel} \cdot \dot{m}_{C,biomass}^{-1}$, energy yield $EY = \dot{m}_{fuel} LHV_{fuel} \cdot \left(\dot{m}_{biomass} LHV_{biomass} + \dot{E}_{SOEL}\right)^{-1}$, and overall net energy efficiency $\eta_E = \dot{m}_{fuel} LHV_{fuel} \cdot \left(\dot{m}_{biomass} LHV_{biomass} + \dot{E}_{SOEL} + \dot{E}_{auxilaries}\right)^{-1}$.

5.1. Evaluation of the integration concepts

The operating behaviour of the SOEL can be influenced by the parameters FU and $\zeta_{CO_2,rcy}$. Suitable operating points for PBtL case I) are summarized for a fuel utilization between FU = 0.5 and 1.0 in Table 3. While U_Z increases only slightly between FU = 0.5 and 0.8, a very large increase is observed when comparing the cell stresses at FU = 0.9 and 1.0. This is due to mass transfer limitation because of high fuel utilization, which causes the over potentials to increase sharply. The ASR, whose value almost doubles for the two operating points starting from 0.25 to 0.47, confirms this assumption. $\dot{m}_{H_2O,SOEL}$ decreases with increasing FU, resulting in an overall lower total fuel flow entering the SOEL. As the inlet flow decreases, so does the area of the SOEL. Since the capital cost of a SOEL stack correlates with the area, this can be reduced because of operation at high fuel utilization. At this point, it should be noted that the conducted cell area determination is only a simple estimate for sizing the SOEL and shortening the computation time. For a comprehensive consideration of the integration concepts in the context of a techno-economic analysis, the choice of a constant active area is necessary.

Since the SOEL is directly integrated into the synthesis gas stream in PBtL case I), the product gas always exits with the same H_2/CO ratio of 2.10. This is not the case with integration at process position II). Here, the gaseous by-products of the FTS are reformed inside the SOEL and then recycled to the syngas stream. Since there is an H_2/CO ratio of about 1 at the outlet of the EFG, the H_2 content must be strongly increased in the used side recycle stream. Therefore, for the exemplary operating points investigated according to Table 3, a significantly higher H_2/CO ratio between 10.55 and 6.70 results, which decreases with increasing FU and $\zeta_{CO_2,rcy}$ and varies due to the composition of the FTS light ends stream.

At the operating points for PBtL case II), a larger additional water flow $\dot{m}_{H_2O,SOEL}$ enters the SOEL compared to case I). This is because the inlet fuel flow is coupled to the active area which decreases with increasing fuel utilization, whereas the supply of additional CO_2 leads to an increase. The ASR is determined to be a constant value of 0.20 for the simulated operating points regardless of the variable parameters FU and $\zeta_{CO_2,rcy}$. This indicates that no mass transfer limitations are simulated at a value of FU=0.9, which is confirmed by the slightly increasing values for cell voltage and DC power, respectively. The global fuel utilization is below the respective fuel utilization for the operating points investigated in the integration concepts. This serves as an input parameter in the simulation, and the difference between the two variables is due to the simplified modelling in co-electrolysis operation. To solve the energy balance around the SOEL, the inlet temperature of the oxygen stream is adjusted. This is limited by the maximum temperature level of the waste heat occurring in the process, which occurs at the exit of the EFG through a raw syngas cooler from 1400 °C to 1200 °C depending on the operating point. To ensure that the waste heat is also used efficiently in the integration concepts and that the temperature of the oxygen stream does not exceed the maximum limit, the mole flow at the oxygen electrode is increased as required for the simulated operating points. The ratio of oxygen and fuel mole flow is included in Table 3.

Table 3. SOEL parameters of selected operating points in PBtL cases.

Parameter	Unit	I.1	I.2	I.3	I.4	II.1	II.2	II.3	II.4
FU	-	0.50	0.80	0.90	1.00	0.50	0.50	0.90	0.90
$\zeta_{CO_2,rcy}$	-	-	-	-	-	0.50	0.90	0.50	0.90
U_Z	V	1.05	1.15	1.20	1.46	1.02	1.02	1.15	1.15
A_Z	m²	14545	13865	13629	13391	22895	27633	14331	15991
j	A/cm²	-0.41	-0.72	-0.83	-0.95	-0.50	-0.49	-0.90	-0.90
W_{DC}	MW_{el}	-63.0	-114.4	-136.4	-186.6	-117.5	-138.5	-148.9	-165.1
FU_{global}	-	0.37	0.65	0.76	0.87	0.46	0.45	0.82	0.82
ASR	Ω·cm²	0.22	0.23	0.25	0.47	0.20	0.20	0.20	0.20
$\dot{m}_{H_2O,SOEL}$	kg/s	6.31	5.42	5.12	4.78	22.47	25.75	14.08	15.16
$\frac{H_2}{CO}$	mol/mol	2.10	2.10	2.10	2.10	10.55	7.48	8.05	6.70
$\frac{O_2}{Fuel}$	mol/mol	1.00	1.00	1.00	1.00	1.50	1.50	1.50	2.00

5.2. Evaluation of the heat integration in the integration concepts

The indirect PBtL process variants developed by Dossow et al. are fully integrated with respect to the integration of the heat flows occurring within the process sequence [8]. The simulation results show that by using EFG, process heat is available at high temperature levels of over 1200 °C. In addition, the gasification, the WGS reaction as well as the FTS are exothermic process steps, whereby large heat flows are released.

These cover the required heat demand of the biomass pretreatment as well as the flue gas cleaning section. Based on the previous investigations, detailed modelling of the heat integration is omitted in this work. The integration of the SOEL into the process heat utilization is estimated using a $\dot{Q}$-T diagram.

For the PBtL case I), the $\dot{Q}$-T diagram representative for the operating point I.3 from Table 3 is shown in Figure 7.a). The curves show that despite the integration of the SOEL, sufficient process heat is available to cover the heat demand of the endothermic process steps. Starting from the maximum temperature level at 1293 °C, the heat is transferred between the occurring hot and cold heat flows. As can be seen from the graph, an excess heat flow of 116 MW_{th} remains at the cold end of the $\dot{Q}$-T diagram. This cannot be used within the process chain and must therefore be dissipated via additional cooling power to be expended. Since part of the waste heat is generated at an almost constant temperature level of approx. 230 °C, it could be used to generate process steam. The remaining heat flow must be removed from the process.

The $\dot{Q}$-T diagram of operating point II.4, which is shown in Figure 7.b), differs significantly from PBtL case I). Although the maximum temperature level of the waste heat present in the process is not exceeded, the curve of the cold heat flows plotted in blue is not completely below the red curve of the hot heat flows. As a result, assuming a minimum pinch point temperature difference of 10 K, additional process heat is required in the form of a cooling capacity of 112 MW_{th} and a heating capacity of 18 MW_{th}. The latter occurs at a very high temperature level of over 1235 °C and, with regard to the use of renewable energies, must be supplied with the aid of electricity or through the combustion of synthetic gases.

One possible reason for the increased heat demand is due to the high internal recycle ratio $\zeta_{CO_2,rcy} = 0.9$. As a result, the rWGS reaction, which is also endothermic, occurs in the SOEL in addition to the endothermic water electrolysis. To maintain the specified temperature difference across the SOEL of 0 K, the heat demand must be balanced by the enthalpy of the incoming oxygen gas stream. A large portion of the high-temperature process heat is transferred to this stream and the SOEL is heated to the operating temperature specified in the assumptions. Aa lower CO_2 recycle flow as well as the adjustment of the SOEL operating temperature can lead to a reduction of the high-temperature heat demand.

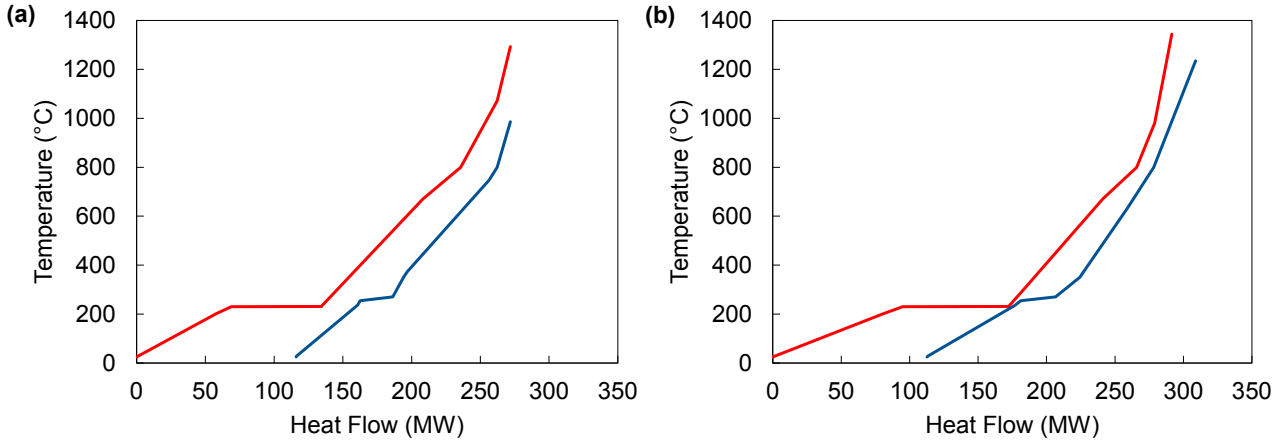

Figure 7. $\dot{Q}$-T diagrams of operating points I.3 (a) and II.4 (b) as a result of heat integration.

5.3. Discussion of the formation of carbon deposits

The SOEL is operated at 800 °C as part of the integration concepts. The risk of carbon deposition is investigated with a ternary diagram. On the fuel side, the recycle stream of the gaseous by-products of the synthesis FTS REC enters the SOEL hierarchy block. Its composition is within the carbon deposition region. With additional water and the CO_2 recycle stream defined by $\zeta_{CO_2,rcy}$ being introduced upstream of the electrolysis, the inlet composition at the SOEL is in a deposition free area. Despite FU = 0.9, the outlet composition is as well below the formation of carbon deposits. The integration into the FTS by-product stream requires a significantly higher H_2/CO ratio in the SOEL product gas to set the required syngas inlet parameters at the FTS reactor. At this point, it should be noted that in the FTS by-product stream, in addition to the unreacted syngas, the CH_4 and the short-chain hydrocarbons, long-chain, saturated and unsaturated hydrocarbons with more than four C atoms also occur in significant concentrations of several 100 ppm. These are not supported by the Cantera input file used in the simulation and are therefore considered inert in the rSOC Python model. In a real system, this is not the case. Here, the components are involved in the reactions taking place, and internal reforming of long-chain hydrocarbons is not possible. To prevent the rapid degeneration of SOEL, it is necessary to have an external pre-reforming step that converts the long-chain impurities.

5.4. Comparison with the Reference Processes

The influence of FU and $\zeta_{CO_2,rcy}$. on the overall process in terms of total electrical power demand, PY, and η_C for part of the operating points is shown in Figure 8. The electrical power requirement of the SOEL increases with fuel utilization. This determines the required electrical power in the overall process, with the additional auxiliary electrical power requirement ranging from 38.3 to 46.2 MW_{el}. With an increase in FU and $\zeta_{CO_2,rcy}$, PY increases and reaches a maximum value between 36.0% and 55.7% at operating point II.4. By incorporating co-electrolysis into the BtL process, the syngas composition can be influenced, and η_c can be more than doubles from 40.5% for the BtL process to 94.4% for the case II.4. Due to η_C and PY, operating points I.3 and II.4 are used for the comparison with the PBtL process variants according to [8].

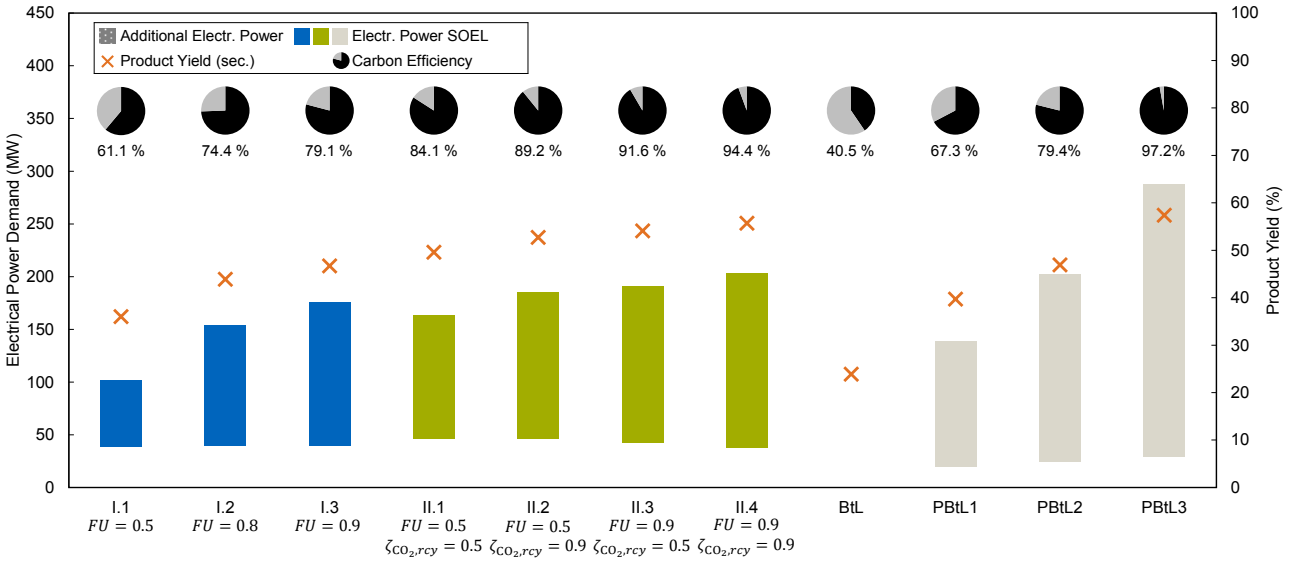

Figure 8. Overall process performance in terms of carbon efficiency, product yield and electrical power requirement for selected operating points of integration concepts I) and II) compared with the indircet (P)BtL process options according to Dossow et al. [8].

When comparing the different process options, it becomes clear how strongly the integration of electrolysis affects the electrical power requirement. While merely 18.7 MW_{el} is required for the BtL process, the value increases depending on the PBtL process variant up to a maximum of 287.4 MW_{el} for the indirect PBtL3 concept. The direct comparison of the integration concepts I.3 and II.4 with the PBtL process variants shows that almost identical product mass flows occur as for the indirect PBtL concepts 2 and 3. However, the power demand of the overall process can be significantly reduced by integrating co-electrolysis. The relative difference is 13.1% and 29.2% for the simulatively investigated cases I) and II), respectively.

Apart from the total electrical power P_{el} large deviations can also be observed in the inlet flows. The co-electrolysis concepts require more than three or four times the molar air flow than the indirect cases. The reason for this is the use of air as a purge gas for discharging the formed O_2 at the oxygen electrode of the SOEL. This is not considered in the PBtL process variants in Dossow et al. [8], so that only the air flow for the pretreatment of the biomass enters the process chain. It can be concluded that O_2 is produced in excess and cannot be further integrated into the process chain within the concepts presented here. When calculating the value, only the oxygen produced in the SOEL and consumed within the process chain is considered. The proportions in the purge gas used, if any, are not included. In addition to the air flow, the incoming hydrogen flow also increases in the integration concepts. This is due to an increased cooling demand in the quench section as well as the additional water flow to adjust the H_2/CO ratio. The latter is highly dependent on the SOEL operating point and can be reduced by adjusting the operating temperature and pressure.

It can be stated that by integrating co-electrolysis into the existing BtL process, large PY s as well as high η_c can be achieved, and the electrical power demand can be significantly reduced compared to the indirect PBtL process variants according to Dossow et al. [8]. A disadvantage is the high additional air and water flow required to operate the SOEL. To summarize to what extent EY and PY can be increased compared to the BtL concept, the relative deviations of both parameters with respect to the initial process are shown in Figure 9. While PY can be increased by up to 140% by incorporating electrolysis water or co-electrolysis, the increase in EY is lower at a maximum of 27%. However, this is strongly dependent on the respective process option, with values greater than 10% being achieved exclusively for the integration concepts developed in this work.

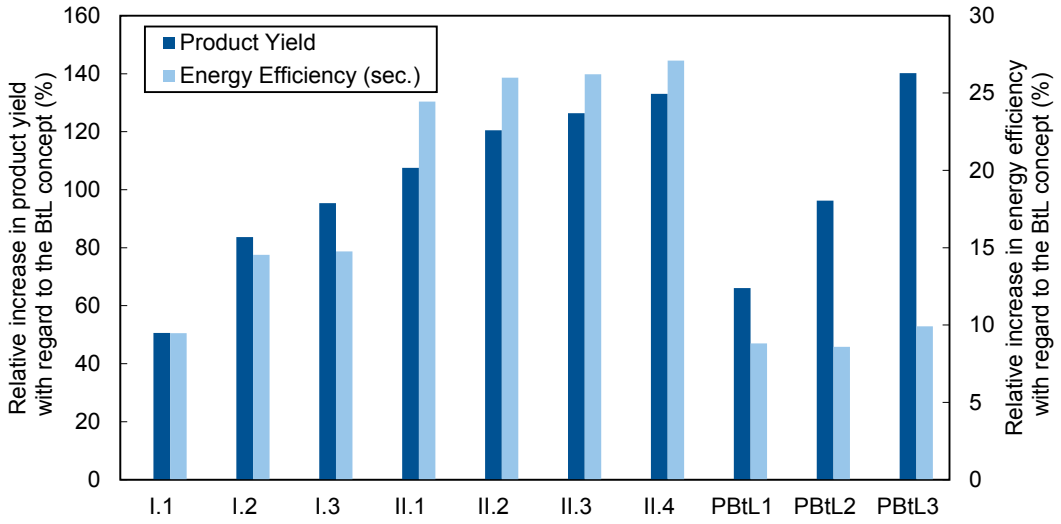

Figure 9. Relative increase in product yield and energy yield compared to the BtL process for the integration of co-electrolysis and the indirect PBtL process variants according to Dossow et al. [8].

6. Conclusion and outlook

To evaluate the suitability of the SOEL in co-electrolysis mode to enhance process efficiency of the BtL process, the newly developed 0D rSOC model is integrated into the existing simulation model. The SOEL replaces the WGS reactor and the additional feed of electrolysis hydrogen in the existing process chain. Two different process options are developed. In process option I, the SOEL is integrated into the syngas stream directly downstream of the ZnO bed, whereas in process option II the internally catalysed thermochemical reactions are used to reform the gaseous by-products of the FTS. In both cases, the SOEL is operated at 800 °C and 1 bar and optimized to set the necessary H_2/CO ratio for the synthesis. This is controlled by an additional water flow and the fuel utilization FU. In the integration concept II, the recirculation of the CO_2 stream separated in the EGR is also possible.

The simulation results of the developed process variants are compared with the PBtL reference processes from Dossow et al. [8]. In a first step, the influence of the fuel utilization FU assumed to be variable, and the CO_2 recycle ratio on the process parameters is investigated. The electrical power demand and PY increase with FU and CO_2 recycle ratio. A possible occurrence of carbon deposits is excluded with the help of the ternary diagram plot and the additional heating and cooling demand, if any, is estimated by a Q-T-diagram. The comparison with the PBtL process variants according to Dossow et al. [8] shows that an almost equal raw PY and η_c can be achieved in the integration concepts. The demand for electrical energy can be reduced by 27 MW_{el} and 84 MW_{el}, respectively, by integrating co-electrolysis for the simulative investigated operating points with an almost identical product flow. This corresponds to an increase in energy efficiency of up to eight percentage points, although the required air and water flow increases sharply. Nevertheless, the integration concepts developed in this work represent a promising alternative to the existing PBtL process variants due to the high product yields and the large potential savings in electrical power.

Numerous simplifying assumptions are made both in the creation of the Python rSOC model and in the integration of the SOEL into the BtL process. There is often the possibility to further develop the existing models and to increase their level of detail. For the Python rSOC model, the primarily concerns are the consideration of CO_2 electrolysis, which is neglected in the existing modelling approach, and the reduced accuracy at high fuel utilizations. Both issues can be addressed with an upgrade into a 1D model. Furthermore, the risk of carbon deposition for concept II is rather high, a more detailed investigation is required as well as the addition of a reformer prior to the SOEL. An investigation of the influence of the impurities at the SOEL to ensure a degradation free operation is required.

In simulative investigations of the integration concepts, constant SOEL operating parameters are assumed. Since these have a major influence on the position of the equilibrium of the internally catalysed reactions and therefore affect the product composition, the identification of an optimal operating range is conceivable. This could reduce the water and heating requirements as well as the associated costs. For a comprehensive comparison with the process variants according to Dossow et al. [8], a comprehensive heat integration as well as techno-economic analysis of the integration concepts is also required. In addition, it must be clarified how the O_2 rich purge gases can be further purified for use in the EFG.

7. Acknowledgments

The investigations have been supported by the Federal Ministry of Education and Research (BMBF) within the project REDEFINE H2E (01DD21005) which is gratefully acknowledged.

8. References

[1] Wenzel H. Breaking the biomass bottleneck of the fossil free society. CONCITO 2010.

[2] Agrawal R, Singh NR, Ribeiro FH, Delgass WN. Sustainable fuel for the transportation sector. Proceedings of the National Academy of Sciences of the United States of America 2007;104(12):4828–33.

[3] Bernical Q, Joulia X, Noirot-Le Borgne I, Floquet P, Baurens P, Boissonnet G. Integrated Design of High Temperature Steam Electrolysis and Biomass to Liquid Fuel Process. In: 11th International Symposium on Process Systems Engineering: Elsevier; 2012, p. 865–869.

[4] Hillestad M, Ostadi M, Alamo Serrano Gd, Rytter E, Austbø B, Pharoah JG et al. Improving carbon efficiency and profitability of the biomass to liquid process with hydrogen from renewable power. Fuel 2018;234:1431–51.

[5] Zhang H, Wang L, van herle J, Maréchal F, Desideri U. Techno-economic evaluation of biomass-to-fuels with solid-oxide electrolyzer. Applied Energy 2020;270:115113.

[6] Isaacs SA, Staples MD, Allroggen F, Mallapragada DS, Falter CP, Barrett SRH. Environmental and Economic Performance of Hybrid Power-to-Liquid and Biomass-to-Liquid Fuel Production in the United States. Environmental science & technology 2021;55(12):8247–57.

[7] Habermeyer F, Kurkela E, Maier S, Dietrich R-U. Techno-Economic Analysis of a Flexible Process Concept for the Production of Transport Fuels and Heat from Biomass and Renewable Electricity. Front. Energy Res. 2021;9.

[8] Dossow M, Dieterich V, Hanel A, Spliethoff H, Fendt S. Improving carbon efficiency for an advanced Biomass-to-Liquid process using hydrogen and oxygen from electrolysis. Renewable and Sustainable Energy Reviews 2021;152:111670.

[9] Pandey U, Putta KR, Rout KR, Rytter E, Blekkan EA, Hillestad M. Conceptual design and techno-economic analysis of biomass to liquid processes. Front. Energy Res. 2022;10.

[10] Dittrich L, Nohl M, Jaekel EE, Foit S, Haart LGJ de, Eichel R-A. High-Temperature Co-Electrolysis: A Versatile Method to Sustainably Produce Tailored Syngas Compositions. J. Electrochem. Soc. 2019;166(13):F971-F975.

[11] Samavati M, Martin A, Santarelli M, Nemanova V. Synthetic Diesel Production as a Form of Renewable Energy Storage. Energies 2018;11(5):1223.

[12] Nielsen AS, Ostadi M, Austbø B, Hillestad M, del Alamo G, Burheim O. Enhancing the efficiency of power- and biomass-to-liquid fuel processes using fuel-assisted solid oxide electrolysis cells. Fuel 2022;321:123987.

[13] Haart LGJ de, Beale SB, Deja R, Dittrich L, Duyster T, Fang Q et al. Forschungszentrum Jülich – Current Activities in SOC Development 2021.

[14] Nguyen VN, Blum L. Reversible fuel cells. In: Compendium of Hydrogen Energy: Elsevier; 2016, p. 115–145.

[15] Schäfer D, Fang Q, Blum L, Stolten D. Syngas production performance and degradation analysis of a solid oxide electrolyzer stack. Journal of Power Sources 2019;433:126666.

[16] Zheng Y, Wang J, Yu B, Zhang W, Chen J, Qiao J et al. A review of high temperature co-electrolysis of H2O and CO2 to produce sustainable fuels using solid oxide electrolysis cells (SOECs): advanced materials and technology. Chemical Society reviews 2017;46(5):1427–63.

[17] Foit S, Dittrich L, Nohl M, Vinke IC, Eichel R-A, Haart LGJ de. Understanding High-Temperature Electrolysis. ECS Trans. 2021;103(1):487–92.

[18] Peters R, Deja R, Blum L, van Nguyen N, Fang Q, Stolten D. Influence of operating parameters on overall system efficiencies using solid oxide electrolysis technology. International Journal of Hydrogen Energy 2015;40(22):7103–13.

[19] Hauck M, Herrmann S, Spliethoff H. Simulation of a reversible SOFC with Aspen Plus. International Journal of Hydrogen Energy 2017;42(15):10329–40.

[20] Hauck M, Schmid M, Herrmann S, Polat B, Steinruecken B, Poblotzki L et al. Modelling of an RSOC with Open Source Tools. European SOFC & SOE Forum Proceedings 2022:792–801.

[21] Preininger M, Stoeckl B, Subotić V, Schauperl R, Hochenauer C. Electrochemical Characterization and Performance Assessment of SOC Stacks in Electrolysis Mode. ECS Trans. 2019;91(1):2589–600.

PROCEEDINGS OF ECOS 2023 - THE 36TH INTERNATIONAL CONFERENCE ON
EFFICIENCY, **C**OST, **O**PTIMIZATION, **S**IMULATION AND ENVIRONMENTAL IMPACT OF ENERGY SYSTEMS
25-30 JUNE 2023, LAS PALMAS DE GRAN CANARIA, SPAIN

Economic and environmental impacts of integrating hydrogen-based technologies in the design optimization of sector-coupling energy systems in residential districts

Mohamed Eldakadosi[a] and Jana Schneeloch[b]

[a] *Fraunhofer UMSICHT, Oberhausen, Germany, mohamed.eldakadosi@umsicht.fraunhofer.de (**CA**)*
[b] *Fraunhofer UMSICHT, Oberhausen, Germany, jana.schneeloch@umsicht.fraunhofer.de*

Abstract:

Recent policies which promote climate-neutral energy systems and rising energy prices overburden the planners of energy supply systems. This leads to an increasing need for cost-effective, yet environmental-friendly, solutions. One interest-arousing approach is utilizing hydrogen-based technologies within cross-sectoral, residential energy systems. However, the economic and environmental potentials of this approach have not yet been fully uncovered. Hence, the aim of this work is to investigate the impacts of considering hydrogen-based technologies on the total costs and CO_2 emissions when designing a residential energy system. For this purpose, we developed a design optimization model using mixed-integer linear programming, whose main objective function is the minimization of total costs. The minimization of total CO_2 emissions is implemented as an epsilon constraint, where a Pareto front is created to represent optimal solutions under both objectives and their trade-off. Consequently, the optimal sizing and operation plan of the considered technologies to fulfill the energy demands of the residents are determined. Besides hydrogen-based fuel cells, electrolyzers, compressors and storage systems, the model includes photovoltaics, batteries, gas-based combined heat and power units, heat pumps, gas boilers and heat storage. For a case study of an exemplary German residential district, we carried out the design optimization for three energy systems, where two involved typical sector-coupling generation units and one included hydrogen technologies. Through the resulting Pareto fronts, we found that the energy system with hydrogen had a comparable, yet limited performance in terms of emissions reduction. However, the hydrogen system showed a poor economic competitiveness.

Keywords:

Cost Minimization, Emission Minimization, Hydrogen Systems, MILP Optimization, Sector Coupling

1. Introduction

Nowadays, planning energy systems for residential districts is facing more challenges. Decision planners must satisfy the rising energy demands while fulfilling other goals. Those goals include maintaining cost efficiency with increasing energy prices, mitigating CO_2 emissions to follow policies promoting climate-neutral energy systems, and integrating renewable energy resources with fluctuating generation. Therefore, it is becoming necessary to consider sector coupling, which describes connecting different energy sectors, such as electricity, gas and heat, while they interact with each other. Solutions to unlock the potential of sector coupling have been discussed in the literature, including electrification of heating, co-generation and power-to-gas [1–3].

Utilizing hydrogen as an energy carrier and involving it in cross-sectoral energy systems has recently attracted researchers and energy systems planners. It has been viewed as an alternative to fossil fuels and a possible storage medium for varying renewable energies. To produce and store hydrogen, electrolyzers and pressurized tanks can be used. Additionally, hydrogen can be fed to a fuel cell, which exploits electrochemical and thermodynamic hydrogen-oxygen reactions to simultaneously generate electricity and heat [4]. Solid oxide fuel cells (SOFC) and proton exchange membrane fuel cells (PEMFC) are the most installed types in residential energy systems. Nonetheless, a major drawback of hydrogen systems is their high capital and operating costs. Compared to other energy generation technologies, investing in fuel cells and electrolyzers is currently not a cost-efficient solution [5]. Another disadvantage for own hydrogen production and utilization is the low round-trip efficiency when converting electricity to hydrogen and then back to electricity [6]

Models to optimally size hydrogen-based technologies along with renewable and decentralized energy equipment have been the focus of multiple publications. For example, the authors in [7] presented a multi-objective design optimization model, using-mixed integer programming (MILP), for a multi-energy system in a neighborhood. The model included PEMFC and SOFC. While the latter could only use natural gas, the PEMFC could additionally consume hydrogen produced by a PEM electrolyzer and stored in high-pressure tanks. It has been

found that gas-based fuel cells were not optimally selected. Another optimization model to design energy hubs was introduced in [8]. It involved a fuel cell, an electrolyzer, a compressor and a refueling station. For the conducted use cases, it was not economic to install fuel cells. Another study in [9] demonstrated a developed model to optimize the sizing of an off-grid energy system for a village. The system contained a hydrogen system besides photovoltaics and batteries. The design of a similar energy system was optimized in [10], where the evolutionary algorithm and MILP were both implemented for the design and operation optimization.

We have observed that those studies focused on sizing hydrogen-based technologies as part of energy systems which also include typical generation and storage units. In most case studies, the hydrogen system was not favorable to be installed. However, it is not clear how the hydrogen systems will perform in terms of cost efficiency and emission reduction when comparing their optimal sizing and operation to typical cross-sectoral energy systems. Therefore, we created three energy systems, where a PEMFC and a PEM electrolyzer are essential elements in one of them. Using a multi-objective design optimization model, we compare the optimal solutions of the three energy systems at different points of optimal costs and emissions.

In this paper, the methodology is described in Section 2., which starts with an overview of the optimization model. Then, the objective function is presented in Section 2.2., followed by an explanation of the epsilon-constraint method in Section 2.3. Next, the model constraints are demonstrated for energy generation and storage in Section 2.4. and specifically for the hydrogen system in Section 2.5. In Section 3., the case study is illustrated. The structure of the energy systems is first clarified in Section 3.1., followed by the description of the input data in Section 3.2.. After that, the results are demonstrated in Section 3.3. and discussed in Section 3.4. Finally, Section 4. summarizes the presented work and suggests future studies as a conclusion.

2. Methodology

2.1. Overview and Implementation

To design residential energy systems under economic and environmental criteria, a multi-objective optimization model, formulated as a MILP problem, has been developed. Its aim is to minimize the total annual costs and total annual CO_2-equivalent emissions. In order to minimize two contradictory objectives, the epsilon-constraint method is utilized [11]. Simply put, the cost-minimization function is implemented as an objective function, while the emission-minimization function is applied as a constraint.

The model has been implemented using the python-based optimization package pyomo and the energy modeling package oemof-solph [12]. It provides modules that enable the modeling of various elements of an energy system. In the presented model, grids of electricity (EG) and gas (GG) are modeled by the *source* module, while the *sink* module portrays the electricity or heat demands of residential buildings. To connect different elements and ensure an energy balance, the *bus* module is added accordingly. Nevertheless, additional modules have been developed to model energy generation and storage units. In other words, decision variables and constraints describing the operation and design limits of a unit are defined inside the respective module. Those units include photovoltaics (PV), gas-based combined heat and power (G-CHP) units, battery storage (BATT), heat pumps (HP), gas boilers (GB), heat storage (HS), hydrogen fuel cell combined heat and power (FC-CHP), electrolyzers (EZ), hydrogen compressor (H2C), and hydrogen storage (H2S). This modular nature is advantageous for flexibly designing energy systems. Figure 1 provides an overview of the optimization model. It also demonstrates the inputs necessary to run the optimization model and the expected outcome of each run.

In the following subsections, a decision variable is denoted by a bold symbol, e.g., $\mathbf{P^{unit}_{out,max}}$, while a model parameter is represented by an italic symbol, e.g., $c^{unit}_{inv,a}$.

2.2. Cost-minimization function

For an optimization run, the decision variables are optimized such that the total annual costs are minimized. The objective function in (1) shows the components of the minimized costs.

$$\min : \sum_{unit} \left(\mathbf{C^{unit}_{inv,a}} + \mathbf{C^{unit}_{op,a}} \right) + \sum_{sto} \left(\mathbf{C^{sto}_{inv,a}} + \mathbf{C^{sto}_{op,a}} \right) + \sum_{grid} \left(\mathbf{C^{grid}_{imp,a}} \right) - \mathbf{R_{tot,a}} \tag{1}$$

For each unit, except for the EZ and H2C units, the annual investment cost $\mathbf{C^{unit}_{inv,a}}$ (Eur/a) is linearly dependent on the maximum output power $\mathbf{P^{unit}_{out,max}}$ (kW) as per (2). The slope of the linear function is the specific variable investment cost $c^{unit}_{inv,var,a}$ (Eur/kW/a), while the intercept is the fixed investment cost $C^{unit}_{inv,fix,a}$ (Eur/a). The latter is multiplied by the binary variable $\mathbf{y^{unit}_{inst}}$, which value decides whether the unit is installed. Regarding the annual operating cost $\mathbf{C^{unit}_{op,a}}$ (Eur/a), equation (3) includes a power-capacity-related operating cost, $c^{unit}_{op,fix,a}$ (Eur), and a variable operating cost, $c^{unit}_{op,var,a}$ (Eur/kWh), which refers to the total output power $\mathbf{P^{unit}_{out,t}}$ (kW) over all time steps t. Regarding EZ and H2C units, the specific investment and operating costs refer to the input power

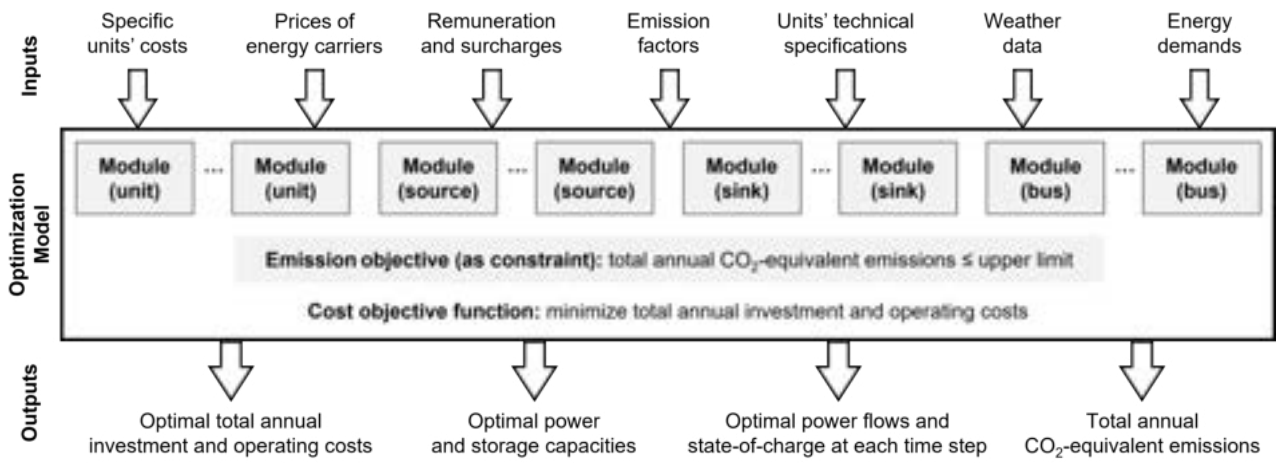

Figure 1: Overview of the developed optimization model including inputs and outputs. The optimization constraints and the decision variables are implemented accordingly in the modules.

of the unit $\mathbf{P^{unit}_{in,t}}$ (kW) or its maximum $\mathbf{P^{unit}_{in,max}}$ (kW) as demonstrated in (4) and (5). Similar to (2) and (3), the investment and operating costs for storage units (sto) are additionally considered in (6) and (7), respectively. In this case, $c^{sto}_{inv,var,a}$ (Eur/kWh/a) and $c^{sto}_{op,fix,a}$ (Eur/kWh/a) refer to the maximum usable energy capacity $\mathbf{E^{sto}_{max}}$ (kWh). Furthermore, the annual costs of importing electricity and gas from their respective grids are taken into account according to (8), where $c^{EG}_{imp,t}$ and $c^{GG}_{imp,t}$ (Eur/kWh) are the prices of electricity and gas, respectively, while $\mathbf{P^{EG}_{imp,t}}$ and $\mathbf{P^{GG}_{imp,t}}$ is the corresponding imported powers at a time step t.

$$\mathbf{C^{unit}_{inv,a}} = c^{unit}_{inv,var,a} \cdot \mathbf{P^{unit}_{out,max}} + C^{unit}_{inv,fix,a} \cdot \mathbf{y^{unit}_{inst}} \quad \text{for } unit \notin \{EZ, H2C\} \tag{2}$$

$$\mathbf{C^{unit}_{op,a}} = c^{unit}_{op,fix,a} \cdot \mathbf{P^{unit}_{out,max}} + c^{unit}_{op,var,a} \sum\nolimits_t \left(\mathbf{P^{unit}_{out,t}} \cdot \Delta t\right) \quad \text{for } unit \notin \{EZ, H2C\} \tag{3}$$

$$\mathbf{C^{unit}_{inv,a}} = c^{unit}_{inv,var,a} \cdot \mathbf{P^{unit}_{in,max}} + C^{unit}_{inv,fix,a} \cdot \mathbf{y^{unit}_{inst}} \quad \text{for } unit \in \{EZ, H2C\} \tag{4}$$

$$\mathbf{C^{unit}_{op,a}} = c^{unit}_{op,fix,a} \cdot \mathbf{P^{unit}_{in,max}} + c^{unit}_{op,var,a} \sum\nolimits_t \left(\mathbf{P^{unit}_{in,t}} \cdot \Delta t\right) \quad \text{for } unit \in \{EZ, H2C\} \tag{5}$$

$$\mathbf{C^{sto}_{inv,a}} = c^{sto}_{inv,var,a} \cdot \mathbf{E^{sto}_{max}} + C^{sto}_{inv,fix,a} \cdot \mathbf{y^{sto}_{inst}} \tag{6}$$

$$\mathbf{C^{sto}_{op,a}} = c^{sto}_{op,fix,a} \cdot \mathbf{E^{sto}_{max}} \tag{7}$$

$$\mathbf{C^{grid}_{imp,a}} = \sum\nolimits_t \left(\left(c^{EG}_{imp,t} \cdot \mathbf{P^{EG}_{imp,t}} + c^{GG}_{imp,t} \cdot \mathbf{P^{GG}_{imp,t}}\right) \cdot \Delta t\right) \tag{8}$$

Moreover, the energy system can generate annual revenues, R_a (Eur/a), by exporting excess electricity from PV and CHP units, denoted by $\mathbf{P^{PV}_{exp,t}}$ and $\mathbf{P^{CHP}_{exp,t}}$ (kW), respectively. For this case, the feed-in tariffs $r^{PV}_{exp,t}$ and $r^{CHP}_{exp,t}$ (Eur/kWh) are applied. Another source of revenues is the remuneration r^{CHP}_{rem} (Eur/kWh) for consuming a kWh of electricity from a CHP unit, symbolized by $\mathbf{P^{CHP}_{dem,t}}$ (kW), according to the CHP Act in Germany [13]. The total annual revenues are calculated as per (9).

$$\mathbf{R_{tot,a}} = \sum\nolimits_t \left(\left(r^{PV}_{exp} \cdot \mathbf{P^{PV}_{exp,t}} + r^{CHP}_{exp} \cdot \mathbf{P^{CHP}_{exp,t}} + r^{CHP}_{rem} \cdot \mathbf{P^{CHP}_{dem,t}}\right) \cdot \Delta t\right) \tag{9}$$

In this paper, the optimization horizon is one year. In order to consider investment costs of units of different lifetimes on an annual basis, they are discounted using the annuity factor as shown in (10). This factor depends on the average weighted cost of capital, *wacc*, and the lifetime of the unit, *LT* (years).

$$c^{unit}_{inv,a} = c^{unit}_{inv} \cdot \frac{wacc \cdot (1 + wacc)^{LT}}{(1 + wacc)^{LT} - 1} \tag{10}$$

2.3. Emission minimization using the epsilon-constraint method

In Fig. 2, the steps to implement the epsilon-constraint method for emission minimization are demonstrated. The aim is to create a Pareto front that shows the trade-off between costs and emissions. In the first step, the

optimization problem is created with the decision variables and the constraints of the energy system components and the cost-minimization objective function as shown in Fig. 1. Next, the constraint in (11) is added (Step 2), which implies that the total annual emissions at the first Pareto iteration, $\varepsilon_{tot,a,1}$ (kg CO_2-equivalent/a), has no limit since it is unknown before carrying out any optimization.

$$0 \leq \varepsilon_{tot,a,1} \leq \infty \tag{11}$$

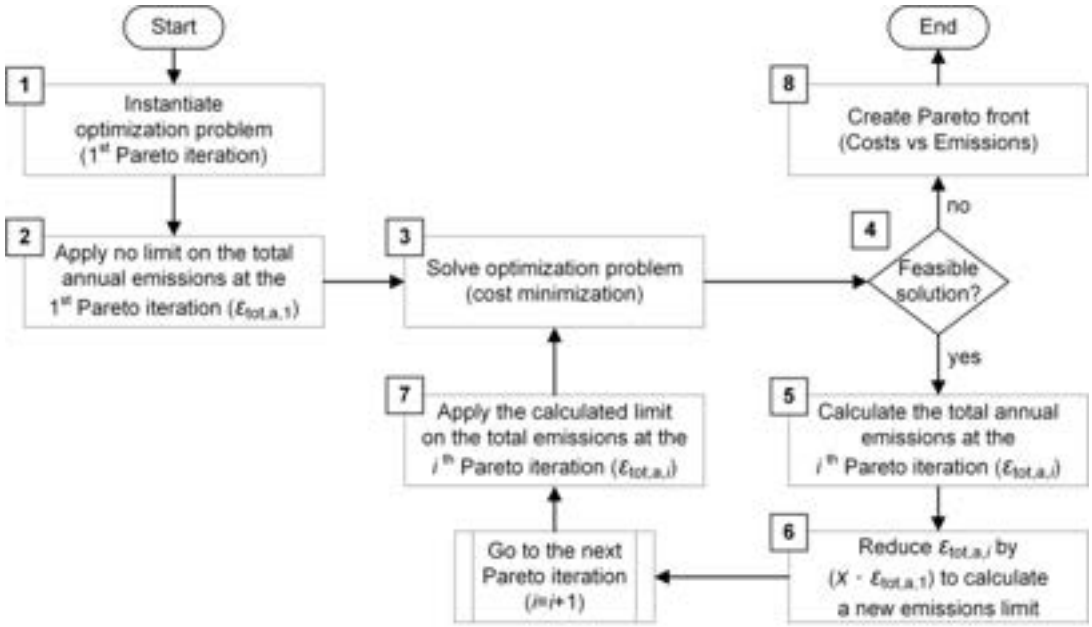

Figure 2: Process flow chart of the epsilon-constraint method.

After solving the optimization problem (Step 3), an if-statement checks whether a feasible solution has been found. If it is true, the total annual emissions at the i^{th} Pareto iteration, $\varepsilon_{tot,a,i}$ (kg CO_2-equivalent/a), is calculated as per (12) (Step 5). It involves the amount of CO_2-equivalent emissions of the district caused by importing electricity and gas, which is determined by the respective emission factors, ε^{EG}_{kWh} and ε^{GG}_{kWh} (kg CO_2-equivalent/kWh). However, the district can reduce these emissions by exporting PV and CHP electricity to the grid, which is represented by a negative emission factor in (12), and, hence, lower the emissions in the grid. For the following Pareto iteration, a new emission limit, $\varepsilon_{tot,max,a,i+1}$, is determined by deducting a percentage x of $\varepsilon_{tot,a,1}$ from $\varepsilon_{tot,a,i}$ as per (13) (Step 6). The new limit is then applied on the total annual emissions according to (14) (Step 7). The optimization is carried out again and the loop continues until the problem has no feasible solution; i.e., the emission-optimal solution has been found. Finally, the Pareto front is created to enable the analysis of the optimal design at different points of optimal costs and emissions (Step 8).

$$\varepsilon_{tot,a,i} = \sum_t \left(\left(\varepsilon^{EG}_{kWh} \cdot \mathbf{P^{EG}_{imp,i,t}} + \varepsilon^{GG}_{kWh} \cdot \mathbf{P^{GG}_{imp,i,t}} - \varepsilon^{EG}_{kWh} \cdot \left(\mathbf{P^{PV}_{exp,i,t}} + \mathbf{P^{grid}_{CHP,i,t}} \right) \right) \cdot \Delta t \right) \tag{12}$$

$$\varepsilon_{tot,max,a,i+1} = \varepsilon_{tot,a,i} - x \cdot \varepsilon_{tot,a,1} \tag{13}$$

$$0 \leq \varepsilon_{tot,a,i} \leq \varepsilon_{tot,max,a,i} \tag{14}$$

2.4. Constraints for energy generation and storage units

Based on a unit's input power, $\mathbf{P^{unit}_{in,t}}$ (kW), and its conversion factor, CF^{unit}, its output power $\mathbf{P^{unit}_{out,t}}$ (kW) is optimized as shown in (15). For instance, the conversion factors of a CHP unit are η^{CHP}_{el} and η^{CHP}_{th}, which describe the electrical and thermal efficiencies of converting the input fuel to electricity and heat, respectively, multiplied by the lower heating value of the input fuel. Another example of a conversion factor is a heat pump's coefficient of performance (COP). In this model, the COP is calculated for each time step based on the source and flow temperatures. Furthermore, the output power cannot surpass $\mathbf{P^{unit}_{out,max}}$ as per (16). In addition, the constraint in (17) implies that $\mathbf{P^{unit}_{out,max}}$ is limited between an upper bound, $P^{unit}_{max,upper}$, and a lower bound $P^{unit}_{max,lower}$, but only if the installation of that unit is optimal; i.e., $\mathbf{y^{unit}_{inst}}$ is selected to be 1.

$$\mathbf{P}^{\mathbf{unit}}_{\mathbf{out,t}} = CF^{unit} \cdot \mathbf{P}^{\mathbf{unit}}_{\mathbf{in,t}} \tag{15}$$

$$0 \leq \mathbf{P}^{\mathbf{unit}}_{\mathbf{out,t}} \leq \mathbf{P}^{\mathbf{unit}}_{\mathbf{out,max}} \tag{16}$$

$$\mathbf{y}^{\mathbf{unit}}_{\mathbf{inst}} \cdot P^{unit}_{out,max,lower} \leq \mathbf{P}^{\mathbf{unit}}_{\mathbf{out,max}} \leq \mathbf{y}^{\mathbf{unit}}_{\mathbf{inst}} \cdot P^{unit}_{out,max,upper} \tag{17}$$

For a PV unit, a time series of normalized output $P^{PV}_{out,norm,t}$ (kW/kWp) is obtained using the solar irradiation and weather data of the geographical location. Based on $P^{PV}_{out,norm,t}$ and the peak power $\mathbf{P}^{\mathbf{PV}}_{\mathbf{out,t}}$ (kWp), the PV output $\mathbf{P}^{\mathbf{PV}}_{\mathbf{out,t}}$ is determined in (18). Besides the constraint in (17), $\mathbf{P}^{\mathbf{PV}}_{\mathbf{out,t}}$ is limited in (19) by the total available area A^{PV}_{tot} (m^2), where A^{PV}_{kWp} (m^2/kWp) is the area of a kWp PV.

$$\mathbf{P}^{\mathbf{PV}}_{\mathbf{out,t}} = P^{PV}_{out,norm,t} \cdot \mathbf{P}^{\mathbf{PV}}_{\mathbf{out,max}} \tag{18}$$

$$A^{PV}_{kWp} \cdot \mathbf{P}^{\mathbf{PV}}_{\mathbf{max}} \leq A^{PV}_{tot} \tag{19}$$

Regarding a storage unit, equation (20) ensures the energy balance between the stored energy $\mathbf{E}^{\mathbf{sto}}_{\mathbf{t}}$ (kWh) at the current and previous time steps, along with the charging and discharging powers $\mathbf{P}^{\mathbf{sto}}_{\mathbf{ch,t}}$ and $\mathbf{P}^{\mathbf{sto}}_{\mathbf{dis,t}}$ (kW), and the respective charging efficiencies η^{sto}_{in} and η^{sto}_{out}. To represent self-discharging losses, the parameter σ^{sto}_{self} represents the percentage of energy lost per hour. The constraints in (21) to (23) represent the bounds for $\mathbf{E}^{\mathbf{sto}}_{\mathbf{t}}$, $\mathbf{P}^{\mathbf{sto}}_{\mathbf{ch,t}}$ and $\mathbf{P}^{\mathbf{sto}}_{\mathbf{dis,t}}$. In order to prevent simultaneous charging and discharging, the binary variable $\mathbf{y}^{\mathbf{sto}}_{\mathbf{ch,t}}$ is utilized in (24) and (25). If it is 1, then the storage unit is being charged. Similar to (17), optimizing $\mathbf{E}^{\mathbf{sto}}_{\mathbf{max}}$ is limited between $E^{sto}_{max,upper}$ and $E^{sto}_{max,lower}$ (kWh) with the association of $\mathbf{y}^{\mathbf{sto}}_{\mathbf{inst}}$.

$$\mathbf{E}^{\mathbf{sto}}_{\mathbf{t}} = \mathbf{E}^{\mathbf{sto}}_{\mathbf{t-1}} \cdot \left(1 - \sigma^{sto}_{self}\right) + \left(\mathbf{P}^{\mathbf{sto}}_{\mathbf{ch,t}} \cdot \eta^{sto}_{ch} - \mathbf{P}^{\mathbf{sto}}_{\mathbf{dis,t}} / \eta^{sto}_{dis}\right) \cdot \Delta t \tag{20}$$

$$0 \leq \mathbf{E}^{\mathbf{sto}}_{\mathbf{t}} \leq \mathbf{E}^{\mathbf{su}}_{\mathbf{max}} \tag{21}$$

$$0 \leq \mathbf{P}^{\mathbf{sto}}_{\mathbf{ch,t}} \leq \mathbf{P}^{\mathbf{sto}}_{\mathbf{max}} \tag{22}$$

$$0 \leq \mathbf{P}^{\mathbf{sto}}_{\mathbf{dis,t}} \leq \mathbf{P}^{\mathbf{sto}}_{\mathbf{max}} \tag{23}$$

$$0 \leq \mathbf{P}^{\mathbf{sto}}_{\mathbf{ch,t}} \leq \mathbf{y}^{\mathbf{sto}}_{\mathbf{ch,t}} \cdot P^{sto}_{max,upper} \tag{24}$$

$$0 \leq \mathbf{P}^{\mathbf{sto}}_{\mathbf{dis,t}} \leq \left(1 - \mathbf{y}^{\mathbf{sto}}_{\mathbf{ch,t}}\right) \cdot P^{sto}_{max,upper} \tag{25}$$

When connecting units, sources and sinks to each other, a bus component is included accordingly in the energy system. Its addition is equivalent to considering (26), which guarantees that the sum of all inflows equals the sum of all outflows at any time step. A special case of the bus component is the heat network (HN) module, where the inflows are multiplied by an efficiency parameter, η_{HN}, to describe distribution losses as per (27).

$$\sum\nolimits_{inflow} \mathbf{P}^{\mathbf{bus}}_{\mathbf{inflow,t}} = \sum\nolimits_{outflow} \mathbf{P}^{\mathbf{bus}}_{\mathbf{outflow,t}} \tag{26}$$

$$\sum\nolimits_{inflow} \mathbf{P}^{\mathbf{HN}}_{\mathbf{inflow,t}} \cdot \eta^{HN} = \sum\nolimits_{outflow} \mathbf{P}^{\mathbf{HN}}_{\mathbf{outflow,t}} \tag{27}$$

2.5. Constraints for hydrogen-based units

The presented constraints for hydrogen-based units are based on the work in [14], where an operation optimization model for energy systems with EZ, H2C, H2S and FC-CHP has been developed. The first component in a hydrogen system is the electrolyzer, which generates the hydrogen gas using electrical work. Equation (28) shows how the output mass flow $\dot{\mathbf{m}}^{\mathbf{EZ}}_{\mathbf{out,t}}$ (kg/h) is dependent on the input power $\mathbf{P}^{\mathbf{EZ}}_{\mathbf{in,t}}$ (kW), the standard density of hydrogen ρ_{h_2} (kg/Nm^3), and the specific energy consumption $e^{EZ}_{h_2}$ (kWh/Nm^3). Moreover, $\mathbf{P}^{\mathbf{EZ}}_{\mathbf{in,t}}$ is limited below $\mathbf{P}^{\mathbf{EZ}}_{\mathbf{max}}$ as formulated in (29). The latter is also confined in (30) by $P^{EZ}_{in,max,upper}$, $P^{EZ}_{in,max,lower}$ and $\mathbf{y}^{\mathbf{EZ}}_{\mathbf{inst}}$.

$$\dot{\mathbf{m}}^{\mathbf{EZ}}_{\mathbf{out,t}} = \mathbf{P}^{\mathbf{EZ}}_{\mathbf{in,t}} \cdot \rho_{h_2} / e^{EZ}_{h_2} \tag{28}$$

$$0 \leq \mathbf{P}^{\mathbf{EZ}}_{\mathbf{in,t}} \leq \mathbf{P}^{\mathbf{EZ}}_{\mathbf{in,max}} \tag{29}$$

$$\mathbf{y}^{\mathbf{EZ}}_{\mathbf{inst}} \cdot P^{EZ}_{in,max,lower} \leq \mathbf{P}^{\mathbf{EZ}}_{\mathbf{in,max}} \leq \mathbf{y}^{\mathbf{EZ}}_{\mathbf{inst}} \cdot P^{EZ}_{in,max,upper} \tag{30}$$

The output of the EZ unit is then fed to an H2C unit to compress the hydrogen and enable its storage in high-pressure tanks. A balance constraint, as shown in (31), is applied to the input and output mass flows. Based

on the hydrogen flow, the necessary power for compression, $\mathbf{P^{H2C}_{in,t}}$, is found in (32) using the electric efficiency η^{H2C}_{el} and the specific enthalpies at the compressor's inlet and outlet, h^{H2C}_{in} and h^{H2C}_{out} (J/kg), respectively. Both parameters depend on the pressure of the input, p^{H2C}_{in} (bar), and the output, p^{H2C}_{out} (bar), as well as the temperature at the inlet, T^{H2C}_{in} (K). The calculation is carried out using the python-based function *PropsSI* [15], which finds the value of a thermophysical property for a selected fluid by inputting the values of two other properties. Additionally, a factor of $3.6 \cdot 10^{-6}$ is used in (32) to obtain the result in kW. Constraints similar to (29) and (30) are applied to $\mathbf{P^{H2C}_{in,t}}$ and $\mathbf{P^{H2C}_{in,max}}$ with the corresponding parameters of the H2C unit.

$$\mathbf{\dot{m}^{H2C}_{in,t}} = \mathbf{\dot{m}^{H2C}_{out,t}} \tag{31}$$

$$\mathbf{P^{H2C}_{in,t}} = 3.6 \cdot 10^{-6} \cdot \mathbf{\dot{m}^{H2C}_{in,t}} \cdot \left(h^{H2C}_{out} - h^{H2C}_{in} \right) / \eta^{H2C}_{el} \tag{32}$$

To identify the charging and discharging powers of the H2S unit, the average storage enthalpy h^{H2S}_{avg} (J/kg) is found using *PropsSI* by inputting the maximum and minimum storage pressures, p^{H2S}_{max} and p^{H2S}_{min} (bar), respectively, and the storage temperature T^{H2S} (K). The operating powers are then determined by (33) and (34). Analogous to (20), the stored energy E^{H2S}_{t} (kWh) is tracked at each time step as per (35). Further, the storage constraints (21) to (25) are applied to the energy and power variables of the H2S unit. Finally, the operation and design constraints of an FC-CHP unit are identical to the generation units' constraints in (15) to (17).

$$\mathbf{P^{H2S}_{in,t}} = 3.6 \cdot 10^{-6} \cdot \mathbf{\dot{m}^{H2S}_{in,t}} \cdot h^{H2S}_{avg} \tag{33}$$

$$\mathbf{P^{H2S}_{out,t}} = 3.6 \cdot 10^{-6} \cdot \mathbf{\dot{m}^{H2S}_{out,t}} \cdot h^{H2S}_{avg} \tag{34}$$

$$\mathbf{E^{H2S}_{t}} = \mathbf{E^{H2S}_{t-1}} + \left(\mathbf{P^{H2S}_{ch,t}} - \mathbf{P^{H2S}_{dis,t}} \right) \cdot \Delta t \tag{35}$$

3. Case Study

3.1. Structure of energy systems under investigation

To examine the hydrogen system economically and environmentally, a case study of an exemplary German residential district is conducted, where three energy systems (ES) are created. Two systems, ES 1 and 2, represent typical sector-coupling approaches. Figure 3 demonstrates the complete energy system, how the units are interconnected and which units are included in each ES. In ES 1, the primary heat supplier is a gas-CHP unit. It can also feed the electricity demand and export excess generation. In ES 2, a heat pump is solely responsible for heat generation. Finally, an FC-CHP unit is taken into account in ES 3. In this energy system, the electrolyzer produces hydrogen at 35 bar, which is then compressed to 300 bar to be stored in the hydrogen storage. In ES 1 and 3, a gas boiler is additionally considered for peak heat demands. In all systems, PV units can be installed to cover the electricity demand, supply the heat pump (in ES 2) or the electrolyzer and the compressor (in ES 3), or export the surplus energy to the grid. Besides, all energy systems can include batteries and heat storage units. The bus component *heat network* connects the central heat generation node to the demand with 5% distribution losses.

3.2. Input data

The district under study includes 13 multi-family houses with electricity and heat demands. The demand profiles were generated based on the guideline VDI 4655 [16] for one year, assuming that the total annual demands amount to 244 MWh of electricity and 1030 MWh of heat. The peak loads of both demands are 48 kW_{el} and 670 kW_{th}. The majority of the input data used, including prices of energy carriers, remunerations, surcharges and weather data, is based on the year 2020. To import electricity from the grid, a time-varying price with a mean of 0.304 Eur/kWh is applied, which is based on day-ahead prices and additional network charges and taxes [17,18]. For importing gas, a constant price of 0.076 Eur/kWh is inputted [19]. In the case of exporting PV or CHP electricity, the energy system receives revenue of 0.065 Eur/kWh [20] and 0.087 Eur/kWh [13, 21], respectively. A remuneration of 0.0305 Eur/kWh is additionally awarded for the own consumption of CHP electricity [13]. Concerning the costs of technologies, linear investment functions and operating costs have been extracted from several studies and market data for PV [22], battery [9], gas CHP, gas boiler, heat pumps, heat storage [23], FC-CHP [24], electrolyzer [25], hydrogen compressor [26] and hydrogen storage [8] units. Furthermore, only emissions from importing electricity and gas from respective grids are taken into account in this study. Hence, emission factors of 0.438 [27] and 0.228 kg CO_2-equivalent [28] per kWh of imported electricity ang gas, respectively, are inputted.

A flat roof area of 4000 m^2 in total is available for the PV modules. These modules can be mounted with two different configurations: a south orientation or an east-west orientation. The available area corresponds to

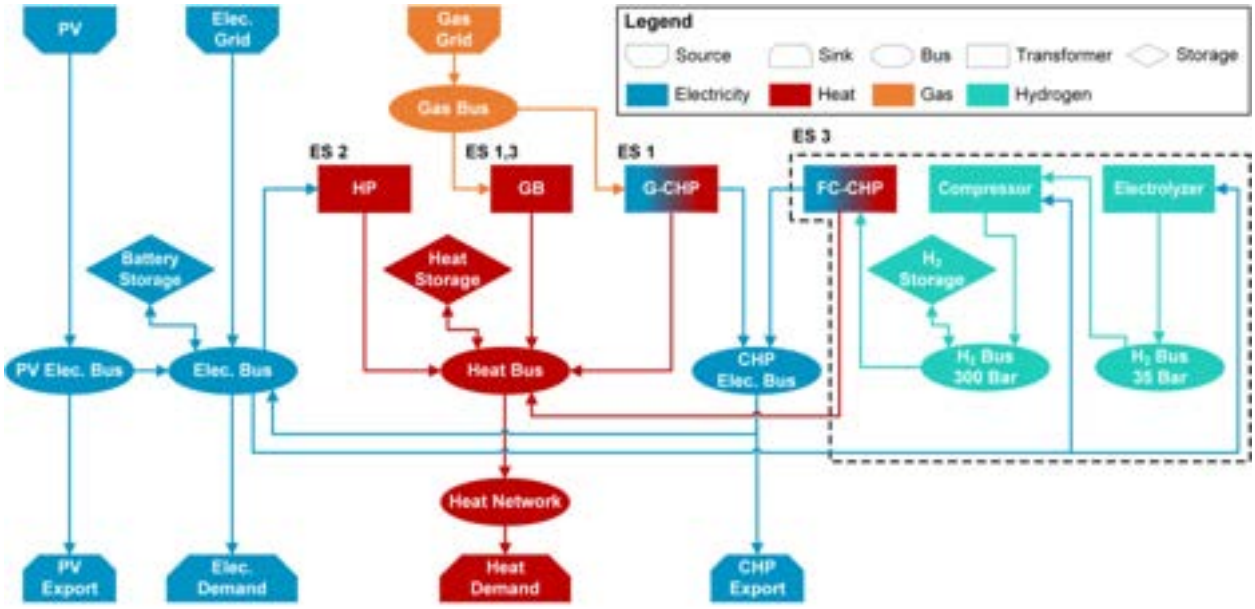

Figure 3: Complete structure of the optimized residential energy systems. Categorization of the elements follows the description in Section 2.1. The abbreviation ES implies in which energy system a unit is considered. ES 1 has a G-CHP and GB, ES 2 has only an HP, and ES 3 has a GB and hydrogen-based units.

331.5 kWp of south-oriented PV or 796 kWp of east-west-oriented PV. The PV output for each configuration, in addition to ambient temperature data, was obtained from PVGIS [29]. For the heat pump, the COP was calculated based on the given data in [30] for a flow temperature of 65 °C. The remaining technical specifications of the units are based on [4, 14, 23]. Since the gas boiler is installed to only support the main heat generator in ES 1 and 3, its sizing is limited to 400 kW.

3.3. Results

The following demonstrated results are obtained by solving the optimization problem with an hourly temporal resolution for each energy system, for multiple iterations, using the solver Gurobi [31]. Following the method presented in Section 2.3., the emission limit is reduced by x = 5% (Step 6 in Fig. 2) of the initial total annual emissions, calculated at the first Pareto iteration. Figure 4 illustrates the Pareto fronts of each energy system. Each point on the plotted curves corresponds to a solution with an optimal total annual cost for a set total annual emission. For each curve, the point on the far right portrays the cost-minimum solution (first Pareto iteration), while the far-left point represents the emission-minimum solution (last Pareto iteration). The curves also depict the best solutions in terms of costs and emissions; i.e., there are no feasible solutions with better cost-emission combinations below or to the left of the curve. For further investigation, the optimal unit sizing in terms of maximum power and maximum storage capacity is plotted for each ES in Fig. 5, while costs and emissions are demonstrated by respective categories in Fig. 6. In both figures, only selected Pareto iterations, including the first and the last, are shown for improved readability.

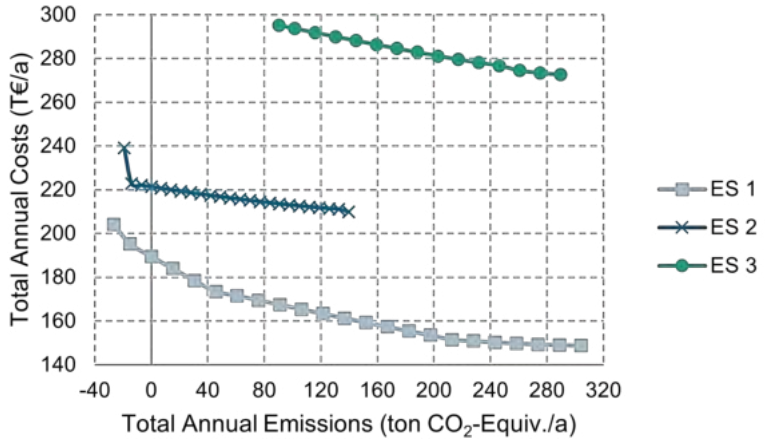

Figure 4: Pareto front (total annual costs vs. total annual emissions) of each energy system.

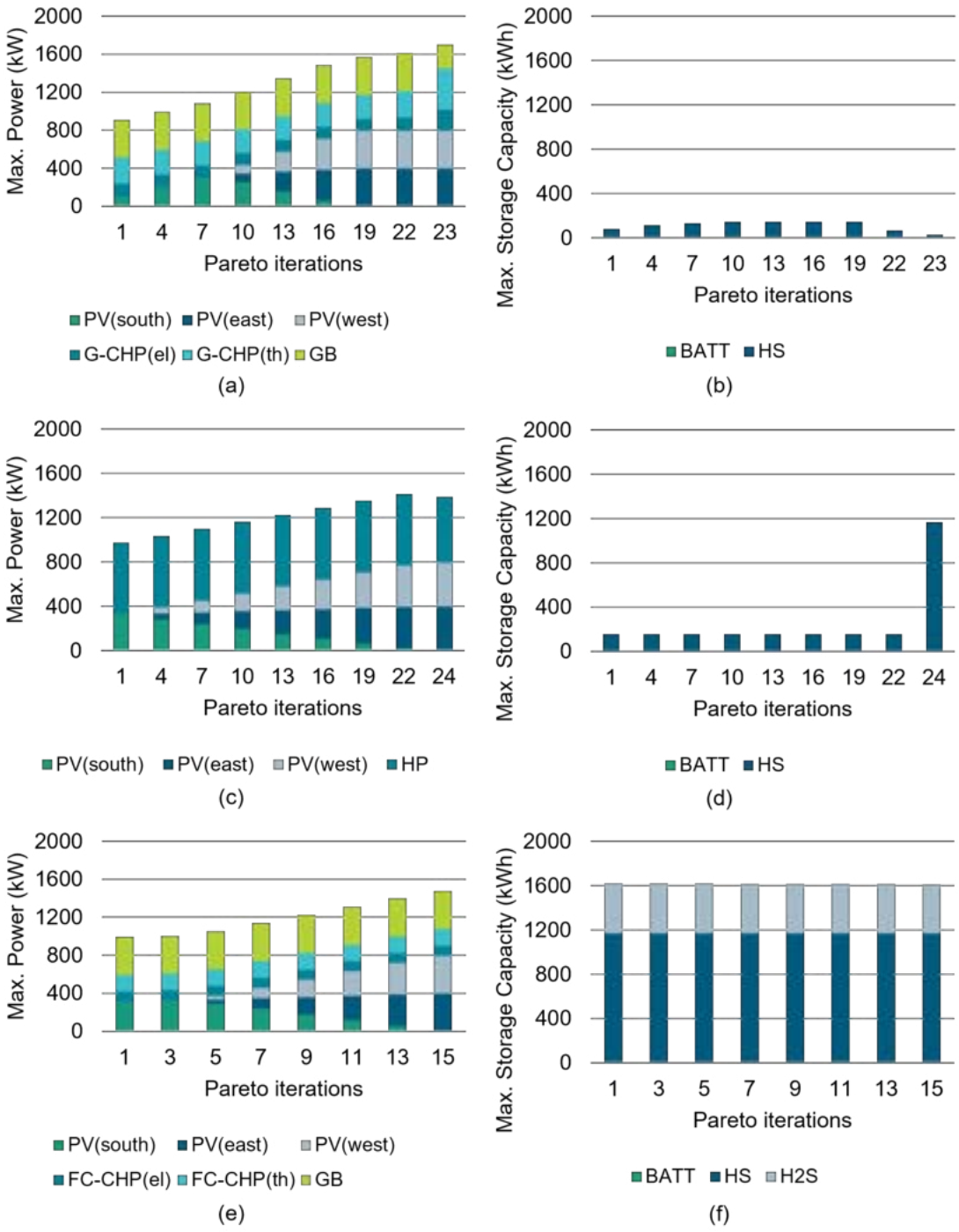

Figure 5: Optimal maximum power of generation units (a, c, e) and optimal storage capacity of storage units (b, d, f) for ES 1 (a, b), ES 2 (c, d) and ES 3 (e, f) among selected Pareto iterations. The first and last iteration corresponds to the cost optimum and the emission optimum, respectively.

3.4. Discussion

In Fig. 4, it is noticeable that the energy system with the hydrogen-based units is remarkably outperformed by the other two in terms of cost efficiency among all the Pareto iterations. In Fig. 6(e), it is evident that ES 3 has notably increased investment and operating costs in comparison to ES 1 and 2. Another observation is the comparable emission-saving performance of the hydrogen system with ES 1 and 2 for a limited number of iterations. Nevertheless, ES 1 and 2 can reduce emissions by 108% and 113%, respectively, in comparison to the first iteration. Exceeding 100% emission reduction implies that the district is producing negative emissions and, consequently, contributing to the emission mitigation in the electricity grid. On the other hand, the hydrogen system can only achieve 68%. Moreover, ES 1 economically surpasses ES 2. The main justification is that the installation of the heat pump leads to additional electricity consumption, which is more expensive than

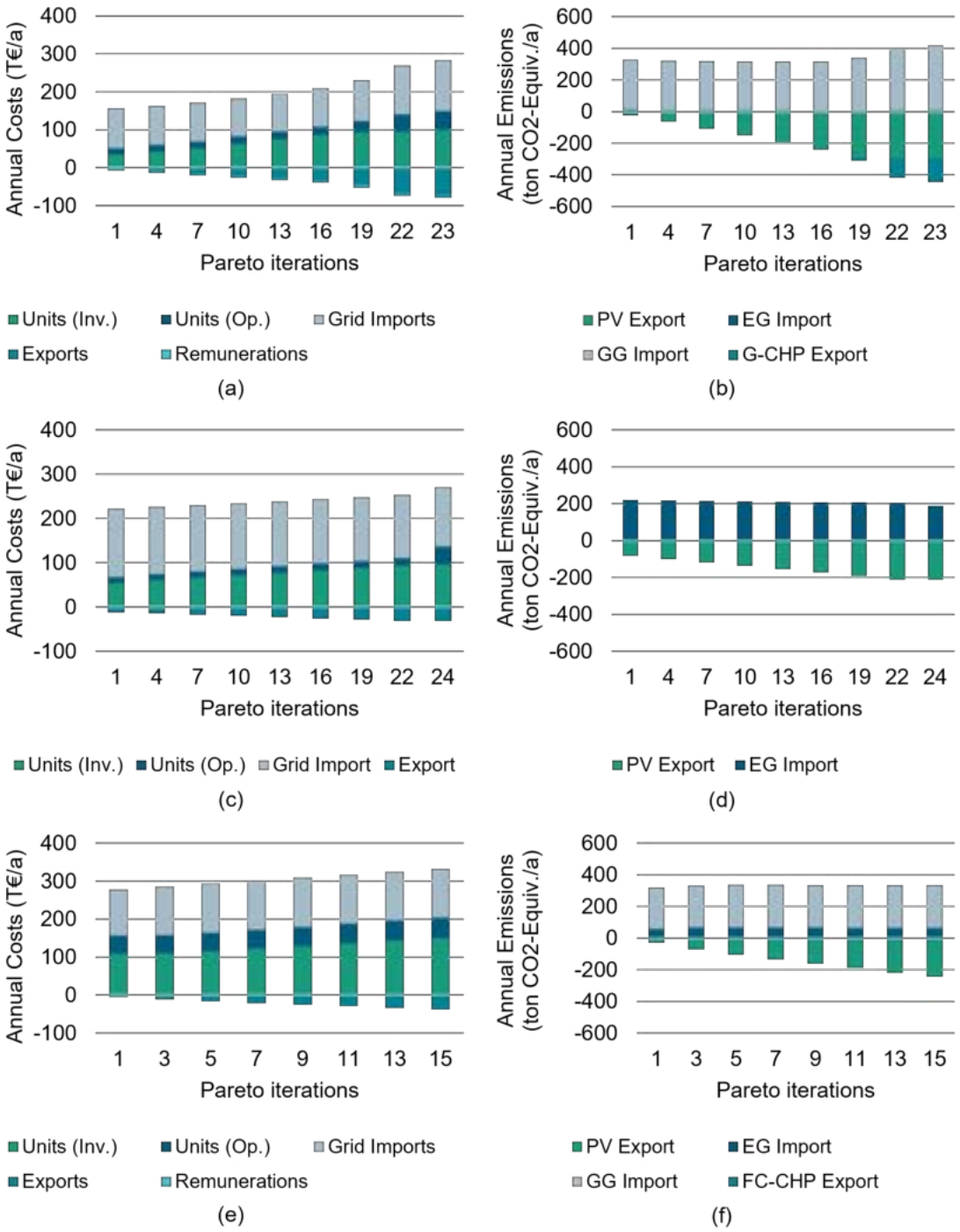

Figure 6: Optimal annual costs (a, c, e) and optimal annual emissions (b, d, f), categorized by source, for ES 1 (a, b), ES 2 (c, d) and ES 3 (e, f) among selected Pareto iterations. The first and last iteration corresponds to the cost optimum and the emission optimum, respectively.

gas, and, hence, results in higher grid import costs as shown in Fig. 6(c).

By observing the trend of reducing emissions in Fig. 4 and the resulting optimal design in Fig. 5, it can be inferred that installing additional PV peak power is the primary strategy for achieving low emission solutions for all energy systems. While lowering the emissions limit to find the emission-optimal solution, the solver attempts to first fully utilize the available area with south-oriented PV modules. After that, those modules are reduced while more east-west-oriented PV modules are recommended, since they require less area to produce the same amount of electricity as the south-oriented area, until the maximum possible peak power is reached. The primary reason is that increasing PV installation can lead to exporting more electricity to the grid and, consequently, increases the negative emissions.

Other strategies can be also noticed among the last Pareto iterations, especially after the first strategy is fully

implemented. For instance, in Fig. 5(a), the maximum power of the gas CHP unit is expanded while the sizing of the gas boiler and the heat storage is reduced in order to produce more electricity and export it to the grid. Another strategy occurs for ES 2, which is noticeable through the last iteration in Fig. 5(a) and (b). The solver recommends decreasing the heat pump's maximum power and increasing the heat storage capacity. This is accompanied by a decrease in emissions from electricity imports and fewer negative emissions from PV exports according to Fig. 6(d). This implies a rising PV supply to feed the heat pump and generate excess heat to be stored, which reduces the amount of imported electricity. However, this strategy causes comparably higher investment costs than the other iterations.

Another remark is the absence of batteries in all energy systems. A possible explanation is that in this district, exporting electricity is more economical than storing it in a battery, which requires an additional investment.

It is important to point out that the demonstrated results correspond exclusively to the input data presented in Section 3.2. Nevertheless, the drawn conclusions agree with recent literature, such as the remarks in [5] regarding the economic disadvantages of hydrogen technologies. In addition, the presented methodology with the multi-objective optimization model can be applied to other residential districts where input data are available as per described in Section 2. and illustrated in Fig. 1. Furthermore, other scenarios can lead to distinctive outcomes. For example, considering an electricity mix with a high share of renewable energy, i.e., a lower emission factor, can result in different Pareto fronts than in Fig. 4.

4. Conclusion

In this paper, we investigated the economic and environmental effects of considering hydrogen-based units on the design optimization of residential energy systems, where sector coupling could be implemented. First, a multi-objective optimization model has been developed to find the cost- and emission-optimal design and operation of different generation and storage technologies in a district, including technologies to produce and utilize hydrogen. The emission minimization has been accomplished by means of the epsilon-constraint method.

To assess the impacts of the hydrogen system, three energy systems for an exemplary district in Germany have been created. The first two involved sector coupling by gas-based co-generation and electrification through a heat pump, while the third included the hydrogen system. By comparing the respective Pareto front, it has been concluded that using hydrogen in a cross-sectoral energy system was unfavorable to obtaining competitive designs in terms of costs and emissions in comparison to typical sector-coupling approaches. It has been also determined that utilizing PV systems was a major factor in mitigating emissions.

Using the developed model, further examinations can be carried out for different energy systems structures. Another possible future work is to conduct sensitivity or scenario analysis to evaluate the performance of hydrogen systems while varying different model inputs. Moreover, further assessment criteria such as degree of self-sufficiency or self-consumption can be investigated for hydrogen systems.

Acknoweldgement

The presented work in this paper has been carried out within the project "ODH@Bochum-Weitmar", which has been funded by the Ministry of Economic Affairs, Industry, Climate Protection and Energy of North-Rhine Westphalia as part of "Program for Rational Energy Use, Renewable Energies and Energy Saving - progres.nrw - Program Area of Innovation (progres.nrw - Innovation)".

Nomenclature

Letter Symbols

C	cost, Eur
c	specific cost, Eur/kW or Eur/kWh
E	energy, kWh
h	enthalpy, J/kg
LT	life time of a unit, years
A	area, m^2
P	power, kW
p	pressure, bar
R	revenue, Eur
r	specific revenue, Eur/kWh
T	temperature, °C or K
$wacc$	weighted average cost of capital
x	reduction in emissions limit
y	binary variable

Greek symbols

Δ	difference
ε	emissions, $kgCO_2$-equiv.
η	efficiency
ρ	density, kg/m^3
σ	self-discharging losses, h^{-1}

Subscripts and superscripts

a	annual
avg	average
BATT	battery
ch	charging
CHP	combined heat and power
dis	discharging
EG	electricity grid
el	electric
exp	export to a grid
EZ	electrolyzer
FC	fuel cell
GG	gas grid
grid	grid of an energy-carrier
H2C	hydrogen compressor
H2S	hydrogen storage
HN	heat network
HS	heat storage
i	Pareto iteration
imp	import from a grid
in	input
inst	installation
inv	investment
max	maximum
norm	normalized
op	operating
out	output
PV	photovoltaics
sto	storage unit
t	time step
th	thermal
tot	total
unit	generation or storage unit

References

[1] Fridgen G, Keller R, Körner M-F, Schöpf M. *A holistic view on sector coupling*. Energy Policy 2020;147:1-8.

[2] Ramsebner J., Haas R., Ajanovic A., Wietschel M. *The sector coupling concept: A critical review*. WIREs Energy and Environment 2021;10;1:27.

[3] Sinsel SR., Riemke RL., Hoffmann VH. *Challenges and solution technologies for the integration of variable renewable energy sources—a review*. Renewable Energy 2020;145:2271–85.

[4] Ramadhani F., Hussain MA., Mokhlis H. *A Comprehensive Review and Technical Guideline for Optimal Design and Operations of Fuel Cell-Based Cogeneration Systems*. Processes 2019;7:950.

[5] Löbberding L., Madlener R. *Techno-economic analysis of micro fuel cell cogeneration and storage in Germany*. Applied Energy. 2019;235:1603–1613.

[6] DiChristopher T. *Hydrogen technology faces efficiency disadvantage in power storage race*. Available at `https://www.spglobal.com/marketintelligence/en/news-insights/latest-news-headlines/hydrogen-technology-faces-efficiency-disadvantage-in-power-storage-race-65162028` [accessed 1.3.2023].

[7] Gabrielli P., Gazzani M., Martelli E., Mazzotti M. *Optimal design of multi-energy systems with seasonal storage*. Applied Energy 2018; 219:408-424.

[8] Götze J., Dancker J., Wolter M. *A general MILP based optimization framework to design Energy Hubs*. Automatisierungstechnik 2019;67:958–71.

[9] Marocco P., Ferrero D., Martelli E., Santarelli M., Lanzini A. *An MILP approach for the optimal design of renewable battery-hydrogen energy systems for off-grid insular communities*. Energy Conversion and Management 2021;245:114564.

[10] Li B., Roche R., Miraoui A. *Microgrid sizing with combined evolutionary algorithm and MILP unit commitment*. Applied Energy 2017;188:547–62.

[11] Becerra RL., Coello CAC. *Solving Hard Multiobjective Optimization Problems Using ε-Constraint with Cultured Differential Evolution*. Differential Evolution 2006;4193:543-542.

[12] oemof developer group. *oemof.solph*, Available at https://oemof-solph.readthedocs.io/en/latest/readme.html [accessed 14.3.2023].

[13] Heimann S. *KWK-Gesetz*. Available at https://www.co2online.de/modernisieren-und-bauen/blockheizkraftwerk-kraft-waerme-kopplung/kwk-gesetz/ [accessed 20.2.2023].

[14] Eisenbach T. *Cross-sektoraler Einsatz von Wasserstofftechnologien - Erhebung des Stands der Technik sowie Modellierung für die wasserstoffbasierte Versorgung eines Wohnquartiers [thesis]* Bochum, Germany: Ruhr University Bochum; 2021.

[15] Maplesoft, *PropsSI*. Available at https://www.maplesoft.com/support/help/maple/view.aspx?path=ThermophysicalData%2FCoolProp%2FPropsSI [accessed 1.3.2023].

[16] VDI. *Reference load profiles of residential buildings for power, heat and domestic hot water as well as reference generation profiles for photovoltaic plants* Dusseldorf: Verein Deutscher Ingenieure; 2021 July.

[17] EPEX SPOT. *Market Data*. Available at https://www.eex.com/de/marktdaten/strom/indizes [accessed 20.1.2023].

[18] STROM-REPORT. *STROMPREISE VERGLEICHEN*. Available at https://strom-report.de/strompreise [accessed 10.1.2023].

[19] BDEW. *BDEW-Gaspreisanalyse Jahresbeginn 2023*. Available at https://www.bdew.de/service/daten-und-grafiken/bdew-gaspreisanalyse/ [accessed 25.2.2023].

[20] Bundesnetzagentur. *Archivierte EEG-Vergütungssätze und Datenmeldungen*. Available at https://www.bundesnetzagentur.de/DE/Fachthemen/ElektrizitaetundGas/ErneuerbareEnergien/ZahlenDatenInformationen/EEG_Registerdaten/ArchivDatenMeldgn/artikel.html[accessed 4.3.2023].

[21] EEX. *Indizes*. Available at https://www.eex.com/de/marktdaten/strom/indizes [accessed 20.1.2023].

[22] Quaschning V. *Abschlussbericht: Beitrag der Photovoltaik zur klimaneutralen Energieversorgung im urbanen Raum (PV2City)*. Available at https://solar.htw-berlin.de/wp-content/uploads/HTW-Abschlussbericht-PV2City.pdf

[23] KEA-BW. *Einführung in Den Technikkatalog*. Available at https://www.kea-bw.de/waermewende/wissensportal/technikkatalog [accessed 1.2.2023].

[24] Wolter M., Beyrau F., Tsotsas E. *Intelligentes Multi-Energie-System(SmartMES)* Magdeburg , Germany: Otto-von-Guericke-Universität Magdeburg, Magdeburger Forum zur Elektrotechnik; 2019 Apr. https://journals.ub.ovgu.de/index.php/MAFO/article/view/1695/1661

[25] Smolinka T, Wiebe N, Sterchele P, Palzer A, Lehner F, Jansen M, et al. *Studie IndWEDe. Industrialisierung der Wasserelektrolyse in Deutschland*. Available at https://www.ipa.fraunhofer.de/content/dam/ipa/de/documents/Publikationen/Studien/Studie-IndWEDe.pdf [accessed 10.1.2023].

[26] Parks G., Boyd R. , Cornish J., Remick R. *Hydrogen Station Compression, Storage, and Dispensing Technical Status and Costs*. Available at https://www.nrel.gov/docs/fy14osti/58564.pdf [accessed 3.3.2023].

[27] Umwelt Bundesamt. *CO2-Emissionen pro Kilowattstunde Strom steigen 2021 wieder an*. Available at https://www.umweltbundesamt.de/themen/co2-emissionen-pro-kilowattstunde-strom-steigen [accessed 25.2.2023].

[28] Zukunft Gas. *Vorkettenemissionen von Erdgas*. Available at https://gas.info/fileadmin/Public/PDF-Download/Faktenblatt-Vorkettenemission-Erdgas.pdf [accessed 30.1.2023].

[29] European Commission. *Photovoltaic Geographical Information System (PVGIS)*. Available at https://re.jrc.ec.europa.eu/pvg_tools/en/ [accessed 3.3.2023].

[30] WAMAK, *Heat Pump Datasheet*. Available at https://www.wamak.eu/wapps/datasheets/v2019/datasheet.php?standard=0&fsource=A&code=WA001047&lang=en-GB. [accessed 1.3.2023].

[31] Gurobi. *Documentation*. Available at https://www.gurobi.com/documentation/ [accessed 1.2.2023].

Implementation of a semi-empirical model for a low-temperature alkaline electrolyzer in Aspen HYSYS®

Paolo Vitulli[a], Andrea Monforti Ferrario[b,c], Mosè Rossi[c], Gabriele Comodi[c]

[a] Marche Polytechnic University, Department of Information Engineering, Ancona, Italy, p.vitulli@pm.univpm.it
[b] ENEA, Italian National Agency for New Technologies, Energy and Sustainable Economic Development, Rome, Italy, andrea.monfortiferrario@enea.it
[c] Marche Polytechnic University, Department of Industrial Engineering and Mathematical Sciences, Ancona, Italy, a.monforti@pm.univpm.it
[c] Marche Polytechnic University, Department of Industrial Engineering and Mathematical Sciences, Ancona, Italy, mose.rossi@staff.univpm.it, CA
[c] Marche Polytechnic University, Department of Industrial Engineering and Mathematical Sciences, Ancona, Italy, g.comodi@staff.univpm.it

Abstract:
Water electrolysis performed by renewables allows to produce green Hydrogen: this process can boost the penetration of clean energy sources into electric grids. This work presents a model developed in Aspen HYSYS® aiming at evaluating the performance of a low-temperature alkaline (ALK) electrolyzer while varying the main operating conditions (e.g., power supply, temperature, and pressure). A Semi-empirical model published in the scientific literature, which describes the physic-chemical processes at the system level, has been implemented in Aspen HYSYS® and used for resembling the operational behaviour of an ALK electrolyzer. The model consists of common system-level blocks with a customized spreadsheet: semi-empirical correlations, which have been calibrated via multiple non-linear regression fittings of experimental data from the scientific literature, allowed to implement the main electro- and thermochemical-equations of the electrolysis process. Simulated results showed a good agreement with respect to the experimental ones for all the studied operating conditions in terms of Normal Root Mean Square Error (NRMSE). Regarding the Hydrogen flow rate, the comparison between the model and the experimental results showed NRMSE values ranging between $4.208e^{-05}$ and $6.415e^{-05}$, where the former is the lowest threshold value obtained in this analysis. On the other hand, as far as the Hydrogen-to-Oxygen (HTO) is concerned, NRSME values vary between $2.486e^{-04}$ and $5.519e^{-04}$, where the latter is the highest threshold value obtained in this analysis. Finally, this model can be considered a good starting point for creating a Hydrogen-integrated system through the connection of the electrolyzer with a Hydrogen storage system and a fuel cell.

Keywords:
Alkaline electrolyzer, Aspen HYSYS®, Green Hydrogen, Water Electrolysis.

1. Introduction

Nowadays, the need to reduce greenhouse gas emissions, which are the main cause of climate change, is urgently needed as well as having energy systems capable of responding fastly to the increasing energy demands [1]. Current research on the energy sector is focused on the development of technologies capable of exploiting renewable sources in different ways (e.g., direct and indirect) to drastically reduce polluting emissions in the upcoming years.

In such a scenario, Hydrogen seems to be a valid option for easing the ecologic transition; in particular, Water electrolysis through the electricity produced by renewables (green Hydrogen) can provide flexibility to the electric grid, thus increasing the penetration of renewables [2]. Water electrolysis was performed for the first time in 1789 [3] and it consists of three components: the anode, the electrolyte, and the cathode. During the oxidation phase of Hydrogen at the anode, cations reach the cathode via the electrolyte and free electrons flow to the external circuit. Cations and electrons reduce Oxygen to Water at the cathode [4]. Hydrogen produced by Water electrolysis has been thought to be the best energy carrier to counteract the variable nature

of renewables and operate as a middle/long-term energy storage solution in different energy applications [5]. Furthermore, Hydrogen is a non-pollutant molecule since it produces only Water when it undergoes a combustion reaction, thus being considered the cleanest, most efficient, and sustainable fossil fuel alternative [6].

The most known and well-established electrolyzers are alkaline (ALK) and Polymer Exchange Membrane (PEM) ones [7], although the ALK electrolysis is the most reliable in terms of cost and ease of use [8]. The modeling of these electrolyzers is fundamental for simulating and properly resembling the behaviour of Hydrogen-generating systems. Realistic modeling of the overall electrolyzer is important when it is coupled to renewables since it has to correctly face the variable power source; furthermore, it also allows to properly analyse, control, size, manage, and optimize this kind of technology. Besides the technologies previously mentioned regarding the ALK and PEM electrolyzers, this technology is also differentiated by low- and high-temperature operating conditions. Typically, ALK electrolyzers operate at a current density of about 400 mA/cm^2, at moderate temperatures of 70-90 °C, with a cell voltage in the range of 1.85-2.2 V, and conversion efficiencies in the range of 50-70%. ALK electrolyzers do not depend upon a noble metal catalyst for Hydrogen production, and they are easily handled due to the low-temperature operation. The PEM electrolyzer can operate at a current density of 2000 mA/cm^2 at 90 °C and with 2.1 V. The kinetics of Hydrogen and Oxygen production reaction is faster than in ALK electrolyzers due to the acidic nature of the electrolyte and the metal surface of the electrodes. PEM electrolyzers do not use caustic electrolytes as in ALK ones, which might be highly toxic for human beings if a failure occurs. In addition, PEM electrolyzers offer the possibility to use high pressure on the cathode side, while the anode can be operated at atmospheric pressure. When dealing with high-temperature electrolysis, it means that the operating temperature range is above 100°C and Water is in vapor form. This operating condition increases considerably the electrolysis efficiency, but it leads to more complex management of the electrolyzer as well as higher costs due to the use of specific materials. However, technologies like Solid Oxide (SO) electrolyzers are still in development and not yet ready for being commercialized [9]. As for the high-temperature electrolysis, Motazedi et al. [10] examined Hydrogen production from both environmental and economic points of view using Aspen HYSYS® models. Along the same line, JaeHwa et al. [11] developed a SO electrolyzer model in Aspen HYSYS® to perform a sensitivity analysis by varying different operating conditions (e.g., current density, temperature, and pressure).

Moving to ALK electrolyzers, Sánchez et al. [12] have developed a model in Aspen Plus® to resemble the behaviour of the ALK electrolyzer. Nevertheless, to the authors' knowledge, in the scientific literature there are no user-friendly models developed in Aspen HYSYS® related to the ALK Water electrolyzers. The novelty of the present work consists of the development of a user-friendly model related to a low-temperature Water ALK electrolysis stack in the Aspen HYSYS® environment, which is capable of providing the main performance parameters (e.g., electric potential and Hydrogen-to-Oxygen (HTO)) according to different input conditions (e.g., pressure, temperature, current density). As previously said, besides being easily used by end-users, this model can be tailored according to the main specific characteristics of the ALK electrolyzer to be resembled.

The model has been calibrated through regression fitting of semi-empirical process relations and validation with respect to experimental data obtained by [12, 13]. In order to model the stack of the ALK electrolyzer and to carry out the regression of experimental data, the authors based the model development on the analysis carried out by Sánchez et al [13] where a semi-empirical model of the electrochemical behavior of a 15 kW ALK electrolyzer has been proposed. In addition, the work performed by Amores et al. [14] has been used as well because they provided a paradigm for modeling the behaviour of an ALK electrolyzer, modifying the Ulleberg equation [15] with the aim of considering the influence of both temperature and pressure, the electrode/diaphragm distance, and the electrolyte concentration.

The paper is structured as follows: Section 2 presents the methodology used to model the ALK electrolyzer analytically, as well as providing an overview of the Aspen HYSYS® model. Section 3 is devoted to the results obtained by the simulations at different operating conditions in terms of both pressure and temperature, which have been then compared to the experimental results available in the scientific literature by making Normal Root Mean Square Error (NRMSE) comparison. Finally, Section 4 reports the conclusions of the work.

2. Methodology

The models that describe the behaviour of a low-temperature ALK electrolyzer stack with different operating conditions (e.g., current density, temperature, and pressure) typically include the simulation of the following

quantities: i) electric potential, ii) Faraday efficiency, iii) HTO, iv) flow rate of produced Hydrogen, v) electric power absorbed by the stack, vi) thermal power generated by the stack, vii) stack efficiency, and viii) specific consumption. The trend of the last five items is obtained by the first two. In the scientific literature, there are multiple mathematical correlations that describe the same physical phenomenon occurring within the stack. Based on the experimental data obtained by [13], a semi-empirical modeling approach has been chosen and used in this work. The mathematical model used for the stack electric potential is the one proposed by Sánchez et al. [12, 13], which is an improvement of the equation proposed by Ulleberg [15] as reported by Eq. (1).

$$U = U(T,P,i) = U_{rev} + [(r_1 + q_1) + r_2 T + q_2 P] \cdot i + s \cdot \log_{10}\left[\left(t_1 + \frac{t_2}{T} + \frac{t_3}{T^2}\right) \cdot i + 1\right] \quad (1)$$

where U is the cell electric potential, T is the temperature in [°C], P is the pressure in [bar], i is the current density [A/cm^2], and r_i, q_i, and t_i are experimental constants. The total potential U is the sum of the reversible potential U_{rev}, which is given by thermodynamics, the activation, and the ohmic overpotentials related to the kinetic losses of the electrolysis process. It is worth noting that the polarization curve is not investigated in the field of concentration overpotential since it would require a more complex model and experimental data at higher current densities.
The cell reversible potential U_{rev} is a purely thermodynamic quantity and depends on the Gibbs free energy variation ΔG between products and reactants as a function of the operating temperature and pressure as reported by Eq. (2).

$$U_{rev}(T,P) = \frac{\Delta G}{zF} = \frac{\Delta G_{H_2}(T,P) + \frac{1}{2}\Delta G_{O_2}(T,P) - \Delta G_{H_2O}(T,P)}{zF} \quad (2)$$

Regarding Water electrolysis, the reversible cell potential U_{rev}^0 under standard conditions (P^0=1bar, T^0=25°C) is equal to 1.229 V. The value of the reversible voltage is a function of temperature and pressure, thus assuming different values from the standard one as expressed by Eq. (3) that is the Nernst's equation [16]:

$$U_{rev} = U_{rev}^0 + \frac{R \cdot T_K}{z \cdot F} \cdot \ln\left(\frac{p_{H2} \cdot \sqrt{p_{O_2}}}{a_{H_2O}}\right) \quad (3)$$

where T_K is the temperature in [K], R is the universal constant of gases (8.314 J/K mol), z is the number of electrons transferred in the electrolysis reaction (2 mol$_{e^-}$/mol$_{H2}$), F is the Faraday constant (96,485 C/mol), a_{H2O} is the coefficient of activity of Water, p_{O2} and p_{H2} are the partial pressure expressed in [bar] of Oxygen and produced Hydrogen, respectively. Assuming that the membrane is subjected to the mechanical equilibrium, the partial pressures of Hydrogen are the same as the Oxygen ones (p_{O2}=p_{H2}=p_{tot}) and, assuming that the coefficient of activity of the Water is approximately equal to 1 [17], Eq. (3) can be written as follows:

$$U_{rev} = U_{rev}^0 + \frac{R \cdot T}{z \cdot F} \cdot \ln\left(P_{tot}^{\frac{3}{2}}\right) \quad (4)$$

The reversible cell potential U_{rev}^0 can be also calculated considering isobaric conditions (at standard pressure P^0 equal to 1 bar) and thus reducing its dependency only on the temperature [17]. In the scientific literature, there are different empirical relationships such as the one proposed by Hammoudi et al. [18] as reported by Eq. (5).

$$U_{rev}^0(T,P^0) = 1.50342 - 9.956 \cdot 10^{-4} T_K + 2.5 \cdot 10^{-7} {T_K}^2 \quad (5)$$

Finally, the reversible potential is calculated by the set of Eq.s (4) and (5). The electrolyzer under investigation consists of 12 cells installed in series; thus, the stack voltage is obtained by multiplying the cell voltage by the number of cells.

$$U_{stack} = N_{cell} \cdot U \tag{6}$$

where N_{cell} is the number of cells installed in series.

The Hydrogen production rate $\dot{n}_{H2}$ [mol/s] is strictly related by the stoichiometry of the reaction and to the applied current *I* [A], which is the same for all the cells connected in series. The Hydrogen production rate is equal to the current density *i* times cell area A_{cell} as reported in Eq. (7) that is the Faraday's equation. As far as the Faraday efficiency η_{Far} is concerned, Sánchez et al. [12, 13] introduced a modification to the η_{Far} Ulleberg's relation [15] with the use of experimental parameters f_{ij} to include also the effect of the temperature as reported by Eq. (8).

$$\dot{n}_{H2} = \eta_{Far} \frac{I}{zF} \tag{7}$$

$$\eta_{Far} = \frac{i^2 \cdot (f_{21} + f_{22} T)}{(f_{11} + f_{12} T) + i^2} \tag{8}$$

As for the HTO, the equation proposed by Hug et al. [19], which describes the HTO dependence on both current density and temperature, has been used by Sánchez et al. [12, 13] and modified by introducing the dependence of pressure as reported by Eq. (9).

$$HTO = C_1 + C_2 T + C_3 T^2 + (C_4 + C_5 T + C_6 T^2) \cdot \exp\left(\frac{C_7 + C_8 T + C_9 T^2}{i}\right) + E_1 + E_2 P + E_3 P^2 + (E_4 + E_5 P + E_6 P^2) \cdot \exp\left(\frac{E_7 + E_8 P + E_9 P^2}{i}\right) \tag{9}$$

where C_1 to C_9 are constants that represent the influence of the temperature in the HTO, and from E_1 to E_9 there are constants that represent the relations between the gas purity and the pressure.

The electrical power absorbed by the stack $\dot{W}_{el}$ allows to evaluate the specific electrical consumption and the stack efficiency as well, as described by Eq. (10).

$$\dot{W}_{el} = U \cdot N_{cell} \cdot i \cdot A_{cell} \tag{10}$$

Regarding the specific consumption c_{sp}, it can be expressed as the ratio between electric power $\dot{W}_{el}$, which is expressed in [kW], and the mass flow rate of the produced Hydrogen $\dot{m}_{H2}$ expressed in [kg/h].

$$c_{sp} = \frac{\dot{W}_{el}}{\dot{m}_{H2}} = \frac{U(i,T,P) \cdot 2F}{10^3 \cdot \eta_F(i,T) \cdot 7.257168} \tag{11}$$

where 7.257168 is a conversion factor in [s•kg/h•mol] that allows to express the molar flow rate of Hydrogen in [kg/h] knowing its value in [mol/s].

Stack electrical efficiency, η_{stack} , is defined as the ratio between the chemical energy contained in the produced hydrogen and the electrical power needed for its production, as shown by Eq. (12).

$$\eta_{stack} = \frac{\dot{n}_{H2} \cdot LHV}{\dot{W}_{el}} \tag{12}$$

where LHV stands for the Lower Heating Value of hydrogen that is equal to 241.82 kJ/mol.

The thermal power $\dot{Q}_{th}$ involved in the electrolysis process, which must be removed to maintain the isothermal condition, is calculated as:

$$\dot{Q}_{th} = i \cdot A_{cell} \cdot (U(i,T,P) - U_{tn}(T,P)) \quad (13)$$

where U_{tn} is the thermoneutral potential of the stack, which is a function of both temperature and pressure.

As previously described, the electrochemical process model is integrated into the Aspen HYSYS® environment using a spreadsheet since the software does not present pre-build blocks for modeling electrochemical components. The rest of the electrolyzer stack (e.g., inlet and outlet fluid management, temperature and pressure settings, etc.) is represented by the common tools made available by the software. Steady-state operations have been considered and the fluid thermodynamic conditions (e.g., pressure and temperature) are set (e.g., isothermal and isobaric conditions are considered for the whole process). The selected *Fluid Package* is the "*Peng-Robinson*". The Water dissociation reaction is defined as a conversion reaction occurring in the "*Electrolysis reactor*", which represents the set of electrodes. Based on the thermodynamic operating conditions (e.g., temperature, pressure) and load current, the reactor sources the main electro- and thermo-chemical equations from the spreadsheet defining the reaction products and the electric power required. U_{rev} is calculated from the thermodynamic fluid property databases, which are embedded in the software, using Eq. (2). The reactor has two material flows at the output: "*Reaction Gas*" and "*Liquid Product*", where the latter is always null since the molar flow rate of the Water entering the model is equal to the molar flow rate of the Hydrogen that is calculated in the spreadsheet using the Faraday equation. The mixture of Hydrogen and Oxygen "*Reaction gas"* is sent to the second component that is the "*Component splitter*" called "*Electrode separator*": through this component it is possible to separate the oxidation and the reduction semi-reactions in the anode and in the cathodic chambers of each cell, respectively. The separator is set up so that the flows are chemically pure at the outputs (no crossover phenomena). The current output flows are corrected with the HTO that is calculated in the spreadsheet: indeed, the amount of Hydrogen separated from the anode flow by the "*Flow splitter",* here called "*Crossover_Tee*", is subsequently mixed to the Oxygen in the anode.

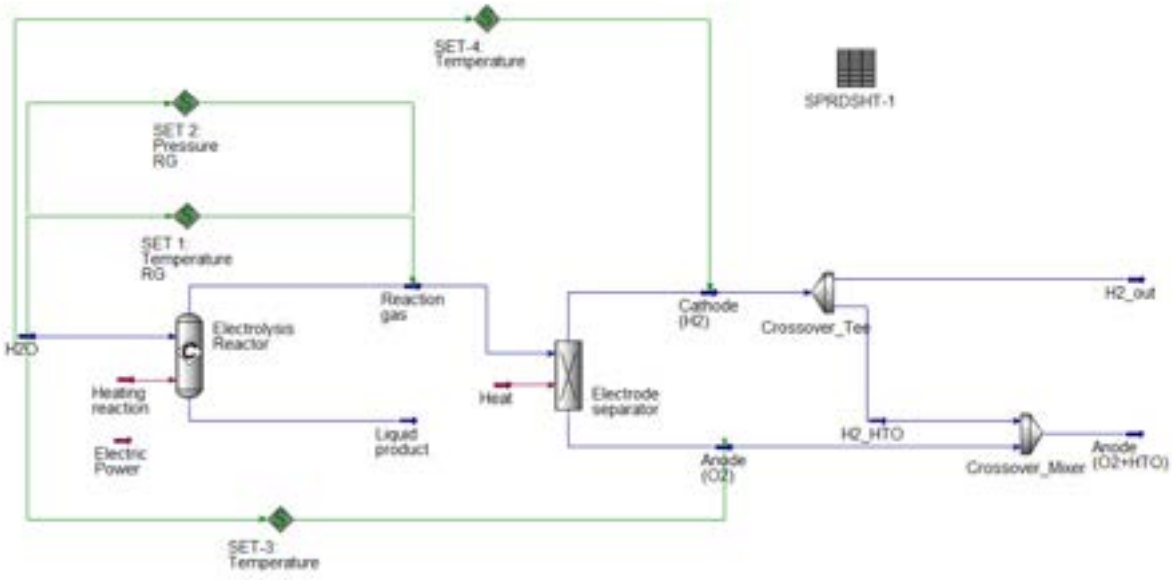

Figure. 1. Model of the low-temperature alkaline electrolyzer developed in Aspen HYSYS®.

In order to obtain comparable simulation results, the electrolyzer that has been modeled is the same one that has been characterized experimentally by Sánchez et al. [12, 13]. It is a small-sized, laboratory scale electrolyzer and its main characteristics are listed in Table 1. To obtain the experimental parameters previously described, the available experimental data have been fitted by using the Matlab® "*Curve Fitting Tool"*. The

regressions are non-linear and multiple, namely two in the case of the Faraday efficiency and three in the case of electric voltage and HTO.

Table 1. Characteristics of the alkaline electrolyzer analysed by Sánchez et al. [12, 13].

Main characteristics	Numerical value	Units of measurement
Hydrogen production flow rate	2.5	m^3/h
Maximum operating pressure	30	bar
Electric potential range	0-120	V
Electric current range	0-500	A
Maximum power	15	kW
The active area of the electrodes	1,000	cm^2
Number of cells	12	-
Electrolyte concentration	30-40	wt% KOH

3. Results and comments

The simulations results, in terms of electrolyzer performance, are evaluated as a function of the current density (between 0-0.5 A/cm^2 with steps of 0.005 A/cm^2) and the parametrization of both pressure and temperature (between 55-85°C with steps of 5°C, and between 1-29 bar with steps of 4 bar). Aspen HYSYS® allows to perform parametric "case studies" and investigate how each variable affects the results while keeping the remained parameters fixed. Figure 2 shows the results related to the stack potential at different values of temperature and pressure. It is worth noting that the trends of the other quantities such as Hydrogen flow rate, etc. have not been here reported.

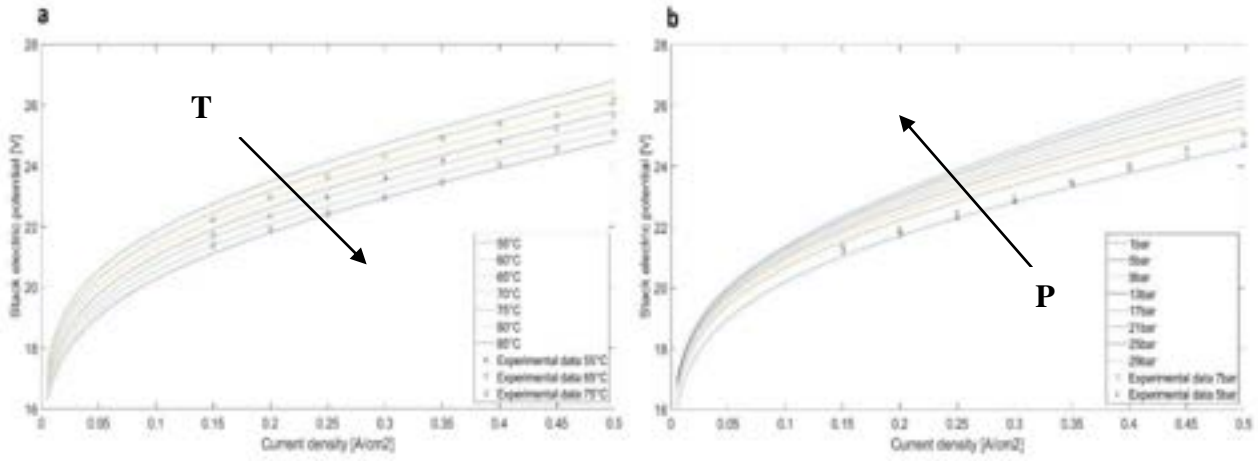

Figure. 2. (a) Stack voltage trend as a function of current density and temperature (pressure equal to 7 bar), and (b) of current density and pressure (temperature equal to 75°C).

In particular, the voltage decreases while the system temperature increases because part of the electric energy required for the electrolysis process is replaced by the associated thermal energy developed during the reaction (see Figure 2). The increase in temperature also improves the reaction kinetics by reducing the activation overpotentials as well as impacting the U_{rev} through the Nernst potential. Furthermore, the electric potential rises when the pressure increases due to the Nernst potential and the one related to the ohmic overpotential.

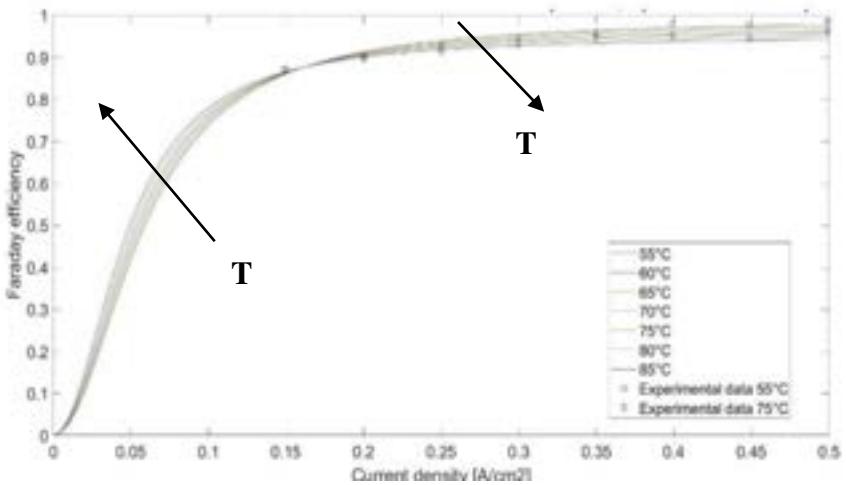

Figure. 3. Faraday efficiency trend as a function of current density and temperature (pressure equal to 7 bar).

Figure 3 shows the trend of the Faraday efficiency as a function of current density and temperature according to Eq. (8). The Faraday efficiency quickly reaches values close to 1 when current density values higher than 0.4 A/cm^2 are used. Conversely, Faraday efficiency decreases when current density values lower than 0.17 A/cm^2 and the increase of temperature leads to lower Faraday efficiency values.

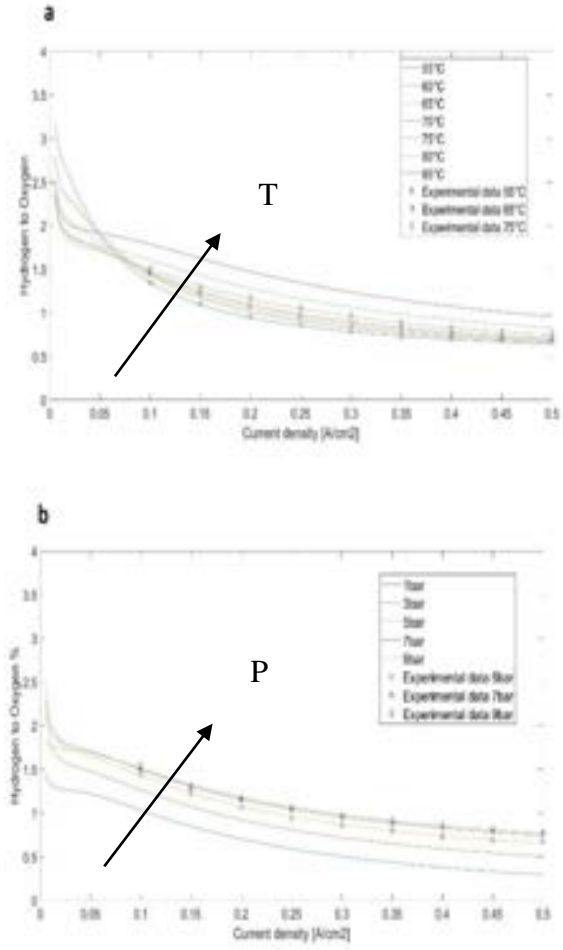

Figure. 4. (a) HTO trend as a function of current density and temperature (pressure equal to 7 bar), and (b) of current density and pressure (temperature equal to 75°C).

Figure 4a shows that the HTO increases when the current density decreases and tends to increase with the increasing temperatures. For this reason, operations with very low values of current density are undesirable because it would be preferable to avoid a HTO beyond the flammability limit of a H_2/O_2 mixture that could lead to combustion or explosion [20]. The higher amount of Hydrogen in the Oxygen stream at higher temperatures is caused by the higher diffusion velocity at elevated temperatures [17]. Figure 4b still shows an increase of the HTO as the current density decreases and as the operating pressure increases. For increasingly small current density values, the HTO model shows an asymptotic behaviour with anomalous variations due to lack of experimental data for very low currents: this means that the model is only valid for the range of density current values for which HTO measurements are available.

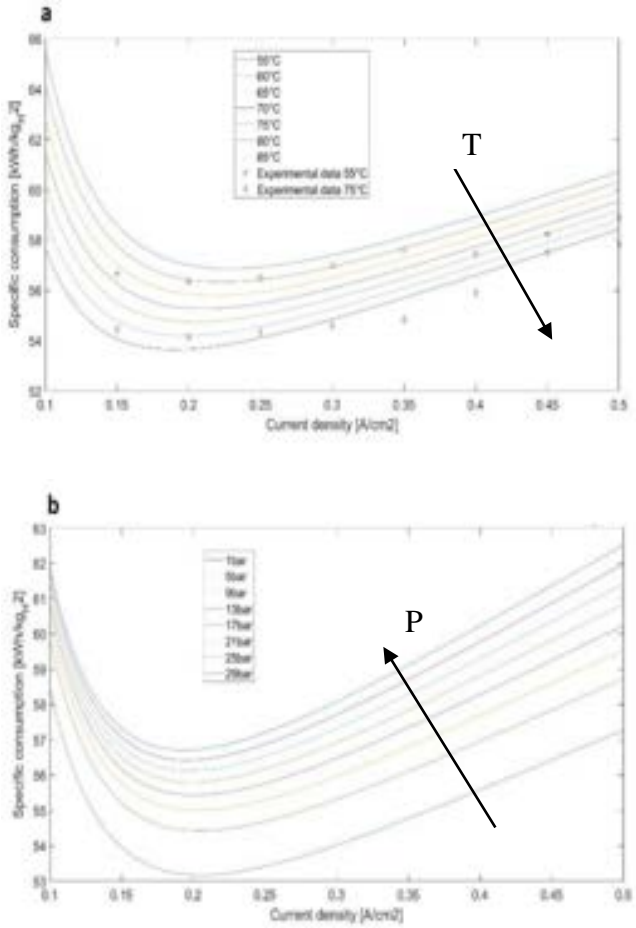

Figure. 5. (a) Specific consumption trend as a function of current density and temperature (pressure equal to 7 bar), and (b) of current density and pressure (temperature equal to 75°C).

Figure 5 shows a non-linear dependence of the specific consumption on the current density. In [13], no experimental data are available for the specific consumption, but these were obtained with data on Faraday efficiency and stack electric potential through Eq. (11). The specific consumption function reaches its minimum value at 0.2 A/cm^2, and it decreases with increasing temperature (see Figure 5a) due to the decrease of the electric potential and increases with the increasing pressure (see Figure 5b) due to the increase of the electric potential. The increase of the specific consumption, when the current density decreases below the threshold of 0.2 A/cm^2, is due to a decrease of the Faraday efficiency that is faster than the electric potential as expressed by Eq. (11). The Faraday efficiency and the electric potential increase with the current density, resulting in an increasing curve for current densities greater than 0.2 A/cm^2. The specific consumption is always between 53 and 63 kWh/kg$_{H2}$.

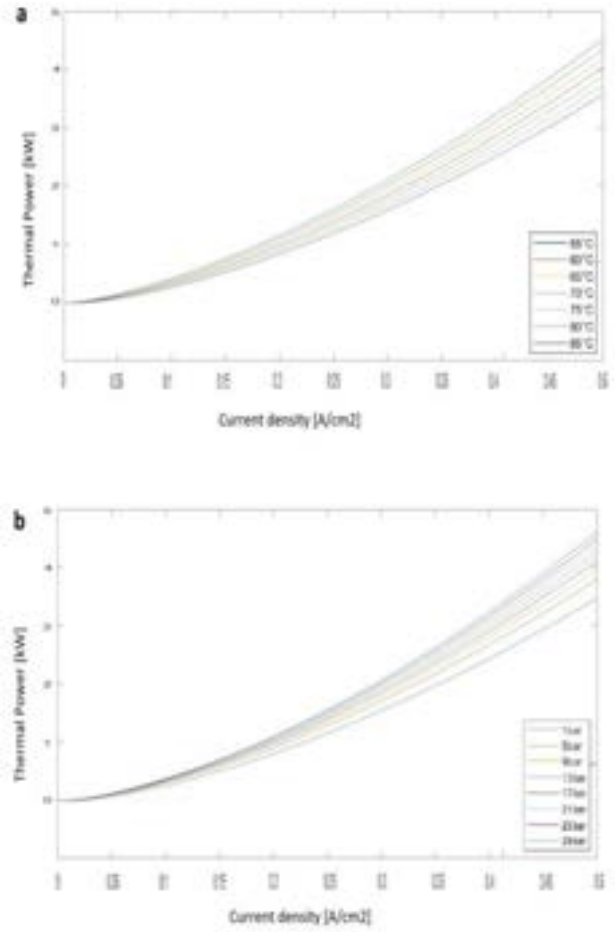

Figure. 6. (a) Thermal power trend as a function of current density and temperature (pressure equal to 7bar), and (b) of current density and pressure (temperature equal to 75°C).

As for the thermal power, Figure 6 shows how it increases with increasing current density and how this trend tends to decrease as the operating temperature increases and to increase as the operating pressure increases. This behaviour can be explained by the influence of both temperature and pressure exert on the stack potential: as the temperature increases the stack potential decreases, while as the pressure increases the potential increases. However, the thermoneutral potential can be considered approximately constant in every case. There are not experimental data for the thermal power. To evaluate the results from the developed model, the *Normal Root Mean Square Error* (NRMSE) has been calculated with respect to the literature experimental values in the same operating conditions reported in [13] (see Table 2).

Table 2. NRMSE values: comparison between model and experimental results.

	7 bar, 55°C	**7 bar, 65°C**	**7 bar, 75°C**	**5 bar, 75°C**	**9 bar, 75°C**
Electric potential	$4.066e^{-04}$	$3.990e^{-04}$	$4.095e^{-04}$	$4.317e^{-04}$	-
Faraday Efficiency	$8.253e^{-05}$	-	$4.871e^{-05}$	-	-
HTO	$5.519e^{-04}$	$2.486e^{-04}$	$3.932e^{-04}$	$4.115e^{-04}$	$3.213e^{-04}$
Specific consumption	$4.859e^{-04}$	-	$4.155e^{-04}$	-	-
Stack efficiency	$4.452e^{-04}$	-	$3.903e^{-04}$	-	-
Electric power	$4.153e^{-04}$	$3.295e^{-04}$	$3.865e^{-04}$	$2.078e^{-05}$	-
Hydrogen flow rate	$6.415e^{-05}$	-	$4.208e^{-05}$	-	-

The regression in Matlab of the cell potential from experimental data was conducted by using the set of Eq.s (4) and (5) where the reversible cell potential U_{rev}^{0} is only a function of the temperature (considering isobaric conditions (at standard pressure P^0 equal to 1 bar) according to [18], while In Aspen HYSYS the reversible cell potential is calculated automatically by implementing Eq. (2). The result is that the numerical value of the reversible cell potential calculated in Aspen HYSYS® is on average greater than the one calculated with the combination of Eq.s. (4) and (5) by 0.0395 V: this is mainly due to the fluid package selected that evaluates the trend of the state function of the components in the system. As a result, an average overestimation of 0.474 V of the electric stack potential of the model developed in Aspen HYSYS® is obtained compared to the experimental data; therefore, also other results are overestimated (e.g., specific consumption and electric power consumed). Conversely, the stack efficiency is underestimated compared to the experimental data. A possible way to increase the accuracy of the model is to perform regressions of the experimental data by firstly calculating the reversible potential according to Eq. (2), and then determining the experimental coefficients from the equation given by the combination of Eq.s. (1) and (2).

4. Conclusions

This work presents and discusses the development of a semi-empirical simulation model developed with Aspen HYSYS® related to a low-temperature Water alkaline electrolysis stack. The main performance parameters (e.g., electric power required and stack efficiency) are evaluated according to different input conditions (e.g., current density, pressure, temperature, etc.).

The trend of the electric potential has been obtained as the sum of the reversible potential and the overpotentials obtained through non-linear multiple regressions performed in Matlab® with the "*Curve Fitting Tool"* of several empirical parameters.

Results show a good agreement with the data made available by the scientific literature (experimental data) for all the analysed quantities within the selected range of operation parameters. Slight differences have been found due to the overestimation of the cell/stack potential related to the electrochemical model: indeed, the comparison between the model and experimental results showed NMRSE values ranging between $3.990e^{-04}$ and $4.317e^{-04}$. Moving to the Faraday efficiency, values ranging between $4.871e^{-05}$ and $8.253e^{-05}$ have been obtained. Then, the specific consumption values varied between $4.155e^{-04}$ and $4.859e^{-04}$, the electric power variation goes from $2.078e^{-05}$ to $4.145e^{-04}$, and the Hydrogen flow rate from $4.208e^{-05}$ to $6.415e^{-05}$ where the former is the lowest threshold value obtained in this analysis. On the other hand, as far as the HTO is concerned, NRSME values vary between $2.486e^{-04}$ and $5.519e^{-04}$, where the latter is the highest threshold value obtained in this analysis. It is worth noting that these results denote that a simple thermodynamic model with the addition of few semi-empirical corrections can represent quite well the operation of the electrolyzer stack without requiring excessive simulation efforts in terms of both kinetic and dynamic behaviours.

The present model will be subsequently implemented in a wider system resembling the behaviour of an integrated Hydrogen system composed by, besides the electrolyzer, a metal hydrides Hydrogen storage and a fuel cell. Furthermore, the future complete model will also take into account both Water recirculation and gas purification processes, which are fundamental in the electrolysis process.

References

[1] EA (2021), Greenhouse Gas Emissions from Energy Data Explorer, IEA, Paris https://www.iea.org/data-and-statistics/data-tools/greenhouse-gas-emissions-from-energy-data-explorer (last accessed 15/05/2023).

[2] IEA (2019), The Future of Hydrogen, IEA, Paris https://www.iea.org/reports/the-future-of-hydrogen, License: CC BY 4.0 (last accessed 15/05/2023).

[3] Jing Zhu, Liangsheng Hu, Pengxiang Zhao, Lawrence Yoon Suk Lee, and Kwok-Yin Wong, Recent Advances in Electrocatalytic Hydrogen Evolution Using Nanoparticles, Chem Rev, Volume 120, 2020, Pages 851-918, https://doi.org/10.1021/acs.chemrev.9b00248.

[4] Lixin Fan, Zhengkai Tu, Siew Hwa Chan, Recent development of hydrogen and fuel cell technologies: A review, Volume 7, 2021, Pages 8421-8446, https://doi.org/10.1016/j.egyr.2021.08.003.

[5] A. Djafour, M. Matoug, H. Bouras, B. Bouchekirma, M.S. Aida, B. Azoui, Photovoltaic-assisted alkaline Water electrolysis: Basic principles, International Journal of Hydrogen Energy, Volume 36, Issue 6, 2011, Pages 4117-4124, https://doi.org/10.1016/j.ijhydene.2010.09.099.

[6] Mingyong Wang, Zhi Wang, Xuzhong Gong, Zhancheng Guo, The intensification technologies to Water electrolysis for hydrogen production – A review, Renewable and Sustainable Energy Reviews, Volume 29, 2014, Pages 573-588, https://doi.org/10.1016/j.rser.2013.08.090.

[7] Z. Abdin, C.J. Webb, E.M. Gray, Modelling and simulation of a proton exchange membrane (PEM) electrolyser cell, International Journal of Hydrogen Energy, Volume 40, Issue 39, 2015, Pages 13243-13257, https://doi.org/10.1016/j.ijhydene.2015.07.129.

[8] Martin David, Carlos Ocampo-Martinez, Ricardo Sanchez-Pena, Advances in alkaline Water electrolyzers: A review, Jounral of Energy Storage, Volume 23, 2019, Pages 392-403, https://doi.org/10.1016/j.est.2019.03.001.

[9] Pierre Millet, Sergey Grigoriev, Chapter 2 – Water Electrolysis Technologies, Renewable Hydrogen Technologies: Production, Purification, Storage, Applications and Safety, 2013, Pages 19-41, https://doi.org/10.1016/B978-0-444-56352-1.00002-7.

[10] Kavan Motazedi, Yaser Khojasteh Salkuyeh, Ian J. Laurenzi, Heather L. MacLean, Joule A. Bergerson, *Economic and environmental competitiveness of high temperature electrolysis for Hydrogen production*, International Journal of Hydrogen Energy, Volume 46, Issue 41, 2021, Pages 21274-21288, ISSN 0360-3199, https://doi.org/10.1016/j.ijhydene.2021.03.226.

[11] JaeHwa KOH, DuckJoo YOON & Chang H. OH (2010) *Simple Electrolyzer Model Development for High-Temperature Electrolysis System Analysis Using Solid Oxide Electrolysis Cell*, Journal of Nuclear Science and Technology, 47:7, 599-607, https://doi.org/10.1080/18811248.2010.9720957.

[12] Mónica Sánchez, Ernesto Amores, David Abad, Lourdes Rodríguez, Carmen Clemente-Jul, *Aspen Plus model of an alkaline electrolysis system for Hydrogen production*, International Journal of Hydrogen Energy, Volume 45, Issue 7, 2020, Pages 3916-3929, ISSN 0360-3199, https://doi.org/10.1016/j.ijhydene.2019.12.027.

[13] Mónica Sánchez, Ernesto Amores, Lourdes Rodríguez, Carmen Clemente-Jul, *Semi-empirical model and experimental validation for the performance evaluation of a 15 kW alkaline Water electrolyzer*, International Journal of Hydrogen Energy, Volume 43, Issue 45, 2018, Pages 20332-20345, ISSN 0360-3199, https://doi.org/10.1016/j.ijhydene.2018.09.029.

[14] Ernesto Amores, Jesús Rodríguez, Christian Carreras*, Influence of operation parameters in the modeling of alkaline Water electrolyzers for hydrogen production*, International Journal of Hydrogen Energy, Volume 39, Issue 25, 2014, Pages 13063-13078, ISSN 0360-3199, https://doi.org/10.1016/j.ijhydene.2014.07.001.

[15] Øystein Ulleberg, *Modeling of advanced alkaline electrolyzers: a system simulation approach*, International Journal of Hydrogen Energy, Volume 28, Issue 1, 2003, Pages 21-33, ISSN 0360-3199, https://doi.org/10.1016/S0360-3199(02)00033-2.

[16] Ernesto Amores, Mónica Sánchez, Nuria Rojas, Margarita Sánchez-Molina, *Renewable hydrogen production by Water electrolysis*, Editor(s): Suman Dutta, Chaudhery Mustansar Hussain, Sustainable Fuel Technologies Handbook, Academic Press, 2021, Pages 271-313, ISBN 9780128229897, https://doi.org/10.1016/B978-0-12-822989-7.00010-X.

[17] Pierre Olivier, Cyril Bourasseau, Pr. Belkacem Bouamama, *Low-temperature electrolysis system modelling: A review*, Renewable and Sustainable Energy Reviews, Volume 78, 2017, Pages 280-300, ISSN 1364-0321, https://doi.org/10.1016/j.rser.2017.03.099.

[18] M. Hammoudi, C. Henao, K. Agbossou, Y. Dubé, M.L. Doumbia, *New multi-physics approach for modelling and design of alkaline electrolyzers*, International Journal of Hydrogen Energy, Volume 37, Issue 19, 2012, Pages 13895-13913, ISSN 0360-3199, https://doi.org/10.1016/j.ijhydene.2012.07.015.

[19] W. Hug, H. Bussmann, A. Brinner, *Intermittent operation and operation modeling of an alkaline electrolyzer*, International Journal of Hydrogen Energy, Volume 18, Issue 12, 1993, Pages 973-977, ISSN 0360-3199, https://doi.org/10.1016/0360-3199(93)90078-O.

[20] H Janssen, J.C Bringmann, B Emonts, V Schroeder, *Safety-related studies on hydrogen production in high-pressure electrolysers*, International Journal of Hydrogen Energy, Volume 29, Issue 7, 2004, Pages 759-770, ISSN 0360-3199, https://doi.org/10.1016/j.ijhydene.2003.08.014.

Implementation of a semi-empirical model for a low-temperature alkaline electrolyzer in Aspen HYSYS®

Paolo Vitulli[a], Andrea Monforti Ferrario[b,c], Mosè Rossi[c], Gabriele Comodi[c]

[a] Marche Polytechnic University, Department of Information Engineering, Ancona, Italy, p.vitulli@pm.univpm.it
[b] ENEA, Italian National Agency for New Technologies, Energy and Sustainable Economic Development, Rome, Italy, andrea.monfortiferrario@enea.it
[c] Marche Polytechnic University, Department of Industrial Engineering and Mathematical Sciences, Ancona, Italy, a.monforti@pm.univpm.it
[c] Marche Polytechnic University, Department of Industrial Engineering and Mathematical Sciences, Ancona, Italy, mose.rossi@staff.univpm.it, CA
[c] Marche Polytechnic University, Department of Industrial Engineering and Mathematical Sciences, Ancona, Italy, g.comodi@staff.univpm.it

Abstract:
Water electrolysis performed by renewables allows to produce green Hydrogen: this process can boost the penetration of clean energy sources into electric grids. This work presents a model developed in Aspen HYSYS® aiming at evaluating the performance of a low-temperature alkaline (ALK) electrolyzer while varying the main operating conditions (e.g., power supply, temperature, and pressure). A Semi-empirical model published in the scientific literature, which describes the physic-chemical processes at the system level, has been implemented in Aspen HYSYS® and used for resembling the operational behaviour of an ALK electrolyzer. The model consists of common system-level blocks with a customized spreadsheet: semi-empirical correlations, which have been calibrated via multiple non-linear regression fittings of experimental data from the scientific literature, allowed to implement the main electro- and thermochemical-equations of the electrolysis process. Simulated results showed a good agreement with respect to the experimental ones for all the studied operating conditions in terms of Normal Root Mean Square Error (NRMSE). Regarding the Hydrogen flow rate, the comparison between the model and the experimental results showed NRMSE values ranging between $4.208e^{-05}$ and $6.415e^{-05}$, where the former is the lowest threshold value obtained in this analysis. On the other hand, as far as the Hydrogen-to-Oxygen (HTO) is concerned, NRSME values vary between $2.486e^{-04}$ and $5.519e^{-04}$, where the latter is the highest threshold value obtained in this analysis. Finally, this model can be considered a good starting point for creating a Hydrogen-integrated system through the connection of the electrolyzer with a Hydrogen storage system and a fuel cell.

Keywords:
Alkaline electrolyzer, Aspen HYSYS®, Green Hydrogen, Water Electrolysis.

1. Introduction

Nowadays, the need to reduce greenhouse gas emissions, which are the main cause of climate change, is urgently needed as well as having energy systems capable of responding fastly to the increasing energy demands [1]. Current research on the energy sector is focused on the development of technologies capable of exploiting renewable sources in different ways (e.g., direct and indirect) to drastically reduce polluting emissions in the upcoming years.

In such a scenario, Hydrogen seems to be a valid option for easing the ecologic transition; in particular, Water electrolysis through the electricity produced by renewables (green Hydrogen) can provide flexibility to the electric grid, thus increasing the penetration of renewables [2]. Water electrolysis was performed for the first time in 1789 [3] and it consists of three components: the anode, the electrolyte, and the cathode. During the oxidation phase of Hydrogen at the anode, cations reach the cathode via the electrolyte and free electrons flow to the external circuit. Cations and electrons reduce Oxygen to Water at the cathode [4]. Hydrogen produced by Water electrolysis has been thought to be the best energy carrier to counteract the variable nature

of renewables and operate as a middle/long-term energy storage solution in different energy applications [5]. Furthermore, Hydrogen is a non-pollutant molecule since it produces only Water when it undergoes a combustion reaction, thus being considered the cleanest, most efficient, and sustainable fossil fuel alternative [6].

The most known and well-established electrolyzers are alkaline (ALK) and Polymer Exchange Membrane (PEM) ones [7], although the ALK electrolysis is the most reliable in terms of cost and ease of use [8]. The modeling of these electrolyzers is fundamental for simulating and properly resembling the behaviour of Hydrogen-generating systems. Realistic modeling of the overall electrolyzer is important when it is coupled to renewables since it has to correctly face the variable power source; furthermore, it also allows to properly analyse, control, size, manage, and optimize this kind of technology. Besides the technologies previously mentioned regarding the ALK and PEM electrolyzers, this technology is also differentiated by low- and high-temperature operating conditions. Typically, ALK electrolyzers operate at a current density of about 400 mA/cm^2, at moderate temperatures of 70-90 °C, with a cell voltage in the range of 1.85-2.2 V, and conversion efficiencies in the range of 50-70%. ALK electrolyzers do not depend upon a noble metal catalyst for Hydrogen production, and they are easily handled due to the low-temperature operation. The PEM electrolyzer can operate at a current density of 2000 mA/cm^2 at 90 °C and with 2.1 V. The kinetics of Hydrogen and Oxygen production reaction is faster than in ALK electrolyzers due to the acidic nature of the electrolyte and the metal surface of the electrodes. PEM electrolyzers do not use caustic electrolytes as in ALK ones, which might be highly toxic for human beings if a failure occurs. In addition, PEM electrolyzers offer the possibility to use high pressure on the cathode side, while the anode can be operated at atmospheric pressure. When dealing with high-temperature electrolysis, it means that the operating temperature range is above 100°C and Water is in vapor form. This operating condition increases considerably the electrolysis efficiency, but it leads to more complex management of the electrolyzer as well as higher costs due to the use of specific materials. However, technologies like Solid Oxide (SO) electrolyzers are still in development and not yet ready for being commercialized [9]. As for the high-temperature electrolysis, Motazedi et al. [10] examined Hydrogen production from both environmental and economic points of view using Aspen HYSYS® models. Along the same line, JaeHwa et al. [11] developed a SO electrolyzer model in Aspen HYSYS® to perform a sensitivity analysis by varying different operating conditions (e.g., current density, temperature, and pressure).

Moving to ALK electrolyzers, Sánchez et al. [12] have developed a model in Aspen Plus® to resemble the behaviour of the ALK electrolyzer. Nevertheless, to the authors' knowledge, in the scientific literature there are no user-friendly models developed in Aspen HYSYS® related to the ALK Water electrolyzers. The novelty of the present work consists of the development of a user-friendly model related to a low-temperature Water ALK electrolysis stack in the Aspen HYSYS® environment, which is capable of providing the main performance parameters (e.g., electric potential and Hydrogen-to-Oxygen (HTO)) according to different input conditions (e.g., pressure, temperature, current density). As previously said, besides being easily used by end-users, this model can be tailored according to the main specific characteristics of the ALK electrolyzer to be resembled.

The model has been calibrated through regression fitting of semi-empirical process relations and validation with respect to experimental data obtained by [12, 13]. In order to model the stack of the ALK electrolyzer and to carry out the regression of experimental data, the authors based the model development on the analysis carried out by Sánchez et al [13] where a semi-empirical model of the electrochemical behavior of a 15 kW ALK electrolyzer has been proposed. In addition, the work performed by Amores et al. [14] has been used as well because they provided a paradigm for modeling the behaviour of an ALK electrolyzer, modifying the Ulleberg equation [15] with the aim of considering the influence of both temperature and pressure, the electrode/diaphragm distance, and the electrolyte concentration.

The paper is structured as follows: Section 2 presents the methodology used to model the ALK electrolyzer analytically, as well as providing an overview of the Aspen HYSYS® model. Section 3 is devoted to the results obtained by the simulations at different operating conditions in terms of both pressure and temperature, which have been then compared to the experimental results available in the scientific literature by making Normal Root Mean Square Error (NRMSE) comparison. Finally, Section 4 reports the conclusions of the work.

2. Methodology

The models that describe the behaviour of a low-temperature ALK electrolyzer stack with different operating conditions (e.g., current density, temperature, and pressure) typically include the simulation of the following

quantities: i) electric potential, ii) Faraday efficiency, iii) HTO, iv) flow rate of produced Hydrogen, v) electric power absorbed by the stack, vi) thermal power generated by the stack, vii) stack efficiency, and viii) specific consumption. The trend of the last five items is obtained by the first two. In the scientific literature, there are multiple mathematical correlations that describe the same physical phenomenon occurring within the stack. Based on the experimental data obtained by [13], a semi-empirical modeling approach has been chosen and used in this work. The mathematical model used for the stack electric potential is the one proposed by Sánchez et al. [12, 13], which is an improvement of the equation proposed by Ulleberg [15] as reported by Eq. (1).

$$U = U(T,P,i) = U_{rev} + [(r_1 + q_1) + r_2 T + q_2 P] \cdot i + s \cdot \log_{10}\left[\left(t_1 + \frac{t_2}{T} + \frac{t_3}{T^2}\right) \cdot i + 1\right] \quad (1)$$

where U is the cell electric potential, T is the temperature in [°C], P is the pressure in [bar], i is the current density [A/cm^2], and r_i, q_i, and t_i are experimental constants. The total potential U is the sum of the reversible potential U_{rev}, which is given by thermodynamics, the activation, and the ohmic overpotentials related to the kinetic losses of the electrolysis process. It is worth noting that the polarization curve is not investigated in the field of concentration overpotential since it would require a more complex model and experimental data at higher current densities.
The cell reversible potential U_{rev} is a purely thermodynamic quantity and depends on the Gibbs free energy variation ΔG between products and reactants as a function of the operating temperature and pressure as reported by Eq. (2).

$$U_{rev}(T,P) = \frac{\Delta G}{zF} = \frac{\Delta G_{H_2}(T,P) + \frac{1}{2}\Delta G_{O_2}(T,P) - \Delta G_{H_2O}(T,P)}{zF} \quad (2)$$

Regarding Water electrolysis, the reversible cell potential U_{rev}^0 under standard conditions (P^0=1bar, T^0=25°C) is equal to 1.229 V. The value of the reversible voltage is a function of temperature and pressure, thus assuming different values from the standard one as expressed by Eq. (3) that is the Nernst's equation [16]:

$$U_{rev} = U_{rev}^0 + \frac{R \cdot T_K}{z \cdot F} \cdot \ln\left(\frac{p_{H2} \cdot \sqrt{p_{O_2}}}{a_{H_2O}}\right) \quad (3)$$

where T_K is the temperature in [K], R is the universal constant of gases (8.314 J/K mol), z is the number of electrons transferred in the electrolysis reaction (2 mol$_{e^-}$/mol$_{H2}$), F is the Faraday constant (96,485 C/mol), a_{H2O} is the coefficient of activity of Water, p_{O2} and p_{H2} are the partial pressure expressed in [bar] of Oxygen and produced Hydrogen, respectively. Assuming that the membrane is subjected to the mechanical equilibrium, the partial pressures of Hydrogen are the same as the Oxygen ones (p_{O2}=p_{H2}=p_{tot}) and, assuming that the coefficient of activity of the Water is approximately equal to 1 [17], Eq. (3) can be written as follows:

$$U_{rev} = U_{rev}^0 + \frac{R \cdot T}{z \cdot F} \cdot \ln\left(P_{tot}^{\frac{3}{2}}\right) \quad (4)$$

The reversible cell potential U_{rev}^0 can be also calculated considering isobaric conditions (at standard pressure P^0 equal to 1 bar) and thus reducing its dependency only on the temperature [17]. In the scientific literature, there are different empirical relationships such as the one proposed by Hammoudi et al. [18] as reported by Eq. (5).

$$U_{rev}^0(T,P^0) = 1.50342 - 9.956 \cdot 10^{-4} T_K + 2.5 \cdot 10^{-7} {T_K}^2 \quad (5)$$

Finally, the reversible potential is calculated by the set of Eq.s (4) and (5). The electrolyzer under investigation consists of 12 cells installed in series; thus, the stack voltage is obtained by multiplying the cell voltage by the number of cells.

$$U_{stack} = N_{cell} \cdot U \tag{6}$$

where N_{cell} is the number of cells installed in series.

The Hydrogen production rate $\dot{n}_{H2}$ [mol/s] is strictly related by the stoichiometry of the reaction and to the applied current *I* [A], which is the same for all the cells connected in series. The Hydrogen production rate is equal to the current density *i* times cell area A_{cell} as reported in Eq. (7) that is the Faraday's equation. As far as the Faraday efficiency η_{Far} is concerned, Sánchez et al. [12, 13] introduced a modification to the η_{Far} Ulleberg's relation [15] with the use of experimental parameters f_{ij} to include also the effect of the temperature as reported by Eq. (8).

$$\dot{n}_{H2} = \eta_{Far} \frac{I}{zF} \tag{7}$$

$$\eta_{Far} = \frac{i^2 \cdot (f_{21} + f_{22} T)}{(f_{11} + f_{12} T) + i^2} \tag{8}$$

As for the HTO, the equation proposed by Hug et al. [19], which describes the HTO dependence on both current density and temperature, has been used by Sánchez et al. [12, 13] and modified by introducing the dependence of pressure as reported by Eq. (9).

$$HTO = C_1 + C_2 T + C_3 T^2 + (C_4 + C_5 T + C_6 T^2) \cdot \exp\left(\frac{C_7 + C_8 T + C_9 T^2}{i}\right) + E_1 + E_2 P + E_3 P^2 + (E_4 + E_5 P + E_6 P^2) \cdot \exp\left(\frac{E_7 + E_8 P + E_9 P^2}{i}\right) \tag{9}$$

where C_1 to C_9 are constants that represent the influence of the temperature in the HTO, and from E_1 to E_9 there are constants that represent the relations between the gas purity and the pressure.

The electrical power absorbed by the stack $\dot{W}_{el}$ allows to evaluate the specific electrical consumption and the stack efficiency as well, as described by Eq. (10).

$$\dot{W}_{el} = U \cdot N_{cell} \cdot i \cdot A_{cell} \tag{10}$$

Regarding the specific consumption c_{sp}, it can be expressed as the ratio between electric power $\dot{W}_{el}$, which is expressed in [kW], and the mass flow rate of the produced Hydrogen $\dot{m}_{H2}$ expressed in [kg/h].

$$c_{sp} = \frac{\dot{W}_{el}}{\dot{m}_{H2}} = \frac{U(i,T,P) \cdot 2F}{10^3 \cdot \eta_F(i,T) \cdot 7.257168} \tag{11}$$

where 7.257168 is a conversion factor in [s•kg/h•mol] that allows to express the molar flow rate of Hydrogen in [kg/h] knowing its value in [mol/s].

Stack electrical efficiency, η_{stack} , is defined as the ratio between the chemical energy contained in the produced hydrogen and the electrical power needed for its production, as shown by Eq. (12).

$$\eta_{stack} = \frac{\dot{n}_{H2} \cdot LHV}{\dot{W}_{el}} \tag{12}$$

where LHV stands for the Lower Heating Value of hydrogen that is equal to 241.82 kJ/mol.

The thermal power $\dot{Q}_{th}$ involved in the electrolysis process, which must be removed to maintain the isothermal condition, is calculated as:

$$\dot{Q}_{th} = i \cdot A_{cell} \cdot (U(i,T,P) - U_{tn}(T,P)) \quad (13)$$

where U_{tn} is the thermoneutral potential of the stack, which is a function of both temperature and pressure.

As previously described, the electrochemical process model is integrated into the Aspen HYSYS® environment using a spreadsheet since the software does not present pre-build blocks for modeling electrochemical components. The rest of the electrolyzer stack (e.g., inlet and outlet fluid management, temperature and pressure settings, etc.) is represented by the common tools made available by the software. Steady-state operations have been considered and the fluid thermodynamic conditions (e.g., pressure and temperature) are set (e.g., isothermal and isobaric conditions are considered for the whole process). The selected *Fluid Package* is the "*Peng-Robinson*". The Water dissociation reaction is defined as a conversion reaction occurring in the "*Electrolysis reactor*", which represents the set of electrodes. Based on the thermodynamic operating conditions (e.g., temperature, pressure) and load current, the reactor sources the main electro- and thermo-chemical equations from the spreadsheet defining the reaction products and the electric power required. U_{rev} is calculated from the thermodynamic fluid property databases, which are embedded in the software, using Eq. (2). The reactor has two material flows at the output: "*Reaction Gas*" and "*Liquid Product*", where the latter is always null since the molar flow rate of the Water entering the model is equal to the molar flow rate of the Hydrogen that is calculated in the spreadsheet using the Faraday equation. The mixture of Hydrogen and Oxygen "*Reaction gas"* is sent to the second component that is the "*Component splitter*" called "*Electrode separator*": through this component it is possible to separate the oxidation and the reduction semi-reactions in the anode and in the cathodic chambers of each cell, respectively. The separator is set up so that the flows are chemically pure at the outputs (no crossover phenomena). The current output flows are corrected with the HTO that is calculated in the spreadsheet: indeed, the amount of Hydrogen separated from the anode flow by the "*Flow splitter",* here called "*Crossover_Tee*", is subsequently mixed to the Oxygen in the anode.

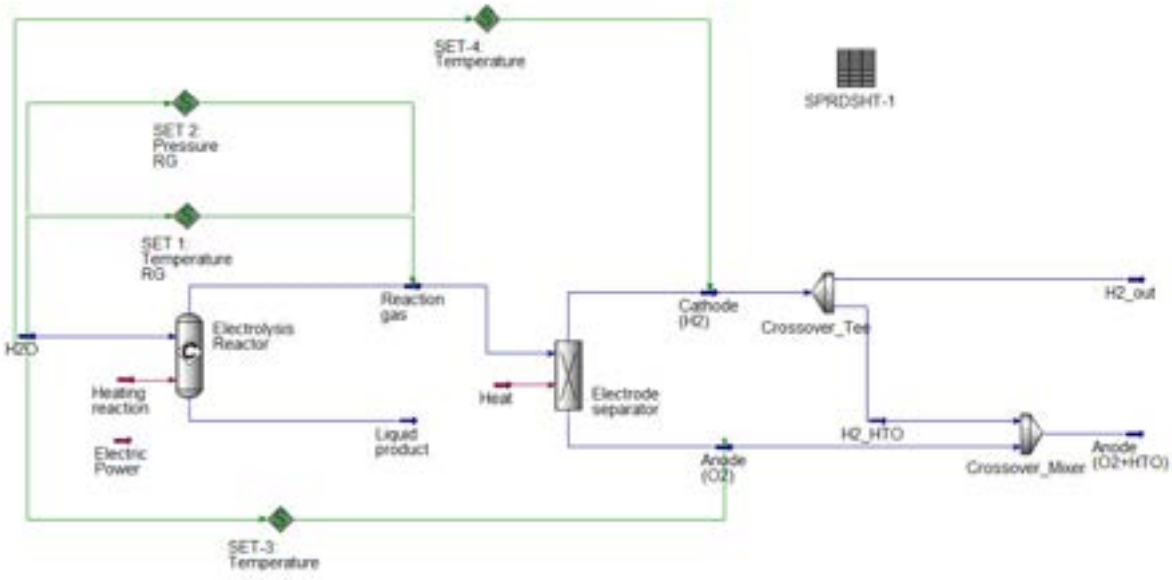

Figure. 1. Model of the low-temperature alkaline electrolyzer developed in Aspen HYSYS®.

In order to obtain comparable simulation results, the electrolyzer that has been modeled is the same one that has been characterized experimentally by Sánchez et al. [12, 13]. It is a small-sized, laboratory scale electrolyzer and its main characteristics are listed in Table 1. To obtain the experimental parameters previously described, the available experimental data have been fitted by using the Matlab® "*Curve Fitting Tool"*. The

regressions are non-linear and multiple, namely two in the case of the Faraday efficiency and three in the case of electric voltage and HTO.

Table 1. Characteristics of the alkaline electrolyzer analysed by Sánchez et al. [12, 13].

Main characteristics	Numerical value	Units of measurement
Hydrogen production flow rate	2.5	m^3/h
Maximum operating pressure	30	bar
Electric potential range	0-120	V
Electric current range	0-500	A
Maximum power	15	kW
The active area of the electrodes	1,000	cm^2
Number of cells	12	-
Electrolyte concentration	30-40	wt% KOH

3. Results and comments

The simulations results, in terms of electrolyzer performance, are evaluated as a function of the current density (between 0-0.5 A/cm^2 with steps of 0.005 A/cm^2) and the parametrization of both pressure and temperature (between 55-85°C with steps of 5°C, and between 1-29 bar with steps of 4 bar). Aspen HYSYS® allows to perform parametric "case studies" and investigate how each variable affects the results while keeping the remained parameters fixed. Figure 2 shows the results related to the stack potential at different values of temperature and pressure. It is worth noting that the trends of the other quantities such as Hydrogen flow rate, etc. have not been here reported.

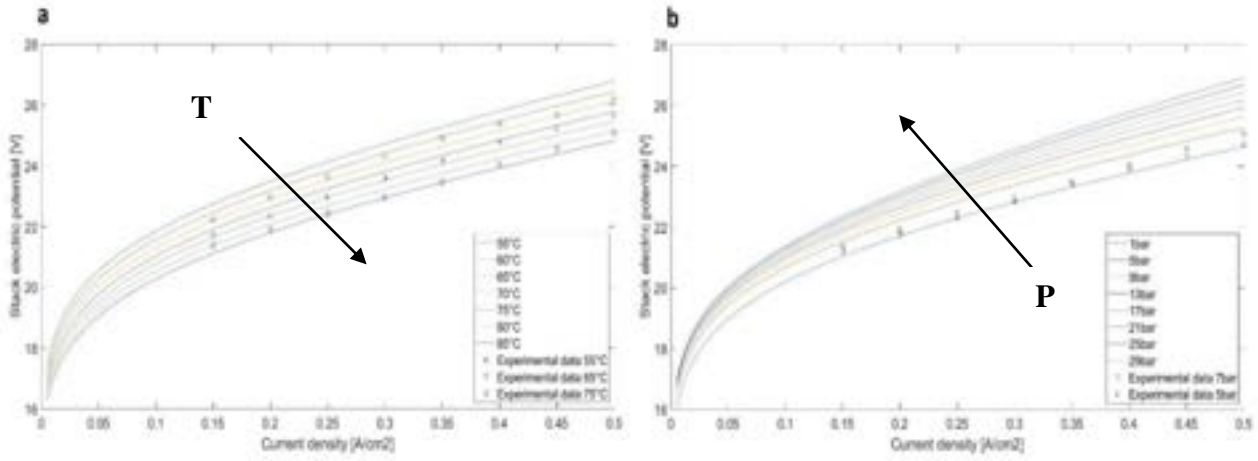

Figure. 2. (a) Stack voltage trend as a function of current density and temperature (pressure equal to 7 bar), and (b) of current density and pressure (temperature equal to 75°C).

In particular, the voltage decreases while the system temperature increases because part of the electric energy required for the electrolysis process is replaced by the associated thermal energy developed during the reaction (see Figure 2). The increase in temperature also improves the reaction kinetics by reducing the activation overpotentials as well as impacting the U_{rev} through the Nernst potential. Furthermore, the electric potential rises when the pressure increases due to the Nernst potential and the one related to the ohmic overpotential.

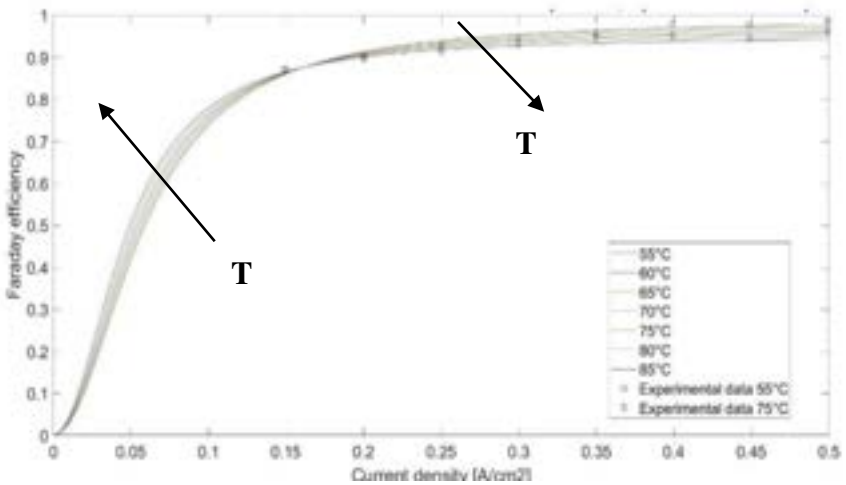

Figure. 3. Faraday efficiency trend as a function of current density and temperature (pressure equal to 7 bar).

Figure 3 shows the trend of the Faraday efficiency as a function of current density and temperature according to Eq. (8). The Faraday efficiency quickly reaches values close to 1 when current density values higher than 0.4 A/cm^2 are used. Conversely, Faraday efficiency decreases when current density values lower than 0.17 A/cm^2 and the increase of temperature leads to lower Faraday efficiency values.

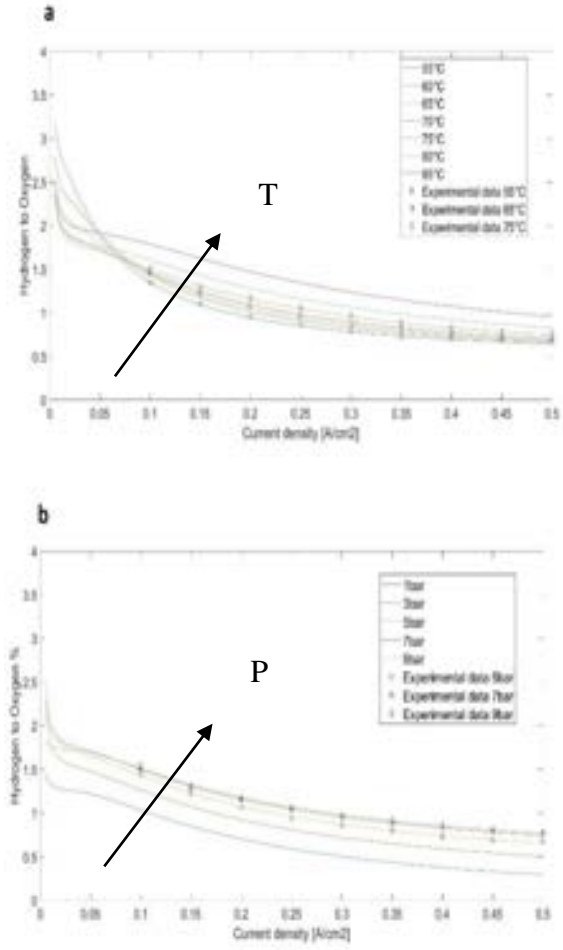

Figure. 4. (a) HTO trend as a function of current density and temperature (pressure equal to 7 bar), and (b) of current density and pressure (temperature equal to 75°C).

Figure 4a shows that the HTO increases when the current density decreases and tends to increase with the increasing temperatures. For this reason, operations with very low values of current density are undesirable because it would be preferable to avoid a HTO beyond the flammability limit of a H_2/O_2 mixture that could lead to combustion or explosion [20]. The higher amount of Hydrogen in the Oxygen stream at higher temperatures is caused by the higher diffusion velocity at elevated temperatures [17]. Figure 4b still shows an increase of the HTO as the current density decreases and as the operating pressure increases. For increasingly small current density values, the HTO model shows an asymptotic behaviour with anomalous variations due to lack of experimental data for very low currents: this means that the model is only valid for the range of density current values for which HTO measurements are available.

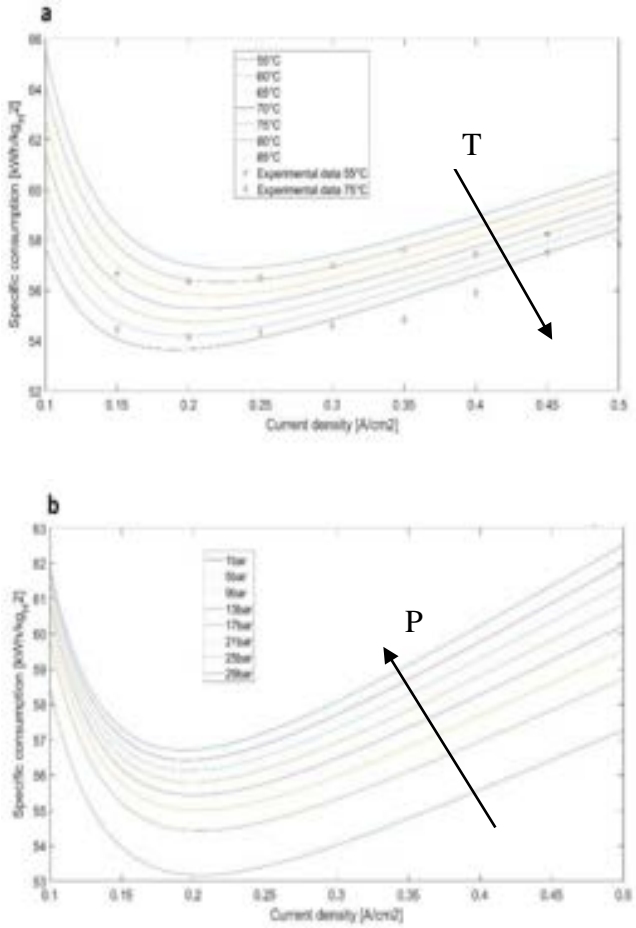

Figure. 5. (a) Specific consumption trend as a function of current density and temperature (pressure equal to 7 bar), and (b) of current density and pressure (temperature equal to 75°C).

Figure 5 shows a non-linear dependence of the specific consumption on the current density. In [13], no experimental data are available for the specific consumption, but these were obtained with data on Faraday efficiency and stack electric potential through Eq. (11). The specific consumption function reaches its minimum value at 0.2 A/cm^2, and it decreases with increasing temperature (see Figure 5a) due to the decrease of the electric potential and increases with the increasing pressure (see Figure 5b) due to the increase of the electric potential. The increase of the specific consumption, when the current density decreases below the threshold of 0.2 A/cm^2, is due to a decrease of the Faraday efficiency that is faster than the electric potential as expressed by Eq. (11). The Faraday efficiency and the electric potential increase with the current density, resulting in an increasing curve for current densities greater than 0.2 A/cm^2. The specific consumption is always between 53 and 63 kWh/kg$_{H2}$.

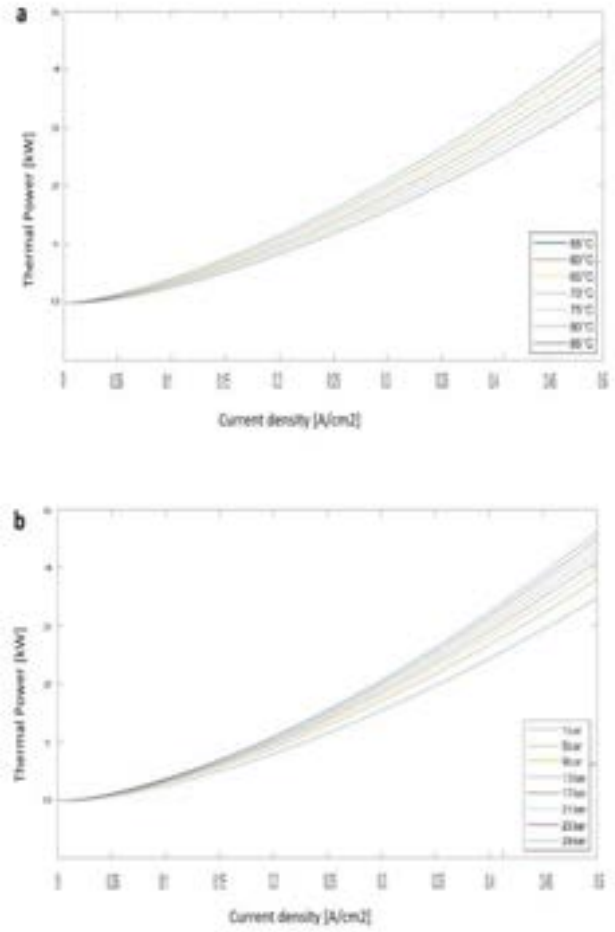

Figure. 6. (a) Thermal power trend as a function of current density and temperature (pressure equal to 7bar), and (b) of current density and pressure (temperature equal to 75°C).

As for the thermal power, Figure 6 shows how it increases with increasing current density and how this trend tends to decrease as the operating temperature increases and to increase as the operating pressure increases. This behaviour can be explained by the influence of both temperature and pressure exert on the stack potential: as the temperature increases the stack potential decreases, while as the pressure increases the potential increases. However, the thermoneutral potential can be considered approximately constant in every case. There are not experimental data for the thermal power. To evaluate the results from the developed model, the *Normal Root Mean Square Error* (NRMSE) has been calculated with respect to the literature experimental values in the same operating conditions reported in [13] (see Table 2).

Table 2. NRMSE values: comparison between model and experimental results.

	7 bar, 55°C	**7 bar, 65°C**	**7 bar, 75°C**	**5 bar, 75°C**	**9 bar, 75°C**
Electric potential	$4.066e^{-04}$	$3.990e^{-04}$	$4.095e^{-04}$	$4.317e^{-04}$	-
Faraday Efficiency	$8.253e^{-05}$	-	$4.871e^{-05}$	-	-
HTO	$5.519e^{-04}$	$2.486e^{-04}$	$3.932e^{-04}$	$4.115e^{-04}$	$3.213e^{-04}$
Specific consumption	$4.859e^{-04}$	-	$4.155e^{-04}$	-	-
Stack efficiency	$4.452e^{-04}$	-	$3.903e^{-04}$	-	-
Electric power	$4.153e^{-04}$	$3.295e^{-04}$	$3.865e^{-04}$	$2.078e^{-05}$	-
Hydrogen flow rate	$6.415e^{-05}$	-	$4.208e^{-05}$	-	-

The regression in Matlab of the cell potential from experimental data was conducted by using the set of Eq.s (4) and (5) where the reversible cell potential U_{rev}^{0} is only a function of the temperature (considering isobaric conditions (at standard pressure P^0 equal to 1 bar) according to [18], while In Aspen HYSYS the reversible cell potential is calculated automatically by implementing Eq. (2). The result is that the numerical value of the reversible cell potential calculated in Aspen HYSYS® is on average greater than the one calculated with the combination of Eq.s. (4) and (5) by 0.0395 V: this is mainly due to the fluid package selected that evaluates the trend of the state function of the components in the system. As a result, an average overestimation of 0.474 V of the electric stack potential of the model developed in Aspen HYSYS® is obtained compared to the experimental data; therefore, also other results are overestimated (e.g., specific consumption and electric power consumed). Conversely, the stack efficiency is underestimated compared to the experimental data. A possible way to increase the accuracy of the model is to perform regressions of the experimental data by firstly calculating the reversible potential according to Eq. (2), and then determining the experimental coefficients from the equation given by the combination of Eq.s. (1) and (2).

4. Conclusions

This work presents and discusses the development of a semi-empirical simulation model developed with Aspen HYSYS® related to a low-temperature Water alkaline electrolysis stack. The main performance parameters (e.g., electric power required and stack efficiency) are evaluated according to different input conditions (e.g., current density, pressure, temperature, etc.).

The trend of the electric potential has been obtained as the sum of the reversible potential and the overpotentials obtained through non-linear multiple regressions performed in Matlab® with the "*Curve Fitting Tool"* of several empirical parameters.

Results show a good agreement with the data made available by the scientific literature (experimental data) for all the analysed quantities within the selected range of operation parameters. Slight differences have been found due to the overestimation of the cell/stack potential related to the electrochemical model: indeed, the comparison between the model and experimental results showed NMRSE values ranging between $3.990e^{-04}$ and $4.317e^{-04}$. Moving to the Faraday efficiency, values ranging between $4.871e^{-05}$ and $8.253e^{-05}$ have been obtained. Then, the specific consumption values varied between $4.155e^{-04}$ and $4.859e^{-04}$, the electric power variation goes from $2.078e^{-05}$ to $4.145e^{-04}$, and the Hydrogen flow rate from $4.208e^{-05}$ to $6.415e^{-05}$ where the former is the lowest threshold value obtained in this analysis. On the other hand, as far as the HTO is concerned, NRSME values vary between $2.486e^{-04}$ and $5.519e^{-04}$, where the latter is the highest threshold value obtained in this analysis. It is worth noting that these results denote that a simple thermodynamic model with the addition of few semi-empirical corrections can represent quite well the operation of the electrolyzer stack without requiring excessive simulation efforts in terms of both kinetic and dynamic behaviours.

The present model will be subsequently implemented in a wider system resembling the behaviour of an integrated Hydrogen system composed by, besides the electrolyzer, a metal hydrides Hydrogen storage and a fuel cell. Furthermore, the future complete model will also take into account both Water recirculation and gas purification processes, which are fundamental in the electrolysis process.

References

[1] EA (2021), Greenhouse Gas Emissions from Energy Data Explorer, IEA, Paris https://www.iea.org/data-and-statistics/data-tools/greenhouse-gas-emissions-from-energy-data-explorer (last accessed 15/05/2023).

[2] IEA (2019), The Future of Hydrogen, IEA, Paris https://www.iea.org/reports/the-future-of-hydrogen, License: CC BY 4.0 (last accessed 15/05/2023).

[3] Jing Zhu, Liangsheng Hu, Pengxiang Zhao, Lawrence Yoon Suk Lee, and Kwok-Yin Wong, Recent Advances in Electrocatalytic Hydrogen Evolution Using Nanoparticles, Chem Rev, Volume 120, 2020, Pages 851-918, https://doi.org/10.1021/acs.chemrev.9b00248.

[4] Lixin Fan, Zhengkai Tu, Siew Hwa Chan, Recent development of hydrogen and fuel cell technologies: A review, Volume 7, 2021, Pages 8421-8446, https://doi.org/10.1016/j.egyr.2021.08.003.

[5] A. Djafour, M. Matoug, H. Bouras, B. Bouchekirma, M.S. Aida, B. Azoui, Photovoltaic-assisted alkaline Water electrolysis: Basic principles, International Journal of Hydrogen Energy, Volume 36, Issue 6, 2011, Pages 4117-4124, https://doi.org/10.1016/j.ijhydene.2010.09.099.

[6] Mingyong Wang, Zhi Wang, Xuzhong Gong, Zhancheng Guo, The intensification technologies to Water electrolysis for hydrogen production – A review, Renewable and Sustainable Energy Reviews, Volume 29, 2014, Pages 573-588, https://doi.org/10.1016/j.rser.2013.08.090.

[7] Z. Abdin, C.J. Webb, E.M. Gray, Modelling and simulation of a proton exchange membrane (PEM) electrolyser cell, International Journal of Hydrogen Energy, Volume 40, Issue 39, 2015, Pages 13243-13257, https://doi.org/10.1016/j.ijhydene.2015.07.129.

[8] Martin David, Carlos Ocampo-Martinez, Ricardo Sanchez-Pena, Advances in alkaline Water electrolyzers: A review, Jounral of Energy Storage, Volume 23, 2019, Pages 392-403, https://doi.org/10.1016/j.est.2019.03.001.

[9] Pierre Millet, Sergey Grigoriev, Chapter 2 – Water Electrolysis Technologies, Renewable Hydrogen Technologies: Production, Purification, Storage, Applications and Safety, 2013, Pages 19-41, https://doi.org/10.1016/B978-0-444-56352-1.00002-7.

[10] Kavan Motazedi, Yaser Khojasteh Salkuyeh, Ian J. Laurenzi, Heather L. MacLean, Joule A. Bergerson, *Economic and environmental competitiveness of high temperature electrolysis for Hydrogen production*, International Journal of Hydrogen Energy, Volume 46, Issue 41, 2021, Pages 21274-21288, ISSN 0360-3199, https://doi.org/10.1016/j.ijhydene.2021.03.226.

[11] JaeHwa KOH, DuckJoo YOON & Chang H. OH (2010) *Simple Electrolyzer Model Development for High-Temperature Electrolysis System Analysis Using Solid Oxide Electrolysis Cell*, Journal of Nuclear Science and Technology, 47:7, 599-607, https://doi.org/10.1080/18811248.2010.9720957.

[12] Mónica Sánchez, Ernesto Amores, David Abad, Lourdes Rodríguez, Carmen Clemente-Jul, *Aspen Plus model of an alkaline electrolysis system for Hydrogen production*, International Journal of Hydrogen Energy, Volume 45, Issue 7, 2020, Pages 3916-3929, ISSN 0360-3199, https://doi.org/10.1016/j.ijhydene.2019.12.027.

[13] Mónica Sánchez, Ernesto Amores, Lourdes Rodríguez, Carmen Clemente-Jul, *Semi-empirical model and experimental validation for the performance evaluation of a 15 kW alkaline Water electrolyzer*, International Journal of Hydrogen Energy, Volume 43, Issue 45, 2018, Pages 20332-20345, ISSN 0360-3199, https://doi.org/10.1016/j.ijhydene.2018.09.029.

[14] Ernesto Amores, Jesús Rodríguez, Christian Carreras*, Influence of operation parameters in the modeling of alkaline Water electrolyzers for hydrogen production*, International Journal of Hydrogen Energy, Volume 39, Issue 25, 2014, Pages 13063-13078, ISSN 0360-3199, https://doi.org/10.1016/j.ijhydene.2014.07.001.

[15] Øystein Ulleberg, *Modeling of advanced alkaline electrolyzers: a system simulation approach*, International Journal of Hydrogen Energy, Volume 28, Issue 1, 2003, Pages 21-33, ISSN 0360-3199, https://doi.org/10.1016/S0360-3199(02)00033-2.

[16] Ernesto Amores, Mónica Sánchez, Nuria Rojas, Margarita Sánchez-Molina, *Renewable hydrogen production by Water electrolysis*, Editor(s): Suman Dutta, Chaudhery Mustansar Hussain, Sustainable Fuel Technologies Handbook, Academic Press, 2021, Pages 271-313, ISBN 9780128229897, https://doi.org/10.1016/B978-0-12-822989-7.00010-X.

[17] Pierre Olivier, Cyril Bourasseau, Pr. Belkacem Bouamama, *Low-temperature electrolysis system modelling: A review*, Renewable and Sustainable Energy Reviews, Volume 78, 2017, Pages 280-300, ISSN 1364-0321, https://doi.org/10.1016/j.rser.2017.03.099.

[18] M. Hammoudi, C. Henao, K. Agbossou, Y. Dubé, M.L. Doumbia, *New multi-physics approach for modelling and design of alkaline electrolyzers*, International Journal of Hydrogen Energy, Volume 37, Issue 19, 2012, Pages 13895-13913, ISSN 0360-3199, https://doi.org/10.1016/j.ijhydene.2012.07.015.

[19] W. Hug, H. Bussmann, A. Brinner, *Intermittent operation and operation modeling of an alkaline electrolyzer*, International Journal of Hydrogen Energy, Volume 18, Issue 12, 1993, Pages 973-977, ISSN 0360-3199, https://doi.org/10.1016/0360-3199(93)90078-O.

[20] H Janssen, J.C Bringmann, B Emonts, V Schroeder, *Safety-related studies on hydrogen production in high-pressure electrolysers*, International Journal of Hydrogen Energy, Volume 29, Issue 7, 2004, Pages 759-770, ISSN 0360-3199, https://doi.org/10.1016/j.ijhydene.2003.08.014.

Hydrothermal Carbonization (HTC) pellets quality assessment: combustion kinetics, efficiency and emissions

Yaniel Garcia Lovella[a,b,g], Abhishek Goel[c,g], Louis Garin[d], Julien Blondeau[e,g] and Svend Bram[e,g]

[a] Vrije Universiteit Brussel (VUB), Faculty of Engineering, Thermo and Fluid dynamics (FLOW), Brussels, Belgium, yaniel.garcia.lovella@vub.be, CA
[b] Universidad Central "Marta Abreu" de Las Villas (UCLV), Faculty of Industrial and Mechanical Engineering, Santa Clara, Cuba, yanielg@uclv.cu
[c] Vrije Universiteit Brussel (VUB), Faculty of Engineering, Thermo and Fluid dynamics (FLOW), Brussels, Belgium, abhishek.goel@vub.be
[d] Université de Namur (UNamur), Nanomaterials Chemistry Research Unit, Namur, Belgium, louis.garin@unamur.be
[e] Vrije Universiteit Brussel (VUB), Faculty of Engineering, Thermo and Fluid dynamics (FLOW), Brussels, Belgium, julien.blondeau@vub.be
[f] Vrije Universiteit Brussel (VUB), Faculty of Engineering, Thermo and Fluid dynamics (FLOW), Brussels, Belgium, svend.bram@vub.be
[g] Brussels Institute for Thermal-Fluid Systems and clean Energy (BRITE), Vrije Universiteit Brussel (VUB) and Université Libre de Bruxelles (ULB), Belgium, svend.bram@vub.be

Abstract:

In current times, climate change due to greenhouse gas (GHG) emissions and rising fossil fuel prices create the need to focus more on renewable energy to become energy independent. The combustion of solid fuels such as biomass is a reliable option for thermal energy production and for combined heat and power production. This work focuses on the quality analysis of carbon-rich solid fuel produced by Hydrothermal Carbonization (HTC) of green waste (such as leaves, small branches, and grass). The combustion and emission performances of the HTC pellets are compared to those of conventional softwood pellets. Thermogravimetric analysis, kinetics assessment, and final use tests on a fixed bed boiler were carried out for both fuels. Combustion efficiency, boiler efficiency, and emissions factors were experimentally determined, computed and compared. Thermogravimetric analyses of the fuels show some qualitative and quantitative differences, in particular a third peak of burning rate corresponding to the oxidation of solid carbon, with a high activation energy. For similar parameters of boiler operation with HTC pellets, a 7% increase in combustion efficiency and a 7% increase in boiler efficiency were observed. However, higher particulate matter and CO emissions were observed. Results suggest that the air/fuel ratio can be further optimized for the use of HTC pellets for this type of boiler. This makes HTC pellets a promising fuel to help tackle climate change.

Keywords:

HTC pellets; softwood pellets; thermogravimetric analysis; boiler efficiency; PM; gaseous emissions.

1. Introduction

In the last few decades, biomass as an energy resource has been considered an attractive alternative to fossil fuels in reaching the European target to reduce carbon dioxide emissions [1]. Nevertheless, others transformation routes of biomass into more valorized goods can be considered, such as biochemical products and raw materials for other industries. This could transform the perspective of biomass as an energy resource, especially woody biomass [2]. Biomass resources from agriculture wastes, grass, leaves, sludge from anaerobic digestion, and urban green wastes have great potential as energy resources. However, such resources with low energy density, high moisture, and high alkali content are still challenging to direct combustion in conventional boilers, especially in issues related to ash formation [3]. Therefore, biomass resource pre-treatments and raw biomasses upgrade into better-quality biofuels have a substantial potential to increase the feasibility of their use for heat and power generation [4, 5].

Hydrothermal carbonization (HTC) has been considered an efficient alternative for upgrading raw combustible material [6], especially for organic feedstock with high moisture contents [7]. Nevertheless, the final use of

such solid fuel, as well as biomass fuels, brings some attention to the emissions issues, especially particulate matter emissions [8, 9]. Therefore, the present study aims to carry out a thermal and emission characterization of HTC pellets through a kinetics description of the fuel, as well as a final use combustion experiment in a 40 kW pellets boiler for efficiency and emission assessment.

2. Material and methods

HTC pellets produced via HTC treatment of green waste were tested and compared to softwood pellets as a reference. The kinetics description was developed by employing Thermogravimetric Analysis (TGA) in a Mettler Toledo TGA/DSC 3+ STARe System. The TGA experiments were conducted under an air atmosphere of 60.0 mL/min, for both softwood pellets and HTC pellets.

The thermal and environmental efficiency of HTC pellets combustion was assessed at the Vrije Universiteit Brussel biomass laboratory on a 40 kW laboratory boiler manufactured by HS TARM (USA). It has a gas-in-tube heat exchanger with helical rods. The boiler is designed for fuels in the form of pellets and chips. It is connected to the thermal network equipped with a PLC control system from Siemens (Desigo CC Compact). It is equipped with various sensors to control and measure the flow rate and temperatures along the network and on the exhaust gas. Two combustion tests were carried out, the first using a high-quality fuel as wood pellets, which was taken as a reference for the second test using HTC pellets. In both tests, the exhaust gas composition was measured with a portable emission analyzer HORIBA PG-250. The particulate matter was measured using an ELPI+ (Electrostatic Low-Pressure Impactor). Additionally, the flue gas temperature and circulation water temperatures were measured. Also, the fuel hopper was continuously weighted to account for the fuel consumption rate.

2.1. Experimental setup for emissions assessment

Figure 1 shows a scheme of the measurement equipment used for conducting the softwood pellets and HTC pellets tests.

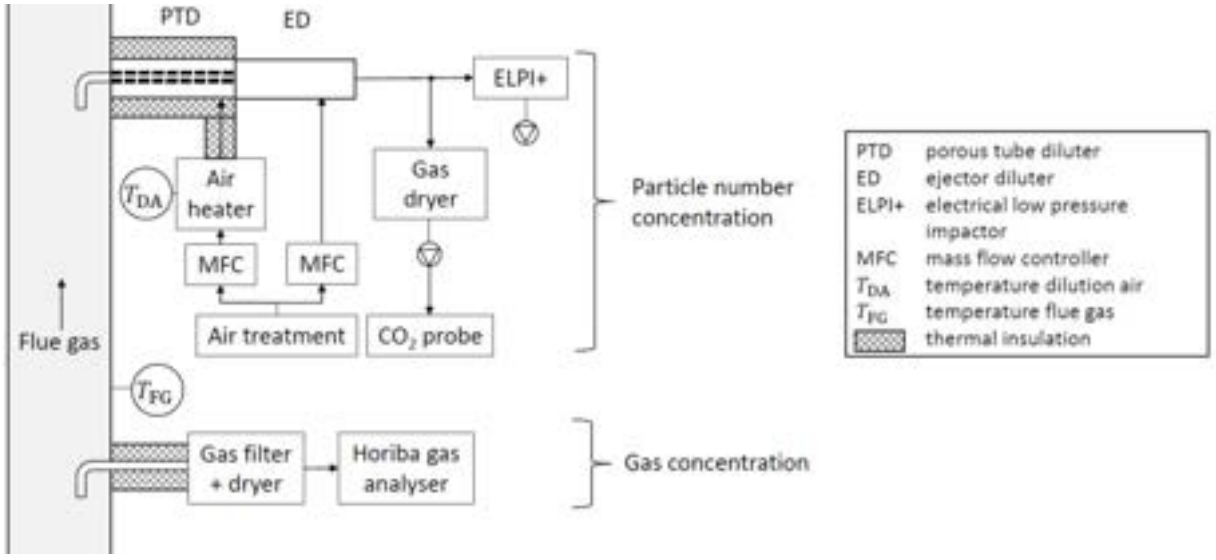

Figure. 1. Scheme of equipment for measuring particulate and gaseous emissions. Source: taken from [10] and modified by the authors.

While performing the particulate matter (PM) measurement with the ELPI+, the flue gases were first diluted in a dilution system to control parameters like temperature, humidity, and particulate concentration according to the specifications of the measuring device. This configuration increases the instrument's life and minimizes the probability of modifications in the PM distribution due to aerosol chemistry during the measurement process. In this particular setup, a two-stage dilution system manufactured by Venacontra has been used, as shown in [11].

2.2. Indexes for combustion characterization and kinetics

The ignition and burnout characteristics of a fuel are commonly related to the ignition temperature (T_{i}) and the burnout temperatures (T_b). Ignition temperatures are estimated graphically (Tangent Method), and the first peak point of the TG first-derivate (DTA) is used as an intersection point with the TG curve, as it is described in [12, 13].

The fuel thermal degradation is expressed as Eq. (1) shows, with W_i being the initial mass fraction of the sample, W the remaining mass fraction of the sample, and W_{f} the final mass fraction of the sample

$$\alpha = \frac{W_i - W}{W_i - W_f}. \quad (1)$$

The burnout temperature can be estimated via the "Conversion Method", suggested by [14]. The method uses a simple criterion for selecting the burnout temperature, which considers T_b at the point where the fuel reaches 99% of thermal degradation $(\alpha = 0.99)$. Also, the tangent method can be used. Nevertheless, authors such as Liu et al. suggest that in cases where the air is used as a carrier gas during TGA two distinct peaks appeared; then the tangent method should be used for the estimation of burnout temperature by using the second DTG peak as intersection point instead of the first DTG peak [12].

Combustion characteristics of biomass fuels can be assessed by the index *S* [15], Eq. (2) shows the formula to compute a comprehensive combustion index

$$S = \frac{(\mathrm{d}X/\mathrm{d}t)_{\max} \cdot (\mathrm{d}X/\mathrm{d}t)_{\mathrm{mean}}}{T_{\mathrm{i}}^2 \cdot T_{\mathrm{b}}}. \quad (2)$$

The index considers the maximum fuel conversion rate $[(\mathrm{d}X/\mathrm{d}t)_{\max}]$ and the average value $[(dX/dt)_{\mathrm{mean}}]$. According to [16], a higher comprehensive combustion index represents a higher fuel reactivity and thus a better combustion performance of the fuel. In a biomass combustion process, pyrolysis is one of the most difficult stages to accurately account for. Nevertheless, some general conversion routes can be assumed, of the form: biomass → char + volatiles + gases. Depending on the pyrolysis regime, the amount of products can vary [17, 18]. In this work, the combustion reaction kinetics of softwood pellets and HTC pellets are studied by using data obtained from TGA experiments. There are several methods available in the literature for modelling the combustion reaction kinetics, such as the Kissinger-Akahira-Sunose (KAS) method [19, 20], Ozawa-Flynn-Wall method (OSF) [21, 22] or Coats – Redfern method [23]. The present study selected the Coats – Redfern method, considering the simplicity of the method and the possibility to estimate the activation energy as well as the pre-exponential factor.

2.3. Efficiency and emission factor calculation

Besides the theoretical study of the combustion reaction kinetics of the HTC pellets, the final use application of this HTC fuel was also assessed experimentally. In the present study, the boiler and combustion efficiencies are calculated from the parameters measured during the experiments, in this case using a more practical approach. Equation (3) shows the efficiency calculation of a boiler using the direct method

$$\eta_B = \frac{\dot{Q}_L}{\dot{Q}_{\mathrm{F}}}. \quad (3)$$

$\dot{Q}_L$ represents the thermal power transferred from the fuel to the feeding water of the boiler. As the water vapour in the exhaust gases is not condensed, the LHV is used to compute the thermal power from the fuel $\dot{Q}_F$. The indirect method for computing the efficiency in the boiler is a more interesting option, considering the possibility to identify the critical point related to all the effects that cause a reduction in boiler efficiency. However, a boiler and combustion efficiency calculation by the indirect method require a representative sampling of bottom and fly ashes in the boiler. In a small fixed-bed boiler, at least 24 hours of operation will be necessary to get an expected amount of bottom ash, completing one cycle of ash out of bed. Nevertheless, Good and Nussbaumer have proposed and simplified method for computing the combustion efficiency of biomass boilers [24, 25]. The method has been successfully applied if CO ≤ 0.5 vol%, CO_2 ≥ 5 vol% and for exhaust gas temperatures below 400°C [26].

$$\eta_C = 100 - L_{\mathrm{Th}} - L_{\mathrm{Ch}}, \quad (4)$$

Equation (4) relates the combustion efficiency to two parameters: the thermal (L_{Th}) and chemical losses (L_{Ch}).

$$L_{\mathrm{Th}} = \frac{(T_{\mathrm{fg}} - T_{\mathrm{A}})\left\{1.39 + \frac{122}{\mathrm{CO_2 + CO}} + 0.02 \cdot u\right\}}{\frac{\mathrm{LHV}}{100} - 0.2442 \cdot \mathrm{u}}, \quad (5)$$

$$L_{\mathrm{Ch}} = \frac{\mathrm{CO}}{\mathrm{CO_2 + CO}} \frac{11800}{\frac{\mathrm{LHV}}{100} - 0.2442 \cdot u}. \quad (6)$$

T_{fg} and T_{A} stand for the temperature of the exhaust gases and atmosphere. CO and $\mathrm{CO_2}$ are the carbon monoxide and carbon dioxide volume fractions of the dry flue gases. *u* represents the fuel moisture expressed in percentage.

Additionally, expressing the energy balance on the boiler, some approximation of the losses regarding unburned carbon on bottom and fly ash can be made. Equation (7) represents the energy balance for a steady-state operation of the boiler

$$\dot{E}_{\mathrm{in}} = \dot{E}_{\mathrm{out}}. \quad (7)$$

Then, identifying all energy flows involved in the process, as Eq. (8) shows, an estimation of energy losses regarding unburned fuel $(\dot{Q}_{\mathrm{UBF}})$ can be computed as

$$\dot{Q}_{\mathrm{F}} = \dot{Q}_{\mathrm{L}} + \dot{Q}_{\mathrm{FG}} + \dot{Q}_{\mathrm{UBF}} + \dot{Q}_{\mathrm{RC}}. \quad (8)$$

The values of the thermal load and thermal power from the fuel are known values from the direct method mentioned earlier. The losses by radiation and convection $(\dot{Q}_{\mathrm{RC}})$ of the boiler can be neglected. However, Lyubov et al. found that for industrial hot-water boilers, the losses by convection and radiation to the environment are less than 0.5% of the thermal power supplied by the fuel to the boiler furnace [27]. Then, with the value of losses by unburned fuel, Eq. 9 can be used to compute the combustion efficiency, which is based on the total power from the fuel and the power not used by unburned fuel.

$$\eta_{\mathrm{C}} = \left(1 - \frac{\dot{Q}_{\mathrm{UBF}}}{\dot{Q}_{\mathrm{F}}}\right), \quad (9)$$

The emission factors (*EF*) are computed on an energy density basis, allowing to compare emissions factors from different combustion tests without considering differences in oxygen concentrations.

$$EF_{\mathrm{e}} = \frac{\dot{m}_{\mathrm{i}}/\Delta t}{(\dot{m}_{\mathrm{f}}/\Delta t)\cdot \mathrm{LHV}}. \quad (10)$$

In Eq. (10), m_{i} represent the mass of each pollutant emitted during the considered time window (Δt). The emissions factors for particle number of $\mathrm{PM}_{2.5}$ and PM_{10} are computed according to Eq. 9-10.

$$n_{\mathrm{PM}} = \mathrm{y_n} \cdot \mathrm{DR}_2 \cdot \dot{V}_{\mathrm{fg,dil,dry}}, \quad (11)$$

$$\mathrm{EF}_{\mathrm{PMx}} = \frac{\mathrm{n}_{\mathrm{PM}}/\Delta t}{(\dot{\mathrm{m}}_{\mathrm{f}}/\Delta t)\cdot \mathrm{LHV}}. \quad (12)$$

In Eq. (11), y_{n} represents the particle number, DR_2 stands for dilution ratio at dilution stage two and $\dot{V}_{\mathrm{fg,dil,dry}}$ represent the volumetric flow of diluted exhaust gases at dry conditions.

3. Results and discussions

3.1. Characterization of fuel combustion

Table 1 summarizes the significant properties of physicochemical characterization of the fuels burned during the TGA experiments and the combustion tests. It can be noticed that HTC pellets have a higher Lower Heating Value (LHV) than softwood pellets, about 18% higher. The higher LHV of the HTC pellet is reflected in the higher fixed carbon content, which is expected in a highly carbonized product obtained from the HTC process. From elemental composition, chlorine compound is present in the tested HTC pellets, in low amounts but still the potential source of corrosion issues.

Table 1. Physicochemical characterization of the analyzed fuels. Source: data adapted from [10, 28, 29].

Property	Units	Softwood pellets	HTC pellets
Bulk density	kg/m^3	≥630	696
Lower Heating Value	MJ/kg_db	≥18.8[a]	23.12
Higher Heating Value	MJ/kg_db	≥20.2[a]	24.36
Moisture content	wt%, ar	<8	5.8
Volatile matter	wt%, ar	(77.7)	69.1
Fixed carbon	wt%, ar	(22.3	30.9
Ash content	wt%, ar	(0.3)	11.0
Carbon (C)	wt%, db	(52.2)	57.9
Hydrogen (H)	wt%, db	(5.9)	5.7
Nitrogen (N)	wt%, db	≤0.3	1.26
Oxygen (O)	wt%, db	(39.1)	23.3
Sulfur (S)	wt%, db	≤0.04	0.137

wt%: percentage on weight basis; ar: as received; db: dry basis; daf: dry basis and ash free. The values in brackets are the median of similar softwood pellets taken for the original author [10] from the public Phyllis2 database. [a]The heating values were computed by the original author [10] using the Boie model [30].

In general, during TGA experiments of lignocellulose-biomass under oxidative conditions, an initial drying step can be observed (of free water, crystal water and absorbed water) which extends from room temperature up to about 170°C (A). The second step is when volatilization and combustion of volatiles start, which could extend from about 120°C up to about 420°C (B). Then, a third step of char oxidation starts from a range temperature

of about 310°C up to about 520°C (C). Finally, the burnout step appears, when all remaining char is depleted, starting at about 480°C (D) [31, 32]. The temperature range of each step of biomass combustion shown by the TGA experiments varies with the type of biomass and is also affected by the heating rate. However, the values showed could be taken as reference values for other biomass samples, considering that the mentioned author analysed 12 different biomass resources with heating rates of $10\,℃/\mathrm{min}$ and $20\,℃/\mathrm{min}$.

Figure 2(b) shows the TGA of softwood pellets and Fig. 2(a) shows the derivative thermogravimetric curve (DTG) of softwood pellets. The drying step extends from 25°C up to 95°C. It is followed by an almost flat zone, where a nearly constant weight loss rate (of about 0.42%) is observed, over a temperature range of about 100°C. The more active drying range and the almost constant weight loss rate were grouped into step A. Step B corresponds to the release and combustion of volatiles, coming from the hemicellulose at the beginning of the step and cellulose at the end of the step. It is where the highest weight loss is observed, between 197°C and 357°C. Step C is in a range of about 357°C to 500°C, where the char coming from the lignin is oxidized, however, some authors point out that some char could appear at the end of step B as well [17, 33, 34]. The burnout step starts from 500°C, where char is completely oxidised. For the purpose of the present analysis, two zones were further studied, zone I (197°C - 357°C) and zone II (357°C - 500°C).

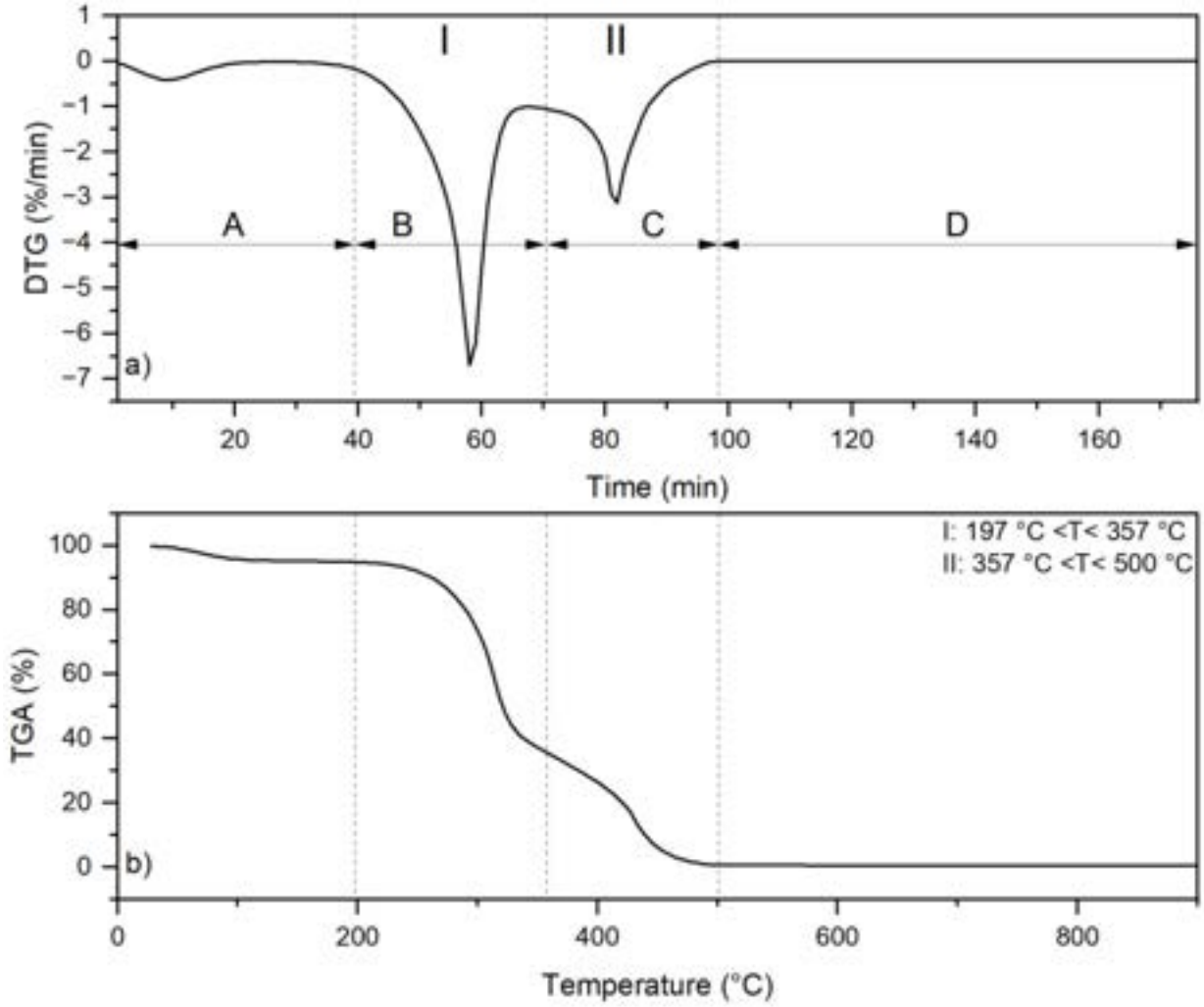

Figure. 2. Thermal degradation of softwood pellets, a) the derivative of thermogravimetry (DTG) analysis and b) thermogravimetry analysis (TGA).

Figure 3(b) shows the TGA of HTC pellets and Figure. 3(a) shows the derivative thermogravimetric curve (DTG) of HTC pellets. As for the softwood pellets, four steps can be identified (A to D), but there are some important differences in these combustion steps. Step A extends in the temperature range of about 15°C more for HTC pellets than for softwood pellets. Additionally, two distinct peaks can be appreciated. The first one is from 25°C to 117°C, which is assumed to correspond to the evaporation of free water in the fuel and the second from 117°C to 212°C, corresponding to the evaporation of the crystal water and absorbed water, contained in the ashes which in this case is about 36 times higher than for softwood pellets. Step B extends from 212°C to 322°C. The temperature span for this step is 50°C less for HTC pellets than for softwood pellets, which suggests a smaller quantity of volatiles released for the HTC pellets case, as confirmed by the volatile contents given in Table 1.

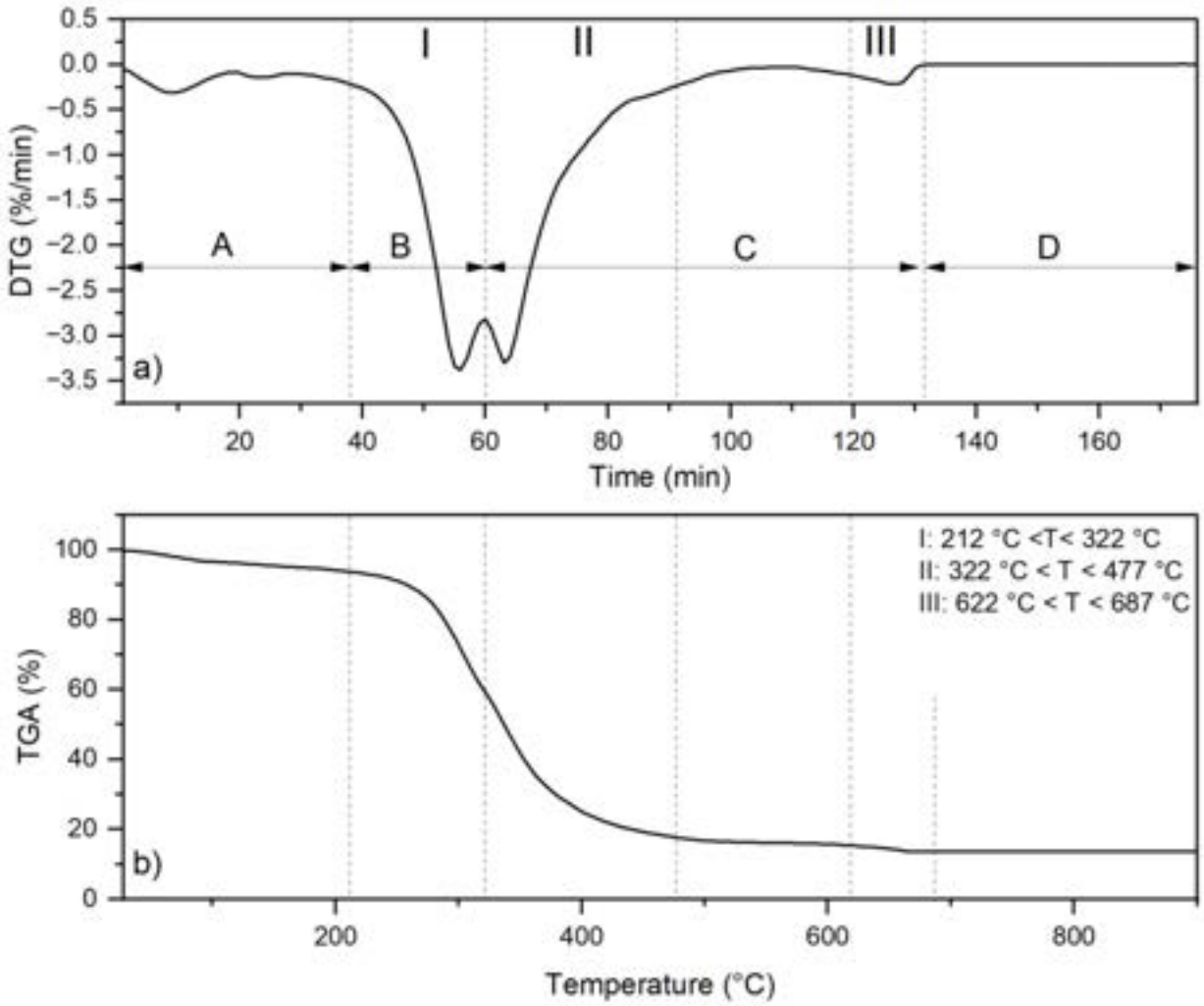

Figure. 3. Thermal degradation of HTC pellets, a) the derivative of thermogravimetry (DTG) analysis and b) thermogravimetry analysis (TGA).

Step C, from Figure 3a, shows a quite different shape for HTC pellets than for softwood pellets. The peak corresponding to the zone of maximum burning rate for step C is similar to the peak observed in step B. Also, the burning rate is quantitatively similar, however, step C starts at 322°C and ends at about 477°C. For the softwood pellets the higher part of the fuel mass is released in step B: 59.3% versus 34.9% during step C. The opposite trend is observed for HTC pellets, 34.5% of the mass is released in step B, versus 45.4% in step C. Another peculiarity of step C is that there is a second peak, after a big peak there is a trend in the TGA (Figure 3b) where the mass burned remains almost constant from 477°C to 622°C, with a weight loss of only 1.8%. But after 622 °C, the weight loss starts to increase making a second peak in step C. It can be noticed in a clearer way from DTG curve (Figure 3a) from 622°C up to 687°C The peaks shown in the DTG curve of HTC pellets were defined as three zones of kinetics interest for further analysis, as pointed out in Figure 3a. In general, the smaller difference in the burning rate of the two peaks showed by the HTC pellets, compared to the bigger difference between the two peaks of step B and C of softwood pellets, strongly suggest a less chaotic burning rate and better combustion stability for the HTC pellet.

Table 2. Characteristic combustion parameters for softwood pellets and HTC pellets.

Biomass sample	Ignition Temperature (°C)	Burnout Temperature (°C)	Temperature at maximum burning rate $(\%/\mathrm{min})$	Index S $(\mathrm{min}^{-2}\cdot\mathrm{K}^{-3})$
Softwood pellets	257	474 (500)[a]	293	$1.45\cdot10^{-10}$ $(1.23\cdot10^{-10})$[b]
HTC pellets	259	392 (687)[a]	301	$1.450\cdot10^{-9}$ $(2.57\cdot10^{-10})$[b]

[a] The value in brackets represents the estimated burnout temperature using conversion methods. [b] The value in brackets corresponds to the recomputed comprehensive combustion index, based on the new burnout temperature.

Table 2 shows the comprehensive combustion index *S*, where it clearly can be seen that the index is bigger by about one order of magnitude for HTC pellets than for softwood pellets. Some authors claim that a higher

S index indicates a higher fuel reactivity and a better fuel combustion performance. The ignition temperature of both fuels is quite similar, which means that HTC pellets are as easy to ignite as softwood pellets.

Nevertheless, the burnout temperature obtained from the tangent method is smaller for HTC than for softwood pellets but considering Figures 2 to 3, it can be noticed that the tangent method showed a poor physical meaning regarding burnout temperature. Then, using the conversion method, as it is suggested by Lu and Chen [14], HTC pellets and softwood pellets burnout temperature can be estimated again, which leads to 500°C and 687°C for softwood pellets and HTC pellets, respectively. The new burnout temperature allows recomputing a comprehensive combustion index, which in this case is for both cases in the same order but slightly better for HTC pellets.

Char oxidation is a multi-phase phenomenon and between 477°C and 722°C the inorganic compounds from the ashes form the bigger part of the remaining fuel mass. It can be that some small amount of char is trapped in the ashes, and as a consequence, a higher temperature and longer time could be required for the diffusion of oxygen to reach the char and be completely depleted. This can be the reason for higher burnout temperatures; in some way, a higher temperature will enhance the porosity of the remaining particles and as result, oxygen diffusion to the char can be enhanced.

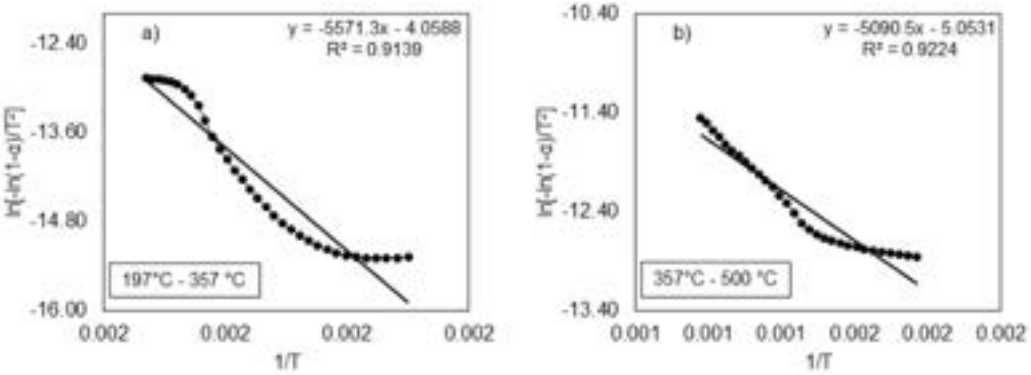

Figure. 4. Fitting curve for thermal reaction stages of softwood pellets.

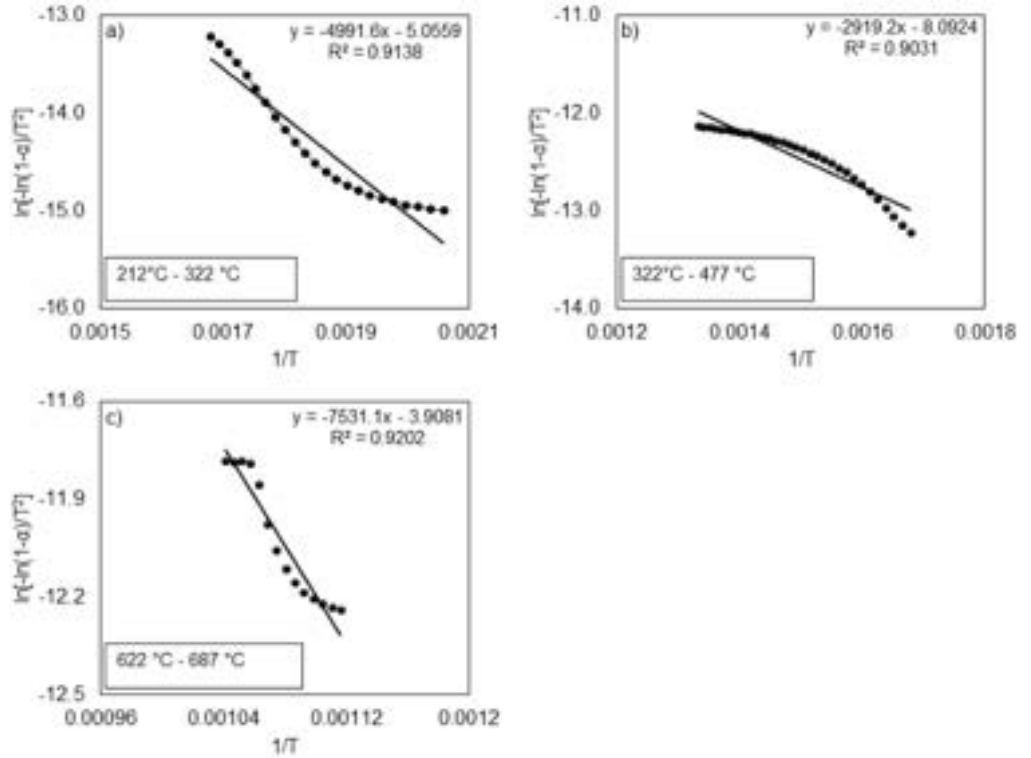

Figure. 5. Fitting curve for reaction stages of HTC pellets.

Figure 4 to 5 show the fitting curves of softwood pellets and HTC pellets for different combustion reaction stages, by means of multiple first-order reactions. The TGA DTG curves for softwood pellets were divided into two main reaction stages or reaction zones, in the temperature range of 197°C to 357°C (zone I in Figure (2a)) and from 357°C to 500°C (zone II in Figure (2a)). In both reaction zones, the correlation coefficients are higher than 0.91, which suggests that the assumption of a first-order reaction might be sufficient for first-order

modelling of the pyrolysis and char oxidation processes. The first reaction zone considers the volatilization and combustion of volatiles and the second is the volatilization and combustion of char. The time of both reaction zones is quite the same, but zone II occurs at a lower burning rate than zone I, about 2.2 times lower than zone I. Table 3 shows the kinetic parameters for tall reaction zones, outlined in Figure 4 to 5. The required activation energy is bigger for zone I than for zone II, suggesting a slower reaction rate for such zones.

Table 3. Kinetic parameters in different temperature ranges.

Biomass sample	Temperature range (°C)	Activation energy $(\mathrm{kJ/mol})$	Pre-exponential factor $(\mathrm{min^{-1}})$
Softwood pellets	197-357	46.32	$1.61 \cdot 10^6$
	357-500	42.32	$3.98 \cdot 10^6$
HTC pellets	212-322	41.50	$3.92 \cdot 10^6$
	322-477	24.27	$4.77 \cdot 10^7$
	622-687	62.61	$1.88 \cdot 10^6$

The TGA DTG curves for HTC pellets were divided into three main reaction zones, showing correlation coefficients above 0.90. The first reaction zone represents the volatilization and combustion of volatile and the second is the volatilization and combustion of the major part of char. In this case, as a highly carbonized fuel obtained by means of the HTC process, the fixed carbon is in a higher quantity than conventional lignocellulosic biomass and therefore burning rate peaks are quite similar. However, the activation energy of the reaction in zone II is 1.7 times smaller than the activation energy in reaction zone I. The combustion zone III can be assumed as an extension of the char volatilization of zone II, which requires the highest activation energy of all zones considered in HTC pellets. The analysis of zone II and III together or even the analysis of zone III alone, suggests that there is a small amount of char that is the reaction rate limiting, which kinetically speaking is the critical route of HTC pellets combustion.

3.2. Characterization of the final use of HTC pellets

Figure 6 shows the difference in boiler efficiencies between the tests performed with softwood pellets and HTC pellets, which is around 6% higher for HTC pellets.

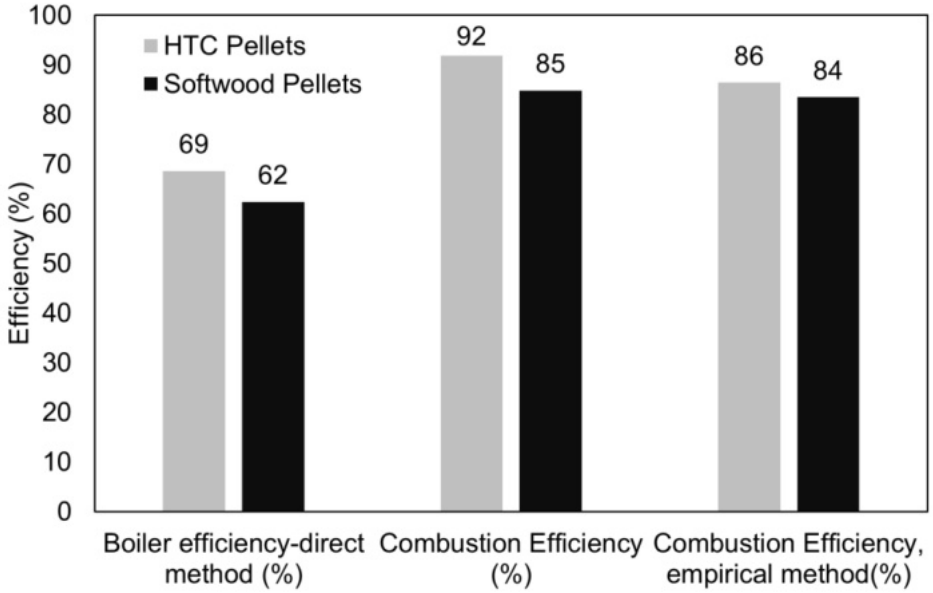

Figure. 6. Boiler efficiency (direct method) and combustion efficiency calculated from indirect method and using the empirical method.

The indirect method for the calculation of the boiler efficiency showed that flue gas losses accounted for about 18% for HTC pellets and 22% for softwood pellets. The losses regarding the unburnt fuel ($\dot{Q}_{\mathrm{UBF}}$ term in Eq. (8)) of HTC pellets and softwood pellets were about 8% and 15%, respectively. Visual observation at the end of the tests confirmed the values obtained for losses by unburned fuel. Figure 7 shows the bottom ash collected at the end of each test. The highly unburnt charcoal in the bottom ash of softwood pellets could suggest the need for more extended boiler operation (more than 3 hours) in steady-state operation for bottom ash sampling. A complete cycle of ash out boiler bed could be necessary. Nevertheless, for the HTC pellets test without complete bottom ash out of the boiler bed, the picture of Figure 7a shows a higher charcoal burnout.

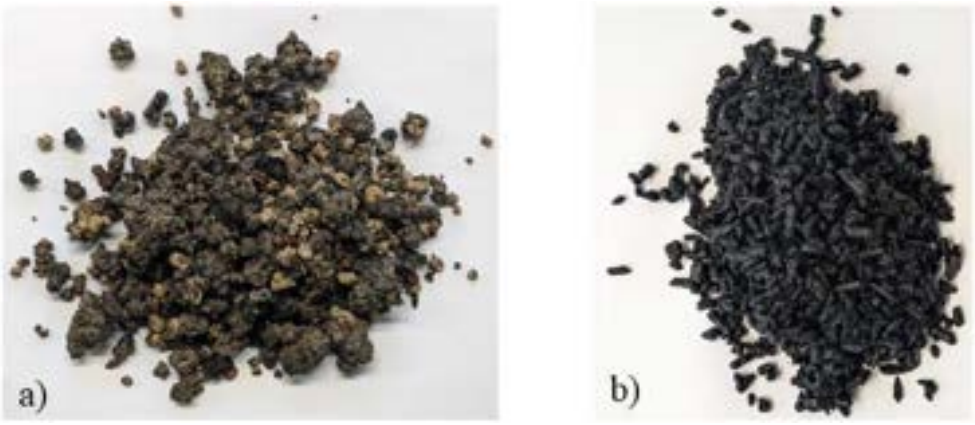

Figure. 7. State of bottom ash at the end of the tests, a): HTC pellets and b): softwood pellets.

The temperature difference between exhaust gases and the environment for both fuel tests is nearly the same, with only two degrees Celsius difference between each test. Still, the difference in a loss regarding hot gases is mostly by the mass flow rate. Both fuels are burned with similar air-fuel ratios (AFR): $29.3\ \mathrm{kg_{air}/kg_{fuel}}$ for softwood pellets and $29.5\ \mathrm{kg_{air}/kg_{fuel}}$ for HTC pellets. Despite AFR for HTC pellets being slightly higher than for softwood pellets, the low energy density of softwood pellets makes it necessary to supply more fuel mass into the combustion chamber than for the other fuel. As a result, more air is needed, and more exhaust gases are obtained, leading to more heat losses to the atmosphere. Figure 3 shows that the combustion efficiency of HTC pellets is higher than the combustion efficiency of softwood pellets. Despite the quantitative differences shown by the methods, consistent results are obtained, as both methods tend to show that HTC pellets are more efficiently burned.

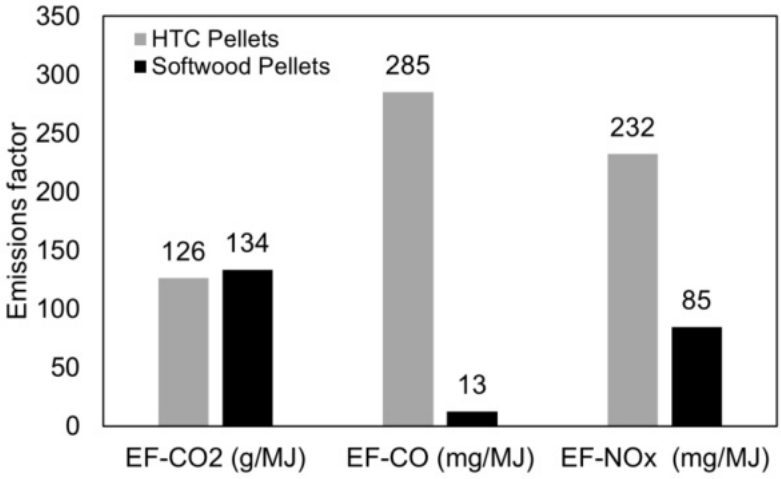

Figure. 8. Emission factor for softwood and HTC pellets.

Figure 8 shows the emission factor (EF) for the measured gaseous emissions, where it can be seen that the softwood pellets emit more carbon dioxide per unit of fuel energy (7 g/MJ). This slightly higher EF for carbon dioxide could mean that softwood pellets tend to convert more carbon during the pyrolysis and gasification phases, see zone II as illustrated in Figure 4a. Indeed, the peak of the char gasification for softwood pellets occurs at a higher temperature than for HTC pellets (416°C for Softwood pellets and 336°C for HTC pellets). The volatiles released during this stage therefore find better kinetics conditions for the complete oxidation of gaseous combustible material. As expected, carbon monoxide EF is bigger for HTC pellets than for softwood pellets, which is related to the slow reaction rate of the kinetics in reaction zone III, shown in Figure 3a. On the other hand, the HTC pellets have a higher fixed-carbon content with 8.6% more fixed carbon than the softwood pellets. In general, the lower combustion efficiency showed by the softwood pellets is related to the amount of unburned char found in the bottom ash. The lower density and lower LHV of softwood pellets than HTC pellets lead to a higher mass flow rate of pellets in the fixed bed of the boiler, making it more difficult for the conditions, in terms of combustion aerodynamics and heat transfer, to reach complete char gasification and consequently oxidation.

The NO_x emissions in the boiler come from two main sources, i.e., thermal NO_x and fuel NO_x. The thermal NO_x formation route is the NO_x source attributed to the high temperature in the furnaces. The second one is associated with nitrogen content in the fuel. The first sources could be minimaxed by managing the boiler's air

supply and reducing the furnace's average temperature. However, regardless of how the fuel is burned, about a third of the nitrogen in solid biofuel is converted to nitrogen monoxide [35]. EF-NO_x of HTC pellets shows a considerably higher value than softwood pellets, which was expected considering that elemental analysis (see Table 1), nitrogen in the fuel is more than four times higher for HTC pellets than softwood pellets. But, considering the higher energy density of HTC pellets, thermal NO_x formation could play an essential role in the NOx emission behaviour shown during the test.

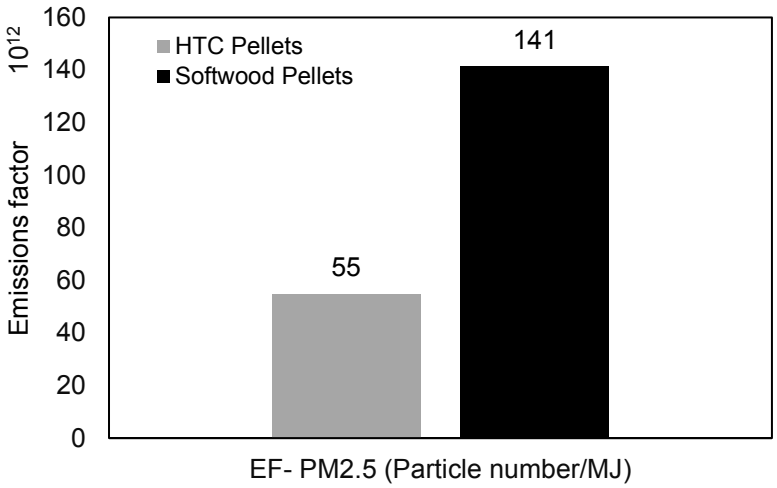

Figure. 9. Emissions factor of softwood and HTC pellets for PM2.5.

The particulate matter measurements show that more than 99% of the particle's emissions were concentrated up to 2 μm. Then, the emission factor for particulate emission was computed only for PM2.5 (see Figure 9). The EF-PM2.5 for HTC pellets was more than two times higher than for softwood pellets. Figure 9 shows that for particles diameter between 0.0091 to 0.0248 μm, PM emission for softwood pellets was higher than for HTC pellets. Still, for particle diameter from 0.0406 to 3.0169 μm HTC pellets, PM2.5 emission was far higher than for softwood pellets. It can be realized that more than 99% of particles' emissions up to 2 μm are concentrated between particle diameters from 0.0091 μm to 0.43 μm.

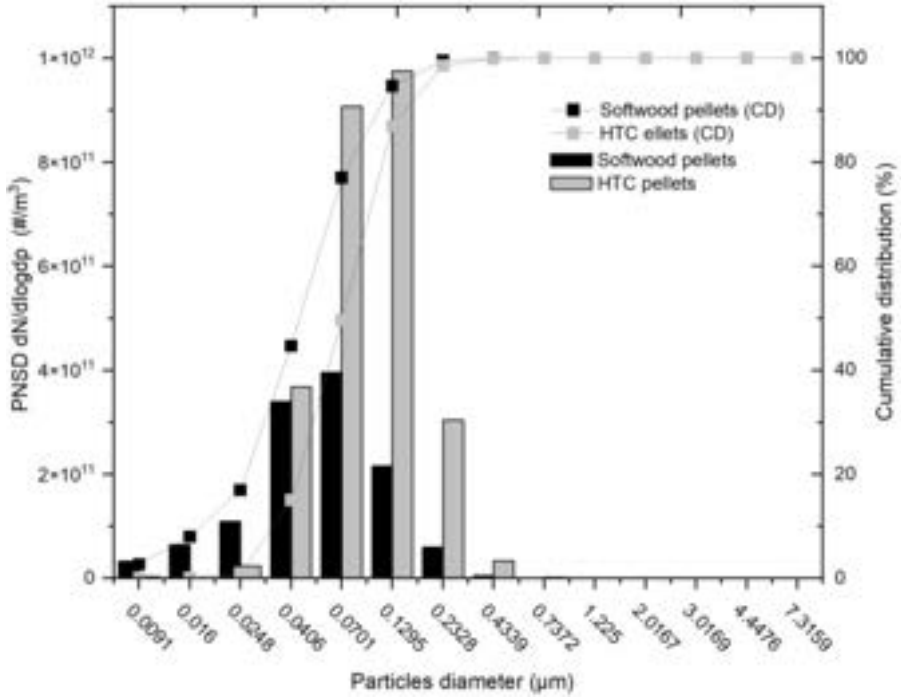

Figure. 10. Particle number distribution and distribution of cumulative particle diameter.

Figure 11 clearly shows how the PM emission of softwood pellets is higher in the zone of smaller particle diameter and higher particle diameter than HTC pellets particles emission. Nevertheless, the total particle number emission was higher for HTC pellets than for softwood pellets.

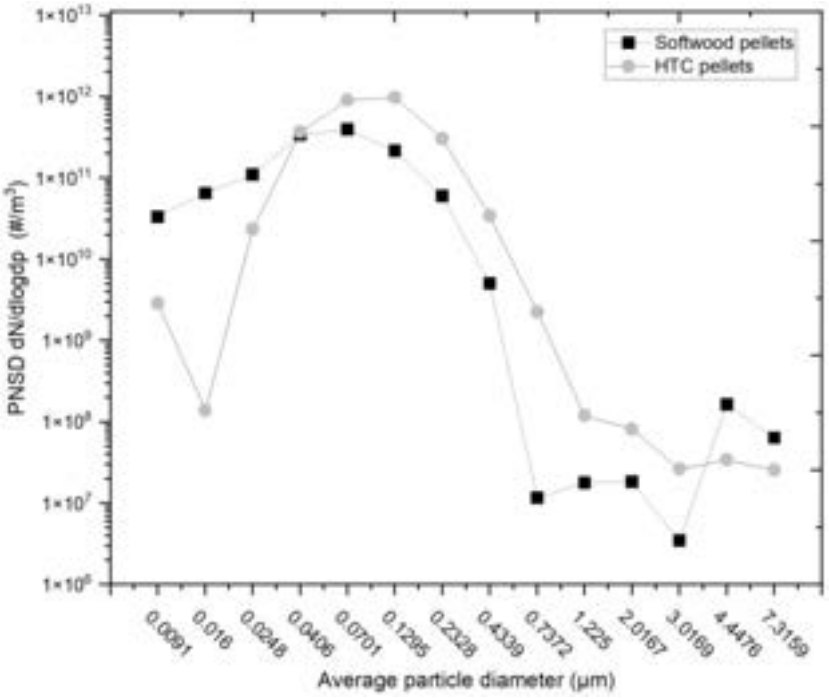

Figure. 11. Particle-number size distribution (PNSD) versus average particle's diameter in logarithm coordinate.

4. Conclusions

In this paper, a comparative study has been carried out on the combustion kinetics, efficiencies and emissions of HTC pellets and softwood pellets.

The kinetics study of softwood pellets showed two characteristic peaks in combustion zone I and II, as expected and the activation energies were found to be quite similar in both reaction zones. However, HTC pellets showed a presumed small amount of char to be gasified in reaction zone III, which takes quite a higher activation energy to start its conversion and therefore gives rise to a very slow reaction rate.

The combustion tests of softwood pellets and HTC pellets have shown that HTC pellets outperform softwood pellets in terms of boiler efficiency and combustion efficiency. However, HTC pellets showed a higher emission factor for carbon monoxide and NOx compared to softwood pellets. For both emission factors, it seems that some optimization in terms of the air-fuel ratio can be performed to reduce the average temperature in the combustion chamber and to increase the mixing of the air and the fuel. Both effects are highly desired to minimize thermal NOx and CO emissions, respectively. Nevertheless, the particulate emission showed a high number of particles in the combustion of HTC pellets. Therefore, special attention is required for the correct setting of the air-fuel ratio during the combustion of HTC pellet fuel.

Acknowledgements

This study was conducted with the support of the VUB University scholarship, which is funded by the VLIR-UOS program of the Flemish government.

References

1. Baul, T.K., et al., *Net climate impacts and economic profitability of forest biomass production and utilization in fossil fuel and fossil-based material substitution under alternative forest management.* Biomass and Bioenergy, 2017. **98**: p. 291-305.
2. Queneau, Y. and B. Han, *Biomass: Renewable carbon resource for chemical and energy industry.* The Innovation, 2022. **3**(1): p. 100184.
3. Lindberg, D., et al., *Towards a comprehensive thermodynamic database for ash-forming elements in biomass and waste combustion — Current situation and future developments.* Fuel Processing Technology, 2013. **105**: p. 129-141.
4. Brigagão, G.V., et al., *A techno-economic analysis of thermochemical pathways for corncob-to-energy: Fast pyrolysis to bio-oil, gasification to methanol and combustion to electricity.* Fuel Processing Technology, 2019. **193**: p. 102-113.
5. Li, Y., et al., *Synergistic effect of combined hydrothermal carbonization of Fenton's reagent and biomass enhances the adsorption and combustion characteristics of sludge towards eco-friendly and efficient sludge treatment.* Science of The Total Environment, 2022. **825**: p. 153854.

6. Basu, P., *Chapter 4 - Torrefaction*, in *Biomass Gasification, Pyrolysis and Torrefaction (Second Edition)*, P. Basu, Editor. 2013, Academic Press: Boston. p. 87-145.
7. Kim, D., K. Lee, and K.Y. Park, *Hydrothermal carbonization of anaerobically digested sludge for solid fuel production and energy recovery.* Fuel, 2014. **130**: p. 120-125.
8. Koppejan, J. and S. Van Loo, *The handbook of biomass combustion and co-firing*. 2012: Routledge.
9. Sitek, T., et al., *Thermogravimetric analysis of solid biomass fuels and corresponding emission of fine particles.* Energy, 2021. **237**: p. 121609.
10. Cornette, J.F.P., et al., *Particulate matter emission reduction in small- and medium-scale biomass boilers equipped with flue gas condensers: Field measurements.* Biomass and Bioenergy, 2021. **148**: p. 106056.
11. Cornette, J., *Experimental and numerical assessment of particle size distributions from solid biomass combustion*, in *Mechanical Departament*. 2022, Vrije Universiteit Brussel: Brussels.
12. Liu, J., et al., *Study of Combustion Characteristics and Kinetics of Agriculture Briquette Using Thermogravimetric Analysis.* ACS Omega, 2021. **6**(24): p. 15827-15833.
13. Escalante, J., et al., *Pyrolysis of lignocellulosic, algal, plastic, and other biomass wastes for biofuel production and circular bioeconomy: A review of thermogravimetric analysis (TGA) approach.* Renewable and Sustainable Energy Reviews, 2022. **169**: p. 112914.
14. Lu, J.-J. and W.-H. Chen, *Investigation on the ignition and burnout temperatures of bamboo and sugarcane bagasse by thermogravimetric analysis.* Applied Energy, 2015. **160**: p. 49-57.
15. Rago, Y.P., et al., *Co-combustion of torrefied biomass-plastic waste blends with coal through TGA: Influence of synergistic behaviour.* Energy, 2022. **239**: p. 121859.
16. Moon, C., et al., *Effect of blending ratio on combustion performance in blends of biomass and coals of different ranks.* Experimental Thermal and Fluid Science, 2013. **47**: p. 232-240.
17. Hoang, A.T., et al., *Progress on the lignocellulosic biomass pyrolysis for biofuel production toward environmental sustainability.* Fuel Processing Technology, 2021. **223**: p. 106997.
18. Bridgwater, A.V., D. Meier, and D. Radlein, *An overview of fast pyrolysis of biomass.* Organic Geochemistry, 1999. **30**(12): p. 1479-1493.
19. Kissinger, H.E., *Reaction Kinetics in Differential Thermal Analysis.* Analytical Chemistry, 1957. **29**(11): p. 1702-1706.
20. Akahira, T. and T. Sunose, *Method of determining activation deterioration constant of electrical insulating materials.* Res Rep Chiba Inst Technol (Sci Technol), 1971. **16**(1971): p. 22-31.
21. Flynn, J.H. and L.A. Wall, *A quick, direct method for the determination of activation energy from thermogravimetric data.* Journal of Polymer Science Part B: Polymer Letters, 1966. **4**(5): p. 323-328.
22. Ozawa, T., *A new method of analyzing thermogravimetric data.* Bulletin of the chemical society of Japan, 1965. **38**(11): p. 1881-1886.
23. Coats, A.W. and J.P. Redfern, *Kinetic Parameters from Thermogravimetric Data.* Nature, 1964. **201**(4914): p. 68-69.
24. Nussbaumer, T. and J. Good. *Determination of the combustion efficiency in biomass furnaces*. in *Proceedings 10th European conference and technology Exhibition biomass for energy, industry and climate protection. Würzburg*. 1998.
25. Good, J. and T. Nussbaumer, *Wirkungsgradbestimmung bei Holzfeuerungen*. 1993: Bezugsquelle.
26. Good, J., et al., *Determination of the efficiencies of automatic biomass combustion plants.* Verenum. International Energy Agency, IEA. Bioenergy Task, 2006. **32**.
27. Lyubov, V.K., et al., *Determining heat loss into the environment based on comprehensive investigation of boiler performance characteristics.* Thermal Engineering, 2015. **62**(8): p. 572-576.
28. TNO, E., *Phyllis2, database for (treated) biomass, algae, feedstocks for biogas production and biochar*. 2020, Von Phyllis2, database for (treated) biomass, algae, feedstocks for biogas ….
29. ENGIE-Laborelec, *Solid biofuel analysis*. 2022, Biomass Lab of Laborelec: Brussels. p. 3.
30. Mason, D.M. and K.N. Gandhi, *Formulas for calculating the calorific value of coal and coal chars: Development, tests, and uses.* Fuel Processing Technology, 1983. **7**(1): p. 11-22.
31. Gil, M.V., et al., *Mechanical durability and combustion characteristics of pellets from biomass blends.* Bioresource Technology, 2010. **101**(22): p. 8859-8867.
32. Jiang, L., et al., *A comparative study of biomass pellet and biomass-sludge mixed pellet: Energy input and pellet properties.* Energy Conversion and Management, 2016. **126**: p. 509-515.
33. Jia, G., *Combustion characteristics and kinetic analysis of biomass pellet fuel using thermogravimetric analysis.* Processes, 2021. **9**(5): p. 868.
34. Chen, D., et al., *Investigation of biomass torrefaction based on three major components: Hemicellulose, cellulose, and lignin.* Energy Conversion and Management, 2018. **169**: p. 228-237.
35. Vakkilainen, E.K., *2 - Solid Biofuels and Combustion*, in *Steam Generation from Biomass*, E.K. Vakkilainen, Editor. 2017, Butterworth-Heinemann. p. 18-56.

Improving the carbon efficiency of two-stage DME synthesis based on wheat-straw gasification

René Kofler [a] *, Lasse Røngaard Clausen [a]

*[a] Section of Thermal Energy, DTU Construct, Technical University of Denmark, Kgs. Lyngby, 2800, Denmark. * renekof@dtu.dk*

Abstract:

For a future fossil-free energy system, solutions for hard-to-abate sectors like maritime transport need to be found. Dimethyl ether (DME) produced from sustainable biomass, like wheat straw, is a promising fuel for substituting fossil Diesel fuels in marine engines. In this work, biorefineries based on wheat straw gasification were designed and analysed. The biorefineries produced DME via two-stage synthesis, where syngas was first synthesized to methanol, before methanol was dehydrated to DME in a second step. In addition, bio-ash was produced, which acts as a soil amendment and carbon sink, when returned to the fields. The biorefineries included alkaline electrolysers for producing hydrogen to increase the carbon and energy efficiency of the plants. In this work, the addition of hydrogen at different process locations was investigated: 1) at high temperatures, enabling the conversion of CO_2 to CO via the reverse water gas shift reaction or 2) at low temperatures. In addition, the amount of hydrogen added through the electrolysers and the amount of gas (containing mainly H_2, CO and CO_2) purged after the methanol reactor were varied. By increasing the amount of hydrogen in the system, carbon efficiencies >98 % were achieved, independent of the location of the hydrogen addition and purge ratios used. Reducing the purge ratio enabled to produce more DME at the same amount of hydrogen added, leading to higher energy efficiencies. Hydrogen addition at low temperature achieved higher energy efficiencies compared to hydrogen addition at high temperatures, because it enabled the operation of the electrolysers at high pressures of 30 bar and reducing the electricity consumption in the compressors. In general, any measures of increasing the energy and carbon efficiency led to an increase in the size of the methanol reactor, leading to a trade-off between investment and operational costs.

Keywords:

Biofuel, Biomass gasification, Dimethyl ether (DME), Hydrogen quench, Power-to-liquid, Wheat straw

1. Introduction

A transition from the fossil fuel based energy system we live in today to an energy system based on renewable energy sources is necessary for reducing climate change. In many sectors this can be achieved by implementing electricity production from renewables, like wind and solar, and electrifying processes. However, there are hard-to-abate sectors like the maritime transport and the aviation sector, where electrification is not possible. Lund et al. [1] show that sustainable use of biomass for producing fuels for these sectors is important for achieving the decarbonization goals. For Denmark, wheat straw has been identified as an important feedstock for a sustainable production of fuels for the maritime transport sector via gasification and similar processes [1], [2].

The use of wheat straw in gasification is challenging due to a high ash content and its low melting temperature. The low-temperature circulating fluidized bed (LT-CFB) gasifier is designed for enabling the efficient conversion of difficult residual biomasses, like straw and manure [3]. In addition to the efficient conversion, the LT-CFB gasifier enables also the production of bio-ash or bio-char, which acts as a carbon sink and improves soil properties, when returned to the fields [4]. The produced gas from the LT-CFB gasifier contains a high tar content, making it unsuitable for downstream fuel synthesis without further treatment.

In our previous works, fuel production plants based on the LT-CFB gasifier were designed and analysed based on their carbon efficiency [5] and exergy efficiency [6]. The carbon efficiency describes, how much of the carbon in the feedstock (i.e. wheat straw) is ending up in the produced fuels and bio-ash. This value is an important measure, because plants with a high carbon efficiency enable to replace a larger part of the fossil-based fuels with the same amount of limited biomass resources. In the studies, the tars are catalytically deoxygenated and then condensed, yielding a high-quality bio-oil. The remaining tar-free gas is used to produce electricity, synthetic natural gas (SNG) or dimethyl ether (DME). In the SNG and the DME production

plant, electrolytic hydrogen is produced and used for increasing the amount of produced fuel. The results show that the SNG production plant reaches the highest carbon and exergy efficiencies, followed by the DME and the electricity production plant. The results show that the DME production plant suffers from an inefficient conversion of tar-free gas to DME, due to the hydrocarbons remaining in the gas after the bio-oil condensation.

The DME production plant was further investigated, because of the promising properties of DME as a substitute for fossil fuels in marine diesel engines [7]. In [8], we showed that the carbon efficiency of a DME production plant based on the LT-CFB gasifier can be increased significantly by changing the plant layout. The carbon efficiency can be improved by using a partial oxidation step after or instead of the tar deoxygenation and condensation. This enables the reforming and cracking of the hydrocarbons (and tars, in the cases without bio-oil condensation) and making the carbon available for DME synthesis. The use of two-stage DME synthesis instead of one-stage synthesis further increases the carbon efficiency. In the two-stage synthesis, methanol is first synthesized from the tar-free gas. The methanol is then dehydrated to DME and water in a second reactor. In the one-stage synthesis, both reactions are taking place in the same reactor, leading to the production of CO_2 as a by-product, reducing the carbon efficiency of the plants. Lastly, a hydrogen quench, where hydrogen is added at high temperatures directly after the partial oxidation step, can further increase the carbon efficiency. The analysis of 14 different plants showed that in most of the cases, an increase of the carbon efficiency also leads to an increase in energy efficiency. Higher efficiencies also mean that more hydrogen and hence more electricity is needed in the plants. While the study showed how the carbon efficiency can be increased by changing the plant layout, the influence of different design parameters was not investigated, due to the complexity of the study, caused by the number of plants included.

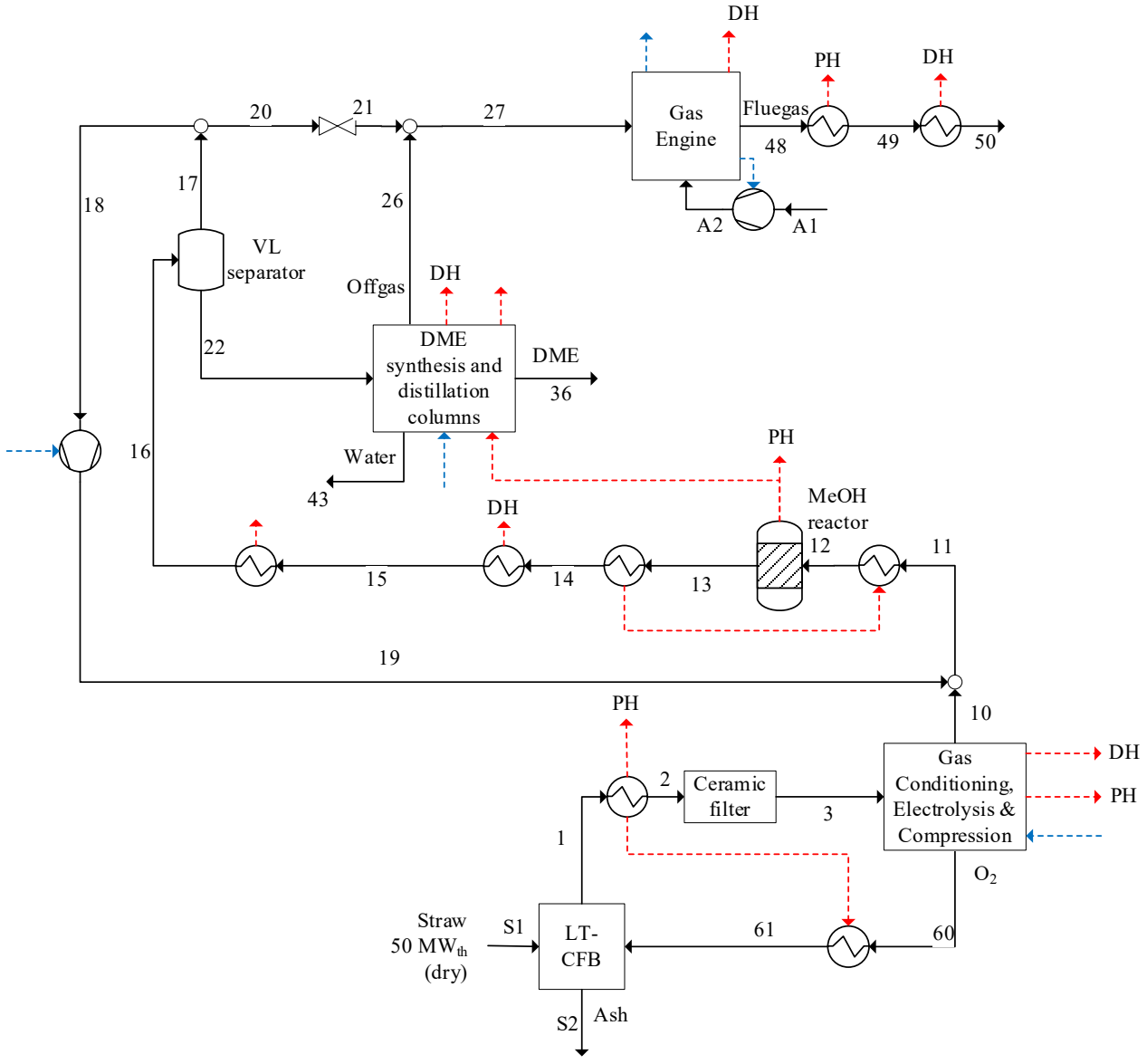

Figure 1. General flowsheet of the investigated plants. Note: The difference between the investigated plants lays in the block "Gas Conditioning, Electrolysis & Compression" as shown in Figure 3

In this work, two of the most promising plants were used for investigating the influence of two important design parameters, the amount of hydrogen addition and the purge ratio in the methanol synthesis loop, on the carbon efficiency and the energy efficiency. In addition, the influence of these parameters on the size of the methanol reactor, a key component in the synthesis part, was evaluated by analysing the change in mole flow rate to the reactor. The two investigated plants as well as the design parameter variation are explained in detail in the following section.

2. Methods

2.1. System layout

In this work, two different plant layouts for the production of DME and bio-ashes from wheat straw were investigated. Figure 1 shows the general plant design of the two different plant layouts. Wheat straw (stream S1) was gasified in the LT-CFB gasifier, using oxygen (61) from an alkaline electrolyser, producing a tar-laden gas (1) and bio-ash (S2). The tar-laden gas was then cooled from 660 °C to 500 °C before any remaining particles were removed in a ceramic filter. After that, the gas (3) entered a block, where the tars and hydrocarbons in the gas were cracked and reformed, before adding electrolytic hydrogen and compressing the gas to the required synthesis pressure. The pressurized gas (10) was then mixed with the recycling stream (19) and preheated before entering the methanol reactor (12).

The mixture of methanol, water and other light fractions out of the methanol reactor was then cooled down (streams 13-16) before entering a vapor-liquid (VL) separator. The vapor exiting the top (17) was split, with the major part (18) being recycled to the methanol reactor and a smaller purge stream (20) being sent to a gas engine in order to avoid the accumulation of inerts in the system. Liquid at the bottom (22) was sent to the block for DME synthesis and distillation columns. The detailed layout of the block is shown in Figure 2. The DME synthesis block yielded a DME stream (36) with a purity of 99.99 %, an offgas from the topping column (26), which is sent to the gas engine and a water stream (43) from the methanol column. The purge gas (21) and the offgas (26) were burned in a turbo charged gas engine, producing electricity and district heating, using air (A1) as oxidant. The exhaust gas (48) from the gas engine was cooled, providing district heating and process heat.

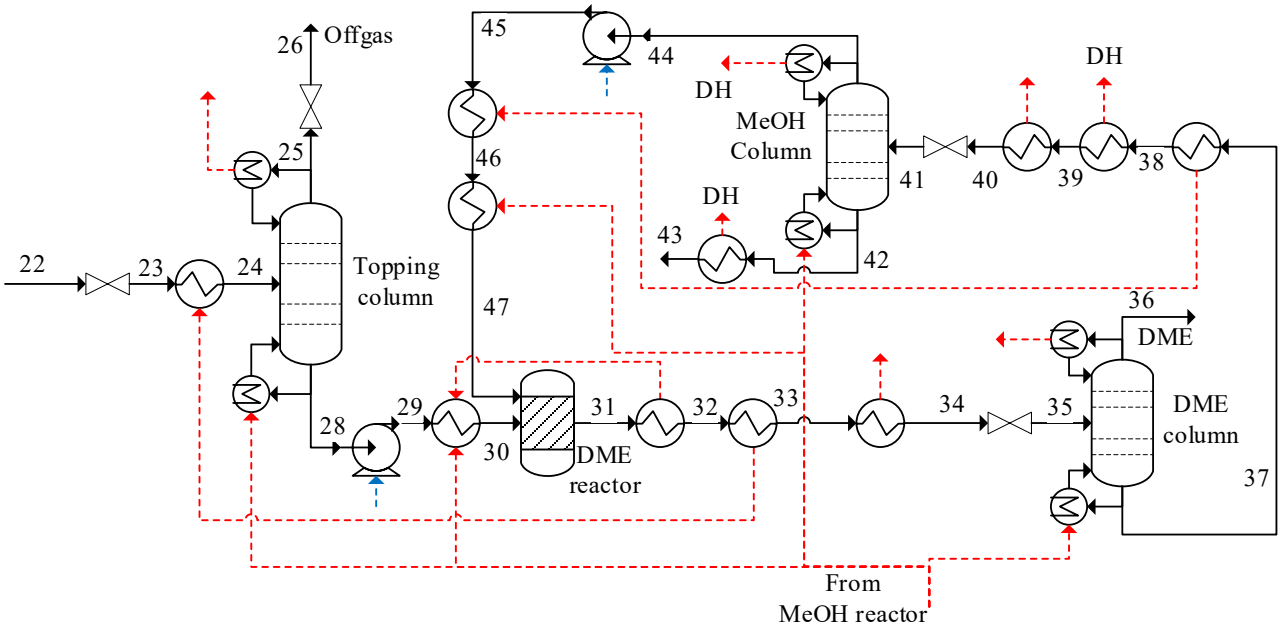

Figure 2. Detailed flowsheet of the DME synthesis and distillation columns section.

Figure 3 depicts the two different layouts for the gas conditioning block. In both cases, the tar-laden gas (stream 3) was first preheated to $T_{\mathrm{POX,preheat}} = 600\ °C$ before entering the partial oxidation (POX) reactor. Pure oxygen (52-57) from the electrolyser was used for the POX. The oxygen was also preheated to $T_{\mathrm{POX,preheat}} = 600\ °C$ and mass flow rate was controlled to reach an outlet temperature of $T_{\mathrm{POX}} = 1200\ °C$.

The differences between the two investigated layouts lay in the location of hydrogen addition. In the first layout (without hydrogen quench), hydrogen was produced in an alkaline electrolyser and added at low temperatures (51). This enabled to operate the electrolyser at a pressure of 30 bar and mixing the hydrogen with the tar-free gas after cooling and compressing the gas in a 4-stage compression with intercooling. The gas and hydrogen mixture (9) was then compressed to a pressure of 85.1 bar in the final compression stage. The high-pressure electrolysis also enabled the expansion of preheated oxygen (53) using turbines, recovering some electricity.

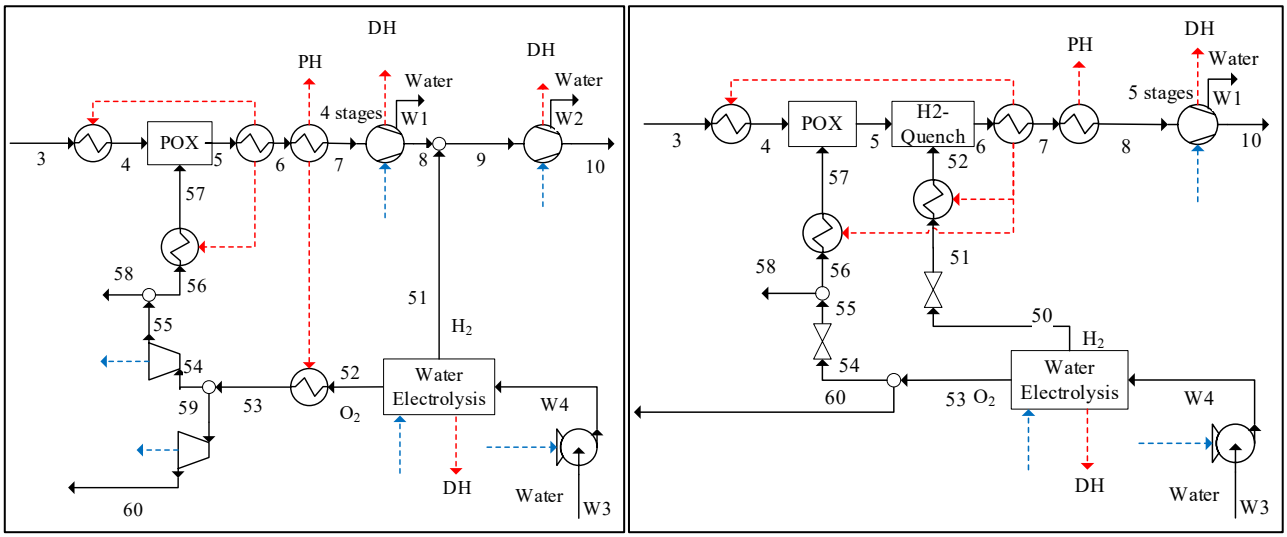

Figure 3. Flowsheet of the gas conditioning block of the two different plant layouts. Left: Plant without hydrogen quench (hydrogen addition at low temperature). Right: Plant with hydrogen quench (hydrogen addition at high temperature directly after POX).

In the second layout (with hydrogen quench), hydrogen was preheated to 600 °C and injected directly after the POX in a hydrogen quench reactor (stream 52). At temperatures above 900 °C, the reverse water gas shift (rWGS) reaction is promoted [9], leading to the conversion of CO_2 to CO, as shown in eq. (1). This process is referred to as hydrogen quench. Due to the addition of hydrogen after the POX at low pressures, the alkaline electrolysis was operated at low pressures as well.

$$CO_2 + H_2 \leftrightarrow \mathrm{CO} + \mathrm{H_2O} \qquad 41\ \mathrm{kJ/mol} \qquad (1)$$

2.2. Modelling and assumptions

The plants were modelled and simulated using the software Aspen Plus V11 [10]. The components were modelled in a zero-dimensional approach [11]. The property method RK-SOAVE (Redlich-Kwong-Soave) [12] was used for the LT-CFB gasifier, gas conditioning and gas engine, including the heat exchangers used before and after these components. SR-POLAR (Schwartzentruber and Renon) [13] was used for the remaining components. Vapor-liquid equilibrium (VLE) was assumed for all streams, except of those, where DME, methanol and water were present. In those streams vapor-liquid-liquid equilibrium (VLLE) was calculated. The solid streams and more complex liquids, namely straw, char, bio-ash, and tars were handled as so-called non-conventional streams. Non-conventional streams are only characterized by a constant heat capacity and a higher heating value (HHV) and are not considered in the chemical equilibrium. The HHV for the non-conventional compounds was estimated using eq. (2) [14], as implemented in Aspen Plus.

$$\mathrm{HHV} = [146.58\ \mathrm{C} + 568.78\ \mathrm{H} + 29.4\ \mathrm{S} - 6.58\ \mathrm{A} - 51.53(\mathrm{O} + \mathrm{N})] \cdot 10^2\ \left[\frac{\mathrm{Btu}}{lb} = 2.326\frac{\mathrm{kJ}}{\mathrm{kg}}\right] \qquad (2)$$

In eq. (2), C, H, S, O, N and A denote the carbon, hydrogen, sulphur, oxygen, nitrogen and ash content in wt.-%, respectively.

For the plants, a wheat straw input of 50 MW_{th} based on the lower heating value (LHV) was used. That corresponded to a mass flow rate of $\dot{m}_{Straw} = 3.41\ kg/s$ with the composition shown in Table 1. The LT-CFB gasifier was modelled for operating temperature of 660 °C and 700 °C in the pyrolysis and char reactor, respectively. The pyrolysis model was based on experimental data [15], while chemical equilibrium was assumed for the char reactor. The resulting gas composition was validated against the experimental results. A detailed description of modelling of the pyrolysis reactor can be found in the supplementary material of our previous work [5].

Table 1. Proximate and ultimate analysis of wheat straw pellets used as feedstock for experiments which the model was calibrated to [15].

Proximate Analysis (wt.%, as received)		**Ultimate analysis (wt.%, dry and ash free)**	
Moisture	8.5 %	N	0.8 %
Volatiles	46.2 %	C	46.2 %
Ash	6.6%	H	6.6 %
Fixed carbon	17.9 %	O	46.4 %

Oxygen for the LT-CFB gasifier, coming from the electrolyser was preheated to 560 °C. For heat exchangers used for preheating and cooling streams, as well as provision of process heat and district heating, $\Delta T_{Gas/Water} = 10\,K$ and $\Delta T_{Gas/Gas} = 30\,K$ were used if no other information are given. Process heat was defined as provision of saturated steam at 200 °C. For district heating, water was heated from 40 °C to 75 °C.

The electrolysers were operated at 30 bar and 1.63 bar, for the system with hydrogen addition at low and high temperatures, respectively. The pressure was set by pumping water to the respective pressure. For pumps, compressors and turbines, isentropic efficiencies of $\eta_{is} = 0.8$ and mechanical efficiencies of $\eta_{mech} = 0.94$ were used. For the electrolysers, an LHV-efficiency of 70 % was used. The electrolysers were operated at 90 °C, enabling the provision of district heating, by cooling the electrolysis stacks.

For the POX, all streams entering the POX were preheated to 600 °C. The outlet temperature was set to 1200 °C by varying the oxygen supply to the POX. The hydrogen for the hydrogen quench was preheated to $T_{\mathrm{H_2,preheat}} = 600\,°\mathrm{C}$. The outlet temperature from the hydrogen quench depended on the amount of hydrogen added. However, in all investigated cases the outlet temperature was higher than 880 °C, and hence high enough for achieving the spontaneous, non-catalytic rWGS reaction [9]. The resulting tar-free gas was then cooled and compressed to 85.1 bar in a 5-stage compression with intercooling.

A boiling-water reactor was used for the methanol synthesis. The outlet temperature was set to $T_{\mathrm{MeOH\ reactor}} = 240\,°C$. Chemical equilibrium with temperature approach was assumed for the occurring reactions shown in eq. (3) and (4).

$$4\,\mathrm{H_2} + 2\,CO \leftrightarrow 2\,CH_3OH \qquad \text{-182 kJ/mol} \qquad \Delta T_{approach} = 15\,K \tag{3}$$

$$\mathrm{CO} + \mathrm{H_2}O \leftrightarrow CO_2 + H_2 \qquad \text{-41 kJ/mol} \qquad \Delta T_{approach} = 15\,K \tag{4}$$

The gas stream flowing to the methanol reactor was preheated to $T_{\mathrm{preheat}} = 210\,°\mathrm{C}$. After the reactor, the stream was cooled in several heat exchangers to 25 °C before entering the vapor-liquid separator. The vapor part was then split. The biggest part was recycled to the methanol reactor, while a smaller purge stream was sent to the gas engine to avoid the accumulation of inerts in the synthesis loop. The remaining CO_2 in the liquid stream from the VL-separator was removed in a topping column after throttling, before the methanol/water mixture was pumped to a pressure of 46.1 bar and preheated to 210 °C for the DME reactor. An adiabatic reactor was used for the DME synthesis. For the methanol dehydration (eq. (5)), chemical equilibrium with temperature approach was assumed. The produced DME was purified in the DME column after cooling and throttling the stream. The bottom stream was sent to the methanol column, where methanol was separated and returned to the DME reactor while the water was disposed.

$$2\,CH_3OH \leftrightarrow CH_3OCH_3 + H_2O \qquad \text{-23 kJ/mol} \qquad \Delta T_{approach} = 100\,K \tag{5}$$

The gas engine was turbo charged to 2 bar. The air mass flow rate to the engine was set to achieve an excess air ratio of $\lambda = 2$, assuming complete combustion. The gas engine was cooled using district heating water. The exhaust gas at 400 °C was cooled to 80 °C providing both process heat and district heating.

A more detailed description of the modelling approach for the different components and the assumptions used can be found in our previous work [8]. The plant layouts investigated in this work correspond to the plants LP_POX-2st and LP_POX-H2_QNCH-2st from [8] for the system with hydrogen addition at low and high temperatures, respectively.

2.3. Parameter variations

In this work, the influence of two key parameters in the plants were investigated: a) the amount of hydrogen added to the system; b) the amount of gas being purged from the methanol synthesis loop.

The amount of hydrogen in the system was varied by increasing the water mass flow rate of stream W3 going to the electrolyser (see Figure 3). The water mass flow rate was gradually increased from the values used in [8] (1.68 kg/s for hydrogen addition at low temperatures and 2.08 kg/s for hydrogen addition at high temperatures) to 5 kg/s. This corresponds to a variation of the hydrogen flow rate of 0.19 – 0.56 kg/s and 0.23 – 0.56 kg/s for the plant with hydrogen addition at low and high temperatures, respectively. The amount of water added to the electrolysers in [8] was determined in order to achieve an H2/CO ratio of two at the inlet of the methanol reactor (stream 12 in Figure 1).

The amount of purged gas after the vapour-liquid separator in the methanol synthesis loop was varied by varying the purge ratio between 5 %, as used in [8], and 1 %, in steps of 1 %. The purge ratio PR is defined according to eq. (6), where the stream numbers in the subscripts reference to the stream numbers shown in Figure 1.

$$\mathrm{PR} = \frac{\dot{m}_{20}}{\dot{m}_{17}} \tag{6}$$

Both variations were conducted simultaneously, meaning that for each value of purge ratio, the amount of hydrogen in the system was varied. The performance of the two plants at different hydrogen mass flows and purge ratios was evaluated by using the energy efficiency η_{main} and the carbon efficiency γ_{tot}, as defined in eq. (7) and eq. (8), respectively.

$$\eta_{\mathrm{main}} = \frac{\dot{m}_{DME} \cdot LHV_{DME}}{\dot{m}_{Straw} \cdot LHV_{Straw} + |\dot{W}_{net}|} \tag{7}$$

$$\gamma_{\mathrm{tot}} = \frac{\dot{m}_{C,DME} + \dot{m}_{C,Bio-ash}}{\dot{m}_{C,Straw}} \tag{8}$$

In addition to the efficiencies, the influence of the variations on the investment cost and the operational cost was estimated. For the investment cost, the biggest variation within each plant was expected to be experienced in a change in methanol reactor size. The size of the reactor was assumed to be proportional to the inlet volume flow rate of the reactor. Since the inlet temperature and pressure were equal for all investigated plants, the volume flow rate was proportional to the inlet mole flow rate to the reactor. In order to estimate the change in reactor size for the different simulations, the relative increase $\varepsilon_{\mathrm{Reactor}}$ was calculated according to eq. (9), where $\dot{n}_{12}$ denotes the inlet mole flow rate to the methanol reactor for the investigated plant and $\dot{n}_{12,\mathrm{ref}}$ denotes the inlet mole flow rate to the methanol reactor for the reference plant. The plant with hydrogen addition at high temperatures (with quench) from [8], corresponding to the plant with hydrogen quench and a purge ratio of 5 % was used as reference case.

$$\varepsilon_{\mathrm{Reactor}} = \frac{\dot{n}_{12} - \dot{n}_{12,\mathrm{ref}}}{\dot{n}_{12,\mathrm{ref}}} \tag{9}$$

For the operational cost, the variation in the net electricity consumption was used as a measure, because the biomass used was kept constant for the investigated plants. The variation was estimated by looking at the increase in net electricity consumption $\varepsilon_{\mathrm{EL}}$, as calculated in eq. (10). $\dot{W}_{\mathrm{net}}$ denotes the net electricity consumption of the investigated plant and $\dot{W}_{\mathrm{net,ref}}$ denotes the net electricity consumption of the reference plant.

$$\varepsilon_{EL} = \frac{\dot{W}_{\mathrm{net}} - \dot{W}_{\mathrm{net,ref}}}{\dot{W}_{\mathrm{net,ref}}} \tag{10}$$

3. Results

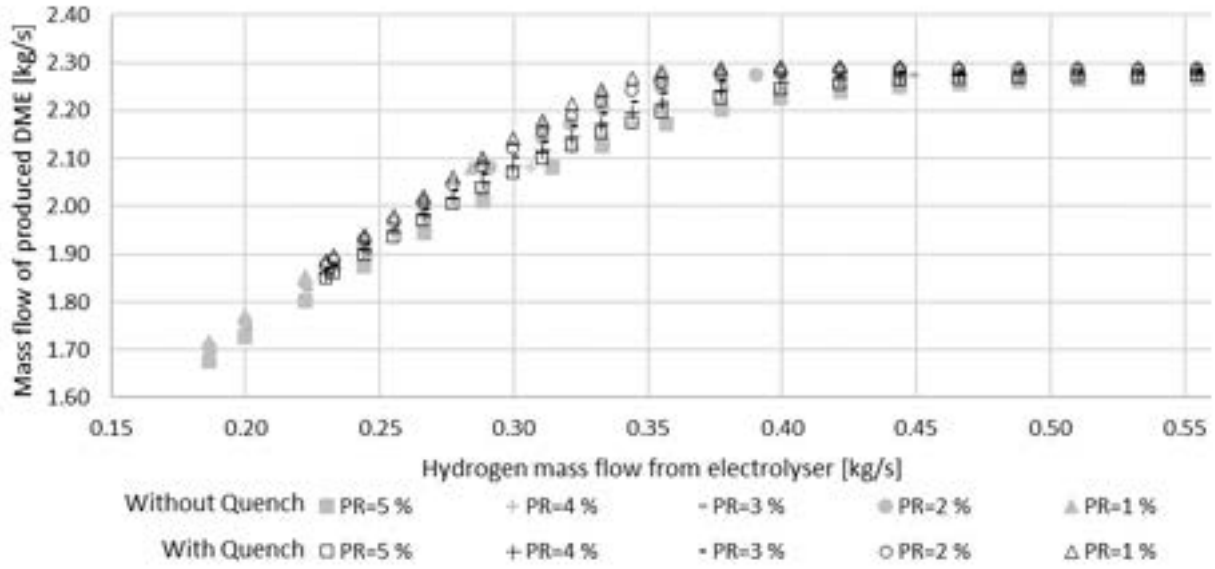

Figure 4. Mass flow rate for produced DME over hydrogen mass flow rate added by the electrolyser for the two different plants at different purge ratios (PR). Note: the grey, filled symbols denote the plant with hydrogen addition at low temperature (without quench), while the black, empty symbols denote the addition at high temperature (with quench).

In this section, the results of the conducted parameter variations are shown. Figure 4 shows the mass flow rate of produced DME for different hydrogen mass flows from the electrolyser. The grey, filled symbols show the results for the plant with hydrogen addition at low temperatures (without quench) and the black, empty symbols show the results for hydrogen addition at high temperatures (with quench). The different symbols denote the different purge rates (PR) used in the methanol synthesis loop.

The amount of produced DME increased with increasing hydrogen addition. The trend of the increase was similar for all the investigated plants and purge ratios with a strong increase in DME production up to a hydrogen addition of around 0.35 kg/s to 0.4 kg/s before flattening towards a maximum achievable DME flow rate. The results show that a decrease in the purge ratio increases the amount of DME produced at constant hydrogen flow rate added as well as the maximum achievable DME mass flow. It can also be seen that in the plants with hydrogen addition at high temperatures (with quench), more DME was produced when adding the same amount of hydrogen, compared to the plants without quench. The difference was more distinct with higher purge ratios, while the difference was almost negligible for a purge ratio of 1 %.

As it can be seen in eq. (8), an increase in DME production led to an increase in carbon efficiency, since the other two carbon flows in the system were kept constant for all plants, i.e. the carbon flows in wheat straw and bio-ash. Hence, an increase in hydrogen addition through the electrolyser led to an increase in carbon efficiency, and a reduction in purge rate led to a higher carbon efficiency at constant hydrogen addition.

Figure 5 shows the energy efficiency of the plants over the carbon efficiency. Based on the results from Figure 4, we know that moving from left to right, i.e. from lower to higher carbon efficiencies, was equivalent to adding more hydrogen to the system. In Figure 5, it can be seen that by reducing the purge rate, higher energy efficiencies were reached for achieving the same carbon efficiency. This was connected to requiring less hydrogen in the system for yielding the same DME production, leading to a reduction in electricity used for the electrolysers and hence a lower net electricity consumption (see also Figure 6). Additionally, the diagonal lines visible in Figure 5 show that reducing PR at constant hydrogen addition led to an increase in both energy and carbon efficiency. That shows that using low purge ratios is very beneficial for improving the performance of the plants.

With increasing carbon efficiencies, the energy efficiency slowly increased until reaching a maximum at different locations for different plants and purge ratios and started decreasing slowly until it reaches a rapid fall at high carbon efficiencies. For a purge ratio of 1 %, the energy efficiency was almost constant for both plants up to a carbon efficiency close to 98 % before rapidly falling at higher carbon efficiencies. This introduced the possibility to yield almost all of the carbon in the straw to end up in DME and bio-ash. For higher purge ratios, the decrease in energy efficiency started earlier. The strongest decrease was seen for a purge ratio of 5 %, where a significant reduction was already seen around a carbon efficiency of 90 %.

At very high carbon efficiencies, a rapid decrease in energy efficiency with little to no increase in carbon efficiency can be observed. This area corresponded to the part of Figure 4, where no additional DME was produced by adding more hydrogen to the system. With purge ratios of 4 % and 5 %, the rapid decrease in energy efficiency occurred earlier, and it was not possible to achieve carbon efficiency of 99 %, no matter how much hydrogen was added to the system.

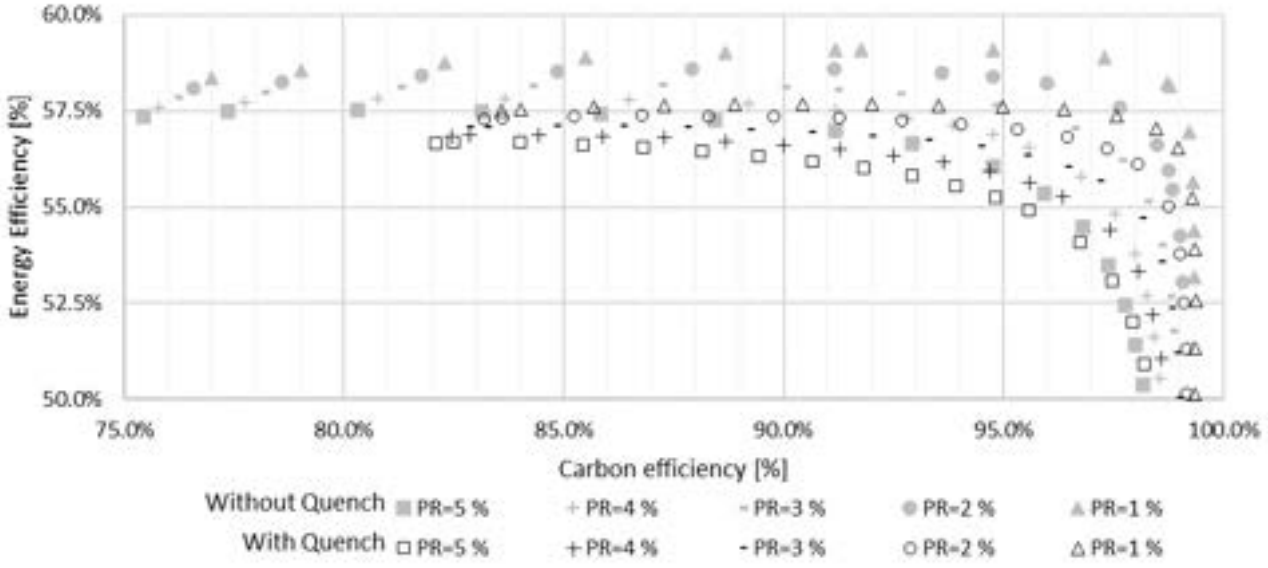

Figure 5. Energy efficiency over carbon efficiency the two different plants at different purge ratios (PR). Note: the grey, filled symbols denote the plant with hydrogen addition at low temperature

(without quench), while the black, empty symbols denote the addition at high temperature (with quench).

Figure 6 shows the electricity consumption in the two different plant layouts for purge ratios of 5 % and 1 %, respectively, for achieving a carbon efficiency of 95 %. It can first be seen that at higher purge ratios (Figure 6, left), more hydrogen was needed for producing the same amount of DME than for lower purge ratios (Figure 6,right), shown by the higher electricity consumption of the electrolyser. The higher amount of hydrogen in the system led also to a higher electricity consumption of the turbomachinery for the plant with hydrogen quench (6.1 vs. 5.7 MW), because more hydrogen needed to be compressed from ambient pressure to the high pressure of 85 bar for methanol synthesis.

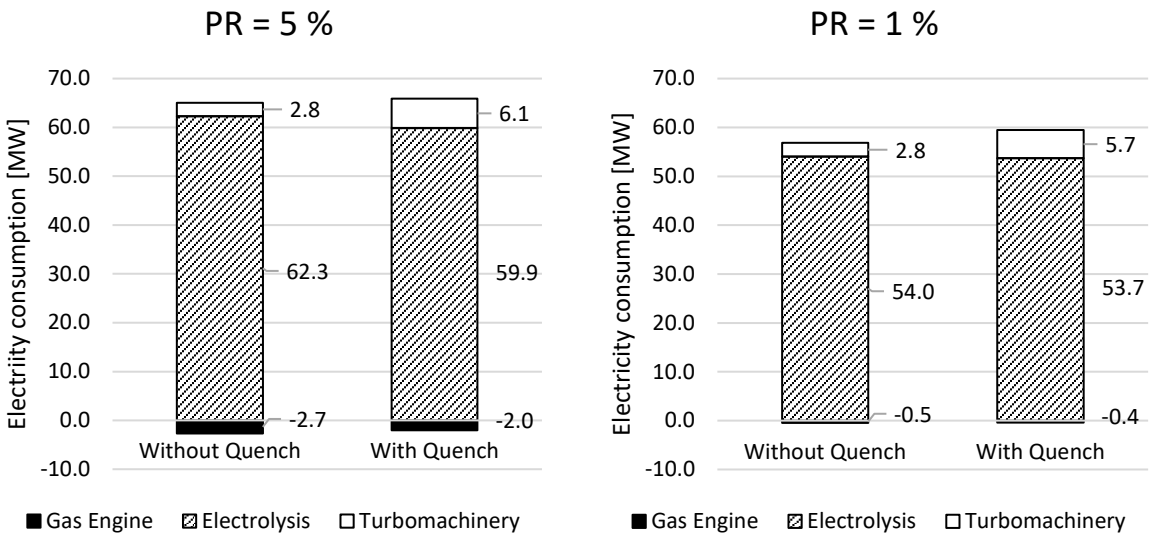

Figure 6. Electricity consumption and production of the different components in plants with a carbon efficiency of $\gamma_{tot} = 95$ %.

This effect was not seen for the plant without hydrogen quench, where the electricity consumption of the turbomachinery remained constant, due to two factors. Firstly, the electrolyser was operated at 30 bar, reducing the influence of the hydrogen on the overall electricity consumption in the turbomachinery. Secondly, the operation at 30 bar introduced the use of turbines for expanding the oxygen produced in the electrolyser, which reduced the electricity consumption with increasing hydrogen production. Additionally, for a purge rate of 5 % the electricity production in the gas engine was higher than at lower purge rate. The higher production derived from significantly more hydrogen and unconverted CO being purged and combusted in the gas engine, leading to both lower energy efficiency and carbon efficiency.

In general, higher energy efficiencies were achieved in the plants with hydrogen addition at low temperatures (without quench), as seen in Figure 5. At first, this may seem surprising, since there was more or equal as much hydrogen required to yield the same amount of DME, as seen in Figure 4. However, in Figure 6 it can be seen that for all purge rates, the higher electricity consumption for electrolysis in the plants without hydrogen quench was compensated by a lower electricity consumption in the turbomachinery, leading to a lower net electricity consumption for the same DME production. The increased electricity consumption for the plants with hydrogen quench derived from the necessity of operating the electrolysers at ambient pressure, leading to compression of hydrogen from ambient pressure to 85.1 bar (instead of 30 bar to 85.1 bar for the plants without hydrogen quench) and not having any electricity generation from expanding the produced oxygen in turbines. The electricity consumption in the 5-stage compression train was increased from 3.81 MW for the plant without hydrogen quench to 6.03 MW for the plant with hydrogen quench at $PR = 5$ % and from 3.70 MW to 5.71 MW for $PR = 1$%. The electricity production in the oxygen turbines for the plant without hydrogen quench was 1.09 MW for $PR = 5$ % and 0.94 MW for $PR = 1$ % . The electricity consumption of the remaining turbomachinery, i.e. pumps and recycling compressor, was significantly smaller than the aforementioned consumption and production and their influence on the variation of the net electricity was negligible.

Lastly, we looked at the influence on the mole flow rate into the methanol reactor for three different carbon efficiencies, i.e. 82 %, 90 % and 95 % (Figure 7). The increases are shown as relative increases compared to a reference case as defined in eqs.(9) and (10). The reference case was the plant with hydrogen addition at high temperatures (with quench) from [8]. It had a purge ratio of 5 % and a carbon efficiency of 82 %.

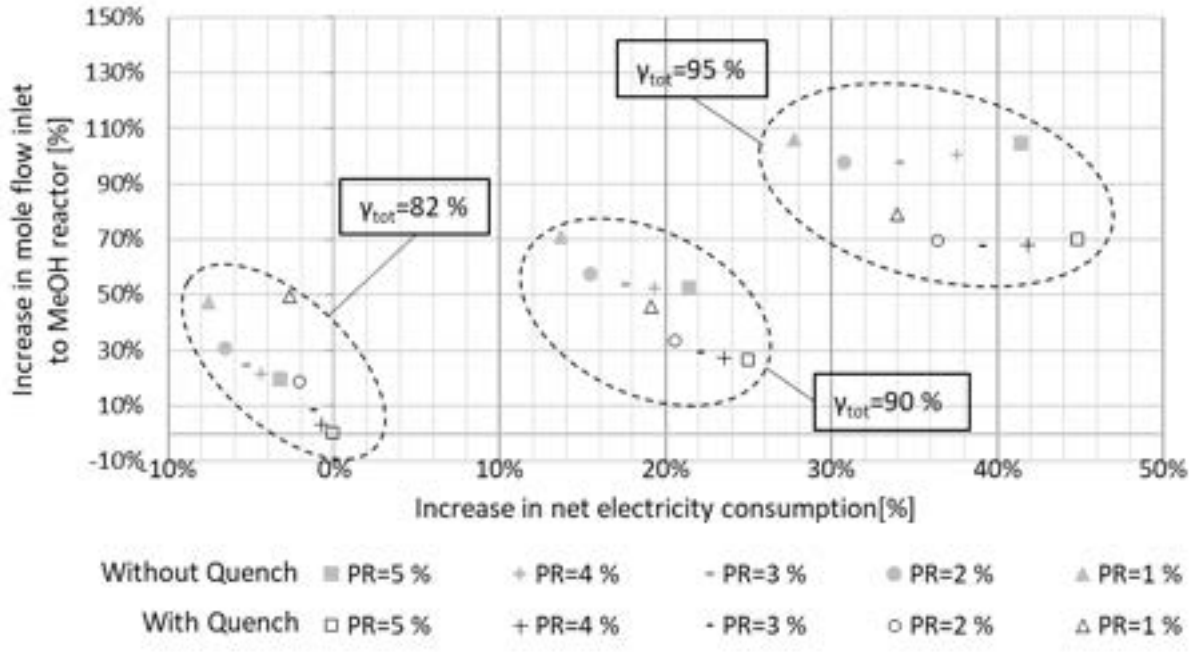

Figure 7. Increase in mole flow rate into the methanol reactor as an indicator for the reactor size over increase in net electricity consumption as an indicator for the operational cost for the different plants at varied purge ratios (PR) for three different carbon efficiencies γ_{tot}. Note: the grey, filled symbols denote the plant with hydrogen addition at low temperature (without quench), while the black, empty symbols denote the addition at high temperature (with quench).

In general, it can be seen that a reduction in purge ratio led to a lower electricity consumption, while the inlet mole flow rate to the methanol reactor increased. The reduction in electricity consumption was already explained above. The increase in mole flow rate to the reactor at lower purge ratios derived mainly from increased recycling the inert nitrogen, but also from a higher CO and CO_2 mole flow rate through the higher recycling. For a carbon efficiency of 95 % a change in the general trend for the mole flow into the reactor was observed, where the inlet mole flow rate initially decreases when reducing the purge ratio from 5 % before starting to increase again for lower purge ratios. The behaviour derived from requiring significantly more hydrogen to achieve a carbon efficiency of 95 % at higher purge ratios, leading to higher mole flow rates into the methanol reactor, despite recycling less nitrogen, CO and CO2.

Looking at the results for the plants with a carbon efficiency of 82 %, for the plant with hydrogen quench, the mole flow rate into the methanol reactor was increased by 50 % by reducing the purge ratio from 5 % to 1 %, while the electricity consumption was reduced by 2.6 %. When not including a hydrogen quench, the electricity consumption was reduced by 3.2 % and the reactor inlet mole flow rate was increased by 20 % for $PR = 5\ \%$, while for $PR = 1\ \%$, a reduction in 7.6 % at a mole flow rate increase of 47 % was achieved. It was observed that all plants without hydrogen quench consumed less electricity than any of the plants with hydrogen quench, while the reactor size was larger at purge ratios between 2 % and 5 %.

For the plants with a carbon efficiency of 90 %, the electricity consumption was higher than for the reference case, as expected, due to the higher hydrogen demand for achieving higher carbon efficiencies. The trends for the two plants looked similar to those for the lower carbon efficiency, but the differences in reactor size were smaller, as seen by the flatter curves. For the plant with hydrogen quench, the electricity consumption was increased by 25 % and 19 % for the plants with $PR = 5\ \%$ and $PR = 1\ \%$, respectively, while the molar flow rate into the methanol reactor was increased by 27 % and 46 % compared to the reference case, respectively. For the plant without hydrogen quench, the increases in electricity consumption were 21 % and 14 % and for the mole flow rate 52 % and 71 %, respectively.

The highest electricity consumption and reactor size were found for the plants with a carbon efficiency of 95 %, due to the amount of hydrogen needed. The increase in electricity consumption was 45 % and 34 % for the plant with hydrogen quench at $PR = 5\ \%$ and $PR = 1\ \%$, respectively, and 41 % and 25 % for the plant without hydrogen quench. The mole flow rate to the methanol reactor was increased by 70 % and 79 % for the plants with hydrogen quench and by 105 % and 106 % without hydrogen quench.

4. Discussion

The results showed that higher energy efficiencies were achieved for plants without hydrogen quench compared to the plants with hydrogen quench (see Figure 5). This derived from avoiding the compression of hydrogen from ambient pressures up to a methanol synthesis pressure of 85 bar. Instead, the hydrogen could be added at 30 bar, enabling pressurized operation of the alkaline electrolyser, reducing the electricity consumption by pumping water to 30 bar instead. Reducing the purge ratio from 5 % increased the energy efficiency of the plants, by better utilizing the hydrogen in the system, leading to a lower hydrogen demand and hence lower electricity consumption. The highest energy efficiency of the investigated plants with $\eta_{\mathrm{main}} = 59.1\ \%$ was achieved with the plant without hydrogen quench and purge ratio of 1 %. This energy efficiency was reached when adding between 0.28 kg/s and 0.32 kg/s of hydrogen to the system, yielding carbon efficiencies of around $\gamma_{tot} = 90 \ldots 95\ \%$. The energy efficiency was almost constant and always larger than $\eta_{\mathrm{main}} \geq 58.3\ \%$ in the range of carbon efficiencies of $\gamma_{tot} = 77 \ldots 98\ \%$. For carbon efficiencies higher than 98 %, the energy efficiency dropped rapidly.

For the plant with hydrogen quench and a purge ratio of 1 %, the energy efficiency was as high as $\eta_{\mathrm{main}} = 57.7\ \%$ in the range of carbon efficiencies $\gamma_{tot} = 88 \ldots 94\ \%$. The energy efficiency was always higher than $\eta_{\mathrm{main}} \geq 57\ \%$ in the range of $\gamma_{tot} = 82 \ldots 98\ \%$. Pressurized operation of the LT-CFB gasifier and the downstream POX would reduce the difference in energy efficiency between the plants with and without hydrogen quench, because this would enable to use pressurized electrolysis also for the plant with hydrogen quench. If the gasifier is pressurised to 30 bar, it is expected that the plants with quench would achieve higher energy efficiency than the plants without quench. Pressurization of the LT-CFB gasifier could be economically feasible for large-scale plants, because it would reduce the size of the component. However, challenges with the biomass feeding may arise. Additionally, it could perhaps impact the tar formation mechanisms in the pyrolysis reactor and increase the risk of tar condensation and subsequent damage of components.

The evaluation of the size of the methanol reactor, described by the mole flow rate into the reactor, showed that for carbon efficiencies of 90 % and lower, a higher energy efficiency (i.e. lower electricity consumption) required a larger methanol reactor. This denotes that there is a trade-off between the investment cost (reactor size) and the operational cost (electricity consumption) of the plants. An economic analysis of the plans would be necessary in order to quantify, which of the factors has a larger influence on the overall plant economics. At higher carbon efficiencies (e.g. 95 %) a different trend was observed, where higher purge ratios led to both higher electricity consumption and larger methanol reactor. There it was clearly beneficial to choose a small purge ratio.

The same trade-off was observed in the comparison between plants with and without hydrogen quench. In order to achieve the same carbon efficiency, the plants with hydrogen quench required more electricity, while the methanol reactor was smaller. It should however be considered, that for the plants with hydrogen quench additional investment would be required for the hydrogen quench. This would consist of either increasing the size of the POX reactor and adding a hydrogen injection or adding an additional reactor for the hydrogen quench after the POX. An economic comparison between the system is necessary for making a clear conclusion.

Lastly, it should be noted that using the mole flow rate into the methanol reactor as a measure for the size of the reactor gives a first estimate of the required investment of the methanol reactor. However, comparing inlet mole flows to the reactor enables only to compare the cross-sectional area of the reactor, i.e. the diameter of or the number of tubes in the reactor, since it is proportional to the volume flow rate into the reactor. The shown results could not be used for making any suggestions on required changes in the length of the reactor, because the length depends strongly on the kinetics of the methanol synthesis reactions. Since the inlet composition to the reactor varied strongly between the different plants, due to the variations in purge ratio, amount of hydrogen addition and the use of hydrogen quench, the use of a kinetic model for estimating the length of the reactor could give further insides into the influence of these parameters on the economic performance of the different plants.

5. Conclusion

In this work we investigated the influence of the amount of electrolytic hydrogen and the purge ratio of the gas after the vapour-liquid separator in the methanol system in two different DME production plants. Both plants produced DME from wheat straw gasification using two-stage DME synthesis, where methanol was synthesized in a first step, and then dehydrated to DME and water in a second step. The plants used a partial oxidation (POX) step after the gasifier for reforming and cracking the tar and hydrocarbons in the produced gas. The difference between the plants was the location of hydrogen addition. In the plants without hydrogen quench, the hydrogen was added after the gas from the POX was cooled and compressed to 30 bar. The gas hydrogen mixture was then compressed to 85 bar. In the plant with hydrogen quench, the hydrogen was added at high temperatures directly after the POX, leading to a spontaneous reverse water gas shift reaction, converting CO_2 and H_2 to CO and H_2O.

The analysis showed that increasing the amount of hydrogen in the system led to a higher DME production and hence a higher carbon efficiency. Carbon efficiencies higher than 98 % were achieved for all plants and

purge ratios. By reducing the purge ratio, the carbon efficiency was increased at constant hydrogen addition, Because the hydrogen in the system was used more efficiently. At the same time, it also increased the energy efficiency of the plants. The plants with hydrogen quench produced more DME then the plants without hydrogen quench, when using the same amount of hydrogen and purge ratio. Despite the lower hydrogen demand, the electricity consumption was higher for the plants with hydrogen quench, due to increased compression work. The compression work was lower for the plants without hydrogen quench, due to adding the hydrogen at 30 bar, enabling to pump water to the electrolyser instead of compressing the hydrogen.

Additionally, the changes in the required size of the methanol synthesis reactor were estimated by comparing the mole flow rate at the inlet of the methanol reactor. The analysis showed that for most of the cases, measures leading to an increase in energy and/or carbon efficiency led also to an increase in reactor size, highlighting a trade-off between investment cost (larger reactor) and operational cost (lower electricity consumption/higher DME production). A detailed economic analysis is proposed to be conducted for further insights into the economic performance of the plants.

6. Acknowledgments

This research project was financially funded by the Danish Ministry of Foreign Affairs under the project “Clean Shipping on Green Fuel” (administered by Danida Fellowship Centre, project code: 18-M10-DTU).

7. Nomenclature

A	Ash content, wt.-%	N	Nitrogen content, wt.-%
C	Carbon content, wt.-%	O	Oxygen content, wt.-%
H	Hydrogen content, wt.-%	PR	Purge ratio, %
HHV	Higher heating value, Btu/lb	S	Sulphur content, wt.-%
LHV	Lower heating value, MJ/kg	T	Temperature, °C
$\dot{m}$	Mass flow rate, kg/s	$\dot{W}$	Electric power, kW
$\dot{n}$	Mole flow rate, mole/s		

Greek symbols

γ	Carbon efficiency, %	η	Energy efficiency, %
ε	Relative increase, %	λ	Excess air ratio, -

Subscripts and superscripts

EL	Electricity consumption	mech	Mechanical
is	Isentropic	Reactor	Methanol reactor
main	Main products	tot	Total system

Abbreviations

DH	District heating	POX	Partial oxidation
DME	Dimethyl ether	PR	Purge ratio
HHV	Higher heating value	rWGS	Reverse water gas shift
LHV	Lower heating value	SNG	Synthetic natural gas
LT-CFB	Low temperature circulating fluidized bed	VL	Vapor-liquid
		VLE	Vapor-liquid equilibrium
MeOH	Methanol	VLLE	Vapor-liquid-liquid equilibrium
PH	Process heat		

8. References

[1] H. Lund *et al.*, “The role of sustainable bioenergy in a fully decarbonised society,” *Renew Energy*, vol. 196, pp. 195–203, Aug. 2022, doi: 10.1016/j.renene.2022.06.026.

[2] G. Venturini, A. Pizarro-Alonso, and M. Münster, “How to maximise the value of residual biomass resources: The case of straw in Denmark,” *Appl Energy*, vol. 250, pp. 369–388, 2019, doi: 10.1016/j.apenergy.2019.04.166.

[3] J. Ahrenfeldt, T. P. Thomsen, U. Henriksen, and L. R. Clausen, “Biomass gasification cogeneration - A review of state of the art technology and near future perspectives,” *Appl Therm Eng*, vol. 50, pp. 1407–1417, 2013, doi: 10.1016/j.applthermaleng.2011.12.040.

[4] V. Hansen, D. Müller-Stöver, J. Ahrenfeldt, J. K. Holm, U. B. Henriksen, and H. Hauggaard-Nielsen, “Gasification biochar as a valuable by-product for carbon sequestration and soil amendment,” *Biomass Bioenergy*, vol. 72, no. 1, pp. 300–308, 2015, doi: 10.1016/j.biombioe.2014.10.013.

[5] R. Kofler and L. R. Clausen, “Wheat straw based polygeneration systems integrating the electricity, heating and transport sector,” *Smart Energy*, vol. 2, 2021, doi: 10.1016/j.segy.2021.100015.

[6] R. Kofler and L. R. Clausen, “Exergy-based comparison of three wheat straw based biorefineries,” in *Proceedings of the 35th International Conference on Efficiency, Cost, Optimization, Simulation and Environmental Impact of Energy Systems 2022*, ECOS, 2022.

[7] T. A. Semelsberger, R. L. Borup, and H. L. Greene, “Dimethyl ether (DME) as an alternative fuel,” *J Power Sources*, vol. 156, no. 2, pp. 497–511, 2006, doi: 10.1016/j.jpowsour.2005.05.082.

[8] R. Kofler and L. R. Clausen, “Increasing carbon efficiency for DME production from wheat straw and renewable electricity – Analysis of 14 system layouts,” *Energy Convers Manag*, vol. 281, p. 116815, Apr. 2023, doi: 10.1016/j.enconman.2023.116815.

[9] F. Bustamante *et al.*, “High-Temperature Kinetics of the Homogeneous Reverse Water-Gas Shift Reaction,” *AIChE Journal*, vol. 50, no. 5, pp. 1028–1041, May 2004, doi: 10.1002/aic.10099.

[10] Aspen Technology, “Aspen Plus,” 2020. https://www.aspentech.com/en/products/engineering/aspen-plus

[11] P. Kaushal, T. Proell, and H. Hofbauer, “Application of a detailed mathematical model to the gasifier unit of the dual fluidized bed gasification plant,” *Biomass Bioenergy*, vol. 35, no. 7, pp. 2491–2498, 2011, doi: 10.1016/j.biombioe.2011.01.025.

[12] G. Soave, “Equilibrium constants from a modified Redkh-Kwong equation of state,” Pergamon Press, 1972.

[13] J. Schwartzentruber and H. Renon, “Extension of UNIFAC to High Pressures and Temperatures by the Use of a Cubic Equation of State,” *Ind Eng Chem Res*, vol. 28, no. 7, pp. 1049–1055, Jul. 1989, doi: 10.1021/ie00091a026.

[14] R. H. Perry and D. W. Green, *Perry’s Chemical Engineers’ Handbook*, 7th ed. McGraw-Hill, 1997.

[15] A. Eschenbacher *et al.*, “Catalytic upgrading of tars generated in a 100 kW th low temperature circulating fluidized bed gasifier for production of liquid bio-fuels in a polygeneration scheme,” *Energy Convers Manag*, vol. 207, 2020, doi: 10.1016/j.enconman.2020.112538.

Hydrogen and fuel cell research community at UPM: A map of infrastructures for the challenge of developing the whole value chain of the hydrogen economy

Alberto Abánades[a], Teresa J. Leo[b], Marcelo F. Ortega[c], Enrique Alcalá[d] and Isabel Carrillo[e]

[a] Universidad Politécnica de Madrid, Madrid, Spain, alberto.abanades@upm.es, CA
[b] Universidad Politécnica de Madrid, Madrid, Spain, teresa.leo.mena@upm.es
[c] Universidad Politécnica de Madrid, Madrid, Spain, mf.ortega@upm.es
[d] Universidad Politécnica de Madrid, Madrid, Spain, enrique.alcala@upm.es
[e] Universidad Politécnica de Madrid, Madrid, Spain, isabel.carrillo@upm.es

Abstract:
A research community to encompass efforts towards the development of the whole value chain of hydrogen and fuel cells related technologies has been set up at UPM. Such community has as main goal to unite the multidisciplinary expertise of the different engineering schools and faculties of UPM (more than 17 in several technological disciplines) to provide research and innovation services to face the challenge of developing medium and high scale hydrogen-related technologies deployment. Such critical mass of knowledge will be needed to highlight the contribution of high education institutions to the technological development for the energy transition. In this communication, we will show a portfolio of research infrastructures at UPM covering the whole value chain of the hydrogen economy: from production to utilization. The knowledge of available infrastructures is a first step to boost collaboration with other institutions.

Keywords:

Hydrogen; Infrastructures; fuel cells; hydrogen storage; hydrogen transport; hydrogen production.

1. Introduction

The climate crisis, that the anthropogenic activity catalyses, is boosting a systemic transformation towards a more sustainable energy system. The main challenge for such transformation is the deep reduction of greenhouse gases emissions, as to avoid expected catastrophic consequences by limiting global warming of the atmosphere below 2 ºC. In such decarbonization process, that should reach every sector, hydrogen is being considered [1] as one of the relevant technologies contributing in the future to comply with emission reduction targets. The deployment of the hydrogen economy needs the development at high scale of its whole value chain, from high capacity production facilities to their consumption at every sector of the society (industry, services, transport, mobility, residential, ...)., Such value chain includes transport/storage infrastructures, market regulation, and sector coupling. To achieve such targets, a paramount funding support has been activated at the highest level [2] as a clear bet for hydrogen to comply with United Nation Sustainable Development Goals [3,4].

The billion-size funding, that will be allocated at national and international level to develop as fast as possible the hydrogen economy, demands a huge coordination effort between different stakeholders to address efficiently such task. A dialogue between several public research funding agencies (including the EU Research & Innovation Framework Programs), industry, research, academic, professional association, technological platforms and social institutions is required. An example of such dialogue is the Clean Hydrogen Partnership [5], that support the European Commission to organise many of the hydrogen related activities in the framework of the EU Green Deal [2].

A significant contribution of a high education institution, as UPM, implies the adaptation to a research and innovation scheme that goes far beyond the classical submission and execution of low Technological Readiness Projects (TRL) for basic research, demanding a modest amount of economic and material resources. The hydrogen economy needs to successfully implement large projects to produce a high impact into the socio-economic structure of the society. In many projections, hydrogen is expected to manage a very significant amount of the worldwide energy demand. For instance, according to some serious prospections, hydrogen is predicted to manage 5% of the energy demand in 2050 in the order of 240 Mton H_2 [6].

At UPM we have created a research community financed by own resources to tackle the challenge to transfer to our socio-economic environment the added value to contribute to the development of the hydrogen related technologies. One of our commitments is to build the human expertise, that is one of the bottlenecks [7] of the fast development of the hydrogen economy. For such purpose, we have designed a master program as one of our activities. We plan to increase our expertise by a close collaboration with the private sector to support their developments with our contribution to project consortia at national and international level, offering the

access and utilization of the experimental infrastructures that are available at UPM. Another relevant action to keep our education standards to comply the needs of the productive sector is to be able to contribute to high scale projects.

The first task in relation within UPM was to create an inventory of our current capacities, that has been created by different groups and institutes, to provide a map of infrastructures. Infrastructures has been classified versus the different stages of the hydrogen value chain. Such classification provides a picture of our capabilities at first sight, and allows to identify weaknesses and strengths in our organization at that respect. The classification of our infrastructure has been done attending to the following position into the hydrogen value chain:

- Hydrogen production
- Storage
- Transport
- End uses
- Skills

The current infrastructures for hydrogen research at UPM are the result of our previous research activity in cooperation with industry and research funding agencies. Our commitment is to upgrade such infrastructures to face the challenges of the new projects to come in the field, in which TRL is expected to be much higher. That means that this portfolio of facilities that will be introduced is being updated depending on the requirements of the current and future projects, and the available funding, mostly in the framework of large-scale projects to develop.

2. Hydrogen production

We are working on several methods for production to extract hydrogen from water or hydrocarbons. Regarding the development of electrolysis, we are working at experimental size to test the sensitivity of electrodes with different water composition, not only to test electrodes, but some biological waste treatment. Such activities are in the first stages of development. Additionally, at UPM we are working testing electrodes and membrane configuration to electrolyse seawater (Figure 1) as well as testing of direct methanol fuel cells and electrolysers (Figure 2) at School of Naval Arquitecture and Marine Engineering (ETSIN).

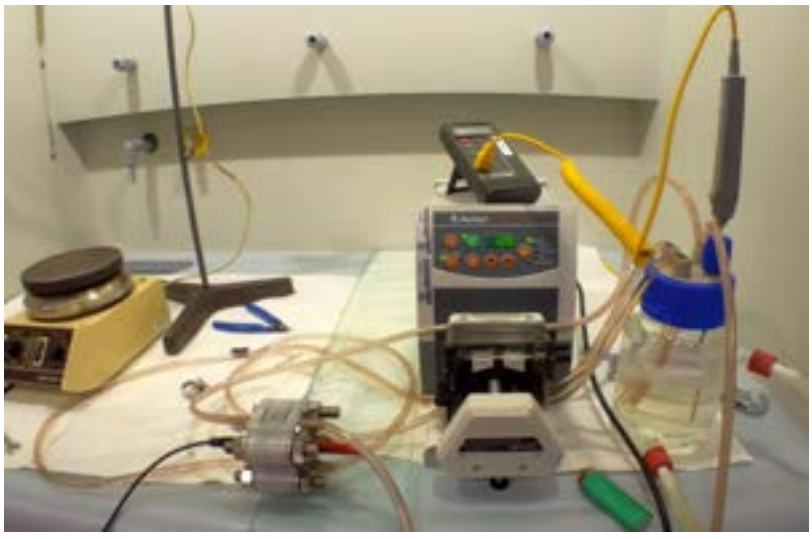

Figure 1: Thermostatic 3d printed alkaline electrolysis cell. Temperature up to 70 °C. Cell used for tests with desalinated seawater as feed

Figure 2: Test bench for direct methanol fuel cell and methanol electrolyser

Regarding Hydrogen integration, it has been installed a demonstration installation in the roof of the School of Engineering and Industrial Design (ETSIDI) consisting of a 260 W PEM electrolyser to produce hydrogen from FV panels located in the roof. In addition, a hydrogen storage system based on metallic hydrides with a capacity of 3 Nm^3 at 6-12 bar is used to manage energy production in combination with a Li-ion battery with a capacity of 2 kWh.

Other capabilities are under development at the School of Industrial Engineering (ETSII), as laboratories for instrumentation testing, or for surface coating that may be applied to the development of materials and temperature or pressure sensors to be integrated in hydrogen production facilities. As an example, we have available sputtering equipment for manufacturing nano-structures for the surface coating of material layers to be used for new electrodes or membranes. A high temperature reactor for methane pyrolysis based on liquid metal technology is also under development, that will constitute a facility for hydrogen production from thermal processes in the future with a capacity of some kW.

Figure 3: Nano-coating sputtering equipment.

3. Hydrogen storage

Hydrogen storage is one of the critical technologies for the development of the hydrogen economy. In particular the availability of high capacity hydrogen tanks and reservoirs is of paramount importance for the viability of hydrogen as energy vector. Hydrogen as reserve storage, even for seasonal storage, depends on the possibility to accumulate large volumes and quantities of hydrogen, for instance, into caverns, what is one of the most recognised expertise at the School of Mines and Energy Engineering (ETSIME). For such purpose, we have specific equipment for rock physical analysis to measure rock density (Accupyc II 1340), porous material envelope (Geopyc 1360), gas permeability (Gasperm), currently used in the UNDERGY project. An example of other equipment for measurement of physical rock properties are presented in Figure 4.

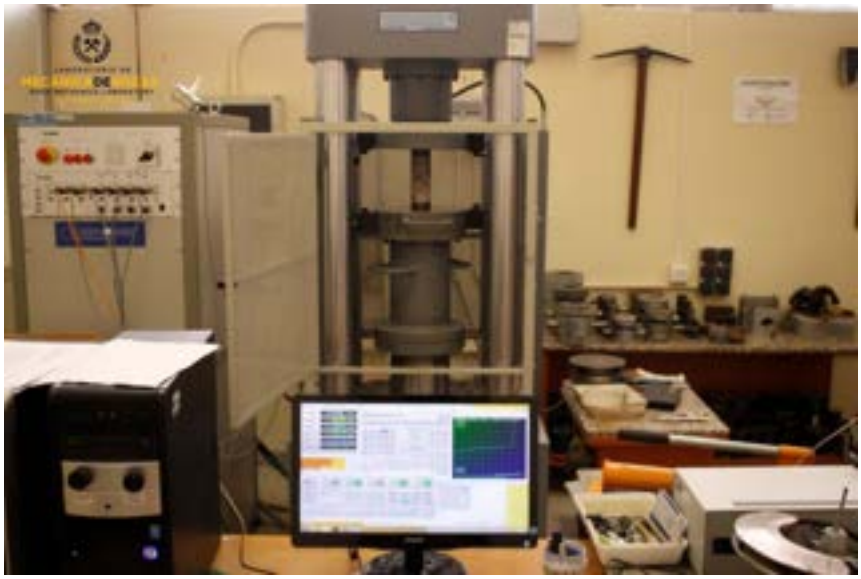

Figure 4: Simple Compressive Strength Measuring Equipment

4. Hydrogen transport

The transport of huge amounts of hydrogen trough dedicated networks, as the existing for oil and natural gas, is on the agenda of many stakeholders related to the hydrogen development and energy supply chain in the European Union and beyond. Research and development in the field of materials, and the effect of high pressure hydrogen in transport ducts are of paramount importance for the technical viability of many projects that are ongoing, The hydrogen corridor proposed [8] by Spain, Portugal and France are the clear example of infrastructure that will need some support in terms of technological development to be safely implemented. At UPM, at the CIME (Centro de de Investigación en Materiales Estructurales/Center for Structural Materials Research) of the School of Civil Engineering (ETSICCP) is available a chamber for high pressure test (up to 100 bar) of structural materials in hydrogen atmospheres, what will be a key information for the choice of structural materials for ducts.

Figure 5: High pressure hydrogen chamber for material testing.

5. Hydrogen end uses

The end use of hydrogen is one of the final steps on its value chain. There are many challenges in this area. One of those challenges is the implementation of hydrogen as energy sources in mobility. That includes, for instance, a test bench for fuel cells operating in hybrid mode for terrestrial vehicle power trains, including Heavy Duty ones. The Test Bench installed at the University Institute of Automobile Research of the UPM (INSIA) can prove Powertrains up to 200 kW and 9600 N.m on each wheel (Figure 6).

Figure 6: Test bench for hybrid power trains.

One of our most important groups, with decades of activity in relation with the development of fuel cells, is PiCOHIMA, of that is currently working in the development of a fuel cell test bench up to a few hundreds of kW (Figure 7), that is expected to be operative at the end of the GreenH2-CM project supported by the Madrid regional government and the Spanish Government trough the “Plan de Recuperación, Transformación y Resiliencia” (PRTR). We have some equipment for evaluating the combustion of gas mixtures, including fraction of H_2, CO_2 and CH_4, that are useful for the characterization of biomass to hydrogen [9,10] conversion and the heating value of the products (Figure 8). Such facility is available at TECMINERGY, a centre depending of the School of Mines and Energy Engineering.

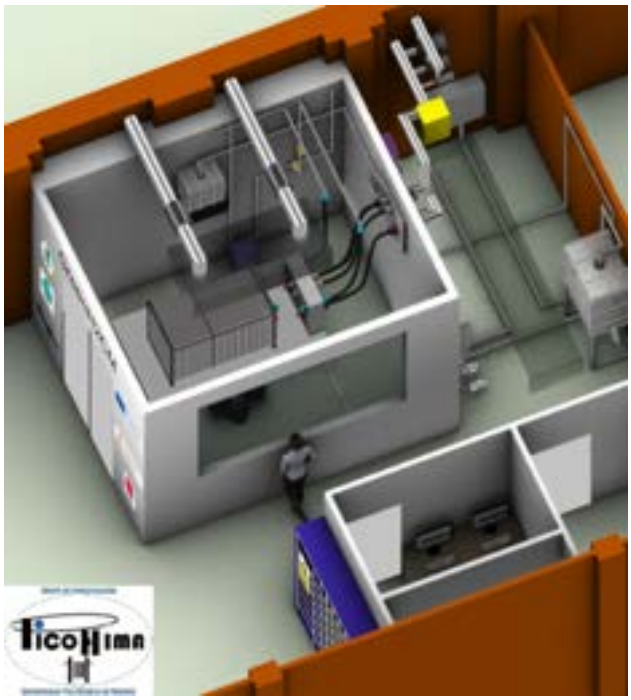

Figure 7: Sketch of the fuel cell test bench under design.

Figure 8: Combustion chamber CO_2 lung (combustion tests of the ternary mixture $CH_4/CO_2/H_2$).

6. Skills

Technology is implemented by people, and the impressive challenge of put into practice the huge projects that are planned to transform the expectations of the hydrogen economy into a reality, demands thousands of skilled people. So many hands will come from fresh young graduates as well as by reskilling of many workers already in related industries. For such purpose, our role as university is to provide tools to allow the access of the Society to the knowledge in order to feed such demand. We have designed a master program [11] of 60 ECTS for the specialization of post-graduated individuals in the whole value chain of the hydrogen economy, from generation to utilization, including regulation and normative as a basic stone for the hydrogen sector.

Conclusion

The hydrogen research and development ecosystem have the societal need to transfer, as fast as possible, knowledge that has been produced for decades into one of the pillars of the energy and productive system.

High education institutions must contribute to the development of high TRL projects in cooperation with industry to transfer such knowledge, as well as for the training of skilled manpower that is needed for such purpose. At UPM we have initiated a process to respond to the needs of a fast implementation of the hydrogen economy in the Society. One of those needs is to gain critical mass and capacity to support large size projects. We have elaborated a first inventory of the existing laboratory infrastructures at UPM to evaluate our own capacity to face such projects. The variety of engineering disciplines at UPM is a strength of the institution to participate in multidisciplinary projects, as required for large scale hydrogen implementation. The expertise at UPM covers the whole value chain of the hydrogen economy. From this first infrastructure inventory, we are trying to upgrade and improve our facilities to face the enormous challenge and contribute to the implementation of a more sustainable society.

Acknowledgments

The authors wish to acknowledge the funding from the Universidad Politécnica de Madrid trough the Project in Modality 1A: Strategic Action in Science and Technology. Disruptive and emerging thematic area, in the frame of the Programa Propio de I+D+I 2022.

References

[1] Seck GS, Hache E, Sabathier J, Guedes F, Reigstad GA, Straus J, et al. Hydrogen and the decarbonization of the energy system in europe in 2050: A detailed model-based analysis. Renew Sustain Energy Rev 2022;167:112779. https://doi.org/https://doi.org/10.1016/j.rser.2022.112779.

[2] European Commision. Green Deal n.d. https://commission.europa.eu/strategy-and-policy/priorities-2019-2024/european-green-deal_en.

[3] Falcone PM, Hiete M, Sapio A. Hydrogen economy and sustainable development goals: Review and policy insights. Curr Opin Green Sustain Chem 2021;31:100506. https://doi.org/10.1016/J.COGSC.2021.100506.

[4] Managi S, Lindner R, Stevens CC. Technology policy for the sustainable development goals: From the global to the local level. Technol Forecast Soc Change 2021;162:120410. https://doi.org/10.1016/j.techfore.2020.120410.

[5] European Commision. Clean Hydrogen Partnership n.d. https://www.clean-hydrogen.europa.eu/index_en (accessed March 13, 2023).

[6] DNV. Energy Transition Outlook 2022. Høvik, Norway: 2022.

[7] Abánades A. Perspectives on Hydrogen. Energies 2023;16. https://doi.org/10.3390/en16010437.

[8] España G de. EUROPE'S FIRST MAJOR GREEN HYDROGEN CORRIDOR 2022. https://www.lamoncloa.gob.es/presidente/actividades/Documents/2022/091222-H2MED.pdf (accessed March 2, 2023).

[9] Amez I, Castells B, Llamas B, Bolonio D, García-Martínez MJ, Lorenzo JL, et al. Experimental Study of Biogas–Hydrogen Mixtures Combustion in Conventional Natural Gas Systems. Appl Sci 2021;11. https://doi.org/10.3390/app11146513.

[10] Amez I, Castells B, Ortega MF, Llamas B, García-Torrent J. Experimental study of flame zones variations of biogas enriched with hydrogen. Int J Hydrogen Energy 2022;47:24212–22. https://doi.org/https://doi.org/10.1016/j.ijhydene.2022.03.251.

[11] UPM. Master propio Hidrógeno y Pilas de Combustible 2022. https://blogs.upm.es/masterhidrogenoypilasdecombustible/ (accessed March 13, 2023).

Performance model of a Proton Exchange Membrane (PEM) fuel cell operating in steady-state conditions with Aspen HYSYS®

Angelo Di Domenico[a], Paolo Vitulli[b], Francesca Mennilli[a], Mosè Rossi[a], Gabriele Comodi[a]

[a] *Marche Polytechnic University, Department of Industrial Engineering and Mathematical Sciences, Ancona, Italy, s1096334@studenti.univpm.it*
[b] *Marche Polytechnic University, Department of Information Engineering, Ancona, Italy, p.vitulli@pm.univpm.it*
[a] *Marche Polytechnic University, Department of Industrial Engineering and Mathematical Sciences, Ancona, Italy, f.mennilli@pm.univpm.it*
[a] *Marche Polytechnic University, Department of Industrial Engineering and Mathematical Sciences, Ancona, Italy, mose.rossi@staff.univpm.it, CA*
[a] *Marche Polytechnic University, Department of Industrial Engineering and Mathematical Sciences, Ancona, Italy, g.comodi@staff.univpm.it*

Abstract:

Nowadays, Hydrogen is considered an important energy vector through which the decarbonization process can be carried out if it is produced by Water electrolysis using renewables. Then, Hydrogen is stored for performing medium- and long-term storage, which is suggested for those sources that face considerable electricity production variability throughout the days/months like renewables, and sent to Fuel Cells (FCs) for producing again electricity. The coupling of the electrolyzer, storage, and FC constitutes an integrated Hydrogen system. This work presents a model of a 5 kW-Proton Exchange Membrane Fuel Cell (PEMFC), which has been developed in Aspen HYSYS®, to evaluate its performance by varying its operating conditions (e.g., current density, temperature, and pressure). The simulation is based on the determination of a semi-empirical mathematical model of the electric potential related to a single 25 cm^2 cell through the regression of experimental data taken from the scientific literature. Normal Root Mean Square Errors (NRMSEs) were obtained by the comparison between the results of the electric potential model of the single cell and the experimental ones, showing a good agreement. The model developed in Aspen HYSYS® allows to predict the behaviour of the PEMFC by identifying the optimal conditions in terms of temperature and pressure. Results showed that the PEMFC performance improves by increasing the temperature up to 80°C, while it is not suggested to operate at pressure values higher than 3 atm due to a lower net electric power and overall system electric efficiency.

Keywords:

Aspen HYSYS®, Fuel cell modeling, Green Hydrogen, Proton Exchange Membrane Fuel Cell.

1. Introduction

In recent years, the issue of environmental sustainability has become increasingly important. Problems related to both pollution and global warming led the international community to pay more attention to the research of new technologies for energy production through the exploitation of renewable sources. In the context of the ecological transition, Hydrogen can play a fundamental role; indeed, governments and companies have focused on this type of chemical element to further contribute to the decarbonization process. Hydrogen is an energy carrier, and it has a higher energy density than fossil fuels. Because of its properties, it represents a valid solution for energy storage and production; in the latter case, Fuel Cells (FCs) use Hydrogen to produce electricity without pollutant emissions.

Nowadays, FCs have considerable attention as they constitute the key technology for further deploying this type of energy carrier [1]. Among the different types, Proton Exchange Membrane Fuel Cells (PEMFCs) are

mostly applied in automotive and small stationary applications due to their high electric efficiency, power density, and reliability. In a PEMFC, the fuel is Hydrogen that reacts with the Oxygen contained in the air to generate electricity, Water, and heat. Electrochemical reactions as well as the transport of ions, electrons, energy, and species in gas and liquid phases across a heterogeneous media are involved. However, this technology is currently developing to further increase its efficiency and applicability ranges, especially when dealing with cogeneration purposes in both residential and industrial sectors [2-4].

To better understand the phenomena behind the operation of FCs, several experiments have been carried out so far and interesting results have been already reported in the scientific literature; however, numerical models aiming to resemble the behaviour of FCs, according to their typology, would fasten and further contribute to the development of this technology, being less time consuming and less economically demanding as well. Among the most known simulation environments, Aspen Technology® is one of the most used since it allows to easily design, manage, and integrate several parts of a system in one macro-system as well as provide preliminary data of how it would run. In this regard, Beheshti et al. [5] developed an Aspen Plus® model to simulate the behavior of an integrated gasification system with a PEMFC stack by coupling the Aspen Plus® software with dedicated FORTRAN subroutines. Effects of critical parameters (e.g., current density, feed gas humidity, equivalence ratio, steam/biomass ratio, and biomass moisture content) on the cell potential and gasification efficiency have been discussed. Results showed that a higher feed humidity at the cathode side is more favorable for the improvement of the voltage output, while the biomass moisture content has a negative impact on the cell potential. Barelli et al. [6] studied a micro-cogeneration Combined Heat and Power (μCHP) energy system based on a PEMFC to evaluate both the performance and energy/economic feasibility of the system to fulfil the thermal and electrical demands of apartments. A zero-dimensional model of the PEMFC has been developed in Aspen Plus® and simulations at different operating conditions have been carried out. Subsequently, optimal operating conditions of the PEMFC have been identified; in particular, these operating conditions have been obtained by fixing constraints to the electricity production/supply as well as to the return temperature and pressure of hot Water at 105 °C and 2 atm, respectively. Zuliani et al. [7] carried out a performance analysis of a 1 kW-High Temperature PEM Fuel Cell (HT-PEMFC). The performance of this FC has been predicted through a zero-dimensional, semi-empirical model implemented in FORTRAN and subsequently integrated into Aspen Plus®. The aim of the work was to perform an energy analysis to investigate how the system operates at partial load operating conditions and assess the difference with Low-Temperature PEM Fuel Cell-based (LT-PEMFC) systems. Results showed that a more reliable balance of plant is obtained with HT-PEMFCs than LT-PEMFCs, while the system efficiency is unchanged.

To the authors' knowledge, as also previously discussed, there are several models of FCs in Aspen Plus® available in the scientific literature, but no references have been found on PEMFCs modeling with Aspen HYSYS®. Aspen Plus® is mostly used with fine chemistry, general chemistry, electrolytes, and polymer modeling, while Aspen HYSYS® is devoted to resemble petrochemical refining, oil assays, and all related industries, thus having wider use in chemical applications. Thus, the modeling of a PEMFC block in this kind of environment can be of interest to those researchers/scientists that would like to use this specific model in a more complex chemical system since it would be easier to be embedded.

This work consists of the development of a numerical model in Aspen HYSYS® related to a stack of a 5 kW-Proton Exchange Membrane Fuel Cell (PEMFC), whose experimental data are available in [8], to study its behaviour by changing its operating conditions (e.g., current density, temperature, and pressure). In particular, the model could be considered as a starting point for then applying an optimization procedure to optimally manage the electricity production of PEMFCs according to a specific load trend. The paper is structured as follows: Section 2 presents the used methodology to analytically model the FC stack, as well as provides an overview of the Aspen HYSYS® model [9]. Section 3 is devoted to the results obtained from the simulations at different operating conditions (e.g., current density, temperature, and pressure). Finally, Section 4 reports the conclusions of the work.

2. Methodology

The models that describe the behaviour of a FC by varying the operating conditions (e.g., current density, temperature, and pressure) typically include the analysis of the following quantities: i) electric potential, ii) net electrical power generation, iii) electrical efficiency, and iv) heat power production. The present analysis has been carried out by considering the experimental data of [8]. The regression of the experimental data allowed to develop a model to predict the performance of the analysed PEMFC. After the validation of the numerical results with the experimental ones, the characteristics of the PEMFC (e.g., dimensions and the number of cells) have been scaled up to analyse the performance of the same PEMFC having a power output of 5 kW. This FC has a stack consisting of 72 cells in series, each of them having an area of 196 cm^2. The modelling of

the PEMFC involves mathematical relationships, thus resulting from empirical or semi-empirical analyses. Figure 1 shows the block diagram that sums up the eight steps used in the present methodology to carry out this study. It is worth noting that some of these steps have been performed in parallel and, for this reason, they have been placed in the same row.

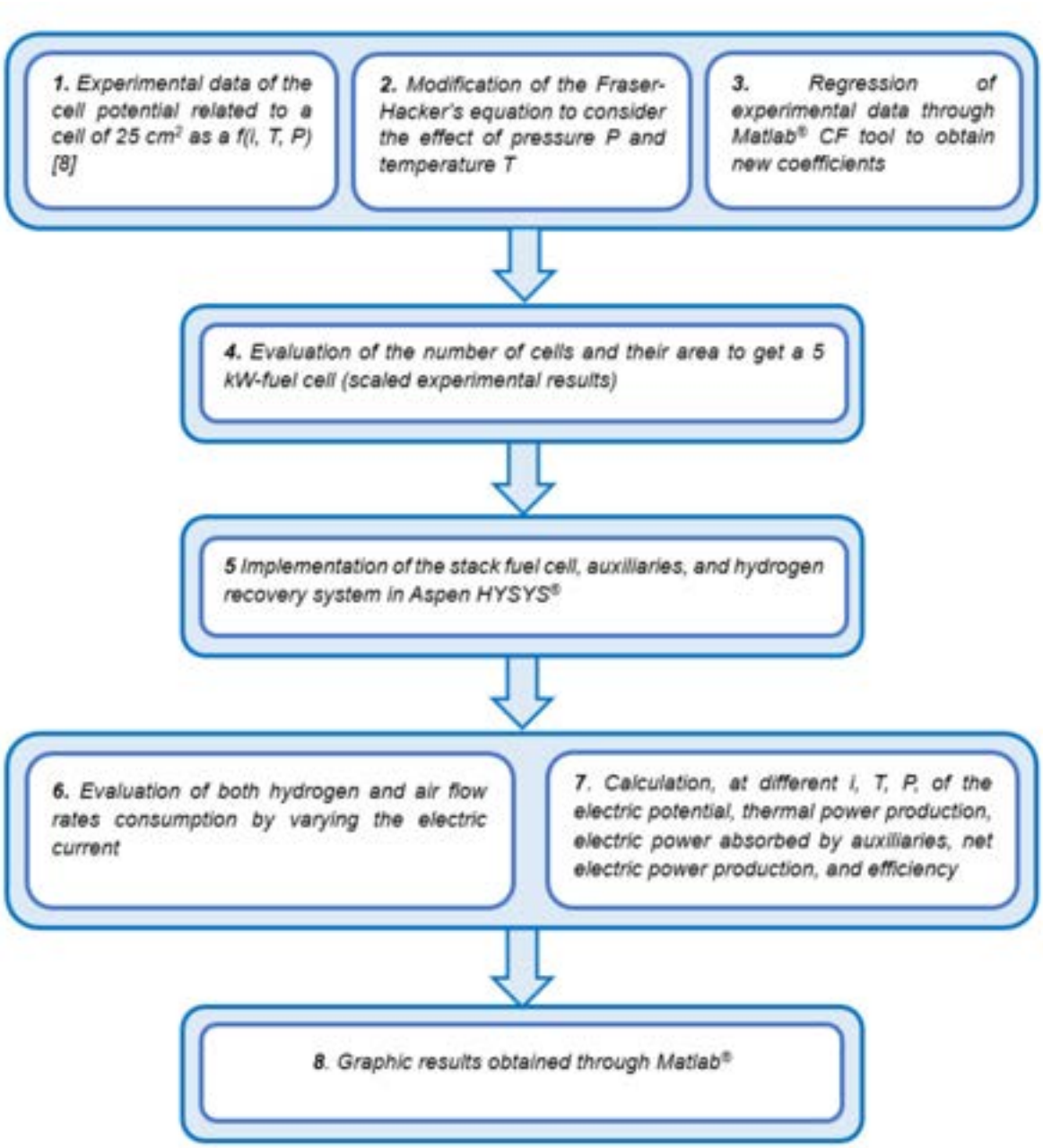

Figure 1. Block diagram with the eight steps used in the present methodology.

The polarization curve that describes the relationship between the output voltage and the current density is a good indicator of the FC performance. The most known semi-empirical fuel cell model to draw up the trend of the electric potential as a function of the current density is Fraser-Hacker's one [10], which is reported in Eq. 1:

$$E_{cell} = E_{rev} - b \cdot log\left(\frac{i+i_{int}}{i_0}\right) - R \cdot i - m \cdot e^{(n \cdot i)} \quad (1)$$

where E_{rev} [V] is the reversible cell voltage and it is computed as a function of the cell temperature and the partial pressures of the active species according to the Nernst's equation, b [V] is the charge transfer overvoltage fitting parameter (V), i_{int} and i_0 [A·cm^{-2}] are charge transfer overvoltage fitting parameters, R [Ω·cm^2] represents the Ohmic overvoltage fitting parameter, m and n are mass transport overvoltage fitting parameter [10] that represent the mass transport limitations and the rapid decrease of E while increasing i, respectively. The reversible thermodynamic voltage E_{rev} is calculated from the modified Nernst's equation that considers both temperature and pressure dependence [11]:

$$E_{rev} = E^0 \cdot \frac{\Delta\hat{s}}{n_e \cdot R}(T - T_0) - \frac{R_g \cdot T}{n \cdot F} \cdot ln\left(\frac{a_{H_2O}}{a_{H_2} \cdot a_{02}^{1/2}}\right) \quad (2)$$

where E^0 is equal to 1.229 V and it is the standard-state reversible cell voltage, Δŝ is the reaction entropy (assuming that it is independent of the temperature and it is equal to -163.28 J·mol^{-1}·K^{-1}), R_g is the universal constant of the gases (8.314 J·mol^{-1}·K^{-1}), n is the number of electrons transferred in the chemical reaction (2 mol$_{e^-}$/mol$_{H2}$), F is the Faraday's constant (96,485 C/mol), a_x is the activity of x that for an ideal gas becomes $a_x = p_x/p_O$ (where p_x is the partial pressure of x, p_o is the standard pressure of 1 atm [11].

It is possible to substitute the constants in Eq. 2 so that the reversible voltage can be also described as a function of both temperature and pressure:

$$E_{rev} = 1.229 - 8.46 \cdot 10^{-4}(T - 298.15) - 4.31 \cdot 10^{-5} \cdot T \cdot ln\left(\frac{1}{p_{H2} \cdot p_{O2}^{1/2}}\right) \quad (3)$$

Fraser-Hacker's equation (Eq. 1) considers only the dependence of the electric potential on the current density [7]. An important step of the present work was the modification of Fraser-Hacker's equation to consider the dependence of the electric potential, as well as the current density, temperature, and pressure. The modified equation is the following:

$$V = E_{rev} - \left(b_t + b_p\right) \cdot log\,10\frac{(i + i_l + i_{lp})}{(i_{0t} + i_{0p})} - \left(r_t + r_p\right) \cdot i - \left(m_t + m_p\right) \cdot e^{[(n_t + n_p) * i]} \quad (4)$$

where the parameters with the subscript t indicate that they are temperature dependent, while those with the subscript p indicate that they are pressure dependent. The dependence of each parameter on both temperature and pressure was derived through the regression of the experimental data of [8], and it has been carried out with the Matlab® Curve Fitting Tool.

The process simulation of the entire system has been developed using Aspen HYSYS® [9]. Regarding the implementation of the model, it is required to identify both involved elements and chemical compounds, the components of the PEMFC, and the methodology to calculate the thermophysical properties of the streams. The selected fluid package is the "*Peng-Robinson*" one [9]. The oxidation-reduction reaction is defined as a *"Conversion reaction"* that takes place in the conversion reactor (CRV-100, see Figure 2), which constitutes the electrode. The mixture of Hydrogen and Oxygen, called reaction gas, is sent to the second component that acts as a membrane (X-100, see Figure 2) and it is capable of perfectly separating the excess of Hydrogen that has not reacted and then recirculating towards the *Mixer*. Based on the thermodynamic operating conditions in terms of both temperature and pressure, the spreadsheet evaluates the value of the main electrochemical and thermochemical equations that define the reaction products and the electrical power produced. Through the spreadsheet, the equations that allow to calculate the fundamental outputs of the model have been implemented such as the stack electric potential, the electrical power produced, the electrical efficiency, and the thermal power to be disposed of. Other relationships have also been implemented such as Faraday's equation (5) for calculating the flow rate of Hydrogen consumed $\dot{n}_{H_2}$ as a function of electric current I.

$$\dot{n}_{H_2} = \frac{I \cdot N_{cell}}{2 \cdot F} \quad (5)$$

where N_{cell} is the number of cells that constitute the stack and F is Faraday's constant, equal to 96,485 C/mol.

The stack electric potential V_{stack} is implemented in the spreadsheet starting from Eq. 4. Eq. 3 is preferred to calculate the reversible potential for ease of implementation. Eq.s 3 and 4 refer to the cell potential, thus to obtain the stack potential the number of cells in series is multiplied by the cell potential. The calculation of the electric potential allows the calculation of the other variables of interest. The net electric power of the PEMFC, $\dot{W}_{el}$, is calculated as the product of its electrical voltage and the electric current minus the electric power required by the air compressor, $\dot{W}_{ac}$. It is worth noting that the electric power of the air compressor is calculated by Aspen HYSYS® and depends on both the pressure ratio and the Hydrogen flow rate. The air compressor allows to maintain the air pressure in the stack equal to that of the Hydrogen, as well as to maintain a stoichiometric ratio between the anode and the cathode.

$$\dot{W}_{el} = \dot{V_{stack}} \cdot I - \dot{W}_{ac} \tag{6}$$

The electric efficiency η_{el} is expressed as the ratio of the net electric power generated by the FC, $\dot{W}_{el}$, and the product between the Lower Heating Value (LHV) of Hydrogen and its molar flow $\dot{n}_{H_2}$ as described in Eq. 5:

$$\eta_{el} = \frac{\dot{W_{el}}}{LHV_{H_2} \cdot \dot{n}_{H_2}} = \frac{V_{stack}}{V_{LHV}} \tag{7}$$

The generated heat power that has to be disposed of $\dot{Q}$ depends on the difference between the thermoneutral potential of the reaction V_{LHV} and the electric stack potential. The thermoneutral potential is related to the Hydrogen Lower Heating Value (LHV) and it is equal to 1.25 V.

$$\dot{Q} = (V_{LHV} - V_{stack}) \cdot N_{cell} \cdot I \tag{8}$$

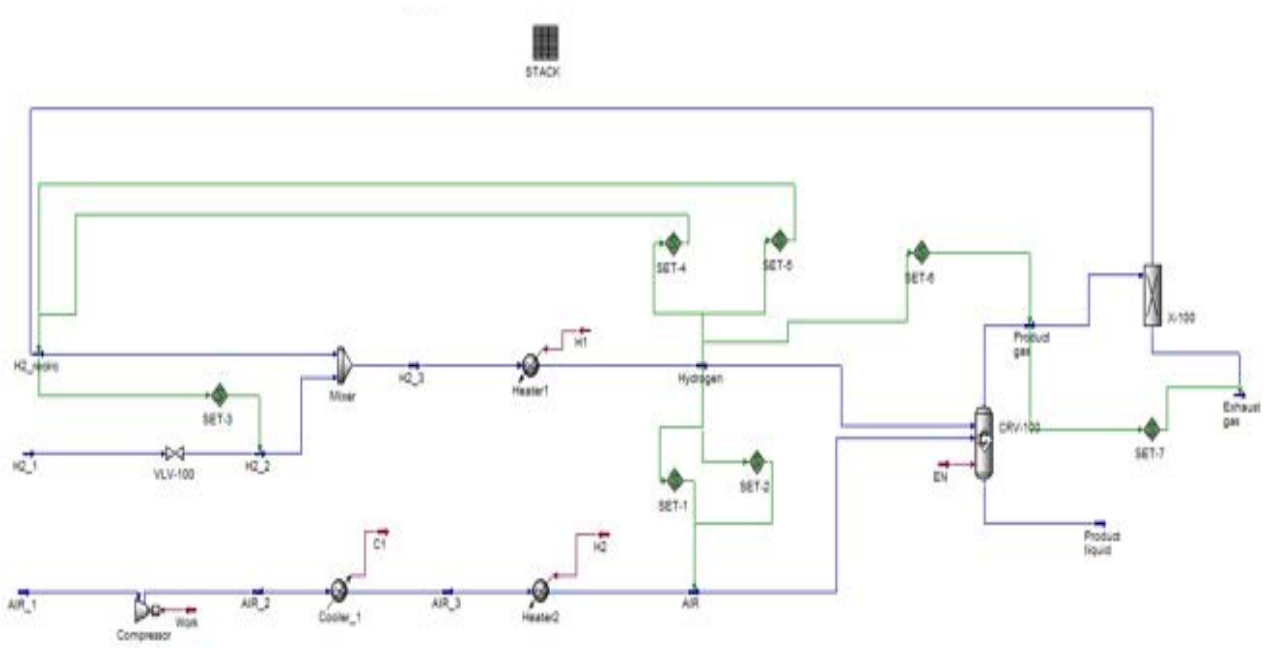

Figure 2. Model of a PEMFC developed in Aspen HYSYS®.

The trends of the performance variables such as temperature, pressure, and current density variation have been obtained by setting up “for cycles” in Aspen HYSYS® called “nested case studies”, which allow to study the trend of multiple dependent variables as a function of multiple independent variables. The numerical results of the analysis were processed in Matlab® to obtain the graphs shown in the next section.

3. Results and comments

The results of the PEMFC performance are evaluated as a function of the current density (range of 0-0.9 A/cm^2), and they depend either on the temperature (range of 60-90°C with steps of 5°C) or the pressure (range of 1-5 atm with steps of 0.5 atm). Precisely, Figure 3, Figure 4, Figure 5, and Figure 6 show the stack electric potential curve, the electric power curve, the electric efficiency curve, and the produced heat trend, respectively.

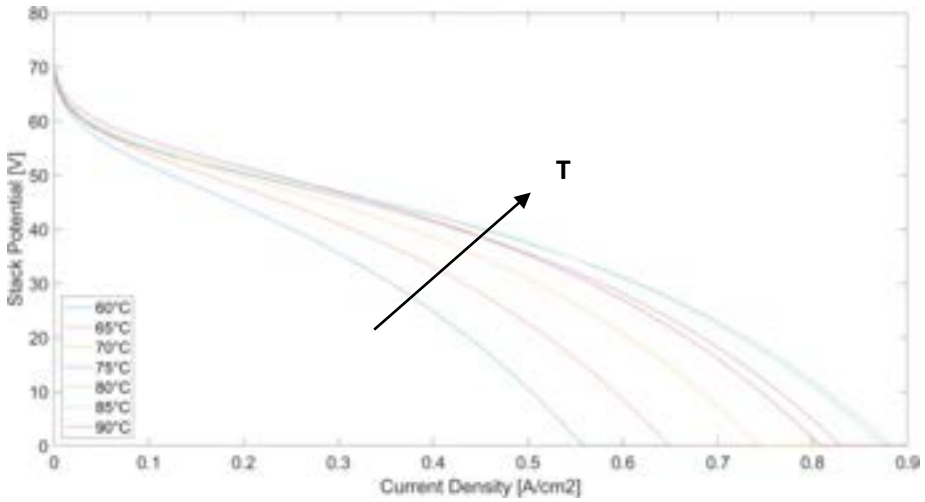

a)

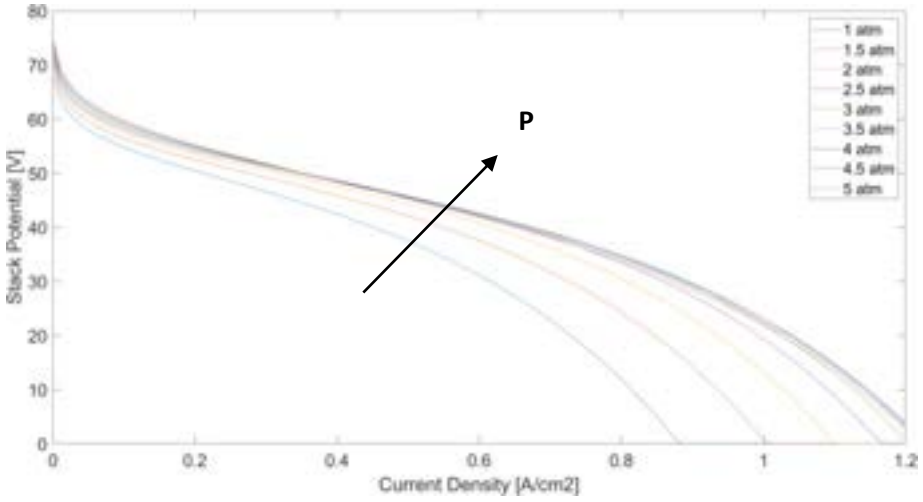

b)

Figure 3. (a) The electric stack potential as a function of both the current density and the temperature (pressure equal to 1 atm), and of (b) both the current density and the pressure (temperature equal to 80°C).

The results confirm the positive effect on the stack performance of increasing both the temperature and the pressure. Figure 3a highlights that the performance of the FC improves while increasing the temperature up to 80°C; beyond this value, it starts to lower due to membrane hydration issues linked to a decrease of the relative humidity in the reaction environment. Polarization curves at different operating pressures show that the performance improves while increasing the pressure (see Figure 3b). The polarization curves undergo a positive increase while increasing the pressure as it produces high partial pressures of the reactants near the electrodes, thus improving the transport phenomena and the solubility of gases in the electrolyte as well.

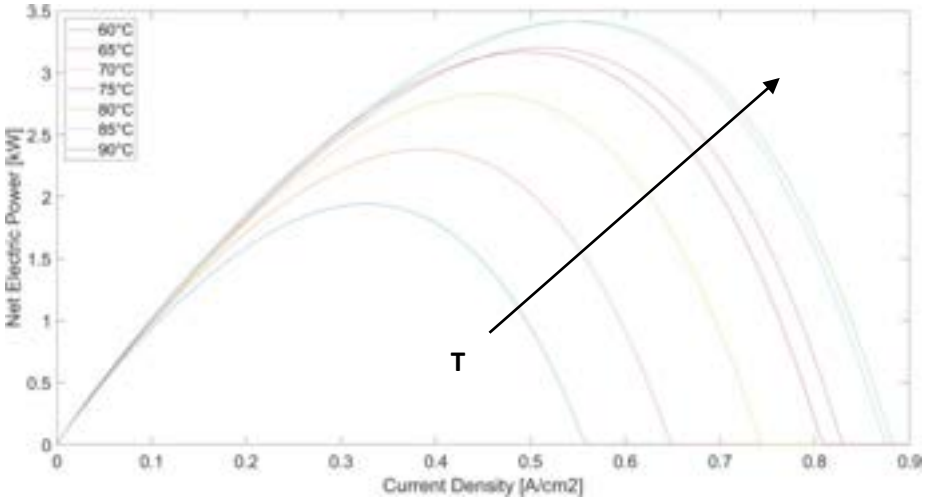

a)

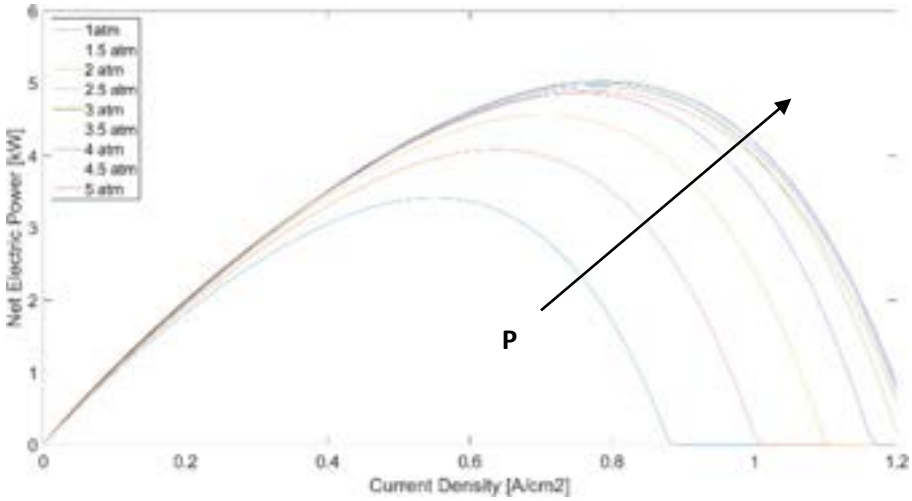

b)

Figure 4. (a) The net electric power as a function of both the current density and the temperature (pressure 1 atm) and of (b) both the current density and the pressure (temperature 80°C).

As it can be noticed in Figure 4a, the net electrical power of the stack improves while increasing the temperature up to 80°C, and then decreases due to the lower electrical potential caused by hydration problems. The net electric power also shows an initial increase with the current density (range 0-0.3 A/cm^2), while it starts to decrease afterward due to the prevalence of the effects due to overvoltage losses.

Figure 4b shows the same trend while changing the operating pressure of the fuel cell, being almost unchanged with pressure values equal to or greater than 3 atm; indeed, higher pressures make the energy power of the compressor increase, thus balancing the electrical production and keeping fixed the net electric power at a constant value.

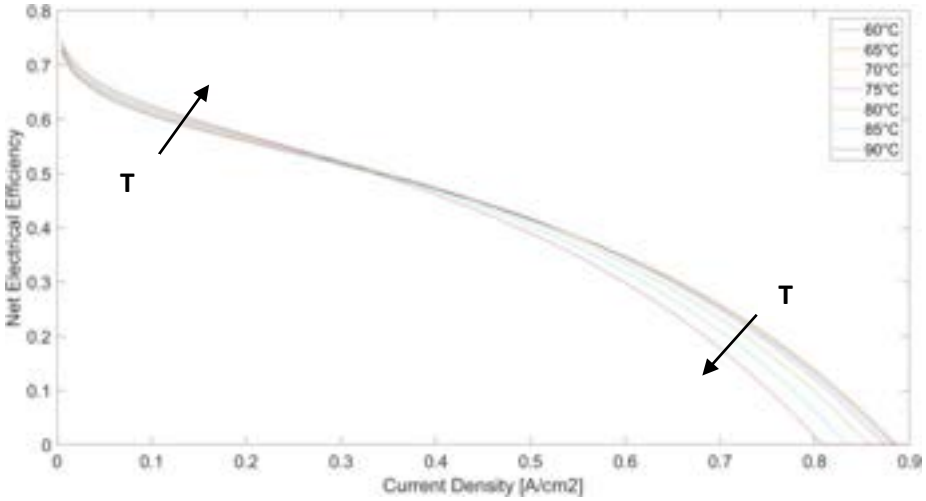

a)

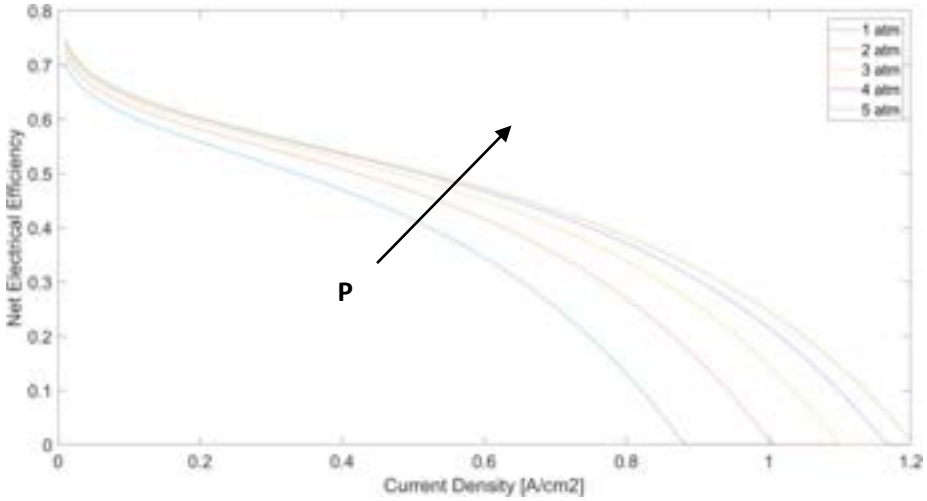

b)

Figure 5. The net electric efficiency as a function of both the current density and the temperature (pressure of 1 atm), and (b) both the current density and the pressure (temperature of 80°C).

Figure 5 shows that the trend of the net electric efficiency depends on the electric potential as it is the result of the ratio between the latter and the thermoneutral potential referred to the LHV, which it can be considered constant in the analysed temperature and pressure ranges.

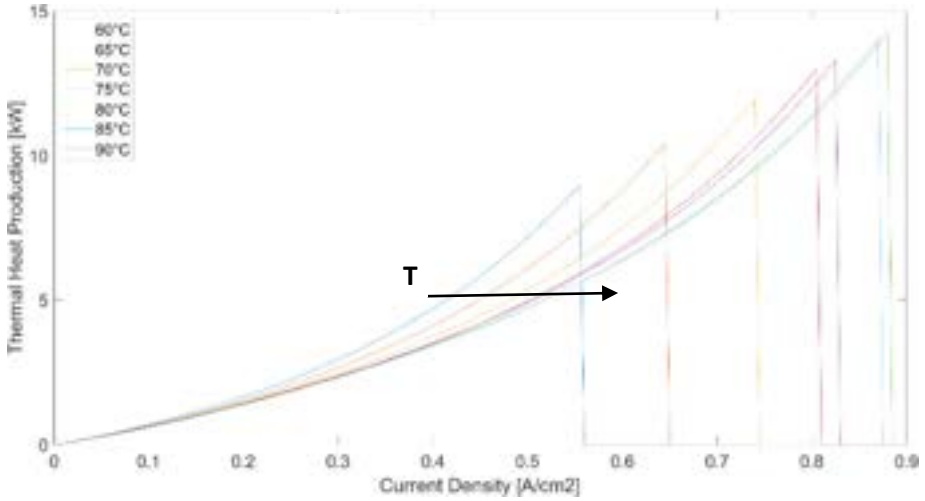

a)

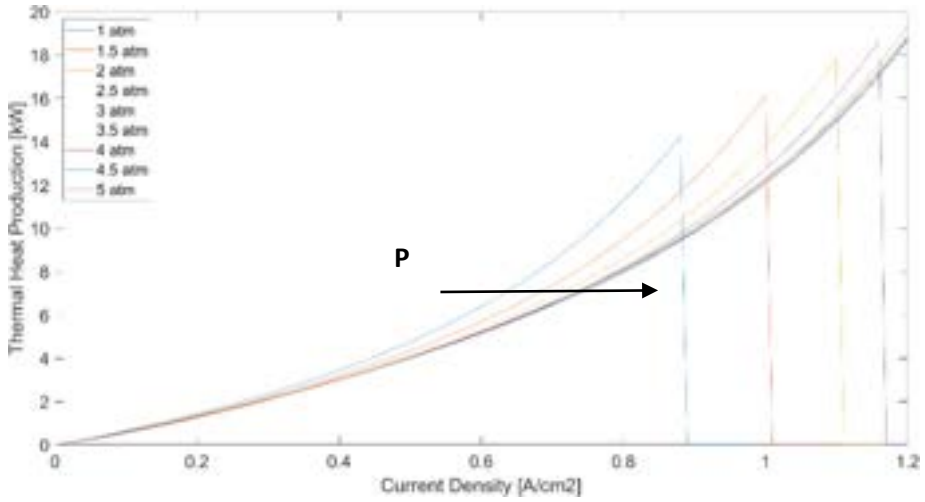

b)

Figure 6. (a) The thermal heat production as a function of both the current density and the temperature (pressure of 1 atm), and (b) both the current density and the pressure (temperature of 80°C).

Figure 6 shows an increase in the thermal power while increasing the current density. As it can be noticed, although the curves seem to drop down sharply toward zero beyond certain current density values, the jump in thermal power production depends on the lack of data available from [8]. The thermal power production decreases while increasing the temperature due to the higher electric potential; however, it increases with temperatures higher than 80°C. The thermal power production, considering the same current density values, decreases as the pressure increases due to the increase of the electric potential.

4. Conclusions

The present work shows the development of a PEMFC model with Aspen HYSYS® to evaluate its performance in terms of electrical potential, net electric power, electric efficiency, and thermal power production by changing its operating conditions in terms of current density, temperature, and pressure. The semi-empirical model developed by modifying Fraser-Hacker's equation showed a good agreement with experimental data taken from [5]. Aspen HYSYS® has proved to be a valid tool to simulate FCs, thus allowing to evaluate the performance of a 5 kW-PEMFC under different operating conditions, starting from the mathematical model developed for the single cell.

Results confirmed the positive effect on the FC stack performance by increasing both temperature and pressure. Indeed, the performance of the FC improves with increasing temperatures up to 80°C; beyond this value, it lowers mainly due to membrane hydration issues. Furthermore, the performance improves with increasing pressure as it enhances the transport phenomena and the solubility of gases in the electrolyte. Consequently, the net electrical power of the stack improves with increasing temperatures up to 80°C, while it decreases due to hydration problems. Regarding the influence of pressure, a pressure equal to or greater than 3 atm leads to higher energy consumption of the air compressor and thus to a lower net electric power and overall system electric efficiency. Regarding thermal power production, the increase of both temperature and pressure leads to its decrease due to a higher electric potential.

The simulation of the PEMFC performed with Aspen HYSYS® allowed to make other evaluations that have not been reported here. A further step of the work could be the coupling of this system with the models of both the electrolyzer and the storage system to form an integrated Hydrogen system, which can provide flexibility to the current electric network increasingly fed by renewables.

References

[1] Andrew Dicks, James Larminie, *Fuel Cell Systems Explained*, II Edition, John Wiley & Sons Ltd, The Atrium, Southern Gate, Chichester, West Sussex PO19 8SQ, England, 2003, ISBN 0-470-84857-X.

[2] Adam Weber, Sivagaminathan Balasubramanian, Prodip Das, Chapter 2 - Proton Exchange Membrane Fuel Cells, Advances in Chemical Engineering, 41, 2012, 65-144, https://doi.org/10.1016/B978-0-12-386874-9.00003-8.

[3] Yun Wang, Daniela Fernanda Ruiz Diaz, Ken Chen, Zhe Wang, Xavier Cordobes Adroher, Materials, technological status, and fundamentals of PEM fuel cells - A review, materialstoday, 32, 2020, 178-203, https://doi.org/10.1016/j.mattod.2019.06.005.

[4] Horng-Wen Wu, A review of recent development: Transport and performance modeling of PEM fuel cells, Applied Energy, 165, 2016, 81-106, https://doi.org/10.1016/j.apenergy.2015.12.075.

[5] S. M. Beheshti, H. Ghassemi, R. Shahsavan-Markadeh, An advanced biomass gasification-proton exchange membrane fuel cell system for power generation, Journal of Cleaner Production, 112, 2016, 995-1000, https://doi.org/10.1016/j.jclepro.2015.05.106.

[6] L. Barelli, G. Bidini, F. Gallorini, A. Ottaviani, An energetic-exergetic analysis of a residential CHP system based on PEM fuel cell, Applied Energy, 88(12), 2011, 4334-4342, https://doi.org/10.1016/j.apenergy.2011.04.059.

[7] Nicola Zuliani, Rodolfo Taccani, Microcogeneration system based on HTPEM fuel cell fueled with natural gas: Performance analysis, Applied Energy, 97, 2012, 802–808, https://doi.org/10.1016/j.apenergy.2011.12.089.

[8] Qiangu Yan, H. Toghiani, Heath Causey, Steady state and dynamic performance of proton exchange membrane fuel cells (PEMFCs) under various operating conditions and load changes, Mississippi State University, United States, 2006.

[9] Aspen Technology, Aspen HYSYS Property Packages Overview and Best Practices for Optimum Simulation.

[10] Viktor Hacker, An empirical fuel cell polarization curve fitting equation for small current densities and no-load operation, Journal of Applied Electrochemistry, Graz University of Technology, April 2008.

[11] Dong Hao, Jianping Shen, Yongping Hou, Yi Zhou, and Hong Wang, *An Improved Empirical Fuel Cell Polarization Curve Model Based on Review Analysis,* Hindawi Publishing Corporation International Journal of Chemical Engineering, Volume 2016, Article ID 4109204.

Sizing of a Green Hydrogen Energy System to power a micro-grid for residential use

Abraham Quintana [a], José A. Carta [b], Fabián Déniz [c]

[a] Industrial and Civil Engineering school, University of Las Palmas de Gran Canaria, Las Palmas, Spain, abraham.quintana101@alu.ulpgc.es
[b] Mechanical Engineering Department, University of Las Palmas de Gran Canaria, Las Palmas, Spain, jose.carta@ulpgc.es
[c] University Institute of Intelligent Systems and Numerical Applications in Engineering (SIANI), University of Las Palmas de Gran Canaria, Las Palmas, Spain, fabian.deniz@ulpgc.es

Abstract:

Storage systems are necessary in microgrids based on renewable energy sources to maintain the balance between production and demand. Currently, hydrogen is being promoted by the European Union to be used as new renewable energy vector (green hydrogen) in order to use it for the generation of electrical power, consequently reducing greenhouse gas emissions. Renewable energy sources used to produce hydrogen, such as photovoltaic and wind, are intermittent, therefore an optimal sizing of the hydrogen storage system is required. Another advantage of using hydrogen as an energy vector is the flexibility obtained in the electrical system. This article proposes a technical and optimal solution to create an electric microgrid for a residential area with 100 dwellings using a green hydrogen storage system powered with renewable energy. Results show that a self-sufficient hybrid photovoltaic and wind turbine microgrid with hydrogen storage system can be economically more attractive than a regular photovoltaic collective self-consumption installation. In addition, the self-sufficient gained with hydrogen as energy vector, means a total decarbonisation of the energy sector.

Keywords:

Green hydrogen, microgrid, decarbonisation, renewable energy, resilience.

1. Introduction

Since the Industrial Revolution, the greenhouse gas emissions have been steadily increasing up to the present day. The rising population, linked to the consumerist society in which we live, has led to an increase of the average temperature in the planet. The European Union has set ambitious targets for renewable energies (REs), energy efficiency and greenhouse gas reduction in order to brake climate change. Today, one of those main objectives pursued by the European Union is to decarbonize the energy sector [1] and become the first climate-neutral continent by 2050. In the particular case of the Canary Islands, it is even more ambitious and aims to bring decarbonisation forward by 10 years [2], so that total decarbonisation in the Canary Islands is set for the year 2040.

To achieve those goals, the European Union and their member states are creating and adapting regulations [3,4] to promote RE generation power plants (GPP), so that clean energy can be attractive to the consumers and be competitive in the market. The most common and available energy resources are solar energy and wind energy. Thus, photovoltaic (PV) and wind turbine (WT) technologies are two of the most widespread technologies used worldwide in renewable energy generation power plants (RE GPP). Nevertheless, the implementation of RE GPP have many challenges and limitations [5] due to the integration into the existing grid infrastructure and the need of huge energy storage systems (ESSs). Because of the excellent solar energy resources available in Spain and the relatively low cost of the PV technology, for the last years, the Spanish government [6] has been working on different policies to facilitate the access to the PV self-consumption to the Spaniards.

This paper intends to provide a solution for the decarbonisation of the Canary Islands. The solution studied consists on a self-sufficient microgrid using PV and WT technologies to generate electricity to feed one hundred dwellings. The self-sufficiency of the microgrid is ensured by a green hydrogen-based energy storage system combined with a battery, to improve the resilience [7] of the microgrid. Whereas an isolated microgrid could be a valid solution, a grid connected GPP could give worth to the excess of electricity generated, reducing the levelized cost of energy (COE) of the consumers. In this sense, a discussion of the Spanish PV collective self-consumption regulation is opened, by comparing the benefits of the legislation if it could be applied to hybrid generation power plants.

To achieve an accurate vision, the rest of the paper is structured in the following way. In section 2, *Background*, the Spanish regulation is exposed identifying weaknesses of PV self-consumption and hydrogen systems legislation. Section 3, *Study area*, identifies a valid location for the microgrid according to the RE resources, the proximity to possible consumptions and the feasible locations according to the current legislation. After this, the section 4, *Methods and modelling of study cases*, shows the methodology followed to build the different study cases using HOMER Energy software [8] and the alternative scenarios proposed. The results from the different scenarios considered are exposed in section 5, *Results*, with a discussion of the findings and its limitations. Finally, section 6, *Conclusion,* summarizes the main ideas concluded from this paper.

2. Background

2.1. Current Spanish self-consumption regulations

In 2019, the Spanish government published the Royal Decree 244/2019 [7], which regulates the administrative, technical and economic conditions for the self-consumption of electrical energy. One of the biggest steps of this regulation is the recognition of different self-consumption modalities [9], distinguishing:

- Self-consumption without surplus
- Self-consumption with surplus
  - Net billing: limited to a maximum GPP of 100 kW, this modality allows to inject the surplus to the general electricity grid (GEG) receiving the prosumer a fixed economic compensation per kWh. The electricity bill cannot have a negative value, this means, the retailer will never pay you for the surplus, but make a discount on your bill. This modality has practically no administrative formalities neither taxes applied to the surplus.
  - Direct Sell (DS): the surplus are sold at market prices, with no constrain. Taxes regarding to the generation and the incomes must be paid. The GPP needs to register as an electricity generator.
- Individual self-consumption
- Collective self-consumption: group of several consumers who are supplied, on an agreed basis, with electrical energy from production facilities close to and associated with those of consumption.

Also, the Royal Decree 244/2019 enables the self-consumption not only to installations connected to the consumers internal grid, but also through the general electricity grid. More in depth, collective self-consumption is allowed in the modality of self-consumption with surplus through the general electricity grid when the generation and the consumers are connected to the low voltage GEG within 500 meters distance of each other.

After the Royal Decree 244/2019, the Spanish government has approved new constraints regarding the self-consumption in the Royal Decree-Law 18/2022 [10] and the Royal Decree-Law 20/2022 [11]. On the one hand, the Royal Decree-Law 18/2022 claims that generation linked to self-consumption is mainly photovoltaic and therefore generated at low voltage, it is the reason why the maximum distance cannot be larger, in order to transport the energy without causing high voltage drops and high losses. At the same time, the regulation promotes self-consumption through the GEG by increasing the distance to the consumption up to 1000 meters in the case of power plants located on the rooftop. On the other hand, the Royal Decree-Law 20/2022 encourages self-consumption through the GEG by increasing the distance of self-consumption up to 2000 meters in the case of photovoltaic power plants located on rooftops, industrial land and artificial structures for other purposes, such as those used to cover parking spaces or other uses.

In a nutshell, the actual Spanish law allows self-consumption with surplus through the general electricity grid when distances between the distance between generation and consumption are under 2000 meters radio and they use PV GPP.

2.2. Current Spanish hydrogen regulations

Although the "Report on current regulations and legislative development needs, November 2019" [12] highlights the need for a new regulation on hydrogen production by hydrolysis, hydrogen production in Spain is currently classified as a chemical industry and is therefore considered an industrial activity, regardless of the production method, storage capacity or purpose of the same. For this reason, until updated regulations are approved, hydrogen production facilities must be located in industrial areas [13].

3. Study area

Self-consumption using RE generation power plants requires critical characteristics of the location, which are:

- High renewable energy resources
- Proximity to residential areas

In addition, the solution proposed in the paper pretends not only to implement self-consumption, but also to ensure the self-sufficiency of the microgrid using a hydrogen-based energy storage system. Therefore, according to the current legislation an extra condition is required:

- Compliance with regulatory requirements, particularly for the hydrogen storage system

Considering those key aspects, the placement chosen for the project is the Arinaga Industrial Estate (Polígono Industrial de Arinaga).

3.1. Location

Arinaga Industrial Estate has good renewable energy resources and different neighbourhoods within 2000 meters radio, as shown in Figure. 1. It is an industrial area which allows chemical industries [14, 15] and energy infrastructure use.

Figure. 1. Location for the proposed microgrid [16]

3.2. Energetic resources

3.2.1. Solar energy

The solar radiation and temperature data were taken from the "PVGIS-SARAH2" database [17] published by the European Commission and correspond to the hourly data for 2006. Figure. 2 shows a monthly average of hourly data on solar radiation and temperature in the location of Arinaga Industrial Park.

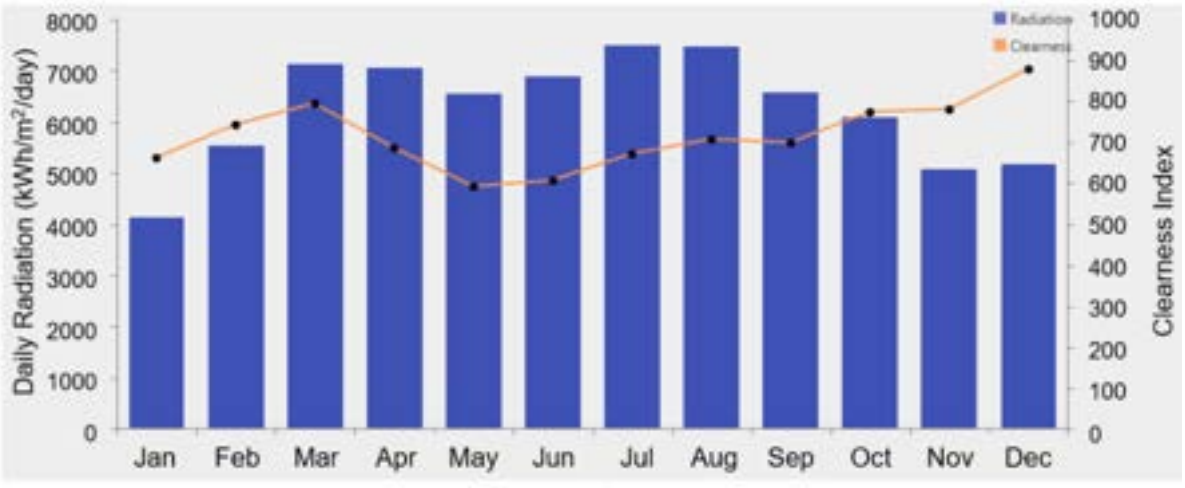

(a)

Figure. 2. Solar radiation and temperature in the Industrial area of Arinaga, year 2006. (a) Average daily solar radiation (kWh/m^2/day). (b) Average daily temperature (ºC)

3.2.2. Wind energy

The wind data taken as a reference correspond to hourly measurements at 10 meters height on the Arinaga dock in 2006. The wind speed data have been corrected due to the variation in height from the anemometer height (10 m) to the wind turbine hub height (65 m) applying the logarithmic variation of the wind speed profile with a roughness factor of 0.1. Figure. 3 shows a monthly average of hourly data on wind speed.

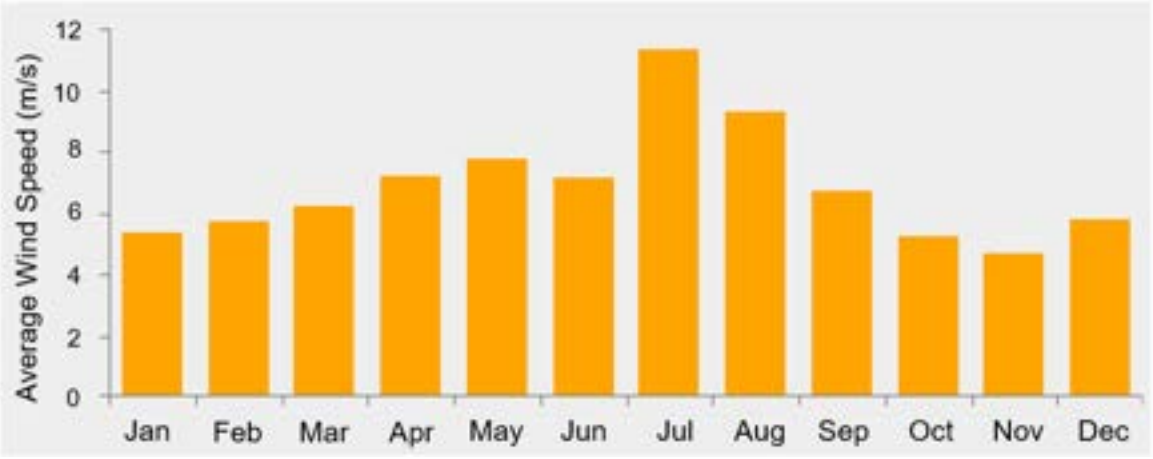

Figure. 3. Wind speed in the Industrial area of Arinaga at 65 m height, year 2006 (m/s)

The chosen year, 2006, had in Gran Canaria an average speed wind under the mean speed during the period 2001-2014, according to Ref. [18]. Taking as reference a year with unfavourable wind resources, the reliability and the resilience of self-sufficiency of the system is increasing.

3.3. Electric demand

To elaborate a base demand power curve profile, real hourly data over the year 2021 for a set of 40 residential meters in the municipality of Alojeró, on the island of La Gomera, were taken as reference. After this, the power curve profile was scaled for a group of 100 dwellings by knowing the minimum power prevision according to the Spanish regulation [19], 5750 W per residence with a simultaneity coefficient of 54.8 %, which results in a total peak power prevision of 315.1 kW. Figure. 4 shows the power curve profile obtained from the reference data. The main electric demand characteristics for 100 dwellings, after scaling the base data according to the minimum installed peak power required, are shown in Table. 1.

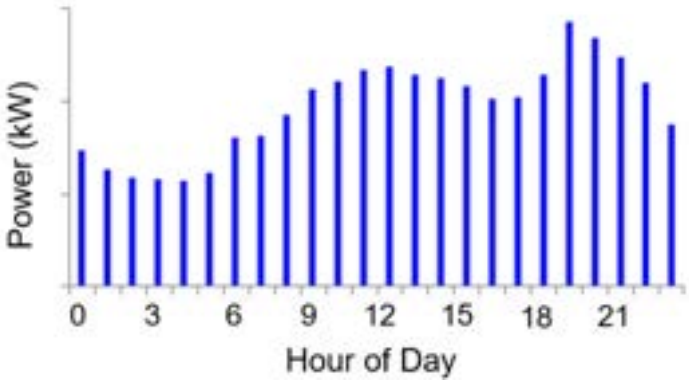

Figure. 4. Daily base demand power curve profile

Table. 1. Electric demand

	Average Energy (kWh/day)	Average Power (kW)	Peak Power (kW)
Base data 40 dwellings	226.5	9.4	21.5
100 dwellings (study case)	3321.1	138.4	315.1

The data presented in Table. 1 show that the base data taken as reference had a very poor electric consumption, the reason behind this fact, is that Alojeró is a municipality where most of the dwellings are second residences and therefore, the mean electrical consumption is very low. Nevertheless, the power curve profile obtained from the data is correct for residential use. The study case has been obtained by scaling the base data until reach the minimum installed power (or Peak Power) for new residences according to the Spanish current regulations, therefore, the scale factor between the real base data and the theoretical study case is nonlinear. Regardless, the study case for 100 dwellings is coherent, with an average power of 1.38 kW per dwelling. This possible oversizing of the demand, just results in a higher resilience of the system and can be justified by the possibility of increasing the number of dwellings attached to the collective self-consumption microgrid in a real case application.

4. Methods and modelling of study cases

The paper's goal is to evaluate the feasibility of a renewable energy self-sufficient green hydrogen microgrid in Gran Canaria to achieve the decarbonisation, attending to the actual legislation, in particular the collective self-consumption and also attending to the actual cost of RE GPP and ESSs technologies.

In order to guarantee the self-sufficiency of the system, an energy storage system is needed to meet the energy demand in the most unfavourable energy resource situations. The solution adopted for this problem is to use green hydrogen as an energy vector. Green hydrogen's greatest virtue is its 100% renewable origin and its small carbon footprint, compared to other storage systems such as conventional batteries. On the other hand, the lack of development of hydrogen technology makes its installation more expensive. At the same time, hydrogen has a great energy density (Wh/kg) but a relatively low power density (W/kg). Whereas a higher energy density indicates a longer autonomy, a low power density means a slower transient response [20]. To solve this problem, another ESS is implemented, a Li-ion battery, which has a lower energy density but a higher power density compared to hydrogen. With the combination of those two ESS, the resilience of the microgrid increases. Furthermore, the minimum power output of proton exchange membrane fuel cells is around 20-30% of its nominal power, for this reason, the use of two ESS is not only justified but also indispensable.

HOMER ENERGY [9] is the software used to design and model different scenarios to determine the best technical solution optimizing the cost of the proposed scenarios. All scenarios are located in the same area, so that all cases have the same RE resources. At the same time, the same electric demand (3.3 Electric demand) is considered for the different scenarios. Same costs of equipment and same lifetime have been considered, which are shown in Table. 2. Equipment costs are set according to the reference bibliography [21,22,23,24,25,26] taken into account.

Table. 2. Equipment, economics and characteristics

Equipment	Symbol	Capital cost	Replacement cost	Lifetime	O&M cost	Other characteristics
Photovoltaic (PV) GPP		1100 €/kW	760 €/kW	25 years	0.1 €/kW year	STC efficiency: 20.9%
Wind turbine (WT)		1180 €/kW	1000 €/kW	25 years	5 €/kW year	Hub height: 65 m
Converter		100 €/kW	100 €/kW	15 years	-	Efficiency: 95%
Electrolyzer		1400 €/kW	1400 €/kW	15 years	28 €/kW year	Efficiency: 75%
Hydrogen tank		669 €/kg	669 €/kg	30 years	6.69 €/kg year	Tank type: IV Pressure: 380 bar
Fuel cell		1800 €/kW	1800 €/kW	25000 hours	0.01 €/op. hr	Slope: 65 g H_2/h/kW Minimum load: 20%
Li-ion battery		650 €/kWh	650 €/kWh	15 years	10 €/kWh year	Minimum SoC: 20%

According to section 2.1 Current Spanish self-consumption regulations & [10], the self-consumption regulation allows the direct sell of the surpluses. Regarding to this, the grid was modelled introducing two different prices of energy:

- Power price: is the price of the energy purchased from the grid (€/kWh). Those data correspond to the monthly mean prices of the voluntary pricing for small consumers tariff 2.0 (PVPC 2.0 TD) [27] during the year 2022. The data used in the study is available on Spanish Consumers and Users Organisation website [28].
- Sellback rate: is the price of the energy dumped on the GEG. Those data correspond to the hourly prices of the day ahead market during 2022. These prices are set by the Spanish market operator (OMIE) [29].

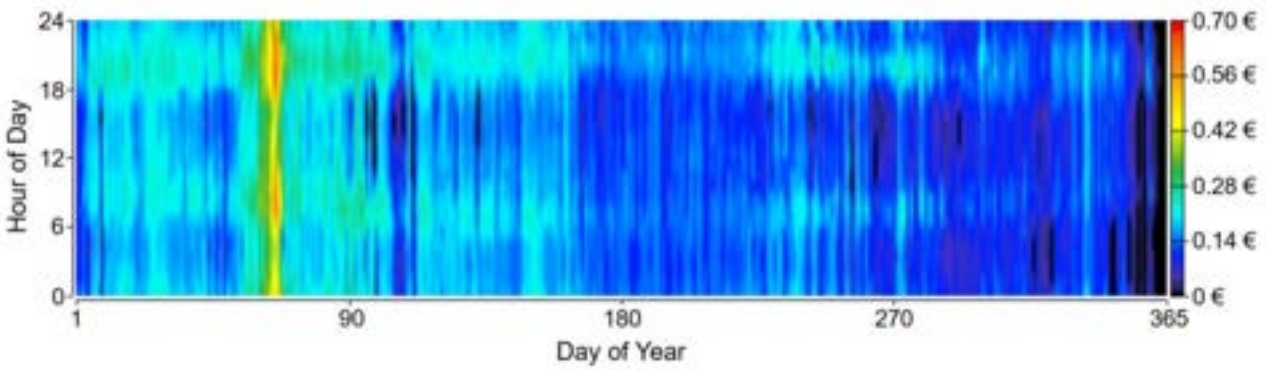

Figure. 5. 2022 Day ahead market prices (OMIE)

The different scenarios Figure. 6, where modelled according to the methodology set out as follows. The first scenario considered, *4.1 Grid connected PV generation plant. Scenario (*A), corresponds to a usual collective self-consumption modality, according to the regulation, which will be the starting point to compare the cost of energy from different alternatives. After this, *Isolated PV self-sufficient microgrid. Scenario (*B), and an *Isolated PV + WT self-sufficient microgrid. Scenario (*C), are modelled to estimate the capacity of the RE GPP and the hydrogen storage capacity in order to satisfy the electrical demand in an isolated self-sufficient microgrid. Whereas scenario (B) makes use of PV technology, scenario (C) utilize a hybrid PV and WT GPP. Lastly, scenario (D) and scenario (E) sections *4.4* and *4.5* respectively, maintain the same self-sufficiency restriction (same ESS capacity and same RE GPP capacity compared to scenarios (B) and (C) respectively)

but are connected to the GEG, with the aim of reducing the cost of energy using the collective self-consumption with surplus through GEG and direct sell modality.

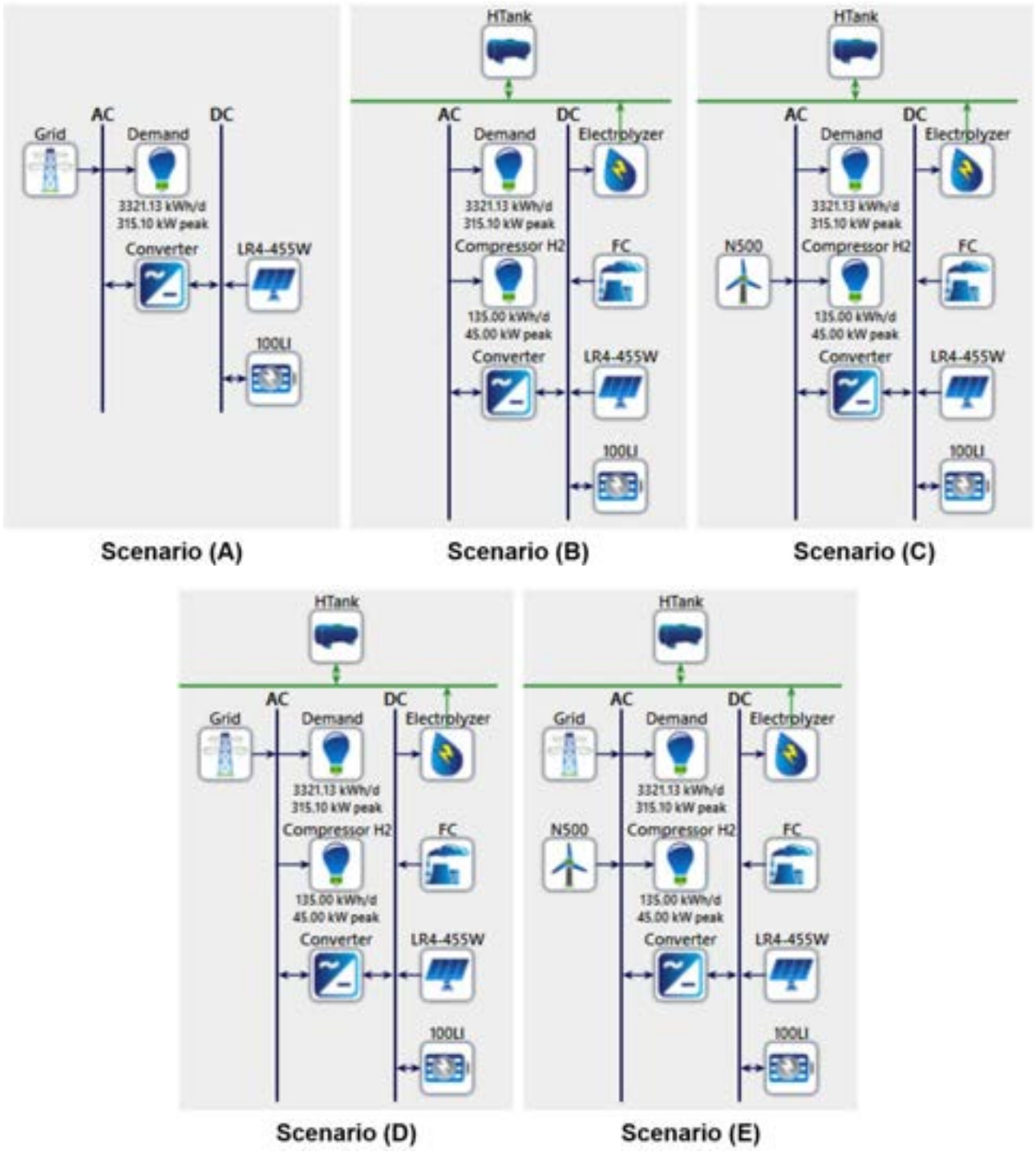

Figure. 6. Study cases scenarios

Table. 3. Study cases scenarios characteristics and equipment capacities

	SS	GEG DS 350 kW	PV (kW)	WT (kW)	Converter (kW)	Li-ion battery (kWh)	Electrolyzer (kW)	H_2 Tank (kg)	FC (kW)
Scenario A	-	✓	1098	-	700	100	-	-	-
Scenario B	✓	-	1665	-	700*	100	1000	1000	250
Scenario C	✓	-	450	500	700*	100	300	1000	250
Scenario D	✓	✓	1665	-	700*	100	1000	1000	250
Scenario E	✓	✓	450	500	700*	100	300	1000	250

*: 700 kW converters are used in every scenario to match the same costs of the equipment required in the most critical scenario.

The GEG is modelled limiting the maximum power output to the grid to 350 kW, so that all systems are equivalent in relation to the access power required and therefore all scenarios can sell the same maximum amount of power. One of the limitations of this methodology is the differentiation made by HOMER between the GEG and the loads, not considering the loads through the GEG, but in a direct line to the consumers. For this reason, a 700 kW converter is chosen in Scenario A, so that the system is able to supply the peak power of the electrical demand considered, and dump up to 350 kW to the GEG at the same time.

All scenarios are compared attending to the levelized cost of energy, which is the average cost per kWh of useful electrical energy produced by the system [9]. With units in €/kWh, HOMER calculates the COE dividing the annualized cost of producing energy by the total electric load served as given in Eq. (1).

$$COE = \frac{C_{ann,tot} - c_{boiler} H_{served}}{E_{served}} \quad (1)$$

Where:

- $C_{ann,tot}$ is the total annualized cost of the system (€/year), which is the annualized value of the total net present cost.
- c_{boiler} is the boiler marginal cost (€/kWh) of thermal energy from the boiler.
- H_{served} is the total thermal load served (kWh/year), which is the total amount of energy that served the thermal load during the year.
- E_{served} is the total electrical load served (kWh/year), which is the total amount of energy that went towards serving the primary and deferrable loads during the year, plus the amount of energy sold to the grid.

As the second term in the numerator results from the thermal load served, this term is zero for RE technologies, as for example PV or WT.

4.1. Grid connected PV generation plant. Scenario (A)

Scenario A is the reference study case. It is an ordinary PV GPP in the modality of collective self-consumption through the general electricity grid with direct sell of the surplus, not being self-sufficient. Scenario A is modelled using HOMER optimiser to size the PV capacity to reach the lowest COE. The sizing of the system is presented in Table. 3.

4.2. Isolated PV self-sufficient microgrid. Scenario (B)

Scenario B intends to model an isolated self-sufficient microgrid by using PV as GPP. The aim of this scenario is to size the PV capacity and ESS needed in order to achieve self-sufficiency, only using PV technology. Two ESS are implemented, hydrogen and Li-ion battery, combined to improve the dynamic response of the system. As shown in Table. 2, the hydrogen tank works at 380 bar pressure, therefore two electrical loads are considered, one hundred dwellings electrical demand and a hydrogen compressor. Hydrogen compressor load refers to the electrical consumption of a 45 kW compressor. This load has been scheduled to work only 3 hours a day. Those 3 hours are the ones with the highest RE penetration.

4.3. Isolated PV + WT self-sufficient microgrid. Scenario (C)

After modelling scenario B, scenario C pretends to size the RE GPP capacity and ESS needed in order to achieve self-sufficiency when two technologies are combined, PV and WT. So, Scenario C, an isolated hybrid microgrid (PV + WT), is dimensioned by HOMER optimizer maintaining the same constrains as scenario B, which are self-sufficiency, combination of green hydrogen and Li-ion battery as ESSs and two electrical loads (100 dwellings electrical demand and hydrogen compressor).

4.4. Grid connected PV self-sufficient microgrid. Scenario (D)

Scenario D matches the same equipment capacities as scenario B differentiating each other in the connection to the GEG. By matching the same generation an ESSs capacities, scenario D ensures self-sufficiency, only using PV technology. In addition, scenario D is in line with the constraints of the regulations, which only allows self-consumption through the general electricity grid when distances between the distance between generation and consumptions are under 2000 meters radio and they use PV GPP. In this scenario, by connecting to the GEG, there is no need to build a private distribution line to the consumers and, at the same time, there is the possibility to sell the surplus.

4.5. Grid connected PV + WT self-sufficient microgrid. Scenario (E)

Scenario E is a hybrid PV and WT microgrid connected to the GEG. With same sizing of the RE GPP and ESSs as Scenario C, this new scenario E, is self-sufficient and at the same time is capable of dumping and selling the surplus to the GEG.

5. Results

A summary of the different scenarios is presented on Table. 4, where the generation of the different technologies are shown not only in MWh/year, but also its percentage out of the total energy production (GEG purchased energy is also considered production). In addition, Table. 4 exhibit two economic parameters, which are the COE and the initial capital cost. These economic parameters are closely related to the total amount of energy discharged to the GEG (GEG sales) of each scenario. All scenarios cover the energy demand of 1261.5 MWh/year required by the 100 dwellings as a whole.

Table. 4. Scenarios analysis: generation, GEG exchange and economics

	SS	PV (MWh/year)	WT (MWh/year)	H_2 FC (MWh/year)	GEG Purchases (MWh/year)	GEG Sales (MWh/year)	Initial capital (€)	COE (€/kWh)
Scenario A	-	2238.2 (78.9 %)	-	-	598.1 (21.1%)	1095.4	1.37 M	0.0503
Scenario B	✓	3393.9 (83.4%)	-	674.3 (16.6%)	-	-	4.50 M	0.409
Scenario C	✓	917.1 (22.9%)	2903.6 (72.4%)	190.8 (4.76%)	-	-	2.76 M	0.217
Scenario D	✓	3392.9 (76.5%)	-	873.4 (19.7%)	171.3 (3.8%)	131.3	4.52 M	0.363
Scenario E	✓	917.1 (20.3%)	2903.6 (64.4%)	570.9 (12.7%)	115.5 (2.6%)	1253.6	2.78 M	0.0450

Scenario A is the only non-self-sufficient study case. As a result, scenario A purchase a total of 598.1 MWh/year energy to cover the total electrical demand. This GEG purchased energy is a 21.1% over the total energy production (as GEG purchased energy is also considered production to the microgrid), but a 47.41 % out of the total load of 1261.5 MWh/year required by the 100 dwellings. Canary Islands power system generates electricity mainly out of diesel groups and combined cycle groups, therefore the GEG purchased energy has an associated CO2 emissions factor of 0.776 kg CO_2/kWh, as [30] states. At the end of the year, scenario A adds to the atmosphere 464062 kg carbon dioxide per year. Although scenario A has the second lower COE because of the difference between the energy sold and the energy purchased, this scenario does not contribute to the target of total decarbonisation set in the Canary Islands for the year 2040.

Scenarios B and C are isolated self-sufficient microgrids. The fact of not being connected to the GEG and being a self-sufficient system out of RE implies that it has no associated emissions from energy purchased from the GEG. Otherwise, compared to scenario A, the initial capital costs of scenarios B and C are higher because of the need for a higher GPP capacity and because of the ESSs implemented to ensure the self-sufficiency of the system. Thus, and because of not having the possibility to sale the surplus to the GEG, the COE are higher for both scenarios, in the particular case of scenario B, it has the highest COE from all cases considered.

Scenarios D and E, pretend to reduce the COE of the systems B and C maintaining the condition of self-sufficiency. Both scenarios, D and E are connected to the GEG, so that the surplus can be sold and therefore, the COE decreases. Scenarios D and E could not have any carbon dioxide emission associated as they are dimensioned with the same generation capacities as both isolated systems, B and C respectively.

When a location matches a good mixture of solar and wind renewable energy sources, a hybrid WT and PV generation power plant is the optimal system [31] increasing the average production among the year. Therefore, a hybrid generation system has the advantage of being able to generate enough electricity those days when one of the energy sources is not available, increasing the reliability and the self-sufficiency of the microgrid. As a result, hybrid GPP in scenarios C and E, generate more energy at the end of the year with a lower power capacity compared to scenarios B and D, which only use PV technology.

When focusing on the economics, there is also a clear tendence in the costs reduction of a self-sufficient system if two generation power plants are used, PV and WT. As a PV and WT hybrid system require a lower generation capacity and less energy storage capacity compared to PV microgrid, the initial capital cost is reduced comparing scenario C and B and comparing scenario E and D. On the other hand, the COE is reduced dramatically when the system is connected to the GEG and can sell the surplus. This can be clearly identified by comparing scenarios D and B and comparing scenarios E and C respectively.

Additionally, a GEG connected microgrid (scenarios D and E) improve the resilience of the power system, so that the electrical demand can be covered at every single moment even the years with lower RE penetration. A grid connected system, also allows the microgrid to stop working for programmed maintenance. The resilience of scenarios B, C, D and E is also increased by the use of two ESS, a Li-ion battery and a green hydrogen based ESSs [32]. The combination of both energy storage system improves the energy storage

capacity and the dynamic response of the microgrid when the hydrogen fuel cell starts up [33], and when the minimal load of the FC is not covered.

5.1. Discussions

The results presented show that a hybrid PV and WT GPP self-sufficient microgrid (scenario E) is a cleaner solution compared to scenario A and it can also can be an economically better solution in comparison with a regular PV self-consumption GPP (scenario A). Because more energy is generated with a lower power capacity in the proposed hybrids microgrids, when the microgrid works in the modality of self-consumption with surplus through the general electricity grid and direct sell, the hybrid microgrid results in a lower COE. Nevertheless, the present Spanish laws Royal Decree 244/2019, Royal Decree-Law 18/2022 and 20/2022 only allow collective self-consumption with surplus through the general electricity grid for PV GPP because it is the most extended technology used in self-consumption. The restriction of a maximum distance of 2000 meters pretends to avoid high voltage drops and high losses. This condition does not make any sense as there is not a restriction on the maximum power of the GPP in the self-consumption DS modality, as the voltage drops depends not only on the distance but also depends on the power. According to the current regulation, only scenarios A and D could work in the modality of self-consumption with surplus through the GEG and DS.

A key aspect of the collective self-consumption consumption with surplus through the general electricity grid and direct sell is the possibility of using the GEG in a radio of 2000 m. This allow a GPP to provide electricity to different locations within an area, which makes the collective self-consumption more accessible to the consumers and at the same time, more attractive to the companies, reducing the costs from building a new distribution line. The current regulation does not provide this opportunity to generation technologies other than photovoltaics, as for example mini wind turbine, biomass or other RE technologies.

If decarbonation is a real objective for the Spanish government, as part of the European Union, it is opened the discussion, whether the collective self-consumption regulation could be applied also for hybrid PV generation power plants. As shown on the results, hybrid microgrids can be economically competitive and with an appropriate energy storage system they can provide 100 % green energy to the society.

5.2. Limitations

The methodology followed to develop this work have some important limitations which conditionate the results presented. The limitations are detailed below:

- No generation taxes are considered: Spanish legislation provides for a tax on generated electricity supplied to GEG of 7 % and a grid access fee of 0.5 €/MWh. HOMER optimizations were not executed considering these generation taxes.
- No construction costs and no land acquisition costs have been considered.
- Simulations have only been carried out over one year. HOMER does not run multi-year simulations with hydrogen systems. Therefore, the COE showed on the results have only been calculated considering direct sales of surpluses over one year and not over the 25-year life of the project.
- Simulations were executed under 2022 electricity prices. 2022 has been the year with the highest energy prices in Europe history, so the direct sell of the surplus turns out in the highest incomes compared to other years. On contrary, the purchased energy in 2022 was the most expensive too.

Although these important limitations denote that the COE obtained is not accurate, they apply equally to all scenarios. Consequently, the simulations are valid to identify which system is the most economically profitable.

6. Conclusion

This work studies different microgrids scenarios to reach the decarbonisation of the energy sector in the Canary Islands attending to the current self-consumption regulations in Spain. To reach the decarbonisation, self-sufficient renewable energy generation power plants microgrids with green hydrogen energy storage systems are proposed. Different combinations of photovoltaic and wind turbines generation technologies are proposed in search of an economic competitive system.

After studying the current Spanish self-consumption and hydrogen regulation, a study area and a location in proposed. The location chosen in the industrial area of Arinaga is in compliance with the regulation and counts with suitable renewable energy resources, which are presented in detail. All microgrids proposed are dimensioned with an electrical demand modelled for 100 dwellings.

The methodology and different scenarios are presented. For the self-sufficient scenarios, two energy storage systems are considered, hydrogen due to the its energetic density and Li-ion battery to improve the dynamic response of the system. The results show that hybrid photovoltaic and wind turbine microgrids are more economic for the particular study case compared to a photovoltaic microgrid. In addition, a self-sufficient hybrid microgrid can be economically more attractive than a self-consumption non-self-sufficient regular photovoltaic power plant. Consequently, a discussion is opened whether the collective self-consumption regulation could be applied also for hybrid photovoltaic generation power plants.

Abbreviations

AC Altern current
COE Cost of energy
DC Direct current
DS Direct sell
ESS Energy storage system
FC Fuel cell
GEG General electricity grid
GPP Generation power plants
H_2 Hydrogen
O&M Operation and maintenance
PV Photovoltaic
RE Renewable energy
SoC State of charge
SS Self-sufficient
STC Standard test conditions
WT Wind turbine

References

[1] MITECO, Estrategia de descarbonización a largo plazo 2050, Spain: Ministerio para la Transición Ecológica y el Reto Demográfico, 2020.

[2] Monitor Deloitte, Los Territorios No Peninsulares 100% descarbonizados en 2040: la vanguardia de la transición energética en España, 2020

[3] El Parlamento Europeo y el Consejo de la Unión Europea, Reglamento (UE) 2021/1119 del Parlamento Europeo y del Consejo de 30 de junio de 2021 por el que se establece el marco para lograr la neutralidad climática y se modifican los Reglamentos (CE) n.o 401/2009 y (UE) 2018/1999 («Legislación europea sobre el clima»)

[4] G. Strbac, et al., Decarbonization of electricity systems in Europe: market design challenges. IEEE Power Energy Mag. 2021; 19 (1) 53–63.

[5] A. Pfeifer, G. Krajaˇci´c, D. Ljubas and N. Dui´c, Increasing the integration of solar photovoltaics in energy mix on the road to low emissions energy system-Economic and environmental implications. Renewable Energy 2019;143 1310–1317.

[6] Ministerio para la transición ecológica, de 5 de abril, por el que se regulan las condiciones administrativas, técnicas y económicas del autoconsumo de energía eléctrica, 2019. Real Decreto 244/2019.

[7] Carlos Bordons, Félix Garcia-Torres and Miguel A. Ridao, Model predictive control of microgrids. Switzerland: Springer International Publishing; 2020.

[8] HOMER (Hybrid Optimization of Multiple Energy Resources) Pro software, version 3.14.5, (2021). Boulder, USA: HOMER Energy, LLC.

[9] Daniel Dasí-Crespo, Carlos Roldán-Blay, Guillermo Escrivá-Escrivá and Carlos Roldán-Porta, Evaluation of the Spanish regulation on self-consumption photovoltaic installations. A case study based on a rural municipality in Spain. Renewable Energy 2023; 204 788–802.

[10] Jefatura del Estado, de 18 de octubre, por el que se aprueban medidas de refuerzo de la protección de los consumidores de energía y de contribución a la reducción del consumo de gas natural en aplicación del "Plan + seguridad para tu energía (+SE)", así como medidas en materia de retribuciones del personal al servicio del sector público y de protección de las personas trabajadoras agrarias eventuales afectadas por la sequía. Real Decreto-ley 18/2022.

[11] Jefatura del Estado, de 27 de diciembre, de medidas de respuesta a las consecuencias económicas y sociales de la Guerra de Ucrania y de apoyo a la reconstrucción de la isla de La Palma y a otras situaciones de vulnerabilidad. Real Decreto-ley 20/2022.

[12] Ministerio de Industria, Comercio y Turismo grupo de trabajo de unidad de mercado subgrupo de trabajo sobre tecnologías del hidrógeno, INFORME SOBRE LA REGLAMENTACIÓN ACTUAL Y NECESIDADES DE DESARROLLO LEGISLATIVO, november 2019.

[13] Ministerio de Economía, Industria y Competitividad, de 23 de junio 2017, por el que se aprueba el Reglamento de Almacenamiento de Productos Químicos y sus Instrucciones Técnicas Complementarias MIE APQ 0 a 10. Real Decreto 656/2017.

[14] Gobierno de Canarias Consejería de política territorial, sostenibilidad y seguridad, Viceconsejería de política territorial dirección general de ordenación del territorio, 2017: Plan General de Ordenación de la Villa de Agüimes, Tomo IV.2. Normas Urbanísticas de Ordenación Pormenorizada.

[15] Decreto de 9 de marzo de 1972, aprobado definitivamente por Orden Ministerial de 15 de diciembre de 1973, anexado en el Plan General de Ordenación de Agüimes, Tomo IV.2 Anexo de Ordenanzas Incorporadas.

[16] Google, Inst. Geogr. Nacional, Data SIO, NOAA, U.S. Navy, NGA, GEBCO, TerraMetrics 2017. - Available at:
<https://earth.google.com/web/@27.86984096,-15.43442157,67.85217502a,8588.0763634d,35y,0h,0t,0r> [accessed 2.2.2023].

[17] European Commission, PHOTOVOLTAIC GEOGRAPHICAL INFORMATION SYSTEM – Available at: <https://re.jrc.ec.europa.eu/pvg_tools/en/> [accessed 10.3.2022].

[18] Julieta Schallenberg-Rodriguez and Nuria Garcia Montesdeoca, Reply to the comments on the article “Spatial planning to estimate the offshore wind energy potential in coastal regions and islands. Practical case: The Canary Islands". Energy 2019; 178 879-886.

[19] Ministerio de Ciencia y Tecnología, de 2 de agosto 2002, por el que se aprueba el Reglamento electrotécnico para baja tensión. Real Decreto 842/2002, ITC-BT-10 PREVISIÓN DE CARGAS PARA SUMINISTROS EN BAJA TENSIÓN.

[20] Javier Tobajas, Félix García-Torres, Pedro Roncero-Sánchez, Javier Vázquez, Ladjel Bellatreche and Emilio Nieto, Resilience-oriented schedule of microgrids with hybrid energy storage system using model predictive control. Applied Energy 2022; 306 118092.

[21] Enock Mulenga, Alan Kabanshi, Henry Mupeta, Musa Ndiaye, Elvis Nyirenda and Kabwe Mulenga, Techno-economic analysis of off-grid PV-Diesel power generation system for rural electrification: A case study of Chilubi district in Zambia. Renewable Energy 2023; 203 601-611.

[22] Wei He, Li Tao, Lei Han, Yasong Sun, Pietro Elia Campana and Jinyue Yan, Optimal analysis of a hybrid renewable power system for a remote island. Renewable Energy 2021; 179 96-104.

[23] Da Huo, Marcos Santos, Ilias Sarantakos, Markus Resch, Neal Wade and David Greenwood, A reliability-aware chance-constrained battery sizing method for island microgrid. Energy 2022; 251 123978.

[24] Robert Förster, Matthias Kaiser and Simon Wenninger, Future vehicle energy supply - sustainable design and operation of hybrid hydrogen and electric microgrids. Applied Energy 2023; 334 120653.

[25] Viktor Walter, Lisa Göransson, Maria Taljegard, Simon Öberg and Mikael Odenberger, Low-cost hydrogen in the future European electricity system – Enabled by flexibility in time and space. Applied Energy 2023; 330 120315.

[26] Yifan Xu, Mengmeng Ji, Jiří Jaromír Klemeš, Hengcong Tao, Baikang Zhu, Petar Sabev Varbanov, Meng Yuan and Bohong Wang, Optimal renewable energy export strategies of islands: Hydrogen or electricity?. Energy 2023; 269 126750.

[27] Comisión Nacional de los Mercados y la Competencia, de 15 de enero 2020, por la que se establece la metodología para el cálculo de los peajes de transporte y distribución de electricidad. Circular 3/2020.

[28] Organización de Consumidores y Usuarios (OCU). El precio de la luz repunta en febrero, El precio de la luz, mes a mes. – Available at: <https://www.ocu.org/vivienda-y-energia/gas-luz/informe/precio-luz> [accessed 5.2.2023].

[29] Operador del Mercado (OMIE). OMIEData Precios horarios del mercado diario en España. Available at: <https://www.omie.es/es/file-access-list?parents%5B0%5D=/&parents%5B1%5D=Mercado%20Diario&parents%5B2%5D=1.%20Precios&dir=Precios%20horarios%20del%20mercado%20diario%20en%20Espa%C3%B1a&realdir=marginalpdbc> [accessed 5.2.2023].

[30] Ministerios de Industria, Energía y Turismo, y Ministerio de Fomento. FACTORES DE EMISIÓN DE CO2 y COEFICIENTES DE PASO A ENERGÍA PRIMARIA DE DIFERENTES FUENTES DE ENERGÍA FINAL CONSUMIDAS EN EL SECTOR DE EDIFICIOS EN ESPAÑA. 14 de enero de 2016.

[31] Domenico Mazzeo, Münür Sacit Herdem, Nicoletta Matera and John Z. Wen, Green hydrogen production: Analysis for different single or combined large-scale photovoltaic and wind renewable systems. Renewable Energy 2022; 200 360-378.

[32] Milad Zamani Gargari, Mehrdad Tarafdar Hagh and Saeid Ghassem Zadeh, Preventive scheduling of a multi-energy microgrid with mobile energy storage to enhance the resiliency of the system. Energy 2023; 263 125597.

[33] Wojciech Uchman, Janusz Kotowicz and Robert Sekret, Investigation on green hydrogen generation devices dedicated for integrates renewable energy farm: Solar and wind. Applied Energy 2022; 328 120170.

Test bench for electricity or hydrogen production from aqueous methanol

Vladimir L. Meca[a,b], Rafael d'Amore-Domenech[a,b], Antonio Villalba-Herreros[a,b], Teresa J. Leo[a,b]

[a] Universidad Politécnica de Madrid, Madrid, Spain, vl.meca@upm.es, CA
[b] Universidad Politécnica de Madrid, Madrid, Spain, r.damore@upm.es
[c] Universidad Politécnica de Madrid, Madrid, Spain, antonio.villalba@upm.es
[d] Universidad Politécnica de Madrid, Madrid, Spain, teresa.leo.mena@upm.es

Abstract:

The growing demand for renewable energy sources, sometimes far from the place of consumption, has led to consider the conversion of these energies into fuels, allowing its transport and storage. This is the case of hydrogen, which can be transported in form of methanol, more suitable for transport and storage, obtained by the synthesis process of CO_2 and hydrogen. In this way, the application of methanol as an energy vector arises. Once methanol reaches its place of use, it can be used as a fuel in Direct Methanol Fuel Cells (DMFC) or transformed back into hydrogen using methanol electrolysis. However, there are at present several challenges to be forced. While DMFC present several still unsolved issues such as poor methanol oxidation reaction, fuel crossover or high demand of noble metal, methanol electrolysers have operational limits produced by problems related to active site blockage by the formation of adsorbed carbonaceous species, sluggish kinetics, or methanol crossover.

For the study of DMFC and methanol electrolysers and implement improvements in their design, a test bench that allows testing both devices independently has been designed and built. It allows plotting polarization curves, analysing crossover and developing electrochemical impedance spectroscopy studies, as well as the control of operating temperature of the devices, the mass flow, pressure and temperature of the oxygen or nitrogen introduced in the DMFC and methanol flow rate. These features will become key factors for the development of technologies for improving the use of methanol as an energy vector.

Keywords:

Methanol electrolysis; hydrogen production; test bench; electricity production; DMFC; methanol

1. Introduction

Renewable energy sources are those obtained from inexhaustible natural resources, such as the sun or wind. These energy sources have the advantage of being cleaner and more sustainable than fossil fuels. However, renewable energies also present some challenges, such as their intermittency. Energy that is not consumed during peak energy production from renewable sources can be stored in chemical form and used when needed. One of the fuels that can be generated using electricity is hydrogen [1]. This is the most abundant element in the universe and can be used to generate electricity or power vehicles [2]. Hydrogen has a high specific energy and its consumption in fuel cells produces only water, making it a very attractive option for reducing greenhouse gas emissions [3]. Green hydrogen, which is produced from renewable energies sources, is environmentally friendly, but also expensive and not easy to store and transport [4].

Methanol is an alcohol that can be used as an alternative fuel for internal combustion engines or fuel cells [5]. This fuel can be produced from a variety of sources, such as hydrogen and carbon dioxide [6]. Methanol has the advantage that it takes up less volume than hydrogen and can be more easily transported and stored because methanol is a liquid chemical compound at ambient temperature and pressure. In addition, methanol can be produced using electricity from wind or solar power to generate hydrogen and then combining it with carbon dioxide captured from the atmosphere or industrial sources [7]. This fuel is known as e-methanol and produces a carbon-neutral fuel that contributes to the decarbonisation of the economy [6].

Methanol can be used to generate electricity or hydrogen. Direct methanol fuel cells (DMFC) are devices that use methanol as fuel and produce electricity, water and carbon dioxide [8]. However, they also present some challenges, such as low efficiency, high methanol permeation loss through the membrane, low CO tolerance and degradation of components [8-9]. DMFC fuel cells are fed with methanol and oxygen to produce direct current electricity. Methanol in aqueous solution is fed to the anode and oxygen is fed to the cathode. The reactions that occur during the operation of a DMFC single cell are shown in Eqs. (R1-R2). Equation (R1)

represents the half-reaction at the anode, Eq. (R2) represents the half-reaction at the cathode and Eq. (R3) represents the overall reaction [10].

Anode: $CH_3OH + H_2O \rightarrow CO_2 + 6H^+ + 6e^-$ (R1)

Cathode: $\frac{3}{2}O_2 + 6H^+ + 6e^- \rightarrow 3H_2O$ (R2)

Overall: $CH_3OH + \frac{3}{2}O_2 \rightarrow 2H_2O + CO_2$ (R3)

Methanol electrolysers are devices that use electricity to produce hydrogen from aqueous methanol. They have the advantage that the hydrogen produced is of high purity. However, they also present some challenges, such as low efficiency [11-12]. Methanol is introduced at the anode, while no reactant is introduced at the cathode. In Eqs. (R4-R6) are presented the half-reactions taking place at the anode, cathode and the overall reaction, respectively [11-12].

Anode: $CH_3OH + H_2O \rightarrow CO_2 + 6H^+ + 6e^-$ (R4)

Cathode: $6H^+ + 6e^- \rightarrow 3H_2$ (R5)

Overall: $CH_3OH + H_2O \rightarrow CO_2 + 3H_2$ (R6)

Several lines of research are underway to improve the performance of DMFC and methanol electrolysers. For example, the development of new membranes with lower permeability to methanol, higher ionic conductivity and higher chemical and mechanical stability [13]. Also, the development of new catalysts with higher activity and selectivity for methanol oxidation and oxygen reduction is undertaken [14]. In addition, the channel configuration of the bipolar plates can be studied to increase the power density of DMFC or to decrease the voltage required for a methanol electrolyser [9,15]. In order to study how these modifications affect the performance of both devices, a test bench is needed.

This work presents the design and operation of a test bench for a DMFC and methanol electrolyser. In the first section, the configuration of the test bench is presented. The second section presents the results obtained for DMFC and methanol electrolyser. Finally, the conclusions are exposed.

2. Configuration of the DMFC and methanol electrolyser test bench

There are several tests that can be conducted to study the performance of DMFC and methanol electrolysers, and the configuration of the test bench depends on these tests. This section presents some of the tests that can be performed and the characteristics of the test bench designed in this work.

2.1. Tests to be performed with the test bench

The aim of this work is to design and build a test bench to investigate the performance of a DMFC and a methanol electrolyser under different operating conditions. To determine this performance, various tests can be carried out for both devices, including polarization curve tracing, crossover tests and electrochemical impedance measurements [16].

A polarization curve test is used to determine the operation and performance of a fuel cell or an electrolyser. With this measurement, the relationship between the voltage and current generated or applied to the cell can be obtained, as well as the voltage losses due to different types of factors. To do this test a DMFC single cell in this work the evolution of the current density generated by the cell is measured as the voltage decreases. To test a methanol electrolyser single cell with this bench the voltage is measured as the current density increases.

A crossover test is used to measure the amount of fuel diffusing through the membrane from the anode to the cathode without being oxidised at the anode. This measurement can provide information on the efficiency and durability of the cell. The test performed consists of feeding the anode with the fuel and the cathode with an inert gas (e.g., nitrogen) and measure the current generated by the reaction of the fuel present in the cathode.

An electrochemical impedance spectroscopy (EIS) test is used to characterise the electrochemical behaviour of a fuel cell. This measurement can provide information on the internal resistance, reaction kinetics and mass transport processes occurring in the fuel cell. The test consists of applying a small sinusoidal current to the cell and measure the frequency response of the system.

All these tests are performed by setting the values of oxygen or nitrogen mass flow rate and pressure, methanol mass flow rate and the temperature at which the device is operating.

2.2. Experimental test bench

Depending on the type of test to be performed and the device under study, the test bench has different configurations. Figure 1 shows the diagram of the test bench for the DMFC study. In this diagram, a dashed line for the supply and treatment of oxygen or nitrogen can be seen. There is a cylinder for each gas used (1) to which a pressure regulator (2) is connected to control the pressure of the gas to be introduced into the system. A flow controller (3) is located downstream of this valve, which allows the flow rate of the gas introduced during the tests to be set. Before being introduced into the DMFC, the oxygen or nitrogen passes through a humidification system (4) so that the DMFC membrane is always wet during the tests (13). This system consists of two scrubber flasks arranged inside a thermostatic bath. After leaving the DMFC, the gas passes through a water trap (5) to prevent liquid water produced during the reaction from reaching the pressure controller (6), which controls the operating pressure of the DMFC. Fuel is supplied to the DMFC from an aqueous methanol tank (7) using a pump (8).

To control the temperature at which the tests are carried out, there are two chambers (9). The device to be tested is placed in the inner chamber and kept at the desired temperature. To achieve this effect, there is a refrigerated and heating circulator (10) which circulates distilled water to a heat exchanger (11) at the temperature required to increase or decrease the temperature inside the chamber. To force the recirculation of air between the two chambers, a fan is connected to the heat exchanger and powered by a power source (12).

Finally, a potentiostat-galvanostat (14) connected to a computer (15) is used to control the voltage values at which the DMFC operates, while the current and impedance parameters are recorded during the tests for subsequent analysis.

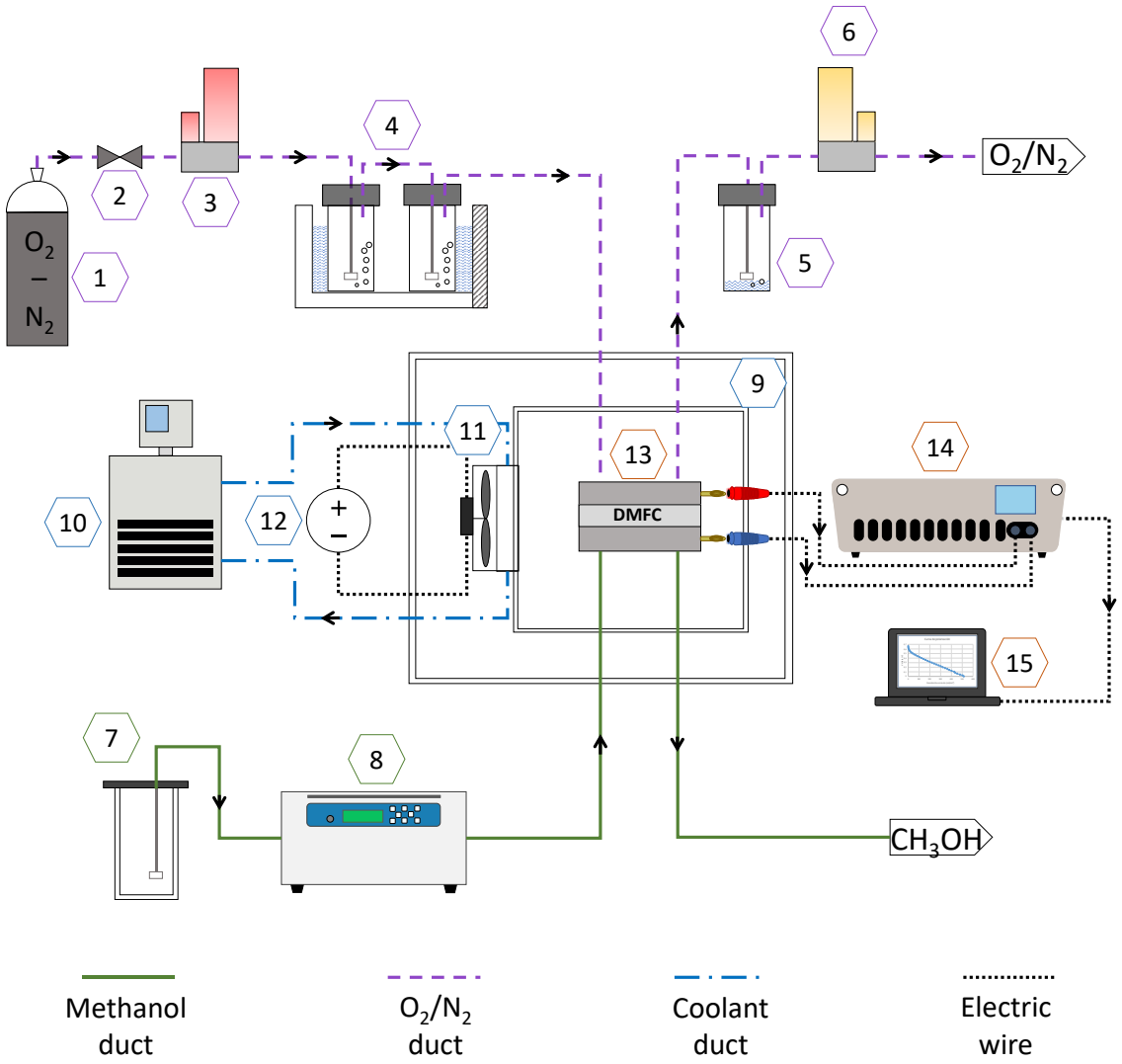

Figure 1. Diagram of the test bench when it is used to test Direct Methanol Fuel Cells. 1 - Compressed O_2/N_2 cylinder. 2 - Pressure reduction valve. 3 - Gas flow controller. 4 - Gas humidification system. 5 - Water trap. 6 - Gas pressure controller. 7 - Aqueous methanol tank. 8 - Methanol pump. 9 - Chamber. 10 - Refrigerated and heating circulator. 11 - Heat exchanger. 12 - Power source. 13 - DMFC. 14 - Potentiostat-galvanostat. 15 - Computer.

3. Results and Discussion

After the assembly and set-up of the test bench presented in Fig. 2, it has been possible to obtain polarization curves of a DMFC single cell and for a methanol electrolyser single cell. The single cells of both devices consist of 316L steel plates with serpentine channels, with an active area of 16 cm^2. The MEA used for each device consists of a Nafion® 117 membrane and commercial electrodes corresponding to the cathode and anode. The cathode uses Freudenberg carbon paper as support with a Pt 1mg/cm^2 catalyst load. For the anode, the same support is used, but with a Pt-Ru charge of 3 mg/cm^2.

Figure 2. The test bench designed and built to study DMFC and methanol electrolysers.

3.1. DMFC polarization curves

Figure 3 shows the polarization and power density curves obtained for the DMFC with the test bench at different oxygen mass flow rates to study the effect of this parameter on the DMFC performance. All curves have been obtained at a temperature of 60 °C, 1 bar pressure and a methanol concentration of 1 M and flow rate of 3 ml/min.

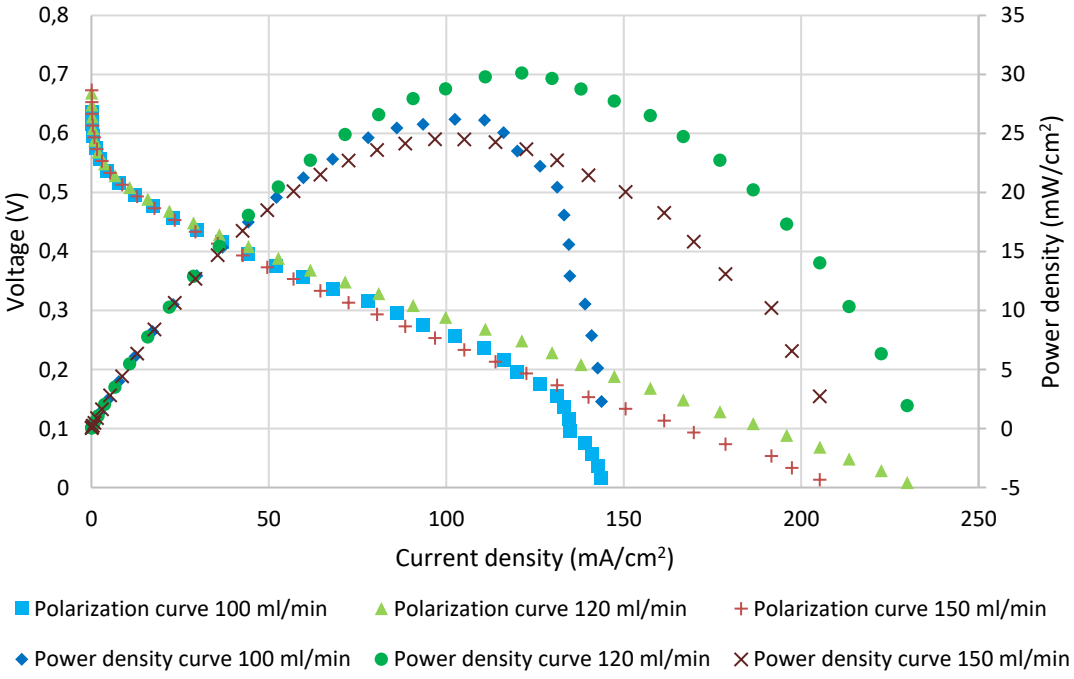

Figure 3. Polarization and power density curves of the DMFC single cell for different oxygen flow rates obtained at a temperature of 60 °C, pressure of 1 bar and a methanol concentration of 1 M and flow rate of 3 ml/min.

It can be seen from Fig. 3 that for a volumetric oxygen flow rate of 110 ml/min the current density increases slightly as the voltage values decrease below 0.23 V, with the current density not following the trend shown up to this voltage value. This results in a large decrease of the power density after having reached the maximum value. This behaviour of the single cell for this volumetric flow of oxygen can be attributed to that this flow is not able to extract from the cathode channels the water that has been generated during the polarization curve, thus blocking the reaction at the last points of the curve. To avoid this, the oxygen flow rate is increased, with best results at 120 ml/min. However, when increasing the flow rate to 150 ml/min, the Nafion® membrane probably starts to dry out during the polarization curve and for this reason the peak power density value is lower.

3.2. Methanol electrolyser polarization curves

Figure 4 shows the polarization curves of the methanol electrolyser obtained with the test bench at different temperatures to evaluate the effect of this parameter in the performance of the electrolyser. The concentration of methanol used to feed the electrolyser is 1 M and the aqueous methanol flow rate is 6 ml/min.

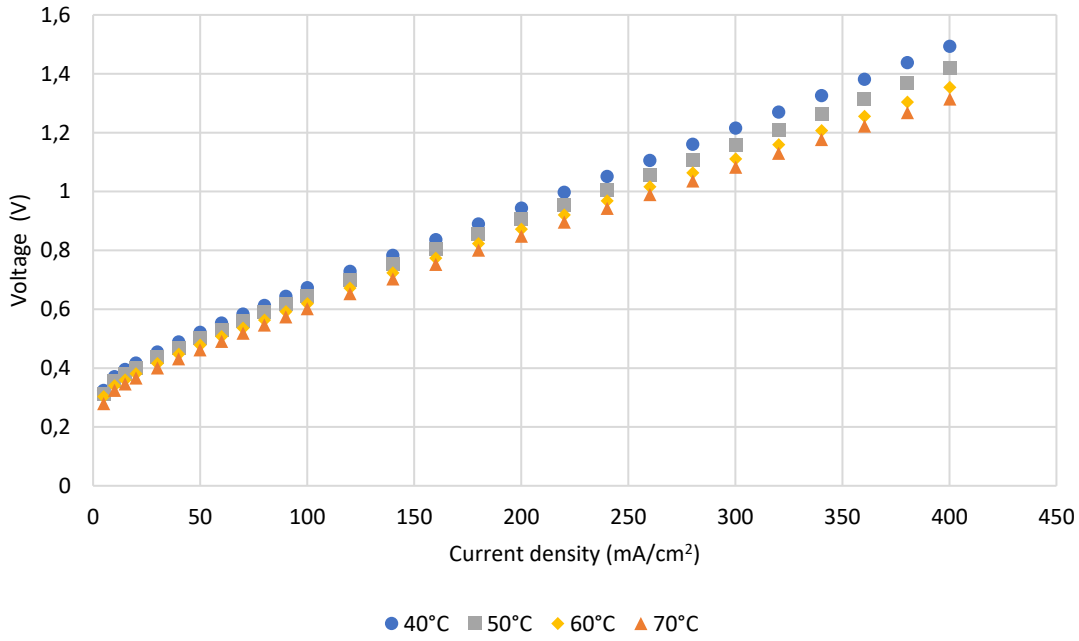

Figure 4. Polarization curves of the methanol electrolyser single cell for temperatures of 40 °C, 50 °C, 60 °C and 70 °C obtained with aqueous methanol of concentration 1 M and methanol flow rate of 6 ml/min.

In Fig. 4 can be observed that while increasing temperature, the voltage decreases for the same current density. This results in a lower electrical energy consumption to produce the same mass of hydrogen with the methanol electrolyser when increasing temperature.

4. Conclusions

This article describes the design and assembly of a test bench to analyse the behaviour of DMFC and methanol electrolysers. The bench makes it possible to control the pressure and flow of oxygen or nitrogen, the flow of methanol in aqueous solution and the temperature at which the tests are carried out.

By performing polarization curves, crossover and EIS measurements with this test bench, the effects of each of the DMFC and electrolyser components, such as membranes, catalysts, electrodes or the flow path of the bipolar plates, on these devices can be evaluated.

From the results obtained so far it can be seen that the choice of the oxygen flow rate is an important parameter for a DMFC, as too little flow rate may indicate that the cathode channels become waterlogged and too much flow rate may indicate that the membrane dries out and blocks the reactions from taking place. It has also been shown that an increase in temperature in the case of the methanol electrolyser implies a decrease in energy consumption to continue producing the same amount of hydrogen with this device.

The test bench presented in this work allows to obtain very useful experimental results to study the influence of different parameters and components, both at experimental and commercial level, on the performance of a DMFC and a methanol electrolyser, allowing to further improve the technology of these devices.

Acknowledgments

This work has been carried out thanks to the Project GreenH2CM funded by MCIN/AEI/10.13039/501100011033, by "NextGenerationEU/PRTR" and the Regional Government of Madrid and to the Grant PID2021-124263OB-I00 funded by MCIN/AEI/10.13039/501100011033 and by "ERDF a way of making Europe".

References

[1] Van Renssen S., The hydrogen solution?. Nature Climate Change 2020; 10(9): 799-801.

[2] Von Zuben, T. W., E.B. Moreira D., L. Germscheidt R., G. Yoshimura R., S. Dorretto D., B. S. de Araujo A., G. Salles Jr. A., A. Bonacin J., Is Hydrogen Indispensable for a Sustainable World? A Review of H2 Applications and Perspectives for the Next Years. Journal of the Brazilian Chemical Society 2022; 33(8): 824-843.

[3] L. Meca V., Villalba-Herreros A., d'Amore-Domenech R., J. Leo T., Zero emissions wellboat powered by hydrogen fuel cells hybridised with batteries. Proceedings of the Institution of Mechanical Engineers, Part M: Journal of Engineering for the Maritime Environment 2022; 236(2): 525-536.

[4] Jang D., Kim J., Kim D., Han W., Kang S., Techno-economic analysis and Monte Carlo simulation of green hydrogen production technology through various water electrolysis technologies. Energy Conversion and Management 2022; 258: 115499.

[5] Korberg A.D., Brynolf S., Grahn M., Skov I.R., Techno-economic assessment of advanced fuels and propulsion systems in future fossil-free ships. Renewable and Sustainable Energy Reviews 2021; 142: 110861.

[6] International Renewable Energy Agency, Methanol Institute, Innovation Outlook: Renewable Methanol. Abu Dhabi; 2021. ISBN 978-92-9260-320-5.

[7] L. Meca V., d'Amore-Domenech R., Crucelaegui A., J. Leo T., Large-Scale Maritime Transport of Hydrogen: Economic Comparison of Liquid Hydrogen and Methanol. ACS Sustainable Chemistry & Engineering 2022; 10(13): 4300-4311.

[8] Majidi P., Altarawneh R. M., Ryan N. D. W., Pickup P. G., Determination of the efficiency of methanol oxidation in a direct methanol fuel cell. Electrochimica Acta 2016; 199: 210-217.

[9] Ramasamy J., Palaniswamy K., Kumaresan T., Chandran M., Chen R., Study of novel flow channels influence on the performance of direct methanol fuel cell. International Journal of Hydrogen Energy 2022; 47 (1): 595-609.

[10] L. Dicks A., A. J. Rand D., Fuel Cell Systems Explained, Third Edition. Glasgow, U.K.: John Wiley & Sons Ltd.; 2018.

[11] Lamy C., Coutanceau C., Baranton S., Production of Clean Hydrogen by Electrochemical Reforming of Oxygenated Organic Compounds. Academic Press; 2020.

[12] Colmati F., Bastos T., Lino F., Linares Leon J., Hydrogen Production via Electroreforming. In: M. Letcher T. editor. Comprehensive Renewable Energy (Second Edition). Elsevier. 2022. P. 566-593.

[13] Santiago O., Mosa J., Escribano P.G., Navarro E., Chinarro E., Aparicio M., J. Leo T., del Río C., 40SiO2–40P2O5–20ZrO2 sol-gel infiltrated sSEBS membranes with improved methanol crossover and cell performance for direct methanol fuel cell applications. International Journal of Hydrogen Energy 2020; 45(40): 20620-20631.

[14] de Sá A.I., Capelo A., Esteves A., Cangueiro L., Almeida A., Vilar R., Rangel C.M., Key issues to high electroactivity for methanol oxidation and oxygen reduction of Pt-based supported catalyst in fuel cells relevant environment. Ciência & Tecnologia dos Materiais 2016; 28(2): 88-98.

[15] S. Pethaiah S., K. Sadasivuni K., Jayakumar A., Ponnamma D., S. Tiwary C., Sasikumar G., Methanol Electrolysis for Hydrogen Production Using Polymer Electrolyte Membrane: A Mini-Review. Energies 2020; 13(22): 5879.

[16] Wang H., Yuan X., Li H., PEM Fuel Cell Diagnostic Tools. CRC Press; 2017.

ULPGC
Universidad de
Las Palmas de
Gran Canaria

grres ULPGC
group for the research on renewable energy systems

H. Process integration, process simulation and optimization, process monitoring & control

ECOS2023

PROCEEDINGS OF ECOS 2023 - THE 36TH INTERNATIONAL CONFERENCE ON
EFFICIENCY, **C**OST, **O**PTIMIZATION, **S**IMULATION AND ENVIRONMENTAL IMPACT OF ENERGY SYSTEMS
25-30 JUNE 2023, LAS PALMAS DE GRAN CANARIA, SPAIN

A Hybrid algorithm based on Bayesian Optimization and Interior Point OPTimizer for Optimal Operation of Energy Conversion Systems

Loukas Kyriakidis[a], Miguel Alfonso Mendez[b] and Martin Bähr[a]

[a] German Aerospace Center, Cottbus, Germany, loukas.kyriakidis@dlr.de (CA), martin.baehr@dlr.de
[b] von Karman Institute for Fluid Dynamics, Sint-Genesius-Rode, Belgium, miguel.alfonso.mendez@vki.ac.be

Abstract:
Optimization methods are essential to improve the operation of energy conversion systems including energy storage equipment and fluctuating renewable energy. Modern systems consist of many components, operating in a wide range of conditions and governed by nonlinear balance equations. Consequently, identifying their optimal operation (e.g. minimizing operational costs) requires solving challenging optimization problems, with the global optimum often hidden behind many local ones. In this work, we propose a hybrid method that advantageously combines Bayesian optimization (BO) and Interior Point OPTimizer (IPOPT). The BO is a global approach which exploits Gaussian process regression to build a surrogate model of the cost function to be optimized, while IPOPT is a local approach which uses quasi-Newton updates. The proposed BO-IPOPT combination allows leveraging the parameter space exploration of the BO with the quasi-Newton convergence of IPOPT once solution candidates are in the neighbourhood of an optimum. Using a challenging constrained test function, we test BO-IPOPT in accuracy, robustness and computational efficiency. Finally, we showcase the proposed hybrid method in the optimal operation of an industrial energy conversion system for renewable steam generation.

Keywords:
Nonlinear global optimization, Bayesian optimization, IPOPT, Hybrid method, Renewable steam generation.

1. Introduction

Numerical optimization is widely used to define the optimal operation [1–4] of energy conversion systems with many component combinations. A large number of system components, their interactions and included control parameters such as temperatures, mass flows or bypasses, combined with their nonlinear response, renders the optimization of these systems that are usually high dimensional and nonconvex. Yet, global optimization is required for model predictive control framework [5–7], where optimization methods with high accuracy and low computational cost are necessary.

Optimization methods can be classified into local and global, see e.g. [8,9]. Local methods use the information in the neighbourhood of a candidate solution to propose an update (improvement). Depending on whether the update relies on the cost function's gradient computation, these can be further classified as gradient-free (e.g. Nelder–Mead) and gradient-based (e.g. quasi-Newton methods). Local methods converge faster (i.e. with fewer cost function evaluations) than global ones if the starting point is sufficiently close to the optimum or if the cost function is (at least locally) convex. However, these methods are more prone to get stuck into local minima. A simple approach to mitigate this risk is to use multi-start (MS) algorithms [10], consisting in repeating the local optimization from multiple starting points. Leveraging the fast convergence of local methods, this approach can capture a large distribution of local optima, from which the one with the best objective function value can be taken as the best guess for the global optimum.

Global methods can be classified into deterministic and stochastic. Deterministic global optimization is mainly based on concepts of enumeration, generating cuts, and bounding to feasible regions that do not contain any optimal solution [9]. Nevertheless, commercial deterministic global solvers, like BARON [11], are extremely computational expensive especially in nonlinear nonconvex problems, where the CPU time increases exponentially with the number of variables and constraints. Common simplifications, which aim to reduce the complexity of the problem so that a global method like BARON can provide the global solution in reasonable time, are the linear modeling of system components [12] and the linearization of nonlinear component equations [13]. However, the former does not always guarantee a realistic system behaviour, whereas the latter requires an appropriate linearization technique depending on the model complexity, where a balance between accuracy and time efficiency must be found for the definition of the grid fineness.

An alternative to the deterministic global search is the random search of stochastic global optimization. These can be further classified into single candidate (e.g. simulated annealing) or population-based (e.g. genetic algorithms or particle swarms) [14] depending on the number of solutions that are iterated upon, or into metaheuristics or surrogate-based depending on the criteria used for the update. Metaheuristic methods (such as genetic algorithms or particle swarms) use a bio-inspired heuristic strategy to advance candidate solutions, while surrogate-based approaches (such as Bayesian optimization [15–18]) build a surrogate model of the function to optimize and use the model to drive the new evaluations. Global stochastic methods can avoid local minima, but tend to require a much larger number of cost-function evaluations than local ones.

The complementary advantages of these methods have motivated various hybrid approaches combining global and local methods [14, 19, 20]; the reader is referred to [21] for an overview of hybridization strategies. While most hybrid methods have combined metaheuristics with local methods, the recent focus seeks to combine surrogate-based methods and gradient-based optimization [22–24] to maximize the sample efficiency of the hybrid formulation.

This work explores the combination of Bayesian optimization and a quasi-Newton local approach to determine the optimal operation of energy conversion systems. In particular, we use the classic BO with Gaussian process regression (GPR) and expected improvement [15] together with the Interior Point OPTimizer (IPOPT) [25, 26]. Our combination is similar to the one proposed in [24], but differs in how the local method is integrated with the GPR, as further detailed in Section 2.3..

This paper is organized as follows: Section 2. gives an overview of the background of the proposed method BO-IPOPT. Section 3. presents the test cases analyzed in this work, namely a constrained test function with known global solution and the constrained optimization problem arising from the operational management of a renewable steam generation system to test the performance of our proposed method. Finally, Section 4. summarizes the main conclusions and provides perspective for future works.

2. Optimization Methods

In this work, we consider the general constrained optimization problem, defined as:

$$\min_{\boldsymbol{x}\in\Omega} \left\{ f(\boldsymbol{x}) \;\text{ s. t. }\; \boldsymbol{h}(\boldsymbol{x}) = \boldsymbol{0}, \boldsymbol{g}(\boldsymbol{x}) \leq \boldsymbol{0} \right\} \tag{1}$$

with $\boldsymbol{x} \in \Omega \subseteq \mathbb{R}^n$ the n-dimensional decision variable contained in set Ω, $f : \mathbb{R}^n \to \mathbb{R}$ the objective function, $\boldsymbol{h} : \mathbb{R}^n \to \mathbb{R}^p$ the set of equality constraints, and $\boldsymbol{g} : \mathbb{R}^n \to \mathbb{R}^q$ the set of inequality constraints. The functions $f, \boldsymbol{h}, \boldsymbol{g}$ can be nonlinear and nonconvex, but are assumed to be sufficiently smooth.

We aim to develop an optimization method that provides a sequence of candidate solutions $\{\boldsymbol{x}_K\}$ converging towards the global minimum $\boldsymbol{x}_K \to \boldsymbol{x}^\star$ with the highest probability and the fewer iterations K. In what follows, we briefly introduce the BO and IPOPT methods and motivate our interest in their combination.

2.1. Bayesian Optimization (BO)

BO is a global black-box optimization approach, i.e. requiring no mathematical definition of the objective function. The main idea is to use the sampling at the candidate solutions $\{\boldsymbol{x}_K\}$ to build a surrogate model of the cost function. Following [15], the surrogate model is usually built with GPR, which is a kernel regression method [27] allowing the analytical computation of both the regression and its uncertainties. The uncertainties of the model can be used to balance exploitation, i.e. the tendency to sample where the surrogate predicts best objective values, with exploration, i.e. the tendency to sample where the surrogate has the highest uncertainty.

An approach to deal with optimization constraints is to augment the objective function as follows according to [14]:

$$u(\boldsymbol{x}) = f(\boldsymbol{x}) + \boldsymbol{\rho}\boldsymbol{h}(\boldsymbol{x})^2 + \boldsymbol{\lambda}\max(\boldsymbol{0}, \boldsymbol{g}(\boldsymbol{x}))^2 \tag{2}$$

where $\boldsymbol{\rho}, \boldsymbol{\lambda} \geq \boldsymbol{0}$ are penalty weight vectors associated with the magnitude of constraint violation. The two ingredients in the BO are described as follows:

1. *GPR*: The GPR builds the surrogate model considering it as a Gaussian process (GP), i.e. a multivariate Gaussian distribution in the domain Ω. This distribution is initialized with a *prior* mean $m(\boldsymbol{x})$ and covariance defined by a kernel function, usually taken as a Gaussian $k(\boldsymbol{x}, \boldsymbol{x}') = \exp(-d(\boldsymbol{x}, \boldsymbol{x}')^2/2l^2)$, with l the length scale of the kernel and $d(\cdot,\cdot)$ the Euclidean distance between points in Ω. As sample points $\{\bar{\boldsymbol{x}}_1, \ldots, \bar{\boldsymbol{x}}_{N_c}\}$ and associated objective values $\bar{u}_n = u(\bar{\boldsymbol{x}}_n)$ are collected, the GPR updates the underlying GP using standard conditioning rules [27] such that the (surrogate) predictions in $\boldsymbol{x} \in \Omega$ become $\hat{u}(\boldsymbol{x}) \sim \text{GP}(\mu(\boldsymbol{x}), \boldsymbol{\Sigma}(\boldsymbol{x}))$ with mean $\mu(\boldsymbol{x})$ and covariance $\boldsymbol{\Sigma}(\boldsymbol{x})$ functions defined as:

$$\mu(\boldsymbol{x}) = \boldsymbol{K}_*^T \left(\boldsymbol{K}_{**} + \alpha \boldsymbol{I}\right)^{-1} u(\bar{\boldsymbol{x}}) \quad \text{and} \quad \boldsymbol{\Sigma}(\boldsymbol{x}) = \boldsymbol{K} - \boldsymbol{K}_*^T \left(\boldsymbol{K}_{**} + \alpha \boldsymbol{I}\right)^{-1} \boldsymbol{K}_* \tag{3}$$

where $\boldsymbol{K} = k(\boldsymbol{x}, \boldsymbol{x})$, $\boldsymbol{K}_* = k(\boldsymbol{x}, \bar{\boldsymbol{x}})$, $\boldsymbol{K}_{**} = k(\bar{\boldsymbol{x}}, \bar{\boldsymbol{x}})$, $\boldsymbol{I}$ is the identity matrix of appropriate size and α is a regularization parameter that avoids the fully interpolative behaviour of the GPR. The main hyperparameters of the regression are the kernel's length scale l and the regularization α; the first determines the smoothness of the function, while the second regularizes the sensitivity of the regression towards noise in the case of stochastic objective functions.

2. *Acquisition function*: This function controls the location of the new candidate solutions. The common approach, also used in this work, is to use the expected improvement (EI) function. This is defined as:

$$\mathrm{EI}(\boldsymbol{x}) = \begin{cases} (\hat{u}(\boldsymbol{x}^+) - \mu(\boldsymbol{x}) - \xi)\Phi(Z) + \sigma(\boldsymbol{x})\phi(Z) & \text{if } \sigma(\boldsymbol{x}) > 0 \\ 0 & \text{if } \sigma(\boldsymbol{x}) = 0 \end{cases} \quad \text{with} \quad Z = \begin{cases} \frac{\hat{u}(\boldsymbol{x}^+) - \mu(\boldsymbol{x}) - \xi}{\sigma(\boldsymbol{x})} & \text{if } \sigma(\boldsymbol{x}) > 0 \\ 0 & \text{if } \sigma(\boldsymbol{x}) = 0 \end{cases} \tag{4}$$

where Φ and ϕ denote the cumulative distribution function and the probability distribution function, respectively. The first term controls the exploitation: this term is large if the new samples are close to the expected optima according to the surrogate model. The second term controls exploration: this term is large if the new samples are in the area of large $\sigma(\boldsymbol{x}) = \mathrm{diag}(\boldsymbol{\Sigma})$. The parameter ξ sets a threshold over the minimal expected improvement that justifies the exploration and is a hyperparameter of the BO; hence the larger this value, the more exploration is produced.

In the classic BO, the algorithm begins with a set of randomly chosen candidate solutions and iterates alternating one update of the GPR and the maximization of EI to define new candidates.

2.2. Interior Point OPTimizer (IPOPT)

The open-source software package IPOPT [25] is a popular tool for solving large-scale nonlinear optimization problems. The solver is mainly based on a primal-dual interior-point method combined with a filter line-search method [26]. IPOPT can also be applied to nonconvex problems, but should be at least once, ideally twice, continuously differentiable.

Algorithmically, IPOPT transforms any inequality constraints of the original problem (1) into natural logarithmic barrier terms in the objective function, including a barrier parameter, thus considering a parametric problem. Based on this, a sequence of equality-constrained problems (barrier problems) is solved for decreasing values of the mentioned barrier parameter. This approach is repeated until a point satisfies the first-order Karush-Kuhn-Tucker optimality conditions. Note that also maximizers and saddle points satisfy the latter optimality conditions, but IPOPT internally uses a Hessian regularization that avoids obtaining maximizers and saddle points. For each barrier sub-problem, a Newton-type algorithm with line search is applied, including the solution of indefinite sparse symmetric linear systems. In particular, the overall performance (runtime, accuracy and robustness) strongly depends on the properties of the chosen sparse linear solver.

Overall, IPOPT is a highly efficient solver to find a local solution of a large-scale nonlinear nonconvex constrained optimization problem. However, the computed local optimum depends strongly on the selected starting point. Consequently, the initialization determines the rate of convergence to a solution and to which optimum the algorithm converges. It should be noted that the local optimization method can also perform poorly and even fail if the initial guess is unfavorable.

2.3. Hybrid Method BO-IPOPT

The proposed BO-IPOPT combination is illustrated in Algorithm 1. The algorithm starts with a set of initialization points to generate a first surrogate model via GPR (cf. lines 1-4). In doing so, the evaluation of the initialization points is possible, since the objective function is assumed to be known. The main part of the algorithm consists of alternating steps of BO and IPOPT until the total number of outer iterations K is satisfied (cf. lines 6-13). More specifically, new candidates for the GPR are first selected by evaluating the acquisition function EI. However, instead of updating the surrogate model directly with the newly selected candidates (as in classical BO), IPOPT is applied to the best candidates, so the surrogate model is then updated based on these local optima. It should be noted that the proposed approach uses only feasible solutions (in line 9): if the solution of IPOPT is not feasible, the algorithm selects the next best candidate.

The advantage of the proposed BO-IPOPT method is that IPOPT increases the convergence of the BO by moving some of the candidate solutions towards optimal locations. When these are local optima, the EI evaluation allows for maintaining global exploration and improving the regression where needed. If any of these is a global optimum, the EI keeps favouring its sampling in the following iterations. Overall, this method is not only efficient for BO to speed up its convergence but also for IPOPT to effectively determine good initial points. It is worth noticing that any local solver could replace IPOPT, which was chosen here because of its efficient, robust, open-source implementation.

As mentioned in Section 1., the recently proposed approach BOwLS [24] (cf. corresponding Algorithm 3 in the mentioned article) is similar to ours. In [24], the BO framework is also used to determine the local solver's

Algorithm 1 Hybrid Method BO-IPOPT

Input: length scale l; regularization term α of GPR; amount of exploration ξ; number of initialization points N_0; number of candidates N_c considering in EI; number of best candidates N_{bc} selected at each iteration; penalty weight vectors $\boldsymbol{\rho}, \boldsymbol{\lambda}$; number of outer iterations K;

1: generate a number of points $\{\boldsymbol{x}_1, \dots, \boldsymbol{x}_{N_0}\}$ in Ω;
2: evaluate $y_n = u(\boldsymbol{x}_n)$ for $n = 1 : N_0$;
3: let $D_0 = \{(\boldsymbol{x}_n, y_n)\}_{n=1}^{N_0}$;
4: construct a GPR model $\hat{u}_0$ from D_0;
5: $n = N_0, j = 0$;
6: **while** $j < K$ **do**
7: generate a new group of points $\{\bar{\boldsymbol{x}}_1, \dots, \bar{\boldsymbol{x}}_{N_c}\}$ in Ω;
8: $\{\boldsymbol{x}_{n+1}, \dots, \boldsymbol{x}_{n+N_{bc}}\} = \arg\max \mathrm{EI}(\bar{\boldsymbol{x}}_i; \hat{u}_n)$ for $i = 1 : N_c$;
9: solve $[y_k^\star, \boldsymbol{x}_k^\star] = \mathrm{IPOPT}(\boldsymbol{x}_k)$ for $k = n+1 : n+N_{bc}$;
10: $D_{j+1} = D_j \cup \{(\boldsymbol{x}_{n+1}^\star, y_{n+1}^\star), \dots, (\boldsymbol{x}_{n+N_{bc}}^\star, y_{n+N_{bc}}^\star)\}$;
11: update GPR model $\hat{u}_{j+1}$ from D_{j+1};
12: $n = n + N_{bc}, j = j + 1$;
13: **end while**
14: **return** $y_{\min} = \min\{y_i\}_{i=1}^n$;

Algorithm 2 MS-IPOPT

Input: Number of outer iterations K;

1: **for** $i = 1 : K$ **do**
2: generate a random point $\boldsymbol{x}_i$ in Ω;
3: solve $[y_i^\star, \boldsymbol{x}_i^\star] = \mathrm{IPOPT}(\boldsymbol{x}_i)$;
4: **end for**
5: **return** $y_{\min} = \min\{y_i^\star\}_{i=1}^K$;

starting points and thus create a suitable MS formulation. However, it should be noted that there are some technical differences to our version. First, the initial GPR model is built from the results of the local searches (not random ones); this brings the risk of restricting the sampling region of the GPR. Second, the initial and updated GPR models are based on the value of the objective function from the local optima but on the inputs of the initial points *before* using the local solver ($\boldsymbol{x}$ instead of $\boldsymbol{x}^\star$). Consequently, the GPR at each iteration does not approximate the underlying function but another one that shares the same local minima identified thus far. Finally, BOwLS uses the conjugate gradient method from the SciPy package as a local search, thus not accounting for constraints and the feasibility set of the problem.

3. Numerical Examples

In this section, we showcase the proposed BO-IPOPT approach on (i) a test function and (ii) the optimization of a renewable steam generation system. In both test cases, the performance of BO-IPOPT is compared with the classical random-based MS-IPOPT (cf. Algorithm 2) and the BOwLS [24] in terms of accuracy, CPU time and robustness. All algorithms were implemented in Python 3.8. More specifically, BO was implemented using the sklearn library [28] for the GPR, while IPOPT is used via the Python Optimization Modeling Objects (Pyomo) software package [29]. To provide the first and second derivative, Pyomo uses the automatic differentiation features in the Ampl Solver Library.

All computations were carried out on a machine with Intel(R) Core(TM) i7-8665U CPU. To allow for a fair comparison between hybrid approaches, we implement IPOPT as the local solver for the BOwLS since the conjugate gradient method from the SciPy package used in [24] is not designed to handle constrained problems. Additionally, for consistency, we consider the same parameters for both hybrid methods, i.e. $N_0 = 10$, $N_c = 1,000$, $N_{bc} = 2$, $\xi = 0.01$, $\alpha = 0.1$, $l = \rho = \lambda = 100$, and the same acquisition function EI. Concerning the random-based MS-IPOPT, we implement it with $N_{bc} = 2$ (cf. line 2 in Algorithm 2), meaning that two random points are generated for each outer iteration K and used as starting points for the IPOPT solver.

3.1. Constrained Ackley Function

The first test case is the well-known Ackley function, often used to test optimization algorithms [30]. This function is nonconvex and highly multi-modal with multiple local minima and one global minimum. Since the Ackley function was originally designed as an unconstrained optimization test case, we add two inequality

constraints as in [30]. The resulting constrained optimization problem is defined as follows:

$$\min \quad -20\exp\left(-0.2\sqrt{\frac{1}{n}\sum_{i=1}^{n}x_i^2}\right)-\exp\left(\frac{1}{n}\sum_{i=1}^{n}\cos(2\pi x_i)\right)+20+e \tag{5}$$

$$\text{s. t.} \sum_{i=1}^{n} x_i \leq 0, \quad \|\boldsymbol{x}\|_2 - 5 \leq 0, \quad \boldsymbol{x} \in [-5,10]^n \tag{6}$$

where n denotes the problem's dimension, set to $n = 100$ for this experimental study. The optimization problem (5)-(6) has a global minimum at $\boldsymbol{x} = \boldsymbol{0}$ with objective function value 0, i.e. $f(\boldsymbol{x}) = 0$. Since all implemented algorithms are based on a certain randomness, our numerical experiments were repeated 100 times with a number of outer iterations $K = 300$.

The optimization results of all three methods are shown in Fig. 1. The figure on the left compares the averaged minimum objective function value, while the figure on the right compares the averaged CPU time versus the number of outer iterations. It can be seen that the proposed BO-IPOPT outperforms the others in convergence and robustness. As expected, MS-IPOPT and BO-IPOPT start with a higher minimum objective function value than BOwLS because both methods use a random initialization, while BOwLS considers local optima as initialization for the initial GPR model. Obviously, BO-IPOPT converges faster towards the global minimum, which can be explained as follows: on the one hand, MS-IPOPT naturally converges more slowly to the global optimum because it strongly depends on its randomly chosen starting points. On the other hand, the GPR in BO-IPOPT has better performance in providing a better surrogate model since the sampling is more spread than in BOwLS, which narrows the sampling near the local optima. Regarding CPU time, the simplest MS-IPOPT outperforms both hybrid methods, as shown on the right side of Fig. 1; this gives an order of magnitude of the costs for training the GPR surrogate model in the two hybrid methods.

It should be underlined that an exhaustive comparison of the two hybrid methods should also include a broader range of hyperparameters; this will be carried out in the extended version of this work. For the investigated test case, the performance gap appears to depend on the outer iterations K: as shown in Fig.1, at $K = 100$, BO-IPOPT is well ahead in the averaged minimum objective function value, but BOwLS reaches similar objectives at $K \approx 170$. The number of initialization points N_0 is a second crucial parameter. It is expected that larger values will favour BO-IPOPT, since they enable better exploration of the solution space, while the local optimization in BOwLS restricts the exploration of the BO. Moreover, increasing N_0 increases the number of (initial) local searches in the BOwLS and thus directly leads to higher computational costs, in contrast to BO-IPOPT. Finally, the number of local searches before the updating of the GPR model is expected to have a significant impact on the balance between accuracy and computational cost and will also be investigated in future work.

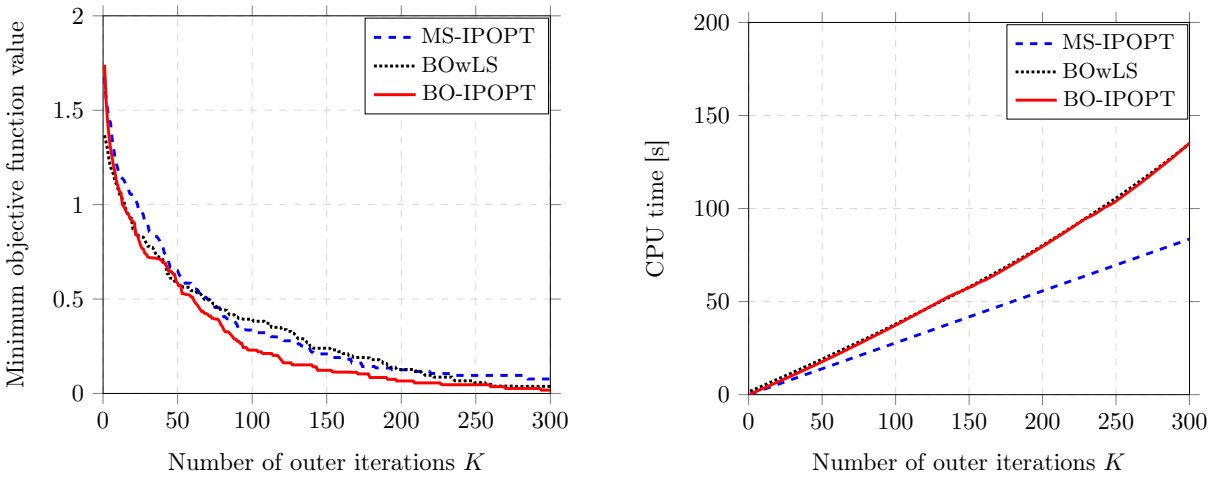

Figure 1: Optimization results for the constrained Ackley function (5)-(6): comparison of the averaged minimum objective function value (**left**) and averaged CPU time (**right**) over 100 trials using MS-IPOPT, BOwLS and BO-IPOPT in relation to the number of outer iterations K.

3.2. Renewable Steam Generation

The second test case is the operation optimization problem of an industrial energy conversion system for renewable steam generation. This power-to-heat system (cf. Fig. 2) was recently proposed in [31] and is currently used as a practical benchmark to evaluate the algorithms. In the following, we first briefly describe the test case and the resulting optimization problem (Section 3.2.1.) and then present and discuss the results of the optimization (Section 3.2.2.).

3.2.1. Problem Description

The considered electrified system shown in Fig. 2 aims to provide constant process heat in the form of superheated steam for an industrial process. The multi-component system mainly consists of 4 units: (i) a wind turbine (WT) to produce renewable electricity driving the system; (ii) a closed reverse Brayton cycle high-temperature heat pump (HTHP), powered by electricity from the WT or the power grid, to generate process heat; (iii) a sensible thermal energy storage (TES) to store excess thermal energy generated during periods of high wind power or low electricity prices; (iv) the steam generator (SG) for providing process steam via an intermediate thermal oil stream and controllable fluid bypasses.

The HTHP and SG models were created with a process simulation software, with the former being able to simulate part load behaviour. The TES model is developed using a lumped capacitance approach, while the WT power output is modeled from the specific power curve at hub height, i.e. the power curve determines the wind power generated as a function of the wind speed extrapolated to the corresponding height.

In the system configuration (cf. Fig. 3), the HTHP provides high-temperature process heat to an intermediate circuit routed through the TES or directly to the SG via a controllable fluid bypass. Thermal oil is chosen as heat transfer fluid (HTF) in the intermediate loop due to its compactness and fluid phase within the temperature range. During the charging process, the temperature in the TES is heated up by the HTF before it enters the SG; discharging operation is vice versa. In discharge mode, the HTHP's power consumption can be significantly reduced since less heat has to be supplied to the intermediate loop to ensure constant steam generation. In idle operation, the TES is completely bypassed by the HTF. The cold outlet stream is not used for cooling applications in the current setup. For more details, we refer the reader to [31].

Optimization aims to determine the cost-optimal operation, i.e. minimizing operational costs considering the fluctuating wind energy and electricity prices. To build an algebraic model problem, the underlying HTHP and SG models are converted into an algebraic form using polynomial surrogate models, as described in [31]. This results in an algebraic nonlinear nonconvex constrained optimization problem that can be formulated in a discrete setting as:

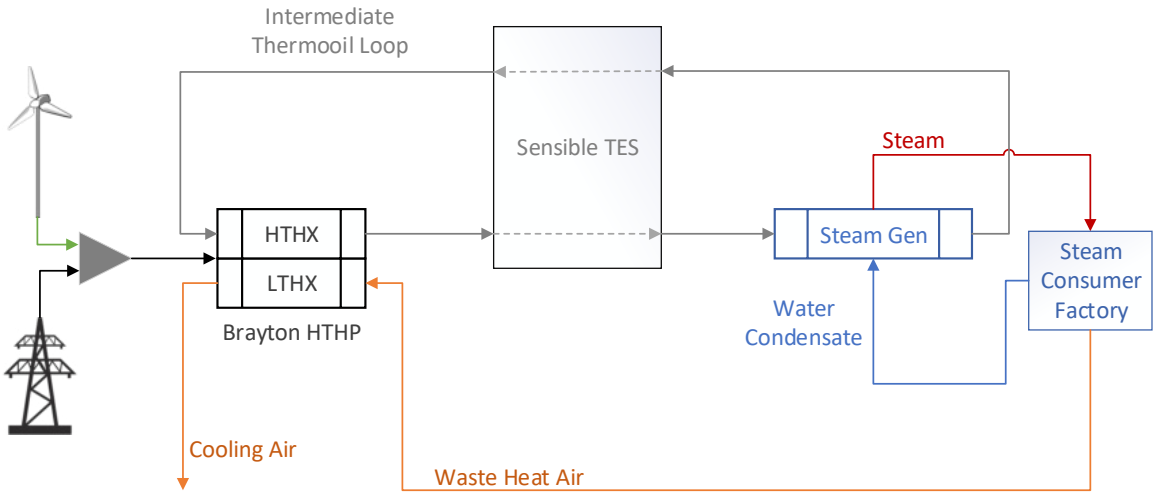

Figure 2: Illustration of the investigated industrial energy conversion system for electrified steam generation recently proposed in [31]. The system consists of a HTHP, a TES and a SG, where the HTHP is powered by electricity from a wind turbine or the power grid. The HTHP uses waste heat air stream as a heat source and enables charging and discharging of the TES via an intermediate thermal oil stream. Furthermore, constant heat demand for the steam consumer factory must be satisfied.

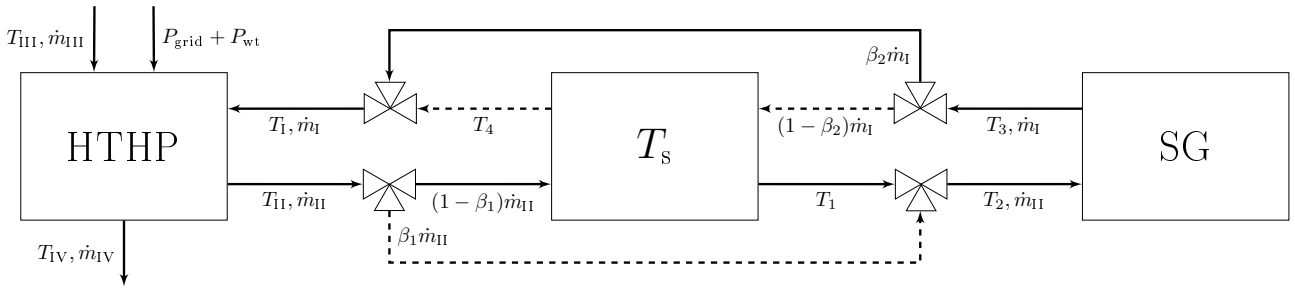

Figure 3: Detailed flow chart [31] of studied system (cf. Fig. 2) including HTHP, TES and SG. HTHP and SG are represented by polynomial surrogate models, while TES is modeled by an effectiveness model. An adjustable fluid bypass $\beta_1 \in [0,1]$ is used to control the heat input to the TES and SG, conversely the bypass $\beta_2 \in [0,1]$ regulates the heat input to the HTHP depending on the thermal state T_{s} of the TES and SG outlet stream. The *solid* and *dashed* lines indicate the charging and discharging mode in a simplified way. In addition, simultaneous charging and discharging is not allowed. For example, *charge* mode is $\beta_1 \in [0,1), \beta_2 = 1$, *discharge* mode implies $\beta_2 \in [0,1), \beta_1 = 1$, and *idle* mode represents $\beta_1 = \beta_2 = 1$.

$$\min\ J(P_{\mathrm{grid}}) = \sum_{k=1}^{n} P_{\mathrm{grid}}^k g_{\mathrm{grid}}^k \Delta t \tag{7}$$

s. t.

$$P_{\mathrm{grid}}^k + P_{\mathrm{wt}}^k = 3F_{\mathrm{HTHP}}\big(T_{\mathrm{I}}^k, \dot{m}_{\mathrm{I}}^k, T_{\mathrm{III}}^k, R^k\big), \quad T_{\mathrm{II}}^k = F_{\mathrm{HTHX}}\big(T_{\mathrm{I}}^k, \dot{m}_{\mathrm{I}}^k, T_{\mathrm{III}}^k, R^k\big), \quad T_{\mathrm{IV}}^k = F_{\mathrm{LTHX}}\big(T_{\mathrm{I}}^k, \dot{m}_{\mathrm{I}}^k, T_{\mathrm{III}}^k, R^k\big) \tag{8}$$

$$T_2^k = T_{\mathrm{II}}^k \beta_1^k + T_1^k\big(1-\beta_1^k\big), \quad T_{\mathrm{I}}^k = T_3^k \beta_2^k + T_4^k\big(1-\beta_2^k\big) \tag{9}$$

$$T_2^k = 201.92 + \tfrac{1819.32}{3\dot{m}_{\mathrm{II}}^k}, \quad T_3^k = 196.3 - \tfrac{188.4}{3\dot{m}_{\mathrm{I}}^k} \tag{10}$$

$$\dot{Q}_{\mathrm{s,ch}}^k = 3\dot{m}_{\mathrm{II}}^k c_{p,\mathrm{f}}\big(T_{\mathrm{II}}^k - T_1^k\big)\big(1-\beta_1^k\big), \quad \dot{Q}_{\mathrm{s,dch}}^k = 3\dot{m}_{\mathrm{I}}^k c_{p,\mathrm{f}}\big(T_4^k - T_3^k\big)\big(1-\beta_2^k\big), \quad \dot{Q}_{\mathrm{s,ch}}^k \dot{Q}_{\mathrm{s,dch}}^k \le \gamma \tag{11}$$

$$T_1^k = T_{\mathrm{II}}^k - \epsilon_{\mathrm{ch}}\big(T_{\mathrm{II}}^k - T_{\mathrm{s}}^{k-1}\big), \quad T_4^k = T_3^k - \epsilon_{\mathrm{dch}}\big(T_3^k - T_{\mathrm{s}}^{k-1}\big), \quad T_{\mathrm{s}}^k = T_{\mathrm{s}}^{k-1} + \tfrac{\dot{Q}_{\mathrm{s,ch}}^k - \dot{Q}_{\mathrm{s,dch}}^k}{m_{\mathrm{s}} c_{p,\mathrm{s}}} \Delta t \tag{12}$$

$$T_{\mathrm{s}}^0 = \widetilde{T}_0, \quad T_{\mathrm{s}}^n = T_{\mathrm{s}}^0 \tag{13}$$

$$T_{\mathrm{I}}^k \in [177, 250],\ \dot{m}_{\mathrm{I}}^k \in [5, 16],\ T_{\mathrm{III}}^k \in [60, 100],\ R^k \in [0.8, 1.53] \tag{14}$$

with a uniformly spaced time grid $t_k = \Delta t_k$ for $k = 1, \ldots, n$, so that the functions are considered only at the discrete time points, i.e. $T_l^k := T_l(t_k)$. The linear objective function (7) relies on the system's operating cost that is directly related to the consumed grid power of the HTHP. The power balance and outlet temperatures of the HTHP are described by (8), where F_{HTHP}, F_{HTHX}, and F_{LTHX} represent the corresponding surrogate models as a function of inlet temperatures, mass flow and rotational shaft speed. The bypass modeling is represented by (9), while (10) reflects the SG surrogate models. The charging and discharging heat flows (11) depend on the HTF mass flow, the temperature level and the fluid flow bypasses. Moreover, charging and discharging at the same time is not allowed. The constraints (12) relate to the TES effectiveness model and the storage temperature change. For a complete set-up, an initial storage temperature $\widetilde{T}_0$ is required, which is assumed to be the same at the end of the operating period (13). The simplified models in (8) are valid within the box constraints in (14), while other variables are naturally limited by the system itself. The factor 3 in (8), (10) and (11) arises because the surrogate models were derived for a single HTHP, but three HTHPs are operated in parallel to keep the component dimensions within a moderate scale.

3.2.2. Optimization Results

This section presents the optimization results of the proposed system for renewable steam generation. We consider a one-day system operation and set the time step to $\Delta t = 1\,\mathrm{h}$, giving the total number of discrete steps $n = 24$. The scenario for the WT power production and the grid electricity price are displayed in Fig. 4

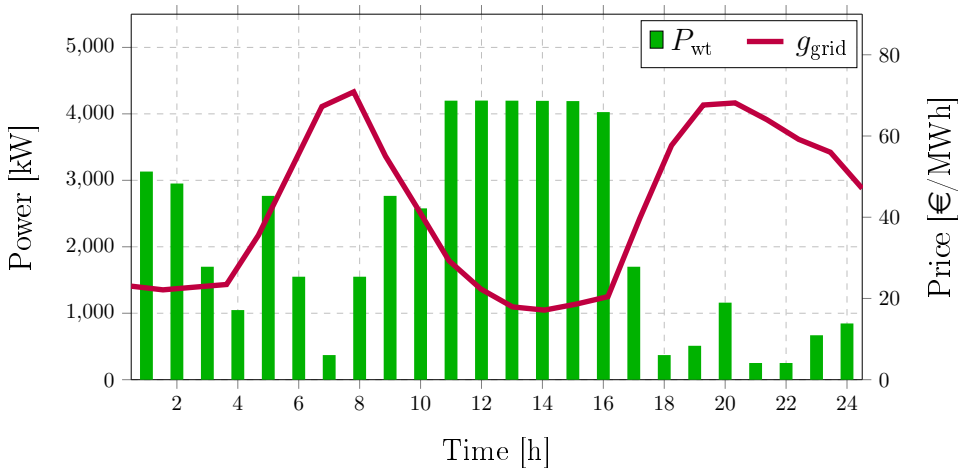

Figure 4: Visualization of 24h reference data P_{wt} (WT power output) and $g_{\text{pr,grid}}$ (electricity price) to minimize operating cost in (7)-(14).

as a function of time during 24h. The time horizon considered, resulting in 408 decision variables controlling the system, makes this test case unfeasible for a commercial global optimization solver like BARON.

The optimization results are presented in Fig. 5. As in Section 3.1., we compare the performance of the proposed BO-IPOPT to MS-IPOPT and BOwLS. The same hyperparameters as in the previous test case are considered. Our numerical experiments are repeated 20 times for averaging out the stochastic nature of the optimizers. We reduce this number with respect to the previous test case because this optimization problem requires larger computational time due to the larger dimension and the large set of equality constraints. Since the global minimum of this optimization problem is unknown, we use MS-IPOPT with 10,000 different initialization points to explore the parameter space. The best result, herein considered as an estimate of the global optimum, lies at 1,046.53€. This optimum is shown in Fig. 5 on the left.

As in the previous test case, BO-IPOPT outperforms the other approaches in convergence and robustness, while both hybrid methods converge faster towards the best reference solution than the MS-IPOPT. The same observations made from the previous test case on the role of the initial point for BO-IPOPT and BOwLS apply to this case. However, it is worth noticing that none of the optimizers approach the best known solution (estimated by the 10,000 IPOPT iterations) within the $K = 300$ outer iterations on average. This, together with the minor improvements achieved by all optimizers, highlights the complexity of the optimization problem at hand. In terms of computational cost, Fig. 5 on the right shows a nearly linear trend for both the hybrid methods and the MS-IPOPT, with the slope being much larger than in the previous test case because of the larger dimensionality of the problem. Nevertheless, this shows that the increased computational cost of the GPR, produced as more samples are available, weighs much less than the objective function evaluation itself for the number of initialization points ($N_0 = 10$) considered in this test case.

The choice of hyperparameters clearly influences the performance of both hybrid methods. Among these, the number of candidates N_{bc} updated via the local solver appears a critical parameter governing the optimization convergence as well as the computational effort. Fig. 6 shows the impact of this hyperparameter in the optimization convergence, both in terms of average convergence and CPU time. A significant increase in the computational cost results in a minor improvement in the convergence. This highlights that much of the cost in the hybrid formulation is due to the local solver and not the GPR updating. Future work will analyze the impact of various hyperparameters in optimization performance with the proposed hybrid method in more depth.

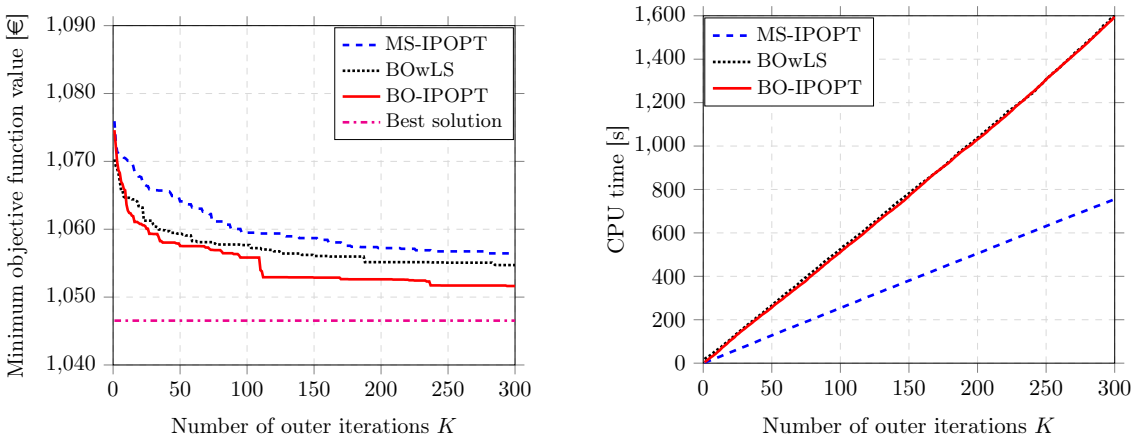

Figure 5: Optimization results for the use case renewable steam generation (7)-(14): comparison of the averaged minimum objective function value (**left**) and averaged CPU time (**right**) over 20 trials using MS-IPOPT, BOwLS and BO-IPOPT in relation to the number of outer iterations K. The best known solution (computed by 10,000 IPOPT iterations) is also visualized as an estimate of the global optimum on the left in the figure.

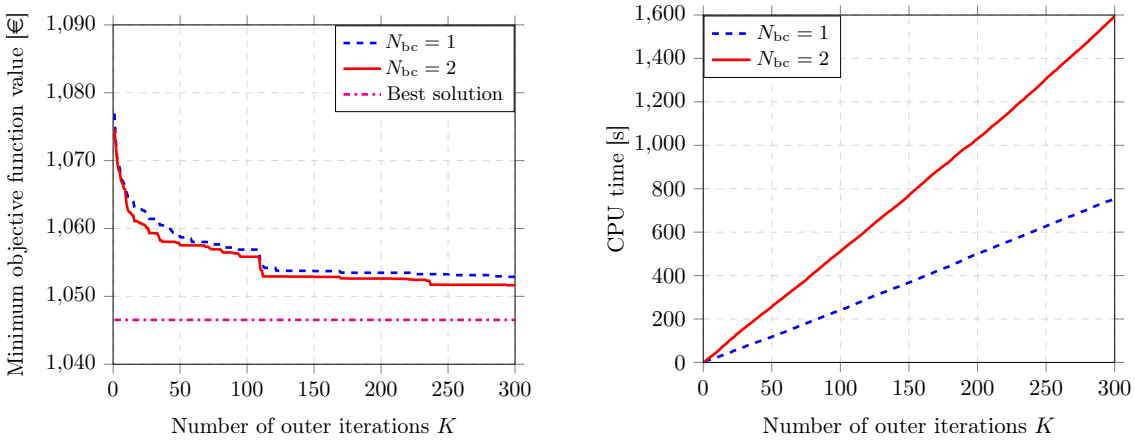

Figure 6: Optimization results for the use case renewable steam generation (7)-(14): comparison of the averaged minimum objective function value (**left**) and averaged CPU time (**right**) over 20 trials using BO-IPOPT with $N_{\mathrm{bc}} = 1$ and $N_{\mathrm{bc}} = 2$ in relation to the number of outer iterations K. The best known solution (computed by 10,000 IPOPT iterations) is also visualized as an estimate of the global optimum on the left in the figure.

4. Conclusion

This work presents a novel method called BO-IPOPT to determine the optimal operation of energy conversion systems. BO-IPOPT beneficially combines Bayesian optimization and Interior Point OPTimizer, allowing profit from the global exploration of the surrogate modelling in the BO with the quasi-Newton local convergence. In BO-IPOPT, BO is made aware of the constraints via penalty terms in the objective function, while IPOPT is naturally aware of the constraints during its updates.

We demonstrate the proposed method in a challenging constrained test case and the optimization of a complex industrial energy conversion system for renewable steam generation. The optimization performance is compared to the classical MS-IPOPT with random initialization and the recently introduced hybrid BOwLS. In both cases, the proposed hybrid method outperforms BOwLS and MS-IPOPT in convergence rate and robustness. The performance gain with respect to BOwLS appears to be linked to the different initialization criteria and the use of surrogate models that approximate the original function. Regarding the computational cost, the overhead of the hybrid methods is mostly linked to the construction of the GPR at each iteration. Nevertheless, this is found to be negligible in both cases. On the other hand, the major increase in the CPU time for both hybrid methods is primarily due to the additional number of best candidates leading directly to more IPOPT evaluations. However, these can be carried out independently and could be easily parallelized. This will be the subject of future work. Finally, future work will address the problem of hyperparameter optimization for BO-IPOPT and consider the sensitivity of its performance to identify the optimal balance between accuracy and computational cost.

Acknowledgments

The authors declare no competing interests. This research did not receive any specific grant from funding agencies in the public, commercial, or not-for-profit sectors.

Nomenclature

Letter symbols

c	specific heat capacity, J/(kgK)
D	set of points
$d(\cdot,\cdot)$	Euclidean distance
EI	expected improvement
F	surrogate model
f	objective function
$\boldsymbol{g}$	set of inequality constraints
g	electricity price, €/(MWh)
$\boldsymbol{h}$	set of equality constraints
$\boldsymbol{I}$	identity matrix
J	operating costs, €
$\boldsymbol{K}$	kernel matrix
K	number of outer iterations
k	kernel function
l	length scale
$\dot{m}$	mass flow, kg/s
m	mass, kg
N	number of points
n	number of dimensions
P	electric power, kW
$\dot{Q}$	heat flow rate, kW
R	rotational shaft speed
T	temperature, °C
$\bar{u}$	objective value of u at $\bar{\boldsymbol{x}}$
$\hat{u}$	GPR model of u
u	objective function with penalty terms
$\bar{\boldsymbol{x}}$	$\boldsymbol{x}$-value of sample points
$\boldsymbol{x}$	n-dimensional decision variable
y	objective value of f at $\boldsymbol{x}$

Greek symbols

α	regularization term of GPR
β	fluid bypass
γ	relaxation parameter
Δt	discrete time step, s
ϵ	effectiveness
$\boldsymbol{\lambda}, \boldsymbol{\rho}$	penalty weight vectors
μ	mean value
ξ	amount of exploration
$\boldsymbol{\Sigma}$	covariance function
σ	standard deviation
Φ	cumulative distribution function
ϕ	probability distribution function
Ω	set of $\mathbb{R}^n$

Subscripts and superscripts

0	starting condition
bc	best candidates
c	candidates
ch	charge mode
dch	discharge mode
f	thermal oil
grid	electricity grid
HTHP	high temperature heat pump
HTHX	high temperature heat exchanger
k	discrete time point
LTHX	low temperature heat exchanger
min	minimum value
p	pressure, N/m^2
s	storage
wt	wind turbine

References

[1] Xu Y., Yan C., Liu H., Wang J., Yang Z., Jiang Y., *Smart energy systems: A critical review on design and operation optimization*. Sustainable Cities and Society 2020;62, Article number:102369.

[2] Lu Y., Wang S., Sun Y., Yan C., *Optimal scheduling of buildings with energy generation and thermal energy storage under dynamic electricity pricing using mixed-integer nonlinear programming*. Applied Energy 2015;147:49-58.

[3] Sass S., Mitsos A., *Optimal operation of dynamic (energy) systems: When are quasi-steady models adequate?*. Computers and Chemical Engineering 2019;124:133-39.

[4] Maleki A., Rosen M.A., Pourfayaz F., *Optimal Operation of a Grid-Connected Hybrid Renewable Energy System for Residential Applications*. Sustainability 2017;9:1-20.

[5] Parisio A., Rikos E., Tzamalis G., Glielmo L., *Use of model predictive control for experimental microgrid optimization*. Applied Energy 2014;115:37-46.

[6] Palma-Behnke R., Benavides C., Lanas F., Severino B., Reyes L., Llanos J., Sáez, D., *A Microgrid Energy Management System Based on the Rolling Horizon Strategy*. IEEE Transactions on Smart Grid 2013;4(2):996-1006.

[7] Ma D., Zhang L., Sun B., *An interval scheduling method for the CCHP system containing renewable energy sources based on model predictive control*. Energy 2021;236, Article number:121418.

[8] Nocedal J., Wright S. J., *Numerical Optimization*. New York, USA:Springer New York; 2006.

[9] Hendrix E. M.T., Tóth B. G., *Introduction to Nonlinear and Global Optimization*. New York, USA:Springer New York; 2010.

[10] Martí R., Lozano J. A., Mendiburu A., Hernando L., *Multi-start Methods*. In: Martí R., Pardalos P. M., Resende M. G. C., editors. Handbook of Heuristics. Springer, Cham. 2018. p. 155-75.

[11] Pardalos P., Tawarmalani M., Sahinidis N. V., *Convexification and Global Optimization in Continuous and Mixed-Integer Nonlinear Programming*. Boston, MA: Springer US; 2002.

[12] Parisio A., Rikos E., Glielmo L., *A Model Predictive Control Approach to Microgrid Operation Optimization*. IEEE Transactions on Control Systems Technology 2014;22(5):1813-27.

[13] Bischi A., Taccari L., Martelli E., Amaldi E., Manzolini G., Silva P., Campanari S., Macchi E., *A detailed MILP optimization model for combined cooling, heat and power system operation planning*. Energy 2014;74:12-26.

[14] Long Q., Wu C., *A Hybrid Method combining Genetic Algorithm and Hooke-Jeeves Method for constrained global optimization*. Journal of Industrial and Management Optimization 2014;10(4):1279–96.

[15] Jeong S, Obayashi S., *Efficient Global Optimization (EGO) for Multi-Objective Problem and Data Mining*. IEEE Congress on Evolutionary Computation; 2005 Sep 02–05; Edinburgh, UK. IEEE:2138-45.

[16] Lan G., Tomczak J. M., Roijers D. M., Eiben A.E., *Time efficiency in optimization with a bayesian-evolutionary algorithm*. Swarm and Evolutionary Computation 2022;69, Article number:100970.

[17] Berk J., Nguyen V., Gupta S., Rana S., Venkatesh S., *Exploration Enhanced Expected Improvement for Bayesian Optimization*. In: Berlingerio M., Bonchi F., Gärtner T., Hurley N., Ifrim G., editors. European Conference: Machine Learning and Knowledge Discovery in Databases; 2018 Sep 10–14; Dublin, Ireland. Springer International Publishing:621-37.

[18] Brochu E., Cora V. M., de Freitas N., *A tutorial on bayesian optimization of expensive cost functions, with application to active user modeling and hierarchical reinforcement learning*. ArXiv 2010;abs/1012.2599.

[19] Hedar A. R., Fukushima M., *Hybrid Simulated Annealing and Direct Search Method for nonlinear unconstrained global optimization*. Optimization Methods and Software 2002;17(5):891-912.

[20] Kelner V., Capitanescu F., Léonard O., Wehenkel L., *A hybrid optimization technique coupling an evolutionary and a local search algorithm*. Journal of Computational and Applied Mathematics 2008;215(2):448-56.

[21] Cherki I., Chaker A., Djidar Z., Khalfallah N., Benzergua F., *A Sequential Hybridization of Genetic Algorithm and Particle Swarm Optimization for the Optimal Reactive Power Flow*. Sustainability 2019;11(14), Article number:3862.

[22] Luo J., Chen Z., Zheng Y., *A gradient-based method assisted by surrogate model for robust optimization of turbomachinery blades*. Chinese Journal of Aeronautics 2022;35(10):1-7.

[23] Zhang D., Zhang B., Wang Z., Zhu X., *An Efficient Surrogate-Based Optimization Method for BWBUG Based on Multifidelity Model and Geometric Constraint Gradients*. Mathematical Problems in Engineering 2021;2021:1-13.

[24] Gao Y., Yu T., Li J., *Bayesian Optimization with Local Search*. In: Nicosia G., Ojha V., La Malfa E., Jansen G., Sciacca V., Pardalos P., Giuffrida G., Umeton R, editors. 6th International Conference: Machine Learning, Optimization, and Data Science; 2020 Jul 19–23; Siena, Italy. Springer International Publishing:350-61.

[25] I. COIN-OR Foundation, *Interior point optimizer (ipopt)* Available at: `https://github.com/coin-or/Ipopt` [accessed 13.3.2023].

[26] Wächter A., Biegler L. T., *On the implementation of an interior-point filter line-search algorithm for large-scale nonlinear programming*. Mathematical Programming 2006;106(1):25-57.

[27] Rasmussen C. E., Williams C. K. I., *Gaussian Processes for Machine Learning*. The MIT Press; 2005.

[28] Pedregosa F., Varoquaux G., Gramfort A., Michel V., Thirion B., Grisel O., Blondel M., Prettenhofer P., Weiss R., Dubourg V., Vanderplas J., Passos A., Cournapeau D., *Scikit-learn: Machine learning in Python*. Journal of machine learning research 2011;12(7):2825-30.

[29] Hart W. E., Watson J. P., Woodruff D. L., *Pyomo: modeling and solving mathematical programs in Python*. Mathematical Programming Computation 2011;3(3):219-60.

[30] Eriksson D., Poloczek M., *Scalable Constrained Bayesian Optimization*. In: Banerjee A., Fukumizu K, editors. Proceedings of The 24th International Conference on Artificial Intelligence and Statistics; 2021 Apr 13-15; San Diego, California, USA. PMLR:730-38.

[31] Walden J. V. M., Bähr M., Glade A., Gollasch J., Tran A. P., Lorenz T., *Nonlinear operational optimization of an industrial power-to-heat system with a high temperature heat pump, a thermal energy storage and wind energy (**accepted**)*. Applied Energy (**online in 2023**).

PROCEEDINGS OF ECOS 2023 - THE 36TH INTERNATIONAL CONFERENCE ON
EFFICIENCY, **C**OST, **O**PTIMIZATION, **S**IMULATION AND ENVIRONMENTAL IMPACT OF ENERGY SYSTEMS
25-30 JUNE 2023, LAS PALMAS DE GRAN CANARIA, SPAIN

Combined Physics-Data Driven Modeling for Design and Operation Optimization of an Energy Concept

Rushit Kansara[a], Michael Lockan[b]

[a] *German Aerospace Center, Institute of Low-Carbon Industrial Processes, Simulation and Virtual Design, Walther-Pauer-Straße 5, Cottbus Germany, rushit.kansara@dlr.de*
[b] *German Aerospace Center, Institute of Low-Carbon Industrial Processes, Simulation and Virtual Design, Walther-Pauer-Straße 5, Cottbus Germany, michael.lockan@dlr.de*

Abstract:
The industrial sector accounts for a huge amount of energy- and process-related CO_2 emissions. One decarbonization strategy is to build an energy concept which provides electricity and heat for industrial processes using combination of different renewable energy sources such as photovoltaic, wind turbine, and solar thermal collector system combined with energy conversion power-to-heat components such as heat pump, electric boiler etc. The challenge for the industries is the economic aspect of the decarbonization, as industries require a cost-efficient solution. The total cost for an industrial energy concept includes investment and operating costs. This complex problem of minimizing cost and emission requires two major tasks: (I) modeling of components and (II) multi-objective coupled design and operation optimization of the energy concept. The optimal design and capacity of the components and optimal system operation depend majorly on the modeling of the components. The modeling of the components is either physics-driven or data-driven. The corresponding multi-objective coupled optimization is a complex problem with a large number of variables and constrains involved. This paper shows different types of physics- and data-driven modeling of energy components for the multi-objective coupled optimization for minimizing cost and emission of an industrial process as a case study. The optimization problem is solved as single-level problem and bi-level problem with different combinations of physics- and data-driven models. Different modeling techniques and their influence on the optimization are compared in terms of computational effort, solution accuracy and optimal capacity of components. The results show that the combination of physics and data-driven models have computational time reduction up to 37% with high accuracy compared to complete physics-driven models for the considered case study. Specific combination of physics-driven and polynomial regression models show the best trade-off between computational speed and accuracy.

Keywords:
energy concept, renewable energy sources, coupled optimization, data-driven modeling

1. Introduction

Sustainable development is one of the most pressing challenges for the industrial sector today. Industrial sector accounts for 34% of the end-energy-related CO_2 emissions in Europe [1]. A very crucial hurdle that needs to be overcome for sustainable future is the immense use of fossil fuels. The associated greenhouse gas emissions require urgent solutions to mitigate their effects on climate. Renewable energy sources (RES) such as wind and solar can be promising alternatives to fossil fuels as they are abundantly available and provide cleaner means of energy [2]. Energy transition concepts such as integrated energy systems (IES) combining RES, conversion components and fuel-based energy generation components could effectively improve the utilization of RES as well as promote the mitigation of CO_2 emissions. Energy-efficiency of such concepts plays a vital role in reducing CO_2 emissions. Efficient design and operation decisions of IES combine ecological and economic aspects; i.e., it does not only have potential for reducing CO_2 emissions, but it also supports significant cost savings as shown in various literature for industrial energy systems [3–5], district and urban energy systems [6–8] and building energy systems [9,10]. The design decisions are determined before and implemented during the development of the energy concept, such as the capacity of the energy components involved. The operation decisions are implemented after development of the energy concept, such as the physical conditions under which the system is operated [11]. However, complex energy component capacity configuration and various operation strategies make further development of such energy concepts for minimizing cost and emission difficult [12].

Multi-objective design and operation optimization is one of the most effective methods for solving such problems [13]. This optimization problem falls under coupled optimization category, where design and operation of the IES have to be optimized together to achieve the multi-objectives such as minimum CO_2 emissions and

minimum costs. Different literature have shown coupled optimization solved with different methods, such as bi-level and single-level optimization. Bi-level solution strategy is where an upper level problem decides the capacity of the components and a lower level decides the operation strategy based on the design decisions from upper level. Single-level solution strategy integrates design and operation optimization in a single mathematical problem. The authors in [7] showed a mixed integer linear program (MILP) of bi-level coupled optimization of district energy systems (DES) for minimizing overall cost as a single objective. In [14] a multi-objective, non-linear coupled optimization with bi-level problem formulation is presented. In [15] single-level MILP multi-objective coupled optimization for buildings is discussed. In [16] topology optimization of DES as MILP single-level formulation with scenario based operating conditions is presented. Above discussed researches have not majorly focused on industrial processes with multi-objective single-level coupled optimization. In this paper the multi-objective coupled design and operation optimization problem of an energy concept is solved using single-level as well as bi-level methods.

Modeling is an important aspect of energy system's design and operation optimization. Physics-driven modeling of energy components are majorly non-linear involving large number of variables and constraints, which makes the coupled optimization computationally expensive [16]. Data-driven models have opened new possibilities for energy system modeling [17]. Data-driven models could imitate the same physical relations hidden in the data sets without focusing on physical description of the process, which makes them quite flexible to use in an optimization problem [18]. The recent advancement in machine learning (ML) has a capability to handle high complexity of such energy system modeling arising from non-linearity of the physics [17]. In this paper data-driven models for solar thermal (ST) collector system and heat pump (HP) are used to formulate reduced order optimization problem and are compared with the physics-driven counterparts in terms of accuracy, computational efforts and optimal capacity of components. Comparison is carried out for both single-level and bi-level multi-objective optimization problem to show the optimization results' consistency.

2. Methods

The coupled design and operation optimization problem in this paper is formulated for a case study energy concept of a small- to medium-sized food and cosmetic company in Germany. Fig. 1 shows the proposed initial energy concept for the case study. It includes RES such as photovoltaic (PV), wind turbine (WT), ST; energy conversion components such as HP, gas boiler (GB), electric boiler (EB); electric grid (EG) and gas grid (GG) to suffice the consumption demand of the production. The heat is required for the steam generation, which is further used for heating and pasteurizing the products in batches. Electricity producing components and electricity consuming components are connected to an electricity hub (EH). In the same manner heat producing and consuming components are connected to a heat hub (HH). Energy storage components such as battery-storage (BAT) and thermal energy storage (TES) are not considered in this paper for the optimization, but can be integrated in future energy concepts for higher flexibility of operation. The coupled optimization

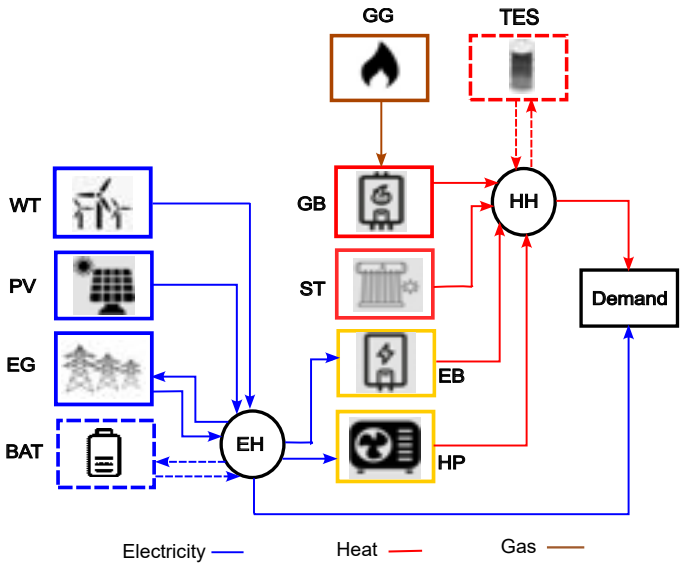

Figure 1: Concept of IES

problem of the energy concept shown in Fig. 1 is complex due to large number of continuous variables such as capacity of the components, power consumption of the components etc., and binary variables such as existence of component in the energy concept are involved with non-linear modeling of the energy components consisting large number of constraints. The total number of variables and constraints involved in this

optimization problem are 1741 and 2748, respectively. It falls under the general category of mixed-integer non-linear programming (MINLP) non-convex problems, which is computationally very expensive to solve [19]. Different types of physics- and data-driven models are integrated into multi-objective coupled optimization. Physics-driven modeling of the components is majorly followed as described in [20]. Solution accuracy and computational efforts of different models in optimization are compared later in section 3. The time horizon for

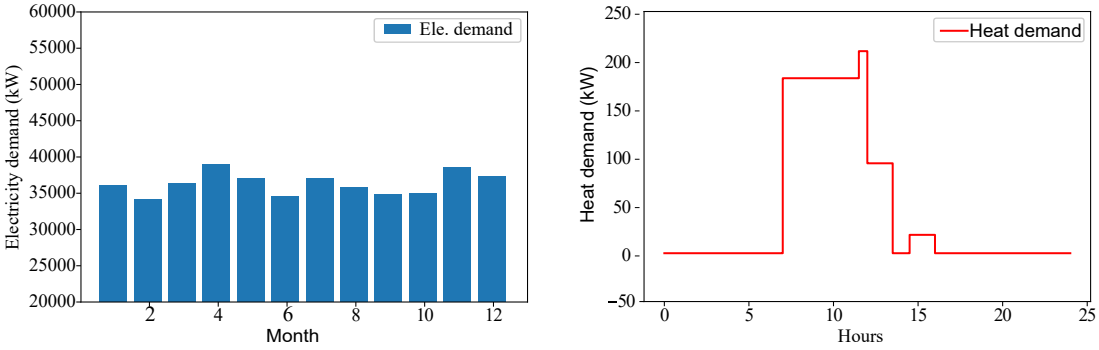

(a) Electricity demand

(b) Heat demand

Figure 2: Monthly electricity and daily heat demand of the case study considered

the operation optimization is 1 year with an hourly time-step. The operation of the plant takes place for 5 days in a week daily for 8 hours. 21 days in a month are working days and 9 days are assumed to be off-days. The operation of the plant is assumed to be scenario-based for the optimization, where 1 working day and 1 off-day in each month are taken as the representative days. The heat demand for working day is shown in Fig. 2 (b). It can be seen that heat demand is divided into 4 operating scenarios for different operating hours on a working day for different batch processes. Off-days have base load requirement of 200 kWh of electricity. Monthly electricity demands are shown in Fig. 2 (a).

2.1. Problem formulation

This case study problem has two objectives to minimize: Total annualized cost (TAC) and global warming impact (GWI). TAC includes investment cost C and operational cost OC. The production facility of the case study is already built. The investment cost for building the facility is excluded. GWI is the measurement of the CO_2 emission. The minimization problem is formulated as

$$\min_{\mathbf{x},\mathbf{y}}[TAC(\mathbf{x},\mathbf{y}), GWI(\mathbf{x},\mathbf{y})], \tag{1}$$

with TAC and GWI as the minimization objectives. The first minimization objective TAC includes operational cost of the energy concept and investment cost of each component, which is defined as

$$TAC(\mathbf{x},\mathbf{y}) = OC(\mathbf{x},\mathbf{y}) + \sum_{i\in S} C^i(x^i), \tag{2}$$

where, the operational costs depends on the net electricity and gas bought from the grids. Which is shown as

$$OC(\mathbf{x},\mathbf{y}) = \sum_{m\in M}(p^{el}_{buy}\cdot E^{el}_{in,m} - p^{el}_{sell}\cdot E^{el}_{out,m}) + p^{gas}_{buy}\cdot E^{gas}_{in,m}), \tag{3}$$

and the investment cost C^i of each component is represented as

$$C^i = \left(\frac{(\beta+1)^\tau\cdot\beta}{(\beta+1)^\tau - 1} + \alpha\right)\cdot CAPEX, \tag{4}$$

which includes capital expenditure $CAPEX$, maintenance cost factor α, interest rate β and time horizon τ for financing cost [20]. $CAPEX$ is calculated based on reference capacity x^i of each component as

$$CAPEX = CAPEX^0\cdot\left(\frac{x^i}{x^0}\right)^\gamma, \tag{5}$$

where, γ represents the scaling exponent for the nominal capacity [20]. The second minimization objective GWI is presented as

$$GWI(\mathbf{x},\mathbf{y}) = \sum_{m\in M}(g^{el}\cdot(E^{el}_{in,m} - E^{el}_{out,m}) + g^{gas}\cdot E^{gas}_{in,m}), \tag{6}$$

where, $M = \{Jan, Feb...., Dec\}$ and $S = \{PV, WT, SH, GB, EB, HP\}$. $\mathbf{x} = [A^{PV}, P^{WT}_{nom}, Q^{GB}_{nom}, Q^{EB}_{nom}, Q^{HP}_{nom}]$ are the design variables and $\mathbf{y} = [E^{el}_{in,m}, E^{el}_{out,m}, E^{gas}_{in,m}]$ are the operational variables for the objective function. GWI is calculated based on the net buying of electricity and gas from the grid. Each net consumed unit of electricity $E^{el}_{in,m} - E^{el}_{out,m}$ and gas $E^{gas}_{in,m}$ has been given corresponding CO_2 factors g^{el} and g^{gas}, respectively, for the calculation of GWI. Parameters for the OC and GWI are shown in Table 1. Table 2 shows the parameters for calculating investment cost of each component and it also shows the minimum part load requirement λ_{min} for the components.

Table 1: Cost and emission parameters for grids taken from [20, 21]

Name	Parameter	Value
electricity buying price	p^{el}_{buy}	0.31 [€]
electricity selling price	p^{el}_{sell}	0.06 [€]
gas buying price	p^{gas}_{buy}	0.15 [€]
CO_2 factor for net consumed electricity	g^{el}	0.349 $[kg - CO_2eq/kWh]$
CO_2 factor for consumed gas	g^{gas}	0.244 $[kg - CO_2eq/kWh]$

The heat demand constraint is shown as

$$Q^{dem} - (Q^{ST} + Q^{GB} + Q^{EB} + Q^{HP}) \leq 0, \tag{7}$$

which indicates that the heat generated from ST, GB, EB and HP should fulfill the heat demand of the production in each time step. Constraint on the capacity of the components is shown as

$$x^i_{min} \cdot z^i \leq x^i \leq x^i_{max} \cdot z^i \qquad \forall i \in \mathbf{x} \quad and \quad z^i \in \{0, 1\}, \tag{8}$$

where, x^i_{min} and x^i_{max} are the lower and upper bounds of the capacity of each components. z is the binary variable, which is linked to the existence of the component in the concept. Equations (1)-(8) represent single-level multi-objective coupled design and operation optimization problem.

Table 2: Component parameters for investment costs and part-load constraints [20]

Components	reference capacity x^0	$CAPEX^0$[€]	γ	α	β	τ[a]	λ_{min}
PV	A^0 $[m^2]$	1400	0.95	0.01	0.03	10	0
WT	P^0_{nom} $[kW]$	5000	0.95	0.03	0.03	10	0.33
ST	A^0 $[m^2]$	400	0.95	0.02	0.03	10	0
GB	Q^0_{nom} $[kWh]$	2700	0.45	0.02	0.03	10	0.2
EB	Q^0_{nom} $[kWh]$	70	0.95	0.01	0.03	10	0
HP	Q^0_{nom} $[kWh]$	1655	0.66	0.02	0.03	10	0

2.2. Modeling of components

Modeling of the components is a crucial part of the optimization problem. In this subsection, for each component integrated in the energy concept either a physics-driven and/or data-driven models are explained. List of all variables, constant parameters and input parameters for physics-driven component modeling is presented in Table 3.

2.2.1. Photovoltaic

The electrical power P^{PV}_{out} generated by the PV unit is constrained by the solar irradiance I, the efficiency of PV unit η^{PV} and total area A^{PV}_{nom} of the PV system. It is represented by

$$P^{PV}_{out} \leq A^{PV}_{nom} \cdot \eta^{PV} \cdot I. \tag{9}$$

The case study facility already has some PV panels built on the terrace, with a tilt angle 5° for the PV model. Moreover, PV unit has the maximum output power limited to its nominal capacity, which is presented as

$$P^{PV}_{out} \leq A^{PV}_{nom} \cdot P^{PV}_{nom}, \tag{10}$$

Table 3: Component variables including binary variables, parameters and inputs for single-level problem

Components	Design variables **x**	Operational variables **y**	Constant parameters **c**	Input paramters in each timestep	Total number of variables
PV	A_{nom}^{PV}	P_{out}^{PV}	η^{PV},P_{nom}^{PV}	I	3
WT	P_{nom}^{WT}	λ^{WT},P_{out}^{WT}	-	v	4
GB	Q_{nom}^{GB}	λ^{GB}, E_{in}^{gas}	η^0	-	4
EB	P_{nom}^{EB}	λ^{EB}, P_{in}^{EB}	η^{EB}	-	4
ST	A_{nom}^{ST}	T_{out}^{w}, T_{out}, T_{in}	I_{AM}, η_0, $\dot{m}^{ST}$	I, T_{amb}, $\dot{m}^{w}$	5
HP	Q_{nom}^{HP}	λ^{HP}, h_{out}^{w}, T_{out}^{w}, P_{in}^{HP}	a, b, c, d, T_{in}^{c}, T_{in}^{w}	$\dot{m}^{w}$	6
Electric grid	-	E_{in}^{el}, E_{out}^{el}	-	-	2
Gas grid	-	E_{in}^{gas}	-	-	1

where, P_{nom}^{PV} is chosen as 0.171 kWm^{-2} [20] and efficiency η^{PV} is chosen to be 0.09 in order to meet the actual output data of PV panels built on the case study facility. P_{out}^{PV} is an operational variable and A_{nom}^{PV} of the unit is a design variable. Total number of variables in Table 3 shows number of design, operational and binary variables to be computed in each time step in optimization problem.

2.2.2. Wind turbine

The power output P_{out}^{WT} of WT is limited by the wind velocity, which in turn determines the part-load behavior of WT and its nominal power [22]. The output power of WT is given by

$$P_{out}^{WT} \leq \eta^{WT}(\lambda^{WT}) \cdot P_{nom}^{WT}, \tag{11}$$

where, P_{out}^{WT} is an operational variable and P_{nom}^{WT} of the wind turbine is a design variable. Operational variable λ^{WT} depends on the wind velocity ($\lambda^{WT} = v/v_{ref}$, where $v_{ref} = 12m/s$ [20]). The efficiency of wind turbine $\eta^{WT}(\lambda^{WT})$ is given by

$$\eta^{WT}(\lambda^{WT}) = \begin{cases} 0 & \text{if } \lambda^{WT} \leq 0.33 \\ 1.5393 \cdot \lambda^{WT} - 0.5091 & 0.33 \leq \lambda^{WT} \leq 1 \\ 1 & \lambda^{WT} \geq 1. \end{cases} \tag{12}$$

2.2.3. Gas boiler

Heat output of the GB is determined by the part-load efficiency, which is given as

$$\eta^{GB}(\lambda^{GB}) = \frac{21.75378 \cdot \lambda^3 - 7.00130 \cdot \lambda^2 + 1.39731 \cdot \lambda - 0.07557}{20.66646 \cdot \lambda^3 - 5.34196 \cdot \lambda^2 + 0.67774 \cdot \lambda + 0.03487} \cdot \eta^0, \tag{13}$$

where η^0 is chosen to be 0.8 [1], which is called nominal efficiency. The heat output depends on the efficiency shown in (13), consumed gas power to heat up the incoming fluid P_{in}^{gas} and nominal capacity Q_{nom}^{GB}, which is presented as

$$Q_{out}^{GB} = \eta^{GB}(\lambda^{GB}) \cdot P_{in}^{gas}, \qquad Q_{out}^{GB} = \lambda^{GB} \cdot Q_{nom}^{GB}. \tag{14}$$

Here, heat output Q_{out}^{GB}, consumed power P_{in}^{gas} and the part-load λ^{GB} are operational variables and nominal capacity Q_{nom}^{GB} is the design variable. The integration of consumed power P_{in}^{gas} over the operation horizon delivers the total energy E_{in}^{gas} consumed from gas grid.

2.2.4. Electric boiler

EB is modeled in the same manner as GB. Efficiency η^{EB} for EB is assumed to be constant at 0.95. The operational variable heat output of the EB depends on operational variables such as consumed electric power P_{in}^{EB}, part-load λ^{EB} and design variable nominal capacity Q_{nom}^{EB}. It is shown as

$$Q_{out}^{EB} = \eta^{EB} \cdot P_{in}^{EB}, \qquad Q_{out}^{EB} = \lambda^{EB} \cdot Q_{nom}^{EB}. \tag{15}$$

2.2.5. Solar thermal collector

There are two kinds of ST collectors generally used in the market, flat plate and evacuated tube. For this case study, flat plate collectors with tilt angle of 40° are chosen to be integrated in the energy concept [23]. ST model is based on the quadratic efficiency model developed by [24], which is shown as

$$\eta^{ST} = \eta_0 - \frac{a_1 \cdot \Delta T}{I} - \frac{a_2 \cdot \Delta T^2}{I}, \tag{16}$$

where η_0 represents optical collector efficiency, a_1 and a_2 are loss coefficients related to linear and quadratic terms, ΔT represents temperature difference between collector fluid temperature and ambient temperature, and I as mentioned before is global solar irradiance on the collector surface. European EN 19275 standards prescribe the collector fluid temperature as average collector temperature of its inlet and outlet temperature [25].

Complete hourly weather data for the location of the case study plant has been gathered from European commission photovoltaic geographical information system [26]. The global solar irradiance and ambient temperatures are the important data for the ST collector model. Complete physical ST collector model is shown in (17) - (20). The ST collector efficiency is shown as

$$\eta^{ST} = \eta_0 \cdot I_{AM} - \frac{a_1 \cdot (T_m - T_{amb})}{I} - \frac{a_2 \cdot (T_m - T_{amb})^2}{I}, \tag{17}$$

where, I_{AM} represents incidence angle modifier, which corrects the optical efficiency for the irradiation not perpendicular to the surfaces [23]. T_m is the average collector fluid temperature, which depends on inlet and outlet temperature T_{in}^{ST} and T_{out}^{ST}, respectively. The optical collector gain is represented by

$$Q_0 = \eta_0 \cdot I_{AM} \cdot I \cdot A_{nom}^{ST}, \tag{18}$$

and thermal losses due to temperature difference between average fluid temperature and ambient temperature is modeled as

$$Q_L = \left(a_1 \cdot (T_m - T_{amb}) - a_2 \cdot (T_m - T_{amb})^2\right) \cdot A_{nom}^{ST}, \tag{19}$$

where, collector surface area is A_{nom}^{ST} of the collector surface is the design variable.

$$Q_u = \begin{cases} Q_0 - Q_L, & \text{if } Q_0 > Q_L \\ 0 & \text{if } Q_0 \leq Q_L \end{cases} \tag{20}$$

Equation (20) shows the useful solar gains with the condition of positive net solar gains. The authors in [23] compared this simplified physical model with detailed simulation model in TRNSYS. The parameters for the physical models are collected in [27], in which extensive research has been carried out for different ST flat collector manufacturers data in Germany and related parameters. Parameters chosen for the case study are shown in Table 4. Fig. 3(a) shows the ST collector with the heat-exchanger (HEX) used in the energy concept. The heat transfer over HEX is given by

$$Q^{ST} = \dot{m}^w \cdot c_p^w \cdot (T_{out}^w - T_{in}^w). \tag{21}$$

For calculating the operational variable heat transfer Q^{ST} over HEX in each time step, 5 different equations (17)-(21) must be solved in the physical model, which consist 3 additional operational variables such as collector inlet temperature T_{in}^{ST}, collector outlet temperature T_{out}^{ST}, water/steam outlet temperature T_{out}^w and one design variable, area A_{nom}^{ST} of the collector surface. Large number of variables and constraints make the optimization expensive. In order to reduce the number of variables and constraints, data-models are trained and used in the optimization.

Data-driven approach to model ST collector could have some advantages over physical model. Proposed data-driven approach is presented as

$$Q^{ST} = f(T_{in}^w, \dot{m}^w, I, A_{nom}^{ST}), \tag{22}$$

where, operational variable heat output of the whole ST collector system depends on 4 inputs. These inputs include only one design variable A_{nom}^{ST}, 3 input parameters T_{in}^w, $\dot{m}^w$, I and none of the operational variables shown before. f in (22) represents a generic data-driven model. This data-driven model represents the relationship between the given input parameters including the design variable area A_{nom}^{ST} with the output variable heat output Q^{ST}. In this paper data-driven models such as linear regression (LR), polynomial regression (PR) and artificial neural network (ANN) are considered. These data-driven models are trained with the input and output data generated from the physical model. In this manner, operational variables to be optimized are reduced to 1 in each time step and all other constraints are eliminated.

Table 4: Parameters for ST flat collector

Collector	η_0	a_1 $[W/(m^2K)]$	a_2 $[W/(m^2K)]$	IAM
Flat plate	0.79	4.03	0.0078	0.86

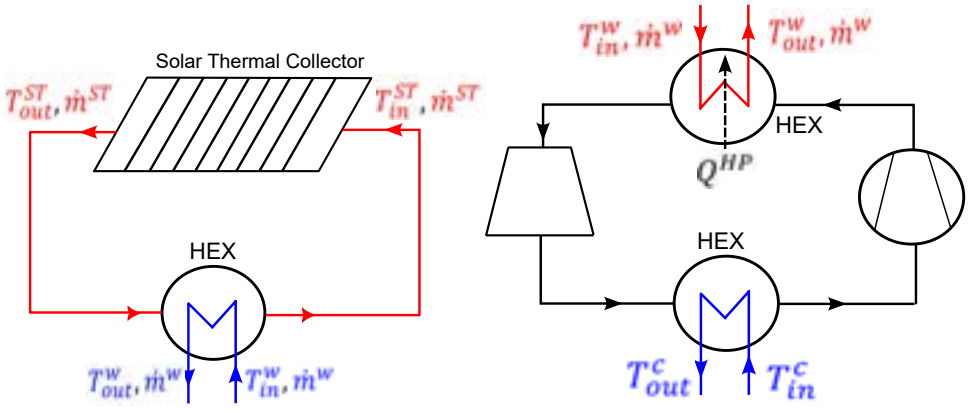

(a) Solar flat plate collector with HEX

(b) HP consisting a compressor, 2 HEX and a turbine

Figure 3: ST collector and HP schematic diagram

2.2.6. Heat pump

HP can use the industrial waste heat as a thermal energy source as well as renewable electricity as the power input to decarbonize industrial thermal processes, which makes it an essential technology [28]. In this case study, waste heat is considered as constant. Renewable electricity is generated from PV and WT. There are many different physical models to describe the performance of the HP. The authors in [28] have investigated different case studies of different types of HPs and came up with different coefficient of performance (COP) regression models. Fig. 3(b) shows a heat pump consisting of two HEXs (condenser and evaporator), a compressor and a turbine. T^c_{in} and T^c_{out} represent input and output temperatures on cold side, whereas T^w_{in} and T^w_{out} are the input and output temperatures on the hot side, respectively. The heat output of the HP depends on its nominal capacity Q^{HP}_{nom} and part-load λ^{HP}, which is shown as

$$Q^{HP}_{out} = \lambda^{HP} \cdot Q^{HP}_{nom}. \tag{23}$$

The output temperature T^w_{out} on the hot side depends on the outlet pressure of water/steam p^w_{out} on hot side and enthalpy h^w_{out} of water/steam, which is a function of heat output Q^{HP}_{out} and inlet temperature T^w_{in} of water on the hot side, shown as

$$T^w_{out} = f(h^w_{out}(Q^{HP}_{out}, T^w_{in}), p^w_{out}). \tag{24}$$

The COP is calculated based on the model

$$COP = a \cdot (\Delta T_{lift} + 2b)^c \cdot (T^w_{out} + b)^d, \tag{25}$$

suggested by [28]. The coefficients a,b,c and d of this model are chosen according to the suitable temperature ranges of the case study ($80°C < T^w_{out} < 160°C$). The heat output is a function of COP and the consumed electrical power P^{HP}_{in}, as well as the input and output enthalpy h^w_{in} and h^w_{out} of water/steam on hot side, which is shown as,

$$Q^{HP}_{out} = COP \cdot P^{HP}_{in}, \qquad Q^{HP}_{out} = \dot{m}^w \cdot (h^w_{out} - h^w_{in}). \tag{26}$$

Equation (23)-(26) represent the physics-driven model of HP. The detailed list of design and operational variables of HP are shown in Table 3. As seen from the physical model, 5 different equations need to be solved in each time step, which include 5 operational variables Q^{HP}_{out}, COP, P^{HP}_{in}, λ^{HP}, T^w_{out} and one design variable Q^{HP}_{nom}. Data-driven approach for HP is shown as

$$COP = f(\dot{m}^w, T^c_{in}, \lambda^{HP}, Q^{HP}_{nom}), \tag{27}$$

which includes 1 design variable Q^{HP}_{nom}, 1 operational variable λ^{HP} and 2 input parameters $\dot{m}^w$ and T^c_{in} as inputs to compute the output variable COP without any constraints. Table 5 shows the total number of variables and

constraints over the whole time-horizon for the single-level multi-objective coupled optimization. It is evident from Table 5 that the total number of variables and constraints involved in coupled optimization problem decreases with the use of data-driven models compared to the complete physics-driven models of ST and HP. Data-driven models for ST and HP reduce the number of variables by 388 and constraints by 504, which is 22% and 18% less than the complete physics-driven models.

Table 5: Total number of variables and constraints in single-level multi-objective coupled optimization problem for different combinations of physics-driven and data-driven models of HP and ST

ST	HP	Total number of variables	Total number of constraints
Physics-driven	Physics-driven	1741	2748
Data-driven	Data-driven	1353	2244
Data-driven	Physics-driven	1525	2316
Physics-driven	Data-driven	1669	2676

3. Results

3.1. Comparison of data-driven models

As shown in Table 5, the data-driven models have fewer variables and constraints to compute in coupled optimization. Table 6 shows the inputs, outputs, number of parameters and amount of data samples. This data samples are divided into training and validation data. 75% of the data samples is used for training the models and 25% of the data samples is used for validating the trained models. Table 7 shows the training time and comparison of accuracy between physical models (actual values) and different data-driven models (predicted values) based on coefficient of determination R^2 method [29]. Three types of data-driven models: LR, PR

Table 6: Data-driven models' input, output and number of samples

Component	Inputs	Output	Number of data samples
ST	T_{in}^{w}, $\dot{m}^{w}$, I, A	Q^{ST}	439199
HP	$\dot{m}^{w}$, T_{in}^{c}, λ^{HP}, Q_{nom}^{HP}	COP	206054

and ANN are trained for ST and HP. In particular, PR models have two variant such as 2^{nd} degree PR (PR-1) and 3^{rd} degree PR (PR-2) models. Furthermore, ANNs are feed forward neural networks with two different specifications: (I) 2 hidden layers, 5 neurons in each hidden layer (ANN-1) (II) 3 hidden layers, 7 neurons in each hidden layer (ANN-2). The number of hidden layers and number of neurons in each hidden layer are optimized using hyper-parameter tuning technique. ANNs are trained with k-fold cross validation method with k=4 [30].

It can be seen from Table 7 that the R^2 score of ST is less for ANN-2 compared to ANN-1. See also Fig. 4 (b), where for ANN-2 the predicted output data does not match properly with actual output data. In contrast, Fig. 5 shows results for the two different ANN models of HP, where ANN-2 showing better fitting performance

Table 7: Data-driven models' training time and accuracy

Model	Specification	Training time for ST [s]	Training time for HP [s]	R^2 for ST	R^2 for HP
LR	degree 1	2.12	1.82	0.96	0.45
PR-1	degree 2	5.33	4.31	0.972	0.68
PR-2	degree 3	11.26	9.25	0.986	0.825
ANN-1	2 hidden layers 5 neurons each	1254	1008	0.999	0.862
ANN-2	3 hidden layers 7 neurons each	1852	1369	0.845	0.982

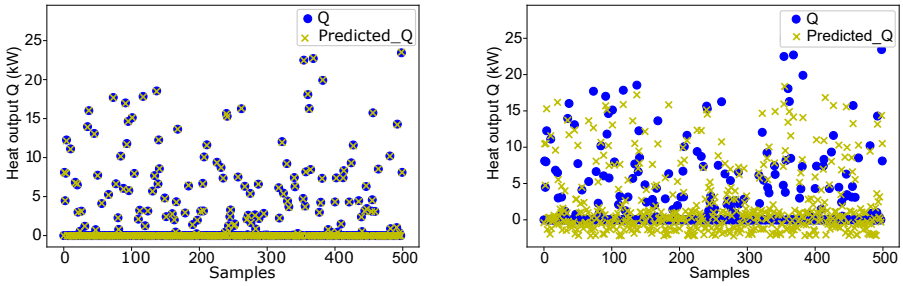

(a) ANN-1 (2 layers, 5 neurons each)

(b) ANN-2 (3 layers, 7 neurons each)

Figure 4: Comparison of ANN models output prediction to actual output of ST

compared to ANN-1. Therefore, the optimized ANN for ST is ANN-1 and for HP is ANN-2. As expected, LR and PR models for HP have lower values of R^2 score compared to ANN models. On the other hand ST has quite higher R^2 score for LR and PR models. Training time for LR and PR models are lesser than their respective ANN models. Training time for ANN is higher due to large number of weights and biases involved in the ANN model. ANN-1 model and ANN-2 model have 35 and 112 such coefficients (and constants), respectively, which makes them time-expensive to compute when these ANN models are integrated into the coupled optimization.

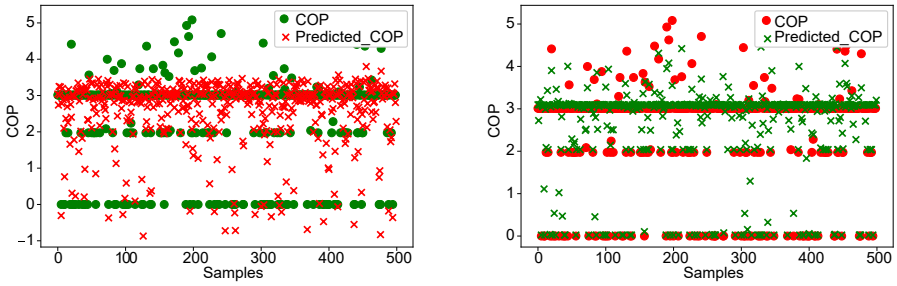

(a) ANN-1 (2 layers, 5 neurons each)

(b) ANN-2 (3 layers, 7 neurons each)

Figure 5: Comparison of ANN models output prediction to actual output of HP

3.2. Comparison of optimization results

Fig. 6 shows several Pareto-fronts of TAC and GWI as results of multi-objective coupled design and operation optimization of the case study energy concept. These pareto-fronts are formed by various combinations of physics- and data-driven models. In particular, Fig. 6 (a) shows the single-level optimization results and (b) shows bi-level optimization results for different combinations of ST and HP models. The optimal Pareto-front of complete physics-driven model (black dots) of the IES is used as the reference solution to evaluate the accuracy and computational effort of the different model combinations.

The original multi-objective MINLP optimization problem is linearized and converted into a MILP optimization problem. The MILP problem is solved with GUROBI solver [31] on PYOMO platform included in COMANDO [22]. More specifically, the single level multi-objective pareto-front is generated by the augmented ϵ-constraint method [32]. Bi-level problem is not linearized and solved on PYMOO platform with non-sorting genetic algorithm (NSGA-II) on the design level and differential evolution on the operation level [33]. Both optimization problems, single-level and bi-level problem, are solved on 11th Gen Intel(R) Core(TM) i7-1185G7 with 16 GB RAM. It can be seen from Fig. 6 (a) and Fig. 6 (b) that the physics-driven model of HP with ANN-1 data-driven model of ST (blue dots) gives the most accurate results, which is close to the complete physics-driven model. The second most accurate result is provided by physics-driven model of HP and PR-2 data-driven model of ST (violet dots). This trend applies to both, single-level and bi-level optimization.

Fig. 7 shows the comparison of computational time and solution accuracy of the coupled optimization results for combination of different models. Accuracy is calculated based on R^2 method, where complete physics-driven model is reference. It can be seen that the best trade-off between computational time and accuracy is found for HP physics-driven model and ST PR-2 model (violet dots). This combination of models reduces the coupled optimization computation time up to 37% with optimization results being approximately 90% accurate

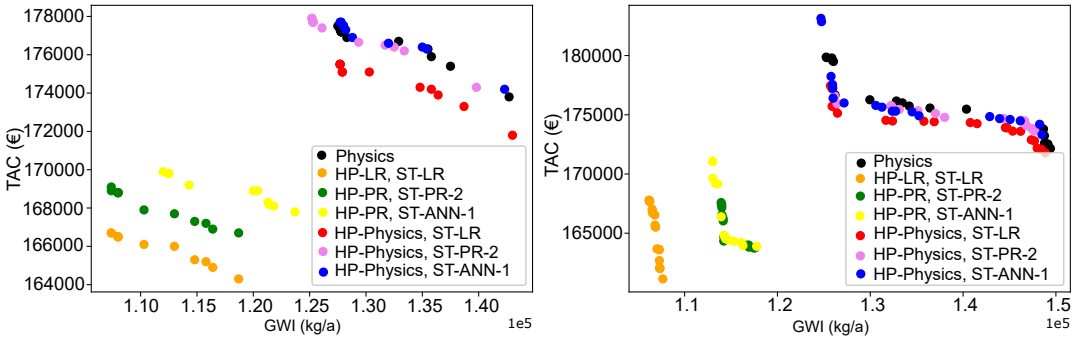

(a) Single-level coupled optimization

(b) Bi-level coupled optimization

Figure 6: Comparison of the optimization results for different model combinations of ST and HP

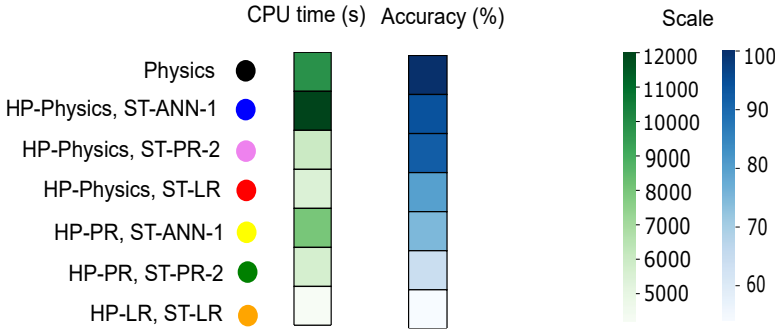

Figure 7: Time and accuracy comparison for different combination of models in single-level multi-objective optimization

compared to complete physics-driven models. In contrast, ST ANN-1 model with HP physics-driven (blue dots) model in coupled optimization is also very accurate, but the computational time for solving the coupled optimization problems with ANN-models are very high due to large number of weights and biases.

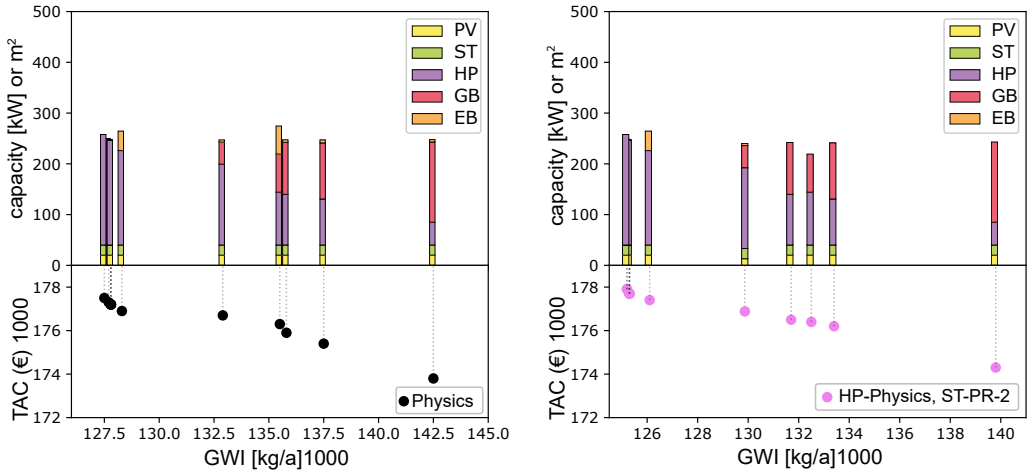

(a) Complete physics-driven model

(b) HP-Physics, ST-PR-2 model

Figure 8: Capacity of components for reference solution and best trade-off solution for single-level coupled optimization

Fig. 8 shows the optimal capacity of the components for the total physics-driven models and the best trade-off combination of physics- and data-driven models, which is chosen based on best trade-off between computational time and solution accuracy according to Fig. 7. Both Fig. 8 (a) and 8 (b) show that for minimum TAC small HP and large GB is required to meet the heating demand, while for minimum GWI large HP is required. The size of ST and PV remains almost constant in all of the Pareto-results. In some solutions, EB is needed

when HP and GB are not sufficient to provide the required heat. The optimal capacity of the components follow a similar trend for complete physics-driven and combined physics-data-driven models, demonstrating the credibility of the combined models.

4. Conclusion and outlook

This paper showed a multi-objective coupled design and operation optimization of an energy concept of a food and cosmetic industry as a case study. Single-level optimization for minimizing TAC and GWI as well as design and operation variables for each component involved is described. The aim of this paper is to compare different types of physics- and data-driven models and to integrate them into a coupled optimization problem to reduce the computational time while maintaining the accuracy of the optimization results. The results showed that the combination of data-driven PR model of ST and physics-driven HP model better than all other combinations in terms of computational time and solution accuracy. The accuracy of the optimization result is up to 90% compared to complete physics-driven model and the computational time is reduced by 37%.

Future work for this case study is to include energy storage models into the energy concept. Integration of thermal and electrical storage can increase the flexibility. Different scenarios such as retrofit designs, greenfield designs, cost neutral solutions and emission free solutions can be optimized for the given case-study and different design-operation solutions can be provided. Combination of physics-data models can be very useful in optimizing these scenarios at less computational efforts and high accuracy.

References

[1] P. Voll, C. Klaffke, M. Hennen, A. Bardow. *Automated superstructure-based synthesis and optimization of distributed energy supply systems*. Energy 2013; 50:374–388; doi:10.1016/j.energy.2012.10.045.

[2] M. J. Mayer, A. Szilagyi, G. Grof. *Ecodesign of ground-mounted photovoltaic power plants: Economic and environmental multi-objective optimization*. Journal of Cleaner Production 2021; 278: 123934; doi:10.1016/j.jclepro.2020.123934.

[3] O. Aguilar, S. J. Perry, J.-K. Kim, R. Smith. *Design and optimization of flexible utility systems subject to variable conditions*. Chemical Engineering Research and Design 2007; 85 (8):1149-1168; doi:10.1205/cherd06063.

[4] P. Velasco-Garcia, P. S. Varbanov, H. Arellano-Garcia, G. Wozny. *Utility systems operation: Optimisation based decision making*. Applied Thermal Engineering 2011; 31 (16):3196-3205; doi:10.1016/j.applthermaleng.2011.05.046.

[5] G. M. Tina, G. Passarello. *Short-term scheduling of industrial co-generation systems for annual revenue maximisation*. Energy 2012; 42(1):46-56; doi:10.1016/j.energy.2011.10.025.

[6] C. Bouvy, K. Lucas. *Multicriterial optimisation of communal energy supply concepts*. Energy Conversion and Management 2007; 48 (11):2827-2835; doi:10.1016/j.enconman.2007.06.046.

[7] C. Weber, N. Shah. *Optimisation based design of a district energy system for an eco-town in the united kingdom*. Energy 2011; 36 (2):1292-1308; doi:10.1016/j.energy.2010.11.014.

[8] J. Keirstead, N. Shah. *Calculating minimum energy urban layouts with mathematical programming and monte carlo analysis techniques*. Computers, Environment and Urban Systems 2011; 35 (5):368-377; doi:10.1016/j.compenvurbsys.2010.12.005.

[9] M. A. Lozano, J. C. Ramos, M. Carvalho, L. M. Serra. *Structure optimization of energy supply systems intertiary sector buildings*. Energy and Buildings 2009; 41 (10):1063-1075; doi:10.1016/j.enbuild.2009.05.008.

[10] P. Liu, E. N. Pistikopoulos, Z. Li. *An energy systems engineering approach to the optimal design of energy systems in commercial buildings*.Energy Policy 2010; 38 (8):4224-4231; doi:10.1016/j.enpol.2010.03.051.

[11] P. Barton, X. Li. *Optimal design and operation of energy systems under uncertainty*. International Symposium on Dynamics and Control of Process Systems 2013; Mumbai, India.

[12] J. Li, H. Zhao. *Multi-objective optimization and performance assessments of an integrated energy system based on fuel, wind and solar energies*. Entropy 2021; 23 (4); doi:10.3390/e23040431.

[13] R. S. Patwal, N. Narang. *Multi-objective generation scheduling of integrated energy system using fuzzy based surrogate worth trade-off approach*.Renewable Energy 2020; 156:864-882; doi:10.1016/j.renene.2020.04.058.

[14] S. Fazlollahi, G. Becker, A. Ashouri, F. Marechal. *Multi-objective, multi-period optimization of district energy systems: Iv – a case study*. Energy 2015; 84:365-381; doi:10.1016/j.energy.2015.03.003.

[15] B. Morvaj, R. Evins, J. Carmeliet. *Optimising urban energy systems: Simultaneous system sizing, operationand district heating network layout*. Energy 2016; 116:619-636; doi:10.1016/j.energy.2016.09.139.

[16] J. Söderman, F. Pettersson. *Structural and operational optimisation of distributed energy systems*. Applied Thermal Engineering 2006; 26 (13) : 1400-1408; doi:10.1016/j.applthermaleng.2005.05.034.

[17] C. Zhang. *Data driven modeling and optimization of energy systems [dissertation]*. Singapore, Nanyang Technological University; 2019.

[18] C. Zhang, L. Cao, A. Romagnoli. *On the feature engineering of building energy data mining*. Sustainable Cities and Society 2018; 39:508-518; doi:10.1016/j.scs.2018.02.016.

[19] G. G. Dimopoulos, A. V. Kougioufas, C. A. Frangopoulos. *Synthesis, design and operation optimization of a marine energy system*. Energy 2008; 33 (2):180-188; doi:10.1016/j.energy.2007.09.004.

[20] S. Sass, T. Faulwasser, D. E. Hollermann, C. D. Kappatou, D. Sauer, T. Schutz, D. Y. Shu, A. Bardow, L. Groll, V. Hagenmeyer, D. Müller, A. Mitsos. *Model compendium, data, and optimization benchmarks for sector-coupled energy systems*. Computers and Chemical Engineering 2020; 135 : 106760; doi:10.1016/j.compchemeng.2020.106760.

[21] Umweltbundesamt *Kohlendioxid-Emissionen 2020*. Available at `https://www.umweltbundesamt.de/daten/klima/treibhausgas-emissionen-in-deutschland/kohlendioxid-emissionen#herkunft-und-minderung-von-kohlendioxid-emissionen`[accessed 07.05.2023]

[22] M. Langiu, D. Y. Shu, F. J. Baader, D. Hering, U. Bau, A. Xhonneux, D. Müller, A. Bardow, A. Mitsos, M. Dahmen. *Comando: A next-generation open-source framework for energy systems optimization*. Computers and Chemical Engineering 2021, 152:107366; doi:10.1016/j.compchemeng.2021.107366.

[23] M. Grahovac, P. Liedl, J. Frisch, P. Tzscheutschler. *Simplified Solar Collector Model: Hourly Simulation of Solar Boundary Condition for Multi-Energy Optimization*. International Congress on Heating, Refrigerating and Air-Conditioning 2011; Belgrade, Serbia.

[24] Duffie, J.,Beckman, W.A.. *Solar engineering of thermal processes*. John Wiley and Sons Inc. 1991.

[25] DIN EN 12975 *Thermische solaranlagen und ihre bauteile – kollektoren – teil 2 : prüfverfahren.*

[26] EU-Science-Hub *Photovoltaic geographical information system 2020*. Available at `https://joint-research-centre.ec.europa.eu/pvgis-online-tool/pvgis-tools/hourly-radiation_en`[accessed 20.01.2023]

[27] SPF Research. *Research and development for sustainable energy systems: Flat plate collectors*. Available at: `https://www.ost.ch/` [accessed 02.02.23]

[28] F. Schlosser, M. Jesper, J. Vogelsang, T. G. Walmsley, C. Arpagaus, J. Hesselbach. *Large-scale heat pumps: Applications, performance, economic feasibility and industrial integration*. Renewable and Sustainable Energy Reviews 2020; 133:110219; doi:10.1016/j.rser.2020.110219.

[29] *Model Selection using R-squared (R^2) Measure*. Available at `https://www.ml-concepts.com/2022/01/19/r-squared-r%C2%B2-measure-for-model-selection/`; [accessed 07.03.23]

[30] F.Y.H. Ahmed, Y. H. Ali, S. M. Shamsuddin. *Using K-Fold Cross Validation Proposed Models for Spikeprop Learning Enhancements*. International Journal of Engineering and Technology 2018; 7 (4.11):145-151.

[31] Non-convex quadratic optimization. *available at `https://www.gurobi.com/events/non-convex-quadratic-optimization/`*; [accessed 27.02.23]

[32] G. Mavrotas. *Effective implementation of the e-constraint method in Multi-Objective Mathematical Programming problems*. Applied Mathematics and Computation 2009; 213:455-465.

[33] A. Slowik, H. Kwasnicka. *Evolutionary algorithms and their applications to engineering problems*. Neural Computing and Applications 2020; 2:12363–12379; doi:10.1007/s00521-020-04832-8.

PROCEEDINGS OF ECOS 2023 - THE 36TH INTERNATIONAL CONFERENCE ON
EFFICIENCY, **C**OST, **O**PTIMIZATION, **S**IMULATION AND ENVIRONMENTAL IMPACT OF ENERGY SYSTEMS
25-30 JUNE 2023, LAS PALMAS DE GRAN CANARIA, SPAIN

Operation planning with thermal storage units using MILP: Comparison of heuristics for approximating non-linear operating behavior

Felix Birkelbach[a], Lukas Kasper[b], Paul Schwarzmayr[c] and René Hofmann[d]

[a] TU Wien, Vienna, Austria, felix.birkelbach@tuwien.ac.at, CA
[b] TU Wien, Vienna, Austria, lukas.kasper@tuwien.ac.at
[c] TU Wien, Vienna, Austria, paul.schwarzmayr@tuwien.ac.at
[d] TU Wien, Vienna, Austria, rene.hofmann@tuwien.ac.at

Abstract:

For operation planning in industrial energy systems mixed integer linear programming (MILP) is the go-to method because of its reliability and the huge advances in MILP algorithms in recent years. MILP is especially well suited for planning the use of storage units, even if including the non-linear operating behavior of thermal storages is still a big challenge – especially if partial load cycles are considered. To model the storage behavior, a multi-variate non-linear function has to be linearized and incorporated into the MILP model. The key for good performance in MILP is using as few linear pieces as possible to achieve the required accuracy. We consider two types of piecewise-linear models: triangulation on a grid and general triangulation.

In this paper, we present different heuristics for computing efficient piecewise-linear approximations of non-linear functions. As a use case we consider the behavior of a thermal storage unit. We apply the heuristics to compute piecewise-linear approximation of the non-linear operating behavior and discuss the results. We then compare the performance of the models in a MILP model for the operation planning of an energy system. For translating the piecewise-linear function to MILP we consider state-of-the-art approaches with a logarithmic number of binary variables.

Our results show that gridded triangulation models in combination with logarithmic MILP formulations can be used for data-driven modeling of non-linear operating behavior of devices. We highlight the potential of this approach for realizing adaptable operation optimization of energy systems.

Keywords:

Thermal energy storage, Packed bed reactor, Unit commitment, MILP, Data-driven modeling.

1. Introduction

In an effort to curb climate change governments are imposing increasingly strict emission targets on industry. The recent increase in energy prices puts additional pressure on companies. Companies, especially in the energy-intensive industries, are forced to reduce primary energy consumption and increase energy efficiency. To do this, companies will have to employ a wide range of different solutions. Re-using excess heat on site, i.e. reducing waste heat, is getting more and more important.

The total global waste heat potential in 2016 was estimated to be more than 68 TW h [1]. Large parts of it can be attributed to the industrial and power generation sectors. In many cases, excess heat remains unused because heat demand occurs at another time than waste heat is available. Thermal energy storage (TES) systems can store a considerable share of the available waste heat and make it available. In this way, TES not only increase the flexibility of energy-intensive industrial processes [2, 3] but they also help increasing the overall energy efficiency and reducing green house gas emissions.

To operate the storage efficiently a lot of planning is required, especially for non-periodic processes. For operation planning in industrial energy systems unit commitment (UC) methods based on mixed integer linear programming (MILP) are the go-to methods because of their reliability [4]. The huge advances in MILP algorithms in recent years allows it to solve UC problems very quickly [5]. MILP has the advantage (compared to genetic algorithms and heuristic storage management techniques) that it reliably finds the optimal storage trajectory because, as a deterministic optimization method, it always converges to the global optimum. UC can be used to organize energy supply in a cost-optimal manner and to ensure that energy demand is always met.

For the present study, we consider a packed bed regenerator (PBR) that is to be used for waste heat recovery from the off-gas in a steel production process [6]. Because of the harsh operating conditions, slag dust is

expected to accumulate inside the storage over time, which will change the operating behavior. In an ongoing research project a digital twin platform is being developed to monitor the PBR and to operate the storage efficiently and reliably during its whole lifetime [7]. The digital twin platform features a thermal model of the PBR that is adapted regularly to model the operating behavior of the storage accurately at all times. This thermal model can be used to predict the behavior of the storage, but it cannot be integrated into the UC model.

To model the behavior of the PBR in the UC model accurately, the dependence of the maximum charging and discharging power on the state of charge has to be considered. The maximum power diminishes, when the storage is almost fully charged or discharged, because the power depends on the position of the thermocline inside the packed bed [4]. When the storage operates in partial charging and discharging cycles (which will usually be the case), the state of charge at the time of switching also has to be considered [4].

A big challenge with modeling the PBR for the UC is automatically deriving an accurate model for its non-linear operating behavior. The model, which was proposed in [4], was set up by hand. For this reason, it cannot be used for the automated model adaption which we intend to realize on our digital twin platform.

In this paper, we discuss different methods for modeling the storage behavior in the UC model and evaluate their performance both in terms of how well they approximate the operating behavior and how they affect the solving time of the UC problem. We show that gridded models are viable for incorporating data driven models in MILP. With this approach, we can adapt the UC model to the changing operating behavior of the PBR and thus realize reliable and accurate operation planning for an energy system with a TES over its whole lifetime.

2. Methods

2.1. Modeling non-linear operation characteristics in MILP

As the name suggests, mixed integer linear programming (MILP) is limited to linear relations between continuous and integer variables. To include non-linear characteristics, they have to be approximated by piecewise-linear functions. These piecewise linear functions are then incorporated into the MILP model by using auxiliary binary variables to distinguish between the individual pieces of the piecewise-linear function.

The ability to (approximately) include non-linear behavior in MILP comes at a price: Since the complexity of MILP problems increases exponentially with the number of binary variables, detailed piecewise-linear functions can severely affect the performance.

Piecewise linear-functions can be incorporated into a MILP problem with different formulations. For functions with one independent variable, the formulation is known as Special Ordered Set of type 2 (SOS2). For functions with more than one independent variable (as in our use case), different formulations were suggested [8,9] which differ in the number of auxiliary binary variables that are required to distinguish the simplices (pieces).

The direct extension of the concepts of SOS2 formulations to higher dimensional functions is known as Convex Combination (CC) [8]. This formulation can be used for any piecewise-linear function that uses simplices and the required number of auxilary binary variables increases linearly with the number of simplices. When the simplices are arranged in a rectangular grid, a more efficient formulation (log CC) can be used, where the number of auxilary binary variables increases only logarithmically with the number of simplices [9]. For piecewise-linear functions with many simplices, this can result in considerable savings.

2.2. Approximating storage behavior for MILP

In a packed bed regenerator, the maximum charging and discharging power depends on the state of charge and and on the initial state of charge of the charging/discharging cycle [4]. This behavior can be described by a non-linear function with two independent variables (state of charge and initial state of charge). To model the storage behavior in a UC problem in MILP, this non-linear function has to be approximated by a piecewise-linear function.

We assume that the non-linear function is given by a data-set (e.g. simulation data from a thermal finite volume model). A general piecewise-linear model with two independent variables is a triangulation of the domain with function values at each vertex. The goal of the approximation is, thus, to determine the optimal triangulation and to estimate the values at the vertices. For this problem, hardly any solutions have been proposed in literature.

From a MILP perspective gridded models have the advantage of more efficient MILP formulations, but with free triangulations (i.e. triangulations that are not confined to a grid) the target accuracy could potentially be achieved with much less simplices. Which modeling approach is more viable thus boils down to how many simplices are needed to achieve the target accuracy and by how much the solving time of the UC problem can be accelerated by using a logarithmic formulation.

For approximating a two dimensional function with a (non-gridded) triangulation, a heuristic was proposed [10]. Starting from an initial triangulation of the domain, the simplices are split according to a specific strategy, until

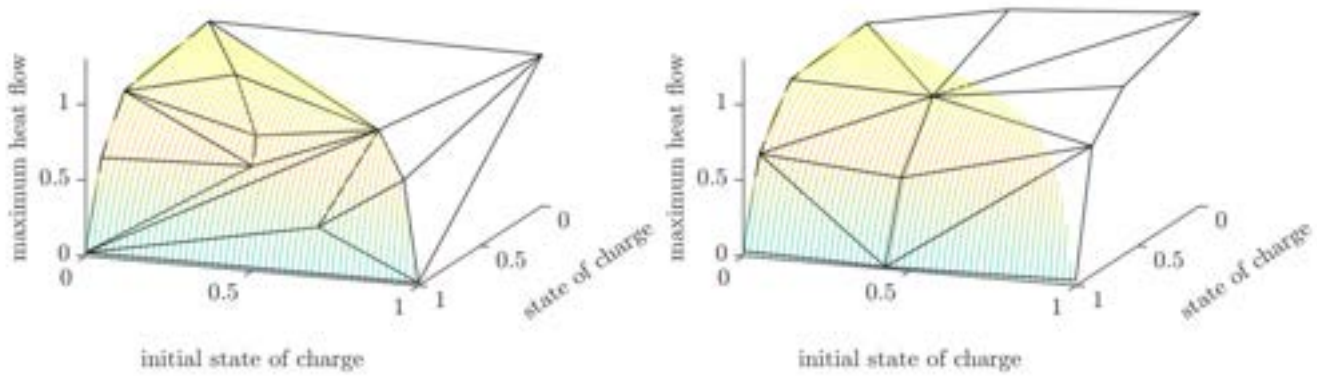

Figure 1: Illustration of the linearization of the maximum charging power with normalized axes. Free triangulation (left) and gridded triangulation (right), both with a root mean square error of $2 \cdot 10^{-2}$.

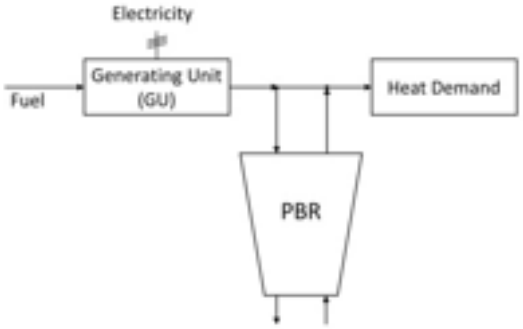

Figure 2: Illustration of the energy system for the unit commitment. Adapted from [4]

the required accuracy is achieved. We found that results with this method were barely satisfactory. Also, this kind of triangulation does not allow for the most efficient logarithmic formulation.

For this reason, we developed our own approximation algorithm for models that use a gridded triangulation. Determining the optimal grid positions and function values at the vertices is posed as a non-linear least-squares problem. As long as the target accuracy is not reached, additional grid lines are added with a heuristic and the optimization is repeated. To improve the convergence, gradients of the non-linear optimization problem are computed analytically. Gradient and grid position regularization is used to improve the quality of the model. A detailed description of the algorithm is beyond the scope of this paper but may be the content of a future publication.

Figure 1 shows an illustration of the piecewise-linear approximation of the maximum charging power of the PBR with each heuristic. In both cases, the target accuracy in terms of the root mean square error (RMSE) was $2 \cdot 10^{-2}$. The model using a free triangulation needed 16 simplices while the one with the gridded triangulation needed only 12. Unfortunately, the heuristic for fitting non-gridded triangulations cannot consistently exploit the additional degrees of freedom and compute better approximations with fewer simplices.

2.3. Unit commitment model

For evaluating the performance of each modeling approach and the effect of the logarithmic formulation, we used the same UC model as Koller et al. [4]. In this UC model, a very simple energy system (see Figure 2) consisting of a generating unit (GU), the PBR as a heat storage and a heat demand is considered. The heat demand of the process has to be covered at all times. The GU produces both heat and electricity. Electricity is sold at the electricity market at a fluctuating but known price. To allow the GU to shut down during times of low electricity prices, the PBR is used to store heat and supply the demand.

The UC model has a prediction horizon of 8 days with time steps of 1 hour. This results in 192 time steps. A detailed documentation of the model and its parameters can be found in [4].

The output of the UC problem is illustrated in Figure 3. The diagram on the top shows how the heat demand is covered by either a heat flow from the GU or from the PBR. The fluctuating electricity price that affects the optimal operation of the GU is also shown. In the bottom diagram, the operating trajectory of the PBR is shown.

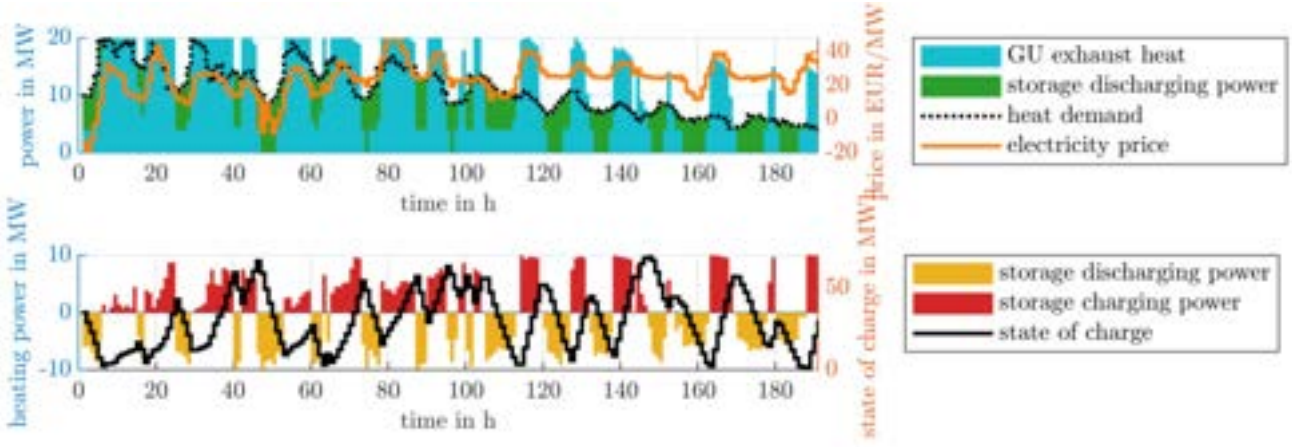

Figure 3: Illustration of the output of the unit commitment problem.

Table 1: Number of simplices, number of auxilary binary variables and resulting solving time in MILP for each model type and MILP formulation.

	RMSE	simplices	auxilary binary variables	solving time in s
free, CC	$1 \cdot 10^{-1}$	10	10	17
	$5 \cdot 10^{-2}$	10	10	18
	$2 \cdot 10^{-2}$	32	32	160
	$1 \cdot 10^{-2}$	64	64	7423
grid, CC	$1 \cdot 10^{-1}$	16	16	49
	$5 \cdot 10^{-2}$	16	16	49
	$2 \cdot 10^{-2}$	24	24	72
	$1 \cdot 10^{-2}$	60	60	1651
grid, log CC	$1 \cdot 10^{-1}$	16	6	5
	$5 \cdot 10^{-2}$	16	6	5
	$2 \cdot 10^{-2}$	24	8	28
	$1 \cdot 10^{-2}$	60	12	54

The bars illustrate heat flow to and from the storage. The line shows the state of charge.

3. Results and discussion

The aim of this study is to determine the most efficient way to derive data-driven models for the operating behavior of a PBR for use in a UC problem.

We consider two types of piecewise-linear models: free triangulation and gridded triangulation. Both types of models can be included with the MILP formulation known as Convex Combination (CC). The gridded model also allows for a logarithmic formulation (log CC). Which approach is more efficient depends 1) on the number of simplices that each modeling heuristic requires to reach the target accuracy and 2) on the speed-up due to the reduced number of auxiliary variables with the log CC formulation.

We used each fitting heuristic with the target accuracies, in terms of the root mean squared error (RMSE), of $1 \cdot 10^{-1}, 5 \cdot 10^{-2}, 1 \cdot 10^{-2}$. The results are aggregated in Table 1. To approximate both the maximum charging and discharging power at an accuracy of $1 \cdot 10^{-1}$ and $5 \cdot 10^{-2}$, 10 simplices were required with the heuristic using a free triangulation, while the heuristic using a gridded triangulation needed 16 simplices. At higher accuracies, the heuristic with free triangulation needed a few more simplices than its gridded couterpart. It could not leverage the additional degrees of freedom to achieve the target accuracy with fewer simplices.

The fourth column in Table 1 shows the number of auxiliary binary variables that is required to include the piecewise-linear function in the UC problem. The number of binary variables can be expected to have a huge impact on the solving time since 1) the complexity of MILP problems increases exponentially with the number of binary variables and 2) the models describing the operating behavior of a device in UC have to be replicated at every timestep. Since our UC problem has 192 timesteps, a model that requires 10 auxiliary binary variables introduces 1920 additional binary variables into the MILP problem.

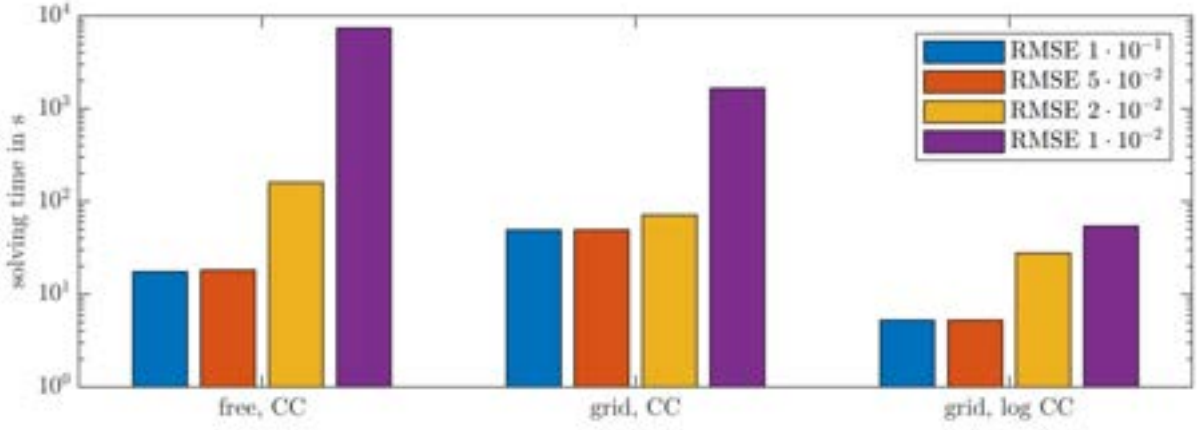

Figure 4: MILP solving time with different models for the operating behavior of the thermal energy storage.

The UC problem was formulated using YALMIP R20210331 [11] in Matlab R2022a. The problems were solved using Gurobi 10.0.0 on a 128-core system (AMD EPYC 7702P) with 256 GB RAM. The results are shown in the last column in Table 1 and are illustrated in Figure 4.

The exponential increase of solving time with the increasing number of simplices and consequently auxiliary binary variables is clearly visible (note the logarithmic scaling of the y-axis). The heuristic using a free triangulation performs slightly better than its gridded counterpart at low accuracies where it managed to make due with fewer simplices. Nevertheless even there it is outperformed by the gridded model using the logarithmic formulation.

4. Conclusion

In this paper we compared two heuristics for deriving data-driven models of the operating behavior of a thermal storage unit in a unit commitment problem. This data-driven modeling approach will be applied in a model adaption service of a digital twin that provides operation planning functionality. The goal is to manage the storage optimally taking into account the degradation of the charging/discharging performance due to harsh operating conditions.

The first heuristic used a free (i.e. non-gridded) triangulation to approximate the non-linear storage behavior, while the other used a grided triangulation. Even if — in theory — the free heuristic should be capable of achieving the target accuracy with fewer simplices than its gridded counterpart, it only did so at low accuracies. Since much more efficient MILP formulations can be used to incorporate gridded models into the unit commitment problem, this model type showed the best performance across the board.

Our results demonstrate that gridded models in combination with the logarithmic MILP formulation are well suited for deriving data-driven models of non-linear functions with multiple independent variables for MILP problems. This allows us to realize adaptable operation optimization on a digital twin platform. Research is already underway to test our approach in a lab test environment and evaluate its potential in a steel mill.

Another interesting direction for future research would be to improve the heuristics for deriving models with a free triangulation. If the additional degrees of freedom can be exploited, this would lead to very efficient models especially if no high accuracy is required or if the function has features that are incompatible with the main grid directions.

References

[1] C. Forman, I. K. Muritala, R. Pardemann, and B. Meyer, “Estimating the global waste heat potential,” *Renewable and Sustainable Energy Reviews*, vol. 57, pp. 1568–1579, May 2016.

[2] G. Manente, Y. Ding, and A. Sciacovelli, “A structured procedure for the selection of thermal energy storage options for utilization and conversion of industrial waste heat,” *Journal of Energy Storage*, vol. 51, p. 104411, July 2022.

[3] D. Le Roux, A. Touzo, T. Esence, and R. Olivès, “Experimental and numerical investigation of the temperature and flow rate variation on an industrial high-temperature thermocline storage for recovering waste heat,” *Journal of Energy Storage*, vol. 55, p. 105656, Nov. 2022.

[4] M. Koller, R. Hofmann, and H. Walter, “MILP model for a packed bed sensible thermal energy storage,” *Computers & Chemical Engineering*, vol. 125, pp. 40–53, Jan. 2019.

[5] T. Koch, T. Berthold, J. Pedersen, and C. Vanaret, “Progress in mathematical programming solvers from 2001 to 2020,” *EURO Journal on Computational Optimization*, vol. 10, p. 100031, 2022.

[6] P. Schwarzmayr, F. Birkelbach, H. Walter, and R. Hofmann, “Standby efficiency and thermocline degradation of a packed bed thermal energy storage: An experimental study,” Jan. 2023. arXiv:2301.01071 [physics].

[7] P. Schwarzmayr, F. Birkelbach, L. Kasper, and R. Hofmann, “Development of a Digital Twin Platform for Industrial Energy Systems,” in *Accelerated Energy Innovations and Emerging Technologies*, vol. 25, (Cambridge, USA), Energy Proceedings, 2022.

[8] J. P. Vielma, S. Ahmed, and G. Nemhauser, “Mixed-Integer Models for Nonseparable Piecewise-Linear Optimization: Unifying Framework and Extensions,” *Operations Research*, vol. 58, pp. 303–315, Jan. 2010.

[9] J. P. Vielma and G. L. Nemhauser, “Modeling disjunctive constraints with a logarithmic number of binary variables and constraints,” *Mathematical Programming*, vol. 128, pp. 49–72, Jan. 2011.

[10] S. Rebennack and J. Kallrath, “Continuous Piecewise Linear Delta-Approximations for Bivariate and Multivariate Functions,” *Journal of Optimization Theory and Applications*, vol. 167, pp. 102–117, Oct. 2015.

[11] J. Löfberg, “YALMIP : a toolbox for modeling and optimization in MATLAB,” in *2004 IEEE International Conference on Robotics and Automation (IEEE Cat. No.04CH37508)*, (Taipei, Taiwan), pp. 284–289, IEEE, 2004.

Acknowledgments

The work that this paper is based on was funded by the Austrian research promotion agency (FFG) in the projects *5DIndustrialTwin* and *IFE* under the grant numbers 881140 and 884340, respectiviely.

PROCEEDINGS OF ECOS 2023 - THE 36TH INTERNATIONAL CONFERENCE ON
EFFICIENCY, **C**OST, **O**PTIMIZATION, **S**IMULATION AND ENVIRONMENTAL IMPACT OF ENERGY SYSTEMS
25-30 JUNE 2023, LAS PALMAS DE GRAN CANARIA, SPAIN

Simulation-based performance assessment for building automation systems

Felix Stegemerten [a], Marwa Maghnie [b], Alexander Kümpel [c] and Dirk Müller [d]

[a] RWTH Aachen University, E.ON Energy Research Center, Institute for Energy Efficient Buildings and Indoor Climate, Aachen, Germany, felix.stegemerten@eonerc.rwth-aachen.de, CA
[b] RWTH Aachen University, E.ON Energy Research Center, Institute for Energy Efficient Buildings and Indoor Climate, Aachen, Germany, marwa.maghnie@eonerc.rwth-aachen.de
[c] RWTH Aachen University, E.ON Energy Research Center, Institute for Energy Efficient Buildings and Indoor Climate, Aachen, Germany, akuempel@eonerc.rwth-aachen.de
[d] RWTH Aachen University, E.ON Energy Research Center, Institute for Energy Efficient Buildings and Indoor Climate, Aachen, Germany, dmueller@eonerc.rwth-aachen.de

Abstract:
The operation of building energy systems contributes significantly to thermal comfort and energy efficiency. In turn, the operation is influenced by the control quality of local closed-loop controllers. However, in practice controllers are often commissioned without sufficient testing, due to the lack of time and budget, leading to reduced performance and energy efficiency. To facilitate controller testing and assessment, this work presents a three-step simulation-based testing method using little user input to provide an automated evaluation of the controller performance. For the assessment, a model of the controlled system is used to enable the evaluation of controller behavior for different scenarios. The controller performance is assessed in each scenario utilizing different Key Performance Indicators (KPIs). The model of the controlled system also allows the estimation of the optimal control behavior, which is used as reference control to provide further feedback for possible improvements to the user. All three steps are implemented and deployed as a cloud service allowing the controller under test to communicate with the controlled system model via an HTTP API. The testing method is applied to two different control loops of an air handling unit. The tested controllers show poor control quality when assessed with different KPIs. The results of the testing method provide direct improvements for both controllers. By applying these improvements to the two controllers, the control quality, assessed with the Integral Time-weighted Absolute Error (ITAE), was improved by 85 % and 63 % respectively.

Keywords:
Controller performance assessment, Simulation-based testing, Air handling unit, Automation, Cloud.

1. Introduction

In 2020, buildings accounted for 36 % of global energy consumption, emphasizing the need for energy-efficient building operations to mitigate climate change [1]. Advanced control strategies like model predictive control (MPC) promise energy savings from 15 % to 50 % [2]. Furthermore, advanced control strategies often rely on local feedback controllers [3]. Additionally, even without advanced control strategies, poor-performing local controllers lead to inefficient operation. Therefore, local controllers highly influence the overall efficiency of buildings. However, in practice, controllers are often not tested sufficiently. One reason is that controller tuning is not done at all or performed manually based on expert knowledge during installation [4]. This can lead to poor performance, especially in operating points not present during the installation period. One promising approach for controller performance assessment is to use models to decrease the required time and cost [5]. In addition, the manual effort can be reduced by clearly defining and automating the testing process.
Jelali identifies a five-step process for controller performance assessment [6]. First, the current control is assessed by performance figures. Second, a benchmark for performance is selected. Afterward, deviations from the benchmark are detected for every control loop inside the system. Fourth, the reason for the deviation is detected. Finally, options for improvement are suggested. The author points out that especially the last two steps are the most challenging and are usually done manually. Matinnejad et. al. present a search-based testing method, which investigates the controller in different scenarios using models [7]. Scenarios are benchmarked against each other based on Key Performance Indicators (KPIs) assessing the controller performance. The aim is to detect worst-case scenarios, which can then be used for further manual testing and improvement of the controller. The BOPTEST framework enables benchmarking different control strategies by providing standardized models as use cases [8]. This allows testing different control strategies on the same system with the same environmental conditions, creating a reference for these use cases. However, the focus

is on advanced control strategies in a building energy management system and not on local controllers like PID. In [9] a framework is presented, which investigates controller performance by step response. The step signals are applied directly to the actual system and are investigated based on monitoring data. This requires an already existing building management system and technical requirements as well as the time to write directly to the system.

In the current literature, a lot of frameworks are developed to assess the performance of modern control and energy management systems. However, these systems often rely on local control loops, which are often not tested sufficiently. Furthermore, the testing process for these local controllers, if conducted, is often costly and time-consuming. Therefore, in this work, we present a three-step simulation-based testing method utilizing minimal user input to assess and, if needed, improve closed-loop controller performance in various scenarios. To benchmark the controller performance, a model of the controlled system is used to calculate a reference controller behavior. As a result of the method, direct suggestions for improvement are given. The testing method is implemented as a cloud service and can be used for the installation of new controllers or during operation since it does not interfere with the actual building. We demonstrate the method by applying it to two local control loops of a reheater of an air handling unit (AHU).

In the following, we explain the testing method and all its processes. Subsequently, the use case and the results of the application are presented and discussed.

2. Methodology

In this section, we first present the nomenclature for this paper and afterward the three steps of the simulation-based testing method for assessing closed-loop controller performance.

The most used controller in building energy systems is still the PID controller [4]. The control behavior of a PID controller is defined by the following equation, with K_p, T_i and T_d being the parameters for the proportional, integral and derivative terms:

$$u(t) = K_p \left[e(t) + \frac{1}{T_i} \int_0^t e(\tau)\mathrm{d}\tau + T_d \frac{\mathrm{d}}{\mathrm{dt}} e(t) \right] \tag{1}$$

In a closed loop, the controller interacts with the controlled system as shown in Fig. 1. The controller output u influences the process variable y, which, together with the setpoint r, is used as feedback for the controller. The controller is therefore directly influenced by the controlled system and the corresponding disturbances z. To fully assess the controller performance, the proposed testing method investigates both, the controller and the system, in various scenarios.

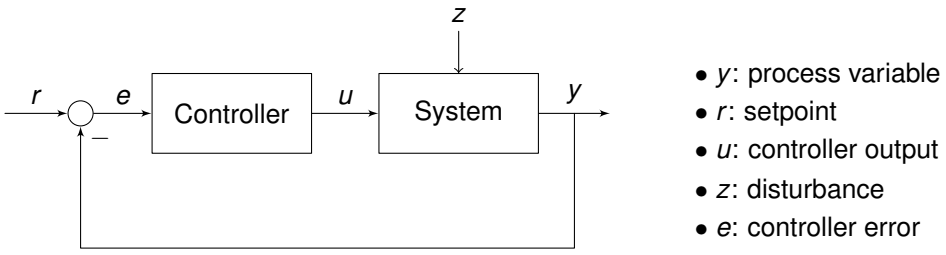

Figure 1: Closed loop control with used nomenclature

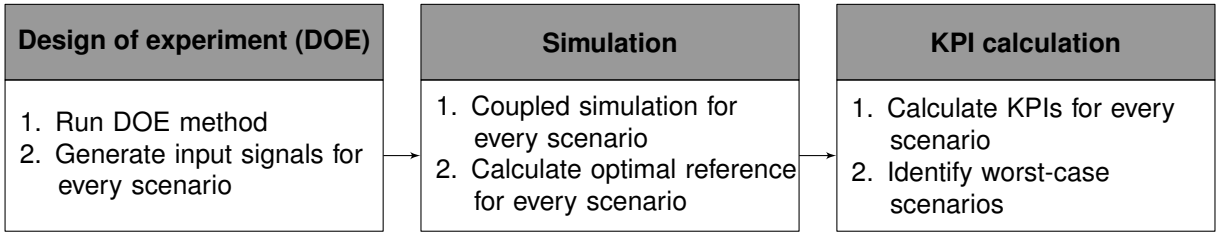

Figure 2: Process of the simulation-based testing method

Figure 2 shows the three different steps of the simulation-based testing method. Each step requires minimal user input and therefore enables an automatic calculation process. As a first step, a Design of Experiment (DOE) method is run, to parametrize the different scenarios in which the controller is assessed. In the second step, the closed loop system is simulated with these scenarios, and for each scenario, an optimal reference

controller is calculated. In the last step, KPIs for each scenario are calculated. This allows the user to identify those scenarios, which performed worst.
In the following, a more detailed description of the three steps of the simulation-based testing method is given.

2.1. Design of experiment

Since a controller's behavior strongly depends on the current operation of the system, a systematic performance assessment needs to investigate controller performance at different operational points. One of the main benefits of using models for controller performance assessment, in comparison to real-world systems, is the ability to easily investigate controller behavior under different environmental conditions. For a control loop, these environmental conditions are specified by the disturbances and the setpoint. Both act as external signals, which can not be influenced by the controller or the system. Therefore, for an assessment of the controller performance, these external signals need to be varied inside the operational boundaries.
Applying constant values for disturbance and setpoint would lead to a static operation, which does not represent the actual operation of a real system. Thus, to keep dynamic operation, a function is parametrized for each external signal resulting in a time series as input for the simulations. We call the combination of an input function for the disturbance and the setpoint a *scenario*. A scenario is defined by the parameter set for the input functions and the type of function.
The parameter sets are chosen from a parameter space, which is limited by the operational boundaries of the corresponding system, by **running a DOE method**. For every parameter set, a scenario is generated. By selecting numerous different parameters for the input functions, long calculation times due to a high number of simulations are needed. Therefore, the combinations of parameters need to be chosen systematically and under consideration of the total amount of combinations. Latin Hypercube Sampling (LHS) is a DOE method that randomly chooses different operational conditions by considering the input dimensions and trying to cover most of the input space [10]. The number of combinations of parameters is defined by an input to the LHS. With this, it is possible to simulate a defined number of parameter combinations while still covering most of the scenario parameter space.
As a result of the DOE method, different sets of parameters are chosen, which are then used **generate input signals for every scenario** by parametrizing functions. Within the methodology, multiple different types of functions can be used for the setpoint and the disturbance. However, in this paper, we focus on two different types of functions: a constant function for the disturbance and a step function for the setpoint. The constant function keeps one value for the whole time period, while the step function changes its value instantly from a start to an end value at a defined time. The combination of these functions allows an isolated assessment of the step response of the controller for different disturbances.
For the DOE, these two functions result in a three-dimensional parameter space: the constant value for the disturbance as well as the start value and end value of the step. The limits of this space, i.e. the operational boundaries, and the time period of the signal are given by the user and depend on the controlled system.
With the created input time series for both the disturbance and the setpoint, the controller and the system model can be simulated.

2.2. Simulation

During the simulation process, the controlled system is simulated separately from the controller. The **coupled simulation for every scenario** is achieved by periodically communicating all necessary variables between the controller and the controlled systems within a specified time step over a defined interface. This interface includes all needed variables for a closed-loop controller: process variable y, setpoint r, disturbance z and controller output u. This allows providing the testing method as a cloud service, by implementing the communication interface as an application programming interface (API). With this, the controller can either be a simulation model or a hardware controller, as long as it is able to send and receive the variables defined by the interface through the API.
In this work, we assess controllers using models that are implemented in the modeling language Modelica [11]. The models are exported as Functional Mock-up Units (FMUs) using the Functional Mock-up Interface (FMI) standard [12]. Within Modelica, the communication interface is realized using the *bus* model, which is based on the expandable connector concept [13]. A *bus* allows the grouping of variables under a specified naming scheme. This naming scheme can then be utilized for communication with external tools like Python. Therefore, a *bus* model is created, which defines the above-mentioned necessary variables for the closed-loop controller. The *bus* model is used to adapt existing models from the Modelica library AixLib, which includes various building energy system models like air handling units and thermal zones and is developed at the Institute for Energy Efficient Buildings and Indoor Climate [14].

Depending on the type of function used to create the input signal for the coupled simulation of the controller and controlled system, different conditions apply to the simulation. For the step function, it is necessary that the system is in a quasi-steady state before the step can occur. Furthermore, it is important to run the simulation long enough to see the effects of the step signal after the step occurs. Therefore, two important parameters for

each simulation are the initialization time and the total simulation time. The initialization time defines the time until the step occurs and the starting time for the assessment. The total simulation time describes the length of the full simulation. Both time values heavily depend on the time constant of the controlled system. For this reason, these values are provided by the user. Additionally, the communication step size for the communication interval between the controller and the system has to be provided by the user.

As a basis for the performance assessment of the controller, the model of the controlled system is also used for the **calculation of an optimal reference**. The calculation is performed for each scenario and in parallel with the coupled simulation. Section 2.3. provides a more detailed description of this process.

2.3. KPI calculation

The KPI calculation is based on the simulation results and evaluates the controller performance by **calculating KPIs for every scenario**. Numerous KPIs for the assessment of controller performance based on different approaches are defined in the literature. Table 1 shows a selection of a few KPIs, which are based on an integral term of the control error $e(t)$. For a more detailed description of these KPIs, the reader is referred to the literature [15].

Table 1: Selection of integral-based KPIs [15]

KPI	Description	Equation
IAE	Integral Absolute Error	$\int \lvert e(t) \rvert \, \mathrm{d}t$
ITAE	Integral Time-weighted Absolute Error	$\int t \cdot \lvert e(t) \rvert \, \mathrm{d}t$
ISE	Integral Squared Error	$\int e(t)^2 \, \mathrm{d}t$

The goal of assessing the controller is to identify the scenarios where the controller performs worst. Since most KPIs represent a single value, it is not possible to directly assess the potential of the tested controller. For example, a controller of a boiler might produce bad KPI values for a downward setpoint step signal, which are not caused by the controller, but by the inability to actively cool. Therefore, to identify these worst-case scenarios, a reference controller is needed. Reference [15] introduces the Harris index, which allows rating the controller performance against minimum variance control (MVC). The index η_{MVC} is defined as:

$$\eta_{MVC} = \frac{\sigma^2_{MVC}}{\sigma^2_y} \tag{2}$$

The variable σ^2_{MVC} describes the variance for the minimum variance control, whereas σ^2_y refers to the variance of the tested controller. MVC describes the best possible controller behavior for achieving the smallest output variance. In analogy to the Harris index, an index can be determined for each KPI, which relates the optimal value to the value of the tested controller. For the ITAE, this leads to the ITAE-Index η_{ITAE}:

$$\eta_{\mathrm{ITAE}} = \frac{\mathrm{ITAE}_{opt}}{\mathrm{ITAE}_y} \tag{3}$$

To estimate the KPI of the optimal reference, an optimization problem is solved by minimizing the corresponding KPI for a coupled simulation of the controlled system and a PID controller. The PID controller is chosen as a reference since it is one of the most used controller types in building energy systems [4]. The optimization problem is shown in (4).

$$\min_{K_p, T_i, T_d} \quad \mathrm{ITAE} \tag{4a}$$

$$\text{subject to} \quad lb \leq K_p, T_i, T_d \leq ub, \tag{4b}$$

The upper boundary (ub) and the lower boundary (lb) for each of the three PID parameters influence the runtime of the optimization. For different systems, default values based on experience are provided, but the user can provide individual values if needed. The ITAE is calculated as a result of the simulation. For every scenario, the optimization leads to optimal PID parameters and the optimal ITAE_{opt}.

The resulting control behavior of the optimal PID heavily depends on the type of KPI that is used for the minimization. Here, the ITAE is used, since [4] shows that the ITAE leads to a low overshoot and a short rise time for heating, ventilation and air conditioning systems.

Based on the ITAE-Index η_{ITAE}, the **worst-case scenarios are identified**. For these scenarios, the behavior of the optimal controller and the tested controller is used as the basis for improving the tested controller. If the tested controller is a PID, the optimal PID parameters can be directly applied.

2.4. User input

The whole three-step process is implemented in a Python framework, which utilizes minimal user input to run an automated performance assessment. The necessary input provided by the user is shown in Table 2. Since this framework aims at testing specific control loops, a lot of the input is also specific for each use case. Nevertheless, some recurring components of building energy systems are modeled and provided with default values for the user input. This enables testing similar systems with low effort.
The user input itself is provided by a config file based on the *JSON Schema*. This setup provides a simple interface, which can be used on a local machine as well as over an HTTP API.

Table 2: Necessary input for the simulation-based testing method provided by the user

Configuration File		
DOE	**Simulation**	**KPI**
• Number of scenarios • operational boundaries • DOE method	• simulation and initialization time • communication step size • system/controller model • optimal PID parameter boundaries	• KPI for index calculation

3. Application to an air handling unit

3.1. Use case description

The simulation-based testing method is tested with a reheater of an air handling unit. The schemata of the reheater as well as the measured variables of the real system are shown in Fig. 3.

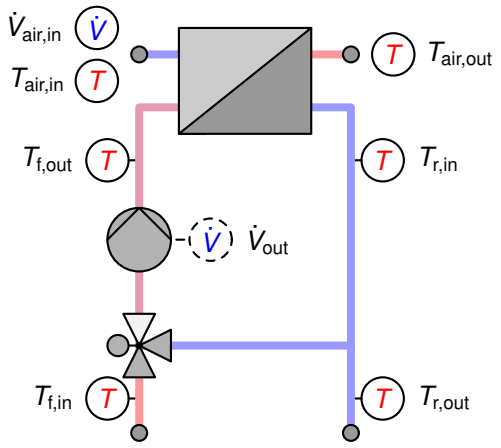

- $T_{f,in}$: primary circuit supply water temperature
- $T_{f,out}$: secondary circuit supply water temperature
- $T_{r,in}$: primary circuit return water temperature
- $T_{r,out}$: secondary circuit return water temperature
- $\dot{V}_{out}$: secondary circuit water volume flow
- $T_{air,in}$: inlet air temperature
- $T_{air,out}$: outlet air temperature
- $\dot{V}_{air,in}$: air volume flow

Figure 3: Reheater structure and measured values

The reheater consists of a heat exchanger and a hydraulic circuit, including two actuators, a three-way valve and a pump. The hydraulic circuit is split into a primary circuit containing the heat exchanger and a secondary circuit, from which the reheater is provided with hot water. The dashed volume flow sensor indicates that this value is not measured directly, but calculated and provided through an interface by the vendor.
The investigated control consists of two different control loops with PID controllers. One control loop controls the outflowing air temperature $T_{air,out}$ with the pump speed, from now on referred to as *pump control loop*. The other controls the inflowing water temperature into the heat exchanger $T_{f,out}$ with the valve position, referred to as *valve control loop*. These two control loops interact with each other resulting in one controller being a disturbance to the other one. A more detailed description of the control can be found in [16].

To analyze the control behavior of the implemented control of the reheater, the step responses for both control loops are investigated. The step responses of the pump and valve control loop are shown in Fig. 4 and Fig. 5. The step occurs at 0 min and both signals are recorded for 30 min. In each, the upper figure shows the step response of the process variable and the corresponding setpoint. The lower figure shows the relative control output between 0 % and 100 %. The installed pump allows relative speeds from 10 % to 100 % and runs on a minimum speed of 500 rpm for values below 10 %.

For the pump control loop, a setpoint step from 292.15 K to 297.55 K leads to an ITAE of 358.66. The control output is not at its maximum value of 100 % even though the process variable does not reach its final value after 30 min. Considering an advanced control strategy, which might send new setpoints every 10 to 15 min, this could lead to high discomfort or energy losses. The valve control loop also doesn't reach the final setpoint value for a step from 295.5 K to 300.5 K with the control output also not utilizing its full range, leading to an ITAE of 333.05.
The step responses indicate that both control loops show significant rise times and need to be adjusted to reach the setpoint within a reasonable amount of time. Therefore, the simulation-based testing method is applied to both control loops. For this, the model used is described in the next section.

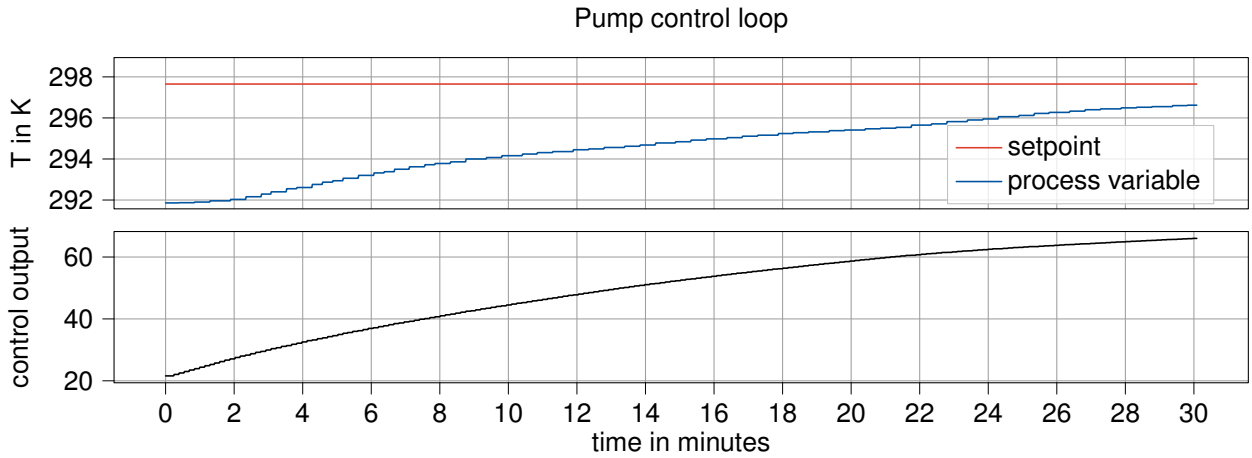

Figure 4: Measured response of the tested pump control loop

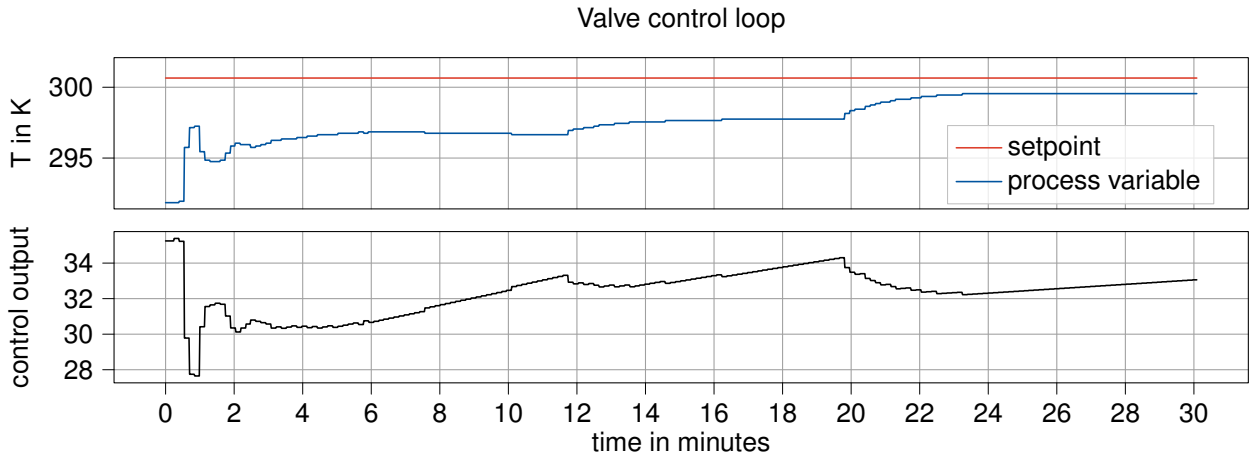

Figure 5: Measured step response of the tested valve control loop

3.2. Models for the reheater

The model for the reheater is created with Modelica using the library AixLib. To reduce the modeling effort, the model is designed so that the user only has to provide parameters that can be found in datasheets. Thus, even a non-professional can use the models. A more detailed description of the model, its assumptions and its application in a use case are given in [13].
The model is calibrated to represent the behavior of the real system. This is done using the AixCaliBuHa framework, which allows the automatic calibration of Modelica models [17]. As input for the calibration, 58 h of measurements of the variables displayed in Fig. 3 are taken. The calibration process is done in two separate steps. First, the volume flow in the secondary circuit is calibrated by varying the pump characteristics and pressure losses of the circuit. In the second step, the outlet air temperature is calibrated by adjusting the parameters of the heat exchanger and temperature losses in the circuit. For both steps, the measured values of the valve position, pump speed and inlet temperatures for the secondary circuit and air are taken as inputs to the model. As the objective for the calibration, the normalized root mean squared error (NRMSE) is used.

With n being the amount of measured data points, y being the measured value and $\hat{y}$ the simulated value, the NRMSE is defined as:

$$\text{NRMSE} = \frac{\sqrt{\frac{1}{n}\Sigma(y_i - \hat{y}_i)^2}}{y_{max} - y_{min}} \tag{5}$$

The results of the calibration for the volume flow and the air temperature are shown in Fig. 6 and Fig. 7 respectively. The calibration resulted in an NRMSE of 0.025 for the volume flow and 0.113 for the air temperature. The bigger NRMSE of the air temperature compared to the volume flow is caused by two major aspects. One

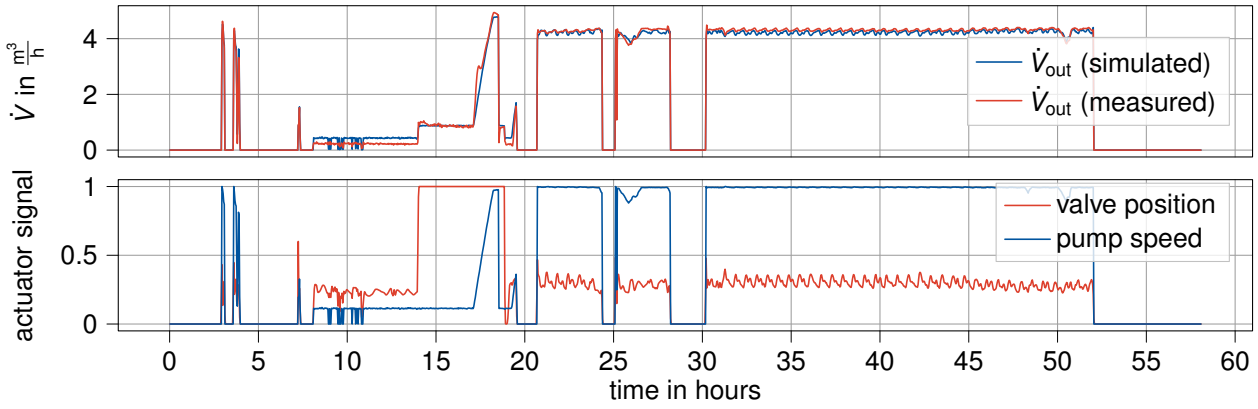

Figure 6: Measured and simulated volume flow in the primary circuit (top) and actuator inputs (bottom) for the calibrated model

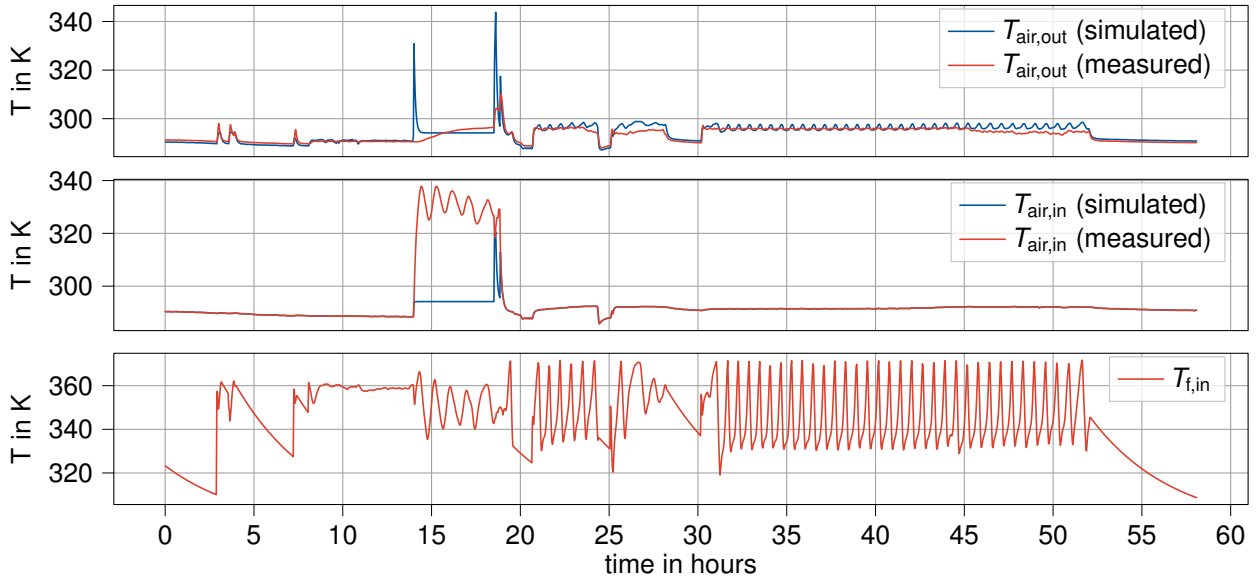

Figure 7: Measured and simulated outlet air temperature (top), measured and simulated inlet air temperature (middle) and water supply temperature as input (bottom) for the calibrated model

aspect is that the temperature sensors of the real system are not calibrated. This leads to high uncertainty of the measurements and fluctuating temperature values over time under otherwise unchanged conditions. The other aspect is the selected time frame for the validation of the calibration. After 14 h, the simulated outlet air temperature rapidly rises, while the measured value only increases slightly over time. A similar behavior occurs after 18 h. Here, two peaks are occurring right after one another. This leads to high deviations and negatively impacts the NRMSE. The deviations are caused by the air volume flow $\dot{V}_{air,in}$ dropping to 0 m^3/h at 14 h and staying at this value until jumping back to 7500 m^3/h at 18 h. Both processes take roughly 300 s. Therefore, during these times, the volume flow reaches values near zero, leading to the first and third peaks in the outlet air temperature due to the unchanged supply water temperature. This behavior is not seen in the measured value. But since this effect only applies to small volume flows, this is only relevant in situations where the AHU is turned on or off. Therefore, this does not influence the model quality for the controller tests.

During the first and third peaks, after the volume flow hits 0 m^3/h, the outlet air temperatures of the simulation and the measurement tend towards the environment temperature of 295.15 K. For the second peak, a rise in the measurement is also seen. This is because the air inside the heat exchanger heats up when the air volume flow is 0 m^3/h and is measured as soon as the air flows again. The measurement shows a similar peak.
The inlet air temperature also shows a deviation from the measurement during the period of 14 h to 18 h. The simulated value tends towards the environment temperature, while the measured value tends towards the supply temperature $T_{f,in}$. This is due to the real temperature sensor being placed near the heat exchanger. Therefore, the air around the heat exchanger heats up according to the supply temperature. In the simulation model, the temperature sensor is only affected by heat losses to the environment.

The NRMSEs for both variables show that the calibrated model sufficiently describes the reheater for the relevant operating points. Therefore, the model is used as input for the testing method.

3.3. Applying the simulation-based testing method

With the calibrated model, the two control loops are investigated using the simulation-based testing method. The method is applied once for each control loop with the tested controller parametrization, which led to the deviations displayed in Fig. 4 and Fig. 5. In the following, the results are presented and discussed using the pump control loop as an example.
As disturbance for the pump control loop, three different variables are possible: the supply temperature at the inlet of the hydraulic module $T_{f,in}$, the volume flow in the air canal $\dot{V}_{air,in}$ and the inlet air temperature $T_{air,in}$. Since monitoring data showed a more or less constant value for the air volume flow over the operation of one year and the supply temperature influences the mixing temperature, controlled by the valve control loop, the inlet air temperature is chosen as the disturbance. For each test run, the other two disturbances are not investigated further and are kept at their average operation values.
The two control loops and the respective actuators influence each other as well. Therefore, the setpoint of one controller is set to a constant value within the operation area, if the other controller is tested. This allows the isolated assessment of each controller.

The value ranges for the different input variables with which the scenarios are generated are given in Table 3. The setpoint represents the setpoint for the outlet air temperature and the disturbance stands for the inlet air temperature. The ranges are based on monitoring data. The control output, here the pump speed, can take values between 0 % and 100 %.

Table 3: Value ranges for the simulation-based testing method

Variable	Value range
setpoint	290 K - 298 K
disturbance	285 K - 295 K

Figure 8 shows the resulting step responses for one exemplary scenario. Each scenario was simulated for 3600 s with an initialization time of 1800 s at which the step occurs. Here, the step function is parametrized with a start value of approximately 291.5 K and an end value of roughly 297 K. The constant function for the disturbance has a value of about 291.55 K. The process variable of the tested controller shows similar behavior to the one displayed in Fig. 4. The outlet air temperature also does not reach its setpoint within the simulation time. Conversely, the optimized controller does reach the setpoint 500 s after the step. The optimal controller reacts more actively to the step by immediately generating a control output of over 60 %, whereas the tested controller never reaches the same output as the optimal controller. This leads to an ITAE for the tested controller of 869 501 K s^2 and for the optimal controller of 9064 K s^2. Thus, the ITAE-index results in 0.01, implying that the tested controller only reaches 1 % of its maximum potential.

Figure 9 highlights the ITAE for every scenario in dependence of the optimal PID parameters (Fig. 9a) and the input function parameters (Fig. 9b). The parameters of the scenarios are given as P_1, the start value of the step signal for the setpoint, P_2, the end value of that signal and P_3, the constant value for the disturbance.
A cluster of low ITAE-indexes η_{ITAE} and therefore worst-case scenarios is located around big values for K_p and small values for T_i and T_d (Fig. 9a). Compared to a PID controller with these values, the tested controller performs worse. Also, the derivative parameter T_d does not seem to have a high impact, since every optimal PID chooses small values for the parameter.
Figure 9b implies that the tested controller performs well for scenarios in which the start value of the step is close to the end value of the step. However, especially for bigger step sizes, the controller performs worse, indicating a passive behavior as seen in Fig. 8.

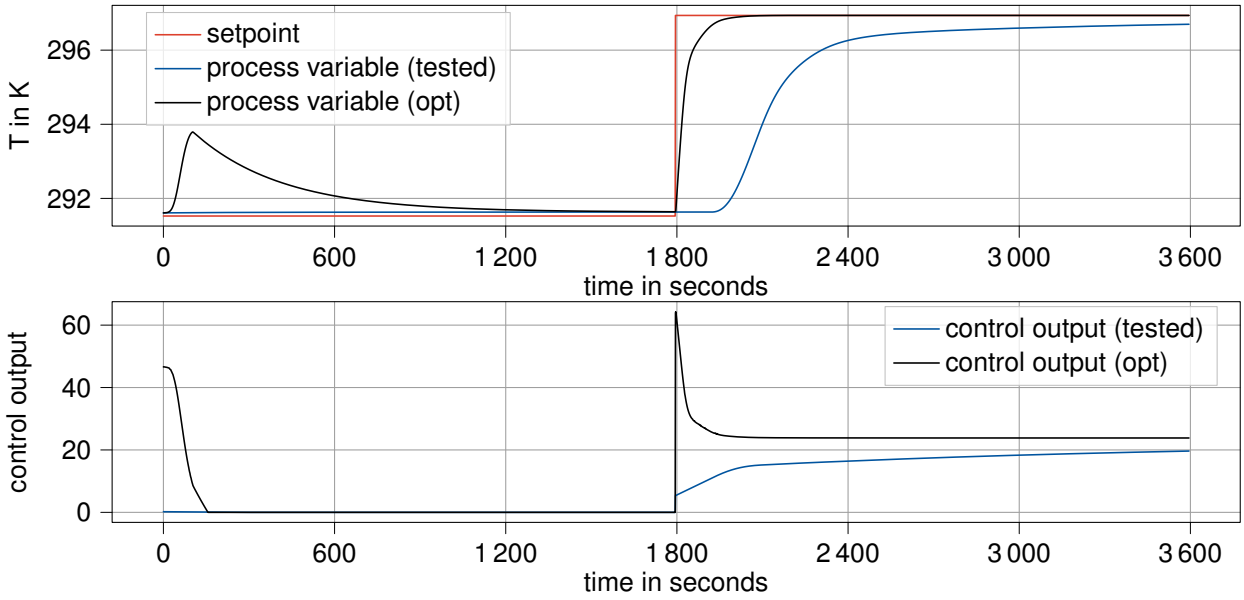

Figure 8: Simulated step response for the tested controller and the optimal reference control

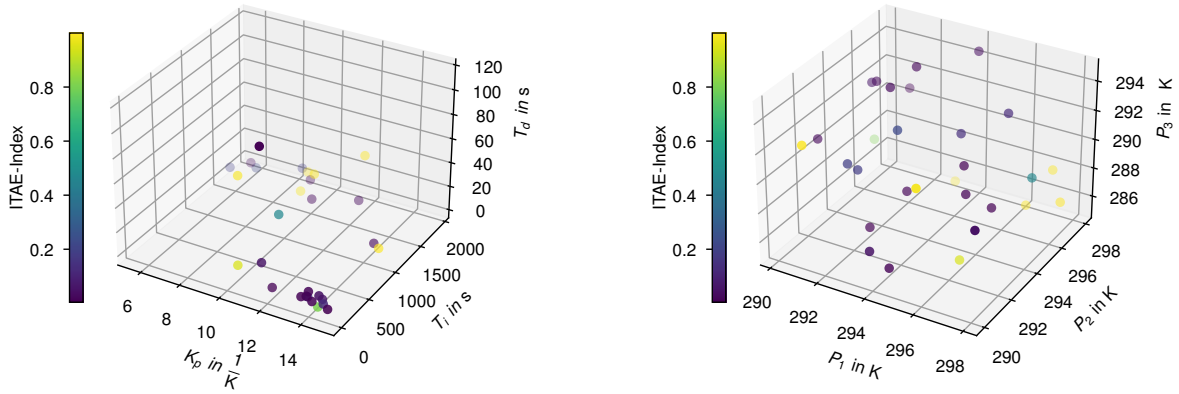

(a) ITAE-Index over optimal PID parameters

(b) ITAE-Index over input function parameters

Figure 9: ITAE-Index for every simulated scenario

Using the graphical representation of the controller performance given in Fig. 9, the tested controller is improved. Since the tested controllers are PIDs, the parameters given by the cluster described in Fig. 9a are applied to improve the controller. The derivative parameter T_d is set to zero since its impact seems to be low. Analog to the pump control loop, the valve parameters are improved. The adapted PID parameters for both control loops are given in Table 4.

Table 4: Different PID Parameters before and after applying the simulation-based testing method

(a) Tested controller

Controller	K_p in $\frac{1}{\mathrm{K}}$	T_i in s	T_d in s
Valve	1.5	850	0
Pump	1.2	130	0

(b) Improved controller

Controller	K_p in $\frac{1}{\mathrm{K}}$	T_i in s	T_d in s
Valve	1	180	0
Pump	11.25	300	0

The initial experiment for the reheater is repeated. The results are shown in Fig. 10 and Fig. 11. With the improved PID parameters, both the outlet air temperature and the primary supply temperature reach their setpoint within a reasonable time. The pump controller shows a small overshoot. The valve control is disturbed by two sudden temperature changes in the secondary supply temperature $T_{f,out}$, leading to two small deviations from the setpoint. Nevertheless, the ITAE of the pump control was reduced to 54.01 K s^2, while the ITAE of the valve has a value of 122.541 K s^2. This results in a relative improvement of approx. 85 % for the pump and approx. 63 % for the valve.

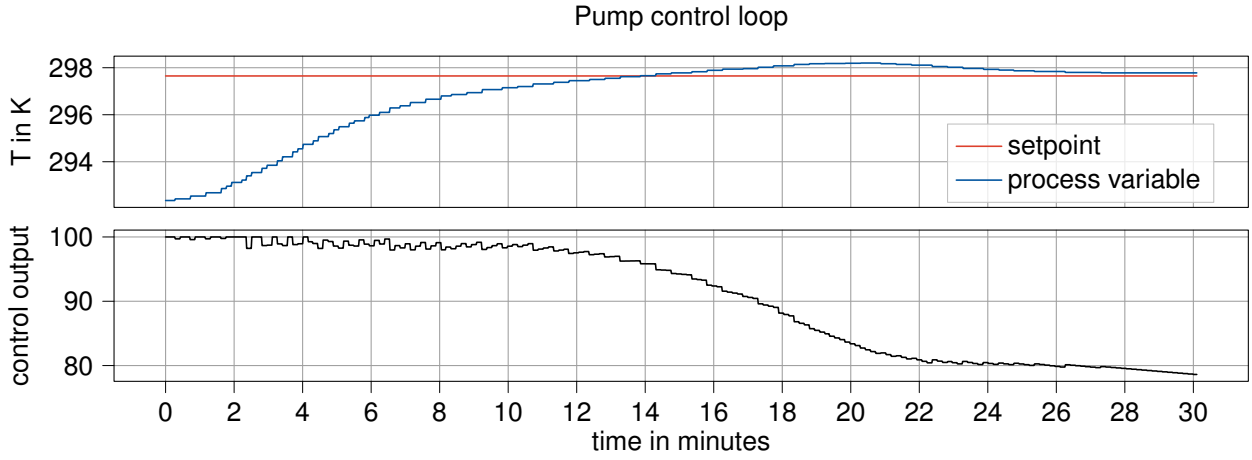

Figure 10: Measured step response of pump control loop with improved PID parameters

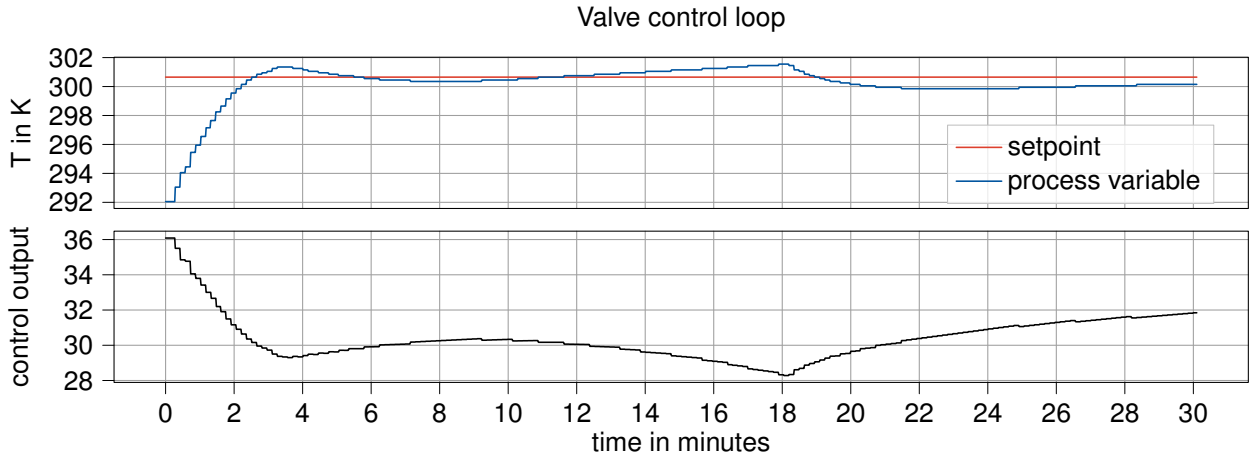

Figure 11: Measured step response of valve control loop with improved PID parameters

4. Conclusion

In this work, we presented a three-step testing method, which utilizes a model of the controlled system to investigate controller performance in various scenarios. The system model is also used to calculate an optimal reference for each scenario to benchmark the tested controller. To receive the optimal control, an optimization problem is solved by varying the parameters of a reference PID controller to minimize the ITAE. With this, the controller performance is assessed in every scenario and worst-case scenarios are identified. These scenarios are then improved utilizing the optimal control.

By applying the method with calibrated models to two different control loops of a reheater of an air handling unit, we have shown that the method can improve the controller behavior. Even when multiple control loops interact with each other, the different scenarios created by the method allowed for isolating and therefore assessing each controller's performance separately. The improved controllers showed enhanced control behavior for two different scenarios, leading to an improvement of the ITAE by 85 % and 63 % respectively.

The presented simulation-based testing method is a promising approach to avoid time-consuming tests on a real system. Even when the used models are not fully calibrated to the real behavior of the controlled system, the derived adjustments improve control behavior. This allows the time-consuming modeling process to be

done once for each type of controlled system and to only invest minimal effort for each specific system the method is applied to. Due to minimal user input, the method can be automated, reducing effort further.
Future work should investigate the automated improvement of controllers or the concrete suggestion of improvement measures based on the optimal reference. In addition, research is needed to assess the disturbance rejection of controllers.

Acknowledgments

We gratefully acknowledge the financial support provided by the BMWK (Federal Ministry for Economic Affairs and Climate Action), promotional reference 03EN1014A. Furthermore, we thank our project partners aedifion GmbH and eurogard GmbH for the good collaboration.

Nomenclature

Abbreviations

AHU	air handling unit,
DOE	Design of Experiment,
KPI	Key Performance Indicator,
LHS	Latin Hypercube sampling,
MPC	model predictive control,
MVC	minimum variance control,
NRMSE	normalized root mean squared error

Letter symbols

$\dot{V}$	volume flow, m^3/h
T	temperature, K

Greek symbols

σ	variance,
η	KPI index

Subscripts and superscripts

p	Proportional,
i	Integral,
d	Derivative,
opt	Optimal value,
f	Forward flow,
r	Return flow,
in	Inlet,
out	Outlet,
air	Air,
max	Maximum value,
min	Minimum value

References

[1] United Nations Environment Programme *Towards a Zero-emission, Efficient and Resilient Buildings and Construction Sector.* Nairobi, Kenia: Global Status Report for Buildings and Construction; 2021;

[2] Drgoňa J., Arroyo J., Cupeiro Figueroa I., Blum D., Arendt K., Kim D., Ollé E., Oravec J., Wetter M., Vrabie D., Helsen L. *All you need to know about model predictive control for buildings*. Annual Reviews in Control. 2020;50:190–232.

[3] Fütterer J. *Tuning of PID controllers within building energy systems* Aachen, Deutschland: RWTH Aachen University, Institute for Energy Efficient Buildings and Indoor Climate; 2017.

[4] Fütterer J., Kraus P., Schmidt M., Müller D. *Demonstration of an easy-to-apply, automated control tuning method for typical PID control loops in building energy systems*. 2015: IEEE 10th Conference on Industrial Electronics and Applications (ICIEA); 2015 Jun 15-17; Auckland, New Zealand. IEEE.

[5] Ceccolini C., Sangi R. *Benchmarking Approaches for Assessing the Performance of Building Control Strategies: A Review*. Energies. 2022;15(4):1270.

[6] Jelali M. *An overview of control performance assessment technology and industrial applications*. Control Engineering Practice. 2006;14(5):441–66.

[7] Matinnejad R., Nejati S., Briand L., Bruckmann T., Poull C. *Search-based automated testing of continuous controllers: Framework, tool support, and case studies*. Information and Software Technology. 2015;57:705-722.

[8] Blum D., Arroyo J., Huang S., Drgoňa J., Jorissen F., Walnum H., Chen Y. Benne K., Vrabie D., Wetter M., Helsen L. *Building optimization testing framework (BOPTEST) for simulation-based benchmarking of control strategies in buildings*. Journal of Building Performance Simulation. 2021;14:586-610.

[9] Santos M., Liu N., Jradi M. *AUSTRET: An Automated Step Response Testing Tool for Building Automation and Control Systems*. Energies. 2021;14:1-20.

[10] McKay, M. D., Beckman, R. J. and Conover, W. J. *A Comparison of Three Methods for Selecting Values of Input Variables in the Analysis of Output from a Computer Code*. Technometrics. 1979;21:239–245.

[11] Modelica Association. *Modelica – A Unified Object-Oriented Language for Systems Modeling* Available at: `https://modelica.org/documents/MLS.pdf` [accessed 28.02.2023].

[12] FMI. *Functional Mock-up Interface for Model Exchange and Co-Simulation* Available at: `https://fmi-standard.org/` [accessed 28.02.2023].

[13] Kümpel A., Teichmann J., Paul Mathis P., Müller D. *Modular hydronic subsystem models for testing and improving control algorithms of air-handling units*. Journal of Building Engineering. 2022;53:104439.

[14] Maier L., Jansen D., Wüllhorst F., Kremer M., Kümpel A., Blacha T., Müller D. *AixLib: An open-source Modelica library for compound building energy systems from component to district level with automated quality management*. Preprint at `https://www.researchgate.net/publication/365475776_AixLib_An_open-source_Modelica_library_for_compound_building_energy_systems_from_component_to_district_level_with_automated_quality_management`

[15] Jelali M. *Control System Performance Monitoring [habilitation]* Germany: Universität Duisburg-Essen; 2010.

[16] Teichmann J., Kümpel A., Mathis P., Müller D. *Improving control quality and reducing pump energy consumption of AHU*. REHVA Journal. 2021;14:586-610.

[17] Wüllhorst F., Storek T., Mehrfeld P., Müller D. *AixCaliBuHA: Automated calibration of building and HVAC systems*. Journal of Open Source Software. 2018;05:30-34.

PROCEEDINGS OF ECOS 2023 - THE 36TH INTERNATIONAL CONFERENCE ON
EFFICIENCY, **C**OST, **O**PTIMIZATION, **S**IMULATION AND ENVIRONMENTAL IMPACT OF ENERGY SYSTEMS
25-30 JUNE 2023, LAS PALMAS DE GRAN CANARIA, SPAIN

Techno-Economic Optimization of an Innovative Plant for Sustainable Iron Reduction

Elisa Corbean[a], Jannik Neumann[b], Frank Dammel[b], Peter Stephan[b], Stefan Ulbrich[a]

[a] Department of Mathematics, Technical University of Darmstadt, Darmstadt, Germany,
{corbean, ulbrich}@mathematik.tu-darmstadt.de
[b] Institute for Technical Thermodynamics, Technical University of Darmstadt, Darmstadt, Germany,
{neumann, dammel, pstephan}@ttd.tu-darmstadt.de

Abstract:

Metal fuels such as iron represent potential energy carriers for large-scale storage and transport of renewable energy. In a circular process renewable energies can be stored in form of iron by thermochemical reduction of iron oxide and the required energy can be released via thermochemical oxidation, time and location independent from the storage process. While existing infrastructure such as coal-fired power plants could be retrofitted to meet the needs for the oxidation process, the conceptualization and construction of new infrastructure for the storage process by reduction is required. This opens up the possibility for a thorough techno-economic assessment of potential processes in order to ensure the optimal process design. Therefore, a techno-economic model of an innovative reduction plant utilizing the flash ironmaking technology for the reduction reactor is developed. The resulting mathematical model describes the operation of the reduction plant in dependence of design variables defining the plant components' dimensions. These design variables together with further process variables are optimized using mathematical optimization with respect to an economic objective function, i.e. the levelized cost of iron, in order to obtain the economically optimal process design. Thorough analyses are performed to assess the impact of changing economic boundary conditions on the optimal process design. Numerical results demonstrate a strong dependence of the cost optimal design on the available renewable energy prices and the obtained levelized cost of iron varies between 0.05 $/kg iron and 0.68 $/kg iron. Thus, choosing appropriate reduction locations with access to low renewable energy prices is crucial for the economic competitiveness of the considered process. The results further confirm an expected trade-off between total investment costs and yearly energy consumption of the plant components. With increasing cost for renewable energy, energetically more efficient system designs also become economically advantageous, i.e. an increase in the energetic efficiency from η_{sys} = 55.6% to η_{sys} = 69.3% is observable. The electrolyzer turns out to be the dominant plant component both, economically and energetically. Future work will take uncertainties into account to ensure a robust process design and couple the reduction plant to location specific renewable energy systems.

Keywords:

Iron as Energy Carrier; Mathematical Optimization; Metal Fuels; Process Design.

1. Introduction

While the ongoing energy crisis sets various challenges, it also acts as an accelerator for the global renewable capacity expansion [1]. Thus, the role of renewable energies (REs) becomes even more important in the endeavor to tackle climate change. However, the potential for RE is not equally distributed around the globe and their availability is subject to fluctuations over time. This turns the efficient global use of REs into a challenge especially for countries with low RE potential.

Suitable carbon-neutral energy carriers could remedy the situation by allowing long-term storage and secure transport of energy from RE sources. This way the energy carrier could be charged with energy from RE sources in locations with high RE potential, transported to locations with low RE potential, but high demand and the energy could be further stored on-site or released according to current demands.

Metal fuels are currently under investigation [2–4] as candidates for such energy carriers due to their high volumetric energy density [3] and their advantageous storage and transport properties. Especially iron seems to be a promising alternative to hydrogen as RE energy carrier [2, 5].

Using iron as an energy carrier, RE can be stored at sites with high RE potential via the thermochemical reduction of iron oxide with green hydrogen to produce iron. The resulting iron can then be transported to regions where energy is required and released via an oxidation reaction through combustion with air. The produced iron oxide is recycled and can again be charged from RE sources (cf. Fig. 1) leading to a circular

energy economy.
While the retrofit of coal-fired power plants for the iron combustion proves to be a promising way for making use of already existing infrastructure and assets [4, 6], the need for developing cost and energy efficient infrastructure at the reduction sites persists. Therefore, this work focuses on an optimal process design for an innovative plant reducing iron oxide to iron using green hydrogen obtained from RE sources.
The considered reduction plant uses a flash ironmaking reactor, which is described in [7] and found to be advantageous with respect to the size and energy requirements compared to common shaft furnace reduction plants. Figure 2 depicts the considered plant with all associated components including the water electrolysis for the production of green hydrogen. The goal of this work is to find an optimal process design for the assessed plant with respect to techno-economic objectives.

Figure 1: The iron energy cycle

Table 1: Design variables of the process components

Component	Design variable	Unit
Flash Reactor	Volume V	m^3
Air Heater Iron Oxide Preheater Hydrogen Preheater Condenser	Area A	m^2
Air Fan Recycle Compressor Electrolyzer	Electric power P_{el}	MW

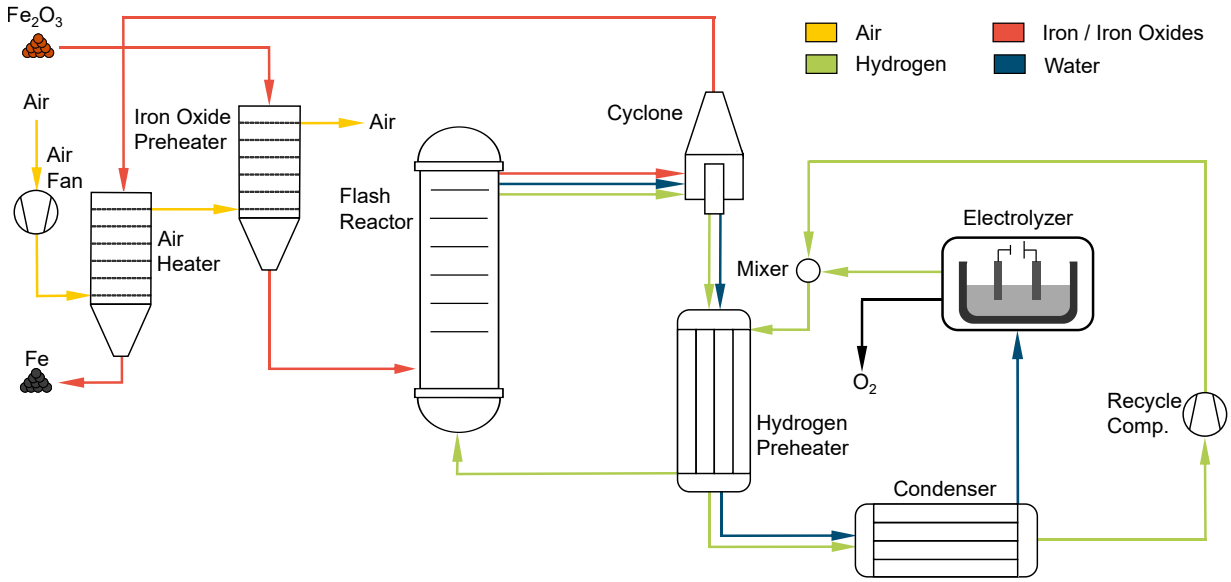

Figure 2: Components of an innovative plant for thermochemical reduction of iron oxides to iron

2. Process description

Blast furnace-based ironmaking remains dominant for steel production, but a more sustainable approach is emerging with the shaft furnace reduction method. Unlike blast furnaces that use coal as a reduction agent, shaft furnaces can reduce CO_2 emissions by utilizing natural gas or green hydrogen. While pure hydrogen-based shaft furnace direct reduction on a large scale has not yet been achieved, it has been technically proven feasible. However, iron oxide pellets are required as feedstock, and must be processed further into iron powder for the oxidation. An alternative technology is the flash ironmaking process [8, 9], which directly utilizes fine iron ore particles without additional pre-treatment, eliminating the need for pelletization and powder production. The flash reactor reduction technology is a high-intensity process that operates at high temperatures, unlike other gas-based ironmaking processes (shaft furnaces or fluidized-bed reactors). To attain these temperatures, the hydrogen reduction of iron oxide requires an external heat source. This heat can be generated internally by burning a portion of the reducing agent.
The reduction process depicted in Fig. 2 starts with fine iron oxide powder, the product of the previous oxidation, which is preheated in a bulk solid heat exchanger (iron oxide preheater). Subsequently, it is fed into the flash reactor where it reacts with a preheated hydrogen stream, yielding iron and water (R1). Heat is supplied

to the reactor, to sustain this endothermic reaction. The reactor effluent is then separated through a cyclone, with the hot iron being cooled down by a bulk solid heat exchanger (air heater) that uses the available heat to preheat the iron oxide feed via heat transfer to a secondary fluid (air). The hot gaseous reaction products (water and unreacted hydrogen) leaving the cyclone are used in a regenerative heat exchanger (hydrogen preheater) to preheat the gaseous reactants and the majority of the water is condensed out in the condenser. The remaining hydrogen is then recycled and merged with hydrogen produced by the electrolyzer, before being fed to the hydrogen preheater and finally entering the flash reactor.

The conversion of iron oxides (Fe_2O_3) to iron (Fe) and water (H_2O) through reduction with hydrogen (H_2) is described by the global reaction (R1). However, it is actually a step wise reaction sequence that involves intermediate iron oxides other than hematite (Fe_2O_3) [10]. These intermediate steps are not taken into account in accordance with the later-used kinetic model [8]. Furthermore, excess hydrogen, which is quantified with a hydrogen equivalence ratio λ_{H_2}, is required due to thermodynamic equilibrium limitations [8, 10] that may inhibit the full conversion.

$$Fe_2O_3 + 3\,\lambda_{H_2} H_2 \longrightarrow 2\,Fe + 3\,\lambda_{H_2} H_2O + 3\,(\lambda_{H_2}\text{-}1)\,H_2 \qquad \Delta H_r(\lambda_{H_2} = 1) = 98.77\,\mathrm{J\,mol^{-1}} \tag{R1}$$

The reaction is modelled on the basis of a global nucleation and growth rate equation for the overall reduction processes derived by Chen et al. [8]:

$$\frac{dX}{dt} = 4.41 \cdot 10^7 e^{\frac{-E_A}{R \cdot T}} \cdot \left(p_{H_2} - \frac{p_{H_2O}}{K_{eq}}\right) \cdot (1 - X), \tag{1}$$

where X is the fractional reduction degree, R is the universal gas constant, T the reaction temperature in K, $E_A = 214\,000\,\mathrm{J/mol}$ the activation energy of the reaction, p_s corresponds to the partial pressures in atm and K_{eq} to the equilibrium constant. From the rate law it becomes clear that the presence of water negatively affects the reduction by lowering the partial pressure of hydrogen but also decreases the thermodynamic reducing power of the gas due to the equilibrium limitations. This can have further implications on the whole process, since the gaseous effluent should be recycled and in ideal case purified into pure hydrogen to inhibit the negative impact. The kinetic law was derived based on hematite particles with an average size of 20 µm and a temperature range between 1423 K-1623 K [8]. This temperature range is used as variable bound for the reactor temperature during the optimization process to assure its correct operation.

3. Mathematical model

Detailed process analyses are crucial in the development of new technologies. Thermodynamic feasibility studies and energetic assessments offer valuable insights into the energetic efficiency of new processes. However, to evaluate the potential profitability and competitiveness of new processes, techno-economic considerations must also be taken into account. Therefore, a techno-economic assessment of the previously described reduction process is performed by directly applying mathematical optimization. This requires an explicit mathematical process description which is then used to obtain the cost optimal design of the system components for varying conditions (i.e. price for RE) by applying mathematical optimization algorithms to an economic objective function. Thus, a cost optimal design refers to a process design minimizing the economic objective, in this case the levelized cost of iron.

Every module in the reduction plant is modelled via incoming and outgoing mass flow rates $\dot{m}_{in,s}$ and $\dot{m}_{out,s}$ associated with species s, temperatures T_{in} and T_{out}, system pressures p_{in} and p_{out} as well as further component specific variables. Appropriate variable bounds on these process variables (e.g. reactor temperature) assure the correct operation of the modules. The underlying processes of each module are then described in terms of (in)equality constraints, including mass, species, and energy balances, as well as pressure changes and equations specific to individual components. The formulation of these technological constraints is closely linked to the cost functions of the equipment, which results in a complex nonlinear interplay between the employed thermodynamic and economic models.

3.1. Design variables

Since the optimization objective aims at finding the cost optimal process design, the functionalities of the modules are described in dependence on design variables, which are summarized in Table 1, responsible for the dimensioning of the modules.

In the case of the heat exchangers and the condenser, their respective area A together with the heat transfer coefficient U, the maximum temperature difference ΔT_{max} and the minimum temperature difference ΔT_{min} determines the heat flow $\dot{Q}_{therm}$ transferred from the hot flow to the cold flow [11]:

$$\dot{Q}_{therm} = \frac{\Delta T_{max} - \Delta T_{min}}{\ln\left(\frac{\Delta T_{max}}{\Delta T_{min}}\right)} \cdot U \cdot A. \tag{2}$$

For compressors, the necessary electric power P_{el} for obtaining an output pressure of p_{out} is determined in dependence of the inlet pressure p_{in}, temperature T_{in}, mass flow rate $\dot{m}_{in}$, specific heat capacity $c_{p,in}$ as well as the electric drive efficiency η_{mot} and the isentropic efficiency η_{is}:

$$P_{el} = \frac{1}{\eta_{mot} \cdot \eta_{is}} \cdot \dot{m}_{in} c_{p,in} T_{in} \cdot \left(\left(\frac{p_{out}}{p_{in}} \right)^{\frac{\kappa-1}{\kappa}} - 1 \right). \tag{3}$$

Lastly, the required electric power for the electrolyzer is determined via the produced mass flow of hydrogen $\dot{m}_{out,H_2}$, its lower heating value $LHV(H_2)$ and the electrolysis efficiency η:

$$P_{el} = \frac{1}{\eta} \cdot \dot{m}_{out,H_2} \cdot LHV(H_2). \tag{4}$$

The reactor modeling including the interplay of its volume V (i.e. residence time) and the time dependent reduction process is addressed in more detail, subsequently.

3.2. Reactor modeling

The flash reactor is at the heart of the reduction plant and its model is therefore crucial for the analysis of the entire process. While the other components do not require a temporal resolution of the residence time, this is crucial for the adequate description of the reduction reaction taking place in the reactor. Recall the global rate equation (1) modeling the time dependent fractional reduction degree X. The considered plug flow reactor model further assumes time dependent partial pressures p_{H_2}, p_{H_2O} within the reactor to account for the impact of the proceeding reaction (i.e. change in partial pressure lead to a change in reaction rate). In the real process the required external heat is provided by partial oxidation of some hydrogen. However, in the deployed reactor model isothermal conditions are assumed, which are achieved by external heat supply. As before, let $\dot{m}_{in,s}$ denote the mass flow rate of species s at the reactor inlet and in addition let $\dot{m}_{R,s}(t)$ denote the mass flow rate of species s throughout the residence time in the reactor R and $\overline{M}_s$ the molar mass of species s. Then, the mass balances of the components considering the global reaction (R1) are described by

$$\dot{m}_{R,Fe_2O_3}(t) = (1 - X(t)) \cdot \dot{m}_{in,Fe_2O_3}, \qquad \dot{m}_{R,Fe}(t) = 2X(t) \cdot \dot{m}_{in,Fe_2O_3} \frac{\overline{M}_{Fe}}{\overline{M}_{Fe_2O_3}}, \tag{5}$$

$$\dot{m}_{R,H_2O}(t) = \dot{m}_{in,H_2O} + 3X(t) \cdot \dot{m}_{in,Fe_2O_3} \frac{\overline{M}_{H_2O}}{\overline{M}_{Fe_2O_3}}, \qquad \dot{m}_{R,H_2}(t) = \dot{m}_{in,H_2} - 3X(t) \cdot \dot{m}_{in,Fe_2O_3} \frac{\overline{M}_{H_2}}{\overline{M}_{Fe_2O_3}}. \tag{6}$$

These representations can be used to define the time dependent partial pressures

$$p_s(X(t)) = p_{in} \frac{\frac{\dot{m}_{in} x_{R,k}(t)}{\overline{M}_k}}{\frac{\dot{m}_{in} x_{R,H_2}(t)}{\overline{M}_{H_2}} + \frac{\dot{m}_{in} x_{R,H_2O}(t)}{\overline{M}_{H_2O}}}, \quad s \in \{H_2, H_2O\}. \tag{7}$$

Using (1) and (5) to (7) the reactor is modelled as follows

$$\frac{dX}{dt} = 4.41 \cdot 10^7 \cdot e^{\frac{-E_A}{R \cdot T}} \cdot \left(p_{H_2}(X(t)) - \frac{p_{H_2O}(X(t))}{K_{eq}(T(t))} \right) \cdot (1 - X(t)), \qquad X(0) = 0. \tag{8}$$

To use the presented reactor model as optimization constraints, the differential equation (8) is discretized using an implicit Euler discretization scheme with a fixed number of discretization steps N and a variable discretization step length h to represent the solution X_ℓ at time steps $t_\ell, \ell = 0, \dots, N-1$. The residence time within the reactor is thus given by t_{N-1} and has to coincide with the ratio of the reactor volume V and the volumetric flow rate $\dot{V}$, i.e. $t_{N-1} = \frac{V}{\dot{V}}$, where $\dot{V}$ is defined by the general gas law.

3.3. Economic objective function

The overall goal of industrial production is to maximize profits, which can be accomplished by either raising the product's selling price or lowering production costs. The latter is typically achieved through the analysis of marginal production costs. To this end, the levelized cost of iron (*LCOI*) serves as the economic objective function, taking into account various costs such as capital expenditures (*CAPEX*), operational expenditures (*OPEX*), energy costs (C_{el}), and transport expenses (C_{trans}), all relative to the yearly production of iron ($m_{Fe,year}$):

$$LCOI = \frac{CAPEX + OPEX + C_{el} + C_{trans}}{m_{Fe,year}}. \qquad [\$/\text{kg iron}] \tag{9}$$

Within the framework of the previously outlined iron-energy cycle (cf. Section 1.), transport costs are linked to long-distance transport costs, while the expenses associated with the feedstock (Fe_2O_3) are not taken into

consideration, as it is continuously recycled. Similarly, costs pertaining to short-distance transport and related logistics are excluded from this investigation. Additionally, it is assumed that the reduction degree of the iron has little effect on its suitability for the generation of high-temperature heat or electricity. Nevertheless, it is important to note that reducing the degree of reduction leads to an increase in the amount of material transported, resulting in higher transportation costs that are taken into account in the objective function.

3.3.1. Capital expenditures

The annuity method is a widely recognized approach for assessing projects from an economic viewpoint because of its simplicity and transparency [12]. It involves computing uniform yearly capital expenditures *CAPEX* that correspond to the present value of the initial investment expenses (*CC*), which can be determined by applying a capital recovery factor (*CRF*), i.e. a constant discount rate i over the project's economic life span n:

$$CAPEX = CRF \cdot CC = \frac{i \cdot (1+i)^n}{(1+i)^n - 1} \cdot CC. \qquad [\$/\text{year}] \tag{10}$$

3.3.2. Operational expenditures

The *OPEX* contrasts the *CAPEX* and comprises maintenance and operating costs. It is commonly provided as a fraction γ of the capital costs: According to [13], the yearly maintenance cost can be estimated to be 6% of the fixed capital cost *CC*. This yields

$$OPEX = \gamma \cdot CC. \qquad [\$/\text{year}] \tag{11}$$

3.3.3. Energy cost

The energy cost for the presented reduction plant refers to the electricity cost c_{el} assumed to come from RE sources and used for the water electrolysis, the compressors, as well as for the heat requirements of the reactor:

$$C_{el} = (P_{el}^{electrolyzer} + P_{el}^{air\ fan} + P_{el}^{recycle\ compressor} + \dot{Q}_{therm}^{reactor}) \cdot c_{el} \cdot t_{year}, \qquad [\$/\text{year}] \tag{12}$$

where P_{el}^{i} denotes the electric power of component i, $\dot{Q}_{therm}^{reactor}$ accounts for the consumed power of the reactor's external heat supply and t_{year} denotes the operation hours within one year.

3.3.4. Transport cost

As previously explained, only long-distance transport costs will be considered. Therefore, it is assumed that the yearly produced iron $m_{Fe,year}$ and the yearly remaining iron oxide $m_{Fe_2O_3,year}$ have to be transported over a long-range distance $dist_{trans}$ at a daily transport cost of $c_{trans,day}$ using n_{ships} with vessel size m_v each travelling with velocity v_{trans}. In total, this yields the following yearly transport costs:

$$C_{trans} = \frac{dist_{trans}}{v_{trans}} \cdot n_{ships} \cdot c_{trans,day} = \frac{dist_{trans}}{v_{trans}} \cdot \frac{m_{Fe,year} + m_{Fe_2O_3,year}}{m_v} \cdot c_{trans,day}. \qquad [\$/\text{year}] \tag{13}$$

3.3.5. Fixed capital cost

The fixed investment costs are based on the cost for the major equipment used in the process (i.e. within the given flow diagram in Fig. 2), which is a common way to derive appropriate estimates in early stages of process synthesis [13, 14]. The cost of each module is determined in dependence of the module size, i.e. the design variables introduced in Section 3.1. The estimated capital cost then results in the sum over all estimated equipment costs. The different components of the capital cost are briefly summarized in the following, for further details please refer to [13].

Costs are commonly represented as power law of capacity, i.e. the equipment cost C_E with capacity Q_E is given by $C_E = C_B\left(\frac{Q_E}{Q_B}\right)^M$, with known base costs C_B of the equipment with base capacity Q_B and an equipment dependent constant M.

Furthermore, the validity of economic data is highly dependent on the publishing date and therefore requires normalization to a common basis which can be done by the means of cost indices (e.g. Chemical Engineering Plant Cost Index (CEPCI) [15]). To account for different materials, design pressures, and temperatures, additional correction factors are used to determine the purchase costs of equipment. These factors include f_M for materials, f_p for design pressure, and f_T for design temperature. In addition, piping costs are accounted for with the factor f_{PIP}, while other direct costs, such as equipment erection and instrumentation, and indirect costs, including engineering and construction, as well as working capital are considered in the total cost calculation with the factor f_{misc}. This leads to the following representation of the fixed capital costs:

$$CC = \sum_j \left(\left(f_M f_p f_T (1 + f_{PIP}) \right)_j + f_{misc} \right) \frac{CEPCI_{year}}{CEPCI_{reference\ year}} C_{B,j} \left(\frac{Q_{E,j}}{Q_{B,j}} \right)^M. \qquad [\$] \tag{14}$$

3.4. Properties and assumptions

Modern ironmaking plants produce between 0.3 Mio and 3 Mio tons of iron per year [7]. Therefore, it is assumed that the continuous Fe_2O_3 feed into the reduction plant amounts 50 kg s^{-1}, leading to 34.97 kg s^{-1} of produced iron when assuming a fractional reduction degree of $X = 1$ and thus to 0.99 Mio tons/year when assuming 328 continuous operating days of the reduction plant and to 1.06 Mio tons/year when assuming 350 continuous operating days.

In the following, several properties and assumptions used in the model definition are summarized. Note that in the computation of numerical results (cf. Section 4.) for properties characterized by feasible ranges, as long as not stated otherwise, the mean value of the range is considered.

Thermodynamic properties such as molar masses are taken from [16]. In order to avoid an increase in the model complexity by modelling discontinuous piecewise polynomial representations for the temperature dependent enthalpy using NASA Glenn coefficients [16], a linear approximation for the enthalpy is computed and used to determine temperature independent constant specific heat capacity values.

When analyzing the numerical results, besides the already presented metrics also the energetic efficiency of the considered system will be assessed. This metric is defined by

$$\eta_{sys} = \frac{HV(Fe) \cdot \dot{m}_{Fe}}{(P_{el}^{electrolyzer} + P_{el}^{air\ fan} + P_{el}^{recycle\ compressor} + \dot{Q}_{therm}^{reactor})}, \tag{15}$$

i.e. the ratio of the energy stored in iron (given by the product of the heating value $HV(Fe)$ of iron and the produced mass flow rate of iron $\dot{m}_{Fe}$) and the total energy supplied to the process as defined in (12).

Table 2: General economic and transport assumptions

Variable	Value/Range	Reference
OPEX fraction γ of *CC*	6%	[13]
Interest rate i	5–8 %	[17]
Economic life time n	20–25 years	[17]
Price for RE c_{el}	0.01–0.10 \$/kWh	[18]
Operational days	328–350 days	[17]
Transport distance	3000–20 000 km	Assumption
Vessel size	160 000 t	[5]
Daily transport costs	5000–50 000 \$/day	[19]
Transport speed	624 km/day	[5]

3.4.1. Technological assumptions

Heat Exchangers

It is assumed that any heat loss originating from other components than the reactor is associated to the heat exchangers, i.e. the air heater, the iron oxide preheater, the hydrogen preheater and the condenser. It is estimated that between 1–5 % of the transferred heat will be lost to the environment instead of being transferred to the cold medium. Further assumptions concerning the heat exchangers are summarized in Table 3.

Cyclone

By assumption, all of the hot reduced iron is separated from the gaseous residual stream within the cyclone. While the cyclone is not specifically designed and optimized for this process, values from a high loaded hot gas cyclone given in [11] are used. Based on this design, the pressure drop is expected to be within the range of $\Delta p = 0.1 - 0.2$ bar.

Electrolyzer

The system efficiency based on the lower heating value of the electrolysis is predicted to be in the range of 50-74 % according to IEA and IRENA [20, 21]. In this use case an efficiency of $\eta = 71\%$ is assumed.

Compressors

For the air fan and the recycle compressor an isentropic efficiency of $\eta_{is} = 85\%$ and an electrical drive efficiency of $\eta_{mot} = 95\%$ is assumed. The heat capacity ratio κ as in (3) is assumed to be $\kappa = 1.4$ for both, the air compressor and the hydrogen recycle compressor.

Table 3: Heat exchanger assumptions including type, pressure drop Δp and heat transfer coefficient U

Component	Type	Δp [bar]	U [W m^{-2} K^{-1}]	References
Iron Oxide Preheater Air Heater	Bulk solid heat exchanger	0.14	100-144	[22–25]
Hydrogen Preheater	Alternating regenerators	0.14	6	[11]
Condenser	Tube and shell	0.05	300-1200	Assumption / [11, 22]

3.4.2. Economic assumptions

As presented in Section 3.3.5. the fixed capital cost includes several correction factors and economic indices for cost normalization. The correction factors are chosen according to [13] and take the following values. For all components except for the electrolyzer the material correction factor f_M is assumed to be f_M = 3.4 (high grade stainless steel), the pressure correction f_p = 1.0, the piping correction factor f_{PIP} = 0.7 and the remaining factors are summarized in f_{misc} = 5.1. The electrolyzer and associated periphery costs are directly taken from the literature. Consequently, the correction factors are set to $f_M = f_p = f_{PIP}$ = 1.0 and f_{misc} = 0. In order to account for potential high process temperatures, a correction factor for temperature is extrapolated based on values given in [13]: $f_T = \max(1,\ 2.75\,^{\circ}\mathrm{C} \cdot 10^{-3} \cdot T_{max} + 0.742)$ with T_{max} denoting the maximum process temperature for each component. The costs are normalized to the year 2021 using the CEPCI of 708.0 [15]. All base costs, base capacities, reference years and indices can be found in Table 4. According to [20, 21] the electrolyzer capital cost can be estimated to be in the range of 450-1400$/kW multiplied by the electric power.

Table 4: Capital costs of equipment; the hydrogen preheater costs are based on [26], the cost of the electrolyzer is estimated based on [20, 21] and the cost functions of all other components are based on [13]

Component	Ref. year /CEPCI	$C_{B,j}$[$]	$Q_{B,j}$	M	$C_{E,j}$
Iron Oxide Preheater Air Heater Condenser	2000 / 391.1	$3.28 \cdot 10^4$	80 m^2	0.68	
Air compressor Recycle Compressor	2000 / 391.1	$9.84 \cdot 10^4$	0.25 MW	0.46	$\frac{CEPCI_{2021}}{CEPCI_{reference\ year}} C_{B,j} \left(\frac{Q_{E,j}}{Q_{B,j}}\right)^M$
Reactor	2000 / 391.1	$1.15 \cdot 10^4$	5 m^3	0.53	
Hydrogen Preheater	1981 / 297.0	$0.85 \cdot 10^6$	6555 m^2	0.6	
Electrolysis	–	–	–	–	925 \$/kW$_{el}$ $\cdot P_{el}$

4. Numerical results and discussion

The presented techno-economical model with the introduced *LCOI* (cf. (9)) as objective is optimized using mathematical optimization algorithms in order to obtain the optimal process design and operation of the reduction plant for varying economic assumptions (i.e. price for RE, *CRF*). Given the significant variation in RE prices depending on the location and type of renewable energy plant [18], and the sensitivity of annualized capital costs to the *CRF* - and consequently to the assumed interest rate and economic lifetime - the impact of these economic constraints on the *LCOI* and the resulting optimized plant designs is evaluated. It should be noted that the *LCOI* is primarily influenced by the total capital cost (*CC*) in terms of both capital expenditure (*CAPEX*) and operating expenditure (*OPEX*), as well as the yearly energy consumption in terms of C_{el}. Additionally, the transportation costs (C_{trans}) and annual iron production ($m_{Fe,year}$) are indirectly impacted by the yearly energy consumption, as the energy consumed during the electrolysis process determines the quantity of produced iron, which subsequently affects the mass fractions of unreduced iron oxide and produced iron, ultimately influencing the transportation costs. Therefore, it is expected that the solutions, obtained by minimizing the *LCOI*, represent trade-offs between the yearly energy consumption and the total capital cost. To investigate and quantify this trade-off, the optimization is performed multiple times with varying values for c_{el} and *CRF* weighting the yearly energy consumption and the total capital costs in the objective function.
The resulting optimization problem is implemented using PySCIPOpt [27], an interface to the mixed-integer nonlinear problem solver SCIP [28], relying on a spatial branch-and-bound algorithm.
Although SCIP is able to perform global optimization, the following results could not be certified to be global solutions within reasonable time due to the complexity of the model characterized by nonlinear model equations as well as the discretized ODE constraint presented in Section 3.2. The solutions are obtained by a local NLP solver used as heuristic in the SCIP framework and therefore constitute local optimal solutions.

4.1. Fixed CRF and varying energy costs

In a first step, the optimization problem is solved for varying energy costs $c_{el} \in \{0, 10, 55, 70, 100, 150, 200\}$ [$/MWh] with a fixed *CRF* $\approx$ 0.085, i.e. assuming an economic life time of n = 23 years and an interest rate of i = 6.5%. The obtained objective values and the corresponding shares of *CAPEX*, *OPEX*, energy and transport costs are depicted in Fig. 3. The resulting *LCOI* varies between 0.05 \$/kg iron and 0.68 \$/kg iron. As to be expected there is a close to linear relation between the energy price and the resulting *LCOI*. The variance in the *LCOI* showcases the high dependency of the competitiveness of the investigated process on suitable locations with low prices for RE. The figure also shows that the transportation costs play an insignificant role for the *LCOI*. This suggests, that it could be beneficial to choose reduction locations with rather high transport distances if in return RE is available at low prices. The results further show that at high prices for RE (e.g.

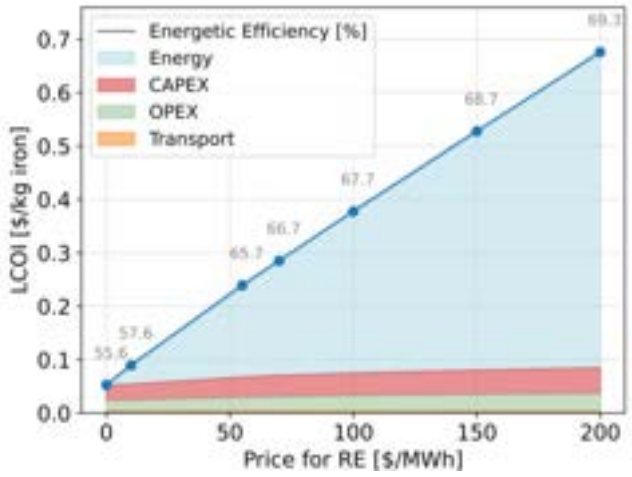

Figure 3: Objective values obtained by minimizing the *LCOI* with a fixed *CRF* ≈ 0.085 and varying values for the energy cost c_{el} of RE

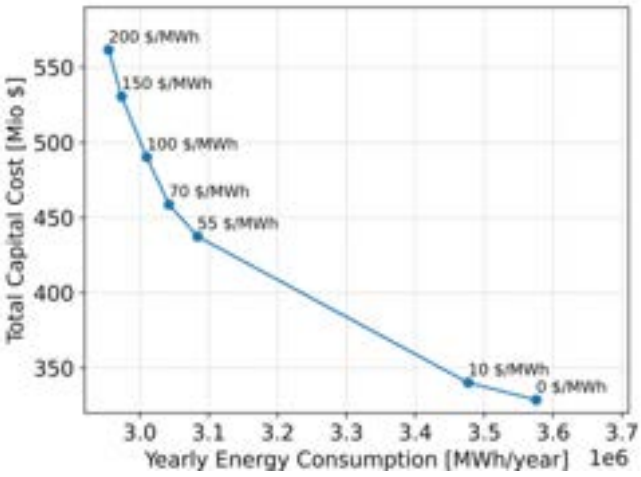

Figure 4: Yearly energy consumption versus total capital cost at the optimization solutions for fixed *CRF* and varying values for c_{el}

200 \$/MWh), energy costs are dominant, accounting for a significant percentage (87.5%) of the *LCOI*. In contrast, at low energy prices (e.g. 10 \$/MWh), a balance is observable between energy and equipment-related costs, with energy costs contributing 39.8% to the *LCOI*. Additionally, with increasing cost for RE, also the energetic efficiency of the system increases from η_{sys} = 55.6% to η_{sys} = 69.3%. For further analyses Fig. 4 shows the relationship between the yearly energy consumption and the total capital cost for the different values of c_{el}. The results indicate that as the price for RE increases, process designs with lower energy demands (and therefore higher energetic efficiencies), but higher total capital costs (due to larger component dimensions) are economically more advantageous. This suggests that an optimal design of the considered reduction plant represents a trade-off between the yearly energy consumption and the total investment costs and is highly dependent on the cost assumptions for RE.

The optimal design variables illustrate the described behaviour. With increasing c_{el} the reactor volume increases from 1574 to 5519 m^3 and the fractional reduction degree X increases from 94.6% to 97.6%, while the reactor temperature remains constant at 1423 K and the hydrogen equivalence ratio λ_{H_2} only varies slightly between 2.55 and 2.32. The increase in the reduction degree is directly related to an increase in the required electrical power $P_{el}^{electrolyzer}$ of the electrolyzer. The condenser area shows an increase from $0.73 \cdot 10^3$ to $1.53 \cdot 10^3$ m^2, the air preheater area an increase from $0.03 \cdot 10^3$ to $3.56 \cdot 10^3$ m^2 and especially the hydrogen preheater an increase from $1.53 \cdot 10^3$ to $55.4 \cdot 10^3$ m^2. The increasing dimensions of the design variables account for the higher total capital cost with increasing RE prices. Regarding the yearly energy consumption, the values for the recycle compressor and the air compressor only vary little, and the yearly energy consumption of the electrolyzer increases from 2.46 to 2.54 TWh due to the increasing reduction degree as explained before. However, the yearly energy consumption of the external heat supply for the reactor decreases from 1.1 to 0.4 TWh. This leads to the overall decreasing yearly energy consumption for increasing RE prices.

Upon examining the shares of the total capital cost of each component, as depicted in Fig. 5, it can be noted that in a scenario where RE is free of charge, the electrolyzer comprises over 80% of the investment cost. As the cost of RE increases, the proportion of investment cost attributed to the electrolyzer declines, yet it still constitutes over 50% of the investment cost at the highest considered cost for RE. Furthermore, the electrolyzer is responsible for nearly 70% of the yearly energy consumption with c_{el} = 0 \$/MWh and for more than 85% with c_{el} = 200 \$/MWh. Considering that the electrolyzer incurs substantial capital costs and energy demand, it has the highest potential for reducing energy demand, capital costs, and consequently the *LCOI* through technological improvements.

Although the costs for turbo-machinery are negligible, the cost shares of the heat recovery equipment, including the air heater, the iron oxide preheater, and the hydrogen preheater experience a significant increase with increasing costs of RE. As the sizes of the associated heat exchangers increase, along with their corresponding costs, a greater amount of the available sensible heat within the reactor effluents can be recovered, resulting in decreased energy dissipation in the condenser and lower residual energy within exiting streams. Ultimately this leads to a reduced energy demand of the reactor. Especially the regenerative hydrogen preheater plays a crucial role for the heat recovery and the reduced energy demand, which is reflected by its increasing share of the capital costs for higher energy costs.

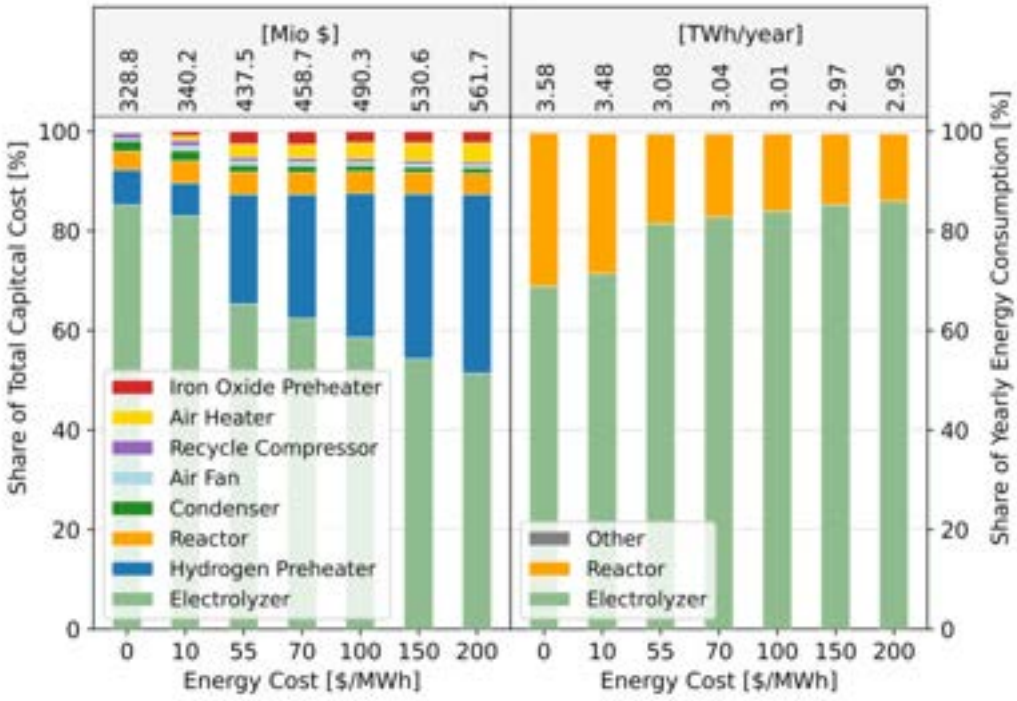

Figure 5: Components' shares of the total capital cost and the yearly energy consumption at the optimization solutions for fixed *CRF* and varying values for c_{el}.

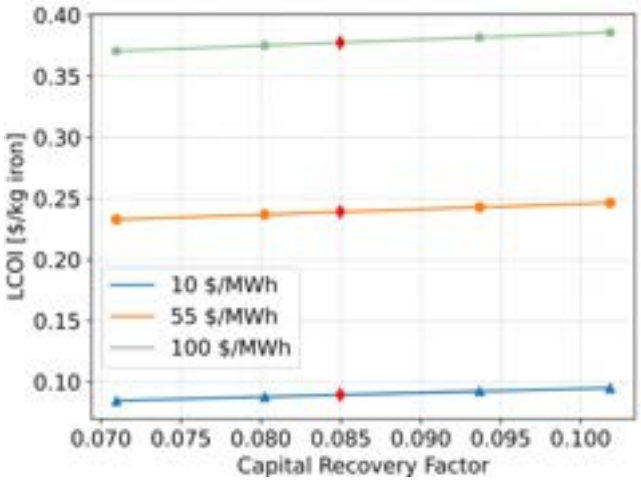

Figure 6: Objective values obtained by minimizing the *LCOI* with varying values for $CRF \in \{0.071, 0.080, 0.094, 0.102\}$ and $c_{el} \in \{10, 55, 100\}$ [$/MWh]; red diamonds represent base *CRF* (n = 23 years, i = 6.5%)

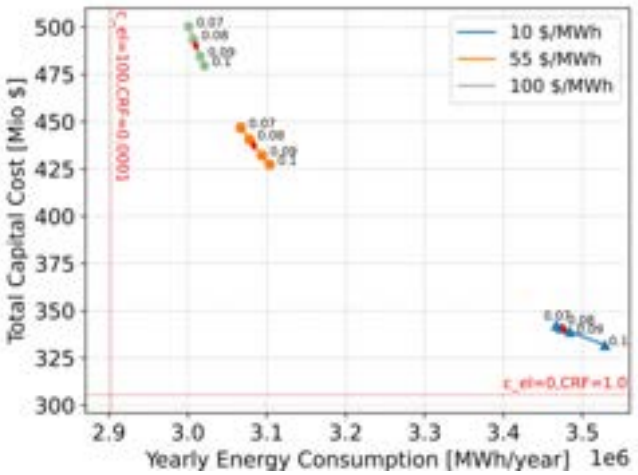

Figure 7: Yearly energy cost versus total capital cost at the optimal solutions for varying values of *CRF* and c_{el}; red diamonds represent base *CRF* (n = 23 years, i = 6.5%); lower bounds obtained by optimization with the specified parameters

4.2. Varying CRF and varying energy costs

As mentioned earlier, the impact of capital costs on the *LCOI* is significant at low to moderate prices for RE. However, the annualized capital costs demonstrate high sensitivity to the assumed *CRF*, and thus, to the assumed interest rate and economic lifetime. To address this uncertainty, the optimization problem was solved for varying energy costs $c_{el} \in \{10, 55, 100\}$ [$/MWh] and varying values for $CRF \in \{0.071, 0.080, 0.094, 0.102\}$ corresponding to economic life times of n = 20 and n = 25 years and interest rates of i = 5 and i = 8%. Figure 6 shows the obtained objective values for the different RE costs in dependence of the *CRF* values together with the *LCOI* for the base case (n = 23 years, i = 6.5%, red diamonds) considered in the previous section. Again

an expected nearly linear relation and a clear shift depending on the energy cost is observable. For c_{el} = 10 \$/MWh, the *LCOI* depending on the *CRF* varies between 0.085 \$/kg iron (-5.5% compared to base *CRF*) and 0.095 \$/kg iron (+6.1% compared to base *CRF*), for c_{el} = 55 \$/MWh between 0.233 \$/kg iron (-2.6%) and 0.246 \$/kg iron (+3.1%) and for c_{el} = 100 \$/MWh between 0.371 \$/kg iron (-1.8%) and 0.386 \$/kg iron (+2.2%) demonstrating the sensitivities of the *LCOI* depending on c_{el} and *CRF*. The results show that the relative impact of the *CRF* assumptions increases for low RE prices.
In addition, the total capital cost is plotted against the yearly energy consumption in Fig. 7 for the varying values of *CRF* and c_{el}. It can be seen, that the total capital cost decreases with increasing values of *CRF* and decreasing values of c_{el}, whereas the yearly energy consumption increases with increasing values of *CRF* and decreasing values of c_{el}. This again indicates the trade-off between the total investment costs and the yearly energy consumption mentioned before. The red lines show the lower bounds for the total capital cost and the yearly energy consumption. On the one hand, the lower bound for the capital cost is obtained by solving the optimization problem with c_{el} = 0 and *CRF* = 1.0, resulting in *CC* = 305.6 Mio \$/year. On the other hand, the lower bound for the yearly energy consumption is obtained by solving the optimization problem with c_{el} = 100, *CRF* = 0.0001 and γ = 0.0 (*OPEX* fraction of *CC*), resulting in a yearly energy consumption of 2.9 TWh/year. These extreme cases result in energetic efficiencies of η_{sys} = 71.6% for high c_{el} and low *CRF* and η_{sys} = 55.4% for low c_{el} and high *CRF* underlining the strong dependence of the optimal process design on the economic boundary conditions and showing the techno-economic limits (highest achievable efficiency vs. lowest achievable capital cost) for the investigated reduction plant.

5. Conclusion and outlook

This work has presented a techno-economic analysis of an innovative reduction plant, based on the flash ironmaking technology, that could be part of a circular energy economy allowing the large-scale storage and transport of RE using iron as energy carrier. The assessment was performed with the goal of investigating the influence of changing economic boundary conditions (price for RE, *CRF*) on the economically optimal process design.
Based on the performed analyses, it can be concluded that the price for RE has a significant impact on the *LCOI*. The resulting *LCOI* varies between 0.05 \$/kg iron and 0.68 \$/kg iron for energy costs between 0 \$/MWh and 200 \$/MWh, respectively. The investigation reveals that changing RE prices lead to noteworthy differences in design parameters such as component dimensions. As the cost of RE rises, effective heat recovery becomes increasingly important with respect to the *LCOI*, resulting in higher capital costs due to larger equipment, but lower energy demands and higher energetic efficiencies (η_{sys} = 55.6% to η_{sys} = 69.3%). In addition, the results emphasize that access to low-cost RE can offset the expenses linked with long-distance transportation. Since RE costs outweigh transport costs, it can be inferred that selecting appropriate reduction sites with access to affordable RE is crucial. Varying *CRF* values (i.e. economic lifetime and interest rate) further reinforce the trade-off between total capital costs and yearly energy consumption, even though the influence of the considered *CRF* values is less prominent than the change in RE prices. Yet, for lower RE prices, the relative effect of changing *CRF* assumptions increases.
Throughout the analysis, the reduction plant was assumed to operate continuously for a fixed number of operating days, assuming continuous availability of RE. However, due to the volatile nature of RE availability, intermediate storage options for green hydrogen and/or RE are necessary to ensure the continuous operation of the reduction plant. In future work, the model will be expanded to integrate such storage options and to couple the reduction plant model with models for RE systems, such as photovoltaic and wind power plants. This would enable the optimization of the entire storage process for the iron energy cycle and result in location specific optimal designs, based on different geographic locations and their RE potential. Additionally, considering uncertainties, e.g. fluctuations in the price or availability of RE, and applying robust optimization strategies to obtain robust process designs, would be a valuable direction for future research.

Acknowledgements

Funding by the Hessian Ministry of Higher Education, Research, Science and the Arts - cluster project Clean Circles is gratefully acknowledged.

Nomenclature

A	area, m^2	$\overline{M}$	molar mass, $kg\,kmol^{-1}$
C	cost, \$	$\dot{m}$	mass flow rate, $kg\,s^{-1}$
c_p	specific heat capacity, $J\,kg^{-1}\,K^{-1}$	p	pressure, bar
E_A	activation energy, $J\,mol^{-1}$	P_{el}	electric power, W

Q capacity,

$\dot{Q}_{therm}$ heat flow, W

R universal gas constant, $\mathrm{J\,kg^{-1}\,K^{-1}}$

T temperature, K

t time, s

U heat transfer coefficient, $\mathrm{W\,m^{-2}\,K^{-1}}$

V volume, $\mathrm{m^3}$

$\dot{V}$ volumetric flow rate, $\mathrm{m^3\,s^{-1}}$

Greek symbols

γ *OPEX* fraction of *CC*

Δ difference

η energetic efficiency

κ heat capacity ratio

λ hydrogen equivalence ratio

Subscripts and superscripts

B base

E equipment

el electrical

eq equilibrium

in incoming

is isentropic

M material

max maximum

min minimum

misc miscellaneous

mot motor

out outgoing

p pressure

PIP piping

R reactor

s species

sys system

T temperature

therm thermal

trans transport

v vessel

References

[1] IEA. *Renewables 2022.* URL: https://www.iea.org/news/renewable-power-s-growth-is-being-turbocharged-as-countries-seek-to-strengthen-energy-security (visited on Jan. 24, 2023).

[2] Bergthorson J. M. *Recyclable metal fuels for clean and compact zero-carbon power*. In: Progress in Energy and Combustion Science 68 (2018), pp. 169–196. DOI: 10.1016/j.pecs.2018.05.001.

[3] Dirven L., Deen N. G., and Golombok M. *Dense energy carrier assessment of four combustible metal powders*. In: Sustainable Energy Technologies and Assessments 30 (2018), pp. 52–58. DOI: 10.1016/j.seta.2018.09.003.

[4] Debiagi P. et al. *Iron as a sustainable chemical carrier of renewable energy: Analysis of opportunities and challenges for retrofitting coal-fired power plants*. In: Renewable and Sustainable Energy Reviews 165 (2022), p. 112579. DOI: 10.1016/j.rser.2022.112579.

[5] Neumann, J. and da Rocha, R. C. et al. *Techno-economic assessment of long-distance supply chains of energy carriers: Comparing hydrogen and iron for carbon-free electricity generation*. In: Applications in Energy and Combustion Science 14 (2023), p. 100128. DOI: 10.1016/j.jaecs.2023.100128.

[6] Janicka J. et al. *The potential of retrofitting existing coal power plants: a case study for operation with green iron*. In: Applied Energy (2023). DOI: 10.1016/j.apenergy.2023.120950.

[7] Sohn H. Y., Fan D.-Q., and Abdelghany A. *Design of Novel Flash Ironmaking Reactors for Greatly Reduced Energy Consumption and CO2 Emissions*. In: Metals 11.2 (2021), p. 332. DOI: 10.3390/met11020332.

[8] Chen F. et al. *Hydrogen Reduction Kinetics of Hematite Concentrate Particles Relevant to a Novel Flash Ironmaking Process*. In: Metallurgical and Materials Transactions B 46.3 (2015), pp. 1133–1145. ISSN: 1073-5615. DOI: 10.1007/s11663-015-0332-z.

[9] Sohn H. Y. *Energy Consumption and CO2 Emissions in Ironmaking and Development of a Novel Flash Technology*. In: Metals 10.1 (2020), p. 54. DOI: 10.3390/met10010054.

[10] Spreitzer D. and Schenk J. *Reduction of Iron Oxides with Hydrogen—A Review*. In: steel research international 90.10 (2019), p. 1900108. ISSN: 1611-3683. DOI: 10.1002/srin.201900108.

[11] *VDI heat atlas*. 2nd ed. VDI-buch. Berlin and New York: Springer, 2010. ISBN: 9783540778769.

[12] Bejan A., Tsatsaronis G., and Moran M. J. *Thermal design and optimization*. New York and Chichester: John Wiley, 1996. ISBN: 0471584673.

[13] Smith R. *Chemical process design and integration*. Second edition. Chichester West Sussex United Kingdom: Wiley, 2016. ISBN: 9781119990147.

[14] Turton R. *Analysis, synthesis, and design of chemical processes*. 3rd ed. Prentice Hall PTR international series in the physical and chemical engineering sciences. Upper Saddle River N.J.: Prentice Hall, 2009. ISBN: 0135129664.

[15] Chemical Engineering. *The Chemical Engineering Plant Cost Index - Chemical Engineering*. 2023. URL: https://www.chemengonline.com/pci-home (visited on Feb. 22, 2023).

[16] McBride B. J., Zehe M. J., and Gordon S. *NASA Glenn Coefficients for Calculating Thermodynamic Properties of Individual Species*. 2002. URL: https://ntrs.nasa.gov/citations/20020085330 (visited on Feb. 22, 2022).

[17] International Energy Agency. *Iron and steel technology roadmap: Towards more sustainable steelmaking*. Energy technology perspectives series. [Paris, France]: IEA Publicatons, 2020. ISBN: 9789264441149. URL: https://iea.blob.core.windows.net/assets/eb0c8ec1-3665-4959-97d0-187ceca189a8/Iron_and_Steel_Technology_Roadmap.pdf (visited on Feb. 21, 2023).

[18] International Renewable Energy Agency. *Renewable power generation costs in 2021*. URL: https://www.irena.org/-/media/Files/IRENA/Agency/Publication/2022/Jul/IRENA_Power_Generation_Costs_2021.pdf?rev=34c22a4b244d434da0accde7de7c73d8 (visited on Feb. 22, 2023).

[19] BIMCO. *Dry bulk - profits surge to multi-year highs as pandemic related demand and disruptions linger*. 2021. URL: https://www.bimco.org/news/market_analysis/2021/20210903-dry-bulk---profits-surge-to-multi-year-highs-as-pandemic-related-demand-and-disruptions-linger (visited on Feb. 22, 2023).

[20] International Energy Agency - IEA. *The Future of Hydrogen: Seizing todays opportunities*. 2019. URL: https://iea.blob.core.windows.net/assets/9e3a3493-b9a6-4b7d-b499-7ca48e357561/The_Future_of_Hydrogen.pdf (visited on Feb. 20, 2023).

[21] The International Renewable Energy Agency. *Green hydrogen cost reduction: Scaling up electrolysers to meet the 1.5C climate goal*. 2020. URL: https://irena.org/-/media/Files/IRENA/Agency/Publication/2020/Dec/IRENA_Green_hydrogen_cost_2020.pdf (visited on June 14, 2021).

[22] Albrecht K. J. and Ho C. K. *Heat Transfer Models of Moving Packed-Bed Particle-to-SCO2 Heat Exchangers*. In: *ASME 2017 11th International Conference on Energy Sustainability*. American Society of Mechanical Engineers, 2017. ISBN: 978-0-7918-5759-5. DOI: 10.1115/ES2017-3377.

[23] Saleh N. S. et al. *Experimental Investigation of a Moving Packed-Bed Heat Exchanger Suitable for Concentrating Solar Power Applications*. In: Applied Sciences 12.8 (2022), p. 4055. DOI: 10.3390/app12084055.

[24] Solex Thermal Sciences. *Solex Thermal Sciences — Energy Efficient Heat Exchanger Technology*. 2023. URL: https://www.solexthermal.com/our-technology/ (visited on Feb. 18, 2023).

[25] John E. Edwards. *Design and Rating of Shell and Tube Heat Exchangers*. 2008. URL: http://www.cit-wulkow.chemstations.com/content/documents/Technical_Articles/shell.pdf (visited on Feb. 20, 2023).

[26] Dastur Engineering International GMBH. *Report on Evaluation of Tender for the Valentine Iron Ore Project in Uruguay*. 1981. URL: https://inis.iaea.org/collection/NCLCollectionStore/_Public/41/076/41076189.pdf (visited on Feb. 20, 2023).

[27] Maher S. et al. *PySCIPOpt: Mathematical Programming in Python with the SCIP Optimization Suite*. In: *Mathematical Software – ICMS 2016*. Springer International Publishing, 2016, pp. 301–307. DOI: 10.1007/978-3-319-42432-3_37.

[28] Bestuzheva K. et al. *The SCIP Optimization Suite 8.0*. ZIB-Report 21-41. Zuse Institute Berlin, Dec. 2021. URL: http://nbn-resolving.de/urn:nbn:de:0297-zib-85309.

Multi-criteria Scenario Development for Linear Optimization Models Utilizing Carbon-Containing Exhaust Gases

Matthias Sadlowski[a], Chae Eon Lim[b]

[a] Fraunhofer Umsicht, Oberhausen, Germany, matthias.sadlowski@umsicht.fraunhofer.de
[b] Fraunhofer Umsicht, Oberhausen, Germany, chae.eon.lim@umsicht.fraunhofer.de

Abstract:

Using the exhaust gases from the steel mill generation to produce chemicals can be a promising carbon capture and utilization (CCU) concept. Applying the model-based mathematical approach with mixed-integer linear programming (MILP) makes it possible to determine the optimal production pathway. However, the MILP aims the uncertain future to evaluate the long-term feasibility. It requires a hypothetical construction to show possible future states. This study aims to develop scenarios as input data for MILP models, representing a comprehensible future description. The investigation domains are determined as the technical, economical, and ecological perspectives to fulfil the multi-criteria evaluation. The factors from domains are projected qualitatively and quantitatively through objective estimations. The mutual relationships between the factors from the different domains such as the electricity price, Carbon footprint, and technical efficiency are implemented properly. The result is represented as five different scenarios: (1) Business as usual (BAU), (2) CO_2 reduction & RE share target (RE-Boom), (3) Technical improvement & Market booming (Market-Boom), (4) Energy & Market crisis (Crisis) and (5) Hydrogen booming (H_2-Boom). The scenarios depict the meaningfully different condition of the CCU concept with the most consistent and plausible combination of the key factors. Additional remarkable results from this study are the rough estimations of the initial capital and operating expenditures through the independently developed method. Consequently, the generated scenarios can be used for MILP models to promote the transparency and traceability of the further decision-making process.

Keywords:

Carbon Capture and Utilization; Multi-criteria Evaluation; Renewable Energy; Scenario Development.

1. Introduction

This study investigates a CCU concept which couples the carbon-emitting steel industry with the chemical and energy industry [1]. Exhaust gases from the blast-furnace, coke oven and basic-oxygen furnace containing large amounts of carbon monoxide, carbon dioxide, methane, hydrogen, and nitrogen serve as raw materials to produce chemicals. Hydrogen is identified as the limiting reactant. Therefore, external supplements utilizing renewable energy (RE) are required to increase its quantity. The exhaust gas can be used to produce products for different markets like methanol (MeOH), acetic acid (AA), ammonia (NH_3) and urea.

The implication of this concept is in a less developed phase. It is still being determined the technical layout of the plant, profitability, and potential environmental impacts. For this reason, a model-based mathematical approach with MILP is suggested to evaluate the long-term feasibility of the system [2]. The target of the MILP model is to find the optimal producing pathway, which includes technologies, design, and time dependent operation conditions. However, the MILP aims for an uncertain future, so the results are depending on the given future situation. From this perspective, this study aims to develop reliably formulated scenarios as input data for MILP. The optimal pathway is represented differently depending on the scenarios. A scenario is presented as a specific part of the future by considering relevant key factors rather than a comprehensive picture. Combining individual factors forms the space of common development of all these aspects. The expanding slice of future developments is described with the scenario funnel in Figure 1.

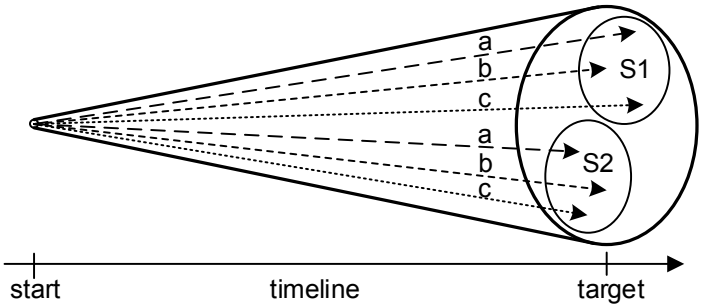

Figure. 1. Scenario funnel for representing the developments from a specific start time to a target time.

Different scenarios in Figure 1, here S1 and S2, now depict the different future possibilities in the target year from the start. For that, the possible projections of the different key factors (a, b, and c) are selected and condensed into scenarios. It should be noted that the meaning of the projection is not identical to the "forecast", which claims the actual probability of the occurrence, but the hypothetical construction to implicitly refer to the possibility of alternative futures [3].

There are some approaches to utilize the scenarios in this CCU context. Here, a short overview of recent contributions and preparatory work in the investigated field is given.

Stießel et al. [4] utilize a single scenario for the target year, 2030. The main target of the research is to identify cross-industrial process concepts of a CCU approach. The authors focus on external influences to formulate the scenarios. The process concept is evaluated in specific desired operating conditions by forcing the factors to be eco-friendly projected. Schlüter et al. [5] investigate a process concept of using steel mill exhaust gases for chemical production in three different operating conditions. The scenarios are developed focusing on the internal technical perspectives. The results are analyzed under time-dependent boundary conditions; thus, the limiting factors for the binding of carbon are identified. Sadlowski et al. [6] discuss the ecological potential of flexible methanol production from steel mill exhaust gases with a MILP model. The authors set up scenarios with three key factors which are external H_2 production, power supply sources and storage capacities. The outcomes are analyzed based on the carbon binding potential for this CCU concept.

In contrast to the concept of recent publications which focusing on a specific perspective to evaluate the CCU approach, the objective from the present work is extended to a multi-criteria evaluation with three different domains. It can be understood as a new and novel approach as the complicated relationships between the different domains are implemented. This approach of scenario development clearly shows the huge difference from the previous studies as it offers more comprehensive future descriptions. In other words, the generated scenarios can be utilized to evaluate the genuine feasibility of the CCU concept with a MILP model.

2. Properties of scenarios for a MILP model

All interconnections for the various technologies and exhaust gas conditions are implemented in the MILP model (e.g., reactors, storages, compressors, separators etc.). The options to be the final products are also set up in the decision point [2]. A detailed description of the model can be found in [6]. The outcome of the model is the optimal pathway, including the selection of technology, products, design and operation of the plants, and it depends on the given future states in form of scenarios.

The generated scenarios from this work can utilized as the input data in a linear optimization model. For that, they involve the special properties which are clearly different from the general scenario development.

First, the scenarios from this study are formulated based on the multi-criteria evaluation. Considering diverse internal and external influences brings reliable results about the technical plant's feasibility, investment decisions, or environmental effects. Secondly, projecting the selected factors from three domains involves the quantitative value in either numeric or linear dependencies to suit the feasibility. The quantitative values are assumed through the independently developed method or mathematically created functions. Finally, the individual relationship between the factors is examined through the software-based method. The cross-impact analysis (CIA) is conducted to find the most consistent and plausible combinations of factors.

3. Scenario development process

An existing method for scenario development is adapted to consider the functions of the scenarios. Based on the scenario technique from von Reibnitz [7]. A modified modelling concept involving the exploratory and quantitative approach is created for generating the five multi-criteria scenarios.

3.1 Premise

Scenario-specific assumptions for further considerations are defined within the premise. The definitions are supplemented by the boundary conditions to form a basis for the scenario development. Table 1 shows a short description of the determined premise.

Table 1. Short overview of the scenario-specific premises.

Parameters	Premise
Time Horizon	25 years (5 years construction + 20 years' operating life span)
Target year	2040 (middle of operating life span)
Maximum generation	40 % of the market volume [8, 9]
Market boundary	European market model
Discount rate	Constant as 2 % annually for life span
Technical parameters	Given from previous studies and project work

The time horizon of the CCU system is estimated as 25 years, with five years of construction and 20 years life span – operating from 2030 to 2050. The target year is 2040, the middle of life span. The maximum generation is restricted under German competition law prohibiting market dominance [9]. The market share-based presumption provides a first indication of dominance where a company's market share exceeds 40 percent [8]. Therefore, the maximum chemical product quantity is 40 percent of its market volume. The overall market assumption in scenario development is based on the system boundaries of and the cross-border trade with European neighbours. The profitability assessment requires the revision of the future cash flows to be compared with the current capital value. The discount rate is assumed to be constant at 2 % annually during the whole amortization period. The technical parameters like possible plant connections, efficiencies, reaction conditions, exhaust gas amounts etc. are given from previous studies, project work and own calculations.

3.2 Key factor selection

First, the domains of influence are determined. For such environmental and energy scenario development, economic, political, ecological, technical, and social influence domains are suggested in practice [10]. However, the social and political influences are excluded from our scenario boundary. The CCU concept can be sensitively affected by adverse social acceptance, which may give policymakers a false sense of security, leading to even a rebound effect [11]. Nevertheless, they are not suitable for our scenario's target. First, the factors from these aspects are often measured in a qualitative approach. For example, political inclination may function importantly in evaluating the feasibility but is formulated qualitative rather than exact values (e.g., left and right orientation). Secondly, the issues depend on subjective assessment. For example, the social acceptance and benefit of CCU concepts can be understood totally different. Based on these reasons, the technical, economic, and ecological domains are determined as the investigation fields' demarcation.

In a first step, 106 internal and external influencing factors from the domains are determined. The importance of the influencing factors is identified through influence analysis. A detailed explanation of the method can be found in [3]. The influence analysis examines the relationships between the factors. All possible pairs of factors are measured on a four-level scale from 0 (no effect) to 3 (strong effect) regarding their mutual impact [10]. As a result, each influencing factor is represented with its active and passive sum. The factors with a high active sum are selected as key factors out of the 106 influencing factors since they have the biggest influence of the overall system [7]. This procedure leads to the final 24 key factors to set up further scenario development.

3.3 Reference scenario

The reference scenario assumes that there will be no new measurements by the target year [10]. The logic is also called "Business as usual" (BAU). The current values are based on well-founded knowledge. Extrapolations in the target years (2040 for operating time and 2025 for investing time) are suggested by a meta-study of different reports about energy and chemical market development scenarios. If a reliable development is unavailable, the assumptions made through trend analysis. It is carried out by collecting historical data as long as possible, and past trends are extended to the future [3].

The time series of the electricity price in 2040 are derived from a forecasting model [12]. This model assumes an energy-only market and calculates the operating plans of the power generation systems. The projected time series of the carbon footprint CF_t for future energy production and RE_t share for 2040 is determined based on the CF_t in 2020 derived with historical data from AGORA [13]. The future CF_t is calculated based on the hourly based data from 2020 and the varied fraction of *RE* share in the German grid mix according to Eq. (1):

$$CF_{t,2040} = CF_{t,2020} \cdot \frac{(100 - RE_{t,2040})}{(100 - RE_{t,2020})} \quad (1)$$

The exemplary results of the projected time series of the CF_t are shown in Figure 2. Figure 2(a) shows the dimensionless sorted annual CF_t of the year 2020 (*RE* = 48 %) and the projection to reference scenario of 2040 (*RE* = 85 %). Figure 2(b) shows an example of a two-week period of the CF_t. The average value for the reference scenario is projected to ca. 110 g_{CO2}/kWh_{el}. Electricity prices are calculated in a similar way.

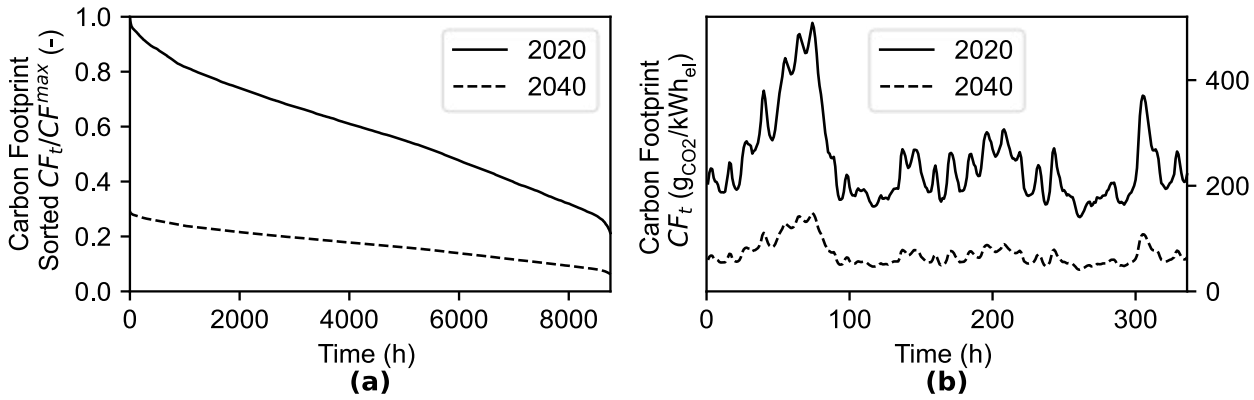

Figure. 2. Time series of carbon footprints (*CF*) for 2020 (48 % *RE*-Share) and BAU projection to 2040 (85 % *RE*-Share): a) Sorted annual dimensionless *CF*, b) exemplary two-week period of the *CF*.

It is necessary to specify fuel prices for natural gas and coal, as well as the CO_2 certificate prices to determine the marginal cost. The prices in the target year are taken from the EU [14] and Bloomberg [15]. H_2 price plays an important role in defining the potential of *RE* and green electricity. The price is derived from the IEA [16].

Market prices of the chemicals are the biggest part of the revenue. Oxygen as by-product from water electrolysis is also considered a part of revenue. The prices are assumed by the trend analysis based on the historical data from 2019 to 2021. Plus, the chemicals' market volumes dramatically affect the size of the plant and expenditure as the maximum generation is regulated by 40 % of the market share limit. They are taken from the IEA [17].

Table 2 shows the data of the most probable BAU scenario. Data from technology domain are shown as relative value (1 = no changes) and are derived from project internal communications and plant development reports. The H_2 generation is a crucial aspect of the system. Therefore, H_2 efficiency, the electricity required to generate the external carbon-free H_2, is considered as a separate factor from the overall energy requirement.

Table 2. Key factors and their values of the reference business-as-usual (BAU) scenario.

Class	Key factor	Current value	Source	BAU-value	Unit
Input	a. Electricity price	41.3	[18, 19]	47.4	€/MWh
	b. Natural gas price	31.4	[19]	46.7	€/MWh
	c. Coal price	7.5	[19]	11.8	€/MWh
	d. H2 price	3000	[16]	2400	€/t
	e. CO2 price	94.5	[4]	135.0	€/t
	f. CO2 certificate price	76.2	[20]	108.8	€/t
	g. CF & RE share (German grid)	373.4	[21, 22]	109.0	g_{CO2}/kWh_{el}
Output	h. O2 price	50	[4]	74.3	€/t
	i. Methanol price	342.0	[19]	401.6	€/t
	j. Urea price	256.3	[19]	428.2	€/t
	k. NH3 price	182.9	[23]	305.5	€/t
	l. Acetic acid (AA) price	605.9	[23]	711.5	€/t
	m. MeOH market vol.	2.2	[19]	3.9	Mt/a
	n. Urea market vol.	4.4	[19]	5.4	Mt/a
	o. NH3 market vol.	12.5	[19]	15.3	Mt/a
	p. Acetic acid (AA) market vol.	1.2	[19]	2.1	Mt/a
Technology	q. Conversion efficiency	1.0	[24]	1.0	-
	r. Energy efficiency	1.0	[24]	1.0	-
	s. H2 efficiency	1.0	[25, 26]	1.0	-
	t. Steel mill energy demand	1.0	-	1.0	-
	u. Part load range	1.0	-	1.0	-
	v. Dynamic operation	1.0	-	1.0	-
Expenditure	w. Investment cost (2025)	-	[27]	1.0	-
	x. Operating cost	1.0	[27]	1.0	-

The target year of the capital expenditures (CAPEX) is set as 2025 following a five-year construction period. CAPEX is calculated for each plant, including the gas conditioning, external H_2 production and chemical synthesis plants. Calculation is based on the capacity method [27]. The CAPEX of a plant C_b and its capacity

S_b is estimated based on the reference CAPEX C_a and its capacity S_a [27]. The reference data is taken from various techno-economic analysis studies and the C_a is extrapolated to the target year of investing 2025. It is extrapolated to 2025 value by applying the chemical engineering plant cost index (CEPCI), as i, to account for inflation rate. The publication years of the studies are between 2006 to 2021. Original CAPEX C_0, capacity S_a and CEPCI i_0 for all technical plants and years are used or derived from these studies. The CEPCI value for the year 2025 i_a is determined through trend analysis from the last five years. Therefore, the reference CAPEX C_a is calculated with Eq. (2):

$$C_a = C_0 \cdot \frac{i_a}{i_0} \tag{2}$$

The CAPEX development of the hydrogen production plants is assumed to be lower in the future. According to [28], it is assumed that the CAPEX for alkaline (ALK) and proton-exchange membrane (PEM) electrolysis are reduced by 14 % and 22.5 % in next five years, caused by reduced manufacturing costs and assumed technological breakthroughs. Based on the updated C_a to 2025, the C_b is calculated via the capacity method in Eq. (3). Where f is the degression coefficient for the economy of scale for chemical plants with a value from 0.6 to 1.0.

$$C_b = C_a \cdot \left(\frac{S_b}{S_a}\right)^f \tag{3}$$

However, the final S_b of the plant is not determined in the scenario development process. Therefore, the C_b of the individual component is represented as the function within possible installed capacity range of S_b^{min} and S_b^{max}. The C_b^{max} of S_b^{max} is where the exhausted gas utilization is maximized based on the market restriction. It should be noted that the S_b^{max} of each plant is differently estimated depending on the final products due to the varied size of the market volume. C_b^{min} is assumed to be 10 % of C_b^{max}. Lower than 10 % of C_b^{max} it's not worth to install these plants because a significant emission reduction is required for the CCU concept. Table 3 shows the range of S_b and C_b of a water gas shift (WGS) plant for each chemical as an example.

Table 3. Range of S_b (capacity) and C_b (CAPEX) of possible water gas shift plants for each chemical.

Final product	S_b^{min}, kg/s	S_b^{max}, kg/s	C_b^{min}, M€	C_b^{max}, M€	Market volume, Mt/a
Acetic acid	2.33	39	0.88	8.8	2.1
Urea	5.2	86	1.7	17	3.9
Methanol	7.2	120	2.2	22	5.4
Ammonia	22.7	376	5.7	57	15.3

The C_b should be represented in a full range of the plants S_b regardless of the production route. In the case of WGS plant, then, the CAPEX is resulted in the function within the overall range of S_b from 2.33 to 376 kg/s.

If f of the component is less than 1 like WGS plant (0.82), the C_b is a root-function. The MILP model requires linearity of C_b and therefore should be revised as a linear approximated function $C_{b,lin}$. The linearized functions maximum relative error tolerance from the original C_b is set as 10 %. If this doesn't match, an additional sampling point for piecewise linear approximation is considered till it reach the <10 % criteria. In the case of the WGS plant, two linear functions are generated with one piecewise sampling point and a maximum relative error of 7.4 %. Figure 3 presents the original C_b function on the left side and the derived piecewise linear functions $C_{b,lin1}$ and $C_{b,lin2}$ on the right for the WGS plant.

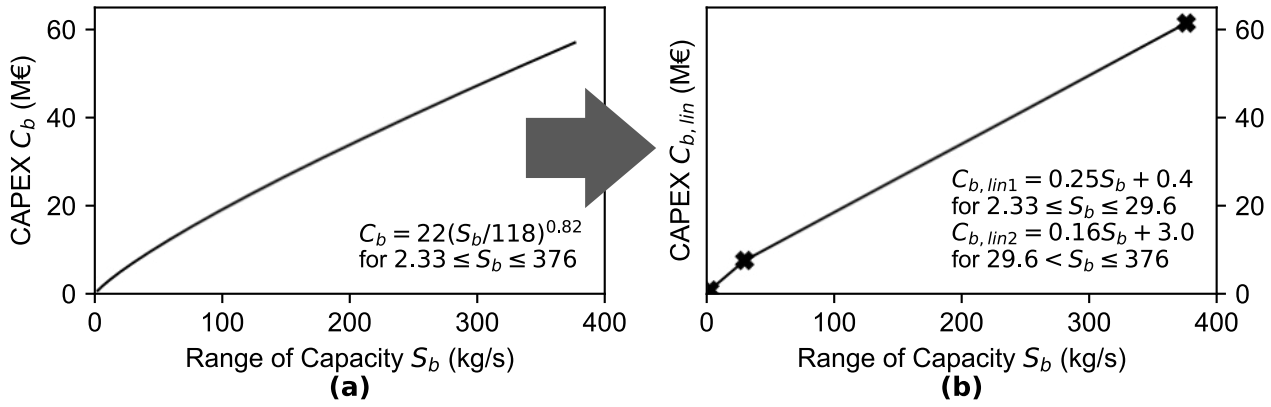

Figure. 3. CAPEX functions of WGS plant: a) Cost function through capacity method C_b, b) linearized cost functions $C_{b,lin}$.

Other plants CAPEX is calculated in a similar way. The maximum relative error is detected in NH_3 synthesis plant as 9.4 %. The range of CAPEX for each plant, regardless of the production pathway, is generated.

The operating cost (OPEX) is the expenditures incurred in the plant. It considers the variable, fixed, and other costs of the system. The variable costs, including the raw and auxiliary materials, are calculated differently depending on the operating time and final production pathway. The fixed and other costs are structured based on [29]. The projected OPEX in BAU scenario is estimated to be constant by the target year.

3.4 Future projection

Each key factor is projected into the future in alternative states. Qualitative projections are created at first. This includes the possible projections of highly decreasing (↓↓), moderately decreasing (↓), constant (-), moderately increasing (↑) and highly increasing (↑↑). Not all projections make sense (e.g., decreasing projection of CO_2 certificate price) so the number of varied projections differs between three or five depending on the key factor. As mentioned, each projection involves quantified numerical values. If the data from the BAU scenario is available, the projection is based on it. The variation rate from the current value to fixed projection of the BAU scenario is applied to other alternative projections identically.

It should be noted that some key factors involve deliberately exaggerated or passive quantification. The factors that contain exaggerated quantification is the “driving factor”. The extreme value of these driving factors brings a clear difference from other projections. On the other hand, the passive quantification is for the case that the value from the BAU scenario is over-predicted. The scenario which involves the projection may cause discord with other elements. Thus, they are quantified at a lower variation rate. Passive quantification makes the combination of the factors more consistent.

If the data from the reference scenario is unavailable, it is quantified based on the independently estimated assumption. For example, the H_2 efficiency has an improving rate of 5 % for projection (↑) and 10 % for (↑↑), according to [16]. The factors, conversion efficiency and energy efficiency, are assumed to be identical in improving rates of H_2 efficiency. It is not plausible to assume that they have greater improvement than external H_2 supplements because these plants are at a state-of-art level.

The investment cost is projected through the independently generated method. A scaling factor, “*s-factor*”, is applied to the generated $C_{b,lin}$ function of each plant to switch the range of CAPEX by multiplying itself. The *s-factor* is derived from the water electrolysis’ CAPEX as it is available to get reliable data on future development. Plus, it can be compared with the current CAPEX as the *f* is equal to 1 - It is not affected by the varied size of the capacity. Table 4 presents the assumed CAPEX of ALK and PEM in diverse future situations.

Table 4. Development of specific CAPEX of ALK and PEM water electrolysis in varied situations.

Unit	Current CAPEX	BAU CAPEX	Future situation	CAPEX in future	**Rate**	Unit	Current CAPEX	BAU CAPEX	Future situation	CAPEX in future	**Rate**
			Pessimistic	1.0	**1.16**				Pessimistic	1.0	**1.29**
ALK	1.0	0.86	Regular	0.79	**0.92**	PEM	1.0	0.775	Regular	0.66	**0.85**
			Optimistic	0.72	**0.84**				Optimistic	0.55	**0.71**

* Rate is the variation rate of future CAPEX from the BAU CAPEX, and it functions as the *s-factor*.
* The higher *s-factor* demonstrates the higher initial expenditures.

In the BAU scenario, the specific CAPEX for ALK and PEM is estimated to be decreased to 86 % or 77.5 % by the target year, respectively [28]. In a pessimistic future, the CAPEX is assumed to be constant as the current value. A regular projection assumes 50 % higher decreasing rate of the CAPEX than the BAU scenario. In the optimistic situation, the decreasing rate is doubled by the BAU scenario. The variation rates of future CAPEX from the BAU CAPEX are the *s-factor.* They are applied to all considered plants of the CCU concept depending on the scenario concept and the result of a cross-impact analysis. Through the process, the range of the component’s CAPEX is newly assigned for each scenario. Another external H_2 supplement option, methane pyrolysis (MP), is applied an identical *s-factor* with the ALK.

3.5 Scenario formation

Based on the projections of key factors, the actual formation of scenarios takes place. The scenario technique of cross-impact analysis (CIA) is applied to ensure consistent combinations [10]. The CIA analyses the relationships between the key factors and the probabilities of occurrence of future events by considering their direct and indirect mutual effects [30].

A cross-impact matrix is first created, which assesses the conditional probability of specific projections if another future event has occurred according to the seven-level scale from -3 (Strong inhibitory influence) to 3 (Strong promoting influence) [30]. After that, the concept of each scenario is developed. The scenario concepts focus on the state of the specific domain to be improved or regressed or the worst or the best operating situations. Based on the concept of the scenarios, the corresponding factors are fixed in a particular projection to fulfil the determined idea. Four different scenarios, excluding the reference scenario, are created. A brief explanation of the different scenario concept and targets is shown below.

3.5.1 CO_2 reduction & RE share target (*RE-Boom*)

The *RE-Boom* depicts the best condition from the ecological perspective. Table 5 presents seven key factors which are forced to demonstrate the scenario.

Table 5. Forced projections for the ecological optimistic scenario *RE-Boom.*

Fixed factor	Projection	Fixed factor	Projection
e. CO_2 price	Highly decreasing (↓↓)	n. Urea market vol.	Highly increasing (↑↑)
f. CO_2 certificate price	Highly increasing (↑↑)	o. Ammonia market vol.	Highly increasing (↑↑)
g. *CF* & *RE* share	Highly decreasing (↓↓)	p. Acetic acid market vol.	Highly increasing (↑↑)
m. Methanol market vol.	Highly increasing (↑↑)		

The key factors, CO_2 certificate price, and *CF* & *RE* share, are forced environment friendly. The chemicals market volume is fixed to be highly increased to remove the market restriction for more possible CCU production. The CO_2 price is defined to be decreased to reduce the availability of direct CO_2 sales options.

3.5.2 Technical improvement & Market Booming (*Market-Boom*)

Scenario *Market-Boom* set the perfect condition from the economic and technical perspectives. Table 6 shows the eleven fixed key factors to fulfil the scenario concept.

Table 6. Forced projections for the economic optimistic scenario *Market-Boom.*

Fixed factor	Projection	Fixed factor	Projection
h. O_2 price	Highly increasing (↑↑)	r. Energy efficiency	Highly increasing (↑↑)
i. Methanol price	Highly increasing (↑↑)	s. Hydrogen efficiency	Moderately increasing (↑)
j. Urea price	Highly increasing (↑↑)	t. Steel mill energy demand	Highly decreasing (↓↓)
k. Ammonia price	Highly increasing (↑↑)	u. Part load range	Highly increasing (↑↑)
l. Acetic acid price	Highly increasing (↑↑)	v. Dynamic operation	Highly increasing (↑↑)
q. Conversion eff.	Highly increasing (↑↑)		

The key factors related to the revenue are all fixed to be highly increased to maximize the profits. The factors in the technology class are defined to be highly advanced. However, the H_2 efficiency is estimated to be moderately increased to make a clear difference with the *H_2-boom* scenario in section 3.5.4.

3.5.3 Energy & Market crisis (*Crisis*)

Crisis scenario projects the worst situation from the economic perspective. The concept refers to the current Ukraine war and an economic crisis. Table 7 presents eight forced factors for the scenario concept.

Table 7. Forced projections for the negative extreme scenario *Crisis*.

Fixed factor	Projection	Fixed factor	Projection
a. Electricity Price	Highly increasing (↑↑)	i. Methanol price	Highly decreasing (↓↓)
b. Natural Gas price	Highly increasing (↑↑)	j. Urea price	Highly decreasing (↓↓)
c. Coal Price	Highly increasing (↑↑)	k. Ammonia price	Highly decreasing (↓↓)
h. O_2 price	Highly decreasing (↓↓)	l. Acetic acid price	Highly decreasing (↓↓)

The factors related to the profitability are all negatively assumed. Prices of raw materials goes up immensely, and revenue of the products is reduced substantially. Regarding the product's market condition, it is evaluated from the perspective of the supplier. In other words, it is assumed that the chemicals market is in depression, so the supplier must sell the product at a lower price.

3.5.4 Hydrogen booming (*H_2-Boom*)

The *H_2-Boom* focuses only on the best condition of H_2 generation from the technical aspects. Table 8 shows six essential key factors to satisfy the scenario concept.

Table 8. Forced projections for Hydrogen optimistic scenario *H2-Boom*.

Fixed factor	Projection	Fixed factor	Projection
d. H_2 Price	Highly decreasing (↓↓)	s. Hydrogen efficiency	Highly increasing (↑↑)
q. Conversion efficiency	Constant (-)	u. Part load range (only H_2)	Moderately increasing (↑)
r. Energy efficiency	Constant (-)	v. Dynamic operation (only H_2)	Moderately increasing (↑)

H_2 price is assumed to be reduced following a drop in generation cost due to highly increasing manufacturing cost and technology breakthroughs. It aims on the hydrogen subdomain from the overall technical domain.

3.6 Scenario generation and selection

Based on the formulated cross-impact matrix and the scenario concepts, the CIA is conducted to determine the most consistent combination. It tests all theoretically possible combinations to analyse their contradictions with the framework conditions. However, the generated matrix involves more than a billion possible combinations. The CIA, thus, can only be checked with algorithm-based software support. For this reason, the *ScenarioWizard*® software is used. Plus, the economic factors related to the chemicals (price and market volume) are combined into a single factor to manage the complexity. It is judged by the fact that the scenario concepts mostly do not involve the comparison of the superiority between the chemicals. A merge does not affect the quantitative values for each factor but merely has an identical qualitative projection. As a result, the bundle containing the possible candidates to be a final scenario is generated for each scenario. In our case, eight options for *RE-boom*, five for *Market-Boom*, two for *Crisis*, and fifteen for *H_2-Boom* are generated.

To select the final most consistent combination out of the candidate's pool, the Consistency Value (CV) and Total Impact Score (TIS) function as the evaluation criteria [30]. TIS means the sum of the impact scores of all selected scenario variants. The CV is the parameter to evaluate if the chosen combination of the factors is consistent. In the case of a positive or zero CV, the combination is accepted as consistent [30]. Based on the scenario selection criteria, the final scenarios are determined. All scenarios have the CV equal to 0 and the highest TIS out of the possible candidates, so they involve the most consistent combination.

4. Results

4.1 Final scenarios

Table 9. Final five scenarios with qualitative (QLT) and quantified values (QNT) for the 24 key factors (a - x).

Key factors with units	BAU		RE-Boom		Market-Boom		Crisis		H2-Boom	
	QLT	QTY	QLT	QTY	QLT	QTY	QLT	QTY	QLT	QTY
a. Electricity price (€/MWh)	(↑)	47.38	(↓↓)	20.66	(-)	41.32	(↑↑)*	72.31	(-)	41.32
b. NG price (€/MWh)	(↑)	46.72	(↓↓)	15.68	(-)	31.35	(↑↑)*	69.63	(-)	31.35
c. Coal price (€/MWh)	(↑)	11.82	(↓)	5.62	(-)	7.49	(↑↑)*	18.67	(-)	7.49
d. H2 price (€/t)	(↓)	2400	(↓)	2400	(-)	3000	(↑↑)	3900	(↓↓)*	1500
e. CO2 price (€/t)	(↑↑)	135.0	(↓↓)*	61.2	(-)	94.5	(↓)	76.1	(↑)	112.9
f. CO2 certificate price (€/t)	(↑)	108.8	(↑↑)*	190.5	(↑)	108.8	(↑↑)	190.5	(↑)	108.8
g. CF & RE share (g_{CO2}/kWh_{el})	(↓)	109	(↓↓)*	0	(↓)	109	(↓↓)	0	(↓)	109
h. O2 price (€/t)	(↑)	74.3	(↓)	25.7	(↑↑)*	110.4	(↓↓)*	13.2	(-)	50.0
i. MeOH price (€/t)	(↑)	401.6	(↓)	282.4	(↑↑)*	471.7	(↓↓)*	233.1	(-)	342.0
j. Urea price (€/t)	(↑)	428.2	(↓)	192.2	(↑↑)*	715.4	(↓↓)*	128.2	(-)	256.3
k. NH3 price (€/t)	(↑)	305.5	(↓)	137.1	(↑↑)*	510.4	(↓↓)*	91.4	(-)	182.9
l. Acetic Acid price (€/t)	(↑)	711.5	(↓)	500.2	(↑↑)*	835.5	(↓↓)*	413.0	(-)	605.9
m. MeOH market vol. (Mt/a)	(↑)	3.85	(↑↑)*	13.36	(-)	2.2	(↓↓)	1.1	(-)	2.2
n. Urea market vol. (Mt/a)	(↑)	5.39	(↑↑)*	25.97	(-)	4.4	(↓↓)	2.64	(-)	4.4
o. NH3 market vol. (Mt/a)	(↑)	15.31	(↑↑)*	18.75	(-)	12.5	(↓↓)	7.51	(-)	12.5
p. Acetic Acid market vol. (Mt/a)	(↑)	2.1	(↑↑)*	3.42	(-)	1.2	(↓↓)	0.6	(-)	1.2
q. Conversion efficiency (-)	(-)	1.0	(↑)	0.95	(↑↑)*	0.9	(-)	1.0	(-)*	1.0
r. Energy efficiency (-)	(-)	1.0	(↑)	0.95	(↑↑)*	0.9	(-)	1.0	(-)*	1.0
s. H2 efficiency (-)	(-)	1.0	(↑)	0.95	(↑)*	0.95	(-)	1.0	(↑↑)*	0.9
t. Steel mill energy demand (-)	(-)	1.0	(↓)	0.9	(↓↓)*	0.8	(-)	1.0	(-)	1.0
u. Part load range (-)	(-)	1.0	(↑)	1.5	(↑↑)*	2.0	(-)	1.0	(↑)*	2.0 (H2)
v. Dynamic operation (-)	(-)	1.0	(↑)	1.5	(↑↑)*	2.0	(-)	1.0	(↑)*	2.0 (H2)
w. Investment costs s-factors (-)	(-)	1.0	(↓)	var[1]	(↓)	var[1]	(↑)	var[1]	(↓)	var[1]
x. Operating cost (-)	(-)	1.0	(↓)	0.75	(↓)	0.5	(↑)	1.5	(↓)	0.75

[1] Scaling factors (s-factors) for investment cost calculations are plant-dependent and shown in Table 10.
* The factors with subscript * denote the predetermined fixed projection.

Additional to Table 9, with all numerical values, the scenarios additional includes the time series for electricity price and *CF* (Figure 2) plus all linearized and scaled CAPEX functions C_s. The explanation for CAPEX, which is determined after CIA, is given below. Table 10 shows different s-factors for all hydrogen production plants.

Table 10. Scaling factor *(s-factor)* to estimate future CAPEX of hydrogen production plants for the scenarios.

Scenario	ALK	PEM	MP	Other components
BAU	1.0	1.0	1.0	1.0
RE-Boom	0.92	0.85	0.92	0.92
Market-Boom	0.92	0.85	0.92	0.85
Crisis	1.16	1.29	1.16	1.23
H2-Boom	0.84	0.71	0.84	1.0

The qualitative projection of CAPEX for the *RE-boom* and *Market-boom* are calculated to be decreased ($s < 1$) through the CIA. The CAPEX of the H_2 supplement is determined to be regularly improved for both scenarios following the projection of H_2 efficiency, moderately increasing. Regarding other components, the *s-factor* is estimated to be identical to the ALK for *RE-boom* and the PEM for *Market-boom*. It is more plausible that *Market-Boom* has a bigger reduction rate than *RE-Boom* as the technical factors of other components is assumed to be improved at a higher rate in *Market-boom*.

Qualitative projection of CAPEX for the *Crisis* scenario is calculated to be increased through the CIA. The CAPEX of the H_2 supplement is decided to be the worst development ($s > 1$). The *s-factor* of other components is assumed as the average value of ALK and PEM.

The CAPEX of the H_2 supplement is determined to be the optimistic future under the projection of H_2 efficiency. The *s-factor* is not applied to other components as the concept of the *H_2-boom* focuses only on the H_2 improvement, so it clarifies the difference with the *RE-boom* and *Market-boom*. It may look illogical that the qualitative projection of CAPEX is calculated to be decreased through the CIA. However, the result of the CIA can be varied depending on the weight of the influence. It is plausible that the CAPEX reduction is mainly because of the H_2 efficiency factor, as it has a more significant impact on the CAPEX.

The s-*factor* is multiplied to $C_{b,lin}$ function for individual plants of each scenario to reach the final scaled CAPEX functions C_s. Figure 4 presents the derived C_s function of the WGS plant for each scenario as an example.

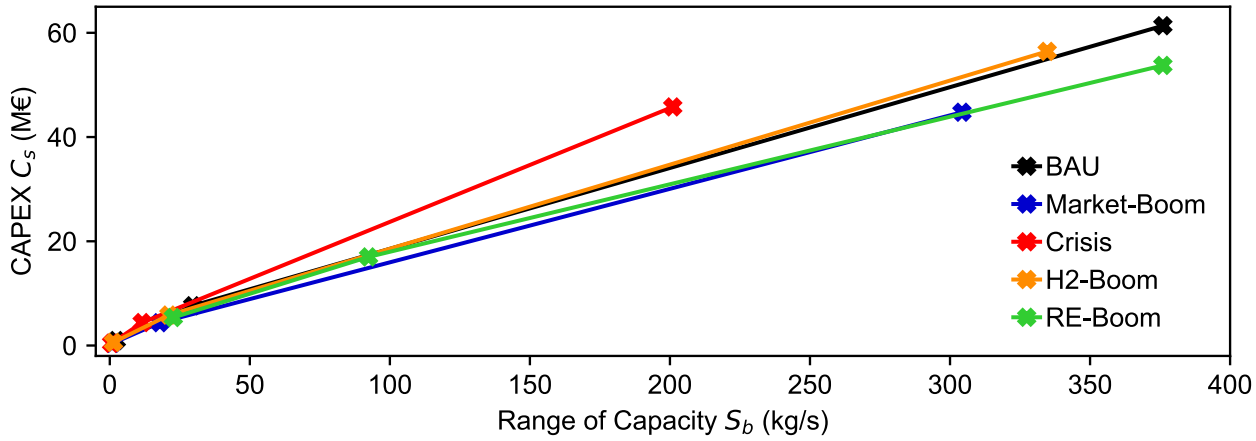

Figure. 4. The five developed linear CAPEX functions Cs of the water gas shift plant for each scenario.

4.2 Scenario evaluation

All combinations from CIA (Table 9) are evaluated based on the three criteria: plausibility, consistency, and differentiation. The BAU scenario is not part of the scenario evaluation due it is generated by the independent method (3.3 Reference scenario). Plus, consistency is already measured in the scenario selection process (3.6 Scenario generation and selection).

4.2.1 Plausibility

Plausibility check of the scenarios is assessed if the combination of the scenario is well matched with the aimed concept and the relationship between the fixed factors and the remaining factors are plausibly formulated.

Scenario *RE-boom* depicts the condition that minimizes the CO_2 emission and simultaneously maximizes the quantity of used exhausted gas. The concept is well satisfied with fixed factors from Table 5. The combination of remaining factors is also well structured. Significantly, the prices of energy raw materials (factors a. to c.) are decreased by the CIA. As the *CF* is assumed to be 0, it is plausible that the prices are decreased accordingly. However, the coal price is less affected as it relates more to steel production.

Main idea of *Market-boom* is the maximization of profitability and technical performance. The concept is well fulfilled by optimizing the product price and technical development in Table 6. Among the remaining factors, the chemicals market volume is resulted to be constant by the CIA even if the prices are incremented. It may

look illogical in general price and market relationship. However, the generated combination results from all factors' mutual interaction, not a pair of two factors. It is plausible to assume that the chemicals market volume is resulted to be constant because of other factors' indirect influences.

The *Crisis* represents the worst situation with the forced factors from Table 7. A discord between the combination of the key factors and the scenario concept is identified. The ecological factors (f. and g.) resulted in highly increased and decreased, respectively, through the CIA calculation as the prices of energy raw materials are forced to be highly increased. It is plausible from the perspective of three considered domains, like the case of *RE-Boom.* However, it does not align with the scenario concept, which refers to the ongoing Ukraine conflict. The current abnormal situation decouples the general relationship of the energy complex. According to the [31], the price of CO_2 permits reached a high of 97 €/kWh_{el} in 2020. After the start of the conflict in 2022, the price dropped to almost 60 €/kWh_{el}. It is reported as the biggest crash since 2014. To elaborate this unique situation, social or political aspects (e.g., acceptance or political trends) should be included. It may function as a "joker", making the retrogress trend plausible.

H_2-boom scenario focuses on the improvement of the overall H_2 generation, a subdomain in the technical and economic field. The concept is fulfilled with the fixed factors from Table 8. Regarding the energy raw materials from the remaining factors may look more plausible to be reduced rather than constant. Assuming that the H_2 price is reduced and the H_2 efficiency is notably advanced, a significant price drop is expected. It is particularly true if a high proportion of green electricity is used, leading to low market prices and *CF*. However, the scenario from this study assumes that the perfect transition to an emission-free system is impossible by the target year. According to the [32], the existing infrastructure has limited application regarding H_2 as an energy source. Germany's current gas supply network can tolerate only 10 % of H_2 by volume in total [32]. However, it is also evident that H_2 gradually contributes to the energy system, simultaneously. It becomes obvious by comparing it with the BAU scenario. As the H_2 price in the BAU scenario decreases at a lower rate than *H_2-boom*, the energy raw materials prices are assumed to be moderately increased. So, even if H_2 as the energy source cannot change the energy system in a flash, it positively influences the gradual transition. Consequently, it is more plausible that the prices of energy raw materials will be constant for *H_2-Boom*.

4.2.2 Differentiation

The differentiation between the scenarios is assessed if the generated scenarios depict the meaningfully varied condition to prevent further calculation results in an identical outcome. *Market-Boom* and *Crisis* scenarios can be understood as the antipodes in the scenario funnel from the economic point of view. The combinations of all the factors in both scenarios are formulated oppositely. They offer different situations in terms of economic conditions. Both, *Market-Boom* and *H_2-Boom,* involve technical improvement by the target year. Because of the similar relationship between the factors, most other elements from the different domains resulted in similar projections. It may be considered a false combination because both slices depict a similar situation. However, the technical concept of these scenarios is distanced - *Market-Boom* for overall improvement, but *H_2-Boom* for mainly H_2 subdomain. Thus, comparing the results from the scenarios bring clearly different results to evaluate the CCU concept. Finally, the *RE-Boom* concentrates on the sole independent domain, the ecological criteria. The combination of *RE-Boom* is conspicuously different. In other words, the generated slice is sketched at a totally distanced area from other scenarios, so it can offer new criteria to evaluate the feasibility of the CCU concept. Figure 5 presents the simplified development process and a qualitative classification to elaborate the differentiation of the scenarios.

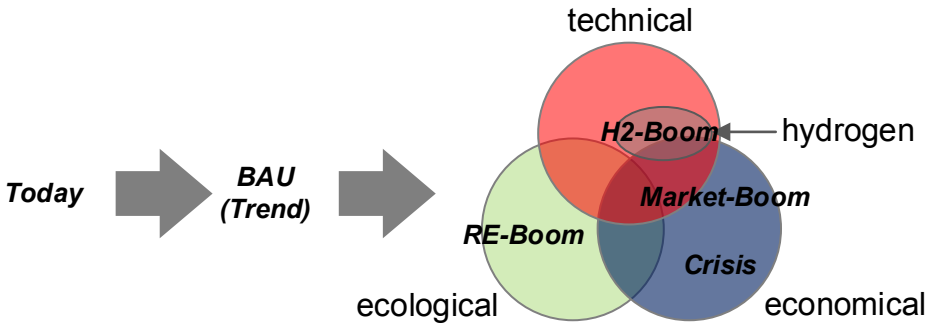

Figure. 5. Simplified development and differentiation of the scenario concepts as a Venn diagram.

5. Conclusion and Outlook

This research aimed to build up consistent, plausible, and meaningfully different scenarios as input data for MILP models to evaluate the long-term feasibility of the desired exhausted gas utilization concept. The generated five scenarios involve internal and external key factors from three main criteria. To build up the BAU scenario, they are extrapolated to the target years for investing (2025) and operating (2040). Especially, the

formulation of the investment cost offers a rough sketch of the initial expenditures. A linear approximation method for CAPEX functions is applied to be suited for the later use in MILP models. It fulfils the criteria for a maximum error tolerance of 10 % from the original nonlinear function.

All 24 key factors are qualitatively and quantitatively projected into the target years to construct the hypothetical future development. The process is carried out in an objective methodology, utilizing the BAU scenario data rather than forecasting the random value. It also involves exaggerated or passive projection so that further evaluation of the CCU approach becomes more evident. If the data from the BAU scenario is unavailable, then the quantification is determined based on independently estimated assumptions. The investment costs are quantitatively projected by applying a scaling factor (*s-factor*). The *s-factor* is derived from the water electrolysis CAPEX and ranges from 0.71 to 1.29. It is applied to other plants to switch the amplitude of CAPEX functions and offering varied economic situations. An s-*factor* greater 1 is represents economically unfavourable scenarios due to higher initial expenditures. This compositional work provides new insight into the probable future development of the "Hot-potato" factors - such as the electricity price, RE share, or the chemicals market.

The concept of each scenario is determined in advance of the scenario formulation. In other words, the scenarios are developed based on the deliberately specified condition. Four scenario concepts are generated: 1. CO_2 reduction & RE share target (*RE-Boom*), 2. Technical improvement & Market booming (*Market-Boom*), 3. Energy & Market crisis (*Crisis*), and 4. Hydrogen booming (*H_2-Boom*). The *RE-Boom* depicts the best condition from the ecological perspective. The *Market-Boom* set the perfect condition from the economic and technical perspective. The *Crisis* projects the worst situation from the economic domain. Finally, the *H_2-Boom* focuses only on the best condition of H_2 generation from the technical and economic aspects.

Based on the predetermined concept, the CIA is carried out to find the most consistent combination of the key factors within the fixed condition. The calculated combinations are considered highly reliable consequences. First, regarding consistency, all scenarios have the desired CV and the highest TIS out of the possible candidates. Secondly, the determinations of the remaining factors' projections through the CIA calculation are also plausible to describe the scenario concept within the investigation domains. Finally, the results also offer meaningfully different operating conditions. These results build on existing evidence of the reliably structured scenarios. The generated scenarios can now be directly utilized in a MILP model for the CCU approach.

In conclusion, the generated five scenarios represent a comprehensible description of the possible situation of the CCU concept in the target years based on a complex network of factors from different impact parameters. All scenarios have consistent, plausible, and meaningfully different combinations of the key factors. Consequently, the optimal solutions for utilizing the exhausted gas are calculated by the MILP optimization model in varied ways depending on the scenarios. It promotes the transparency and traceability of the further decision-making process of the CCU concept.

Acknowledgements

This work was carried within in the Carbon2Chem® project. The authors thank the German Federal Ministry of Education and Research (BMBF) for financial support of the project.

Nomenclature

C Capital expenditures of the plants, M€

CF Carbon footprint, g/kWh

f Degression coefficient, -

RE Renewable energy share, %

S Capacity of the plant, kg/s

s Scaling factor, -

Subscripts and Superscripts

0 Index for reference year of data source

a,b Index for reference year (2025) before (a) and after (b) scaling with degression coefficient

lin Linearized function

min/max Minimum and Maximum value

s,t Index for scenario number and time series

References

[1] Deerberg G, Oles M, Schlögl R. The Project Carbon2Chem®. Chemie Ingenieur Technik 2018; 90(10): 1365–8.

[2] Sadlowski M, van Beek M. Integration und strukturelle Optimierung verschiedener chemischer Syntheserouten zur Abgasnutzung bestehender Stahlproduktionsanlagen. Internationale Energiewirtschaftstagung (IEWT): TU Wien 2019.

[3] Kosow H, Gaßner R. Methoden der Zukunfts- und Szenarioanalyse: Überblick, Bewertung und Auswahlkriterien. Bonn 2008.
[4] Stießel S. Entwicklung eines Referenzmodells zur multikriteriellen Bewertung von cross-industriellen Systemen. Dissertation, Bochum University 2020.
[5] Schlüter S, Geitner C. Simulation of Methanol and Urea Production from Catalytic Conversion of Steel Mill Gases. Chemie Ingenieur Technik 2020; 92(10): 1403–15.
[6] Sadlowski M, van Beek M. Ecologic Potential for Flexible Methanol Production from Steel Mill Off-gases. Chemie Ingenieur Technik 2020; 92(10): 1416–24.
[7] von Reibnitz U, Hammond P. Scenario Techniques. Hamburg, Germany: McGraw-Hill 1988.
[8] Polley R, Apel K, editors. The Dominance and Monopolies Review: Germany. Cleary Gottlieb Steen & Hamilton LLP; 2022.
[9] Bundesministerium der Justiz. Competition Act: Gesetz gegen Wettbewerbsbeschränkungen. Berlin 2022 Jul 19.
[10] Gausemeier J, Fink A, Schlake O. Szenariomanagement: Planen und Führen mit Szenarien. München: Paderborner Universität 1996.
[11] Vreys K, Lizin S, van Dael M, Tharakan J, Malina R. Exploring the Future of Carbon Capture and Utilisation by Combining an International Delphi Study with Local Scenario Development. Resources, Convervation and Recycling 2019; 146: 484–501.
[12] Raths S, Koopmann S, Müller C*, et al., editors.* The Energy System Development Plan. Bonn: Institute of Electrical and Electronics Engineers Inc.; 2015.
[13] Agora Energiewende. German Net Power Generation, Consumption, and Exports 2020.
[14] European Commission. EU Reference Scenario 2020: Energy, Transport and GHG emissions Trends to 2050. Luxemburg: European Union; 2021.
[15] Henze V. Carbon Offset Prices Could Increase Fifty-Fold by 2050: Bloomberg NEF; 2022 Oct 1.
[16] International Energy Agency. Global Hydrogen Review 2021. Paris: IEA; 2021.
[17] International Energy Agency. The Future of Petrochemicals. Paris: IEA; 2018.
[18] Fraunhofer ISE. Annual Electricity Spot Market Prices in Germany: Fraunhofer; 2022 [cited 2022 August 10] Available from: URL: https://energy-charts.info/?l=en&c=DE.
[19] Statistical Office of the European Union (EUROSTAT). Statistics on the production of goods (Prodcom): EUROSTAT; 2021.
[20] Trading Economics. Chemicals Price Trend; 2021 [cited 2022 August 5] Available from: URL: https://tradingeconomics.com/commodity/.
[21] Umweltbundesamt. Indicator: Greenhouse gas emissions: Umweltbundesamt; 2021 [cited 2022 November 4] Available from: URL: umweltbundesamt.de/en/data/environmental-indicators/indicator-greenhouse-gas-emissions.
[22] Prognos, Öko-Institut, Wuppertal Institut. Towards a Climate-Neutral Germany by 2045: How Germany can reach its climate targets before 2050: Executive Summary conducted for Stiftung Klimaneutralität, Agora Energiewende and Agora Verkehrswende; 2021.
[23] Procurement Resource. Chemicals Price Trend; 2021 [cited 2022 August 5] Available from: URL: https://www.procurementresource.com/resource-center/.
[24] William. L. L. Chemical Reactor Design and Control. California: John Wiley & Sons 2007.
[25] Nel Hydrogen Electrolysers. The World's Most Efficient and Reliable Electrolysers: Nel; 2018 [cited 2022 September 12] Available from: URL: https://nelhydrogen.com/assets/uploads/2017/01/Nel_Electrolyser_brochure.pdf.
[26] International Energy Agency. The Future of Hydrogen. 2019: IEA; Paris.
[27] Towler G, Sinnott R. Chemical Engineering Design: principles, practice and economics of plant and process design. Butterworth-Heinemann 2021.
[28] Zauner A, Böhm H, Rosenfeld D, Tichler R. Innovative Large-scale Energy Storage Technologies and Power-to-Gas Concepts After Optimization: European Union; 2019. Analysis on future technology options and on techno-economic optimization 2019.
[29] Geldermann J. Anlagen- und Energiewirtschaft: Kosten- und Investitionsschätzung sowie Technikbewertung von Industrieanlagen. Munich: Franz Vahlen 2014.
[30] Weimer-Jehle W. ScenarioWizard 4.4: Constructing Consistent Scenarios Using Cross-impact Balance Analysis. Stuttgart 2021.
[31] Ambrose T. EU carbon permit prices crash after Russian invasion of Ukraine. The guardian 2022 Mar 2.
[32] Agora Verkehrswende, Agora Energiewende, and Frontier Economics. The Future Cost of Electricity-Based Synthetic Fuels; 2018.

Development and assessment of an IoT system for monitoring air and soil quality in the agricultural sector

Pedro R. Gomes[a], António Nicolau[b], Ana Cristina Ferreira[c], Bruna Ramos[d], João Ferreira[e], José Costa[f], Filipe Santos[g], Eduardo Santos[h] and Gonçalo Teixeira[i]

[a]COMEGI, Universidade Lusíada, Portugal, pedroreis@fam.ulusiada.pt (CA)
[b]CITAD, Universidade Lusíada, Portugal, anicolau@por.ulusiada.pt
[c]MEtRICs and ALGORITMI, Universityof Minho, Guimarães, Portugal; COMEGI, Universidade Lusíada, Portugal, acferreira@dps.uminho.pt
[d]ALGORITMI, Universityof Minho, Guimarães, Portugal; COMEGI, Universidade Lusíada, Portugal, bruna.ramos@fam.ulusiada.pt
[e]COMEGI, Universidade Lusíada, Portugal, a31719020@fam.ulusiada.pt
[f]COMEGI, Universidade Lusíada, Portugal, a31725014@fam.ulusiada.pt
[g]COMEGI, Universidade Lusíada, Portugal, filipesantos__12@hotmail.com
[h]COMEGI, Universidade Lusíada, Portugal, a31709317@fam.ulusiada.pt
[i]COMEGI, Universidade Lusíada, Portugal, a31705116@fam.ulusiada.pt

Abstract:

Currently, there is a set of variables that directly and indirectly influence the level and quality of life of human beings. Climate change, pandemic situations and wars raise questions about their survival. Thus, the development of systems allowing efficient monitoring of the surrounding environment seems appropriate. In this sense, since the agricultural sector is a pillar of modern societies, the application of technologies such as IoT (Internet of Things), for its sustainable development is the motivation for this multidisciplinary work. The work carried out uses emerging technologies, wireless communication networks, alternative energy sources, control systems and friendly human-machine interfaces. Communication between the devices uses LoRa (Long Range) technology due to its low consumption. Depending on the location to be monitored, alternative sources of energy, solar and hydropower, are selected individually, using an algorithm that monitors the power available at each instant. Data acquired such as temperature and humidity by several network nodes (peripheral towers), communicate to a gateway (main tower). These data are stored, treated statistically, and presented in a user-friendly application for different users. The system was installed in an urban vegetable garden in the Vila Nova de Famalicão municipality. After its operational validation, the temperatures and humidity values were registered. In conclusion, the developed system is low cost, autonomous, modular, flexible, has a low energy consumption and uses alternative energies, allowing the optimization of techniques and types of cultivation.

Keywords:

IoT systems; LoRa technology; Renewable energy; Agricultural sector; Sustainability.

1. Introduction

The internet of things, also known as IoT, is a current concept that continues to demonstrate great relevance, mostly because it allows autonomous interaction between different entities of a system endowed with technology. In practice, the IoT consists of a system of devices that are related to each other, which can represent equipment with a mechanical or digital operation, intelligent objects and people or animals monitored by sensors. Each entity in the system must have a unique identifier in order to enable communication/data transfer over a network without the need for human interaction. According to Fortino et al.[1], the IoT represents a seamless interaction between dynamic communities of users, smart objects and traditional computer systems that have the possibility to interact with each other and with the surrounding environment. When building an IoT system from smart objects, another important aspect is being able to differentiate several types of smart objects.

In [2], Kortuem and his co-authors present a classification of these types of objects where they highlight their most relevant differences. The authors refer to three fundamental aspects of intelligent objects, such as "Awareness", "Representation" and "Interaction". The first represents the ability of an object to interpret and react to events and activities that occur in a real physical context. The second denotes the digital representation of the object obtained through an applied programming model. The latter represents the ability of the object to interact with the user concerning the input, output and data visualization. The authors also mention that IoT systems based on smart objects raise research questions such as *"What is the right balance for the distribution of functionality between smart objects and the supporting infrastructure? How do we model and represent smart objects' intelligence? What are appropriate programming models? And how can people make sense of and interact with smart physical objects?".* These questions may have different answers according to the context of the problem. However, they must be considered when defining the project objectives.

Over time, different architectures for IoT systems have been defined, some more detailed than others (number of layers in the model) that are being adapted to emerging technologies. An exhaustive literature review of the IoT architecture evolution and main concerns was provided by [3]. The review considered architectures from 2008 to 2018 and the IoT challenges, for example, security and privacy issues. More attention to data security is being paid over the last years due to the massive data gathering and analysis. IoT can be applied to different areas of activity, however, all systems provide an architecture where data collection and transport, data storage, processing and data availability are required [4]. In general, the most comprehensive system must incorporate the requirements identified in Table 1 that are associated with an inherent technological process.

Table 1. Summary of IoT system requirements and respective process description

IoT system requirements	Process description and inherent methods or technology
Transport and collect data	The system in real physical context contains objects connected to local data collection points that can establish communication through wired technology such as fibre optics or ethernet or through wireless networks such as Wi-Fi or LoRaWAN.
Storage data	The transmitted information is stored in databases appropriate to the context of the problem, using database management systems as MongoDB or SQLServer.
Processing data	Data processing occurs through data analysis techniques, based on statistical procedures, data mining, programming models and artificial intelligence techniques. Several methods can be used, such as exploratory data analysis, exact methods, heuristics, among others.
Make data available	The data must be made available to the user in a summarized form, providing only the information necessary for the process under analysis. This can be available through APIs or GUIs, such as a web application or a dashboard.

In the agriculture sector, IoT systems are increasingly used to allow better monitoring, support decision-making and, consequently, an increase of the business value. IoT can be applied in different ways in agriculture, from telemetry systems, computational software, data collection and efficient automation control. IoT enables data generation, which can be analysed to improve how agricultural activities are carried out [5]. The applications in irrigation are emerging in the literature [6–8]. Syrmos et al [5] presented an intelligent modular water monitoring IoT system for real-time data collection to sustain operational reliability. The authors discuss the relevance of IoT communications and infrastructure maturity, which are the foundation for a robust smart water metering solution. The proposed system uses LoRaWAN as the communication protocol and the flowmeter is equipped with a gyroscope for detecting movements. The limitation of the system is the cost since the proposed system cannot be adopted for domestic use due to frequent sensor replacement costs and an increased energy consumption. LoRaWAN defines the communication protocol and system architecture for the network, while the LoRa physical layer enables the long-range communication link. LoRaWAN is also responsible for managing the communication frequencies, data rate, and power for all devices [9]. Cheema et al. [10] proposed an IoT applied in a farm, based smart system equipped with accessible and economical devices and sensors to capture real-time parameters, such as temperature, soil moisture and pH level or humidity at frequent intervals of time. The IoT system evaluates these environmental factors, facilitating the decision-making.

Ragnoli et al. [11] proved that implementing low power wide area network technologies in IoT-oriented wireless sensor grids because it can help to good energetic performances, which are essential for energy harvesting in powered devices.

Thus, there is a need for emerging technologies to reduce energy consumption and cost-effectiveness in control and monitoring systems [12,13]. It has been predicted that the global energy consumption of IoT edge devices will reach of about 46TWh by 2025 [14]. Thus, it is of utmost importance to use renewable energy sources to power IoT devices, in line with the ambitioned sustainable development of modern society. Outdoor IoT devices can use photovoltaic panels to power themselves. Liu and Ansari [14] presented an example of a green energy solution to power IoT devices.

This study proposes the development and implementation of a monitoring system based on open IoT hardware and software platforms. Also, a LoRa supporting low-power long-distance network is applied through a low-cost solution. The IoT system can be powered by alternative energy sources, solar panels and a μhydroelectric plant. An algorithm was developed to monitor and collect several parameters, such as temperature and humidity by the different network towers, which communicate with the main gateway. These data are stored, statistically treated and presented in a user-friendly application.

This system's novelty is related to the possibility of using different renewable energy sources since the microcontroller can switch from solar to hydroelectric, which ensures constant battery power. Also, to increase their efficiency, the peripheral towers were programmed to remain in active mode only during the data sending and receiving. Otherwise, the microcontroller of the peripheral tower remains on standby. This aspect also enhances the batteries' useful life span.

2. System design and architecture

The IoT monitoring system consists of three main parts: the First is an energy IoT node that collects data, a second is IoT gateway that receives and stores data from nodes at remote locations, and the last is the low-cost LoRa network which is support wide area networking and low costed wireless solution. In this research work, when referring to IoT systems, one should keep in mind their properties and limitations. In this sense, an IoT system should be, when possible, battery-powered, have a small size, low cost and perform simple tasks. The assigned restrictions imply a study of consumption, autonomy, computational power, and specific tasks.

2.1. Schematics of the system design

The methodology used in this work for monitoring air and soil quality in an agricultural environment is based on the principles of IoT systems in which it seeks to find adequate solutions for its limitations. Figure 1 presents a general design of the developed system. The system is composed by peripheral towers for acquisition of soil-related variables; a main tower for monitoring variables related to air quality and to serve as a gateway of all information; a server to store and analyse data and an informatic application to query and monitor it.

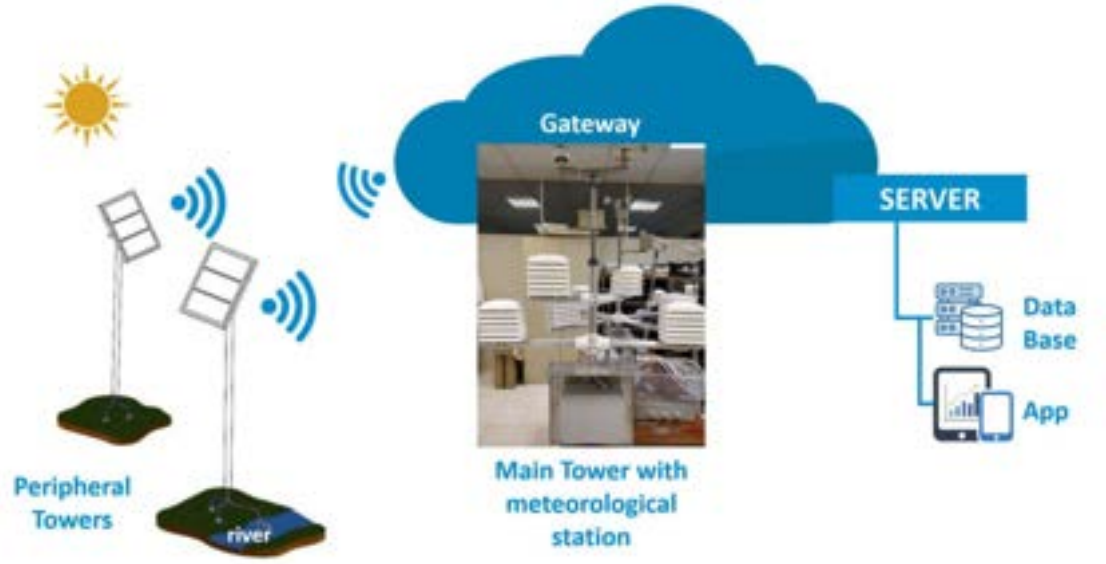

Figure. 1. Schematics of the system design.

2.2. Characterization of data acquisition towers

The data acquisition subsystem includes the main tower and the peripheral towers, both equipped with sensors and communication systems. Each peripheral tower, Figure 2 (a), is composed of temperature and soil humidity sensors. These sensors are connected to a data acquisition developed board capable of communicating with the main tower through a wireless network (LoRA at 868 MHz).

Regarding the power supply of each tower (battery), this is charged by using renewable energy that comes from the solar panel installed. Figure 2(b) depicts a peripheral tower installed to collect soil parameters.

The main tower, Figure 2(c), serves as a gateway to the data acquisition system. In this tower, there is also a meteorological station that provides information on atmospheric pressure, air temperature and humidity, wind direction and speed and precipitation rate, as well as, CO_2, O_3 or particles (e.g., PM2.5, PM10). The air quality information is provided through sensors installed. Data is sent over the internet to a remote server.

(a) (b) (c)

Figure. 2. Data acquisition subsystem: (a) detail of peripheral tower with the solar panel to feed the battery and the antenna; (b) peripheral tower installed in the urban garden near the river flow; (c) main tower with the meteorological station.

2.3. Architecture of the energy feeding system

One of the requirements of this project is that the peripheral towers are powered by using renewable energy. Renewable energy sources cause some disturbances in electrical power grids. In this sense, designing a system that monitors the available power in real time is required, whereas the energy is provided from solar panels or hydroelectric plants, with the use of small generators.

The monitoring system comprises two components: hardware and software. Regarding the hardware, it is necessary the physical interfaces connected to the current and voltage intensity sensors, necessary for the calculation of the available power. Power drives were also developed to charge the battery responsible for powering the electronic system (microcontrollers, relays, development board and others) implemented in each peripheral tower. In addition to the software that controls the hardware, an algorithm was also developed to articulate historical or via satellite information regarding the seasonality and predictability of the variables to be monitored, for a specific location (agricultural zone) with the data coming from physically implemented sensors. Figure 3 shows the flowchart of the developed algorithm.

The algorithm developed is based on the history of available information and it was created to consider two types of energy input, i.e., solar energy and/or hydroelectricity. For instance, on a summer day, the hours from sunrise to sunset and the hours of highest solar irradiance are both known. So, if the power available from the solar panel is below the nominal power to charge the battery, then, the algorithm commutes to the alternative energy source. In case there is only solar energy available, its current intensity is calculated to power the system during the night.

Figure 4 shows the flow of information between the different components. The available power from each of the alternative energy sources are measured (product of the current intensity by the voltage) and compared to determine the highest one. Afterwards, the microcontroller (development board) activates an output for the relay drive. Through a relay contact, the current intensity is physically routed to the circuit that charges the battery. Once the alternative energy source has been chosen, the others are blocked by the auxiliary contacts of the relay associated with that source. A hysteresis cycle was also implemented in the algorithm, which prevents the switch whenever the instantaneous power available is of a higher energy than the current one that is charging the battery.

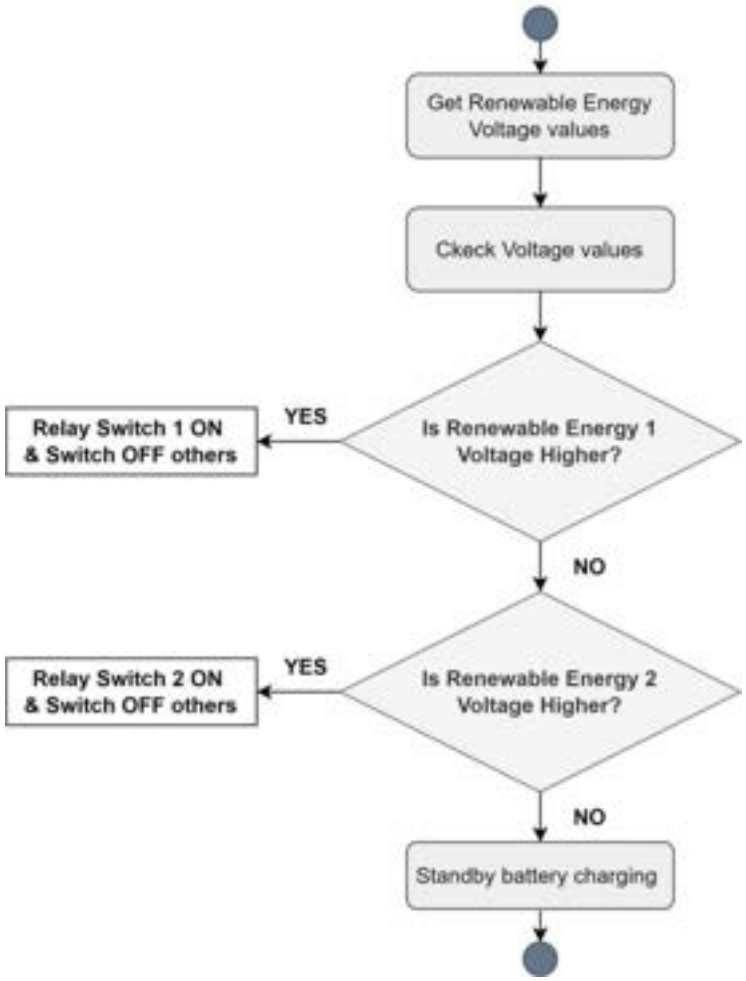

Figure. 3. Flowchart of the developed algorithm to manage the architecture of the energy feeding system.

The implementation of renewable energies in the project facilitates the acquisition of data in remote locations, mostly where there are no conventional energy sources. The supplying companies offer a set of equipment solutions with several sizes and available capacities. However, regarding the hydroelectric production, it is difficult to obtain components with potentials available for IoT applications. In this sense, this project includes the design of an innovative μhydroelectric plant.

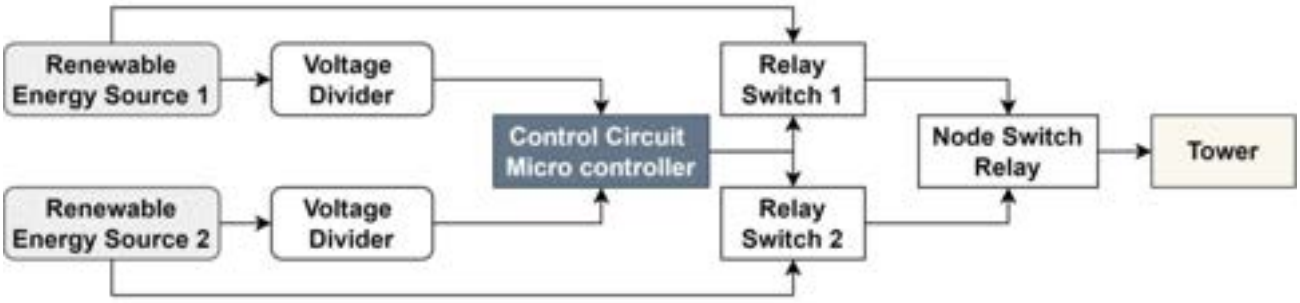

Figure. 4. Information flowchart between the system components.

An optimized printed circuit board was developed with hardware improvements, allowing a better efficiency of the switch system between alternative energy sources. Despite to the fact that, in this study, only solar and hydroelectric energy sources are assessed, the developed printed circuit board allows the switch between 3 different types of alternative energies. The optimized printed circuit board layout is presented in Figure 5.

Figure. 5. Optimized printed circuit board layout.

The μhydroelectric plant was designed based on a modular architecture, capable of adapting to the most diverse scenarios related to its installation. Different configurations were studied, according to the environmental conditions related to natural water courses. The two basic configurations, turbines arranged in series (Figure 6(a)) or in parallel (Figure 6(b)), can be adapted to different natural river bed scenarios. The number of turbines can also change according to the intensity of electrical current required to power IoT devices.

As technical specifications, the turbines used in this work have the output Voltage of 5V DC and a maximum intensity of electrical current output of 150 mA for a constant water flow rate (4L/min). Solidworks® software was used for the development and testing of components. Depending on where the water is collected, for example, in a small river, if the bed is flat, the best turbine configuration is in series. That is, a use of the kinetic energy caused by the natural current of the river. On the other hand, if the riverbed is uneven, the best configuration is parallel. That is, the use of potential energy at a height of about one meter of distance towards to the turbine position. Mixed configurations (series/parallel) of turbines are also possible.

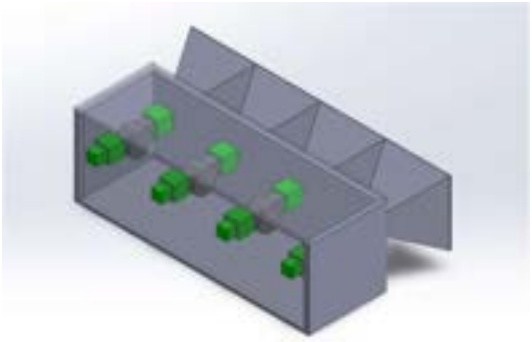

(a)

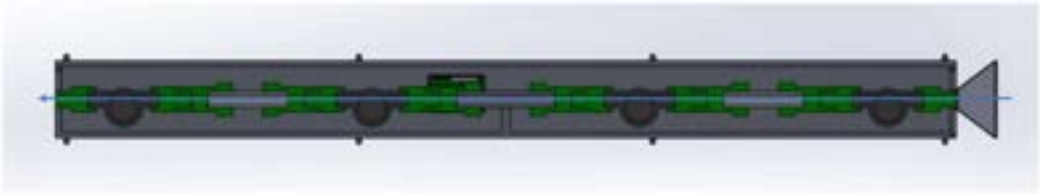

(b)

Figure. 6. CAD files of turbines developed for the project: (a) turbines arranged with a parallel flow architecture; (b) turbines arranged with a series flow architecture.

2.4. Definition of the communication protocols

Recent studies show a wide variety of IoT applications using the LoRaWAN Protocol. This defines the system architecture as well as the communication parameters in relation to LoRa technology.

In this work, the technologies involved were considered, seeking to standardize the power supply voltages of the devices, powers involved and communication networks. In this sense, the WEMOS TTGO ESP32 SX1276 LoRa development board was chosen. As main features, this board is low cost, composed by the ESP32 microcontroller and a LoRa SX1276 radio communication module.

The ESP32 is a 32-bit microcontroller with integrated Wi-Fi and Bluetooth connectivity, which has several advantages, such as low power consumption associated with high processing performance. The SX1276 LoRa radio communication module allows you to communicate with other LoRa devices over long distances, usually in the range of a few kilometres (about 10 km with an unobstructed view), depending on the environment and device configuration. It is usually used in projects that require long-range wireless communication with low data transfer rate and low power consumption.

The TTGO development board allows the use of an external antenna, in order to provide a greater performance of the LoRa technology. When choosing an outdoor antenna, it is important to consider the type of antenna that will best meet the specific needs of each project. There are two main types of antennas: omnidirectional and directional. Omnidirectional antennas emit signals in all directions, while directional antennas emit signals in a specific direction. Omnidirectional antennas are ideal in situations that require signal coverage in all directions, such as in urban areas or places with many obstacles. On the other hand, directional antennas are best suited in situations that require a strong signal in a specific direction, such as in rural areas or places where there are few obstacles. As presented in Figure 7, an omnidirectional antenna was chosen. Omnidirectional antennas provide easier installation compared to directional antennas, which require prior positioning in relation to the other nodes in the network. It is possible to add new nodes (sensors) to the LoRa network, which is one of the objectives of future work. The solar panel as a nominal capacity of 20 W.

The use of the TTGO development board that integrates the ESP32 microcontroller has the advantage of allowing operation in different energy modes. There are five power modes available on the ESP32, ordered from highest to lowest consumption: active mode (pre-set mode by default), modem-sleep mode, light-sleep mode, deep-sleep mode, and hibernation mode.

Figure. 7. Omnidirectional antenna installed in the peripheral towers.

The monitoring of the environmental variables and their transmission by the peripheral towers are carried out every 10 minutes, which makes it unnecessary to keep the microcontroller constantly in active mode. In this work, the efficiency of the peripheral towers is a relevant aspect, since they are powered by batteries, and it is important to guarantee their efficiency. To increase their efficiency, the peripheral towers were programmed to remain in active mode while reading and sending environmental variables. After this process, the microcontroller of the peripheral tower goes into sleep mode, leaving only the sensors connected to the GPIO (programmable input and output ports) and an RTC timer responsible for waking it up after 10 minutes. With this procedure, it is possible to improve the efficiency of the microcontroller, reducing the current consumption from 50 mA to 10 mA during the respective period of 10 minutes.

2.5. Development of the application interface

On the server, data is stored in a non-relational database DB (Mongo DB) created for this purpose. Some of the attributes that contributed to its choice were: easy adaptation to new data, open source, and familiarization with this DB. Data is treated statistically and presented in the form of an application (App) for users. This application is a user-friendly application because it was thought and designed considering the different ages of users. The system architecture for data storage and visualization is divided into three main components: backend, frontend, and database. The backend is composed by a NodeJS application that provides two different API's considering the requests that are served. Indeed, there is a specific API to receive and store the data provided by the central control tower.

The second API have methods to provide the necessary data or validations for the frontend application. The communication is based on HTTP requests and considers the different GET, POST, DELETE and PUT methods. The information is stored in a non-relational database (MongoDB). Finally, the frontend provides, through several HTML, CSS and Javascript files, the information to the user. A dashboard is made available through a web application accessible with an Internet connection. Such information contains plots with, for example, temperature and humidity data and has methods that enables the user to change the visualized data by a temporal period (e.g., reset the zoom of an axis). By separating the backend from the frontend, the system may be more responsive since the backend has the only goal of providing the information, whereas the frontend is responsible for formatting and display such information. Indeed, the backend server is not overloaded with graphical requests.

3. Results and discussion

The results obtained with this work are presented taking into account the validation of each component of the IoT monitoring system architecture, considering the improvements of each subcomponent. In this section, the process for data acquisition and communication protocol validation is presented, as well as the assessment of the μhydroelectric plant operation and the variables measurement which can be accessed by the dashboard developed for the informatic application.

3.1. Data acquisition and communication protocol validation

Although the main tower is prepared to operate, in a remote location, with a current intensity of 600 mA, for technical reasons related to the compatibility of the developed system and the existing internet devices in the urban garden, the power supply to the tower was carried out using the mains. The data from the peripheral towers are sent together with the data acquired in the tower to a remote server located in the University Laboratories. The sending cadence corresponds to a 10 minutes interval period.

Regarding the battery charging, the initial calculations were carried out for a battery capable of supplying the designed circuits for each one of the peripheral towers. It was determined a current intensity value of 480 mA. This current intensity would be required for the constant and continuous system operation.

Nevertheless, during the project development, improvements were made at both hardware and software levels, which lowered the initially calculated value to around 250 mA. Taking into account the values initially calculated for the current intensity and the inclusion of more sensors in the near future, the average current intensity stipulated for the development of battery charging systems is 600 mA.

Regarding the sensors calibration, the system was also optimized for the application in study. The sensors that are part of the peripheral towers to measure soil temperature (SONOFF SENSOR-DS18B20) and moisture (SKU: SEN0193 Analog Capacitive Soil Moisture Sensor) were calibrated according to the manufacturer's specifications.

The temperature sensors were calibrated with ice (for a reference temperature of 0ºC) and with boiling water (for the reference temperature of 100ºC) in order to maintain their linearity in the measurements taken. The humidity sensors were calibrated according to the resolution of the analogue to digital converter (ADC) of the development board microcontroller. For a 12-bit ADC resolution, the value of 1490 corresponds to 100% humidity (immersed in water) and the value of 2980 corresponds to 0% (dry value). Figure 8 shows a cycle of reading and sending temperature and humidity values from the peripheral tower to the main tower. After the RTC timer wakes up the device, the program reads the humidity and temperature and sends the information through LoRa. Afterwards, the system enters in deep-sleep again.

Figure. 8. Cycle of reading and sending temperature and humidity values.

3.2. Assessment of μhydroelectric plant operation

As previously stated, a μhydroelectric plant was developed as the second renewable energy source of the IoT monitoring system. Prior to the tests to monitor the turbines behaviour, they were calibrated individually, according to the manufacturer's specifications, using information from a flow sensor and an ammeter. This process ensured an output current intensity of 150 mA. The water supply pipe diameter of was also sized to guarantee a constant flow rate of 4 L/min.

Regarding the series configuration of the 4 turbines (Table 2), it was verified that the first turbine was producing 150.0 mA, the second turbine 147.9 mA, the third 145.8 mA and the fourth turbine 142.6 mA. The fact that all the turbines were not producing all 150 mA was caused by mechanical losses and junction losses. One of the solutions to solve the problem may be to increase the flow rate. Yet, the flow rate increase results in higher wear rates of the first and second turbines since, by increasing the flow rate, the maximum intensity of the current does not increase as they are already in saturation.

Regarding the parallel configuration of the 4 turbines, the performance improves, as it was possible to obtain a maximum current intensity of 600 mA through a summation circuit. The problem lies in the need for a gap of about one meter in the riverbed.

Table 2. Intensity of current produced by the turbines considering the series configuration

Generator equipment ID	Current intensity (mA)
Turbine 1	150.0
Turbine 2	147.9
Turbine 3	145.8
Turbine 4	142.6

At the moment, a hybrid system is being developed with the architecture of a parallel system of two turbines in series, capable of producing 600 mA. With this architecture it is possible to solve the problems described above. This configuration is being tested, so the data will be subject to future analysis.

3.3. Temperature and humidity measurements

The IoT system developed in this study aims to monitor environmental parameters registered at an urban vegetable garden located in the vicinity of a river stream in the Vila Nova de Famalicão municipality. Figure 9 shows the visualization dashboard obtained from the data of temperature and humidity registered in March 16th of 2023, between 10 a.m. and 11 p.m. The developed interface is able to estimate the mean obtained values.

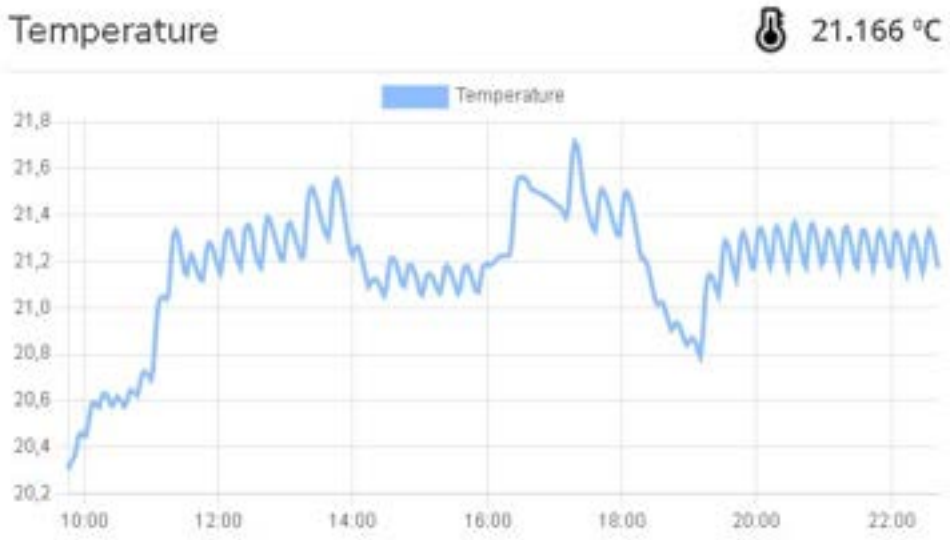

(a)

(b)

Figure. 8. Temperature (a) and humidity (b) registered by the IoT monitoring system in March 16th of 2023, between 10 a.m. and 11 p.m.

Like the Portuguese national meteorological service (Portuguese Institute of the Sea and Atmosphere -IPMA) the interface is very user-friendly, since it uses a coloured code for variables range classification: light green (very good), green (Good), yellow (medium), orange (weak) and red (bad). In addition, the interface was programmed to disclose the collected data with statistically treated. The dashboard detailed by Figure 9 shows the average, maximum and minimum values for both temperature and humidity during the time of data acquisition. For instance, regarding the temperature data from March 16th, the application reported an average value of 21.18 ºC, with an amplitude ranging from 20.30 ºC to 21.72 ºC. The temperature standard deviation corresponds to ±0.25.

Statistic

Variable	Average	Standard Deviation	Max	Min
Temperature (°C)	21.18	0.25	21.72	20.30
Humidity (%)	54.37	2.03	58.37	50.48

Figure. 9. Print of the statistic information provided by the interface application dashboard, regarding the registered temperature and humidity values.

Thus, with this IoT monitoring system it is possible to define the best techniques and types of agricultural crops for a certain environmental pattern. Soil humidity sensors are used in detecting the changes which are required and to adjust the irrigation practices. Minor changes in irrigation practices increases the cultures growth and saves water.

For instance, a proper irrigation management using soil humidity level variation depends on the specific soil type. The modularity of the developed system also allows to design and size an economical, appropriate and a low maintenance solution for agricultural small-scale applications, mainly in rural areas.

4. Conclusions and final remarks

This paper presented the architecture and development of an IoT monitoring system to effectively collect environmental data such as temperature and soil humidity to facilitate agriculture activities. A LoRa supporting low power long distance network was applied through a low-cost solution, the WEMOS TTGO ESP32 SX1276 LoRa. The system can be powered by alternative energy sources, solar energy and hydroelectric and it uses an algorithm that monitors and collects several parameters by the different network towers, which communicate with the main gateway tower, which is equipped with an atmospheric station to collect air quality data.

All the stored data are statistically treated and presented in a user-friendly application that can be used by different users. The system was installed in an urban vegetable garden in the Vila Nova de Famalicão municipality.

The monitoring of the environmental variables and their transmission by the peripheral towers are carried out every 10 minutes. Since these towers are battery powered, the control circuit was optimized to reduce the current consumption, from 50 mA in activated mode to 10 mA in sleeping mode. The peripheral towers can also be feed by hydroelectricity, since an optimized printed circuit board was conceived allowing a better efficiency of the switch system between alternative energy sources. Due to the irregularities of the river bed, two configurations for the turbine connexion were studied – in series and in parallel. In series configuration, due to mechanical and junction losses, it is not possible to guarantee the intensity of 150 mA from all turbines. Hybrid configurations need to be implemented. Through the dashboard developed as the informatic application interface, it was possible to validate the IoT system by monitoring the temperature and humidity.

The use of different renewable energies makes this project thrive in all weather conditions and seasons, with wind and hydro energy for nights and winters and solar energy during the day and especially in summer. The implementation of renewable energies in the project facilitates the collection of data from remote places where there are no conventional energy sources. As future work, the IoT monitoring system will be able to select the most appropriate source from wind, water or solar, since the defined architecture allows to adapt the system to operate with three renewable energy inputs.

Acknowledgments

This work has been supported by FCT within the R&D Units Project Scope UIDP/04005/2020 (COMEGI) and R&D Unit Project Scope UIDP/04077/2020 (METRICS).

References

[1] Fortino G, Savaglio C, Spezzano G, Zhou M. Internet of Things as System of Systems: A Review of Methodologies, Frameworks, Platforms, and Tools. IEEE Trans Syst Man, Cybern Syst 2021;51:223–36. https://doi.org/10.1109/TSMC.2020.3042898.

[2] Kortuem G, Kawsar F, Sundramoorthy V, Fitton D. Smart objects as building blocks for the Internet of things. IEEE Internet Comput 2010;14:44–51. https://doi.org/10.1109/MIC.2009.143.

[3] Alshohoumi F, Sarrab M, AlHamadani A, Al-Abri D. Systematic Review of Existing IoT Architectures Security and Privacy Issues and Concerns. Int J Adv Comput Sci Appl 2019;10. https://doi.org/10.14569/IJACSA.2019.0100733.

[4] Dorsemaine B, Gaulier J-P, Wary J-P, Kheir N, Urien P. Internet of Things: A Definition & Taxonomy. 2015 9th Int. Conf. Next Gener. Mob. Appl. Serv. Technol., IEEE; 2015, p. 72–7. https://doi.org/10.1109/NGMAST.2015.71.

[5] Syrmos E, Sidiropoulos V, Bechtsis D, Stergiopoulos F, Aivazidou E, Vrakas D, et al. An Intelligent Modular Water Monitoring IoT System for Real-Time Quantitative and Qualitative Measurements. Sustain 2023;15. https://doi.org/10.3390/su15032127.

[6] Cheema SM, Khalid M, Rehman A, Sarwar N. Plant Irrigation and Recommender System–IoT Based Digital Solution for Home Garden. vol. 932. Springer Singapore; 2019. https://doi.org/10.1007/978-981-13-6052-7_44.

[7] Chilundo RJ, Neves D, Mahanjane US. Photovoltaic water pumping systems for horticultural crops irrigation : Advancements and opportunities towards a green energy strategy for Mozambique. Sustain Energy Technol Assessments 2019;33:1–8. https://doi.org/10.1016/j.seta.2019.03.004.

[8] Moura J, Ferreira AC, Costa C, Martins L. Design and Operational Analysis of a Photovoltaic Irrigation System. Proc. ASME 2022 Int. Mech. Eng. Congr. Expo., Columbus, Ohio, USA: American Society of Mechanical Engineers; 2022, p. 1–7. https://doi.org/10.1115/IMECE2022-95967.

[9] Choi C-S, Jeong J-D, Lee I-W, Park W-K. LoRa based renewable energy monitoring system with open IoT platform. 2018 Int. Conf. Electron. Information, Commun., vol. 2018- Janua, IEEE; 2018, p. 1–2. https://doi.org/10.23919/ELINFOCOM.2018.8330550.

[10] Cheema SM, Ali M, Pires IM, Gonçalves NJ, Naqvi MH, Hassan M. IoAT Enabled Smart Farming: Urdu Language-Based Solution for Low-Literate Farmers. Agric 2022;12:1–23. https://doi.org/10.3390/agriculture12081277.

[11] Ragnoli M, Colaiuda D, Leoni A, Ferri G, Barile G, Rotilio M, et al. A LoRaWAN Multi-Technological Architecture for Construction Site Monitoring. Sensors 2022;22. https://doi.org/10.3390/s22228685.

[12] Saban M, Bekkour M, Amdaouch I, Gueri J El, Ahmed BA, Chaari MZ, et al. Computing Web Application Using LoRa and LoRaWan 2023:1–16.

[13] Prasanna Rani DD, Suresh D, Rao Kapula P, Mohammad Akram CH, Hemalatha N, Kumar Soni P. IoT based smart solar energy monitoring systems. Mater Today Proc 2021. https://doi.org/10.1016/j.matpr.2021.07.293.

[14] Liu X, Ansari N. Toward Green IoT: Energy Solutions and Key Challenges. IEEE Commun Mag 2019;57:104–10. https://doi.org/10.1109/MCOM.2019.1800175.

Optimization of energy systems sizing and operation including heat integration and storage

Rafael Nogueira Nakashima[a], Peter Vang Hendriksen[b], Henrik Lund Frandsen[c]

[a] Technical University of Denmark, Kgs. Lyngby, Denmark, rafnn@dtu.dk, CA
[b] Technical University of Denmark, Kgs. Lyngby, Denmark, pvhe@dtu.dk
[c] Technical University of Denmark, Kgs. Lyngby, Denmark, hlfr@dtu.dk

Abstract:

Sustainable energy solutions are highly dependent on the availability and costs of resources during their operation. For instance, power output of solar cells and wind turbines vary over time which impacts the technical, economic, and environmental feasibility of Power-to-X (P2X) systems. In addition, efficient system solutions for energy conversion will require an optimal heat integration between several technologies and conversion routes. Thus, several methods have been proposed to conceptualize and optimize the design and operation of process plants. However, the possibilities of heat integration and storage during dynamic operation of different P2X-processes have been rarely evaluated by existing methods in literature. In this context, this research aims to provide an optimization framework, based on linear optimization and pinch analysis, to fill this knowledge gap, crucial to the development of dynamic renewable systems. The novel method is exemplified in the optimization of a Power-to-Methanol plant using solid oxide cells (SOCs) subjected to varying electricity production of wind turbines. The optimization estimates a minimal methanol production cost of 1772-1793 USD/ton for integrated scenarios and 1820-1807 USD/ton for non-integrated cases. Thus, heat integration plays a crucial role in cutting up to 2% of fuel production cost, while storage and optimal operation reduces further 3.3 % of the electrolysis size compared with reference scenarios.

Keywords:

energy integration; energy storage; optimization; pinch analysis; power-to-methanol.

1. Introduction

The increasing capacity of renewable electricity generation, combined with goals to reduce the dependency on fossil fuels in the global economy, has driven interest in the electrification of the industry. For instance, by replacing natural gas with wind or solar power as the main source of energy in hydrogen production, several chemical products (such as ammonia, methanol, natural gas, etc.) could be produced sustainably, with regional security and possibly at a lower cost. Processes plants that focus on using electricity to produce chemical goods have been called Power-to-X plants in the literature. Recent studies indicate that Power-to-X systems will play a major role in energy storage and industry decarbonization, and several large-scale projects are currently under development [1].

In this context, research has been focusing on different challenges associated with the design and optimization of Power-to-X plants. Most of these studies rely on thermodynamic models and mixed integer linear optimization problems (MILP) to estimate and optimize key performance indicators of novel system solutions. With regards to the optimization framework, these works can be categorized by their methods into two major types: energy integration and multi-period optimization studies. The first aims to assess the best technology types and sizes that can be integrated using a heat exchanger network [2,3]. On the other hand, the second type focus on optimizing equipment sizes under variable production profiles and market prices [4,5].

However, energy integration studies usually disregard the effects of intermittent resources, partial load efficiencies and storage solutions. In addition, multi-period optimization usually oversimplifies the heat integration problem (i.e., reduced number of temperature levels) or assume lumped models with fixed heat connections. Thus, each optimization approach has gaps that could be fulfilled by combining the two approaches. For instance, recently Li et. al [6] has proposed a complex optimization that merges both approaches to optimize distributed energy systems. Nonetheless, the optimization of Power-to-X systems including the variability of resources, storage and detailed heat integration opportunities have seldom been studied in literature. For example, a Power-to-X operating solely with wind power may benefit from power

and heat storage to stabilize energy supply. However, the optimal size of storage and utility systems is interconnected with operation and therefore both aspects should be considered to minimize production costs.

Thus, this research aims to address this research gap by proposing a simple and generalized optimization framework merging pinch analysis and multi-period optimization for energy systems like Power-to-X plants. The method allows to select and size technologies while ensuring an optimal heat integration at each time step. To exemplify the method and assess its possible gains, the design and optimization of a Power-to-Methanol system is evaluated using the optimization framework and the results are compared with non-integrated solutions.

2. Case study: Power-to-methanol

The optimization framework proposed in this section is applied to design an off-grid Power-to-Methanol plant comprised of wind turbines, solid oxide electrolysis system, methanol synthesis and distillation, as illustrated in Fig. 1. Each technology is represented by a linear model based on previous investigations using different modelling environments (e.g., Julia, Aspen Plus, etc.) [7]. The lists of every technology input, output, heat transfer and costs considered in this analysis are provided in Appendix A. In addition, a brief description of the main technologies employed in this case study is given in this subsection.

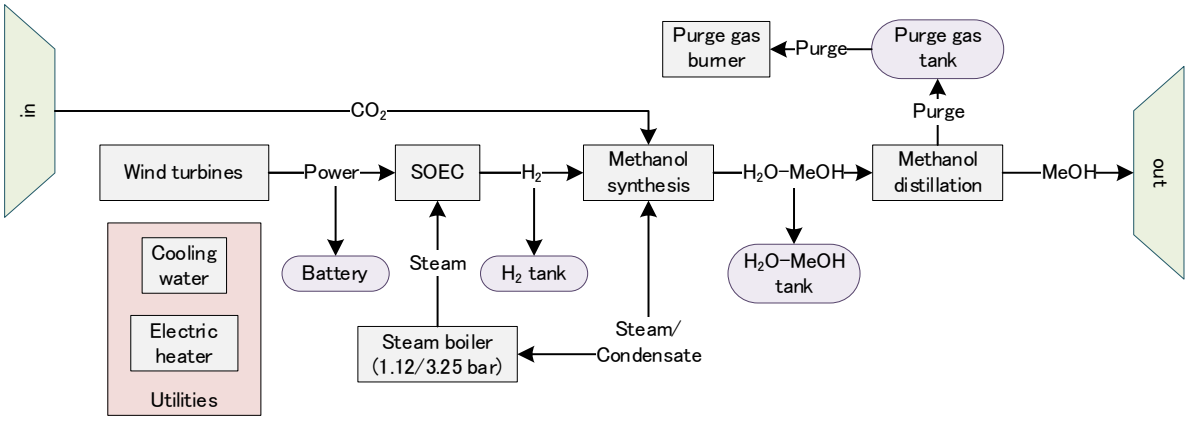

Figure. 1. Flowchart of the study case for a Power-to-Methanol plant (some resources and heat transfer were omitted for clarity)

The data of wind power generation reported by Champion, et al. [4] for an onshore wind turbine located in Esbjerg, Denmark was used to simulate the hourly power generation of a wind turbine. The main information about the wind turbine is reproduced in Table 1 from the source reference [4].

Table 1. Reference wind turbine parameters

Parameter	Value
Nominal power generation	3.15 MW
Rotor diameter (D)	142 m
Hub height	100 m
CAPEX	1.76 M€$_{2019}$/MW
Fixed OPEX	14.4 €$_{2019}$/kW/y
Variable OPEX	1.56 €$_{2019}$/MWh

The electrolysis system, Fig. 2, uses solid oxide cells to efficiently convert steam at high temperature (750 °C) and close to atmospheric pressure (1.12 bar) into hydrogen, which is compressed for storage and methanol production. A small portion of the products from the cathode of each cell are recirculated to maintain a minimal hydrogen concentration of 10% vol. in the reactants, which helps to control the electrochemical reaction, degradation, and thermal management. A detailed description of the process and modelling assumptions can be referenced in our previous works [7–9].

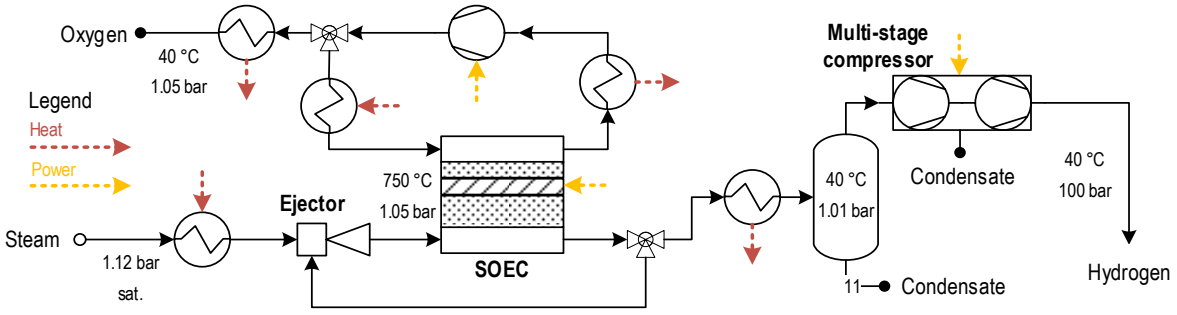

Figure. 2. Flowchart of the electrolysis system based on solid oxide cells (SOEC)

Methanol is produced in a quasi-isothermal reactor (265 °C, 90 bar) from the stoichiometric mixture of carbon dioxide and hydrogen ($CO_2+3H_2 \rightarrow CH_3OH+H_2O$). The chemical reactor is designed to achieve the same product's composition of 20 °C below the chemical equilibrium condition, as it is reported by previous works [10]. The reaction rate is estimated based on the model proposed by Bussche and Froment [11] for a copper/zinc oxide catalyst [12]. The methanol synthesis and distillation are divided as shown in Fig. 3 to include the possibility to store the water-methanol mixture (H_2O-MeOH) and operate the distillation on demand. Methanol distillation is an energy intensive process with little operational flexibility, therefore modelling it separately allows the optimization to reach more precise solutions. The detailed description of the process parameters and additional assumptions can be referenced in our previous work [7].

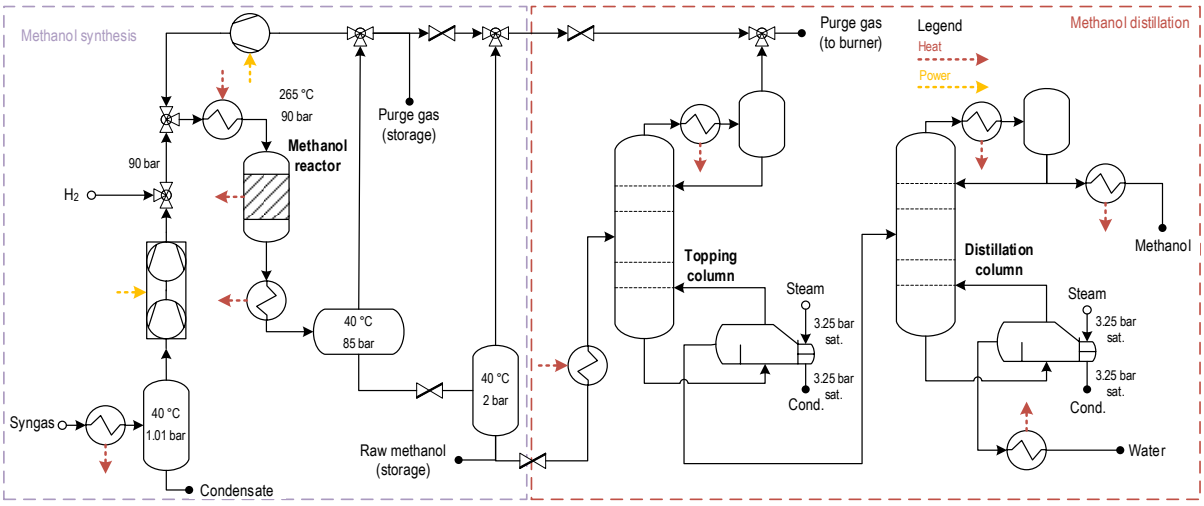

Figure. 3. Flowchart of the methanol synthesis and distillation units based on the isothermal reactor design.

The same technology and storage solutions shown in Fig. 1 and detailed in Appendix A are assumed to analyse optimal configurations under the same conditions, which are summarized in Table 2. In total, five scenarios are proposed to examinate how the wind power profile, heat integration and storage impact on the results. A summary of these scenarios is provided in Table 3.

Table 2. Summary of common parameters for optimization scenarios

Parameter	Value
Annual production of methanol (t/year)	54750
CO_2 cost (USD/ton)	30
Plant lifetime (years)	20
Interest rate of return (%/year)	8 %/year
Partial load limits (% nominal capacity)	0-100%
Installed capacity limits	≥ 0
Storage efficiency	100%
Ramping limits (% nominal capacity / h)	
Solid oxide electrolysis system	20 %/h
Methanol synthesis	20 %/h
Methanol distillation	20 %/h

Table 3. Summary of scenarios description

	Scenario acronym				
Characteristics	*AVG*	*NI-NS*	*NI-S*	*I-NS*	*I-S*
Wind power profile	No	Yes	Yes	Yes	Yes
SOEC/Methanol heat integration	Yes	No	No	Yes	Yes
Storage technologies	No	No	Yes	No	Yes

The base scenario, AVG, represents the usual energy integration optimization at steady-state conditions, where only an average of the power supply and costs is assumed. The other four scenarios include the possibility to heat integrate the electrolysis and fuel production (I – integrated; NI – non-integrated), as well as the use of storage to allow the processes to operate out of sync (S – storage; NS – no storage).

2. Methods

The objective function of the proposed optimization problem is the operating revenues of a process plant over a year discounting the amortized investment cost and fixed expenses, as expressed in Eq. (1). In this equation, $r_{i,t}^{in}$ and $r_{i,t}^{out}$ represent the rate of resources imported and exported by the process plant, respectively, while $c_{i,t}^{in}$ and $c_{i,t}^{out}$ denote their associated cost. In addition, the investment repayment and fixed expenses are estimated based on the grassroot cost for each technology (C_{GR}^{τ}) multiplied by the scale factor (f^{τ}) and capital recovery factor (β_{CRF}).

$$\max\left\{\sum_{t}^{T}\left[\sum_{i}^{I}\left(r_{i,t}^{out}c_{i,t}^{out}-r_{i,t}^{in}c_{i,t}^{in}\right)\right]-\sum_{\tau}^{\tau_n}f^{\tau}C_{GR}^{\tau}\beta_{CRF}\right\} \quad (1)$$

Technologies are divided into two categories, conversion and storage, which are denoted by the superscripts κ and σ, respectively. Each converting technology (κ) is represented by a black-box model consisted of a set of inlet resources ($r_i^{\kappa,in}$), outlet resources ($r_i^{\kappa,out}$) and heat transfers divided into temperature intervals (Q_k^{κ}), as exemplified in Figure 1. The main constraints of the optimization problem, Eq. (2) and (3), represent the balance of resources and heat between the boundary conditions of the process plant and its components (i.e., technologies). Moreover, resources and heat balances are influenced by transfers between technologies, which are affected by a temporal size factor (f_t^{κ}). This reflects the partial-load conditions of a technology in a particular timeframe (t).

$$r_{i,t}^{in}+\sum_{\sigma}^{\sigma_n}s_{i,t-1}^{\sigma}\eta_i^{\sigma}+\sum_{\kappa}^{\kappa_n}f_t^{\kappa}(r_i^{\kappa,in}-r_i^{\kappa,out})=r_{i,t}^{out}+\sum_{\sigma}^{\sigma_n}s_{i,t}^{\sigma}\quad\forall i,t \quad (2)$$

$$R_{k-1,t}+\sum_{\omega}^{\Omega}f_t^{\omega}\left(\sum_{n}^{N}Q_k^{\omega}\right)=R_{k,t}\quad\forall k,t \quad (3)$$

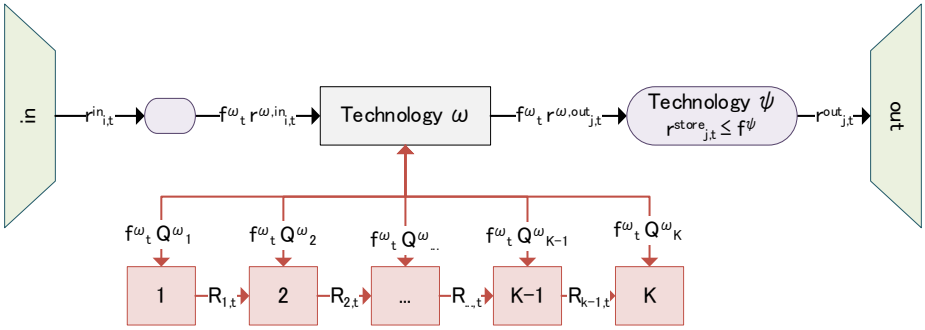

Figure. 2. Generalized sketch of a technology model in the optimization framework (where multiple technologies are coupled).

The heat cascade constraint, Eq. (3), is based on the work of Marechal and Kalitventzeff [13] and recently adapted by Li, et al. [6]. The heat transferred in a temperature interval, *k*, in a specific timestep ($R_{k,t}$) is positive to indicate a possible exchange from higher to a lower temperature level, and null in the extremes of the heat cascade (0 and K) [14]. These variable limits are represented in Eq. (4).

$$\begin{aligned} R_{k,t} &= 0, \quad k = 0, K \\ R_{k,t} &\geq 0, \quad otherwise \end{aligned} \tag{4}$$

On the other hand, storage technologies relate to accumulation variables ($s_{i,t}$) in Eq. (2) by limiting their maximum value to a size factor (f^{σ}), as written in Eq. (5). It's important to notice that storage losses can be modelled throughout an efficiency factor (η_i^{σ}) in Eq. (2), while inefficiencies in charging and discharging processes can be described by conversion technologies with an unequal balance of resources ($r_i^{\kappa,in} \geq r_i^{\kappa,out}$).

$$s_{i,t}^{\sigma} \leq f^{\sigma} \tag{5}$$

Resources can be imported or exported by the process plant under limited conditions that may vary depending on the problem analysed. For instance, a certain amount of product "*i*" may be delivered after a finite number of time steps (e.g., yearly demand of fuel), which can be represented by a constraint like Eq. (6). Another common scenario is that the supply and/or demand for each timestep is defined (e.g., hourly power generation or heat demand), as exemplified in Eq. (7).

$$\sum_t r_{i,t} = cte \tag{6}$$

$$r_{i,t} = cte \tag{7}$$

The technology size factors (f) are limited by upper and lower bounds, Eq. (8), while the temporal size factors for converting technologies (f_t) are restricted by maximum and minimal loads relative to their size (l_{min} and l_{max}, respectively), Eq. (9). In addition, some converting technologies may have ramping limits proportional to their size (r_{down} and r_{up}), which can be represented by Eq. (10).

$$f_{min} \leq f \leq f_{max} \tag{8}$$

$$l_{min} f \leq f_t \leq l_{max} f \tag{9}$$

$$r_{down} f \leq f_t - f_{t-1} \leq r_{up} f \tag{10}$$

The constraints described in Eq. (8) and (9) have been proposed by different authors [4,15] and they allow to optimize the technology sizes and operation loads simultaneously. However, these constraints don't allow to model operational discontinuities such as shutdown and standby periods without fixing the technology size. A possible alternative is to use a reformulation strategy as proposed by Voll et. al. [16] and recently employed by Li et al. [6].

3. Results

The main results for the optimization of each scenario are presented in Table 4. The cost estimates for methanol production and CAPEX excluding wind turbines vary between 1290-1820 USD/ton and 5123-8918 USD/t/y, respectively. Due to the current high investment of SOECs ($/kg$_{H2}$), these numbers are in the upper end range of those reported by IRENA and Methanol Institute [17] for e-methanol production through CO_2 from renewable sources (820-1620 USD/ton and 2000-9720 USD/t/y). The optimization results also exemplify how the variability of wind, heat integration and storage solutions can lead to different designs and costs.

For instance, the estimated costs for fuel production in the base scenario (AVG) are 27-29 % lower than other cases in which the influence of the wind power variability is considered. This difference can be explained by the need to oversize wind turbines, to compensate curtailment losses, and the Power-to-MeOH system, to match the varying rating of power generation, as it can be observed in Table 4. Figure 5 illustrates the distribution of CAPEX investments among all the technologies in each scenario. It is noticeable that the increase of SOEC size, due to the variability of wind power, represents the lion share (56-59%, 2766-2981 USD/t/y) of the CAPEX increase relative to the AVG scenario.

The optimization results also indicate the possibility to reduce 1-2% of methanol costs by integrating high temperature electrolysis with a methanol plant. This cost reduction can be attributed to the lower power consumption in the electric heaters for the integrated cases, as depicted in the Figure 6, which lowers the wind turbine sizes and, consequently, the total CAPEX investment. As can be observed by the integrated composite curves, heat provided by the condensation of the methanol reactor's products could be used to generate steam for the electrolysis system, reducing approximately 22% of electric heaters rating at steady state conditions (~1.5 MW).

Table 4. Main optimization results for each scenario proposed

	Scenarios				
Result	*AVG*	*NI-NS*	*NI-S*	*I-NS*	*I-S*
Size factors					
Wind turbine	1.00	1.25	1.24	1.22	1.21
SOEC	1.00	1.74	1.71	1.73	1.67
MeOH synthesis	1.00	1.74	1.71	1.73	1.66
MeOH distillation	1.00	1.74	1.59	1.73	1.66
Steam boiler (1.12 bar)	1.00	0	0	1.73	1.67
Steam boiler (3.25 bar)	1.00	1.74	1.59	1.73	1.66
Purge gas burner	1.00	1.74	2.00	1.73	3.48
Electric heaters	1.00	0.18	0.59	1.73	2.30
Cooling water	1.00	1.47	1.41	1.73	1.66
Battery (MWh)	0	0	6.79	0	3.85
Hydrogen (m^3)	0	0	0	0	1.49
Purge gas (m^3)	0	0	6.33	0	13.18
Water-MeOH (m^3)	0	0	167	0	57.32
*Economics**					
Annual costs (MMUSD/y)	70.62	99.65	98.9	98.16	96.99
CAPEX (MMUSD)	625.97	919.49	911.98	905.58	894.29
CAPEX (USD/t/y)	11433	16794	16537	16540	16334
CAPEX excluding wind turbines (USD/t/y)	5124	8919	8846	8857	8705
Methanol cost (USD/t)	1290	1820	1807	1793	1772

*The year base for economic values presented in this research is 2022

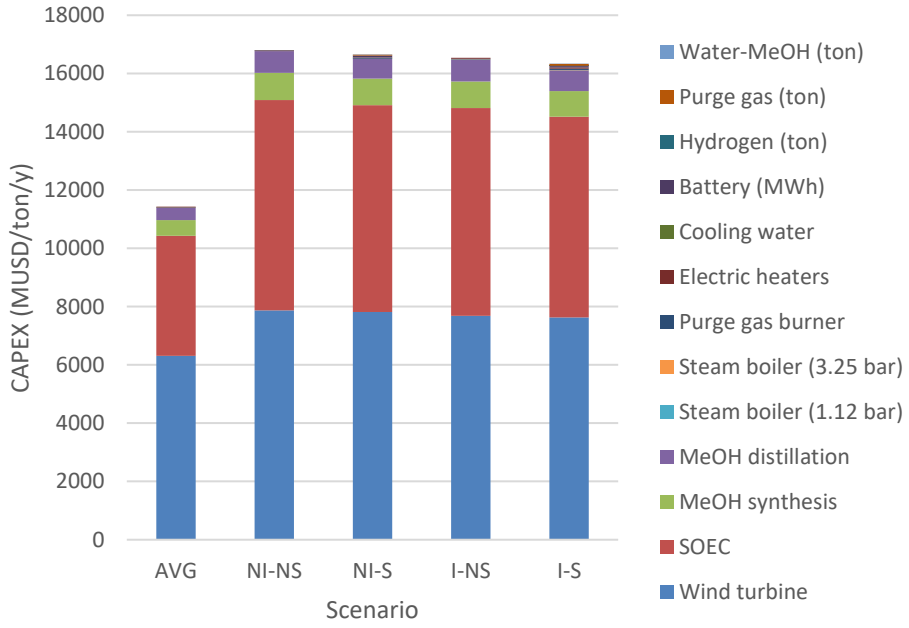

Figure. 5. Distribution of CAPEX investment for each scenario

The inclusion of storage solutions in scenarios NI-S and I-S allows an additional reduction in size of the wind turbines and electrolysis system and, consequently, lower the fuel costs in 0.7-1.2% compared with NI-NS and I-NS scenarios. It is important to highlight that a larger reduction in the electrolysis size is observed for the integrated scenario (3.3% against 1,6% for the non-integrated), which indicates that excluding heat integration during operating optimization could hide significant improvement opportunities. In particular, the I-S scenario operates differently depending on the wind power availability, as can be observed in Figure 7. For

instance, the system stores purge gas when wind power is close to maximum to be used when electricity availability is diminished. In addition, the optimal configuration also shuts-down the distillation process to reduce power consumption in electric heaters. This effect on the utility's consumption can be more clearly examined from the integrated composite curves depicted in Figure 8

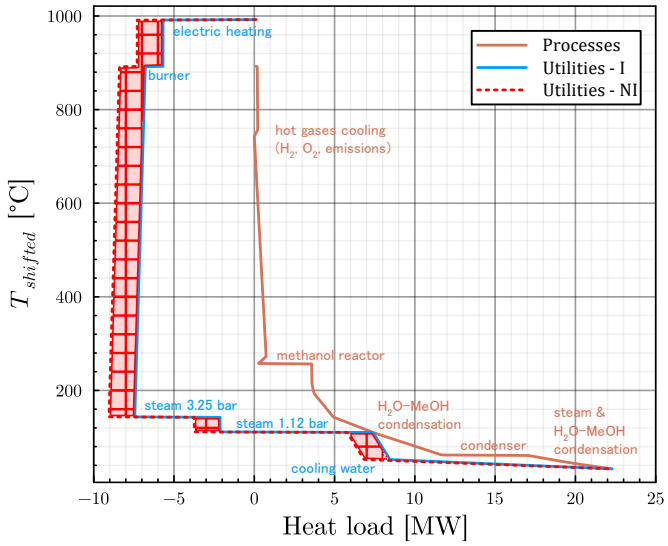

Figure. 6. Heat integration between utilities and processes for scenarios I and NI

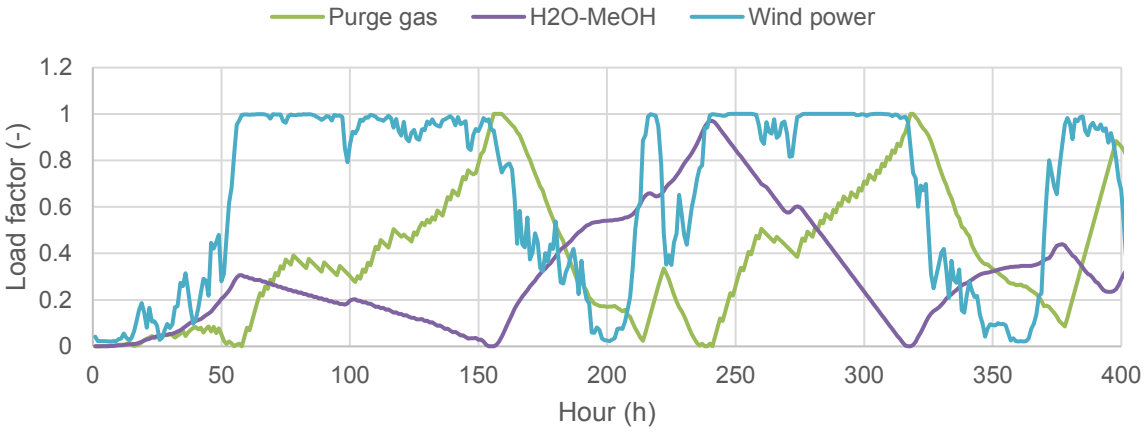

Figure. 7. Wind power and storage load variation of purge gas and H_2O-MeOH for the I-S scenario

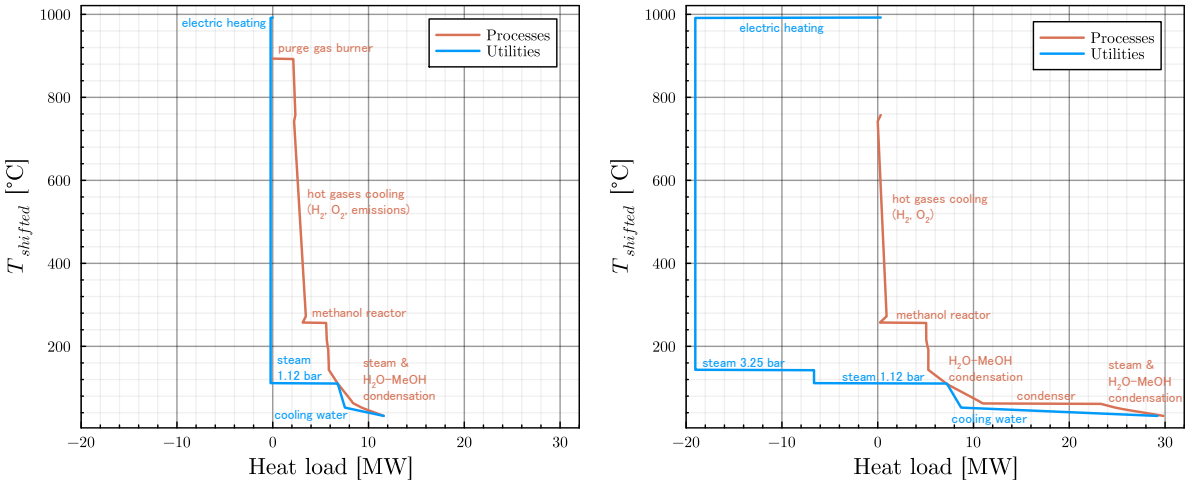

(a) Low wind power (t = 170 h) (b) High wind power (t = 277 h)

Figure. 8. Integrated composite curves for I-S scenario at different hours

3.1. Discussions

The results of the optimization study presented in the previous subsection exemplify how the steady-state assumption may hide costs and inefficiencies linked with the variability of renewable energies such as wind and solar power. This underestimation may also diminish the possible benefits of using biomass energy, which is usually less efficient than wind/solar power, but it can supply a stable source of energy. For instance, a possible alternative to further reduce the SOECs and wind turbine sizes is to complement wind power with biomass energy. The impact of this hybridization in the product costs, which could be assessed by the optimization framework proposed here, can't be fully evaluated from traditional steady-state integration studies.

In addition, the Power-to-Methanol example also demonstrates how heat integration is a crucial part of high temperature electrolysis systems such as SOECs. On the other hand, this may not be an important factor for traditional technologies, such as alkaline electrolysis, which may lead to unfavourable designs of Power-to-X plants for the future. For example, choosing to produce hydrogen separated from its use may not impact on product's cost today, but it may hinder the possibly benefits of switching from alkaline/PEM electrolysis to SOEC technology in the future. A similar observation can be drawn from the storage optimization scenarios, which may require oversized process parts (e.g., distillation and burners) from conception to reduce operating costs.

Previous studies have also pointed to possible improvements by generating steam from heat integration and proposed to reduce steam consumption by using co-electrolysis [2]. Other suggested modification indicated by Zhang et al. [3] is to operate at strongly exothermal conditions (0.9-1.1 A/cm^2, 1.42 V, 750-870 °C) to provide enough heat for steam generation and reduce cells size. However, the operation under exothermal conditions may severely increase cells degradation, which mostly likely will limit this optimization solution. On the other hand, the impacts of wind power variability and storage in the optimization of plant design and operation, as demonstrated in this study, have seldom been evaluated.

The optimization framework proposed in this study has several limitations, which can be overcome by including additional modelling strategies. For instance, the nonlinear properties of certain systems (e.g., efficiency and costs) can be approximated by a series of lines for specific intervals [16]. Another example is the details of the heat exchanger network, which can be designed to minimize the number of units to indirectly reduce the cost of the energy integration [8,14]. An extended version of this research work will focus on including these improvements and extending the Power-to-Methanol analysis.

4. Conclusions

An optimization framework is proposed to evaluate opportunities for heat integration on energy conversion and storage systems operating at dynamic conditions (e.g., fluctuating power loads, seasonal resources, etc.). The method aims to merge techniques from multi-period optimization with energy integration methods derived from pinch analysis to assist in the optimization of size and operation of future energy systems such as Power-to-X. The optimization of a Power-to-Methanol plant operating off-grid using wind power is used to exemplify the different insights provided by the optimization framework. For instance, the results indicate that conventional heat integration studies assuming constant power supply and costs may significantly underestimate technology sizes and costs (27-29 %). In addition, heat integration between high temperature electrolysis and methanol production may reduce up to 2% of fuel costs by reducing the required electric heating for steam generation. Moreover, a reduction of up to 4% in the electrolysis systems can be achieved by optimizing storage and operation including heat integration. This is possible by storing purge gas during high wind power periods and shutting down methanol distillation during low wind power generation. It is important to highlight that this size reduction is reduced by half in the case without including the possibility of heat integration, exemplifying the hidden opportunities for design in Power-to-X compared with previous studies of multi-period optimization.

Acknowledgments

The authors thank the Energy Technology Development and Demonstration Program (EUDP) at the Danish Energy Agency for financial support via the "SkyClean 2MW Process Development and Industrial Demonstration" project (project no. 64021-1114) and the project Power-to-X of Greenlab Skive.

Appendix A – Technologies details

The main details of each technology and storage options assumed in the optimization study are presented in Tables 5-8. The balance of resources and heat transfer, Tables A.1 and A.2, are based on thermodynamic models described in a previous study. The cost of investment, maintenance, and operation (Tables A.3 and A.4) were estimated following the equations proposed by Turton, et. al. [18] and Seader et. al. [19], except for the SOEC system and storage, which was determined based on values proposed by Refs. [4,20].

Table A.1. Balance of resources for each technology at reference size

	Inputs			**Outputs**		
Technology	*Type*	*Qnt.*	*Unit*	*Type*	*Qnt.*	*Unit*
Wind turbines				Electricity	0-130.5	MW
SOEC thermoneutral	Steam 1.12 bar	365.37	ton/d	Hydrogen	29.84	ton/d
	Electricity	46.06	MW			
SOEC thermoneutral / independent system	Electricity	52.91	MW	Hydrogen	29.84	ton/d
Methanol synthesis	Hydrogen	29.84	ton/d	H2O-MeOH	237.07	ton/d
	CO2	217.02	ton/d	Purge gas	4.76	ton/d
	Electricity	1.19	MW			
Methanol distillation	H2O-MeOH	237.07	ton/d	MeOH	150.00	ton/d
	Steam 3.25 bar	212.63	ton/d	Cond. 3.25 bar	212.63	ton/d
Steam boiler (1.12 bar)				Steam 1.12 bar	365.31	ton/d
Steam boiler (3.25 bar)	Cond. 2.5 bar	212.63	ton/d	Steam 3.25 bar	212.63	ton/d
Purge gas burner	Purge gas	4.76	ton/d			
	Electricity	3.79	kW			
Electric heater	Electricity	5.77	MW			
Cooling water	Electricity	0.19	MW			

Table A.2. Heat transfers associated with each technology at reference size

	Heat transfers			
Technology	*Type*	*Rate (MW)*	*T source (K)*	*T target (K)*
SOEC thermoneutral	Steam heating	5.77	376	1023
	H2 cooler	-5.05	1023	344
	H2 condenser	-2.66	344	313
	O2 1st cooling	-4.56	1023	473
	O2 2nd cooling	-0.43	481	313
	O2 reheat	2.96	480	1023
	H2 compression	-3.80	473	313
Methanol synthesis	CO2 compression	-1.37	422	313
	Preheater	7.71	308	538
	Reactor	-3.35	538	537
	Cooling	-3.66	537	424
	Condenser	-7.94	424	313
Methanol distillation	Preheater	0.16	314	328
	1st Condenser	-0.01	323	322
	2nd Condenser	-5.17	343	342
	MeOH cooling	-0.20	343	313
	H2O cooling	-0.35	388	313
Steam boiler (1.12 bar)	Liquid heating	1.38	298	376
	Phase change	9.51	376	377
Steam boiler (3.25 bar)	Evaporating	5.30	408	409
Purge gas burner	Air preheater	0.06	304	398
	Radiative	-1.10	1174	1173
	Convective	-0.65	1173	433
Electric heater	Heating	5.77	1273	1272
Cooling water	Cooling	13.46	298	318

Table A.3. Estimated costs for each technology at refence size

	Costs		
Technology	*Type*	*Value (MMUSD)*	*Lifetime (years)*
Wind turbines	C_{GR}	345.45	20
SOEC thermoneutral	C_{GR}	225.76	20
SOEC thermoneutral / independent system	C_{GR}	227.45	20
Methanol synthesis	C_{GR}	29.16	20
Methanol distillation	C_{GR}	23.49	20
Steam boiler (1.12 bar)	C_{GR}	0.13	20
Steam boiler (3.25 bar)	C_{GR}	0.07	20
Purge gas burner	C_{GR}	0.70	20
Electric heater	C_{GR}	1.21	20
Cooling tower	C_{GR}	0.54	20

Table A.4. Estimated costs for each storage technology at reference size

	Resource			Cost		
Technology	*Type*	*Qnt.*	*Unit*	*Type*	*Cost (MMUSD)*	*Lifetime*
Battery	Electricity	100	MWh	C_{GR}	54.43	20
H2 tank	Hydrogen	1	T	C_{GR}	0.69	20
Purge gas tank	Purge gas	1	t	C_{GR}	0.25	20
Raw MeOH tank	Raw MeOH	1000	t	C_{GR}	3.24	20

Nomenclature

c specific cost, USD/kg or USD/MWh or -

C_{GR} investment cost, USD

β_{CRF} capital recovery factor $(i/(1-(1+i)^{-years}))$, year $^{-1}$

D rotor diameter, m

f size factor, -

r resource amount, kg or MWh or m^3, or rate, kg/h or MW or USD/h.

$ramp$ ramp limit factor, -

R heat transfer rate between temperature intervals, kW

s stored amount, kg or MWh or m^3.

$\dot{Q}$ heat transfer rate, kW

Greek symbols

κ converting technology index

κ_n number of converting technologies

σ storage technology index

σ_n number of storage technologies

η efficiency, -

ρ specific mass, kg/m^3

v velocity, m/s

Subscripts and superscripts

$down$ discharge rate

fix fix rate

i resource index

I	number of resources
in	inlet
k	temperature interval index
K	number of temperature intervals
$rate$	design condition
T	number of time frames
t	time index
n	stream index
N	number of streams
min	minimal size or load
max	maximum size or load
out	outlet
up	charging rate

References

[1] IEA. The Future of Hydrogen [Internet]. Paris: IEA; 2019 [cited 2021 Feb 28]. Available from: https://www.iea.org/reports/the-future-of-hydrogen

[2] Wang L, Chen M, Küngas R, Lin TE, Diethelm S, Maréchal F, et al. Power-to-fuels via solid-oxide electrolyzer: Operating window and techno-economics. [Renewable and Sustainable Energy Reviews] 2019 Aug;110:174–87.

[3] Zhang H, Wang L, Van herle J, Maréchal F, Desideri U. Techno-Economic Optimization of CO2-to-Methanol with Solid-Oxide Electrolyzer. [Energies] 2019 Sep 30;12(19):3742.

[4] Campion N, Nami H, Swisher PR, Vang Hendriksen P, Münster M. Techno-economic assessment of green ammonia production with different wind and solar potentials. [Renewable and Sustainable Energy Reviews] 2023 Mar;173:113057.

[5] Zheng Y, You S, Bindner HW, Münster M. Optimal day-ahead dispatch of an alkaline electrolyser system concerning thermal–electric properties and state-transitional dynamics. [Applied Energy] 2022 Feb;307:118091.

[6] Li C, Wang L, Zhang Y, Yu H, Wang Z, Li L, et al. A multi-objective planning method for multi-energy complementary distributed energy system: Tackling thermal integration and process synergy. [Journal of Cleaner Production] 2023 Mar;390:135905.

[7] Nogueira Nakashima R, Nami H, Nemati A, Butera G, Hendriksen PV, Oliveira Jr. S de, et al. Integration of electrolysis with pyrolysis: effects of carbon conversion in methanol production. In: [7th International Conference on Contemporary Problems of Thermal Engineering] Warsaw, Poland; 2022.

[8] Nogueira Nakashima R, Oliveira Junior S. Multi-objective optimization of biogas systems producing hydrogen and electricity with solid oxide fuel cells. [International Journal of Hydrogen Energy] 2021 Sep;S036031992103442X.

[9] NogueiRa NakashiMa R, De OliVeiRa S. Thermodynamic Evaluation Of Solid Oxide Fuel Cells Converting Biogas Into Hydrogen And Electricity. [International Journal of Thermodynamics] 2021 Aug 29;24(3):204–14.

[10] Blumberg T, Morosuk T, Tsatsaronis G. Exergy-based evaluation of methanol production from natural gas with CO2 utilization. [Energy] 2017 Dec;141:2528–39.

[11] Bussche KMV, Froment GF. A Steady-State Kinetic Model for Methanol Synthesis and the Water Gas Shift Reaction on a Commercial Cu/ZnO/Al2O3Catalyst. [Journal of Catalysis] 1996 Jun;161(1):1–10.

[12] Aspen Technology, Inc. Aspen Plus Methanol Synthesis Mode. Bedford, United States: Aspen Technolgy, Inc.; 2018.

[13] Marechal F, Kalitventzeff B. Targeting the minimum cost of energy requirements: A new graphical technique for evaluating the integration of utility systems. [Computers & Chemical Engineering] 1996 Jan;20:S225–30.

[14] Papoulias SA, Grossmann IE. A structural optimization approach in process synthesis—II. [Computers & Chemical Engineering] 1983 Jan;7(6):707–21.

[15] Limpens G, Moret S, Jeanmart H, Maréchal F. EnergyScope TD: A novel open-source model for regional energy systems. [Applied Energy] 2019 Dec;255:113729.

[16] Voll P, Klaffke C, Hennen M, Bardow A. Automated superstructure-based synthesis and optimization of distributed energy supply systems. [Energy] 2013 Feb;50:374–88.

[17] IRENA, Methanol Institute. Innovation Outlook : Renewable Methanol. Abu Dhabi: International Renewable Energy Agency; 2021.

[18] Turton R, Bailie RC, Whiting WB, Shaeiwitz JA. Analysis, synthesis, and design of chemical processes. 3th ed. Upper Saddle River, NJ: Prentice Hall; 2009. 1007 p.

[19] Seider WD, Lewin DR, Seader JD, Widagdo S, Gani R, Ng KM. Product and process design principles: synthesis, analysis and evaluation. Fourth edition. New York: Wiley; 2017. 738 p.

[20] Nami H, Rizvandi OB, Chatzichristodoulou C, Hendriksen PV, Frandsen HL. Techno-economic analysis of current and emerging electrolysis technologies for green hydrogen production. [Energy Conversion and Management] 2022 Oct;269:116162.

A novel two-bed reactor for a chemical looping combustion system with a moving bed

Anna Zylka[a], Jaroslaw Krzywanski[a],Tomasz Czakiert[b], Marcin Sosnowski[a], Karolina Grabowska[a], Anna Kulakowska[a], Dorian Skrobek[a], Wojciech Nowak[c], Yunfei Gao[d]

[a] Jan Dlugosz University in Czestochowa, Faculty of Science and Technology, Armii Krajowej 13/15, 42-200 Czestochowa, Poland, e-mail: a.zylka@ujd.edu.pl; j.krzywanski@ujd.edu.pl; m.sosnowski@ujd.edu.pl; k.grabowska@ujd.edu.pl; d.skrobek@ujd.edu.pl; a.kulakowska@ujd.edu.pl
[b] Czestochowa University of Technology, Department of Advanced Energy Technologies, Dabrowskiego 73, 42-200 Czestochowa, Poland, e-mail tczakiert@is.pcz.czest.pl;
[c] AGH University of Science and Technology, Faculty of Energy and Fuels, A. Mickiewicza 30, 30-059 Cracow, Poland, e-mail: wnowak@agh.edu.pl
[d] Institute of Clean Coal Technology, East China University of Science and Technology, Shanghai 200237, PR China, e-mail: yunfeigao@ecust.edu.pl

Abstract:
This work presents a novel concept of reactor design in CLC technology. This is the second concept in a series of patents on the construction of air and fuel reactors. The first patent ”The combustion chamber design of a duo-fluidized bed reactor with circulating solid oxygen carriers of the CLOU type” was presented at the 6th International Conference on Chemical Looping in Zaragoza, Spain in September 2022.
The purpose of the presented solution according to the invention was to develop a simple reactor structure for the optimization of the chemical looping combustion process. According to the invention, the presented reactor dedicated to solid fuels combustion in the CLC system has two chambers of identical conical-cylindrical shapes, which are symmetrically and permanently attached with their upper conical parts to rotatably fixed transport pipes located on a common axis.
The simple and compact design of the reactor makes it economic & easy to manufacture and takes up significantly less space than a classical unit designed for the chemical looping combustion process. The proposed design enables uncomplicated process control due to fewer auxiliary devices as compared to the previous designs used for process control. Moreover, the reactor according to the invention has a lower energy expenditure because it uses lower gas velocities for effective operation than in a traditional CLC unit.

Keywords:
Chemical looping combustion, fuel reactor, oxygen carrier, moving bed.

1. Introduction

The currently visible climate changes encourage the reduction of pollutant emissions and the search for low-emission combustion technologies. There are many ways to mitigate climate change, but two are the most common. The first method includes all means that reduce CO_2 emissions into the atmosphere while increasing energy efficiency or using zero or low-carbon fuel sources. Another, also effective method is the use of negative emissions (NET) to reduce carbon dioxide from the atmosphere using sequestration techniques [1]. Commonly known and used CO_2 capture methods are: pre-combustion, oxy-fuel combustion, and post-combustion separation [2]. Another method of reducing carbon dioxide emissions into the atmosphere is oxy-fuel combustion. In this method, the combustion process takes place in a mixture of oxygen and CO_2 [3].

All of the above methods are effective, but at the same time energy-intensive, resulting in a significant decrease in overall combustion efficiency and consequently leading to higher energy prices [4].

1.1. CLC technology a brief characteristics

The Chemical Looping Combustion (CLC) technology is one of the methods of reducing CO_2 emissions. In the combustion process, fossil fuels release pollutants responsible for the greenhouse effect into the

atmosphere. Fossil fuels are estimated to be responsible for as much as one-third of global CO_2 emissions [5–7]. This undoubtedly has a significant impact on climate change. CLC allows to obtain a high concentration of CO_2 in flue gases, therefore it eliminates the need to use Carbon Capture and Storage (CCS) methods. This type of combustion can be classified under the category of oxy-combustion techniques, it has the advantage of producing nitrogen-free flue gases from the combustion air. It is an environmentally friendly method that reduces costs and time while reducing CO_2 emissions into the atmosphere [8–10].

A typical CLC unit consists of two separate reactors: an air reactor and a fuel reactor, which form two separate circulation contours (Figure. 1). In the literature, a system for chemical looping combustion of fuels is known, which was designed by Chalmers University of Technology (Sweden). A conventional unit consists of fuel and air reactors, a cyclone and two loop seals connecting the reactors. Each of the reactors has a different structure and dynamics of the fluidized bed, characteristic for a given chamber: a circulating fluidized bed in an air reactor and a bubble fluidized bed in a fuel reactor. The reactors are located parallel to each other, and the entire unit has a stationary structure [9,11].

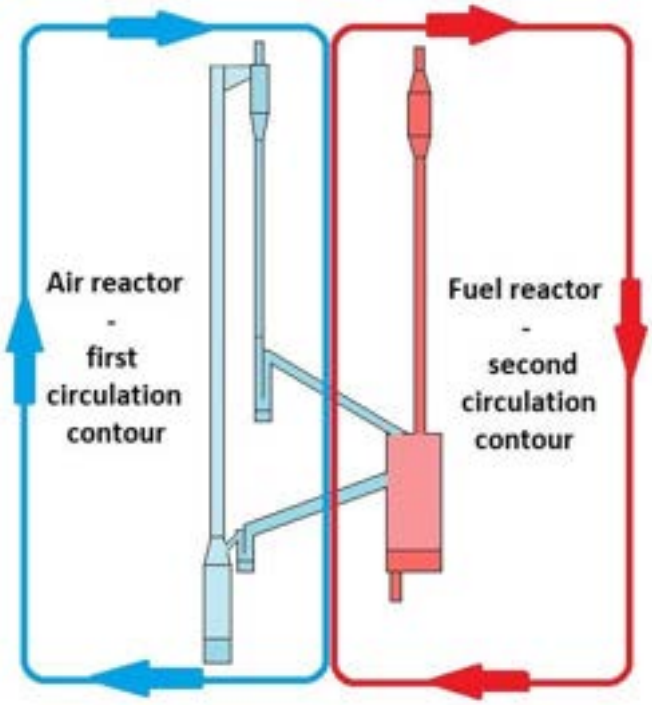

Figure. 1. Typical scheme of a CLC unit divided into circulation contours.

CLC technology applies solid oxygen carriers in the fuel combustion process, which are metals or metal oxides that carry oxygen between the air reactor and fuel reactor. Oxygen carriers play a vital role in the overall process because their oxygen-carrying capacity eliminates direct contact between air and fuel [12].

The selection of the appropriate oxygen carrier is a very important issue in the design of CLC combustion, as its properties affect the entire process. Therefore, the oxygen carrier should be: environmentally friendly, economically viable, resistant to abrasion and agglomeration. Additionally, the oxygen carrier should be characterized by the following features: high oxygen carrying capacity, reactivity, both during the oxidation and reduction stages, high melting point, ease of fluidization and mechanical resistance [13–16].

1.2. CLC pilot facilities

One of the largest pilot CLC installations with a capacity of 1MW is located at Darmstadt University of Technology. The air reactor and fuel reactor are designed as two separate circulating fluidized bed reactors. The inner diameter of the fuel reactor is 0.40 m, while the air reactor is 0.59 m. The height of the fuel reactor structure is 11.35 m, while that of the air reactor is 8.66 m. In addition, the entire system has been covered with insulating material to minimize heat losses. The use of insulation of the entire system is crucial because the reactors are not additionally heated with electric heaters. Tests studies were carried out on the pilot plant in Darmstadt using coal as fuel and Fe, Cu, Mn and ilmenite as oxygen carriers [17–19].

Another example is CLC pilot plant which is located at the Vienna University of Technology. The 120 kW test stand is dedicated to burn gaseous fuels [20]. The structure of the fuel reactor is designed to operate in a turbulent fluidization regime. This ensures better mixing of the gaseous fuel with the oxygen carriers in the

fluidized bed. In studies conducted on this pilot unit used nickel and ilmenite as oxygen carriers, while the fuel was natural gas and a gas mixture of CH_4, CO, H_2 and C_3H_8 [8,20,21].

Another well-known CLC pilot unit is located at Chalmers University in Sweden. The designed 100 kW system is dedicated to burn solid fuels. The pilot plant was developed as part of the European ÉCLAIR project coordinated by the ALSTOM concern. Tests were conducted using hard coal and ilmenite as oxygen carriers. During the test studies, a temperature of 1000°C was maintained in the fuel reactor and 970°C in the air reactor. A good CO_2 capture rate of 98 – 99% was achieved [17].

There are two CLC units in Poland. The first one is located at the Institute for Chemical Processing of Coal in Zabrze (IChPW). The second one is located at the Czestochowa University of Technology. The CLC unit located in the IChPW is dedicated for the combustion of gaseous fuels. The following gases are supplied to the installation: nitrogen, methane and process gases. The CLC plant operates at atmospheric pressure, at temperatures 800°C - 1000°C. The maximum feed rates for fuel, air and oxygen carrier are 1 m^3/h, 15 m^3/h and 40 kg/h, respectively. The height of fluidized bed reactors are 1 m high and 0.133 m in diameter [16].

The second unit for Chemical looping combustion of solid fuels is located at the Institute of Advanced Energy Technologies, Czestochowa University of Technology [5].

The CLC system for solid fuels consists of two main circulating contours [11]:

(1) an air reactor with a circulating fluidized bed, an ascending section and a return system comprising a cyclone and a precipitation section,

(2) a bubbling fluidized bed fuel reactor and a particulate collector.

The air reactor is constructed as a cylinder, which transitions into a cone at the top. In contrast, building a fuel reactor is more complex (Figure 2), as the structure is a cuboid with incomplete internal baffles. These baffles are designed to improve mixing processes and increase the residence time of the gas and material grains. The CLC stand is equipped with electric heaters with a total output of 72 kW. The heating system is located at full height on both sides of the stand [5,11,22,23].

a) b)

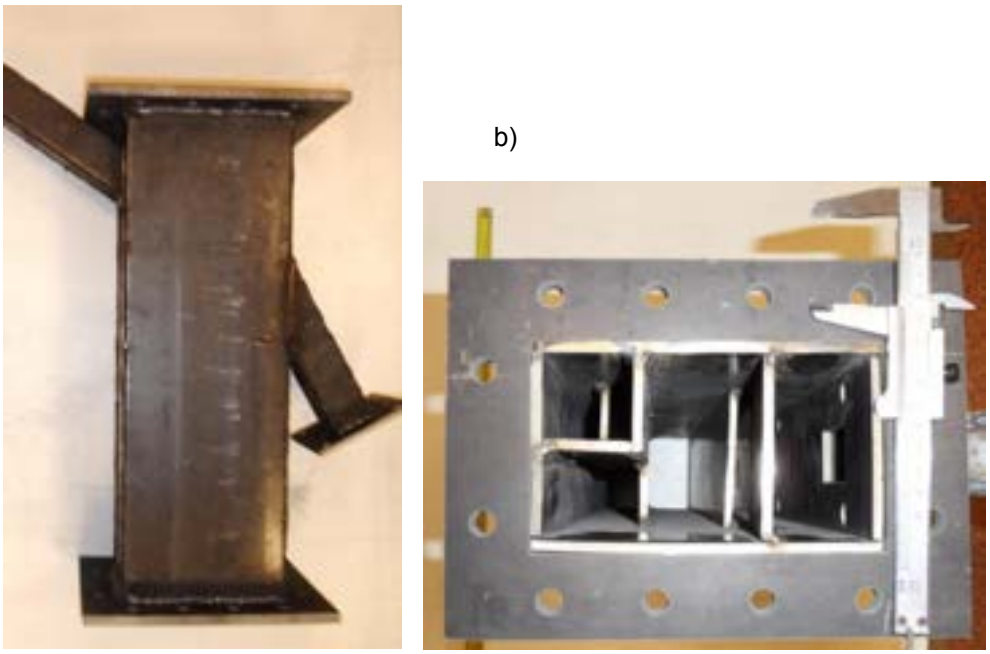

Figure. 2. Photo of the fuel reactor: a) side view; b) cross-section of the fuel reactor.

1.3. Motivation and scope of research

The proposed idea concerns the new design of the fuel reactor with a moving bed and is dedicated to solid fuels. It can be used in power plants and research laboratories. This reactor design allows for the implementation of subsequent processes of solid fuel combustion and regeneration of the oxygen carrier. In addition, this reactor design increases the efficiency of the system.

The reactor for solid fuels in a chemical looping combustion system, according to the invention has chambers of identical conical-cylindrical shapes, which are symmetrically and permanently fixed with their upper, conical parts to rotatably fixed transport pipes located on a common axis. In the channel narrowing between the conical parts of the chambers there is a material flow control valve, and in the conical part of the air chamber there are air supply nozzles. In the conical part of the combustion chamber there are gas

nozzles, while the outlets of the chute channels are located in both chambers in their conical parts from the side of the cylindrical parts.

2. Results and discussion

2.1. Two-bed reactor design

A novel two-bed reactor for a chemical looping combustion system with a moving bed is presented in this paper. The invention is the subject of patent No. PL 234783 (Czakiert et al., 2017). The novel fuel reactor is designed to ensure the more efficient performance of the CLC process in general. The idea of the construction is shown in Figure 3, and the details are provided below [24].

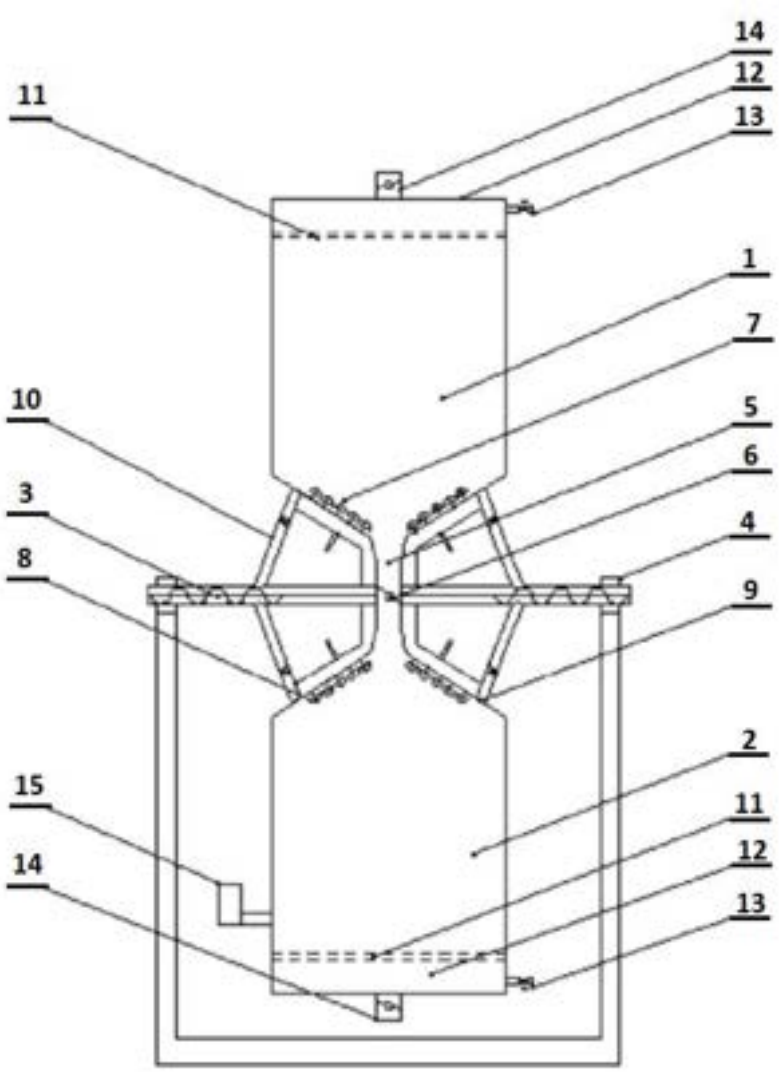

1 – air chamber
2 – combustion chamber
3 – transport pipes
4 – the supports of the frame structure
5 – channelled constriction
6 – control valve
7 – air nozzles
8 – gas nozzles
9 – outlets
10 – ash chute channels
11 – grate
12 – air box
13 – gas inlet port
14 – gas outlet stack
15 – fuel feeder

Figure. 3. Schematic of two-bed reactor for a chemical looping combustion system with a moving bed.

The chemical looping combustion reactor for solid fuels has two chambers (1) and (2) of identical conical-cylindrical shapes, with one chamber being air chamber (1) and the other combustion chamber (2).

Chambers (1) and (2) are symmetrically and permanently fixed with their upper conical parts to pivotally fixed transport tubes 3, for removing ash from the reactor, situated on a common axis. The transport tubes (3) are connected by bearings to the supports of the frame structure (4). The mobile connection of transport pipes (3) ensures that the entire reactor can rotate around the horizontal axis. Between the conical parts of chambers (1) and (2), which are connected to each other, there is a channelled constriction (5) in which a control valve (6) for the flow of material during the combustion process is fitted. In the conical part of the air chamber (1), nozzles (7) are fixed to supply air to the inside of the air chamber (1) and in the conical part of the combustion chamber (2) there are gas nozzles (8). Gas nozzles (8) in the combustion chamber allow air to be supplied when combustion chamber (2) is above air chamber (1), while, after the rotation of chambers (1) and (2), when combustion chamber (2) is below air chamber (1), gas nozzles (8) allow exhaust gases to exit combustion chamber (2). Both chambers (1) and (2) are equipped with outlets (9) of chute channels of ash (10) connected to transport pipes (3). The outlets (9) of chute channels (10) in chambers (1) and (2) are located in their conical parts on the side of the cylindrical parts. The positioning of the outlets (9) of the ash chute channels (10) close to the vertical walls of the cylindrical section allows efficient ash removal during reactor operation.

In the lower cylindrical part in each chamber (1) and (2), above the bottom, there is a grate (11) with an air box (12) equipped with a gas inlet port (13) and a gas outlet stack (14). Above the grate (11) in combustion chamber (2) there is a fuel feeder (15).

The reactor according to the invention, shown in Figure 3, allows pendulum movements during which, in an alternating cycle, once the air chamber (1) and once the combustion chamber (2) are in the upper position, while the other chamber is in its lower position. Depending on the position of chambers (1) and (2) in relation to each other, their functions change. The chamber in the lower position becomes combustion chamber (2), while the chamber at the top of the reactor becomes air chamber (1).

When the upper air chamber (1) of the reactor is emptied, chambers (1) and (2) rotate 180 degrees around the horizontal axis - the transport pipe (3). The lower chamber (2), which acted as the combustion chamber (2) and was fluidized with an inert gas in the form of carbon dioxide, henceforth becomes air chamber (1) and is fluidized with air. A channelled constriction (5) connecting chambers (1) and (2) equipped with a control valve (6) allows the flow of material between chambers (1) and (2). The gas in the lower chamber of the reactor constituting combustion chamber (2) is fed through a gas inlet port (13) via an air box (12) and grate (11), while in the upper chamber of the reactor constituting air chamber (2) it is fed through nozzles (7). Gas is discharged from air chamber (1) through a gas outlet stack (14) and from combustion chamber (2) through gas nozzles (8).

The solution according to the invention allows for the implementation of subsequent processes of solid fuel combustion and regeneration of the oxygen carrier.

To summarise the novel design concept of the CLC unit, the innovative reactor is characterised by:

1. The fuel and air reactors are made in the form of identical cylindrical-conical chambers connected by a flow channel.
2. The flow channel connecting the tops of the reactors is equipped with a valve to regulate the flow of material between the reactors.
3. The rigidly connected reactors, after emptying the upper chamber, perform a pendulum motion - a rotation of 180 degrees around the horizontal axis.
4. Nozzles are used in the reactors, which in the air reactor supply air to the chamber, while in the fuel reactor they are used to exhaust the flue gases.

The fuel combustion reactor design is simple and compact, so it is cheap to produce and takes up much less space than a classical unit designed for a chemical looping combustion process. The developed design allows for easier process control due to the smaller number of auxiliary devices previously used to control the process. In addition, the reactor according to the invention is characterised by lower energy expenditure because lower gas velocities are used in the reactor than in a traditional CLC unit to lift the fluidised layer. In addition, the reactor during operation is characterised by a lower consumption of the media and gases necessary for the fluidisation process needed for the chemical looping combustion process. The advantages mentioned above will affect the faster dissemination of ecological CLC technology in various industrial applications.

3. Conclusions

The CLC concept generally offers a highly concentrated CO_2 stream at the outlet of the power unit without any additional energy-consuming systems for gas separation (oxygen fractionations from atmospheric air or carbon dioxide capture from conventional flue gases), which makes this technology competitive with other

pro-CCSU (Carbon Capture, Storage and Utilization) technologies. However, the presented novel fluidized-bed fuel reactor, which is tailored to the use of solid oxygen carriers and the utilization of solid fuels, provides further reduction of operating costs with even higher inherent CO_2 capture efficiency.
The new fuel reactor concept was designed for solid oxygen carriers. Solid fuels, such as coal, and biomass, can be used as fuel. The proposed idea is characterised by an innovative reactor design that makes it economic and easy to manufacture. In addition, such a design takes up significantly less space than a classical unit designed for the chemical looping combustion process. These are undoubtedly the most significant advantages of the presented idea. As a result, the new fuel reactor concept ensures more efficient operation of the CLC processes.

Acknowledgments

This study was funded from Norway Grants in the Polish-Norwegian Research Programme operated by the National Centre for Research and Development, project: Innovative Idea for Combustion of Solid Fuels via Chemical Looping Technology, agreement number POL-NOR/235083/104/2014. The support is gratefully acknowledged.

The work was also funded by the statute subvention of the Czestochowa University of Technology, Faculty of Infrastructure and Environment.

References

[1] Tsai W-H., Carbon Emission Reduction—Carbon Tax, Carbon Trading, and Carbon Offset. Energies 2020;13:6128. https://doi.org/10.3390/en13226128.
[2] Gibbins J., Chalmers H., Carbon capture and storage. Energy Policy 2008;36:4317–22. https://doi.org/10.1016/j.enpol.2008.09.058.
[3] Jansen D., Gazzani M., Manzolini G., Dijk E van., Carbo M., Pre-combustion CO2 capture. International Journal of Greenhouse Gas Control 2015;40:167–87. https://doi.org/10.1016/j.ijggc.2015.05.028.
[4] Hossain MM., de Lasa HI., Chemical-looping combustion (CLC) for inherent CO2 separations—a review. Chemical Engineering Science 2008;63:4433–51. https://doi.org/10.1016/j.ces.2008.05.028.
[5] Zylka A., Krzywanski J., Czakiert T., Idziak K., Sosnowski M., et al. Modeling of the Chemical Looping Combustion of Hard Coal and Biomass Using Ilmenite as the Oxygen Carrier. Energies 2020. https://doi.org/10.3390/en13205394.
[6] Krzywanski J., Ashraf WM., Czakiert T., Sosnowski M., Grabowska K., Zylka A., et al. CO2 Capture by Virgin Ivy Plants Growing Up on the External Covers of Houses as a Rapid Complementary Route to Achieve Global GHG Reduction Targets. Energies 2022;15:1683. https://doi.org/10.3390/en15051683.
[7] Song T., Shen L., Review of reactor for chemical looping combustion of solid fuels. International Journal of Greenhouse Gas Control 2018;76:92–110. https://doi.org/10.1016/j.ijggc.2018.06.004.
[8] Lyngfelt A., Chemical Looping Combustion: Status and Development Challenges. Energy Fuels 2020;34:9077–93. https://doi.org/10.1021/acs.energyfuels.0c01454.
[9] Adanez J., Abad A., Garcia-Labiano F., Gayan P., de Diego LF., Progress in Chemical-Looping Combustion and Reforming technologies. Progress in Energy and Combustion Science 2012;38:215–82. https://doi.org/10.1016/j.pecs.2011.09.001.
[10] Moghtaderi B., Review of the Recent Chemical Looping Process Developments for Novel Energy and Fuel Applications. Energy Fuels 2012;26:15–40. https://doi.org/10.1021/ef201303d.
[11] Zylka A., Krzywanski J., Czakiert T., Idziak K., Sosnowski M., Grabowska K., et al. The 4th Generation of CeSFaMB in numerical simulations for CuO-based oxygen carrier in CLC system. Fuel 2019;255.
[12] Krzywanski J., Czakiert T., Nowak W., Shimizu T., Zylka A., Idziak K., et al. Gaseous emissions from advanced CLC and oxyfuel fluidized bed combustion of coal and biomass in a complex geometry facility:A comprehensive model. Energy 2022;251:123896. https://doi.org/10.1016/j.energy.2022.123896.
[13] Cormos C-C., Chemical Looping with Oxygen Uncoupling (CLOU) concepts for high energy efficient power generation with near total fuel decarbonisation. Applied Thermal Engineering 2017;112:924–31. https://doi.org/10.1016/j.applthermaleng.2016.10.156.
[14] Adánez J., Abad A., Chemical-looping combustion: Status and research needs. Proceedings of the Combustion Institute 2019;37:4303–17. https://doi.org/10.1016/j.proci.2018.09.002.
[15] Yüzbasi NS., Kierzkowska A., Müller C., Development of Fe2O3-based, Al2O3-stabilized Oxygen Carriers using Sol-gel Technique for H2 Production via Chemical Looping. Energy Procedia 2017;114:436–45. https://doi.org/10.1016/j.egypro.2017.03.1186.
[16] Ksepko E., Klimontko J., Kwiecinska A., Industrial wastewater treatment wastes used as oxygen carriers in energy generation processes. J Therm Anal Calorim 2019;138:4247–60. https://doi.org/10.1007/s10973-019-08214-8.

[17] Lyngfelt A., Linderholm C., Chemical-Looping Combustion of Solid Fuels – Status and Recent Progress. Energy Procedia 2017;114:371–86. https://doi.org/10.1016/j.egypro.2017.03.1179.
[18] Ströhle J., Orth M., Epple B., Design and operation of a 1MWth chemical looping plant. Applied Energy 2014;113:1490–5. https://doi.org/10.1016/j.apenergy.2013.09.008.
[19] Wang X., Gong Y., Wang X., Jin B., Experimental and kinetics investigations of separated-gasification chemical looping combustion of char with an iron ore as the oxygen carrier. Fuel Processing Technology 2020;210:106554. https://doi.org/10.1016/j.fuproc.2020.106554.
[20] Kolbitsch P., Bolhàr-Nordenkampf J., Pröll T., Hofbauer H., Operating experience with chemical looping combustion in a 120kW dual circulating fluidized bed (DCFB) unit. International Journal of Greenhouse Gas Control 2010;4:180–5. https://doi.org/10.1016/j.ijggc.2009.09.014.
[21] Lyngfelt A., Oxygen Carriers for Chemical Looping Combustion - 4 000 h of Operational Experience. Oil & Gas Science and Technology - Revue d'IFP Energies Nouvelles 2011;66:161–72. https://doi.org/10.2516/ogst/2010038.
[22] Czakiert T., Kulicki K., Idziak K., Krzywanski J., Zylka A., Jankowska S., et al. Experiences from the Operation of a Fluidized-Bed Chemical-Looping-Combustion Solid-Fuels Test Rig. Proc. of the 12th International Conference on Fluidized Bed Technology CFB-12, Cracow, Poland: 2017, p. 1045–6.
[23] Zylka A., Krzywanski J., Czakiert T., Idziak K., Kulicki K., Jankowska S., et al. A 1.5 D Model for the Chemical Looping Combustion System with Ilmenite. Proc. of the 8th European Combustion Meeting, Dubrovnik, Croatia, Dubrovnik, Croatia: Adria Section of the Combustion Institute; 2017, p. 1785–90.
[24] Czakiert T., Krzywanski J., Zylka A., Idziak K., Nowak W., Jankowska S., Kulicki K., Patent: Reactor for solid fuels combustion in chemical looping system (Pl: Reaktor do spalania paliw stałych w pętli chemicznej), 2017. P.234783.

Modeling of Submerged Membrane Bioreactor Filtration using Deep Learning Neural Networks

Nur Sakinah Ahmad Yasmin[a], Norhaliza Abdul Wahab[b], Kumerasan A. Danapalasingam[c], M. Meneses[d] and R. Vilanova[d]

[a] Faculty of Electrical Engineering Universiti Teknologi Malaysia, 81310 Skudai Johor Bahru, Malaysia, nursakinahyasmin@gmail.com
[b] Faculty of Electrical Engineering Universiti Teknologi Malaysia, 81310 Skudai Johor Bahru, Malaysia, norhaliza@utm.my, CA
[c] Faculty of Electrical Engineering Universiti Teknologi Malaysia, 81310 Skudai Johor Bahru, Malaysia, kumeresan@fke.utm.my
[d] Department Telecommunications and Systems Engineering Universitat Autònoma de Barcelona, Spain,{Montse.Meneses, Ramon.Vilanova}@uab.cat

Abstract:

Wastewater treatment (WWTP) is one of the major challenges due to the growing global population. Despite the complexity of the non-linearity and dynamic of environmental data, deep learning technologies should be created for WWTP. In this study, deep learning of long short-term memory (LSTM) is adopted to forecast permeate flux in membrane bioreactor of WWTP with five parameters involved such as permeate flux, transmembrane pressure (TMP), air flow, pump (voltage) and backwash. Three deep learning models derived from LSTM namely vanilla LSTM, bidirectional LSTM, and stacked LSTM including recurrent neural network (RNN) were constructed. The proposed LSTM's models provide promising results with 90 % accuracy of the predicted permeate flux model and can aid in establishing fouling backwashing process strategies, leading to reduced capital, energy consumption, and operational cost. Therefore, the proposed LSTM model is an adequate interpolation tool to predict the permeate flux of membrane bioreactor process in WWTP systems.

Keywords:

LSTM; Deep Learning; Neural Network; WWTP.

1. Introduction

One of the promising 21st-century technologies is the membrane bioreactor, which combines a biological process with permeable membranes. Since then, this technology has experienced constant advancement, and its uses have covered a wide range of industries, including water treatment, wastewater reclamation, juice concentration, dairy production, medical use, and cell harvesting [1-5]. But a serious issue that continues to restrict this technique's potential is membrane fouling. Fouling lead to an increase in operational costs due to more labour expenses for maintenance, increase energy demand, increase cleaning chemical expenses that will lead to shorter membrane life [6, 7]. It needs to be controlled and minimized through effective and efficient approaches.

The formation of fouling includes several mechanisms including adsorption, pore blockage and the formation of cake on the membrane [6]. Adsorption takes place when there is certain interaction between solutes/particles with the membrane. It results from the surface energy process and thermodynamic equilibrium process. Internal fouling caused by in-pore adsorption can contribute to overall flux drop as well as rise in transmembrane pressure (TMP) since the pore of membrane are equivalent to those of many macromolecules [8] [9]. Meanwhile the pore blockage is caused by entire or partial blockage by colloids and particles that cause pore obstruction [10]. Cake formation is the process by which particles accumulate on a membrane outside surface layer by layer, increasing the flow of permeates resistance. The additional resistance is known as a cake resistance, and the process is frequently referred to as the development of a fouling cake.

In order to maintain the membranes' ability to function sustainably, routine operations must include cleaning the membranes—both physically and chemically. Chemical cleaning is recommended to be avoided or limited in frequency in the full-scale application of submerged membranes due to the detrimental effects it has on the membrane [11]. However, by using efficient physical cleaning techniques, which would lengthen the membrane lifetime, the use of cleaning agents can be decreased. Procedures for backwashing are essential to the longevity and effective operation of low-pressure membranes. As a result, this operating technique has become essential to ensuring reliable, consistent, and high-quality water [12]. Backwashing is a vital

component of physical cleaning and is done by pushing a reversed flow through a membrane from the permeate side to the feed side while utilizing a specific kind of medium. Backwashing causes foulants that were deposited or adsorbed on the membrane surface or pores to become loosened or detached.

The widespread application of artificial intelligence (AI) in areas including healthcare, smart cities, intelligent search, big data, and pattern recognition, as well as its rapid development, present a huge chance to accomplish this goal. One of the most popular AI method used for water quality prediction is artificial neural network (ANN) [13]. ANNs are feedforward neural networks consisting of multiple layers of interconnected nodes, or neurons. They are primarily used for supervised learning tasks, such as image classification and regression, and are not well-suited for handling sequential data. As a typical representative of ANN, the conventional feed-forward neural network (FFNN) and its upgraded algorithm are a classic example of neural networks and have been successfully used to predict water quality [14-16]. Another neural network that has been extensively used in model prediction in various water environment is radial basis function (RBF), as it has a straightforward structure, quick training time and capacity to estimate any functions globally with arbitrary precision [17-19]. However, the above ANN's model are not designed to consider the sequential nature of data, and thus are not well-suited for tasks such as time-series prediction problems. Hence, the so-called time series is a collection of observations that have been made in a time. Compared to automatic water quality monitoring plant, automatically collects the quality water parameters at a defined time interval such as once per day and uploads it into a server to reflect the variations of water quality. As a result, time series data is presented for water quality metrics.

On the other hand, one of deep learning neural networks that are designed to handle sequential data, such as time series-data is known as long short-term memory (LSTM) is highly recommended for time-series prediction [20-22]. LSTMs are specifically designed to address the problem of vanishing gradients in recurrent neural networks (RNN), which can make it difficult to train models that rely on long-term dependencies in the input data. LSTMs use a gating mechanism to selectively remember or forget information over time, which makes them particularly useful for tasks such as speech recognition, machine translation, and sentiment analysis. In summary, while ANNs are used for a wide range of tasks and have a general-purpose architecture, LSTMs are specifically designed to handle sequential data and have a unique architecture that enables them to model long-term dependencies in the input data. Due to those characteristics of LSTM, the research has grown significantly as a result of their successful time-series prediction ability [23]. In our knowing, just a few research have used LSTM models to predict permeate flux in membrane for drinking water quality process [20, 24].

The main objective of the current study is to develop and validate the capabilities of deep learning neural network models based on LSTMs, including vanilla-LSTM, bi-directional LSTM, and stacked LSTM, in predicting the permeate flux in a submerged membrane bioreactor. In addition to LSTM models, a comparison will be made with another neural network model called RNN. The study utilizes a dataset consisting of approximately 4021 samples, encompassing five key parameters: permeate flux, transmembrane pressure (TMP), air flow, pump voltage, and backwash. These parameters are utilized to construct the predictive models. The results of the study demonstrate the potential of deep learning LSTM models in accurately predicting time series data, particularly within the context of a submerged membrane filtration system. The ability of LSTMs to capture long-term dependencies and model complex dynamics makes them suitable for accurately forecasting the permeate flux over time in this specific application.

2. Modeling methodology

2.1. Long short-term memory (LSTM)

Long short-term memory (LSTM) is a type of recurrent neural network (RNN) that specifically designed for time-series problem and their long-range dependencies more accurately than conventional RNNs [25]. Figure 1(a) shows the architecture of RNN network. An RNN can be viewed as the design of a normal feedforward MLP network with loops added. Recurrent neural networks have cycles that feed previous time step activations into the network as inputs to influence predictions at the current time step. The network's internal states, which are theoretically capable of storing long-term temporal contextual information, store these activations. As a result of this process, RNNs can take use of a contextual window that changes dynamically over the course of the input sequence history [25].

A LSTM memory cell contains one tanh layer in addition to three sigmoid layers. The input, forget, and output gates of the LSTM are used to maintain and refresh the memory cells while filtering out extraneous data. The forget gate first chooses whether data should be kept or removed from the model. The input gate also manages the reserve of data on the current cycle input. The input gate has two responsibilities. Finding the state of the cell that needs to be updated is the first task; the sigmoid function chooses the value that needs to be updated. The second duty is updating the data to reflect the current condition of the cell. The output gate is the final gate. The following hidden state is determined by the output gate.

2.2. Vanilla LSTM

A vanilla LSTM is a most basic LSTM model as it has a straightforward LSTM configuration as shown in Figure 1(b). LSTM have a input layer and output layer that directly connected to single hidden layer of LSTM memory cells to create predictions [26]. The LSTM architecture described in the original LSTM study from 1997 is the one that will perform well on the majority of minor sequence prediction challenges. Contrary to its extensions, vanilla LSTM still performs brilliantly on a range of datasets more than 20 years after its launch, according to Greff and K. et al. [27]. Nelson et al. [28] used Vanilla LSTM to predict stock prices for the first time, and they were encouraged by the findings.

2.3 Stacked LSTM

Stacked LSTM were introduced by Graves et al. [29], in their application of LSTMs to speech recognition, beating a benchmark on a challenging standard problem. In the same work, it was found that the depth of the network was more crucial to accurately modelling rather than the number of memory cell. A stacked LSTM architecture is made up from multiple LSTM layers. Instead of sending a single value to the LSTM layer below, an LSTM layer above sends a sequence of values. Instead of having one output time step for all input time steps, specifically, one output per input time step [30]. Figure 1© shows the architecture of stacked LSTM.

2.4 Bidirectional LSTM

In order to maximise the use of the input sequence, bidirectional LSTMs walk through input time steps in both the forward and backward directions [31]. In order to implement this design, the first recurrent layer of the network is duplicated so that there are now two layers side by side. The input sequence is then provided as-is to the first layer as input, and a reversed copy is provided to the second layer. This method was created in the past as a broad method for improving the effectiveness of recurrent neural networks (RNNs). Figure 1(d) shows the architecture of bidirectional of LSTM network.

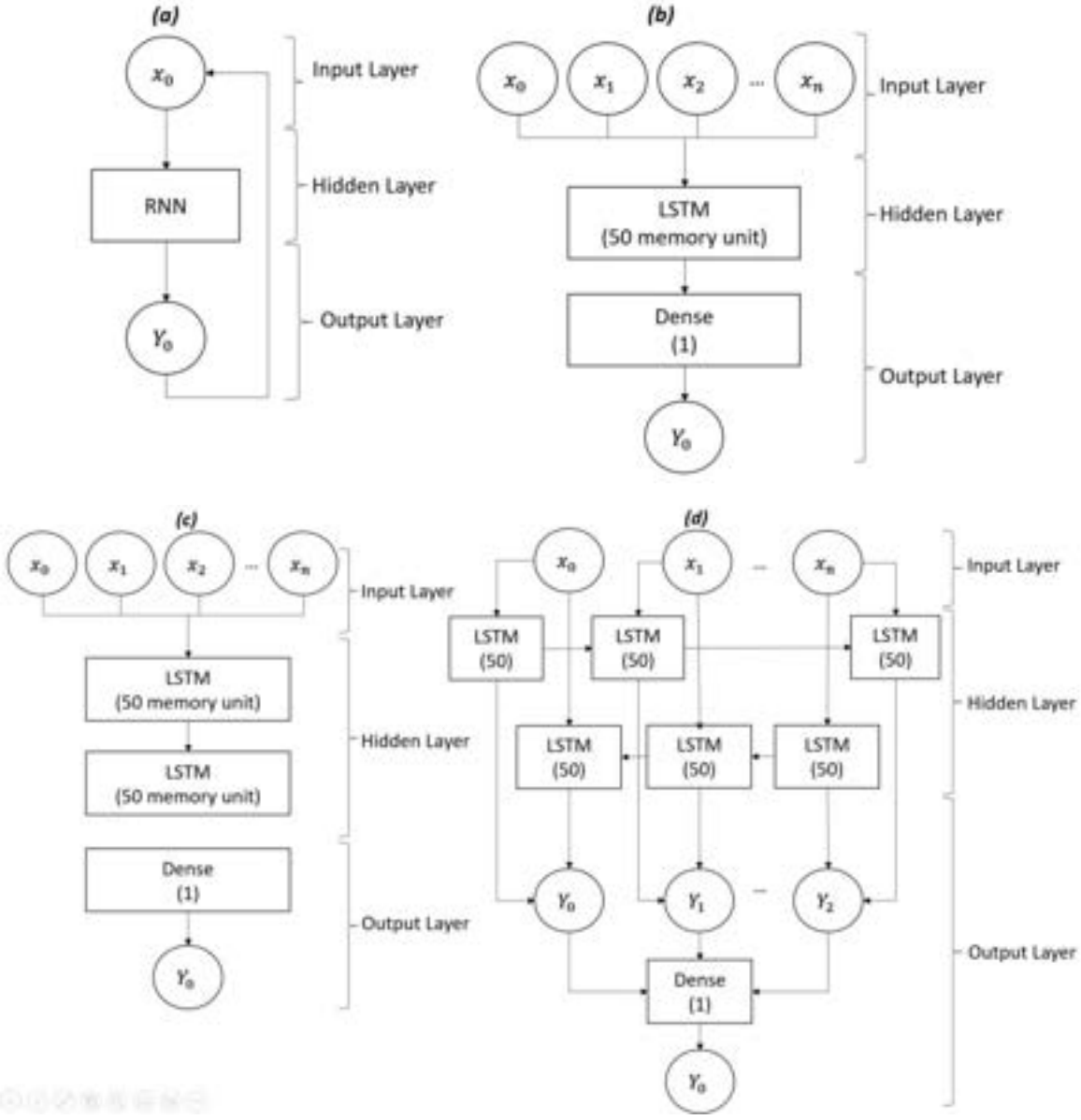

Figure. 1. Architecture of: (a) RNN (b) Vanilla LSTM (c) Stacked LSTM (d) Bidirectional LSTM.

3. Organization of paper

3.1. Pilot source water

A schematic diagram of submerged membrane bioreactor (SMBR) with four configurations of inlet stream, permeate stream, aeration and backwashing stream is illustrated in Figure 2. The permeate stream used diluted palm oil mill effluent (POME) collected from Mahamurni Plantation palm oil Sdn. Bhd., Wastewater treatment plant, located in Sedenak Johor Bahru as its source. The plant comprises of a single bioreactor tank that has been fitted inside with submerged hollow fibre and Polyethersulfone (PES) material is used to construct the hollow fibre membrane.

The POME was supplied into the 20 L bioreactor tank through the inlet stream. When the level reaches the specified level, the influent supply to the bioreactor will be stopped off by a mechanical level controller. The filtered influent is then pumped to the effluent tank down the pipe using a peristaltic pump (P-101). During permeate stream, the P-101 is activated to open the valve (SV-101). Electronic flow sensors are used to detect the permeate flux flow rate (FM-101). This part employs an electronic pressure sensor to monitor the transmembrane pressure (TMP) (P-101).

In order to study the long-term effects on transmembrane pressure (TMP) and membrane flux, the membranes were cleaned using just physical cleaning which are backwashing and aeration stream. The membrane was cleansed from the inside out in the backwash stream. When pump (P-102) is activated and valve (SV-102) is opened, the backwash procedure is complete. The membrane was cleaned by the backwash using filtered tap water that was kept in the backwash tank. The air that was pumped into the bioreactor using an air compressor (C-101). Electronic flow sensors are used to measure the air velocity under proportional valve (PV-101) control (FA-101). To produce bubbles, the air from the compressor is sent through the air diffuser.

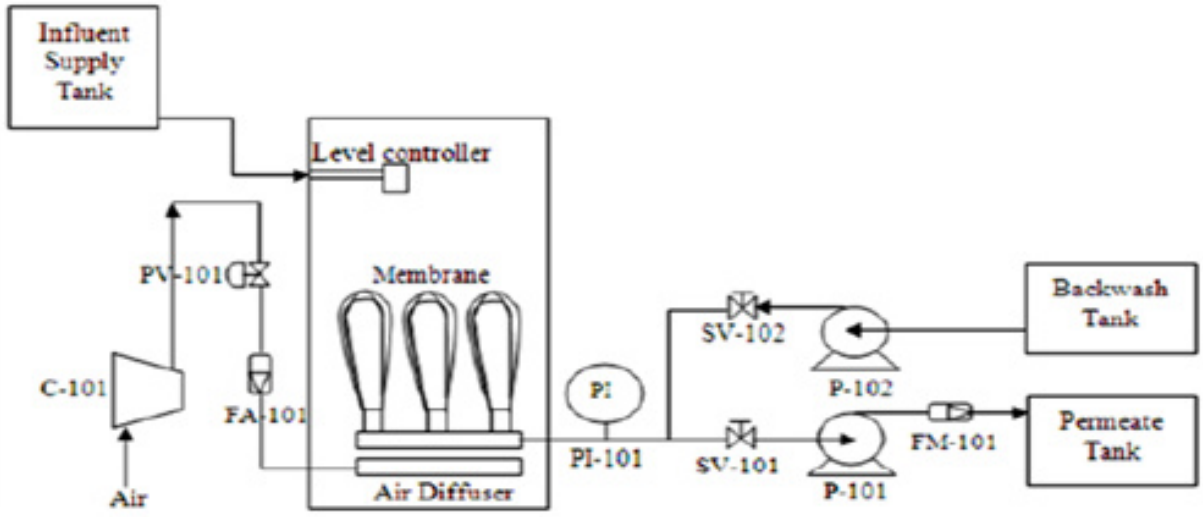

Figure. 2. Schematic diagram of submerged membrane pilot plant.

The pilot plant system was equipped with full monitoring and control using a data acquisition of National Instrument. Supervisory Control and Data Acquisition (SCADA) software is a type of graphical language-based programme that can be used with LabVIEW. For the aim of modelling, the software was created to record the collected data in the pilot plant. In this research, POME is used to generate fouling in the MBR filtration process. Figure 3 shows the actual sample used in the filtration process.

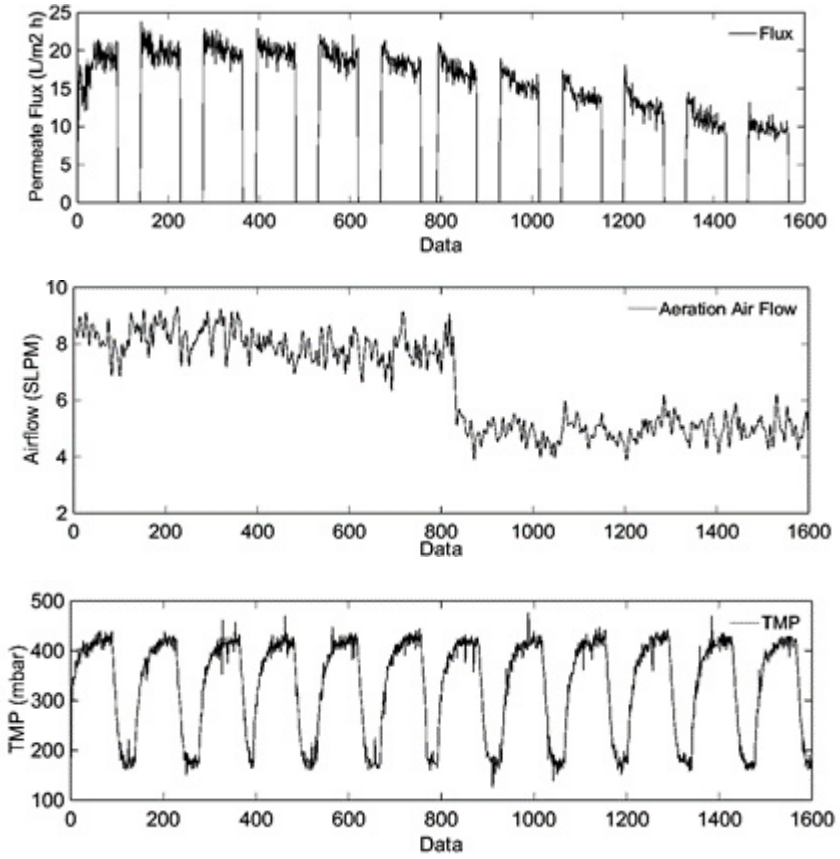

Figure. 3. Samples of the collected data using submerged membrane bioreactor plant.

3.2. Data pre-processing

Data pre-processing involved normalization or standardization of the data before they were used to train models. The normalization data is a method of scaled down the collected data that in the original range, so all values fall between 0 and 1. Meanwhile, standardize means rescaling the distribution values to have a mean of 0 and a standard deviation of 1. This can be thought of as subtracting the mean value or centering the data. Like normalization, standardization can be useful and required in machine learning algorithm when the data contains input values with different scale. Standardization makes the underlying assumption that your data has a Gaussian distribution (bell curve) with a well-behaved mean and standard deviation. If this assumption is not satisfied, an accurate result might not be able to achieve. The collected data was normalise using scikit-learn object MinMaxScaler and standardization can both be achieved using scikit-learn machine learning library in Python programming [32].

3.3. Transform time series data

A key function in Pandas library that is crucial tool for converting time series data into a supervised problems is Pandas shift () function. The shift() function can be used to make copies of columns that are pushed forward (rows of NaN values are added to the front) or pulled back (rows of NaN values added to the end). This is to generate columns of lag observations as well as columns of prediction observations. In terms of time series forecasting, forecasts are made using prior observations (t-1, t-n) and the current time (t), as well as future times (t+1, t+n). We can see how a time series containing sequences of input and output patterns can be utilised to generate a new DataFrame for a supervised learning task [32].

4. Result and discussion

4.1 Model performance

In this study, three different architecture of LSTM models such as Vanilla LSTM, Stacked LSTM and Bidirectional LSTM including RNN were developed to predict the permeate flux in submerged membrane bioreactor. During training these models, two loss function was used which are mean absolute error (MAE) and mean square error (MSE) to evaluate the performance of the models as it is suitable and recommended for time series problems. In this work, 100 epoch and 50 batch size were used. An epoch is an iteration over the entire training dataset. The model was iterating over the training data, multiple times until it achieves 100 epochs and updating the model's parameters at each time. The accuracy metric will be reported at each training epoch to reflect the performance of the model in addition to the loss function. The dataset consists of 4021 samples, and it were divided into 60/40 for each training and testing dataset. Figure 4 shows the loss

function graph of RNN, Vanilla LSTM, Stacked LSTM and Bidirectional LSTM models that were iterates for 100 epochs. From the graph, we can clearly seen that the model learned the problem by achieving towards zero error. A train (blue) and test (orange) line is created showing the MSE over the training epochs converged up to three decimal places which is a good sign for training models. The performance of the model suggests that the MAE and MSE error is a good match for a deep learning neural network LSTM's model as compared to RNN model which achieved MAE slightly lower than the others LSTM's model.

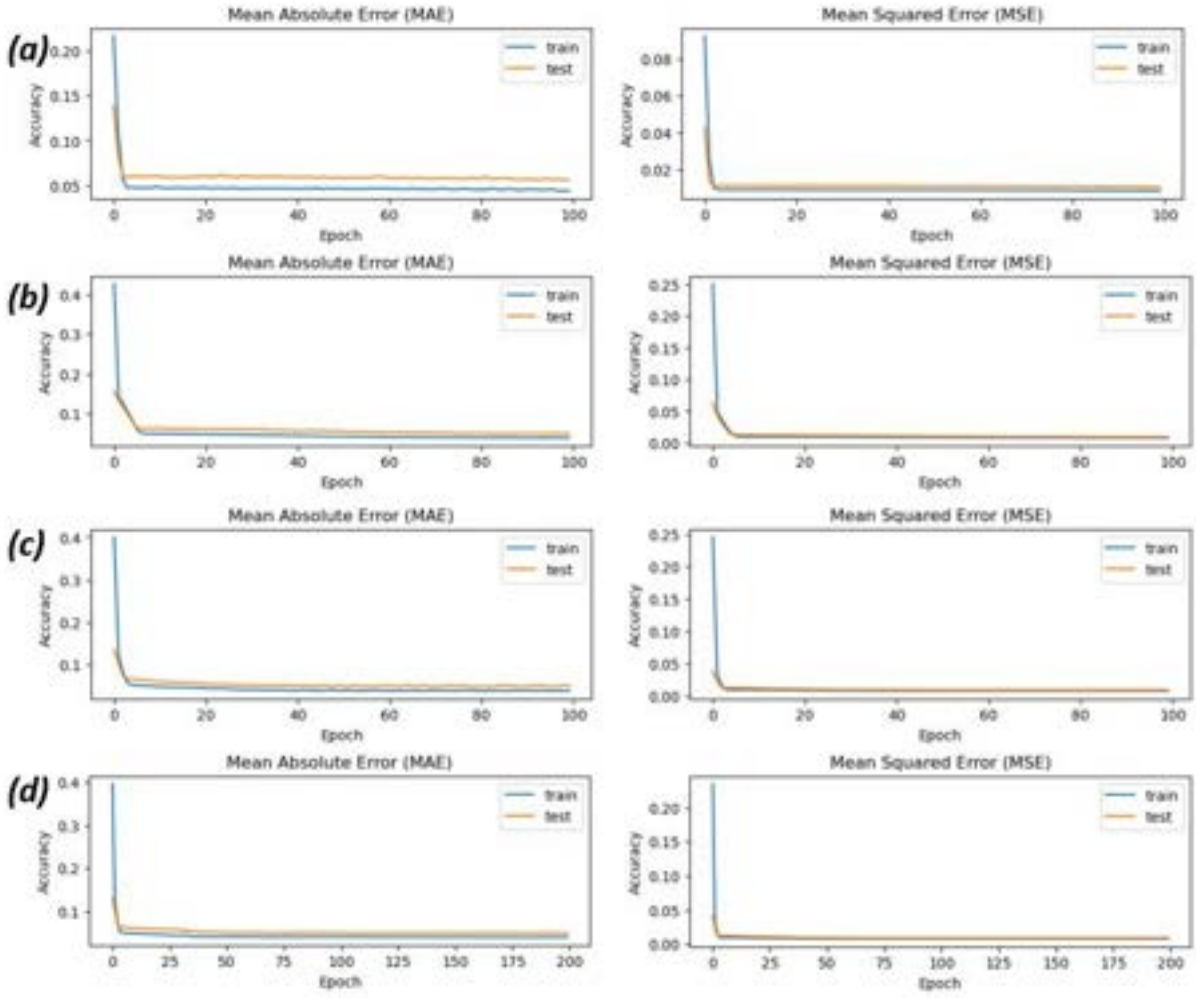

Figure. 4. (a) RNN, (b) Vanilla LSTM (c) Stacked LSTM (d) Bidirectional LSTM

After training using 60 % of dataset, the rest 40 % of the samples were used to predict the models. Figure 5 shows the plotted graph of training and testing dataset for RNN model. RNN model has the simplest architecture with 50 memory units, and it takes inputs from previous time steps direct to the output. From the training graph, RNN are able to forecast the training data set with 92.4 %. Meanwhile, the testing dataset only able to forecast the testing dataset with 89.0 %. Figure 6 shows the graph of vanilla LSTM. The architecture of Vanilla LSTM used 50 memory unit with 1 dense and batch size of 32. For training and testing dataset, it achieves 93.2% and 90.6 % respectively. As compared to RNN, Vanilla LSTM are able to improve the accuracy performance better when predicting the unknown model. Figure 7 shows the training and testing graph of stacked LSTM. For stacked LSTM, 50 memory unit were stacked with another 100 memory unit and 1 dense for its architecture. The results shows that 93.2% were achieve during training plot while 90.7% during the testing plot. The same result was obtained for bidirectional LSTM for both training and testing graph as shown in Figure 8. The overall accuracy performance results were also evaluated using root mean square error (RMSE) and it was tabulated in Table 1.

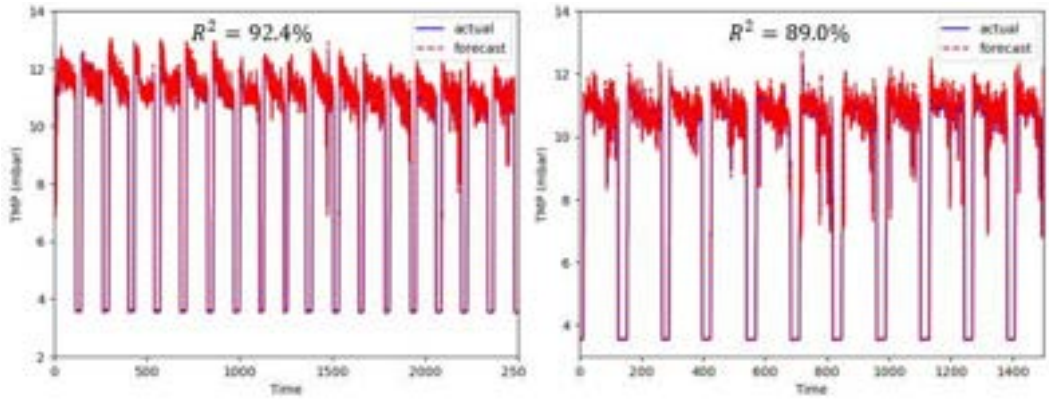

Figure. 5. The graph of training and testing dataset for RNN model.

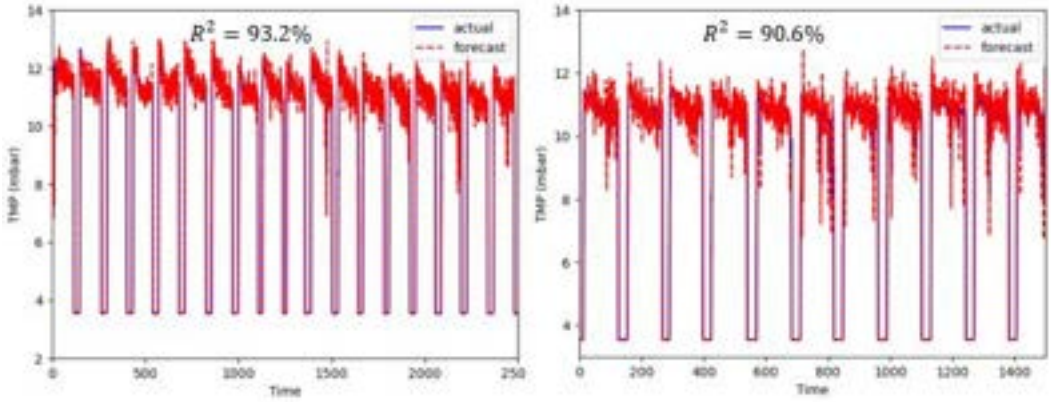

Figure. 6. The graph of training and testing dataset for Vanilla LSTM model.

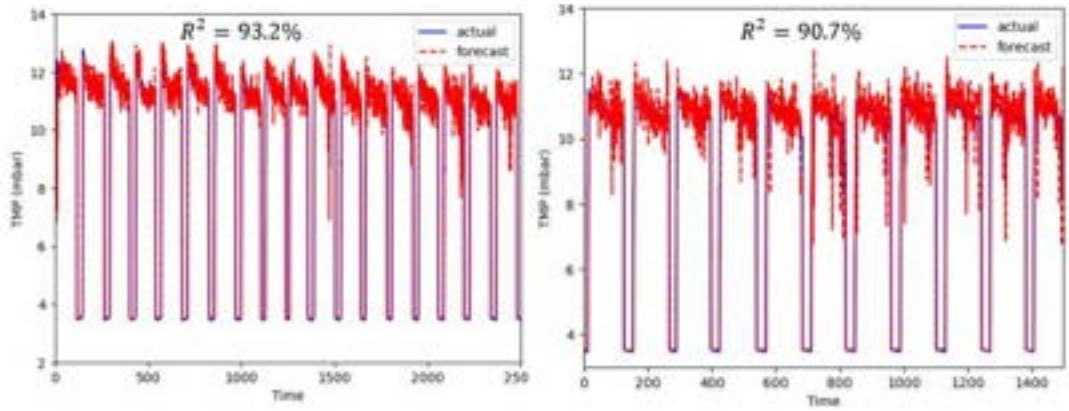

Figure. 7. The graph of training and testing dataset for Stacked LSTM model.

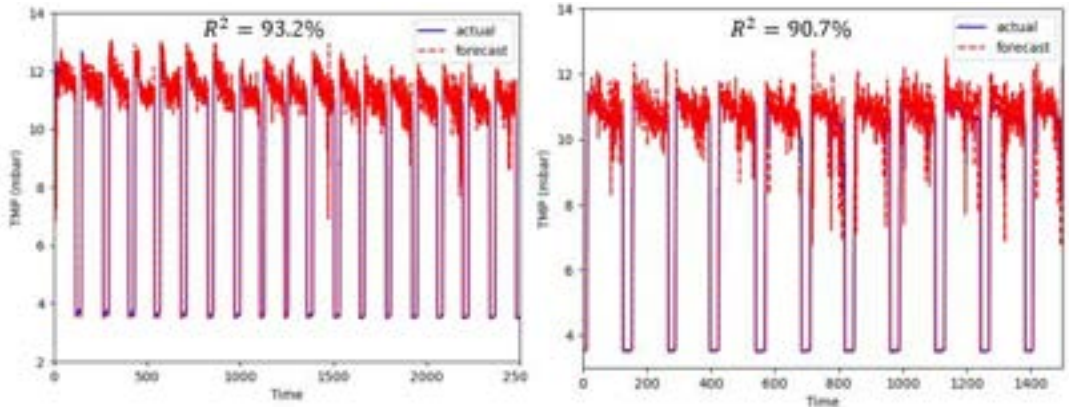

Figure. 8. The graph of training and testing dataset for Bidirectional LSTM model.

Table 1. Overall performance results of the models.

Model	Accuracy	Training	Testing
Vanilla LSTM	MSE	0.679	0.818
Epoch: 100	$RMSE$	0.824	0.905
Batch Size: 32	MAE	0.360	0.465
	R^2	0.932	0.906
Stacked LSTM	MSE	0.683	0.808
Epoch: 100	$RMSE$	0.826	0.899
Batch Size:32	MAE	0.363	0.466
	R^2	0.932	0.907
Bi-Directional LSTM	MSE	0.676	0.806
Epoch: 200	$RMSE$	0.822	0.898
Batch Size: 64	MAE	0.367	0.467
	R^2	0.932	0.907
RNN	MSE	0.762	0.955
Epoch: 100	$RMSE$	0.873	0.977
Batch Size: 32	MAE	0.414	0.534
	R^2	0.924	0.890

4.2 Conclusion

The good prediction model of submerged membrane filtration process can be a good useful in order to analysing backwashing strategies and helps to gaining some understanding on the fouling phenomena.

The main objective of the study is to compare the performance of two popular neural network architectures: RNN (Recurrent Neural Network) and LSTM (Long Short-Term Memory). Specifically, the researchers explored different types of LSTM models, including Vanilla LSTM, Stacked LSTM, and Bidirectional LSTM, to assess their effectiveness in comparison to RNN. Upon conducting the experiments, the researchers found that all three types of LSTM models Vanilla LSTM, Stacked LSTM, and Bidirectional LSTM yielded similar results. Despite their architectural differences, these variations of LSTM exhibited comparable performance, indicating that the core LSTM mechanisms were effective in capturing the underlying patterns in the data. However, when comparing these LSTM models with the RNN architecture, it was evident that the different types of LSTM consistently outperformed RNN. This suggests that LSTM's specialized design, which incorporates memory cells and gates to selectively retain and forget information, offers distinct advantages over the basic RNN architecture.

The improved performance of LSTM models can be attributed to their ability to capture and remember long-term dependencies in sequential data, thereby mitigating the vanishing gradient problem that hampers RNN performance. Vanilla LSTM, Stacked LSTM (which includes multiple LSTM layers), and Bidirectional LSTM (which processes input sequences in both forward and backward directions) all leverage these capabilities to achieve better results compared to RNN. These findings underscore the significance of employing LSTM architectures, in their various forms, for tasks involving sequential data or temporal dependencies. By utilizing the memory cells and gating mechanisms, LSTM models are better equipped to handle complex patterns and long-range dependencies in the data, leading to improved performance and more accurate predictions.

The performance of LSTM models can be further enhanced through various optimization strategies, including tuning the number of epochs, batch size, memory units, and dense architecture network. These adjustments aim to improve the accuracy and reliability of predictions. Additionally, the effectiveness of LSTM can be further amplified by integrating optimization techniques such as particle swarm optimization (PSO) or genetic algorithms (GA). These optimization methods assist in identifying the optimal architecture for the LSTM network, ensuring its efficiency and effectiveness in capturing complex patterns and delivering robust predictions. By leveraging these optimization approaches, LSTM models can be fine-tuned to achieve superior performance and more accurate results.

Acknowledgments

This work was financially supported by the Universiti Teknologi Malaysia High Impact Research Grant (UTMHR) vote Q.J130000.2451.08G74 and the Ministry of Higher Education under Prototype Research Grant Scheme (PRGS/1/2019/TK04/UTM/02/3). Also, the the support of the Spanish Government through the coordinate MICINN projects PID2019-105434RB-C31 and PID2019-105434RB-C33, project TED2021-129201B-I00 are acknowledged.

Nomenclature

MSE mean square error

RMSE root mean square error

$M\dot{A}E$ mean absolute error

R^2 correlation coefficient

References

[1] S. Vinardell *et al.*, "Advances in anaerobic membrane bioreactor technology for municipal wastewater treatment: A 2020 updated review," *Renewable and Sustainable Energy Reviews,* vol. 130, p. 109936, 2020.

[2] J. Ma, R. Dai, M. Chen, S. J. Khan, and Z. Wang, "Applications of membrane bioreactors for water reclamation: micropollutant removal, mechanisms and perspectives," *Bioresource technology,* vol. 269, pp. 532-543, 2018.

[3] S. Güneş-Durak, A. Ciggin, and N. Tüfekci, "Fabrication, characterization and treatment of polymeric membranes with submerged membrane bioreactor system: fruit juice industry wastewater," *International Journal of Environmental Science and Technology,* pp. 1-14, 2022.

[4] F. A. Fraga, H. A. García, C. M. Hooijmans, D. Míguez, and D. Brdjanovic, "Evaluation of a membrane bioreactor on dairy wastewater treatment and reuse in Uruguay," *International Biodeterioration & Biodegradation,* vol. 119, pp. 552-564, 2017.

[5] N. Wung, S. M. Acott, D. Tosh, and M. J. Ellis, "Hollow fibre membrane bioreactors for tissue engineering applications," *Biotechnology letters,* vol. 36, pp. 2357-2366, 2014.

[6] X. Shi, G. Tal, N. P. Hankins, and V. Gitis, "Fouling and cleaning of ultrafiltration membranes: A review," *Journal of Water Process Engineering,* vol. 1, pp. 121-138, 2014.

[7] M. B. Asif and Z. Zhang, "Ceramic membrane technology for water and wastewater treatment: A critical review of performance, full-scale applications, membrane fouling and prospects," *Chemical Engineering Journal,* vol. 418, p. 129481, 2021.

[8] W. Guo, H.-H. Ngo, and J. Li, "A mini-review on membrane fouling," *Bioresource technology,* vol. 122, pp. 27-34, 2012.

[9] Q. Li and M. Elimelech, "Natural organic matter fouling and chemical cleaning of nanofiltration membranes," *Water Science and Technology: Water Supply,* vol. 4, no. 5-6, pp. 245-251, 2004.

[10] N. Delouche, B. Dersoir, A. Schofield, and H. Tabuteau, "Flow decline during pore clogging by colloidal particles," *Physical Review Fluids,* vol. 7, no. 3, p. 034304, 2022.

[11] G. Crozes, J. Jacangelo, C. Anselme, and J. Laine, "Impact of ultrafiltration operating conditions on membrane irreversible fouling," *Journal of Membrane Science,* vol. 124, no. 1, pp. 63-76, 1997.

[12] Z. Cui *et al.*, "Investigation of backwashing effectiveness in membrane bioreactor (MBR) based on different membrane fouling stages," *Bioresource technology,* vol. 269, pp. 355-362, 2018.

[13] K. B. Newhart, R. W. Holloway, A. S. Hering, and T. Y. Cath, "Data-driven performance analyses of wastewater treatment plants: A review," *Water research,* vol. 157, pp. 498-513, 2019.

[14] Y. Xie *et al.*, "Enhancing real-time prediction of effluent water quality of wastewater treatment plant based on improved feedforward neural network coupled with optimization algorithm," *Water,* vol. 14, no. 7, p. 1053, 2022.

[15] R. Huang, C. Ma, J. Ma, X. Huangfu, and Q. He, "Machine learning in natural and engineered water systems," *Water Research,* vol. 205, p. 117666, 2021.

[16] L. Zhao, T. Dai, Z. Qiao, P. Sun, J. Hao, and Y. Yang, "Application of artificial intelligence to wastewater treatment: A bibliometric analysis and systematic review of technology, economy, management, and wastewater reuse," *Process Safety and Environmental Protection,* vol. 133, pp. 169-182, 2020.

[17] X. Meng, Y. Zhang, and J. Qiao, "An adaptive task-oriented RBF network for key water quality parameters prediction in wastewater treatment process," *Neural Computing and Applications,* pp. 1-14, 2021.

[18] M. Zeinolabedini and M. Najafzadeh, "Comparative study of different wavelet-based neural network models to predict sewage sludge quantity in wastewater treatment plant," *Environmental monitoring and assessment,* vol. 191, no. 3, p. 163, 2019.

[19] G. Wang, Q.-S. Jia, M. Zhou, J. Bi, J. Qiao, and A. Abusorrah, "Artificial neural networks for water quality soft-sensing in wastewater treatment: a review," *Artificial Intelligence Review,* vol. 55, no. 1, pp. 565-587, 2022.

[20] D. J. Kovacs *et al.*, "Membrane fouling prediction and uncertainty analysis using machine learning: A wastewater treatment plant case study," *Journal of Membrane Science,* vol. 660, p. 120817, 2022.

[21] F. Harrou, T. Cheng, Y. Sun, T. Leiknes, and N. Ghaffour, "A data-driven soft sensor to forecast energy consumption in wastewater treatment plants: A case study," *IEEE Sensors Journal,* vol. 21, no. 4, pp. 4908-4917, 2020.

[22] S. A. Khadem and A. D. Rey, "Nucleation and growth of cholesteric collagen tactoids: A time-series statistical analysis based on integration of direct numerical simulation (DNS) and long short-term memory recurrent neural network (LSTM-RNN)," *Journal of Colloid and Interface Science,* vol. 582, pp. 859-873, 2021.
[23] C.-J. Huang and P.-H. Kuo, "A deep CNN-LSTM model for particulate matter (PM2. 5) forecasting in smart cities," *Sensors,* vol. 18, no. 7, p. 2220, 2018.
[24] J. Shim, S. Park, and K. H. Cho, "Deep learning model for simulating influence of natural organic matter in nanofiltration," *Water Research,* vol. 197, p. 117070, 2021.
[25] H. Sak, A. W. Senior, and F. Beaufays, "Long short-term memory recurrent neural network architectures for large scale acoustic modeling," 2014.
[26] J. Brownlee, *Deep learning with Python: develop deep learning models on Theano and TensorFlow using Keras*. Machine Learning Mastery, 2016.
[27] K. Greff, R. K. Srivastava, J. Koutnik, B. R. Steunebrink, and J. Schmidhuber, "LSTM: a search space odyssey (2015)," *arXiv preprint arXiv:1503.04069,* 2016.
[28] D. M. Nelson, A. C. Pereira, and A. Renato, "de Oliveira. 2017. Stock market's price movement prediction with LSTM neural networks," in *International Joint Conference on Neural Networks (IJCNN), Anchorage, AK, USA, May*, pp. 14-19.
[29] A. Graves, N. Jaitly, and A.-r. Mohamed, "Hybrid speech recognition with deep bidirectional LSTM," in *2013 IEEE workshop on automatic speech recognition and understanding*, 2013, pp. 273-278: IEEE.
[30] M. V. Sebt, S. Ghasemi, and S. Mehrkian, "Predicting the number of customer transactions using stacked LSTM recurrent neural networks," *Social Network Analysis and Mining,* vol. 11, pp. 1-13, 2021.
[31] J. Brownlee, *Long short-term memory networks with python: develop sequence prediction models with deep learning*. Machine Learning Mastery, 2017.
[32] "Ultrafiltration Membranes: Technologies and Global Markets," BCC PublishingJuly 2020 2020.

A MILP approach for hybrid energy systems design for sustainable maritime mobility

Matteo Cavo[a], Luca Mantelli[b], Massimo Rivarolo[c] and Andriy Vasylyev[d]

[a] Thermochemical Power Group, DIME, University of Genova, Italy, matteo.cavo@edu.unige.it,
[b] Thermochemical Power Group, DIME, University of Genova, Italy, luca.mantelli@edu.unige.it,
[c] Thermochemical Power Group, DIME, University of Genova, Italy, massimo.rivarolo@unige.it,
[d] Thermochemical Power Group, DIME, University of Genova, Italy, andriy.vasylyev@edu.unige.it.

Abstract:

In this paper, an optimization algorithm based on a Mixed-Integer Linear Programming (MILP) solver is developed to determine the best energy generation solutions for marine applications. Environmentally sustainable systems (e.g., fuel cells and batteries), heat recovery devices (e.g., HRSG and Organic Rankine Cycles) and traditional power technologies (e.g., diesel generators and fired boilers) are modelled as linear systems to simulate their off-design performance. The tool considers thermal, electrical and propulsion power demands, space constraints, fuel type and availability for up to three main-vertical zones of the ship. From this information, the optimizer identifies the energy system configuration which minimizes a cost optimization function. The objective function considers the actualized capital costs of each technology (based on real market data and updated literature review), fuel costs and CO_2 emissions taxes.

In this article, the case study of a cruise ship is considered. The optimization is performed referring to real historical load demands of the cruise ship and several typical mission profiles are considered to simulate a whole operational year.

Then, the same optimization is performed after a reduction of the price of H2, which is expected in the near future according to the latest market forecasts. Thanks to this analysis, it is possible to determine the influence of this economic parameter on the optimal on-board power generation configuration.

It is worth noting that the approach presented here has a general validity and can be applied for the optimization of various typologies of maritime vessels. Moreover, the MILP algorithm could be easily expanded to consider additional demands (e.g. cooling power), constraints (e.g., weight), and power systems.

Keywords:

MILP; Energy systems; optimization model; sustainability; alternative fuels.

1. Introduction

It is a matter of fact that, as total final energy consumption is increasing more and more at global level (298 EJ in 2000, 365 EJ in 2010 and 418 EJ in 2019), CO_2 emissions are growing as well (22.3 Gtons in 2000, 30.6 Gtons in 2010, 33.6 Gtons in 2019) [1]. Despite recent international energy policies that are trying to limit the increase, it is evident that further efforts must be done to comply with the 2015 Paris agreement (COP21). According to IEA data, electricity and heat production is the most impactful sector (14.0 Gtons), followed by transports (8.2 Gtons). The maritime sector represents an important contributor, responsible for the emissions of nearly 3% in terms of CO_2 (1 Gton/year). In order to decrease the impact of this sector, the International Maritime Organization (IMO) set a long-term strategy in 2018, with the ambitious goal of reducing transport-related CO_2 emissions of 40% by 2030, with the final target cut of 70% by 2050, compared to 2008 levels [2]. In 2023 the strategy is going to be revised, with the possibility of introducing further reduction targets. Furthermore, the European Commission has recently proposed adding maritime transport to the EU Emissions Trading System (EU-ETS) [3]. More in detail, The Commission is proposing to extend the scope of the EU-ETS to cover CO_2 emissions from all cargo vessels and passenger ships above 5000 gross tons, regardless of the flag they fly. The extension will include, starting from 2024: (i) all emissions from ships calling at an EU port for voyages within the EU; (ii) 50% of the emissions from voyages starting or ending outside of the EU; (iii) emissions that occur when ships are at berth in EU ports [3]. To reach the ambitious targets of emissions reduction, many parallel strategies can be adopted [4][5], including optimization in vessel design, speed reduction in navigation, use of alternative systems for power propulsion (i.e. fuel cells) and alternative fuels (i.e. biofuels, e-fuels) [6][7]. As far as power systems are concerned, the use of different kinds of fuel cells has been investigated in recent literature [8][9][10], focusing on: (i) high temperature Solid Oxide Fuel Cells

(SOFC), usually in hybrid systems configuration to increase efficiency [11] (up to 60%); (ii) low temperature Proton Exchange Membrane Fuel Cells (PEMFC), directly fuelled by hydrogen, which represent a zero emissions solution. The latter solution is the most employed today, in particular in research vessels as reported in recent literature. Regarding fuels, many alternatives are possible to replace Heavy Fuel Oil (HFO) and Marine Diesel Oil (MDO), which are the most employed today and have high CO_2 emissions (about 3.1 $kgCO_2$/kg fuel). Natural gas is an alternative [12], however larger volumes are required for storage on-board and it only allows for a limited reduction (specific emission 2.75 $kgCO_2$/kg fuel). The use of hydrogen [13], ammonia [14], or other low carbon fuels is under investigation for several types of vessel [15].

To compare the different possible solutions in terms of power propulsion and storage technologies, it is important to develop reliable tools and models able to identify the best alternatives [16][17][18], taking into proper account the constraints of the problem, such as the volume and weight constraints of the vessel, the navigation route and the required performance in terms of autonomy and maximum power. The use of Mixed-Integer Linear Programming (MILP) models is largely recognized to optimize the distributed energy systems [19], also in presence of energy storage systems and not programmable renewable energy sources [20]. However, only a few applications of MILP models for power propulsion and fuel storage on-board maritime vessels are available in literature [21]. MILP models have never been developed before to investigate a wide spectrum of innovative technologies for a maritime application considering a time-dependent simulation on one year. In this paper, the tool developed by the Authors aims at: (i) choosing the optimal installation mix to meet the energy demands of the ship (electrical and thermal), while considering the most relevant constraints; (ii) minimizing an objective function which represents the annual costs.

2. Model Description

This section describes the optimization model developed for this study. It was designed as a tool capable of supporting the preliminary design phase of the energy systems installed on a ship. The optimization is performed by comparing different technologies for the generation of onboard electric and thermal power. The ship layout is split into three Main-Vertical-Zones (MVZ): each main-vertical-zone respects the tool constrains in order to identify the optimum location for each technology. The optimization model was tested considering a cost-based optimization function, which includes taxes on CO_2 emissions.

2.1. Library and user-interface

The optimization model was developed in MATLAB, while the optimization procedure relies on the BNB built-in solver of the Yalmip toolbox [19]. Within Yalmip, the GUROBI optimizer was adopted. This optimizer implements a standard branch & bound algorithm [20] to solve different kinds of mixed-integer problems [20][21]. The following technologies have been considered for electrical and thermal energy production:

- Internal Combustion Engines: Diesel Generators (DG).
- Heat Recovery System Generators (HRSG).
- Organic Rankine Cycles (ORC).
- Fire Boilers (FB).
- Heat Pump (HP)
- Battery Electrical Storage (BES).
- Proton-Exchange Membrane Fuel Cells (PEMFC).

Each technology requires a certain amount of primary energy source. Heat recovery systems (HRSG, ORC) or storages (BES) interact with the ship balance depending on their efficiency and usage. Then, Diesel Generators, Fired Boilers and PEMFCs require a primary energy source. The fuel of these technologies is considered by the tool as a limited energy source: if the fuel tank is empty, the associated technology is shut down. The type of fuel and storage systems implemented are:

- Tank for liquid storage: HFO, MDO, LNG, liquid hydrogen.
- Tank for gas storage: compressed hydrogen.
- Metal Hydrides (MH) for solid hydrogen storage.

Some system contributes to the production of both thermal and electrical power, which are requested to satisfy the demands of the ship. Assuming that a propulsion unit driven by an electric generator is installed on the ship, the propulsive power is included in the electricity balance. The propulsive demand is increased to consider an overall efficiency for energy transformation of 95%.

The user interfaces with an Excel worksheet (Figure 1) to specify which technologies will be considered in the simulation, the volumes allocated to each technology and their distribution in each main vertical zone.

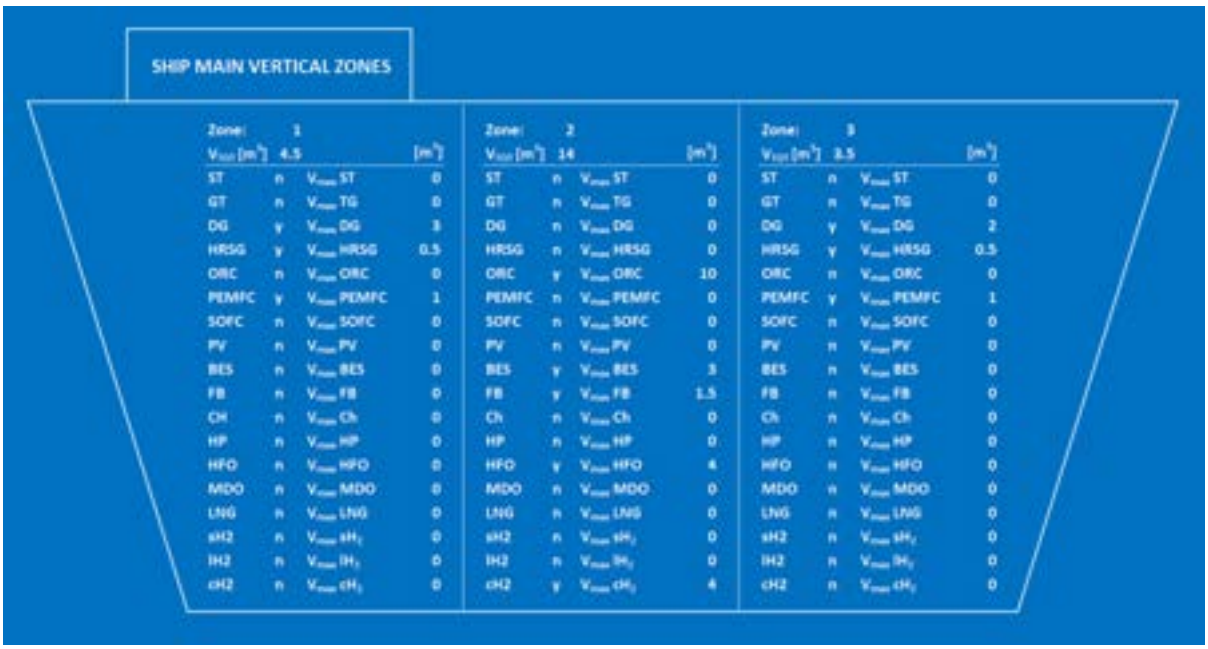

Figure 1 – The Excel user interface where the inputs of the MILP model can be defined.

Then, the user selects from a database the models to be compared during the simulation for each technology. The database contains the information required for optimisation computation and performance estimation of energy systems. **Appendix A** lists the data stored in the database. The model determines certain technical working characteristics of the systems under investigation based on their performance and thermal/electricity demands.

2.2. Constraints

The solution found by the MILP model is limited by four different types of constraints that are implemented on the algorithm:

- Operative constraints.
- Size constraints.
- Specific constraints of each energy system.
- Balance constraints: they allow the balance constraints of electrical and thermal demand and ensure continuity in the energy flow where energy systems interact (i.e. DG, HRSG ORC). They also verify the overall plant volume against the available space.

Operative constrains are necessary to guarantee that every variable under consideration have physical limits. Usually, all the technology considered in this tool have a minimum power output and a maximum power output. Size constraints ensure that each energy system respects an overall volume constraint. For each main vertical zone, the user defines both the volume dedicated to each specific technology and the total volume available in that main-vertical-zone. So, over imposing a total main-vertical-zone constraint is possible to guarantee that all the technologies installed don't exceed the volume available.
Every energy system must respect the constraints characteristic of the physics representing it, which correlate power (thermal and electrical), efficiency, current, consumption, etc (Table 1). In order to maintain the problem linear, the tool considers a linear correlation to evaluate the technologies off-design, as presented in the following table. Also, binary variables are limited to guarantee that a technology installed can be set on or off by the tool just in case it is installed.

Table 1 – System constrains description.

System constraints	
DG $\nabla d = 1 \dots N_{model}^{DG}$; $\nabla \mathrm{g} = 1 \dots N_{max}^{DG}$	$x^{DG} \leq y^{DG}$ $\eta^{DG} = \alpha\, P_{el}^{DG} + \beta\, x^{DG}$; $P_{th,diss}^{DG} = P_{el}^{DG}(1-\eta^{DG})$; $\dot{m}_{fuel}^{DG} = \frac{P_{el}^{DG}}{\eta^{DG} LHV_{fuel}}$
HRSG $\nabla \mathrm{h} = 1 \dots N_{model}^{HRSG}$; $\nabla \mathrm{r} = 1 \dots N_{max}^{HRSG}$	$x^{HRSG} \leq y^{HRSG}$ $\eta^{HRSG} = \alpha\, P_{th,out}^{HRSG} + \beta\, x^{HRSG}$; $P_{th,in}^{HRSG} = \frac{P_{th,out}^{HRSG}}{\eta^{HRSG}}$

ORC $\nabla o = 1 \dots N_{model}^{ORC}$; $\nabla c = 1 \dots N_{max}^{ORC}$	$x^{ORC} \leq y^{ORC}$ $\eta^{ORC} = \alpha\, P_{el}^{ORC} + \beta\, x^{ORC}$; $P_{th,in}^{ORC} = \frac{P_{el}^{ORC}}{\eta^{ORC}}$
FB $\nabla f = 1 \dots N_{model}^{FB}$; $\nabla b = 1 \dots N_{max}^{FB}$	$x^{FB} \leq y^{FB}$ $\eta^{FB} = \alpha\, P_{th}^{FB} + \beta\, x^{FB}$; $\dot{m}_{fuel}^{FB} = \frac{P_{th}^{FB}}{\eta^{FB} LHV_{fuel}}$
HP $\nabla h = 1 \dots N_{model}^{HP}$; $\nabla p = 1 \dots N_{max}^{HP}$	$x_{cool}^{HP} + x_{heat}^{HP} \leq y^{FB}$ $COP^{HP} = \alpha\, P_{heat}^{HP} + \beta\, x_{heat}^{HP}$; $EER^{HP} = \alpha\, P_{cool}^{HP} + \beta\, x_{cool}^{HP}$ $P_{el,in}^{HP} = (\alpha\, P_{heat}^{HP} + \beta\, x_{heat}^{HP}) + (\alpha\, P_{cool}^{HP} + \beta\, x_{cool}^{HP})$
PEMFC $\nabla p = 1 \dots N_{model}^{PEMFC}$ $\nabla e = 1 \dots N_{max}^{PEMFC}$	$x^{PEMFC} \leq y^{PEMFC}$ $\eta^{PEMFC} = \alpha\, P_{el}^{PEMFC} + \beta\, x^{PEMFC}$; $\dot{m}_{H_2}^{PEMFC} = \frac{P_{el}^{PEMFC}}{\eta^{PEMFC} LHV_{H_2}}$
BES $\nabla b = 1 \dots N_{model}^{BES}$ $\nabla s = 1 \dots N_{max}^{BES}$	$x_{ch}^{BES} + x_{disch}^{BES} \leq y^{BES}$ $C_{(t,w+1)}^{BES} = C_{(t,w)}^{BES} + \Delta t \left(P_{ch,(t,w)}^{BES} \eta_{ch}^{BES} - \frac{P_{disch,(t,w)}^{BES}}{\eta_{disch}^{BES}} \right)$; $C_{(t,1)}^{BES} = C_{max}^{BES}$ $\sum_w \left(P_{ch}^{BES} \eta_{ch}^{BES} - \frac{P_{disch}^{BES}}{\eta_{disch}^{BES}} \right) \geq 0$
FUELS	$SoC_{(t,w+1)} = SoC_{(t,w)} - \sum_{i=1}^{Numb.Techn.} \dot{m}_{fuel}^{i}$; $SoC_{(t,1)} = SoC_{max}$

2.2.1. Balance constraints

Balance constraints are presented in Table 2. These constraints have been introduced in order to guarantee the overall thermal and electrical energy balances of the ship. Also cooling demand has been introduced but it's not considered by the model at this stage.

Table 2 – Balance constraints description.

Balance Constraints
Electrical Balance
$\sum_d \sum_g P_{el}^{DG} + \sum_o \sum_r P_{el}^{ORC} + \sum_f \sum_c P_{el}^{PEMFC} + \sum_b \sum_s P_{disch}^{BES} - D_{el} - \sum_h \sum_p P_{el,in}^{HP} - \sum_b \sum_s P_{ch}^{BES} = 0$
Thermal Balance
$\sum_h \sum_r P_{th,out}^{HRSG} + \sum_f \sum_b P_{th}^{FB} + \sum_h \sum_p P_{heat}^{HP} - D_{th} = 0$ $\sum_d \sum_g P_{th}^{DG} - \sum_o \sum_r P_{th,in}^{ORC} = 0$

2.3. Optimization Function

The objective function adopted aims to minimise the costs of the ship considered. Furthermore, the tool includes fuel costs and CO_2 taxes. The main technologies costs considered by the objective function are:

- The total Installation Cost (1) obtained by the Capital Cost (CC) of each technology considered (s) and installed (i) adjusted by the Capital Recovery Factor (CRF).
- The total cost of the fuel consumed (2) during navigation into the time-lap considered (t) and every cruise profile (w). This equation takes into account the different costs for each fuel considered (f).
- Taxes due to CO_2 emissions (3).

$$Tot.Inst.Cost = \sum_s \sum_i CC_i\, CRF_i \qquad (1)$$
$$where, \quad CRF = \frac{(1-r)^{UL}}{(1+r)^{UL} - 1}$$

$$Tot.FuelCost. = \sum_w \sum_t \sum_f \dot{m}_f\, \Delta t\, c_{fuel} \qquad (2)$$

$$EmissionCost. = \sum_w \sum_t \dot{m}_{CO_2} \Delta t \; c_{tax} \quad (3)$$

The time lap adopted for simulation considers a whole cruise from port to port for one year. Costs are influenced by the number of cruise that the ship schedule during the year

3. Analysis and Results

3.1. Case study

To verify the correct operation of the MILP optimizer presented in Section 2, the case study of a passenger ferry boat was considered. The specifications of the boat, as well as its daily path and load profile were derived from the study by Rafiei et al. [22][5]. The ferry boat has an overall length of 47 m and in this specific scenario it sails with an average speed of 11 knots and a maximum speed of 13 knots. To guarantee the correct operation of the ferry boat, a propulsion system with at least 600 kW nominal power must be installed onboard. Moreover, the electrical power required by the auxiliary systems must be taken into account, both during navigation and while docked in port.

The ferry boat is used to carry passengers across a bay, following the same navigation plan every day:

- 06.00: departure from the port A
- 10.00: arrival at port B
- 13.00: departure from the port B
- 18.00: arrival at port C
- 20.00: departure from the port C
- 01.00: arrival at port A

Figure 2 shows the propulsion and auxiliary power demands for each hour of the navigation plan, specifying if the ferry boat is sailing or is docked in that moment.

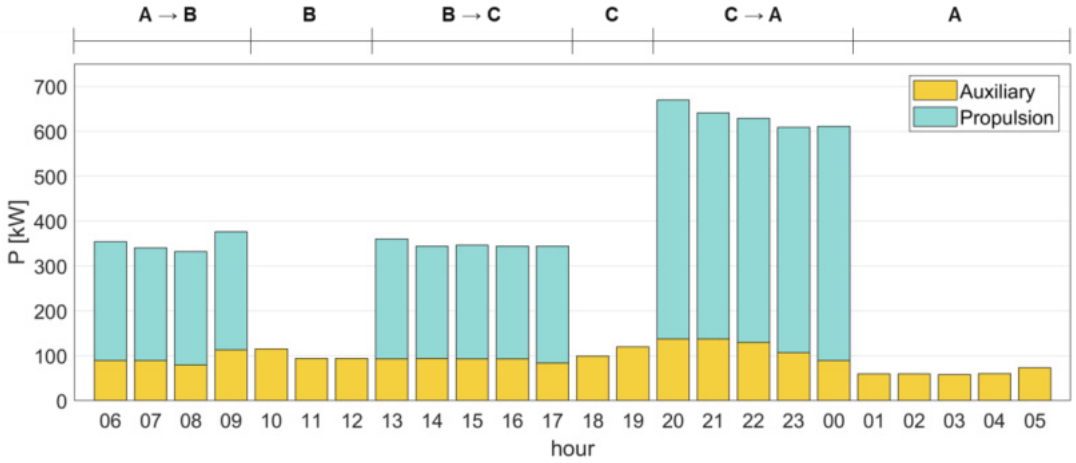

Figure 2 – Load profile of propulsive power and electrical power of the auxiliary systems; on the top it is specified if the ferry boat is sailing between ports or if it is docked.

For this analysis, only the port A is supposed to be equipped for cold ironing, and the BES are always completely charged at the beginning of each daily path (6.00).

The data used in [22] include only information of propulsive and auxiliary electrical loads. However, the MILP algorithm was designed to optimize the generation onboard of both electric and thermal power. Therefore, three possible daily weather conditions (i.e., hot, mild, cold) were defined, associating a different thermal load profile to each one of them:

- Hot weather: no thermal load – 92 days a year
- Mild weather: low thermal load – 151 days a year
- Cold weather: high thermal load – 122 days a year

Similarly to the electrical load of the auxiliary systems, the thermal load is present also when the ferry boat is docked. Figure 3 show the thermal load profiles for mild and cold weather, respectively.

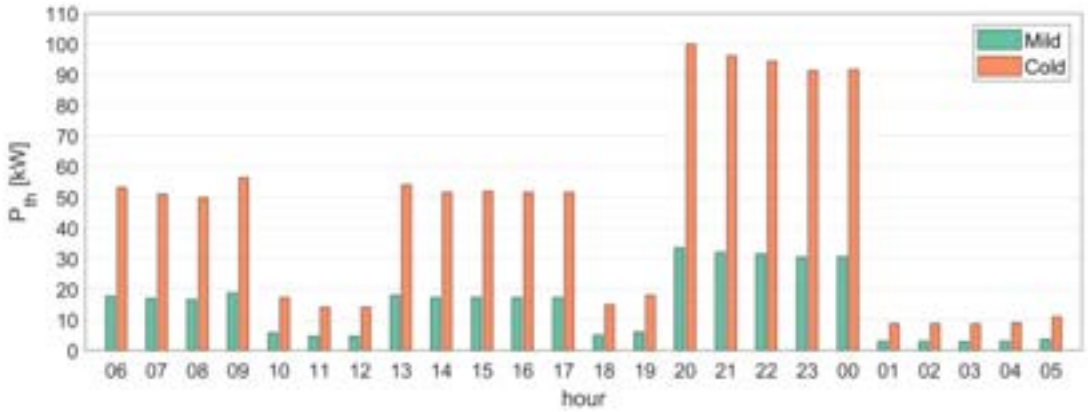

Figure 3 – Load profiles of thermal power for days with mild and cold weather.

3.2. Current scenario optimal solution

This section presents the results of a simulation using the current scenario: CO_2 tax 100€/ton, according to recent ETS [23] and hydrogen cost 6€/kg [24]. The technologies considered by the tool to minimise the objective function are listed in the Table 3, together with the best resulting configuration.

Table 3 – Optimization results, considering the actual scenario.

Supplier	Model	N° of elements installed	CAPEX / FuelCost [€/unit] / [€/y]
	Diesel Generator		
Solè Diesel	SDZ-205	1	35750
Solè Diesel	L1306C2 MSD	1	147500
Isotta Fraschini	SDZ-280	0	-
	Organic Rankine Cycle		
Orcan Energy	eP M 050.100 HP	0	-
Zuccato Energia	ZE-30-ULH	0	-
	Proton Exchange membrane Fuel Cell		
Genevos	HPM-15	0	-
Nuvera	E-45-HD	0	-
Nuvera	E-60-HD	0	-
	Battery Electrical Storage		
Corvus Energy	Orca Pack249	0	-
Nidec	Marine battery pack	3	48000
	Heat Recovery System Generators		
Siemens Energy	100	2	9900
Siemens Energy	10	1	990
	Fired Boiler		
AlphaLaval	Aalbotg CHB	0	-
AlphaLaval	Aalbotg CHB	1	4000
	Fuel Considered		
DG:	Heavy Fuel Oil		249150
FB:	Heavy Fuel Oil		
PEMFC:	Compressed green hydrogen		-
	Emissions		
CO_2			177190

The selection of these items is the outcome of some preliminary tests necessary to roughly identify the size of the systems which may potentially be installed. Therefore, some technologies have been excluded as too small or too large for this case study.

The results (Figure 4 and Figure 5) led to a configuration where the PEMFC technology is not present due to the high fuel cost. However, three battery modules were installed to manage the electrical load in combination with a smart modulation of the diesel engines. The capital cost of this technology is offset by the lower fuel consumption of the engines and the reduction in annual CO_2 emissions. The configuration also includes the installation of 3 HRSGs and 1 FB. It is clear that in the current scenario the most competitive technology is still the Diesel Generator due to its compactness, low cost per unit of power and low fuel cost.

The tool also determines the best strategy for using these technologies to cover the electricity and heat demands. It is important to observe that the electrical load distribution in the first two mission profiles (hot and

mild weather) is similar, so it is presented only once in this article. On the other hand, in the third mission profile (cold weather), the electrical power generation strategy is notably influenced by the high thermal demand of the ferry boat.

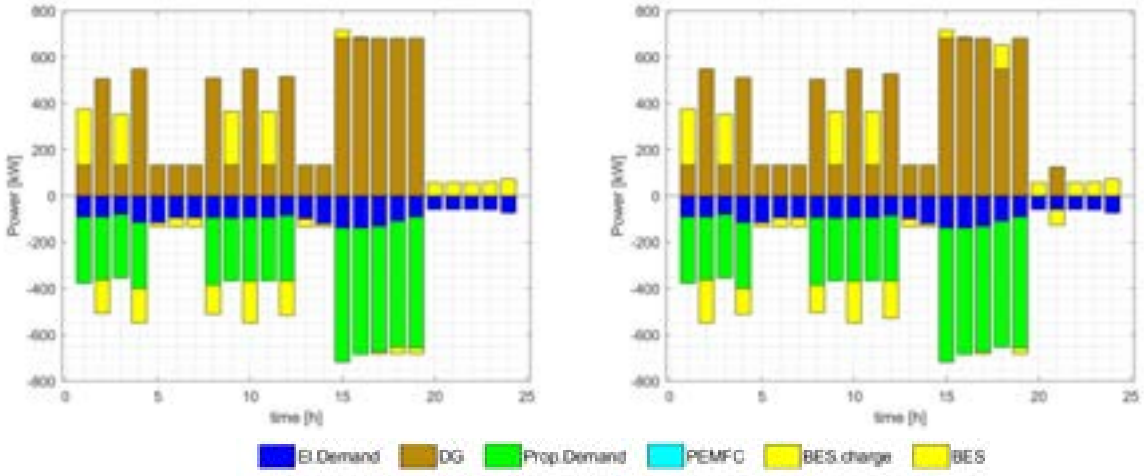

Figure 4 – Electrical load profile solutions for current scenario for mild (left) and cold weather (right).

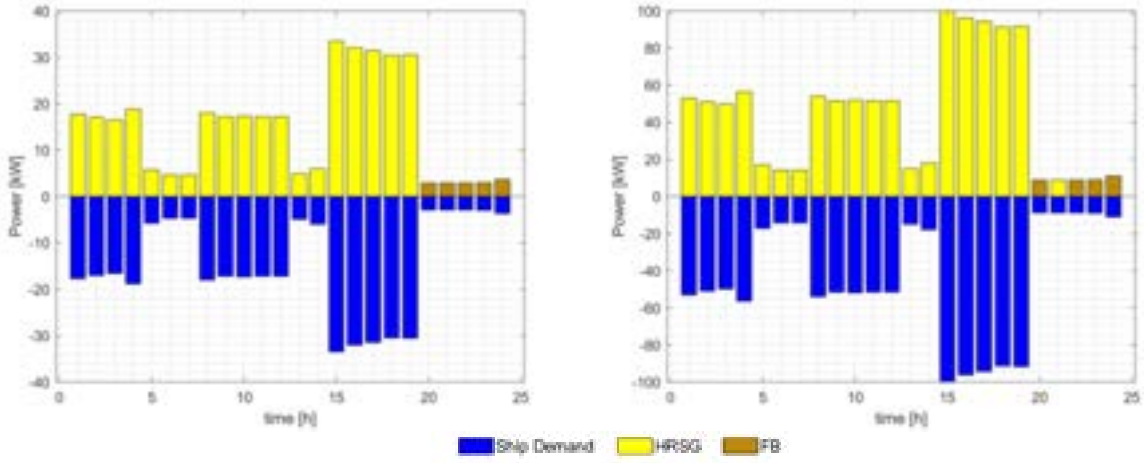

Figure 5 – Thermal load profile solutions for current scenario for mild (left) and cold weather (right).

Analysing the results, it can be observed that the batteries are used to operate DG technology as close as possible to the optimum point, in order to maximise the efficiency of the system by decreasing both consumptions and emissions. Regarding the thermal demand, HRSG units from DGs heat waste are used whenever possible. This technology requires a considerably higher investment compared to the fired boiler solution; however, it is justified by the fact that it saves fuel and reduces emission taxes. Turning on a fired boiler is necessary when demand is below the technical minimum.

3.3. Near future scenario optimal solution

This section presents the results of a simulation using a near future scenario, characterized by CO_2 tax [23] 100€/tons and hydrogen cost 1.5 €/kg, according to recent forecasts [25].
The technologies considered by the tool to minimise the objective function are listed in the Table 4 together with the best resulting configuration.

Table 4 - Optimization results, considering the actual scenario.

Supplier	Model	N° of elements installed	CAPEX / FuelCost [€/unit] / [€/y]
	Diesel Generator		
Solè Diesel	SDZ-205	1	35750
Solè Diesel	L1306C2 MSD	1	147500
Isotta Fraschini	SDZ-280	0	-
	Organic Rankine Cycle		

Orcan Energy	eP M 050.100 HP	0	-
Zuccato Energia	ZE-30-ULH	0	-
	Proton Exchange membrane Fuel Cell		
Genevos	HPM-15	0	-
Nuvera	E-45-HD	0	-
Nuvera	E-60-HD	1	88500
	Battery Electrical Storage		
Corvus Energy	Orca Pack249	0	-
Nidec	Marine battery pack	3	48000
	Heat Recovery System Generators		
Siemens Energy	100	2	9900
Siemens Energy	10	1	990
	Fired Boiler		
AlphaLaval	Aalbotg CHB	0	-
AlphaLaval	Aalbotg CHB	1	4000
	Fuel Considered		
DG:	Heavy Fuel Oil		213810
FB:	Heavy Fuel Oil		
PEMFC:	Compressed green hydrogen		40089
	Emissions		
CO_2			152230

According to the results of the tool, it appears that the price drop of hydrogen had a significant influence on the optimal energy mix. In this configuration, a PEMFC of 60 kWe is installed. Therefore, this technology currently has a major weakness: the price of fuel. However, the expected reduction of H2 price in the near future will make it a competitive solution, not only for their zero-emissions, but also from an economical point of view.

As shown by the load profile solution (Figure 6), the tool highlights that PEMFCs cannot be operated at maximum load all the time. This result is due to the SoC of the hydrogen stored in the ship: its energy density is fairly low, so the volume dedicated to hydrogen storage does not allow for a more intensive use of the fuel cells. However, it can be observed in Figure 6 how the fuel cells replace the batteries during the port stays.

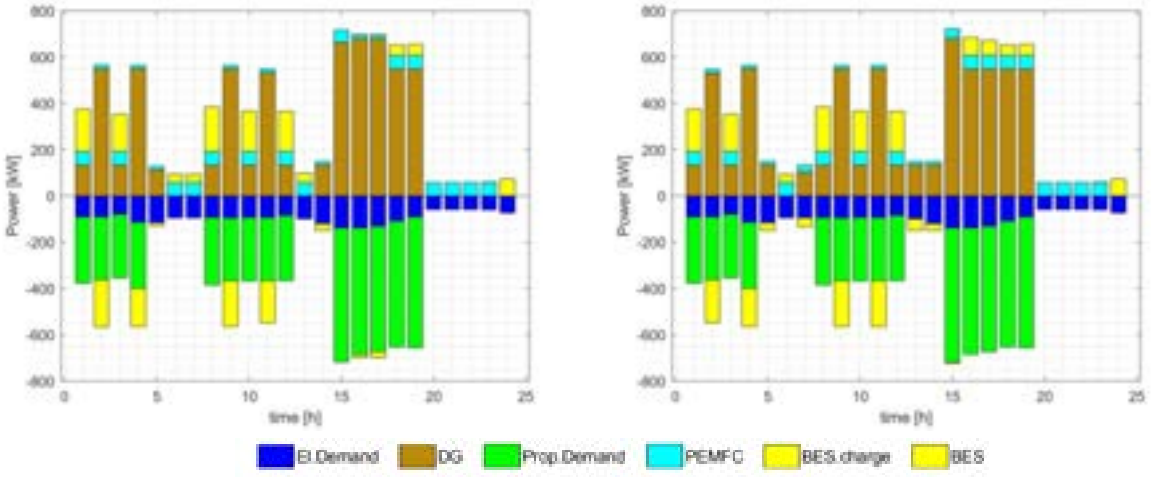

Figure 6 – Electrical load profile solution for the near future scenario for mild (left) and cold weather (right).

Figure 7 shows that the installation of the PEMFCs did not affect significantly the thermal power generation, compared to the results shown in Figure 5 for the current scenario. In fact, the thermal power is mostly supplied by the HRSG, with the FB that is turned on only when necessary.

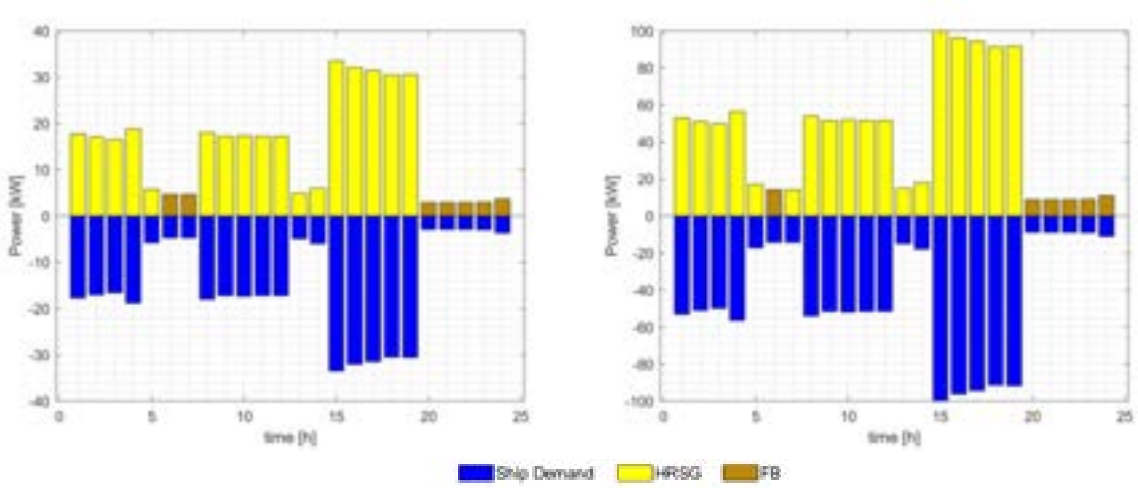

Figure 7 – Thermal load profile solutions for the near future scenario for mild (left) and cold weather (right).

4. Conclusions

This paper presented a MILP model designed to determine the best power generation mix to be installed on a ship and, at the same time, to optimize the operation of each energy system. The MILP model was developed in MATLAB environment relying on the Yalmip optimization toolbox. The model compares different technologies to find the layout that minimizes an objective function, representing the annual costs necessary to cover the electrical and thermal energy demands of the vessel. The analysis is performed considering the specific constraints of the problem, related to the available volume on-board, technical limitations for each technology and overall energy balances (electrical and thermal) to satisfy the demand in each period (hour) of the navigation year. Fixed costs, fuel costs and CO_2 taxation are included in the objective function. The case study of a small passenger ferry boat is considered, taking into account three different representative energy demand profiles, for hot, mild and cold season respectively. Different possible market technologies are considered for on-board installation and electrical (diesel generators, PEMFC, batteries, ORC) and thermal (HRSG, fire boilers) energy production. The following conclusions can be drawn from the results:

- In the current scenario, the optimal configuration mostly relies on traditional and consolidated technologies, i.e. DG and HRSG. These systems are installed and employed to satisfy the largest part of the demand, with a small contribute by electrical batteries.
- In the near future scenario, characterized by lower hydrogen price, PEMFC are installed as well on-board to generate a part of electrical energy. This fact leads to CAPEX increase, but also allows for a reduction in terms of CO_2 emissions and related fees.
- In all the scenarios, the largest costs are due to fuel and CO_2 taxes, which are both strongly dependent on international markets and environmental/energy policies: an increase in CO_2 fees or in fossil fuel prices, or a decrease in hydrogen production cost, can represent one of the key points for economic feasibility of more sustainable solutions.

In the future, the MILP model will be used to assess more precisely the impact of CO_2 taxation on the optimal energy solution. The library of components considered by the tool will be expanded, introducing electric boiler technology as an alternative to HFO-fuelled boilers. This solution expected to further reduce CO_2 emissions.

Moreover, the MILP tool will be tested on different types of vessels, to understand how different sizes and navigation plans change the best power generation strategy.

References

[1] International Energy Agency (IEA) website, available at https://www.iea.org/regions/world [accessed 1/3/2023].

[2] International Maritime Organization (IMO) website, 4th Greenhouse Gas study 2020, available at https://www.imo.org/en/OurWork/Environment/Pages/Fourth-IMO-Greenhouse-Gas-Study-2020.aspx [accessed 1/3/2023].

[3] European Commission website, Reducing emissions for maritime sector, available at https://climate.ec.europa.eu/eu-action/transport-emissions/reducing-emissions-shipping-sector_en [accessed 1/3/2023].

[4] Maritime forecast to 2050-Energy transition outlook (2021), DNV Maritime.

[5] Elkafas A.G., Rivarolo M., Massardo A.F., Assessment of alternative marine fuels from environmental, technical, and economic perspectives onboard ultra large container, Int. J. of Maritime Eng. 2022;164(A2).

[6] Balcombe P., Brierley J., Lewis C., Skatvedt L., Speirs J., et al., How to decarbonise international shipping: Options for fuels, technologies and policies, Energy Conversion and Management 2019;182:72-88.

[7] Bouman E.A., Lindstrad E., Rialland A.I., Strømman A.H., State-of-the-art technologies, measures, and potential for reducing GHG emissions from shipping – A review, Transportation Research Part D: Transport and environment 2017;52:408-421.

[8] Xing H., Stuart C., Spence S., Chen, H. Fuel Cell Power Systems for Maritime Applications : Progress and Perspectives, Sustainability 2021;13:1213.

[9] Elkafas A.G., Rivarolo M., Gadducci E., Magistri L., Massardo A.F., Fuel Cell Systems for Maritime: A Review of Research Development, Commercial Products, Applications, and Perspectives, Processes 2023;11(1):97.

[10] van Biert L., Godjevac M., Visser K., Aravind P.V., A review of fuel cell systems for maritime applications, Journal of Power Sources 2016;327:345-364.

[11] Mantelli L, Ferrari M.L., Traverso A., Dynamics and control of a turbocharged solid oxide fuel cell system. Applied Thermal Engineering 2021;191:116862.

[12] Ouyang T., Tan J., Xie S., Wu W., Su Z., A new scheme for large marine vessels LNG cold energy utilization from thermodynamic and thermoeconomic viewpoints, Energy Conv. and Manag. 2021;229:113770.

[13] M. Rivarolo, D. Rattazzi, T. Lamberti, L. Magistri, Clean energy production by PEM fuel cells on tourist ships: a time-dependent analysis, International Journal of Hydrogen Energy 2020;45:25747-25757.

[14] Z. Wan, Y. Tao, J. Shao, Y. Zhang, H. You, Ammonia as an effective hydrogen carrier and a clean fuel for solid oxide fuel cells, Energy Conversion and Management 2021;228:113729.

[15] Prussi M., Scarlat N., Acciaro M., Kosmas V., Potential and limiting factors in the use of alternative fuels in the European maritime sector, Journal of Cleaner Production 201;291:125849.

[16] Al-Breiki M., Bicer Y., Investigating the technical feasibility of various energy carriers for alternative and sustainable overseas energy transport scenarios, Energy Conv. and Management 2020;209: 112652.

[17] Pesce M., Terzi S., Al-Jawasreh R.I.M., Bommarito C., Calgaro L., Fogarin S., et al., Selecting sustainable alternatives for cruise ships in Venice using multi-criteria decision analysis, Science of the Total Environment 2018;642:668-678.

[18] Rivarolo M, Rattazzi D, Magistri L, Massardo AF, Multi-criteria comparison of power generation and fuel storage solutions for maritime application, Energy Conversion and Management 2021;244:114506.

[19] Lofberg, J. (2004). YALMIP: A toolbox for modeling and optimization in MATLAB. In 2004 IEEE international conference on robotics and automation (IEEE Cat. No. 04CH37508) (pp. 284-289).

[20] https://www.gurobi.com/ [accessed 22/03/2023]

[21] https://yalmip.github.io/solver/bnb/ [accessed 22/03/2023]

[22] Rafiei, M., Boudjadar, J., & Khooban, M. H. (2020). Energy management of a zero-emission ferry boat with a fuel-cell-based hybrid energy system: Feasibility assessment. *IEEE Transactions on Industrial Electronics*, *68*(2), 1739-1748.

[23] https://ember-climate.org/data/data-tools/carbon-price-viewer/ [last accessed 15/03/2023].

[24] Global Hydrogen Review 2021, International Energy Agency (IEA), 2021.

[25] Green Hydrogen Cost Reduction: Scaling up Electrolysers to Meet the 1.5ºC Climate Goal, International Renewable Energy Agency, Abu Dhabi, IRENA 2020.

Appendix A

Table A.1. Database of main technologies implemented and available in the tool.

Diesel Generators							
Supplier	Model	Brake Power (max-min) [kW]	Efficiency (max-min) [%]	Kcost [€/kW]	Kgrav [t/kW]	Kvol [m^3/kW]	Useful Life [y]
Wartsila	8L25	3000-900	55-30	250	0.0089	0.0167	25
Wartsila	8V31F	4880-1464	55-30	250	0.0117	0.0184	25
Wartsila	10V31F	6100-1830	55-30	250	0.0106	0.0163	25
Wartsila	14V31	8540-2562	55-30	250	0.0099	0.0163	25
Wartsila	16V31	9760-2928	55-30	250	0.0095	0.0154	25
Wartsila	8L46F	9600-2880	55-30	250	0.0129	0.0108	25
Wartsila	12V46F	14400-4320	55-30	250	0.0123	0.0155	25
Wartsila	14V46F	16800-5040	55-30	250	0.0129	0.0191	25
Wartsila	16V46F	19200-5760	55-30	250	0.0121	0.0184	25
Rolls-Royce MTU	12V 4000 P63	1350-405	55-30	250	0.0054	0.0062	25
Rolls-Royce MTU	16V 4000 P63	180-540	55-30	250	0.0049	0.0055	25
Rolls-Royce MTU	20V 4000 P63	2245-674	55-30	250	0.0048	0.0051	25
MAN	14V51/60DF	14700-4410	55-30	250	0.0151	0.0199	25
Isotta Fraschini	V1712C2 MLH	1350-405	55-30	250	0.0034	0.0062	25
Isotta Fraschini	V1708C2 MLL	815-245	55-30	250	0.0044	0.0061	25
Solé Diesel	SDZ-280	200-60	55-30	250	0.0034	0.0056	25
Solé Diesel	SDZ-205	143-43	55-30	250	0.0045	0.0076	25
Organic Rankine Cycles							
Supplier	Model	El.Power Output (max-min) [kW]	Efficiency (max-min) [%]	Kcost [€/kW]	Kgrav [t/kW]	Kvol [m^3/kW]	Useful Life [y]
Zuccato Energia	ZE-30-ULH	30-15	8.5-4	2500	0.103	0.323	15
Zuccato Energia	ZE-40-ULH	40-20	8.9-4	2500	0.078	0.243	15

Zuccato Energia	ZE-50-ULH	50-25	9.1-4	2500	0.090	0.206	15
Zuccato Energia	ZE-100-ULH	100-50	8.3-4	2500	0.065	0.348	15
Orcan Energy	eP M 050.100 HP	100-50	9-4	2500	0.023	0.033	15
Orcan Energy	eP M 150.200	200-100	9.5-4	2500	0.023	0.037	15

Proton Exchange Membrane Fuel Cell

Supplier	Model	El.Power Output (max-min) [kW]	Syst.Efficiency (max-min) [%]	Kcost [€/kW]	Kgrav [t/kW]	Kvol [m^3/kW]	Useful Life [y]
Ballard	FCWave	200-55	40-53.5	50	0.0050	0.0098	10
Nuvera	E-45-HD	45-13	37-50	50	0.0042	0.0067	10
Nuvera	E-60-HD	59-16	40-53	50	0.0032	0.0051	10
Ned Stack	PemGen MT-FCPI-100	100-28	37-50	50	0.0250	0.0462	10
Ned Stack	PemGen MT-FCPI-500	500-138	37-50	50	0.0300	0.0858	10
Powercell	Marine System 200	200-55	45-60	50	0.0035	0.0063	10
Proton Motor	HyShip	213-59	40-50	50	0.0035	0.0063	10
Genevos	HPM-40	40-11	40-52	50	0.0048	0.0130	10
Genevos	HPM-80	78-22	40-52	50	0.0042	0.0115	10

Battery Energy Storage

Supplier	Model	Capacity [kWh]	El.Power Max (Charge-Discharge) [kW]	Efficiency (Charge-Discharge) [%]	Kcost [€/kWh]		Kgrav [t/kWh]	Kvol [m^3/kWh]	Useful Life [y]
Corvus Energy	Orca Pack249	249	747	70-80	400	0.013	0.011	10	
Corvus Energy	Orca Pack992	992	2976	70-80	400	0.013	0.011	10	
ABB	containerized ESS	1100	1100	70-80	400	0.027	0.049	10	
ABB	eStorage Flex 10-190	190	160	70-80	400	0.028	0.114	10	
ABB	eStorage Flex 10-240	240	160	70-80	400	0.024	0.090	10	
Nidec	marine battery pack	120	120	70-80	400	0.007	0.007	10	
Forsee power	Pulse15 146	146	572	70-80	400		0.018	0.017	10
Forsee power	Pulse15 219	219	857	70-80	400		0.018	0.017	10

Eco-efficiency dependencies for Wastewater Treatment Plant operation

S. Revollar[a], M. Meneses[b], P. Vega[a], M. Francisco[a] and R. Vilanova[b]

[a] University of Salamanca, Salamanca, Spain, {srevolla,pvega,mfs}@usal.es
[b] Universitat Autonoma Barcelona, Barcelona, Spain, {Montse.Meneses,Ramon.Vilanova@uab.cat}

Abstract:
The operation of wastewater treatment plants (WWTP) faces numerous challenges. These facilities must guarantee effluent quality requirements addressing also economic and environmental issues in the presence of variable influent conditions. This work presents a comprehensive analysis of the influence of climate and meteorological conditions into the eco-efficiency aspects of control/operational strategies applied in WWTPs. The main novelty of this work is the consideration of dynamic environmental performance in the assessment method, which allows to identify the impact on eco-efficiency of the eventual and seasonal variations of temperature and precipitations. Different operation scenarios, with different wastewater temperature profiles and precipitation levels are defined, and eco-efficiency is evaluated in terms of emissions to water and energy consumption. Annual and monthly performance indicators are computed to provide a general view of plant behaviour in the different conditions. The Benchmark Simulation Model (BSM2) has been selected as a reference WWTP model. The analysis is performed from a plant-wide perspective, since the effects on different units of the plant are considered. The analysis makes possible to identify the operational issues and control problems that should be tackled to address environmental impacts as eutrophication and global warming potential, resulting in an improvement of WWTP eco-efficiency.

Keywords:
Wastewater treatment plants, eco-efficiency, sustainability, process control.

1. Introduction

The operation of wastewater treatment plants (WWTP) faces numerous challenges. These facilities must guarantee the imposed effluent quality standards, while attempting to address economic issues and environmental impact of the operation. These three aspects: emissions to water, environmental impact and economics have to be considered in a sustainability framework. In this study a comprehensive analysis of the influence of climate and meteorological conditions into the eco-efficiency aspects of control/operational strategies is performed.

The attainment of eco-efficiency targets when running WWTPs is a complex task because it includes the evaluation of environmental and economic performance indicators which are usually in conflict [1-3]. Then, a holistic viewpoint is necessary [4, 5] in the search for sustainable solutions for WWTP operation. Several performance indicators and assessment criteria for the evaluation of the eco-efficiency of WWTPs are available in the literature [1-5]. Among the different environmental performance indicators, measurements and criteria of a standardized procedure as the Life Cycle Assessment (LCA) are particularly interesting [1].

The variability of the characteristics of the incoming wastewater is one of the main issues that affect the operation of WWTPs. The influent flowrate and pollutants load are affected by different factors such as population activities, precipitations, sewer management, and industrial discharges [6]. Furthermore, wastewater temperature, that depends on ambient temperature and hot water discharges, is a relevant parameter [7-9] with a significant influence on biological processes kinetics, oxygen transfer processes and heating requirements of some WWTP processes. Therefore, WWTP operation should be accommodated to deal with the eco-efficiency, depending on the influent characteristics, while maintaining quality/cost aspects.

This study aims to determine the influence of climatological and meteorological conditions on treatment effectiveness and energy consumption in a conventional WWTP. The analysis is performed from a plant-wide perspective, since the effects on different units of the plant are considered. Some typical performance indicators [5, 10-12] and complementary efficiency indexes are selected to evaluate the effect of precipitations and temperature variations on the throughput of the WWTP. Dynamic evaluation of WWTP of performance [13] considering monthly operational windows for different weather scenarios is proposed to observe the influence of different operating conditions (and therefore costs) on the eco-efficiency of the operation. The Benchmark Simulation Model (BSM2) [10-12] has been selected as a reference WWTP model to drive the

study. The main idea is to provide an assessment tool that facilitates the integration of meteorological insights in the formulation of the WWTP operation strategy.

The remainder of this paper is organized as follows. The BSM2 simulation platform, its control system and the eco-efficiency indicators are described in section 2. Section 3 introduces the methodology for the eco-efficiency assessment under different meteorological conditions. The results of the simulations of BSM2 plant under different meteorological conditions and the analysis of performance are presented in section 4. Conclusions are presented in section 4.

2. Process and control system

The BSM2 simulation platform is selected to describe the behaviour of a conventional WWTP with activated sludge biological treatment and anaerobic digestion. This is a widely recognized simulation platform designed as a benchmark to test control strategies applied to wastewater treatment facilities from a plantwide perspective [10-12]. The BSM2 version used in this work [12] represents only nitrogen removal processes. The phosphorous removal processes are not considered.

The influent data available in the BSM2 platform is obtained from influent generation models [6] that contemplates temperature, influent flow and pollutants concentration variations characteristic of a WWTP in the Northern Europe region. The analysis presented in this paper concentrates on the effect generated by temperature variations and precipitations.

2.1. Process description

The BSM2 plant model, the simulation platform and the evaluation protocol are described in [10-12]. BSM2 layout includes primary clarification and activated sludge process units in the water line, and anaerobic digestion, thickening, dewatering units and a storage tank in the sludge line (Fig.1). The influent model is described in [6], temperature variation is represented using a combination of sine functions that represents daily and seasonal variations, and load data represents influent flow and pollutants concentration variations associated with population activities, industrial activities, sewer effects and rain effects. Table 1 summarizes characteristic influent parameters.

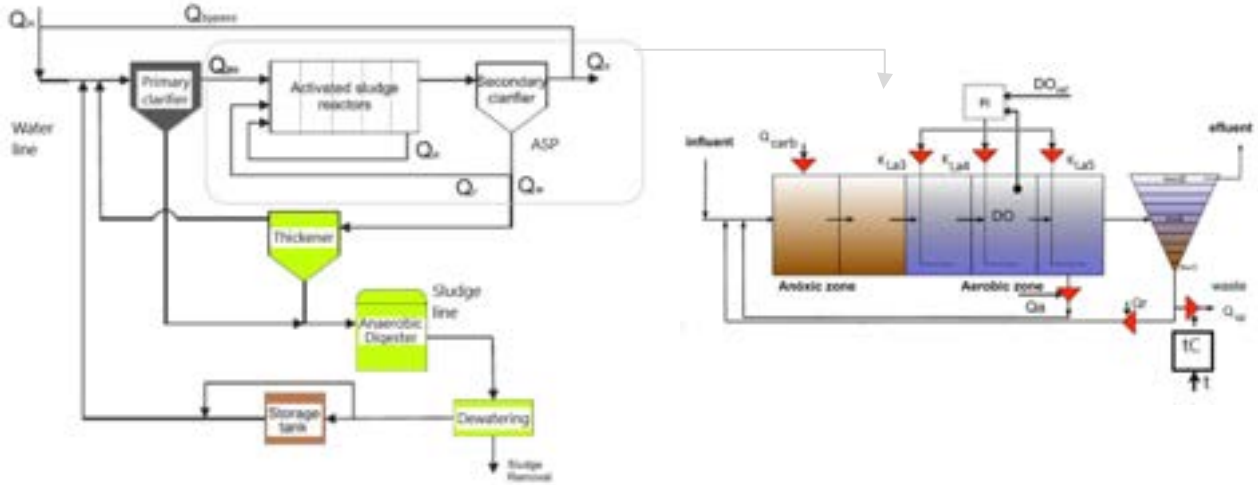

Figure. 1. BSM2 simulation platform layout and default control strategy

Table 1. Characteristic values of the significant variables of the influent profile

Variable	Average	Maximum	Minimum
T (ºC)	15	20.5	9.5
Q_{in} (m^3/d)	20648	85841	5146
N_{tot} influent (gN/m^3)	55.2	114.2	7.7
COD influent ($gCOD/m^3$)	592.2	1213.0	36.5

BSM2 activated sludge process (ASP) [10-12] is described here to facilitate comprehension of the paper. There are five bioreactors, denitrification process occurs first in two anoxic and perfectly mixed reactors. External carbon dosage (Q_{carb}) is required to keep denitrification, and internal recirculation (Q_a) is used to transfer nitrates from aerobic reactors. The 3rd to 5th reactors are aerobic to promote nitrification process. Oxygen is provided by an aeration system and the oxygen transfer is represented by oxygen transfer coefficients: KLa3, KLa4, Kla5 of each aerobic reactor. A settler separates the clean water (Q_e) that is discharged, and the sludge,

that is divided: wastage flow (Q_w) is fed to the sludge line thickener, and external recycle flow Q_r returns to the head of ASP.

The anaerobic digester produces biogas and stabilizes the sludge. An operation temperature of 35ºC is necessary, then BSM2 considers a micro gas turbine to produce the heat required by the digester [12] and immediate electricity. The energy content of biogas is estimated as 13.89kWh/kgCH_4, a biogas to electricity efficiency of 43% and a biogas to heat efficiency of 50% is considered in BSM2 performance evaluation.

2.2. Control strategy

The predetermined control strategy provided with the BSM2 platform [10-12] is employed for all the case studies presented in this paper. It consists on DO control in the 4th reactor and timer-based control of Q_w. In the aerobic reactors, the levels of dissolved oxygen (DO) should be between 1 to 2 gCOD/m^3 to promote nitrification. Then, BSM2 applies a control system for the regulation of DO in the 4th reactor manipulating the oxygen transfer coefficient of the fourth reactor (KLa4). A PID controller is implemented in the proposed control loop, the tuning parameters can be found in [13]. The coefficients KLa3 and KLa5 depends on KLa4, with proportional gains of 1 and 0.5, respectively. The DO concentration in the 3rd and 5th reactor is affected by control actions applied in the fourth reactor.

Sludge purge flow (Q_w) affects the sludge age or solids retention time (SRT). In the BSM2 platform a timer-based control of Q_w is applied. If the wastewater temperature is below 15ºC (colder season) wastage flow (Q_w) is set to 300 m^3/d, else Q_w is set to 450 m^3/d.

2.3. Eco-efficiency indicators

The eco-efficiency assessment of WWTPs includes the evaluation of environmental and economic performance indicators which are usually in conflict [1-3], then, the search for sustainable solutions for the operation of these facilities results in an interesting multi-objective problem. Several performance indicators and assessment criteria for the evaluation of the eco-efficiency of WWTPs are available in the literature [1-3]. The consideration of measurements and criteria of a standardized procedure as the Life Cycle Assessment (LCA) is recommended, especially, the metrics in the impact categories of Eutrophication Potential and Global Warming Potential [1] which are important issues for these facilities. The Eutrophication Potential is associated with the emissions to water, and Global Warming Potential is associated with the energy consumption and the corresponding indirect emissions to air in the energy sources.

BSM2 platform provides a systematic evaluation protocol of plant performance under the different control strategies tested in the plant. Relevant variables such as the load and concentration of pollutants in the influent and the effluent, production of biogas and sludge are computed for a given evaluation period, as well as indicators of the suitability of the WWTP operation, as influent and effluent quality, violations of the effluent requirements, energy consumption and operation costs.

In this work, some of the performance indicators proposed in BSM2 platform are used to evaluate the environmental performance of the WWTP. The selected indicators are focused on the level of pollutants in the influent and the effluent, the use of energy and production of biogas in the plant, and in the operation costs. A general description of the indicators is presented below, a detailed description including equations can be found in [5,12].

2.3.1. Environmental indicators associated with emissions to water

- Effluent Quality Index, EQI (kg/d): it is a measure of the total pollution load of the plant discharge for a given operation period (i.e.one year). It includes the following measurements of pollutants in the effluent: total Nitrogen (N_{tot}), ammonium (S_{NH}), nitrates (S_{NO}), total Chemical Oxygen Demand (COD), total Suspended Solids (TSS) and Biological Oxygen Demand (BOD5) [5, 12].
- Influent Quality Index, IQI (kg/d): it is a measure of the total pollution load of the influent for a given operation period (i.e.one year). It includes N_{tot}, S_{NH}, S_{NO}, COD, TSS and BOD5 load in the influent [5, 12].
- Violations of effluent requirements. Desirable limits of pollutants in the effluent (Total nitrogen, ammonium concentration, total Chemical Oxygen Demand (COD) and total suspended solids (TSS)) are given in BSM2 platform [1-3]: N_{tot} < 18 gN/m^3, S_{NH} < 4 gN/m^3, COD <100 gCOD/m^3, TSS<30 g/m^3.These values are in concordance with current effluent requirements in European countries. Deviation of the levels of pollutants in the effluent from desired limits are quantified in terms of number of events, extension of time of the infringements (absolute and relative), and magnitude of the violation [5, 12].

2.3.2. Environmental indicators associated with energy consumption

- Pumping energy, PE (kWh/d): it is computed considering the pumps available on each unit: the internal recycle flow Q_a, the external recirculation flow Q_r, the wastage flow Q_w, the primary clarifier bottom flow, the thickener feed flow and the dewatering unit bottom flow [5, 12].

- Aeration energy, AE (kWh/d): it depends on aeration system characteristics: type of diffuser, bubble size, depth of submersion. It is computed from oxygen transfer coefficient on each reactor and the volume of each reactor for Degrémont DP230 porous disks at an immersion depth of 4 m [5, 12].
- Mixing energy, ME (kWh/d): it is computed for activated sludge reactors if KLa<20 d^{-1} (ME_{AS}) and anaerobic digester (ME_{AD}), considering the volume of each reactor and digester volume, respectively [5, 12].
- Heating energy, HE (kWh/d) and heating energy net (HE_{net}): HE is the energy necessary to heat the sludge to the operation temperature required in the anaerobic digester, and HE_{net} is zero if methane produced in anaerobic digester (AD) covers its heating requirements, otherwise, HE_{net}=HE-7MET_{prod} [5, 12], it is computed considering that energy content of biogas is 13.89 kWh/kgCH_4 and biogas to heat efficiency is 50% [10]. MET_{prod} (kg/d) is the amount of biogas produced in AD.
- Electricity from biogas (EB, kWh/d): biogas is used in BSM2 to heat AD and to produce electricity simultaneously with an efficiency of 43%, then electricity from biogas is computed as 6MET_{prod} [10].

2.3.3. Economic indicators

- Operational Cost Index (OCI): it is defined in BSM2 as the net energy costs, the sludge production for disposal (SP) costs and external carbon addition (EC) costs [5, 12].

$$OCI=AE+PE+3SP+3EC-6MET_{prod}+HE_{net} \quad (1)$$

2.3.4. Efficiency indicators

Efficiency indices formulated as the ratio between interesting indicators are considered [10, 11].

The energy efficiency (EE), defined here as the ratio between pollution removed by BSM2 plant in kg and the energy consumed to achieve such objective (kWh):

$$EE=\frac{IQI-EQI}{Electricity}\ (kg/kWh) \quad (2)$$

This performance indicator has been used in previous works [4-5] however, interpretation of the evolution of the index should be cautious. Increments of the index are supposed to indicate efficiency improvement, but in some cases the index increases due to limitations of the control system that affect the energy use, then the index increases, but elimination of pollution is incomplete.

The treatment efficiency (TE) that is the ratio between the load of pollutants removed and the load of pollutants in the influent:

$$TE=\frac{IQI-EQI}{IQI} \quad (3)$$

The heating methane harnessing (HMH) that is the ratio between available heating energy from methane 7MET_{prod} and anaerobic digester heating requirements:

$$HMH=\frac{7MET_{prod}}{HE} \quad (4)$$

The electrical methane harnessing that is the ratio between the electrical energy obtained from methane and the electricity requirements of ASP (E_{ASP}):

$$E_{ASP}=PE+AE+ME_{AS}\ (kW) \quad (5)$$

$$EMH=\frac{6MET_{prod}}{E_{ASP}} \quad (6)$$

3. Description of eco-efficiency assessment procedure under different meteorological conditions

Four scenarios characterised by different influent conditions have been defined to evaluate the influence of climate and meteorological conditions on treatment effectiveness and energy consumption in BSM2 plant. Then, fifth case studies are considered including the default BSM2 scenario. The predeterminate BSM2 control strategy described in section 2.2 is applied in all cases.

- Scenario 1. Default. The BSM2 influent characteristics as described in table 1.
- Scenario 2. Wider temperature profile variation (W. T.). Mean temperature: 15ºC, minimum temperature: 5ºC and maximum temperature: 25ºC.
- Scenario 3. Higher temperature profile (H.T.). Mean temperature: 19ºC, minimum temperature: 10ºC and maximum temperature: 27ºC.

- Scenario 4. Rainy year (R.Y.). The BSM2 influent data is modified copying and inserting data corresponding to rain events in the dry periods of the default influent profile.
- Scenario 5. Dry year (D.Y.). The BSM2 influent data is modified copying and inserting data corresponding to dry periods events in the rainy periods of the default influent profile.

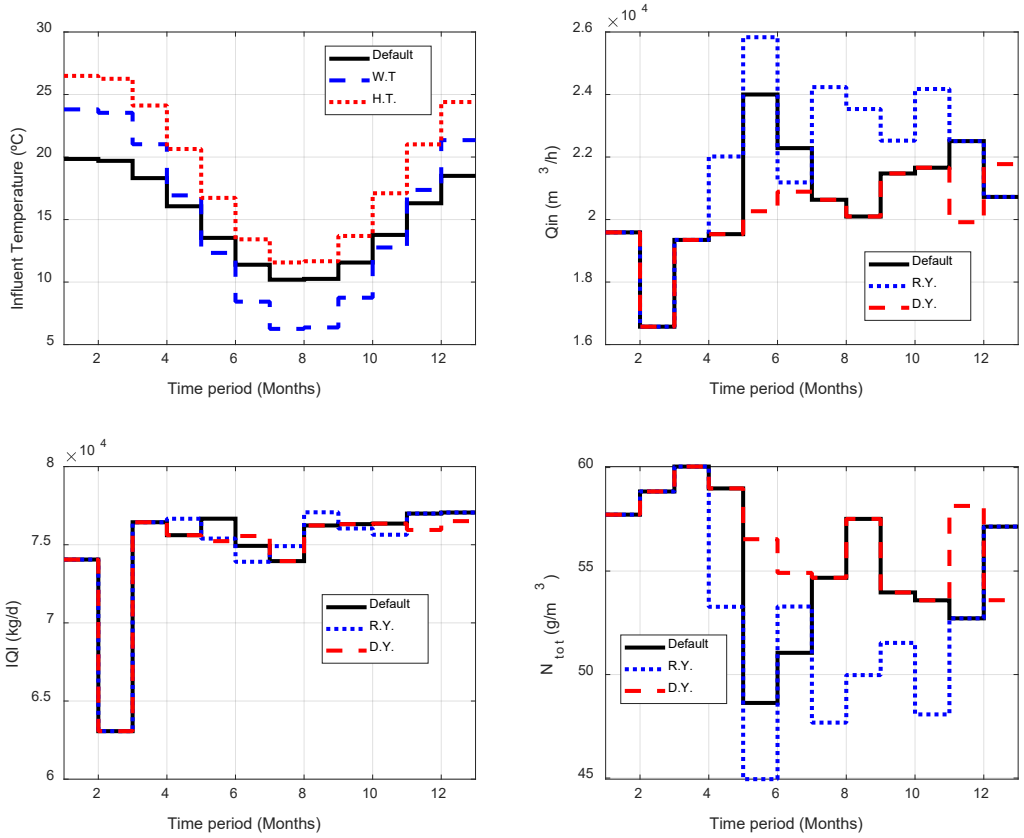

Figure. 2. Temperature and influent flow influent profiles for the different scenarios proposed to study the impact of meteorological conditions on WWTP performance.

An evaluation period of one year is recommended in the BSM2 protocol, the evaluation period starts the 1rst of July. A sample time of 15min is set in BSM2 platform, however monthly temporal windows are used here, to show the evolution of relevant variables. The monthly average profile of influent temperature and flowrate, Influent Quality (IQI) and total Nitrogen (N_{tot}) for the different scenarios is presented in Fig. 2.

The use of monthly windows facilitates the observation of seasonal changes of climate and meteorological conditions. In figure 2, in the representation of influent temperature, it is observed a step descend of temperature from summer season (1rst of July in the northern hemisphere) to winter (months 6 to 9) and the return to warmer periods at the end of the year. This trend is maintained in W.T. and H.T. scenarios within their corresponding range of variation. Regarding the influent flow, the first two months (July and August) are equal in all scenarios (dry weather and reduced influent flow due to holiday period), but average influent flow increases for precipitations, almost in all months in the R.Y. scenario, and decreases in winter and the beginning of summer in the D.Y. scenario. Precipitations affect the load of pollutants in the effluent as observed in IQI and N_{tot} profiles, N_{tot} concentration diminish in the rainy periods. Temperature variations do not affect influent pollutants concentration in BSM2 model.

4. Results

Simulations of plant behaviour, using the default BSM2 influent profile and the data adjusted according to the four scenarios describing temperature and precipitation changes, have been executed. Annual average performance and dynamic performance is evaluated and compared for the different scenarios. Control system performance is examined in the case that exhibits the worst behaviour associated with temperature and precipitations changes, to determine the possible drawbacks of the control system in these situations and to contemplate possible solutions.

4.1. Performance analysis in the different climate and meteorological scenarios

The annual average values of some performance indicators were computed to evaluate the overall performance in one year of operation. On the other hand, the dynamic evolution of relevant variables along

the year is represented using monthly average values. Dynamic analysis makes possible to observe the seasonal effects of the influent variations in the operation period.

4.1.1. Comparison of the annual average performance

The annual average values of selected indicators of performance are presented in table 2. IQI is used as indicator of the load of pollutants in the influent to be removed. Environmental indicators associated with emissions to water are EQI, N_{tot} and S_{NH} violations and TE. S_{NH} violations are measured as the period of time out the desired limits. Energy consumption is measured with indicators of electricity use in ASP (E_{ASP}) and heating energy of AD (HE), and the ratios: EE, HMH and EMH, that measure of the amount of electricity used for removing pollution, and the usefulness of biogas to produce the heat and electricity required for the plant operation. Evaluation of emissions to water and energy consumption are associated with the eutrophication potential and global warming potential, that are environmental impacts in the recognized Life Cycle Assessment. OCI indicates the overall operation costs.

According to annual average values presented in Table 1, in H.T. scenario the operation at higher temperatures is favourable for environmental performance. Heating efficiency (HMH, HE) improves because the difference between the operation temperature of AD (35ºC) and the temperature of the sludge decreases. Electrical efficiency increases (EE), but consumption of electricity in ASP (E_{ASP}) is the highest compared with the other evaluated scenarios. Then, the EE index increases due to the improvement of pollutants removal.

On the other hand, W.T scenario exhibits the minimum consumption of electricity (E_{ASP}) but the worst electrical efficiency (EE), which indicates a lower removal of pollutants. This is corroborated by environmental indicators with extremely long violation periods of S_{NH} and N_{tot} limits. This W.T. scenario exhibits the minimum OCI among the different cases studies, probably because it presents the minimum consumption of electricity (E_{ASP}). Then, the conditions that provoke the minimum operations costs, produce the poorer environmental performance.

In the case of the Rainy Year scenario (R.Y.), the indicators of violations of the S_{NH} and N_{tot} requirements in the effluent are acceptable, but it exhibits the worst EQI values, with an increment of 7.3% with respect to the Default scenario. The temperature profile is equal for the Rainy and the Default scenarios, but a lower heating efficiency (HE) is observed in the former, indicating that the Rainy influent profile produces changes in the load of the anaerobic digester that increases the energy demand.

Table 2. Annual average values of selected performance indicators

	Default	W.T	H.T.	R.Y	D.Y.
IQI (kg/d)	74783	74783	74783	74747	74584
EQI (kg/d)	5576.7	5809.1	5218.2	5984.0	5375.0
OCI (EUR/d)	9450.0	9368.4	9650.3	9462.7	9437.2
Electricity ($E_{ASP,}$ kWh/d)	5017.1	4941.0	5126.3	5012.3	5009.2
Heating energy (HE, kWh/d)	4225.3	4260.7	3357.2	4437.4	4130.6
N_{tot} violation (time d)	4.28	7.48	1.19	5.56	4.23
S_{NH} violation (time d)	1.49	19.20	0.51	4.17	0.98
Treatment Efficiency (TE)	0.93	0.92	0.93	0.92	0.93
Electrical Efficiency (EE)	12.72	12.86	12.54	12.65	12.74
Heat from methane/HE (HMH)	1.80	1.79	2.17	1.69	1.84
Electricity from methane/ E_{ASP} (EMH)	0.24	0.24	0.28	0.22	0.25

4.1.2. Comparison of the dynamic performance of BSM2 in the proposed scenarios

The evolution of environmental indicators: Effluent Quality, N_{tot} concentration, S_{NH} concentration and Treatment Efficiency (TE) is presented in Fig. 3. In the figure, it is noticed a superior performance of the WWTP in the W.T. scenario compared with Default scenario in the warmer months (months: 1-4, 10-12). In the colder months (5-9), temperature of W.T scenario ranges between 13-6ºC (Fig. 2), while the minimum temperature of Default and H.T scenarios is 10ºC. In this colder period of operation, EQI, N_{tot} and S_{NH} for the W.T scenario experiment a significant increase with respect to H.T and Default conditions. Moreover, the treatment efficiency (TE) representation shows how pollutants removal efficacy decreases in the colder period in all the cases studied, but the reduction in the W.T. scenario is significant due to the lower temperatures. This behaviour cannot be appreciated in an analysis based on annual average indicators.

Regarding energy consumption and methane exploitation, Fig. 4 shows the dynamic evolution of the corresponding indicators. Electricity consumption in the ASP presents an important reduction in the colder month for the W.T. scenario, that is reflected as an increment of the EE and EMH ratios. In this case, larger values of these indicators could be interpreted as an improvement in the electrical efficiency of the plant, however, the observation of the environmental metrics leads to detect an operation problem in the colder period of W.T scenario. The HMH ratio, in the fourth subplot, is related with the use of methane to cover heating

requirements of digester; it varies between scenarios in the periods of higher temperature, but attain similar values in the colder periods.

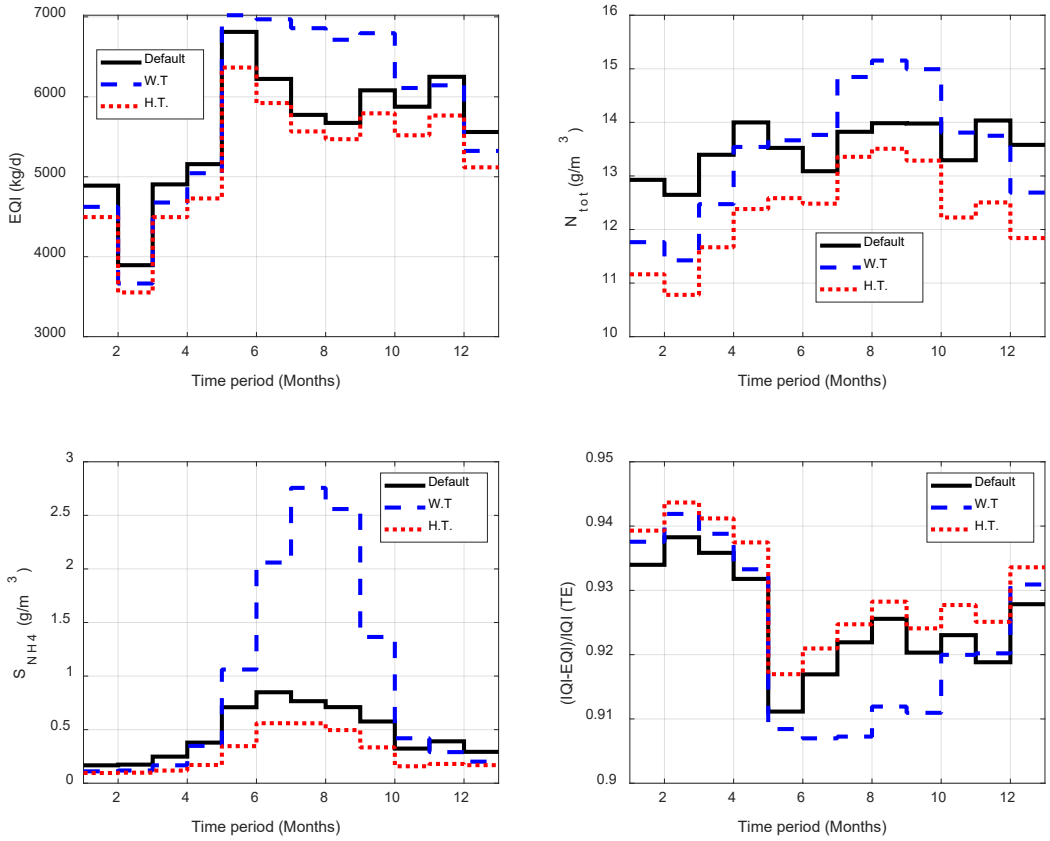

Figure. 3. Comparison of the effluent quality indicators for the operation scenarios focused on temperature variation (W.T., H.T.).

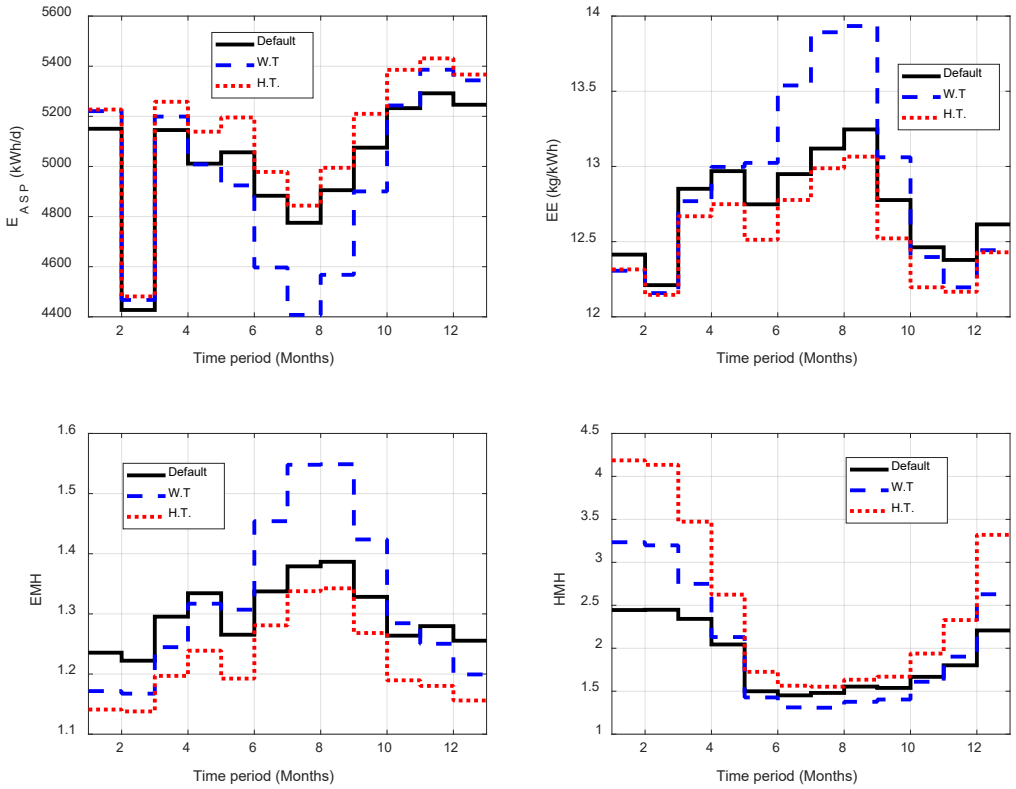

Figure. 4. Comparison of the energy efficiency indicators for the operation scenarios focused on temperature variation (W.T., H.T).

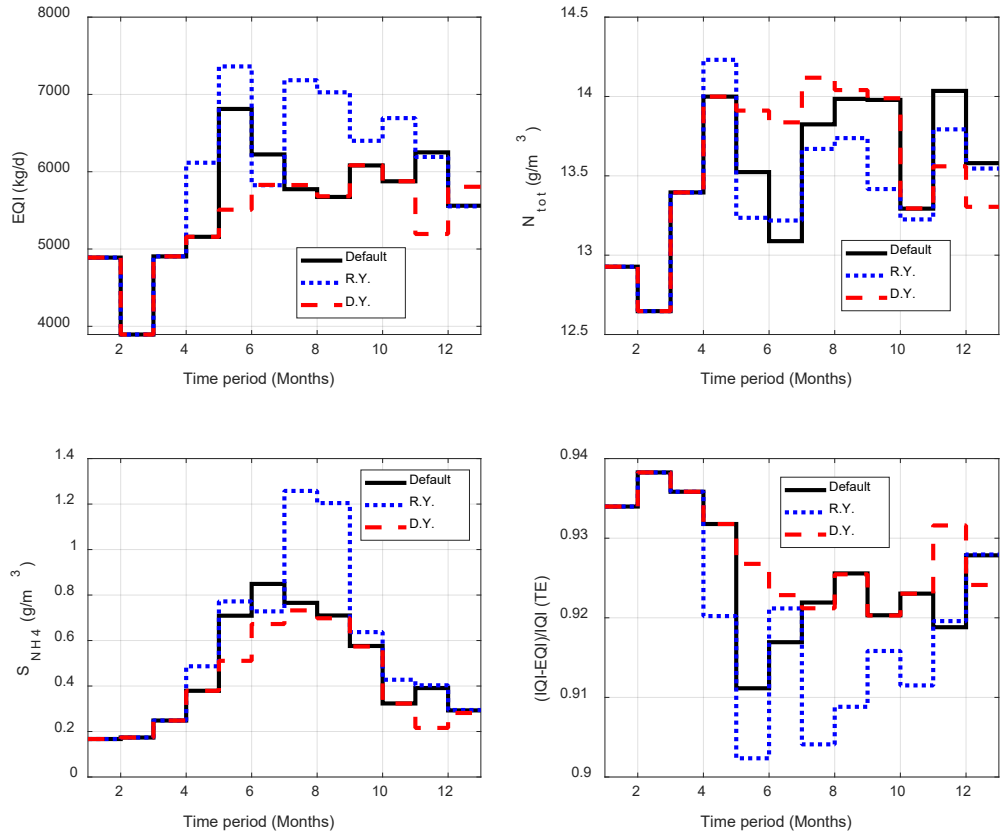

Figure. 5. Comparison of the effluent quality indicators for the operation scenarios focused on variation of precipitations (R.Y., D.Y.)

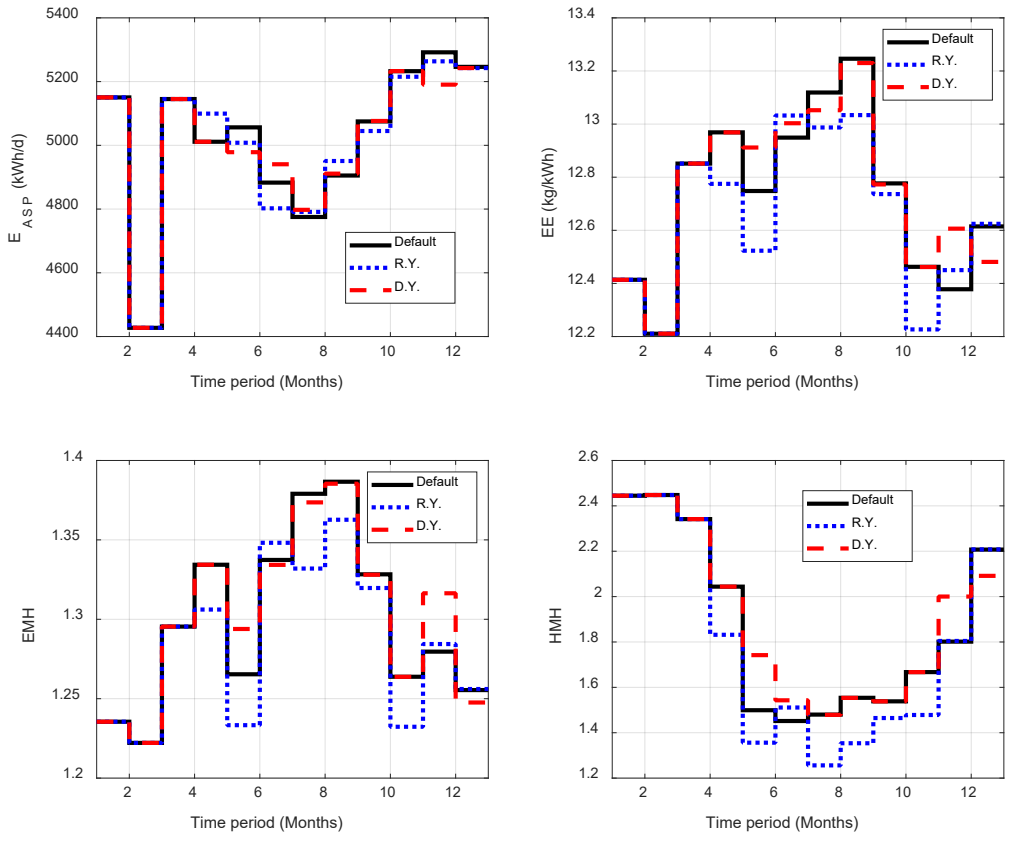

Figure. 6. Comparison of the energy efficiency indicators for the operation scenarios focused on variation of precipitations (R.Y., D.Y.).

Figure 5 shows the comparison of the environmental performance indicators for the Default, Rainy Year (R.Y) and Dry Year (D.Y.) scenarios. It is observed that continuous precipitations affect negatively the indicators of effluent quality, specially S_{NH} concentration and the Treatment Efficiency (TE), although total nitrogen (N_{tot}) is slightly improved. The dynamic evolution of the energy consumption indicators is presented in Fig. 6. Electricity consumption is similar for the three scenarios and the effect of precipitations on the efficiency indicators is not clear. The effect of precipitations requires a detailed analysis considering separately the effect of precipitations and the effect of human activities. In this study both effects are combined in the R.Y. and D.Y. scenarios.

4.2. Comparison of control system performance in the W.T. and Default scenario.

Dynamic control system performance is studied to find the issues behind the atypical behaviour observed for the operation in the W.T. scenario in the colder periods. Figure 5 and Fig.6 shows the control variables: KLa4, SO_4, SO_3 and SO_5 in the Default and W.T. scenarios, respectively.

In both scenarios, good tracking of SO_4 reference is achieved with reasonable movements of the manipulated variable Kla4, there are no saturations nor instabilities. It is noticed that average KLa4 decreases between the days 275-300, that correspond with the second month (August), that is the period with the lower load (see Fig.2). In the colder months (days: 400-500d, months 6-9), a slight reduction of KLa4 is observed in the Default scenario, that is significant in the W. T. scenario (blue lines). This behavior explain the reduction of the energy consumption in the W.T. scenario. Furthermore, controlled SO_4 is not affected by KLa4 reduction in the colder days, and good reference tracking is maintained, but SO_3 and SO_5 concentrations are affected.SO_3 increases and SO_5 decreases in the colder period. This effect is amplified in the W.T: scenario, with SO_5 concentration approaching to the minimum allowed DO levels (see Fig. 6) This situation possibly produces the poor environmental performance in the W.T. scenario that reaches the lower temperatures.

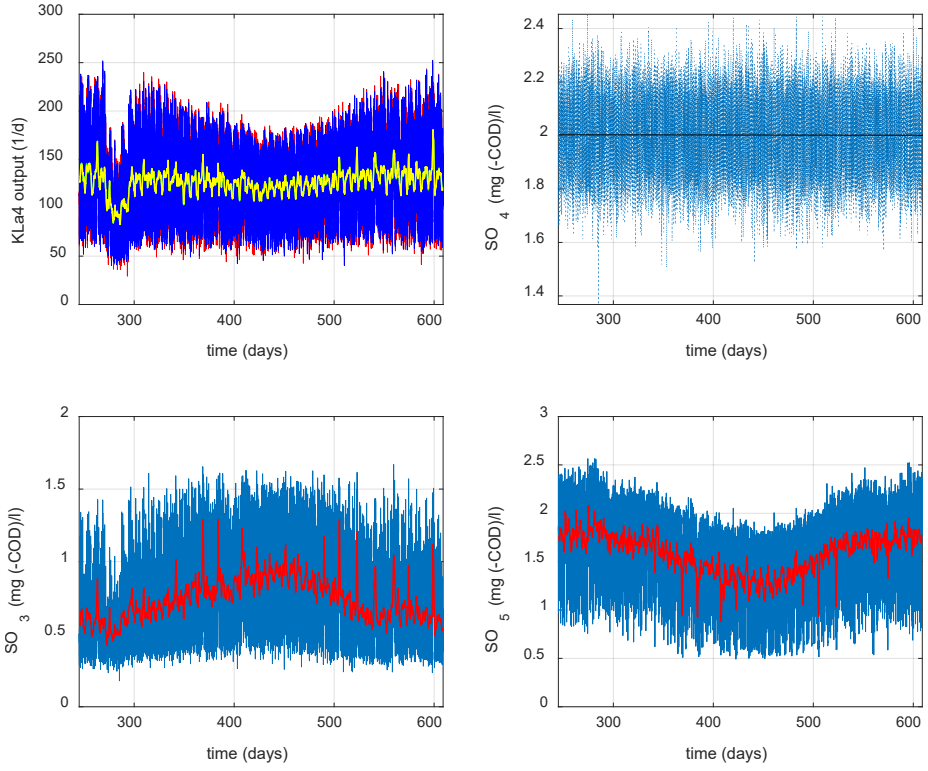

Figure. 5. Dynamic response of the plant in the default operation scenario. (SO_4 set-point: 2mgCOD/l. Yellow and red lines: filtered signals. Blue lines: samples obtained each 15min)

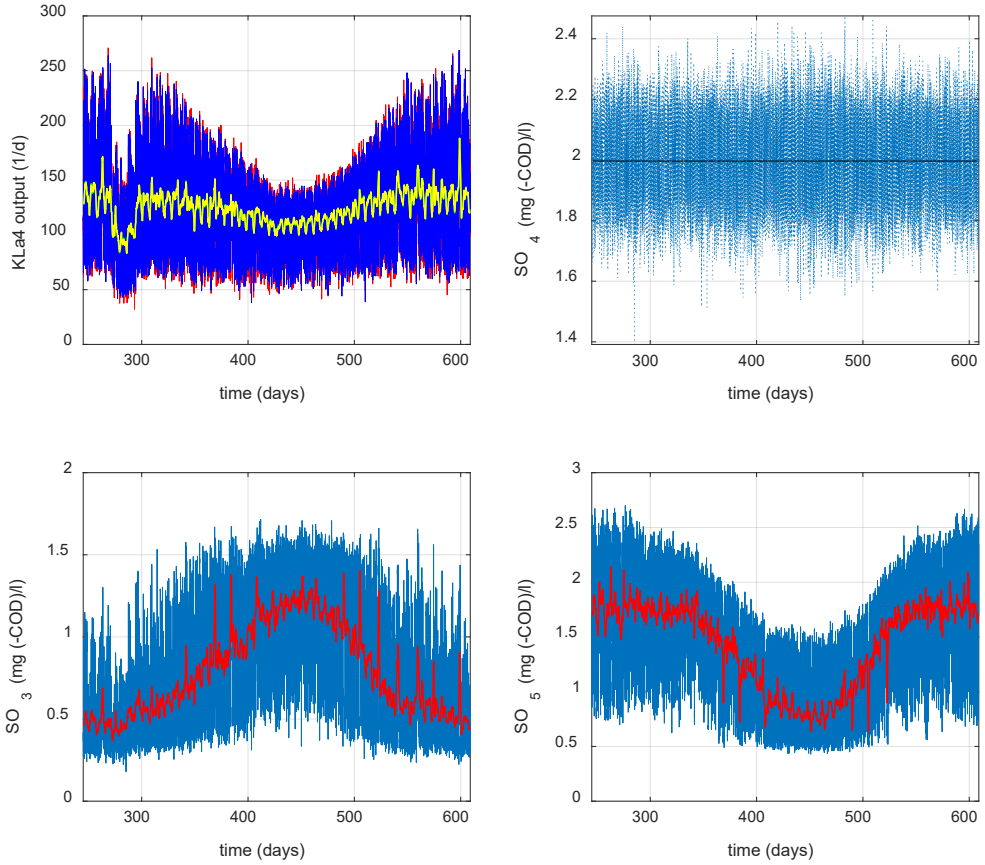

Figure. 6. Dynamic response of the plant in the W.T scenario (Wider temperature variation with respect to default scenario). (SO4 set-point: 2mgCOD/l. Yellow and red lines: filtered signals. Blue lines: samples obtained each 15min)

5. Conclusions

The evaluation of plant behaviour under different climate and meteorological scenarios has been carried out portraying annual performance, computing annual average eco-efficiency indicators, and dynamic performance, considering monthly operation windows. The analysis was performed from a plant-wide perspective, since the effects on different units of the plant were considered. The effect of weather conditions on environmental performance, in terms of emissions to water and energy consumption, an energy consumption was evaluated with appropriated indicators. The analysis showed that temperature variations affect significantly the environmental performance of the plant. Operational issues and control problems were detected in the periods of lower temperatures, that affect energy consumption. On the other hand, an influence of precipitations on indicators of emissions to water and energy consumption is observed, but deeper study of influent variations of concentration and influent flowrate is necessary. These problems should be tackled to address environmental impacts as eutrophication and global warming potential, save energy and reduce operation costs to make WWTP operation more eco-efficiency.

Acknowledgments

The authors wish to thank the support of the Spanish Government through the coordinate MICINN projects PID2019-105434RB-C31 and PID2019-105434RB-C33, project TED2021-129201B-I00, the Samuel Solórzano Foundation through project FS/11-2021 and the support from the Catalan Government under Project 2021 SGR 00197. The authors acknowledge the WWTP of Salamanca (Aqualia) for allowing our research group visiting the plant and the IWA Task Group from the Department of Industrial Electrical Engineering and Automation (IEA), Lund University, Sweden (Ulf Jeppsson, Christian Rosen) for the BSM2 models.

Nomenclature

Temperature (ºC)	T	Activated Sludge Process	ASP
Influent flow (m^3/d)	Q_{in}	Anaerobic Digestion	AD
Total nitrogen (gN/m^3 o mgN/l)	N_{tot}	Wider Temperature	W.T.
Chemical oxygen demand ($gCOD/m^3$)	COD	Higher Temperature	H.T.
Influent Quality Index (kg/d)	IQI	Rainy year	R.Y.
Effluent Quality Index (kg/d)	EQI	Dry year	D.Y.
Operational Cost Index (EUR/d)	OCI	Oxygen Transfer Coefficient for i reactor	KLai
Electrical Efficiency (kg/kWh)	EE	Oxygen concentration reactor i	SO_i
Heat from methane (kWh/d)	HE	Dissolved Oxygen	DO
Treatment Efficiency (Dimensionless)	TE	Total Suspended Solids	TSS
Electricity from methane (Dimensionless)	EMH	Aeration Energy	AE
Heat from methane (Dimensionless)	HMH	Mixing Energy	ME
Electricity consumption in ASP (kWh/d)	E_{ASP}	Pumping Energy	PE

References

[1] Lorenzo Toja, Y.; Vázquez-Rowe, I.; Amores, M.; Termes-Rife, M.; Marín-Navarro, D.; Moreira, M.; Gumersindo, F. Benchmarking wastewater treatment plants under an eco-efficiency perspective. *Science of The Total Environment* **2016**, 566-567. 10.1016/j.scitotenv.2016.05.110.

[2] Molinos-Senante, M., Gémar, G., Gómez, T., Caballero, R., Sala-Garrido, R. Ecoefficiency assessment of wastewater treatment plants using a weighted Russell directional distance model. *J. Clean. Production **2016***. 137, 1066e1075. https://doi.org/ 10.1016/j.jclepro.2016.07.057

[3] Balkema, A. J.; Preisig, H. A.; Otterpohl, R.; Lambert, F. Indicators for the sustainability assessment of wastewater treatment systems. *Urban Water* **2002**; 4(2), 153–61.

[4] Revollar, S.; Vilanova, R.; Vega, P.; Francisco, M.; Meneses, M. (2020). Wastewater Treatment Plant Operation: Simple Control Schemes with a Holistic Perspective. *Sustainability*, *12*, 768.

[5] Revollar, S.; Meneses, M.; Vilanova, R.; Vega, P.; Francisco, M. Eco-Efficiency Assessment of control Actions in Wastewater Treatment Plants. Water **2021**, *13*, 612.

[6] Gernaey, K.V. ; Rosén, Christian ; Jeppsson, Ulf. / BSM2: A Model for Dynamic Influent Data Generation. Lund University, 2005. 73

[7] Alisawi, H.A. Performance of wastewater treatment during variable temperature. Applied Water Science. 2020. 10:89.

[8] Kruglova, A.; Kesulahti, J.; Minh Le, K.; Gonzalez-Martinez, A.; Mikola, A.; Vahala, R. Low-Temperature Adapted Nitrifying Microbial Communities of Finnish Wastewater Treatment Systems. *Water* **2020**, *12*, 2450

[9] Hülsen, T; Barry, E.; Lu, Y; l Puyol, D; Batstone, D. Low temperature treatment of domestic wastewater by purple phototrophic bacteria: Performance, activity, and community. Water Research, 2016, 100, 537-545.

[10] Gernaey, K., Jeppsson, U., Vanrolleghem, P., Copp, J., Steyer, J. Benchmarking of control strategies for wastewater treatment plants., IWA Publishing, Colchester, UK, **2010**.

[11] Alex, J.; Benedetti, L.; Copp, J.; Gernaey, K.; Jeppsson, U.; Nopens, I.; Pons, M.; Rosen, C.; Steyer, J.; Vanrolleghem, P.A. Benchmark Simulation Model No. 2 (BSM2), Technical report No 3. IWA Taskgroup on Benchmarking of Control Strategies for WWTPs. **2018**

[12] Jeppsson, U., M. N. Pons, I. Nopens, J. Alex, J. B. Copp, K. V. Gernaey, C. Rosen, J. P. Steyer, and P. Vanrolleghem. Benchmark simulation model no 2: general protocol and exploratory case studies. Water Science and Technology, 2007. 56, p. 67-78.

[13] Revollar, S.; Meneses, M.; Vilanova, R.; Vega, P.; Francisco, M. Quantifying the Benefit of a Dynamic Performance Assessment of WWTP. *Processes* **2020**, *8*, 206.

Oil tanker speed optimization based on grey-box fuel consumption prediction model

Xianwei Xie[a], Xiaohe Li[b,c], Baozhi Sun[a] and Fredrik Ahlgren[d]

[a] *College of Power and Energy Engineering, Harbin Engineering University, Harbin 150001, Heilongjiang, China,* xiexianwei163@163.com (X.Xie), sunbaozhi@163.com (B. Sun, CA),

[b] China Ship Scientific Research Center, Wuxi, 214082, China, lxhcsmx@163.com,

[c] Taihu Laboratory of Deepsea Technological Science, Wuxi, 214082, China,

[d] Department of Computer Science and Media Technology, Linnaeus University, Kalmar, 39354, Sweden, fredrik.ahlgren@lnu.se

Abstract:

An accurate ship fuel consumption prediction model is the basis for ship energy analysis. Based on an established ship fuel consumption prediction model with input navigational features. We use the Gurobi solver to optimize the ship's speed to minimize fuel consumption on a given route. In addition, We compare the changes in the fuel-saving rate before and after applying the smoothing method and discuss the pros and cons. Compared with the historical average speed, the speed optimization can save 7.9% and 3.2% of fuel consumption before and after smoothing, respectively. Proved by experiments that ship speed optimization considering the influence of weather conditions can significantly reduce ship fuel consumption and provide decision support for shipping companies' operations.

Keywords:

Machine learning; Grey-box model; Ship fuel consumption prediction; Ship speed optimization; Data smoothing.

1. Introduction

In recent years, with the gradual warming of the global climate, the international community has paid more attention to the issue of greenhouse gas emissions. According to the Fourth International Maritime Organization (IMO) Greenhouse Gas (GHG) Study, the carbon intensity (i.e., CO_2 emissions per unit of Gross Domestic Product(GDP)) of international shipping decreased by about 11% between 2012 and 2018. Still, annual greenhouse gas emissions increased from 977 million tons to 1,076 million tons ([1], [2]). The emission of GHG is closely related to the fuel consumption of ships. As the carrier of waterway transportation, ships consume massive amounts of energy every year, producing a large amount of GHG. The IMO has already set strict limits on air pollutants to reduce GHG emissions from the shipping industry. At the same time, shipping companies are paying more attention than ever to the energy efficiency of their ships as fuel costs become an increasing proportion of their operating costs. Improving ship energy efficiency and reducing fuel consumption and GHG emissions through various energy efficiency optimization measures are essential for shipping companies to reduce ship operating costs and improve their competitiveness. Therefore, these resources need to be managed and utilized more effectively.

With the continuous development of ship intelligence and digitization, as well as the continuous improvement of machine learning, data mining, and other methods, through the intelligent and diversified monitoring of various parameters and indicators generated during the ship's navigation, as well as the weather, sea conditions and other information encountered and analysis, the decision support system can make more realistic suggestions for different situations in the course of the ship's navigation. Using data analysis to study ship fuel consumption has become a research hotspot. It is applied to analyze the massive data generated during ship navigation as a fuel consumption optimization analysis and decision support system [3].

The rest of the paper is organized as follows. Section 2 is an introduction to published articles in related fields. Section 3 is the data pre-processing and a short introduction to the proposed model, which we have covered in detail in another paper. Section 4 developed the function model of speed optimization and the introduction of Gurobi. Section 5 introduces the solution results of Gurobi before and after data smoothing using the EWMA. Finally, conclusions are drawn in Section 6.

2. Related work

Many researchers have devoted themselves to optimizing the navigation process of ships through mathematical formulas and calculation methods of ship energy consumption terms of ship energy consumption. Zaccone [4] proposed a three-dimensional dynamic planning-based ship navigation optimization method, which takes the minimum fuel consumption as the goal and selects the best route and speed for the ship's navigation according to the weather forecast map. The results show that the fuel-saving effect is very significant. Still, the percentage of fuel-saving and the influence of related parameters (trim, draft, etc.) on fuel consumption have yet to be reported. The mathematical model, the white-box model, derives the fuel consumption by calculating the resistance in different wind and wave conditions. Because of the derivation and superposition of the formula, the error will be magnified, and detailed hull parameters are required, which requires high accuracy.

Statistical data analysis is a prevalent and widely accepted method in optimizing ship energy consumption. It is necessary to study the data generated by ships in different states during operation through additional classification and clustering methods. Perera [5] analyzed different trim values of engine fuel consumption rates based on statistical data analysis and achieved optimal sailing conditions by identifying different draft values. In addition, he proposed a data processing framework, including data pre-processing with the data-driven model, sensor, and fault identification and post-processing. This data processing framework laid a foundation for the ship's data analysis platform [6].

Data analysis methods extract hidden information and knowledge by analysing various datasets to help explain information and make decisions [7]. Lu [8] discussed voyage optimization, which involved selecting the best route for a ship's voyage to increase energy efficiency and reduce greenhouse gas emissions, and proposes a semi-empirical ship operational performance prediction model that can accurately predict a ship's performance under different conditions. Venturini [9] proposed a mathematical model to solve the Berth Allocation Problem (BAP) in the container shipping industry, which extends to cover multiple ports in a shipping network, optimizes speed on all sailing legs, and reduces the total time of operation and fuel consumption, and emissions. Compared with the ship fuel consumption prediction model based on ship propulsion principles and mathematical formulas (white-box model) ([10]), the model based on the machine learning method (black-box model) ([11]) usually has higher prediction accuracy and can relatively accurately capture the impact of various weather/sea conditions and other external factors on the ship fuel consumption. Jeon [12] proposed a big data analysis approach for smart ships, using artificial neural network (ANN) to accurately predict the fuel consumption of main engines, after testing various hidden layers, neurons, and activation functions, which outperforms polynomial regression and support vector machine methods. Kee [13] proposes the multiple linear regression (MLR) methods to construct fuel efficiency profiles for working tugboats and the development of a Fuel Consumption Analysis System for real-time fuel consumption monitoring and operation at optimal fuel efficiency, demonstrating up to 37.1% fuel savings in real operational data. Omer [14] proposed a tree-based modeling approach using high-dimensional data to monitor ship performance under operational conditions. This model uses publicly accessible data, and the results show that the proposed model outperforms other methods, such as ANN and GP, in ship performance monitoring. The findings contribute to ship management companies in monitoring ship operational performance. The high accuracy of the black-box model has laid a solid foundation for multiple measures of ship energy efficiency optimization.

The inexplicability inside the black box model has caused many researchers to have concerns. However, its high accuracy and simple method for ship fuel consumption prediction provide a good example and research prospect for ship energy consumption analysis. Bialystocki and Konovessis [15] calibrated ship fuel consumption-speed curves by polynomial regression method based on 418-noon report data of transport ships, thus obtaining a set of ship fuel consumption-speed curves that can be used under most weather conditions and loading conditions. Yan [16]used the Hadoop framework and the MapReduce method based on the ship sensor data and realized the fine segmentation of the ship route. They optimized the engine speed of inland ships by obtaining the optimal segment set by the particle swarm optimization algorithm. Du [17] built an Artificial Neural Network (ANN) model to predict the ship fuel consumption by using the noon report data of ships and then optimized the speed and trim of ships during navigation by two-stage optimization method of shore-based and offshore. Because of the high nonlinearity of the ANN model, they proposed a dynamic programming algorithm to solve the objective function of the optimization problem. Their results show that optimizing speed and trim can reduce ships' fuel consumption by 2% - 7% in actual navigation. Yan [18] proposed a Random Forest model for fuel consumption prediction of dry bulk carriers based on 242 noon-report data. The Mean Absolute Percentage Error (MAPE) reached 7.91% in the model evaluation results. They used a linear programming solver to solve the speed optimization problem and the Savitzky Golay filtering method (SG) [19] to smooth the predicted fuel consumption and make the optimization result more reliable. Their results show that fuel consumption can be saved by 6.53% after speed optimization.

Through the above literature analysis, most researchers use the noon report data as the modeling dataset for the fuel consumption prediction model. In contrast, the sensor data is collected within a few seconds or minutes and can reflect the changes in fuel consumption during the ship's voyage than the noon report data collected by days and have a better modeling effect. Although there are studies using sensor data to build ship fuel consumption prediction models in speed optimization, their research objects are inland ships. Compared with inland ships, ocean-going ships have numbers and substantial power, and they have significant potential for energy conservation and emission reduction. Given the above reasons, We have established a gray-box model with meteorological conditions as input, combining the black-box model (XGBoost) with the Kwon formula in the white-box model. On this basis, we simulated the actual meteorological conditions (wind and waves) and the external parameters of the ship (trim, bow, stern draft, etc.). We applied the Gurobi solver to optimize the speed of a voyage with an ocean-going carrier as the research target. The Exponential Weighted Moving Average (EWMA) method is proposed for the prediction model to smooth the prediction results.

3 Data pre-processing and proposed model

Data pre-processing has a crucial impact on the establishment of models. This section briefly introduces a data pre-processing method and machine learning model proposed in previous work [27].

3.1 Data description and pre-processing

In this study, we analyzed a sailing test case from an oil tanker consisting of 496 data features, but due to sensor failure, some of the collected data had fault signals. We kept the remaining 378,468 (4.38 days) data records collected at one-second intervals. Raw data often contain noise that can negatively impact the model's generalization ability by causing over-fitting or leading to misleading decisions [20]. Hence, data pre-processing plays a vital role in improving the generalization performance of a supervised machine-learning algorithm [21].

This dataset includes alarm signal detection points, temperature, pressure, flow, and other signals, collected during a sailing test case from an oil tanker. Fuel consumption optimization is of utmost importance to shipping companies since it directly impacts the navigation economy, surpassing rpm and power. Therefore, the study aims to filter the data and select relevant features for modelings, such as speed, engine power, trim, and draft. The chosen parameters' influence on fuel consumption must be considered. The correlation between engine power and fuel consumption already thinks the impact of ship speed and other features. The modeling features include speed, fuel consumption rate (FCR), trim, fore and aft draft, and external features such as wind and waves. As the sensor dataset lacks wave and current features, wave data (wave high and wave direction) was obtained from ECMWF and matched into the sensor data using geographical location (latitude and longitude) and collection time. To consider the relative relationship between absolute wind direction and ship heading, the angle between the absolute-wind direction and heading was calculated as the relative wind direction. The wind from the port side and starboard side has an identical impact, so the relative wind direction was converted from 0° ~ 360° to 0° ~ 180°, with 0° meaning the wind is from the bow and 180° from the stern.

After extracting the above data features from the sensor dataset, the following data pre-processing is carried out: the data of FCR, wind speed, and wind direction less than 0 are removed; the data of speed beyond the range of 10~16.8 knots are removed. The dataset includes nine features: ship speed (V), fore draft (D_f), aft draft (D_a), trim (T), wave high ($Wave_h$), wave direction ($Wave_d$), absolute wind speed ($Wind_s$), wind direction ($Wind_d$) and FCR, 147845 rows after these steps. The data distribution of ship speed and fuel consumption is shown in Figure. 1. The data statistics are shown in Table 1.

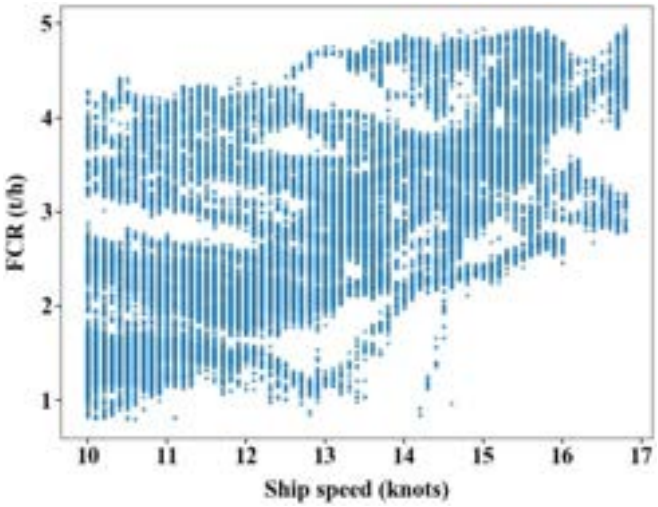

Figure. 1. Speed - fuel consumption data distribution after preliminary data pre-processing.

Table 1. Statistical of the modeling input features.

	V (knots)	$Wind_s$ (knots)	$Wind_d$ (°)	D_a (m)	D_f (m)	T (m)	$Wave_h$ (m)	$Wave_d$ (°)	FCR (tons/h)
Count	147845	147845	147845	147845	147845	147845	147845	147845	147845
Mean	13.14	9.42	84.49	18.80	17.23	1.57	0.37	192.57	2.78
Std	1.92	5.23	44.46	2.92	4.22	1,44	0.25	30.53	0.97
Min	10.00	0.00	0.00	11.83	7.17	-0.64	0.12	133.20	0.81
25%	11.5	5.40	54.70	19.11	16.30	0.65	0.17	200.02	2.03
50%	13.20	8.60	79.50	20.30	19.46	0.91	0.24	204.49	2.77
75%	14.90	11.90	113.00	20.40	19.69	2.29	0.35	211.72	3.51
Max	16.80	25.60	180.00	20.70	20.03	5.55	0.85	218.20	4.98

3.2. Proposed model

In this part, we use a grey-box model that have been proposed before [27], which is combined with the black box model (XGBoost) and the Kwon formula of the white box model. The white-box model is based on this ship's structural and main-engine parameters [10]. Kwon proposed corresponding formulas for calculating ship speed loss and additional effective power ([22], [23]):

$$\frac{\Delta P_E}{P_E} = (n{+}1)\frac{\Delta v}{v_1} \quad (1)$$

$$\frac{\Delta v}{v_1} \times 100\% = C_\beta C_U C_F \quad (2)$$

$$\Delta v = v_1 - v_2 \quad (3)$$

$$v_1 = F_r \cdot \sqrt{L_{PP} \cdot g} \quad (4)$$

where n is an empirical constant, related to ship type and loading status; P_E is the effective power of the ship in calm water; Δv is the speed loss caused by wind and waves, m/s; v_1 is the speed in calm water, m/s; v_2 is ship speed in selected weather (wind and irregular waves), m/s; C_β is direction reduction coefficient, related to weather direction angle (concerning the ship's bow) and Beaufort number (BN); C_U is the speed reduction coefficient, which is related to the ship's block coefficient (C_B), Froude number (F_r), and loading conditions; C_F is the ship form factor related to ship type, ship displacement (∇), and BN; L_{PP} is the ship length between perpendiculars, m; g is the local acceleration of gravity, m/s^2.

Black box model Based on the scale of sensor data, we select the XGBoost model based on decision trees. Xgboost is a distributed gradient boosting algorithm based on the gradient boosting framework, which aims to build boosting trees in order, efficiently, flexibly, and conveniently to solve the regression problem. We integrate the Kwon formula into the black box model's pre-processing process, calculate the ship's additional fuel consumption under the maximum wind value (Beaufort number (Bn) = 6) in the data, and remove it accordingly. Since we only consider the steady-state navigation process of the ship in the speed optimization process, the speed change process does not need to take into account (for ocean-going ships, the duration of this process is concise and can be ignored).

In the hyperparameter optimization (HPO), we used the grid search method to perform 5-fold cross-validation, and optimized the hyperparameters, 'n_estimators' and 'max_depth' together. The optimization range of the two parameters we specified is as follows: 'n_estimators' ranges from 100 to 3000, and every 200 is one step-size, resulting in a total of 15 parameter values; 'max_depth' ranges from 3 to 15, and each value is one step-size, resulting in a total of 12 parameter values. From this, HPO requires fitting five folds for each of the 180 candidates, totaling 900 fits. Regarding accuracy, we use R^2 to validate the model. Figure 2 shows the result of the optimization. And after the HPO, 'max_depth' is 9, and 'n_estimators' is 100."

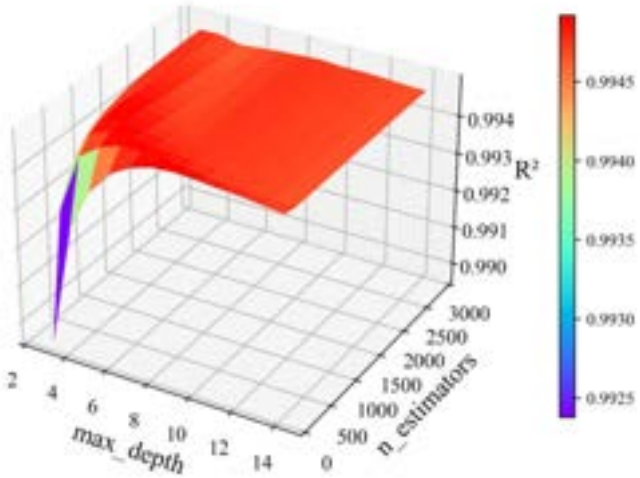

Figure 2. HPO result of the grey-box model

In order to comprehensively compare the prediction performance of the model, Mean Square Error (MSE), Root Mean Square Error (RMSE), Mean Absolute Error (MAE), MAPE, and R-Square (R^2) are used to evaluate the accuracy of the models, the evaluation index formulas are as follows:

$$MSE=\frac{1}{n}\sum_{i=1}^{n}(y_i'-y_i)^2 \tag{5}$$

$$RMSE=\sqrt{\frac{1}{n}\sum_{i=1}^{n}(y_i'-y_i)^2} \tag{6}$$

$$MAE=\frac{1}{n}\sum_{i=1}^{n}\left|y_i'-y_i\right| \tag{7}$$

$$MAPE=100\%\cdot\frac{1}{n}\sum_{i=1}^{n}\left|\frac{y_i'-y_i}{y_i}\right| \tag{8}$$

$$R^2=1-\frac{\sum_{i=1}^{n}(y_i'-y_i)^2}{\sum_{i=1}^{n}(\overline{y_i}-y_i)^2} \tag{9}$$

where n is the number of samples; y_i is the true value; y_i' is the predicted output value of the model; $\overline{y_i}$ is the average value of the samples."

The model results were evaluated ten times by randomly splitting the training–test dataset (training–test split) and calculating the result each time [27]. **Table 2** shows the model evaluation results that the model can achieve acceptable accuracy for predicting ship fuel consumption rate.

Table 2. Grey-box model evaluation results.

	Grey-box model
MSE	0.0018

RMSE	0.0432
MAE	0.0296
MAPE	1.7461
R^2	0.9954

Note: MSE: Mean Square Error; RMSE: Root Mean Square Error; MAE: Mean Absolute Error; MAPE: Mean Absolute Percentage Error; R^2: R-Square.

4. Ship speed optimization model

We study the ship speed optimization problem on a given route between two ports under a given time window constraint and speed constraints. And then, the ship's minimum fuel consumption is used as the objective function for speed optimization. The weather data (wind speed and wind direction) used in the research are all collected in real-time by sensors during the actual navigation of the ship. Usually, the route is divided into several segments according to the estimated sailing time or weather conditions. Therefore, divided according to the principle that the ship sails for about one day on each segment, and it is assumed that a segment has the same weather conditions (more segments can also be divided).

4.1. Objective function and constraints

The case route of speed optimization is the ocean route from Ceuta port in Spain to Miami port in the United States. The estimated sailing time on the route is 237 hours, excluding entering and leaving the port and only the sailing time between anchorages. The route is shown in Figure. 3, divided into ten segments according to the sailing days. The distance of each segment is calculated according to the longitude and latitude coordinates of the start and end of each segment by using the great circle route formula:

$$L_{Km} = 2R \cdot arcsin\left(\sqrt{sin^2\left(\frac{latA - latB}{2}\right) + cos(latA) \cdot cos(latB) \cdot sin^2\left(\frac{lonA - lonB}{2}\right)}\right) \quad (5)$$

$$L_{Nm} = 0.54 \cdot L_{Km} \quad (6)$$

where R=6378.14 km is the equatorial radius of the earth; $lonA$, $latA$, $lonB$, and $latB$ are respectively the longitude and latitude coordinates of point A and point B; $L_{Nm}$is the voyage of the great circle route between coordinates A and B, n mile. The distance and sailing time of each segment calculated by combining the average speed on the route and the above formula are shown in Table 3.

Figure. 3. Route map.

Table 3. Sailing segment distance and sailing time

Segment	Distance (n mile)	Time (h)
1	366	23.6
2	381	24.5
3	380	24.2
4	375	23.6
5	357	24.6
6	357	23.8
7	389	24.3
8	372	24.4
9	376	23.0
10	316	20.0

Under the dual pressure of economic interests and environmental protection, shipping companies are eager to reduce ships' fuel consumptions through various energy efficiency optimization measures. Ship speed optimization is such an energy efficiency optimization measure with fuel-saving potential. Currently, the objective functions of ship speed optimization mainly include the minimum ship fuel consumption, the minimum ship operating cost, the maximum ship revenue, and the minimum ship CO_2 emission. Considering that the fuel consumption of the main engine largely determines the fuel consumption, operating cost, and CO_2 emission of the ship, speed optimization is carried out to minimize the fuel consumption of the main engine. Therefore, the speed optimization objective function based on the grey-box fuel consumption prediction model is as follows:

$$M_{Gb} = f_i^{Grey-box}(v_i, t_i, wd_i, ws_i, fd_i, ad_i, wvd_i, wvh_i) \tag{10}$$

$$TotalFC = min\{\sum_{i=1}^{10} M_{Gb} \cdot (d_i/v_i)\} \tag{11}$$

where M_{Gb} is the grey-box model; $i = 1,\ 2,\ \ldots,\ 10$ represents the segment of the route; v_i is the ship speed on the segment i (knots); $t_i, wd_i, ws_i, fd_i, ad_i, wvd_i, wvh_i$ are the trim (m), wind direction (°), wind speed (knots), fore draft (m), aft draft (m), wave direction (°), and wave high (m) on the segment i, respectively; d_i is the distance of the segment i, calculated by latitude and longitude (n mile); $TotalFC$ is the total fuel consumption of the ship on the route (tons).

When ships sail on a given route, shipping companies usually provide a time for the latest arrival at the port of destination, so there is a time constraint in speed optimization. In addition, considering the operating performance of the main engine under low operating conditions and the main engine rated power limit, speed optimization usually has minimum and maximum speed constraints. The constraints of the latest arrival time and the minimum and maximum speed are as follows:

$$Speed_{lim}: \begin{cases} v_i \le v_{max} \\ v_i \ge v_{min} \end{cases} \tag{12}$$

$$Time_{lim}: \sum_{i=1}^{10} (d_i/v_i) \le T_{max} \tag{13}$$

Where, v_{max} and v_{min} are the maximum speed and minimum speed of the ship, which are determined by the ship test data. In this study,v_{max}=16.8 knots, v_{min} =10 knots; T_{max} is the latest arrival time, for this route set as T_{max}=237 h.

4.2. Transformation and solution of the speed optimization model

After obtaining the speed optimization objective function and constraints, the optimal speed of the ship can be obtained by applying appropriate optimization algorithms. For optimization problems involving machine learning models, conventional nonlinear numerical optimization algorithms (e.g., linear approximation method and interior point method) are difficult to solve effectively due to the highly nonlinear characteristics of machine learning models. Although emerging heuristic optimization algorithms (e.g., genetic algorithms [24] and differential evolution algorithms [25]) can obtain a well acceptable solution in a relatively short period, they cannot obtain the exact optimal solution of the optimization problem. Considering that the ship speed in actual navigation is usually accurate to 0.1 knots, the continuous optimization range of the ship speed [10, 16.8] is discretized according to 0.1 knots, and 0-1 variables are introduced at the same time to convert the nonlinear speed optimization problem to mixed-integer linear programming problem. Furthermore, this speed optimization problem can be solved by linear programming solvers such as Gurobi.

5. Results and discussion

We simulated the meteorological conditions of the ship's navigation process under actual conditions and used the model to predict the fuel consumption rate and optimize the speed.

5.1. Weather conditions and model prediction results

To evaluate the fuel-saving potential of speed optimization, the ship's historical voyage data on the research route are extracted from sensor data, as shown in **Table 4**. An established grey-box model is used to predict the ship fuel consumption rate at different speeds, and the results are shown in **Figure. 4**.

Table 4. The ship's historical voyage data on the route

Segment	Trim (m)	Draft aft (m)	Draft fore (m)	Wind direction (°)	Wind speed (knots)
1	4	22	18	56.3	5.8
2				128.5	13.6

3	48.9	12.1
4	162.3	14.6
5	146.3	18.3
6	65.4	21.3
7	175.3	22.9
8	170.3	16.3
9	140.3	15.2
10	100.6	10.6

Note: Segment is represented by S, for example, S1 represents segment 1.

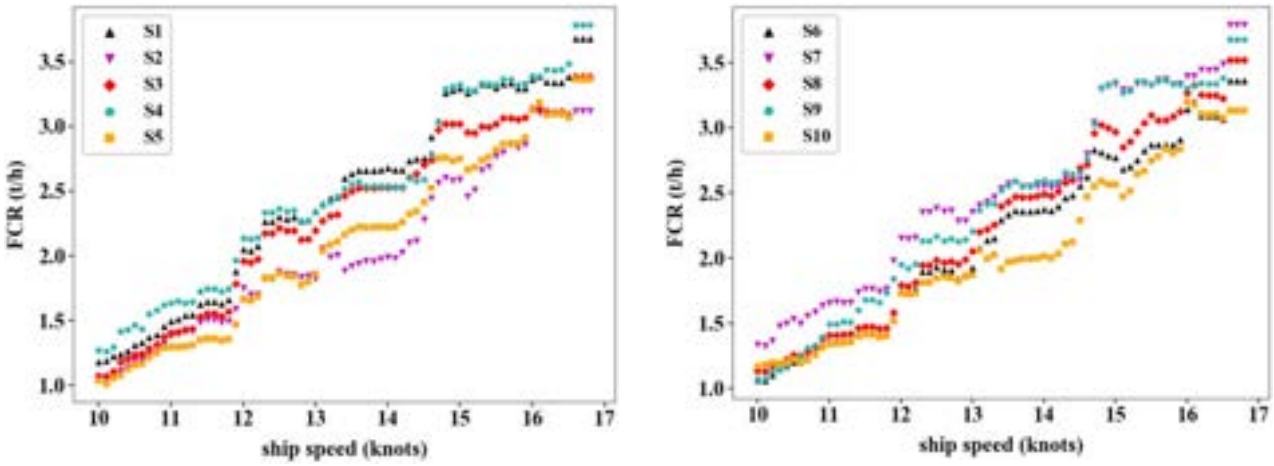

(a) S1 ~ S5 **(b)** S6 ~ S10

Figure. 4. The predicted fuel consumption rate at different speeds in each segment.

The predicted results of the model conform to the cubic relationship between speed and fuel consumption. Due to different weather conditions, the results are different in different segments. At the speed of 14.5 and 16.5 knots, there is a step phenomenon in fuel consumption. This is because the data is not evenly distributed, there is missing data at this speed, which can also be seen in Figure. 1. The lack of speed data will lead to an abnormal step in the prediction result of the model to a certain extent.

5.2. Speed optimization results

To obtain the optimal speed of each segment and the minimum fuel consumption of the ship on the route, the corresponding optimization algorithm is developed using Python programming to call the Gurobi 9.0.2 solver to solve the speed optimization problem. Comparing the speed before and after optimization can reveal the reasons for the reduction of fuel consumption after optimization to a certain extent. Therefore, to evaluate the fuel-saving effect of speed optimization, the optimal speed is compared with the historical average speed in the segment. The speed on the segments before and after optimization and the fuel consumption (FC) predicted by the model are shown in Figure. 5 and Figure. 6, respectively.

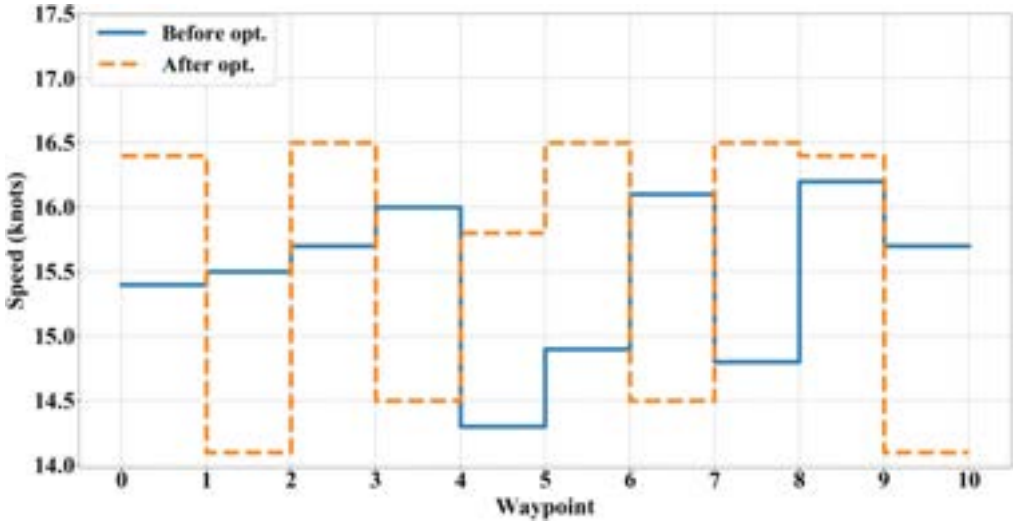

Figure. 5. Comparison of optimized speed results.

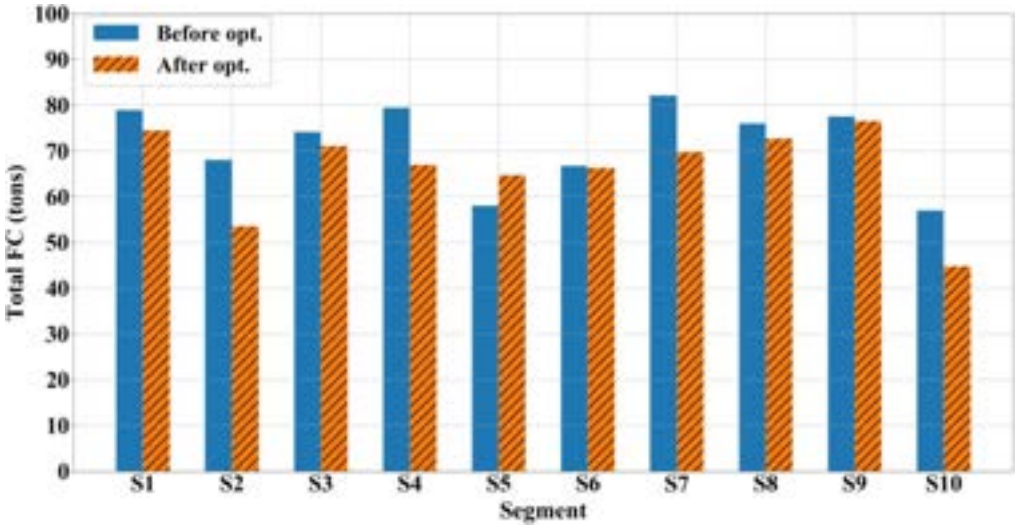

Figure. 6. Comparison of fuel consumption results.

The fluctuation of the optimized speed is mainly caused by the different weather conditions of each segment. Combined with Figure. 5 and Figure. 6, when the optimized speed is higher than the historical average speed, the fuel consumption after optimization is still saved than the historical average speed (segments 1, 3, 6, and 8). This is due to the small amount of data within the range of 16 ~ 16.5 knots speed, which leads to no significant upward trend of fuel consumption rate so the predicted fuel consumption rate is low at high speed. When the optimized speed is lower than the historical average speed, the fuel-saving effect is significant (segments 2, 4, 7, and 10), indicating that the model fully reflects the fuel-saving effect of the ship's slow-down sailing.

The ship speed, fuel consumption, and the fuel-saving rate on the route before and after optimization are shown in Table 5. Among them, the fuel consumption of the ship before and after speed optimization is FC1 and FC2, respectively. During the entire voyage, the total fuel consumption is reduced from 717.9 tons to 661.0 tons after optimization, the overall fuel saving is 56.9 tons, and the fuel-saving rate reached 7.9%. With the current price of marine fuel oil at US$500 per ton, the fuel-saving rate of 7.9% can save US$28,450 in fuel expenses during a single voyage. That's substantial for a single voyage.

Table 5. Fuel consumption before and after optimization

	S1	S2	S3	S4	S5	S6	S7	S8	S9	S10	Total
FC1 (t)	78.9	68.1	74.1	79.5	58.0	66.7	82.1	76.0	77.5	57.0	717.9
FC2 (t)	74.5	53.6	71.0	67.0	64.8	66.3	69.8	72.7	76.5	44.8	661.0
Fuel-saving (tons)											56.9
Fuel-saving rate (%)											7.9

5.3. Optimization results after data smoothing

As shown in the prediction results in Figure. 4, ship fuel consumption rate has a certain degree of step in the speed range of 12~13 knots and 14~15 knots, which is due to the uneven distribution of the speed data used in the modeling. The step phenomenon of fuel consumption affects the reliability of the optimization results. For example, when the speed changes from 11.9 knots to 12 knots, there is a step in the fuel consumption rate. The fuel consumption savings brought by the 0.1 knots reduction in speed are considerable, which is not in line with the actual situation. To make the speed optimization results reasonable and reliable, it is necessary to smooth the fuel consumption results predicted by the model. The Exponential Weighted Moving Average (EWMA) [26] is used to process the predicted fuel consumption. EWMA gives different weights to the observed values, obtains the moving average according to different weights, and determines the predicted value based on the final moving average.

The data in a range under the same sailing speed and weather conditions are regarded as a window capacity, and certain weights are given. Different weights are used to determine that the current prediction result is close to the true value, which can make the prediction result more accurate. As shown in Figure. 7, After using the EWMA to smooth the prediction results of fuel consumption rate, the step phenomenon of fuel consumption rate is significantly alleviated. The optimization results are shown in Figure. 8 and Figure. 9 after smoothing the data.

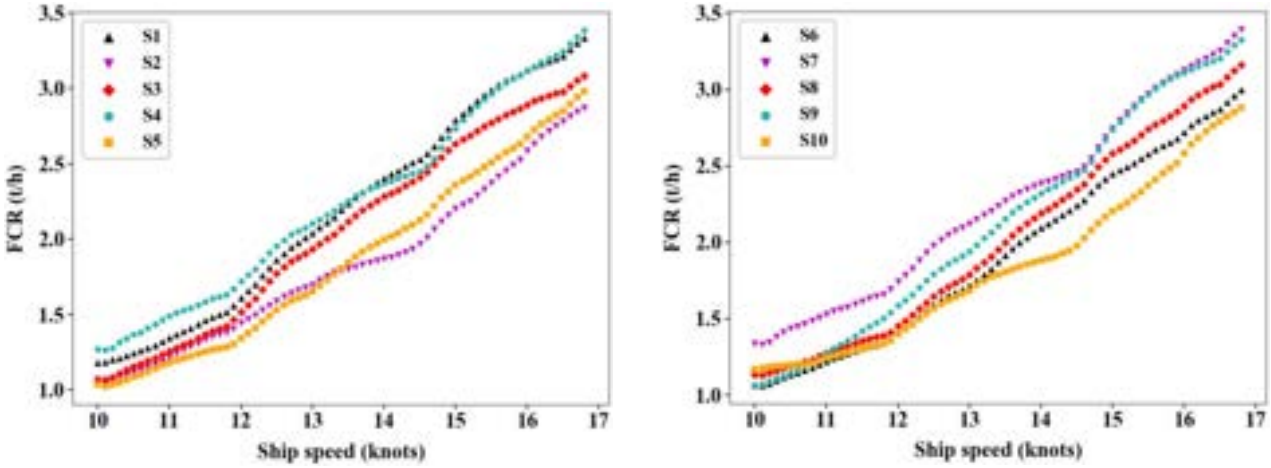

(a) S1 ~ S5 **(b)** S6 ~ S10

Figure. 7. Fuel consumption prediction results after smoothing.

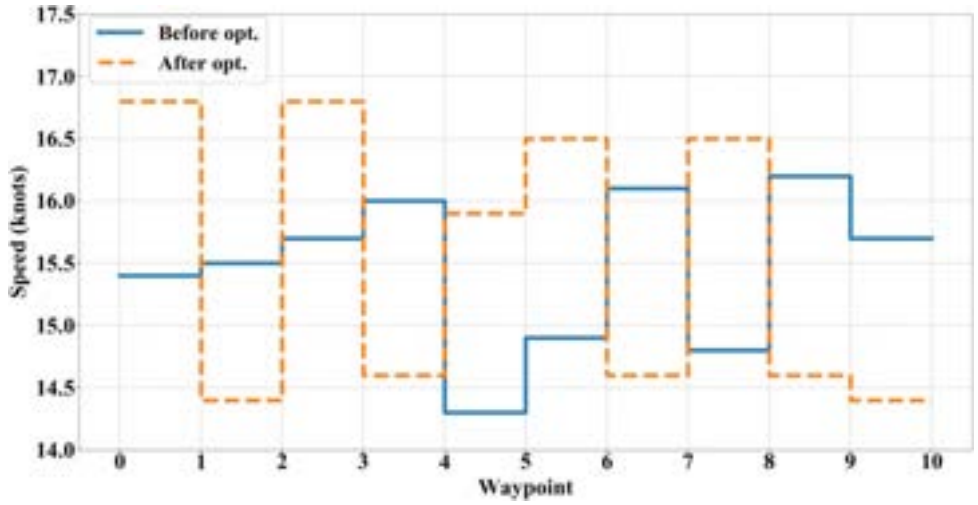

Figure. 8. Comparison of speed optimization results after smoothing.

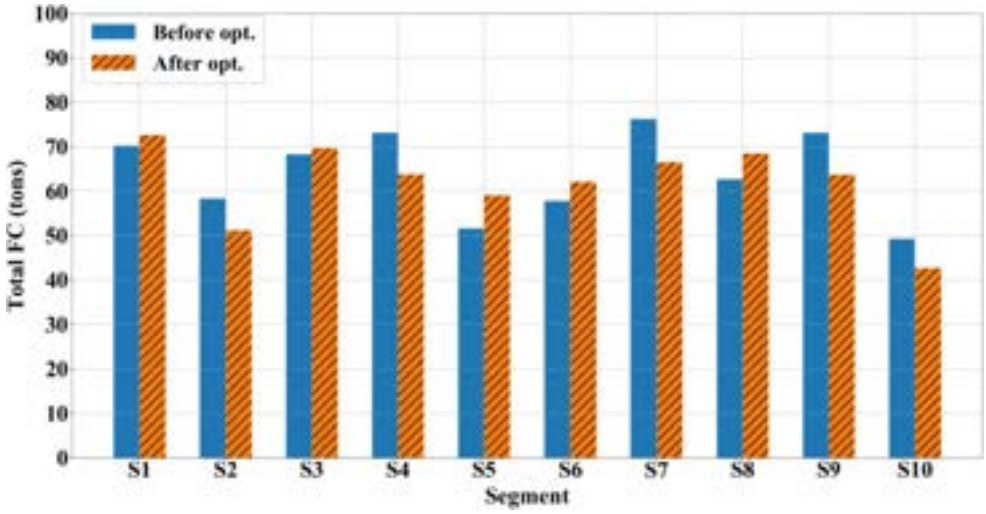

Figure. 9. Comparison of fuel consumption results after smoothing.

After smoothing, the fuel consumption of each segment rises smoothly with the increase of ship speed, the step phenomenon of fuel consumption at certain speeds has been significantly alleviated. At the same time, it also alleviates the insignificant upward trend of fuel consumption rate due to a lack of data under high-speed conditions (16~16.5 knots).

Table 6. Fuel consumption before and after optimization after smoothing

	S1	S2	S3	S4	S5	S6	S7	S8	S9	S10	Total
FC3 (t)	70.2	58.4	68.3	73.1	51.6	57.9	76.2	62.7	73.2	49.3	640.9
FC4 (t)	72.6	51.2	69.7	63.8	64.0	59.1	62.1	66.5	68.5	42.7	620.2
Fuel-saving (tons)											20.7
Fuel-saving rate (%)											3.2

The fuel consumption results before and after optimization are compared and shown in Table 6. The actual fuel consumption and optimized fuel consumption after data smoothing are FC3 and FC4, respectively. The fuel-saving rate for speed optimization after data smoothing is 4.7% lower than that before, but even so, it still reaches 3.2%. In the case of a 3.2% fuel-saving effect, speed optimization can still save $10,350 in fuel expenses. Speed optimization experiments confirm that ship speed optimization can significantly reduce ship fuel consumption, which can provide reliable decision support for shipping companies' ship operations.

6. Conclusion

Ship speed optimization is a crucial aspect of the shipping industry, directly affecting navigation economics. The cost of fuel consumption constitutes a significant portion of a shipping company's expenses, and reducing it by even a small percentage can result in substantial cost savings. In this paper, we based on the sensor data and ship parameters of an oil tanker, using the proposed grey-box ship fuel consumption model, consider the speed of the oil tanker is optimized in consideration of the influence of weather conditions to reduce the fuel consumption of the ship's navigation. Moreover, the data smoothing process is carried out for the model prediction step problem. The main conclusions obtained are as follows:

EWMA method is used to smooth the model prediction result, which can effectively solve the problem of fuel consumption rate step with the increase of ship speed. The relationship between fuel consumption rate and sailing speed is more continuous after smoothing, and the reliability of speed optimization results is improved.

The speed optimization results show that speed optimization considering the influence of weather conditions can save 3.2% and 7.9% of fuel for a single voyage, also $10,350 and $28,450, respectively. Although this study is only aimed at optimizing the speed of a tanker, the modeling and optimization methods used can also be extended to other ship types, which is foreseeable. Ship speed optimization based on actual ship operation data can provide strong support for ship energy saving and emission reduction decision-making.

Acknowledgments

This study was supported by Harbin Engineering University, China Scholarship Council, and Linnaeus University IoT lab, which we gratefully acknowledge.

References

[1] Joung T H, Kang S G, Lee J K, et al. The IMO initial strategy for reducing Greenhouse Gas (GHG) emissions, and its follow-up actions towards 2050[J]. Journal of International Maritime Safety, Environmental Affairs, and Shipping, 2020, 4(1): 1-7

[2] International Shipping. International Energy Agency – Available at:< https://www.iea.org/reports/international-shipping/> [accessed 2022].

[3] Rudzki K, Tarelko W. A decision-making system supporting selection of commanded outputs for a ship's propulsion system with a controllable pitch propeller[J]. Ocean Engineering, 2016, 126: 254-264.

[4] Zaccone R, Ottaviani E, Figari M, et al. Ship voyage optimization for safe and energy-efficient navigation: A dynamic programming approach[J]. Ocean engineering, 2018, 153: 215-224.

[5] Perera L P. Handling big data in ship performance and navigation monitoring[J]. Smart Ship Technology, 2017: 89-97.

[6] Perera L P, Mo B, Kristjánsson L A. Identification of optimal trim configurations to improve energy efficiency in ships[J]. IFAC-PapersOnLine, 2015, 48(16): 267-272.

[7] Silverman B W. Density estimation for statistics and data analysis[M]. CRC press, 1986.

[8] Lu, R., Turan, O., Boulougouris, E., Banks, C., Incecik, A., 2015. A semi-empirical ship operational performance prediction model for voyage optimization towards energy efficient shipping. Ocean Engineering 110, 18-28.

[9] Venturini, G., Iris, Kontovas, C.A., Larsen, A., 2017. The multi-port berth allocation problem with speed optimization and emission considerations. Transportation Research Part D Transport & Environment 54, 142-159.

[10] Li, X., Sun, B., Zhao, Q., Li, Y., Shen, Z., Wei, D., Nan, X., 2018. Model of speed optimization of oil tanker with irregular winds and waves for given route. Ocean Engineering 164 (SEP.15), 628-639.

[11] Cheng, X., Li, G., Skulstad, R., Chen, S., Zhang, H., 2019. A Neural-Network-Based Sensitivity Analysis Approach for Data-Driven Modeling of Ship Motion. IEEE Journal of Oceanic Engineering PP (99), 1-11.

[12] Jeon, M., Noh, Y., Shin, Y., Lim, O.K., Lee, I., Cho, D., 2018. Prediction of ship fuel consumption by using an artificial neural network. Journal of Mechanical Science and Technology.

[13] Kee, K.K., Simon, B.Y.L., Renco, K.H.Y., 2018. Prediction of Ship Fuel Consumption and Speed Curve by Using Statistical Method, The 7th International Conference on Computer Science and Computational Mathematics 2018 (ICCSCM 2018).

[14] Omer, S., Emre, A., Metin, C., 2018. Use of tree based methods in ship performance monitoring under operating conditions. Ocean Engineering 166, S0029801818314446-.

[15] Bialystocki, N., Konovessis, D., 2016. On the estimation of ship's fuel consumption and speed curve: A statistical approach. Journal of Ocean Engineering and Science 1 (2), 157-166.

[16] Yan, X., Wang, K., Yuan, Y., Jiang, X., Negenborn, R.R., 2018. Energy-efficient shipping: An application of big data analysis for optimizing engine speed of inland ships considering multiple environmental factors. Ocean Engineering 169 (DEC.1), 457-468.

[17] Du, Y., Meng, Q., Wang, S., Kuang, H., 2019. Two-phase optimal solutions for ship speed and trim optimization over a voyage using voyage report data. Transportation Research Part B: Methodological 122 (APR.), 88-114.

[18] Yan, R., Wang, S., Du, Y., 2020. Development of a two-stage ship fuel consumption prediction and reduction model for a dry bulk ship. Transportation Research Part E-Logistics and Transportation Review 138.

[19] Press, W.H., Flannery, B.P., Teukolsky, S.A., Vetterling, W.T., 1990. Savitzky-Golay Smoothing Filters. Computers in Physics 4 (6), 669-672.

[20] Hand D J. Principles of data mining[J]. Drug safety, 2007, 30: 621-622.

[21] Alexandropoulos S A N, Kotsiantis S B, Vrahatis M N. Data preprocessing in predictive data mining[J]. The Knowledge Engineering Review, 2019, 34: e1.

[22] Kwon, Y.J., 2008. Speed loss due to added resistance in wind and waves. Naval Architect, 14-16.

[23] Townsin R L, Kwon Y J. Approximate formulae for the speed loss due to added resistance in wind and waves[J]. 1983.

[24] Goldberg, D.E., Holland, J.H., 1988. Genetic algorithms and machine learning.

[25] Storn, R., Price, K., 1997. Differential evolution–a simple and efficient heuristic for global optimization over continuous spaces. Journal of global optimization 11 (4), 341-359.

[26] Frisén M, De Maré J. Optimal surveillance[J]. Biometrika, 1991, 78(2): 271-280.

[27] Xie, Xianwei, Baozhi Sun, Xiaohe Li, Tobias Olsson, Neda Maleki, and Fredrik Ahlgren. 2023. "Fuel Consumption Prediction Models Based on Machine Learning and Mathematical Methods" *Journal of Marine Science and Engineering* 11, no. 4: 738. https://doi.org/10.3390/jmse11040738

Evaluation and optimization of the integration of ice energy storage systems in interconnected supply networks for non-residential buildings

Marco Griesbach[a], Andreas König-Haagen[a,b], Florian Heberle[a] and Dieter Brüggemann[a]

[a] Chair of Engineering Thermodynamics and Transport Processes (LTTT), Center of Energy Technology (ZET), University of Bayreuth, Bayreuth, Germany, lttt@uni-bayreuth.de
[b] ENEDI Research Group, University of the Basque Country – UPV/EHU, Bilbao, Spain

Abstract:

Ice energy storage systems (ICES) in non-residential buildings are a promising technology for utilizing waste heat arising inside the building to efficiently provide heating and cooling without solar assistance. However, there are currently no recommendations for the dimensioning and operation of ICES in interconnected systems with a high level of supply security. Therefore, a detailed numerical investigation of a 500 m³ ICES in a research building is performed and compared with measurement data over one year within this work. Besides, an economic and ecological analysis, a multi-objective evaluation including direct and social costs caused by climate change damages is conducted. An optimization of different operation approaches is examined, ranging from a simple constant operating strategy over a year or representative week, to seasonal control, to an elaborate weekly varying strategy. Moreover, to determine an optimal storage sizing different system combinations are investigated, using a downhill simplex algorithm for each given configuration. Frameworks for Germany, France and EU27 average are used, whereby their influence is investigated by means of a sensitivity analysis. Through an optimized operation, the CO_2 emissions can be reduced by 37 % compared to a conventional system. The adaptation of the plant concept and the determination of an optimal storage dimensioning can also significantly increase the economic feasibility of the realization, whereby a high dependence on the prevailing boundary conditions is evident. The use of ICES leads to an ecological improvement in all regions considered, whereas the methodology can be applied to further building types in the future.

Keywords:

Ice energy storage; thermal storage; heat pump; optimization; dimensioning; non-residential building; waste heat

1. Introduction

The progressive climate change and its negative consequences represent an increasingly important challenge for society, which is why a more sustainable energy supply is unavoidable in all areas. The building sector is currently responsible for 15 % of direct CO_2 emissions from the end-use sector, and in fact, its share of emissions increases to about 30 % if indirect emissions from building electricity and heat consumption are considered [1]. According to the International Energy Agency (IEA), global emissions from space heating are steadily declining while cooling is becoming increasingly important. Thus, appliances and cooling are the fastest-growing uses of energy in buildings, and their growth is expected to continue. In 2019, only 15 % of the energy used for heating was required to meet space cooling demand in the building sector, with about 1 $GtCO_2$ generated through the use of electricity. Nevertheless, based on stated policy intentions, cooling demand is assumed to grow by more than 3 % per year over the next several decades. [2] Beside the higher requirements for air conditioning, especially in non-residential buildings (NRB), there are more and more technical devices like servers that require cooling. Rather than releasing this waste heat unused into the environment and operating refrigeration machines, its utilization represents an auspicious alternative. However, the main challenge is the mostly low-temperature level, complicating the search for technical solutions. [3]

A promising concept is the combined supply of heating and cooling, in which waste heat generated in the building is used directly. Especially NRBs can be suitable for this task, since unlike residential buildings, the demand for cooling does not only occur in the warmer half of the year and often there is even a simultaneous demand for heating and cooling. Nevertheless, Ghoubali et al. [4] show that the important ratio of simultaneous

heating and cooling demand is often insufficient even in these buildings due to temporal mismatch. In order to minimize the effects of this time offset, storage systems come into focus.

In this context, especially in recent years, there has been an increase in the amount of research. At this point, borehole systems, which are coupled with a heat pump, are often considered in order to achieve the required high storage capacity. Applications can range from industrial low-temperature waste heat [5] to ice rink and waste incineration [6] to data centers [7]. In the cases mentioned, both ecological and economic improvements can be achieved. However, the common feature of having borehole installations can be a constraint as well. Beside the high investment costs, more and more countries have stricter regulations for drilling, whereby these types of systems could not be deployed at all locations.

A promising extension or even alternative is provided by ice energy storage systems (ICES), which are not affected by any regulations. Contrary to numerous other phase change materials (PCM), water is an affordable alternative that is neither toxic nor flammable, has long-term stability, and offers a high storage density. The first attempts of applying an ice storage for waste heat utilization and simultaneous heat and cold supply already dates back to the year 1980 by Shipper [8]. Recently, for example, Philippen et al. [9] have investigated the use of waste heat from an air ventilation system in a multi-family house. In a previous paper, the use of an ICES entirely without solar support was considered in detail for the first time by Griesbach et al. [10]. In this paper, an ICES with a volume of 500 m³ in a research building and a corresponding numerical model are examined in detail. Over an evaluation period of 13 months, the ICES can provide therein a considerable share of 34 % of the cooling and 31 % of the heating demand. [10]

In an NRB requiring high security of supply, components such as the ice storage and the associated HP are generally integrated in conjunction with other heating and cooling equipment. However, complex mutual reciprocal interactions of the interconnected system complicate the identification of an optimal operating strategy. In addition, there are no recommendations in the literature so far for the dimensioning of the ICES and a prediction on the components which it should be combined with.

At that point this work sets in, whereby this gap should be filled. For this purpose, the existing model of the previous work [10] is supplemented by all generation plants of the compound system and in this context, for the first time, it is investigated as a case study. Over a period of one year (1st October 2020 to 30th September 2021), real plant and consumption data are monitored and compared with numerical results. For this purpose, a numerical model is introduced in MATLAB Simulink [11] with the help of the Carnot component library [12]. In a first step, the detailed numerical model, which considers the complex mutual interactions, is used to investigate the effects of different operating strategies and approaches for optimizing the operation. In addition, various plant configurations are investigated for which an optimal storage system is identified with the application of a downhill simplex algorithm [13]. To evaluate the operation as well as the dimensioning, an economic, an ecological as well as a combined consideration by social costs takes place. The boundary conditions of economic and ecological parameters from different locations on the optimization process are examined and concluded by a sensitivity analysis.

2. Description of the system

Within the framework of this work, a case study is presented, which is located at the Center of Energy Technology (ZET) at the University of Bayreuth in the Technology Alliance of Upper Franconia (TAO) building. From the 5,600 m² of the research building, about 4,000 m² can be attributed to laboratories and workshops. In addition to the heat demand for space heating, the non-residential building has a particularly high cooling demand, which occurs during the whole year. In addition to air conditioning, a high proportion is attributable to laboratory cooling water for machine cooling. Since the building is not connected to any district heating or cooling pipelines, all the required energy is supplied within the building itself. The nominal capacities of all loads and producers are provided in a previous publication [10]. This paper focused on the ice energy storage system and the development of a numerical model, including analytical validation and comparison with long-term measurement data. In the present work, on the other hand, the entire system is considered for the first time, whereby all plants are considered in a combined model.

An overview of the whole system is shown schematically in Figure 1. All heat consumers are supplied by a common heat distribution network, which is supplied by a conventional gas boiler (GB) and gas-fired combined heat and power plant (CHP). The cooling supply of the laboratory cooling water is carried out together with the air conditioning via a common network. As conventional generators, a compression chiller (CC) and the possibility of free cooling (FC) via dry coolers (DC) at low ambient temperatures are installed.

The ICES is located as an innovative interface between these two networks. The heat pump (HP) is able to act as the main heat generator, if its capacity is sufficient to cover the entire demand. In this case, the required flow temperature on the hot water side is set by a mixing valve. If the capacity is not enough, the HP is operated in combination with the GB and/or CHP. Then the HP is used to preheat the return flow of heating water, which reduces the load on the subsequent producers. The source of the HP is the ice storage or the chilled water network directly, the latter assuming that the appropriate heating and cooling demand prevails simultaneously. The ice storage is regenerated via the cold water network, which enables it to provide cooling in a time-shifted

manner. Since all components interact with each other in a complex way, the entire system is considered in a common interconnected system.

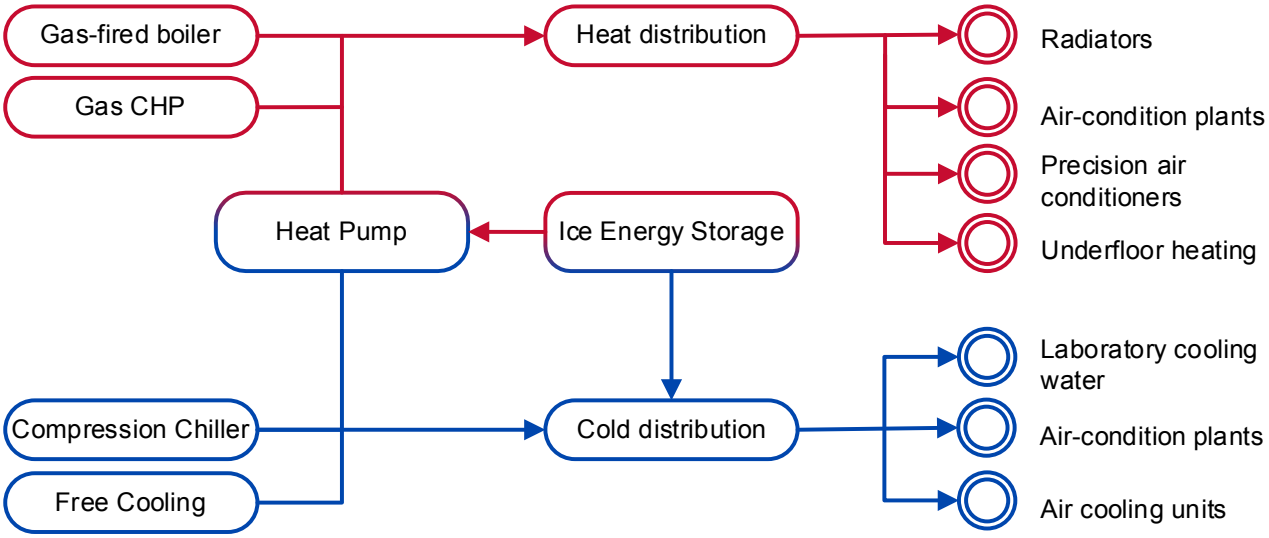

Figure. 1. Simplified scheme of the heat and cold supply system at the University of Bayreuth

A detailed data recording of the entire interconnected system up to the distribution takes place. For this purpose, over 150 data points are continuously logged with a resolution of 1 minute. These comprise all relevant temperatures and flow rates of the respective feed and return lines. The heat meters used are PolluWatt Duo II with an uncertainty of ±0.3 %; PolluStat E with an uncertainty ≤±1.5 % at all producers. At the sub-distribution, 22 PolluStat E are also installed to record in detail the demand of the different consumers. In addition to the provision of load profiles and the analysis of the realized system, the data can be used to validate the numerical models.

3. Methodology

3.1. Formulation of the numerical model

The heating and cooling supply system is entirely implemented in a numerical model in terms of the producers. The simulation environment applied is MATLAB Simulink [11] including the Carnot Toolbox [12]. The components contained therein are mostly adopted unchanged, for instance, the GB, buffer tank according to Patankar [14] and hydraulic components. The models of the HP as well as the CHP are extended by lookup tables, which are parameterized according to the manufacturer's specifications. To determine the electrical power consumption of the DC, the fan characteristic is calculated as a function of the airflow rate. The model of Griesbach et al. [10] is used for the ICES, which has been validated analytically in detail and compared with real long-term measurement data of over one year. Since it is adaptable in terms of dimension, it can also be used in the context of this work to analyse the effects of the dimensioning of the storage.

3.2. Evaluation of the numerical results

The evaluation of the plant operation and dimensioning is performed with regard to economic and ecological criteria as well as a combined evaluation including social costs. The economic consideration is carried out according to the guideline VDI 2067 [15], which combines single as well as recurring payments in a consideration period in a so-called annuity. The recommendation of 20 years is used as the period under consideration. The interest factor q is set at 3 %, the general price increase rate r at 3.1 % and the rate for electric power at 2 %. In addition, the energy tax refund for the CHP and the EEG surcharge of 40 % for self-consumed electricity are applied in the case of Germany. Using the methodology from [15], capital-related costs A_K are calculated including the initial investment and possible residual value as well as replacements. Demand-related costs are determined by the purchase of natural gas $A_{V,gas}$ and electricity $A_{V,el}$ from the power grid. Operating costs A_B include maintenance, inspection and operation of the plants. In addition, other costs A_S such as insurance or taxes can be considered. Proceeds A_E from self-production of electricity are subtracted from the costs. The Chemical Engineering Plant Cost Index (CEPCI) is used to relate the investment costs of the plants to the same reference year [16]. A summary of the costs and parameters used is shown in Table 1.

Table 1. Economic parameters of the heat and cold generators and the ice energy storage [15,17,18].

Component	A_0, €	T_N, yr	n	f_{Inst}, %	f_{W+Insp}, %	f_{Op}, h/a	$CEPCI$
GB	39,598	20	0	1	2	20	2012-2020
CHP	224,298	15	1	6	2	100	2012-2020
CHP (117 kW)	111,913	15	1	6	2	100	2012-2020
HP	60,180	20	0	1	1.5	5	2012-2020
CC	316,428	15	1	2	1.5	1	2012-2020
FC	13,387	20	1	2	1.5	0	2002-2020
ICES	498,031	50	0	1	1	0	2018-2020

In contrast to the established plants, there is no general cost function available for the relatively new technology of ice energy storages. The publication of Allan et al. [19] in which a function for a storage volume of 10 to 270 m³ is contained constitutes an exception. Since within the framework of this work also larger storage systems up to 750 m³ will be considered, an own function based on real costs from the system of the University of Bayreuth will be presented. In order to derive from the realized configuration to others, the so-called six tenth rule [20] with the default value of 0.6 is used. In addition to the storage volume V_{st}, the sum of the pipe length of the charging and discharging circuit l_{CH+DC} can be varied:

$$A_{0,ICES} = 44151 + 134769 \left(\frac{V_{st}}{443\ \mathrm{m}^3}\right)^{0.6} + 152862 \left(\frac{l_{CH+DC}}{6000\ \mathrm{m}}\right)^{0.6} \quad (1)$$

The ecological assessment considers CO_2 emissions from gas $\dot{Q}_{gas}$ and electricity consumption $\dot{Q}_{el,con}$ and power generation by the CHP $\dot{Q}_{el,gen}$. The total emission A_{CO_2} is calculated by means of CO_2 factors for gas $a_{CO_2,gas}$ and electricity $a_{CO_2,el}$ for the respective electricity mix of the grid. Since the entire electricity is self-consumed, a subtraction with the grid factor is performed:

$$A_{CO_2,i} = a_{CO_2,gas,i} \int \left(\dot{Q}_{gas,i}\right) \mathrm{d}t + a_{CO_2,el,i} \int \left(\dot{Q}_{el,con,i} - \dot{Q}_{el,gen,i}\right) \mathrm{d}t \quad (2)$$

The reference cases Germany (DEU), European average (EU27) and France (FRA) are utilized to identify the influence of the boundary conditions on the evaluation and optimization. A summary overview of the parameters applied is given in Table 2.

Table 2. Economic and ecological parameters [21–25].

Location	$A_{V,gas}$, €/kWh	$A_{V,el}$, €/kWh	$a_{CO2,gas}$, g_{CO_2}/kWh_{gas}	$a_{CO2,el}$, g_{CO_2}/kWh_{el}	hr, €/h
DEU	0.0564	0.2016		366	
EU27	0.0613	0.1584	194.3	226	73
FRA	0.0660	0.1099		57	

Frequently, an economic and ecological evaluation might not move in the same direction and may even be contrary to each other. In order to perform a combined evaluation, there is the challenge of applying a non-arbitrary weighting. Therefore, in this work, CO_2 emissions are attributed a price as a consequence of social costs in the form of climate consequential damages a_{clim,CO_2} in accordance with the German federal environmental agency [26]. These can be added to the direct costs of the plant operator, allowing a multi-criteria evaluation to be carried out. Two different values are given for the costs incurred to society by CO_2 emissions in Waldhoff et al. [27]. These differ in terms of the pure time preference rate (PTPR) and thus a weighting between the welfare of current and future generations. With a rate of PTPR of 1 %, only 74 % of the damage for the next generation (30 years) and 55 % of the damage for the generation after that (60 years) is considered. At a rate of 0%, on the other hand, the costs are weighted equally for all generations, resulting in higher values for a_{clim,CO_2}. The recommended values depending on the year under consideration are summarized in Table 3.

Table 3. German federal environmental agency recommendation on climate costs [26].

Year of consideration	a_{clim,CO_2} at PTPR=1 %, €/t CO_2	a_{clim,CO_2} at PTPR=0 %, €/t CO_2
2020	195	680
2030	215	700
2050	250	765

In order to obtain a combined evaluation parameter, the annuity of the overall system is added to the total CO_2 emissions, which are multiplied by a_{clim,CO_2}.

3.3. Plant operation optimization

Through the number of the different plants there are 24 possible rank orders of the possible plant operation on the cooling side (CCC) and 6 on the heating side (HCC), illustrated in Figure 2. Since these can be combined together in any desired way, there is a total of 144 possibilities for operating the compound system. The respective aggregate with the highest priority of the rank order under consideration is used first. Should its capacity not be sufficient, or if it is not available, the plant with the next higher priority is activated and further on. Generally, FC can only be enabled at ambient temperatures below 6.6 °C and the CHP at a heat demand of at least 70 % of its nominal capacity. HE CH can only operate at an average storage temperature below 5 °C in order to achieve a sufficient temperature difference to the cold-water network. HE HP is only applicable up to a maximum icing degree of 10 %. The HP can operate up to a degree of icing of 80 % or a minimum inlet temperature on the brine side of -9 °C. No separate restrictions exist for the GB and CC.

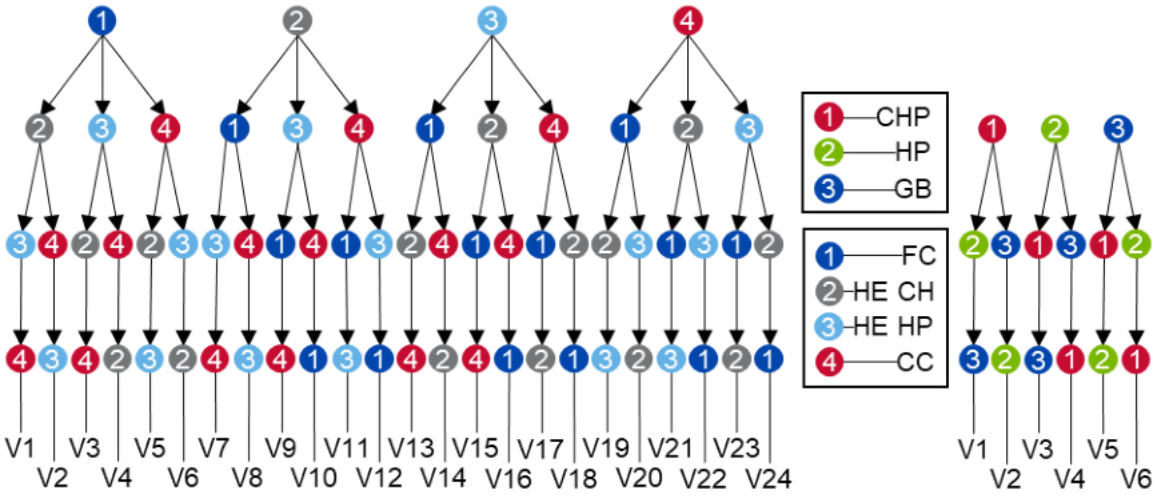

Figure. 2. Possible rank orders of the CCC (left) and HCC (right)

Since mutual interactions exist between the plants and the plant efficiency depends on the state of charge of the storage tank, no simple analytical solution can be formulated for identifying the optimal operation strategy considering all mentioned aspects. Therefore, different numerical optimization approaches to determine an optimal mode of operation are presented and investigated. In Figure 3 these approaches are summarized schematically.

The first and simplest variant is the constant control over the whole year (CCY). For each of the 144 possible combinations, an annual simulation is performed and the best one is selected. Henceforth, this will be enabled constantly over the entire year. In the second variant, on the other hand, only a simulation period of one week is used, i.e. summer (CCS), winter (CCW) and transition (CCT). In order to account for different states of charge of the storage, the model of the storage is initialized with four different degrees of icing. In each case, one week is simulated and the best variant is chosen in the process. Only with the best one a yearly simulation is carried out, which significantly reduces the simulation effort. In the third variant of the seasonal control (SC), an ice-building period $P_{i,b}$ is first defined. During this period, the priority of HE CH is reduced so that the storage is only charged if otherwise the CC has to be activated. The remaining time of the simulation period of one year, the respective strategy is used constantly, resulting in the same effort as for CCY. The best variant is then selected, which needs to be adjusted by the plant operator at the beginning and end of $P_{i,b}$. The fourth variant is the weekly adjusted control (WAC), which is also the most complex one. This is basically equivalent to a model predictive control with a perfect predictive model. Initially, the first week is simulated with all modes of operation and an optimum is selected. The next week is initialized with the final conditions of the previous week and an optimum is identified again. The procedure is repeated until a full year has been examined. For all strategies, both an economical and an ecological objective function can be defined.

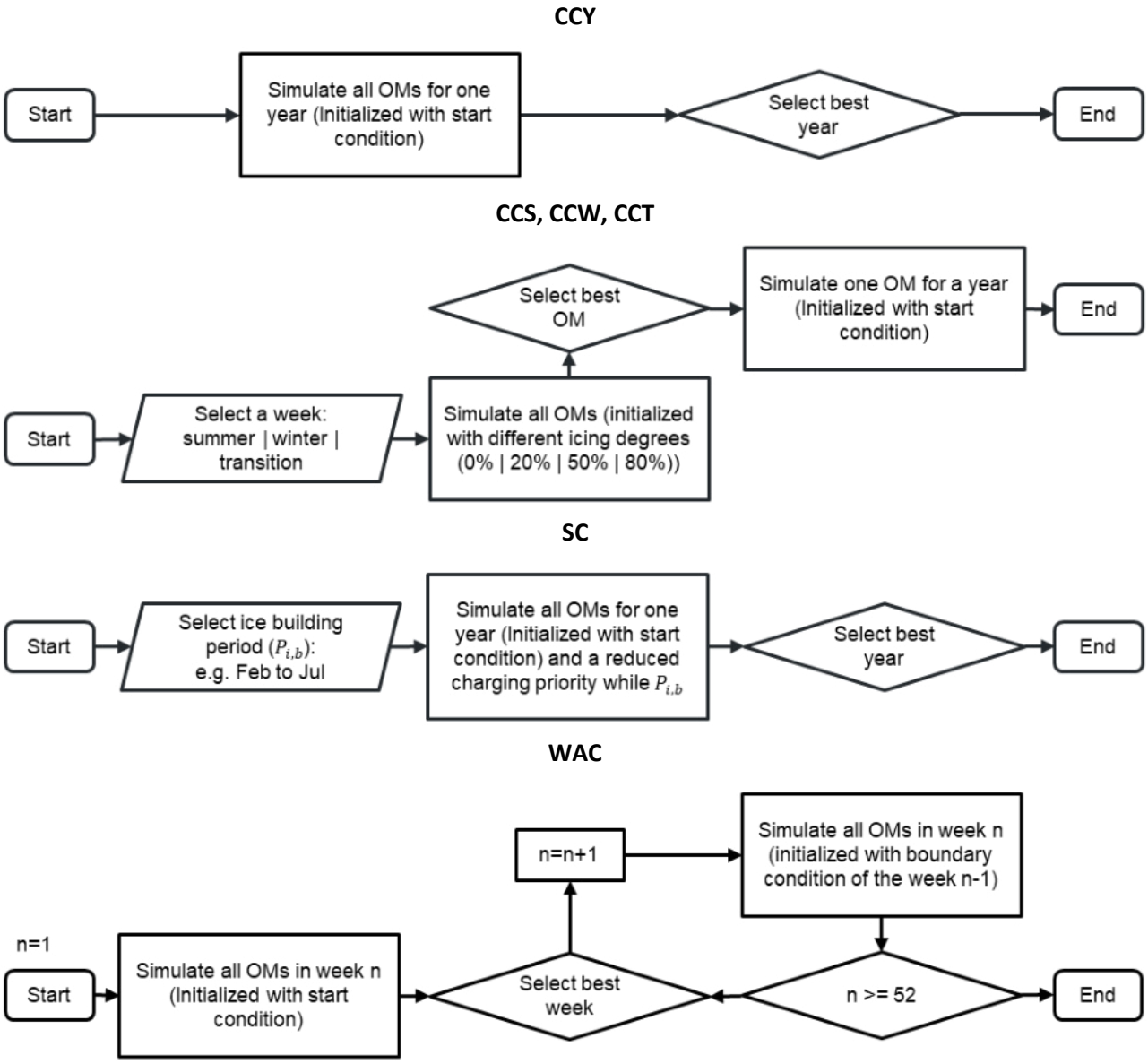

Figure. 3. Flowchart of the CCY (first), CCS, CCW, CCT (second), SC (third) and the WAC (last)

3.4. Plant dimensioning optimization

In addition to the analysis and optimization of the operation of the realized configuration, the influence of different plant dimensioning and configuration is investigated. The focus lies on the ICES here, so the remaining components are dimensioned according to established standard procedures. As the security of supply must be guaranteed, these must be able to cover the complete demand even if the storage tank is completely charged or discharged. Two reference variants (r) are defined and two variants with ICES (I) are considered, which are schematically illustrated in Figure 4. In each variant, the case without (S) and with CHP (C) is considered. FC is used in the S(r) and C(r) cases, whereas it is not applied in S(I) and C(I) in order to utilize as much of the waste heat as possible through the ICES. In the C cases, a CHP with a nominal power of 117 kW is utilized, allowing approximately 4500 full load hours to be obtained. The remaining components correspond to the realization, with the exception of the storage.

With the selected plant concept the dimensioning of the ice storage itself is carried out by a downhill simplex method [13], illustrated in Figure 5. Annual simulations with CCY (HCC: 1 & CCC: 15) are carried out during the optimization. The storage volume as well as the pipe lengths of both hydraulic circuits are continuously varied. The volume is mainly decisive for the storage capacity, which is especially relevant for seasonal considerations. The length of CH essentially influences the achievable regeneration power. The pipe length of DC determines not only the extraction capacity but also the ice layer thickness that forms around the pipes.

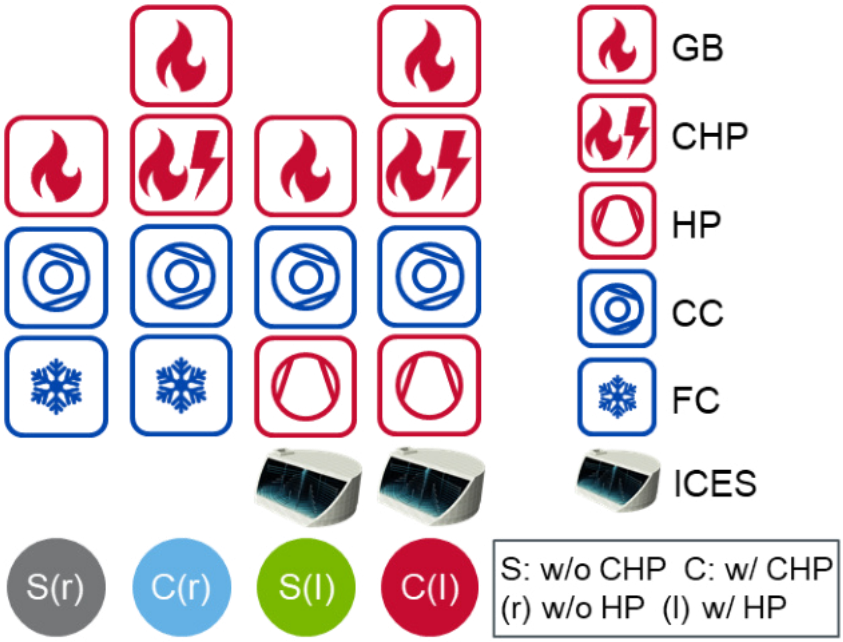

Figure. 4. Schematic overview of the examined combinations

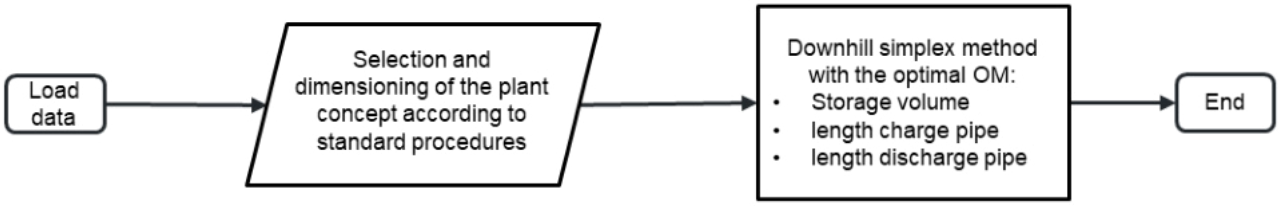

Figure. 5. Flowchart of the dimensioning optimization strategy

4. Results

In this chapter, the results of the plant operation and optimization of the realization concerning the real case study are presented first. Subsequently, different plant dimensions and configurations are investigated, identifying an optimal storage system for each of it. Finally, the chapter concludes with a sensitivity analysis to consider future developments of energy prices and CO_2 emissions of the electricity mix.

4.1. Plant operation

The results of the numerical optimization of the plant operation of the installed system at the TAO building of the University of Bayreuth are presented first. For this purpose, different optimization approaches are presented here instead of all prioritization variants, since especially weekly simulations result in too many variants to present them explicitly at this point. For this purpose, the resulting CO_2 emissions and the annuity for all strategies from chapter 3.3. for an economic (econ.) and an ecological (ecol.) optimization are indicated in Figure 6. The annuity ranges from 212 to 255 k€ and the CO_2 emissions from 148 to 195 metric tons per year.

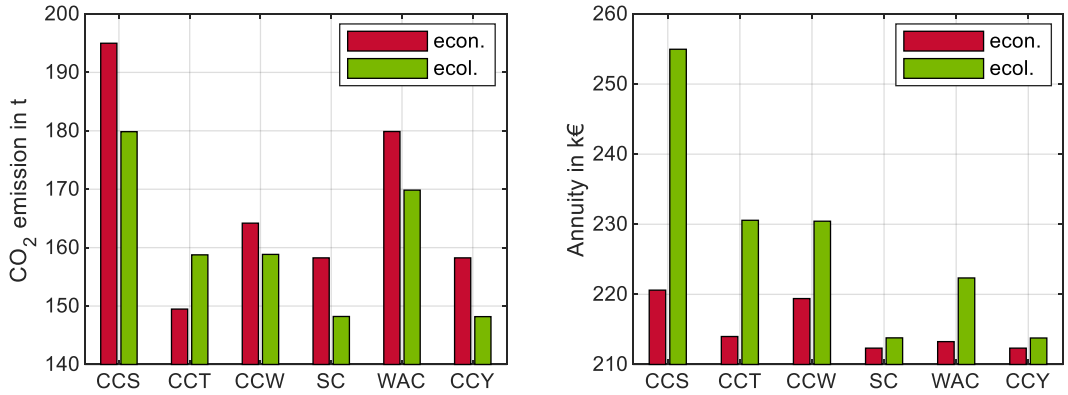

Figure. 6. CO_2 emissions (left) and the annuity (right) of all control strategies considered.

In general, using CCY yields the best results, however, an annual simulation must be conducted for each strategy to obtain these values. For the CCS, CCT and CCW variants, one week each is simulated with 4 different boundary conditions, resulting in the shortest computation time. Using the summer week in CCS performs worst for both optimization objectives from an economic as well as an ecological point of view. This can be explained by the fact that the full potential of the plant diversity cannot be exploited during this period. The heat demand is not sufficient for the use of the CHP and FC cannot be operated due to too high ambient temperatures. These limitations are not present in CCT, which provides a significantly better representation of potential annual plant usage. With an economic objective function, the ecological and economic optimum from CCY can be met with a distance of less than 1 %. From an environmental point of view, CCW can compete with CCT, while from an economic perspective it is noticeably less competitive. In SC, one annual simulation is also performed in each case, whereby the storage is charged with low priority during the ice build-up period. However, no improvement compared to CCY can be achieved, since in each case a variant is selected in which the ice build-up plays a subordinate role. The main reason stated for this is the complex mutual interactions of the system and the fact that the demand for cooling is relatively constant during the whole year. The last examined variant is the WAC, which is also the most complex one. This corresponds to a model predictive control with perfect prediction with a time horizon of one week. The economic objective function comes close to the optimum of the CCY, but from an ecological point of view it performs considerably worse. An ecological target function is not competitive regarding both evaluation parameters. This can be explained by the fact that for a time horizon of one week, the capacity of the long-term storage is not fully utilized. Due to the fact that the storage tank is not sufficiently cooled during economic optimization, it can hardly provide cold. However, the competitive ability of the system only increases with the combined provision of heating and cooling. In the case of ecological optimization, on the other hand, the CHP is increasingly displaced by the HP as the base load generator, thus noticeably limiting its operating time.

4.2. Plant dimensioning

In the second section of the results, the findings on plant dimensioning according to chapter 3.4. are presented. First, two reference simulations with and without CHP are performed, each with three different boundary conditions. As operating strategies, CCC 15 and HCC 1, which represent the optimum from chapter 4.1, are selected as fixed and non-existing components are omitted. A downhill simplex algorithm is utilized to optimize the storage configuration. The sum of annuity and climate impact costs with PTPR = 0 % is adopted as the objective function of this computationally intensive procedure. Similar to the reference simulations, the boundary conditions for DEU, FRA and EU27 are applied.

The identified optimal storage configuration in dependence of the location, the respective storage volume as well as the determined pipe lengths are listed in Table 1. In the S(I) scenario, the compound system consists of a GB and a CC in addition to the ICES. Using the DEU and EU27 boundary conditions, highly similar storage configurations are determined. In both cases, a significantly longer pipe length is also determined for DC compared to CH. Contrary to the FRA case, an ~5 times larger storage volume is adopted. However, also in this instance, a significantly increased pipe length is identified for CH compared to CH. In conclusion, relatively similar ratios between pipe length and storage volume are selected in all three situations.

In addition to the components from S(I), a CHP is applied in C(I). By means of DEU boundary conditions, a storage volume of 20 m³ is identified, which represents the lowest constraint of the optimization algorithm. Furthermore, a minimum pipe length is chosen, which makes the ICES contribution to the energy supply almost negligible. With the EU27 conditions, a larger storage is chosen than in S(I), whereby the length of CH is hardly shorter than that of DC. The subsequent FRA case identifies a smaller volume that is relatively comparable in scale to the S(I) cases of DEU and EU27.

In conclusion, the prevailing boundary conditions have a considerable influence on the resulting storage. While for S(I) the findings for DEU and EU27 are relatively similar, a significantly larger system is preferred for FRA. The higher investment costs are more rapidly compensated for by savings on the high $A_{V,gas}$ for GB, while the consumption of electricity by HP with low $A_{V,el}$ and $a_{CO2,el}$ is significantly less relevant. In combination with CHP, which represents an additional investment, a smaller ICES is generally identified. In the case of DEU, where CHP electricity generation is highly attractive due to high $A_{V,el}$ and $a_{CO2,el}$ and relatively low $A_{V,gas}$, the contribution by HP is minimized as it displaces the CHP and the additional investment is not viable. In FRA, the ICES advantage may not be as significant due to the CHP as the base load generator, so a significantly small system is identified.

Table 1. Pipe length and storage volume of all configurations for optimization with the boundary condition DEU, EU27 and FRA

Variant	Location	Storage volume, m³	Pipe length charge, m	Pipe length discharge, m
	DEU	142	562	1047
S(I)	EU27	149	589	1099
	FRA	732	2897	6126
	DEU	20	79	56
C(I)	EU27	213	843	974
	FRA	141	558	1060

A comparison of the annuity and the climate impact costs is presented in Figure 7 for all combinations. The reference case S(r) appears in all regions quite similar, as basically higher $A_{V,gas}$ are compensated by lower $A_{V,el}$ and the investment is equal. In addition, CO_2 emissions and thus the climate impact costs are primarily determined by $a_{CO2,gas}$, a factor that is independent of the location. In C(r), descending competitiveness from DEU over EU27 to FRA is clearly visible. For the annuity, this is largely determined by increasing $A_{V,gas}$ and simultaneously decreasing $A_{V,el}$, making the CHP less profitable. Parallel to this, the climate impact costs also increase due to lower $a_{CO2,el}$, making grid-related electricity savings less attractive. For S(I), the annuity is higher than for S(r), essentially determined by the additional investment of the ICES, which is not compensated by savings in demand-related costs. On the other hand, the CO_2 emissions and thus also the climate impact costs are significantly lower, resulting in benefits in a combined assessment. The most obvious outcome is for FRA, where the investment for the large storage increases the annuity, but minimal climate impact costs prevail at the same time. In C(I), the progression tends to be analogous to C(r) with the same reasons as in this case. For DEU, the annuity turns worse with no decrease in climate impact costs, as the additional investment hardly achieves any changes due to its low contribution. For EU27, the annuity increases while the climate impact costs decrease, yielding in sum similar results as in C(r). Finally, while with FRA constraints an altogether improvement of C(I) over C(r) can be considered, it is not preferable to the S cases, especially due to the highest annuity.

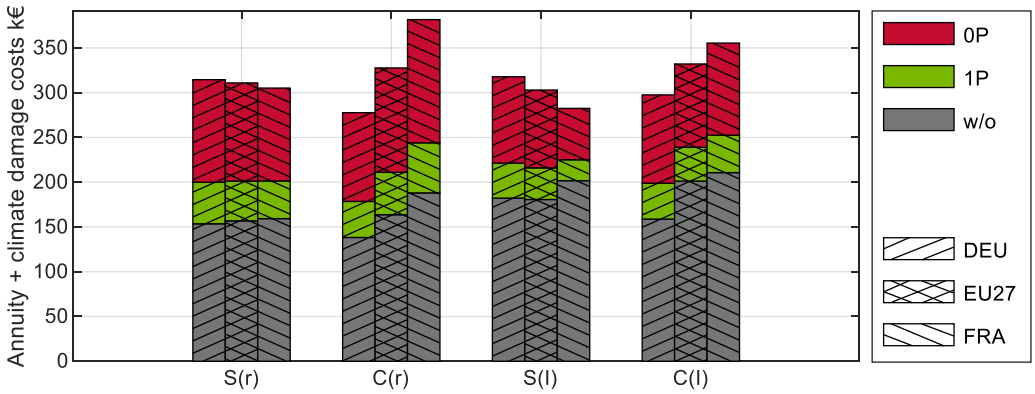

Figure. 7. Annuity plus climate damage costs for all considered regions and configurations.

4.4. Sensitivity analysis

In this last part of the results section, a sensitivity analysis is performed in order to consider the effects of varying boundary conditions. For this purpose, the gas and electricity prices as well as the CO_2 emissions of the electricity mix are varied by ±10 %. The parameter impact on costs or CO_2 emissions is determined according to Saltelli et al. [28] and illustrated in Figure 8. Negative values, as in the C cases, signify that an increase in the input parameter leads to a decrease in the output value.

For S(r), all regions are characterized by a similarly strong dependence on the gas price $A_{V,gas}$. In contrast, the influence of $A_{V,el}$ plays a subordinate role, which decreases slightly with the prevailing value. The influence of $a_{CO2,el}$ is similar, whereas it is almost negligible at FRA due to the low values of the CO_2 emissions of the electricity mix. In C(r), the dependence on $A_{V,gas}$ is reduced compared to S(r), whereas the dependence on the regional price is stronger. On the other hand, due to the self-production of electricity by the CHP, it is possible to benefit from rising electricity prices. As with $a_{CO2,el}$, there is a dependence on the location, which is determined by the respective absolute values. The negative values will increase the CO_2 emissions of the system when $a_{CO2,el}$ decreases due to the expansion of renewable energies in the electricity mix. For S(I), the ICES application results in a decrease in dependence on $A_{V,gas}$ compared to S(r), with an increase in dependence on $A_{V,el}$. However, at the same time, from an environmental point of view, it is also possible to

benefit from falling $a_{CO2,el}$, which are expected in the future. Finally, the distribution of the impact in C(I) looks similar to C(r). The reduced generation of electricity by the CHP and the increased consumption of electricity by the HP can reduce the impact of $A_{V,el}$ and $a_{CO2,el}$.

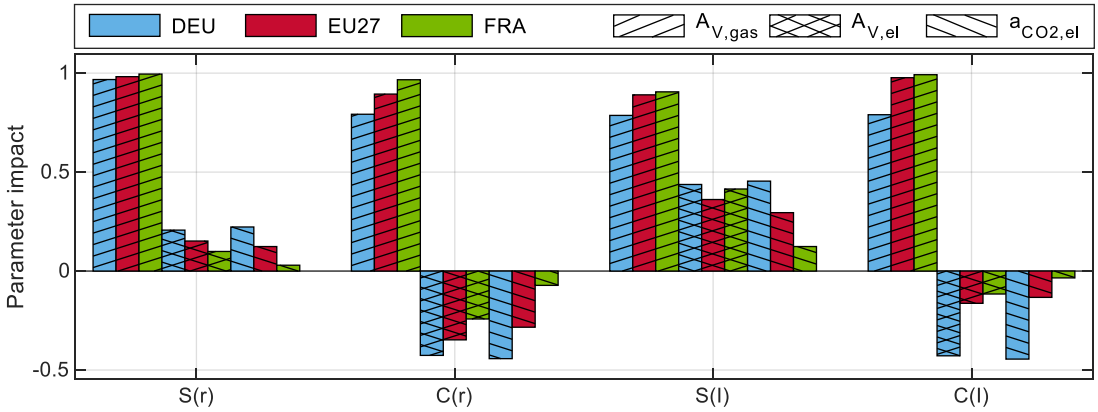

Figure. 8. Parameter impact of the gas and electricity price on the cost and CO_2 emission factor of the electricity mix on the CO_2 emission for all configurations and boundary conditions

5. Conclusion

A detailed numerical investigation of an ICES for the combined supply of heating and cooling energy to a research building is carried out. Therefore, the entire supply system including ice energy storage is implemented in MATLAB Simulink and validated with real long-term measurement data. By means of this, both approaches for the optimization of plant operation and dimensioning can be investigated. To evaluate them, an economic, an ecological as well as a combined analysis with the help of social costs is performed. The optimization of the operation, ranges from a simple constant operating strategy over a year or typical week, to seasonal control, to a sophisticated weekly varying strategy. Moreover, for the boundary conditions of DEU, EU27 and FRA, an optimal storage dimensioning with and without additional CHP is identified using a downhill simplex algorithm. This work is concluded by a sensitivity analysis of the constraints.

Depending on the approach, optimization results for plant operation range from 212 to 255 k€ for the annuity and from 148 to 195 t for CO_2 emissions. The best results can be achieved with a constant operating strategy over the whole year. Whereas computationally efficient weekly simulations are well suited for pre-estimation, neither a seasonal control nor a weekly adjusted strategy with perfect forecasting, both of which are complex to implement, can improve the performance. An ICES can reduce CO_2 emissions noticeably, wherefore an optimal storage is identified within the context of this work, depending on the plant location. Nevertheless, from an economic point of view, a higher annuity must be accepted for systems with ICES due to the additional investment. Combining these with social costs in the form of climate impact damages, an improvement compared to conventional systems can be achieved. Furthermore, the ICES can reduce dependence on natural gas and benefit from the future expansion of renewable energies in the electricity mix.
The approach can be applied in the future to other building types, such as hospitals or office buildings, which are characterized by high heating and cooling requirements. The determining parameters such as the absolute heating and cooling demand as well as the time shift between them should be identified.

Declaration of Competing Interest

The authors declare that there is no conflict of interest.

Acknowledgments

The authors gratefully acknowledge the financial support of the Bavarian State Ministry of Education, Science and the Arts within the framework Graduiertenkolleg Energieautarke Gebäude of the TechnologieAllianzOberfranken (TAO). Additionally, the authors gratefully acknowledge the financial support of the Upper Franconian Trust (Oberfrankenstiftung) within the framework KomWEisS. Andreas König-Haagen is grateful for the financial support of the Deutsche Forschungsgemeinschaft, (DFG, German Research Foundation) under Grant no KO 6286/1-1 / 444616738.

Nomenclature

A_0 investment amount, €

A_{CO_2} amount of emitted CO_2, kg

A_V costs of consumed natural gas and electricity, €

a_{clim,CO_2} climate costs, €/t_{CO2}

a_{CO2} CO_2 factor, kg_{CO2}/kWh

hr hourly rate for staff, €/h

l pipe length, m

n replacements, (-)

$P_{i,b}$ ice-building period, (-)

$\dot{Q}$ demand, kW

q interest factor, (-)

R_W residual value, €

r general price change factor, (-)

T observation period, a

T_N service life of the installation component, a

$V_{storage}$ storage volume, m³

Subscripts and superscripts

B operation-related costs

CH charge

con consumption

DC discharge

E proceeds

el electricity

gas natural gas

gen generation

$inst$ repair effort

K capital-related costs

op operating effort

S other costs

V demand-related costs

$W + Insp$ servicing and inspection

References

[1] International Energy Agency. World Energy Outlook 2021. IEA, Paris. 2021. https://www.iea.org/reports/world-energy-outlook-2021, Accessed 05.09.2022.

[2] International Energy Agency. Is cooling the future of heating. IEA, Paris. 2020. https://www.iea.org/commentaries/is-cooling-the-future-of-heating, Accessed 07.09.2022.

[3] Forman C, Muritala IK, Pardemann R, Meyer B. Estimating the global waste heat potential. Renewable and Sustainable Energy Reviews 2016;57(1):1568–79. https://doi.org/10.1016/j.rser.2015.12.192.

[4] Ghoubali R, Byrne P, Miriel J, Bazantay F. Simulation study of a heat pump for simultaneous heating and cooling coupled to buildings. Energy and Buildings 2014;72(5):141–9. https://doi.org/10.1016/j.enbuild.2013.12.047.

[5] Wang S, Qu R, Zhang X, Li Y, Chen J. Thermal performance analysis of ground source heat pump system for low-temperature waste heat recovery storage. Case Studies in Thermal Engineering 2022;35(4):102131. https://doi.org/10.1016/j.csite.2022.102131.

[6] Egging-Bratseth R, Kauko H, Knudsen BR, Bakke SA, Ettayebi A, Haufe IR. Seasonal storage and demand side management in district heating systems with demand uncertainty. Applied Energy 2021;285(2):116392. https://doi.org/10.1016/j.apenergy.2020.116392.

[7] Li H, Hou J, Hong T, Ding Y, Nord N. Energy, economic, and environmental analysis of integration of thermal energy storage into district heating systems using waste heat from data centres. Energy 2021;219(12):119582. https://doi.org/10.1016/j.energy.2020.119582.

[8] Shipper KE, Energy Development Fund. Demonstration ice storage with waste heat recovery project final report. [Austin, Tex.]: The Council; 1980.

[9] Philippen D, Carbonell D, Battaglia M, Thissen B, Kunath L. Validation of an Ice Storage Model and Its Integration Into a Solar-Ice System. In: Häberle A, editor. Proceedings of EuroSun 2018. Freiburg, Germany: International Solar Energy Society; 2018 - 2018, p. 1–12.

[10] Griesbach M, König-Haagen A, Brüggemann D. Numerical analysis of a combined heat pump ice energy storage system without solar benefit – Analytical validation and comparison with long term experimental data over one year. Applied Thermal Engineering 2022;213(1):118696. https://doi.org/10.1016/j.applthermaleng.2022.118696.

[11] Matlab and Simulink Release 2020b. Natick, Massachusetts, United States.: The MathWorks, Inc; 2020.

[12] CARNOT Toolbox Ver. 6.3, /2018 for Matlab/Simulink 2016b, © Solar-Institut Jülich.

[13] Nelder JA, Mead R. A Simplex Method for Function Minimization. The Computer Journal 1965;7(4):308–13. https://doi.org/10.1093/comjnl/7.4.308.

[14] Patankar SV. Numerical Heat Transfer and Fluid Flow. Boca Raton, FL: CRC Press; 1980.

[15] Association of German Engineers. VDI 4655 Part 1: Reference load profiles of residential buildings for power, heat and domestic hot water as well as reference generation profiles for photovoltaic plants. Beuth Verlag, Berlin, 2019.

[16] Chemical Engineering. The Chemical Engineering Plant Cost Index. https://www.chemengonline.com/pci-home, Accessed 05.04.2022.

[17] Bundesministerium für Verkehr, Bau und Stadtentwicklung (BMVBS): Ermittlung von spezifischen Kosten energiesparender Bauteil-, Beleuchtungs-, Heizungs- und Klimatechnikausführungen bei Nichtwohngebäuden für die Wirtschaftlichkeitsuntersuchungen zur EnEV 2012.

[18] M. Gebhardt, H. Kohl, T. Steinrötter. Ableitung von Kostenfunktionen für Komponenten der rationellen Energienutzung (in German). Duisburg-Rheinhausen, 2002.

[19] Allan J, Croce L, Dott R, Georges G, Heer P. Calculating the heat loss coefficients for performance modelling of seasonal ice thermal storage. Journal of Energy Storage 2022;52:104528. https://doi.org/10.1016/j.est.2022.104528.

[20] Tribe MA, Alpine RLW. Scale economies and the “0.6 rule”. Engineering Costs and Production Economics 1986;10(1):271–8. https://doi.org/10.1016/0167-188X(86)90053-4.

[21] Bundesnetzagentur für Elektrizität, Gas, Telekommunikation, Post und Eisenbahnen; Bundeskartellamt. Monitoringbericht 2021 (in German). Bonn. 2022. https://www.bundesnetzagentur.de/SharedDocs/Mediathek/Monitoringberichte/Monitoringbericht_Energie2021.pdf?__blob=publicationFile&v=7, Accessed 05.04.2022.

[22] Bundesministerium für Wirtschaft und Ausfuhrkontrolle. Informationsblatt CO_2-Faktoren (in German). 2021. https://www.bafa.de/SharedDocs/Downloads/DE/Energie/eew_infoblatt_co2_faktoren_2021.pdf?__blob=publicationFile&v=5, Accessed 05.04.2022.

[23] Weltenergierat - Deutschland e. V. Energie in der Europäischen Union: Zahlen und Fakten (in German). Berlin. 2022. https://www.weltenergierat.de/publikationen/energie-fuer-deutschland/energie-fuer-deutschland-2021/energie-in-der-europaeischen-union-zahlen-und-fakten/?cn-reloaded=1, Accessed 22.04.2022.

[24] Aurora Energy Research. Carbon intensity outlook of the power sector in France from 2020 to 2050. Berlin. 2022.

[25] Bundesministerium für Wirtschaft und Klimaschutz. Zahlen und Fakten: Energiedaten (in German). Berlin. 2022. https://www.bmwk.de/Redaktion/DE/Artikel/Energie/energiedaten-gesamtausgabe.html, Accessed 23.05.2022.

[26] Umweltbundesamt. Methodenkonvention 3.1 zur Ermittlung von Umweltkosten - Kostensätze (in German). Dessau-Roßlau. 2020. https://www.umweltbundesamt.de/sites/default/files/medien/1410/publikationen/2020-12-21_methodenkonvention_3_1_kostensaetze.pdf, Accessed 12.04.2022.

[27] Waldhoff S, Anthoff D, Rose S, Tol RSJ. The Marginal Damage Costs of Different Greenhouse Gases: An Application of FUND. Economics 2014;8(1). https://doi.org/10.5018/economics-ejournal.ja.2014-31.

[28] Saltelli A, Ratto M, Andres T, Campolongo F, Cariboni J, Gatelli D et al. Global Sensitivity Analysis. The Primer. Chichester, UK: John Wiley & Sons, Ltd; 2007.

Metamodels for economically optimized closed Brayton cycles

Andreas Siman Menzel[a], Francesco Witte[b], Julio Augusto Mendes da Silva[c], Icaro Vilasboas Figueiredo[d] and Armando Sá Ribeiro Jr.[e]

[a] UFBA (Polytechnic School of UFBA), Salvador, Brazil, menzel.andreas@outlook.com, CA
[b] German Aerospace Center (DLR), Institute of Networked Energy Systems, Oldenburg, Germany, francesco.witte@dlr.de,
[c] UFBA PEI (Industrial Engineering Post-graduate Program), Salvador, Brazil, jamsilva08@gmail.com
[d] UFBA (Polytechnic School of UFBA), Salvador, Brazil, icarofvilasboas@gmail.com
[e] UFBA (Polytechnic School of UFBA), Salvador, Brazil, asrj@ufba.br

Abstract:
Closed Brayton Cycles (CBC) can be integrated with many different energy sources, such as heliothermic, biomass, geothermal, etc. However, simplified models for the cycle components are required to optimize the system in its entirety due to all possible cycle configurations like the use of recuperation, intercooling, reheating, etc, together with operating variables such as rate of heat input and its temperature. This work discusses, therefore, the development of a surrogate model for a supercritical CO_2 CBC with recuperation, intercooling and reheating. It can indicate the optimal CBC from an economic point of view under varying boundary conditions. The cycle is first optimized for different heat inputs through its operational parameters (mass flow, minimum cycle pressure and cycle pressure ratios) and heat exchangers area. Compressor and expanders costs are obtained as a function of power while heat exchangers cost is obtained as a function of their area and pressure. Each solution is used to train a surrogate model that will act as an approximator for the optimized CBC and predict cost based on heat input.

Keywords:
CBC; Economic analysis; Machine learning; Surrogate; Thermodynamic analysis.

1. Introduction

Population growth, technological and industrial development are linked to increasing demand for energy, especially in recent years. The continuous reliance on fossil fuels to meet this demand on a global scale is causing negative impacts on the environment, meaning a more robust and sustainable energy matrix is necessary. Because of this, many renewable energy sources are being searched and some of them have become economically feasible such as wind and photovoltaic thanks to continuous investment in recent years. The heliothermic energy, or Concentrating Solar Power (CSP), is one of the first solar technologies to demonstrate grid potential and that could effectively reduce carbon dioxide emissions [1, 2]. That being said, the Closed Brayton Cycle (CBC) has been gaining much attention for its efficiency and possible application as a CSP Power block [3–5].

A CBC is typically more efficient and has a lower cost per power than more conventional cycles such as Rankine and Organic Rankine for heat sources in a temperature range of 600 to 1000°C [6–8]. The CBC also favours the construction of plants in arid locations with higher levels of insolation, i.e., no water is needed, thus being ideal for power generation with CSP.

Variations of the closed Brayton cycle using CO_2 as working fluid at supercritical condition (S-CO_2) are usually studied for heliothermic sources. They are dominant in the few works available in the literature on the use of CBCs to harness solar thermal energy below 600C [8–12]. This is because the closed Brayton cycle with minimum temperature and pressure values near the critical point of the working fluid experience a large reduction in compression work, increasing the thermal efficiency of the cycle [13]. The use of CO_2 as a working fluid stems from the proximity of its critical temperature ($T_c = 31.1$°C) to the ambient temperature [9–11].

The compatibility of CBC with heat sources below 600°C is uncertain. Garg et al [14] investigate a supercritical Brayton cycle using CO_2 with an efficiency potentially greater than 30% even for 820 K (~547°C)

sources. Milani et al. [11] evaluated several configurations of a Brayton Cycle using supercritical CO_2 as the working fluid for a hybridized CSP power source. The optimal configuration has a turbine inlet temperature (TIT) of 600°C and can reach a thermal efficiency of 52.7%. Utamura and Tamaura [9] studied the application of a CBC with S-CO_2, recuperation and pre-and inter-cooling in solar thermal sources with a TIT of up to 577°C. The authors found that the cycle can reach thermal efficiencies of up to 47%.

A widely explored option to optimize the performance of the closed Brayton cycle is the use of multistage (intercooling and/or reheating) compression and expansion plus recuperation. This is a common way to increase efficiency and reduce irreversibilities, which can improve the applicability of the cycle at heat source temperatures below 600C [15, 16]. In this case, a small pressure ratio enables high thermal efficiency and increases the recuperation potential, decreasing the size of the recuperator that would be required for a single-stage cycle.

The use of multistage compression and expansion will require the evaluation of multiple configurations of the cycle to determine the optimal or most economically feasible one. The optimization uses input data from the available heat source, i.e., inlet temperature and mass flow rate of the heat source fluid, as well as the rate in which heat is supplied. However, evaluating all possible configurations for each instance of the decision variables, like heat exchanger area, turbine inlet temperature, pressure ratio, etc., in the optimization process is computationally expensive. Thus, this work proposes an alternate method of optimization using Surrogates to reduce the processing time of the optimal CBC configuration while maintaining convergence to a global minimum specific cost value. Surrogate models, also known as metamodels, response surfaces, approximation models, etc., map an input-output relationship from data associated with some phenomenon to reproduce it in an approximate and often faster way [17, 18].

Using metamodels for complex process optimization is common for several engineering disciplines. Urquhart et al. [19] investigate the performance of two methods based on the construction of response surfaces for the optimization of aerodynamic shapes. Huang et al. [20] propose and study the use of Kriging models to perform global optimizations of stochastic systems. Carranza-Abaid et al. [21] created thermodynamically consistent Machine Learning-based Surrogate models to represent phase equilibria with multiple components.

In this work, a surrogate is created to replace the overall CBC model, reducing computational time, and allowing its use in broader optimization codes.

2. System Description

2.1. CBC Layout

Figure 1 displays a schematic of the proposed S-CO_2 CBC, while Fig. 2. shows its T-s diagram. The thermal and working fluids used are DOWTHERM A (in red) and CO_2 (in black), respectively. The optimal configuration and operating condition of the CBC varies depending on: (i) thermal fluid inlet temperature (T_Q^{in}); (ii) thermal fluid mass flow rate ($\dot{m}_Q$); and (iii) total heat transfer rate ($\dot{Q}_H = \dot{Q}_{H,0} + \dot{Q}_{H,1}$).

The working fluid at supercritical pressures goes through the compression process with intercooling (1-4) and then to the recuperator (4-5) as a cold stream. In the recuperator its temperature is increased by residual heat from the working fluid after expansion process. The CO_2 is heated up to turbine inlet temperature - TIT (5-6) before entering the re-heated expansion system (6-9) and the recuperator as hot stream (9-10). The working fluid is then cooled in (10-1) and returns to the cycle starting point (1).

The thermal fluid enters the reheaters and the main heat exchanger with the same temperature (T_Q^{in}). Different mass flow rates and output temperatures are allowed, which serve as decision variables chosen during optimization. The lower and upper boundaries of each global input are shown on Table 1.

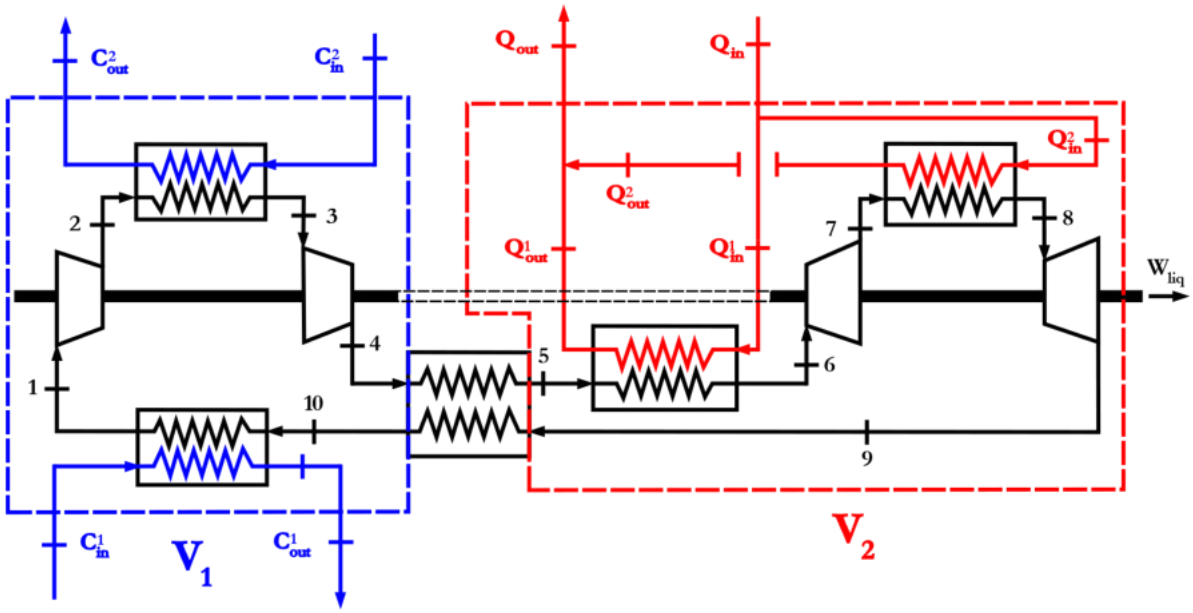

Figure 1. CBC diagram with supercritical CO_2.

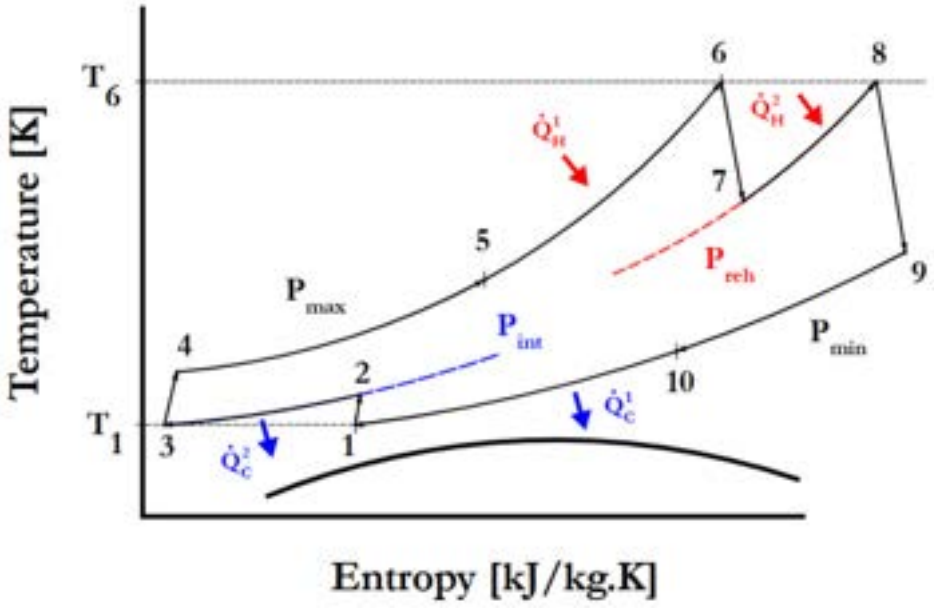

Figure 2. T-s diagram of CBC with supercritical CO_2.

Table 1. Operating range of the CBC input parameters.

	Lower boundary	Upper boundary
T_Q^{in}	200°C	390°C
$\dot{m}_Q$	100 kg/s	200 kg/s
$\dot{Q}_H$	100 kW	50000 kW

3. Thermodynamic Modelling

All components were modelled in a permanent regime, disregarding kinetic and potential energy effects and pressure drop in heat exchangers and piping. Table 2 presents the fixed parameters considered in the calculation of the thermodynamic states for CBC [22–24].

Table 2. Fixed parameters used to model CBC.

	Description	Value
$\eta_{ise,comp}$	Isentropic Compressor Efficiency	85%
$\eta_{ise,turb}$	Isentropic Turbine Efficiency	85%
η_e	Generator Efficiency	95%
T_C^{in}	Cooling Water inlet temperature	35°C
T_C^{out}	Cooling Water outlet temperature	42.55°C
$\overline{U}_{g/g}$	Overall heat transfer coefficient (gas/gas)	47.5 $W/(m^2 \cdot K)$
$\overline{U}_{g/w}$	Overall heat transfer coefficient (gas/water)	177.5 $W/(m^2 \cdot K)$
$\overline{U}_{g/o}$	Overall heat transfer coefficient (gas/oil)	274.5 $W/(m^2 \cdot K)$

The isentropic efficiencies of the compressor ($\eta_{ise,comp}$) and turbine ($\eta_{ise,turb}$) are calculated according to Eqs. (1) - (2), respectively. Their energy balances are represented by Eqs. (3) - (4). The energy balance of the recuperator is presented by Eq. (5) and assumes no heat losses to the environment.

$$\eta_{ise,comp} = \frac{h_{2s} - h_1}{h_2 - h_1} = \frac{h_{4s} - h_3}{h_4 - h_3} \quad (1)$$

$$\eta_{ise,turb} = \frac{h_6 - h_7}{h_6 - h_{7s}} = \frac{h_8 - h_9}{h_8 - h_{9s}} \quad (2)$$

$$\dot{W}_{turb,n} = \dot{m}_{CO2}(h_{in} - h_{out}) \quad (3)$$

$$\dot{W}_{comp,n} = \dot{m}_{CO2}(h_{out} - h_{in}) \quad (4)$$

$$\dot{m}_{CO2}(h_5 - h_4) = \dot{m}_{CO2}(h_9 - h_{10}) \quad (5)$$

Equations (6) - (7) show the energy balances of the cycle remaining heat exchangers.

$$\dot{m}_{CO2}(h_{out} - h_{in}) = \dot{m}_Q\left(h_{in}^Q - h_{out}^Q\right) \quad (6)$$

$$\dot{m}_{CO2}(h_{in} - h_{out}) = \dot{m}_{water}(h_{water}^{out} - h_{water}^{in}) \quad (7)$$

Liquid electric power ($\dot{W}_{liq}$) and cycle total efficiency (η_t) are given by Eqs. (8) – (10).

$$\dot{W}_{liq} = \sum_{i=1}^{n} \dot{W}_{turb,i} - \sum_{i=1}^{n} \dot{W}_{comp,i} \quad (8)$$

$$\dot{W}_{liq,e} = \eta_e \dot{W}_{liq} \quad (9)$$

$$\eta_e = \frac{\dot{W}_{liq,e}}{\dot{Q}_H} \quad (10)$$

Equations (11) – (13) are used to calculate the area for each heat exchanger present in the cycle.

$$\begin{cases} \Delta T_{in} = T_h^{in} - T_c^{out} \\ \Delta T_{out} = T_h^{out} - T_c^{in} \end{cases} \quad (11)$$

$$\Delta T_{ml} = (\Delta T_{out} - \Delta T_{in})/ln(\Delta T_{out}/\Delta T_{in}) \quad (12)$$

$$A_{hx} = \frac{\dot{Q}_H}{\overline{U} \cdot \Delta T_{ml}} \quad (13)$$

Most of the working fluid's thermodynamic properties were calculated through the use of CoolProp, a module dedicated to the calculation of thermodynamic states, and TesPy, a thermodynamic cycle simulation toolkit that was used to model the different components of the proposed CBC configuration [25, 26].

4. Economic Models

According to the literature, there are many different methods to estimate the acquisition cost of industrial equipment [27, 28]. The cost estimates in this work came from Eq. (14) of exponential cost of Bejan et al. [27]. Cost data from Peters et al. [28] for a centrifugal compressor, axial turbine and double-pipe and U-tube heat exchangers was used to adjust the equation.

$$C = C_{ref}\left(\frac{X}{X_{ref}}\right)^{\alpha}\left(\frac{CEPCI}{CEPCI_{ref}}\right) \quad (14)$$

Equation (14) indicates the equipment acquisition cost (C) using reference values for equipment size (X_{ref}) and cost (C_{ref}), the current size parameter (X) and an adjustable exponent (α). The ratio between $CEPCI$ (Chemical Engineering Plant Cost Index) and $CEPCI_{ref}$ serves as a correction factor for the cost of equipment in years other than the base year, which in this case is the year 2021 with $CEPCI_{ref} = 607.5$.
The total acquisition cost of CBC encompassing compression and expansion systems, is obtained by summing their respective individual equipment costs.
Table 3 displays the cost parameters of compressors and turbines used in the CBC. The heat exchangers acquisition cost varies according to the thermal load, operating pressure, and area. Tables 4 - 5 present the operational ranges in which each heat exchanger type has the lowest cost per area [27, 28].

Table 3. Cost estimation parameters for compression and expansion equipment.

Equipment	Size Parameter	Reference Size	Reference Cost [$]	α
Axial Turbine	Electric Power	10 kWe	16955.23	0.611
Centrifugue Compressor	Electric Power	100 kWe	105240.35	0.943

Table 4. General cost estimation parameters for heat exchangers.

Type	Exchanger Area [m²]	Size Parameter	Reference Size [m²]	α
Double-Pipe	0.25 – 20	Exchanger Area [m²]	0.25	0.063
U-Tube	20 – 1000	Exchanger Area [m²]	20	0.479

Table 5. Operating conditions and reference cost for heat exchangers.

Type	Pressure Range [MPa]	Reference Cost [$]
Double-Pipe	10 – 20	2321.89
	20 – 30	3605.73
	30 – 40	5494.36
U-Tube	10 - 20	9831.35
	20 – 30	10591.46
	30 - 40	11015.60

The cheapest heat exchangers were investigated and selected based on cost data from Peters et al. [28]. Figure 3 compares the specific cost curves of the cheapest exchangers with an operational pressure from 0.1 to 5 MPa. The plate exchangers (Welded and Gasketed Plate) have the lowest specific cost. However, their operating pressure limit goes up to 2.5 MPa, thus, in operating pressures above this value, Double-Pipe and U-Tube exchangers may be required.

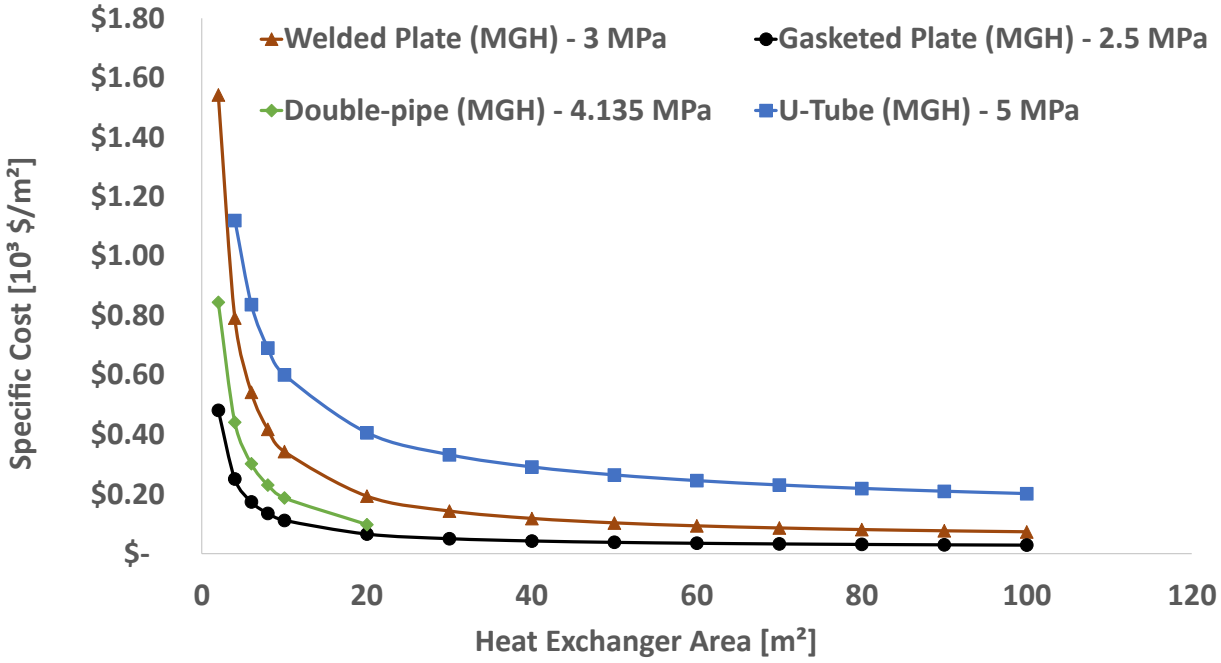

Figure 3. Specific cost curves comparison of different types of heat exchangers with operating pressure between 0.1 – 5 MPa.

5. CBC Optimization

The optimal cycle considered in this work is the one that has the greatest energy output for the lowest acquisition cost for its given heat input. Therefore, the CBCs objective function to be minimized is its specific cost, as per Eq. (15).

$$\min C_{e,CBC} = \frac{C_{total}}{\dot{W}_{liq,e}} \tag{15}$$

The optimizations were performed using Particle Swarm Optimization, implemented through the Pygmo library in Python, developing 50 individuals over a course of 30 generations [29, 30]. To facilitate data transfer between the power plant simulation in TESPy and the optimization a dedicated API was developed based on the work of Chen et al. [31] and made available in the most recent version of the software [32].

Many decision variables with general boundaries have been initially considered in the optimization process, such as working fluid mass flow rate, minimum cycle pressure, compression and expansion pressure ratios, thermal fluid split value between the heater and reheater, minimum temperature difference in the recuperator, main heater, and cooler, etc. To restrict their boundaries, 25 runs resulting in 25 champions have been performed and each of the decision variables was plotted against the obtained objective function values. The variables whose variation was of no consequence to the final result were set to a specific value. The final set of decision variables can be found in Table 6.

Table 6. Decision variables considered.

Decision Variable	Description	Value Interval
P_{min}	Minimum cycle pressure	10.1 – 13.0 MPa
ΔP	Total cycle pressure variation	2.0 – 8.0 MPa
$\dot{m}_{CO2}$	CO_2 mass flow rate	100.0 – 350.0 kg/s
ΔT_{min}^{reh}	Minimum Reheater temperature difference	3.0-20.0 ºC
f_q	Thermal fluid mass flow rate fractions	0 - 1
P_{int}^{comp}	Compression system intermediate pressures	P_{min} - P_{max} MPa
P_{int}^{exp}	Expansion system intermediate pressures	P_{min} - P_{max} MPa

6. Surrogate Model Development

This work used Scikit-Learn, one of the most used Machine Learning (ML) libraries in Python [33], to build the CBCs response surface. This approach used a supervised learning model with offline training. Unsupervised learning was implemented for dimensionality reduction of each model training set [34–36]. A regression model was trained on the champion population obtained as a result of the optimization process to predict the value of optimum specific cost for a given set of input variables.

Dimensionality reduction was performed using a Stratified Latin Hypercube (LHS) with *CenterMaximin* from the PyDOE2 library in Python which is a widely used technique in surrogate modelling [17, 37–39]. LHS is, by itself, used to generate smaller data sets with more information. *CenterMaximin* is a stratification criterion that allows LHS to further spread out those samples within their data regions [18, 37].

The surrogate was built using linear regression with a polynomial and a normalizing pre-processing step. These steps highlights trends and relationships in the data previously unknown to the ML model, augmenting their capacity [36, 40, 41]. The model was validated using *Cross-Validation* [17, 18, 36] which allows the exploration of the entire data set for both training and validation, through the use of an R^2 score.

7. Results and Discussion

7.1. Optimization Results

A total of 832 champions were obtained through the optimization process with an average of 8 champions/hour while using an Intel Core i7 processor computer with 16 GB of RAM memory and 8 logic cores. Although the champions are not always guaranteed to be global optima, they can still be used to verify the thermodynamic consistency of the developed objective function. As shown in Figure 4, the obtained values of specific cost tend to decrease with greater values of thermal input to the cycle, when considering a constant average heat source temperature of $200°C$. Figure 5 highlights that the optimum cycle efficiency tends to increase with a higher average heat source temperature, considering a constant Heat input of $20000\ kW$, as was to be expected.

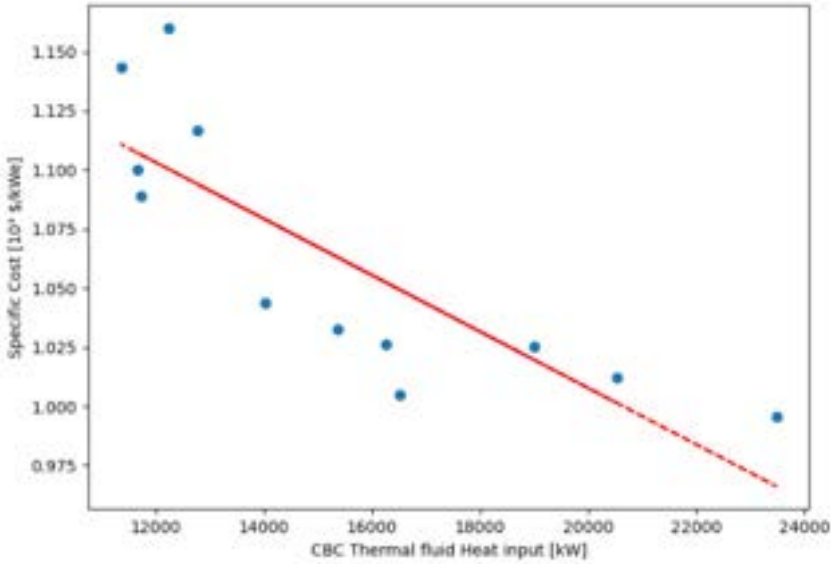

Figure 4. Specific cost versus CBC heat input, considering an average heat source temperature at 200°C.

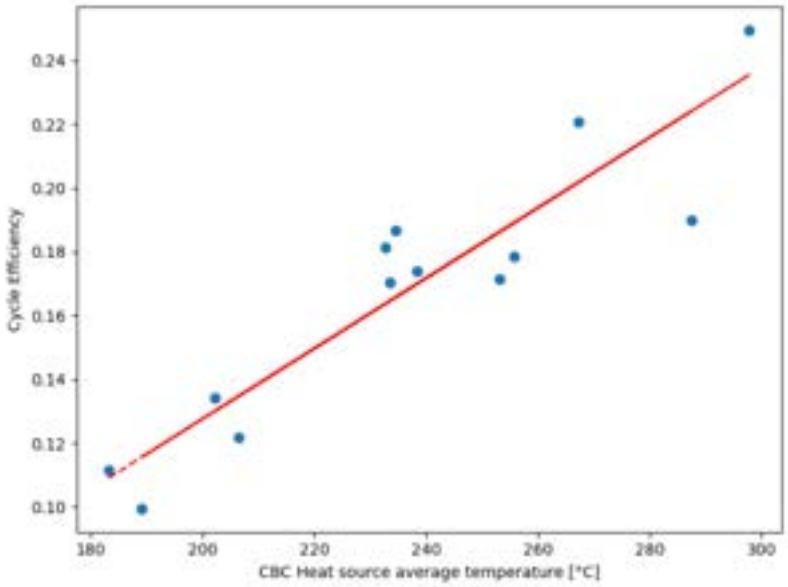

Figure 5. Optimum cycle efficiency versus heat source average temperature, considering a heat input of 20000 kW.

7.2. Surrogate Results

The most informative input format for training the Surrogate model was shown to be a combination of the original input variables (T_Q^{in}, $\dot{m}_Q$ and $\dot{Q}_H$) and implicit variables, calculated considering that the heat fluid possesses a constant pressure of $P_Q = 10.49\ MPa$, such as outlet thermal fluid temperature (T_Q^{out}) and the arithmetic average of the heat source temperature ($\overline{T}_Q$). Figure 6 is a correlation plot of each set of values for the mentioned variables and their respective optimal specific cost.

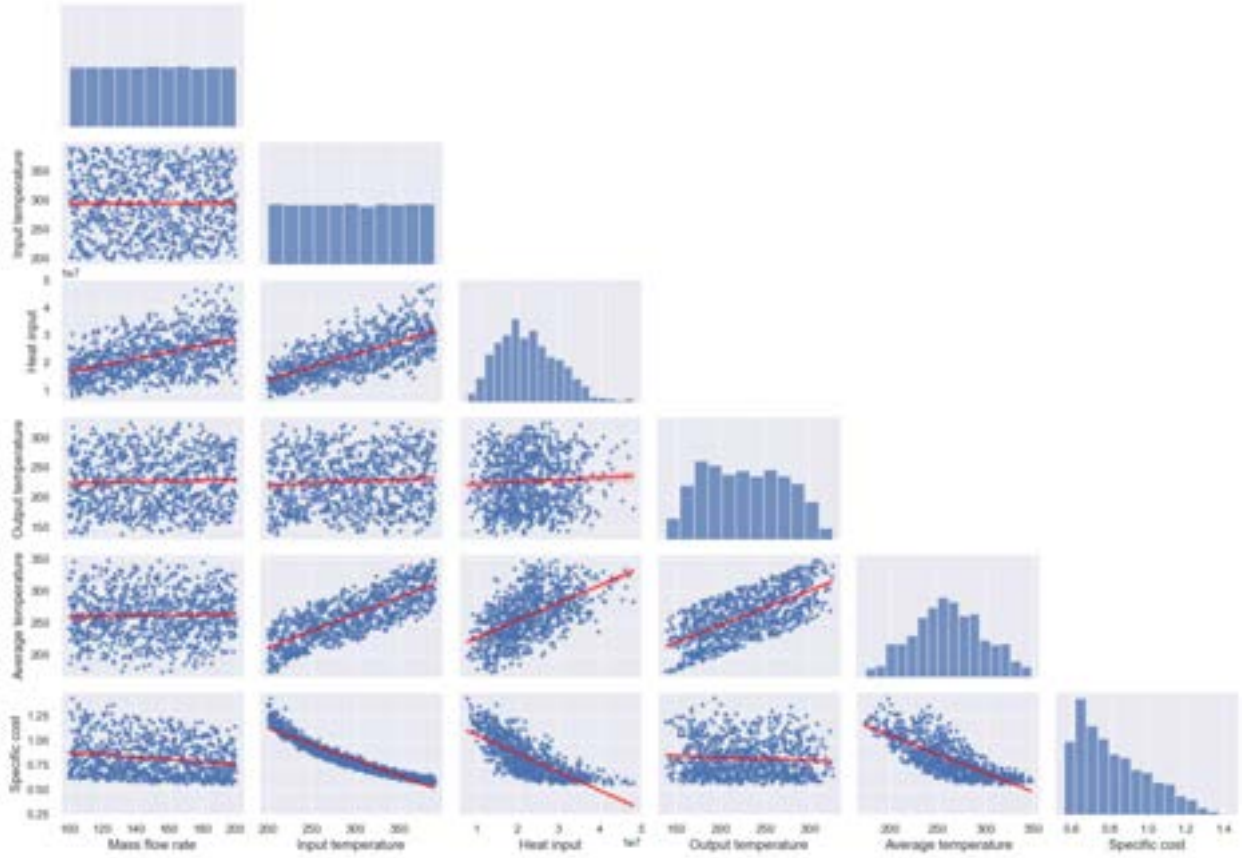

Figure 6. Correlation and distribution plot between Thermal fluid input variables (mass flow rate, input temperature, heat input, output temperature and average temperature) and optimum CBC specific cost.

Using variables with a clear relationship to the objective tend to improve the final cross-validation score of the model [34, 36].

The regression Model in question is of the second degree and utilizes a normalizing pre-processing feature from Scikit-Learn to allow for a model with a higher R^2. All champions have been used to train the model, with its final cross-validation score being $R^2 = 0.9911 \pm 0.0022$. Figures 7(a) and (b) display the residuals and prediction versus real value plots for the trained model when predicting its training set, respectively. While the model has a precision score of 99.11%, there is still an amount of residual error that varies in its majority between $(-150, 50)\ \$/kW_e$. The model took approximately $0.004\ s$ to predict the specific cost of 832 different sets of input variables.

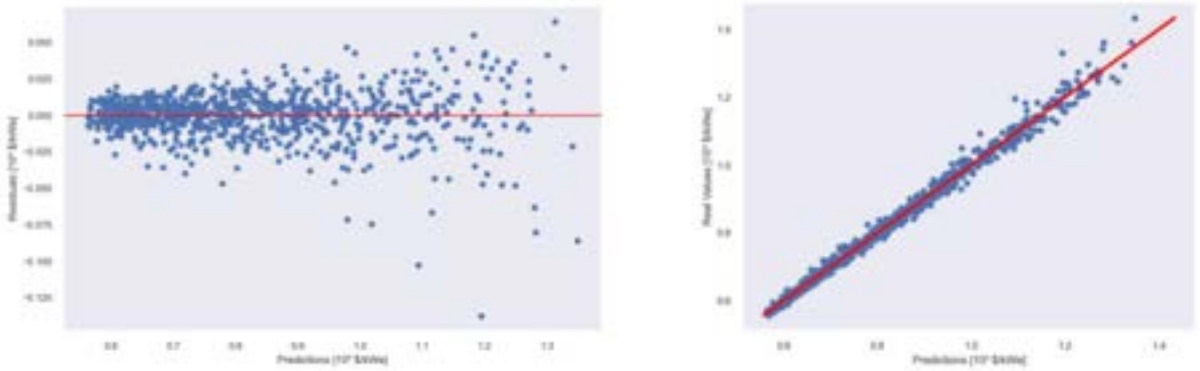

(a) *(b)*

Figure 7. Surrogate model (a) specific cost prediction residual plot, (b) specific cost prediction versus real values plot.

The created surrogate model is shown to be much faster to determine the optimum minimal specific cost of the CBC than the optimization method, at a very low precision cost, even though it only utilized 832 Champions to be created. The method presented in this work allowed for the creation of a deployable representation of the proposed Thermodynamic cycle that, while in this case was used to investigate the minimal specific cost, could also be used to evaluate other parameters of interest, such as number of intercoolers/reheaters, maximum cycle pressure, etc. as a function of a set of input variables.
It should be noted that an interesting application would be to use the model to perform a preliminary evaluation of the solution space for optimum CBC configuration and then perform a single optimization on the region most inclined to contain the minimum. This way the global solution space can be more thoroughly investigated at a very low computational burden. It should also be brought to attention that optimum CBC configurations can have a typical specific cost ranging from 600 to $1400\ \$/kW_e$ under the proposed ranges of input variables. Therefore, the closed Brayton cycle with Heat input from a low temperature source might be economically feasible given the right conditions.

8. Conclusion

The present work has shown that it is possible to create estimators that can allow for precise evaluations of a supercritical CBC using intercooling, reheating and a recuperator. First, the proposed cycle was optimized for multiple combinations of input variables, i.e. thermal fluid input temperature, mass flow rate and exchanged heat, so as to minimize the cycle's specific cost. After 832 champions were acquired, they were used to train a surrogate model that predicts optimum specific cost for the CBC based on a set of input variables. The difference in time between the optimization and the evaluation through the surrogate model on the specified machine is in the order of $10^8 s$. With a 99.11% cross-validation score, it can be considered as a viable estimator for the supercritical CBC.

Acknowledgements

The authors would like to thank Grupo Global Participações em Energia (GPE) for the financial support under Agência Nacional de Energia Elétrica (ANEEL) P&D program, project number PD-06961-0011/2019.

References

[1] Goswami DY. *Principles of solar engineering*. 3rd ed. Boca Raton: CRC Press, 2015.

[2] Santos JJCS, Palacio JCE, Reyes AMM, et al. Concentrating Solar Power. In: *Advances in Renewable Energies and Power Technologies*. Elsevier, pp. 373–402.

[3] Iverson BD, Conboy TM, Pasch JJ, et al. Supercritical CO2 Brayton cycles for solar-thermal energy. *Appl Energy* 2013; 111: 957–970.

[4] Khatoon S, Kim MH. Potential improvement and comparative assessment of supercritical Brayton cycles for arid climate. *Energy Convers Manag* 2019; 200: 112082.

[5] Mahmoudi SMS, Akbari AD, Rosen MA. Thermoeconomic analysis and optimization of a new combined supercritical carbon dioxide recompression Brayton/Kalina cycle. *Sustain*; 8. Epub ahead of print 2016. DOI: 10.3390/su8101079.

[6] Najjar YSH, Zaamout MS. Comparative performance of closed cycle gas turbine engine with heat recovery using different gases. *Heat Recover Syst CHP* 1992; 12: 489–495.

[7] Yu SC, Chen L, Zhao Y, et al. A brief review study of various thermodynamic cycles for high temperature power generation systems. *Energy Convers Manag* 2015; 94: 68–83.

[8] Dunham MT, Iverson BD. High-efficiency thermodynamic power cycles for concentrated solar power systems. *Renew Sustain Energy Rev* 2014; 30: 758–770.

[9] Utamura M, Tamaura Y. A solar gas turbine cycle with super-critical carbon dioxide as a working fluid. *Proc ASME Turbo Expo* 2006; 4: 329–335.

[10] Rovira A, Muñoz-Antón J, Montes MJ, et al. Optimization of Brayton cycles for low-to-moderate grade thermal energy sources. *Energy* 2013; 55: 403–416.

[11] Milani D, Tri M, Mcnaughton R, et al. Optimizing an advanced hybrid of solar-assisted supercritical CO 2 Brayton cycle : A vital transition for low-carbon power generation industry. *Energy Convers Manag* 2017; 148: 1317–1331.

[12] Binotti M, Astolfi M, Campanari S, et al. Preliminary assessment of sCO2 cycles for power generation in CSP solar tower plants. *Appl Energy* 2017; 204: 1007–1017.

[13] Invernizzi CM. Prospects of mixtures as working fluids in real-gas Brayton cycles. *Energies*; 10. Epub

ahead of print 2017. DOI: 10.3390/en10101649.

[14] Garg P, Kumar P, Srinivasan K. The Journal of Supercritical Fluids Supercritical carbon dioxide Brayton cycle for concentrated solar power. *J Supercrit Fluids* 2013; 76: 54–60.

[15] Le Roux WG, Bello-Ochende T, Meyer JP. A review on the thermodynamic optimisation and modelling of the solar thermal Brayton cycle. *Renew Sustain Energy Rev* 2013; 28: 677–690.

[16] Mohammadi K, McGowan JG, Saghafifar M. Thermoeconomic analysis of multi-stage recuperative Brayton power cycles: Part I- hybridization with a solar power tower system. *Energy Convers Manag* 2019; 185: 898–919.

[17] Jiang P, Zhou Q, Shao X. *Surrogate-Model-Based Design and Optimization*. 2020. Epub ahead of print 2020. DOI: 10.1007/978-981-15-0731-1_7.

[18] Forrester AIJ, Sóbester A, Keane AJ. *Engineering Design via Surrogate Modelling*. 2008. Epub ahead of print 2008. DOI: 10.1002/9780470770801.

[19] Urquhart M, Ljungskog E, Sebben S. Surrogate-based optimisation using adaptively scaled radial basis functions. *Appl Soft Comput J* 2020; 88: 106050.

[20] Huang D, Allen TT, Notz WI, et al. Global optimization of stochastic black-box systems via sequential kriging meta-models. *J Glob Optim* 2006; 34: 441–466.

[21] Carranza-Abaid A, Svendsen HF, Jakobsen JP. Surrogate modelling of VLE: Integrating machine learning with thermodynamic constraints. *Chem Eng Sci X* 2020; 8: 100080.

[22] Çengel YA, Ghajar AJ. *Heat and Mass Transfer*.

[23] Kakaç S, Liu H, Pramuanjaroenkij A. *Heat Exchangers: Selection, Rating, and Thermal Design, Third Edition*. 2012.

[24] Shah RK, Sekuli DP. *Selection of Heat Exchangers and Their Components*. 2007. Epub ahead of print 2007. DOI: 10.1002/9780470172605.ch10.

[25] Witte F, Tuschy I. TESPy: Thermal Engineering Systems in Python. *J Open Source Softw* 2020; 5: 2178.

[26] Bell IH, Wronski J, Quoilin S, et al. Pure and Pseudo-pure Fluid Thermophysical Property Evaluation and the Open-Source Thermophysical Property Library CoolProp. Epub ahead of print 2014. DOI: 10.1021/ie4033999.

[27] Bejan A, Tsatsaronis G, Moran M. *Thermal Design and Optimization*. 1st ed. John Wiley & Sons, Inc., 1995.

[28] Peters MS, Timmerhaus KD, West RE. *Plant Design and Economics for Chemical Engineers*. 5th ed. 2003. Epub ahead of print 2003. DOI: 10.16309/j.cnki.issn.1007-1776.2003.03.004.

[29] Arora JS. *Introduction to Optimum Design*. 4th ed. Elsevier. Epub ahead of print 2017. DOI: 10.1016/C2013-0-15344-5.

[30] Biscani F, Izzo D. A parallel global multiobjective framework for optimization: pagmo. *J Open Source Softw* 2020; 5: 2338.

[31] Chen C, Witte F, Tuschy I, et al. Parametric optimization and comparative study of an organic Rankine cycle power plant for two-phase geothermal sources. *Energy* 2022; 252: 123910.

[32] Witte F. TESPy: Thermal Engineering Systems in Python. Epub ahead of print 2022. DOI: 10.5281/ZENODO.7134696.

[33] Pedregosa F, Varoquaux G, Gramfort A, et al. Scikit-learn: Machine Learning in Python. *J Mach Learn Res* 2011; 2825–2830.

[34] Goodfellow I, Bengio Y, Courville A. *Deep Learning*. 2017.

[35] Bishop CM. *Pattern Recognition and Machine Learning*. Springer, 2006. Epub ahead of print 2006. DOI: 10.13109/9783666604409.185.

[36] Hastie T, Tibshirani R, Friedman J. *The Elements of Statistical Learning - Data Mining, Inference, and Prediction*. 2008. Epub ahead of print 2008. DOI: 10.1007/978-0-387-84858-7.

[37] Garud SS, Karimi IA, Kraft M. Design of computer experiments: A review. *Comput Chem Eng* 2017; 106: 71–95.

[38] Jin R, Chen W, Sudjianto A. On sequential sampling for global metamodeling in engineering design. *Proc ASME Des Eng Tech Conf* 2002; 2: 539–548.

[39] Giunta AA, Wojtkiewicz SFJ, Eldred MS. Overview of Modern Design of Experiments Methods for Computational Simulations. *41st Aerosp Sci Meet Exhib* 2003; 1–18.

[40] Koziel S, Yang X-S. *Computational Optimization, Methods and Algorithms*. Springer Berlin Heidelberg, 2011.

[41] García S, Luengo J, Herrera F. *Data Preprocessing in Data Mining*. 2015.

Optimization tools for the operational dispatch of power generation systems to reduce diesel fuel consumption

Daniel Felipe Sempértegui-Tapia[a], Cesar Alberto Ayma-Ramos[b], Filiberto Soto Encinas[c] and Renán Orelllana Lafuente[d]

[a]Universidad Privada Boliviana, Cochabamba, Bolivia, dsempertegui@upb.edu, CA
[b]Universidad Privada Boliviana, Cochabamba, Bolivia, cesaralberto1996@gmail.com
[c] Ende Transmisión S.A., Cochabamba, Bolivia, filiberto.soto@endetransmision.bo
[d]Universidad Privada Boliviana, Cochabamba, Bolivia, renanorellana@upb.edu

Abstract:

Bolivia, despite being a relatively small country, has several small cities far away for the National Interconnected System. For this reason, these cities have Isolated Systems and almost 70% of their installed power are generated through thermoelectric plants, which ended up being a problem because of the high diesel fuel consumption. The diesel fuel supply in Bolivia is not guaranteed because the country depends on importation at very high prices. In this sense, this study intends to reduce the diesel consumption of the isolated power generation systems in Bolivia using an operational dispatch optimization model. First, there were chosen 3 Isolated systems in Bolivia, the Cobija Hybrid System, the Sena Hybrid System and the Gonzalo Moreno System. The latter is a purely thermal system, while the other two are hybrid systems (thermal and photovoltaic plants). Then, a comprehensive analysis of the power demand and supply has been completed for the three cases. Subsequently, an optimization model has been developed using the software Matlab and its complementary package knows as the Optimization Tool Box. Using this model, a comparison has been made between the operational dispatch of the energy system with and without optimization. The results indicate that it would be possible to save 2211 L/day, 182 L/day and 73 L/day of diesel consumption with an optimization process for the Cobija Hybrid System, the Sena Hybrid System and the Gonzalo Moreno Systems, respectively. These diesel fuel savings would represent more than 1.31 MM$ in money savings for the Bolivian Government.

Keywords: Optimization, hybrid energy system, diesel fuel consumption.

1. Introduction

In Bolivia, a country in South America, the largest population is concentrated in its main cities. The energy supply in the main cities is guaranteed because these cities are part of the National Interconnected System (NIS). The NIS connects 8 out of 9 departments in Bolivia, the only department that is not part of the NIS is Pando, which is located in the northern part of Bolivia in the middle of the Amazon forest.

Considering that there is a Department of Bolivia that is not connected to the NIS, the cities of this department have Isolated Systems (IS). Most of the isolated systems are thermoelectric plants that work with diesel fuel due to the difficulty of the natural gas transportation to these cities since most of them are in the middle of the Amazon Forest. The Isolated Systems in Bolivia are Cobija, El Sena, Gonzalo Moreno, Baures and Guayaramerin. Some of them are hybrid energy systems, which combines two or more types of energy generation.

According to [1], hybrid generation systems are a viable solution for electricity supplying especially when there are access difficulties to the location or when the city is too far away of the National Interconnected System. In the region, there are some examples of hybrid generation systems. For example, there is a photovoltaic-diesel hybrid system in Campinas, Amazonas – Brazil with a power capacity of 99.2 kW. In Rondonia - Brazil, the hybrid system of Araras presents an installed diesel power of 162 kW and 20.48 kW of power in the photovoltaic plant. On the other hand, there is also examples of hybrid generation system between wind generation and diesel thermoelectric generation like the energy system in Vila de Praia Grande, Brazil. In Bolivia, the hybrid systems are Cobija and El Sena, which are photovoltaic-diesel hybrid systems. Cobija has an installed capacity of 24.16 MW in diesel and 5.10 MW in photovoltaic, and El Sena has a total installed capacity of 4.62 MW [2].

As mentioned before, the hybrid systems in Bolivia use diesel as the source of energy. For this reason, the consumption of diesel in Bolivia in general has increased a lot the last decades. Figure 1 shows that the diesel consumption in the isolated systems System has been increasing rapidly the last ten years. In 2021, the isolated systems have expended approximately 57,800 m3 of diesel fuel.

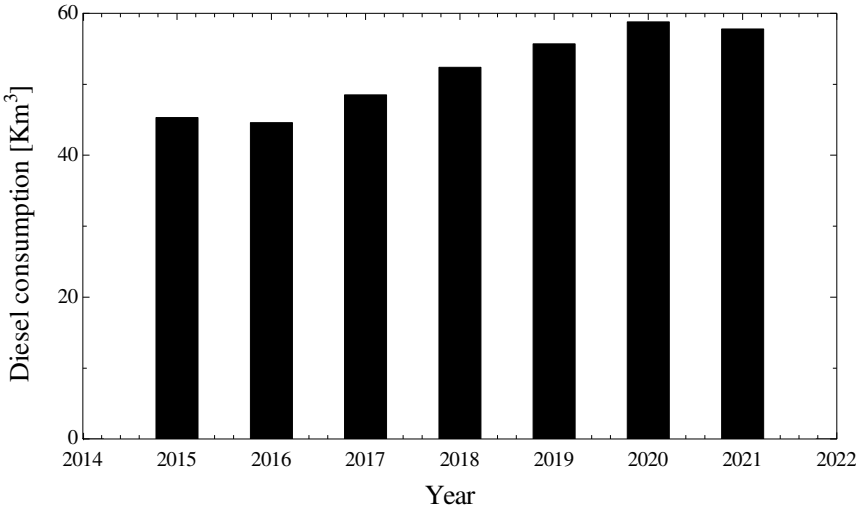

Figure. 1. Isolated systems diesel consumption in Bolivia per year.

Unfortunately, Bolivia does not produce diesel fuel. Hence, the country depends on the importation of this fuel and, therefore, on the international prices of the diesel. Figure 2 shows that the diesel in 2022 was approximately 10.1 Bs per liter (1.45 $ per liter). It's also worth to mention that the price of diesel is increasing since 2020 (8.6 Bs/liter), so it´s possible that the next years the price of the diesel is going to be even more than 10.1 Bs per liter.

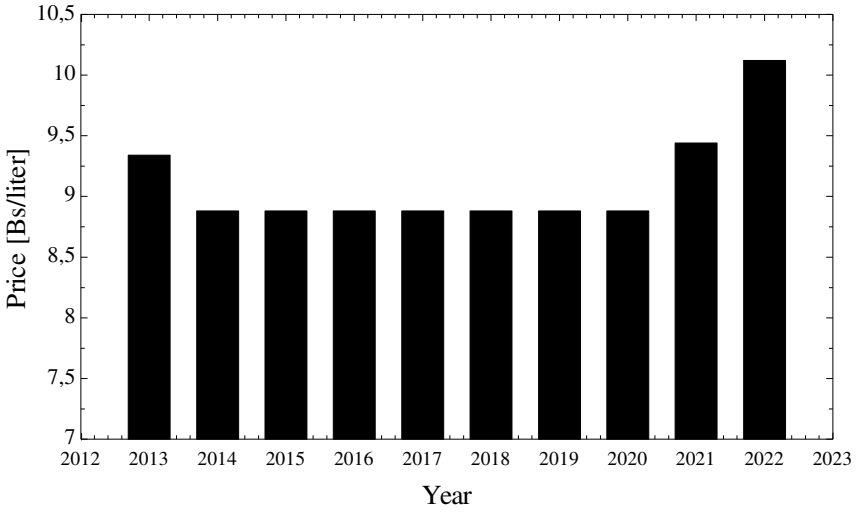

Figure. 2. Diesel price evolution [2], [3], [4].

On the other hand, the installed power of the Isolated Systems reached a value of 216.71 MW, of which 67.54% was thermally generated. So, Bolivia needs approximately 57800 m3/year of diesel fuel, which represents 84.5 MM$/year in order to keep the isolated systems working, and consequently, providing electric energy to a lot of small cities in the country.

Sempértegui-Tapia et al. [5] presented a case of study for the optimization of the Cobija Hybrid System. The authors recommended some changes in the operational dispatch of the energy system which allowed them to save 2622 L/day of diesel consumption. In this paper, we intend to further the mentioned study by including the analysis of 3 out of 5 isolated systems in the country. The Cobija Hybrid System will be analysed again, with updated data. Also, El Sena Hybrid System and the purely thermal Gonzalo Moreno System are going to be optimized. This way, the proposed optimization tool proposed by [5] is going to be validated and assessed using it for three different energy systems, which have very unique characteristics like number of generating units, installed power, load and demand factors, etc.

2. Mathematical model of the operational dispatch optimization

The mathematical model of the optimal operational dispatch consists on an objective function (OF), equality constraints (EC) and inequality constraints (IC), as shown in Eq. (1).

$$\text{Minimize} \rightarrow \mathbf{OF} \text{ subject to} \begin{cases} EC \\ IC \end{cases} \tag{1}$$

The modelling requires the objective function, which is formed by the energy consumption equations of the generating units; the equality constraints of the energy balance between demand and supply of the generating units and the inequality constraints that limit the power delivery of the generating units. Thus, taking into account that the energy consumption equations are second degree polynomial, the problem results in a non-linear program. Considering the characteristics of the "n" generating units in the IS (energy consumption equation and on-site effective power) and the isolated system type (hybrid or purely thermal), the mathematical model of the optimal operational dispatch is shown in Eq. (2).

$$\text{minf}(\mathrm{P}) = \sum_{\mathrm{i}=1}^{n} \mathrm{C_i} \text{ subject to} \begin{cases} \mathrm{d} - \sum_{\mathrm{i}=1}^{n} \mathrm{p_i} - \mathrm{p_s} = 0 \\ 0 \leq \mathrm{p_1} \leq \mathrm{p_{e1}} \\ \vdots \\ 0 \leq \mathrm{p}_n \leq \mathrm{p_{en}} \end{cases} \tag{2}$$

Equation (2) defines the operational dispatch problem. In order to solve this problem, the objective function has to be defined first and then the interior point algorithm will be used.

2.1. Objective function

The behaviour of a generating unit is described by the overall ratio of the heat input to the thermal unit in Btu/h vs the power output in MW. These behaviour is mathematically modelled by a second degree polynomial equation:

$$\mathrm{C_i} = \mathrm{a_i P_i^2} + \mathrm{b_i P_i} + \mathrm{c_i} \tag{3}$$

Therefore, the objective function will be composed by the sum of "n" energy consumption equations, one for each generating unit present in the isolated system.

2.2. Interior point algorithm

The interior point algorithm is normally used in nonlinear programming due to the speed of convergence and the ease of handling the inequality constraints. Besides, this method has advantages with quadratic-type constraints.

In this method, the approximation process starts from an initial point inside the plausible zone, moving internally until the global optimum point is found. In the case of the operational dispatch in thermal generation systems, 2nd order polynomial equations are presented to form the objective function and to determine the constraints. In other words, this method works with the Lagrange function modified by the inequality constraints present, the Karush Kuhn Tucker conditions and finally uses Newton Raphson to approximate the problem to an optimal solution.

Matlab and the Optimization Toolbox add-on provide a number of algorithms for solving a wide range of optimization problems. The optimal operational dispatch problem converges using the *fmincon* routine, that operates the interior point algorithm.

2.3. Multidimensional matrix

As mentioned before, the interior point algorithm is an iterative tool that starts from an initial point and travels through the interior of the solution space considering the constraints of the problem. In this way, the interior point algorithm must solve the following multidimensional matrix:

$$\begin{bmatrix} \mathrm{W_K} & \nabla \mathrm{R(P)} & -\mathrm{I} \\ \nabla \mathrm{R(P)^T} & 0 & 0 \\ \mathrm{Z} & 0 & \mathrm{P} \end{bmatrix} \begin{bmatrix} \mathrm{d_P} \\ \mathrm{d_\lambda} \\ \mathrm{d_z} \end{bmatrix} = - \begin{bmatrix} (\nabla \mathrm{f(P)} - \lambda \nabla \mathrm{R(P)} - \mathrm{z}) \\ \mathrm{R(P)} \\ (\mathrm{zPe} - \mu \mathrm{e}) \end{bmatrix} \tag{5}$$

It should be noted that the system has the form Ax=b, with the difference that the components of the matrix A and b are also matrices that will change size according to the dimension of the problem and its restrictions. The iterations will stop when d_p^{n-1}-d_p^n approaches 0.

For more detailed information about the mathematical model for this optimization dispatch problem, Sempértegui-Tapia et al. [5] should be consulted.

3. Optimization dispatch solver

The operational dispatch solver (ODIS) has 11 graphic windows elaborated with the help of Guide Matlab. These windows also have programming code where all the instruction for the correct operation of the tool are written. This way, this operational dispatch solver is very friendly with the user even more considering the graphical interface.

One of the main features of the program are the ability to work with a hybrid system and also with a thermal system. Also, the program allows the user to stablish a maintenance plan for the generating units and also allows the user to modify the maximum power delivery for the process.

On the other hand, the program provides the user with a power table that describes the optimum economic dispatch profile. More importantly, the solution includes an hourly consumption graphic that could be displayed globally for the isolated system of more detailed, considering all the components of the system.

The input and output parameters for the optimization dispatch solver are discussed next.

3.1. Input parameters

The parameters needed in order to optimize an energy system are:

1. Energy consumption equation: The behavior of a generating unit is considered through the general ratio between the heat input and the power output.
2. Characteristic days of demand: the user can select the characteristic days of demand of the energy system.
3. Available solar power: It refers to the photovoltaic solar power installed, which interacts with the thermal power plant.
4. Maintenance program: This program provides the information about the periods of time where some generating units will not be available.
5. List of available units: Determines the list of available generating unit to be considered to perform the optimization.
6. Effective power: The status condition of each generating unit is determine don site.
7. Rotating reserve: Corresponds to the percentage of the demand that is predicted to absorb the variation of the distribution system. The user can select this value up to 15%.

3.2. Output parameters

The first output parameter is the optimized power of the generating units. The tool also calculates the diesel consumption in liters and the hourly operating cost of the thermoelectric plant. With these output parameters, the program presents different kinds of figures to the user in the graphical interface.

4. Optimization tools applied to real hybrid power generation systems

The optimization tools were applied to three different isolated systems in Bolivia. Two of them are hybrid system (thermal and solar) and one of them is purely thermal.

4.1. General description of the isolated systems

4.1.1. Cobija Hybrid System (CHS)

The CHS is located in the Northern part of Bolivia, more specifically in the department of Pando. Also, it is one of the oldest and largest isolated systems in the country. Furthermore, is under the management of the National Electricity Company (ENDE) since 1990. This company not only supplies electricity to the city of Cobija, but also, to the towns that are within its operational area. Currently the Cobija System is a Hybrid System; due to the combination of two generation technologies; a diesel thermoelectric plant and a photovoltaic solar plant. Figure 3 shows a complete scheme of the CHS illustrating both plants.

The thermoelectric plant has diesel generating units of the Caterpillar brand. Until 2018, this thermoelectric plant had a total of 14 diesel generating units, with an approximate growth in demand of one generating unit per year (approx. 1.4 MW). The electric company ENDE, in order to properly identify the generating units, labelled each generating unit beginning with the code of the pant “BAH” and a numerical value according to the order of commissioning. As observed in the figure, the thermoelectric plant has two voltage levels in generation: 6.6 kV and 0.315 kV. The units that generate in 0.315 kV require a transformer that raises the voltage to 6.6 kV, so that they can be coupled to the 6.6 KV rigid busbar in the electrical substation.

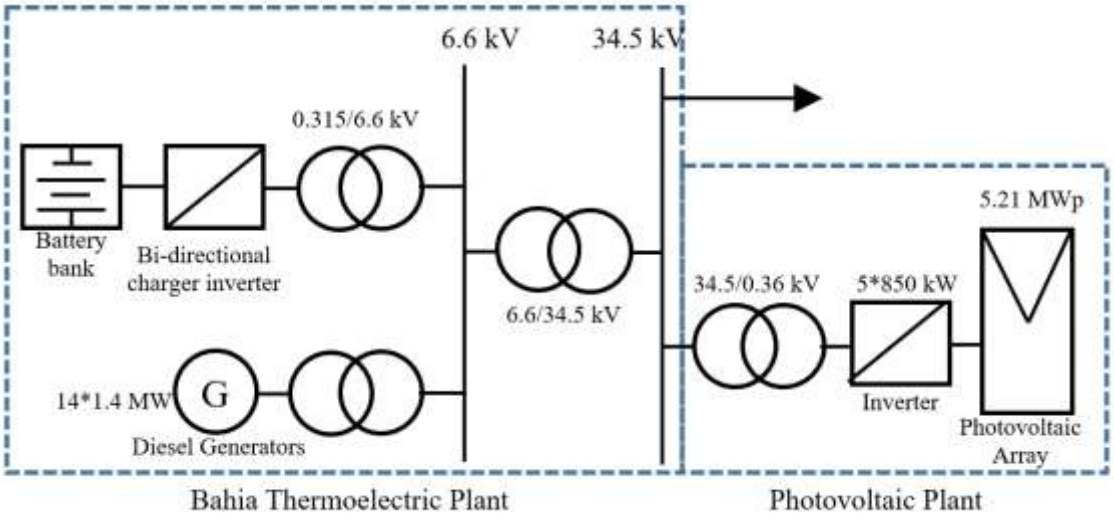

Figure. 3. Scheme of the Cobija Hybrid System.

The photovoltaic plant is comprised of 17,352 solar panels of 300 W. The total installed power is 5.21 MW. It is located about 7 km away from the city. Moreover, it is connected with the BAHÍA thermoelectric plant through a 34.5 KV sub-transmission line that reaches a 34.5 KV flexible bus from the substation (see Figure 3).

Also, a battery bank is located at the thermoelectric plant and uses energy generated by the CATERPILLAR generating units for its own consumption and also constantly supplies the grid. The SAFT brand battery bank is made up of 2 containers with Li-ion batteries.

Table 1 shows the operational limits and the 2nd degree equation of energy consumption for each generating unit of the CHS.

Table 1. Operational limits and 2nd degree equation of energy consumption for each generating unit, CHS.

Generating Unit	Operation limits	a	b	c
BAH01	P_{01}≤1400	-0.2528	10.05	-0.0092
BAH02	P_{02}≤1600	-0.1909	10.118	-0.0016
BAH04	P_{04}≤1200	-0.2435	9.7298	-0.007
BAH05	P_{05}≤1400	-0.0979	10.5298	-0.0069
BAH06	P_{06}≤1400	-0.0632	10.2078	-0.005
BAH07	P_{07}≤1400	-0.27	10.237	-0.0142
BAH08	P_{08}≤1200	-0.3675	10.005	-0.0063
BAH09	P_{09}≤1400	-0.3675	10.005	-0.0063
BAH10	P_{10}≤1400	-0.2835	9.8879	-0.0087
BAH11	P_{11}≤1400	-0.1	10.423	-0.0007
BAH13	P_{13}≤1400	-0.4923	10.511	-0.0009
BAH14	P_{14}≤1400	-0.1472	10.095	-0.0004
BAH15	P_{15}≤1600	-0.1448	9.96388	-0.004
BAH16	P_{16}≤1600	-0.1022	9.9368	-0.0061

For more information on the Cobija Hybrid System see Sempértegui-Tapia et al. [5].

4.1.2. Sena Hybrid System (SHS)

The SHS is located in the Sena Municipality of the Madre de Dios Province in the Department of Pando, on the banks of the Manuripi River. This system has 9 generating units; two of them are Scania brand, 2 are CAT brand and 5 VOLVO brand. This system has also a photovoltaic plant of 436 kW of installed power. The configuration of this hybrid system can be observed in Figure 4.

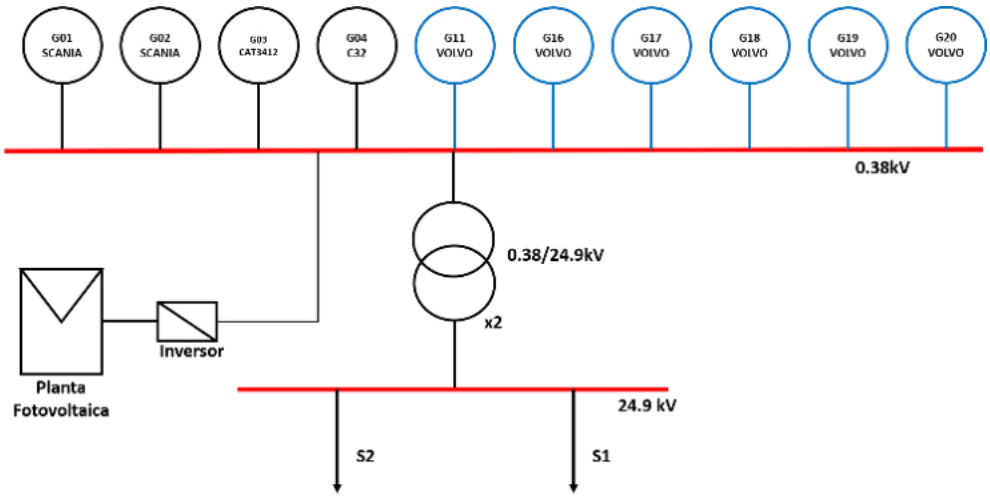

Figure. 4. Scheme of the Sena Hybrid System.

Table 2 shows the operational limits and the 2nd degree equation of energy consumption for each generating unit of the SHS.

Table 2. Operational limits and 2nd degree equation of energy consumption for each generating unit, SHS.

Generating Unit	Operation limits	a	b	c
G01(Scania)	$P_{G01} \leq 350$	-5.8857	11.934	-1.60E-03
G02(Scania)	$P_{G02} \leq 350$	-0.6945	11.577	0.0015
G03(CAT3412)	$P_{G03} \leq 350$	0.2951	11.6	-0.003
G04(C32)	$P_{G04} \leq 500$	0.2951	11.6	-3.00E-03
G11(VOLVO)	$P_{G11} \leq 200$	7.4646	10.783	8.60E-03
G16(VOLVO)	$P_{G16} \leq 200$	1.1231	11.483	1.90E-03
G17(VOLVO)	$P_{G17} \leq 200$	1.1231	11.483	1.90E-03
G18(VOLVO)	$P_{G18} \leq 200$	-2.2623	11.915	-1.10E-02
G19(VOLVO)	$P_{G19} \leq 200$	5.1106	10.646	2.43E-02
G20(VOLVO)	$P_{G20} \leq 200$	0.1113	11.623	-0.0015

4.1.3. Gonzalo Moreno System (GMS)

The GMS is located in the Municipality of Puerto Gonzalo Moreno in the province of Madre de Dios in the Department of Pando. It is responsible of three activities; generation, distribution and commercialization of electric energy. It has a powerhouse of 3 Volvo generating units (see Figure 4).

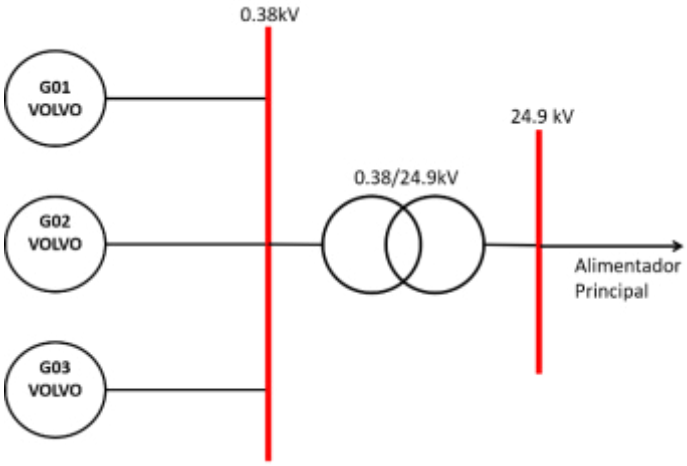

Figure. 5. Scheme of the GMS.

Table 3 shows the operational limits and the 2nd degree equation of energy consumption for each generating unit of the GMS.

Table 3. Operational limits and 2nd degree equation of energy consumption for each generating unit, GMS.

Generating Unit	Operation limits	a	b	c
G01(VOLVO)	$P_{G01} \leq 200$	-32.805	12.73	-4.00E-05
G02(VOLVO)	$P_{G02} \leq 200$	-0.357	10.722	0.0049
G03(VOLVO)	$P_{G03} \leq 200$	0	0	0
G04(VOLVO)	$P_{G04} \leq 200$	-1.8357	10.661	-4.00E-05
G09(VOLVO)	$P_{G05} \leq 200$	-3.5981	10.272	0.0002

4.2. Power demand analysis

Electricity demand is distributed by categories, the most important ones for their incidence are: industrial, commercial and residential. But also, there are other categories like public lighting, police, pumps, whose participation are not comparable to the aforementioned.

Typical demand curves have characteristics that differ from one another, a residential curve will rapidly increase its demand in the period from 18 to 21 hours; a commercial curve will slightly increase its demand in the same period; while an industrial curve will not have a noticeable demand between this period.

Figure 6 illustrates the demand of the three energy systems. Gonzalo Moreno is purely residential, Cobija has a demand associated with the commercial sector and Sena shows an intermediate behavior between residential with the commercial sector. Is worth to mention that neither of this cities show an industrial demand.

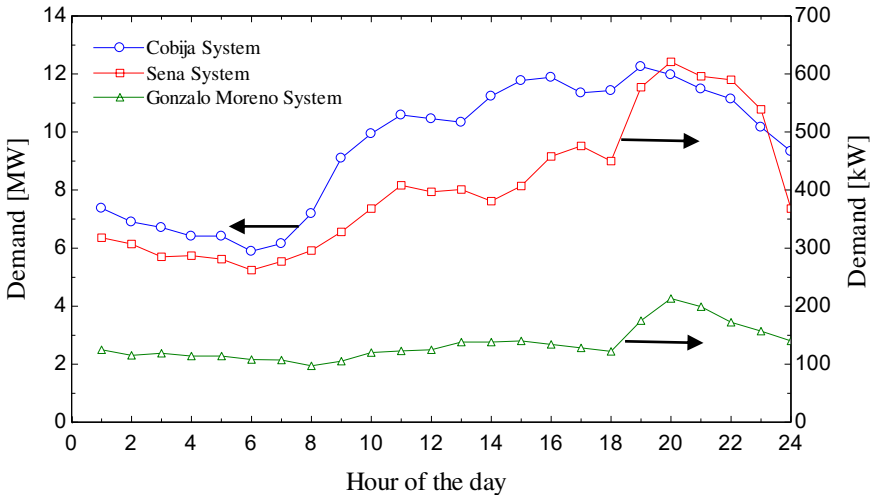

Figure. 6. One-day operational dispatch without optimizing.

To characterize the demand of the energy systems, representative curves were carefully calculated and plotted according to the procedure suggested by [6]. This analysis resulted in a total of 17 representative curves. Eight curves belong to business and non-business days, five curves related to the recorded temperature and four curves for operational events. All the generated curves are summarized in Figure 7 (see [5] for more detailed information).

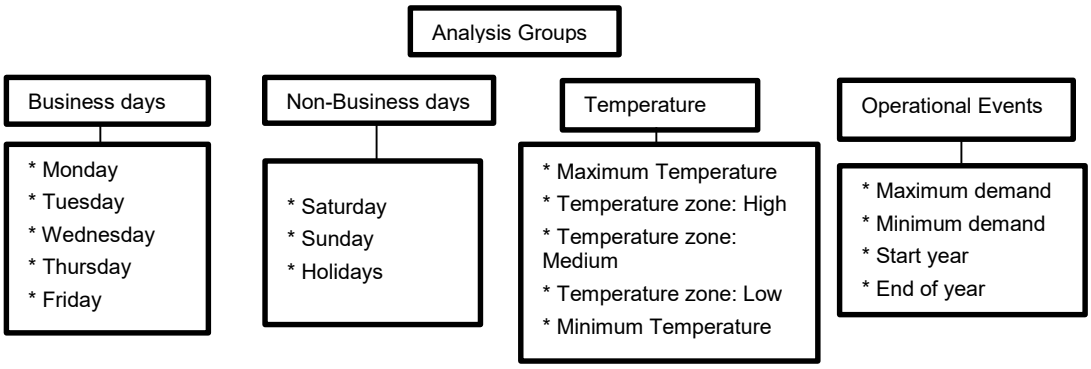

Figure. 7. One-day operational dispatch without optimizing.

4.3. Power supply analysis

Table 4 shows a summary of the important operating data for the three energy systems that are being analyzed.

Table 4. Operating data of the three energy systems.

Operating Data	CHS	SHS	GMS
Energy [MWh]	60160	2824	1019
Diesel consumption [m^3]	15981	878	287
Generating units	14	9	3
Installed thermal power [KW]	19800	2550	600
Photovoltaic panels	17352	1292	0
Installed solar power [KW]	5206	426	0
Maximum demand [KW]	12262	621	213

In order to analyze the power supply of the energy systems, three important variables were calculated for each of them. These performance indicators are the load factor, the demand factor and the specific consumption and can be observed in Figure 8.

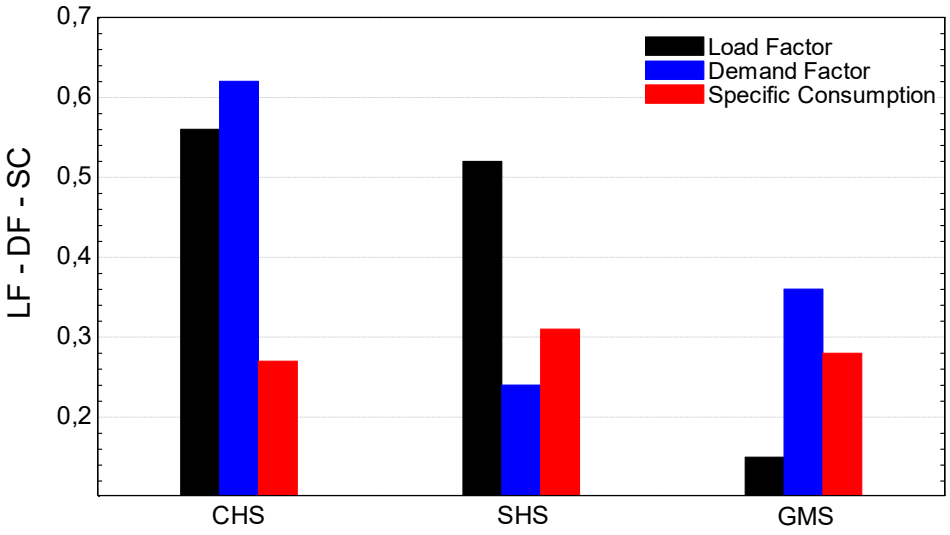

Figure. 8. Performance indicators for the three energy systems.

As it can be observed in the figure, the CHS has a very satisfactory relationship between demand and supply. On the other hand, the SHS has an installed power that exceeds the demand almost four times.

5. Results and discussions

To obtain the results, the three systems were run with the program. All the necessary data, including the demand analysis, operational availability, and others were the input parameters to obtain an optimized energy system. The rotating reserve used for the operation was 10%. Table 5 shows the general results of the optimization model for the three energy systems.

Table 5. Summary of the optimization results.

Indicators	CHS	SHS	GMS
S.C. (Actual) [L/KWh]	0.27	0.31	0.28
S.C. (Optimized) [L/KWh]	0.252	0.287	0.256
Savings [m^3/año]	807	66	27
Savings without subsidizing [KBs/year]	888	73	29
Savings with subsidizing [KBs/year]	8223	677	272

As observed in the table, the optimization results show savings in the fuel consumption for the 3 cases. It can be observed a reduction of the specific consumption for the optimized system compared to the real system. This indicates that the electricity demand could be meet by optimizing the energy resource. In economic terms,

it can be observed annual savings of 9172 KBs for the 3 energy systems. More detailed information about each one of the energy systems are discussed below.

5.1. Cobija Hybrid System (CHS)

Figure 9 shows an operational dispatch in a period of 24 hours for the CHS without the use of the optimization program. The shallow area represents the photovoltaic generation, and every other colour in the figure represent one generation unit added to the system. It can be noted that in order to meet the demand, eleven generating units must be working in addition to the photovoltaic plant. These 13 generating units consume 44260 liters of diesel fuel.

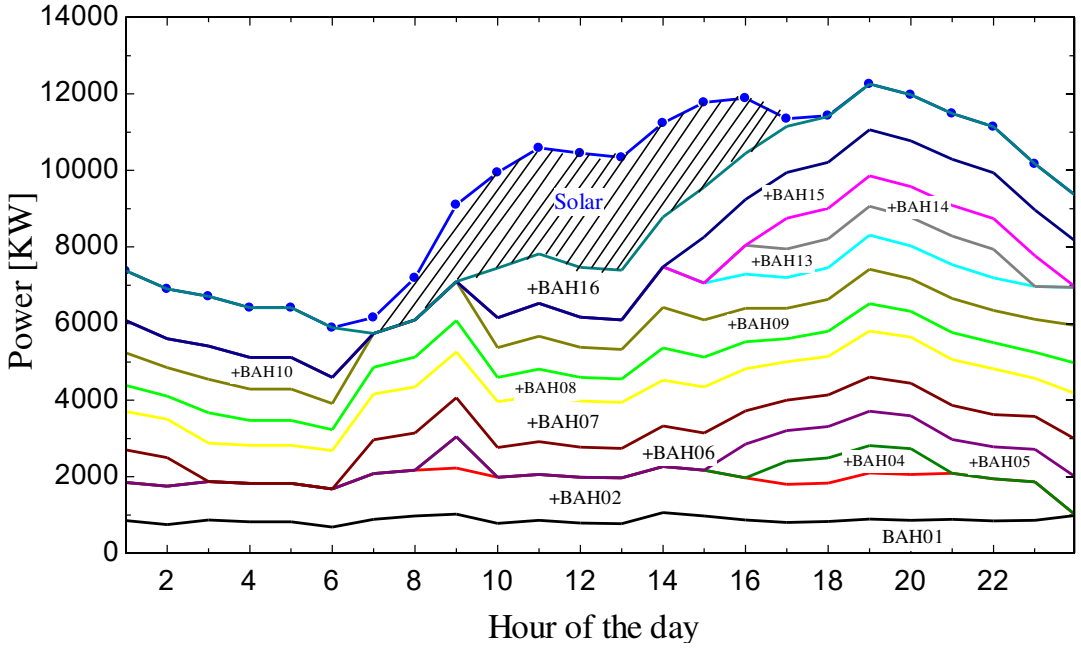

Figure. 9. One-day operational dispatch at the CHS without optimizing.

On the other hand, using the optimization algorithm, it´s possible to reduce the number of generating units dispatched on the same day to 10 (see Figure 10). Also, a better load factor of this equipment is achieved, which is demonstrated by the height of the areas shown by each generating unit. Furthermore, a better distribution of the service of generating units is achieved, minimizing the starts and taking full advantage of the contribution of the photovoltaic solar plant (shallow area). Finally, the CHS with the optimization model needs 42049 liter of diesel consumption, which means 2211 liters of diesel on savings.

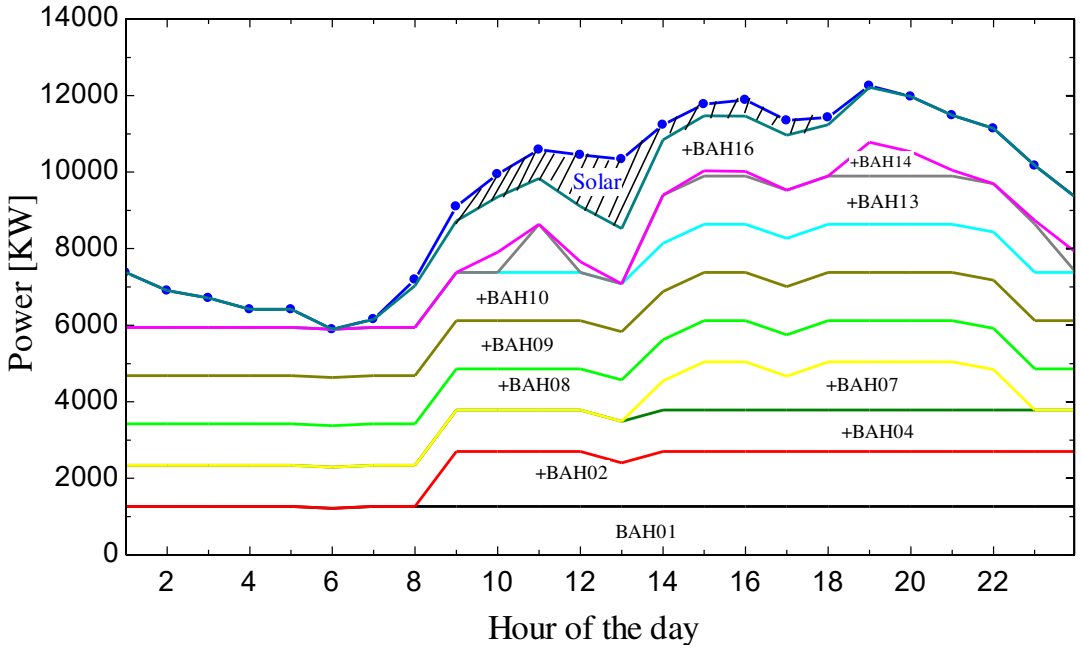

Figure. 10. One-day operational dispatch at the CHS with optimizing.

5.2. Sena Hybrid System

As observed in Figure 11, the Sena Hybrid System needed the operation of four generating units in addition to the solar energy contribution.

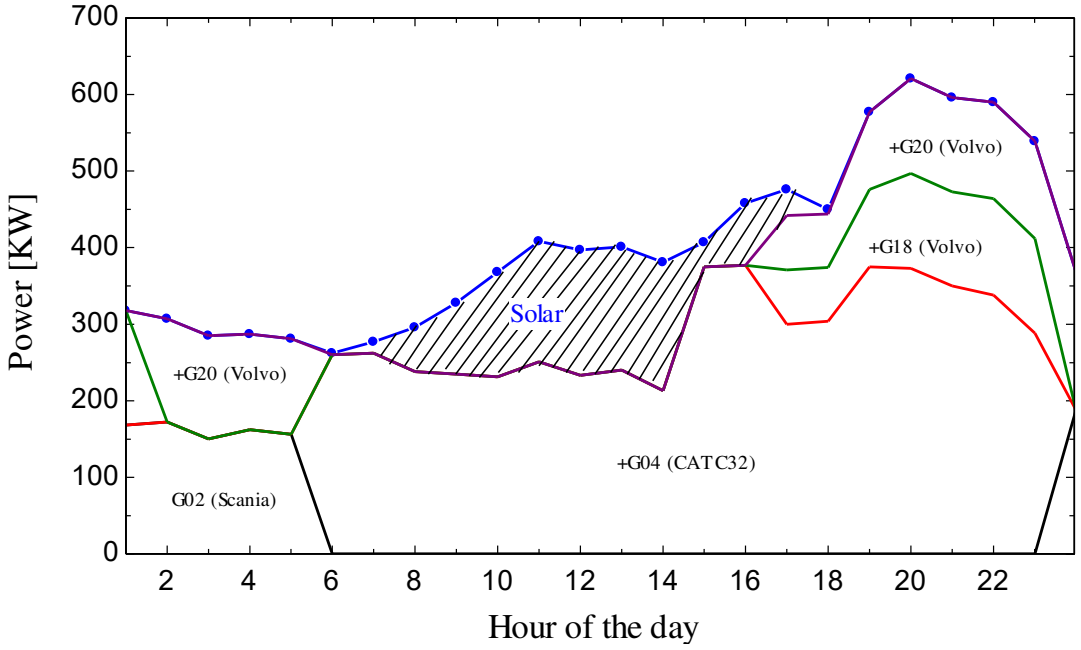

Figure. 11. One-day operational dispatch at the SHS without optimizing.

With the optimized model, the requirement reduces to 3 generating units, reducing at the same time the operative charge and use of personnel.

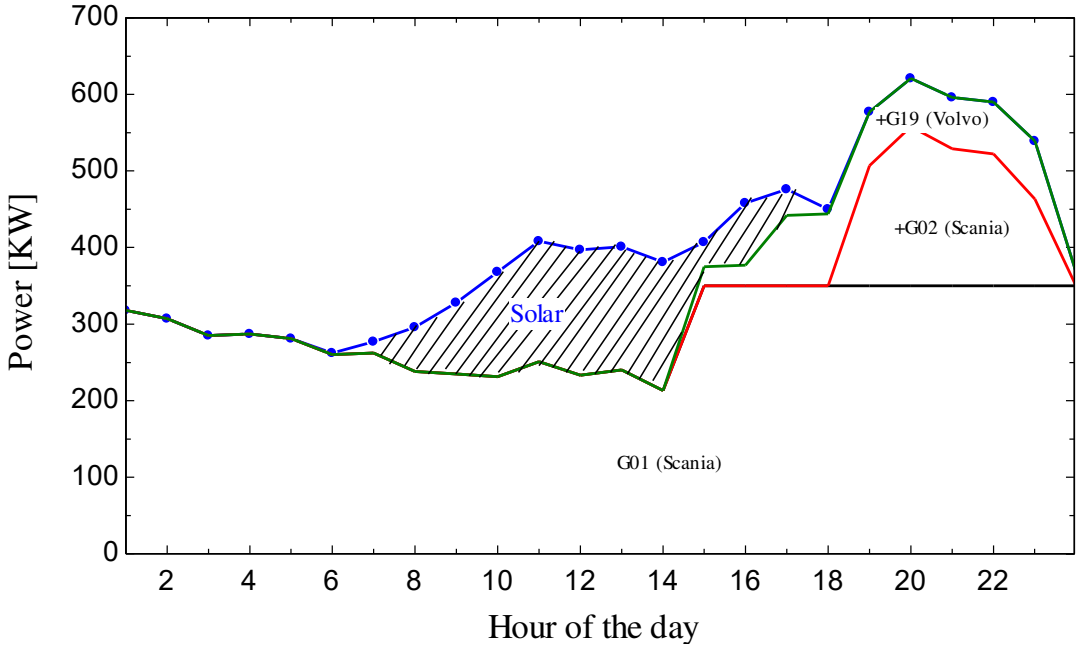

Figure. 12. One-day operational dispatch at the SHS with optimizing.

5.3. Gonzalo Moreno System

The Gonzalo Moreno System is a low-demand system, consequently, start-ups can create periods of time with no generation at all. As observed in Figure 13a, without the optimization the GMS required two units (G02 and G09) in one day, furthermore, the unit G02 was required on two occasions the same day. On the other hand, with the optimization model (see Figure 13b), the equipment should be connected 24 hours and produce a single start-up at least every three or four days, which is considered an appropriate period of time to make routine equipment inspections. Moreover, this slight change would allow us to save 73 L/day according to the optimization program.

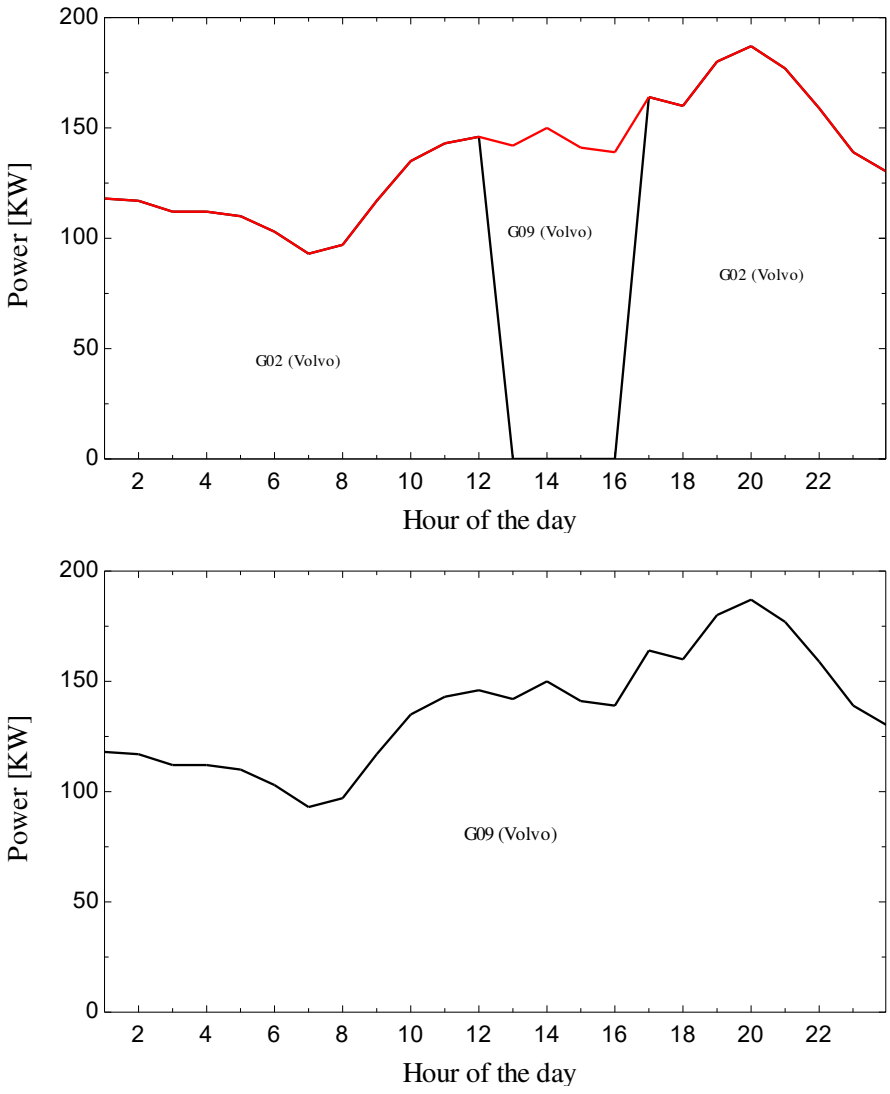

Figure. 13. *One-day operational dispatch at GMS, a) Without optimizing, b) With Optimizing*

7. Conclusions

The optimization tools for energy systems developed by Sempértegui-Tapia et al. [5] has been validated for three very different energy systems. The model works regarding the type (hybrid or purely thermal), the installed power (medium size cities or very small cities) or the demand characteristics (industrial, commercial or residential). The optimized energy systems provided an average daily savings in fuel consumption of 2211 L/day for the CHS, 182 L/day for the SHS and 73 L/day for the GMS. Which represent annual savings of 1.18 MM$ (CHS), 97 K$ (SHS) and 39 K$ (GMS). Thus, the savings obtained are between 5 and 9% of the annual cost of diesel fuel in Bolivia considering the international diesel fuel price (1.46 $/L).

References

[1] J. T. Pinho *et al.*, *Sistemas Híbridos: Soluções Energéticas para a Amazônia*. 2008.

[2] AETN (Autoridad de Fiscalizacion de Electricidad y Tecnologia Nuclear), “Anuario Estadistico 2019,” 2019.

[3] AETN (Autoridad de Fiscalizacion de Electricidad y Tecnologia Nuclear), “Anuario Estadistico 2020,” 2020.

[4] AETN (Autoridad de Fiscalizacion de Electricidad y Tecnologia Nuclear), “Anuario Estadistico 2021,” 2021.

[5] D. F. Sempertegui-Tapia, C. A. Ayma-Ramos, F. S. Encinas, and R. O. Lafuente, “Case study : Optimization tools for the operational dispatch of a hybrid power generation system to reduce diesel fuel consumption,” in *23rd International Conference on Enviroment and Electrical Engineering*, 2023.

[6] A. Vuorinen, *Planning of optiomal power systems*. Ekoenergo Oy, 2007.

Superheated steam drying for paper production: process efficiency assessment

Veronika Wilk[a], Sophie Knöttner[b], Gerwin Drexler-Schmid[c] and Tilman Barz[d]

[a] AIT Austrian Institute of Technology GmbH, Vienna, Austria, veronika.wilk@ait.ac.at, CA
[b] AIT Austrian Institute of Technology GmbH, Vienna, Austria, sophie.knoettner@ait.ac.at
[c] AIT Austrian Institute of Technology GmbH, Vienna, Austria, gerwin.drexler-schmid@ait.ac.at
[d] AIT Austrian Institute of Technology GmbH, Vienna, Austria, tilman.barz@ait.ac.at

Abstract:

Compared with hot air as drying medium, superheated steam has several advantages as drying agent, such as faster drying rates due to a higher overall heat transfer coefficient and lower viscosity allowing for better penetration of pores. It is already an established technology in drying processes in the food industry, as well as for biomass and pet food. In state-of-the-art paper production, the most energy intensive process step is drying with hot air. Using superheated steam for paper drying is an interesting alternative technology enabling more efficient heat recovery. This contribution presents different drying and heat recovery concepts, including air and steam drying as well as conventional energy supply by fossil fired boilers and heat pumps. It evaluates the potential reduction in final and primary energy consumption and CO_2 emissions based on process simulation in IPSEpro and compares the applicability of unused waste heat. Drying in steam atmosphere including steam compression for heat recovery was identified as the most beneficial concept. It allows for primary energy savings of 70% and CO_2 emission reductions of 88% compared to the benchmark concept with air drying.

Keywords:

Heat pumps; Heat recovery; Optimization; Paper drying; Process simulation.

1. Introduction

In the EU, the paper, pulp and printing industry consumed 1326 PJ or 13.7 % of the total final energy consumption in industry. Thus, it is the third largest final energy consumer after chemical and petrochemical industry (2121 PJ in 2020) and non-metallic minerals (1372 PJ). Most of the energy consumption is related to paper and paper products. To cover this demand, 30% of natural gas, 34% of renewables and biofuels and 21% of electricity are used. Minor shares are covered with other fossil fuels, such as oil or solid fuels. [1]

Typically, the type of produced goods in a paper mill has an impact on used energy carriers for energy supply. Factories producing both, pulp and paper, are often referred to as integrated factories. In comparison to factories producing only paper or board, in integrated factories a typical by-product is liquor from the chemical pulp production (cooking process) which is assessed as biogenous fuel. After pulp making, the used liquor is usually concentrated and burned afterwards in a liquor-boiler producing steam and in combination with a steam turbine also electricity. This leads to a high share of non-fossil energy supply for so called integrated factories.

However, other typical energy carriers for steam production in the pulp and paper sector, e.g., at sites using recycled fibres or (dry) pulp purchased from an external source, are natural gas, external waste streams, solid biomass, other biogenous residues or by-products from the production process such as internal waste streams, sludge or bark. Other possible, but less commonly used energy carriers are oil or coal. In order to provide energy in an efficient way, the following energy conversion technologies are often applied in those factories: steam turbines (often back pressure) in combination with gas turbines and / or different types of boilers, e.g. natural gas fired, but also using solids such as bark, sludge, coal or biomass as fuel. In general, the share of onsite electricity auto-production in the pulp and paper sector is rather high, usually realized with co-generation units. This is emphasized by an example from the Austrian pulp and paper sector. In 2021, 16000 GWh of energy were consumed, about 70% in the form of steam and 30% in the form of electricity. The on-site electricity production covered 65% of the electricity consumption. A total of 95% thereof was provided in co-generation units. [2]

The 2050 Roadmap of the Forest Fibre Industry [3], which covers pulp and paper as well as wood-based products in Europe, outlines how to reduce CO_2 emissions to reach an 80% reduction by 2050. A large impact is achieved by substituting fossil fuels, more electricity-based installations using renewable energy and efficiency increase due to the application of BAT – best available technologies. However, without breakthrough technologies only a reduction of 50-60% CO_2 emissions is achievable. The aim of the breakthrough technologies is to lower the heat demand in paper making, by reducing water use and improving drying processes. Paper drying accounts for 70% of fossil energy consumption and is therefore an important field of action.

In state-of-the-art paper mills, paper is first dewatered mechanically in the press section followed by the drying section. Most commonly, multicylinder dryers are used [4]. Cylinder dryers consist of a series of cylinders that are heated on the inside by condensation of steam. The paper is moved around the cylinders and water is evaporated. Thus, humid exhaust gas is formed that leaves the hood of the dryer. The principle is shown in Figure 1. A recent technology review of paper drying by Stenström [4] showed that the multicylinder design has not undergone significant changes in the last 20 years. The most important new developments are impingement dryers using hot air that is blown onto the paper and the development of new steel cylinders for through air drying (TAD), as shown in Figure 2. In the analysis of Stenström [4], energy use is considered as very important with special focus on the recovery of humid exhaust air from the hood. However, there was no progress on new drying technologies, such as the use of superheated steam that has been studied in the past by several researchers. There are no industrial units installed so far.

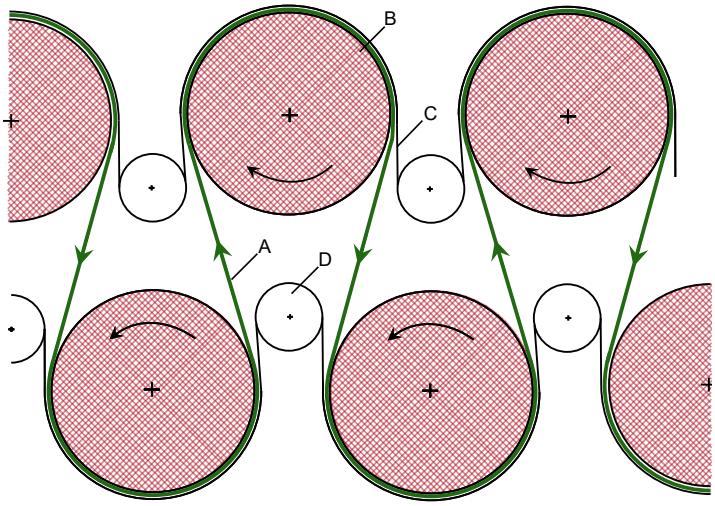

Figure 1. *Schematic visualization of steam heated cylinders in typical paper machines (A - paper, B - steam, C - felt, D - deflector roll)*

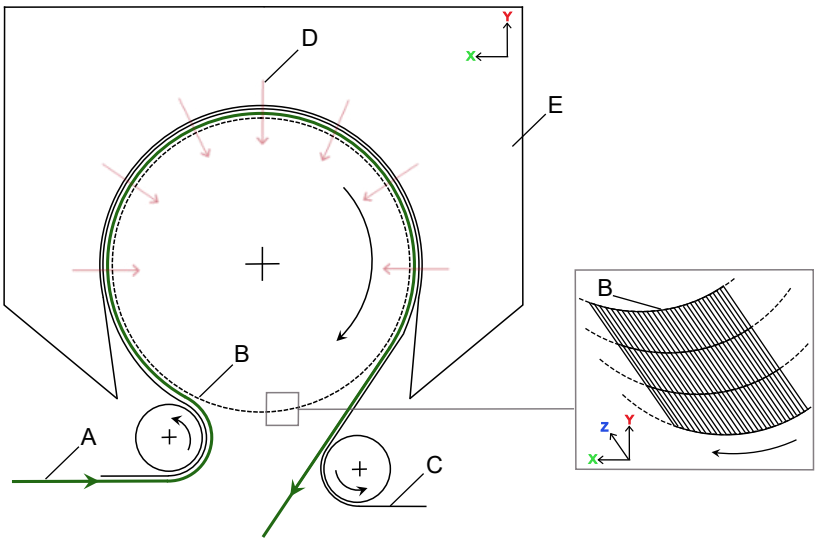

Figure 2. *Schematic visualization of Through-Air Drying (TAD) (A – TAD fabric, B – TAD cylinder, C – paper web, D – air flow, E – dryer hood)*

Superheated steam drying is already an established technology in the food industry, e.g. for distiller grains, beet pulp, rice, sea grass, dried fruit, potato products and tea, as well as for biomass and pet food. The main drivers to use superheated steam are an increase in product quality, less severe conditions for sensitive products and shorter duration of the drying process. [5-10] Recently an e-book [11] on superheated steam drying was published compiling the most important references in the field. The authors stated that activity was sporadic in the past, but it is now gaining momentum due to the potential energy savings.

In the field of paper production, superheated steam drying was studied experimentally by Kiiskinen et al. [12] in 2002 as steam drying offers many advantages, such as the potential to save energy and improve paper quality. It was a continuous steam dryer with a high velocity hood for steam impingement, that was operated with steam at 250°C. They studied paper quality, start up, the effect of non-condensable gases on heat transfer related to air intake and steam quality and impurities. It was found that steam drying offers advantages in terms of energy economy, if the exhaust steam can be used elsewhere in the process, e.g. in the drying cylinders, to heat the supply air in the dryer section, shower water, buildings, wire pits, paper web in the press section or in the calender, pulp, and to heat air or water in the power plant. The energy saving potential is 15-85% depending on the selected further use of the exhaust steam. Thus, heat recovery is based on cascaded use of steam provided in the conventional fossil fuel power plant.

This contribution presents different drying and heat recovery concepts, including air and steam drying as well as conventional energy supply by fossil fired boilers and heat pumps. It evaluates the potential reduction in energy consumption and CO_2 emissions based on process simulation in IPSEpro. The aim is identifying the most efficient process configuration as a contribution to the breakthrough technologies needed for efficient, decarbonized paper production.

2. Methodology

2.1. Process simulation in IPSEpro

The paper drying process, as well as the integration of heat recovery equipment, were investigated using the simulation software IPSEpro (Integrated Process Simulation Environment), which was developed for process simulations in the field of power plant and energy technology. It uses an equation-oriented solver for the calculation of mass and energy balances of steady state processes. [13]

The setup implemented as a flowsheet in IPSEpro corresponds to the actual process layout. The individual components of the process (unit operations such as the dryer, compressors, heat exchangers, etc.) are connected by streams that transfer mass and energy. The components are balanced according to conservation of mass and energy and the balances are strictly fulfilled for each component. The components can either be taken from the model library provided with the simulation software or they can be created by the user. Customized developed models for the dryer and the heat pump were used here.

Process data based on literature was used for the dryer model, which is explained in more detail in section 2.2. For the simulations, a simplified heat pump model was used. The model uses the temperature of the heat source and heat sink and the second law efficiency based on Carnot efficiency to calculate the power consumption, heat input and heat output of the heat pump. It is not necessary to specify the refrigerant or type of compressor in this model, so it can be used for potential assessment in a wide range of temperatures. The second law efficiency was chosen to be 0.45 based on the authors' experience.

2.2. Definition of benchmark process

A joint paper by the European Heat Pump Association (EHPA) and the Confederation of the European Paper Industries (Cepi) [14] published in 2023 is used to define the benchmark process of air drying for paper production as it summarizes the current status in the paper industry. According to [14], the dew point of the exhaust air is 60°C and typical steam pressures in the cylinders range from 1 to 9 bara. Typically, low pressures are used in the first cylinders and higher pressures in the last. Pressure levels are also influenced by paper grades and grammatures (max. 20%). It is found that 70% of steam use is below 6 bara and 50% below 5 bara in European paper mills, as it is illustrated in Figure 3.

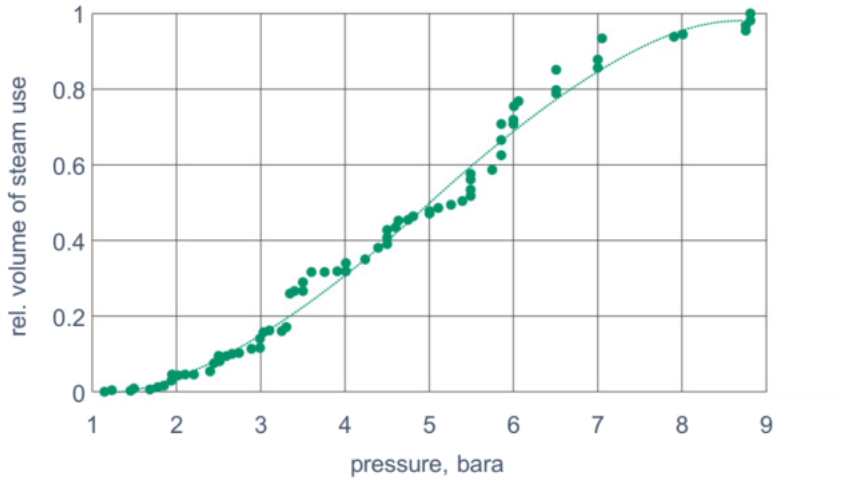

Figure 3. *Range of typical steam pressures in a paper machine, data from [14]*

In the benchmark process, 1 t/h of water is evaporated from the paper. When entering the drying section, the water in the paper has a temperature of 30°C. In the dryer, water is evaporated. For the sake of simplicity, only the enthalpy of evaporation for pure water is considered and enthalpy of sorption of water in the paper fibre structure is neglected. The enthalpy of evaporation amounts to 2257 kJ/kg for pure water at 1 bar. For example, enthalpy of sorption adds another 300 kJ/kg to reach 90% dry content and increases to 700 kJ/kg for 97-98% dry content [15]. In this evaluation, paper properties are kept constant for all concepts and are described by evaporation of 1 t/h. Thermal losses are neglected.

The steam cylinders in the dryer are supplied with saturated steam at 5 bara and 151.8°C. Steam is supplied from a combustion process operated with natural gas and a thermal efficiency of 90%.

Air is supplied from the production hall with a temperature of 30°C and is preheated with steam. The exhaust air from the dryer has a dew point of 60°C. It is assumed that it leaves the hood with 80°C followed by optional heat recovery using heat exchangers to preheat drying air. A total of 7454 kg/h of exhaust gas are formed when evaporating 1 t/h water from the paper. A pressure of 1 bar in the air system is assumed, pressure losses are neglected.

2.3. Environmental impact evaluation

Primary energy consumption:

Final energy is converted into primary energy using the primary energy factor f_{PE}. Primary energy also includes the production of the energy carrier itself, such as extraction, processing, storage, transport, conversion, transmission, and distribution to provide end energy. Primary energy consumption for electricity is predominantly influenced by the energy carriers and efficiencies used for electricity generation. For this comparison, factors based on current European averages are used. In 2019, the European Parliament defined the primary energy factor to be used for the calculation of the energy efficiency targets to 2.1 kWh/kWh for electricity [16], for natural gas, the factor amounts to 1.1 [17]

CO_2 emissions:

Like the primary energy consumption, CO_2 emissions are calculated based on the final energy demand and the emission factor f_{CO2} for CO_2-equivalent also considering other greenhouse gases such as methane or nitrous oxide. The emission factors f_{CO2} includes the production of the energy carrier itself, such as extraction, processing, storage, transport, conversion, transmission, and distribution to provide end energy. The CO_2 emissions from electricity are predominantly influenced by the energy carriers used for electricity generation. Currently, the use of electricity in the EU leads to 275 g_{CO2eq}/kWh [18], use of natural gas accounts for 268 g/kWh [19]. All factors are compiled in Table 1.

Table 1. Factors for the calculation of emissions, primary energy, and costs

	Unit	Electricity	Natural gas
CO_2 emissions factors (f_{co2})	g_{CO2eq}/kWh	275	268
Primary energy factors (f_{PE})	kWh/kWh	2.1	1.1

3. Results

3.1. Air drying

A1 is the benchmark process described above. Paper is dried in air atmosphere on drying cylinders that are supplied with steam at 5 bara (Figure 4). Steam is condensed in the cylinders at 151.8 and the condensate returns to the boiler in a closed cycle. The boiler is operated on natural gas and has a thermal efficiency of 90%. In this process, 876 kW of natural gas are required. Exhaust gas at 80°C leaves the hood of the dryer containing the latent energy of the water evaporated from the paper. A total of 754 kW can be recovered if the exhaust gas is cooled to 20°C ($\dot{Q}_{Rmax}$), thereof 47 kW above the dew point temperature of 60°C.

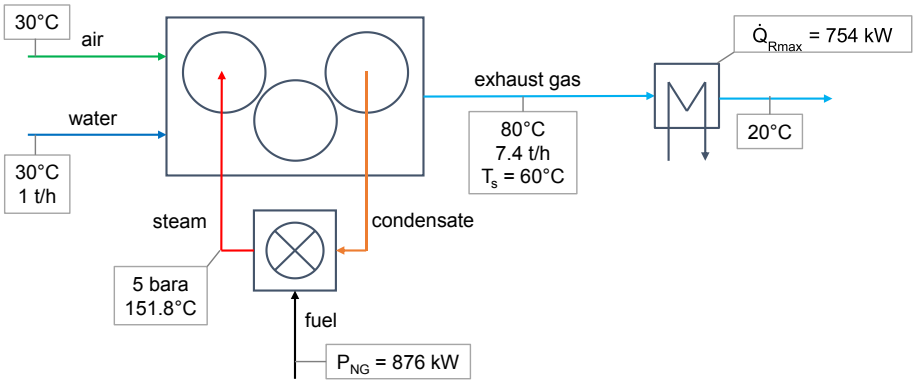

Figure 4. *Air drying with drying cylinders and steam from natural gas combustion (A1, benchmark)*

A2 accounts for heat recovery that is frequently implemented in paper mills (Figure 5). The exhaust gas is cooled to 55°C, a part of the heat is used to preheat the drying air to 65°C. Thereby, the natural gas demand is decreased to 805 kW. The remaining heat can be used for other sinks, such as preheating of water in other parts of the process.

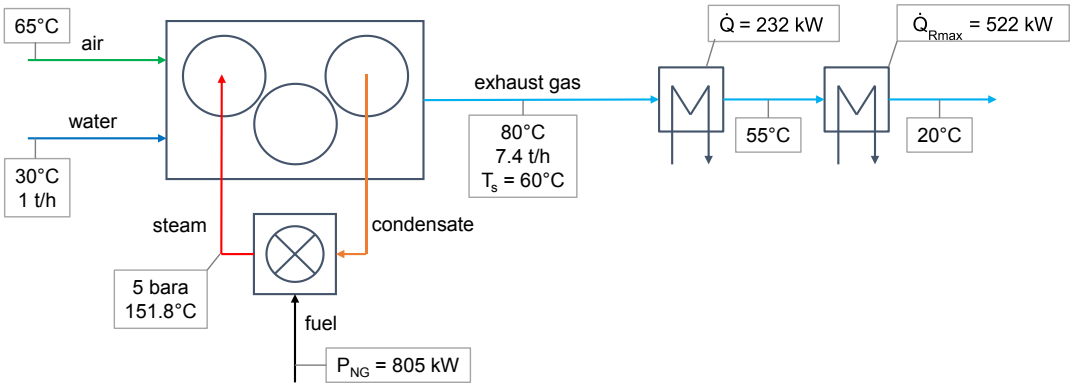

Figure 5. *Air drying with drying cylinders and steam from natural gas combustion and heat recovery (A2)*

In A3, heat from the exhaust gas is recovered with a heat pump (Figure 6). First, the exhaust gas is cooled to 38.7°C by an intermediate water cycle. The water cycle is the heat source of the heat pump, which is cooled by the evaporator of the heat pump. In the condenser, the heat pump produces saturated steam at a pressure of 1.05 bara (111°C) from the condensate of the cylinders. The steam is further compressed in steam compressors to 5 bara. In practise, a pressure difference of ca. 5 bar would require several compression stages with liquid injection to desuperheat the steam. About 5% of the steam are generated by injection for desuperheating. In the simulation, the setup is simplified to only one compressor with an isentropic efficiency of 70% without liquid injection.

In A3, the heat supply is fully electrified, the energy consumption amounts to 386 kW. The remaining heat recovery potential from the exhaust gas is 173 kW.

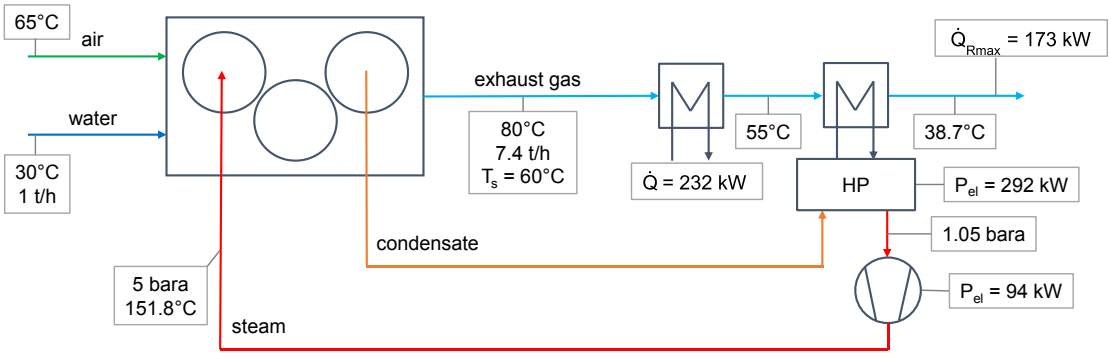

Figure 6. *Air drying with drying cylinders, heat recovery and heat pump (A3)*

In A4, there is no heat exchanger in the exhaust gas upstream of the heat pump (Figure 7). The exhaust gas is cooled by the intermediate water cycle that is the heat source of the heat pump. Thereby, the exhaust gas temperature after the heat pump is increased to 47.9°C. Due to the smaller temperature lift of the heat pump, it requires less energy. However, the drying air is preheated with steam in this concept, which increases the steam demand and the electricity consumption of the steam compressor. In total, 383 kW of electricity are needed. The remaining heat recovery potential from the exhaust gas is 333 kW.

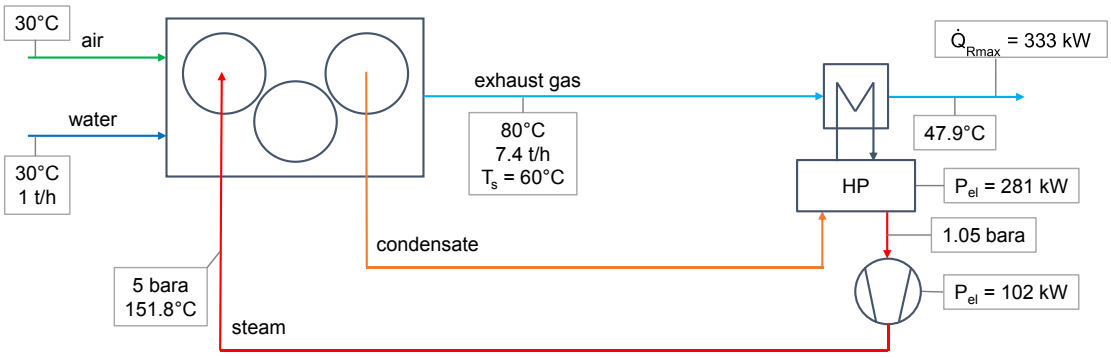

Figure 7. *Air drying with drying cylinders and heat pump (A4)*

3.2. Steam drying

In S1, the air atmosphere is changed to steam (Figure 8). Instead of drying air, superheated steam is supplied to the dryer with 151.8°C and a slight over-pressure of 1.05 bar to avoid air intake. To keep the inlet velocities constant, the drying steam volume flow is the same as the drying air flow in A1 (6261 m³/h). At the outlet of the dryer, the steam has a temperature of 111°C and has 10 K of superheat to avoid condensation on the paper. Water evaporated from the paper is present as excess steam which is discharged. The rest of the steam is reheated in the boiler and is recycled to the dryer.

Like A1, the cylinders are heated by another flow of saturated steam at 5 bara and 151.8°C. This stream is condensed in the cylinders and is reevaporated in the natural gas boiler. It is not in contact with the steam atmosphere.

In total, 794 kW of natural gas are needed. Heat recovery amounts to 726 kW if the excess steam is cooled to 20°C, whereas most of the heat occurs at the condensation temperature of 101°C.

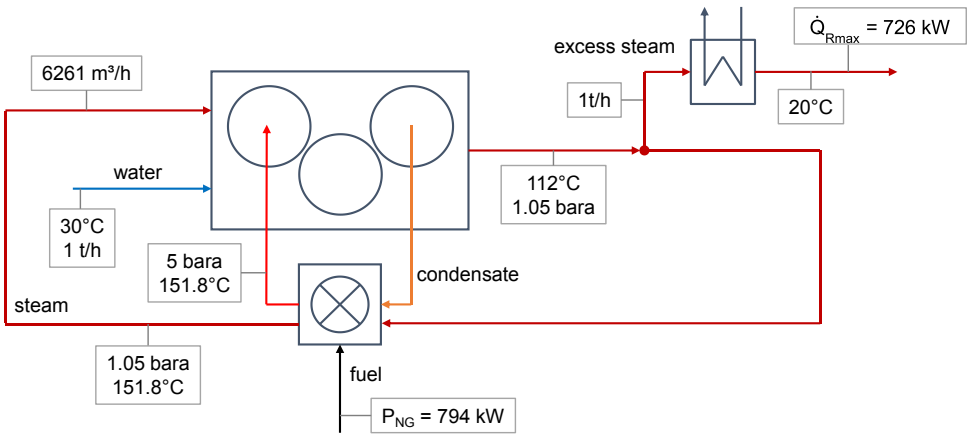

Figure 8. *Superheated steam drying with drying cylinders (S1)*

In S2, there are no cylinders, all energy for drying is supplied by steam like in impingement dryers or through-air-dryers (TAD). Thus, the heat distribution in the dryer is changed. However, there is no change in energy flows in this simple balance model (Figure 9). Natural gas demand amounts to 794 kW and the heat recovery potential to 726 kW as in S1.

The steam volume flow increases drastically by nine times to 59464 m³/h if steam is supplied at 151.8°C. If steam is supplied at 250°C, as it was in the lab test of Kiiskinen et al. [12], the volume flow is 21466 m³/h (3-fold increase compared to air drying). The increase in steam temperature lowers the volume flow of steam but has no relevant impact on the energy consumption of the natural gas boiler.

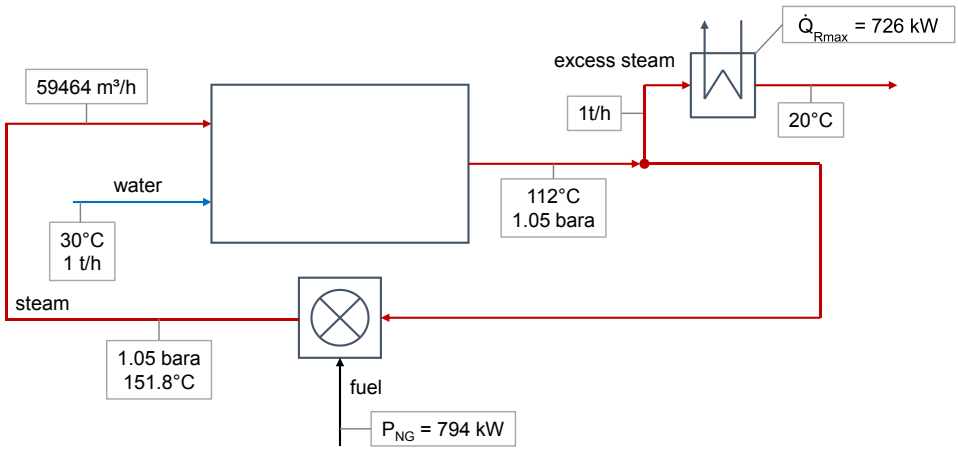

Figure 9. *Superheated steam drying without cylinders (S2)*

S3 is a full electric concept with superheated steam drying and cylinders (Figure 10). After the dryer, a slip stream of 1 t/h of steam is separated. It is the mass flow originating from the water in the paper. It is compressed in a steam compressor to 5.4 bar, thereby the condensation temperature of steam increases to 155°C. The slip stream is condensed and transfers the heat to the second steam cycle in the cylinders. Then, the slip stream condensate heats the steam for the steam atmosphere to 145°C. As in S1, the steam volume flow for the steam atmosphere amounts to 6261 m³/h. After heating the steam atmosphere, the slip stream condensate still has a temperature of 149°C.

The steam compressor requires 139 kW of electricity. The heat recovery potential from the slip stream condensate is 151 kW.

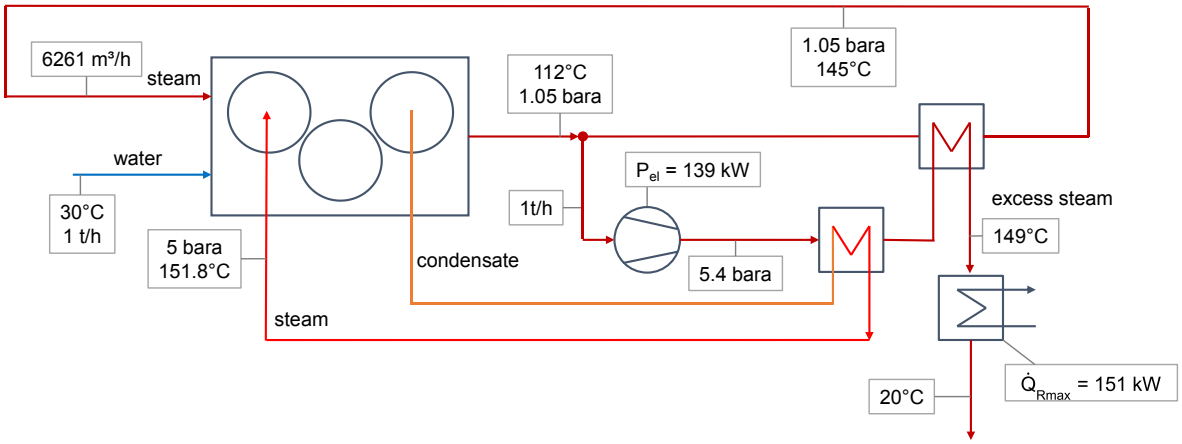

Figure 10. *Superheated steam drying with cylinders and steam compression (S3)*

S4 is another full electric concept based on a heat pump (Figure 11). The slip stream (1 t/h) is the heat source for the heat pump and it is partly condensed. The heat pump produces steam from the condensate returning from the cylinders at 1.5 bara. The outlet pressure on the sink side of the heat pump was set to 1.5 bara to have a small temperature lift over the heat pump. The steam compressor further increases the pressure to 5 bara. A part of the superheat is used to reheat the steam for the steam atmosphere, then the steam is sent to the cylinders, where it is condensed. Energy consumption amounts to 154 kW. From the slip stream, 166 kW can be recovered, if it is further cooled to 20°C.

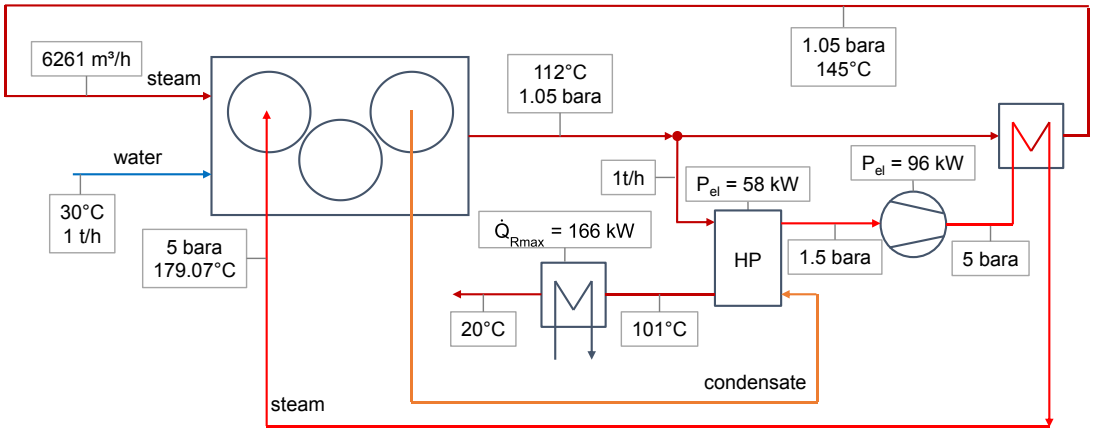

Figure 11. *Superheated steam drying with cylinders and a heat pump (S4)*

3.3. Discussion

Figure 12, Figure 13 and Figure 14 compare the concepts in terms of final energy consumption, CO_2 emissions and primary energy consumption. Final energy consumption decreases considerably for all concepts with heat pumps or steam compression (A3, A4, S3, S4), as they allow for recovery of the latent heat of the evaporated water from the paper. The same effect is found for CO_2 emissions. In terms of primary energy, the concepts A3, A4, S3 and S4 are still beneficial, but the difference to the concepts based on natural gas is smaller. The reason is the European primary energy factor, that is based on an electricity mix with less renewable energy than the one currently available in the EU.

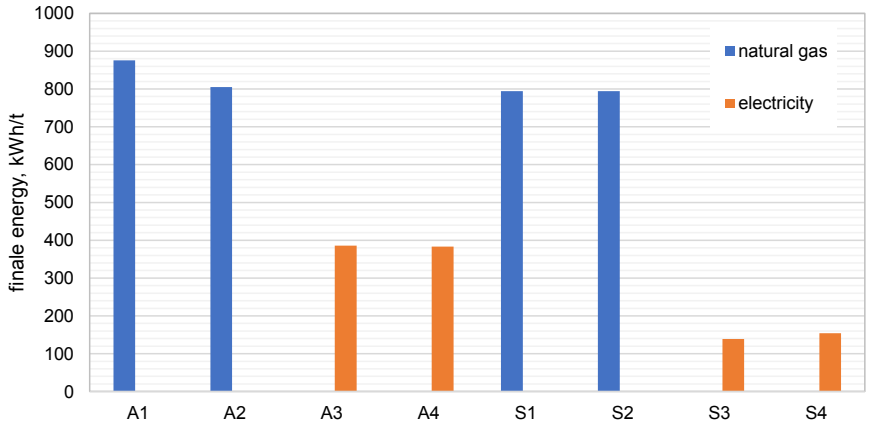

Figure 12. *Comparison of final energy consumption to evaporate 1 t/h water*

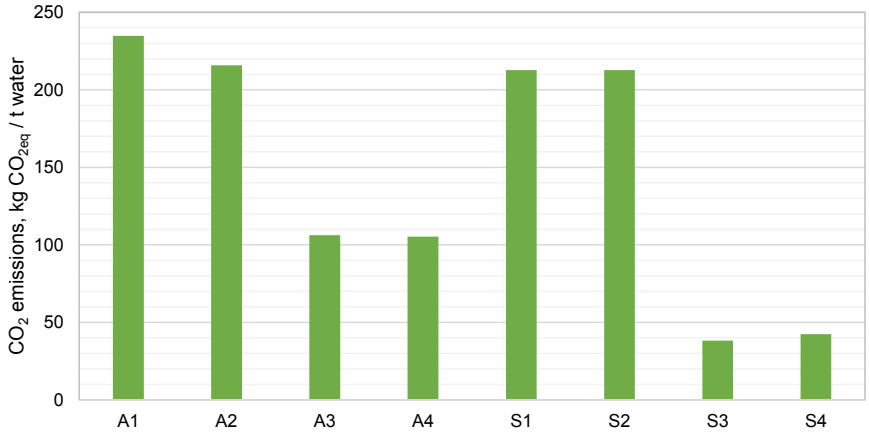

Figure 13*. Comparison of CO_2 emissions to evaporate 1 t/h water*

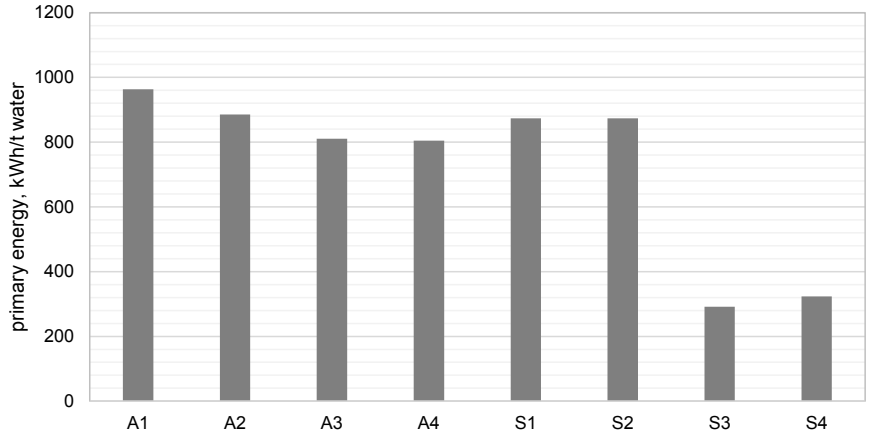

Figure 14. *Comparison of primary energy consumption to evaporate 1 t/h water*

The main difference between air and steam drying is that the dew point of the exhaust air is limiting heat recovery to low temperatures. A1 yields 754 kW, but mostly below 60°C. S1 and S2 yield 726 kW of excess steam that can be condensed at ca. 100°C. In the concept S3, the highest heat recovery temperature is available. Figure 15 visualises the heat recovery potential. The higher the temperature, the easier it is to find a suitable application. In A4, the heat pump is the only heat recovery measure. Compared to A3 (heat exchanger, then heat pump), more heat is available in A4 at a higher temperature. Energy consumption of A3 and A4 is in a comparable range. If there is no further heat demand at the paper mill, waste heat from steam drying can used for district heating, which is not possible for air drying.

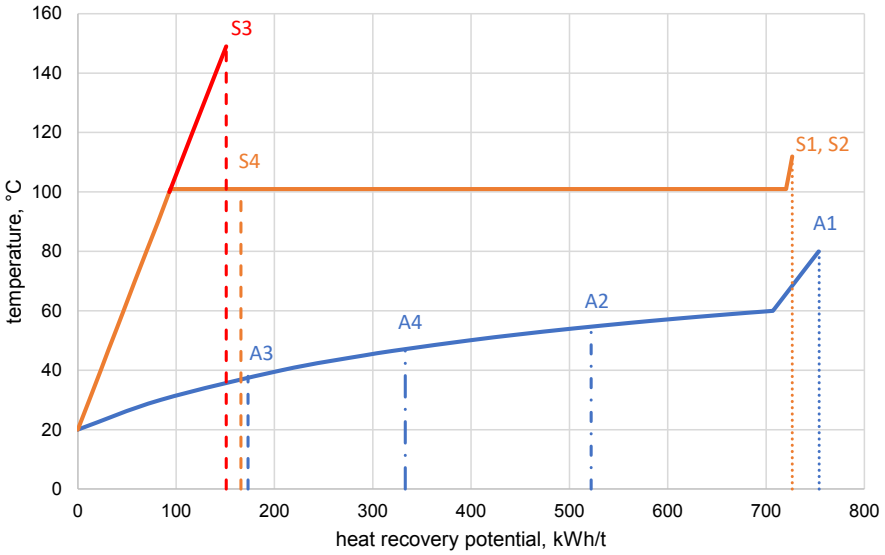

Figure 15. *Comparison of heat recovery potential for air and steam drying*

4. Conclusions and outlook

The most beneficial concept is S3 with steam atmosphere and steam compression for heat recovery. It reduces primary energy consumption by 70% and CO_2 emissions by 88% compared to A1, the benchmark concept with air drying. It also provides the highest excess steam temperature of 145°C that is well suited for further use.

The use of cylinders in the dryer is recommended to allow for low steam temperatures in the system. If the steam temperature is increased to 250°C, the volume flow is decreased. However, energy recovery with steam compression is more difficult, as the operation point moves closer to the boundaries of the operation envelope of steam compressors. The maximum allowable temperatures are typically at ca. 280°C, furthermore it must be considered that steam superheats strongly during compression.

To realize the concept S3, further research and demonstration is needed as an important part of the concept is that the steam for steam atmosphere is reheated and recycled. It has to be studied, what kind of impurities accumulate in the steam and how to remove them if necessary. Also, air intake should be avoided as it was already shown by Kiiskinen et al. [12]. In the simulation, a slight over-pressure of 1.05 bara was chosen for that reason. If the steam cannot be recycled, it can be condensed to evaporate clean steam. This would result in a more complex setup and in another temperature difference to overcome, which reduces the savings.

The simulation has shown that there is a huge potential in energy and emission savings if paper is dried in steam atmosphere using steam compression and condensation for heat recovery. Thereby drying is based on electricity only. The concept S3 is a suitable breakthrough technology to considerably improve paper drying.

5. References

[1] Eurostat: Final energy consumption in industry - detailed statistics – Available at: https://ec.europa.eu/eurostat/statistics-explained/index.php?title=Final_energy_consumption_in_industry_-_detailed_statistics#The_largest_industrial_energy_consumers_in_the_EU. [Accessed on 2023-03-19]

[2] Austropapier - Vereinigung der Österreichischen Papierindustrie, Branchenbericht 2021/2022, 2022.

[3] CEPI: unfold the future: The Forest Fibre Industry 2050 Roadmap to a low-carbon bio-economy - Available at: https://www.cepi.org/wp-content/uploads/2020/08/2050_roadmap_final.pdf [Accessed 2023-03-19]

[4] Stenström, S., Drying of paper: A review 2000–2018, Drying Technology 2020;38(7):825-845.

[5] Padel et Bade (2015): A Review on Superheated Steam As a Potential Drying Medium, 10th Asia Pacific Drying Conference, Vadodara, India, Dec. 14-17, 2019

[6] IGB Fraunhofer - Available at: https://www.igb.fraunhofer.de/content/dam/igb/documents/brochures/thermische-trennung/1803_BR_dampftrocknung_de.pdf, [Accessed 2021-04-20]

[7] Jittanit,W., Angkaew, K., Effect of superheated-steam drying compared to conventional parboiling on chalkiness, head rice yield and quality of chalky rice kernels, Journal of Stored Products Research 2020; 87; 101627. ISSN 0022-474X, https://doi.org/10.1016/j.jspr.2020.101627.

[8] Rumaisa, N., Hanim, M. & Hii, C.Superheated Steam Drying of Black Tea and Quality Improvement. International Journal of Food Engineering 2018;14(9-10); 20180185. https://doi.org/10.1515/ijfe-2018-0185

[9] Adamski, R., Siuta, D., Kukfisz, B., Mitkowski, P.T., Szaferski, W., Influence of process parameters in superheated steam drying on fire and explosion parameters of woody biomass, Fuel Processing Technology 2021; 211; 106597; ISSN 0378-3820, https://doi.org/10.1016/j.fuproc.2020.106597

[10] Stenström, S. Drying of biofuels from the forest—A review, Drying Technology 2017; 35(10);1167-1181. DOI: 10.1080/07373937.2016.1258571

[11] Shivanand S. Shirkole (2021), Literature resources on superheated steam drying – Available at https://arunmujumdar.com/wp-content/uploads/2021/09/Literature-Resources-on-Superheated-Steam-Drying.pdf [accessed 2023-03-18].

[12] Kiiskinen, H.T., Edelmann, K.E., Superheated Steam Drying of Paper Web. Dev. Chem. Eng. Mineral Process. 2002;10;349-365. https://doi.org/10.1002/apj.5500100408

[13] Perz, E., A Computer Method for Thermal Power Cycle Calculation, Journal of Engineering for Gas Turbines and Power 1991;113(2);184.

[14] EHPA, CEPI: Through pumps to pulp: greening the paper industry's heat (2023) - available at https://www.cepi.org/wp-content/uploads/2023/02/Cepi-x-EHPA.pdf [accessed 2023-03-10].

[15] Schneeberger, M., Leuk, P., Hirn U., Bauer, W., The heat of sorption in paper drying – an investigation of measurement methods and influence of pulp parameters. In: Advances in Pulp and Paper Research, Cambridge 2013, Trans. of the XVth Fund. Res. Symp. Cambridge, 2013, (S.J. l'Anson, ed.), pp 469–492, FRC, Manchester, 2018. DOI: 10.15376/frc.2013.1.469

[16] European Parliament, 2018c, Position of the European Parliament, 13 November 2018, first reading 2016/0376(COD) adopted at first reading on 13 November 2018 with a view to the adoption of Directive (EU) 2018/… of the European Parliament and of the Council amending Directive 2012/27/EU on energy efficiency (EP-PE_TC1-COD(2016)0376)

[17] EN ISO 52000. Energy performance of buildings - Overarching EPB assessment - Part 1: General framework and procedures (ISO 52000-1:2017), Edition: 2018-02-01

[18] European Environment Agency, Greenhouse gas emission intensity of electricity generation, published on 2022-10-26 - available at https://www.eea.europa.eu/data-and-maps/daviz/co2-emission-intensity-12#tab-googlechartid_chart_11 [Accessed 2023-03-20]

[19] Umweltbundesamt, Calculation of green house gas emissions for different energy carriers in Austria, updated in November 2022 - available at https://secure.umweltbundesamt.at/co2mon/co2mon.html [Accessed 2023-03-20]

Improving Computation Time for Optimization Runs of Modelica-based Energy Systems

Sven Klute[a], Markus Hadam[b], Mathias van Beek[c] and Marcus Budt[d]

[a] Fraunhofer Institute for Environmental, Safety, and Energy Technology UMSICHT, 46047 Oberhausen, Germany, sven.klute@umsicht.fraunhofer.de, CA
[b] Fraunhofer Institute for Environmental, Safety, and Energy Technology UMSICHT, 46047 Oberhausen, Germany, markus.hadam@umsicht.fraunhofer.de
[c] Fraunhofer Institute for Environmental, Safety, and Energy Technology UMSICHT, 46047 Oberhausen, Germany, mathias.van.Beek@umsicht.fraunhofer.de
[d] Fraunhofer Institute for Environmental, Safety, and Energy Technology UMSICHT, 46047 Oberhausen, Germany, marcus.budt@umsicht.fraunhofer.de

Abstract:
Mathematical optimization is a widespread method in order to improve, for instance, the efficiency of energy systems. A simulation approach based on partial differential equations can typically not be formulated as an optimization problem, thus requiring interfacing to an external optimization environment. This is, amongst others, also true for the programming language Modelica. Because of high computation time, such coupled approaches are often limited to small scale optimization problems. Since simulation models tend to get more complex, simulation time and, in turn, associated optimization time rise significantly. To enable proper sampling of the search space, individual optimization runs need to be solved in acceptable times. This paper addresses the search for a proper optimization approach and tool to couple with Modelica/Dymola. The optimization is carried out on an exemplary power plant model from the ClaRa-Library using an evolutionary algorithm (SPEA2-based) with Ansys optiSlang. To verify and evaluate the results, a comparison with the standard Dymola optimization library is performed. Both parallelization and indirect optimization with surrogate models achieved a significant runtime reduction by a factor of up to 5.4. The use of meta models is particularly advantageous for repetitive optimization runs of the same optimization problem but may lead to deviations due to the calculated approximations.

Keywords:
Mathematical Optimization, Runtime Reduction, Parallelization Methods, Energy Systems, Meta-model, Modelica, Dymola, Ansys optiSLang

1. Introduction

Process modeling and simulation is becoming increasingly important to achieve improvements in today´s complex energy systems and technologies [1]. The model formulation can be carried out via several programming languages. A frequently used language is the object- and equation-oriented programming language Modelica, which is particularly suitable for the representation of dynamic processes [2, 3]. To improve the handling of the modeling process, usually simulation environments such as Dymola are used [4]. Based on these models, extensive investigations such as design or control optimizations can be performed. A wide used method is the parameter variation, which is quite simple to perform, but becomes more time consuming as the complexity of the model increases. In these cases, mathematic optimization is used instead. Therefore, an optimization problem has to be defined and solved with the help of algorithms. The programming language Modelica, which is designed for simulation tasks, does not allow the formulation of such optimization problems. Thus, a coupling with external optimization languages or optimization environments is necessary [2]. In the field of energy systems, a wide variety of such environments have already been used for coupling with Dymola (see Section 3). This paper presents the first-time coupling of Dymola and Ansys optiSLang [5] in order to solve static optimization problems. For this purpose, the implemented workflow and its main features as well as the used algorithm are presented in Section 4 and 5. The verification of the results is finally done by a comparison with the standard Dymola optimization library (DLR Optimization Library [6]). This library offers a wide range of different optimization techniques that are easy to apply. However, a huge disadvantage is the

required runtime for optimization which will be further discussed in Section 6. For a better understanding of the results, relevant basics of mathematical optimization are presented first.

2. Mathematical optimization

The first step when dealing with optimization is the definition of the problem itself. Therefore, the objective function f(x), the optimization variable x and possible restrictions must be defined [7, 8]. For this study, we split optimization into the static and transient type, depending on the contents of the optimization variable. A typical application for static optimization is design optimization, where an optimal design of a component is determined disregarding transient features [9, 10]. Transient optimization is, for instance, used to calculate optimal process control strategies [11].

When choosing the appropriate algorithm, the specific properties of the algorithm as well as the specifications of the optimization problem must be considered [9, 12]. In application-related problems, multi-objective optimization tasks are the most common. In contrast to the single-objective optimization, several objective functions are optimized simultaneously. Usually, these functions are in conflict with each other. As a result, there is no solution where both objective functions reach their individual optimum [9, 13–15]. This context can be described by the so-called Pareto-Front (see Figure 1). Illustrated are the two fictitious objective functions $f_1(x)$ and $f_2(x)$, which are to be minimized by a variation of x. By using the single optima (x_1 and x_2), three characteristic ranges can be identified. While an increase of x in the range $x < x_1$ leads to an improvement of both functions, an increase for $x > x_2$ causes a deterioration of both functions. The relevant range is thus located between the two individual optima ($x_1 < x < x_2$). Within this range, an improvement of one objective function can only be realized by a deterioration of the other criterion. This means, that there is no longer a single optimum as in the case of the single-objective optimization. Instead, there is a set of different optima, also called the Pareto-Optimal set or Pareto-Solutions. By comparing the two objective functions, this set can be represented as a subset of the boundary curve (Pareto-Front on the right). By selecting a weighting factor, a problem-specific overall solution can then be determined. [9, 13–15]

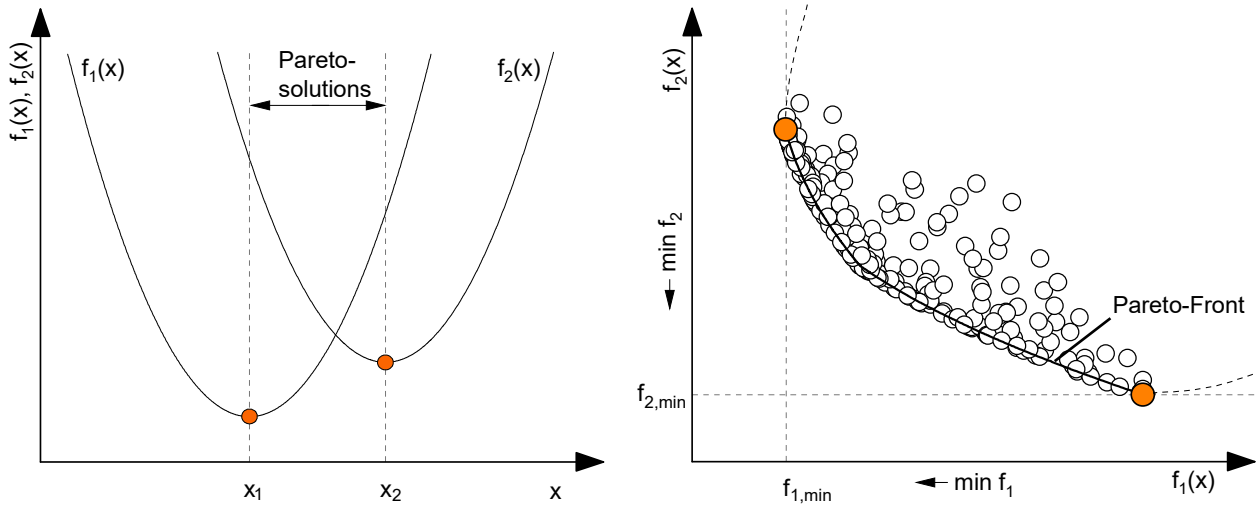

Figure. 1. Target function values of the fictitious functions $f_1(x)$ and $f_2(x)$ (left) and Pareto-Front of the fictitious functions (right) according to [9]

3. Optimization with Dymola

In the area of energy systems, various couplings between Dymola and different optimization environments have already been implemented. The choice of the appropriate environment is problem-specific and depends primarily on the type of optimization problem. Table 1 shows an overview of published investigations and lists the used optimization-tool. The DLR Optimization Library is fully integrated in Dymola and can be used to define multicriteria and trajectory optimization problems. In the three listed examples [16–18] different types of Models and optimization problems were investigated. Dymola is one of currently over 170 tools which support the FMI standard. It allows the export and exchange of simulation models into other simulation or optimization environments. The studies [19–21] are using this standard for an optimization in Matlab and Simulink with the focus on optimal control. In the study [22] Matlab is used as an optimization platform. Instead of FMI, an optimization workflow is presented. The workflow is using a Dymola script to run the simulation with different input parameters. The results are imported into Matlab from result files (dsres.mat) using pre-implemented functions. The study [23] is using the optimization environment OMOptim and Dymola as a simulation tool. To excess the model structure and adapt the input variables, OpenModelica is used. In the shown example, a

design optimization of a heat pump is presented. The optimization program GenOpt is a text-based system which uses the input and output files of a simulation software to perform the optimization. The studies [24–26] are presenting an optimal control problem and [27] are solving a design optimization with GenOpt. Pfeiffer [28] utilize the FISEMO environment to perform a numerical sensitivity analysis of Modelica models. Dymola is used for the modeling process and the export of the model into C-Code. The integration into the FISEMO environment is done by using the DASPK3.1 package.

Table 1. Couplings of Dymola and optimization environments in the field of energy systems.

Model	Method	Optimization-tool	Ref.
Chilled water plant	Real-Time Optimization	DLR Optimization Library	[16]
CO_2 heat pump and thermal storage	Optimal Control	DLR Optimization Library	[17]
Osmosis hybrid system	Design Optimization	DLR Optimization Library	[18]
Hybrid Energy systems (HES)	Optimal Control	Matlab	[19]
Decentralised energy supply	Optimal Control	Simulink	[20]
Thermal management system	Optimal Control	MUSCOD-II	[21]
Chiller plant	Optimal Control	Matlab	[22]
Heat pump	Design Optimization	OMOptim	[23]
Combined heat and power plant (CHP)	Optimal Control	GenOpt	[24]
Central cooling plant	Optimal Control	GenOpt	[26]
Chiller plant	Optimal Control	GenOpt	[25]
Chilled water system	System configuration	GenOpt	[27]
Discontinuously Models	Sensitivity analysis	Fisemo	[28]

Most of the listed publications deal with transient optimization and focus on optimal control problems. The static optimization is less frequent and only addressed in two publications with small scale problems. In order to test the optimization framework optiSLang and contribute to the landscape of investigations of static optimization-simulation coupling, a proof of concept with a model of a coal-fired power plant is set up and carried out in this paper. One of the main advantages of optiSLang is the support of high-order parameter spaces, and thus, extensive sensitivity analysis as well as comparatively complex design optimization calculations. In the field of mechanical construction, for instance, optimization problems with up to 30,000 independent variables were solved [29]. Since there is currently no direct connection to Dymola, a workflow will be presented in the first step (Section 4). Solving dynamic optimization problems with optiSLang is possible as well but will not be further discussed within this paper.

4. Coupling of Dymola and Ansys optiSLang

Since there is no direct coupling option for Dymola and optiSLang yet, an appropriate workflow had to be developed. The implemented workflow presented in this paper enables an automatic data exchange between Dymola and optiSLang (see Figure 2). optiSLang works according to the principle of variance calculation, which is why several model simulations and modifications of the model have to be performed [5]. Therefore, a text-based solver chain is implemented within the optiSLang environment.

Dymola is used for the modeling process of the respective system in the programming language Modelica. The model can then be translated into C-Code and saved as an executable file with an associated input file. The input file contains essential initial values, model parameters and simulation settings which are needed for the simulation run of the model. After a successful simulation, the results are saved into output files. By modifying the input file, different model parametrizations and therefore results can be generated.

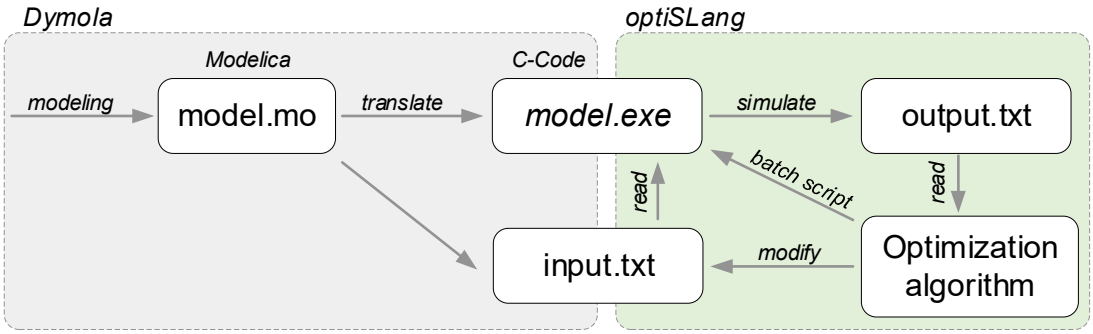

Figure. 2. Basic principle of the workflow for coupling Dymola and optiSLang

optiSlang is using these three files to perform the optimization. As a first step, the optimization problem must be defined in the optiSLang environment. In contrast to the original mathematical optimization, it is not necessary to develop a complex mathematical objective function. Instead, the optimization is performed using a black box model of the Dymola model (executable file). The input variables are set as optimization variables while the output variables are set as target criteria. The optimization variables (tuners) must be extracted from the input file. For each evaluation of the algorithm, one modified input file is created. Each of these files has different tuning values which are varied in a defined range in order to achieve the optimum. The validation of the optimum is done by using target criteria which are integrated in the model and calculated through a simulation (via batch-script). The results of each simulation are saved into individual output files. optiSLang extracts these values and evaluates them according to the chosen algorithm.

Although the black box model simplifies the definition of the optimization problem, it also means that there is no knowledge of the mathematical structure of the problem. However, this knowledge is usually necessary for the choice of a suitable algorithm. To counteract this problem, optiSLang offers the user a traffic light system which recommends an algorithm based on the determined internal optimization problem (number of inputs, single- or multi-objective problem etc.). It must be taken into account, that this recommendation depends on the mathematical solvability of the problem and does not guarantee the best possible result. Thus, it is still necessary to know about the functionality of the individual algorithms to select a suitable one for a given optimization problem.

5. Case study: coal-fired power plant

In order to validate the implemented workflow, an optimization run is performed using an example model of the open source library ClaRa [30]. The chosen model represents a coal-fired power plant with eight turbine stages including feedwater preheating. Fig. 3 shows a simplified schematic of the plant. After passing the boiler, the generated steam flows through the individual turbine stages until it is expanded to the condenser pressure. The collected condensate is then preheated by the four low-pressure preheaters (LP-PH) before it enters the steam-heated feedwatertank. The feedwater is preheated by the high-pressure preheater (HP-PH) before it enters the boiler. The power plant is designed to provide 580 MW_{el}. In the simulation scenario two load reductions to 70 percent load are performed. One simulation run of 10.000 seconds requires around 118 seconds simulation time.

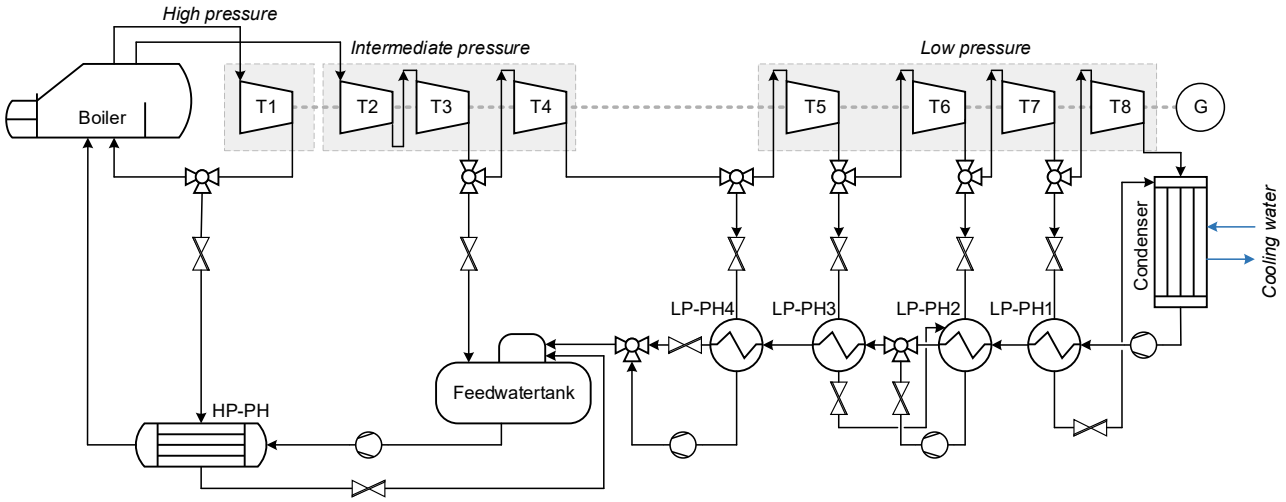

Figure. 3. *Simplified schematic of the coal fired power plant model SteamPowerPlant_01 from the open-source library ClaRa*

The optimization is carried out using the HP preheater as an example component due to its huge impact on the preheating section. The HP-PH model is a shell-and-tube heat exchanger for which selected tube parameters are to be optimized. Further information about the model can be obtained from the open source library ClaRa [30].

Table 2. Specifications of the optimization variables d_i, d_o and l.

Tuner	lower boundary [m]	initial value [m]	upper boundary [m]
d_i	0.015	0.020	0.024
d_o	0.025	0.028	0.031
l	9	10	11

The aim of the optimization is the improvement of the overall power plant efficiency with respect to the investment costs of the heat exchanger. Therefore, inner tube diameter d_i, outer tube diameter d_o and tube length l are to be optimized (Eq. (1)). The resulting multi-objective optimization problem is shown below. In many cases, optimization tools simplify a multi-objective problem to a single-objective problem by combining the multiple functions into a single sum-function with individual weights or by focusing on one function and introducing the remaining as constraints [31]. However, optiSLang is using an interactive method (see Section 2) instead, which allows to deal with several functions simultaneously. The resulting Pareto-Front can be used to identify the area of interest where focused optimization runs can be performed.

A simple degression function is implemented for estimating the investment costs (see Eq. (2)) [32, 33]. Therefore, the heat transfer surface is set in relation to a theoretical reference heat exchanger (A_{ref} = 1,500 m² and $K_{i,ref}$ = 800,000 €) and is simplified by Eq. (3) The degression exponent n was set to 0.6 [32, 33]. The price index effect from PI and PI_{ref} is neglected in this example. The efficiency is automatically calculated within in the model and is equal to the outlet-power and inlet-power ratio (see Eq. (4)). The negative equation sign is used to transform the maximization problem into a minimization problem. Table 2 shows the individual limits of the tuner variables. The initial values of the overall system efficiency η_{ref} and the investment costs $K_{i,ref}$ are 51,58 % and 802,545 €.

$$x = (d_o, d_i, l)^T \tag{1}$$

$$\min f_1(x) = K_{i,ref} \cdot \left(\frac{A(x)}{A_{ref}}\right)^n \cdot \left(\frac{PI}{PI_{ref}}\right) \tag{2}$$

$$A(x) = 2\pi \cdot \frac{d_o + d_i}{2} \cdot l \cdot n_T \tag{3}$$

$$\min f_2 = -P_{out}/P_{in} \tag{4}$$

5.1. Optimization algorithm

As solving algorithm a modified implementation of the Strength Pareto Evolutionary Algorithm 2 (SPEA2 [34]) is used. Figure 4 shows the general flowchart of the algorithm and indicates the interaction with the implemented workflow from Section 4.

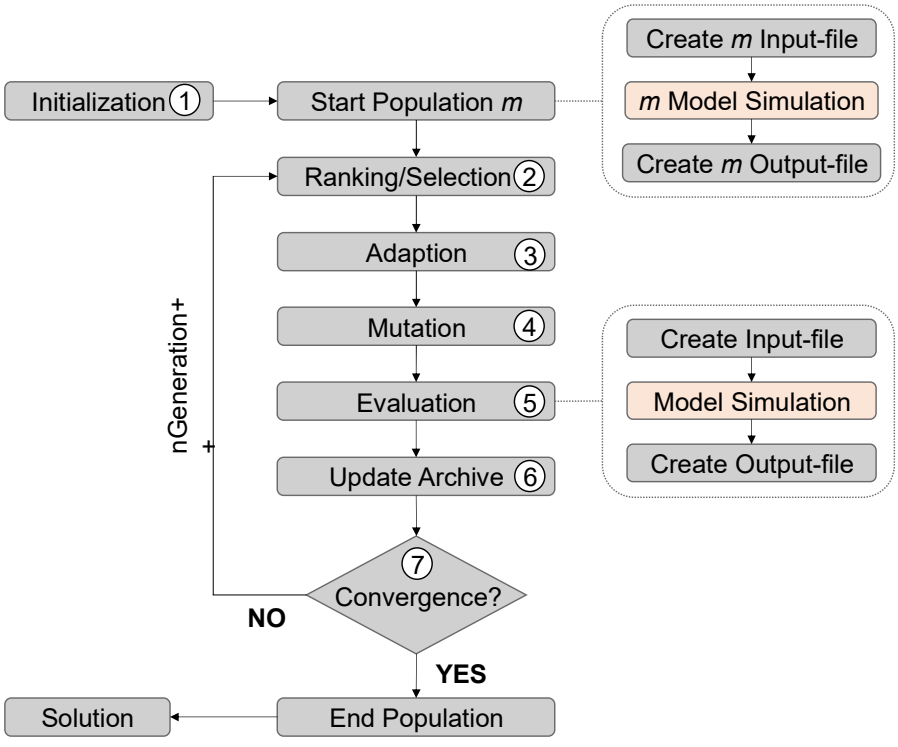

Figure. 4. General flowchart of the evolutionary algorithm (according to [14] and [35]) and the interaction with the implemented workflow

After initialization of the simulation model, a start population of the size *m* is generated (Step 1). Therefore, *m* modified input-files are created and *m* respective simulation runs are performed. A dominance-based ranking system is used to assign a corresponding fitness factor to each solution, which are extracted from the *m* output-files (Step 2). The iteration loop starts after the assignment process is done by using adaption (e.g. crossover or swarm movement) and mutation methods. The additional designs must be evaluated and ranked once more (Step 5). Therefore, new model simulations are required. Beneficial solutions are used to update the archive (containment for good solutions) and checked for convergence (Step 7). If the convergence criteria is reached, the optimization terminates and the end population is stated. In the negative case, step 2 to 7 are repeated until convergence or a termination criterion are reached. Since each evaluation requires one simulation of the model, optimization runtime is highly affected by simulation runtime and the number of total simulations. For a time-efficient optimization, both should be reduced as far as possible.

The described steps can be modified further by changing the algorithm parameter (e.g. mutation-rate or crossover method). This allows the user to adapt the algorithm to the specific problem. The optimization runs presented in this paper use the optiSLang standard settings. All calculations are carried out under Windows 10 on an Intel Core i5-6500 (3.2 GHz processor) with 8 GB RAM.

6. Results

6.1. Direct and indirect optimization

The optimization can be done as a direct or indirect optimization (Figure 5). In case of the direct optimization, an individual model simulation is carried out for each evaluation of the algorithm. The indirect optimization, on the other hand, uses a surrogate model (meta-model) of the simulation model. The meta-model is determined based on n model simulations (100 by default) via a sensitivity analysis (SA). The SA provides several response surfaces which mathematically describe the correlation between the target criteria and the chosen optimization variables. Both variants have individual advantages and disadvantages which are described in more detail below.

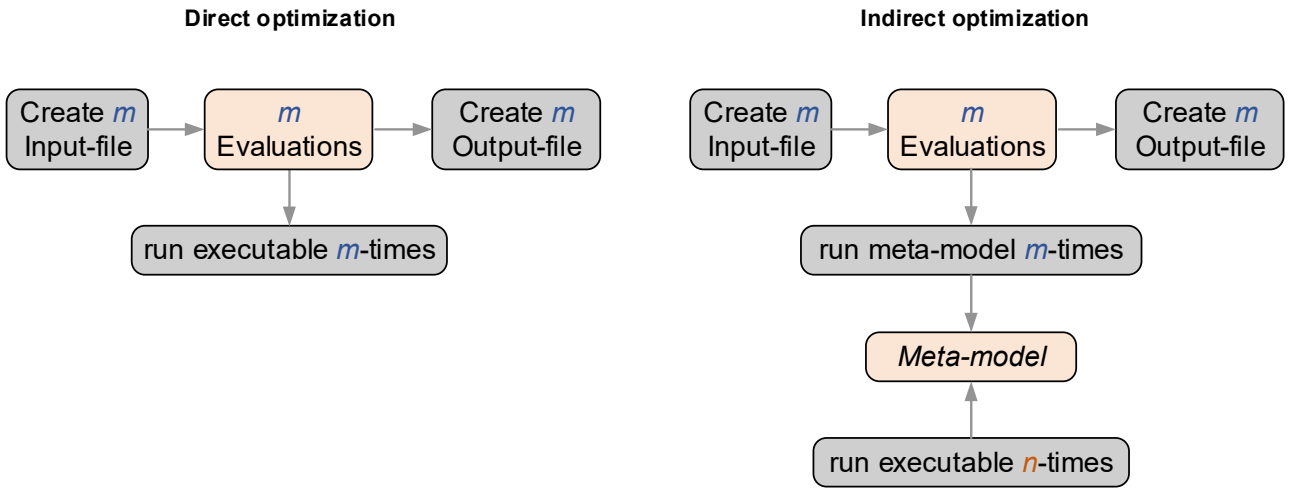

Figure. 5. Direct and indirect optimization using the executable file and surrogate models

Figure 6 shows an example response surface of the overall system efficiency and its correlation to the tube length and the inner tube diameter of the HP-PH. For the approximation a combination of several approximation techniques such as Kriging or neuronal networks are used. In this case the color scale indicates the local forecast quality of the approximation. Therefore, the so-called Coefficient of Prognosis (COP) is used. This value is a validation criterion developed by optiSLang to describe the quality of the approximation. It is calculated by using a cross-validation procedure [5]. In this case the COP is on a very high level across the entire surface. In systems with more complex and discontinuous process behavior generally lower COP values are reached. In such cases, it is possible to use other Design of Experiment (DoE) methods and/or to increase the number of samples (*n*). Another feature of the SA is the filtering of non-relevant parameters to simplify the optimization problem.

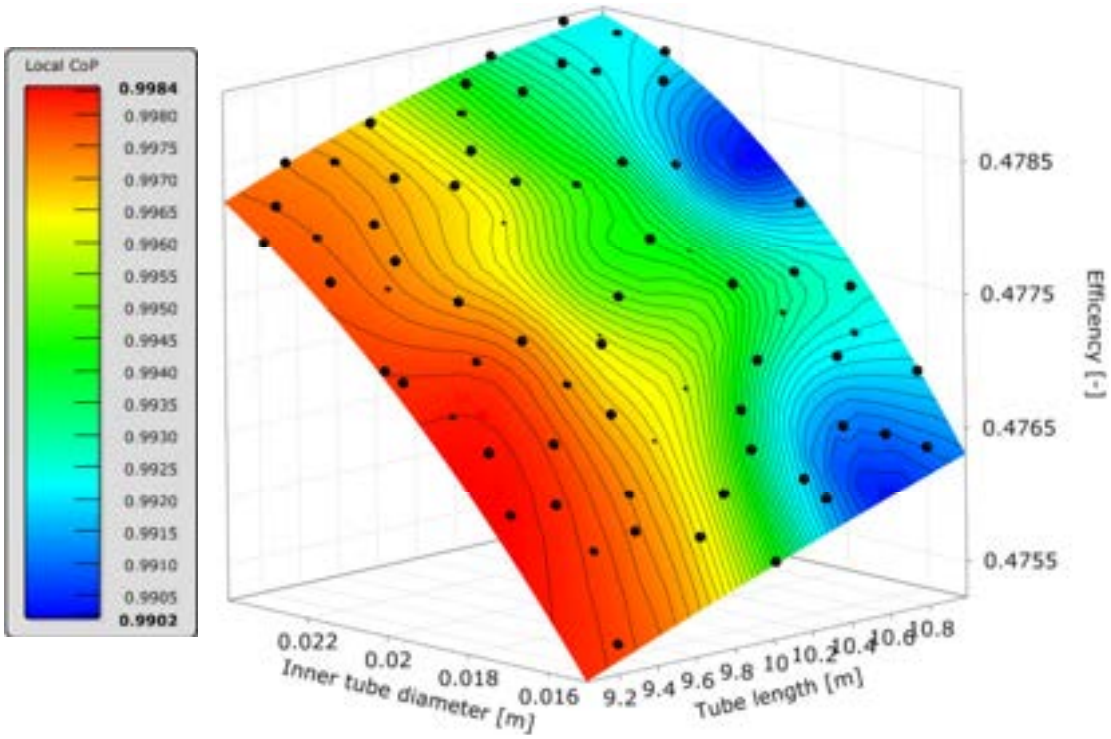

Figure. 6. Change of overall system efficiency depending on the tube length and the inner tube diameter of the HP preheater. Indication of the local COP by means of color scale

6.2. Runtime comparison of direct and indirect optimization

A comparison of the direct and indirect optimization method indicates a time advantage in favor of the indirect method. Both calculations are carried out with the same number of model simulations and algorithm evaluations. For the comparison, the overall runtime (t_{dir} and t_{indir}) is further separated into different categories (see Eq. (5) and Eq. (6)). Hereby a more detailed understanding of the optimization processes is achieved. The different categories are defined as the simulation time, the approximation time and the optimization time. The simulation time t_{sim} equals the total time for model simulation and can be calculated from the runtime for one simulation t_{model} and the total number of model simulations n_s (see Eq. (7)). The approximation time t_{approx} of the indirect variant corresponds to the time period for generating the surrogate model and is affected by the number of simulation and the complexity of the correlations. The remaining time is assigned to the optimization time. Both, the approximation time and the total runtime can be taken from the optiSLang log file.

$$t_{dir} = t_{sim} + t_{opt,dir} \tag{5}$$

$$t_{indir} = t_{sim} + t_{opt,indir} + t_{approx} \tag{6}$$

$$t_{sim} = t_{model} \cdot n_s \tag{7}$$

The resulting runtimes of the direct and indirect method are shown in Figure 7. The displayed percentage values describe the share of the respective category in the total runtime of the method. Due to the fixed number of model simulations, the direct and indirect optimization require the same simulation time. Although the indirect variant requires additional time due to the creation of the meta-model, the optimization can be done significantly faster because no further time-consuming simulation runs are needed. Compared to the direct method, the optimization time can be reduced by 97 % and the total runtime by 12 %. With increasing number of evaluations this time advantage increases even more. In addition, simulation and approximation are omitted in a new optimization run of the same problem since the determined approximation is reusable.

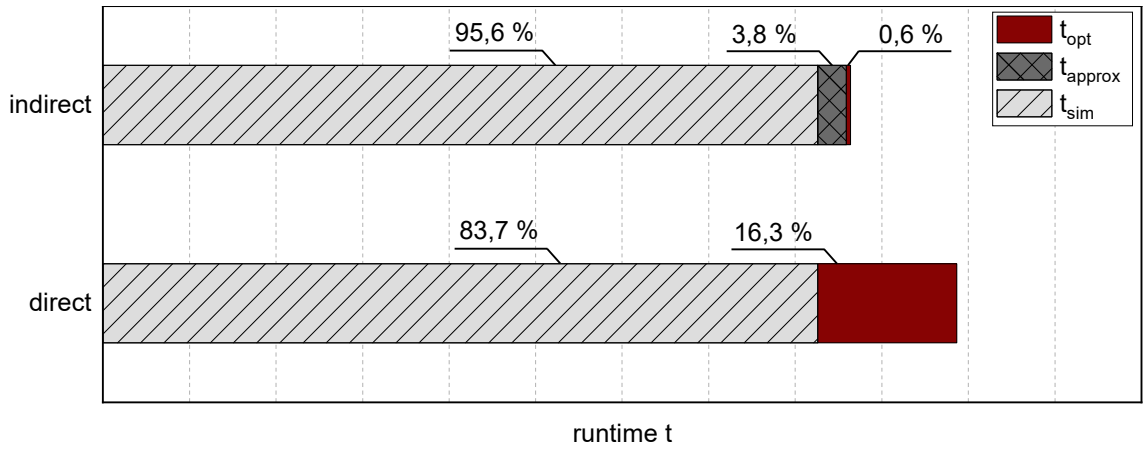

Figure. 7. Overall runtime of the direct and indirect optimization and the respective proportions of the simulation, approximation and optimization time

When using approximations, it must be taken into account that the results are affected by an error seen in Figure 8 which compares the Pareto-Front of the two methods. While the indirect Pareto-Front generates a very smooth graph, the direct method shows a much more complex behavior. The use of the approximation simplifies the system response, which in this example leads to areas where the investment costs are underestimated or overestimated. Because of these discrepancies, the indirect method should be used primarily as a first optimization step in order to reduce the overall computing time and to locate/constrain the relevant solution space [5].

With increasing model runtime, shortening methods are becoming more important. If no pre-optimization is desired, parallelization methods can be used alternatively. Since the simulations of each evaluation loop are executed parallel instead of sequentially, runtime reductions can be achieved without affecting the result. In the present work the runtime of the direct method could be reduced by up to 75 % using parallelization. A further reduction can be realized by using a computing cluster which grants access to more cores.

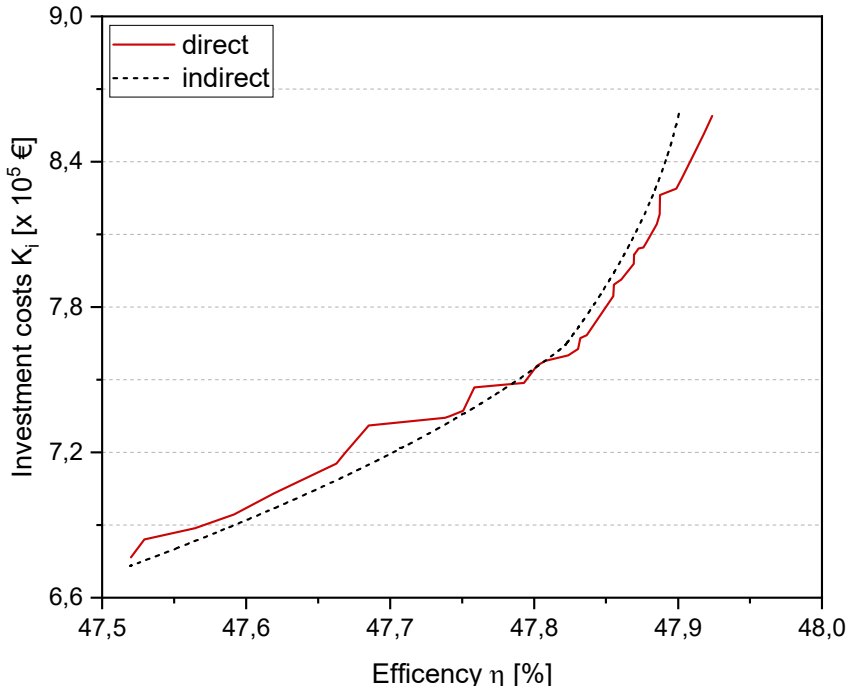

Figure. 8. Comparison of the direct and indirect Pareto-Front of the overall system efficiency and the investment costs of the HP preheater

6.3. Comparison of the DLR Optimization Library and optiSLang

In the following section, a comparison of the optiSLang workflow and the DLR Optimization Library is presented. Since the DLR Optimization Library uses weighting factors to transform multi-objective problems into single-objective problems, no comparison to the previous results could be made. Instead, a single-

objective optimization using the overall efficiency as the optimization goal is carried out. An evolutionary algorithm with standard specifications is used for the calculation and parallelization methods are considered.

All setups manage to improve the overall system efficiency (see Table 3). The optimized efficiency η_{opt} as well as the difference to the initial value $\Delta\eta$ are shown in the second column of the table and only differ slightly. For the further comparisons of the setups, the direct DLR setup is defined as reference. With regard to the optimized efficiency only minimal changes occur. On the other hand, large differences in the runtime were found. The direct optimization of the DLR Optimization Library is the most time-consuming setup. However, by using parallelization, the runtime can be more than halved. The direct optiSLang setup reduces the runtime by almost 40 %. By using additional parallelization, the runtime can be further reduced by a factor of four without influencing the results. The indirect optiSLang setup is faster than the direct DLR and direct optiSLang setup but slightly influences the optimized results negatively. A benefit of this setup is the generated surrogate model, which can be reused for further optimization runs.

Table 3. Overall runtime and maximum efficiency of the investigated setups for the single-objective optimization of the HP Preheater.

Method	$\boldsymbol{\eta_{opt}}$ $(\Delta\boldsymbol{\eta})$ [%]	$\boldsymbol{\eta_{DLR,direct} - \eta_{opt}}$ [%]	$\boldsymbol{t}$ [h]	$\frac{\boldsymbol{t}}{\boldsymbol{t_{DLR,direct}}}$ [-]
DLR Optimization Library direct	51.688 (+ 0.105)	0	11.4	1
DLR Optimization Library direct and parallel	51.688 (+ 0.105)	0	5.3	0.46
optiSLang direct	51.689 (+ 0.106)	0.001	8.2	0.72
optiSLang direct and parallel	51.689 (+ 0.106)	0.001	2.1	0.18
optiSLang indirect	51.686 (+ 0.103)	- 0.002	7.2	0.63

7. Conclusion

Since the programming language Modelica does not allow the definition of optimization problems, it is necessary to link up with external optimization environments or optimization languages. The simulation environment Dymola offers the integrated DLR Optimization Library which contains ready-made methods for static and transient optimization. These optimization methods are easy to use but only customizable to a limited extent. Therefore, it is barely possible to adapt the algorithm individually for different optimization tasks. Since the optimization is done directly, large simulation models cause long optimization times. For a runtime reduction parallelization can be used. To ensure a better optimization performance with higher flexibility, tools such as Ansys optiSLang can be used. An implementation of an appropriate workflow for coupling Modelica/Dymola and optiSLang is presented in this paper. It has been shown that the optimization via optiSLang can be more time efficient compared to the Dymola standard DLR Optimization Library. When using parallelization methods, the runtime of the examined test case has been reduced by the factor 4. This improvement is necessary to deal with large scale optimization problems in a suitable time. By using the sensitivity analysis, it is possible to obtain additional information about the system behavior. The determined surrogate model (meta-model) can also be used for an indirect optimization which is especially advantageous for a repeated optimization of the same model. Due to the deviations from the model behavior indirect methods should only be used for pre-optimizations.

The comparison with the DLR Optimization Library shows that the developed workflow makes it possible to solve static optimization problems very efficiently. Further investigations should focus on optimization problems with a higher complexity to identify the limits of the presented workflow. In addition, first investigations showed that dynamic optimization problems may be realized by adjusting the workflow. For this, the input signals/vectors need to be discretized into a finite number of static points, which can later be used like the tuners of the static optimization.

Nomenclature

f	Objective function	[-]
x	Optimization variable	[-]
d_i	Inner tube diameter	[m]
d_o	Outer tube diameter	[m]
l	Tube length	[m]

η	Overall system efficiency in nominal operation	[%]
η_{opt}	Optimized overall system efficiency in nominal operation	[%]
K_i	Investment costs	[€]
$K_{i,ref}$	Reference investment costs	[€]
A	Heat exchange surface	[m^2]
A_{ref}	Reference heat exchange surface	[m^2]
PI	Price index	[-]
PI_{ref}	Reference price index	[-]
P_{in}	Input Power	[MWh]
P_{out}	Output Power	[MWh]
n	Degression exponent	[-]
n_T	Number of tubes	[-]
n_s	Number of model simulations	[-]
t	Runtime	[h]
t_{model}	Model runtime	[h]
t_{sim}	Simulation time	[h]
t_{approx}	Approximation time	[h]
t_{opt}	Optimization time	[h]
t_{dir}	Runtime of the direct method	[h]
t_{indir}	Runtime of the indirect method	[h]
$t_{DLR,direct}$	Runtime of the direct DLR optimization Library method	[h]

References

[1] A. Subramanian, T. Gundersen, and T. Adams, Eds., *Modeling and Simulation of Energy Systems: A Review*. Processes, 2018, doi: 10.3390/pr6120238.

[2] J. Akesson, *Optimica - An Extension of Modelica Supporting Dynamic Optimization*. The Modelica Association, 2008. [Online]. Available: https://www.researchgate.net/publication/253089188_Optimica-An_Extension_of_Modelica_Supporting_Dynamic_Optimization

[3] Modelica Association, *Modelica - A Unified Object-Oriented Language for Physical Systems Modeling Version 3.2 Revision 2*, 2013. [Online]. Available: https://www.modelica.org/

[4] Dassault Systèmes, *Dymola - Dynamic Modeling Laboratory: Dymola Release Notes*, 2022. [Online]. Available: https://www.3ds.com/

[5] Dynardo. “optiSLang - Produktübersicht.” https://www.dynardo.de/software/optislang.html (accessed Jan. 28, 2020).

[6] A. Pfeiffer, *Documentation, Optimization Library for Dymola: Version 2.2.2 - Tutorial*, 2016.

[7] K. Siebertz, D. van Bebber, and Thomas Hochkirchen, *Statistische Versuchsplanung: Design of Experiments (DoE)*. Springer-Verlag Berlin Heidelberg, 2010.

[8] L. Göllmann *et al., Mathematik für Ingenieure: Verstehen Rechnen Anwenden: Band 2: Analysis in mehreren Variablen, Differenzialgleichungen, Optimierung* (Lehrbuch). Berlin: Springer Vieweg, 2017.

[9] A. Wünsch, “Effizienter Einsatz von Optimierungsmethoden in der Produktentwicklung durch dynamische Parallelisierung,” Dissertation, Fakultät für Maschinenbau, Otto-von-Guericke-Universität Magdeburg, 2016.

[10] A. M. Vogelsang, “Mehrzieloptimierung von solarthermischen Parabolrinnenkraftwerken unter Berücksichtigung variabler Vergütungsschemata mit Hilfe technischer Auslegungsparameter,” Dissertation, Universität Flensburg, 2014.

[11] K. Graichen, “Methoden der Optimierung und optimalen Steuerung (WS 2017/2018),” Skriptum, Institut für Mess–; Regel– und Mikrotechnik, Universität Ulm, Institut für Mess–, Regel– und Mikrotechnik, Universität Ulm, 2017.

[12] S. Vajna, H. Bley, P. Hehenberger, C. Weber, and K. Zeman, *CAx für Ingenieure: Eine praxisbezogene Einführung,* 2nd ed. Berlin, Heidelberg: Springer Berlin Heidelberg, 2009. [Online]. Available: http://site.ebrary.com/lib/alltitles/docDetail.action?docID=10274774

[13] J. Kallrath, *Gemischt-ganzzahlige Optimierung: Modellierung in der Praxis: Mit Fallstudien aus Chemie, Energiewirtschaft, Papierindustrie, Metallgewerbe, Produktion und Logistik,* 2nd ed., 2013.

[14] A. Schumacher, *Optimierung mechanischer Strukturen: Grundlagen und industrielle Anwendungen,* 2nd ed. Berlin, Heidelberg: Springer, 2013.

[15] M. Pieper, *Mathematische Optimierung: Eine Einführung in die kontinuierliche Optimierung mit Beispielen* (essentials). Wiesbaden: Springer Spektrum, 2017.
[16] B. Mu, Y. Li, J. M. House, and T. I. Salsbury, Eds., *Real-time optimization of a chilled water plant with parallel chillers based on extremum seeking control*. Applied Energy, 2017, doi: 10.1016/j.apenergy.2017.09.072.
[17] F. Liu, J. Deng, and W. Pan, Eds., *Model-based Dynamic Optimal Control of an Ejector Expansion CO2 Heat Pump Coupled with Thermal Storages*. Energy Procedia, 2018, doi: 10.1016/j.egypro.2018.09.074.
[18] S. Senthil and S. Senthilmurugan, Eds., *Reverse Osmosis–Pressure Retarded Osmosis hybrid system: Modelling, simulation and optimization*. Desalination 389, 2016, doi: 10.1016/j.desal.2016.01.027.
[19] J. Chen and H. E. Garcia, Eds., *Economic optimization of operations for hybrid energy systems under variable markets*. Applied Energy, 2016, doi: 10.1016/j.apenergy.2016.05.056.
[20] C. Hoffmann and H. Puta, Eds., *Dynamic optimization of energy supply systems with modelica models: Energy saving control in plants and buildings*, 2006, doi: 10.3182/20061002-4-BG-4905.00009.
[21] M. Gräber, Ed., *A tool chain for the efficient solution of optimal control point*. Linköping University Electronic Press, 2017, doi: 10.3384/ecp17132249.
[22] M. Karami and L. Wang, Eds., *Particle Swarm optimization for control operation of an all-variable speed water-cooled chiller plant*. Applied Thermal Engineering, 2018, doi: 10.1016/j.applthermaleng.2017.11.037.
[23] H. Thieriot. “Towards Design Optimization with OpenModelica Emphasizing Parameter Optimization with Genetic Algorithms.” https://ep.liu.se/ecp/063/084/ecp11063084.pdf
[24] G. Delikaya, “Supervisory control of a combined heat and power plant by economic optimization,” Masterarbeit, Fraunhofer ISE, 2015.
[25] S. Huang, W. Zuo, and M. D. Sohn, Eds., *Improved cooling tower control of legacy chiller plants by optimizing the condenser water set point*. Buildings and Enviroment, 2017, doi: 10.1016/j.buildenv.2016.10.011.
[26] J. Granderson, G. Lin, D. Blum, J. Page, M. Spears, and M. A. Piette, Eds., *Integrating diagnostics and model-based optimization*. Energy & Buildings, 2019, doi: 10.1016/j.enbuild.2018.10.015.
[27] M. Ali, V. Vukovic, M. H. Sahir, and G. Fontanella, Eds., *Energy analysis of chilled water system configurations using simulation-based optimization*. Energy and Buildings, 2013, doi: 10.1016/j.enbuild.2012.12.011.
[28] A. Pfeiffer, *Numerische Sensitivitätsanalyse unstetiger multidisziplinärer Modelle mit Anwendungen in der gradientenbasierten Optimierung* (Zugl.: Halle, Univ., Naturwissenschaftliche Fak. III, Diss.) (Berichte aus dem Institut für Robotik und Mechatronik 417). Düsseldorf: VDI-Verl., 2008.
[29] J. Riedel, *Gewichtsoptimierung eines Kreuzfahrtschiffes unter Spannungsrestriktionen*. Institutskolloquium: Dynardo, 2000. Accessed: Jan. 25, 2020. [Online]. Available: www.dynardo.de
[30] TLK-Thermo GmbH and XRG-Simulation GmbH, *Clara Lib - Version 1.4.0*. Accessed 20 March 2020, 2019. [Online]. Available: https://www.claralib.com/
[31] J. Branke, K. Deb, K. Miettinen, and R. Słowiński, *Multiobjective Optimization* (5252). Berlin, Heidelberg: Springer Berlin Heidelberg, 2008.
[32] Lehner. “Betriebstechnik - BET -Wirtschaftlichkeitsrechnungen und Betriebliches Rechnungswesen.” https://docplayer.org/14249839-Betriebstechnik-bet-teil-2-wirtschaftlichkeitsrechnungen-und-betriebliches-rechnungswesen.html (accessed Jan. 16, 2023).
[33] C. Lühe, “Modulare Kostenschätzung als Unterstützung der Anlagenplanung für die Angebots- und frühe Basic Engineering Phase,” Dissertation, Technischen Universität Berlin, 2013.
[34] E. Zitzler, M. Laumanns, and L. Thiele, Eds., *SPEA2: Improving the strength pareto evolutionary algorithm*. ETH Zurich, 2001, doi: 10.3929/ethz-a-004284029.

PROCEEDINGS OF ECOS 2023 - THE 36TH INTERNATIONAL CONFERENCE ON
EFFICIENCY, **C**OST, **O**PTIMIZATION, **S**IMULATION AND ENVIRONMENTAL IMPACT OF ENERGY SYSTEMS
25-30 JUNE 2023, LAS PALMAS DE GRAN CANARIA, SPAIN

Rolling horizon Dynamic Real-Time Optimization of a solar thermal plant with a planning phase

Alix Untrau[a], Sabine Sochard[b], Frédéric Marias[c], Jean-Michel Reneaume[d], Galo A.C. Le Roux [e] and Sylvain Serra[f]

[a,b,c,d,f] Universite de Pau et des Pays de l'Adour, E2S UPPA, LaTEP, Pau, France
[a] alix.untrau@univ-pau.fr, CA, [b] sabine.sochard@univ-pau.fr, [c] frederic.marias@univ-pau.fr, [d] jean-michel.reneaume@univ-pau.fr, [f] sylvain.serra@univ-pau.fr
[e] Universidade de São Paulo, Escola Politécnica, São Paulo, Brazil, galoroux@usp.br

Abstract:
Solar thermal plants operate in a highly variable environment, with variations in both the energy source and the heat demand. Moreover, weather and load forecasts contain uncertainty. Thermal energy storage helps to decouple the heat production from the heat supply and gives the solar thermal plant more flexibility while complexifying its operation. In this work, a Dynamic Real-Time Optimization (DRTO) methodology is presented. Firstly, a planning phase determines the best storage management policy, given the estimated weather and load forecasts. An economic DRTO algorithm is then used to update the optimal trajectories to minimize the operating costs of the plant while respecting the storage management policy determined at the planning level, despite disturbances in the weather conditions. This stage uses updated forecasts and real-time information to update the optimal trajectories. This methodology is tested on a "virtual solar plant" (a detailed dynamic model of an existing plant) in a case study, with real data for the weather forecasts and measurements and a variable heat demand. Results obtained without and with DRTO adjustment are compared. In the first case, the virtual plant is operated using trajectories computed with offline dynamic optimization (DO) at the planning phase and undergoing the real-time weather and load conditions, while in the second case, real-time modification of the operating trajectories is performed. We observe an improvement in the solar fraction used to satisfy the heat demand and a reduction in the operating costs with DRTO compared to DO, without degrading the storage management significantly. The results are promising for an application to an existing plant.

Keywords:
Dynamic Real-Time Optimization, Solar thermal energy, Simulation

1. Introduction

Greenhouse gases emissions need to be reduced to mitigate climate change. An efficient energy transition is crucial to achieve carbon neutrality. Heat represents a large part of the final energy consumption and mostly relies on fossil fuels for its production nowadays. Solar thermal plants are a good alternative to fossil fuels because they allow the production of heat from the solar irradiation, and thus without direct CO_2 emissions.

1.1. Solar thermal plants challenges and opportunities

In a solar thermal plant, the solar irradiance heats up a fluid flowing through solar collectors. High temperatures, suitable for steam and electricity generation can be achieved by concentrating the solar radiation with mirrors. In the present work, we consider a non-concentrating solar thermal plant for low temperature heat production suitable for space heating, domestic hot water and some industrial processes. Nevertheless, the methodology presented in the remaining parts of the paper could be applied to other solar thermal plants. Solar energy is intermittent, with daily and seasonal variations. On the other hand, the heat demand also varies, and generally its variations are not synchronized with the variations in solar heat production. To help to decouple solar heat production and supply, Thermal Energy Storage (TES) solutions are developed. Both daily and seasonal storage solutions exist, but only daily storage is considered in this work, in the form of a stratified water tank. The association of a variable energy source and a storage solution makes the solar thermal operation complex and with several operating modes possible: direct supply, storage discharge, storage charge, shut down. Optimization methodologies are particularly promising for a system with such degrees of freedom.

1.2. Solar thermal plants optimization

Mathematical optimization is a useful tool to make the most of a system. For example, it can reduce the investment and operation costs, or the environmental impact of a system. Given the large cost of a solar thermal plant, optimizing its design and operation can help to reduce its cost and thus can improve its competitiveness

against fossil fuels. The design of the system, such as solar panels area, storage tank volume, etc., can be optimized to minimize the investment cost while making sure that the heat demand can be met. Once the system is designed accordingly to the consumer needs, the operation of the solar thermal plant can also be optimized in order to help to meet the heat demand despite variable weather conditions, reduce the operating cost and cut down the fossil fuel consumption in heat production.

Nowadays, most solar thermal plants are operated with logic control rules, such as a constant temperature at the outlet of the solar field, the equality of calorific fluxes in heat exchangers or the discharge of the storage tank as soon as the heat demand is not met. To track the set points determined by these logic rules, basic controllers are mostly implemented [1]. However, a solar thermal plant is a highly non-linear system, with various dynamics and ever-changing environmental conditions. Hence, more advanced controllers are developed, with predictive features for example. In the recent years, an economic objective has been incorporated in complex controllers in order to optimize the operation of systems [2]. This has been tested for a solar thermal system with storage in [3], where the back-up fossil fuel consumption was minimized. A linear control oriented model was employed to reduce the computational time since the economic optimization has to be performed at each control time step. Moreover, the control time horizon is not long enough to plan a good storage management, since the storage tank has much slower dynamics than the rest of the plant. The economic optimization and the control of the system could be performed separately to avoid the over-simplification of the dynamic model of the system.

Dynamic optimization (DO) has been applied to solar thermal plants in order to determine optimal trajectories for the control variables over a given time horizon. This is also known as planning. For example, in [4], the flow rates in the different parts of the solar thermal plant were optimized over 36 hours using weather and heat demand forecasts. In particular, the use of storage was optimized. Dynamic optimization has been more commonly applied to concentrating solar thermal plants for electricity generation. For example in [5], the income from electricity selling is maximized, with a variable electricity price and TES to shift the electricity production. A hybrid system composed of a solar thermal plant and a back up fossil fuel burner has also been optimized, in [6] for example. These studies on dynamic optimizations allowed to improve the performances of the solar thermal plants by increasing the income and reducing the back-up fossil fuel consumption. However, they relied on weather and load forecasts which are uncertain. Dynamic optimization does not adapt the optimal strategy to the current disturbances. Thus, the trajectories determined might become sub-optimal or even impossible to track by the controllers.

An intermediate level between planning and control in the hierarchical operation of the plant is real-time optimization. For a solar thermal plant, Dynamic Real-Time Optimization (DRTO) could be applied to determine the optimal trajectories of the control variables, that will be tracked by controllers [7]. These trajectories are updated regularly with a new dynamic optimization run based on updated forecasts and current measurements of state variables and disturbances. This has been tested for a concentrating solar thermal field, without considering the storage tank, in [8]. Another work focused on the daily storage management of a solar district heating system [9], by optimizing the flow rate between a long term and a short term storage tanks. These two studies only optimized in real-time a single flow rate and not the complete solar thermal plant operation, although DRTO seems well-suited to optimize such a complex system operated in an ever-changing environment.

Storage management is a particularly challenging part of the operation of a solar thermal plant. Indeed, the optimal operation of the TES has to be determined over several days, since it has slow dynamics and its optimal operation requires a long term strategic vision. However, running a new accurate dynamic optimization regularly with a time horizon of several days might lead to prohibitive computational times. A hierarchical approach might improve storage management, as shown in [10] for an electric system with storage. In this paper, a top layer is in charge of planning the storage state over a longer time horizon and a bottom layer optimizes the operation of the electric system in real-time. A similar approach could be used for a solar thermal plant, as suggested in [11]. The association of a planning phase for storage management and DRTO for the operation of the plant was only tested in one paper [16] in a theoretical case study. Reduction in the operating cost compared to DO was achieved. These promising results need to be confirmed in a more realistic case study.

Based on this literature review, there is a lack of studies focusing on the DRTO of a solar thermal plant to optimize its performances despite varying environmental conditions and consumer needs and uncertain forecasts. Moreover, a methodology to ensure a good storage management, through hierarchical optimization layers should be developed and tested in realistic case studies.

1.3. Paper contents

In the present paper, a DRTO methodology in association with a planning phase for storage management is developed. The planned storage state is incorporated into the DRTO economic objective function. The methodology is tested in a realistic case study on a simulation model. Real data are used for the weather forecasts and measurements. The test is carried out over 96 hours, showing better performances than DO without real-time adaptation.

Section 2. presents the solar thermal plant layout and its modeling. Section 3. details the input information for the algorithm. Section 4. explains the methodology with the two-layer optimization algorithm. Section 5. presents the case study chosen to test the methodology and Section 6. shows the results obtained. Finally, Section 7. gives some conclusions and perspectives for this work.

2. System description and modeling

2.1. Presentation of the solar thermal plant considered

The solar thermal plant considered in this study is presented in Fig. 1 and corresponds to an initial design of a real system provided by our industrial partner NEWHEAT. It is composed of a solar circuit, with 12 loops of 15 flat plate collectors each, where the fluid is heated up by the solar irradiation. This represents an equivalent surface of 2873m^2 of solar collectors. The fluid inside the solar circuit is composed of 70% of water and 30% of glycol in volume. The fluid can by-pass the first heat exchanger by flowing through the recirculation loop. This allows a faster warm-up of the solar circuit. Once the temperature at the outlet of the solar field is high enough for the consumer needs, the fluid flows through the heat exchanger 1, to transfer the solar heat to the secondary circuit, filled with water. The main part of the secondary circuit is a short term thermal energy storage. The technology chosen is a stratified water tank with a volume of 500m^3 and a height of 12m. The storage tank can be charged, discharged and by-passed depending on the consumer need and weather conditions. For example, the storage tank can be charged when the solar heat produced exceeds the heat demand. It can be discharged when the storage tank contains valuable energy and not enough heat is produced in the solar field. Finally, it can be by-passed to deliver directly the solar heat produced to the consumer when the heat production and demand happen simultaneously. The temperature of the fluid flowing through the second heat exchanger can be adjusted by diluting the fluid from the solar field or the storage tank with fluid exiting the second heat exchanger after having transferred its heat to the consumer. This avoids exceeding the heat demand. Three variable speed pumps are used to move the fluid in the different parts of the system and three-way valves ensure the fluid distribution in the pipes. The different operational modes of the solar thermal plant make its operation flexible but also complex. In this context, optimizing the operation of the plant should be promising because of the large number of degrees of freedom in the system. In case the heat demand is not fully satisfied by solar energy, a gas burner will be used by the consumer to reach the target temperature. The gas burner is not represented in Fig. 1 and is not modeled in our work. However, the gas consumption will be computed in order to obtain the operational cost of the heat production.

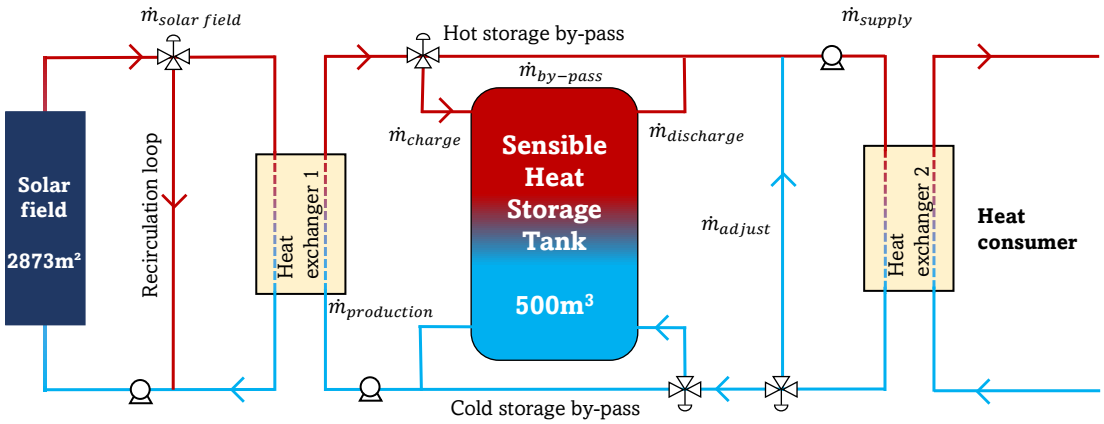

Figure 1: Solar thermal plant architecture

2.2. Modeling of the solar thermal plant

A solar thermal plant is intrinsically dynamic, with variations in the energy source and demand. The elements of the solar thermal plants have various dynamics. For instance, the solar field has fast variations while the storage tank state varies less rapidly. For these reasons, a dynamic model was chosen to represent the solar thermal plant. Moreover, nonlinear phenomena need to be represented. For example, power terms are written as the product of a flow rate and a temperature, which are both important to characterize the solar thermal plant operation. Hence, a nonlinear model was chosen. Since the optimization methodology will be tested on a simulation model, both an optimization and a simulation models are necessary. Both models are similar but some additional simplifying assumptions are made in the optimization model to keep the computational time low, as presented hereafter. The model for the solar thermal plant was developed in [4] and the main equations are detailed below, as well as some simplifying assumptions made to the original model.

2.2.1. Solar field

The solar field in this work is modeled as a single equivalent solar panel, with a total area A_{eq} equal to the sum of the areas of all the flat plate collectors in the solar field. The original model in [4] represented an equivalent loop of the solar field but considering a single equivalent solar panel speeds up the calculations without deteriorating the accuracy of the model significantly [12]. No spatial discretization of the collector and no heat losses between the collectors within a loop are considered. Moreover, the fluid distribution is assumed uniform between the loops. The equation modeling the solar field is the one node capacitance model written for the equivalent solar panel as follows:

$$\frac{\dot{Q}_{SF}}{A_{eq}} = \left(\eta_{0,b}(\eta_{sh}K_b(\theta)G_b + K_d G_d) - c_1(T_{mean} - T_{amb}) - c_2(T_{mean} - T_{amb})^2 - c_5\frac{dT_{mean}}{dt}\right) \quad (1)$$

This energy conservation equation allows us to calculate the mean temperature T_{mean} inside the solar field, taking into account the heat gain from the solar irradiance, using both the direct irradiation G_b and the diffuse irradiation G_d in the plane of the collectors, the heat losses to the ambient at the temperature T_{amb} and the equivalent inertia of the collectors. $\dot{Q}_{SF}$ is the power transmitted from the sun to the heating fluid in the solar field. $\eta_{0,b}$, c_1, c_2, c_5, $K_b(\theta)$ and K_d characterize the solar collectors and are provided by the manufacturer. $\eta_{0,b}$ is the optical efficiency of the collectors, c_1 is the heat loss coefficient in the collector at $T_{mean} = T_{amb}$, c_2 is the temperature dependence of the heat loss coefficient, c_5 is the effective thermal capacity, $K_b(\theta)$ is the incidence angle modifier for the direct irradiation and K_d is the incidence angle modifier for the diffuse irradiation. η_{sh} represents the reduction in efficiency due to the shading effect. The outlet temperature of the solar field is computed assuming a linear temperature distribution in the collectors. This simplified model can represent the transient behavior of the solar field in a short computational time.

2.2.2. Storage tank

The storage tank is modeled in 1D, only the variations of the temperature along the vertical axis are considered. The storage tank is divided into N layers of same height Δz. The temperature inside each layer is assumed uniform. The energy balance can be written for each layer i, numbered from 1 at the bottom of the tank to N at the top, composed of the stored fluid and the tank wall assumed in thermal equilibrium:

$$\rho C_p A \Delta z \frac{dT_i}{dt} = US_l * (T_{amb} - T_i) + \frac{k^* A}{\Delta z}(T_{i-1} - 2T_i + T_{i+1}) + \dot{m}_{charge}C_p(T_{i+1} - T_i) + \dot{m}_{discharge}C_p(T_{i-1} - T_i) \quad (2)$$

T_i is the temperature of the layer i. The charging flux enters the top of the tank at the temperature T_{charge} and flow rate $\dot{m}_{charge}$ while the return flow enters the bottom of the tank at the temperature T_{return} and flow rate $\dot{m}_{discharge}$. C_p is the specific heat capacity of the water only because the mass of water is larger than the mass of metallic wall and the heat capacity of the metal is smaller than the heat capacity of water. ρ is the fluid density. k^* is the effective conductivity of the fluid and the tank wall, because conduction through the wall participates in destratification of the tank fluid. Heat losses between each layer and the ambient air at T_{amb} are computed with an overall heat transfer coefficient U. The exchange surface is the lateral surface of a tank layer S_l. For the top and bottom layers, the exchange surfaces and heat transfer coefficients are different than for the interior layers.

The number of layers used in the model has a great impact on the accuracy of the vertical temperature profile computed, as shown in [13] for example. The effect of numerical diffusion tends to smooth the temperature profile when a small number of layers is chosen. However, a larger number of layers increases the computational time. For the accurate simulation model used in this work to test the methodology, 1000 layers are chosen. For the optimizations, a simplified model is required to ensure reasonable computational times. Hence, only 10 layers are used, similarly to [4].

One phenomenon not represented in Eq. 2 is the natural convection. When solar irradiation goes down, at the end of the day for example, it happens that the solar heat produced is at a temperature lower than the one achieved earlier in the day. Nevertheless, its temperature is still high enough for the consumer needs. Hence, this lower temperature heat can be charged and will arrive on top of warmer stored fluid. Due to buoyancy forces, the lower temperature fluid will sink inside the tank and exchange energy with the surrounding stored fluid. This phenomenon was neglected in the optimization model for simplicity and to reduce computational time [13]. For the simulation model, the temperatures inside the tank are regularly re-organized to ensure that the top of the tank is the warmest zone and the bottom of the tank is the coldest [14].

2.2.3. Heat exchangers

The two heat exchangers are the same, both plate heat exchangers with 97 plates of 1.5m^2 each. The model used for the heat exchangers is simple to keep the computational time low: no spatial discretization, no accumulation and no heat losses are considered. The ϵ-NUT model is used to compute the exchanged energy and the two outlet temperatures. A constant global heat transfer coefficient is chosen, $U = 4000 W.m^{-2}.K^{-1}$, to reduce the nonlinearities in the model.

2.2.4. Pipes

Each pipe in the system is modeled by developing the energy balance equation in 1D without spatial discretization but considering accumulation in the fluid. Heat losses are computed with either circulating fluid or static fluid. A thermal resistance is calculated to account for external convection and conduction through the insulation layer. The external convection coefficient is computed using Hilpert correlation. Internal convection and conduction through the wall are not modeled because we assume a very large heat transfer coefficient and thus a perfect heat transfer. For the mixing valves and the flow divisions, the mass and energy balances are developed neglecting the accumulation and heat losses.

2.2.5. Pumps

Part of the operational cost of the solar thermal plant is the electricity consumption of the variable speed pumps used to move the fluid in the different circuits of the plant. First, the maximum pumping power $\dot{P}_{hydrau}$ is computed with Eq. 3, when the pressure drop in the circuit is the highest ΔP_{max}, which corresponds to the maximum flow rate allowed in the pump $\dot{m}_{max}$. Then, the actual flow rate in the circuit $\dot{m}$ is used to compute the electric power $\dot{P}_{elec}$ with the overall efficiency η_{pump} of the pump in Eq. 4.

$$\dot{P}_{hydrau} = \frac{\dot{m}_{max}}{\rho} \Delta P_{max}(\dot{m}_{max}) \quad (3) \qquad \dot{P}_{elec} = \frac{\dot{P}_{hydrau}}{\eta_{pump}} \left(\frac{\dot{m}}{\dot{m}_{max}} \right)^3 \quad (4)$$

2.2.6. Representation of the various operating modes

The complete solar thermal plant model is built by connecting the models for the solar field, storage tank, heat exchangers, pipes and pumps. The difficulty of modeling a solar thermal plant operation is the existence of various operating modes depending on the heat demand, the state of the system and the environmental conditions. Sigmoid functions are used to represent the existence of a flow in an element with a continuous formulation, allowing to neglect very small flow rates that would not be implementable in the real plant (if the flow rate is near zero, the sigmoid function is 0, otherwise it is 1). A sigmoid function is expressed as follows, with β characterizing the steepness of the function and δ the threshold:

$$sig(x) = \frac{1}{1 + exp^{-\beta(x-\delta)}} \quad (5)$$

For example, this is necessary to represent the heat exchangers through which heat can be transferred. Big M formulations are used to represent the existence of an exchanged power $\dot{Q}_{hx}$ or not, in the optimization model. If the flow rate in the heat exchanger is negligible (for example lower than $\delta = 0.5 kg.s^{-1}$), then the exchanged power is zero, otherwise it is computed with the ϵ-NUT model, with ΔT_e the difference between the inlet temperatures on each side. This is expressed as follows, with M a scalar to adjust (10^8 here) :

$$-M\ sig \leq \dot{Q}_{hx} \leq M\ sig \quad (6)$$

$$-(1 - sig)M + \epsilon(\dot{m}C_p)_{min}\Delta T_e \leq \dot{Q}_{hx} \leq (1 - sig)M + \epsilon(\dot{m}C_p)_{min}\Delta T_e \quad (7)$$

If no energy is exchanged in the heat exchanger, the outlet temperature is equal to the inlet temperature on each side. These continuous formulations allow us to represent the different working modes of the solar thermal plant. In particular, the night mode when the solar circuit is shut down and no heat is transferred in heat exchanger 1, or a mode where no solar heat is supplied to the consumer through heat exchanger 2 because the storage tank is empty and the solar irradiation is too low.

3. Input data

The study is conducted for the city of Trappes (78), France (48° 46' 39.0000" N, 2° 0' 9.0000" E). In addition to the design parameters of the system, described in Section 2., the environmental conditions and the heat demand are the inputs of the model.

3.1. Weather data

Weather forecasts as well as meteorological measurements were provided by Météo-France for the whole year of 2021 at this location. The parameters of interest are the Global Horizontal Irradiance (GHI), the Direct Normal Irradiance (DNI), the ambient temperature and the wind speed (which impacts the convection coefficient used to compute the heat losses). The weather forecasts are computed with the ARPEGE model and updated every 6 hours. Their time horizon varies depending on the run: 103h for the run at 12am, 73h for the run at 6am, 103h for the run at 12pm and 61h for the run at 6pm. Hourly values are provided for each parameter. The forecasts will be used in the optimization algorithm, to determine the best operational strategy of the solar thermal plant for a given time horizon. The same 4 parameters are measured every hour with a meteorological station. The measurements differ from the forecasts and will impact the actual solar thermal plant operation.

3.2. Heat demand

The consumer considered in this work is a District Heating Network (DHN) supplying heat to a residential area. In a DHN, the heat demand varies throughout the day and throughout the year. It is not easy to find available public data on the heat consumption of a DHN. Moreover, the solar thermal plant considered should be sized accordingly for the specific DHN it supplies the heat to. To simplify this case study, the same daily heat demand profile is considered for every day of the year. The real heat demand would be greater in winter than in summer due to the space heating need. The daily profile has been created in order to be consistent with the specific solar thermal plant considered. The general shape of the daily profile was retrieved from [15]. We chose that the storage tank from the solar thermal plant can supply heat to the DHN for two days when it is full. The heat demand values were then adjusted accordingly. The daily heat demand profile created is presented in Fig. 2. We observe a peak in the heat demand around 8am, and the demand is the lowest around 4pm.

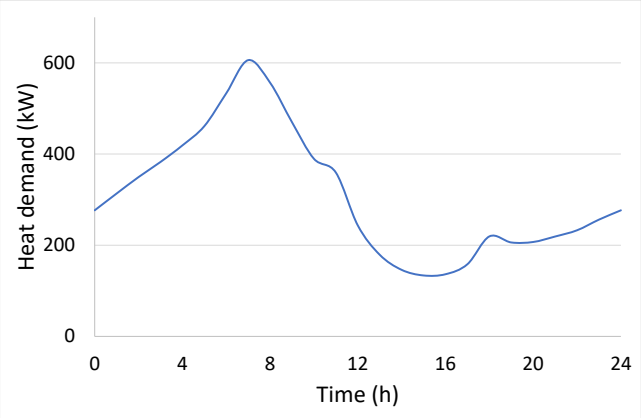

Figure 2: Daily heat demand

We consider that the DHN return temperature $T_{DHN\ return}$ is at 55°C, so the consumer inlet flow in Fig. 1 enters the heat exchanger 2 at 55°C. The target temperature T_{target} for the consumer flow after collecting the solar heat is 65°C. The flow rate of the consumer flow is variable depending on the heat demand, according to the following equation:

$$\dot{Q}_{demand} = \dot{m}_{consumer} * Cp * (T_{target} - T_{DHN\ return}) \quad (8)$$

$T_{DHN\ return}$ and $\dot{m}_{consumer}$ are both inputs of the system. The outlet temperature on the consumer side of heat exchanger 2 is calculated and should be as close as possible to T_{target} without ever exceeding it.

The variable heat demand is considered perfectly known in this work. No disturbance in the heat demand is introduced even though the methodology could be applied to an uncertain heat demand similarly to the uncertain weather conditions presented in subsection 3.1..

4. Optimization methodology

4.1. Two-level Algorithm

As explained in Section 1., the optimization methodology developed is composed of two hierarchical optimization layers to improve storage management. The methodology is tested in real-time on a simulation model, receiving the optimal trajectories and simulating the solar thermal plant actual behavior. The two-level optimization algorithm is presented in Fig. 3. The initial state of the system is that all temperatures are equal to the ambient temperature and the storage tank is half charged. The first step is the planning phase, which will be described in more details in Subsection 4.2.. It is an economic dynamic optimization that will optimize the operation of the solar thermal plant based on weather forecasts. As presented in Section 3., the longest time horizon for the weather forecasts obtained is 103 hours at 12am. Hence, the planning phase is implemented over 103 hours, starting at 0:00. The simulation model follows the optimal trajectories from the planning phase for the next 6 hours, since no weather forecast update is available. Then, the DRTO starts. Every 6 hours, a new weather forecast is available so a new DRTO is run to determine updated optimal trajectories for the next 12 hours. The DRTO economic objective function incorporates the planned storage state at the end of the DRTO time horizon. Planning is therefore used for storage management. Details on the DRTO will be provided in Subsection 4.3.. Between each DRTO run, the behavior of the system is simulated with the actual weather over the 6 hours before an update, and the simulation provides feedback to the DRTO algorithm. Details on the simulation are given in Subsection 4.4.. The complete simulation ends after 96 hours because no planned storage state is available for the next DRTO run. In a real implementation, this algorithm would be repeated continuously to optimize the operation of a solar thermal plant throughout the year, with a new planning computed regularly. In this work, the methodology was only tested for 96 hours.

4.2. Planning

The planning phase, which is an offline economic dynamic optimization follows the method developed in [4]. The degrees of freedom in the system are the 6 independent flow rates in the solar thermal plant at each time instant. The time discretization of the dynamic model for optimization is done with orthogonal collocation on

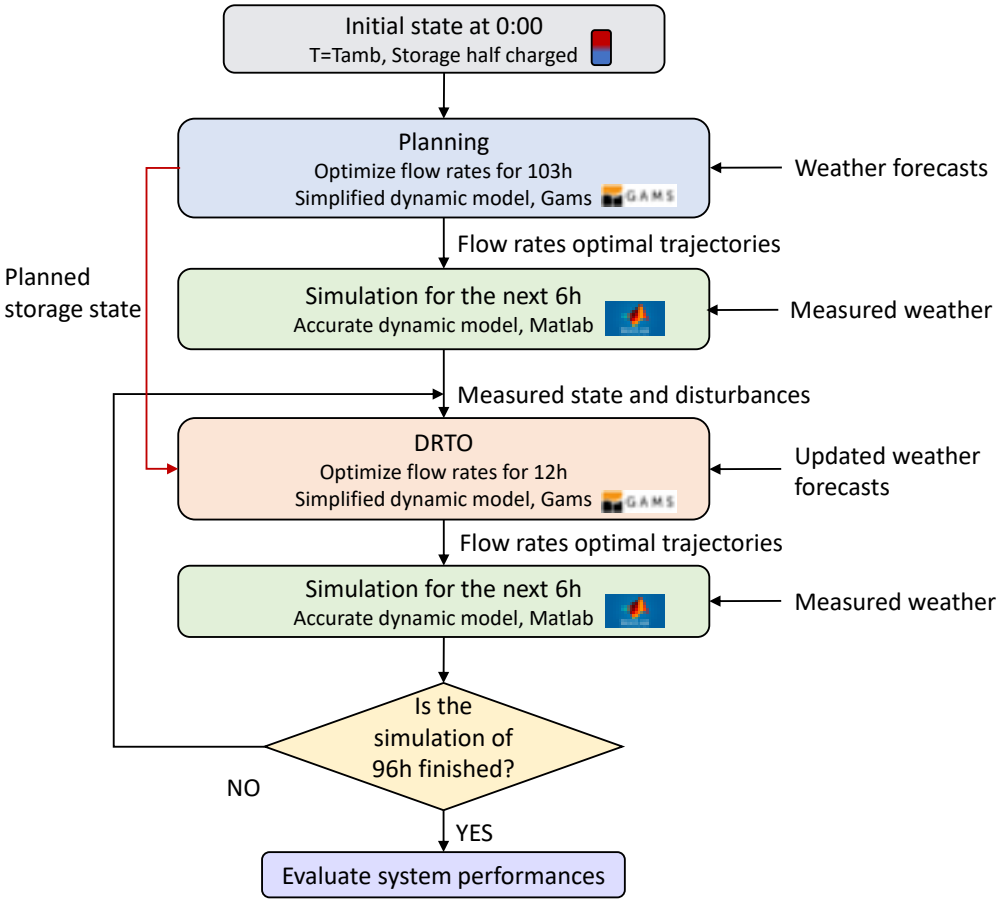

Figure 3: Two-level optimization algorithm

finite elements, with 1 hour long elements containing 9 collocation points each. The constraints in the dynamic optimization are the following:

- $T \leq 95°C$ for all temperatures T
- The flow rate in each pump is defined as follows:

$$\begin{cases} \dot{m} = 0 \text{ (corresponding to the pump turned off)} \\ \text{or} \\ 0.3\dot{m}_{max} \leq \dot{m} \leq \dot{m}_{max} \text{ (corresponding to the pump turned on, with } \dot{m}_{max} \text{ determined by the pump specifications)} \end{cases}$$

- $T_{consumer\ out} \leq T_{target}$ forbidding the heat supply to exceed the heat demand ($T_{consumer\ out}$ is the temperature of the consumer stream after collecting the solar heat)

The objective function to be minimized is the operating costs of the solar thermal plant, which are the electricity consumption of the pumps and the gas consumption of the back up burner. It includes the maximization of the stored energy at the end of the time horizon since it represents useful energy for the next hours and will allow to cut down the gas consumption. An additional term is added to smooth the trajectories obtained for the flow rates Φ_{var} and is affected by a weight γ_{var} that needs to be adjusted to achieve a good compromise between smooth flow rates trajectories and a good economic objective OF_{eco}. The formulation of the dynamic optimization problem is presented hereafter:

$$\min_{free\ \dot{m}} OF_{eco} - \gamma_{var}\Phi_{var}, \text{ with} \tag{9}$$

$$OF_{eco} = -GasPrice \int_0^{t_f} \dot{Q}_{gas}(t)\mathrm{d}t - ElecPrice \int_0^{t_f} \dot{P}_{elec}(t)\mathrm{d}t + 0.7 HeatPrice\ E_{stored}(t = t_f) \tag{10}$$

The prices used are the following: $GasPrice$ = 80€/MWh, $ElecPrice$ = 130€/MWh and $HeatPrice$ = 25€/MWh. The benefits associated to the stored energy are affected by a weight of 0.7 found appropriate in [4]. This

weight represents the decrease in energy quality between the moment it is stored and the moment it will be supplied. This dynamic optimization is solved with the NLP solver CONOPT in the software GAMS. The optimization is initialized with standard operating strategies ensuring that the local optimum found by CONOPT is implementable on the real plant. The planning phase takes around 2 hours to converge to an optimal solution on a laptop with the following characteristics: Intel Core i7-1065G7 1.3GHz. The stored energy throughout time determined during this planning phase will be passed to the next optimization level.

4.3. DRTO

The DRTO is also an economic dynamic optimization and is built similarly to the planning phase. Only the differences with the planning phase are presented hereafter. The time discretization is the same as planning but the time horizon is much shorter: 12 hours. With this time horizon, the methodology is applicable in real-time with a maximum computational time of 10 minutes for a DRTO on the same laptop. The economic objective function is also the same as the planning phase except for the term on the storage. In the planning phase, the stored energy at the end of the time horizon is maximized because it will be useful in the future. For the DRTO, the aim is to follow the plan established previously based on a long term strategic vision and weather forecasts. Hence, the difference between the planned stored energy and the actual storage state at the end of the DRTO time horizon is minimized. The difference is multiplied by the price of gas to obtain the order of magnitude of the cost of the non-respect of the plan, since the energy which should have been stored but was not will be replaced by gas. Finally, this term is affected by a weight ω which has been adjusted in [16] to obtain a good compromise between the following of the plan and the lowest operating costs. The value of 0.5 was chosen. This term is written as follows:

$$\omega.GasPrice.|E_{stored\ planning}(t = t_{f\ DRTO}) - E_{stored\ DRTO}(t = t_{f\ DRTO})| \tag{11}$$

Each DRTO run starts with an initial state retrieved from the simulation model, as explained in the next subsection.

4.4. Simulation

The online methodology needs to be tested on an actual plant. In this work, we replace the actual plant with a simulation performed with the solver ode15s in MATLAB. In the simulation model, perfect control is assumed so the controllers are not modeled and we assume that the optimal trajectories are perfectly tracked. The simulation model provides feedback to the DRTO algorithm. We assume that all states are measured and no state estimation step is included in the methodology. The simulation model undergoes the actual weather. It uses a more precise model for the storage tank, as explained in Subsection 2.2.2.. Since the DRTO algorithm regularly starts over with the actual system state, model error propagation due to the simplifying assumptions in the optimization model is mitigated.

5. Case study

The methodology was tested for one case study in Trappes in 2021, using the meteorological data from Météo-France. The period from the 12^{th} to the 15^{th} of May was chosen because the solar irradiance was not well predicted for this period, as shown in Fig. 4.

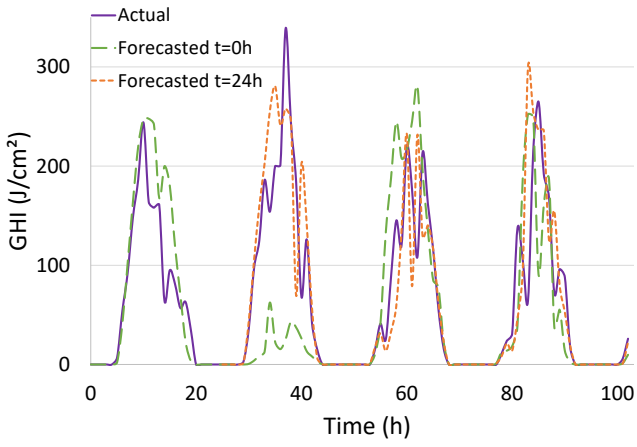

Figure 4: Predicted and actual solar irradiance for the test period in May

In this figure, the forecasted GHI plotted in dashed green line is the one used for the planning phase, at the beginning of the algorithm, while the solid purple line corresponds to the measured GHI. The solar irradiance was greatly underestimated for the second day. Forecasts are updated every 6 hours, and this underestimation is corrected in the next forecasts, which are used at the DRTO level. For example, the forecasted GHI at 24 hours is plotted in dotted orange line in Fig. 4. This forecasted GHI is closer to the measured GHI for the second day than the one predicted at 0 hours. The solar irradiation is quite variable during these four days, and the fast variations during the day are not perfectly estimated even a few hours in advance. Only the GHI was shown in Fig. 4 but a similar analysis can be conducted for the DNI.

The forecasts for the wind speed and ambient temperature are also uncertain but the differences between

forecasted values and measurements are not as large and these parameters do not impact the solar thermal plant operation as significantly as the GHI and DNI.

6. Results

6.1. Comparison between planning only and planning with DRTO

In order to assess the performances of the methodology developed, it will be compared with offline dynamic optimization (DO) without real-time adjustment, for the case study presented previously. Fig. 5 shows the comparison made.

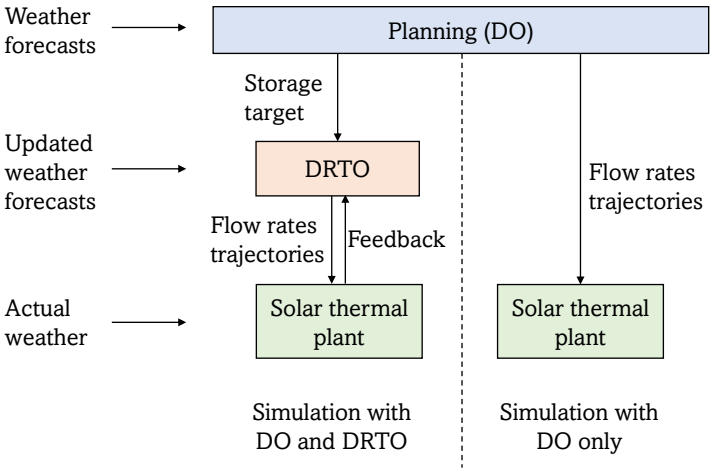

Figure 5: Comparison of simulations based on DO with DRTO and DO only

On one hand, our DRTO methodology is tested in a simulation undergoing the actual weather. The planning phase is used for storage management only, using weather forecasts. The simulation follows the optimal trajectories determined by the DRTO and regularly updated using updated forecasts. This is presented on the left side of Fig. 5. On the other hand, a simulation following the optimal trajectories determined during the planning phase (DO) is performed, with no update in the trajectories during the whole simulation undergoing the actual weather. This corresponds to the right side of Fig. 5. It was shown in the literature that offline dynamic optimization outperforms standard control strategies based on logic control rules [4]. In this section we show the interest of having real-time updates of the optimal trajectories.

6.2. Outputs

The results from the two simulations presented in the previous paragraph are compared. In Fig. 6, the flow rates in the solar field are plotted. The solid blue line corresponds to the flow rate determined during the planning phase (DO), without any update. The dash-dotted red line corresponds to the flow rate determined with our DRTO methodology. This curve is composed of sixteen portions, each six hours long, and determined by a new DRTO call. In Fig. 6, the flow rate determined by DO is zero for the second day. This is because a very low solar irradiation was predicted for that day, as shown in Fig. 4. When using our DRTO methodology, the flow rate determined during the second day is not zero because the updated weather forecasts used for the DRTO predicted a solar irradiation high enough for solar heat production. This shows that the DRTO allows the modification of the optimal trajectories when the weather forecasts are corrected.

Fig. 7 presents the temperature of the consumer stream after collecting the solar heat, $T_{consumer\ out}$, achieved for both simulations. It should be greater than the return temperature of the DHN of 55°C but lower than the target temperature of 65°C. We observe in Fig. 7 a few occurrences of a temperature lower than the DHN return temperature. This might be due to a sudden release of solar heat after a period with no supply from the source (either direct supply of from the storage). The pump is turned on but the temperature of the fluid inside the pipe has decreased due to heat losses. It takes a little time before the warm fluid reaches the second heat exchanger. There are also periods with a temperature exceeding the target temperature. For example, the temperature for DO on day 4 is much larger than 65°C. This is because the solar irradiation for this period was greatly underestimated, as shown in Fig. 4. The forecasted GHI presented a sudden decrease around hour 85 but the GHI measured actually presented a peak at that time. Hence, the operating strategy determined during planning led to exceeding the heat demand. On day 2, the solar irradiation was also greatly underestimated for the DO calculations. However, the heat demand was not exceeded on this day because the solar irradiation predicted was too low to start collecting solar heat and the storage tank was already empty at that time. Hence, the complete solar thermal plant was shut down, no solar heat was supplied and the

demand was thus not exceeded. However, for DRTO, the solar thermal plant was operated on day 2, delivering solar heat to the consumer. The heat demand was exceeded for part of the day because the updated forecast for the solar irradiation, although more accurate than the one used for planning and determined earlier, still underestimated the actual solar irradiation. In a real system, this behavior would be prevented thanks to local controllers forbidding to exceed the heat demand. Since our simulation model did not include controllers, nothing prevented the temperatures to go high. Adding the local controllers to our simulation model could improve the methodology before it can be tested on an actual plant. In order to avoid an optimal operating strategy that could lead to overheating, more frequent re-optimizations should be employed, based on more accurate forecasts. However, this requires access to updated forecasts very regularly. In this work, we were limited in the frequency of our DRTO runs because the weather forecasts were provided every six hours. Accurate forecasting of solar irradiation is an active area for research and new methods are developed. For example, sky imagers provide regular forecasts accounting for local clouds, or machine learning could help recomputing forecasts regularly. Figs. 6 and 7 showed that DRTO can adapt the optimal operating strategy to the actual conditions, thanks to regular re-optimizations using updated forecasts. In the next paragraph, the performances of the solar thermal plant in the two simulations are compared.

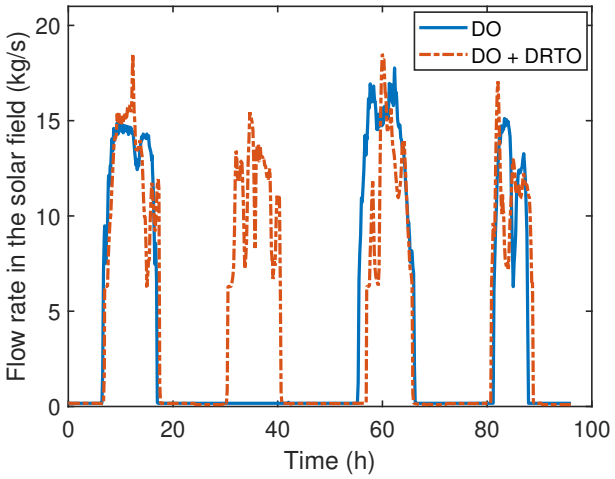

Figure 6: Comparison of the flow rates in the solar field

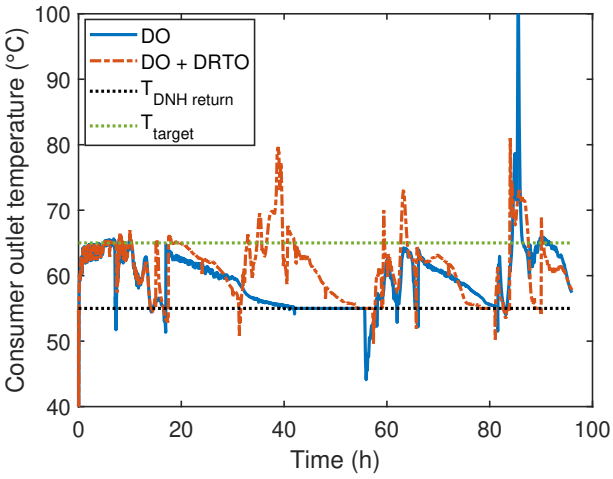

Figure 7: Comparison of the temperatures at the outlet of the consumer stream

6.3. Performances

The performances of the solar thermal plant are determined using several indicators:

- $E_{supplied}$ corresponds to the quantity of solar heat supplied at a temperature lower than the target temperature. This should be as high as possible to reduce gas consumption.
- E_{excess} corresponds to the quantity of solar heat delivered that exceeded the heat demand.
- E_{elec} corresponds to the electric consumption of the pumps.
- C_{tot} corresponds to the total operating costs of the plant (electricity and gas consumption)
- $E_{stock\ final}$ corresponds to the quantity of valuable energy inside the storage tank at the end of the simulation.

The value of each indicator for the two simulations are presented in Table 1. The total heat demand for the 96 hours of simulation is 29.8 MWh.

We observe an increase in the quantity of solar heat delivered to the consumer of about 31% with DRTO compared to DO only. This is mostly due to the solar heat supplied on the second day with DRTO, while no solar heat was produced for that day with DO. Our DRTO methodology led to more excess energy delivered in this case study, because the updated forecasts still contained inaccuracies. But this excess energy should not be delivered in a real system thanks to local controllers preventing this behavior. The electricity consumption is similar for both simulations. The total cost was reduced by 19% thanks to our DRTO methodology, because less gas was required to complete the heat demand. Finally, the quantity of energy inside the storage tank is only slightly decreased, by 1.4% of the storage capacity. However, in this case study, the storage tank is almost emptied at the end of both simulations because the solar irradiation is not very high. There is a need to study the best way to integrate storage management in the DRTO. There is probably no interest in following

Table 1: Comparison of the performances of the simulated solar thermal plant using DO only or DO+DRTO

Performance indicator	Simulation with DO only	Simulation with DO and DRTO
$E_{supplied}$ (MWh)	11.42	14.98
E_{excess} (MWh)	0.40	0.93
E_{elec} (MWh)	0.12	0.12
C_{tot} (€)	1487	1203
$E_{stock\ final}$ (MWh)	0.42	0.22

a plan determined with very inaccurate forecasts. The planning phase should be re-computed whenever the weather forecasts differ too much from the measured weather. This will be investigated in future work, with several case studies showing various levels of solar irradiation.

7. Conclusion and Perspectives

In this work, we presented a DRTO methodology using a planning phase for storage management to optimize the operation of a solar thermal plant providing heat to a DHN. The methodology was tested in a realistic case study, using real weather forecasts and measurements and a variable heat demand for four days in mid-season. The results obtained show the interest of having a real-time adaptation phase of the optimal trajectories to correct uncertainties in the weather forecasts. Thanks to DRTO, the quantity of solar heat supplied to the consumer increased, leading to a decrease in gas consumption and thus in the operating costs. The methodology developed includes the tracking of the storage state determined during the planning phase, which benefits from a better strategic vision. Thus, the DRTO is able to follow the plan while minimizing the operating costs. However, if the weather forecasts used during the planning phase are very inaccurate, following the plan is probably not optimal. A new plan should then be computed. In the mean time, a new storage management policy for the DRTO needs to be employed. Future investigations will focus on finding the best way to use the planning phase in order to improve storage management in the DRTO method. This will require testing of the methodology in various case studies.

Acknowledgments

The project leading to this publication has received funding from Excellence Initiative of Université de Pau et des Pays de l'Adour – I-Site E2S UPPA, a French "Investissements d'Avenir" programme.

Nomenclature

Abbreviations

GHI Global Horizontal Irradiance

DHN District Heating Network

DNI Direct Normal Irradiance

DO Dynamic Optimization

DRTO Dynamic Real-Time Optimization

TES Thermal Energy Storage

Latin symbols

A Tank cross sectional area, m^2

A_{eq} Area of the equivalent surface panel representing the solar field, m^2

c_1 Heat loss coefficient in the collector at $T_m = T_{amb}$, $W.m^{-2}.K^{-1}$

c_2 Temperature dependence of the heat loss coefficient, $W.m^{-2}.K^{-1}$

c_5 Effective thermal capacity, $J.m^{-2}.K^{-1}$

C_p Fluid specific heat capacity, $J.kg^{-1}.K^{-1}$

E Energy, MWh

G_b Direct irradiation (beam) in the plane of a collector, $W.m^{-2}$

G_d Diffuse irradiation in the plane of a collector, $W.m^{-2}$

k^* Effective thermal conductivity, $W.m^{-1}.K^{-1}$

$K_b(\theta)$ Incidence angle modifier for the direct irradiation (beam)

K_d Incidence angle modifier for the diffuse irradiation

$\dot{m}$ mass flow rate, kg/s

N Number of discretization layers in the storage tank

$\dot{P}$ Power, W

$\dot{Q}_{SF}$ Power transmitted from the sun to the heating fluid in the whole solar field, W

S_l Lateral surface of a tank layer, m^2

t Time, s

T Temperature, °C

U Tank fluid to ambient overall heat transfer coefficient, $W.m^{-2}.K^{-1}$

z Tank height from the bottom of the tank, m

Greek symbols

Δz Height of a discretization layer in the storage tank, m

ΔP Pressure drop in a circuit, Pa

$\eta_{0,b}$ Optical efficiency of a collector

η_{pump} Overall efficiency of a pump

η_{sh} Shading effect of a solar field loop onto the next loop

ρ Fluid density, $kg.m^{-3}$

References

[1] Camacho E., Rubio F., Berenguel M., Valenzuela L., *A survey on control schemes for distributed solar collector fields. Part I: Modeling and basic control approaches*. Solar Energy 2007;81:1240–1251.

[2] Engell S., *Feedback control for optimal process operation*. Journal of Process Control 2007;17:203-219.

[3] Serale G., Fiorentini M., Capozzoli A., Cooper P., Perino M., *Formulation of a model predictive control algorithm to enhance the performance of a latent heat solar thermal system*. Energy Conversion and Management 2018;173:438-449.

[4] Scolan S., Serra S., Sochard S., Delmas P., Reneaume J-M., *Dynamic optimization of the operation of a solar thermal plant*. Solar Energy 2020;198:643–657.

[5] Wittmann M., Eck M., Pitz-Paal R.,Müller-Steinhagen H., *Methodology for optimized operation strategies of solar thermal power plants with integrated heat storage*. Solar Energy 2011;85:653–659.

[6] Powell K.M., Edgar T.F, *An adaptive-grid model for dynamic simulation of thermocline thermal energy storage systems*. Energy Conversion and Management 2013;76:865-873.

[7] Kadam J.V., Schlegel M. Marquardt W., Tousain R.L., Van Hessen D.H., Van Den Berg J. Bosgra O.H., *A Two-Level Strategy of Integrated Dynamic Optimization and Control of Industrial Processes - a Case Study*. European Symposium on Computer Aided Process Engineering 2002;12:511–516.

[8] Pataro I.M.L., Roca L., Sanches J.L.G., Berenguel M., *An economic D-RTO for thermal solar plant: analysis and simulations based on a feedback linearization control case*. XXIII Congresso Brasileiro de Automatica 2020.

[9] Saloux E., Candanedo J.A., *Model-based predictive control to minimize primary energy use in a solar district heating system with seasonal thermal energy storage*. Applied Energy 2021;291:116840.

[10] Clarke W.C., Manzie C., Brear M.J., *Hierarchical economic MPC for systems with storage states*. Automatica 2018;94:138–150.

[11] Untrau A., Sochard S., Marias F., Reneaume J-M., Le Roux G., Serra S., *Analysis and future perspectives for the application of Dynamic Real-Time Optimization to solar thermal plants: A review*. Solar Energy 2022;241:275-291.

[12] Scolan S., *Développement d'un outil de simulation et d'optimisation dynamique d'une centrale solaire thermique*. Doctoral thesis, Universite de Pau et des Pays de l'Adour, Pau, France. Retrieved from https://www.theses.fr/2020PAUU3007.

[13] Untrau A., Sochard S., Marias F., Reneaume J-M., Le Roux G., Serra S., *A fast and accurate 1-dimensional model for dynamic simulation and optimization of a stratified thermal energy storage*. Applied Energy 2023;333:120614.

[14] Franke R., *Object-oriented modeling of solar heating systems*. Solar Energy 1997;60:171–180.

[15] Petkov I., Gabrielli P., *Power-to-hydrogen as seasonal energy storage: an uncertainty analysis for optimal design of low-carbon multi-energy systems*. Applied Energy 2020;274:115197.

[16] Untrau A., Sochard S., Marias F., Reneaume J-M., Le Roux G., Serra S., *Dynamic Real-Time Optimization of a Solar Thermal Plant during daytime*. Computers and Chemical Engineering 2023;172:108184.

PROCEEDINGS OF ECOS 2023 - THE 36TH INTERNATIONAL CONFERENCE ON
EFFICIENCY, **C**OST, **O**PTIMIZATION, **S**IMULATION AND ENVIRONMENTAL IMPACT OF ENERGY SYSTEMS
25-30 JUNE, 2023, LAS PALMAS DE GRAN CANARIA, SPAIN

A seasonal assessment of a hybrid combined heat and power system with green hydrogen storage in Rio de Janeiro (Brazil) through an energetic, exergetic, exergoeconomic, and environmental analysis

José Eduardo Sanson Portella de Carvalho[a], Romuald Rullière[b], Rémi Revellin[c] and Florian Pradelle[d]

[a] Pontifícia Universidade Católica do Rio de Janeiro, Rio de Janeiro, Brazil, Univ Lyon, INSA Lyon, CNRS, CETHIL, UMR5008, 69621 Villeurbanne, France, zecarvalho07@gmail.com
[b] Univ Lyon, INSA Lyon, CNRS, CETHIL, UMR5008, 69621 Villeurbanne, France, romuald.rulliere@insa-lyon.fr,
[c] Univ Lyon, INSA Lyon, CNRS, CETHIL, UMR5008, 69621 Villeurbanne, France, remi.revellin@insa-lyon.fr,
[d] Pontifícia Universidade Católica do Rio de Janeiro, Rio de Janeiro, Brazil, pradelle@puc-rio.br,

Abstract:
The increasing energy and environmental crises require a shift in worldwide energy management, with the broader use of energy storage, and an increase in the share of renewable energy sources, in particular for electricity generation. Such a process is called energy transition. Thus, low-carbon (or green) hydrogen produced by water electrolysis from renewable electricity is one of the most promising options, since it can be used in fuel cells, with a high-efficiency operation, and without harmful emissions. Thus, this work investigates through a numerical simulation in Matlab, a cogeneration system used to supply electricity and heat demands for an on-grid residence in the city of Rio de Janeiro, Brazil. The original configuration for the hybrid combined heat and power (CHP) system is composed of photovoltaic (PV) panels, which exceeding energy feeds a proton exchange membrane electrolyzer cells (PEMEC) to produce hydrogen that is compressed and then stored. When the PV system is not able to supply the demand, the produced green hydrogen is then blended with natural gas to feed a solid oxide fuel cell (SOFC). Natural gas burner is used as an auxiliary source for heat generation when the SOFC is not operating. The energetic, exergetic, exergoeconomic, and environmental (4E) performances are assessed on a typical day of each season. Results indicate that the system can stably operate with moderate energy and exergy efficiencies for both the SOFC and PEMEC. Blending hydrogen with natural gas also allow a reduction of CHP specific emissions. The high availability of unused heat also strongly suggests the addition of an absorption chiller to increase the global system efficiency.

Keywords:
Proton exchange membrane electrolyzer cells (PEMEC); Solid oxide fuel cell (SOFC); Hydrogen compression, Renewable energy; 4E analysis; Numerical study.

Nomenclature

A	Area, m²	f_k	Exergoeconomic factor
$\dot{C}$	Cost rate, $/s	F	Faraday constant. C/mol
c	Unit cost, $/GJ	h	Specific enthalpy, kJ/kg
e	Specific entropy, kJ/(kg.K)	I	Electric current, A
$\dot{E}$	Exergy Rate, W	I_L	Light current, A

I_0	Reversible saturation current, A
J	Current density, A/m²
k	Boltzmann constant, m².kg/(s².K)
K	Equilibrium constant
LHV	Lower heating value, MJ/kg
$\dot{m}$	Mass flow rate, kg/s
N	Number of cells
$\dot{n}$	Molar flow rate, mol/s
P	Pressure, kPa
$\dot{P}$	Electric Power, W
q	Electron charge, C
$\dot{Q}$	Heat exchange rate, W
r	Recirculation factor
R	Resistance, Ω
R_u	Universal Gas Constant, J/(K.mol)
T	Temperature, K
U	Utilization factor
V	Voltage, V
V_{act}	Activation voltage, V
V_{ohm}	Ohmic voltage, V
V_{conc}	Concentration voltage, V
$\dot{W}$	Power, kW
X	Molar fraction
$\dot{Z}$	Levelized cost, $/s

Greek symbols

η	Efficiency
v	Stoichiometry coefficient

Subscript

bu	Burner
c	Compressor
cell	Cell
con	Consumption
d	Destruction
dem	Demand
ele	Electric
f	Fuel
gen	Generation
hxc	Heat exchanger's cold stream
hxh	Heat exchanger's hot stream
i	Inlet
j	Surrounding
p	Pump
PV	Photovoltaic
q	Heat
rh	Recoverable heat
ther	Thermal
W	Work

1. Introduction

The demand for low environmental impact and renewable power sources is steadily increasing. Thus, there is a growing installed capacity of power generation from renewable resources, particularly wind turbines (WT) and photovoltaic panels (PV), which are widely adopted. During the day, PV systems convert incident solar radiation into electricity, while WT systems harness the wind's favorable conditions to rotate the blades and produce electricity. Combining these two systems offers a viable solution for enhancing the reliability of power generation, even though they increased the complexity of the grid management. Since both PV and WT are intermittent energy sources, it is crucial to incorporate a storage system to enhance overall efficiency and provide the demand during the whole day. Hydrogen emerges as a promising alternative due to its high energy density in weight basis, minimal energy loss, well-established technology, on-site provision capability, and reliability comparable to conventional fuels such as coal, nuclear, and natural gas [1]. Among the most promising methods for hydrogen production is water electrolysis, while the current predominant approach involves fossil fuel conversion (mainly by steam reforming of natural gas). The resulting hydrogen, known as green hydrogen, has emerged as a potential solution for future decarbonization efforts [2].

Additionally, the interest in efficient technology that offers a wide range of useful energy products and services, such as polygeneration, is increasing significantly. Polygeneration system involves an integrated process that produces multiple energy outputs from a single energy source. Among the possible technology, the fuel cells are energy conversion devices that play a key role in generating electricity through an electrochemical reaction between a fuel (mainly hydrogen) and an oxidant. This direct conversion of chemical energy into electricity eliminates the need for a combustion process. Significant attention has been directed towards Solid Oxide Fuel Cells (SOFC) due to their superior efficiency, long-term stability, and low emissions during operation. Operating at high temperatures (ranging from 650 to 1000 °C), SOFCs enable the reforming process to occur within the cell itself. This allows the SOFCs to be fed with natural gas and remove the need to reduce the carbon monoxide content of the reformate, making them an excellent choice for cogeneration, trigeneration, and multigeneration applications [3]. Numerous studies have examined the feasibility and thermal performance of SOFCs within complex systems. In trigeneration systems, where electricity generation is the primary function of SOFCs, previous studies have observed the utilization of heat exchangers to recover exhaust gas heat, along with refrigeration systems (typically with absorption chillers) to provide cold demand [4–7]. Parameters such as current density [4,7–16] and SOFC operating temperature [4,8–10,14,17] have been extensively investigated in the literature. Furthermore, some studies have conducted exergoeconomic evaluations of the system [9–16,18], while a few have undertaken environmental analyses [10,12,14,18].

Many studies have focused on the utilization of electrolysis to produce hydrogen. Among the electrolyser technologies, the polymer electrolyte membrane electrolyser (PEMEC) is the most widely used in the recent projects and the literature showed that it is adaptable for integration with different systems. The advantage of PEMEC is its rapid response, making it suitable for transient conditions, while producing high-purity hydrogen at relatively low temperatures (around 50 to 90°C) [19]. Literature reviews have demonstrated the integration of PEMEC in systems that harness renewable resources [20–23]. Similarly to SOFCs, the process parameters investigated for the optimization of the PEMEC operation include current density [20,22,24] and operating temperature [21–23].

Even though the renewables reached 44.7% of the energy mix, with sugarcane biomass and hydroelectricity accounting for the largest shares at 16.4% and 11% respectively, a recent study examining the Brazilian energy matrix highlighted a decline in the contribution of renewable energy sources due to water scarcity and an increased reliance on thermoelectric plants. Despite solar and wind power having a smaller share at 2.5% and 10.6% respectively, they experienced significant year-on-year increases of 55.9% and 26.7%. In terms of energy consumption, the residential sector accounted for approximately 10.9% of Brazil's energy use, while the transport and industrial sectors combined represented a consumption of 64.5%. The installed capacity for energy generation demonstrated an overall increase of 3.9%, with solar and wind power leading the growth at 40.9% and 21.2% respectively. In the realm of micro/mini distributed generation, solar power witnessed a remarkable 88.3% increase compared to the previous year [25].

Regarding hydrogen in the country, the Energy National Plan 2050 (PNE 2050) recognizes hydrogen as a disruptive technology and a crucial element for the decarbonization of the energy matrix. The plan highlights the diverse uses and applications of hydrogen and provides recommendations for energy policies to promote the development of the chain values, including production, transport, storage, and consumption, in the country. Key guidelines include assessing opportunities for blue hydrogen production from natural gas and green hydrogen production using renewable energy sources, called “rainbow” approach. Additionally, the plan emphasizes exploring the production of hydrogen from biofuels (bioethanol, biomethane and glycerine) and using existing infrastructure for the transition, such as incorporating hydrogen into the natural gas pipeline network [26,27]. The integration of hydrogen into natural gas has the potential to enhance the role of natural gas, abundant in the Pre-salt fields, as a low-carbon transition fuel while simultaneously scaling up hydrogen production, particularly from renewable sources [2].

As demonstrated earlier, there are a limited number of studies in the literature that conduct a energetic, exergetic, economic, and environmental (4E) analysis of a cogeneration system. Furthermore, no research has been found that specifically examines the impact of seasonality on a hybrid system that integrates renewable power generation and consumption using both PEMEC and SOFC technologies. Although the share of solar power is not so expressive into the Brazilian energy matrix, its growth is noticeable, along with an increasing interest for hydrogen production. In light of these factors, this study aims to evaluate a hybrid combined heat and power (CHP) system with green hydrogen storage in Rio de Janeiro, Brazil. The evaluation focuses on a typical day from each season for a residential building. An hourly-based analysis is performed, considering the electricity and heat demand of a standard building. The study specifically assesses the energetic, exergetic, exergoeconomic, and environmental aspects of the system through a comprehensive 4E analysis. To achieve this, various parameters are examined, including system efficiencies, carbon dioxide emission rates, cost per unit of exergy, and the exergoeconomic factor. The aim is to provide a thorough understanding of the system's performance and quantify its impact in terms of energy, exergy, economics, and the environment.

2. System description

The representation of the hydrogen storage system is shown in Figure 1. A renewable module comprised of a set of photovoltaic panels in series and parallel is responsible for extracting energy from the sun and supplying an electric demand. If there is a surplus of power in this process, the system operates in what is called the generation mode, otherwise, if there is a shortage, it works in the consumption mode. In the first mode, the surplus energy from the renewable module is used to supply power for an electrolyzer which together with water, generates green hydrogen and oxygen. The hydrogen is compressed into a pressurized tank, to be later used in any case of need. To supply the heat demand, a natural gas burner is triggered. For the other mode of operation, hydrogen from the tank is withdrawn and goes through the expansion valve to be mixed with natural gas and then preheated in a heat exchange before entering the reformer. Water is also preheated before entering the reformer, and after the reforming process, the products and a preheated air feed the solid oxide fuel cell for the electrochemical process. The generated electricity passes through the inverter priorly to being supplied to the final user. The depleted fuel and air from the SOFC go into an afterburner for complete combustion of carbon monoxide, methane, and hydrogen, and the exhaust gases are used for preheating the mixture (hydrogen-natural gas), water, and air. Then, the exhaust gases pass by a heat exchanger to supply the user’s heat demand. This module consists of a hot tank, a pump, and a pair of heat exchangers (exhaust gas and hot water). The tank is assumed to be sufficiently large to be considered isothermal. Finally, the hot exhaust gases from the afterburner are cooled down to ambient temperature.

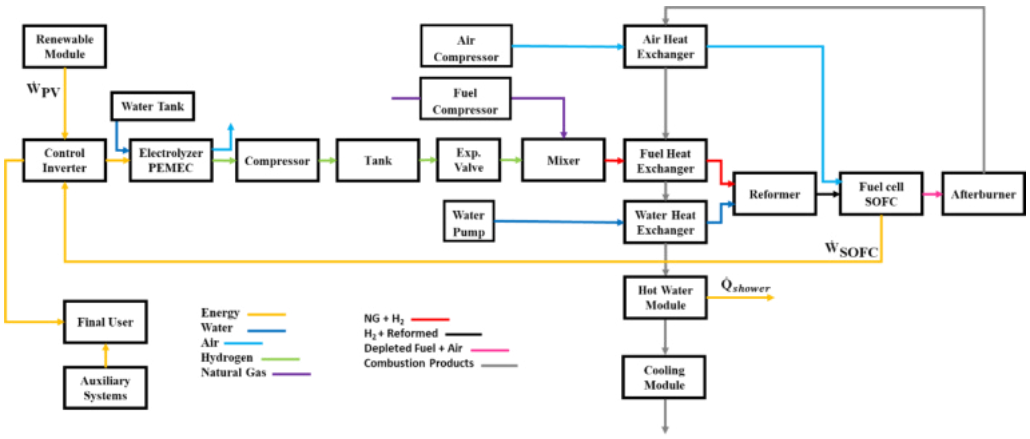

Figure 1. Schematic representation of the hydrogen storage system.

For this system's simulation, a steady-state condition under thermodynamic equilibrium is assumed for each investigated instant of time. All components are assumed to be well insulated, thus no heat loss from equipment to the environment is considered. Compressors and pumps operate with isentropic efficiency equal to 0.85, and the heat exchangers have a constant efficiency during operation of 0.9 with no pressure drop. The mixing chamber, reformer, natural gas burner, and afterburner operate at constant pressure, and their outlet species composition and temperature are calculated using energy and mass balance. The inverter has a constant efficiency of 0.95. All gases are treated as an ideal gas, dry air composition is considered 21% O_2 and 79% N_2, and natural gas is considered as pure methane. The compressed hydrogen is stored at 300 bar and ambient temperature. The properties of all fluids are based on the Peng-Robinson equation of state, having as reference state for gases temperature at 298.15 K and 0.101325 MPa.

3. Modeling

This section focuses on displaying the main equations for the system's components. The extensive equating can be found in Appendix A, and the parameters for the system in Appendix B [28].

3.1. Renewable module: photovoltaic panels (PV)

This module consists of a combination of photovoltaic panels producing electric power at an optimized current and voltage [29,30]. This system's performance presents a non-linear current-voltage curve, Eq. (1):

$$I=I_L-I_0\left(\exp\left(\frac{q(V+IR)}{\gamma k T_{cell}}\right)-1\right) \quad (1)$$

The panels are set to work at maximum power output adjusting both voltage and current to reach such conditions

3.2. Proton exchange membrane electrolyzer (PEMEC)

A proton exchange membrane electrolyzer is used to generate hydrogen using the surplus energy from the renewable module. The rate of the produced hydrogen is defined by a function of the current density and number of electrolyzers considered, Eq. (2) [5,31]:

$$\dot{n}_{H_2}=\eta_f\frac{NI}{2F} \quad (2)$$

The actual voltage of the electrolyzer is defined by a function of its reversible voltage and losses, Eq. (3) [11,32]:

$$V=V_0+V_{act}+V_{ohm} \quad (3)$$

3.3. Solid oxide fuel cell (SOFC)

The amount of hydrogen entering the anode in the electric reaction of the solid oxide fuel cell is also described by the current density operation, Eq. (4) [33]:

$$\dot{n}_{H_2}=\frac{JA\,(1-r+rU_f)n}{2\,F\,U_f} \quad (4)$$

The process for calculating the inlet on the cathode side and the outlet of both the anode and cathode are described in Colpan et al. [33].

The actual voltage of the solid oxide fuel cell is described in Eq. (5) [4,11,32]:

$$V=V_0-V_{act}-V_{ohm}-V_{conc} \quad (5)$$

3.4. Reformer

Fuel reforming reactions allow the conversion of fuel (natural gas blended with hydrogen into another one through a catalytic reaction, from a less active one into one more active. Thermodynamic equilibrium is assumed for the considered chemical reactions and described by the general equilibrium constant, Eq. (6):

$$K_{e,i} = \prod_i x_i^{v_i} \left(\frac{P}{P_0}\right)^{\sum_i v_i} \quad (6)$$

3.5. 4E analysis

Such analysis comprehends assessing the components, and the whole system, as control volumes through an energetic, exergetic, exergoeconomic, and environmental point of view. To do so, mass, energy exergy, and cost balances are considered, Eqs. (7-11) [34]:

$$\sum \dot{m}_o = \sum \dot{m}_i \quad (7)$$

$$\dot{Q} - \dot{W} = \sum_o \dot{m}_o h_o - \sum_i \dot{m}_i h_i \quad (8)$$

$$\dot{E}_D = \sum_j \left(1 - \frac{T_0}{T_j}\right) \dot{Q}_j - \dot{W} + \sum_i \dot{m}_i e_i - \sum_o \dot{m}_o e_o \quad (9)$$

$$\sum \dot{C}_i + \dot{C}_q + \dot{Z} = \sum \dot{C}_o + \dot{C}_w \quad (10)$$

$$\dot{C} = c\dot{E} \quad (11)$$

Table B.1 displays the capital equation of each component [28].

The environmental analysis considers the amount of carbon dioxide emitted during the system operation, through the combustion of natural gas and the depleted fuel of the solid oxide fuel cell, and its mitigation due to the addition of hydrogen in the blend with natural gas.

The electric and thermal efficiencies of the system are used to assess the system's performance. They are described as follows in Eqs. (12-15):

$$\eta_{ele,gen} = \frac{\dot{P}_{dem} + \dot{m}_{H_2} LHV_{H_2} + \dot{W}_{c,H_2}}{\dot{W}_{PV} + \dot{W}_{c,H_2}} \quad (12)$$

$$\eta_{ele.con} = \frac{\dot{P}_{dem} + \dot{W}_{c,all} + \dot{W}_{p,all}}{\dot{W}_{PV} + \dot{W}_{Grid} + \dot{m}_{H_2} LHV_{H_2} + \dot{W}_{c,all} + \dot{W}_{p,all}} \quad (13)$$

$$\eta_{ther,gen} = \frac{\dot{Q}_{dem}}{\dot{Q}_{bu}} \quad (14)$$

$$\eta_{ther,con} = \frac{\dot{Q}_{hxc,all} + \dot{Q}_{dem}}{\dot{Q}_{hxh,all} + \dot{Q}_{ts} + \dot{Q}_{rh} + \dot{Q}_{bu}} \quad (15)$$

For the exergoeconomic evaluation, the exergoeconomic factor, Eqs. (16-17), and unit cost of the SOFC and PEMEC are considered.

$$f_k = \frac{\dot{Z}}{\dot{Z} + \dot{C}_d} \quad (16)$$

$$\dot{C}_d = c_f \dot{E}_d \quad (17)$$

The unit cost expresses the average cost at which each unit of fuel is supplied to a component or the average cost at which exergy unit was supplied to a product. The exergoeconomy factor expresses the contribution of the capital cost to the sum of capital cost and exergy destruction, providing a measurement of the component cost-effectiveness.

4. Numerical solution

The solution of the system relies on the hourly interaction between the solar radiation and the electric demand of the building through one day for each season of the year. Figure 2 displays the flowchart of the steps taken for solving the system. The parameters considered in this work concerning the building, photovoltaic panels, SOFC, and PEMEC dimensioning are shown in Appendix B [28].

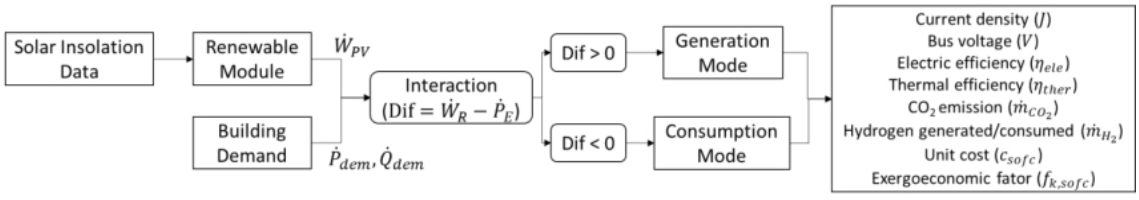

Figure 2: System's solution flowchart.

4.1. Electric power and heat demands

The electricity demand of a typical residential building from Rio de Janeiro is evaluated using the typical profile curve of residential consumption together with the historical average value for each month [35]. It is possible to observe a higher consumption in summer due to the hot temperatures in the country, as a higher amount of air conditioners are working. Spring and Autumn have similar electric demands. Water heating for showers is the only source of heat demand in the Rio de Janeiro context [36]. Both demands are displayed in Figure 3.

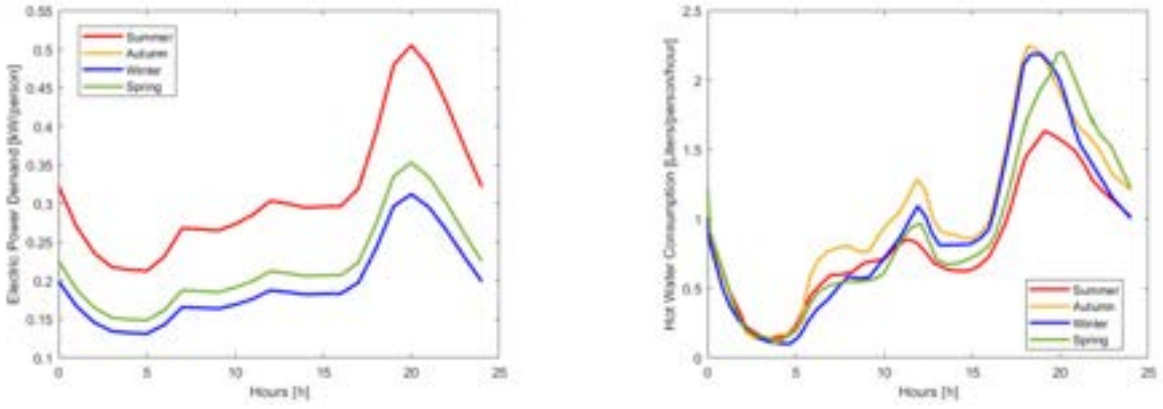

(a) (b)

Figure. 3. a) Electric power demand per person. b) Hot water profile of a typical Brazilian residential building.

4.2. Solar Radiation and interaction

As previously said, the difference between the electric power coming from the renewable module and the electricity demands dictates the functioning of the system. Figure 4 presents both the solar radiation for a characteristic day of each season in Rio de Janeiro and the aforementioned difference for the Summer. The area above the zero line (orange) corresponds to the generation mode, while the area under the line (blue) corresponds to the consumption mode.

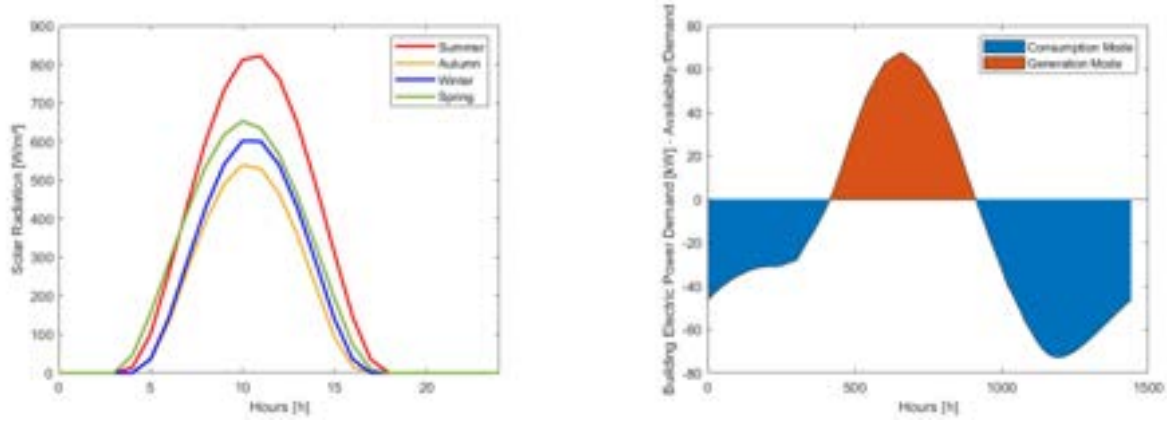

(a) (b)

Figure. 4. a) Solar radiation in Rio de Janeiro for the characteristic day of each season. b) Data regarding availability and demand of electric power.

4.3. Generation path

The stacks of PEMEC work accordingly to the amount of available power, turning on and off to the necessary number of stacks for the operation. Both current density and the stack's bus voltage are adjusted in this process so the system can operate at the highest efficiency. Having the final condition set, the amount of green hydrogen produced and the electrolyzer's parameter can be calculated. The variables considered in this study for the PEMEC are displayed in Table B.4.

4.4. Consumption path

When the electric power from the renewable module is not enough to meet the user's demand, the stacks of solid oxide fuel cells are required to generate the missing power. Similarly to the generation path, the stacks can be turned on and off, as a function of the missing electric power, and the stack's current density and bus voltage are adjusted so the system can operate at the highest efficiency. The rate of hydrogen consumption is

calculated in function of the SOFC module's electric power output, and with that, it is possible to infer the amount of natural gas withdrawn from the grid, hydrogen from the tank, and steam necessary for the reforming process using a mass balance on the SOFC reformer. The parameters of the SOFC are shown in Table B.5. After the process in the SOFC, the depleted air and fuel passes through an afterburner for a complete combustion reaction. The hot combustion products are used to heat the hydrogen-natural gas blend and water entering the reformer, and the air entering the cell.

5. Results

5.1. Validation

Both PEMEC and SOFC were modeled according to data taken from the literature [37,38], and results are shown in Appendix B [28]. Tables B.6 and B.7 display a comparison with the values for voltages of each component, and it can be seen a good agreement between this study and the corresponding experimental data.

5.2. Season analysis

To assess the seasonality effect on the system, a characteristic day of each season was chosen, being in the middle of February, May, August, and November to represent Summer, Autumn, Winter, and Spring respectively. Thus, in each case, the current density and bus voltage of both SOFC and PEMEC are controlled and adjusted to supply and use the exact amount of electric power and operate at the highest efficiency. The adjustment for the current density is seen in Figure 5.

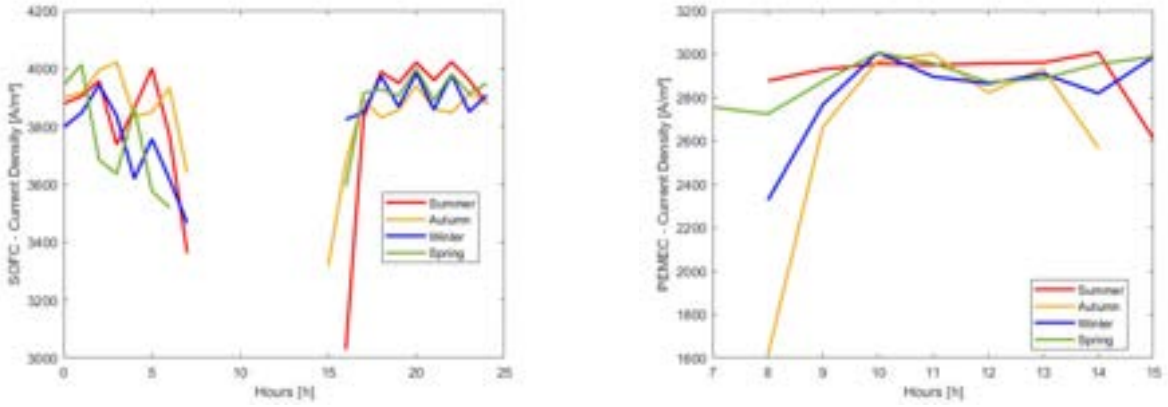

(a) (b)

Figure. 5. Current density. a) SOFC. b) PEMEC.

Figure 5 illustrates a distinct behavior in controlling the current density of both components. In the case of the SOFC, a decrease in current density corresponds to an expected increase in bus voltage, whereas for the PEMEC, the bus voltage decreases as the current density decreases. This phenomenon can be attributed to the nature of the actual voltage definitions for both components, as described in Sections 3.2 and 3.3. Specifically, a lower current density for the SOFC leads to higher voltages, while the opposite is observed for the PEMEC. The values of current density are determined by the electric power to be supplied or utilized by the components, where lower electric power results in lower current density.Hydrogen consumption and generation during operation are also a consequence of the electric power, as shown in Figure 6.

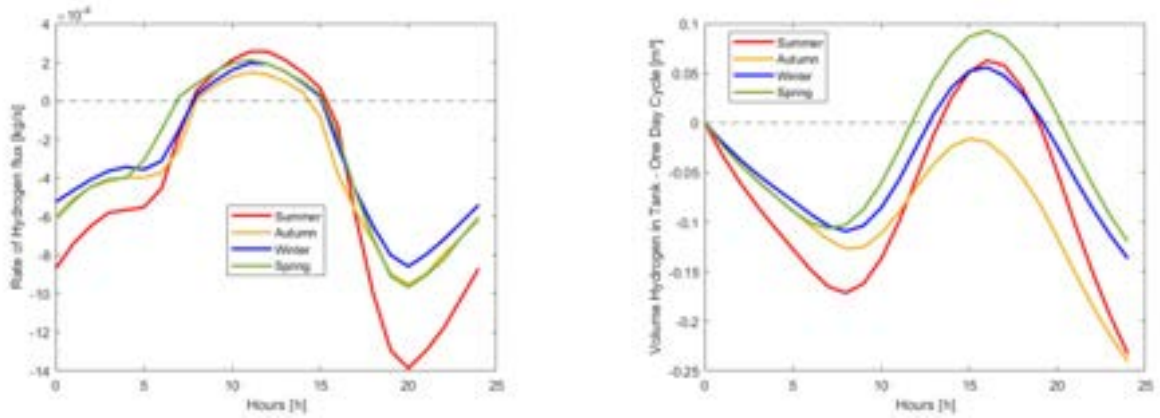

(a) (b)

Figure. 6. Rate of hydrogen generated and consumed. b) Hydrogen volume variation inside the tank.

In Figure 6a, when the curve has a negative or positive value, it corresponds to hydrogen consumption or generation, respectively. During the summer, higher generation and consumption are observed, as expected due to increased electric power demand and solar insolation, as shown in Figures 3a and 4a. Figure 6b illustrates the amount of hydrogen that entered or left the tank after a full day of operation. The greatest variations are observed in the summer, reflecting higher consumption and solar insolation. Consequently, there is a greater fluctuation in the hydrogen level within the tank. These results indicate that, under the given conditions, more hydrogen is consumed than generated each day during every season. By integrating the curve in Figure 6a, the total amount consumed can be calculated, confirming that summer has the highest consumption, followed by autumn, spring, and winter. These findings enable the design of storage tank autonomy and the development of a strategy to control hydrogen availability, such as limiting generation to specific times or blending hydrogen with natural gas in lower quantities.

Figure 7 helps to understand the behavior of the system to supply electricity, and consequently the heat demands.

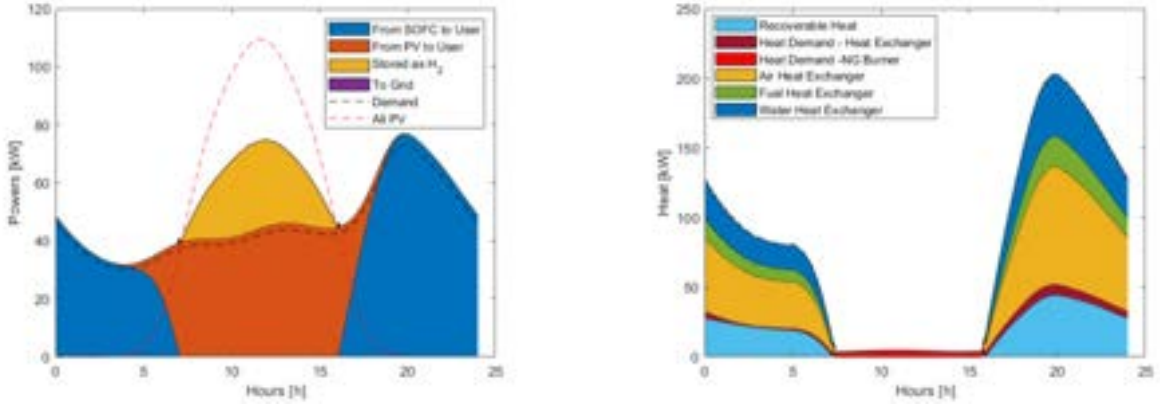

(a) (b)

Figure. 7. Month of February. a) Electric power supply. b) Heat supply.

When there is no energy being generated by the renewable module, the solid oxide fuel cell becomes responsible for supplying all the electric power (blue area). Its contribution gradually decreases as the photovoltaic system begins to supply a portion of the demand (orange area), until a point is reached where the photovoltaic system supplies all the energy, resulting in an excess. When there is an excess, the energy is converted into hydrogen (yellow area) and stored in a tank. Figure 7a shows the losses associated with hydrogen generation by comparing the total power supplied by the photovoltaic system (red dashed line) with the yellow area. It is important to note that both the solid oxide fuel cell and the photovoltaic system deliver more power than the electric demand to account for losses in the inverter. The heat response (Figure 7b) is directly proportional to the number of fuel cells in operation and exhibits a similar behavior to the electric power shown in Figure 7a. The exhaust gases from the afterburner can preheat the fuel, air, and water used in the process and fulfil the building's heat demand. The curve labelled "Recoverable Heat" represents the cooling of the exhaust gases to ambient conditions and could be utilized for a trigeneration process, such as powering an absorption chiller to meet the cooling demand.

The system's electric and thermal efficiencies are assessed in Figure 8.

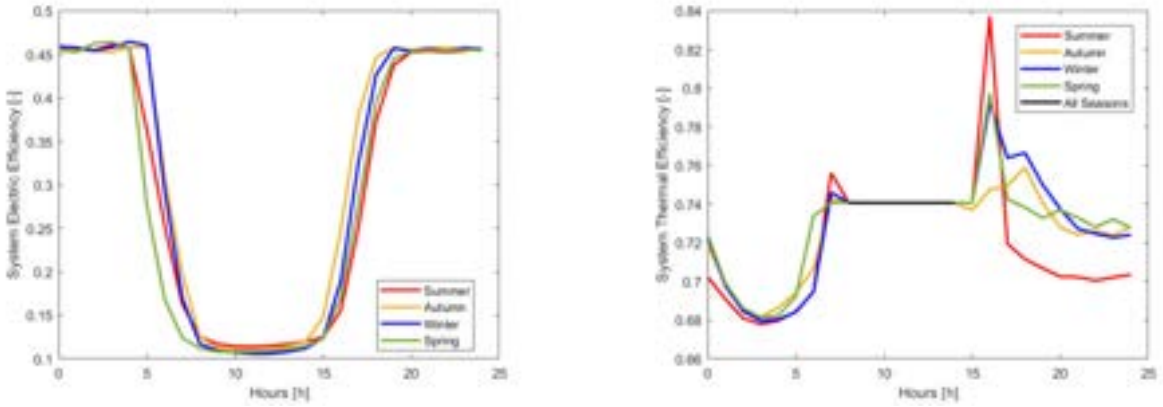

(a) (b)

Figure. 8. a) System's electric efficiency. b) System's thermal efficiency.

Figure 8a demonstrates that the system maintains a steady efficiency when only the SOFC operates to supply the electric power. This behavior is attributed to the control method, which adjusts both the current density and bus voltage to meet the electric power demand. As the photovoltaic panels begin to contribute to the electric power supply, the overall efficiency of the system starts to decrease due to the panels' lower efficiency. Additionally, in the energy surplus region, there is a further decrease in efficiency caused by losses in hydrogen generation through the PEMEC. By examining Figure 8b, it can be observed that the thermal efficiency of the system remains constant during the generation mode, with a natural gas burner efficiency of 0.74. However, during the consumption mode, the variations among seasons primarily stem from different hot water profiles and the number of operational cells.

Figure 9 displays the results for both the rate of CO_2 emitted and the influence of hydrogen in the blend during summer.

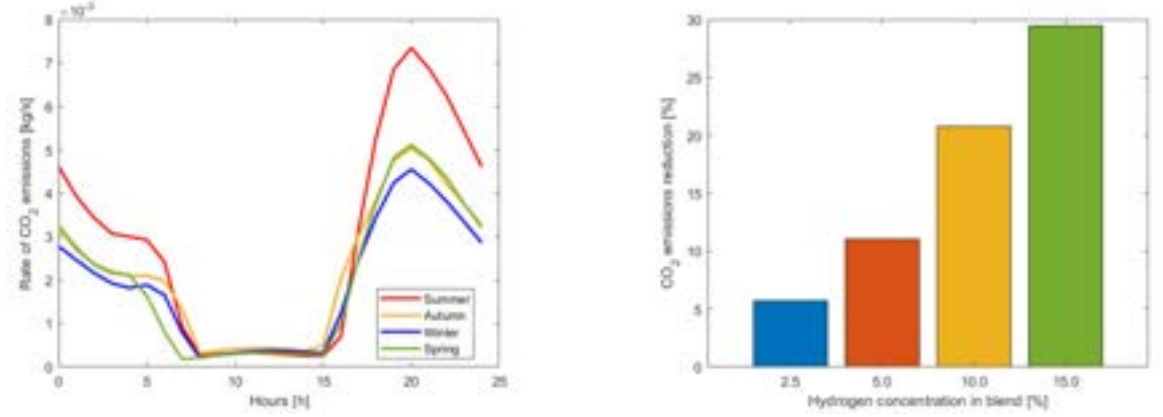

(a) (b)

Figure. 9. a) Rate of CO_2 emission. b) Carbon dioxide emission reduction due to hydrogen addition to the blend.

The carbon dioxide emission, Figure 9a, is described as a function of the electricity demand of the consumption mode, and as a function of heat demand of the generation mode. A higher amount of functioning fuel cells would imply a higher amount of hydrogen being withdrawn from the tank and natural gas from the grid. Consequently, after the whole process, higher emissions would be seen. It is expected to have a higher emission during the Summer, as the electric demand from the building is also higher. In the generation mode, the amount of emissions is dictated by the heat demand which is supplied by the natural gas burner. Figure 9b displays the influence of adding hydrogen to the blend with natural gas. A higher participation of hydrogen would reduce the emissions of carbon dioxide due to a lesser amount of CO_2 after the reforming process, and consequently after the electrochemical reaction in the SOFC. The addition of 15% of hydrogen, on a mass basis, to the blend would reduce up to 29% of these emissions.

Figure 10 shows the unit cost for both SOFC and PEMEC.

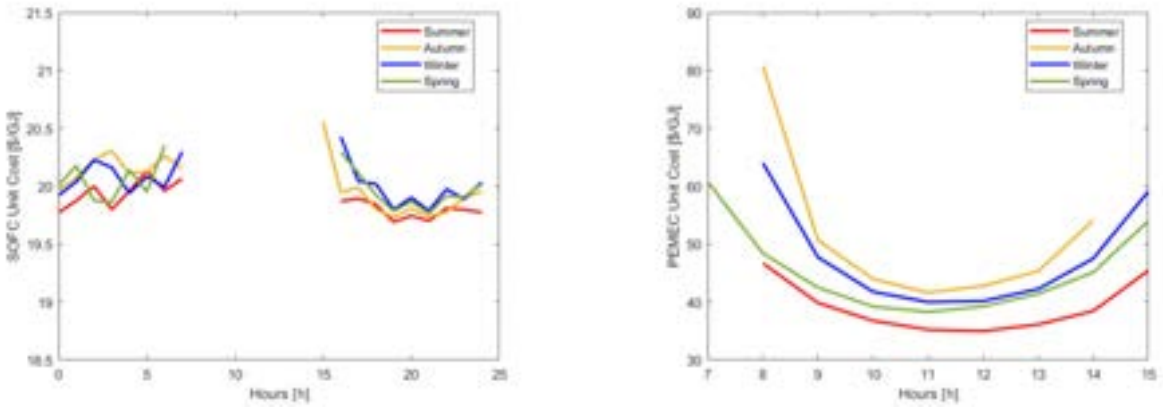

(a) (b)

Figure. 10. Unit cost. a) SOFC. b) PEMEC.

The unit cost of the SOFC shows only minor variations based on seasonality and the time of day. The capital cost of the SOFC is determined by the number of active cells, which is in turn influenced by the user's electric power requirements. Consequently, the relatively stable unit cost arises from the consistent operational efficiency of the system, where the current density is adjusted to meet the electric demand. On the other hand, the unit cost of operation for the PEMEC is greatly impacted by the excess electric power supplied by the PV system. During midday, when solar radiation reaches its peak, the unit cost of operation is lower due to increased hydrogen generation, despite the higher capital cost associated with the PEMECs.

Figure 11 displays the exergoeconomic factor for both components.

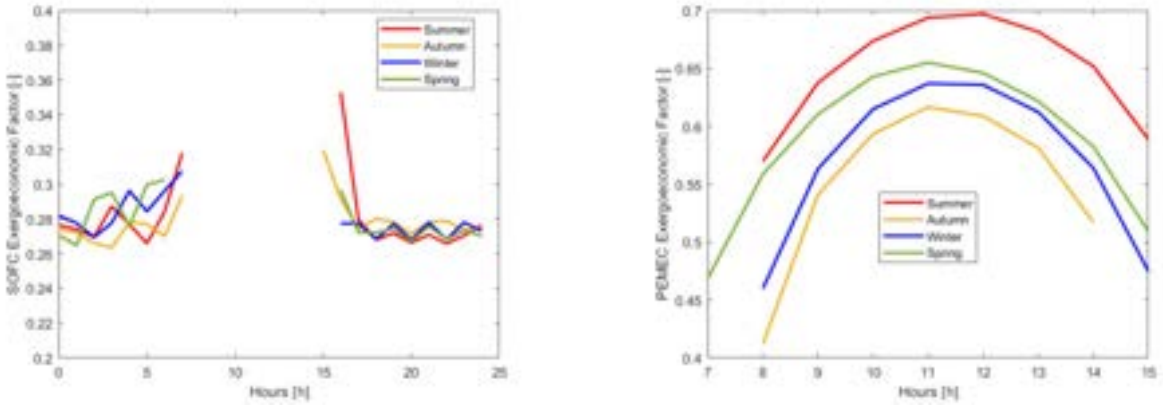

(a) (b)

Figure. 11. Exergoeconomic factor. (a) SOFC. (b) PEMEC.

The behavior of the exergoeconomic factor is similar to the unit cost. Regarding the SOFC, its value is constant for most of the operation, which fluctuations are a result of the current density adjustments. For the PEMEC, the exergoeconomic factor is highly influenced by the supplied electric power, due to the higher values at midday and due to the seasonality, where the summer has a higher radiation compared to the other seasons. A low value of the exergoeconomic factor indicates potential cost savings for the system by reducing exergy destruction, which can be achieved by improving component efficiency, even if it entails increased capital investment. Conversely, a high value of the factor suggests the possibility of reducing the investment cost of the component at the expense of its exergetic efficiency.

6. Conclusion

A hybrid combined CHP system using green hydrogen storage is evaluated in the city of Rio de Janeiro, Brazil. The system is assessed through a 4E standpoint while supplying both electric power and the heat demand of a typical building. The system is mainly composed of a photovoltaic system, a proton exchange membrane electrolyzer, and a solid oxide fuel cell. The system can perform at the rated electricity demand at maximum and stable efficiency while supplying all the heat necessary for its running and hot shower. The amount of hydrogen produced and consumed is estimated and it was seen that during summer, due to a higher solar insulation and electric demand, the variations inside the tank are higher when compared with any other season. Pollutant emissions are strictly related to the number of operating fuel cells, as they would require a higher

amount of fuel, and the addition of hydrogen would reduce the number of such emissions, as less natural gas would be burnt. Recalling the exergoeconomic, it has been shown that seasonality has little effect on the solid oxide fuel cell parameters, while the proton exchange membrane is highly affected by solar radiation. Finally, the system showed the possibility of introducing a cooling system utilizing the recoverable heat in an absorption chiller.

The system seems to be a good option to diversify the use of renewable resources in Brazil, which has hydropower as the main source. With the right design of the tank, the system would be able to sustain both the electricity and heat demand of a typical residential building. In the future, it is desired to analyze the system's functioning during a whole year, compare the results found with demands and weather conditions of other countries, and optimize the system to find the best functioning condition. Additionally, a comparison with other energy storage systems, such as compressed air (CAES), would allow a better understanding of the feasibility of these systems to substitute the ongoing ones.

References

[1] Khalilnejad A, Sundararajan A, Sarwat AI. Optimal design of hybrid wind/photovoltaic electrolyzer for maximum hydrogen production using imperialist competitive algorithm. J Mod Power Syst Clean Energy 2018;6:40–9. https://doi.org/10.1007/s40565-017-0293-0.

[2] IRENA. Hydrogen: A renewable energy perspective. International Renewable Energy Agency; 2019.

[3] Mehr AS, Lanzini A, Santarelli M, Rosen MA. Polygeneration systems based on high temperature fuel cell (MCFC and SOFC) technology: System design, fuel types, modeling and analysis approaches. Energy 2021;228:120613. https://doi.org/10.1016/j.energy.2021.120613.

[4] Chitsaz A, Hosseinpour J, Assadi M. Effect of recycling on the thermodynamic and thermoeconomic performances of SOFC based on trigeneration systems; A comparative study. Energy 2017;124:613–24. https://doi.org/10.1016/j.energy.2017.02.019.

[5] Ranjbar F, Chitsaz A, Mahmoudi SMS, Khalilarya S, Rosen MA. Energy and exergy assessments of a novel trigeneration system based on a solid oxide fuel cell. Energy Conversion and Management 2014;87:318–27. https://doi.org/10.1016/j.enconman.2014.07.014.

[6] Sadeghi M, Chitsaz A, Mahmoudi SMS, Rosen MA. Thermoeconomic optimization using an evolutionary algorithm of a trigeneration system driven by a solid oxide fuel cell. Energy 2015;89:191–204. https://doi.org/10.1016/j.energy.2015.07.067.

[7] Tian M, Yu Z, Zhao H, Yin J. Thermodynamic analysis of an integrated solid oxide fuel cell, Organic Rankine Cycle and absorption chiller trigeneration system with CO2 capture. Energy Conversion and Management 2018;171:350–60. https://doi.org/10.1016/j.enconman.2018.05.108.

[8] Ahmadi S, Ghaebi H, Shokri A. A comprehensive thermodynamic analysis of a novel CHP system based on SOFC and APC cycles. Energy 2019;186:115899. https://doi.org/10.1016/j.energy.2019.115899.

[9] Sadat SMS, Mirabdolah Lavasani A, Ghaebi H. Economic and thermodynamic evaluation of a new solid oxide fuel cell based polygeneration system. Energy 2019;175:515–33. https://doi.org/10.1016/j.energy.2019.03.093.

[10] Hosseinpour J, Chitsaz A, Liu L, Gao Y. Simulation of eco-friendly and affordable energy production via solid oxide fuel cell integrated with biomass gasification plant using various gasification agents. Renewable Energy 2020;145:757–71. https://doi.org/10.1016/j.renene.2019.06.033.

[11] Chitgar N, Moghimi M. Design and evaluation of a novel multi-generation system based on SOFC-GT for electricity, fresh water and hydrogen production. Energy 2020;197:117162. https://doi.org/10.1016/j.energy.2020.117162.

[12] Wu Z, Zhu P, Yao J, Zhang S, Ren J, Yang F, et al. Combined biomass gasification, SOFC, IC engine, and waste heat recovery system for power and heat generation: Energy, exergy, exergoeconomic, environmental (4E) evaluations. Applied Energy 2020;279:115794. https://doi.org/10.1016/j.apenergy.2020.115794.

[13] Habibollahzade A, Gholamian E, Behzadi A. Multi-objective optimization and comparative performance analysis of hybrid biomass-based solid oxide fuel cell/solid oxide electrolyzer cell/gas turbine using different gasification agents. Applied Energy 2019;233–234:985–1002. https://doi.org/10.1016/j.apenergy.2018.10.075.

[14] Xu Y, Luo X, Tu Z. 4E analysis of a SOFC-CCHP system with a LiBr absorption chiller. Energy Reports 2022;8:5284–95. https://doi.org/10.1016/j.egyr.2022.03.202.

[15] Chitsaz A, Mehr AS, Mahmoudi SMS. Exergoeconomic analysis of a trigeneration system driven by a solid oxide fuel cell. Energy Conversion and Management 2015;106:921–31. https://doi.org/10.1016/j.enconman.2015.10.009.

[16] Khani L, Mahmoudi SMS, Chitsaz A, Rosen MA. Energy and exergoeconomic evaluation of a new power/cooling cogeneration system based on a solid oxide fuel cell. Energy 2016;94:64–77. https://doi.org/10.1016/j.energy.2015.11.001.

[17] Wang H, Yu Z, Wang D, Li G, Xu G. Energy, exergetic and economic analysis and multi-objective optimization of atmospheric and pressurized SOFC based trigeneration systems. Energy Conversion and Management 2021;239:114183. https://doi.org/10.1016/j.enconman.2021.114183.
[18] Ghorbani Sh, Khoshgoftar-Manesh MH, Nourpour M, Blanco-Marigorta AM. Exergoeconomic and exergoenvironmental analyses of an integrated SOFC-GT-ORC hybrid system. Energy 2020;206:118151. https://doi.org/10.1016/j.energy.2020.118151.
[19] Ozturk M, Dincer I. A comprehensive review on power-to-gas with hydrogen options for cleaner applications. International Journal of Hydrogen Energy 2021;46:31511–22. https://doi.org/10.1016/j.ijhydene.2021.07.066.
[20] Nafchi FM, Baniasadi E, Afshari E, Javani N. Performance assessment of a solar hydrogen and electricity production plant using high temperature PEM electrolyzer and energy storage. International Journal of Hydrogen Energy 2018;43:5820–31. https://doi.org/10.1016/j.ijhydene.2017.09.058.
[21] Zheng N, Duan L, Wang X, Lu Z, Zhang H. Thermodynamic performance analysis of a novel PEMEC-SOFC-based poly-generation system integrated mechanical compression and thermal energy storage. Energy Conversion and Management 2022;265:115770. https://doi.org/10.1016/j.enconman.2022.115770.
[22] Zhang X, Zeng R, Du T, He Y, Tian H, Mu K, et al. Conventional and energy level based exergoeconomic analysis of biomass and natural gas fired polygeneration system integrated with ground source heat pump and PEM electrolyzer. Energy Conversion and Management 2019;195:313–27. https://doi.org/10.1016/j.enconman.2019.05.017.
[23] Zhang F, Wang B, Gong Z, Zhang X, Qin Z, Jiao K. Development of photovoltaic-electrolyzer-fuel cell system for hydrogen production and power generation. Energy 2023;263:125566. https://doi.org/10.1016/j.energy.2022.125566.
[24] Chitsaz A, Haghghi MA, Hosseinpour J. Thermodynamic and exergoeconomic analyses of a proton exchange membrane fuel cell (PEMFC) system and the feasibility evaluation of integrating with a proton exchange membrane electrolyzer (PEME). Energy Conversion and Management 2019;186:487–99. https://doi.org/10.1016/j.enconman.2019.03.004.
[25] Ministério de Minas e Energia, Empresa de Pesquisa Energética. BEN - Relatório Sínteses 2022 2022.
[26] Ministério de Minas e Energia, Empresa de Pesquisa Energética. Bases para a Consolidação da Estratégia Brasileira do Hidrogênio 2021.
[27] Ministério de Minas e Energia, Empresa de Pesquisa Energética. Programa Nacional do Hidrogenio 2021.
[28] Carvalho JESP, Rullière R, Revellin R, Pradelle FAY. Supplementary data for ECOS 23 2023. https://www.researchgate.net/publication/369503049_Supplementary_Data_-_ECOS23_f804.
[29] Chenni R, Makhlouf M, Kerbache T, Bouzid A. A detailed modeling method for photovoltaic cells. Energy 2007;32:1724–30. https://doi.org/10.1016/j.energy.2006.12.006.
[30] Hosseini M, Dincer I, Rosen MA. Hybrid solar–fuel cell combined heat and power systems for residential applications: Energy and exergy analyses. Journal of Power Sources 2013;221:372–80. https://doi.org/10.1016/j.jpowsour.2012.08.047.
[31] Sánchez M, Amores E, Rodríguez L, Clemente-Jul C. Semi-empirical model and experimental validation for the performance evaluation of a 15 kW alkaline water electrolyzer. International Journal of Hydrogen Energy 2018;43:20332–45. https://doi.org/10.1016/j.ijhydene.2018.09.029.
[32] Gholamian E, Hanafizadeh P, Habibollahzade A, Ahmadi P. Evolutionary based multi-criteria optimization of an integrated energy system with SOFC, gas turbine, and hydrogen production via electrolysis. International Journal of Hydrogen Energy 2018;43:16201–14. https://doi.org/10.1016/j.ijhydene.2018.06.130.
[33] Colpan C, Dincer I, Hamdullahpur F. Thermodynamic modeling of direct internal reforming solid oxide fuel cells operating with syngas. International Journal of Hydrogen Energy 2007;32:787–95. https://doi.org/10.1016/j.ijhydene.2006.10.059.
[34] Bejan A, Tsatsaronis G, Moran M. Thermal Design & Optimization. First. John Wiley & Sons Ltd; 1996.
[35] Empresa de Pesquisa Energética. Metodologia: projeção de curva de carga horária 2020.
[36] Sborz J, Cominato C, Kalbusch A, Henning E. Hourly and daily domestic hot water consumption in social housing dwellings: An analysis in apartment buildings in Southern Brazil. Solar Energy 2022;232:459–70. https://doi.org/10.1016/j.solener.2021.12.067.
[37] Tao G, Virkar A. Intermediate temperature solid oxide fuel cell (IT-SOFC) research and development activities at MSRI. Nineteenth Annual ACERC&ICES Conference, Utah 2005.
[38] Ni M, Leung MKH, Leung DYC. Energy and exergy analysis of hydrogen production by a proton exchange membrane (PEM) electrolyzer plant. Energy Conversion and Management 2008;49:2748–56. https://doi.org/10.1016/j.enconman.2008.03.018.

Robust Optimization of the Energy Concept of an Industrial Process w.r.t. Uncertain Energy Costs and Environmental Conditions

Michael Lockan[a], Rushit Kansara[a]

[a] German Aerospace Centre (DLR),
Institute of Low-Carbon Industrial Processes, Cottbus, Germany,
michael.lockan@dlr.de

Abstract:

Due to the required CO_2 reduction to achieve global climate goals, the political, social, and economic pressure for decarbonizing industry increases rapidly. An essential step towards this goal is the replacement of fossil fuels by renewable energy sources making changes in technology for generating electricity, steam, and process heat an inevitable requirement. This raises the question about the combination of energy supply technologies (such as photovoltaic systems, wind turbines or solar thermal systems) with energy conversion units (such as heat pumps or electric boilers) to cover the demand of an industrial process at minimal cost. Optimization methods are increasingly used for the selection and dimensioning of such units. These methods can systematically and efficiently determine optimal energy concepts according to the multicriterial requirements of a specific industrial process.

The results of such deterministic optimizations depend heavily on assumptions of environmental conditions such as solar radiation and wind speed, the cost of purchasing and selling revenue of electric power, local infrastructure, and the demand of the industrial plant. Changes in these assumptions can result in significantly different costs or lead to an energy system, which is eventually incapable of covering the process demand. In this paper, the modelling of the required components is briefly described and a robust optimization approach is presented taking uncertainties of the assumptions into account during the optimization process. After a robust optimization for an industrial process is performed, the results are compared and discussed to those of a deterministic optimization. It can be shown, that the robust optimization allows to find energy concepts with less sensitivity and higher reliability when uncertainties are considered.

Keywords:

decarbonization of industry, energy concept, robust optimization, component modelling.

Nomenclature

A area [m^2]
C capital expenditures [€]
c constant, specific heat [kJ/(kg K)]
E energy [kWh]
f performance, uncertainty factor [-]
g specific global warming index [$\mathrm{g_{CO2eq}/kWh}$]
$\dot{m}$ mass flow rate [kg/s]
m mass [kg]
P power [kW], probability, quantile [-]
p specific price [€/kWh]
$\mathbf{p}$ parameter vector [-]
Q thermal energy [kWh]
$\dot{Q}$ thermal power [kW]
S solar radiation [kWh/(m^2)]
T temperature [K]

Abbreviations

EB electric boiler
GB gas boiler
GWI global warming index
HP heat pump
PV photovoltaic
ST solar thermal unit
TAC total annual cost
TES thermal energy storage
WT wind turbine

Greek symbols

α maintenance factor
β panel tilt angle, interest rate
γ scaling exponent
δ declination angle of the sun
η efficiency
τ time horizon
λ load fraction
φ latitude industrial site

Subscripts and superscripts

d daily
det deterministic
hor horizontal
in inlet
inc incidence
nom nominal
out output
pan penal
rob robust

1. Introduction

For a successful decarbonization of industrial processes it is essential to integrate renewable energies in an appropriate way considering economic as well as environmental aspects. For this purpose, it is necessary to model the required units of the considered process and the energy concept sufficiently to gain an understanding of their interaction and characteristics. Due to the huge number of parameters involved describing an energy concept it is necessary and to use numerical optimization strategies in order to find optimal configurations.

1.1. Optimization of energy concepts

With the increasing complexity of the investigated systems and the associated number of parameters to be defined, as well as with increasing requirements, optimization processes are increasingly used. This includes almost all industrial areas in which designs and systems are consistently pushed to the limits of feasibility. Thus, the need for design and operational optimizations of energy concepts for industrial processes is also increasing due to the global economic competition and increasing political and social pressure to reduce CO_2 emissions. The design of an energy concept is typically formulated as mixed integer nonlinear problem, where the nominal capacity of the units is described by real number whereas with the integer variable the number of units used defined, [1]. In the context of this paper, the units used are specified, so that the complexity of the optimization problem can be reduced, while still using nonlinear modelling of the units, *Figure 1*. A more accurate unit modelling is usually used for operational optimizations involving e.g. non-linear model predictive control with real-time weather data or forecasts, [2]. Such a complex operational optimization is not carried out here, but a simplified operational optimization is need to determine the operating costs, which results in a two-level optimization problem. Thus, a stationary modelling of the components is sufficient for the design optimization of the energy concept.

1.2. Robust optimization strategies

Optimized systems often only behave ideally under the given boundary conditions, so that deviations can lead to undesired system behaviour or a loss of performance. The goal of a robust optimization is to consider uncertainties or possible deviations directly during design optimization process. There are many definitions regarding robustness, like a small scatter in the objectives or low failure probabilities, [3]. For each of the defined robust criteria there are sophisticated methods for their efficient estimation. In any case, the consideration of conditions away from the design point requires a number of function evaluations to determine the robust objectives. To avoid this, usually only selected scenarios are considered in current energy concept design processes [4]. However, response surface methods in connection with robust optimizations are often very suitable, which can be created on the basis of a few function evaluations and then used to carry out extensive statistical evaluations efficiently [5]. In this paper local response surfaces are used for the robust optimization of an energy concept, which are created around the design point in every design evaluation.

1.3. Structure of the paper

In the following section the mathematical modelling of the units under consideration is described and the corresponding analysis of the entire energy concept is explained*, Figure 1*. An electrical batterie is not directly considered in this paper, but since the energy balances are calculated on a daily basis, it is assumed that the corresponding amount of electricity can be stored for a short time. The unit modelling serves as the basis for the energy concept design process, in which the nominal capacities of the units are optimized. Finally, the robust optimization problem is presented and its solution is compared with a deterministic optimum.

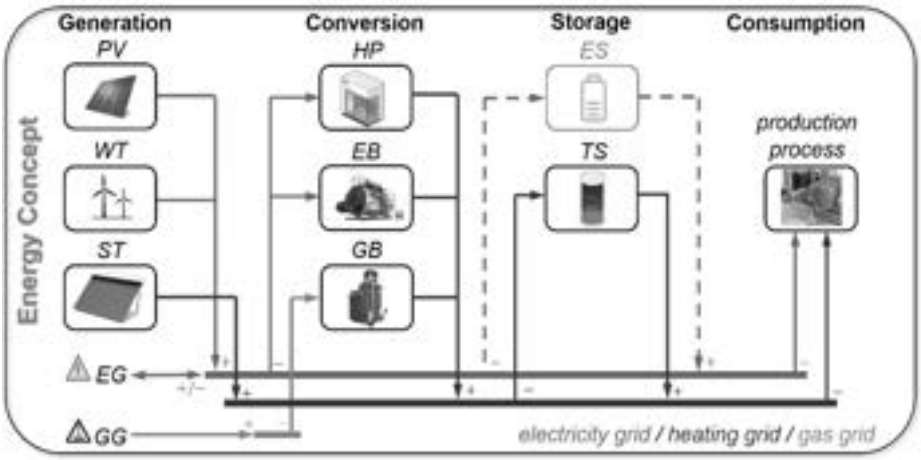

Figure 1 *overview of the energy concept to be optimized showing the electricity, gas and heating grid*

2. Modelling of the energy concept

In order to design and dimension the units shown in *Figure 1*, it is necessary to model them by an energetic point of view. The modelling then forms the basis for determining the electrical energy and heat produced in order to cover the production needs at all times. For this purpose, the formulations of the generation, conversion and storage units are first described in the following sections before the evaluation of the overall system is explained.

2.1. Generation units

The output of the generation units essentially depends on the installed capacity, solar radiations and wind speeds. The installed capacity is described by the area of the panels for the PV and ST units and by the nominal power for the wind turbine. The electrical power P^{PV} provided by the PV unit is thus calculated according to [2] by

$$P^{PV} = A^{PV}\eta^{PV}S^{pan} \tag{1}$$

with the unit area A^{PV}, penal efficiency η^{PV} and solar radiation S^{pan} which summarizes direct and diffuse radiations. The electrical power is limited by the nominal capacity P^{PV}_{nom}, such that

$$P^{PV} \leq P^{PV}_{nom} \qquad \text{with} \qquad P^{PV}_{nom} = A^{PV}P^{PV}_{nom,rel} = A^{PV}0.171. \tag{2}$$

Values for solar radiation are taken from monthly totals $S^{hor}_{\mathcal{M}}$ for a horizontal surface for the region of the industrial site from the DWD, [6]. Using the geometric relationships in *Figure 2a*, the corresponding solar radiation S^{inc} of the sun can be measured using its declination angle δ as well as the latitude φ of the industrial site:

$$S^{inc} = \frac{S^{hor}}{\sin\alpha} \qquad \text{with} \qquad \alpha = 90° - \varphi + \delta. \tag{3}$$

A tilt angle β of the PV module then corresponds to a decrease in latitude φ, so that the solar radiation on the module is calculated by

$$S^{pan} = S^{inc}\,sin(\alpha+\beta) = S^{hor}\frac{sin(\alpha+\beta)}{\sin\alpha}. \tag{4}$$

The efficiency of the PV unit was chosen with $\eta^{PV} = 0.09$ in such a way that calculated values correspond to the measurements of a PV unit already installed at the industrial site.

The electrical power provided by the wind turbine unit is determined by the nominal power P^{WT}_{nom} and a wind load fraction λ^{WT} dependent efficiency η^{WT}:

$$P^{WT} = \eta^{WT}(\lambda^{WT})P^{WT}_{nom} \qquad \text{with} \qquad \lambda^{WT} = \frac{v^{wind}}{v^{wind,0}} \tag{5}$$

where a reference wind speed of $v^{wind,0} = 12ms^{-1}$ is chosen for the present study. Due to the linear dependency in (5), only a single representative wind turbine unit is considered at this point, a separation into several wind turbines with different capacities does not take place here. The efficiency function is selected according to [2]

$$\eta^{WT}(\lambda^{WT}) = \begin{cases} 0 & if \quad \lambda^{WT} < 0.33 \\ 1.5393\lambda^{WT} - 0.5091 & if \quad 0.33 \leq \lambda^{WT} \leq 1.0 \\ 1 & if \quad \lambda^{WT} > 1.0 \end{cases} \tag{6}$$

and displayed *Figure 2b*. The wind speeds used here are taken from measurements at the industrial site. The same distributions of wind speeds and thus the same output of the wind turbine unit is assumed for each day in this paper. A distinction between days with a lot and little wind does not take place for the design of the wind turbine unit.

To determine the output of the solar thermal unit, a single equivalent solar panel is usually considered, for which the inlet and outlet temperatures w.r.t a given the mass flow are calculated, [7]. However, to find an appropriate design an optimization of the mass flow in the panels is required, which may necessary for an operational consideration, but not for the design. For the design, the calculation of the thermal performance

$$\dot{Q}^{ST} = A^{ST}\eta_0^{ST}S^{pan}f^{ST} \qquad \text{with} \qquad f^{ST} = 0.97 - 0.0367\left(\frac{a^*}{\eta_0^{ST}}\right) + 0.0006\left(\frac{a^*}{\eta_0^{ST}}\right)^2 \tag{7}$$

using the panel area A^{ST}, the zero-loss panel efficiency η_0^{ST}, the solar radiation on the penal S^{pan} as in (4) and a collector performance factor f^{ST}, [8]. Heat losses from the panel are considered using the performance

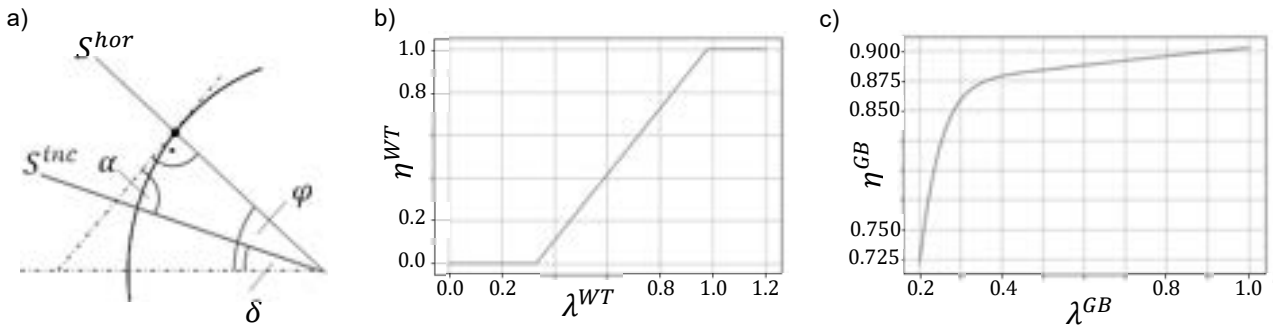

Figure 2 a) angles to calculate the solar radiation b) efficiency of wind turbines depending on the wind load and c) efficiency of the gas boiler depending on the load fraction

factor f^{ST}, which depends on the type of panel. For this paper, evacuated tubes with $\eta_0^{ST} = 0.6$ and $a^* = 3$ are used.

2.2. Conversion units

The task of the conversion units is to provide the heat required for the industrial process using electricity or gas. There are a lot of ways to generate heat, e.g. using combined heat and power units, but firstly only the components described below were considered in this work. The thermal output $\dot{Q}^{GB}$ of the gas boiler is calculated according to

$$\dot{Q}^{GB} = \dot{Q}_{nom}^{GB} \lambda^{GB} \tag{8}$$

with the nominal capacity $\dot{Q}_{nom}^{GB}$ and the load fraction λ^{GB} limited by lower and upper bounds $0.2 \leq \lambda^{GB} \leq 1.0$. The power P^{GB} required for generating $\dot{Q}^{GB}$ is calculated based on the efficiency η^{GB}, so that the behavior in part load can also be considered, [2]:

$$P^{GB} = \frac{\dot{Q}^{GB}}{\eta^{GB}} \quad \text{with} \quad \eta^{GB} = \frac{21.754\lambda^{GB^3} - 7.001\lambda^{GB^3} + 1.397\lambda^{GB} - 0.076}{20.666\lambda^{GB^3} - 5.342\lambda^{GB^3} + 0.678\lambda^{GB} + 0.035}\eta_{nom}^{GB} \tag{9}$$

and a nominal efficiency of $\eta_{nom}^{GB} = 0.8$, *Figure 2c.* In the calculation, λ^{GB} is set to $\lambda^{GB} = 0.2$ if $0.01 \leq \lambda^{GB} \leq 0.2$ and $\lambda^{GB} = 0.0$ if $\lambda^{GB} < 0.01$ to also consider the non-use of the gas boiler.

The electric boiler is calculated in the same way as the gas boiler. Thus, the thermal output $\dot{Q}^{EB}$ is determined according to

$$\dot{Q}^{EB} = \dot{Q}_{nom}^{EB} \lambda^{EB} \tag{10}$$

with the nominal capacity $\dot{Q}_{nom}^{EB}$ and the load fraction $0.0 \leq \lambda^{EB} \leq 1.0$. In contrast to the gas boiler, the entire range of the nominal capacity $\dot{Q}_{nom}^{EB}$ can be used. Furthermore, a constant efficiency $\eta^{EB} = 0.95$ is assumed, so that a required power is calculated by

$$P^{EB} = \frac{\dot{Q}^{EB}}{\eta^{EB}} = \frac{\dot{Q}^{EB}}{0.95}. \tag{11}$$

Finally, heat pumps are also considered for the heat supply, as these offer the possibility of providing heat very efficiently and on the basis of renewable energy sources, especially in connection with thermal energy storages and solar thermal systems. The thermal output $\dot{Q}^{HP}$ of the heat pump is also calculated by

$$\dot{Q}^{HP} = \dot{Q}_{nom}^{HP} \lambda^{HP} \tag{12}$$

with the nominal capacity $\dot{Q}_{nom}^{HP}$ and the load fraction λ^{HP}. As by the gas boilers, the load fraction is limited by an upper and lower bound, such that $0.2 \leq \lambda^{HP} \leq 1.0$. The efficiency of the heat pump is calculated according to [2] as the product of a constant 2nd law efficiency $\eta_{2nd}^{HP} = 0.36$ and the Carnot efficiency η^{carnot} that serves as theoretical maximum:

$$\eta^{HP} = \eta_{2nd}^{HP} \eta^{carnot} = \eta_{2nd}^{HP} \frac{T_{h,out}^{HP}}{T_{h,out}^{HP} - T_{c,in}^{HP}} \tag{13}$$

with the heat sink temperature $T_{h,out}^{HP}$ as output and the heat source temperature $T_{c,in}^{HP}$ as input of the heat pump. In (13) it becomes clear that a heat pump can work most effective when an appropriate high-quality

heat source is available and the difference between $T_{h,out}^{HP}$ and $T_{c,in}^{HP}$ is as small as possible. The required electrical power P^{HP} of the heat pump is then determined by

$$P^{HP} = \frac{\dot{Q}^{HP}}{\eta^{HP}}. \tag{14}$$

In addition to a minimum temperature difference of $T_{h,out}^{HP} - T_{c,in}^{HP} \geq 25K$ and a maximum output temperature $T_{h,out}^{HP} \leq 160°C$ are also taken into account, [9]. Using (13) and (14) the required thermal power $\dot{Q}_{TES}^{HP}$ taken from a connected thermal energy storage can be calculated for a given temperature difference:

$$\eta_{2nd}^{HP} \frac{T_{h,out}^{HP}}{T_{h,out}^{HP} - T_{c,in}^{HP}} = \frac{\dot{Q}^{HP}}{P^{HP}} = \frac{\dot{Q}^{HP}}{\dot{Q}^{HP} - \dot{Q}_{TES}^{HP}} \Longrightarrow \dot{Q}_{TES}^{HP} = \dot{Q}^{HP}\left(1 - \frac{T_{h,out}^{HP} - T_{c,in}^{HP}}{\eta_{2nd}^{HP} T_{h,out}^{HP}}\right). \tag{15}$$

Usually, only constant efficiencies of the heat pump are applied during the design process. However, this means that solar thermal unit, thermal energy storage and heat pump are considered separately, which can lead to an incorrect evaluation of the overall system.

2.3. Thermal energy storage

The thermal energy storage is used to store the thermal output generated by e.g. the solar thermal unit and to make it available for the generation of the required heat. It is used on the one hand for preheating but also as a source for the heat pump, *Figure 3a*. Starting from the currently stored thermal energy Q_0^{TES}, available thermal performance $\dot{Q}$ during the considered time frame Δt is used to charge the storage tank

$$Q^{TES} = Q_0^{TES} + \dot{Q}\Delta t. \qquad \text{with} \qquad Q^{TES} \leq Q_{nom}^{TES} \tag{16}$$

ensuring that the nominal capacity Q_{nom}^{TES} of storage is not exceeded. Due to the fact, only a hot water storage is used in this paper the temperature T^{TES} of the storage tank can be determined based on the stored thermal energy Q^{TES}, the storage mass m^{TES}, the specific heat capacity of the storage medium c_p^{TES} and initial temperature T_0^{TES}:

$$Q^{TES} = c_p^{TES} m^{TES}(T^{TES} - T_0^{TES}) \qquad \Longrightarrow \qquad T^{TES} = T_0^{TES} + \frac{Q^{TES}}{c_p^{TES} m^{TES}} \tag{17}$$

When discharging the storage, a simple calculation as in (16) is not suitable, because with the discharging of the storage, the storage temperature reduces and according to (15) also the thermal power taken from the storage by the heat pump. In order to be able to better describe the discharging, it is necessary to consider the power used for preheating $\dot{Q}_{TES}^{w}$ and for the heat pump $\dot{Q}_{TES}^{HP}$ within a single formulation

$$\dot{Q}^{TES} = -\dot{Q}_{TES}^{w} - \dot{Q}_{TES}^{HP} = -c_p^w \dot{m}^w (T^{TES} - \Delta T - T_{in}^w) + \dot{Q}^{HP}\left(\frac{T_{h,out}^{HP} - T^{TES}}{\eta_{2nd}^{HP} T_{h,out}^{HP}} - 1\right) \tag{18}$$

where the source temperature for the heat pump is set to the storage temperature $T_{c,in}^{HP} = T^{TES}$ and the output temperature for the preheating is chosen to be $T_{out}^{w} = T^{TES} - \Delta T$ in order to ensure a pinch in the heat exchangers of ΔT. By rearranging (18), formulation

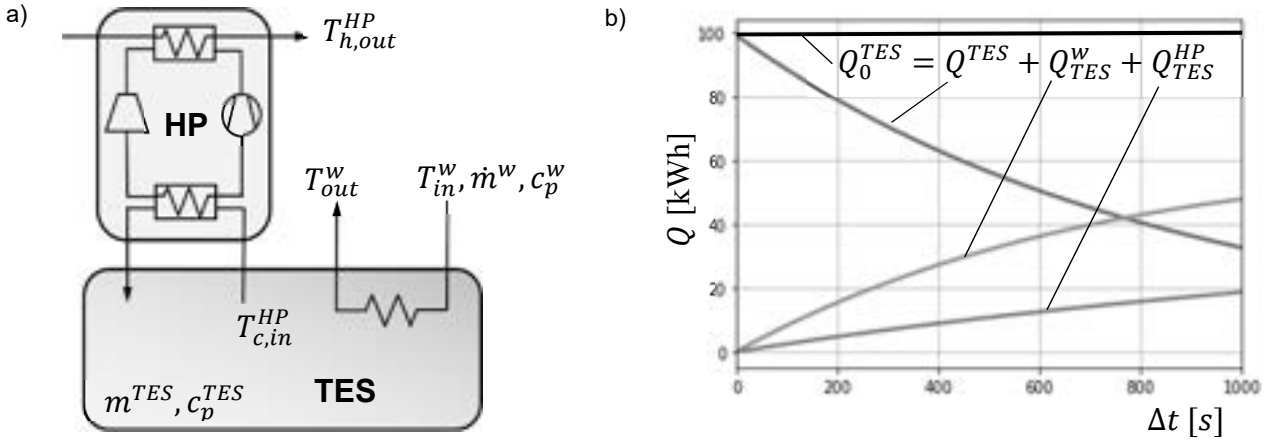

Figure 3 description of the two options for discharging the storage (a) and discharging of the storage according to (22) using $m^{TES} = 1000kg$, $c_p^{TES} = 4.19\,kJ/kgK$, $T_0^{TES} = 15°C$, $c_p^w = 4.19\,kJ/kgK$, $\dot{m}^w = 1.0\,kg/s$, $\dot{Q}^{HP} = 100kW$ and $T_{h,out}^{HP} = 100°C$ (b)

$$\dot{Q}^{TES} = \underbrace{\left[c_p^w \dot{m}^w (\Delta T + T_{in}^w) + \dot{Q}^{HP}\left(\frac{T_{h,out}^{HP}}{\eta_{2nd}^{HP} T_{h,out}^{HP}} - 1\right)\right]}_{c_1} - \underbrace{\left[c_p^w \dot{m}^w + \frac{\dot{Q}^{HP}}{\eta_{2nd}^{HP} T_{h,out}^{HP}}\right]}_{c_2} T^{TES} \tag{19}$$

is obtained, where the terms in the square brackets, that are assumed to be constant with time, are summarized by the constants c_1 and c_2. If the formulation of T^{TES} in (17) is used, equation (19) can be formulated such as

$$\dot{Q}^{TES} = c_1 - c_2 T^{TES} = c_1 - c_2\left(T_0^{TES} + \frac{Q^{TES}}{c_p^{TES} m^{TES}}\right) = \underbrace{c_1 - c_2 T_0^{TES}}_{c_3} - \underbrace{\frac{c_2}{c_p^{TES} m^{TES}}}_{c_4} Q^{TES} \tag{20}$$

with the constants c_3 and c_4, where (20) now depends on Q^{TES}. With this, the following problem can be formulated

$$\dot{Q}^{TES} = \frac{dQ^{TES}}{dt} = c_3 - c_4 Q^{TES} \qquad \Longrightarrow \qquad \frac{dQ^{TES}}{c_3 - c_4 Q^{TES}} = dt \tag{21}$$

which can be solved by integrating separately from Q_0^{TES} to Q^{TES} and t_1 to t_2, where $\Delta t = t_2 - t_1$:

$$Q^{TES} = \left(-\frac{c_3}{c_4} + Q_0^{TES}\right) e^{-c_4 \Delta t} + \frac{c_3}{c_4} \tag{22}$$

Using (22), the energy provided by the storage $Q^{TES} - Q_0^{TES}$ and $\dot{Q}_{TES}^{w}$ as well as $\dot{Q}_{TES}^{HP}$ can be calculated over different time ranges, taking into account the effect of (15) and the fact that also with decreasing storage temperature T^{TES} in the preheating less energy can be transferred, *Figure3b*. During the discharging of the thermal energy storage it is checked that $Q^{TES} \geq 0$.

2.4. Integration of the components

To model the entire energy concept of the industrial process, the components described in the previous chapter must be integrated to check whether the demand of the production process can be covered at any time. The heat requirement considered here corresponds to the batch process of an existing food processing process shown in *Figure 4*a, whereby this is only applicable on weekdays, due to the fact that there is no production at off days. Here the day is divided into 7 sections, with different time periods $\Delta t^{(i)}$ and heat requirements $\dot{Q}^{dem,(i)}$ with a peak load that is only required for a short period of time.

For the analysis of the system consisting of the described components with their nominal capacity, representative weeks are evaluated for each month of the year. This is necessary because the solar radiation and thus also the power of the PV and ST unit change greatly over the course of a year. To determine the daily solar radiation $S_{\mathcal{M},d}^{hor}$ for a specific month, the monthly values $S_{\mathcal{M}}^{hor}$ are divided by the corresponding number of days per month. The analysis of each week starts on Saturday with an empty thermal energy storage. This means that the storage can be charged over the weekend, since there is no heat demand for the production process here. In general, the charging level of the storage is calculated according to the sections in *Figure 4a* by

$$Q^{TES,(i+1)} = Q^{TES,(i)} - \left(\dot{Q}_{TES}^{w,(i)} + \dot{Q}_{TES}^{HP,(i)} - \dot{Q}^{ST,(i)}\right)\Delta t^{(i)} \quad \text{w.r.t.} \quad Q^{TES,(i+1)} \leq Q_{nom}^{TES} \tag{23}$$

where at weekends $\dot{Q}_{TES}^{w,(i)} = \dot{Q}_{TES}^{HP,(i)} = 0$. In order to determine $\dot{Q}_{TES}^{HP,(i)}$, according to (18) it is necessary to define the thermal output of the heat pump $\dot{Q}^{HP}$. Since the components in the batch process under consideration have to be operated at partial load, in sections with a lower heat demand $\dot{Q}^{dem,(i)}$ it is necessary to determine appropriate load fractions $\lambda^{GB}, \lambda^{EB}$ and $\lambda^{HP}$of the units. In this paper, this is realized by a load optimization with regard to minimal operating costs:

$$\min_{\boldsymbol{\lambda} \in L} f \qquad \text{s.t.} \qquad h = \dot{Q}^{dem,(i)} - \dot{Q}^{GB,(i)} - \dot{Q}^{EB,(i)} - \dot{Q}^{HP,(i)} - \dot{Q}_{TES}^{w,(i)} \leq 0 \tag{24}$$

with $f = p_{buy}^{el} E^{el,(i)} + p_{buy}^{gas} E^{gas,(i)}$, the price for electricity $p_{buy}^{el}$and for natural gas p_{buy}^{gas} as well as

$$E^{el,(i)} = \left(P^{HP,(i)} + P^{EB,(i)}\right)\Delta t^{(i)}, \qquad E^{gas,(i)} = P^{GB,(i)} \Delta t^{(i)}, \tag{25}$$

$$L = \{\boldsymbol{\lambda} = [\lambda^{GB}, \lambda^{EB}, \lambda^{HP}]^T \in \mathbb{R}^3 | h \leq 0, \boldsymbol{\lambda}^l \leq \boldsymbol{\lambda} \leq \boldsymbol{\lambda}^u\}. \tag{26}$$

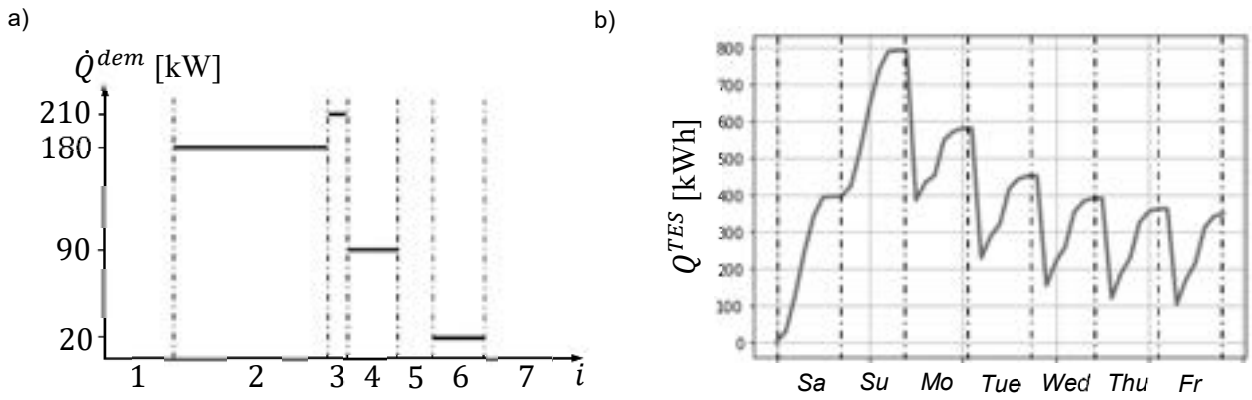

Figure 4 a) considered batch process with daily heat demand sections i and b) charging level of the thermal energy storage for one week in November and an exemplary energy concept

Due to $h \leq 0$ it can be ensured that the heat demand of the production process is covered with minimal operational cost. When calculating the required electrical energy $E^{el,(i)}$, the energy of the PV and WT unit is also taken into account, which is not required to cover the electricity demand of the production process. The total electricity demand of a day is then calculated according to

$$E_d^{el} = E_d^{BL} + E_d^{WL} - E_d^{PV} - E_d^{WT} + \sum_{j=1}^{7} \left(P^{HP,(j)} + P^{EB,(j)}\right) \Delta t^{(j)} \tag{27}$$

with daily energy generated by the PV unit E_d^{PV} and the WT unit E_d^{WT} as well as daily base load E_d^{BL} and load E_d^{WL} on the working days, which is needed e.g. to use the electrical machines. The daily gas demand is calculated according to

$$E_d^{gas} = \sum_{j=1}^{7} P^{GB,(j)} \Delta t^{(j)}. \tag{28}$$

The calculation of the daily demands is carried out consecutively for all days of the week. A negative energy demand means that more energy has been produced than is needed and this amount can be sold, a positive energy demand means that the corresponding amount has to be bought. The charging level of the storage is taken over from one day to the next, as shown exemplarily in *Figure 4b*. Since representative weeks with five working days are analysed for all months, a total of $4 \times 5 \times 12 = 240$ load optimizations (24) are required for an evaluation of the energy concept.

3. Deterministic optimization of the energy concept

The results of the analysis of the energy concept from section 2.4 essentially depend on the dimensioning or the nominal capacities of the units used. For example, larger PV or WT units lead to a larger amount of electrical energy being produced, which, according to (27), can reduce the energy demand. Furthermore, a larger ST unit with a corresponding thermal energy storage means that, according to (23), the heat pump also has a high-temperature source available or the energy in the storage can be used for preheating, so that less additional energy is needed. In addition, the CO_2 emissions can also be reduced by using renewable energy sources like PV, WT and ST units, although an increase in the normal capacities is also associated with increased investment costs. In order to find suitable trade-offs between economic criteria such as costs and ecological criteria such as CO_2 emissions, optimization processes are applied. Therefore, in the next section, the considered criteria will first be explained before the corresponding optimization problem is formulated and the optimization result is discussed.

3.1. Determination of the objectives

As already described, economic as well as ecological criteria are considered in the design process. The total annual costs TAC, which are calculated on the one hand from the required operating costs and on the other hand from the investment costs, are chosen as ecological criterion. The annual investment cost for each unit c^i , $i \in \{PV, WT, ST, GB, EB, HP, TES\}$ is determined according to

$$c^i = \left(\frac{(\beta+1)^\tau \beta}{(\beta+1)^\tau - 1} + \alpha^i\right) C^i \qquad \text{with} \qquad C^i = C^{i,0} \left(\frac{\dot{Q}_{nom}^i / Q_{nom}^i / P_{nom}^i / A^i}{\dot{Q}_{nom}^{i,0} / Q_{nom}^{i,0} / P_{nom}^{i,0} / A^{i,0}}\right)^\gamma \tag{29}$$

with total capital expenditure C^i for unit with nominal capacity $\dot{Q}^i_{nom}/Q^i_{nom}/P^i_{nom}/A^i$, cost $C^{i,0}$ and nominal capacity $\dot{Q}^{i,0}_{nom}/Q^{i,0}_{nom}/P^{i,0}_{nom}/A^{i,0}$ of a reference unit, scaling exponent γ, maintenance cost factor α^i and interest rate β as well as time horizon τ at financing, [10]. Thus, in c^i the annual rate for financing is combined with the maintenance costs. The values used here for the individual units are summarized in *Table 1*, [2], [11].

Table 1 values for calculating annual component costs c^i

	reference capacity	$CAPEX^0$[€]	γ [−]	α [−]	τ [−]	β [−]
PV unit	$P^{PV,0}_{nom} = 1$ kW	1400	0.95	0.01	10	0.03
WT unit	$P^{WT,0}_{nom} = 1$ kW	5000	0.95	0.03	10	0.03
ST unit	$A^{ST,0} = 1\ m^2$	240	0.95	0.5	10	0.03
GB unit	$\dot{Q}^{GB,0}_{nom} = 1$ kW	2700	0.45	0.015	10	0.03
EB system	$\dot{Q}^{EB,0}_{nom} = 1$ kW	70	0.66	0.02	10	0.03
HP system	$P^{HP,0}_{nom} = 1$ kW	2650	0.95	0.02	10	0.03
TES system	$Q^{TES,0}_{nom} = 1$ kWh	80	0.87	0.02	10	0.03

To calculate the operating costs, days with positive and negative energy demand E^{el}_d must be considered separately. Thus, in $E^{el}_{in,m}$, all positive energy demands of the considered representative week of each month m are summarized and in $E^{el}_{out,m}$ all negative ones. For the calculation of the weekly gas demand $E^{gas}_{in,m}$, however, the daily values E^{gas}_d are simply summed up. The total annual costs TAC can then be calculated:

$$TAC = \sum_{m\in\mathcal{M}} \left(p^{el}_{buy}E^{el}_{in,m} - p^{el}_{sell}E^{el}_{out,m} + p^{gas}_{buy}E^{gas}_{in,m}\right)4.3 + \sum_{i\in\mathfrak{I}} c^i \tag{30}$$

with $\mathcal{M} = \{Jan,\ Feb,\ \cdots,\ Dec\}$, $\mathfrak{I} = \{PV, WT, ST, GB, EB, HP, TES\}$, revenue for the sale $p^{el}_{sell} = 0.06\,€/\text{kW}$ and price for the purchase $p^{el}_{buy} = 0.35\,€/\text{kW}$ of electrical energy as well as price for natural gas $p^{gas}_{buy} = 0.13\,€/\text{kW}$. The weekly values are multiplied by 4.3 to get estimated monthly values.

The global warming impact GWI is considered as ecological criterion

$$GWI = \sum_{m\in\mathcal{M}} \left(g^{el}\left(E^{el}_{in,m} - E^{el}_{out,m}\right) + g^{gas}E^{gas}_{in,m}\right) \tag{31}$$

with the specific global warming impacts $g^{el} = 349\ \text{g}_{\text{CO2eq}}/\text{kWh}$ and $g^{gas} = 244\ \text{g}_{\text{CO2eq}}/\text{kWh}$ of electricity and natural gas, respectively [2]. It should be noted that the specific global warming impact from purchased energy is actually varying greatly over time, depending on the shares of e.g. renewable energies. Formulation (31) reduces the GWI through the purchase of energy to emphasize the positive contribution. It should be noted at this point that the manufacture of components or units also has an effect on the GWI, which, according to [12], is significantly lower than that caused by operation. However, the contribution of manufacturing to the GWI is not considered here.

3.2. Optimization problem formulation

The two optimization objectives (30) and (31) depend on the one hand on the investment costs of the installed units and on the other hand on the consumption of electrical energy and natural gas. Both criteria therefore depend on the nominal capacities of the installed units, which are to be determined as part of an optimal design. Thus, the design parameters $\mathbf{p}_{nom}$ of the energy concept are:

$$\mathbf{p}_{nom} = \left[A^{PV}, P^{WT}_{nom}, A^{ST}, \dot{Q}^{GB}_{nom}, \dot{Q}^{EB}_{nom}, \dot{Q}^{HP}_{nom}, Q^{TES}_{nom}\right]^T. \tag{32}$$

The multi-objective optimization problem for minimizing both objectives simultaneously is

$$\min_{\mathbf{p}_{nom}\in P} \begin{bmatrix} TAC \\ GWI \end{bmatrix} \qquad \text{with} \qquad P = \{\mathbf{p}_{nom} \in \mathbb{R}^7 | h_{max} \le 0, \mathbf{p}^l_{nom} \le \mathbf{p}_{nom} \le \mathbf{p}^u_{nom}\} \tag{33}$$

with the constraint $h_{max} = max\left(\dot{Q}^{dem,(i)} - \dot{Q}^{GB,(i)} - \dot{Q}^{EB,(i)} - \dot{Q}^{HP,(i)}\right)$, which is the maximum of all constraints h of the optimal solution of the problem (24). It can happen, that if the nominal capacities of the GB, EB and HP units are chosen too small, a valid solution of (24) is not possible, which result in $h > 0$. This constraint is essential, since the units are chosen to be as small as possible, particularly to reduce the investment costs. The lower limits for the design parameters are chosen to be $\mathbf{p}^l_{nom} = [0, 0, 0, 0, 0, 0, 0]^T$ and the upper limits to be $\mathbf{p}^u_{nom} = [4000, 24, 2000, 250, 250, 250,\ 5000]^T$. This means that individual units do

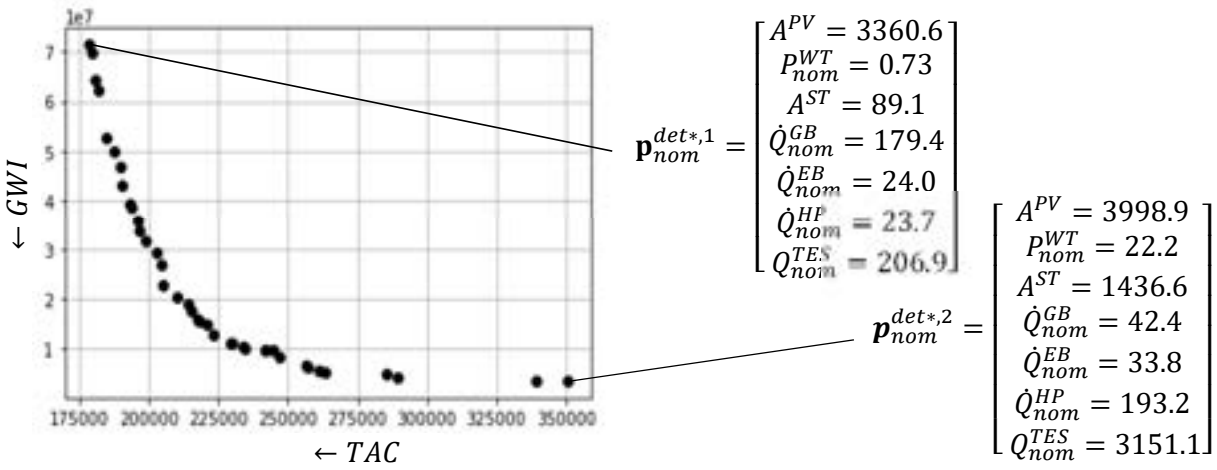

Figure 5 Pareto-front as solution of the multi-objective problem (33)

not have to be used and the entire heat requirement can be covered by GB, EB or HP. It should be noted here that the capacity of the units is modelled continuously, so that the results may not be directly implemented in practice, since e.g. PV units are only available in a certain size.

3.3. Discussion of the results

The optimization problem (33) is solved by the genetic algorithm NSGA2 which is implemented like the modelling of the units and the energy concept in Python, [13]. The result is a Pareto-front consisting of optimal compromises between the objectives, *Figure 5.* Here it can be clearly seen that the objectives TAC and GWI are contradictory and the design $\mathbf{p}_{nom}^{det*,1}$ for a minimum TAC causes only about half the annual costs as the design $\boldsymbol{p}_{nom}^{det*,2}$ for a minimum GWI. However, there are also compromises in between that can be chosen for implementation. The low TAC is realized mainly due to a low gas price p_{buy}^{gas} compared to the price of electricity p_{buy}^{el} and a high nominal capacity $\dot{Q}_{nom}^{GB}$ of the GB unit, while a low GWI is achieved through a high use of renewable energy sources, a large thermal energy storage and a high nominal capacity $\dot{Q}_{nom}^{HP}$ of the HP unit.

4. Robust optimization approach

The result of the optimization from chapter 3.3 depend decisively on the assumptions about e.g. prices for electricity and gas, unit performances, investment costs as well as assumptions about environmental influences such as wind speeds and solar radiation. Uncertainties in these assumptions can lead to deviating and undesirable system behaviour. It is the task of robust optimization to take this into account in the design process. In the following sections, the uncertainties assumed here are presented, the corresponding robust optimization concept is explained and finally the solution from deterministic and robust optimization is compared.

4.1. Description of uncertainties

In this paper uncertainties in the price of gas p_{buy}^{gas} and in the solar radiation S^{pan} on the panels are considered for a first investigation. This is realized in the form of two uncertainty factors f_1 and f_2 such that:

$$\tilde{S}^{pan} = S^{pan} f_1 \qquad \text{and} \qquad \tilde{p}_{buy}^{gas} = p_{buy}^{gas} f_2 \tag{34}$$

with $0.9 \leq f_1 \leq 1.0$ and $1.0 \leq f_2 \leq 2.0$. Thus, the gas price will change with an assumed increase of up to 100%. Solar radiation is assumed to be reduced by up to 10%, which corresponds to degraded panel performance, additional shading, or overestimation of solar radiation.

Local response surfaces are used to assess the influence of f_1 and f_2 on the optimization objectives (30) and (31), [14]. Response surfaces enable the relationship between input parameters and output of a function to be approximated on the basis of a few function evaluations in order to subsequently carrying out extensive statistical studies very efficiently. To set up the response surfaces, a random sample $\left[f_1^{(i)}, f_2^{(i)}\right], i = 1(1)4$ based on a Latin Hypercube Sampling is defined and analysed with $\mathbf{p}_{nom} = \mathbf{p}_{nom}^{det*,1} = const.$ Kriging models $\hat{y}_{TAC}$ and $\hat{y}_{GWI}$ are then created using the calculated values of $TAC^{(i)}$ and $GWI^{(i)}$, [15]. The response surface $\hat{y}_{TAC}$ is shown in *Figure 6a* as an example. A sample with $N = 1e3$ sampling points is then defined and

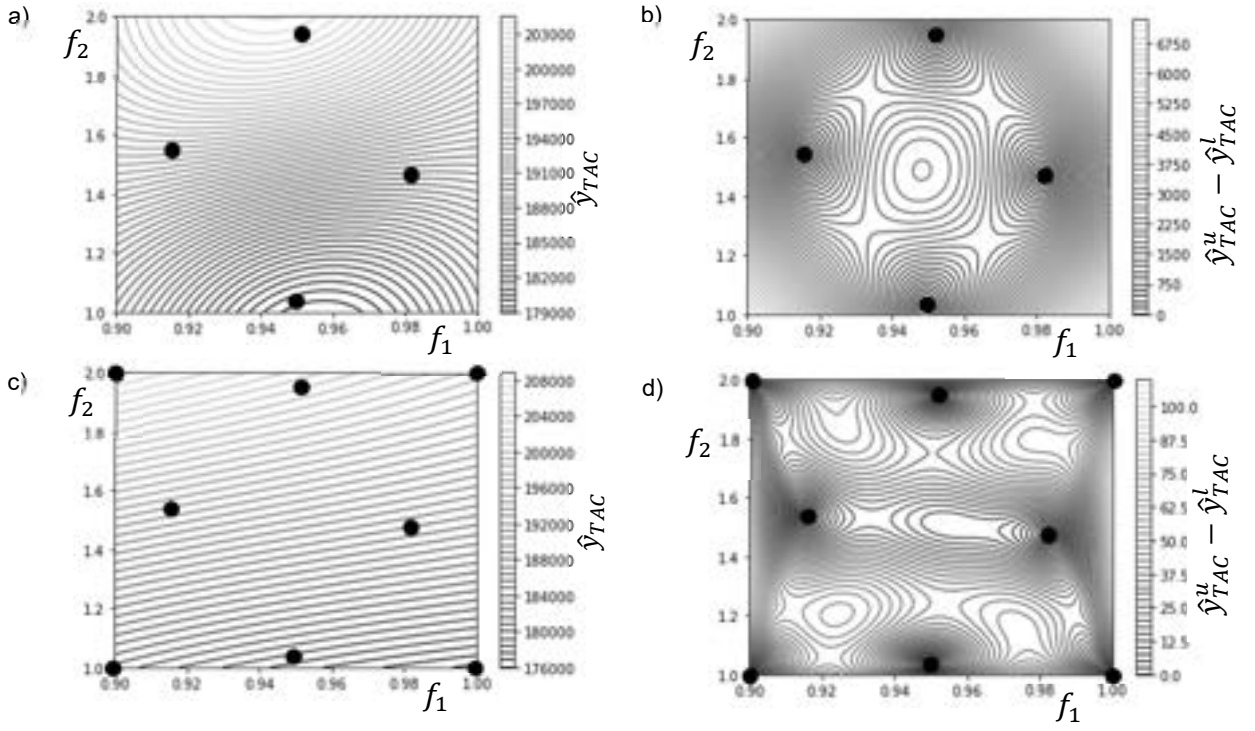

Figure 6 approximation of $\hat{y}_{TAC}$ using a) four and c) eight design evaluations (●) and the associated differences $\hat{y}^u_{TAC} - \hat{y}^l_{TAC}$ between upper and lower bound (b) and (d)

evaluated just using the response surfaces in order to determine the robust criteria. The 95% quantiles P_{95}^{TAC} and P_{95}^{GWI} of the objectives are chosen as criteria, which e.g. for TAC is defined as follows:

$$\frac{1}{N}\sum_{i=1}^{N} I(\hat{y}_{TAC}^{(i)}) = 0.95 \qquad \text{with} \qquad I(\hat{y}_{TAC}^{(i)}) = \begin{cases} 1 & \hat{y}_{TAC}^{(i)} \leq P_{95}^{TAC} \\ 0 & else \end{cases}, \tag{35}$$

and describes a value under which 95% of all elements of the sample are located. However, since the criteria were only determined on the basis of the response surfaces, the question arises as to how accurate these estimates were. For this purpose, the variances $\hat{s}_{TAC}$ and $\hat{s}_{GWI}$ of the Kriging estimates $\hat{y}_{TAC}$ and $\hat{y}_{GWI}$ can be used, [16]. This allows to define lower and upper limits, e.g.

$$\hat{y}_{TAC}^{l,(i)} = \hat{y}_{TAC}^{(i)} - 3\hat{s}_{TAC}^{(i)} \qquad \text{and} \qquad \hat{y}_{TAC}^{u,(i)} = \hat{y}_{TAC}^{(i)} + 3\hat{s}_{TAC}^{(i)}\,, \tag{36}$$

which define a range in which the actual value $TAC^{(i)}$ is within a probability of $\approx 99.99\%$, *Figure 6b*. With these lower and upper limits, the quantiles can then be determined according to (35) and thus a quantile range

$$R_{P,95}^{TAC} = P_{95}^{u,TAC} - P_{95}^{l,TAC} \tag{37}$$

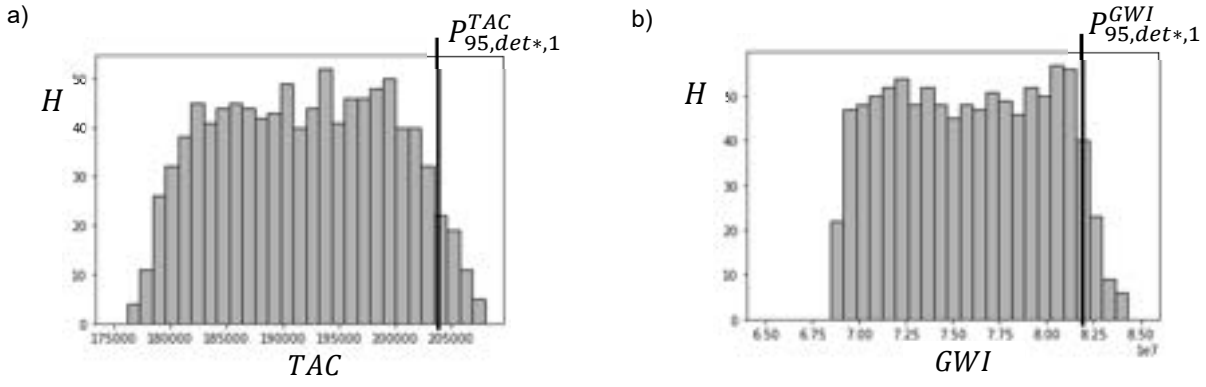

Figure 7 frequency distributions of the optimal solution $\boldsymbol{p}_{nom}^{det*,1}$ with respect to a) TAC and b) GWI

can be estimated. If this range is above a 1% limit of P_{95}^{TAC}, the response surface has to be refined. Appropriate update points are defined by solving the optimization problem

$$\max_{f_1,f_2} \hat{s}_{TAC} \qquad \text{with} \qquad 0.9 \leq f_1 \leq 1.0 \qquad \text{and} \quad 1.0 \leq f_2 \leq 2.0 \tag{38}$$

which finds the point where the estimation $\hat{y}_{TAC}$ has the greatest variance $\hat{s}_{TAC}$. This update process is carried out until the quantile range (37) is sufficiently small, *Figure 6c* and *d*. As can be seen, the response surface can thus be updated very efficiently using just a few iterations. The distributions and estimates for the quantiles $P_{95,det*,1}^{TAC}$ and $P_{95,det*,1}^{GWI}$ determined for the design $\mathbf{p}_{nom}^{det*,1}$ for minimal TAC using the updated response surfaces are shown exemplarily in *Figure 7,* where the spread in the TAC covers a range of $30\text{k}€$.

4.2. Robust optimization concept

As reference for the robust optimization the optimal design $\mathbf{p}_{nom}^{det*,1}$ of the deterministic optimization (33) is chosen, because it may be an appropriate choice from an economic perspective. Due to the fact, that the robust assessment is performed according to the adaptive local response surface procedure described in the previous section, where a number of energy concept evaluations are needed for a single design, just a single objective robust optimization approach is chosen in order to reduce the computational effort. This results in the optimization problem

$$\min_{\mathbf{p}_{nom} \in P} P_{95}^{TAC} \quad \text{with} \quad P = \left\{ \mathbf{p}_{nom} \in \mathbb{R}^7 \left| \begin{bmatrix} h_{max} \\ P_{95}^{GWI} - P_{95,det*,1}^{GWI} \end{bmatrix} \leq \mathbf{0}, \mathbf{p}_{nom}^{l} \leq \mathbf{p}_{nom} \leq \mathbf{p}_{nom}^{u} \right. \right\}, \tag{39}$$

where in addition to (33) a further constraint is added to ensure that an improvement of P_{95}^{TAC} is not be achieved by an increase of P_{95}^{GWI} and a comparability with the design $\mathbf{p}_{nom}^{det*,1}$ can be guaranteed.

4.3. Comparison of optimization results

The optimization problem (39) is solved using a differential evolution algorithm implemented in Python, whereby the computing time was approximately twice as high as with the deterministic multi-objective optimization (33). In contrast to multi-objective optimization, the result is not a set of optimal compromises but a single design

$$\begin{aligned} \boldsymbol{p}_{nom}^{rob*} &= \left[A^{PV}, P_{nom}^{WT}, A^{ST}, \dot{Q}_{nom}^{GB}, \dot{Q}_{nom}^{EB}, \dot{Q}_{nom}^{HP}, Q_{nom}^{TES}\right]^T \\ &= [3539.7,\ 0.3,\ 173.7,\ 3.5,\ 57.6,\ 161.9,\ 755.3]^T. \end{aligned} \tag{40}$$

Compared to the deterministic optimum $\mathbf{p}_{nom}^{det*,1}$, *Figure 5*, the TES and the ST unit were significantly increased and the nominal capacity of the GB unit was reduced to a small value. According to the selected robust criterion, the quantile value P_{95}^{TAC} and thus the high costs to be expected could be reduced, *Figure 8a*. However, over a wide range, the deterministic optimum $\mathbf{p}_{nom}^{det*,1}$ results in low TAC, whereas the robust optimum has a significantly smaller variance in the TAC. In any case, the robust optimum $\boldsymbol{p}_{nom}^{rob*}$ results in a significantly smaller GWI, *Figure 8b,* which was not a goal of the optimization but is an effect due to an increase in the share of renewable energies. The choice of a specific objective of the robust optimization or the desired properties of the energy concept depend heavily on individual factors and must be redetermined depending on the situation.

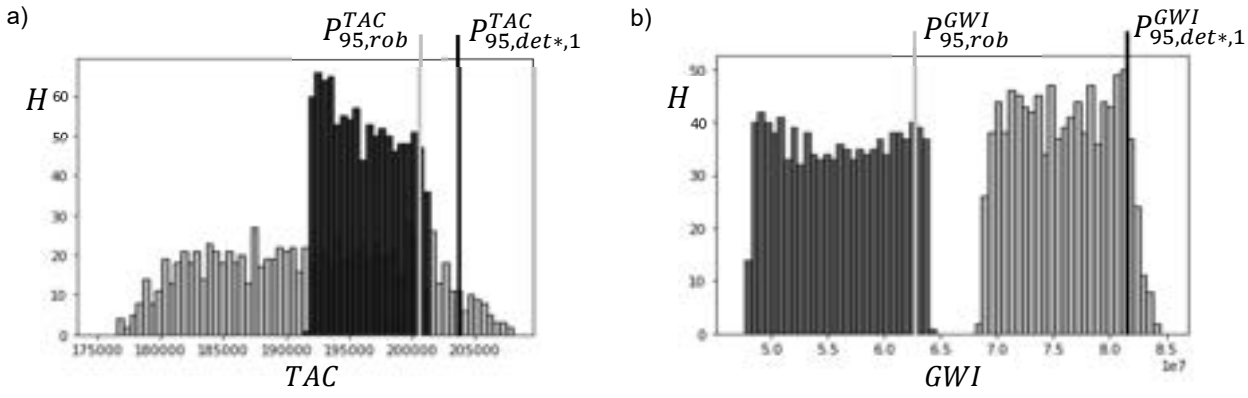

Figure 8 frequency distributions of the optimal solutions $\boldsymbol{p}_{nom}^{det*,1}$ (grey) and $\boldsymbol{p}_{nom}^{rob*}$ (dark grey) with respect to a) TAC and b) GWI

5. Conclusions

In this paper, the modelling of units of an energy concept was described and the procedure for the integrated analysis with regard to economic and environmental criteria was explained. Based on the analysis, a deterministic multi-objective and a robust single-objective optimization problem for the dimensioning of the units used were defined and corresponding optimizations were carried out.

It turns out that the results of the deterministic optimization depend strongly on the assumptions and boundary conditions used and deviations can lead to a large scatter in the objective functions. Furthermore, changes in the boundary conditions of the optimization can lead to different optimal configurations. As part of a robust optimization, assumptions about uncertainties in the price of natural gas and the solar radiation were considered and a design was found that has a lower scatter in the TAC and reduces the expected high costs compared to a selected reference design from the deterministic multi-objective optimization. This shows that the consideration of uncertainties is particularly necessary for long planning periods. In general, the result of a robust optimization strongly depends on the criteria and uncertainties considered, so that different criteria and more realistic assumptions of the uncertainties are investigated in further studies.

References

[1] P. Voll, C. Klaffke, M. Hennen and A Bardow: Automated Superstructure-based Synthesis and Optimization of Distributed Energy Supply Systems. *Energy*, Volume 50, pp. 374-388, 2013.

[2] S. Sass, T. Faulwasser, D.E. Hollermann, C.D. Kappatou, D. Sauer, T. Schütz, D.Y. Shu, A. Bardow, L. Gröll, V. Hagenmeyer, D. Müller and A. Mitsos: Model Compendium, Data and Optimization Benchmarks for Sector-Coupled Energy Systems. *Computers and Chemical Engineering*, Volume 135, 106760, 2020.

[3] A.J. Keane and P.B. Nair: Computational Approaches in Aerospace Design, The Pursuit to Excellence. *John Wiley & Sons*, New York, 2005.

[4] D.E. Majewski, M. Wirtz, M. Lampe and A. Bardow: Robust Multi-Objective Optimization for Sustainable Design of distributed Energy Supply Systems. *Computers and Chemical Engineering*, Volume *102*, pp. 26-39, 2017.

[5] G. Dellino, J.P.C. Kleijnen and C. Meloni: Robust Optimization in Simulation: Taguchi and Response Surface Methodology. *International Journal of Production Economics*, Volume 125 (1), pp. 52-59, 2010.

[6] DWD – Deutscher Wetter Dienst: Average 30-Year Monthly and Annual Sums of Global Radiation – *available at: https://www.dwd.de/DE/leistungen/solarenergie/strahlungskarten_mvs.html?nn=16102* [accesed 13.03.2023]

[7] R. Debulac, S. Serra, S. Sochard and J.-M. Reneaume: A Dynamic Optimization Tool to Size and Operate Solar Thermal District Heating Networks Production Plants. *Energies*, Volume 14, 8003, 2021.

[8] G.B. Murphy, M. Kummert, B.R. Anderson and J. Counsell: A Comparision of the UK Standard Assessment Proceure (SAP) and detailed Simulation of Building-integrated Renewable Energy Systems. *Journal of Building Performance Simulation*, Volume 4 (1), pp.75-90, 2011.

[9] F. Schlosser, M. Jesper, J. Vogelsang, T.G. Walmsley, C. Arpagaus and J. Hesselbach: Large-scale Heat pumps: Applications, Performance, Economic Feasibility and Industrial Integration. *Renewable and Sustainable Energy Reviews*, Volume 133, 110219, 2020.

[10] R. Smith: Chemical Process: Design and Integration. *John Wiley & Sons*, Chichester, 2005.

[11] M. Seitz, H. von Storch, A. Nechache and D. Bauer: Techno Economic Design of a Solid Oxide Electrolysis System with Solar Thermal Steam Supply and Thermal Energy Storage for the Generation of Renewable Hydrogen. *International Journal of Hydrogen Energy*, Volume 42 (42), pp. 26192-26202, 2017.

[12] G. Guillèn-Gosálbez: A noval MILP-based Objective Reduction Method for Multi-Objective Optimization: Application to Environmental Problems. *Computers and Chemical Engineering*, Volume 35 (8), pp. 1469-1477, 2011.

[13] K. Deb, S. Agrawal, A. Pratap and T. Meyarivan: A Fast Elitist Non-Dominated Sorting Genetic Algorithm for Multi-Objective Optmization: NSGAII. *Proceedings of the 6th International Conference on Parallel Problem Solving from Nature*, Paris, France, pp. 849-858, 2000.

[14] D. Bestle, P. Flassig and A.K. Dutta: *Optimal* Aerodynamik Compressor Blade Design Considering Manufacturing Noise. *Proceedings of the 9th European Conference on Turbomachinery*, Istanbul, Turkey, 2011.

[15] D.R. Jones, M. Schonlau and W.J. Welch: Efficient Global Optimization of Expensive Black-Box Functions. *Journal of Global Optimization*, Volume 13, pp. 455-492, 1998.

[16] D.R. Jones: A Taxonomy of Global Optimization Methods based on Response Surfaces. *Journal of Global Optimization*, Volume 21, pp. 348-383, 2001.

Integration of the Compression Units of the Processing Plant with an Organic Rankin Cycle for Power Generation and Cooling Process

Ali Allahyarzadeh Bidgoli[a], Jurandir Itizo Yanagihara[b]

[a] Department of Mechanical Engineering, Polytechnic School, University of São Paulo, São Paulo, Brazil, ali@usp.br

[b] Department of Mechanical Engineering, Polytechnic School, University of São Paulo, São Paulo, Brazil, jiy@usp.br,

Abstract:

The gas compression units in the processing plant are used for various purposes. Compression of the associated gas is designed to adjust for the different operating pressures. In addition, the injection of CO_2 into oil reservoirs is used for enhanced oil recovery (EOR) and/or reduction of environmental impact. These systems utilize dozens of megawatts of electrical energy and intercooling for each compression stage. Therefore, the equipment used is energy-intensive and not thermodynamically efficient. An Organic Rankine Cycle (ORC) technology produces electrical energy from heat sources with low to medium temperature levels (90°C - 150°C). In the present work, a model of an ORC integrated with the intercoolers of the compression units is used to simulate the energy conversion of the system. Next, various working fluids, such as R123, n-butane, n-pentane, hexane, and n-heptane, are considered. The results show a possibility of net power generation by R123 ORC of up to 40 MW. Furthermore, only an increase of 0.95% in the CO_2 molar fraction of the flue gas leads to an increase of 1.29E8 kJ/h in the cooling demands of the CO_2 removal and compression units. Moreover, the presented increase in cooling demands creates the possibility of net power generation of up to 41 MW by ORC. Furthermore, in terms of footprint, this integrated system can be implemented in onshore structures and with some modifications in the condenser in offshore plants. Finally, this integrated system reduces environmental impacts by generating power from waste heat sources.

Keywords:

Multi-stage compression, Intercooling, Organic Rankine Cycle, Power production, Thermodynamic efficiency.

1. Introduction

Based on the IPCC Climate Change 2022 report, it is estimated that there will be a decrease of one billion tonnes of carbon dioxide emissions by 2050 [1]. Accordingly, decarbonization is no longer a prestige option in industries but is also an obligation for several industries, especially oil and gas industries with massive GHG emissions. In addition to the CO_2 removal unit of the oil and gas industries, the proper processing plant needs high cooling demands for the different cooling steps in gas compression units [2]. Attending to these demands and considering the environmental impacts is a dual challenge for the future of processing plants.

Typical processing plants consist of more than five gas compression steps to prepare the desired condition for exportation or injection [3, 4]. These steps need precooling, intercooling, and cooling to meet the required operating temperature. Therefore, the required cooling demands reach 100 MW for a typical processing plant [5, 6]. Conversely, due to the high operating pressure and temperature of the gas compression unit, the equipment used is energy-intensive and is not thermodynamically efficient [7].

An Organic Rankine Cycle (ORC) system is a thermodynamic process utilized for small to medium-scale implementations in several operating temperature ranges and electricity productions using small to intermediate and high-temperature heat supplies varying from 80 to 400°C. With the help of a closed cycle, the limited heat that might otherwise be wasted can be used effectively [8, 9] for power generation. This technology can also mitigate environmental impacts by managing and using waste heating sources [10].

Vilarini et al. [8] and Morais et al. [11] show that the selection of an organic fluid for a system depends on the evaporation enthalpy, dry, isentropic (or wet) characterization, and the slope of the saturation vapor curve of the T-s diagram of the working fluid. In addition to traditional hydrocarbons as working fluids of ORC, such as

n-butane, heptane, propane, etc, the refrigerants of the R12XX family present outstanding performance [12, 13] for certain operating conditions. This positive effect on thermodynamic performance is more prominent when applying regenerative ORC [12].

To the author's knowledge, no other research group evaluated the performance of different working fluids for the cooling process of an ORC that uses the waste heat of compression units of a typical processing plant as the heating source. Moreover, the impact of the CO_2 molar fraction in the flue gas on the cooling demand of a processing plant and the analysis of using this waste heating for power production by ORC is not presented in the open literature.

Therefore, to fill the existing gaps and evaluate possible solutions, a model of an ORC integrated with the intercoolers of the compression units is used to simulate the energy conversion of the system. Next, various working fluids, such as R123, n-butane, n-pentane, hexane, and n-heptane, are considered. In addition, the impact of the variation of the CO_2 molar fraction in the process stream is investigated, and its effect on the cooling demands of the compression unit and the power generated for each working fluid is calculated. Finally, the dimensions of the installation for application in onshore and offshore structures and the environmental impacts of this integration are discussed.

2. Process Simulator and Problem Setup

2.1. System description

2.1.1 Compression units

As Figure 1 shows, the organic Rankin cycle uses the waste heating of the following unit to meet cooling and power generation demands:

1- **Main gas compression**
This unit is responsible for compressing the associated gas of the fluid reservoirs, including CO_2 and natural gas components, for the following processing units at operating pressures of up to 8500 kPa. The suction pressure of compression is 2000 kPa. This unit has precooling and cooling heat exchangers [3].

2- **Vapor recovery unit**
The vapor recovery unit increases and adjusts the operating pressure of the separated gas in different steps of the separation train and the suction temperature of the main gas compressor. This unit comprises two compressor stages with two operating conditions and cooling heat exchangers [14].

3- **Exportation Gas Compression**
The exportation gas system receives gas with the suction pressure of the compressors at 250 bar. Note that the cooling steps of the compression system provide heating sources for a Rankine cycle for power generation [15].

4- **CO_2 compression**
The gases separated in membrane CO_2 separators from the fluid reservoir and the CO_2 captured by the MEA solution-based mechanism from the combustion product are prepared in these systems. The discharge pressure of these units can reach up to 25 MPa. These units comprise four compression stages and the corresponding intercoolers [7].

5- **Carbon capture**
The carbon capture unit or the CO_2 removal unit presents a huge cooling demand for the condenser of the stripper tower, which is a significant source of waste heat for use in the organic Rankine cycle [5].

Table 1 shows the operating conditions of the compression unit of a typical processing plant (offshore and FPSO) that works with many gas and CO_2 in reservoir fluid.

Table 1. Specification of gas compression units [16].

Main unit	Description	Value
Gas treatment	Number of the main units	5
Vapor recovery	Operating pressure of suction-discharge (kPa)	770–2000
Main compression	Operating pressure of suction-discharge (kPa)	2000 –8500
	Compression capacity (Sm^3/d)	6,000,000
	Number of stages	2
Gas exportation	Operating pressure of suction-discharge (kPa)	4500–25,000
	Compression capacity (Sm^3/d)	3,000,000
CO_2 treatment	Number of main units	3
	Number of stages	4
CO_2 compression	Operating pressure of suction-discharge (kPa)	400–25,000

As shown in Figure 1, the heat transferred from three systems is the heat source for the organic Rankine cycle. In fact, in each unit, there are a number of heat exchangers (pre-coolers, intercoolers, and coolers) connected to the ORC system. From the point of view of the ORC system, the heating is absorbed in three stages: economizer, evaporator, and superheater. Furthermore, the ORC uses a regenerative heat exchanger to increase energy efficiency.

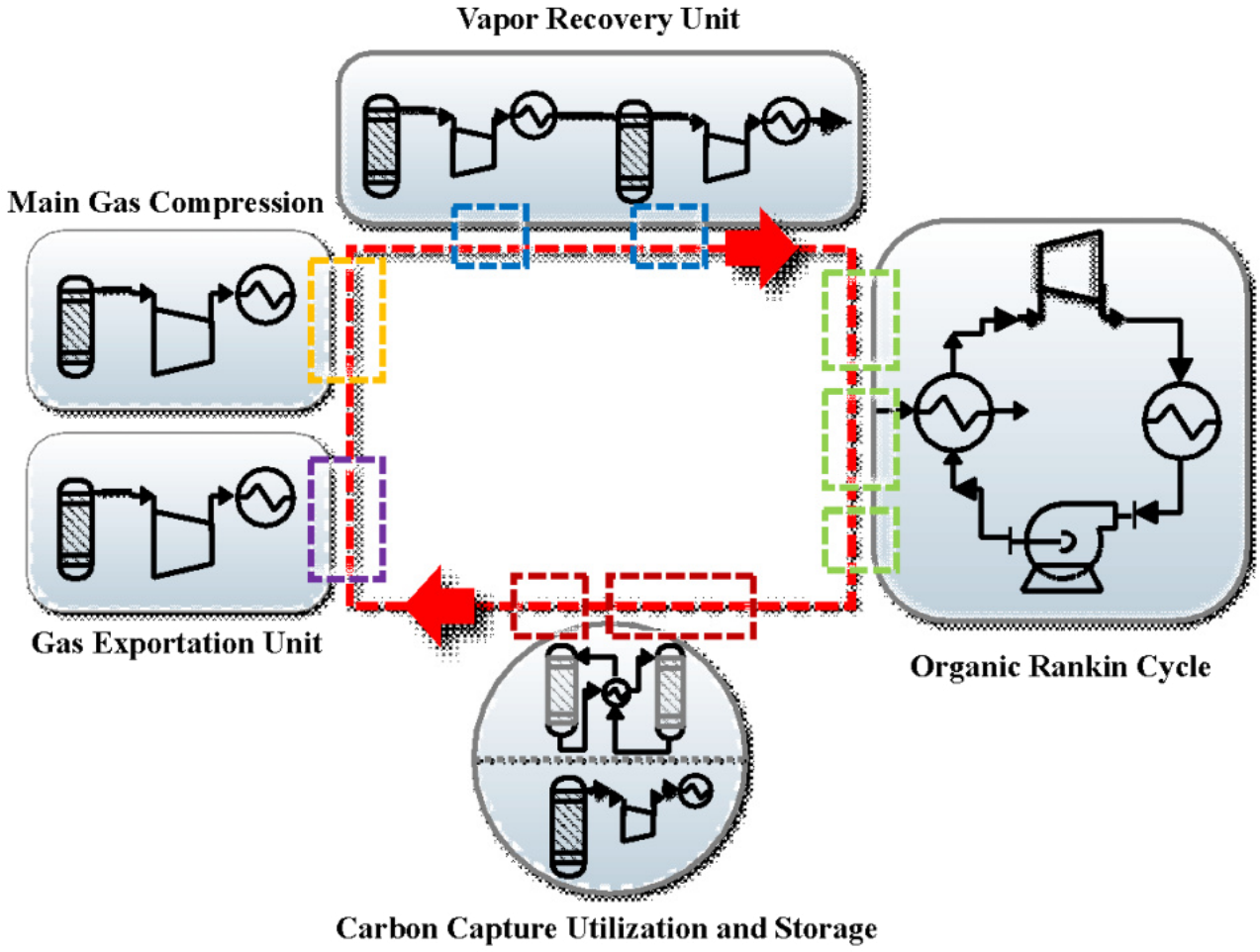

Figure 1. A Conceptual flow diagram of compression units and Organic Rankin Cycle

2.1.2 Organic Rankin Cycle

In this study, as previously mentioned, a regenerative ORC is simulated. To evaluate the performance of different working fluids with respect to the operating condition of the cooling heat exchangers, four distinct fluids with different thermodynamic properties are implemented, as seen in Table 2. In this case, n-butane presents the minimum boiling point and critical temperature, while the lowest critical pressure belongs to n-heptane. After R123, the next lowest critical temperature is for n-hexane. Figure 2 presents the temperature vs. entropy diagrams calculated for n-pentane in this study. Figure 2 also shows the quality lines, different pressure lines, and connected saturate states.

Table 2. Boiling point, critical temperature, and critical pressure of applied working fluids

Fluid	Boiling Point (°C)	Critical Temperature (°C)	Critical Pressure (kPa)
n-pentane	36.06	196	3367
n-butane	-0.50	152	3797
n-hexane	68.73	234.7	3032
n-heptane	98.4	267	2736
R123	27.8	183.6	3661

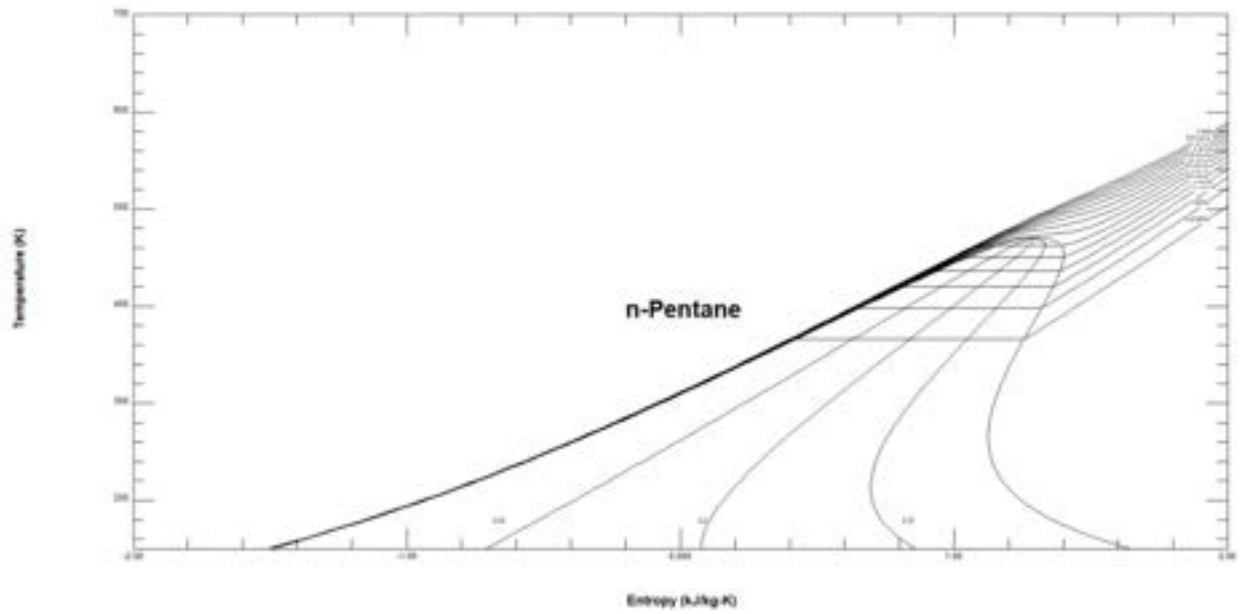

Figure 2. T-s diagram of the applied working fluid (n-pentane)

2.2 Assumptions and numerical modeling

The following assumptions are considered or adopted for numerical simulations:

- The environmental pressure is considered to be 101 kPa, and the ambient temperature is 25 ^{o}C [11].
- A polytropic efficiency of 85% is considered for all centrifugal compressors [7];
- The isentropic efficiency of the steam turbine is considered to be 90% [11];
- Aspen HYSYS [17] is used for model development. Due to the different operating pressures, temperatures, and compositions of each unit, a multi-EoS simulation (PR [18], Span-Wagner [19], and Acid Gas [20]) is considered for the calculation of thermodynamic properties;
- Heat loss and fluid leakage are considered negligible for the heat exchangers.
- The pressure drop of pre-coolers, intercoolers, and coolers is adjusted for 50 kPa based on technical documents, and the pressure drop in other heat exchangers is negligible [16];
- To avoid the temperature cross in the heat exchangers, the minimum temperature approach is set at 2 ^{o}C [3].

3. Methodologies

3.1. Thermodynamic analysis process

Equations 1 and 2 are the mass and energy balances for volume control in a steady state

$$\sum \dot{m}_{in} - \sum \dot{m}_{out} = 0 \tag{1}$$

$$\dot{Q} - \dot{W} + \sum \dot{m}_{in} h_{in} - \sum \dot{m}_{out} h_{out} = 0 \tag{2}$$

where $\dot{m}$ = mass flow rate

$\dot{Q}$ = heat generated or rejected

$\dot{W}$ = work consumed or produced

h = specific enthalpy

in and *out*= input and output.

The total heat transferred between the tube and shell sides (Heat Exchanger duty) can be defined in terms of the overall heat transfer coefficient, the area available for heat exchange, and the log mean temperature difference as Equation 3 presents

$$Q = UA\Delta T_{LM} F_t \tag{3}$$

where

U = overall heat transfer coefficient

A = surface area available for heat transfer

ΔT_{LM} = logarithmic mean temperature difference (LMTD)

F_t = LMTD correction factor

The following general relation applies to the shell side of the heat exchanger.

$$m_{shell}(h_{in} - h_{out})_{shell} - Q_{loss} + Q = \rho \frac{d(Vh_{out})_{shell}}{dt} \tag{4}$$

For the tube side

$$m_{tube}(h_{in} - h_{out})_{tube} + Q = \rho \frac{d(Vh_{out})_{tube}}{dt} \tag{5}$$

where:

m_{shell} = shell fluid flow rate

m_{tube} = tube fluid flow rate

ρ = specific mass

h = enthalpy

Q_{loss} = heat loss

Q = heat transfer from the tube side to the shell side

V = volume of shell or tube holdup

4. Results

This section presents and discusses the results of the integration of the compression unit with ORC. First, the calculated duty of each unit's heat exchangers that can be used as the heat source for the ORC is presented. Then, the power generated and applied operating conditions for the ORC are shown. In addition, the variation of the CO_2 molar faction in the process stream is discussed, and finally, a discussion regarding weight and footprint is presented.

4.1 Waste heat of compression units

Hydrocarbon fluid can be extracted directly from the processing plant for use as the working fluid in the ORC. As the operating conditions of precooling, intercooling, and condensers are different**,** it is essential to adjust the heat exchanger for feasible and acceptable heat transfer. For example, avoiding temperature cross is an important matter for using the waste heat of the compression unit in the ORC.

Figure 3 shows the waste heat available for recovery in the compression and CO_2 removal units. In that, a MEA-based solution to separate CO_2 presents a cooling demand of approximately 1.4 X 10^8 kJ/h that can be used for ORC. Figure 3 shows that this waste heat is more than 37% of the total heating source, being the highest. Next, the heat exchangers for precooling, intercooling, and cooling of the CO_2 compression unit, the exportation gas compression, the main gas compression, and the vapor recovery unit represent, respectively, 23.5%, 23.1%, 13.7 %, and 2.4% of waste heat recovery, as can be seen in Figure 3.

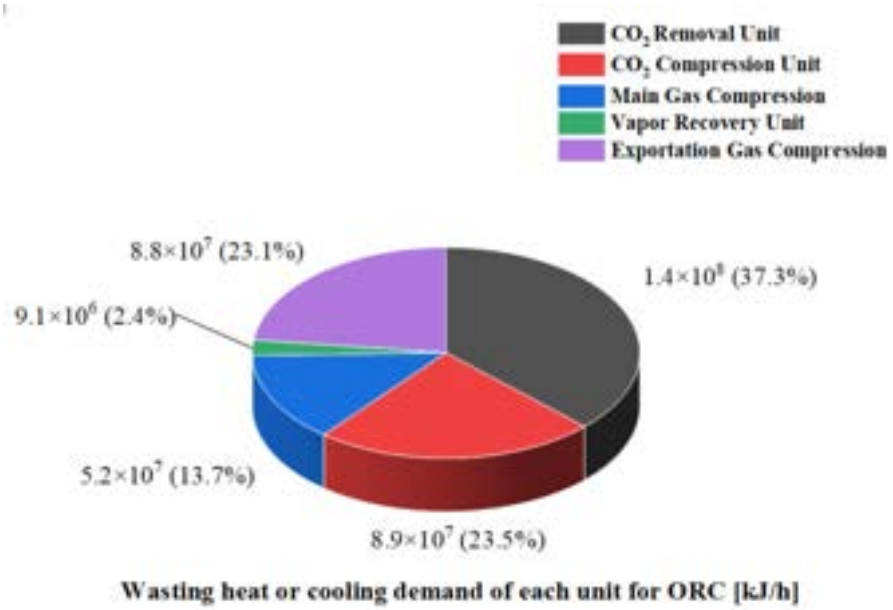

Figure 3. Existing duty of the applied heat exchanger for using the waste heat of coolers as the heat source of the ORC

Figure 4 shows the power generated by the different working fluids in Table 2. The performance of N-pentane, n-butane, hexane, n-heptane, and R123 is evaluated and presented in Figure 4. Figure 4 shows that R123 yields a power of 41 MW, and n-hexane achieves a power generation of 34.7 MW, which is more than 32% of the total power demand of a typical offshore structure [3, 15]. After n-hexane, n-pentane presents a power generation close to 32 MW and is in third place in terms of power generation. Furthermore, as shown in Figure 4, n-butane and n-heptane present a power generation of 18.6 and 27.8 MW, respectively. As can be seen here, R123 presents the highest power generated for the present operating conditions and the existing waste heat of a typical processing plant.

Figure 5 presents the work consumed by the pumps of ORCs. In that, an ORC with R123 as the working fluid needs a pump that consumes 973 kW of electrical energy. Next, the shaft work of pumps of the ORC working with n-pentane, n-butane, n-hexane, and n-heptane are 546, 375, 318, and 147 kW, respectively.

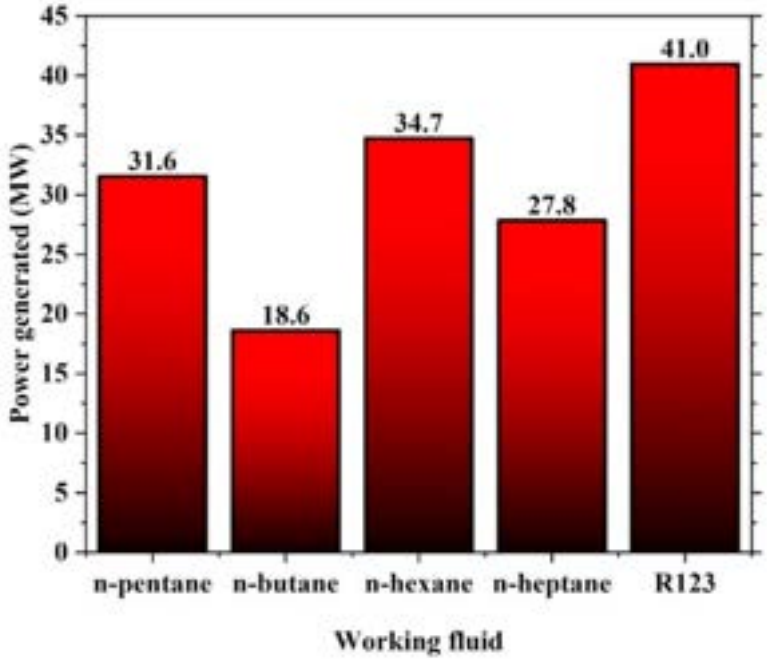

Figure 4. Power generated by working fluid applied in a typical processing plant of this study

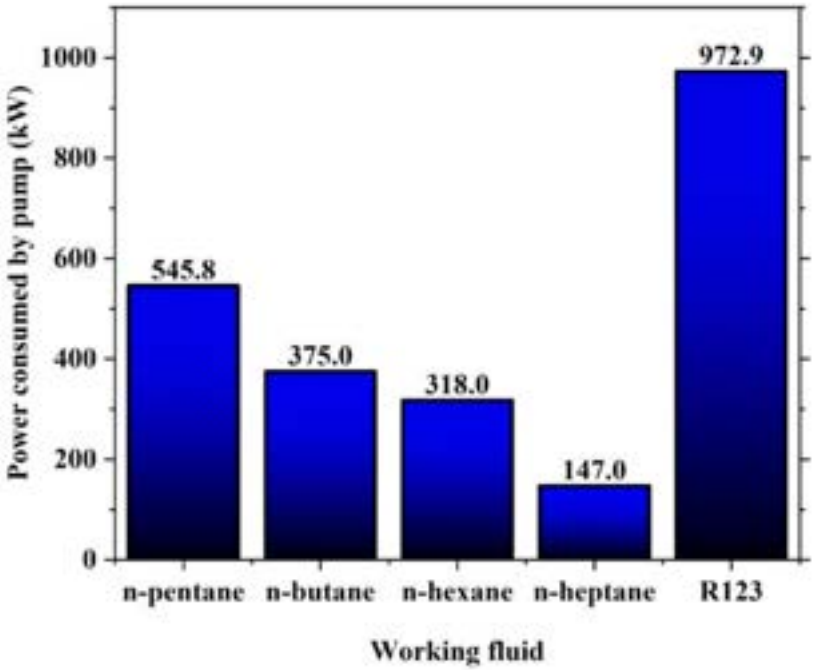

Figure 5. Power consumed by pumps of ORC working fluid applied in a typical processing plant of this study

Table 3 shows the operating condition of R123 ORC with the maximum power generated compared to other fluids. Based on that, the outlet temperature of the cold fluid from the regenerator is 36 °C, and the inlet temperature of the steam turbine is 123.3 °C, as can be observed in Table 3. The cooling demands of 10 heat exchangers from different units are used as the heat sources for the ORC. Table 3 shows that this arrangement generates 40 MW of power.

Table 3. Specification of R123 ORC

Section	Description	value
Organic Rankin Cycle	Operating fluid	R123
	Type of ORC	Regenerative
	Outlet temperature of cold fluid from the regenerator	36 °C
	Inlet temperature of steam turbine	123.3 °C
	Type of heating sources	Precooling, intercooling and cooling shell and tube HE
	Number of heating sources	10
	Net Power generation	40 MW
	Overall required power	973 kPa

4.2 Sensitivity analysis of CO_2 molar fraction on the power generation and heating sources of compression units

Figure 6 shows the effect of the CO_2 molar fraction of the flue gas on the power generation of the applied working fluids. In this case, CO_2 molar fractions of 2.65%, 3.1%, and 3.6% in the flue gas input mass flow rate are evaluated. This flue gas enters the CO_2 removal units, and then the separated CO_2 is sent to storage or utilization purposes. Note that as the mass flow rate increases, the required cooling demands increase for the condenser in the stripper tower of the CO_2 removal unit and the intercoolers of the CO_2 compression unit.

The increase in the heat provided to the ORC results in a higher temperature of the working fluid in the input of the steam turbine and ends with more power generated, as can be observed in Figure 6. In detail, with an

increase of 0.95% in the CO_2 molar fraction of flue gas, the power generated by R123 can increase to approximately 2% (41.81 MW), as can be seen in Figure 6. Moreover, Figure 6 presents the increase in CO_2 processing from the baseline of 2.63% to 3.6%, leading to an increase in the power generated by n-butane ORC of up to 20 MW (an increase of 1.45 MW).

Figure 7 introduces the effect of the CO_2 molar fraction of the flue gas on the waste heat of CO_2 processing plants, such as the CO_2 removal unit and the CO_2 compression unit. With a 0.02% increase in the CO_2 molar fraction of the flue gas, the cooling demand of the plants increases from 7.99E8 kJ/h to 8.28E8 kJ/h, as shown in Figure 7. Moreover, Figure 7 shows that an increase of 0.95% in the CO_2 molar fraction results in a waste heat of 9.19E9 kJ/h, which presents an increase of 15% (1.29E8 kJ/h).

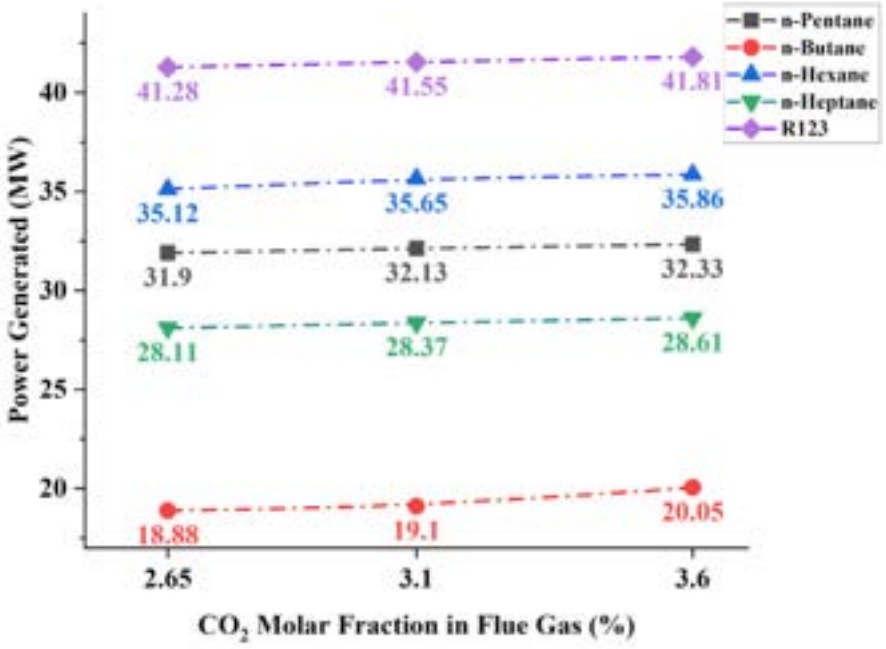

Figure 6. The effect of the CO_2 molar fraction of the flue gas on the power generation of working fluids.

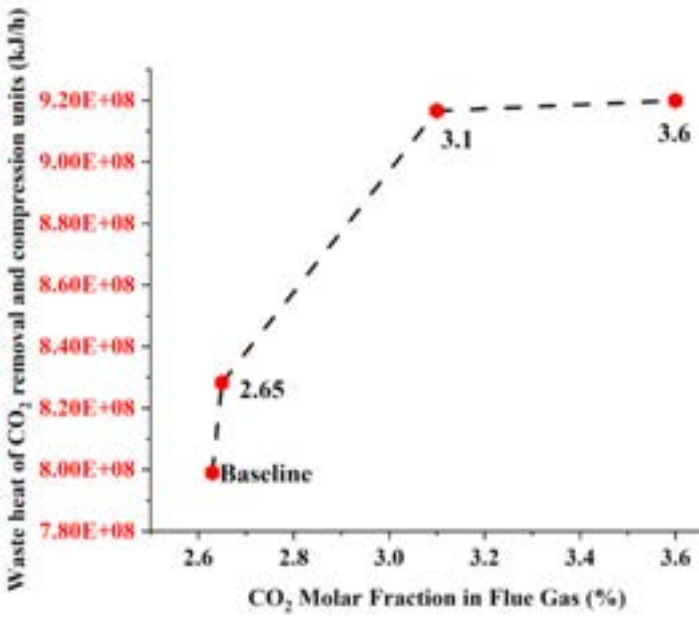

Figure 7. The effect of CO_2 molar fraction of flue gas on the waste heat of regarding processing plant to CO_2.

4.3 Footprint analysis of the proposed Organic Rankin Cycle

As a novelty of this work, there is no research in the open literature focused on the integration of compression units with an ORC for power generation and process cooling in an offshore processing plant. For such applications, the footprint and weight of any added system are crucial because they may imply a complete redesign of the whole haul [21].

For onshore applications, we present the following information. In terms of required footprint, based on the commercial data of an existing ORC system (without indicating the working fluid), for a geothermal heating source with an inlet steam temperature of 130 ^{o}C, a footprint for two 22.5 MW ORCs is approximately 30,000 m^2 [22]. These plants use radial outflow turbines that can work with two operating pressures.

As the satellite figures show (Figure 8, a and b), more than half the occupied footprint of these plants belongs to the air coolers of the condenser. In ORC integrated systems in processing plants, these air coolers can be replaced by shell and tube heat exchangers to meet the cooling demand, with a much smaller footprint. Although further studies focused on the topsides configuration are needed for offshore applications, the potential of this system for energy saving was clearly demonstrated.

(a) (b)

Figure 8. ORC plants of up to 50 MW with geothermal heat sources: a) one of 22.5 MW, of two (Ken Kipaş), b) two of 24 MW (Kubilay I, II)

5. Conclusions

In this research, a model of an ORC integrated with the intercoolers of the compression units was used to simulate the energy conversion of the system. Next, various working fluids, such as R123, n-butane, n-pentane, hexane, and n-heptane, were applied for ORC to evaluate the most efficient with respect to power generation. Then, the variation of the CO_2 molar fraction in the flue gas was analyzed, and its effect on the cooling demands of the compression unit and the power generated for each working fluid was presented.

Integration was carried out successfully with ten heat exchangers, and R123 obtained up to 40 MW of net power generation. In addition, an increase of 0.95% in the CO_2 molar fraction of flue gas resulted in an increase of 15% in cooling demands of the units for CO_2 processing and the possibility of power generation of 41.81 MW by R123 ORC.

Regarding the required footprint for the presented ORC, it may be feasible to use it in onshore structures. Moreover, an offshore application can be made by redesigning the air cooler for the ORC condenser to use this heat source.

Furthermore, the presented system significantly decreases the environmental impact, namely the global warming effect of the compression units, because the cooling demands can be addressed by atmospheric air or seawater. On the other hand, any increase in the capacity of the CO_2 removal unit and its increase in cooling demands can be managed and converted to power generation. Finally, this system can be implemented for several industries with large gas compression units, and the recovered heat can be used to generate power.

Acknowledgments

Jurandir Itizo Yanagihara would like to acknowledge CNPq (National Council for Scientific and Technological Development - Brazil) for the research grant 306364/2020-4.

Nomenclature

A	Surface area available for heat transfer (m^2)
F_t	LMTD correction factor
FPSO	Floating Production Storage and Offloading
h	Specific enthalpy (kJ/kg)
$\dot{m}$	Mass flow rate (kg/s)
MEA	Monoethanolamine
PR	Peng-Robinson
$\dot{Q}$	Heat rate (kW)
T	Temperature (°C)
U	Overall heat transfer coefficient ($W/(m^2.K)$)
V	Volume, (m^3)
$\dot{W}$	Work, (kW)

Greek symbols

ρ	Specific mass (kg/m^3)
ΔT_{LM}	Log mean temperature difference (LMTD)

Subscripts and superscripts

in	input
out	output

References

[1] Pörtner, H.-O., et al., IPCC, 2022: Summary for policymakers. 2022.

[2] Allahyarzadeh Bidgoli, A., N. Hamidishad, and J.I. Yanagihara, The impact of carbon capture storage and utilization on energy efficiency, sustainability, and production of an offshore platform: thermodynamic and sensitivity analyses. Journal of Energy Resources Technology, 2022. **144**(11): p. 112102.

[3] Bidgoli, A.A., Simulation and optimization of primary oil and gas processing plant of FPSO operating in pre-salt oil field. 2018, Universidade de São Paulo.

[4] Nguyen, T.-V., et al., A novel methodology for the design and optimisation of oil and gas offshore platforms. Energy, 2019. **185**: p. 158-175.

[5] Allahyarzadeh-Bidgoli, A., N. Hamidishad, and J.I. Yanagihara, Carbon capture and storage energy consumption and performance optimization using metamodels and response surface methodology. Journal of Energy Resources Technology, 2022. **144**(5).

[6] Hunt, J.D., et al., Deep seawater cooling and desalination: Combining seawater air conditioning and desalination. Sustainable Cities and Society, 2021. **74**: p. 103257.

[7] Allahyarzadeh-Bidgoli, A., et al., Thermodynamic analysis and optimization of a multi-stage compression system for CO 2 injection unit: NSGA-II and gradient-based methods. Journal of the Brazilian Society of Mechanical Sciences and Engineering, 2021. **43**: p. 1-19.

[8] Villarini, M., et al., Influence of the incident radiation on the energy performance of two small-scale solar Organic Rankine Cycle trigenerative systems: A simulation analysis. Applied Energy, 2019. **242**: p. 1176-1188.

[9] Ahmadi, A., et al., Applications of geothermal organic Rankine Cycle for electricity production. Journal of Cleaner Production, 2020. **274**: p. 122950.

[10] Imran, M., et al., Optimization of organic rankine cycle power systems for waste heat recovery on heavy-duty vehicles considering the performance, cost, mass and volume of the system. Energy, 2019. **180**: p. 229-241.
[11] da Silva Morais, P.H., et al., Energy, exergetic and economic analyses of a combined solar-biomass-ORC cooling cogeneration systems for a Brazilian small plant. Renewable Energy, 2020. **157**: p. 1131-1147.
[12] Zhar, R., et al., A comparative study and sensitivity analysis of different ORC configurations for waste heat recovery. Case Studies in Thermal Engineering, 2021. **28**: p. 101608.
[13] Ata, S., A. Kahraman, and R. Şahin, Prediction and sensitivity analysis under different performance indices of R1234ze ORC with Taguchi's multi-objective optimization. Case Studies in Thermal Engineering, 2020. **22**: p. 100785.
[14] Allahyarzadeh-Bidgoli, A., et al., Energy optimization of an FPSO operating in the Brazilian Pre-salt region. Energy, 2018. **164**: p. 390-399.
[15] Allahyarzadeh-Bidgoli, A., et al., FPSO fuel consumption and hydrocarbon liquids recovery optimization over the lifetime of a deep-water oil field. Energy, 2019. **181**: p. 927-942.
[16] Allahyarzadeh-Bidgoli, A. and J.I. Yanagihara, Energy efficiency, sustainability, and operating cost optimization of an FPSO with CCUS: An innovation in CO2 compression and injection systems. Energy, 2023. **267**: p. 126493.
[17] Aspen HYSYS 2017, Aspen Technology Inc. .
[18] Peng DY, R.D., A new two-constant equation of state. . Ind Eng Chem Res, 1976. **15**: p. 59-64.
[19] Span R, W.W., A new equation of state for carbon dioxide covering the fluid region from the triple-point temperature to 1100 K at pressures up to 800 MPa. J Phys Chem Ref Data, 1996. **25**(61): p. 509–9.
[20] Austgen DM, R.G., Peng X, Chen CC., Model of vapor-liquid equilibria for aqueous acid gas-alkanolamine systems using the electrolyte-NRTL equation. Ind Eng Chem Res, 1989. **28**(7): p. 1060–73.
[21] Pereira, L.A.G., J.I. Yanagihara, Sensitivity analysis and optimization to reduce dry weight and footprint of FPSO processing plants in a high CO2 oil field. Comp & Chemical Eng, 2022. **156**: p. 107576.
[22] SRL, E.I. GREENECO ENERJI. [cited 2023; Available from: https://www.exergy-orc.com/casi-studio/greeneco-enerji/.

PROCEEDINGS OF ECOS 2023 - THE 36TH INTERNATIONAL CONFERENCE ON
EFFICIENCY, **C**OST, **O**PTIMIZATION, **S**IMULATION AND ENVIRONMENTAL IMPACT OF ENERGY SYSTEMS
25-30 JUNE 2023, LAS PALMAS DE GRAN CANARIA, SPAIN

A fast heuristic algorithm for multi-energy system design

Antoine Mallégol[a], Arwa Khannoussi[b], Mehrdad Mohammadi[c], Bruno Lacarrière[d], Patrick Meyer[c]

[a] IMT Atlantique, Lab-STICC, UMR CNRS 6285, F-29238 Brest, France, antoine.mallegol@imt-atlantique.fr, CA
[b] IMT Atlantique, LS2N, UMR CNRS 6004, F-44307 Nantes, France,
[c] IMT Atlantique, Lab-STICC, UMR CNRS 6285, F-29238 Brest, France,
[d] IMT Atlantique, GEPEA, UMR CNRS 6144, F-44307 Nantes, France

Abstract:

The optimization of multi-energy systems (MESs) in which multiple energy carriers interact with each other is a complex problem. Their optimal operation and design can be determined through mathematical programming. A classical technology used in MESs is the combined heat and power units (CHP) whose efficiency is modeled through non-linear equations. These non-linear functions are approximated through piecewise linear ones by introducing binary decision variables, which generates a mixed-integer linear program (MILP). Consequently, optimizing such systems over a long time period with a high temporal resolution becomes infeasible in a reasonable amount of time. In this work, we propose a fast heuristic algorithm to optimize the design and operation of such an MES. Our case study is an MES at the scale of a district with five types of generation units, including a CHP, over a time period of one year with a temporal resolution of one hour. Comparison of the proposed heuristic and a state-of-the-art MILP solver over smaller time periods shows that the heuristic is up to 99.9 % faster, with a mean error of 2.3×10^{-4} % compared to the optimal solution. The heuristic can also solve the optimal design and operation problem over a year in about 10 minutes.

Keywords:

Combined Heat and Power, Part-Load Efficiency, Heuristic, Linearization, Multi-Objective Optimization.

1. Introduction

Energy systems may include several types of energy carriers, such as electricity or heat. However, these carriers are classically considered as separate systems. Combining them into a single multi-energy system (MES) can increase the energy efficiency of the system by taking advantage of the synergies and interactions between the energy carriers [1]. It helps to reduce costs or reduce environmental impact by integrating renewable energy sources (RES) more easily in the form of intermittent energy sources [2].

An MES can be optimized using techniques from Operational Research by modeling the system as a mathematical program. Optimization of an MES generally focuses on improving two main areas of the system: its *design*, and its *operation*. Optimizing the design aims to select which production technologies to use in the system, along with their installed capacity, configuration, etc. Optimizing the operation deals with planning the use of the technologies to meet the energy demands by choosing at each time step how much energy each technology produces [3].

Two important points to consider when optimizing an MES are the time horizon and the temporal resolution of the optimization problem [4]. A large time horizon is more accurate to optimize the design, but more complex to solve. Similarly, high temporal resolution impacts the accuracy, especially when intermittent RES are considered in the system [5].

Two main approaches are typically used to solve such optimization problems: *exact* or *approximate* methods. Exact methods (e.g., branch-and-bound) solve the problem to optimality; however, they are computationally expensive and may not be able to even solve medium and large instances of the problem due to the high complexity of MES models. [6] review different exact methods and their properties to solve an MES. On the other hand, approximate methods employ approximate algorithms (e.g., heuristics or metaheuristics) to solve the problem. As their name implies, the approximate algorithms do not guarantee optimality but are able to provide good solutions (i.e., close to optimal) in a reasonable computation time for complex MES models. As an example, [7] use Particle Swarm Optimization algorithm, as a metaheuristic algorithm, to minimize the cost of an MES with three energy carriers.

To deal with the high complexity of MES models, simplifications are sometimes necessary [8]. An example is the use of design days to make the model less complex. Instead of solving the model over a long time period (e.g. a full year), it is solved over smaller time periods of one or a few days that represent typical days (i.e.,

design days) of the year. [9] divide the year into 12 representative periods with a resolution of one hour, plus an extreme event, prior to the optimization. [10] represent the year using shiftable 24-hour periods.

There can also be simplifications in the mathematical model. Modeling an MES typically generates some non-linearities. Considering the difficulties in solving non-linear models, it can be more efficient to linearize the non-linear parts of a model to solve it using linear solvers. [11] linearizes the part-load efficiency of a combined heat and power unit (CHP) and optimizes the model over several typical 24-hour periods.

In this work, we aim to optimize a non-linear MES over a time period of one year with a temporal resolution of one hour. To do so, the system is first formulated as a non-linear mathematical programming model, which is then linearized using a set of auxiliary binary decision variables. Finally, the initial non-linear model is transformed into a mixed-integer linear programming (MILP) model. Solving the proposed MILP model for a period of one year with a temporal resolution of one hour is practically impossible using exact methods. Consequently, an innovative heuristic algorithm is proposed to solve the linearized model. Our proposed algorithm is significantly faster than commercial exact solvers (e.g., branch-and-bound) to solve the problem, while still obtaining good solutions very close to optimal ones.

The rest of this paper is organized as follows: Section 2. introduces the definition of the optimization problem and its mathematical formulation. Section 3. presents the proposed heuristic algorithm used to solve the problem. In Section 4. we employ the proposed algorithm to solve a real case study and compare the results of our algorithm with exact methods. Finally, Section 5. concludes the paper and provides further perspectives.

2. Problem definition

In this work, we study an MES with three energy carriers: electricity, heat, and gas, the latter being only used as fuel. The goal is to meet the energy demand of the system by optimizing the design and operation of the MES with a time resolution of one hour over a time horizon of one year.

The system is characterized by different generation technologies: a combined heat and power unit (CHP) to provide heat and electricity from gas using an internal combustion engine and a heat recovery system [12]; an electric boiler (EB) and a gas boiler (GB) to provide heat; two renewable energy sources (RES) that are photovoltaic (PV) panels to provide electricity and solar thermal (ST) panels to provide heat. The system can also interact with the grid to buy electricity or sell the surplus electricity produced by PV panels.

The system must provide energy to respond to the heat and electricity demands while optimizing two objectives: minimizing the cost of the system and maximizing the rate of RES. Therefore, the aim is to determine the design and operation of the MES while optimizing the two objectives and respecting the energy balance of the system.

2.1. Mathematical formulation

To perform the optimization, the MES is modeled as a mathematical program, shown in Equations (1a) to (1l). In this program and in the rest of this article, independent decision variables, which represent the optimal values to determine, are shown in bold (e.g. $\boldsymbol{P_{e,PV,t}}$). The other elements are parameters, i.e. fixed input data of the model.

$$\text{maximize} \quad ATCR = 100 * (1 - \frac{ATC_{MES}}{ATC_{ref}}) \tag{1a}$$

$$\tau_{RES} = 100 * \frac{\sum_{t\in\mathcal{T}}(\boldsymbol{P_{e,PV,t}} + \boldsymbol{P_{h,ST,t}})}{\sum_{t\in\mathcal{T}}(L_{e,t} + L_{h,t})} \tag{1b}$$

subject to

$$\boldsymbol{A_{PV}} + \boldsymbol{A_{ST}} \leq A_{total} \tag{1c}$$

$$\boldsymbol{P_{e,CHP,t}} \leq \boldsymbol{P_{CHP,nom}} \qquad \forall t \in \mathcal{T} \tag{1d}$$

$$\boldsymbol{P_{h,GB,t}} \leq \boldsymbol{P_{GB,nom}} \qquad \forall t \in \mathcal{T} \tag{1e}$$

$$\boldsymbol{P_{h,EB,t}} \leq \boldsymbol{P_{EB,nom}} \qquad \forall t \in \mathcal{T} \tag{1f}$$

$$\boldsymbol{P_{e,CHP,t}} = (a + b(\frac{\boldsymbol{P_{e,CHP,t}}}{\boldsymbol{P_{CHP,nom}}}) + c(\frac{\boldsymbol{P_{e,CHP,t}}}{\boldsymbol{P_{CHP,nom}}})^2)\boldsymbol{F_{g,CHP,t}} \qquad \forall t \in \mathcal{T} \tag{1g}$$

$$\boldsymbol{P_{h,CHP,t}} \leq \eta_{th,CHP}(\boldsymbol{F_{g,CHP,t}} - \boldsymbol{P_{e,CHP,t}}) \qquad \forall t \in \mathcal{T} \tag{1h}$$

$$\boldsymbol{V_{e,t}} + \boldsymbol{P_{e,PV,t}} = \boldsymbol{A_{PV}}\eta_{DC/AC}\eta_{ref}(1 - \alpha(30 + 0.0175(G_{\beta,t} - 300) + 1.14(T_{a,t} - 25) - T_{ref}))G_{\beta,t} \qquad \forall t \in \mathcal{T} \tag{1i}$$

$$\boldsymbol{P_{h,ST,t}} \leq \boldsymbol{A_{ST}}(G_{\beta,t}\eta_0 - U_{loss}(T_{w,m} - T_{a,t})) \qquad \forall t \in \mathcal{T} \tag{1j}$$

$$\boldsymbol{P_{e,CHP,t}} + \boldsymbol{P_{e,PV,t}} + \boldsymbol{U_{e,t}} - \frac{\boldsymbol{P_{h,EB,t}}}{\eta_{EB}} = L_{e,t} \qquad \forall t \in \mathcal{T} \tag{1k}$$

$$\boldsymbol{P_{h,CHP,t}} + \boldsymbol{P_{h,GB,t}} + \boldsymbol{P_{h,EB,t}} + \boldsymbol{P_{h,ST,t}} = L_{h,t} \qquad \forall t \in \mathcal{T} \tag{1l}$$

$$\boldsymbol{A_j} \in [A_j^{\min}, A_j^{\max}] \qquad \forall j \in \{PV, ST\} \tag{1m}$$

$$\boldsymbol{P_{j,nom}} \in [P^{\min}_{j,nom}, P^{\max}_{j,nom}] \qquad \forall j \in \{CHP, GB, EB\} \tag{1n}$$

$$\boldsymbol{P_{e,CHP,t}}, \boldsymbol{P_{h,CHP,t}}, \boldsymbol{F_{g,CHP,t}}, \boldsymbol{P_{h,GB,t}}, \boldsymbol{P_{e,PV,t}}, \boldsymbol{P_{h,ST,t}}, \boldsymbol{U_{e,t}}, \boldsymbol{V_{e,t}} \geq 0 \quad \forall t \in \mathcal{T} \tag{1o}$$

The first two formulas are the objective functions that are maximized: (1a) as the annual total cost reduction of the MES compared to a reference cost ATC_{ref}, and (1b) as the rate of RES used to respond to the energy demand. The annual total cost ATC_{MES} in (1a) is expressed as (2):

$$ATC_{MES} = \sum_{j \in \mathcal{M}} (C_{O\&M,j} + crf \cdot C_{inv,j}) - \sum_{t \in \mathcal{T}} I_{gr} \boldsymbol{V_{e,t}} + \sum_{t \in \mathcal{T}} (C_{gr,t} \boldsymbol{U_{e,t}} + C_g (\boldsymbol{F_{g,CHP,t}} + \frac{\boldsymbol{P_{h,GB,t}}}{\eta_{GB}})) \tag{2}$$

with $\mathcal{M} = \{CHP, GB, EB, PV, ST\}$ the set of technologies, $\mathcal{T} = (1, ..., 8760)$ the set of time steps of the year. I_g is the price of electricity sold, $\boldsymbol{V_{e,t}}$ the electricity sold at time t, $C_{gr,t}$ the cost of the electricity bought depending on the time of day t, $\boldsymbol{U_{e,t}}$ the electricity bought at time t, C_g the cost of gas bought, $\boldsymbol{F_{g,CHP,t}}$ the gas used by the CHP at time t, $\boldsymbol{P_{h,GB,t}}$ the heat of the GB at time t, and η_{GB} the efficiency of the GB.

The dependent variables $C_{O\&M,j}$ and $C_{inv,j}$ represent the operation and maintenance cost and the investment cost of each technology $j \in \mathcal{M}$, summarized in Table 1. *crf* is the capital recovery factor and represents the value of an annuity based on the number of annuities n and a discount factor i. It is expressed as $crf = i(1+i)^n/((1+i)^n - 1)$. Each technology j has an investment cost $\gamma_{inv,j}$, and an operation and maintenance cost with a fixed part $\gamma_{O\&M,j,f}$ and a variable part $\gamma_{O\&M,j,v}$. $P_{panel,nom}$ is the nominal power of a PV panel.

Table 1: Investment and operation costs of the technologies

Technology j	$C_{inv,j}$	$C_{O\&M,j}$
CHP	$\gamma_{inv,CHP} \boldsymbol{P_{CHP,nom}}$	$\gamma_{O\&M,CHP,v} \sum_{t \in \mathcal{T}} \boldsymbol{P_{e,CHP,t}}$
GB	$\gamma_{inv,GB} \boldsymbol{P_{GB,nom}}$	$\gamma_{O\&M,GB,f} \boldsymbol{P_{GB,nom}}$
EB	$\gamma_{inv,EB} \boldsymbol{P_{EB,nom}}$	$\gamma_{O\&M,EB,f} \boldsymbol{P_{EB,nom}} + \gamma_{O\&M,EB,v} \sum_{t \in \mathcal{T}} \boldsymbol{P_{h,EB,t}}$
PV	$\gamma_{inv,PV} P_{panel,nom} \boldsymbol{A_{PV}} / A_{panel}$	$\gamma_{O\&M,PV,f} P_{panel,nom} \boldsymbol{A_{PV}} / A_{panel}$
ST	$\gamma_{inv,ST} \boldsymbol{A_{ST}}$	$\gamma_{O\&M,ST,f} \boldsymbol{A_{ST}}$

The reference cost is calculated as the cost of responding to the demand using only the GB to generate heat and only buying electricity from the grid, calculated as (3):

$$ATC_{ref} = \gamma_{O\&M,GB,f} \max(L_{h,t}) + crf \cdot \gamma_{inv,GB} \cdot \max(L_{h,t}) + \sum_{t \in \mathcal{T}} (C_{gr,t} L_{e,t} + C_g \frac{L_{h,t}}{\eta_{GB}}) \tag{3}$$

The other equations and inequations in the model represent physical constraints. Equation (1c) constrains the maximum area of solar panels, with $\boldsymbol{A_{PV}}$ and $\boldsymbol{A_{ST}}$ the area of PV and ST panels and A_{total} the total area available for solar panels. (1d) to (1f) represent the limitation of the production by the installed capacity of the technologies with $P_{e,j,t}$ the electricity generated by technology j at time t, $P_{h,j,t}$ the heat generated by technology j at time t, and $P_{j,nom}$ the installed capacity of technology j. Equations (1g) and (1h) represent the power and heat production of the CHP. $\boldsymbol{F_{g,CHP,t}}$ is the gas consumption of the CHP, a, b, and c are the coefficients of electrical efficiency of the CHP, used by the function $a + b(\boldsymbol{P_{e,CHP,t}}/\boldsymbol{P_{CHP,nom}}) + c(\boldsymbol{P_{e,CHP,t}}/\boldsymbol{P_{CHP,nom}})^2$ that represents the electrical efficiency, depending on the part-load ratio of the CHP [12]. $\eta_{th,CHP}$ is the thermal efficiency of the CHP. Equation (1i) represents the electricity production from the PV panels. PV panels can sell the surplus produced power to the grid, represented by the variable $\boldsymbol{V_{e,t}}$. $\eta_{DC/AC}$ is the efficiency of PV inverters, η_{ref} is a reference efficiency for PV, α the temperature coefficient of the PV, $G_{\beta,t}$ the global solar radiation at time t, $T_{a,t}$ the ambient temperature at time t, and T_{ref} a reference temperature. (1j) is the production of heat from ST panels. η_0 is the optical efficiency of ST, U_{loss} the thermal loss coefficient, $T_{w,m}$ the mean water temperature in the ST collector. Equations (1k) and (1l) force the power and heat balance of the MES, with η_{EB} the efficiency of the EB, $L_{e,t}$ the electricity demand at time t, and $L_{h,t}$ the heat demand at time t. Finally, (1m), (1n), and (1o) represent the domain of the design and operation variables, respectively.

However, as seen in (1g), the CHP is governed by a non-linear efficiency function representing the part-load efficiency of the power generation of the CHP. Using a non-linear solver to solve a non-linear problem does not guarantee the optimality of the solution. We, therefore, propose to approximate this non-linear function by a piece-wise linear function to be able to model the system as a MILP.

2.2. Linearization

The efficiency function of the CHP in (1g) is linearized through a piece-wise linearization with two decision variables, adapted to the shape of the function. The proposed method of this paper is inspired by the so-called "triangle method" proposed by [13], which we adapt to the problem at hand. This type of method works by

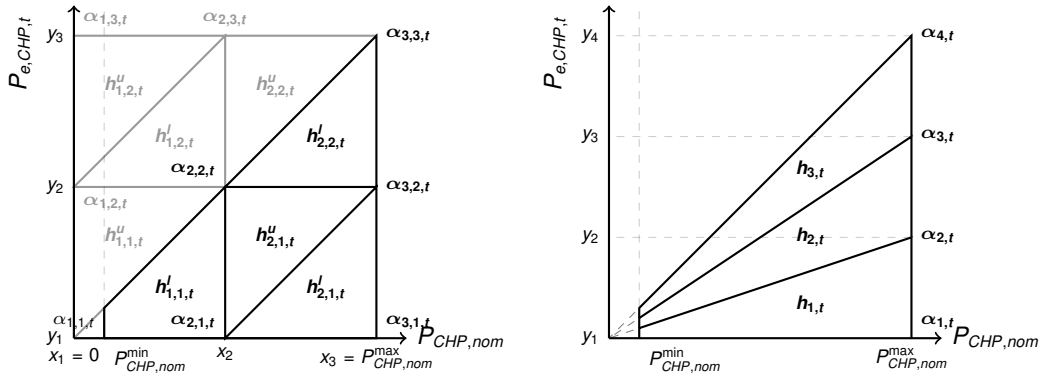

(a) "Triangle" method with $N = 3$ and $M = 3$ breakpoints (b) Adapted method with $N = 4$ breakpoints

Figure 1: Linearization methods examples

adding binary variables in the mathematical model to know which linear piece is selected. The mathematical program resulting from the addition of these binary variables is a MILP model, which can be solved by exact methods (e.g., branch-and-bound, branch-and-cut) [14], guaranteeing the optimality of the solution found.

The "triangle method" of [13] linearizes a function by introducing piece-wise linear parts in the form of triangles. However, in this work, half of those triangles are outside the feasible region of the problem. Figure 1a is an example of the application of the "triangle method". The x-axis is the variable $P_{CHP,nom}$, the y-axis the variable $P_{e,CHP,t}$, and the z-axis would be the function $F_{g,CHP,t}$ to linearize. $\alpha_{n,m,t}$ and $h_{n,m,t}$ represent the variables introduced in the model by this linearization method, N and M being the number of breakpoints on the x and y axes, respectively. As can be seen, half of the triangles are grayed out because they are outside the feasible region in our problem, enforced by Constraint (1d) of the model. This means that some variables and constraints would be added to the model without being useful in the present study. It also needs a large number of triangles to work with a small installed capacity of the CHP for this problem. Looking again at Fig 1a, for the linearization to be effective, the value of $\boldsymbol{P_{CHP,nom}}$ must be greater than x_2, otherwise it would be equivalent to a linearization with a single triangle. Furthermore, a MILP model, with binary or integer variables, while being able to be solved to optimality, is still harder to solve than a linear program (LP) with only continuous variables. Accordingly, reducing the number of binary variables can greatly reduce the complexity of the problem.

We therefore propose an "adapted" version of the triangle method to use fewer triangles and ignore the area outside the feasible region. The adapted method better follows the function we are looking to linearize and uses fewer binary variables, and it is not subject to the inaccurate linearization mentioned for the triangle method when there is a small installed capacity. It introduces continuous variables, noted $\boldsymbol{\alpha_{n,t}} \in [0,1],\ \forall n \in \{1,...,N\}, t \in \mathcal{T}$, and binary variables, noted $\boldsymbol{h_{n,t}} \in \{0,1\},\ \forall n \in \{1,...,N-1\}, t \in \mathcal{T}$, for each breakpoint $n \in \{1,...,N\}$ in the linearization and at each time step $t \in \mathcal{T}$. N is a parameter of the linearization and is the number of breakpoints introduced (and therefore $N-1$ is the number of triangles). We choose to linearize the function $F_{g,CHP,t}$ written as (4).

$$F_{g,CHP,t} = \frac{P_{e,CHP,t}}{a + b\frac{P_{e,CHP,t}}{P_{CHP,nom}} + c(\frac{P_{e,CHP,t}}{P_{CHP,nom}})^2} \tag{4}$$

We need the value of this function at different breakpoints over $P_{e,CHP,t}$, noted $y_n = P^{max}_{CHP,nom} \times (n-1)/(N-1)$:

$$f(y_n) = \frac{y_n}{a + b\frac{y_n}{P^{max}_{CHP,nom}} + c(\frac{y_n}{P^{max}_{CHP,nom}})^2} \tag{5}$$

Equations (6a) to (6f) represent the linearization constraints used to replace (1g). We consider N breakpoints, and a convex combination of the values $\boldsymbol{\alpha_{n,t}}$ can approximate the values of the linearized variables $\boldsymbol{P_{CHP,nom}}$, $\boldsymbol{P_{e,CHP,t}}$, and $\boldsymbol{F_{g,CHP,t}}$. Equation (6e) ensures that only one triangle h is selected at each time step, and (6f) ensures that only the coefficients α associated with the selected triangle have non-zero values, with dummy values $h_{0,t} = 0$ and $h_{N,t} = 0$. (6g) and (6h) constrain the domain of the linearization variables. An example with

N = 4 breakpoints is presented in Fig 1b.

$$\sum_{n=1}^{N} \boldsymbol{\alpha_{n,t}} \leq 1 \qquad \forall t \in \mathcal{T} \tag{6a}$$

$$\boldsymbol{P_{CHP,nom}} = \sum_{n=1}^{N} \boldsymbol{\alpha_{n,t}} P_{CHP,nom}^{\max} \qquad \forall t \in \mathcal{T} \tag{6b}$$

$$\boldsymbol{P_{e,CHP,t}} = \sum_{n=1}^{N} \boldsymbol{\alpha_{n,t}} y_n \qquad \forall t \in \mathcal{T} \tag{6c}$$

$$\boldsymbol{F_{g,CHP,t}} = \sum_{n=1}^{N} \boldsymbol{\alpha_{n,t}} f(y_n) \qquad \forall t \in \mathcal{T} \tag{6d}$$

$$\sum_{n=1}^{N-1} \boldsymbol{h_{n,t}} = 1 \qquad \forall t \in \mathcal{T} \tag{6e}$$

$$\boldsymbol{\alpha_{n,t}} \leq \boldsymbol{h_{n,t}} + \boldsymbol{h_{n-1,t}} \qquad \forall n \in \{1, ..., N\}, t \in \mathcal{T} \tag{6f}$$

$$\boldsymbol{\alpha_{n,t}} \in [0, 1] \qquad \forall n \in \{1, ..., N\}, t \in \mathcal{T} \tag{6g}$$

$$\boldsymbol{h_{n,t}} \in \{0, 1\} \qquad \forall n \in \{1, ..., N-1\}, t \in \mathcal{T} \tag{6h}$$

The problem is studied through a multi-objective perspective, optimizing both the cost of the MES and the rate of RES producing energy. It is not possible to improve both objectives at the same time, since the improvement of one objective implies a degradation of another one. Therefore, we calculate a set of non-dominated solutions on the so-called Pareto front. The ϵ-constraint method [15] is used to calculate a set of solutions on the Pareto front, from which the decision maker can choose the solution that best corresponds to his or her preferences, as a trade-off between the two objective functions. This method works by maximizing one objective function while setting a constraint on the other objective function. Modifying the value of this constraint allows us to obtain several optimal solutions.

Although linearizing the non-linear model makes it computationally easier to be solved, solving the proposed MILP model is still challenging. The binary variables introduced to the model make it combinatorial and NP-hard to solve. It is possible to obtain optimal solutions for shorter time horizons, up to a few weeks, but the resolution of the model over the time horizon of one year is intractable in a reasonable computation time.

In this work, our goal is therefore to improve the resolution time of this model while obtaining good quality solutions. To this end, we propose in the next section a heuristic to solve the problem over long time horizons while maintaining good-quality solutions.

3. Solution approach

We propose a heuristic algorithm to reduce the complexity of the model by letting the binary variables be continuous while guaranteeing the binary value of these variables. Heuristics are approximate algorithms that aim to provide good solutions to a specific problem in a limited computation time [16]. They do not guarantee the optimality of the solution, but are generally faster than exact methods.

The proposed heuristic is composed of two subsequent steps: 1) Initialization and 2) Iterative local search. The initialization generates an initial solution by relaxing the binary variables of the proposed MILP model, and the local search aims to iteratively improve the generated initial solution toward the optimal solution.

These two high-level steps are summarized in Algorithm 1. First, the MILP model is generated with the set of parameters $\mathcal{P}$ of the case study (line 2). A relaxed MILP model, detailed in Section 3.1., is then created from the MILP (line 3), and an initial solution is found after solving this model (line 4). Second, a local search, described in Section 3.2., is used iteratively on the initial solution until there is no improvement. The values of the objective functions are compared to their best values so far (line 5 of Algorithm 1), and if the new solution is better, the next iteration of the local search starts.

As there are two objective functions *ATCR* and τ_{RES} in the model, subscripts 1 and 2 indicate the first and second objective functions, respectively. In the proposed heuristic algorithm, the vector $(bestObj_1, bestObj_2)$ represents the best value of the objective functions found so far, and (obj_1, obj_2) is the vector of the objective functions of the current solution. We consider that the solution *a* is better than the solution *b* if the first objective function of *a* is better, or if the second objective function of *a* is better and the first objective function of *a* is at least as good. As an example, consider *ATCR* and τ_{RES} as the first and second objective functions, respectively. Solution *a* is better than *b* if $ATCR^a > ATCR^b$, or $\tau_{RES}^a > \tau_{RES}^b$ and $ATCR^a \geq ATCR^b$.

3.1. Initialization

As the first step of the heuristic algorithm, a relaxation method is used to generate an initial solution to the problem: the binary variables that allow knowing which triangle is selected at each time step are relaxed to be continuous (i.e., have a value between zero and one), transforming the MILP model into an LP model which is much easier to solve by using, for example, the Simplex class of algorithms. All other variables and constraints remain unchanged. The relaxed MILP model is solved as a linear model and, therefore, the continuous relaxed variables $\boldsymbol{h_{n,t}}$ have a value in $[0, 1]$.

This process is explained in Algorithm 2. The first relaxed MILP model is solved on line 2. Then, at each time

Algorithm 1 High-level algorithm

1: $(bestObj_1, bestObj_2) \leftarrow (-\infty, -\infty)$
2: $MILP \leftarrow$ GENERATEMILP($\mathcal{P}$)
3: $relaxedMILP \leftarrow$ RELAX($MILP$)
4: $(obj_1, obj_2),\ sol \leftarrow$ CREATEINITIALSOLUTION($relaxedMILP$) ▷ Find initial solution
5: **while** $obj_1 > bestObj_1$ or $obj_1 \geq bestObj_1$ and $obj_2 > bestObj_2$ **do**
6: $(bestObj_1, bestObj_2),\ bestSol \leftarrow (obj_1, obj_2),\ sol$
7: $(obj_1, obj_2),\ sol \leftarrow$ LOCALSEARCH($relaxedMILP$, $bestSol$) ▷ Improve the solution
8: **end while**
9: **return** *bestSol*

step $t \in \mathcal{T}$, the variable with the highest value among $\boldsymbol{h_{1,t}}, ..., \boldsymbol{h_{N-1,t}}$ is selected, and a constraint is added to the model to force this variable to be equal to 1, on line 3 of the algorithm. The relaxed MILP model is again solved with these additional constraints on line 4, obtaining this time a feasible solution with all the relaxed variables $\boldsymbol{h_{n,t}}$ having a value of 0 or 1, which gives us the initial solution for the heuristic.

In these algorithms, $\mathcal{N}$ is the ordered set of the triangle indices: $\mathcal{N} = (1, ..., N-1)$. H is the set of variables representing the triangles selected: $H = \{\boldsymbol{h_{n,t}},\ \forall n \in \mathcal{N}, t \in \mathcal{T}\}$. They have binary values in the MILP model or real values in the relaxed MILP model. *sol* is a vector of the index n of the triangle selected at each time step, i.e. $sol = (\{n : \boldsymbol{h_{n,t}} = 1, \forall n \in \mathcal{N}\},\ \forall t \in \mathcal{T})$ if the variables are binary.

Algorithm 2 Initial solution search algorithm

1: **function** CREATEINITIALSOLUTION($relaxedMILP$)
2: $(obj_1, obj_2),\ H \leftarrow$ SOLVE($relaxedMILP$) ▷ Solve relaxed MILP
3: $H_N^{\max} \leftarrow (\arg\max_n(\boldsymbol{h_{n,t}}),\ \forall t \in \mathcal{T})$ ▷ Get the max. argument n for each time step
4: $C \leftarrow \{\boldsymbol{h_{n,t}} = 1,\ \forall n \in H_N^{\max}, t \in \mathcal{T}\}$ ▷ Construct set of constraints to force a triangle to 1 at each time step
5: $(obj_1, obj_2),\ H \leftarrow$ SOLVE($relaxedMILP \cup C$) ▷ Solve relaxed MILP with additional constraints C
6: $sol \leftarrow (\{n : \boldsymbol{h_{n,t}} = 1, \forall n \in \mathcal{N}\},\ \forall t \in \mathcal{T})$ ▷ Get vector of arguments n where $\boldsymbol{h_{n,t}} = 1$ for each time step
7: **return** $(obj_1, obj_2),\ sol$
8: **end function**

3.2. Local search

The second step is to improve the initial solution found. For this aim, we developed a local search method to improve the initial solution by looking at its neighborhood. A local search method works by applying small local changes to a solution with the aim of improving the solution and is applied iteratively until a stopping criterion is reached, e.g. the solution does not improve further, or a time limit fixed in advance is exceeded.

In this work, the local search starts from the initial solution found previously using Algorithm 2. Adjacent linearization triangles of this initial solution are selected to obtain a better solution. For example, in Fig 1b, we can see that if $\boldsymbol{h_{1,t}} = 1$, the first triangle is selected, and if $\boldsymbol{\alpha_{2,t}} > 0$ and $\boldsymbol{\alpha_{1,t}} = 0$, that would mean that the point selected is on the edge between the first and second triangle, and we could choose to select the second triangle without degrading the solution.

Using this knowledge, our local search method selects the other triangle each time a value of the linearization is on the edge of a triangle, executed on lines 2 to 9 of Algorithm 3. For each time step $t \in \mathcal{T}$, for each triangle n selected, if the value of $\alpha_{n,t} = 0$ we select the next triangle, and otherwise if the value of $\alpha_{n+1,t} = 0$ we select the previous triangle. If no value $\alpha_{n,t}$ or $\alpha_{n+1,t}$ is null, we are not on the edge of the triangle and therefore keep the same triangle selected. The selected triangles become constraints in the linear program, i.e. a constraint $h_{n,t} = 1$ is added for the triangle n selected at time step t, $\forall t \in \mathcal{T}$. The linear model is again solved with the newly selected triangles. The new constraints to force the selected triangles are created on line 10, the relaxed MILP model is solved with these constraints on line 11, and the new solution is then constructed on line 12.

A new iteration of the local search is started if the new solution is better than the previous one. Otherwise, the algorithm stops and the best solution found is considered as the solution of the algorithm.

4. Case study

4.1. Description

An instance of the problem defined in Section 2. is used to compare the solutions of the heuristic algorithm and the MILP resolution with real-world data. The MES studied in the present case study covers an area of 33.5 hectares in the vicinity of Nantes, France. It includes the campus of IMT Atlantique, a French technological university, and 45 single-family houses. There are two objective functions to optimize: the maximization of the cost reduction of the MES (i.e. the minimization of the cost of the MES compared to a reference cost), and the maximization of the rate or RES used to respond to the energy demand. The values of the parameters of the

Algorithm 3 Local search algorithm

function LOCALSEARCH(*relaxedMILP*, *sol*)
  for all $t \in \mathcal{T}$ **do**
    $n \leftarrow sol_t$ ▷ Index n of triangle selected for time t
    if $\alpha_{n,t} = 0$ and $n < N - 1$ **then**
      $sol_t \leftarrow sol_t + 1$
    else if $\alpha_{n+1,t} = 0$ and $n + 1 > 1$ **then**
      $sol_t \leftarrow sol_t - 1$
    end if
  end for
  $C \leftarrow \{\boldsymbol{h}_{\boldsymbol{sol_t},t} = 1,\ \forall t \in \mathcal{T}\}$ ▷ Construct set of constraints for the new triangles
  $newObj,\ H \leftarrow$ SOLVE($relaxedMILP \cup C$) ▷ Solve relaxed MILP with selected triangles *sol*
  $newSol \leftarrow (\{n : \boldsymbol{h}_{n,t} = 1, \forall n \in \mathcal{N}\},\ \forall t \in \mathcal{T})$
  return *newObj*, *newSol*
end function

model for this case study are summarized in Tables 2 and 3. The energy demands, the temperature, and the global solar radiation over the year are time series parameters.

Table 2: Cost (investment and operation) parameters per technology

Technology j	$\gamma_{inv,j}$	$\gamma_{O\&M,j,f}$	$\gamma_{O\&M,j,v}$
CHP	1140 €/kW	-	21 €/MWh
GB	90 €/kW	3.15 €/(kW year)	-
EB	100 €/kW	1 €/(kW year)	0.8 €/MWh
PV	1000 €/kW	15 €/(kW year)	-
ST	615 €/m^2	10 €/(m^2 year)	-

4.2. Methodology

The model is solved using an MILP solver and the proposed heuristic algorithm to compare the two resolution methods. Three periods of the year of one week are studied: one week in winter when there is high demand variability and low RES generation, one week in summer when there are lower demands and high RES potential, and one week in mid-season when the demand is lower but there is still a high RES potential.

The time horizon of one week allows us to obtain the optimal solution for the MILP model, and therefore, by comparison, to evaluate the quality of the output of the proposed heuristic algorithm. For each of the three periods, 10 solutions are calculated on the Pareto front using the ϵ-constraint method explained in Section 2., with solution 1 being the solution with the most RES and solution 10 the solution with the highest cost reduction. The number of breakpoints for the linearization was set by trial and error at a value $N = 10$ (i.e. $N - 1 = 9$ triangles), giving a good trade-off between the precision of the linearization and the complexity of the model.

The two methods are compared in terms of the quality of the solution using a *Mean Ideal Distance* indicator to compare the Pareto fronts obtained. This indicator compares the solutions of the two Pareto fronts, as the mean difference of the distance of each solution to an ideal point at the origin, as detailed in (7), with $\mathcal{S} = \{1, ..., 10\}$ the 10 solutions calculated.

$$mean\ distance = \frac{1}{|\mathcal{S}|} \sum_{s \in \mathcal{S}} \left(\sqrt{ATCR_s^{optimal^2} + \tau_{RES}{}_s^{optimal^2}} - \sqrt{ATCR_s^{heuristic^2} + \tau_{RES}{}_s^{heuristic^2}} \right) \tag{7}$$

An error indicator also allows us to compare the result of the heuristic algorithm with the optimal solution, by calculating the error between the heuristic solution and the MILP solution for the two objective functions and the $|\mathcal{S}|$ solutions, as in (8).

$$error = \left\{ \left| \frac{f_s^{optimal} - f_s^{heuristic}}{f_s^{optimal}} \right|, \quad \forall f \in \{ATCR, \tau_{RES}\}, s \in \mathcal{S} \right\} \tag{8}$$

The maximum, mean, and standard deviation are calculated and shown in the table.

The solutions are also compared in terms of the total computation time for the $|\mathcal{S}|$ solutions.

An energy analysis is also performed to compare the two methods. The difference between the values of the operation variables for the two variables is presented at each time step, in the form of a boxplot. As an example, the set $v = \{P_{e,CHP,t}^{heuristic} - P_{e,CHP,t}^{optimal},\ \forall t \in \mathcal{T}\}$ would be presented as a boxplot for the electricity produced by the CHP. Whiskers are represented to show the 5th and 95th percentiles of each set. These figures are

Table 3: General parameters of the case study

$P^{min}_{CHP,nom}$ = 100 kW, $P^{max}_{CHP,nom}$ = 1000 kW	Minimum and maximum nominal power of the CHP
$P^{min}_{GB,nom}$ = 100 kW, $P^{max}_{GB,nom}$ = 3000 kW	Minimum and maximum nominal power of the GB
$P^{min}_{EB,nom}$ = 100 kW, $P^{max}_{EB,nom}$ = 3000 kW	Minimum and maximum nominal power of the EB
A^{min}_{PV} = 0 m^2, A^{max}_{PV} = 10 000 m^2	Minimum and maximum area of the PV panels
A^{min}_{ST} = 0 m^2, A^{max}_{ST} = 10 000 m^2	Minimum and maximum area of the ST panels
$L_{e,t}$ (kW)	Electricity demand of the system
$L_{h,t}$ (kW)	Heat demand of the system
a = 0.1, b = 0.4, c = -0.2	Electrical efficiency coefficients of the CHP
β = 0.3	Constant CHP electrical efficiency
$\eta_{th,CHP}$ = 0.8	Thermal efficiency of the heat recuperation system of the CHP
η_{GB} = 0.8	Efficiency of the GB
η_{EB} = 0.8	Efficiency of the EB
$\eta_{DC/AC}$ = 0.9	PV inverters' efficiency
η_{ref} = 0.155	Reference efficiency for PV
$G_{\beta,t}$ (W m^{-2})	Global solar radiation
α = 0.43 %/ ℃	Temperature coefficient of PV
T_{ref} = 25 ℃	Reference temperature
$T_{a,t}$ (℃)	Outdoor temperature
$P_{panel,nom}$ = 250 W	Nominal power of a PV panel
A_{panel} = 1.6 m^2	Area of a PV panel
η_0 = 0.8	Optical efficiency of ST
U_{loss} = 5 W m^{-2} ℃$^{-1}$	Thermal loss coefficient of ST
$T_{w,m}$ = 45 ℃	Mean water temperature in the ST collector
A_{total} = 10 000 m^2	Total area available for solar panels
$C_{gr,t}$ = 0.13 €/kWh	Cost of electricity bought from the grid (0h–7h)
$C_{gr,t}$ = 0.17 €/kWh	Cost of electricity bought from the grid (8h–23h)
C_g = 0.076 €/kWh	Cost of gas bought
I_{gr} = 0.1 €/kWh	Price of electricity sold to the grid

presented for each of the three one-week periods, each time for the $|\mathcal{S}| = 10$ solutions of the Pareto set. These figures will show the difference in the MILP and heuristic solutions from an operation standpoint by highlighting the difference in the power generated by the different technologies.

An energetic analysis will also be presented, with the energy balance of each technology being calculated for the worst solution of each season. Energy is calculated as the integral of the power generated by each technology over the time period, e.g. $E_{e,CHP} = \sum_{t\in\mathcal{T}} P_{e,CHP,t}$ for the electric energy balance of the CHP.

Capacity factors are also presented, showing the difference in the usage of each technology between the MILP and heuristic solutions. It is the ratio of the energy output of a technology over the maximum theoretical energy output based on the installed capacity. As an example for the GB, it is calculated as (9):

$$\mathrm{CF}_{GB} = 100 \times \frac{\sum_{t\in\mathcal{T}} \boldsymbol{P_{h,GB,t}}}{|\mathcal{T}|\boldsymbol{P_{GB,nom}}} \tag{9}$$

For the RES the maximum theoretical energy depends on the environmental conditions, as in 10 for the ST:

$$\mathrm{CF}_{ST} = 100 \times \frac{\sum_{t\in\mathcal{T}} \boldsymbol{P_{h,ST,t}}}{\sum_{t\in\mathcal{T}} \boldsymbol{A_{ST}}(G_{\beta,t}\eta_0 - U_{loss}(T_{w,m} - T_{a,t}))} \tag{10}$$

The installed capacity of the CHP is expressed in its electrical installed capacity, so the maximum theoretical heat energy is calculated using $\eta_{e,CHP} = 0.3$, which is the best theoretical electrical efficiency given the values of the parameters a, b, and c, which gives a capacity factor for the heat of the CHP calculated as (11):

$$\mathrm{CF}_{h,CHP} = 100 \times \frac{\sum_{t\in\mathcal{T}} \boldsymbol{P_{h,CHP,t}}}{|\mathcal{T}|\boldsymbol{P_{CHP,nom}}\eta_{th,CHP}(1-0.3)} \tag{11}$$

Finally, a resolution of the model is performed over the full year using the proposed heuristic algorithm. The computation time is compared with the resolution of the full year using a MILP solver with an optimality gap as a stop criterion, to have an idea of the time required to solve the full year to optimality.

4.3. Results

The optimal solutions are obtained using the Gurobi solver (version 9.5.2), and the heuristic was implemented in Python with the same version of Gurobi used to solve the relaxed MILP. All the solutions were computed

on a computation server with 400GB RAM and Intel Xeon Gold 6138 @ 2.00GHz CPUs, using 32 threads for Gurobi and one thread in Python.

Table 4 shows the computation times of the two methods for the three different periods (winter, summer, and mid-season). The optimal time and the heuristic time are the total time necessary to obtain the 10 solutions for each method and each period. The improvement is the relative difference between the two durations.

Table 4: Comparison of the total computation time over 3 one-week periods

Period	Optimal time	Heuristic time	Improvement
Winter	1182.4 s	4.1 s	99.7 %
Summer	42.3 s	1.1 s	97.4 %
Mid-season	1802.0 s	2.0 s	99.9 %

As can be seen for the mid-season period, the MILP solver can take a really long time to find the solution. This period is especially complex because it is the season where the energy demand varies the most from day to day, but there is still enough solar radiation to make the RES a good option to generate energy. On average, for the three periods computed here, the heuristic algorithm is 99.0 % faster than the MILP solver.

Table 5 shows the error of the heuristic method compared to the optimal solutions found when solving the MILP model, i.e. the maximum, mean, and standard deviation of the errors calculated from (8). It also shows how many times the heuristic algorithm found the optimal solution.

Table 5: Precision of the heuristic algorithm

Period	Error			Nbr. optimal solutions
	Max.	Mean	SD	(out of 10)
Winter	6.6×10^{-5}	6.8×10^{-6}	1.6×10^{-5}	4
Summer	2.5×10^{-15}	7.2×10^{-16}	6.9×10^{-16}	6
Mid-season	3.1×10^{-10}	1.6×10^{-11}	7.0×10^{-11}	4

We can see that the heuristic obtains good solutions, the maximum error being 6.6×10^{-5} and the average mean error 2.3×10^{-6}. Furthermore, the heuristic found the optimal solution 14 times out of the 30 solutions computed.

This shows that the heuristic method works well for small time periods, giving good-quality solutions with a much smaller computation time than the MILP.

Figure 2 presents boxplots of the difference between the values of the operation variables of the MILP and the heuristic resolutions. The x-axis of each subplot represents the 10 solutions of the Pareto front, and the y-axis is the difference in the operation's variables. When there is no symbol for ST, that means that no ST panels are installed for this solution. We can see that the ST panels are installed only in winter and on the first solutions, when we focus on maximizing the RES. In these boxplots, the whiskers represent the 5th and 95th percentiles, and the points are the outliers outside this range. As can be seen in the figure, the "box" is never visible, meaning that the first and third quartiles always coincide with the median; therefore, at least 50 % of the operation variables of each technology are identical between the solutions of the MILP and of the heuristic. Most of the time, the 5th and 95th percentile whiskers also coincide with the median, meaning that more than 90 % of the solutions are the same. The difference is larger in winter and smaller in summer. This can be explained because the energy demands have a larger variability with a greater maximum demand in winter.

Another analysis that can be drawn from Fig 2 is that the two resolution methods can have different operation plans but still be optimal in terms of the mathematical program. During the winter week, for solutions 2, 3, 4, and 5 the MILP solver and the heuristic give the same values for the two objective functions, the same installed capacities, and the same triangles selected for the linearization. However, solutions 2, 3, and 4 on the boxplots 2a show that the operation variables are slightly different. The same is true for the summer week, with solutions 1, 2, 3, 4, 5, and 10 being optimal but having different values for the operation variables for solutions 2, 3, 4, and 5 on 2b, and for the mid-season week, with solutions 1, 2, 3, and 10 being optimal but solutions 2 and 3 having different operation values on 2c. This can happen because the energy balance is identical, but the energy might be used at different times of the week.

It can also be observed that ST panels are not installed during the summer and mid-season weeks, and ST panels appear in winter only when there is a high value for the objective function τ_{RES}.

Table 6 presents the energy balance of the solution with the largest difference between the MILP and the heuristic solution for each time period. The underlined cells show the technologies with a difference between the two solutions. The relative differences in the values of the objectives functions for these solutions are

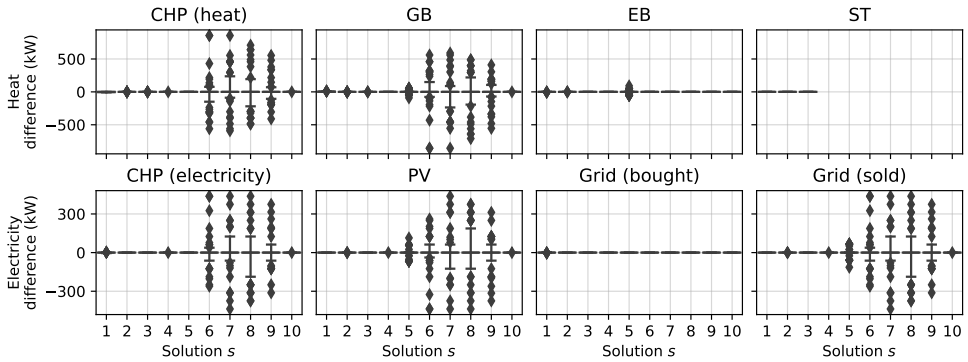

(a) 1 week in winter

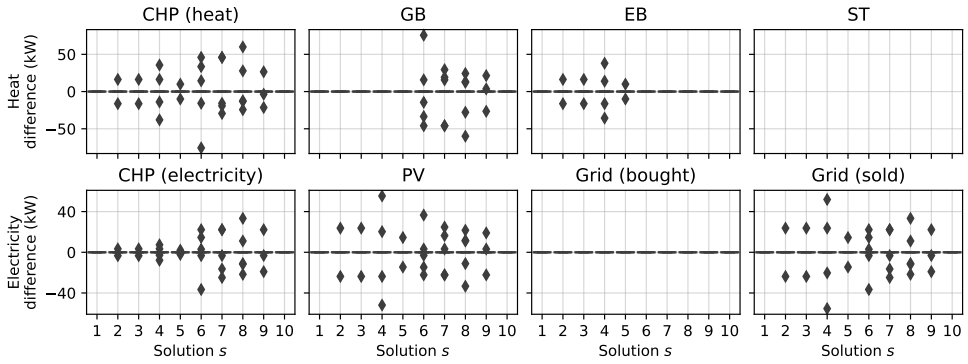

(b) 1 week in summer

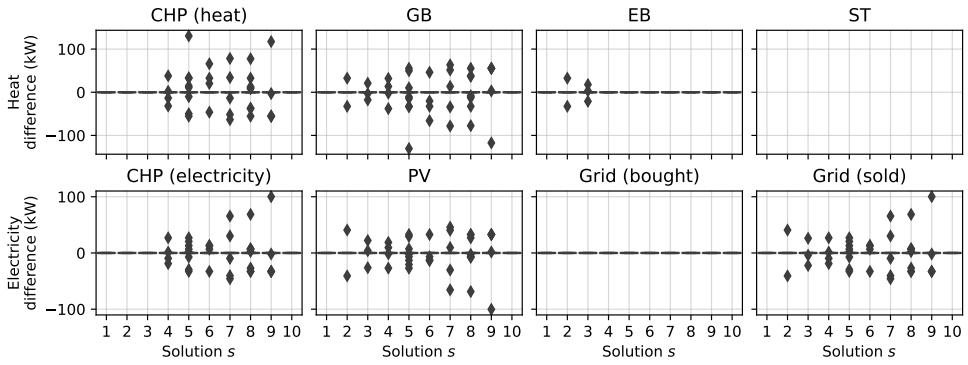

(c) 1 week in mid-season

Figure 2: Difference in the operation of the MILP and heuristic resolutions

6.6×10^{-3} %, 1.6×10^{-13} %, and 3.1×10^{-8} % for *ATCR*, and 0 %, 3.3×10^{-14} %, and 1.9×10^{-14} % for τ_{RES}, for the winter, summer, and mid-season week presented, respectively. As can be seen, the difference is small even in the worst cases. For the summer and mid-season solutions, only the heat produced by the CHP and the GB are different between the MILP and the heuristic solution, with the CHP heat energy being slightly higher for the heuristic and the GB energy slightly lower. For the winter week, the energy produced by the EB is also different, and there is also a difference in the electrical energy produced by the CHP and the electricity imported from the grid.

Table 7 presents the capacity factors, calculated using (9), (10), and (11), for the same selected solutions. For these solutions, the installed capacity is the same for the summer and mid-season solutions. The installed capacity is different for some of the technologies for the winter week, with the largest difference being only 11 kW for the GB or a relative difference of 0.8 %. The capacity factor is also very similar, the largest difference being 0.4 % for the electrical capacity factor of the CHP for the winter solution.

As an example, Fig 3 shows the operation of the 8th solution of the winter week for the MILP model and the heuristic algorithm. As can be seen in the figure, the operation can be different at certain time steps. However, the values of the objective functions are very similar, with a relative difference of 6.9×10^{-6} % for *ATCR* and 8.4×10^{-4} % for τ_{RES}. This can be explained by the fact that the operation variables intervene always as the sum of the variables over the time period considered, i.e. as the energy over the time period. Two solutions can be very similar in terms of energy but have different operation plans to reach the same energy. In other words,

Table 6: Energy balance of the most different solutions

Technology	Winter, solution 1 MILP	Winter, solution 1 Heuristic	Summer, solution 7 MILP	Summer, solution 7 Heuristic	Mid-season, solution 5 MILP	Mid-season, solution 5 Heuristic
CHP (heat)	135.65 MWh	135.21 MWh	8.89 MWh	8.92 MWh	46.27 MWh	46.38 MWh
GB	84.78 MWh	85.25 MWh	273.60 kWh	246.06 kWh	18.32 MWh	18.22 MWh
EB	261.66 kWh	245.40 kWh	0.00 Wh	0.00 Wh	132.62 kWh	132.62 kWh
ST	24.47 MWh	24.47 MWh	0.00 Wh	0.00 Wh	0.00 Wh	0.00 Wh
CHP (elec)	69.10 MWh	68.97 MWh	3.58 MWh	3.58 MWh	23.60 MWh	23.60 MWh
PV	16.51 MWh	16.51 MWh	27.01 MWh	27.01 MWh	22.62 MWh	22.62 MWh
Grid (bought)	3.00 MWh	3.11 MWh	23.48 MWh	23.48 MWh	8.63 MWh	8.63 MWh

Table 7: Capacity factors of the most different solutions

	Winter, solution 1				Summer, solution 7				Mid-season, solution 5			
	MILP		Heuristic		MILP		Heuristic		MILP		Heuristic	
Technology	Factor	Capacity	Factor	Capacity	Factor	Capacity	Factor	Capacity	Factor	Capacity	Factor	Capacity
CHP (heat)	82.0 %	–	82.3 %	–	29.6 %	–	29.7 %	–	52.2 %	–	52.4 %	–
GB	36.2 %	1395 kW	36.1 %	1406 kW	1.6 %	100 kW	1.5 %	100 kW	22.4 %	486 kW	22.3 %	486 kW
EB	1.6 %	100 kW	1.5 %	100 kW	0.0 %	100 kW	0.0 %	100 kW	0.8 %	100 kW	0.8 %	100 kW
CHP (elec)	74.6 %	552 kW	75.0 %	547 kW	21.3 %	100 kW	21.3 %	100 kW	47.6 %	295 kW	47.6 %	295 kW
ST	67.9 %	4756 m^2	67.9 %	4756 m^2	–	0 m^2	–	0 m^2	–	0 m^2	–	0 m^2
PV	100.0 %	5244 m^2	100.0 %	5244 m^2	63.6 %	10 000 m^2	63.6 %	10 000 m^2	58.8 %	10 000 m^2	58.8 %	10 000 m^2

the technologies produce almost the same energy at different time steps over the time period. However, the difference is acceptable in the objective of optimal design taking into account the operation (control aspects being out of the scope of this work).

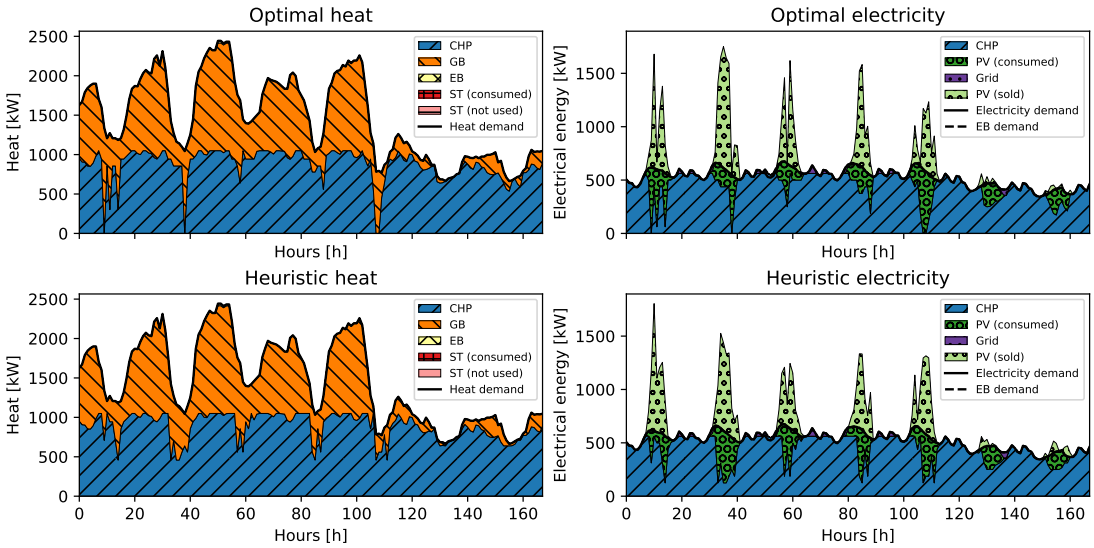

Figure 3: Operation for a MILP and heuristic solution (winter week, solution 8)

Finally, the model was solved with the heuristic algorithm for the full time period of one year, and a MILP solver was used to try to solve the same model for the entire year. The solver was stopped when its optimality gap reached 0.1 %, as it is not possible to obtain an optimal solution in a reasonable time.

The heuristic algorithm took 549.9 s to find results for the 10 solutions of the Pareto front. The MILP solver took 5.6×10^5 s, or 156.7 h to find the 10 solutions. That represents an improvement of 99.9 %. The average relative differences for the 10 solutions of the Pareto front are 1.1 % and -1.7 % for *ATCR* and τ_{RES}, respectively, with the heuristic giving better solutions than the MILP solver for *ATCR*. However the MILP solver was stopped before obtaining an optimal solution.

5. Conclusion and perspectives

This paper presented the modeling of an MES as a non-linear mathematical programming model. A piece-wise linearization method was used to linearize the model and obtain a MILP model. However, it has been shown that the computation time can be intractable for optimizing the MILP model over a long time period of one year. Consequently, a heuristic algorithm was proposed to solve the MILP model. The proposed algorithm finds an

initial solution through a relaxed MILP model, then uses a local search to iteratively improve the initial solution by finding which piece of the linearization to select.

A comparison of the resolution of small time periods of one week of the model through a MILP solver and through the heuristic algorithm showed that the heuristic is capable of finding solutions close to the optimum. It has also been shown that different operations of the MES can be optimal with regard to the mathematical program. Even when the solution found by the heuristic is not optimal, the capacity factors of the different technologies are close to the optimum values. The heuristic algorithm was shown to be faster than the resolution using a MILP solver, with an improvement of more than 99.9 % when solving a long time period of a year.

Although the proposed heuristic algorithm is very fast on the MES model presented in this article, further experimentation on other linearized models is still needed to determine if this method is generalizable for solving other problems. Additional work is also needed to evaluate the robustness of the initialization method and the local search, as relaxation of the MILP model could theoretically lead to infeasible solutions. Further experiments should also be conducted to compare the solutions of the heuristic algorithm and the MILP resolution over the full year, to assess whether the heuristic is still efficient when solving long time periods.

References

[1] Geidl M. et al. *Energy hubs for the future*. In: "IEEE Power and Energy Magazine" 5.1 (Jan. 2007), pp. 24–30. DOI: 10.1109/mpae.2007.264850.

[2] Fabrizio E., Filippi M., and Virgone J. *Trade-off between environmental and economic objectives in the optimization of multi-energy systems*. In: "Building Simulation" 2.1 (Mar. 2009), pp. 29–40. DOI: 10.1007/s12273-009-9202-4.

[3] Frangopoulos C. A., Spakovsky M. R. von, and Sciubba E. *A Brief Review of Methods for the Design and Synthesis Optimization of Energy Systems*. In: "International Journal of Applied Thermodynamics" 5.4 (Dec. 2002), pp. 151–160. ISSN: 1301-9724. DOI: 10.5541/ijot.97.

[4] Wirtz M. et al. *Design optimization of multi-energy systems using mixed-integer linear programming: Which model complexity and level of detail is sufficient?* In: "Energy Conversion and Management" 240 (July 2021), p. 114249. ISSN: 0196-8904. DOI: 10.1016/j.enconman.2021.114249.

[5] Poncelet K. et al. *Impact of the level of temporal and operational detail in energy-system planning models*. In: "Applied Energy" 162 (Jan. 2016), pp. 631–643. DOI: 10.1016/j.apenergy.2015.10.100.

[6] Klemm C. and Vennemann P. *Modeling and optimization of multi-energy systems in mixed-use districts: A review of existing methods and approaches*. In: "Renewable and Sustainable Energy Reviews" 135 (Jan. 2021), p. 110206. ISSN: 1364-0321. DOI: 10.1016/j.rser.2020.110206.

[7] Wu M. et al. *An integrated energy system optimization strategy based on particle swarm optimization algorithm*. In: "Energy Reports" 8 (Nov. 2022), pp. 679–691. DOI: 10.1016/j.egyr.2022.10.034.

[8] Kotzur L. et al. *A modeler's guide to handle complexity in energy systems optimization*. In: "Advances in Applied Energy" 4 (Nov. 2021), p. 100063. DOI: 10.1016/j.adapen.2021.100063.

[9] Fazlollahi S. et al. *Methods for multi-objective investment and operating optimization of complex energy systems*. In: "Energy" 45.1 (Sept. 2012), pp. 12–22. DOI: 10.1016/j.energy.2012.02.046.

[10] Salpakari J., Mikkola J., and Lund P. D. *Improved flexibility with large-scale variable renewable power in cities through optimal demand side management and power-to-heat conversion*. In: "Energy Conversion and Management" 126 (Oct. 2016), pp. 649–661. DOI: 10.1016/j.enconman.2016.08.041.

[11] Milan C. et al. *Modeling of non-linear CHP efficiency curves in distributed energy systems*. In: "Applied Energy" 148 (June 2015), pp. 334–347. DOI: 10.1016/j.apenergy.2015.03.053.

[12] Yousefi H., Ghodusinejad M. H., and Noorollahi Y. *GA/AHP-based optimal design of a hybrid CCHP system considering economy, energy and emission*. In: "Energy and Buildings" 138 (Mar. 2017), pp. 309–317. DOI: 10.1016/j.enbuild.2016.12.048.

[13] D'Ambrosio C., Lodi A., and Martello S. *Piecewise linear approximation of functions of two variables in MILP models*. In: "Operations Research Letters" 38.1 (Jan. 2010), pp. 39–46. DOI: 10.1016/j.orl.2009.09.005.

[14] Conforti M., Cornuéjols G., and Zambelli G. *Integer Programming*. Springer International Publishing, 2014. DOI: 10.1007/978-3-319-11008-0.

[15] Haimes Y. Y., Lasdon L. S., and Wismer D. A. *On a Bicriterion Formulation of the Problems of Integrated System Identification and System Optimization*. In: "IEEE Transactions on Systems, Man, and Cybernetics" SMC-1.3 (July 1971), pp. 296–297. DOI: 10.1109/tsmc.1971.4308298.

[16] Lin S. *Heuristic Programming as an Aid to Network Design*. In: "Networks" 5.1 (Jan. 1975), pp. 33–43. DOI: 10.1002/net.1975.5.1.33.

PROCEEDINGS OF ECOS 2023 - THE 36TH INTERNATIONAL CONFERENCE ON
EFFICIENCY, **C**OST, **O**PTIMIZATION, **S**IMULATION AND ENVIRONMENTAL IMPACT OF ENERGY SYSTEMS
25-30 JUNE 2023, LAS PALMAS DE GRAN CANARIA, SPAIN

Highly efficient heat integration of a power-to-liquid process using MILP

David Huber[a], Kathrin Werdinig[a], Felix Birkelbach[a] and René Hofmann[a]

[a] Institute of Energy Systems and Thermodynamics, TU Wien, Getreidemarkt 9/BA, Wien, 1060, Austria
david.huber@tuwien.ac.at

Abstract:
Synthetic fuels are needed to decarbonize the non-electrifiable parts of the transportation sector, such as shipping and aviation. The synthesis of fuels using power-to-liquid (PtL) processes has already been investigated and tested. However, economic implementation has failed to gain traction due to high plant and product costs and insufficient PtL-efficiencies. In this paper, we will use heat exchanger network synthesis (HENS) to optimize the heat integration of a novel 1 MW PtL-process. A unique feature of this case study is that the internal heat is supplied by oxidizing a Fischer-Tropsch tail gas within a combustion system (CS). The inlet and outlet temperatures of the exhaust gas flow of the three serially connected CS can be adjusted by the mass flow of excess air and the tail gas. Using HENS implies specifying inlet and outlet temperatures. We apply an adaptation of the HENS that allows for variable stream temperatures and flow capacities. This allows the CS, an internal hot utility, to be optimally tailored to the specific process. Linearization of the non-linear relations, such as stream- and stage-wise energy balance, is done with simplices. The linear approximation is transferred to MILP using highly efficient logarithmic coding. We show that implementing the CS in HENS significantly improves the total annual costs and PtL-efficiency. With the developed method, the design engineering of highly efficient PtL-processes can be successfully supported and the technology can be brought closer to an economically viable market maturity.

Keywords:
synthetic fuels, power-to-liquid, heat exchanger network synthesis, mixed-integer linear programming.

1. Introduction

In 2019, about 16.6 % of the global CO_2 emissions were caused by the transport sector. About three quarters of that are caused by road traffic [1]. The electrification of road traffic will lead to long-term emission reduction. However, replacing vehicles before they reach their lifetime will lead to higher emissions in the medium term. Climate-neutral transportation, using emission-free synthetic fuels (also known as eFuels), offers the possibility to continue using existing vehicles. Furthermore, due to the high energy density of liquid fuels, shipping and aviation will presumably continue to rely on them in the long term.

Despite a technology readiness level (TRL) greater than 7, large-scale industrial production of eFuels has yet not taken off [2]. The first commercial integrated PtL-plant Haru Oni was built by the lead developing company HIF and its partner network in Punta Arenas, Chile. In December 2022, the first tank was filled with eFuel, which was produced with one 3.4 MW wind turbine in the pilot phase. From March 2023, the goal is to produce 130 000 L liters of synthetic fuel per year.

A key inhibitor of this technology are the costs. A significant share of the costs arises from the energy required to heat and cool process streams. Efficient heat integration is a crucial element for cost-effectiveness. With heat exchanger network synthesis (HENS), cost-optimal heat integration can be realized using mathematical programming. Using the non-linear superstructure formulation from Yee & Grossmann [3], all stream and utility temperatures and flow capacities must be defined a priori. Furthermore, the utility heat transfer is only possible in one stage and without stream splits. Huber et al. [4] presented an extension of the superstructure formulation from Yee & Grossmann, which allows the implementation of utilities as streams with variable temperatures and flow capacities. It has been shown that significant cost savings result from variable temperatures and multi-stage heat exchanges with stream splits of utilities [4]. Utilizing only the sensible heat of a fluid such as thermal oil, water or flue gas, allow flexibility in selecting temperatures. As long as technical limitations are considered, both the outlet and inlet temperatures can be varied within a certain range. When designing new plants, integrating the design of the utilities into the HENS formulation offers significant advantages in terms of efficiency and total annual costs (TAC).

In this paper, we adapt the method presented by Huber et al. [4] to simultaneously optimize the internal heat supply and the heat exchanger network (HEN). As a use case, the design of a novel 1 MW PtL-plant is opti-

mized. The PtL-plant combines solid co-electrolysis (co-SOEC) with efficient CO_2 processing and a Fischer-Tropsch (FT) reactor. The internal heat supply is provided by three combustion systems (CS) where a process tail gas from the FT-reactor is oxidized. The hot exhaust gas streams from the CS are used as an internal hot utility. In this paper, we compare the design case with the results applying classical HENS. We additionally demonstrate that previously untapped potential for optimization can be activated by optimizing the CS stream temperatures and heat capacity flows. The results show that the TAC can be reduced, and the efficiency can be increased simultaneously. Thus, production costs of synthetic fuels can be lowered, and large-scale industrial deployment can be strengthened.

2. Methods

2.1. HENS superstructure formulation

The objective of the optimization is to minimize the total annual costs (TAC) of the heat exchanger network according to Equation (1).

$$\begin{aligned}\min TAC = {} & \underbrace{\sum_i c_{\mathrm{uc}}\, q_{\mathrm{uc},i}}_{\text{cold utility costs}} + \underbrace{\sum_j c_{\mathrm{uh}}\, q_{\mathrm{uh},j}}_{\text{hot utility costs}} \\ & + \underbrace{\sum_i \sum_j \sum_k c_{\mathrm{f}}\, z_{ijk} + \sum_i c_{\mathrm{f}}\, z_{\mathrm{uc},i} + \sum_j c_{\mathrm{f}}\, z_{\mathrm{uh},j}}_{\text{step-fixed investment costs}} \\ & + \underbrace{\sum_i \sum_j \sum_k c_{\mathrm{v}} \left(\frac{q_{ijk}}{U_{ij}\, LMTD_{ijk}} \right)^{\beta}}_{\text{variable HEX stream costs}} + \underbrace{\sum_i c_{\mathrm{v}} \left(\frac{q_{\mathrm{uc},i}}{U_{\mathrm{uc},i}\, LMTD_{\mathrm{uc},i}} \right)^{\beta}}_{\text{variable HEX cold utility costs}} + \underbrace{\sum_j c_{\mathrm{v}} \left(\frac{q_{\mathrm{uh},j}}{U_{\mathrm{uh},j}\, LMTD_{\mathrm{uh},j}} \right)^{\beta}}_{\text{variable HEX hot utility costs}}\end{aligned} \tag{1}$$

The mathematical formulation of the optimization problem is based on the superstructure formulation of Yee & Grossmann [3]. Huber et al. [4] extended this HENS formulation to implement utilities as streams with variable temperatures and flow capacities. Consequently, the utility heat exchange is possible in multiple stages with stream splits. In this context, utilities implemented as multi-stage streams are referred to as utility streams. Different sets of constraints were added to the Yee & Grossmann formulation, which are activated depending on the utility stream definition. This ensures that no utilities can be placed at the stream ends. Further constraints have been added to limit the heat capacity flows, inlet and outlet temperature to pre-defined ranges. The modifications to the superstructure formulation as well as all necessary constraints can be found in [4].

2.2. Piecewise-linear approximation

To apply fast MILP solvers and to prevent the solver from getting stuck in local optima, all non-linear terms such as reduced HEX areas for streams and utilities, LMTD and energy balances are piecewise-linear approximated and transferred to MILP. To increase the accuracy of the linearization and to decrease the number of binaries, the functions of the reduced HEX areas are trimmed to the feasible domain according to Beck et al. [5]. The three-dimensional function of the stream‘s reduced HEX area is piecewise-linear approximated with superpositioned planes, see Figure 3 (left) in Appendix A. The two-dimensional function of the reduced utility HEX area is approximated piecewise-linear with straight lines and transferred to MILP with an SOS2 approach, see Figure 3 (right) in Appendix A. The piecewise-linear approximation of the three-dimensional function for the LMTD, stage- and stream-wise energy balances is done with plane triangles, see Figure 4 in Appendix A. The plane equations are transferred to MILP with a highly efficient logarithmic coding according to Vielma & Nemhauser [6]. In all piecewise linear approximations, lines, planes, or triangles are added until a root-mean-square error (RMSE) of less than 1 % is reached.

2.3. PtL-efficiency

The performance of the PtL-process is evaluated from an economic point of view by TAC and from a technical point of view with the PTL-efficiency. The PtL-efficiency η_{PtL} is calculated with the ratio of the electrical energy input to the sum of the lower heating values, see Equation (2).

Since the output of synthetic fuels is independent of the heat integration, the PtL-efficiency is only affected by the additional required electrical energy. Depending on the heat integration, P_{base} is increased by the electrical energy demand for hot P_{uh} and cold utilities P_{uc}. For the cooling of hot streams, energy is dissipated to the environment, while the energy for hot utilities is provided by an electric steam generator. For both processes, it is assumed that an additional 5 % of electric energy must be supplied to operate the circulation pumps and

to cover losses. With these assumptions, the PtL-efficiency is calculated according to Equation (2).

$$\eta_{\mathrm{PtL}} = \frac{\sum LHV}{P_{\mathrm{base}} + P_{\mathrm{uh}} + P_{\mathrm{uc}}} = \frac{\sum LHV}{P_{\mathrm{base}} + 1.05 \cdot \sum q_{\mathrm{uh}} + 0.05 \cdot \sum q_{\mathrm{uc}}} \tag{2}$$

3. PtL-process

Within the research project *IFE* (Innovation Flüssige Energie, engl.: innovation liquid energy), a two-stage PtL-process with a H_2O + CO_2 high-temperature solid oxide co-electrolysis (co-SOEC) and Fischer-Tropsch (FT) synthesis is being fully conceptualized and basically engineered. The plant, powered by renewable electricity, has a total electric load of approximately 1 MW. A schematic diagram of the six major components is shown in Figure 1. In the stationary process, an industrial offgas from a cement production plant containing about 15 wt% CO_2 and N is conditioned and reformed together with steam in the co-SOEC to a gas of H_2 and CO. In the downstream FT-reactor, a syngas is reformed. The subsequent strippers separate the syngas into the components, naphtha, diesel and FT-wax. Annually, about 160 000 L of naphtha, 100 000 L of diesel and 360 000 L of Fischer-Tropsch wax are produced climate-neutrally. The sum of the lower heating values $\sum LHV$ is 650.31 kW. The electrical energy requirement of the system without utilities P_{base} is 1135.90 kW. A significant part of this, viz. 992.32 kW, is used by the co-SOEC. 143.59 kW are required for compressors, pumps and to cover losses.

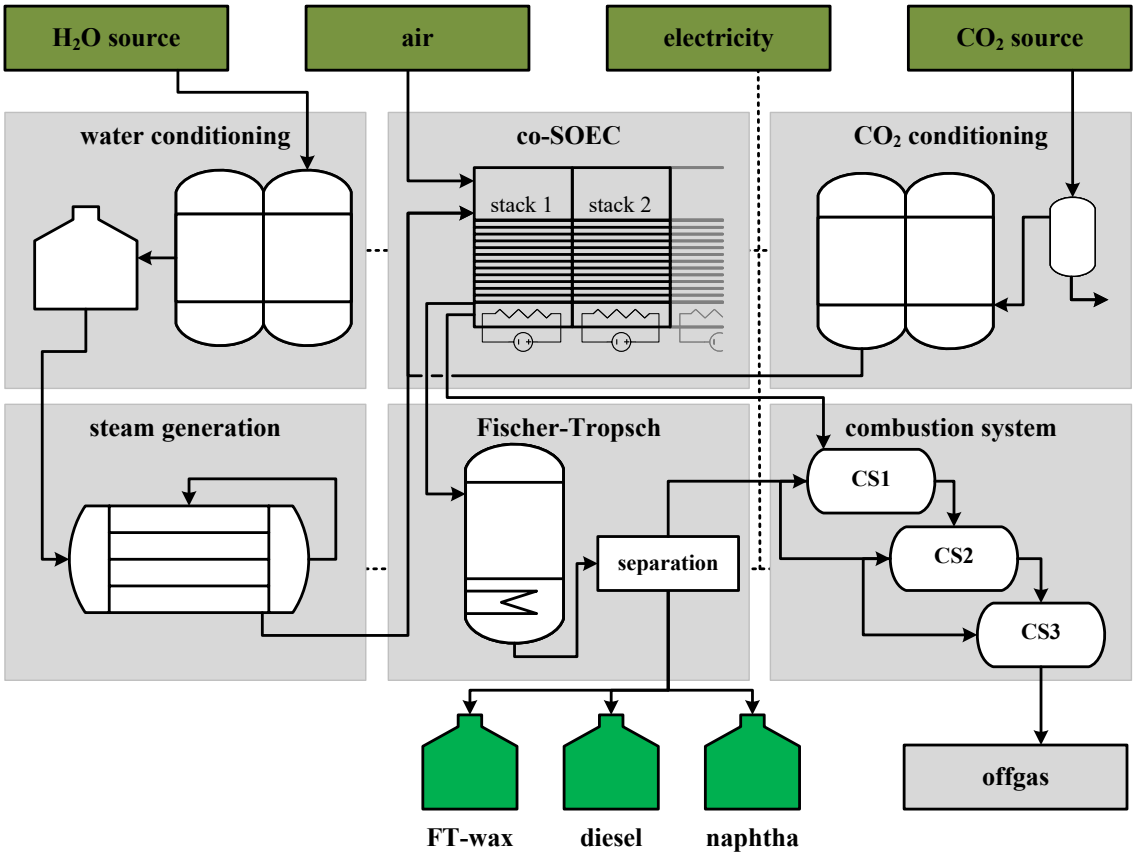

Figure 1: Schematic representation of the 1 MW PtL-process with the main components: water conditioning, CO_2 conditioning, steam generation, co-SOEC, Fischer-Tropsch reactor and combustion systems.

As a starting point for basic engineering, the entire PtL-process was modeled and simulated using Aspen HYSYS. The crucial process streams for heat integration can be reduced to 15 hot and 7 cold process streams. The stream data can be found in Table 1. The necessary energy for heating the cold process streams is provided by oxidizing a tail gas from the FT-reactor. The tail gas cannot be further circulated and must otherwise be flared. Together with the exhaust air from the co-SOEC, the tail gas is oxidized in three combustion systems (CS). The exhaust air of the co-SOEC has a temperature of almost 900 °C. Due to the high amount of sensible heat, the entire exhaust air is used for oxidation. The three CS are connected in series, with new tail gas being added at each stage. Regarding HENS, the CS's exhaust gas streams CS1 to CS3 are used as hot utilities to provide heating energy. The inlet temperatures of the CS streams of 848.90 °C, 893.16 °C and 492.60 °C result from the empirical definition of the fuel quantity at each stage. Additionally, a high-temperature electric steam generator serves as a hot utility. The energy needed to cool the hot process streams is provided by

Table 1: Stream and cost data for the PtL-process

stream	T^{in} / °C	T^{out} / °C	F / kW/K	h / kW/(m^2 K)
H1	40.00	35.00	2.1558	1.0
H2	131.09	35.00	0.1174	1.0
H3	174.05	35.00	0.1190	1.0
H4	209.98	190.00	0.2801	1.0
H5	190.00	120.00	0.5767	1.0
H6	120.00	30.00	0.4978	1.0
H7	56.96	31.00	2.9471	1.0
H8	139.86	138.86	188.7246	1.0
H9	825.45	35.00	0.1297	1.0
H10	50.72	35.00	0.8830	1.0
H11	101.80	30.00	0.6404	1.0
H12	190.00	189.00	153.7523	1.0
CS1	848.90	786.71	0.4203	1.0
CS2	893.16	278.50	0.4122	1.0
CS3	492.60	132.88	0.4025	1.0
CS1^v	900.00	[890.00, 150.00]	[0.0349, 2.6138]	1.0
CS2^v	900.00	[890.00, 150.00]	[0.3377, 25.3284]	1.0
CS3^v	900.00	[890.00, 150.00]	[0.1930, 14.4781]	1.0
C1	319.18	824.96	0.1816	1.0
C2	116.90	124.40	25.1158	1.0
C3	58.79	825.00	0.3306	1.0
C4	138.86	139.86	285.2732	1.0
C5	138.86	426.62	0.1039	1.0
C6	35.00	145.42	0.0566	1.0
C7	20.27	189.47	0.2110	1.0
uh	600.00	598.00	-	1.0
uc	15.00	20.00	-	1.0

HEX costs: c_f = 1013 €/y, c_v = 62 €/(m$^{2\beta}$ y), β = 0.8
utility costs: c_{uh} = 200 €/(kW y), c_{uc} = 10 €/(kW y)
min. approach temperature: ΔT_{min} = 1 °C

cooling water. The cost parameters for utilities and HEX are shown at the bottom of Table 1. Parameterization of the degressive HEX cost function was performed using cost information from the DACE Price Booklet [7] and multiple feedback rounds with the project partners.

3.1. Case study

With this paper, we show that HENS is a highly efficient tool for determining cost-optimal heat integration. Applied to the actual design problem of a novel PtL-plant, basic engineering can be actively supported and the potential of HENS can be quantified. Implementing the CS's exhaust gas stream as utilities with variable outlet temperatures and heat capacity flows, the utility design problem can be optimized holistically using mathematical optimization. The following cases are investigated to quantify the method's potential in terms of cost reduction and efficiency increase.

base This case represents the plant design from basic engineering. The HEN and the temperatures of the CS streams were determined empirically. This case serves as a reference to evaluate the achievable improvements.

baseHENS Only the HEN configuration is optimized. The stream temperatures resulting from the process simulation remain unchanged. With these assumptions, we demonstrate the potential of classical HENS and provide a cost-optimal heat integration.

advancedHENS Both the HEN and the CS are optimized. The outlet temperatures and the flow capacities of the CS streams are included as variables in the optimization problem. In Table 1, the CS streams are shown with the allowed ranges for temperature and flow. The inlet temperatures of the streams CS1^v to CS3^v are set to the material-specific limit of 900 °C. The outlet temperature can range from 150 °C to 890 °C. The permissible range of the flow capacity F was determined to ensure that no energy balances were violated.

4. Results

The optimization problem in this paper was modeled in MATLAB R2022a [8] using Yalmip R20210331 [9]. Gurobi 9.5.2 [10] was used as the MILP solver on a 128-core system (AMD EPYC 7702P) with 256 GB RAM. As a termination criterion, a relative gap of less than 0.01 % was set. The relative gap is defined as the gap between the best feasible solution objective and the best bound.

4.1. Optimization

The results of the case study are summarized in Table 2. The corresponding stream plots are shown in Appendix B. Remarkably, no hot utility is needed in all three cases.

Table 2: Comparison of costs, PtL-efficiency, heat loads and HEX area.

case	TAC / €/y	η_{PtL} / %	q_{UC} / kW	q_{UH} / kW	A_{HEX} / m^2
base	29 394.70	56.04	244.60	0	60.15
baseHENS	27 213.00	56.04	244.30	0	55.68
advancedHENS	23 576.13	56.16	219.78	0	49.35

The base case with TAC of 29 394.70 €/y and a PtL-efficiency of 56.04 % is the most expensive case. With identical PtL-efficiency, the TAC for the baseHENS case are 27 213.00 €/y. Using HENS, a reduction of the TAC by 8.01 % can already be achieved. In both cases, the capacity of the cold utilities are almost identical at 244.60 kW and 244.30 kW, respectively. The base case requires 21 HEX and the baseHENS case requires 22 HEX. Despite the larger number of HEX in the baseHENS case, less HEX area is required, 60.15 m^2 compared to 55.68 m^2. It can be concluded that the savings from a smaller HEX area outweigh the increased fixed costs due to one additional stream match. Counter-intuitively, a HEN with more HEX can still lead to lower TAC.

The advancedHENS case is based on different stream data. As shown in Figure 7, the solution of the optimization problem results in outlet temperatures of 877.4 °C, 878.3 °C and 887.5 °C at the streams CS1^v to CS3^v, respectively. The high temperatures close to the inlet temperature of 900 °C ensure a large LMTD at the HEX. A large LMTD reduces the HEX area required for the same amount of heat to be transferred. Compared to the base case, the HEX area is reduced from 60.15 m^2 to 49.35 m^2. Also, instead of 21 or 22 HEX, only 19 HEX are required. The smaller HEX area and number of HEX are the main reasons for the significant cost savings. With TAC of 23 576.13 €/y, 24.68 % of the costs can be saved compared to the base case. Approx. 4.27 % of the cost savings, i.e. 248.20 €/y, result from the lower cold utility load. 95.73 % of the cost savings, i.e. 5570.37 €/y, results from the fewer HEX and the decreased HEX area.

4.2. Composite curves & PtL-efficiency

According to Equation (2), the highest possible PtL-efficiency would be 57.25 % if no utilities are required. Evaluation of the composite curves (CC) at different minimum temperature differences shows that the theoretically achievable PtL-efficiency can not be achieved and must be lowered. Figure 2 on the left shows the CC of the process for a fictive minimum temperature difference of 0 K. It should be noted that the cases base, respectively baseHENS (solid lines) and advancedHENS (dashed line), show different composite and PtL-efficiency curves due to the different stream data. The results show that in the advancedHENS case, considerably more heat is transferred in the upper-temperature range due to the higher temperatures of the CS streams. The higher temperature difference between the streams generally results in higher LMTD at the HEX. Therefore, less HEX area is needed and costs can be saved.

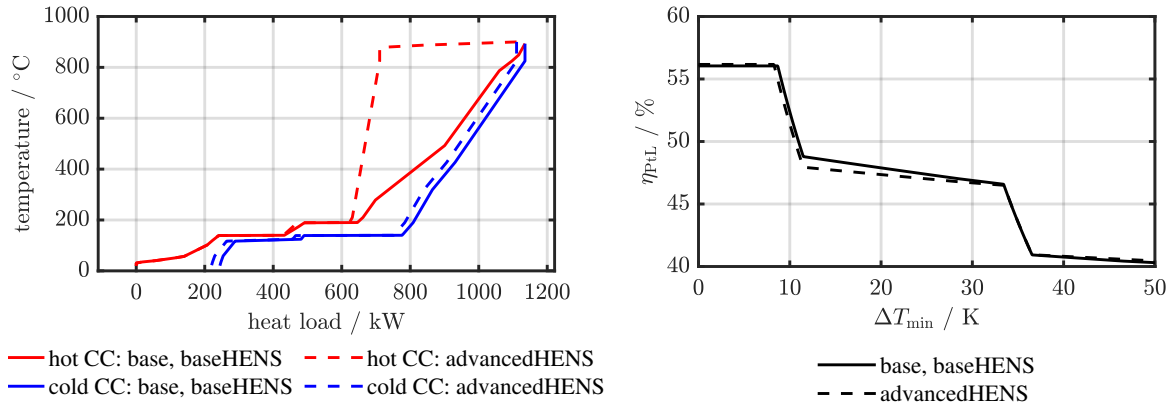

Figure 2: Left: Composite curve at a minimum temperature difference of ΔT_{min} = 0 K. Right: Maximum achievable efficiency as a function of the minimum temperature difference.

Figure 2 on the right shows the maximum achievable efficiency as a function of the minimum temperature difference. Up to a minimum temperature difference of 9 K, the pinch point is located at the upper right end of the CC. Consequently, no hot utilities are needed for the threshold problem. Up to ΔT_{min} of less than 9 K, a maximum efficiency of 56.04 % can be achieved for the base and baseHENS case. Due to optimized temperatures and flow capacities of the CS streams, the maximum achievable efficiency for the advancedHENS case can be increased to 56.16 %. Additional hot utilities are needed for ΔT_{min} higher than 9 K and the efficiency drops below 50.00 % for all cases. In all cases of the case study, the theoretical upper limit of the PtL-efficiency is reached.

5. Conclusion

Synthetic fuels are necessary to decarbonize the non-electrifiable transport sectors such as aviation and shipping. They also serve as a transitional solution for existing vehicles. High fuel production costs inhibit large-scale synthetic fuel production because of high total annual costs (TAC) and low PtL-efficiency. In this paper, we used an adapted HENS formulation and implemented the combustion systems (CS) of a novel 1 MW PtL-plant as internal hot utilities in the heat exchanger network design problem. The outlet temperatures and flow capacities of the internal hot utilities are implemented as optimization variables, unlike conventional HENS, and optimized simultaneously with the HEN. By coupling the optimization, a holistic examination is made possible, which opens up new potential for cost reduction and efficiency increase.

In the base case, the design case from the process simulation with Aspen HYSYS, as well as the baseHENS case, a PtL-efficiency of 56.04 % could be achieved. Using HENS in the baseHENS case, it was possible to find a HEN that is 8.01 % less expensive with TAC of 27 213.00 €/y. In the advancedHENS case, the inlet temperature of the CS streams has been set to the upper technical limit of 900 °C. The outlet temperatures resulting from the optimization problem are above 850 °C, compared to the base and baseHENS case. The high temperatures and the small temperature differences between the feed and return ensure a large LMTD at the heat exchangers. This allows smaller and also less expensive HEX to be used. TAC can be reduced by 24.68 % to 23 576.13 €/y. It can be concluded that the temperature of hot utilities should always be set as high as possible as long as the utility costs are not affected. Optimizing the temperature and flow capacity of the CS streams, allows the CS streams' heat flow to be reduced. The resulting shift in composite curves subsequently reduces the need for cold utilities. Therefore, the PtL-efficiency can be increased to 56.16 % and cold utility costs can be lowered.

In this paper, we showed that for given stream parameters, TAC can be significantly reduced using classical HENS. A key finding is that the coupled optimization of stream parameters and HEN lead to significant cost reductions and efficiency improvements simultaneously. From the results, it can be concluded that the main cost reduction stems from the higher temperatures of the hot utilities and the simultaneously optimized lower-cost HEN. With this paper, we show that the coupled optimization of utility parameters and HEN enables the activation of previously untapped potential for optimization. Applied to the use case of a PtL-plant, we can accelerate the economically viable production of synthetic fuels. Therefore, decarbonization of the transport sector can be achieved more quickly and emissions can be reduced in the long term.

Acknowledgments

The work this paper is based on was funded by the Austrian research promotion agency (FFG) under grant number 884340.

Appendix A Piecewise-linear approximation

Figure 3 (left) shows the piecewise linear approximated reduced heat exchanger area for a stream HEX with the following stream data:

- Hot stream: $T^{\text{in}} = 270\,^{\circ}\text{C}$, $T^{\text{out}} = 160\,^{\circ}\text{C}$, $F = 18\,\text{kW/K}$, $h = 1\,\text{kW}/(\text{m}^2\,\text{K})$
- Cold stream: $T^{\text{in}} = 50\,^{\circ}\text{C}$, $T^{\text{out}} = 210\,^{\circ}\text{C}$, $F = 20\,\text{kW/K}$, $h = 1\,\text{kW}/(\text{m}^2\,\text{K})$
- $\beta = 0.8$

Figure 3 (right) shows the piecewise linear approximated reduced heat exchanger area for a utility HEX with the following stream data:

- Hot stream: $T^{\text{in}} = 270\,^{\circ}\text{C}$, $T^{\text{out}} = 160\,^{\circ}\text{C}$, $F = 18\,\text{kW/K}$, $h = 1\,\text{kW}/(\text{m}^2\,\text{K})$
- Cold utility: $T^{\text{in}} = 10\,^{\circ}\text{C}$, $T^{\text{out}} = 30\,^{\circ}\text{C}$, $h = 1\,\text{kW}/(\text{m}^2\,\text{K})$
- $\beta = 0.8$

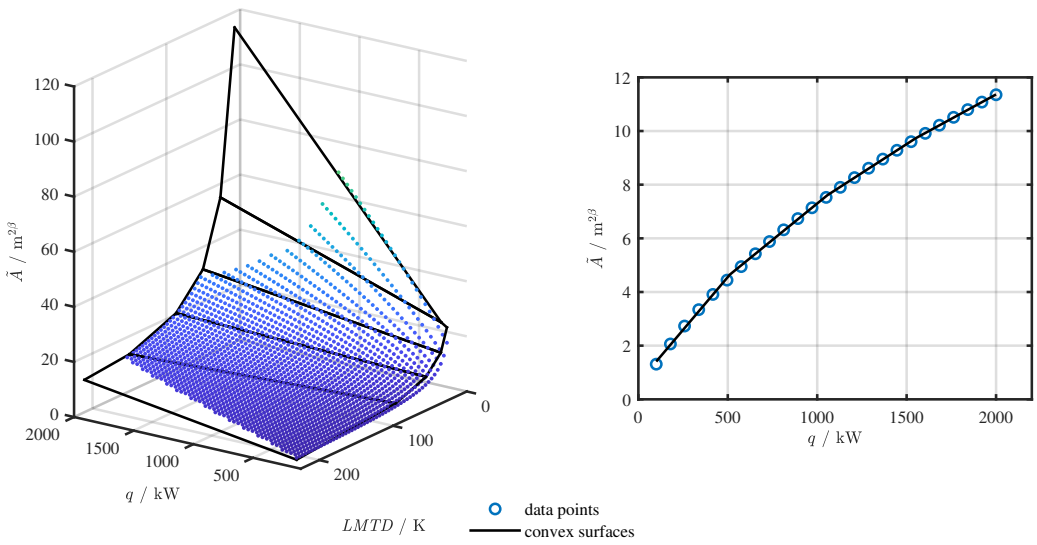

Figure 3: Piecewise linear approximation of the reduced stream HEX area $\tilde{A}$ as a function of the heat flow q and $LMTD$ with five hyperplanes ($RMSE$ = 1.26 %). Right: Piecewise linear approximation of the reduced utility HEX area $\bar{A}$ as a function of the heat flow q with four lines ($RMSE$ = 0.38 %).

Figure 4 (left) shows the piecewise linear approximated function of the $LMTD$ within a temperature range of 10 K to 200 K. Figure 4 (right) shows the piecewise linear approximated function of the stream-wise energy balance within the following stream data:

- Hot stream: T^{in} = 270 °C, T^{out} = [50, 160] °C, F = [2, 20] kW/K.

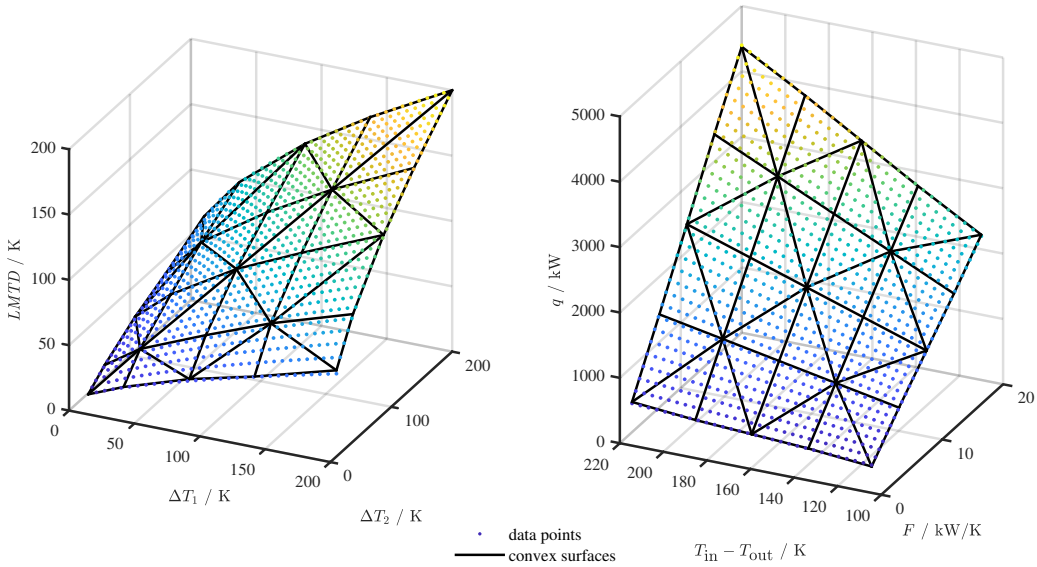

Figure 4: Left: Piecewise linear approximation of the $LMTD$ as a function of the two temperature differences ΔT_1 and ΔT_2 ($RMSE$ = 0.34 %). Right: Piecewise linear approximation of the stream-wise energy balance as a function of the flow capacity F and the temperature difference $T_{\text{in}} - T_{\text{out}}$ with 32 simplices ($RMSE$ = 0.28 %).

Appendix B Stream plots

Figure 5 to 7 shows the stream plots. Red arrows represent hot process streams that need to be cooled down. Blue arrows represent cold process streams that need to be heated. Utilities are characterized by dark gray circles at the stream ends. Light gray circles and black lines represent connected heat exchangers between hot and cold streams.

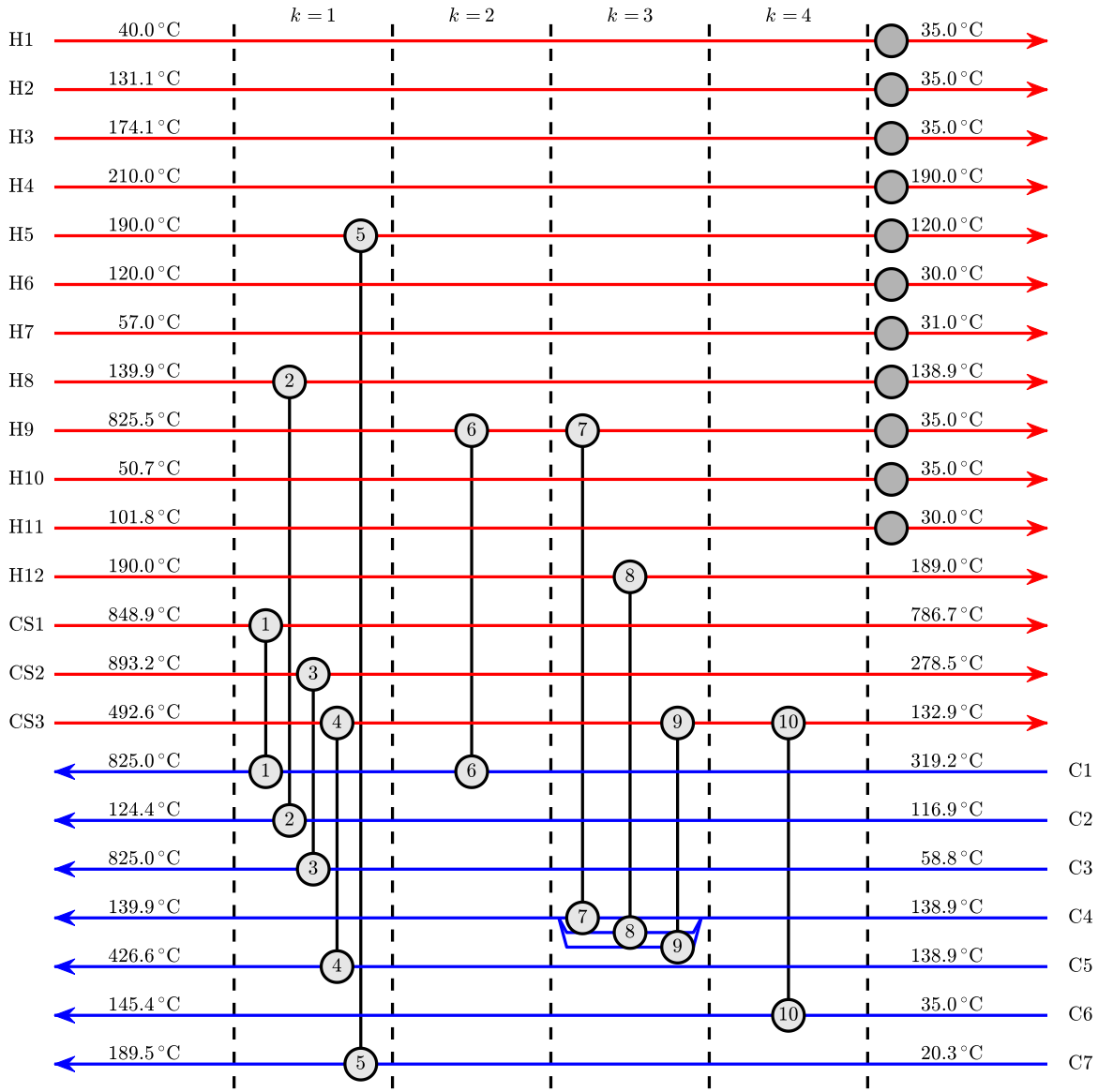

Figure 5: Stream plot of the case *base*. *TAC* = 29 394.70 €/y. η_{PtL} = 56.04 %.

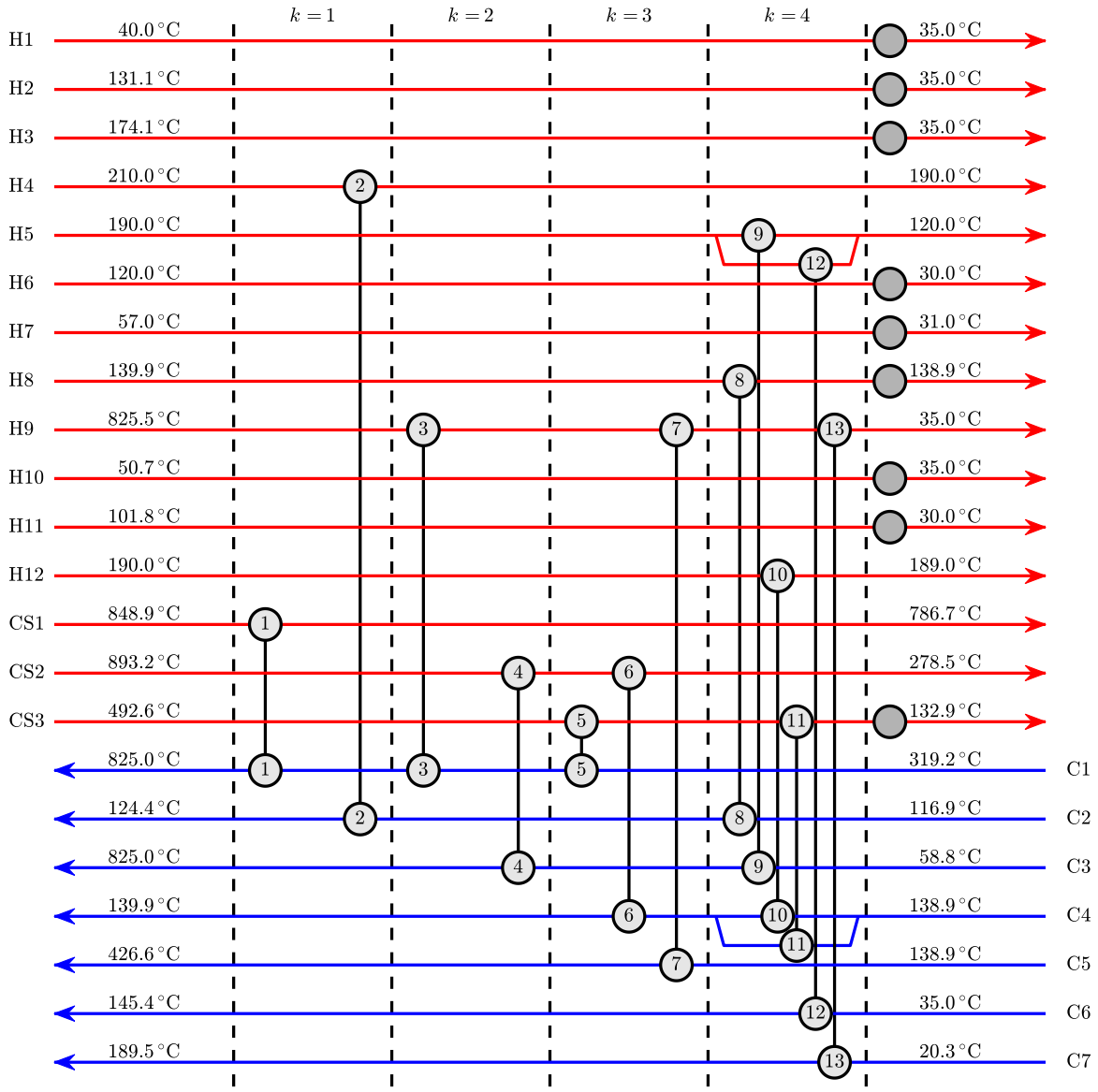

Figure 6: Stream plot of the case *baseHENS*. *TAC* = 27 213.00 €/y. η_{PtL} = 56.04 %.

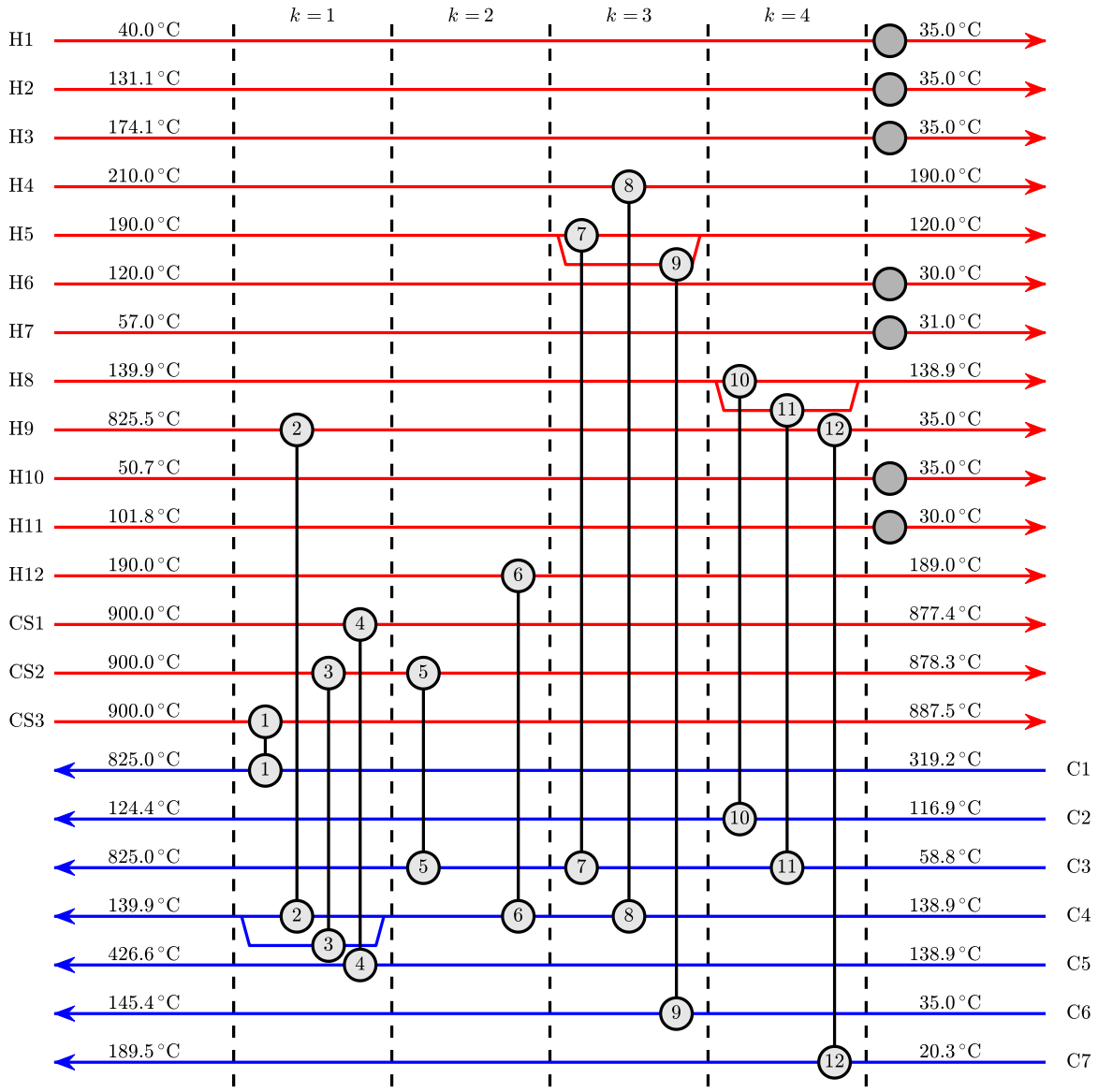

Figure 7: Stream plot of the case *advancedHENS*. *TAC* = 23 576.13 €/y. η_{PtL} = 56.16 %.

Nomenclature

Letter symbols

$\tilde{A}$	reduced HEX area, m^2
F	flow capacity, kW/K
h	heat transfer coefficient, kW/m^2K
k	stage, –
LMTD	logarithmic mean temperature difference, K
n	number of plane triangles, –
q	heat flow, kW
P	load, kW
RMSE	root mean square error, %
T	temperature, °C
U	heat transfer coefficient for stream matches, $kW/m^2/K$

Greek symbols

β cost exponent, $-$

ΔT temperature difference, K

η efficiency, %

Subscripts and superscripts

base electric consumption of the PtL plant without utilities

f fixed

i hot stream

j cold streams

k stage

uc cold utility

uh hot utility

v streams with variable outlet temperature and flow capacity, variable

in inlet

out outlet

References

[1] Mengpin Ge, Johannes Friedrich and Leandro Vigna. World Resources Institute: World Greenhouse Gas Emissions in 2019; 2022. [Accessed 09.02.2023]. Available from: https://www.wri.org/insights/4-charts-explain-greenhouse-gas-emissions-countries-and-sectors.

[2] Quante G, Bullerdiek N, Bube S, Neuling U, Kaltschmitt M. Renewable fuel options for aviation – A System-Wide comparison of Drop-In and non Drop-In fuel options. Fuel. 2023 Feb;333:126269.

[3] Yee TF, Grossmann IE. Simultaneous optimization models for heat integration—II. Heat exchanger network synthesis. Computers & Chemical Engineering. 1990 Oct;14(10):1165-84.

[4] Huber D, Birkelbach F, Hofmann R. HENS unchained: MILP implementation of multi-stage utilities with stream splits, variable temperatures and flow capacities. 2023. Publisher: arXiv Version Number: 1. Available from: https://arxiv.org/abs/2302.08912.

[5] Beck A, Hofmann R. A Novel Approach for Linearization of a MINLP Stage-Wise Superstructure Formulation. Computers & Chemical Engineering. 2018 Apr;112:17-26.

[6] Vielma JP, Nemhauser GL. Modeling disjunctive constraints with a logarithmic number of binary variables and constraints. Mathematical Programming. 2011 Jun;128(1):49-72.

[7] DACE price booklet: cost information for estimation and comparison. Edition 35 ed. Nijkerk: DACE Cost and Value; 2021. OCLC: 1303572720.

[8] The MathWorks Inc . MATLAB version: 9.13.0 (R2022b). Natick, Massachusetts, United States; 2022. Available from: https://www.mathworks.com.

[9] Löfberg J. A toolbox for modeling and optimization in MATLAB. Proceedings of the CACSD Conference. 2004 Oct:289.

[10] Gurobi Optimization, LLC. Gurobi Optimizer Reference Manual; 2023. Available from: https://www.gurobi.com.

Identifying the ideal process configuration for a green methanol production plant dependent on economic boundary conditions

Simon Maier[a], Yoga Pranata Rahmat[a], Ralph-Uwe Dietrich[a]

[a] German Aerospace Center (DLR), Institute of Engineering Thermodynamics, 70569 Stuttgart, Germany, simon.maier@dlr.de

Abstract:

The production of second-generation biofuels from agricultural waste products represent a sustainable option for future fuel and chemical industry. Yet, due to the local biomass availability, the identification of process designs dependent on the site-specific boundary conditions is mandatory to assess their potential contribution to a sustainable transition. While biomass-based routes have the advantage of mature technologies, the combination with renewably-generated hydrogen provides the opportunity to significantly increase the extent of carbon utilisation. Via dual fluidized bed gasification, gas cleaning, and a subsequent methanol synthesis and purification, grade AA methanol can be synthesised. With its ability of a direct CO_2-conversion at a high selectivity towards methanol, the methanol synthesis constitutes a promising option to chemically store fluctuating renewable energy. The potential of a biomass-to-liquid concept is analysed incorporating economic constraints into the process design to allow the identification of regionally adjusted process designs. The production costs of the concepts are estimated by setting up a detailed flowsheet simulation in AspenPlus®. A techno-economic evaluation methodology has been extended by an automated utility integration to identify European sweet spots. The conducted evaluation includes two different process configurations for two different biogenic feedstocks, including the integration of hydrogen produced through renewable sources. A correlation between economic boundary conditions such as the electricity and heat market, and the process design will be presented. Finally, the potential contribution of the investigated (power&)biomass-to-liquid process to a green methanol economy is discussed.

Keywords:

Techno-economic analysis, Green methanol, Second-generation biofuels, Process design

1. Introduction

The Intergovernmental Panel on Climate Change (IPCC) is once again urging the energy, transport, and agriculture sectors to take decisive action to achieve the Paris climate targets of reducing greenhouse gas emissions by 80 to 95 % by 2050 compared to 2010 [1]. To promote the use of renewable energy sources in the transport sector, the European Union has adopted the Renewable Energy Directive (RED) in 2009 [2], and its 2018 revision (RED II) [3], which require EU member states to achieve minimum shares of alternative and renewable energy sources in the transport sector (RED: 10 % by 2020, RED II: 14 % by 2030). The Fuel Quality Directive (FQD) [2] is another instrument used to monitor energy carriers in the transport sector, which aims to reduce the lifecycle greenhouse gases of fuels and defines greenhouse gas reduction targets for fuels placed on the market [2]. Fuel suppliers are obligated to report GHG emissions for the fuels they place on the market. As a result, there is an increased interest in renewable alternative fuels that can be produced from renewable power sources or waste materials derived from municipal, forestry, or agricultural wastes.

Methanol synthesis from biomass is a promising approach to meet the future demand for renewable fuels. Synthetic methanol can be produced through biomass-to-liquid (BtL) processes using a methanol synthesis and purification system, to achieve high methanol purity [4].

Renewable power-based methods are facing challenges in scaling up their technologies, particularly in water electrolysis and running a chemical production plant with varying feed sources [5, 6]. In contrast, biomass-based methods have a higher technology readiness level and require limited adaptations to use biomass as a feedstock, benefiting from the experience gained from coal gasification and large-scale fuel synthesis in coal-to-liquid plants like Sasol in South Africa [7-9]. However, there are also scalability concerns with biomass-to-liquid (BtL) processes due to the availability and transportation distance of biomass, which impacts overall greenhouse gas emissions and production costs. To overcome these challenges, BtL plant size can be kept small to medium or located near waste material sources. Alternatively, an efficient and ecologically friendly method to provide enough biomass is needed to benefit from economies of scale.

Based on the gasification and gas cleaning track described in [10] a decentralised process configuration for a biomass-to-methanol process is set up and extended by a proton exchange membrane electrolyser. For the methanol synthesis two different reactor concepts are investigated in order to analyse their performance for different boundary conditions.

In contrast to the work of Poluzzi et al. [11], two different feedstocks are investigated. Nevertheless, since the process setups are very similar to the ones modelled by Poluzzi et al. they are used as a benchmark for the conducted analyses.

Other studies looking into the biomass-to-liquid process often have Fischer-Tropsch syncrude as their product since it can easily integrated into the existing refinery structure [12, 13]. Another difference is the plant scale, since the biomass transport is a main driver for the feedstock's costs and its global warming potential, the investigated plant size is limited to 200 MW_{th} [14].

Simply evaluating pre-defined process configurations for multiple boundary conditions to find economically viable plant locations may not result in optimal designs, as there is no way to adjust the process itself. Therefore, this study aims to analyse the potential of multiple configurations under different economic boundary conditions while ensuring flexibility. This has been enabled by changed way of how TEPET accesses the AspenPlus® simulation files and to allow the modification of certain parameters through TEPET. To evaluate the process potential and its ideal configuration for achieving the lowest production costs, data was gathered on regional biomass potential, prices for straw and bark, other raw material prices, labour and transportation costs, and applicable revenues in the heat market.

2. Methodology

To evaluate the different process design a detailed flowsheet model [10] is utilized and adapted for the conducted investigation of methanol production. The process models are linked to the DLR inhouse tool TEPET [15] and its extension described in [10].

2.1. Flowsheet model

The basic flowsheet model is well described in the previous work of Maier et al. [10] which is based on the work within the EU-project COMSYN [16] and the experimental and simulative work of [17, 18]. The process schemes for the biomass-to-liquid and the power&biomass-to-liquid process can be seen in Figure 1.

The main difference is the introduction of an electrolyser into the model to provide some additional hydrogen for the methanol synthesis and to replace the air for the reformer by pure oxygen.

While the settings for the gasification and gas cleaning steps are well described by Maier et al. [10], the electrolyser, the methanol synthesis, and the purification units are described in the following chapters. The two investigated biomass types, bark and straw, differ the most in the assumed moisture content and a slight difference in the carbon, oxygen and ash contents. While bark is received with 50 wt.% moisture and its dry matter analysis results in 52.5 wt.% carbon, 38.5 wt.% oxygen and 2.6 wt.% of ash, straw is received with 10 wt.% moisture and 47.3 wt.% carbon, 41.4 wt.% oxygen and 4.7 wt.% ash. Hence, the bark is firstly led into a drying section to reduce its moisture content to 12 wt.% [10, 19]. In case of using straw as the feedstock, a certain amount of chlorine content is assumed which needs to be removed before the reformer by quenching the raw syngas before the filtration step from 730 °C to 550 °C.

Electrolyser

The PEM electrolytic cell was modelled through a black box approach with conversion factor 1 (with regard to water) and operating conditions of 40 bar and 80 °C. The electrical energy demand of 61.6 kWh per kg of H_2 was used for electrolysis corresponding to an electrical efficiency (power to HHV_{H2}) of approximately 64 % [20]. It was assumed that pure oxygen can be separated from the anode, which is utilized to operate the reformer with pure oxygen, significantly reducing the amount of inerts in the syngas. The amount of hydrogen is adjusted to achieve a H/C ratio of 3 at the entrance of the MeOH synthesis loop.

Methanol synthesis

The methanol section consists of a compression to the 90 bar operating pressure, a plug flow reactor model (RPlug) with an isothermal cooling liquid at 240 °C. The reactor model is representing a tube-and-shell reactor concept as it is commonly used for large methanol production plants. The entering temperature is set to 235 °C. The pressure drop is calculated using the Ergun equation [21]. A recycle with a purge rate of 5 % ensures that impurities such as nitrogen are not accumulating within the recycle loop. For the reaction modelling the simplified kinetic model from Van-Dal and Bouallou [22] of the in-depth model of Vanden Bussche and Froment [23] with the readjusted parameters from Mignard and Pritchard [24] is implemented. The whole section is modelled with the IDEAL property method as suggested by Graaf et al. [25].

Methanol purification

For the purification a two-column approach is applied. While the first column divides the gaseous side-products from the methanol, the second column separates the methanol from the water. The methanol is purified until

a purity of grade AA (99.85 wt.%) is achieved. The methanol purification section is modelled using ELECNRTL to achieve a better description of the azeotropic methanol-water separation.

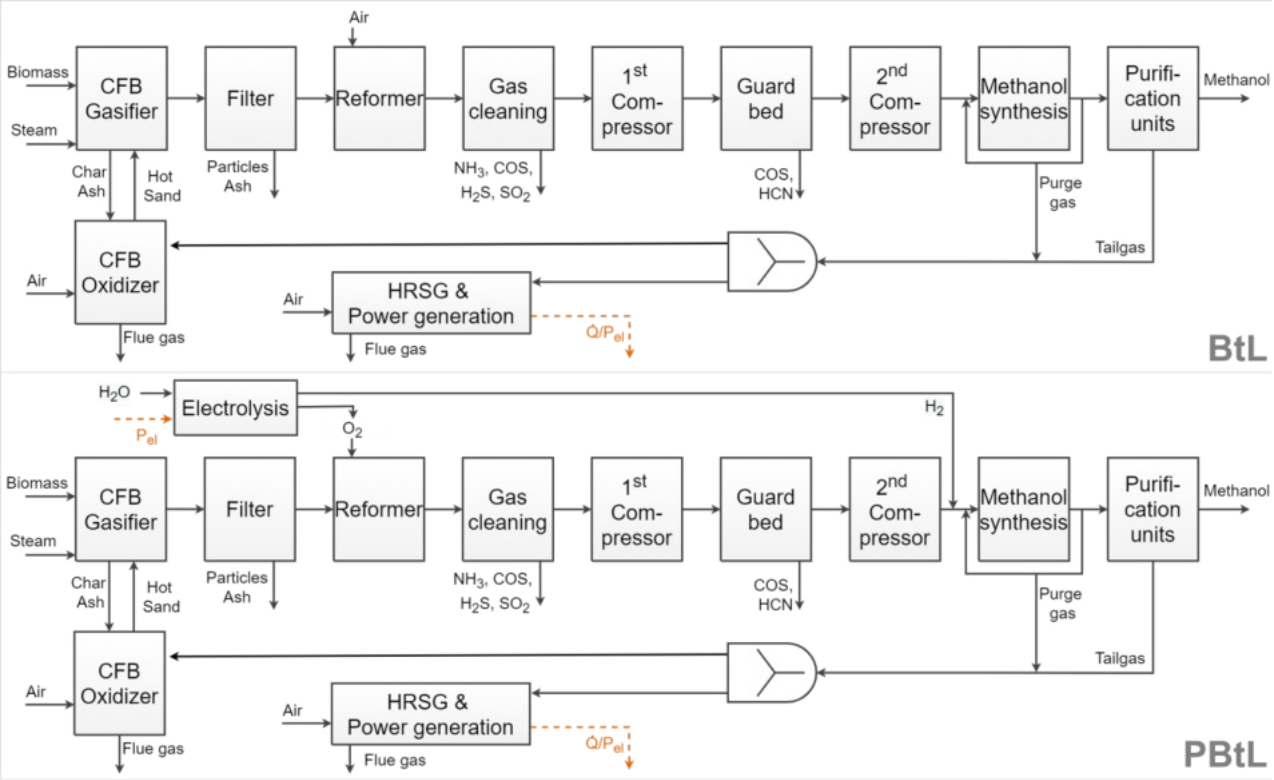

Figure 1. Process schemes for the biomass-to-liquid (BtL) and the power&biomass-to-liquid (PBtL) process.

2.2. Technical analysis

The process configurations are evaluated according to their ability to convert the stored energy of the biomass into the desired product methanol. To compare the different setups according to this performance indicator, the biomass-to-liquid efficiency is defined as follows:

Biomass-to-liquid efficiency: $$\eta_{PBtL} = \frac{\dot{m}_{CH_3OH} \cdot LHV_{CH_3OH}}{\dot{m}_{biomass}\, LHV_{biomass} + P_{el}}$$

2.3. Techno-economic analysis

The economic evaluation of the concept follows the approach of Peters, Timmerhaus, and West [26], which has been utilized in several previous techno-economic studies [15, 27, 28]. To apply this methodology, a database of reference equipment costs is needed to account for changes in the process configuration and its impact on capital and operational expenses. The AspenPlus® process model previously described is used to scale equipment sizes, as well as raw material and by-product streams, based on the material and energy flows. For the main equipment the cost functions of Maier et al. [10] are applied to the current biomass-to-methanol process concepts. The formulas utilized to calculate the production costs are listed below [15]:

- Equipment costs: $EC_i = EC_{ref,i} \cdot \left(\frac{D_i}{D_{ref,i}}\right)^{d_i} \cdot \left(\frac{CEPCI_{2020}}{CEPCI_{ref}}\right)$
- Fixed capital investment: $FCI = \sum_{i=1}^{m} EC_i \cdot \left(1 + \sum_{j=1}^{12} F_{eco,i,j}\right),\ TCI = \frac{FCI}{0.9}$
- Annualized capital costs: $ACC = FCI \cdot IR \cdot \left(\frac{(1+IR)^{PL}}{(1+IR)^{PL}-1} + \frac{1}{1-0.1} - 1\right)$
- Net production costs: $NPC = \frac{ACC + \sum OPEX_{ind} + OPEX_{dir} + N_P \cdot c_{labour}}{\dot{m}_{fuel}}$

The equipment costs are calculated by setting the actual unit capacity *D* into relation with a reference equipment capacity D_{ref} and its reference costs EC_{ref} and applying a defined digression factor *d* to it. To account for price differences between the reference and the base year the Chemical Engineering Plant Costs Index (CEPCI) is applied to the equipment costs. After including the Lang factors [26] for additional costs such as piping, engineering etc. the fixed capital investment (FCI) is estimated. To calculate the final net production costs, the direct and indirect operational expenditures (OPEX) are sum up together with the annualized capital costs and the labour costs. Finally, the whole yearly expenses are divided by the product output per year.

3. Results and discussion

Assessing the different process concepts regarding their biomass-to-methanol efficiency, it becomes clear that the power&biomass-based process routes yield in a higher energetic efficiency (Table 1). By enabling additional product formation, more biogenic carbon is converted to methanol, which increases the overall process efficiency. Furthermore, it can be seen, that the choice of the biomass feedstock has a significant impact on the technical potential of the process. Due to the higher ash content and higher oxygen content in the straw, the resulting syngas has a lower potential [10], since more hydrogen is required to remove the oxygen in form of water out of the system. Furthermore, due to the potential chlorine in the straw, the particle filter after the gasifier has to be operated at 550 °C which leads to further energy losses, since part of the reaction enthalpy in the autothermal reformer is used to heat the syngas up to 850 °C again. The disadvantageous composition is also the reason for the additional electricity demand in case of the straw-based PBtL concept, since more hydrogen is required to achieve the desired H/C ratio for the MeOH synthesis of 3.

Table 1. Technical results for the BtL and PBtL concepts with bark and straw as their feedstock

		BtL-B	PBtL-B	BtL-S	PBtL-S
Biomass moisture content	wt.%	50	50	12	12
Biomass input (mass flow)	kg/h	39.1	39.1	24.4	24.4
Biomass input (energy content)	MW_{th}	100	100	100	100
Electricity consumption	MW_{el}	14.6	103.9	15.8	121.4
Product output (mass flow)	kg/h	10,210	18,604	8,478	18,532
Product output (energy content)	MW_{th}	64.9	118.3	53.9	117.9
PBtL-efficiency	%	56.7	58.0	46.6	53.2

Compared to previous studies such as Peduzzi et al [4] the proposed biomass-to-liquid concept presents an 5% higher BtL efficiency for the bark case. The calculated efficiency for the bark-based PBtL case are in very good alignment with the work of [11], who estimated an efficiency of 57.5% for their process setup. Yet, the conducted analyses of this work highlight the potential of a power-enhanced setup for other biomass feedstocks. While for bark the PBtL efficiency has been increased by only 1.3%, the efficiency for converting straw into methanol can be increased by 6.6% which shows that especially for biogenic waste materials with a disadvantageous composition, the implementation of additional hydrogen generation is highly beneficial for its conversion rate.

To investigate the different concepts economically, the net production costs (NPC) are calculated (Figure 2) with the economic boundary conditions given in Table 2. With Germany as the selected region the biomass-to-methanol plant's costs are calculated for a country with relatively high raw material prices compared to other European regions such as Poland, Czech Republic or Slovenia [10].

Table 2. Economic boundary conditions.

Base year	-	2020	
Plant size	MW_{th}	100	
Interest rate (*IR*)	%	10	
Persons per shift (N_P)	-	10	
Full load hours (*flh*)	h/a	8260	
Plant lifetime (*PL*)	a	20	
Plant location	Germany		
Electricity costs/revenue (c_{EL})	€/MWh_{el}	106.5	[29]
Biomass costs ($c_{Bio,b}$)	€/GJ	8.4	[30]
District heating revenue (r_{DH})	€/MWh	21.0	[31]
Process steam revenue (r_{PS})	€/MWh	36.0	[31]
Labor costs (c_L)	€/h	29.0	[32]

Due to the process configuration, which contains an internal recycle within the methanol synthesis but no further re-activation of the process' tailgas, the process yields in a high amount of excess heat. Its utilisation is very dependent on the given boundary conditions. In the conducted techno-economic analysis, it is assumed that high pressure steam, as well as district heating can be provided. Hence, the methanol production costs can be decreased by achieving a quite high by-product revenue on the heat market. While the prices for

electricity and biomass are extracted from literature, the revenue for potential heat market products is calculated based on the assumption that they have to compete with a provision based on biomass- or natural-gas fuelled boilers. Therefore, the costs are calculated according to Ulrich et al. [31], where the price for the fuels is assumed to be the average between the local natural gas price and the biomass price [10].

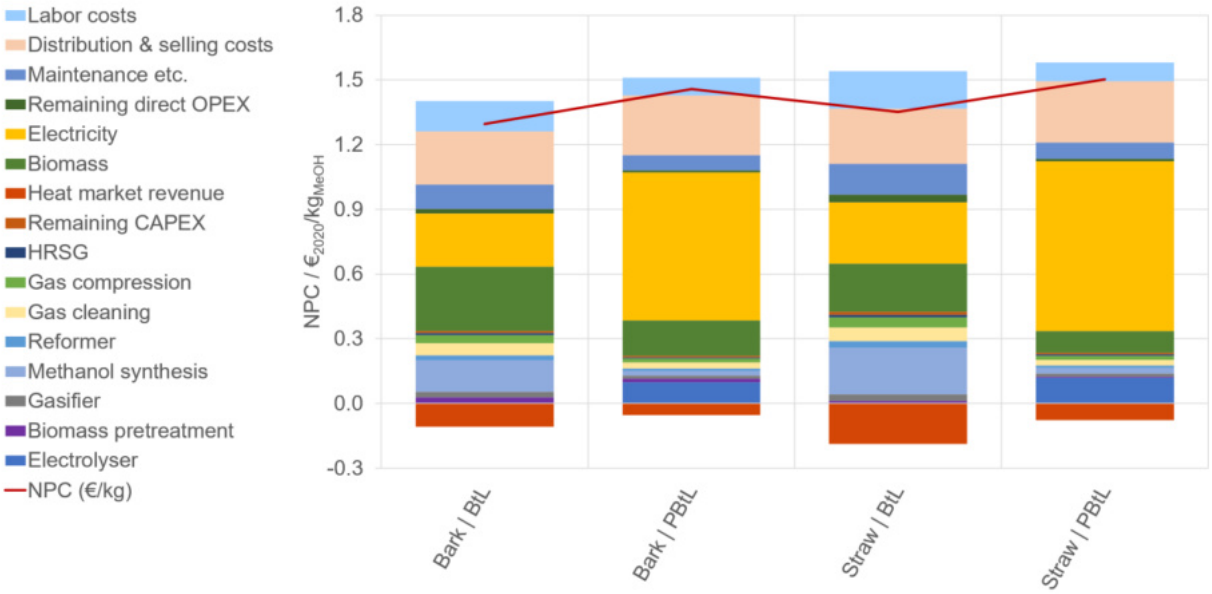

Figure 2. Net production costs for straw and bark for the two different process concepts biomass/power&biomass-to-liquid

In contrast to the prior technical results, the economic analysis of the concepts shows that the BtL process is more economic than the PBtL concepts. The main reasons can be found in the high additional expenses for the required electrical power and the additional investment for the electrolyser. The estimated NPC for all concepts differs within a range of 0.21 €$_{2020}$/kg$_{MeOH}$.

In order to identify at which conditions the PBtL concept might be able to compete with the BtL process, a sensitivity analysis with bark as feedstock is conducted and shown in Figure 3.

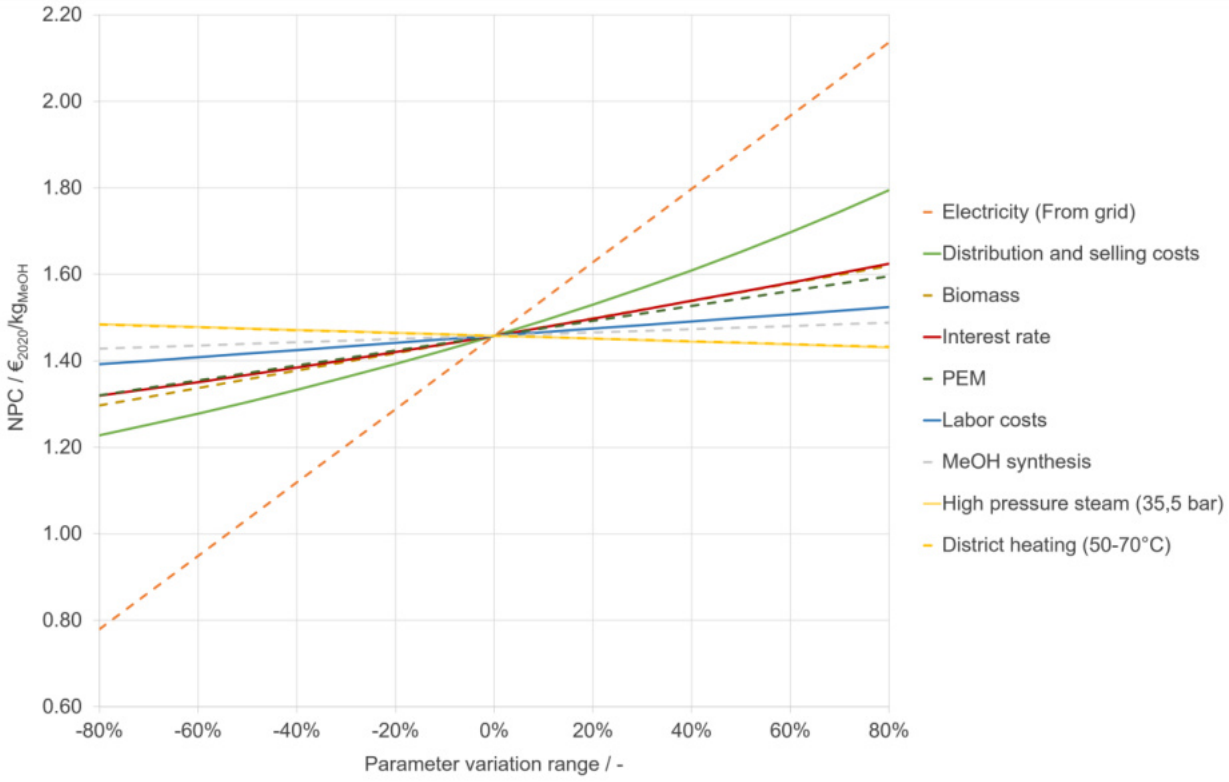

Figure 3. Sensitivity study for power&biomass-to-methanol concept using bark as feedstock

The presented sensitivity analysis is performed by varying each of the most relevant cost drivers within a range of -80% and +80%. Since the additional costs for distribution and selling of the product is dependent on the overall production costs and the interest rate affects the annualized capital costs their variations result in non-linear impacts on the net production costs. The remaining raw materials, utilities and equipment costs are having a linear effect on the calculated net productions.

In dependence on the electricity and biomass price, the PBtL concept gains more attraction. With a reduction of the electricity price, the productions costs can be reduced significantly. As it can already be seen in Figure 2, the electricity prices are the most dominant cost driver for the PBtL concepts, followed by the product distribution and the raw material: Biomass. In case of an electricity price of lower than 40 €/MWh_e, the production costs for the PBtL case are dropping below the methanol commodity prices of around 1 $€_{2020}/kg_{MeOH}$.

Figure 3 shows how the required subsidies for power demand or renewable methanol sales will change with feedstock and electricity costs. Future reduction of renewable electricity costs might favour the power-assisted biofuels production in the coming years. Furthermore, the increase of renewable energy in the electricity mix is required to achieve a positive environmental impact with the PBtL cases. Recent studies of Habermeyer et al. [27] and Weyand et al. [14] showed that utilizing the electricity from the German grid to generate the hydrogen, yields in an even higher greenhouse gas emission than using the fossil alternatives. Hence, PBtL concepts imply a potential alternative for an increased production of alternative fuels by an increased carbon efficiency but strongly depend on the availability of renewable and inexpensive electricity. Until then, only off-grid solutions may contribute to a reduction of the global warming potential or the exclusive use of biogenic waste materials as a feedstock together with a reduction of society's fuel consumption.

4. Conclusion and outlook

The study presented a promising approach for the production of sustainable methanol using two biogenetic waste materials, straw and bark. By combining highly efficient process units and by avoiding a recycle to the reformer stage, the equipment sizes can be kept small, while still achieving (power&)biomass-to-liquid efficiencies of up to 58.0%. An AspenPlus® flowsheet model was set up to model multiple process configurations which were evaluated using the DLR software-tool TEPET. Through automated heat integration, different process configurations were assessed, and a trade-off was identified between maximizing the BtL efficiency and minimizing net production costs. Even though the PBtL concepts come with high process efficiencies, the additional investment and costs for electricity lead to higher production costs in Germany in 2020. Furthermore, the shown work shows the potential of a hydrogen-enhanced biomass-to-liquid process especially for preliminary unattractive biogenic waste materials such as straw.

With an increasing investment into renewable energy sources and a ramp-up of cheap renewable electricity generation technologies, the PBtL concept might contribute to a carbon-neutral domestic transport by ensuring that the biogenic carbon is utilized best possible. To minimize the investment risk associated with the introduction of the technology, one approach could be to start the market introduction with biomass-to-methanol plants. These plants could then be expanded to include a hydrogen production plant and a second methanol synthesis reactor once a sufficient supply of renewable electricity is available.

Appendix A

Heat integration has been conducted with the automated heat and utilisation feature of the DLR-inhouse tool TEPET [10]:

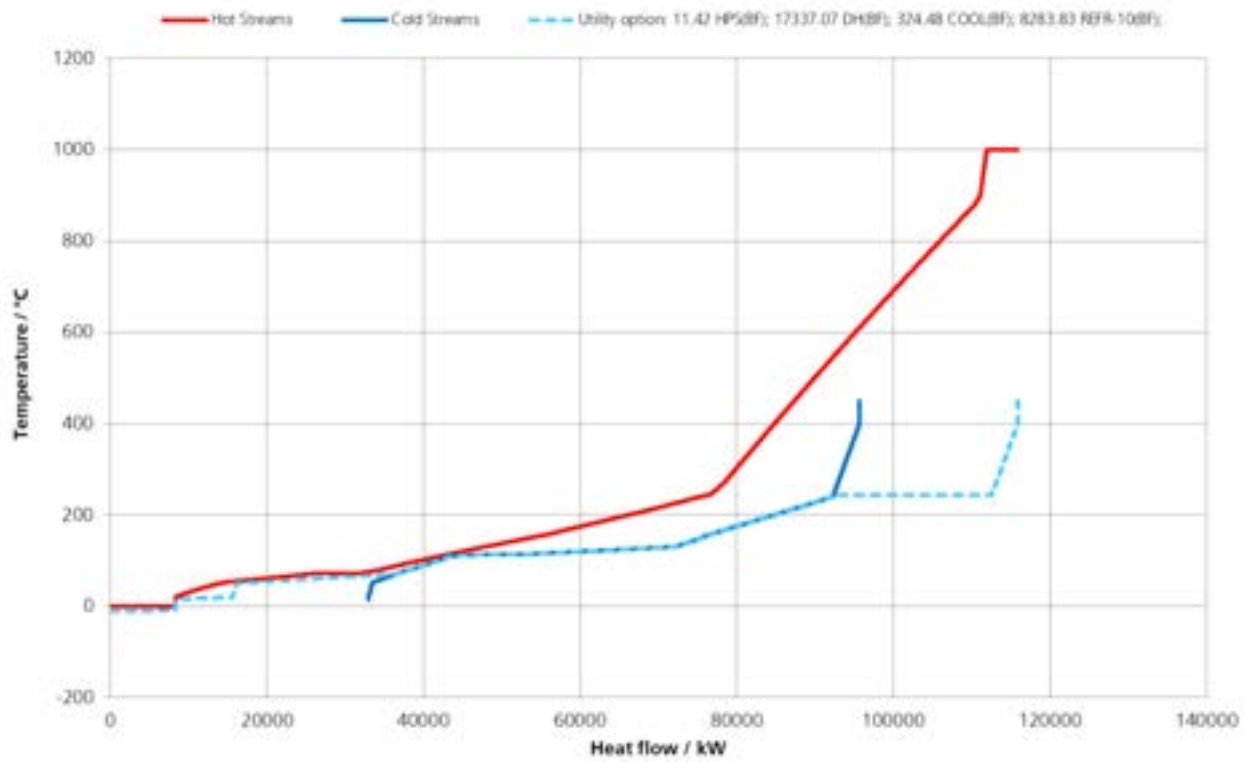

Figure 4. Heat integration for the bark-based biomass-to-liquid process.

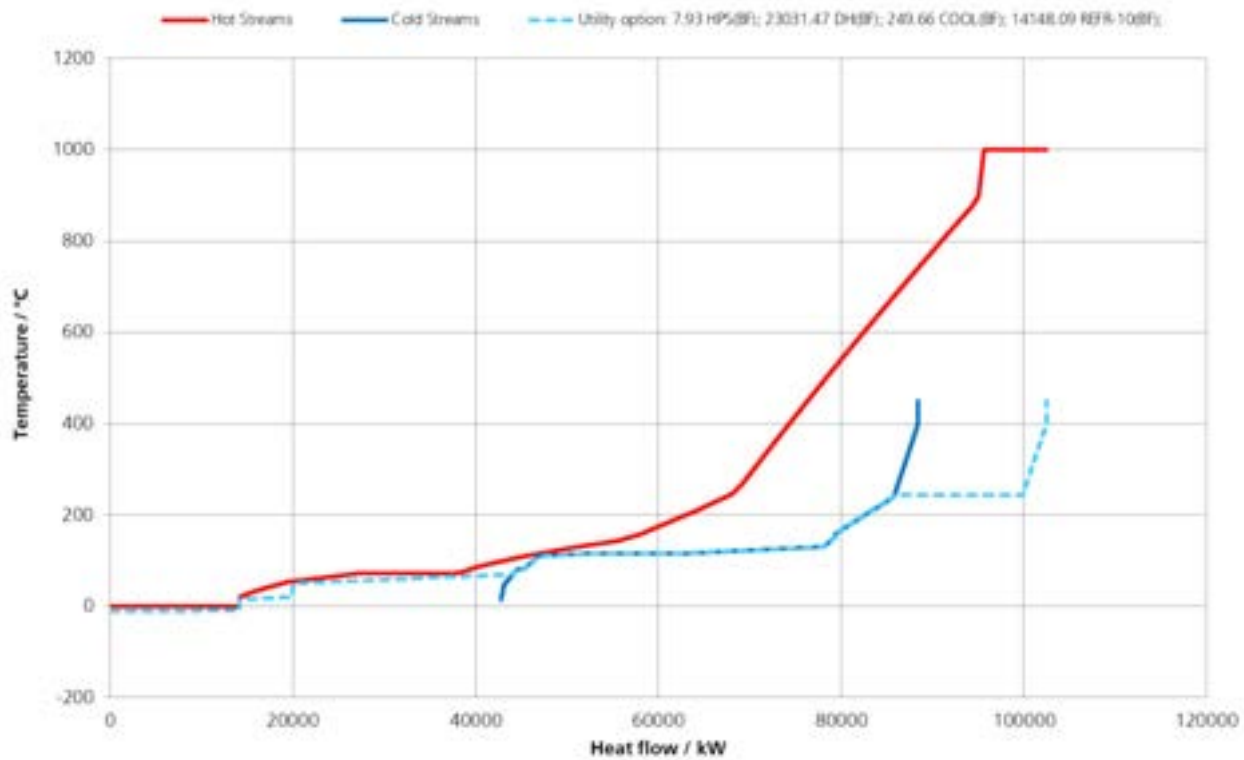

Figure 5. Heat integration for the bark-based power&biomass-to-liquid process.

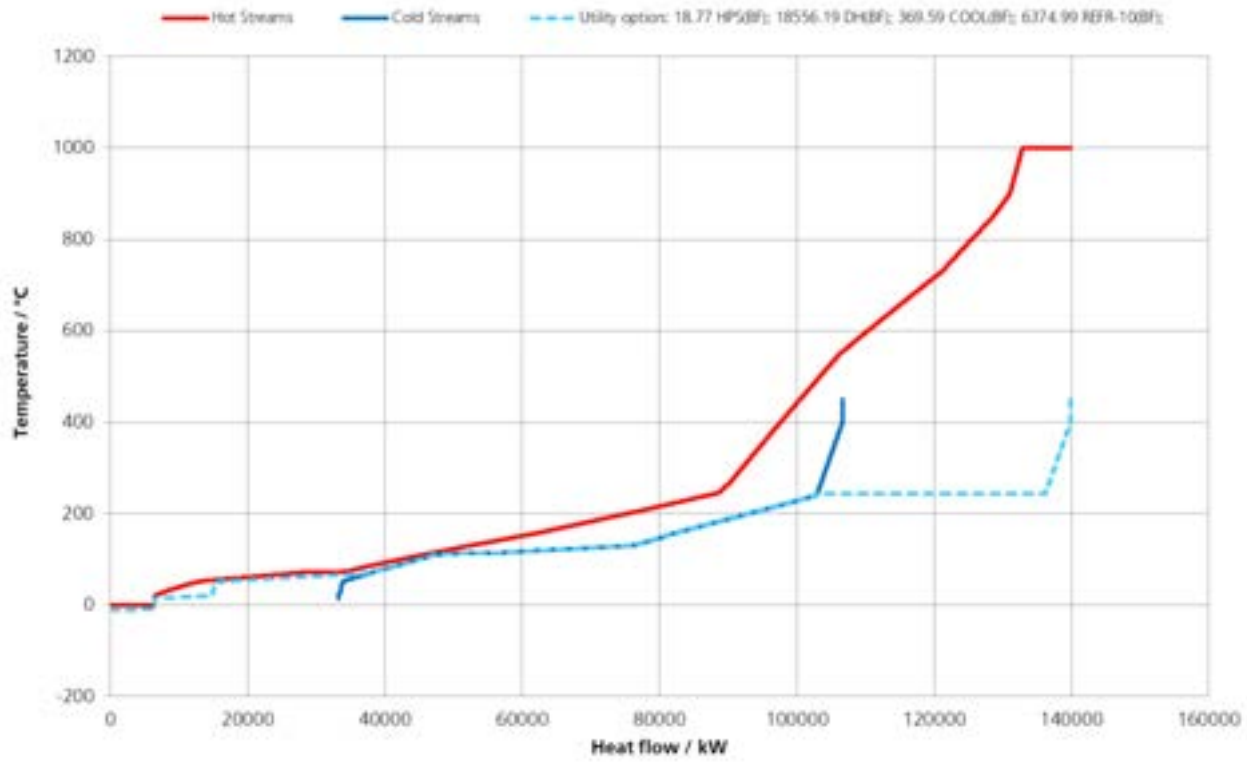

Figure 6. Heat integration for the straw-based biomass-to-liquid process.

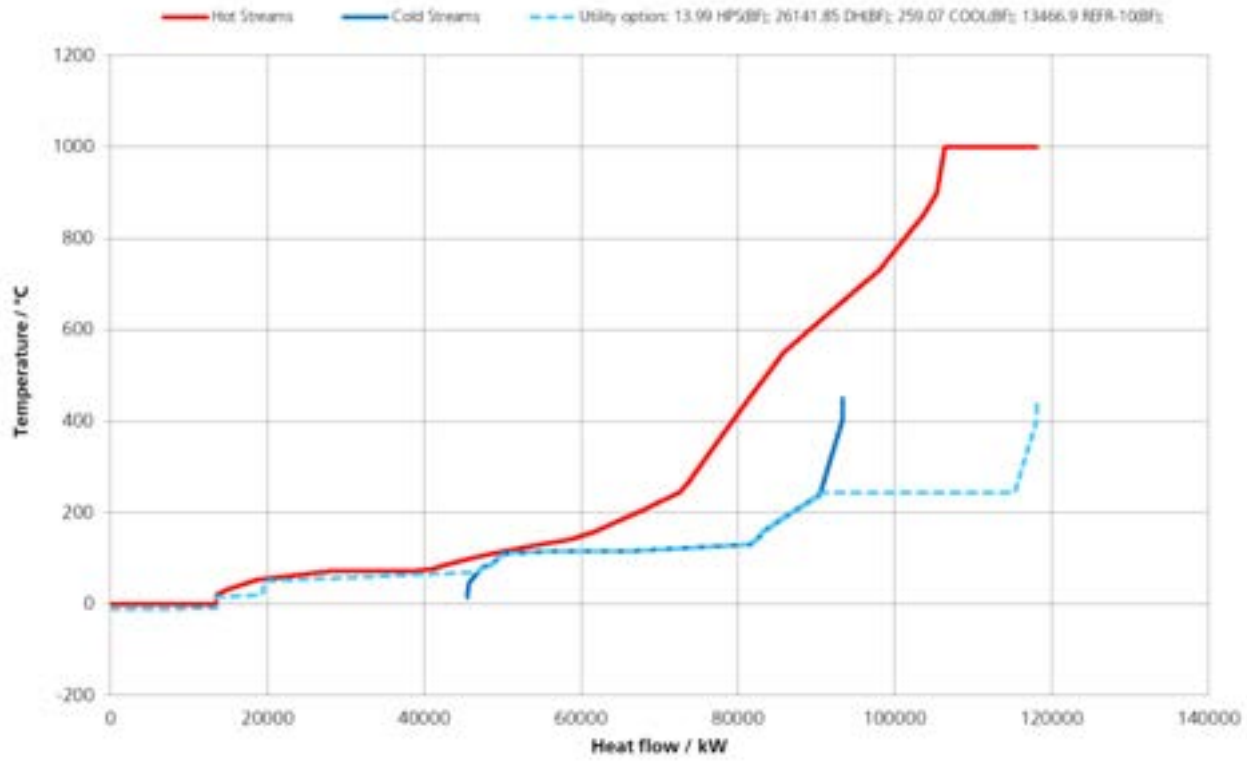

Figure 7. Heat integration for the straw-based power&biomass-to-liquid process.

Nomenclature

Abbreviations	
CAPEX	Capital investment expenditures
OPEX	Operational expenditures
Acronyms	
ACC	Annualized capital costs
BtL	Biomass-to-Liquid
DFB	Dual fluidized bed
DH	District heating
EC	Equipment cost
FCI	Fixed capital investment
FLH	Full load hours
HHV	Higher heating value
IR	Interest rate
LHV	Lower heating value
NPC	Net production costs
PL	Plant lifetime
PBtL	Power&Biomass-to-Liquid
TCI	Total capital investment
TEPET	Techno-Economic Process Evaluation Tool
Greek letters & variables	
α	Capital cost factor for utility cost calculation
β	Operational cost factor for utility cost calculation
η	Plant efficiency
c_i	Costs for i = [raw material, heat, power]
C_{plant}	Plant capacity, MW_{th}
d_i	Degression factor
D_i	Equipment capacity
$\dot{m}$	Mass flow, t/h
N_P	Number of persons per shift
P_e	Power, MW_e
r_i	Revenue for i = [by-product, heat, power]

References

[1] IPCC, Climate Change and Land: an IPCC special report on climate change, desertification, land degradation, sustainable land management, food security, and greenhouse gas fluxes in terrestrial ecosystems, in, 2019.

[2] E. Union, Directive 2009/30/EC of the European Parliament and of the Council of 23 April 2009 amending Directive 98/70/EC as regards the specification of petrol, diesel and gas-oil and introducing a mechanism to monitor and reduce greenhouse gas emissions and amending Council Directive 1999/32/EC as regards the specification of fuel used by inland waterway vessels and repealing Directive 93/12/EEC, (2016).

[3] E. Union, On the promotion of the use of energy from renewable sources, in, 2018.

[4] E. Peduzzi, L. Tock, G. Boissonnet, F. Marechal, Thermo-economic evaluation and optimization of the thermo-chemical conversion of biomass into methanol, Energy, 58 (2013) 9-16.

[5] O. Schmidt, A. Gambhir, I. Staffell, A. Hawkes, J. Nelson, S. Few, Future cost and performance of water electrolysis: An expert elicitation study, International Journal of Hydrogen Energy, 42 (2017) 30470-30492.

[6] G. Herz, C. Rix, E. Jacobasch, N. Müller, E. Reichelt, M. Jahn, A. Michaelis, Economic assessment of Power-to-Liquid processes – Influence of electrolysis technology and operating conditions, Applied Energy, 292 (2021).

[7] V.S. Sikarwar, M. Zhao, P.S. Fennell, N. Shah, E.J. Anthony, Progress in biofuel production from gasification, Progress in Energy and Combustion Science, 61 (2017) 189-248.

[8] A.S. Snehesh, H.S. Mukunda, S. Mahapatra, S. Dasappa, Fischer-Tropsch route for the conversion of biomass to liquid fuels - Technical and economic analysis, Energy, 130 (2017) 182-191.

[9] R.L. Espinoza, A.P. Steynberg, B. Jager, A.C. Vosloo, Low temperature Fischer–Tropsch synthesis from a Sasol perspective, Applied Catalysis A: General, 186 (1999) 13-26.
[10] S. Maier, S. Tuomi, J. Kihlman, E. Kurkela, R.-U. Dietrich, Techno-economically-driven identification of ideal plant configurations for a new biomass-to-liquid process – A case study for Central-Europe, Energy Conversion and Management, 247 (2021).
[11] A. Poluzzi, G. Guandalini, S. Guffanti, M. Martinelli, S. Moioli, P. Huttenhuis, G. Rexwinkel, J. Palonen, E. Martelli, G. Groppi, M.C. Romano, Flexible Power and Biomass-To-Methanol Plants With Different Gasification Technologies, Frontiers in Energy Research, 9 (2022).
[12] G. Haarlemmer, G. Boissonnet, E. Peduzzi, P.-A. Setier, Investment and production costs of synthetic fuels – A literature survey, Energy, 66 (2014) 667-676.
[13] M. Ostadi, E. Rytter, M. Hillestad, Boosting carbon efficiency of the biomass to liquid process with hydrogen from power: The effect of H2/CO ratio to the Fischer-Tropsch reactors on the production and power consumption, Biomass and Bioenergy, 127 (2019).
[14] J. Weyand, F. Habermeyer, R.-U. Dietrich, Process design analysis of a hybrid power-and-biomass-to-liquid process – An approach combining life cycle and techno-economic assessment, Fuel, 342 (2023).
[15] F.G. Albrecht, D.H. König, N. Baucks, R.-U. Dietrich, A standardized methodology for the techno-economic evaluation of alternative fuels – A case study, Fuel, 194 (2017) 511-526.
[16] COMSYN - Webpage, in, VTT Technical Research Centre of Finland Ltd, 2017, pp. COMSYN project has received funding from the European Union's Horizon 2020 research and innovation programme under grant agreement No 727476.
[17] I. Hannula, Hydrogen enhancement potential of synthetic biofuels manufacture in the European context: A techno-economic assessment, Energy, 104 (2016) 199-212.
[18] E. Kurkela, M. Kurkela, S. Tuomi, C. Frilund, I. Hiltunen, Efficient use of biomass residues for combined production of transport fuels and heat, in: VTT Technology, VTT Technical Reserach Centre of Finland Ltd, 2019, pp. 63.
[19] E. Alakangas, M. Hurskainen, J. Laatikainen-Luntama, J. Korhonen, Properties of indigenous fuels in Finland, VTT Technology, 272 (2016).
[20] T. Smolinka, M. Günther, J. Garche, Stand und Entwicklungspotenzial der Wasserelektrolyse zur Herstellung von Wasserstoff aus regenerativen Energien, in: NOW-Studie, Fraunhofer ISE, FCBAT, 2011.
[21] S. Ergun, Determination of geometric surface area of crushed porous solids, Analytical Chemistry, 24 (1952) 388-393.
[22] É.S. Van-Dal, C. Bouallou, Design and simulation of a methanol production plant from CO2 hydrogenation, Journal of Cleaner Production, 57 (2013) 38-45.
[23] K.M. Vanden Bussche, G.F. Froment, A Steady-State Kinetic Model for Methanol Synthesis and the Water Gas Shift Reaction on a Commercial Cu/ZnO/Al2O3 Catalyst, JOURNAL OF CATALYSIS, 161 (1996) 1-10.
[24] M. Dimitri, P. Colin, On the use of electrolytic hydrogen from variable renewable energies for the enhanced conversion of biomass to fuels, Chemical Engineering Research and Design, 86 (2008) 473-487.
[25] G.H. Graaf, A.A.C.M. Beenackers, Comparison of two-phase and three-phase methanol synthesis processes, Chem Eng Process, 35 (1996) 413-427.
[26] M.S. Peters, K.D. Timmerhaus, R.E. West, Plant Design and Economics for Chemical Engineers, 2002.
[27] F. Habermeyer, J. Weyand, S. Maier, E. Kurkela, R.-U. Dietrich, Power Biomass to Liquid — an option for Europe's sustainable and independent aviation fuel production, Biomass Conversion and Biorefinery, (2023).
[28] I. Hannula, Co-production of synthetic fuels and district heat from biomass residues, carbon dioxide and electricity: Performance and cost analysis, Biomass and Bioenergy, 74 (2015) 26-46.
[29] E. Union, Electricity prices for non-household consumers - bi-annual data (from 2007 onwards) [NRG_PC_205], in: E. Commission (Ed.) Electricity prices for non-household consumers - bi-annual data (from 2007 onwards), European Union, 2019.
[30] A.S. Pablo Ruiz, Wouter Nijs,, C. Thiel, IET-JRC, T.K. Francesco Dalla Longa, ECN, G.H. Berien Elbersen, Alterra, The JRC-EU-TIMES model. Bioenergy potentials for EU and neighbouring countries, in, 2015, pp. 176.
[31] G.D. Ulrich, P.T. Vasudevan, How To Estimate Utility Costs, Engineering Practice, (2006).
[32] E. Commission, Labour cost, wages and salaries, direct remuneration (excluding apprentices) by NACE Rev. 2 activity) - LCS surveys 2008, 2012 and 2016, in: E. Union (Ed.), 2021.

Design and operational optimisation of a combined cooling, heating and power plant to enable waste heat integration into an existing district heating network

Jan Stock[a], Malte Berrenberg[a], André Xhonneux[a], Dirk Müller[a, b]

[a] Forschungszentrum Jülich, Institute of Energy and Climate Research, Energy Systems Engineering (IEK-10), Jülich, Germany, j.stock@fz-juelich.de, CA
[b] RWTH Aachen University, E.ON Energy Research Center, Institute for Energy Efficient Buildings and Indoor Climate, Aachen, Germany

Abstract:

The substitution of fossil fuels in current energy systems is essential on the path to carbon neutrality. In the building sector, different renewable and waste heat sources could be used in district heating systems to replace fossil-based heating plants. However, if new heat sources are integrated into multi-energy systems, the profitability of present heating plants could decrease. At the Forschungszentrum Jülich, the waste heat from a new high-performance computer is to be integrated into the local district heating system in order to reduce overall CO_2 emissions. This waste heat integration will have an impact on the holistic multi-energy system of the campus, which is mainly supplied by a combined cooling heat and power plant (CCHP). This paper investigates the described waste heat integration using a bi-objective optimisation approach. The proposed model optimises the operation of the overall multi-energy supply system with waste heat integration. Furthermore, the optimisation model allows for the optimal design of the required heat pump system and additional absorption chiller capacity that enable efficient CCHP heat usage despite the waste heat integration. In addition, the effects of lowering district heating temperatures and changed energy prices are studied. The results show that integrating waste heat reduces the overall CO_2 emissions of the multi-energy system and even more if the integration is combined with a lowering of district heating temperatures. Furthermore, the optimisation shows that a cost reduction is feasible by increasing the absorption chiller capacity that uses the produced heat of the CCHP.

Keywords:

Waste Heat Integration, Bi-Objective Optimisation, Multi-Energy System, CCHP, District Heating

1. Introduction

The endeavour to decarbonise the building sector offers great potential for achieving the European Union's climate targets. The heat supply is mainly based on fossil fuels such as gas or oil to supply boiler systems in buildings. However, also many district heating systems are supplied by fossil-based energy plants, like 74 % of the combined heat and power plants (CHP) in Europe are based on coal and gas [1]. As an important contribution to the overall energy transition, heating plants in district heating systems need to be replaced by sustainable heat sources in order to reduce carbon dioxide emissions in the building sector. Renewable energy sources such as solar or geothermal energy as well as (low-temperature) waste heat sources from industry or cooling processes are examples of sustainable heat sources. Depending on the quality of the waste heat, the utilisation of waste heat sources could reduce CHP operation and, thus, save fuel and operating costs [2]. However, replacing existing, operating heating plants with sustainable heat sources could be challenging for many reasons.

Most heating plants in district heating systems have large nominal thermal capacities that cannot be easily replaced since the potential heat sources for replacement have limited heat capacities, are geographically inconveniently located, or the heat availability fluctuates due to scheduled processes. Zhang et al. show the difficulties of waste heat usage by optimising the utilisation rate for a district heating system and a cooling process depending on the availability of heat and the seasonal demand. Furthermore, they also consider how many consumers can be supplied with the available heat capacity [3].

The economic constraints make it challenging to replace current heating plants, as the profitability depends on different boundary conditions, such as the fuel prices or the investment required to integrate the sustainable heat source. Dorotić et al. perform an economic assessment of waste heat utilisation in an urban area by investigating the available waste heat from supermarkets and power substations. They show that the costs

of waste heat integration into district heating systems depend not only on the waste heat process itself, but also on the waste heat temperature and the current temperature level of the district heating system [4]. In [5], the possibilities of integrating solar heat with the help of heat pumps into Helsinki's existing district heating system are examined and evaluated from an economic point of view. In this particular case, the operation of the CHP is less advantageous than the operation of the heat pumps due to the electricity price level. However, Durán et al. point out that the conversion of existing district heating systems towards sustainable systems is technically possible, but the substitution of CHP with sustainable heat sources is an economic challenge. Therefore, they propose to establish economic and political regulations to facilitate the economic realisation of such projects [6]. The challenging utilisation of sustainable heat sources depends on the boundary conditions of the respective use case.

Optimisation models are helpful in showing optimal adaptions of energy systems, from a design or an operational point of view, to e.g. enable the usage of sustainable energy sources. The consideration of different objectives is necessary in order to take into account ecological and economic interests. The objective functions of such mathematical optimisation problems can be the minimisation of emitted CO_2 emissions or the minimisation of total costs. Capone et al. develop a multi-objective optimisation model to optimise the operation of producers and consumers in a district heating system, taking into account different objectives, such as reducing CO_2 emissions or minimising the total costs [7]. However, the additional integration of sustainable heat sources in the existing district heating system is not considered.

The integration of a waste heat source into a fossil-fuelled district heating system takes place at the Forschungszentrum Jülich (FZJ), a research facility in Germany. On the campus of the FZJ, the integration of waste heat of an upcoming high-performance computer in the local district heating system is studied. However, the use of the waste heat source reduces the supply of the currently operated CHP units. Due to the fact that the CHP units are operated heat-led, the electricity production for the campus is lowered, which affects the economic profitability of the entire energy system. Therefore, the usage of the waste heat source in the energy system of the campus leads to ecological benefits, but may result in higher operating costs.

The impact of a possible waste heat utilisation at the FZJ is simulated for different shares of waste heat integration and evaluated for the ecological and economic effects in previous work [8]. In addition, [8] presents different measures on the energy system to improve the efficiency of waste heat utilisation are presented, such as lowering the district heating supply temperature and extending the absorption cooling production. However, as campus' heat and cooling demand fluctuates throughout the year, the operation of the existing energy plants is very dynamic, so the targeted waste heat utilisation could be further optimised. Therefore, we develop an optimisation model in this study to optimise the waste heat utilisation in the existing energy system design of the FZJ in order to show optimal system measures and optimal operation of the involved energy components under ecological but also economic aspects.

The paper is structured as follows: In Section 2., we first give an overview of the multi-energy system of the FZJ and describe the planned waste heat utilisation. Following, we describe the optimisation model and show the modelling approach of the energy components, which represent the different energy plants on the campus. Furthermore, we show the investigated scenarios and summarise the assumptions of the modelling approach. Section 3. shows the optimisation results for the different studied scenarios. After discussing the results and the limitation of the model in Section 4., Section 5. summarises the study.

2. Methods

In the following, we first explain the use case of waste heat utilisation on the FZJ campus. After that, we present the developed optimisation model and the objective functions. Thirdly, we show the scenarios studied and the corresponding boundary conditions.

2.1. Multi-energy system and waste heat utilisation

The campus of the FZJ is a research facility in North Rhine-Westphalia, Germany, with many buildings used as offices and laboratories. A local multi-energy system supplies the various energy demands on the campus with different energy components. The main energy plant of the multi-energy system is a gas-fired combined cooling, heat and power system (CCHP) consisting of three CHP units, two heat-only boilers (HOB) and an absorption chiller (AC). The CHP units supply electricity and heat to the campus and should operate at a high load for a cost-efficient operation. The electricity generated by the CHP is less expensive than the electricity supplied by the public power grid, which supplies the remaining electricity demand. The CHP units cover the heat demand in the base load. If the heat demand of the campus exceeds the capacity of the three CHP units, two HOB units support the heat supply. When the heat demand of the campus is low, the surplus heat from the CHP units is used to operate the AC to generate cooling for the campus. A district cooling network distributes the cooling to the buildings. Since the AC in the CCHP cannot meet the entire cooling demand of the campus, three additional compression chiller (CC) plants located on the campus also supply cooling to the

district cooling network.

A new high-performance computer is being built on the FZJ campus, which generates a lot of waste heat through its operation. This waste heat source is being integrated into the multi-energy system of the campus to partially replace the heat supply from the gas-fired heating plants in the CCHP. However, the emitted waste heat will be available at a low-temperature level. Therefore, a heat pump (HP) system is required to raise the waste heat temperature to a higher level to make it usable in the local district heating system.

Different measures are described in [8] to enable more efficient waste heat usage. First, the supply temperature in the district heating system could be reduced to improve the efficiency of heat pump operation for waste heat integration. Second, the possibility to utilise more high-temperature heat by the CHP in the AC for cooling production is presented. Integrating waste heat into the district heating system reduces the supplied heat by the CHP and HOB units. Suppose the CHP units decrease their operation because the produced heat is not used anymore. In that case, electricity production will also decrease, leading to higher electricity consumption of the public grid and, thus, to higher operating costs. The CHP workload could be maintained at a high level by using the CHP surplus heat for additional AC cooling production. In addition, the extended AC operation partially replaces the cooling supply of the CC plants, which reduces the electricity demand for the cooling supply. However, as the ability to extend the operation of the current AC is limited, the construction of additional AC capacities can improve the ability to utilise high-temperature heat by the CHP units.

The dynamic operation of the various components of the energy system, in combination with the integration of waste heat, can be improved by optimising the multi-energy system at the campus. Therefore, an optimisation model is developed that both optimises the CCHP operation and takes into account possible design adaptation, such as the installation of heat pumps for waste heat utilisation and the expansion of the AC cooling supply. In the following, we describe the developed optimisation model.

2.2. Optimisation model

The campus' current energy supply system forms the basis for modelling the multi-energy system. However, the district heating and cooling network are not considered in the optimisation model, as we want to investigate the effects of waste heat utilisation on the overall energy production in this study. The main objective is the utilisation of waste heat in order to reduce carbon dioxide emissions taking into account the economic profitability of the overall energy system. Therefore, we apply a bi-objective optimisation approach that optimises the global warming impact (GWI) and the total annualised costs (TAC) of the multi-energy system, which are described more in detail in Section 2.2.3.

We use the COMANDO framework, which is written in Python [9]. COMANDO is an open-source modeling and optimisation framework for modelling energy components and linking them to an holistic energy system. The resulting energy system model is passed to a solver that optimises the design or operation regarding the set objective functions. The model in this study is based on a two-stage stochastic programming, which allows the design of components and the simultaneous operation optimisation based on a few typical time steps, i.e. operating points [9]. The typical operating points are determined by a clustering approach (see Section 2.3.).

In Fig. 1, the structure of the FZJ multi-energy system is shown. The different energy components, represented by submodels, are described in the following section. First, we give an overview about the main formulations and assumptions of modelling, followed by a more detailed description of the existing components and optional components for waste heat utilisation.

2.2.1. General model formulations

All energy components in the multi-energy system are modelled in terms of their operation efficiency η_{part}, which determines the quantity of energy output as a function of the amount of consumed energy. The general formulation of the components' part load efficiency is

$$\eta_{\text{part}} = \eta_{\text{base}} \cdot \mathcal{P}(out_{\text{rel}}), \tag{1}$$

where the base efficiency η_{base} is multiplied with $\mathcal{P}(out_{\text{rel}})$ that approximates the part load behaviour using two polynomial equations. The polynomials are determined by the specific energy components and depend on the relative energy output out_{rel}, which refers to the nominal capacity.

The modelling approach of the part load behaviour (1) leads to non-linear equations that increase the computation time for solving. Therefore, the resulting efficiency formulations of the energy components are simplified by using piecewise linear functions if necessary. The output of the components is an operational variable, and so is the efficiency, since it depends on out_{rel}. Thus, the input-output correlation is a multiplication of two variables and results in a quadratic equation. Since this correlation is set as a constraint in the energy components, the resulting optimisation problem is a quadratically constrained program.

The existing energy plants are modelled according to the currently installed components on site. The optional components, i.e. the HP for waste heat utilisation and the additional AC, can be built or not and are, there-

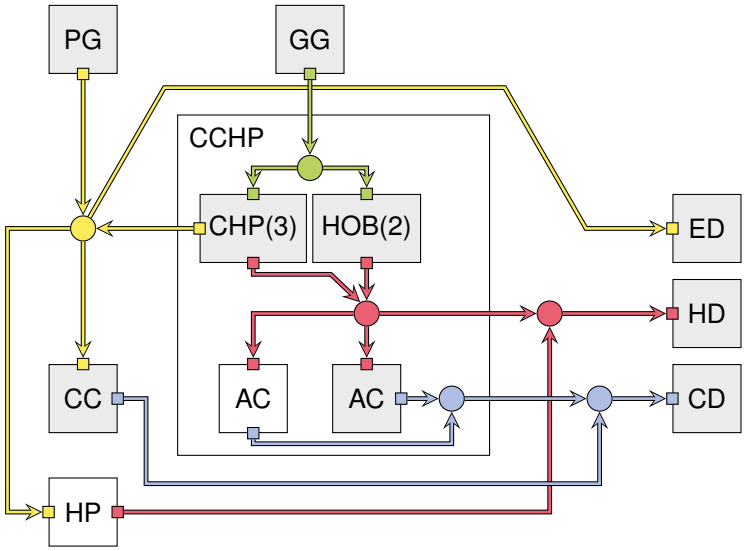

Figure 1: The different energy components of the multi-energy system are symbolised as grey boxes for existing and as white boxes for optional components. The CCHP includes three CHP units, two HOB units and an AC. The optional AC extension is shown as an additional AC in the CCHP. The CHP and HOB units are connected to the gas grid (GG). Electricity is supplied by the power grid (PG) and the CHP units to the CC and the electrical demand (ED) of the campus. The CHP and HOB units supply the heat demand (HD). The AC and the CC supply cooling to the cooling demand (CD). The AC is supplied by heat from the CHP units. A HP component is optional for waste heat utilisation, which consumes electricity from the PG and supplies heat to the HD. The waste heat source of the HP is not visualised.

fore, a design decision for the optimisation problem. In addition, the nominal output capacity of the optional components is a design variable.

For both existing and additional components of the energy system, the maintenance costs are taken into account through a maintenance coefficient and the initial investment of the component. The maintenance factors are based on [11].

2.2.2. Modelling of energy component

CHP

All three installed CHP units in the CCHP are identical in construction. The parameters set for the CHP model are based on manufacturer specifications. The nominal electrical output is 4.3 MW. At part load, the electrical efficiency decreases while the thermal efficiency increases. The manufacturer provides efficiency data for 100 % at full load (η_{heat}=0.437 and η_{el}=0.432) down to minimum part load of 50 %. The efficiency of the CHP between these operating points, with an additional available data point at 75 % part load, are linearly approximated.

HOB

The two HOB units in the CCHP have a nominal heat capacity of 16 MW each. The thermal efficiency is assumed to be constant at 80 % while considering a minimal part load of 20 %.

AC

The AC submodel is used for the installed AC in the CCHP and the optional AC capacity extension, i.e. an additional AC machine. For the already installed AC component, the design variable is set to one and the nominal cooling capacity to 5.7 MW. Furthermore, it is also considered that only the CHP units supply the AC, but not the HOB units.

The design variables for construction decision and dimensioning the nominal cooling capacity are used for the optional AC component. However, the minimal possible cooling capacity is set at 1 MW, as the investment for too small capacities is uneconomical for the studied energy system [12]. The part load efficiency of the AC components is modelled according to manufacture specifications, taking into account a minimal part load of 20 %. The specific investment of the AC is estimated following [12] at 200 EUR/kW.

HP

The waste heat utilisation in the multi-energy system is modelled as an optional HP. The HP increases the temperature of the waste heat to a sufficient level to integrate it into the local district heating system. Since the HP is not yet part of the multi-energy system, the HP component is a design decision subject to optimisation. In addition, the heat supply of the HP on the condenser side $\dot{Q}_{\text{HP,con}}$ is an operational variable to determine the

optimal amount of waste heat utilisation depending on the fluctuating demand.

The efficiency of the HP system is modelled by the coefficient of performance (COP). The COP of the HP COP_{HP} depends on the temperature difference between the heat source on the evaporator (eva) side, i.e. the waste heat source, and the heat sink on the condenser (con) side, i.e. the district heating system. The COP is calculated by

$$COP_{\mathrm{HP}} = \frac{T_{\mathrm{lm,con}}}{T_{\mathrm{lm,con}} - T_{\mathrm{lm,eva}}} \cdot \eta_{\mathrm{HP,system}} \cdot \eta_{\mathrm{HP,part}}, \tag{2}$$

where T_{lm} is the logarithmic mean temperature according to

$$T_{\mathrm{lm}} = \frac{T_{\mathrm{out}} - T_{\mathrm{in}}}{\ln T_{\mathrm{out}} - \ln T_{\mathrm{in}}}, \tag{3}$$

with the incoming (in) and outgoing (out) fluid temperature at the corresponding heat exchanger. The system efficiency $\eta_{\mathrm{HP,system}}$ is used to account for the system losses of the HP and is set to 0.5 [13]. The part load efficiency $\eta_{\mathrm{HP,part}}$ is based on [14] and linearised with the behaviour about 20 % part load. This linearised part load is considered down to the minimal set part load of 5 %. This is done, since the part load efficiency drops drastically below 20 % according to [14], however, the HP would not be operated in such inefficiently operating regimes in reality. The HP system is modelled as one component to reduce model complexity. In reality, however, the heat capacities required in this study would be realised by several HP units. The multiple HP units would allow for more efficient operation by avoiding the inefficient part loads under 20 %. Therefore, the linearised behaviour is used for the one HP system model.

The HP heat output $\dot{Q}_{\mathrm{HP,con}}$ is calculated by an energy balance and $COP_{\mathrm{HP}} = \frac{\dot{Q}_{\mathrm{HP,con}}}{P_{\mathrm{HP,el}}}$ to

$$\dot{Q}_{\mathrm{HP,con}} = \dot{Q}_{\mathrm{HP,eva}} + P_{\mathrm{HP,el}} = \frac{\dot{Q}_{\mathrm{HP,eva}}}{1 - COP_{\mathrm{HP}}^{-1}}, \tag{4}$$

where $\dot{Q}_{\mathrm{HP,eva}}$ represents the heat input of the waste heat source and $P_{\mathrm{HP,el}}$ the required electricity for operation.

Based on an anticipated waste heat capacity of 18 MW, a constant temperature level of the waste heat source at 44 °C [8], and the current supply temperature of the district heating system (see Section 2.3.), the upper limit of the design variable determining the thermal HP capacity is set to 22 MW. The lower limit of the HP capacity is set to 1 MW to avoid installing too small HP systems. The specific investment of the HP system is based on estimations by [15] and is set at 700 EUR/kW.

CC

The cooling demand of the campus is also met by three CC plants with a combined cooling capacity of 21 MW. Each CC plant comprises two or three CC units. In addition, no detailed manufacturer data of the individual chillers are available for these components. Since the district cooling network is not modelled and only the overall cooling supply is considered, all CC units on the campus are simplified into one CC component model. Therefore, a detailed analysis of the CC operational measurement data is performed to model the average behaviour of the summarised CC cooling supply.

The analysed measurement data of overall CC supply and consumed electricity for the CC operation does not show any significant correlation of the energy efficiency to the cooling load or the ambient temperature. The several CC units are from different years of construction, have various nominal capacities, and a control strategy for an optimal combined operation of the units is missing. Therefore, the analysed measurement data show a relatively constant COP over the year, which results from various superimposed COP characteristics of the individual CC units. Thus, the efficiency of the overall CC cooling supply is assumed to be constant and set at 3.7, as a COP formulation based on the temperature levels would not represent the actual CC operation on the campus.

The CC supply model consists of several small units, which is why the minimal part load of the comprised model is negligible. As no detailed information about the different CC units is available, the maintenance costs of the CC component are neglected.

GG, PG, ED, HD, CD

The external energy consumption by the GG and the PG (see Fig. 1) is modelled by considering specific energy prices and CO_2 factors that are defined in Section 2.3. Since the FZJ is not allowed to sell electricity to the grid, the energy flow from the PG model is limited to one direction. No restrictions on electricity and gas consumption are set for either grid model.

The demand models symbolise the consumption of the multi-energy system. The ED, CD and HD have a single input that represents the demand to be met (see Fig. 1). The energy demand symbolises the required

supply by the energy plants, as the distribution losses are not considered. The assumed data for the energy demand is described in Section 2.3..

2.2.3. Optimisation problem and objective functions

The defined optimisation model is solved considering two objectives, minimising the TAC and the GWI of the multi-energy system. The TAC is expressed as

$$TAC = \frac{(1+i)^n \cdot i}{(1+i)^n - 1} \cdot I + R, \tag{5}$$

with i for the interest rate of 0.7 %, n for the project duration of 20 a, I for the investment of HP installation and AC extension. The operational costs R are calculated according to the energy prices (see Section 2.3.) for energy consumption from the grids and the maintenance costs of the energy components. Gas is consumed to supply the CHP and HOB units, and electricity is consumed from the grid to cover the HP, CC and electricity demand of the campus that is not met by the CHP units.

Furthermore, the second objective GWI is formulated as

$$GWI = \dot{Q}_{\mathrm{GG}} \cdot CO_{2,gas} + P_{\mathrm{PG}} \cdot CO_{2,el}, \tag{6}$$

where $CO_{2,gas}$ and $CO_{2,el}$ represent the CO_2 emission factors for gas and electricity consumption supplied by the grids. The resulting bi-objective problem is solved by using the ε-constraint method.

The formulated energy system optimisation problem results in a Mixed Integer Quadratically Constrained Programming. The problem is passed to the Gurobi solver [16] via the implemented interface of COMANDO and solved for both objectives [9].

2.3. Studied scenarios

We define different scenarios for investigating waste heat utilisation in the FZJ multi-energy system. First, we optimise the energy system based on the current design without waste heat utilisation, i.e. an operational optimisation (Ref). Second, we consider the design option for an additional AC extension and HP installation for waste heat utilisation. Currently, the district heating network operates at high supply temperatures (HT) from 95 to 132 °C, controlled by a heating curve that depends on the ambient temperature. The first optimisation with optimal waste heat utilisation is carried out with these high supply temperature requirements at the HP system (WH_{HT}).

The HP operates much more efficiently if the temperature difference between waste heat and network supply temperature is reduced. Therefore, we investigate another scenario with lower supply temperatures (LT) in the district heating network of 80 to 100 °C (WH_{LT}). The technical feasibility of district heating operation and the sufficient heat supply to the connected consumers at these lower supply temperatures is already studied in [17].

In addition, we consider a changed energy price situation for gas and electricity consumption. As energy prices have changed significantly at the beginning of 2022, we estimate the changed energy prices for the FZJ supply ($WH_{HT,price}$ and $WH_{LT,price}$) in contrast to former energy prices used in [8]. Table 1 summarises all optimisation scenarios, including their considered option for waste heat utilisation, supply temperatures for HP operation and energy prices.

Table 1: Studied optimisation scenarios of the multi-energy system at the FZJ campus.

Scenario	Waste heat utilisation and AC extension	HP supply temperatures	Energy prices
Ref	No	95-132 °C	$c_{\mathrm{gas,old}}$ & $c_{\mathrm{el,old}}$
WH_{HT}	Yes	95-132 °C	$c_{\mathrm{gas,old}}$ & $c_{\mathrm{el,old}}$
WH_{LT}	Yes	80-100 °C	$c_{\mathrm{gas,old}}$ & $c_{\mathrm{el,old}}$
$WH_{HT,price}$	Yes	95-132 °C	$c_{\mathrm{gas,new}}$ & $c_{\mathrm{el,new}}$
$WH_{LT,price}$	Yes	80-100 °C	$c_{\mathrm{gas,new}}$ & $c_{\mathrm{el,new}}$

The energy prices in the period before 2022 ($c_{\mathrm{gas,old}}$=26.89 EUR/MWh and $c_{\mathrm{el,old}}$=149.54 EUR/MWh) are taken from [10] and used for the first scenarios. As the current energy prices of the FZJ were not made available, we estimate the energy prices increase based on the German gas and electricity prices of 2020 and calculate an average increase compared to December 2022. The average price increase for gas is calculated

to 280 % [18] and to 126 % for electricity [19]. Thus, the increased energy prices for consumption from the energy grids are assumed to be $c_{gas,new}$=75.51 EUR/MWh and $c_{el,new}$=188.37 EUR/MWh, resulting in a lower price ratio between gas and electricity. Furthermore, the CO_2 emission factors are determined to $CO_{2,gas}$=201.24 kg/MWh for gas consumption and to $CO_{2,el}$=408 kg/MWh for electricity consumption [20, 21]. The energy demand data of the FZJ campus are taken from [10] since the consumption data from recent years are not representative due to the Corona-related basic operation with reduced on-site operation at the campus. Since the model is optimised for typical operating points that occur during one year of operation (see Section 2.2.), the demand data for heating, cooling and electricity are clustered. The demand data is clustered using the k-means algorithm [9]. The number of clusters is determined by the elbow-method, which evaluates the sum of squared errors within a cluster. Through this analysis, the number of clusters is set to ten. An additional cluster with a weight of zero represents the summed up nominal demand of the campus to account for the required design capacity [9]. The ambient temperature data, required for the district heating curve to calculate the HP condenser temperature, is matched to the identified clusters.

3. Results

We first present the optimisation results for the reference design of the multi-energy system. Then we show the results of waste heat utilisation with optional AC extension for both considered district heating supply temperatures. Finally, we show the influence of changed energy prices on the results of waste heat utilisation.

3.1. CCHP optimisation without waste heat utilisation

Figure 2a shows the multi-objective results of operational optimisation of the CCHP. The optimisation results are presented for both objectives resulting in multiple pareto-optimal solutions labelled as solution 1-6, with the resulting TAC on the vertical axis and the corresponding GWI on the horizontal axis. Solution 1 represents the minimal GWI, and solution 6 shows the minimal TAC. The energy output of the different energy components is presented in a stacked bar chart above each pareto solution.

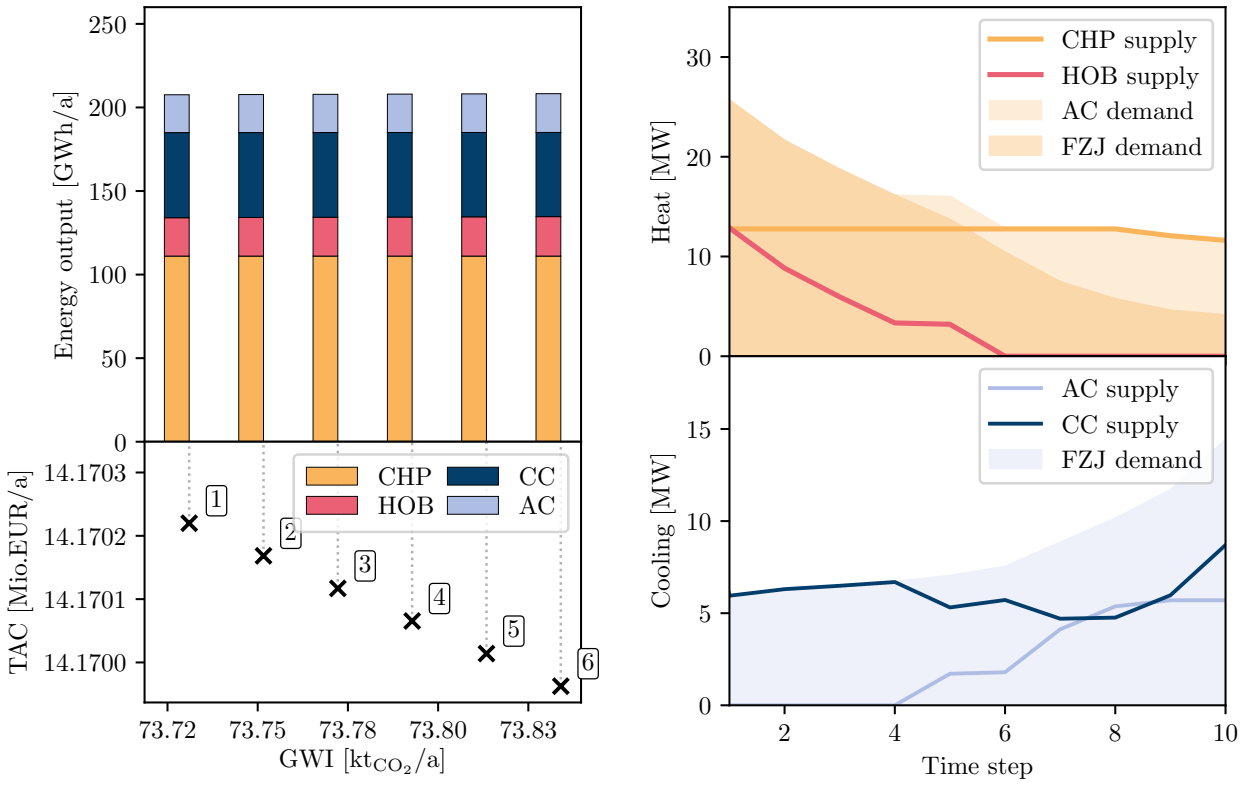

(a) Pareto solutions (Ref)

(b) Operation over clustered time steps (solution 1)

Figure 2: Operational optimisation of the CCHP without waste heat utilisation (Ref); Pareto solutions (6) for GWI, TAC and the corresponding energy output of the components (2a); Campus demand and supply of energy components for heat and cooling over clustered time steps of pareto solution 1 (2b).

The bi-objective optimisation shows only minor deviations between the solutions (see Fig. 2a) and therefore

confirms that the current energy system is well designed to achieve the best economical and ecological result. Since the six solutions differ only minimally, the CCHP operational optimisation result is exemplary explained for solution 1.

In Fig. 2b, the energy demand of the campus and the energy supply of the different energy components over the clustered time steps are shown for solution 1. The clustered time steps are sorted from left to right by decreasing heat demand. The corresponding cooling demand is shown below the heat demand. The CHP units operate at full power to produce heat and electricity for the campus, while the HOB units cover the peak heat demands. Only in time steps 9 and 10 the CHP units operate in part load somewhat, as the heat demand of the FZJ and the AC demand are below the nominal heat output of all CHP units. The CC component covers the main cooling demand of the campus, especially when the heat demand is high. However, when the heat demand decreases, the heat from the CHP units is used to run the AC, which supplies cooling and replaces part of the CC supply (time step 7 and 8). In case the heat demand decreases and the cooling demand increases, the AC supply is extended as more CHP produced heat is available. At time step 8, the maximal cooling capacity of the AC is reached, so the CC cooling supply increases.

3.2. Waste heat utilisation and AC extension

The optimisation results for the additional waste heat utilisation, i.e. the optional HP installation and AC extension, are shown in Fig. 3a for the high supply temperature requirements at the HP system (WH_{HT}) and in Fig. 3b for the lowered supply temperatures (WH_{LT}). In addition, the installed system capacities for HP and AC extension are shown as stacked hatched bar charts above the corresponding solution.

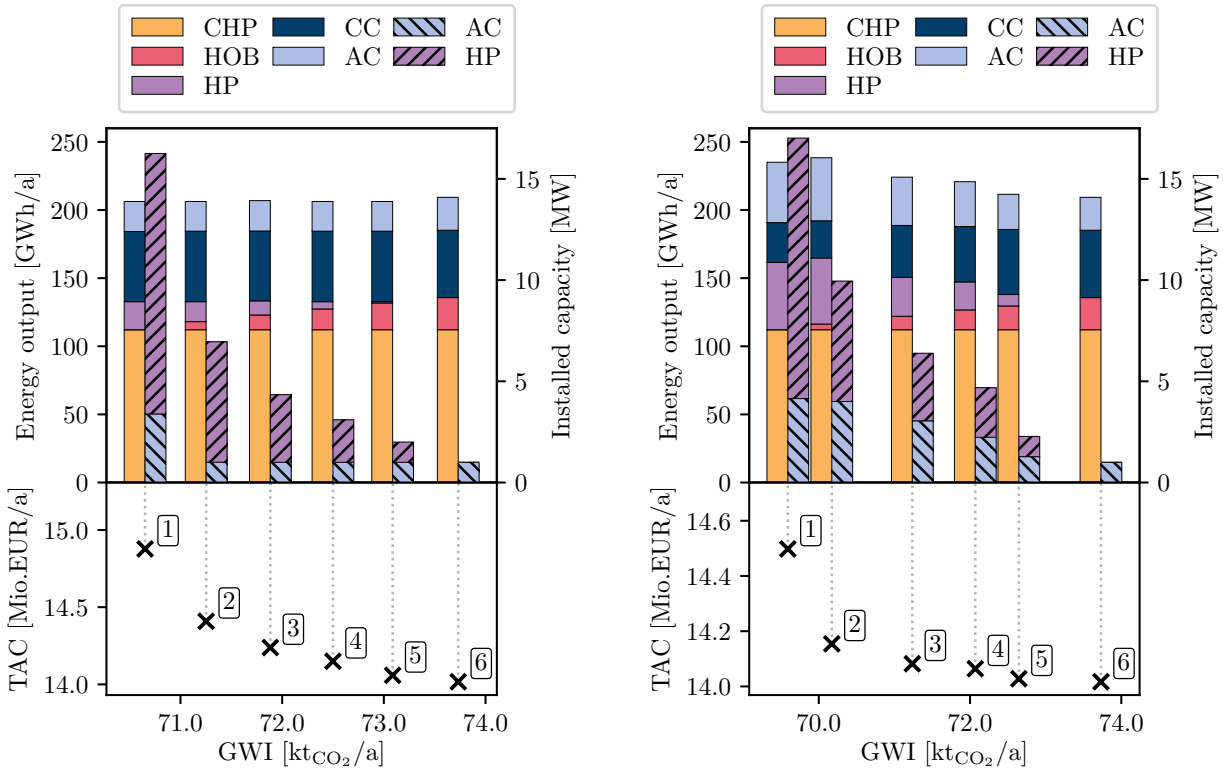

(a) High-temperature requirements (WH_{HT})

(b) Low-temperature requirements (WH_{LT})

Figure 3: Optimisation of the CCHP with optional waste heat utilisation and AC extension.

The pareto solutions 1-6 differ significantly for the high supply temperature scenario WH_{HT} in Fig. 3a. For the lowest TAC, no waste heat is used. However, compared to the Ref results (see Fig. 2a), an additional AC capacity of 1 MW is installed to allow higher AC cooling production. When the GWI is lowered (solutions 5 to 2), the HOB heat supply is reduced while the waste heat usage, represented by the HP, increases. The HP supply increases for lower GWI, leading to an increased HP capacity installation and, thus, to higher TACs. The minimal GWI is reached at the maximal TAC (solution 1), leading to the largest installed HP capacity and increased AC capacity extension. However, the HP heat supply in solution 1 is not much higher than in solution 2. From solution 2 to 1, the HP even replaces peak supply of the HOB, but therefore additional HP capacity is

needed to cover the highest peak demands. The waste heat utilisation at high temperatures enables a GWI reduction of up to 4.2 % while the TAC increases by 4.7 % compared to the Ref scenario. However, although the waste heat utilisation is expanded to reduce GWI, waste heat does not replace the CHP heat supply. This is due to the high CO_2 factor of the power grid, which is why the HP heat supply still leads to relatively high GWI compared to the more ecological combined electricity and heat supply of the CHP units.

For lower supply temperatures in the district heating network (WH_{LT}) and thus more efficient HP operation, the HOB heat supply is replaced by the HP supply much earlier (see Fig. 3b). Compared to the WH_{HT} scenario, the HP heat supply is much higher for lower temperature requirements and therefore results in lower GWI values in WH_{LT}. In addition, the AC cooling supply rises for lower GWI while the CC cooling supply decreases. The CHP units continue to operate at full load as they produce priceless electricity for the campus. The high-temperature heat is not used to cover the heat demand as the HP supports the supply and is therefore used to supply the AC. Lowering the supply temperatures of the district heating network therefore leads to a more efficient use of waste heat and, thus, to an extended HP supply, while the high-temperature heat generated by the CHP units is used to operate the extended AC capacity. Compared to the current energy system design (Ref), the waste heat utilisation at low supply temperatures (WH_{LT}) lead to a GWI reduction of 5.6 % while the TAC increases by 2.3 %.

3.3. Changed energy prices

For the results of the changed energy price situation ($WH_{HT,price}$ and $WH_{LT,price}$), we show only two solutions (minimal TAC and minimal GWI) for each investigated supply temperature since the solutions only differ slightly and the effects for reaching lower GWI are the same as described before. The optimisation results of the changed energy prices are presented in Fig. 4a for the high supply temperatures and in Fig. 4b for the lowered supply temperatures.

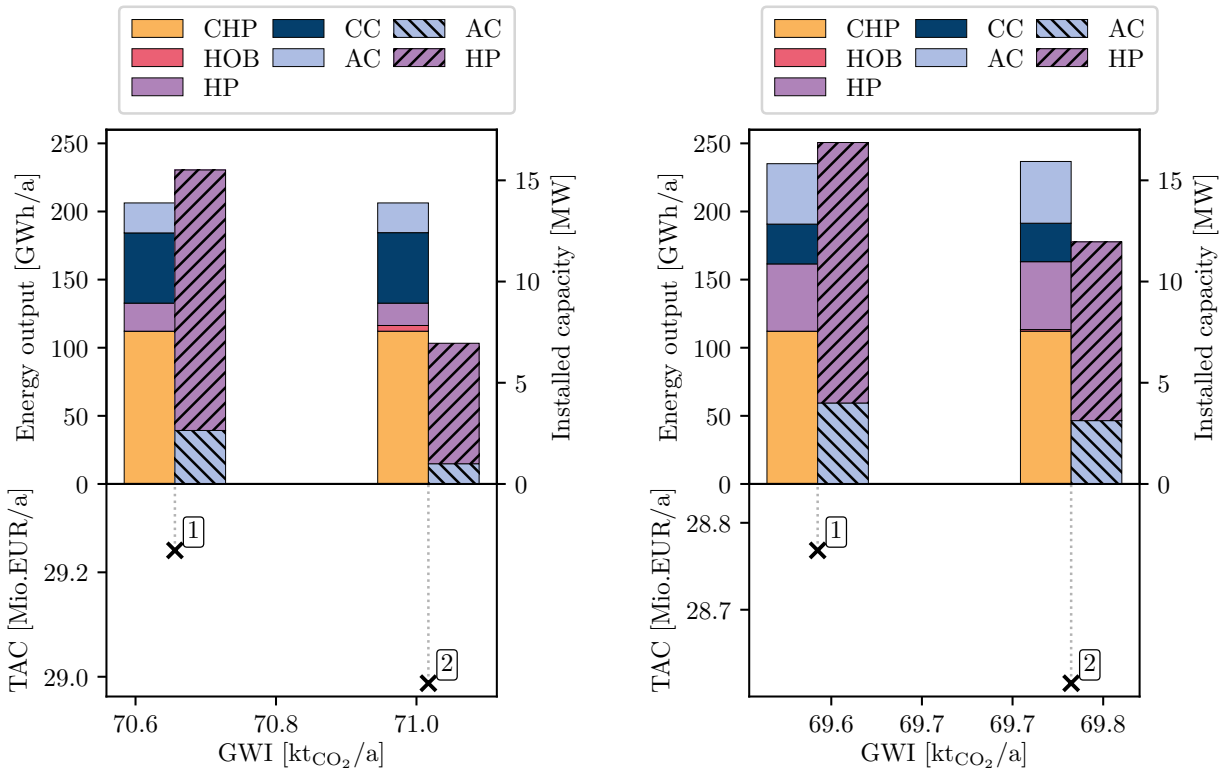

(a) High-temperature requirements $WT_{HT,price}$

(b) Low-temperature requirements $WT_{LT,price}$

Figure 4: Optimisation of the CCHP with optional waste heat utilisation and AC extension and increased energy prices.

In scenario $WT_{HT,price}$, waste heat is already used in the case of minimising TAC (solution 2), despite the necessary investment for HP installation, which indicates an uneconomic operation of gas-fired plants. However, the peak heat demand is still supplied by the HOB to avoid the installation of large HP capacities. Whereas for minimal GWI (solution 1), the peak heat demand is also partly covered by the HP, accepting the high investment

for the large HP capacity.

Lowering the supply temperatures in scenario $WT_{LT,price}$ also positively affects waste heat utilisation for increased energy prices (see Fig. 4b). For the minimal TAC (solution 2), a larger HP capacity is installed than in $WT_{HT,price}$ as the waste heat can be used more efficiently and, thus, already replaces the HOB heat supply to minimise the costs. To minimise GWI, the HP capacity installation is expanded to replace even the HOB peak supply (solution 1).

However, as the CHP units continue to operate at full load also for increased energy prices, the CHP heat is used to supply the extended AC. The AC capacity extension is more distinctive for lower supply temperatures, as waste heat utilisation is more efficient and, thus, more CHP heat is shifted to cooling production.

4. Discussion

The presented optimisation model confirms that the current CCHP is designed to operate at optimal ecological and economical performance, as the minimal TAC and GWI solutions are close to each other. The additional waste heat utilisation in the multi-energy system enables an increased ecological operation, as the waste heat replaces the HOB heat supply. However, the required investment for HP installation reduces the economic profit, as no waste heat is utilised for minimal TAC. Lowering the temperature in the district heating network has a positive effect on the efficiency of the HP, so that additional GWI and TAC savings can be achieved. Given the changed energy price situation, the waste heat is already being used for minimal TAC. As the gas price increases relatively more than the electricity price, the HP installation is more profitable for the HOB replacement in this price situation. Thus, the results show that a lower price ratio between gas and electricity strengthens the use of waste heat in the current energy system concept. To reduce the GWI, an extended HP heat supply becomes more attractive than a gas-fired heat supply. However, as the CHP units continue to operate at a high workload for producing electricity, additional AC capacity is installed to utilise the high-temperature heat of the CHP units. Thus, the option of AC extension enables continuous economic operation of the CHP units, as favourable electricity is produced, and the produced heat is used for cooling production and, thus, partially replaces the current CC supply.

The high CO_2 factor of the power grid leads to high emissions for waste heat utilisation, as the additional electricity for HP operation is supplied by the grid. In addition, the CHP produced electricity has a lower GWI than the electricity supplied by the power grid due to the assumed CO_2 factor. Thus, the waste heat does not replace the CHP heat supply, as the relative emissions of CHP produced heat and electricity, coupled with the cooling production via the AC, are lower than the emissions from the alternative supply by the HP and power grid. However, a changed electricity supply situation for the campus, e.g. through renewable electricity supply or a decreased CO_2 factor of the power grid, would reduce the emissions associated with waste heat utilisation and make the electricity supplied by the power grid more ecological than the electricity from the CHP plant. A more CO_2 neutral electricity supply by the grid could therefore increase the waste heat utilisation, as CHP operation would be replaced from an ecological point of view.

In the optimisation model, the CC component represents the total CC cooling supply from several individual CC units. The CC cooling supply model could be improved by collecting more detailed information about the installed CC units and parameterising several individual CC models to represent the different installed units. In this way, also the partially rather inefficient operation of the CC units on the campus could be improved. However, an adapted control strategy of the individual CC units, recommended by the optimisation, must be evaluated for a feasible district cooling operation, as the CC units are located decentrally on the campus.

5. Conclusion

In this study, we develop a model of a multi-energy system to optimise waste heat utilisation. Therefore, we model the existing components for heat, cooling and electricity supply and add an optional HP system to enable the usage of an available heat source. Additionally, we add the option to extend the AC cooling capacity to continue the CHP heat usage and, thus, maintain an economical CHP operation.

The optimisation model shows promising results for waste heat utilisation in the multi-energy system. To reduce the TAC, the CHP units operate at full load, and the HOB units cover the peak loads as these plants are already installed at the campus, and no investment is required. However, for minimal GWI, the waste heat utilisation by the installed HP system increases to replace the HOB heat supply. Lowering the district heating temperatures leads to a more efficient HP operation and, thus, to an increased waste heat usage to cover the heat demands of the campus. In contrast to the reference operation, the minimal GWI for the multi-energy system could be decreased by 4.2 % for high temperature requirements and by 5.6 % for lower supply temperature requirements at the HP system. The changed energy price situation leads to a smaller ratio between gas and electricity prices and strengthens the case of waste heat usage since, in this case, a HP installation is recommended to minimise costs as it replaces expensive gas-fired HOB heat supply.

With the developed optimisation model, different adaptations to the multi-energy system could be additionally studied to improve waste heat utilisation. For example, a more CO_2 neutral electricity supply to the HP system would favorise an expansion of waste heat usage. Overall, the model is applicable for investigating the general effects and possible measures for waste heat utilisation in an existing multi-energy system.

Nomenclature

c	Specific costs, EUR/MWh
CO_2	Carbon dioxide factor, kg/MWh
COP	Coefficient of Performance, -
GWI	Global warming impact, t_{CO_2}/a
i	Interest rate, %
I	Investment, EUR
n	Project time span, a
P	Electric power, W
$\mathcal{P}$	Factor part load behaviour, -
$\dot{Q}$	Heat flow, W
R	Annual operating costs, EUR/a
T	Temperature, K
TAC	Total Annualized Costs, EUR/a

Abbreviations

AC	Absorption Chiller
CC	Compression Chiller
CCHP	Combined Cooling Heat and Power
CD	Cooling Demand
CHP	Combined Heat and Power
ED	Electrical Demand
FZJ	Forschungszentrum Jülich
GG	Gas Grid
HD	Heat Demand
HOB	Heat-Only Boiler
HP	Heat Pump
HT	High District Heating Temperatures
LT	Lower District Heating Temperatures
PG	Power Grid
WH	Waste Heat Utilisation

Greek symbols

η	Efficiency, -

Subscripts and superscripts

con	Condenser
el	Electricity
eva	Evaporator
in	Incoming quantity
lm	Logarithmic mean
nom	Nominal
out	Outgoing quantity
part	Part-load
Ref	Reference optimisation
rel	Relative

References

[1] Sayegh M., Danielewicz J., Nannou T., Miniewicz M., Jadwiszczak P., Piekarska K., Jouhara H. *Trends of European research and development in district heating technologies*. Renewable and Sustainable Energy Reviews 2017;68(2):1183-1192.

[2] Lund H., Østergaard P., Chang M., Werner S., Svendsen S., Sorknæs P., Thorsen J., Hvelplund F., Mortensen B., Mathiesen B., Bojesen C., Duic N., Zhang X., Möller B. *The status of 4th generation district heating: Research and results*. Energy 2018;164:147-159.

[3] Zhang L., Wang Y., Feng X. *A Framework for Design and Operation Optimization for Utilizing Low-Grade Industrial Waste Heat in District Heating and Cooling*. Energies 2021;14(8):511–516.

[4] Dorotić H., Čuljak K., Miškić J., Pukšec T., Duić N. *Technical and Economic Assessment of Supermarket and Power Substation Waste Heat Integration into Existing District Heating Systems*. Energies 2022;15(5):1666.

[5] Rämä M., Wahlroos M. *Introduction of new decentralised renewable heat supply in an existing district heating system*. Energy 2018;154:68-79.

[6] Durán P., Torio H., Schönfeldt P., Klement P., Hanke B., Maydell K., Agert C. *Technology Pathways and Economic Analysis for Transforming High Temperature to Low Temperature District Heating Systems*. Energies 2021;14(11):3218.

[7] Capone M., Guelpa E., Verda V. *Multi-objective optimization of district energy systems with demand response*. Energy 2021;227:120472.

[8] Stock J., Xhonneux A., Müller D. *Low-Grade Waste Heat Integration into an Existing High-Temperature District Heating System at the Research Centre in Jülich, Germany*. In: B. Elmegaard, E. Sciubba, A. M. Blanco-Marigorta, J. K. Jensen, W. B. Markussen, W. Meesenburg, N. Arjomand Kermnai, 755 T. Zhu, R. Kofler (Eds.), Proceedings of ECOS 2022: The 35th International Conference on Efficiency, Cost, Optimization, Simulation and Environmental Impact of Energy Systems: Technical University of Denmark, 2023; 2022 July 03-07; Copenhagen, Denmark.

[9] Langiu M., Shu D., Baader F., Hering D., Bau U., Xhonneux A., Müller D., Bardow A., Mitsos A., Dahmen M. *COMANDO: A Next-Generation Open-Source Framework for Energy Systems Optimization*. Computers & Chemical Engineering 2021;152:107366.

[10] BFT Planung GmbH. *Neubau der Wärmevollversorgungszentrale des Forschungszentrums Jülich*. Aachen, Germany: BFT Planung GmbH; 2017 June.

[11] Sass S., Faulwasser T., Hollermann D., Kappatou C., Sauer D., Schütz T., Shu D., Bardow A., Gröll L., Hagenmeyer V., Müller D., and Mitsos A. *Model compendium, data, and optimization benchmarks for sector-coupled energy systems*. Computers & Chemical Engineering 2020;135:106760.

[12] Berliner Energieagentur GmbH *Meeting cooling demands in SUMMER by applying HEAT from cogeneration*. 2009 April.

[13] Arpagaus C., Bless F., Uhlmann M., Schiffmann J., Bertsch S. *High temperature heat pumps: Market overview, state of the art, research status, refrigerants, and application potentials*. Energy 2018;152:985-1010.

[14] Fuentes E., Waddicor D., Salom J. *Improved characterization of water-to-water heat pumps part load performance*. REHVA Journal 2016;4:45–49.

[15] Pieper H., Ommen T., Buhler F., Paaske B. L., Elmegaard B., Markussen W. B. *Allocation of investment costs for large-scale heat pumps supplying district heating*. Energy Procedia 2018;147:385-367.

[16] Gurobi Optimization Inc. *Gurobi Optimizer* Available at: `https://www.gurobi.com/` [accessed 20.2.2023].

[17] Stock J., Arjuna F., Xhonneux A., Müller D. *Modelling of Waste Heat Integration into an Existing District Heating Network Operating at Different Supply Temperatures*. Smart Energy 2023; 100104

[18] Bundesverband der Energie- und Wasserwirtschaft. *BDEW Gaspreisanalyse Dezember 2022* Available at: `https://www.bdew.de/media/documents/221207_BDEW-Gaspreisanalyse_Dez_2022_07.12.2022_003_fkuXtZW.pdf` [accessed 20.2.2023].

[19] Bundesverband der Energie- und Wasserwirtschaft. *BDEW Strompreisanalyse Dezember 2022* Available at: `https://www.bdew.de/media/documents/221208_BDEW-Strompreisanalyse_Dez2022_08.12.2022_korr_vx5gByn.pdf` [accessed 20.2.2023].

[20] Jurich K. *CO2-Emissionsfaktoren für fossile Brennstoffe*. Dessau-Roßlau, Germany: Umweltbundesamt; 2016 June, ISSN 1862-4359.

[21] Umweltbundesamt. *Spezifische Emissionsfaktoren für den deutschen Strommix* Available at: `https://www.umweltbundesamt.de/themen/luft/emissionen-von-luftschadstoffen/spezifische-emissionsfaktoren-fuer-den-deutschen` [accessed 20.2.2023].

ULPGC
Universidad de
Las Palmas de
Gran Canaria

grres ULPGC
group for the research on renewable energy systems

I. Renewable energy

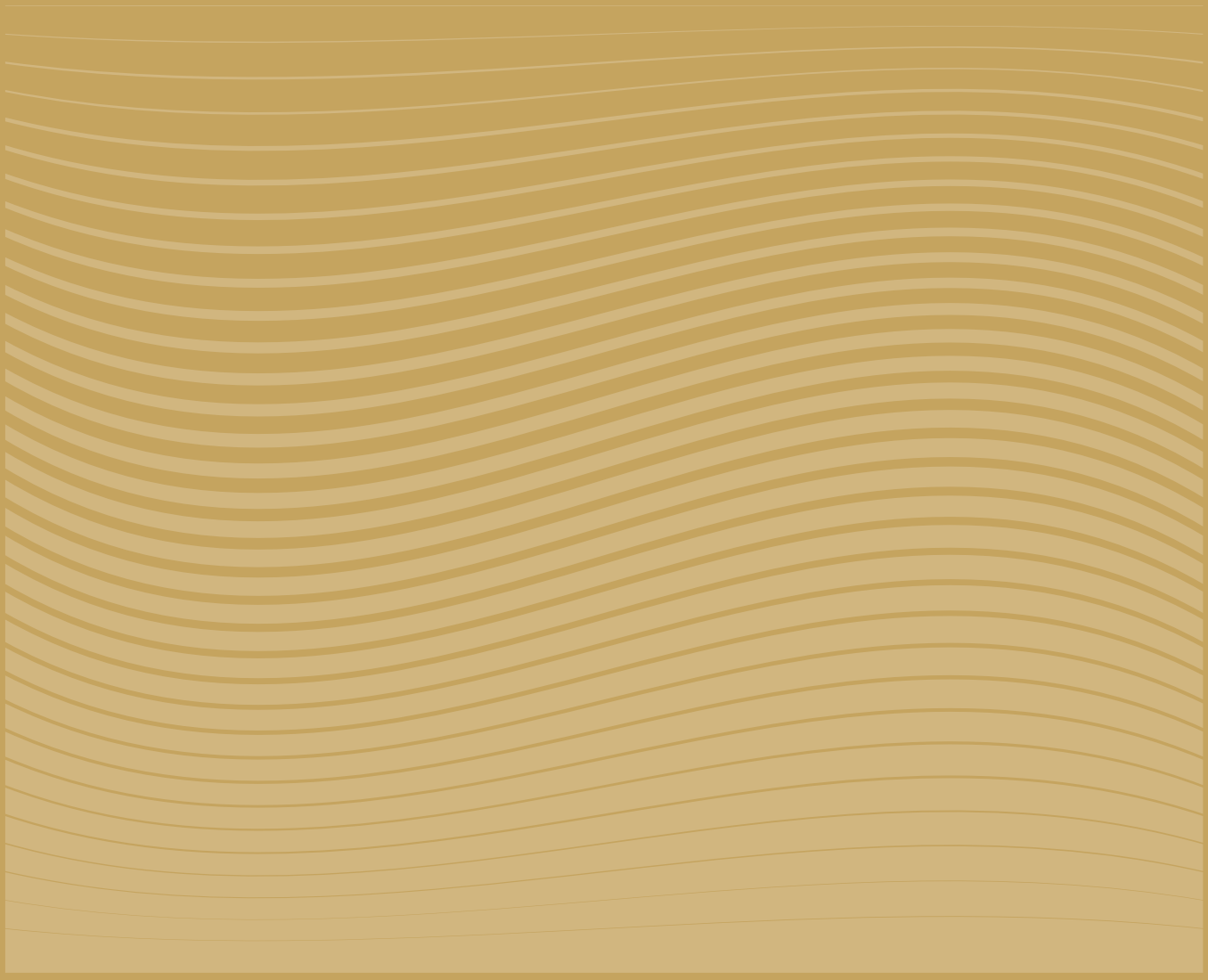

ECOS2023

ECOS 2023: A state-of-the-art review of Geographic Information System applications, the main criteria of selection, and available data that may be used in the process

Krzysztof Szczepaniec[a], Fergal O'Rourke[b], Peter Ryan[c]

[a]Centre for Renewables and Energy at Dundalk Institute of Technology, School of Engineering, Dundalk, Ireland, krzysztof.szczepaniec@dkit.ie, CA
[b]Centre for Renewables and Energy at Dundalk Institute of Technology, School of Engineering, Dundalk, Ireland, fergal.orourke@dkit.ie
[c]Centre for Renewables and Energy at Dundalk Institute of Technology, School of Engineering, Dundalk, Ireland, peter.ryan@dkit.ie

Abstract:

The energy crisis, global warming, and rising energy consumption have positioned renewable energy as a priority from national and international planning perspectives. Not only to reach the goals of the renewable energy mix, but also as part of overall energy security strategy. Rising energy prices and supply concerns have made the need for energy changes that are tangible for society and have increased public awareness of renewable energy. In order to achieve its renewable energy targets, Ireland has placed a focus on the development of offshore wind energy project, due to its massive potential. Other regions have already commenced the deployment of large-scale offshore wind farms and the technology is now competitive with fossil fuels. This work presents a comparison of Geographic Information System (GIS) applications and Multi-Criteria Decision-Making (MCDM) methods applied in the process of multicriteria site selection for Floating Offshore Wind Farms (FOWF). This work presents a reflection on current trends of FOWF site selection, the most suitable and efficient methods, and outlines critical limitations. Finally, the work attempts to map the next steps that shall be taken to improve the methodology.

Keywords:

Geographic Information System (GIS), Floating Offshore Wind Farm (FOWF), Multi-Criteria Decision-Making (MCDM), Analytic Hierarchy Process (AHP), Fuzzy Analytic Hierarchy Process (FAHP), Monte Carlo Analytic Hierarchy Process (MAHP), Evidence Reasoning (ER), Multiple Attribute Decision Analysis (MADA), ECOS Conference;

1. Introduction

The energy crisis, global warming, and rising energy consumption have prioritised renewable energy from national and international planning perspectives. Not only to reach the goals of the renewable energy mix but also as part of the overall energy security strategy. Rising energy prices and supply concerns have made the need for changes tangible for society and have increased public awareness of renewable energy. In order to achieve its renewable energy targets, Ireland has begun to shift its attention to offshore wind developments, for a number of reasons. The government has introduced the new Maritime Area Planning Act [1] that streamlines the planning process. Other regions have already begun to deploy large-scale offshore wind energy projects. In January 2023, the Crown Estate signed Lease Agreements for six offshore wind projects, with a total capacity of 8.0 GW located in the waters around England and Wales [2]. The Scottish Government has even more progressive plans. The Net-Zero target has been set to 2045, five years before the consensus reached under the Paris Agreement [3]. To reach this ambitious target, in 2022 the Crown Estate Scotland conducted the ScotWind Leasing auction of 17 offshore projects with a total capacity of 24.8 GW, ten of those projects involve floating technology with a total capacity of 14.6 GW [4].

The energy crisis has accelerated the legislation and set new objectives dictating the pace of offshore wind development. In May of 2022, The European Commission defined the steps leading to independence from Russian fossil fuels before 2030. The Esbjerg Offshore Wind Declaration [5] signed in May of 2022 by representatives of Denmark, Belgium, Netherlands and Germany set out new targets of at least 65 GW by 2030 and 150 GW by 2050. The European region is not the only one to put offshore wind energy in the spotlight, ambitious objectives have been set out by the USA, China, South Korea, Vietnam, India and Brazil [6].

In 2021, 21.1 GW of offshore wind energy was connected globally to the grid [6] setting a new record. However, according to [7] to achieve Net-Zero before 2050, annual installations should increase to 28 GW by 2030 and then to 45 GW by 2050. The unprecedented shift towards offshore wind technology as one of the main renewable energy sources in the energy mix, and the new technology that must be implemented on a commercial scale to reach the targets, will bring new challenges that must be addressed. The vast majority of wind resources, estimated at about 80%, are located in waters deeper than 60 m [9]. From a technological development perspective, the fixed-bottom offshore wind turbine deployment is constrained to a water depth of approximately 60 m [7,8]. Hence to unlock the offshore wind potential and reach the ambitious objectives, the deployment of floating wind turbines on a commercial scale is inevitable.

The rapid growth of installed offshore wind turbines may, however, come at a price. Pressure to act quickly could potentially compromise stakeholders' interests and harm the natural environment, leading to conflicts and negative perceptions of offshore wind by society. In order to mitigate these potential issues, an efficient methodology and toolset to extract the most suitable locations for development projects is crucial. Site selection for the deployment of floating offshore wind farms off the Irish coast requires careful analysis. Careful site selection requires adequate technics that allow data integration with geographical location, analysis of data, and results visualisation. The Geographic Information System (GIS) addresses all of these requirements. Furthermore, it is widely used in spatial environmental studies since it supports the decision-making process by linking it with multicriteria evaluation methods [11]. Environmental and maritime spatial studies are complex and many interests must be considered. Therefore, sufficient criteria prioritisation and alternative comparison methods are highly desirable to implement alongside GIS.

A good example of how critical the preliminary site selection might be is the 400 MW offshore wind farm Anholt, located off the Danish coast on the Baltic Sea. This location was prioritised by authorities in the planning procedure. However, the risk of construction of the wind farm assessed by three potential bidders was so high, that two bidders gave up the race. As a result, only one offer was submitted with the price per kWh twice as high as for other offshore projects at the time [14]. Floating offshore technology is at a relatively early stage of commercialisation, the first commercial-scale floating wind farm, Hywind Scotland has been in operation since 2017; The farm consists of five floating wind turbines with a total capacity of 30 MW [13]. Another project of 3 wind turbines and total capacity of 25 MW called Windfloat Atlantic has operated since 2020 [12]. The largest operating floating wind farm is the Kincardine Offshore Windfarm located off the east coast of Scotland, consisting of five Vestas V164-9.5MW wind turbines and one Vestas V80-2.0MW wind turbine with a total capacity of nearly 50 MW [12].

2. Geographic Information System

2.1. Methods of spatial analysis

The Geographic Information System (GIS) is a data management and processing tool in the spatial domain. Hence, most researchers use GIS as the primary tool because it allows for the convenient organising of data in a spatial grid and its complex processing capability. It is also a flexible tool allowing advanced users to programme new features. Today, because of the large amount of available data, GIS plays an important role in many aspects of the modern economy. In principle, the vector or raster system of data analysis may be used in GIS. The chosen approach depends on the objectives, the results will differ depending on the chosen method [11]. The first common method of vector-based analysis is the conversion of the criteria to true or false values and then using Boolean operators. This approach leads to the results of a crisp spatial mapping of areas that are either included or excluded from a designated set [11]. This method is suitable to process hard constraints as an exclusion area. The second method is based on raster-based analysis where quantitative criteria are processed as continuous variables rather than simplified to a Boolean's true or false approach [11]. Very often two methods are applicable in one study. Examples of vector and raster methods application can be found in [11,17]. The constraints may have a form of exclusion areas like military zones or designated wildlife areas where offshore wind farm development is prohibited. Criteria can also be a continuous factor where development is not prohibited but less or more favourable because of other factors like wind speed, water depth, distance to the port and many others [11,14].

The key to effectively achieving the objectives is a proper definition of criteria that form the attractors and set the boundaries of the study. Criterion is the basis of decision-making; it represents the objectives and methodology and also serves as evidence of the reasoning behind the decision [22]. Hence, diligent criteria selection is a crucial part of the spatial assessment. Furthermore, the selection should also concern the appropriateness and quality of data they are based on.

2.2. State-of-the-art GIS applications

Due to open access to many valuable data sets and GIS tools, the usage of geographical information system in marine spatial planning has gained momentum. The importance of spatial planning is also acknowledged by authorities. In 2014 the European Commission adopted the directive establishing a framework for maritime spatial planning [15]. The main objectives of the directive are to support the sustainable development of the marine sector by consideration of economic, social and environmental aspects and applying the ecosystem-

based approach to ensure the coexistence of various activities and uses. Moreover, the marine spatial plans shall contribute to the sustainable development of the energy sector on the sea, transportation and fisheries with respect to the preservation and protection of the environment.

For the region of the Celtic Sea off the southwest coast of England and Wales, [16,17] have conducted an extensive GIS spatial analysis to identify project development areas to be offered on tender for Floating Offshore Wind Farm (FOWF) deployment. The central axis of the study was the engagement of the stakeholders at an early stage of the study to participate in the process. The study has a discrete structure that could be divided into five steps. In the first step, the authors defined the area of study and defined main assumptions that were implemented in GIS and visualised. In the second step, the hard constraints were defined. The hard constraints consist of nineteen criteria where only nine of them effectively influence the analysed area, and ten of them don't contribute to the model. Despite not ultimately contributing to the model it is important to acknowledge that they were considered in the study. Step three is the restriction model, based on soft constraints. It includes twenty-six criteria with only two of them not affecting the analysed area. Soft and hard constraints have been listed in Table 1 and Table 2.

Table 1 Hard constraints, exclusion zones

Study	[16, 17]		[18, 19]		[20]		[21]	
Criterion	Applied	Exclusion	Applied	Exclusion	Applied	Exclusion	Applied	Exclusion
Exclusive Economic Zone	Yes	-	Yes	-	No	-	No	-
Distance	Yes	>200 km from grid connection	Yes	>200 NM from shore	No	-	No	-
Protected Wrecks / Heritage	Yes	-	Yes	-	No	-	Yes	-
Environmental protected areas	No	-	Yes	-	Yes	-	Yes	-
Nuclear Power Stations	Yes	Buffer 1NM	No	-	No	-	No	-
Navigational Dredging	Yes	-	No	-	No	-	No	-
Cables agreements	Yes	-	No	-	No	-	No	-
Infrastructure Oil and Gas Agreements	Yes	-	No	-	No	-	No	-
Meteorological Equipment Agreements	Yes	-	No	-	No	-	No	-
Minerals and Aggregates Agreements	Yes	-	Yes	-	No	-	No	-
Minerals Capital and Navigation Agreements	Yes	-	Yes	-	No	-	No	-
Natural Gas Storage Agreements	Yes	-	No	-	No	-	No	-
Pipelines Agreements	Yes	-	Yes	-	No	-	No	-
Tidal stream, wave, wind agreements	Yes	-	Yes	-	No	-	No	-
Aquaculture agreements	Yes	-	Yes	-	Yes	-	Yes	-
Outfall leases	Yes	Buffer 250 m	No	-	No	-	No	-
Active cables Infrastructure	Yes	Buffer of 250 m	Yes	Buffer 500 m	No	-	No	-
Active Pipelines Infrastructure	Yes	-	Yes	Buffer 500 m	No	-	No	-
Traffic Separations Schemes	Yes	Buffer 1.77 NM	Yes	Buffer 500 m	Yes	-	Yes	-
Platform Helicopter Safety Zones	Yes	-	No	-	No	-	No	-
Military areas	No	-	Yes	-	No	-	No	-

Wind Velocity	Yes	<9.5 m/s @ hh	Yes	Excluded <4 m/s @ 10 m	No	-	Yes	<4 m/s and >25 m/s
Water Depth	Yes	<50 m >250 m	Yes	<50 m >1000 m	Yes	<62 m >1000 m	Yes	<100 m
Significant wave height	Yes	Not excluded but 2 groups identified: <14 m >14 m	No	-	No	-	Yes	>8 m
Islands / Rocks	No	-	No	Unkonwn	Yes	-	Yes	-
Seismic fault lines	No	-	No	-	Yes	-	No	-

Table 2 Soft constraints, evaluation criteria

Ref.	General Criteria Tier 1	Weight	Basic Criteria Tier 2	Weight	Basic Criteria Tier 3
[17]	Economic	0.5	Navigation	0.1	AIS density (Tier 4)
					Harbor authorities
					Anchorage areas
					Open disposal sites
			Sub-surface infrastructure	0.225	Evaporites agreements
					CCUS agreements
					O&G Fields
					O&G awarded blocks
			Infrastructure	0.175	Out of service pipelines
					Out of service cables
					Wells
			Fisheries	AIS data, linear weight	AIS density (Tier4)
	Environmental	0.2	Environmental designations	0.11	SACs
					SPAs
					Ramsar
					MCZ & NNRs
					SSSIs
			Environmental features	AIS data, linear weight	Fish spawning & nursery areas (Tier 4)
			Contamination	0.09	Closed disposal sites
	Social	0.3	Leisure	0.045	AIS density (Tier 4)
					Recreational Yachting Training Areas
					Marinas
			Visual	0.075	Visibility
			Historic	0.075	Wrecks (unprotected)
					World Heritage Sites
			Bathing	0.09	Bathing beaches
[18]	General Criteria	Weight	Basic Criteria		Weight
	Met-ocean	0.295	Wind velocity		0.073
			Wind potential		0.094
			Water depth		0.038
			Wave conditions		0.051
			Marine currents		0.028

			Temperature	0.01
	Viability	0.104	Technical feasibility	0.066
			Sufficient study times	0.038
	Logistics	0.102	Distance to local electrical grid	0.053
			Distance from coastal facilities	0.048
	Facilities	0.237	Distance from shore	0.033
			Distance from residential areas	0.032
			Distance from the maritime routes	0.03
			Distance from underwater lines	0.042
			Distance to marine recreational activities	0.035
			Distance from airport	0.065
	Marine environment	0.148	Distance from protected areas	0.064
			Proximity to migratory bird paths	0.043
			Proximity to migratory marine life paths	0.041
	Techno-economic	0.114	Area of the territory	0.035
			Proximity to the area of electric demand	0.031
			Population served	0.017
			Multiple resources	0.031
[21]	Met-ocean	0.515	Wind velocity	0.3697
			Potential power output	0.3344
			Significant wave height	0.2441
			Tidal range	0.0518
	Logistics	0.1756	Vicinity to ports maintenance	0.3212
			Sub-station vicinity	0.2384
			Depth range	0.4404
	Facilities and environment	0.3094	Minimum distance to land	0.0669
			Proximity to fisheries	0.0688
			Proximity to shipping lanes	0.2722
			Proximity to shipwrecks	0.0424
			Proximity to MPAs	0.2774
			Proximity to aquatic habitats	0.2722

AIS - Automatic Identification System, CCUS - Carbon Capture Utilisation and Storage, O&G - Oli and Gas, SACs - Special Areas of Conservation, SPAs - Special Protection Areas, MCZ - Marine Conservation Zone, NNRs - National Nature Reserves, SSSIs - Sites of Special Scientific Interest

Step four is based on the application and processing data applied to models in previous steps. As a result of running the exclusion and restriction models in the GIS, the map presenting more or less favourable to FOWFs deployment locations was created. The soft constraints criteria were organised into groups and subgroups and then pairwise compared. The analytic hierarchy process (AHP) was used to assess their relative importance and to calculate the weights of soft constraints. Finally, the weights were applied to the soft constraints model. The combined output has been normalised from 0 to 100 to reflect the percentage of constraints. Then the considered area has been divided into equal cells of the seabed. The constraints have been organised into ten groups ranging from the least constraints of 10% to the most constraint 90% and 100%. Cells constrained in 50% or less were chosen for further proceedings. Then neighbouring cells were organised forming five large areas representing 11,000 km^2, of potential FOWF sites, which will be a subject of a detailed study in step five which has not been completed yet. The selection of the project development areas (PDAs) is based on the assessment of technical risks, cost of energy and environmental and social impact. This step will identify smaller areas of the PDAs that will be offered on public auctions for particular FOWF projects. Therefore, a detailed study of technical risks and the cost of energy is required. To fully understand the technical challenges and cost of the energy the authors are aiming to:

- study wake effect to shape project parameters and forecast energy yield;
- recognise the relationship between the energy density, turbine layout and mechanical fatigue loading;
- analyse mooring and anchoring systems and their limitation in terms of geotechnical and met-ocean site characteristics;
- recognise energy export options and related costs as well as onshore grid reinforcement.

Finally, based on the information above fine tune Levelised Cost of Energy (LCOE) layer will be used in the final PDAs ranking.

For the region of the European Atlantic coast of Portugal, Spain and France the [18] has proposed an integrated GIS approach of multicriteria site selection for floating offshore wind farms. Researchers conducted the literature review in the field of offshore wind farms site selection based on GIS and Multi-Criteria Decision-Making (MCDM) methods and proposed their proprietary approach of an integrated GIS tool built using the Phyton language. The site selection is performed in three stages. In the first stage data from various regulatory bodies, like national marine spatial plans and issued concessions are collected and processed to feed the GIS model. The second stage is narrowing the area of search by the addition of hard constraints as a result of step one. The hard constraints or in other words exclusion zones can be divided in this study into two main categories. The first is the regulatory, infrastructural and maritime usage while the second is related to social-economic aspects reflected in wind speed, water depth and distance from shore. The locations with an average wind speed below 4 m/s at 10 m height are considered as not suitable therefore form the exclusion zone. As a suitable area to deploy FOWF the water depth range between 50 m to 1000 m has been considered as well as a minimum distance from shore in case of the regions where such regulations are in place. The third step of the study aims to assess the feasible locations defined in the previous step. Each site may have a different characteristic that shall be recognised and represented by the quantitative, objective measure to allow for choice of the best alternative from a technical and socio-economic perspective. To rank sites, a set of evaluation criteria or in other words soft constraints have been proposed by the researchers. With the help of industry experts and as per a review of existing studies, the twenty-three evaluation criteria grouped into six categories have been chosen and applied to the model. Soft and hard constraints have been listed in Table 1 and Table 2. As a result of the study, the forty-two locations suitable for floating offshore farms have been identified and evaluated. The area of potential FOWF development covers 7230 km^2. To ease site comparison, each site has been characterised by the fixed set of evaluation criteria like: average wind speed, wind potential, water depth and others. The researchers have also estimated the number of wind turbines and annual energy yield together with CO_2 and SO_2 reduction as well as direct and indirect job creation. The advantage of the procedure is its flexibility in terms of applied criteria and transparency however since there are just a few examples of operating small-scale floating wind farms, there is no reliable operational data that include the power curve changes and availability factors. Therefore, performance estimates have a large component of uncertainty and shall be treated just as an indication factor. In [18], no MCDM methods have been implemented.

In the follow-up article [19] written by the same authors, the site selection of forty-two potential floating wind sites has been supplemented with the MCDM method to ease and streamline the multi-criteria decision-making process. In that research, scholars utilised the twenty-three evaluation criteria formed in the previous study. The relative importance of each criterion has been estimated in a pairwise comparison process with the AHP methodology. The criteria's weights were assigned based on the opinion of five industry experts representing different fields of the offshore wind industry. The pairwise comparison method was used not only to weight criteria but also to evaluate alternatives which are in this case forty-two locations grouped by region. All feasible locations were compared concerning each criterion therefore with known criterion weight derived in the previous step the most suitable location in each group could be identified.

Castro-Santos et al. [20] have proposed the application of GIS for selecting the site for the floating offshore farm in the North-West of Spain. The GIS method is similar to the above studies and comprises two steps. The first is defining the exclusion zones, and the second step defines the soft constraints. As a hard constraint where development is not permitted or desirable the following restrictions are considered: fishing banks and grounds, navigation areas, Spanish marine development plans, environmental protection areas, underwater rocks and seismic fault lines. Noteworthy is the application of bathymetry as a hard constraint that can be adjusted to the given platform technology addressing different draft requirements. The area of the search will vary depending on the considered technology.

The soft constraints are based on local ports and shipyards' characteristics. The draft, storage area and lifting capability have been considered. In the case study described in [20], the ports and shipyards draft has been set between 3.0 m to 12.5 m which is suitable for installation vessels and tugboats but not for semisubmersible platforms where the draft oscillates around 20 m [10]. Low draft of the shipyards and ports that may not be suitable for towing to site some platform types or preassembled turbines on platforms. A higher draft and study of overhead clearance would contribute to the output of [20].

The final areas of interest are shaped based on hard and soft constraints as per desirable water depth or port and shipyard characteristics. As an output not only feasible areas of development are plotted but also the distance to the suitable port or shipyard and the economic indexes of internal rate of return, levelised cost of energy and others. The economic indexes are presented in the form of a heat map covering only areas that are resultant of the application of exclusion zones and soft constraints. The input parameters that are used to calculate the economic indexes have not been presented in [20]. No MCDM method has been applied in the study, however, the estimation of economic factors and depicture results on maps support decision-making based on economic criteria.

Nonetheless, due to the immaturity of floating wind farm technology, and other factors that have a significant impact on costs and energy yield, it is expected that large uncertainty is assigned to these factors. Therefore, they shall be considered as indications rather than precise values. Nonetheless, it is important to incorporate this information in the study as ultimately, it is one of the key decision drivers. Graphical presentation of economic indexes is a clear advantage of the study [20] and may be used as an input to GIS overlay analysis. However, the lack of clarity on how the indexes were obtained adds extra uncertainty to the results.

For the western part of the Irish coast, [21] has outlined a multiple attribute decision-analysis methodology for selecting the most suitable location to deploy the floating offshore wind farm. In order to limit the search area, researchers conducted a literature review, identified sites that are either developed or in planning procedure, investigated the grid connection possibilities and held meetings and consultations with experts in the renewable and legislation field. This procedure led to the selection of the area of interest of Shannon Foynes Bay off the coast of Galway. Instead of dedicated GIS software typically used in spatial analysis, researchers utilised Microsoft Excel. The Excel cells play the same role as the raster cells in GIS assessments. It allows the assignment of multiple attributes reflecting criteria to each cell and the application of Excel formulas. Usage of Excel where more suitable tools are available may not be the best choice. However, in cases where no high-resolution data are available or the research doesn't require a large spatial precision Excel may serve well. In [21] usage of proper GIS tools would contribute in a positive way to the conducted research. Here also criteria are divided into two main groups of hard and soft constraints. The nine hard constraints and thirteen soft constraints organised into three main groups have been identified. It is unclear if all of the listed constraints have contributed to the final output. After the limitation of the search area by the application of hard constraints the researchers with the help of five experts in the offshore wind industry prioritised soft criteria in the pairwise comparison procedure as a part of the AHP method. Then the MCDM method of Evidence Reasoning (ER) was applied. Soft and hard constraints have been listed in Table 1 and Table 2.

3. Multi-Criteria Decision Making

The Multi-Criteria Decision Making (MCDM) methods are used to support the decision-making aiming to achieve the objective by choosing the best alternative among all alternatives under multiple evaluation criteria. The increase in the number of MCDM methods took place in the 1970s, while the origins of modern MCDM date back to the 1950s [23]. Over one hundred MCDM methods have been developed, moreover, recently hybrid and modular methods are frequently used to eliminate the basic methods' drawbacks. An example is an application of fuzzy set theory to the Analytic Hierarchy Process (AHP), implemented in [29,30]. The MCDM methods are widely used in the financial sector, medical diagnostic, engineering, spatial planning, management and other fields where multiple criteria must be handled in the decision process. The choice of the method depends on the scenario that is analysed. Some of the methods are suitable for certain problem-solving, but there is no single universal method to address all scenarios [24].

3.1. MCDM methods used in site selection

A floating offshore wind farm site selection requires detailed consideration of multiple criteria in order to achieve the objectives. In FOWF site selection one of the most popular methods is the AHP introduced by Saaty in 1971 [25]. Application of AHP requires deconstructing problems in a hierarchical or network structure followed by the Pairwise Comparison (PC) of elements regarding their importance. To score relative importance, Saaty's fundamental scale has been applied as presented in Table 3. In the typical AHP process of site selection, the criteria would be pairwise compared to reaching the goal and separately the alternatives (feasible sites) concerning criteria.

The relative intensity of importance	Name	Explanation
1	Equal importance	Equal contribution
3	Moderate importance	Experience and judgment strongly favour one over another
5	Essential importance	Experience and judgment strongly favour one over another
7	Very strong importance	One is strongly favoured and its dominance is verified in practice
9	Extreme importance	Strong evidence exists in favour of one over another

2,4,6,8	Intermediate values	The comprise solution
Reciprocal	-	If *i* has one of the importance numbers when compared with *j,* then *j* has a reciprocal value of *i*

Table 3 The Saaty's fundamental scale [25]

The AHP is a relatively easy and transparent method, it introduces a structural and logical division of complex problems and a pairwise comparison of its elements step by step. It also allows for group decision-making and evaluation of quantitative and qualitative criteria as well as an application of subjective and objective measures.

Among the weaknesses of the method is a rapid increase in pairwise comparisons with criteria and alternatives to be considered [25]. The number of pairwise comparisons needed for a particular matrix of order *n,* is *n(n-1)/2* because it is reciprocal as well as its diagonal elements are comparisons of the same elements and therefore equal to one [25]. Let the A_1 , A_2 ,…, A_n , be the set of criteria. The comparison of criteria is represented by n-by-n matrix $A = (a_{ij})$, $ij = 1,2, \dots, n$. The quantified pairwise comparison on pairs of (A_i, A_j) is represented by numerical entries a_{ij} in matrix A [28]. The entries a_{ij} to (1) follow two general rules:

if $a_{ij} = a$, then $a_{ji} = 1/a$, $a \neq 0$;

and,

if relative importance intensity $A_i = A_j$, then $a_{ij} = 1$, $a_{ji} = 1$, as well as $a_{ii} = 1$.

The comparison matrix *A* has the form:

$$A = \begin{bmatrix} 1 & \cdots & a_{1n} \\ \vdots & \ddots & \vdots \\ \frac{1}{a_{1n}} & \cdots & 1 \end{bmatrix} \quad (1)\ [28]$$

Besides human error, bias, or subjectivity, the final result will also be influenced by the presentation of Saaty's scale, the number of degrees used (eg. five instead of nine) and their form of verbal degrees or numerical as well as the graphical presentation of scale. Also, the method of obtaining the judgments is important, whether as an administrated interview or without the influence of the researcher [26]. The main advantages and disadvantages of the AHP method are listed below.

Among the main advantages of the AHP method are:

- Relative simplicity and transparency [25];
- Useful for organising the complex problem into a structured hierarchy [25];
- Offer the possibility of application of quantitative and qualitative criteria as well as an objective and subjective evaluation of each on one scale [19];
- Support of group judgments [25];
- Consistency check allows for verification of errors in the pairwise comparison process [25,28].

However, the AHP method does have some disadvantages:

- It is based on experts' opinions therefore it may be subjective [27];
- Each group of elements that are pairwise compared should not exceed seven, therefore in the case of many criteria division in many subgroups is required [28];
- The number of pairwise comparisons increases rapidly with the number of criteria [25];
- Presentation of Saaty's fundamental scale and form of gathering expert's opinions may influence results [26];

The AHP procedure supported by GIS was used by The Crown Estate [17]. The pairwise comparison of criteria concerning their risk of achieving the objective was introduced. The criteria selection and weighting are a result of consultations with stakeholders and industry experts. Twenty-six soft constraints were identified and organised in the logic hierarchy. The soft constraints were relatively compared with respect to the risk posed to achieve a goal. Therefore, the higher the weight of the criterion then the higher the risk is. The result of this process is weights were normalised from 0 to 100 and divided into ten groups. Finally, they were fed to the GIS model as the attributes of raster cells, where weights were summed-up as an overlay of multiple data layers of each soft constraint. The higher the score the more constraint the raster cell is. The cells with a score of 50% or less were chosen for further proceedings followed by grouping neighbouring cells to form larger areas. In that manner, the areas with the lowest development risk were identified, so further assessment with the concern of the performance and costs of the FOWF can be conducted.

For the Atlantic coastal region of Spain, France and Portugal, Diaz and Guedos Soares [19], conducted an extensive multicriteria floating site evaluation. Their work comprises not only criteria weighting but also an

evaluation of forty-two sites that have been outlined as a result of the GIS procedure conducted in the preceding study [18]. The pairwise comparisons of constraints were conducted by five experts experienced and competent in broad offshore energy areas. Nonetheless, the evaluation of the importance of certain criteria varied between experts, which indicates the bias made by their area of expertise. The way of objectifying experts' input or at least the measurement of ambiguity and ignorance would contribute in a positive way to the study and assessment of the results. The authors also identified this downside and therefore explored other MCDM methods in the further studies [29].

To reflect the central tendency of the results of pairwise comparisons conducted by the experts, their judgments were averaged throughout the geometric mean. Unlike in [17] the criteria weights calculated in [19] are reflecting risks by minimising weight with the proximity to certain elements (eg. maritime routes) and the opportunities by maximising weight where higher wind speed occurs. The higher the combined weight the better the location is from an economic and risk perspective.

The AHP method assumes that the decision maker in the pairwise comparison process can select a clear winner which may not be the case in many situations. In these cases, the probabilistic approach would provide additional information [30]. Therefore, the AHP is not recommended for scenarios with high uncertainty of judgments. Also, if the final rank of alternatives is convergent, there are no statistical measures to differentiate alternatives and support decision-making [31].

To address issues inherently related to the application of AHP, the study [19] has been extended by Diaz et al. [29] with the addition of the Monte Carlo simulations and Fuzzy Set theory to determine the relative preference of wind farm locations. The fuzzy set theory applied to AHP forming the FAHP allows for ambiguity in decisions, where there are no clear boundaries therefore the decisions are closer to natural human decisions [29,30]. The application of the fuzzy set is executed by replacing the standard Saaty's scale with Triangular Fuzzy Numbers (TFNs).

The AHP and FAHP do not provide a measure for the imprecision and disagreement between decision-makers. The Monte Carlo Analytic Hierarchy Process (MAHP) provides information about the influence on results of judgment variability of decision-makers. The application of Monte Carlo simulation is recommended when there is a large uncertainty associated with the ranking of alternatives. However, the exact level of uncertainty over which the Monte Carlo Analytic Hierarchy Process (MAHP) outperforms the AHP is not clearly defined [31,32]. In [29] nine different locations were ranked based on twenty-three criteria resulting in twenty-three separate sets of pairwise comparisons for each location. Finally, the ranking of each location was performed with three methods: AHP. FAHP and MAHP. The same results were derived for locations ranked at first, second and third place. Seven out of nine locations were ranked the same by AHP and MAHP, the only differences being locations ranked as seven (Bilbao) and eight (Mutriku). Five out of nine locations were ranked the same by AHP and FAHP, where the highest difference in ranking is by two places, the location ranked by AHP is in seventh position while using the FHAP method is in ninth position. In All three methods, changes by one to two locations in the ranking occurred between Bilbao, Mutriku and San Vicente sites. The probability distribution derived from MAHP shows that the probability of ranking those three locations at the place of seventh, eighth and ninth is very close oscillating around 30%. That explains slight differences in final results between the three methods. Convergent results especially between the AHP and MAHP and slight variance between AHP and FAHP indicates that in the given example, the AHP method itself performs equally or if not better considering its simplicity than FAHP and MAHP. The clear advantage of study is application of MAHP resulting with an additional data to be used in interpretation of the results. The Table 4 lists the results of the [29].

Table 4. Comparison of AHP, FAHP and MAHP results from [29].

No.	Site name	Ranking			Probability of occurrence at a given ranking place					
		AHP	FAHP	MAHP	Ranking No.	Probability	Ranking No.	Probability	Ranking No.	Probability
1	Ribadeo	1	1	1	1	87%	2	6%	3	4%
2	Navia	2	2	2	2	40%	3	36%	4	10%
3	A Guarda1	3	3	3	3	35%	4	24%	2	21%
4	Huelva	4	5	4	4	24%	2	21%	6	20%
5	A Guarda2	5	4	5	5	33%	4	25%	6	22%
6	Santander	6	6	6	6	43%	5	29%	4	13%
7	Bilbao	7	9	8	9	32%	7	28%	8	28%
8	Mutriku	8	8	7	8	31%	9	30%	7	29%
9	San Vicente	9	7	9	8	32%	9	30%	7	29%

A slightly different approach to multi-criteria site selection of FOWF is presented in [21]. Researchers applied the AHP method to calculate weights of general and basic criteria and then employed the Evidence Reasoning (ER) method to rank the sites. The AHP method combined with ER is also named Multiple Attribute Decision Analysis (MADA). The ER is an evidence-based primary MCDM method developed in the early nineties. It applies to solving problems having quantitative and qualitative criteria [21]. Unlike in the AHP, the ignorance and uncertainty of decision-makers can be assessed. The downside of this method is its complexity, therefore non specialists may not be able to apply it or interpret results [33]. In [21] the MADA method was applied to rank forty-three sites of Shannon Foynes Bay off the coast of Galway. The utility ranking derived in the MADA method vary in the range of 0.6193 for the site ranked at first place to 0.5421 for the site at forty-third place which results in an average step per rank of 0.002. As a result of the study, the most suitable site has been determined along with other sites where five of the most suitable sites are adjacent. The site named F16 is the most favourable site among all forty-three sites explored. Furthermore, this site was ranked high in all three general criteria. However, site G14 ranked third position was ranked twelve and nineteenth in terms of the general criteria of met-ocean and facilities and environment but first in general criteria of logistics. The general criteria weighting has been distributed in [21] as follows: met-ocean 51.50%, facilities and environment 30.94% and logistic 17.56%. It is seen that combination weighting has a profound effect on the final assessment of site suitability [21]. The very small average step per place in rank and therefore high sensitivity to criteria alteration and resulting high uncertainty indicate that MADA method may not suit well in ranking adjacent sites of similar characteristics. To support the result interpretation, the ignorance and uncertainty of decision-makers shall be assessed in [21].

In [34] the researchers compared AHP and MADA methods. The comparison has been performed based on the case study of twenty-two feasible sites off the coast of Scotland and three sites off the Madeira Islands. The locations used in the case study were derived from other studies performed by Loughney et al. [35] and Diaz and Guedes Soares [18,19]. The final results of ranking sites off Scotland's shore show no substantial differences in location suitability assessment. Results up to eight in rank vary by one place. Results of ranking sites off the Madeira Islands are the same for the first place in ranking however the second and third places are reversed between AHP and MADA.

The weights range for the ranking of the Scottish sites is very narrow for the AHP method ranging between 0.9984 for the site ranked at first place to 0.9866 for the site ranked at the twenty-second place. It means that the average step of weight per place in the ranking is 0.0006. The range of weights derived in the MADA method vary in range of 0.7565 for the site ranked at first place to 0.6325 for the site at twenty-second place which results in an average step per rank of 0.006. The range of weights in the ranking of the Madeira Islands is wider than for Scottish sites the weights range from 0.697 to 0.567 in the AHP method and from 0.392 to 0.300 in the MADA method. Respectively the average step of weight per place of rank is then 0.065 and 0.046. The relatively narrow weight range in the case study of Scottish [35] sites are compared to Irish sites as in [21] which were also grouped in a relatively small area is probably the result of lower differentiation of sites' characteristics. The very small average step per place in rank, high sensitivity and resultant high uncertainty indicate that AHP and MADA methods may not suit well in ranking adjacent sites of similar characteristics.

The comparison shows that both methods are suitable to support multi-criteria decision-making and allow for the engagement of the industry experts and stakeholders considering all interests because both methods support group-decision making. The inherent subjectivity of preferences between criteria is one of the disadvantages of the AHP method. Limited involvement of experts in the final steps of the MADA method, which requires a detail study of criteria by the methodology developer, may reduce the influence of the subjectivity of the experts [34]. One of the advantages of the MADA method is its ability to measure ignorance, however this factor has not been estimated in reviewed studies. [21,34].

The AHP method requires less computations, is easier to implement, and more intuitive, therefore in this regard, it outperforms the MADA method. Because of this the AHP may be the preferred method to be applied where stakeholders and non-specialists are engaged in the process of site selection. Results indicate that the value of the weight across all sites is very similar, therefore there is no clear winner. In this case, the uncertainty of the results is high. This can raise confusion among stakeholders that no clear information for decision-making has been obtained as a result of the study. Ranking sites of similar characteristics using the AHP and MADA methods requires a diligent approach because of large uncertainty of the results.

4. Conclusion and further research

The complexity of this task is reflected in different sets of soft and hard criteria chosen by researchers as listed in Table 1 and Table 2. Some of the discrepancies in the criteria selection result from the methodology and some from the geographical region that is analysed but most of them are caused by lack of standardisation and immaturity of technology therefore lack of clear guidance that would set the framework to floating offshore farm site selection.

The methods of site selection are evolving and researchers use various GIS techniques, different criteria sets, as well as various combinations of MCDM methods. Very often the AHP method has been used to derive the criteria weights and rank sites.

The inherent disadvantage of the AHP method is its subjectivity and lack of possibility to measure ignorance and ambiguity of the expert's input. Some researchers applied a combination of the AHP method with other methods like fuzzy set theory, Monte Carlo simulations and evidence reasoning. A comparison of the results shows that there is no clear winner among those methods. Some of them like ER method add extra layers of complexity that its application is limited to advanced users and therefore would work as a black box for non-specialists. One of the advantages of the ER method is its ability to measure ignorance however this estimation has not been performed in reviewed studies [21,34].

The application of Monte Carlo simulations adds extra information to the site selection process. Despite its complexity, the probability distribution of rank place of various alternatives may be very important information in the decision-making process. However, very similar results between AHP and MAHP in the reviewed study [29] as presented in Table 4 together with the simplicity of AHP compared to MAHP are questioning the application of this method.

The application of MCDM methods to rank sites of very similar characteristics may result in convergent results for the sites, however, the uncertainty of the results is high and the final site ranking may be questionable. Therefore, the GIS and MCDM methods perform well in high-level spatial analysis over a large area on a national or international scale. While assessing adjacent sites on a local level different methods or at least different sets of criteria shall be considered.

Further research on site selection for floating wind farms should be focused on creating the standards reflecting the technical specification of floating platforms supported by operational data. That would decrease the level of experts' judgment subjectivity as well as allow for test robustness of various MCDM methods using the same criteria and possibly a quantitative comparison of them.

Future research shall also be conducted towards the economic aspects concerning the Levelised Cost of Energy (LCOE) from floating offshore wind farms. The success and pace of implementation of this technology are strongly correlated with this factor.

References

[1] Electronic Irish Statute Book (eISB) – Available at:<https://www.irishstatutebook.ie/eli/2021/act/50/enacted/en/html> [accessed 23.1.2023].

[2] The Crown Estate, Offshore Wind Leasing Round 4 – Available at:<https://www.thecrownestate.co.uk/round-4/> [accessed 25.1.2023].

[3] Act of the Scottish Parliament. Climate Change (Emissions Reduction Targets) (Scotland) Act 2019 (asp 15).

[4] The Crown Estate Scotland, ScotWind Leasing – Available at:<https://www.crownestatescotland.com/news/scotwind-offshore-wind-leasing-delivers-major-boost-to-scotlands-net-zero-aspirations> [accessed 25.1.2023].

[5] The Esbjerg Offshore Wind Declaration - Available at:<https://windeurope.org/policy/joint-statements/the-esbjerg-offshore-wind-declaration/> [accessed 26.1.2023].

[6] Williams R, Zhao F, & Lee J. (2022). *GWEC GLOBAL OFFSHORE WIND REPORT 2022*

[7] IRENA (2019), Future of wind: Deployment, investment, technology, grid integration and socio-economic aspects (A Global Energy Transformation paper), International Renewable Energy Agency, Abu Dhabi.

[8] Jiang, Z. (2021). Installation of offshore wind turbines: A technical review. *Renewable and Sustainable Energy Reviews*, *139*, 110576. https://doi.org/10.1016/J.RSER.2020.110576

[9] The Global Wind Atlas – Available at:<https://globalwindatlas.info/en> [accessed 23.1.2023].

[10] Sergiienko, N. Y., da Silva, L. S. P., Bachynski-Polić, E. E., Cazzolato, B. S., Arjomandi, M., & Ding, B. (2022). Review of scaling laws applied to floating offshore wind turbines. In *Renewable and Sustainable Energy Reviews* (Vol. 162). Elsevier Ltd. https://doi.org/10.1016/j.rser.2022.112477

[11] Eastman, J. R. (1999). Multi-criteria evaluation and GIS. *John Wiley and Sons*, 493–502.

[12] Principle Power the official website – Available at:<https://www.principlepower.com/windfloat> [accessed 27.1.2023].

[13] Equinor the official website – Available at:<https://www.equinor.com/energy/hywind-scotland> [accessed 27.1.2023].

[14] Möller Bernd, B. (2011). Continuous spatial modelling to analyse planning and economic consequences of offshore wind energy. *Energy Policy*, *39*(2), 511–517. https://doi.org/10.1016/j.enpol.2010.10.031

[15] European Commission. Directive 2014/89/EU of the European Parliament and of the Council of 23 July 2014 establishing a framework for maritime spatial planning.

[16] Fitch-Roy, O., Baldock, N., Gibberd, G., & Phillips, J. (2020). BROAD HORIZONS: Key resource areas for offshore wind Summary Report An Everoze Report, commissioned by The Crown Estate.

[17] The Crown Estate. (2022). *Celtic Sea Floating Wind Programme: Draft Site Selection Methodology*. https://www.thecrownestate.co.uk/media/4150/2022-floating-wind-site-selection-methodology-report.pdf

[18] Díaz, H., & Guedes Soares, C. (2020). An integrated GIS approach for site selection of floating offshore wind farms in the Atlantic continental European coastline. *Renewable and Sustainable Energy Reviews*, *134*. https://doi.org/10.1016/j.rser.2020.110328

[19] Díaz, H., & Guedes Soares, C. (2022). A novel multi-criteria decision-making model to evaluate floating wind farm locations. *Renewable Energy*, *185*, 431–454. https://doi.org/10.1016/j.renene.2021.12.014

[20] Castro-Santos, L., Lamas-Galdo, M. I., & Filgueira-Vizoso, A. (2020). Managing the oceans: Site selection of a floating offshore wind farm based on GIS spatial analysis. *Marine Policy*, *113*. https://doi.org/10.1016/j.marpol.2019.103803

[21] Loughney, S., Wang, J., Bashir, M., Armin, M., & Yang, Y. (2021). Application of a multiple-attribute decision-analysis methodology for site selection of floating offshore wind farms off the West coast of Ireland. *Developments in Renewable Energies Offshore - Proceedings the 4th International Conference on Renewable Energies Offshore, RENEW 2020*, 389–398. https://doi.org/10.1201/9781003134572-45

[22] Eastman, L. R., Jin, W., K' Kyem, P. A., & Toledano, J. (1995). Raster Procedures for Multi-Criteria /Multi-0biective Decisions. In *Photogrammetric Engineering & Remote Sensing* (Vol. 61, Issue 5).

[23] Mardani, A., Jusoh, A., Nor, K. M. D., Khalifah, Z., Zakwan, N., & Valipour, A. (2015). Multiple criteria decision-making techniques and their applications - A review of the literature from 2000 to 2014. In *Economic Research-Ekonomska Istrazivanja* (Vol. 28, Issue 1, pp. 516–571). Taylor and Francis Ltd. https://doi.org/10.1080/1331677X.2015.1075139

[24] Baydaş, M., & Pamučar, D. (2022). Determining Objective Characteristics of MCDM Methods under Uncertainty: An Exploration Study with Financial Data. *Mathematics*, *10*(7). https://doi.org/10.3390/math10071115

[25] Saaty, R. W. (1987). THE ANALYTIC HIERARCHY PROCESS-WHAT IT IS AND HOW IT IS USED (Vol. 9, Issue 5).

[26] Prusak, A., Stefanów, P., & Strojny, J. (n.d.). Monica GARCIA-MELON 4 THE INFLUENCE OF THE FORM OF THE 9-POINT SCALE IN THE AHP METHOD ON THE CONSISTENCY OF JUDGMENTS: Vol. XXI. www.superdecisions.com

[27] Saaty, T. L., & Vargas, L. G. (2001). *The Seven Pillars of the Analytic Hierarchy Process* (pp. 27–46). https://doi.org/10.1007/978-1-4615-1665-1_2

[28] Saaty, T. L., & Ozdemir, M. S. (2003). Why the Magic Number Seven Plus or Minus Two. In *MATHEMATICAL coMPuTEa MODELLING Mathematical and Computer Modelling* (Vol. 38). www.elsevier.com/locatp!mcm

[29] Díaz, H., Teixeira, A. P., & Guedes Soares, C. (2022). Application of Monte Carlo and Fuzzy Analytic Hierarchy Processes for ranking floating wind farm locations. *Ocean Engineering*, *245*. https://doi.org/10.1016/j.oceaneng.2021.110453

[30] Taoufik, M., & Fekri, A. (2021). GIS-based multi-criteria analysis of offshore wind farm development in Morocco. *Energy Conversion and Management: X*, *11*, 100103. https://doi.org/10.1016/J.ECMX.2021.100103

[31] Rosenbloom, E. S. (1996). EUROPEAN JOURNAL OF OPERATIONAL RESEARCH A probabilistic interpretation of the final rankings in AHP. In *European Journal of Operational Research* (Vol. 96).

[32] Yaraghi, N., Tabesh, P., Guan, P., & Zhuang, J. (2015). Comparison of AHP and Monte Carlo AHP under different levels of uncertainty. *IEEE Transactions on Engineering Management*, *62*(1), 122–132. https://doi.org/10.1109/TEM.2014.2360082

[33] Ngan, S. C. (2015). Evidential Reasoning approach for multiple-criteria decision making: A simulation-based formulation. *Expert Systems with Applications*, *42*(9), 4381–4396. https://doi.org/10.1016/j.eswa.2014.12.053

[34] Díaz, H., Loughney, S., Wang, J., & Guedes Soares, C. (2022). Comparison of multicriteria analysis techniques for decision making on floating offshore wind farms site selection. *Ocean Engineering*, *248*. https://doi.org/10.1016/j.oceaneng.2022.110751

[35] Loughney, S., Wang, J., Bashir, M., Armin, M., & Yang, Y. (2021). Development and application of a multiple-attribute decision-analysis methodology for site selection of floating offshore wind farms on the UK Continental Shelf. *Sustainable Energy Technologies and Assessments*, *47*. https://doi.org/10.1016/j.seta.2021.101440

Energy evaluation of hydrogen production integrated into the ethanol and sugar production process

Maria Luisa Fernandes da Silva[a], Rogério Luis Aguilera[b], Milagros Cecilia Palacios-Bereche[c], Antonio Garrido Gallego[d], Silvia Azucena Nebra[e] and Reynaldo Palacios-Bereche[f]

[a] Federal University of ABC, Santo Andre, Brazil, maria.fernandes@aluno.ufabc.edu.br
[b] Federal University of ABC, Santo Andre, Brazil, rogerio.aguilera@ufabc.edu.br
[c] Energy Engineering Modeling and Simulation Laboratory, Federal University of ABC, Santo Andre, Brazil, milagros.palacios@ufabc.edu.br
[d] Federal University of ABC, Santo Andre, Brazil, a.gallego@ufabc.edu.br
[e] Federal University of ABC, Santo Andre, Brazil, silvia.nebra@ufabc.edu.br
[f] Federal University of ABC, Santo Andre, Brazil, reynaldo.palacios@ufabc.edu.br

Abstract:

The sugarcane industrial sector is one of the main Brazilian economic activities due to its high efficiency and competitiveness, producing ethanol and sugar for internal and external markets. On the other hand, green hydrogen, produced from renewable energy, has emerged as a promising climate-neutral energy carrier over the last years; thus, several countries have published hydrogen roadmaps and are supporting the development of a hydrogen economy. Currently, hydrogen is produced mainly from natural gas through a reformation process; the refineries and the chemical industry are the main hydrogen consumers on the demand side. This hydrogen, produced from natural gas or methane without capturing the greenhouse gases made in the process, is classified as Grey hydrogen. In this way, in this study, the integration of Green hydrogen production into the conventional ethanol and sugar production process is proposed to use in the hydrotreatment of bio-oil produced via fast pyrolysis of sugarcane straw. Nevertheless, the sustainability and efficiency of the integrated process depend on the route adopted for hydrogen production. Thus, this study aims to perform an energy evaluation of different routes of hydrogen production and their integration into the ethanol and sugar production process from sugarcane. The different alternatives evaluated are: i) electrolysis using the surplus electricity in the process; ii) steam reforming of biogas produced from vinasse; iii) steam reforming of part of the ethanol produced. Furthermore, the impacts on the cogeneration system of the production process will also be evaluated.From the evaluated cases, ethanol reforming presented the lowest water consumption (14.1 L/t cane) and the lowest impact in cogeneration system (-6.3% in surplus electricity). Nevertheless Case III requires the consumption of 27.7% of the total ethanol produced in the mill.

Keywords:

Sugarcane; hydrogen; heat integration; hydrotreatment.

1. Introduction

In recent decades, debates have grown significantly about the use and dependence on fossil fuels as a result of the release of gases that intensify the greenhouse effect and global warming. Because of this, studies and research involving the use of alternative fuels have gained increasing prominence. Among these, hydrogen production has shown positive results and attracted the attention of the international market.

Hydrogen (H_2) has several advantages, such as its combustion only results in water, which makes its use especially attractive as a fuel since it is considered a clean energy. In addition, its heating value on a mass basis is significantly higher than that of fossil fuels, approximately three times that of fossil fuels [1], [2] . Given this, H_2 is an alternative energy source already widely studied, mainly for application in fuel cells. Moreover, H_2 is used as a reactant in the chemical and petroleum industries, for instance, ammonia production, petroleum processing and methanol production. However, H_2 is not found in free form in nature. Therefore, technologies such as water electrolysis, methane reforming and ethanol reforming have been

widely studied in order to obtain hydrogen. Another possibility for applying H_2 is upgrading biofuels, such as the pyrolysis bio-oil.

Mechanical harvesting of sugarcane increased the availability of straw in the field, which can be used as fuel in boilers or as raw material for second-generation biofuel production through biochemical and thermochemical routes. Regarding the thermochemical routes, the fast pyrolysis allows to production of bio-oil from sugarcane straw that can be used for heating applications. However, there are limitations to the use of pyrolysis bio-oils as fuel in the transport sector because of its high oxygen content (35–40 wt%), which gives bio-oil unwanted properties such as low energy content, corrosiveness, high viscosity and aging [3].

There are several technologies for bio-oil upgrading, according to Sharifzadeh et al. [4], these processes can be classified into physical and chemical technologies. Concerning the chemical processes, hydrodeoxygenation (HDO), also known as hydrogenation or simply hydrotreatment, is the leading technology for upgrading pyrolysis oils, moreover compounds contained in gasoline and diesel can be obtained through this process; however, significant amounts of hydrogen are required as well as high temperatures and pressures.

In the existing literature, there are several studies regarding H_2 production in sugarcane production plants; however, these studies do not compare technologies, nor evaluate heat integration between processes or impacts in the cogeneration system. Thus, this work aims to evaluate the possibilities and opportunities of integrating hydrogen production into the sugarcane processing plants to use the produced hydrogen to upgrade pyrolysis bio-oil aiming at the production of synthetic gasoline and diesel. For this purpose, three technologies for H_2 production were studied: water electrolysis, methane reforming and ethanol reforming. Thus, mass and energy balances were performed with the objective of analysing how much H_2 is necessary for the upgrading process, as well as how much it is possible to obtain through each technological route, from the raw materials available in sugarcane factories, in addition to the possibility of analysing the impacts within the sugar and ethanol production process. The novelty of this study is to present the potential of renewable H_2, from feedstocks available from a sugarcane processing plant, for the specific application of bio-oil upgrading in the context of a biorefinery, as well as investigating the opportunities of heat integration aiming at a more efficient and sustainable production process.

2. Hydrogen production processes and feedstocks

According to IEA [5], in 2021, almost total global H2 production came mainly from fossil fuels, 62% from natural gas without CCUS (Carbon Capture, utilisation and storage), 19% from coal, mainly in China and 18% as a by-product from naphtha reforming at refineries, approximately 0.7% from oil and approximately 0.04% from water electricity. Regarding the low emission H2 production, it accounted for less than 0.7%, almost all from fossil fuels with CCUS.

There are several technologies and routes for hydrogen production, which depends mainly on the material that contains the hydrogen (hydrocarbon or non-hydrocarbon), energy source and catalyst material. The selection of feedstock and production pathway determines the cleanness, cost-effectiveness, efficacy, and feasibility of hydrogen production [6]. The cleanness of a hydrogen production pathway depends on the GHG emissions associated with the life cycle of produced hydrogen determined through LCA (Life Cycle Assessment). Furthermore, some studies in the literature classify the hydrogen production pathways in colours based on their associated emissions. For instance, grey hydrogen is associated with dirty and polluting production, such as natural gas reforming without CCUS, blue hydrogen considers the use of CCS (Carbon Capture and Storage), while green hydrogen refers to renewable energy for hydrogen production.

This study focused the hydrogen production from renewable raw materials and energy sources that are products and by-products of sugarcane processing, such as ethanol, the biogas produced from anaerobic digestion of vinasse, and the surplus bioelectricity from cogeneration system that can be used for water electrolysis. Next, there is a summary description of the production routes that were assumed in this study:

2.1. Water electrolysis

Water electrolysis is the process responsible for the breakdown of the H_2O molecule into H_2 and O_2 from the application of a continuous current of electricity that, through redox reactions, dissociates the water. It is considered an endothermic process because energy is absorbed and converted into heat in the electrodes, subsequently converted into chemical energy resulting in gaseous H_2. This technology can be described by the reaction:

$$H_2O_{(l)} + \text{energy} \rightarrow H_{2(g)} + 1/2\ O_{2(g)} \quad (1)$$

The reactions that take place at the cathode and anode, respectively, are:

$$2H_2O + 2e^- \rightarrow H_2 + 2OH^- \quad (2)$$

$$2OH^- \rightarrow 1/2\ O_2 + H_2O + 2e^- \quad (3)$$

According to [2], modern electrolysers have the capacity to reach an efficiency that varies from 75% to 90%, which is equivalent to a consumption of 4.0 to 5.0 kWh/Nm^3 of H_2.

2.2 Methane reform from biogas

Biogas is the result of the anaerobic digestion process, and their main components are methane (CH_4) and carbon dioxide (CO_2). Because of its high methane content (between 50 and 60 % in molar basis), biogas can be subjected to methane reforming to produce hydrogen. The methane reforming processes that can be applied for hydrogen production are: steam reforming, partial oxidation, autothermal reforming and dry reforming. Among them, steam reforming is one of the most used, representing 48% worldwide [7]. This process can be described globally through the following reaction:

$$CH_4 + H_2O \leftrightarrow CO + 3H_2$$

2.3 Ethanol reforming

Ethanol is considered a raw material with a strong potential to produce hydrogen. This is due to its well-established handling, transport and storage technologies, low toxicity and volatility characteristics, and economic and thermodynamic viability.

To obtain hydrogen from ethanol, steam reforming of ethanol is used. This is an endothermic process characterized by the reaction of ethanol with water when they are in the presence of catalysts. In this environment, the reactions will be intensified, producing a gas mixture (syngas) that contains H_2, CO and H_2O [8].

According to Teixeira et al. [8], the ethanol conversion into hydrogen has an efficiency of 93.7%, and the suitable temperature range for this process took place is between 800 K and 1000 K. However, the conversion depends on the physic-chemical characteristic of fuel and the conditions of temperature, pressure, fuel-steam ratio and reforming techniques.

Two stages mark the steam reforming of ethanol: steam reforming reactions and water-gas shift reactions, the first of which is characterized by high temperatures and the second by low temperatures.

The reactions below represent the two steps, respectively:

Steam reforming: $C_2H_5OH_{(v)} + H_2O \rightarrow 2CO + 4H_2$

Water-gas shift reaction (WGS): $2CO_{(g)} + 2H_2O \rightarrow 2CO_2 + 2H_2$

The reaction that encompasses the entire process can be written as follows:

Overall reaction: $C_2H_5OH_{(v)} + 3H_2O_{(v)} \rightarrow 2CO_2 + 6H_2$, $\Delta H = 207.7$ kJ/mol

The choice of catalysts and supports is an important factor to be considered since their choice will impact the amount of H_2 that will be obtained. According to [8], the combination of Cu and Ni achieved the best efficiency: 90% H_2.

3. Methods

In order to analyse the feasibility of hydrogen production in sugar and ethanol production plants, mass and energy balances were performed in order to quantify the amount of H_2 that is possible to produce from available inputs through the proposed methods. The first analysis focuses on the potential of H2 production. In contrast, the second aims to evaluate the amount of raw materials and energy necessary to produce a certain amount of H_2, which is needed for a hydrotreatment plant that upgrades the bio-oil produced from the fast pyrolysis of sugarcane straw.

3.1. Evaluated cases

3.1.1. Case 0 – Base case

The base case corresponds to the production process of sugar, ethanol and bioelectricity from sugarcane. In it, the starting point is the processing of 500 t/h of sugarcane. Mass and energy balances in this process were performed in previous research studies [9],[10]. Figure 1 shows the main flows of the production process.

In this process, it was assumed that 50% of total recovery sugars from sugarcane were sent to sugar production while the remaining was directed to hydrous ethanol production. Regarding the bagasse usage, from the total produced (136 t/h), 5% (6.8 t/h) is reserved for start-up operations, 5 kg/t cane, equivalent to 2.5 t/h, is used in filters, while the remaining (126.7 t/h) is used as fuel in the boiler of the cogeneration

system, which is based on a steam cycle with condensing extracting steam turbines (CEST) in order to maximise the electricity production; thus no surplus bagasse is obtained. The cogeneration system supplies steam and power to the production process (Fig. 1), and the main parameters of the cogeneration system are presented in Table 1.

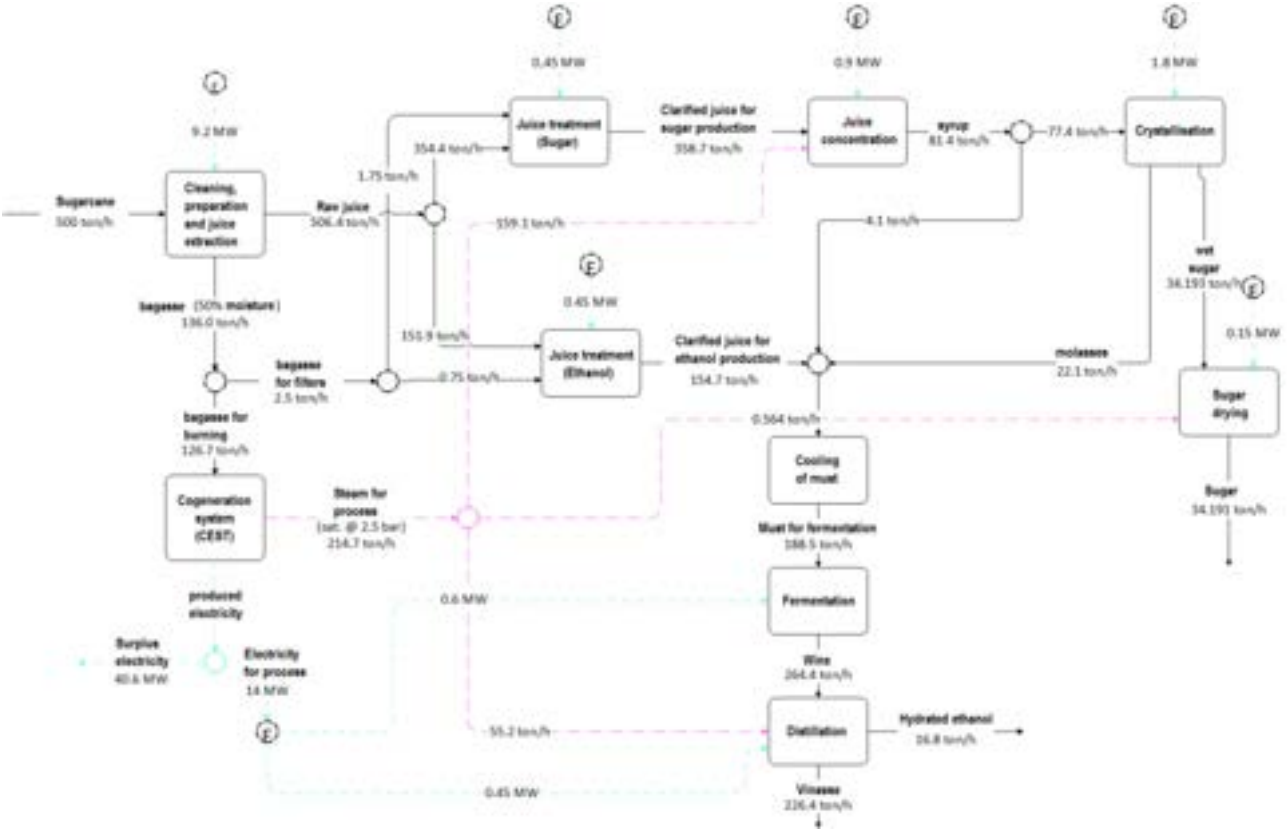

Figure. 1. Fowsheet of the conventional ethanol and sugar production process

Table 1. Main parameters of the cogeneration system of conventional process

Parameter	Value
Steam consumption, kg/t cane	437.6
Bagasse LHV (50% moisture content), MJ/kg	7.64
Electricity consumption in the conventional process, kWh/t cane	28
Boiler thermal efficiency, LHV basis,%	85
Isentropic efficiency of turbines and pumps, %	80
Condensing pressure, kPa	10
Temperature of live steam, °C	520
Pressure of live steam, bar	65
Process steam pressure, bar	2.5

Source: Palacios-Bereche et al. [10]

3.1.1. Case I - Water electrolysis

Table 2 presents the main parameters assumed for water electrolysis evaluation. The specific electricity consumption was assumed from the manufacturer Norsk Hydro A.S. according to [2] and [11].

Table 2. Main parameters of water electrolysis assessment

Parameter	Value
Energy consumption of electrolyser[a], kWh/Nm^3 of hydrogen	4.3
Ultrapure water requirement for electrolysis[b], L of water/kg of hydrogen	9
Cooling water requirement[b,c], (L/h) per MW of electrolyser capacity	400
Water recovery in standard filtration (pre-treatment)[b,d], %	98
Water recovery in polishing to ultrapure standard[b], %	75
Energy consumption in water treatment system [b,d], kWh/m^3 of water	2
Energy consumption related to cooling water system, kWh/m^3 cooling water	0.0465

[a]Norsk Hydro A.S., [b]Madsen [11], [c]For evaporative cooling tower, [d]For groundwater,

Concerning to the water treatment, it was assumed a pre-treatment with standard filtration and further polishing to achieve the ultrapure standard. Water consumption for electrolysis as well as make-up water for the cooling water system in an evaporative tower, were taken into account.

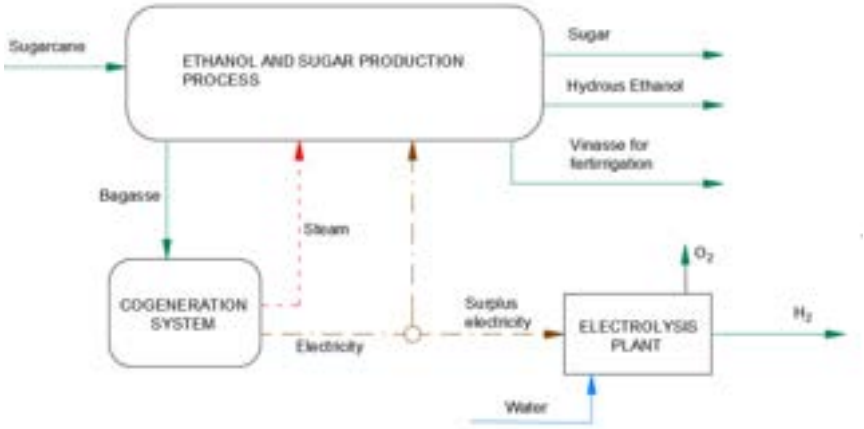

Figure. 2. Hydrogen production through water electrolysis using the surplus electricity of the mill

3.1.2. Case II - Biogas reforming

The biogas production from sugarcane was estimated according procedure presented in [10], which resulted in 2359.1Nm^3/h of raw biogas. In order to prevent reformer catalyst poisoning, a dessulphurisation system is necessary to remove H_2S; thus, a chemical scrubbing system (THIOPAQ system) was assumed in this study. Figure 3 presents a flowsheet for the H_2 production from biogas produced from vinasse biodigestion, while Table 3 shows the main parameters considered for simulation and evaluation.

Table 3. Main parameters assumed for biogas reforming

Parameter	Value
Biogas dessulphurisation	
Flow reduction in dessulphurisation process[a], %	15
Specific power consumption[a], kWh/Nm^3 of raw biogas	0.024
Biogas reforming[b]	
Reforming reactor temperature,°C	850
Reforming reactor pressure, bar	20.1
Steam/Carbon ratio in reforming (mol/mol)	2.87
Water-gas-shift reactor temperature[c], °C	400
Conversion of CO in WGS reactor[d], %	75
Efficiency of pumps and compressors, %	70
Hydrogen recovery in PSA (% of inlet H2)	75
H2 inlet concentration for PSA (% molar)	74
Temperature of preheated air, °C	315
Temperature of exhaust gases at burner outlet, °C	1400

[a]Flores-Zavala [12]; [b]Nakashima [13]; [c]Operating pressure 20.05 bar; [d]tese Peters

The desulphurised biogas composition was assumed in 64.4% of CH_4, 35% of CO_2, 0.6% N_2 and 40 ppm of H_2S in molar basis according to [12]. The biogas reforming process was simulated in Aspen Plus software

according to the flowsheet and specifications supplied by [13] and [14]. In order to maximise the hydrogen production, it was assumed that all available biogas would be sent to the reforming reactor while the heating requirements of the process were fulfilled by burning the off-gas from the PSA system with sugarcane bagasse. Heat integration through Pinch Analysis was applied in order to determine the minimum requirements of external utilities, thus minimising the amount of bagasse necessary.

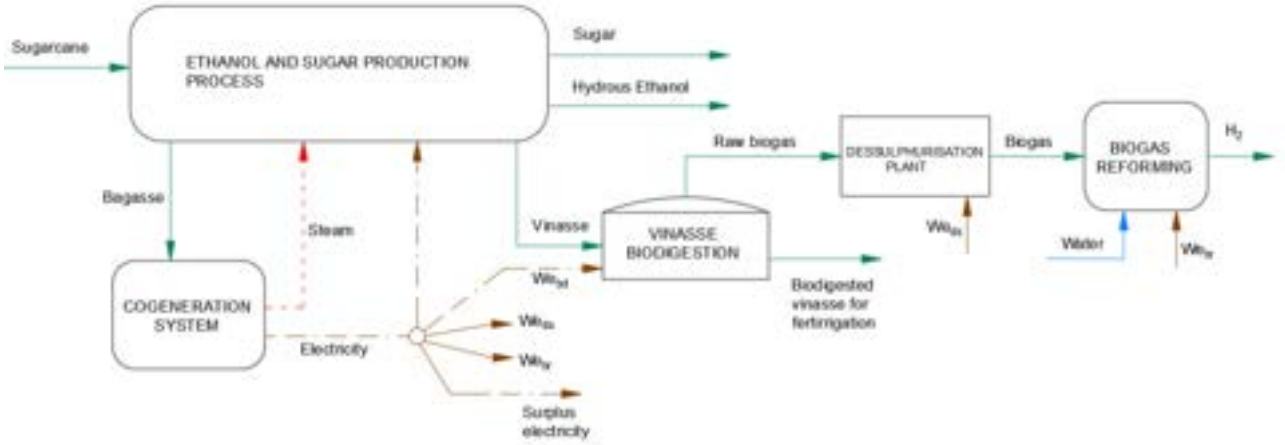

Figure. 3. Hydrogen production through biogas reforming

3.1.3. Case III - Ethanol reforming

Ethanol reforming was another technology analysed to obtain H_2. For this analysis, data from Souza et al. [15] was used to estimate the H_2 production and their energy requirements. In the same way, as in Case II, ethanol is sent to the reforming reactor, while the thermal energy demands were fulfil burning the off-gas from PSA and sugarcane bagasse. Using the simulation supplied by [15] performed in Aspen Hysys, it was possible to apply the heat integration procedure to determine the minimum amount of bagasse necessary. Figure 4 presents the flowsheet of H_2 production from ethanol, while Table 4 shows the main parameters adopted from [15] for evaluation

Table 4. Main parameters assumed for ethanol reforming [15]

Parameter	Value
Specific H_2 production from ethanol, kg H2/kg ethanol	0.219
Water consumption, kg water/kg ethanol	1.6
Additional heat supply, kWh/kg ethanol	1.25
Specific power consumption, kWh/kg ethanol	0.0441

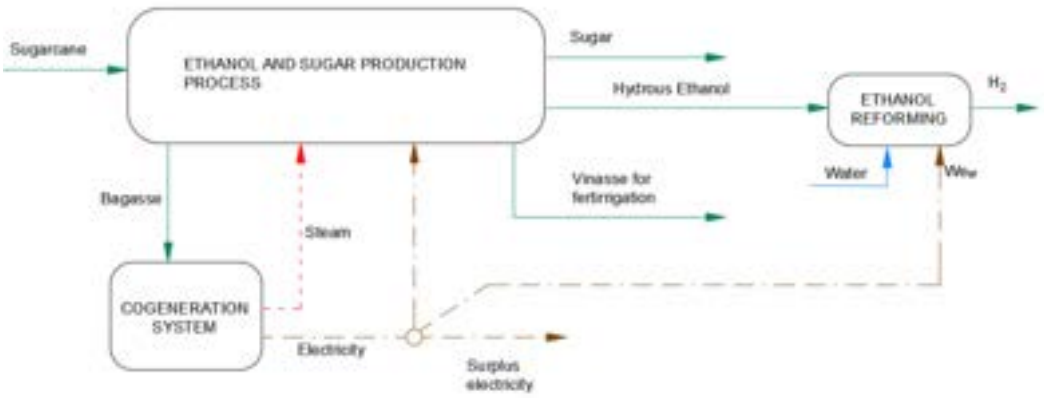

Figure. 4. Hydrogen production through water electrolysis using the surplus electricity of the mill

3.2. Hydrogen consumption in hydrotreating and hydrocracking

This analysis aims to evaluate the raw materials and energy requirements necessary to produce hydrogen for a bio-oil upgrading plant, which processes bio-oil produced from the fast pyrolysis of sugarcane straw. The fast pyrolysis of straw was simulated in Aspen Plus software in a previous study [16], while the hydrotreatment was simulated according to Peters [17]. Figure 5 presents the flowsheet of the hydrotreatment process followed by the distillation step with hydrocracking of the bottom product of the C-DIST2 column. Table 5 shows the main parameters assumed for hydrogen production analyses. Figure 5 shows that the organic phase produced in hydrotreatment is depressurized in a flash. The gaseous stream (FLSHGAS) has a significant amount of hydrogen recovered in a PSA system. This study assumed an H2 recovery of 85% in the PSA system; thus, hydrogen make-up results in 0.04651 kg H_2/kg bio-oil equivalent to 10,938 Nm^3/h.

Table 5. Main parameters assumed in the bio-oil upgrading system

Parameter	Value
Sugarcane straw recovery from field, %	50
Sugarcane straw processing rate in pyrolysis plant[a], t/h	47
Bio-oil produced in pyrolysis plant[b], t/h	21.1
Specific consumption of hydrogen in hydrotreatment[c], kg H_2/kg bio-oil	0.09
Specific consumption of hydrogen in hydrocracking[c], kg H_2/kg bio-oil	0.0032
Mass flow of FLSHGAS, kg/s	1.43
Hydrogen content in FLSHGAS, wt.%	22.6
Recycling rate of H_2 [d], %	55.8

[a]15% of moisture content, [b]artigo Fernando, [c]Tese Peters; [d]Simulation

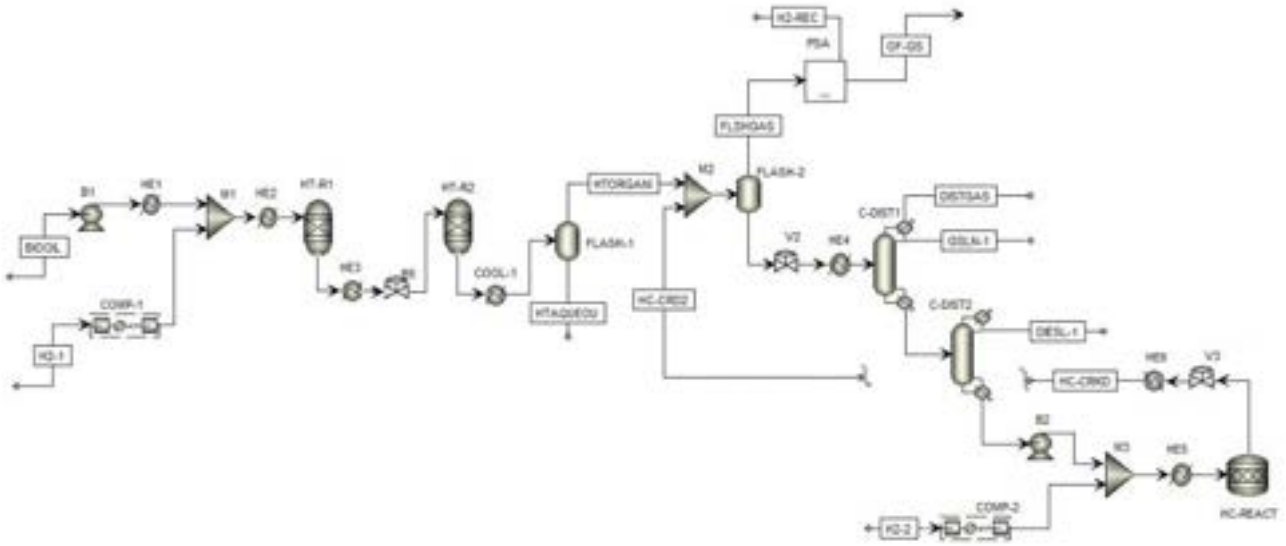

Figure. 5. Flowsheet of upgrading boi-oil plant in Aspen Plus software.

4. Results

4.1. Potential of hydrogen production from products and by-products of sugarcane processing plant

Figure 6 presents the results of hydrogen production from available inputs in the mill; it can be observed that only Case III (ethanol reforming) can supplied all the hydrogen necessary for hydrotreatment.

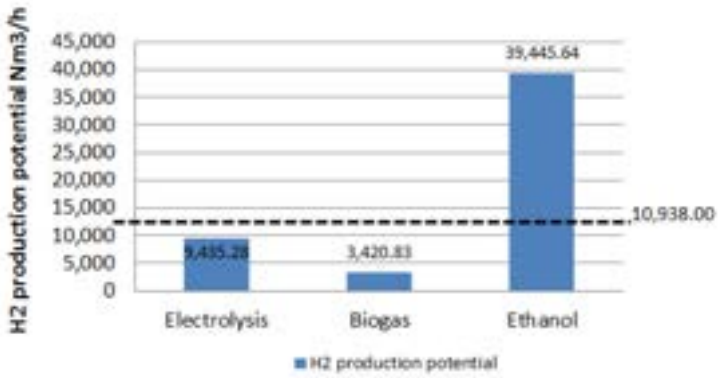

Figure. 6. Hydrogen production potential from available inputs in sugar and ethanol production process.

Thus, surplus electricity from the cogeneration system (40.6 MW) can produce 86.3% of the H2 necessary (Case I). Biogas reforming can achieve 31.3% (Case II) while considering all available ethanol produced in the plant (16.2 t/h), it is possible to produce 3.6 times the amount of hydrogen necessary (Case III). It represents a specific hydrogen production of 18.9, 6.8 and 78.9 Nm^3 of H_2 per t of cane for cases I, II and III, respectively. Regarding ethanol reforming, to produce the necessary hydrogen for hydrotreatment would be required only 4.5 t/h, which is equivalent to 27.7% of the ethanol produced in the mill.

Figure 7 shows the Grand Composite Curves obtained from Pinch Analysis for (a) biogas reforming (2,359.1Nm^3/h of raw biogas) and ethanol reforming (4.5 t/h of ethanol). Stream data for CC and GCC construction is presented in Appendix A

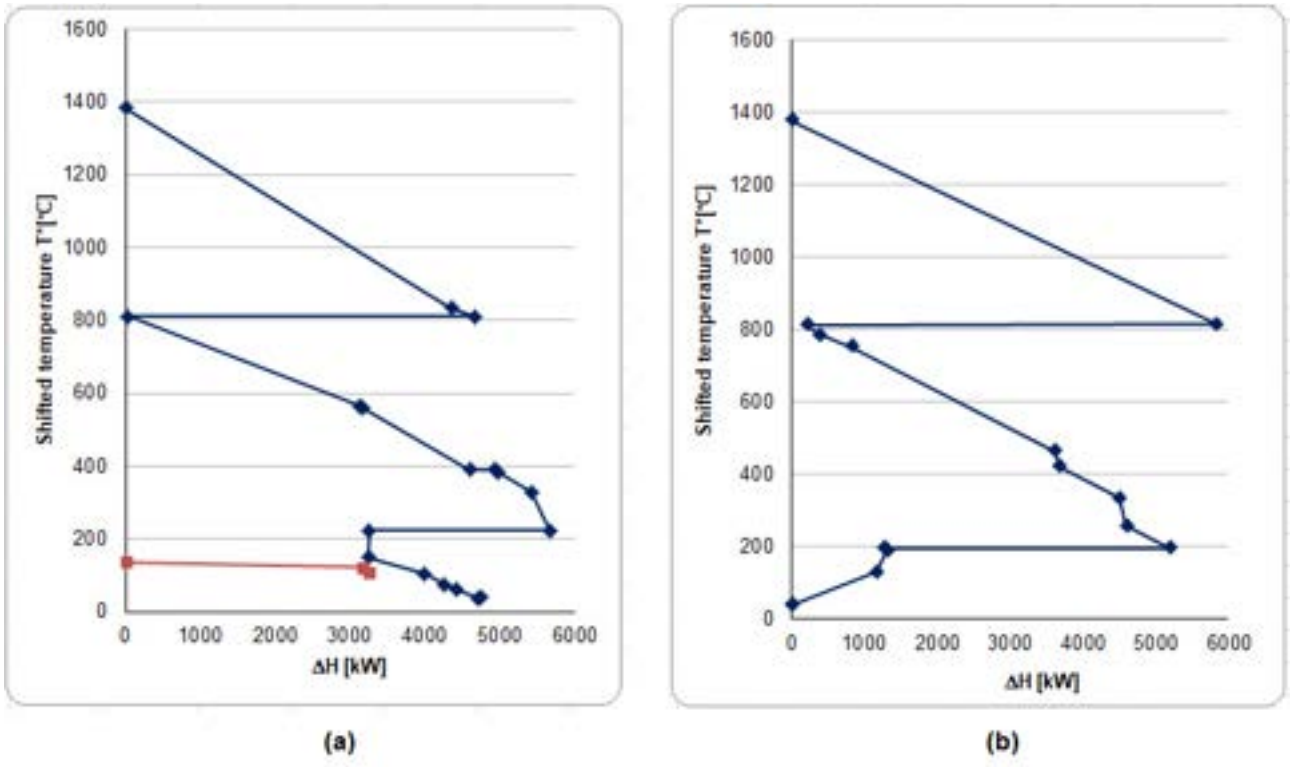

Figure. 7. GCC for (a) biogas reforming and (b) ethanol reforming process

From Fig. 7a, it can be observed that there is a significant amount of heat available at a relatively high temperature (below the reformer reactor temperature, 850°C); thus, it is possible to produce steam (at 2.5 bar and 127.4°C) and use it in ethanol and sugar production process, the red line in Fig. 7a represents this heat recovery potential. On the other hand, in Fig. 7b, better integration is observed because this configuration needs more heat at low temperatures (no hot and cold utilities are required for this case). Moreover, the heat integration procedure allows determining the amount of bagasse necessary to complete the heat demand in the reforming process for these cases. Table 6 presents the main results for these cases.

Table 6. Main results for H_2 production potential

Parameter	Case I	Case II	Case III
H_2 production, Nm^3/h	9,435.3	3,420.8	10,938.0
% of the total H_2 required	86.3	31.3	100.0
Biogas consumption[a], Nm^3/h	0	2,359.1	0
Ethanol consumption, t/h	0	0	4.5
Electricity consumption, kW	40,600	423	198
Water consumption, m^3/h	10.9	4.6	7.0
Bagasse consumption[b], t/h	0	2.0	4.0
Impacts in the cogeneration system			
Steam supplied for the production process[c], t/h	0	5.1	0
Surplus electricity, kW	0	39,443	38,023

[a]Raw biogas; [b]Bagasse to fulfil the heat demand in the reforming process, 50% of moisture content, wet basis, [c]Saturated steam at 2.5 bar.

4.2. Production of H2 necessary for bio-oil upgrading plant and its impact in the cogeneration system

Table 7 presents the main results of this analysis. Regarding Case I, it would be necessary to buy from the electrical grid 6,466 kW (12.9 kWh/tcane) to achieve the required H_2 production. This electricity represents 11.8% of the total power produced by steam turbines of the cogeneration system. On the other hand, Case II requires an additional supply of 5,184 Nm^3/h of biogas or an equivalent of 2940.7 Nm^3/h of natural gas or biomethane (CH_4 content of 96.5% mol).

Regarding water consumption, biogas reforming presents the highest value, equivalent to 29.4L/t cane. According to Pina et al. [18], this value represents 7.1% of effective water collecting in the sugarcane processing plant (414 L/t cane). Finally, the case with the lowest impact in surplus electricity as well as water consumption is Case III; however, this case requires 27.7% of the total hydrated ethanol produced in the mill.

Table 7. Main results for H_2 production necessary to meet the bio-oil upgrading plant

Parameter	Case I	Case II	Case III
H_2 production, Nm^3/h	10,938.0	10,938.0	10,938.0
Biogas consumption[a], Nm^3/h	0	7,543.2	0
Ethanol consumption, t/h	0	0	4.5
Electricity consumption, kW	47,066.4	1,353.0	198
Water consumption, m^3/h	12.6	14.7	7.0
Bagasse consumption[b], t/h	0	6.4	4.0
Impacts in the cogeneration system			
Steam supplied for the production process[c], t/h	0	16.3	0
Surplus electricity, kW	-6,466	36880	38,023
ΔSurplus electricity[d] %	-115.9	-9.2	-6.3

[a]Raw biogas; [b]Bagasse to fulfil the heat demand in the reforming process, 50% of moisture content, wet basis, [c]Saturated steam at 2.5 bar, [d]In comparison to the Base Case (surplus electricity of 40.6 MW).

5. Conclusions

Three routes of hydrogen production were evaluated in this study assuming as feedstock products and by-products available in sugar and ethanol production process aiming to match the hydrogen consumption of a bio-oil upgrading plant. Furthermore, its integration to the conventional sugar and ethanol production process was analysed as well as the impacts in cogeneration system. All evaluated cases presented feasibility; however there are advantages and disadvantages in each one. Case I (electrolysis) presented a significant impact in cogeneration system because the high electricity consumption of this technology. Case II (biogas reforming) presented the highest water consumption (29.4 L/t cane), while Case I presented the second highest (25.2 L/t cane), moreover, it would be necessary to acquire a significant amount of external biogas or natural gas, because the biogas available from anaerobic digestion of vinasse only can produce 31.3% of the required hydrogen for the upgrading plant. Case III (ethanol reforming) presents the lowest water consumption (14.1 L/t cane) and the lowest impact in cogeneration system (-6.3% in surplus electricity). Nevertheless Case III requires the consumption of 27.7% of the total ethanol produced in the mill, impacting significantly the revenues of the plant. In this way a more detailed analysis is needed, for instance an economic assessment or an exergoeconomic analysis to help in choosing the best proposal or proposals.

Acknowledgments

The authors wish to thank the Coordenação de Aperfeiçoamento de Pessoal de Nível Superior (CAPES) and the Conselho Nacional de Desenvolvimento Científico e Tecnológico (CNPq) (Process PQ 306303/2014-0 and PQ 309588/2019-7) for the researcher fellowship; and for the Research Project Grant (Process 407175/2018-0 and 429938/2018-7).

Appendix A

Table A.1 Stream data for heat integration – Case II – Biogas reforming (2,359.1 Nm^3/h)

Stream Name	Supply Temp.	Target Temp.	dT Min Contrib.	Heat Duty
	°C	°C	°C	kW
Biogas preheating - HE1	60	550	15	609.2
Water heating HE2	25.31	212.6	10	1024.0
Water vaporization HE2	212.6	212.61	10	2413.0
Water superheating HE2	212.6	550	10	997.3
Product of reforming reactor - HE3	850	400	15	2097.8
Product WGS reactor - HE4 (1)	400	163.4	15	1046.7
Product WGS reactor - HE4 (2)	163.4	55	15	2346.3
Reforming reactor - REFORM	800	800,01	10	4625.3
Water-Gas-Shift reactor - WGS	400	399,9	10	331.6
Off-gas and air preheater - HE6	45.37	315	15	1563.9
Exhaust- gases - HE5	1400	120	15	10125.0

Table A.2 Stream data for heat integration – Case III – Ethanol reforming

Stream Name	Supply Temp.	Target Temp.	dT Min Contrib.	Heat Duty
	°C	°C	°C	kW
Ethanol preheating (2=>4)	25,22	740	15	3327
Product reforming reactor (13=>14)	800	350	15	3737
Product WGS-HT reactor (15=>16)	436.4	200	15	1874
Water heating (22=>25)	25.08	179.9	15	1283
Water vaporization	179.9	179.9	15	3939
Water superheating	179.9	800	15	2696
Product WGS-LT reactor (15=>16)	245.4	450	15	1651
Reforming reactor	799.1	800	15	5636
Exhaust gases	1400	150	20	12921

References

[1] P. D.A.F., “Produção de hidrogênio por eletrólise alcaline da água e energia solar,” Universidade Federal de Uberlândia, 2016.

[2] J. R. L. Neto and J. R. S. Moreira, “Geração e Combustão do Hidrogênio Obtido Através do Processo de Eletrólise da Água,” *Trab. conclusão Curso. Univ. São Paulo*, pp. 1–9, 2007.

[3] S. Czernik and A. V. Bridgwater, “Overview of applications of biomass fast pyrolysis oil,” *Energy and Fuels*, vol. 18, no. 2, pp. 590–598, 2004, doi: 10.1021/ef034067u.

[4] M. Sharifzadeh *et al.*, “The multi-scale challenges of biomass fast pyrolysis and bio-oil upgrading: Review of the state of art and future research directions,” *Prog. Energy Combust. Sci.*, vol. 71, pp. 1–

80, 2019, doi: https://doi.org/10.1016/j.pecs.2018.10.006.

[5] IEA, “Global Hydrogen Review 2021,” 2021. doi: 10.1787/39351842-en.

[6] F. Dawood, M. Anda, and G. M. Shafiullah, “Hydrogen production for energy: An overview,” *Int. J. Hydrogen Energy*, vol. 45, no. 7, pp. 3847–3869, 2020, doi: 10.1016/j.ijhydene.2019.12.059.

[7] E. Léo Schultz, I. P. Soares, and F. B. Noronha, “Produção de hidrogênio a partir do biogás,” 2013. [Online]. Available: https://www.embrapa.br/documents/1355242/0/BiogásFert+-+Resultados+PA06.pdf.

[8] A. C. R. TEIXEIRA, C. H. G. de BRITO, C. B. MAIA, and J. R. SODRÉ, “Uma revisão sobre a reforma de etanol a vapor com foco na produção de hidrogênio,” in *XXIV Simpósio Internacional de Engenharia Automotiva*, 2016, pp. 541–550, doi: 10.5151/engpro-simea2016-pap76.

[9] M. C. Palacios-Bereche, “Análise energética e exergética de diferentes processos de disposição/aproveitamento energético da vinhaça em usinas sucroalcooleiras,” Universidade Federal do ABC, 2019.

[10] M. C. Palacios-Bereche, R. Palacios-Bereche, and S. A. Nebra, “Techno-Economic Evaluation and GHG Emission Assessment of Different Options for Vinasse Treatment and Disposal Aiming at Reducing Transport Expenses and Its Energy Use,” *BioEnergy Res.*, 2021.

[11] H. T. Madsen, “Water treatment for green hydrogen: what you need to know.” [Online]. Available: https://hydrogentechworld.com/water-treatment-for-green-hydrogen-what-you-need-to-know.

[12] B. A. Flores-Zavala, “Beneficiamento do biogás produzido em biodigestores anaeróbios para produção de biometano e energia elétrica,” Universidade Federal do ABC, 2016.

[13] R. N. Nakashima, “Modelling, simulation and optimization of biogas conversion routes integrated with fuel cell technology,” University of Sao Paulo, 2022.

[14] R. Nogueira Nakashima and S. Oliveira Junior, “Multi-objective optimization of biogas systems producing hydrogen and electricity with solid oxide fuel cells,” *Int. J. Hydrogen Energy*, no. xxxx, 2021, doi: 10.1016/j.ijhydene.2021.08.195.

[15] T. A. Z. de Souza *et al.*, “Exergoenvironmental assessment of hydrogen water footprint via steam reforming in Brazil,” *J. Clean. Prod.*, vol. 311, no. February, p. 127577, 2021, doi: 10.1016/j.jclepro.2021.127577.

[16] F. H. Salina, F. B. Molina, A. G. Gallego, and R. Palacios-Bereche, “Fast pyrolysis of sugarcane straw and its integration into the conventional ethanol production process through Pinch Analysis,” *Energy*, vol. 215, p. 119066, 2021, doi: 10.1016/j.energy.2020.119066.

[17] J. F. Peters, “Pyrolysis for biofuels or biochar? A thermodynamic, environmental and economic assessment,” Universidad Rey Juan Carlos, 2015.

[18] E. A. Pina, R. Palacios-Bereche, M. F. Chavez-Rodriguez, A. V. Ensinas, M. Modesto, and S. A. Nebra, “Reduction of process steam demand and water-usage through heat integration in sugar and ethanol production from sugarcane – Evaluation of different plant configurations,” *Energy*, vol. 138, pp. 1263–1280, 2017, doi: 10.1016/j.energy.2015.06.054.

Energy assessment of biofuels production from fast pyrolysis of sugarcane straw, and upgrading of the bio-oil produced through hydrotreatment

Bruna Stella De Freitas Santos[a], Milagros Cecilia Palacios-Bereche[c], Antonio Garrido Gallego[d], Silvia Azucena Nebra[e] and Reynaldo Palacios-Bereche[f]

[a] Federal University of ABC, Santo Andre, Brazil, bruna.stella@ufabc.edu.br
[c] Energy Engineering Modeling and Simulation Laboratory, Federal University od ABC, Santo Andre, Brazil, milagros.palacios@ufabc.edu.br
[d] Federal University of ABC, Santo Andre, Brazil, a.gallego@ufabc.edu.br
[e] Federal University of ABC, Santo Andre, Brazil, silvia.nebra@ufabc.edu.br
[f] Federal University of ABC, Santo Andre, Brazil, reynaldo.palacios@ufabc.edu.br

Abstract:

Second-generation biofuels are produced from non-food biomass such as the lignocellulosic residues of sugarcane processing, namely, bagasse and straw. Sugarcane processing is one of the most important economic activities in Brazil, producing ethanol and sugar for domestic and international markets. The use of these lignocellulosic residues would increase the second-generation biofuel production without increasing the sugarcane planted area. Among the second-generation technologies available nowadays, the fast pyrolysis is a thermochemical process that produces mainly bio-oil, which is a liquid that has several advantages in transportation, pumping, storage and handling, in comparison to solid biomass. Moreover, the bio-oil can be upgraded in order to obtain biofuels of higher added-value. Among feasible upgrading technologies for bio-oil, the hydrotreatment is one of the most promising for eliminating the reactive functionalities of the bio-oil by removing oxygen or cracking large molecules in the presence of hydrogen; however, the hydrogen consumption is significant. In this way, the aim of this study is to evaluate the biofuel production by means of fast pyrolysis of sugarcane straw, followed by a hydrotreatment to upgrade the produced bio-oil. The evaluation is performed through an energy assessment. The energy and mass balances of the processes were performed using the software Aspen Plus. Furthermore, the possibilities of the integration of the bio-oil production and upgrading into the conventional ethanol and sugar production process will also be evaluated. The final products of bio-oil upgrading plant showed a yield of 0.086 kg/kg of dry straw and 0.080 kg/kg of dry straw for renewable gasoline and diesel respectively. The heat integration of pyrolysis process, hydrotreating and hydrogen production process presented a significant potential for steam production. This could be integrated into the conventional sugar and ethanol production process, which could save 28.6% of steam and increase the surplus electricity in 6%.

Keywords:

Sugarcane; fast pyrolysis; bio-oil; hydrotreatment; energy analysis.

1. Introduction

The production of biofuels from lignocellulosic residues of sugarcane (bagasse and straw) is presented as a desirable alternative since it would increase the biofuel production without the need to increase the area planted with sugarcane. Thus, these biofuels diversify the Brazilian energy matrix and contribute to the reduction of greenhouse gases (GHG) emissions. In this context, the introduction of the fast pyrolysis of lignocellulosic residues into the conventional sugarcane process plant for bio-oil production, aiming at its further processing, can improve the productivity and sustainability indexes of the integrated process. Pyrolysis is the physico-chemical process of thermal degradation of a material in a non-oxidizing atmosphere, resulting in the formation of a solid residue rich in carbon (charcoal or char) and a volatile fraction composed of condensable organic gases and vapours. The proportions of these products depend on the pyrolysis conditions and the characteristics of the feedstock. Fast pyrolysis is characterised by low residence times in the reactor, high heating rate at moderate temperatures (400 to 600ºC). The formation of

bio-oil is prioritised, as it can be used as fuel for boilers or serve as raw material for the production of vehicles fuels. In the literature, some studies have already regarded the fast pyrolysis of lignocellulosic biomass, such as the study of Mesa-Perez et al.[1], where the oxidative fast pyrolysis of sugarcane straw in a fluidised bed reactor was analysed. In addition, Ferreira et al. [2] carried out a study to evaluate the influence of some parameters on the oxidative pyrolysis of sugarcane straw, while Alves et al. [3] experimentally evaluated and compared the fast pyrolysis of sugarcane straw and eucalyptus bark in a fluidised bed reactor at 500°C. Still, raw bio-oil is not suitable as fuel for the transport sector because of some undesirable characteristics such as low energy content, corrosiveness, high viscosity, incomplete volatility and chemical instability. These unfavourable properties are consequences of the high water content and oxygenated compounds [4]. Thus, the bio-oil requires upgrading and fine-tuning in order to achieve product specifications commensurate with existing transportation infrastructures. The upgrading methods aim at stabilising the crude bio-oil by removing its oxygen content and reducing its viscosity, ageing potential, and solid content [5]. Among the different available methods, the hydrodeoxygenation (HDO), also known as hydrogenation or simply hydrotreatment, is the main technology for upgrading pyrolysis oils due to its effectiveness. It was originally inspired by the hydrodesulphurisation (HDS) and hydrodenitrogenation (HDN) used in petroleum refineries. A catalytic reaction of crude bio-oil with hydrogen can significantly reduce the oxygenated compounds through the formation of water. The involved reactions in this process include hydrogenation, hydrodeoxygenation, decarboxylation, hydrogenolysis, hydrocracking, and dehydration. The optimal combination of these reactions requires significantly higher pressures (> 20 MPa) and moderate temperatures (around 400°C) [5]. HDO yields high quality hydrocarbon products for gasoline and diesel substitution, but requires important amounts of hydrogen at high pressure, which affects costs and energy balances. Process conditions and catalyst type have to be carefully adjusted in order to minimise hydrogen consumption and to achieve the desired product [6]. According to Sharifzadeh et al. [5], it is recommended to first stabilise the bio-oil through hydrogenation at a lower temperature, followed by more intense HDO at higher temperatures. Some studies regarding bio-oil upgrading can be found in the literature, for instance, Jones et al. [7] presented a report about process design and economic assessment for fast pyrolysis of woody biomass and bio-oil hydrotreating; in Zacher et al. [8], a study regarding technology advancements in hydroprocessing of bio-oils was accomplished, while Peters [6] evaluated the fast pyrolysis, including the bio-oil upgrading, for the production of second-generation biofuels from thermodynamic, environmental, and economic approaches.

Thus, the present study aims at evaluating the biofuel production by means of fast pyrolysis of sugarcane straw, followed by its upgrading through hydrotreatment. The evaluation being performed through an energy assessment. The energy and mass balances of the processes were performed using the software Aspen Plus v12 [9]. Furthermore, the possibilities of integrating the bio-oil production and upgrading into the conventional ethanol and sugar production process will also be evaluated through the Pinch Analysis.

2. Biofuels production from fast pyrolysis of sugarcane straw

2.1. Fast pyrolysis of sugarcane straw

This section presents the main characteristics of the fast pyrolysis plant assumed in this study, whose flowchart is shown in Figure 1. This plant, receiving sugarcane straw as raw material, is comprised of the following components: reactor (1), cyclone (2), quench (3), condensers (4), heat exchanger (5), compressors (6), coal and synthesis gas combustor (7), heat recovery steam generator (HRSG) (8), fluidising gas preheater (9), and biomass dryer (10). In this configuration, the pyrolysis process is characterised as autothermal [10], burning the char and syngas to supply energy to the pyrolysis reactor. Furthermore, it is possible to produce steam in the HRSG (8), which is used in a Rankine cycle to produce electricity for the process. The bio-oil produced in this plant is then sent to the upgrading plant.

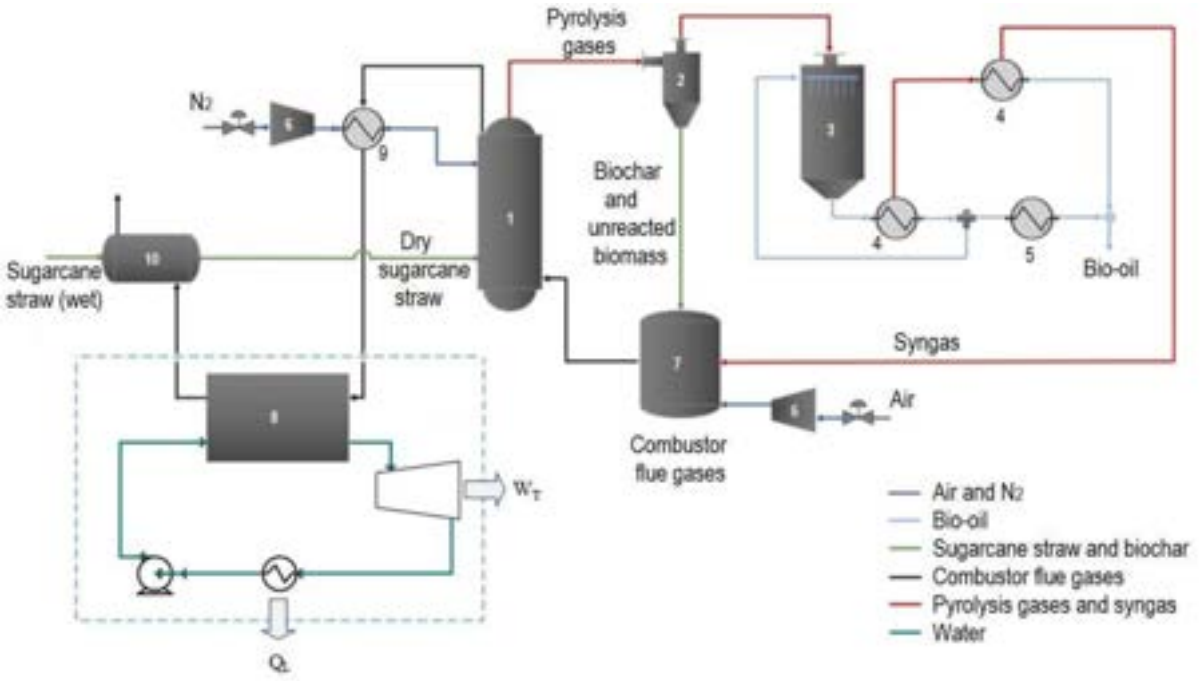

Figure. 1. Fast pyrolysis process diagram [10]

2.2. Bio-oil upgrading through hydrotreatment

The bio-oil upgrading plant was divided into three subsystems: hydrotreatment, distillation and hydrocracking, and hydrogen production. Figure 2 presents the flowsheet of the hydrotreatment section.

2.1. Hydrotreating section

The bio-oil supplied by the pyrolysis plant is pressurised in pump B1 and preheated in the heat exchanger HE1; after that, it is mixed with pressurised hydrogen in M1. The mixture is preheated in the heat exchanger HE2 before entering the first hydrotreating reactor HT-R1, whose operating conditions were assumed at 170 bar and 250°C, according to Peters [6]. This reactor aims at stabilising the bio-oil sufficiently to be suited for a more severe treatment in the second reactor. The product of HT-R1 is heated till 370°C and decompressed to 140 bar before entering the second hydrotreating reactor HT-R2. The operating conditions in HT-R2 were assumed at 370°C and 140 bar [6]. The aim of this second reactor is to deeply deoxygenate and stabilise the bio-oil up to an oxygen content of <2% [11],[12]. Both reactors HT-R1 and HT-R2 were assumed to operate with a standard Co-Mo catalyst, according to [6].

The product of HT-R2 is cooled to 137.4°C, in the heat exchanger COOL-1, before entering the flash tank, which operates at 35 bar, where the organic vapours (HTORGANI) are separated from the aqueous liquid phase (HTAQUEOU). The organic vapours are sent to the following subsystem (Distillation and Hydrocracking), while the aqueous stream enters the hydrogen production subsystem.

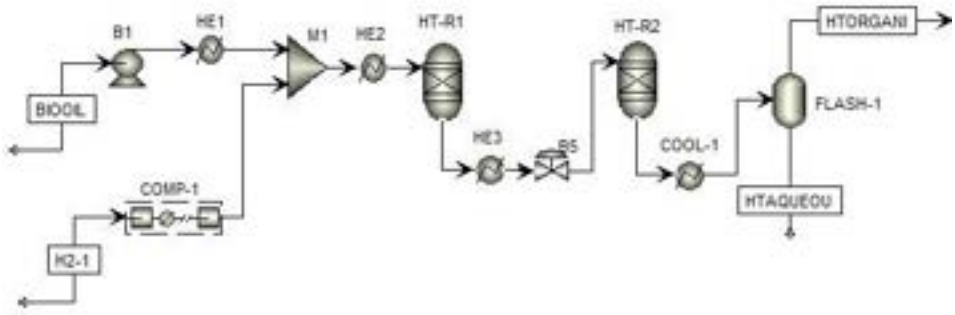

Figure. 2. Flowsheet of bio-oil hydrotreatment in Aspen Plus

2.2. Distillation and hydrocracking

Figure 3 presents the flowsheet of the Distillation and Hydrocracking subsystem. It can be observed that the products of the hydrotreatment step (stream HTORGANI) and the hydrocracking reactor (HC-CRD2) are mixed before being sent to a flash tank (FLASH-2) operating at 20 bar. The liquid phase is preheated in the heat exchanger HE4 and fed to the first distillation column (C-DIST1), while the gaseous phase, containing a significant amount of unreacted hydrogen, is sent to a PSA (Pressure Swing Adsorption) system for hydrogen recovery and recycling. This configuration was assumed according to Zacher et al. [8] and Jones et al. [7]. In this study, it was assumed that a part of the tail gas from the PSA system (OF-GS) is used as fuel in the utility system while the remaining is integrated into the hydrogen production system. In the first distillation column (C-DIST1), renewable gasoline is obtained at the top, while the bottom product is sent to the second distillation column (C-DIST-2). Moreover, in the top of C-DIST1, distillation gases (DISTGAS) are also obtained, which are used as fuel in the utility system.

In the second distillation column (C-DIST2), renewable diesel (stream DIESL-1) is obtained at the top, while the heavier product at the bottom is mixed with preheated hydrogen and sent to the hydrocracking reactor (HC-REACT). In the hydrocracking (HC) reactor, under severe conditions (677°C, 170 bar) and a hydrogen atmosphere, the heavy tar fraction is catalytically split up into smaller chain components, producing hydrocarbons in the range of C1-C18 [6].

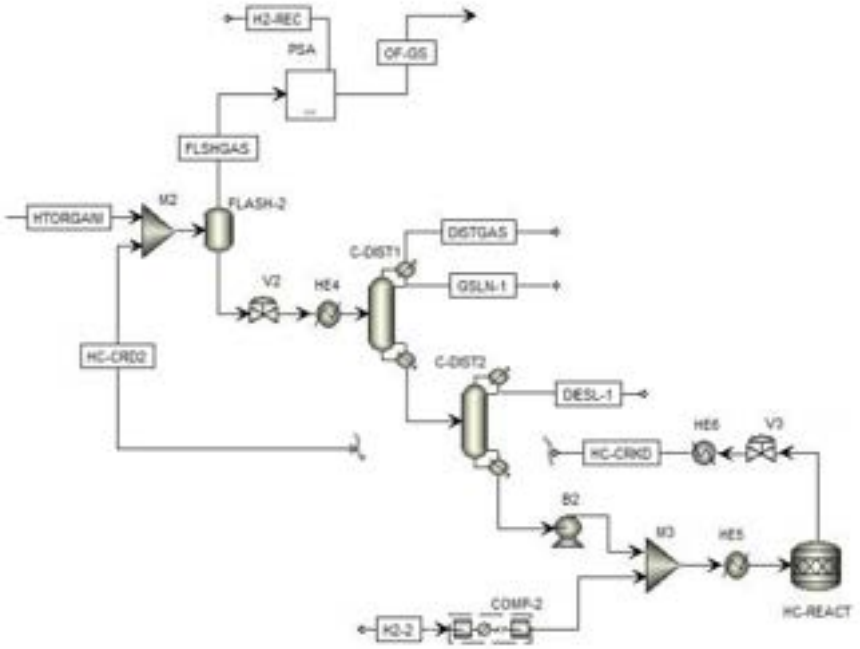

Figure. 3. Flowsheet of the distillation and hydrocracking processes in Aspen Plus

2.3. Hydrogen production

Figure 4 presents the flowsheet of the hydrogen production section. This study considered the steam reforming of desulphurised biogas (DS-BIOG1), produced from the anaerobic digestion of vinasse, in combination with external natural gas acquired from the grid (SRCH4EXT). The components removed together with some hydrogen lost in the PSA system are obtained as tail gas. Part of this tail gas (stream FLSHGAS2) is used as fuel to meet the energy requirements of the hydrotreatment and distillation sections, while the remaining (FLSHGAS3) is sent to hydrogen production. One part of the FLSHGAS3 stream is compressed till 50 bar and sent to the reform reactor, while the other part is used as fuel in a combustor (COMB), whose exhaust gases are used as hot utility to meet the heat requirements of the reformer. Furthermore, the aqueous liquid stream (HTAQUEOU) obtained in the hydrotreatment section is also sent to the hydrogen production system; where it is mixed with part of the condensate recovered (SRH2O-IN stream) in FLASH-3. Afterwards, the liquid mixture is pumped and heated in HE7 and sent to the reforming reactor (SR-REACT). Biogas and natural gas are sent to the reforming reactor as well. The feed of the reforming reactor is preheated in the heat exchanger HE8 till 500°C, the product of which is then cooled to 310°C and sent to the WGS (Water-Gas-Shift) reactor, which operates at 350°C and 48 bar. The product of the WGS reactor is then cooled to 77°C before entering the FLASH-3, which operates at 46 bar. The gaseous product of FLASH-3 is sent to the second PSA system (PSA-II) in order to separate the hydrogen from the other gases. The tail-gas from the PSA-II system (OFFGS stream), the gaseous product of the

distillation column (DISTGAS stream), and part of the tail gas from the PSA-I system (remaining part of FLSHGAS3) are preheated with combustion air in HE11 before entering to the combustor COMB to be burnt.

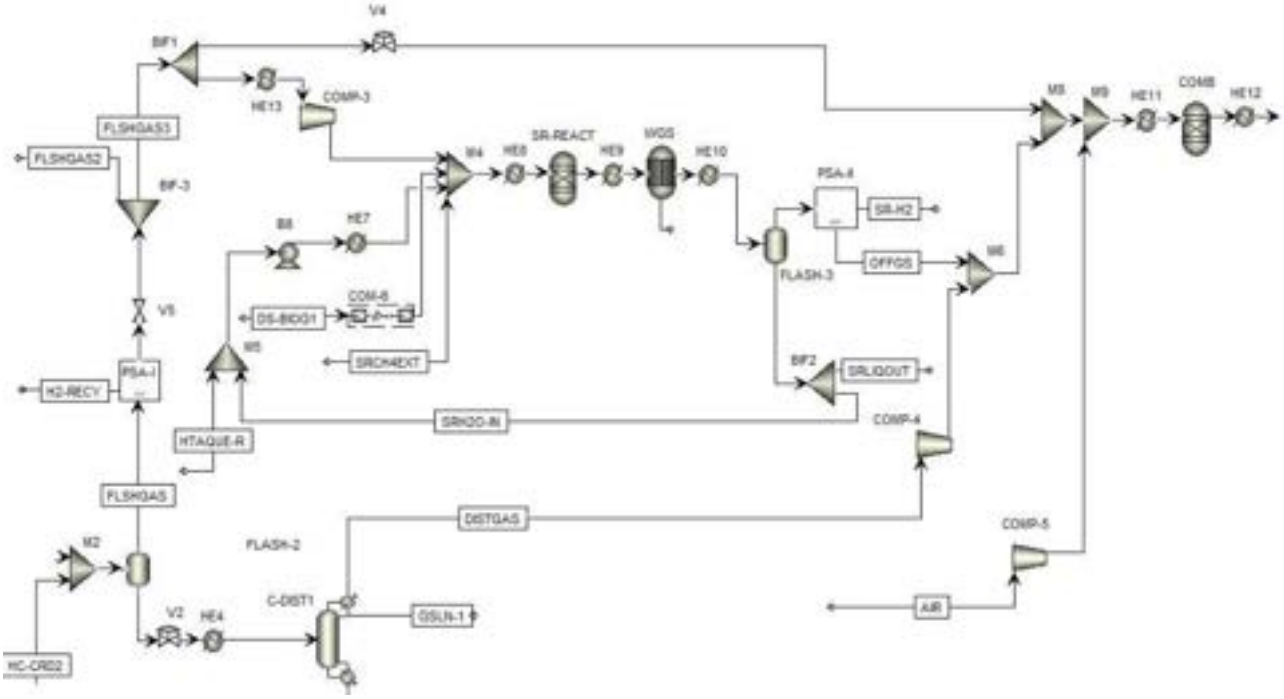

Figure. 4. Flowsheet of the hydrogen production process

3. Methods

3.1. Fast pyrolysis plant

The simulation of the fast pyrolysis plant using sugarcane straw as feedstock was performed in the Aspen Plus software, according to [10]. The Peng-Robinson equation of state with Boston-Mathias modification (PR-BM) was selected as the preferred method for properties calculation in the reactor and combustor system, while the NRTL method was selected in the separation system. A straw availability of 160 kg of dry matter per tonne of cane stalks [13] in the field was considered, the pyrolysis plant processing 50% of this total potential. The kinetic model developed by [14] was applied in this study. Table 1 presents the main parameters assumed in the simulation.

Table 1. Main parameters of sugarcane straw pyrolysis

Parameter	Value
Sugarcane straw, as received (15% moisture content), t/h	47.1
Sugarcane straw, dried (5% moisture content), t/h	42.1
Pyrolysis reactor temperature, °C	475
Pyrolysis reactor pressure, bar	1.5
Residence time, s	20
Fluidising gas and biomass ratio, (mass/mass)	0.5
Outlet temperature in first condenser, °C	75
Outlet temperature in second condenser, °C	25

3.2. Bio-oil upgrading plant

The bio-oil upgrading plant was simulated in the Aspen Plus software, according to the procedure presented in [6]. The composition of the bio-oil obtained in the fast pyrolysis simulation was adjusted in order to take into account the same components considered by Peters [6]; in addition, the Pen-Robinson with Boston-Mathias modification (PR-BM) method was selected [15], [16].

3.2.1. Hydrotreating section

In the hydrotreating section, the crude bio-oil from the pyrolysis process is upgraded in a two-stage catalytic hydrotreatment to almost oxygen-free hydrocarbon. Seeing as hydrotreating reactors were modelled as RYield blocks in the Aspen Plus software, the composition of reactor products were a necessary input. Since

there is not detailed information regarding the composition of hydrotreating reactors products from sugarcane straw, the composition presented by [6], who evaluated hybrid poplar wood chips, was taken as a reference. These values are based on a typical bio-oil hydrotreatment with Co-Mo catalyst, based on the literature [11]. In this way, taking into account these data and the specific bio-oil composition obtained in the pyrolysis simulation, a mass balance procedure was performed in MS Excel for each element present in the bio-oil, using proportionality factors, aiming at following a similar product distribution.

Table 2 presents the main parameters assumed in the modelling of the Hydrotreating section.

Table 2. Main parameters in the Hydrotreating section

Parameter	Value
Outlet pressure – pump B1, bar	170
Outlet pressure – compressor COMP-1, bar	170
Number of stages – compressor COMP-1	2
Outlet temperature – HE1, °C	100
Outlet temperature – HE2, °C	250
Operating pressure – hydrotreating reactor HT-R1, bar	170
Operating temperature – hydrotreating reactor HT-R1, °C	250
Outlet temperature – HE3, °C	370
Operating pressure – hydrotreating reactor HT-R2, bar	140
Operating temperature – hydrotreating reactor HT-R2, °C	370
Outlet temperature – COOL-1, °C	35
Operating pressure – FLASH-1, bar	35
Heat duty – FLASH-1, kW	0
Hydrogen consumption in hydrotreating section, kg H_2/kg bio-oil	0.09

3.2.2. Distillation and Hydrocracking section

Distillation columns were modelled as RadFrac blocks in the Aspen Plus software, while a stoichiometric block represented the hydrocracking reactor, and the reactions assumed thereof were adopted from [6]. In Table 3, the main parameters assumed in this stage for the modelling in the Aspen Plus software are presented.

Table 3. Main parameters for distillation and hydrocracking

Parameter	Value
Operating pressure in FLASH-2, bar	20
Outlet temperature in HE4, °C	212
Number of stages in C-DIST1	8
Reflux ratio (mass basis) in C-DIST1	1.2
Distillate to feed ratio (mass basis) in C-DIST1	0.48
Operating pressure in C-DIST1 (stage 1), bar	2.5
Condenser temperature[(a)], C-DIST1, °C	32
Number of stages in C-DIST2	7
Reflux ratio (mass basis) in C-DIST2	1.2
Distillate to feed ratio (mass basis) in C-DIST2	0.85
Operating pressure in C-DIST2 (stage 1), bar	0.01
Outlet pressure in pump B2, bar	90
Operating temperature in the hydrocracking reactor, °C	430
Operating pressure in the hydrocracking reactor, bar	90
Outlet pressure in valve V3, bar	36
Outlet temperature in HE6, °C	32
Hydrogen consumption in the hydrocracking section, kg H_2/kg bio-oil	0.0032

[(a)]C-DIST1 was assumed with a partial condenser, while in C-DIST2 there is a total condenser

3.3. Hydrogen production plant

The PSA systems (PSA I and II) were modelled as separators. Regarding the steam reforming assumed in this simulation, the reforming reactor considered a conventional nickel catalyst, as it is widely used in this type of reactors, and was modelled as a RGibbs reactor type in the Aspen Plus software, while a REquil type reactor was used in the modelling of the WGS reactor. The reactions within the WGS reactor were limited to the WGS reaction ($H_2O+CO<-->CO_2+H_2$), according to [6]. The temperature approach in the WGS reactor was adjusted in order to achieve a CO conversion in the range of 75%. The combustor COMB was modelled as a RGibbs reactor type as well. The mass flow of combustion air (AIR stream) was adjusted to achieve a temperature of 1500°C at the outlet of COMB, while the split fraction of stream SR2O-IN in the bifurcation BIF2, which determines the amount of liquid condensate recycled to the reforming reactor, was adjusted to achieve a Steam to Carbon ratio (S/C) of 4.5 (mol basis). The split fraction of the FLSHGAS stream specified in the bifurcation 1 (BIF1), which determines the mass flow of FLSHGAS destined for the reforming reactor, was determined from the energy balance. Thus, it was adjusted aiming at calculating the heat duty in HE12 to meet the required heat duty in SR-REACT, maintaining a ΔT_{min} of 30°C. Table 4 presents the main parameters assumed in the simulation of the hydrogen production plant. The composition of the desulphurised biogas was assumed as 35.4% CO_2 and 64.4% CH_4 (molar basis) [17], while the composition of the external natural gas was assumed as 3.5% CO2 and 96.5% CH4 (molar basis).

Table 4. Main parameters for the hydrogen production plant

Parameter	Value
Outlet pressure, valve V4, bar	2.3
Outlet pressure, compressor COMP-3, bar	50
Outlet pressure, pump B8, bar	50
Outlet temperature, HE7, °C	259.9
Outlet temperature, HE8, °C	500
Operating pressure, SR-REACT, bar	49
Operating temperature, SR-REACT, °C	950
Outlet temperature, HE9, °C	310
Operating temperature, WGS reactor, °C	350
Operating pressure, WGS reactor, bar	48
Outlet temperature, HE10, °C	77
Operating pressure FLASH-3, bar	46
H_2 recovery in PSA system, %	90
Outlet pressure, compressors COMP-4 and COMP-5, bar	2.2
Outlet temperature, HE11, °C	300
Operating pressure, COMB, bar	1.01325
Heat duty, COMB, kW	0

3.4. Integration into the conventional ethanol and sugar production process

The heat integration was accomplished according to the Pinch method [18], performing the following steps: data extraction from the evaluated processes, composite curves construction, evaluation of steam generation, and integration of the cogeneration system, which meets the heat and power demands of the processes.

4. Results

4.1. Bio-oil composition

Figure 5 shows the main components of bio-oil produced in the fast pyrolysis of sugarcane straw. The amount of sugar derived, which includes levoglucosan, hydroxyimethylfurfural, xilan and intermediate compounds derived from cellulose and hemicellulose represents almost 50% of the amount of bio-oil. This can be explained because the assumed kinetic model for fast pyrolysis only assumed primary reactions. In second place, the water content reaches 17.8%, followed by the aldehydes with 15.5%, which include

acetaldehyde, glyceraldehyde, formaldehyde, glyoxal, furfural, and acrolein. This composition presents a slightly divergence from the experimental data presented by [6] for bio-oil obtained from fast pyrolysis of pine wood, which contains sugar derived 33%, water 24%, and aldehydes and ketones 21%. Nevertheless, further research is needed in order to try taking into account secondary reactions.

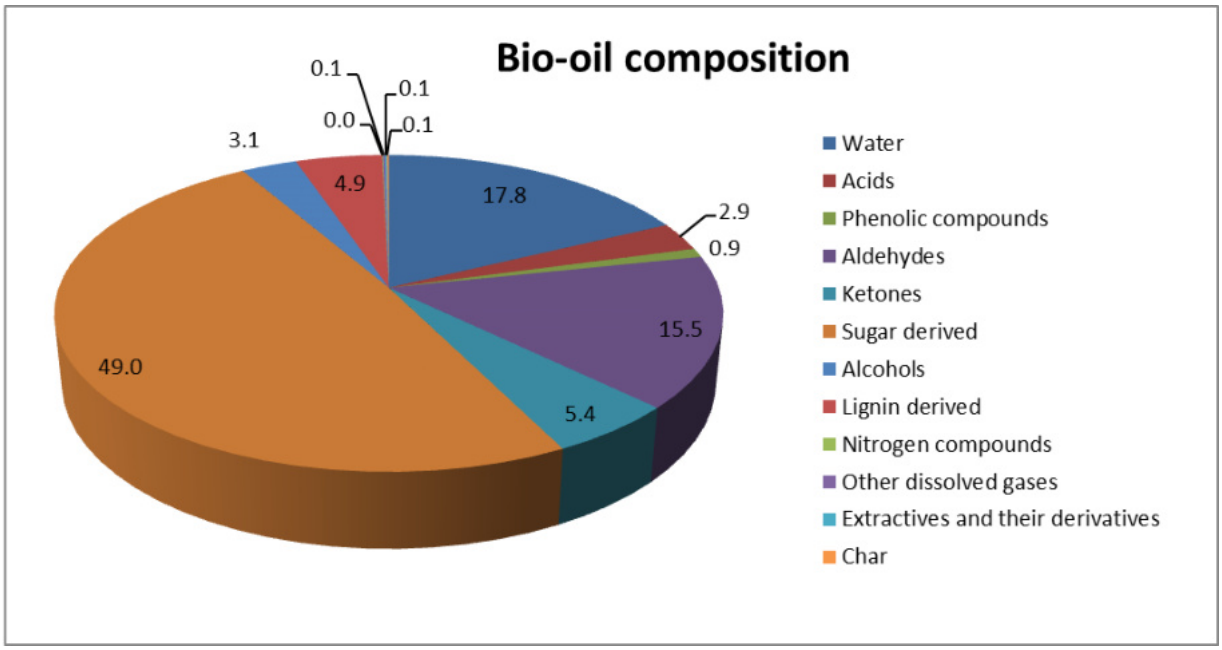

Figure. 5. Main compounds in bio-oil produced from fast pyrolysis

4.2 Bio-oil upgrading plant

This section presents the results of the bio-oil upgrading plant simulation. Table 5 presents the main results of this analysis.

Table 5. Main results of the hydrotreatment, and distillation and hydrocracking sections

Parameter	Value
Hydrotreatment	
Bio-oil production in fast pyrolysis plant[a], t/h	21.1
Hydrogen consumption in hydrotreatment, t/h	1.8
Water content at the outlet of HT1 reactor (mass basis), %	36.3
Water content at the outlet of HT2 reactor (mass basis), %	49.4
Organic phase stream (HTORGANIC) at the vapour outlet of FALSH-1, t/h	11.49
Water content in HTORGANIC stream (mass basis), %	0.1
Aqueous phase stream (HTAQUEOUS) at the liquid outlet of FLASH-1, t/h	11.43
Water content in HTAQUEOUS (mass basis), %	99.05
Power consumption in hydrotreatment section, kW	3,310.9
Distillation and hydrocracking	
Vapour product of FLASH-2 (FLSHGAS stream), t/h	5.11
Hydrogen content in FLSHGAS stream (mass basis), %	22.37
Hydrogen recovery in H2-RECY stream[b], t/h	0.97
Hydrogen consumption in Hydrocracking, t/h	0.28
Renewable gasoline (GSLN-1 stream)[d], t/h	3.45
Renewable diesel (DISEL-1 stream)[e], t/h	3.2
Power consumption in distillation and hydrocracking section, kW	125.4

[a]17.8% of moisture content; [b]85% of H_2 recovery in PSA system; [c]LHV at 15°C 34.4 MJ/kg; [d]LHV at 15°C 44.3MJ/kg; [e]LHV at 15°C 33.5MJ/kg

It can be observed, in Table 5, that the power consumption in the Hydrotreatment section resulted significantly higher in comparison to the Distillation and Hydrocracking section, because of the high power consumption in the hydrogen compressor COMP-1 (3.18 MW). The final products of the bio-oil upgrading plant showed a yield of 0.086 and 0.080 kg/kg of dry straw for renewable gasoline and diesel, respectively. The reboiler temperatures of columns C-DIST1 and C-DIST2 resulted 283.3°C and 254.6°C, respectively, these operating conditions being important for evaluating the heat requirements and heat integration opportunities. Regarding the hydrogen production, section Table 6 presents the main results.

Table 6. Main results of the hydrogen production process

Parameter	Value
External consumption of natural gas, (or biomethane)[a,b], kg/h	1232.7
Desulphurised biogas consumption[c,d,e], kg/h	2325.1
Water consumption in reforming process, t/h	18.1
Recirculation rate of SRH2OIN stream[f], %	55.9
Condensate sent to waste water treatment system (SRLIQOUT stream), t/h	5.4
Fraction of FLSHGAS3 stream sent to reforming reactor[g], %	28.6
Hydrogen production in PSA-II system, t/h	1.1
Fuels used in combustor COMB	
Off-gas from PSA-I system[h,i], t/h	2.8
Off-gas from PSA-II system[j], t/h	9.6
Gas from distillation (DISTGAS stream)[k], t/h	0.024
Power consumption in hydrogen production process, kW	2,884.7

[a]96.5% of CH_4 (mol basis); [b]equivalent to 72.4 kmol/h; [c]produced from anaerobic digestion of vinasse; [d]64.4% of CH_4 (mol basis); [e]equivalent to 89.46 kmol/h; [f]split fraction of condensate recycled to reforming process specified in bifurcation BIF2; [g]split fraction of FLSHGAS specified in bifurcation BIF1; [h]Fraction of FLSHGAS3 stream; [i]LHV at 15°C of 34.4MJ/kg; [j]LHV at 15°C, 3.84 MJ/kg; [k]LHV at 15°C, 32.9MJ/kg

4.3 Heat integration results

Stream data adopted for heat integration is presented in Tables A1 and A2 of Appendix A, for the Hydrotreatment coupled with Distillation and Hydrocracking processes, and the hydrogen production process. Simulation results showed that the hydrotreating and the hydrocracking reactors are exothermic. In order to make use of this thermal energy, it was assumed that heat released from exothermic reactors is used to heat thermal oil that can be used as hot utility. Thus, these streams of thermal oil were taking into account for Composite Curves (CCs) and Grand Composite Curves (GCCs) construction. Because of the large amount of gaseous streams in the processes, the contribution to the ΔT_{min} was assumed to be 15°C for almost all streams. Process streams with phase change were divided into ranges in order to properly consider the available heat at different temperature levels. Figure 6a presents the GCC for the Hydrotreatment coupled with Distillation and Hydrocracking processes, while the GCC for the hydrogen production process is presented in Figure 6b.

According to Fig. 6a, the target of minimum hot utility consumption above the Pinch resulted in 1328.34 kW, thus, combustion gases with an adiabatic flame temperature of 1500°C were assumed as hot utility to meet this energy requirement using part of FLASHGAS as fuel. Considering that combustion gases are cooled till the Pinch temperature of 320°C, the fuel consumption resulted in 0.0486 kg/s (0.18 t/h) (mass flow of FLSHGAS2 stream in Fig.4).

On the other hand, both GCCs present available heat below the Pinch temperature that can be used to produce steam for the ethanol and sugar production process. The red lines in Figures 6a and 6b show these potentials. Since in Fig. 6a there is heat available at lower temperatures (below to 300°C), in comparison to Fig. 6b, the production of saturated steam at 2.5 bar (127.4°C) from available heat of hydrotreating and hydrocracking sections was assumed. On the other hand, the production of superheated steam at 500°C and 65 bar was assumed in Fig. 6b (represented by the red line). The steam mass flow resulted in 17.1 t/h and 20.9 t/h in Figures 6a and 6b, respectively. Moreover, from the superheated steam obtained in Fig. 6b, there is a power production potential of 3655 kW, using a back-pressure steam turbine. Thus, the exhaust steam from the turbine can be used to meet heat demands in the sugar and ethanol production process.

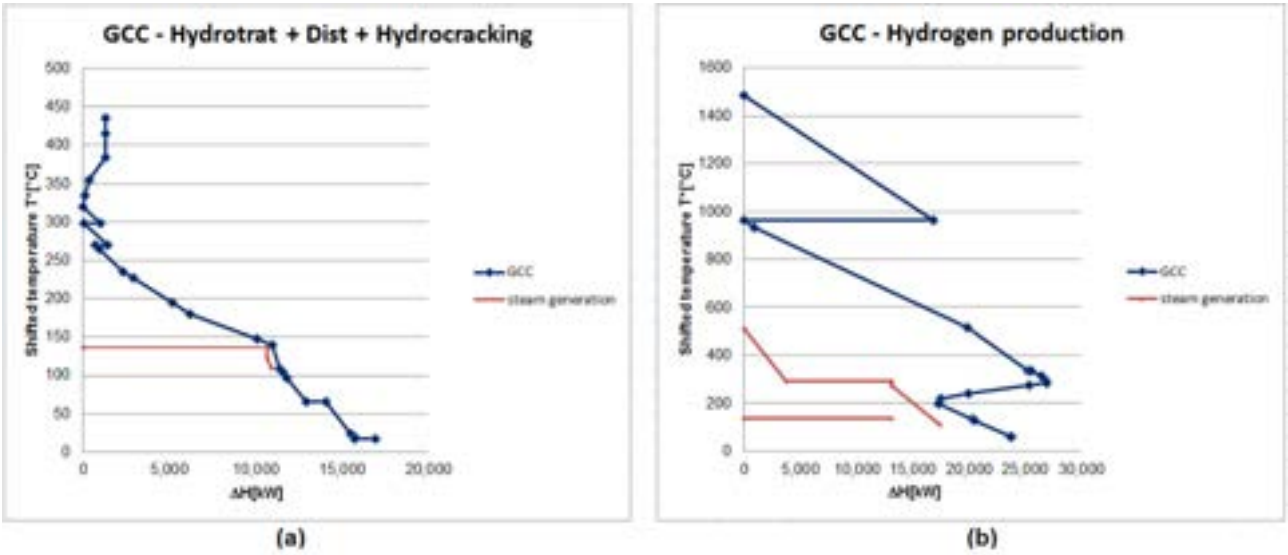

Figure. 6. Grand Composite Curves (GCC) for (a) the Hydrotreatment with Distillation and Hydrocracking processes, and (b) the hydrogen production process

Finally, Table 7 presents the impacts on the cogeneration system; detailed impacts regarding pyrolysis plant integration can be found in [19].

Table 7. Impacts on the cogeneration system

Description	Base Case	Integrated process
Steam consumption in cogeneration system, t/h	214.8	153.4
Steam produced in pyrolysis process, t/h	0	23.4
Steam produced in upgrading plant, t/h	0	38.0
Power consumption in pyrolysis process, kW	0	3,448.3
Power consumption in upgrading plant, kW	0	6,321.0
Power production in pyrolysis process, kW	0	2279
Power production in H_2 production process, kW	0	3655
Surplus electricity, kW	40,600.0	43,060.7

5. Conclusions

The modelling and simulation of a bio-oil upgrading plant was performed in this study; moreover, the integration of an upgrading plant into the sugar and ethanol production process was evaluated including the impacts on the cogeneration system. Bio-oil upgrading through hydrotreatment requires high amounts of hydrogen (4.16 kg of H_2/t cane for 50% of straw recovery from the field), and in this initial assessment, the steam reforming was assumed for H_2 production, taking the biogas produced from the anaerobic digestion of vinasse as feedstock. Nevertheless, from the hypotheses assumed (availability of vinasse in a plant that uses 50% of recoverable sugars in ethanol production), an additional methane source was necessary to complete the required H_2 production (2.47 kg/t cane of biomethane 96.5% mol). Regarding the energy assessment, the pyrolysis process, as well as the hydrotreating and hydrogen production process, presented a significant potential for steam production (28.6% of total steam consumption in the conventional mill), that can be integrated into the conventional sugar and ethanol production process. This could allow the reduction of process steam extraction in the cogeneration system of the conventional plant that operates with sugarcane bagasse as fuel. Thus, the electric energy production in the cycle that operates with condensing-extraction steam turbines would increase. After the power balance, it is possible to achieve a 6% increase in surplus electricity.

Acknowledgments

The authors wish to thank the Coordenação de Aperfeiçoamento de Pessoal de Nível Superior (CAPES) and the Conselho Nacional de Desenvolvimento Científico e Tecnológico (CNPq) (Process PQ 306303/2014-0

and PQ 309588/2019-7) for the researcher fellowship; and for the Research Project Grant (Process 407175/2018-0 and 429938/2018-7).

Appendix A

Table A1. Stream data for heat integration of the Hydrotreatment and Distillation and Hydrocracking processes

Stream Name	Supply Temp. (°C)	Target Temp. (°C)	dT Min Contrib (°C)	Heat Duty (kW)
Bio-oil preheating – (HE1)	18.8	100		1202.9
Feed stream reactor HT-R1 – (HE2)	93.9	250	15	5094.9
Thermal oil – Reactor HT-R1	210	170	30	4324.2
Feed stream reactor HT-R2 – (HE3)	250	370	15	3709.1
Thermal oil – Reactor HT-R2	350	210	30	7873.8
Product of reactor HT-R2 (1) – (COOL-1)	370	250	15	2332.1
Product of reactor HT-R2 (2) – (COOL-1)	250	35	15	10494.0
Feed stream of column C-DIST1 – (HE4)	81.9	212	15	614.0
Feed stream reactor HC-REACT – (HE5)	132.7	420	15	451.1
Product of reactor HC-REACT – (HE-6)	430.5	32	15	573.8
Hydrocracking reactor – HC-REACT	350	210	15	406.4
Reboiler of column C-DIST1	283.3	283.3	15	1002.5
Condenser of column C-DIST1	32	31.9	15	1213.6
Reboiler of column C-DIST2	254.6	254.58	15	667.4
Condenser of column C-DIST2	80.5	80.48	15	1122.9

Table A2. Stream data for heat integration of the hydrogen production process

Stream Name	Supply Temp. (°C)	Target Temp. (°C)	dT Min Contrib (°C)	Heat Duty (kW)
Water preheating (HE7)	44.6	259.9	15	5353.0
Feed stream SR-REACTOR (1) – (HE8)	204.3	227.7	15	2308.6
Feed stream SR-REACTOR (2) – (HE8)	227.7	270.3	15	6925.8
Feed stream SR-REACTOR (2) – (HE8)	270.3	500	15	3462.9
Steam reforming reactor SR-REACT	949.99	950	15	16841.3
Product of SR-REACT – (HE9)	950	310	15	10457.3
Water-Gas-Shift reactor (WGS)	350	349.9	15	-250.3
Product of WGS (1) – (HE10)	350	210.6	15	2186.7
Product of WGS (2) – (HE10)	211	77	15	9839.9
Feed stream of combustor – (HE11)	115.4	300	15	4947.0
Exhaust gases – (HE12)	1500	980	15	16841.3
Exhaust gases – (HE14)	980	150	15	24002.8

References

[1] J. M. Mesa-Pérez, J. D. Rocha, L. A. Barbosa-Cortez, M. Penedo-Medina, C. A. Luengo, and E. Cascarosa, “Fast oxidative pyrolysis of sugar cane straw in a fluidized bed reactor,” *Appl. Therm. Eng.*, vol. 56, no. 1–2, pp. 167–175, 2013, doi: 10.1016/j.applthermaleng.2013.03.017.

[2] R. A. dos R. Ferreira, C. da S. Meireles, R. M. N. Assunção, M. A. S. Barrozo, and R. R. Soares, “Optimization of the oxidative fast pyrolysis process of sugarcane straw by TGA and DSC analyses,” *Biomass and Bioenergy*, vol. 134, no. January, pp. 1–7, 2020, doi: 10.1016/j.biombioe.2019.105456.

[3] V. Alves, A. P. S. Silva, J. P. Lacerda, A. Garcia, and A. Ushima, “Fast Pyrolysis of Sugarcane Straw and Eucalyptus Bark in a Fluidized Bed Reactor,” *Eur. Biomass Conf. Exhib. Proc.*, no. May, pp. 960–965, 2022.

[4] L. Faba, E. Díaz, and S. Ordóñez, “Recent developments on the catalytic technologies for the transformation of biomass into biofuels: A patent survey,” *Renew. Sustain. Energy Rev.*, vol. 51, pp. 273–287, 2015, doi: 10.1016/j.rser.2015.06.020.

[5] M. Sharifzadeh *et al.*, “The multi-scale challenges of biomass fast pyrolysis and bio-oil upgrading: Review of the state of art and future research directions,” *Prog. Energy Combust. Sci.*, vol. 71, pp. 1–80, 2019, doi: 10.1016/j.pecs.2018.10.006.

[6] J. F. Peters, “Pyrolysis for biofuels or biochar? A thermodynamic, environmental and economic assessment,” Universidad Rey Juan Carlos, 2015.

[7] S. Jones *et al.*, “Process design and economics for the conversion of lignocellulosic biomass to hydrocarbon fuels: Fast pyrolysis and hydrotreating bio-oil pathway,” 2013. [Online]. Available: http://www.pnnl.gov/main/publications/external/technical_reports/PNNL-23053.pdf%5Cnhttp://www.nrel.gov/docs/fy14osti/61178.pdf.

[8] A. H. Zacher, D. C. Elliott, M. V. Olarte, H. Wang, S. B. Jones, and P. A. Meyer, “Technology advancements in hydroprocessing of bio-oils,” *Biomass and Bioenergy*, vol. 125, no. April, pp. 151–168, 2019, doi: 10.1016/j.biombioe.2019.04.015.

[9] aspentech, “Aspen Plus,” 2018. https://www.aspentech.com/products/engineering/aspen-plus (accessed Sep. 23, 2018).

[10] F. H. Salina, F. B. Molina, A. G. Gallego, and R. Palacios-Bereche, “Fast pyrolysis of sugarcane straw and its integration into the conventional ethanol production process through Pinch Analysis,” *Energy*, vol. 215, p. 119066, 2021, doi: 10.1016/j.energy.2020.119066.

[11] D. C. Elliott, “Historical developments in hydroprocessing bio-oils,” *Energy and Fuels*, vol. 21, no. 3, pp. 1792–1815, 2007, doi: 10.1021/ef070044u.

[12] S. Jones, C. Valkenburg, and C. Walton, “Production of gasoline and diesel from biomass via fast pyrolysis, hydrotreating and hydrocracking: a design case,” 2009. doi: PNNL-22684.pdf.

[13] D. J. Carvalho, J. P. S. Veiga, and W. A. Bizzo, “Analysis of energy consumption in three systems for collecting sugarcane straw for use in power generation,” *Energy*, vol. 119, pp. 178–187, 2017, doi: 10.1016/j.energy.2016.12.067.

[14] E. Ranzi, T. Faravelli, P. Gaffuri, E. Garavaglia, and A. Goldaniga, “Primary Pyrolysis and Oxidation Reactions of Linear and Branched Alkanes,” *Ind. Eng. Chem. Res.*, vol. 36, no. 8, pp. 3336–3344, 1997, doi: 10.1021/ie960603c.

[15] G. G. Zaimes, K. Soratana, C. L. Harden, A. E. Landis, and V. Khanna, “Biofuels via Fast Pyrolysis of Perennial Grasses: A Life Cycle Evaluation of Energy Consumption and Greenhouse Gas Emissions,” *Environ. Sci. Technol.*, vol. 49, no. 16, pp. 10007–10018, 2015, doi: 10.1021/acs.est.5b00129.

[16] I. N. Zaini, N. Sophonrat, K. Sjöblom, and W. Yang, “Creating values from biomass pyrolysis in Sweden: Co-production of H2, biocarbon and bio-oil,” *Processes*, vol. 9, no. 3, pp. 1–21, 2021, doi: 10.3390/pr9030415.

[17] B. A. Flores-Zavala, “Beneficiamento do biogás produzido em biodigestores anaeróbios para produção de biometano e energia elétrica,” Universidade Federal do ABC, 2016.

[18] R. Smith, *Chemical Process Design and Integration*. England: John Wiley & Sons, Ltd, 2005.

[19] F. H. Salina, M. C. Palacios-Bereche, A. G. Gallego, S. A. Nebra, and R. Palacios-Bereche, “Energy and exergy assessment of fast pyrolysis of sugarcane straw integrated and non-integrated into the conventional ethanol production process,” in *ECOS 2021 - 34th International Conference on Efficency, Cost, Optimization, Simulation and Environmental Impact of Energy Systems*, 2021, pp. 1329–1341, doi: 10.52202/062738-0117.

PROCEEDINGS OF ECOS 2023 - THE 36TH INTERNATIONAL CONFERENCE ON
EFFICIENCY, **C**OST, **O**PTIMIZATION, **S**IMULATION AND ENVIRONMENTAL IMPACT OF ENERGY SYSTEMS
25-30 JUNE 2023, LAS PALMAS DE GRAN CANARIA, SPAIN

Economical and ecological optimization of renewable energy solutions for thermal demands of livestock barns

Manon Everaert[a], Willem Faes[b], Jarissa Maselyne[c] and Steven Lecompte[d]

[a] Ghent University and ILVO, Ghent, Belgium, manon.everaert@ilvo.vlaanderen.be, CA
[b] Ghent University, Ghent, Belgium, willem.faes@ugent.be
[c] ILVO, Merelbeke, Belgium, jarissa.maselyne@ilvo.vlaanderen.be
[d] Ghent University, Ghent, Belgium, steven.lecompte@ugent.be

Abstract:

This work targets sustainable livestock farming, with the aid of cost-effective, novel renewable energy sources (RESs). A literature review showed that evaluating the energy consumption in the livestock sector is not straightforward. Therefore, a model was made to estimate the heating and cooling demands of a pig farm throughout the year. Various combinations of RES technologies are compared with respect to the current installation and an economic and ecological assessment is performed. The possible technologies are: PV panels, PVT panels, solar collectors, heat pumps, wind energy and batteries (both thermal and electrical). The assessment allows estimating the investment cost, life-cycle cost (LCC) and greenhouse gas (GHG) emissions from energy usage of different selections and sizes of renewable technologies. The boundary conditions for the studies are taken from an actual pig farm in Belgium. Autonomous energy creation with solar energy and/or wind generation in combination with a heat pump proves to be the most promising solution to reduce GHG emissions according to the model. The model and results will be evaluated with actual performance data by means of installing heat pumps, PVT panels and thermal storage at the pig farm.

Keywords:

Renewable energy, livestock, pig farm, energy optimization, economical assessment, prediction model

1. Introduction

According to Paris et al. [1], the livestock sector is one of the main energy consumers in the European Union (EU). A large part of this energy is still provided by fuel oils and natural gas. The goal of RES4LIVE[1], a project that received funding from the European Union's Horizon 2020 research and innovation program (grant agreement No 101000785), is to defossilize the livestock industry by researching the implementation of optimized designs and combinations of RES. Looking at the energy needs of different farms, an optimal solution based on investment cost, life-cycle cost (LCC) and greenhouse gas (GHG) emissions should be calculated. In the current work, the model developed for this purpose is explained and some initial results are presented.

The goal of Section 2. is to frame the energy consumption of livestock in the EU and Flanders (a region in Belgium). In 2021, a survey was held in Flanders about energy consumption in pig farming whose results can be found at the end of the section. In Section 3., the calculation model (made in Python) is explained as well as its application to a pig farm in Belgium called the 'Varkenscampus', together with the corresponding sensitivity analysis. At the end, some remarks about future work are presented.

2. Energy consumption in livestock

Even though the livestock sector is claimed to be one of the main energy consumers in the EU by Paris et al. [1], there is no standardized methodology to measure the energy usage in livestock. At the moment, the livestock's energy consumption pattern is derived from literature reviews or by performing analyses in a local environment. There is no detailed database available yet. In this section, the currently known energy usage in the livestock sector is discussed on three different levels. First, a literature review is performed to frame the energy consumption in livestock across the EU. Secondly, a biennial study performed by the Department of Agriculture and Fisheries about agriculture in Flanders (Belgium) is discussed. Thirdly, a recent survey was launched whose results are reported in this work.

2.1. Energy consumption in livestock across the EU

In Paris et al. [1], a literature review was conducted by the Agricultural University of Athens that gathered some papers on the subject. The review summarizes several direct and indirect energy uses from several livestock

[1] res4live.eu/

farms including dairy cattle, beef cattle, pigs, laying hens and broilers. Direct energy covers all energy used on the farm, while indirect energy refers to all outside usage, e.g. feed processing. To be able to equally compare energy consumption across all types of livestock farms, it is scaled per amount of end product produced by the farm. For all livestock categories, this is done per kg produced meat or eggs, except for milk production. To obtain similar values for milk, a unit is needed that takes into account the extra fat and protein production. The energy corrected milk production (ECM), expressed in kg, is the unit that fulfills this purpose. The total energy consumption can be roughly estimated by taking the mean of the results reported by Paris et al. [1] and multiplying these with the total production in Europe. This is done to obtain the total energy usage mentioned in Table 1.

Table 1: Estimation of the total energy consumption of different livestock farms across Europe in one year according to Paris et al. [1], the † indicates a number that could not be retrieved from Paris et al. [1] and was extracted from the Eurostat database [2] instead, with the mean weight of an egg assumed to be 60g.

Livestock type	Total production in the EU [10^9 kg]	Avg. energy per kg production [MJ/kg]	Total energy usage in the EU [10^{10} MJ]	Direct energy [%]
Dairy cattle	158	3.7	58	15-48
Beef cattle	7.9	49.9	39	60-70
Pork	23.8	19.3	46	20
Poultry meat	15.29	14.36	22	25
Laying hens	4.35 †	22	9.6	25-46

From the results reported by Paris et al. [1], it can also be concluded that the main contributor to energy consumption is the feed (indirect). In this paper however, the focus lies on the direct energy consumption. The percentage of direct energy consumption is indicated in Table 1. Although it is not as large as the contribution of the feed, it is still significant, especially in laying hens and beef production. A large share of this on-farm energy consumption is still produced by fossil fuels. Other energy sources are the electricity grid (still lacking green sources in many countries) and natural gas. By converting this direct energy consumption to renewable energy sources (RESs), a noteworthy improvement can be made in the climate impact of livestock.

2.2. Energy consumption in livestock across Flanders (Belgium)

In Flanders, the Department of Agriculture and Fisheries publishes an exhaustive report every two years about all agricultural related activities. Their most recent report [3] was written in 2017, but biannual updates can be consulted at [4]. In Fig. 1, a brief summary of the results concerning energy consumption in livestock is given. Pork, dairy and beef take up about 20% of the total energy consumption in Flanders. Poultry has been left out of this discussion due to insufficient data available.

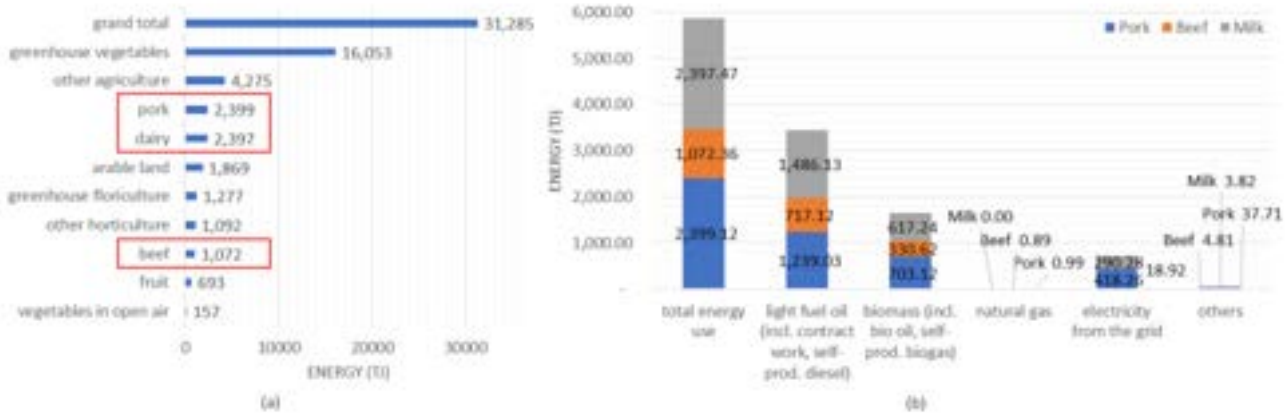

Figure 1: Results adapted from the Department of Agriculture and Fisheries [4] about (a) the energy consumption of agriculture in Flanders per sector with livestock indicated by red rectangles and (b) the energy consumption in livestock per carrier, poultry is not mentioned in this data since there is no detailed data available yet.

As can be seen in Fig. 1b, most energy comes from light fuel oils, such as gasoline and diesel fuel. The main consumers of these fuel oils are tractors for tillage. Another purpose is additional heating during winter by

e.g. heat canons. The latter is mostly for pigs, since cows do not need as much heat. Runner up is biomass, which shows that Flemish farmers have been making efforts in using cleaner energy. The energy balance [4] reported by the Department of Agriculture and Fisheries over the past 10 years, shows a rise of about 10 000 TJ in biomass energy generation across all agriculture. The biggest consumer of natural gas in Flanders is the pig industry. This phenomena can be attributed to the use of hot water systems for floor heating, providing the high heating needs for piglets, and sanitary hot water, used for cleaning and showers. According to Paris et al. [1], electricity from the grid is mainly used for ventilation, present in all livestock farms; heat lamps, appearing mostly in pig farms; and milk cooling for dairy cattle. Beef cattle requires the least amount of electricity. The Department of Agriculture and Fisheries [4] shows that during the last 10 years, the latter sector even produced a net amount of electricity by installing photovoltaic (PV) panels on their large roofs. Other energy sources are thus mainly solar panels, but can also be small wind turbines, heat pumps etc.

2.3. Energy survey in pig farming across Flanders

In 2021, a survey was launched by Flanders Research Institute for Agriculture, Fisheries and Food (ILVO) for Flemish pig farmers. This survey was meant to probe their current energy installations. There were 38 correspondents composed of 25 farrow-to-finish (farmers that have a sow herd to breed piglets and rear these from birth to slaughter - so the entire life-cycle of the pig), 11 fattening pig farmers (farmers that buy piglets and rear them until slaughter) and 2 sow farmers (farmers that have a sow herd to breed piglets and sell these piglets). In this subsection, the results are presented. Initially, the heating system of the participants' farms was asked. Heating is the main energy consumer in pig farming, since newborn piglets need a high temperature of about 35°C. In intensive pig farms, it is not unusual to have new piglets every three weeks meaning this high temperature demand is often required. Therefore, knowing the heating system offers valuable information about the energy consumption of the farm. The results about current installations can be found in Fig. 2. Most of the pig farmers still use fuel oil to heat up their farms. This result is in line with the literature review performed by Paris et al. [1]. It indicates that improvement is still possible in many farms. Almost all participants already took measures to reduce their energy consumption, especially on electricity.

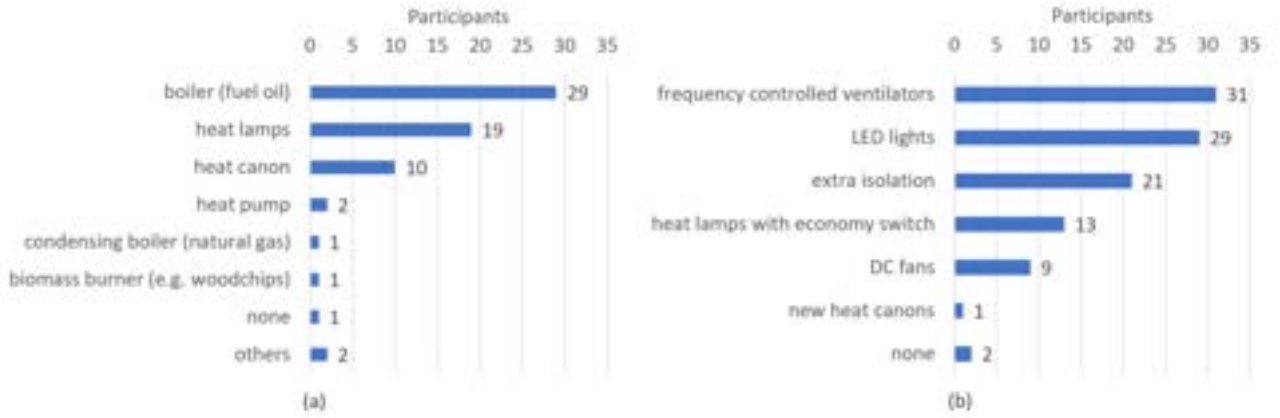

Figure 2: Survey results about energy consumption in pig farming with the horizontal axes representing the amount of participants (38 in total): (a) presents the currently installed heating systems on the participants farms and (b) which measures they already took to reduce their energy consumption.

In the next part of the survey, the participant's motivation about switching to renewable energy sources was questioned. All participants were asked to rate the importance of a project on introducing renewable energy in pig farming on a 5-point scale. The results of the survey were that 76.3% of participating pig farmers scores this type of project with an importance of 4 or 5 out of 5. Of the respondents, 92.1% thinks more energy saving measures are possible on their farm and 76.3% already owns a renewable energy source. These numbers conclude that switching to renewable energy is deemed important among pig farmers. Most of the farmers already made some efforts, but still think more energy saving measures are possible on their farms. This can also be concluded from the results in Fig. 3, in which their encountered difficulties were questioned. Lack of investment budget and insufficient knowledge about the needed capacity, system requirements and current legislation are the main obstacles for farmers.

From this section, it can be concluded that livestock in general has a high energy demand and a lot of improvement can still be made to convert to clean energy. In the residential and industrial sector, many optimized and adapted RESs are already present. The goal of this work is to evaluate these solutions for the livestock sector. A generally applicable calculation tool was created to optimize the combination and design of RESs

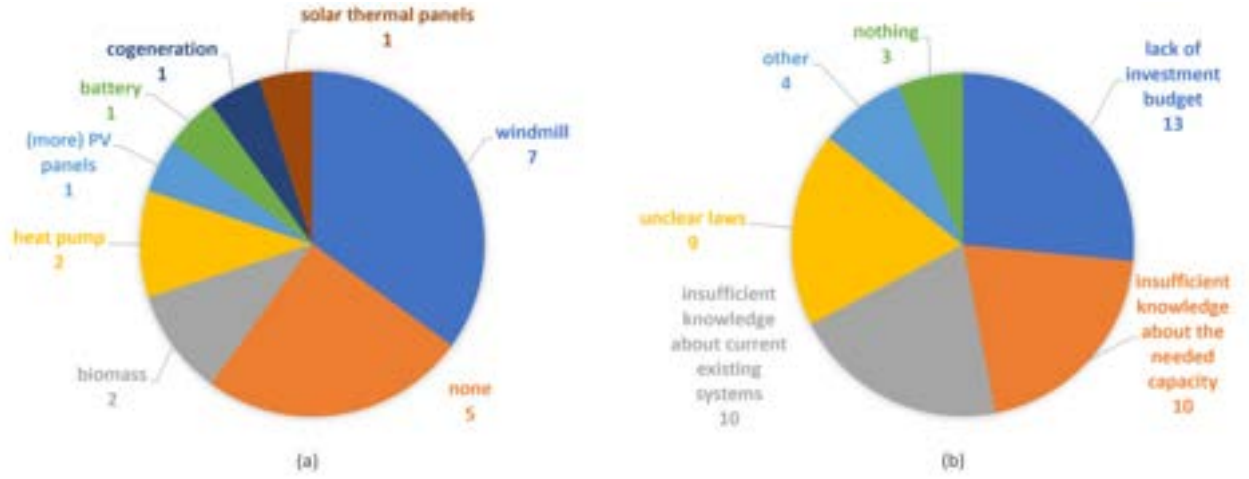

Figure 3: Survey results about energy consumption among pig farmers (38 participants): (a) which RESs the participants are considering and (b) the barriers they encounter to install (more) RESs.

for farm-specific cases. In the next part of this paper, the simulation methodology is explained and applied to a pig farm in Belgium, called the 'Varkenscampus'. The calculated parameters are investment cost, LCC and GHG emissions. Such a tool could fill the gap of insufficient knowledge about system requirements and needed capacities of RESs by livestock holders.

3. Calculation tool

A calculation tool was made in Python to find optimal combinations of RESs that are fine-tuned to the specific energy demands of livestock farms. A first version was made by Faes [5]. This paper expands further upon this tool and tests its sensitivity to several parameters. The calculation is based on the Varkenscampus, located in Melle (Belgium). This is a commercial farrow-to-finish pig farm with a maximum capacity of 136 sows, 576 piglets, 640 fattening pigs, 12 young sows and 2 boars. This puts the Varkenscampus into the category of a small to medium pork producer. Currently, the energy demand of the farm is provided by a connection to the grid and a condensing natural gas boiler. The electricity is mainly used for ventilation and heat lamps, while the condensing boiler provides hot water for floor heating, air heating and sanitary hot water. The tool takes into account past energy consumption patterns and satisfies this demand with predefined combinations of RESs. Subsequently, the investment cost, LCC and GHG emissions can be calculated for every combination. Finally, the optimal combinations are found by using Pareto optimization.

3.1. Explanation of the tool

The Python tool consists of multiple parts, each of which is explained below. The starting point is the construction of an hourly energy demand of the farm. These energy requirements must always be met, otherwise there would be discomfort for the animals. A reference case is obtained by implementing parameters of the current (existing) condensing gas boiler. Finally, the calculated output parameters of all the possible installations are scaled to this reference case.

3.1.1. Estimation of the energy demand

An hourly energy demand is required as input for the tool. To achieve this, the energy demand is separated into two flows: the electricity demand and the heat demand.

Electricity demand

The electricity demand profile of the farm is constructed based on monthly measurements at the Varkenscampus. The monthly usage was averaged out to obtain an hourly mean value. The total electricity demand of the farm in the year 2020 was 107 MWh.

Heat demand

The calculation of the heat demand is less straightforward since it cannot be measured directly and many factors need to be taken into account. These factors, among other things, consist of:

- The farm's building materials and isolation.
- The amount of pigs per compartment and their heat production.
- The complete heating system (sanitary hot water, air heating, floor heating etc.).
- The required heating and/or cooling for the pigs.
- Ventilation and relative humidity at which the pigs feel comfortable.

- The weather conditions outside.

In 2021, the calculations were performed by De Win [6] and eventually adjusted by Faes [7]. They created a steady-state model, which calculates the heat flow in and out of the barn. Documentation of the barn's building process provided the necessary information on the building's properties. From a literature study [8], the heat production and comfort requirements of pigs can be found. Subsequently, the hourly heating/cooling demands for air and underfloor heating can be estimated. This is done per compartment to take into account the occupation rate, age of the pigs and existing heating system. For example, some compartments have no air heating installed, while other ones require both air and floor heating. Different compartments will also have different ages of pigs at any time, which effects the heat production and comfort needs in that compartment at that moment.

In the end, two separate hourly heat demands were obtained: one for the high temperature water cycle (60°C) used for air heating (twin tubes), and one for the low temperature water cycle (40°C) used for floor heating. The high temperature heat demand is calculated by taking the required heat demand of every zone. It takes into account all of the above-mentioned factors. The low temperature heat demand is calculated with the characteristics of the heating mats in combination with the weekly occupation rate of newborn piglets of the farm in 2020. When piglets are present and they are younger than 4 days, the 16 available heating mats (each able to deliver 180W) are put at full power. When the piglets have the age of 4 to 7 days, the mats are put at half their power. In 2020, new piglets were born every 21 days. Consequently, the low temperature heat demand follows a periodic cycle of 21 days with 3 separate values per zone depending on the age of the piglets. In the end, the calculated heat demand in 2020 is about 212 MWh corresponding to an estimated consumption of 20,000 m^3 natural gas.

3.1.2. Selection of RES

In a next step, the model adds a selected combination of RESs to the current installation. These combinations are shown in Table 2. The currently installed natural gas boiler is included in the first row and taken as the reference point. The selection is made by taking the size of the Varkenscampus into account. As can be seen, the heat pump options are chosen in pairs indicated by a pair of brackets. Considering the two different heat demand profiles, it is more efficient to have two separate heat pumps with one operating continuously than one of a bigger size operating in on/off mode [6]. Running over every possible combination results in 123,480 possible scenarios, however not every scenario is sensible. Batteries are useless without an autonomous source of electricity and are therefore left out of the calculation if no such source is present in the scenario.

Table 2: Selection of energy systems to be calculated by the model, the square brackets are used to indicate a pair of heat pumps in the configuration, with first the high temperature heat pump (60℃), and second the low temperature heat pump (40℃).

Energy system	Unit	Options
natural gas boiler	kW	60
PV panels	m^2	$0 - 10 - 50 - 100 - 500 - 1000$
ST panels	m^2	$0 - 10 - 50 - 100 - 500 - 1000$
PVT panels	m^2	$0 - 10 - 50 - 100 - 500 - 1000$
heat pump(s)	kW	$0 - [60, 0] - [55, 15] - [30, 30]$
electrical battery	kWh	$0 - 2 - 5 - 10 - 100$
thermal storage (water)	liter	$0 - 250 - 800 - 1000 - 2500 - 3000$
wind turbines	kW	$0 - 15 - 30$

For every scenario, a steady-state model for the energy flow over a period of one year is performed. Besides the electricity and heat demand of the barn (see 3.1.1.) and the sizing of possible RESs combinations (Table 2), several other input parameters are needed. These include set parameters related to the steady-state model and weather parameters describing the boundary conditions of the RES (Table 3). The latter consists of the local solar irradiance (q_{sun} in W/m^2) and the wind velocity (v_{wind} in m/s). At the Varkenscampus, a weather station is installed that measures these at an hourly basis.

The RESs' hourly energy generating functions depending on the measured weather conditions are described by Eq. (1) to Eq. (5). Eq. (1) calculates the power P [W] generated by a surface size A [m^2] of PV panels. The model uses PV panels that generate 1 kWp per 7 m^2.

$$P_{PV} = q_{sun} \frac{A_{PV}}{7} \tag{1}$$

Table 3: Chosen parameters to create the steady-state model.

Parameter	Value
time step	1 hour
simulated period	1 year
boiler efficiency	95%
low temperature heating	40 °C
high temperature heating	60 °C
low temperature nominal COP	5
high temperature nominal COP	3.5
COP nominal temperature	17 °C
initial battery charge	0 kWh
initial thermal storage temperature	40 °C
maximal thermal storage temperature	90 °C

Eq. (2) describes the heat Q [W] generating profile of solar thermal (ST) panels. These panels generate 4 times the solar irradiance per surface size of 7 m^2, which results in an energy production of 500 $kWh/m^2/year$.

$$Q_{ST} = q_{sun}\ 4\ \frac{A_{ST}}{7} \tag{2}$$

For practical reasons, the generating profile of the photovoltaic thermal (PVT) panels is seen as a hybrid between PV and ST panels, relatively described by Eq. (3) and Eq. (4). They generate 80% of the electricity that PV panels would generate and 70% of the heat generated by the ST panels.

$$P_{PVT} = 0.8\ q_{sun} \frac{A_{PVT}}{7} \tag{3}$$

$$Q_{PVT} = 0.7\ q_{sun}\ 4\ \frac{A_{ST}}{7} \tag{4}$$

Finally the electricity generated by n small wind turbines with each a power P_{unit} of 15kW is given by Eq. (5). The measured wind speed at a height of 10m is multiplied by a factor 1.3 to correct for the height of the wind turbine's blades, which is 15m. The nominal wind speed at which nominal power is reached, is 7.8 m/s.

$$P_{wind} = n\ P_{unit}\ \left(\frac{1.3\ v_{wind}}{7.8\ m/s}\right)^3 \tag{5}$$

3.1.3. Simulation methodology

Starting from the energy demand mentioned in section 3.1.1., the tool tries to satisfy this demand in subsequent order:

1. Fulfill the heat demand by using heat pumps, if any are installed.
2. If PV, ST, PVT panels and/or wind turbines are installed, their energy is used to its full capacity. Without heat pumps installed, their produced energy goes to the heating or electricity systems of the farm. If heat pumps are present, their energy is first provided to the heat pumps. If the energy production exceeds the total demand, the excess is put back onto the grid or lost in case of heat excess. If the heat demand is not fulfilled, electricity is taken from the grid if heat pumps are present, else the condensing gas boiler is used.
3. If storage systems are present, they are filled to their maximum capacity before sending electricity to the grid or losing heat.

Subsequently, an hourly energy balance of all 123,480 scenarios can be calculated.

3.1.4. Cost and emission functions

The energy consumption pattern is now known for every scenario. Next, the parameters necessary to calculate the investment cost, LCC and GHG emissions are introduced in this subsection.

Investment cost

The investment cost is estimated from selling prices of local vendors. The condensing boiler and wind turbine are easiest to define since they exist as one unit. The prices chosen are:

- Condensing gas boiler: €15k (purchase price at Varkenscampus).
- Wind turbine: €60k (estimated from a commercial wind turbine [9]).

The other cost functions depend on the size of the installation. This phenomena can be attributed to the initial installation cost. They are represented by the functions in Fig. 4. To estimate these functions, the prices of several installation sizes were consulted. PV panel prices [10] and ST panel prices [11] were obtained from online sources. Prices of PVT panels are derived from these two and calculated with Eq. (6).

$$\text{PVT} = \text{PV} + \frac{\text{ST}}{2} \tag{6}$$

The heat pump prices were obtained from De Win's dissertation [6]. The prices for thermal storage tanks [12] and batteries [10] were also obtained online.

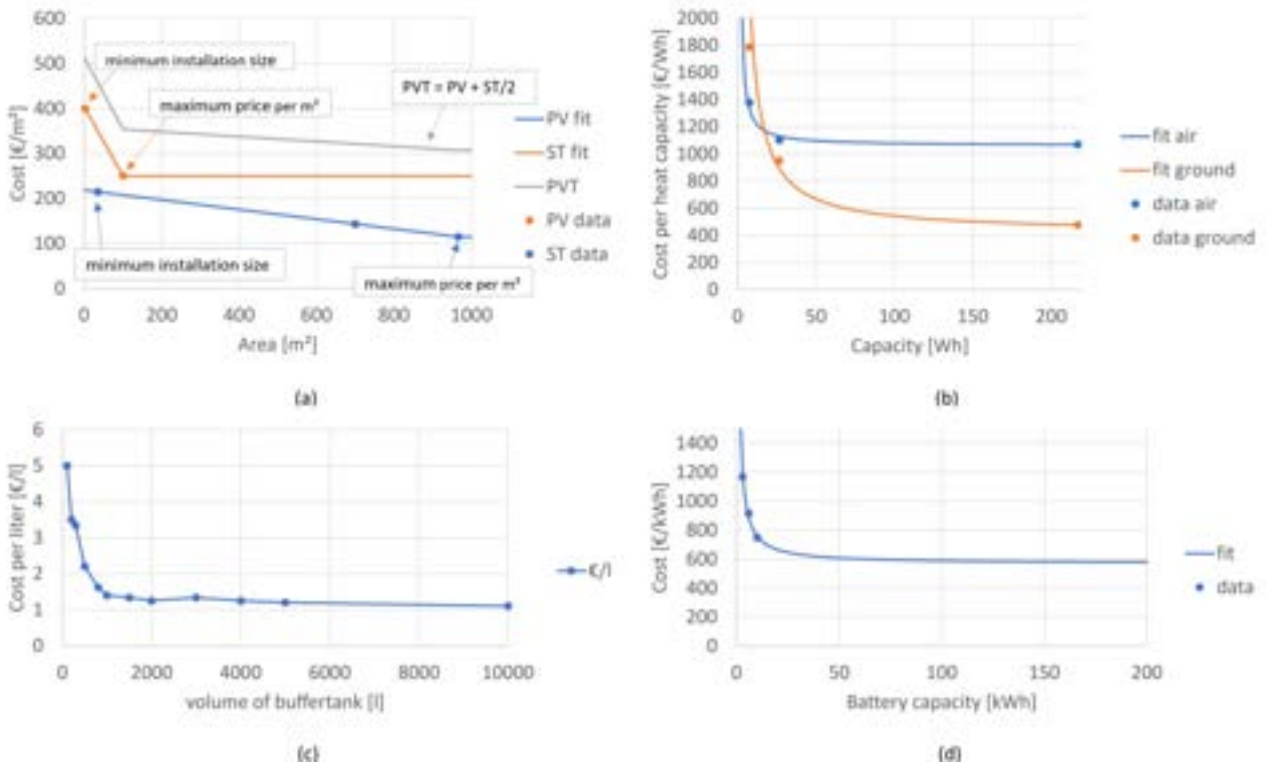

Figure 4: Cost functions of the renewable energy sources with prices depending on the size, the functions are interpolated from local vendor prices with (a) price function of PV panels [10], ST panels [11] and PVT panels according to Eq. 6, (b) heat pump prices [6], (c) prices of thermal storage tanks (water) prices [12] and (d) battery price function [10].

Life-cycle cost

The LCC takes into account the lifetime of the RES and their operational cost. When energy prices are high, it is self explanatory that autonomous energy generation would become more economical in the long run. The LCC is calculated using Eq. (7)

$$LCC = IC_0 + \sum_{i=0}^{n} \frac{EC_i + IC_i}{(1+r)^i} \tag{7}$$

The summation is done over a period of $n = 20$ years. Every year, the operational cost and potential replacement cost of the total combined system is calculated. IC_0 is the initial investment cost, calculated with the cost functions in Fig. 4. This cost reoccurs when the energy system's life is shorter than the 20 years, indicated in the sum by the term IC_i. In Table 4, an overview of the chosen lifetimes is given. Next in line is the operational cost, which is indicated by EC_i. It is calculated by multiplying the current energy tariffs and the yearly energy consumption resulting from the steady-state model. The energy tariffs can be found in Table 5 and were obtained from the VREG (Energy Regulator in Flanders) database [13]. At last, the reduction factor $\frac{1}{(1+r)^i}$ appearing in Eq. (7) represents the reduction in monetary value over the years. The parameter r is the internal rate of return and is chosen to be 6%.

Table 4: Lifetimes for the selected energy systems

Energy system	Lifetime (years)
condensing gas boiler	15
PV panels	25
ST and PVT panels	20
heat pump	20
electrical battery	8
thermal storage tank	20
wind turbine	20

Table 5: Energy tariffs in Flanders in 2022 [13].

Energy source	Cost [€/kWh]
electricity cost	0.5
gas cost	0.2
injection cost	-0.15

Greenhouse gas emissions
Just like the operational cost, the GHG emission is calculated by multiplying the energy demand from the steady-state model with the relevant parameters representing the GHG emissions. This is just a simple estimate without taking into account the GHGs emitted during the creation process of the RESs. For electricity from the grid and natural gas consumption, the equivalent CO_2 per kWh is given in Table 6 and were respectively obtained from the European Environment Agency [14] and Casasso et al. [15].

Table 6: Equivalent CO_2 emissions of the Belgian grid and the consumption of natural gas by a condensing boiler.

Energy source	Effective CO_2 [kg/kWh]
electricity grid	0.20 [14]
gas boiler	0.25 [15]

3.2. Results

In Fig. 5 the results of the calculation are shown. All three parameters are represented in this graph (i.e. investment cost, LCC and GHG emissions). To better investigate the results, an interactive version (in Plotly) was made to observe which RESs are present in a selected scenario.

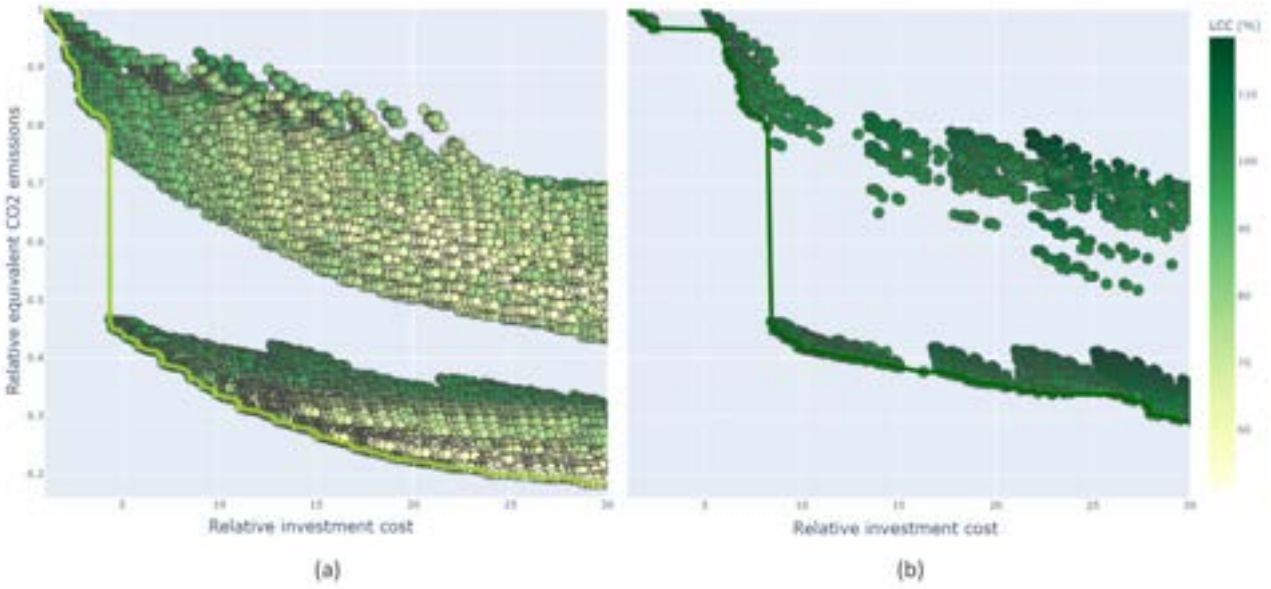

Figure 5: Scatter plots containing all 123,480 combinations from Table 2 with every dot representing a scenario for which the calculation was performed over one year, the results are expressed relative to the current installation which can be found at (1,1,1). In (a) results with a lower LCC compared to the current installation are plotted and in (b) those with a higher LCC, the optimal solutions can be found on the plotted lines (Pareto front).

A first observation is the separation into two clouds. The upper one has the most GHG emissions, but starts at the lowest investment cost compared to the lower cloud (only starting at a relative investment cost of 4 times the original scenario). This is due to a lack of heat pumps in the upper clouds, while the lower cloud

represents all scenarios where heat pumps are present. To find the optimized solutions, the Pareto front was calculated for GHG emissions and investment cost for the selection of results with a lower relative LCC (Fig. 5a) compared to the original installation (in other words LCC $<$ 100%) and with a relatively higher LCC (Fig. 5b). This division was made to take into account the third parameter, since the Pareto front is only calculated with two parameters. The principle is based on Pareto optimality in which two parameters are compared. If one parameter improves, it is imposed onto the other parameter that it cannot degrade. If one parameter improves to the detriment of the other one, the solution is discarded. This results in a front along the minima of both parameters, as can be observed in Fig. 5. By walking down this Pareto front, the optimized combinations can be recognized. For a lower LCC, the order is as follows:

$$PV > ST > PVT > \textit{thermal storage} > \textit{heat pumps} > \textit{electrical battery} > \textit{wind turbine}$$

and for a higher LCC:

$$PV > \textit{electrical battery} > PVT > ST > \textit{thermal storage} > \textit{heat pumps} > \textit{wind turbine.}$$

For clarity, these Pareto fronts are visualized in Fig. 6.

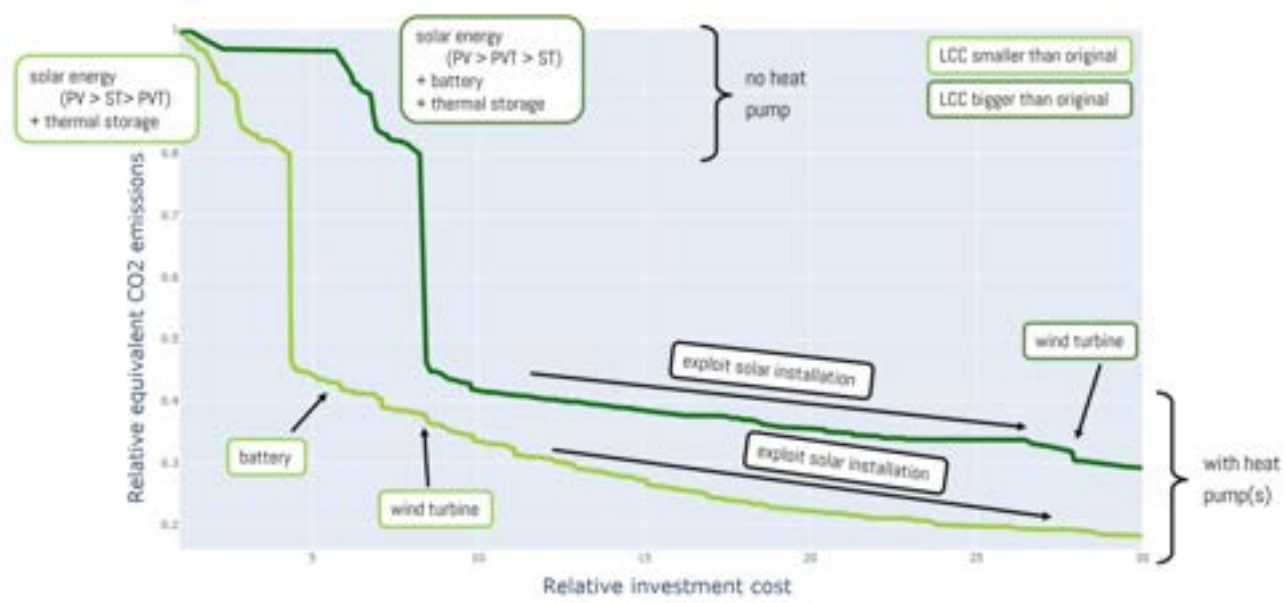

Figure 6: Pareto fronts representing an optimization of greenhouse gas emissions and investment cost, to take into account the third parameter (LCC) a separation was made between a relatively higher or lower LCC than the original installation at the Varkenscampus (natural gas boiler and grid connection), the boxes indicate the energy sources encountered in the configurations when walking along the fronts.

From these observations, it can be concluded that both Pareto fronts agree on installing solar panels first, preferably with heat production and storage. Taking this into consideration it seems that renewable energy systems are best integrated before installing a heat pump. Furthermore, installing a heat pump results into a large jump of 35% in the reduction of GHG emissions. Combining a heat pump with green energy, the GHG emissions are reduced by 55%. With the chosen parameters, the lower LCC Pareto front also results into the best case scenario for reducing GHG emissions compared to the higher LCC Pareto front. However, changing some parameters can cause the opposite to be true. This will be discussed in section 3.3. Batteries emerge sooner when walking along the front for higher LCC, which might be due to their short lifetime in the LCC calculation. Configurations with wind turbines appear last (starting at a relative investment cost of 8) on both fronts as their installation cost is the highest of all resources. However, they appear much sooner for lower LCCs indicating an economic advantage over longer periods.

3.3. Sensitivity analysis

A sensitivity study was made to see how the results behave when inserting different parameters. The changes are compared to a base case, for which the previously explained result is chosen. The adjusted parameters are shown in Table 7 with a variation in the relevant ranges. The influence of these variations on the optimized solutions can be derived from their influence on the Pareto fronts. This is shown in Fig. 7. The influence of the parameters corresponding to GHG emissions and energy costs will be discussed separately.

Table 7: Used alterations to the tweaked parameters.

parameter	[unit]	ref. case	variation in relevant range	%
CO_2-eq. emissions of the grid	[kg/kWh]	0.20	$\pm$ 0.05	25
CO_2-eq. emissions of the gas	[kg/kWh]	0.25	$\pm$ 0.05	20
electricity price	[€/kWh]	0.50	$\pm$ 0.25	50
gas price	[€/kWh]	0.20	$\pm$ 0.1	50
injection cost	[€/kWh]	0.15	$\pm$ 0.1	67

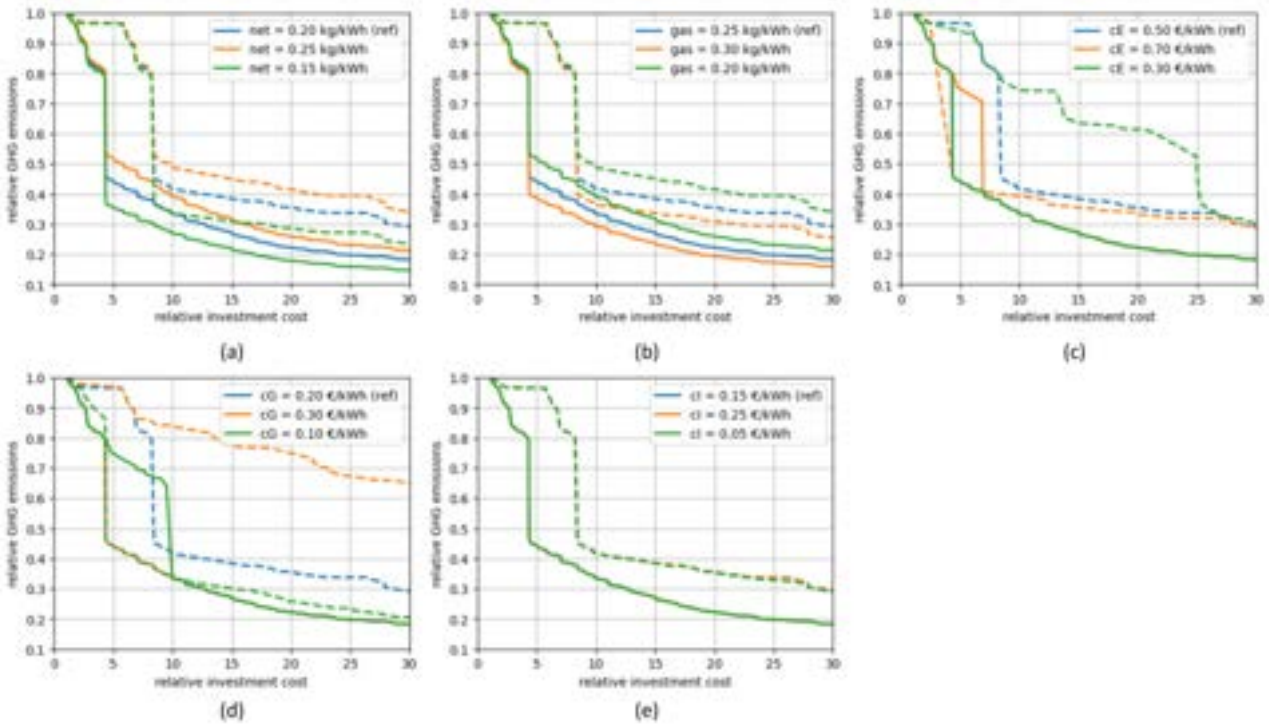

Figure 7: Influence of different parameters on the optimized solutions or Pareto fronts, the reference case from Fig. 5 is given in blue (in some cases, these blue lines are covered but they are the same everywhere), with a full line representing fronts with a lower LCC compared to the original scenario (where LCC = 1) and the dashed lines fronts with higher LCC, the studied parameters are (a) GHG emissions from the electricity network (b) GHG emissions from the natural gas boiler (c) electricity cost (d) gas price and (e) injection cost.

Influence of the equivalent CO_2 emission

The variation of the equivalent CO_2 emissions for the electricity and natural gas causes a vertical shift in the dispersion of the 123,480 scenarios. Their effect is inversely proportional. While a lower GHG emission factor for the grid (Fig. 7a) drives the clouds together, the opposite is true for the GHG emission related to natural gas burning (Fig. 7b). Therefore, these parameters additionally influence the reduction in GHG emissions when installing heat pumps. In the reference case, a reduction of 35% was seen. A variation of 20% on the electricity emission factor can cause this jump to reduce or increase by 8%. Further analysis indicates that a relative variation of the gas emission factor has a bigger influence on the data than the grid emission factor. The LCC and investment cost are left unchanged.

Influence of the energy prices

The variation in energy prices has a significantly higher effect on the results, especially on the Pareto fronts. Some variations even flip around the high and low LCC fronts, making configurations with a higher LCC more beneficial to reduce GHG emissions. This event occurs for high electricity prices (Fig. 7c: cE = 0.70 €/kWh) or low gas prices (Fig. 7d: cG = 0.10 €/kWh), causing a higher LCC for all scenarios containing heat pumps. The order encountered when walking along the Pareto fronts are the same as mentioned before (section 3.2.), but investing in a heat pump when electricity prices are high is detrimental for the LCC. This causes the front with higher LCCs to jump to heat pumps already at a lower investment cost than the front with lower LCCs. A higher investment cost is thus needed to make the reduction in GHG (by installing heat pumps) and simultaneously be beneficial to the LCC. When the electricity price is low (Fig. 7c: cE = 0.30 €/kWh) or the gas price high (Fig. 7d: cG = 0.30 €/kWh), the two Pareto fronts disperse until heat pumps no longer occur into the optimized

configurations with a higher LCC (the dashed line never reaches into the lower cloud at acceptable investment costs). In such scenario, heat pumps come out on top both economically and ecologically. Further analysis indicates that the influence of electricity and gas prices on the LCC is opposite: a low electricity price causes a generally higher LCC and vice versa. Again, a relative variation of the gas price a bigger influence on the results than the electricity price. The injection cost barely has any influence (Fig. 7e), since this cost only occurs for overproducing configurations and is relatively small compared to the other costs.

It can be concluded that realistically occurring changes in energy prices result in different optimal solutions. This is not very convenient if the tool is to be used to calculate economically optimized configurations. A solution could be to better predict the LCC by improving Eq. (7) and introducing life-cycle assessments. On a more positive note, the jump in GHG emissions owing to heat pumps is consistent throughout all parameter ranges.

4. Conclusion

A tool was made to calculate the influence of different combinations of RESs on livestock barns. From the simulations some preliminary conclusions can be drawn. The installation of a heat pump is most effective on GHG emissions when green energy sources are already present. This causes a reduction in GHG emissions of 55% compared to the current gas boiler installation at the Varkenscampus (reference case). Due to their high investment cost, scenarios containing heat pumps only start occurring at relative investment costs of 4 times that of the gas boiler or higher. However, with moderate energy prices they are beneficial to the LCC except when electricity prices are high or gas prices are low. All optimized solutions agree on investing in solar energy first, preferably with heat production and storage. This is a sensible result, since the Varkenscampus and pig farms in general, require a lot of heat. The best investment would be a wind turbine resulting in scenarios with the lowest LCCs. Unfortunately, they only come into the picture at a relative investment cost of 8.

Future work

The calculation tool requires further testing and fine-tuning. In the near future, two heat pumps, 50 m^2 PVT panels and a buffer tank of 800 liters will be installed at the Varkenscampus. This will be the calculation tool's first validation. Secondly, the tool needs to be expanded to other type of farms. As for the fine-tuning aspect, the cost and emission functions are pretty rough estimations at the moment. More sensitivity analyses must be performed on other parameters as well. It might be useful to connect the tool to energy price predictions on the web. Taking life-cycle assessments of the relevant RESs into account, would be an improvement as well. Many improvements are still to be made to the tool, but it already produces some sensible results. Fine-tuning, testing and adapting the tool to other farms can result into a positive contribution to the energy transition in livestock.

Acknowledgments

The RES4LIVE project has received funding from the European Union's Horizon 2020 research and innovation programme under grant agreement No 101000785. Lastly, I would like to thank Robin Tassenoy, Jera Van Nieuwenhuyse and Petros Demissie Tegenaw for their useful inputs during our monthly discussions on the subject and for thoroughly proofreading this work.

Nomenclature

Abbreviations

RES renewable energy source

GHG greenhouse gas

LCC life-cycle cost

PV photovoltaic

PVT photovoltaic thermal

ST solar thermal

COP coefficient of performance

References

[1] Paris B., Vandorou F., Tyris D., Balafoutis A.T., Vaiopoulos K., Kyriakarakos G., Manolakos D., Papadakis G. *Energy Use in the EU Livestock Sector: A Review Recommending Energy Efficiency Measures and Renewable Energy Sources Adoption.* Applied Sciences 2022;12(4):2142.

[2] Eurostat. *Production of eggs for consumption (million eggs, 2021).* Available at: https://ec.europa.eu/eurostat/statistics-explained/index.php?title=File:Production_of_eggs_for_consumption_(million_eggs,_2021)_20-12-2022_rev.png#filelinks [accessed 06.03.2023].

[3] Lenders S. and Deuninck J. *Gebruik van energie, gewasbescherming, water en kunstmest in de Vlaamse landbouw. Resultaten op basis van het Landbouwmonitoringsnetwerk 2007-2014*. Departement Landbouw en Visserij, Brussel; 2016.

[4] Department of Agriculture and Fisheries. *Energiebalans.* Available at: `https://landbouwcijfers.vlaanderen.be/landbouw/totale-landbouw/energiebalans` [accessed 16.02.2023]

[5] Faes W., Lecompte S. and Maselyne J. *Cost-effective implementation of renewable energy sources in livestock barns* AgEng-LAND.TECHNIK 2022; p. 245-251.

[6] De Win W. *Modelling the thermal load of pig stables and integrating renewable energy sources [dissertation]* Ghent, Belgium: Ghent University; 2021.

[7] RES4LIVE project. *D2.2: Integration schemes of RES4LIVE adapted technologies with commercial solutions (version 1)*; 2022 Jun. 30; Zenodo; https://doi.org/10.5281/zenodo.6855901 [accessed 20.02.2023]

[8] Bartali E., Bruce J., Dolby C.M., Menella V., O'Neill D., Pedersen S., Sallvik K. Sokhansanj S., Souty J.C., Tillie M. *CIGR Handbook of Agricultural Engineering, Volume II Animal Production & Aquacultural Engineering.* Gainesville FL, United States of America; 1999.

[9] EAZ wind. *Onze windmolen.* Available at: https://www.eazwind.be/onzewindmolen [accessed 06.03.2023]

[10] Zonnepanelen-gids.be. *Zonnepanelen: soorten, prijs, premie en rendement.* Available at: https://www.zonnepanelen-gids.be/ [accessed 23.06.2022]

[11] Zonneboilertips.be. *Soorten zonneboilers en hun prijzen in 2021.* Available at: https://zonneboilertips.be/zonnecollector/ [accessed 23.06.2022]

[12] Dimeco.be. *Buffervaten.* Available at: https://www.dimeco.be/soort/boilers-en-buffervaten/buffervat/ [accessed 23.06.2022]

[13] VREG. *Energiemarkt in cijfers.* Available at: https://www.vreg.be/nl/energiemarkt-cijfers#2 [accessed 26.01.2023]

[14] European Environment Agency. *Greenhouse gas emission intensity of electricity generation.* Available at: https://www.eea.europa.eu/data-and-maps/daviz/co2-emission-intensity-12/#tab-chart_2 [accessed 26.01.2023]

[15] Casasso A., Capodaglio P., Simonetto F., Sethi R. *Environmental and Economic Benefits from the Phase-out of Residential Oil Heating: A Study from the Aosta Valley Region (Italy).* Sustainability 2019;11(13):3633.

Exergy cost assessment of Very High Gravity (VHG) Fermentation in the sugarcane industry

Milagros Cecilia Palacios-Bereche[a], Reynaldo Palacios-Bereche[b], Antonio Garrido Gallego[c], Luis M. Serra[d], Miguel A. Lozano[e] and Silvia Azucena Nebra[f]

[a] Energy Engineering Modeling and Simulation Laboratory, Federal University of ABC, Santo André, S.P., Brazil, milagros.palacios@ufabc.edu.br,
[b] Federal University of ABC, Santo André, SP., Brazil, reynaldo.palacios@ufabc.edu.br,
[c] Federal University of ABC, Santo André, SP., Brazil, a.gallego@ufabc.edu.br,
[d] GITSE-I3A, Department of Mechanical Engineering, Universidad de Zaragoza, Spain, serra@unizar.es,
[e] GITSE-I3A, Department of Mechanical Engineering, Universidad de Zaragoza, Spain, miguel.lozano@unizar.es,
[f] Federal University of ABC, Santo André, S.P., Brazil/ University of Campinas, Campinas, S. P., Brazil, silvia.nebra@ufabc.edu.br

Abstract:

The vinasse, produced as the bottom product of the distillation column of the ethanol production process, is the main liquid residue of this industry, whose disposition represents a problem for the industry because of its high production rate, which ranges from 10 to 15 litres of vinasse per litre of ethanol produced. In this way, the evaluation of technologies that could reduce the vinasse volume—either reducing its production during ethanol production process or its volume once already produced—is advantageous to the process and its sustainability, seeing as a lower amount of vinasse would allow a better and appropriate disposal of this effluent. This way, this work addresses the vinasse problem by a preliminary exergy cost analysis of two different technologies for vinasse volume reduction and a Base Case for comparison purposes; being the analysed cases: i) a Base Case (conventional production process), ii) the introduction of the VHG (Very High Gravity) fermentation with the use of ejectors as complementary refrigeration system, aiming at utilising a more concentrated most during fermentation to produce a wine with a higher ethanol content, thus reducing the amount of vinasse produced in the distillation step. The analysis aims at comparing the unitary exergy costs of the main products and by-products of the different alternatives, and identifying the processes with the highest irreversibilities associated, which resulted in the fermentation with distillation volume control, with values of 37.1% and 41%, for the conventional and VHG cases, respectively.

Keywords:

Vinasse; VHG fermentation; Exergy cost.

1. Introduction

The sugar and ethanol industry from sugarcane has an important role in the Brazilian agribusiness, being the ethanol demand quite significant in the Brazilian market [1], [2]; resulting in a desire of a more efficient ethanol production. Thus, seeing as the fermentation is a crucial step in ethanol production, where it is formed through a biochemical reaction lead by yeast, a more efficient fermentation process will lead, therefore, to an improved ethanol production. In this way, maintaining an adequate fermentation temperature is essential to favour ethanol production, as one of the most important parameters in this process. That being so, a low-temperature fermentation has been proved to result in higher ethanol yields since a more concentrated substrate can be used [3].

By lowering the fermentation temperature, a higher ethanol concentration in the wine is obtained, since the inhibition of organic acids and ethanol is reduced, and the flocculation and bacterial contamination is better controlled. In addition, a fermentation temperature lower than the conventional one, also allows the use of a high substrate concentration in the must, leading, in turn, to a Very High Gravity (VHG) fermentation, which is an emerging and versatile technology that offers great savings in process water and energy requirements during the distillation and fermentation steps, by reducing the size of distillation columns and decreasing the power consumption of yeast centrifugation, respectively, because of the higher concentrations of sugar in the

substrate, which leads to a higher final ethanol concentration in the medium. In addition, seeing as the ethanol content is higher in the wine, the amount of water and impurities is reduced, thus producing a lower amount of vinasse [3]–[5].

That being said, a cooling system is necessary to reach and maintain an adequate temperature. Since the fermentation process is an exothermic reaction, cooling towers have been conventionally used to control and maintain a fermentation temperature of around 34°C. Nevertheless, sometimes, the cooling water provided by cooling towers cannot achieve a temperature low enough to reach an appropriate fermentation temperature range because of adverse environmental conditions. In this way, alternative refrigeration systems are necessary when a fermentation with high sugar concentration in the substrate is applied.In this way, this work assesses the VHG fermentation against the conventional production process through a preliminary exergy cost analysis. In order to mantain the fermentation temperature in appropriate levels that make viable the VHG fermentation, a complementary refrigeration system based on ejectors was assumed for this case. Regarding the exergy cost assessment, this is a tool that aims at identifying the location, magnitude and source of thermodynamic losses (irreversibilities) in an energy system. Furthermore, it calculates the cost associated with the exergy destruction and exergy losses; besides assessing the production costs of each product in an energy-conversion system that has more than one product. The exergoeconomics is also used to compare technical alternatives and facilitates feasibility and optimisation studies [6]. Although the application of ejectors in cooling systems, as well as the assessment of the VHG fermentation, have already been regarded in the literature separately, there is a lack of studies either combining these technologies or evaluating the impacts of the VHG fermentation in the production and cogeneration systems; besides, studies evaluating these systems from exergy and exergy cost approaches are yet to be found.

2. Processes description and evaluated cases

2.1. Case i: Conventional fermentation – Base Case

A conventional fermentation was considered as a “Base Case,” according to Figure 1.

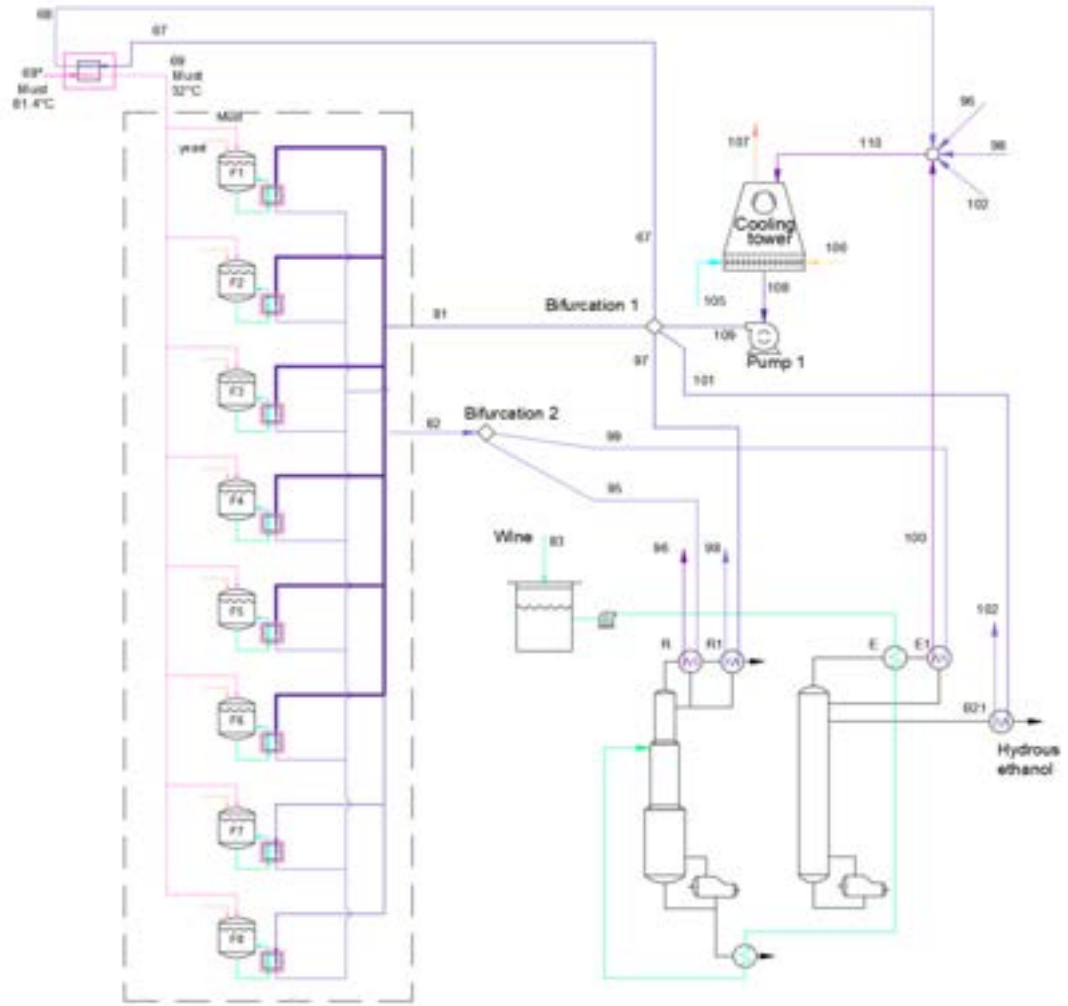

Figure. 1. Conventional fermentation operating with 8 fermentation vats, using water from the cooling tower as the only cold utility.

A cooling tower was adopted to supply water to meet the requirements of cold utilities in the plant, including removing the heat from the fermentation exothermic reaction, since this is a cooling system that is usually adopted in the industry. In this system, cooling water is used in the heat exchangers of fermentation vats, must cooling, and distillation system. A fermentation system operation with 8 vats was assumed, where 6 vats are being cooled simultaneously.

2.2. Case ii: VHG fermentation using an ejector system

Refrigeration systems based on the use of ejectors are an attractive alternative to compression vapour and absorption refrigeration systems because of their mechanical simplicity, which represents an easy maintenance and operation. Notwithstanding, some drawbacks of these systems include an increase in steam and energy consumption, as well as the high vacuum required in the evaporator [3]. In this study, a two-stage ejector system was chosen to aid the cooling tower, according to Figure 2. First, the chilled water (14°C) from the ejector system is used to refrigerate the fermentation vats and cool the must down to 28°C. Then, the cooling water that returns from the fermentation vats and must heat exchangers (stream 122) is mixed with the return water from the cooling tower (stream 121); this mixture is sent to a first flash tank at 20°C, where the first ejector is driven using steam at 9 bar. Next, the cooled water in this first stage is sent to a second flash tank at 14°C, whose low temperature is maintained by the vacuum generated by the second ejector. The chilled water is then sent to a buffer tank for storage before use. Afterwards, the steam at the ejectors' outlet (streams 119 and 120), at an intermediate pressure, is condensed in a barometric condenser. Finally, a fraction of this condensed water (stream 113) is sent to the cogeneration system of the mill, while the rest is cooled in the cooling tower. The fermentation operation assumed 8 vats, where 3 vats are cooled with chilled water and 3 are cooled with cold water from the cooling tower, simultaneously.

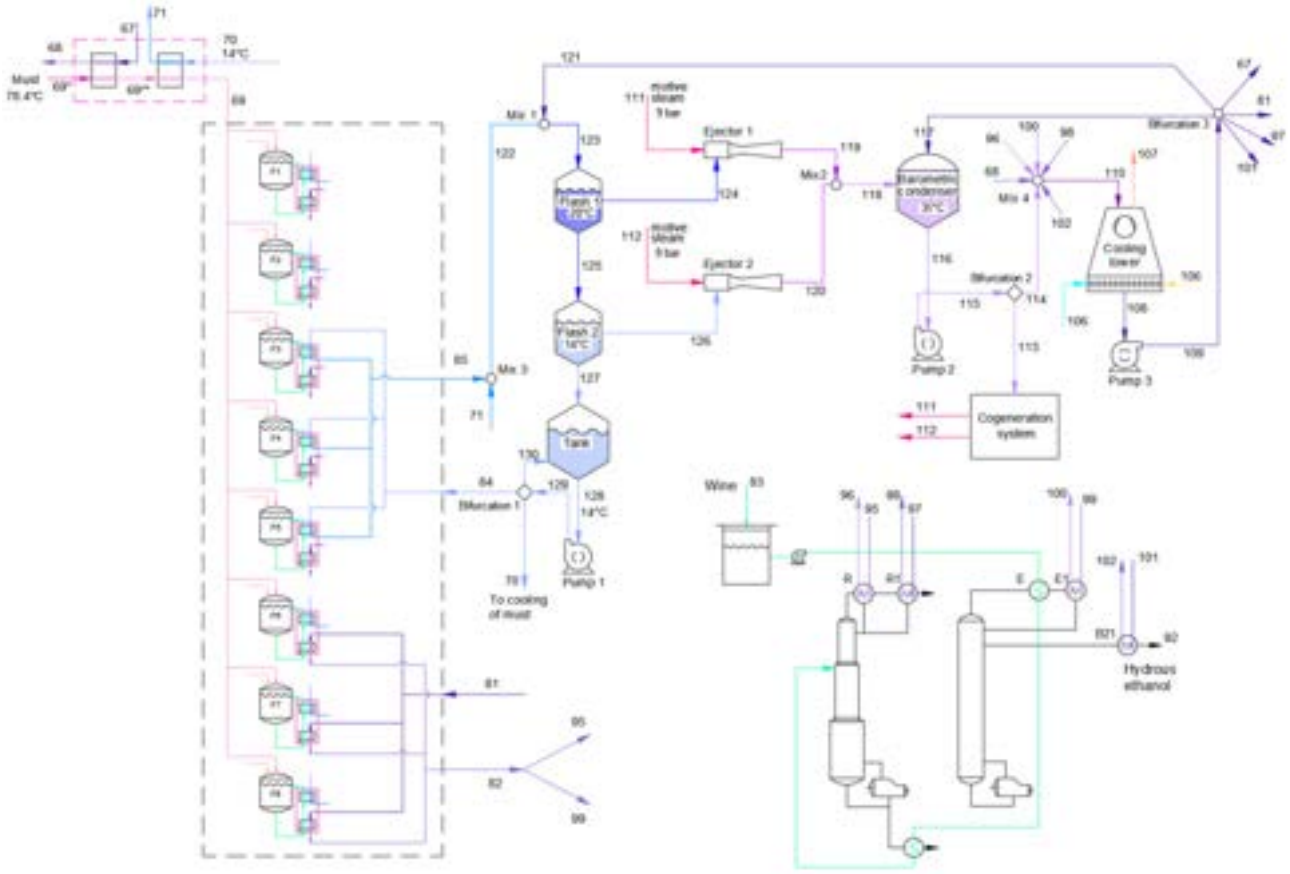

Figure. 2. Low-temperature fermentation operating with 8 fermentation vats, using cold and chilled water from the cooling tower and ejector system, respectively, as cold utilities.

2.3. Cogeneration system

The cogeneration system adopted was based on a Rankine cycle, considering back-pressure steam turbines, where the steam generation depends on the steam consumption of the overall production process. Figure 3 (a) presents a scheme of the cogeneration system for the conventional fermentation (Case i), while Figure 3 (b) shows a scheme of the cogeneration system when the VHG fermentation is considered (Case ii), where a steam bleed at 9 bar is needed to operate the ejector cooling system. The boiler pressure and temperature were

adopted at 65 bar and 520°C, according to [7], considering a boiler efficiency of 85%, according to [8], and turbine and pump efficiencies of 80%, as stated in [9].

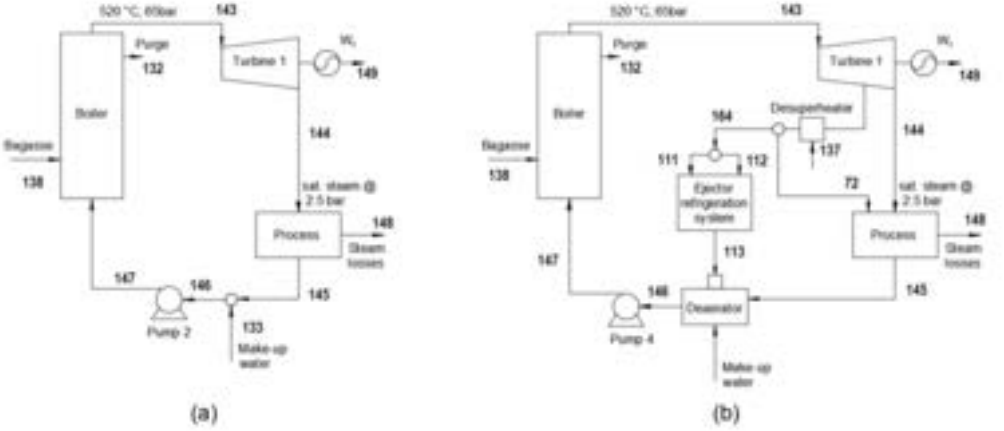

Figure. 3. Cogeneration system for (a) Case i and (b) Case ii.

3. Methodology

The main steps performed in the present work are listed below:

- Modelling and simulation of the conventional production process (Base Case), VHG fermentation integrated thereof, and cogeneration system;
- exergy analysis;
- exergy cost assessment.

3.1. Modelling and simulation

Two cases of a conventional ethanol and sugar production process were simulated using the software Aspen Plus v9 [10], according to [11], considering a sugar concentration of 16% and 35% (m/m) in the must for the conventional and VHG fermentation cases, respectively. Table 1 shows the main data assumed in the aforementioned simulation.

Table 1. Main parameters for the simulation of the ethanol and sugar production process.

Parameter	Value
Sugarcane processing rate, t/h	500
Bagasse production in mills, kg/t cane	272
Bagasse for filters, kg/t cane	5
Bagasse for self-consumption, %	5
Sugar production, kg/t cane	68.4
Hydrous ethanol, m^3/h	21.1
Vinasse production, m^3/h	247.8
Electricity consumption in conventional process, kWh/t cane	28
Steam consumption in conventional process, kg/t cane	437.6

Source: Palacios-Bereche et al. [11]

3.2. Kinetic modelling for conventional and VHG fermentation

First, the modelling of both, the conventional and VHG fermentation, was performed using the software Scilab. The kinetic model from [12] was chosen for the conventional fermentation, seeing that the best results were obtained since the model used a high cellular density and a cell recycle that were closer to the actual concentration used in the commercial process, which resulted in a better convergence than other models that used a low-cell concentration, and a more realistic modelling [12]–[17]. On the other hand, the kinetic model from [18] was used for the VHG fermentation, as this model was validated for very-high-gravity (VHG) fermentation conditions.

Then, an analysis of the heat exchanger of the fermentation vat was performed using the effectiveness approach, according to [19]. This method allows the calculation of the outlet temperatures of the heat exchanger for off-design conditions keeping constant the parameters R (relation of heat capacities) and P (effectiveness). In the conventional fermentation, these parameters (R and P) were calculated assuming the data from [20]. The temperature of the cooled wine that returns to the fermenter (T_{16}) is used as feedback for the energy balance in

the fermentation vat. Finally, the cold water mass flow is calculated through an energy balance in the heat exchanger. The same approach was assumed when the chilled water from the ejector system was used in the VHG fermentation case.

Finally, the ejector was modelled following the procedure presented in [21], due to its simplicity and the possibility of performing a thermodynamic analysis of the ejector system, without dimensioning the equipment. It is highlighted some design parameters that were considered for the simulations: a nozzle efficiency of 71.2% and 73.5%, a compression efficiency in the diffuser of 67.8% and 71.3%, and an efficiency of momentum transfer of 60.0% and 63.8%, all of them for ejectors 1 and 2, respectively. These values were used so that the steam consumption results obtained were similar to real systems that operate at the same thermal capacity.

Table 2 presents the fermentation parameters and initial conditions assumed for the fermentation process in the conventional and VHG fermentation processes.

Table 2. Main parameters for the fermentation modelling.

Parameter	Case i (Conventional)	Case ii (VHG fermentation)
Must feed		
Substrate feed volume rate, $\dot{F}$ [m^3/h]	67.1[*(a)]	42.0[*(a)]
Feed substrate concentration, S_in [kg/m^3]	169.7[(a)]	407.2[(b)]
Inlet must temperature, T_{18} [°C]	32.0[(a)]	28.0[(a)]
Specific heat capacity, cp_{in} [kJ/kg-K]	3.8[(c)]	3.34[(c)]
Density, ρ_{in} [kg/m^3]	1060.4[(c)]	1151.6[(c)]
Fermentation parameters		
Fermentation time, t [h]	8	15[(b)]
Feed time, t_{feed} [h]	4	5
Initial conditions		
Initial substrate concentration, S_0 [kg/m^3]	0	0
Initial ethanol concentration, P_0, [kg/m^3]	40[(b)]	26.96[(b)]
Initial cell concentration, X_0 [kg/m^3]	120[(b)]	52.08[(b)]
Initial temperature, T15_0 [°C]	32.0[(d)]	28.0[(d)]
Cooling		
Water temperature from the cooling tower, T_{cw} [°C]	28.0	28.0
Volume flow rate of fermenter recycle, V_{15} [m^3/h]	500[**(b)]	308[**(b)]
Water temperature from ejector system T_8, [°C]	-	14[(d)]
Operating time of ejector[***], [h]		7.5

[(a)] From simulation in Aspen Plus v9; [(b)] [17]; [(c)] Calculated from [22]; [(d)] [23]

[*] Corresponding to a 50/50 sugarcane-processing plant that uses 50% of the total recoverable sugars (TRS) to produce sugar and the other 50% to produce ethanol, which is made from a mixture of cane juice, syrup, and molasses.

[**] 1 hour of feeding

[***] The ejector was set to start operating two hours and a half after finishing the feeding time (7.5 h) until the end of the fermentation process.

3.3. Exergy calculation

The exergy of each stream of the evaluated processes was calculated according to previous studies [24], [25]. A reference level was chosen at 25°C and 1.01325 bar, according to [26]. The total thermal exergy (ex_{tot}) was calculated as the sum of the physical (ex_{phy}) and chemical (ex_{ch}) exergies [26]:

$$ex_{tot} = ex_{phy} + ex_{ch}. \quad (1)$$

The physical exergy was calculated according to (2), neglecting the potential and kinetic components:

$$ex_{phy} = h - h_0 - T_0(s - s_0), \quad (2)$$

where the subscript 0 indicated the reference level.

The chemical exergy is calculated, generally, considering the activity of the stream, as can be observed in (3), considering the standard chemical exergy of pure components (first term) and the losses of chemical exergy due to the dissolution process (second term), according to [26]:

$$ex_{ch} = \left(\frac{1}{\overline{M}}\right) \cdot \left[\sum_{i=1}^{n} y_i \cdot ex_i^{\circ} + \overline{R}_u \cdot T_0 \sum_{i=1}^{n} y_i \cdot \ln(a_i)\right]. \quad (3)$$

Nevertheless, other approaches were followed for certain streams. Thus, when sucrose-containing streams were contemplated (sugarcane, bagasse, juice, syrup, molasses, sugar), the specific exergy was calculated

according to the guidelines presented in [27]. On the other hand, for ethanol-containing streams, the guidelines in [28] were followed.

3.4. Exergy cost assessment

Since the exergy is an objective measure of the thermodynamic value of an energy carrier, it is also closely related to the economic value of said carrier, because users pay for the potential of energy to cause changes [6]. Thus, the exergoeconomic approach was utilised, since it integrates thermodynamic and economic analysis through the exergy costing, which is the assignment of costs to the exergy content of an energy carrier [6]. The Theory of Exergetic Cost [29] was followed to perform the exergy cost assessment in this study.

An exergetic cost balance was performed in each sub-system of the production process of the proposed cases (4), to calculate the exergetic cost of a flow:

$$\sum \dot{B}_{in} = \sum \dot{B}_{out}, \tag{4}$$

where $\dot{B}$ represents the exergetic cost of each flow that enters (*in*) to, and goes out (*out*) from the control volume.

According to [29], the exergetic cost of a flow ($\dot{B}$) is defined as the amount of exergy required to produce said flow (5):

$$\dot{B}_i = k_i \cdot \dot{E}x_i, \tag{5}$$

where the exergetic cost of an *i* stream is determined by its unit exergetic cost (k_i) and its total exergy $(\dot{E}x_i)$. The total exergy of a stream is calculated by its specific exergy (calculated in the previous section) and the mass flow of the stream, which is given by the process simulation.

Applying (4) to all the sub-systems of the production processes of all the considered cases results in a system of linear equations, where the unit exergetic cost (k_i) remains unknown. Thus, assumptions were made by following the propositions of the Theory of the Exergetic Cost [29], resulting in additional equations that are required to resolve the equation system.

- A unitary value is assigned as the unit exergy cost (k_i) of external inputs (sugarcane, freshwater, chemicals).

$$k_{externalinput} = 1. \tag{6}$$

- By-products of the control volume are assigned a unit exergy cost (k_i) equal to the input (P4a).

$$k_{by-product} = k_{input}. \tag{7}$$

As was the case of bagasse, molasses, phlegmasse, and vinasse, were the following were considered:

$$k_{bagasse} = k_{sugarcane}, \tag{7.1}$$

$$k_{molasses} = k_{syrup}, \tag{7.2}$$

$$k_{vinasse} = k_{phlegmasse} = k_{must}. \tag{7.3}$$

- If a control volume has two or more product streams, then the same unit exergy cost (k_i) is assigned to all of them (P4b).

$$k_{product1} = k_{product2} = ... = k_{productn}. \tag{8}$$

As in the case of second-grade ethanol and fusel oils, that were considered co-products and assigned an unit exergy cost equal to that of the hydrated ethanol

- The unit exergy cost (k_i) of the energy carrier (steam, condensates, vapour bleeds) is determined during its generation (at the boiler of the cogeneration system) and do not change throughout the process.

$$k_{live\ steam} = k_{processsteam} = k_{condensate} = k_{vapourbleeds}. \tag{9}$$

The cost of the irreversibility associated with the operation of the condenser in the cogeneration system, is added to the turbine control volume, thus increasing the unit exergy cost (k_i) of the electricity.

4. Results and discussion

In Table 3, the main results of the evaluated processes are presented, from which it can be highlighted the significant reduction of 60% in vinasse production when the VHG fermentation was considered, which can significantly reduce transport and disposal costs related to this effluent. In addition, this technology also allowed a reduction in the effective water withdrawal of 72%, which would lead to environmental and economic advantages. Still, the use of the VHG fermentation required an increased steam consumption at 2.5 bar, although not significant (0.8%), which can be explained due to the increased consumption during the concentration step, as more raw juice needed to be concentrated; in this way, even though there was a steam consumption was lower in the distillation stage, it could not compensate the juice concentration steam demand; moreover, there is an additional steam consumption at 9 bar for thermal juice sterilisation, a necessary step in the VHG fermentation, and for the ejector system (motive steam). Regarding the surplus electricity, an increase of 6.8% was observed in the VHG case, in comparison to the Conventional case, due to the higher steam consumption in the first one (the electricity produced in backpressure steam turbines is directly proportional to the flow of steam being expanded). Thus, there is an increase in fuel consumption in the boiler, which is reflected in a reduction of 52.6% in surplus bagasse in the VHG case, when compared to the Conventional case.

Table 3. Main results of evaluated processes

Parameter	Case i Conventional	Case ii VHG fermentation
Sugarcane, processed, t/h	500	500
Raw juice for sugar production, %	70	91.4
Sugar production, kg/t cane	68	68
Must for fermentation, kg/t cane	427.2	195.5
Must for fermentation, Brix	19.42	42.47
Ethanol content in wine, % (wt.)	6.15	12.37
Hydrated ethanol production[a], L/t cane	43.8	43.8
Steam consumption in process at 2.5 bar, kg/t cane	435.6	439.3
Steam consumption in process at 9 bar, kg/t cane	0	18.8
Vinasse production, kg/t cana	511.6	203.0
Vinasse production, L/L hydrated ethanol	12.8	5.1
Effective water collection, kg/t cane	418.7	116.2
Surplus electricity in cogeneration system, kWh/t cane	47.2	50.4
Surplus bagasse, kg/t cane	25.1	11.9

[a]At 35°C

Figure 4 shows the distribution and the connexion between the analysed subsystems in this study, for Cases I and II. In both cases, the fermentation and distillation processes were evaluated together, including the cold utility production system for these processes (cooling tower and chilled water) in the exergy and exergy cost assessments.

Table 4 presents the irreversibilities (kWh/t cane) calculated through the exergy balance in each sub-system considered in the analysis. The boiler subsystem presented the highest irreversibility for both cases, accounting for 62% and 60% of the total irreversibility for the Conventional and VHG cases, respectively, mainly due to the high irreversibilities in the combustion process. In second place, the Fermentation + Distillation subsystem represents 14.1 and 16.4% for the Conventional and VHG cases, respectively, this can be explained due to of the biochemical reaction in the fermentation process and the significant steam consumption in distillation columns; moreover, the cooling towers and the cooling ejector system in the VHG case were incorporated into this control volume. Next, the Juice extraction subsystem amounts to 12 and 10.9% for the Conventional and VHG cases, respectively, in this sub-system there is a significant power consumption in the mills. The following subsystem is the Juice treatment for sugar, which accounts for 4.7 and 6.8% for the Conventional and VHG cases, respectively. The following subsystems present a low irreversibility in comparison to the total.

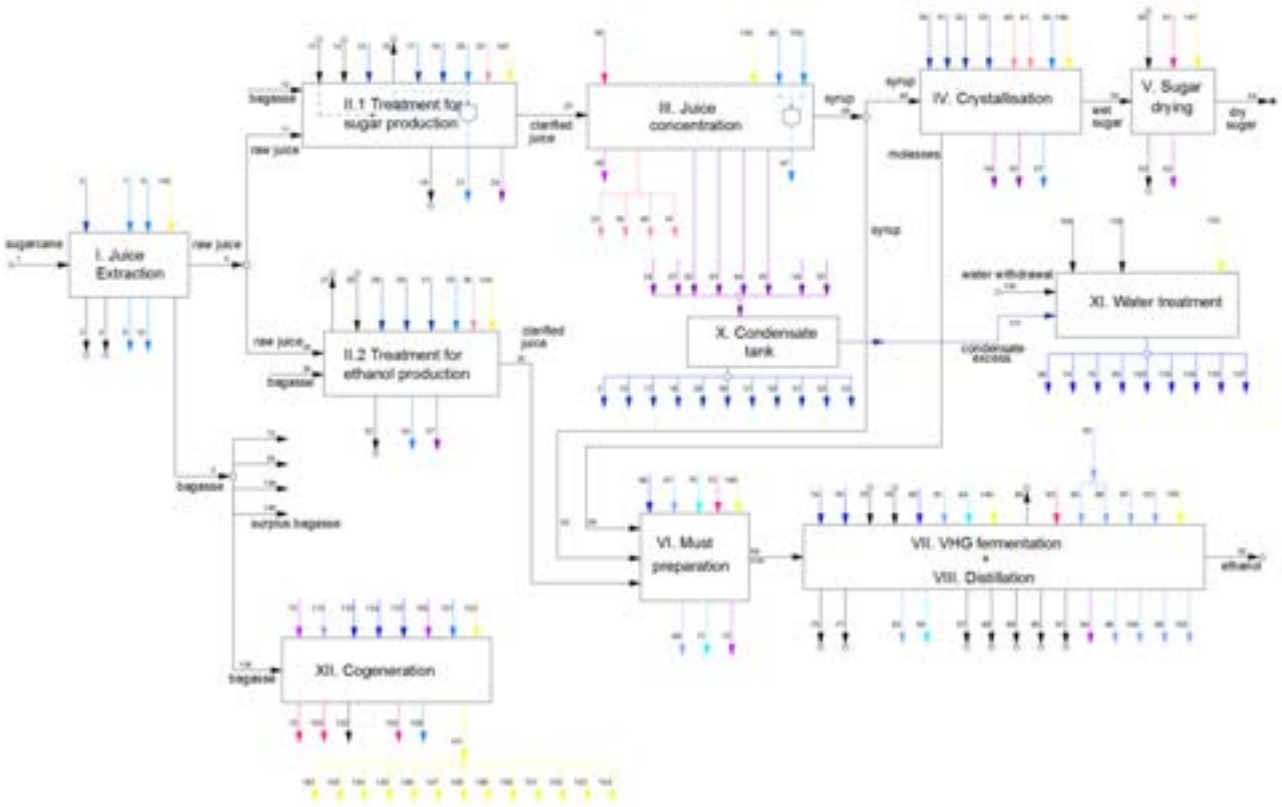

Figure. 5. Block diagram of the evaluated subsystems in the exergy and exergy cost assessments

Analysing the differences between the Conventional and VHG cases, an increase of 10.5% in total irreversibility can be observed, which can be explained by the additional requirements in the VHG case, such as the additional steam consumption in the must sterilisation in the fermentation process, and the steam demand in the cooling system based on ejectors. Moreover, there is a significant increase in the irreversibilities of the Juice treatment-sugar and Juice concentration subsystems, due to the larger amount of juice being concentrated and the layout assumed in this assessment.

Table 4. Irreversibilities in each sub-system for Conventional and VHG cases in kWh/t cane

Parameter	Case i Conventional (kWh/tcane)	Case ii VHG fermentation (kWh/tcane)
Juice extraction	91.4	91.4
Juice treatment - sugar	35.8	57.5
Juice treatment - ethanol	15.5	6.4
Juice concentration	14.9	19.5
Crystallisation	13.7	14.0
Sugar drying	1.6	1.6
Must preparation	4.1	2.9
Fermentation + Distillation	107.1	137.8
Water treatment	1.6	1.3
Boiler	472.4	504.8
Turbine	3.0	3.4
TOTAL	761.0	840.6

The results verification in the Base Case (Case i) can be done comparing results from other studies; however for VHG case verification of results was performed by calculating irreversibilities of the processes, in order to evaluate their thermodynamic feasibility from 2nd Law of Thermodynamic approach. In Figure 5,

the irreversibilities are presented in percentage, without taking into account the boiler, aiming at a better visualisation of the contribution of each subsystem.

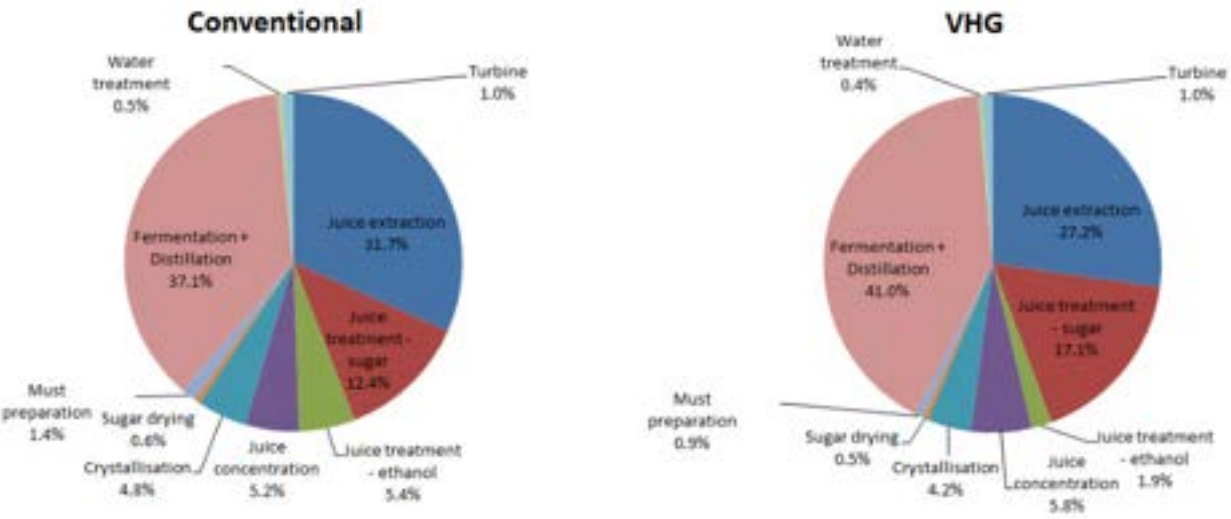

Figure. 5. Irreversibilities, in % without considering the boiler

Figure 6 presents the unitary exergy costs (kJ/kJ) of the main products and by-products of the analysed sub-systems for the Conventional and VHG fermentation cases. It can be observed that the highest unitary exergy cost corresponds to the hydrated ethanol because of the significant amount of processes required to produce it and the high irreversibilities associated to obtain this product; moreover, it can also be observed that the unitary exergy cost in the VHG case is higher than the Conventional case, mainly due to the higher costs of utilities produced in the cogeneration system, such as electricity and steam.

Regarding the other streams the difference between the Conventional and VHG cases is not significant (difference lower that 5.6%)

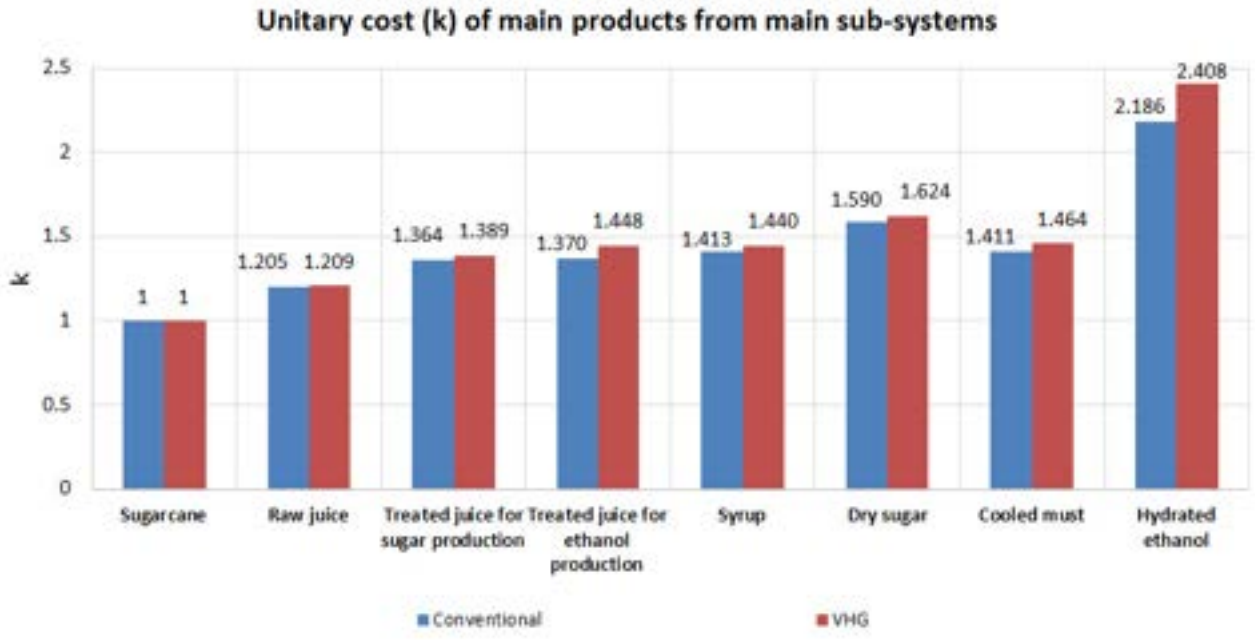

Figure. 6. Unitary exergy cost of main products and by-products for Conventional and VHG cases

Figure 7 presents the unitary exergy costs for the utilities produced in the process. It can be observed that the unitary exergy costs of steam, electricity and treated water are higher in the VHG case, in comparison to the Conventional case.

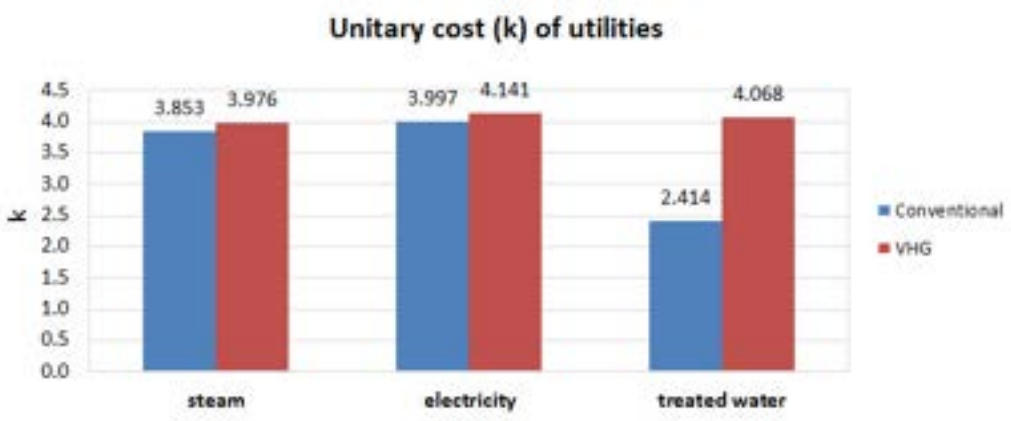

Figure. 7. Unitary exergy costs of the utilities produced in the process

Regarding the steam, its unitary exergy cost resulted higher in the VHG case, because the irreversibilities in the boiler, were the steam is produced, resulted higher as well, since more steam is necessary in this case, and more fuel is being burned. Regarding the electricity, the irreversibilities in the steam turbines are higher in the VHG case, as well; because more steam is being expanded through them; thus, the exergy cost to produce this electricity results higher as well. Concerning the treated water, although a smaller amount of water (33% of the total water use) is captured from the environment in the VHG case, in comparison to Conventional case (80% is captured in the conventional case), the exergy cost of the treated water was significantly higher (68.5%) in the VHG case. This can be explained by the fact that recycled and reused water streams come from the spray pond system and condensate tank, whose exergy cost was assumed equal to the steam ($k_{condensate}=k_{steam}$); in addition, the electricity consumption in the treated water system, where reverse osmosis membranes were assumed, had a specific energy consumption of 2.58 kWh/m^3 of water according to [30].

Conclusions

From the results, it is observed that the implementation of the VHG fermentation, using an ejector cooling system as auxiliary cooling utility, presents several advantages over the conventional production process, such as a significant reduction of the vinasse produced and a lower water withdrawal for the process, leading to economic and environmental advantages. Regarding the vinasse reduction, its volume could be further reduced when coupled with other technologies such as concentration by evaporation or incineration, or even membrane technologies; furthermore, the energy required in these technologies would be lesser than the energy needed when considering the volume and concentration of the vinasse produced in the conventional process. On the other hand, the exergy analysis revealed that the use of the VHG fermentation increased the irreversibilities of the overall process, besides impacting negatively in the cogeneration system, by increasing the unitary exergy costs of the utilities (steam and electricity), as well as increasing the unitary exergy cost of the hydrated ethanol. Moreover, even though there was an increase in surplus electricity, due to the higher consumption of steam, it leads to an also increased fuel (bagasse) consumption. Although the availability of bagasse surplus is desired when further processing of this residue is considered, such a production of second-generation ethanol, among others, further research and analyses are needed, in order to determine if the advantages here presented compensate this issue, such as economic and environmental assessments.

Acknowledgments

The authors wish to thank the Coordenação de Aperfeiçoamento de Pessoal de Nível Superior (CAPES) and the Conselho Nacional de Desenvolvimento Científico e Tecnológico (CNPq) (Process PQ 306303/2014-0 and PQ 309588/2019-7) for the researcher fellowship; and for the Research Project Grant (Process 407175/2018-0 and 429938/2018-7).

References

[1] X. Du and M. A. Carriquiry, 'Flex-fuel vehicle adoption and dynamics of ethanol prices: Lessons from Brazil', *Energy Policy*, vol. 59, pp. 507–512, 2013, doi: 10.1016/j.enpol.2013.04.008.

[2] A. L. Ferreira, F. P. de A. Prado, and J. J. da Silveira, 'Flex cars and the alcohol price', *Energy Econ.*, vol. 31, no. 3, pp. 382–394, 2009, doi: 10.1016/j.eneco.2009.01.007.

[3] M. O. S. Dias, R. Maciel Filho, and C. E. V. Rossell, 'Efficient Cooling of Fermentation Vats in Ethanol Production – Part 1', in *XXVI congress - International Society of Sugar Cane Technologists: ICC, Durban, SouthAfrica, 29 July - 2 August 2007; papers (English)*, 2007, vol. 26, no. December, pp. 1210–1217.

[4] L. A. B. Cortez, C. E. V. Rossell, R. A. Jordan, M. R. L. V. Leal, and E. E. S. Lora, 'R&D needs in the industrial production of vinasse', in *Sugarcane bioethanol: R&D for productivity and Sustainability*, 1st ed., L. A. B. Cortez, Ed. São Paulo: Blucher, 2010, pp. 619–636.

[5] P. Puligundla, D. Smogrovicova, V. S. R. Obulam, and S. Ko, 'Very high gravity (VHG) ethanolic brewing and fermentation: a research update', *J. Ind. Microbiol. Biotechnol.*, vol. 38, no. 9, pp. 1133–1144, Sep. 2011, doi: 10.1007/s10295-011-0999-3.

[6] G. Tsatsaronis, 'Thermoeconomic analysis and optimization of energy systems', *Prog. Energy Combust. Sci.*, vol. 19, no. 3, pp. 227–257, 1993, doi: 10.1016/0360-1285(93)90016-8.

[7] J. H. Sosa-Arnao, 'Personal communication', 2018.

[8] E. F. Cortes-Rodríguez, S. A. Nebra, and J. H. Sosa-Arnao, 'Experimental efficiency analysis of sugarcane bagasse boilers based on the first law of thermodynamics', *J. Brazilian Soc. Mech. Sci. Eng.*, vol. 39, no. 3, pp. 1033–1044, 2017, doi: 10.1007/s40430-016-0590-y.

[9] A. V. Ensinas, S. A. Nebra, M. A. Lozano, and L. M. Serra, 'Analysis of process steam demand reduction and electricity generation in sugar and ethanol production from sugarcane', *Energy Convers. Manag.*, vol. 48, no. 11, pp. 2978–2987, 2007, doi: 10.1016/j.enconman.2007.06.038.

[10] aspentech, 'Aspen Plus', 2018. https://www.aspentech.com/products/engineering/aspen-plus (accessed Sep. 23, 2018).

[11] M. C. Palacios-Bereche, R. Palacios-Bereche, and S. A. Nebra, 'Comparison through energy, exergy and economic analyses of two alternatives for the energy exploitation of vinasse', *Energy*, vol. 197, p. 117231, 2020, doi: 10.1016/j.energy.2020.117231.

[12] I. I. K. Veloso, K. C. S. Rodrigues, J. L. S. Sonego, A. J. G. Cruz, and A. C. Badino, 'Fed-batch ethanol fermentation at low temperature as a way to obtain highly concentrated alcoholic wines: Modeling and optimization', *Biochem. Eng. J.*, vol. 141, pp. 60–70, 2019, doi: 10.1016/j.bej.2018.10.005.

[13] M. V. A. Da Costa Filho, J. B. Monteiro, F. C. Magazoni, and S. Colle, 'Modeling, simulation and analysis of ethanol fermentation process with control structure in industrial scale', in *Proceedings of ECOS 2009 - 22nd International Conference on Efficiency, Cost, Optimization, Simulation and Environmental Impact of Energy Systems*, 2009, no. August 2009, pp. 1351–1360.

[14] D. I. P. Atala, 'Fermentação alcoólica com alta densidade celular: Modelagem cinética, convalidação de parâmetros e otimização do processo', Universidade Estadual de Campinas, 2000.

[15] G. C. Fonseca, C. B. B. Costa, and A. J. G. Cruz, 'Comparing a dynamic fed-batch and a continuous steady-state simulation of ethanol fermentation in a distillery to a stoichiometric conversion simulation', *Brazilian J. Chem. Eng.*, vol. 34, no. 4, pp. 1121–1131, 2017, doi: 10.1590/0104-6632.20170344s20160155.

[16] F. C. Magazoni, J. B. Monteiro, J. M. Cardemil, and S. Colle, 'Cooling of Ethanol Fermentation Process Using Absorption Chillers', *Int. J. Thermodyn.*, vol. 13, no. 3, pp. 111–118, 2010, doi: 10.5541/IJOT.1034000167.

[17] C. E. V. Rossell, 'Personal communication', 2020.

[18] E. Ccopa Rivera *et al.*, 'Effect of temperature on sugarcane ethanol fermentation: Kinetic modeling and validation under very-high-gravity fermentation conditions', *Biochem. Eng. J.*, vol. 119, pp. 42–51, 2017, doi: 10.1016/j.bej.2016.12.002.

[19] N. Kayansayan, 'Thermal behavior of heat exchangers in off-design conditions', *Heat Recover. Syst. CHP*, vol. 9, no. 3, pp. 265–273, 1989, doi: 10.1016/0890-4332(89)90010-0.

[20] C. K. Yamakawa, 'Avaliação da fermentação alcoólica com reciclo de células de hidrolisado celulósico de bagaço de cana-de-açúcar em unidade integrada e autônoma', Universidade Estadual de Campinas, 2016.

[21] D. Q. Kern, *Procesos de Transferencia De Calor*, 31st ed. México, D.F.: McGraw Hill Book Company, 1999.

[22] S. A. Nebra and M. I. Fernández-Parra, 'The Exergy of Sucrose-Water Solutions: Proposal of a Calculation Method', in *Proceedings of ECOS 2005 - The 18th International Conference on Efficiency, Cost, Optimization, Simulation and Environmental Impact of Energy Systems*, 2005, pp. 385–392.

[23] C. E. V. Rossell, 'Melhoramento dos processos de produção de etanol de cana de açúcar. P,D&I', 2019.

[24] M. C. Palacios-Bereche, R. Palacios-Bereche, and S. A. Nebra, ‘Comparison through exergy assessment of two alternatives for the energy use of vinasse : Concentration with incineration vs . Biodigestion’, in *Proceedings of ECOS 2018 - The 31st International Conference on Efficiency, Cost, Optimisation, Simulation and Environmental Impact of Energy Systems*, 2018, pp. 1–14.

[25] M. C. Palacios-Bereche, A. C. Medina-jimenez, R. Palacios-Bereche, and S. A. Nebra, ‘Comparison between two alternatives for the energy use of vinasse: Concentration-Incineration vs Biodigestion’, in *Proceedings of the 17th Brazilian Congress of Thermal Sciences and Engineering*, 2018, pp. 1–13.

[26] J. Szargut, D. R. Morris, and F. R. Steward, *Exergy Analysis of Thermal, Chemical, and Metallurgical Processes*. New York, USA: Hemisphere Publishing Corporation, 1988.

[27] A. V. Ensinas and S. A. Nebra, ‘Exergy Analysis as a Tool for Sugar and Ethanol Process Improvement’, in *Handbook of Exergy, Hydrogen Energy and Hydropower Research*, G. Pélissier and A. Calvet, Eds. Nova Science Publishers, 2009, pp. 125–160.

[28] M. Modesto, S. A. Nebra, and R. J. Zemp, ‘A Proposal to Calculate the Exergy of Non Ideal Mixtures Ethanol-Water Using Properties of Excess’, in *14th European Biomass Conference*, 2005, no. October, pp. 1924–1927, doi: 88-89407-07-7.

[29] M. A. Lozano and A. Valero, ‘Theory of the Exergetic Cost’, *Energy*, vol. 18, no. 9, pp. 939–960, 1993.

[30] D. Ryan, A. Gadd, J. Kavanagh, and G. W. Barton, ‘Integrated biorefinery wastewater design’, *Chem. Eng. Res. Des.*, vol. 87, no. 9, pp. 1261–1268, 2009, doi: 10.1016/j.cherd.2009.04.016.

Field and central receiver design methodology based on multi-parameter optimization by the design of experiments (DOE) technique

Rubén Barbero[a], Guillermo Ortega[b], Fernando Varela[c], Antonio Rovira[d]

[a] Universidad Nacional de Educación a Distancia (UNED), Madrid, Spain, rbarbero@ind.uned.es. (CA)
[b] Universidad de Huelva (UHU) Huelva, Spain. guillermo@didp.uhu.es
[c] Universidad Nacional de Educación a Distancia (UNED), c/ Juan del Rosal, 12, 28040 Madrid, Spain, fvarela@ind.uned.es
[d] Universidad Nacional de Educación a Distancia (UNED), c/ Juan del Rosal, 12, 28040 Madrid, Spain, rovira@ind.uned.es

Abstract:

This manuscript presents a novel methodology for the design of Central Tower Receivers (CTR), which involves simplified models for optical and thermal calculations and evaluation of design constraints. The proposed methodology optimizes the total yearly energy production as the criterion, considering a multi-parameter analysis. This design is part of the AdInCCSol (Advanced Integration of Combined Cycles in Solar thermal power plants) project, which aims to integrate advanced thermodynamic cycles in solar thermal power plants to improve efficiencies and lower LCOE. Specifically, the manuscript presents the optimization of a 100 MW CTR plant based on a conventional cylindrical receiver that operates at an outlet temperature of 565 ºC. Unlike previous studies, the proposed methodology considers yearly calculations and takes into account most of the parameters that affect thermal and optical efficiencies, including tube diameter, receiver diameter, height, and the number of faces. The aiming strategy for each design was also optimized to achieve the best balance between optical and thermal losses while meeting stress and corrosion limits. The study was conducted using two in-house codes that integrate thermal and optic performance calculations and models for estimating design constraints, providing accurate results with low running times. The findings of the study indicate the presence of an optimal receiver area that optimizes the design for a target power of concentrated radiation flux density. Moreover, certain combinations of parameters yield similar yearly energy productions, enabling the development of designs with comparable performance and reduced costs.

Keywords:

Central Tower Receiver (CTR), aiming strategy, receiver design optimization, heliostat field

1. Introduction

This paper presents a study focused on designing an optimized central tower receiver for the AdInCCSol project. The objective is to analyze multiple parameters and optimize the receiver design in terms of yearly performance.

Designing a solar thermal power plant is a complex task that requires the integration of multiple models and tools from various multidisciplinary fields since the optimal solution depends on several parameters. One of the key challenges is that the optical and thermal performance cannot be optimized independently. Also, structural stresses or corrosion inside the tubes can cause receiver failure [1-3], while pressure drop and flow stability inside the tubes can lead to operational issues [2,4]. Therefore, it is essential to integrate all these calculations into the design process to achieve the desired performance.

The heliostat field design and aiming strategy are crucial for an optimal design. Firstly, it is important to establish the Allowable Density Flux (AFD) [5-6], to adapt the flux maps to this limit, maximizing thermal

performance and minimizing ray spillages. The strategy of adapting the aiming points of the heliostats can vary from different authors from more simple approximations [7] to more complex ones like the one based on Deviation-based Aiming Strategy (DBA) [8-9]. Again, the optimization of the aiming strategy involves the integrated analysis of the optical and thermal performances.

Over the last four decades, some algorithms have been developed oriented toward the optimization of the heliostat field [10]. However, up to the authors' knowledge, there are no studies that proposed a receiver design based on an optimization process coupling heliostat field and aiming strategy optimization with thermal performance analysis and considering stress and corrosion limits.

The present study describes the design of a solar thermal power plant with a standard configuration of 100 MWe in Seville. To achieve this, the power output is divided into two towers and their respective fields to avoid very large distances from the heliostats to the receiver that would be subjected to an important attenuation. In addition, the flexibility that adds a dual-tower system [11] is another aspect that can be considered in this project. Specifically, each tower is designed to produce 340 MW of concentrated radiation and 300 MWt of thermal output for the fluid, resulting in a Solar Multiple (SM) of 1.2. Doubling the tower produces an optimal SM of 2.4, which is suitable for 8 hours of storage [12].

Two already developed tools were adapted to this methodology and are described in section 2, while the methodology for the design is established in section 3. The results are introduced an analyzed in section 4 to obtain an optimum combination of design parameters and orientate the final design of the receiver.

This work represents a significant contribution to the field of Central Tower Systems (CTS) design for Concentrated Solar Power (CSP) by presenting an efficient methodology for designing CTRs and considering multiple parameters in the optimization. One of the novelties is the use of a Design of Experiments (DOE) methodology for the optimization, which contributes to having more information about the effect of the different parameters over the global performances.

2. Heliostat field and receiver modeling

In this project, two different tools have been used to facilitate the design process. One of the tools was specifically adapted for the optical optimization of the field and receiver aiming strategy. The other tool was dedicated to the thermal performance of the receiver and included integrated calculations to predict structural limits, flow stability issues, and pressure drops. By utilizing these tools in combination, a more comprehensive understanding of the solar thermal power plant design was achieved, allowing for an optimized solution that meets the requirements.

The subsequent sub-sections outline the models and tools utilized in the study, while the methodology section describes their integration and iterative process to obtain an optimal solution.

2.1. Optical modeling and optimization of the heliostat field. Aiming strategy.

Two software applications developed in Matlab 2022b have been employed.

- An application for optimizing the layout of heliostats.
- An application for optimizing the aiming strategy.

The first one, HRT (Homology Ray-Tracing) code is used for the optics optimization and is based on the yearly insolation weighted efficiency as a Function Of Merit (FOM), which according to [13] and [14], is given by Eq. (1):

$$\eta_{yearly\_w} = \frac{\sum_{d=1}^{365} \int_{orto}^{ocaso} \eta(t) \cdot IND(t)}{\sum_{d=1}^{365} \int_{orto}^{ocaso} IND(t)}, \quad (1)$$

where η (t) is the instantaneous optical efficiency and IND (t) represents the instantaneous beam insolation, Eq. (2).

$$\eta_{(t)} = \frac{\sum_{1}^{N} (\eta_{cos} \cdot \eta_{ref} \cdot \eta_{s\&b} \cdot \eta_{aa} \cdot \eta_{int})}{N}. \quad (2)$$

In general, the optimization code operates by proposing an array or pattern of heliostats in the field, according to parameterized expressions. These allow the location of each of the heliostats in the array to be determined within geometric limits on the horizontal plane, which are usually a function of the tower height and the geometry of the receiver [15, 16]. Typically, the proposed field layout comprises a greater number of heliostats than those required to reach the target power at the design point [13, 14, 17].

Next, the subset of heliostats of the proposed field is determined that, with greater optical efficiency, allows obtaining the target power on the receiver at the design point (autumn equinox at solar noon). Subsequently, operating with this subset of heliostats, the merit function is evaluated using multiple sample points. Since the initial field is as compact as possible, the overall efficiency can be improved, as significant losses due to

shading and blockages will occur, while the remaining elementary efficiencies (cosine factor, reflection, atmospheric attenuation, and interception) are very high. Then, the optimization code proposes another configuration or pattern, differing slightly from the previous one, and the calculations are repeated.

To reduce computation time, the code implements various resources, such as techniques to reduce the number of candidates in determining to shade and blocking performances [18], homographic techniques for determining interception and shading and blocking performance [19] and [20], or evaluating the merit function using numerical integration methods [21].

Starting from an optimized layout, the aiming strategy is optimized using the aforementioned second application. For this purpose, an iterative process is used, which consists of the following steps:

1. Several sample points are used to simulate in detail each of the heliostats in the solar field aiming at the receiver center and determine the power density matrices of each heliostat.
2. Correct the aiming in the vertical direction.
3. Recalculate the power density matrices and efficiencies of each heliostat.

In this case, a detailed Monte-Carlo Ray Tracing (MCRT) is used, with few simplifications. 10,000 rays per heliostat have been used. Other features of this ray-tracing include:

- Uses the MCRT methodology.
- Assumes that the surface of the heliostat has a rectangular shape and elliptical quadric curvature without holes or discontinuities (a spherical surface is considered in this case with on-axis cant).
- Incident rays are randomly generated following a Standard Solar Model (SSM). A Gaussian SSM with σ = 2.325 mrad has been considered.
- The incident rays are randomly generated uniformly over the surface of the heliostat.
- The optical errors (macroscopic and microscopic) associated with the reflecting surface of the heliostat are considered by using Gaussian distributions in both cases. Values of σ = 2.0 and 1.0 mrad for the macroscopic and microscopic, respectively, are used.
- The reflectivity of the heliostat, as well as the losses due to atmospheric attenuation, are applied in a non-deterministic manner.
- Both the methodology used for preselecting candidates for shading and blocking, as well as the methodology used for determining to shade and blocking, are defined in [19].

This sub-process dedicated to correcting the aiming in the vertical direction consists of the following steps: a ϕ_{obj} matrix of size m·n is defined, whose cells have the value given by Eq. (3).

$$\phi_{obj} = coef \cdot \frac{Total\ power\ over\ the\ receiver}{receiver\ area}. \quad (3)$$

Where *coef* is a user-defined value. The φ matrix of size m·n is initialized with null values, where m represents half of the number of vertical cells and n is the number of heliostats. An iterative process is started that goes through the n heliostats of the solar field ordered from highest to lowest total optical efficiency. The vertical location of the power density matrix of the i-th heliostat ϕ_i that minimizes the Root Mean Square (RMS) value is determined, by minimizing Eq. (4).

$$RMS = \sqrt{\sum_1^m \left(\sum_1^n \varphi + \phi_i - \phi_{obj}\right)/(m \cdot n)}. \quad (4)$$

Once the RMS is minimized the aiming vertical position for each heliostat is updated, using Eq. (5).

$$\varphi = \varphi + \phi_i. \quad (5)$$

The aiming vertical correction for the i-th heliostat is determined trigonometrically and stored. This is repeated for different values of coef.

2.2. Thermal modeling of the receiver

The thermal performance for a region of uniform absorbed radiation can be obtained using Eq. (6) [22].

$$\eta(x^*) = \frac{\eta_0 \cdot g'(Z)}{(1-g'(Z))} \cdot \frac{1}{NTU \cdot x^*} \cdot \left(e^{\frac{1-g'(Z)}{g'(Z)} \cdot NTU \cdot x^*} - 1 \right), \quad (6)$$

The thermal efficiency at the inlet denoted as η_0, is a key performance parameter for a thermal system. In this context, the derivative of the characteristic function, g'(z), and z, the variable of this function, are defined in [22], while NTU (Number of Transfer Units) is a characteristic parameter of the thermal system and x^* is the non-dimensional coordinate.

To model the system, external heat transfer coefficients are required to evaluate the different terms of the characteristic function. However, it should be noted that the heat transfer mechanisms at the receiver are

complex due to the non-uniform absorption of radiation. Consequently, a dense mesh is needed to precisely evaluate the temperature at the tube surfaces. Furthermore, the receiver tubes are exposed to ambient air at the front and are insulated at the back with a panel that is separated from them. As a result, the air can enter through the gaps situated among the tubes and refrigerate them. The complexity of the convective currents around the receiver tubes, the coupling with radiation, the large dimensions of the receiver, and its open configuration are some of the reasons that support the idea that to accurately capture convection heat transfer it is required to perform unaffordable simulations by Computational Fluid Dynamics (CFD). The radiation mechanisms are also complex because different sections of the surface have varying view factors concerning the sky, the heliostats, the ground, the neighbor tubes, or the insulation at the back part. In this study, it was decided to introduce some simplifications as the purpose is not to achieve precise results, but rather approximations that allow comparison of different designs with rapid yearly calculations to optimize the design. To this end, the following hypotheses are considered for radiation and convection heat transfer:

- The tube is painted with Pyromark, with a constant emissivity of 0.87 in the range of temperatures of the receiver, and a solar absorptivity of 0.96 [23].
- The front face of the tube exchanges radiation with an equivalent surface at ambient temperature.
- The back face of the tube is considered insulated.
- Heat transfer by convection is assumed to be constant and equal to 14 W/(m^{2}K), as it is proposed in [24] for the DELSOL code.

The same set of hypotheses for the evaluation of thermal losses was considered and validated in [25], with the only difference of the values of the convective heat transfer coefficient that could vary.

Due to the non-uniform absorption of radiation in the receiver, the tube length is discretized into slices of 0.5 m where radiation flux density is averaged.

The fluid used is the "Solar salt", 60% $NaNO_3$ and 40% KNO_3, which thermo-physical properties are based on [1]. The fluid flow rate is adjusted to achieve the desired outlet temperature (565 ºC). However, under conditions of low absorbed radiation, the fluid flow may not be sufficient to adequately cool the receiver tube, leading to potential structural or corrosion limitations being exceeded. To prevent this, a threshold concentration of radiation at 160 MW (47% of the nominal value) has been established, below which the fluid flow rate is maintained at a constant value and the outlet temperature is allowed to vary accordingly.

The Direct Normal Irradiance (DNI) and temperature data for the location of Seville were obtained from the Typical Meteorological Year International Weather for Energy Calculation (TMY IWEC) database [26] and used as inputs in the simulations for all cases analyzed.

2.3. Design constraints

In concentrated solar power systems, receiver tubes are exposed to solar radiation and undergo thermal stresses that can lead to failure. The axial thermal stresses in the tubes can be eliminated with proper design. However, the temperature gradient in the tubes leads to maximum thermal stresses at the front or crown, estimated via a superposition of circumferential and radial gradients. Equation (7) has been adopted by multiple authors [4, 6-7].

$$\sigma_c = \gamma \cdot E \cdot \left[(\bar{T}_c - \bar{T}_w) + \frac{\Delta T_c}{2 \cdot (1-\nu)} \right]. \quad (7)$$

Where ν is the Poisson's ratio, γ is the coefficient of thermal expansion (mm/m·K) and σ_c is the thermal stress at the crown (MPa). The radial temperature difference at the crown (ΔT_c), the mean temperature at the crown (T_c), and the average tube temperature (T_w) are based on the local absorbed radiation and assuming that the backside temperature of the tube wall is the same as the working fluid temperature [4, 6-7]. These values are compared with Ultimate Tensile Strength (UTS) values for the tube material [27]. In this case Inconel 625 is selected for the tubes as it presents better performance to corrosion than, for example, Haynes 230, although this alternative presents better mechanical performance [7].

The corrosion of tubes is also a significant concern as it is accelerated by high temperatures. The material loss due to corrosion is limited to 0.5 mm over 10 years, and the temperature limit for corrosion of Inconel 625, used for the tubes, is 628 ºC [7]. These two limits are used to calculate the Allowable Flux Densities (AFD) for each node along the tube [7]. The radiation flux density at each node is compared to its allowable value, and the flux is reduced uniformly to meet this criterion. Although selective defocusing could be included in future studies.

Pressure loss is another critical factor, as a pressure of 20 bar is required to ensure correct solar field operation. Pressure losses are estimated for receiver tubes, headers, and elbows that appear in a standard, using the models proposed in [2].

Finally, downward flow inside the tubes may be subject to instabilities due to the upward buoyancy force, which tends to increase as flow velocity decreases. Perturbations in a downward-flow tube lead to the increased temperature inside the tube and buoyancy force, further decreasing the flow rate and potentially leading to

flow imbalance and operational problems in the receiver. The stability criterion proposed in [4] is included in the model to ensure that the downward flow inside the tubes is not subjected to instabilities. The criterion is expressed as follows, Eq. (8).

$$\frac{32 \cdot f}{\pi^2 \cdot d_i^5 \cdot \rho^2 \cdot g \cdot \beta} \cdot \dot{m}^2 / \Delta T \geq 1. \quad (8)$$

where f is the friction factor (-), di is the internal tube diameter (m), ρ is the fluid density in (kg/m3), $\dot{m}$ is the mass flow (kg/s), ΔT is the temperature difference (K), and L is the length of the tube (m).

3. Methodology

As was already introduced the proposed methodology was developed to optimize the heliostat field and receiver designs for a power plant located in Seville with a target thermal power of 300 MWt for each receiver, which implies a SM of 2.4. The design involves the analysis and optimization of three key parameters of the receiver, namely the receiver diameter (D), receiver height (H), and the number of faces (N). The optimization process is carried out in three steps. Firstly, the heliostat field is optimized for each of the receiver's diameters and heights using the code described in the previous section. Secondly, an appropriate aiming strategy is determined to maximize yearly energy production, and finally, a response surface is constructed and optimized using the results from all the simulations.

It is noteworthy that the effect of radiation flux densities changes from high to low temperatures, as shown in Fig. 1. The thermal performance for low temperatures due to a four-times reduction in radiation flux densities is found to be around 8%. In contrast, a two-times reduction for high temperatures leads to a significant reduction in performance, up to 20%. Thus, it is crucial to adopt a concentration level that optimizes thermal efficiency while avoiding optical losses for the operation over the whole year.

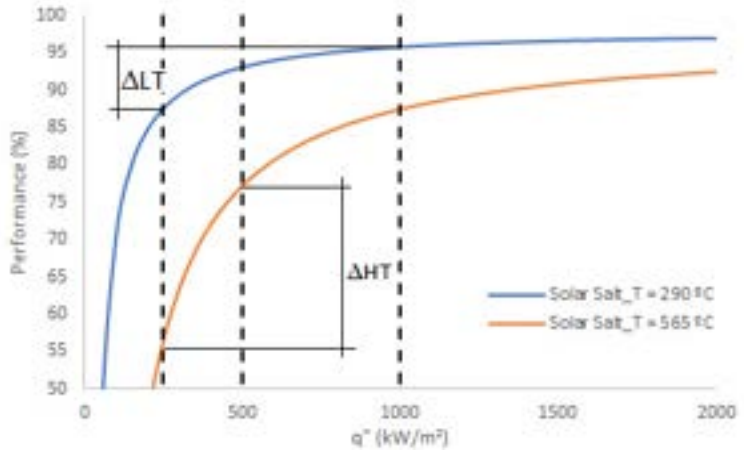

Figure 1. Thermal performance as a function of radiation flux density

To address the non-uniform distribution of the flux densities along the height of the receiver, a correction coefficient is proposed in this study, as described in section 2.1. This coefficient is designed in such a way that lower values indicate a tendency towards a uniform distribution (Figure 2 and Table 2). However, such uniformity can lead to an increase in optical losses due to ray spillage. On the other hand, higher values of the correction coefficient generate a narrower distribution with improved optical efficiency, but problems with the limits for tube failure. Thermal efficiency can increase or decrease depending on the shape of the distribution and receiver height. As a result, a search for the optimal value of this coefficient can be performed for a given set of parameters. Figure 2 shows the density flux maps for different values of the coefficient, while Table 2 summarizes the performance values of each of the maps.

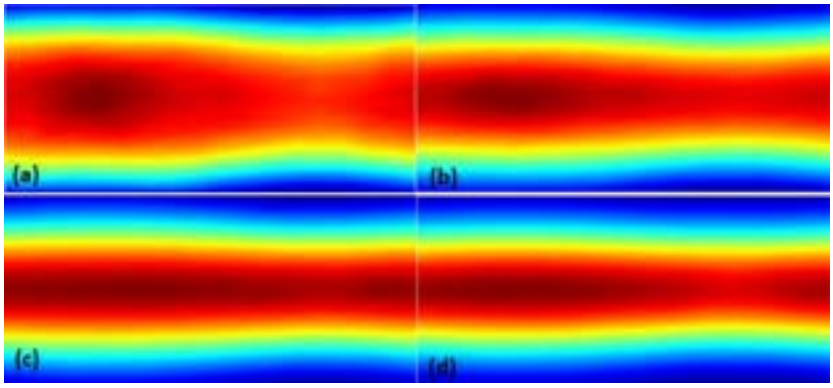

Figure 2. Density flux maps for different values of the coefficient

Table 2. Performance values for different coefficients in a general case

Coefficient	Thermal efficiency (%)	Optical efficiency (%)	Total efficiency (%)	Number of hours operation over the limit (h)
0.8	85.95	51.16	43.97	0
1.0	86.4	55.46	47.92	144
1.2	86.76	55.46	48.12	412
1.4	87.08	55.46	48.3	600

As it was said before, the operation over the tube failure limit is not permitted and radiation flux density is reduced for these instants, so the yearly energy produced would be diminished as this number increased, although optical and thermal efficiencies are greater. The operation under these conditions was limited to a maximum value of 10%, except in those cases with a small receiver, because the radiation flux density is very high. In any case, the influence of these cases on the optimization process is very limited, as It is shown in the next sections.

The optimization of the receiver design is carried out based on the yearly energy produced by the system, which is the main objective of this study. It is crucial to consider the system's performance under non-nominal conditions, as demonstrated in Fig. 1. The system's efficiency drops significantly when the absorbed radiation falls below a certain threshold, which is higher in the case of high temperatures.

The proposed methodology involves computationally expensive and time-consuming simulations. Therefore, the Design Of Experiments (DOE) methodology is preferred in this study due to its ability to reduce computational cost while providing a comprehensive understanding of the system's performance over a year. A face-centered central composite design algorithm is used to establish the case matrix which is composed of 15 cases (Table 3). The results of these cases are used to construct a second-grade polynomial function of three variables as a response surface for the yearly energy produced, which is then optimized.

Table 3. Case matrix from the face-centered central composite algorithm.

Cases	D (m)	H (m)	Number of faces	D tube (mm)	Gap (mm)	Number of tubes
1	8	10	10	36	0.9	670
2	15	10	10	22	1.06	2010
3	8	18	10	36	0.9	670
4	15	18	10	22	1.18	2000
5	8	10	18	57	2.4	414
6	15	10	18	34	1.2	1332
7	8	18	18	57	2.4	414
8	15	18	18	34	1.2	1332
9	8	14	14	46	0.85	532
10	15	14	14	28	1.28	1596
11	11.5	10	14	34	1.05	1022
12	11.5	18	14	34	1.05	1022
13	11.5	14	10	27	1.2	1260
14	11.5	14	18	43	1.38	810
15	11.5	14	14	34	1.05	1022

In all cases, the diameter of the tubes is established such that the mass flow velocity of the Heat Transfer Fluid (HTF) at nominal conditions is set at 3.6 m/s, with some margin from the maximum velocity. This is a critical factor that influences the overall efficiency of the system and needs to be maximized to achieve the highest possible thermal efficiency. So the tube diameter is a variable of our design which is previously established.

It can be observed that as the receiver diameter increases, the tube diameter decreases. This is because for lower receiver diameters, the radiation flux density is higher, and the total absorbed energy along the HTF path is also higher. An increase in tube diameter results in an increase in flow, which depends on the squared diameter, and an increase in the total amount of energy, which depends linearly on the tube diameter, so an increase in tube diameter tends to keep constant the temperature increment. The same principle applies to the number of faces; as this number increases, the length of the path that the HTF follows increases, and also does the total amount of energy, necessitating an increase in tube diameter to compensate for this.

The number of tubes primarily increases with the receiver diameter because the receiver is larger, and the tube diameter is lower. This number decreases as the number of faces increases since the tube diameter

increases and the receiver area only slightly increases. Meanwhile, the height of the receiver does not affect the number of tubes.

The gaps among the tubes are adjusted to cover the entire panel length with a minimum value to avoid tube contact.

The number of circuits considered for all the designs is 2 with no crossovers and the flow path for both circuits goes from N to S. This flow path reduces film temperatures and so the defocusing of the mirrors optimizing the yearly energy produced [2]. It is planned to analyze also these parameters in future works, but it is not expected important results modifications.

4. Results discussion and optimization

The heliostat field is optimized in the initial stage of the optimization process. For this purpose, heliostats of 12·10 m were considered and the optimized tower height was 250 m for all the cases. The layout for each case is summarized in Table 4.

Table 4. Heliostat layout for each case.

Cases	D (m)	H (m)	Number of faces (-)	Number of heliostats (-)	Number of rows (-)
1	8	10	10	6451	55
2	15	10	10	5644	51
3	8	18	10	5918	52
4	15	18	10	5390	48
5	8	10	18	6451	55
6	15	10	18	5644	51
7	8	18	18	5918	52
8	15	18	18	5390	48
9	8	14	14	6003	53
10	15	14	14	5451	49
11	11.5	10	14	5780	52
12	11.5	18	14	5390	48
13	11.5	14	10	5451	49
14	11.5	14	18	5451	49
15	11.5	14	14	5451	49

This layout only varies with receiver diameter and height.

Once the heliostat field is optimized for each case, the aiming coefficient is determined, which maximizes the yearly thermal energy output. As an illustration, an optimization example for case 12 is depicted in Fig. 3. The yearly energy production is normalized with the maximum value.

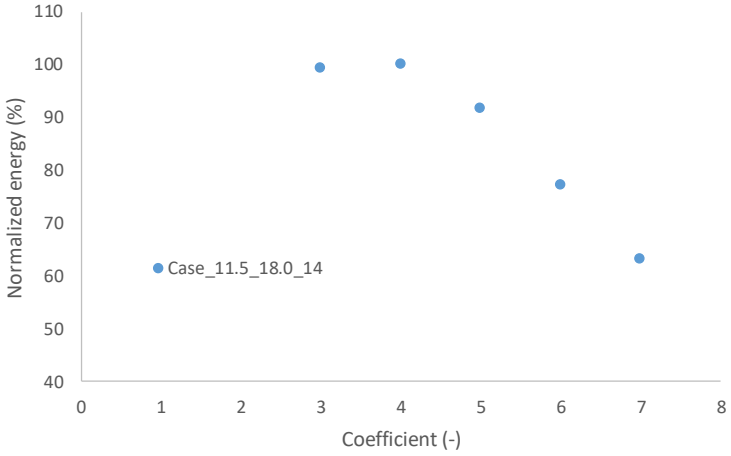

Figure 3. Normalized energy production for case 12

The results for, considering an optimum aiming strategy for each case are summarized in Table 5.

Table 5. Case matrix main results.

Cases	D (m)	H (m)	N. of faces (-)	Number of tubes (-)	Total energy (GWh/y)	η_{opt} (-)	η_t (-)	ΔP (bar)
1	8	10	10	670	497.60	47.28	81.33	1.14
2	15	10	10	2010	552.03	54.44	81.44	2.12
3	8	18	10	670	558.10	53.87	83.72	5.70
4	15	18	10	2000	531.56	54.19	78.11	5.47
5	8	10	18	432	513.15	47.42	84.64	23.28
6	15	10	18	1332	549.76	53.01	83.08	8.18
7	8	18	18	432	519.01	53.83	78.96	16.82
8	15	18	18	1332	542.07	53.96	80.34	15.86
9	8	14	14	532	509.10	50.56	81.06	5.53
10	15	14	14	1596	553.77	54.00	81.40	7.34
11	11.5	10	14	1022	544.25	53.82	81.42	2.53
12	11.5	18	14	1022	557.69	53.96	82.88	12.16
13	11.5	14	10	1260	562.14	54.00	82.82	4.32
14	11.5	14	18	810	563.23	53.90	83.79	24.01
15	11.5	14	14	1022	565.86	53.96	84.10	9.85

Only two cases have a greater pressure drop than the limit. This situation is considered for the optimum design.

It has been observed that the optical efficiency is optimized for each case, and the values are mostly similar, except for the cases with the lowest receiver areas. In such cases (i.e., cases 1, 5, and 9), the distribution is made more uniform to avoid exceeding the structural and corrosion limits at the radiation flux peak. As the area is small, spillage losses are high. As the receiver area increases, more rays hit the receiver with more uniform distributions, which helps avoid exceeding the structural and corrosion limits. For these cases, the thermal efficiency is high, and the slope of optical efficiency becomes lower with the growing area. However, if we continue to increase the receiver area, the radiation concentration is reduced, and thus the thermal efficiency drops, while the optical efficiency only marginally increases. Based on this analysis, it can be inferred that there exists a maximum yearly performance that is related to the receiver area (as shown in Fig. 4).

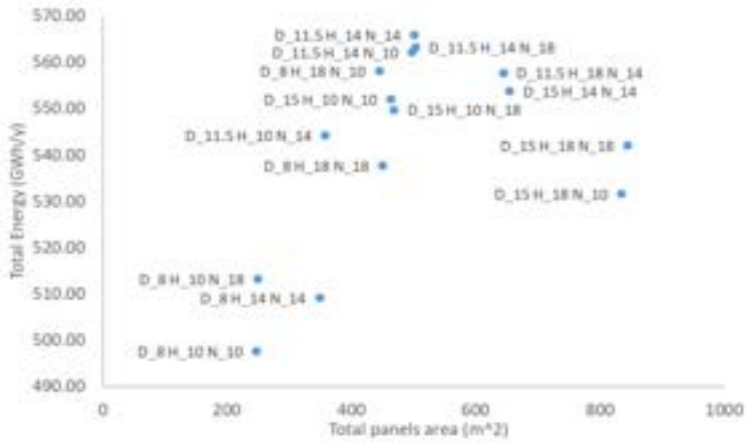

Figure 4. Yearly energy produced as a function of the receiver area.

It can be observed that the total energy produced increases with the total area of the panels up to the maximum value in the region near 500 m^2. For receiver areas greater than this value, the total energy drops. The result is not the same if the area is obtained with different combinations of values, as expected, it seems that, around the maximum value, it could exist some different combinations with similar yearly energy yield.

Once the results are obtained and analyzed, an expression that represents the yearly thermal energy as a function of the receiver diameter (D), height (H), and the number of faces (N) is obtained, Eq. (9).

$$f(D,H,N) = C_0 + C_1 \cdot D + C_2 \cdot H + C_3 \cdot N + C_4 \cdot D \cdot H + C_5 \cdot D \cdot N + C_6 \cdot H \cdot N + C_7 \cdot D^2 + C_8 \cdot H^2 + C_7 \cdot N^2 \quad (9)$$

The coefficients C_0 through C_9 are determined using the least squares method to fit the function to the data obtained from the DOE methodology. Once the coefficients are determined, this function can be potted to analyze the performance of the system as a function of the considered parameters. Figures 5(a), 5(b), and 5(c) depict the yearly energy production for cases with N = 18, N=14, and N=10, respectively. It can be noted that as the number of faces increases, the receiver height is higher and the receiver diameter is lower for the maximum value of the energy produced. So the receiver area tends to keep constant but with a different aspect ratio.

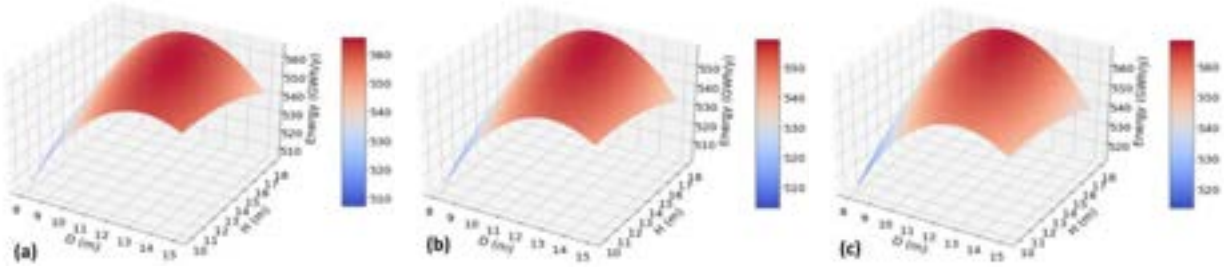

Figure 5. Total energy produced as a function of D and H for N = 18 (a), N=14 (b), and N=10 (c).

Figure 6 depicts a three-dimensional (3D) volume that displays the function value for each variable point within the considered range, represented by a color scale on the right. The volume illustrates the region where the function attains a maximum.

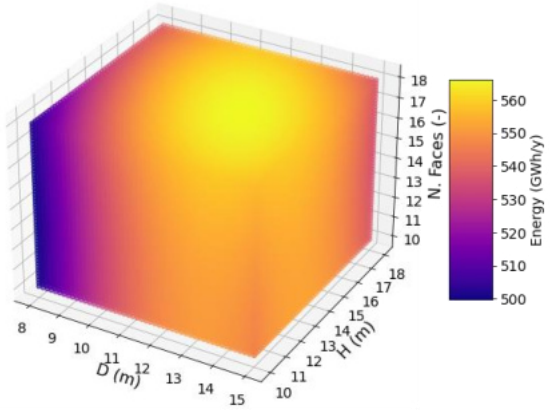

Figure 6. Total energy produced as a function of D, H, and N.

The function can be optimized to find the combination of the receiver parameters that yield the maximum yearly thermal energy. This optimization can be done using various optimization techniques, such as gradient-based methods or genetic algorithms, depending on the complexity and nonlinearity of the function. In this case, the Nelder-Mead method in Python was utilized to optimize the function within the specified range. The optimal values of the variables were determined to be (D = 12.63 m, H = 13.96 m, N = 18) which resulted in a total energy yield of 566.15 GWh/y and a receiver area of 550.3 m^2. This value is close to case 15 (D = 11.5 m, H = 14 m, N = 14), with a difference of only 0.05%. Figures 7(a) and 7(b) illustrate the areas where the response surface lies between this maximum value and yearly energy production that is 1% and 0.5% lower, respectively.

The optimal design resulting from the Nelder-Mead method would require a tube with a diameter of 40 mm and 972 tubes, which is less than the requirement for case 15. However, the receiver diameter is higher. It should be noted that the cost of the receiver is influenced by both the receiver diameter and the number of tubes required. Therefore, from a techno-economic analysis point of view, the response surface must be evaluated by taking into account the cost information to determine the optimal design. What is observed in Figures 7(a) and 7(b) is that there is an important number of combinations with similar yearly energy produced, so there is room to search for a design with a balanced cost and energy production which at the same time uses a nominal pipe size that can further reduce the costs and with a pressure drop less than 20 bar.

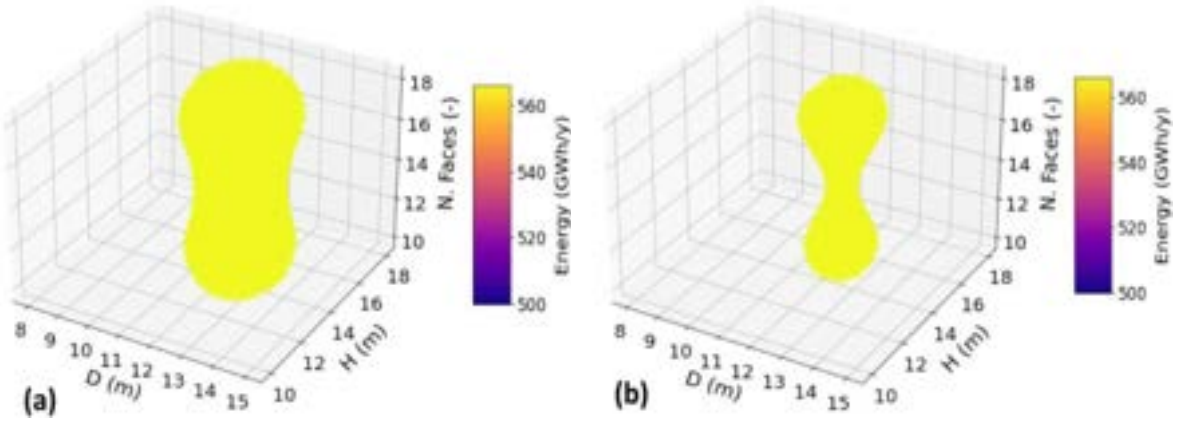

Figure 7. A volume that contains the combination of values that have yearly energy produced higher than 99% of the highest value (a) and higher than 99.5% of the highest value (b).

5. Conclusions

A methodology for the design of a CTR is proposed in this study, employing simplified models that encompass optical and thermal calculations, along with evaluations of other design constraints such as tube-failure predictions by stress or corrosion, and stable operation, which is ensured by limiting pressure drop and ensuring balanced flow among the receiver tubes. The methodology employs the yearly energy produced as the optimization criterion and considers the three primary parameters of receiver design, namely receiver diameter and height, and the number of panels. The tube diameter is predetermined for the optimization of thermal performance by controlling the HTF flow velocity.

The proposed methodology is developed in two steps, where the heliostat field is optimized for each design, followed by the optimization of the aiming strategy for the concrete heliostat field and receiver design. The employment of simplified models and DOE methodology to optimize the design enables the objective to be achieved within a reasonable time and with reduced computational resources. The response surface function obtained provides useful information for designing and optimizing solar receivers for maximum yearly thermal energy.

The results of the study indicate that for a target power of concentrated radiation flux density of 340 MWt (for one of the towers), the receiver area that optimizes the design is around 550 m^2, with an average value of 618 kWt/m^2. The results also reflect that some combinations of parameters will output similar yearly energy productions, thereby enabling the proposal of a design with similar performance and reduced costs.

Future work will include sensitivity analysis for the thermal-performance-related parameters to analyze their effect on the region for optimal designs. Furthermore, the inclusion of receiver costs as a function of the design parameters to obtain a response surface weighted by these cost estimations, oriented to reduce the Levelized Cost of Electricity (LCOE) for the optimized design will be explored. The implementation of more complex aiming strategies that can adjust heliostat aiming longitudinally in addition to vertically, to adapt the distribution to comply with the AFD without defocusing, will also be investigated.

Acknowledgments

This work has been supported by the Spanish Ministry of Economy and Competitiveness through the PID2019-110283RB-C31 project.

Nomenclature

C	response surface coefficient
coef	optimization coefeccient for the aiming strategy
f	friction factor,
d	diameter, m
E	Young Modulus, GPa
$G'(z)$	derivative of the characteristic function
H	receiver height, m
N	number of panels,
NTU	Number of Transfer Units
IND (t)	instantaneous beam insolation

L tube length, m

$\dot{m}$ mass flow rate, kg/s

T temperature, K

UTS Ultimate tensile strength, MPa

x^* non-dimensional coordinate,

z characteristic variable for the thermal performance equation

Greek symbols

β thermal expansion coefficient, K^{-1}

Δ difference,

γ coefficient of thermal expansion, mm/m·K

η efficiency,

ϕ radiation flux matrix for each node, kW/m^2

φ aiming point correction matrix, $kW/m^{2,}$

ν Poisson's ratio,

ρ fluid density, kg/m^3

σ thermal stress, MPa; aiming error,

Subscripts and superscripts

0 inlet

aa atmospheric attenuation

c crown

cos cosine factor

int interception

obj objective

ref reflection

$s\&b$ shading and blockages

w wall

References

[1] Pacheco JE. Results of molten salt panel and component experiments for solar central receivers: cold fill, freeze/thaw, thermal cycling and shock, and instrumentation tests. Sandia National Laboratories; 1995

[2] María de los Reyes Rodríguez Sánchez. On the design of solar external receivers. PhD thesis. Universidad Carlos III, September 2015.

[3] Abe, Osami, Utsunomiya, Taizo & Hoshino, Yoshio 1984 The thermal stability of binary alkali metal nitrates. Thermochimica Acta 78 (1-3), 251–260.

[4] Babcock & Wilcox Company, 1984. Molten Salt Receiver Subsystem Research Experiment Phase 1 – Final Report, Volume 1 – Technical. Barberton, Ohio.

[5] L.L. Vant-Hull, The role of "allowable flux density" in the design and operation of molten-salt solar central receivers, J. Sol. Energy Eng. 124 (2) (2002) 165, doi:10.1115/1.1464124, http://solarenergyengineering.asmedigitalcollection.asme.org/article.aspx?articleid¼1456457.

[6] Z. Liao, X. Li, C. Xu, C. Chang, Z. Wang. Allowable flux density on a solar central receiver, Renew. Energy 62 (2014) 747–753, doi:10.1016/j.renene.2013.08.044, http://linkinghub.elsevier.com/retrieve/pii/S0960148113004606.

[7] Alberto Sánchez-González *, María Reyes Rodríguez-Sánchez, Domingo Santana. Allowable solar flux densities for molten-salt receivers: Input to the aiming strategy. Results in Engineering 5 (2020) 100074

[8] G. Augsburger, "Thermo-economic optimisation of large solar tower power plants," Tech. Rep. (EPFL, 2013).

[9] Shuang Wang, Charles-Alexis Asselineau, John Pye, et al.An efficient method for aiming heliostats using ray-tracing. AIP Conference Proceedings 2445, 120023 (2022); https://doi.org/10.1063/5.0085672

[10] Arslan A. Rizvi, Syed N. Danish, Abdelrahman El-Leathy, Hany Al-Ansary, Dong Yang. A review and classification of layouts and optimization techniques used in design of heliostat fields in solar central receiver systems. Solar Energy 218 (2021) 296–311; https://doi.org/10.1016/j.solener.2021.02.011

[11] J. Serrano-Arrabal, J.J. Serrano-Aguilera, A. Sánchez-González. Dual-tower CSP plants: optical assessment and optimization with a novel cone-tracing model Renewable Energy 178 (2021) 429e442.

[12] Praveen R. P. Performance Analysis and Optimization of Central Receiver Solar Thermal Power Plants for Utility Scale Power Generation. Sustainability 2020, 12, 127; doi:10.3390/su12010127.

[13] S.M. Besarati, D. Yogi Goswami, A computationally efficient method for the design of the heliostat field for solar power tower plant, Renew. Energy 69 (2014) 226-232.

[14] C.J. Noone, M. Torrilhon, A. Mitsos, Heliostat field optimization: a new computationally efficient model and biomimetic layout, Sol. Energy 86 (2) (2012) 792-803.

[15] X. Wei, Z. Lu, Z. Wang, W. Yu, H. Zhang, Z. Yao: A new method for the design of the heliostat field layout for solar tower power plant, Renew. Energy 35 (9) (2010a) 1970-1975.

[16] X. Wei, Z. Lu, W. Yu, Z. Wang: A new code for the design and analysis of the heliostat field layout for power tower system, Sol. Energy 84 (4) (2010b) 685-690.

[17] Schwarzbözl, P., Pitz-Paal, R., Schmitz, M., Visual HFLCAL – A Software Tool for Layout and Optimization of Heliostats Fields. Presented at SolarPACES (2009), Berlin, Germany.

[18] G. Ortega, A. Rovira, A new method for the selection of candidates for shading and blocking in central receiver systems, Renew. Energy 152 (2020) 961-973.

[19] G. Ortega, A. Rovira, Proposal and analysis of different methodologies for the shading and blocking efficiency in central receivers systems, Sol. Energy 144 (2017) 475-488.

[20] G. Ortega, A. Rovira, Advanced methodologies for the calculation of shading & blocking and interception efficiency in central receiver systems, Presented at SolarPACES (2017), Santiago de Chile, Chile.

[21] Ortega, G. Transformaciones homográficas aplicadas a la simulación y optimización del subsistema óptico en centrales termosolares de torre. Ph.D. Thesis, Universidad Nacional de Educación a Distancia, Madrid, Spain, June 2017. (In Spanish)

[22] R Barbero, A. Rovira, M. J. Montes, J. M. Martínez Val, (2016). A new approach for the prediction of thermal efficiency in solar receivers. Energy Conversion and Management 2016, 123: 498–511.

[23] Rodríguez-Sánchez, M.R.; Soria-Verdugo, A.; Almendros-Ibáñez J.A; Acosta-Iborra A. & Santana, D. 2014a Thermal design guidelines of solar power towers. Applied Thermal Engineering 63 (1), 428–438.

[24] Kistler BL. A user's manual for DELSOL3: a computer code for calculating the optical performance and optimal system design for solar thermal central receiver plants. USA: Sandia National Laboratories; 1986. Sandia Report, SAND-86-8018.

[25] Robert Flesch, Cathy Frantz, Daniel Maldonado Quinto, Peter Schwarzbozl.Towards an optimal aiming for molten salt power towers. Solar Energy 155 (2017) 1273–1281; http://dx.doi.org/10.1016/j.solener.2017.07.067.

[26] Typical Meteorological Year International Weather for Energy Calculation (TMY IWEC). Available at: https://bigladdersoftware.com/epx/docs/8-3/auxiliary-programs/source-weather-data-formats.html#:~:text=The%20IWEC%20data%20files%20are,U%20S%20National%20Climatic%20Data%20Center.

[27] The ASME Boiler and Pressure Vessel Code Section III American Society of Mechanical Engineers. ASME boiler and pressure vessel code e section III, rules for construction of nuclear power plant components, Div. 1, Subsection NH; 2007. New York.

PROCEEDINGS OF ECOS 2023 - THE 36TH INTERNATIONAL CONFERENCE ON
EFFICIENCY, **C**OST, **O**PTIMIZATION, **S**IMULATION AND ENVIRONMENTAL IMPACT OF ENERGY SYSTEMS
25-30 JUNE 2023, LAS PALMAS DE GRAN CANARIA, SPAIN

A simple truncation criterion in CPCs using constructal theory

Eduardo González-Mora[a], Eduardo A. Rincón-Mejía[b]

[a] Facultad de Ingeniería, Universidad Autónoma del Estado de México, Toluca, México, egonzalezmo@uaemex.mx
[b] Programa de Energía, Universidad Autónoma de la Ciudad de México CDMX, México, eduardo.rincon@uacm.edu.mx

Abstract:
Compound parabolic concentrators (CPCs), whose origin dates back to the mid-1960s, gave rise to anidolic optics. Systems of this type allow the thermodynamic limit of solar concentration to be reached; however, in the case of CPCs, they involve systems with a very large height in relation to the aperture area (svelteness). Thus, arbitrary criteria have been proposed to reduce the height of the systems (truncation) and to be able to give them a real application. These truncation criteria establish the elimination of the upper part of the CPCs at a certain height in order to considerably reduce the height, but this has certainly undesirable consequences, since the geometric concentration (ratio of aperture area to receiver area) decreases with respect to the original design, which can limit the operating temperatures. Alternatively, a geometrical criterion has been proposed to truncate the CPCs without losing geometrical concentration, and still manage to reduce the height of the system by approximately 30%. This criterion consists of avoiding that the parabolic section mirrors do not block the incident rays that enter the aperture area with the maximum acceptance angle, thus defining an optimum truncation angle of 3 times the acceptance angle. However, now, with the help of the constructal law, it is possible to demonstrate that this angle is the optimum from a geometric viewpoint. Additionally, a new dimensionless number is defined for solar concentrating systems, relating the entropy generation distribution ratio, allowing to demonstrate that the Rincón criterion is the optimum for $C_g > 2.28$.

Keywords:
CPC truncation, entropy generation, étendue, constructal law

1. Introduction

The origin of compound parabolic concentrators (CPC) can be traced back to the mid-'60s by the developments of different researchers around the world: Baranov and Melinkov in the URSS [1], Ploke in Germany [2], and Hinterberger and Winston in the US [3], who independently described a novel optical system, unlike traditional systems, were based on the optimal transfer of radiation from the source to the objective, even if this implies forming aberrations and losing the shape of the source at the end of the system. This characteristic led to the coinage of the name non-imaging optics [4], to differentiate it from classical optics, where the image of the source must be conserved [5, 6]. As a result, in nonimaging optics, the light propagation is analyzed in terms of phase-space quantities and energy flow patterns This new optics has some advantages, but the possibility to reach the thermodynamic limit for solar concentrators systems is the principal [7]. Since mid-70s, their potential as collectors of solar energy was pointed out by Winston [8], and the widespread of this technologies has been fruitful.

Today, there is already a wide development of CPCs for solar applications, and several geometries have been generated that take advantage of non-imaging optics to concentrate solar energy on receivers of different shapes (circular, square, triangular, wedge, flat, elliptical...) [4, 9], Fig. 1 shows four typical CPC designs. All these geometries had been used for different purposes, like photovoltaics, solar heating and cooling, solar cooking, solar distillation, among others, that a complete summary of most of the works is out of the scope of the present paper, but several reviews [10–14] summarize some of the many developments, both experimental and commercial, that have been developed to date.

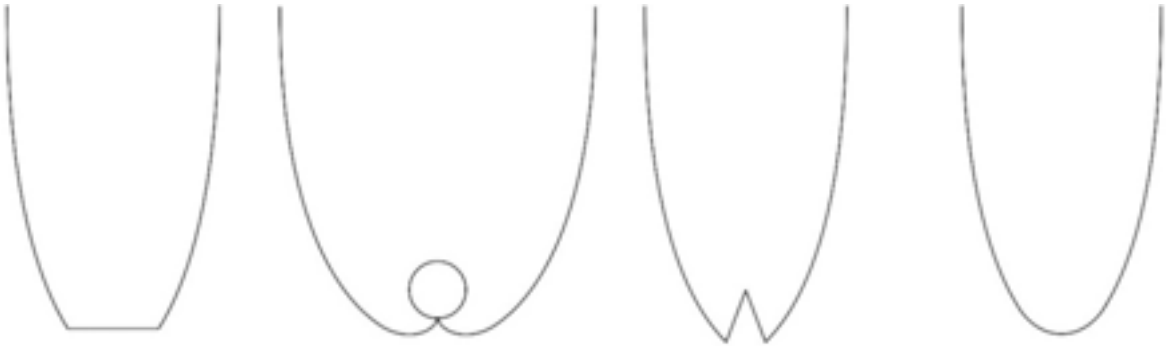

(a) Flat. (b) Circular. (c) Wedge. (d) Elliptical.

Figure 1: Different CPC receiver designs.

The main drawback of the CPCs, is that the ratio of height vs the receiver's area (svelteness) is too large, i.e. these concentrators are too high, and this ultimately limits their application even for fixed concentrators [4]. To overcome this problem, different truncation criteria have been proposed to decrease the total height [15–18] and consequently reduce the use of mirrors. These criteria had been developed from a purely geometrical perspective. Therefore, a formal analysis of the geometrical, optical, and thermodynamic aspects is necessary to establish which of the criteria is the most appropriate. This is fulfilled in the present work analyzing the original 2D flat receiver CPC with its geometric related parameters (height-aperture ratio and reflector area-aperture area ratio), optical-energy parameters (average number of reflections and étendue loss) and entropy related parameters (entropy generation number, optimum concentrator temperature and optimum efficiency) with the use of Bejan's constructal law [19, 20]. Although the analysis is done on a flat receiver CPC, the present work can be extended to any CPC design.

2. Brief description of the CPC

Regardless of the type of absorber the CPC may have, rays entering the concentrator with a maximum half acceptance angle θ_{max} (extreme rays), must be reflected by the mirror so that they are incident tangent to the absorber; while all rays entering with an angle θ less than the maximum half acceptance angle (i.e. within the angular full acceptance angle $2\theta_{max}$), are directed to the absorber after passing through the internal optics of the CPC (reflection or refraction).

With this definition, several receivers can be used, but only the flat receiver uses properly parabolas. In the present work, the flat receiver CPCs are considered. Equation 1 are the parametric equations to describe a flat receiver CPC with full height, schematically shown in Fig. 2., where it is assumed that the length of the trough CPC is l. The geometric parameters that define CPCs are the half-acceptance angle θ_0 and receiver size $2a'$. The subscript t stands for the truncated parameter.

$$\begin{cases} x(t) = \dfrac{2a'\,(1+\sin\theta_0)\cos t}{1-\sin\,(t-\theta_0)} \\ y(t) = \dfrac{2a'\,(1+\sin\theta_0)\sin t}{1-\sin\,(t-\theta_0)} \end{cases} \qquad t \in \left[0, \frac{\pi}{2}-\theta_0\right] \tag{1}$$

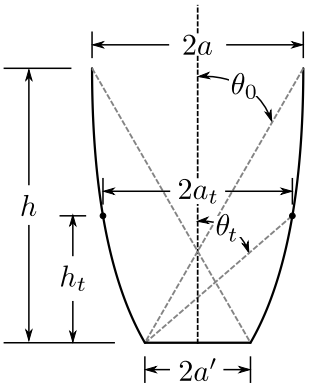

Figure 2: Schematic of the CPC with flat receiver.

From 1, it can easily be demonstrated that the concentration ratio (C_g) for a full CPC is simply:

$$C_g = \frac{A}{A'} = \frac{2al}{2a'l} = \frac{2x\left(\frac{\pi}{2} - \theta_0\right) - 2a'}{2a'} = \frac{1}{\sin\theta_0} \tag{2}$$

With the parametric equations given in 1, the svelteness Sv (height-aperture ratio) and the reflector area-aperture area ratio $r_{m,a}$ can be determined by.

$$Sv = \frac{y(t)}{2x(t) - 2a'} \tag{3}$$

$$r_{m,a} = \frac{\int_0^{t_{max}} \sqrt{x'^2 + y'^2}\mathrm{d}t}{2x(t) - 2a'} \tag{4}$$

2.1. Truncation of the CPC

As mentioned previously, one of the disadvantages of CPCs is the height of the concentrator; however, as seen in Fig. 2, the upper part of the mirrors does not contribute substantially to C_g. For this reason, it is recommended to remove a portion of the mirror to reduce height; this is known as truncation. While truncating the CPCs, material savings are achieved, but on the other hand, C_g will be reduced too since $2a_t < 2a$.

Winston, Rabl, and O'Gallagher recommend truncating the CPCs about half the fully developed height [7, 8, 17] (named Winston's criterion), while it can be found that some CPC can be truncated up to 2/3 the full height to reduce the loss in C_g. Independently, Rincón et al. [18] have proposed to truncate the CPCs to $3\theta_0$, because at this angle the mirror will not block light in the half-acceptance angle range $\pm\theta_0$ (Rincón criterion).

2.2. Optical energy related parameters

The thermal power that reaches the absorber can be described by a relation $\dot{Q}_u \sim G_b C_g \eta_o$, where G_b is the beam solar radiation and η_o is the optical efficiency, being a function of the average number of reflections n in the mirrors with reflectivity ρ as $\eta_o \sim \rho^n$. As can be seen, the lower the average number of reflections, the higher the optical efficiency and the higher the power that reaches the absorber.

Originally, Rabl [15] studied the average number of reflections , where it was shown that reducing the value of n led to an increase in the useful energy of the receiver. A summary of Rabl's equations for n can be found in [21]. Briefly, the average number of reflections in the CPC is a function of the type:

$$n = \max\left(F\left(\theta_0, x, y, t\right), 1 - \frac{1}{C_g}\right) \tag{5}$$

However, the most important parameter in optics is the étendue $\mathcal{E}$, defined as a geometric quantity that measures the amount of "place" available for light to pass [9], as a measure of the power transmitted along a beam of light. For 2D systems, the étendue is defined as [4, 9, 17, 22]:

$$\mathcal{E} = 2An_{ref} \sin\theta \cos\phi \tag{6}$$

where A is the area where the light passes, n_{ref} is the refractive index, θ is the solid angle where light enters in A and ϕ is the incidence angle. Recalling the concept of steady-state balance equations for any physical property ψ, the imbalance of the property can be determined as $\psi_{imb} = \psi_{in} - \psi_{out}$ [23, 24], where the subscript imb stands for the imbalance (destruction in the case of a negative value, generation for a positive value).

According to the definition of 6, if the rays enter an optical system with imperfections (the étendue is not preserved), then, at the output the rays will tend to scatter over the output area, consequently $\mathcal{E}_{out} > \mathcal{E}_{in}$, thus the imbalance term will be defined as scattered instead of generated. For full CPCs, the étendue is conserved [4, 9, 17, 22]. Any scattering in the étendue will cause the optics to fail to properly redirect the incoming light through the concentrator aperture, so the étendue scattering can be defined as:

$$\mathcal{E}_{sc} = \mathcal{E}_{out} - \mathcal{E}_{in} \tag{7}$$

or as a normalized scattering value as:

$$\mathcal{E}^*_{sc} = \frac{\mathcal{E}_{out} - \mathcal{E}_{in}}{\mathcal{E}_{in}} \tag{8}$$

which will have a value of 0, if there is no light scattering (perfect system, with conserved étendue); or 1 if the light is completely scattered (imperfect system, with non-conserved étendue).

2.3. Entropy related parameters

As described by Bejan [25], the minimization of the entropy generation rate implies the maximization of the useful power. In general, the entropy generation in a concentrating solar system, as in the thermal devices, will be due to the heat transfer process ($\dot{S}^{th}_{gen}$) and the fluid friction ($\dot{S}^{fl}_{gen}$) [25], but the étendue loss also contributes to an entropy generation $\dot{S}^{\mathcal{E}_{sc}}_{gen}$, so the total entropy generation has the basic form $\dot{S}^{total}_{gen} = \dot{S}^{fl}_{gen} + \dot{S}^{th}_{gen} + \dot{S}^{\mathcal{E}_{sc}}_{gen}$.
Considering an isothermal concentrator with no flow of mass on the concentrator (i.e., heating a plate), it is possible to eliminate the fluid friction entropy generation. The thermal entropy generation, as described by Bejan [25], includes the heat transfer coefficient U_r, the net solar transfer rate $\dot{Q}_s$ captured by the concentrator with an aperture A and receiver A' areas, the ambient temperature T_0, and the apparent sun temperature as an exergy source $T^* = \frac{3}{4}T_s$, as suggested by Petela [26], by:

$$\dot{S}^{th}_{gen} = \frac{U_r A' (T_r - T_0)}{T_0} - \frac{\dot{Q}_s}{T^*} + \frac{\dot{Q}_s - U_r A' (T_r - T_0)}{T_r} \tag{9}$$

The entropy generation for the etendue loss can be related trough the concepts of statistical thermodynamics, resembling that in general $S = k \log \Omega (E, V, N) + \text{const.}$ [27], and since the étendue is a measure of the transmitted power along a beam of light, a proper relation between this two variables can be developed. Winston et al. [28] have stated an entropy-étendue per photon relation as:

$$S^{\mathcal{E}} = k \log \mathcal{E} + \text{const.} \tag{10}$$

where the constant is related to a thermal quantity that can be set aside, since it applies only in the case of a wavelength shift [28, 29] or computed independently as done in 9, so the relation between entropy and étendue is firmly established. The entropy change for an irreversible process is equal to the entropy generation, so the entropy generation in terms of the étendue:

$$\dot{S}^{\mathcal{E}_{sc}}_{gen} = \dot{S}^{\mathcal{E}_{out}}_{out} - \dot{S}^{\mathcal{E}_{in}}_{in} = \dot{N}k \ln (1 + \mathcal{E}^*_{sc}) \tag{11}$$

where $\dot{N}$ is the number of photons per unit time that cross the aperture area of the concentrator. Note that under the numerical conditions of 8, the value of the entropy generation due to étendue scattering is always positive. The number of photons can be determined with $\dot{Q}_s$ and the average photon energy $E_{ph} \sim 10^{-19}$J as $\dot{N} = \dot{Q}_s / E_{ph}$.

Therefore, the total entropy generation rate in the concentrator is

$$\dot{S}_{gen}^{total} = \frac{U_r\,(2a')\,(T_r - T_0)}{T_0} - \frac{\dot{Q}_s}{T^*} + \frac{\dot{Q}_s - U_r\,(2a')\,(T_r - T_0)}{T_r} + \frac{\dot{Q}_s}{E_{ph}}\,k\ln\left(1 + \mathcal{E}_{sc}^*\right) \tag{12}$$

In view of this two discussed entropy generation terms, a dimensionless parameter relating the entropy (irreversibility) distribution ratio can be defined as $\dot{S}_{gen}^{\mathcal{E}_{sc}}/\dot{S}_{gen}^{total}$, with extreme values of 1 when the étendue scattering irreversibility dominates, 0 is the opposite limit at which irreversibility is dominated by heat transfer effects, and 0.5 is the case in which the heat transfer and the étendue scattering entropy generation rates are equal. In addition, when the entropy distribution ratio is zero, the étendue conservation condition is fulfilled. Thus, it is justified to define this parameter from the étendue concept and not from the heat transfer perspective.

Caution must be taken, since this relation can be confused with the Bejan number (Be) defined by Paoletti et al. [30] for the generation of entropy through heat and flow. This new relationship involves an optical parameter (the étendue) as an element that also generates entropy. This dimensionless parameter was originally proposed for entropy analysis in CPCs by González-Mora [31] but can be further generalized to any concentration geometry, since étendue conservation is a major concern when designing optical systems [4, 9, 22]. Consequently, it is suggested to call the entropy distribution ratio as Mo. The Mo number can then be expressed with the help of 12 as:

$$\mathrm{Mo} = \frac{\gamma\,(\theta_{max} - 1)\ln\left(1 + \mathcal{E}_{sc}^*\right)}{\theta^*\left[\theta_r^2 - 2\theta_r + \theta_{max}\right] + \theta_r\,(\theta_{max} - 1)\left[\gamma\theta^*\ln\left(1 + \mathcal{E}_{sc}^*\right) - 1\right]} \tag{13}$$

where $\theta_r = T_r/T_0$, $\theta^* = T^*/T_0$, $\theta_{max} = T_{r,max}/T_0 = 1 + \dot{Q}_s/U_r A' T_0$ and $\gamma = T_0 k/E_{ph}$. Furthermore, from 12 the optimal receiver temperature can be defined as the one that minimizes the total entropy generation rate, i.e. $\mathrm{d}\dot{S}_{gen}^{total}/\mathrm{d}\theta_r = 0$, resulting:

$$\theta_{r,opt} = \theta_{max}^{1/2} \quad \Leftrightarrow \quad T_{r,opt} = \sqrt{T_0\,T_{r,max}} \tag{14}$$

2.4. Constructal law

The aforementioned truncation criteria were established only through a purely geometrical approach. However, Rincón's criterion was recently demonstrated on a simplified parametric energy basis with a first approach of the constructal law [32]; while González-Mora [31] gave the first approach for entropy related parameters suggesting the evaluation of the so-called Mo number, as a response to several inquiries to rename the Rincón criterion. Therefore, a complete discussion of the geometric, optical and entropy parameters of CPCs is required for an objective comparison of the truncation criteria. To compare these criteria, constructal theory is used to define a constructal truncation criterion.

In 1997, Bejan [19] stated "For a finite-size system to persist in time (to live), it must evolve in such a way that it provides easier access to the imposed currents that flow through it", which is known today as constructal law, with a vast theory under it [20, 33]. The constructal law has been applied to various engineering systems [34], and recently in renewable energy systems analyzing a solar chimney and an oscillating water column [35], in addition to the first approaches in CPCs [31, 32], so the path for the constructal law in sustainable energy systems is clear and ongoing.

The fundamental concept of the constructal law is to establish the configuration that facilitates the flows in the system, by defining different parametric relations that establish the system degrees' of freedom and evaluating the behavior of the system with its proper restrictions. In the present analysis, the degrees of freedom are C_g and θ_r for the parametric relations that are described in the previous sections. Thus, accoring to the different truncation criteria, different configurations can be easily compared , where the main objective function is the Mo number described in 13.

3. Results

These results are shown graphically below, including the constructal law results applied with the PIKAIA genetic algorithm [36]. Although the objective function is the Mo number, all parameters were evaluated and discussed below. In all the plots, the same color palette is used: black for the full CPC, purple for the truncated CPCs, red for the truncated CPC under the Rincón criteria, blue for the truncated CPC under the Winston criteria, and green for the CPC results using the constructal law.

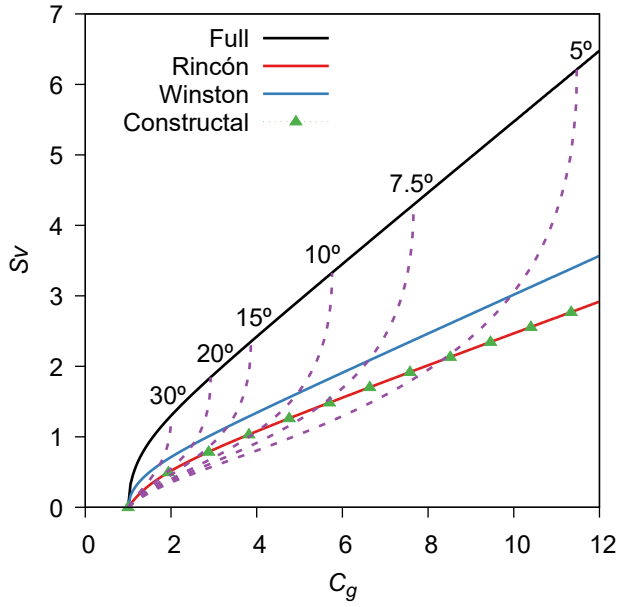

(a) Svelteness for different CPC designs.

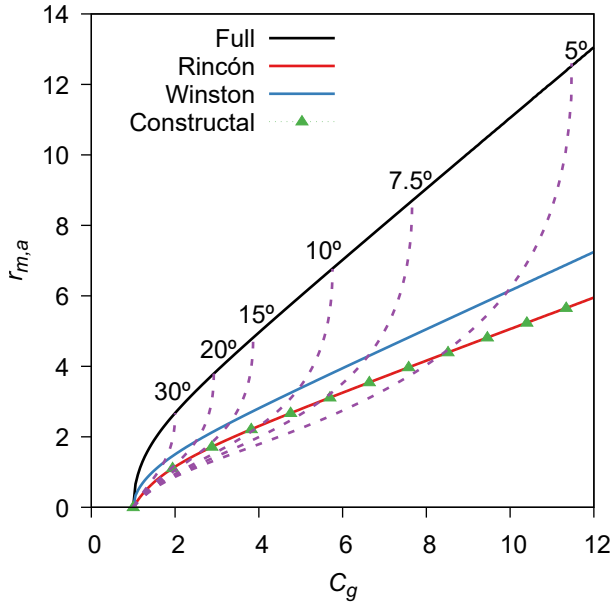

(b) Reflector area-aperture area for different CPC designs.

Figure 3: Geometric results.

3.1. Geometric results

In Fig. 3, the svelteness Sv and the reflector area-aperture area $r_{m,a}$ are plotted as a function of the concentration ratio C_g. As can be seen, Winston's criterion (blue line) reduces the height of CPCs, but Rincón's criterion (red line) reduces the height even further compared to the full CPC (black line). Here, a remark must be done for this, and all the following plots, since Winston's criterion reduces the concentration ratio one must find the intersection of the blue curve with the green curves to read the desired parameter, while the Rincón criterion attains no reduction in concentration ratio since a new acceptance angle must be determined to keep the original C_g value, and parameters can be read directly.

When applying the constructal law to the geometric parameters (green line), the same result is obtained as the Rincón criterion. Therefore, from a purely geometric perspective, the Rincón criterion is a geometric result justified by the constructal law.

3.2. Optical-energy results

The average number of reflections and the étendue scattering are shown in Fig. 4 and can be read like the previous plots. As can be seen, the Winston criterion (blue line) considerably reduces the average number of reflections, but the Rincón criterion (red line) reduces even more the average number of reflections, being the same for C_g between 2.04 and 5.01; however, Rincón's criterion maintains an almost average value n close to the minimum average number of reflections. An interesting behavior occurs for the étendue loss, since the Rincón criterion results in beneficial results only for $C_g > 2.28$, otherwise the light will start to spread over the receiver. In view of these results, the optical efficiency will be maximum for the CPC that is truncated with the Rincón criterion due to a greater reduction of n and, in general a minimum loss of the étendue.

Similarly, the application of the constructal law (green line) to the optical energy parameters yields a curious behavior. For the average number of reflections, the results are in agreement with the Rincón criterion, but not so for the étendue scattering. The behavior of the truncation criterion according to the constructal law shows that the Winston criterion is beneficial up to C_g = 2.28, and subsequently, the Rincón criterion is the one that minimizes the dispersion of the étendue in the optical system for $C_g > 2.28$.

3.3. Entropy results

In this case, in addition to C_g, θ_r is another degree of freedom. Although a 3D surface could be generated, its interpretation would be complicated. The parameter θ_r is the dimensionless temperature of the receiver, so it is greater than 1, and necessarily less than θ_{max}, with the possibility of being $\theta_{r,opt}$. Under these constraints, in the present analysis θ_r is proposed as an average of these values.

The entropy parameters under the described conditions are shown in Fig. 5. As expected, for the full CPC (black line), Mo=0 regardless of C_g. In the case of the Winston criterion (blue line), Mo results lower up to

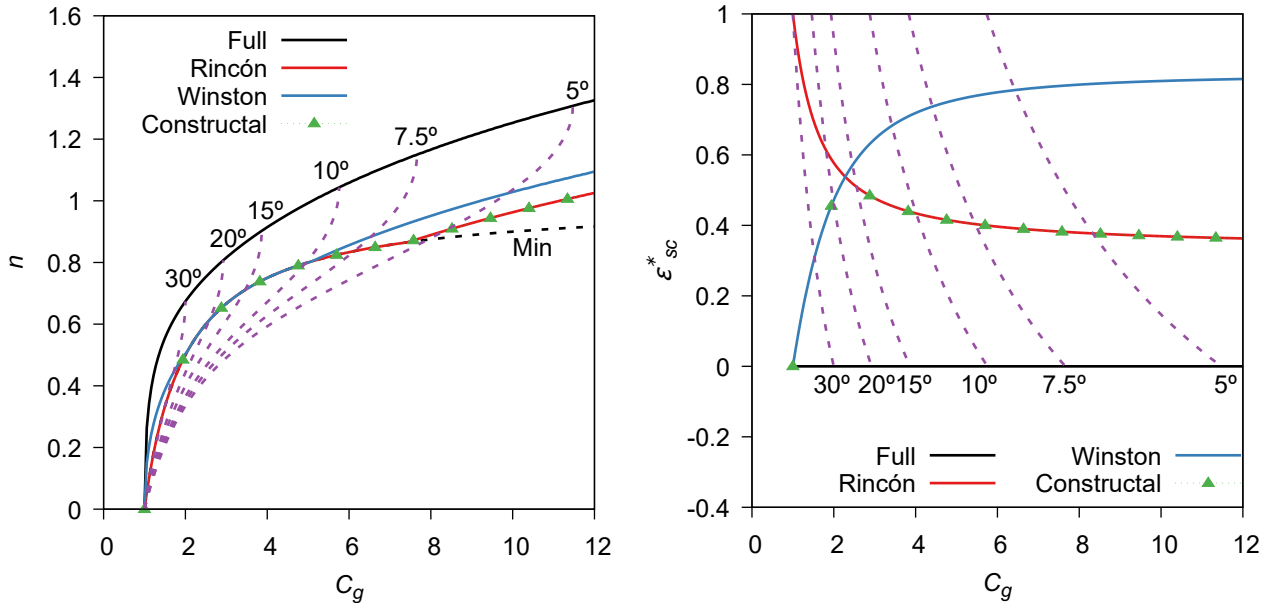

(a) Average number of reflections for different CPC designs.

(b) Étendue scattering for different CPC designs.

Figure 4: Optical-energy results.

$Cg < 2.28$, subsequently, the Rincón criterion (red line) presents lower values. Applying the constructal law (green line) gives a result very similar to the dispersion of the étendue, since the truncation of the CPC is optimized as a function of C_g. As can be seen in the graph of the optimum temperature, the Rincón criterion allows the optimum temperature of the complete CPC to be reached, just as if the constructal law were applied.

4. Conclusions

The CPC has several advantages for concentration systems; principally the possibility to get mid temperature ranges with a fixed concentrator, however, its height is the major drawback for its application. As a result, several truncation criteria had been proposed to increase its use, but, up to date, all had been justified by its height reduction, despite a first approximation with a simplified energy analysis.

Now, the analysis has been extended to include the rate of entropy generation, identifying that this production occurs by two factors: dispersion of the étendue and heat transfer process; leaving aside the entropy generation by fluid friction when considering only the heating of a flat plate for CPC with flat receivers. However, this analysis can be extended to any receiver geometry.

The present analysis has focused on comparing the behavior of the concentration ratio (C_g) for full CPCs with respect to truncated CPCs according to Winston's and Rincón's criteria and by applying Bejan's constructal law. This comparison is made by means of six parameters: two geometrical (svelteness and reflector area-aperture area ratio), two optical-energy (average number of reflections and étendue dispersion) and entropy (a new dimensionless group proposed Mo that relates the entropy generation distribution and the optimum receiver temperature).

When the study is carried out for different values C_g for the geometric parameters, the results of the constructal law and the Rincón criterion are optimal as Sv and $r_{m,a}$ decrease significantly to a value close to $1/3$ of the full CPC. With respect to the optical-energy parameters, the Rincon criterion and the construct law can be identified as the conditions for minimizing n; however, with respect to the dispersion of the étendue, the Rincon criterion is only beneficial for $C_g > 2.28$, for lower concentrations, the Winston criterion is a better choice, as shown by the constructal law. For the entropy results, again the Rincon criterion is only beneficial for $C_g > 2.28$, as shown by the constructal law; while for the optimal temperature, the Rincón criterion allows reaching the full CPC temperature.

In view of the results obtained, Rincón's criterion, although proposed from a purely geometric perspective, is practically a result of the construction law, provided that $C_g > 2.28$. This allows, without any doubt, to establish that, for the great majority of low- and medium-temperature applications, using the Rincon criterion allows obtaining the best performance in CPCs, as had been stated as an assumption (without a formal demonstration) in other previous works.

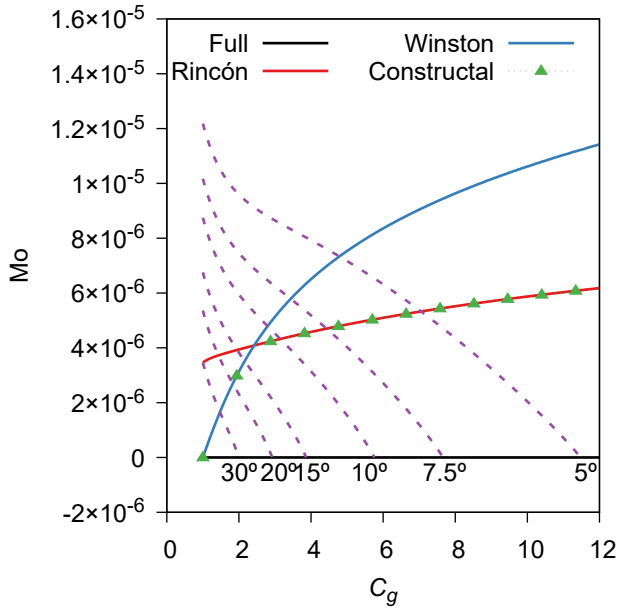

(a) Mo number for different CPC designs.

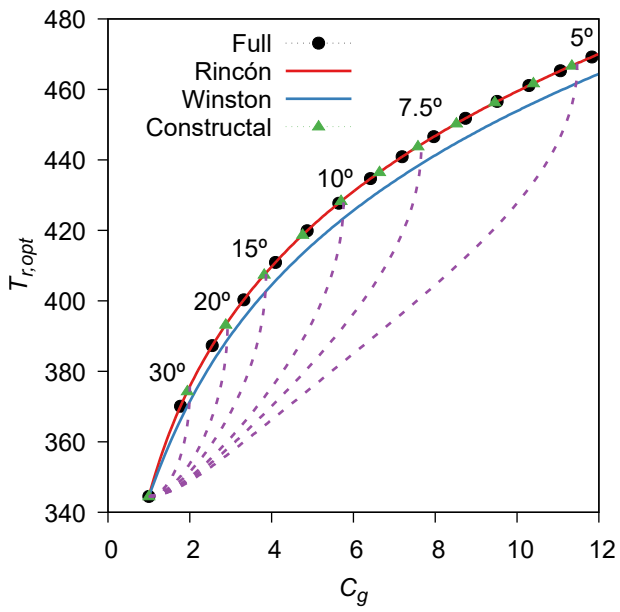

(b) Optimal temperature for different CPC designs.

Figure 5: Entropy results.

Acknowledgments

EGM would like to acknowledge PhD Diogo Canavarro (Universidade de Évora) for his insight and explanation of étendue. Although he may not agree with all the interpretation of this paper, any error is by the authors, and should not tarnish the reputation of this esteemed colleague.

Nomenclature

Letter symbols

A	aperture area, m^2
a	aperture width, m
A'	receiver area, m^2
a'	receiver width, m
Cg	concentration ratio, -
F	function, -
l	CPC length, m
E	energy, J
G	irradiation, W/m^2
h	heat transfer coefficient, W/m^2K; specific enthalpy, kJ/kg
k	Boltzmann constant, J/K
L	lenght, m
Mo	Mora number, -
$\dot{N}$	number of photons per unit time, photons$/m^2 \cdot s$
n	average number of reflections, -
$\dot{Q}$	heat transfer rate, W

r reflector area-aperture area ratio, -

$\dot{S}$ entropy rate, W/K

Sv svelteness, -

T temperature, K

t parameter (angle), rad

U heat transfer coefficient, $\mathrm{W}/\mathrm{m}^2 \cdot \mathrm{K}$

x parametric equation, m

y parametric equation, m

Greek symbols

γ dimensionless photon energy

$\mathcal{E}$ étendue, m^2

θ half acceptance angle, dimensionless temperature, -

ϕ incidence angle, -

Subscripts and superscripts

$*$ sun

0 ambient

ap aperture

bn beam normal

fl flow

gen generated

imb imbalance

in inlet

out outlet

ph photon

r receiver

s solar

sc scattering

t truncated

th thermal

total total

References

[1] V. K. Baranov and G. K. Melnikov, "Study of the illumination characteristics of hollow focons," *Sov. J. Opt. Technol*, vol. 33, no. 5, pp. 408–411, 1966.

[2] M. Ploke, "LICHTFUHRUNGSEINRICHTUNGEN MIT STARKER KONZENTRATIONSWIRKUNG," *Optik*, vol. 25, no. 1, p. 31, 1967, ISSN: 0030-4026.

[3] H. Hinterberger and R. Winston, "Efficient Light Coupler for Threshold Čerenkov Counters," *Review of Scientific Instruments*, vol. 37, no. 8, pp. 1094–1095, Aug. 1966, ISSN: 0034-6748. DOI: 10.1063/1.1720428.

[4] R. Winston, L. Jiang, and V. Oliker, *Nonimaging Optics: Solar and Illumination System Methods, Design, and Performance*. CRC Press, 2020, ISBN: 1466589841.

[5] C. A. DiMarzio, *Optics for engineers*. CRC Press, 2011, ISBN: 1439897042.

[6] J. Hecht, *Optics*, 5th ed. Pearson Education, 2017, ISBN: 1511445653.

[7] Y. D. Goswami, *Principles of Solar Engineering*, 3rd ed. Boca Raton: CRC Press, 2015, p. 822, ISBN: 1466563796. DOI: 10.1017/CBO9781107415324.004.

[8] R. Winston, "Principles of solar concentrators of a novel design," *Solar Energy*, vol. 16, no. 2, pp. 89–95, Oct. 1974, ISSN: 0038092X. DOI: 10.1016/0038-092X(74)90004-8.

[9] J. Chaves, *Introduction to NONIMAGING OPTICS*, 2nd ed. New York: CRC Press, 2017, p. 786, ISBN: 9781138747906.

[10] J. O'Gallagher and R. Winston, "Development of compound parabolic concentrators for solar energy," *International Journal of Ambient Energy*, vol. 4, no. 4, pp. 171–186, Oct. 1983, ISSN: 0143-0750. DOI: 10.1080/01430750.1983.9675885.

[11] D. K. Patel, P. K. Brahmbhatt, and H. Panchal, "A review on compound parabolic solar concentrator for sustainable development," *International Journal of Ambient Energy*, vol. 39, no. 5, pp. 533–546, Jul. 2018, ISSN: 0143-0750. DOI: 10.1080/01430750.2017.1318786.

[12] M. Tian, Y. Su, H. Zheng, G. Pei, G. Li, and S. Riffat, "A review on the recent research progress in the compound parabolic concentrator (CPC) for solar energy applications," *Renewable and Sustainable Energy Reviews*, vol. 82, pp. 1272–1296, Feb. 2018, ISSN: 13640321. DOI: 10.1016/j.rser.2017.09.050.

[13] S. M. Mortazavi and A. Maleki, "A review of solar compound parabolic collectors in water desalination systems," *International Journal of Modelling and Simulation*, vol. 40, no. 5, pp. 339–354, Sep. 2020, ISSN: 0228-6203. DOI: 10.1080/02286203.2019.1626539.

[14] Jiang *et al.*, "A Review of the Compound Parabolic Concentrator (CPC) with a Tubular Absorber," *Energies*, vol. 13, no. 3, p. 695, Feb. 2020, ISSN: 1996-1073. DOI: 10.3390/en13030695.

[15] A. Rabl, "Optical and thermal properties of compound parabolic concentrators," *Solar Energy*, vol. 18, no. 6, pp. 497–511, Jan. 1976, ISSN: 0038-092X. DOI: 10.1016/0038-092X(76)90069-4.

[16] A. Rabl, N. B. Goodman, and R. Winston, "Practical design considerations for CPC solar collectors," *Solar Energy*, vol. 22, no. 4, pp. 373–381, 1979, ISSN: 0038092X. DOI: 10.1016/0038-092X(79)90192-0.

[17] J. O'Gallagher, *Nonimaging Optics in Solar Energy* (Synthesis Lectures on Energy and the Environment: Technology, Science, and Society), 1st ed. Morgan & Claypool Publishers, 2008, ISBN: 9781598293302.

[18] E. A. Rincón Mejía, M. D. Durán García, and Á. Lentz Herrera, "New Solar Air Heater Based on Non-Imaging Optics for High-Temperature Applications," in *ASME 2009 3rd International Conference on Energy Sustainability, Volume 2*, 2009, pp. 839–844, ISBN: 978-0-7918-4890-6. DOI: 10.1115/ES2009-90306.

[19] A. Bejan, "Constructal-theory network of conducting paths for cooling a heat generating volume," *International Journal of Heat and Mass Transfer*, vol. 40, no. 4, pp. 799–816, Mar. 1997, ISSN: 0017-9310. DOI: 10.1016/0017-9310(96)00175-5.

[20] A. Bejan and S. Lorente, *Design with Constructal Theory*, A. Bejan and S. Lorente, Eds. Hoboken, NJ, USA: John Wiley & Sons, Inc., Sep. 2008, ISBN: 9780470432709. DOI: 10.1002/9780470432709. [Online]. Available: http://doi.wiley.com/10.1002/9780470432709.

[21] J. A. Duffie and W. A. Beckman, *Solar Engineering of Thermal Processes*, 4th ed. John Wiley & Sons, Inc., 2013, p. 936, ISBN: 1118418123.

[22] R. Winston, J. Miñano, and P. Benítez, *Nonimaging optics*, 1st ed. New Jersey: Elsevier, 2005, p. 509, ISBN: 0127597514.

[23] R. B. Bird, W. E. Stewart, and E. N. Lightfoot, *Transport phenomena*, 2nd ed. New York: John Wiley & Sons, Inc., 2002, p. 920, ISBN: 978-0-470-11539-8.

[24] G. T. Mase, R. E. Smelser, and J. S. Rossmann, *Continuum Mechanics for Engineers*. CRC Press, 2020, ISBN: 9781482238693.

[25] A. Bejan, *Entropy generation through heat and fluid flow*. Wiley, 1982, vol. 1, p. 248, ISBN: 0-471-09438-2.

[26] R. Petela, "Exergy of Heat Radiation," *Journal of Heat Transfer*, vol. 86, no. 2, pp. 187–192, May 1964, ISSN: 0022-1481. DOI: 10.1115/1.3687092.

[27] W. Greiner, D. Rischke, L. Neise, and H. Stöcker, *Thermodynamics and Statistical Mechanics* (Classical Theoretical Physics). Springer New York, 2012, ISBN: 9781461208273.

[28] R. Winston, C. Wang, and W. Zhang, "Beating the optical Liouville theorem: How does geometrical optics know the second law of thermodynamics?," R. Winston and J. M. Gordon, Eds., Aug. 2009, p. 742 309. DOI: 10.1117/12.836029.

[29] T. Markvart, "Counting sunrays: From optics to the thermodynamics of light," in *Physics of Nanostructured Solar Cells*, V. Badescu and M. Paulescu, Eds., 1st ed., New York: Nova Science Publishers, 2010, ch. 2, pp. 43–68.

[30] S. Paoletti, F. Rispoli, and E. Sciubba, "Calculation of exergetic losses in compact heat exchanger passages," in *ASME AES*, vol. 10, 1989, pp. 21–29.

[31] E. González-Mora, "Optimal trunation criterion for compound parabolic collectors: A thermodynamic justification," Book of Abstracts Thermodynamics 2.0 — 2022 (preprint), available at https://iaisae.org.

[32] E. González-Mora, E. A. Rincón-Mejía, and D. Morillón Gálvez, "Diseño constructal de CPCs y la evolución de los diseños Tolokatsin," in *XVII Congreso Ibérico y XIII Congreso Iberoamericano de Energía Solar*, H. Gonçalves and M. Romero, Eds., Lisboa, 2020, pp. 131–136. DOI: https://doi.org/10.34637/cies2020.1.2013.

[33] A. Bejan, *Shape and Structure, from Engineering to Nature* (Shape and Structure, from Engineering to Nature). Cambridge University Press, 2000, ISBN: 9780521793889.

[34] L. A. O. Rocha, S. Lorente, and A. Bejan, *Constructal Law and the Unifying Principle of Design* (Understanding Complex Systems). Springer New York, 2012, ISBN: 9781461450498.

[35] E. Dos Santos, L. Isoldi, M. Gomes, and L. Rocha, "The constructal design applied to renewable energy systems," in *Sustainable Energy Technologies*, E. Rincón-Mejía and A. de las Heras, Eds., 1st ed., Boca Raton: CRC Press, 2017, ch. 4, pp. 45–59.

[36] P. Charbonneau and B. Knapp, "A User's Guide to PIKAIA 1.0," Tech. Rep., 1995. DOI: 10.5065/D69P2ZKK. [Online]. Available: http://n2t.net/ark:/85065/d74m93xb.

Alternative Methodology for Modeling Direct Steam Generation in Parabolic Collectors: A Study Case in Northweast Mexico

Eduardo González-Mora[a], Ma. Dolores Durán-García[a]

[a] Facultad de Ingeniería, Universidad Autónoma del Estado de México, Toluca, México, egonzalezmo@uaemex.mx

Abstract:

The possible implementation of direct steam generation (DSG) in parabolic troughs in the Northweast region of Mexico is very limited, since there are no analyses of this type to try to define a first proposal for a solar plant. Recently, a methodology has been implemented to eliminate the convective coefficient *h* in order to model the DSG process in a simpler way. This methodology has been validated with experimental data from the DISS results from PSA. This methodology allows to evaluate the temperature evolution along the loop, the pressure drop and the flow pattern in a short time and with low computational resources. This allows generating the first evaluation of a solar field with parabolic troughs. Additionally, by applying a new practical efficiency limit for the conversion of solar radiation into work, the exergetic efficiency of the installation is evaluated. The results show that this first evaluation, seems to be adecuate acording to the results suggested in the open literature.

Keywords:

Direct steam generation modeling, parabolic collector, flow pattern, heat transfer, boiling

1. Introduction

The consequences of the socioeconomic model based on the consumption of fossil fuels have been so dramatic in recent years that no one denies that the current energy model is in crisis and, therefore, in the process of a fast and unstoppable transformation [1, 2]. It is urgent to shift from the current centralized system based on fossil fuels toward a system that is distributed, and based on renewable energies [3]. Among the energies that should make up an important part of the world's energy mix, solar energy undoubtedly stands out. Solar energy is clean, environmentally friendly, and freely available over the planet.

Concentrating solar power (CSP) plants, also known as solar thermal, is a commercial alternative to non-renewable energy sources such as oil, coal and nuclear power for the production of electricity, mainly with the use of parabolic trough solar fields. Most CSP facilities to date have implemented synthetic or mineral oil as a working fluid in the solar field. The main limitation of thermal oil is that at 400°C it begins to degrade, thus imposing a limitation on the maximum operating temperature of the thermodynamics power cycle, generally a steam Rankine cycle [4–6].

Alternatively, thanks to DISS loop at Plataforma Solar de Almería [7–10], it has been demonstrated that it is possible to work with the concept of direct steam generation (DSG), in which steam is generated directly in the solar field and then redirected to the power block turbine. The DSG has some technical advantages that must be considered [5, 7, 11]:

- There is no danger of contamination or fire due to the use of thermal oil
- Possibility of raising the maximum temperature of the Rankine cycle above 400°C, which is the limit imposed by the thermal oil currently used
- Reduction of the size of the solar field, thus reducing the investment cost
- Reduction of operating and maintenance costs, as thermal oil based systems require a certain amount of oil inventory that must be changed every year, as well as antifreeze protection when the air temperature is below 14 °C

However, the DSG process have several problems. For example, Almanza et al. operated a parabolic trough collector (PTC) plant to feed a low-power steam engine, highlighting the deflection problems suffered by low-temperature systems and controllability of the flow pattern [12, 13]. It is therefore necessary to carry out simulations to understand the thermohydraulics of the process. Up to date, there is considerable progress in

DSG analysis [11, 14, 15]. However, they all resort to the concept of classical heat transfer with the calculation of the convective coefficient *h*, in combination with the friction factor *f*, to understand the thermo-hydraulic behavior of the installation, even in CFD models [16, 17].

Nevertheless, the use of these parameters demands high computational power because the methodology to obtain these parameters requires an iterative process [18]. In this work, we apply the recently proposed and validated methodology for the analysis of DSG in PTC [19], with low computational times and high confidence, in which the use of the convective coefficients *h* is eliminated. The analysis is performed on a 10 MW conceptual plant located in northwestern Mexico.

1.1. Structure and scope

This article is organized in two parts. The first part outlines the thermohydraulic model and, subsequently, its application to the case study. This allows us to identify that the proposed methodology can be used without complications in the analysis of solar plants for direct steam generation in parabolic troughs.

2. Thermohydraulic modeling for DSG in PTC

The model to be developed takes as a reference the one described by other authors [20–25]. The present, uses the typical 1D modeling technique based on a steady-state energy balance over the receiver. The receiver is divided into smaller parts called Heat Collector Elements (HCE). The balance equations comprises direct normal solar irradiation, optical losses, HCE thermal losses, and the working fluid gains. The distinction of this model lies for the use of the heat transfer methodology developed by Adiutori [26]. This methodology does not require iteration to solve the heat fluxes and associated temperatures in the thermal model.

2.1. Energy balance equations

The working fluid temperature increases as the energy is absorbed by the HCE. Heat losses will occur as a result of differences between the average fluid temperature in each cross section and the ambient temperature. With Fig. 1, the following balance equations can be written:

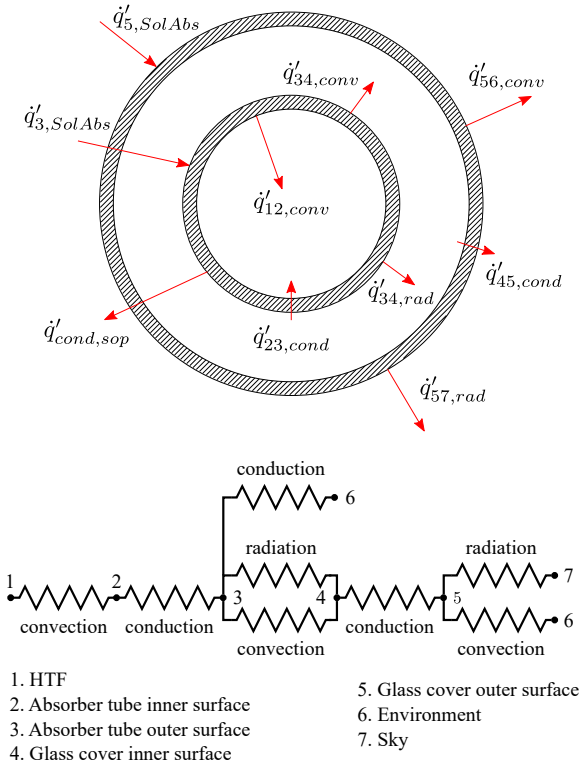

Figure 1: Heat fluxes over the parabolic trough.

$$\dot{q}'_{12,conv} = \dot{q}'_{23,cond} \tag{1a}$$

$$\dot{q}'_{3,SolAbs} = \dot{q}'_{34,conv} + \dot{q}'_{34,rad} + \dot{q}'_{23,cond} + \dot{q}'_{38,cond} \tag{1b}$$

$$\dot{q}'_{45,cond} = \dot{q}'_{34,conv} + \dot{q}'_{34,rad} \tag{1c}$$

$$\dot{q}'_{45,cond} + \dot{q}'_{5,SolAbs} = \dot{q}'_{56,conv} + \dot{q}'_{57,rad} \tag{1d}$$

$$\dot{q}'_{12,conv} = \frac{\dot{m}}{L_{HCE}} \left(h_{in} - h_{out}\right) \tag{1e}$$

For the five equations of 1, the radiation absorption phenomena in the absorber tube and the transparent cover are treated as surface heat fluxes. In addition, the temperatures, heat fluxes and all thermodynamic properties are uniform around the cross-sectional area (1D model) [27]. These simplifications lead to theoretical values larger than the real ones, but with adequate results [21]. Under these conditions, each heat flux can be expressed as:

$$\dot{q}'_{i,SolAbs} = \eta_o W G_{bn} \tag{2a}$$

$$\dot{q}'_{ij,cond} = \frac{2\pi k_{ij} \left(T_i - T_j\right)}{\ln\left(\frac{D_j}{D_i}\right)} \tag{2b}$$

$$\dot{q}'_{ij,rad} = \frac{\sigma\pi D_i \left(T_i^4 - T_j^4\right)}{\frac{1}{\varepsilon_i} + \frac{\left(1-\varepsilon_j\right) D_i}{\varepsilon_j D_j}} \tag{2c}$$

$$\dot{q}'_{ij,conv} = f\left(\Delta T\right) \tag{2d}$$

where $\eta_o = IAM\Gamma\rho\tau\alpha$ is the optical efficiency, W is the trough width, G_{bn} is the incident solar radiation in the normal direction, k is the conductivity, T is the temperature, D is the diameter, σ is the Stefan-Boltzmann constant, and ε is the emittance. The subscripts i and j allow us to identify each of the surfaces, according to Fig. 1.

Notice that 2d, omits the use of the convective heat transfer coefficient h, and a particular function of the temperature difference should be used. These functions must be obtained from the expressions of the Nusselt number, by means of a transformation of the dimensionless groups, as explained in [26].

The annulus formed between the absorber tube and the glass envelope is modeled as free convection between two cylinders because the receiver is evacuated. Between the glass cover and the environment the convection can be forced or natural. In the first case, the Žhukauskas equation is used, while the Churchill-Chu equation is adequate for the second case [28]. For the convection between the absorber tube and the heat transfer fluid, there are two cases: the Pethukhov or Gnielisnki equation [28] for the single phase fluid and the Gungor and Winterton correlation for the two-phase flow [29]. The transformation of the two-phase flow equation is described in [27], resulting in the following:

$$\Delta T = C_1 \dot{q}'_{12,conv} \left[C_2 \left(C_3 + C_4 \dot{q}'^{1.16}_{12,conv} \right)^2 + C_5 - \frac{C_6 \dot{q}'^{0.67}_{12,conv}}{C_7 \left(C_3 + C_4 \dot{q}'^{1.16}_{12,conv} \right)^2 - 1} \right]^{-1} \tag{3}$$

where each C_i is a functional parameter of the temperature, obviously positive ($C_i > 0$), which can be obtained from any database of thermodynamic properties. This equation can be used with confidence, as validated in [27] with data recovered from the DISS loop [10, 16].

3. Study case

A conceptual regenerative Rankine cycle with parabolic trough collectors using the DSG concept is under consideration. The power block is designed to produce 10 MW of net power output, fixing the conditions at the turbine inlet 100 bar and 673.15 K (400 °C), and 0.08 bar at the turbine outlet. A generic turbine with a nominal isentropic efficiency of 80% is selected, as it is a value suggested by other similar analyses [30]. The Rankine cycle employs two internal regenerations (see Fig. 2), which allow the inlet temperature of the solar field to be higher (496.121 K) and consequently the size of the parabolic trough loops to be smaller. The tubine steam extractions have been determined with the premise of minimizing the exergy destruction and consequently maximizing the second law efficiency. The process of this optimization can be found in [31, 32].

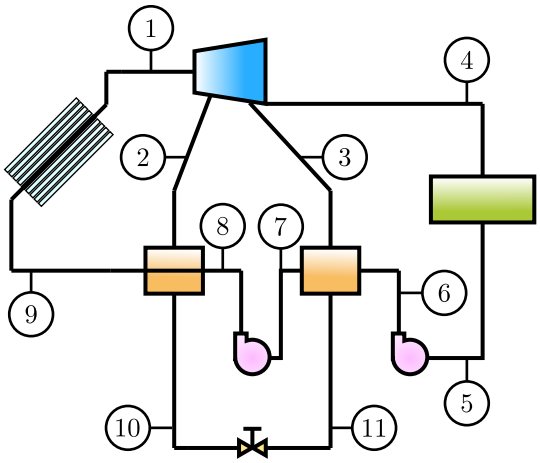

Figure 2: Schematic of the conceptual DSG Rankine power plant. Adapted from [31, 32].

With the operating conditions of the power block, 12.8058 kg/s of steam is needed to produce 10 MW of nominal power. Two conditions should be taken into account for DSG plants. The first is a mass flow rate that allows turbulent flow ($\mathrm{Re} > 2 \times 10^5$) to ensure an appropriate heat transfer between the absorber and the water/steam [9, 21]. Second, the annular flow pattern should be sought to avoid overheating in the absorber. However, at the beginning of the boiling process, the flow pattern may be intermittent and annular, as in the DUKE loop [33]. Dividing the mass flow rate into a certain number of loops allows us to fulfill the first consideration. At the end of the thermohydraulic characterization, the second consideration can be verified.

The analysis is carried out considering three days: June 21 (summer solstice), May 21 (highest insolation condition), and September 21 (lowest insolation condition). Therefore, there are a total of 24 simulations to be carried out. In all the cases, the HCE is fixed to 2 m. The weather conditions for the selected days in Agua Prieta (northwest Mexico) are described in Table 1. For the present analysis, the mass flow is divided into 8 loops; therefore, the mass flow rate per loop is 1.6007 kg/s, with Re = 3.699×10^5, fulfilling the first flow condition.

Table 1: Weather conditions for the selected simulation days in Agua Prieta, México. Data obtained from [34].

Parameter	21st june	21st may	21st september
DNI (W/m^2)	856.4815	889.6396	628.8580
Atmospheric pressure (bar)	0.886	0.884	0.885
Ambient temperature (K)	300.05	295.95	300.05
Sky temperature (K)	271.95	265.75	277.75
Wind speed (m/s)	4	4.1	3.2

For the two-steam extractions, the subcooled water must enter the solar field at 496.121 K. Once the fluid input conditions to the solar field are known, together with the normal weather conditions described in Table 1, it is possible to start with the simulations to thermo-hydraulically characterize the solar field, simultaneously solving 1. Knowing all the initial parameters and having defined the size of the HCE, the fluid starts its path along the loop, increasing its temperature and evidently suffering a pressure drop; until it reaches the saturated liquid condition. The fluid then undergoes a phase change from saturated liquid to saturated vapor in a non-isobaric process. An intermittent flow at the beginning of the boiling and annular in the rest of the process is expected. Finally, the fluid is superheated to a temperature of 673.15 K.

Figure 3 shows the temperature evolution along the loop. It is important to note that, as expected, the temperature during the phase change does not remain constant due to the pressure drop (as shown in detail in Fig. 4). The pressure drop decreases slightly the saturation temperature, which also affects the vapor-liquid mixture quality. It is evident that in the three days, the evaporation zone has a larger size since the phase change processes require a high demand of thermal energy to achieve this task.

As seen in Figure 4a, the pressure along the loop decreases until it reaches the required conditions at the turbine inlet (100 bar and 673.15 K). Figure 4b shows that the phase change region presents the highest pressure drop. It is important to note that the curve obtained shows an abrupt change in its slope, as occurs in the DISS loop [35].

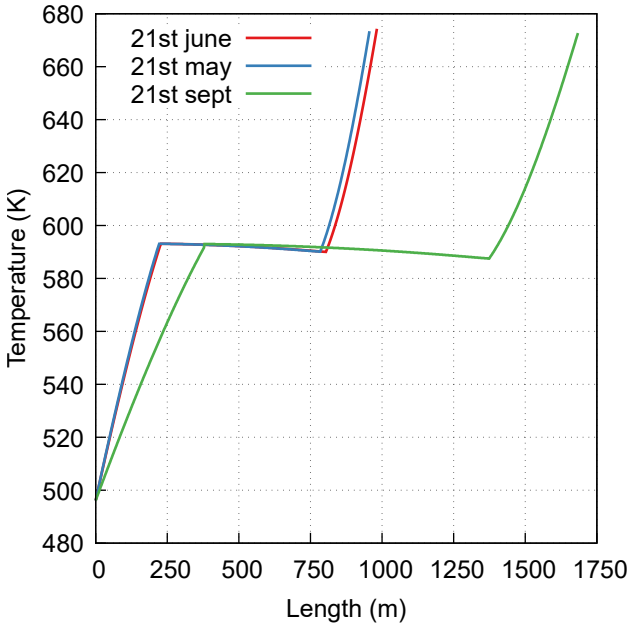

Figure 3: Evolution of the temperature increase along the loop.

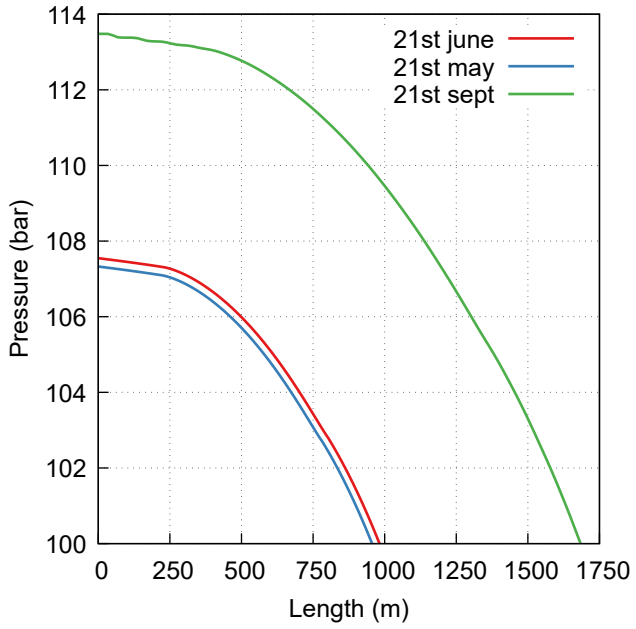

(a) Pressure evolution along the loop.

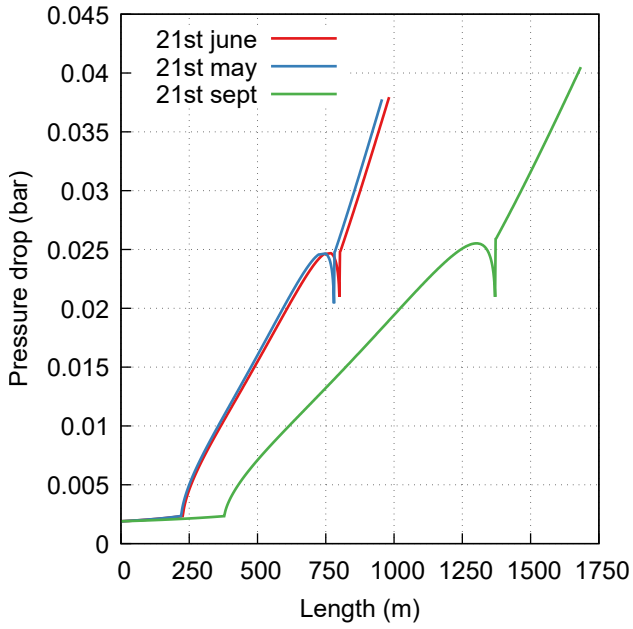

(b) Pressure drop along the loop.

Figure 4: Loop pressure characterization.

The flow pattern in the boiling process along the loop must be verified, as stated previously. Figure 5 shows the flow pattern in the two-phase flow region in the Taitel and Dukler flow map. While analyzing the graph for the Martinelli parameter X, an intermittent flow (high values of X) is present at the beginning of the boiling process, then changes to an annular flow as the steam quality increases (low values of X). Doing this verifies that the mass flow is adequate and meets the two established conditions: a high Re number to ensure a high heat transfer rate and a flow pattern that reduces overheating in the absorber.

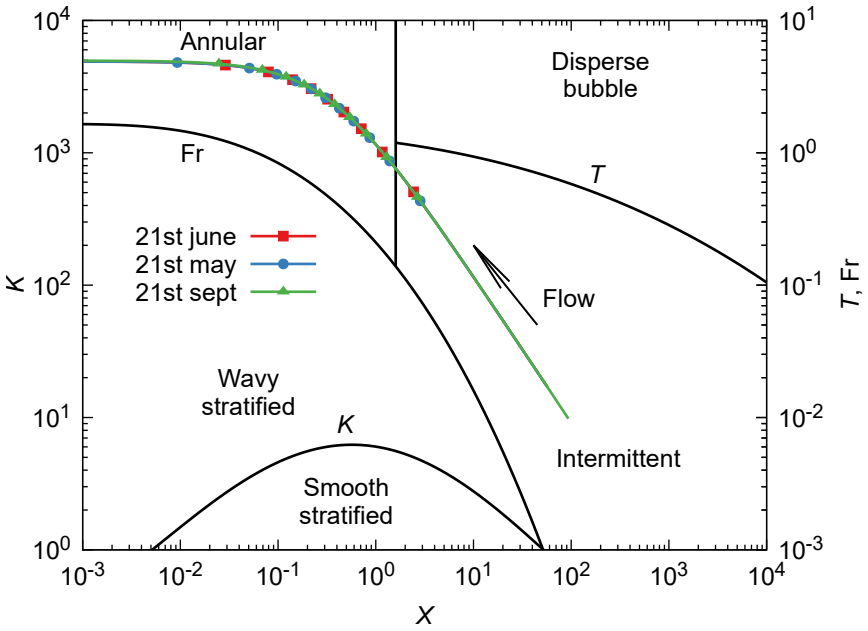

Figure 5: Flow pattern in the two-phase region.

When analyzing Figure 3, and as expected, the solar field has a longer length on the day of less insolation (September 21), being shorter for the day of greater insolation (May 21) although there is no substantial difference concerning the summer solstice (June 21). Since the total mass flow rate of the Rankine cycle was divided into eight loops, the total length of the PTC field must be multiplied by 8. It is possible to define the total concentration area for the solar field. These will allow us to define the type of arrangement of the loops in the solar field, since for areas greater than 40 ha, an "H" arrangement is recommended, while for less than 40 ha an "I" arrangement can be used [21, 36]. In Table 2, the precise loop length is shown, including the total area of the solar field, in addition, the pressure at the inlet of the solar field is also shown. In these three cases, the arrangement "H" is recommended.

Table 2: Solar field description.

Parameter	21st june	21st may	21st september
Preheater length per loop (m)	226	220	378
Evaportor length per loop (m)	578	570	1016
Superheater length per loop (m)	178	164	290
Total length per loop (m)	982	954	1684
Total concentrating area (ha)	4.53	4.41	7.78
Inlet pressure (bar)	107.55	107.33	113.48

The pressure evolution along the loop presents a similar behavior (Figure 4a). Since the September 21 loop is the longest, it will have higher pressure drops, so the solar field must be operated at a higher pressure (almost 114 bar). Figure 4b shows that the highest pressure drop occurs in the two-phase flow zone. The behavior at the phase change interfaces (saturated liquid and saturated vapor) presents an abrupt change in its slope (nondifferentiability condition), although as reported in [37], it is continuous.

Once all the operating parameters in the solar field (temperature and pressure) are known, it is possible to identify the flow pattern in the phase-change region. Although the loops have different lengths and pressure drops in the three cases of analysis, the flow at the beginning of boiling is intermittent. As the liquid transforms

into steam, the flow behaves as an annular. This behavior is desired in plants with the direct steam generation, so the feasibility of this loop is adequate.

Four additional parameters of great interest are usually computed for CSP plants: solar multiple (SM, 4), thermal energy storage size ($\dot{Q}_{TES}$, 5), energy (η_I, 6) and exergy (η_{II}, 7) efficiency of the PTC solar field. Considering that on September 21st, the loop is the largest, this day is considered as the design condition. If $SM > 1$, it is possible to include thermal energy storage (TES). For PTC, the SM must be below of 2 [6]. To date, there are no commercial TESs for DSG. However, a generic TES size system can be defined and rated accordingly. These four parameters are defined as:

$$SM = \frac{\dot{Q}_{solar\ field,design}}{\dot{Q}_{solar\ field}} = \frac{A_{ap} G_{bn}}{A_{ap,september} G_{bn}} \tag{4}$$

$$\dot{Q}_{TES} = (SM - 1)\, \dot{Q}_{solar\ field} \tag{5}$$

$$\eta_I = \frac{\dot{Q}_{HTF}}{\dot{Q}_{inc}} = \frac{\dot{m}\,(h_{out} - h_{in})}{A_{ap} G_{bn}} \tag{6}$$

$$\eta_{II} = \frac{\Delta \dot{E}x_{HTF}}{\dot{E}x_{inc}} = \frac{\dot{m}\,(ex_{out} - ex_{in})}{A_{ap} \dot{E}x_{solar}} \tag{7}$$

The exergy of solar thermal radiation is calculated with González-Mora formula [38]:

$$\eta = \left(1 - \frac{1}{\xi}\left[\frac{T_r}{T_{sun}}\right]^4\right)\left(1 - \frac{\lambda_c T_{amb}}{\lambda_c T_r + \xi\sigma T_{sun}^4 - \sigma T_r^4}\right) \tag{8}$$

where the optimum receiver temperature T_r must be obtained by solving $4\sigma^2 T_r^{11} - 8\sigma\lambda_c T_r^8 - 8\sigma^2\xi T_{sun}^4 T_r^7 + 4\lambda_c^2 T_r^5 - T_r^4\left(4T_{amb}\lambda_c^2 - 8\lambda_c\sigma\xi T_{sun}^4 - \lambda_c^2 T_{amb}\right) - \lambda_c^2 T_{amb}\xi T_{sun}^4 = 0$. In [38], it has been demonstrated that the exergy of solar radiation is $0.8391 G_{bn}$. Table 3 shows the solar multiple, the TES size, the energy efficiency and the exergy efficiency of the PTC solar field.

Table 3: Solar multiple and efficiencies of the solar loop.

Parameter	21st june	21st may	21st september
SM	1.72	1.77	1
TES (MW_t)	3.49	3.76	0
Energy efficiency (%)	70.38	69.49	56.05
Exergy efficiency (%)	40.71	40.78	32.23

4. Conclusions

The modeling of parabolic trough solar plants in direct steam generation remains crucial to understanding the operating behavior and, consequently, in their implementation. In this work, an alternative methodology for thermo-hydraulic characterization of these types of systems is used to characterize the solar field. The developed model, unlike other models, eliminates the use of the convective coefficient h and the friction factor f. This allows a fast computation, with confident results.

The thermohydraulic model was applied for the analysis of the conceptual direct steam generation plant in Agua Prieta (Northwestern Mexico). The 10 MW Rankine cycle was previously optimized to minimize the destruction of exergy. As a result, 12.8058 kg/s of steam at 100 bar and 673.15 K (400 °C) is required. With the restriction of maintaining a turbulent flow, the mass flow rate has been divided into 8 loops; each loop circulating 1.6007 kg/s of water/steam entering at 496,121 K, with a maximum pressure of 113.48 bar.

Three days have been analyzed for the conditions of highest insolation (21st may), minimum insolation (21st september) and the summer solstice (21st june), considering their respective weather conditions for each day. As a result, the total length of each loop has been defined first, where it turns out that the longest loop is for

21st september (1684 m, 7.78 ha in total). This loop is considered as the design field. Once the loop length has been defined, the flow pattern type in the two-phase zone has been characterized. It is identified that for the three days of analysis, the flow at the beginning of the boiling is intermittent and later evolves towards an annular flow, which is the one suggested in DSG plants.

Finally, the solar multiple has been calculated, showing that for the design condition, the solar multiple is not excessively large, so the loop is adequate, with a capacity of 3.76 MW. Similarly, the PTC energy efficiency has a maximum value of 70.38% (and 56.05% minimum), while the PTC exergy efficiency has a maximum value of 40.78% (and 32.23% minimum).

Acknowledgments

Authors acknowledge CONACyT for a graduate scholarship for EGM (863595).

Nomenclature

Letter symbols

- A area, m^2
- C temperature functional parameter, -
- D diameter, m
- ex specific exergy, kJ/kg
- $\dot{E}x$ total exergy rate, W
- G irradiation, W/m^2
- h heat transfer coefficient, W/m^2K; specific enthalpy, kJ/kg
- IAM incidence angle modifier, -
- k conductivity, $W/m \cdot K$
- L lenght, m
- $\dot{m}$ mass flow rate, kg/s
- $\dot{q}'$ heat flux per unit length, W/m
- $\dot{Q}$ heat transfer rate, W
- Re Reynolds number, -
- SM solar multiple, -
- T temperature, K
- W parabolic collector aperture, m
- X Martinelli parameter, -

Greek symbols

- α receiver absorptivity
- Γ intercept factor
- ε receiver emittance
- η efficiency
- λ thermal conductance per unit length, $W/m \cdot K$
- χ concentration acceptance product
- ρ mirror reflectivity
- σ Stefan-Boltzmann constant

Subscripts and superscripts

amb ambient

ap aperture

bn beam normal

cond conduction

conv convection

HCE heat collector element

i generic counter

I first law

II second law

j generic counter

in inlet

inc incident

o optic

out oulet

r receiver

solar solar

SolAbs slar absorption

Solar field, design solar field in design conditions

Solar field solar field

rad radiation

References

[1] A. Leon-Grossmann, "Renewables—the politics and economics behind them," in *Sustainable Energy Technologies*, CRC Press, 2017, pp. 29–44.

[2] IRENA, "Global Energy Transformation: A roadmap to 2050," International Renewable Energy Agency, Abu Dhabi, Tech. Rep., 2018.

[3] B. Cozen, D. Endres, T. R. Peterson, C. Horton, and J. T. Barnett, "Energy communication: Theory and praxis towards a sustainable energy future," *Environmental Communication*, vol. 12, no. 3, pp. 289–294, 2018.

[4] IEA, "Technology Roadmap – Solar Thermal Electricity," Paris, France, Tech. Rep., 2014, p. 52. [Online]. Available: www.iea.org.

[5] M. Romero, J. Gonzalez-Aguilar, and E. Zarza, "Concentrating Solar Thermal Power," in *Energy Efficiency and Renewable Energy Handbook, Second Edition*, ser. The CRC Press Series in Mechanical and Aerospace Engineering, CRC Press, Sep. 2015, pp. 1237–1345, ISBN: 978-1-4665-8508-9. DOI: 10.1201/b18947-47.

[6] E. Z. Moya, "Chapter 7 - parabolic-trough concentrating solar power systems," in *Concentrating Solar Power Technology*, K. Lovegrove and W. Stein, Eds., Second Edition, UK: Woodhead Publishing, 2021, pp. 219–266. DOI: https://doi.org/10.1016/B978-0-12-819970-1.00009-8.

[7] M. Eck and W.-D. Steinmann, "Direct Steam Generation in Parabolic Troughs: First Results of the DISS Project," *Journal of Solar Energy Engineering*, vol. 124, no. 2, pp. 134–139, Apr. 2002, ISSN: 01996231. DOI: 10.1115/1.1464125. [Online]. Available: http://solarenergyengineering.asmedigitalcollection.asme.org/article.aspx?articleid=1456439%20https://doi.org/10.1115/1.1464125.

[8] M. Eck, E. Zarza, M. Eickhoff, J. Rheinländer, and L. Valenzuela, "Applied research concerning the direct steam generation in parabolic troughs," *Solar Energy*, vol. 74, no. 4, pp. 341–351, Apr. 2003, ISSN: 0038-092X. DOI: 10.1016/S0038-092X(03)00111-7. [Online]. Available: https://www.sciencedirect.com/science/article/pii/S0038092X03001117.

[9] E. Zarza Moya, "Generación directa de vapor con colectores solares cilindro parabólicos. Proyecto DIrect Solar Steam (DISS).," Ph.D. dissertation, Universidad de Sevilla, 2003, pp. 1–480. [Online]. Available: http://www.tdx.cat/handle/10803/114351.

[10] M. Eck and W.-D. Steinmann, "Modelling and Design of Direct Solar Steam Generating Collector Fields," *Journal of Solar Energy Engineering*, vol. 127, no. 3, pp. 371–380, Aug. 2005, ISSN: 0199-6231. DOI: 10.1115/1.1849225.

[11] A. Giglio, A. Lanzini, P. Leone, M. M. Rodríguez García, and E. Zarza Moya, "Direct steam generation in parabolic-trough collectors: A review about the technology and a thermo-economic analysis of a hybrid system," *Renewable and Sustainable Energy Reviews*, vol. 74, no. March 2016, pp. 453–473, 2017, ISSN: 18790690. DOI: 10.1016/j.rser.2017.01.176. [Online]. Available: http://dx.doi.org/10.1016/j.rser.2017.01.176.

[12] R. Almanza, A. Lentz, and G. Jiménez, "Receiver behavior in direct steam generation with parabolic troughs," *Solar Energy*, vol. 61, no. 4, pp. 275–278, 1997, ISSN: 0038-092X. DOI: https://doi.org/10.1016/S0038-092X(97)88854-8. [Online]. Available: https://www.sciencedirect.com/science/article/pii/S0038092X97888548.

[13] R. Almanza and A. Lentz, "Electricity production at low powers by direct steam generation with parabolic troughs," *Solar Energy*, vol. 64, no. 1, pp. 115–120, 1998, ISSN: 0038-092X. DOI: https://doi.org/10.1016/S0038-092X(98)00046-2. [Online]. Available: https://www.sciencedirect.com/science/article/pii/S0038092X98000462.

[14] M. T. Islam, N. Huda, A. B. Abdullah, and R. Saidur, "A comprehensive review of state-of-the-art concentrating solar power (CSP) technologies: Current status and research trends," *Renewable and Sustainable Energy Reviews*, vol. 91, pp. 987–1018, Aug. 2018, ISSN: 1364-0321. DOI: 10.1016/J.RSER.2018.04.097.

[15] A. Sandá, S. L. Moya, and L. Valenzuela, "Modelling and simulation tools for direct steam generation in parabolic-trough solar collectors: A review," *Renewable and Sustainable Energy Reviews*, vol. 113, p. 109 226, Oct. 2019, ISSN: 1364-0321. DOI: 10.1016/J.RSER.2019.06.033. [Online]. Available: https://www.sciencedirect.com/science/article/pii/S1364032119304265?via%7B%5C%%7D3Dihub.

[16] D. H. Lobón, E. Baglietto, L. Valenzuela, and E. Zarza, "Modeling direct steam generation in solar collectors with multiphase CFD," *Applied Energy*, vol. 113, pp. 1338–1348, Jan. 2014, ISSN: 03062619. DOI: 10.1016/j.apenergy.2013.08.046.

[17] R. K. Pal and K. Ravi Kumar, "Thermo-hydrodynamic modeling of direct steam generation in parabolic trough solar collector," in *Proceedings of the 7th International Conference on Advances in Energy Research*, M. Bose and A. Modi, Eds., Singapore: Springer Singapore, 2021, pp. 131–140, ISBN: 978-981-15-5955-6.

[18] A. Bejan, *Heat Transfer: Evolution, Design and Performance*. Hoboken: John Wiley & Sons, 2022.

[19] E. González-Mora and M. D. Duran García, "Propuesta de eliminación del coeficiente convectivo h para el modelado de flujo bifásico en concentradores parabólicos," in *XVIII Congreso Ibérico y XIV Congreso Iberoamericano de Energía Solar*, Mallorca, 2022.

[20] R. Forristall, "Heat Transfer Analysis and Modeling of a Parabolic Trough Solar Receiver Implemented in Engineering Equation Solver," National Renewable Energy Laboratory, Colorado, Tech. Rep., 2003. [Online]. Available: https://www.nrel.gov/docs/fy04osti/34169.pdf.

[21] M. J. Montes Pita, "Análisis Y Propuestas De Sistemas Solares De Alta Exergía Que Emplean Agua Como Fluido Calorífero," Ph.D. dissertation, Universidad Politécnica de Madrid, 2008, p. 323.

[22] R. Vasquez Padilla, "Simplified Methodology for Designing Parabolic Trough Solar Power Plants," Dissertation, University of South Florida, 2011, p. 283. [Online]. Available: https://scholarcommons.usf.edu/etd/3390.

[23] J. Sun, Q. Liu, and H. Hong, "Numerical study of parabolic-trough direct steam generation loop in recirculation mode: Characteristics, performance and general operation strategy," *Energy Conversion and Management*, vol. 96, pp. 287–302, May 2015, ISSN: 01968904. DOI: 10.1016/j.enconman.2015.02.080. [Online]. Available: https://www.sciencedirect.com/science/article/pii/S0196890415002010?via%7B%5C%%7D3Dihub%20http://dx.doi.org/10.1016/j.enconman.2015.02.080.

[24] P. D. Tagle Salazar, “Thermo-hydraulic performance modeling of thermal energy systems using parabolic trough solar collectors,” Ph.D. dissertation, Instituto Tecnológico y de Estudios Superiores de Monterrey, 2018. [Online]. Available: http://hdl.handle.net/11285/632662.

[25] A. A. Hachicha, I. Rodríguez, and C. Ghenai, “Thermo-hydraulic analysis and numerical simulation of a parabolic trough solar collector for direct steam generation,” *Applied Energy*, vol. 214, pp. 152–165, Mar. 2018, ISSN: 0306-2619. DOI: 10.1016/J.APENERGY.2018.01.054. [Online]. Available: https://www.sciencedirect.com/science/article/pii/S0306261918300667?via%7B%5C%%7D3Dihub.

[26] E. Adiutori, *The New Engineering*, 3rd ed. Naples, FL: Ventuno Press, 2017, p. 315, ISBN: 978-0-9626220-4-5.

[27] E. González-Mora and M. D. Duran García, “Validation of an Alternative Methodology for Direct Steam Generation Modelling in Parabolic Collectors,” in *EUROSUN2022*, 2022.

[28] T. L. Bergman, A. S. Lavine, F. P. Incropera, and D. P. Dewitt, *Fundamentals of Heat and Mass Transfer*, 7th ed. New York: John Wiley & Sons, Inc., 2011, p. 1048, ISBN: 9780470501979.

[29] K. Gungor and R. Winterton, “A general correlation for flow boiling in tubes and annuli,” *International Journal of Heat and Mass Transfer*, vol. 29, no. 3, pp. 351–358, 1986, ISSN: 0017-9310. DOI: https://doi.org/10.1016/0017-9310(86)90205-X. [Online]. Available: https://www.sciencedirect.com/science/article/pii/001793108690205X.

[30] L. Coco-Enríquez, J. Muñoz-Antón, and J. M. Martínez-Val, “Innovations on direct steam generation in linear Fresnel collectors,” in *SolarPACES2013*, vol. 00, 2013, p. 45 721.

[31] E. González-Mora and M. D. Durán-García, “Energy and Exergy (2E) Analysis of an Optimized Solar Field of Linear Fresnel Reflectors for a Conceptual Direct Steam Generation Power Plant,” *Energies*, vol. 14, no. 14, p. 4234, Jul. 2021, ISSN: 1996-1073. DOI: 10.3390/en14144234.

[32] E. González-Mora and M. D. Durán-García, “Approaching a lfr direct steam generation power plant towards an endoreversible heat engine,” in *Advanced Energy Technologies and Systems I*, A. Zaporozhets, Ed. Cham: Springer International Publishing, 2022, pp. 21–44, ISBN: 978-3-030-85746-2. DOI: 10.1007/978-3-030-85746-2_2. [Online]. Available: https://doi.org/10.1007/978-3-030-85746-2_2.

[33] J. F. Feldhoff, T. Hirsch, R. Pitz-Paal, and L. Valenzuela, “Analysis and potential of once-through steam generators in line focus systems – Final results of the DUKE project,” *AIP Conference Proceedings*, vol. 1734, no. 1, p. 100 006, 2016, ISSN: 0094-243X. DOI: 10.1063/1.4949194.

[34] Meteotest, *Meteonorm*, Bern, Switzerland, 2018. [Online]. Available: https://www.meteonorm.com/.

[35] M. Eickhoff, “Incident angle modifier of the ls-3-diss-collectors,” Internal report of the DISS project. Doc. ID: DISS-SC-SF-30, Tech. Rep., 2002.

[36] E. González-Mora, “Análisis 2E de diferentes configuraciones de plantas solares de generación directa de vapor empleando reflectores Fresnel,” M.S. thesis, Universidad Autónoma del Estado de México, 2019, p. 179.

[37] G. L. Tomei, *Steam: its generation and use*. Ohio: Babcock & Wilcox Company, 2015.

[38] E. González-Mora, R. Poudel, and M. D. Durán-García, “A practical upper-bound efficiency model for solar power plants,” *Journal of Non-Equilibrium Thermodynamics*, Feb. 2023, ISSN: 0340-0204. DOI: 10.1515/jnet-2022-0080. [Online]. Available: https://www.degruyter.com/document/doi/10.1515/jnet-2022-0080/html.

Feasibility of solar photovoltaic energy as an energy source for the electrowinning of zinc in South Africa

Ricardo Magdalena[a], Nicole Uys[b], and Jochen Petersen[c]

[a] Research Centre for Energy Resources and Consumption (CIRCE) - Universidad de Zaragoza, Zaragoza, Spain; rmagdalena@unizar.es CA
[b] Mineral to Metals Initiative, Department of Chemical Engineering, University of Cape Town, Cape Town, South Africa, uysnic002@myuct.ac.za
[c] Mineral to Metals Initiative, Department of Chemical Engineering, University of Cape Town, Cape Town, South Africa, jochen.petersen@uct.ac.za

Abstract:

Energy consumption for metal extraction and beneficiation is substantial and is expected to keep growing due to increased demand. With rising worldwide energy prices and the continued energy crisis in South Africa, there is a need to decrease the dependence on the national energy grid. Among the refining processes, electrowinning is one of the most energy intensive unit operations. In the context of zinc, electrowinning can consume on average 2,900-3,300 kWh/t-zinc, approximately accounting for 60% of the total electricity consumption of refined zinc production. Industrial and economic growth, a major focus of Southern African countries, is positively correlated with zinc demand due to its role in general construction, electricity transmission, and telecommunications. South Africa is endowed with 14 Mt of zinc content within 200-300 Mt of zinc ore reserves and expanding internal zinc production capacity is a current focus. Since electrowinning units operate with low-voltage direct current, photovoltaic solar energy appears to be an applicable green energy source due to its electricity output also being low-voltage direct current. In addition, South Africa has an attractively high solar irradiance (220 W/m^2 compared with Europe's 100 W/m^2). Hence, an investigation into the technical and economic feasibility of substituting or supplementing the energy demand, using solar energy for the electrowinning unit of a theoretical zinc refinery operating in the Northern Cape of South Africa, is warranted. A high-level carbon footprint analysis is included. The findings from this study could assist in stabilising the energy supply for the beneficiation of zinc in South Africa, as well as contribute to the decarbonisation of the industry.

Keywords:

Zinc refining, electrowinning, solar energy, photovoltaic cells, South Africa

1. Introduction

The applications of metals within society are ubiquitous [1]. This continued, and increasing, demand for metals results in a substantial consumption of energy related to metal extraction and beneficiation. The embodied energy associated with metal production (mining, beneficiation and refining) can range from 20 MJ/kg refined metal (Pb, steel) to 200 MJ/kg refined metal (Al, Ni) and should be taken into consideration in conjunction with the annual production of metals when determining the total annual energy consumption per metal. While mining is reported to account for between 2-11% [2] (average reported value is 3.5% [3], [4]) of total global energy consumption, the energy consumption associated with metal refining processes (leaching, smelting, electrowinning etc.) typically far exceed that of mining activities. For instance, the following metals and alloys, namely copper nickel, zinc, lead, aluminium and steel, collectively consume approximately 6% of the annual global energy production, while depending on the source of energy production, they can account for up to 10% of the global greenhouse gas emissions [5], [6].

The following trends are the major driving factors for the increasing metal demand: population growth, increased urbanisation, electrification and renewable energy technologies [7], [8]. In conjunction with the United Nations prediction [9] that in the next 30 years the world's population may increase by 2 billion people, the World Bank [10] anticipates that the urban population will more than double by 2050. In order to accommodate this trend, there will be a focus on building infrastructure which will increase demand for certain metals, such as zinc (galvanised steel) [11]. In addition, societies focus on electrification, in the aim of achieving carbon neutrality, will not only increase demands for metals associated with green energy generation technologies but also on those for energy storage [12], [13]).

Several authors have already studied and predicted this increasing demand [14], [15], with Figure 1 illustrating the predictions from the last decades until 2100 [1]. Other authors have corroborated these trends with predictions for zinc [16] and copper [17] being of the same order of magnitude. This increased demand for metals will translate into increased metal production. However, one must ensure this is achieved in a 'sustainable' manner with due regard for the sources of energy used which will impact the industries' energy stability and carbon footprint.

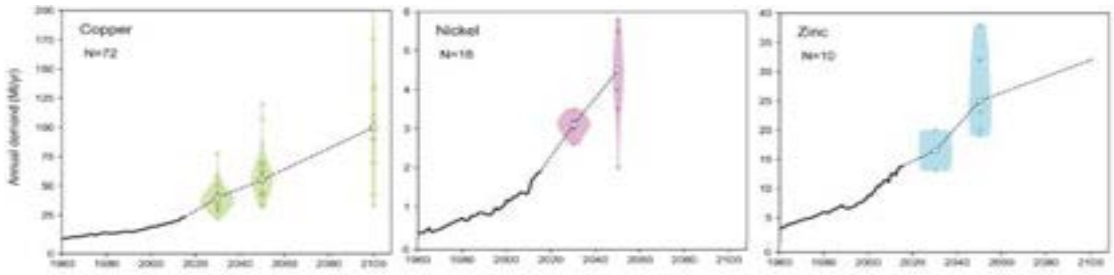

Figure 1. Historical and projected future outlook demand for copper, nickel and zinc from 1960 to 2100 [1].

To meet the demand created by electrification and population growth the global power consumption is also projected to increase by 50% between 2020 and 2050 [18], [19]. However, the world is currently in a Global Energy Crisis [7]. What started in 2021 as a supply and demand imbalance, emerging out of the COVID pandemic, has been exacerbated, primarily, by the invasion of Ukraine by Russia in February 2022. As Russia is seen as the world's largest exporter of fossil fuels and thus the interplay of sanctions and supply curtailment has exposed Europe's historic dependence on Russia for natural gas, oil and coal [7]. In some countries additional environmental factors such as droughts (Brazil and China) have also contributed to the crisis at a more local scale [20]–[22]. As a result of the current Global Energy Crisis there has been a high volatility in the prices for metals, gas and electricity. As a result of the high electricity prices, there are refineries in Europe which have been forced to either halt or reduce production capacity. The Budel refinery in Belgium, from the company Nyrstar, is one such example [23]. The IEA emphasised that this energy crisis is not a "clean energy crisis" as it believes the world should be relying on larger quantities of "green energy" to address this crisis and thereby creating more secure energy systems [7]. The hope is that this Global Energy Crisis will serve as a catalyst for policy makers and consumers to fast track the implementation of renewable green energy technologies.

Figure 2. Annual electricity generation (in thousands of GWh/yr) by source, in South Africa in 2020. Energy sources, other than coal and oil, are characterised further by % [7].

South Africa is also facing an energy crisis, although this crisis predated the current Global Energy Crisis. In 1998, a White Paper on the Energy Policy of the Republic of South Africa predicted that electricity demand would exceed generation capacity by 2007 [24]. As this warning was not heeded, the country started experiencing nationwide blackouts (referred to as load-shedding) in the latter part of 2007 and which continues to this day. Eskom is the state-owned utility company which has a monopoly on the electricity generation within South Africa, which is also highly centralised. The country has historically and continues to be primarily reliant on coal as its source of electricity generation [7]. As of 2020, coal represents 88% of energy generation, with nuclear and renewables representing 4% and 7% respectively (Figure 2). This is in comparison with the world average dependence on coal being 36.5% and renewable energies being 26% [25]. Despite South Africa's attractively high solar irradiance (220 W/m2 compared with Europe's 100 W/m2), solar PV only represents 1.5% of the electricity generation capacity at an estimated 3600 GWh/yr [24], [26]. The authors believe the application of solar PV within the local metals beneficiation and refining industries represents an opportunity for South Africa.

At the end of 2007, the National Energy Regulator of South Africa (NERSA) commissioned a Renewable Energy Feed in Tariff (REFiT), which was approved in March 2009, as a mechanism to promote the generation

of renewable energy within South Africa by creating certainty for investors. Effectively the REFiT was a purchase power agreement at fixed prices, which varied according to the renewable energy source. As of 2008, over 36 other countries (including Spain, Germany, certain states in the USA, Brazil, and even Kenya) had REFiT's [27], [28]. However, in 2011, the Department of Energy revised this scheme and replaced it with a more conventional procurement process, called the Renewable Energy Independent Power Producer Programme (REIPPP), which was based on a competitive pricing model, where independent power producers bid for the development of renewable power plants [28].. In particular, the application of Feed in Tariff (FIT) for small-scale embedded generation systems (SSEG) rests with the individual municipality / city. The City of Cape Town (CoCT) is one of the few South African cities which has successfully implemented a FiT for SSEG where households can receive approximately 0.04 $/kWh with the caveat that the household/business must be a net consumer of electricity (from the CoCT) over a 12-month period.

Load-shedding is a scheduled means of rotating the available electricity amongst Eskom's customers. The reason load-shedding is implemented is to prevent the entire electricity system from failing [29]. As a result, mining contracted by 9% in 2022 and many industries and companies are at the point of closure [30]. The need to stabilise the national energy system and ensure stability of energy availability is paramount to the minerals and metals industry. In response to their inability to provide a stable power supply and to incentivise private sector participation in addressing the continued load-shedding, in 2021 the South Africa government increased the embedded generation (self-generation) capacity licensing threshold from 1 MW to 100 MW [31].

While there are many metals which could be considered within the South African context, the refining of zinc has been chosen for this particular study. Zinc is the fourth most consumed metal globally [32] and as it readily reacts with oxygen, forming a protective zinc oxide layer, its primary use (>50%) is for galvanising of steel [33]. Other major uses include zinc-based alloys and brass production [33]. For the same aforementioned reasons that metal demand is expected to increase, the demand for zinc is also expected to increase. Zinc demand has been positively correlated with industrial and economic growth by White [34] and as both are key focus areas for Southern African countries the demand for zinc consumption is expected to increase. In order to obtain zinc at an economically competitive price, the focus on local production is expected to increase. South Africa is endowed with 14 Mt of zinc content [35] within 200-300 Mt of zinc ore reserves [36] which it is in the process of beneficiating (at Gamsberg with proposals to re-explore the Prieska Copper-Zinc Project). However, since the closure of Exxaro's Zincor Plant in 2011/2012, it no longer locally refines zinc metal. Zincor closed due to rising 'administrative costs', of which a contributing factor may have been the 2008/2009 zinc metal price depression [37] and in addition is speculated to have been due to rising electricity costs [34]. Given the renewed interest in exploring the refining of zinc and given the current energy supply crisis faced by the country, it is proposed to explore the potential application of solar PV within the zinc refining process within the context of South Africa.

The most energy intensive step in the traditional refining process (Roast-Leach-Electrowinning process) for zinc is electrowinning, which uses direct current (DC) to deposit zinc, typically from a purified zinc sulphate solution, onto cathodes. It consumes on average 2,900-3,300 kWh/t-zinc, accounting for approximately 60% of the total electricity consumption of refined zinc production [38]. As photovoltaic (PV) systems represent an established 'green' energy technology to produce DC electricity, it appears that a solar PV system is the most appropriate 'green' technology to generate electricity for this purpose. The application of solar PV for the provision of electricity for the zinc electrowinning unit operation would mean that losses in the electricity generation system would be minimised as no rectification from DC/AC is required, contributing to energy efficiency and loss minimisation, as well as contributing to the decarbonisation of the industry.

2. Case study

As previously mentioned, the Minerals Council of South Africa estimates that South Africa has 14 Mt of zinc content [35] within its 200-250 Mt of zinc ore reserves with the Northern Cape Province (specifically near the mining town of Aggeneys) containing significant deposits of these Lead-Zinc ores [39]. In particular the Gamsberg deposit, located approximately 30 km from Aggeneys, which is one of the largest zinc deposits in the world, is estimated to have approximately 12.8-13.9 Mt of Zinc content within its 214 Mt ore body (6-6.5% Zn) and a life of mine (LoM) of over 30 years [40]. As this one area accounts for nearly all the estimated zinc content within South Africa it is the most likely location for a future zinc refining facility and will thus form the focus area for this case study. This theoretical refinery, proposed in this study, would use the Roast-Leach-Electrowinning process, as this process accounts for 80-95% of all zinc production, with a production capacity of 50,000 tons of refined zinc per year. As zinc refineries can range in capacity from 30,000 tons refined zinc produced per year to 450,000 tons per year, the proposed 50,000 tons per year would be considered a small refinery.

Aggeneys is a copper, zinc, silver lead mining complex and was developed to service the Black Mountain Mine. Vedanta is the current majority owner of both Black Mountain and Gamsberg. With respect to climate Aggeneys is classified as semi-desert [41] and water is pumped from the Orange River (approximately 40 km away). In terms of Photovoltaic Power potential, Aggeneys is one of the world's prime locations with high solar irradiance (daily totals of 5.6 h corresponding to approximately 2,000 kWh/kWp) [42].

There is already a 46 MW (117 GWh/yr) solar PV power project which was commissioned in July 2020 in Aggeneys (Aggeneys Solar PV Park) and is designed to power 20,000 homes. It is owned by BioTherm Energy, cost $54.7m to build, and has a 20-year contract with Eskom under a power purchase agreement. It consists of 140,640 single axis tracking polycrystalline silicon PV modules and covers an area of 110 hectares [43]. This indicates the theoretical feasibility of designing and installing a solar PV plant in this location and the possibility of power purchase agreements with Eskom to possibly sell excess energy back to the grid if need be.

3. Methodology

Traditionally, solar resource / solar irradiance maps, which provide the average available hours of sun per day, were used for this purpose. However, there are now software packages available which can provide this and other important data, such as irradiance depending on the angle, azimuth, temperature, etc. Once the location, in this instance the Northern Cape, and other parameters such as the angle and azimuth are identified, it is possible to obtain the data monthly, daily, or even hourly. The software used in this project was the Photovoltaic Geographical Information System (PVGIS), provided as a free tool for the European Commission (EC) and the Joint Research Centre (JRC). As a general rule, solar PV installations located in the Southern hemisphere must face North (Northern hemisphere must face South) in order to maximise the amount of irradiation received. Furthermore, depending on the purpose of the installation, the slope angle must be equal to the latitude, or plus / minus 10º, depending on whether more irradiation is required in winter or summer.

For this study, the azimuth chosen is 180° (North facing), while the optimum angle, determined after a sensitivity analysis carried out, has been set up as 30°. This sensitivity analysis is shown in Figure 3, where it is possible to see the irradiation with different azimuth and angles. There are two figures which illustrate the best configuration in terms of azimuth. As can be seen, Figure 3a (left) has the least variance, having more or less the same irradiation during the whole year. Conversely, Figure 3b (right) shows an inverted Gauss bell, obtaining high irradiation (>265 kW/m2) during the summer months (from October to March), while in winter months (from April to September) the irradiation is very low (<20 kW/m2). Since the electrowinning plant is designed to work during the whole year, the most applicable configuration is Figure 3a (180° azimuth) which results in approximately the same amount of irradiation every month of the year (i.e. least deviation from the average irradiance value).

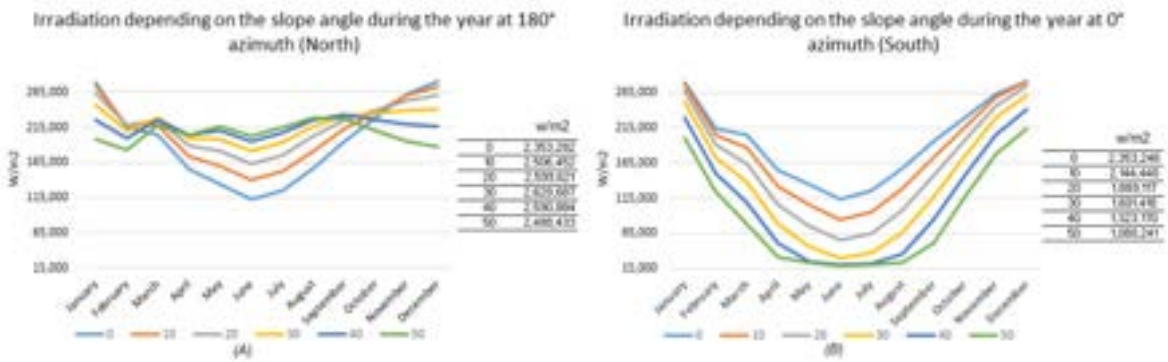

Figure 3. Annual irradiation in the Northern Cape, South Africa, with two different angles of azimuth chosen (180º and 0º). Tables on the right of the Figures summarize the total amount of irradiance per year depending on the slope of the solar panels.

Once the azimuth has been chosen, the angle of the solar panels needs to be determined. As aforementioned, this slope can vary according to the specifications of the facility. For the purpose of this study, the best configuration will be considered as the one with the highest irradiance. Thus, it has been decided to use all the irradiation for every hour in the year 2020, to obtain the cumulative irradiation at the end of the year. As it is possible to see in the data table included in Figure 3a, the highest irradiation occurs when the solar panels are inclined 30º. Therefore, and following this criterion, the configuration chosen for the solar plant is 180º for the azimuth, and 30º for the slope.

Different scenarios have been identified to analyse the performance of the solar plant according to the power installed and the operating time. Currently, the plant is assumed to be operating 24 h/day. However, this is not possible to carry out a 24h/day operation exclusively using solar PV technology as other technologies would be needed to supply electricity during the night, either as power generation (grid supply) or additional storage capacity (batteries).

Accordingly, two more scenarios have been analysed to determine the feasibility of the plant with respect to its hours of operation, while keeping annual zinc production the same. The first is operating the electrowinning plant for only 6 h/day. This operation time is designed around maximising the hours of sun per day that is possible to obtain, during wintertime. This means that even in winter it could be possible to produce the quantity

of zinc required, with the possibility of increasing the operation time in summer months, as more hours of sun per day are available. The second scenario is operating for 12 h/day and trying to strike a balance between maximising solar PV electricity generation while balancing the costs of storage capacity / alternative energy sources. In this way, it has been proposed that there will be three different operating durations for the electrowinning plant: 24 h/day, 12 h/day, and 6 h/day.

The electrowinning plant is designed to achieve a production of at least 50,000 tons per year, which is the current production, operating 24 h/day. For all scenarios considered, this annual production value must be reached by the end of the year, irrespective of whether operation times change. For that purpose, if the operation times are reduced, the capacity of the electrowinning plant must be increased, being multiplied two times if the operation time is reduced to 12 h/day and four times if the plant is reduced to 6 h/day. With the above three different operating time scenarios, an energy and economic assessment will be carried out taking into account that the scenarios are applied in the following cases: 1) Grid tie only (basis for comparison as this is the benchmark), 2) Solar plant and grid tie, 3) Solar Plant and Batteries (off grid), 4) Solar Plant with no Batteries (off grid).

3.1. Grid tie only

Electrowinning units worldwide are typically connected through a country's national / regional electricity grid. Grid tie is therefore the benchmark for all other scenario comparisons detailed below. Since no additional technologies (additional energy generation nor energy storage) are used in this option, the electrowinning process will be designed to operate 24 h/day. The capacity of the plant would be costed for a production of 50,000 tons refined Zn/day. The economic assessment in this case, in terms of electricity cost, would be simply multiplying the electricity demanded by the electrowinning plant with the current price of the electricity. Operating the electrowinning plant 12 h/day or 6 h/day would result in an unnecessary doubling and quadrupling of the capacity of the electrowinning unit, if the same annual production is to be achieved. In this event, the economic assessment would be calculated similarly to the 24 h/day case, however, additional electrowinning capacity would be needed (increased CAPEX costs), solely increasing the final economic costs without any perceived financial gain.

3.2. Solar PV plant and grid tie

This scenario is the most widespread when supplementing electricity supply with solar PV, in particular for households and businesses that are located in close proximity to the grid. This scenario combines a new solar PV plant with the traditional way of obtaining electricity from the grid. One of the main reasons to keep the connection to the grid, is to ensure that in principle there will always be electricity for the plant. This assumes there is no load-shedding. The grid connection mitigates a scenario where there is a drop in embedded generation due to cloudy and rainy days and accommodates for during the night without the necessity to invest in storage capacity or other power generation technologies. It is anticipated that all three operation times are applicable and achievable with this configuration. When the operation times are reduced, the capacity of the electrowinning plant must increase in order to reach the required production throughput. In addition, the power capacity of the proposed solar PV plant must increase in order to produce the increased electricity supply required to maintain annual production. Therefore, the CAPEX of the additional electrowinning units and the increased size of the solar PV plant must be included and added to the final price calculated. This scenario is therefore about balancing the increased capital expense of an increased electrowinning plant and increased solar PV plant with a lower payment for electricity from the grid. The break-even point of each of these scenarios would need to be determined.

3.3. Solar PV plant and batteries

There are currently limited technologies available for storing energy at large scale. The largest being dammed hydroelectricity, however, this application is location specific requiring the available land and water to make it viable. As Aggeneys is classified as semi-desert, dammed hydroelectricity production does not appear to be a viable option. Another option which is starting to make an appearance within the mining industry is the production and storage of hydrogen with excess electricity which can then be converted back to electricity when needed. This should be explored further in future studies, particularly for large scale projects. Although batteries are capable of storing a certain amount of energy, they are widely used in small (household) solar plants. They are unfortunately still very inefficient, since batteries based on lead cannot be discharged more than 40%, while those based on lithium it is possible to use up to 80% [44]. Depending on the type of battery utilised, some metals used for their manufacture are classified as ‘critical’ and may therefore be expensive due to limited supply. Despite their high cost, batteries were deemed by the authors to be the simplest storage option for this study.

There are different technologies in batteries that can be applied to store energy. The most known are the based on lead-acid (considered the traditional) and those based on lithium [44]. The batteries based on lead-acid are very inefficient since they cannot be discharged more than 40%, otherwise the lifespan could be shortened, being already not very long, since the best technology for this kind of batteries is gel, with a lifespan lower than 750 cycles [44]. On the other side, batteries based on lithium have an efficiency higher than 80%,

spotting the LTO (variation of the crystalline structure), which has a lifespan higher than 5,000 cycles [44]. The main disadvantage of this battery is that is very expensive (six more times than lead-acid), and this can increase the initial investment. However, this study, lithium batteries have been chosen due to them being the most efficient energy storage system. However, other options should be explored in future studies.

3.4. Solar PV plant with no batteries

This option would only make sense for the configuration of the lowest operation time, namely 6 h/day, since 12 h/day and 24 h/day would inherently require a storage capacity or an alternative source of energy supply because the sun is not available for that length of time. Running an electrowinning plant solely with a solar plant must therefore be carried out during the day, when the sun is shining. The reason for proposing this scenario is due to the well-known fact that batteries (energy storage) represent a significant cost and therefore the feasibility of operating without storage capacity was proposed. However, given that solar irradiance fluctuates within a day and with the seasons, it is already known that a consistent throughput is impossible to maintain. The authors are not anticipating that this scenario will be technically feasible to achieve without a more detailed design where throughput can be increased during the peak solar irradiance hours.

4. Design and performance of the plant

4.1. Power of the solar PV plant

The capacity of the solar plant will dictate the amount of electricity which can be generated. For this study, the solar plant must be designed to achieve the production expected at the end of the year, namely 50,000 tons of refined zinc. The first step to start the design is calculating the power capacity. To that aim, it is needed to convert the zinc generated at the end of the year into power units. It has been taken from the literature review the specific energy to produce 1 ton of zinc in an electrowinning cell, being a range from 2,900 kWh to 3,300 kWh. 2,900 kWh was chosen as the best-case scenario for the initial investigation. If these values are multiplied by total annual tons of zinc produced and divided by the total hours working during the year (the current operation time is 8760 h/yr), it is possible to determine the power needed in 1 h (see Equation 1).

$$Power\ Demand = \frac{50{,}000\ tons\ Zn \times \frac{2{,}900\ kWh}{tons\ Zn}}{8760\ h} = 17\ MW \quad (1)$$

This means that it is necessary to install a solar plant of 17 MW to achieve the specified zinc production. However, and for the reasons explained in the next section, this power must be higher due to losses incurred, as well as the fluctuating electricity produced during the day and depending on the season. To determine the most appropriate power capacity for each of the three operation times proposed, Figure 4 has been presented.

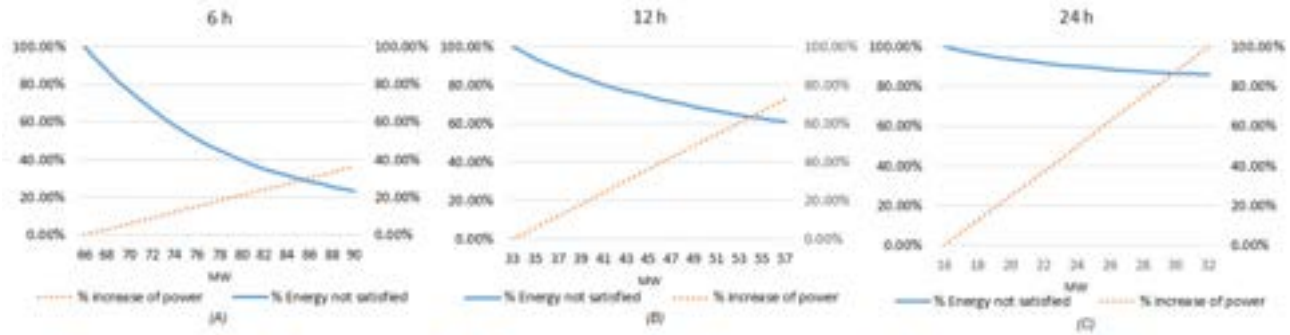

Figure 4. Comparison between the increased power capacity of the solar PV plant (left axis) with the electricity demand not-satisfied by the solar plant as a % (right axis).

As shown, the power required for 24 h operation starts with the 17 MW calculated, while for the 12 h and 6 h are 33 MW and 66 MW, respectively. From these power capacities, as a starting point, the power capacity will be linearly increasing and compared with the electricity not-satisfied from the solar plant, starting at 100% and being reduced when the power installed increases. The electricity not-satisfied can be defined as the electricity needed to supply from another alternative source, either from a green energy or from grid, due to the solar plant not being able to supply all the electricity demanded at certain times.

Although it would make sense to choose the best/optimal power capacity of each solar PV plant as the point at which a % increase in power capacity is no longer greater or equal to the % decrease in energy not-satisfied, given the curvature of the graph, this point is reached very quickly with the 12 h scenario and is never possible with the 24 h scenario. The optimal/best power capacity was therefore chosen as the intersection point between the curve for energy not-satisfied and the line for increasing power capacity of the solar PV plant. The authors felt that for this high-level study this approach balanced the increasing CAPEX association with increasing the power capacity of the proposed solar PV plant while still achieving a reasonable electricity production.

In this way, it is seen that for the 24 h operation time it is needed to increase the power by 90%, to 30 MW, to reduce this electricity by approximately 20% (i.e., 80% of the energy requirements are still not-satisfied). In the case of the 12 h operation time, the power must be increased by 60% approximately to decrease the electricity not-satisfied by 40%. The last chart could be the most interesting option, in terms of electricity exploitation, since increasing the power installed only 25%, the electricity not-satisfied can be reduced by 75%.

This could be explained by the fact that the solar plant works only 6 h, most of the time is running when the sun is out. This means that the exploitation of the solar plant could have a higher efficiency with this operation time. Nevertheless, since an assessment of the performance and economic will be carried out with all scenarios, it has decided to choose the best power for each operation time, being 30 MW for 24 h, 55 MW for 12 h and 85 MW for 6 h, as can be seen in Figure 4.

4.2. Electricity generation

The performance of the solar plant electricity production depends on the power installed and how this electricity can be used to supply the energy to the electrowinning plant. Once the irradiance has been calculated for the specific location and the power selected for the different operation times, it is necessary to know the specifications of the solar panels to install. For this analysis, solar panels from a local supplier were chosen, with the details summarised in Table 1, and the electricity generated per hour calculated with equation 2.

Table 1. Specifications of the solar panels.

Type	Lifetime	Power	Surface	Efficiency
Monocrystalline	25 years	400 W	2 m^2	21%

$$Electricity\ Generated = Irradiance \times Surface \times Efficiency \quad (2)$$

By cumulating the electricity generated every hour of the year (determined using Equation 2), it is possible to analyse the quantity of energy which can (1) be produced, (2) is self-consumed and (3) the excess electricity. Figure 5 and Table 2 summarise the above data, calculated for the different operation times proposed.

Figure 5. Performance of the solar PV plant designed according to the operation times.

As can be seen in Figure 5, the highest electricity generation (due to solar PV) is produced when the operation time is smaller since the power capacity installed is higher. This makes sense as the higher the power capacity installed, the more panels have been installed and therefore the surface to absorb the irradiance from the sun is larger which translates into higher electricity generation. However, in order to see the performance of the three different operation times, it is important to check how much electricity is not being satisfied by the solar plant. While the demand is constant for the three scenarios, it is shown that the electricity not-satisfied is increasing when the operation time is longer. This is explained by the fact that there is an electricity demand when it is dark with the operation times of 12 h and 24 h. These numbers can be seen in Table 2, where the energy not-satisfied from the total demand is 26.68 % and 62.41 %, for 12 h/day and 24 h/day, respectively. On the other hand, this number drops to less than 5 % when it is operated 6 h/day. Therefore, it is not possible to accomplish these requirements for 12 h/day and 24 h/day with the solar plant alone, so an alternative energy source is required to supplement the electricity demand and keep the electrowinning unit operating.

One of the most important disadvantages of running the electrowinning plant for only 6 h/day is the amount of excess energy generated. Since the plant is only working for 6 h, there are hours during the day that some electricity is being produced and cannot be used, so it would either be (1) wasted, (2) stored in batteries, or (3) sold back to the grid. This is reflected in the self-consumption data being the lowest of the three cases analysed.

Table 2. Annual data calculated according to the solar PV power capacity installed.

Operation time	Power installed	Energy generated	Excess Energy	Self-consumption	Energy not-satisfied	Energy not-satisfied
6 h/day	85 MW	215,845 MWh	77,250 MWh	64.21 %	4.42 %	6,408 MWh
12 h/day	55 MW	139,662 MWh	33,352 MWh	76.12 %	26.68 %	38,690 MWh
24 h/day	30 MW	76,179 MWh	21,670 MWh	71,55 %	62.41 %	90,491 MWh

The following should be noted for the 6 h/day operation. For the combination of solar PV and grid tie backup power, it can be seen from Table 2 that very little energy is needed from the grid (4.42%) to supplement electricity supply and given that excess energy far exceeds the energy not-satisfied (77,250>>6,408 MWh) that the plant is actually likely to be a net provider of electricity to the grid. A Feed in Tariff (FiT) would need to be negotiated with Eskom or the local municipality. There is a similar situation with batteries, as opposed to grid tie, in that excess energy significantly outweighs energy not-satisfied at all times of the year. Therefore, the addition of battery storage capacity should comfortably allow the operation of the electrowinning plant for the 6 hour/day operational schedule. Unfortunately, as there is no tie to the grid, the excess energy which does not need to be stored will be wasted unless an alternative use can be found. It is recommended that further studies investigate lowering the power capacity installed (<85 MW) and increase battery capacity to minimise energy losses. Finally, with respect to solar only (no batteries and no grid tie) unfortunately at this specific power capacity it is unable to entirely meet demand. This is evident by the fact that there is a % of energy not-satisfied. The only way to still meet the annual demand for zinc is firstly to increase the power capacity of the plant ensure the total energy is always satisfied, however this will increase the excess energy which is wasted. The other alternative is to increase the capacity of the electrowinning unit such that during the middle of the day the throughput can be increased to compensate for lower throughput at the beginning and end of the day. However, the economic feasibility of this trade-off would need to be explored in a further study.

The following should be noted for the 12 h/day operation. For the combination of solar PV and grid tie backup power, it can be seen from Table 2 that the energy not-satisfied is fairly significant at 26.68% and electricity from the grid is therefore essential to maintain operations. In addition, as the energy not-satisfied is similar, although still slightly larger than the excess energy (38,690>33,352 MWh), the plant will be a net importer of electricity from the grid. A negotiated FiT is still encouraged to minimise the expense of buying energy from the grid. When using batteries as a storage capacity it can be seen that there is insufficient excess energy generated to be able to be stored and resupplied by the batteries to the plant. The power capacity of the solar plant would need to be increased (at least by 3 MW) above the proposed 55 MW and would also need to account for losses involved in storing the DC energy in the DC batteries. Luckily the high losses associated with DC/AC conversion can be avoided in this process. A solar only supply is unfeasible as can be seen by the aforementioned 26.68%.

The following should be noted for the 24 h/day operation. For the combination of solar PV and grid tie backup power, it can be seen from Table 3 that the energy not-satisfied is high at 62.41% and significantly greater than the excess energy (90,491>>21,670 MWh) meaning that once again the plant is a net importer of electricity from the grid. At the current power capacity of 30 MW, the battery scenario is therefore unfeasible and would require at least an additional 30 MW of capacity to generate sufficient electricity to charge at the batteries. Once again, the scenario with a stand-alone solar operation is unfeasible due to the large amount of energy not-satisfied within the system.

Table 3. Summary of the technical feasibility of the various scenarios under the current constraints**.**

	Electrowinning operating hours and solar PV power capacity (if applicable)		
	6 h/day (85MW)	12 h/day (55 MW)	24 h/day (30 MW)
Grid Only	N/A	N/A	✔
Grid + Solar	✔	✔	✔
Solar + Batteries	✔	?	X
Solar Only	?	N/A	N/A

N/A= not applicable / scenario not investigated; ✓ = technically feasible; ? = not technically feasible under the current conditions, however, requires further investigation as technical feasibility was borderline; X = not technically feasible under the current conditions.

4.3. Key assumptions and limitations of the study

The following key assumptions have been made during this investigation. The plant operates for 365 days a year with no down time and the effect of loadshedding is not taken into account. Electricity use within the zinc plant, other than electrowinning, is not included. The cost of electricity was assumed to stay constant

throughout the day and year. A 25-year lifespan was assumed for all economic calculations. Lastly, it is assumed that the quality of zinc will be unaffected if the electrowinning unit runs for only 12 h/day or 6 h/day. It is acknowledged that if some of the above parameters were altered the results may be affected and that further investigations with sensitivity analyses are needed to determine the effect that each assumption has on the results.

5. Economic assessment

The aim of this study is to determine the most economically feasible option(s) of the aforementioned scenarios. To be able to implement an economic assessment, certain factors must be included, such as the price of solar panels and batteries, the capital cost of an electrowinning unit at different scales, electricity price from the grid, price for the compensation of extra energy being fed back into the grid (Feed in Tariff) etc. In addition, the methodology of Levelized Cost of Energy (LCOE) has been applied. This methodology was applied in order to obtain a value to measure the average cost of generating one kilowatt hour (Megawatt hour in this case, MWh) of electricity over the lifetime of a generating asset. The LCOE takes into account the costs associated with a system, including installation, operation, maintenance, and fuel. The average cost per year (over 25 years) has also been determined in Table 5 to provide the easiest comparison amongst the scenarios.

As obtaining electricity solely from the grid has been deemed the benchmark, this value will be calculated first. It must be noted that the price for the power supplied from the grid (Eskom) is assumed to remain constant (no peak hour costs), even though it varies in quantity amongst the different operating times. Based on this, it has been calculated that the electricity cost (OPEX) associated with obtaining electricity solely from the grid is $ 10,585,000 ($ 10.585 M) for the 2022/2023 year. Further Eskom electricity price increases are expected as outlined in Table 4.

The capital cost of the zinc electrowinning unit was estimated using capital cost data from a copper electrowinning unit [45]. The CAPEX for the solar PV plant was taken as the 2021 worldwide estimate for solar installations which is $ 857 per kW [46] which was comparable to the $/kWh value quoted by Green Pro Consulting of $ 778/kWh [47]. The prices applied to the various scenarios, are summarised in Table 4.

Table 4. Costs associated with the various solar PV plant designs.

Price of grid (Eskom) supplied electricity [39]	FiT (based on CoCT) [48]	CAPEX associated with different scales of the Electrowinning Unit			CAPEX for Solar PV plant [46]	CAPEX for battery storage (Lithium)
		6 h/day (85 MW)	12 h/day (55 MW)	24 h/day (30 MW)		
$ 73 / MWh*	$ 18 / MWh	$ 150 M	$ 75 M	$ 35 M	$ 857,000 / MW	1,005 $/kWh

The final LCOE price is determined by the power installed, as the more power installed the more panels are needed. Accordingly, it is also necessary to include the operation and maintenance (O&M) costs, which is usually calculated as the 10% per year of the capital cost. Using these values and the LCOE method, to calculate the feasibility of the design for a 25 years of lifespan, it has been calculated that the LCOE price for the 6 h/day, 12 h/day and 24 h/day are $ 80.66 /MWh, $ 65.77 /MWh and $ 57.87 /MWh, respectively (without taking into account the batteries). Although the price calculated for the 6 h/day scenario is higher than the price from the grid in 2022, it should be noted that once the proposed 18% price increase takes effect, all scenarios will be cheaper ($/MWh) than the grid-only price. In addition, having the embedded generation capacity (through solar PV) provides additional advantages compared with solely relying on the grid connection for electricity supply. As discussed in the introduction, as South Africa continues to experience load-shedding it results in interrupted power supply on almost a daily basis which is affecting the production of all industries including mining and refining of metals. Having an independent embedded electricity generation capacity will therefore reduce / eliminate this situation while also having the advantage of decreasing the pressure on the national grid. If excess “green” electricity can be returned to the grid it will also have an added benefit to the stabilising of the grid as well as contributing to meeting renewable energy targets.

Table 5. Summary of the average total cost per year (25 years) for the various scenarios [million $/year].

	Electrowinning operating hours and solar PV power capacity (if applicable)		
	6 h/day (85MW)	12 h/day (55 MW)	24 h/day (30 MW)
Grid Only	N/A	N/A	10.59
Grid + Solar	13.79	10.38	9.79
Solar + Batteries	1,045	6,230	14,555
Solar Only	14.79	N/A	N/A

The most economical configuration is therefore operating a solar plant for 24 h/day with a combination of grid and solar energy supply. It should be noted that the grid only price of $ 10.59 million/year is expected to increase to $ 12.47 million/year in 2023/2024 as an 18% increase is expected and to $14.07 million/year by 2025 when a further 12% increase is expected. The Eskom supplied electricity cost is expected to continue to increase. With this understanding one can see that all solar and grid options will become more economical than only being supplied by the grid over the 25-year life of the project. With respect to different operating times, the grid and solar option at longer operating times makes more economic sense as it requires less additional capital expenditure in the form of additional electrowinning capacity and additional solar capacity. As can be seen, under no circumstances is the scenario of solar and batteries economically feasible. However, in this scenario it can be seen that, as expected, shorter operating times results in a smaller capital cost (less batteries required) and thus is more economical than longer operating times. Lastly, the reason the solar and grid combination for 6 h/day is more economical than solar stand alone is the benefit gained from selling electricity back to the grid.

6. Conclusions

A stable (and economical) electricity supply is one of the key necessities that society (households and companies) requires. Unfortunately, there are a number of factors which are generating volatility in terms of the supply and cost of electricity. Globally, a major factor in the increasing price of electricity is the Russian-Ukrainian war, with some European countries experiencing an increase of up to 200%, while on a local scale South Africa is struggling with insufficient generation capacity, ageing infrastructure amongst other factors. The hope is that globally and at the local level, these challenges will promote the implementation of increasing quantities of alternative (renewable) energy sources to alleviate dependence on fossil fuels and or countries' national energy grids.

Different scenarios were analysed to determine the optimal incorporation of solar PV for the electricity substitution for zinc electrowinning, namely: grid only, solar and grid supply, solar and battery storage, and a stand-alone solar supply. Although the ideal would be to maximise reliance on embedded generation capacity, it needed to be determined as to where this optimal point currently is. It should be acknowledged that this optimal may change over time. In addition, the operational times were varied (24h, 12h and 6h) in order to determine the trade-off between increased capital costs associated with increasing the size of electrowinning units and solar plant power capacity as the operational time decreased) and the increased costs of energy storage (as operational timeless increased). Accordingly, it has been demonstrated that the best orientation for the solar panel is facing South with a slope of 30º, obtaining the highest electricity production within a year, and ensuring similar monthly generation.

With this configuration, the most promising scenario to maximise reliance on embedded energy generation, is running the electrowinning plant for 6 hours per day. The reason being that it had the lowest energy not-satisfied (< 5% of the total electricity demanded in a year), while the 12 h and 24 h scenarios resulted in 27% and 64% energy not-satisfied. In addition, since the power installed in 6h case is higher than the other scenarios, there will also be excess energy that can be introduced into the grid which may assist in stabilising the grid while the company owning the zinc plant may derive economic benefit. While the 6 h/day solar can feasibly be combined with a grid or battery supply to cover the energy not-satisfied, under the current solar power capacity of 85 MW, running on a stand-alone solar PV plant (no batteries) is not feasible. The power capacity of the solar PV plant would either need to be increased or there would need to be an increase in the capacity of the electrowinning plant to allow for a higher throughput during peak irradiation hours.

The most economical configuration is operating a solar plant for 24 h/day with a combination of grid and solar energy supply. Further studies should investigate how varying only the size of the solar plant will affect the economics in this scenario. Under no circumstances was the solar and battery scenarios economically feasible with the current price of lithium batteries. Future studies should explore alternative energy store options.

One of the main disadvantages of installing solar plants is the amount of land that is needed to produce the electricity expected. For the best-case scenario (6 h/day), from an energy generation perspective, the land use would be 0.425 km2, taken into account only the panels. This number can increase from 30-50%, up to 0.64 km2 after adding the separation between panels and rest of equipment. Choosing the option of installing the lowest number of panels (30 MW plant operating for 24 h/day), the land use can still be in excess of 0.25 km2, which is still significant. However, compared to the existing 46 MW solar PV plant in Aggeneys, which is 110 hectares (1.1 km2) the proposed land area per MW installed is significantly less. In addition, Aggeneys as a town not pressurised for space (i.e., it is not densely populated), therefore the space requirements are not anticipated to be problematic.

One benefit from this study is that the approach can be applied to similar industries/unit operations where the electricity is needed in direct current form, which avoids additional losses incurred when converting from DC to AC and vice versa. For instance, it could be applied to electrowinning plants for other metals located in other areas such as Europe. Other locations may have advantages or face different challenges, for instance in

Europe although there are established FiT schemes, the solar irradiance is significantly lower and there may be more space constraints.

This study has demonstrated that the incorporation of solar PV into the energy supply mix for a zinc electrowinning plant can be beneficial. To that end, governments such as South African government must incentivize the continued investigation and investment into solar PV and other renewable energy sources which can improve the energy stability of the country as well as meet the increasing worldwide expectations on decarbonation within the minerals and metals industry.

Acknowledgement

This paper has received funding from a European Commission project called Treasure, with Gran Agreement Number: 101003587.

References

[1] T. Watari, K. Nansai, and K. Nakajima, “Major metals demand, supply, and environmental impacts to 2100: A critical review,” *Resour. Conserv. Recycl.*, vol. 164, no. August 2020, p. 105107, 2021, doi: 10.1016/j.resconrec.2020.105107.

[2] E. B. Oussama, “The Role of the Mining Industry in the Energy Transition,” *InfoMineo*, 2020. https://infomineo.com/mining-industry-in-energy-transition/ (accessed Mar. 08, 2023).

[3] M. Allen, “Mining Energy Consumption 2021,” 2021.

[4] Engineering and Mining Journal, “New Report Defines Mining’s Energy Intensity,” 2021. [Online]. Available: https://www.e-mj.com/breaking-news/new-report-defines-minings-energy-intensity/.

[5] J. Rankin Csiro, “Energy Use in Metal Production,” *High Temp. Process. Symp.*, no. Table 1, pp. 7–9, 2012, [Online]. Available: https://publications.csiro.au/rpr/download?pid=csiro:EP12183&dsid=DS3.

[6] H. Ritchie, M. Roser, and P. Rosado, “Energy,” *OurWorldInData.org*, 2021. https://ourworldindata.org/energy (accessed Feb. 03, 2023).

[7] International Energy Agency, “Database Documentation,” 2023.

[8] IEA, “Key World Energy Statistics 2020,” 2020. [Online]. Available: https://www.iea.org/reports/key-world-energy-statistics-2020.

[9] “WORLD POPULATION TO 2300,” *United Nations*, p. 254, 2004.

[10] Worldbank, “Urban development,” *The World Bank*, 2022. https://www.worldbank.org/en/topic/urbandevelopment/overview (accessed Jan. 03, 2023).

[11] G. G. Graf, “Zinc Ullmann’s encyclopedia,” *Encycl. Ind. Chem.*, p. 23, 2005.

[12] McKinsey and Company, “Global Energy Perspective 2022 McKinsey ’ s Global Energy Perspective is a collaboration between Energy Insights and adjacent practices,” *Exec. Summ.*, no. April, 2022, [Online]. Available: https://www.mckinsey.com/~/media/McKinsey/Industries/Oil and Gas/Our Insights/Global Energy Perspective 2022/Global-Energy-Perspective-2022-Executive-Summary.pdf.

[13] L. Grandell, A. Lehtilä, M. Kivinen, T. Koljonen, S. Kihlman, and L. S. Lauri, “Role of critical metals in the future markets of clean energy technologies,” *Renew. Energy*, vol. 95, pp. 53–62, 2016, doi: 10.1016/j.renene.2016.03.102.

[14] ILZSG, “International Lead and Zinc Study Group,” *Int. Organ.*, vol. April, no. Press Release, p. 4, 2018, doi: 10.1017/s0020818300009838.

[15] International Energy Agency, “Total cobalt demand by sector and scenario, 2020-2040,” *The Role of Critical Minerals in Clean Energy Transitions*, 2021. .

[16] R. Magdalena, A. Valero, A. Valero, and J. Palacios, “Mining energy consumption as a function of ore grade decline: the case of lead and zinc,” *J. Sustain. Min.*, vol. 20, no. 2, pp. 109–121, 2021, doi: https://doi.org/10.46873/2300-3960.1060.

[17] P. Jose-Luis *et al.*, “The energy needed to concentrate minerals from common rocks: The case of copper ore,” *Energy*, vol. 181, no. August, pp. 494–503, 2019, doi: 10.1016/j.energy.2019.05.145.

[18] C. Sourmehi, “EIA projects nearly 50% increase in world energy use by 2050, led by growth in renewables,” *Today in Energy*, 2021. https://www.eia.gov/todayinenergy/detail.php?id=49876# (accessed Feb. 03, 2023).

[19] H. Bauer, L. Gigliotti, F. Liebacj, B. Smeets, C. Tryggestad, and R. Winter, “Unlocking opportunities from industrial electrification,” *McKinsey’s Advanced Industries and Global Energy & Materials Practices*, p. 1, Jul. 18, 2022.

[20] Reuters, “Brazil warns of energy crisis with record drought,” *Aljazeera. Business and economy*, 2021. https://www.aljazeera.com/economy/2021/9/1/brazil-warns-of-energy-crisis-with-record-drought (accessed Mar. 05, 2023).

[21] P. Trevisani and J. Lewis, “Brazil’s Drought Pressures Power Grid, Boosting Case for Renewables—and Fossil Fuels,” *The Wall Street Journal*, p. 1, Oct. 11, 2021.

[22] L. Scott, “China’s Drought Threatens Nation’s Energy, Food and Economic Security,” *Climate change*, 2022. https://www.voanews.com/a/china-s-drought-threatens-nation-s-energy-food-and-economic-security-/6725241.html.

[23] M. F. F. Achmad Ali Fikri, Syamsul Arifin, “Metals: at the heart of Europe,” 2022.

[24] Department of Energy, *White Paper on the Energy Policy of the Republic of South Africa*, no. December. 1998.

[25] Statista, “Distribution of electricity generation worldwide in 2021, by energy source.” p. 1, 2021.

[26] South African Government, “Overview of Solar power,” *Energy Sources. Renewable Energy*, 2023. https://www.energy.gov.za/files/renewables_frame.html.

[27] International Energy Agency and International Renewable Energy Agency, “Renewable Energy Feed-in Tariff (REFIT),” 2013. [Online]. Available: https://www.iea.org/policies/4786-renewable-energy-feed-in-tariff-refit.

[28] R. E. Feed, “NERSA Consultation Paper Renewable Energy Feed - In Tariff,” *Renew. Energy*, no. December, pp. 1–14, 2008.

[29] Joburg Department, “What is Load Shedding?” https://www.joburg.org.za/departments_/Pages/MOEs/city power/What-is-load-shedding.aspx.

[30] A. Madubela, “Load-shedding hits mining output,” *Mail & Guardian*, p. 1, 2023.

[31] The Presidency, “President announces major reform to enable investment in embedded generation and promote energy security,” 2021.

[32] T. Christie and B. Brathwaite, “Mineral Commodity Report 6 — Lead and Zinc,” *New Zeal. Min.*, vol. 16, pp. 22–30, 1995, [Online]. Available: https://www.nzpam.govt.nz/assets/Uploads/doing-business/mineral-potential/zinc.pdf.

[33] R. J. Sinclair, “The Extractive Metallurgy of Zinc,” *Australas. Inst. Min. Metall.*, vol. 13, p. 297, 2005.

[34] T. Creamer, “SA’s power prices approaching affordability ‘tipping point,” *Polity*, 2011. https://www.polity.org.za/article/sas-power-prices-approaching-affordability-tipping-point.

[35] M. E. Best, “Mineral Resources,” *Treatise Geophys. Second Ed.*, vol. 11, pp. 525–556, 2015, doi: 10.1016/B978-0-444-53802-4.00200-1.

[36] C. J. Van Niekerk and C. . Begley, “Zinc in South Africa,” *J. South African Inst. Min. Metall.*, vol. 91, no. 7, pp. 233–248, 1991.

[37] Trading Economics, “Zinc Trade,” *Commodities*, 2023. https://tradingeconomics.com/commodity/zinc (accessed Oct. 03, 2023).

[38] R. J. Sinclair, “The Australasian Institute of Mining and Metallurgy spectrum series.” 2005, [Online]. Available: https://catalogue.nla.gov.au/Record/3106763.

[39] Global Petrol Prices, “Electricity prices,” 2023. [Online]. Available: https://www.globalpetrolprices.com/electricity_prices/.

[40] Vedanta, “Gamsber, more than a mine,” vol. 44, no. 0. pp. 1–4, 2019.

[41] C. Grobler, “Aggeneys Information,” *Info South Africa*. https://www.infosa.co.za/provinces/northern-cape/northern-cape-town-cities/aggeneys/.

[42] Global Solar Atlas, “Western Cape Government,” 2023. https://globalsolaratlas.info/download/south-africa.

[43] B. Renewables, “Aggeneys Solar,” *Press release*, 2021. https://bterenewables.com/aggeneys-solar-pv/.

[44] A. Townsend and R. Gouws, “A Comparative Review of Lead-Acid, Lithium-Ion and Ultra-Capacitor Technologies and Their Degradation Mechanisms,” *Energies*, vol. 15, no. 13, 2022, doi: 10.3390/en15134930.

[45] 911 Metallurgist, “SX EW Capital & Operating Cost of Solvent Extraction & Electrowinning,” 2017. [Online]. Available: https://www.911metallurgist.com/sx-ew-capital-operating-cost/.

[46] Statista, “Average installed cost for solar photovoltaics worldwide from 2010 to 2021.” p. 1, 2021.

[47] GreenPro Consulting, “Solar Power Systems,” 2013. [Online]. Available: http://www.greenpro.co.za/pv systems.htm.

[48] W. C. Government, “Small-Scale Embedded Generation (SSEG) Feed-In Tariff Map,” 2023. https://www.westerncape.gov.za/static/solar-pv-mapping/ (accessed May 03, 2023).

Design and simulation of a Banki cross-flow wind turbine for highways under high turbulence and high altitude conditions

Eduard Matheo Alave-Vargas[a], Valentina Rita Villarroel-Beltrán[a], Renán Orelllana Lafuente[a], Cecilia Tapia-Siles[b] and Daniel Felipe Sempértegui-Tapia[a]

[a] Laboratorio de Energías Alternativas, Centro de Investigaciones Ópticas y Energía, Universidad Privada Boliviana, Cochabamba, Bolivia, dsempertegui@upb.edu, CA
[b] Laboratorio de Innovación Tecnológica Industrial y Robótica, Universidad Privada Boliviana, Cochabamba, Bolivia.

Abstract:

The objective of this study is to design an optimal vertical axis wind turbine (VAWT) for electric generation on a high-density urban highway in Cochabamba, Bolivia, taking into account the special functional conditions due to the characteristics of the high altitude area. Based on the literature, it was initially determined that the Banki cross-flow turbine is the most suitable VAWT for use on highways. An in-situ measurement of the wind velocity spectra was conducted to assess the typical wind characteristics along the highway using statistical analysis and selected optimal values for testing and optimization. The diameter of the Banki wind turbine was then determined and fixed considering the width of the space between the two lanes of the highway as a limitation. Three geometrical aspects were assessed as variables for finding the optimal power coefficient; attack angle, number of blades and height. Computational fluid dynamics (CFD) simulations were carried out with every turbine combination to determine the optimal characteristics. From C_p and TSR values obtained from the simulations a multivariate analysis was carried out optimizing these values. The response of C_p and TSR were obtained, prioritizing C_p results. Finally, an ultimate design for the Banki wind turbine is proposed. The optimized Banki cross flow turbine has 11.5495° attack angle, 12 number of blades and 0.9 m of height.

Keywords: Vertical Axis Wind Turbine, Energy harvesting, Highway wind turbine, Banki Cross-flow

1. Introduction

Nowadays, the world is facing an energy crisis resulting from a shortage of traditional energy resources. As a result, many countries have started to shift their focus towards renewable energy alternatives such as solar thermal and photovoltaic energy, hydro energy, geothermal energy and wind energy to generate power.

Recent technological advances and diversification of types of wind turbines show a reduction in the risk of these installations and present more efficient systems in electrical conversion. Nevertheless, wind energy generation has shown to be a risky investment for the development of an interconnected power grid due to wind energy variability and uncertainty, its effect on power fluctuations, voltage drops, and as a consequence, grid instability.

The trend within wind turbines falls on a horizontal configuration of their axes or HAWT (horizontal axis wind turbine), mainly due to their large generation capacities within a specific area. However, horizontal-axis wind turbines are complex projects that cannot compete in micro-scale markets due to demanding operating conditions, large investments and studies, and high maintenance costs. A more relegated but no less important technology is the vertical axis wind turbine or VAWT (vertical axis wind turbine), which has an increased demand due to the need to take advantage of resources in limited environments. These turbines allow easy integration into the market of products for electricity generation and installation in urban areas for micro-generation and self-sustainability of products. The VAWT stands out due to the possibility of self-starting the generation as well as the omnidirectional capacity to harvest winds; factors that are limiting for horizontal axis wind turbines. In addition, new studies consider the use of sets of VAWTs in different configurations to increase efficiency or new types of airfoils with the same purpose, taking advantage of fluid mechanics and phenomena occurring during their operation.

In the literature, the principal focus of the research on VAWTs is the geometrical design, consequently, the VAWTs are continually being adapted and redesigned to achieve maximum benefits in power generation. Geometrical design of a Nautilus wind turbine [1], a comparison between helical and straight blades [2] and a

nature-inspired shape blades proposal for a VAWT [3] are some examples. Likewise, VAWTs have been researched to suit specific applications, such as subsidized houses [4] and highways [5], [6]. On highways, the authors are exploring the possibility of using VAWTs for electricity generation and street lighting, with certain types of turbines, with the cross-flow Banki wind turbine appearing to be the most effective option. Recent developments have also focused on enhancing the efficiency of arrays of vertical wind turbines [6], [7], [8]. Moreover, wind deflectors or guiding vanes are being studied as a solution to the performance challenges of some turbines [9]. Additional details and discussion on the state-of-the-art of VAWTs can be found on a recent review done by Alave-Vargas et al. [10].

In this sense, the present article will propose the design of an optimal Banki-type vertical axis wind turbine according to specific wind conditions and data analysis of in-situ measurements of the location within Blanco Galindo highway in Cochabamba, Bolivia; a city that is located at 2558 m.a.s.l., which implies a high altitude condition that has effects on the viscosity and density of air. The experiment consists on the geometrical design based on the angle of attack, height, and the number of blades of the turbine. The experiment will be carried out on computational fluid dynamics (CFD) recording moment and angular velocity to perform an efficiency analysis, obtaining an optimal Banki wind turbine that can be used in-site.

2. Types of vertical axis wind turbines

Although horizontal axis wind turbines have been extensively studied and are currently used as the prime wind energy generation turbine in the world, new advances and studies have emerged related to the construction and application of vertical axis wind turbines and emphasize the optimal values of tip-speed ratio (TSR), power coefficient (C_p), thrust coefficient (C_t) and the cut-in speed at which the turbine starts generating [1].

The values of TSR for VAWTs are determined by the turbine geometry, installation conditions and required power output. TSR is defined as the relation between the blade tip velocity and the wind speed. A high TSR value means higher power output, but it can cause mechanical issues. The C_p measures the turbine's efficiency converting the kinetic energy of the wind into electrical energy, and its maximum value occurs at a specific TSR value. The calculation of C_p is defined by Eq. (1). The C_t also measures the efficiency of the turbine extracting energy from the wind, and depends on the thrust force produced by the turbine, air density, wind speed, and swept area of the turbine, this value is represented by Eq. (2). A high C_t value indicates higher efficiency, but it could cause the turbine to fail mechanically as suggested by [11] and [5].

$$C_p = \frac{P}{\frac{1}{2}\cdot\rho\cdot S\cdot V^3}, \tag{1}$$

$$C_t = \frac{\tau}{\frac{1}{4}\cdot\rho\cdot S\cdot V^2\cdot D_1}, \tag{2}$$

The types of vertical axis wind turbines, according to recent literature, can be divided on:

2.1. Darrieus turbine

Darrieus rotors were invented in the third decade of the 20th century in France. They consist of 2 or 3 blades parallel to the axis of the rotor [12]. Regarding sub-types, there are Darrieus turbines with straight blades, with H rotor and with curved blades. They are considered the most efficient vertical-axis turbines [5], [6], and also very trustful [13].

The Darrieus turbines generate power from the lift produced by the rotating airfoils and have a higher power coefficient than the Savonius turbine [14]. They are recommended for use in areas with high and constant wind speeds without noticeable variations [15].

2.2. Savonius turbine

The Savonius turbine is used for variable wind flows in different ranges and requires a minimum wind speed to start working [15]. Despite being less efficient than the Darrieus turbines, it has been shown to have higher starting torque and good starting performance [5], [13].

2.3. Banki turbine

The Michell-Banki or Banki turbine is a cross-flow wind turbine type. Experiments have shown that it outperforms the Savonius and Darrieus vertical axis turbines in certain conditions and on highway applications [16]. It has a low autostart of around 1.2 m/s, relatively high torque and a rigid structure [13]. The remarkable efficiency of this turbine is due to the fact that the wind passes through two stages. In the first stage, the wind enters the turbine hitting the blades facing the wind and in the second stage, it leaves the turbine hitting the blades facing backwards. A large number of blades gives the turbine the ability to have low connection speed and high starting torque [11].

The construction of Banki turbines adapted for wind applications can be designed following a series of guidelines and equations, proposed by Al-Maaitah [11]. They define the maximum efficiency or C_p of the turbine

for the given context, where the geometry of the exposed blades is specifically designed using a velocity triangle as shown in Figure 1.

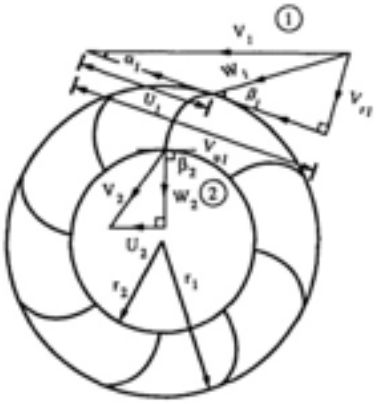

Figure. 1. *Velocity triangle diagram of wind input and output of the rotor* [11].

Through a geometric analysis of the velocity triangles of the input speed (system 1) and the output speed (system 2), Eq. (3) and Eq. (4) are obtained, where r_2 corresponds to the inner radius, r_1 is the outer radius, α_1 represents the angle of attack, and β_1 represent the input blade angle.

$$\left(\frac{r_2}{r_1}\right)^4 + 4 \cdot \left(\frac{r_2}{r_1}\right)^2 \cdot tan^2(\alpha_1) - tan^2(\alpha_1) = 0, \tag{3}$$

$$tan\ \beta_1 = 2 \cdot tan\ \alpha_1, \tag{4}$$

With the definition of the radius, Sammartano et al. [17] proposed the Eq. (5) and Eq. (6) to calculate the radius of curvature of ρ_b and degree of curvature of the blade δ, this geometry is shown in Figure 2.

$$\rho_b = \frac{D_1}{4} \cdot \left[1 - \left(\frac{D_2}{D_1}\right)^2\right] \cdot cos\ (\beta_1)^{-1}, \tag{5}$$

$$tan\left(\frac{\delta}{2}\right) = \frac{cos(\beta_1)}{sin(\beta_1)}, \tag{6}$$

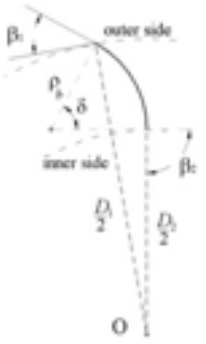

Figure. 2. *Blade geometry* [17].

3. In-site wind resource analysis

In order to carry out a design based on real conditions, wind speed measurements were taken on the Blanco Galindo highway in the city of Cochabamba, Bolivia. This avenue has a double lane with one lane going east and the other going west, and a space of 1.86 m separating the lanes of opposite circulation.

The data collection was carried out at 3.5 km of the highway, 460 metres from the distributor of another important avenue, Beijing avenue (the exact location can be seen in Figure 3). The criteria for determining the location for data collection were based on the observation of high vehicular flow, circulation of trucks and heavy vehicles coming from the distributor, and the absence of traffic lights within a radius of at least 400 metres.

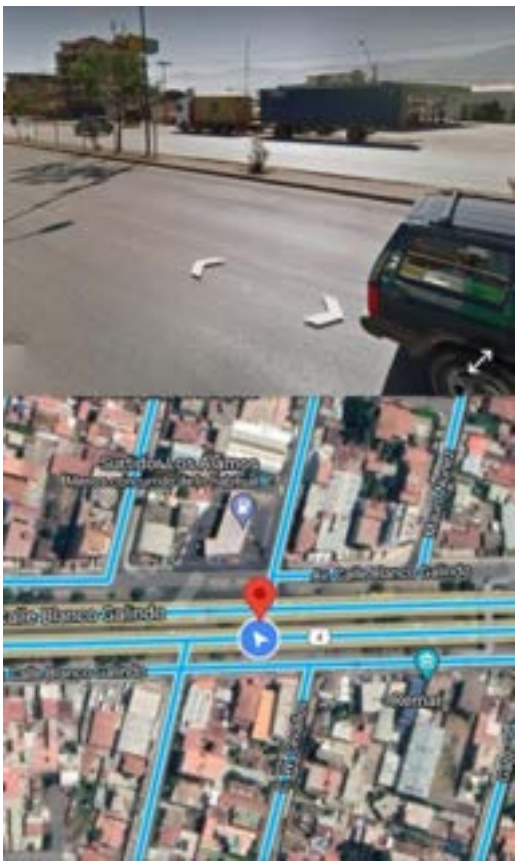

Figure. 3. *Location of the data gathering point (-17.393004, -66.188506).*

Wind data were collected for four days at different periods, taking into account high traffic periods caused by rush hours. During the measurement days, there was no rain or significant variations in temperature and humidity. Anemometers with data loggers and Bluetooth were used with a collection frequency of 1 data/s. The data was measured at 1 m from the ground; this selection is based on a study by Al-Aqel et al. [18]. They concluded that the maximum recorded wind speed is found at that height because of the formation of trailing vortices behind and at the sides of vehicles. The results obtained for periods, in terms of maximum wind speeds and average speeds, are shown in Table 1.

Table 1. *Summary of wind speed data.*

Period	Day	From	To	Maximum wind velocity north side, m/s	Maximum wind velocity south side, m/s	Average wind speed north side, m/s	Average wind speed south side, m/s
Period 1	Wednesday	08:58 am	10:00 am	7.29	3.49	1.598	1.226
Period 2	Wednesday	11:47 am	12:55 pm	7.64	7.63	2.237	1.898
Period 3	Thursday	08:58 am	09:58 am	6.31	6.35	1.305	1.445
Period 4	Thursday	12:06 am	01:08 pm	5.94	4.42	1.806	0.655
Period 5	Friday	08:22 am	10:00 am	10.14	0.00	2.050	0.000
Period 6	Friday	12:04 pm	01:08 pm	9.47	4.42	2.180	0.655
Period 7	Friday	04:09 pm	05:01 pm	7.23	6.17	1.494	1.722
Period 8	Saturday	07:42 am	08:45 am	7.75	5.79	2.622	0.938

For a better understanding of the data, Table 2 presents the percentage of data that corresponds to a specific range of wind speed.

Table 2. *Range wind speed percentage.*

Wind speed range , m/s	Data percentage north side, %	Data percentage south side, %
0.1 - 1.1	27.20	57.58
1.2 - 2.1	41.01	27.52
2.2 - 3.1	19.97	12.26
3.2 - 5-1	7.920	2.540
5.2 - 10.2	3.900	0.100

As shown in Table 2, the entirety of the collected data is concentrated between 0.1 and 2.1 m/s, with at least 68% of the measurements on both sides falling within this range. There are some variations between the south and north side measurements, with higher values consistently recorded on the north side. However, while the data is consistent, the measured wind speeds are limited to specific periods and have a low magnitude, which limits their potential as a good wind resource [13], [18]. Therefore, for the purpose of obtaining an optimal turbine design, a higher wind speed value will be used. During the Saturday measurements, higher wind speeds were recorded on the north side, with every measurement greater than 5 m/s, with a mean value of 6.15 m/s. The first measured speed on the north side with this value has a 1.98 m/s speed on the south side. These two values were used for the development of all CFD simulations.

4. Experimental design

To obtain the most efficient turbine possible, a series of parameters and limitations must be defined. Since the turbine must be located in the middle of the highway and the maximum width is 1.86 m, the diameter will be limited to 1.4 m, taking into consideration safety factors to prevent risking human lives during its operation. Other considerations for the site include the local density and viscosity of the air, which were extracted from the EES software library, corresponding to the air pressure at 2,558 m.a.s.l. with a value of 0.8913 kg/m^3 and 1.82E-5 m^2/s, respectively. The experiment will not focus on power production and will analyse the optimal turbine with the dimensionless coefficient C_p. This parameter will enable the comparison of turbines with different configurations and give an idea of the raw power they can produce [5], [19] , [20]. Since the experiment will be conducted on a double duct wind tunnel, the defined TSR concept will be adapted to consider wind speed as the sum of the speed in both lanes; C_t and C_p will have a similar variation using the sum of wind speeds as the parameter. Finally, a factorial statistical analysis will be carried out using the peak values obtained from the parameters of each turbine to obtain the optimal values for each turbine's geometrical parameters.

4.1. Turbine type selection

Many types of turbines have been studied, each with its advantages and disadvantages in different situations and wind characteristics. Highways have a wind resource that is not related to climate phenomena and has high turbulence and a mixture of air, as well as short bursts of air that require the use of low-starting torque turbines. Tian et al. [6] conducted a study comparing the Savonius, Darrieus, and Banki turbine designs for highway energy recovery applications. The results showed that the Banki wind turbine is the most efficient for energy production on a turbine situated on a highway due to its drag characteristics, which allow it to perform at low wind speeds and high torque. This is why in the current study, this turbine will be analysed and used for highway energy recovery.

Considering that there is an interest in building a functional prototype of the wind turbine, the material selection was carefully considered. While many authors utilize models with aluminium or composite materials, these materials can be both high-density and expensive. To mitigate these issues, a solid polyvinyl chloride (PVC) with a density of 1.4 g/cm³ was chosen for its ease at manufacturing, natural material resistance, low cost, and availability in the local Bolivian market. This choice of material allows for the turbine's geometrical properties to be easily constructed while still maintaining its functionality [21], [22], [23].

4.2. Geometric design parameters

After selecting the Banki wind turbine for simulation to find the geometric design parameters for the operating conditions, parameters such as height, angle of attack, and number of blades for Banki turbines with similar characteristics are presented. Tian et al. [6] used 18 blades, a radius of 0.25 m, and a height of 0.21 m for the Banki turbine design. Al-Maaitah [11] used an angle of attack of 16°, a height of 1 m, and 8 blades. However, Ushiyama et al. [24] suggest that the turbine must have a minimum of 12 blades to be more effective. Andrade et al. [25] have demonstrated through experiments that the angle of attack can vary from 7° to 23°. On the other hand, Sammartano et al. [17] use a design with 35 blades, an angle of attack of 22°, and a height of 1 m.

Based on these experiences, it was decided to establish three angles of attack (6°, 10°, and 14°), rotor heights of 0.9 m and 1.1 m, and numbers of blades of 12, 16, and 20. Therefore, 18 possible turbine designs were created. For all these combinations, calculations were made using the proposed equations for Banki turbine design. The outer radius r_1 was defined based on the available space of 1.86 m where wind speed measurements were taken, with a fixed value of 0.7 m. Equation (3) was used to calculate the inner radius r_2 and Eq. (4) to obtain the blade angle β_1. The geometric parameters that complete the blade geometry, the radius of curvature and the curvature angle, were calculated using Eq. (5) and Eq. (6). The geometrical design parameters are shown in Figure 4a and the computer model of a specific Banki turbine is illustrated in Figure 4b.

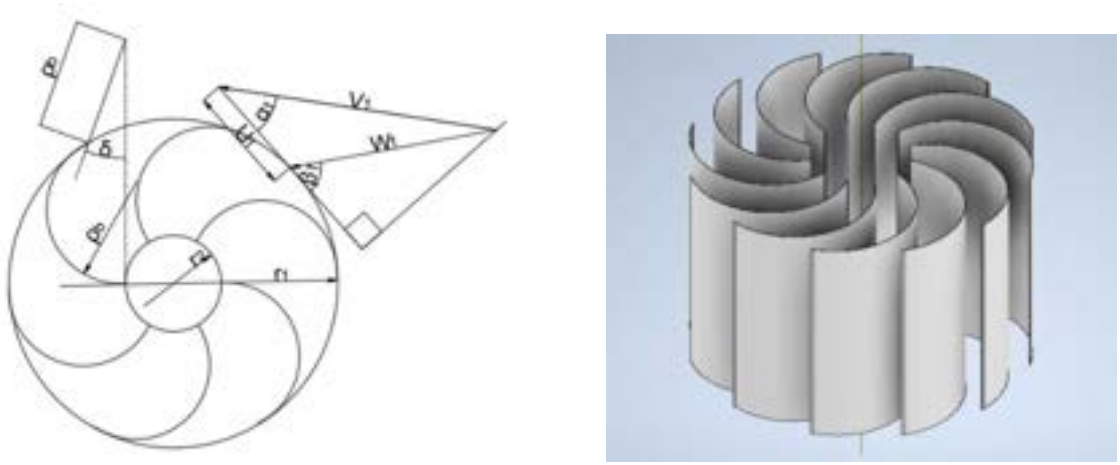

a) *b)*

Figure. 4. *a) Geometric design parameters for a Banki wind turbine, b) 3D model of the Banki turbine.*

For the 18 turbines geometries, using 3D computer design software with the selected material, their mass and moment of inertia were obtained. These results for all possible combinations are presented in Table 3.

Table 3. *Design parameters.*

Part name	Angle of attack α_1	Number of blades	Height, cm	Blade angle β_1	Radius of curvature ρ_b, m	Degree of curvature δ	r_1, m	r_2, m	Mass turbine kg	Inertia moment kg m^2
TS-01	6°	12	90	11.87°	0.327	23.72°	0.7	0.204	32.543	8.8820
TS-02	6°	12	110	11.87°	0.327	23.72°	0.7	0.204	39.774	10.856
TS-03	6°	16	90	11.87°	0.327	23.72°	0.7	0.204	43.390	11.843
TS-04	6°	16	110	11.87°	0.327	23.72°	0.7	0.204	55.032	14.475
TS-05	6°	20	90	11.87°	0.327	23.72°	0.7	0.204	54.238	14.804
TS-06	6°	20	110	11.87°	0.327	23.72°	0.7	0.204	66.290	18.094
TS-07	10°	12	90	19.42°	0.325	38.85°	0.7	0.247	27.608	7.6210
TS-08	10°	12	110	19.42°	0.325	38.85°	0.7	0.247	33.743	9.3140
TS-09	10°	16	90	19.42°	0.325	38.85°	0.7	0.247	36.810	10.161
TS-10	10°	16	110	19.42°	0.325	38.85°	0.7	0.247	44.990	12.419
TS-11	10°	20	90	19.42°	0.325	38.85°	0.7	0.247	46.013	12.701
TS-12	10°	20	110	19.42°	0.325	38.85°	0.7	0.247	56.238	15.524
TS-13	14°	12	90	26.50°	0.330	53.00°	0.7	0.274	24.404	6.7910
TS-14	14°	12	110	26.50°	0.330	53.00°	0.7	0.274	29.827	8.3000
TS-15	14°	16	90	26.50°	0.330	53.00°	0.7	0.274	32.539	9.0550
TS-16	14°	16	110	26.50°	0.330	53.00°	0.7	0.274	39.769	11.067
TS-17	14°	20	90	26.50°	0.330	53.00°	0.7	0.274	40.673	11.318
TS-18	14°	20	110	26.50°	0.330	53.00°	0.7	0.274	49.712	13.833

With the 18 possibilities of wind turbines a multivariable analysis will be carried out. The study will analyse the influence of the angle of attack, number of blades, and height in power production; correlating these parameters to the C_p and TSR of the turbine. From this analysis, an optimal geometrically designed turbine will be obtained. Integer steps were proposed to evaluate a high number of transient analyses, covering a broad range of values. While smaller steps in all variables would increase the precision of the statistical analysis allowing us to reach more specific values, there are limitations to do it without increasing the length of the study.

4.3. Performance simulations

4.3.1. Numerical methods and computational domain

A CFD simulation has been conducted using Ansys Fluent. The numerical simulation was performed with a k - ε turbulence model due to its accuracy; the enhanced wall treatment condition was applied. The simulations used dynamic mesh and included the mass and inertia data from each turbine to generate the movement in the respective flow. A pressure-based solver was chosen and velocity inlets were defined, with inlet 1 having a value of 6.15 m/s and inlet 2 having a value of 1.98 m/s with their disposition shown in Figure 5. Both outlets were pressure based with a gauge pressure of 0 and assumed no loss [26].

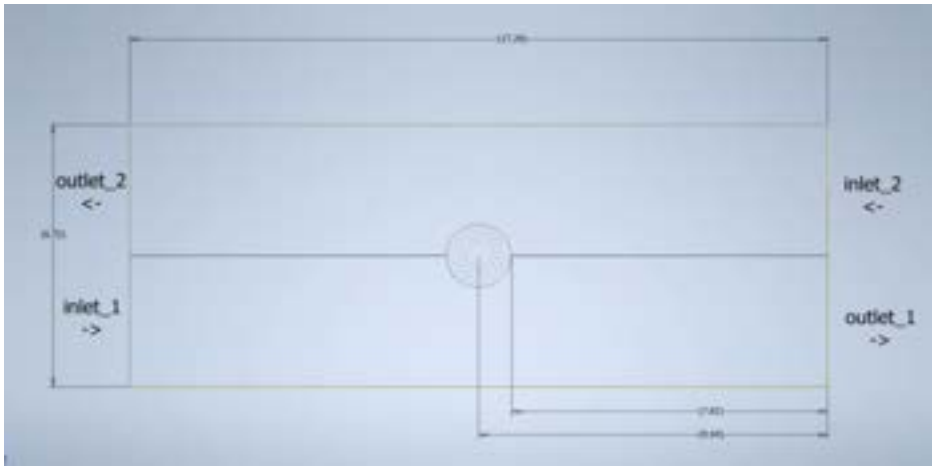

Figure. 5. *Computational domains for CFD simulations (dimensions are m).*

For the current analysis, the turbine was isolated from interaction with vehicles, and a separator in the middle was used for the flows to develop completely. This separator is a thin wall 20 mm thick, allowing the turbine to be analysed without mixing the flows and obtaining the optimal design based solely on performance under similar conditions to those on the highway, not including elevated turbulence of air. Creating an adequate computational domain is necessary to generate real results from the data input into the simulation. When the computational domain is too short, the flow does not resemble a real flow, and when it is too large, the duration of the computational process is considerably long [20]. The computational domains are analogous to Toudasrbari et al. [20], and consist of a rectangle of 17.28 m x 6.72 m. The values were decreased from other studies due to the crossflow characteristics of the domain as shown in Figure 5. The thin wall that separates both flows and avoids interaction between them before reaching the turbine is 7.82 m from the lateral wall, allowing a small gap that generates the resultant mixture of air due to the turbine interacting with the flow. The domain is 1.5 m tall since it is not necessary to analyse the flow in the y-axis.

4.3.2. Mesh generation and simulation setup

The meshing type and size are crucial in every CFD simulation to generate good results and accuracy. The meshing generation uses multizone generation for the wind turbine, where the resultant mesh has a free mesh type of tetrahedral elements and hexa/prism elements for the whole domain. As shown in Figure 6, the number of elements has a higher density over the turbine to correctly calculate the flow and to resemble a real one. On average, the whole domain has approximately 362240 nodes. This value fluctuates for every turbine and geometrical model, but the pre-set is the same for every evaluation. To further increase the quality of the results, an inflation layer was generated for the blades of the turbine, further diminishing the size of the mesh and gaining precision in the calculation.

Figure. 6. *Mesh of tetrahedral elements over the turbine.*

As a final step previous running the simulations a time step must be defined. To avoid long computational processes and according to Tourdarbi et al. [20], a series of time steps must be defined as a translation of angle: $\Delta\theta = 1°$, $\Delta\theta = 0.5°$ or $\Delta\theta = 0.25°$. This is translated into the simulation as a time step of 0.005 s [20]. Another parameter for the simulation is limiting the number of iterations to 50 which allows the solver to converge into a result.

4.3.3. Simulation results and final selection

CFD simulations were carried out for the 18 generated models, and the graphical results obtained for the TS-01 simulation are shown in Figure 7.

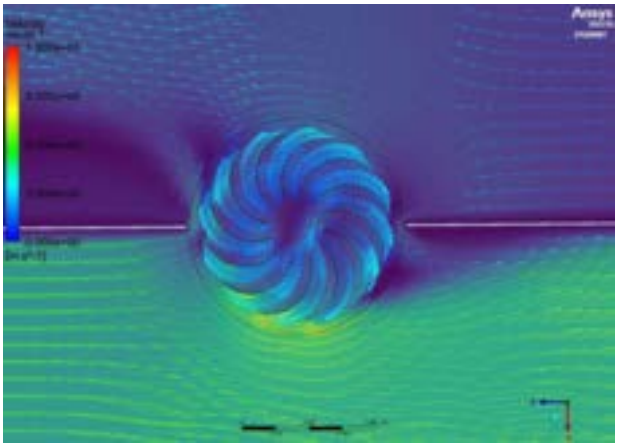

Figure. 7. *Velocity and vector contour for TS-01 model.*

Reports were generated for all simulations for the analysis of the relevant parameters in MatLab. The speed of the turbine's tip was obtained through CFD and the no-slip boundary condition, while the moment was obtained through FEA (Finite element analysis). From these simulations, TSR, C_t, and C_p were calculated with the assistance of Eq. (1) and Eq. (2).

The turbines were grouped by attack angle to show the graphed results in Figure 8 and Figure 9. The maximum C_p value of the 6° angle group was obtained with TS05 at 0.0594 and a TSR of 0.2456. In the group of 10° angle, the maximum C_p was 0.5686 from TS07 and a TSR of 0.2903 and from the 14° angle group the maximum C_p was 0.0583 with a TSR of 0.3094 corresponding to TS13. Overall, the C_p and C_t values show low efficiency, but high starting torque, which is a good value for the current wind resource measured in-site. The generated vortices in the turbine show unbalance and indicate the need for higher structural resistance. The crossflow functionally of the turbine is neglected and instead, the re-entry angle becomes sharper, inducing a lower efficiency of the turbine.

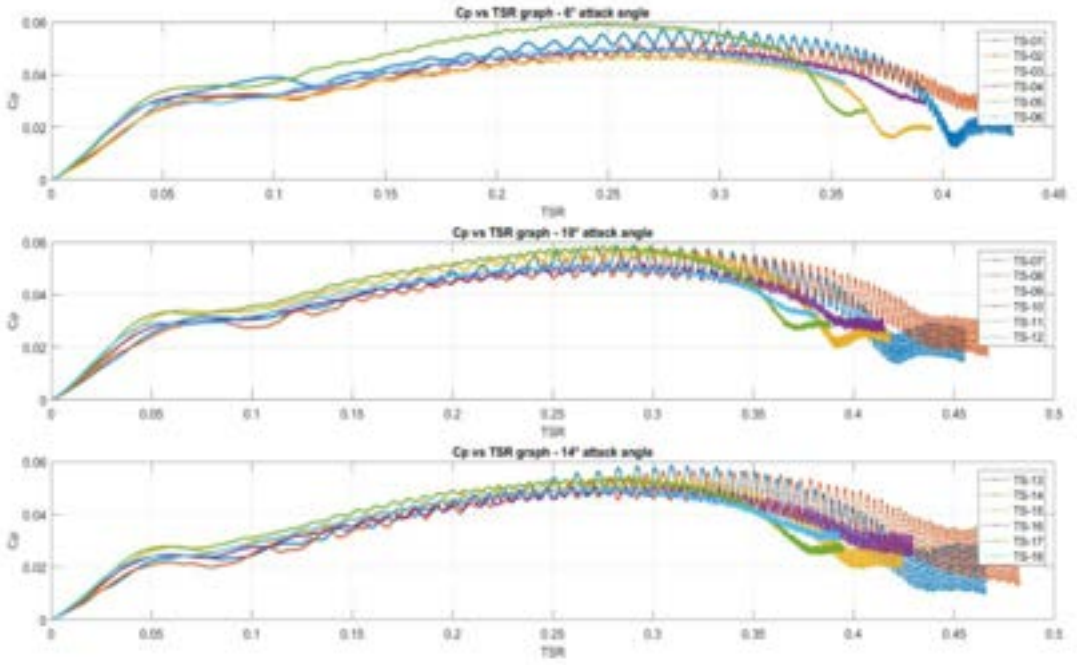

Figure. 8. *Resultant* C_p *vs TSR plot grouped by attack angle.*

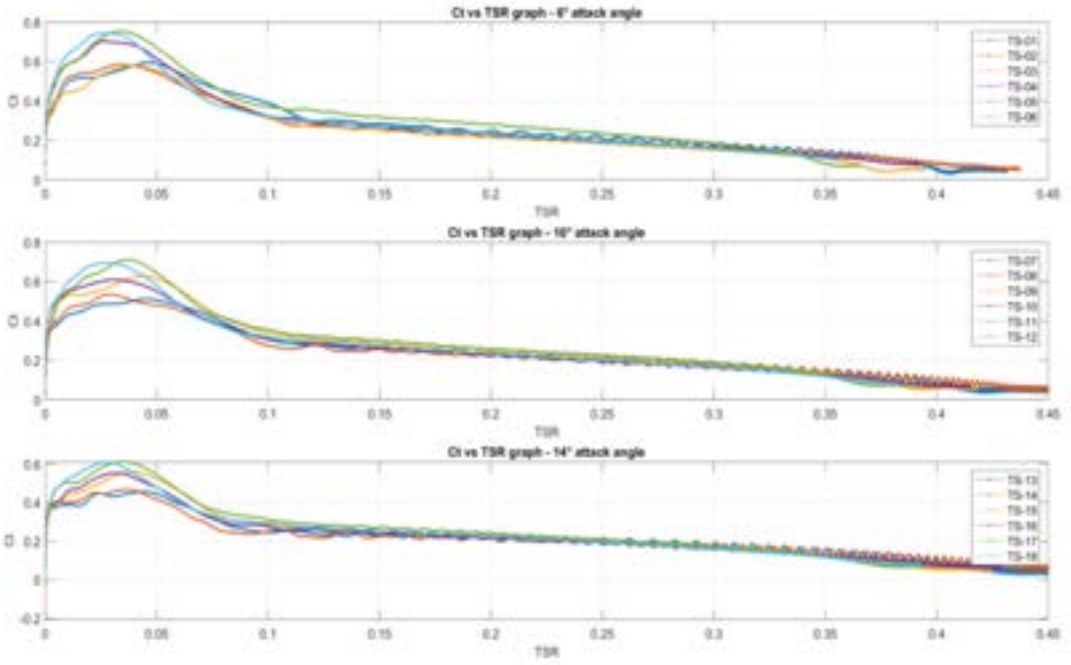

Figure. 9. *Resultant* C_t *vs TSR plot grouped by attack angle.*

From all these values a multivariate statistical analysis was carried out with C_p and their related TSR. The data input is given in Table 4. The software STATGRAPHICS 19 Centurion was used to carry out the multivariate analysis.

Table 4. *Data for factorial analysis.*

Part name	Angle of attack α_1	Number of blades	Height, m	C_p	TSR
TS-01	6°	12	0.9	0.0570	0.2742
TS-02	6°	12	1.1	0.0520	0.3161
TS-03	6°	16	0.9	0.0474	0.2456
TS-04	6°	16	1.1	0.0505	0.2701
TS-05	6°	20	0.9	0.0594	0.2456
TS-06	6°	20	1.1	0.0500	0.2639
TS-07	10°	12	0.9	0.0586	0.2903
TS-08	10°	12	1.1	0.0566	0.3002
TS-09	10°	16	0.9	0.0580	0.2973
TS-10	10°	16	1.1	0.0518	0.2868
TS-11	10°	20	0.9	0.0583	0.2755
TS-12	10°	20	1.1	0.0511	0.2542
TS-13	14°	12	0.9	0.0583	0.3094
TS-14	14°	12	1.1	0.0564	0.3202
TS-15	14°	16	0.9	0.0545	0.2871
TS-16	14°	16	1.1	0.0512	0.3006
TS-17	14°	20	0.9	0.0537	0.2834
TS-18	14°	20	1.1	0.0502	0.2763

The first conducted analysis was the optimization for C_p, where the desired behaviour is to maximise this value. Table 5 summarises the obtained values and optimization results. The optimal geometrical properties for energy production were found to be an angle of attack of 11.5495°, a minimum height of 0.9 m and a number of blades of 12.0058, resulting in a C_p prediction of 0.05944. Although the recorded values are low for the given wind speed, this behaviour may be expected due to the lower air density and the definition of TSR and C_p, where the global speed is considered to be the sum of each lane's speed. The surface plot resembles a saddle-back, indicating that higher C_p values may exist on the extreme ends of the number of blades and near 10° attack angle.

Table 5. *Optimization results for* C_p.

Factor	Lower limit	Upper limit	Optimum value
Angle of attack α_1	6°	14°	11.5495°
Number of blades	12	20	12.0058
Height, m	0.9	1.1	0.9

After obtaining the C_p analysis, a similar analysis was performed for TSR, trying to minimise this value due to the low wind speed present in the selected location. This analysis didn't provide any interesting results. So, an additional analysis was carried out considering both responses. Table 6 shows the resultant values to minimise the TSR and maximise the C_p. The height is the same as for the optimal results in Table 5, but the condition to minimise TSR imposes a higher blade number of blades and lower attack angle, obtaining the value of 20 and 6.4656° respectively. From the response analysis, the predicted C_p is 0.05725 and a TSR of 0.49881.

Table 6. *Optimization results for multiresponse analysis.*

Factor	Lower limit	Upper limit	Optimum value
Angle of attack α_1	6°	14°	6.46562°
Number of blades	12	20	20
Height, m	0.9	1.1	0.90075

Figure 10 shows the response surface and has a similar shape as the one generated for C_p, but shifted to benefit higher blade numbers and with a sharper slope. The resultant height is the mean between both values, upper and lower limit. This is the default option from the software to avoid dependence of the third variable and since the response from the height is not significant the figure is valid and represents the correct behaviour of the system.

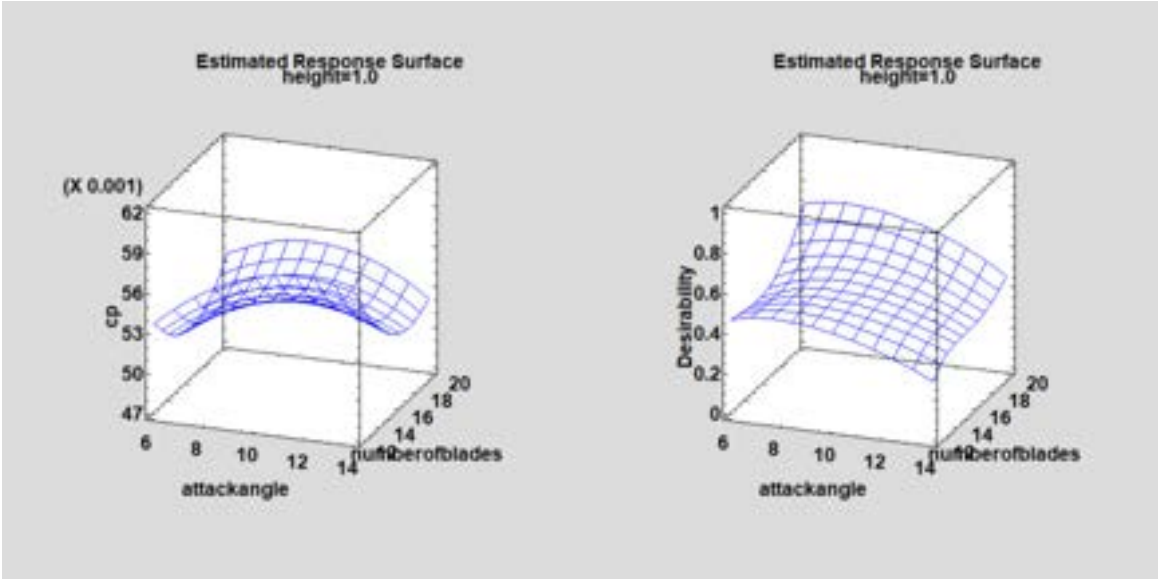

Figure. 10. *Estimated response surface for* C_p *optimization and Multiresponse analysis at height 1 m.*

5. Conclusions and recommendations

The design and simulation of a Banki cross-flow wind turbine for highways under high turbulence and high altitude conditions was developed in this work. The results include the following conclusions:

- The number of blades, attack angle and height were optimized for maximum energy production. The results indicate that the number of blades should be 12 and the attack angle and height should be 11.55° and 0.9, respectively.
- The predicted maximum C_p value is 0.05944, which indicates low efficiency. Results that could be improved with the addition of concentrators. The TSR value for this maximum C_p must be minimised to improve turbine performance at lower wind speeds, which is important considering the location and high altitude conditions.
- The optimal value for the combination of the Cp and TSR fluctuates in terms of blade numbers, where higher values indicate higher starting torque and lower self-start speed of the turbine, resulting in a higher Cp shortly after the turbine's cut-in speed. The predicted C_p, in this case is 0.05735 and the optimal blade number is 20 and 6.46° angle.

- The attack angle seems to have a maximum efficiency point for the conditions where the most beneficial angle for energy production appears to be in the middle of the considered parameters. Overall and considering that the difference between C_p's in both analysis is low, the optimal geometrical designs for the turbine are the ones related to the C_p analysis.

The design of the turbine was successful and has a similar approach to other authors in the literature regarding limitations and parametrical design. Nevertheless, we have some recommendations and future work to do:

- The results must be improved with better instruments of measurement and larger intervals of wind speed measurements in order to obtain a more accurate prediction of the resource and to assess the feasibility of installing the turbine over the Blanco Galindo highway.
- The construction of a prototype is also recommended. The prototype should be made from a durable material with a high Young modulus that will enable the turbine to operate correctly. Composite materials offer an advantage in this regard.
- Also, in order to increase the reliability of the study a more realistic CFD analysis should be carried out taking into account the aerodynamics of a moving vehicle, with a higher number of elements and better-quality meshing for a group of turbines (energy harvesting). Moreover, future studies could also consider wind deflectors or other passive elements to increase turbine efficiency.

It is also important to mention that the next steps in this work include manufacturing a couple of prototypes to validate their performance in different conditions and to gather information from at least two sites where the altitude is a predominant factor for eolic generation efficiency. The construction and manufacturing of these prototypes would involve a improvement on Bolivia's renewable energy matrix and distributed generation. The sites chosen for the next stage of the project are the Blanco Galindo Avenue in Cochabamba, Bolivia (2558 m.a.s.l.) and the El Alto - Mallasilla road in La Paz, Bolivia (3500 m.a.s.l.).

Nomenclature

ρ	air density, kg/m^3
α_1	angle of attack, °
β_1	blade angle, °
δ	degree of curvature, °
D_2	inner diameter, m
r_2	inner radius, m
D_1	outer diameter, m
r_1	outer radius, m
P	output power from the turbine, W
S	projected area of the turbine, m^2
c_p	power coefficient
ρ_b	radius of curvature, m
c_t	thrust coefficient
TSR	tip-speed ratio
V	wind speed, m/s

References

[1] R. Pramod, G. B. V. Kumar, P. S. S. Harsha, and K. A. U. Kumar, "Design and development of nautilus whorl-wind turbine," *AIP Conf. Proc.*, vol. 1859, 2017, doi: 10.1063/1.4990246.

[2] T. Q. Le, K. S. Lee, J. S. Park, and J. H. Ko, "Flow-driven rotor simulation of vertical axis tidal turbines: A comparison of helical and straight blades," *Int. J. Nav. Archit. Ocean Eng.*, vol. 6, no. 2, pp. 257–268, 2014, doi: 10.2478/IJNAOE-2013-0177.

[3] J. Blanco, J. de D. Rodriguez, A. Couce, and M. I. Lamas, "Proposal of a nature-inspired shape for a vertical axis wind turbine and comparison of its performance with a semicircular blade profile," *Appl. Sci.*, vol. 11, no. 13, 2021, doi: 10.3390/app11136198.

[4] R. D. Maldonado *et al.*, "Design, simulation and construction of a Savonius wind rotor for subsidized houses in Mexico," *Energy Procedia*, vol. 57, pp. 691–697, 2014, doi: 10.1016/j.egypro.2014.10.224.

[5] W. Tian, Z. Mao, X. An, B. Zhang, and H. Wen, "Numerical study of energy recovery from the wakes of moving vehicles on highways by using a vertical axis wind turbine," *Energy*, vol. 141, pp. 715–728, 2017, doi: 10.1016/j.energy.2017.07.172.

[6] W. Tian, B. Song, and Z. Mao, "Numerical investigation of wind turbines and turbine arrays on highways," *Renew. Energy*, vol. 147, pp. 384–398, 2020, doi: 10.1016/j.renene.2019.08.123.

[7] I. D. Brownstein, N. J. Wei, and J. O. Dabiri, "Aerodynamically Interacting Vertical-Axis Wind Turbines:

Performance Enhancement and Three-Dimensional Flow," *Energies*, vol. 12, no. 14, p. 2724, 2019, doi: 10.3390/en12142724.
[8] J. Durkacz *et al.*, "CFD modelling and prototype testing of a Vertical Axis Wind Turbines in planetary cluster formation," *Energy Reports*, vol. 7, pp. 119–126, 2021, doi: 10.1016/j.egyr.2021.06.019.
[9] A. H. Rajpar, I. Ali, A. E. Eladwi, and M. B. A. Bashir, "Recent development in the design of wind deflectors for vertical axis wind turbine: A review," *Energies*, vol. 14, no. 16, 2021, doi: 10.3390/en14165140.
[10] E. M. Alave-Vargas, R. Orellana Lafuente, and D. F. Sempértegui-Tapia, "ESTADO DEL ARTE SOBRE AEROGENERADORES DE EJE VERTICAL (Monografía)," *Investig. Desarro.*, vol. 22, no. 1, pp. 161–172, 2022, doi: 10.23881/idupbo.022.1-13i.
[11] A. A. Al-Maaitah, "The design of the Banki wind turbine and its testing in real wind conditions," *Renew. Energy*, vol. 3, no. 6–7, pp. 781–786, 1993, doi: 10.1016/0960-1481(93)90085-U.
[12] F. Alqurashi and M. H. Mohamed, "Aerodynamic forces affecting the H-rotor darrieus wind turbine," *Model. Simul. Eng.*, vol. 2020, 2020, doi: 10.1155/2020/1368369.
[13] T. A. Ismaeel, S. Aljabair, O. A. Abdulrazzaq, and Y. A. Abood, "Energy recovery of moving vehicles' wakes in highways by vertical axis wind turbines," *FME Trans.*, vol. 48, no. 3, pp. 557–565, 2020, doi: 10.5937/fme2003557I.
[14] W. YAMAZAKI and Y. ARAKAWA, "Inexpensive airfoil shape optimization for vertical axis wind turbine and its validation," *J. Fluid Sci. Technol.*, vol. 10, no. 2, pp. JFST0015–JFST0015, 2015, doi: 10.1299/jfst.2015jfst0015.
[15] J. J. N. Quispe, J. H. Nina, and S. T. Jara, "Study and application of wind rose for vertical and horizontal axis wind turbine installation in Lima," *Proc. 2020 IEEE Eng. Int. Res. Conf. EIRCON 2020*, pp. 16–19, 2020, doi: 10.1109/EIRCON51178.2020.9254076.
[16] I. J. T. Matias, L. A. M. Danao, and B. E. Abuan, "Numerical investigation on the effects of varying the arc length of a windshield on the performance of a highway installed Banki wind turbine," *Fluids*, vol. 6, no. 8, 2021, doi: 10.3390/FLUIDS6080285.
[17] V. Sammartano, C. Aricò, A. Carravetta, O. Fecarotta, and T. Tucciarelli, "Banki-Michell optimal design by computational fluid dynamics testing and hydrodynamic analysis," *Energies*, vol. 6, no. 5, pp. 2362–2385, 2013, doi: 10.3390/en6052362.
[18] A. A. Al-Aqel, B. K. Lim, E. E. M. Noor, T. C. Yap, and S. A. Alkaff, "Potentiality of small wind turbines along highway in Malaysia," *Proc. 2016 Int. Conf. Robot. Autom. Sci. ICORAS 2016*, 2017, doi: 10.1109/ICORAS.2016.7872634.
[19] D. D. D. P. Tjahjana, P. Purbaningrum, S. Hadi, Y. A. Wicaksono, and D. Adiputra, "The study of the influence of the diameter ratio and blade number to the performance of the cross flow wind turbine by using 2D computational fluid dynamics modeling," *AIP Conf. Proc.*, vol. 1931, pp. 2–7, 2018, doi: 10.1063/1.5024093.
[20] S. Toudarbari, M. J. Maghrebi, and A. Hashemzadeh, "Evaluation of Darrieus wind turbine for different highway settings using CFD simulation," *Sustain. Energy Technol. Assessments*, vol. 45, no. November 2020, p. 101077, 2021, doi: 10.1016/j.seta.2021.101077.
[21] S. Singh Rathore, R. Dalmia, K. Tamakuwala, and S. Manavalla, "Design, Fabrication and Testing of a Low Cost Vertical Axis Wind Mill for Low End Power Generation," *Int. Res. J. Eng. Technol.*, pp. 1524–1528, 2016, [Online]. Available: www.irjet.net.
[22] A. R. Gatlewar, N. K. Mandavgade, M. T. Kanojiya, and V. N. Kalbande, "Material selection for rotor blade of vertical axis wind turbine," *Mater. Today Proc.*, vol. 46, no. xxxx, pp. 8489–8493, 2021, doi: 10.1016/j.matpr.2021.03.505.
[23] ISO. 4439:1979, "Unplasticized polyvinyl chloride (PVC) pipes and fittings — Determination and specification of density," 1979. https://www.iso.org/standard/10341.html.
[24] I. Ushiyama, I. Isshiki, and G. Z. Chai, "Experimentally evaluating the design and performance of cross-flow wind rotors," *Energy Environ. into 1990´s*, vol. 3, pp. 1499–1504, 1990.
[25] J. De Andrade, C. Curiel, F. Kenyery, O. Aguilln, A. Vásquez, and M. Asuaje, "Numerical investigation of the internal flow in a Banki turbine," *Int. J. Rotating Mach.*, vol. 2011, 2011, doi: 10.1155/2011/841214.
[26] M. H. Mohamed, A. M. Ali, and A. A. Hafiz, "CFD analysis for H-rotor Darrieus turbine as a low speed wind energy converter," *Eng. Sci. Technol. an Int. J.*, vol. 18, no. 1, pp. 1–13, 2015, doi: 10.1016/j.jestch.2014.08.002.

Dynamic Analysis Of A Power Plant Producing Liquefied Biomethane For Heavy Road Transport

Francesco Calise[a], Francesco Liberato Cappiello[b], Luca Cimmino[c] and Maria Vicidomini[d]

[a] Univesità degli studi "Federico II", Napoli (NA), Italy, frcalise@unina.it
[b] Univesità degli studi "Federico II", Napoli (NA), Italy, francescoliberato.cappiello@unina.it
[c] Univesità degli studi "Federico II", Napoli (NA), Italy, luca.cimmino@unina.it, CA
[d] Univesità degli studi "Federico II", Napoli (NA), Italy, maria.vicidomini@unina.it

Abstract:

In the recent years, European Countries are paying more and more attention to the issue of greenhouse gases emissions due to the road transport sector. In particular, the fuel consumption due to the heavy road transport is one of the most relevant issues both for the weight and the long distances that they cover. In addition, the cost of the natural gas dramatically increased in many European countries due to recent international crisis. Thus, finding alternative ways of producing natural gas from renewable sources would be of great economic and environmental impact for the current global asset. In this work, a dynamic thermoeconomic analysis of a plant producing bio liquefied natural gas (bio-LNG), driven by renewable sources, to meet the fuel demand of a fleet of heavy trucks is proposed. The plant consists of a plug flow reactor digesting the organic fraction of municipal solid wastes in mesophilic conditions. The biogas upgrading model and the biomethane liquefaction models are in detail developed in MATLAB. The whole system is integrated in TRNSYS for dynamic simulation purpose. Then, the bio-LNG is used to meet the fuel demand of heavy trucks which cover relevant distances all over the region of Campania, in the South of Italy. The environmental impact related to the avoided emissions due to the use of bio-LNG is analysed together with the economic feasibility of the proposed system. The results of the thermoeconomic simulation show that the system has high capital costs, close to 85 M€ despite the fundings granted for bioLNG trucks purchasing. However, the fundings for the biomethane production and selling are enough to guarantee a remarkable economic feasibility with a Simple Payback period of less than 2 years and a Net Present Value of 402 M€. Furthermore, the solution proposed is effective for the pathway of the green mobility, with a Primary Energy Saving of 91% and a reduction of CO_2 emissions by 86%.

Keywords:

Liquefied biomethane; plug flow reactor; renewable energy; heavy-duty truck; Linde cycle.

1. Introduction

To achieve the goal of the climate neutrality by 2050, the European Commission of the European Union (EU) issued several directives that must be mandatorily attended by all the EU Countries [1]. To this scope, a first key set of proposals to revise EU Legislation was signed in 2021, known as "fit for 55" package [2]. The main purpose of this package is to reduce by 55% CO_2 emissions by the end of year 2030, compared to the year 1990. The proposals include a significant revision in EU policies on energy taxation, carbon border adjustment mechanisms and emissions trading systems. In this framework, particular attention was paid to the transport sector, which is still responsible for over 25% of greenhouse gases (GHG) emissions, by including a strict alternative fuels infrastructure regulation [3]. Nowadays, there are 13.4 million of alternative fuel road vehicles in the EU, around 5% of the total number, but estimations predict an exponential increasing trend of alternative fuels spreading in the next 20 years [4]. More specifically, large attention is paid to the installation of alternative refuelling points on the main roads, to allow vehicles, especially heavy-duty trucks, to circulate throughout the EU countries [5].

The environmental impact of the heavy-duty trucks is indeed widely acknowledged and the main reason lies behind the ever increasing spreading of worldwide freight shipments [6]. The current globalized market allows the trade of products among the most remote parts of the world by means of containers which carry out tons of consumer goods. These goods are then overwhelmingly land transported by heavy trucks for internal moving among the ports of the same country [7]. Unfortunately, the sustainability of this market is jeopardized by the increasing connections of ports for the exchange of containers, that comes with the increase of the number of

heavy-duty trucks for road transport of containers. In this framework, among the proposals for the EU Legislation revision for a sustainable development, the installation of alternative fuels refuelling stations in the busiest seaports was indeed considered [8]. This strategy mainly involves electric batteries recharging, but the usage of liquefied natural gas (LNG) is also taken into account. Unfortunately, latest directives in terms of road transport vehicles circulation are aiming to the utter replacement of internal combustion engine vehicles with electric vehicles by 2035 []. However, these directives are still under discussion since several EU Countries are concerned that this pathway is not at all the most efficient and sustainable for the road to the full decarbonisation. In fact, cutting-edge solutions for the progress towards a green mobility not only include electric road transport [9], but also hydrogen vehicles [10] and vehicles fuelled with compressed natural gas (CNG) and liquefied natural gas (LNG), even produced starting from biomass, respectively named bio-CNG and bio-LNG. In fact, the scientific literature shows an increasing number of studies involving produced emission analyses and economic feasibility of these solutions compared to Diesel fuelled heavy trucks [11]. A case study with real drive cycles was conducted in British Columbia [12] and it was estimated that CNG trucks emit 15% less CO_2 than Diesel trucks, primarily depending on drivetrain technology rather than operating conditions. The same results is found in similar works [13].

However, what is mostly catching the eye nowadays is the possibility of exploiting the biomasses to produce fuels that are utterly eco-friendly [14]. In fact, electric road transport is a solution which is still not sustainable as a unique for the advancement towards the “green mobility” and alternative solutions are increasingly pursued. This, in particular, is shown by the ever and ever growing interest for the study of power-to-fuels (PtF) technologies [15]. The anaerobic digestion (AD) process for the production of biogas from the municipal wastes is a well-known technology and it is suited for PtF systems. In fact, it allows one to combine the urban waste recycling and the necessity of producing natural gas from renewable sources. The biogas produced by the AD is a gaseous compound mainly consisting of methane (CH_4) and carbon dioxide (CO_2), with other minor impurities [16]. After a process of clean up, required for the poisoning components included in the biogas, this gas may undergo an upgrading process to separate, with a high grade of purity, the CH_4 from the CO_2 [17].

On the one hand, the most commonly adopted solution for the biogas upgrading is the membrane separation process [18]. This solution provides biomethane with a still significant gas purity (around 95%) and is the less expensive, so it is vastly adopted for the production of CNG. On the other hand, the biogas upgrading process with the highest percentage purity of the final biomethane obtained as by-product is the liquefaction [19]. The LNG is mainly obtained by means of the cryogenic separation process. However, this process is high-energy demanding since the biogas must be compressed up to 20 MPa and cooled down to -161°C [20]. Naquash et al. [21] provided an energy and exergy analysis of the biomethane liquefaction process with mixed-refrigerant followed by CO_2 solidification. The process simulated in Aspen and validated with experimental data showed a 68.6% of energy saving with respect to the case in absence of CO_2 solidification. Furthermore, a beneficial specific consumption of 0.49 kWh/kg was observed with respect to the base case where 1.57 kWh/kg were required. The greatest exergy rate is due to the cryogenic heat exchangers. In [22] the authors compare two different upgrading options, namely cryogenic separation and ammine absorption, combined with liquefaction for LNG production. Models were simulated in Aspen and optimized for minimization of energy consumption. In case of cryogenic upgrading, the specific consumption resulted of 2.07 kWh/kg whereas for ammine absorption, a value of 3.35 kWh/kg was obtained, also considering the heat required for regenerating the ammines. In reference [23], a comparative energy, environmental and economic analysis is proposed for the biogas upgrading and distribution of CNG and LNG. As a result of the analysis, it was obtained that differences among different biogas upgrading and biomethane liquefaction technologies, using a life cycle analysis, are marginal, especially in case of long-distance transportation of the gas. However, the longer the distance to the customer, the more convenient the bio-LNG with respect to the bio-CNG.

The aim and novelty of the work here proposed can be summarized in the following points:

- Development of an innovative layout based on a plug flow reactor fed by organic fraction of municipal solid waste for the production of biogas, equipped with biogas upgrading unit and biomethane liquefaction unit
- Adoption of a solar PV system with lithium-ion battery for analysis of the specific energy consumption for the production of the bio-LNG
- Thermoeconomic analysis of the model in dynamic operating conditions with specific case study for meeting the fuel demand of a fleet of heavy-duty trucks

2. Layout

The layout of the system is shown in figure 1.

In the proposed system configuration, the whole liquefied biomethane production is based on the anaerobic digestion (AD) of the organic fraction of municipal solid wastes (OFMSW) within a plug flow reactor (PFR). The PFR is fed by the biomass, converted in biogas by the AD process. The biogas production is almost constant in rated operating conditions and a buffer is equipped downstream the PFR to ensure constant operating

conditions of the biogas upgrading unit [24]. The thermal demand of the digester is partially met by evacuated tube solar collectors (ETC), the integration occurs by means of a biomass-fed auxiliary boiler.

The biogas upgrading unit is a hollow fiber three-stage membrane compression system which separates the methane from the carbon dioxide. The three-stage compression is intercooled by means of sea water heat exchangers, so the inlet temperature from the cold side continuously changes. Thus, the energy consumption of the process is not constant despite the constant operating flow rate of biogas. The biomethane obtained as a by-product from the separation of the carbon dioxide is supplied to the liquefaction unit, operating according to the Linde industrial process [25]. Details of the models are discussed in the following section. Here only the final result of the process is explained. In fact, the biomethane is cooled down to the saturation temperature at ambient pressure and the liquid phase is separated from the steam phase. The former one is captured and sold as LNG, the latter is instead used to refill the process and repeat the cycle. The precooling of the biomethane is realized by means of an ammonia electric chiller, then a lamination valve realizes the final cooling. This whole cycle of biomethane production and liquefaction is also equipped with a PV system and a Lithium-Ion battery (LIB). This equipment is considered to partially meet the energy demand of the process and increase the share of renewables in the overall bio-LNG production. The PV system coupled with the LIB is responsible for meeting the load of the upgrading unit and the liquefaction unit, together with the auxiliary electricity-driven devices.

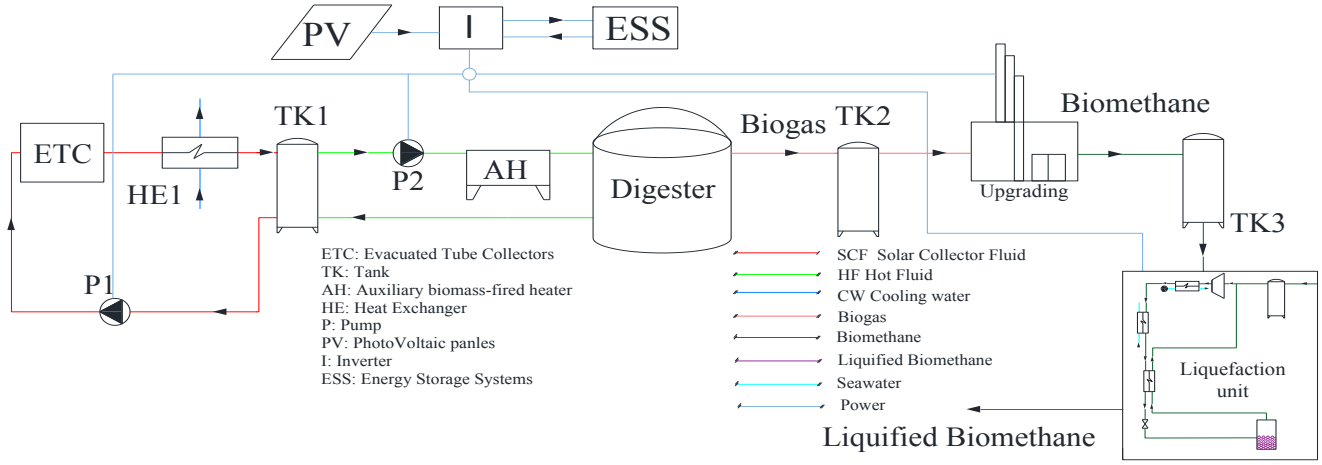

Figure. 1. Layout of the plant.

3. Model

In this section the main models developed by the authors are shown and discussed. The models are first developed in MatLab and then integrated in TRNSYS environment to perform the dynamic simulation of the plant including all the technologies proposed. Furthermore, the thermoeconomic model adopted to perform the energy, environmental and feasibility analysis of the solution proposed is shown. The following models are proposed by the authors and discussed in this work:

- Plug Flow reactor for the biogas production
- Membrane separation for the biogas upgrading
- Biomethane liquefaction

3.1. Plug Flow reactor

The plug flow reactor (PFR) model here developed is based on the discretization of the system of partial differential equations for the anaerobic digestion and the heat transfer phenomena occurring in the reactor. The model has been widely explained by the authors in previous works [26], together with its validation. The biological model is based on the anaerobic digestion model n.1 (ADM1) with some simplified assumptions on the number of species taking part to the process, eq.(1) [26]. The thermal model is instead based on the well-known heat transfer equation for heat exchangers, eq.(2) [27]. In addition, the thermal balance between the digester and the environment is considered, see eq.(3) to understand how dynamically varies the thermal demand basing on the heat loss to the ambient. The main equations involved in the model are thus the following:

$$\frac{dC_{w,i}}{dt} = \frac{\dot{V}_{w,in}}{V_w}\left(C_{w,i,in} - C_{w,i}\right) + \sum_j \rho_j \nu_{i,j} \tag{1}$$

$$\dot{m}_{wat} C_{p,wat} \left(T_{in,wat} - T_{out,wat} \right) = n U_{HE,n} A_{HE,n} (\overline{T}_{in,wat} - \overline{T}_{react}) \tag{2}$$

$$\dot{m}_{OFMSW} C_{p,OFMSW} T_{in,OFMSW} + \dot{m}_{wat} C_{p,wat} \left(T_{in,wat} - T_{out,wat} \right) - \dot{m}_{dig} C_{p,dig} T_{react} + \\ -\dot{m}_{biogas} C_{p,biogas} T_{react} - \dot{Q}_{loss} = \rho_{OFMSW} V_{OFMSW} C_{p,OFMSW} \frac{dT_{react}}{d\vartheta} \tag{3}$$

Where $C_{w,i}$ is the concentration of the bacterial species considered, $V_{w,in}$ is the input waste volumetric flow rate, V_w is the volume occupied by the biomass in the digester, $C_{w,i,in}$ is the concentration of the i-th species in the input flow rate. The last term is the sum on the j-th process of all the kinetics terms times the reaction coefficient of the i-th biochemical species involved in the j-th process. The temperature at which the kinetic terms of the biological process are iteratively calculated according to the thermal balance on the digester and the heat exchange with the inner water heat exchanger.

3.2. Membrane separation

The biogas upgrading process is based on a three-stage hollow fiber membrane compression unit in which each stage includes a double stage compression with inter-refrigeration by means of seawater heat exchangers, see figure 2.

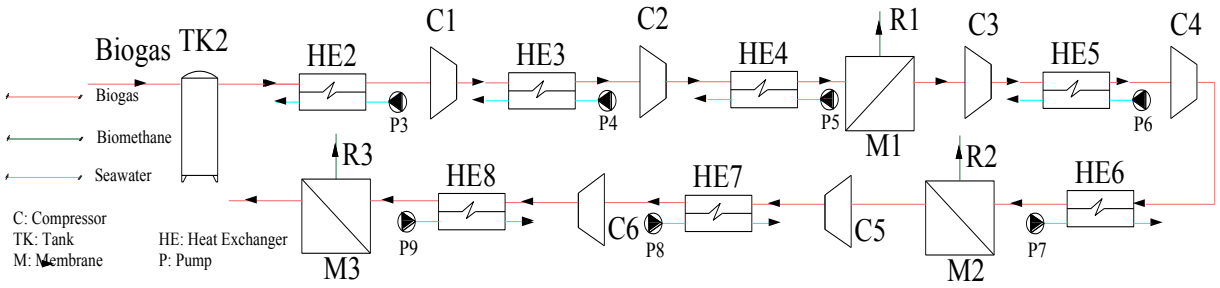

Figure. 2. Membrane separation unit.

The gaseous compound compressed is sent to the membrane at the end of each stage and the different permeability of CH_4 and CO_2 at a given operating pressure and temperature drive the separation process. In fact, due to the different permeability of the gases, two different streams are obtained, one rich in CH_4 (retentate) and one rich in CO_2 (permeate) [28]. The detailed model of the system of equations describing the process is discussed in [29].

3.3. Biomethane liquefaction

The biomethane obtained from the biogas upgrading process is the liquefied by means of a Linde cycle where the biomethane itself is the working fluid, see figure 3.

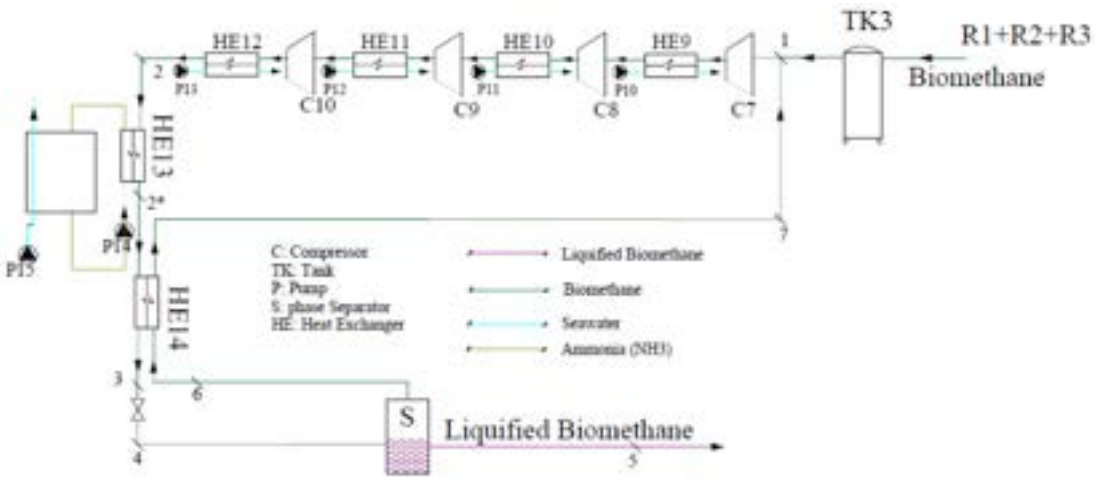

Figure. 3. Biomethane liquefaction unit.

The biomethane first undergoes an inter-refrigerated multi-stage compression up to the rated operating pressure of the cycle of 20 MPa. Here, the temperature is still the ambient temperature, T = 25°C. Then, the biomethane is cooled down to the temperature of -50°C through the evaporator of an ammonia electric chiller.

This heat exchanger HE13 is pivotal to drive the operation of the cycle in the transient conditions, since after this precooling the biomethane is furtherly cooled down by means of the regenerative heat exchanger HE14. After this, a throttling valve is used to decrease the pressure of the biomethane down to the ambient pressure and obtained saturated steam. The liquid fraction of the biomethane is spilled and stored, whereas the steam is used as cold fluid for the HE14 and then as a refill for the cycle. The model is developed in MatLab and iteratively calculates the variables T_3, T_7 and x_4 by means of the following system:

$$\begin{cases} h_4 = h_6 x_4 + h_5 \cdot (1 - x_4) \\ \dot{Q}_{HE14} = \dot{m} \cdot x_4 \cdot (h_7 \cdot - \cdot h_6) \\ \dot{Q}_{HE14} = \dot{m} \cdot (h_{2^*} \cdot - \cdot h_3) \end{cases} \quad (4)$$

Where Q is the heat transfer rate and h is the enthalpy of a specific state point.

There is no direct validation of these models against experimental data but each of them is based on well-known and globally accepted equations for the calculation of the biogas production, the membrane separation, and the Linde cycle. Therefore, the model as a whole can be considered intrinsically valid, since all the results are also consistent with data available from literature.

3.4. Thermoeconomic model

The thermoeconomic analysis is based on a widely adopted approach which allows to evaluate the energy, environmental, and economic performance of the proposed system (PS) with respect to the reference system (RS) by means of few key performance indicators [30]. The RS in this case is the one including the heavy-duty trucks equipped with Diesel engines, with the fuel provided by the GPL stations. In the PS, the heavy-duty trucks are equipped with LNG engines whose fuel demand is partially met by the renewable plant described. The Primary Energy Saving (PES) is calculated as $\Delta PE/PE_{,RS}$ where ΔPE is:

$$\Delta PE = PE_{RS} - PE_{PS} = \left(M_{Diesel} LHV_{Diesel}\right)_{RS} - \left[\frac{E_{el,fromGRID} - E_{el,toGRID}}{\eta_{el,grid}}\right]_{PS} \quad (5)$$

Where $\eta_{el,grid}$ is the efficiency of the national electric grid, $M_{LNG,dem}$ is the fuel demand of the heavy-duty trucks adopting LNG engines and $M_{LNG,prod}$ is the LNG produced by the renewable plant proposed. The CO_2 emissions saved are calculated according to the emissions factors of electricity and diesel consumed [31]:

$$\Delta CO_2 = CO_{2,RS} - CO_{2,PS} = \delta_{trucks} f_{trucks,D} - \left(E_{el,fromGRID} - E_{el,toGRID}\right) f_{EE} \quad (6)$$

Where δ_{trucks} is the total distance covered by the heavy-duty trucks and $f_{trucks,D}$ is the CO_2 equivalent emission factor for Diesel fuel trucks [31].

The economic feasibility is instead evaluated by means of the cost savings due to the PS:

$$\begin{aligned} \Delta C &= C_{RS} - C_{PS} \\ &= (V_{Diesel} c_{u,Diesel})_{RS} - (E_{el,fromGRID} c_{u,EE} + M_{wc} c_{wc} + E_{el,toGRID} p_{u,EE} - CIC + M)_{PS} \end{aligned} \quad (7)$$

Where the term M represents the maintenance costs whereas CIC is referred to the fundings granted by the Italian Government for the production of biomethane from municipal organic wastes [24]. More precisely, for the calculation of the operative costs for both the RS and the PS, the carbon tax for the CO_2 emissions due to fossil fuels consumption is considered [32].

The capital cost of the system includes the cost for the replacement of the trucks, the digesters, the collectors, the photovoltaics, the storage units, the liquefaction units, the membranes, the heat exchangers, and all the auxiliary components. The correlations for the costs of all of the components can be found in previous works of the authors [33]. From the values calculated, is possible to calculate the main thermoeconomic indicators such as the Primary Energy Saving (PES), the Simple Payback (SPB), and the Net Present Value (NPV) [24]. Table 1 shows the main parameters used for the thermoeconomic analysis. More information about the costs of the components can be found in previous works of the authors [33].

Table 1. Parameters used in the thermoeconomic analysis.

Parameter	Description	Value	Unit
$c_{u,EE}$	Electricity purchasing cost	0.20	€/kWh
$p_{u,EE}$	Electricity energy exporting cost	0.05	€/kWh
c_{wc}	Woodchip purchasing cost	0.06	€/kg
$c_{u,Diesel}$	Diesel purchasing cost	0.805	€/L

LHV_{Diesel}	Diesel lower heating value	12.67	kWh/kg
LHV_{wc}	Biomass lower heating value	3.70	kWh/kg
LHV_{LNG}	LNG lower heating value	15.33	kWh/kg
LHV_{biogas}	Biogas lower heating value	5.86	kWh/Sm^3
J_{ETC}	Evacuated thermal collectors unit capital cost	300	€/m^2
J_{PV}	PV panels unit capital cost	1000	€/kW
J_{LIB}	Lithium-ion battery unit capital cost	200	€/kWh
J_{CH-NH3}	Ammonia chiller specific cost	2076	€/kW
J_{mem}	Membrane unit capital cost	50	€/m^2
J_{D2LNG}	Replacement unit cost from Diesel to LNG truck	84.72	k€/truck
M_{plant}	Plant yearly maintenance	1.5	%/year
K_{mr}	Membrane replacement price	25	€/m^2
v	Replacement rate	0.25	1/year
$\eta_{el,Grid}$	Electric efficiency of the public power grid	0.46	-
$\eta_{th,boiler}$	Thermal efficiency of the auxiliary heater	0.95	-
f_{EE}	Electric energy equivalent CO_2 emission factor	0.483	$kgCO_2$/kWhel
$f_{trucks,D}$	Diesel truck equivalent CO_2 emission factor	0.942	$kgCO_2$/km
CIC	Certificate of release for consumption	375	€/CIC

4. Case study

The techno-economic analysis of the proposed system is evaluated for a case study in the region of Campania, in the South of Italy. More specifically, the liquefied biomethane produced with the layout described is supposed to fully meet the fuel demand of a fleet of heavy-duty trucks. The trucks considered for the case study are the ones that everyday transport the containers (TEU) arriving as freight shipments in the port of Naples. The TEU are handled in the port and transported by means of heavy-duty trucks to the several distribution points where other TEU are withdrawn, in a continuous back-and-forth trading. According to the latest report of the Port System Authority [34], the total number of hinterland TEU daily handled in the port of Naples in 2022 was around 1440 TEU/day. The assumption of the model proposed is that half of these are incoming and half are outgoing, thus for each trade considered the trucks move one TEU from Naples to the distribution point and viceversa. On the base of this assumption, 720 heavy-duty trucks everyday take part to this trading system. The distribution points considered for the reference year are the cities of Caserta, Benevento, Isernia, Frosinone, Latina, and Salerno, see figure 4.

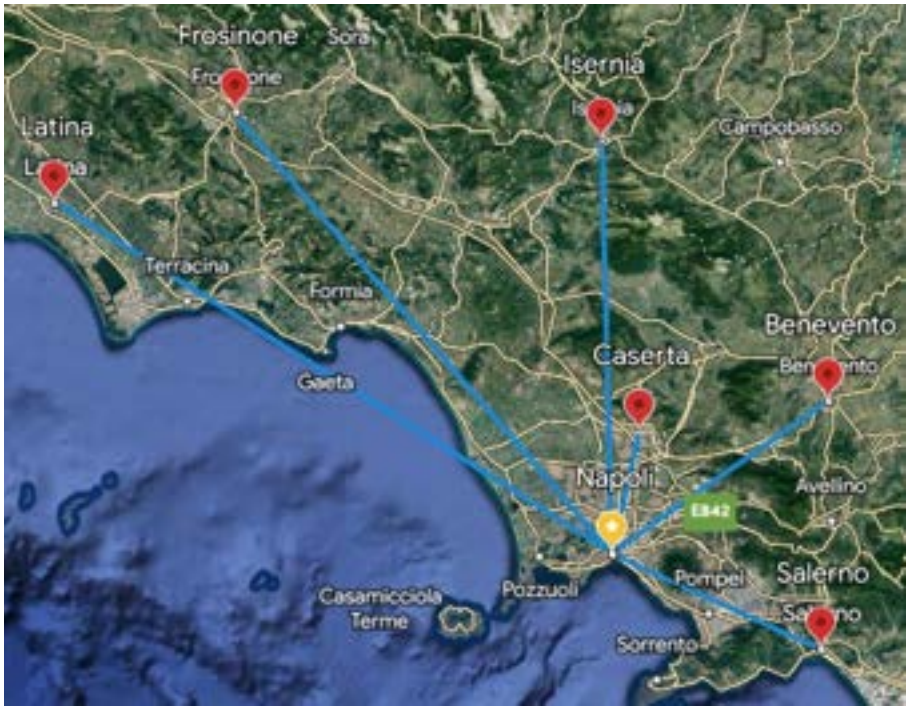

Figure. 4. Distribution map of the heavy-duty tracks transporting the containers.

Each truck runs for an average of 200 km every day mainly on highway roads, which means that the total distance daily covered by the fleet is 144´000 km/day. To cover this distance in the RS, 90´000 L/day of Diesel fuel are required, given a specific fuel consumption of 0.623 L/km [31]. According to data in table 1 and table

2, this fuel demand is equivalent to roughly $3.5x10^8$ kWh of primary energy, which is equivalent to roughly 23´000 tons/year of LNG. To meet this demand with the PS, the necessary amount of OFMSW needed is roughly 353´200 tons/year. According to data discussed in the "Report on Management of Municipal Waste in Campania" [35], around 625´000 tons/year of OFMSW are harvested, 65% of which come from the area of Naples, Caserta, and Salerno. Therefore, the biomass demand is fully met by the region and the collection points are possibly located very close to the TEU distribution points. In this case, 5 massive bio digestion plants are supposed to be dislocated in these areas, neglecting the energy costs for the fuel displacement due to the position with respect to the trucks displacements. Each plant is composed of 4 parallel PFRs of 2´580 m^3 operating with 2´016 kg/h of biomass and producing an average of 1´231 Sm3/h of biogas each. The biogas is then collected and sent to a membrane upgrading unit of roughly 2´850 m^2. Each plant is thus able to produce an average of roughly 530 kg/h which is sufficient to fully meet the LNG demand of the fleet. Detailed data regarding the case study are shown in table 2 and table 3.

Table 2. Main technical features of the case study proposed.

Parameter	Description	Value	Unit
δ_{trucks}	Distance covered by trucks	200	km/day
$Cs_{,Diesel}$	Diesel fuel truck specific consumption	0.623	L/km
ρ_{Diesel}	Density of the Diesel fuel	0.85	kg/L
M_{Diesel}	Mass of Diesel fuel required	27´922.5	tons/year
M_{LNG}	Mass of LNG required	23´077.5	tons/year
X	Rated quality of Linde Cycle	0.58	-
M_{bioCH4}	Rated flow rate of biomethane	6´272	kg/h
M_{OFMSW}	Organic municipal waste harvested in Campania	625´000	tons/year

Table 3. Technical data of the digesters.

Parameter	Description	Value	Unit
$\dot{m}_{OFMSW}$	Mass flow rate of OFMSW	2016	kg/h
ρ_{OFMSW}	Density of OFMSW	750	kg/m^3
$C_{p,\,OFMSW}$	Specific heat of OFMSW	2.72	kJ/(kg K)
$\dot{m}_{W,\,in}$	Mass flow rate of the inlet hot water range	1400÷9000	kg/h
T_{amb}	Ambient temperature range	-2 ÷ 35	°C
$T_{W,\,in}$	Inlet hot water temperature range	40 ÷ 60	°C
HRT	Hydraulic Retention Time	30	days
T_{dig}	Digester temperature	38	°C
H_{react}	Height of digester	10	m
n_{react}	Number of reactors operating in parallel	4	-
n_{plant}	Number of plants in operation	5	-

4. Results

The hourly, monthly, and yearly results of the simulation are presented and discussed in this section. Figure 5 shows the dynamic results for the electricity flow rates.

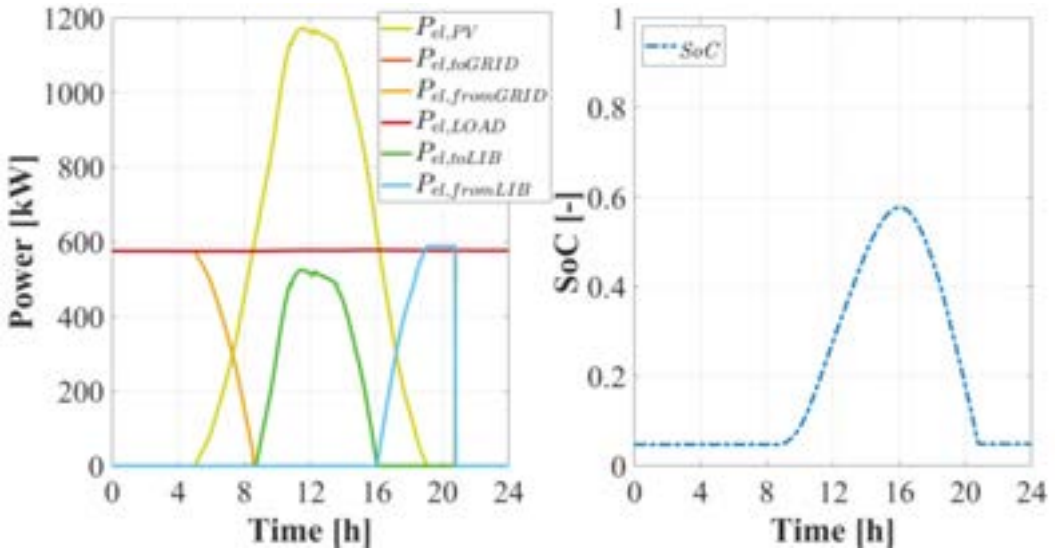

Figure. 5. Dynamic results for power flow rates.

The electricity flows shown here regard a single plant with 4 digesters operating with the biogas upgrading unit and the liquefaction cycle. The load of the plant is almost constant due to the possibility of operation in rated conditions, as it is common for optimal management of these technologies [29]. The day shown in figure 4 is a summer day so the electricity demand is met by the PV for large part of the day – 5 AM to 5 PM – with a remarkable fraction integrated with the battery in the other hours. In fact, the PV excess is relevant and the battery is filled up to roughly 60% allowing to extend the share of renewable power until 9 PM.

Figure 6 shows the monthly results of the simulation considering the total amount of energy for all the plants proposed.

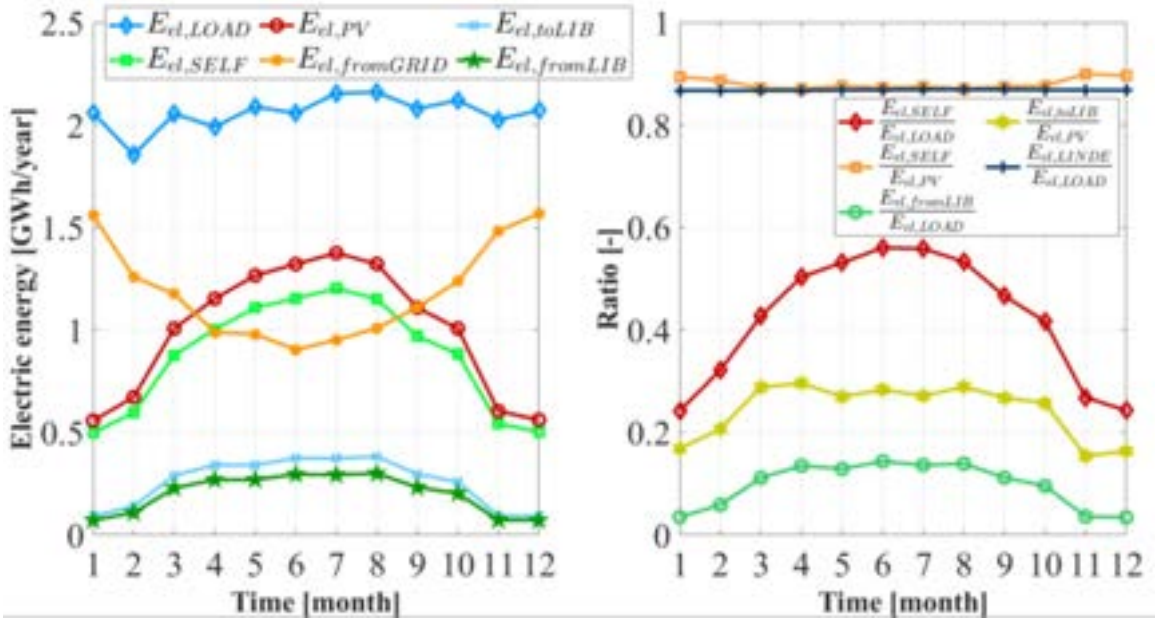

Figure. 6. Monthly results for the electric energies.

In the proposed system, the usage of the battery is pivotal to increase the share of renewables, since almost 30% of the PV energy is collected by the battery each month. The renewable fraction with respect to the PV energy, in fact, is constantly higher than 85%, see $E_{el,SELF}/E_{el,PV}$, and it reaches a peak of roughly 60% with respect to the total load in the summer period, see $E_{el,SELF}/E_{el,LOAD}$. The dynamic trend is thus confirmed and the battery is almost always fully exploited, with just a slight energy dispatching of few kWh in the summer period. However, the electricity sent to the grid is always negligible. This result is crucial since the production of bioLNG with this PS does not affect the electric grid and allows a great reduction of fossil fuel energy consumption. Furthermore, monthly trends also show that large fraction of the energy consumption is due to the liquefaction cycle, see $E_{el,LINDE}/Ee_{l,LOAD}$, as it was expected.

The trends discussed are confirmed by the results shown in Table 4. Furthermore, yearly results show a great economic feasibility of the solution presented.

Table 4. Results of the yearly analysis.

Parameter	Value	Unit
$E_{el,Upgrading}$	3.24	GWh
$E_{el,Linde}$	21.44	GWh
$E_{el,LOAD}$	24.71	GWh
$E_{el,fromGRID}$	14.22	GWh
$E_{el,toGRID}$	0.00	GWh
$E_{el,self}$	10.49	GWh
$E_{el,PV}$	11.95	GWh
$E_{el,toLIB}$	3.08	GWh
$E_{el,fromLIB}$	2.42	GWh
$E_{el,self}/E_{el,LOAD}$	0.424	-
$E_{el,fromLIB}/E_{el,LOAD}$	0.098	-
$E_{el,fromGRID}/E_{el,LOAD}$	0.575	-
$E_{el,toGRID}/E_{el,PV}$	0.000	-
$E_{el,self}/E_{el,PV}$	0.878	-
$E_{el,Upgrading}/E_{el,LOAD}$	0.131	-
$E_{el,Linde}/E_{el,LOAD}$	0.868	-
PE_{RS}	353.78	GWh
PE_{PS}	30.91	GWh
ΔPE	322.87	GWh
PES	0.91	-
$CO_{2,RS}$	49511.5	tons/year
$CO_{2,PS}$	6868.5	tons/year
ΔCO_2	0.86	-
$M_{biomethane}$	$5.5\ 10^7$	kg/year
M_{LNG}	$2.3\ 10^7$	kg/year
$M_{LNG}/M_{LNG,demand}$	1.00	-
C_{inv}	84.19	M€
C_{RS}	26.44	M€/year
C_{PS}	-20.33	M€/year
ΔC	46.77	M€/year
SPB	1.80	years
NPV	402.22	M€
PI	4.78	-

The primary energy consumption in the RS, when the Diesel fuel required is considered, is by far larger than the one of the PS. In fact, in this case only the amount of electricity withdrawn from the grid is responsible for fossil fuel consumption since the bioLNG produced meets all the fuel demand of the fleet of trucks, and the PES is equal to 91%. At the same time, the CO_2 emissions are reduced by 86%, also due to the fact that the thermal energy demand of the digesters is fully met by renewables, ETC and auxiliary biomass-fed boilers.

The economic feasibility is due to strong incentives both for the usage of bio-fuelled trucks and the production of biomethane from organic municipal wastes. In fact, Italian Government provides double fundings both for the purchase of bioLNG trucks and the dismissal of old Diesel fuelled trucks, and for the production and selling of “advanced” biomethane produced from organic wastes. In this case, the relevant capital costs of such a proposed solution, higher than 84 M€, are widely justified by the great reduction of the operative costs which lead to a yearly money saving of 46.77 M€/year. The fundings due to the CIC for biomethane vastly overcome the extra costs necessary for the maintaining of the plants and the withdrawal of electricity form the grid. The outstanding result in terms of profitability of the solution is highlighted by the NPV which is equal to 402 M€, almost five times the initial investment.

Figure 7 shows a parametric analysis considering different prices for the purchasing of urban waste for the disposal. In fact, Government may pay the ones who assume the responsibility of the urban wastes disposal.

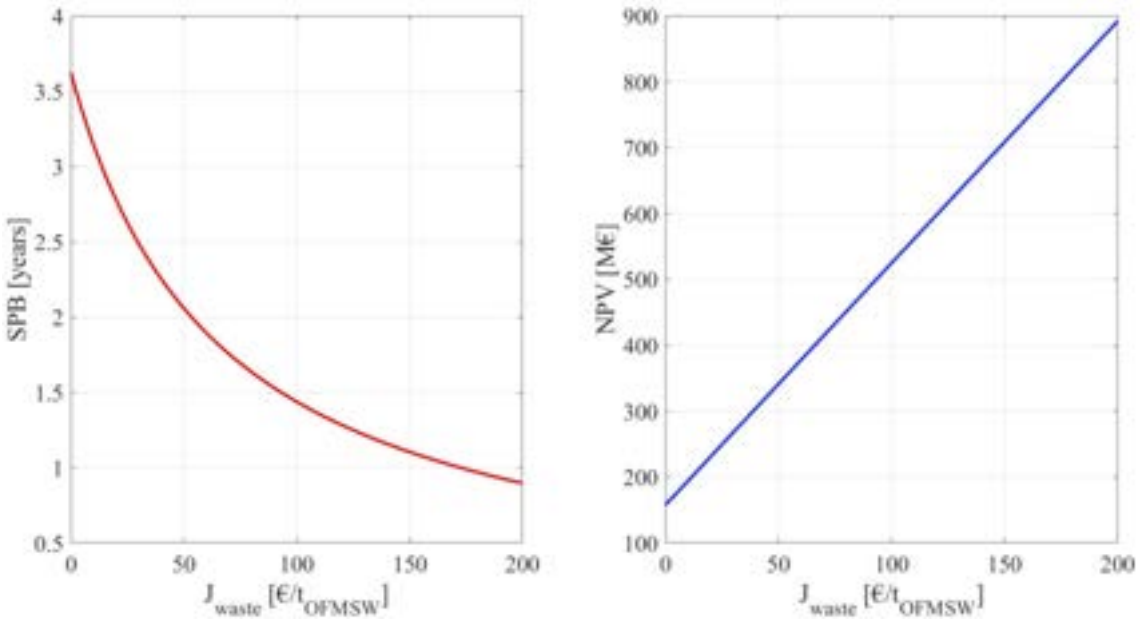

Figure. 7. Dynamic results for power flow rates.

The purchasing price for the disposal (J_{waste}) ranges from 0 to 200 €/ton of waste, treated to be used as biomass for the anaerobic digestion plants. In this case the CIC were not considered in the calculation of the economic indexes since with CIC the biomethane produced is already paid twice because of the treatment of the organic fraction of municipal solid wastes. In this case the SPB of the system could be even more profitable when the value of J_{waste} is greater than 70 €/ton. The same occurs for the NPV, with a constantly linear increase. It is worth noting that further increasing of J_{waste} over 250 €/ton would not come with relevant beneficial effect on the SPB of the system.

5. Conclusion

This work proposed a thermoeconomic analysis of a liquefied biomethane production plant proposed for several cities in the region of Campania, in the South of Italy. The proposal of these plants was to meet the fuel demand of a fleet of Diesel fuelled heavy-duty trucks which transport containers back and forth from the port of Naples. The main results obtained from the dynamic simulation and thermoeconomic analysis of the model proposed are the following:

- Five plants each one including four plug flow reactors operating 2016 kg/h of organic fraction of municipal solid wastes are able to fully meet the fuel demand of the fleet, equal to roughly 23000 tons/year of liquefied biomethane.
- The system proposed has large share of renewables since the thermal demand of the digesters is met by evacuated tube collectors and biomass fed boilers. In fact the Primary Energy Saving is remarkable and equal to 91%. At the same time the CO2 equivalent emissions avoided are equal to 86%.
- In addition, the system shows also great economic feasibility due to the grants provided by the Italian Government for the production of biomethane. Furthermore, relevant discounts are offered for the purchasing of green trucks, resulting in a Simple Payback of 1.8 years. The profitability is also shown by the Net Present Value equal to roughly 422 M€.
- Considering a premium tariff for the purchase of the urban wastes would increase the profitability of the system even more than the incentives for the selling of biomethane. In this case the Simple Payback and the Net Present Value would be even higher with a value of this tariff greater than 70 €/ton of waste.

Acknowledgments

Italian national research project:

PRIN 2020: OPTIMISM – Optimal refurbishment design and management of small energy micro-grids, funded by the Italian Ministry of University and Research (MUR).

Nomenclature

c specific cost [euro/kWh]

C operating cost [euro/y]
E energy [kWh/y]
h specific enthalpy [kJ/kg]
J capital cost [euro]
LHV lower heating value [kWh/kg]
M maintenance [euro/year]
m mass flow rate [kg/s]
M mass flow rate [kg/y]
OFMSW organic fraction of municipal solid wastes
PE primary energy [kWh/y]
T temperature [°C]
x quality [-]

Subscript

c compressor
dig digester
el electric
f emission factor [$kgCO_2/kWh$ or $kgCO_2/kg$]
HE heat exchanger
iso isentropic
LNG liquified natural gas
D diesel
p pressure
PS proposed system
RS reference system
TK tank

Greek symbol

β compression ratio [-]
ε heat exchanger effectiveness [-]
ω heat capacity ratio [-]
η efficiency [-]

References

1. Parliament, E., *Resolution of the European Green Deal. p. RSP.* 2019.
2. Köhl, M., et al., *The EU climate package "Fit for 55" - a double-edged sword for Europeans and their forests and timber industry.* Forest Policy and Economics, 2021. **132**: p. 102596.
3. EEA. *Share of transport GHG emissions*. 2020; Available from: <https://www.eea.europa.eu/data-and-maps/daviz/sds/share-of-transport-ghg-emissions-4/@@view>.
4. Chiaramonti, D., et al., *The challenge of forecasting the role of biofuel in EU transport decarbonisation at 2050: A meta-analysis review of published scenarios.* Renewable and Sustainable Energy Reviews, 2021. **139**: p. 110715.
5. Mandley, S.J., et al., *EU bioenergy development to 2050.* Renewable and Sustainable Energy Reviews, 2020. **127**: p. 109858.
6. Goetz, A.R., *Intermodality*, in *International Encyclopedia of Human Geography*, R. Kitchin and N. Thrift, Editors. 2009, Elsevier: Oxford. p. 529-535.
7. Giuliano, G., et al., *Heavy-duty trucks: The challenge of getting to zero.* Transportation Research Part D: Transport and Environment, 2021. **93**: p. 102742.
8. Council, E. *Fit for 55: towards more sustainable transport*. 2022; Available from: https://www.consilium.europa.eu/en/infographics/fit-for-55-afir-alternative-fuels-infrastructure-regulation/.

9. Feng, Y. and Z. Dong, *Comparative lifecycle costs and emissions of electrified powertrains for light-duty logistics trucks.* Transportation Research Part D: Transport and Environment, 2023. **117**: p. 103672.
10. Küffner, C., *Multi-level perspective for the development and diffusion of fuel cell heavy-duty trucks.* Transportation Research Part D: Transport and Environment, 2022. **111**: p. 103460.
11. Scopus. *Article search*. 2023; Available from: https://www.scopus.com/term/analyzer.uri?sort=plf-f&src=s&sid=4fd4e27465bd22d7fe2a51c2d07679ab&sot=a&sdt=a&sl=27&s=TITLE-ABS-KEY%28green+trucks%29&origin=resultslist&count=10&analyzeResults=Analyze+results.
12. Lajevardi, S.M., J. Axsen, and C. Crawford, *Examining the role of natural gas and advanced vehicle technologies in mitigating CO2 emissions of heavy-duty trucks: Modeling prototypical British Columbia routes with road grades.* Transportation Research Part D: Transport and Environment, 2018. **62**: p. 186-211.
13. Quiros, D.C., et al., *Greenhouse gas emissions from heavy-duty natural gas, hybrid, and conventional diesel on-road trucks during freight transport.* Atmospheric Environment, 2017. **168**: p. 36-45.
14. Kiehbadroudinezhad, M., et al., *The role of biofuels for sustainable MicrogridsF: A path towards carbon neutrality and the green economy.* Heliyon, 2023. **9**(2): p. e13407.
15. Wang, L., et al., *Power-to-fuels via solid-oxide electrolyzer: Operating window and techno-economics.* Renewable and Sustainable Energy Reviews, 2019. **110**: p. 174-187.
16. Barros, R.S., et al., *Evaluation of the methanogenic potential of anaerobic digestion of agro-industrial wastes.* Heliyon, 2023: p. e14317.
17. Hosseini, S.S., et al., *Progress in high performance membrane materials and processes for biogas production, upgrading and conversion.* Separation and Purification Technology, 2023. **310**: p. 123139.
18. Gkotsis, P., et al., *Biogas upgrading technologies – Recent advances in membrane-based processes.* International Journal of Hydrogen Energy, 2023. **48**(10): p. 3965-3993.
19. Naquash, A., et al., *State-of-the-art assessment of cryogenic technologies for biogas upgrading: Energy, economic, and environmental perspectives.* Renewable and Sustainable Energy Reviews, 2022. **154**: p. 111826.
20. Baccioli, A., et al., *Small scale bio-LNG plant: Comparison of different biogas upgrading techniques.* Applied Energy, 2018. **217**: p. 328-335.
21. Naquash, A., et al., *Renewable LNG production: Biogas upgrading through CO2 solidification integrated with single-loop mixed refrigerant biomethane liquefaction process.* Energy Conversion and Management, 2021. **243**: p. 114363.
22. Hashemi, S.E., et al., *Cryogenic vs. absorption biogas upgrading in liquefied biomethane production – An energy efficiency analysis.* Fuel, 2019. **245**: p. 294-304.
23. Gustafsson, M., et al., *Scenarios for upgrading and distribution of compressed and liquefied biogas — Energy, environmental, and economic analysis.* Journal of Cleaner Production, 2020. **256**: p. 120473.
24. Calise, F., et al., *Concentrating photovoltaic/thermal collectors coupled with an anaerobic digestion process: Dynamic simulation and energy and economic analysis.* Journal of Cleaner Production, 2021. **311**: p. 127363.
25. Ghorbani, B., et al., *Energy, exergy and pinch analyses of a novel energy storage structure using post-combustion CO2 separation unit, dual pressure Linde-Hampson liquefaction system, two-stage organic Rankine cycle and geothermal energy.* Energy, 2021. **233**: p. 121051.
26. Calise, F., et al. *Modeling of the Anaerobic Digestion of Organic Wastes: Integration of Heat Transfer and Biochemical Aspects*. Energies, 2020. **13**, DOI: 10.3390/en13112702.
27. Calise, F., et al., *Dynamic analysis and investigation of the thermal transient effects in a CSTR reactor producing biogas.* Energy, 2023. **263**: p. 126010.
28. Al-Obaidi, M.A., C. Kara-Zaïtri, and I.M. Mujtaba, *Performance evaluation of multi-stage reverse osmosis process with permeate and retentate recycling strategy for the removal of chlorophenol from wastewater.* Computers & Chemical Engineering, 2019. **121**: p. 12-26.
29. Cappiello, F.L., et al. *Thermoeconomic Analysis of Biomethane Production Plants: A Dynamic Approach*. Sustainability, 2022. **14**, DOI: 10.3390/su14105744.
30. Calise, F., et al., *A novel tool for thermoeconomic analysis and optimization of trigeneration systems: A case study for a hospital building in Italy.* Energy, 2017. **126**: p. 64-87.
31. Tratzi, P., et al., *Liquefied biomethane for heavy-duty transport in Italy: A well-to-wheels approach.* Transportation Research Part D: Transport and Environment, 2022. **107**: p. 103288.
32. Hartmann, P., A. Marcos, and J.M. Barrutia, *Carbon tax salience counteracts price effects through moral licensing.* Global Environmental Change, 2023. **78**: p. 102635.
33. Calise, F., et al., *Dynamic simulation modelling of reversible solid oxide fuel cells for energy storage purpose.* Energy, 2022. **260**: p. 124893.
34. Authority, P.S., *Port of Naples displacements - updated to 22-12-22*. 2022.
35. region, C., *Report on Management of Municipal Waste in Campania*. 2020.

Segmental application of two heat absorption intensification methods in parabolic trough collector solar loop

Bartosz Stanek[a], Daniel Węcel[b], Łukasz Bartela[c]

[a] Silesian University of Technology, Gliwice, Poland, bartosz.stanek@polsl.pl, CA
[b] Silesian University of Technology, Gliwice, Poland, daniel.wecel@polsl.pl,
[c] Silesian University of Technology, Gliwice, Poland, lukasz.bartela@polsl.pl

Abstract:

Due to climate change and worldwide policies, the importance of renewable energy sources is increasing significantly. Increasing its share of total energy consumption is essential to reduce CO_2 emissions and achieve energy independence. A commonly available source of heat is solar energy, which can be efficiently used and converted using a specific technology. For the generation of medium and high-temperature heat, CSP technologies are used, with parabolic trough collectors (PTC) being the most mature. In heat industrial power, this technology is used on a reduced scale, with a smaller aperture. The scale-down of the geometry and the lower temperature stage compared to traditional high aperture PTCs provides opportunities for optimisation and the use of alternative materials. As the temperature and heat flow parameters change in different sections of the absorber, it is optimal to introduce different methods in different areas of the solar loop. This article presents the optimization results of the use of non-selective but highly absorptive and cost-effective solar coating and twisted tape inserts in solar loop sections. The research was conducted for a case study which was a medium-sized industrial facility with a heat demand of a maximum of 250 °C. A numerical model was used for this study, validated by a previously performed experiment using a solar simulator. The results showed that both methods lead to an intensification of heat absorption, almost 45% of the absorbers can have a low-cost non-selective coating and twisted tapes with a twisted ratio of 1 and 2 can be applied inside the absorber pipes. The maximum efficiency gain was 1.3%.

Keywords:

solar energy; parabolic trough collectors; renewable energy; heat absorption; concentrated solar power.

1. Introduction

The development of renewable energy sources in parallel with energy storage is necessary to increase energy independence from fossil fuels, the availability and price of which have been strongly influenced by international policy in recent years [1,2].Due to rising raw material prices, the profitability of most technologies previously not considered due to their relatively high cost and the long payback period is increasing [3]. Another but extremely important aspect in favour of increasing the share of low- and zero-carbon sources is the positive impact on the environment [4]. Energy requirements can be roughly divided into two, in the form of electricity and heat [5]. Considering only solar energy as a clean energy source, for electricity generation the most common sources are photovoltaic panels. Heat can be generated using PV panels and heat pumps, but this solution is mainly considered for small domestic installations [6].

The greatest need for heat is in industry, which uses it in various processes. Depending on the characteristics of the company, heat can be used for manufacture of food and dairy products [7,8], drying and sterilization [9], steam production [10]. Heat, in the temperature range up to about 300 °C, can be efficiently generated by parabolic trough collectors with a low concentration ratio. It is a mature technology that has recently been scaled down and adapted to produce heat at lower temperature levels [11,12].

Reducing the temperature level opens up opportunities to increase the efficiency of these installations and reduce their manufacturing cost. It is therefore necessary to look for solutions that can be easily applied to this scaled-down version of a mature technology. These treatments are intended to increase the popularity of solar technologies mainly in the industry sector.

The methods proposed in this article for intensifying heat absorption can be divided according to their location of application: outside and inside the absorber. The first is the use of the no-selective and cost-effective coating in the individual preliminary sections of the absorber, in such a way as to increase efficiency and reduce the investment cost of the installation. The proposed coating differs from the regularly used one

in that it is not selective, so radiation losses are high but are compensated by the extremely high absorptivity of this coating. The methodology associated with such a coating application has been presented in previous work [13]. A second method of heat intensification is the use of twisted tape inserts, which is a fairly popular and mature research topic [14–16]. Twisted tapes have been tested experimentally and numerically for a wide range of parameters [17,18]. Solutions that modify traditional twisted tapes, such as the application of perforation [18] or peripherally cut [19] as well as double application [20], are also analysed. However, the literature provides no sufficient data on the application of twisted tapes for low-concentrated parabolic trough collectors, which are characterised by different boundary conditions, such as radiation distribution, temperature range or mass flow.

In this analysis, a numerical study supported by experimental results has been carried out, where we propose to use the two previously described methods sequentially in an absorber loop. The research questions that this article answers are as follows.

- Does the application of the two proposed methods increase the efficiency of the installation?
- How can both methods of heat intensification be used optimally?

2. Methods

An analysis of the combination of the two heat intensification methods developed was carried out using a mathematical model and the results of numerical tests and experimental study. Figure 1 shows the assumptions accompanying the analysis. Three absorber configurations were tested in the absorber loop. The case 1, also called the reference case, was the use of tubular absorbers with a selective coating throughout the whole absorber loop. Case 2, involved included partial application of non-selective, but cost-effective coatings in part of the absorbers in such a way that the efficiency of the installation did not decrease. Case 3 shows the addition of twisted tapes inserts to the previous (from case 2) results. In summary, the analysis first aimed to determine the number of absorbers that could be covered with a no-selective coating and then to add an additional method of intensifying heat collection through twisted tapes applied inside the absorber.

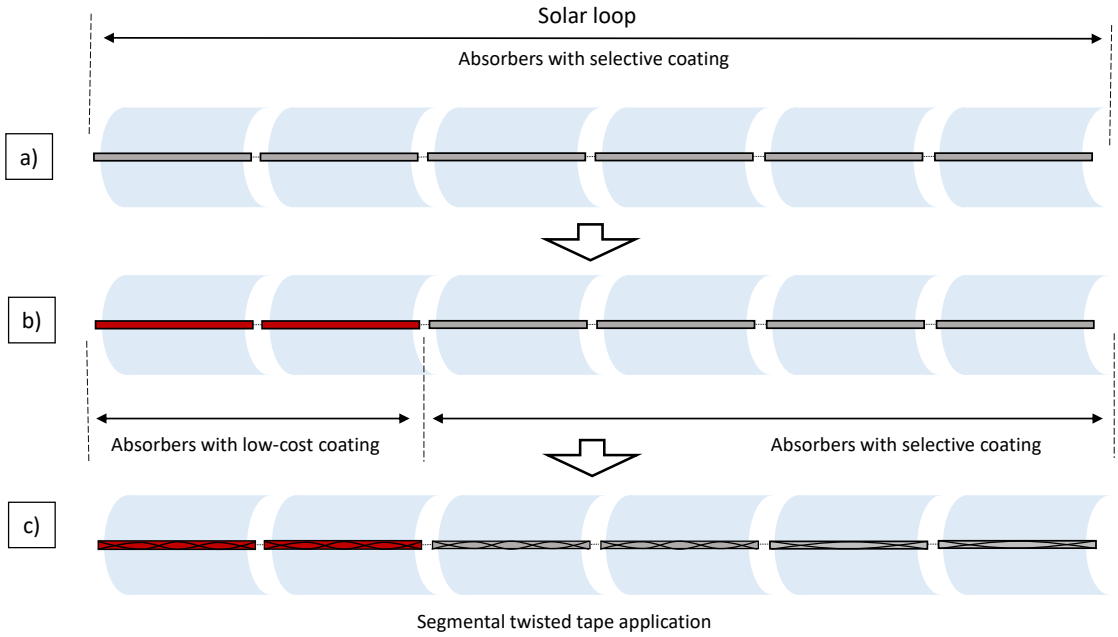

Figure. 1. Coating and twisted tapes application strategy: a) refence CASE 1 (all absorbers covered by selective coatings), b) CASE 2 with no-selective and selective coatings, c) CASE 3: combination of coatings applications and segmental twisted tapes coatings (in configuration as case 2).

2.1. Analysis assumptions

The following section outlines the assumptions that were used in the model.

2.1.1. Parabolic trough collector – geometry and operation parameters

The analysis considers a low-concentration parabolic trough collector that can produce heat for industrial applications. The geometric and optical parameters are shown in Table 1, and the most important ones which are particularly important are: aperture width 1800 mm, absorber length 1000 mm, absorber external diameter 33.7 mm. The assumed parameters are based on parabolic trough collectors manufactured serially [21].

Table 1. Geometrical and optical parameters of analysed parabolic trough collector.

Parameter	Symbol	Value	Unit
Focal length	f	0.647	m
Aperture width	W_{ap}	1.8	m
Absorber length	L_{abs}	1	m
Absorber external diameter	$d_{abs,e}$	33.7	mm
Absorber internal diameter	$d_{abs,i}$	30.7	mm
Absorber wall thickness	th_{abs}	1.5	mm
Glass env. external diameter	$d_{c,e}$	56	mm
Glass env. internal diameter	$d_{c,i}$	51	mm
Glass env. wall thickness	th_c	2.5	mm
Transmittance of glass envelope	τ_c	0.93	-
Clean mirror reflectance	η_{ref}	0.9	-
Dirt factor	η_{dirt}	0.96	-

The installation was assumed to consist of 90 absorbers connected in series, with an inlet temperature of 60 °C and a maximum outlet temperature depending on weather conditions but not exceeding 250 °C. For the analyses, the mass flow was assumed to be constant at 0.3 kg/s.

2.1.2. Heat transfer fluid

The heat transfer fluid used in the analysis was Therminol VP-1, an Eastman product widely used in solar installations and successfully used in our previous publications [22]. The operating temperature of this fluid is 12 – 400 °C. In the analysis, the data of this fluid as a function of temperature was used, based on the manufacturer's data [23]. Table 2 presents, as an example, the fluid parameters for extreme temperatures occurring in the system, i.e. 60 °C and 250 °C.

Table 2. Example Therminol VP-1 parameters [23].

Temperature, °C	Density, kg/m^3	Heat capacity, kJ/kg	Thermal conductivity, W/(m·K)	Viscosity, mPa·s
60	1032	1.662	0.1323	1.76
250	867	2.181	0.1055	0.288

2.1.3. Coatings assumptions

The analysis examined the effect of two coatings on the absorber surface. The first one was selective coating reported by Lu et al. [24] as suitable for SHIP installations. It has high absorptivity and low emissivity which reduces radiation losses. The alternative coating analysed is Pyromark 2500, which is a non-selective coating but with extremely high absorption [25]. Due to its lack of selectivity, the emissivity of the Pyromark is also high, but it is characterised by low cost and very simple application. The parameters of both these coatings are shown in Table 3.

Table 3. Coatings parameters.

Coating type	Coating name	Absorptivity	Emissivity
Selective	Mo/Al_2O_3	0.9	0.08
No-selective	Pyromark	0.965	~0.8

2.1.4. Twisted tapes

Two geometries of twisted tapes were analysed in this work, first one with twisted ratio (Tr) 1 and the second one with 2, the width of each twisted ratio was assumed equal to 28 mm and thickness 1 mm. The material used is steel. The insert is assumed to be centred on the axis of the absorber, which in reality can be realised by a specially shaped handle that centres the twisted insert. The study analysed inserts with a low twisted ratio to find the limit for which there is a benefit to its use. The twisted ratio was defines as Eq. (1):

$$Tr = H/d_{abs,i} \quad (1)$$

where, H is 180° turn length and $d_{abs,i}$ is internal diameter of absorber.

2.2. CFD model

Numerical calculations were performed in ANSYS Fluent using a discretised 3D domain. The analysis was performed for the steady state. CFD tests were performed in the heat transfer fluid region, where constant mass flow and inlet temperature were assumed. It was assumed that twisted tape is used as a swirl flow forming element and is not involved in heat transfer. In the analysis, the k-ω SST turbulence model listed in the literature as the most optimal for this type of analysis was used [26]. To determine the influence of the numerical grid on the results, a grid independence test was performed, analysing five grids with the parameters shown in Table 4.

Table 4. Analysed numerical meshes.

Grid no.	Number of elements	Average Nusselt number
1	244 283	273.6
2	1 320 067	286.6
3	1 933 627	290.0
4	2 337 226	290.4
5	3 076 697	290.6

The results showed that the difference between grids 3 - 5 is about 0.2%, so it was decided to choose grid number 4, which is shown in Figure 2.

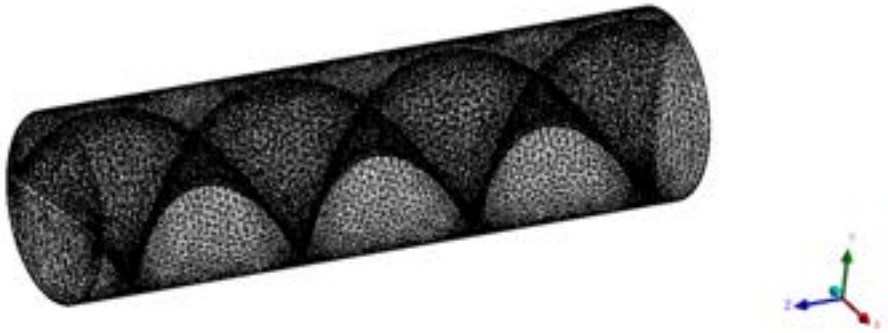

Figure. 2. Mesh used in CFD for absorber and twisted tape.

The parabolic trough collector is an installation based on a tracking system which makes it possible to utilise direct solar radiation during operation. Thus, the concentrated radiation reaching the surface of the absorber is not uniform. In CFD studies, this factor should be considered and a polynomial described distribution of radiation should be introduced by using a defined function. To obtain this distribution, optical studies were performed using the Monte Carlo Ray Tracing Method in APEX software, which has been successfully used in our previous studies [27]. An absorber with applied radiation distribution is shown in Figure 3.

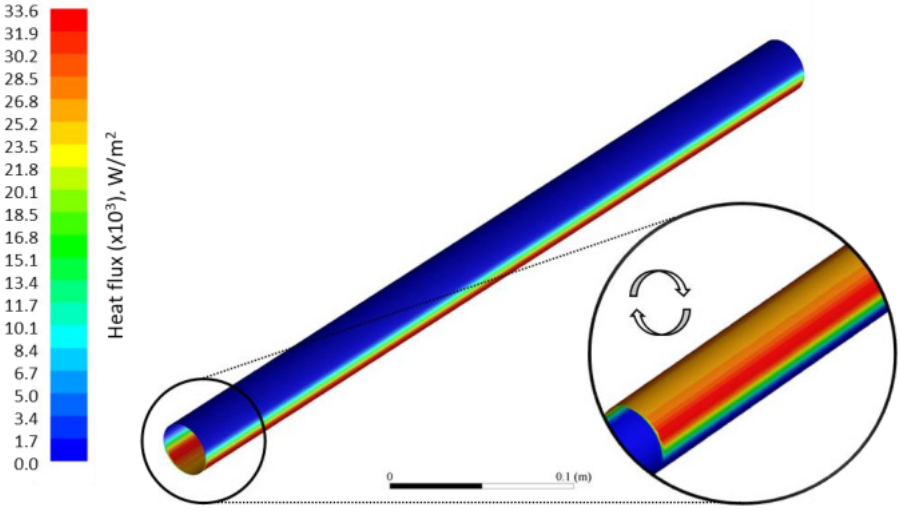

Figure. 3. Heat flux distribution on external absorber surface.

2.3. Mathematical model

In this study, a previously developed mathematical model of a parabolic solar concentrator was used, which is described in detail and validated in publication [13]. The distinguishing feature of this model from others available in the literature of the subject is the separation of heat absorbed by concentrated radiation and direct radiation (which was not reflected from the parabolic mirror). This radiation passes through a different pathway, therefore the efficiency must be calculated separately. For the high aperture PTC analysis, the influence of this factor is small, but for the low concentrated PTC, the contribution of direct radiation is more significant. The heat absorbed by the absorber is defined as Eq. (2) – (4):

$$Q_u = \dot{m} \cdot c_p \cdot (T_{out} - T_{in}), \tag{2}$$

$$Q_u = (Q_{u,CSP} + Q_{u,SP}) - Q_{loss}, \tag{3}$$

$$Q_u = ((A_{ap} - d_{abs,e} \cdot L) \cdot G_B \cdot \eta_{opt,CSP} \cdot cos\,\theta \cdot IAM + (d_{abs,e} \cdot L) \cdot G_B \cdot \eta_{opt,SP}) - Q_{loss} \tag{4}$$

where, $\dot{m}$ is mass flow rate, c_p is specific heat, T_{in} and T_{out} are inlet and outlet temperatures, $Q_{u,CSP}$ is the concentrated solar energy, $Q_{u,SP}$ is the non-concentrated solar energy, Q_{loss}- energy losses, A_{ap} is the aperture surface area, $d_{abs,e}$ is the absorber external diameter, G_B is the direct solar irradiance, $\eta_{opt,CSP}$ is the optical efficiency for CSP, θ is the incident angle, IAM is the incidence angle modifier, L is absorber length, $\eta_{opt,SP}$ is the optical efficiency for solar power. The individual efficiencies for concentrated irradiance and non concentrated irradiance, their components and how they are calculated are presented in a previous paper [13].

Furthermore, when twisted tapes are used, it is necessary to consider the effect of the pressure drop on the requirements of the circulating pump. For this purpose, efficiency of PTC is defined as Eq. (5):

$$\eta_{PTC} = \frac{Q_u - \frac{W_p}{\eta_{el}}}{Q_s} \tag{5}$$

where, W_p is required pump power, Q_s is heat from sun and η_{el} is average reference electricity production efficiency. For purposes of this analysis, the value 32.7% is selected [28].

A pumping work demand for the fluid movement is calculated as Eq. (6):

$$W_p = \frac{\dot{m} \cdot \Delta P}{\rho} \tag{6}$$

where, ΔP is pressure drop, ρ is fluid density. The pressure drop was determined using the Darcy-Weisbach equation.

2.4. Models validation

Validation of the numerical model presented in section 2.3 was performed using the solar radiation simulator test rig and parabolic trough collectors presented in previous publications [29] and conference presentations [30]. The test stand is shown in Figure 4.

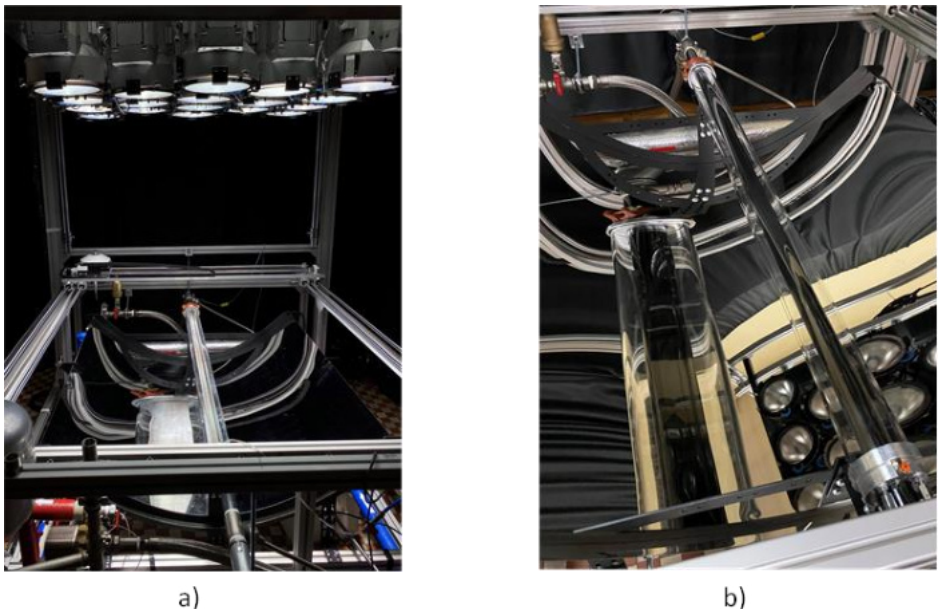

a) b)

Figure. 4. Experimental test stand: a) solar simulator and parabolic trough collector under experimental campaign, b) linear absorber covered by Pyromark coating in collector focal length.

The test rig consists of 18 metal halide lamps, each with a nominal power of 575 W, and a parabolic solar concentrator with aperture and length of 1000 mm, and absorber with diameter of 33.7 mm covered by Pyromark coating with glass envelope and vacuum in between. For temperature incensement for plane absorber the RMSD was 1.02, for absorber with twisted tape with twisted ratio 3.8 RMSD was 1.43. For pressure drop measurement RMSD was as follows: plane absorber RMSD = 5.8, absorber with insert Tr = 3.8 RMSD = 7.5.

Validation of the mathematical model presented in section 2.4 was performed using experimental data provided by the National Renewable Energy Laboratory (NREL) [31] and indicated an RMSD of 2.54 for absorber temperature and 3.52 for heat loss, which confirms its agreement with reality.

3. Results and discussion

The first part of the analysis was to determine the maximum number of absorbers in preliminary sections of the solar loop that would not result in a reduction in efficiency compared to the reference value (all absorbers covered with selective coating CASE 1). Tests were carried out for various values of direct radiation and the results are shown in Figure 5. For $G_B \geq 300$ W/m^2, the potential for partial replacement of absorbers with low-cost coatings is clearly visible. For $G_B = 300$ W/m^2, the maximum number of absorbers with Pyromark coating that can be used is 40. For higher radiation values, the possible number of absorbers increases, but assuming a worst-case scenario, a value of 40 was chosen for further consideration.

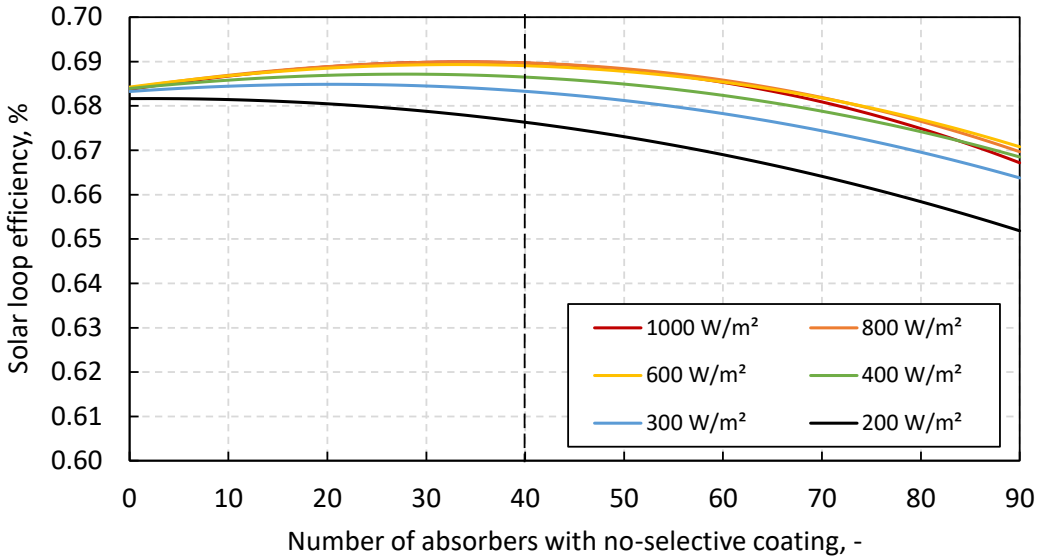

Figure. 5. Absorber loop efficiency as a function of absorber numbers with no-selective coating.

The next stage of the analysis was to test the effect of twisted tapes on increasing the intensity of heat absorption by the fluid. Twisted tapes cause swirl flow, which intensively mixes the fluid inside, resulting in an increase in velocity and thus in the number of Reynolds and an intensification of heat absorption. What is more, this flow character results in a reduction in the temperature difference at the absorber surface, which reduces material stress and increases the life span of the installation. However, the placement of any element inside the tubular absorber results in increased pressure losses which force higher own energy needs to drive the circulation pump.

Considering the pumping demand (Eq. (6)) in the efficiency of the PTC loop (Eq. (5)), it is possible to determine the efficiency increment resulting from the use of an insert with a specific twisted ratio. Fig. 6 shows the increase in efficiency ratio relative to the reference case for a specific thermal fluid temperature. The graph highlights two data series, for twisted ratio 1 and 2. It can be seen that the use of both these inserts results in an efficiency gain relative to the reference case. However, it was observed that for fluid temperatures above 200 °C the efficiency of PTC with twisted ratio 1 decreases significantly. This is due to the high velocity and relatively high-pressure drop relative to the increased intensification of heat absorption and the increased power requirement of the pump. It was therefore decided that for temperatures up to 200 °C it was appropriate to use tape with ratio 1, and above this temperature tape with ratio 2.

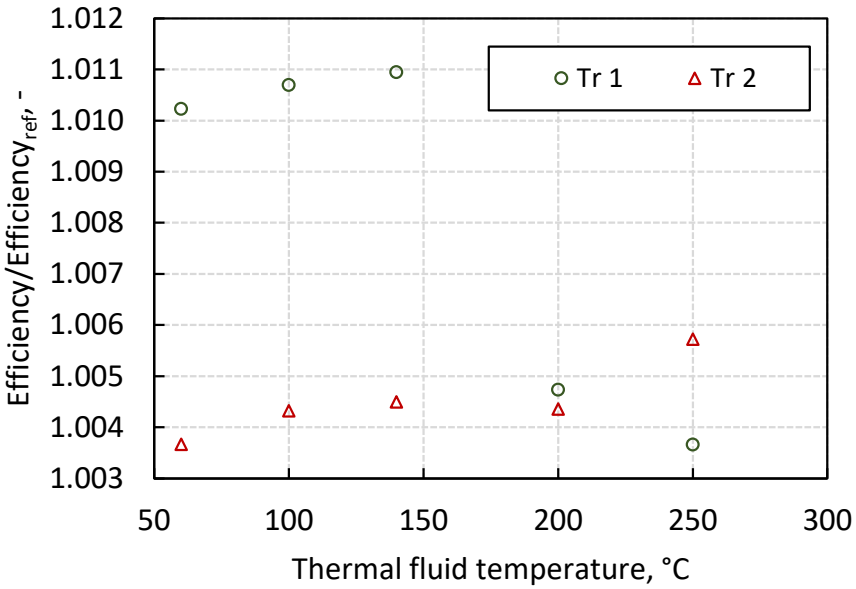

Figure. 6. Efficiency with twisted tapes to reference efficiency ratio as a function of heat transfer fluid temperature for different twisted ratio inserts.

As the application of twisted tapes has to be done for specific sections of the PTC, the next part of the analysis was, for a predefined sequence of specific absorber types, to determine where to apply which type of twisted tape. For this purpose, it was determined that a temperature above 200 °C of fluid would occur in the furthest sections of the absorbers for the case of the highest radiation value. The efficiency of absorber loop and thermal oil temperature along loop length were therefore determined and presented in Fig. 7. Based on the results, it was determined that defined temperature in the absorber loop, consisting of 90 absorbers, could occur after the 60 absorbers, so it was decided to use inserts with twisted ratio 1 in preliminary 60 metres. After the 60th absorber, twisted tape with Tr = 2 was used.

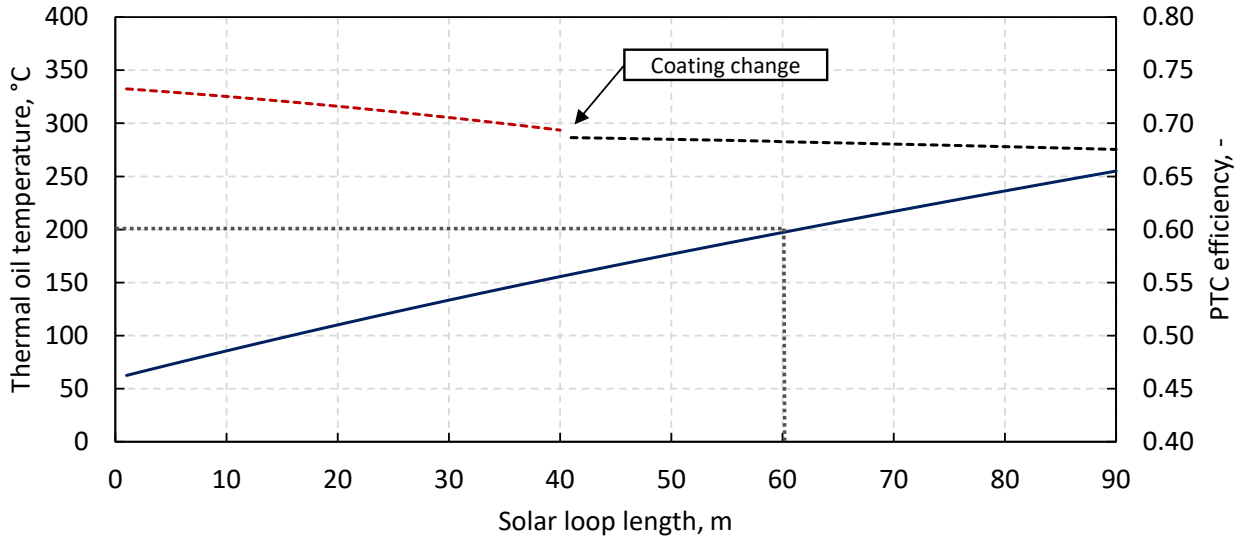

Figure. 7. Thermal oil temperature and efficiency along solar loop for G_B = 1000 W/m^2 and T_{amb} = 23°C.

To directly compare the results, a wide-parameter analysis was performed for G_B ranging from 300 to 1000 W/m^2, T_{amb} from 2 to 35 °C and wind speed of 0.1 - 5 m/s while maintaining a constant mass flow of 0.3 kg/s and T_{in} 60 °C. Case 1 has the lowest efficiency, but the most constant curve. As the parameter represented on the x axis increases, the efficiency slightly decreases. Each of the methods analysed intensifies heat absorption and increases the overall efficiency of the installation. By using absorbers with a high absorptivity value, the highest efficiency gains when the installation is operating in high solar radiation is visible. The increased absorptivity along the length of the installation largely contributes to increased heat collection and efficiency. Emission losses are largely compensated by the high absorptivity. For periods with low insolation and temperature, there is no increased heat absorption and losses to the environment are high, but no greater than the reference case. The use of twisted tapes has the effect of intensifying heat absorption throughout the whole analysed range. In periods of high solar radiation, swirl flow reduces the

temperature of the absorber wall and intensively mixes the heat transfer fluid. During periods of low insolation, twisted tape has the effect of increasing the velocity and the Reynolds number and increases heat extraction. Using only the method related to the coatings, the maximum efficiency gain will be around 0.7%, for using both methods in the configuration presented, the efficiency gain is between 0.3% and 1.3%.

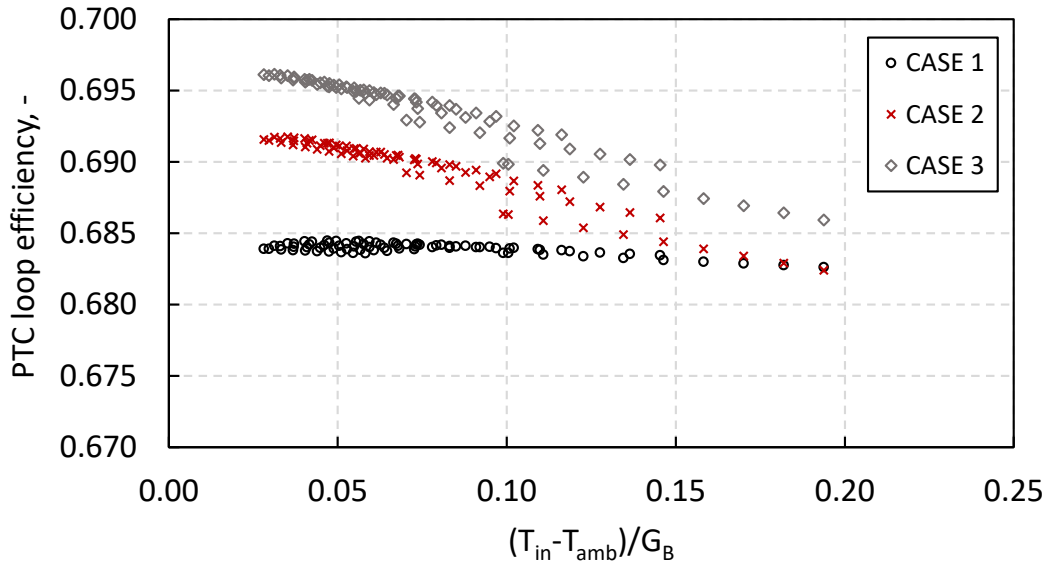

Figure. 8. PTC loop efficiency curves for 3 analysed cases.

4. Conclusions

This paper presents two methods to intensify heat absorption: externally by using a highly absorptive coating, and internally by using twisted tapes to increase flow turbulence. The following conclusions can be drawn.

- Both of the proposed methods intensify the heat collection in the absorber.
- It has been shown that it is optimal to cover 40 of the 90 absorbers with a no-selective coating.
- Besides the increased heat uptake of the absorber in this configuration, it is possible to reduce investment costs due to the low price and simplicity of the Pyromark coating application.
- Numerical tests have shown that both inserts analysed increase the heat absorption efficiency and that up to a temperature of heat transfer of 200 °C it is optimal to use an insert with twisted ratio 1, above this temperature with twisted ratio 2.
- Analysing the entire solar loop consisting of 90 absorbers, the following parameter combinations were determined: non-selective coating up to 40 absorbers, from 41 absorbers selective coating, insert with twisted ratio 1 up to 60 absorbers, from 61 absorbers twisted ratio 2.
- Efficiency increment after proposing Pyromark coatings increased from 0% to 0.7% with both methods, from 0.3% to 1.3%.

Acknowledgments

The scientific work is funded by the European Union through the European Social Fund (grant POWR.03.05.00-00-Z305).

Nomenclature

A	area, m²
c_p	specific heat, J/(kgK)
CSP	concentrated solar power
d	diameter, m
f	focal length, mm or m
G	direct normal irradiance, W/m²
H	180° turn length
IAM	incidence angle modifier
L	length, m
$\dot{m}$	mass flow
PTC	parabolic trough collector
Q	heat
RMSD	Root mean square deviation
T	temperature, °C
th	thickness, mm
Tr	twisted ratio
W	width, mm or m; or power, W
ΔP	pressure drop, Pa

Greek symbols

η	efficiency
ρ	density, kg/m3
τ	transmittance

Subscripts and superscripts

abs	absorber
amb	ambient
ap	aperture
B	beam
c	envelope
CSP	concentrated solar power
dirt	dirt factor
e	external
el	electrical
i	internal
in	inlet
loss	loss
opt	optical
out	outlet
p	pumping
ref	reflectance
s	solar
SP	solar power
u	useful

References

[1] Fossil Fuels Consumption Subsidies 2022 – Analysis - IEA – Available at:<https://www.iea.org/reports/fossil-fuels-consumption-subsidies-2022 > [accessed 15.3.2023].

[2] Renewable and Energy Storage Solutions – Available at:<https://process.honeywell.com/us/en/industries/renewable-and-energy-storage-solutions> [accessed 02.6.2022].

[3] Renewable Power Generation Costs in 2020 – Available at:<https://www.irena.org/publications/2021/Jun/Renewable-Power-Costs-in-2020> [accessed 03.6.2022].

[4] IEA, Renewables 2021: Analysis and forecast to 2026 – Available at:<https://www.iea.org/reports/renewables-2021> [accessed 03.6.2022].

[5] Hess S., Solar Thermal Process Heat (SPH) Generation, in: Renewable Heating and Cooling: Technologies and Applications, Elsevier Inc., 2016: pp. 41–66.

[6] Stanek B., Grzywnowicz K., Bartela Ł., Węcel D., Uchman W., A system analysis of hybrid solar PTC-CPV absorber operation, Renew Energy. 174 2021 635–653.

[7] IMPLEMENTED PROJECTS - Inventive Power 2026 – Available at:<https://inventivepower.com.mx/english/implemented-projects/> [accessed 02.6.2022].

[8] Products and Equipment from NEP Solar Pty Ltd | Energy XPRT – Available at:< https://www.energy-xprt.com/companies/nep-solar-pty-ltd-32087/products > [accessed 02.6.2022].

[9] CSHINDIA || HOME– Available at:< http://www.cshindia.in/> [accessed 02.6.2022].

[10] Häberle A., Krüger D., Concentrating solar technologies for industrial process heat, in: Concentrating Solar Power Technology: Principles, Developments, and Applications, Elsevier, 2020: pp. 659–675.

[11] Chen Q.F., Yuan Z.X., Guo Z.Q., Zhao Y., Practical performance of a small PTC solar heating system in winter, Solar Energy. 179, 2019.

[12] Schoeneberger C.A., McMillan C.A., Kurup P., Akar S., Margolis R., Masanet E., Solar for industrial process heat: A review of technologies, analysis approaches, and potential applications in the United States, Energy. 206, 2020.

[13] Stanek B., Wang W., Bartela Ł., A potential solution in reducing the parabolic trough based solar industrial process heat system cost by partially replacing absorbers coatings with non-selective ones in initial loop sections, Appl Energy. 331, 2023,120472.

[14] Varun, Garg M.O., Nautiyal H., Khurana S., Shukla M.K., Heat transfer augmentation using twisted tape inserts: A review, Renewable and Sustainable Energy Reviews. 63, 2016 193–225.

[15] Cabello R., Plesu Popescu A.E., Bonet-Ruiz J., Curcó Cantarell D., Llorens J., Heat transfer in pipes with twisted tapes: CFD simulations and validation, Comput Chem Eng. 166, 2022.

[16] Mwesigye A., Bello-Ochende T., Meyer J.P., Heat transfer and entropy generation in a parabolic trough receiver with wall-detached twisted tape inserts, International Journal of Thermal Sciences. 99, 2016 238–257.

[17] Hasanpour A., Farhadi M., Sedighi K., A review study on twisted tape inserts on turbulent flow heat exchangers: The overall enhancement ratio criteria, International Communications in Heat and Mass Transfer. 55, 2014, 53–62.

[18] Bhuiya M.M.K., Chowdhury M.S.U., Saha M., Islam M.T., Heat transfer and friction factor characteristics in turbulent flow through a tube fitted with perforated twisted tape inserts, International Communications in Heat and Mass Transfer. 46, 2013, 49–57.

[19] Seemawute P., Eiamsa-ard S., Thermohydraulics of turbulent flow through a round tube by a peripherally-cut twisted tape with an alternate axis, International Communications in Heat and Mass Transfer. 37, 2010, 652–659.

[20] Eiamsa-ard S., Thianpong C., Eiamsa-ard P., Promvonge P., Thermal characteristics in a heat exchanger tube fitted with dual twisted tape elements in tandem, International Communications in Heat and Mass Transfer. 37, 2010, 39–46.

[21] Ibarra M., Rovira A., Alarcón-Padilla D.C., Zaragoza G., Blanco J., Performance of a 5 kWe Solar-only Organic Rankine Unit Coupled to a Reverse Osmosis Plant, Energy Procedia. 49, 2014, 2251–2260.

[22] Grzywnowicz K., Bartela Ł., Remiorz L., Stanek B., Modeling of influence of vibration on intensification of heat transfer within the absorber of the vacuum solar collector, E3S Web of Conferences. 137, 2019, 01034.

[23] Therminol VP-1 Heat Transfer Fluid | Therminol | Eastman, – Available at:<https://www.therminol.com/product/71093459> [accessed 01.2.2022].

[24] Lu J.Z., Chen B.H., Jin L.H., Fang Z., Liu G., Gao X.H., Thermal stability investigation of the SS/MO/Al2O3 spectrally selective solar absorber coatings, 35, 2018, 565–572.

[25] Ho C.K., Mahoney A.R., Ambrosini A., Bencomo M., Hall A., Lambert T.N., Characterization of Pyromark 2500 Paint for High-Temperature Solar Receivers, J Sol Energy Eng. 136, 2014.

[26] Menter F.R., Two-equation eddy-viscosity turbulence models for engineering applications, AIAA Journal. 32, 1994, 1598–1605.

[27] Stanek B., Węcel D., Bartela Ł., Rulik S., Solar tracker error impact on linear absorbers efficiency in parabolic trough collector – Optical and thermodynamic study, Renew Energy. 196, 2022, 598–609.

[28] Wirz M., Petit J., Haselbacher A., Steinfeld A., Potential improvements in the optical and thermal efficiencies of parabolic trough concentrators, Solar Energy. 107, 2014, 398–414.

[29] Stanek B., Bartela Ł., Węcel D., Rulik S., An experimental study on parabolic trough collector in simulated conditions by metal-halide solar radiation simulator, Archives of Thermodynamics. 43, 2022, 47–61.

[30] Stanek B., Bartela Ł., Numerical and experimental study on 10 kWe metal-halide solar simulator for parabolic-trough collector testing, ECOS 2021 Conference Proceedings, in: 34th International Conference on Efficiency, Cost, Optimization, Simulation and Environmental Impact of Energy Systems (ECOS21), Taormina, 2021: pp. 1198–1209.

[31] Burkholder F., Kutscher C., Heat Loss Testing of Schott's 2008 PTR70 Parabolic Trough Receiver, 2008, Technical report: Available at:< http://www.osti.gov/bridge>.

An Investigation of the Synthesis and Optical Properties of a Novel Ag/ZnO Hybrid Nanofluid for Spectral Splitting in Photovoltaic-Thermal Systems

Sandesh S. Chougule[a], Gaurav G. Bolegave[b], Bhaskar Soni[c], Chandan Pandey[a], Vinayak Kamble[b] and Christos N. Markides[a]

[a] Clean Energy Processes (CEP) Laboratory, Department of Chemical Engineering, Imperial College London, London SW72AZ, United Kingdom,
[b] School of Physics, Indian Institute of Science Education and Research, Thiruvananthapuram, Kerala 695551, India,
[c] Department of Physics, Faculty of Science, The Maharaja Sayajirao University of Baroda, Vadodara, Gujrat 390002, India,
[*] Corresponding author: s.chougule@imperial.ac.uk

Abstract:

The deficient utilisation of the solar spectrum in conventional hybrid concentrating photovoltaic-thermal (CPV-T) technologies leads to a detrimental decrease in PV efficiency due to elevated temperatures. Solar spectral beam splitting (SBS) is an advancement in PV-T system design, which aims to use the full solar spectrum with minimal optical losses. The implementation of fluid-based SBS designs is economically feasible, with optical features that can be tuned by selecting suitable nanofluids with a desired concentration. Fluid-based SBS filters are advantageous over other filters for PV-T systems due to their ability to operate simultaneously as thermal storage as well as heat transfer media in these systems. In the present study, we report on the optical and thermophysical properties of a novel water-based Ag-ZnO hybrid nanofluid. The filter is synthesised by adding Ag to ZnO nanoparticles by a wet chemical method for improved stability. Silver (Ag) allows visible light harvesting (down conversion of UV to the visible region of the solar spectrum) and good optical properties in the visible and near-IR regions. An Ag shell can be embedded into the core of zinc oxide (ZnO) nanoparticles for improved stability. The presence of ZnO enables excellent optical properties, including high visible transmittance and high UV absorption. The presence of structural defects in ZnO induces colour centres which are deep traps emitting in the visible. Ag-ZnO nanofluids with different nanoparticle concentrations were tested to measure absorbance and transmittance using UV spectroscopy. These nanofluid filters can be used for full spectrum utilisation (by SBS) which helps in achieving: (i) down conversion in the UV region, (ii) transmit visible and near IR (NIR) region (desired wavelength of Si PV cell optoelectronic efficiency) ,and (iii) absorb (filter) the IR region of the solar spectrum (for downstream thermal use/applications).

Keywords:

CPV-T; Colour Centres; Light Harvesting; Nanofluid; Solar Spectral Beam Splitting.

1. Introduction

In the 21st century, the energy crisis and climate change are both among the most pressing global issues. Fossil fuels derived from carbon are responsible for both problems. In the future, energy demand will undoubtedly increase, so how to balance energy supply and CO2 emissions will become a global concern. In this case, it's essential to focus on emerging technologies involving new energies and decarbonization. As one of the most important renewable energy sources, solar power could play a crucial role in solving the energy crisis and cutting down on pollution. It may be utilised in two important ways, namely through direct production of electricity via photovoltaic conversion (PV) and through the conversion of heat i.e. photothermal (PT) conversion. Solar photovoltaic panels use only a small fraction of the solar spectrum for the generation of charge carriers, while the remainder causes undesirable heating of the panels, reducing their efficiency [1]. A hybrid photovoltaic-thermal (PV-T) system was therefore proposed in which the heat generated by the PVs is dissipated by a heat exchanger fluid, commonly called a coolant, thus resulting in a PV-T hybrid system [2]. The hybrid system is also more energy-efficient than individual photovoltaic or thermal systems. The performance of PV-Ts has improved significantly with the emergence of alternative heat exchange fluids

[3]. However, the emerging spectral splitting PV-T technology can produce greater fluid temperature and higher total efficiencies by separating the PV and thermal units.

In the spectral splitting method, the part of sunlight that cannot be converted into electricity is filtered out before it reaches the PV cells. Solar radiation is split into ultraviolet (UV), visible, and infrared (IR) spectrums by this technique, which requires matching the spectral bands of the cells and the wavelengths absorbed by the filter. A solar PV system uses the visible spectrum to produce electricity, while UV and IR spectra are absorbed and collected elsewhere as heat. It has been reported in previous studies that fluid-based spectral beam splitters (SBS) are more efficient than other kinds of splitters, such as interference filters and holographic filters [4]. Furthermore, fluid based SBS can be implemented economically, and its filtering features can be easily altered by choosing suitable by varying fluid properties. The fluid-based filter is also advantageous over other filters for PV-T systems since it can simultaneously serve as a thermal storage medium and a heat transfer medium. There have been experimental studies conducted with water as a filter for PV-T collectors in the past. Water is a common liquid, used conventionally in such systems and has excellent thermal and optical properties. There has been evidence that water improves the performance of PV-T, and many researchers have explored the ability of traditional fluids to absorb solar irradiance not effectively utilised by PV cells [4,5], including water, inorganic salts, glycols, and oils. Pure fluids can only absorb a portion of the infrared light, while they perform poorly in the UV region of the solar spectrum, so PV-T systems with pure fluid filters are inefficient.

Water-based nanofluids have been recommended by many studies as beam splitters in PV-T systems [6,7]. PV modules will heat up unnecessarily when they are exposed to wavelengths that are outside of their spectral ranges, thereby reducing efficiency. Nanofluids may solve the challenges discussed above because of their tunable optical properties. A nanofluid comprises a stable suspension of nanoparticles in a base fluid (e.g., water). In addition, nanoparticles allow the splitter to adjust its bandwidth and absorption peak continuously according to the amount of bandgap energy needed for converting solar energy into electricity [8]. Several experimental studies have so far investigated the performance of nanofluid filtered PV-T systems. This led to an ideal nanofluid filter for a particular solar cell [4, 5]. An interesting method for improving nanofluid beam splitting involves plasmonic metal nanomaterials. Plasmonic nanoparticles that manipulate, guide, and localise the incident light. Silver (Ag) is among the most important metals for plasmonic particles, it has demonstrated capabilities for visible light harvesting [9] as well as support in the visible and near-infrared spectrum. A silver nanofluid is highly effective in both thermal and electrical conversions in previous studies involving beam splitting applications such as- Silver nanoparticles are also highly suitable for industrialization and commercialisation. Zhang et al. [10] conducted an indoor experiment to optimise the heat/electricity production of a PV-T system filtered by Ag/water nanofluid. The results confirmed that arranging the nanofluid above PV modules is beneficial for heat collection and cell temperature regulation. The performance of a PV-T system with nanofluid filter consisting of silver-silica nanoplates as visible light absorbers and silica-coated gold and gold-copper nanorods as infrared absorbers was evaluated through an indoor test [9]. The results showed that the c-Si PV cells based PV-T system with Ag-SiO2 nanofluids achieved the highest combined efficiency of 40%, while the electrical efficiency was only 6%. Han et al. [11] developed a high-performance optical filter using water-based Ag-CoSO4 nanofluid for SBS PV/T systems. The measured transmittance indicated that water-based Ag-CoSO4 nanofluid is superior to Ag/water nanofluid in terms of performance. A PV-T system with water based rGO-Ag nanofluid filters was experimentally investigated by Abdelrazik et al. [12]. As a result of the experimental results, the proposed system showed better performance than a PV system with only PV cells, and the electrical efficiency was generally less than 10%, whereas the thermal efficiency ranged between 24-30%. Despite these advantages, the readily oxidising nature of silver in air restricts its use. This drawback may be overcome by embedding Ag nanoparticles into stable oxides such as zinc oxide (ZnO). As an optoelectronic material, ZnO exhibits excellent optical properties like transmittance, suggesting the possibility of using it with Ag nanoparticles [13,14].

This work presents plasmonic silver metal with ZnO nanoparticles, made using simple wet chemical methods. The hybrid material has excellent spectral splitting properties that can be used in PVs to harvest visible light and convert it into electrical power. The narrow bandwidth of transparency (400-1000 nm) also leads to heat absorption by filtering UV and infrared rays. The water-based Ag-ZnO nanofluids has been assessed with optical transmission measurements, whereas Ag-ZnO hybrid nanomaterials is examined about structure, morphology, and chemical composition, which helps confirm the observed optical properties with those of the material. The preliminary results reported could be useful in providing a better insight in the optical and thermal processes that leads to SBS. Localised surface plasmons of Ag nanostructures are observed in the visible region (400 nm), ZnO band edge absorption is observed above 375 nm, and IR absorption, particularly for low-energy photons, is observed. More work is required for selection of the nanofluid filter parameters, including nanoparticle type, size, mass fraction, base fluid type, etc. Nevertheless, the results are promising to demonstrate a spectral beam splitting with environment friendly, benign and economical composition.

2. Experimental details

2.1. Materials

Zinc nitrate hexahydrate [$Zn(NO_3)_2.6H_2O$, mol. wt. = 297.49 g/mol, 99.99% pure, from Sigma Aldrich], Silver nitrate [$AgNO_3$, mol. wt. = 169.87 g/mol, 99.90% pure, from Sigma Aldrich], PVA [mol. wt. = 96800 g/mol, degree of polymerization = 2000, from Fischer Scientific], ammonia solution (NH_4OH, conc. 25%, from Merck), and sucrose ($C_{12}H_{22}O_{11}$, mol. wt. = 342.30 g/mol, 99.95% pure, from Merck) were used for the synthesis of ZnO -Ag hybrid nanoparticles.

2.2. Synthesis method

The process of synthesis of *Ag coated ZnO hybrid nanoparticles* has been shown in Fig 1. There were two main stages in the synthesis procedure of ZnO:Ag nanoparticles. In the first stage, Zn^{2+}-PVA-sucrose precursor powders were created by a chemical reaction between aqueous solutions of Zn^{2+} salt and PVA-sucrose polymer, as described in reference [15–18]. The next step involved further processing the precursor powders to create ZnO:Ag core-shell nanoparticles. A comprehensive explanation is given below.

In synthesis, 1:10 mass ratio of PVA and sucrose was mixed in water at reaction temperature of 60–65 ^oC with continuous magnetic stirring to disperse 0.2 M aqueous Zn^{2+} salt solution. The PVA-sucrose used in this process acts as a surfactant and offers a stable medium for the nanoparticles'-controlled growth through encapsulation in polymer micelles [19,20]. The sucrose additive improves the average viscosity of the reaction solution. It was noted that in the solution, the salts had an endothermic reaction with the PVA-sucrose molecules. By adding NH_4OH solution in the required quantity to support the hydrogenation of Zn^{2+} ions in the reaction solution, the pH of the mixed solution was maintained at 9 throughout the reaction. Following the reaction, the mixture was cooled to room temperature and aged at 20-25 °C for 24 hours before the transparent, colourless top layer of PVA-sucrose was decanted out. To obtain the fluffy, voluminous, whitish mass of polymer capped precursor powders, the obtained precipitate was dried at a controlled temperature of 50–60 °C after being washed with methanol to remove any unreacted residual PVA–sucrose. After pulverising the polymer precursor powders in a mortar and pestle, they were heated for two hours at 400–600 °C to produce refined ZnO nanoparticles. The final size of the particles is largely controlled by the heat treatment temperature.

In the next step, 5.0 g of the dried ZnO precursor powders were mixed with 100 ml of a 0.25 M solution of $AgNO_3$ in water. This was done in the dark at 60 °C under constant stirring. After about 30 minutes of reaction time at this temperature, the powders were recovered by decanting the $AgNO_3$ solution, washing them at least twice in hot water, and then drying them under low pressure (10 to 100 mbar) at 25 °C. The dried powders were then heated for 2 hours in ambient air at 500 °C. Followed by recrystallization, the ZnO nanoparticles are encapsulated by a stable, thin layer of Ag.

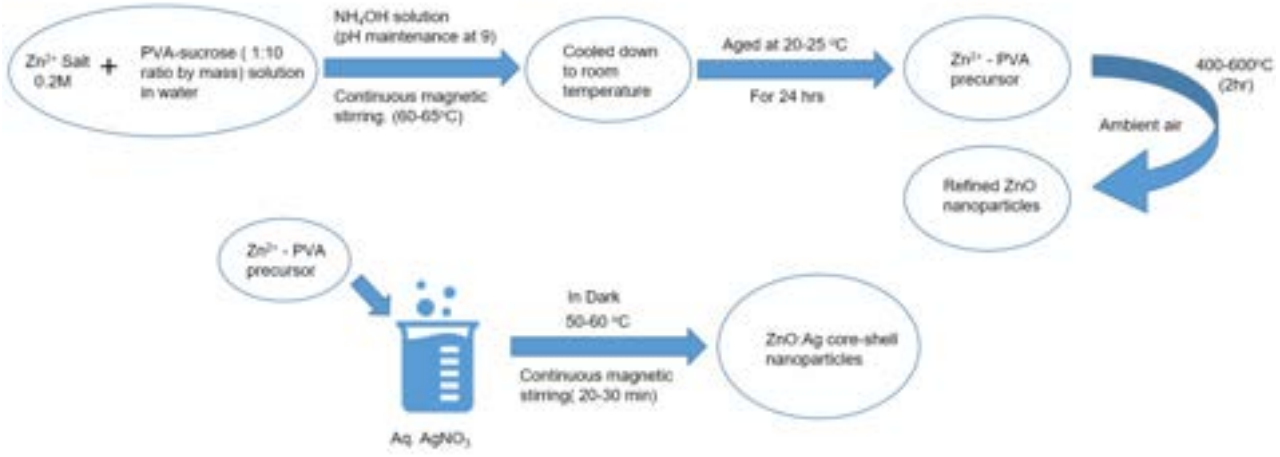

Figure 1. *Synthesis route of Ag coated ZnO hybrid nanoparticles.*

2.3. Characterisation

The crystalline nature and structure of synthesised Ag coated ZnO hybrid nanoparticles was examined under Bruker D8 powder X-ray diffractometer using Cu K_α source of radiation wavelength 1.5406 °A in the range 5 ° to 90 ° with a step size of 0.02 °. The particle morphology and elemental composition of the samples was analysed using FEI Nova Nanosem 450 Field Emission SEM equipped with Energy Dispersive X-ray spectroscopy (EDS). The individual particle morphology was investigated with FEI Tecnai G2 sprit Bio-Twin TEM at an accelerated voltage of 120 kV. To probe at the local structures of the chosen regions under investigation, an in-situ study of electron diffraction from selected areas (SAED) and high-resolution TEM imaging was carried out with FEI Tecnai G2 F30 S-Twin TEM at an accelerated voltage of 300 kV. The Raman spectra were captured on a Horiba Jobin

Vyon LabRam HR Raman by exciting with a 532 nm laser at room temperature. The optical transmittance spectra of the sample were taken in aqueous solution at room temperature with Perkin Elmer Lambda 950. The sample was sonicated for 30 minutes for well dispersion of nanoparticles in water. ZnO:Ag/Water nanofluids of mass fractions 50 ppm, 30 ppm, 15 ppm, and 5 ppm were made. Transmittance and absorption spectra were taken in the cuvette of 10 mm optical length.

3. Results and discussion

Figure 2 (a) shows the XRD pattern of the as-prepared ZnO-Ag sample. The pattern shows broad and distinct peaks which marks the nanocrystalline nature of the sample. The pattern is indexed to the hexagonal wurtzite type (space group P63mc) crystal structure of ZnO [JCPDS card # 036-1451]. Three distinct peaks corresponding to metallic silver of face-centred-cubic (fcc) crystal structure [JCPDS card # 04-0783] have been identified. The same have been marked as Ag with given (*hkl*) indices. The peaks are sufficiently broad in either case, which denotes the small particle size.

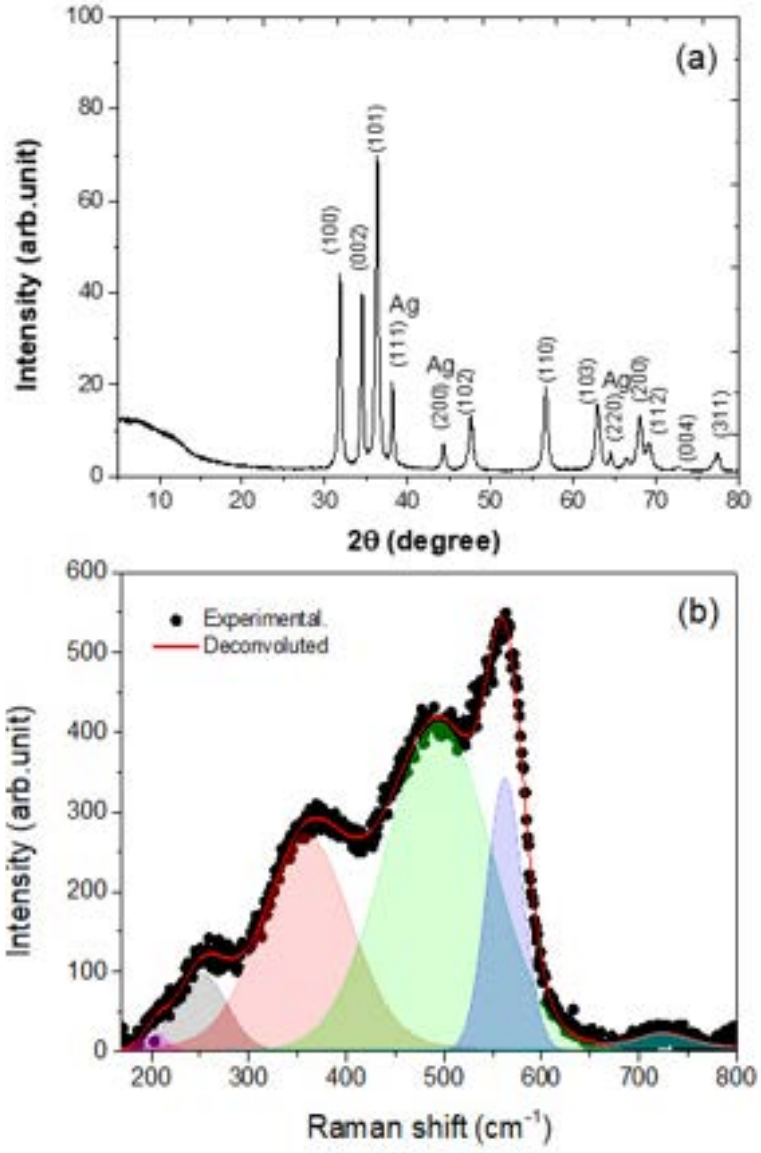

Figure 2. *(a) X-ray diffraction patterns, and (b) room temperature Raman spectrum of Ag-ZnO hybrids.*

The room temperature Raman spectra of Ag-ZnO as shown in Figure 2(b). The spectrum shows five distinct peaks that are listed in Table 1 along with their probable assignments [21–23]. Overall, from the comparison of observed data with that of reported literature, it can be observed that the Raman modes are significantly broadened in the present sample and the usual high intense peak of 438 cm^{-1} $E_{2(high)}$ is suppressed and the 563.2 cm^{-1} peak is observed to rise which is often ascribed to either high oxygen defects, substitutional impurities [21] or even lower particle sizes. [22] In this case, the smaller crystallite size along with presence of Ag additives may have resulted into such highly dispersive Raman absorption bands.

Table 1. Comparison of observed Raman peaks and probable modes reported in literature.

Peak position (cm^{-1})	Probable mode
205.1	2 $E_{2(low)}$ at 210 cm^{-1}
252.8	Not found
357.3	$E_{2(high)}$-$E_{2(low)}$ at ~340 cm-1 and E1(TO) at ~380 cm^{-1}
493.9	$E_{2(high)}$ at 440 cm^{-1}
563.2	A_1(low optical) or E_1 (low optical)) at 576 cm^{-1}

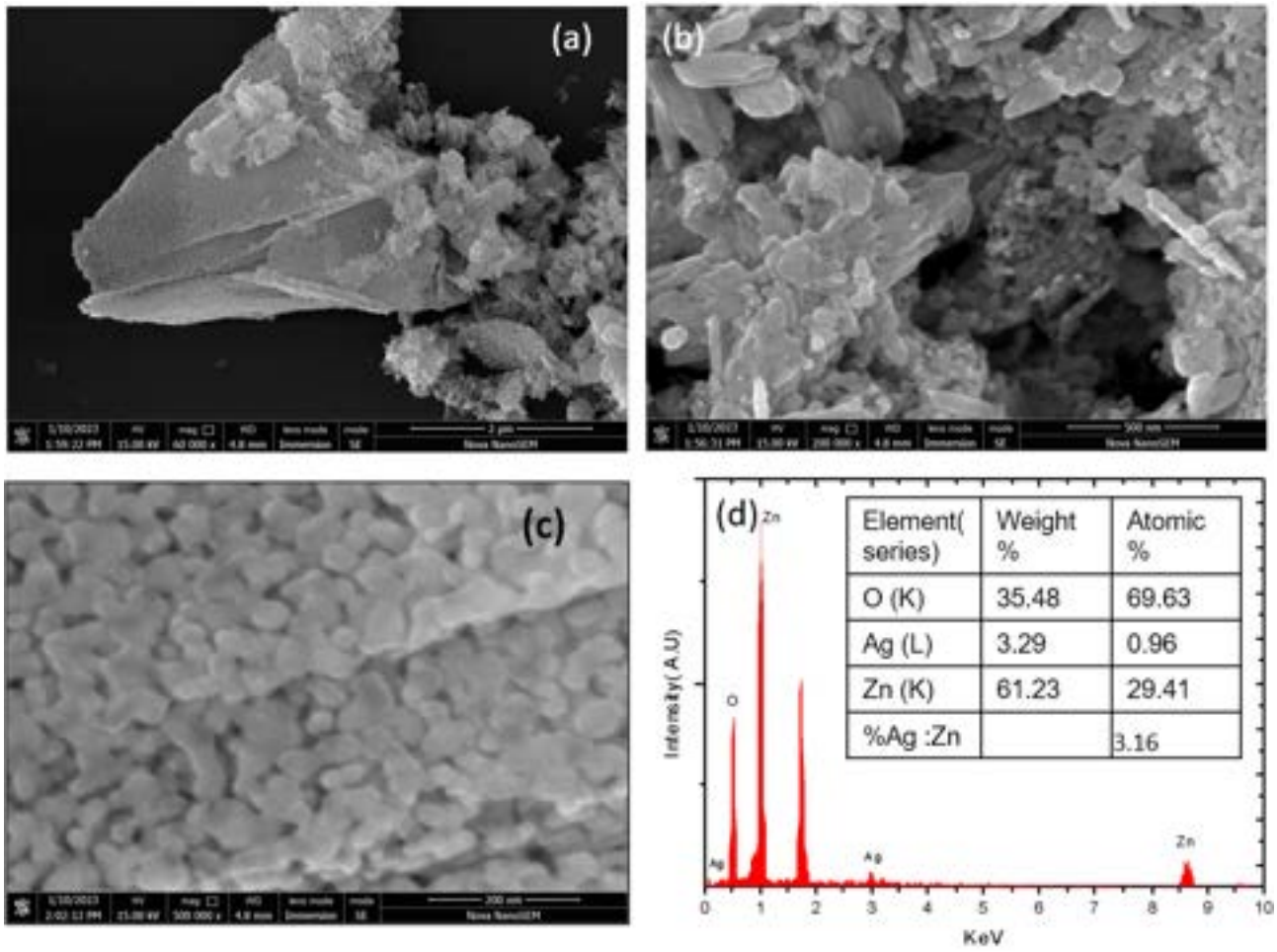

Figure 3. *Scanning electron micrographs of Ag-ZnO hybrid at: (a) low ,and (b, c) high magnifications showing the nanoscale particles (~50 nm). (d) energy dispersive spectrum of the Ag-ZnO sample with the quantification shown inset.*

Figure 3 shows the FESEM images of Ag-ZnO hybrid nanoparticles synthesised at 500 °C after heating the precursor for 2h in air. The loose agglomerates can be seen in the micrographs of the sample (Figure 3 a, b). In the particle clusters, a magnified view (Figure 3. b) reveals particles arranged in petal-like structures. Figure 3(d) depicts the elemental composition of the Ag-ZnO nanoparticles obtained at 500 °C. The presence of Zn, O, and Ag elements is confirmed in the samples, according to the EDS spectrum. The quantitative analysis indicates that Zn and Ag elements have atomic contents of 29.41%, and 0.96%, respectively.

Figure 4 shows the typical TEM images (a-d) and HRTEM (e) of Ag-ZnO nanoparticles. Figure 4 shows well dispersed particles. The average particle size was calculated from a histogram shown in Figure 4(f) and it is found to be 25–30 nm, with a narrow size distribution (±20 nm). The high-resolution TEM (HRTEM) image of a single particle is shown in Figure 4(e) it reveals that the particles may have facets with regular shape which gives them a thickness contrast. Nevertheless, the hexagonal shape is evident from Figure 4(a) also. The visible lattice reflections are close to an interplanar spacing of 0.27 nm (as shown in Figure 4 (e)). The results demonstrate the Ag along with ZnO nanoparticles. A typical selected area electron diffraction pattern (SAED) of nanoparticles is provided in Figure 4(g). It is made up of ZnO and Ag lattices that look like separate, concentric rings with spots in between. There are six characteristic rings of d_{hkl} values 0.2851 nm, 0.2503 nm, 0.1938 nm, 0.1659 nm, 0.1503 nm, and 0.1394 nm that correspond to the (100), (101), (102), (110), (103), and (112) planes of ZnO respectively, and the two characteristic rings of d_{hkl} values 0.2099 nm and 0.1112 nm correspond to the (200) and (222) planes of Ag. The d_{hkl} values derived from the SAED pattern and those

derived from the X-ray diffractograms are in close agreement. Due to the lower intensity of the diffraction spots, some reflections of ZnO and Ag could not be distinguished.

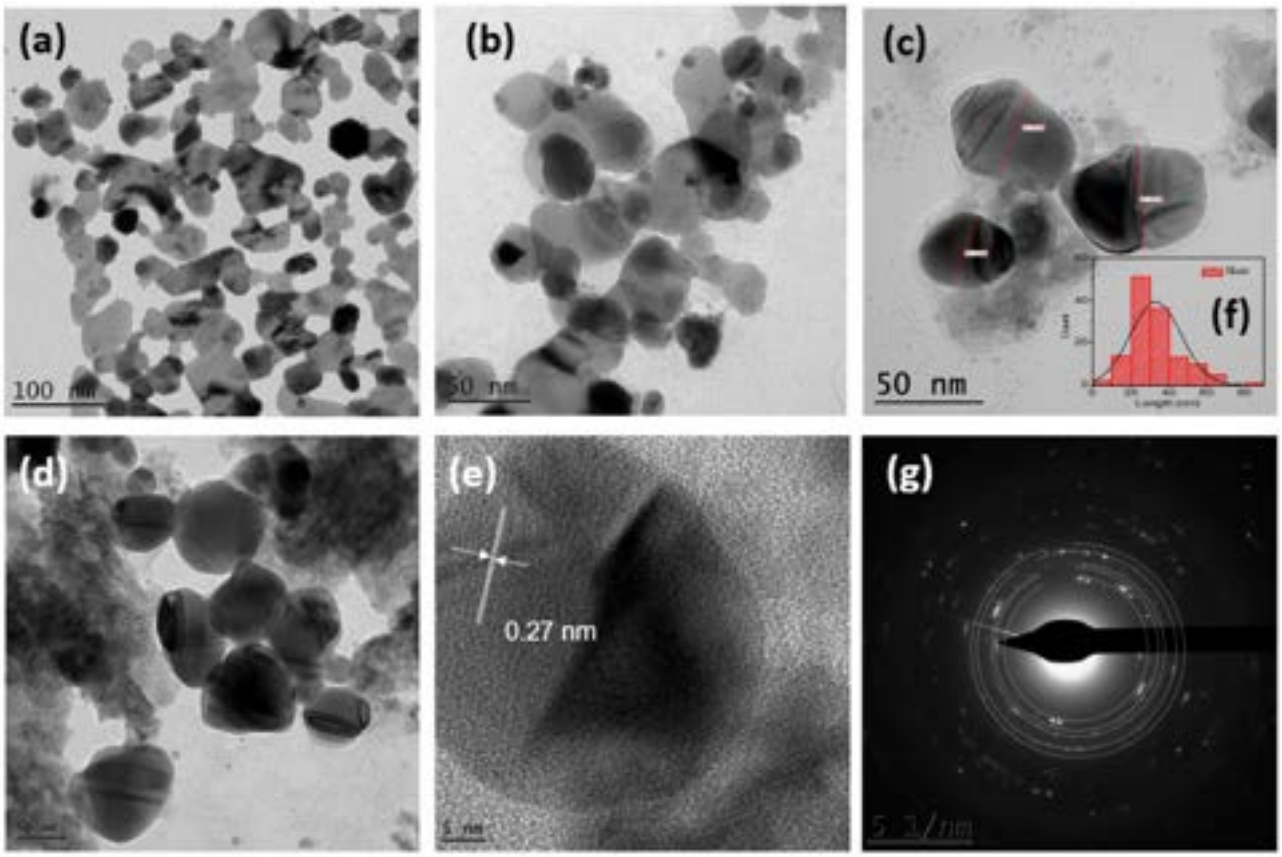

Figure 4. *Transmission electron micrographs of the Ag-ZnO showing: (a-d) the typical morphology of the powder at nanoscale, (e) high-resolution image of the individual nanoparticles, (g) selected area electron diffraction pattern, and (f) the size distribution histogram.*

Figure 5 shows the optical transmittance of Ag-ZnO/Water nanofluid with four mass fractions: 50 ppm, 30 ppm, 15 ppm, and 5 ppm. As the concentration of Ag-ZnO increases from 5 to 50 ppm in the nanofluid, the transmittance in the UV region of the spectrum decreases. The effect of the mass fraction of the nanofluid is found to be insignificant in the 400–1100 nm range. The majority of spectral energy between 400 nm and 1100 nm can pass through the Ag-ZnO /water nanofluid, while the remaining energy is absorbed. As a result of this nanofluid's ability to absorb spectral energy that is not used by the solar cell, heat harvesting has improved. Therefore, it may be regarded as a suitable optical nanofluid for PV-T systems that use spectral splitting, as the working area of PV/T systems is reported to be between 400 nm and 1200 nm.

ZnO has a wide bandgap of nearly 3.3 eV in bulk. In nanoscale morphologies this may increase slightly depending on the size, shape, etc. Because of this band gap, the absorption edge of ZnO is 3.3 eV which corresponds to about 375 nm [24]. Therefore, ZnO absorbs significantly in the UV region and the peak is observed near band edges that decreases gradually on either side. ZnO may be completely transparent in the wavelength below 400 nm if there exist no energy states within the gap [23]. These gap states usually arise because of donors for n-type (or acceptors for p-type) which lie just below the conduction band (or above valence band for p-type). ZnO shows intrinsically n-type character due to unintentionally doped oxygen vacancies and zinc interstitials [21, 25]. These crystal defects have low formation energies in the ZnO lattice and hence readily nucleate. Zinc interstitial (Zni) lies just below conduction band whereas oxygen vacancies depending on their charged state can lie shallow or deep within the gap. These states are referred to as gap states and they may lead to photo-absorption and emission of energies equivalent to the difference between the defect state and the valence band maximum. Therefore, they may increase the visible emission as their energies are 1-2 eV above valence band maxima.

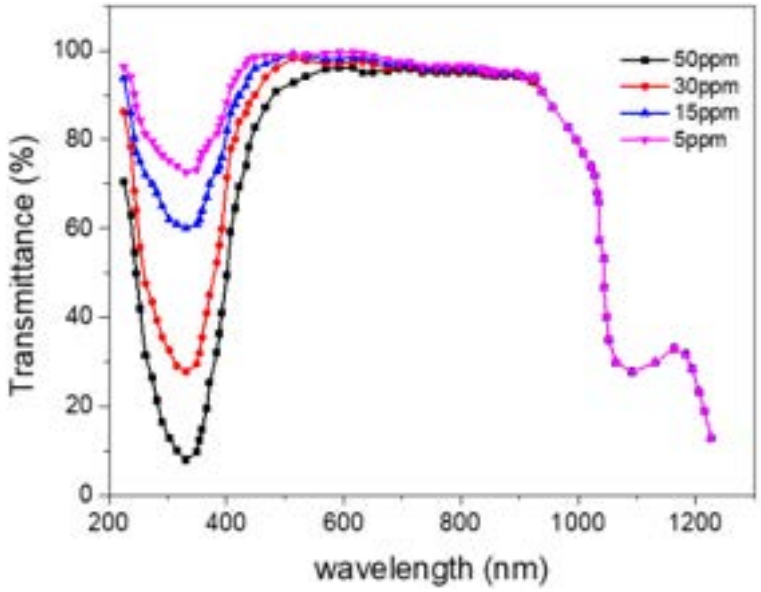

Figure 5. *UV-visible transmittance spectra of the Ag-ZnO nanoparticles at different dilutions in water.*

On the other hand, the silver lattice may show significant absorption that is usually caused in noble metals due to presence of surface plasmon resonance (SPR). The SPR is called collective oscillations of the free electron in metals which is the result of excitation due to electromagnetic radiation of appropriate energy (frequency); For Silver, this absorption mostly occurs at about 400 nm. Therefore, the corresponding amount of energy is called the plasmon absorption energy. In this case, the work function of Ag (fermi level is only slightly smaller than that of ZnO). Thus, any electron excited to a virtual SPR level is higher in energy that conduction band of ZnO and hence the charge transfer from Ag to ZnO is highly likely. This configuration of Ag-ZnO not only allows the absorption of near UV regions but may also result in visible emission as the charges transferred to ZnO may undergo a radiative transition and emit photons of smaller energy which happens to be in the visible region. Thus, this offers a win-win situation where the Ag absorbs the near UV and ZnO emits the visible light. This Additional visible light emitted can be beneficial to the PV sell and enhance the efficiency.

Conclusions

In this paper, results were presented relating to the use of Ag-ZnO nanofluids (nanoparticles suspended in water as the base fluid) for spectral-splitting PV-T applications. Ag-ZnO nanoparticles were synthesised by the solvothermal method. Several characterization techniques were utilised, including electron microscopy, X-ray diffraction and Raman spectroscopy. The XRD patterns revealed that Ag may coexist with the ZnO nanoparticles and these may have poor crystalline nature. The presence of Ag has also been confirmed by energy dispersive spectroscopy. The optical properties of the proposed nanofluids were investigated over a range of concentrations. The nanofluids exhibited a high degree of spectral selectivity, in the UV and IR regions which were absorbed or reflected respectively. In the visible region, a good transmittance was observed, which promotes higher PV cell efficiencies. In future work, visual inspection and dynamic light scattering techniques will be applied to evaluate the long-term stability of these nanofluids.

Acknowledgments

This work was supported by the Marie Skłodowska-Curie Individual Fellowships under the European Union's Horizon 2020 research and innovation program, grant agreement no. 101028904 — NANOSPLIT — H2020-MSCA-IF-2020. The authors are thankful to the central instrumentation facility of IISER Thiruvananthapuram for access to various characterization facilities. This work was also supported by the UK Engineering and Physical Sciences Research Council (EPSRC) [grant numbers EP/M025012/1, and EP/R045518/1] and by the Royal Society under an International Collaboration Award 2020 [grant number ICA\R1\201302]. The authors would like to thank UK company Solar Flow Ltd. (www.solar-flow.co.uk). Data supporting this publication can be obtained on request from cep-lab@imperial.ac.uk. For the purpose of Open Access, the authors have applied a CC BY public copyright licence to any Author Accepted Manuscript version arising from this submission.

References

[1] Al-Shohani W.A.M., Al-Dadah R., Mahmoud S., Reducing the thermal load of a photovoltaic module through an optical water filter. Appl Therm Eng 2016;109:475–486.

[2] Chow T.T., A review on photovoltaic/thermal hybrid solar technology. Appl Energy 2010;87:365–379.

[3] Candadai A.A., Kumar V.P., Barshilia H.C., Performance evaluation of a natural convective-cooled concentration solar thermoelectric generator coupled with a spectrally selective high temperature absorber coating. Solar Energy Materials and Solar Cells 2016;P3:333–341.

[4] Huang G., Curt S.R., Wang K., et al., Challenges and opportunities for nanomaterials in spectral splitting for high-performance hybrid solar photovoltaic-thermal applications: A review. Nano Materials Science 2020;2:183–203.

[5] Hong W., Li B., Li H., et al., Recent progress in thermal energy recovery from the decoupled photovoltaic/thermal system equipped with spectral splitters. Renewable and Sustainable Energy Reviews 2022;167:112824.

[6] Zachariah R., Amalnath V.N., Feasibility Study of Liquid-Based Spectral Beam Splitting Technique for Solar Panel Cooling. 2020;3–18.

[7] Abdelrazik A.S., The potential of liquid-based spectrally-selective optical filtration and its use in hybrid photovoltaic/thermal solar systems. Solar Energy 2023;249:569–605.

[8] Stanley C., Mojiri A., Rosengarten G., Spectral light management for solar energy conversion systems. Nanophotonics 2016;5:161–179.

[9] Hjerrild N.E., Crisostomo F., Chin R.L., et al., Experimental Results for Tailored Spectrum Splitting Metallic Nanofluids for c-Si, GaAs, and Ge Solar Cells. IEEE J Photovolt 2019;9:385–390.

[10] Zhang C., Shen C., Zhang Y., et al., Optimization of the electricity/heat production of a PV/T system based on spectral splitting with Ag nanofluid. Renew Energy 2021;180:30–39.

[11] Han X., Chen X., Wang Q., et al., Investigation of CoSO4-based Ag nanofluids as spectral beam splitters for hybrid PV/T applications. Solar Energy 2019;177:387–394.

[12] Abdelrazik A.S., Tan K.H., Aslfattahi N., et al., Optical properties and stability of water-based nanofluids mixed with reduced graphene oxide decorated with silver and energy performance investigation in hybrid photovoltaic/thermal solar systems. Int J Energy Res 2020;44:11487–11508.

[13] Huaxu L., Fuqiang W., Dong L., et al., Optical properties and transmittances of ZnO-containing nanofluids in spectral splitting photovoltaic/thermal systems. Int J Heat Mass Transf 2019;128:668–678.

[14] Huaxu L., Fuqiang W., Dong Z., et al., Experimental investigation of cost-effective ZnO nanofluid based spectral splitting CPV/T system. Energy 2020;194:116913.

[15] Khan M., Wei C., Chen M., et al., CTAB-mediated synthesis and characterization of ZnO/Ag core–shell nanocomposites. J Alloys Compd 2014;612:306–314.

[16] Barewar S.D., Chougule S.S., Heat transfer characteristics and boiling heat transfer performance of novel Ag/ZnO hybrid nanofluid using free surface jet impingement. Experimental Heat Transfer 2021;34:531–546.

[17] Barewar S.D., Tawri S., Chougule S.S., Experimental investigation of thermal conductivity and its ANN modeling for glycol-based Ag/ZnO hybrid nanofluids with low concentration. J Therm Anal Calorim 2020;139:1779–1790.

[18] Barewar S.D., Chougule S.S., Jadhav J., et al., Synthesis and thermo-physical properties of water-based novel Ag/ZnO hybrid nanofluids. J Therm Anal Calorim 2018;134:1493–1504.

[19] Biswas S., Ram S., Morphology and stability in a half-metallic ferromagnetic CrO2 compound of nanoparticles synthesized via a polymer precursor. Chem Phys 2004;306:163–169.

[20] Biswas S., Ram S., Synthesis of shape-controlled ferromagnetic CrO2 nanoparticles by reaction in micelles of Cr6+–PVA polymer chelates. Mater Chem Phys 2006;100:6–9.

[21] Biswas S., Singh S., Singh S., et al., Selective Enhancement in Phonon Scattering Leads to a High Thermoelectric Figure-of-Merit in Graphene Oxide-Encapsulated ZnO Nanocomposites. ACS Appl Mater Interfaces 2021;13:23771–23786.

[22] Song Y., Zhang S., Zhang C., et al., Raman Spectra and Microstructure of Zinc Oxide irradiated with Swift Heavy Ion. Crystals 2019;9:395.

[23] Srinatha N., No Y.S., Kamble V.B., et al., Effect of RF power on the structural, optical and gas sensing properties of RF-sputtered Al doped ZnO thin films. RSC Adv 2016;6:9779–9788.

[24] Urs K.M.B., Kamble V., Surface photovoltage response of zinc oxide microrods on prismatic planes: effect of UV, temperature and oxygen ambience. Journal of Materials Science: Materials in Electronics 2021;32:6414–6424.

[25] Xu PS, Sun YM, Shi CS, et al. The electronic structure and spectral properties of ZnO and its defects. Nucl Instrum Methods Phys Res B 2003; 199: 286–290.

PV potential of the public building stock of the Basque Country

Mikel Garro-Aguilar[a*], Ana Picallo-Perez[a], Pablo Hernandez-Cruz[a], Juan Mª Hidalgo-Betanzos[b], JM Sala-Lizarraga[a] and Imanol Ruiz de Vergara-Ruiz de Azua[b]

[a] Research group ENEDI, Department of Energy Engineering, University of the Basque Country (UPV/EHU); Alameda Urquijo, S/N, 48013 Bilbao, Vizcaya, Spain; e-mail: mikel.garro@ehu.eus
[b] Thermal Area of the Laboratory of Quality Control of Buildings of the Basque Government; Aguirrelanda 10, Vitoria-Gasteiz, Spain

Abstract:
The energy consumption of buildings is constantly increasing and not only impacts on resources, but also emits polluting gases into the atmosphere. For this reason, there is a great commitment to integrate renewable energies, as well as to renovate and hybridize the energy facilities of existing buildings. Spain has a large potential to exploit solar energy and this is reflected in the PV integration in buildings, as PV self-consumption has risen to 1,203MW installed. However, buildings still have a high potential for improving photovoltaic applications and can help to increase the exploitation of renewable resources. Following European recommendations and Spanish directives, the Basque Government is analysing how to conduct the renovation of the existing public housing stock to achieve more sustainable housing and take into account the quality of life of the users. To this end, the project Plan ZERO-Plana, led by ALOKABIDE "Public institution of the Basque Government", was developed to, among others, increase renewable energy implementation for self-consumption. This work takes a step forward and analyses the photovoltaic potential of the public building stock of the Basque Country based on a GIS application. The objective is to, on the one hand, account for the PV potential in each of the public housing units themselves and, on the other hand, to analyse the possibility of implementing energy communities in the Basque Country to supply the energy use of these buildings, as well as to compare the viability of both options.

Keywords:
ALOKABIDE; PV potential; energy community; Vitoria-Gasteiz; QGIS; renewable energy; rooftops.

1. Introduction

Spain, due to its climate and geographical location, has a significant number of sun-hours during the year, which allows the exploitation of clean energy with significant potential to meet energy needs. Given that a large part of the world's population is concentrated in cities, it is necessary to establish urban plans to ensure the sustainable development of urban environments, using available human resources and technology. In addition, Buildings are responsible for approximately 40% of the energy consumption of the European Union (EU) [1]. Residential buildings in particular accounted for the 27% of the final energy consumption of the EU in 2020 [2], so one of the options is to produce energy through solar technology, such as placing photovoltaic panels on building rooftops. Therefore, this work assesses the solar potential of the city of Vitoria-Gasteiz, as a geographical area with suitable characteristics for the installation of solar panels and the possibility to create different energy communities in this area.

1.1. State of the art

Accordingly, some studies have identified areas of high population density, such as urban centres, as places with high potential for solar production, such as Ávila and Zamora [3], Miraflores de la Sierra (Madrid, Spain), Gassar and Cha [4] in Geneva (Switzerland), Guevara [5] (Perú) and Haegermark and Dalenbäck [6] (Sweden).

In terms of feasibility analysis, analysis is frequently restricted to figuring out solar radiation, although the environment is still crucial. In addition, the study can be further detailed, as it is done in the case of housing in Valencia (Spain), Aparisi [7], where the orientation of the roof and the adjacent buildings are taken into account, as well as the tilt of the roof. On the other hand, the polytechnic school of engineering in Gijón studied photovoltaic feasibility in Asturias (Spain), Guerrero [8].

The PV potential can be estimated by using different models or methods. In this study, the method used is based on a Geographic Information System (GIS). This method or tool has been employed in numerous studies for various purposes, including the estimation of PV potential in rooftops. Examples include Quiros-Tortos et al.'s [9] consideration of various factors when integrating GIS data sources in a PV analysis and Khan and Arsalan's [10] use of the GIS tool to determine the best rooftops for solar PV applications in Karachi. Baiocchi et al. [11] also uses this tool to study the effect of defining different PV criteria, and Davybida et al. [12] uses GIS to design a PV system for a built-up roof in Poland, which generates an electrical power of around 100 MWh/year.

Moreover, this tool can be used to determine the influence of different elements on PV solar energy generation, and Silveire Júnior et al. [13] uses GIS to determine the influence of aerosol in the state of Goiás (Brazil).

Apart from GIS there are different models that can be used to analyse the PV potential of an area. For instance, of Mohajeri et al. [14], used Machine Learning to classify urban characteristics for solar applications, including the impacts of different roof shapes on annual solar PV electricity production.

The electricity obtained from the PV installation can be used in different ways. Current policies are promoting the combination of technologies such as heat pumps or solar thermal collectors, and these possibilities have been studied in articles such as Wang et al. [15]. This last work analyses three different configurations to supply the heating and DHW demands of a dwelling (ST, PV/T and PV with ASHP). Herrando et al. [16] analyses the possibilities of using solar thermal collectors to meet the heating and DHW demands of a dwelling (ST, PV/T and PV with ASHP), and Ayadi and Al-Dahidi [17] compares how to implement heating and cooling in a building with solar thermal and solar electric power.

In addition, some countries are also promoting energy communities, which is a relatively new concept. Frieden et al. [18], Jeriha [19] and Gjorgievski et al. [20] reviewed the current regulatory framework and analyse the social arrangements, technical designs and impacts of an energy community. As it is known, with energy communities the heating, cooling and electrical demand can be assessed, so this could be a great opportunity for the public house stock of Vitoria-Gasteiz to introduce this kind of initiative into work, due to its geographical and distributional situation.

1.2. Regulatory framework

This section briefly explains the European, Spanish and regional regulatory framework.

1.2.1. European framework

In Europe, the recent directives are seeking to promote new roles for citizens who produce and use energy by promoting local energy markets and introducing the concept of energy communities.

One of the most remarkable directives, is the Directive (EU) 2018/2001 of the European Parliament and of the Council of 11 December 2018 [21], on the promotion of the use of energy from renewable sources. This directive defines Renewable Energy Communities (REC) as "*A legal entity; which, in accordance with the applicable national law, is based on open and voluntary participation, is autonomous, and is effectively controlled by shareholders or members that are located in the proximity of the renewable energy projects that are owned and developed by that legal entity;. The shareholders or members of which are natural persons, SMEs, or local authorities, including municipalities; the primary purpose of which is to provide environmental, economic, or social community benefits for its shareholders or members or for the local areas where it operates, rather than financial profits*.".

This directive establishes that the Renewable Energy Communities (RECs) have the right to produce, consume, store, or sell renewable energy, or to share what is generated by producing units owned by that community and to access all energy markets. It also mandates member states to provide a framework to encourage and facilitate the development of RECs, as well as to guarantee the right of consumers to participate in a REC.

Another remarkable directive is the Directive (EU) 2019/944 of the European Parliament and of the Council of 5 June 2019 [22], which defines the common rules for internal market for electricity in Citizen Energy Communities (CEC) as follows. "*A legal entity that: is based on voluntary and open participation and is effectively controlled by members or shareholders that are natural persons, local authorities, including municipalities, or small enterprises; has for its primary purpose to provide environmental, economic or social community benefits to its members or shareholders or to the local areas where it operates rather than to generate financial profits; and may engage in generation, including from renewable sources, distribution, supply, consumption, aggregation, energy storage, energy efficiency services or charging services for electric vehicles or provide other energy services to its members or shareholders*."

This directive establishes the obligation for member states to provide a favourable legal framework for CECs that ensures that: (1) participation in CECs is open and voluntary; (2) the distribution system operator cooperates, in return for fair compensation, to facilitate the transfer of electricity between different CECs; (3) CECs are subject to procedures and charges that ensure that they contribute adequately and in a balanced way to the overall sharing of system costs.

These two directives are included in the “Clean Energy Package” [23], which proposes an adaptation of the European energy policy framework to facilitate the transition away from fossil fuels toward cleaner energy.

1.2.2. Country framework

In Spain, the most recent regulations related to electricity self-consumption are “*Real Decreto-ley 15/2018*” [24], which establishes urgent measures for energy transition and consumer protection, and “*Real Decreto-ley 244/2019*” [25], which regulates the administrative, technical and economic conditions for electricity self-consumption, promoting the consumption of km0 energy.

In addition to these regulations, the Spanish state proposes the "*Plan Nacional Integrado de Energía y Clima 2021-2030*" [26], which describes several measures for the penetration of renewable energies and energy efficiency, as well as introduces local energy communities and the importance of citizen participation in the energy field. For the latter, lines of action are set out to develop the appropriate regulatory framework to define these legal entities and encourage their development.

In addition to this national plan, the Spanish government in 2020 proposed the document "*Estrategia de Descarbonización a Largo Plazo 2050*" [27] with the aim of becoming a climate neutral country by 2050 by transforming the energy and economic system in a stable and joint manner with the help of citizens.

1.2.2. Regional framework

In the Basque Country, there are different regulations and strategies that establish guidelines to favour the use of renewable energies and sustainable development.

This is the case of Ley 4/2019, of 21 February [28], on energy sustainability in the Basque Autonomous Community and its development decree, “*Decreto 254/2020”*, of 10 November [29], whose objective is to promote energy saving and efficiency measures, and the promotion and implementation of renewable energies. The spatial planning guidelines, approved by “*Decreto 128/2019”* of 30 July [30], state that renewable energies must be increasingly incorporated into the construction of our territory.

The Basque Energy Strategy 2030 [31] identifies, after a full analysis of the surrounding, elements that will be key to the transition towards a sustainable energy system in the Basque Country. This analysis includes: energy saving and efficiency; renewable energies; infrastructures and networks; distributed energy, self-consumption and energy cooperatives; non-conventional gas; energy and environmental taxation; policy integration; governance; adaptation to climate change in the energy system; and the importance of health co-benefits.

2. Case study

This work examines 157 sections of 31 public housing buildings, managed by ALOKABIDE, in the city of Vitoria-Gasteiz (Basque Country, Spain), with an average age of 16-year-old. In addition, 84% of the 31 buildings have a D and E labels in primary energy consumption or CO2 emissions [32], which means they have relatively low values.

This analysis focuses on electrical consumption and considers the available data obtained from previous works. Therefore, after averaging the number of households and consumption in Vitoria-Gasteiz, we obtain the average monthly consumption profile of a household, see Figure 1. It is also taken into account that 21 out of 31 buildings already have renewable energy solar thermal systems installed, but there is still space to expand the facility and increase the renewable production.

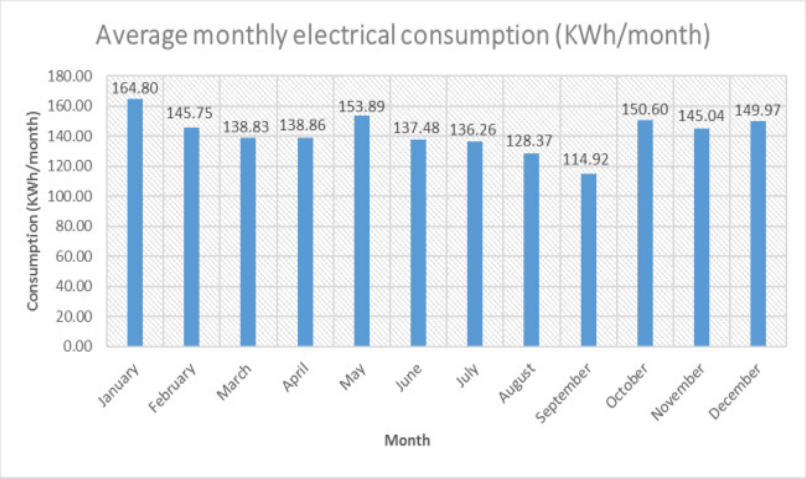

Figure. 2. Average monthly electrical consumption of the buildings studied in Vitoria-Gasteiz.

Due to technical limitations, only a specific number of buildings will be analysed in this work, which are collected and depicted in Figure 2. The analysis of the rest of the public building stock can be done in an analogous way.

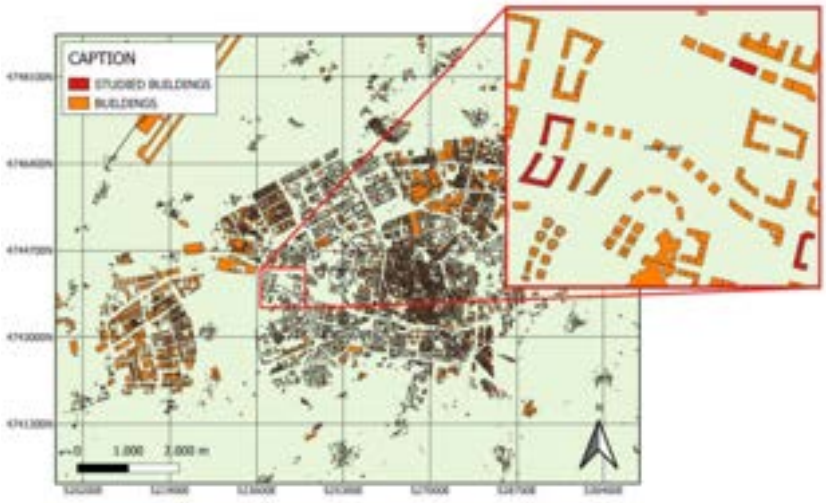

Figure. 2. Buildings studied in Vitoria-Gasteiz.

3. Methodology

QGIS Georeferencing Software (Open Access Geographic Information System) has been used for studying solar radiation from the rooftops of public buildings in Vitoria-Gasteiz. This tool organizes large volumes of data from a particular place in the world, allowing data to be stored, manipulated, analysed and modelled.

3.1. Data

Topographic data have been obtained from GeoEuskadi [33], which collects data from the entire Autonomous Community of the Basque Country. These are LIDAR (L*aser Imaging, Detection, And Ranging*) type and are obtained by optical remote sensing through a laser light. That is, with accurate x-y measurements, they define a compact sample of the Earth's surface as in cartographic applications of aerial laser images. These data contain cadastral information on all the localities of the Basque Country, such as buildings, urban centres, rural areas, railway lines, roads, etc., as well as data on the boundaries of each municipality. It also contains other data on the DSM sheets (Digital Surface Model) representing all the elements of the soil surface, such as vegetation, buildings, infrastructure, and soil itself.

3.2. Methods and indicators

Once the topographic data have been obtained and downloaded into the software, they are assigned a reference system of type ETRS89/UTM zone 30N, and are also assigned to the other layers of QGIS.

Between these layers, radiation accumulates by means of a device called Potential Incoming Solar Radiation. This device simulates accumulated radiation over a time-period, taking into account the type of radiation selected. In the case of this study, a period of one year, 2018, has been set by months, with a 7-day and 1-hour jump, and takes into account total or global radiation, i.e., the sum of direct, diffuse, incident, reflected and absorbed radiation. Therefore, monthly layers are obtained, for example, the total radiation of August and December is gathered in Figure 3 and Figure 4.

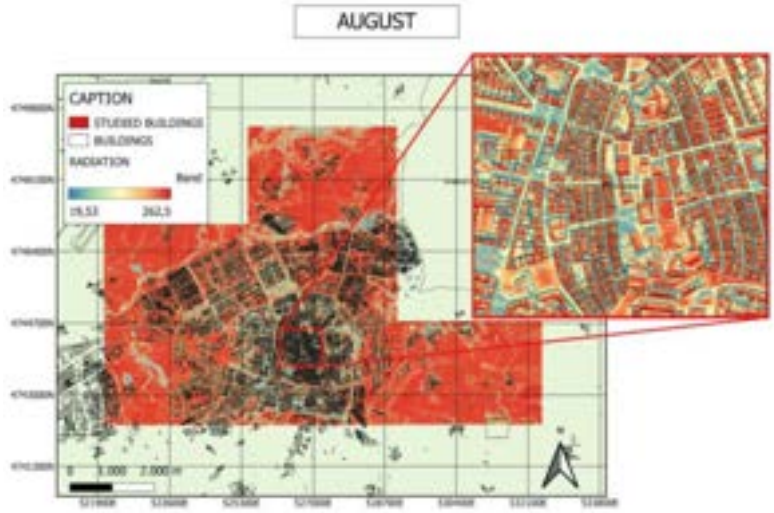

Figure. 3. Accumulated radiation during August.

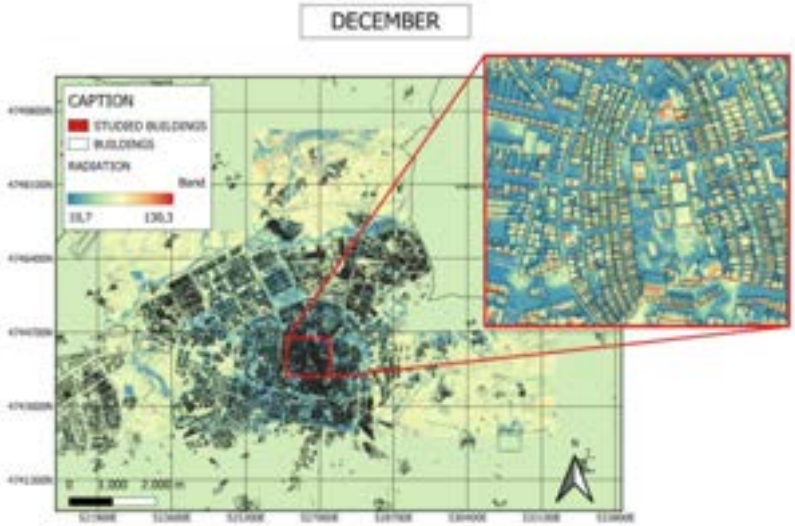

Figure. 4. Radiation accumulated on December.

As it can be seen, there is a huge difference between the maximum and minimum total radiation reaching the layers in both months of August and December.

The layer of the same size as the DSM simulation sheet is then cut to collect only radiation data consistent with buildings (public houses); see figure 5.

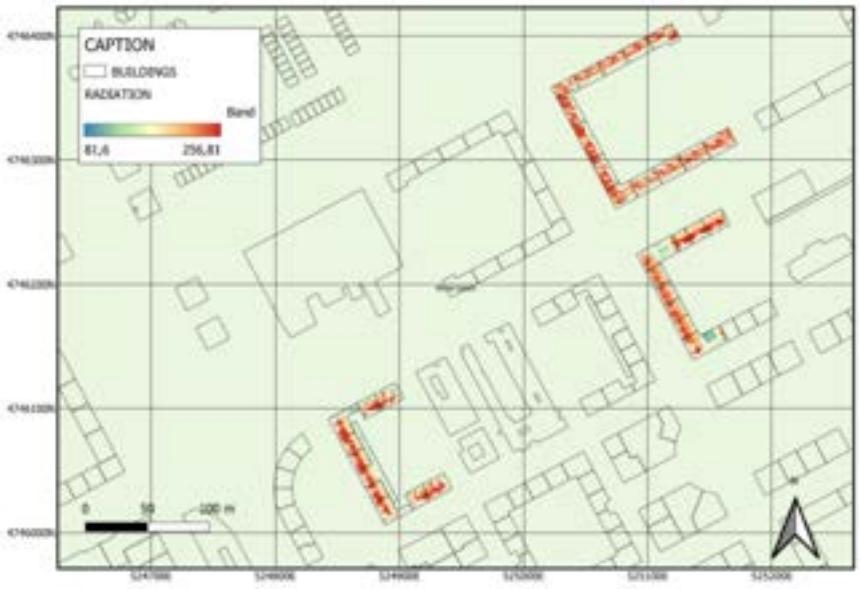

Figure. 5. Radiation accumulated on building rooftops.

Thus, once the radiation potential of residential rooftops has been achieved, three criteria are proposed to identify the suitable rooftops, as Delphine Khana mentions [34]:

- C.1) The rooftops must contain at least 65 kWh/m^2 of accumulated solar radiation in one month.
- C.2) The slope of suitable roofs must be less than or equal to 45 degrees, as steep slopes tend to receive less sunlight. The 45 degree limit is defined according to the latitude of Vitoria-Gasteiz, which is 42.85 °, since the optimal inclination is ± 10 ° compared to the local latitude.
- C.3) The rooftops, which are oriented north and receive less sunlight, are rejected.

Once the appropriate rooftops are identified and their radiation potential is obtained, the next step deals with analysing the possibilities of establishing energy communities, taking into account the location of the buildings of the public houding stock, since the consumption points must be at a maximum distance of 500 metres from the production point. Following these instructions, seven energy communities are proposed in Figure 6.

Figure. 5. Energy communities proposed in Vitoria-Gasteiz.

From now on, considering the seven energy communities, only 134 buildings out of the original 157 will be analysed (since the rest are outside of the circles), and for this analysis, several indicators have been determined to better understand the analysis:

- Optimal surface of section rooftops [m^2]

Indicates the appropriate surface of the PV panel installation rooftop according to the predefined criteria.

- Percentage of optimal surface [%]

It is the ratio between the optimal surface of the building and the total.

$$Percen.opt.surf.(\%) = \frac{Opt.surf.\ (m^2)}{Total\ surf.\ (m^2)} \quad (1)$$

- Photovoltaic efficiency [%]

It relates the photovoltaic capacity of each section to the electrical consumption. This indicator allows a detailed analysis of the context of each building.

$$PV\ eff.(\%) = \frac{PV\ capacity\ (KWh)}{Elec.consumption\ (KWh)} \quad (2)$$

4. Results

The most significant results are related to the following:

- Histograms of radiation based on the first calculation.
- Optimal surface of the buildings, after applying the three criteria to the rooftops.
- Radiation percentage of each cover for the introduction of a PV facility.
- Photovoltaic efficiency of the proposed energy community.

4.1. Histograms

Accordingly, Figure 6 shows the histograms of August and December associated with the buildings of Figure 5, where the most repeated value of the accumulated radiation in August is around 240 kWh/m^2 and in December around 65 kWh/m^2.

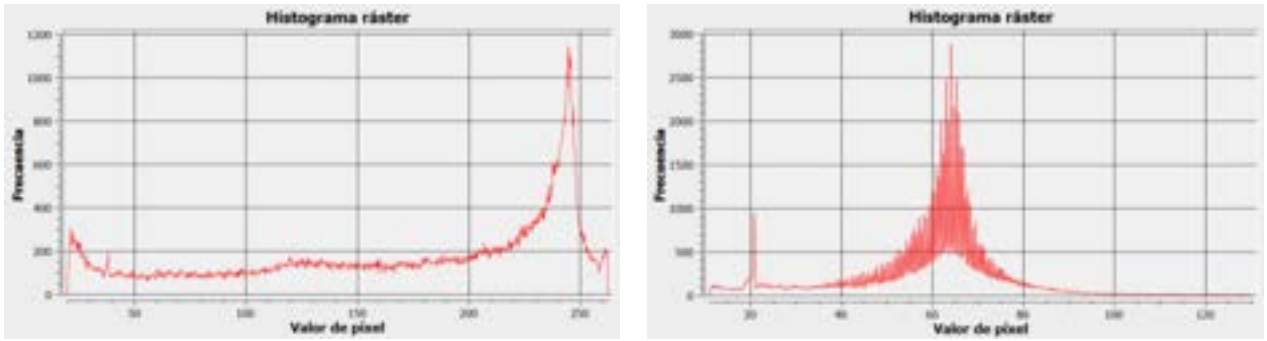

(a) (b)

Figure. 6. Histogram of the accumulated radiation: a) August, b) December.

4.2. Optimal Surface

As it has been said, each building is examined according to three criteria (C.1, C.2 and C.3) to identify suitable rooftops. A building-by-building analysis has been carried out and the global results are gathered in Table 1.

Table 1. Summary based on three criteria

Optimal surface (m^2)	Total surface (m^2)	Percentage (%)
25,076.20	52,804.88	47.49

Consequently, only 47.49% of the total roof capacity is considered adequate for installing PV panels.

But what is more, some parts of this area are not suitable for installing a photovoltaic panel, since there are also areas with obstacles, such as chimneys, antennas, etc. Because of that, the results are afterwards filtered and analysed more precisely in order to identify the specific areas of the rooftop detecting the obstacles, according to the following three criteria:

- C.4) Buildings with an adequate area of less than 25% are excluded.
- C.5) Buildings with an optimal surface area of less than 30% and an optimal surface area of less than 100 m^2 are eliminated.
- C.6) Suitable areas of less than 10 m^2 are excluded.

Based on these extra criteria (considering C.1-C.6), the number of the optimal percentage falls from 47.49% to 47.10%, as shown in Table 2.

Table 2. Summary based on all six criteria

Optimal surface (m2)	Total surface (m2)	Percentage (%)
24,871.76	52,804.88	47.1

4.3. Including PV facility

In addition, on the one hand, only 25% of the optimal surface can be covered with photovoltaic panels (in order to avoid panel loss of shadow, inclination, structure, space for maintenance, etc.). On the other hand, photovoltaic panels are estimated to have 15% performance and 86% PR (Performance Ratio). Thus, the monthly electricity contribution on public residence decks has been calculated with this equation:

$$Elec.production\ (KWh) = Surf_{opt} \cdot 0.25 \cdot Rad_{mean} \cdot 0.15 \cdot 0.86 \quad (3)$$

Accordingly, the results of electricity PV production of the selected public buildings of Vitoria-Gasteiz are shown in Table 3.

Table 3. Monthly electricity production

Month	Electricity produced (kWh)
January	43,940.12
February	66,805.28
March	139,575.64
April	191,039.39
May	226,364.23
June	242,116.29
July	235,092.65
August	206,475.89
September	161,275.77
October	110,118.26
November	59,850.77
December	27,482.56

Once the PV electricity production of each of the roofs has been calculated, the electricity consumption of each dwelling and the number of dwellings in each of the buildings need to be considered in order to obtain the percentages of electricity that could be self-consumed.

4.4. Energy Communities

Apart from that and going further, seven energy communities are proposed, which take into account the proximity of the buildings and the criterion of 500 metres (mentioned in section "*3.2 Methods and indicators"*).

As the same conclusions are obtained for all energy communities, and because of technical limitations, only the most representative one will be analysed in this paper, the one shown in Figure 7.

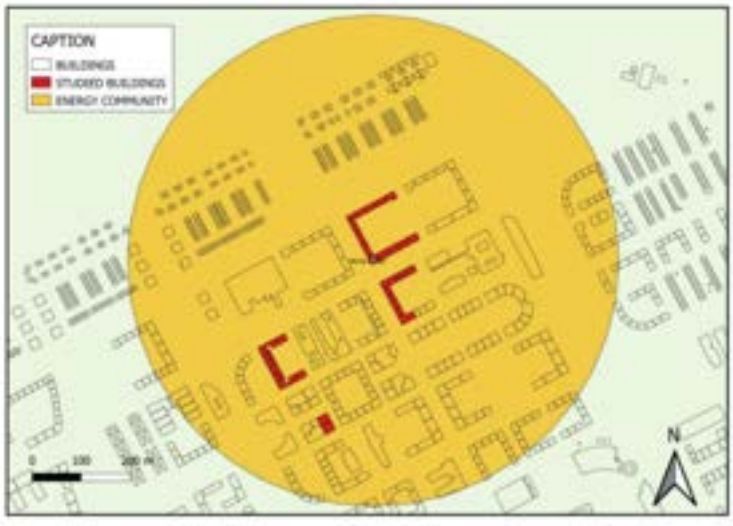

Figure. 7. Selected energy community.

The chosen energy community has the characteristics shown in Table 4:

Table 4. Energy community characteristics

Description (name of the building)	Number of households
Lakua 30	30
Lakua 110	110
Lakua 90	90
Ibaiondo 228	228

Moreover, the monthly electricity produced in the corresponding rooftops (obtained from the previous analysis) and the consumptions of the households (calculated with the corresponding consumption data of 2018) of this energy community are shown in Table 5 and is graphically represented in Figure 8:

Table 5. Production vs Consumption

Month	Total production (KWh)	Total consumption (KWh)	Photovoltaic efficiency (%)
January	7,924.77	75,478.25	10.5
February	15,676.17	66,751.97	23.48
March	28,054.36	63,586.10	44.12
April	38,414.26	63,597.44	60.4
May	45,512.82	70,480.53	64.58
June	48,704.16	62,964.97	77.35
July	47,276.88	62,408.82	75.75
August	41,509.91	58,794.55	70.6
September	32,450.38	52,632.10	61.66
October	21,996.25	68,973.49	31.89
November	11,048.48	66,429.19	16.63
December	5,462.89	68,684.48	7,95

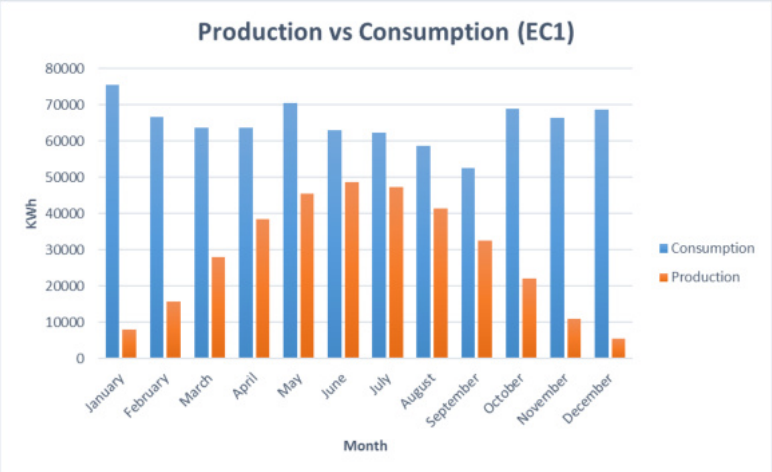

Figure. 8. Production vs Consumption in the selected energy community.

As it can be seen, the selected energy community, composed only by the public residential buildings, is not capable of supplying the total electricity demand in any of the months of the year, although it does supply part of the demand.

Without making an economic analysis of the study, it is too early to conclude whether it is economically viable or not, but at least it can be seen that in the central months of the year the installation of PV panels and the concept of the energy community is an option to be taken into account.

5. Conclusions and next steps

In summary, the study determines that 47.1% of the total roof surface area of the social housing buildings in Vitoria-Gasteiz is suitable for a photovoltaic installation. Furthermore, by adding the criterion that only 25% of the optimum surface area can be used for photovoltaic installations, it is still possible that all these potential PV installations together could produce more than 1,700 MWh per year, see Table 6.

Table 6. Summary table

Percentage of optimal surface (%)	Electricity production (MWh)
47.1	1,710.14

Furthermore, if an energy community is proposed, the electricity consumption cannot be completely compensated or supplied by the PV electricity production. However, PV production could be increased by adding more buildings' roofs to these communities, following the 500 metres criterion, such as other public tertiary-use buildings.

Therefore, the main conclusions of this study are, on the one hand, that introducing photovoltaic panels in social housing buildings is a viable option, and on the other hand, that implementing energy communities in Vitoria-Gasteiz could be an interesting option but requires further analysis, being the beginning of a community or municipality with a vision towards the future of sustainability.

Considering all this, the next steps would be, at first, to make an economical study of the energy community proposed, and then, to evaluate the possibility of making a hybridization between PV panels and heat pumps, to benefit from their potential as energy storage.

6. Acknowledgments

The authors would like to thank the Basque Government's Laboratory for the Quality Control of Buildings and ALOKABIDE SA for the provided information and help for this study.

7. References

[1] European Commission, "Making our homes and buildings fit for a greener future," 2021. doi: 10.2775/03938.

[2] Eurostat, "Energy consumption in households," 2022. [Online]. Available: https://ec.europa.eu/eurostat/statistics-explained/index.php?title=Energy_consumption_in_households#Energy_products_used_in_the_residential_sector%0Ahttps://ec.europa.eu/eurostat/statistics-explained/index.php?title=Energy_consumption_in_households#Energy.

[3] Ávila, A. M. M., & Zamora, A. B. (2015). Estudio del potencial fotovoltaico sobre los tejados del núcleo urbano de Miraflores de la Sierra. Ciemat.

[4] Gassar, A. A. A., & Cha, S. H. (2021). Review of geographic information systems-based rooftop solar photovoltaic potential estimation approaches at urban scales. Applied Energy, 291, 116817. https://doi.org/10.1016/j.apenergy.2021.116817

[5] Guevara Sempertegui, C. I. (2018). Viabilidad de un sistema fotovoltaico para suministrar energía eléctrica a la estación base celular de la empresa Claro ubicado en el Caserío Santa Rosa-Sallique-Jaén Cajamarca.

[6] Haegermark, M., Kovacs, P., & Dalenbäck, J. O. (2017). Economic feasibility of solar photovoltaic rooftop systems in a complex setting: A Swedish case study. Energy, 127, 18-29.

[7] Aparisi Cerdá, I. (2019). Estudio de viabilidad económica de instalaciones fotovoltaicas en entorno urbano. Aplicación a 4 casos de estudio en la provincia de Valencia (Doktorego tesia, Universitat Politècnica de València).

[8] Guerrero Gallego, A. J. (2021). Viabilidad de uso de paneles fotovoltaicos como mecanismo de ahorro energético/CO2 en Asturias.

[9] Quiros-Tortos, J., Valverde, G., Arguello, A., & Ochoa, L. N. (2017). Geo-Information Is Power: Using Geographical Information Systems to Assess Rooftop Photovoltaics in Costa Rica. IEEE Power and Energy Magazine, 15(2), 48-56. https://doi.org/10.1109/MPE.2016.2637158

[10] Khan, J., & Arsalan, M. H. (s. f.). Use of Open Source GIS Tools to Identify Bright Rooftops for Solar PV Applications in Karachi.

[11] Baiocchi, V., Lelo, K., Marzaioli, V., & Vatore, F. (2022). SIMULATION OF THE EFFECTS OF POSSIBLE REGULATIONS FOR THE LOCATION OF WIND AND PHOTOVOLTAIC POWER PLANTS IN THE LAZIO REGIONAL ADMINISTRATION (ITALY). The International Archives of the Photogrammetry,

Remote Sensing and Spatial Information Sciences, XLVIII-4/W1-2022, 43-49. https://doi.org/10.5194/isprs-archives-XLVIII-4-W1-2022-43-2022

[12] Davybida, L., Wyczałek, I., & Plichta, A. (2022). Using GIS and SDSS Tools in the Design of a Photovoltaic System for a Built-up Roof. Geomatics and Environmental Engineering, Vol. 16(4). https://doi.org/10.7494/geom.2022.16.4.31

[13] Silveira Júnior, C. R., Luiz, G. C., Barbosa, G. A. S., & Sousa, L. G. C. (2020). Aerosol Influence on Photovoltaic Solar Energy Generation for the State of Goiás (BRAZIL). 2020 IEEE Latin American GRSS & ISPRS Remote Sensing Conference (LAGIRS), 345-350. https://doi.org/10.1109/LAGIRS48042.2020.9165629

[14] Mohajeri, N., Assouline, D., Guiboud, B., Bill, A., Gudmundsson, A., & Scartezzini, J.-L. (2018). A city-scale roof shape classification using machine learning for solar energy applications. Renewable Energy, 121, 81-93. https://doi.org/10.1016/j.renene.2017.12.096

[15] Wang, X., Xia, L., Bales, C., Zhang, X., Copertaro, B., Pan, S., & Wu, J. (2020). A systematic review of recent air source heat pump (ASHP) systems assisted by solar thermal, photovoltaic and photovoltaic/thermal sources. Renewable Energy, 146, 2472-2487. https://doi.org/10.1016/j.renene.2019.08.096

[16] Herrando, M., Pantaleo, A. M., Wang, K., & Markides, C. N. (2019). Solar combined cooling, heating and power systems based on hybrid PVT, PV or solar-thermal collectors for building applications. Renewable Energy, 143, 637-647.

[17] Ayadi, O., & Al-Dahidi, S. (2019). Comparison of solar thermal and solar electric space heating and cooling systems for buildings in different climatic regions. Solar Energy, 188, 545-560. https://doi.org/10.1016/j.solener.2019.06.033

[18] Frieden, D., Tuerk, A., Roberts, J., D'Herbemont, S., Gubina, A. F., & Komel, B. (2019). Overview of emerging regulatory frameworks on collective self-consumption and energy communities in Europe. 2019 16th International Conference on the European Energy Market (EEM), 1-6. https://doi.org/10.1109/EEM.2019.8916222

[19] Jeriha, J. (2019). Collective self-consumption and energy communities. Compile, 23.

[20] Gjorgievski, V. Z., Cundeva, S., & Georghiou, G. E. (2021). Social arrangements, technical designs and impacts of energy communities: A review. Renewable Energy, 169, 1138-1156. https://doi.org/10.1016/j.renene.2021.01.078

[21] DIRECTIVE (EU) 2018/ 2001 OF THE EUROPEAN PARLIAMENT AND OF THE COUNCIL - of 11 December 2018—On the promotion of the use of energy from renewable sources. (n. d.).

[22] DIRECTIVE (EU) 2019/ 944 OF THE EUROPEAN PARLIAMENT AND OF THE COUNCIL - of 5 June 2019—On common rules for the internal market for electricity and amending Directive 2012/ 27/ EU. (n. d.).

[23] Directorate-General for Energy (European Commission). (2019). Clean energy for all Europeans. Publications Office of the European Union. https://data.europa.eu/doi/10.2833/9937

[24] Royal Decree-Law 15/2018 of 5 October on urgent measures for energy transition and consumer protection, Pub. L. No. Royal Decree-Law 15/2018, in Spanish, Real Decreto-ley 15/2018, de 5 de octubre, de medidas urgentes para la transición energética y la protección de los consumidores, Pub. L. No. Real Decreto-ley 15/2018, BOE-A-2018-13593 97430 (2018). https://www.boe.es/eli/es/rdl/2018/10/05/15

[25] Royal Decree 244/2019, of 5 April, regulating the administrative, technical and economic conditions for the self-consumption of electricity, Pub. L. No. Royal Decree 244/2019,, in Spanish, Real Decreto 244/2019, de 5 de abril, por el que se regulan las condiciones administrativas, técnicas y económicas del autoconsumo de energía eléctrica, Pub. L. No. Real Decreto 244/2019, BOE-A-2019-5089 35674 (2019). https://www.boe.es/eli/es/rd/2019/04/05/244

[26] National Integrated Energy and Climate Plan (PNIEC) 2021-2030, in Spanish, Plan Nacional Integrado de Energía y Clima (PNIEC) 2021-2030. (n. d.). Retrievered March 6, 2023, from https://www.miteco.gob.es/es/prensa/pniec.aspx

[27] Long Term Decarbonisation Strategy 2050, in Spanish, Estrategia de Descarbonización a Largo Plazo 2050. (n. d.). Retrievered March 6, 2023, from https://www.miteco.gob.es/es/prensa/documentoelp_tcm30-516109.pdf

[28] Law 4/2019, of 21 February, on energy sustainability of the Basque Autonomous Community, Pub. L. No. Law 4/2019, BOE-A-2019-3705 25577, in Spanish, Ley 4/2019, de 21 de febrero, de sostenibilidad energética de la Comunidad Autónoma Vasca, Pub. L. No. Ley 4/2019, BOE-A-2019-3705 25577 (2019). https://www.boe.es/eli/es-pv/l/2019/02/21/4

[29] DECREE 254/2020, of 10 November, on Energy Sustainability in the Basque Autonomous Community. - Law Day: Regulations of the Basque Country-Basque Government-Euskadi.eus , in Spanish, DECRETO 254/2020, de 10 de noviembre, sobre Sostenibilidad Energética de la Comunidad Autónoma Vasca. - Legegunea: Normativa del Pais Vasco—Gobierno Vasco—Euskadi.eus. (n. d.). Retrieved March 6, 2023, from https://www.legegunea.euskadi.eus/eli/es-pv/d/2020/11/10/254/dof/spa/html/webleg00-contfich/es/

[30] DECREE 128/2019, of 30 July, by which the Spatial Planning Guidelines of the Autonomous Community of the Basque Country are definitively approved (September 25, 2019). - Legegunea: Normativa del Pais Vasco-Gobierno Vasco-Euskadi.eus in Spanish, DECRETO 128/2019, de 30 de julio, por el que se aprueban definitivamente las Directrices de Ordenación Territorial de la Comunidad Autónoma del País Vasco. (2019, septiembre 25). - Legegunea: Normativa del Pais Vasco—Gobierno Vasco—Euskadi.eus. (n. d.). Retrieved March 6, 2023, from https://www.legegunea.euskadi.eus/eli/espv/d/2019/07/30/128/dof/spa/html/webleg00-contfich/es/

[31] Energy Policy 2030—EVE. (n. d.). Retrieved March 6, 2023, from https://www.eve.eus/Conoce-la-Energia/La-energia-en-Euskadi/Energy-Policy-2030?lang=en-gb

[32] Plan de Ciencia, Tecnología e Innovación—PLAN ZERO PLANA. . (September 1, 2022). https://www.alokabide.euskadi.eus/plan-de-ciencia-tecnologia-e-innovacion-plan-zero-plana/

[33] GeoEuskadi. Datu Espazialen Egitura—Euskadiko DEA. (n. d.). Retrieved March 6, 2023, from https://www.geo.euskadi.eus/webgeo00-inicio/eu

[34] Estimar el potencial de energía solar | Learn ArcGIS. (d. d.). Retrieved March 6, 2023, from https://learn.arcgis.com/es/projects/estimate-solar-power-potential/

Proceedings of ECOS 2023 - The 36th International Conference On
Efficiency, **C**ost, **O**ptimization, **S**imulation and Environmental Impact of Energy Systems
25-30 June, 2023, LAS PALMAS DE GRAN CANARIA, SPAIN

Energy, Exergy and Exergo-economic analyses of supercritical CO_2 cycles for the exploitation of a geothermal resource in the Mt. Amiata region

N. Di Michele[b], L. Talluri[a], P. Ungar[c], D. Fiaschi[d,*]

Department of Industrial Engineering, University of Florence, Florence, Viale Morgagni 40-44, 50134, Italy
[a]lorenzo.talluri@unifi.it
[b]nicola.dimichele@stud.unifi.it
[c] pietro.ungar@unifi.it
[d] daniele.fiaschi@unifi.it

Abstract:

An alternative powerplant layout to the commonly applied flash technology is proposed for the geothermal location of Monte Amiata, Italy. The reservoir conditions correspond to a pressurized brine field, with relevant contents of CO_2, acid gases/contaminants, and dissolved salts. The present solution avoids flashing the brine stream, proposing instead to install a borehole pump capable of maintaining pressurized conditions. By applying this solution, the amount of non-condensable gases released when reaching the ground level with reduced pressure can be conveniently limited; the gas stream is recovered, compressed and reduced in liquid conditions, suitable for complete reinjection into the reservoir. The necessity of a gas treatment section is thus completely avoided. The heat recovered from the hot brine, placed at ground level, is transferred to the supercritical CO_2 cycle. Different CO_2 cycle configurations were considered. Exergy and exergo-economic analyses of the whole system are carried out. The optimal calculated exergy efficiency of 45.5% was achieved for the recuperative cycle with intercooling and reheat configuration and the lowest obtained produced cost of electricity was 7.4 c€/kWh for the recuperative cycle configuration. Furthermore, the influence of the pressure losses to the heat exchanger has been assessed, allowing evaluating of the loss in efficiency for each cycle.

Keywords:

Geothermal energy; binary cycle; sCO2; Exergo Economic; Electricity production cost

1. Introduction

The energy demand has increased exponentially in recent years due to the strong increase in economic development and population growth. This led to an increased concern on sustainability issues and environmental deterioration [1]. The exploitation of renewable energy technologies has therefore bloomed, allowing an increase in the efficiency of the conversion systems. Among renewables, geothermal energy has the advantage of having the highest resource availability, not depending on the weather conditions. Geothermal energy systems exploit the heat content of the earth's interior, as the earth is slowly cooling down. The total global output of the Earth's heat flow is over $4x10^{13}$ W [2], which is four times higher than the actual energy consumption; however, only a small part of this heat flux can be exploited. Geothermal power plants can be categorized in shallow geothermal and deep geothermal. The first exploits low temperature heat sources at the surface, with a maximum of well drilling in the range of 250 m and are suitable for low temperature heat generation. On the other hand, deep geothermal is considered when wells are drilled deep, from 1 to 5 km within the Earth, or even deeper with the newest drilling technologies. Deep geothermal allows reaching higher temperature, which enables the conversion of the geothermal heat in electricity. Another way to categorize geothermal power plant is to classify it on the enthalpy content of the flow: low, medium or high enthalpy. Medium and high enthalpy resources are the most common exploited and have almost reached its maximum potential, while low or moderate enthalpy fields are still yet to be fully utilized. Typical power plant for the exploitation of medium high temperature fields are single, double and triple flash power plants (for a water dominant reservoirs) and direct steam power plants (for vapor dominant reservoirs). These power plants have several advantages, such as relatively high conversion efficiencies, several years of operation which led to a solid know-how, well-known safety measures which are not critical thanks to low pressure and temperatures involved, and economic feasibility. On the other hand, they present a significant disadvantage when considering the environmental sustainability; indeed, a relevant documented issue is the release of non-condensable gases NCGs (mainly CO_2 plus several kind of contaminants) to the environment [3, 4]. The current solution to reduce the environmental impact of geothermal power plant is the utilization of AMIS

technology in Italy, developed by ENEL GP [5]. This allows reducing the Hg and SO_2 content from the NCGs stream, and thus the environmental impact of the power plants. Several studies have been developed on the environmental sustainability of geothermal energy conversion systems though the application of life cycle assessment [6]. In [8] a 20 MW single flash power plant is evaluated and compared with similar size power plants operating with wind and solar. It was found that the geothermal power plant, which includes the AMIS technology, performs well against other renewables, and has only a slightly higher environmental footprint, due to larger values of the global warming category (Recipe 2016 Midpoint). In [9] enhanced geothermal systems (EGS) were considered, estimating several design scenarios and compared to other renewable energies environmental impacts. The results indicated that EGS power plant environmental footprint is in the same range of other renewables and it was confirmed that the highest contribution to the environmental impact comes from the drilling of the wells, in particular by the diesel burned in the drilling process. In [10], the environmental impact of a combined heat and power double flash geothermal power plant was estimated. Their studies confirmed that the drilling process is the main responsible for most of the impact category results. However, it was also found that the global warming and acidification category are significantly affected by the operation phase. Indeed, during the operational lifetime of the power plant, continuous emissions of CO_2 and H_2S provide a significant environmental impact. In [11] the definition of harmonized LCA guidelines for the comparison of geothermal power plant have been drought. Particularly, the aim of their study was to increase the comparability of the results of LCA studies on geothermal system, by proposing a consistent methodology with several indications of the critical aspects of the analysis.

From the above mentioned studies, it seems that only the use of binary cycles (like ORCs, Kalina or trans-critical and super critical CO_2) coupled to the complete reinjection of NCGs could give a valuable answer to the improvement of sustainability of geothermal power plants, particularly in the operational phase [12]. ORC and Kalina cycles work with novel and environmentally friendly fluids (low GWP), which are adapt for the exploitation of low temperature resources. Several studies on the coupling of ORC or Kalina cycles with low temperature or medium-high temperature [13-17] geothermal resources have been performed. These studies involved the optimal selection of the working fluid [18], including zeotropic mixtures [19], the optimal configuration of the power plant [20, 21], as well as thermo-economic analysis [22]. In [23] an energy and exergy analysis is carried out for a dual fluid ORC. Isobutane and Isopentane were selected as working fluids, allowing a production of almost 3.5 MW of electricity, almost equally shared between the high temperature isopentane cycle and the low temperature isobutane cycle. The most critical components for this power cycle configuration were found to be the low and high pressure vapor generators, due to the not optimal match of the heat curves. An interesting study on the profitability of geothermal electricity production from several ORC configurations have been carried out in [24]. In their study, an optimization of cycle configurations, working fluid selection and thermodynamic conditions was carried out in order to investigate the most performing configuration, based on levelized cost of electricity, return of investment and payback period. They performed the analysis taking into account for the economic calculation the corporate tax rates and the average electricity prices of 20 countries and found that is the country with the highest return of investment due to the high electricity price. A focus on the design and optimization of the evaporator for ORCs for low temperature geothermal application has been developed in [25]. In their study a Pareto front solution has been found in order to assess the proper compromise between costs and pressure drop in the heat exchanger; finally evaluating the performance of the ORC.

While several studies on ORC and Kalina cycle for geothermal applications have been developed, on the other hand, few studies on the coupling of super critical CO_2 cycles with geothermal energy resources have been carried out. In [26] a trans critical power cycle for low temperature geothermal power plants has been investigated, with a particular focus of the influence of the recuperator performance in both design and off-design operation. It was found that the recuperator allows an improvement in the off-design performance of the system, particularly enhancing the performance of the CO_2 pump.

In [27], an innovative supercritical CO_2 cycle configuration was evaluated, and its performance compared to a ORC working with R245fa or R1233zd(E). The cycle configuration exploits the thermosiphon concept, therefore utilizing the CO2 both as heat medium in the reservoir and as the working fluid in the power cycle. The results obtained indicated that the ORC cycle with R245fa as working fluid allowed the highest power production for one year of operation (8% more than the sCO_2 thermosiphon cycle). In [28] a low temperature geothermal case study, the Sidirokastron field in Greece was studied with the objective of coupling a super critical CO2 power plant. Particularly, the maximum temperature achieved by the geothermal fluid is of 75°C, which is a very low value, hindering the thermodynamic efficiency. In these conditions, the sCO_2 cycle achieved a maximum thermal efficiency of over 6%. Another interesting study by [29] deals with the thermodynamic analysis of a low temperature geothermal power plant utilizing a mixture of SF_6 and CO_2 as working fluid. The maximum achieved efficiency of the binary geothermal cycles was found to be 15% with a 20% SF_6-80% CO_2 composition, with a resource temperature of 160°C. The results therefore indicated that the utilization of zeotropic CO_2 mixtures could allow to increase the thermal efficiency of the sCO_2 power plants for geothermal applications.

While few studies were focused on the coupling of super critical CO_2 cycles with low temperature geothermal application, on the other hand several studies are available in literature dealing with high temperature applications, like solar power generation [30], coal fired power plants [31] or waste heat recovery [32,33]. This is due to the very good behaviour of the CO_2 for high temperature applications, nonetheless, it seems that further studies are needed to provide a clear assessment on the application of CO_2 cycle to low temperature resource. Indeed, the selection of CO_2 as working fluid is a due to its main characteristics, such as non-toxic, non-flammable, not suffering any thermal degradation at high temperature (unlike ORCs fluids) and optimal environmental traits, with a nil ODP and a GWP of 1. Furthermore, in the supercritical region, the high density of the CO_2 allows a smaller and more compact design of the components, which could allow a "miniaturize" design of geothermal power plants. Finally, for variable temperature heat source, super critical CO_2 allow a better match of the profiles, guaranteeing a higher efficiency of the heat exchange and thus reducing the exergy destructions in the heat exchanger.

1.1. A Case study for a sustainable Geothermal Energy power plant (Mount Amiata, Italy)

The properties of the geothermal resource are variable depending on the location in terms of pressure, temperature, state of the fluid, and amount and composition of NCGs as well as of dissolved mineral salts. The nature of contaminants released by GECS usually includes H_2S, NH_3, CH_4, and in some cases Hg [34 – 36]. Each potential location deserves careful study, possibly leading to different issues when selecting the best available technology.

The area of Mount Amiata, Italy, represents a significant challenging application. This region of Southern Tuscany is historically one of the reference sites for the development of geothermal conversion systems; currently, about 120 MW of geothermal electricity are installed there. The Amiata reservoir is water-dominant type [37]; the current conversion technology applies single or double-flash power plant layouts, in one case also combined to an ORC to recover the energy content in brines. The composition of the geofluid includes relevant amounts of NCGs (CO_2, H_2S, NH_3, CH_4), mercury sulphide, HgS and dissolved salts (mainly stibnite and silica salts). The reservoir is located at 3000–3500 m depth, thereby determining supercritical pressure conditions (p >250 bar); however, the fluid is not in critical conditions, since the reservoir temperature is in the 300–350 °C range. Consequently, flashing in the well takes place at a depth between 600 and 1500 m, with two-phase flow in the upper section. In the current technology, a throttling valve/separator assembly is located at the wellhead [38, 39]. Despite the attractiveness of the region in terms of energy generation potential, local opposition is present in the area against further development of geothermal energy. The main concerns of the opponents are long-term sanitary effects (mainly traceable to Hg and H_2S emissions, even after the introduction of catalytic gas treatment [5]), as well as the water balance and the greenhouse gas emissions. Within this context, even if the resource can be classified as high-enthalpy and therefore traditionally converted using flash power plant solutions, it makes sense to explore different possible options, investigating the potential to mitigate these specific issues.

1.2. Reference case

As a specific reference case, the available data from the Bagnore 3 power plant were considered. A flow rate of 122 kg/s is assumed to be available at an enthalpy level of 1200 kJ/kg, corresponding to about 275 °C at 250 bar, which are the estimated reservoir conditions for the deep reservoir in the Mt. Amiata region at a depth z>3000 m. The CO_2 content of the brine is evaluated at 2% mass fraction [40]. The current power plant applies a wellhead separator set at 20 bar, determining a saturated steam flow rate of 36 kg/s (with 7% CO_2 content), while a hot brine (enriched with salts causing considerable scaling problems) of about 86 kg/s is directed to reinjection. The power plant is a single-flash unit equipped with an ORC recovery section on a secondary (low-pressure) flash of the brine, providing a total power output of about 23 MWe (actually, at present 3 MWe less because a smaller ORC unit is installed, with incomplete heat recovery from the reinjection brine). The separator setting determines the flash conditions inside the well, which take place at a depth of about 600 m. The considerable amount of CO_2 in the flash steam is accompanied by minor contaminants (H_2S, Hg and NH_3 with minor traces of CH_4); while the steam is condensed in the steam cycle, the NCGs are discharged to the atmosphere; however, before the final release, the emissions treatment is applied, with extensive capture of H_2S, Hg and NH_3. The following emissions levels were calculated: e_{CO2} = 396 g/kWh; e_{H2S} = 1.21 g/kWh; e_{Hg} = 1.3 g/kWh; these figures correspond to measurements taken by the pollution control authority. It should be underlined that the CO_2 emissions are of natural origin; however, they are of similar level to those obtained by the most advanced fossil fuel power plants and could be avoided if the resource was not extracted from the reservoir.

For the above reasons, a number of improved solutions were developed, leading finally to identifying guideline the complete reinjection of NCGs in the reservoir as a possible best practice to exploit this geothermal resource [40].

To summarize, the literature review and the analysis of the presented case study has indicated a significant gap in the study of supercritical CO_2 cycle for the exploitation of geothermal resources.

Specifically, in the present study a relatively simple solution is proposed, inspired by the guideline of completely avoiding the practice of flashing the geothermal stream by the means of a borehole pump located at suitable depth, coupled to an advanced (supercritical) binary cycle.

The aim of this study is therefore to **evaluate the energy, exergy and economic performance** of the proposed advanced CO_2 power plant, which guarantee a relevant step ahead in the environmental behaviour of the geothermal powerplants, but they could result into a not economically viable options if compared to the current single and double flash technologies.

The main goal of this study is, therefore, the investigation and comparison of optimized solutions adopting supercritical CO_2 cycles configurations to the selected case study, in order to assess the *most suitable ones to compete with the current single flash +ORC power plant,* either from thermodynamic and exergo-economic points of view. Figure 1 presents the schematic of the current power plant and table 1 summarizes its main performance parameters.

Table 1. Bagnore 3 single flash + ORC power plant performance parameters

Parameter	Value
First Law efficiency η	0.19
Second Law efficiency η_{II}	0.46
Net power output W_{net}	20
Cost of energy €/kWh	0.04

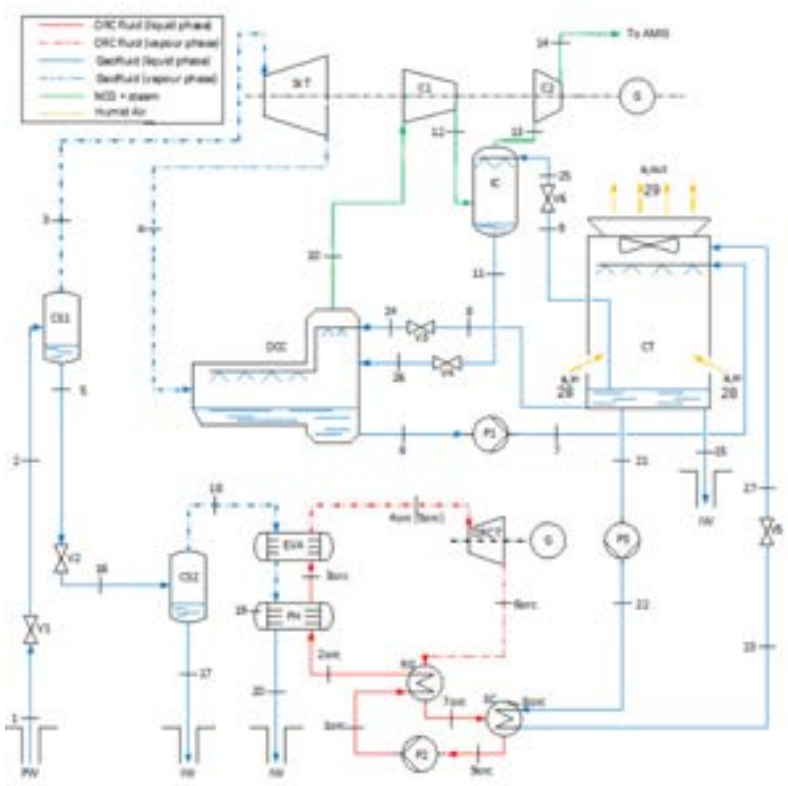

Figure 1. Schematic of Bagnore 3 power plant [40]

2. Methodology

The Amiata geothermal field was selected as a case study because of the difficulties encountered in using the local resource with flash power plant technology. The brine is particularly rich in antimony sulphide (Stibnite), which precipitates in the flash drain at temperature below 140°C and is responsible for the scaling of the ducts, causing drastic reductions of the passage sections. In order to prevent the scaling of Stibnite, the introduction of a borehole pump upstream the flash point located inside the well at 800 m depth from the ground level was proposed, thereby maintaining the geothermal fluid under pressurized liquid conditions, from the extraction to the re-injection reservoir. The required pump head and power were calculated modelling the friction and heat losses in the geothermal fluid extraction duct. The pressurized fluid, after having delivered its sensible heat to the working fluid, is re-injected at a fixed 150°C temperature, in order to avoid any sedimentation of stibnite while ensuring, at the same time, a correct management of the geothermal field. A guideline applied in this research is to maintain the geothermal fluid under pressurized liquid conditions: this includes the modelling of the well thermo-fluid dynamics and of the borehole pump. A model was thus developed in EES [41] in order to calculate the heat transfer and pressure losses, while the fluid (geothermal brine in liquid conditions) is ascending the well duct. A steel cladding is included only in the first 500 m from the surface. Once the geometry is fixed, the head losses, which must be overcome by the borehole pump in order to maintain the geothermal fluid in liquid phase were calculated; the same was done for the heat losses. The Colebrook formula for the

calculation of the friction factor was utilized. The temperature of the ground is assumed to vary linearly with a gradient of 50°C per km of depth, from the starting value of the ambient temperature of 285 K.

Table 2 and Figure 2 show the main thermodynamic and performance parameters and the configuration of the borehole pump respectively.

Table 2. Main borehole pump parameters

Parameter	Value
η	0.8
W_{bp}	0.87 [MW]
T_{inBH}	273 [C]
P_{inBH}	5758 [kPa]
T_{outBH}	274.6 [C]
P_{outBH}	10258 [kPa]

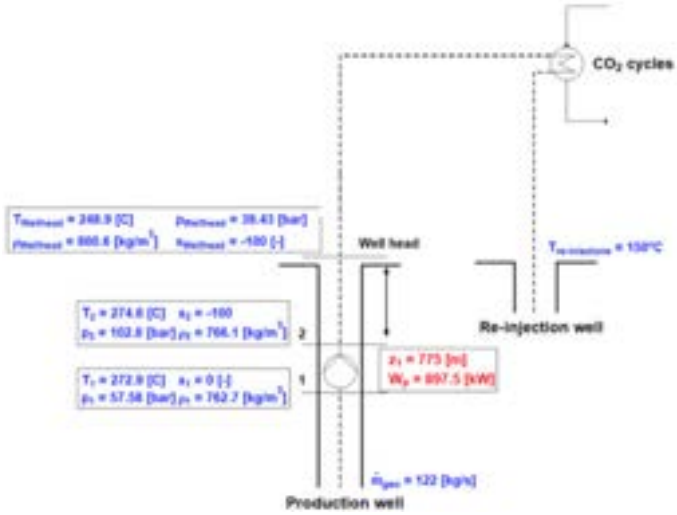

Figure 2 Borehole Pump schematic

2.1. Power plants schematic

In these work several power plant configurations were considered in order to evaluate the optimal power plant layout to be applied to the investigated medium temperature geothermal resource. Clearly, it is general for many different aspects, so that it may be representative of many other cases of exploitation of medium – high temperature geothermal resource with trans and supercritical CO2 binary cycles. Figure 3 shows the analysed configurations and figure 4 represents the corresponding temperature-entropy diagrams. Particularly, the assessed configurations comprehend a recuperative cycle, a recuperative cycle with reheating, a recuperative cycle with reheating and intercooling, a precompression cycle, a recompression cycle with two recuperation and a recompression cycle with one recuperator.

For each developed power plant, it was assumed that: (i) the cycles work in steady state conditions; (ii) the geothermal fluid is modelled as pure water; (iii) the difference in kinetic and potential energy between the input and output of turbomachines and heat exchangers is ne-glected; (iv) the isentropic efficiency of turbomachines is fixed.

The real fluids thermodynamic properties were evaluated from EES internal libraries [41].

For each component, mass end energy balance equations were applied, as displayed in Eqns. (1)-(2).

$$\sum \dot{m}_{in} = \sum \dot{m}_{out} \qquad (1) \qquad \dot{W} + \dot{Q} = \sum \dot{m}_{out} h_{out} - \sum \dot{m}_{in} h_{in} \qquad (2)$$

The first law efficiency was then defined, as shown Eq. (3).

$$\eta_I = \frac{\dot{W}_{net}}{\dot{Q}_{in}} \qquad (3)$$

2.2. Exergy and exergo-economic analysis

Exergy is the ability of a system, a flow of matter or an energy interaction (such as heat, work or potential energy) to produce work as a result of interaction with the environment. For a completely reversible system, the maximum obtainable work is equal to the total exergy of the initial thermodynamic state.

Exergy is, therefore, the combination of the First and Second Laws of Thermodynamic, which allow to properly assess the energy efficiency of a system and to correctly identified the associated irreversibilities [42].

Exergy analysis is considered as one of the most robust method for the design and assessment of energy systems [43]. Indeed, the concept of exergy allows to estimate the effective thermodynamic values of energy flows. In the present work, the exergy is calculated at each point of the system by Eq (4).

$$\dot{E}x_j = \dot{m}_j[(h_j - h_o) - T_o(s_j - s_o)] \qquad (4)$$

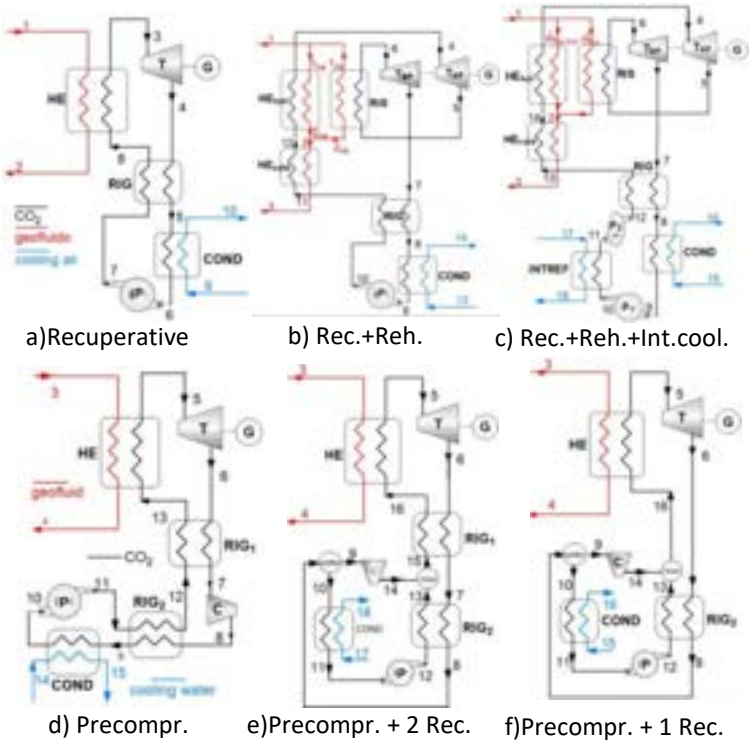

Figure 3 Schematic of super critical cycles

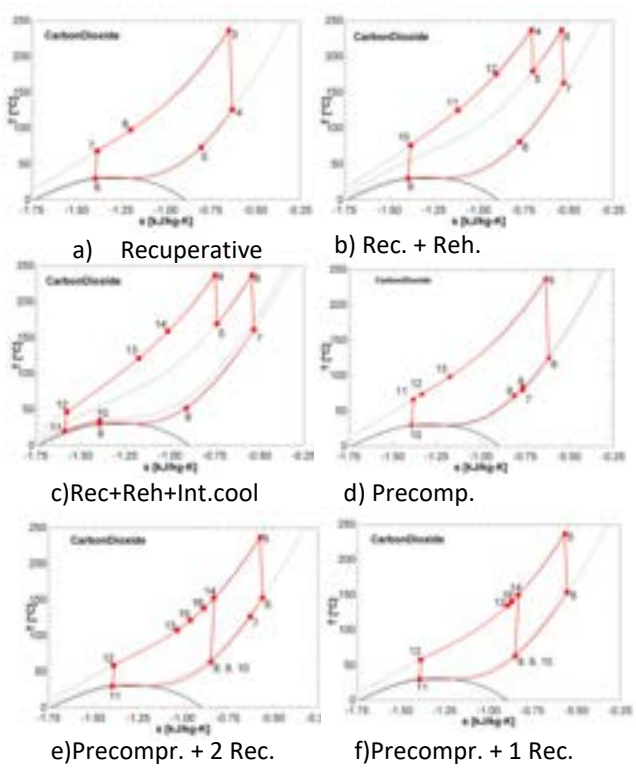

Figure 4 T-s diagram of super critical cycles

Combining the economic and exergy analysis (e.g. exergo-economic methodology) allows providing an efficient evaluation of the power plant and components cost-effectiveness, by introducing the costs per exergy unit [44]. The exergo-economic approach outlined in [45] was applied in this work by defining, for each component k, a cost balance equation, expressed in the following equations (5).

$$\dot{C}_{P,k} = \dot{C}_{F,k} + \dot{Z}_k$$
$$c_{P,k}\,\dot{E}x_{P,k} = c_{F,k}\,\dot{E}x_{F,k} + \dot{Z}_k \qquad (5)$$

Where:

$\dot{C}_{P,k}$ and $\dot{C}_{F,k}$ are the cost rates associated with exergy products and fuels respectively

$c_{P,k}$ and $c_{F,k}$ are the costs per unit of exergy of product or fuel respectively.

$\dot{Z}_k$is the sum of cost rates associated with investments and O&M for the k-th component.

In order to determine the investment and O&M costs ($\dot{Z}_{tot}^{CI} + \dot{Z}_{tot}^{OM}$) of the two proposed power plants, an economic analysis was carried out. The cost functions applicable to the system components were obtained from [46, 16]. Costs were actualized to 2019 values, by using the CEPCI indexes [47]. The Operation and Maintenance costs (O&M) of each component were determined following the best practises in literature [48, 16].

Finally, Table 2 summarizes the exergo-economic balances and the auxiliary equations [44], which are logic statements that allow defining the missing number of conditions to solve the cost equations applied to each component for the recuperative cycle.

Table 2. Exergo-economic balance equations of power plant components for the recuperative configuration

	Recuperative
Borehole pump	$c_{21}\cdot\dot{E}x_{21} = c_{20}\cdot\dot{E}x_{20} + c_{Wp_{kJ}}\cdot\dot{W}_{BHpump} + \dot{Z}_1 \qquad c_{Wp_{kJ}} = c_{Wt_{kJ}} \qquad c_{20} = c_{fuel_{kJ}}$
Condenser	$c_6\cdot\dot{E}x_6 + c_{10}\cdot\dot{E}x_{10} = c_5\cdot\dot{E}x_5 + c_9\cdot\dot{E}x_9 + \dot{Z}_2 \qquad c_9 = 0 \qquad c_{10} = c_9$
Recuperator	$c_8\cdot\dot{E}x_8 + c_5\cdot\dot{E}x_5 = c_7\cdot\dot{E}x_7 + c_4\cdot\dot{E}x_4 + \dot{Z}_3 \qquad c_4 = c_5$
Heater$_{geo}$	$c_2 * \dot{E}x_2 + c_3 * \dot{E}x_3 = c_1 * \dot{E}x_1 + c_8 * \dot{E}x_8 + \dot{Z}_4 \qquad c_1 = c_{21} * \frac{\dot{E}x_{21}}{\dot{E}x_1} \qquad c_1 = c_2$
Turbine	$c_{Wt_{kJ}}\cdot\dot{W}_T + c_4\cdot\dot{E}x_4 = c_3\cdot\dot{E}x_3 + \dot{Z}_5 \qquad c_4 = c_3$
Compressor	$c_7\cdot\dot{E}x_7 = c_6\cdot\dot{E}x_6 + c_{Wp_{kJ}}\cdot\dot{W}_{pump} + \dot{Z}_6$

3. Results

3.1. Power Cycles Optimization

The main parameters influencing the cycles efficiency are the maximum pressure and temperature. Specifically, a very wide range of maximum cycle pressures was investigated, with a wider range for the recuperative cycle with reheating and intercooling, in order to assess the optimal configuration of the power plants. On the other hand, the maximum temperature of the cycle was defined by the geothermal source at 249 °C, therefore the ΔT approach was varied in order to investigate its influence on both efficiency and cost.

Figure 5 shows the behaviour of the first law efficiency and unit electricity exergo-economic cost at variable maximum pressure (a and b) and ΔT approach (c and d) of the investigated power cycles configurations reported in figures 3 and 4. The figures clearly show that the recuperative configuration with reheating and intercooling is the highest efficiency one, followed by the recuperative and reheating configuration. For all the proposed cycles, an optimizing efficiency range of maximum pressure exists. It is essentially due to the variable shape of the cycles at different p_{max}, which is rather remarkable in the range of 15000 to 30000 kPa. On the other hand, the First Law efficiency and unit energy cost are less sensitive to ΔT approach, with the costs monotonically decreasing with increasing ΔT, due to the dominant effect of heat exchanger cost on the slightly improved performance at low ΔT. The efficiency of the cycles also shows a slight optimization at ΔT in the 3 to 8 degrees, because of the increase of the compressors work for very low ΔT approach due to the increase of the exchange area (and therefore of the pressure losses) of the heat exchanger.

Conversely to the efficiency behavior, the lowest exergo-economic cost is achieved from the less efficient configuration which, however, is also the simplest one, namely the recuperative layout. This was expectable, as the other configurations allow indeed improved performance, but not so high to counterbalance the increased costs due to the additional required equipment. This is more remarkable for the recompression configurations, allowing a modest increase of efficiency at the price of much larger exergo-economic costs. Another interesting feature of the recompression configurations, is their optimal efficiency at lower maximum pressures, while the recuperative and the precompression layouts require higher maximum pressure in order to achieve high cycle efficiencies and low exergo-economic costs.

The performance data of the optimized power cycles are summarized in table 4. The considered configuration allows a 249°C geothermal fluid temperature at the inlet of the main HE, also considering the temperature increase given by the pumping process. The geothermal fluid is re-injected at 150°C in order to avoid the precipitation of stibnite while guaranteeing, at the same time, a correct management of the geothermal field. The best performing thermodynamic cycle is the recuperative with reheating and intercooling, which achieves an efficiency, even including the pumping power from the borehole pump and the heat losses of the ascending geothermal fluid in the well close to that of the currently installed single flash unit (19%). However, the maximum achievable power is much lower than the reference case, with a dramatic 40% reduction in power output. Indeed, all the configurations loose an amount of power output between 40 and 50% when compared to the traditional flash solutions.

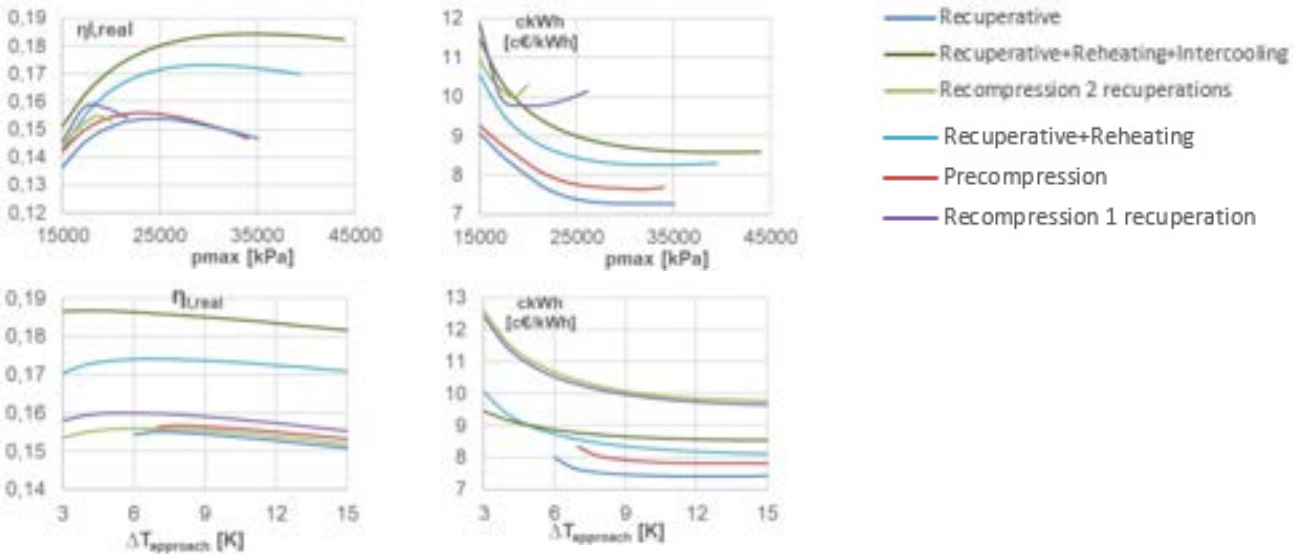

Figure 5 Efficiency and produced energy unit cost as a function of max pressure and $\Delta T_{approach}$ with geothermal fluid

The largest gross power production was achieved with the recompression cycles. However, these layouts have the main drawback of requiring the highest compressor power, exceeding 12 MW, which is almost double than

all the other configurations. These ones, however, guarantee the lowest maximum pressure of the cycle at 18.9 and 18.6 [MPa] respectively, for the configurations 1 and 2 with recuperation.

Finally, the recuperative cycle is the one generating the lowest amount of power, and therefore it is also the less efficient one. It should be remarked that the considered overall power plant efficiency takes into account the heat losses in the ascending well pipe. If the analysis was carried out from the well-head input, the overall efficiency would be closer to the cycle efficiency, and therefore higher than the reference case with flash.

Table 4 Performance comparison of each supercritical CO_2 cycle configuration

Performance Parameter	**Recuperative**	**Recuperative with reheating**	**Recuperative with reheating and intercooling**	**Precompression**	**Recompression with 2 recuperations**	**Recompression with 1 recuperation**
Turbines [kW]	17605	20053	20151	18138	23339	23926
Compressors [kW]	6401	7545	6887.9	6784.7	12048	12371
Borehole pump [kW]	873.2	873.2	873.2	873.2	873.2	873.2
Net Power [kW]	10331	11635	12390	10480	10418	10682
Maximum Pressure [kPa]	24931	30661	35171	23670	18976	18611
CO_2 Cycle Efficiency [-]	0.2162	0.2414	0.2559	0.2191	0.2179	0.223
Global Power Plant Efficiency [-]	**0.1539**	**0.1733**	**0.1845**	**0.1561**	**0.1552**	**0.1591**

3.2. Exergy analysis: results

Figure 6 shows the non-dimensional exergy destruction and losses of each components of the power cycles. The exergy input from the geothermal resource, was fixed at the same value for each thermodynamic cycle. As it is evident from figure 6a, the highest exergy loss comes from the production well (29%). Indeed, this loss is common to all the considered cycles and cannot be avoided. On the other hand, the exergy losses at the condenser to the environment, are not the main contributors to the inefficiency of the cycles, as they are in the range of 2%. These levels of losses are clearly related to the largely different exergy value of the two heat losses.

The source of highest exergy destruction is differently located for the considered cycles: for example, in the recuperative and precompression cycles the highest values belong to the main heater (HE). Furthermore, the exergy destructions in the condenser represent the second main contributor to the inefficiency of the cycles, with values higher than 7.5% for all the configurations except the recuperative one with reheat and intercooling, as it allows a further heat recuperation from the exhaust stream of the turbine.

From the sum of the exergy destructions, it is possible to address the best and worst performing power cycles configurations. The highest exergy efficiency (45.4%) belongs to the recuperative cycle with reheat and intercooling, as clearly shown on figure 6b. As clear from the comparison of the exergy destruction sources in the different cycles, this is mainly due to the lower values found in the heaters and the condenser. Moreover, the good coupling of the fluids heat capacities (water and CO_2) allows achieving a satisfactory value of exergy efficiency in the main HE for this power plant layout. On the contrary, for the same reason (e.g. the weak coupling of heat capacities in the main HE) the recuperative cycle configuration shows the lowest overall value of exergy efficiency.

3.3. Exergo-economic analysis: results

The cost of electricity generation for the proposed power plant configuration can be obtained from an exergo-economic assessment. The levelized cost of electricity for geothermal power plants project installed (or in progress) between 2007 and 2021 varies depending on technology and size. Particularly, for binary cycle configuration the cost of electricity varies between 4 c€/kWh for very big power plants (>300 MW), to values close to 14 c€/kWh for power plants with a nominal capacity of 1 MW. The mean range value of electricity production from geothermal power plants is between 6 and 10 c€/kWh [49].

In the here presented power plant case studies, the range of installed power is between 10 and 15 MW. These lead to a relatively high cost of electricity for some of the investigated configurations (recompression), but still very close or in line with the expected electricity production values. Particularly, the lowest electricity cost (7.42 c€/kWh) was achieved with the recuperative configuration. On the contrary, the highest electricity cost (9.98 c€/kWh) was obtained for the recompression cycle layout with one recuperation level. The configuration achieving the highest efficiency (recuperative with reheating and intercooling) achieves electricity production at 8.6 €/kWh, which is a proper value for this power range. However, if we compare the obtained electricity costs with the reference power plant (Bagnore 3, single flash + ORC), the costs are doubled and the power produced is lower. This kind of power plants can be nonetheless attractive, as they can achieve an almost zero environmental impact configuration during the operation phase. Figure 7 summarizes the calculated electricity cost for all the analysed power cycles.

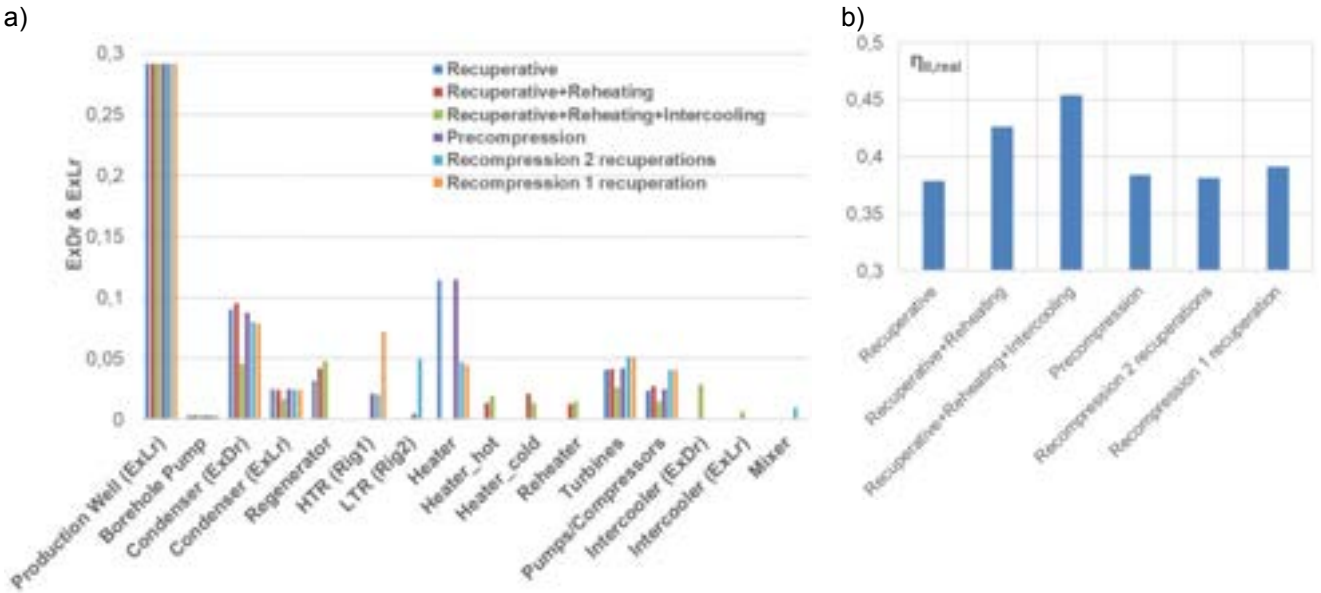

Figure 6 a) comparison of components exergy destruction of the different configurations overall; **b)** comparison of overall Second Law efficiency of the different configurations

3.4. Influence of heat exchangers pressure losses on cycles performance and electricity cost

Finally, given the primary importance of the heat exchangers performance, size and cost on the cycle efficiency and electricity cost, the influence of the pressure losses of the heat exchangers was carried out. In fact, when dealing with heat exchangers network in power cycles, the counteracting effects of their efficiency, generally enhanced with high specific area per unit volume with the induced enhanced pressure losses, negatively affect the cycle performance. Indeed, here the recent very efficient and compact Printed Circuit Heat Exchangers (PCHE, [50 – 52]) were considered, so deserving an accurate addressing of the pressure losses against their high heat transfer performance. The results presented so far included the evaluation of the pressure losses within the circuit, calculated through the developed model of the heat exchangers. The influence of the heat exchangers pressure losses is, on the whole, not negligible, as they reduce the efficiency in a relevant amount, especially for the recompression cycles where the efficiency drops by almost 5 percentage points, as clear from Figure 8.

The drop in efficiency is directly related to the increase of the produced electricity cost. Indeed, as can be grasped from Figure 9, the associated increase of the produced electricity cost is more remarkable for the recompression cycles, because of the relevant decrease in efficiency due to friction pressure losses, leading to an increase of costs higher than 1 c€/kWh. On the other hand, the lowest increase in electricity cost due to HX pressure losses belongs to the recuperative cycle configuration, as it is the simplest one from this point of view.

Conclusions

In this study an exergo-economic assessment of different supercritical CO_2 power cycles configurations for the exploitation of water dominant geothermal resources in place of traditional flash based technologies was carried out by the means of energy, exergy and exergo-economic analysis. The proposed power cycle configurations adopted the efficient PCHE which, on the other hand, may negatively affect the cycle

performance due to their possible relevant pressure losses. The results confirmed that the supercritical CO_2 cycles may be valuable binary cycles solutions for the exploitation of low temperature geothermal resources, as the produced cost of electricity is in line with the existing binary cycle costs [49].

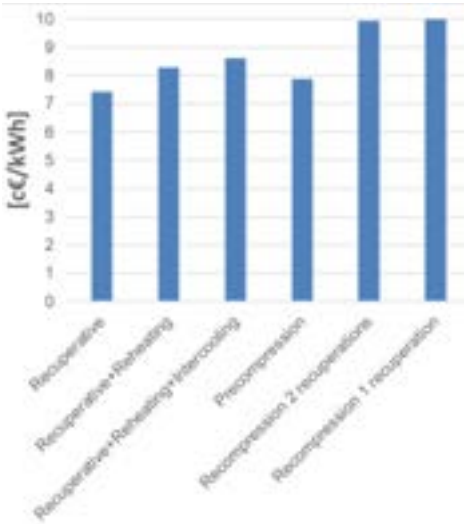

Figure 7 Comparison of electricity costs for the analysed power plants

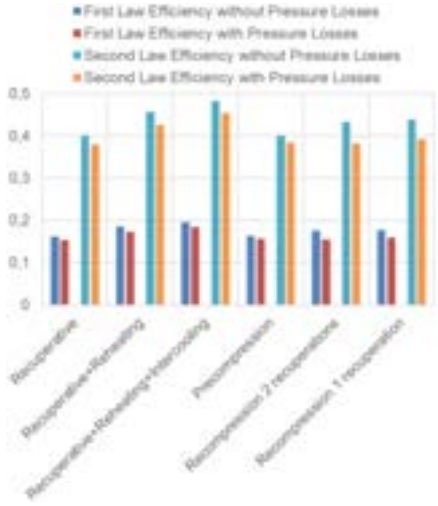

Figure 8 Sensitivity of first and second low efficiencies of the proposed cycles to the pressure losses in the heat exchangers (bars with and without considering them).

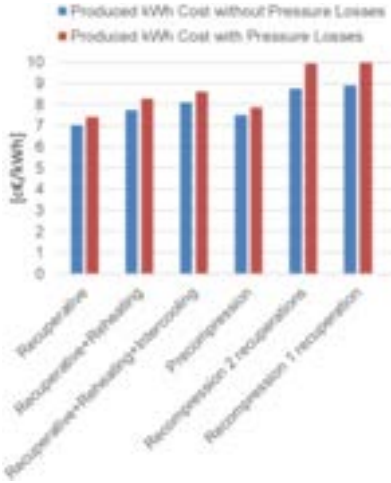

Figure 9 Sensitivity of electricity cost of the proposed cycles to the pressure losses in the heat exchangers (bars with and without considering them)

The most remarkable outcomes from the present research are the costs of electricity related to the adoption of supercritical power cycles under six different configurations, exploiting the same fixed geothermal resource:

- The lowest cost of electricity was achieved for the simplest recuperative cycle configurations, at 7.4 c€/kWh, which is in line with the level of current geothermal binary cycles.
- The configuration allowing the highest thermodynamic efficiency was the recuperative with intercooling and reheating, which gave First and Second Law efficiencies of 18.5% and 45.4% respectively. However, due to the increase in complexity of the power plant configurations, especially related to the “heavier” heat exchangers network, the cost of electricity becomes slightly higher (8.092 c€/kWh), even though still competitive with that of current binary cycles.
- The recompression configurations are hindered by the high required compressors work, having therefore the highest produced electricity costs and the lowest efficiencies. Nonetheless, it should be remarked that these configurations guarantee the lowest maximum cycles pressures (around 190 bar).
- All the binary configurations show lower performance when compared to the currently adopted single flash +ORC power cycle, with a reduction of the power output in the range of 40-50% and an almost doubled cost of the electricity. On the other hand, these CO_2 power plants could guarantee an almost zero environmental impact during the operation phase.

As a concluding remark, this analysis well addresses the importance of including the effect of pressure losses in the heat exchangers, also considering the fact that the high efficiency and compact PCHE were adopted, where this issue may be typically relevant. It is shown, here, that this aspect might lead to a significant increase of the produced electricity costs, related to the entailed drop of power cycles efficiency, especially in the most complex configurations.

The results of this research introduce, in the context of known configurations of CO_2 based binary cycles to exploit geothermal resources, the novelties related to two main aspects which are missing in literature:

1) The accurate evaluation and comparison of electricity production costs by the means of exergo-economic methodology;
2) This methodology was applied to cycles equipped with PCHEs, which is a novel proposal in these applications, particularly for the aspects addressing the influence of the related pressure losses on the cycle's performance.

Acknowledgments

The present research was partially supported by the European Commission H2020 Program, GA Nr 963530 (*LEAP-RE JA Project*) and partially by Italian *PNRR NEST* Spoke 5 "Energy Conversion”

References

[1] Song J., Ren X., Tian H., Shu G., Gu C., Markides CN., Thermodynamic and economic investigations of transcritical CO2-cycle systems with integrated radial-inflow turbine performance predictions, *Applied Thermal Engineering*, 165, 2020.

[2] Galgaro A., Di Sipio E., Teza G., Destro E., De Carli M., Zarrella A., Emmi G., Manzella A., Empirical modeling of maps of geo-exchange potential for shallow geothermal energy at regional scale, *Geothermics*, 57, 173-184, 2015.

[3] Bravi M., Basosi R., Environmental impact of electricity from selected geothermal power plants in Italy*, J. Clean. Prod.*, 66, 301–308, 2014.

[4] Saner D., Juraske R., Kubert M., Blum P., Hellweg S., Bayer P., *Is it only CO_2 that matters? A life cycle perspective on shallow geothermal systems*, Renew. Sustain. Energy Rev. 2010, 14, 1798–1813.

[5] Baldacci A., Mannari M., Sansone, F., "Greening of Geothermal Power: An Innovative Technology for Abatement of Hydrogen Sulphide and Mercury Emission", in: *Proceedings World Geothermal Congress 2005, Antalya, Turkey, 24-29 April,* 2005.

[6] Bayer P., Rybach L., Blum P.H., Brauchler R., "Review of Life Cycle Environmental effects of geothermal power generation", in: *Renew. Sustain. Energy Rev.*, 26, 446–463, 2013.

[7] Frick S., Kaltschmitt M., Schorder G., *A Life cycle assessment of geothermal binary power plants using enhanced low-temperature reservoirs*, Energy 2010, 35, 2281–2294.

[8] Basosi R., Bonciani R., Frosali D., Manfrida G., Parisi ML., Sansone F., Life Cycle Analysis of a Geothermal Power Plant: comparison of the environmental performance with other renewable energy systems, *Sustainability*, 12, 2786, 2020.

[9] Lacirignola, M.; Blanc, I. Environmental analysis of practical design options for enhanced geothermal systems (EGS) through life-cycle assessment. Renew. Energy 2013, 50, 901–914.

[10] Karlsdottir MR., Heinonen J., Palsson H., Palsson OP., Life cycle assessment of a geothermal combined heat and power plant based on high temperature utilization, *Geothermics*, 84, 2020.

[11] Parisi ML., Douziech M., Tosti L., Pérez-Lopez P., Mendecka B., Ulgiati S., Fiaschi D., Manfrida G., Blanc I., Definition of LCA guidelines in the geothermal sector to enhance result comparability, *Energies*, 13, 3534, 2020.

[12] Paulillo A., Cotton L., Raw R., Striolo A., Lettieri P., Geothermal energy in the UK: The life-cycle environmental impacts of electricity production from the United Downs Deep Geothermal Power project, *Journal of Cleaner Production*, 249, 2020.

[13] Astolfi M., Noto La Diega L., Romano MC., Merlo U., Filippini S., Macchi E., Techno-economic optimization of a geothermal ORC with novel "Emeritus" heat rejection units in hot climates", *Renewable Energy*, 147, 2810-2821, 2020.

[14] Fiaschi, D., Lifshitz, A., Manfrida, G., Tempesti, D., "An innovative ORC power plant layout for heat and power generation from medium to low-temperature geothermal resources", in: *Energy Conversion and Management*, Vol. 88, pp. 883-893, 2014.

[15] Fiaschi, D., Manfrida, G., Talluri, L., "Water-ammonia cycles for the utilization of low temperature geothermal resources", in: *ASME 2015 Power Conference*, San Diego, United States, 2015.

[16] Fiaschi D., Manfrida G., Rogai E., Talluri L., Exergoeconomic analysis comparison between ORC and Kalina cycles to exploit low and medium-high temperature heat from two different geothermal sites, *Energy Conversion and Management*, 154, 503-516, 2017.

[17] Yari, M., Mehr A.S., Zare, V., Mahmoudi, S.M.S., Rosen, M.A., "Exergoeconomic comparison of TLC (trilateral Rankine cycle), ORC (organic Rankine cycle) and Kalina cycle using a low-grade heat source", in: *Energy*, vol. 83 pp. 712-722, 2015.

[18] Liu, Q., Duan, Y., Yang, Z., "Performance analyses of geothermal organic Rankine cycles with selected hydrocarbon working fluids", in *Energy*, Vol. 63, pp. 123-132, 2013.

[19] Liu, Q., Duan, Y., Yang, Z., "Effect of condensation temperature glide on the performance of organic Rankine cycles with zeotropic mixture working fluids, in: Applied Energy, Vol. 115, pp. 394-404, 2014.

[20] Eyerer S., Dawo F., Wieand C., Spliethoff H., Advanced ORC architecture for geothermal combined heat and power generation, *Energy*, 205, 2020.

[21] Prananto LA., Zaini IN., Mahendranata BI., Juangsa FB., Aziz M., Soelaiman TAF., Use of Kalina cycle as a bottoming cycle in a geothermal power plant: Case studynof the Wayang Windu geothermal power plant, *Applied Thermal Engineering*, 132, 686-696, 2018.

[22] Liu X., Wei M., Yang L., Wang X., Thermo-economic analysis and optimization selection of ORC system configurations for low temperature binary-cycle geothermal plant, *Applied Thermal Engineering*, 125, 153-164, 2017.

[23] Nami H., Nemati A., Fard FJ., Conventional and advanced exergy analyses of a geothermal driven dual fluid organic Rankine cycle (ORC), *Applied Thermal Engineering*, 122, 59-70, 2017.

[24] Karimi S., Mansouri S., A comparative profitability study of geothermal electricity production in developed and developing countries: Exergoeconomic analysis and optimization of different ORC configurations, *Renewable Energy*, 115, 600-619, 2018.

[25] Imran M., Usman M., Park BS., Kim HJ., Lee DH., Multi-objective optimization of evaporatator of organic Rankine cycle (ORC) for low temperature geothermal heat source, *Applied Thermal Engineering*, 80, 1-9, 2015.

[26] Wu C., Wang SS., Li J., Parametric study on the effects of a recuperator on the design and off-design performances for a CO2 transcritical power cycle for low temperature geothermal plants, *Applied Thermal Engineering*, 137, 644-658, 2018.

[27] Schifflechner, C., Dawo F., Eyerer S., Wieland C., Spliethoff H., Thermodynamic comparison of direct supercritical CO2 and indirect brine-ORCconcepts for geothermal combined heat and power generation, *Renewable Energy*, 2020.

[28] Chasapis D., Misirlis D., Papadopoulos PA., Kleidis K., Thermodynamic analysis on the performance of a low-enthalpy geothermal fields using a CO_2 supercritical binary cycle, *Chemical Engineering Transactions*, 76, 2019.

[29] Yin H., Sabau AS., Conklin JC., McFarlane J., Qualls AL., Mixtures of SF6-CO2 as working fluids for geothermal power plants, *Applied Energy*, 106, 243-253, 2013

[30] Qiu Y., Li MJ., He YL., Tao WQ., Thermal performance analysis of a parabolic trough solar collector using supercritical CO_2 as heat transfer fluid under non-uniform solar flux, *Applied Thermal Engineering*, 115, 1255-1265, 2017.

[31] Li H., Zhang Y., Yang Y., Han W., Yao M., Bai W., Zhang L., Preliminary design assessment of supercritical CO2 cycle for commercial scale coal-fired power plants, *Applied Thermal Engineering*, 158, 2019.

[32] Ayub A., Invernizzi CM., Di Marcoberardino G., Iora p., Manzolini G., Carbon dioxide mixtures as working fluid for high-temperature heat recovery: A thermodynamic comparison with transcritical organic Rankine cycles, *Energies*, 13, 4014, 2020.

[33] Lecompte S., Ntavou E., Tchanche B., Kosmadakis G., Pillai A., Manolakos D., De Paepe M., Review of experimental research on supercritical and transcritical thermodynamic cycles designed for heat recovery application, *Applied Sciences*, 9, 2571, 2019.

[34] Kagel A., Bates D., Gawell K., A Guide to Geothermal Energy and the Environment; Geothermal Energy Association: Washington, DC, USA, 2005. Available online: https://www.osti.gov/servlets/purl/897425-q5NDer/ (accessed on 06 August 2020).

[35] Niknam P., Talluri L., Fiaschi D., Manfrida G., Gas purification process in a geothermal power plant with total reinjection designed for the Larderello area, *Geothermics*, 88, 2020.

[36] Peralta O., Castro, T., Durón M., Salcido A., Celada-Murillo A.-T., Márquez C., Navarro-González R., García J., de la Rosa J., Torres R., H_2S emissions from Cerro Prieto geothermal power plant, Mexico, and air pollutants measurements in the area, *Geothermics* 2013, 46, 55–65.

[37] Barelli A., Ceccarelli A., Dini I., Fiordelisi A., Giorgi N., Lovari F., Romagnoli P., A Review of the Mt. Amiata Geothermal System (Italy), *Proceedings of the World Geothermal Congress*, Bali, Indonesia, 25–29 April 2010.

[38] Di Pippo R., Geothermal Power Plants—Principles, Applications, Case Studies and Environmental Impact, 3rd ed.; Elsevier: Oxford, UK, 2012.

[39] Zarrouk S.J., Purnanto M.H., Geothermal steam-water separators: Design overview, *Geothermics*, 53, 236–254, 2015.

[40] Bruscoli L., Fiaschi D., Manfrida G., Tempesti D., Improving the Environmental Sustainability of Flash Geothermal Power Plants—A Case Study, Sustainability 2015, 7, 15262-15283; doi:10.3390/su71115262

[41] Engineering Equation Solver, EES, F-Chart software, Po Box 444042, Madison, WI 53744, www.fchart.com (accessed on 07 August 2020).

[42] Szargut, J., Morris, D.R., Steward, F.R., *Exergy analysis of thermal, chemical, and metallurgical processes*, Hemisphere Publishing Corporation, 1988.

[43] Kotas, T.J., *The Exergy Method of Thermal Plant Analysis*, Butterworths, 1985.

[44] Bejan, A., Tsatsaronis, G., Moran, M. Thermal design and optimization, *John Wiley & Sons, Inc*.: New York, USA, 1996.

[45] Lazzaretto A., Tsatsaronis G., SPECO: A systematic and general methodology for calculating efficiencies and costs in thermal systems, *Energy*, 2006, *31*, 1257-1289.

[46] Turton R., Bailie R., Whiting W., Shaeiwitz J., Analysis, synthesis and design of chemical processes, *Prentice Hall PTR*, 2003.

[47] Chemical Engineering, Economic Indicators. https://www.chemengonline.com/site/plant-cost-index/ (accessed on 28/09/2020).

[48] Schuster, A., Karellas, S., Kakaras, E., Spliethoff, H., "Energetic and economic investigation of Organic Rankine Cycle applications", in:*Applied Thermal Engineering*, pp.1809–1817, 2009.

[49] IRENA, Renewable power generation costs in 2019. https://www.irena.org/publications/2020/Jun/Renewable-Power-Costs-in-2019 (accessed on 28/09/2020).

[50] Chu WX., Li XH., Ma T., Chen YT., Wang QW., Experimental investigation on SCO_2-water heat transfer characteristics in a printed circuit heat exchanger with straight channels, International Journal of Heat and Mass Transfer, 113, 184-194, 2017.

[51] Jiang Y., Liese E., Zitney SE., Bhattacharyya D., Design and dynamic modeling of printed circuit heat exchangers for supercritical carbon dioxide Brayton power cycles, *Applied Energy*, 231, 1019-1032, 2018.

[52] Le Pierres R., Southall D., Osborne S., Impact of mechanical design issues on printed circuit heat exchangers, *Proceedings of SCO2 Power cycle symposium*, 2011.

The new role of sustainable hydropower in flexible energy systems and its technical evolution through innovation and digitalization

Elena Vagnoni[a], Dogan Gezer[b], Ioannis Anagnostopoulos[c], Giovanna Cavazzini[d], Eduard Doujak[e], Marko Hočevar[f] and Pavel Rudolf[g]

[a] École Polytechnique Fédérale de Lausanne, Lausanne, Switzerland, elena.vagnoni@epfl.ch
[b] Tubitak, Ankara, Turkey, dogan.gezer@tubitak.gov.tr
[c] National Technical University of Athens, Athens, Greece, anagno@fluid.mech.ntua.gr
[d] University of Padova, Padova, Italy, giovanna.cavazzini@unipd.it, CA
[e] TU Wien, Wien, Austria, eduard.doujak@tuwien.ac.at
[f] University of Ljubljana, Ljubljana, Slovenia, Marko.Hocevar@fs.uni-lj.si
[g] Brno University of Technology, Brno, Czech Republic, rudolf@fme.vutbr.cz

Abstract:

Hydropower (HP) has played an important role in Europe in recent decades, offering a unique combination of safe, low-cost and clean power generation. Today, it is still one of the largest renewable energy sources (RES), accounting for about 35% of RES electricity generation and its share is estimated to reach 50% by 2025. However, grid stability is threatened by the increasing amount of unregulated energy (wind and solar). Flexibility and dynamics such as energy storage and rapid response are urgently needed to achieve EU policy goals. In such a context, HP can play a key role, not only as a provider of regulated renewable energy, but also due to its ability to balance a renewable energy system in the short term (seconds to minutes) and in the medium/long term (months or even years) through the use of pumped storage technology. All these aspects underline the new role of hydropower, which aims to strengthen grid stability and power supply resilience, and to enable higher penetration of volatile RES.

The study provides an overview of the preliminary results obtained by the working groups of the COST Pen@hydropower action. In particular, it presents a first assessment of the flexibility offered by hydropower today at the European level, focusing on different geographical areas, and confirms the key role of hydropower in future scenarios (30% of the flexibility demand at all time scales met by hydropower). An overview of the digitalization solutions and innovative technologies that support the growth of a new generation of sustainable hydropower and the modernization of existing hydropower plants is also provided.

Keywords:

Hydropower; Energy; Sustainability; Flexibility; Digitalization.

1. Introduction

Many countries in the world have introduced specific installation targets and financial incentives for further wind and solar power development, but few have policies to support the sustainability of existing and facilitate the addition of new hydropower plants (HPPs). However, hydropower is the most appropriate technology to provide the future power systems at RES with the emission-free flexibility they need. This new, crucial role that hydropower is expected to play in future power systems should be recognized by governments, energy stakeholders, and society, and reflected in long-term expansion targets and investment plans.

The sustainable use of water resources for hydropower to support this new role is the goal of some initiatives and international associations, such as the Technology Cooperation Program on Hydropower of the International Energy Association [1], which is a working group of some member countries and organizations from Europe, the Americas, and Asia; the International Hydropower Association [2], whose members are hydropower developers, operators, and manufacturers from many countries around the world, and the Joint Research Program on Hydropower of the European Energy Research Alliance [3], which consists mainly of universities and research organizations in Europe.

In this sense, the main objective of the Pen@hydropower Cost Action [4] is to build and establish a Pan-European network for sustainable, digitalized and flexible hydropower in order to contribute to the Clean

Energy Transition (CET) and climate change mitigation, and to promote the development of a sustainable society. Pen@hydropower engages members on a more personal level and aims to create an interdisciplinary consortium that brings together researchers, scientists, and other stakeholders from engineering, social, economic, legal, and environmental sciences who will work towards the above goal through various activities. A key objective of the Action is to engage and build the capacity of many young researchers to bridge generations and prepare the hydropower experts of tomorrow.
To achieve this goal, there are some recognized challenges and identified barriers that need to be addressed and overcome. First, EU support for the scientific environment of HP is low. Over the past 15 years, only about 15 HP projects have been funded [5], and today only about 0.7% of EU funding for RES development goes to HP to improve the performance, efficiency, and flexible operation of hydropower plants, to support the use of other RES and electricity storage, and to address important environmental issues related to river hydraulics and ecology. As a result, there are few technological innovations to promote sustainability and resilient operation of old and new power plants to meet the increasing demands of power systems and environmental and social requirements.:

- Research coordination objectives that include a scientific support framework for HP producers and investors, a platform for collaboration among scientists and stakeholders from different disciplines, mapping of current EU legislation, market and CET scenarios, and identification of policy gaps and barriers to create a unique knowledge base currently lacking in the scientific community, and to develop a novel holistic scientific HP community strategy with new approaches to support sustainable development.
- Capacity building objectives to expand the existing technical network by incorporating additional disciplines (engineering, ICT, environment and climate, hydrology, social, finance, etc.), promote career development of young scientists through joint PhD programs, knowledge transfer, and training schools, and increase awareness among policy makers and industry of the importance of HP in the energy mix.

The Pen@Hydropower management committee consists of members from 33 European countries, including 20 COST Inclusiveness Target Countries (ITC), and there are more than 160 members in the 5 working groups, ranging from young researchers and early career investigators (ECI) to experienced researchers. During the 4-year duration of the project, several funded activities are planned for researchers or innovators from all fields HP. Each year, a training school for PhD students and ECI will be organized in different European regions to broaden their knowledge and deepen their teamwork in the field of hydropower. This year, the training school will be organized in Timisoara, Romania (May 9-12, 2023), on the topic of "Sustainable Hydropower" [6].

Researchers can also apply for short-term scientific missions to visit and work at a host institution in another country to gain new knowledge or access equipment or techniques not available at their home institution. In addition, the Action offers conference grants that enable young researchers to attend international conferences, as well as grants to attend high-level conferences to present their activities and results under this Action and to establish new contacts and potential future collaborations [7].

This article presents some initial results of the Pen@Hydropower working groups since the launch in September 2022. These results provide for the first time a pan-European overview of the hydropower technology status from an holistic perspective, exploiting information and data collected among stakeholders spread in several different Countries. Section 2 discusses the future flexibility requirements for power systems in different European countries with a time horizon from 2030 to 2050 and the contribution of hydropower to meet these needs. Section 3 then presents some technical innovations and digitization technology that can be used to modernize the existing HP power plant fleet and to design new plants so that they can more effectively support the power systems of the future.

2. The flexibility of hydropower in the European context

It is well known that transitioning our energy system to one dominated by renewable energy sources is an increasing challenge. This includes volatile renewable energy sources (VRE), which increase the demands on the system to balance supply and demand. For example, the increasing use of power converters to generate solar and wind energy is reducing grid inertia and challenging traditional approaches to limiting and restoring frequency. The Australian Energy Market Operator (AEMO) has found that a lack of frequency limiting by conventional power plants leads to difficulties in managing frequency and scheduling system reserves [8]. Similarly, the California Independent System Operator (CAISO) experienced a progressive degradation of its frequency containment and restoration performance: the frequency response measure (FRM) decreased by 122 MW /0.1 Hz in 4 years [9].

In Europe, forecast scenarios for the 2030 horizon show that effective management of large-scale VRE, flexibility on multiple time scales from short-term to seasonal, as shown in Figure 1.

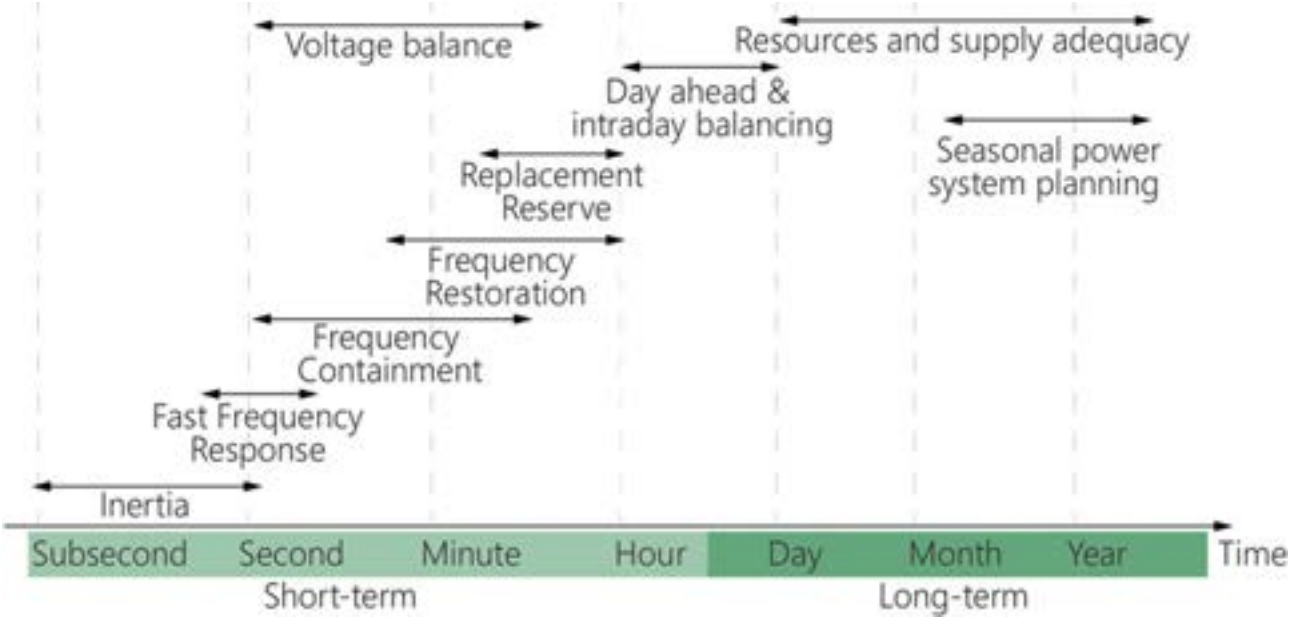

Figure. 1. Time-horizon of the flexibility services that hydropower can provide. Adapted from IEA [10].

In particular, the simulations projected the residual load curve in 2030 in the European Union (EU), which serves as a parameter for assessing flexibility requirements [11]. As can be seen in Figure 2, the residual load curve has a peak in the morning and evening, which coincides with hours of increasing demand, and a significant drop in the midday when solar production increases. By measuring and predicting this parameter, the flexibility demand can be quantified in terms of energy per day, week, and month. Figure 3 shows the daily flexibility demand per country in Europe in 2021, 2030, and 2050. The daily flexibility demand will be 288 TWh in 2030 and will increase by an average of 133% between 2021 and 2030 in all countries. Weekly and monthly flexibility needs are lower (258 TWh on a weekly basis and 173 TWh on a monthly basis), but they increase faster over the next decade: weekly flexibility is projected to increase by 166% and monthly flexibility by 300%. From these results, it is clear that flexibility must be used in all areas of the power system, from power generation to stronger transmission and distribution systems to storage and more flexible demand.

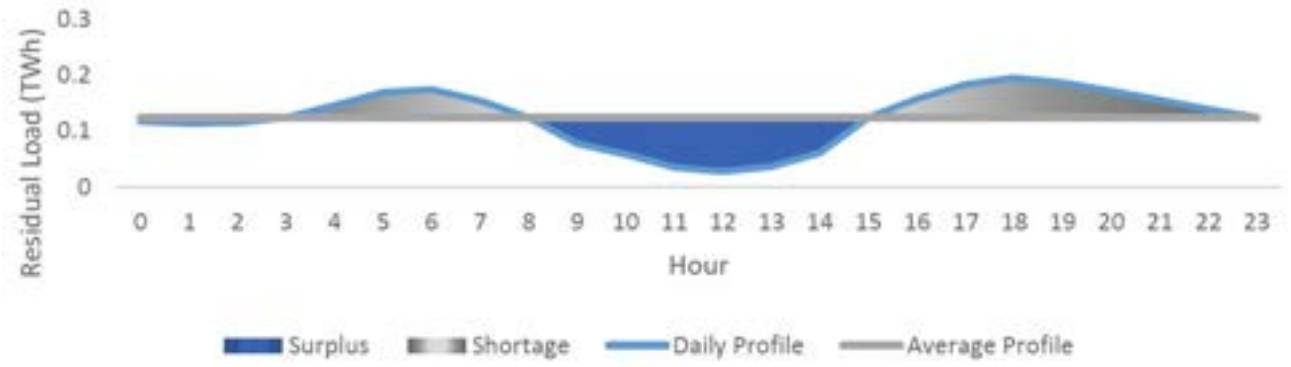

Figure. 2. Flexibility requirements based on hourly-averaged daily EU residual load curve in 2030 (Source: Joint Research Centre [11])

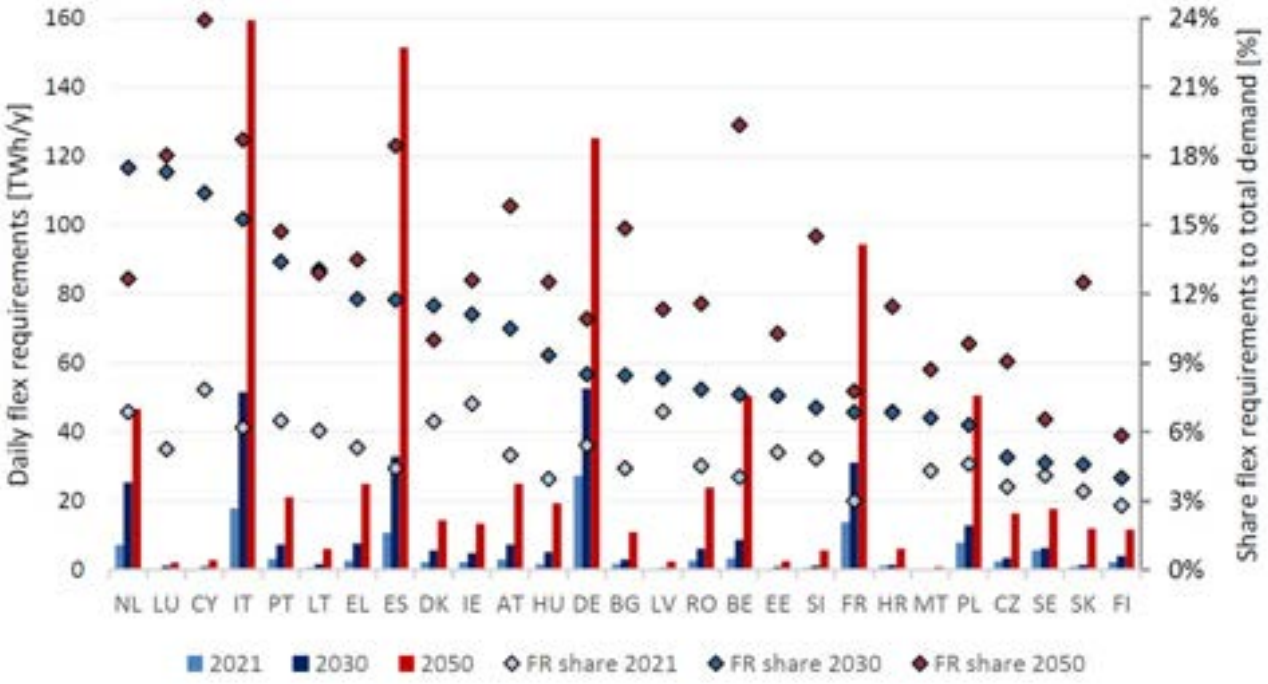

Figure. 3. Daily flexibility requirements in 2021, 2030 and 2050, ordered by 2030 flexibility requirements share to total demand (Source: Joint Research Centre [11])

With dispatchable power generation and high potential for storage capacity, hydropower is already providing these essential services to the grid. Even though the simulations predict a decrease in the share of hydropower in these services by 2050 (about -7% for hydropower including pumped storage), this technology will be needed to meet the increasing demand for these services, which will require higher flexibility of hydropower plant (HPP) operation, higher availability, and higher electricity capacity and storage capacity of the hydropower fleet. In the 2030 scenario for the European Union, more than 30% of the flexibility demand at all time scales is met by hydropower. Another study on the optimization of storage needs and market profitability has shown that, considering the previous scenario for 2030 and excluding gas-fired power plants from the options, the optimal additional capacity of pumped storage is 1.3 GW (and + 14.5 GW batteries), with an additional storage capacity of 62.2 GWh, of which 7% comes from hydropower.

A study conducted by the IEA [12] presents several case studies around the world in which hydropower contributes to power system flexibility by demonstrating its ability to support almost all the systems studied at the different time horizons, from short-term grid services to long-term storage. In the selected countries in Europe (Germany, Norway, Switzerland and Finland), the share of hydropower depends on the country, as it is a geographically limited resource. This also reflects a different market structure, which seems to be particularly pronounced in the countries where the share of hydropower is highest, such as Norway and Switzerland, even for short-term sub-hourly services.

According to these studies, it is clear that hydropower is a key resource to enable the energy transition and achieve the 2030 and 2050 sustainability targets. Therefore, there are new opportunities for this technology in terms of market participation and further increasing its production. This requires, for example, an increasing share in the auxiliary services under the hour, by increasing the availability of balancing energy of the hydropower plant with multiple units, if available, both in generation and pumping mode.

3. Technological Evolution through Innovation & Digitalization

As explained above, flexible operation is one of the challenges facing hydropower, and technological development to achieve this goal and others (e.g., related to increasing sustainability in terms of river hydraulics and ecology) must come through advances in digitalization and innovation. The PEN @Hydropower action has a working group dedicated to these aspects, with the aim of raising awareness of digitalization and other innovative technologies, sharing experiences between operators, manufacturers and universities, and imagining the new generation of hydropower plants.

In the first grant period, one of the objectives of Pen@Hydropower is to identify trend technologies and the needs of the hydropower sector in terms of digitalization, flexibility and efficiency. To this end, a survey will be conducted to identify the current situation of members in their countries in terms of technological

developments and common practices. This survey, described in detail below, can be considered representative of the European context and the different disciplines, as the PEN @Hydropower working group has 97 members from 27 different countries (70% of the members are under 40 years old and 12% of the members are female), whose expertise spans a wide spectrum that includes electrical, mechanical, environmental, computer science and civil disciplines.

3.1 Methodology

Surveys are used to gather information from respondents to answer research questions. Conducting surveys is a very convenient way to gather information from a large number of people in a given period of time. Due to the locations of the respondents, an Internet survey is chosen as the survey type. A conceptual framework consisting of innovative technologies and digitalization in hydropower is constructed. Many of the questions are prepared as closed-ended. Some of the questions in the survey are asked as open-ended questions. The choices in closed-ended questions are determined based on the experience of the preparers. The questionnaire is validated through sharing the questionnaire with the experts in the COST Action before publishing the questionnaire. The questions in the survey were created to understand the technological level of hydropower plants in the different European countries and to identify what technological advances the new investments in hydropower plants should include.

The structure of the questionnaire was optimized to facilitate completion by members from different disciplines. The final form of the questionnaire is shown in Figure 4, and its explanation with the survey results is given in the following section. There are some open-ended questions as well as most of the closed-ended questions.

Participant's Information • Name • Surname • Country Unmanned Operation of Hydropower Plants • 0% • Below 10% • 10% to 25% • 25% to 50% • Above 50% Presence of Modern SCADA Systems • 0% • Below 10% • 10% to 25% • 25% to 50% • Above 50% Number of pumped storage hydropower plants • 0 • 1-5 • 6-10 • 11-20 • Above 20 Fish friendliness of hydropower plants • There exist fish passages • The turbine design is fish friendly • Not fish friendly Presence of variable speed operated hydropower	Presence of any hydropower plants in drinking water supply system for pressure energy recovery or any projects related to hydropower plant in drinking water supply system • Yes/No If yes, typical output of recovery units? • Below 10 kW • 11-100 kW • 101 – 500 kW • more than 500 kW The average age of hydropower plants • 0-10 • 11-20 • 21-35 • 36-50 • Older than 50 The percentage of the hydropower plants have technical documents in digital media • 0% • Below 10% • 10% to 25% • 25% to 50% • Above 50% Presence of any recent hydropower installations or major hydropower refurbishments, any installation of significant technological innovations or adopting up-to-date digitalization approaches.

plant or any project on variable speed operation • Yes/No	Any (realistic) plans for building new hydropower in near future, any plans to adopt digitalization approaches or any major technological innovations.

Figure 4. Questionnaire Structure

3.2 Results and Discussions

During one of the regular meetings of the Working Group, the questionnaire is explained to members of the group and the questionnaire link is shared with the members through the data sharing platform. The questionnaire is open before the submission of the manuscript. So far, ten respondents from nine different countries fill the questionnaire.

It is well known that unmanned operation increases operational efficiency in hydropower plants and protects plant operations from human error, but it also requires an advanced control system that collects all sensor data on site. It also requires a communication infrastructure with a reliable communication protocol. The control algorithms of the hydropower plant should be sophisticated enough to allow the control system to operate the plant satisfactorily even when there is no operator on site.

The first question aims to analyze the prevalence of unmanned operation of hydropower plants in Europe. The respondents are experts and academicians who give consultancy to plant owners and operators in their countries such that they are aware of the general situation in their countries. The results are shown in Figure 5. 60% of the respondents indicate that at least 50% of the power plants in their country are operated unmanned. On the other hand, 30% of the respondents indicate that at most 10% of the power plants in their country are operated unmanned. This question shows that the unmanned operation of the hydropower plants is quite high among the participants.

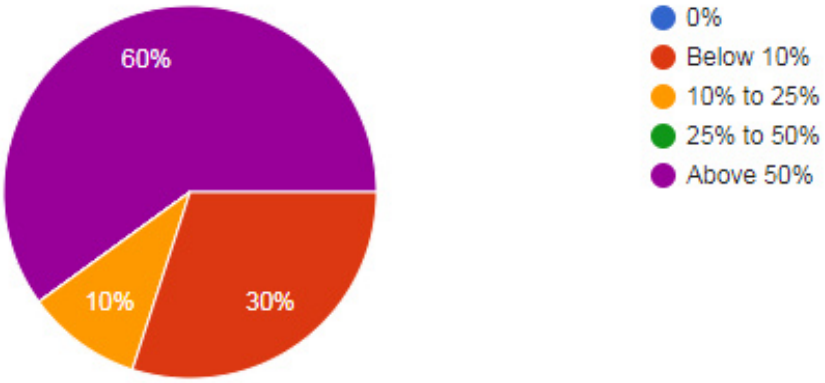

Figure 5. Distribution of Unmanned Operated Hydropower Plants

Unmanned operation requires that the facility's communications infrastructure and other control algorithms are set up accordingly. Supervisory Control and Data Acquisition (SCADA) systems are used to collect information from sensors in the plant, log that information, visualize it based on trends, and list it as alarms and events. The operator monitors and controls the plant remotely or on-site via man-machine interfaces. Regarding this aspect, it appears that the majority of hydropower plants have modern SCADA systems, as shown by the results in Figure 6, which perfectly reflect the results of the first question (Figure 5): 60% of the respondents say that at least half of the power plants in their country have modern SCADA systems, while 10% of the respondents say that up to 25% of the hydropower plants in their country have modern SCADA systems. These results show that most hydropower plants are unmanned and have modern control systems. This situation will allow the hydropower industry and developers to access historical data in a structural way

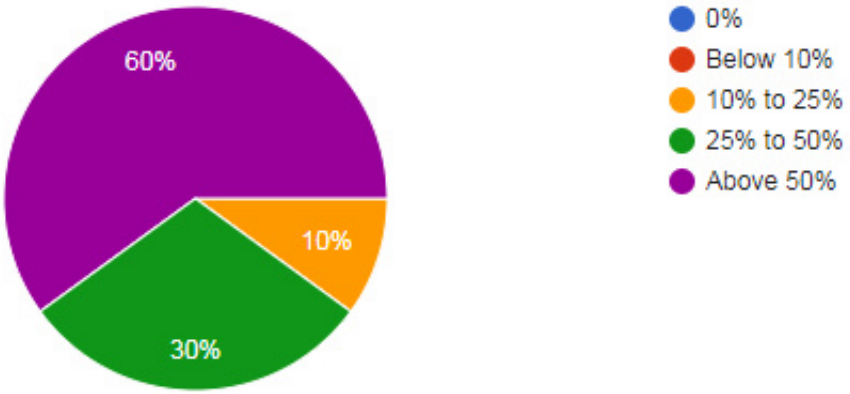

Figure 6. Presence of Modern SCADA Systems in Hydropower Plants

A pumped storage power plant is an efficient way to store electrical energy by pumping it to a higher reservoir when demand is low and by generating power to a lower reservoir during peak periods when demand is high. The next question asks about the presence of pumped storage power plants and the results are shown in Figure 7. 20% of the respondents have more than 20 pumped storage power plants in their country. On the other hand, 40% of the respondents have 1 to 5 pumped storage power plants in their country and 20% of the respondents have none. This question shows that the number of pumped storage power plants is variable and there is no common installation in the different countries when looking at the numbers.

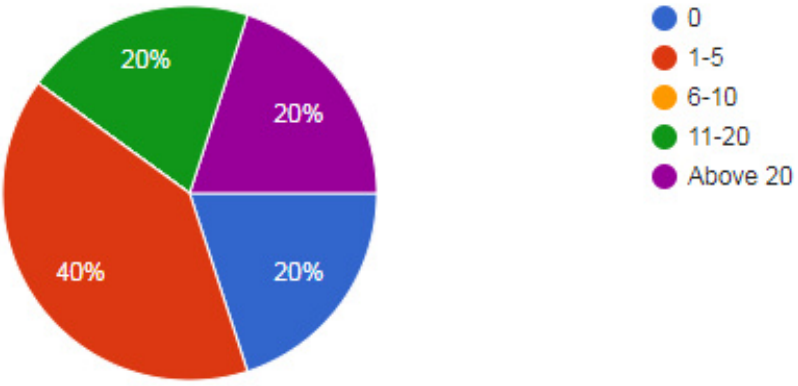

Figure 7. Number of pumped storage hydropower plants

Regarding the interaction between hydropower plants and the environment, new approaches have been developed in recent years to ensure accurate and rapid monitoring of fish. The use of digital tools combined with machine learning and artificial intelligence algorithms (e.g. convolutional neural networks) for automatic image-based detection and classification of species in different environments has been a breakthrough. Deep neural networks have already been successfully applied in various fields for fish monitoring [13]. In addition to image-based detection systems, molecular techniques such as environmental DNA have emerged as a tool for monitoring various aquatic species, particularly fish [14]. For example, a single eDNA study at the Spjutmo hydropower plant (Sweden) detected twice as many fish species as several electrofishing studies [15].

Fish-friendliness is a must for sustainable hydropower. To this end, there are many ways to provide fish safety, including fish passages, turbine designs, and fish tracking. When asked about the fish-friendliness of hydropower plants in their country, most of the respondents confirmed the presence of a fish passage in their country's hydropower plants. Few of them also indicated that the turbine design is fish friendly, and only a small proportion of respondents indicated that the hydropower in their country is not fish friendly. It can be concluded that most of the hydropower plants care about fish passage.

Regarding the presence of variable speed operation, which is extremely efficient in pumping mode, it was found that this is common throughout Europe. 60% of the respondents confirmed the introduction of variable speed operation in their country. The use of variable speed turbines is not very common in the hydropower industry in Europe.

Hydropower in the drinking water system is an untapped potential for green and sustainable cities. In the questionnaire, respondents are asked about the existence of hydropower plants in the drinking water supply for the recovery of pressurised energy or about the existence of projects related to hydropower plants in the drinking water supply. 90% of respondents indicate that there is a hydropower plant in the drinking water system in their country. As can be seen in Figure 8, the typical capacity of recovery plants ranges from 11-100 kW. This suggests that while the majority of countries have hydropower facilities in their drinking water systems, the potential of hydropower in the drinking water system needs to be explored more thoroughly.

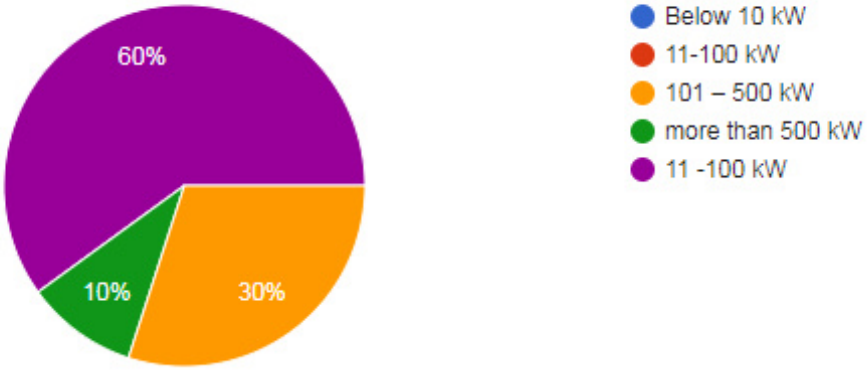

Figure 8. Typical Outputs of Recovery Units

The average age of the hydropower plant fleet can give an indication of the future potential for refurbishment in a country. When power plants are modernized, new technologies can be easily adapted and integrated into the newly modernized system. The results summarized in Figure 9 show that for 50% of the respondents, the power plants in their country are on average between 21 and 35 years old, while for 20% they are over 50 years old. 30% of the respondents indicate that the average age of the hydropower plants in their country is between 36 and 50 years. These results show that the hydropower fleet in Europe is quite old and the hydropower industry should develop new solutions based on innovation and digitalization for refurbishment.

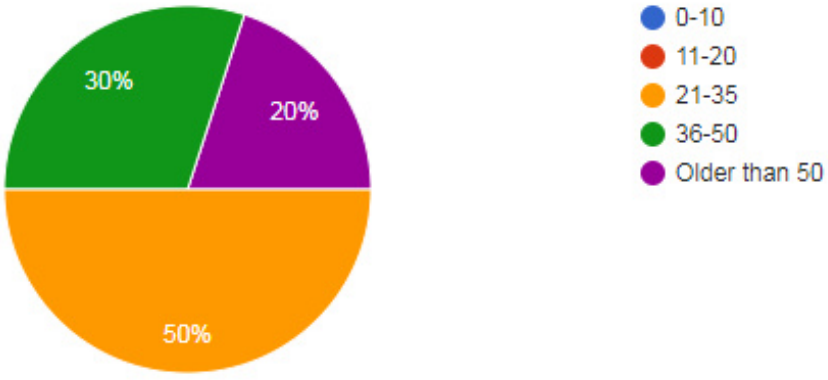

Figure 9. Average age of Hydropower plants

In the context of digitization, technical documents are stored and organised on digital media in order to digitise them. The last question asks respondents how much of the technical documents in their countries' hydropower plants are stored in digital media. As shown in Figure 10, 40% indicate that more than 50% of the technical documents of the hydropower plants in their countries are stored on digital media. On the other hand, 30% of the respondents indicate that this rate is less than 10%. This confirms that the hydropower

industry and developers need to spend more time to digitise the technical documents for technological progress, such as the digital twin.

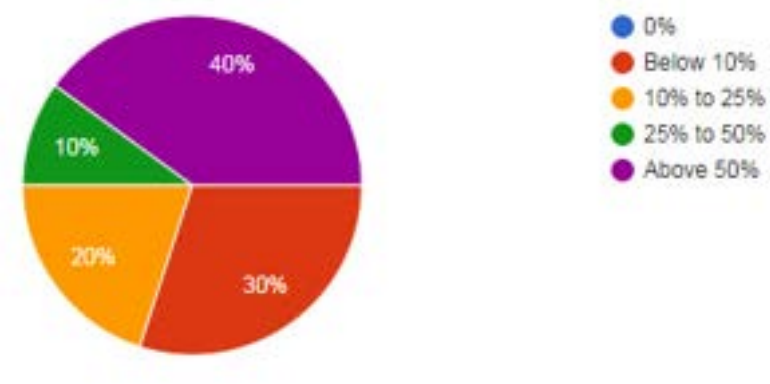

Figure 10. Technical documents in digital media

In the open-ended questions, respondents refer to major modernization works, including hydropower plants with an installed capacity of more than 500 MW. There are some power plants that are being renovated to make them compatible for variable speed control.

4. Conclusions

The PEN @Hydropower action laid the foundation for a pan-European collaborative platform of scientists and stakeholders from different disciplines, whose initial goal was to map the current state of the hydropower sector in Europe.

This study summarizes the results of the first activities carried out in the framework of PEN @Hydropower. In particular, we focused on the European energy framework and on the challenges of the Clean Energy Transition. Several studies have confirmed that one of the key requirements for the successful implementation of this zero emissions scenario is flexibility in all areas of the energy system, from power generation to stronger transmission and distribution systems, storage and more flexible demand. In this context, the key role of hydropower has been highlighted by several authors, along with the technological advances that are still needed for hydropower to play this role successfully. One of the most important is certainly to increase sustainability to make these advances technically feasible and economically viable, minimize environmental impacts, and increase society's awareness of the importance of hydropower technology to the CET.

This technological development must occur through advances in digitization and innovation, the mapping of which was the second short-term goal of PEN @Hydropower. Using its multidisciplinary network (engineering, ICT, environment and climate, hydrology, social, financing, etc.), the state of hydropower technology was studied, with some interesting results. The European hydropower sector confirms a good level of digitalization, but this is not fully exploited for technological advances. The latest technological solutions do not seem to have been uniformly adopted across European countries, confirming the need for knowledge transfer between stakeholders. For instance, the unmanned operation of hydropower plants has to be improved in Turkiye, Crotia, Albania and Bosnia Herzegova. Another figure to improve is the number of pumped storage type hydropower plants, e.g. there is no pumped storage type hydropower plant in Turkiye and Albania. Moreover, the fleet is quite old, which offers a great opportunity for promoting innovative refurbishment strategies to increase the sustainability of hydropower worldwide.

Acknowledgments

This article is based upon work from COST Action PEN@Hydropower (CA21104), supported by COST (European Cooperation in Science and Technology).

References

[1] IEA, The International Energy Agency Technology Collaboration Programme on Hydropower – Available at: <www.ieahydro.org>

[2] IHA, International Hydropower Association – Available at: <www.hydropower.org>

[3] EERA, European Energy Research Alliance, Joint Programme Hydropower – Available at: <www.eera-hydropower.eu>

[4] Pen@Hydropower, Pan-European Network for Sustainable Hydropower – Available at: <www.pen-hydropower.eu>

[5] Hoogland O, Veenstra E, Guevara Opinska L, Torres Vega PC, Rademaekers K (2019). Study on impacts of EU actions supporting the development of renewable energy technologies. PP-05441-2017. Ed. European Commission. Directorate-General for Research and Innovation. Brussels.

[6] Pen@Hydropower, Pan-European Network for Sustainable Hydropower – Available at: <www.pen-hydropower.eu/training-schools>

[7] Pen@Hydropower, Pan-European Network for Sustainable Hydropower – Available at: <www.pen-hydropower.eu/short-term-scientific-missions >

[8] AEMO, 2020, Renewable Integration Study: Stage 1 Report: Tech. Rep.

[9] CAISO, 2016, Frequency Response Phase 2: Tech Rep.

[10] International Energy Agency (IEA) (2021). Hydropower Special Market Report. Analysis and forecast to 2030

[11] Joint Research Centre, 2022, Flexibility requirements and the role of storage in the future European power system

[12] International Energy Agency (IEA) (2021). Valuing Flexibility in Evolving Electricity Markets: Current Status and Future Outlook for Hydropower.

[13] Kandimalla V, Richard M, Smith F, Quirion J, Torgo L and Whidden C (2022) Automated Detection, Classification and Counting of Fish in Fish Passages With Deep Learning. Front. Mar. Sci. 8:823173. doi: 10.3389/fmars.2021.823173

[14] Stefanni S, et.al. Framing Cutting-Edge Integrative Deep-Sea Biodiversity Monitoring via Environmental DNA and Optoacoustic Augmented Infrastructures. Front. Mar. Sci. 8:797140. doi: 10.3389/fmars.2021.797140

[15] Hellmér E. (2018) Using eDNA to improve environmental monitoring for water bodies effected by hydropower in Sweden, Dissertation, 2018.

Exergy assessment of electricity generation via biomass gasification by neural network algorithm.

Gabriel Gomes Vargas[a], Silvio de Oliveira Junior[b]

[a] University of São Paulo, São Paulo, Brazil, gabrielvargas@usp.br
[b] University of São Paulo, São Paulo, Brazil, soj@usp.br

Abstract

The main objective of this study was to develop a prediction model using artificial neural networks (ANNs) and analyze the performance indicators of a green electric energy generation process based on the gasification of Brazilian biomass residues. The recovery of energy from renewable resources is a promising avenue for efficiently delivering valuable products. To achieve this, sugarcane and orange bagasse, residues from the sugarcane harvest, sewage sludge, residues from the corn harvest, coffee residues, eucalyptus residues, and municipal urban waste were used in the proposed process. The Aspen Plus software was used to generate simulation data to predict the energy conversion for each biomass, and a three-layer feed-forward neural network algorithm was employed to build the model. The developed model showed good training and test data accuracy, with an R^2 greater than 0.993. Regarding the performance of the generation plant, the gasification unit provided a maximum of 18.12 MJ/kg of HHV for sewage sludge. Urban and orange waste had the highest cold gas efficiency at 82.21% and 80.66%, respectively. Meanwhile, in the gasification process, sugarcane bagasse and orange residue showed the highest carbon conversion efficiency at 92.88% and 91.17%, respectively. The results indicated that eucalyptus waste gasification could generate more electricity at 12.86 MW. In overall, the study highlights the potential of using ANNs to predict energy conversion and analyze the performance of gasification-based green electric energy generation processes using Brazilian biomass residues.

Keywords:

Biomass gasification, Artificial neural network, Power generation, Exergy analysis.

1. Introduction

Biomass is a significant source of renewable energy that has the potential to reduce fossil fuel dependence and CO_2 emissions. Biofuels have accounted for almost 70% of renewable energy production globally, and biomass was responsible for 25.5% of Brazil's domestic energy supply [1]. Brazil has enormous biomass potential, and biomass wastes could be converted into valuable energy products like hydrogen, ammonia, and electrical energy. This way, energy consumption and greenhouse gas emissions could be reduced, along with waste disposal costs and environmental impact. Brazil has a vast biomass potential, including sugarcane bagasse, orange bagasse, corn, and coffee residues that could be used to produce bioenergy.

Waste-to-energy systems produce electrical and thermal energy using a variety of processes, including combustion, gasification, and power cycles [2]. Sapali and Raibhole [3] examined the combination of air separation and biomass gasification techniques. Because it uses less energy, the low-pressure column's pressure is close to the surrounding atmosphere's pressure of around 1.2 bar, while the high-pressure column operates at about 4 bar. To use less energy than the standard procedure, Wu et al. [4] also modeled a multi-column cryogenic air separation (i.e., high-pressure, low-pressure, and mixed fluid cascade columns) in combination with LNG regasification.

Banerjee et al. [5] also demonstrated a biomass gasification system under various oxygen and vapor ratio circumstances. Five biomass types, including pine, corn, coffee, maple, and straw, were used as fuel for the gasification unit. The fluid bed's gasification temperature was 800°C. Dhanavath et al. [6] have conducted various tests on corn straw, sawdust, and sunflower shells in a fixed bed reactor to study the gasification with stea. The outcomes were contrasted with the process modeling in Aspen Plus. They concluded by reporting that increasing the gasification temperature to 1000ºC produced cold gas with an efficiency of 95% for all inputs. A combined floatation gasification unit and power generation system were described by Lan et al. [7]. They discovered that gradually raising the gasifier's temperature boosted the hydrogen and methane output. In any case, the synthesis gas stream's carbon dioxide content decreased, but the amount of carbon monoxide produced grew considerably.

Artificial neural networks (ANNs) are one of the alternative modeling techniques most utilized at the moment; when compared to other techniques, they may be used to forecast and optimize system outputs in a shorter amount of CPU (Central Processing Unit) time [8]. Although ANN may learn and predict non-linear correlations between the output and input parameters, memorizing the data for training should be avoided [64]. A well-developed ANN model requires careful consideration of the transfer function, training algorithm, and model structure. A powerful and popular analytical technique for the non-linear model is the multi-layer network structure and feed-forward ANN with the backpropagation method [9]. Many studies have adopted ANN models because of their superior effectiveness in predicting the parameters associated

with the gasification process. An ANN model was created by Mikulandric et al. [10] to forecast gasification process parameters, and the findings demonstrated a good correlation with experimental research. The study realized of Serrano et al [11], used an artificial neural network model to predict gas composition and gas yield in a biomass gasification process in a bubbling fluidized bed. The effect of different bed materials was included as a new input, and different network topologies were simulated to determine the best configuration. The developed models were able to predict gas composition and gas yield accurately, indicating that this approach is a powerful tool for efficient design, operation, and control of bubbling fluidized bed gasifiers with different operating conditions, including the effect of bed material.. An ANN model for a combined biomass gasifier-power system was utilized by Safarian et al. [12] to evaluate power output utilizing the features of the biomass and gasifier operation. An ANN model was used by Sozen et al. [13] to look into the energy losses of the heat transformer.

Integrating neural networks and Aspen Plus models present a promising approach to improving the accuracy of power generation predictions. Neural networks can learn complex patterns from operational variables and historical data, making them helpful in predicting generated power. With that in mind, the primary goal of this research was to convert Brazilian waste biomass into renewable energy using waste-to-energy systems, including gasification plants and combined cycles. An Aspen Plus simulation program was used to simulate the bubbling fluidized bed gasifier and combined cycle to achieve this goal. This simulation generated data on the gasification and power generation process, which were used to create a general artificial neural network (ANN) pattern. Some of the significant contributions of this study include proposing a new method for evaluating cycle power generation, implementing machine learning methods on simulation data, and calculating performance indicators as crucial parameters. Finally, the study achieved a new method for generating renewable electricity from waste biomass by integrating these concepts.

2. Methods

2.1. Hypotheses for simulation

In this study, the combustion of volatile and biomass materials is assumed to occur with complete mixing. The Gibbs reactor is used to simplify the simulation, assuming that the gasification reactor is in equilibrium. These assumptions and the software's capabilities allow for accurate predictions of chemical process behaviour, including the physical and chemical properties of mixtures under various operating conditions.

It is important to note that utilizing Aspen Plus for process simulation has limitations. For example, the software cannot account for every factor, such as pressure drops in pipelines or other equipment, and all process-related calculations. However, despite these limitations, Aspen Plus is a powerful and valuable tool for predicting the behaviour of chemical processes, and its use is widespread in the industry.

Also, the following assumptions are considered in the simulation:

1. The system is in a steady state operating condition.
2. Kinetic energy and potential energy changes are neglected.
3. All heat exchangers are assumed to have counter-current flow.
4. Biomass only contains carbon and ash.
5. The volatile materials in the final product of the gasification process are mainly composed of carbon dioxide, carbon monoxide, hydrogen, methane, and water.
6. The pressure drop in the pipelines and other simulation equipment and process-related calculations are ignored.

2.2. Drying and milling process

The flow rate data used in this study were collected through a bibliographic review and data provided by the Basic Sanitation Company of the State of São Paulo [14]. The simulations assumed a constant biomass mass flow rate of 26,400 kg/h, which was kept the same across all simulations, including those performed using neural network analysis.

Figure 1 illustrates the production route that was proposed and analyzed in this study. The process begins with a rotary dryer that removes moisture from the biomass, consuming approximately 15 kWh per wet ton of biomass [15]. The dryer reduces the water content of the biomass to 7% [16]. Following the drying process, the biomass is chipped, and the specific electricity consumption required for the grinding process to obtain 0.5 mm particle diameters [17] was estimated to be approximately 3% of the thermal input of the biomass, based on its lower heating value.

2.3. Waste gasification process

Moving on to the next stage, shown in Fig 1, the gasification unit model was employed using the ultimate and proximate biomass analyses, as illustrated in Table 1. The gasifier model proposed by Battelle Columbus Laboratory (BCL) [18]–[20] was utilized, which is based on an indirect gasification process carried out at atmospheric pressure. This process prevents dilution between the nitrogen present in the produced syngas and the combustion gases. The combustion and gasification processes are carried out separately in a double-column system, with steam serving as the gasification medium.

During the combustion process, a portion of the char produced in the biomass pyrolysis step provides the heat necessary for endothermic drying, pyrolysis, and gasification reactions. Once these reactions are complete, the syngas exits the gasifier, and the produced tar undergoes thermal catalytic cracking. The syngas is then cooled to 400°C and scrubbed with water to remove any impurities that could affect downstream equipment. Finally, the syngas is compressed to 30 bar.

Table 1: Proximate and Ultimate analysis used for different biomass (dry basis) %

Biomass	M_{db}	FC_{db}	VM_{db}	Ash_{db}	C	H	N	S	Cl	O	REF.
Sugar cane bagasse	50.00	14.32	83.54	2.14	46.70	6.02	0.17	0.02	0	44.95	[21]
Sewage sludge	18.40	7.60	64.90	27.50	33.90	6.30	5.88	0.67	0.21	25.50	[22]
Sugar cane straw waste	31.30	12.80	20.60	13.00	49.00	5.60	0.80	0.30	0	44.00	[23]
Coffee waste	8.88	14.48	75.85	0.79	49.33	5.86	0.66	0.04	0	43.24	[24]
Eucalyptus waste	7.73	16.38	74.91	0.98	48.65	6.16	0.28	0	0	44.91	[25]
MSW	49.16	13.94	71.83	14.23	42.04	5.90	0.66	0.10	0	29.87	[26]
Orange bagasse	9.23	13.20	30.60	6.20	46.40	5.54	1.70	0	0	40.15	[27]
Corn waste	60.29	12.62	84.22	0	47.54	6.33	1.32	0.08	0	42.22	[28]

M, moisture content; VM, volatile matter content; FC, fixed carbon content; db, dry basis.

The base of gasification is composed of sequential process pre-treatment (dryer and chipping), pyrolysis, reduction, and combustion processes. Besides, the moisture removal simulation uses a FORTRAN subroutine [18]. To estimate the yield rates of H_2, CO, CO_2, methane, tar, char, and water in the pyrolysis reaction, step one uses empirical correlations reported in the literature as a function of temperature [29]. For this, it is employed an Aspen-embedded Excel spreadsheet.

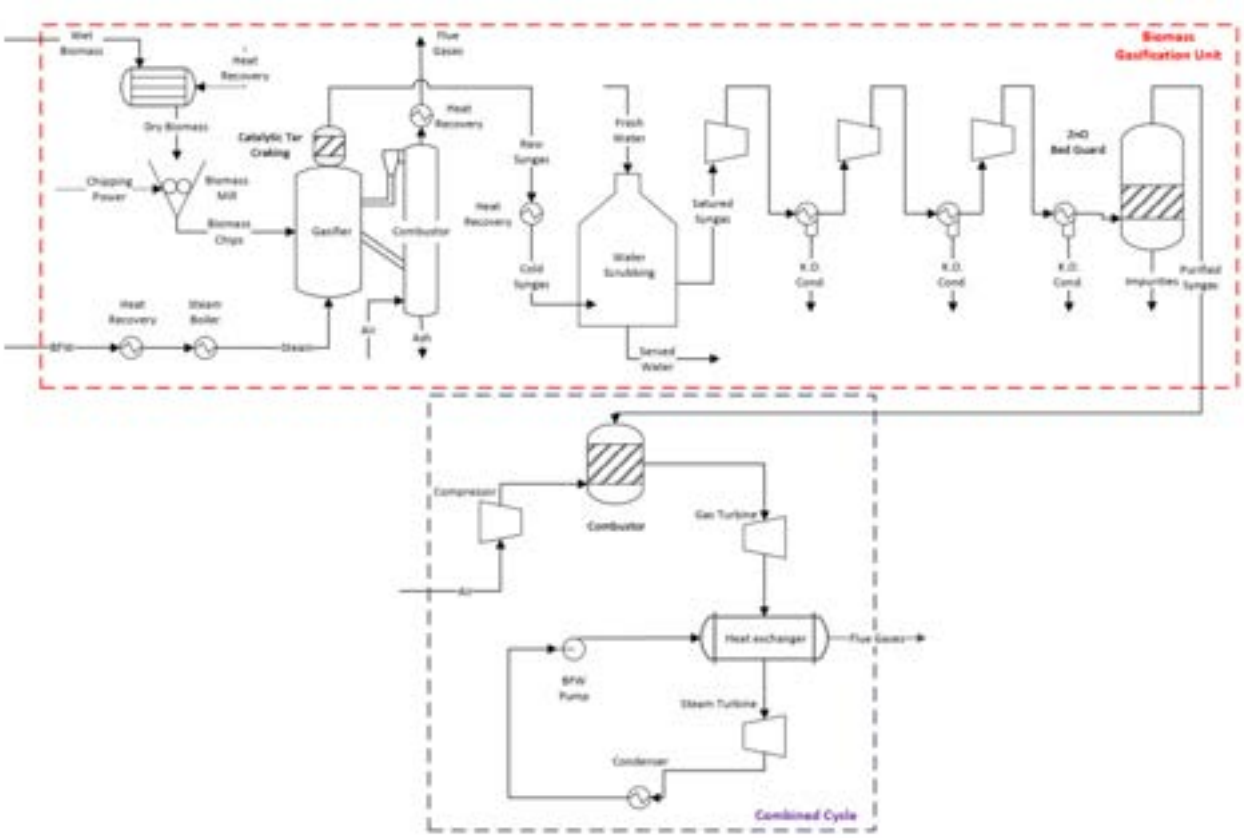

Fig. 1. Superstructure used in the process power conversion of the biomass-based.

2.4. Combined cycle

Figure 1 presents a comprehensive diagram of the combined cycle, depicting the various stages involved. The gas turbine utilized in this system is designed to simulate a Brayton Cycle and is based on the Alstom GT11N2 engine. The specifications for this turbine include mass flow, temperature, and pressure ratio. The steam turbine, on the other hand, operates using a conventional Rankine Cycle, with the simulation parameters being outlined in Table 2. It's worth noting that the same set of assumptions utilized by Silva Ortiz [30] and Medeiros et al [31] have been employed in this study.

To achieve a desired total exit flow rate of 400 kg/s, it is necessary to determine the mass flow rate of air based on the design specifications. The syngas produced during the gasification process serves as the inlet stream in the combustion chamber, where the air and syngas streams are directed to a RStoic reactor for combustion at a prescribed pressure ratio and constant pressure, as presented in Table 2. The gas turbine is designed to maintain the outlet temperature at 526°C. Once the steam temperature is attained, the output gases from the turbine undergo heat exchange with a compressed liquid water stream. Posteriorly, the steam follows to the steam turbine, that operates at an 83% isentropic efficiency and an outlet pressure of 0.1 bar, follows the previously stated pressure and isentropic efficiency assumptions [48, 49]. Ultimately, the water will be cooled in a heat exchanger and pumped back to start a new cycle.

Table 2: Combined cycle variables

Variable	Unit	Value
Compressor pressure ratio	-	15.9:1
Temperature after the gas turbine	°C	526
Pressure after the gas turbine	bar	1
Flue gas temperature	°C	~130
Temperature entering the turbine	°C	510
Pressure entering the turbine	bar	81
Isentropic efficiency of steam turbine	-	83
Pressure after steam turbine	bar	0.1

2.5. Validation

In this study, gasification represents a critical unit operation, given its significant impact on the quality of the final product. To validate the results obtained from the gasification system, It was utilized parameters from Almond shell biomass. Specifically, It was compared our findings with those from a previous study conducted by Marcantonio et al. [32]. and the comparative results are presented in Table 3. The most notable deviation was observed for CO_2, with a discrepancy of approximately 2.13%. However, the deviations for the other substances were relatively minor, with CH_4 showing a deviation of only 0.52%.

Table 3: Gasification results validation.

Parameter	Experimental results [32]	Simulation results	Standard deviation
Proximate analysis (%)			
FC	18.2	18.2	0.00
VM	80.6	80.6	0.00
Moisture	12	12	0.00
Ultimate Analysis (%)			
C	47.9	47.9	0.00
H	6.3	6.3	0.00
O	44.27	44.27	0.00
N	0.32	0.32	0.00
Ash	1.2	1.2	0.00
Volume Fraction (% vol)			
CO	28	29.35	0.95
CO_2	18	14.99	2.13
H_2	44	46.44	1.69
CH_4	10	9.27	0.52

2.6. Artificial neural network

A three-layer feed-forward neural network was employed to model the process of connecting each layer to the one below it. Unlike feedback neural networks, the information in this architecture flows only in one direction, from the input to the output layer. It was assumed that the data gathered accurately represented the system under investigation, a common assumption when working with neural networks. The neural network follows the same structure as described in the work of Cavalcanti et al. [33], with modifications to the inputs and outputs.

To represent the category or categorical-quantitative input variables, one-dimensional zero-arrays were used with a composition value of the component other than zero. This means that nine input neurons were used to represent a proximate and ultimate analysis of biomass, as well as temperature and steam biomass ratio. The ANN design was then expanded to include four neurons in the hidden layer, resulting in 11 input neurons and one output neuron.

To adjust the data, it was used the *NeuralNet package* available in the R software environment [34]. The package trains an ANN by estimating the weights between two neurons in successive layers, which simulate synapses. During training, information is transferred from one neuron to another. The ANN is trained using a sufficiently large dataset to compare its predictions. The training procedure stops when all partial derivatives of the error function E/w concerning the weights are smaller than a specified tolerance, such as 0.01. To compute the error function, it was summed the quadratic errors between observed and predicted values by the ANN.

To mitigate the impact of variable magnitudes on the model predictions, we pre-processed the data using min-max normalization, scaling their values between 0 and 1. The dataset was then randomly split into two subsets: 20% for the

test set, which was solely used to evaluate the ANN's performance, and 80% for the training set, which was used to estimate the ANN weights.

It is important to note that the test data used to evaluate the performance of the ANN must be representative of the same data domain used for training to avoid extrapolations that may result in uncertain predictions. In our case, the ANN included a bias neuron that served as an intercept with sigmoid activation characteristics.

The Resilient Backpropagation with Weight Backtracking (RPROP+) algorithm was used to train the network. Unlike the conventional Backpropagation algorithm, RPROP+ uses a different learning rate for each weight and can be modified during training. This allows for setting a global learning rate suitable for the entire network. RPROP+ only uses the sign of the gradient to update the weights instead of their magnitude, ensuring that the learning rate has an equal impact on the entire network. Weight backtracking refers to erasing the previous weight iteration and adding a smaller value to it in the subsequent step, preventing repeatedly jumping over the minimum. It is important to note that this algorithm is designed to avoid overfitting and improve the model's generalisation ability.

The number of neurons in the hidden layer (NH) was determined to prevent overfitting using the k-fold cross-validation procedure. This technique aims to run the ANN calculations multiple times with different training and test dataset combinations to identify the NH value that results in the lowest mean squared error (MSE) for the test set. This approach helps to ensure that the data used in the analysis are suitable for the ANN model, considering that all data from the articles were employed for training the ANN [35]. The MSE is calculated using Eq. 1.

$$\mathrm{MSE} = \frac{\sum_{i=1}^{a}(P_i - R_i)^2}{a} \tag{1}$$

where for the calculation of MSE; a is the number of data, P_i and R_i are the predicted and real values of the model, respectively.

The topology of the ANN used in this study is shown in Figure 2. The ANN comprises one input layer, one hidden layer with four neurons (NH=4), and one output layer. The inputs to the ANN are gasification temperature (labeled as "temperature" in °C), steam biomass ratio (labeled as "s/b ratio" in %), ultimate analysis of biomass (labeled as "moisture," "volatile material," "fixed carbon," and "ash"), and proximate analysis of biomasses in wt% (labeled as "carbon," "hydrogen," "nitrogen," "sulfur," and "oxygen"). In total, there are 11 input neurons and one output neuron. The ANN topology was generated using the *neuralnet* package available in the R software environment [34]

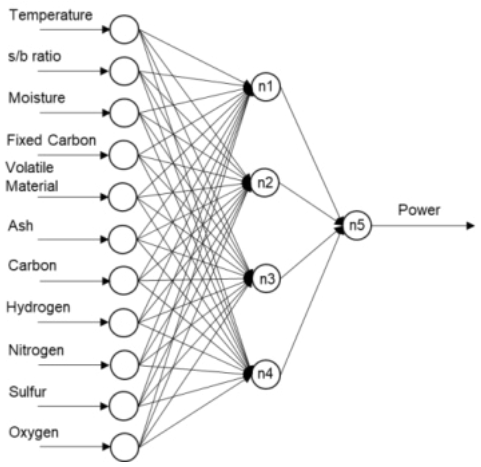

Figure 2. Three-Layer Feedforward Neural Network employed in this work

It is worth noting that none of the covariates directly affect the bias neurons (whose initial value is equal to one) existent to the intercept. The estimated weights calculated during the training phase are also presented in Table 4, where the "From" column indicates the source neuron and the "To" column indicates the destination neuron, as shown in Figure 2.

Table 4: Weights values for each neuron of naeural network

from	to	weight	from	to	weight
Baias	n1	-0.753261712	s/b ratio	n3	0.284048
Temp	n1	0.961899079	Moisture	n3	1.55496
s/b ratio	n1	0.21014481	Fixed Carbon	n3	-0.50962
Moisture	n1	-1.711559624	Volatile Material	n3	-2.5561
Fixed Carbon	n1	-1.538194587	Ash	n3	0.318489
Volatile Material	n1	-0.940108411	Carbon	n3	0.09278
Ash	n1	0.918331711	Hydrogen	n3	0.228348
Carbon	n1	0.207191253	Nitrogen	n3	-0.78659
Hydrogen	n1	-1.386894776	Sulfur	n3	-2.62901
Nitrogen	n1	-0.941899465	Oxygen	n3	-0.8421
Sulfur	n1	-2.042446266	Baias	n4	0.195908
Oxygen	n1	-1.305202095	Temp	n4	-0.2577
Baias	n2	-0.029572741	s/b ratio	n4	0.00124
Temp	n2	0.036312963	Moisture	n4	-1.76798
s/b ratio	n2	-0.483953217	Fixed Carbon	n4	-0.24548
Moisture	n2	3.970044275	Volatile Material	n4	0.110772
Fixed Carbon	n2	0.661251307	Ash	n4	0.157837
Volatile Material	n2	0.106854669	Carbon	n4	-1.10524
Ash	n2	-0.008101265	Hydrogen	n4	-0.6584
Carbon	n2	-0.447942202	Nitrogen	n4	1.105558
Hydrogen	n2	-0.108357221	Sulfur	n4	-0.06553
Nitrogen	n2	1.225302782	Oxygen	n4	0.005014
Sulfur	n2	0.095169143	Baias	n5	1.162488
Oxygen	n2	-0.009455786	n1	n5	1.139094
Baias	n3	-0.602606332	n2	n5	-1.18583
Temp	n3	-0.28335936	n3	n5	0.826087
			n4	n5	0.642381

2.7. Performance indicators

To assess the overall performance of production plants [20], [36], two performance indicators are proposed by Florez-Orrego et al [37] to allow systematic comparisons among the different designed setups: rational and relative exergy efficiencies. The rational efficiency is defined according to Eq. (2), and the relative efficiency by Eq. (3).

$$\eta_{rational} = \frac{B_{useful\,,output}}{B_{\,input}} = 1 - \frac{B_{Dest}}{B_{\,input}} = 1 - \frac{B_{Dest}}{B_{biomass} + W_{input}} \quad (2)$$

$$\eta_{relative} = \frac{B_{consumed\,,ideal}}{B_{\,consumed,actual}} = \frac{B_{power}}{B_{biomass} + W_{input}} \quad (3)$$

where, B is the exergy flow rate (kW) and B_{Dest} represents the exergy destroyed rate, while W is the electrical power input to the plant.

The efficiency of a gasifier is typically investigated in terms of two types of efficiency: carbon conversion efficiency and cold gas efficiency. The carbon conversion efficiency (η_{cc}) (Eq. (4)) is defined as the ratio of the reaction carbon ($\boldsymbol{M}_{c_{re}}$) to the feed carbon in the gasifier ($\boldsymbol{M}_{c_{in}}$).

$$\eta_{cc}(\%) = \frac{\boldsymbol{M}_{c_{re}}}{\boldsymbol{M}_{c_{in}}} \quad (4)$$

The higher heating value (HHV) of fuels, including coal, coke, biomass, and municipal wastes, emanates from the heat released from the complete combustion of a unit of mass of fuel at a specific temperature and pressure [38]. Based on HHVs, the cold gas efficiency (η_{cg}) (Eq. (5)) is also expressed as the ratio of the chemical energy of the gas products released from the gasifier to the chemical energy of the input biomass.

$$\eta_{cg}(\%) = \frac{HHV_{syngas} \times M_{syngas}}{HHV_{biomass} \times M_{biomass}} \times 100 \quad (5)$$

The evaluation of each flow's thermodynamic properties and the mass, energy, and exergy balances of each operating unit are evaluated using the Aspen Plus® V8.8 software [39] . Compressors and pumps are modeled using 60% and 80% isentropic efficiencies, respectively. Furthermore, pressure and heat losses are not considered in any process. The ratio of specific chemical exergy (b ^{ch}) to the lower heating value is calculated employing the correlation proposed by [40] for solid fuels with specified mass ratios, Eq. (6)

$$\beta = \frac{b^{ch}}{LHV} = \frac{1.0438 + 0.1882\frac{y_H}{y_C} - 0.2509(1 + 0.7256\frac{y_H}{y_C})}{1 - 0.30350.1882\frac{y_O}{y_C}} \quad (6)$$

where the biomass lower heating value (LHV, MJ/kg) is estimated based on the correlations reported by [41] in Eq. (7)

$$LHV = 349.1y_C + 1178.3y_H + 100.5y_s - 103.4\,y_O - 15.1y_N - 21.5y_{ashes} - 0.0894h_{lv}y_H \quad (7)$$

and y_i are the mass fractions of carbon (C), hydrogen (H), sulfur (S), oxygen (O), nitrogen (N), and ashes (A) in the dry biomass and h_{lv} is the enthalpy of evaporation of water at standard conditions (2442.3 kJ/kg).

Finally, the biomass higher heating value (HHV, MJ/kg) is estimated based on the correlations reported by Parikh et al. [42] in Eq. 8

$$HHV = 0.3536\text{FC} + 0.1559\text{VM} - 0.0078\text{ASH} \quad (8)$$

where FC (%dry basis) is the fixed carbon, and VM is the volatile matter (%dry basis) ASH (%dry basis). The lower heating, high heating, and chemical exergy of biomasses are shown in Table 5.

Table 5: Calculated lower heating value (LHV) and specific chemical exergy value (b^{CH}) for selected materials and fuels streams.

Biomass	HHV (MJ/kg)	LHV (MJ/kg)	b^{CH} (MJ/kg)
Sugar cane bagasse	16.89	15.25	19.50
Sewage sludge	20.28	18.12	16.13
sugar cane waste	16.43	14.89	19.28
Coffee waste	17.06	15.45	19.84
eucalyptus waste	17.19	15.54	21.75
MSW	18.92	17.08	18.32
Orange bagasse	16.79	15.20	20.26
Corn waste	17.87	16.13	19.93

3. Results and discussion

To determine the number of neurons in the hidden layer of the ANN, the data were divided into ten sets using the k-fold cross-validation technique. Each set was then used for training and testing purposes. The mean squared error (MSE) for the testing set was plotted against the number of neurons in the hidden layer (NH), as shown in Fig. 3a. The graph indicates that the MSE value drops to its lowest point at NH = 4 before rising and oscillating, which could be due to overfitting.

Based on the prediction graphs, it was decided that four neurons were sufficient for the ANN hidden layer without compromising the system representation performance. It should be noted that the MSE value for the training set (Fig. 3b) tends to decrease as more neurons and parameters are added to the model, resulting in model overestimation.

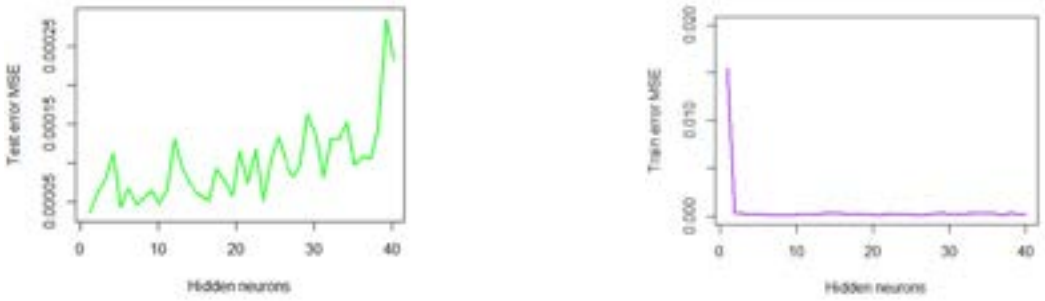

(a) (b)

Figure 3. Mean squared error versus the number of neurons in the hidden layer (a) for the testing set and (b) for the training set.

The training procedure converged after 3309 steps, resulting in an error of 0.04368 for the ANN weights. The accuracy of the ANN model for the training set can be seen in Fig. 4a, which shows an excellent match to the data, as indicated by the high R^2 value of 0.996. The mean square error (MSE) between the observed and projected values was 0.000366. The training set consisted of 80% of the overall dataset, and these data were used to estimate the ANN weights, explaining the good values for R^2 and MSE. Moreover, the residues histogram (Fig. 4b) displayed typical behaviour with an average of roughly zero, further confirming the high agreement between the observed and predicted values.

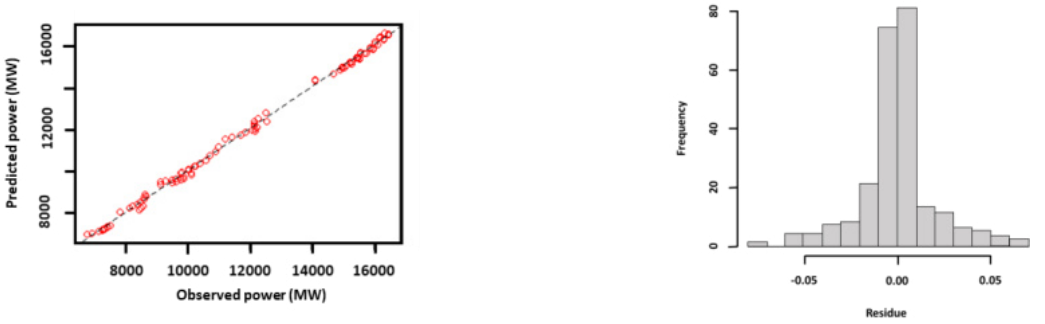

(a) (b)

Figure 4. (a) Comparison between prediction and observed power conversion values for the training set (b) Histogram of residues for the training set.

Fig. 5a demonstrates that the ANN model was validated using the test set. The results indicate that the network can accurately predict data not used in weight estimation, with an R2 value of 0.994 and an MSE of 0.00909. While these metrics are slightly worse than those obtained from the training set, they still reflect a highly credible performance. The corresponding histogram of residuals for this validation, as shown in Fig. 5b, reveals a more significant normal distribution with a less frequent zero-centred average compared to the training set, further corroborating the accuracy of these results.

(a) (b)

Figure 5. (a) Comparison between prediction and observed power conversion values for the testing set (b) Histogram of residues for the testing set.

The results presented in Fig. 6 are based on the entire dataset. A residuals histogram displaying a standard shape and an R^2 value of 0.993 and MSE of 0.00172, indicating a good match between predicted and observed values without any noticeable bias in the fit. These performance metrics lie between those obtained from the training and testing sets but are closer to the former, given that the training set contained 80% of the total data and was used to estimate the ANN parameters. Overall, the ANN model exhibits good predictive ability across the entire dataset.

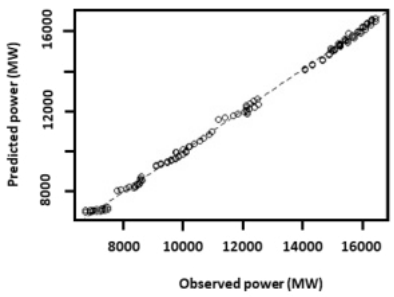

(a)

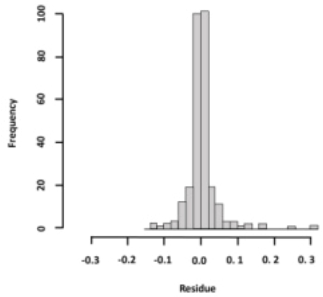

(b)

Figure 6. (a) Comparison between prediction and observed power conversion values for all datasets (b) Histogram of residues for all datasets

To investigate the gasification unit's performance with different fuels, the reactor's initial biomass mass flow rate (26,640kg/h), temperature (850°C), s/b ratio (0.5), and operating pressure were kept constant. The quality of the produced synthesis gas for each fuel was then compared by examining the quantity of its main constituents: H_2, H_2O, CO, and CH_4. Fig. 7 displays the mole fraction of hydrogen and carbon monoxide, the two primary syngas components, in the gasifier's output stream for each fuel. The results reveal that corn waste and sewage sludge produce a high amount of hydrogen but a low mole fraction of carbon monoxide compared to the other biomass fuels.

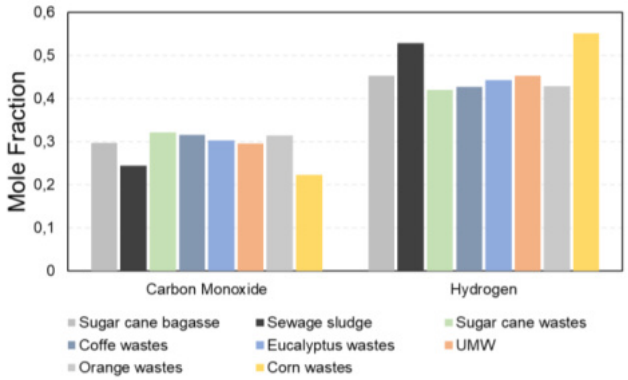

Figure 7 Comparison of syngas quality by the mole fraction of hydrogen and carbon monoxide.

Fig. 8 provides valuable insight into the net power production of different waste materials after the gasification process. The graphic shows that eucalyptus waste, sewage sludge, and sugar cane bagasse have the highest power production potential in the gas turbine section, with 15.86 MW, 15.06 MW, and 14.73 MW, respectively.

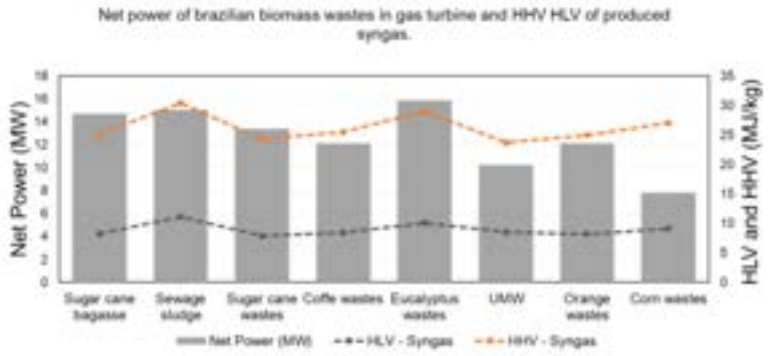

Figure 8. Net power of Brazilian biomass wastes in combined cycle and HHV and LHV of produced syngas

This highlights the importance of utilizing these waste materials as potential energy sources, which can generate significant amounts of power. Additionally, Fig. 8 suggests that the higher the HHV (Higher Heating Value) and LHV (Lower Heating Value) of the produced syngas, the greater the power output from the gas turbine. This underscores the importance of selecting appropriate waste materials for gasification, as those with higher HHV and HLV values can provide greater energy yield and efficiency. Moreover, it is crucial to note that using waste materials for energy production can positively impact the environment by reducing greenhouse gas emissions and mitigating the negative impacts of waste disposal.

Based on the information provided in Fig. 9, It can observe that urban municipal waste has the highest cold gas efficiency (82.21%) among all waste materials studied. This indicates that a significant proportion of the energy content of the waste

material is converted into syngas during the gasification process. On the other hand, sugar cane bagasse exhibits the highest carbon conversion efficiency (92.88%), indicating that most of the carbon content in the waste material is converted into syngas during gasification.

It is important to note that cold gas efficiency (CGE) is affected by various factors, such as the HHV and mass flow rate of waste and syngas. As depicted in Fig. 9, there is a positive correlation between the HHV of syngas and CGE, implying that waste materials with higher HHV values can result in more efficient gasification processes. However, it is also worth mentioning that coffee waste has the lowest cold gas (61.88%) and carbon conversion (72.35%) efficiencies among the waste materials studied. This highlights the need to carefully consider the waste material selection for gasification to ensure optimal efficiency and energy yield.

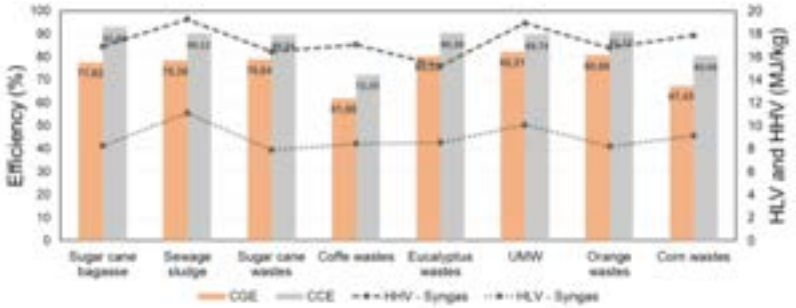

Figure 9: LHV and HHV of syngas, cold gas efficiency (CGE), and carbon conversion efficiency (CCE) of Brazilian biomass wastes in the gasification process.

Figure 10 presents a more detailed view of the destroyed exergy, considering each residual biomasses' leading equipment and processes. Thus, when analyzing these data, it can be noted that the gasifier and the combustor of the combined cycle contribute the largest share of the destruction compared to all biomasses. In addition, it is worth remembering that the syngas' grinding, drying, scrubbing, and compression are also processed internally by the gasification unit. However, compared to the gasification process, they present a small share in the contribution of the exergy destruction of the unit. In addition, it is worth citing the works of Florez-Orrego et al. [18], where the gasification of sugarcane bagasse was studied, and Domingos et al. [19], studying black liquor, obtained similar results.

Observing only the gasifier for the different waste biomasses, the process representing the highest exergy destruction was via RMU, with 68.79%, followed by coffee waste and orange bagasse, with 67.53% and 65.78%, respectively. On the other hand, gasification via sugarcane bagasse had the lowest exergy destruction rate, approximately 58.61%. Also, the combustion process of the combined cycle corresponds to a variation of 22.95% to 30.63% of the exergy destroyed by the entire power conversion process. In other words, exergy destruction in the gasifier is caused by the reactions that decompose the large biomolecules into smaller gas molecules presenting the most considerable exergy destruction compared with combustor burning only syngas.Another essential point to be highlighted is the compression systems, which present intermediate values of exergy destruction. These systems are divided into 3 parts: compression of syngas typical to all conversion plants, air compression of the gas cycle, and pump for the Rankine cycle. The highest proportion of exergy destruction was located in the sewage sludge (2.78%). This happened because the flow rate of syngas after the gasifier is the biggest one compared with other biomasses.

A way to help reduce the amount of exergy destroyed in biomass-based production plants is to employ better technologies to remove the bagasse moisture, hot catalytic cleaning of the syngas, and increase gasifier pressure [43].

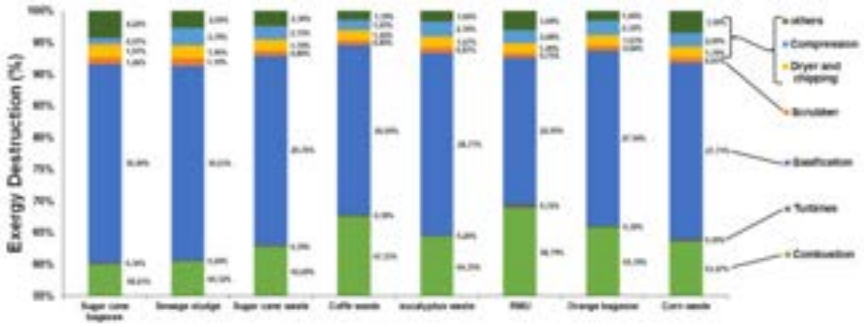

Figure 10: Exergy destroyed by equipment or conversion processes for different biomass waste selected types.

Fig. 11 presents the calculated plantwide efficiencies for different waste materials, revealing that the relative exergy efficiencies ranged from 24.42% for sugar cane straw waste to 42.57% for sugar cane bagasse. Similarly, the rational exergy efficiencies ranged from 23.71% for coffee waste to 39.09% for sugar cane bagasse. These results highlight the significant variability in the energy efficiency of different waste materials. However, it is worth noting that the performance of different biomasses was impaired, likely due to differences in the proximate and ultimate analysis of the waste materials.

Factors such as moisture content and volatile materials can significantly affect the gasification process, leading to variations in energy efficiency. Therefore, it is essential to thoroughly analyse the waste materials before selecting them for gasification to ensure optimal performance and energy yield. By understanding the composition of the waste materials strategies can be developed to optimize the gasification process and improve the energy efficiency of the overall plant.

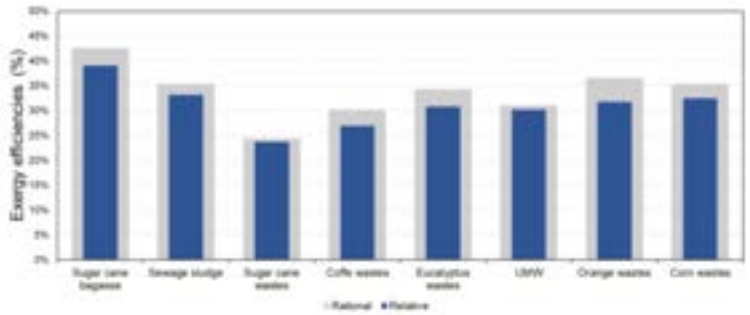

Figure 11. Comparison between the exergy efficiencies of conversion processes for different types of selected biomass.

4. Conclusions

The current research aimed to develop a predictive model using artificial neural networks (ANNs) to analyze the performance indicators of a green electric energy generation process based on the gasification of Brazilian biomass residues. The results indicated that the highest cold gas and carbon conversion efficiencies were achieved using urban municipal waste and sugar cane bagasse with 82.1% and 92.89%, respectively. On the other hand, coffee waste had a relatively low carbon conversion efficiency of about 72.35%, with cold gas efficiency of 61.88%. Eucalyptus waste was found to have the highest renewable power capacity, with 12.86 MW. The relative and rational exergy efficiencies were determined for different waste types, ranging from 24.42% to 42.57% for sugar cane straw waste and sugar cane bagasse, respectively, and from 23.71% to 39.09% for coffee waste and sugar cane bagasse. Furthermore, the study demonstrated the effective use of environmental resources by mapping the exergy destruction reaction to produce a clean and valuable energy source. The study's findings provide important insights into the sustainable utilization of environmental resources by mapping exergy destruction reactions for producing a clean and valuable energy source. These outcomes can be used to guide future research and improve the performance of similar models. However, further studies are necessary to enhance the robustness of ANN models in predicting power generation. More research should be reported in the literature to develop more reliable models. It is worth noting that the ANN model developed in this study exhibited high accuracy in predicting power generation, with R^2 values greater than 0.993 for both training and test datasets. Finally, using neural networks and Aspen Plus models provides a viable solution to improve power generation predictions and reduce computational costs. Applying these methods in this study demonstrates the potential of waste-to-energy systems to generate renewable electricity from waste biomass, promoting a more sustainable energy future.

Acknowledgements

This study was financed in part by the Coordenação de Aperfeiçoamento de Pessoal de Nível Superior - Brasil (CAPES) - Finance Code 001. The first author acknowledges CAPES for his PhD grant. The second author acknowledges CNPq (Brazilian National Council for Scientific and Technological Development) for grant 306484/2020-0.

References

[1] D. Thraen and kay Shaubach, “Global Wood Pellet Industry and Trade Study 2017,” *IEA Bioenergia*, 2017.

[2] W. Foster *et al.*, “Waste-to-energy conversion technologies in the UK: Processes and barriers – A review,” *Renew. Sustain. Energy Rev.*, vol. 135, p. 110226, Jan. 2021, doi: 10.1016/J.RSER.2020.110226.

[3] R. V. Sapali S, “Exergy analysis of cryogenic air separation unit integrated with biomass gasifier.,” *Congr. Eng. Comput. Sci.*, vol. 2, 2013.

[4] Y. Wu, Y. Xiang, L. Cai, H. Liu, and Y. Liang, “Optimization of a novel cryogenic air separation process based on cold energy recovery of LNG with exergoeconomic analysis,” *J. Clean. Prod.*, vol. 275, p. 123027, Dec. 2020, doi: 10.1016/J.JCLEPRO.2020.123027.

[5] S. Banerjee, J. A. Tiarks, and S. C. Kong, “Modeling biomass gasification system using multistep kinetics under various oxygen–steam conditions,” *Environ. Prog. Sustain. Energy*, vol. 34, no. 4, pp. 1148–1155, Jul. 2015, doi: 10.1002/EP.12109.

[6] K. N. Dhanavath, K. Shah, S. K. Bhargava, S. Bankupalli, and R. Parthasarathy, “Oxygen–steam gasification of karanja press seed cake: Fixed bed experiments, ASPEN Plus process model development and benchmarking with saw dust, rice husk and sunflower husk,” *J. Environ. Chem. Eng.*, vol. 6, no. 2, pp. 3061–3069, Apr. 2018, doi: 10.1016/J.JECE.2018.04.046.

[7] W. Lan, G. Chen, X. Zhu, X. Wang, C. Liu, and B. Xu, “Biomass gasification-gas turbine combustion for power generation system model based on ASPEN PLUS,” *Sci. Total Environ.*, vol. 628–629, pp. 1278–1286, Jul. 2018, doi: 10.1016/J.SCITOTENV.2018.02.159.

[8] M. H. Sahraei, M. A. Duchesne, P. G. Boisvert, R. W. Hughes, and L. A. Ricardez-Sandoval, “Reduced-Order Modeling of a Commercial-Scale Gasifier Using a Multielement Injector Feed System,” *Ind. Eng. Chem. Res.*, vol.

56, no. 25, pp. 7285–7300, Jun. 2017, doi: 10.1021/ACS.IECR.7B00693/ASSET/IMAGES/MEDIUM/IE-2017-00693B_0014.GIF.

[9] H. Wang, D. Chaffart, and L. A. Ricardez-Sandoval, “Modelling and optimization of a pilot-scale entrained-flow gasifier using artificial neural networks,” *Energy*, vol. 188, p. 116076, Dec. 2019, doi: 10.1016/J.ENERGY.2019.116076.

[10] R. Mikulandrić, D. Lončar, D. Böhning, R. Böhme, and M. Beckmann, “Artificial neural network modelling approach for a biomass gasification process in fixed bed gasifiers,” *Energy Convers. Manag.*, vol. 87, pp. 1210–1223, Nov. 2014, doi: 10.1016/J.ENCONMAN.2014.03.036.

[11] D. Serrano, I. Golpour, and S. Sánchez-Delgado, “Predicting the effect of bed materials in bubbling fluidized bed gasification using artificial neural networks (ANNs) modeling approach,” *Fuel*, vol. 266, p. 117021, Apr. 2020, doi: 10.1016/J.FUEL.2020.117021.

[12] S. Safarian, S. M. Ebrahimi Saryazdi, R. Unnthorsson, and C. Richter, “Artificial neural network integrated with thermodynamic equilibrium modeling of downdraft biomass gasification-power production plant,” *Energy*, vol. 213, p. 118800, Dec. 2020, doi: 10.1016/J.ENERGY.2020.118800.

[13] A. Sözen and E. Arcaklioğlu, “Exergy analysis of an ejector-absorption heat transformer using artificial neural network approach,” *Appl. Therm. Eng.*, vol. 27, no. 2–3, pp. 481–491, Feb. 2007, doi: 10.1016/J.APPLTHERMALENG.2006.06.012.

[14] SABESP, “State Basic Sanitation Company From Sao Paulo (in portugese).” São Paulo, [Online]. Available: www.sabesp.gov.br.

[15] A. Sues Caula, “Are European bioenergy targets achievable? : an evaluation based on thermoeconomic and environmental indicators,” Technische Universiteit Eindhoven, 2011.

[16] P. Basu, “Biomass Gasification and Pyrolysis,” *Biomass Gasif. Pyrolysis*, 2010, doi: 10.1016/C2009-0-20099-7.

[17] P. C. A. Bergman *et al.*, “Torrefaction for entrained-flow gasification of biomass Revisions A B Made by,” Accessed: Aug. 11, 2021. [Online]. Available: www.ecn.nl/biomass.

[18] D. Flórez-Orrego, F. Maréchal, and S. de Oliveira Junior, “Comparative exergy and economic assessment of fossil and biomass-based routes for ammonia production,” *Energy Convers. Manag.*, vol. 194, pp. 22–36, 2019, doi: https://doi.org/10.1016/j.enconman.2019.04.072.

[19] M. E. G. R. Domingos, D. Flórez-Orrego, M. T. dos Santos, H. I. Velásquez, and S. de Oliveira, “Exergy and environmental analysis of black liquor upgrading gasification in an integrated kraft pulp and ammonia production plant,” *Int. J. Exergy*, vol. 35, no. 1, pp. 35–65, 2021, doi: 10.1504/IJEX.2021.115083.

[20] R. Nakashima, D. Flórez-Orrego, and S. de Oliveira Junior, “Integrated anaerobic digestion and gasification processes for upgrade of ethanol biorefinery residues,” *J. Power Technol.*, vol. 99, no. 2, pp. 104–114, 2019.

[21] Y. C. Ardila, J. E. J. Figueroa, B. H. Lunelli, R. M. Filho, and M. R. W. Maciel, “Syngas production from sugar cane bagasse in a circulating fluidized bed gasifier using Aspen Plus™: Modelling and Simulation,” *Comput. Aided Chem. Eng.*, vol. 30, pp. 1093–1097, Jan. 2012, doi: 10.1016/B978-0-444-59520-1.50077-4.

[22] M. P. Languer *et al.*, “Insights into pyrolysis characteristics of Brazilian high-ash sewage sludges using thermogravimetric analysis and bench-scale experiments with GC-MS to evaluate their bioenergy potential,” *Biomass and Bioenergy*, vol. 138, p. 105614, Jul. 2020, doi: 10.1016/J.BIOMBIOE.2020.105614.

[23] D. L. 1986- Franco Jacome, “Caracterização físico-química das cinzas da palha de cana-de-açúcar através de análises térmicas simultâneas (STA),” 2014, Accessed: Aug. 17, 2021. [Online]. Available: http://repositorio.unicamp.br/jspui/handle/REPOSIP/265950.

[24] R. Manrique, D. Vásquez, F. Chejne, and A. Pinzón, “Energy analysis of a proposed hybrid solar–biomass coffee bean drying system,” *Energy*, vol. 202, pp. 1–8, 2020, doi: 10.1016/j.energy.2020.117720.

[25] M. Guerrero, M. P. Ruiz, M. U. Alzueta, R. Bilbao, and A. Millera, “Pyrolysis of eucalyptus at different heating rates: studies of char characterization and oxidative reactivity,” *J. Anal. Appl. Pyrolysis*, vol. 74, no. 1–2, pp. 307–314, Aug. 2005, doi: 10.1016/J.JAAP.2004.12.008.

[26] A. C. Gutierrez-Gomez, A. G. Gallego, R. Palacios-Bereche, J. Tofano de Campos Leite, and A. M. Pereira Neto, “Energy recovery potential from Brazilian municipal solid waste via combustion process based on its thermochemical characterization,” *J. Clean. Prod.*, vol. 293, p. 126145, Apr. 2021, doi: 10.1016/J.JCLEPRO.2021.126145.

[27] J. L. F. Alves *et al.*, “Lignocellulosic Residues from the Brazilian Juice Processing Industry as Novel Sustainable Sources for Bioenergy Production: Preliminary Assessment Using Physicochemical Characteristics,” *Artic. J. Braz. Chem. Soc*, vol. 31, no. 9, 2020, doi: 10.21577/0103-5053.20200094.

[28] S. Pan-In and N. Sukasem, “Methane production potential from anaerobic co-digestions of different animal dungs and sweet corn residuals,” *Energy Procedia*, vol. 138, pp. 943–948, 2017, doi: 10.1016/j.egypro.2017.10.062.

[29] M. Puig-Arnavat, J. C. Bruno, and A. Coronas, “Modified Thermodynamic Equilibrium Model for Biomass Gasification: A Study of the Influence of Operating Conditions,” *Energy \& Fuels*, vol. 26, no. 2, pp. 1385–1394, 2012, doi: 10.1021/ef2019462.

[30] P. A. Silva Ortiz, “Hierarquização exergética e ambiental de rotas de produção de bioetanol.,” Biblioteca Digital de Teses e Dissertações da Universidade de São Paulo, São Paulo, 2017.

[31] E. M. Medeiros *et al.*, “Preliminary assessment by the Virtual Sugarcane Biorefinary framework of syngas production and power generation from a first-generation sugacane plant lignocellulosic biomass.,” *5th Int. Conf. Eng. Waste Biomass Valoris.*, no. September 2015, 2014.

[32] V. Marcantonio, M. De Falco, M. Capocelli, E. Bocci, A. Colantoni, and M. Villarini, “Process analysis of hydrogen production from biomass gasification in fluidized bed reactor with different separation systems,” *Int. J. Hydrogen Energy*, vol. 44, no. 21, pp. 10350–10360, 2019, doi: https://doi.org/10.1016/j.ijhydene.2019.02.121.

[33] F. M. Cavalcanti, M. Schmal, R. Giudici, and R. M. Brito Alves, “A catalyst selection method for hydrogen production through Water-Gas Shift Reaction using artificial neural networks,” *J. Environ. Manage.*, vol. 237, pp. 585–594, May 2019, doi: 10.1016/J.JENVMAN.2019.02.092.

[34] F. Günther and S. Fritsch, “neuralnet: Training of Neural Networks,” *R J.*, vol. 2, no. 1, pp. 30–38, 2010, doi: 10.1109/SP.2010.25.

[35] G. Rothenberg, “Data mining in catalysis: Separating knowledge from garbage,” *Catal. Today*, vol. 137, no. 1, pp. 2–10, Aug. 2008, doi: 10.1016/J.CATTOD.2008.02.014.

[36] D. Flórez-Orrego and S. de Oliveira Junior, “On the efficiency, exergy costs and CO2 emission cost allocation for an integrated syngas and ammonia production plant,” *Energy*, vol. 117, pp. 341–360, 2016, doi: https://doi.org/10.1016/j.energy.2016.05.096.

[37] D. Flórez-Orrego, F. Nascimento Silva, and S. de Oliveira Junior, “Syngas production with thermo-chemically recuperated gas expansion systems: An exergy analysis and energy integration study,” *Energy*, vol. 178, pp. 293–308, Jul. 2019, doi: 10.1016/J.ENERGY.2019.04.147.

[38] M. Bagheri, R. Esfilar, M. Sina Golchi, and C. A. Kennedy, “Towards a circular economy: A comprehensive study of higher heat values and emission potential of various municipal solid wastes,” *Waste Manag.*, vol. 101, pp. 210–221, Jan. 2020, doi: 10.1016/J.WASMAN.2019.09.042.

[39] ASPENTECH, “Aspen Plus V8.8.” 2011.

[40] J. Szargut, D. R. Morris, and F. R. Steward, “Exergy analysis of thermal, chemical, and metallurgical processes,” 1987.

[41] S. A. Channiwala and P. P. Parikh, “A unified correlation for estimating HHV of solid, liquid and gaseous fuels,” *Fuel*, vol. 81, no. 8, pp. 1051–1063, 2002, doi: https://doi.org/10.1016/S0016-2361(01)00131-4.

[42] J. Parikh, S. A. Channiwala, and G. K. Ghosal, “A correlation for calculating HHV from proximate analysis of solid fuels,” *Fuel*, vol. 84, no. 5, pp. 487–494, 2005, doi: 10.1016/j.fuel.2004.10.010.

[43] A. C. Caetano de Souza, J. Luz-Silveira, and M. I. Sosa, “Physical-Chemical and Thermodynamic Analyses of Ethanol Steam Reforming for Hydrogen Production,” *J. Fuel Cell Sci. Technol.*, vol. 3, no. 3, pp. 346–350, Aug. 2006, doi: 10.1115/1.2217957.

Adaptive Radiative Collectors and Emitters (AD-RCE) to improve the efficiency of heat pumps

Roger Vilà[a], Jesús Monterrubio[a], Mohammed Reda Haddouche[a], Lídia Rincón[a], Marc Medrano[a*]

[a] Sustainable Energy, Machinery and Buildings (SEMB) Research Group, INSPIRES Research Centre, Universitat de Lleida, Pere de Cabrera s/n, 25001 Lleida, Spain,
**marc.medrano@udl.cat*

Abstract:

A Radiative Collector and Emitter (RCE) is a device which combines solar collection and radiative cooling functionalities to provide both heat and cold from renewable sources. In solar collection mode, fluids are heated up using the incoming solar radiation. In radiative cooling mode, it takes advantage of the atmospheric window transparency to dissipate infrared radiation towards the outer space at nights, allowing to cool down fluids circulating through it. However, the heat production of the RCE is about 10 times higher than the cold production, and the cold water can only be produced a few degrees below ambient temperature (4-8 ºC). An evolution of the RCE, the adaptive RCE (ad-RCE) is capable to adapt its behaviour to the energy requirements, producing either heat or cold during daytime, as well as cold during night-time. To further enhance the cooling potential, we suggest coupling the ad-RCE with a compression heat pump (HP) that utilizes the cold produced by the ad-RCE as a heat sink for the condenser. In this study, we numerically estimate the performance of a water-to-water compression heat pump coupled with an ad-RCE. Our results indicate a yearly average improvement of the coefficient of performance (COP) of 3.89%, which translates to an annual electricity savings of 3.70%.

Keywords:
radiative cooling, solar thermal collection, adaptive energy production, renewable energy, heat-pump, COP.

1. Introduction

The building sector is considered to have a significant impact on energy consumption, with estimates indicating that it accounts for 40% of final energy consumption in Europe and generates 36% of CO_2 emissions [1]. Space conditioning, including DHW, cooling, and heating, constitutes the largest share of 80% of the total energy consumption in buildings. This trend is expected to continue, with rising global temperatures and heat waves leading to increase the energy consumption for refrigeration in households. Unfortunately, this will contribute to a vicious cycle of CO_2 emissions, further exacerbating the problem.

While renewable energies have become more important in recent years, cooling comfort is still achieved through electricity consumption [1]. However, new technologies based on radiative cooling have emerged in recent years, enabling the production of cold in a renewable way [2–4]. Radiative cooling (RC) is the process by which terrestrial bodies reduce their surface temperature by emitting infrared radiation towards outer space, taking advantage of the transparency of the infrared atmospheric window at certain wavelengths (7-14 μm). The low effective temperature of the space makes it possible to cool down below ambient temperature [5]. At the beginning, it was only possible to achieve RC during the night, in absence of solar radiation. New materials, called Daytime Radiative Cooling (DRC) materials, have been developed in the last decade, which enable the achievement of RC during daytime hours [6–11]. These materials reflect most of the incident solar radiation [10–12], thus the surface is able to cool down. This phenomenon, which is known as all-day radiative cooling, has been achieved using low-cost materials in recent years [13, 14].

Radiative coolers present low cooling rates, between 20 and 80 W/m^2 with peak values of 120 W/m^2 [15], which represent an order of magnitude lower than those that can be achieved in solar heating, representing a limitation of this type of technology. In order to make the technology attractive to markets, Vall et al. [15]

introduced the Radiative Collector and Emitter (RCE) as a novel technology that integrates, in a single device, solar collection and radiative cooling to produce both heat and cold through renewable means. The RCE operates by circulating a heat transfer fluid through pipes that are in contact with a radiative surface. During the day, the radiative surface heats up and transfers heat to the fluid. At night, the heat from the fluid is transmitted back to the radiative surface and radiated away. By using this technology, the dependence on fossil fuels can be greatly reduced, leading to a smaller carbon footprint.

The integration of radiative cooling systems with the built environment is still a field under study. One of the proposal is that the low power rates of cold generated in the RCE can be used to improve the performance of a water-water heat pump by increasing its coefficient of performance (COP), thereby decreasing electricity consumption. Goldstein et al [16] showed electricity savings up to 21% in an office building when a heat pump was combined with radiative cooling. In 2023, Vilà et al. [17] presented a study that simulated different configurations of RCE coupled with heat pumps, where the RCE produced cold during the night in combination with the heat pump, while during the day the RCE was decoupled and used to produce DHW independently by means of solar heating. The study examined various cities and climates and found an improvement in the system performance. However, the hot water production during solar heating mode far exceeded the domestic hot water (DHW) demand.

To minimize the underutilization of the solar collection mode while increasing the production of cold water, we propose an evolution of the RCE, the adaptive RCE (ad-RCE). The RCE takes advantage of the above-mentioned DRC materials to modify its behaviour to produce hot or cold water during the day and cold water during the night, as required. By reducing the solar heating mode to 1 or 2 hours, the ad-RCE can optimize cold production during the day.

This study builds upon the previous research conducted by Vilà et al. by implementing the advanced version ad-RCE. The aim of this study is to present a preliminary evaluation of the improvement of the COP of a water-water heat pump coupled with an ad-RCE in the condenser's side. In this study, we evaluate the performance of the combined system ad-RCE+HP integrated in a hotel in Brisbane (Australia) to cover the cold and DHW requirements of the building. The results are compared with a reference case of a conventional heat pump, and the potential energy savings are discussed.

2. Methodology

2.1. Description of the configurations

2.1.1. Studied case: ad-RCE+HP

An ad-RCE was coupled to the condenser of a water-to-water compression heat pump (**Figure *1***). The proposed configuration consisted of two modes of operation. In the first mode, the radiative cooling mode, the heat transfer fluid was initially pre-cooled through an air-water heat exchanger where its temperature decreases close to ambient temperature. The fluid was then circulated through the ad-RCE circuit, where it was further cooled, and finally, it was used as the condenser heat sink. In the second mode of operation, the heating mode, the ad-RCE field was disconnected from the heat pump. During the day, the heat transfer fluid was circulated through the ad-RCE field, heating up the fluid, and directly supplying the DHW demand.

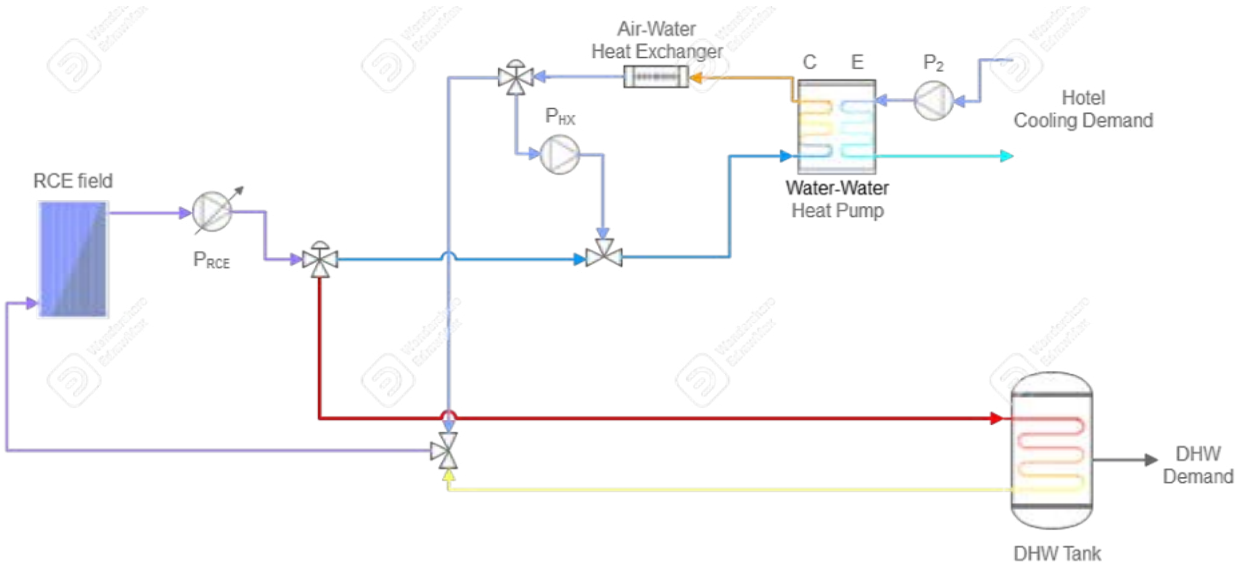

Figure 1. Conceptual scheme of the proposed configuration of an ad-RCE field with a water-to-water heat pump.

2.1.2. Reference case: water-to-water heat pump

The conventional cooling circuit, which employs a water-to-water heat pump, was used as the reference case to assess the improvement provided by the ad-RCE (**Figure 2**). The condenser side comprised a closed circuit with a single speed pump and an air-water heat exchanger. The heat transfer fluid was cooled down to temperatures close to ambient in the heat exchanger (5 ºC above the ambient), releasing the heat of condensation in the heat pump to the surrounding air.

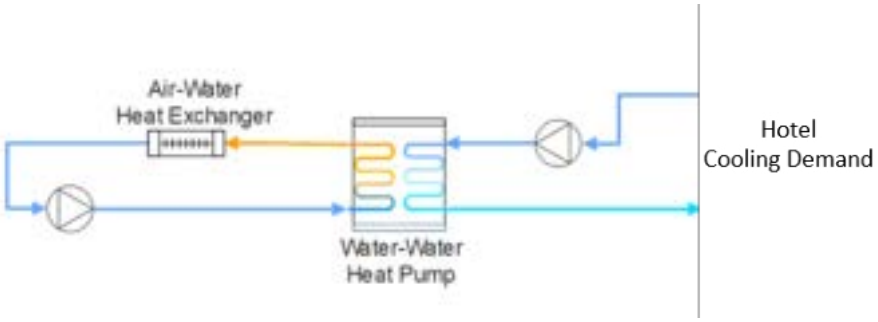

Figure 2. Conceptual scheme of the reference case of conventional water-to-water heat pump.

2.2. Building Load Demands and simulation condition

The studied facilities were designed to meet the load demand for cooling and DHW of a small hotel located in Brisbane (Australia). To determine the energy demands, numerical simulations were conducted using EnergyPlus software [33]. The building models used in the simulation were adapted from those published by the US Department of Energy (DOE). The small hotel consisted of a rectangular floor plant spanning 4 floors, with a net conditioning area of 4,013.6 m^2 and a roof area equivalent to 1,003.4 m^2 (**Figure *3***). The hotel's facades were oriented towards each of the four cardinal points, and the set point temperature was set at 25 ºC. Brisbane's climate is classified as Cfa in the Koppen-Geigger classification, which is characterized by relatively high temperatures and evenly distributed precipitation throughout the year.

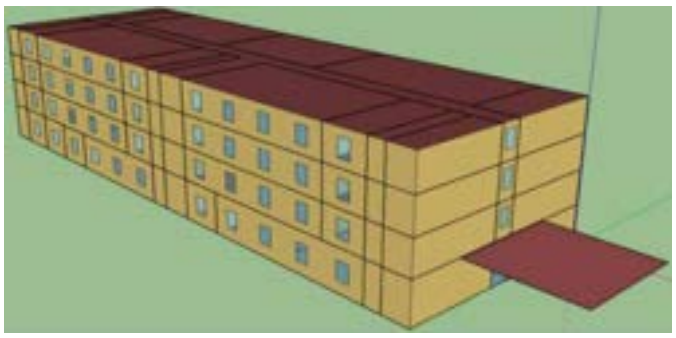

Figure 3. Small hotel simulated in EnergyPlus.

Prior to evaluate the integration of the heat pump system, an extensive energy analysis was conducted through a year-long numerical simulation to assess the building's energy requirements. Results were organized on a monthly basis. As shown in **Figure *4***, the cooling demand greatly surpasses the DHW demand in almost all the months, except for the months of June, July, and August in Brisbane, which is worth noting that are the winter months in Australia. January, December, and February have peak values of cooling demand, exceeding 30,000 kWh. In contrast, the DHW demand remained barely constant throughout the year, with an average of around 10,000 kWh per month. This finding emphasizes the importance of focusing on cooling demand in the design and implementation of the system.

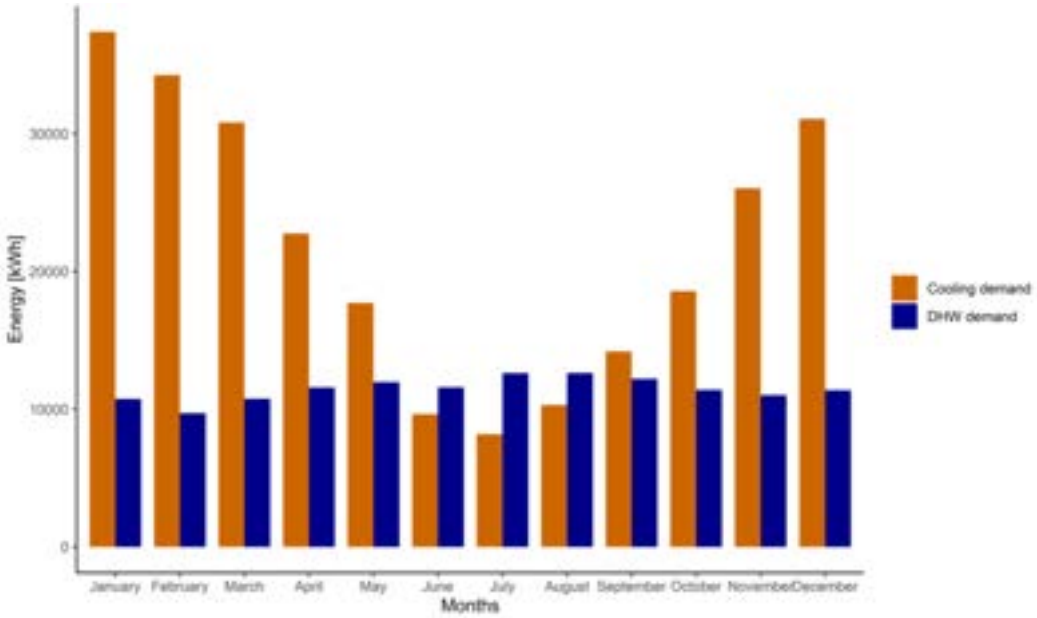

Figure 4. Yearly energy loads (cooling and DHW) in a small hotel in Brisbane.

2.3. Sizing

In the present study, an ad-RCE was considered which could switch its optical properties perfectly between each of the two modes. During the solar heating mode, the devices absorbed the totality of the incoming solar radiation while blocking the long-infrared radiation. During the radiative cooling mode, the device was able to reflect the totality of the incoming solar radiation, while perfectly emitting in the 7-14 μm range (atmospheric window). For the calculations, the following assumptions were also made:

- A steady-state model was used.
- The efficiency of the ad-RCE accounted for the conductive and convective losses.
- The tilt angle for the ad-RCE was assumed horizontal, maximizing the cold production.

The number of ad-RCE installed on the horizontal roof was determined by the required water flowrate for the case when the maximum cooling was demanded. 349 ad-RCE were used which corresponded to a total surface (A) of 698 m^2, representing 69.5% of the total roof area. All the months produced the required DHW from 11 a.m. to 12 a.m., except from April to September, when an additional hour was added (from 11 a.m. to 13 a.m.); the remaining hours were dedicated to radiative cooling mode.

The heat pump was sized so that its evaporator could match the peak value of the year demand, which corresponded to 93.9 kW. The flowrate for the RC mode was set to 5.84 kg·s^{-1}, while a lower flowrate of 4.17 kg/s was set for the solar heating mode. As both modes had different design parameters, the different flowrates were represented by a variable speed pump in the diagram.

2.4. Heating Mode

To determine the DHW production, the hourly Global Horizontal Irradiance (GHI) data was used along with the efficiency of the ad-RCE in solar collection mode, which is calculated using Eq. 1. This method of calculating solar collector efficiency is widely accepted and it takes into account various inefficiencies of the system, including optical and thermal losses. In line with previous research [15], an annual average efficiency η_{sc} of 0.6 was used in the calculations.

$$P_{solar,net}\left[\frac{W}{m^2}\right] = GHI \cdot \eta_{sc} \quad (1)$$

Once the average thermal power for each hour of the year was calculated, the next step was to determine the amount of energy produced. This was done by multiplying the average thermal power by the time step of 1 hour. To calculate the daily DHW production, the values obtained for each hour of the day were integrated over the course of a day. This allowed for a more accurate determination of the DHW production on a daily basis. The monthly production was then calculated by integrating the daily production values for a month. The formula used to calculate monthly production is presented in Eq. 2.

$$E_{solar,month}\left[\frac{Wh}{month}\right] = A \cdot \sum_{month} P_{solar,net} \cdot \Delta t \quad (2)$$

2.5. Cooling Mode

The maximum achievable RC power was determined using Eq. 3, which takes into account the infrared atmospheric radiation (Q_{atm}) and the absorbed radiation from the Sun (Q_{sun}) - both available in the weather data file- the radiation emitted on the surface of the ad-RCE (Q_s) – expressed in Eq.4., and the conductive and convective heat transfer. The approximation was made that the conductive and convective transfer were included in the efficiency parameter of the ad-RCE and therefore were assumed to be zero in Eq. 3. To determine the useful cooling power (Eq. 5), an efficiency of 60% was used.

$$Q_{net}[W] = [Q_s(T_s) - Q_{atm}(T_{atm}) - Q_{sun}(T_{sun}) - Q_{cond} - Q_{conv}] \cdot A \quad (3)$$

$$Q_s\left[\frac{W}{m^2}\right] = \varepsilon_s \sigma T^4 \quad (4)$$

$$P_{RC,net}[W] = Q_{net} \cdot \eta_{RC} \quad (5)$$

The temperature at the outlet of the ad-RCE (T_{out}) was calculated with the Eq. 6, where T_{in} represents the inlet temperature, $\dot{m}_{in}$ is the inlet flowrate and C_p is the water specific heat. The temperature at the inlet (T_{in}) was assumed to be equal to the pre-cooled temperature in the heat exchanger, which was set 5 ºC above the ambient temperature.

$$T_{out}[°C] = T_{in} - \frac{P_{RC,net}}{\dot{m}_{in} \cdot C_p} \quad (6)$$

A correlation was developed to model the performance of a water-to-water heat pump in TRNSYS. The correlation, expressed in Eq. 7, calculates the coefficient of performance (COP) of the heat pump as a function of the inlet temperature of the condenser (T_{cond}), assuming a constant evaporator temperature of 12 ºC.

$$COP = 7.45 - 0.116 \cdot T_{cond} - 0.00234 \cdot T_{cond}^2 + 0.0000852 \cdot T_{cond}^3 - 6.67 \cdot 10^{-7} \cdot T_{cond}^4 \quad (7)$$

The *COP* was calculated, for each time-step, both for the reference configuration and the ad-RCE+HP configuration. In the ad-RCE+HP configuration T_{cond} was set to be the same temperature as the outlet of the RCE (T_{out}). In the reference case, T_{cond} was assumed to be equal to the temperature at the outlet of the heat exchanger (5 ºC above the ambient temperature). The electrical energy of the compressor (E_{comp}) was determined using the energy supplied by the evaporator (E_{evap}, cooling demand) and the COP (Eq. 8).

$$E_{comp}[Wh] = \frac{E_{evap}}{COP} \quad (8)$$

3. Results and discussion

3.1. Heating Analysis

In **Figure *5***, the DHW production from the ad-RCE and the DHW demand of a small hotel are presented. As mentioned earlier, the DHW production is limited to two hours per day from April to September and one hour per day during the remaining months. On average, the system can produce 12,233 kWh of DHW per month. From April to September, the DHW production from the ad-RCE is higher than the hotel's demand. During the rest of the year, although the demand exceeds the potential production, the system has been sized to ensure a coverage of at least 80% of the demand, with actual coverage ranging from 85.25% to 95.52%.

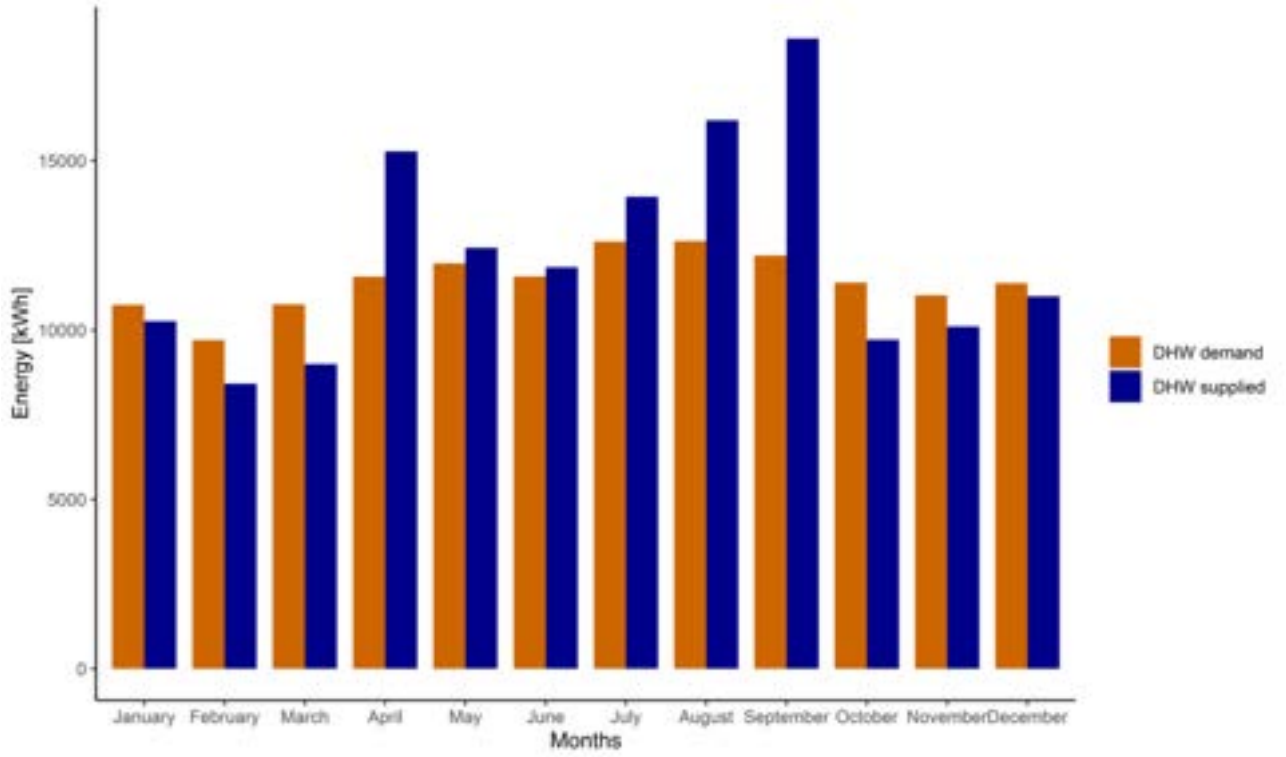

Figure 5. DHW energy loads in a small hotel in Brisbane and DHW produced in the ad-RCE.

3.2. Cooling Analysis

Through the implementation of radiative cooling, the average reduction in the temperature at the condenser inlet of the heat pump is found to be 1.4 ºC. The highest decrease is recorded in June with a value of 1.49 ºC, while the lowest reduction is observed in May, with a value of 1.31 ºC. A graphical representation of the monthly average temperature decrease at the condenser inlet is presented in **Figure *6***.

Additionally, the integration of the ad-RCE system with the heat pump leads to an increase in the yearly average coefficient of performance (COP) from 4.15 to 4.42 (**Figure *7***). The greatest improvements are observed during the winter months in Brisbane (**Figure *6.*** Temperature difference between inlet and outlet temperature in the ad-RCE over a year (orange) and improvement of the COP in the new configuration (blue). Cooling of water by more than 1.3 ºC is achieved in all the months.). The average increase in performance is 3.89%, with relatively constant values throughout the year ranging from 3.64% to 4.10%, as demonstrated in **Figure 6**.

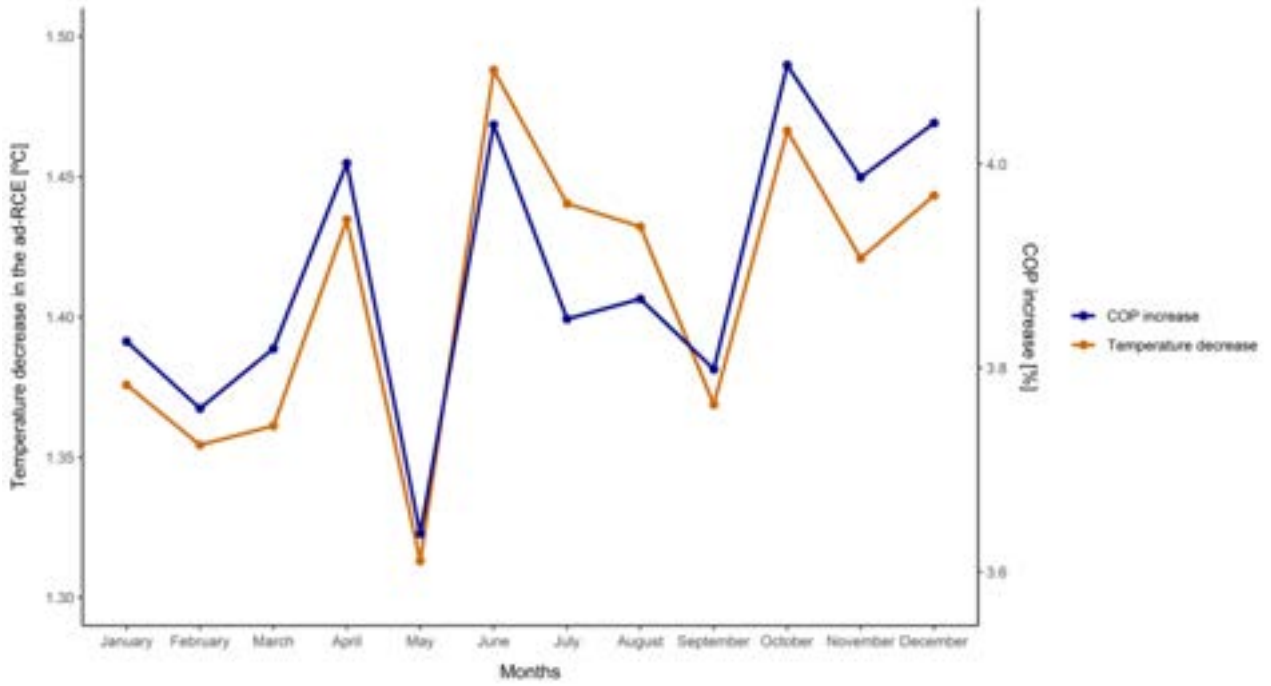

Figure 6. Temperature difference between inlet and outlet temperature in the ad-RCE over a year (orange) and improvement of the COP in the new configuration (blue). Cooling of water by more than 1.3 ºC is achieved in all the months.

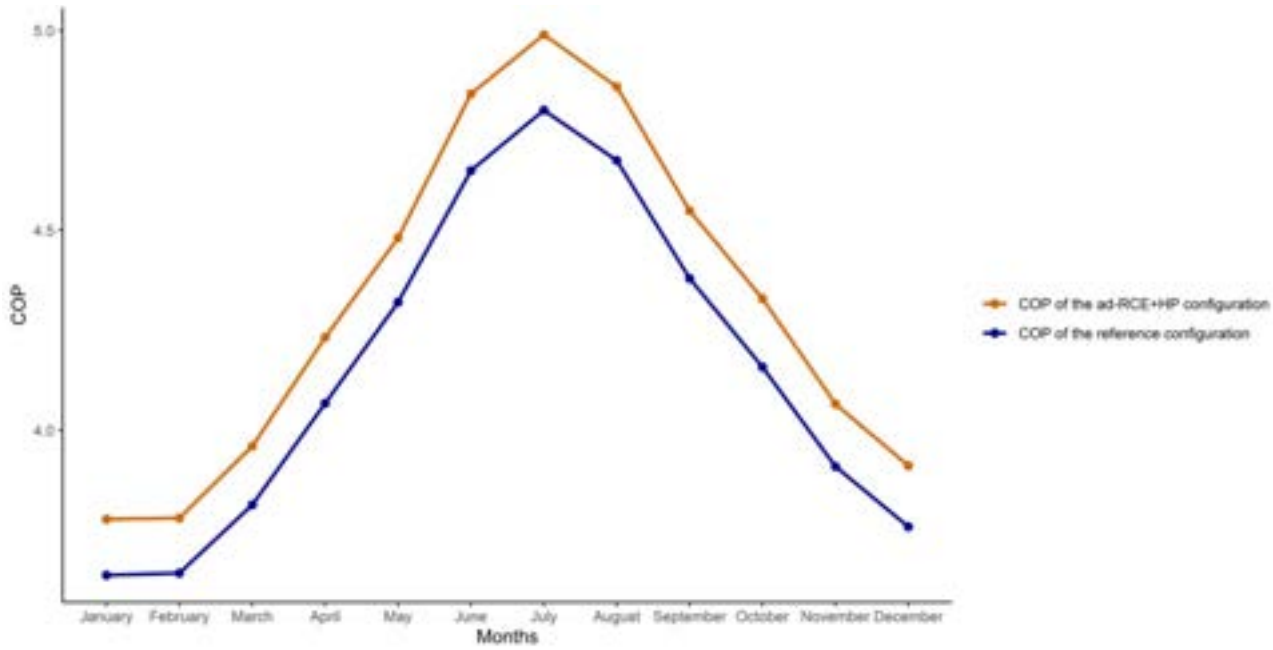

Figure 7. Evolution of the COP of the reference configuration and the studied configuration.

The integration of the ad-RCE with the heat pump system resulted in estimated total electricity savings of 2,533.3 kWh per year, which represents a reduction of 3.7%, the greatest savings are found during the summer months in Brisbane (**Figure *8***). This finding is consistent with literature reports which suggest that electricity consumption of a heat pump is reduced by approximately 3.5% for every degree Celsius reduction in the condenser's temperature [18]. In our study, the average reduction in the inlet temperature achieved with the ad-RCE is 1.4 ºC, resulting in a slightly lower condenser temperature. The monthly energy savings remained relatively constant throughout the year, ranging between 3.34% and 3.92%, which could contribute to a decrease in fossil fuel dependency of the system.

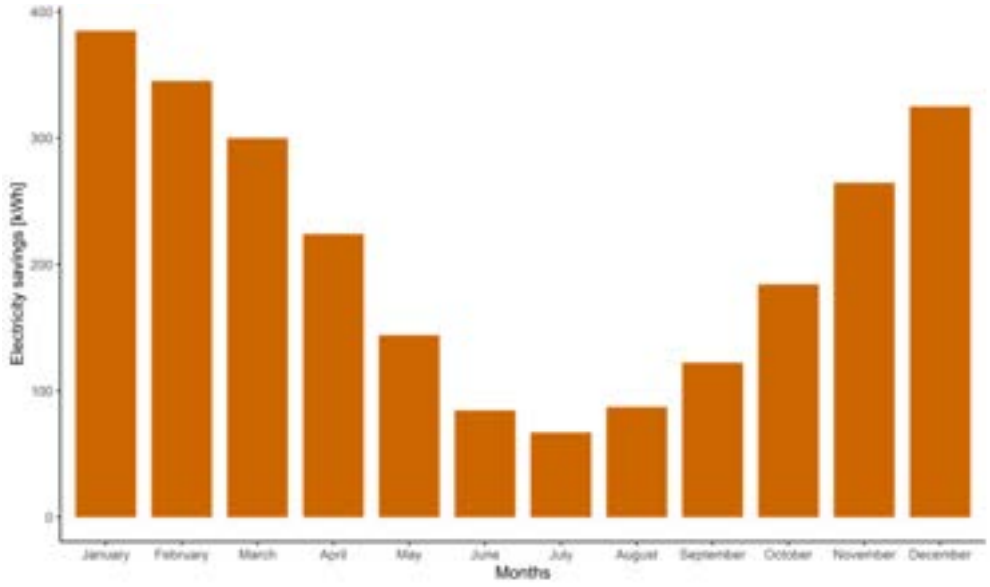

Figure 8. Electricity savings in the ad-RCE+HP configuration.

These results are preliminary estimates, and future work involves developing a validated ad-RCE model, similar to the RCE model previously developed [19] – and implementing effective control strategies to maximize energy savings. Additionally, a promising approach to improve energy savings would be to develop an efficient control system that anticipates the energy demand and operates the ad-RCE during optimal radiative cooling conditions. Another potential strategy is to integrate storage tanks, such as sensible heat water tanks and latent heat phase change materials tanks, to store the cold produced by the ad-RCE during favourable radiative cooling periods for later use during less favourable weather conditions. These strategies will be investigated in detail in the following stages of our research.

4. Conclusions

In this paper, we present a numerical analysis of the performance improvement of a water-to-water compression heat pump when combined with an adaptive Radiative Collector and Emitter (ad-RCE). The ad-RCE is an advancement of the Radiative Collector and Emitter (RCE), a device capable of producing hot water by solar thermal collection during the day and cold water by radiative cooling at night. The ad-RCE is a redesigned version of the RCE that offers users the option of selecting either daytime radiative cooling mode or solar collection mode, depending on the daily energy demands. By coupling the heat pump with the ad-RCE, higher COPs can be achieved compared to conventional heat pump reference systems. Our results demonstrate an average yearly COP improvement of 3.89% in a small hotel in Brisbane (Australia), leading to annual electricity savings of 3.70%.

Acknowledgments

This publication is part of the grant PID2021-126643OB-I00, funded by MCIN/ AEI/10.13039/501100011033/ and by “ERDF A way of making Europe”. This publication is also part of the grant PDC2022-133215-I00, funded by MCIN/ AEI/10.13039/501100011033/ and by the “European Union NextGenerationEU/PRTR”. The authors would like to thank Generalitat de Catalunya for the project awarded to their research group (2021 SGR 01370). Jesús Monterrubio would like to thank the University of Lleida for his “Introduction to research BIR 2022-2023” fellowship of collaboration with research groups. Mohammed Reda Haddouche would like to thank the project INVESTIGO-AGAUR for his postdoc funding.

Nomenclature

$\boldsymbol{A}$	Radiator/Absorber surface	(m^2)
$\boldsymbol{E_{solar,month}}$	Net monthly heating energy thanks to solar collection	(Wh/m^2/month)
$\boldsymbol{E_{cool,month}}$	Net monthly cooling energy thanks to RC	(Wh/m^2/month)
$\boldsymbol{Q_{atm}}$	Absorbed infrared radiation from atmosphere	(W)
$\boldsymbol{Q_{cond}}$	Conduction heat power	(W)
$\boldsymbol{Q_{conv}}$	Convective heat power	(W)
$\boldsymbol{Q_{net}}$	Net balance radiation power	(W)
$\boldsymbol{Q_s}$	Infrared radiation power emitted by a radiative surface	(W)
$\boldsymbol{Q_{sun}}$	Incident solar radiation power	(W)
$\boldsymbol{T_{atm}}$	Ambient and atmosphere temperature	(K)
$\boldsymbol{T_s}$	Surface temperature	(K)
$\boldsymbol{\sigma}$	Stefan-Boltzmann's constant: $5.6704 \cdot 10^{-8}$	($W/m^2 \cdot K^4$)
$\boldsymbol{\varepsilon_s}$	Surface emissivity	(-)

References

[1] Eurostat, «Energy consumption in households», maig 2019. https://ec.europa.eu/eurostat/statistics-explained/index.php?title=Energy_consumption_in_households#Use_of_energy_products_in_households_by_purpose

[2] S. Vall i A. Castell, «Radiative cooling as low-grade energy source: A literature review», *Renewable and Sustainable Energy Reviews*, vol. 77, p. 803-820, set. 2017, doi: 10.1016/j.rser.2017.04.010.

[3] B. Ko, D. Lee, T. Badloe, i J. Rho, «Metamaterial-Based Radiative Cooling: Towards Energy-Free All-Day Cooling», *Energies*, vol. 12, núm. 1, p. 89, des. 2018, doi: 10.3390/en12010089.

[4] G. N. Nwaji, C. A. Okoronkwo, N. V. Ogueke, i E. E. Anyanwu, «Hybrid Solar Water Heating/Nocturnal Radiation Cooling System I: A Review of the Progress, Prospects and Challenges», *Energy and Buildings*, p. S0378778818338179, juny 2019, doi: 10.1016/j.enbuild.2019.06.017.

[5] S. Catalanotti, V. Cuomo, G. Piro, D. Ruggi, V. Silvestrini, i G. Troise, «The radiative cooling of selective surfaces», *Solar Energy*, vol. 17, núm. 2, p. 83-89, 1975, doi: 10.1016/0038-092X(75)90062-6.

[6] S. Catalanotti, V. Cuomo, G. Piro, D. Ruggi, V. Silvestrini, i G. Troise, «The radiative cooling of selective surfaces», *Solar Energy*, vol. 17, núm. 2, p. 83-89, maig 1975, doi: 10.1016/0038-092X(75)90062-6.

[7] M. A. Kecebas, M. P. Menguc, A. Kosar, i K. Sendur, «Passive radiative cooling design with broadband optical thin-film filters», *Journal of Quantitative Spectroscopy and Radiative Transfer*, vol. 198, p. 179-186, set. 2017, doi: 10.1016/j.jqsrt.2017.03.046.

[8] J. Mandal *et al.*, «Hierarchically porous polymer coatings for highly efficient passive daytime radiative cooling», *Science*, vol. 362, núm. 6412, p. 315-319, oct. 2018, doi: 10.1126/science.aat9513.

[9] J.-W. Cho, T.-I. Lee, D.-S. Kim, K.-H. Park, Y.-S. Kim, i S.-K. Kim, «Visible to near-infrared thermal radiation from nanostructured tungsten anntennas», *J. Opt.*, vol. 20, núm. 9, p. 09LT01, ago. 2018, doi: 10.1088/2040-8986/aad708.

[10] A. P. Raman, M. A. Anoma, L. Zhu, E. Rephaeli, i S. Fan, «Passive radiative cooling below ambient air temperature under direct sunlight», *Nature*, vol. 515, núm. 7528, p. 540-544, nov. 2014, doi: 10.1038/nature13883.

[11] B. Ko, D. Lee, T. Badloe, i J. Rho, «Metamaterial-Based Radiative Cooling: Towards Energy-Free All-Day Cooling», *Energies*, vol. 12, núm. 1, p. 89, des. 2018, doi: 10.3390/en12010089.

[12] Y. Cui, X. Luo, F. Zhang, L. Sun, N. Jin, i W. Yang, «Progress of passive daytime radiative cooling technologies towards commercial applications», *Particuology*, vol. 67, p. 57-67, ago. 2022, doi: 10.1016/j.partic.2021.10.004.

[13] Y. Dong *et al.*, «A low-cost sustainable coating: Improving passive daytime radiative cooling performance using the spectral band complementarity method», *Renewable Energy*, vol. 192, p. 606-616, juny 2022, doi: 10.1016/j.renene.2022.04.093.

[14] S. Zhang *et al.*, «Full daytime sub-ambient radiative cooling film with high efficiency and low cost», *Renewable Energy*, vol. 194, p. 850-857, jul. 2022, doi: 10.1016/j.renene.2022.05.151.
[15] S. Vall, A. Castell, i M. Medrano, «Energy Savings Potential of a Novel Radiative Cooling and Solar Thermal Collection Concept in Buildings for Various World Climates», *Energy Technol.*, vol. 6, núm. 11, p. 2200-2209, nov. 2018, doi: 10.1002/ente.201800164.
[16] E. A. Goldstein, A. P. Raman, i S. Fan, «Sub-ambient non-evaporative fluid cooling with the sky», *Nature Energy*, vol. 2, núm. 9, p. 17143, set. 2017, doi: 10.1038/nenergy.2017.143.
[17] R. Vilà, M. Medrano, i A. Castell, «Numerical analysis of the combination of radiative collectors and emitters to improve the performance of water-water compression heat pumps under different climates», *Energy*, vol. 266, p. 126445, març 2023, doi: 10.1016/j.energy.2022.126445.
[18] T. Facius, «Benefits of Water Cooled vs Air Cooled Equipment in Air Conditioning Applications», *Cooling Technology Institute*, p. 50, 2011.
[19] S. Vall, K. Johannes, D. David, i A. Castell, «A new flat-plate radiative cooling and solar collector numerical model: Evaluation and metamodeling», *Energy*, vol. 202, p. 117750, jul. 2020, doi: 10.1016/j.energy.2020.117750.

Covering energy demands of buildings with an Adaptive Radiative Collector and Emitter (AD-RCE)

Jesús Monterrubio[a], Roger Vilà[a], Jonathan Cofré[a], Cristian Solé[a], Albert Castell[a], Ingrid Martorell[a*]

[a] Sustainable Energy, Machinery and Buildings (SEMB) Research Group, INSPIRES Research Centre, Universitat de Lleida, Pere de Cabrera s/n, 25001 Lleida, Spain,
ingrid.martorell@udl.cat

Abstract:

The building sector is one of the main consumers of energy, being the heating and cooling, as well as the Domestic Hot Water (DHW), the highest demands. The Radiative Collector and Emitter (RCE) is a renewable technology capable of providing both heating and cooling in a single device. This innovative technology reduces the dependency on fossil fuels, as well as diminishes the carbon footprint. An evolution of the RCE, the adaptive RCE (ad-RCE), which allows night-time radiative cooling and either daytime solar collection or daytime radiative cooling is presented for a single-family house in Johannesburg, South Africa. This new concept is capable to adapt its behaviour to the energy requirements, producing either heat or cold during daytime, as well as cold during night-time. Thus, the production of heat and cold adapts to the demands of the building. By means of numerical simulation, the relation between cooling and Domestic Hot Water (DHW) demands are compared with the renewable energy produced by the ad-RCE to determine the suitability of such technology to cover the energy demands of buildings by means of renewable energy. Results show that with a proper decision on the number of hours in solar collection mode and the rest for daytime or night-time radiative cooling, the ad-RCE field could yield to annual coverages of the cooling demand of 83% and of 100% for the DHW.

Keywords:

Radiative cooling, solar thermal collection, adaptive energy production, renewable energy, energy demand, single-family house.

1. Introduction

In the European Union, 40% of the final energy consumption and 36% of the CO_2 emissions are associated to the building sector [1]. The Eurostat [2] concludes that space heating represents 64.1% of the total consumption in buildings, Domestic Hot Water (DHW) 14.8%, and space cooling 0.4%. Although space cooling is a small fraction in the total energy consumption of households, [3] predicts that refrigeration demands will triple worldwide by 2050 if no action is taken. Today, the operating refrigeration systems account for 18.5% of the world's electricity consumption [4]. Most current cooling systems run on compression cooling cycles, consuming a lot of electricity, especially in the summer heat peaks. Typically, space heating and domestic hot water is produced by natural gas in households, whereas space cooling is all achieved by electricity consumption [5]. Both natural gas and non-renewable electricity production, contributes negatively to climate change and an alternative renewable production of these energy needs should be fostered.

The Radiative Collector and Emitter (RCE) is a renewable technology capable of providing both heating and cooling in a single device [6]–[8]. This innovative technology reduces the dependency on fossil fuels, as well as diminishes the carbon footprint. It combines in a single device the ability of solar collection during the day and radiative cooling (RC) during the night. Solar thermal collectors are a mature and commercially implemented technology to produce hot water from renewable energy. They rely on exposing an absorber to solar radiation to heat up a fluid circulating through different internal pipes [9]. On the other hand, radiative coolers are not mature yet. RC is the process by which a surface reduces its temperature by emitting thermal radiation (long wave) into the deep space, taking advantage of the transparency of the infrared atmospheric window at certain wavelengths (7-14 μm). The low effective temperature of the space makes it possible to cool down below ambient temperature [10]. Initially, RC was only possible at night, since the energy balance during the day resulted in gains due to solar radiation, but with the appearance of new materials it is also possible to

cool a surface during the day by RC [11], [12]. Several papers have been published recently proposing different types of materials for daytime radiative cooling (DRC), such as nanoparticles, metamaterials, bio-inspired materials, photonic structures, and hierarchically porous polymers [15]. However, these new materials do not allow to take advantage of solar energy during the day.

Vall et. al [6] showed how the RCE device could be integrated in several residential and commercial building types and in various cities located in different Köppen-Geiger climate classification regions over the world, covering most of the DHW usage. However, with the RCE surface sized for this DHW coverage, the covered fraction of the cooling demands was modest, being below 25% in 10 of the 15 climates studied. Besides, a not realistic 100 % efficiency for the radiative cooling mode was applied in this maximum cooling potential study, so even less cooling production and less coverage is expected for a real RCE prototype. The production of cooling could be increased mainly with two different strategies. On the one hand, the RCE efficiency should be substantially enhanced, as the achieved experimental values in a RCE prototype are only in the order of 25%, with peaks of 32%. This means that most of the cooling power generated in the RCE emitter is not used to cool down the circulating water but cools down the surrounding air and surfaces. On the other hand, the above mentioned daytime radiative cooling materials could be exploited, generating cold water also during the day. In summertime, when cooling is more necessary, DRC could reach a three-fold increase of the number of cooling hours.

An evolution of the RCE, the adaptive RCE (ad-RCE), which allows night-time radiative cooling and either daytime solar collection or daytime radiative cooling is presented in this study for one of the cities and one of the buildings used in [6]: a single-family house in Johannesburg (Africa). This new concept is capable to adapt its behaviour to the energy requirements, producing either heat or cold during daytime, as well as cold during night-time. Hence, this new equipment, which is still under development, avoids over-sizing the installation while maintaining high levels of energy coverage.

In this study, both the feasibility of the ad-RCE and the improvement it offers, compared to its predecessor, (RCE) is analysed. With this objective, this work presents a simple methodology to estimate the minimum operating hours of solar heating mode needed to cover DHW demands and for determining the hourly, daily and monthly production of heat and cold with the ad-RCE. As expected, the increase of cooling hours within a day thanks to daytime RC predicts a significant raise in annual cooling coverage, reducing the dependency on traditional CO_2 emitting cooling and heating systems.

2. Evolving the concept of RCE to ad-RCE

Figure 1 shows the conceptual differences between the original Radiative Collector and Emitter (RCE), which produces cold water during the night by radiative cooling and hot water during the day by solar thermal collection (Figure 1, a), and the evolution to the adaptive RCE (Figure 1, b) with a new design capable of producing both solar heating and radiative cooling at daytime, together with night-time radiative cooling. Thus, during the day the user can decide to apply it to heat up water or cool it down, adapting to variable energy demands of the building. The RCE concept has already been demonstrated experimentally with a prototype [7] and a model has been validated [8], whereas the ad-RCE is still under development. We aim to develop and validate a new ad-RCE model and to design, build and test a new ad-RCE prototype in the following 2 years.

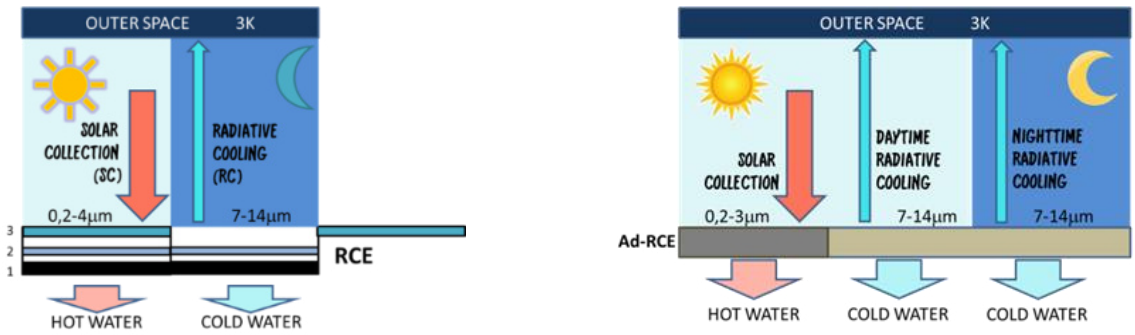

Figure. 1. Conceptual differences between the RCE (a) and the ad-RCE (b), which includes DRC.

3. Methodology

A simple steady state method was used to estimate the DHW and cooling production of the ad-RCE for a whole year in Johannesburg. The house energy demands were obtained from a whole-building energy simulation. Daily productions and demands were used to calculate the daily and monthly coverages of the ad-RCE.

3.1. Calculation of DHW and cooling building demands

Meteorological information for Johannesburg was obtained from the Meteonorm database [16], which corresponds with the radiation period 1991-2010 and the temperature period 2000-2009. The DHW and cooling demands for the simulated single-family house were obtained from the EnergyPlus building energy simulation software. The single-family house (Figure 2) is a template taken from the USA Department of Energy, DOE [17]. It consists of a two-floor, pitched gabled roof, detached house with a net conditioned area of 223.1 m^2. The original house model was modified to include additional active and passive strategies such as set point temperature schedules at 25ºC, summer night ventilation and overhangs. The same procedure as the presented in [6] was followed.

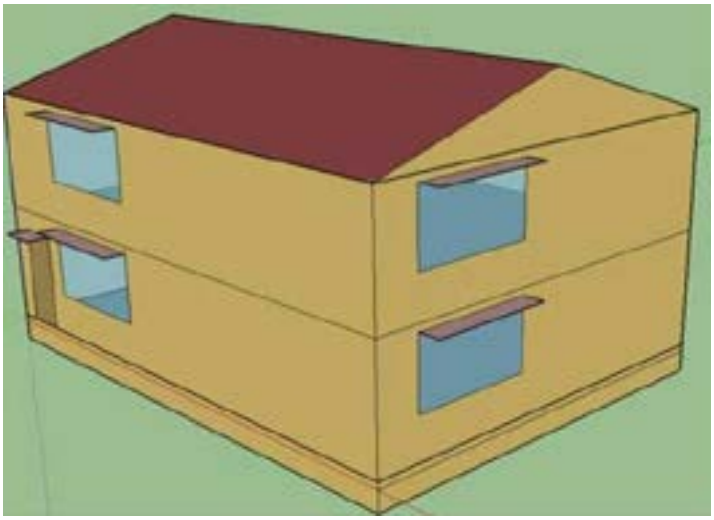

Figure. 2. Simulated single-family house in Johannesburg.

3.2. ad-RCE production

A very similar procedure to the one explained in [6] has been applied in this paper. A summary of the assumptions for the production of DHW and cooling, used both in [6] and in this work, is presented as follows:

- Steady state model.
- Conductive and convective losses are included in the ad-RCE efficiencies.
- Tilt angle for the ad-RCE is assumed horizontal, for maximum production of cooling.
- Wind-shield cover for solar collection mode with 100% transmittance in solar spectrum and 0% transmittance in the thermal spectrum is considered.

Contrary to the previous work, the daytime RC capability of the ad-RCE forces the wind-shield cover in DRC mode to have 100% reflectivity in solar spectrum and 100% transmittance in the thermal spectrum.

The DHW production thanks to solar collection was determined considering the hourly Global Horizontal Irradiance (GHI) given in the data file and the RCE efficiency in solar collection mode (Eq. 1). The solar collector efficiency is a common methodology and considers in a single parameter all the inefficiencies of the system (solar collector efficiency, losses due to inclination and shadows, etc.). The same annual average efficiency η_{sc} of 0.6 used in [6] was applied in this work for the solar collection calculations.

$$P_{solar,net}\left[\frac{W}{m^2}\right] = GHI \cdot \eta_{sc} \quad (1)$$

The average thermal power calculated for each hour of the year is then converted into energy produced simply multiplying by the time step (1 hour). The integration of these values along a day will determine the daily DHW production and along a month, the monthly production. Eq. 2 presents the calculation of this monthly production:

$$E_{solar,month}\left[\frac{Wh}{m^2 \cdot month}\right] = \sum_{month} P_{solar,net} \cdot \Delta t \quad (2)$$

The assumed efficiency for cooling production by daytime and night-time RC in the ad-RCE is also 60%. The justification for this value is that it is expected that the achieved 32% efficiency in the first prototype could be improved with better design that reduces the heat gains by conduction and convection to the emitter. This RC efficiency η_{RC} is defined as the cooling power achieved by the circulating water and the maximum cooling power achieved on the surface of the radiative cooler. This maximum cooling power can be calculated as an energy balance on the radiative surface, as presented in Eq. 3 and in Figure 3:

$$Q_{net} = Q_s(T_s) - Q_{atm}(T_{atm}) - Q_{sun}(T_{sun}) - Q_{cond} - Q_{conv} \quad (3)$$

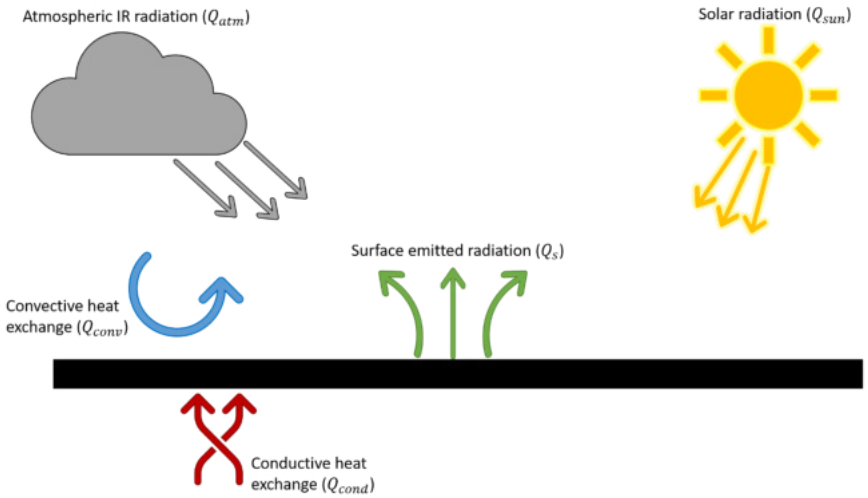

Figure. 3. Scheme of the thermal exchanges between the radiative surface (black) and its surroundings.

For this calculation, heat gains/losses by conduction Q_{cond} and convection Q_{conv}, are taken as 0. The infrared radiation coming down from the atmosphere Q_{atm} and the absorbed radiation from the Sun Q_{sun} are direct readings from the weather file, as the absorptivity of the surface is assumed equal to 1 in this study.

The amount of energy emitted from a surface with an average emissivity ε_s (in this study equal to 1) is given by Eq. 4.

$$Q_s = \varepsilon_s \sigma T^4 \quad (4)$$

Eq. 5 gives the useful cooling power given to the water, as the product of Q_{net} and the RC efficiency η_{RC}:

$$P_{RC,net}\left[\frac{W}{m^2}\right] = Q_{net} \cdot \eta_{RC} \quad (5)$$

The integration of the $P_{RC,net}$ values along a day will give us the daily cooling production and along a month, the monthly production. Eq. 6 presents the calculation of this monthly production:

$$E_{cool,month}\left[\frac{Wh}{m^2 \cdot month}\right] = \sum_{month} P_{RC,net} \cdot \Delta t \quad (6)$$

The energy coverage is calculated as the ratio between the cooling or heating energy produced in a day divided by the daily demand. If this ratio is over 1 (or 100% in percentage), we take a coverage percentage of 100% for that day. When there is an excess of daily energy production, this excess is lost; it is not used in the following days. The monthly coverage is the average of the daily coverage. Note that this simplified approach, without considering energy storage tanks, is underestimating the potential maximum coverage. So, we are on the safe side of the coverage predictions. A correctly designed thermal energy storage system would slightly raise the coverage figures presented next in the results section.

All the meteorological data processing, all the above hourly calculations and the daily and monthly integrations are carried out with the Rstudio, version 1.3R.

3.2. ad-RCE sizing

A similar approach as the one proposed in [6] is followed in this work. Indivisible units of 2 m^2 are assumed for the ad-RCE and the number of ad-RCE installed on the roof should cover at least 75% of the DHW demands. In the case of Johannesburg, the RCE sizing resulted in 4 m^2 of surface area and 2 units of RCE, with 2 m^2 each [6]. Thus, in this study, 2 ad-RCEs of the same area used. However, an additional degree of freedom is available with the ad-RCE that was not present in the traditional RCE [6]. The number of solar collection hours during the day can be reduced while increasing the RC hours. Starting at 11.00 h, we have increased the number of hours of solar collection (and decreased the RC hours) until all the months had at least 80% DHW coverage with the ad-RCE. In this case study, running in solar heating mode from 11.00 h to 17.00 h is enough for the target DHW coverage for all the months, but May, June and July (winter months in Johannesburg), which need 12 h of solar heating instead of 6 h, from 7.00 to 19.00 h. The remaining 18 h (12 h for the latter three months) of the day are dedicated to RC, both in daytime and nighttime, increasing the cooling production with respect to pure night RC.

3. Results and discussion

Figure 4 shows the comparison of the DHW monthly demand with the ad-RCE monthly hot water energy production over one year in the selected single-family house in Johannesburg. As explained in the previous section, the DHW production is realized only during 6 hours with high insolation, in the middle of the day, from 11.00 h to 17.00 h (12 hours for May, June and July). The rest of the time the ad-RCE works in RC mode, producing cold water both at daytime and night-time thanks to the use of advanced daytime radiative cooling materials. The fine-tuned optical properties of these materials make them capable of reflecting barely all sunlight and emitting, almost as a black body, to the deep space. In most of the months, the monthly supplied DHW production surpasses the monthly demands, with the only exception of April, July and August, where the fraction of demand not supplied by the ad-RCE is small (in the range 1-10%). DHW demands are relatively constant in the house, ranging from 250 and 315 kWh/month. The expected increase in DHW demand in winter months due to the lower water grid temperatures is compensated by the above-mentioned increase in the number of hours in solar mode. Adding up the monthly demands and productions of DHW and making the ratio, the annual coverage reaches 108%. However, this coverage is an upper limit for the actual coverage as a non-realistic, large DHW tank, would be necessary to store all the excess heat that is not used in a particular day.

Regarding the cooling demand and supply, Figure 5 presents the cooling covered by the ad-RCE each month of the year. For months with modest, or almost inexistent cooling needs, the ad-RCE cooling generation clearly exceeds the demands. On the other hand, in the months with the highest cooling demands (January, February, March, November and December), the ad-RCEs cooling productions are well below the house cooling needs, being the monthly productions between 26 and 60% of the monthly demands. Adding up the monthly demands and productions of cooling and making the ratio, the annual coverage reaches 83%. The 37% yearly cooling coverage obtained in [6] for the same single-family house in Johannesburg with normal RCEs is clearly surpassed with the same surface of ad-RCEs. This is achieved due to the extra hours of DRC offered by the ad-RCE. However, more surface of ad-RCEs should be necessary if a higher percentage of RC fraction is targeted for the hot summer months.

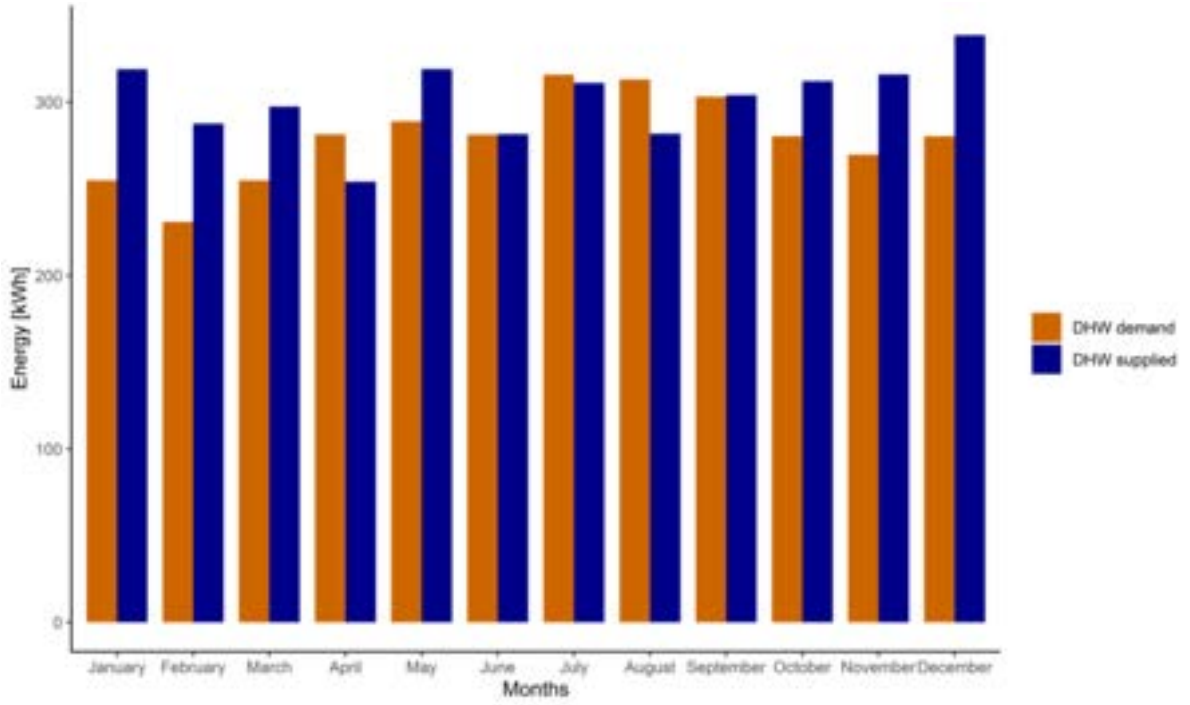

Figure. 4. Comparison of monthly DHW demand versus RCE DHW production.

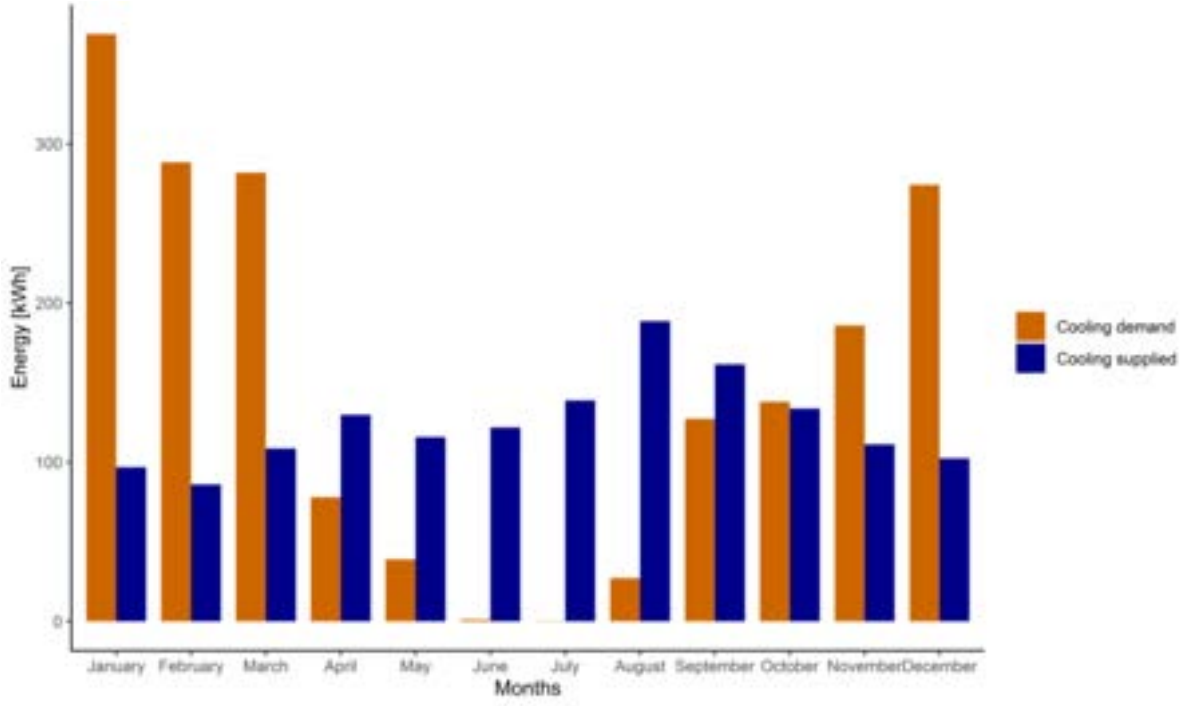

Figure. 5. Comparison of monthly cooling demand versus RCE cooling production.

It is important to note that these comparisons of Figure 4 and Figure 5 of annual demands over annual productions are overestimating the real coverage because we are assuming that any excess production of one day can be used in the following days of the month. Next, we will compare the monthly coverages as the average of the daily coverages, which is the lower end of the estimation, as the excess production of one day is not used in the following days of the month. In a real situation, with DHW and cooling storage tanks, the actual monthly coverage should be between these two extreme values.

The monthly energy coverage for both DHW and cooling is shown in Figure 6. These coverages are calculated as the average of the daily coverages. DHW coverages lie in the range 83-94%, meaning that, even in the sunny summer months, there may be some cloudy days when the DHW demand is not reached. As for the

cooling, the coverages are above 90% in the central cold months (May, June, July and August) and it goes down to 32 % for February, the month with the lowest cooling coverage. Note that an easy strategy to increase the cooling coverage in summer months, without increasing the ad-RCE total surface, may be the reduction of the number of hours in solar collection mode, sacrificing in that way the DHW coverage. Nevertheless, it is out of the scope of this study the optimization of the number of operating hours per day to minimize the house operating costs and/or the environmental impacts of the consumed energy.

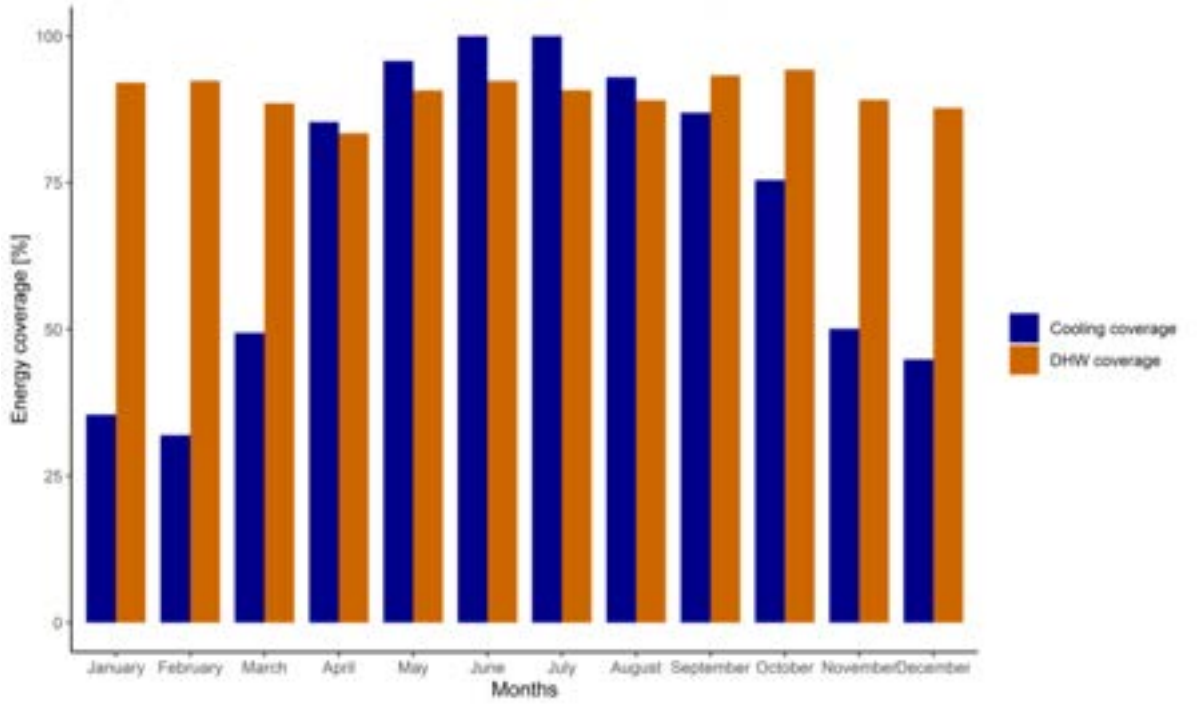

Figure. 6. DHW and cooling coverage of demands achieved by the ad-RCE.

Figure 7 illustrates the substantial increase in cooling coverage thanks to the substitution of normal RCEs by new ad-RCEs. In the hottest months of the year in Johannesburg, where the cooling is more needed, the growth in cooling production is in the range of 65-70%. This implies an increase in cooling coverage between 36 and 56%. These increases could even be higher for locations in the world where the difference of daily and night hours in summer are more pronounced than in Johannesburg.

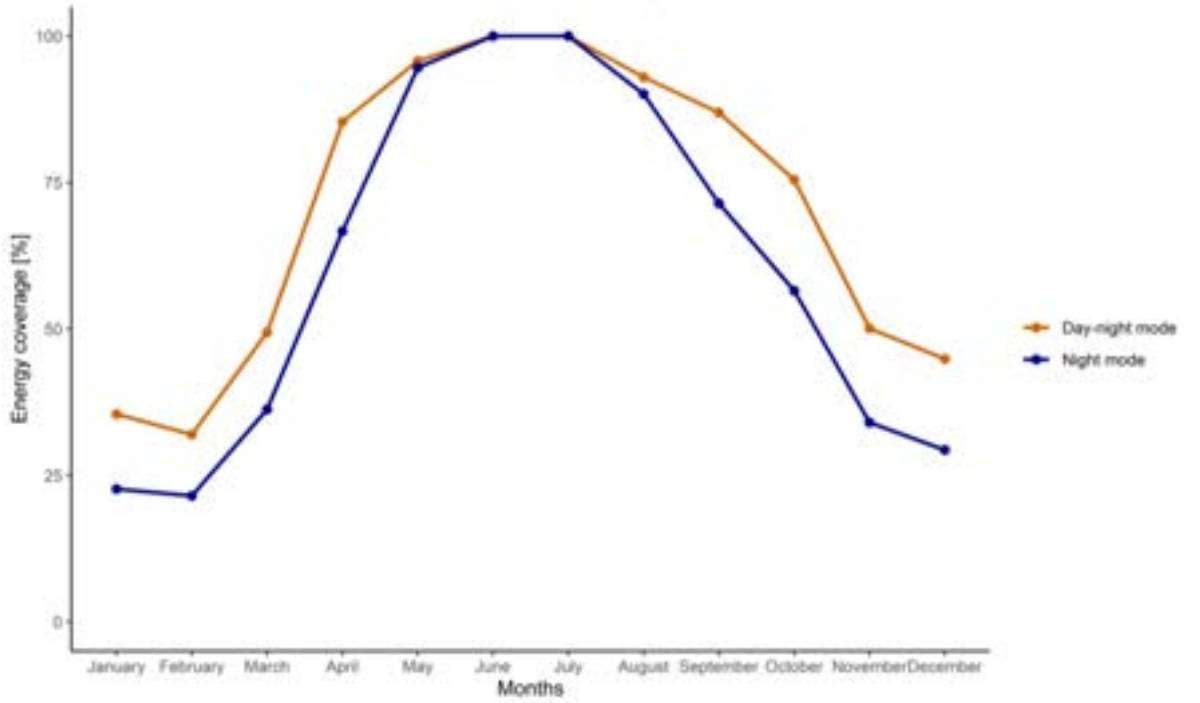

Figure. 7. Cooling coverage of ad-RCE with DRC and NRC, and normal RCE with only NRC.

4. Conclusions

In this study a new renewable energy device, the ad-RCE, is presented. The ad-RCE is an evolution of the Radiative Collector and Emitter (RCE), which is a single device able to produce cold water by radiative cooling at night and hot water by solar thermal collection at daytime. The ad-RCE is a new redesign of the RCE that enables the user to choose between daytime radiative cooling mode and solar collection mode, depending on the daily demands. The new ad-RCE is integrated in a house in Johannesburg, South Africa, to analyse the level of DHW and cooling monthly coverages for the house. Energy plus is used to calculate the DHW and cooling demands of the house and R studio is applied for the dynamic hourly simulation of the ad-RCE. The increased hours of radiative cooling in daytime enables a better match between the demand and production of cooling, increasing the annual production by 66%, while keeping the DHW coverage above 80%.

Acknowledgments

This publication is part of the grant PID2021-126643OB-I00, funded by MCIN/ AEI/10.13039/501100011033/ and by "ERDF A way of making Europe". This publication is also part of the grant PDC2022-133215-I00, funded by MCIN/ AEI/10.13039/501100011033/ and by the "European Union NextGenerationEU/PRTR". The authors would like to thank Generalitat de Catalunya for the project awarded to their research group (2021 SGR 01370). Jesús Monterrubio would like to thank the University of Lleida for his "Introduction to research BIR 2022-2023" fellowship of collaboration with research groups.

Nomenclature

$\boldsymbol{A}$	Radiator/Absorber surface	(m^2)
$\boldsymbol{E_{solar,month}}$	Net monthly heating energy thanks to solar collection	(Wh/m^2/month)
$\boldsymbol{E_{cool,month}}$	Net monthly cooling energy thanks to RC	(Wh/m^2/month)
$\boldsymbol{Q_{atm}}$	Absorbed infrared radiation from atmosphere	(W/m^2)
$\boldsymbol{Q_{cond}}$	Conduction heat power	(W/m^2)
$\boldsymbol{Q_{conv}}$	Convective heat power	(W/m^2)
$\boldsymbol{Q_{net}}$	Net balance radiation power	(W/m^2)
$\boldsymbol{Q_s}$	Infrared radiation power emitted by a radiative surface	(W/m^2)
$\boldsymbol{Q_{sun}}$	Incident solar radiation power	(W/m^2)
$\boldsymbol{T_{atm}}$	Ambient and atmosphere temperature	(K)
$\boldsymbol{T_s}$	Surface temperature	(K)
$\boldsymbol{\sigma}$	Stefan-Boltzmann's constant: $5.6704 \cdot 10^{-8}$	($W/m^2 \cdot K^4$)
$\boldsymbol{\varepsilon_s}$	Surface emissivity	(-)

References

[1] 'Directive (EU) 2018/ of the European Parliament and of the Council of 30 May 2018 amending Directive 2010/31/EU on the energy performance of buildings and Directive 2012/27/EU on energy efficiency', p. 17.

[2] Eurostat, 'Energy consumption in households', May 2019. https://ec.europa.eu/eurostat/statistics-explained/index.php?title=Energy_consumption_in_households#Use_of_energy_products_in_households_by_purpose

[3] 'The Future of Cooling. Opportunities for energy-efficient air-conditioning', IEA, 2018.

[4] Consejo de la Unión Europea, *Project Europe 2030: challenges and opportunities: a report to the European Council by the Reflection Group on the Future of the EU 2030*. Luxemburg: Publications Office of the European Union, 2010.

[5] 'Commission Recommendation (EU) 2019/786 of 8 May 2019 on building renovation (notified under document C(2019) 3352) (Text with EEA relevance.) (OJ L 127 16.05.2019, p. 34.' [Online]. Available: http://data.europa.eu/eli/reco/2019/786/oj)

[6] S. Vall, A. Castell, and M. Medrano, 'Energy Savings Potential of a Novel Radiative Cooling and Solar Thermal Collection Concept in Buildings for Various World Climates', *Energy Technol.*, vol. 6, no. 11, pp. 2200–2209, Nov. 2018, doi: 10.1002/ente.201800164.

[7] S. Vall, M. Medrano, C. Solé, and A. Castell, 'Combined Radiative Cooling and Solar Thermal Collection: Experimental Proof of Concept', *Energies*, vol. 13, no. 4, p. 893, Feb. 2020, doi: 10.3390/en13040893.

[8] S. Vall, K. Johannes, D. David, and A. Castell, 'A new flat-plate radiative cooling and solar collector numerical model: Evaluation and metamodeling', *Energy*, vol. 202, p. 117750, Jul. 2020, doi: 10.1016/j.energy.2020.117750.

[9] S. A. Sakhaei and M. S. Valipour, 'Performance enhancement analysis of The flat plate collectors: A comprehensive review', *Renewable and Sustainable Energy Reviews*, vol. 102, pp. 186–204, Mar. 2019, doi: 10.1016/j.rser.2018.11.014.

[10] S. Catalanotti, V. Cuomo, G. Piro, D. Ruggi, V. Silvestrini, and G. Troise, 'The radiative cooling of selective surfaces', *Solar Energy*, vol. 17, no. 2, pp. 83–89, 1975, doi: 10.1016/0038-092X(75)90062-6.

[11] A. P. Raman, M. A. Anoma, L. Zhu, E. Rephaeli, and S. Fan, 'Passive radiative cooling below ambient air temperature under direct sunlight', *Nature*, vol. 515, no. 7528, pp. 540–544, Nov. 2014, doi: 10.1038/nature13883.

[12] Y. Zhai *et al.*, 'Scalable-manufactured randomized glass-polymer hybrid metamaterial for daytime radiative cooling', *Science*, vol. 355, no. 6329, pp. 1062–1066, Mar. 2017, doi: 10.1126/science.aai7899.

[13] X. Wang *et al.*, 'Scalable Flexible Hybrid Membranes with Photonic Structures for Daytime Radiative Cooling', *Adv. Funct. Mater.*, p. 1907562, Nov. 2019, doi: 10.1002/adfm.201907562.

[14] H. Ma *et al.*, 'Multilayered SiO2/Si3N4 photonic emitter to achieve high-performance all-day radiative cooling', *Solar Energy Materials and Solar Cells*, vol. 212, p. 110584, Aug. 2020, doi: 10.1016/j.solmat.2020.110584.

[15] X. Yu, J. Chan, and C. Chen, 'Review of radiative cooling materials: Performance evaluation and design approaches', *Nano Energy*, vol. 88, p. 106259, Oct. 2021, doi: 10.1016/j.nanoen.2021.106259.

[16] J. Remund, S. Müller, S. Kunz, B. Huguenin-Landl, C. Studer, and R. Cattin, 'Meteonorm'. Meteotest, Switzerland, Jul. 23, 2019. [Windows Vista/7/8/10 32/64 bit]. Available: https://meteonorm.com/en/download

[17] 'Prototype Building Models | Building Energy Codes Program'. https://www.energycodes.gov/prototype-building-models#Commercial (accessed Mar. 10, 2023).

TECHNICAL ECONOMIC STUDY: A Collective Photovoltaic Installation

Daniela Contreras Uribe [a], Luis Mazorra Aguiar [b], Eduardo Vega Fuentes [c]

[a] University of Las Palmas de Gran Canaria, Las Palmas de Gran Canaria, Spain, danielacuribe2.0@gmail.com
[b] University Institute for Intelligent Systems and Numerical Applications in Engineering. Department of Electrical Engineering, University of Las Palmas de Gran Canaria, Spain, luis.mazorra@ulpgc.es
[c] University of Las Palmas de Gran Canaria, Las Palmas de Gran Canaria, Spain, danielacuribe2.0@gmail.com

Abstract:

Since the recognition of self-consumption in Spain in 2019, self-consumption photovoltaic installations have experienced significant growth. This fact, together with a rise in energy prices, has allowed the development of both individual and collective distributed photovoltaic generation. Collective installations allow several consumers to benefit from a single photovoltaic installation. The use of dynamic distribution coefficients of the photovoltaic energy among the different consumers for each hour of the period is allowed and can be determined according to the criteria considered most appropriate by the participants. This article makes a technical and economic study of a photovoltaic installation for collective self-consumption of a group of houses located in Tafira - Gran Canaria, with different possibilities of photovoltaic energy distribution coefficients, both fixed and dynamic, to study the profitability of the different energy distribution and optimize the energy distribution, taking into account the different consumption curves and electricity contracts of each of the consumers. Eight cases of energy sharing are studied, the most characteristic and with which the best results are the cases with coefficients based on previous consumptions and current consumptions (in situ).

Keywords:

Shared Self-Consumption, Photovoltaic Energy, Renewable Energy.

1. Introduction

The Canary Islands are rich in natural resources, especially the wind and sun. The Canary Islands has abundant hours of light that allow the production of a photovoltaic panel installation to be much higher than in other areas, photovoltaic energy in the Canary Islands is an opportunity for the economy since, the installations of photovoltaic panels in hotels or other establishments provide savings and companies can offer more competitive prices.

Anthony Roy [1], Jean-Christophe Olivier, François Auger [1], Bruno Auvity [1], Salvy Bourguet [1], and Emmanuel Schaeffer [1] mention that collective self-consumption is especially useful in places that lack lands such as the Canary Islands, the Balearic Islands, large cities such as Madrid and Barcelona, or industrial estates. Thanks to this mode of self-consumption, consumers can benefit from a shared investment, which means that many consumers can have clean electricity at an affordable price. On the other hand, with collective self-consumption, you can obtain savings of up to 70% in the electricity bill, and reduce greenhouse gas emissions, and emissions of polluting gases, therefore, the carbon footprint of consumers. In addition, this type of facility will allow us to move towards a market of real flexibility, cleaner, decentralized, and less dependent on fossil fuels.

The collective self-consumption of photovoltaic solar energy has great advantages for the consumer, however, there are many unknowns when executing a project of this type. For example, the calculation and allocation of the distribution coefficient β among final consumers, which represents the proportion of the net energy generated that corresponds to each consumer.

On April 5, 2019, Royal Decree 244/2019 was approved, which regulates electricity self-consumption in Spain. This Royal Decree recognized collective self-consumption for the first time [2]. This change in the regulations allows several people to join and consume from the same generation plant. Royal Decree 244/2019 provides for the existence of coefficients to distribute energy in collective self-consumption. The value of these partition coefficients depends on the agreement between the participants, with the only requirement that they be constant values. These criteria and coefficients must be included in the agreement between the participants

and each consumer must send to the distributor or through its marketing company. The annex I of Royal Decree 244/2019, of April 5, establishes that: [2]

"The value of these coefficients may be determined according to the power to be billed by each of the participating associated consumers, the economic contribution of each of the consumers for the generation facility, or any other criterion provided that there is an agreement signed by all the participants and provided that the sum of these coefficients β i of all consumers who participate in collective self-consumption is the unit. In any case, the value of these coefficients must be constant" In addition, on November 15, 2021, Annex I was modified, which allows each participant to have a dynamic energy distribution coefficient under any criterion, as long as all consumers agree.

Villalonga [3], Serrano [3], Riquellme [3], Alvarez [3] and Roldan [3] mention that despite the fact that this normative represents ¨an advance over the previous regulatory framework, this new regulation introduces a series of inefficiencies with respect to the criteria for sharing the energy produced by the collective generation system. These inefficiencies are associated with an economic cost for the members of the collective self-consumption community, which to a certain extent may discourage its deployment, with the consequent negative impact on the development of renewable energies and the achievement of climate objectives´´.

That said, taking into account Royal Decree 244/2019 and order TED/1247/2021 [4] , an analysis is carried out to determine the different benefits that can be obtained with permanent and dynamic energy distribution coefficients for the case of collective self-consumption of 15 homes located on the Island of Gran Canaria (Spain). Using these homes, the economic viability and benefits of each of the dwellings obtained from different methods of distributing the PV energy generated will be analysed.

2. Methodology:

In this work, a technical economic study of a photovoltaic installation for collective self-consumption in a housing development with 15 houses located in Tafira - Las Palmas De Gran Canaria (Spain) is carried out.

For this study, 2 main scenarios have been considered. The first scenario assumes that the neighbours decide to invest in a self-consumption installation individually. Each one contracts the same installation company. In turn, as it is individual self-consumption, each house will have its own single-phase inverter and photovoltaic panels.

The second scenario is collective self-consumption, in which all the neighbours make a joint investment in photovoltaic solar panels and a connection inverter for all the installed power. Making a joint investment could reduce costs since the purchase and installation is cheaper the larger the investment.

In order to carry out this work, a series of steps were followed. First, we obtained the actual consumption of the fifteen houses, hour by hour during the period of one year. After this, we studied the consumption profiles, from which we obtained the percentage of consumption in hours of sunshine, the houses with the highest percentage will take more advantage of the energy produced by the photovoltaic panels.

In each of the houses, we chose to study their annual energy consumption and the availability of the roofs to estimate the peak power installed in the individual case. In the case of collective installation, an identical installation was simulated for each house. In order to study the electricity generation obtained in each installation, the photovoltaic production is estimated based on the solar radiation of the area. Table 1 shows the peak power that would correspond to each house according to the annual energy consumption, both for the individual case and the cases of collective self-consumption.

Table 1. Summary peak power to be installed in each home in the case of individual and collective self-consumption.

House N.º	Consumption Annual (kWh/year)	Hsp	P. Peak individual (kW)	P. Peak Collective (kW)
House 1	9948	2025	5.46	3.51
House 2	6000,6	2025	3.51	3.51
House 3	5397	2025	3.12	3.51
House 4	4599	2025	2.8	3.51
House 5	5610	2025	3.12	3.51
House 6	3361	2025	2.34	3.51
House 7	7970	2025	4.68	3.51
House 8	5610	2025	3.12	3.51
House 9	5610	2025	3.12	3.51
House 10	3361	2025	2.34	3.51
House 11	9948	2025	5.46	3.51
House 12	4599	2025	2.8	3.51
House 13	5610	2025	3.12	3.51
House 14	5610	2025	3.12	3.51
House 15	5610	2025	3.12	3.51
Total consumption	88844		51.23	52.65

Once the peak photovoltaic power for each case study has been estimated, we use the data obtained in the weather stations installed by the University of Las Palmas de Gran Canaria in the city of Las Palmas. From these data, the electrical energy produced using the described model is calculated. [5] [6] [7]

On the other hand, the different types of electricity billing that the owners had, according to the electricity market, which can be free market or regulated market (PVPC) were studied. The difference between these two markets is that the free market allows having a constant energy price during the contracting period, while in the regulated market the price of electricity changes hour by hour and day by day according to the supply and demand between the producers and marketers. In addition, the compensation price of surpluses also depends on the type of contract of the owner, in the same way as the purchase price of energy.

For the calculations, the data for the purchase and sale of electricity in the regulated market were obtained from the Sistema De Información Del Operador Del Sistema (eSios) website [7], while for the free market, a fixed purchase price of 0.16 €/kWh and a fixed sale price of 0.06 €/kWh were established. Once all these data were obtained for each of the homes, different cases of coefficients of distribution of energy generated by collective self-consumption were studied. From these coefficients, the calculations of the net energy balance were made in each hour, surplus (€) and network consumption (€) with which we will study the profitability of the installation in each case. In addition, other terms of the electricity bill such as power or electricity tax were studied, in order to make an approximate calculation of the price of this for each home in order to determine the savings in the electricity bill. In order to decide the best installation in each case, budgets were made, the economic feasibility study (NPV) and the results obtained were analyzed.

3. Cases of study

According to [2] "the net hourly energy generated individualized of those subjects 'i' that carry out collective or consumer self-consumption associated with a nearby installation through the network, ENG h, 'i' it Will be:

$$\boldsymbol{ENGh, i = \beta i . ENGh}$$

$ENGh$: total net hourly energy produced by the generator(s).

βi: Coefficient of distribution of the energy generated among consumers who participate in collective self-consumption.

For each consumer '*i*' participant of collective self-consumption, this coefficient will take the value that appears in an agreement signed by all consumers participating in collective self-consumption and notified to the distribution company as responsible for reading consumption. The value of these coefficients can be determined with any criterion, provided that there is a signed agreement for all participants and provided that the sum of the beta coefficient of all consumers participating in collective self-consumption is unity."

The generic formula established by the royal decree to find the coefficient of energy distribution is as follows:

$$\beta i = \frac{Pci}{\sum Pcj}$$

Pci: Maximum power contracted to the associated consumer i.

∑PCJ: Sum of the maximum powers contracted by all consumers who participate in collective self-consumption.

Based on the above, the following cases of energy distribution coefficient are proposed:

1. **Individual Self-consumption with surplus and Compensation (ISC):** Each owner of a home invests in a photovoltaic self-consumption installation individually, that is, each home will have its own single-phase inverter and photovoltaic panels.
2. **Collective self-consumption with distribution coefficient according to the number of houses (CFC-NH):** In this case, it has been decided that the beta energy distribution coefficient will be the same for all houses at all times of the year and the criterion is the total number of houses that will participate in self-consumption (15 dwellings), the way to calculate it is as follows:

$$\beta i = \frac{1}{15} = 0.06666666667$$

3. **Collective self-consumption with a distribution coefficient based on the contracted power in the electricity bill (CFC-PEB):** In this case, the criterion for choosing the beta coefficient of energy distribution will be according to the contracted power that each of the 15 dwellings has in the electricity contract, in this way each dwelling will have its own beta coefficient that will be the same for each hour of the year. The formula for calculating the beta coefficient is as follows:

$$\beta i = \frac{contracted\ power\ i}{\sum contracted\ power\ of\ the\ dwelling\ j}$$

4. **Collective self-consumption with distribution coefficient according to peak installed (CFC-IPP):** For this case study it has been decided that the criterion for calculating the beta coefficient will be the peak installed power of each of the dwellings, this power will be the same as that used for the case of individual self-consumption. In this case, the formula used for calculating the beta coefficient for energy distribution is the following:

$$\beta i = \frac{PV\ power\ installed\ i}{\sum \text{PV power installed of the dwelling } j}$$

5. **Collective self-consumption with dynamic distribution coefficient according to monthly consumption ex ante (CFC-MCE):** As mentioned in section No. 5, on November 15, 2021, Annex I of RD 244/2019 [3] was modified. Said modification allows the use of dynamic distribution coefficients, these coefficients may be different for each hour of the billing period as long as the coefficient βi is unity. The ex-ante monthly consumption is the criteria selected to determine the dynamic allocation coefficient.

   The term ex-ante means "before the event", in the case of collective self-consumption it will be a coefficient of distribution prior to the energy consumption. For calculating this coefficient we have decided to take the monthly consumption ex-ante for two months. The coefficient will be constant for all the hours of the same month but will adopt a different value for each month.

   It is taken as ex-ante data for two previous months because normally the billing comes every two months. In this way, the process for the new allocation of the betas coefficients would not be delayed every month. The formula to find the ex-ante dynamic allocation coefficient is:

$$\beta i(marzo) = \frac{January\ dwelling\ consuption\ i}{\sum January\ dwelling\ consuption\ j}$$

   The previous formula indicates that if we want to know what the coefficient βi is for the month of March I will have to use the consumption for the month of January.

6. **Collective self-consumption with distribution coefficient according to hourly consumption ex-ante (CFC-HCEA):** This coefficient is similar to the dynamic monthly ex-ante with the difference that there will be a different distribution coefficient for each hour. For the calculation of this coefficient we have decided to take the ex-ante hourly consumption two months prior to the month for which we want to calculate the coefficient, i.e., if we want to find the distribution coefficient in January, we will use the hourly consumption for the month of November. The formula to find the dynamic ex-ante allocation coefficient is:

$$\beta i = \frac{hourly\ ex\ ante\ consuption\ of\ dwelling\ i}{\sum hourly\ ex\ ante\ consuption\ of\ dwlling\ j}$$

7. **Collective self-consumption with distribution coefficient according to hourly consumption ex-post (CFC-HCEP)**: Despite the current regulation does not allow using these distribution coefficients, as a study, this work will calculate the ex-post dynamic coefficient in order to compare them in the future with the other cases of energy distribution coefficients and see which of them is more convenient for collective self-consumption. The term ex post refers to consumptions based on real and on-site readings. The calculation will be the same as the one used to find the dynamic distribution coefficient ex with the only difference that we take the hourly consumptions of the same hour from which we want to calculate the coefficient, i.e., if we want to find the distribution coefficient at 13 o'clock we will use the consumptions of that same hour 13. The formula to find the dynamic distribution coefficient ex-post is:

$$\beta i = \frac{hourly\ home\ consuption\ per\ hour\ i}{\sum hourly\ home\ consuption\ per\ hour\ j}$$

8. **Collective self-consumption with distribution coefficient according to hourly consumption ex-post with consumption improvement in a dwelling (CFC-IMP):** Solar energy generation occurs during daylight hours, so it is crucial to self-consume as much of the energy produced as possible since surplus energy is not paid for at the same price as the energy purchased. Therefore, the best option is to use as much of the energy produced by solar panels as possible.

   In order to demonstrate that consumers adapt their consumption to sunny hours the results will improve. For the demonstration, we have chosen house No. 1 for the ex-post sharing coefficient case.

   .

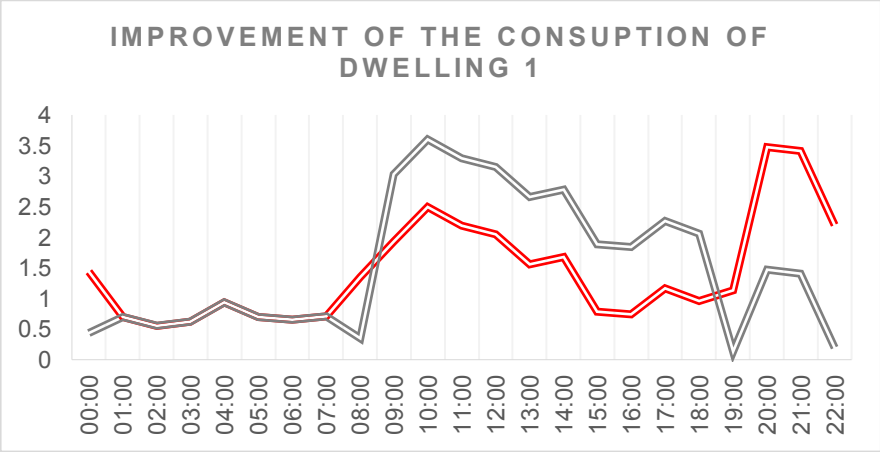

Figure. 1. Consumption before (red) and after (grey) the improvement of the consumption of dwelling No. 1 for 02/28/2021.

In the case of the ex-post dynamic distribution coefficient, as house 1 will adapt its consumption to the hours of sunshine, its beta coefficient will be higher compared to the rest of the houses. This will result in a higher energy distribution, a decrease in grid consumption, an increase in surpluses and an increase in the percentage of self-consumption over total consumption.

4. Economic study

4.1. Electricity bill

The changes suffered by electricity bills if the photovoltaic installation is carried out will be analyzed in order to visualize the economic savings that it would mean for the owners in each of the cases studied. As mentioned above, the electric bill has fixed terms that will be present even with no electricity consumption. The variable term is where the economic savings for self-consumption are visualized. Greater self-consumption translates into a decrease in the energy purchased from the grid, and therefore lower cost. In addition, to the variable term is added the fact that if there are surpluses of the photovoltaic generation they can be compensated in the monthly bill.

The term variable shall adopt the following formula:

- No photovoltaic installation:

  Variable term= Network consumption (kWh) x Price (€/kWh)

- With photovoltaic installation:

  Variable term= Network consumption (kWh) x Price (€/kWh)- Compensable surplus (€/kWh)

For the estimation of the annual bills of the houses, the following price assumptions have been used:

Table 2. Data used for electricity bills on the regulated market

Electricity tax	5.11%
Canary Tax	7.0%
Power	0.083 €/kWh
Energy Price	eSios
Compensated energy price	eSios

The regulated market prices correspond to the year 2021 and, as mentioned above, were obtained from the website of Red Eléctrica [8] de España eSios [9]. While the data used for the free market electricity bill are shown in Table 3.

Table 3. Data used for the free market electricity bill.

Electricity tax	5.11%
IGIC	7.00%
Contracted power	0.083 €/kWh
Energy Price	0.168662
Compensated energy price	0.0663 €/kWh

4.2. Investment

An estimated budget is made for the case of individual installation and collective self-consumption. In addition, ways to distribute investment in cases of collective self-consumption are proposed.

The economic distribution is made as follows:

$$\boldsymbol{Individual\ investment\ for\ fixed\ coefficents\ \beta i} = \textbf{total}\ \boldsymbol{investment\ x\ \beta\ fixed\ i}$$

$$\boldsymbol{Individual\ investment\ for\ dynamic\ coefficents\ \beta i} = \frac{\boldsymbol{total\ investment}}{\boldsymbol{\sum dwelling}}$$

in the following table, we can see a summary of the investment for each case and each home.

Table 4. Summary of the investments of each of the houses for the different case studies.

House N.º	CASE 1	CASE 2,5,6,7	CASE 4	CASE 3
House 1	9.454 €	4.621 €	7.763 €	4.666 €
House 2	7.841 €	4.621 €	4.683 €	4.666 €
House 3	7.810 €	4.621 €	4.212 €	4.243 €
House 4	6.738 €	4.621 €	3.589 €	4.243 €
House 5	7.810 €	4.621 €	4.378 €	4.874 €
House 6	6.473 €	4.621 €	2.623 €	4.243 €
House 7	8.579 €	4.621 €	6.219 €	4.874 €
House 8	7.810 €	4.621 €	4.378 €	4.874 €
House 9	7.810 €	4.621 €	4.378 €	4.874 €
House 10	7.810 €	4.621 €	4.378 €	4.874 €
House 11	9.454 €	4.621 €	7.763 €	4.666 €
House 12	6.738 €	4.621 €	3.589 €	4.243 €
House 13	7.810 €	4.621 €	4.378 €	4.874 €
House 14	7.810 €	4.621 €	4.378 €	4.874 €
House 15	7.810 €	4.621 €	4.378 €	4.874 €

5. Results

Several conclusions can be drawn from the cases studied, either from an economic point of view, referring to the NPV, or from the point of view of savings in the electricity bill, which will depend on several factors such as consumption, type of market or contracted power.
In order to be able to understand the reason for the results, Table 5 shows the data for each house, which will be used to identify them and see their main differences:

Table 5. Summary of characteristic data of the dwellings

House N.º	Annual consumption (kWh/Año)	% Sun Hours Consumption	Contracted power (kW)	Electricy market	Electricity Bill no PV (€)
House 1	9948	48%	5.5	Free	2084
House 2	6000	61%	5.5	Regulated	1481
House 3	5397	61%	5	Regulated	1338
House 4	4599	52%	5	Regulated	1143
House 5	5610	54%	5.75	Free	1272
House 6	3361	56%	5	Regulated	938
House 7	7970	63%	5.75	Free	1719

The importance of the % consumption in hours of sunshine was mentioned previously since the consumers who have a higher percentage will benefit more because they will consume more energy from the photovoltaic panels than energy from the electric grid. House No. 7, 2 and 3 have the highest consumption in sunlight hours; on the contrary, houses No. 1, 4, 5 and 6 have a slightly lower percentage, meaning that they consume more energy at night than during the day.

5.1. Economic feasibility

Several economic parameters were studied to determine the feasibility of each case, such as NPV, ERP and savings obtained in the electricity bill. Below, we can see the results obtained for the houses with the highest consumption (1;11) and the houses with the lowest consumption (6;10)

***Table* 6.** Summary of economic results obtained from housing 1 and 6.

Colours scale from worst to best.

Nº DWELLING	1	6	1	6	1	6
	NPV €		SAVINGS%		ERP	
Cfc-Nh	10048	4835	55%	52%	9	9
Cfc-Peb	9511	6687	40%	71%	6	8
Cfc-Ipp	8679	9655	38%	66%	6	6
Cfc-Mce	9501	5581	53%	52%	7	6
Cfc-Hcea	15329	3633	56%	53%	4	10
Cfc-Hcep	14604	4530	54%	58%	4	9
Cfc-Imp	13724	4410	48%	57%	5	9

Table 6 shows that cases with fixed coefficients benefit homes with higher consumption, while houses with low consumption obtain better benefits with fixed distribution coefficients.

5.2. Percentage of distribution of electrical energy over the total produced

This percentage indicates the electrical energy that corresponds to each dwelling annually as agreed. The following table shows how the distribution of energy improves or worsens according to the distribution coefficients adopted. The homes that have a higher percentage mean that it corresponds to more photovoltaic energy.

Table 7. Percentage of distribution of photovoltaic energy of each dwelling part of the total energy production of the installation.

% PV allocation energy/ Total PV production						
	CFC-NH	CFC-PEB	CFC-IPP	CFC-MCE	CFC-HCEA	CFC-HCEP
House 1	7%	7%	11%	11%	10%	9%
House 2	7%	7%	7%	8%	8%	8%
House 3	7%	6%	6%	7%	7%	7%
House 4	7%	6%	5%	5%	6%	6%
House 5	7%	7%	6%	6%	6%	6%
House 6	7%	6%	4%	4%	4%	4%
House 7	7%	7%	9%	9%	11%	11%
House 8	7%	7%	6%	6%	6%	6%
House 9	7%	7%	6%	6%	6%	6%
House 10	7%	6%	4%	4%	4%	4%
House 11	7%	7%	11%	11%	10%	9%
House 12	7%	6%	5%	5%	6%	6%
House 13	7%	7%	6%	6%	6%	6%
House 14	7%	7%	6%	6%	6%	6%
House 15	7%	7%	6%	6%	6%	6%
Total	100%	100%	100%	100%	100%	100%

We can see that the CFC-NH case is the same for everyone, this is because the distribution is made equally. The CFC-PEB case depends on the contracted power that each house has, we can see that there is not much variation, the reason is that all houses have a very similar power (between 5 to 5.75 kW).

$$\uparrow \boldsymbol{Contracted\ power} \uparrow \%\ \boldsymbol{PV\ energy\ allocation}$$

In the case of CFC-IPP, if we can see the difference, the houses that have greater installed power will have a higher percentage.

$$\uparrow \boldsymbol{Power\ installed} \uparrow \%\boldsymbol{PV\ energy\ allocation}$$

The CFC-MCE case benefits more households with the highest monthly consumption. House 1 has the highest consumption in all months of the year, which is the reason why this house corresponds to a higher percentage of photovoltaic energy.

$$\uparrow \boldsymbol{Monthly\ consumption} \uparrow \%\ \boldsymbol{PV\ energy\ allocation}$$

For the cases CFC-HCEA and CFC-HCEP the order of preference that will define whether a house corresponds to more or less a percentage of the distribution of photovoltaic energy will be:

1. Houses with high consumption and also do it on sunny hours.
2. Houses with high consumption, but do most of it at night
3. Houses with low consumption, but make most of it in sunny hours

5.3. Percentage of self-consumption over total consumption

Having a higher percentage of self-consumption means having greater savings in the electricity bill, since the consumption of the network is reduced, in addition, knowing that the compensable energy is paid worse than the price of energy from the network, the importance of everything generated is self-consumption is visualized and surpluses are avoided. The table below shows the percentages of self-consumption, these percentages correspond to the fraction of total consumption that is consumed during the hours in which the PV system is generating energy and the remaining percentage is obtained from the grid.

Table 8. Percentage of self-consumption for each of the case studies

	CFC-NH	CFC-PEB	CFC-IPP	CFC-MCE	CFC-HCEA	CFC-HCEP	CFC-IMP
House 1	35%	33%	32%	35%	38%	35%	39%
House 2	40%	38%	38%	35%	44%	46%	50%
House 3	42%	42%	41%	43%	40%	33%	50%
House 4	43%	47%	46%	4%	42	46%	46%
House 5	41%	42%	40%	40%	41%	47%	44%
House 6	43%	47%	30%	44%	43%	45%	47%

5.4. Overall results

In view of the results of the investments shown in Table 5, it can be concluded that opting for any case of collective self-consumption is more economical than individual self-consumption since savings of up to 50% can be made on the investment.

The cases with fixed coefficients, especially CFC-NH and CFC-PEB are the ones that benefit less to houses with high consumption because the distribution is made in equal parts without taking into account the consumption of the house, in these cases, it can happen that while a house with low consumption produces surpluses, another with high consumption will need to consume from the electricity grid.

We have taken the consumption and energy distribution of houses 1 and 6 for case 2, in this case, the two houses have the same amount of energy, house 6 has more energy than it consumes and house 1 needs to consume energy from the grid to meet its demand. This is the reason why these cases obtain the lowest savings in the electricity bill. The houses with low consumption, which in turn consume energy during sunlight hours, tend to have better results with fixed coefficients.

Table *9*. Comparison of houses 1 and 6 for Cfc-Peb case.

House	Hour	Hourly Consumption (kWh)	Cast Fv (kWh)	Net Balance (kWh)	Energy Price (€/kWh)	Compensation Price (€/kWh)	Network (€)	Surplus (€)
House	10	2.21	1.79	-0.41	0.168662	0.0663	0.07	0
House	10	0.25	1.79	1.54	0.22122	0.08266	0	0.128

Table 9 compares a house with high consumption versus a house with low consumption for the cases with fixed coefficients, it is observed that the house with low consumption is supplied with photovoltaic energy and even has surpluses. On the contrary, house 1 has a higher consumption and cannot be supplied with photovoltaic energy, so it has to consume energy from the electric grid.

Houses with a higher percentage of sunshine hours will obtain greater benefits with dynamic distribution coefficients. Since they have a higher beta coefficient compared to the rest of the houses and, therefore, they have a higher energy distribution.

consumers who adapt their electricity consumption to the hours of sunshine will be able to achieve a higher percentage of self-consumption and therefore greater savings. In addition, they will obtain better economic results and will recover their photovoltaic investment in less time. The study was carried out in the months of January and February with house 1.

The results are shown in Table 10, comparing the case of self-consumption with ex-post coefficient without improvement versus ex-post with improvement in the months of January and February.

Table 10. *Comparison of the results obtained before and after the improvement in consumption.*

House 1	January		February	
	No Improvement	With improvement	No Improvement	With improvement
Consumption Month (kWh)	1305	1305	999	999
Energy Distribution (kWh)	792	1235	837	1241
Mains consumption (kWh)	861	615	584	389
Surpluses (kWh)	25	545	29	630
% Self-consumption	32%	53%	40%	61%

Energy consumption through the grid decreased by 30% in both January and February. However, surpluses increased by 31% due to the increase in energy sharing. In addition, energy sharing increases because the sharing coefficient increases. Table 11 shows the variation of the energy sharing percentage, while for house 1 it increases from 12.59% to 19%, and for the rest of the houses it decreases

Table 11. photovoltaic energy allocation percentage before and after the improvement of the consumption of house 1.

% Energy Distribution		
	No Improvement	With improvement
House 1	12.59%	19,00%
House 2	6.09%	5.98%
House 3	5.48%	5.14%
House 4	5.38%	5.1%
House 5	4.86%	4.35%
House 6	4.66%	4.15%
House 7	14.45%	14.01%
House 8	4.86%	4.35%
House 9	4.86%	4.35%
House 10	4.66%	4.15%
House 11	12.59%	12.21%
House 12	5.38%	5.1%
House 13	4.86%	4.35%
House 14	4.86%	4.35%
House 15	4.86%	4.35%
Total	100%	100%

6. Conclusions

In view of the economic results, it is concluded that opting for collective self-consumption is an economically more beneficial decision than individual self-consumption.

The cases with dynamic coefficients are better than permanent coefficients. Because dynamic coefficients take into account the consumptions of the houses, then the distribution of energy will be done in an efficient way. On the other hand, fixed coefficients distribute the energy equally, without taking into account this important aspect.

The cases of collective self-consumption with permanent distribution coefficients are suitable for houses with low consumption during sunlight hours. If the consumptions are very low, these houses will have many surpluses and this will not be convenient because the purchase price of these surpluses is very low. On the other hand, houses with high consumption do not benefit from this coefficient because the distribution of energy is not very efficient since, while the houses with low consumption produce surpluses, the houses with high consumption will have to consume from the grid.

The problem of the efficient distribution of consumption is solved with the dynamic coefficients, these coefficients optimize the allocation of energy that corresponds to the different consumers. For example, they allow adjusting the distribution of photovoltaic energy to different casuistry, for example, to adjust to different daily consumption habits.

In addition, if consumers adapt their electricity consumption to the hours when the installation is generating energy, it is found that self-consumption increases and therefore the savings on the electricity bill is higher.

The results obtained in this study will help communities of neighbours to make a decision on which distribution coefficient to choose. However, the ex-post coefficient is recommended because the distribution of energy is made according to instantaneous consumption, thus, if a house increases its consumption in sunny hours, it will obtain greater energy savings.

The acceptance of dynamic coefficients is an important step towards the ecological transition in Spain. Even so, governments must continue to take measures and seek solutions to encourage photovoltaic self-consumption if they Xant to meet the targets set.

7. Acknowledgements

This research was partially supported by ACIISI-Gobierno de canarias and European Feder Funds Grant EIS

202104.

7. References

[1] Anthony Roy, "A comparison of energy allocation rules for a collective self-consumption operation in an industrial multi-energy microgrid," *ELSEVIER,* vol. 1, p. 14, 2023.

[2] RD 244/2019, « Spanish Official Gazette, Real Decreto 244/2019, de 5 de abril, por el que se regulan las condiciones administrativas, técnicas y económicas del autoconsumo de energía eléctrica, 2019.,» 15 marzo 2022. [En línea]. Available: https://www.boe.es/eli/es/rd/2019/04/05/244.

[3] Joan Tomás Villalonga Palou, "Sharing approaches in collective self-consumption systems: A techno-economic analysis of the Spanish regulatory framework," *ELSEVIER,* vol. 1, no. 1, p. 11, 2023.

[4] IDAE.ES, «Orden TED/1247/2021, de 15 de noviembre, por la que se modifica, para la implementación de coeficientes de reparto variables en autoconsumo colectivo, el anexo I del Real Decreto 244/2019, de 5 de abril, por el que se regulan las condiciones administrativ,» 2021. [En línea]. Available: https://www.idae.es/sites/default/files/documentos/publicaciones_idae/2022-06_Guia_Profesional_Tramitacion_autoconsumo_v.4.1.pdf. [Último acceso: 6 MAYO 2022].

[5] Tsai., «Insolation-oriented model of photovoltaic module using Matlab/Simulink, Solar Energy,» p. 318–1326.

[6] TaoMa n, "Solar photovoltaic system modelling and performance prediction, Renewable and Sustainable Energy Reviews," *ELSEVIER,* vol. 1, no. 1, p. 35, 2014.

[7] Vera Davila, «Validación del modelo matematico de un panel solar empleando la herramienta Simulink de Matlab.,» (2018).

[8] Red Electrica de España, S.A., «Ministerio para la Transición Ecológica y el Reto Demográfico,» 2022. [En línea].

[9] Sistema de Información del Operador del Sistema (esios), «esios,» 2022. [En línea]. Available: https://www.esios.ree.es/es.

[10] Agencia Estatal Boletín Oficial del Estado, «BOE,» 16 noviembre 2021. [En línea]. Available: https://boe.es. [Último acceso: 18 febrero 2021].

Evaluation and possible direct utilization of low- to medium-enthalpy geothermal resources for the sustainable development of the African continent

Claudio Zuffi[a-b], Luca Socci[a], Andrea Rocchetti[a], Giampaolo Manfrida[a] and Daniele Fiaschi[a]

[a] Department of Industrial Engineering, University of Florence (Italy),
[b] claudio.zuffi@unifi.it, CA

Abstract:

Low- and high-enthalpy geothermal resources exist throughout the African continent, but their utilization is still minimal. The rift valley area includes several high-enthalpy resource manifestations, but numerous medium- and low-enthalpy resources characterize the mainland. Geothermal resources offer a large energy potential suitable for several users. The main goal of this article is the assessment of the energy potential of the geothermal resources in Africa for direct use. The analysis of different types of medium- and low-enthalpy resources is carried out. The use of absorption cycles for cold production is considered here. A parametric analysis of the resource conditions, with special reference to the temperature level, allowed the estimation of the cooling power potential connected to the low to medium geothermal energy resources available in the African continent. On the other hand, possible end users of this resource are identified cold room storage and building cooling. The present study covers several aspects, from thermodynamic modelling to environmental analysis. The mathematical model allows the simulation of the cooling system and, through parametric analyses, the most suitable cycle characteristics are determined in compliance with the potential of the available geothermal resource. The Life Cycle Assessment (LCA) methodology is adopted for the sustainability analysis and the assessment of environmental compatibility of the proposed solutions. A parametric Life Cycle Inventory (LCI) is developed, modeling the components according to the required size for each use. The main outcome of the present work is that the low enthalpy Geothermal available in the African continent can offer significant energy savings and large environmental benefits, which may play a fundamental role in the sustainable development of this area.

Keywords:

Geothermal energy, direct use, Absorption Refrigeration System, Life Cycle Assessment

1. Introduction

Geothermal energy is acknowledged as a renewable source with a very relevant potential, and technologies to exploit it are at a rather advanced stage of development [1]. The use of this source is mainly classified into two categories: *indirect*, in which electricity is produced by power plants; direct, which directly exploits the geothermal heat flow for several applications, from residential to industrial heating [2]. Over the years, the installed geothermal powerplant capacity has grown extensively. In 2000, the worldwide installed capacity was 7.97 GWe producing about 49.30 GWh/y [3], while at 2020 the installed capacity had roughly doubled to 15.95 GWe producing about 95.10 GWh/y electricity [4]. The currently available technologies for electricity production are dry steam, flash steam and binary cycles, usually for medium-high enthalpy resources ranging from 120° C to 350° C. On the other hand, in a 20 years range period, the direct use of the resource has also grown extensively, from 15.14 GWt in 2000 to 107.73 GWt in 2020 installed capacity, with a growth in the produced heat from 1.9E+5 TJ/y to 1.02E+6 TJ/y at worldwide level [5]. The direct heat uses can vary widely, often involving space heating and cooling for building or industrial applications: Heat pumps, Heat Exchangers, Absorption cooling and refrigeration, greenhouses, agricultural drying, fish farming and others. The choice is highly related to the temperature level of the resource and to that required for the specific applications [6]. Generally, the direct heat use technologies belong to medium-low enthalpy resources, usually ranging between 20° C and 150° C.

The African continent, and in particular the East Area where Rift valley is located, has a very high geothermal potential (over 15 GW) but the exploitation of this resource is still limited to extremely low fractions [7]. In 2020, data on the installed geothermal power in Africa amounted to 830 MWe, of which 823 MW in Kenya and 7 MW in Ethiopia. On the other hand, direct use of geothermal heat in the African continent is about 198 MWt, shared between several countries. Direct use applications are more equally distributed across the entire continent (Algeria, Burundi, Egypt, Ethiopia, Kenya, Madagascar, Malawi, Morocco, Nigeria, South Africa and Tunisia) [5].

In this context, investigating direct-use applications of geothermal heat for low to medium-enthalpy resources in the African scenario is of relevant interest. In the 40 – 150 °C heat range, the Absorption Refrigeration System (ARS) is economically and environmentally promising [8]. Several studies were conducted considering different conditions of the geothermal resource. Tugcu et al. analysed an ARS with ammonia-water mixture fed by a geothermal resource at 133°C [9]; Kairouani et al. evaluated an ARS with a mixture of ammonia and water and the geothermal resource in a range between 72°C and 75°C [10]; Velàzquez et al. have designed a single- and double-effect ARS which utilises a geothermal resource at 80°C and 163°C respectively [11].

Similarly, some paper in literature analyse the sustainability of geothermal heat for refrigeration and chilling, evaluating the coupling of the generator to different renewable sources with the Life Cycle Assessment methodology. Solano-Olivares et al. and Bukoski et al. evaluated an absorption cycle coupled with a solar system for building cooling [12], [13]. Hamedani et al. analysed the energy and environmental aspects through LCA of a biomass-fuelled heating and cooling system [14]. On the other hand, Maione et al. and Chaiyat, assessed the environmental impacts of coupling the ARS to a geothermal resource [15], [16].

In numerous regions of Africa, electricity is not easily accessible and distributed. As a result, geothermal energy plays a crucial role in the country's development. Thus, investigating systems that harness the existing heat from geothermal resources facilitates the implementation of multiple systems that would be considerably more challenging if powered by electricity. The objective of this work is modelling and evaluating the thermodynamic behaviour and the environmental impact of an ARS for different possible geothermal conditions. It is designed to cover the cooling load of a cold room (for food storage or other industrial use) or a building. The thermodynamic performance of an absorption cycle with a mixture of water and ammonia under different geothermal resource conditions have been evaluated. At the same time, the environmental impact assessment of the investigated ARS has been carried out by the means of Life Cycle Assessment (LCA), considering the construction and operation phase of the system.

This work is done in the framework of the European Horizon 2020 project Long-Term Joint EU-AU Research and Innovation Partnership on Renewable Energy *(LEAP-RE)* [17].

2. Materials and methods

The analysed ARS is an absorption cycle with a mixture of water and ammonia (NH_3/H_2O mixture) for the refrigeration of a cold room or cooling of a building. The proposed mathematical model of the ARS takes into account the chemical characterization of the mixture, the mass and energy balances. In order to realize a model suitable and easily applicable to different conditions of the African continent, several wide range variable parameters were considered. The parametric analyses focused on condensation temperature (T_{cond}), evaporation temperature (T_{evap}), mass ratio of NH_3 to the whole mixture (y), and finally the temperature of the geothermal resource (T_{geo}).

An environmental analysis was performed by the Life Cycle Assessment of the ARS, following the ISO 14040 and ISO 14044 standards [18], [19] The regulations define 4 key steps in this analysis: Goal and scope definition, Life Cycle Inventory (LCI), Life Cycle Impact Assessment (LCIA), Interpretation. In this work, the focus was on the second step, consisting in the development of a parametric LCI representing the construction phase of the absorption cycle. The goal is to provide the assessment of materials needed for construction in relation to the cooling power of the ARS, refereed to the installed kW unit. In addition, some parameters used in the thermodynamic model are set to evaluate the operation phase as well. Then, by combining the results obtained from the thermodynamic model and using them as inputs of the LCA model, it is possible to perform a comprehensive analysis of system performance and sustainability. This is done by varying the external conditions such as outdoor temperatures T_{air}, and target temperatures T_{aim}. The next sections describe the thermodynamic model and the LCA model of the considered plant, outlined in Figure 1.

The mathematical model of the absorption cycle was implemented in Engineering Equation Solver (EES) software [20], whereas the environmental analysis was conducted with OpenLCA software [21] and Ecoinvent 3.7 datatbase [22].

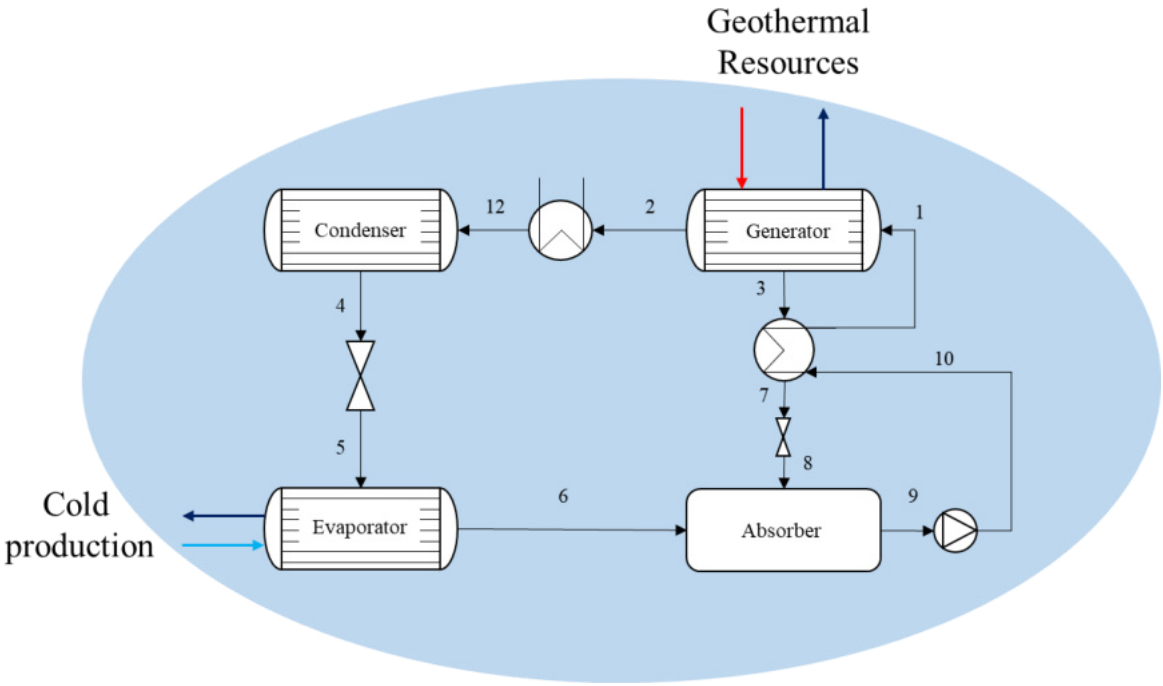

Figure 1 - Geothermal absorption cycle for refrigeration, with a mixture of water and ammonia

2.1 Energy modelling

The ARS is a single-effect cycle, mainly consisting of generator, desuperheater (DSH), condenser, evaporator, absorber, and heat recovery unit (RH). The system is shifted in two lines, differently modelled according to the working fluid. At the generator outlet, from point 2 to point 6, the working fluid is pure ammonia starting as superheated vapor in 2, saturated vapor in 12, saturated liquid in 4 and saturated vapor in 6. From the generator outlet at point 3 (line 3-8) and the absorber outlet at point 9 (line 9-1) the working fluid is in the liquid state, consisting in a mixture of NH_3/H_2O at the concentration y. The working fluid is at a high concentration y in line 9-1 (strong solution), corresponding to the design concentration of the cycle, and at low concentration

in line 3-8. With reference to the external conditions, two parameters mainly influence the cycle, namely the temperatures at point 4 (T_{cond}) and the NH_3 mass ration at point 9 (y), as they set the two pressure levels of the cycle:

- High pressure corresponding to the saturation pressure of ammonia at T_{cond};
- Low pressure corresponding to the saturation pressure of the mixture evaluated at temperature T_{cond} with mass ratio y.

T_{cond} is determined by the external conditions (1), hence the environmental air temperature, while y is set and evaluated at different level. The reason for setting the temperature T_9 equal to the temperature T_{cond} is that the absorber exchanges heat with the outside air. T_{evap} is evaluated from the low-pressure level as the saturation temperature at low pressure and also defines the aim temperature (T_{aim}) achievable in the cold room or in the building (e.g. cold utility temperature) (2). Thus, these parameters uniquely set the cycle and a changing one of them leads to a variation in temperatures and pressures of the other components (Figure 2 - Temperature-pressure graph with constant water-ammonia concentration curves of the Absorption Refrigeration System), as will be seen in the Results section.

$$T_{cond} = T_{air} + \Delta T_{cond} \quad (1)$$

$$T_{evap} = T_{aim} + \Delta T_{evap} \quad (2)$$

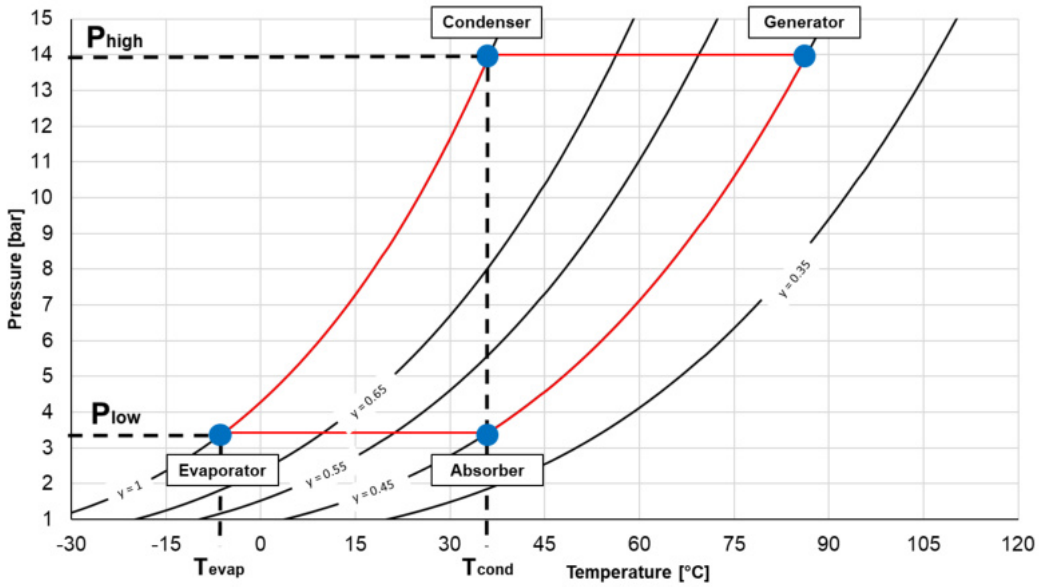

Figure 2 - Temperature-pressure graph with constant water-ammonia concentration curves of the Absorption Refrigeration System

The whole cycle is calculated around these two fixed pressure levels. In Point 1, the water-ammonia mixture enters into the generator, which is heated by the geothermal resource. The temperature level at the generator output (point 3) is evaluated according to equation (3), where T_{geo} is the temperature of the geothermal resource entering the generator.

$$T_2 = T_3 = T_{geo} - \Delta T_{gen} \quad (3)$$

Thus, from point 2 the ammonia in the superheated vapour state passes through the desuperheater (DSH) and successively condenses at point 4. Downstream the isenthalpic throttling valve (4-5), the ammonia evaporates into the evaporator (5-6), providing the required refrigeration effect. At the same time, in point 3 the weak water / ammonia solution under the liquid state releases heat (thus recovered) to the NH_3/H_2O strong solution from the absorber. The regeneration level R of this recuperator is defined in equation (4).

$$R = (h_3 - h_7) / (h_1 - h_{10}) \quad (4)$$

The equations governing the energy balances of the main points of the cycle are given below from (5 to 14).

$$Q_{geo} = \dot{m}_{geo} * (h_{15} - h_{16}) \quad (5)$$

$$Q_{geo} = \dot{m}_2 * h_2 + \dot{m}_3 * h_3 - \dot{m}_1 * h_1 \quad (6)$$

$$Q_{DSH} = \dot{m}_2 * (h_{12} - h_2) \quad (7)$$

$$Q_{cond} = \dot{m}_2 * (h_{12} - h_4) \quad (8)$$

$$Q_{evap} = \dot{m}_2 * (h_4 - h_6) \quad (9)$$

$$Q_{abs} = \dot{m}_2 * h_6 + \dot{m}_3 * h_8 - \dot{m}_1 * h_9 \quad (10)$$

$$\dot{m}_1 * (h_1 - h_{10}) = \dot{m}_3 * (h_3 - h_7) \quad (11)$$

$$Q_{abs} = \dot{m}_2 * h_6 + \dot{m}_3 * h_8 - \dot{m}_1 * h_9 \quad (12)$$

$$W_p = \dot{m}_1 * (h_{10} - h_9) \quad (13)$$

$$COP = {Q_{evap}}/{(Q_{geo} + W_p)} \quad (14)$$

The model relies on some fixed parameters set during the analysis, while other ones are allowed to vary. Table 1 shows all fixed and variable parameters and their values or ranges. T_{cond} and T_{evap} are evaluated to analyse their influence on the Coefficient of Performance (*COP*) of the whole system. The sensitivity analysis to the NH3/H2O solution concentration *y* is carried out to determine the most suitable ammonia concentration for the cycle in relationship to the available low-temperature level of the geothermal resources. Finally, T_{geo} allows defining the performance level achievable referred to the heat input to the system.

Table 1 - Range of parameters used in the parametric analysis of the system

Name	***Parameter***	***Unit***	***Value /range***
Hot-cold side temperature difference at the condenser	ΔT_{cond}	°C	10
Hot-cold side temperature difference at the evaporator	ΔT_{evap}	°C	5
Hot-cold side temperature difference at the generator	ΔT_{geo}	°C	5
RH regeneration level	*R*	-	0.8
Condenser temperature	T_{cond}	°C	25 – 50
Evaporator temperature	T_{evap}	°C	-10 – 0
Mass fraction Ammonia/mixture	*y*	kg $_{NH3}$/kg $_{mixture}$	0.3 – 0.8
Geothermal mass flow rate	m_{geo}	kg/s	0.5 – 10
Temperature of resources	T_{geo}	°C	50 – 120

2.2 LCA Modelling

The surface plant for refrigeration defines the system boundaries of the analysis. Geothermal wells or the drawdown point are not considered because they are strongly site dependent. The cold room or the building are as well not considered at the analysis, as out of the focus of this work. The electricity consumption of the pumps is taken into account, and it's impact is modelled using Kenya's electricity energy mix as a reference. The assumed functional unit is 1 kW of installed cooling power.

The parametric LCI consisted in two basic steps:

- Finding a reference process representative of the construction materials of the absorption cycle;
- Finding enough data to establish a relationship between the installed cooling capacity and the weight of the device.

For the first step, a literature review was conducted, and several LCIs were compared [12]–[16]. It turned out that many of them were either incomplete or referred directly to secondary processes in the database. For this reason, to consider a consistent reference, the process of the Absorption cycle provided by the Ecoinvent 3.7 database [22] was adopted as a reference model. This process was the starting point to obtain the typical composition of materials for the devices of the case study. Indeed, by neglecting the materials not closely related to the construction phase of the devices, a relative mass fraction (%) of construction materials was made per each considered unit. The second step was finding reliable catalogues of Absorber manufacturing companies. The purpose of this step is achieving information on weight and cooling power. Once obtained the necessary data, a distribution of points outlining the relationship between the weight of the devices and the nominal ARS cooling power (kW) may be traced. The *World Energy Absorption Chillers Europe Ltd* catalogues available online[23] were used which allowed to obtain 140 number of points.

With the distribution of this data in hands, it was possible to achieve a satisfactory second-degree polynomial fitting function. The second-degree function was selected in order to limit its complexity, increasing with the polynomial degree, without entailing an appreciable reduction of the uncertainty. Figure 3 shows the point distribution and the related 2nd degree polynomial power-weight fitting function.

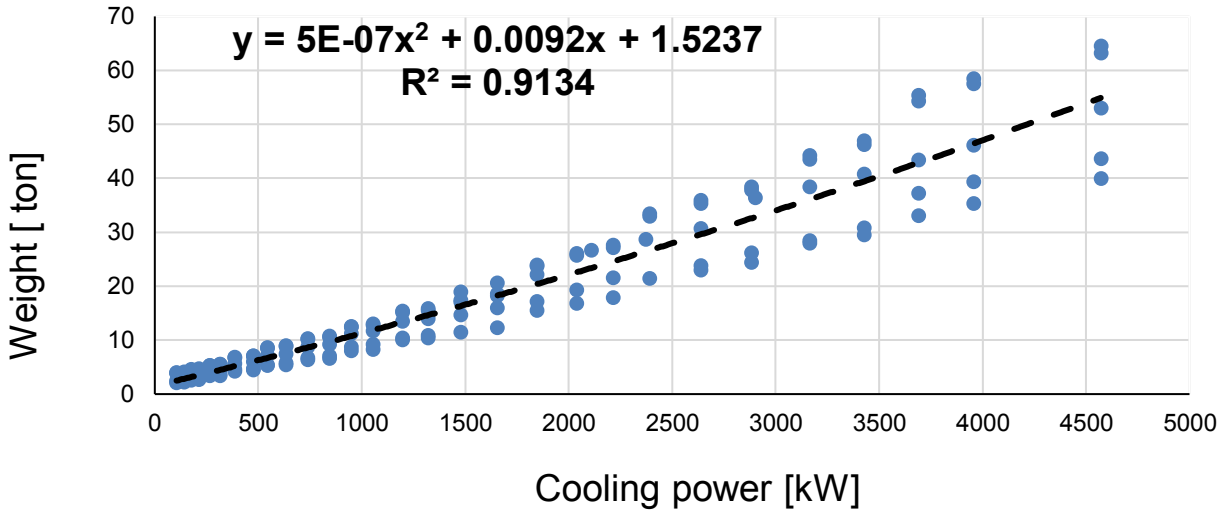

Figure 3 - Descriptive function of installed cooling power-weight trend

The conducted analysis adopts the Environmental Footprint (EF) 3.0 methodology, adapted to the Ecoinvent database. Specifically, the analysis develops on two levels: (i) Analysis of the environmental indicator Climate Change (CC) in terms of kg CO_2 equivalent emitted and (ii) analysis of the single score in terms of Environmental Points (Pt). The latter is achieved following normalization and weighting of all indicators evaluated by EF3.0, therefore it represents the overall environmental impact of the system.

3. Results

In this section, the results coming from energy parametric analysis and LCA study are presented. In particular:

- The parametric analysis shows the sensitivity of the absorption refrigeration cycle to the ammonia concentration in the mixture, condensation temperature and geothermal resource temperature.
- The LCA study shows the contributions analysis of the environmental indicator Climate Change (CC), as well as an analysis of the most impactful categories at single score level.

3.1 Effect of ammonia concentration

Figure 4 shows the temperature trend of the NH_3/H_2O mixture at the generator inlet T_1 and the evaporation temperature T_{evap} with respect to different y_1 levels. In this case, the analysis was carried out by keeping the T_{geo} set at different temperature levels: a) 120°C; b) 100°C; c) 80°C; d) 60°C. The y analysis highlights a key aspect of low-, and medium-enthalpy geothermal resources and the target temperature. The first aspect that results is that as y_1 increases, the temperature T_1 decreases and T_{evap} increases. Respecting the constant

concentration curves of the ammonia-water mixture shown in Figure 2, it is denoted that as the selected curve in the Aborber-Generator stream varies, the temperature levels at the generator and evaporator also vary. This means that increasing y_1 allows geothermal resources to be exploited at lower temperatures. However, it must be considered that the refrigeration effect for cold room can be obtained at most for T_{evap} in the order of 5°C while, for the cooling of a building, T_{evap} must be higher than this level. As a reference, it must be considered that a satisfying refrigeration effect for a cold room can be obtained for T_{evap} not higher of 5°C (while, for the cooling of a building, Tevap could be higher). Taking this graph into account, it is easy to identify the NH_3/H_2O concentration y_1 which allows the required performance to be obtained with respect to the temperature of the geothermal resource. There is a grey area in the graphs, the low side of this area represents the temperature level of geothermal resource. This implies that the T_1 profile is not acceptable when it crosses this area and it can only assume values below that level. For low-temperature resources, the variation of y_1 is very limited and therefore also the terminal uses forcing only one type of application such as the cooling of buildings. Conversely, for higher temperature levels, such as a) and b), it is possible to choose both applications of cold storage and building cooling.

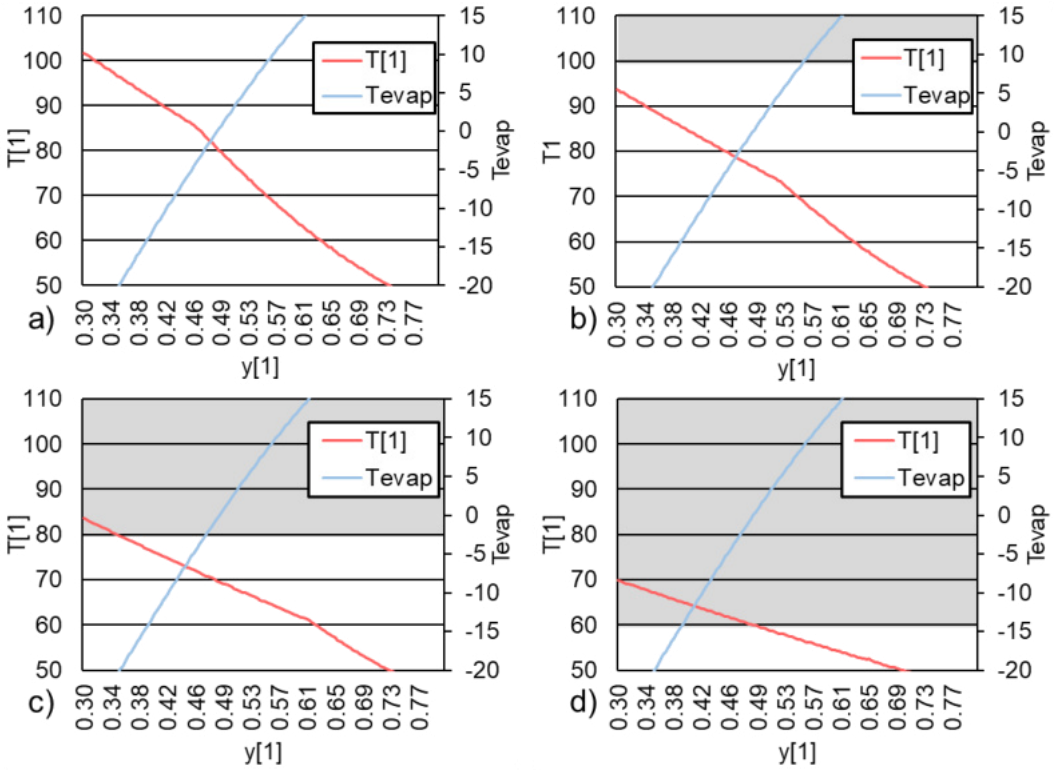

Figure 4 - Parametric analysis of T_1 and T_{evap} as a function of y_1 at different level of T_{geo}: a) T_{geo} =120°C; b) T_{geo} = 100°C; c) T_{geo} = 80°C; d) T_{geo} = 60°C.

3.2 Effects of condensation temperature

Through the parametric analysis of T_{cond}, the trend of the system's COP)is investigated using a function that is also dependent on y_1. In order to explore various T_{cond} variations, T_{geo} was set to its maximum level of 120°C. Figure 5 illustrates the relationship between COP and T_{cond} at different levels of y_1. It can be observed that at lower levels of y_1, higher COP values are achieved with lower T_{cond}, but as y_1 increases, the system's performance tends to decline.

However, for higher levels of y_1 ranging from 0.5 to 0.6, it appears that T_{cond} has minimal influence on COP. Since T_{cond} is influenced by external air temperatures, this indicates that these particular cases are minimally affected by external temperature changes, maintaining their performance almost unchanged within the typical temperature ranges of the African continent. Conversely, for cases where y_1 is below 0.45 to 0.35, variations in external temperatures significantly impact the system's performance, leading to a drastic drop in COP.

Another consideration is that the different y_1 levels correspond to a specific T_{evap} level, which are presented in Table 2. The cases relevant to refrigeration purposes focus on y_1 = 0.5. Realistically, considering the outdoor temperatures commonly encountered in East Africa, the design T_{cond} would fall within the range of 30-40°C [24], where the COP exhibits a declining phase. Furthermore, it should be noted that a slight increase in T_{evap} can slightly enhance the system's performance, but it may require applications beyond refrigeration, such as building cooling. Thus, considering all the aforementioned factors, the performance of the system is highly

dependent on its final application, as well as the external temperatures prevailing at the specific African site where the geothermal resource is located.

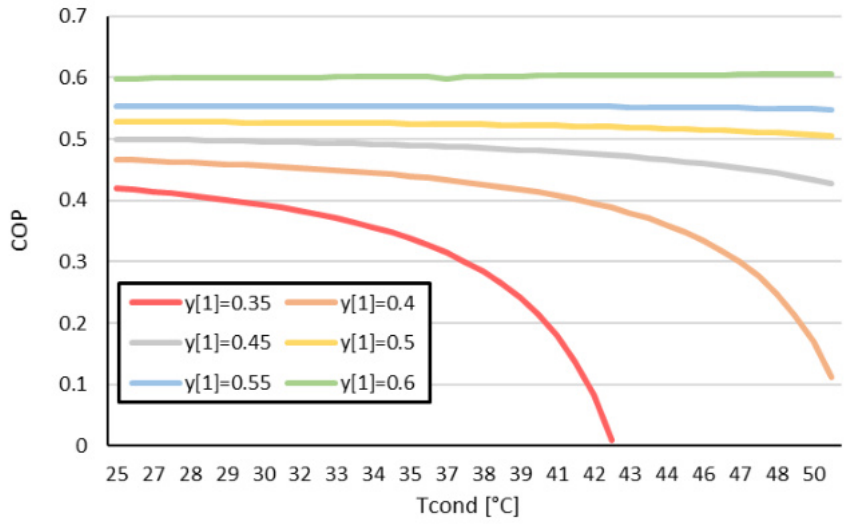

Figure 5 - Parametric analysis of COP as a function of T_{cond} and T_{evap}

3.3 Geothermal resource

The parametric analysis performed on the geothermal resource explores the trends of the COP at various y_1 levels. Figure 6 depicts the overall pattern, characterized by a substantial performance increase until reaching the temperature that maximizes COP, followed by a gradual decline. The lowest point of each curve corresponds to the geothermal resource temperature at which the absorption cycle initiates operation.
Considering the values presented in Table 2 and setting y_1 to 0.5 as the threshold for applications related to food refrigeration, it becomes evident that the minimum geothermal resource temperature is 83°C (lowest point of y_1 = 0.5 curve). As y_1 increases, corresponding to lower T_{evap} temperatures, the required geothermal resource temperature approaches the maximum value at a medium-low enthalpy level. In essence, lower y_1 levels in the cycle necessitate higher geothermal resource temperatures. This highlights the fact that refrigeration-type applications demand minimum temperatures around 80°C, which are only available in select regions of Africa, particularly in the East Africa Rift Valley (EARV) area.
Conversely, for higher y_1 levels, corresponding to higher Tevap temperatures, lower-temperature resources can be exploited, which are present in both the EARV and North Africa (e.g., Algeria and Morocco).
Hence, it is crucial to determine the optimal ammonia concentration, y_1, that maximizes COP as a function of the geothermal resource. For this reason, Table 2 provides the respective COP_{max} and T_{geo} values for each y_1 level.

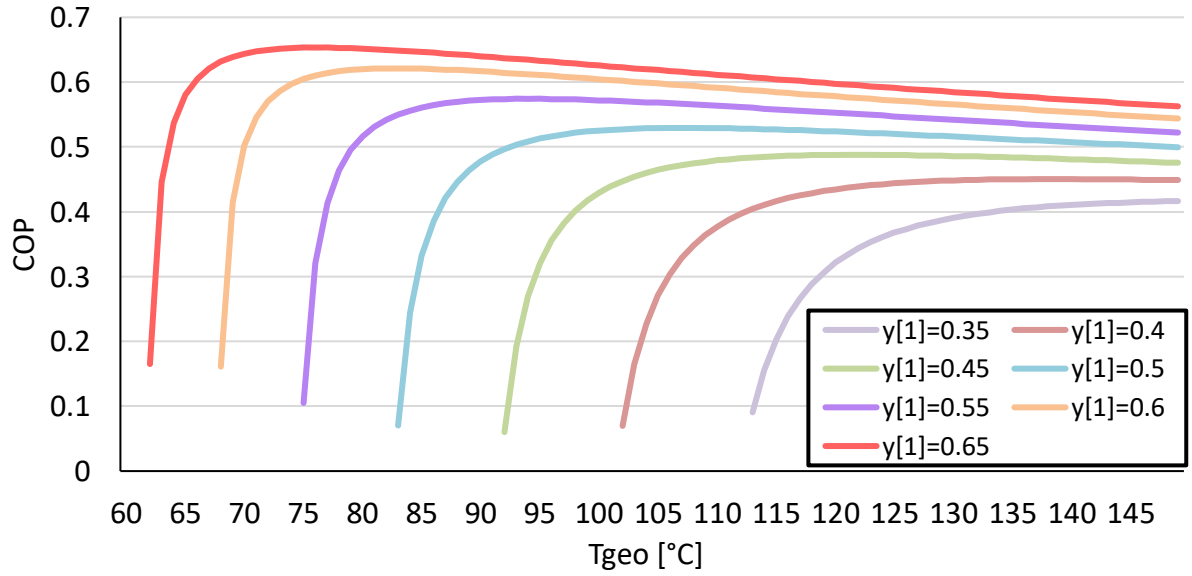

Figure 6 - Parametric analysis of COP as a function of T_{geo} and y_1

Table 2 - Evaluation of the maximum COP with respect to the temperature of the resource and the resulting cooling power

	y_1						
	0.35	**0.40**	**0.45**	**0.50**	**0.55**	**0.60**	**0.65**
T_{geo} [°C]	140	137	121	106	94	83	76
T_{evap} [°C]	-20.00	-12.56	-5.34	1.50	7.85	13.60	18.63
COP_{max}	0.41	0.45	0.48	0.52	0.57	0.62	0.65

3.4 Final application

Two cases are taken as reference: a) the first has the conditions set at y_1=0.5 and therefore T_{evap}=1.5° C for the refrigeration of a cold room for food storage purposes; b) the second has the conditions set at y_1=0.6 and therefore T_{evap}=13.60° C for the cooling of a building. In Figure 7 an analysis is shown on the heat loads of the main components, as the geothermal resource variations. As the two graphs show, for the cooling of the building it is possible to exploit a resource at temperatures above 70°C, while for the cold room it must be above 85°C. Analysing the point at which COP is maximum for both configurations show that for case a) the cold load is 21.34 kW while for load b) it is 22.27 kW.

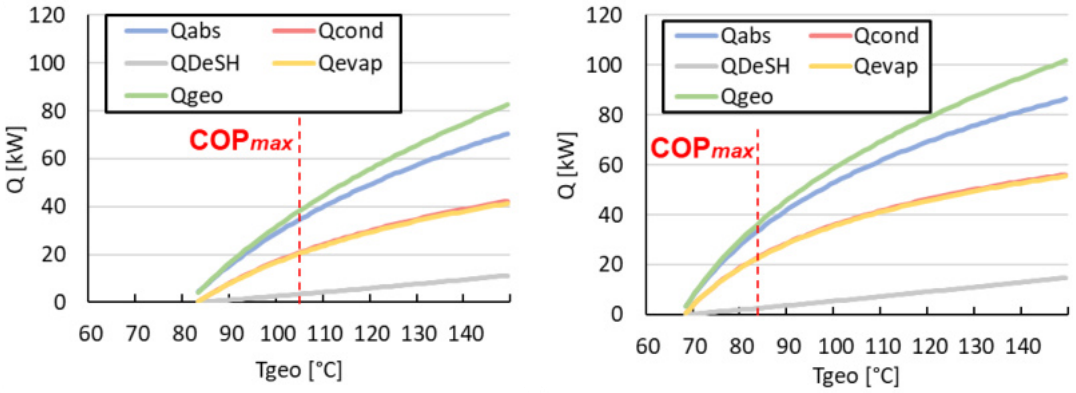

Figure 7 - Evaluation of heat level of two different cases: On the left a) for the application of a cold room, on the right b) for the cooling of a building

A preliminary dimensioning of a cold room was carried out to evaluate the output of the refrigeration and cooling system. Using equation 15 to estimate the annual cooling energy ($E_{cooling}$) in terms of kWh/y in a cold room for food storage. Where CF_a is the total number of hours per years of about 8000 [25], and F_r is a reduction factor of about 0.5. The results obtained for the reference case is approximately 85.360 MWh. Given data from literature 73 kWh/m^3 per year [26] for cold room is required, so a hypothetical cold room that is met by this system is 1169 m^3. At the same time, approximately 0.21kW/m^2 of cooling power is required for cooling a building with an internal temperature of 23°C [27]. Therefore, it can be estimated that with the analysed system a building of approximately 106 m^2 can be cooled. To make a point in support of these results, consider the case of the cold room. Taking as reference the results obtained from Evans et al. 2014 [28], an estimation can be made that suggests the consumption of around 56 kWh/m3 per year for cold room. It is crucial to emphasize that the availability of electricity poses challenges in numerous African regions, which underscores the necessity to devise a system that ensures access to electricity. In this context, the utilization of the geothermal resource in Africa assumes even greater significance.

$$E_{cooling} = Q_{evap} * CF_a * F_r \quad (15)$$

3.5 Life Cycle Impact Assessment

The analysis carried out on the environmental indicator CC, is shown in figure Figure 8. Here it is shown that the larger the installed cooling power of the device, the more CO_2 eq per kW of installed cooling power is reduced. In particular, the largest contribution of the impact comes from the electricity consumption of the operation phase, which is in the range of 60-65 % of the impact. In addition, the ammonia mixture makes a very low contribution ranging from 1.6-3.5 % of the impact. The construction phase results in approximately 1.94E+02-1.89E+021 kg CO2/kW, contributing 33-36% of the impacts.

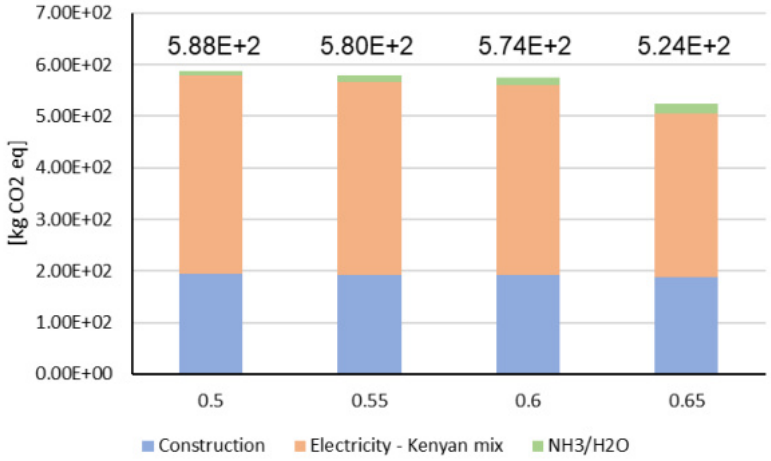

Figure 8 - Climate change evaluation

Finally, a single score analysis is shown in Figure 9, highlighting the contribution of the most impactful categories. The trend that was achieved for the CC indicator also persists at the overall system level. In fact, even at single score there is a decrease in impacts for systems with higher ammonia concentrations in the working fluid. Furthermore, globally, the most impactful categories are Resource use, minerals and metals, which impact in the range of 55-52%%. Two other indicators such as CC and Ecotoxicity, freshwater have a significant weight of about 9-11% and 11-12% respectively. While acidification, Particulate matter and Resource use, fossil impact about 3-6%, while the other indicators have negligible impact percentages.

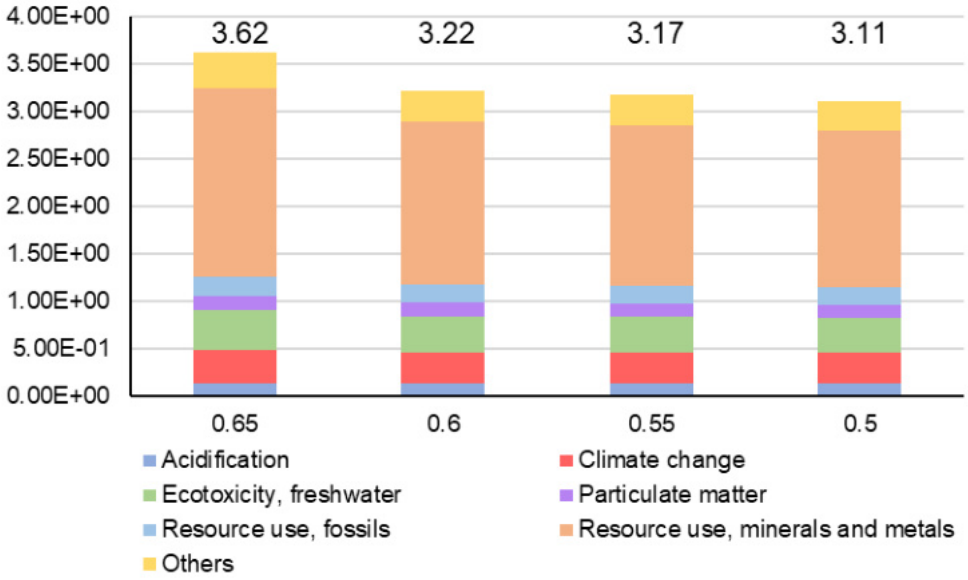

Figure 9 - Single score evaluation

4. Conclusion

In this paper, an application of direct use of the geothermal resource for medium and low enthalpy is analyzed. In particular, an absorption refrigeration system using a mixture of NH_3/H_2O is taken as a reference system for col room or building cooling. The analysis that has been conducted aims to highlight aspects concerning achievable thermodynamic performance and aspects concerning sustainability. For this reason, a thermodynamic model of the system was developed using the EES software to assess the performance of the cycle with several parametric analyses. From the analysis of the ammonia concentration, it can be deduced that increasing y_1 decreases the temperature of the mixture feeding the generator but at the same time increases the temperature level at the evaporator. This makes it possible to exploit a geothermal resource at a lower temperature but to increase the target temperature. The condenser temperature analysis shows that for low y_1, the increase in T_{cond} strongly reduces COP performance, whereas, for higher levels of y_1, the cycle is not influenced by these effects. The range of air temperatures in Africa limits T_{cond} to the 30-40°C range where the COP trend is decreasing. From the analysis of the geothermal resource, the minimum temperature values T_{geo} are set at different values of y_1. Furthermore, it is possible to evaluate the T_{geo} that maximizes the COP for each type of application. In particular, for refrigeration purposes, concentrations below 0.5 are required and COP_{max} is obtained for temperatures above 106°C. For the purposes of building cooling, on the other hand, y_1 greater than 0.55 is preferred and allows resources to be exploited at temperatures below 94°C. The results obtained dimension a cold room of 1169 m^3 at 5°C, using a resource at 106°C, and a building to be cooled of 106 m^2 at 23°C, with a resource at 86°C. To analyze the sustainability of the considered system, an LCA was conducted developing a parametric LCI to represent the construction and operation phase of the system. It was used OpenLCA software and the EF3.0 methodology adapted to the Ecoinvent 3.7 database. LCA uses the cooling power installed of the system as functional unit. Only the cooling system is analyzed, neglecting the entire system outside it (geothermal resource extraction point, cold room, building).

The outputs obtained from the thermodynamic model, in terms of cooling power, energy consumption, mass flow rate of ammonia mixture, are taking as input for the parametric LCI. The analysis of the environmental indicator CC shows a reduction in impacts corresponding to the increase in installed cold power of the system. The main contribution comes from electricity consumption and accounts for about 60-65%, while the construction phase of the device accounts for 33-36%. The single score analysis determines the same trend as for CC, and it is also established that the environmental indicator with the highest impact is Resource use, minerals and metals for about 52-55%. The environmental impact of CC accounts for 9-11%.

5. Bibliography

[1] I. W. Johnston, G. A. Narsilio, and S. Colls, “Emerging geothermal energy technologies,” *KSCE Journal of Civil Engineering*, vol. 15, no. 4, pp. 643–653, Apr. 2011, doi: 10.1007/s12205-011-0005-7.

[2] M. T. Islam *et al.*, “Trends and prospects of geothermal energy as an alternative source of power: A comprehensive review,” *Heliyon*, vol. 8, no. 12. Elsevier Ltd, Dec. 01, 2022. doi: 10.1016/j.heliyon.2022.e11836.

[3] E. Barbier, “Geothermal energy technology and current status: an overview,” 2002. [Online]. Available: www.elsevier.com/locate/rser

[4] J. W. Lund, G. W. Huttrer, and A. N. Toth, “Characteristics and trends in geothermal development and use, 1995 to 2020,” *Geothermics*, vol. 105, Nov. 2022, doi: 10.1016/j.geothermics.2022.102522.

[5] J. W. Lund and A. N. Toth, “Direct utilization of geothermal energy 2020 worldwide review,” *Geothermics*, vol. 90, Feb. 2021, doi: 10.1016/j.geothermics.2020.101915.

[6] D. Moya, C. Aldás, and P. Kaparaju, “Geothermal energy: Power plant technology and direct heat applications,” *Renewable and Sustainable Energy Reviews*, vol. 94. Elsevier Ltd, pp. 889–901, Oct. 01, 2018. doi: 10.1016/j.rser.2018.06.047.

[7] E. Y. Kombe and J. Muguthu, “Geothermal Energy Development in East Africa: Barriers and Strategies,” *Journal of Energy Research and Reviews*, vol. 2, no. 1, pp. 1–6, 2019, doi: 10.9734/JENRR/2019/45278.

[8] A. Keçeciler, H. I. Acar, and A. Dogan, “Thermodynamic analysis of the absorption refrigeration system with geothermal energy: an experimental study,” *Energy Conversion & Menagement*, vol. 41, pp. 37–48, 2000, [Online]. Available: www.elsevier.com/locate/enconman

[9] A. Tugcu and O. Arslan, “Optimization of geothermal energy aided absorption refrigeration system—GAARS: A novel ANN-based approach,” *Geothermics*, vol. 65, pp. 210–221, Jan. 2017, doi: 10.1016/j.geothermics.2016.10.004.

[10] L. Kairouani and E. Nehdi, “Cooling performance and energy saving of a compression-absorption refrigeration system assisted by geothermal energy,” *Appl Therm Eng*, vol. 26, no. 2–3, pp. 288–294, Feb. 2006, doi: 10.1016/j.applthermaleng.2005.05.001.

[11] J. Saucedo-Velázquez, G. Gutiérrez-Urueta, A. Pacheco-Reyes, and W. Rivera, “Case study: Design of an absorption refrigeration system for milk preservation in Jalisco, Mexico,” *Case Studies in Thermal Engineering*, vol. 44, p. 102866, Apr. 2023, doi: 10.1016/j.csite.2023.102866.

[12] K. Solano–Olivares *et al.*, “Life cycle assessment of a solar absorption air-conditioning system,” *J Clean Prod*, vol. 240, Dec. 2019, doi: 10.1016/j.jclepro.2019.118206.

[13] J. Bukoski, S. H. Gheewala, A. Mui, M. Smead, and S. Chirarattananon, “The life cycle assessment of a solar-assisted absorption chilling system in Bangkok, Thailand,” *Energy Build*, vol. 72, pp. 150–156, Apr. 2014, doi: 10.1016/j.enbuild.2013.12.034.

[14] S. Rajabi Hamedani, M. Villarini, V. Marcantonio, U. di Matteo, D. Monarca, and A. Colantoni, “Comparative energy and environmental analysis of different small-scale biomass-fueled CCHP systems,” *Energy*, vol. 263, Jan. 2023, doi: 10.1016/j.energy.2022.125846.

[15] A. Maione, N. Massarotti, R. Santagata, and L. Vanoli, “Environmental assessment of a heating, cooling and electric energy grid from a geothermal source in Southern Italy,” *J Clean Prod*, vol. 375, Nov. 2022, doi: 10.1016/j.jclepro.2022.134198.

[16] N. Chaiyat, “A multigeneration system of combined cooling, heating, and power (CCHP) for low-temperature geothermal system by using air cooling,” *Thermal Science and Engineering Progress*, vol. 21, Mar. 2021, doi: 10.1016/j.tsep.2020.100786.

[17] Horizon 2020, “Long-Term Joint EU-AU Research and Innovation Partnership on Renewable Energy - LEAP-RE project,” *European Commission*, 2021. https://www.leap-re.eu/project-context/ (accessed Mar. 20, 2023).

[18] International Organization for Standardization (ISO), “ISO 14040:2021—Environmental management — Life cycle assessment — Principles and framework. Environ. Manage.,” *Geneva, Switzerland*, 2021.

[19] International Organization for Standardization (ISO), “ISO 14044:2021 Environmental management - Life cycle assessment - Requirements and guidelines. Environ. Manage.,” *Geneva, Switzerland*, 2021.

[20] “EES: Engineering Equation Solver. http://www.fchart.com/.”

[21] “OpenLCA: Open source Life Cycle and Sustainability Assessment software. https://www.openlca.org/.”

[22] E. Moreno-Ruiz *et al.*, “ Documentation of changes implemented in ecoinvent database v3.6. ecoinvent Association,” Zürich, Switzerland, 2019.

[23] “The World Energy Absorption Chillers Europe Ltd,” *https://www.worldenergyeurope.eu/index.html*.

[24] B. O. Ayugi and G. Tan, “Recent trends of surface air temperatures over Kenya from 1971 to 2010,” *Meteorology and Atmospheric Physics*, vol. 131, no. 5, pp. 1401–1413, Oct. 2019, doi: 10.1007/s00703-018-0644-z.

[25] S. M. S. Mahmoudi and M. Akbari Kordlar, “A new flexible geothermal based cogeneration system producing power and refrigeration,” *Renew Energy*, vol. 123, pp. 499–512, Aug. 2018, doi: 10.1016/j.renene.2018.02.060.

[26] J. A. Evans *et al.*, “Specific energy consumption values for various refrigerated food cold stores,” *Energy Build*, vol. 74, pp. 141–151, May 2014, doi: 10.1016/j.enbuild.2013.11.075.

[27] M. El Haj Assad *et al.*, “Space cooling using geothermal single-effect water/lithium bromide absorption chiller,” *Energy Sci Eng*, vol. 9, no. 10, pp. 1747–1760, Oct. 2021, doi: 10.1002/ese3.946.

[28] J. A. Evans *et al.*, “Specific energy consumption values for various refrigerated food cold stores,” *Energy Build*, vol. 74, pp. 141–151, May 2014, doi: 10.1016/j.enbuild.2013.11.075.

Exergy and Environmental Analysis of the Substitution of Coal for Biomass in Thermal Power Plants in Brazil

Leonardo A. Ferraresi Bassi[a], Silvio de Oliveira Junior[b]

[a] Polytechnic School of the University of São Paulo, São Paulo, Brazil, leobassi@gmail.com
[b] Polytechnic School of the University of São Paulo, São Paulo, Brazil, soj@usp.br

Abstract:

In the last decade, biomass consumption for thermal and electrical energy generation presented significant growth, as part of the plan to reduce greenhouse gas emissions through the gradual substitution of fossil fuels for renewable sources. In Brazil, although coal burning is still allowed in thermal power plants, the environmental demand is imminent for its substitution for less polluting sources and financial institutions already take a stand against coal investments, rising the pressure over existing consumers. This paper intends to identify and model coal-based power generation plants and compare its performance to that of different types of biomass available in Brazil – wood chips, wood pellets, sugarcane bagasse pellets – which are candidates to substitute coal in a large scale. Energy and exergy approaches are used to assess the full life cycle efficiency of these fuels, with a focus on the fuel combustion for steam generation, enabling the identification of inefficiencies and the selection of the most interesting operational opportunities. Despite of the life cycle specific energy consumption of biomass being higher than that of coal, its environmental performance is highly advantageous, drastically reducing fossil CO_2 emissions in the combustion process. When comparing pellets to dry wood chips, under the aspect of life cycle specific energy, biomass pellets result in a significantly higher specific energy consumption compared to dry wood chips, due to the thermal energy demand of drying and pelletizing stages. Such distinction between the performance of different types of low moisture biomass may only be detected if the life cycle approach is utilized. From the perspective of life cycle energy efficiency, the use of less processed types of biomass such as dried wood chips is preferrable over pellets.

Keywords:

Biomass; Thermal power plants; Coal substitution; Exergy analysis.

1. Introduction

Climate changes have encouraged efforts worldwide to reduce greenhouse gas emissions through the gradual insertion of renewable energy sources in substitution of fossil fuels, among which coal stands out as a major emitter to be controlled.

Coal substitution is an alternative to the reform of existing coal-based power plants for controlling NOx and SOx emissions limits, which tends to be an expensive solution, or even to their shutdown. Required investment for NOx and SOx control might be prohibitive and force these plants to interrupt operation [1].

Large scale power plants in the European Union have stricter atmospheric emissions limits to attend in the current decade, as described in BREF – Best Available Techniques Reference Documents – regarding not only CO_2 emissions, but also NOx and SOx emissions. IEEFA [1] shows that, from a sample of 600 solid fuel based power plants with capacities higher than 50 MW, more than 43% are not in conformity with new limits for SOx (180-320 mg/Nm³) and 69% were considered in non conformity with new limits for NOx (150-175 mg/Nm³).

In that context, as it is reported by Escobar [2], since 2010 biomass consumption in the European Union has presented significant growth. In opposition to the intermittent behavior of solar and wind-based power generation, biomass is adequate as a fuel for base load power plants.

In the United Kingdom, for instance, Drax power plant is one of the largest base load units, with an installed capacity of 4.0 GW, originally coal-based. From this total, approximately 2.6 GW have been converted to burn biomass pellets, which are mostly wood-based and imported from North America [3]. Other examples of

coal to biomass conversions are reported by boiler manufacturers and contractors such as Mitsubishi Power [4], Hofor [5] and AET [6], which also list well succeeded conversions in Denmark, Finland and Canada.

By sharing physical characteristics with coal, biomass might be applied in existing coal-based power plants after adaptations in the fuel storage and combustion systems, which would result in a significant impact in the Brazilian electricity matrix. Although mineral coal represents a small fraction of the Brazilian matrix, it causes the highest specific CO_2 emissions for each MWh of generated electricity [7].

The Brazilian electricity matrix currently reports 6 operational coal-based pure power plants, with capacities ranging from 350 MW to 720 MW, and 3 coal-based cogeneration plants, with capacities from 75 MW to 104 MW [8], [9]. These plants are concentrated in the southern region, for which coal is mainly provided by national mines, and in the northern coast, for which coal is imported from Colombia and the USA.

At least since 2009, there have been reports pointing out that coal substitution or co-firing with biomass would be a promising alternative for clean electric generation in Brazil [10], but until this time there have not been yet registers of coal-based cogeneration or pure power plants to have firmly migrated to biomass. In the meantime, however, the potential of utilizing biomass for energy purposes has been extensively reported, usually highlighting *Eucalyptus* chips or pellets [2], [11], sugarcane bagasse pellets [12], [13] and straw pellets derived from many sources, such as rice, soy and corn [11].

The objective of this work is to compare the processes of electricity generation by coal combustion and biomass combustion, in several forms, in order to identify and quantify the potential of utilizing biomass as an energy source to substitute coal. This analysis uses energy and exergy approaches to evaluate the performance of the technological route for each fuel, as well as calculating CO_2 emissions resulting from their life cycle. This study should assess what are the impacts of substituting coal for biomass and what are the resulting efficiencies in each case.

2. Materials and methods

The simulations of typical thermal power plants are carried out in PowerFNESS® software [14], which contains a thermodynamic database for the working fluids used in power cycles and acts as an equation solver for mass and energy balances, given the inputs for equipment efficiencies and operational boundary conditions (flow, pressure and temperature).

The software is based on the construction of thermal cycles consisting of equipment, nodes and lines. The nodes represent boundary conditions and the union or separation of flow currents; in each node, fluid properties are calculated and updated on every simulation step. The lines serve as connections between nodes, which correspond mainly to the pipe sections and connections from the real system. When running the model, mass and energy balance equations are linearized and solved by the finite element method, until convergence to a steady state flow condition is reached.

A model description is presented in the following sections.

2.1. Process modeling

Typical plants for power and heat cogeneration or pure power generation are presented in Figure 1. Energy and exergy efficiencies will further be calculated based on these configurations.

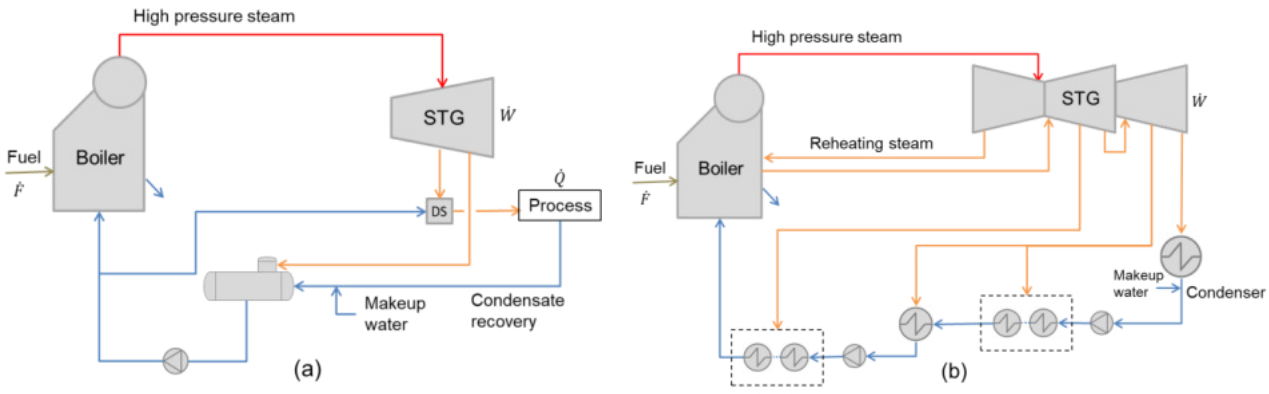

Figure 1. Thermodynamic cycles for power generation plants: a) Cogeneration of power and heat; b) Pure power generation.

Table 2. Main operation parameters for cogeneration and pure power generation configurations.

Process parameter	Unit	Cogeneration Plant	Pure Power Plant
Boiler			
Type	-	Circulating Fluidized Bed / Pulverized Fuel	Pulverized Fuel
Operating steam pressure	bar a	85	170
Operating steam temperature	°C	485	540
Thermal efficiency	%	91	93
Turbogenerator			
Exhaust steam pressure	bar a	15	0.085
Thermal efficiency	%	84	86
Generator / Reductor losses	%	3	2
Process heat demand			
Steam flow	t/h	500	-
Steam pressure	bar a	15	-
Steam temperature	°C	210	-
Condensate Recovery			
Recovery rate	%	90	100
Temperature	°C	100	43
Makeup water			
Temperature	°C	25	25

Since 2 out of the 3 coal-based cogeneration plants listed by the Brazilian National Electric Power Agency are part of alumina refineries [8-9], in the Cogeneration scenario it is assumed that the process demands low pressure steam at 15 bar a, as this is representative of such refineries [15].

Regarding the boiler technology, typical configurations for Brazilian coal-based plants considered in this study are equipped with pulverized coal boilers, whose full conversion to biomass is arguably viable and has been applied in the previously mentioned cases [4], [5], [6]. The same premise could not be adopted for fluidized bed or grate boilers. Biomass has lower carbon content than coal, therefore producing less CO_2 in combustion, which is a gas that highly contributes to radiation heat exchange. Since grate boilers are the most dependent on radiation heat exchange, their performance would be the most harmed after fuel migration. Also, good performance in fluidized bed boilers is deeply related to fuel ash content, which is much lower for most types of biomass when compared to coal. Fluidized bed boilers that were originally designed to burn coal, exclusively, would hardly be able to maintain design bed temperature and achieve design capacity after the conversion to biomass.

2.2. Fuel characterization

Both *Eucalyptus* and sugarcane bagasse derived fuels are selected as substitute fuels for coal, given their abundancy as residues and potential to be grown in large scale sustainable forest plantations [2], [11].

Elemental compositions and moisture content for each fuel are presented in Table 2.

Table 2. Elemental composition of the selected fuels (dry basis).

Element	Coal	*Eucalyptus [16]*	Sugarcane bagasse [16]
C	72.7%	47.5%	46.5%
H	4.4%	6.1%	6.2%
N	1.1%	1.5%	1.2%
O	8.0%	43.8%	44.4%
S	2.4%	0.0%	0.0%

Ashes	11.4%	1.1%	1.8%
Moisture	12.0%	15.0% (dry chips) 7.0% (pellets)	7.0% (pellets)

Ambient conditions are $T_0 = 25$ °C and $p_0 = 1$ bar.

Regarding fuel chemical exergy, Szargut [17] expressions for solid fuels are utilized, taking as inputs fuel LHV, moisture content and elemental composition:

$$b_{q,biom} = \beta.\left(LHV_{fuel} + x_w.h_{lv}\right) + x_w.b_{q,H2O,l} + x_S.\left(b_{q,S} - LHV_S\right) + x_{ash}.b_{q,ash} \quad (1)$$

Factor β varies according to mass composition of the respective fuel. The following correlations are established: any solid fuel, Eq. (2); coal, Eq. (3); wood, Eq. (4).

$$\beta = \frac{1.044 + 0.016(H/C) - 0.3493(O/C)[1 + 0.531(H/C)] + 0.0493(N/C)}{1 - 0.4124(O/C)} \quad (2)$$

$$\beta = 1.0437 + 0.1896\left(x_{H_2}/x_C\right) + 0.2499\left(x_{O_2}/x_C\right) + 0.0428\left(\frac{x_{N_2}}{x_C}\right) \quad (3)$$

$$\beta = \frac{1.0412 + 0.216\left(x_{H_2}/x_C\right) + 0.2499\left(x_{O_2}/x_C\right)\left[1 + 0.7884\left(x_{H_2}/x_C\right)\right] + 0.045\left(x_{N_2}/x_C\right)}{1 + 0.3035\left(x_{O_2}/x_C\right)} \quad (4)$$

From Eq. (1) to Eq. (4) and elemental compositions presented in Table 2, the chemical exergy for each fuel is calculated, as shown in Table 3, as well as the chemical exergy to LHV ratio.

Table 3. LHV and chemical exergy for each selected fuel.

Property	**Unit**	**Coal**	***Eucalyptus* dry chips**	***Eucalyptus* pellets**	**Sugarcane bag. pellets**
Moisture	%	12%	15%	7%	7%
Bulk density	kg/m³	900	350	657	726
LHV (per mass)	MJ/kg	25.6	14.8	17.2	18.3
LHV (per vol.)	MJ/m³	23040	5180	11300	13311
$LHV_{biomass}$ / LHV_{coal} (per vol.)	-	-	22%	49%	58%
bq	MJ/kg	28.4	15.7	18.0	19.1
bq/LHV	-	1.110	1.061	1.045	1.043

Aiming for operating the boilers at their original design capacities, substitute fuels shall have heating values and densities as close as possible to those of coal. The volumetric energy density of solid fuels has impacts both to the storage system design and to the boiler itself, whose furnace volume defines how much fuel can be introduced and how much heat can be generated. This hinders the utilization of *in natura* biomass at high moisture, due to its lower volumetric energy density. Dry wood chips at 15% moisture content were selected so that their LHV and density properties would be closer to pellets and coal. The necessary heat for drying wood chips from 40% down to 15% will further be considered in its life cycle analysis, as discussed in section 3.2. Wood chips would not serve as an alternative fuel for pulverized fuel boilers, but only for circulating fluidized bed boilers.

As presented in Table 3, all three types of biomass resulted in low values of chemical exergy to LHV ratio, ranging from 1.043 to 1.061, which is caused by their low moisture content. *In natura* wood chips with moisture content up to 40% would result in even higher ratios, up to 1.17, which would significantly harm the exergy efficiency of power plants.

Although dry wood chips and pellets are types of biomass with relatively high energy densities, they are still less dense than coal and would require the expansion of fuel storage, handling systems and the adaptation of burners, in the case of pulverized fuel boilers. Fuel silo (or bunker) and the pulverizing mill shall be adapted, as well as forced and induced air fans, since flue gas flow is expected to rise for higher moisture content fuels.

2.3. Efficiencies

In cogeneration plants, both electric power and useful heat for process consumption are considered when calculating the plant efficiency, as shown in Eq. (5):

$$\eta_e = \frac{\dot{W} + \dot{Q}_u}{\dot{F}} \tag{5}$$

In which:

- $\dot{W}$ is gross electric power
- $\dot{Q}_u = \dot{m}_{stm}(h_{stm} - h_{mup})$;
- $\dot{F} = \dot{m}_{coal}.LHV_{coal}$ or $\dot{F} = \dot{m}_{bio}.LHV_{bio}$

In analogy, exergetic efficiency is calculated as in Eq. (6):

$$\eta_b = \frac{\dot{W} + \Delta\dot{B}_f}{\dot{B}_q} \tag{6}$$

In which:

- $\dot{W}$ is gross electric power
- $\Delta\dot{B}_f = \dot{m}_{stm}(b_{stm} - b_{mup}) = \dot{m}_{stm}[(h_{stm} - h_{mup}) - T_0.(s_{stm} - s_{mup})]$;
- $\dot{B}_q = \dot{m}_{coal}.b_{q,coal}$ or $\dot{B}_q = \dot{m}_{bio}.b_{q,bio}$

2.4. Life Cycle Analysis

2.4.1. Coal route

Figure 2 shows the most relevant stages in mineral coal life cycle, as well as resources consumed and gas effluents produced in each stage. As a premise in this study, only existing power plants will be evaluated, therefore both the plant construction and decommissioning are excluded from the routes considered.

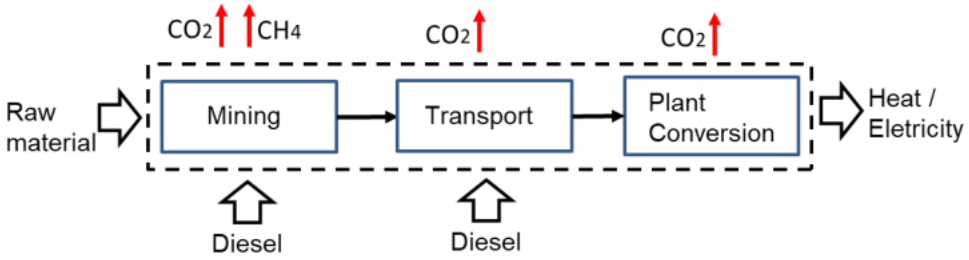

Figure 2. Mineral coal route to be consumed in existing power plants. Adapted from [18].

Figure 2 shows that, besides CO2 resulting from coal combustion and Diesel consumption in transportation vehicles, it is also relevant to count CH_4 emissions in mining stage. Methane is produced during coal formation process and is gradually liberated to the atmosphere as coal layers shatter and gas deconfines. Methane contribution in total equivalent CO_2 emissions equals 1% to 9% [18].

The tracking of mineral coal allows to calculate specific energy consumption rates and CO_2 emissions in terms of electric power generated as the final product of the power plant.

The following premises are considered [18]:

- Power plant life time: 30 years;
- Transportation logistics: road transport, 100 km radius;
- Equivalency from CH_4 to CO_2: 21 kg CH_4 / 1 kg CO_2 (100 year period);
- CH_4 contribution in total equivalent CO_2 emissions: 3%.

2.4.2. Biomass route

Figure 3 shows the most relevant stages in biomass life cycle. After wood extraction and chipping, wet wood chips are dried to 15% before being transported to the power plants. Both for wood and sugarcane bagasse pellets, not only the material is dried, but also compacted to pellets. Besides Diesel consumption in extraction and transport stages before reaching to the power plant, drying and pelletizing stages also demand relevant heat and electricity.

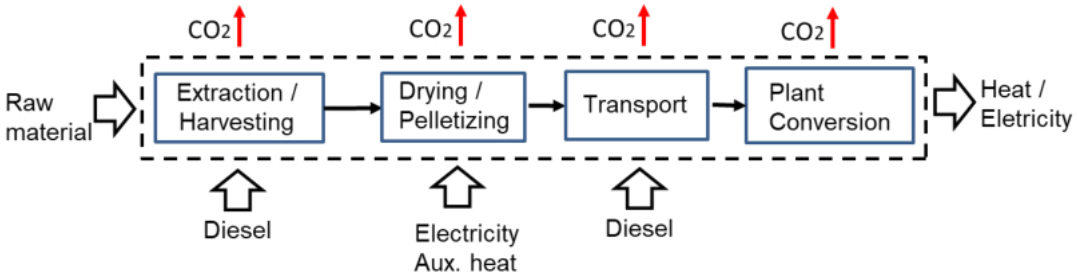

Figure 3. Biomass route to be consumed in existing power plants. Adapted from [19].

Premises for energy consumption and CO_2 emissions along biomass life cycle are the following [19]:

- Extraction executed by field harvesters, forwarders and chargers;
- Transportation logistics: road transport, 100 km radius;

As commented by [19], since silvicultural activities have a low level of mechanization compared to biomass extraction, harvesting and transport, then Diesel consumption at that stage is assumed to be not relevant to this analysis. Silviculture is therefore omitted from the biomass route illustrated in Figure 3.

3. Results and discussion

3.1. Thermal power plants

Table 4 shows the calculates efficiencies for each fuel and both plant configurations.

Table 4. Calculated efficiencies for each configuration.

Process parameter	Unit	Coal	Dry wood chips	Wood pellets	Sugarcane bag. pellets
Cogeneration Plant					
Fuel consumption	t/h	60.3	104.3	90.0	84.5
Fuel energy	MWh	430.2	428.8	429.8	429.7
Fuel exergy	MWh	475.5	454.9	449.2	449.1
Electricity generated	MWh	52.3	52.3	52.3	52.3
Steam to process	t/h	500.0	500.0	500.0	500.0
Thermal energy	MWh	338.5	338.5	338.5	338.5
Thermal exergy	MWh	136.6	136.6	136.6	136.6
Energy efficiency	%	90.9%	90.9%	90.9%	90.9%
Exergy efficiency	%	39.7%	41.5%	42.1%	42.1%
Pure Power Plant					
Fuel consumption	t/h	125.6	218.1	187.7	176.4
Fuel energy	MWh	896.6	896.6	896.6	896.6
Fuel exergy	MWh	991.0	951.2	937.2	936.9
Electricity generated	MWh	365	365.0	365.0	365.0
Energy efficiency	%	40.7%	40.7%	40.7%	40.7%
Exergy efficiency	%	36.8%	38.4%	38.9%	39.0%

The calculated values shown in Table 4 refer to gross electric power generation and energy efficiency, therefore not considering impacts on electricity consumption by auxiliary systems within the power plants, such as fuel milling before pulverization or induced and forced draft fans. Although it is expected that the fans demand will increase due to higher flue gas flows resulting from wet biomass compared to coal, such impact would represent less than 0,1% of total power generation and may be neglected in this preliminary approach. Auxiliary systems electric load and general losses in a pulverized fuel fired power plant would typically represent up to 10% of gross electric power generation, therefore resulting in a net energy efficiency of 35% to 37% [18], which is consistent with the calculated gross energy efficiency of 40.7% as shown in Table 4. Analogously, exergy efficiency for pure power plants would be reduced to the range between 33% and 35% when net electricity generation is considered.

Impacts on boiler efficiency due to biomass moisture content were minimized in this study due to the selection of low moisture (<15%) types of biomass, but this would be a major factor in the case of *Eucalyptus* and sugarcane bagasse *in natura*, harming the efficiency and making it not viable to convert and still preserve the boiler design capacity.

From the exergy approach, the advantage is clear for the use of dry types of biomass instead of coal. As shown previously in Table 3, all three types of biomass with low moisture content resulted in close values of chemical exergy comparing their own LHV, which positively affects the exergy efficiencies. Energy and exergy losses due to the process of drying biomass are not detected in the thermal plant analysis, making it necessary to analyze the fuel life cycle to correctly quantify its influence.

Regarding the cogeneration configuration, exergy efficiencies are remarkably lower than energy efficiencies, as expected, since exergy approach calculates process steam as a low value stream, with low potential for electric power generation (15 bar a, 210°C).

3.2. Fuel life cycle

Coal and biomass life cycle performances are presented in Table 5. Each line shows the contribution of the most relevant energy sources consumed – Diesel (as fuel for extraction, handling and transportation vehicles), heat (for biomass drying), electricity – at specific energy consumption rates and equivalent CO_2 emissions along the fuel cycle from extraction stages to electricity conversion process.

Specific energy is calculated as the energy input to the energy output ratio, which is the inverse of the efficiency. The CO_2 emissions for coal and biomass life cycles are calculated according to [18] and [19], respectively, as the sum of direct, indirect and life cycle emissions.

Table 5. Calculated energy consumption and CO_2 emissions for each configuration.

Life cycle stage	Unit	Coal	Dry wood chips	Wood pellets	Sugarcane bag. pellets
Diesel					
Specific Energy	MJ/MWh	389	319	293	220
CO2 emissions	$kgCO_2$/MWh	28.2	22.4	21.2	16.0
Heat					
Specific Energy	MJ/MWh	0	969	1681	3778
CO_2 emissions	$kgCO_2$/MWh	0	0.3	0.5	1.1
Electricity					
Specific Energy	MJ/MWh	1590	766	571	403
CO_2 emissions	$kgCO_2$/MWh	2.2	1.1	0.8	0.6
Fuel					
Specific Energy	MJ/MWh	10073	10286	10286	10286
CO_2 emissions	$kgCO_2$/MWh	905.0	0.3	1.4	1.3
Total specific energy	MJ/MWh	12052	12340	12831	14687
Total CO_2 emissions	$kgCO_2$/MWh	935.4	24.0	23.9	18.9

Energy consumption and equivalent CO_2 emissions due to fuel extraction and distribution stages highly depend on the characteristics of the mining area (in the case of coal) and the distances to the power plant sites. The premises presented in section 2.3 are estimations based on the main Brazilian power plants, but they should be revised when studying specific cases. In any respect, such values represent a small fraction of total energy and emissions, therefore not harming final conclusions here stated.

As Table 5 shows, biomass processing stage (chipping, drying, compaction) represents a significant fraction of total specific energy consumed, from 8% in the case of dry wood chips to 25% in the case of sugarcane bagasse pellets, resulting in higher values of total specific energy consumption than that of coal. Although an economical study is beyond the scope of this paper, it is relevant to mention that biomass processing also implies in higher production costs, which may inhibit the selection of dry versions of biomass. Conversions of this type will most probably take place in cogeneration and power plants which must preserve and guarantee the current heat and electric power generation capacities in the future scenarios. Otherwise, wet versions of wood and sugarcane bagasse would be acceptable, even if requiring an expansion in the storage area or causing derating in the boiler thermal capacity.

Both for coal and biomass, the energy conversion stage is dominant in the life cycle, representing from 70% to 84% of total energy consumption. This indicates that the biggest efforts to achieve higher efficiencies should be focused on this stage, through the correct evaluation and selection of the burner technology, biomass properties and operation routines.

In contrast to the energy efficiency performance, the environmental performances of all three types of biomass show significant benefits when compared to coal performance. Table 5 shows that wood chips, wood pellets and sugarcane bagasse pellets emit from 19.0 to 24.0 equivalent kg CO_2 for each electric MWh generated, which represents less than 3% of mineral coal specific emissions. When multiplying this difference for the annual coal-based electricity generation in the Brazilian matrix in 2022, of 15327 GWh [40], it results in avoiding up to 14.0 equivalent Mt CO_2 each year, when converting 50% of the total installed coal-based capacity. Although coal currently represents only 3.3% of Brazilian electricity generation, it is responsible for around 24.4% of CO_2 emissions in that sector. The conversion of 50% of coal-based installed capacity to dry types of biomass would result represent an annual reduction of around 12% in annual CO_2 emissions in the electricity generation sector.

4. Conclusions

Under the global tendency of reducing CO_2 emissions and adhering to net-zero targets, it is expected that large scale coal-based systems will have to be converted to the use of renewable fuels, at least partially. In that decision, long term technical and environmental impacts need to be evaluated. This paper approaches the life cycle assessment of coal and different types of biomass when applied in typical configurations of the main coal-based power plants and cogeneration installed in Brazil.

Empirical correlations found in literature were utilized to calculate the chemical exergy of coal and biomass, reassuring that the resulting exergies for low moisture fuels deviate less from their LHV, which slightly increases the exergy efficiency of the thermal power plants from 38,4% to around 39,0% when comparing dry wood chips to pellets. Nevertheless, under the aspect of life cycle specific energy, biomass pellets result in a 19% higher specific energy consumption compared to dry wood chips, due to the significant thermal energy demand of drying and pelletizing stages. Such distinction between the performance of different types of low moisture biomass may only be detected if the life cycle approach is utilized, since energy efficiency within the power plant cycle may be very similar among them.

The analysis of large scale coal-based plants shows that the conversion to dry types of biomass (up to 15% of moisture content) is viable and demands relatively low intervention in the existing infrastructure for coal, as it has been previously demonstrated mainly in European plants. Particularly in Brazil, this kind of conversion is greatly motivated by the high availability and diversity of biomass residues and land for sustainable plantation. From the perspective of life cycle energy efficiency, the use of residues and less processed types of biomass is highly preferrable over pellets.

Nomenclature

b specific exergy, kJ/kg
$\dot{B}$ exergy flow, kW
$\dot{F}$ fuel energy flow, kW
h specific enthalpy, kJ/kg
$\dot{m}$ mass flow, kg/s
LHV lower heating value, kJ/kg
$\dot{Q}$ heat rate, kW
s specific entropy, kJ/kg K
T_0 Ambient temperature, K
$\dot{W}$ Net power generated, kW
x Mass fraction

Greek symbols

η efficiency
Δ change

Subscripts and superscripts

b exergetic
bio biomass
C carbon
ash ashes
e energetic
f physical
H_2 hydrogen
H_2O water
N_2 nitrogen
O_2 oxygen
q chemical
mup make-up
S sulphur
u useful
stm steam
w water (moisture)

References

[1] IEEFA – Institute for Energy Economics and Financial Analysis. Europe's Coal-Fired Power Plants: Rough Times Ahead, 2017 - Available at: <https://ieefa.org/wp-content/uploads/2017/05/Europe-Coal-Fired-Plants_Rough-Times-Ahead_May-2017.pdf> [accessed 10.03.2023].

[2] Escobar, J. F., Sustainable wood production for energy in Brazil. The case of wood pellets [doctoral thesis]. São Paulo, Brazil: Graduate Program in Energy at the University of São Paulo – PPGE, 2016.

[3] Drax. Drax closer to coal-free future with fourth biomass unit conversion, 2018 - Available at: <https://www.drax.com/press_release/drax-closer-coal-free-future-fourth-biomass-unit-conversion/> [accessed 10.03.2023].

[4] Mitsubishi Power. Pulverized Biomass Fired Boiler Technology - Available at: https://power.mhi.com/products/boilers/technology/pulverized-biomass-fired [accessed 10.03.2023].

[5] Hofor: About Amager Power Station - Available at: <https://www.hofor.dk/baeredygtige-byer/fremtidens-fjernvarme/amagervaerket/om-amagervaerket/> [accessed 10.03.2023].

[6] AET Biomass: Retrofitting and biomass fuel conversion. Bioenergy Insight, 32-33, 2020 - Available at: <https://www.aet-biomass.com/Admin/Public/DWSDownload.aspx?File=%2FFiles%2FFiles%2FPDF%2FArticles%2Faet_Bioenergy-Insight_MayJune_2020.pdf> [accessed 10.03.2023].

[7] Flórez-Orrego, D., Silva, J.A.M, Oliveira JR., S. Renewable and Non-Renewable Exergy Cost and Specific CO_2 Emission of Electricity Generation: The Brazilian Case. Energy Conversion and Management 85 (2014) 619-629.

[8] EPE. Brazilian Energy Balance Year 2021 - Available at: <https://www.epe.gov.br/sites-pt/publicacoes-dados-abertos/publicacoes/PublicacoesArquivos/publicacao-479/topico-521/Relato%CC%81rio%20Si%CC%81ntese%20BEN%202020-ab%202019_Final.pdf> [accessed 10.03.2023].

[9] ANEEL – National Electric Power Agency. ANEEL's Generation Information System (SIGA), 2020 - Available at: <https://www.aneel.gov.br/siga> [accessed 10.03.2023].

[10] Pereira, F. L.; Bazzo, E.; Oliveira Jr, A. A. M. Biomass Co-Firing as an Alternative Technology for a Clean Coal Electric Generation in Brazil. Gramado, Brazil - 20th International Congress of Mechanical Engineering, November 15-20, 2009.

[11] EPE. Technical Note 17/18: Energy potential of sustainable forest residues and wood industrialization residues, 2018 - Available at: <https://www.epe.gov.br/sites-pt/publicacoes-dados-abertos/publicacoes/PublicacoesArquivos/publicacao-312/NT-EPE_17-2018_Biomassa-Lenhosa-Residual_2018-10-17.pdf> [accessed 10.03.2023].

[12] Silva, F. T. F. Assessment of agricultural residues torrefaction and densification in Brazil [dissertation]. Rio de Janeiro, Brazil - COPPE, Federal University of Rio de Janeiro, 2017.

[13] Nova Cana. Raizen sugarcane bagasse pellets are exported to the UK, 2021 - Available at: <https://www.novacana.com/n/etanol/mercado/exportacao/pellets-bagaco-cana-raizen-exportados-reino-unido-130121> [accessed 10.03.2023].

[14] PowerFNESS®, version 7.1.8.2. Licensed by FIGENER, 2023.

[15] EPE. Energy efficiency analysis in selected industrial sectors – Aluminium sector, 2017 – Available at: <https://www.epe.gov.br/sites-pt/publicacoes-dados-abertos/publicacoes/PublicacoesArquivos/publicacao-314/topico-407/PRODUTO%203_Vpublicacao.pdf> [accessed 10.03.2023].

[16] Pereira, B. L. C. Properties of pellets: biomass, additives and heat treatment [doctoral thesis]. Viçosa, Brazil - Universidade Federal de Viçosa, 2014.

[17] Szargut, J. Exergy Method: Technical and Ecological Applications. Boston, WIT Press, 2005.

[18] Lenzen, M. Life cycle energy and greenhouse gas emissions of nuclear energy: A review. Energy Conversion and Management 49, 2178-2199, 2008.

[19] Pereira, M. F. Exergoenvironmental analysis concerning the wood chips and wood pellets production chains [doctoral thesis]. Florianopolis, Brazil –Federal University of Santa Catarina, 2018.

Experimental study of an ultrasonic spray atomiser as an evaporative cooler

Pedro Martínez[a], Javier Ruiz[a], Manuel Lucas[a], Jonás Pérez[a], Pedro Navarro[b] and Alberto Rodríguez[a]

[a] Miguel Hernández University of Elche, Avda. de la Universidad, s/n, 03202 Elche, Spain, j.ruiz@umh.es, CA
[b] Technical University of Cartagena, Dr. Fleming, s/n, 30202 Cartagena, Spain

Abstract:

The use of evaporative cooling techniques for pre-cooling the inlet air of a condenser used in air conditioning applications has proven to be very effective in improving its performance. Ultrasonic techniques constitute a promising alternative to improve the design of evaporative pre-cooling systems. Compared to direct spray cooling applications, not only they eliminate the pressure loss induced in the inlet air stream but also, they are capable of generating smaller droplet sizes with reduced power consumption than a high-pressure spray nozzle. This paper deals with an experimental investigation of an ultrasonic spray atomiser used to pre-cool the air entering to the condenser of a heat pump used in air-conditioning applications. A set of 12 experimental tests were conducted on a test bench consisting of a subsonic wind tunnel with an ultrasonic spray atomiser installed in the test section. The influence of the air velocity and mass flow rate of sprayed water (depending on the number of active atomisers) on the performance of the system was investigated. The results of the study show the pre-cooling capacity of this system, under different operating conditions, through several performance indicators: evaporative cooling efficiency (saturation efficiency), temperature drop, wet bulb depression and evaporated water efficiency. The highest values of evaporative cooling efficiency occur in the low speed range of the tested airflows, for configurations of the atomisation system with a high number of active atomisers, and it has been found that the evaporative pre-cooling process is not homogeneous throughout the airflow for some operating conditions.

Keywords:

Evaporative cooling, ultrasonic spray atomiser, cooling efficiency, air conditioning

1. Introduction

Evaporative cooling techniques applied to the condenser of a refrigerating machine represent one of the most effective and immediately applicable solutions for improving the efficiency of domestic and commercial air conditioning systems worldwide. With these techniques it is possible to reduce significantly, mainly in countries with hot-dry climates, the energy demand and the high consumption peaks. Energy savings contribute to reducing the dependence on fossil fuel in any country and have a direct impact on its economic development and growth, as well as decreasing greenhouse gas emissions.

A considerable amount of studies in the literature show the benefits of pre-cooling techniques applied to different air conditioning systems. There are different strategies to reduce the temperature of the air entering the condenser. The most widely studied systems can be classified into: evaporative packings or pads and spray or mist generators. For direct evaporative coolers, Martínez et al. [1] investigated how different thicknesses of cooling pads influenced the energy performance of a split-type air-conditioner. They found that the highest increase of 10.6% in the overall coefficient of performance (COP) was achieved by a thickness of about 100 mm. The main drawback of pre-cooling systems based on evaporative pads is the additional pressure drop produced in the condenser air stream. Furthermore, this effect is present even if pre-cooling is not activated. Pressure drop causes a reduction in the air flow rate through the condenser and a decrease in its ability to reject heat to the environment. This means an increase in the condensation pressure, an additional compressor consumption and a reduced cooling capacity of the air-conditioning system, [2]. When water is sprayed over the evaporative pads and pre-cooling is activated, the temperature drop of the intake air to the condenser far outweighs both effects, the pressure drop and the air flow rate reduction, and results in savings of energy consumed by the compressor. However, when the water injection is not activated, the evaporative pads still generate a pressure loss that penalises the energy consumption in the compressor. Compared with direct evaporative coolers, mist or deluge systems give further installation flexibility because of their low profile piping network and provide negligible flow resistance to the air stream. Yu et al. [3] analysed the cooling effectiveness of mist in pre-cooling condenser air for an air-cooled chiller. In a subtropical climate, pre-cooling the condenser air by mist brought an increase of 0.36–8.86% and 0.34–10.19% in the coefficient of performance of the chiller

under the normal mode (conventional head pressure control) and the VSD mode (variable speed control for the condenser fans), respectively. However, the use of water spray or deluge can cause corrosion, scaling, and fouling on the heat exchanger bundles if water droplets are carried by the airstream to the heat exchanger bundles of the condenser. To avoid this, the system is required to evaporate all water in the airstream to prevent water droplet contact with the heat exchanger surface. Special wet media or spray nozzles may be required to meet the requirement. High-pressure nozzles provide small water droplets but at a higher cost. Water quality affects the performance of the nozzles and their maintenance cost, [4]. In view of the drawbacks found in current techniques for pre-cooling, a search for alternatives seems appropriate.

Applications of ultrasonic energy to enhance a wide variety of processes or to improve system efficiency have been explored in recent years. Yao [5] reviewed the studies addressing the applications of ultrasound as a new technology in the field of Heating, Ventilation and Air-Conditioning (HVAC). The author claimed that, from a general point of view, all the effects produced by ultrasound could be interesting in applications involving heat or mass transport, decreasing both the external and internal resistance to transport. Yao et al. [6] presented a review of the state-of-the-art of high-intensity ultrasound and its applications. However, the authors did not specifically cite evaporative cooling as an application of ultrasound, denoting the little attention they have received to date. Up to the knowledge of the authors, the studies conducted by Ruiz et al. [7] and Martinez et al. [8] were the first attempt to apply ultrasonic techniques (mist generator) to pre-cool the air entering the condenser in an air conditioning application. The authors experimentally analysed the performance of an ultrasonic mist generation system in [8]. Its thermal performance and its water mist production capacity were assessed in terms of the mass flow rate of atomised water and size distribution of the droplets generated. A CFD model of an ultrasonic mist generator specifically designed for HVAC applications was reported in [7]. The model was validated using the results obtained in [8], and the authors conducted a parametric analysis including some physical variables involved in the cooling process, and, finally, carried out an optimisation process regarding the overall cooling performance of the ultrasonic generator.

However, although the tests were satisfactory and their scientific interest has been revealed by the recent publications achieved, there are still many aspects related to the search for the optimal design of the pre-cooling system based on ultrasound techniques (reduce wet length and water power consumption). In conclusion, the works referring to the pre-cooling of the inlet air with ultrasonic atomisation techniques have been reviewed and it has been observed that this technique has received limited attention for this application, with few references found in the literature to date. Despite this, it has been proven that ultrasound technology constitute a promising method to improve the design of evaporative pre-cooling systems. Therefore, the main objective of this paper is to study the performance of an ultrasonic spray atomiser used to pre-cool the air entering to the condenser of a heat pump used in air-conditioning applications. The influence of the air velocity and mass flow rate of sprayed water (number of atomisers) on the performance of the system was investigated.

2. Materials and methods

2.1. Experimental test facility

To evaluate the performance and cooling capacity of the water mist produced by the ultrasonic atomiser, a set of tests has been conducted on a redesigned test bench specifically adapted for this purpose. The test rig mainly consists of two components: ultrasonic spray atomisers and a subsonic wind tunnel where evaporative cooling takes place.

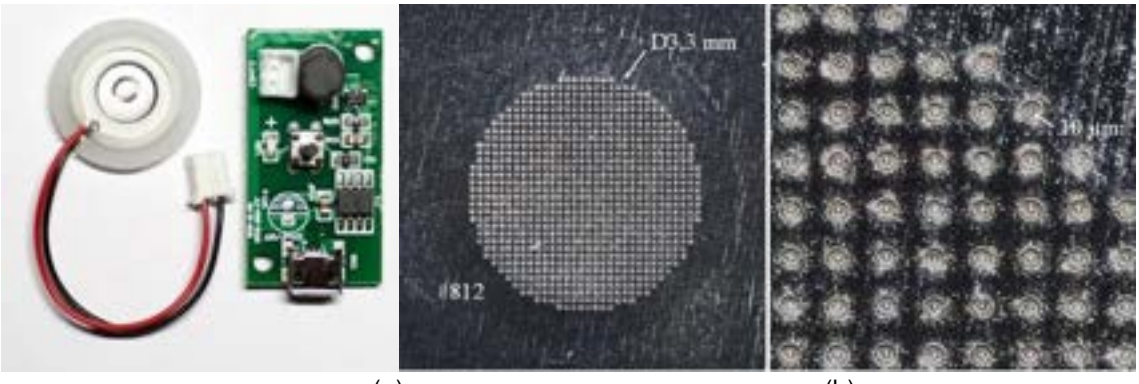

(a) (b)

Figure 1: (a) Used ultrasonic spray atomisers and an oscillator circuit PCB. (b) Microscopic image of the water outlet holes in the spray atomisers used.

The device used in the system is a ultrasound spray atomiser (Fig. 1 (a)). This is composed of a ceramic piezoelectric, which surrounds a porous metallic membrane, and an oscillator circuit PCB that generates a pulse signal at a frequency of 108 kHz for the spray atomiser. When the current is supplied, the piezoelectric initiates an expansion/contraction cycle. This oscillation allows the water to pass through its microscopic holes (around 10 μm, Fig. 1 (b)) , and pushes the drops forming a column of water spray. The mass flow rate is approximately $1.95 \cdot 10^{-5}$ kg s^{-1}. This component is characterised by having a low cost and consumption (1.3 W). Table 1 shows the operating conditions and technical specifications of a spray atomiser.

Table 1: Spray atomiser technical specifications.

Magnitude	Value
Disc diameter	15.5 mm
Ceramic core diameter	8.5 mm
Porous membrane diameter	3.3 mm
Microscopic Holes Diameter	10 μm
Input voltage	DC 5 V
Power	1.3 W
Resonance frequency	108 kHz
Mass flow rate	$1.95 \cdot 10^{-5}$ kg s^{-1}
Exit speed of the drops	2.5 m s^{-1}

In this research, several atomisers work at the same time, therefore, a hydraulic installation was built to supply several units at the same time. For this, an ABS plastic body was used for the connection of the atomisers with a system of flexible silicone pipes. On the other hand, to avoid creating bubbles in the pipes, it was decided to use a low-flow pump (RS PRO 20) for the recirculation of the water. It has a maximum flow rate of 650 ml min^{-1} and a consumption of 5 W. Fig. 2 shows a schematic representation of the configuration of 5 $\times$ 5 atomisers (rows $\times$ columns) with which the experimental tests were carried out.

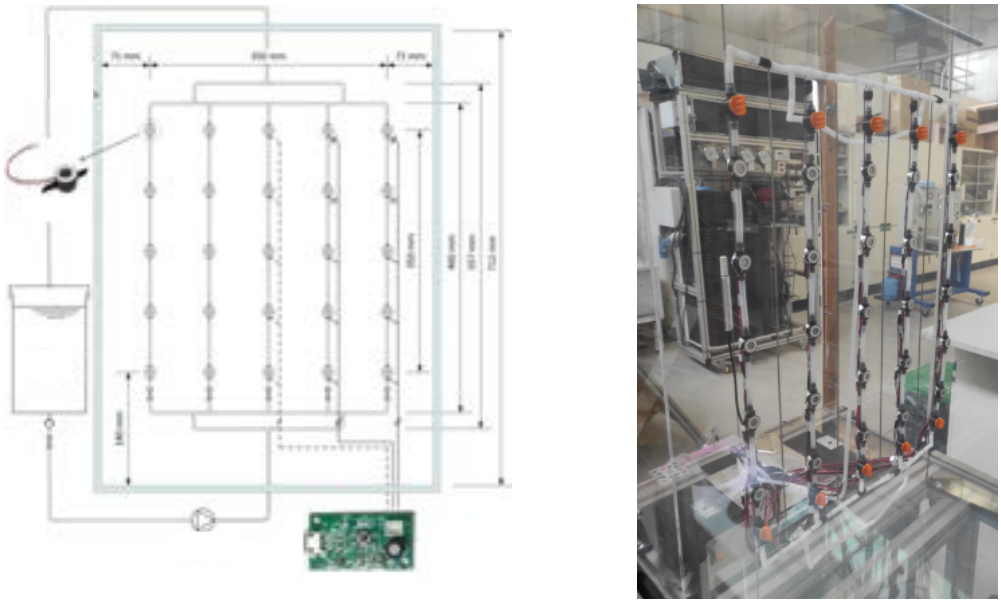

Figure 2: Scheme of the distribution of the spray atomisers in the form of a 5 $\times$ 5 manifold.

To carry out the experimental tests of ultrasonic evaporative cooling, the open-circuit subsonic wind tunnel shown in Fig. 3 was used. To ensure stable and uniform velocity profiles of the air flow, a nozzle was used along the honeycomb baffle (anti-turbulence screen), which was adapted for the tunnel entrance (leftmost part). It is not shown in the Fig. 3 because it is removed when modifications are made to the atomiser system. This nozzle has dimensions of 1.2 $\times$ 1.7 m^2 (cross-sectional) and a length of 1.55 m. While the test section of the wind tunnel has a cross section of 0.492 $\times$ 0.712 m^2 and a length of 5.3 m. A axial fan of 0.55-kW has been used to create the air flow inside the tunnel, which is located at the tunnel exit. This is associated with a variable-frequency drive that allows different air flows to be configured (from 0–3 m s^{-1}). The maximum

volumetric air flow rate allowed by the fan is 3783 m^3 h^{-1}. A detailed description of the wind tunnel can be found in [9, 10].

Figure 3: Subsonic wind tunnel facility in which the experimental tests are carried out.

2.2. Experimental procedure

A number of tests have been carried out to evaluate the performance of the ultrasonic spray system. Firstly, the flow rate of atomised water that the system is able to supply as a function of the number of working ultrasonic transducers has been studied by means of a gravimetric measurement method. A photographic technique with digital image processing has also been used to determine the size, emission speed and distribution of the droplets generated in the atomisation process. Finally, the pre-cooling capacity of atomised water when sprayed into an air stream has been evaluated as a function of both air flow velocity and atomised water flow rate (depending on the number of atomisers).

In order to reproduce in the wind tunnel the real operating conditions of the atomisation system when used to pre-cool the inlet air to a condenser of a conventional split-type air-conditioning system, tests were carried out with four different air flow rates covering the usual range of flow rates of this type of equipment: 0.5 m s^{-1}, 1 m s^{-1}, 1.5 m s^{-1} and 2 m s^{-1}. Different flow rates of atomised water were used in the tests using three configurations of the ultrasonic atomisation system with 5, 15 and 25 active atomisers, respectively, in order to determine the performance of the system in terms of water consumption and taking into account the power consumption of the ultrasonic transducers. Counting the different configurations of the atomisation system and the air flow velocities established in the wind tunnel, a total of 12 tests were carried out.

For each test, dry bulb temperature and relative humidity were measured at various positions along the central axis of the wind tunnel, as can be seen in Fig. 4, which shows a schematic of the location of the different sensors installed in the wind tunnel. On the other hand, a set of nine thermo-hygrometers was used to record the temperature and relative humidity distribution in a measurement cross section. T_{ms} and ϕ_{ms} refer to the average temperature and relative humidity at the measurement section. Finally, a hot-wire anemometer was used to measure the airflow peak velocity (v_a) at the centre of the wind tunnel. By means of a calibration test of the air flow through the tunnel, an experimental correlation was obtained to determine the mean velocity and the volumetric flow rate from this central peak velocity.

Table 2 shows the technical specifications and accuracy of the test bench probes used in both the wind tunnel calibration tests and during the experimental characterization tests of the ultrasonic spray atomiser. All measurements were recorded with a Keysight DAQ970A data acquisition unit incorporating two Keysight DAQM901A 20-channel multiplexer modules.

In accordance with UNE-EN 13741 [11], steady-state conditions were maintained throughout the wind tunnel tests. A maximum variation of ± 0.2°C at each of the temperature probes during a continuous measurement recording period of 5 minutes was set as the steady-state criterion for the tests. The temperature of the water supplied to the atomisation system was maintained in the same range of variation. Before the start of each test, all the equipment and instrumentation is started up with a stabilisation period of at least 20 minutes during which measurements are taken to correct the zero error of the temperature and relative humidity probes. In order to guarantee the repeatability of the measurements, each test lasted approximately 40 minutes, during

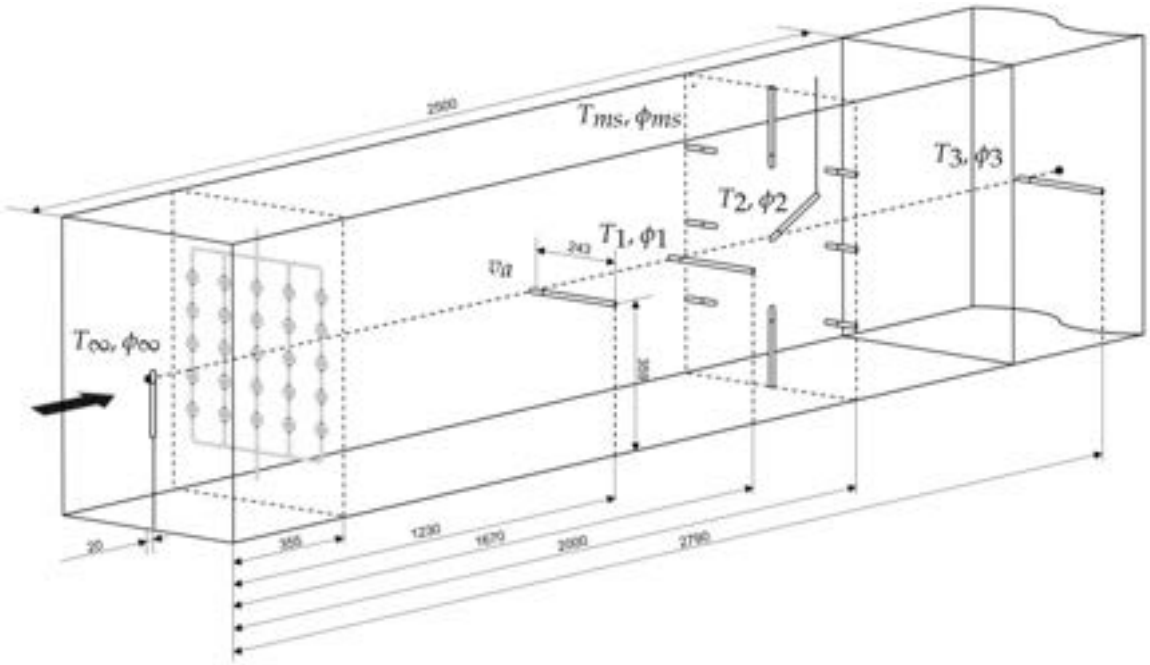

Figure 4: Schematic layout of the ultrasonic atomisation system and location of the probes and the measuring section in the wind tunnel.

Table 2: Specifications and characteristics of the test bench probes used during the experimental tests

Measurement	Measuring device	Brand	Model	Measuring range	Output signal	Accuracy
Air temperature	Thermohygrometer	E+E Elektronik	EE210-HT6xPBFxB	-20 to 80 °C	4–20 mA	± 0.2 °C
Air humidity	Thermohygrometer	E+E Elektronik	EE210-HT6xPBFxB	0–100% RH	4–20 mA	± (1.3+0.3% RD)% RH
Air temperature	Thermohygrometer	E+E Elektronik	EE210-HT6xPCxx	-20 to 80 °C	4–20 mA	± 0.2 °C
Air humidity	Thermohygrometer	E+E Elektronik	EE210-HT6xPCxx	0–100% RH	4–20 mA	± 2.5% RH
Air flow velocity	Anemometer	E+E Elektronik	EE65-VCD02	0–20 m/s	4–20 mA	± (0.2 m/s + 3% RD)
Air flow rate	Flow hood balometer	Testo	0563 4200	40–4000 m^3/h	USB port	± (12 m^3/h + 3% RD)
Power consump.	Power quality analyzer	Chauvin Arnoux	8334		USB port	± 1% RD
Water temperature	RTD-Pt100	Desin	ST-FFH PT100	-200 to 600°C	4-wires	± 0.05 °C
Water weight	Benchtop scale	PCE Instruments	PCE-TB 3	0–3 kg	4–20 mA	± 0.1 g

which measurements were taken every 7 seconds.

The atomised water flow rate was determined using a gravimetric method, measuring the initial and final mass of water supplied during each test with a benchtop scale and recording the time elapsed during the test. The average power consumption of the ultrasonic transducers was also determined by averaging the instantaneous power measured every 5 minutes.

3. Results and discussion

3.1. Measurement of water droplet size and spray emission speed

To determine the average size of the water droplets produced by the ultrasonic spray atomiser, a technique of high-speed photography and subsequent digital image processing has been used, similar to the method described by Ramisetty et al. [12]. A Pentax K-1 DSLR camera with a shutter speed of 1/8000s and a Tamron SP AF 90 mm F2.8 Di Macro 1:1 lens were used to measure the size of the droplets produced in the ultrasonic atomisation process. Due to the micrometric size of the droplets, it was necessary to attach an 18 cm extension tube to the lens to achieve a higher magnification of the captured images. The lighting was performed with a Pentax AF-360 FGZ automatic flash in TTL mode to achieve a t.5 peak duration time of approximately 1/20000 s.

Shots were taken over a reference atomiser, by placing the plume of atomised water between the lens and the flash and using a remote shutter release. The light emitted by the flash was filtered through a honey comb and then passed through a 3 mm grid to create a narrow illumination plane and thus reduce the number of drops that appear in each shot, as only the drops that cross the illumination plane are captured by the camera. An f-stop number of f/2.8 was used to provide a pronounced defocusing of the out-of-focus drops, so that some drops are isolated from others, which simplifies further digital processing.

The pictures taken with the camera were then processed with a graphic editor to increase contrast and acutance. An image analysis technique was used to measure the diameter of the droplets with both ImageJ and Fiji software. Fig. 5 shows an example of a high-speed shutter photography in which the movement of the droplets is frozen and diameter measurements can be made.

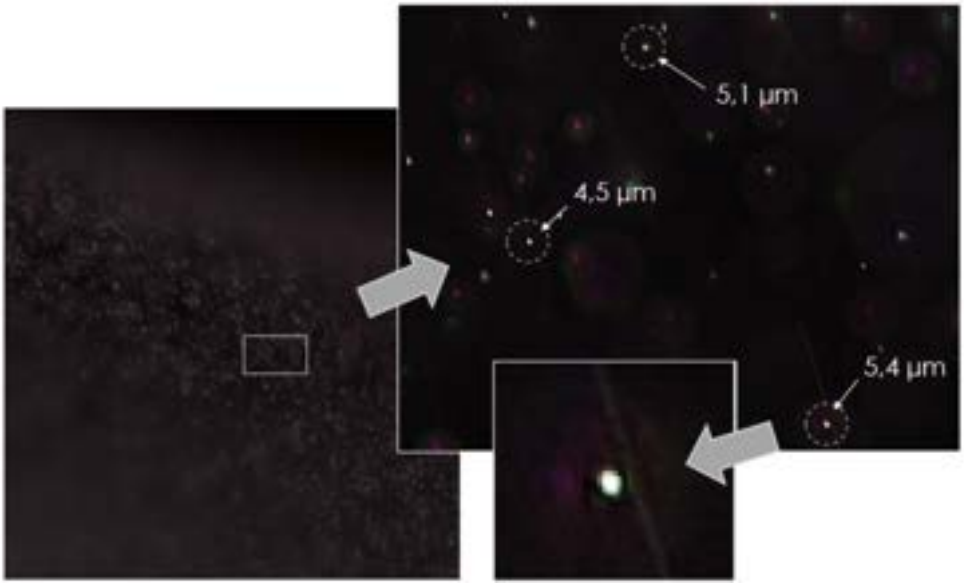

Figure 5: Example of a digitally processed high-speed photograph showing droplet diameter and size distribution.

The arithmetic mean diameter ($D_{1,0}$) and Sauter's mean diameter ($D_{3,2}$) of the droplets produced by the ultrasonic atomiser have been calculated according to the following general equation of the mean diameter:

$$D_{p,q} = \left[\frac{\sum_{i=1}^{N} n_i d_i^p}{\sum_{i=1}^{N} n_i d_i^q} \right]^{\frac{1}{p-q}} \tag{1}$$

where n_i stands for the number of droplets with a diameter d_i.

Finally, the arithmetic mean diameter of the droplets emitted by the ultrasonic atomiser under the test conditions is approximately $D_{1,0}$ = 5.0 μm and the Sauter mean diameter is $D_{3,2}$ = 5.2 μm. The uncertainty of this measurement method was calculated by considering a $\pm$1 pixel variation in the droplet diameter measurement by digital image processing. Taking into account the native camera resolution of 7360$\times$4912 pixels and the lens magnification factor, the maximum uncertainty was estimated to be $\pm$1.6 μm.

With this photographic technique it was also possible to measure the emission speed of the droplets generated in the ultrasonic atomisation process. From high-speed images showing the starting sequence of the atomised water injection (see Fig. 6), an approximate spray emission speed of 2.4 m s^{-1} was determined. This value is important to be able to perform a CFD simulation of the process and to determine the boundary conditions of the numerical model.

3.2. Thermal performance of the ultrasonic spray system

Table 3 summarises the operating conditions and configuration of the ultrasonic atomisation system in the conducted thermal performance tests and the experimental measurements obtained by the probes.

Based on the measurements obtained, a first study of the thermal behaviour of the atomisation system was carried out, taking into account the temperature drop reached in the air flow as it moves longitudinally through the wind tunnel. In this case, the temperature measurements obtained by the T_∞, T_1, T_2 and T_3 probes located on the central axis of the wind tunnel have been considered. A visual inspection of the water mist plume was also carried out during the tests to approximately determine the degree of evaporation of the supplied water flow, since as long as it is visible it indicates that there are still non-evaporated droplets that may be able to produce additional evaporative cooling within the air flow.

Fig. 7 shows the results of the longitudinal evolution of the temperature drop for the three configurations of 5, 15 and 25 active atomisers and for the different levels of air flow velocity considered in the tests. These graphs

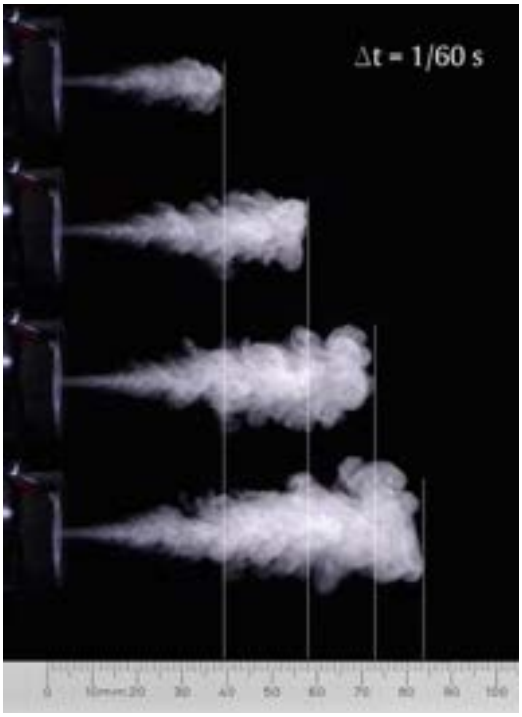

Figure 6: High-speed images showing the initial sequence of atomised water injection used to determine the spray emission speed.

Table 3: Summary of experimental tests of thermal performance on the ultrasonic atomisation system

Test run	config.	v_a (m s^{-1})	$\dot{m}_w$ (kg s^{-1})	T_∞ (°C)	ϕ_∞ (%)	T_1 (°C)	ϕ_1 (%)	T_2 (°C)	ϕ_2 (%)	T_{ms} (°C)	ϕ_{ms} (%)	T_3 (°C)	ϕ_3 (%)
1	5×1	0.5	9.8×10^{-5}	29.3	54.7	27.3	65.1	28.6	55.0	28.1	60.4	28.5	56.2
2	5×1	1.0	9.8×10^{-5}	28.8	47.3	27.9	50.5	28.0	47.4	28.3	48.7	27.9	48.9
3	5×1	1.5	9.8×10^{-5}	28.1	60.1	27.1	65.8	27.1	62.4	27.6	62.1	27.0	64.3
4	5×1	2.0	9.8×10^{-5}	28.8	57.0	28.0	61.0	28.0	58.2	28.4	58.4	27.9	59.5
5	5×3	0.5	2.9×10^{-4}	29.5	54.8	25.2	79.4	25.3	75.0	26.3	73.2	24.9	81.2
6	5×3	1.0	2.9×10^{-4}	28.7	49.4	26.9	57.7	26.8	55.4	27.2	56.4	26.5	57.3
7	5×3	1.5	2.9×10^{-4}	29.2	53.9	27.5	62.2	27.6	58.5	28.1	58.6	27.3	60.8
8	5×3	2.0	2.9×10^{-4}	29.6	53.0	28.3	58.8	28.3	55.7	28.6	56.7	27.9	58.7
9	5×5	0.5	4.9×10^{-4}	29.5	45.4	22.7	85.3	23.0	78.0	24.3	73.9	24.1	75.0
10	5×5	1.0	4.9×10^{-4}	30.9	36.3	26.3	55.4	26.2	52.5	28.5	44.1	26.8	50.4
11	5×5	1.5	4.9×10^{-4}	29.4	40.4	26.2	53.5	26.2	50.9	27.7	46.0	26.5	52.0
12	5×5	2.0	4.9×10^{-4}	29.2	40.7	26.8	50.6	26.7	47.7	27.9	44.7	26.8	50.2

show, as expected, that the largest temperature drops occur at lower levels of air velocity, since low velocity leads to an increase in the residence time of the water droplets in the air, which allows a higher transfer of sensible and latent heat between the water and the air.

For low air velocity levels (0.5–1 m s^{-1}), the largest longitudinal temperature drop occurs in almost all cases at probe T_1, the first one downstream of the atomisation section. From that moment on, the temperature drop of the air evolves along the tunnel, slightly decreasing its value. This effect is caused by the fact that the volume of atomised water is more concentrated at the centre of the tunnel and, therefore, this is where the evaporative cooling of the air is most intense, whereas at points away from the centre, the air temperature does not decrease as much. Far away from the atomisation section, a progressive temperature equilibrium is established in the air flow, which causes the temperature value measured at the central axis to be closer to the average temperature of the air flow cross-section at that location. The resulting non-homogeneity in the atomisation process is the reason for the longitudinal decrease in temperature drop observed in the graphs for the different levels of air velocity.

On the other hand, for higher air velocities (1.5–2 m s^{-1}) the highest temperature drop occurs at a distance further away from the atomisation section, between the probes T_1 and T_2, because at these velocities the droplets travel a longer distance before evaporating completely.

In the results for the configuration of 5 active atomisers, some anomalous behaviours are observed, such as a sharp drop in the temperature drop at the end of the tunnel for the velocity of 0.5 m s^{-1}. This may be due to

the lack of uniformity in the generation of atomised water, which is more pronounced the smaller the number of active atomisers.

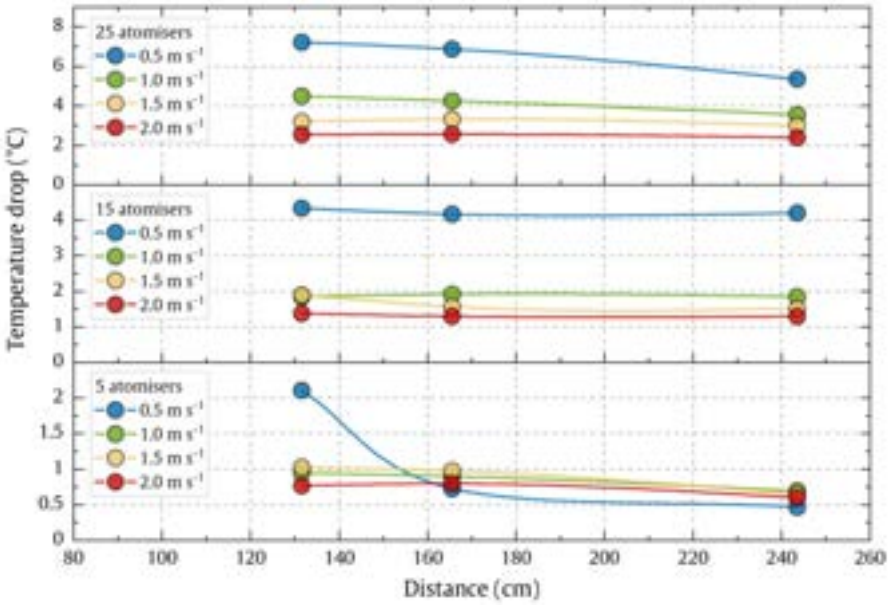

Figure 7: Temperature drop measured by the thermo-hygrometers located on the longitudinal axis of the wind tunnel, as a function of the distance of the probes from the atomisation section and the velocity of the air flow.

A study of the thermal behaviour of the atomisation system was then carried out, centred on a measurement cross-section in which a total of 9 thermo-hygrometers were installed to record the level of homogeneity of the evaporative cooling caused in the air flow. Table 4 and Fig. 8 show the values of the temperature drop recorded in each of the thermohygrometers that constitute the measurement section, for the three configurations of the atomisation system (5, 15 and 25 active atomisers) and for the four levels of air flow velocity.

Table 4: Temperature drop (°C) recorded on the 9 thermo-hygrometers located in the measuring cross-section of the wind tunnel, as a function of the active number of atomisers and the different levels of air flow velocity.

	Air flow velocity											
	0.5 m s^{-1}			1 m s^{-1}			1.5 m s^{-1}			2 m s^{-1}		
25 atomisers	1.0	3.8	2.8	1.6	0.8	2.3	0.9	0.4	1.2	0.9	0.3	1.3
	6.1	6.9	6.0	2.6	4.3	3.6	1.9	3.3	2.6	1.7	2.6	2.1
	6.4	7.2	6.5	1.6	3.6	2.1	0.8	2.1	0.9	0.6	1.6	1.0
15 atomisers	0.3	0.5	0.7	1.2	1.3	0.9	0.3	0.3	1.5	0.4	0.1	1.3
	3.8	4.2	4.8	2.0	1.9	2.1	1.1	1.6	1.9	0.9	1.3	1.4
	4.3	5.0	4.9	1.2	2.4	1.9	1.0	1.2	1.0	0.9	1.1	1.1
5 atomisers	0.2	0.1	0.4	0.5	0.4	0.2	0.2	0.1	0.1	0.4	0.1	0.2
	0.4	0.7	1.2	0.9	0.9	0.4	1.0	1.0	0.3	0.3	0.8	0.4
	2.7	2.7	2.9	0.7	1.7	0.3	0.3	0.9	0.4	0.3	1.1	0.5

From the temperature drop measurements, it can be seen that, for low velocities, very significant temperature drops are obtained in all the tests. However, as the number of active atomisers decreases, the temperature drop registered on the upper thermo-hygrometers and those located in the central area decreases. A lack of uniformity in the temperature drop can also be observed and, for example, the temperature drop in the upper right area of the measurement section is usually higher than that obtained in the upper left area. This situation may be caused by non-uniform atomisation of water or also by the development of turbulent vortices in the air flow. For all three configurations of the atomisation system, as the velocity increases, the temperature drop in the measurement section decreases, because the air mass flow rate is higher.

Fig. 9 shows a comparison of the calculated average values of the evaporative cooling efficiency or saturation efficiency (η_{sat}) and the wet bulb depression (WBD) for the three configurations of the atomisation system and

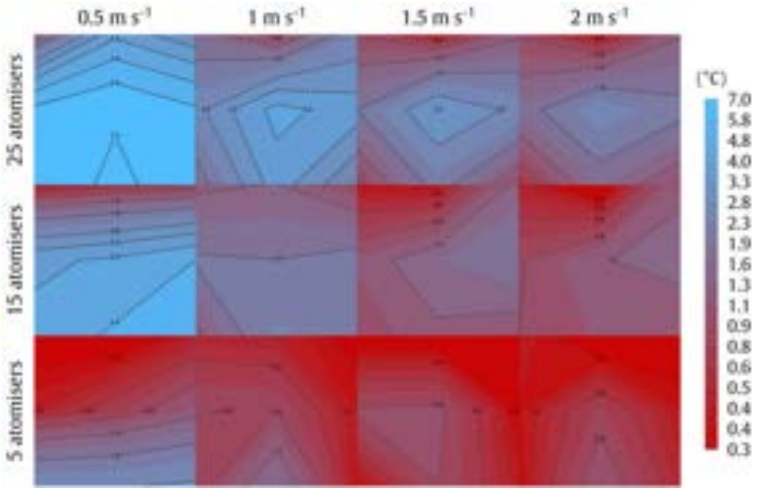

Figure 8: Contour plot of data presented in Table 4.

as a function of different air flow velocities. The saturation efficiency and the wet bulb depression have been calculated from the following expressions:

$$\eta_{sat} = \frac{\omega_{ms} - \omega_{\infty}}{\omega_s^* - \omega_{\infty}} = \frac{T_{\infty} - T_{ms}}{WBD} \tag{2}$$

$$WBD = T_{\infty} - T_{wb} \tag{3}$$

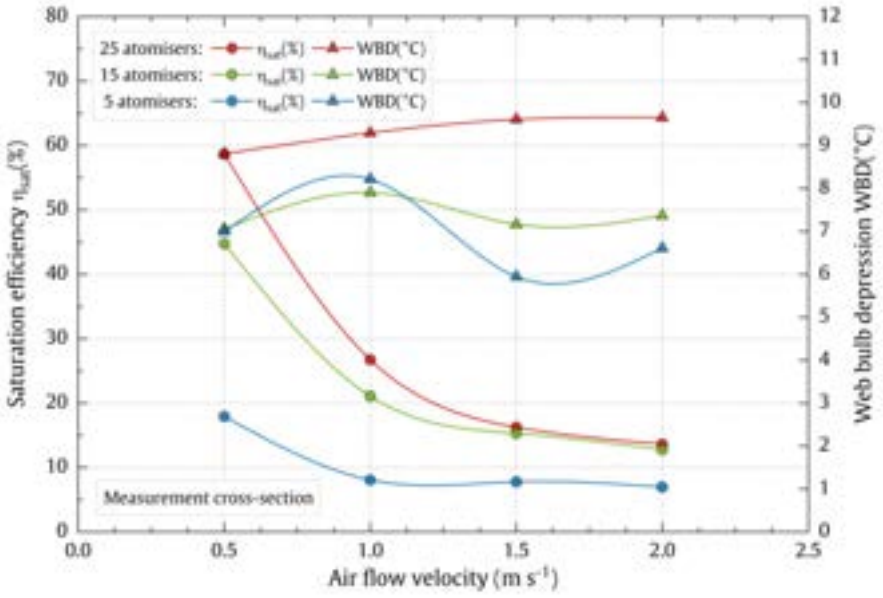

Figure 9: Comparison of the saturation efficiency (η_{sat}) and the wet bulb depression (WBD) for the three configurations of the atomisation system and as a function of different air flow velocities.

In Fig. 9 we can see that for high air flow velocities (1.5 m s^{-1} and 2 m s^{-1}) the results are very similar in the configurations of 25 and 15 atomisers. However, the saturation efficiency alone may be insufficient to obtain a clear interpretation of the evaporative cooling phenomenon taking place and it is necessary to include in the graph the wet bulb depression, which represents the largest possible temperature drop, i.e., the difference between the dry bulb temperature of the incoming air and its wet bulb temperature. Thus, if we compare the configurations of 15 and 25 atomisers for high air flow velocities we can see that, although they have a very similar saturation efficiency, as the web bulb depression is higher in the case of 25 atomisers, this implies that the temperature drop will also be higher for the configuration of 25 atomisers.

Finally, Fig. 10 shows a comparative study for the configuration of 25 atomisers of the evaporative cooling achieved in the measurement cross-section with respect to the maximum cooling that could be obtained if the entire flow of atomised water were evaporated before reaching the measurement cross-section. For this study, a novel performance indicator called evaporated water efficiency (η_{evap}) was considered, that denotes the extent to which the temperature in a particular region of the air flow (T_{ms}) approaches the minimum temperature (T_{min}) that would be reached if all the atomised water evaporates, defined as:

$$\eta_{evap} = \frac{T_\infty - T_{ms}}{T_\infty - T_{min}} = \frac{T_\infty - T_{ms}}{\frac{\dot{m}_w h_{fg}}{\dot{m}_a c_{pma}}} = \frac{1}{r_w} \frac{c_{pa} + \omega_a c_{pv}}{h_{fg}} (T_\infty - T_{ms}) \tag{4}$$

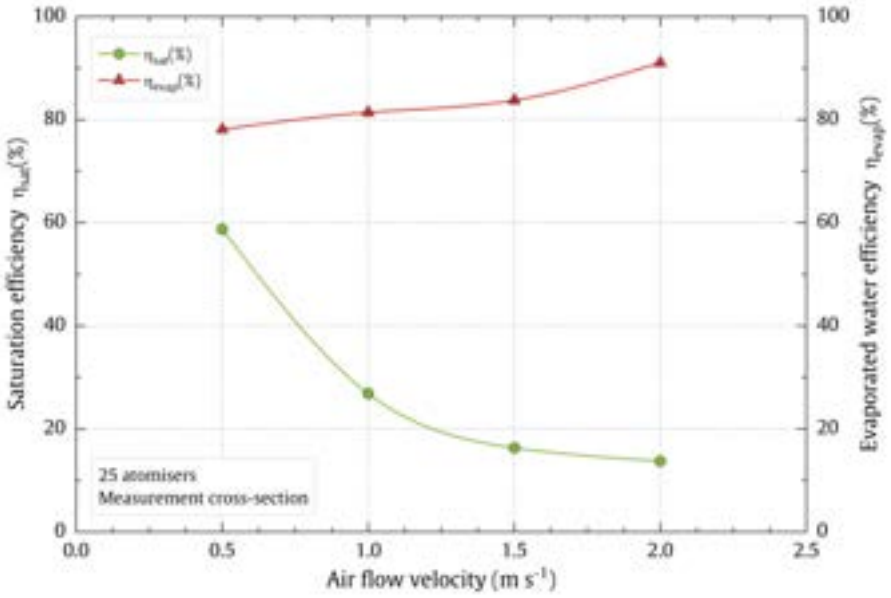

Figure 10: Comparative study of the saturation efficiency and the evaporated water efficiency for the configuration of 25 atomisers. Values close to η_{evap} = 100% indicate a more uniform distribution of the evaporative cooling effect.

The evaporated water efficiency can be used to identify the operating conditions of the atomisation system that lead to the most uniform and homogeneous evaporative cooling (η_{evap} = 100%) throughout the air flow, with complete utilisation of the supplied water.

4. Conclusions

In this article, an experimental study of the operating conditions and thermal behaviour of an ultrasonic atomisation system for evaporative pre-cooling of the inlet air of a condenser in air conditioning applications has been carried out.

Firstly, a measurement of the water droplet size and the emission speed of the atomiser was conducted using a high-speed photography technique and digital image processing to determine the average size of the water droplets produced by the ultrasonic atomiser and the emission speed of the atomiser. As a result, it has been obtained that the arithmetic mean diameter of the droplets emitted by the ultrasonic atomiser under the test conditions is approximately $D_{1,0}$ = 5.0 μm, the Sauter mean diameter is $D_{3,2}$ = 5.2 μm, and the approximate spray emission speed is 2.4 m s^{-1}.

An experimental study of the thermal behaviour of the atomisation system was then carried out in a wind tunnel to determine the longitudinal and transversal evolution of the temperature drop, specific humidity and saturation efficiency at different locations along the central axis of the wind tunnel and at a specific cross-section downstream of the atomisation section. The results of this study have provided information on the configurations of the atomisation system and the air flow velocities that provide the greatest potential of pre-cooling.

A maximum temperature drop of 7.2℃ was obtained for a configuration of 25 atomisers and 0.5 m s^{-1} at the temperature probe T_1, located at 131.5 cm from the atomisation section. Under the same operating con-

ditions, the maximum saturation efficiency, calculated from the 9 thermo-hygrometers in the measurement cross-section, was 58.7% and the wet bulb depression value was 8.8°C.

It has been noticed that the lowest air velocities lead to the highest saturation efficiencies in the measurement cross-section. Furthermore, it has been found that for velocities of 0.5 m s^{-1} and 1 m s^{-1}, and for a configuration of 25 atomisers, the supplied water is almost completely evaporated when the air flow reaches the measurement cross-section, located 164.5 cm downstream of the atomisation section.

Finally, it has been found that the evaporative cooling process is not homogeneous throughout the air flow under many operating conditions, so a new performance indicator called evaporated water efficiency (η_{evap}) has been defined to specifically evaluate this phenomenon.

From the results of this study, it is concluded that an ultrasonic atomisation system is a promising alternative to conventional evaporative cooling systems that can be used to pre-cool the incoming air flow into a condenser with the following advantages: no pressure loss in the air flow; no maintenance, cleaning or replacement of evaporative pads and no accumulation of salts; no recirculation or storage of a large volume of water. However, there are a number of issues that still need to be addressed in future research, such as optimising the energy consumption of the ultrasonic transducers and increasing the evaporation rate of the droplets to reduce the wet length and reduce the potential impact of droplets on the condenser heat exchanger. A final issue to be solved is the optimisation of the atomised water distribution to ensure a more homogeneous pre-cooling throughout the air flow.

Acknowledgments

The authors acknowledge the financial support received from the Government of Valencia (Generalitat Valenciana), through project AICO/2021/190 (Subvenciones para grupos de investigación consolidables).

Nomenclature

c_{pa} specific heat at constant pressure of dry air, J kg^{-1} K^{-1}

c_{pv} , specific heat at constant pressure of water vapour, J kg^{-1} K^{-1}

$D_{1,0}$, arithmetic mean diameter, m

$D_{3,2}$, Sauter mean diameter, m

h_{fg} , enthalpy of vaporization, J kg^{-1}

$\dot{m}_a$, inlet air mass flow rate at wind tunnel, kg s^{-1}

$\dot{m}_w$, mass flow rate of spray atomisers, kg s^{-1}

r_w , water mist to air mass flow ratio

T , dry bulb temperature, °C

T_{wb} , wet bulb temperature of moist air, °C

v_a , air flow velocity, m s^{-1}

Greek symbols

η_{evap} , evaporated water efficiency

η_{sat} , saturation efficiency

ω , humidity ratio of moist air, kg_w kg_a^{-1}

ω_s^* , humidity ratio of saturated moist air evaluated at T_{wb}, kg_w kg_a^{-1}

ϕ , relative humidity

Subscripts and superscripts

a air

∞ , ambient conditions

ma , moist air

ms , measurement section

v , water vapour

w , water

wb , wet bulb

Abbreviations

CFD , computational fluid dynamics

COP , coefficient of performance

PCB , printed circuit board

WBD , wet bulb depression

References

[1] Martínez P, Ruiz J, Cutillas CG, Martínez PJ, Kaiser AS, Lucas M. Experimental study on energy performance of a split air-conditioner by using variable thickness evaporative cooling pads coupled to the condenser. Applied Thermal Engineering. 2016;105:1041 1050. Available from: http://www.sciencedirect.com/science/article/pii/S1359431116300175.

[2] Mehrabi M, Yuill D. Generalized effects of faults on normalized performance variables of air conditioners and heat pumps. International Journal of Refrigeration. 2018;85:409 430. Available from: http://www.sciencedirect.com/science/article/pii/S0140700717304012.

[3] Yu FW, Ho WT, Chan KT, Sit RKY. Theoretical and experimental analyses of mist precooling for an air-cooled chiller. Applied Thermal Engineering. 2018;130:112 119. Available from: http://www.sciencedirect.com/science/article/pii/S1359431116321895.

[4] Hooman K, Guan Z, Gurgenci H. 9 - Advances in dry cooling for concentrating solar thermal (CST) power plants. In: Blanco MJ, Santigosa LR, editors. Advances in Concentrating Solar Thermal Research and Technology. Woodhead Publishing Series in Energy. Woodhead Publishing; 2017. p. 179 212. Available from: http://www.sciencedirect.com/science/article/pii/B9780081005163000095.

[5] Yao Y. Research and applications of ultrasound in HVAC field: A review. Renewable and Sustainable Energy Reviews. 2016;58:52 68. Available from: http://www.sciencedirect.com/science/article/pii/S1364032115016056.

[6] Yao Y, Pan Y, Liu S. Power ultrasound and its applications: A state-of-the-art review. Ultrasonics Sonochemistry. 2020;62:104722. Available from: http://www.sciencedirect.com/science/article/pii/S1350417719308995.

[7] Ruiz J, Martínez P, Martín I, Lucas M. Numerical Characterization of an Ultrasonic Mist Generator as an Evaporative Cooler. Energies. 2020;13(11). Available from: https://www.mdpi.com/1996-1073/13/11/2971.

[8] Martínez P, Ruiz J, Íñigo Martín, Lucas M. Experimental study of an ultrasonic mist generator as an evaporative cooler. Applied Thermal Engineering. 2020;181:116057. Available from: https://www.sciencedirect.com/science/article/pii/S1359431120335377.

[9] Martínez P, Ruiz J, Martínez PJ, Kaiser AS, Lucas M. Experimental study of the energy and exergy performance of a plastic mesh evaporative pad used in air conditioning applications. Applied Thermal Engineering. 2018;138:675 685. Available from: http://www.sciencedirect.com/science/article/pii/S1359431117378225.

[10] Ruiz J, Cutillas CG, Kaiser AS, Zamora B, Sadafi H, Lucas M. Experimental study on pressure loss and collection efficiency of drift eliminators. Applied Thermal Engineering. 2019;149:94 104. Available from: http://www.sciencedirect.com/science/article/pii/S1359431118355388.

[11] UNE-EN 13741:2004 Thermal performance acceptance testing of mechanical draught series wet cooling towers. Spanish Standardization; 2004.

[12] Ramisetty K, Pandit A, Gogate P. Investigations into ultrasound induced atomization. Ultrasonics sonochemistry. 2012 05;20:254-64.

PROCEEDINGS OF ECOS 2023 - THE 36TH INTERNATIONAL CONFERENCE ON
EFFICIENCY, **C**OST, **O**PTIMIZATION, **S**IMULATION AND ENVIRONMENTAL IMPACT OF ENERGY SYSTEMS
25-30 JUNE 2023, LAS PALMAS DE GRAN CANARIA, SPAIN

Comparison between an artificial neural network and Poppe's model for wet cooling tower performance prediction in CSP plants

Pedro Navarro[a], Juan Miguel Serrano[b], Lidia Roca[b], Patricia Palenzuela[b], Manuel Lucas[c] and Javier Ruiz[c]

[a] Technical University of Cartagena, Dr. Fleming, s/n, 30202 Cartagena, Spain
[b] CIEMAT-Plataforma Solar de Almería-CIESOL, Ctra. de Senés s/n, 04200 Tabernas, Almería, Spain
[c] Miguel Hernández University of Elche, Avda. de la Universidad, s/n, 03202 Elche, Spain, j.ruiz@umh.es, CA

Abstract:

The efficiency of a Concentrated Solar Power (CSP) plant strongly depends on the temperature at what the steam is condensed. To date, the conventional systems used to remove the heat from CSP plants are either water (wet) or air-cooled (dry). The use of wet cooling in CSP plants results in the best plant performance. This efficiency increase, however, comes at a high cost: huge water use. This fact is crucial since CSP plants are, in general, located in arid areas where water is scarce. Dry cooling eliminates the water use but suffers from lower efficiency when ambient air temperature is high. Those hot periods are often the periods of peak system demand and higher electricity sale price. A combined cooling system (combination of dry and wet cooling) offers the advantages of each process in terms of lower water consumption and higher electricity production. The ultimate goal of this research is to model and optimise the performance of a CSP plant operating alongside with a combined cooling system in terms of water consumption and net power generation. This paper focuses on the wet cooling tower modelling validated with experimental data from a pilot plant. In this sense, two different models are compared: the Poppe model and an artificial neural network (ANN). Both models are compared in terms of performance prediction (water outlet temperature and water use), experimental requirements and applications. Although both models are reliable (for outlet water temperature, R^2 = 0.97 and RMSE= 1.01°C with the ANN, and $R^2 \approx 1$ and RMSE$<$ 0.36°C for with the Poppe model), it was found that depending on the variable, each model had its strengths and weaknesses.

Keywords:

Concentrated solar power, Combined cooling systems, Cooling tower, Neuronal networks, Poppe model

1. Introduction

Concentrated Solar Power (CSP) plants use mirrors to concentrate the sun's energy to drive steam turbines that create electricity. This technology currently represents a minor part of renewable energy generation in Europe. Only approximately 5 GW are installed globally (of which 2.3 GW in Europe, concentrated in Spain). However, the potential for growth is significant given the capability of CSP to provide renewable electricity when needed, unlike other technologies that are dependent on the availability of the energy source. This dispatchability is possible thanks to in-built energy storage and enables plants to respond to peaks in demand, continue production even in the absence of sunlight, and provide ancillary services to the grid. According to the International Energy Agency forecasts, CSP has a huge potential in the long term, ranging from the 986 TWh by 2030 up to 4186 TWh by 2050 according to the Sustainable Development hi-Ren scenario (Energy Technology Perspectives 2014), meaning CSP will account for 11% of the electricity generated worldwide and 4% in Europe. As the technological leader in the sector, the EU has much to gain from such expansion. To remain a global leader, the European industry needs to stay ahead with more advanced, competitive technologies. CSP plants are, in general, located in arid areas, where water is scarce. The efficiency of these plants strongly depends on the temperature at what the steam is condensed. To date, the conventional systems used to remove the heat from CSP plants are either water (wet) or air-cooled (dry). The lowest attainable condensing temperature is the wet-bulb temperature (wet system). This efficiency increase comes at a high cost: huge water use. Dry cooling eliminates the water use but suffers from lower efficiency when ambient air temperature is high. Those hot periods are often the periods of peak system demand and higher electricity sale price.

There are different types of innovative cooling systems that can reduce the water consumption: those that integrate the dry and wet cooling systems into the same cooling device, which are called hybrid cooling systems [1–3] and those that combine a dry and a wet cooling system, which are called combined systems. In the last case, different configurations can be found.The most proposed in the literature is the one considering an Air

Cooled Condenser (ACC) in parallel with a Wet Cooling Tower (WCT) [4, 5]. In this case, the exhaust steam from the turbine is condensed either through the ACC or through a surface condenser coupled with the WCT. Another configuration, recently proposed in Palenzuela et al. [6] is a wet and a dry cooling tower (type air cooled heat exchanger) sharing a surface condenser. In this case, the exhaust steam from the turbine is condensed through the surface condenser and the heated cooling water is cooled either through the WCT or through the dry cooling tower. Combined systems are the most suitable option for a flexible operation as a function of the ambient conditions, allowing to select the best operation strategies to achieve an optimum water and electricity consumption [7]. To optimise the operation of this kind of refrigeration systems, modelling each one of its components is required as a first step.

Regarding WCT modelling, two kind of models can be distinguished: those based on physical equations and black-box model such as artificial neuronal networks (ANN). The analysis of wet cooling towers through modelling (physical equations) has its origin in [8], where the theory for the performance evaluation of wet cooling towers was developed. The author proposed a model based on several critical assumptions to reduce the solution of heat and mass transfer in wet-cooling towers to a simple hand calculation. Because of these assumptions, however, the Merkel method does not accurately represent the physics of the heat and mass transfer process in the cooling tower. Bourillot [9] stated that the Merkel method is simple to use and can correctly predict cold water temperature when an appropriate value of the coefficient of evaporation is used. In contrast, it is insufficient for the estimation of the characteristics of the warm air leaving the fill and for the calculation of changes in the water flow rate due to evaporation. These quantities are important to estimate water consumption and to predict the behaviour of plumes exiting the cooling tower. Jaber and Webb [10] developed the equations necessary to apply the effectiveness-NTU method directly to counterflow or crossflow cooling towers. This approach is particularly useful in the latter case and simplifies the method of solution when compared to a more conventional numerical procedure. The effectiveness-NTU method is based on the same simplifying assumptions as the Merkel method. Poppe and Rögener [11] developed the Poppe method. They derived the governing equations for heat and mass transfer in a wet cooling tower and did not make any simplifying assumptions as in the Merkel theory. Predictions from the Poppe formulation result in values of evaporated water flow rate that are in good agreement with full scale cooling tower test results. In addition, the Poppe method predicts the water content of the exiting air accurately.

Although the theoretical analysis of WCT has demonstrated successful results with not excessive complexity, black box models based on experimental data are also available in the literature. Numerous authors have designed ANN models for WCT with different objectives, such as performance prediction, simulation and optimisation. One of the first works in this area is the one described in [12] where an ANN model was developed to predict the performance of a forced-counter flow cooling tower at lab scale. In this case, the input variables were the dry bulb temperature, relative humidity of the air stream entering the tower, the temperature of the water entering the tower, the air volume flow rate and the water mass flow rate. The outputs of this model were the heat rejection rate at the tower, the mass flow rate of water evaporated, the temperature of the water at the tower outlet and the dry bulb temperature and relative humidity of the air stream leaving the tower. The results obtained with a 5-5-5[1] ANN demonstrated that cooling towers at lab-scale can be modelled using ANNs within a high degree of accuracy. At lab-scale there are also ANN models for Natural Draft Counter-flow Wet Cooling Towers (NDWCT) such as the one proposed by [13]. In this case, the authors used a 4-8-6 ANN structure and considered some additional variables, such as air gravity, wind velocity, heat transfer coefficients and efficiency as outputs. All these works at lab-scale can be useful to validate the model development methodology but may fail predicting the performance of WCT at larger scale. In this sense, special attention deserves the study carried out by [14] where an 8-14-2 ANN model was proposed to predict the performance (the cooling number and the evaporative loss proportion) of NDWCTs at commercial scale. The model is based on 638 sets of field experimental data collected from 36 diverse NDWCTs used in power plants. It is a very challenging work since it covers samples from a wide range of tower sizes and capacities but the results show that the Mean Relative Error (MRE) is below 5%. From the ANN models found in the literature, it can be concluded that these computational models are able to predict WCT performance with satisfactory results, but it is necessary to deepen and reflect when it is convenient to develop models of this type or to use others, either based on experimental data or based on physical equations. In the literature, comparisons between ANN and Response Surface Methodology (RSM) models for WCT can also be found [15], such as the case of where ANN model is compared with one obtained with the RSM. Although the results obtained show that ANN model predictions are better than RSM model, the study is based on data from a WCT lab-scale system, with only one output (the cooling temperature) and no ambient conditions variability.

Based on the previous discussion, the ultimate goal of this research is to optimise the operation of combined cooling systems integrated into CSP plants in terms of water consumption avoiding a penalty in the plant performance . This paper presents a comparison between the Poppe model (based on physical equations) and

[1] The notation n_1-...-n_l represents the architecture of the ANN model, where l is the number of layers and n_i are the nodes in each one of the layers.

a model based on an ANN for performance evaluation of wet cooling towers. For the calibration of the physical model and for the development of the neural network model, experiments have been performed in a 200 kW_{th} WCT integrated into a combined cooling system pilot plant, located at Plataforma Solar de Almería (PSA). The comparison between models not only evaluates the outputs accuracy obtained with both models, but also discusses other aspects such as required inputs/outputs and parameters, minimal number of experiments and possibility of applying these models for different purposes.

This paper is organised as follows: section 2. contains the description of the experimental facility, the mathematical modelling, and the experimental procedure for the performance tests. Next, the results obtained in the tests are presented and discussed in section 3. Finally, the the most important findings of the research are summarised in section 4.

2. Methodology

2.1. Description of the pilot plant

The pilot plant of combined cooling systems located at PSA (see the layout in Figure 1) consists of three circuits: cooling, exchange and heating. In the cooling circuit (see a picture in Figure 2), refrigeration water circulating inside the tube bundle of a Surface Condenser (SC) can be cooled through a Wet Cooling Tower and/or a Dry Cooling Tower (type Air Cooled Heat Exchanger), both with a designed thermal power of 204 kW_{th}. In the exchange circuit, a saturated steam generator of 80 kWth (on the design point), generates steam at different pressures (in the range between 82 and 200 mbar), which is in turn condensed in the surface condenser that has a thermal power at design conditions of 80 kW_{th}. In this way, the steam transfers its latent heat of condensation to the refrigeration water, that is heated. Finally, in the heating circuit, a solar field with a thermal power of 300 kW_{th} at the design point, provides the energy source required by the steam generator, in the form of hot water. It is a unique, very flexible, fully instrumented and versatile facility, able to operate in different operation modes: series and parallel mode, conventional dry-only mode (all water flow is cooled through the dry cooling tower) and wet-only mode (all water flow is cooled through the wet cooling tower). For this work, the wet-only operation mode has been used, in which the cooling water (FT-003) is pumped by Pump 1 from the basin of the WCT to the surface condenser, circulating through Valve 2 position I up to the entrance of the WCT where water is sprayed. The velocity of air going through the tower is regulated by variable frequency drive (SC-001). The water losses by evaporation in the tower are replaced by demineralised water (FT-004) when the basin level decreases. The sensors used in this operation mode and their characteristics in terms of errors are shown in Table 1.

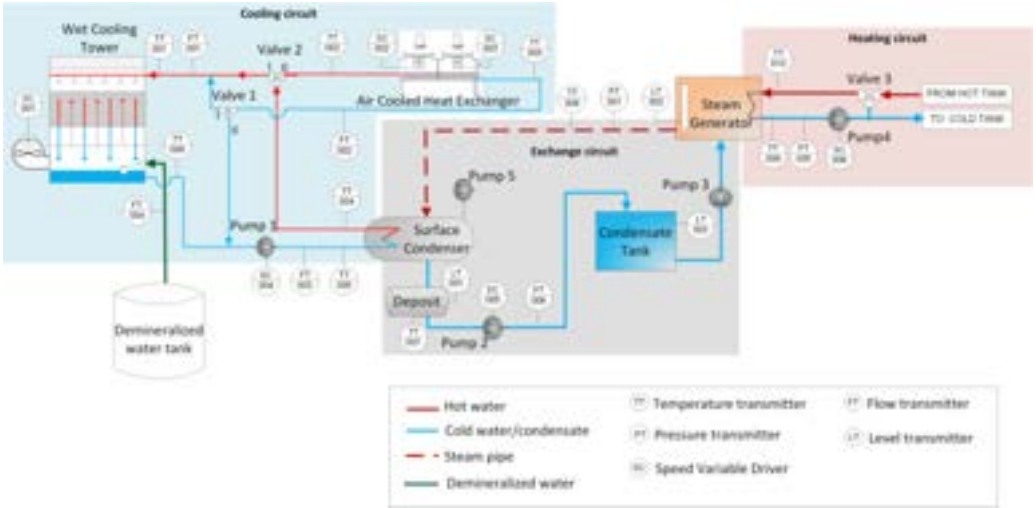

Figure 1: Layout of combined cooling systems pilot plant at PSA.

2.2. Experimental campaign

As mentioned in section 1., two models have been developed for performance evaluation of a WCT: the Poppe model (based on physical equations) and ANN (based on experimental data). With the aim of calibrating and validating both models, 19 experimental tests were performed at the combined cooling pilot plant located at PSA. The physical model focuses on the calculation of the Merkel number, which according to the literature depends on the water-to-air mass flow ratio ($\dot{m}_w/\dot{m}_a$). Therefore, the experimental camping has been designed to cover different water-to-air mass flow ratios. This criterion is also valid with the neural network model, since varying $\dot{m}_w/\dot{m}_a$ allows obtaining different operating points, which helps in collecting information from different

Figure 2: Picture of the cooling circuit in the combined cooling pilot plant at PSA.

Table 1: Characteristics of instrumentation ([a] value of the temperature in °C, [b] of reading, [c] full scale, [d] mean value).

Measured variable	Instrument	Range	Measurement uncertainty
Water temperature, TT-001, TT-006	Pt100	0 - 100°C	$0.3 + 0.005 \cdot T^a$
Cooling water flow rate, FT-001	Vortex flow meter	9.8 - 25 m^3/h	$\pm$ 0.65% o.r.[b]
Water flow rate, FT-004	Paddle wheel flow meter	0.05 - 2 m^3/h	$\pm$ 0.5% of F.S[c] + 2.5% o.r
Ambient temperature	Pt1000	-40 - 60°C	$\pm$ 0.4 @20°C
Relative humidity	Capacitive sensor	0 - 98%	$\pm$ 3 % o.r @20°C
Air velocity	Impeller anemometer	0.1-15 m/s	$\pm$ 0.1 m/s + 1.5% m.v.[d]

scenarios that can occur in tower. At the experimental facility, $\dot{m}_w/\dot{m}_a$ can be modified in two ways, with Pump 1 ($\dot{m}_w$) and with the fan frequency SC-001 ($\dot{m}_a$). Both variables were varied within the allowable range for plant operation. In the case of the water flow, it ranged from 8 to 22 m^3/h. The air mass flow rate was modified by changing the frequency from 12.5 to a maximum of 50 Hz. Therefore, the experimental values of $\dot{m}_w/\dot{m}_a$ obtained were in the range 0.5-5. The thermal load was $\approx$ 170 kW_{th} in all tests conducted.

The standards UNE 13741 "Thermal performance acceptance testing of mechanical draught series wet cooling towers" [16] and CTI "Acceptance Test Code for Water Cooling Towers" [17] were taken as a reference to evaluate that stationary conditions were achieved during the tests, in which it is established that the duration of the test should not be less than one hour. During the test, the maximum deviation of circulating (or cooling) water flow rate, heat load and range cannot be more than 5%. For the wet-bulb temperature and dry-bulb temperature, the linear least-squares trends should not exceed 1°C and 3°C, respectively. Both variables shall not have a deviation greater than $\pm$1.5°C and $\pm$4.5°C, respectively. Finally, it must be verified that the average wind velocity did not exceed 4.5 m/s throughout the test and punctually (for a minute) the 7 m/s.

2.3. Modelling

The models presented in this section have been developed to predict two main outputs, the water temperature at the outlet of the WCT, $T_{wct,out}$, and the water consumption, $\dot{m}_{wct,lost}$. As inputs, both models require five variables: the cooling water flow rate ($\dot{m}_w$), inlet water temperature ($T_{wct,in}$), ambient temperature (T_∞), ambient relative humidity (ϕ_∞) and the frequency level of the fan (f_{fan}) (or the air mass flow rate[2] ($\dot{m}_a$).

2.3.1. Poppe model

The well-known Merkel number is accepted as the performance coefficient of a wet cooling tower, [18]. This dimensionless number is defined in Equation 1, and it measures the degree of difficulty of the mass transfer processes occurring in the exchange area of a cooling tower.

[2]ANN uses as input f whereas Poppe's model uses $\dot{m}_a$.

$$\mathrm{Me} = \frac{h_D a_v V}{\dot{m}_w}, \tag{1}$$

where the variables and parameters involved are described in the Nomenclature Section.
The Merkel number can be calculated using the Merkel and Poppe theories for performance evaluation of cooling towers. The Merkel theory [8] relies on several critical assumptions, such as the Lewis factor (Le) being equal to 1, the air exiting the tower being saturated with water vapour and neglecting the reduction of water flow rate by evaporation in the energy balance. For this reason, the Poppe theory [11] is usually preferred. In this theory, the authors derived the governing equations for heat and mass transfer in the transfer region of the cooling tower (control volume shown in Figure 3, one dimensional problem). The detailed derivation process and simplification of the previously-mentioned governing equations can be found in [18]

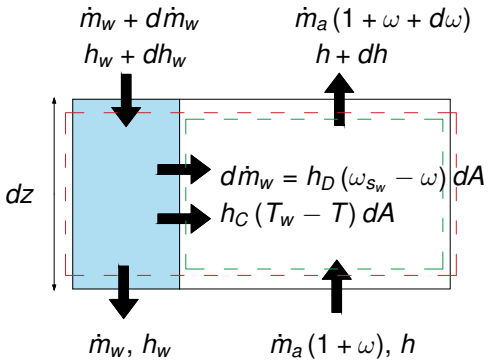

Figure 3: Control volume in the exchange area of a wet cooling tower for counterflow arrangement.

According to the Poppe theory, the major following equations for the heat and mass transfer are obtained:

$$\frac{d\omega}{dT_w} = \frac{c_{p_w}\frac{\dot{m}_w}{\dot{m}_a}\,(\omega_{s_w} - \omega)}{(h_{s_w} - h) + (\mathrm{Le} - 1)\,[(h_{s_w} - h) - (\omega_{s_w} - \omega)\,h_v] - (\omega_{s_w} - \omega)\,h_w} \tag{2}$$

$$\frac{dh}{dT_w} = c_{p_w}\frac{\dot{m}_w}{\dot{m}_a}\left[1 + \frac{(\omega_{s_w} - \omega)\,c_{p_w}\,T_w}{(h_{s_w} - h) + (\mathrm{Le} - 1)\,[(h_{s_w} - h) - (\omega_{s_w} - \omega)\,h_v] - (\omega_{s_w} - \omega)\,h_w}\right] \tag{3}$$

$$\frac{d\,\mathrm{Me}}{dT_w} = \frac{c_{p_w}}{(h_{s_w} - h) + (\mathrm{Le} - 1)\,[(h_{s_w} - h) - (\omega_{s_w} - \omega)\,h_v] - (\omega_{s_w} - \omega)\,h_w} \tag{4}$$

where Me in Equation 4, is the Merkel number according to the Poppe theory. The above described governing equations can be solved by the fourth order Runge-Kutta method. Refer to [18] for additional information concerning the calculation procedure.

2.3.2. Neural Network model

Machine learning algorithms are unique in their ability to obtain models and extract patterns from data, without being explicitly programmed to do so. They are more effective with large volumes of data but can also be applied for steady state modelling with fewer information. Artificial neural networks are part of this set of algorithms and, as the name suggests, have a behaviour similar to biological neurons. Its structure is formed by a succession of layers, each one composed by nodes (or neurons) and receiving as input the output of the previous layer. With this input a calculation is performed and its output is fed as the input for the subsequent layers.

The training process was done making use of the *Neural Network Toolbox* of MATLAB, using the Lavenberg-Marquardt BP algorithm [19]. Several ANN architectures were tested varying the number of hidden layers between 1 and 2 and the number of neurons in each layer between 1 and 10. The transfer function adopted in the hidden layers was the *logsig*, whereas the one employed in the output layer was the *purelin*. The optimal architecture was selected according to the performance function (Mean Square Error, MSE).

2.4. Procedure

Figure 4 schematically depicts the steps taken to perform the comparison procedure. Different tests are carried out with a variety of values in the system inputs (mainly cooling water mass flow rate and fan speed), while the system timeseries outputs are monitored and stored. The processing of the experimental data is done

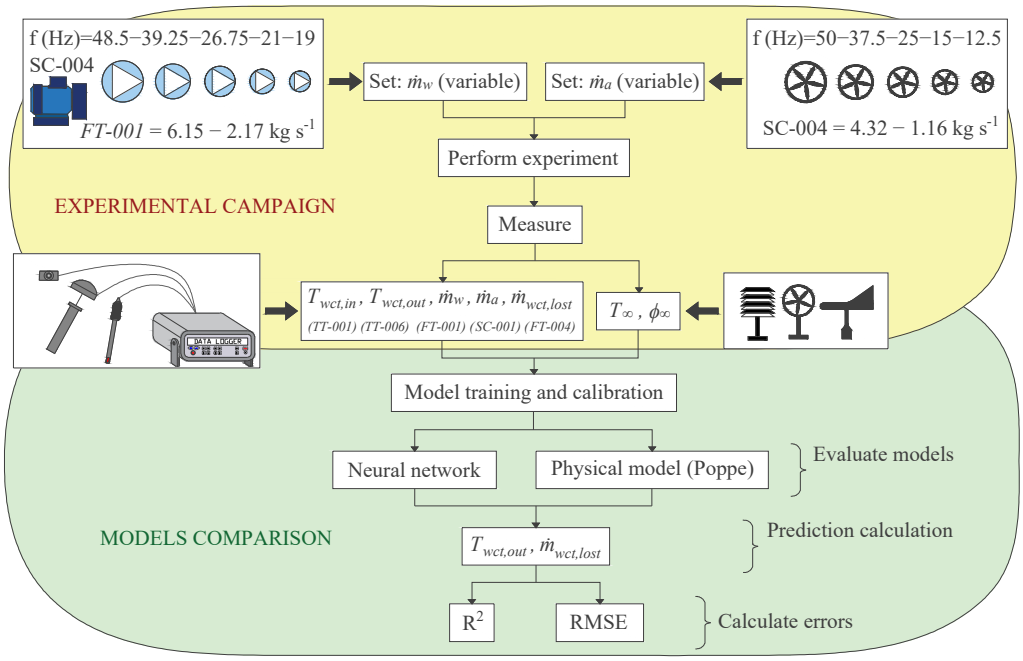

Figure 4: Methodology scheme for experimental procedure and model calibration and evaluation.

as mentioned in subsection 2.2., when the plant achieves steady state conditions according to UNE 13741 specifications.

Once the experimental campaign is done and the steady state operation points identified, different case studies are presented. Each case study takes the available operation points and divides them in two subsets: one is used for calibration/training of the modelling approaches and the second one for testing their performance. The case studies start with a low amount of points selected for training while the remaining are used for validation and increase up to a maximum, to have a minimum of 5 points for validation.

The performance metrics used to evaluate the fitness of the models to the experimental data are the Root Mean Square Error (RMSE) and R-squared (R^2). RMSE is a statistical measure of the difference between the values predicted by a model and the observed values. It is calculated as the square root of the mean of the squared differences between the predicted and observed values:

$$\text{RMSE} = \sqrt{\frac{1}{N}\sum_{i=1}^{N}(y_i - \hat{y}_i)^2}$$

where y_i is the measurement variable for the $i-th$ data point, $\hat{y}_i$ is the estimated value of the same variable and N is the number of data points.

R-squared [20] is a statistical measure that represents the proportion of the variance in the predicted variable that can be explained by the independent variable in a regression model, the measured output in this case, with value equal to 1 indicating the best fit. It is calculated as follows:

$$R^2 = 1 - \frac{\sum_{i=1}^{n}(y_i - \hat{y}_i)^2}{\sum_{i=1}^{n}(y_i - \bar{y})^2},$$

where $\bar{y}$ is the mean value of the experimental values.

3. Results and discussion

Table 2 shows the average values of the variables required by both models, which were obtained from the experimental campaign described in subsection 2.2.. As can be observed, the range of air and water mass

flow rates are 1.16-4.32 kg/s and 2.17-6.15 kg/s, respectively. Regarding the environmental conditions, these were quite similar for all tests: high ambient temperatures (ranging between 32°C and 41°C), and low ambient relative humidities (between 13% and 40%) since it was carried out during the summer season. The table also lists the output variables: $T_{wct,out}$ and $\dot{m}_{wct,lost}$.

Table 2: Averaged values in the experimental test runs.

Test	Q_{pump} (m^3/h)	f_{fan}(%)	T_∞ (°C)	ϕ_∞ (%)	T_{wb_∞} (°C)	$T_{wct,in}$ (°C)	$T_{wct,out}$ (°C)	$\dot{m}_a$ (kg/s)	$\dot{m}_w$ (kg/s)	$\dot{m}_{wct,lost}$ (kg/s)
1	≈8	12.5	33.31	39.58	22.53	48.88	34.79	1.193	2.173	0.050
2		15	35.05	32.38	22.16	46.87	32.95	1.481	2.176	0.081
3		50	36.02	29.94	22.23	43.74	25.43	4.248	2.170	0.091
4	≈9	25	36.76	14.76	18.39	42.56	26.74	2.636	2.449	0.073
5		37.5	36.59	17.43	19.11	39.58	23.74	3.668	2.445	0.080
6		50	34.77	18.46	18.30	39.15	22.26	4.248	2.445	0.092
7	≈12	12.5	40.50	13.11	19.97	46.85	36.94	1.157	3.263	0.058
8		25	39.75	12.97	19.50	40.30	28.42	2.588	3.272	0.075
9		37.5	36.93	22.39	20.79	38.13	26.25	3.648	3.266	0.097
10		50	35.79	16.13	18.24	35.34	23.32	4.319	3.268	0.087
11		50	34.40	23.07	19.32	35.82	23.79	4.312	3.267	0.084
12	≈18	12.5	34.69	32.55	21.94	46.53	39.44	1.177	4.895	0.058
13		25	33.57	27.24	19.83	38.37	30.15	2.619	4.914	0.071
14		37.5	35.66	25.14	20.71	35.39	27.57	3.637	4.942	0.075
15		50	33.53	29.29	20.30	34.50	26.27	4.292	4.940	0.086
16	≈22	12.5	32.84	38.77	21.99	46.25	40.57	1.186	6.096	0.057
17		25	34.25	16.50	17.42	36.41	29.81	2.596	6.127	0.072
18		37.5	35.99	16.91	18.59	33.54	27.04	3.651	6.133	0.078
19		50	35.80	14.73	17.83	31.30	24.87	4.302	6.147	0.085

3.1. Poppe model

Figure 5 shows the variation of the Merkel number as a function of the water-to-air mass flow ratio ($\dot{m}_w/\dot{m}_a$) for two case studies. It can be seen that the expected trend is observed: decreasing Me for increasing $\dot{m}_w/\dot{m}_a$ values (linear trend on log-log scale).

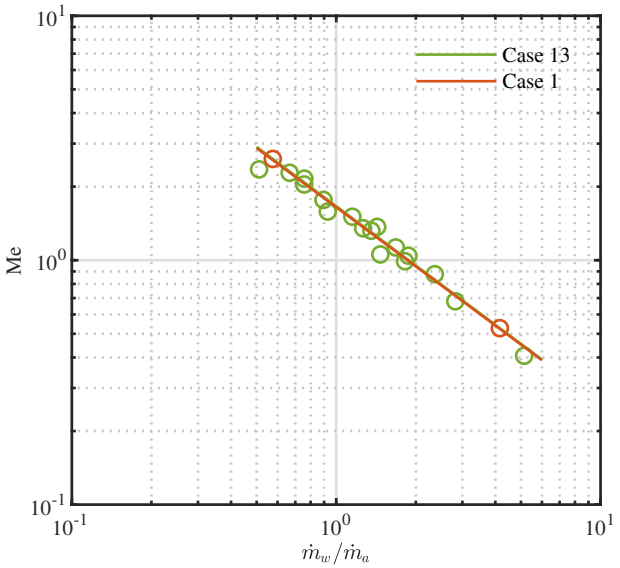

Figure 5: Experimental results for the Me number as a function of $\dot{m}_w/\dot{m}_a$.

The model based on the physical equations (Merkel number) can be obtained by correlating the values of Me with the water-to-air mass flow ratio as an independent variable, described by an equation of the form $\text{Me} = c\,(\dot{m}_w/\dot{m}_a)^{-n}$. Constants c and n in the previous equation have been calculated for the different case studies. In the Case 1, only 2 tests are considered for the fit (solid red line in Figure 5). Subsequently, more

Table 3: Comparison of results and parameters for each case study between an ANN model and a physical model based on Poppe equations.

Case studies	Train set size	Test set size	ANN					Poppe					
			Topology	$T_{wct,out}$		$\dot{m}_{wct,lost}$		Params		$T_{wct,out}$		$\dot{m}_{wct,lost}$	
				RMSE (°C)	R²	RMSE (l/min)	R²	c	n	RMSE (°C)	R²	RMSE (l/min)	R²
1	2	17	5-4-2	5.23	-0.19	0.73	-0.01	1.663	-0.806	0.33	1.00	0.75	-0.06
2	3	16	5-2-2	5.35	-0.19	0.77	-0.06	1.651	-0.817	0.29	1.00	0.78	-0.09
3	4	15	5-5-2	2.11	0.83	0.47	0.62	1.595	-0.850	0.30	1.00	0.84	-0.19
4	5	14	5-5-2	2.03	0.85	0.56	0.50	1.618	-0.823	0.29	1.00	.085	-0.14
5	6	13	5-2-2	1.13	0.95	0.61	0.43	1.631	-0.802	0.31	1.00	0.84	-0.10
6	7	12	5-3-2	1.45	0.93	0.43	0.67	1.631	-0.802	0.32	1.00	0.75	0.00
7	8	11	5-10-2	1.67	0.91	0.46	0.66	1.629	-0.803	0.33	1.00	0.78	0.01
8	9	10	5-2-2	1.74	0.91	0.46	0.65	1.635	-0.790	0.35	1.00	0.76	0.06
9	10	9	5-10-2	1.69	0.91	0.49	0.62	1.640	-0.786	0.37	1.00	0.77	0.06
10	11	8	5-10-2	2.01	0.88	0.54	0.36	1.652	-0.769	0.41	1.00	0.81	-0.43
11	12	7	5-5-2	2.41	0.85	0.44	0.62	1.648	-0.776	0.32	1.00	0.55	0.40
12	13	6	5-5-2	2.72	0.81	0.47	0.59	1.636	-0.793	0.32	1.00	0.51	0.51
13	14	5	5-10-2	1.01	0.97	0.25	0.85	1.647	-0.804	0.36	1.00	0.55	0.31

tests are progressively added for the fit, up to a total of 14 tests in Case 13 (green series). These data are presented in Table 3.

As can be seen in the Figure 5 and in Table 3, the fit is practically the same for cases 1 and 13. This suggests that not much tests will be needed to get a reliable model of the tower. To evaluate the goodness of the correlation, the differences between the data calculated with these correlations and those measured experimentally for the outlet water temperature and water consumption of the tower can be verified. The results of the comparison for both models is presented in subsection 3.3..

3.2. ANN

In Table 3 - Topology column, the configuration of the best obtained networks for each case study are shown. In the first case study, the data available for training the neural network were too sparse to obtain significant results, but it was still done to show the strengths of the model based on the first principle. More interesting results are obtained for the latter case studies that make use of more data for its training, even though better results could be obtained with a more extensive campaign and thus obtaining more points to work with. For all of them, one hidden layer was always the best design, which is in accordance with results from literature [12–15] since there is not enough data to adjust a more complex ANN. Also, the number of neurons tends to be low, though the most performant networks make use of a higher number of neurons in the hidden layer (10). As expected, the optimal network, considering as optimal the one that performs best with the available data, is the one using the maximum amount of available data for training, while leaving enough points for testing. A high error is obtained for the scarce available data networks.

Detailed parameters for the best obtained model are shown at Table 4. It is composed of five inputs, one hidden layer containing ten neurons, and two outputs. It is a feedforward neural network (FFNN) that can be described as 5-10-2 and its predicted output expression is: $\hat{Y} = \Phi_{(2)}(LW_{(1)}\Phi_{(1)}\left(IW_{(1)}x + b_{(1)}\right) + b_{(2)})$, where Φ_i is the layer i transfer function, b the bias matrices, LW and IW are the layer weight matrices (output and input respectively), x is the network input and $\hat{Y}$. The subscripts corresponds with the notation used in the table.

3.3. Comparison between both approaches: prediction, abilities and requirements

3.3.1. Prediction

Table 3 shows the results obtained with both models. Each row shows a case study, which corresponds to a number of data used for the training (or calibration) of the models. As one progresses through the case studies, the number of data used for calibration increases. For each case the performance metrics (*RSME* and R^2) are calculated. Looking at the case of study with the best results (case study 16), the error obtained in the prediction of the water outlet temperature ($T_{wct,out}$) is almost null using the Poppe model ($R^2 \approx 1$ and RMSE = 0.36°C) whereas the error with ANN model is slightly higher (R^2 = 0.97 and RMSE = 1.01°C). This comparison is also observed in Figure 6 (b), where the perfect fit is depicted together with the results obtained with both models. On the contrary, in the case of the water consumption, the results with the ANN model are better than those provided by Poppe's model, being the RMSE with ANN model less than half that obtained with Poppe's model (0.25 to 0.55 l/min). This is because Poppe's model predicts the water lost by evaporation during the process, but it does not consider the water lost as drift (emission of droplets into the atmosphere) nor other losses such as windage , splash-out, leaks or overflow.

Table 4: Best performing network parameters.

Input weight matrix $IW_{(1)}^{(10x5)} = \begin{pmatrix} 0.0016 & 0.0418 & 0.1239 & 0.1353 & -0.1324 \\ 0.0011 & -0.0348 & -0.1022 & -0.1104 & 0.1098 \\ 0.0064 & -0.0066 & -0.0297 & -0.0294 & 0.0334 \\ -0.0015 & 0.0252 & 0.0697 & 0.0740 & -0.0748 \\ -0.0056 & 0.0109 & 0.0389 & 0.0394 & -0.0430 \\ 0.0035 & 0.0454 & 0.1362 & 0.1494 & -0.1452 \\ 0.2361 & 0.1815 & 0.4889 & 0.3339 & -0.4397 \\ 0.0209 & 0.0641 & 0.1763 & 0.1930 & -0.1823 \\ -0.0079 & -0.0505 & -0.1457 & -0.1602 & 0.1539 \\ 0.0024 & -0.0319 & -0.0953 & -0.1023 & 0.1026 \end{pmatrix}$

Hidden layer bias vector $b_{(1)} = \begin{pmatrix} 0.0041 \\ -0.0062 \\ -0.0040 \\ 0.0064 \\ 0.0048 \\ 0.0022 \\ -0.2480 \\ -0.0086 \\ -0.0001 \\ -0.0066 \end{pmatrix}$

Output layer weight matrix $LW_{(1)}^{(2x10)^T} = \begin{pmatrix} 0.1648 & -0.1636 \\ -0.1349 & 0.1351 \\ -0.0335 & 0.0430 \\ 0.0922 & -0.0908 \\ 0.0467 & -0.0540 \\ 0.1814 & -0.1799 \\ 0.6502 & -0.5160 \\ 0.2428 & -0.2231 \\ -0.1969 & 0.1897 \\ -0.1246 & 0.1265 \end{pmatrix}$

Output layer bias vector $b_{(2)} = \begin{pmatrix} -0.0051 \\ -0.1031 \end{pmatrix}$

3.3.2. Experimental requirements

As previously mentioned, Table 3 shows the results obtained varying the number of training experimental points. Regarding the water outlet temperature ($T_{wct,out}$), it can be seen that the error is almost null for the Poppe model even using the lowest number of train points ($R^2 \approx 1$ and RMSE = 0.33°C), whilst is not the case for the ANN one ($R^2 = -0.19$ and RMSE = 5.23°C), as expected. This is reflected in Figure 6 (a), there is not enough information to adjust the weights and biases in the network and therefore it is unable to capture the system dynamics. By increasing the available information during training, the results get better obtaining the best results explained in subsubsection 3.3.1.. In the case of the ANN model, this trend is similar for ($\dot{m}_{wct,lost}$) predictions; increasing the training point, the results improve (RMSE decreases more than 80% and R^2 changes from being negative to approaching 1). With the Poppe model and the $\dot{m}_{wct,lost}$ predictions, it can be observed that, increasing the number of tests, the prediction improvement is low (RMSE decreases less than 27 % and R^2 changes from being negative to 0.31). Therefore, while the ANN model benefits from as much data as possible, the Poppe model is already able to produce satisfactory results with just two properly selected points. These two points are easy to identify in advance because they are related to the maximum and minimum $\dot{m}_w/\dot{m}_a$ ratio. In the practice, to minimise the error prediction, ≈5 points are often used.

Regarding the instrumentation, Poppe's model requires measurement of the air flow rate at the outlet of the WCT, while the ANN model uses as input the frequency of the WCT fan. In addition, to improve the water consumption estimations provided by Poppe's model, it would be necessary to carry out an experimental campaign to measure the water losses due to drift.

3.3.3. Scalability, operating and weather conditions

One important advantage of the Poppe model is its adaptability to large scale systems, as long as the system configuration remains the same. This allows to study and analyse pilot scale plants and extrapolate the results to industrial sized plants. In addition, the model obtained is also capable of accurately predicting the behaviour of the WCT in conditions that have not been tested (different environmental conditions or inlet water temperatures). It would even be valid for unknown $\dot{m}_w/\dot{m}_a$, although the reliability of the model will be lower if this ratio moves away from those experimentally used for calibration. This is not the case for ANN models that are only applicable to the system and operating ranges they are trained for. Even though there are techniques to create new ANN models from previously trained ones [21], this is not as straightforward, requires expertise and additional experimental data.

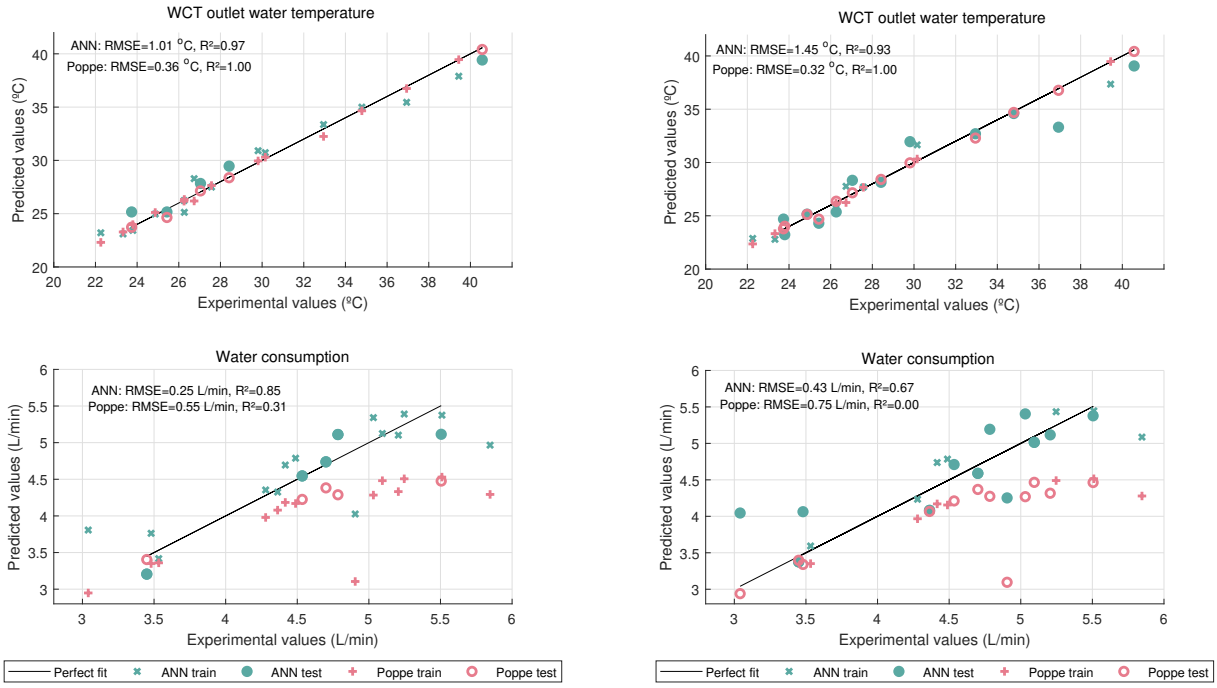

(a) Larger set for training. Case study: 13

(b) Scarce train data. Case study: 6

Figure 6: Models performance comparison with different dataset distribution.

3.3.4. Implementation

In the recent years and due to the increase popularity of artificial intelligence, there are many libraries of easy access for most common programming languages, which makes the development and implementation of ANN models achievable by non experts or specialised teams. The need of extensive data can be mitigated if an online steady-state identification is implemented [22], which allows updating the model with a growing dataset. In the case of the Poppe model, although the number of tests is not a problem, it is necessary to know the governing equations described in the subsubsection 2.3.1.. Solving the system of differential equations requires a non linear solver, which nowadays it is not a problem since there is a wide variety of software tools and packages available to face it.

3.3.5. Execution time

The execution time in the case of the ANN model is very low (in the order of milliseconds) and independent of the input conditions. This is not the case for the Poppe model because it depends on the non-linear solver used. This issue can have an impact in optimisation applications, such as the determination of optimal operating conditions to minimise the water consumption of combined cooling systems for CSP plants.

4. Conclusions

In this study, a comparison between an artificial neural network and Poppe model for wet cooling tower performance prediction in CSP plants has been performed. The results obtained during the investigation can be summarised as follows:

Both models reported good results predicting the outlet water temperature, since the errors were quite low (R^2 = 0.97 and RMSE= 1.01°C for the best case with the ANN, and $R^2 \approx 1$ and RMSE$<$ 0.36°C for all cases with the Poppe model). However, the Poppe model reached confidence levels with only 2 tests, while the ANN needed the maximum number of points available.

For the measurements of water consumption, it was shown that the Poppe model does not accurately predict this magnitude (R^2 = 0.51 and RMSE= 0.51 l/min for the best case), since it does not account for the water lost by drift or other losses. On the other hand, the ANN does present good results in this aspect (R^2 = 0.85 and RMSE= 0.25 l/min for the best case), since it only depends on the results measured in similar tests.

The strengths and weaknesses of each model have also been compared. As for the Poppe model, it is capable of predicting the operation of the tower, regardless of the tested conditions. It is also possible to adapt it to large-scale systems, as long as the system configuration remains the same. Unlike the ANN model that can only be used for the conditions and the tower for which it was developed.

As for the ANN model, it has the advantage of being able to be developed and implemented by non expert or specialised teams (who do not know the physical process that takes place in a cooling tower). Another advantage is in the execution time, the ANN model is faster and more constant independently of the input conditions (in the order of milliseconds for simple networks like the ones presented in this work).

As future lines of work, drift measurements could be carried out on the tower so that the prediction of $\dot{m}_{wct,lost}$ can be improved for the Poppe model. Another way could be to parameterise and adjust this model output to reduce the error. Other possible lines of work would consist of checking other output variables ($\phi_{a,o}$ and $T_{a,o}$) or evaluating the models under different conditions (other seasons). Finally, these models will be used for optimisation purposes in combined cooling systems for CSP plants.

Acknowledgments

This publication is part of the R&D project PID2021-126452OA-I00, funded by MCIN/ AEI/10.13039/501100011033/ and "ERDF A way of making Europe. The authors thank the Plataforma Solar de Almeria for providing access to its installations.

Nomenclature

a_V	surface area of exchange per unit of volume (m^2/m^3)
c_p	specific heat (J/kg K)
f	frequency level (Hz)
h	enthalpy (J/kg)
h_C	heat transfer coefficient (W/m^2 K)
h_D	mass transfer coefficient (kg/m^2 s)
Le	Lewis number (= $h_C/\left(h_D c_{p_{ma}}\right)$)
$\dot{m}$	mass flow rate (kg/s)
Me	Merkel number (= $h_D a_V V/\dot{m}_w$)
N	number of data points
R^2	R-squared
T	temperature (K)
T_{wb}	wet bulb temperature (°C)
V	volume of the transfer region (m^3)
y_i	measurement variable for the $i-th$ data point
$\hat{y}_i$	estimated value of variable y_i
$\bar{y}$	mean value of the experimental values
z	height (m)

Greek symbols

ϕ	relative humidity (%)
ω	humidity ratio (kg/kg)

Subscripts and superscripts

a	air
∞	ambient
fan	fan
i	inlet
$lost$	consumption
o	outlet
s	saturated
v	vapour
w	water

Abbreviations

ACC	Air Cooled Condenser
ANN	Artificial Neural Network
CSP	Concentrated Solar Power
NDWCT	Natural Draft Counter-flow Wet Cooling Towers
PSA	Plataforma Solar de Almería
RMSE	Root Mean Square Error
WCT	Wet Cooling Tower

References

[1] Rezaei E, Shafiei S, Abdollahnezhad A. Reducing Water Consumption of an Industrial Plant Cooling Unit Using Hybrid Cooling Tower. Energy Conversion and Management. 2010 Feb;51(2):311-9.

[2] Asvapoositkul W, Kuansathan M. Comparative Evaluation of Hybrid (Dry/Wet) Cooling Tower Performance. Applied Thermal Engineering. 2014 Oct;71(1):83-93.

[3] Hu H, Li Z, Jiang Y, Du X. Thermodynamic Characteristics of Thermal Power Plant with Hybrid (Dry/Wet) Cooling System. Energy. 2018 Mar;147:729-41.

[4] Barigozzi G, Perdichizzi A, Ravelli S. Wet and Dry Cooling Systems Optimization Applied to a Modern Waste-to-Energy Cogeneration Heat and Power Plant. Applied Energy. 2011 Apr;88(4):1366-76.

[5] Barigozzi G, Perdichizzi A, Ravelli S. Performance Prediction and Optimization of a Waste-to-Energy Cogeneration Plant with Combined Wet and Dry Cooling System. Applied Energy. 2014 Feb;115:65-74.

[6] Palenzuela P, Roca L, Asfand F, Patchigolla K. Experimental Assessment of a Pilot Scale Hybrid Cooling System for Water Consumption Reduction in CSP Plants. Energy. 2022 Mar;242:122948.

[7] Asfand F, Palenzuela P, Roca L, Caron A, Lemarié CA, Gillard J, et al. Thermodynamic Performance and Water Consumption of Hybrid Cooling System Configurations for Concentrated Solar Power Plants. Sustainability. 2020;12(11).

[8] Merkel F. Verdunstungskühlung. VDI Zeitschriff Deutscher Ingenieure, Berlin, Alemania. 1925:123-8.

[9] Bourillot C. Hypotheses of Calculation of the Water Flow Rate Evaporated in a Wet Cooling Tower. 1983 Aug.

[10] Jaber H, Webb RL. Design of Cooling Towers by the Effectiveness-NTU Method. Journal of Heat Transfer. 1989 Nov;111(4):837-43.

[11] Poppe M, Rögener H. Berechnung von Rückkühlwerken. VDI wärmeatlas. 1991:Mi 1.

[12] Hosoz M, Ertunc HM, Bulgurcu H. Performance Prediction of a Cooling Tower Using Artificial Neural Network. Energy Conversion and Management. 2007 Apr;48(4):1349-59.

[13] Gao M, Shi Yt, Wang Nn, Zhao Yb, Sun Fz. Artificial Neural Network Model Research on Effects of Cross-Wind to Performance Parameters of Wet Cooling Tower Based on Level Froude Number. Applied Thermal Engineering. 2013 Mar;51(1):1226-34.

[14] Song J, Chen Y, Wu X, Ruan S, Zhang Z. A Novel Approach for Energy Efficiency Prediction of Various Natural Draft Wet Cooling Towers Using ANN. Journal of Thermal Science. 2021 May;30(3):859-68.

[15] Ramakrishnan R, Arumugam R. Optimization of Operating Parameters and Performance Evaluation of Forced Draft Cooling Tower Using Response Surface Methodology (RSM) and Artificial Neural Network (ANN). Journal of Mechanical Science and Technology. 2012 May;26(5):1643-50.

[16] UNE. Thermal Performance Acceptance Testing of Mechanical Draught Series Wet Cooling Towers [Manual]; 2004.

[17] CTI. Code Tower, Standard Specifications. Acceptance Test Code for Water Cooling Towers [Manual]; 2000.

[18] Navarro P, Ruiz J, Hernández M, Kaiser AS, Lucas M. Critical Evaluation of the Thermal Performance Analysis of a New Cooling Tower Prototype. Applied Thermal Engineering. 2022;213:118719.

[19] Beale MH, Hagan MT, Demuth HB. Neural Network Toolbox. User's Guide, MathWorks. 2010;2:77-81.

[20] Chicco D, Warrens MJ, Jurman G. The Coefficient of Determination R-squared Is More Informative than SMAPE, MAE, MAPE, MSE and RMSE in Regression Analysis Evaluation. PeerJ Computer Science. 2021;7:e623.

[21] Zhuang F, Qi Z, Duan K, Xi D, Zhu Y, Zhu H, et al. A Comprehensive Survey on Transfer Learning. Proceedings of the IEEE. 2020;109(1):43-76.

[22] Pérez-Sánchez B, Fontenla-Romero O, Guijarro-Berdiñas B. A Review of Adaptive Online Learning for Artificial Neural Networks. Artificial Intelligence Review. 2018;49:281-99.

Design rules for a PV-inverter in Belgium: evaluation of actual rules of thumb

Hugo Monteyne[a], Wim Beyne[b], Rik Koch[c] and Michel De Paepe[d]

[a] Department of Electrical Energy, Metals, Mechanical Constructions & Systems, University Ghent, Ghent, Belgium, Hugo.Monteyne@UGent.be CA
[b] Department of Electrical Energy, Metals, Mechanical Constructions & Systems, University Ghent, Ghent, Belgium, Wim.Beyne@UGent.be,
[c] Intellisol, Maaseik, Belgium, Rik.Koch@Intellisol.be,
[d] Department of Electrical Energy, Metals, Mechanical Constructions & Systems, University Ghent, Ghent, Belgium, Michel.DePaepe@UGent.be

Abstract:
An optimized inverter sizing depends on the installed photovoltaic capacity, the azimuth and zenith of the panels, the latitude and the efficiency curve of the inverter. Simplified inverter sizing rules are generally used and can be narrowed to two rules of thumb. The first rule aims a maximum PV-production and uses an inverter according to the PV power, the second rule aims a maximum self-sufficiency and uses an inverter size ratio of 0.7. Simulations are performed to quantify the production loss or self-sufficiency loss when the rule of thumb is used instead of the optimized inverter power for a load profile with only household appliances. In a second part, the energy system is extended with a heat pump, a battery or both combined. This study checks if the refurbishment of residential PV systems with heat pump and/or battery still can use the same rules of thumb or is a new sizing method preferred to replace the inverter. Detailed models for load, PV-inverter, battery and battery-converter are developed. The PV-production and the self-sufficiency are determined for 6 azimuths and 7 zenith positions. A final evaluation of the rules of thumb is made.

Keywords:

Inverter, Photovoltaics, renewable energy, electrical storage, heat pump

1. Introduction

The energy transition is progressing and boosts the sales of photovoltaic solar systems (PV). Between 2015 and 2021, the installed PV capacity in Belgium is more than doubled[1]. The heat pump market grew with factor 10[2] and in 2021 the number of installed home batteries exceeded 11000 units where in 2020 hardly 337 units were installed[3].The inverter is an important component of the PV system. Since several years, the Flemish government advises to size the inverter power on 70% of the installed PV power at standard reference conditions to get a maximum self-sufficiency [4-6], the Walloon government advises 70 to 100%[7], the Brussels region advises 80% [8]. Belgium's neighbouring countries do not give an unambiguously advice. In France, the government advises 80% [9], in the Netherlands 90 to 110% [10] is advised to have a maximum production and in Germany [11] 100% for maximum production and 70% for maximum financial benefit. All those rules of thumb can be narrowed to two rules. When a maximum PV production is the target, the inverter is sized with an inverter ratio of 1[12]. When a maximum self-sufficiency or self-consumption is targeted, the inverter ratio is 0.7.The optimized inverter power to get a maximum PV production is described by Burger [13], Nofuentes[14] and Van Der Borg [15]. They investigated the inverter power for different zeniths and azimuths to maximize the PV production. Their results show that the ideal inverter power, for maximum PV production vary from 0.3 to 1.1. The rules of thumb give just one fixed figure, namely a ratio of 1. What is the production loss if the rule of thumb is used? Maximizing the self-sufficiency or self-consumption is another target to optimize the inverter power[4] .The previous target, maximizing the PV production, is maximizing the energy output of the inverter which is independent of the loads connected to the inverter. Once maximizing the self-sufficiency becomes the main objective, the load profile of the energy user becomes an extra parameter. Since every end user has a different consumption profile, different equipment, different PV technologies, orientations, inverters etc. it is impossible to state that there is one optimal inverter power. This includes that the resulting optimized inverter power in this case is indicative and can state a trend. Although the authors could not trace the original documents that formed the basis of the rule of thumb where 70 to 80% of the installed PV power is used, in each case this rule was made when heat pumps and batteries were not frequent applied [16], now they are. Adding a heat pump to a residential energy system will increase the energy use during the winter

and mid-season, just in the period that less solar energy is available. The load profile of the heat pump is even the opposite of the PV production profile. It can be questioned if it is not better to optimize the inverter for the energy use during winter. A similar question can be asked in case of adding a battery to the residential energy system. The battery can take energy during the full period with daylight. As long as there is daylight a battery can charge energy. The battery can be considered as a load that can take energy during the moments with maximum solar radiation. Is a larger inverter power beneficial in that case? Optimized inverter sizing to maximize the PV production is described by different authors [13-15, 17] but optimized inverter sizing to maximize the self-sufficiency related to orientation and panel zenith or the impact of a heat pump, or battery, on the optimized inverter power is not yet described. In this study the different rules of thumb are investigated for residential buildings in the Belgian climate. Different scenarios are investigated starting with a reference case with only household appliances, called ‘appliances’ in this paper. Next, the energy system is extended with a heat pump and/or a battery. Evaluating the impact of the heat pump and the battery on the optimal sizing of the inverter compared to the rules of thumb is the main contribution of this research. The optimized inverter is determined for the full range of both, zenith and azimuth. For each case the maximum self-sufficiency, using the optimized inverter power, is compared to the self-sufficiency obtained by using the rules of thumb.

2. Methodology

2.1. Residential energy system

The reference case (case 1) is a realistic example of a standard family in Belgium. The family counts 4persons. The energy system is used for a residential house where space heating and domestic hot water production is realized with fossil fuel combustion technology. The energy use for the appliances is 5000kWh/a. A PV system of 5 kWp is installed. The optimized inverter power is determined for this system as reference for a panel zenith of 0° to 90° in steps of 15° and 6 orientations are considered with steps of 60°. Case2 to case 4 are based on this reference case where the system is extended with a heat pump, a battery or the combination of the two. Case 5 is similar to case 1 but with an high efficiency inverter (Table 1). In each case, the PV production and self-sufficiency obtained with the optimized inverter power is compared to the one resulting with the rule of thumb inverter power.

2.2. Components overview

2.2.1. Photovoltaic panels

The power output of a PV area is simulated in Trnsys, using type 94. The simulations were performed with the technical specifications of the polycrystalline solar panel type Q.Plus-G4.1 275. The power P_{pv} , in Watt is a function of:

$$P_{pv} = f\left(n, \mathrm{W}_p, \Phi_{solar}, T_{module}\right) \quad (1)$$

2.2.2. Inverter

The inverter transforms the DC-voltage coming from the PV panels to AC 230V which can be used by the appliances. The inverter efficiency varies with the load. Faranda [18] presented a few typical inverter curves. Two of them are used in this study (see Fig. 1). ’ Inverter 1’ has a pronounced efficiency drop for low part loads. ‘Inverter 2’ has a significant higher efficiency in that part. The impact of a high efficient inverter will be evaluated. Each curve is characterized by two sections. A low part load ,below 10% of the nominal power, results in a low inverter efficiency due to the relative high self-consumption losses compared to the input. Once the load is above 10% of the nominal power, the efficiency reaches maximum values of up to 96%. The inverter efficiency curves presented in Fig. 1contain already the information to predict the trend which can be expected as end result:

- An inverter sized too small will have high part loads with high efficiency but the limited inverter power will not be able to handle the loads above the nominal inverter power. The load will be limited to the nominal inverter power and the overshoot becomes an extra production loss.
- An inverter sized too large will result in small part loads which gives a low inverter efficiency

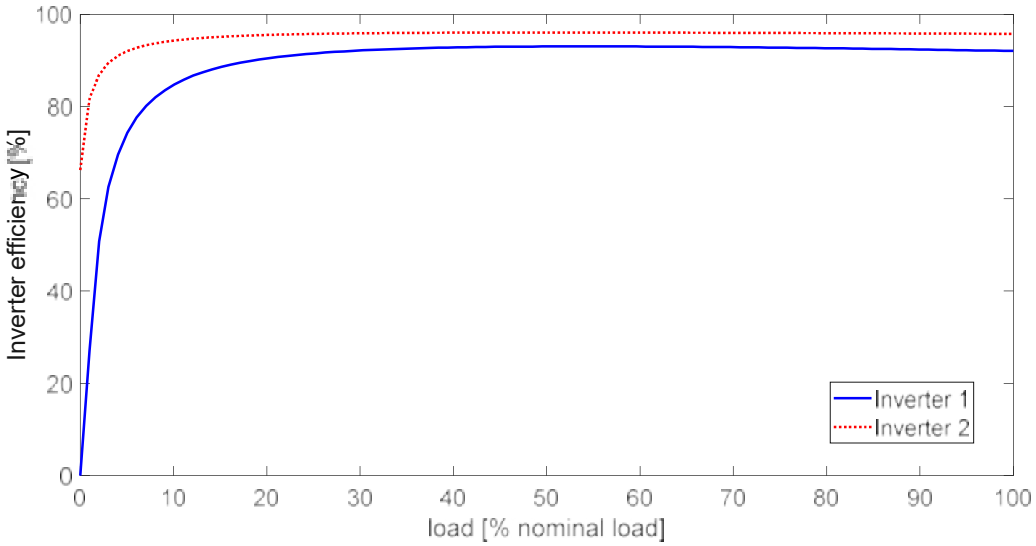

Figure. 1. Typical inverter efficiency curves from different manufacturers[18]

The presented inverters have a maximum efficiency between 90 and 96%. New technology is already available with 99% inverter efficiency [19, 20]. The simulations are made with inverter model 1. Inverter model 2 is used as alternative to check the influence of a high efficient inverter. Adding a heat pump to the system for space heating and domestic hot water makes that the winter period will have the highest energy use, just when the PV production is lower and where the efficiency of the inverter at low part load becomes more important. The results show the impact of the heat pump on the inverter selection.
The power of an inverter is therefore a function of:

$$P_{inverter} = f(\eta_{eff}, P_{pv}) \tag{2}$$

2.2.3. Heat pump

The heat pump is an air to water inverter system used for space heating and production of domestic hot water. The heat pump model calculates the needed energy input for the given outdoor temperature, heating curve and needed capacity for space heating. Manufacturer data is used to make the model. The start-up sequence and switch off sequence of the heat pump is integrated into the model to get realistic electric peak loads in the load profile. Each 3 minutes, the part load ratio can increase or decrease with 10% to get a balance with the energy demand. The minimum part load ratio is 30%. The production of domestic hot water always happens on full load.

$$P_{hp} = f(PLR_{HP}, T_{outdoor}, T_{lwt}) \tag{3}$$

2.2.4. Battery converter

The battery converter is characterized by its efficiency curve and its capacity. The same considerations as for the PV inverter are applied. The efficiency curve presented by Weniger [21] is used with a nominal capacity of 5kW. Previous simulations showed that the self-sufficiency achieved with a converter power of 5kW reaches an optimized point within the range of 0.5% loss due to not optimized battery converter for the considered load profiles, PV area and different PV panel positions.

$$P_{batt\ conv} = f(E_{bat\ conv}, PLR_{bat\ conv}) \tag{4}$$

2.2.5. Battery

A battery model described by Brivio [22] is modelled in Matlab to calculate the battery performance. The model is represented by a RC circuit. The R and C value is related to the state of charge. The model calculates the available charge or discharge capacity which is function of the C-rate. The battery is determined by its nominal capacity, the maximum depth of discharge (80%), maximum state of charge90%, self-discharge 3%/month, charge capacity factor 0.5kW/kWh and discharge capacity factor0.55kW/kWh.

$$P_{batt} = f(E_{bat}, C_{bat}, C_{dr}, R_f, SOC, E_{loss}) \tag{5}$$

2.2.6. Grid

The generated PV energy is converted by the inverter to be used by the appliances and/or the battery system. The surplus of energy is supplied to the grid. In case the PV system nor the battery can deliver enough energy, the deficit is supplied by the grid. It is assumed that there is no feed-in limitation.

$$\frac{d\,E_{bat}}{dt} = P_{inverter} + P_{grid} - P_{appliances} - P_{hp} \tag{6}$$

2.3. Load profiles

2.3.1. Appliances

A synthetic load profile is developed for a household of four persons, one full time working parent, apart-time working parent, a student and a young child. The load profile of the base case only contains appliances, assuming that space heating and DHW is done with fossil fuels. A probability curve is used to identify the start of use of 19 different appliances [23] [24]. Reinhardt measured the energy use of different appliances , for several actions, on a 1 second timestep [25]. His results are the building blocks of the synthetic profile. The energy use profiles are composed out of appliances with different measured performances to get a load profile of 5000kWh/a. The synthetic load profile is generated with a 1 sec time step and rescheduled to a 3 minute time step. The synthetic profile is verified with the results of measured data. Fig. 2 shows 4 load duration curves of load profiles of 5000kWh/a. All curves are presented on a 3 minute time step. One measured profile is a similar household measured in the Lineas project[26] with time step 15 minutes. The second verification is the average of 50 load profiles of 5000kWh/a from the distribution network operator Fluvius. The synthetic profile is presented with a time step of 15 minutes and also with a time step of 3 minutes. The different curves show that the 15 minute time step synthetic profile matches the average values. The 3 minutes time step synthetic profile shows more peak loads. The larger the time step the more that peak loads disappear in the average values.

2.3.2. Domestic hot water

The daily DHW-profile of the European Directive EU813/2013 is used (Medium user profile - 3XS user profile Ecodesign)) [27]. To use a maximum of solar energy, the charging of the DHW buffer is programmed to start at 14h00.

2.3.3. Heating demand

An archetypical Belgium dwelling[28] is used to calculate the heating demand. The heating demand is simulated in Trnsys[29] for a south oriented building. The air infiltration is simulated with Trnflow[30].The resulting heating demand includes the inertia of the building mass and the under floor heating. The appliances and the persons (presence is coupled with the probability determination used for the load profile) are considered as an internal heat gain and are assigned to a specific room. A predefined heat gain factor is used per appliance to deduct the not used energy such as the hot water drain of a laundry machine.

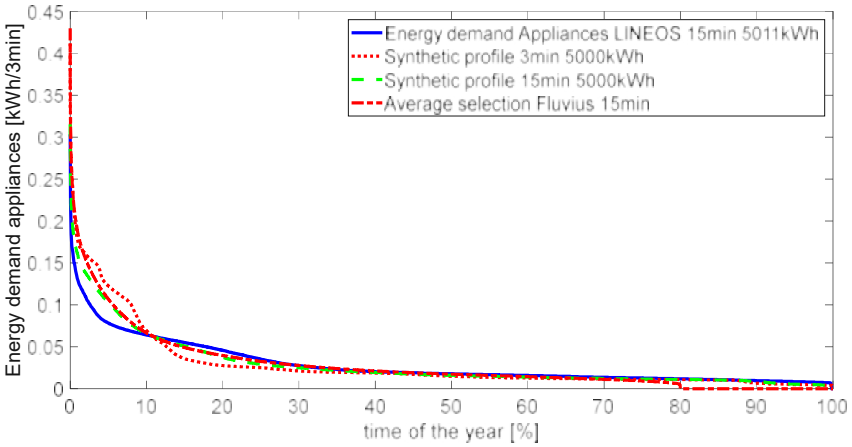

Figure. 2. Load duration curves of different load profiles

2.4. Climate data

The Meteonorm climate data of the reference year of Uccle (Belgium), time step 1 hour, is used to simulate the PV performance and the heating demand. The PV generation and the heat demand is simulated in Trnsys

using the Meteonorm data using interpolated time steps of 3 minutes. To check the impact of 3 minute interpolated time steps using 1 hour data compared to 3 minute time step, measured data with time step 1 minute is used. The self-sufficiency calculated with the interpolated data had a maximum difference of 0.6% compared to the self-sufficiency calculated with 3 minute data. Using the 3minute interpolated hourly climate data gives no significant difference when 3 minute appliance data is used.

2.5. Simulation method

The simulations of the energy flows between the different components are performed in Matlab. Several authors investigated the impact of the time step [31] [32] [33] [34] and conclude that a time step of less than 5 minutes reduces the error to 2% and even less than 1% in case a battery is used. All inputs (PV production, electrical load, heating demand, domestic hot water production) are on a 3 minute time step. All simulations are done for a full year. To investigate one case, 7 inverter powers are simulated for 7 zeniths and 6 orientations. The load is determined by the sum of the energy use of the appliances and the energy use of the heat pump if available. If there is renewable energy available, it is first used to compensate the energy demand of the appliances and the heat pump, a shortage is supplied from the grid, a surplus is supplied to the battery (if available) as far as the battery can take the surplus in quantity and power. The leftover is supplied to the grid. All efficiencies (inverter, converter, battery) are calculated per time step.

2.6. Case study selection

The 5 selected cases could be a timeline of one residential energy system starting with a PV system that can cover the energy use of the appliances. The following cases could be the refurbishment of the energy system, namely adding or a heat pump, or a battery, or both. For each case the results are checked to see if the inverter has a different power as in the reference case. The reference case is an energy system with only appliances (5000kWh/a) with 5kWp PV, no heat pump, no battery. The optimized inverter is calculated for the targets of the two main rules of thumb, namely maximum PV production and maximum self-sufficiency. The results are compared with the rules of thumb.

Table 1. Overview cases

Case	Appliances	Heat pump	Battery	Inverter model
1	5000 kWh/a	no	0 kWh	1
2	5000 kWh/a	no	8 kWh	1
3	5000kWh/a	yes	0 kWh	1
4	5000 kWh/a	yes	8kWh	1
5	5000 kWh/a	no	0 kWh	2

Two solar panel positions are picked out to follow up each case, respectively due south (azimuth 0°) and azimuth -120°.

3. Results

3.1. Case 1

3.1.1. Maximum PV production

To maximize the PV production, the rule of thumb advises to use an inverter ratio of 1. The maximum PV production is evaluated at the output of the inverter. This is the sum of used PV energy in the residential energy system and the energy supplied to the grid.

$$0 = P_{inverter} + P_{grid} - P_{appliances} \quad (7)$$

This is only evaluated for case 1 but is equal for all other cases. Fig. 3 gives the resulting inverter output in kWh/a in relation to the inverter power for different zeniths with 0° azimuth and a PV area of 5kWp. Each curve is characterized by a fast decreasing inverter output for an inverter power lower than 4 kW and a slightly decreasing efficiency above an inverter power of 4 kW. The fast inverter output decrease in the left side of the curve is caused by the peak shaving due to the limited inverter power. All produced energy above the nominal capacity of the inverter is a loss. The slow decreasing right part of the curve is caused by the low efficiencies during small part loads. The larger the inverter power the more the inverter will operate in the region of the low part loads which results in low inverter efficiency. The 90° zenith has less high irradiation than the 0° zenith. The lower irradiation is a lower part load of the inverter and results in a lower inverter efficiency. Over-sizing the inverter power is less critical than under-sizing. The best performing PV panel position (due south, zenith

between 30 and 60°) gives an ideal inverter ratio of 0.99 and 1.01. For this positions, the rule of thumb is perfect. The 90° zenith gives an optimized inverter ratio of 0.81. Using the rule of thumb is a 19% oversizing but results in a loss of 0.6% of the yearly production.

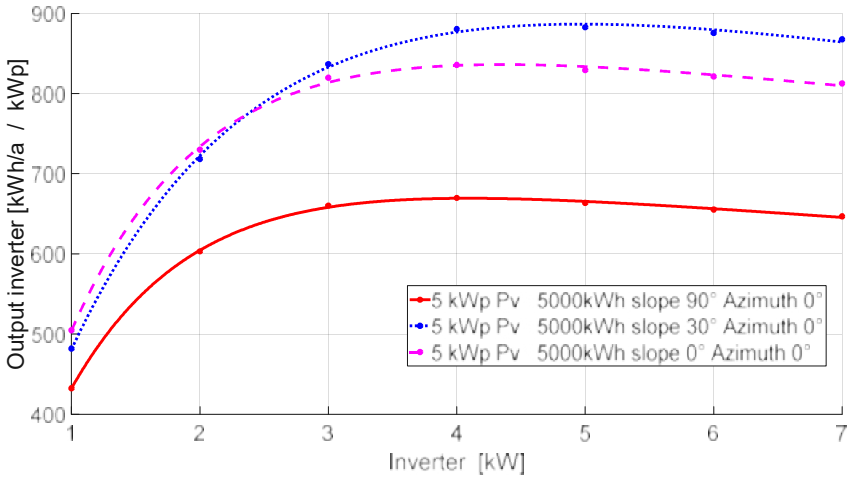

Figure. 3. Output inverter for inverter model 1, 5kWp PV, no heat pump, no battery, azimuth 0°

Table 2 gives the optimized inverter power per kWp installed PV at reference conditions to get the maximum yearly production. In case of azimuth -120° and a 90° zenith, the optimized inverter power is0.54kW/kWp instead of 1kW/kWp (rule of thumb). The optimized inverter ratio 0.54, results in 3.7%more PV production. Due to the lower irradiation, a smaller inverter is needed.

Table 2. Optimized inverter power kW/kWp for maximum energy production, inverter model 1, 5kWp PV, no heat pump, no battery

azimuth	-180	-120	-60	0	60	120	180
zenith							
90	0,30	0,54	0,78	0,81	0,78	0,54	0,30
75	0,35	0,61	0,89	0,93	0,88	0,61	0,35
60	0,38	0,67	0,94	0,99	0,93	0,67	0,38
45	0,41	0,72	0,96	1,01	0,95	0,71	0,41
30	0,56	0,77	0,95	0,99	0,94	0,76	0,56
15	0,74	0,82	0,92	0,95	0,91	0,81	0,74
0	0,87	0,87	0,87	0,87	0,87	0,87	0,87

Most rules of thumb advice 1kW inverter power/kWp to get the highest production. The results show that the rule of thumb fits for a south orientation. Deviating from the best zenith decreases the inverter power for the south direction up to 20%, changing the azimuth to east or west can decrease the inverter power up to 50%. The mentioned design rules can be considered as a good first estimation. Using the simulated optimum as design criteria can bring an extra production up to 3.7% (azimuth between 120° and -120°)and gives an additional saving due to the lower inverter power to be installed. A pure north orientation, zenith 90° , results in a loss of 8.8%. North facing solar panels are rare but there is a growing interest, especially for building integrated PV panels [35] [36] [37].

3.1.2. Maximum self-sufficiency

To maximize the self-sufficiency, the advised inverter ratio is 0.7. Fig. 4 show the self-sufficiency for different inverter powers and zeniths for azimuth 0. The optimized values are listed in Table 3. If the aim of the PV system is to maximize the self-sufficiency, an optimized inverter size ratio of 0.7 to 0.77is calculated for azimuth 0° . The azimuth -120° has enough with an inverter size ratio down to 0.33.A higher self-sufficiency for the same PV capacity means that the energy production is better fitting with the energy demand. The chosen load

profile is for a standard family with standard behaviour. This means an average daily energy demand profile is characterized by a peak in the morning and a peak in the evening. The PV production peak at noon happens most of the time during a low energy demand which makes that the high inverter power is not needed for the high peaks at noon. In contrary the high inverter power makes that the low PV generation in the morning and the evening is transformed at a lower inverter efficiency. A lower inverter power brings the average inverter efficiency to a higher level when the solar energy can be used. In case an inverter ratio of 1 is used (gives the maximum PV production) when a maximum self-sufficiency is targeted, less PV energy can be used. The maximum extra loss is 6.2% when the inverter ratio 1 is used and the 0.7 inverter ratio gives a maximum extra loss of 3% (see Table 4).

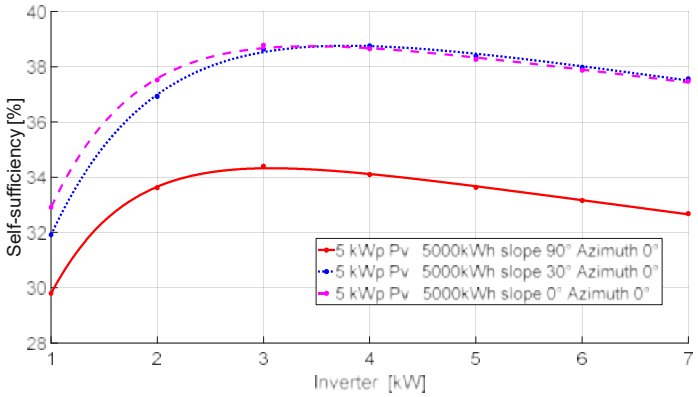

Figure. 4. Self-sufficiency load inverter 5000kWh/a, inverter model 1, 5kWp PV, no heat pump, no battery, azimuth 0°

As long as the azimuth is between -60° and 60° , the loss in self-sufficiency remains smaller than 1%using the 0.7 inverter ratio.

Table 3. Optimized inverter power kW/kWp in function of azimuth and panel zenith for maximum self-sufficiency, load 5000kWh/a, inverter model 1, 5kWp PV, no heat pump, no battery

azimuth	-180	-120	-60	0	60	120	180
zenith							
90	0,23	0,33	0,49	0,61	0,54	0,32	0,23
75	0,29	0,38	0,56	0,70	0,62	0,38	0,29
60	0,32	0,42	0,62	0,75	0,68	0,44	0,32
45	0,36	0,48	0,66	0,77	0,71	0,50	0,36
30	0,46	0,55	0,69	0,77	0,72	0,58	0,46
15	0,59	0,63	0,70	0,74	0,72	0,64	0,59
0	0,69	0,69	0,69	0,69	0,69	0,69	0,69

Table 4. Evaluation loss caused by rules of thumb

sizing method		ideal inverter	inverter ratio 0,7		inverter ratio 1	
Azimuth	zenith	Self-sufficiency [%]				
		Result	Result	% Loss	Result	% Loss
-120°	0°	38,7	38,7	0,0	38,3	1,1
	30°	31,6	31,1	1,6	30,3	4,2
	90°	27,9	27,0	3,0	26,1	6,2
0°	0°	38,7	38,7	0,0	38,3	1,1
	30°	38,8	38,7	0,0	38,5	0,7
	90°	34,4	34,3	0,3	33,7	2,1

Considering each target, the rule of thumb is in both cases a good robust sizing method for a load profile with only residential appliances.

3.2. Case 2

Case 2 is the energy system of case 1 with an extra battery of 8kWh useful battery capacity. The nominal battery capacity is 11.4kWh with a maximum state of charge of 90% and maximum depth of discharge of 80%. Adding a battery will not change the maximum PV production but will increase the self-sufficiency from 40% to 68% for azimuth 0° zenith 30° . Table 5 gives the optimized inverter ratio for the this extended energy system.

$$\frac{d\,E_{bat}}{dt} = P_{inverter} + P_{grid} - P_{appliances} - 0 \tag{8}$$

Table 5 shows that the optimized inverter power to maximize the self-sufficiency is between 0.5 and 0.77 for the values of azimuth -120° to +120° . This brings the average inverter power value on 0.64 instead of 0.6 for the values of azimuth -120° to +120° , so 6% closer to the rule of thumb of 0.7.

Table 5. Optimized inverter power kW/kWp in function of azimuth and panel zenith for maximum self-sufficiency, load 5000kWh/a appliances, inverter model 1, 5kWp PV, heat pump 1691 kWh/a, 8kWh battery

azimuth	-180°	-120°	-60°	0°	60°	120°	180°
zenith							
90°	0,30	0,50	0,65	0,68	0,68	0,49	0,30
75°	0,35	0,51	0,67	0,71	0,70	0,51	0,35
60°	0,38	0,51	0,66	0,69	0,69	0,52	0,38
45°	0,40	0,51	0,64	0,68	0,67	0,53	0,40
30°	0,42	0,52	0,62	0,65	0,63	0,52	0,42
15°	0,49	0,54	0,59	0,60	0,60	0,54	0,49
0°	0,57	0,57	0,57	0,57	0,57	0,57	0,57

Table 6 gives the relative increase of the optimized inverter power of case 2 compared to case 1. Zeniths above 45° have a significant increase of the inverter power up to 53%, zeniths below 45° have a smaller inverter power up to 19% smaller. The vertical installed panels have the largest increase. Without battery, the inverter is determined by the match between solar production and energy demand. Using a large battery, produced energy can be used as long as the battery is not full charged. This means that the vertical panel has only a short period of the day that beam irradiation can be captured. The lower the zenith the larger the period of the day that beam irradiation can be captured which can even result in a smaller optimized inverter power.

Table 6. Increase of inverter power in percentage case 2 compared to case 1

azimuth	-180°	-120°	-60°	0°	60°	120°	180°
zenith							
90°	33	53	33	12	26	51	33
75°	20	36	19	1	13	34	20
60°	17	22	7	-8	2	20	17
45°	11	7	-3	-13	-6	4	11
30°	-9	-6	-11	-16	-12	-11	-9
15°	-17	-14	-16	-19	-17	-16	-17
0°	-17	-17	-17	-17	-17	-17	-17

Adding a battery to the energy system brings for most positions the optimized inverter power closer to the inverter ratio of the rule of thumb. The energy loss due to a not optimized inverter power is even smaller.

3.3. Case 3

Case 3 is case 1 extended with a heat pump. Table 7 shows the percentage increase of the inverter power compared to the base case.

$$0 = P_{inverter} + P_{grid} - P_{appliances} - P_{hp} \tag{9}$$

The orientations influenced by the rising sun have a small increase of inverter power, the orientations influenced by the sunset have a small decrease of inverter power. The morning has the coldest temperature of the day and will make that the heat pump is more activated which makes that the resulting load during the morning will be higher. When the solar panels are oriented to the west makes that they only have diffuse irradiation during the morning. A smaller inverter power will increase the efficiency of the small part loads that occur in the morning. On the level of sizing can be concluded that the extra load of the heat pump does not influence the optimized inverter power significant. For example azimuth -60° , zenith 75° , brings the optimized inverter from 0.56kW/kWp to0.62kW/kWp. Adding a heat pump makes the loss smaller when the rule of thumb is used.

Table 7. Percentage increase of inverter power, case 2 compared to case 1

azimuth	-180°	-120°	-60°	0°	60°	120°	180°
zenith							
90°	1	5	11	2	1	1	1
75°	0	7	9	0	0	1	0
60°	0	9	7	0	0	-1	0
45°	1	8	5	0	-1	-1	1
30°	0	4	3	0	-2	-1	0
15°	0	2	2	-1	-1	-1	0
0°	0	0	0	0	0	0	0

3.4. Case 4

In case 4 the energy system is extended with a heat pump and a battery.

$$\frac{d\,E_{bat}}{dt} = P_{inverter} + P_{grid} - P_{appliances} - P_{hp} \tag{10}$$

Table 8 shows the optimal inverter for maximum self-sufficiency for the reference system extended with a heat pump and a battery. Most values come even closer to the rule of thumb value of 0.7.
Table 9 gives the relative increase of the optimized inverter power of case 4 compared to case 1 in percentage. The increased load due to the added heat pump and the extra battery that charges the surplus makes that a larger inverter power can be used for zeniths which have a limited time to capture beam irradiation. The orientations having larger periods access to beam radiation have more time to charge the battery resulting in a smaller inverter power. Case 4 combines the effects of case 2 and case 4: decrease for zeniths below 45° and increase for zeniths above 45° , increase for sunrise sensible positions and decrease for sunset sensible positions. The statements are mentioned in case 2 and case 3.

Table 8. Optimized inverter power kW/kWp in function of azimuth and panel zenith for maximum self-sufficiency, load 5000kWh/a appliances, inverter model 1, 5kWp PV, heat pump 1691 kWh/a, 8kWh battery

azimuth	-180°	-120°	-60°	0°	60°	120°	180°
zenith							
90°	0,30	0,52	0,69	0,72	0,69	0,50	0,30
75°	0,35	0,56	0,72	0,77	0,73	0,53	0,35
60°	0,38	0,56	0,72	0,76	0,73	0,55	0,38
45°	0,41	0,56	0,71	0,75	0,71	0,57	0,41
30°	0,44	0,56	0,68	0,71	0,68	0,56	0,44
15°	0,52	0,57	0,65	0,66	0,64	0,56	0,52
0°	0,61	0,61	0,61	0,61	0,61	0,61	0,61

Table 9. Increase inverter power in percentage case 4 versus case 1

azimuth	-180°	-120°	-60°	0°	60°	120°	180°
zenith							
90°	32	58	41	17	28	55	32
75°	21	48	28	9	17	38	21
60°	17	33	17	2	7	26	17
45°	13	18	6	-4	-1	13	13
30°	-4	3	-2	-7	-7	-3	-4
15°	-11	-8	-7	-11	-11	-12	-11
0°	-12	-12	-12	-12	-12	-12	-12

3.5. Case 5

Case 5 is equal to case 1 but using a more energy efficient inverter (see Fig.1). Inverter model 1 has an EU-efficiency of 91.1%, where inverter model 2 has an EU-efficiency of 95.6%. Table 10 shows the optimized inverter power for inverter model 2 to maximize the self-sufficiency. In the previous cases the inverter power is often reduced to limit the inverter losses during low part loads. The higher the inverter efficiency during low part load the less there is a need to reduce the inverter power. The rule of thumb is in this case an under-sizing for the south orientation. The loss in self-sufficiency is maximum0.2%.

Table 10. Optimized inverter power kW/kWp in function of azimuth and panel zenith for maximum self-sufficiency, load 5000kWh/a appliances, inverter model 5, 5kWp PV, no heat pump , no battery

azimuth	-180°	-120°	-60°	0°	60°	120°	180°
zenith							
90°	0,32	0,43	0,63	0,77	0,70	0,43	0,32
75°	0,35	0,48	0,72	0,86	0,79	0,49	0,35
60°	0,37	0,52	0,78	0,90	0,84	0,56	0,37
45°	0,39	0,60	0,82	0,92	0,87	0,65	0,39
30°	0,57	0,69	0,84	0,91	0,88	0,73	0,57
15°	0,73	0,78	0,85	0,89	0,87	0,80	0,73
0°	0,83	0,83	0,83	0,83	0,83	0,83	0,83

4. Conclusion

The optimized inverter power is determined for a reference system without battery or heat pump, as well as for the extended systems with heat pump and battery. Adding a battery, or adding a heat pump, or both, results in a different optimized inverter power but the gains compared to the inverter power determined by the rule of thumb are small.

Two rules of thumb to select the inverter power are used by contractors in Belgium, namely 70% and100% of the installed PV power expressed in kWp regarding the standard conditions. The 70% rule aims a maximum self-sufficiency, the 100% rule aims a maximum PV production. The results show that the rules of thumb are valid for the ‘best’ orientation in Belgium, namely due south and 30° zenith. A deviation of this position results in an extra loss of self-sufficiency or extra loss in production. Those losses are smaller than 1%. Adding a heat pump, a battery or both gives a small shift to a larger or smaller inverter power depending the orientation and zenith. Even with a changing load profile by adding heat pump and/or battery, the rule of thumb remains a good selection method of the inverter power. For an azimuth out of the range [-60°,60°] the optimized inverter will have a smaller power as the one determined by the rule of thumb and will reduce the investment with a better performance on top.

Nomenclature

C_{bat}	charge/discharge rate of the battery [h^{-1}]
C_{dr}	Capacitance of the battery cell in function of the open circuit voltage [F]
E_{bat}	Nominal capacity battery [kWh]
E_{loss}	Capacity loss of the battery in function of the SOC [kWh]
n	number of solar panels
$P_{appliances}$	Power of all appliances [W]
P_{batt}	Power charge/discharge battery [W]
$P_{batt\ conv}$	Power battery converter [W]
P_{grid}	Power supplied by the grid [W]
P_{hp}	Heating power heat pump [W]
$P_{inverter}$	Power output of the inverter [W]
P_{pv}	Power generated by the solar panels [W]
$PLR_{bat\ conv}$	Part load ratio battery converter [%]
PLR_{HP}	part load ratio heat pump [%]
R_f	Resistance of the battery cell in function of the open circuit voltage [mOhm]
SOC	State of charge of the battery [%]
T_{lwt}	Leaving water temperature heat pump [K]
T_{module}	Temperature of the solar panel [K]
$T_{outdoor}$	Outdoor temperature [K]
W_p	peak power of the solar panel at standard conditions [W/panel]
Φ_{solar}	Solar irradiation [W/m²]
η_{eff}	Efficiency of inverter [%]

References

[1] M. Schmela, W. Hemetsberger, and G. Chianetta, "Global Market Outlook for Solar Power 2021–2025," *SolarPower Europe, July,* 2021.

[2] WPP, "Marktcijfers Belgische warmtepompsector," ed. Nieuwsflits 2021/13: Warmtepomp Platform, 2021, p. 1.

[3] E. S. Edwin van Gastel. (2021, 08/11/2021) In 2021 al 11174 thuisbatterijen geïnstalleerd in Vlaanderen. *Solarmagazine*. 1.

[4] V. E.-e. Klimaatagentschap. "Berekening van de besparing en terugverdientijd voor zonnepanelen tot 10kVA." Vlaams Energie- en Klimaatagentschap
https://www.energiesparen.be/sites/default/files/atoms/files/Calculator-zonnepanelen-tot-10-kVA-versie-april%202021.xlsx (accessed 12/03/2022, 2022).

[5] M. Meuris *et al.*, "Managing PV power injection and storage, enabling a larger direct consumption of renewable energy: A case study for the Belgian electricity system," *Progress in Photovoltaics: Research and Applications,* vol. 27, no. 11, pp. 905-917, 2019.

[6] S. Chen, P. Li, D. Brady, and B. Lehman, "Determining the optimum grid-connected photovoltaic inverter size," *Solar Energy,* vol. 87, pp. 96-116, 2013/01/01/ 2013, doi: https://doi.org/10.1016/j.solener.2012.09.012.

[7] S. P. d. Wallonie. "Simulateur photovoltaïque financier pour particuliers en Wallonie." Energie Commune Région Wallone. http://sifpv.apere.org/ (accessed 12/03/2022, 2022).

[8] I. B. p. l. g. d. l'environnement, "Le photovoltaïque dimensionnement d'une installation PV," (in French), infos fiches-énergie p. 8, November 2010 2010. [Online]. Available: https://document.environnement.brussels/opac_css/elecfile/IF%20ENERGIE%20Mod5%20Dimensionnement%20PV%20FR.

[9] Hespul. "Performance des onduleurs." Le centre de ressources Photovoltaïque. https://www.photovoltaique.info/fr/realiser-une-installation/choix-du-materiel/fonctionnement-et-categories-des-onduleurs-photovoltaiques/rendement-et-performance-des-onduleurs/#performance_des_onduleurs (accessed 12/03/2022, 2022).

[10] P. v. d. Wilt. "Hoeveel zonnepanelen heb ik nodig?" Consumentenbond. https://www.consumentenbond.nl/zonnepanelen/hoeveel-zonnepanelen (accessed 12/03/2022, 2022).

[11] C. Märtel. "So wählen Sie Wechselrichter für Ihre PV-Anlage aus." https://www.photovoltaik-web.de/photovoltaik/wechselrichter (accessed 12/03/2022, 2022).

[12] J. D. Mondol, Y. G. Yohanis, and B. Norton, "Optimal sizing of array and inverter for grid-connected photovoltaic systems," *Solar Energy,* vol. 80, no. 12, pp. 1517-1539, 2006/12/01/ 2006, doi: https://doi.org/10.1016/j.solener.2006.01.006.

[13] B. Burger and R. Rüther, "Inverter sizing of grid-connected photovoltaic systems in the light of local solar resource distribution characteristics and temperature," *Solar Energy,* vol. 80, no. 1, pp. 32-45, 2006/01/01/ 2006, doi: https://doi.org/10.1016/j.solener.2005.08.012.

[14] G. Nofuentes and G. Almonacid, "Design tools for the electrical configuration of architecturally-integrated PV in buildings," *Progress in photovoltaics: research and applications,* vol. 7, no. 6, pp. 475-488, 1999.

[15] N. Van Der Borg and A. Burgers, "Inverter undersizing in PV systems," in *3rd World Conference onPhotovoltaic Energy Conversion, 2003. Proceedings of*, 2003, vol. 2: IEEE, pp. 2066-2069.

[16] S. Islam, A. Woyte, R. Belmans, P. Heskes, and P. Rooij, "Investigating performance, reliability and safety parameters of photovoltaic module inverter: Test results and compliances with the standards," *Renewable Energy,* vol. 31, no. 8, pp. 1157-1181, 2006.

[17] G. Notton, V. Lazarov, and L. Stoyanov, "Optimal sizing of a grid-connected PV system for various PV module technologies and inclinations, inverter efficiency characteristics and locations," *Renewable Energy,* vol. 35, no. 2, pp. 541-554, 2010.

[18] R. S. Faranda, H. Hafezi, S. Leva, M. Mussetta, and E. Ogliari, "The optimum PV plant for a given solar DC/AC converter," *Energies,* vol. 8, no. 6, pp. 4853-4870, 2015.

[19] F. Obeidat, "A comprehensive review of future photovoltaic systems," *Solar Energy,* vol. 163, pp. 545-551, 2018/03/15/ 2018, doi: https://doi.org/10.1016/j.solener.2018.01.050.

[20] Y. Shi, L. Wang, R. Xie, Y. Shi, and H. Li, "A 60-kW 3-kW/kg five-level T-type SiC PV inverter with 99.2% peak efficiency," *IEEE Transactions on Industrial Electronics,* vol. 64, no. 11, pp. 9144-9154, 2017.

[21] J. Weniger, T. Tjaden, J. Bergner, and V. Quaschning, "Sizing of battery converters for residential PV storage systems," *Energy Procedia,* vol. 99, pp. 3-10, 2016.

[22] C. Brivio, V. Musolino, M. Merlo, and C. Ballif, "A physically-based electrical model for lithium-ion cells," *IEEE Transactions on Energy Conversion,* vol. 34, no. 2, pp. 594-603, 2018.

Data-driven techno-economic analysis of rooftop photovoltaic systems in the Spanish residential sector at municipal level

Raul Saez[a], Dieter Boer[b], Adedamola Shobo[c], Manel Vallès[d]

[a]Universitat Rovira i Virgili, Tarragona, Spain, raul.saez@urv.cat
[b]Universitat Rovira i Virgili, Tarragona, Spain, dieter.boer@urv.cat,
[c]Universitat Rovira i Virgili, Tarragona, Spain, adedamolababajide.shobo@urv.cat,
[d]Universitat Rovira i Virgili, Tarragona, Spain, manel.valles@urv.cat, CA

Abstract

The current energy transition goals set by Spain in the PNIEC 2021-2030 anticipate a photovoltaic (PV) installed capacity of 39 GW by 2030, against the installed capacity of about 9 GW in 2020. The global improvement of PV systems' cost-effectiveness coupled with the current escalation in energy prices and the high annual solar energy potential of Spain are positive drivers. Thus, there has been an acceleration in the deployment of PV in the country, where the installed capacity has increased by 72% in the last two years, up to 15 GW. To study the potential contribution of residential rooftop PV systems in the future Spanish electricity mix, a data-driven multi-regional tool has been developed in Python. The hourly net electricity production-consumption balance is obtained for one year by using specific hourly solar irradiation data and real hourly electricity consumption data for each of the 8,131 municipalities in Spain. Furthermore, the economic potential of such installations is evaluated with the consideration of different electricity market scenarios as well as surplus electricity compensation policies. The analysis of the results shows a capacity for self-consumption which is 3 to 4 times higher in rural areas than in urban areas when energy storage is not considered. Furthermore, the current compensation policies may negatively affect the economic profitability of PV systems in the areas with the most significant PV potential.

Keywords

Data-driven tool; Regional analysis; Rooftop photovoltaic; Self-consumption potential; Techno-economical assessment.

1. Introduction

According to *PNIEC 2021-2030* national plan [1], Spain aims to deploy 39 GW of PV power by 2030 in the country, a significant increase from the 9 GW capacity in 2020. To encourage self-production of energy through PV systems in the residential sector, legal changes and fiscal measures have been implemented recently, including a law passed in 2019 to regulate surplus energy fed into the grid [2] and subsidies announced in 2021 to cover a percentage of the cost of new installations [3]. These measures, combined with the improving cost-effectiveness of PV systems and rising electricity prices [4], have led to an increase in PV system installations for self-consumption in Spain of 72% over the past two years [5].

Spain has a heterogeneous population distribution, with 16% residing in rural areas and occupying 84% of the land, while 84% live in urban areas and occupy 16% of the land [6]. According to [7-10], this distribution will affect the deployment of PV systems in the country, as some areas have low population densities but large surface areas to install PV while others have high population densities but small surface areas to install PV. Therefore, challenges remain in optimizing the deployment and integration of solar PV systems into different regional energy systems. Decision-makers in Spain need to address key questions, including the contribution of individual PV systems to the energy transition, promotion of larger-scale solutions such as energy communities, and how solutions should differ in rural and urban areas.

Previous studies have examined the potential of solar PV systems in specific regions of Spain, such as the Canary Islands. One study [11] found that the islands' potential solar fraction (i.e., percentage of the total energy demand satisfied by solar energy) is about 150%, meaning that there will be an overproduction of energy from PV compared to current demand. The same study concludes that PV systems would be economically profitable on the islands even without policies to compensate for electricity surpluses. Another recent study [12] focused on Gran Canary Island examined a theoretical hybrid energy system based on PV, offshore wind turbines, and energy storage to support local electricity self-consumption, with positive results. However, its analysis of future electrification scenarios showed that the optimal weight of solar PV generation systems decreases as electricity demand increases in contrast to wind turbines.

Moreover, other studies have focused on PV self-consumption capacity at the municipal scale in urban areas of Spain, such as the cases of Seville [13], Irun [14], and Valencia [15]. In Seville, PV systems installed on the roofs of buildings (residential, services, and industrial) could virtually meet the electricity demand of the city.

However, in Irun, only 59% of the city's demand could be covered by PV on building rooftops due to the prevailing climatic conditions. The study presented a sensitivity analysis of PV systems' economic profitability under three different surplus compensation policies: sole self-consumption, net-metering, and electricity transactions between buildings. The results showed that to achieve an investment return rate below 12 years, 27% to 71% of the roof surface area would need to be used, depending on the compensation policy. Meanwhile, the study of Valencia developed a multiple linear regression model to determine the economic payback of PV installations on residential buildings. The model identified shadow losses and power unit cost as the main factors affecting the payback period, which ranged between 7 and 15 years in most cases. High electricity demand buildings with low surpluses were found to be more profitable than those with large surpluses, due to the low economic compensation when injecting surplus electricity to the grid. The study suggested the promotion of energy communities to improve the profitability of PV systems.

At the national level, Gomez-Exposito et al. [16] evaluated Spain's potential for sustainable energy systems based on rooftop PV systems. The study highlighted the model's limitations due to the lack of hourly resolution energy demand data although it showed promising possibilities regarding a greener future in Spain.

With a careful review of the previous works on self-generation of electricity through PV systems, no work is yet to assess the impact of current Spanish surplus compensation policies on economic profitability and adoption. Additionally, no regional-level study has been conducted on the self-consumption capacity of the residential sector using massive data of real electricity consumption with hourly resolution. To address this gap, this work proposes a novel data-driven method to analyze the economic profitability and electricity self-production capacity using PV modules on residential rooftops, considering different compensation policies and flexible electricity prices. The analysis uses real hourly electricity consumption data from individual smart meters for all municipalities in Spain, allowing for higher resolution energy balances and individual analyses for each municipality. This enables the assessment and comparison of the capacity and profitability of rooftop PV between rural and urban areas.

2. Material and methods

Data from online databases are used to estimate the average electricity demand, rooftop surface availability, PV generation capacity, and solar fraction at different scales and regions. An economic analysis is conducted to find the optimal PV investment, calculating Net Present Value, Total Annual Cost, and Payback Period at the dwelling scale. Sensitivity analyses are performed for different scenarios of electricity prices and surplus electricity compensation policies. A Python-based software is developed to extract and process data automatically and generate tabular and graphic outputs for ease of analysis.

2.1 Architecture of the solution

Figure 1 illustrates the four main steps of the workflow: 1) Data collection, 2) Pre-processing, 3) Modeling, and 4) Analysis and visualization. Input datasets such as electricity consumption data, cadastral data, weather data, PV performance data, and economic data are collected in step one. Step two involves cleaning, filtering, and normalizing the collected data. In step three, the normalized datasets are combined to build the energetic and economic models. Finally, the techno-economic indicators are computed for all regions in Spain at the municipality level at hourly resolution.

2.2 Data processing

Hourly electricity demand per dwelling: Equation (1) can be used to obtain the Average Electricity Consumption per Dwelling, E_{dw}, by assuming one electricity contract per dwelling. E_{dw} is derived from the hourly electricity consumption in a municipality, E_T, and is influenced by the number of consumers in the area, C.

$$E_{dw} = \frac{E_T}{C}. \quad (1)$$

Rooftop availability per dwelling: The average amount of available rooftop surface per dwelling in square meters has been determined for each of the 15 typical housing clusters proposed by [17] in Spain. This calculation utilized the "void fraction coefficient," "shadowing fraction coefficient," and "facility coefficient" proposed by [18]. These coefficients consider factors such as empty space, shading, and obstacles in rooftops.

Hourly solar irradiation per square meter: Hourly solar irradiation data G in kWh·m^{-2} is obtained from the PVGIS platform [19]. Municipalities are reduced to one point (latitude and longitude) for simplicity when retrieving data. Solar PV modules are assumed to be installed horizontally to simplify the model by discarding the dependency of irradiation on the panel's azimuth angle and considering the associated decrease in efficiency for this configuration.

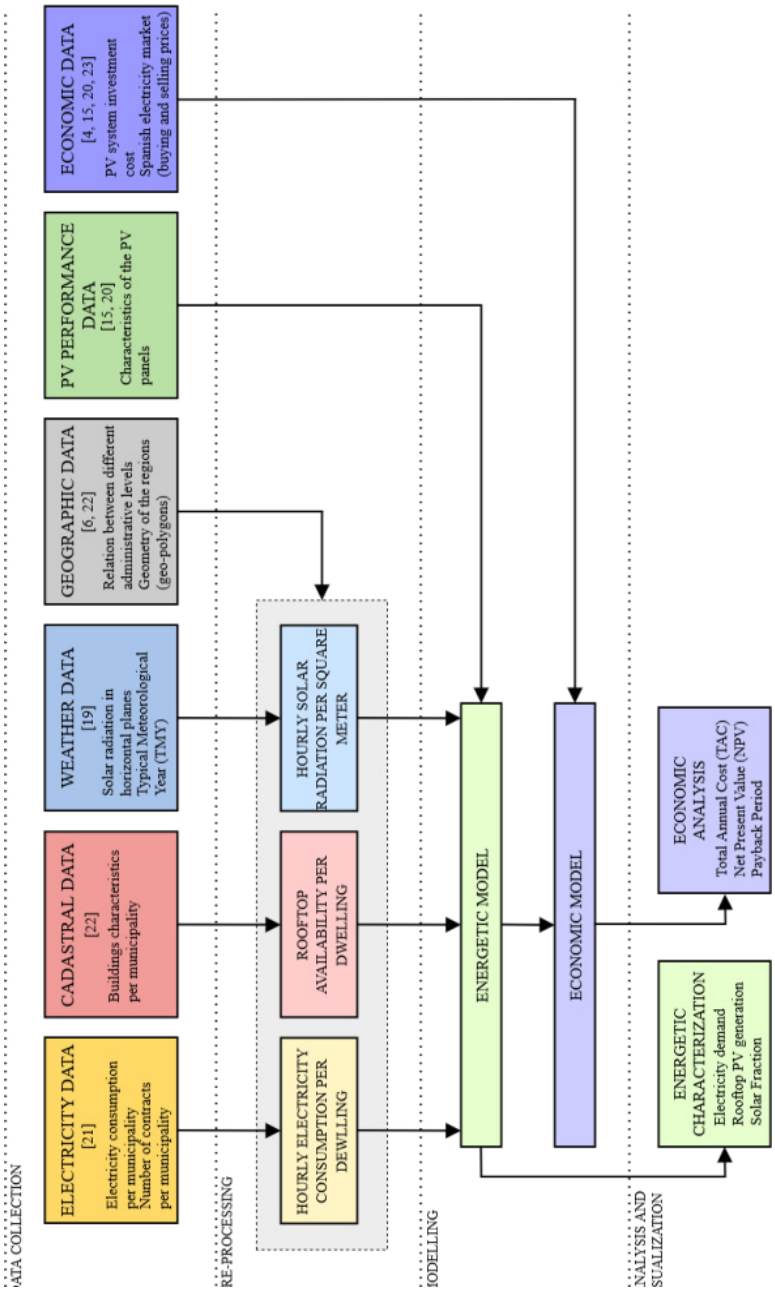

Figure 1. Workflow of the proposed method.

2.3 Techno-economic model

PV potential generation per dwelling. The PV potential per dwelling (in kWh) is determined by the percentage of rooftop surface (S_{PV}) covered by solar modules (load factor), hourly solar radiation (G) in kWh·m^{-2}, and the PV system performance factor (η). In the developed model, the rooftop load factor (α) ranges from 0% (no PV module) to 100% (full coverage of available roof surface). Equation (2) calculates the PV potential per dwelling (in kWh) for each observed hour i.

$$E_{PV,i} = G_i \cdot \alpha \cdot S_{PV} \cdot \eta. \quad (2)$$

Solar Fraction. The Solar Fraction represents the proportion of the annual energy demand that can be met by solar energy. Typically, this balance is calculated using annual average data of demand and PV production. However, studies have shown that analyzing the balance using hourly average data can provide valuable insights into the region's self-consumption estimation [16]. This study includes both methods: the one based on annual averages (SF_a, Eq. 3) and the one based on hourly averages (SF_h, Eq. 4).

$$SF_a = \frac{\sum_{i=1}^{j} E_{PV,i}}{\sum_{i=1}^{j} E_{d,i}} \cdot 100\%. \quad (3)$$

$$SF_h = \frac{\sum_{i=1}^{j} \frac{E_{PV,i}}{E_{d,i}}}{j} \cdot 100\%. \quad (4)$$

where $E_{d,i}$ is the hourly electricity demand (in kWh) at each hour *i*, $E_{PV,i}$ is the hourly PV electricity production (in kWh) at each hour *i*, and *j* is the total number of hours in a year.

Net money flow. The hourly money flow (C_h) in EUR is determined in Eq. (6) at each hour *i* according to the price of electricity and the net hourly energy balance (E_h), calculated in Eq. (5) as the difference between electricity consumed (E_d) and produced (E_{PV}) in an hour. When the net hourly energy balance (E_h) is positive, the purchase price (P_p) is used in Eq. (6); but when the balance is negative, selling price is used (P_s).

$$E_{h,i} = E_{d,i} - E_{PV,i}. \quad (5)$$

$$C_{h,i} = \begin{cases} E_{h,i} \cdot P_p \ \ if E_{h,i} > 0 \\ E_{h,i} \cdot P_s \ \ if E_{h,i} < 0 \end{cases}. \quad (6)$$

Accordingly, the monthly money flow (C_M) in EUR is an aggregate of all the hourly money flows for the month for the number of hours *I* observed in that month:

$$C_M = \sum_{i=1}^{I} C_{h,i}. \quad (7)$$

Total Annual Cost TAC The Total Annual Cost (*TAC*) for a PV system in EUR includes the annualized costs of owning, operating, and maintaining the system. *TAC* is the sum of Investment Annual Cost (*IAC*) in EUR and operational cost (C_{ope}) in EUR, as shown in Eq. (8):

$$TAC = IAC + C_{ope}. \quad (8)$$

The *IAC,* as given by Eq. (9), is the result of the *TIC* after applying the Capital Recovery Factor (*CRF*) which is given by Eq. (10):

$$IAC = TIC \cdot CRF, \quad (9)$$

$$CRF = \frac{ir \cdot (1+ir)^n}{(1+ir)^n - 1}. \quad (10)$$

where *IAC* is the Investment Annual Cost in EUR; *TIC* is the Total Investment Cost in EUR; *CRF* is the Capital Recovery Factor; *ir* is the Interest Rate in %; and *n* is the lifetime of the project in years. In Eq. (8), C_{ope} refers the cost of electricity consumption, i.e., the electricity bill, where C_{fix} is the Monthly fixed costs in EUR by using Eq. (11):

$$C_{ope} = \sum_{y=1}^{12} \left[(C_{fix,y} + C_{M,y}) \cdot (1 + VAT) \right]. \quad (11)$$

It is worth mentioning that each state, region, etc., has its own policies and laws on surpluses that may affect Eq. (11). For instance, in the current Spanish scenario, the monthly money flow (C_M) is restricted to be a positive value [2].

Total Investment Cost TIC The total investment cost for one PV system includes the cost of all the hardware, the installation cost, and the maintenance cost, in Euro per peak watt (EUR/Wp) and it is obtained by using Eq. (12):

$$TIC = (1 + F_{ind}) \sum_{k=1}^{K} \left[C_c \cdot (1 + FNPV_k) \cdot \left(1 + F_{m,k}\right) \cdot (1 + VAT) \right]. \quad (12)$$

where:

- F_{ind} — Factor for the indirect costs of the project (e.g., engineering cost) and it is estimated as 0.2 [20].
- FNPV — Net Present Value Factor for the possible repositions of components during the lifetime of the project.
- F_m — Factor for installation and maintenance costs and it estimated as 0.01 [20].
- VAT — Value-added tax (specific for each country)
- K — the number of all the different components of in system

Net Present Value NPV. The Net Present Value for one PV system (in EUR) as determined by Eq. (13), gives the time value of money invested and the economic risk of the project.

$$NPV = -TIC + \sum_{y=1}^{n} \frac{C_Y}{(1+ir)^y} \quad (13)$$

where C_Y is the Net Money Flow for one year in EUR.

3. Case study

This methodology was applied to assess the PV potential and self-consumption capacity in all 8,131 municipalities in Spain, covering both rural and urban areas. The study estimated the net energy balance over one calendar year and evaluated the economic profitability of PV systems over a 20-year projection. Hourly electricity demand data for 2019 was obtained from the Datadis database [21] for each municipality, while solar radiation data was collected from meteorological data series from 2006 to 2015 [19]. The availability of rooftop surface was estimated using the latest data from the INE database (dated 2011) [22]. Electricity prices were based on trends in the Spanish wholesale electricity market from 2015 to 2021 [4], while the performance and investment costs of the PV system were based on up-to-date global benchmarking reports and other referential works [14,15,20].

It should be noted that complete data on electric demand and housing stock is not available for all 8,131 municipalities in Spain. 326 municipalities, mostly with populations under 500 and representing 0.79% of the country's population, lack complete electricity demand data for 2019 [21]. Meanwhile, 138 municipalities representing 0.09% of the population have no statistical data on the housing stock [22].

In order to facilitate the analysis, all municipalities have been classified into 11 hotspots based on their population size, as shown in Table 1.

Table 1. Population distribution of the municipalities in Spain.

Number of municipalities	Size of the municipality (Number of inhabitants)
1233	< 100
2521	101 to 500
968	501 to 1,000
848	1,001 to 2,000
931	2,001 to 5,000
548	5,001 to 10,000
499	10,001 to 20,000
110	20,001 to 50,000
84	50,001 to 100,000
57	100,001 to 500,000
6	> 500,000

3.1 PV systems' parameters

Table 2 presents the PV system performance parameters used in the techno-economic analyses, including peak power per square meter, system efficiency, and lifetime.

Table 2. Performance parameters of the PV systems considered for the analyses.

PV performance parameters	Value
PV system output peak power	200 W_p/m^2 [20]
PV system efficiency	20 % [20]
PV system lifetime	20 years [13,14,20]

Table 3 summarizes the economic parameters considered in the analysis, including the cost in EUR per peak watt installed, the operation and maintenance costs in EUR per watt per year, and the VAT rate.

Table *3.* Economic parameters of the PV systems considered in the analyses.

PV economic parameters	Value
Residential PV system cost (VAT excl.)	1.6 EUR/Wp [14,15,20]
O&M cost (VAT excl.)	0.02 EUR/W·year [20]
VAT	21%

3.2 Electricity market scenarios

Table 4 outlines the proposed hybrid tariffs for electricity prices, which are based on REE's Active Energy Billing Term of the Voluntary Price for the Small Consumer (PVPC) [23] and the average prices in Spain from 2015-2021 [4]. The prices are divided into three hourly sections during the week with no differentiation on weekends. Three scenarios are considered: a downward trend, average trend, and an upward trend price.

Table 4. The three scenarios of hourly electricity prices considered in the analyses.

Period of the day (hours)	Downward trend (EUR/kWh)	Average trend (EUR/kWh)	Upward trend (EUR/kWh)
0-8	0.06	0.12	0.17
8-10; 14-18; 22-24	0.10	0.18	0.26
10-14; 18-22	0.14	0.24	0.34
Weekends	0.06	0.12	0.17

3.3 Surplus compensation policy scenarios

In Spain, the self-production surplus policy restricts profits from selling excess production as the monthly money flow (C_M) cannot be negative [2]. This means compensation for surplus sale cannot provide economic gains to consumers. To account for this constraint, Eq. (11) is redefined as Eq. (11b). However, to evaluate the impact of this policy on PV system profitability, both equations are computed, and their results compared.

$$C_{ope} = \begin{cases} \sum_{y=1}^{12}\left[(C_{fix,y} + C_{M,y}) \cdot (1 + VAT)\right] \; if \; C_{M,y} > 0 \\ \sum_{y=1}^{12}\left[(C_{fix,y} + 0) \cdot (1 + VAT)\right] \; if \; C_{M,y} < 0 \end{cases} . \quad (11b)$$

4. Results and discussion

4.1. Hourly electricity demand

Figure 2 displays the average electricity demand per dwelling per year (E_{dw}) in kWh for 7,828 municipalities in Spain. These municipalities were categorized into 11 population groups using Table 1 in Section 3.1. The average daily electricity demand in Spain is 7.6 kWh per dwelling per day, increasing to 8.5 kWh during winter and decreasing to 7.3 kWh during summer. Urban areas with over 30,000 inhabitants exhibit similar consumption patterns as the average. However, rural areas tend to have lower consumption, likely due to factors such as electrification levels and local alternative energy availability.

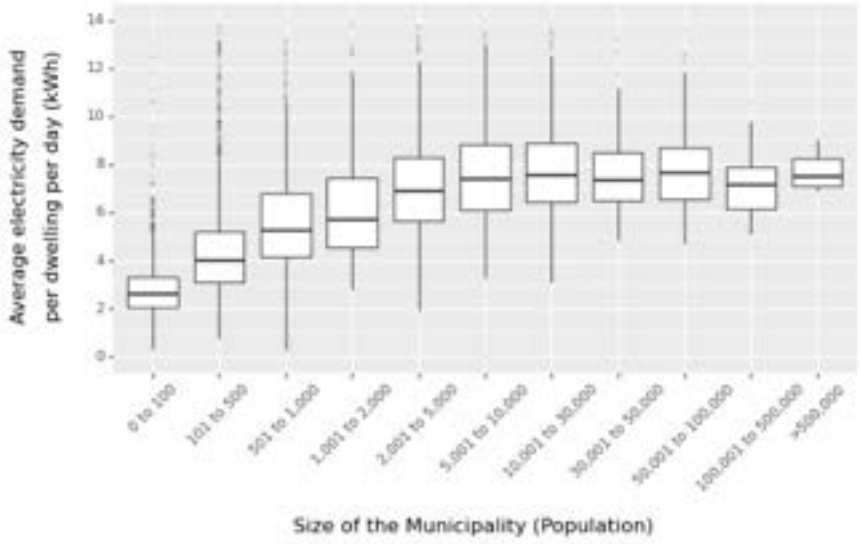

Figure 2. Average electricity demand per dwelling per day, in kWh, in the 7,828 municipalities in Spain with available data (>99% population representativity) grouped by population.

4.2 PV rooftop potential

Figure 3 displays the estimated useful rooftop surface to install PV per dwelling for the 7,828 municipalities with available data in Spain, calculated using the methodology described in Section 2.2. Small rural

municipalities (less than 5,000 inhabitants and 12% of the total population) have a consistent 10 m^2 of surface per dwelling in average, while larger urban areas (over 100,000 inhabitants and 40% of the population) have only between 3 – 4 m^2. This is due to a higher concentration of single-family buildings in rural areas compared to urban areas, where the proportion of multi-story housing blocks is significantly higher. Expressed in PV power terms, smaller rural areas can accommodate up to 5 solar panels per dwelling in average, equivalent to around 1.5 – 2.0 kWp of installed power, while larger urban areas can only accommodate up to 2 solar panels per dwelling in average, approximately 0.8 – 1.2 kWp. These results will be further discussed in the next section in relation to electricity demand.

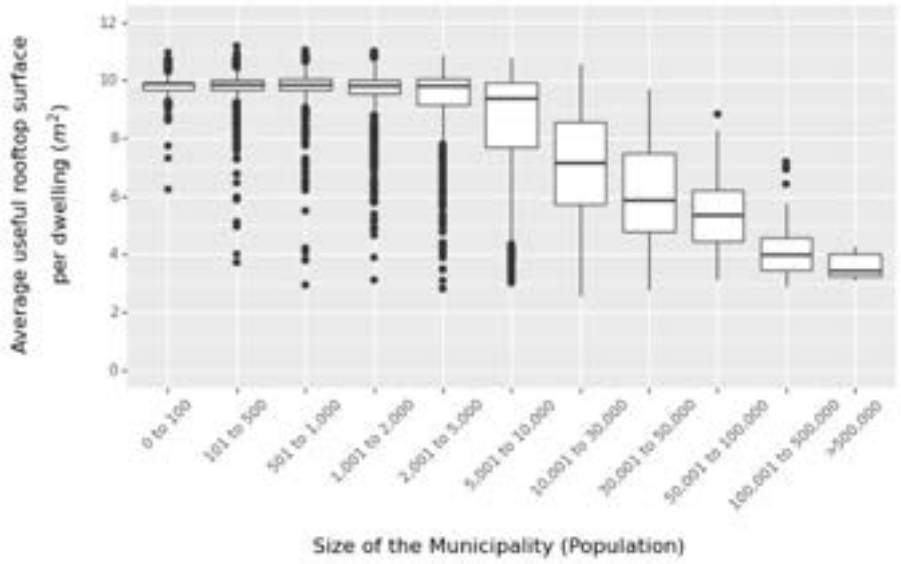

Figure 3. Available rooftop surface per dwelling, in square meters, for the installation of PV panels in the 7,828 municipalities in Spain with available data (>99% population representativity) grouped by population.

4.3 Solar Fraction

When estimating the solar fraction for municipalities in Spain, the annual balance method driven by Eq. (3) assume that surplus solar energy can be stored for on-demand use. However, this is not realistic due to current storage technology limitations. Therefore, a more practical approach is determined by using the hourly balance method driven by Eq. (4), which only considers immediate consumption. Figure 5 shows the results using this method, which demonstrate a decrease in self-production capacity for all municipalities compared to the annual balance method (Figure 4). With the hourly method, rural areas are no longer 100% self-sufficient, and all municipalities will remain between 30 and 55% solar fraction. Specifically, large urban areas experience a 30% drop, while rural areas see a 50 – 75% drop.

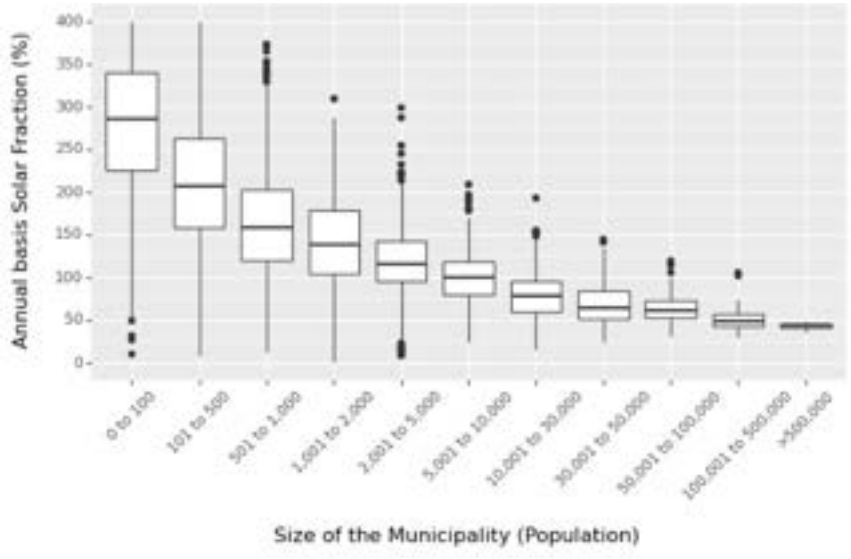

Figure 4. Solar fraction per dwelling (%) obtained with the annual balance method in the 7,828 municipalities in Spain with available data (>99% population representativity) grouped by population.

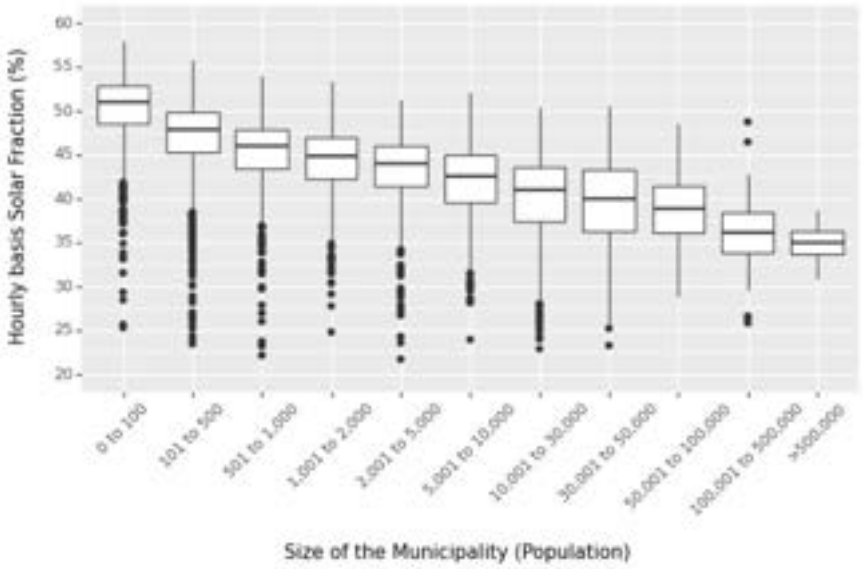

Figure 5. Solar fraction per dwelling (%) obtained with the hourly balance method in the 7,828 municipalities in Spain with available data (>99% population representativity) grouped by population.

4.4 Economic analysis

The economic optimization of 7,828 municipalities was conducted employing Total Annualized Cost (TAC), Net Present Value (NPV), and Payback Period (PBP) as key metrics. Figure 6 illustrates the outcomes for a selection of six municipalities distributed across various regions and diverse population sizes, thereby enabling a comparative study between urban and rural morphologies and also between different prevailing climate conditions. This selection encompasses Bilbao and Sopuerta in the north, Madrid and Ajalvir in the center, and Sevilla and Pruna in the south. Each pair of cities symbolizes urban and rural morphologies, respectively. Three distinct electricity price scenarios, as outlined in Table 4, were assessed, in conjunction with two surplus compensation policies, elucidated in section 3.3. The outcomes are portrayed for green (downward trend), orange (average trend), and red (upward trend) electricity price scenarios. The compensation policies considered include one that permits economic gains and another that aligns with the current Spanish regulations, devoid of economic incentives. The x-axis signifies the percentage of rooftop occupancy or load factor, which ranges from 0% (indicating no PV system installation) to 100% (indicating full occupancy). For this analysis, an interest rate of 3% and a projected lifespan of 20 years were presumed. Neither inflation nor owners' risk factor were considered in the study.

The TAC results, as shown in the first row, demonstrate that all six municipalities could obtain economic benefits from the installation of solar panels. However, the optimal rooftop load factor is subject to variations on the size of the municipality and the surplus compensation policy considered. Large urban municipalities such as Bilbao, Madrid, and Sevilla, generally have less rooftop surface availability compared to their rural counterparts, Sopuerta, Ajalvir, and Pruna. This constraint in urban areas diminishes the PV potential capacity, and consequently, the potential economic gains, as depicted by the marginal decrease of TAC with increasing load factor. Furthermore, the limited PV potential implies that surplus in urban municipalities are inadequate to reap the benefits of more generous compensation policies for PV system owners. Hence, both policy scenarios exhibit similar behavior. In contrast, rural municipalities, with generally larger rooftop surface availability per dwelling, yield superior economic performance and more significant surpluses. Consequently, they stand to gain the most from a hypothetical, more favorable surplus compensation policy.

The second row presents the NPV values, which supplement the TAC analysis by suggesting the optimal rooftop load factor for PV investment. The Payback period values also exhibit variability, dependent on the size of the municipality, electricity prices, and compensation policy. It is evident that current compensation policies could potentially hinder the complete deployment (100% load factor) of PV in rural areas. In an average market scenario, a dwelling in the rural areas could attain a PBP between 8 and 10 years under the current compensation policy. However, this could be reduced to between 6 and 8 years if a more favorable policy were implemented.

In summary, the analysis indicates that all municipalities could profit economically from the installation of solar panels. However, the optimal rooftop load factor and investment return timing are subject to multiple influencing factors. Moreover, current compensation policies negatively impact dwellings with more than 6 – 8m2 of available surface for installing PV.

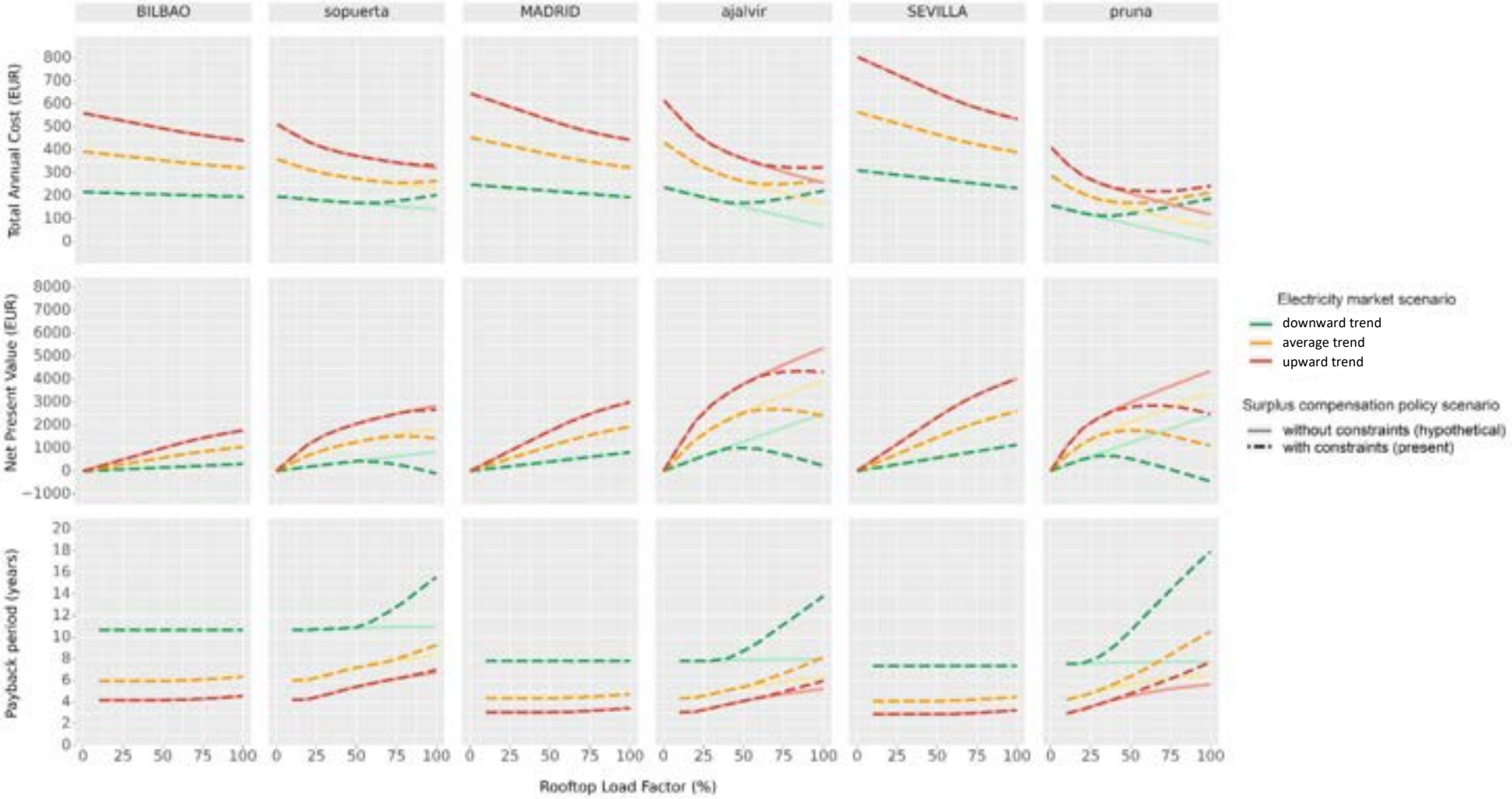

Figure 6. Total Annual Cost, Net Present Value, and Payback Period associated with installing solar panels on residential rooftops in different regions of Spain, under different electricity market and surplus compensation policy scenarios. Capitalized municipality names indicate urban morphology municipalities, while lowercase names indicate rural morphology municipalities.

5. Conclusions

This study introduces a new hourly data-driven method to assess the feasibility of residential solar PV systems for electricity self-consumption in Spain. The method employs mathematical models to estimate the electricity demand, self-consumption capacity, and economic profitability of rooftop-based PV systems at the municipal level, considering different surplus compensation policies and flexible electricity prices. The most relevant conclusions of this work are presented below:

- Rural areas have up to three times more rooftop surface per dwelling than urban areas, resulting in higher rooftop PV generation capacity. This correlation is linked to population size and rooftop availability per dwelling in a municipality.

- High-resolution hourly data is crucial for estimating self-consumption capacity when planning PV deployment. Analyzing hourly data reduces the potential by up to 75% in rural and 30% in urban municipalities compared to yearly data analysis.

- Current policies do not fully compensate for surplus electricity generated by PV systems, limiting potential investments in residential PV systems by 40 – 60% of their maximum capacity and reducing economic profitability.

Acknowledgments

The authors would like to acknowledge financial support from the “Agència de Gestió d’Ajuts Universitaris i de Recerca (AGAUR)” from “Generalitat de Catalunya” [2022-FISDU-00128]; “Diputació de Tarragona” [2021PGR-DIPTA-URV01]; the “Ministerio de Ciencia, Innovación y Universidades” of Spain [PID2021-127713OA-I00, PID2021-123511OB-C33, PID2021-124139NB-C22 - MCIN/AEI/10.13039/501100011033/FEDER, UE, & TED2021-129851B-I00]; “Ministerio de Universidades” of Spain through the Recovery, Transformation and Resilience Plan; “The European Union – NextGenerationEU”; and “Universitat Rovira i Virgili” [2021URV-MZ-11].

References

[1] Ministerio para la Transición Ecológica y el Reto Demográfico. Plan nacional Integrado de Energía y Clima (PNIEC) 2021-2030 2020. – Available at: <https://www.miteco.gob.es/es/ministerio/planes-estrategias/plan-nacional-integrado-energia-clima/plannacionalintegradodeenergiayclima2021-2030_tcm30-546623.pdf> [1.12.2022]

[2] Ministerio para la Transición Ecológica. RD 244/2019, 5 abril, por el que se regulan las condiciones administrativas, técnicas y económicas del autoconsumo de energía eléctrica. Boletín Oficial Del Estado 2019 – Available at: <https://www.boe.es/eli/es/rd/2019/04/05/244>. [accessed 1.12.2022].

[3] Ministerio para la Transición Ecológica y el Reto Demográfico. RD 477/2021, de 29 de junio, por el que se aprueba la concesión directa a las comunidades autónomas y a las ciudades de Ceuta y Melilla de ayudas para la ejecución de diversos programas de incentivos ligados al autoconsumo y al almacenamiento 2020 – Available at: <https://www.boe.es/eli/es/rd/2021/06/29/477> [accessed 1.12.2022].

[4] Eurostat. Electricity prices for household consumers-bi-annual data (from 2007 onwards) – Available at: <https://ec.europa.eu/eurostat/databrowser/view/nrg_pc_204/default/table?lang=en> [accessed 1.12.2022].

[5] Red Eléctrica de España. Potencia instalada renovable por tecnología/combustible (MW) – Available at: <https://www.ree.es/es/datos/generacion/potencia-estructura-renovables> [1.12.2022].

[6] Instituto Nacional de Estadística (INE). Cifras oficiales de población de los municipios españoles: Revisión del Padrón Municipal 2022 – Available at: <https://www.ine.es/dyngs/INEbase/es/operacion.htm?c=Estadistica_C&cid=1254736177011&menu=resultados&idp=1254734710990> [accessed 1.12.2022].

[7] Westacott P., Candelise C., Assessing the impacts of photovoltaic penetration across an entire low-voltage distribution network containing 1.5 million customers. IET Renew Power Generation 2016;10:460–6.

[8] Few S., Djapic P., Strbac G., Nelson J., Candelise C., Assessing local costs and impacts of distributed solar PV using high resolution data from across Great Britain. Renew Energy 2020;162:1140–50.

[9] Balta-Ozkan N., Yildirim J,. Connor P.M., Regional distribution of photovoltaic deployment in the UK and its determinants: A spatial econometric approach. Energy Econ 2015;51:417–29.

[10] Torres-Rivas A., Palumbo M., Jiménez L,. Boer D., Self-consumption possibilities by rooftop PV and building retrofit requirements for a regional building stock: The case of Catalonia. Sol Energy 2022;238:150–61.

[11] Schallenberg-Rodriguez J., Photovoltaic techno-economical potential on roofs in the Canary Islands. J Sustain Develop Energy Water Environ Syst 2014;2:68–87.

[12] Berna-Escriche C., Vargas-Salgado C., Alfonso-Solar D., Escrivá-Castells A., Can a fully renewable system with storage cost-effectively cover the total demand of a big scale standalone grid? Analysis of three scenarios applied to the Grand Canary Island, Spain by 2040. J Energy Stor 2022;52.

[13] Arcos-Vargas A., Gomez-Exposito A., Gutierrez-Garcia F., Self-sufficient renewable energy supply in urban areas: Application to the city of Seville. Sustain Cities Soc 2019;46.

[14] Pedrero J., Hermoso N., Hernández P., Munoz I., Arrizabalaga E., Mabe L., et al. Assessment of urban-scale potential for solar PV generation and consumption. IOP Conf Ser Earth Environ Sci 2019;323:1–11.

[15] Fuster-Palop E., Prades-Gil C,. Masip X., Viana-Fons J.D,. Payá J., Innovative regression-based methodology to assess the techno-economic performance of photovoltaic installations in urban areas. Renew Sust Energ Rev 2021;149.

[16] Gomez-Exposito A., Arcos-Vargas A., Gutierrez-Garcia F., On the potential contribution of rooftop PV to a sustainable electricity mix: The case of Spain. Renew Sust Energ Rev 2020;132.

[17] Arcas-Abella, J., Pagès-Ramon, A., Larrumbide, E., & Huerta, D., Segmentación del parque residencial de viviendas en España en clústeres tipológicos. Dirección General de Arquitectura, Vivienda y Suelo. Ministerio de Fomento 2019, 01.

[18] Izquierdo S., Rodrigues M., Fueyo N., A method for estimating the geographical distribution of the available roof surface area for large-scale photovoltaic energy-potential evaluations. Sol Energy 2008;82:929–39.

[19] European Comission. JRC Photovoltaic Geographical Information System (PVGIS) – Available at: <https://re.jrc.ec.europa.eu/pvg_tools/en/> [accessed 1.12.2022].

[20] Feldman D., Fu R., Margolis R., Woodhouse M., Ardani K., U.S. Solar Photovoltaic System and Energy Storage Cost Benchmarks: Q1 2021. 2021.

[21] Asociación de Empresas Eléctricas (ASEME). DATADIS. La plataforma de datos de consumo eléctrico – Available at:<https://datadis.es/> [accessed 1.12.2022].

[22] Instituto Nacional de Estadística (INE). Censos de Población y Viviendas 2011. Población residente en establecimientos colectivos – Available at: <https://www.ine.es/censos2011/tablas/Inicio.do> [accessed 1.12.2022].

[23] ESIOS - Electricidad datos y transparencia. Término de facturación de energía activa del PVPC – Available at: <https://www.esios.ree.es/es/pvpc> [accessed 1.12.2022].

Evaluation of weather datasets for rural energy communities simulation

Raul Saez[a], Rasool Kazemi[b], Manel Vallès[c], Dieter Boer[d] and Adedamola Shobo[e]

[a] Universitat Rovira i Virgili, Tarragona, Spain, raul.saez@urv.cat,
[b] Universitat Rovira i Virgili, Tarragona, Spain, rasool.kazemi@estudiants.urv.cat,
[c] Universitat Rovira i Virgili, Tarragona, Spain, manel.valles@urv.cat, CA
[d] Universitat Rovira i Virgili, Tarragona, Spain, dieter.boer@urv.cat,
[e] Universitat Rovira i Virgili, Tarragona, Spain, adedamolababajide.shobo@urv.cat

Abstract:

Rural areas are strategic assets to ensure sustainable energy transition due to their potential to implement renewable energy production. In this context, the EU seeks to promote synergies between renewable energy deployment and rural development, through several funding programs and supporting policies that benefit both parties. Consequently, the number of rural Energy Communities is increasing, and researchers are focusing on optimizing their designs. In this regard, one critical aspect when simulating the energy demand of Energy Communities is the use of weather data which are mostly not available for specific locations. In these cases, data from nearby urban centers are typically used, if available. But these data may not be representative of the typical weather conditions of the specific rural area under study which will negatively affect such design. In this context, this paper studies the impact of using urban areas' weather data when designing Energy Communities in the nearby rural areas. Therefore, the case study of the Tarragona province in Spain is presented, driven by 43 weather stations homogeneously distributed across the region. Findings reveal higher correlation in temperature and solar irradiation between local data and province's capital data than with third-party data, despite climatic differences. Heating degree day analysis indicates third-party's data closer to reality. Given Spain's heating demand, accurate data is crucial for HDD, therefore, when local data is unavailable, third-party data is recommended, despite lower correlation.

Keywords:

Renewable energy; Rural energy communities; TMY (Typical Meteorological Year); Weather datasets.

1. Introduction

Increasing global energy demand and costs have been catalyzed by growths in global population and in the technological input required to drive economies [1]. This is also projected to be amplified by the rising global temperatures due to global warming. Resultant effects have been seen in rising energy prices due to the domination of energy supply from non-renewable resources. International agreement was reached, with clear road maps to reduce the emission of greenhouse gases (GHGs) with clean and renewable energy resources [2]. The UNEP Emissions Gap Report 2022 [3] indicates that to attain the goal outlined in the Paris Agreement [4] to reduce global temperatures increase to below 1.5 ^{o}C, the current global emissions of GHGs must be cut by 45%. This calls for greater penetration of cleaner energy into the global energy scenario. Following this, the European Union (EU) has committed to the attainment of 32 % renewable energy inclusion in its member states by 2030 [5]. An even bolder commitment of attaining 42% inclusion of renewable energy inputs into its nation energy mix by 2030 has been made by Spain [6]. Realizing these goals will require paradigm shift in all sectors, especially in electricity production as the supply of electricity drives many sectors (industrial, residential, services, transportation, etc). Hence, there is a need to deviate from the traditional centralized system of power generation to a distributed one which is capable of flexibly accommodating inputs from complimentary renewable energy sources. The creation of energy communities has been demonstrated to be a viable approach to meeting energy targets in the EU [7]. The EU in its Green deal commitment to meet emission targets, recognizes and supports Renewable Energy Communities (RECs) as essential components of energy transition [8]. This energy model also has the potentials of promoting self-consumption, reducing energy cost to consumers, and job creation. Thus, a demand is placed on member states to develop national policies and legal frameworks to promote participation of their stakeholders. However, the current Spanish energy regulatory framework has limited widespread roll-out of these RECs [9-10].

To maximize self-consumption and stabilize the national electricity grid, different types of renewable systems can be combined into a hybrid renewable energy system (HRES) [11]. Spain possesses vast renewable energy potentials which places it at advantage of benefiting from the HRES scenario [12]. On the other hand, the building sector accounts for about 43% of the total final energy consumption with about two-thirds of this from the residential buildings [13]. According to the International Energy Agency (IEA), the Spanish residential sector reliance on energy from fossil fuels still accounts for more than 50% of the sectors' final energy consumption [14]. This is even more prominent in the rural areas of the country. Therefore, energy transition efforts from the angle of the building sector are crucial. To this end, the EU directive 2010/31/EU and its amendment 2018/844/EU are legislative frameworks binding on member states to improve the energy efficiency of their buildings. Apart from participating in the energy demand side, buildings are also expected to participate in the supply side through the incorporation of available renewable energy technologies [15]. The idea is to achieve nearly zero energy buildings (NZEBs) or even positive energy buildings (PEBs) [16]. The excess energy generated by a PEB may then be consumed by another member of its HRES or exported to the national grid.

Dynamic numerical simulation has for some time, been an indispensable tool for HRES and NZEB researchers/designers in improving buildings' and HRES' energy efficiencies. The energy models utilized are usually run with weather data generated for the climatic conditions around the facility and they are often with some measure of uncertainties [17]. Different procedures have been used to construct typical annual weather data by statistically processing a multi-year (usually 10 years or more) actual weather data set as means of forecasting future weather conditions [18]. The Typical Meteorological Year (TMY) method was developed by Hall et al. [19] at Scandia laboratories, using Filkenstien-Schafer method, was modified into TMY2 and later, TMY3, by the National Renewable Energy Laboratory (NREL). The American society of Heating, Refrigerating and Air-Conditioning Engineers (ASHRAE) commissioned the International Weather Energy Calculations (IWEC) which was later updated to International Weather Energy Calculations 2 (IWEC2) [20]. The International Organization for Standards (ISO) also presented a procedure (ISO 15927-4:2005) for constructing a reference year of hourly values of meteorological data [21].

The reliability of the results obtainable from a building's or/and HRES' energy performance simulation depends on the accuracy of the weather data file utilized for the corresponding facility's location. The weather data used to compute typical weather conditions are typically obtained from historical measurements from weather stations which are usually situated at capital cities or airports. Since rural communities are usually far from such locations, their climatic conditions may differ from those around the weather stations. This will introduce errors when assessing energy performances in the rural areas [22]. However, generating the weather data for a specific location through any of the established procedures can be very demanding. A simpler alternative is to patronize the services of a third-party company which will generate the needed weather files while specifying the preferred meteorological model and the geographic location of concern.

In summary, the constitution of energy communities in the rural areas requires a precise evaluation of the energy performance of the involved buildings. However, according to the literature reviewed, no studies have yet to specifically investigate the impact of utilizing non-local meteorological data on these communities' design. This paper, therefore, seeks to fill this research gap by examining the implications of using data from various common sources, such as the capital city of the region or third-party providers, in comparison to employing local weather data in the design of rural energy communities.

2. Methodology

2.1. Data gathering and preparation.

The multi-year weather data supporting this work have been recorded by the weather stations owned by METEOCAT (Meteorological Service of Catalonia) during the period 2010 - 2019 at the 12 different locations around the province of Tarragona in Spain. The locations and main characteristics of these are presented in Figure 1.

The METEOCAT weather dataset include among others, 30-minutes measures of the following meteorological variables: dry-bulb temperature, wind velocity, relative humidity, global solar irradiance, maximum dry-bulb temperature, minimum dry-bulb temperature, maximum relative humidity, and minimum relative humidity. Despite the good quality of these measured weather data, it contained small gaps of usually a few hours, mainly in the wind speed data. Therefore, the linear interpolation technique was employed to fill in the missing data.

In building energy simulation, typical meteorological year weather data is usually a synthesized single year of weather data that represents multiple years of historical weather data. The collected weather data were then used to construct typical weather years according to the TMY. This method extracted a monthly weather dataset each, for all the calendar months, which typifies the weather characteristics of each location, from the historical data. The twelve selected typical months, which do not necessarily belong to the same year, were then concatenated to create a typical year.

municipalities	population	altitude	latitude	longitude
Amposta	**21317**	**3 m**	**40.7078**	**0.6321**
El Perelló	2846	179 m	40.8729	0.7158
El Vendrell	38891	59 m	41.2155	1.5212
Falset	**2724**	**359 m**	**41.1537**	**0.8195**
Horta de Sant Joan	1138	515 m	40.9513	0.3056
L'Espluga de Francolí	3717	446 m	41.3924	1.0989
Prades	**602**	**926 m**	**41.3148**	**0.9816**
Roquetes	8159	1055 m	40.797	0.3182
Tarragona	**135436**	**5 m**	**41.1039**	**1.201**
Vila-rodona	1299	287 m	41.3073	1.3626
Vinebre	427	53 m	41.185	0.5938
Vinyols i els Arcs	2193	29 m	41.0802	1.0666

Figure. 1. A map of the province of Tarragona, indicating the locations of the weather stations analyzed in this study and their key characteristics. The four stations examined in this paper are highlighted for reference.

The TMY methodologies build upon the original method by Hall et al. [23] which utilizes the following nine parameters that are considered with daily frequency: minimum, maximum and mean values of dry bulb air temperature (ºC) and dew point temperatures (ºC); maximum and mean values of the wind speed (m/s); and the cumulative global horizontal solar radiation (Wh/m^2). The weather data obtained from the different meteorological stations did not include the data for dew point temperature but this was determined from the data for relative humidity and dry bulb through psychrometrics.

In the TMY procedure, the Finkelstein-Schafer (FS) [24] statistic was calculated to determine the typical weather months for a calendar year. The FS statistic defines the absolute value of the difference between long-term data and each of the historical candidate months. That is, for each weather data month, all historical months were evaluated and the month which matched most statistically to the long-term weather pattern was selected. The procedure is summarized below.

a) The daily means $\bar{p}$ were calculated from the parameter *p* values of the data series.

b) For each calendar month, the cumulative distribution function ($CDF_{p,m,i}$) of the daily means for all the years in the dataset was calculated by sorting all the daily means values in increasing order and then ranking them using Eq. (1):

$$CDF_{p,m,i} = \left(\frac{K(i)}{N+1}\right), \quad (1)$$

where *K*(*i*) is the rank order of the *i* values of the daily means of a month *m* in the total data set and *N* is number of days for the month in the total data set.

c) For each year of the dataset, the cumulative distribution function ($CDF_{p,m,y,i}$) of the daily means within each month was calculated by sorting all values for that month *m* and year *y* in increasing order and then ranking them using Eq. (2),

$$CDF_{p,y,m,i} = \left(\frac{J(i)}{n+1}\right), \quad (2)$$

where *J(i)* is the hierarchical order of the values *i* of the daily means within that month and year while *n* the number of days in the specific month.

d) For each month, the FS statistic were then calculated for each parameter according to Eq. (3) & (4):

$$FS_{(p)} = \frac{1}{n}\sum_i^n \delta_i\,, \quad (3)$$

where δ_i is absolute difference between the long-term data CDF and the historical candidate month data CDF, and *n* is the number of readings in a month.

$$\delta_i = \sum_{i=1}^{n}\left|CDF_{p,y,m,i} - CDF_{p,m,i}\right| \quad (4)$$

e) The TMY procedures introduced a weighted sum of the single FS statistics calculated for every parameter for each month as in Eq. (5). The weighting factors W_p attributed to each of the nine weather parameters vary according to their importance on building energy demandand are presented in Table 1. The month with minimum weighted sum of FS displays the most similar weather pattern to the long-term historical weather.

$$WS_p = \sum W_p * FS_{(p)} \quad (5)$$

The hourly weather data belonging to the minimum WS were then used to fill up the corresponding month of the twelve-month weather file.

Table 1. Weighting factor used for each meteorological parameter.

Meteorological Parameter	**TMY** [24]
Maximum dry-bulb temperature	0.042
Minimum dry-bulb temperature	0.042
Mean dry-bulb temperature	0.083
Maximum dew point temperature	0.042
Minimum dew point temperature	0.042
Mean dew point temperature	0.083
Maximum wind speed	0.083
Mean wind speed	0.083
Global horizontal solar radiation	0.500

Also, the TMY for each of the 12 municipalities were obtained with the Meteonorm software which has a database with information from more than 7700 weather stations distributed around the world. The main advantage of the Meteonorm software is its ability to generate weather date for user-defined locations by interpolating data from nearby weather stations in combination with data obtained from satellites [25, 26].

2.2. Data analysis

The four locations selected for this study, are each considered to be representative of the 12 different climatic typologies of the province. Tarragona's (the capital) station is coastal, Amposta stations is pre-coastal, Falset is inland at 259 meters above sea level, and Prades is also inland but at the highest altitude of about 926 meters. It should also be noted that the weather station at Prades usually records the lowest temperatures during winter in the province.

A correlational analysis of weather parameters (ambient temperature, relative humidity and total solar irradiation) from the TMY of Tarragona, which was determined from historical data; the TMY for each of the three locations as determined from their historical data and also the TMY obtained for each location from Meteonorm, was performed. The Taylor Diagram provides a second approach for comparing weather data from the on-site weather station, Meteonorm, and the province capital's weather station. This method uses statistical metrics, such as the Pearson correlation coefficient (R), the centered root-mean-squared error (RMSE), and the normalized standard deviation (σ), to visually represent how closely a weather parameter sample matches the local observation.

A comparative study of the Heating Degree Days (HDD) and the Cooling Degree Days (CDD) were then conducted for the municipalities. The HDD relative to a base outdoor temperature of 18 ^{o}C were integrated from mid-October to mid-April, while the CDD relative to a base outdoor temperature of 24 ^{o}C were integrated from mid-April to mid-October. For each municipality, the values of the HDD and the CDD obtained from the TMY built using the climatic data of its meteorological station were compared with the TMY of the capital (Tarragona) and with the TMY obtained from the Meteonorm software. The method used for calculating the degree days are as defined in [27].

3. Results and discussion

3.1. Typical Meteorological Months

Table 2 shows the monthly weather data that were selected to assemble the typical meteorological year for each of the location considered in this study, based on the TMY procedure.

Table 2. Selected typical months for the different locations based on the TMY procedure.

Location	Jan	Feb	Mar	Apr	May	Jun	Jul	Aug	Sep	Oct	Nov	Dec
Amposta	2018	2013	2014	2016	2012	2018	2013	2015	2016	2012	2016	2012
Falset	2015	2015	2014	2016	2012	2016	2013	2017	2016	2019	2016	2014
Prades	2013	2015	2014	2018	2014	2016	2013	2015	2016	2015	2016	2012
Tarragona	2013	2013	2014	2016	2016	2018	2010	2015	2016	2019	2016	2012

3.2. Taylor Diagram

The Taylor diagram is a useful graphical display of the statitiscal summary of how different models' performances match each other in terms of correlation, root-mean-square difference and ratio of variance [28].

The weather data from on-site weather stations, the province capital's weather station, and third-party software (Meteonorm) are compared using the previously introduced statistical metrics and displayed in a Taylor diagram for each of the three selected municipalities (Amposta, Falset, and Prades), based on three meteorological variables (temperature T, relative humidity RH, and global horizontal irradiance GHI).

In Amposta (Figure 2), T and GHI from the province capital's weather station have higher correlation with the on-site data (R=0.92 and R=0.93) than the Meteonorm's data (R=0.82 and R=0.73) obtained for the location.

RH however, generally showed much lower correlation (R=0.65 for the capital and R=0.21 for Meteonorm). The standard deviations are similar in all cases, below the 10% compared with the reference, except for the T of Meteonorm's data, around 21%.

In Falset (Figure 3) and Prades (Figure 4), T and GHI from the province capital's weather station also have higher correlations with the on-site data than Meteonorm's data, while RH has lower correlations. In these two locations, the standard deviation for all parameters is within acceptable values in all cases, less than 20% different from the reference data. It is noteworthy that Meteonorm's data are worse than the province capital's data in all locations, despite significant climatic differences between some of the municipalities. Although it is expected that Amposta and the province capital would have similar data, as they are both located on the coast with a Mediterranean climate, Prades and Falset have different climates and are located at higher altitudes than the capital.

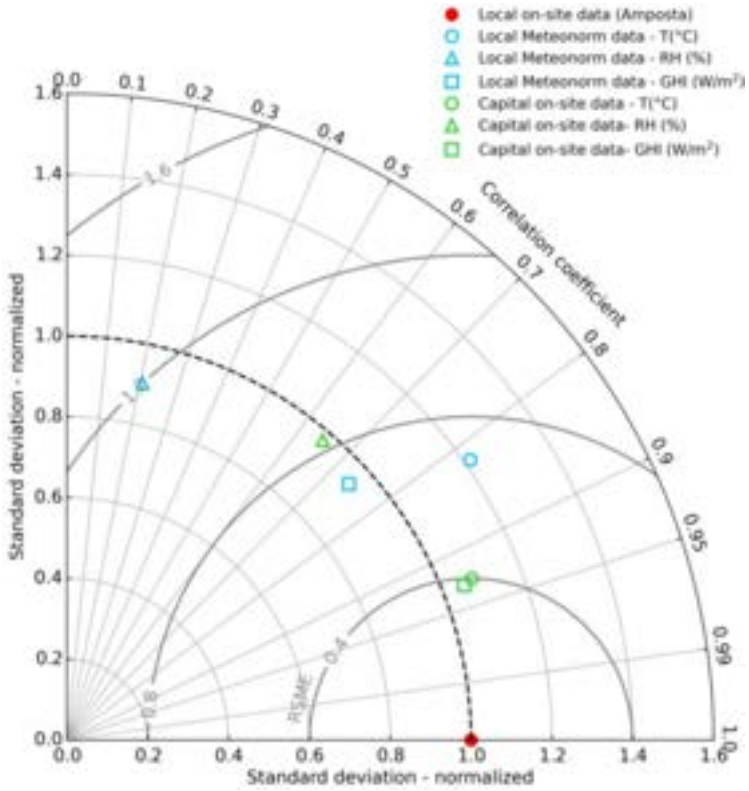

Figure. 2. Normalized Taylor Diagram for Amposta municipality, which compares the Amposta on-site weather station data (as reference) with Amposta third-party Meteonorm data, and with the province capital's weather station data for the TMY 2010-2019.

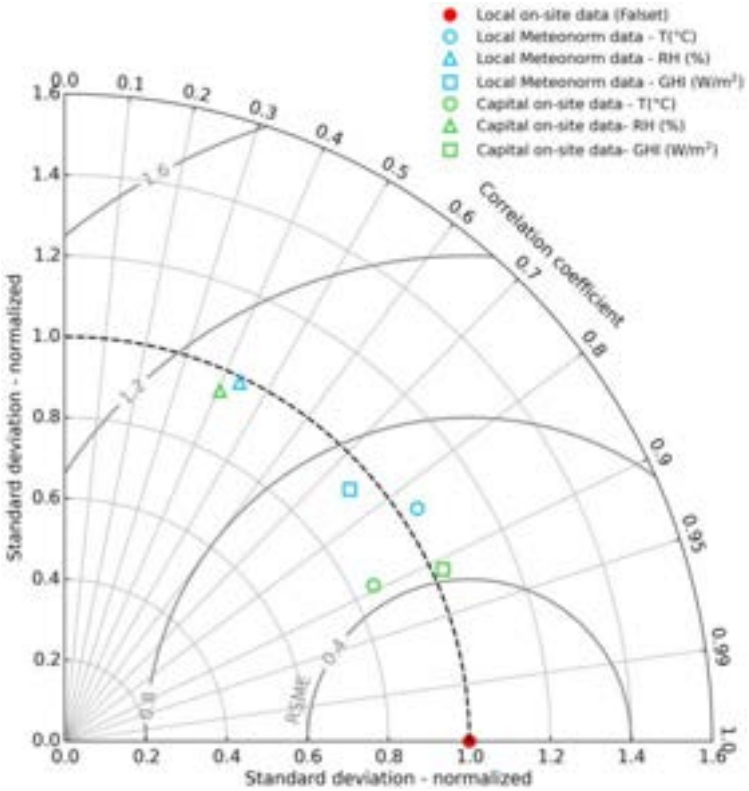

Figure. 3. Normalized Taylor Diagram for Falset municipality, which compares the Falset on-site weather station data (as reference), Falset third-party Meteonorm data, and the province capital's weather station data for the TMY 2010-2019.

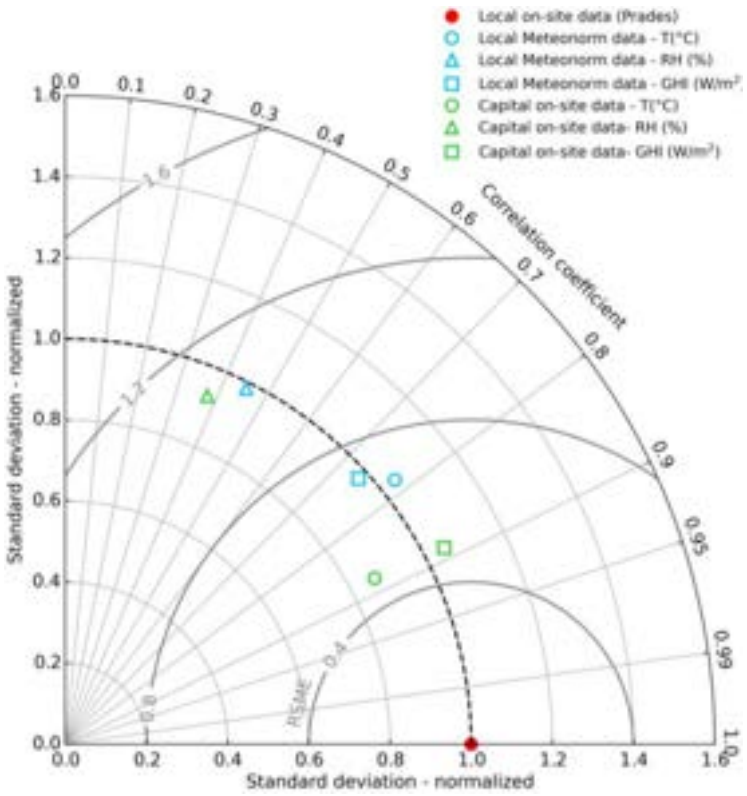

Figure. 4. Normalized Taylor Diagram for Prades municipality, which compares the Prades on-site weather station data (as reference), Prades third-party Meteonorm data, and the province capital's weather station data for the TMY 2010-2019.

3.3. Heating degree days (HDD) and Cooling degree days (CDD)

To evaluate the impact of typical weather data sources on building energy demand prediction for the three locations (Amposta, Falset, and Prades), it is crucial to analyze the representative Cooling Degree Days (CDD) and Heating Degree Days (HDD) of the different weather datasets. To this end, Figure 5 presents a comparison of the HDD and CDD values obtained from the TMY built using climatic data from each local weather station (On-site TMY), the TMY built using climatic data from the province's capital weather station (Capital TMY), and the TMY generated for each location using the Meteonorm software (Meteonorm TMY).

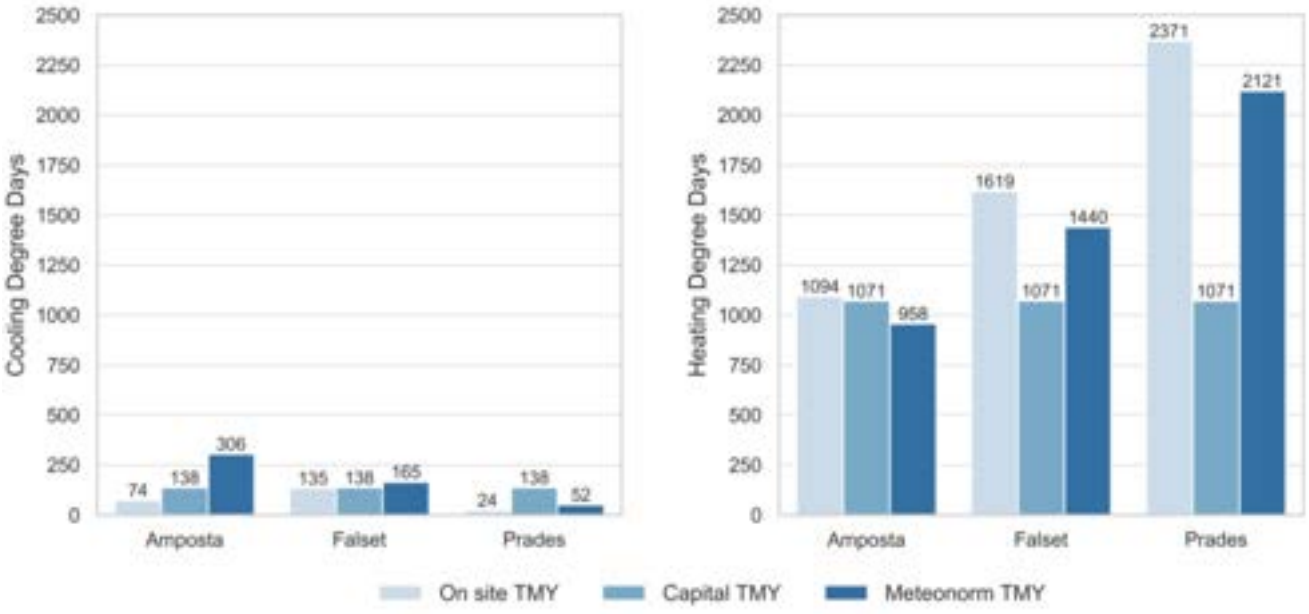

Figure. 5. Cooling Degree Days (left) and Heating Degree Days (right) for the 3 municipalities in the study (Amposta, Falset and Prades), computed from 3 different TMY 2010-2019 datasets: on-site weather station data, province capital's weather station data, and third-party Meteonorm data.

For the coastal municipality of Amposta, which is assumed to be more climatically similar to the provincial capital, the CDD values show significant deviations. Specifically, the onsite weather dataset resulted in CDD

which deviated from those from Tarragona's weather dataset by -86%, and even larger deviation of -300% from those given by the Meteonorm weather dataset. With respect to HDD, the onsite weather dataset minimally deviated from Tarragona's weather dataset by +2% while significant deviation of +12% from the Meteonorm's dataset is observed. These deviations are consistent with the Degree Days presented on the METEOCAT website for Amposta and Tarragona [29]. Concerning the implications for building energy demand, using the weather datasets from both the capital or Meteonorm would result in a large overestimation of cooling energy demands of buildings in summer. On the other hand marginal underestimation of heating demand of buldings in winter would result from the use of weather dataset from the capial while significant underestimation would result with the use of Meteonorm's dataset.

The CDD from the onsite weather dataset at Falset, which is located inland and at an altitude of 359 meters, are similar to those resulting from the capital's dataset with a minor deviation of about -2% while a larger deviation of about -22% resulted compared to the Meteonorm's dataset. However, the onsite weather data HDD show a larger deviation of about +34% from the capital's dataset and about +11% from the Meteonorm's dataset. This imply that using weather dataset from Meteonorm will result in significant overestimation of buildings' cooling demands in summer while datasets from both the province's capital and Meteonorm will result in significant underestimation of buildings' heating demands in winter.

Finally on Prades, which experiences considerably colder winters than the other locations (as evidenced by the onsite HDD values in Figure 5), the onsite weather dataset's CDD deviates with +475% and +116% with respect to the capital's and Meteonorm weather datasets respectively. The HDD from the onsite weather dataset on the other hand, deviates with +55% and +11% from the capital's and meteonorm's datasets respectively. Therefore, there is the risk of significantly underestimating buildings' heating demands during winter if the local weather dataset are not utilized, especially by using the weather dataset from the provincial capital. Additionally, significant overestimation of buildings'cooling energy demands will result from using weather datasets from both the province's capital and Meteonorm in summer.

Overall, and considering that in the period between 2010-2020, heating accounted for 41.5% of the total energy consumption in the residential sector in Spain, while air conditioning only accounted for 1% [31], it is crucial to properly size the heating system as opposed to the cooling system. Thus, in cases of extreme winter temperatures, it is more advisable to use Meteonorm data instead of relying on data from the provincial capital.

3.4. Conclusions

The objective of this research is to show the impact of using approximate meteorological data instead of using real local weather data in the design of rural energy communities. The study was conducted in twelve rural municipalities in the province of Tarragona, which have on-site data from local weather stations, with focus on three of them. Thus, for each location, the data from the local Typical Meteorological Year (TMY) computed from the on-site data were statistically compared, in terms of correlation, root-mean-square difference and ratio of variance, with data from the TMY of the province's capital and the TMY obtained using third-party software, Meteonorm. Additionally, the typical cooling and heating demands in buildings at each location were estimated using Cooling Degree Days (CDD) and Heating Degree Days (HDD) for the three meteorological datasets: referencial on-site data, province's capital data, and Meteonorm's data. The results show that, in all three case studies, the correlation of temperature and solar irradiation parameters between the local data and the data from the province's capital was higher (R=0.85-0.90) than with those from Meteonorm (R=0.70-0.85). This is despite the apparent climatic differences between the capital, in the coast, and the inland municipalities of higher-altitude. It should also be noted that the relative humidity data had correlation values lower than R=0.5 with respect to both the province's and Metenorm's data, indicating that they are unreliable for replacing the on-site data in any case. Furthermore, the analysis of CDD indicates that the data from the provincial capital is closer to the real local data than the data provided by Meteonorm. However, for HDD, the opposite is true, as the data from Meteonorm was found to be closer to real data, with deviations of 11%, compared to the deviation of 34-55% with the data from the provincial capital. Given that the heating energy demand in the residential sector in Spain represents 41.5% of energy consumption in average, while cooling demand barely reaches 1%, it is vital to use the data that best approximates reality with respect to HDD. Therefore, when local meteorological data is not available, third-party data yields better results in HDD analysis than the weather data of the provincial capital, though with low worse correlation. However, it is advisable to study to what extent the deviations found affect the definition of specific building design parameters for rural energy communities.

Acknowledgments

The authors would like to acknowledge financial support from the "Agència de Gestió d'Ajuts Universitaris i de Recerca (AGAUR)" from "Generalitat de Catalunya" [2022-FISDU-00128]; the "Ministerio de Ciencia, Innovación y Universidades" of Spain [PID2021-127713OA-I00, PID2021-123511OB-C33, PID2021-

124139NB-C22 & TED2021-129851B-I00]; and “Ministerio de Ciencia, Innovación y Universidades” of Spain through the Recovery, Transformation and Resilience Plan; “The European Union – NextGenerationEU”; and “Universitat Rovira i Virgili” [2021URV-MZ-11].

References

[1] van Ruijven, B.J., De Cian, E., Sue Wing, I., Amplification of future energy demand growth due to climate change. *Nat Commun* 2019;10: 2762.

[2] Edenhofer, O., Madruga, R.P., Sokona, Y., Seyboth, K., Matschoss, P.R., Kadner, S., Zwickel, T., Eickemeier, P., Hansen, G., Schlömer, S., Stechow, C.V., Summary for Policymakers. In: IPCC Special Report on Renewable Energy Sources and Climate Change Mitigation. Special report of the Intergovernmental Panel on Climate Change, 2011.

[3] United Nations Environment Programme. Emissions Gap Report 2022 – Available at: <https://doi.org/10.18356/9789210023993> [accessed 12.01.2023].

[4] UNFCCC. “Paris Agreement: Decision 1/CP.17 - UNFCCC Document FCCC/CP/2015/L.9/Rev.1” – Available at:<http://unfccc.int/resource/docs/2015/cop21/eng/l09r01.pdf> [Accessed 12.01.2023].

[5] European Commission. The European Green Deal – Available at:<https://eur-lex.europa.eu/resource.html?uri=cellar:b828d165-1c22-11ea-8c1f-01aa75ed71a1.0002.02/DOC_1&format=PDF> [accessed 12.01.2023].

[6] IEA. Country report on Spain – Available at: <https://www.iea.org/reports/spain-2021 https://www.iea.org/reports/spain-2021> [accessed 12.01.2023].

[7] Stian Backe, Sebastian Zwickl-Bernhard, Daniel Schwabeneder, Hans Auer, Magnus Korpås, Asgeir Tomasgard, Impact of energy communities on the European electricity and heating system decarbonization pathway: Comparing local and global flexibility responses. Appl Energy 2022; 323: 119470.

[8] Steininger, K.W., Williges, K., Meyer, L.H. et al., Sharing the effort of the European Green Deal among countries. Nat Commun 2022; 13: 3673.

[9] Manso-Burgos, Á., Ribó-Pérez, D., Alcázar-Ortega, M., Gómez-Navarro, T. Local Energy Communities in Spain: Economic Implications of the New Tariff and Variable Coefficients. Sustainability 2021; 13: 10555.

[10] Gallego-Castillo C., Heleno M., Victoria M., Self-consumption for energy communities in Spain: A regional analysis under the new legal framework. Energy Policy 2021; 150: 112144.

[11] Hossain Lipu M. S. H, Miah Md. S., Ansari S., Hannan M. A., Hasan K., Sarker M. R., Mahmud Md. S., Hussain A., Mansor M., Data-driven hybrid approaches for renewable power prediction toward grid decarbonization: Applications, issues and suggestions. J Clean Prod 2021; 328: 129476.

[12] Francisco G. Montoya, Maria J. Aguilera, Francisco Manzano-Agugliaro (2014). Renewable energy production in Spain: A review. Renewable Sustainable Energy Rev 2014; 33: 509-31.

[13] Tsemekidi-Tzeiranaki S., Bertoldi P., Castellezzi L., Gonzales Torres M., Clementi E., Paci D., Energy Consumption and Energy Efficiency Trends in the EU-28 for the Period 2000-2020. Luxemburg; Publications Office of the European Union; 2022 – Available at: <https://doi.org/10.2760/727548> [accessed 16.01.2023].

[14] IEA. Spain 2021: Energy Policy Review in IEA Energy Policy Reviews. Paris, France; OECD Publishing; 2021.

[15] Borge-Diez D., Icaza D., Trujillo-Cueva D. F., Açıkkalp E., Renewable energy driven heat pumps decarbonization potential in existing residential buildings: Roadmap and case study of Spain. Energy 2022; 247: 123481.

[16] Magrini A., Lentini G., Cuman S., Bodrato A., Marenco L., (2020). From nearly zero energy buildings (NZEB) to positive energy buildings (PEB): The next challenge - The most recent European trends with some notes on the energy analysis of a forerunner PEB example. Developments in the Built Environment 2020; 3: 100019.

[17] Yu J., Chang,W.-S., Dong, Y., Building Energy Prediction Models and Related Uncertainties: A Review. Buildings 2022; 12: 1284.

[18] Gutiérrez G. V., Ramos R. G.; Du H., Sánchez-Ostiz, A., Bandera F. C., Weather Files for the Calibration of Building Energy Models. Appl. Sci. 2022; 12: 7361.

[19] Hall I. J., Prairie R. R., Anderson H. E., Boes E. C., Generation of a typical meteorological year. Albuquerque, New Mexico; USA: Sandia Laboratories; 1978. Technical Report No.: SAND-78-1096C and CONF-780639-1.

[20] Huang Y.J., Su F., Seo D. & Moncef K., Development of 3012 IWEC2 weather files for international locations (RP-1477). ASHRAE Trans 2014; 120, 340-355.

[21] Pernigotto, G., Prada, A., Gasparella, A., Hensen J. L. M., Analysis and improvement of the representativeness of EN ISO 15927-4 reference years for building energy simulation. J Build Perform Simul 2014; 7: 391-410.

[22] Yu J., Chang W.-S., Dong, Y., Building Energy Prediction Models and Related Uncertainties: A Review. Buildings 2022; 12(8): 1284.

[23] Hall I. J., Prairie R., Anderson H., Boes E., Generation of a typical meteorological year for 26 SOLMET stations. Albuquerque, New Mexico; USA: Sandia Laboratories; 1978. Technical Report No.: SAND-78-1601.

[24] Hosseini M., Bigtashi A., Lee B., A systematic approach in constructing typical meteorological year weather files using machine learning, Energy Build 2020; 226: 110375.

[25] Remund J., Müller S., Schilter C., Rihm B. (2010). The use of Meteonorm weather generator for climate change studies. EMS Annu Meet Abstr 2010; 7.

[26] Hassan R., A comparison of the accuracy of building energy analysis in Bahrain using data from different weather periods. Renewable Energy 2009; 34 (3): 869-875.

[27] ASHRAE, 2009 ASHRAE Handbook- Fundamentals, ASHRAE, 2009.

[28] Taylor K. E., Summarizing multiple aspects of model performance in a single diagram. J Geophys Res 2001; 106(D7): 7183-92.

[29] Servie Meteorolgical Catalunya. Graus-dia de calefacció i de refrigeració – Available at:< https://www.meteo.cat/wpweb/climatologia/dades-i-productes-climatics/graus-dia-de-calefaccio-i-de-refrigeracio/> [accessed 01.03.2023].

[30] <https://www.meteo.cat/wpweb/climatologia/dades-i-productes-climatics/graus-dia-de-calefaccio-i-de-refrigeracio/> [accessed 01.03.2023]

[31] IDAE. Informe annual de consumos por usos del sector residencial 2022 – Available at < https://informesweb.idae.es/consumo-usos-residencial/informe.php> [accessed 01.03.2023]

Thermo-economic Assessment of an Organic Rankine Cycle System for Repowering Application in a Landfill Biogas Power Plant

Lucas Rodrigues Loyola[a], Lucas Antônio Silveira Silva[b], Átila Pavan Vasconcellos[c], José Joaquim Conceição Soares Santos[d], João Luiz Marcon Donatelli[e], Carla César Martins Cunha[f]

[a]Federal University of Espírito Santo, Vitória, Brazil, lucasloyola730@gmail.com
[b]Federal University of Espírito Santo, Vitória, Brazil, lucasa@ucl.br,
[c] Federal University of Espírito Santo, Vitória, Brazil, atilapavanv@gmail.com
[d] Federal University of Espírito Santo, Vitória, Brazil, jjcssantos@yahoo.com.br
[e] Federal University of Espírito Santo, Vitória, Brazil, donatelliufes@gmail.com
[f] Federal University of Espírito Santo, Vitória, Brazil, carlacmcunha@gmail.com

Abstract:
Marca Ambiental is a Brazilian company that collects and treats solid waste from Grande Vitória, state of Espírito Santo, since 1997. In order to recovery this waste energy, mainly the landfill biogas, the company installed a steam power plant, in 2008, generating 1 MW of electricity. A study showed that greater efficiency and electric power, by recovering the landfill biogas energy, would be possible using internal combustion engines (ICE). This first repowering has already occurred using three internal combustion engine gensets, generating more than 3 MW of electricity. This work carried out a thermo-economic analyse for this plant new repowering, using organic Rankine cycle (ORC) systems. The energy and exergy balances showed that, although more than 40% of the biogas energy is converted into electricity, more than 54% is lost through exhaust gases (27.2%) and cooling water (27.4%), which represent, respectively, 14.13% and 4.12% of the biogas total exergy. The simulation and economic evaluation of this repowering, using ORC systems, shows technical and economic feasibility, respectively, for 400 kW and 300 kW of additional electricity generation.
Keywords:
Energy Efficiency, Repowering, Exergy Balance, Energy Recovery.

1. Introduction

According to [1], in 2021 the Brazilian electric energy demand was 497 TWh, an increase of 4.6% in relation to the year of 2020. In the same period, the participation of thermoelectric power plants in electricity generation was 23.5%. Nowadays, thermoelectric generation is mostly using fossil fuels. The use of landfill biogas from Urban Solid Waste (USW) landfills may be one of the alternatives to improve this scenario. One of the technologies for thermoelectric generation is Internal Combustion Engines (ICE). According to [2], the waste heat energy from these engine gensets, due to the cooling system (of the engine block, lubricating oil and intercooler) and exhaust gases, is generally rejected to the atmosphere. This waste heat, from exhaust gas and cooling water can be effectively recovered, for the system efficiency improvement and repowering.

Repowering is defined by [3] as an important alternative to achieve improvements in systems and thermoelectric generation. Among the improvements, there are: reduction of the specific fuel consumption and/or costs, reduction of the emissions and least cost option for increasing generation capacity. The repowering methodology presented by [3] is summarized with the following steps: determine the generation system goals; identify the generation system information and restrictions; identify the candidates repowering technologies; Evaluate and select the most feasible technology. In consideration of repowering thermal power plants through the usage of waste heat, a study was conducted by [4] in order to survey waste heat recovery technologies for power plants equipped with internal combustion engines (ICE) aiming at increasing the produced net power and overall efficiency. Among the alternatives, the following were chosen as interesting based on commercial availability and low impact on engine operation:

- Combined cycle with Conventional Rankine Cycle (CRC).
- Combined cycle with Organic Rankine Cycle (ORC).
- Combined cycle with Kalina Cycle (KA).
- Absorption cycle for intake air cooling.

The results of a study by [4] showed that the Organic Rankine Cycle, using the exhaust gases heat from an ICE) presented the best performance for repowering purposes, considering the maximum power produced, achieving 5.3% in additional power produced. According to [5] ORC involves the same components of a conventional Rankine cycle: evaporator, expander, condenser and pump. One study [6] affirmed ORC is considered a simple technology because most of the heat addition and rejection happens during the phase change of the working fluid in the evaporator and condenser, respectively. The fundamental difference between CRC and ORC is the working fluid. As seen in [6], in ORC the fluid is an organic compound characterized by a lower boiling temperature than water, allowing power generation using heat sources with lower temperatures than in the conventional Rankine cycle. [8] affirms that, consequently, for low temperature waste heat recovery, ORC is a more suitable technology. One study [4] claims that organic fluids are high molecular mass fluids, compared to water, which allows compact equipment and low pipe diameter, for higher mass flow and higher isentropic efficiency of the expander.

In [5], parameter optimizations were performed, considering evaporation and condensation temperature, evaporator pinch-point and different types of organic fluids, as decision variables, in two configurations of ORC systems (simple and regenerative) to recover waste heat from an internal combustion engine. Considering the lowest specific costs for the power generated, as objective function, the best working fluid were selected, Toluene for waste heat recovery from engine exhaust gases and R141b for engine cooling water recovery. In [5], the maximum increase in efficiency and additional power generated was about 7%.

A study [6] was conducted to compare the efficiency of different working fluids in the heat recovery of exhaust gases from an internal combustion engine operating with biogas. The study examined pure organic fluids as well as their mixtures. The findings revealed that the Organic Rankine Cycle (ORC) system operating with toluene demonstrated the highest net electrical energy production, achieving an efficiency of 19.9%. In a related study [7], the use of toluene and cyclohexane in recovering waste heat from the flue gas of a reheat furnace was compared. The results indicated that under similar conditions, the ORC system with toluene exhibited a lower gross electricity production of 30 kW, but a higher energy efficiency of 17.08%. It is worth noting that neither of these studies explored the heat recovery potential from engine cooling water nor conducted an economic feasibility analysis of implementing the ORC technology.

With this in mind, the present work aims to recover both waste heat from the exhaust gases and cooling water of gensets in a Brazilian company involved in the collection and treatment of municipal waste. This company operates a thermal power plant based on three internal combustion engine gensets for landfill biogas energy recovery, generating over 3 MW of electricity. This paper outlines the procedures and discusses the results of a thermo-economic assessment of organic Rankine cycle systems for repowering applications in this landfill biogas power plant. The main contribution and novelty of this work lie in conducting an economic analysis of this plant under Brazilian conditions, as well as utilizing the engine cooling water as an input for a secondary ORC system.

To perform the energy and exergy balance analysis of the gensets, Engineering Equation Solver (EES) software was employed. IPSEpro was used for simulation purposes, and Excel was utilized for the economic evaluation of the ORC systems. Importantly, this work proposes advancements in the utilization of residual heat from an engine by providing a detailed explanation of the economic analysis using Brazilian economic conditions. Furthermore, the utilization of engine cooling water as a heat source is investigated in a real plant setting, with actual operating conditions that have not been previously explored.

2. Case Study Description

Marca Ambiental is an urban solid waste (MSW) recovery company, which has been collecting and treating municipal waste from Grande Vitória, in the state of Espírito Santo, Brazil, since 1997. According to [8], the urban solid waste is deposited in the landfill and then covered with layers of soil from the site itself, isolating it from the environment. Chambers are then formed, in which microbial activity, mainly of anaerobic bacteria that, through their metabolism, transform organic matter into combustible products, such as methane gas and released leachate. The slurry is captured through pipes and drained into treatment tanks.

In 2011, the company installed a steam cycle thermal power plant, generating 1 MW of electric power. Later, as shown in Figure 1, the original system was replaced by three ICE gensets (Genset 1, 2 and 3), generating more than 3 MW of electric power. Figure 1 shows the pipelines for capturing the biogas and directs it to the three engine-generator sets (EG's). There is a forecast for the future installation of two more generator groups. Nowadays, the thermoelectric plant has 3 ICE gensets modules, Jenbacher J416 GS models, 4-stroke Otto engines with mixture compression and exhaust gas turbocharging.

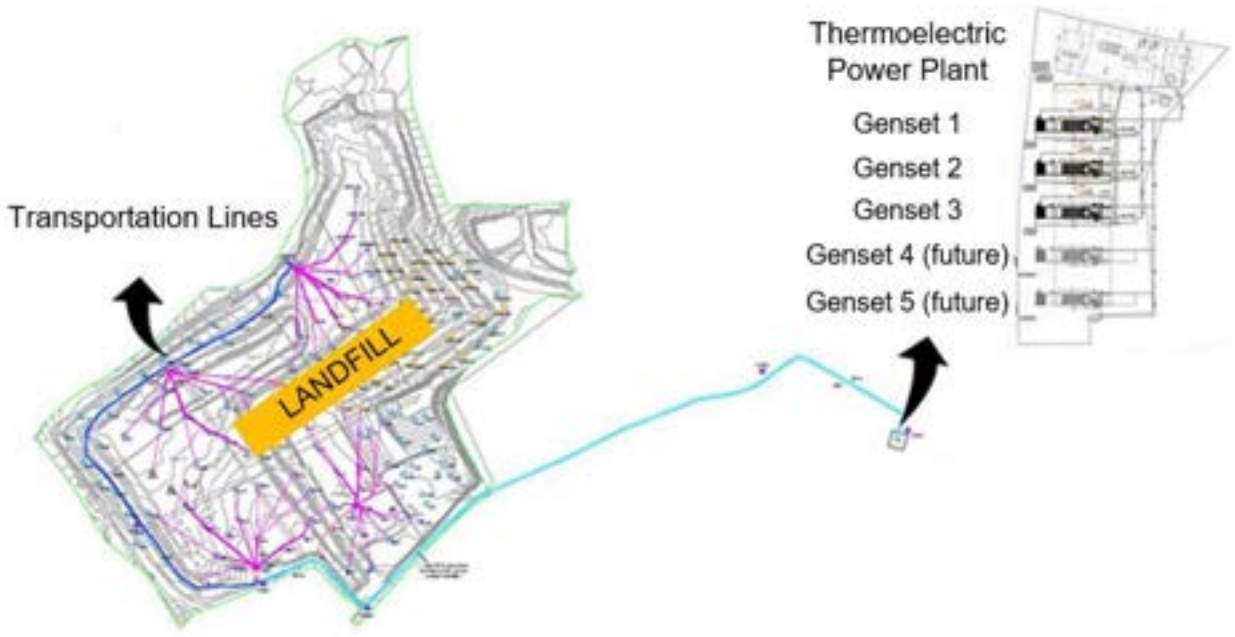

Figure 1 - Marca Ambiental's Biogas Capture and Thermoelectric System.

The average chemical characterization of the biogas generated at the Marca Ambiental landfill is shown in Table 1, as well the air composition, considering the average onsite conditions (25°C, 1 atm and 60% RH).

Table 1 - Biogas Characterization and Environmental Conditions.

Parameters			Value	Unit
Biogas Composition	CH_4		47.57	%
	CO_2		47.34	
	N_2		4.02	
	O_2		1.07	
	Heating Value	Lower (LHV)	12,753	kJ/kg
		Higher (HHV)	14,153	
Onsite Average Conditions	Pressure		1.013	bar
	Temperature		25	°C
	Relative Humidity		60	%

2.1. Gas Exhaust System

Each genset releases exhaust gases through the stack at a temperature of approximately 457 °C and a mass flow rate of 1.54 kg/s. This is the main source of heat with the potential to be recovered. It is important to stress the fact that there is a limit temperature for cooling the exhaust gases in their recovery process, due to the possible presence of sulfur in the fuel composition, which is considered 180ºC, in this work. The molar composition of the exhaust gases, shown in Table 2, was previously calculated with the aid of Engineering Equation Solver (EES) software using a complete combustion model with excess of wet air.

Table 2 - Molar Composition of the Exhaust Gases.

CO_2 (%)	H_2O(%)	N_2(%)	O_2(%)
12.85	14.49	67.57	5.09

2.2. Engine Cooling System

The cooling system of the generating units is done by means of demineralized water in two closed circuits, high temperature (HT) and low temperature (LT), with very low makeup during operation. The heat removed from the two aftercoolers, the lube oil and jacket water must be dissipated in a cooling system in order to allow the closing of the circuit. In the case of the thermoelectric plant, the cooling method adopted, depending on environmental conditions and water availability, is the use of a bank of radiators, with each generator set having two radiators. A thermal scheme of the cooling system, with water, biogas and exhaust gas flow values, can be seen in the engine flowchart, collected from the company documents, in Figure 2.

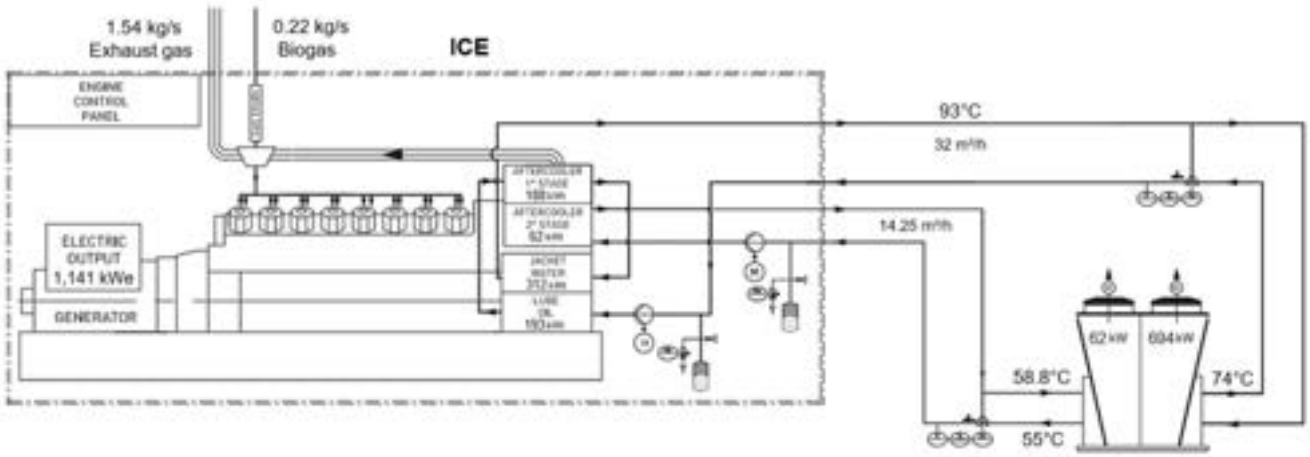

Figure 2 - Engine Flowsheet.

3. Engine Energy and Exergy Balance Methodology

The biogas energy rate is expressed by Eq. (1), as function of lower heating value (*LHV*) and mass flow ($\dot{m}_b$). The exergy rate of the biogas is calculated by Eq. (2), where $\dot{n}_b$ is the molar flow rate of the fuel, e_i^{ch} is the standard specific chemical exergy of each element, $\bar{R}$ the universal gas constant on a molar basis and T_0 is the reference temperature (dead state) in Kelvin scale.

$$\dot{Q}_b = \dot{m}_b \,.\, LHV \tag{1}$$

$$\dot{Ex}_b = \dot{n}_b \left(\sum_{i=1}^{j} y_i e_i^{ch} + \bar{R} T_0 \sum_{i=1}^{j} y_i \ln y_i\right) \tag{2}$$

The recoverable heat of each engine cooling water circuit is expressed by Eq. (3), where h_O and h_i are the specific enthalpy of the outgoing and incoming water stream, respectively. The sum of the two circuit recoverable heats, due to the two cooling water circuit, is the total recoverable cooling water heat ($\dot{Q}_{cw}$).

$$\dot{Q}_i = \dot{m}_i \,.\, (h_o - h_i) \tag{3}$$

The exergy of each engine cooling water flow is expressed by Eq. (4). The sum of the two circuit recoverable exergy is the total exergy loss, due two both cooling water circuit ($\dot{Ex}_{cw}$).

$$\dot{Ex}_i = \dot{m}_i \,.\, (\Delta h_i - T_0 \Delta s_i) \tag{4}$$

The energy contained in the exhaust gases ($\dot{Q}_{eg}$) is calculated using Eq. (5) Where $\dot{n}_{eg}$ is the molar flow rate of the exhaust gases, y_i is the molar fraction of each component in the exhaust gases, and $\Delta\bar{h}_i$ the variation of the specific enthalpy between the standard state and the state of interest.

$$\dot{Q}_{eg} = \dot{n}_{eg} \,.\, \sum y_i \,.\, \Delta\bar{h}_i \tag{5}$$

To calculate the exergy of the exhaust gas, its chemical and physical parts are calculated ($\dot{Ex}_g^{ch} + \dot{Ex}_g^{phi}$) represented by Eqs. (6) and (7), respectively, where y_i^e represents the molar fraction of the component in the air.

$$\dot{Ex}_g^{ch} = \dot{n}_b \, \bar{R} T_0 \sum_{i=1}^{j} y_i \ln \frac{y_i}{y_i^e} \tag{6}$$

$$\dot{Ex}_g^{phi} = \dot{n}_b \sum_{i=1}^{j} y_i (\Delta h_i - T_0 \Delta s_i) \tag{7}$$

$$\dot{E}x_g = \dot{E}x_g^{ch} + \dot{E}x_g^{phi} \quad (8)$$

Since the mechanical power is pure exergy, then the exergy of this stream is represented by $\dot{E}x_M$. Finally, the overall energy and exergy balance are represented by Eqs. (9) and (10) respectively.

$$\dot{Q}_b = \dot{W}_M + \dot{Q}_{cw} + \dot{Q}_{eg} + \dot{Q}_l \quad (9)$$

$$\dot{E}x_b = \dot{E}x_M + \dot{E}x_{cw} + \dot{E}x_{eg} + \dot{E}_d \quad (10)$$

In Equations 9 and 10, $\dot{Q}_l$ is other heat losses from the internal system and $\dot{E}_d$ is the destroyed exergy involving engine irreversibility and other losses.

4. Recoverable Waste Heat using Reversible Bottoming Cycles

The heat available to be used by each heat source in an engine if the minimum recoverable temperature is reached is shown in Table 3, considering that the heat sink temperature ranges from 27 °C to 32 °C.

Table 3 - Amount of heat available at each source to be recovered.

Range Temperature of the Recoverable Heat Source	Total Heat (kW)
Exhaust Gases (457 °C – 180 °C)	511
Cooling Water HT (93 °C – 74 °C)	694
Cooling Water LT (58.8 °C – 55 °C)	62

In an optimist scenario, where the heat addition line of the bottoming cycle is very close to the hot source line and the heat rejection line is close to the heat sink, one has the maximum technical potential presented in Table 4, considering that the recoverable would be converted into net power using a total reversible cycle.

Table 4 - Maximum Technological Potential of Repowering.

Range Temperature of the Recoverable Heat Source	Net Power (kW)
Exhaust Gases (457 °C – 180 °C)	250
Cooling Water HT (93 °C – 74 °C)	105
Cooling Water LT (58.8 °C – 55 °C)	5

It can be seen that the LT cooling circuit has a small flow rate and temperature variation compared to the remaining heat sources, so this water flow has a very small heat amount. Therefore, only the HT circuit heat source is chosen to be model for repowering purposes using the ORC with cooling water hot source.

4.1. Proposed Heat Recovery Thermal Scheme

The configuration of the ORCs coupled to the ICEs is proposed by joining the flows of the 3 gensets units and proposed to model one ORC for each of the available recoverable heat sources, as shown in Figure 3.

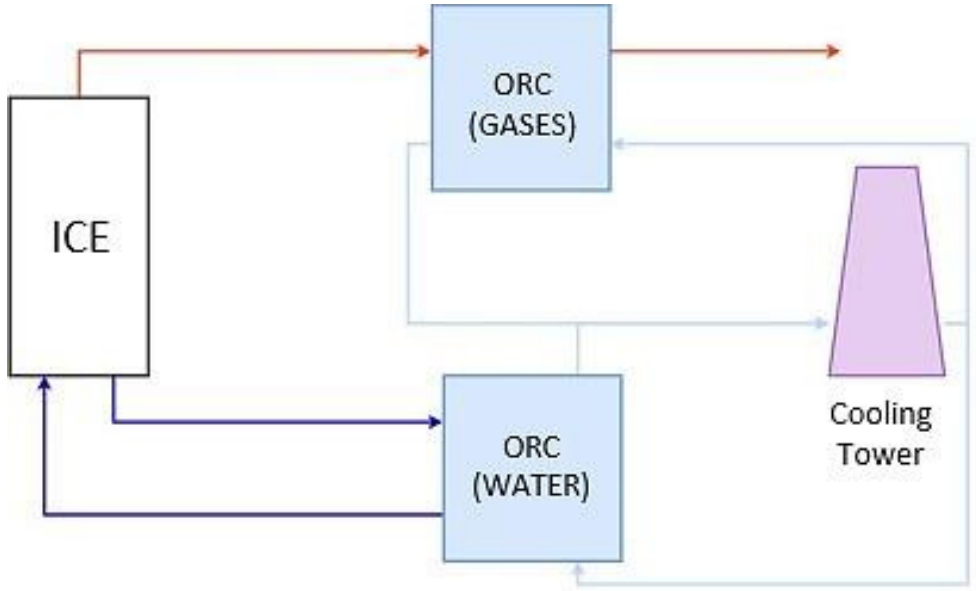

Figure 3 - Configuration of the ORCs to be coupled at the Marca Ambiental Thermal Power Plant.

5. Thermo-Economic of the ORCs

From the optimization data of [5], which caried out a similar case study, the implementation of the simple ORC was defined. This same study tested several working fluids for the different heat sources for recovery and reached a conclusion that in terms of power production with the lowest specific cost, the best fluids were Toluene and R141b, for the cycle recovering exhaust gases heat source and for the cycle recovering cooling water heat source, respectively. Based on that work, other parameters were taken into account to start modeling the ORCs, such as evaporation and condensation temperature and isentropic efficiencies of turbines and pumps, for each modeled ORC. These parameters are presented in Table 5.

Table 5 - ORC parameters.

Parameter	Fluid	
	Toluene	R141b
T_{evap} (ºC)	242.60	62.63
T_{cond} (ºC)	57.45	38.35
η_b (%)	71.54	71.10
η_t (%)	81.52	86.27

With the set of equations of the mass and energy balance of the Organic Rankine Cycle it was possible to obtain all the thermodynamic properties (pressure, temperature, enthalpy and entropy) of each state of the cycle, which was obtained as described, according to the configuration represented in Figure 4.

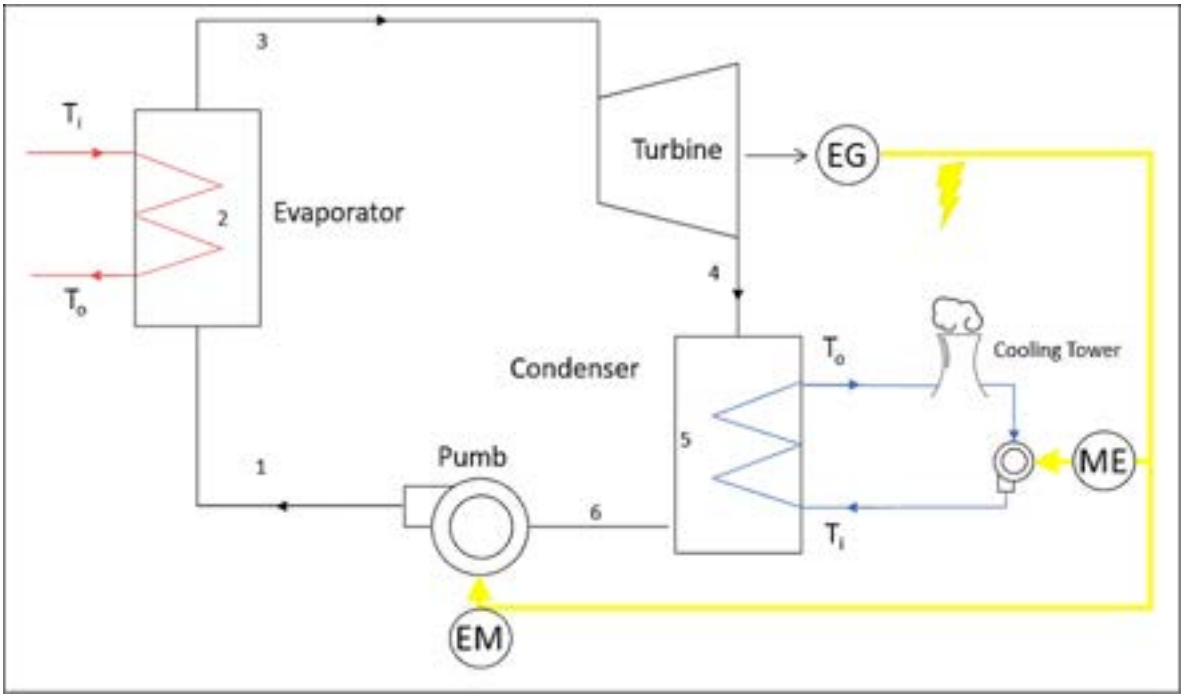

Figure 4 – ORC System Flowsheet.

The successful completion of a thermal design project requires estimation of the major costs involved in the project. Therefore, good cost estimation is a key factor in successfully completing a design project, as shown in [11]. There are many types of capital cost estimations and various methods often provide different results. The economic evaluation in this work is performed according to the module costing technique (MCT), extensively used for preliminary cost estimates of plants by [12]. This technique relates all direct and indirect costs to the purchased equipment cost evaluated for base conditions (C_{PE}) at ambient pressure, and carbon steel construction expressed by Eq. (11), where K_i are constants depending on the equipment type and A is the capacity or size parameter.

$$log_{10} C_{PE} = K_1 + K_2 log_{10}(A) + K_3[log_{10}(A)]^2 \quad (11)$$

Deviations from these base conditions are handled by multiplying pressure (F_P) and material (F_M) factors. The pressure factor is given by Eq. (12), where P is the pressure and c_i are constants depending on equipment type.

$$log_{10} F_P = C_1 + C_2\, log_{10}(P) + C_3[log_{10}(P)]^2 \quad (12)$$

The additional direct and indirect costs are considered through the bare module factor (F_{BM}) in the module costing technique. The bare module cost is the sum of all direct and indirect cost and can be calculated by Eq. (13).

$$C_{BM} = C_{PE} \cdot F_{BM} \quad [US\$] \quad (13)$$

The values of the bare module cost factors are given for different types of equipment. For heat exchangers and pumps the expression of the bare module cost factor is given by Eq. (14), where B_i are constants depending of the heat exchanger or pump type.

$$F_{BM} = B_1 + B_2 \cdot F_P \cdot F_M \quad (14)$$

For other components the F_{BM} is directly given as a multiplier that accounts for equipment type, operating pressure and construction material. The coefficients for Eq. (11) to (14) are obtain from [12] for carbon steel turbines, pumps and shell and tube heat exchangers. The parameters to estimate the cost of the colling tower was not considered in [11]. Thus, for this equipment, the methodology by [13], was employed in this work, as shown in Equation (15).

$$C_P = C_{ref,i} \cdot \left(\frac{X}{X_{ref}}\right)^m \quad (15)$$

For modifications and expansions of existing thermal systems, there are also other costs that need to be accounted for, like taxes and contingencies costs. According [14] when there are no other recommendations, these costs are 3% and 15% of the bare cost module respectively. Adding these remaining costs, the total module cost is calculated by Eq. (16), where *n* represents the number of the project equipment.

$$C_{TM} = 1.18 \cdot \sum_{i=1}^{n} C_{BM,i}\ [US\$] \quad (16)$$

All the data available in [12] are referenced in 2001. According to [14] the calculated cost updated is made through an appropriated cost index. The cost index is an inflation indicator used to correct the cost of equipment items, material, labor, and supplies to the date of the estimation. For thermal design projects the Chemical Engineering Cost Index (CEPCI) is recommended for total plants, or groups of components. It's adopted the CEPCI of 2022 ($CEPCI_{2022}$ = 821.3). Thus, the correct total cost is given by Eq. (17), where the $CEPCI_{2001}$ is 397.

$$C_{Total} = (C_{TM})\ \frac{CEPCI_{2022}}{CEPCI_{2001}}\ [US\$] \quad (17)$$

6. Results and Discussions

The thermodynamic evaluations of the repowering alternative were carried out on energy and exergy basis aiming at providing more support to the analysis, since exergy efficiency, exergy losses and irreversibilities allow a better understanding of the improvement opportunities in the waste heat recovery for power production, once that power is pure exergy. Exergy allows the evaluation of waste heat according to its maximum potential for power conversion, which is not possible using only an energy evaluation, as it overestimates the available heat potential for recovery and repowering. The economic evaluation allows the estimation of the specific capital cost for the repowering technology.

6.1. Recoverable Waste Heat

Based on the balances performed on the engine, the equations were implemented in the EES software. Thus, the results were found for a Jenbacher J416 GS engine of the EG of the Marca Ambiental Thermal Power Plant (TPP). In Figure 5 are the energy and exergy balances of an engine. The available heat energy is 54.60% of the energy provided by the biogas. However, the exergetic heat potential is 18.25% only.

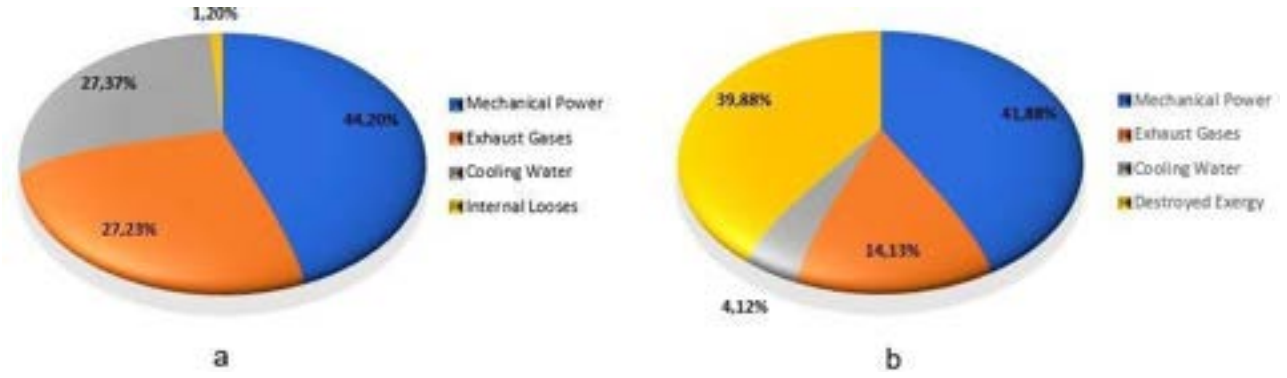

Figure 5 - UTE Marca Ambiental EG balances: a) energy balance, b) exergy balance

6.2. ORC Utilizing the Exhaust Gases Heat

Given the thermodynamic properties of toluene calculated in the EES it is possible to plot the T x s plot of the cycle, as seen in Figure 6. the values of the properties for each point are shown in the Table 6. The cycle has a net electric power production of 300.87 kW. In Table 7 there are the capacities and costs of each equipment.

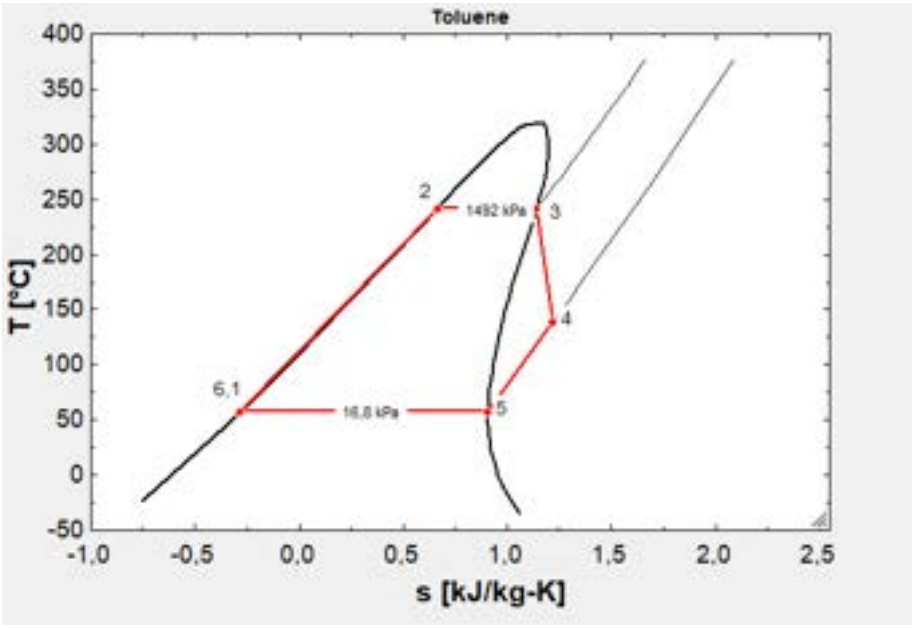

Figure 6 - Toluene T x s Diagram.

Table 6 - Thermodynamic Properties of Toluene at the ORC State for 2.38 kg/s of Mass Flow.

State	Temperature (°C)	Pressure (kPa)	Enthalpy (kJ/kg)	Entropy (kJ/kg.K)
1	58.2	1492.4	-98.8	-0.281
2	242.6	1492.4	301.7	0.667
3	242.6	1492.4	545.7	1.140
4	139.0	16.8	407.9	1.218
5	57.5	16.8	292.8	0.908
6	57.5	16.8	-101.3	-0.283

Table 7 - Capacity and Cost of Each Equipment.

Equipment	Capacity [unit]	C_{BM} [US$]
Evaporator	46.85 [m²]	149,190.03
Condenser	99.52 [m²]	203,466.40
Turbine	328.03 [kW]	543,019.03
ORC Pump	5.90 [kW]	13,469.85
Condenser Pump	2.06 [kW]	10,681.43
Cooling Tower	3.48 [m³/min]	29,867.1

Inserting the fees and updating the values to 2022 the total cost of the project is US$ 2,318,339.01.

Starting from the total cost of the project, we can apply some methods of economic feasibility analysis, such as: payback, NPV (Net Present Value) and IRR (Internal Rate of Return). For this we need the interest rate per year on the investment, the value of the electric energy and the life time of the project. The interest rate of the investment which was adopted is 12% and the life time of the equipment adopted was 20 years. Unitary Variable Cost (UVC), that is, the cost of selling electricity to the grid was US$ 0.130/kWh. The obtained payback was 15.36 years, showing that the initial investment will be paid, even if it is in a time close to the useful life of the equipment of 20 years. The IRR is was approximately 13.38%, greater than 12%.

6.3. ORC Utilizing Cooling Water

Faced with the thermodynamic properties of toluene calculated in the EES it is possible to plot the T x s plot of the cycle, as seen in Figure 7. the values of the properties for each point are shown in the Table 8.

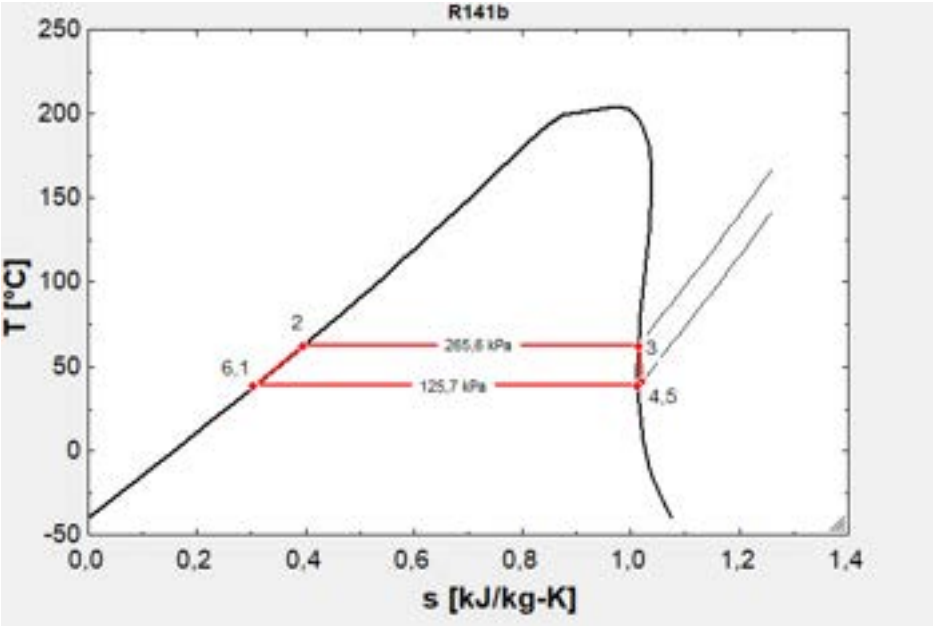

Figure 7 - R141b T x s Diagram.

Table 8 - Thermodynamic Properties of R141b at the ORC State for 8.35 kg/s of Mass Flow.

State	Temperature (°C)	Pressure (kPa)	Enthalpy (kJ/kg)	Entropy (kJ/kg.K)
1	38.50	265.59	83.27	0.306
2	62.63	265.59	112.86	0.397
3	62.63	265.59	320.09	1.014
4	41.58	125.74	306.10	1.021
5	38.35	125.74	303.52	1.013
6	38.35	125.74	83.09	0.305

The cycle has a net electric power production of 100.42kW. In Table 9 re defined the capacities and costs of each equipment.

Table 9 - Capacity and Cost of Each Equipment.

Equipment	Capacity [unit]	C_{BM} [US$]
Evaporator	300.71 [m²]	106,597.48
Condenser	891.53 [m²]	143,471.47
Turbine	116.74 [kW]	284,450.35
ORC Pump	1.47 [kW]	10,231.25
Condenser Pump	3.07 [kW]	11,462.07
Cooling Tower	5.34 [m³/min]	45,830.55

Inserting the fees and updating the values to 2022 the total cost of the project is US$ 1,469,673.82.

In this case, the ORC system is not able to return the money invested within the useful life of the equipment of 20 year. The find the IRR, which was approximately 4.06%, comparing to the MARR of 12 %, it can be stated that the IRR rate is extremely lower than the MARR, show the unfeasibility of the project.

7. Conclusions

This paper aimed to perform the thermodynamic modeling of ORC systems, and then analyze the additional power generated, repowering performance, in order to carry out an economic feasibility analysis of the implementation of the ORC systems, using some economic indexes: payback, Net Present Value (NPV), Internal Rate of Return (IRR). Two separately ORC system was simulated for this repowering purpose.

Firstly, energy and exergy balance were performed in order to evaluate the thermodynamic repowering potential, obtaining more than 43% of repowering potential. However, it is important to notice the limitations of the recoverable waste heat sources, which make the repowering potential drop down to approximately 32%. Additionally, it was observed that the LT colling water circuit has a very small repowering potential, representing approximately 5% of the HT cooling water circuit or 1% of the exhaust gas repowering potential.

Bearing this in mind, an ORC system was modeled for the exhaust gases from the 3 engines, operating with toluene as working fluid, generating 300.87 kW, which represents almost 8.8% of repowering. Another ORC was modeled for the HT colling water circuits heat of the 3 engines, operating with R141b as working fluid, generating 100.42 kW of additional electric power, representing 2.9% of repowering. The net efficiencies obtained for each cycle were 20.99% for exhaust gases ORC system and 5.83% for the cooling water ORC.

The economic analyses indexes obtained demonstrated the economic feasibility for the exhaust gases heat ORC system only, with total investment cost of US$ 2,318,339.01 and payback of approximately 15.5 years.

Acknowledgments

The authors would like to thank the Federal University of Espírito Santo (UFES), the Eficácia Consultoria, the Marca Ambiental, this study was financed in part by the Coordenação de Aprefeiçoamento de Pessoal de Nível Superior – Brasil (CAPES), the Support Foundation of Espírito Santo Research (FAPES), Conselho Nacional de Desenvolvimento Científico e Tecnológico (CNPq) and Rodrigo Guedes for the technical revision and formatting of the article.

Nomenclature

Symbols

A	capacity or size parameter, kW, m² or m³/min
B	bare module factor coefficient
C	pressure factor coefficient
E	exergy rate, kW
h	enthalpy, kJ/kg
K	equipment type coefficient
$\dot{m}$	mass flow rate, kg/s
P	pressure, bar
$\dot{Q}$	energy rate, kW
s	entropy, kJ/(kg.C)
T	temperature, °C
$\dot{W}$	power, kW
y	mole fraction
η	efficiency

Subscripts and superscripts

BM	bare module
cond	condensation
b	biogas
cw	cooling water

evap	evaporation	i	in
eg	exhaust gases	o	out
ex	exergetic	wf	working fluid
ge	generator efficiency		

References

[1] EPE - Empresa de Pesquisa Energética. Anuário Estatístico De Energia Elétrica 2022, ano base 2021. Rio de Janeiro, junho de 2022. Disponível em:< https://www.epe.gov.br/pt/publicacoes-dados-abertos/publicacoes/anuario-estatistico-de-energia-eletrica >. Acesso em 19 de dezembro de 2022.

[2] Domingues, A. Avaliação do potencial de aproveitamento da energia contida nos gases de escape de automóveis. Dissertação de Mestrado. Universidade Técnica de Lisboa, 2011.

[3] Stenzel WC, Sopocy DM, Pace SE. Repowering Existing Fossil Steam Plants. EPRI - Electric Power Research Intitute 1997:1–22.

[4] Morawski A. Avaliação da Repotenciação de uma Termelétrica Equipada com Motores de Combustão Interna Diesel por Meio de Recuperação de Calor Residual 2016.

[5] Ribeiro, L. C. (2017), Determinação da Configuração Ótima de Ciclo Rankine Orgânico para Aproveitamento do Calor Rejeitado em Usinas Termelétricas com Motores de Combustão Interna, Vitória, 108p. Dissertação (Mestrado em Engenharia Mecânica) – Centro Tecnológico, Universidade Federal do Espírito Santo.

[6] Benato, A.; Macor, A. Biogas Engine Waste Heat Recovery Using Organic Rankine Cycle. *Energies* 2017, *10*, 327.

[7] Yagli, H., Koc, A., Karakus, C. and Koc, Y. (2016) 'Comparison of toluene and cyclohexane as a working fluid of an organic Rankine cycle used for reheat furnace waste heat recovery', Int. J. Exergy, Vol. 19, No. 3, pp.420–438.

[8] Roy, J. P.; Mishra, M. K.; Misra, A. Parametric optimization and performance analysis of a waste heat recovery system using Organic Rankine Cycle. Energy, v. 35, n. 12, p. 5049–5062, 2010.

[9] Clemente, S. Small Scale Cogeneration Systems Based On Organic Rankine Cycle Technology. Tese de Doutorado, 2015.

[10] Quoilin, S. et al. Techno-economic survey of organic rankine cycle (ORC) systems. Renewable and Sustainable Energy Reviews, v. 22, p. 168–186, 2013.

[11] Figueiredo, N. J. V. d. (2007). Utilização do Biogás de aterros sanitários para geração de energia elétrica e iluminação a gás - Estudo de caso. Escola de Engenharia - Engenharia Mecânica. São Paulo, Universidade Presbiteriana Mackenzie.

[12] Bejan A, Tsatsaronis G, Moran M. Thermal Design and Optimization. New York: Wiley; 1996.

[13] Turton RA, Bailie RC, Whiting WB, Shaeiwitz JA, Bhattacharyya D. Analysis, Synthesis and Design of Chemical Processes. 4th ed. Pearson Education; 2012.

[14] Boehm, R, F. Design analysis of thermal systems. John Wiley & Sons Inc, 1987.

[15] Morawski, A. P. (2021), Otimização de Superestruturas Para a Recuperação de Calor Residual de Uma Termelétrica Brasileira à Motores Alternativos de Combustão Interna, Vitória, 314p. Tese (Doutorado em Engenharia Mecânica) – Centro Tecnológico, Universidade Federal do Espírito Santo.

[16] Bejan A.; Tsatsaronis G.; Moran M. Thermal Design and Optimization. (S.l.): John Wiley & Sons, INC, 1996.

[17] Fenergia - Feira e Fórum de Energia XII. UTE A Biogás Cariacica/Es "Operações da Liberum Energia em GD no ES", 2021. Espirito Santo.

[18] Jenbacher (2023) – Available at:<www.jenbacher.com> [accessed 02.17.2023].

[19] Lecompte, S. et al. Review of organic Rankine cycle (ORC) architectures for waste heat recovery. Renewable and Sustainable Energy Reviews, v. 47, p. 448–461, 2015.

[20] Marca Ambiental (2023) – Available at:< www.marcaambiental.com.br> [accessed 02.17.2023].

[21] Passos, G. C.; Bonelle, S. S. (2011), Estudo da Utilização de Resíduos Urbanos Para a Geração Termelétrica e Distribuída, Vitória, 81p. Trabalho de Conclusão de Curso (Graduação em Engenharia Mecânica) – Centro Tecnológico, Universidade Federal do Espírito Santo.

[22] Quoilin, S. An introduction to thermodynamics applied to organic Rankine cycles. Faculty of Applied Science of the University of Liège (Bélgica), 2008.